ECOS2012

THE 25TH INTERNATIONAL CONFERENCE ON EFFICIENCY, COST, OPTIMIZATION AND SIMULATION OF ENERGY CONVERSION SYSTEMS AND PROCESSES

Perugia, June 26th-June 29th, 2012

a cura di
Umberto Desideri
Giampaolo Manfrida
Enrico Sciubba

FIRENZE UNIVERSITY PRESS

ECOS 2012

The 25th International Conference on Efficiency, Cost, Optimization and Simulation of Energy Conversion Systems and Processes

(Perugia, June 26th-June 29th, 2012)

edited by
Umberto Desideri, Giampaolo Manfrida,
Enrico Sciubba

firenze university press
2012

ECOS 2012 : the 25th International Conference on Efficiency, Cost, Optimization and Simulation of Energy Conversion Systems and Processes (Perugia, June 26th-June 29th, 2012) / edited by Umberto Desideri, Giampaolo Manfrida, Enrico Sciubba. – Firenze : Firenze University Press, 2012.
(Proceedings e report ; 90)

http://digital.casalini.it/9788866553229

ISBN 978-88-6655-322-9 (online)

Progetto grafico di copertina Alberto Pizarro, Pagina Maestra snc
Immagine di copertina: © Kts | Dreamstime.com

Peer Review Process
All publications are submitted to an external refereeing process under the responsibility of the FUP Editorial Board and the Scientific Committees of the individual series. The works published in the FUP catalogue are evaluated and approved by the Editorial Board of the publishing house. For a more detailed description of the refereeing process we refer to the official documents published on the website and in the online catalogue of the FUP (http://www.fupress.com).

Firenze University Press Editorial Board
G. Nigro (Co-ordinator), M.T. Bartoli, M. Boddi, F. Cambi, R. Casalbuoni, C. Ciappei, R. Del Punta, A. Dolfi, V. Fargion, S. Ferrone, M. Garzaniti, P. Guarnieri, G. Mari, M. Marini, M. Verga, A. Zorzi.

© 2012 Firenze University Press
Università degli Studi di Firenze
Firenze University Press
Borgo Albizi, 28, 50122 Firenze, Italy
http://www.fupress.com/
Printed in Italy

ECOS 2012

The 25th International Conference on

Efficiency, Cost, Optimization and Simulation
of Energy Conversion Systems and Processes

Perugia, June 26th-June 29th, 2012

Book of Proceedings - Volume I

Edited by:
Umberto Desideri, Università degli Studi di Perugia
Giampaolo Manfrida, Università degli Studi di Firenze
Enrico Sciubba, Università degli Studi di Roma "Sapienza"

ECOS 2012 - THE 25TH INTERNATIONAL CONFERENCE ON
EFFICIENCY, COST, OPTIMIZATION, SIMULATION AND ENVIRONMENTAL IMPACT OF ENERGY SYSTEMS
JUNE 26-29, 2012, PERUGIA, ITALY
EDITED BY UMBERTO DESIDERI, GIAMPAOLO MANFRIDA, ENRICO SCIUBBA
FIRENZE UNIVERSITY PRESS, 2012, ISBN ONLINE : 978-88-6655-322-9

Advisory Committee (Track Organizers)

Building, Urban and Complex Energy Systems
V. Ismet Ugursal
Dalhousie University, Nova Scotia, Canada

Combustion, Chemical Reactors, Carbon Capture and Sequestration
Giuseppe Girardi
ENEA-Casaccia, Italy

Energy Systems: Environmental and Sustainability Issues
Christos A. Frangopoulos
National Technical University of Athens, Greece

Exergy Analysis and Second Law Analysis
Silvio de Oliveira Junior
Polytechnical University of Sao Paulo, Sao Paulo, Brazil

Fluid Dynamics and Power Plant Components
Sotirios Karellas
National Technical University of Athens, Athens, Greece

Fuel Cells
Umberto Desideri
University of Perugia, Perugia, Italy

Heat and Mass Transfer
Francesco Asdrubali, **Cinzia Buratti**
University of Perugia, Perugia, Italy

Industrial Ecology
Stefan Goessling-Reisemann
University of Bremen, Germany

Poster Session
Enrico Sciubba
University Roma 1 “Sapienza”, Italy

Process Integration and Heat Exchanger Networks
Francois Marechal
EPFL, Lausanne, *Switzerland*

Renewable Energy Conversion Systems
David Chiaramonti
University of Firenze, Firenze, Italy

Simulation of Energy Conversion Systems
Marcin Liszka
Polytechnica Slaska, Gliwice, Poland

System Operation, Control, Diagnosis and Prognosis
Vittorio Verda
Politecnico di Torino, Italy

Thermodynamics
A. Özer Arnas
United States Military Academy at West Point, U.S.A.

Thermo-Economic Analysis and Optimisation
Andrea Lazzaretto
University of Padova, Padova, Italy

Water Desalination and Use of Water Resources
Corrado Sommariva
ILF Consulting M.E., U.K

Scientific Committee

Riccardo Basosi, University of Siena, Italy
Gino Bella, University of Roma Tor Vergata, Italy
Asfaw Beyene, San Diego State University, United States
Ryszard Bialecki, Silesian Institute of Tecnology, Poland
Gianni Bidini, University of Perugia, Italy
Ana M. Blanco-Marigorta, University of Las Palmas de Gran Canaria, Spain
Olav Bolland, University of Science and Technology (NTNU), Norway
Renè Cornelissen, Cornelissen Consulting, The Netherlands
Franco Cotana, University of Perugia, Italy
Alexandru Dobrovicescu, Polytechnical University of Bucharest, Romania
Gheorghe Dumitrascu, Technical University of Iasi, Romania
Brian Elmegaard, Technical University of Denmark , Denmark
Daniel Favrat, EPFL, Switzerland
Michel Feidt, ENSEM - LEMTA University Henri Poincaré, France
Daniele Fiaschi, University of Florence, Italy
Marco Frey, Scuola Superiore S. Anna, Italy
Richard A Gaggioli, Marquette University, USA
Carlo N. Grimaldi, University of Perugia, Italy
Simon Harvey, Chalmers University of Technology, Sweden
Hasan Heperkan, Yildiz Technical University, Turkey
Abel Abel Hernandez-Guerrero, University of Guanajuato, Mexico
Jiri Jaromir Klemeš, University of Pannonia, Hungary
Zornitza V. Kirova-Yordanova, University "Prof. Assen Zlatarov", Bulgaria
Noam Lior, University of Pennsylvania, United States
Francesco Martelli, University of Florence, Italy
Aristide Massardo, University of Genova, Italy
Jim McGovern, Dublin Institute of Technology, Ireland
Alberto Mirandola, University of Padova, Italy
Michael J. Moran, The Ohio State University, United States
Tatiana Morosuk, Technical University of Berlin, Germany
Pericles Pilidis, University of Cranfield, United Kingdom
Constantine D. Rakopoulos, National Technical University of Athens, Greece
Predrag Raskovic, University of Nis, Serbia and Montenegro
Mauro Reini, University of Trieste, Italy
Gianfranco Rizzo, University of Salerno, Italy
Marc A. Rosen, University of Ontario, Canada
Luis M. Serra, University of Zaragoza, Spain
Gordana Stefanovic, University of Nis, Serbia and Montenegro
Andrea Toffolo, Luleå University of Technology, Sweden
Wojciech Stanek, Silesian University of Technology, Poland
George Tsatsaronis, Technical University Berlin, Germany
Antonio Valero, University of Zaragoza, Spain
Michael R. von Spakovsky, Virginia Tech, USA
Stefano Ubertini, Parthenope University of Naples, Italy
Sergio Ulgiati, Parthenope University of Naples, Italy
Sergio Usón, Universidad de Zaragoza, Spain
Roman Weber, Clausthal University of Technology, Germany
Ryohei Yokoyama, Osaka Prefecture University, Japan
Na Zhang, Institute of Engineering Thermophysics, Chinese Academy of Sciences, China

The 25th ECOS Conference 1987-2012: leaving a mark

The introduction to the ECOS series of Conferences states that "ECOS is a series of international conferences that focus on all aspects of Thermal Sciences, with particular emphasis on Thermodynamics and its applications in energy conversion systems and processes". Well, ECOS is much more than that, and its history proves it!

The idea of starting a series of such conferences was put forth at an informal meeting of the Advanced Energy Systems Division of the American Society of Mechanical Engineers (ASME) at the November 1985 Winter Annual Meeting (WAM), in Miami Beach, Florida, then chaired by Richard Gaggioli. The resolution was to organize an annual Symposium on the Analysis and Design of Thermal Systems at each ASME WAM, and to try to involve a larger number of scientists and engineers worldwide by organizing conferences outside of the United States. Besides Rich other participants were Ozer Arnas, Adrian Bejan, Yehia El-Sayed, Robert Evans, Francis Huang, Mike Moran, Gordon Reistad, Enrico Sciubba and George Tsatsaronis.

Ever since 1985, a Symposium of 8-16 sessions has been organized by the Systems Analysis Technical Committee every year, at the ASME Winter Annual Meeting (now ASME-IMECE). The first overseas conference took place in Rome, twenty-five years ago (in July 1987), with the support of the U.S. National Science Foundation and of the Italian National Research Council. In that occasion, Christos Frangopoulos, Yalcin Gogus, Elias Gyftopoulos, Dominick Sama, Sergio Stecco, Antonio Valero, and many others, already active at the ASME meetings, joined the core-group.

The name ECOS was used for the first time in Zaragoza, in 1992: it is an acronym for **Efficiency, Cost, Optimization and Simulation** (of energy conversion systems and processes), keywords that best describe the contents of the presentations and discussions taking place in these conferences. Some years ago, Christos Frangopoulos inserted in the official website the note that "ècos" ('οικος) means "home" in Greek and it ought to be attributed the very same meaning as the prefix "Eco-" in environmental sciences.
The last 25 years have witnessed an almost incredible growth of the ECOS community: more and more Colleagues are actively participating in our meetings, several international Journals routinely publish selected papers from our Proceedings, fruitful interdisciplinary and international cooperation projects have blossomed from our meetings. Meetings that have spanned three continents (Africa and Australia ought to be our next targets, perhaps!) and influenced in a way or another much of modern Engineering Thermodynamics.
After 25 years, if we do not want to become embalmed in our own success and lose momentum, it is mandatory to aim our efforts in two directions: first, encourage the participation of younger academicians to our meetings, and second, stimulate creative and useful discussions in our sessions. Looking at this years' registration roster (250 papers of which 50 authored or co-authored by junior Authors), the first objective seems to have been attained, and thus we have just to continue in that direction; the second one involves allowing space to "voices that sing out of the choir", fostering new methods and approaches, and establishing or reinforcing connections to other scientific communities. It is important that our technical sessions represent a place of active confrontation, rather than academic "lecturing".
In this spirit, we welcome you in Perugia, and wish you a scientifically stimulating, touristically interesting, and culinarily rewarding experience. In line with our 25 years old scientific excellency and friendship!

Umberto Desideri, Giampaolo Manfrida, Enrico Sciubba

CONTENT MANAGEMENT

The index lists all the papers contained all the eight volumes of the Proceedings of the ECOS 2012 International Conference.
Page numbers are listed only for papers within the Volume you are looking at. The ID code allows to trace back the identification number assigned to the paper within the Conference submission, review and track organization processes.

CONTENT

VOLUME I

I . 1 – SIMULATION OF ENERGY CONVERSION SYSTEMS

» A novel hybrid-fuel compressed air energy storage system for China's situation (ID 531) ……..... *Pag. 1*
Wenyi Liu, Yongping Yang, Weide Zhang, Gang Xu,and Ying Wu

» A review of Stirling engine technologies applied to micro-cogeneration systems (ID 338) ……..... *Pag. 17*
Ana C Ferreira, Manuel L Nunes, Luís B Martins, Senhorinha F Teixeira

» An organic Rankine cycle off-design model for the search of the optimal control strategy (ID 295) ……..... *Pag. 28*
Andrea Toffolo, Andrea Lazzaretto, Giovanni Manente, Marco Paci

» Automated superstructure generation and optimization of distributed energy supply systems (ID 518) ……..... *Pag. 42*
Philip Voll, Carsten Klaffke, Maike Hennen, André Bardow

» Characterisation and classification of solid recovered fuels (SRF) and model development of a novel thermal utilization concept through air-gasification (ID 506) ……..... *Pag. 55*
Panagiotis Vounatsos, Konstantinos Atsonios, Mihalis Agraniotis, Kyriakos D. Panopoulos, George Koufodimos,Panagiotis Grammelis, Emmanuel Kakaras

» Design and modelling of a novel compact power cycle for low temperature heat sources (ID 177) ……..... *Pag. 70*
Jorrit Wronski, Morten Juel Skovrup, Brian Elmegaard, Harald Nes Rislå, Fredrik Haglind

» Dynamic simulation of combined cycles operating in transient conditions: an innovative approach to determine the steam drums life consumption (ID 439) ……..... *Pag. 85*
Stefano Bracco

» Effect of auxiliary electrical power consumptions on organic Rankine cycle system with low-temperature waste heat source (ID 235) ……..... *Pag. 100*
Samer Maalouf, Elias Boulawz Ksayer, Denis Clodic

» Energetic and exergetic analysis of waste heat recovery systems in the cement industry (ID 228) ……..... *Pag. 114*
Sotirios Karellas, Aris Dimitrios Leontaritis, Georgios Panousis, Evangelos Bellos, Emmanuel Kakaras

» Energy and exergy analysis of repowering options for Greek lignite-fired power plants (ID 230) ……..... *Pag. 128*
Sotirios Karellas, Aggelos Doukelis, Grammatiki Zanni, Emmanuel Kakaras

» Energy saving by a simple solar collector with reflective panels and boiler (ID 366) ……..... *Pag. 143*
Anna Stoppato, Renzo Tosato

» Exergetic analysis of biomass fired double-stage Organic Rankine Cycle (ORC) (ID 37) ……..... *Pag. 155*
Markus Preißinger, Florian Heberle, Dieter Brüggemann

FIRENZE UNIVERSITY PRESS, 2012, ISBN ONLINE : 978-88-6655-322-9

» **Experimental tests and modelization of a domestic-scale organic Rankine cycle (ID 156)** ……..... *Pag. 166*
Roberto Bracco, Stefano Clemente, Diego Micheli, Mauro Reini

» **Model of a small steam engine for renewable domestic CHP system (ID 31)** ……..... *Pag. 178*
Giampaolo Manfrida, Giovanni Ferrara, Alessandro Pescioni

» **Model of vacuum glass heat pipe solar collectors (ID 312)** ……..... *Pag. 194*
Daniele Fiaschi, Giampaolo Manfrida

» **Modelling and exergy analysis of a plasma furnace for aluminum melting process (ID 254)** ……..... *Pag. 206*
Luis Enrique Acevedo, Sergio Usón, Javier Uche, Patxi Rodríguez

» **Modelling and experimental validation of a solar cooling installation (ID 296)** ……..... *Pag.221*
Guillaume Anies, Pascal Stouffs, Jean Castaing-Lasvignottes

» **The influence of operating parameters and occupancy rate of thermoelectric modules on the electricity generation (ID 314)** ……..... *Pag. 233*
Camille Favarel, Jean-Pierre Bédécarrats, Tarik Kousksou, Daniel Champier

» **Thermodynamic and heat transfer analysis of rice straw co-firing in a Brazilian pulverised coal boiler (ID 236)** ……..... *Pag. 245*
Raphael Miyake, Alvaro Restrepo, Fábio Kleveston Edson Bazzo, Marcelo Bzuneck

» **Thermophotovoltaic generation: A state of the art review (ID 88)** ……..... *Pag. 258*
Matteo Bosi, Claudio Ferrari, Francesco Melino, Michele Pinelli, Pier Ruggero Spina, Mauro Venturini

I . 2 – HEAT AND MASS TRANSFER

» **A DNS method for particle motion to establish boundary conditions in coal gasifiers (ID 49)** ……..... *Pag. 279*
Efstathios E Michaelides, Zhigang Feng

» **Effective thermal conductivity with convection and radiation in packed bed (ID 60)** ……..... *Pag. 291*
Yusuke Asakuma

» **Experimental and CFD study of a single phase cone-shaped helical coiled heat exchanger: an empirical correlation (ID 375)** ……..... *Pag. 302*
Daniel Flórez-Orrego, Walter Arias, Diego López, Héctor Velásquez

» **Thermofluiddynamic model for control analysis of latent heat thermal storage system (ID 207)** ……..... *Pag. 321*
Adriano Sciacovelli, Vittorio Verda, Flavio Gagliardi

» **Towards the development of an efficient immersed particle heat exchanger: particle transfer from low to high pressure (ID 202)** ……..... *Pag. 334*
Luciano A. Catalano, Riccardo Amirante, Stefano Copertino, Paolo Tamburrano, Fabio De Bellis

I . 3 – INDUSTRIAL ECOLOGY

» **Anthropogenic heat and exergy balance of the atmosphere (ID 122)** ……..... *Pag. 348*
Asfaw Beyene, David MacPhee, Ron Zevenhoven

» **Determination of environmental remediation cost of municipal waste in terms of extended exergy (ID 63)** ……..... *Pag. 363*
Candeniz Seckin, Ahmet R. Bayulken

» **Development of product category rules for the application of life cycle assessment to carbon capture and storage (537)** ……..... *Pag. 377*
Carlo Strazza, Adriana Del Borghi, Michela Gallo

» **Electricity production from renewable and non-renewable energy sources: a comparison of environmental, economic and social sustainability indicators with exergy losses throughout the supply chain (ID 247)** ……..... *Pag. 391*
Lydia Stougie, Hedzer van der Kooi, Rob Stikkelman

» **Exergy analysis of the industrial symbiosis model in Kalundborg (ID 218)** ……..... *Pag. 406*
Alicia Valero Delgado, Sergio Usón, Jorge Costa

» **Global gold mining: is technological learning overcoming the declining in ore grades? (ID 277)** ……..... *Pag. 417*
Adriana Domínguez, Alicia Valero

» **Personal transportation energy consumption (ID305)** ……..... *Pag. 434*
Matteo Muratori, Emmanuele Serra, Vincenzo Marano, Michael Moran

» **Resource use evaluation of Turkish transportation sector via the extended exergy accounting method (ID 43)** ……..... *Pag. 448*
Candeniz Seckin, Enrico Sciubba, Ahmet R. Bayulken

» **The impact of higher energy prices on socio-economic inequalities of German social groups (ID 80)** ……..... *Pag. 466*
Holger Schlör, Wolfgang Fischer, Jürgen-Friedrich Hake

CONTENTS OF ALL THE VOLUMES

VOLUME II

II . 1 – EXERGY ANALYSIS AND 2ND LAW ANALYSIS

» **A comparative analysis of cryogenic recuperative heat exchangers based on exergy destruction (ID 129)**
Adina Teodora Gheorghian, Alexandru Dobrovicescu, Lavinia Grosu, Bogdan Popescu, Claudia Ionita

» **A critical exploration of the usefulness of rational efficiency as a performance parameter for heat exchangers (ID 307)**
Jim McGovern, Georgiana Tirca-Dragomirescu, Michel Feidt, Alexandru Dobrovicescu

» **A new procedure for the design of LNG processes by combining exergy and pinch analyses (ID 238)**
Danahe Marmolejo-Correa, Truls Gundersen

» **Advances in the distribution of environmental cost of water bodies through the exergy concept in the Ebro river (ID 258)**
Javier Uche Marcuello, Amaya Martínez Gracia, Beatriz Carrasquer Álvarez, Antonio Valero Capilla

» **Application of the entropy generation minimization method to a solar heat exchanger: a pseudo-optimization design process based on the analysis of the local entropy generation maps (ID 357)**
Giorgio Giangaspero, Enrico Sciubba

» **Comparative analysis of ammonia and carbon dioxide two-stage cycles for simultaneous cooling and heating (ID 84)**
Alexandru Dobrovicescu, Ciprian Filipoiu, Emilia Cerna Mladin, Valentin Apostol, Liviu Drughean

» Comparison between traditional methodologies and advanced exergy analyses for evaluating efficiency and externalities of energy systems (ID 515)
Gabriele Cassetti, Emanuela Colombo

» Comparison of entropy generation figures using entropy maps and entropy transport equation for an air cooled gas turbine blade (ID 468)
Omer Emre Orhan, Oguz Uzol

» Conventional and advanced exergetic evaluation of a supercritical coal-fired power plant (ID 377)
Ligang Wang, Yongping Yang, Tatiana Morosuk, George Tsatsaronis

» Energy and exergy analyses of the charging process in encapsulted ice thermal energy storage (ID 164)
David MacPhee, Ibrahim Dincer, Asfaw Beyene

» Energy integration and cogeneration in nitrogen fertilizers industry: thermodynamic estimation of the efficiency, potentials, limitations and environmental impact. Part 1: energy integration in ammonia production plants (ID 303)
Zornitza Vassileva Kirova-Yordanova

» Evaluation of the oil and gas processing at a real production day on a North Sea oil platform using exergy analysis (ID 260)
Mari Voldsund, Wei He, Audun Røsjorde, Ivar Ståle Ertesvåg, Signe Kjelstrup

» Exergetic and economic analysis of Kalina cycle for low temperature geothermal sources in Brazil (ID 345)
Carlos Eymel Campos Rodriguez, José Carlos Escobar Palacios, Cesar Adolfo Rodríguez Sotomonte, Marcio Leme, Osvaldo José Venturini, Electo Eduardo Silva Lora, Vladimir Melián Cobasa, Daniel Marques dos Santos, Fábio R. Lofrano Dotto, Vernei Gialluca

» Exergy analysis and comparison of CO2 heat pumps (ID 242)
Argyro Papadaki, Athina Stegou - Sagia

» Exergy analysis of a CO2 Recovery plant for a brewery (ID 72)
Daniel Rønne Nielsen, Brian Elmegaard, C. Bang-Møller

» Exergy analysis of the silicon production process (ID 118)
Marit Takla, Leiv Kolbeinsen, Halvard Tveit, Signe Kjelstrup

» Exergy based indicators for cardiopulmonary exercise test evaluation (ID 159)
Carlos Eduardo Keutenedjian Mady, Cyro Albuquerque Neto, Tiago Lazzaretti Fernandes, Arnaldo Jose Hernandez, Paulo Hilário Nascimento Saldiva, Jurandir Itizo Yanagihara, Silvio de Oliveira Junior

» Exergy disaggregation as an alternative for system disaggregation in thermoeconomics (ID 483)
José Joaquim Conceição Soares Santos, Atilio Lourenço, Julio Mendes da Silva, João Donatelli, José Escobar Palacio

» Exergy intensity of petroleum derived fuels (ID 117)
Julio Augusto Mendes da Silva, Maurício Sugiyama, Claudio Rucker, Silvio de Oliveira Junior

» Exergy-based sustainability evaluation of a wind power generation system (ID 542)
Jin Yang, B. Chen, Enrico Sciubba

» Human body exergy metabolism (ID 160)
Carlos Eduardo Keutenedjian Mady, Silvio de Oliveira Junior

» Integrating an ORC into a natural gas expansion plant supplied with a co-generation unit (ID 273)
Sergio Usón, Wojciech Juliusz Kostowski

» One-dimensional model of an optimal ejector and parametric study of ejector efficiency (ID 323)
Ronan Killian McGovern, Kartik Bulusu, Mohammed Antar, John H. Lienhard

» Optimization and design of pin-fin heat sinks based on minimum entropy generation (ID 6)
Jose-Luis Zuniga-Cerroblanco, Abel Hernandez-Guerrero, Carlos A. Rubio-Jimenez, Cuauhtemoc Rubio-Arana, Sosimo E. Diaz-Mendez

» Performance analysis of a district heating system (ID 271)
Andrej Ljubenko, Alojz Poredoš, Tatiana Morosuk, George Tsatsaronis

» System analysis of exergy losses in an integrated oxy-fuel combustion power plant (ID 64)
Andrzej Ziębik, Paweł Gładysz

» What is the cost of losing irreversibly the mineral capital on Earth? (ID 220)
Alicia Valero Delgado, Antonio Valero

II . 2 – THERMODYNAMICS

» A new polygeneration system for methanol and power based on coke oven gas and coal gas (ID 252)
Hu Lin, Hongguang Jin, Lin Gao, Rumou Li

» Argon-Water closed gas cycle (ID 67)
Federico Fionelli, Giovanni Molinari

» Binary alkane mixtures as fluids in Rankine cycles (ID 246)
M. Aslam Siddiqi, Burak Atakan

» Excess enthalpies of second generation biofuels (ID 308)
Alejandro Moreau, José Juan Segovia, M. Carmen Martín, Miguel Ángel Villamañán, César R. Chamorro, Rosa M. Villamañán

» Local stability analysis of a Curzon-Ahlborn engine considering the Van der Waals equation state in the maximum ecological regime (ID 281)
Ricardo Richard Páez-Hernández, Pedro Portillo-Díaz, Delfino Ladino-Luna, Marco Antonio Barranco-Jiménez

» Some remarks on the Carnot's theorem (ID 325)
Julian Gonzalez Ayala, Fernando Angulo-Brown

» The Dead State (ID 340)
Richard A. Gaggioli

» The magnetocaloric energy conversion (ID 97)
Andrej Kitanovski, Jaka Tusek, Alojz Poredos

VOLUME III

THERMO-ECONOMIC ANALYSIS AND OPTIMIZATION

» A comparison of optimal operation of residential energy systems using clustered demand patterns based on Kullback-Leibler divergence (ID 142)
Akira Yoshida, Yoshiharu Amano, Noboru Murata, Koichi Ito, Takumi Hashizume

» A Model for Simulation and Optimal Design of a Solar Heating System with Seasonal Storage (ID 51)
Gianfranco Rizzo

» A thermodynamic and economic comparative analysis of combined gas-steam and gas turbine air bottoming cycle (ID 232)
Tadeusz Chmielniak, Daniel Czaja, Sebastian Lepszy

» Application of an alternative thermoeconomic approach to a two-stage vapor compression refrigeration cycle with intercooling (ID 135)
Atilio Barbosa Lourenço, José Joaquim Conceição Soares Santos, João Luiz Marcon Donatelli

» Comparative performance of advanced power cycles for low temperature heat sources (ID 109)
Guillaume Becquin, Sebastian Freund

» Comparison of nuclear steam power plant and conventional steam power plant through energy level and thermoeconomic analysis (ID 251)
S. Khamis Abadi, Mohammad Hasan Khoshgoftar Manesh, M. Baghestani, H. Ghalami, Majid Amidpour

» Economic and exergoeconomic analysis of micro GT and ORC cogeneration systems (ID 87)
Audrius Bagdanavicius, Robert Sansom, Nick Jenkins, Goran Strbac

» Exergoeconomic comparison of wet and dry cooling technologies for the Rankine cycle of a solar thermal power plant (ID 300)
Philipp Habl, Ana M. Blanco-Marigorta, Berit Erlach

» Influence of renewable generators on the thermo-economic multi-level optimization of a poly-generation smart grid (101)
Massimo Rivarolo, Andrea Greco, Francesca Travi, Aristide F. Massardo

» Local stability analysis of a thermoeconomic model of an irreversible heat engine working at different criteria of performance (ID 289)
Marco A. Barranco-Jiménez, Norma Sánchez-Salas, Israel Reyes-Ramírez, Lev Guzmán-Vargas

» Multicriteria optimization of a distributed trigeneration system in an industrial area (ID 154)
Dario Buoro, Melchiorre Casisi, Alberto de Nardi, Piero Pinamonti, Mauro Reini

» On the effect of eco-indicator selection on the conclusions obtained from an exergoenvironmental analysis (ID 275)
Tatiana Morosuk, George Tsatsaronis, Christopher Koroneos

» Optimisation of supply temperature and mass flow rate for a district heating network (ID 104)
Marouf Pirouti, Audrius Bagdanavicius, Jianzhong Wu, Janaka Ekanayake

» Optimization of energy supply systems in consideration of hierarchical relationship between design and operation (ID 389)
Ryohei Yokoyama, Shuhei Ose

» The fuel impact formula revisited (ID 279)
Cesar Torres, Antonio Valero

» The introduction of exergy analysis to the thermo-economic modelling and optimisation of a marine combined cycle system (ID 61)
George G. Dimopoulos, Chariklia A. Georgopoulou, Nikolaos M.P. Kakalis

» The relationship between costs and environmental impacts in power plants: an exergy-based study (ID 272)
Fontina Petrakopoulou, Yolanda Lara, Tatiana Morosuk, Alicia Boyano, George Tsatsaronis

» Thermo-ecological evaluation of biomass integrated gasification gas turbine based cogeneration technology (ID 441)
Wojciech Stanek, Lucyna Czarnowska, Jacek Kalina

» Thermo-ecological optimization of a heat exchanger through empirical modeling (ID 501)
Ireneusz Szczygieł, Wojciech Stanek, Lucyna Czarnowska, Marek Rojczyk

» Thermoeconomic analysis and optimization in a combined cycle power plant including a heat transformer for energy saving (ID 399)
Elizabeth Cortés Rodríguez, José Luis Castilla Carrillo, Claudia A. Ruiz Mercado, Wilfrido Rivera Gómez-Franco

» Thermoeconomic analysis and optimization of a hybrid solar-electric heating in a fluidized bed dryer (ID 400)
Elizabeth Cortés Rodríguez, Felipe de Jesús Ojeda Cámara, Isaac Pilatowsky Figueroa

» Thermoeconomic approach for the analysis of low temperature district heating systems (ID 208)
Vittorio Verda, Albana Kona

» Thermo-economic assessment of a micro CHP systems fuelled by geothermal and solar energy (ID 166)
Duccio Tempesti, Daniele Fiaschi, Filippo Gabuzzini

» Thermo-economic evaluation and optimization of the thermo-chemical conversion of biomass into methanol (ID 194)
Emanuela Peduzzi, Laurence Tock, Guillaume Boissonnet, François Marechal

» Thermoeconomic fuel impact approach for assessing resources savings in industrial symbiosis: application to Kalundborg Eco-industrial Park (ID 256)
Sergio Usón, Antonio Valero, Alicia Valero, Jorge Costa

» Thermoeconomics of a ground-based CAES plant for peak-load energy production system (ID 32)
Simon Kemble, Giampaolo Manfrida, Adriano Milazzo, Francesco Buffa

VOLUME IV

IV . 1 – FLUID DYNAMICS AND POWER PLANT COMPONENTS

» A control oriented simulation model of a multistage axial compressor (ID 444)
Lorenzo Damiani, Giampaolo Crosa, Angela Trucco

» A flexible and simple device for in-cylinder flow measurements: experimental and numerical validation (ID 181)
Andrea Dai Zotti, Massimo Masi, Marco Antonello

» CFD Simulation of Entropy Generation in Pipeline for Steam Transport in Real Industrial Plant (ID 543)
Goran Vučković, Gradimir Ilić, Mića Vukić, Milan Banić, Gordana Stefanović

» Feasibility Study of Turbo expander Installation in City Gate Station (ID 168)
Navid Zehtabiyan Rezaie, Majid Saffar-Avval

» GTL and RME combustion analysis in a transparent CI engine by means of IR digital imaging (ID 460)
Ezio Mancaruso, Luigi Sequino, Bianca Maria Vaglieco

» Some aspects concerning fluid flow and turbulence modeling in 4-valve engines (ID 116)
Zoran Stevan Jovanovic, Zoran Masonicic, Miroljub Tomic

IV . 2 – SYSTEM OPERATION CONTROL DIAGNOSIS AND PROGNOSIS

» Adapting the operation regimes of trigeneration systems to renewable energy systems integration (ID 188)
Liviu Ruieneanu, Mihai Paul Mircea

» Advanced electromagnetic sensors for sustainable monitoring of industrial processes (ID 145)
Uroš Puc, Andreja Abina, Anton Jeglič, Pavel Cevc, Aleksander Zidanšek

» Assessment of stresses and residual life of plant components in view of life-time extension of power plants (ID 453)
Anna Stoppato, Alberto Benato and Alberto Mirandola

» Control strategy for minimizing the electric power consumption of hybrid ground source heat pump system (ID 244)
Zoi Sagia, Constantinos Rakopoulos

» Exergetic evaluation of heat pump booster configurations in a low temperature district heating network (ID 148)
Torben Ommen, Brian Elmegaard

» **Exergoeconomic diagnosis: a thermo-characterization method by using irreversibility analysis (ID 523)**
Abraham Olivares-Arriaga, Alejandro Zaleta-Aguilar, Rangel-Hernández V. H, Juan Manuel Belman-Flores

» **Optimal structural design of residential cogeneration systems considering their operational restrictions (ID 224)**
Tetsuya Wakui, Ryohei Yokoyama

» **Performance estimation and optimal operation of a CO2 heat pump water heating system (ID 344)**
Ryohei Yokoyama, Ryosuke Kato, Tetsuya Wakui, Kazuhisa Takemura

» **Performances of a common-rail Diesel engine fuelled with rapeseed and waste cooking oils (ID 213)**
Alessandro Corsini, Valerio Giovannoni, Stefano Nardecchia, Franco Rispoli, Fabrizio Sciulli, Paolo Venturini

» **Reduced energy cost through the furnace pressure control in power plants (ID 367)**
Vojislav Filipović, Novak Nedić, Saša Prodanović

» **Short-term scheduling model for a wind-hydro-thermal electricity system (ID 464)**
Sérgio Pereira, Paula Ferreira, A. Ismael Freitas Vaz

VOLUME V

V . 1 – RENEWABLE ENERGY CONVERSION SYSTEMS

» **A co-powered concentrated solar power Rankine cycle concept for small size combined heat and power (ID 276)**
Alessandro Corsini, Domenico Borello, Franco Rispoli, Eileen Tortora

» **A novel non-tracking solar collector for high temperature application (ID 466)**
Wattana Ratismith, Anusorn Inthongkhum

» **Absorption heat transformers (AHT) as a way to enhance low enthalpy geothermal resources (ID 311)**
Daniele Fiaschi, Duccio Tempesti, Giampaolo Manfrida, Daniele Di Rosa

» **Alternative feedstock for the biodiesel and energy production: the OVEST project (ID 98)**
Matteo Prussi, David Chiaramonti, Lucia Recchia, Francesco Martelli, Fabio Guidotti

» **Assessing repowering and update scenarios for wind energy converters (ID 158)**
Till Zimmermann

» **Biogas from mechanical pulping industry – potential improvement for increased biomass vehicle fuels (ID 54)**
Mimmi Magnusson, Per Alvfors

» **Biogas or electricity as vehicle fuels derived from food waste - the case of Stockholm (ID 27)**
Martina Wikström, Per Alvfors

» **Compressibility factor as evaluation parameter of expansion processes in organic Rankine cycles (ID 292)**
Giovanni Manente, Andrea Lazzaretto

» **Design of solar heating system for methane generation (ID 445)**
Lucía Mónica Gutiérrez, P. Quinto Diez, L. R. Tovar Gálvez

» **Economic feasibility of PV systems in hotels in Mexico (ID 346)**
Augusto Sanchez, Sergio Quezada

» Effect of a back surface roughness on annual performance of an air-cooled PV module (ID 193)
Riccardo Secchi, Duccio Tempesti, Jacek Smolka

» Energy and exergy analysis of the first hybrid solar-gas power plant in Algeria (ID 176)
Fouad Khaldi

» Energy recovery from MSW treatment by gasification and melting technology (ID 393)
Fabrizio Strobino, Alessandro Pini Prato, Diego Ventura, Marco Damonte

» Ethanol production by enzymatic hydrolysis process from sugarcane biomass - the integration with the conventional process (ID 189)
Reynaldo Palacios-Bereche, Adriano Ensinas, Marcelo Modesto, Silvia Azucena Nebra

» Evaluation of gas in an industrial anaerobic digester by means of biochemical methane potential of organic municipal solid waste components (ID 57)
Isabella Pecorini, Tommaso Olivieri, Donata Bacchi, Alessandro Paradisi, Lidia Lombardi, Andrea Corti, Ennio Carnevale

» Exergy analysis and genetic algorithms for the optimization of flat-plate solar collectors (ID 423)
Soteris A. Kalogirou

» Experimental study of tar and particles content of the produced gas in a double stage downdraft gasifier (ID 487)
Ana Lisbeth Galindo Noguera, Sandra Yamile Giraldo, Rene Lesme-Jaén, Vladimir Melian Cobas, Rubenildo Viera Andrade, Electo Silva Lora

» Feasibility study to realize an anaerobic digester fed with vegetables matrices in central Italy (ID 425)
Umberto Desideri, Francesco Zepparelli, Livia Arcioni, Ornella Calderini, Francesco Panara, Matteo Todini

» Investigations on the use of biogas for small scale decentralized CHP applications with a focus on stability and emissions (ID 140)
Steven MacLean, Eren Tali, Anne Giese, Jörg Leicher

» Kinetic energy recovery system for sailing yachts (ID 427)
Giuseppe Leo Guizzi, Michele Manno

» Mirrors in the sky: status and some supporting materials experiments (ID 184)
Noam Lior

» Numerical parametric study for different cold storage designs and strategies of a solar driven thermoacoustic cooler system (ID 284)
Maxime Perier-Muzet, Pascal Stouffs, Jean-Pierre Bedecarrats, Jean Castaing-Lasvignottes

» Parabolic trough photovoltaic/thermal collectors. Part I: design and simulation model (ID 102)
Francesco Calise, Laura Vanoli

» Parabolic trough photovoltaic/thermal collectors. Part II: dynamic simulation of a solar trigeneration system (ID 488)
Francesco Calise, Laura Vanoli

» Performance analysis of downdraft gasifier - reciprocating engine biomass fired small-scale cogeneration system (ID 368)
Jacek Kalina

» Proposing offshore photovoltaic (PV) technology to the energy mix of the Maltese islands (ID 262)
Kim Trapani, Dean Lee Millar

» Research of integrated biomass gasification system with a piston engine (ID 414)
Janusz Kotowicz, Aleksander Sobolewski, Tomasz Iluk

» Start up of a pre-industrial scale solid state anaerobic digestion cell for the co-treatment of animal and agricultural residues (ID 34)
Francesco Di Maria, Giovanni Gigliotti, Alessio Sordi, Caterina Micale, Luisa Massaccesi

» The role of biomass in the renewable energy system (ID 390)
Ruben Laleman, Ludovico Balduccio, Johan Albrecht

» Vegetable oils of soybean, sunflower and tung as alternative fuels for compression ignition engines (ID 500)
Ricardo Morel Hartmann, Nury Nieto Garzón, Eduardo Morel Hartmann, Amir Antonio Martins Oliveira Jr, Edson Bazzo, Bruno Okuda, Joselia Piluski

» Wind energy conversion performance and atmosphere stability (ID 283)
Francesco Castellani, Emanuele Piccioni, Lorenzo Biondi, Marcello Marconi

V. 2 – FUEL CELLS

» Comparison study on different SOFC hybrid systems with zero-CO2 emission (ID 196)
Liqiang Duan, Kexin Huang, Xiaoyuan Zhang and Yongping Yang

» Exergy analysis and optimisation of a steam methane pre-reforming system (ID 62)
George G. Dimopoulos, Iason C. Stefanatos, Nikolaos M.P. Kakalis

» Modelling of a CHP SOFC power system fed with biogas from anaerobic digestion of municipal wastes integrated with a solar collector and storage units (ID 491)
Domenico Borello, Sara Evangelisti, Eileen Tortora

VOLUME VI

VI . 1 – CARBON CAPTURE AND SEQUESTRATION

» A novel coal-based polygeneration system cogenerating power, natural gas and liquid fuel with CO2 capture (ID 96)
Sheng Li, Hongguang Jin, Lin Gao

» Analysis and optimization of CO2 capture in a China's existing coal-fired power plant (ID 532)
Gang Xu, Yongping Yang, Shoucheng Li, Wenyi Liu and Ying Wu

» Analysys of four-end high temperature membrane air separator in a supercritical power plant with oxy-type pulverized fuel boiler (ID 442)
Janusz Kotowicz, Sebastian Stanisław Michalski

» Analysis of potential improvements to the lignite-fired oxy-fuel power unit (ID 413)
Marcin Liszka, Jakub Tuka, Grzegorz Nowak, Grzegorz Szapajko

» Biogas Upgrading: Global Warming Potential of Conventional and Innovative Technologies (ID 240)
Katherine Starr, Xavier Gabarrell Durany, Gara Villalba Mendez, Laura Talens Peiro, Lidia Lombardi

» Capture of carbon dioxide using gas hydrate technology (ID 103)
Beatrice Castellani, Mirko Filipponi, Sara Rinaldi, Federico Rossi

» Carbon dioxide mineralisation and integration with flue gas desulphurisation applied to a modern coal-fired power plant (ID 179)
Ron Zevenhoven, Johan Fagerlund, Thomas Björklöf, Magdalena Mäkelä, Olav Eklund

» Carbon dioxide storage by mineralisation applied to a lime kiln (ID 226)
Inês Sofia Soares Romão, Matias Eriksson, Experience Nduagu, Johan Fagerlund, Licínio Manuel Gando-Ferreira, Ron Zevenhoven

» Comparison of IGCC and CFB cogeneration plants equipped with CO2 removal (ID 380)
Marcin Liszka, Tomasz Malik, Michał Budnik, Andrzej Ziębik

» Concept of a "capture ready" combined heat and power plant (ID 231)
Piotr Henryk Lukowicz, Lukasz Bartela

» Cryogenic method for H2 and CH4 recovery from a rich CO2 stream in pre-combustion CCS schemes (ID 508)
Konstantinos Atsonios, Kyriakos D. Panopoulos, Angelos Doukelis, Antonis Koumanakos, Emmanuel Kakaras

» Design and optimization of ITM oxy-combustion power plant (ID 495)
Surekha Gunasekaran, Nicholas David Mancini, Alexander Mitsos

» Implementation of a CCS technology: the ZECOMIX experimental platform (ID 222)
Antonio Calabrò, Stefano Cassani, Leandro Pagliari, Stefano Stendardo

» Influence of regeneration condition on cyclic CO2 capture using pre-treated dispersed CaO as high temperature sorbent (ID 221)
Stefano Stendardo, Antonio Calabrò

» Investigation of an innovative process for biogas up-grading – pilot plant preliminary results (ID 56)
Lidia Lombardi, Renato Baciocchi, Ennio Antonio Carnevale, Andrea Corti, Giulia Costa, Tommaso Olivieri, Alessandro Paradisi, Daniela Zingaretti

» Method of increasing the efficiency of a supercritical lignite-fired oxy-type fluidized bed boiler and high-temperature three - end membrane for air separation (ID 438)
Janusz Kotowicz, Adrian Balicki

» Monitoring of carbon dioxide uptake in accelerated carbonation processes applied to air pollution control residues (ID 539)
Felice Alfieri, Peter J Gunning, Michela Gallo, Adriana Del Borghi, Colin D Hills

» Process efficiency and optimization of precipitated calcium carbonate (PCC) production from steel converter slag (ID 114)
Hannu-Petteri Mattila, Inga Grigaliūnaitė, Arshe Said, Sami Filppula, Carl-Johan Fogelholm, Ron Zevenhoven

» Production of Mg(OH)2 for CO2 Emissions Removal Applications: Parametric and Process Evaluation (ID 245)
Experience Ikechukwu Nduagu, Inês Romão, Ron Zevenhoven

» Thermodynamic analysis of a supercritical power plant with oxy type pulverized fuel boiler, carbon dioxide capture system (CC) and four-end high temperature membrane air seprator (ID 411)
Janusz Kotowicz, Sebastian Stanisław Michalski

VI . 2 – PROCESS INTEGRATION AND HEAT EXCHANGER NETWORKS

» A multi-objective optimization technique for co- processing in the cement production (ID 42)
Maria Luiza Grillo Renó, Rogério José da Silva, Mirian de Lourdes Noronha Motta Melo, José Joaquim Conceição Soares Santos

» Comparison of options for debottlenecking the recovery boiler at kraft pulp mills – Economic performance and CO2 emissions (ID 449)
Johanna Jönsson, Karin Pettersson, Simon Harvey, Thore Berntsson

» Demonstrating an integral approach for industrial energy saving (ID 541)
René Cornelissen, Geert van Rens, Jos Sentjens, Henk Akse, Ton Backx, Arjan van der Weiden, Jo Vandenbroucke

» Maximising the use of renewables with variable availability (ID 494)
Andreja Nemet, Jiri Jaromír Klemeš, Petar Sabev Varbanov, Zdravko Kravanja

» Methodology for the improvement of large district heating networks (ID 46)
Anna Volkova, Vladislav Mashatin, Aleksander Hlebnikov, Andres Siirde

» Optimal mine site energy supply (ID 306)
Monica Carvalho, Dean Lee Millar

» Simulation of synthesis gas production from steam oxygen gasification of Colombian bituminous coal using Aspen Plus® (ID 395)
John Jairo Ortiz, Juan Camilo González, Jorge Enrique Preciado, Rocío Sierra, Gerardo Gordillo

VOLUME VII

VII . 1 - BUILDING, URBAN AND COMPLEX ENERGY SYSTEMS

» A linear programming model for the optimal assessment of sustainable energy action plans (ID 398)
Gianfranco Rizzo, Giancarlo Savino

» A natural gas fuelled 10 kW electric power unit based on a Diesel automotive internal combustion engine and suitable for cogeneration (ID 477)
Pietro Capaldi

» Adjustment of envelopes characteristics to climatic conditions for saving heating and cooling energy in buildings (ID 430)
Christos Tzivanidis, Kimon Antonopoulos, Foteini Gioti

» An exergy based method for the optimal integration of a building and its heating plant. Part 1: comparison of domestic heating systems based on renewable sources (ID 81)
Marta Cianfrini, Enrico Sciubba, Claudia Toro

» Analysis of different typologies of natural insulation materials with economic and performances evaluation of the same buildings (ID 28)
Umberto Desideri, Daniela Leonardi, Livia Arcioni

» Complex networks approach to the Italian photovoltaic energy distribution system (ID 470)
Luca Valori, Giovanni Luca Giannuzzi, Tiziano Squartini, Diego Garlaschelli, Riccardo Basosi

» Design of a multi-purpose building "to zero energy consumption" according to European Directive 2010/31/CE: Architectural and plant solutions (ID 29)
Umberto Desideri, Livia Arcioni, Daniela Leonardi, Luca Cesaretti ,Perla Perugini, Elena Agabitini, Nicola Evangelisti

» Effect of initial systems on the renewal planning of energy supply systems for a hospital (ID 107)
Shu Yoshida, Koichi Ito, Yoshiharu Amano, Shintaro Ishikawa, Takahiro Sushi, Takumi Hashizume

» Effects of insulation and phase change materials (PCM) combinations on the energy consumption for buildings indoor thermal comfort (ID 387)
Christos Tzivanidis, Kimon Antonopoulos, Eleutherios Krawvaritis

» Energetic evaluation of a smart controlled greenhouse for tomato cultivation (ID 150)
Nickey Van den Bulck, Mathias Coomans, Lieve Wittemans, Kris Goen, Jochen Hanssens, Kathy Steppe, Herman Marien, Johan Desmedt

» Energy networks in sustainable cities: temperature and energy consumption monitoring in urban area (ID 190)
Luca Giaccone, Alessandra Guerrisi, Paolo Lazzeroni and Michele Tartaglia

» Extended exergy analysis of the economy of Nova Scotia, Canada (ID 215)
David C Bligh, V.Ismet Ugursal

» Feasibility study and design of a low-energy residential unit in Sagarmatha Park (Nepal) for envirnomental impact reduction of high altitude buildings (ID 223)
Umberto Desideri, Stefania Proietti, Paolo Sdringola, Elisa Vuillermoz

» Fire and smoke spread in low-income housing in Mexico (ID 379)
Raul R. Flores-Rodriguez, Abel Hernandez-Guerrero, Cuauhtemoc Rubio-Arana, Consuelo A. Caldera-Briseño

» Optimal lighting control strategies in supermarkets for energy efficiency applications via digital dimmable technology (ID 136)
Salvador Acha, Nilay Shah, Jon Ashford, David Penfold

» Optimising the arrangement of finance towards large scale refurbishment of housing stock using mathematical programming and optimisationg (ID 127)
Mark Gerard Jennings, Nilay Shah, David Fisk

» Optimization of thermal insulation to save energy in buildings (ID 174)
Milorad Bojić, Marko Miletić, Vesna Marjanović, Danijela Nikolić, Jasmina Skerlić

» Residential solar-based seasonal thermal storage system in cold climate: building envelope and thermal storage (ID 342)
Alexandre Hugo and Radu Zmeureanu

» Simultaneous production of domestic hot water and space cooling with a heat pump in a Swedish Passive House (ID 55)
Johannes Persson, Mats Westermark

» SOFC micro-CHP integration in residential buildings (ID 201)
Umberto Desideri, Giovanni Cinti, Gabriele Discepoli, Elena Sisani, Daniele Penchini

» The effect of shading of building integrated photovoltaics on roof surface temperature and heat transfer in buildings (ID 83)
Eftychios Vardoulakis, Dimitrios Karamanis

» The influence of glazing systems on energy performance and thermal comfort in non-residential buildings (ID 206)
Cinzia Buratti, Elisa Moretti, Elisa Belloni

» Thermal analysis of a greenhouse heated by solar energy and seasonal thermal energy storage in soil (ID 405)
Yong Li, Jin Xu, Ru-Zhu Wang

» Thermodynamic analysis of a combined cooling, heating and power system under part load condition (ID 476)
Qiang Chen, Jianjiao Zheng, Wei Han, Jun Sui, Hong-guang Jin

VII . 2 – COMBUSTION, CHEMICAL REACTORS

» Baffle as a cost-effective design improvement for volatile combustion rate increase in biomass boilers of simple construction (ID 233)
Borivoj Stepanov, Ivan Pešenjanski, Biljana Miljković

» Characterization of CH4-H2-air mixtures in the high-pressure DHARMA reactor (ID 287)
Vincenzo Moccia, Jacopo D'Alessio

» Development of a concept for efficiency improvement and decreased NOx production for natural gas-fired glass melting furnaces by switching to a propane exhaust gas fired process (ID 146)
Jörn Benthin, Anne Giese

» Experimental analysis of inhibition phenomenon management for Solid Anaerobic Digestion Batch process (ID 348)
Francesco Di Maria, Giovanni Gigliotti, Alessio Sordi, Caterina Micale, Claudia Zadra, Luisa Massaccesi

» Experimental investigations of the combustion process of n-butanol/diesel blend in an optical high swirl CI engine (ID 85)
Simona Silvia Merola, G. Valentino, C. Tornatore, L. Marchitto , F. E. Corcione

» Flameless oxidation as a means to reduce NOx emissions in glass melting furnaces (ID 141)
Jörg Leicher, Anne Giese

» Mechanism of damage by high temperature of the tubes, exposed to the atmosphere characteristic of a furnace of pyrolysis of ethane for ethylene production in the petrochemical industry (ID 65)
Jaqueline Saavedra Rueda, Francisco Javier Perez Trujillo, Lourdes Isabel Meriño Stand, Harbey Alexi Escobar, Luis Eduardo Navas, Juan Carlos Amezquita

» Steam reforming of methane over Pt/Rh based wire mesh catalyst in single channel reformer for small scale syngas production (ID 317)
Haftor Orn Sigurdsson, Søren Knudsen Kær

VOLUME VIII

VIII . 1 - ENERGY SYSTEMS : ENVIRONMENTAL AND SUSTAINABILITY ISSUES

» A multi-criteria decision analysis tool to support electricity planning (ID 467)
Fernando Ribeiro, Paula Ferreira, Madalena Araújo

» Comparison of sophisticated life cycle impact assessment methods for assessing environmental impacts in a LCA study of electricity production (ID 259)
Jens Buchgeister

» Defossilisation assessment of biodiesel life cycle production using the ExROI indicator (ID 304)
Emilio Font de Mora, César Torres, Antonio Valero, David Zambrana

» Design strategy of geothermal plants for water dominant medium-low temperature reservoirs based on sustainability issues (ID 99)
Alessandro Franco, Maurizio Vaccaro

» Energetic and environmental benefits from waste management: experimental analysis of the sustainable landfill (ID 33)
Francesco Di Maria, Alessandro Canovai, Federico Valentini, Alessio Sordi, Caterina Micale

» Environmental assessment of energy recovery technologies for the treatment and disposal of municipal solid waste using life cycle assessment (LCA): a case study of Brazil (ID 512)
Marcio Montagnana Vicente Leme, Mateus Henrique Rocha, Electo Eduardo Silva Lora,Osvaldo José Venturini, Bruno Marciano Lopes, Claudio Homero Ferreira

» How will renewable power generation be affected by climate change? – The case of a metropolitan region in Northwest Germany (ID 503)
Jakob Wachsmuth, Andrew Blohm, Stefan Gößling-Reisemann, Tobias Eickemeier, Rebecca Gasper, Matthias Ruth, Sönke Stührmann

» Impact of nuclear power plant on Thailand power development plan (ID 474)
Raksanai Nidhiritdhikrai, Bundhit Eua-arporn

» Improving sustainability of maritime transport through utilization of liquefied natural gas (LNG) for propulsion (ID 496)
Fabio Burel, Rodolfo Taccani, Nicola Zuliani

» Life cycle assessment of thin film non conventional photovoltaics: the case of dye sensitized solar cells (ID 471)
Maria Laura Parisi, Adalgisa Sinicropi, Riccardo Basosi

» Low CO2 emission hybrid solar CC power system (ID 175)
Yuanyuan Li, Na Zhang, Ruixian Cai

» Low exergy solutions as a contribution to climate adapted and resilient power supply (ID 489)
Stefan Goessling-Reisemann, Thomas Bloethe

» On the use of MPT to derive optimal RES electricity generation mixes (ID 459)
Paula Ferreira, Jorge Cunha

» Stability and limit cycles in an exergy-based model of population dynamics (ID 128)
Enrico Sciubba, Federico Zullo

» The influence of primary measures for reducing NOx emissions on energy steam boiler efficiency (ID 125)
Goran Stupar, Dragan Tucaković, Titoslav Živanović, Miloš Banjac, Srđan Belošević,Vladimir Beljanski, Ivan Tomanović, Nenad Crnomarković, Miroslav Sijerčić

» The Lethe city car of the University of Roma 1: final proposed configuration (ID 45)
Roberto Capata, Enrico Sciubba

VIII . 2 - POSTER SESSION

» A variational optimization of a finite-time thermal cycle with a Stefan-Boltzmann heat transfer law (ID 333)
Juan C.Chimal-Eguia, Norma Sanchez-Salas

» Modeling and simulation of a boiler unit for steam power plants (ID 545)
Luca Moliterno, Claudia Toro

» Numerical Modelling of straw combustion in a moving bed combustor (ID 412)
Biljana Miljkoviü, Ivan Pešenjanski, Borivoj Stepanov, Vladimir Milosavljeviü, Vladimir Rajs

» Physicochemical evaluation of the properties of the coke formed at radiation area of light hydrocarbons pyrolysis furnace in petrochemical industry (ID 10)
Jaqueline Saavedra Rueda , Angélica María Carreño Parra, María del Rosario Pérez Trejos, Dionisio Laverde Cataño, Diego Bonilla Duarte, Jorge Leonardo Rodríguez Jiménez, Laura María Díaz Burgos

» Rotor TG cooled (ID 121)
Chiara Durastante, Paolo Petroni, Michela Spagnoli, Vincenzo Rizzica, Jörg Helge Wirfs

» Study of the phase change in binary alloy (ID 534)
Aroussia Jaouahdou, Mohamed J. Safi, Herve Muhr

» Technip initiatives in renewable energies and sustainable technologies (ID 527)
Pierfrancesco Palazzo, Corrado Pigna

ECOS 2012

VOLUME I

A Novel hybrid-fuel Compressed Air Energy Storage System for China's Situation

Wenyi Liu[a], Yongping Yang[b] Weide Zhang[c], Gang Xu[b],and Ying Wu[e]

[a] *Key Lab of Education Ministry for Power Plant Equipments Conditions Monitoring and Fault Diagnosis, North China Electric Power University, Beijing, China, lwy@ncepu.edu.cn*

[b] *Key Lab of Education Ministry for Power Plant Equipments Conditions Monitoring and Fault Diagnosis, North China Electric Power University, Beijing, China, yyp@ncepu.edu.cn*

[c] *Key Lab of Education Ministry for Power Plant Equipments Conditions Monitoring and Fault Diagnosis, North China Electric Power University, Beijing, China, wadezhang2006@126.com*

[d] *Key Lab of Education Ministry for Power Plant Equipments Conditions Monitoring and Fault Diagnosis, North China Electric Power University, Beijing, China, xg2008@ncepu.edu.cn*

[e] *Key Lab of Education Ministry for Power Plant Equipments Conditions Monitoring and Fault Diagnosis, North China Electric Power University, Beijing, China, 837469236@qq.com*

Abstract:

China is one of the world's top industrial sources of CO_2. Enormous coal-fired power plants in China make up almost half of the total CO_2 emissions. So cleaner energy sources, such as wind energy and solar energy, need to be developed at a fast rate. China has 45GW of wind power installed by 2011, which ranks no.1 in the world. Wind power is variable and intermittent. Compressed air energy storage(CAES) systems have increasingly been expected as a means of load levelling of wind power. China is a country with rich coal but deficient natural gas. So a novel hybrid-fuel compressed air energy storage is proposed and analysed. Air is compressed with a motor/generator using low cost, off-peak or discarded electricity from wind power or off-peak energy and is stored underground in caverns or porous media. This pressurized air is released from the ground and heated in recuperator, external combustion heater and combustion chamber. Then the hot air drives the high-pressure air turbine and low-pressure gas turbine to run a motor/generator which, in turn, produces electricity during peak demand periods. Through this system, coal can be used efficiently in CAES plant. An exergy and techno-economic analysis is also performed for this novel system.

Key words:

Compressed air energy storage(CAES), hybrid-fuel, techno-economic analysis of China's situation.

1. Introduction

Global warming was initiated by the increasing concentrations of CO2 and other greenhouse gases (GHG) in the atmosphere[1-2]. Using wind energy and other cleaner, less polluting, technologies will make a significant contribution to reversing the worse situation of world global warming [3-4]. But wind power is variable and intermittent. Electric energy storage has the ability to complement wind and overcome many challenges noted above. Current available electric energy storage technologies contain potential energy (e.g. CAES, pumped hydro storage (PHS)) [5-6], kinetic, thermal, chemical energy storage. For large scale storage applications, PHS and CAES are the most viable technologies.

Pumped hydro storage is the largest-capacity form of grid energy storage now available. PHS needs special hydrologic and geographic condition and is found to have certain adverse environmental effects [7]. In addition of PHS, CAES is a technically proven solution for bulk energy storage[8]. According to reported data, the investment of CAES power plant is far lower than PHS power plant with equivalent capacity.

CAES technology has been in use for over 30 years. The first CAES plant, a 290 MW facility, was started in Huntorf, Germany in 1978, and a 110 MW plant commenced operation in McIntosh,

Alabama in 1991[9-10]. The McIntosh plant made some improvements compared to the Huntorf design by incorporating a recuperator (air to air heat exchanger) to preheat air from the cavern with waste heat from the turbines. After overcoming some startup issues, the plant has functioned with over 95% reliability. The successful operation of the McIntosh and Huntorf plants has demonstrated the technical viability of CAES technology in supplying ancillary services, load following, and intermediate power generation.

Nowadays, CAES is still in hot research due to its vital role in power grid. The main research focuses on system analysis and optimization, different kinds of fuels, integration with wind power and techno-economic analysis.

Some novel CAES systems have been analyzed and optimized. A hybrid wind–diesel-compressed air energy storage system has been studied and designed[11].Victor de Biasi has proposed some improvement solutions for energy storage[12-13]. It is concluded that the second-generation CAES technology provides unique load management of renewable energy, smart grid regulation, synchronous reserve, demand power and peak shaving management. And adiabatic CAES plants (3rd-generation CAES technology) ACAES plants can be optimized to operate with over 70% efficiencies.

Energy, exergy analysis and economic analysis of CAES have been analyzed in some papers[14-19]. It is estimated that the rate of wind +CAES system with a greenhouse gas (GHG) emission, is one fourth of that for natural gas combined cycle plants and about one-tenth of that for pulverized coal plants[20]. With utilization of the computer model, the economic advantages of using large-scale energy to complement a wind farm in a base-load dominated electricity grid have been theoretically studied. It has been found that CAES is the most profitable storage medium. Different energy storage methods have been compared. It is therefore highly recommended that CAES should be further investigated with the aim of introducing large-scale energy storage to some similar wind turbine installations.

China has 45GW of wind power installed by 2011 which ranks no.1 in the world[21]. Wind power is growing at the rate of 30% annually in China. Wind energy source has made great strides in penetrating into the grid. Large scale storage applications have to be developed to meet the demand of wind power. But some rich wind energy resources places, like north China and northwest China, are lack of conditions to develop PHS. On the contrary, most of Chinese stable geographic structure regions are suitable for developing CAES. There exist a large number of salt mines, coal mines, natural gas mines and other metal mines. The utilization of depleted mines will cut investment cost in CAES. China needs CAES to meet its demand of renewable energy. So many power groups have planned to develop CAES.Although a large body of researches involving CAES have been undertaken and reported during the past few years, few researches of CAES have been studied linked with China’s situation.

In view of these factors, this paper proposes a novel hybrid-fuel compressed air energy storage(CAES) system combined with China’s situation. Additionally, the thermodynamic and techno-economic performance of this CAES system will also be studied.

2. The novel CAES system with China’s situation

2.1. The development of CAES technology

2.1.1 The first-generation CAES system

The first-generation CAES system was commercially used about 30 years ago. It has been proved that this technology is practical. This CAES technology is similar with gas turbine power plant. Air is compressed with a motor using low cost, off-peak electricity and is stored underground in caverns or porous media. The pressurized air is released from the ground and then be mixed and burned with gas in a combustor. The hot gas drive a turbo expander and run a generator which, in turn, produces electricity during peak demand periods. The compressor series and gas turbine are respectively linked with motor/generator using clusters. The conceptual diagram is shown in figure

1.

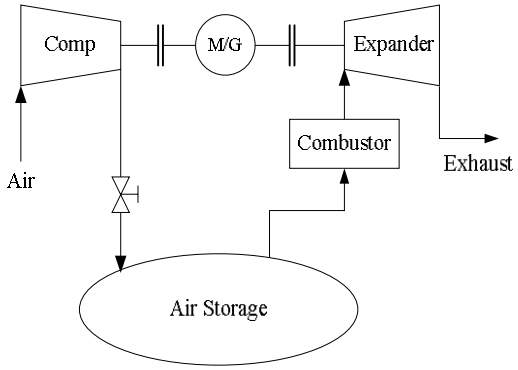

Fig. 1. Conceptual diagram of Huntorf CAES power plant

2.1.2 The second-generation CAES system[12]

The second-generation CAES is similar to the first-generation technology [12]. Figure 2 is a typical configuration of the second-generation CAES technology. The design utilizes standard, industrial proven equipment components to deliver a reliable and economic CAES plant. Some technologies for gas turbine have been improved to some extent. One improvement lies in the drop of heat rate; another improvement is overall efficiency enhancement, with about 54% efficiency compared to 48-50% for the first-generation CAES technology. The second-generation CAES technology is an open cycle and makes use of traditional gas turbine. The leakage air from the turbine is used to preheat air before putting into the expander.

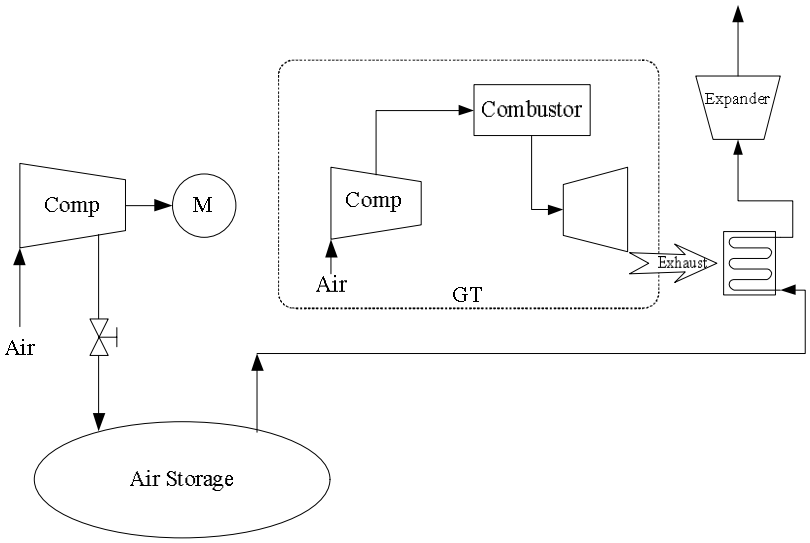

Fig. 2. Diagram of the second generation CAES technology

2.1.3 The third-generation CAES system[13,22]

The third-generation CAES technology is called adiabatic CAES technology. The typical configuration of the 3rd-generation CAES technology is shown in figure 3. The design is based on using standard, industry proven equipment components. The key components are motor driven compressors, thermal oil, heat exchanger, and air expanders. All key components are available with commercial guaranties and warranties. Adiabatic CAES uses no fuel to convert stored compressed air into peak-electricity power. Cooling of the compressors and heating of the stored air for power

production are achieved with thermal energy storage. During storage operations, "cold oil" is used to intercool the compressed air, and produces "hot oil" for use during power production. This "hot oil" is then delivered to heat the stored air from the air storage reservoir before compressed air enters the expander for power production. Overall conversion efficiency from off-peak electricity to on-peak electricity varied in the range from 70% to 75%.The main problem of 3rd-generation CAES is thermal energy storage and this problem is still under research until now. The novel design of thermal energy storage material is high temperature molten salt which is used in Concentrating Solar Power(CSP).

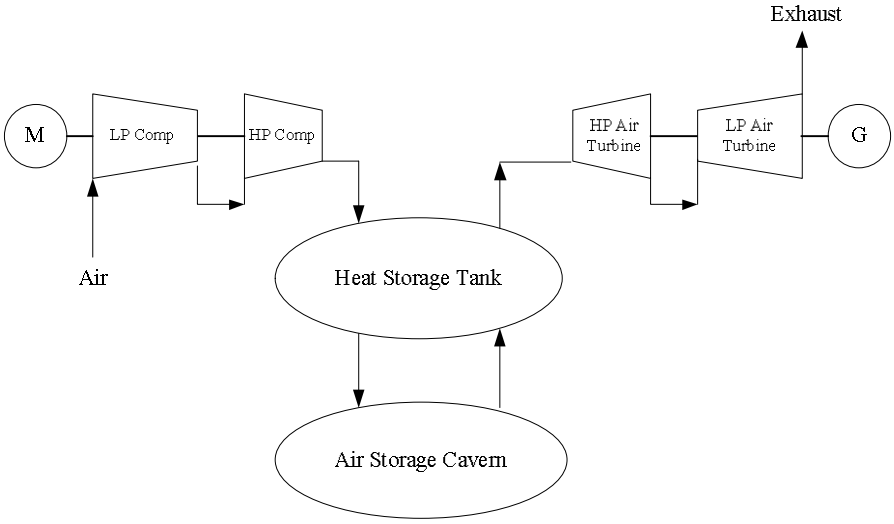

Fig. 3. Diagram of the third generation CAES technology

2.1.4 The comparison of 3 generations CAES

The 3 generations CAES technologies have their own characteristics. The comparison of main parameters for 3 generations CAES is illustrated in table 1.

Table 1. The main parameters for 3 generations CAES

Name	1st-generation CAES	2nd-generation CAES	3rd-generation CAES
location	Huntorf, Germany	No practical plant	No practical plant
output	290MW over 2 hours	With air injection power augment, Total CAES2 plant power 172MW CAES2 expander power 108MW	114.5MW
Compressor power	60MW(≤12hours)	71	157.6MW
commissioned	1978	No	No
pressure tolerance	50~70bar	No	No
HR	1.6kW.h gas	1.105kW.h gas	0
Cavern storage capacity	310,000m3	No	No
Energy ratio	1.0kW.h out/0.8kW.h in	1.0kW.h out/0.65~0.68kW.h in	0.727kW.h out/1.0kW.h in
fuel	natural gas(NG)	natural gas(NG)	No fuel

2.2. China's energy source structure and technology character

2.2.1 The energy source structure of China[23-25]

The distribution of energy sources and industry in China is extremely uneven. Statistics show that the coal reserve is 5.6 trillion ton and natural gas reserve is 50 trillion m^3 in China. The coal reserves structure is rich in the western and northern region but poor in the eastern and southern region. And the coal reserve is mainly concentrated in undeveloped provinces. The coal reserve in Shanxi, Inner Mongolia, Shaanxi, Xinjiang, Guizhou and Ningxia is about 4.63 trillion ton , and it accounts for about 82.8% of nation's total reserves. The coal character in coal-rich regions is versatile and of good quality. However, the eastern region, particularly, the southeastern coastal area, is an industrially-developed area but is short of energy sources. There is only about 5.3% of the nation's total reserves in Beijing, Shanghai, Tianjin, Shandong, Hebei, Liaoning, Jiangsu, Zhejiang, Guangdong, Fujian, Guangxi, Hainan, Hongkong and Taiwan. And These 14 provinces, cities and autonomous regions consume more than 50% energy sources. The natural gas reserves are abundant in Ordos basin and Sichuan Basin, Northern China region, Tarim Basin, Tu-Ha basin, Zhungeer Basin in Xinjiang Uygur Autonomous Region, Chadamu basin in Qinghai province, Eastern-Sea basin and Yunnan-Guizhou region. Natural gas reserve in these region accounts for nearly 80% national reserve.

2.2.2 The industry situation of rich wind energy regions in China

The areas with the richest wind energy sources are mainly located in the northern and the south-eastern coastal areas and their adjacent islands. The geographical distribution of wind energy source doesn't match the country's power load profile however. The heavy power loads are concentrated in the economic centers along eastern coastal provinces, where inland wind sources are scarce. Consequently, wind power development is amplifying the present imbalance of power production and consumption. For the northern regions, where wind sources are abundant, the power loads are small and the grid infrastructure is weak.

The regions with rich water resources are mainly situated in the south of China[26]. The boundary line is Kunlun mountain, Qinling mountain, Dabie mountain. The northern part of the boundary line is poor in water resource. The 17 north provinces(cities, autonomous regions) account for 21.4% national water resource with 600.8 billion m^3 every year. Taihang mountain is the boundary line in Northern China. Eastern regions are more abundant than western regions in water resource. For example, Shanxi, Gansu and Ningxia only account for 7.5% northern water resource. The rainfall quantity is below 500mm in these three provinces(autonomous regions) and its adjacent provinces(autonomous regions), including Shaanxi, Inner Mongolia and Xinjiang. Thus, the water resource is very poor in these areas.

It is showed that the abundant energy source regions are relatively undeveloped, while the developed regions is noticeably short of energy sources. The rich wind energy source regions are also rich in coals. Wind power is growing at the rate of 30% annually in China. But these wind rich regions are lack of hydrologic and geographic condition for pumped hydro power plants. Consequently, a lot of CAES power plants will be needed in west China.

Based on the above analyses, we believe that CAES development in China should consider these factors: (1) using more coal as fuel. China is a country with rich coal and deficient natural gas. Considering energy source distribution, coal should become main energy source in China. In addition of energy source distribution, the price of coal is relatively lower than that of natural gas. (2)The power capacity for leveling peak and off-peak is large. The power grid is extremely large in China with large amounts of wind power capacity. As a consequence, the power capacity for leveling peak and off-peak should be large enough to the best of its ability. (3) Simple structure and relatively proven technology. China is a developing country with poor overall industry base and limit economic support. Combined with China's situation, a hybrid-fuel CAES system should be considered.

2.3. The design of novel CAES system

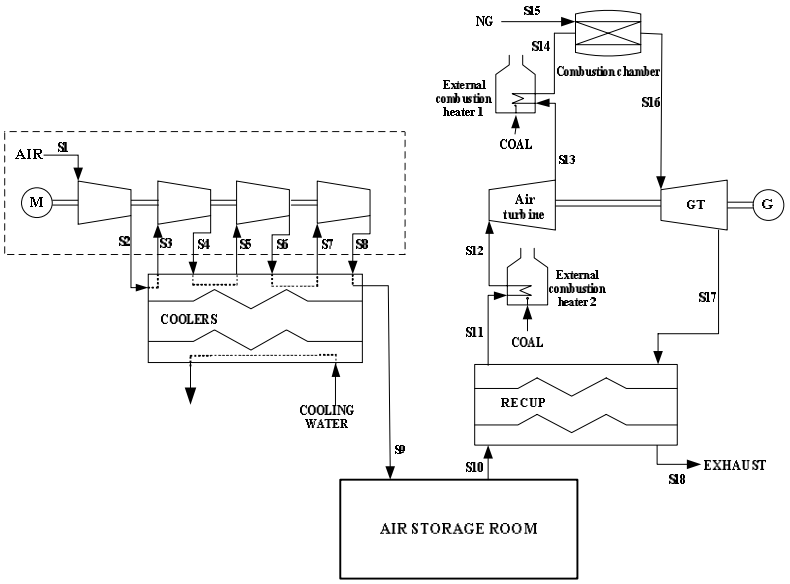

Fig. 4. flow sheet of the novel hybrid-fuel CAES system

Based on above analyses, a novel hybrid-fuel CAES system for China's situation is proposed. A conceptual configuration of the novel CAES system is shown in Fig. 4. This CAES system includes a compressed air energy storage sub-system and a turbine electricity-generating sub-system. Air is compressed with a motor using low cost, off-peak electricity and is stored underground in caverns or porous media, just like the 1st-generation CAES. The pressurized air is released from the ground and then heated by the recuperator and external combustion heater 2 and finally put into high pressure air turbine. The hot expanding air drives a high-pressure air turbine. After leaving the high-pressure air turbine, air is heated by external combustion heater 1 then mixed and burned in combustor. The hot gases will drive a low-pressure gas turbine. The high-pressure air turbine and low-pressure gas turbine will operate a generator which, in turn, produces electricity during peak demand periods.

Compressed air energy storage sub-system consists of a motor and compression system which includes a 4-stage coaxial compressor train. Through the 4-stage coaxial compressor train, each stage operates with a cooler which helps to cool the hot air to ambient temperature. All of compression system input and output tubes are placed in a thermal storage exchanger to transfer heat. The first compressor output is linked to the second compressor input, the second compressor output is linked to the third compressor input, the third compressor output is linked to the fourth compressor input. After the 4th compressor system and the corresponding after-cooler, the air is compressed to about 70bar. And the compressed air is stored in the air room through pipelines.

Turbine electricity-generating sub-system consists of air-turbine, gas turbine, external combustion heater 1, external combustion heater 2, combustor and generator. During the peak power consumption periods, high-pressure air is released from air room. It is first preheated in the recuperator, absorbing heat from the gas turbine exhaust. Then the preheated air passes through external combustion heater 2 and is further heated to a higher temperature. After the 2-stage heating processes, the heated air enters the air turbine to generate electricity. Both the pressure and temperature of the air turbine exhaust drops to a lower level. The air turbine exhaust is reheated in external combustion heater 1. This heated air with a proper high-pressure, accompanied by high-pressure natural gas, enters the combustion chamber. The combustor output is linked with gas turbine. After the combustion process, gas is heated to high temperature. The gas enters the gas turbine which is coaxial with the air turbine so as to generate more electricity. As the heat source of the low-temperature compressed air, the gas turbine exhaust passes through the recuperator, and cools down to about 100 ℃。

The design is based on the usage of standard, industry proven equipment components to deliver a reliable and economic compressed air energy cycle. All key components are available with commercial guaranties and warranties. Compared with conventional CAES plant, 1 or 2 external combustion heater is added. In addition of natural gas, more than 1/3 fuel is coal. Using coal as part of fuel is suitable for China's energy source structure.

3. Performance evaluation of novel hybrid-fuel CAES system

3.1. Evaluation criteria

Since the CAES plant is a dual purpose (peak power generation and energy storage) plant, it has two energy inputs (electric energy and fuel during the charging and discharging phases, respectively) which are of different qualities. The evaluation criteria of CAES plants differ from the ones usually applied for conventional power plants. Specific fuel consumption (SFC), for example, cannot identify the thermodynamic merits of the CAES plant as in a conventional power cycle. So some evaluation criteria will be introduced.

3.1.1.The energy rate

The energy rate expresses the ratio of pumping energy at the off-peak period to the generated energy during the peak period:

$$ER = \frac{W_c}{W_t} \tag{1}$$

though not accounting for fuel consumption, is unique to CAES plants. Thereby, *ER* is used as another performance parameter in addition to W_t which equals the net electric energy output during the discharge phase.

3.1.2.The heat rate

The heat rate is expressed as the number of kW.h of heat required to produce a kilowatt-hour of energy:

$$HR = \frac{Q_f}{W_t} \tag{2}$$

where Q_f is the total fuel energy (kW.h) used in the combustors and in the boilers during the generation period.

3.1.3. Plant Energy Efficiency [28]

The output from a CAES plant is work. This may be compared to the input energy to the plant consisting of natural gas and compressor work:

$$\eta_{ee} = \frac{W_t}{Q_f + W_c} \tag{3}$$

This may be seen as an expression of the storage efficiency, but it may be questioned, which consists of two different types of energy that are consumed by different parts of the process and at different point in time. The fuel cannot be seen as a part of the electricity storage but is only required due to the heating of the air to the turbine.

3.1.4. Electricity Storage Efficiency

The electricity energy efficiency may be defined as below.

$$\eta_{es} = \frac{W_t - \eta_{sys} Q_f}{W_c} \tag{4}$$

The system efficiency η_{sys} is a measure of the thermal efficiency of the energy system. Its value will depend on which system the CAES plant is used in. For a coal-fired power plant or a gas turbine

power plant, the value is between 30% and 55%. The value of 40% is used for a coal-fired power plant and the value of 55% is used for a gas turbine power plant in this paper. The total system efficiency of this hybrid-fuel system (η_{sys}) is 50% in this paper.

3.2. System simulation

In the novel hybrid-fuel CAES system, the air turbine electricity-generating sub-system consists of an air turbine and a gas turbine. The basic conditions and assumptions of the system process simulation are given in Table 2.

Table 2. Basic conditions and assumptions for simulation

Fuel information	
LHV of Coal(MJ/kg)	29.3
LHV of Natural Gas(MJ/kg)	50
Compressors	
Parameter	Value
Number of stages	4
Number of intercoolers	3
Number of after-coolers	1
Pressure ratio of each stage	2.90
Isentropic efficiency of compressors(%)	86.00
Air Turbine & Gas Turbine	
Parameter	Value
Inlet temperature of air turbine (℃)	540
Inlet temperature of gas turbine (℃)	1200
Pressure ratio of air turbine	3
Pressure ratio of gas turbine	18
Isentropic efficiency of air turbine (%)	88.00
Isentropic efficiency of gas turbine (%)	90.00
Other assumptions	
Parameter	Value
efficiency of external combustion heater (%)	90.00
efficiency of generators (%)	99.00
efficiency of motors (%)	99.00
total hybrid-fuel system efficiency η_{sys} (%)	50.00
system efficiency $\eta_{syscoal}$ (%)	40.00
system efficiency η_{sysgas} (%)	55.00

The novel hybrid-fuel CAES system was evaluated by commercial software, Aspen Plus. During the physical and chemical processes involved in the simulation, all the equations of state adopts the Peng-Robinson base method.

Peng-Robinson base method can calculate all the thermodynamic properties except molar volume of liquid. It is recommended for gas processing, oil refining and chemical applications. The nature of the method can be used to calculate thermodynamic properties of pure component, especially suitable for high temperature and pressure range, thus we can get a reasonable calculation results in the critical region. For gas mixtures, the P-R equation can calculate the thermodynamic properties of the fugacity coefficient, density, enthalpy, entropy, Gibbs free energy and so on.

The pressure, temperature, mole flow and the composition of each stream corresponding to the points indicated in Fig. 4 is listed in Table 3.

Table 3. Parameters of main points of novel hybrid-fuel CAES system

Streams	Temperature (^oC)	Pressure (bar)	Mass Flow (kg/s)	Mole Frac. (%)				
				N_2	O_2	CH_4	CO_2	H_2O
S1	35.00	1.03	400.00	79.00	21.00	0.00	0.00	0.00
S2	161.28	2.90	400.00	79.00	21.00	0.00	0.00	0.00
S3	35.00	2.90	400.00	79.00	21.00	0.00	0.00	0.00
S4	161.40	8.41	400.00	79.00	21.00	0.00	0.00	0.00
S5	35.00	8.41	400.00	79.00	21.00	0.00	0.00	0.00
S6	161.70	24.39	400.00	79.00	21.00	0.00	0.00	0.00
S7	35.00	24.39	400.00	79.00	21.00	0.00	0.00	0.00
S8	162.25	70.73	400.00	79.00	21.00	0.00	0.00	0.00
S9	35.00	70.73	400.00	79.00	21.00	0.00	0.00	0.00
S10	50.00	57.00	400.00	79.00	21.00	0.00	0.00	0.00
S11	500.84	57.00	400.00	79.00	21.00	0.00	0.00	0.00
S12	540.00	57.00	400.00	79.00	21.00	0.00	0.00	0.00
S13	359.11	19.00	400.00	79.00	21.00	0.00	0.00	0.00
S14	580.00	19.00	400.00	79.00	21.00	0.00	0.00	0.00
S15	50	19.00	6.42	0.00	0.00	100.0	0.00	0.00
S16	1200.03	19.00	406.42	76.78	14.80	0.00	2.81	5.61
S17	537.09	1.06	406.42	76.78	14.80	0.00	2.81	5.61
S18	100.00	1.06	406.42	76.78	14.80	0.00	2.81	5.61

3.3. Performance evaluation

The simulation results of the novel hybrid-fuel CAES system are presented in Table 4.

Table 4. Results for novel hybrid-fuel CAES system

Coal input (MW)	114.3
Natural gas input (MW)	321.2
Total fuel input (MW)	435.5
Power generation (MW)	
Air turbine	79.5
Gas turbine	329.7
Subtotal	409.2
Internal power consumption (MW)	
Compressors	205.7
Subtotal	205.7
Net power output (MW)	203.5
ER	0.50
HR	1.10
η_{ee}	62.58%
η_{es}	80.24%

It can be seen from Table 4 that, the results of *ER* and *HR* is 0.50 and 1.10, respectively. It means that compared with the 1st-generation CAES system, to produce a kilowatt-hour of energy, both the power consumed by compressors and the thermal energy needed from fuel are relatively lower. The plant energy efficiency of 62.58% is also higher accordingly. The electric storage efficiency is 80.24%, which illustrates that this novel CAES system is more efficient. In a word, this novel hybrid-fuel system exhibits high performance.

4. Discussion

4.1. Exergy analysis

To better reveal the internal phenomena of the novel hybrid-fuel CAES system, an exergy analysis is performed for the system. The results are listed in table 5.

Table 5. Exergy analysis of Novel hybrid-fuel CAES system

	Novel hybrid-fuel CAES system		Huntorf CAES system	
	Value MWh	Proportion of exergy input %	Value MWh	Proportion of exergy input %
Exergy input:				
Air	0.77	0.06	1.98	0.14
Power consumption by compressors	411.33	31.37	463.21	31.84
Thermal energy input of coal	228.66	17.44		
Thermal energy input of NG	670.54	51.14	989.43	68.02
Subtotal	1311.29	100.00	1454.63	100.00
Exergy output:				
Electricity Power generation	818.51	62.42	584.49	40.18
Exergy loss:				
Energy storage sub-system:				
Compressors	40.29	3.07	40.04	2.75
Coolers	80.29	6.12	122.18	8.40
Air storage room	13.80	1.05	33.57	2.31
Subtotal	134.38	10.25	195.79	13.46
Electricity-generating sub-system :				
HP turbine	10.44	0.80	17.50	1.20
LP turbine	28.36	2.16	36.64	2.52
External combustion heater 1	13.12	1.00		
External combustion heater 2	78.27	5.97		
Combustion chamber	191.05	14.57	460.18	31.64
Recuperator	19.91	1.52		
Subtotal	341.15	26.02	514.32	35.36
Exergy of exhaust stream	15.89	1.21	152.89	10.51
Total exergy output	1309.93	99.90	1447.49	99.51
Error of exergy input and output (%)	0.10		0.49	
Exergy efficiency (%)	62.42		40.18	

As shown in Table 5, the exergy efficiency of the novel system is 62.42%, the exergy efficiency of the Huntorf CAES system is 40.18%, which is approximately 20% higher than the 1st-generation Huntorf CAES system; and this number is much higher than the general gas turbine power plant, it greatly demonstrated the high performance advantage of the novel system.

The main exergy loss comes from the combustion chamber, the external combustion heater and the coolers in the energy storage sub-system.

Compared with the typical 1st-gegeration CAES system, the exergy loss of the turbine electricity-generating sub-system of the novel system was decreased. The main reason lies in several aspects as follows: firstly, the addition of the heating process greatly decreased the exergy loss of the exhaust gas from the gas turbine. Secondly, the installation of the external combustion heaters, which are

fuelled by coal, also make contribution to the reduction of exergy loss, in the typical 1st-generation CAES system, the exergy loss of 1st stage combustion chamber is much higher. Thirdly, the thermal energy derived from the coal makes thermodynamic properties of the air higher to match with the high parameters(1200℃) of the gas turbine, thus，the power generation sub-system could generates more power.

4.2 Techno-economic analysis

4.2.1 Fundamental parameters for CAES plant

Based on the novel CAES system, a typical CAES power plant can be analyzed. The volume of air storage required for a typical CAES plant is most economically provided by geological structures. Salt caverns, aquifers, depleted oil，gas reservoirs and rock mines have all been considered as possibilities for air storage in a CAES application. The CAES investment cost is tightly associated with the construction of air storage domes. Total capital investment costs are among $436/kW~$739/kW for 10h air storage cavities [27].

Standard compression blocks of 205 MW each can be combined with standard generation blocks of 410MW each in order to configure a plant that optimizes the ability of the facility to capture the market opportunities present at any given location. The use of multi-unit trains, each with a wide span and speed of response, on both the compression and generation side，gives the operator maximum flexibility to manage the load, storage, and generation aspects of CAES in a very efficient and cost effective manner.

Therefore, this study was performed based on the following equipment configuration:

Compression – a 205MW train allows a plant to operate in the range of 103 MW to 205 MW load and result injection into storage.

Generation – a 410 MW train allows a plant to operate in the range of 205 MW to 410 MW generation and result withdrawal from storage.

Storage volume is optimally sized to allow a daily exchange of injection and withdrawal volumes. The storage volume was designed to accommodate a maximum of 10 hours of rated injection into storage. The resulting CAES plant with 410 MW generation, 205 MW of compression, and 2,050 MW of storage is a size . The following table 6 summarizes the main assumptions about the 410 MW CAES plant, which the rate of €/￥ is 8.4 and $/￥ is 6.5.

Table 6. 410 MW CAES plant fundamental parameters

Name	Value and unit	Name	value and unit
generation range per unit	205~410MW	Overnight Cost – above ground equipment	3250￥/kW
Compression range per unit	103~205MW	Overnight Cost – cavern development	650￥/kW
Cavern storage capacity	2050MW.h	Total Overnight Cost	3900￥/kW
ER(kW.h in /(kW.h out)	0.50	Annual VOM cost	2% of total investment cost
HR (kW.h in /(kW.h out)	1.09	Annual FOM cost	2% of total investment cost
LHV of natural gas(NG)	36MJ/Nm^3	price of natural gas	3￥/Nm^3
LHV of coal	29.3MJ/kg	price of coal	800￥/t
Equivalent base-load time	2500h		

Overnight cost for above ground equipment includes all equipment costs, engineering, procurement and construction, spare parts, interconnects for gas, air, water, and electricity, and contingency. Costs are included to enable one of the generators to be disconnected from the turbine via a clutch so that it can operate as a synchronous condenser.

Cavern development costs include all the costs associated with acquisition of the land and mineral rights, solution mining of the caverns, well drilling and completion costs, and piping and casing costs.

FOM (fixed operations and maintenance) cost includes plant personnel and major maintenance accrual associated with start costs, as well as ancillary costs such as auxiliary power and water treatment.

VOM (variable operations and maintenance) cost mostly consists of accrual for major maintenance based on utilization of the turbines.

4.2.2 Economic data

In fact, the calculation of the levelized cost of electricity for power plant is highly complicated[29]. Based on the assumption that the energy production and the operation and maintenance costs for each year are the same, a simplified expression for the levelized cost of electricity calculation can be described as,

$$COE = \frac{[(CRF)(Total \quad investment \quad \cos t) + (Annual \quad O\,\&\,M \quad \cos t) + AFC + AOEC}{Annual \quad on-peak \quad electricity \quad ouput} \tag{5}$$

where, AOEC is annual off-peak electricity cost, AFC is annual fuel cost, COE is the levelized cost of electricity (￥/kWh); CRF is capital recovery factor, which is related to the discounted rate (k) and the life of equipments, and is calculated as: $CRF = \left[k \cdot (1+k)^n\right] \Big/ \left[(1+k)^n - 1\right]$.

Linked with above data and Chinese characteristics, the generation cost of CAES can be calculated. The annual VOM and annual FOM cost are assumed as 2% respectively of total investment cost. Low cost off-peak energy from the grid or discarded wind energy would be used to supplement the compression requirements. Its price is assumed as 0.2￥/kWh. Natural gas cost and coal cost are calculated according to LHV of NG and coal and their heat rate. The related data are listed in table 7.

Table 7. 445 MW CAES plant economic data

Name	Value and unit	Name	value and unit
Total investment cost	1.60billion ￥	CRF	0.12
NG fuel rate	2.83MJ/kW.h	NG cost	0.236￥/kWh
Coal fuel rate	1.12 MJ/kW.h	Coal cost	0.031￥/kWh
Annual VOM cost	31.98million ￥	VOM cost	0.031 ￥/kWh
Annual FOM cost	31.98million ￥	FOM cost	0.031 ￥/kWh
Annual Off peak electricity cost	102.5 million ￥	Off peak electricity cost	0.10￥/kWh
Annual CAES total electricity output	1.03×10^6MW.h	COE	0.616￥/kW.h
Off peak electricity price	0.2￥/ kW.h	On peak electricity price	0.7￥/ kW.h

4.2.3 Sensitivity analysis

According to table 7, the *COE* of CAES is 0.616￥/kWh. It is too expensive to integrate with the grid. In a competitive market, plant developers would not have an incentive to build generation to meet reserve requirements unless they were paid enough by the market to cover the fixed costs (capital and operating costs) on average over the life of the plant. So the price of off-peak energy, natural gas price, coal price and *CRF* should be variables. Then the sensitivity analysis data are listed in Table 8. Investment cost and variable *O&M* cost are fixed.

Table 8. Sensitivity analysis of COE for the novel CAES

Variable off-peak power price								
Off-peak energy price	0.16	0.20	0.24	0.28	0.32	0.36	0.40	￥/kW.h
Off-peak energy cost	0.08	0.10	0.12	0.14	0.16	0.18	0.2	￥/kW.h
COE	0.596	0.616	0.636	0.656	0.676	0.696	0.716	￥/kW.h
variable natural gas price								
natural gas price	1.5	2.0	2.5	3.0	3.5	4.0	4.5	￥/ Nm^3
natural gas cost	0.118	0.157	0.197	0.238	0.275	0.314	0.354	￥/kW.h
COE	0.498	0.537	0.577	0.616	0.655	0.695	0.734	￥/kW.h
variable coal price								
coal price	500	600	700	800	900	1000	1100	￥/t
coal cost	0.019	0.023	0.027	0.031	0.034	0.038	0.042	￥/kW.h
COE	0.605	0.608	0.612	0.616	0.620	0.624	0.628	￥/kW.h
variable *CRF*								
CRF	0.10	0.11	0.12	0.13	0.14	0.15	0.16	
investment cost	0.156	0.170	0.187	0.203	0.218	0.234	0.250	￥/kW.h
COE	0.585	0.599	0.616	0.632	0.647	0.663	0.678	￥/kW.h

According to table 8, the COE of the novel CAES is among 0.596￥/kWh and 0.716￥/kW.h if off-peak energy prices are among 0.16￥/kW.h and 0.40￥/kW.h. If the off-peak energy price is more than 0.36￥/kW.h, the COE of the novel CAES will exceed the sale price. The CAES power plant will not be economic. The COE of the novel CAES is among 0.598￥/kWh and 0.734￥/kW.h while NG prices are among 1.50￥/ Nm^3 and 4.50￥/ Nm^3.

The grid construction cost also must be considered. Because most of CAES power plants are constructed in undeveloped regions and far away from developed regions, the transforming grid must be constructed. The grid investment will be much more than the power plant investment. With energy storage, the maximum power output can be levelled, the investment of power grid will be reduced. Taking into account this cost, the COE of the novel CAES will be reduced accordingly. This cost is competent in Chinese energy market. This techno-economic analysis proved that the hybrid-fuel CAES is competent in Chinese energy market.

5. Conclusion

In this paper, a novel hybrid-fuel CAES system for China's situation is proposed. The design is based on using standard, industry proven equipment components to deliver a reliable and economic compressed air energy cycle. Compared with conventional CAES plant, 1 or 2 external heater is added. In addition of natural gas, more than 1/3 fuel is coal. Using coal as part of fuel is suitable for China's energy source structure.

An exergy analysis is also performed for the novel system. The results show that the exergy efficiency of the novel system is 62.43%, which is approximately 20% higher than the average 1st-generation conventional CAES system; and this number is much higher than the general gas turbine power plant, it well demonstrated the high performance advantage of the novel system. The main reason lies in the addition of the heating process from exhaust gas, the installation of the external combustion heaters and the thermal energy derived from the coal makes thermodynamic properties of the air higher to match with the high parameters(1200℃) of the gas turbine. The main exergy loss comes from the combustion chamber, the external combustion heaters and the coolers in the energy storage sub-system.

Linked with related data and China's situation, the COE of the novel CAES is calculated, the value is 0.616￥/kWh. It is too expensive to integrate with the grid. So the price of off-peak energy, natural gas price, coal price and CRF should be variables Then the sensitivity analysis data are studied. These data show if the on-peak energy price is more than 0.7￥/ kW.h, the hybrid-fuel CAES power plant is competent in Chinese energy market.

Therefore, the novel CAES system is simple, proven technological, high-efficient, coal-utilized and economic system. It will bring great benefits for CAES used in China and promote the sustainable development of western China.

Acknowledgements

The paper is supported by National Nature Science Fund of China (No. 51006034), and the National Major Fundamental Research Program of China (No.2009CB219801, No. 2011CB710706).

Nomenclature

ER energy rate [kW.h/ kW.h]

HR heat rate [kW.h/ kW.h]

W_c Compressor work [kW.h]

W_t Turbine work [kW.h]

Q_f the total fuel energy [kW.h]

η_{ee} Energy efficiency

η_{es} Electricity storage efficiency

η_{sys} System efficiency

$\eta_{syscoal}$ System efficiency for coal-fired power plant

η_{sysgas} System efficiency for gas turbine power plant

LHV lower heating value[MJ/kg]

AOEC annual off-peak electricity cost[￥]

AFC annual fuel cost[￥]

COE the levelized cost of electricity [￥/kWh]

CRF capital recovery factor

References

[1] Tong Liu, Gang Xu, Peng Cai, Longhu Tian, Qili Huang, Development forecast of renewable energy power generation in China and its influence on the GHG control strategy of the country, Renewable Energy 2011:36: 1284-1292.

[2] Working Group III of the Intergovernmental Panel on Climate Change (IPCC), IPCC's fourth assessment report (AR4): mitigation of climate change. Cambridge, UK: Cambridge University Press; 2007.

[3] EU rethinks nuclear energy policy after Japanese accident-Available at:< http://english.peopledaily.com.cn/index.html> [accessed 17.3.2011].

[4] Jeff Mason, Will Dunham, Japan nuclear woes cast shadow over US energy policy. cn_reuters_com.mht, WASHINGTON (Reuters) –Available at: <http://cn.reuters.com>.

[5] Mandhapati Raju, Siddhartha Kumar Khaitan, Modeling and simulation of compressed air storage in caverns: A case study of the Huntorf plant, Applied Energy 2012:89: 474–481.

[6] Lerch E., Storage of fluctuating wind energy. In: Eur Conf Power Electron Appl, 2007 sept.

[7] Makarov YV, et al. Wide-area energy storage and management system to balance intermittent resources in the Booneville power administration and California ISO control areas. 2008 June. PNNL Report; <http://www.electricitystorage.org/images/uploads/docs/ Wide_Area_EMS_Report_V7.pdf>.

[8] Ridge Energy Storage & Grid Services L.P., The Economic Impact of CAES on Wind in TX, OK, and NM, Final Report. 2005 June 27. REPORT FOR: Texas State Energy Conservation Office.

[9] Wen-yi Liu, Yong-ping Yang, Zhi-ping Song, Optimization and performance simulation of different CAES systems, Journal of Engineering Thermo-physics, 2005:26(Supp.): 25–28 (in Chinese).

[10] Wen-yi Liu, Simulation Analysis of Thermal Performance for Compressed Air Energy Storage (CAES) Power Plant [dissertation]. Beijing, China: North China Electric Power University; 2008. (in Chinese).

[11] A. Ilinca, M. Dimitrova, J. Perron, Study and design of a hybrid wind–diesel-compressed air energy storage system for remote areas, Applied Energy 2010:87: 1749-1762.

[12] Victor de Biasi, New solutions for energy storage and smart grid load management, GAS TURBINE WORLD: 2009: 22-26.

[13] Victor de Biasi, Fundamental analyses to optimize adiabatic CAES plant efficiencies, GAS TURBINE WORLD: September - October 2009.

[14] Mir-Akbar Hessami, David R. Bowly, Economic feasibility and optimisation of an energy storage system for Portland Wind Farm (Victoria, Australia), Applied Energy 2011:1-9.

[15] D. Zafirakis, J.K. Kaldellis, Economic evaluation of the dual mode CAES solution for increased wind energy contribution in autonomous island networks, Energy Policy 2009: 1958–1969.

[16] Y.M. Kim, D. Favrat, Energy and exergy analysis of a micro-compressed air energy storage and air cycle heating and cooling system, Energy Energy 2012:35: 213–220.

[17] Giuseppe Grazzini, Adriano Milazzo, A Thermodynamic Analysis of Multistage Adiabatic CAES, Proceedings of the IEEE 2011, pp:1-11.

[18] Georges Salgi, Henrik Lund, System behaviour of compressed-air energy-storage in Denmark with a high penetration of renewable energy sources, Applied Energy 2008:85: 182–189.

[19] Giuseppe Grazzini, Adriano Milazzo, Thermodynamic analysis of CAES/TES systems for renewable energy plants, Renewable Energy 2008:33:1998–2006.

[20] Jeffery B. G, Samir S., David C. D.,Etc. Modelling the competition between gas turbines and compressed air energy storage for supplemental generation, Energy Policy 2007:35: 1474–1492.

[21] Wind power in the People's Republic of China, http://en.wikipedia.org/wiki/, 10 January 2012

[22] Adiabatic CAES concept-Available at :<http://www.espcinc.com/>

[23] 2010 coal resource of China, http://www.sxcoal.com/coal/2324065/articlenew.html. (in Chinese).

[24] A survey of coal resource for different regions in China, http://www.coal.com.cn/Coal_Resource_1_070307040706_.htm. (in Chinese).

[25] 2010-2030 natural gas resource potential reserve analysis in China. http://www.askci.com/freereports/2011/07/271559325678.shtml. (in Chinese).

[26] http://news.xinhuanet.com/fortune/2005-09/19/content_3512629.htm. (in Chinese).

[27] Ridge Energy Storage & Grid Services L.P., The Economic Impact of CAES on Wind in TX, OK, and NM, Final Report. 2005 June 27; pp:71-88

[28] Brian Elmegaard, Wiebke Brix, Efficiency of Compressed Air Energy Storage, ECOS 2011: 2512-2523.

[29] Tong Liu, Gang Xu, Peng Cai, etc., Development forecast of renewable energy power generation in China and its influence on the GHG control strategy of the country, Renewable Energy 2011:36:1284-1292.

A Review of Stirling Engine Technologies applied to micro-Cogeneration Systems

Ana C.M. Ferreira[a], Manuel L. Nunes[b], Luís A. S. B. Martins[c] and Senhorinha F.C.F. Teixeira[d]

[a] *Department of Production and Systems, School of Engineering, University of Minho, Guimarães, Portugal, acferreira@dps.uminho.pt*

[b] *Department of Production and Systems, School of Engineering, University of Minho, Guimarães, Portugal, lnunes@dps.uminho.pt*

[c] *Department of Mechanical Engineering, School of Engineering, University of Minho, Guimarães, Portugal, lmartins@dem.uminho.pt*

[d] *Department of Production and Systems, School of Engineering, University of Minho, Guimarães, Portugal, st@dps.uminho.pt*

Abstract:

This paper presents a review on Stirling engines used in micro-CHP system applications. The aim of this review is to investigate and identify the commercial solutions available in the market based on Stirling engine technology. This should represent a preliminary study to understand what are the best configurations to use with this technology in combined heat and power production for the building sector. A number of Stirling engine configurations and designs, including the engine's development is provided and discussed.
Stirling engines have been identified as a promising technology for energy conversion due to their high efficiency levels, low pollutant emissions, low noise levels and due to their flexibility in terms of fuel sources. Micro-CHP systems based on Stirling engines could be suitable for applications where multi-fuelled characteristics and high thermal efficiencies are needed. Stirling engines are flexible and consistent with the requirements for a sustainable development.

Keywords:

Combined Heat and Power, Efficiency, Stirling Engine, Primary Energy Savings, Equivalent Carbon Avoided Emissions.

1. Introduction

The use of cogeneration systems in micro scale applications has recently gained expression in the energy market. As matter of fact, Combined Heat and Power (CHP) is a well proven concept relying on a variety of technologies and energy sources. These decentralized energy systems have been recognized as an effective method to improve the efficiency of energy conversion, reducing the pollutant emissions and the impact on climate change [1-4]. They are typically designed to provide electricity in a range of 1-10kW$_e$ and able to cover similar heat loads, which appears to be a good opportunity to meet the energy needs for the residential sector. Different technologies are been studied based on their complexity, range of power and efficiency [5]. The most common technologies for this type of applications are: reciprocating engines, Organic Rankine cycles, Fuel Cells and the Stirling engines [2, 5]. These technologies are usually compared considering technical, ecological and economic aspects in order to assess their performance and viability in penetrating the market for domestic and micro-scale applications [1, 6].
The Stirling engine has interesting characteristics for micro-CHP applications. Although this technology is not fully developed yet and thus in very limited use, it shows a great potential due to its intrinsic high efficiency, fuel flexibility, low emissions and noise/vibration levels and good performance at partial load. A number of Stirling engine developers for micro-CHP applications are available. Stirling engine manufactures that are focused on micro-CHP applications are worldwide dispersed. *WhisperTech*®, from New Zealand, produces a four-cylinder alpha-type Stirling engine and self-integrates the engine in a complete micro-CHP system [7]. *Enatec*® from the Netherlands

builds Stirling driven domestic CHP plants [8]. *Cleanergy*® from Sweden recently acquired the rights and patents of the previously known SOLO engine from Germany[9]. There is the MicroGen Engine, which is being developed by a consortium of Baxi Group and other players in the European heating market [10].

The main purpose of this work is to develop a preliminary study on the application of Stirling engines in the modelling of micro-CHP systems. Therefore, it is intended to include a comprehensive review of the state-of-the-art based on the technological knowledge about the performance characteristics (electrical efficiency, heat recovery capacity, gas emissions), quality of supplied electricity, specific maintenance requirements, systems lifetime and fuel types.

2. The Stirling Engine

Since the presentation of the patent by Robert Stirling in 1816, Stirling engines have been developed for different purposes and applications. This versatility is due to the fact that the heat source in Stirling engines is external and thus can accept a wide variety of fuels, including fossil fuels, biomass, solar, geothermal and nuclear energy. Another good point is that the combustion process can occur in steady state and therefore is easier to control. Stirling engines are very flexible and its most outstanding feature is related to their capacity to work at low temperatures. In this way, they can use some energy sources that are usually widespread, for instance, hot water [1]. Also, Stirling engines have low pollutant emissions, low noise levels and long maintenance free operating periods.

2.1. Principle of Operation

An elementary Stirling engine consists of an engine piston, an exchanger piston and three heat exchangers: a cooler, a regenerator and a heater. The piston converts gas pressure into mechanical power, whereas the exchanger piston is used to move the working gas between the hot and cold sources. Stirling engines are usually classified according to its mechanical configuration: the Alpha, Beta and the Gamma arrangements (Fig. 1).

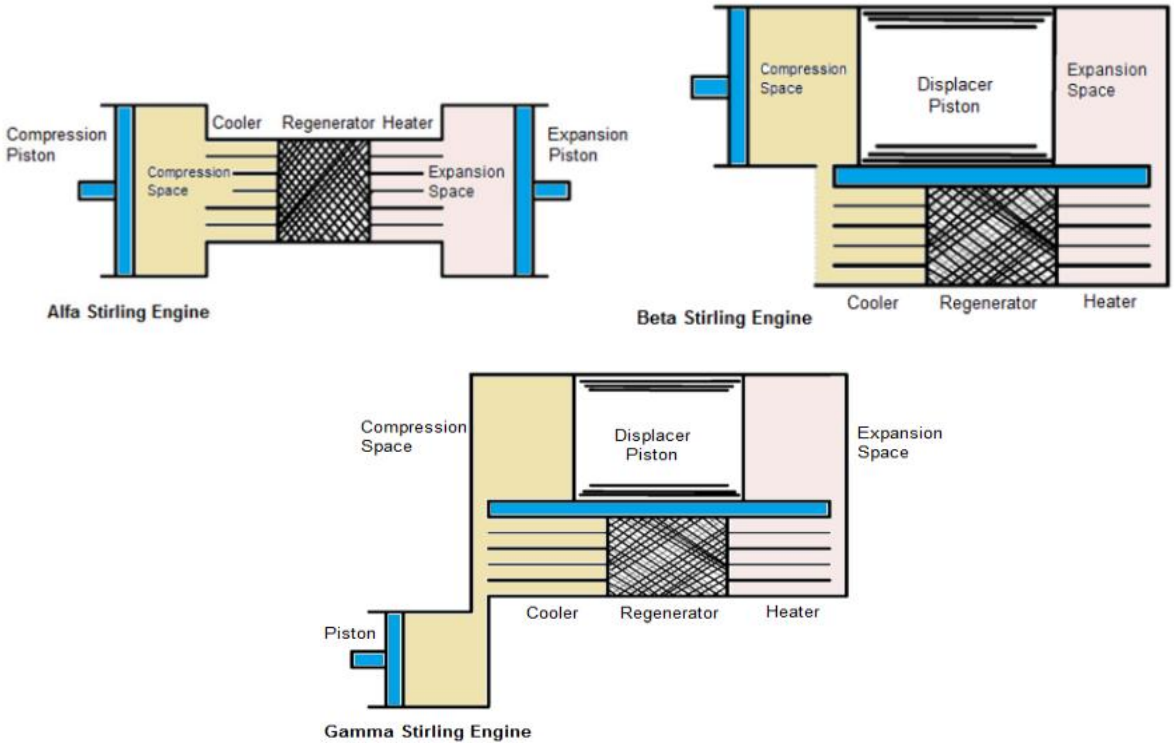

Fig. 1. Schematic representation of Stirling engine configurations.

The Alpha configuration has two mechanically linked pistons (compression and expansion pistons) in separate cylinders connected in series by the cooler, the regenerator and the heater. The Beta configuration corresponds to the classic Stirling engine, having a power/compression piston arranged within a single cylinder with a displacer/expansion piston, both connected to the same shaft in a rather complex manner. The existence of a displacer aims to move the working gas between the expansion and the compression spaces at constant volume. Similar to what happens in the Beta configuration, Gamma engines use displacer-piston arrangements. The main difference between these two configurations is that, in the Gamma engine, the power piston is mounted in a separate cylinder alongside the displacer-piston cylinder and the working gas can flow freely between them. This configuration produces a lower compression ratio, but allows an easier mechanical linkage between the pistons and a convenient separation between the heat exchangers which are associated to the displacer cylinder and the compression work space associated with the power piston [11].

Stirling engine drive methods are based on two distinct principles of operation: the kinematic drive and the free piston drive method. Kinematic Stirling engines use the mechanical elements to convert the reciprocal piston motion to a rotational output, say to drive a generator. The kinematic drives require special sealing to avoid leaks due to high pressures at which the working gas is subject. Free-piston Stirling engines move the reciprocating elements using the pressure variations in the space beneath the piston. As the linear alternator is tightly attached, the mechanical friction is minimized and, as a result, the leakage of the working gas is substantial reduced. So, the free piston engine does not require large maintenance costs, allowing a continuous power operation and a great potential for high efficiency [12].

Stirling engines have the potential of achieving higher efficiencies because they closely approach the Carnot cycle. Presently, these engines are able to get an electrical efficiency of about 30% and a total efficiency of 85-98% operating in cogeneration mode. Stirling engines also have good capability to operate under part-load conditions.

In theory, the Stirling engine is the most efficient technology for converting heat into mechanical work, being its efficiency limited by the Carnot cycle (ideal engine) efficiency.

2.2. Stirling engine thermodynamic cycle

The Stirling cycle engines have been developed in recent years as external combustion engines with regeneration. It is a closed cycle and it contains a fixed mass of a working gas.

The ideal Stirling cycle combines four thermodynamic distinct processes: two constant-temperature processes and two constant-volume processes. In the ideal Stirling engine cycle, the working gas is alternately heated and cooled as it is compressed and expanded. The first process of the ideal Stirling engine cycle is the isothermal compression process. During this stage work (W_{1-2}) is done on the working fluid, while an equal amount of heat (Q_{1-2}) is rejected by the system to the cooling source. As there is no change of gas temperature, the transferred heat to this process is the same ($Q_{1-2}=W_{1-2}$). At the second step, a constant-volume process occurs with heat addiction (Q_{2-3}) and no work is done ($W_{2-3}=0$). Then the working fluid suffers an isothermal expansion at constant temperature, as heat is added (Q_{3-4}) to the system from the heating source. Work is done by the working fluid (W_{3-4}). Finally heat (Q_{4-1}) is rejected by the working fluid and gas temperature decreases when it passes through the regenerator. No work is done ($W_{4-1}=0$). Figure 2 represents the pressure/volume diagram of the ideal Stirling engine [13].

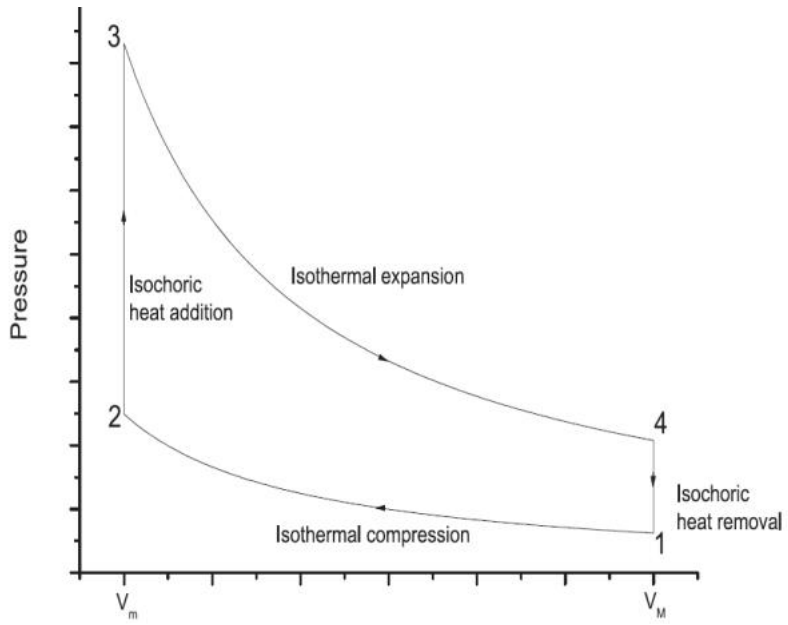

Fig. 2. Pressure/volume diagram of the ideal Stirling engine cycle {adapted from [14]}.

The efficiency of a real Stirling Engine is lower when compared with the ideal cycle. One of the causes for inefficiency of the real Stirling cycle is due to the regenerator because it adds friction to the flow of the working gas. The other major cause of Stirling cycle inefficiency is the fact that not all the gas in the engine participates in the cycle, since there is a certain amount of gas that remains in the regenerator, heater or cooler. The reduction of cycle efficiency is related with the percentage of this "dead volume" of gas in the engine, which is always present because of the addition of heat exchangers, transfer ducts, and regenerators. Many authors have studied the effect of heat losses, irreversibilities and design parameters on the thermodynamic performance of Stirling engines. Timoumi and co-workers [11] presented a study where a numerical simulation was developed using the experimental data from the General Motor (GPU-3) Stirling engine. The model was used to determine the influence of geometrical and physical parameters in the engine performance. Puech and Tishkova [14] performed a theoretical analysis on the thermodynamic analysis of a Stirling engine with linear and sinusoidal variations of the volume. The authors concluded that the dead volume strongly amplifies the imperfect regeneration effect and, therefore, the regenerator effectiveness. Kongtragool and Wongwises [15] also studied the effects of dead volume and regenerator effectiveness on thermal Stirling efficiency and concluded that the dead volume conduces to the reduction of engine network and the thermal efficiency.

The nature and the pressure of the working fluid influence the power performance of the Stirling engine. Gases such as helium and hydrogen, which allows rapid heat transfer and do not change phase, are typically used in high-performance Stirling engines [2]. Hydrogen, thermodynamically a better choice, has a higher thermal diffusivity and has a lower viscosity and therefore lower flow losses than helium. On other hand, helium has fewer material compatibility problems and it is safer to work with. Also, air can be used as the working fluid but with a prejudice on performance [16].

2.3. Review on Stirling Engines Optimization

In the design of Stirling engines, two aspects are currently considered: the maximum efficiency and the maximum power production. Markman and co-workers [11] conducted an experiment using a beta-configuration Stirling engine to measure the heat fluxes and the power losses, aiming to the optimization of the engine efficiency. Wu et al. [2] analysed the optimal performance of a Stirling engine. In their Study, the influence of heat transfer and regeneration time on the Stirling engine

cycle performance was discussed. Puech and Tishkova [14] performed a thermodynamic analysis of a Stirling engine conducting an investigation about the influence of regenerator dead volume variations. The results showed that the dead volume amplifies the imperfect regeneration effect.

Petrescu et al. [5] presented a method for calculating the efficiency and power of a Stirling engine.

Boucher et al. [12] related a theoretical study of the dynamic behaviour of a dual free-piston Stirling engine coupled with an asynchronous linear alternator. The objective was the evaluation of the thermo-mechanical conditions for a stable operation of the engine.

Formosa and Despesse [17] developed an analytical thermodynamic model to study a free-piston Stirling engine architecture. The model integrated the analysis of the regenerator efficiency and conduction losses, the pressure drops and the heat exchangers effectiveness. The model was validated using the whole range of the experimental data available from the General Motor GPU-3 Stirling engine prototype. The influence of the technological and operating parameters on Stirling engine performance was investigated. The results from the simplified model and the data from the experiment showed a reasonable correlation. Rogdakis et al. [18] studied a Solo Stirling Engine V161 cogeneration module via a thermodynamic analysis. Calculations were conducted using different operational conditions concerning the heat load of the engine and the produced electrical power. The authors achieved good results in terms of electrical and thermal efficiencies as well as good primary energy savings.

3. Stirling engine based micro-CHP systems

Stirling engines have been developed in a wide range of power capacity, from 1 W to 1MW. Both engine drive types show a great potential for combined heat and power systems. The kinematic Stirling units are able to produce 1.1 to 500 kW of electrical capacity, while free piston Stirling engines can be found in the range between 1 and 25 kW of electrical capacity [17]. This makes free piston Stirling engines an attractive technology suitable for small- and micro-scale applications. There are some commercially available cogeneration systems, based on Stirling engines, in development. The company *WhisperTech*® (New Zealand) developed an alpha kinematic engine called WhisperGen™ with a capacity of up to 1.2 kW of electrical power and 7.5-14.5 kW of heat. It is a four cylinder unit with the option to interface with the electrical grid. *WhisperGen*™ provides a low electrical efficiency of 12% but an total efficiency of 80%, leading to smooth and vibration free operation [1, 7].

Microgen™ unit, developed by BG Group from a US (*Sunpower*) design, contains a supplementary burner which enables it to meet the full heating requirements for larger homes. *MicroGen*™ is a cogeneration unit for residential and small-office use. The unit is based on free piston Stirling engine and it is fuelled by natural gas. This unit is able to produce 1.1 kW of electricity and a thermal output range of 15-36 kW_{th}. However, when the demand is low, the unit has the capacity of modulating down to 5 kW_{th}. According to BG Group, the *MicroGen*™ unit can reduce CO_2 emissions in 25% [10].

Cleanergy® is a leading engine manufacturer in the Stirling technology field. It offers two variants of small power plants: one for biogas and one for solar power, the Solo Stirling model. The units are of open source configuration and have the maximum electrical capacity of 9kW. The combined heat and power unit for biogas also generates 26 kW of thermal power. Cleanergy's Stirling units have a very long lifetime and high efficiency. In 2009 *Cleanergy*® moved the production of Stirling engines to the newly refurbished company in Sweden from Germany in order to scale-up the production [9, 18].

The *Enatec*® consortium in the Netherlands and Rinnai in Japan both use Infinia Stirling generator technology in their residential CHP systems. Their free-piston Stirling generators are designed to deliver energy in a way that is virtually silent, long-lasting, economical, environmentally-friendly and exceptionally low-maintenance [10]. *Infinia Corporation*® recently launched a new system, the *PowerDish*™, which uses a parabolic concentrator dish to concentrate the sun's energy onto the hot end of a free-piston Stirling engine. This concentrated solar energy creates a temperature

differential across the engine, causing the expansion and the contraction of the working gas which leads to the piston motion and the alternator generates electricity [19]

Inspirit® has been developing a micro-CHP unit based on a kinematic Stirling engine design. The beta configuration Stirling engine uses helium as its working gas and utilises an external heat source, to provide energy. The micro-CHP unit is capable of simultaneous generation of 15kW thermal and 3kW electrical output, exporting this electricity back to the utility grid. The appliance offers a total efficiency of up to 92%, comparing to an electrical efficiency of 16% and a thermal efficiency of 76% [20].

Stirling BioPower®, previously called STM Power, is a North American company which designs and manufactures Stirling engines. The company developed the *PowerUnit*™ which uses a Stirling engine to create a prime mover designed for renewable energy and distributed generation applications. The system was designed to operate on natural gas, propane, alcohol, renewable energy such as biomass or hot air as heat source. *PowerUnit*™ is able to reach a net electrical efficiency of 27-28% and, used in cogeneration mode, the total efficiency can achieve the 75-80% [21].

Sigma Elektroteknisk (Norway) developed a Stirling engine, PCP 1-130, to be used in co-generating applications. The beta-type Stirling uses helium as the working fluid, producing 1.5 kW of electrical power and 9 kW of thermal power with a total efficiency of 95% [22].

The use of Stirling technology applied to combined heat and power production is still under development. The Table 1 compares the power and the efficiencies for commercial models with greater significance in terms of commercialization.

Table 1. Power and Efficiency of micro-CHP commercial systems based on Stirling technology

Technical Specifications	*WhisperGen*™	*MicroGen*™	*Solo Stirling*	*Inspirit micro-CHP appliance*
Fuel	Natural Gas	Natural Gas	Biogas/Solar	Gas
Heat Production	7.5 -14.5(1) kW	15-36 kW	8-26 kW	12-15 kW
Electrical Production	1-1.2 kW	1.1 kW	2-9.5 kW	0.5-3 kW
Electrical Efficiency	12%	13.5%	24%	16%
Thermal Efficiency	77%	(2)	72%	76%
CO_2 Emission Savings[24]	11%	25%	*	20%

(1) Including the burner; *Information not found

Stirling Denmark has also developed a micro-CHP unit, the SM5A, which is not yet available in the market. The unit, based on a beta-type Stirling engine, delivers, at nominal condition, 8.1kWof electric power and 24.9kWof thermal power. The unit uses helium as working gas and was developed for utilization of biogas.

According to the presented values, it seems that micro-CHP systems are suitable for residential, commercial or institutional buildings, where the demand for thermal energy is more amplified: hot water consumption and space heating.

4. Comparison with other technologies

A number of prime mover technologies have been proposed for micro-CHP applications, based on ICE (Internal Combustion Engine), Stirling engines, Fuel Cells and Rankine cycles [23].

For micro-CHP applications, spark ignition engines are used where the exhaust heat as well as the heat from the oil and engine cooling are recovered using heat exchangers. Reciprocating engines are produced and commercialized in large scale by a variety of companies worldwide. One of the most sold systems is the *Dachs* model by *Senertec*® model, which generates 5.5 kW of electricity and 14 kW of thermal energy. It achieves 25% and 80% of electrical and total efficiency, respectively. An interesting unit for single-family house applications is the Honda´s *Ecowill*™ unit which delivers 1 kW of electricity [24].

Fuel Cells, which convert the chemical energy into electrical energy, are under development by several companies. Leading examples include the Plug Power PEM (Polymer Exchange Membrane) unit with a production of 4.6 kW of electricity, plus 7 kW of heat and the Sulzer Hexis SOFC (Solid Oxide Fuel Cell) 1kW_e unit with integral gas burner to provide flexible thermal output. The main disadvantages of this technology are that the heat cannot be extracted at well-defined points in the system, investment costs are extremely high and reliability issues are still a problematic [25].

A recent technological development is the Organic Rankine units. The most familiar Rankine engine is the steam engine in which water is boiled by an external heat source, expands and exerts pressure on a piston or turbine rotor and hence does useful work. Some of these systems use an organic fluid and operates at temperatures and pressures much closer to conventional heating and refrigeration purposes [24]. An example of this of these units is the *Energetix Genlec* system, based on the Inergia prototype developed by the Battelle Institute in the USA. This system is able to produce 1 kW of electricity and 10 kW of heat. Although having rather low electrical efficiency, it is well matched to many domestic applications and appears to offer relatively low manufacturing costs and good service life characteristics. As of 2011, the system is still in laboratory tests [26].

Micro gas turbines are also used as prime movers for cogeneration applications, but not at the micro-scale level due to the fact that these systems are only available for higher power outputs (30kW_e). In Table 2, different technologies are compared considering the electrical and thermal efficiencies, the stage of the technology development, fuel versatility, investment costs for each technology and the specific power [1, 17, 24].

Table 2. Comparison of different micro cogeneration technologies

Technology	η_{el} (%)	η_{th} (%)	*Energy Source*	*Stage of Technology*	*Investment Costs (€/kW_e)*	*Specific Power (W/kg)*
Reciprocating Engine	20-30	> 85	Liquid fuel Natural gas	Commercially available	2100[(1)] – 4500	10 - 18
Stirling Engine	**11-35**	**> 85**	**Any type of fuel, solar radiation**	**Some models are already commercially available**	**2800[(2)] – 10 000**	7.3 - 9.1 [(3)]
Fuel Cells	28-30	80-85	Hydrogen hydrocarbon	In R&D and test prototypes	>30 000	-
Rankine Engines	10-20	70-85	Any type of Fuel	In R&D	-	-

(1) For a 15 kW_e unit; (2) Solo 161 not currently available; (3) not including Solo 161

Considering the data from Table 2, it can be said that Stirling engines offer a high variety of fuels with which it is possible to operate, allowing in particular the use of bio fuels or solar energy. Stirling engines have a great potential to achieve high overall efficiencies despite the moderate electrical efficiency. Also, the Stirling engines have good performance at partial load. The reciprocating engines are the technology with higher maturity, which represents a great advantage with respect to their diffusion in the market. Reciprocating engines have similar values for electrical

efficiency when compared with the Stirling engines, but theoretically require more periodic maintenance representing a cost increase. In addition, reciprocating engines have high noise levels and pollutant emissions. Fuel Cells and Rankine engines are still under development with some pilot plants being currently tested. The major potential of these two technologies lies in the highest electrical efficiency and the almost zero pollutant emissions. However, and due to fact that both are emerging technologies, their capital costs are considerable. As a result, their competitiveness remains unclear until they could be distributed in the market [27].

5. Economics of micro-CHP systems

The technical and economic challenges are significantly higher for micro-CHP than for larger scale systems. The economic viability of the micro CHP systems is fully related to the capacity of manufacturing the systems at a cost that can be recovered from the savings and incomes during the operating lifetime. In fact, the production costs per unit of power tend to rise exponentially as size reduces. In addition, micro-CHP depends on both the capital investment and the value of electricity produced by the unit. This latter represents the most valuable income from the systems operation. Therefore, for any given system, the payback relies on the unit's operating hours and consequently the total electricity produced annually. Clearly, it is not only the system purchase costs that are important to assess. The maintenance, the installation and the frequency of service intervals over the system working lifetime have to be quantified [28]. Because Stirling engines have sealed operating chambers, these systems have low wear and, as a consequence, long maintenance intervals. The result is the reduction of operating costs.

The economic viability analysis of cogeneration systems at mini- and micro-scale level have to consider, necessarily, the social and environmental benefits arising from its use. In practical terms micro-CHP plants also need to match the operational aspects with the respective energy needs. At least in Europe, micro CHP operation is thermally led, which means that the micro-CHP systems run when there is a demand for heat production.

In fact, the introduction of these systems in the building sector brought several challenges in order to determine the real needs in terms of electrical and thermal energy. Each household has a specific energy demand depending on many variables such as climate characteristics, building features, the number and the behaviour of the dwellers. A number of earlier studies have used diverging approaches to investigate this. Some authors [29, 30] simulated the behaviour of entire buildings using whole-building and systems simulation tools. Other authors [31, 32] used approaches that are based on established load profiles, not explaining how this residential energy load is composed. Hawkes et al. [30] developed techno-economic modelling of micro-CHP to determine the minimum annual cost of meeting a given residential electricity and heat demand profile through optimal sizing of micro-CHP generation capacity.

Effectively the electricity and heat generated from micro-CHP systems does not impose an additional combustion process, being reduced the carbon emissions in producing both electricity and heat. According to Onovwiona [1], emissions from Stirling burners can be 10 times lower than those emitted from gas Otto engines with catalytic a converter. The actual "savings" in CO_2 as well as pollutant emissions (e.g. SO_x, NO_x emissions) depend on the annual operating hours. In addition to the economic benefits, there is potential in strategic terms of reducing fuel dependency, although there are complications regarding the funding of this energy efficiency measure.

Many authors defend the theory that the success of micro-CHP systems in the residential sector requires a multi-criteria evaluation where consumers identify the different parameters that may influence the acquisition of such systems as viable solution to meet their energy demands. Generally, the micro-CHP units must be of small dimensions, unobtrusive visually and acoustically silent [1, 4]. The benefits of micro-CHP over conventional power production can be summarized in a few points: *(i)* micro-CHP produces heat and power at point on demand which fulfil the domestic electric and heating needs; *(ii)* the on-site power production reduces transmission and distribution losses; *(iii)* the utilization of primary energy is maximized by reducing waste heat; and finally *(iv)*

micro-CHP offers significant contribution to gas emissions reduction, also because of the possibility of using renewable sources.

Perhaps, of more significance though, is the benefit which micro CHP offers in conjunction with other beneficial technologies. One example of this is the impact it's the integration of the micro-CHP systems with the national grid, which is led by thermal demand and therefore greater when network demand tends to be the highest. This will therefore reduce peak generation and network capacity demand, reducing energy distribution costs [33].

6. Conclusions

The present paper presents a review of the state-of-the-art based on the technological knowledge about the Stirling cycle, performance characteristics such as the electrical efficiency, the heat recovery capacity and the fuels used by micro-CHP systems centred on Stirling engines. A comparison between Stirling engine and other technologies used in to micro-scale applications was also performed. The thermal efficiency is better for the micro-CHP systems with Stirling engines and reciprocating engines when compared with the Fuel Cells for instance. Many systems based on kinematic drive and free-piston engines show a great potential for the combined production of heat and power.

Stirling engines have been identified as a promising technology for the conversion of primary energy into useful power due to their high efficiency levels, low pollutant emissions, low noise levels and mostly due to their flexibility in terms of fuel sources. The use of a renewable energy source is very important from the view point of the primary energy savings. However, these systems present some disadvantages. One of them is the relatively high capital costs of those plants.

The review on Stirling engine technology presented in this paper intends to be a preliminary study on all micro cogeneration systems commercially available (or about to be marketed) in order to understand what are the best configurations and settings of this technology to be applied in combined heat and power production for the building sector. The main purpose behind this study is the definition of a numerical cost-benefit model applied to a cogeneration system for a micro-scale application. The system that is intended to be modelled is based on Stirling engine technology combined with a solar collector by proposing the use of a renewable energy source. After defining the numerical model, optimization methods will be used with the aim to achieve the best technical and economic output of the system in analysis. The relevance of the study is to prove that the use of numerical optimization in the design of technical systems could be of utmost importance, allowing the improvement of performance and the reliability of the power plants, prior to their introduction in the market.

Acknowledgments

The first author would like to express her acknowledgments for the support given by the Portuguese Foundation for Science and Technology (FCT) through the PhD grant SFRH/BD/62287/2009. This work was financed by National Funds-Portuguese Foundation for Science and Technology, under Strategic Project and PEst-OE/EME/UI0252/2011.

References

[1] Onovwiona H.I., Ugursal V.I., Residential cogeneration systems: review of the current technology. Renewable and Sustainable Energy Reviews 2006; 10(5): 389-431.

[2] Wu D., Wang R., Combined cooling, heating and power: A review. Progress in Energy and Combustion Science 2006; 32(5-6): 459-495.

[3] Jackson J., Ensuring emergency power for critical municipal services with natural gas-fired combined heat and power (CHP) systems: A cost-benefit analysis of preemptive strategy. Energy Policy 2007; 35:5931-5937.

[4] Huangfu Y., Wu J., Wang R., Kong X., Wei B., Evaluation and analysis of novel micro-scale combined cooling, heating and power (MCCHP) system. Energy Conversion and Management 2007; 48:1703-1709.

[5] Ptrescu S., Costea M., Harman C., Florea T., Application of the direct method to irreversiblr Stirling cycles with finite speed. International Journal of Energy Research 2002; 26:589-609.

[6] Alanne K., Saari A., Sustainable small-scale CHP technologies for buildings: the basis for multi-level decision making. Renewable and Sustainable Energy Reviews 2004; 8:401–431.

[7] WhisperGen CHP System from WhisperTech Company Web Site. Available at: <http://www.whispergen.com > [accessed 12.01.2012].

[8] Enatec Company Web Site. Available at:< http://www.enatec.org/> [accessed 12.01.2012].

[9] Cleanenergy Web Site at:< http://www.cleanergy.com/> [accessed 12.01.2012].

[10] Baxi Group and De Dietrich Remeha Group official Web Site Available at: http://www.bdrthermea.com/home.html [accessed 07.02.2012].

[11] Timoumi Y., Tlili I., Nasrallah, B.S., Performance optimization of Stirling engines. Renewable Energy 2008; 33(7): 2134-2144.

[12] Boucher J., Lanzetta F., Nika P., Optimization of a dual free piston Stirling engine. Applie Thermal Engineering 2007; 27:802-811.

[13] Ferreira C.M.C., Ante-Projecto de um Motor Stirling [dissertation in portuguse]. Guimarães, Portugal: University of Minho; 2010.

[14] Puech P., Tishkova V., Thermodynamic analysis of a Stirling engine including regenerator dead volume. Renewable Energy 2011; 36(2): 872-878.

[15] Kongtragool B., Wongwises S., Thermodynamic analysis of a Stirling engine including dead volumes of hot space, cold space and regenerator. Renewable Energy 2006; 31: 345-359.

[16] Scollo L., Valdez P., Baron J., Design and construction of a Stirling engine prototype. International Journal of Hydrogen Energy 2008; 33(13): 3506-3510.

[17] Formosa F., Despesse G., Analytical model for Stirling cycle machine design. Energy Conversion and Management 2010; 51:1855-1863.

[18] Rogdakis E.D., Antonakos G.D., Koronaki I.P., Thermodynamic analysis and experimental investigation of SOLO V161 Stirling cogeneration unit. ECOS 2011: Proceedings of the 24th International Conference on Efficiency, Cost, Optimization, Simulation, and Environmental Impact of Energy Systems; 2011 Jul 4-7; Novi Sad, Serbia.

[19] Infinia Corporation Web Site Available at: <http://www.infiniacorp.com> [accessed 12.01.2012].

[20] Inspirit Web Site Available at: http://www.inspiritenergy.com/producttechnology.html [accessed 31.01.2012].

[21] Stirling BioPower Web Site. Available at: <http://www.stirlingbiopower.com> [accessed 31.01.2012].

[22] Scarpete D.A.N., Uzuneanu K., Stirling Engines in Generating Heat and Electricity for micro - CHP Systems. 11th WSEAS: Proceedings of Recent Researches in Multimedia Systems, Signal Processing, Robotics, Control and Manufacturing Technology International Conference; (pp. 149-154). WSEAS Press; 2011 March 8-10, Venice, Italy.

[23] Krawinkler R., Trnka G., Simader G.R., Micro CHP systems: State-of-the-art. Austrian Energy Agency 2006; 8:1-68 Vienna, Austria.

[24] Pehnt M., Cames M., Fisher C., Praetorius B., Schneider L., Schumacher K., Micro Cogeneration Technology. In: Micro Cogeneration towards Decentralized Energy Systems. Berlin, Germany. Springer Publisher. 2006. p. 1-16.

[25] Worldwide fuel cell installations. Fuel Cells 2000. Available at: <htt://www.fuelcells.org> [accessed 7.02.2012].

[26] Energetix Group Web Site Available at: <http://www.energetixgroup.com> [accessed 7.02.2012].

[27] Pehnt M., Environmental impacts of distributed energy systems - The case of micro cogeneration. Environmental science & policy 2008; 25-37.

[28] Ren H., Gao W., Economic and environmental evaluation of micro CHP systems with different operating modes for residential buildings in Japan. Energy and Buildings 2010; 42:853-861.

[29] Alanne K., Soderholm N., Sirén K., Beausolei-Morrison I., Techno-economic assessment and optimization of Stirling engine micro-cogeneration systems in residential buildings. Energy Conversion and Management 2010; 51:2635-2646.

[30] Dorer V., & Weber, A., Energy and CO_2 emissions performance assessment of residential micro-cogeneration systems with dynamic whole-building programs. Energy Conversion and Management 2009; 50: 648–657.

[31] Voorspools K., D'Haeseleer W. The evaluation of small cogeneration for residential heating. International Journal of Energy Research 2002; 26:1175–1190.

[32] Hawkes A., Leach, M., Impacts of temporal precision in optimisation modelling of micro-Combined Heat and Power. Energy 2005; 30: 1759–1779.

[33] Hawkes A., & Leach, M., Cost-effective operation strategy for residential micro- combined heat and power. Energy 2007; 32: 711-723.

An Organic Rankine Cycle off-design model for the search of the optimal control strategy

Andrea Toffolo[a], Andrea Lazzaretto[b], Giovanni Manente[c] and Marco Paci[d]

*[a] Luleå University of Technology, Luleå, Sweden, andrea.toffolo@ltu.se, **CA***
[b] University of Padova, Padova, Italy, andrea.lazzaretto@unipd.it
[c] University of Padova, Padova, Italy, giovanni.manente@unipd.it
[d] ENEL Engineering and Innovation, Pisa, Italy, marco.paci@enel.it

Abstract:

Power generation from low enthalpy geothermal resources using Organic Rankine Cycle systems is markedly influenced by the temperature level of the heat source and heat sink. During plant operation the actual temperature of the geofluid may be different from the value assumed in the design phase. In addition, the seasonal and daily variations of the ambient temperature greatly affect the power output especially when a dry condensation system is used. This paper presents a detailed off-design model of an Organic Rankine Cycle that includes the performance curves of the main plant components. Two capacitive components in the model have the key function of damping the temporary disequilibrium of mass and energy inside the system. Isobutane and R134a are considered as working fluids, mainly operating in subcritical and supercritical cycles, respectively. The off-design model is used to find the optimal operating parameters that maximize the electricity production in response to changes of the ambient temperatures between 0 and 30°C and geofluid temperatures between 130 and 180°C. This optimal operation strategy can be conveniently applied both to already existing plants and in the choice of new design plant configurations.

Keywords:

Organic Rankine Cycle, Off-Design, Dynamic Model, Control Strategy.

1. Introduction

Organic Rankine Cycles are a viable option for high efficiency/low cost exploitation of low temperature geothermal flows for electricity production. Some studies in the literature searched for parameters which are most suitable to correctly analyze the overall system performance. Among them, the works [1], [2] and [3] emphasized the importance of using a heat recovery efficiency in addition to thermal efficiency to correctly quantify the system capability of using the available energy/exergy content of the geothermal source. Other studies [4], [5] and [6] focused mainly on the best choice of the cycle operating fluids both in terms of efficiency and costs. The common approach in these studies consists in building system models and in comparing the obtained results for a given inlet temperature of the sensible heat source. Only few works [7] and [8] present instead a comparison between calculated and experimental values.

A different approach was used by the authors in [9] to search for the optimal and sub-optimal design conditions of Organic Rankine Cycle systems, which consists in keeping the design of the "heat transfer section" within the system (which appears as a black-box including hot and cold thermal streams, see Fig. 1a) independent of the design of the rest of the system itself (which is called basic plant configuration). This is done using the so called HEATSEP method [10] which considers the temperatures at the boundaries of the two parts of the systems as decision variables in the design optimization procedure. So, the design of the heat exchanger network can be performed only after these optimal temperature values are calculated.

In [11] the optimal thermodynamic solutions found in [9] for the working fluids isobutane and R134a were evaluated from the economic point of view. For various temperature values of the geothermal source in the range 130-180 °C, the heat exchanger network, previously left undefined

inside the black box, was obtained (Fig. 1b). It was composed by a preheater-vaporizer or a supercritical evaporator, an air cooled condenser and, only in some cases, a recuperator. The recuperator was "introduced" in the system structure by the optimization procedure when the thermal energy required to heat the operating fluid between pump outlet and turbine inlet was greater than the thermal energy made available by the geothermal source.

Although ORC systems are rather easy to operate, particular care must be taken in controlling and monitoring the system during transient conditions when the load demand or the quality or flow of the low temperature heat source changes. These conditions can be profitably predicted by off-design models. In [7] one of the present authors built an off-design stationary model of an existing 30 MW ORC plant in Aspen® environment using real characteristic curves. The model was then used to calculate the values of the operating parameters which maximize the power output from the available geothermal resource, and to change the actual operating criterion accordingly. Dynamic off-design models of ORC plants were recently proposed in [12] and [13]. In [12] the authors focused on the correct representation of evaporator and condenser dynamic behavior. The model was validated against experimental data available from a pilot 100kW ORC system using R245fa as working fluid. In [13] a dynamic model was built for a small scale Organic Rankine Cycle including a volumetric expander. The model was used to find the optimal control strategy to recover energy from a variable flow rate and temperature waste heat source using R245fa as working fluid. In particular, the authors developed dynamic models for the evaporator and the "receiver" (an accumulator) at the condenser exhaust whereas they used a steady state model for the expander.

In this paper an innovative off-design dynamic model of the ORC system is presented. Design conditions are assumed to be the optimal ones obtained in [9], and real characteristic curves are included in the model. When the ambient temperature and/or the geofluid temperature depart from the design values new operating parameters and thermodynamic cycles can be found by the model, which depend on the performance curves of the components and the plant control criterion. On this basis, an optimal control strategy is suggested to search for the values of the operating parameters which maximize the power generated at any predictable off-design conditions.

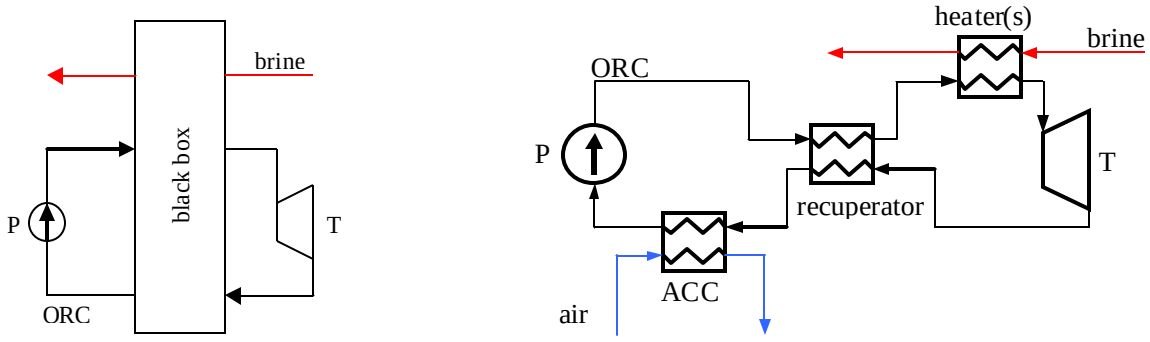

(a) *(b)*

Fig. 1. Configuration of the single pressure level ORC: a) basic plant configuration according to the HEATSEP method [10], b) plant configuration which includes the heat exchanger network.

2. The off-design model

2.1. General description

The off-design model built to simulate the system is composed by the sequence of components shown in Fig. 2. Each of these components is described by a performance curve previously set in the design phase. The operating point of the system is the equilibrium point obtained at given ambient conditions and control philosophy of the components. The point of equilibrium is obtained by balancing the reactions that each component provides in response to the thermodynamic conditions at the boundary of its control volume (both inlet and outlet) and by calculating the new

conditions according to its performance curve. Two key components of the system are the capacities at low and high pressure that can either exist in the real system as separate components or be only included in the model to calculate the equilibrium point. The capacities are filled and drained by the two main streams in the system: the stream flowing through the pump (from the low pressure capacity to the high pressure capacity) and the stream flowing through the turbine (from the high pressure capacity to the low pressure capacity). The mass flow rates of both these streams are obtained using the performance curves of the pump and turbine and the pressures inside the two capacities. However, the pressure inside the capacities depends in turn on the mass flows entering and leaving the capacities (actually the summation of the mass and enthalpy flows). Thus, after a transient from fixed initial conditions for each component a general equilibrium is found among all components, which describes the steady operating point of the system.

The following variables, shown in Fig. 2 using blue labels, are assumed as control variables in the system:

- Pump rotational speed (*npump*);
- Turbine capacity factor defined as a multiplier of the corrected mass flow rate at nominal conditions, controlled by opening of the nozzle vanes (*fcap*);
- Air mass flow rate in the ACC (*mA*).

The control variables are optimized to maximize the net power output (P_{net}), which is defined as the difference between the power generated by the turbine (P_{gen}) and the power absorbed by the feed pumps (P_{pump}) and the ACC fans (P_{ACC}):

$$P_{net} = P_{gen} - P_{pump} - P_{ACC} \qquad (1)$$

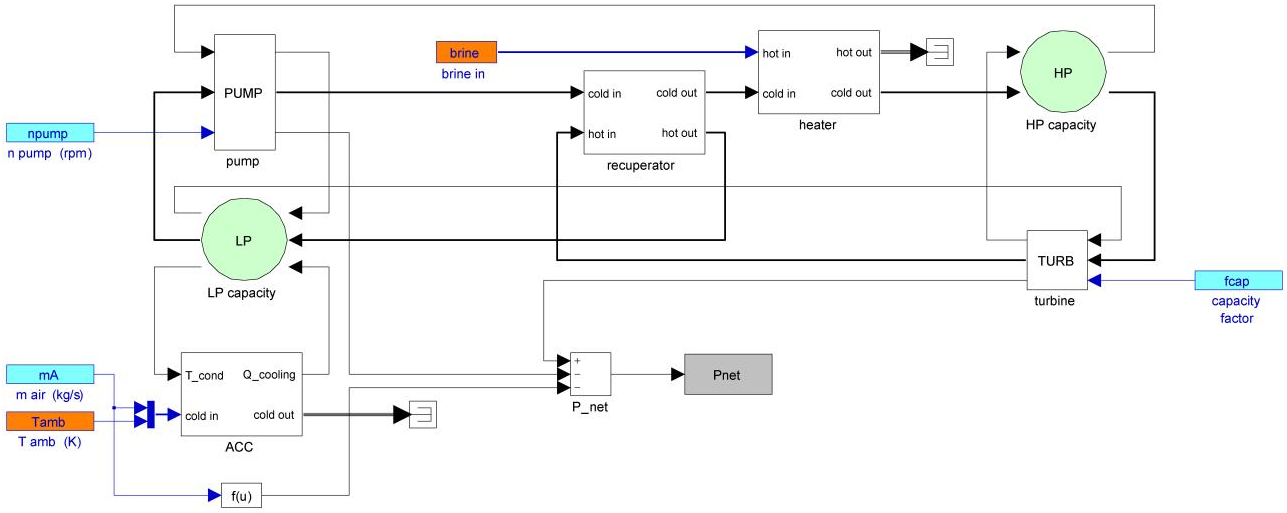

Fig. 2. Schematic of the off-design model of the ORC system. Note the two capacities in addition to the main plant components.

2.2. Capacity

The capacity has the main function of damping the temporary mass and energy imbalance inside the system. A capacity is usually represented in the Simulink model as a high level block where mass and energy flows converge and depart. This volume can either be included in the model to help in the attainment of the equilibrium condition increasing the stability of the system or it can represent a really existing volume like a tank. In the latter case the transient toward the equilibrium condition represents the transient occurring in the real system.

Inside the block capacity the transient mass and energy balances are solved (as a function of mass and energy transfers of the capacities with the outside environment), which set the physical,

thermodynamic and chemical conditions inside the same capacity (the conditions of the flows leaving the capacity are identical to the conditions inside the same capacity).

The mass balance is:

$$V\frac{d\rho}{dt}=\sum\dot{m} \qquad (2)$$

The energy balance is:

$$\frac{dU}{dt}=\sum(\dot{m}\cdot h) \qquad (3)$$

According to these mass and energy balances the time variation of pressure and specific internal energy are obtained, which are then integrated to calculate the instantaneous parameters, from which all the other fluid properties are obtained.

2.3. Feed pump

The pump sets the flow rate that passes through the upper branch of the loop shown in Fig. 2. The pump performance curve included in the model, shown in Fig. 3, was derived from a multi-speed performance curve of a pump operating in a real geothermal binary plant. The maximum efficiency of the pump, which is set equal to 70%, was assumed to occur at the design flow rate and design head at the nominal speed of rotation of the pump. The nominal speed of rotation is fixed in the design phase and it is here conventionally assumed equal to 1500 rpm. The speed of rotation of the pump (*npump*) is among the model operating parameters that are varied to maximize the power production in off-design conditions: when this parameter varies the pump performance curve is scaled down in head and flow rate according to the affinity laws. The input to the block pump is given by the difference between the pressures in the two capacities: this information, combined with the information on the speed of rotation allows to enter in a non-dimensional curve from which the non-dimensional mass flow rate and pump efficiency are obtained. The mass flow rate through the pump is then obtained from the non-dimensional flow rate and pump speed of rotation.

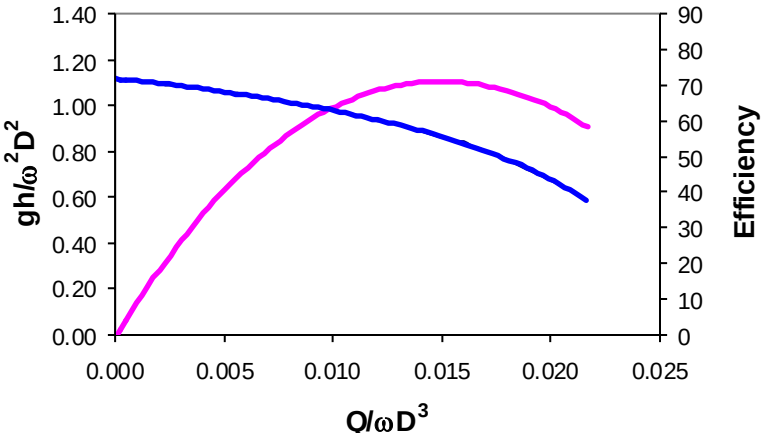

Fig. 3. Pump performance curve used in the model.

2.4. Expander

The expander sets the mass flow rate in the lower branch of the loop in Fig. 2. Since the expansion ratios are generally high, it is assumed that the turbine works at sonic conditions with choking conditions in the nozzle. This implies that for a given opening of the nozzle vanes the "corrected mass flow" ($\dot{m}_c=\frac{\dot{m}\sqrt{T_{01}}}{p_{01}}$) is constant, so that the mass flow rate depends only on the nominal mass flow rate and the pressure and temperature values of the high pressure capacity, whereas it does not depend on the enthalpy drop and speed of rotation.

The trend of the performance curve with the opening of the nozzle vanes is shown in Fig. 4, and it is simulated by applying a multiplying factor lower, equal or higher than one to the nominal corrected mass flow. This multiplying factor sets the mass flow rate in the turbine and contributes in setting the mass flow rate of the whole system, therefore it was selected as the second operating parameter (*fcap*) that is varied to maximize the power output in off-design conditions.

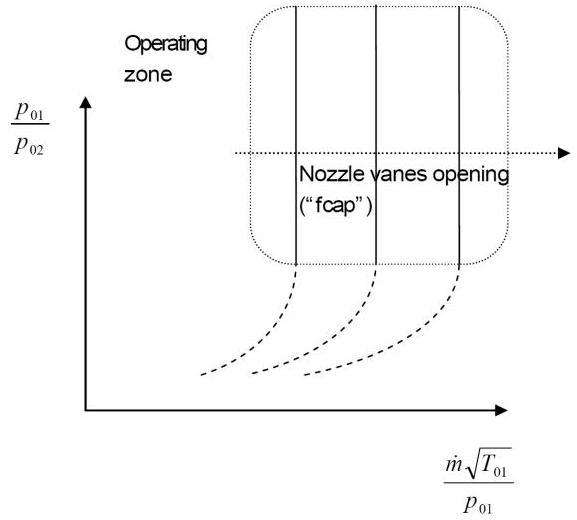

Fig. 4. Turbine maps. In the operating zone (circled) the corrected mass flow rate increases due to the opening of the nozzle vanes only.

The isentropic efficiency of the turbine is calculated starting from the isentropic efficiency at design conditions (0.85) and multiplying it by two correction factors. The first correction factor, shown in Fig. 5a, is related to the variation of u/c_0 that results from the variation of the isentropic enthalpy drop (Δh_{IS}) at off-design conditions. Optimal u/c_0 values, where c_0 is the "spouting velocity" ($c_0 = \sqrt{2 \cdot \Delta h_{IS}}$) are around 0.7. The second factor is related to the variation of the mass flow rate from the design value, as shown in Fig. 5b.

Inputs to the turbine block are the pressures of the two capacities and the temperature of the high pressure capacity at the operating conditions considered. From these information the isentropic enthalpy drop and the mass flow rate flowing through the turbine (still using the flow multiplying factor associated with the position of the vanes) are calculated. These variables are then used in the calculation of the two correction factors in Figs 5a and 5b, that multiply the expander isentropic efficiency at design conditions (85%).

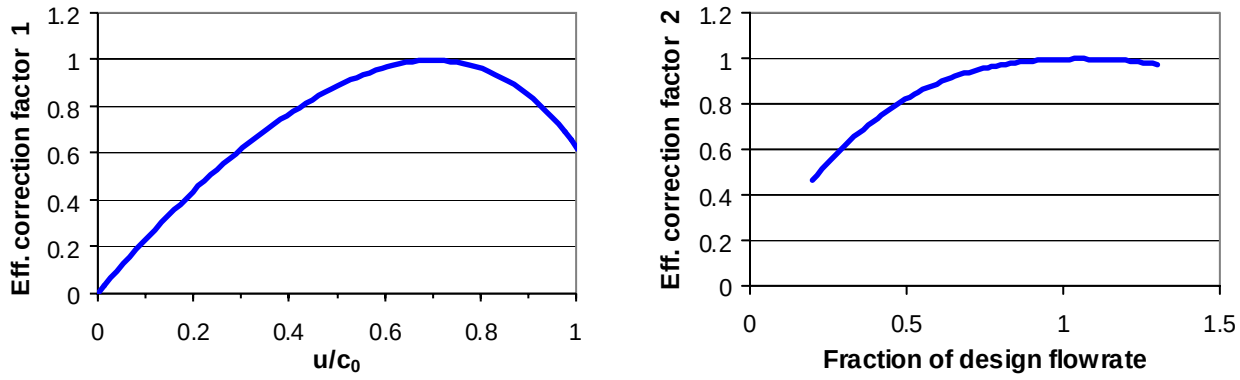

(a) *(b)*

Fig. 5. Correction factors of design turbine isentropic efficiency due to: a) variation of ΔH_{IS} from the design value, b) variation of working fluid mass flow rate from the design value.

2.5. Heat exchangers

The model assumes that the mass flow rate and pressure of the hot and cold streams inside the heat exchangers do not vary. The heat duty is calculated from the surface area, the overall heat transfer coefficients, and the inlet temperatures of the hot and cold streams. The overall heat transfer coefficient varies with the flow rate simply according to the following correlation:

$$U = U_{DP} \cdot \left(\frac{\dot{m}}{\dot{m}_{DP}} \right)^n \qquad (4)$$

where *DP* refers to the design point, $\dot{m}$ is the mass flow rate and the exponent *n* was calculated by modeling the heat exchangers using the software Aspen Shell&Tube. The values shown in Table 1 were used for the exponent *n*, and they apply to the air flow rate for the air cooled condenser and to the working fluid for the remaining components (preheater, vaporizer, supercritical evaporator, recuperator). On the basis of these data the temperatures and the remaining properties of the flows leaving the heat exchangers are obtained.

Table 1. Values used for exponent n in (4).

Heat exchanger	Exponent *n*
Air cooled condenser	0.4
Preheater + vaporizer (subcritical case)	0.15
Evaporator (supercritical case)	0.66
Recuperator	0.67

2.6. Air cooled condenser

The air cooled condenser is considered as a part of the low pressure capacity. The vapor leaving the turbine (or the recuperator) enters the low pressure capacity, is condensed and leaves the capacity as a subcooled liquid (2°C below the saturation temperature). The saturation temperature depends on the condensing pressure, that is the pressure of the low pressure capacity. The equilibrium of the capacity depends on the mass balance and the enthalpy balance where, in addition to the enthalpy of the working fluid, the heat removed by the cooling air should be considered. This heat load is calculated in a heat exchanger where air enters at ambient temperature while the working fluid remains at saturated conditions. The third parameter that is varied to maximize the power output at off-design conditions is the cooling air mass flow rate (*mA*). The specific power consumption of the air cooled condenser fans is assumed to be 0.15 kW/(kg/s of air).

3. Simulation results

The optimization problem described in Section 2.1 is solved using the optimization algorithm SQP (sequential quadratic programming) that is included in MATLAB optimization toolbox. The optimization algorithm maximizes the net power output by modifying the values of the following control variables: pump speed of rotation, multiplying factor of the nominal turbine corrected mass flow rate, air mass flow rate in the air cooled condenser. In the optimization problem the following constraints are considered: the minimum brine reinjection temperature is 70°C; in the subcritical cases the working fluid is completely vaporized at the outlet of the vaporizer; the vapor fraction at the outlet of the expander should be higher than 0.9. Consistently with the design basis assumptions, the mass flow rate of geothermal fluid is 100 kg/s.

3.1. Optimal response to ambient temperature variations

The optimal values of the operating plant parameters in response to variations of the ambient temperature are shown in Figs 6 to 11 where the brine temperature is considered as a parameter.

The results for isobutane are presented first (Figs 6 to 8), followed by those obtained for R134a (Figs 9 to 11). Different symbols are used to underline the activation of the operation constraints, as described in Table 2.

Table 2. Meaning of symbols associated with plant operation constraints used in Figs 6 to 11.

Symbol	Meaning
Small dots	The constraint on the minimum brine outlet temperature is active (i.e. the brine leaves the plant at exactly 70°C)
Big dots	The brine outlet temperature is higher than 70°C
Empty dots	The constraint on the minimum vapor fraction at turbine inlet is active (the turbine inlet temperature must be at least 1°C higher than the saturation temperature corresponding to the cycle maximum pressure)
Full dots	The vapor at the turbine inlet is superheated (in supercritical cycles all dots are full)

It is interesting to note that in the off-design optimization the constraint on the minimum temperature difference between the heat exchanger profiles does not apply as it was in the design optimization performed in [9]. This results in optimal power output in all scenarios at 20°C slightly higher (a few kW, i.e. about 1%) than that obtained in the design optimization. In fact, in the different scenarios air flow rate, pump speed of rotation and turbine capacity factor may assume values that are higher or lower than the nominal ones, affecting therefore in different ways turbine power output and power absorbed by pump and air cooled condenser, but improving in any case the net power output.

The trend of variation of the main parameters with the ambient temperature is explained in the following:

- Working fluid mass flow rate (Figs 6a and 9a) decreases at low ambient temperatures to satisfy the constraint on the minimum brine reinjection temperature (70°C). If this constraint were not included, the net power output would be higher and the brine would leave the plant at much lower temperature;
- Condensing pressure (Figs 6b and 9b) decreases in response to a reduction of the ambient temperature and it is only slightly influenced by the inlet temperature of the geothermal fluid;
- Maximum cycle pressure (Figs 7a and 10a) decreases in response to a reduction of the ambient temperature for supercritical cycles; on the other hand, it increases when the cycle is saturated due to the change of the thermodynamic cycle under the combined effect of the heat transfer with the brine and the operating constraints considered;
- Turbine inlet temperature is roughly constant for any variation of the ambient temperature for each value of brine temperature considered;
- Recuperator heat load increases when the ambient temperature is decreased; however, the recuperator heat load remains low if it is low at design conditions.

The increase in net power output (Figs 7b and 10b) in response to a reduction of the ambient temperature is due to:

- Increase in turbine power output due to the reduction in the condensing pressure, which more than compensates the reduction of working fluid flow rate;
- Decrease in power absorbed by the ACC fans due to the reduction of working fluid flow rate;
- Decrease in power absorbed by the feed pump due to the reduction of working fluid flow rate (only in the supercritical cases).

As regards the optimal control strategy there is a substantial difference between supercritical and subcritical cycles associated with both the pump and the turbine:

- In the subcritical case (Fig. 8a) the pump rotational speed increases with the decrease of the ambient temperature; in the supercritical case (Figs 8a and 11a) the pump rotational speed decreases with the decrease of the ambient temperature;
- In the subcritical case (Fig. 8b) the turbine capacity factor (i.e. the opening of the guide vanes) decreases in response to a decrease of the ambient temperature whereas in the supercritical case (Fig. 8b and 11b) the turbine capacity factor remains constant or limited within a narrow range.

An additional consideration is about the operational flexibility of the plants in the considered scenarios intended as the capacity of generating power in front of variation of the external conditions (in this case only the ambient temperature). In general, in all scenarios, without any distinction about working fluid, sub or supercritical cycle, presence of the recuperator, the optimal control strategy results in a power output at 0°C that is about 130% the net power output at nominal conditions (ambient temperature 20°C), and a power output at 30°C that is about 80% the power output at nominal conditions. Thus, the advantage of the R134a supercritical cycles over the isobutane subcritical cycles found at design conditions [9] still remains at off-design conditions.

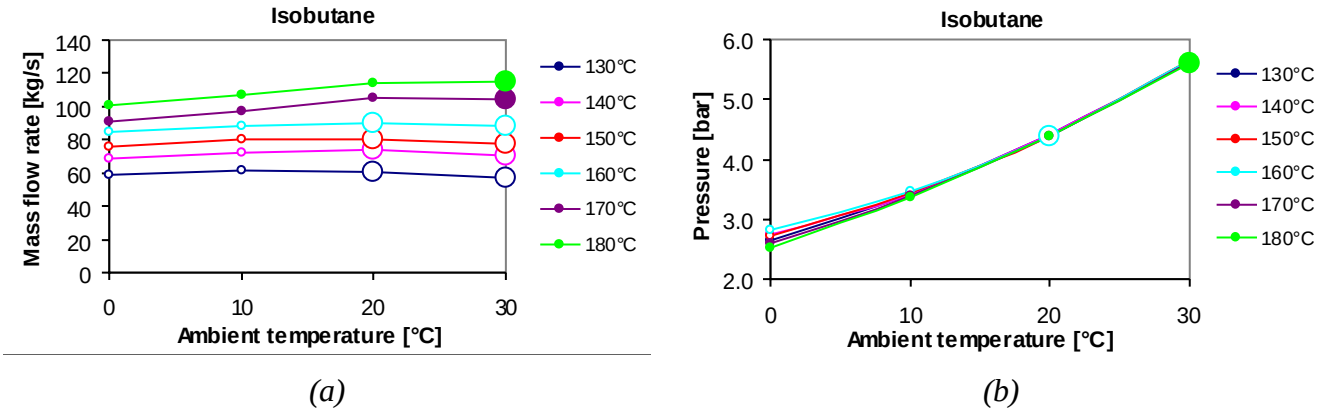

(a) *(b)*

Fig. 6. Optimal variation of isobutane cycle parameters with ambient temperature: a) working fluid mass flow rate, b) condensing pressure.

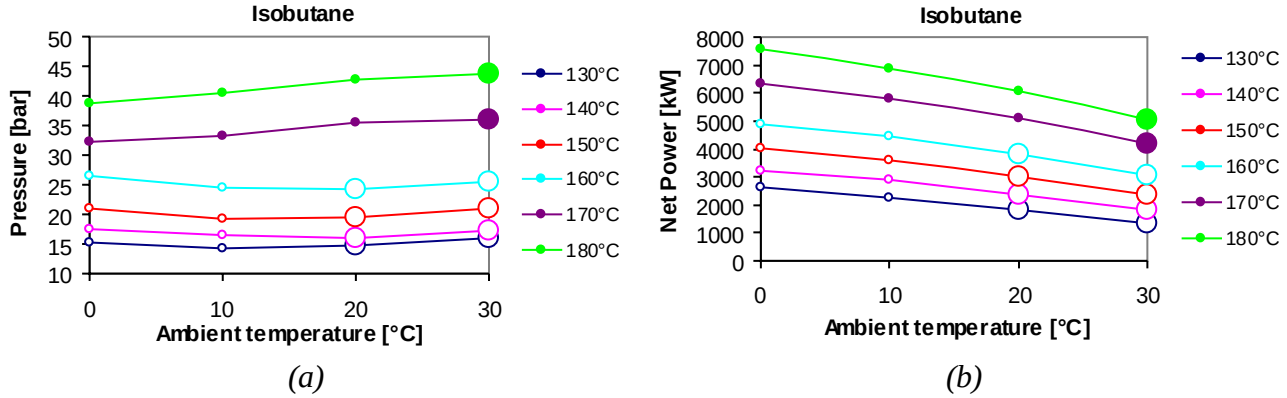

(a) *(b)*

Fig. 7. Optimal variation of isobutane cycle parameters with ambient temperature: a) cycle maximum pressure, b) net power output.

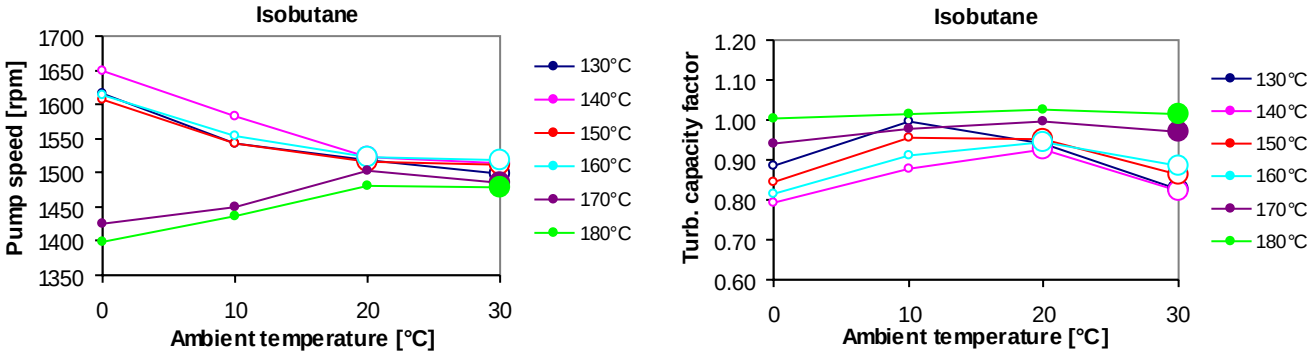

(a) *(b)*

Fig. 8. Optimal variation of isobutane cycle parameters with ambient temperature: a) pump rotational speed, b) turbine capacity factor.

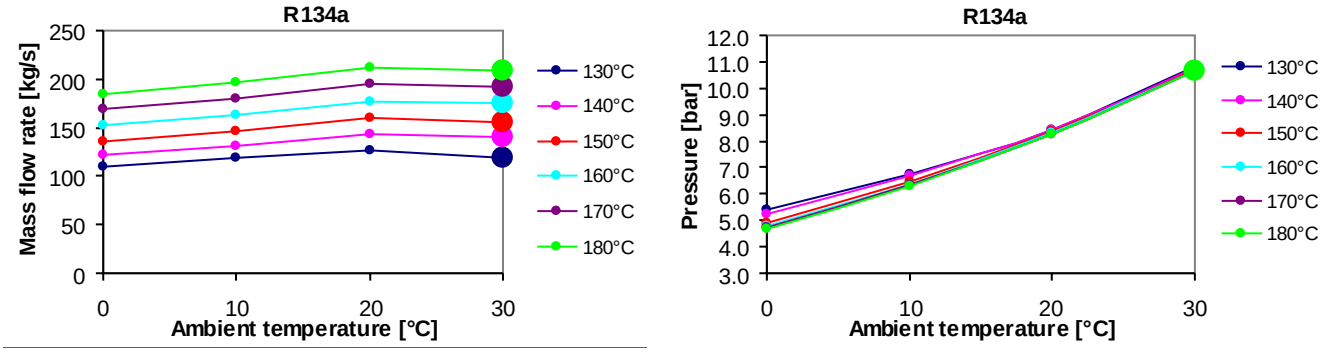

(a) *(b)*

Fig. 9. Optimal variation of R134a cycle parameters with ambient temperature: a) working fluid mass flow rate, b) condensing pressure.

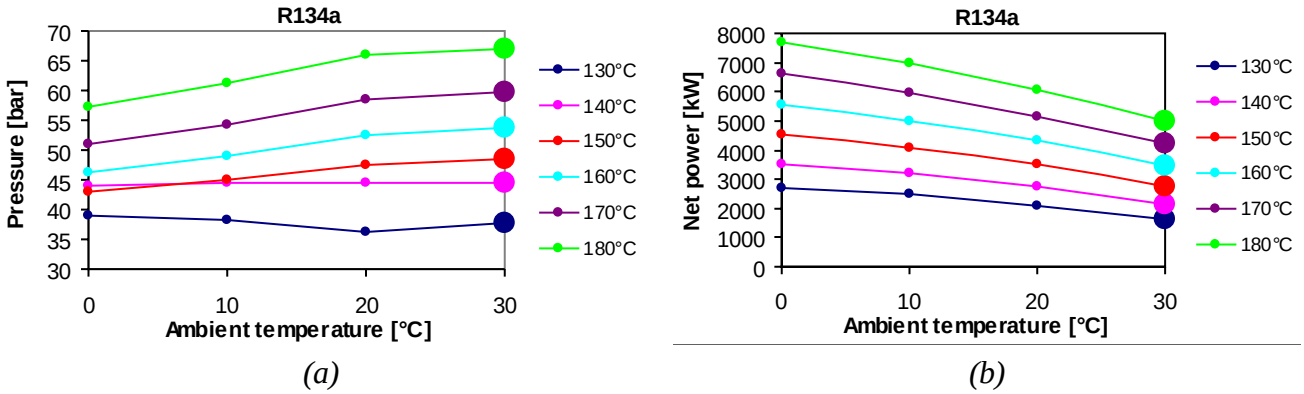

(a) *(b)*

Fig. 10. Optimal variation of R134a cycle parameters with ambient temperature: a) cycle maximum pressure, b) net power output.

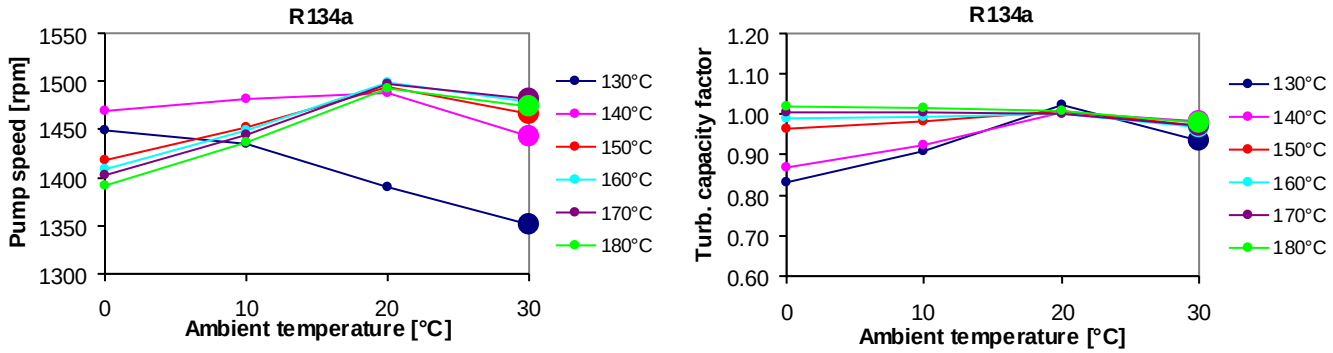

Fig. 11. Optimal variation of R134a cycle parameters with ambient temperature: a) pump rotational speed, b) turbine capacity factor.

3.2. Optimal response to brine temperature variations

The optimal values of the plant parameters in response to variations of the brine inlet temperature from the assumed design value of 160°C are shown in Figs 12 to 15. The subcritical and supercritical cycles show a similar trend: by increasing the brine inlet temperature, the mass flow rate (Figs 12a and 13a), the cycle maximum pressure (Figs 12b and 13b) and maximum temperature increase and the condensation pressure slightly increases. This implies a significant increase of the net power output (Figs 14a and 14b) since the increased turbine power output more than compensates the increase in power absorbed by the ACC fans due to the higher working fluid flow rate and the increase in power absorbed by the feed pump due to the increase of both flow rate and head.

Concerning the control parameters both the air flow rate and the pump rotational speed increase with the increase of the brine inlet temperature. This is due to the increase of the working fluid flow rate and the difference between the cycle high pressure and the condensing pressure.

It is interesting to note the operating range of the two power plants. On the one hand in the R134a supercritical plant the decrease of brine inlet temperature to 140°C leads to the decrease of the cycle high pressure up to values very close the critical pressure (41.2 bar against a critical pressure of 40.6 bar). On the other hand in the isobutane subcritical plant the maximum pressure increases approaching the critical pressure of the working fluid (36.3 bar); as brine temperature is increased the vaporization temperature increases steeply, while the latent heat of vaporization decreases. These modifications caused instability problems that resulted in difficulties in getting the convergence of the model; to better describe the changes in the control strategy the temperature discretization interval was reduced from 5°C to 1°C in the temperature range between 170 and 180°C. The cycle maximum pressure curve (Fig. 12b) markedly increases around a brine inlet temperature of 170°C whereas the values assumed by the turbine capacity factor (Fig. 15b) suggest that the nozzle vanes should close more and more, which probably is the first cause of the operational instability hindering model convergence. Because of that, it was necessary to introduce a further constraint that does not allow the cycle high pressure to exceed the 34 bar threshold. This constraint is activated at brine inlet temperatures equal or higher than 172°C. This new constraint forces the search of new strategies to maximize the power output, which are different from the increase in the cycle high pressure. At first the heat from the brine is completely exploited (the brine outlet temperature is 70°C at temperatures slightly higher than 174°C) and then the working fluid is slightly superheated (at brine temperatures equal or higher than 178°C). The activation/deactivation of these three constraints (cycle high pressure lower than 34 bar; minimum brine outlet temperature equal to 70°C; saturated or superheated vapor at turbine inlet) produces discontinuities in the control parameters and main cycle parameters, as it appears in the temperature range between 170 and 180°C. The results obtained put some doubts on the operational flexibility of isobutane

subcritical cycle, which are not due to the margin of variation of the net power output (that is very similar to that of the R134a supercritical cycle), but to positive variations of the geothermal fluid temperature which causes the cycle to operate at maximum cycle pressures close to the critical pressure.

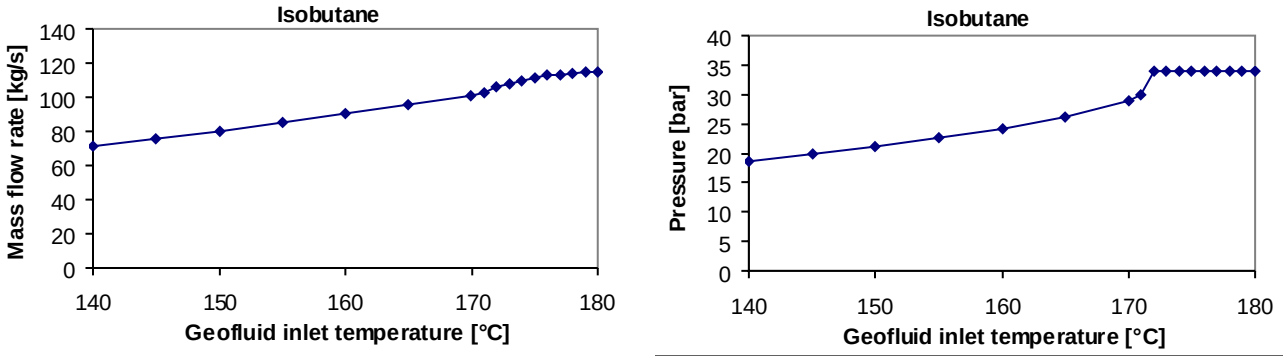

(a) *(b)*

Fig. 12. Optimal variation of isobutane cycle parameters with geofluid inlet temperature: a) working fluid mass flow rate, b) maximum pressure.

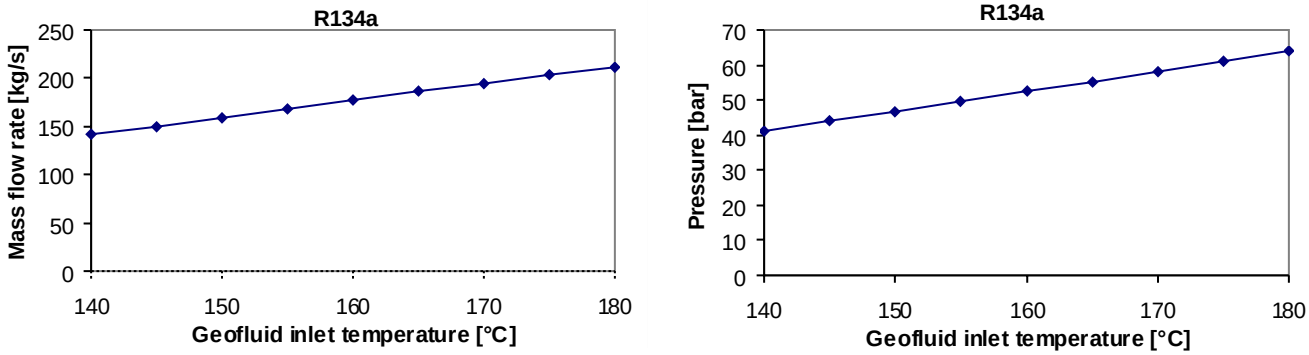

(a) *(b)*

Fig. 13. Optimal variation of R134a cycle parameters with geofluid inlet temperature: a) working fluid mass flow rate, b) maximum pressure.

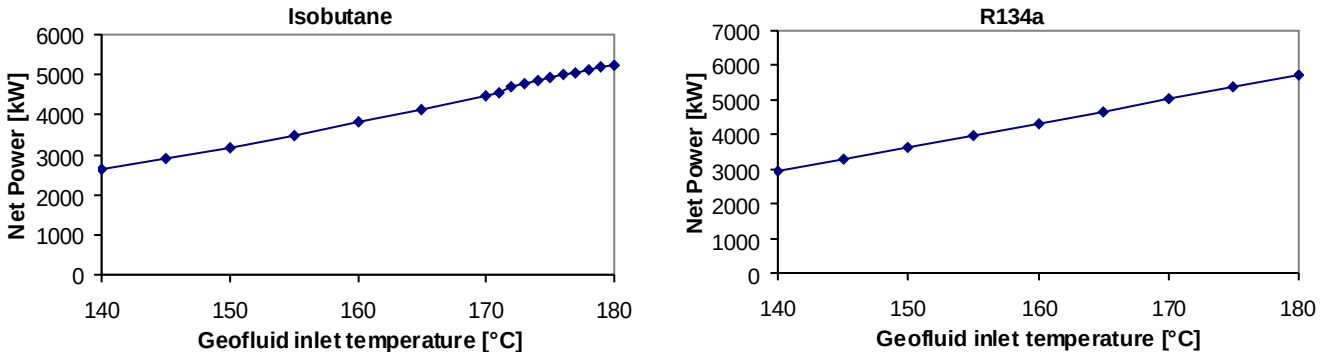

(a) *(b)*

Fig. 14. Optimal variation of net power output with geofluid inlet temperature: a) isobutane, b) R134a.

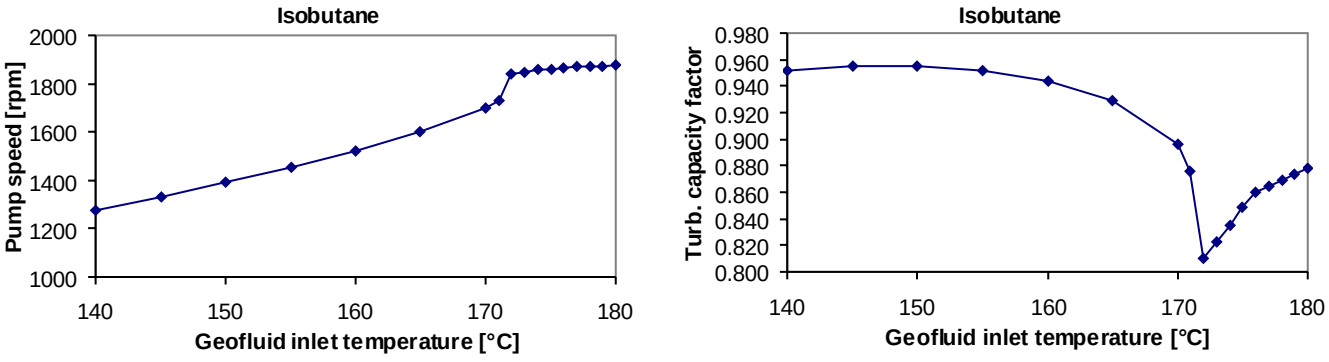

Fig. 15. Optimal variation of isobutane cycle parameters with geofluid inlet temperature: a) pump rotational speed, b) turbine capacity factor.

4. Conclusions

An off-design model was built to find the optimal control strategy of an Organic Rankine Cycle system in response to variations of the boundary conditions from the design values. The model includes two dynamic components, the low and high pressure capacities for the evaluation of the equilibrium point.

Results show that the ambient temperature greatly influences the power output due to the air cooling system. At low ambient temperature the net power output is much higher than at warm ambient temperature and the difference would be even higher without a constraint on the minimum brine outlet temperature.

Results obtained under variable geofluid inlet temperature show that the power output markedly increases with the increase of the geothermal fluid inlet temperature mainly due to the increase of the cycle maximum pressure (and temperature) and the working fluid flow rate. However, the optimal cycle maximum pressure may approach the critical pressure in both subcritical and supercritical cycles, which requires a change in the control strategy as described for the subcritical isobutane cycle.

The optimal operation strategy is obtained by varying the control variables in different ways for subcritical and supercritical cycles. However, the percentage increase or decrease in power output due to variations of ambient temperature or geofluid inlet temperature from the design values is similar for both subcritical and supercritical cycles. This strategy can be conveniently used both for already existing plants and in the design phase of new plants to choose among the available design options those which supply the highest electricity production during the expected life according to predictable variations of brine and ambient temperatures.

Acknowledgments

The authors wish to thank Dr. Nicola Rossi of ENEL Engineering and Innovation for helpful discussions and suggestions.

Nomenclature

ACC	air cooled condenser
c_0	spouting velocity, m/s

D	impeller diameter, m
$fcap$	turbine capacity factor
g	acceleration of gravity, m/s^2
h	enthalpy
h	pump head, m
HP	high pressure
LP	low pressure
mA	air mass flow rate, kg/s
$\dot{m}$	mass flow rate, kg/s
$npump$	pump rotational speed, rpm
ORC	Organic Rankine Cycle
p	pressure, bar
P	pump
P	power, kW
Q	heat load, kW
Q	volumetric flow rate, m^3/s
t	time, s
T	turbine
T	temperature, °C
u	wheel tip speed, m/s
U	overall heat transfer coefficient, W/m^2-K
U	internal energy, J
V	volume, m^3

Greek symbols

η	efficiency
ρ	density, kg/m^3
ω	pump rotational speed, rad/s

Subscripts and superscripts

ACC	air cooled condenser
amb	ambient
c	corrected
$cond$	condenser
DP	design point
gen	generated by the turbine
in	inlet
IS	isentropic
net	net
out	outlet
$pump$	feed pump
$turb$	turbine
01	total conditions at turbine inlet

References

[1] Liu B.-T., Chen K.-H., Wang C.-C, Effect of working fluids on organic Rankine cycle for waste heat recovery. Energy 2004;29:1207-1217.

[2] Schuster A., Karellas S., Aumann R., Efficiency optimization potential in supercritical Organic Rankine Cycles. Energy 2010;35:1033-1039.

[3] Zyhowski G.J., Brown A.P., Achaichia A., HFC-245fa Working Fluid in Organic Rankine Cycle - A Safe and Economic Way to Generate Electricity from Waste Heat. ECOS2010: Proceedings of the 23rd International Conference on Efficiency, Cost, Optimization, Simulation and Environmental Impact of Energy Systems; 2010 June 14-17; Lausanne, Switzerland.

[4] Dai Y., Wang J., Gao L., Parametric optimization and comparative study of organic Rankine cycle (ORC) for low grade waste heat recovery. Energy Conversion and Management 2009;50:576-582.

[5] Shengjun Z., Huaixin W., Tao G., Performance comparison and parametric optimization of subcritical Organic Rankine Cycle (ORC) and transcritical power cycle system for low-temperature geothermal power generation. Applied Energy 2011;88:2740-2754.

[6] Quoilin S, Declaye S., Tchanche B.F., Lemort V., Thermo-economic optimization of waste heat recovery Organic Rankine Cycles. Applied Thermal Engineering 2011;31:2885-2893.

[7] Manente G., Field R., DiPippo R., Tester J.W., Paci M., Rossi N., "Hybrid Solar-Geothermal Power Generation to Increase the Energy Production from a Binary Geothermal Plant", IMECE 2011 conference proceedings, Denver, November 11-17.

[8] Pei G., Li J., Li Y. Wang D., Ji J., Construction and dynamic test of a small-scale organic rankine cycle. Energy 2011;36:3215-3223.

[9] Toffolo A., Lazzaretto A., Manente G., Rossi N., 2010, Synthesis/Design Optimization of Organic Rankine Cycles for Low Temperature Geothermal Sources with the HEATSEP Method. ECOS2010: Proceedings of the 23rd International Conference on Efficiency, Cost, Optimization, Simulation and Environmental Impact of Energy Systems; 2010 June 14-17; Lausanne, Switzerland.

[10] Lazzaretto A., Toffolo, A., A method to separate the problem of heat transfer interactions in the synthesis of thermal system. Energy 2008;33:163-170.

[11] Lazzaretto A., Toffolo A., Manente G., Rossi N., Paci M., Cost Evaluation of Organic Rankine Cycles for Low Temperature Geothermal Sources. ECOS2011: Proceedings of the 24th International Conference on Efficiency, Cost, Optimization, Simulation and Environmental Impact of Energy Systems; 2011 July 4-7; Novi Sad, Serbia.

[12] Wei D., Lu X., Lu Z., Gu J., Dynamic modeling and simulation of an Organic Rankine Cycle (ORC) system for waste heat recovery. Applied Thermal Engineering 2008;28:1216-1224.

[13] Quoilin S., Aumann R., Grill A., Schuster A., Lemort V., Spliethoff H., Dynamic modeling and optimal control strategy of waste heat recovery Organic Rankine Cycles. Applied Energy 2011;88:2183-2190.

Automated Superstructure Generation and Optimization of Distributed Energy Supply Systems

Philip Voll[a], Carsten Klaffke[b], Maike Hennen[c] and André Bardow[d]

[a] RWTH Aachen University, Aachen, Germany, philip.voll@ltt.rwth-aachen.de,
[b] RWTH Aachen University, Aachen, Germany, carsten.klaffke@ltt.rwth-aachen.de,
[c] RWTH Aachen University, Aachen, Germany, maike.hennen@ltt.rwth-aachen.de,
*[d] RWTH Aachen University, Aachen, Germany, andre.bardow@ltt.rwth-aachen.de (**CA**)*

Abstract:

A novel framework is proposed for the automated generation and optimization of models representing superstructures of distributed energy supply systems (DESS). Based on a basic problem description specifying load cases, available technologies, and topographical constraints, the presented framework employs the P-graph approach as an initialization step. Since DESS require accounting for time-varying load profiles and part-load dependent operating efficiencies, the P-graph superstructure is automatically extended, as necessary, to include multiple redundant energy conversion units. The proposed framework employs a robust MILP formulation to automatically derive the optimization model representing the generated superstructure. In the present implementation, a GAMS model is generated that can be readily optimized. In a case study, the synthesis optimization of an industrial site is analyzed. It is shown that the framework conveniently and efficiently enables the automated grassroots and retrofit synthesis of DESS identifying unexpected and complex designs with multiple redundant units and trigeneration systems.

Keywords:

Distributed Energy Supply Systems, MILP, P-graph, Structural Optimization, Superstructure Generation, Superstructure Optimization, Synthesis and Optimization.

1. Introduction

Distributed energy supply systems (DESS) are highly integrated and complex systems containing a multitude of technical components including energy conversion plants, energy distribution infrastructure, and energy storage facilities. This makes DESS synthesis an inherently difficult problem as a most simple example already shows: Consider the total cost optimization of a heating system for a single time-varying heating demand (Fig. 1 b).

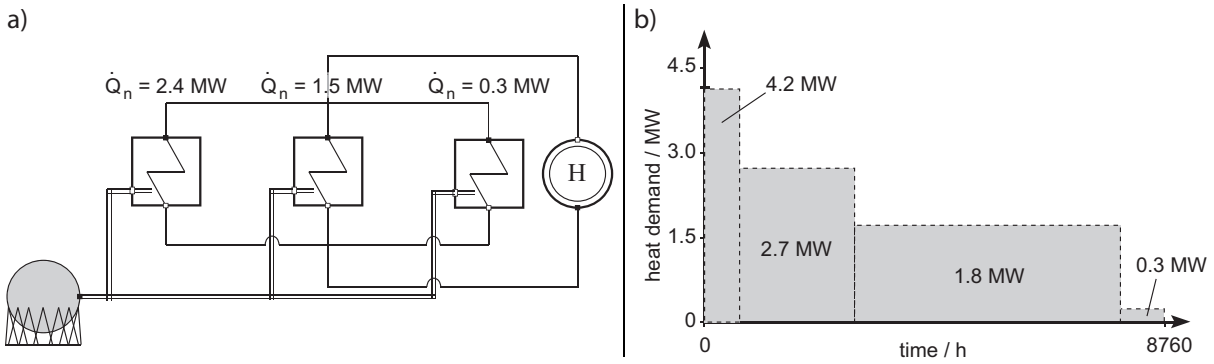

Fig. 1. Optimal heating system (a) covering time-varying heat demand (b).

Even if only a single technology such as a simple boiler is considered, the grassroots design problem becomes challenging due to the trade-offs between

- economy of scale of the equipment investments,

- limited capacities of standardized equipment,
- equipment performance in part-load operation, and
- minimum operation loads of the equipment.

On the one hand, the boilers' total capacity has to cover the maximum heat demand, and economy of scale favors large over small equipment; on the other hand, off-the-shelf boilers are available only within certain capacity ranges, and hence exceptionally large boilers become disproportionately expensive. Then again, the boilers' efficiencies drop at part-load operation, and thus a sizing enabling full-load operation is beneficial. Moreover, boilers must not be operated below their minimum part-loads, and therefore need to be sized sufficiently small to cover the minimum loads. For the considered example (Fig. 1), these trade-offs enforce the installation of three redundant boilers in the optimal configuration (Fig. 1 a). Thus, multiple redundant units are generally to be expected in DESS. This is in stark contrast to classical process network synthesis (PNS) problems, for which, multiplicity and redundancy are often regarded as shortcomings of the problem formulation [1].

For solving DESS synthesis problems, the intrinsic properties of DESS have to be reflected in the optimization model. Both the superstructure generation and optimization are difficult tasks leading to MINLP problems with time-dependent constraints (e.g., demand profiles, ambient temperature curves); moreover, the problem is multi-modal in the way that for each system structure a local optimal solution can be found for the equipment dimensioning and operation. For solving these problems, algorithmic approaches rely on the use of mathematical programming techniques [2-3] to optimize a given superstructure. Thus, the designer needs to decide *a priori* which alternatives should be encoded in the superstructure, and thereby runs the risk to exclude the optimum from consideration. If the number of equipment considered in the superstructure is enlarged, the complexity of the optimization problem substantially increases. Above all, manual superstructure modeling is an error-prone task making automated methods desirable.

For PNS problems, Friedler et al. [4] developed the P-graph based PNS framework for automated and efficient superstructure generation [5] and optimization [6]. Recently, the P-graph approach has been applied successfully to the synthesis of energy systems [7]. However, since the current PNS framework has been developed for synthesizing chemical plants, it does not consider time-varying boundary conditions and part-load dependent equipment performance – features that have a strong impact on the performance of DESS as demonstrated above. The current PNS framework therefore requires manual manipulations to incorporate multiple redundant equipment in the superstructure.

In this paper, a framework for automated superstructure generation and optimization is presented. This framework accounts for time-dependent boundary conditions, part-load performance, as well as multiple redundant energy conversion units as key features of DESS.

2. Automated superstructure generation and optimization

This section presents the framework for automated DESS superstructure generation and optimization. A major difficulty of DESS synthesis problems is that the designer does not know *a priori* how many redundant energy conversion units have to be included in the superstructure to guarantee the inclusion of the global optimal solution. On the other hand, the inclusion of too many redundant units leads to prohibitive computational effort. To address this problem, this paper proposes a successive approach for the automated superstructure generation and subsequent optimization.

Section 2.1 describes the algorithm for automated superstructure and model generation. Section 2.2 describes the successive approach for superstructure generation and optimization. Finally, section 2.3 describes an MILP formulation for DESS superstructure optimization employed in this work.

2.1. Automated superstructure and model generation

This section presents an automated approach for the generation of DESS superstructures represented as MI(N)LP models (Fig. 2).

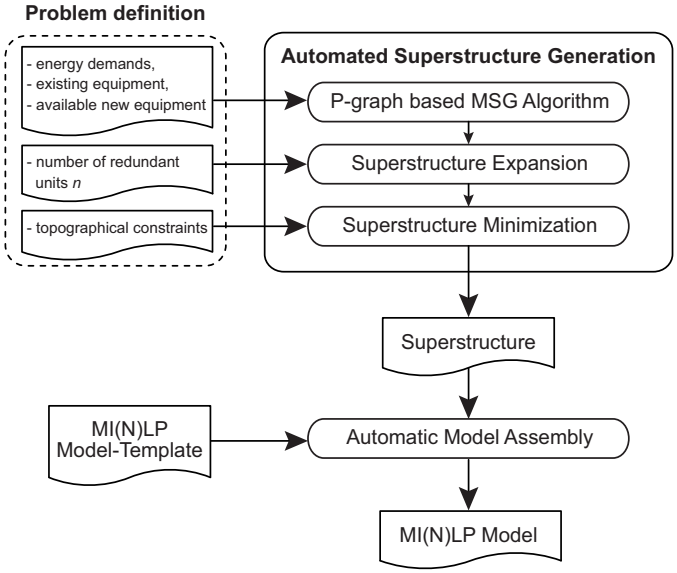

Fig. 2. Flowchart representing the algorithm for automated superstructure and model generation.

The algorithm relies on a basic problem definition including demand time series, specification of the existing equipment as well as available new equipment, topographical constraints (if any), and the number of redundant units n to be considered in the superstructure. First, the algorithm employs the P-graph based *maximal structure generation* (MSG) algorithm [5] generating a P-graph superstructure including all feasible technologies. However, this superstructure contains only one unit of each technology. Next, this superstructure is therefore expanded to incorporate n redundant units: For this purpose, the generated superstructure is represented as a connectivity matrix **C**. Its rows and columns represent final energy users (e.g., demands for heating and cooling) and generators (e.g., boilers, absorption and compression chillers), respectively. The entries c_{lk} of the connectivity matrix represent the connectivity between users and generators: If a generator l is connected to a user k, the entry in the corresponding row and column is $c_{lk} = 1$; otherwise, it is 0.

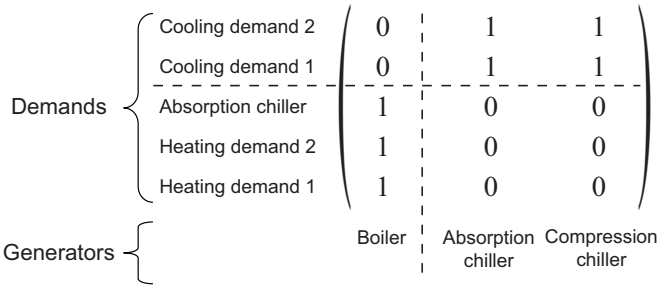

Fig. 3. Example connectivity matrix representing a superstructure incorporating two heating and cooling demands, and one boiler, one absorption chiller and one compression chiller.

Fig. 3 shows a connectivity matrix representing a fully connected superstructure incorporating two heating and cooling demands, as well as one boiler, one absorption chiller and one compression chiller. It can be seen that absorption chillers take a special role since they represent both final energy users (driving heat) and generators (refrigeration). For superstructure expansion, all columns representing generators are copied n-times. The same applies to the rows representing the demand for driving heat of absorption chillers.

If specified, topographical constraints are taken into account to reduce the generated superstructure by cutting infeasible connections, or more technically, assigning zeros to the corresponding matrix entries. To assemble the final model, the user can use arbitrary MI(N)LP model-templates, which are parameterized by the generated connectivity matrix. In the present implementation, a GAMS model [8] is generated that can be readily optimized using standard solvers. This model is based on an MILP formulation described in section 2.3.

2.2. Successive superstructure generation and optimization

This section presents an algorithm for successive superstructure generation and optimization of DESS. As stated above, a major difficulty when solving DESS synthesis problems is that the designer does not know *a priori* how many redundant conversion units have to be included in the superstructure to include the global optimal solution. Then again, if too many units are included, the computational effort becomes prohibitively large. Thus, in this approach, the number of units included in the superstructure is continuously increased until the global optimal solution is found.

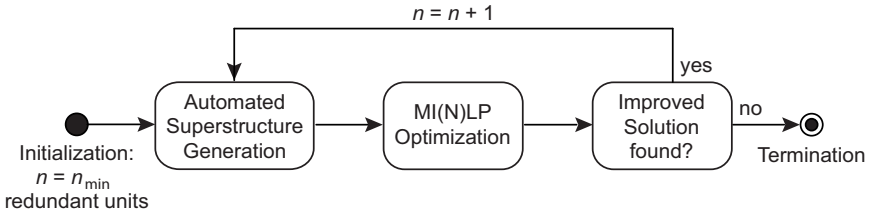

Fig. 4. Flowchart representing the successive algorithm for automated superstructure generation and optimization of DESS synthesis problems.

The proposed approach (Fig. 4) employs the automated superstructure and model generation algorithm (section 2.1) and subsequently optimizes the generated model by means of mathematical programming techniques. Next, it expands the superstructure by inclusion of more redundant units and optimizes the new superstructure. Then, the algorithm compares the objective function values of the new and the previous solutions: If the new solution is better than the previous one, the superstructure is further expanded and another optimization is performed; if not, the loop is terminated. The algorithm is initialized with a minimum number of $n = n_{\min}$ redundant units. In the present study, the thinkable simplest strategy for superstructure expansion has been realized: It increases the number of redundant units to be considered in the superstructure by one for each loop: $n = n + 1$. In our experience, this simple strategy usually yields the global optimal solution in practical applications; i.e., in all test cases, superstructure expansions beyond the above described termination criterion did not improve the optimal solution found.

2.3. An MILP formulation for DESS synthesis problems

For modeling DESS synthesis problems, this work employs an MILP formulation similar to the one presented by Yokoyama et al. [9]. The present formulation is based on quasi-stationary energy balances accounting for multiperiod discrete-time load profiles. Part-load performance and investment cost of the equipment are modeled by piecewise linearized performance and cost functions. The quality levels, i.e. temperatures and pressures, at which the different energy forms are provided are assumed to be constant. To employ this MILP formulation in the successive approach (section 2.2), a generic component-based modeling design is developed enabling an easy model specification (demand data, number of units and their interconnections, etc.) to represent the automatically generated superstructures. This is realized by establishing the energy balances in each particular superstructure according to the corresponding connectivity matrices (section 2.1).

Kasaš et al. [10] identified the net present value as the best suited economic criterion for single-objective flowsheet optimization. Accordingly, in this work, the objective function to be maximized is the net present value,

$$C_t = \frac{(i+1)^{t_{CF}} - 1}{i(i+1)^{t_{CF}}} \cdot R_t - \sum I_0 . \qquad (1)$$

It is calculated from the net cash flow R_t (annual revenues from feed-in electricity minus annual energy delivery and maintenance costs), total investments $\sum I_0$, the cash flow time t_{CF}, and the discount rate i. Typically, energy delivery costs outbalance feed-in revenues, and thus the net present value becomes negative for DESS.

3. Numerical example

The proposed framework is applied to the synthesis optimization of an industrial distributed energy supply system. Section 3.1 describes the considered site. In section 3.2, a retrofit synthesis of this site is performed. Section 3.3 analyzes the potential of a grassroots synthesis. In section 3.4, the result of the retrofit and the grassroots synthesis are compared. For calculation of the net present value, a cash flow time of 10 years and a discount rate of 8 % are assumed.

Table 1. Considered energy conversion technologies including their power and cost ranges, and nominal efficiencies η_N (for boilers and CHP engines) and COPs (for chillers).

Technology	Thermal power range / MW	Price range / 10^3 €	η_N, COP_N / -
Boiler	0.1 - 14.0	34 - 380	0.90
CHP engine	0.5 - 3.2	230 - 850	0.87
Absorption chiller	0.1 - 6.5	75 - 520	0.67
Turbo-driven chiller	0.4 - 10.0	89 - 1570	5.54

The set of equipment models employed in this study comprises of boilers, CHP engines, compression and absorption chillers. For simplicity, cooling towers are assumed to be part of the chiller units. Table 1 lists capacity and cost ranges of the considered technologies as well as their nominal efficiencies and COPs. Investment costs are calculated by capacity power laws [11]:

$$I_0 = I_B \cdot (\dot{Q}_N / \dot{Q}_B)^M , \qquad (2)$$

and modeled as piecewise linearized functions for the employed MILP formulation (section 2.3). In (2) I_0 represents the equipment cost with capacity $\dot{Q}_N$, I_B the reference cost for equipment with capacity $\dot{Q}_B$, and M a constant parameter depending on the equipment type. If available, the necessary parameters are taken from the German market [12-13], or else they were provided by industry partners.

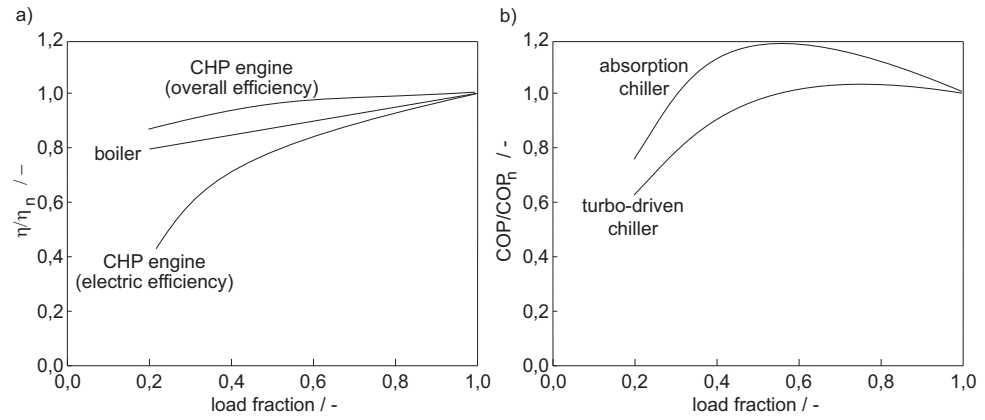

Fig. 5. Characteristic performance curves of heat generators (a) and chillers (b).

In this study, only standardized equipment is considered. Thus, for the underlining performance models, it is justified to assume a characteristic behavior for all units of a certain technology: Therefore, all units' part-load efficiency curves are scaled to their nominal efficiencies. These characteristic performance curves are then assumed to be valid for a technology regardless of the single units' capacities. Fig. 5 shows the characteristic performance curves assumed in this study. These include the relative boiler efficiency, η/η_N, the relative CHP engine's overall and electrical efficiencies, η/η_N and $\eta_{el}/\eta_{el,N}$, and the chillers' relative coefficients of performance, COP/COP_N. The minimum part-load is assumed to be 20 % for all technologies. While boilers and CHP engines are subject to efficiency losses at part-load operation, the COPs of absorption and turbo-driven compression chillers gain maximum values at 55 % and 70 % part-load, respectively. The performance curves are taken from the German market [12-13], or else provided by industry partners.

3.1 Site description

The following case study is based on a real-world application. The considered industrial site comprises of six buildings with time-varying demands for heating and cooling (Fig. 6). The site has access to the regional natural gas distribution network (gas tariff: 6 ct/kWh). Electricity can be drawn from an on-site power supply (electricity tariff: 16 ct/kWh; feed-in tariff: 10 ct/kWh).

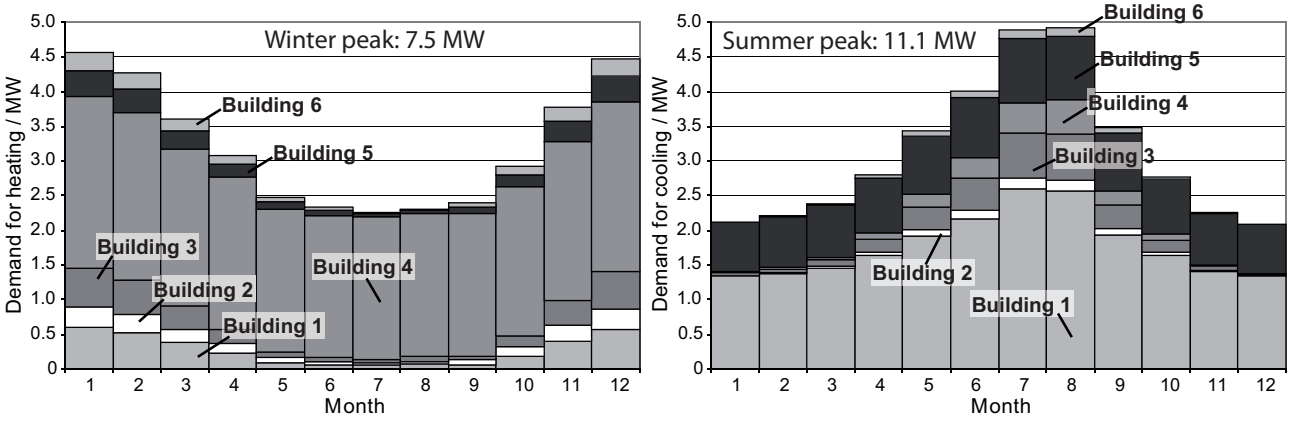

Fig. 6. Monthly-averaged demand profiles for heating and cooling of the industrial site.

The existing supply system comprises of two boilers, one CHP engine, one absorption and one compression chiller. Table 2 lists these units including their nominal thermal powers, overall efficiencies, and COPs.

Table 2. Nominal thermal powers, overall efficiencies, and COPs of the existing (E) equipment.

	Boiler E1	Boiler E2	CHP engine E1	Absorption chiller E1	Turbo-chiller E1
Thermal power / MW	7.0	7.0	3.0	4.0	8.0
η_N, COP_N / -	0.8	0.75	0.7	0.5	2.8

3.2 Retrofit synthesis

This section describes the optimal retrofit synthesis of the described site employing the proposed framework for automated superstructure generation and optimization. Available technologies are boilers, CHP engines, absorption chillers, and turbo-driven compression chillers. The minimum number of redundant units to be considered in the superstructure is $n = 0$ (initial case). No topographical constraints are defined.

Fig. 7 shows a flowsheet of the optimal solution and the corresponding superstructure. The superstructure incorporating this solution includes $n = 3$ redundant units. It incorporates existing as well as new equipment. In optimal configuration (C_t = -13.4 Mio. €), one of the two existing

boilers, the CHP engine and the absorption chillers are removed from the flowsheet. Two new CHP engines, and three new turbo-driven compression chillers are installed on-site.

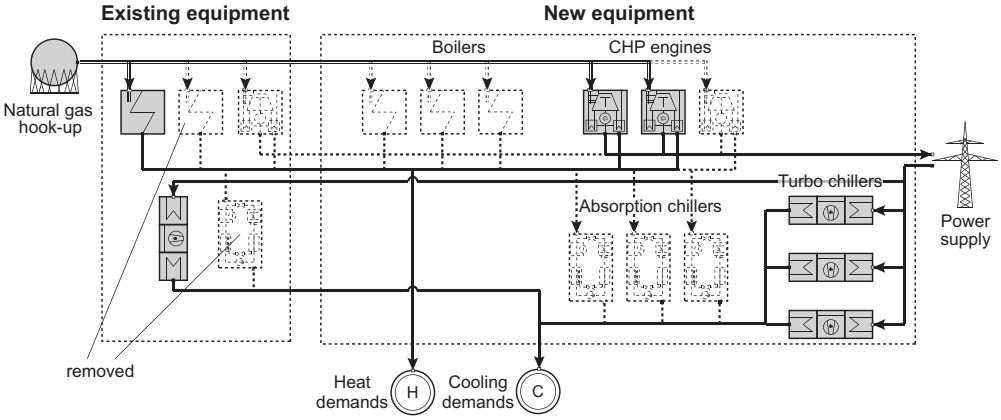

Fig. 7. Superstructure incorporating three redundant units of each technology and optimal solution (units in grey) for the retrofit synthesis problem.

Table 3 lists all units of the optimal solution including their nominal thermal powers, overall efficiencies, COPs, and investment cost. Note that the new equipment (N) has better performance than the existing equipment (E).

Table 3. Nominal thermal powers, overall efficiencies, COPs, investment cost, operating times and annual average part-loads of the equipment installed in the optimal retrofit solution (E: Existing equipment. N: New equipment).

	Boiler E1	CHP engine N1	CHP engine N2	Turbo-chiller E1	Turbo-chiller N1	Turbo-chiller N2	Turbo-chiller N3
Thermal power / MW	7.0	2.4	1.8	8.0	1.8	1.3	1.8
Investment / 10^3 €	0	673	530	0	310	230	310
η_N, COP_N / -	0.8	0.87	0.87	2.8	5.54	5.54	5.54
operating time / h/a	< 100	8,760	5,110	< 100	8,760	6,570	5,840
average part-load	46 %	99 %	77 %	78 %	75 %	80 %	79 %

Fig. 8 shows the reduced connectivity matrix representing the optimal retrofit solution. For clarity, technologies not selected in the optimal solution are not given in the reduced matrix. In optimal configuration, the new *CHP engine N1* and *CHP engine N2* are operated as central heat generators. In contrast, *Boiler E1* supplies heat to buildings 3 and 4, only. For the cooling system, the situation is quite different: Three of the four chillers are operated as central refrigerators for all buildings. *Turbo-chiller E1* is reserved to produce cooling for buildings 1 and 4.

Table 3 also lists the operating times and annual average part-loads of the installed equipment. Most of the units are run at loads close to their operating points with maximum efficiency. *CHP engine N1* is operated year-round at maximum load. *CHP engine N2* is also operated at high loads, but only in winter. The existing *Boiler E1* is reserved to solely meet the peak load requirements during winter at 46 % part-load. The chiller configuration allows for load sharing enabling to run all four units close to their maximum COP: While the existing *Turbo-Chiller E1* is operated only in summer, the other three chillers are run year-round with operating times between 5,840 h/a and 8,760 h/a. It should be noted that in the optimal solution, three compression chillers are purchased to enable their operation close to their optimal part-load of 70 %. This result shows the importance

of incorporating multiple redundant units in the superstructure. Furthermore, the suggested successive approach allows to conveniently assess the trade-offs between cost and the number of redundant units.

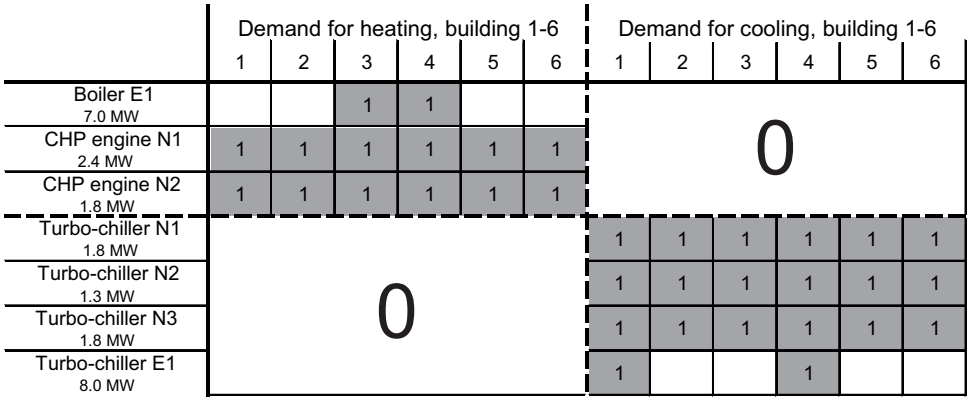

Fig. 8 Reduced connectivity matrix (transposed) representing the optimal retrofit solution

Fig. 9 shows the progress of the successive approach for automated superstructure generation and optimization for the retrofit synthesis problem. Clearly, for the initial situation ($n = 0$), the net present value takes its worst value (-25.9 Mio. €). At the same time, the annual energy cost take their maximum value (3.9 Mio. €/a). When redundant units are considered ($n = 1$) and new equipment is added to the superstructure, the net present value of the optimal solution is reduced to -13.9 Mio. €, which is an improvement of 46 % compared to the initial situation. For this solution, the investment sum amounts to 1.8 Mio. €, annual energy cost are reduced by 54 % and amount to 1.8 Mio. €. Further superstructure expansions only marginally improve the net present value. The optimal solution is found for a superstructure with $n = 3$: The optimal net present value amounts to -13.4 Mio. €, which is an improvement of another 4 % compared to the superstructure with $n = 1$. For larger superstructures ($n = 4, 5$), no further improvements were found; moreover, the successive approach converges faster to the optimal solution when compared to a one-time optimization of an oversized superstructure with $n = 5$ redundant units.

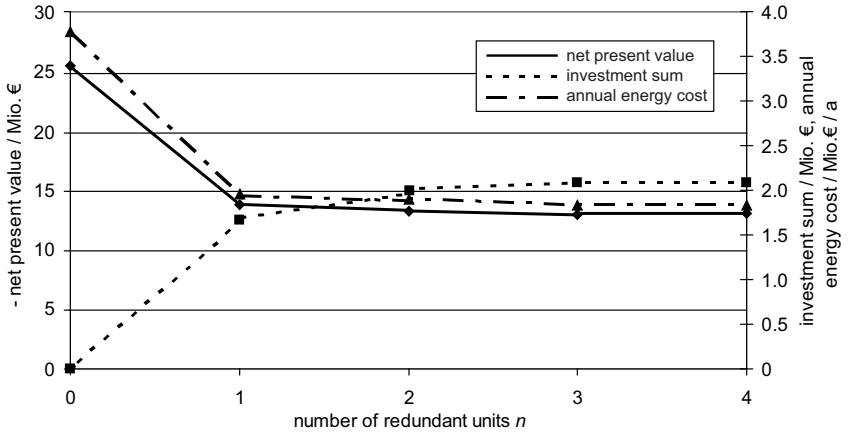

Fig. 9. Progress of the successive approach for the automated superstructure generation and optimization for the retrofit synthesis problem. Net present value, investment sum, and annual energy cost of each optimal solution are plotted against the number redundant units included in the corresponding superstructures.

3.3 Grassroots synthesis

In the second case study, the presented framework is applied to the grassroots synthesis of the considered site assuming that no equipment is installed on-site yet. Fig. 10 shows the flowsheet of the optimal solution and the corresponding superstructure. The structure of the grassroots solution differs considerably from the retrofit solution. In contrast to the retrofit synthesis, in optimal

configuration (C_t = -14 Mio. €), only one boiler is installed; moreover, one compression chiller is replaced by an absorption chiller. Table 4 lists all units of the optimal solution.

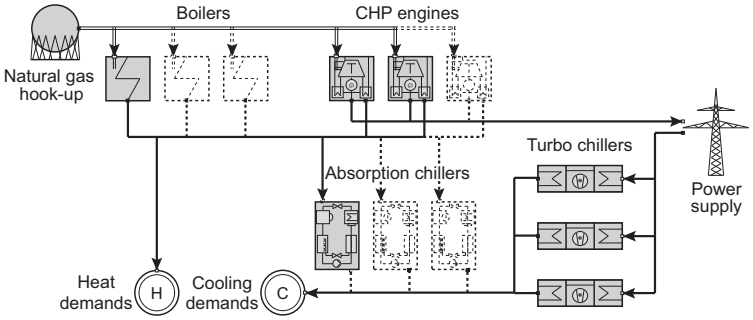

Fig. 10. Superstructure incorporating three redundant units of each technology and optimal solution (units in grey) for the grassroots synthesis problem.

Table 4. Nominal thermal powers, overall efficiencies, COPs, investment cost, operating times and annual average part-loads of the equipment installed in the optimal grassroots solution (E: Existing equipment. N: New equipment).

	Boiler N1	CHP engine N1	CHP engine N2	Absorption chiller N1	Turbo-chiller N1	Turbo-chiller N2	Turbo-chiller N3
Thermal power / MW	4.3	1.8	2.4	4.3	2.0	1.1	3.7
Investment / 10^3 €	140	530	650	390	340	200	600
η_N, COP_N / -	0.9	0.87	0.87	0.67	5.54	5.54	5.54
operating time / h/a	< 100	5,100	8,760	< 100	5,100	5,800	5,800
average part-load	88 %	77 %	98 %	100 %	70 %	70 %	70 %

Fig. 11 shows the reduced connectivity matrix of the optimal grassroots solution. In optimal configuration, *CHP engine N2* is operated as central heat generator. *CHP engine N1* and *Boiler N1* are reserved to cover the heat demands of buildings 1, 3, and 4 (*CHP engine N1*), and buildings 2, and 4-6 (*Boiler N1*). Moreover, *CHP engine N2* and *Boiler N1* provide the heat for driving *Absorption chiller N1*. For the cooling system, two of the three turbo-driven compression chillers (*Turbo-chiller N1* and *N3*) are operated as central cooling generator for all buildings. *Turbo-chiller N2* supplies cooling energy to the buildings 1 and 5. *Absorption chiller N1* provides cooling energy for the buildings 3, 4, and 6.

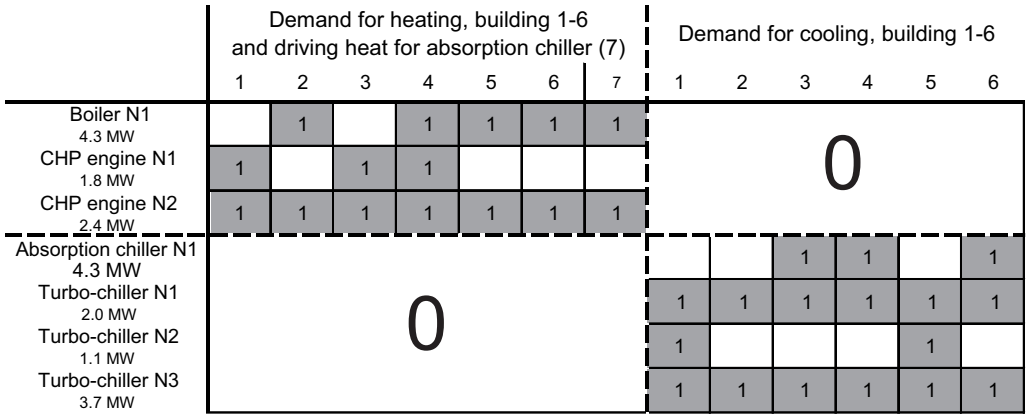

Fig. 11. Reduced connectivity matrix (transposed) representing the optimal grassroots solution.

Table 4 lists the operating times and annual average part-loads of the installed equipment: In particular, *CHP engine N2* is sized as to enable a year-round full-load operation. *CHP engine N1* covers the remaining heat demand. *Boiler N1* is reserved to solely meet the peak load requirements in winter, and to supply driving heat for *Absorption chiller N1*. The chiller configuration allows for a load sharing enabling to run the three turbo-driven chillers always exactly at maximum COP. Their operating times are within a range of 5,100 h/a and 5,800 h/a. As in the retrofit solution, three compression chillers are purchased to realize their operation at optimum part-loads.

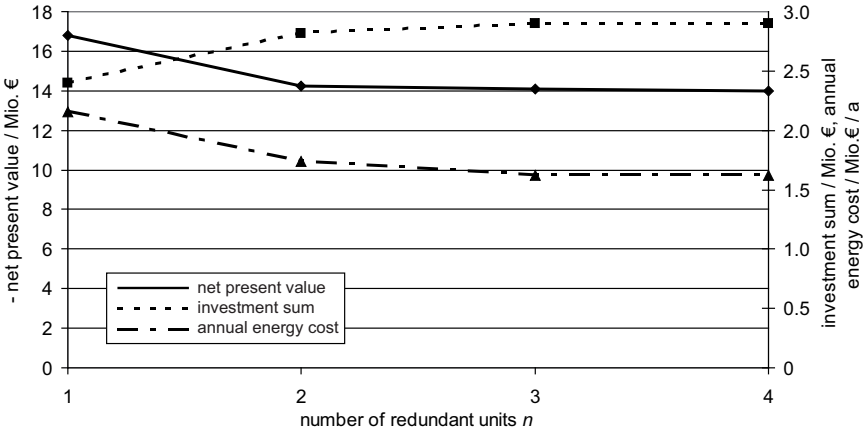

Fig. 12. Progress of the successive approach for the automated superstructure generation and optimization for the grassroots optimization. Net present value, investment sum, and annual energy cost of each optimal solution are plotted against the number redundant units included in the corresponding superstructures.

Fig. 12 shows the progress of the successive approach for automated superstructure generation and optimization of the grassroots problem: If only one unit of each technology is considered in the superstructure ($n = 1$), the net present value takes its worst value (-16.7 Mio. €). Allowing for redundant units ($n = 2$) leads to a significant improvement of the net present value (15 %). The optimal solution (C_t = -14 Mio. €) is found for a superstructure with $n = 3$. For larger superstructures ($n = 4, 5$), no further improvements were found; moreover, the successive approach converges faster to the optimal solution when compared to a one-time optimization of an oversized superstructure with $n = 5$ redundant units.

3.4 Comparison of the retrofit and the grassroots solution

This section compares the optimal solutions of the retrofit and the grassroots synthesis problems. Table 5 lists the net present value, the annual energy cost, and the investment sum of both solutions.

Table 5. Net present value, annual energy cost, and investment sum of the optimal solutions of the retrofit and the grassroots synthesis problems.

	Retrofit solution	Grassroots solution
Net present value / Mio. €	-13.4	-14.0
Annual energy cost / Mio. €/a	1.7	1.7
Investment sum / Mio. €	2.1	2.9

The annual energy cost of the grassroots solution are the same as those of the retrofit solution. At the same time, the investments of the grassroots solution are 38 % higher than for the retrofit case (2.9 Mio € compared to 2.1 Mio. €). In total, the net present value of the retrofit solution is 4 % (0.6 Mio. €) higher than for the grassroots solution. Basically, this is to be expected as the grassroots problem is a sub-problem of the retrofit problem. However, interestingly enough, the two solutions differ considerably from a structural point of view: In particular, the optimal solutions differ with regard to the chiller selection. In both solutions, three high-performance (COP = 5.54)

turbo-driven compression chillers are installed. But, while in the retrofit solution, the existing low-performance absorption chiller (COP = 0.5) is removed in favor of keeping the low-performance turbo-chiller (COP = 2.8), in the grassroots solution, a new absorption chiller (COP = 0.67) is installed together with the three turbo-driven chillers. This nontrivial behavior underlines the complexity of the addressed problem:

In the retrofit case, a large heat generation capacity is already installed on-site. On the one hand, this allows to produce driving heat for the existing absorption chiller without requiring to purchase extra heat generators. On the other side, both the existing absorption chiller and the existing heat generators have low efficiencies. Furthermore, the sizing of the absorption chiller does not allow an operation close to its optimum part-load. While the existing compression chiller has a low COP as well, its capacity fits for a close-to-optimum operation in summer.

In contrast, in the grassroots case, new heat generators have to be purchased anyway. The proportions of heating and cooling demands in summer and winter also allow for an optimal exploitation of the trigeneration potential in summer. Moreover, the investments for the absorption chiller are lower than for a turbo-driven compression chiller of comparable size. The proposed framework allows for the convenient and rigorous assessment of these complex trade-offs.

4. Summary and conclusions

This paper proposes a generic framework for the automated generation and optimization of superstructures representing distributed energy supply systems (DESS). Considering basic input data comprised of demand time series, existing and available new technologies, and topographical constraints, the framework employs the P-graph approach as an initialization step. As required for DESS, the generated superstructure is automatically extended to include multiple redundant energy conversion units. The algorithm derives the optimization model representing the generated superstructure. In this paper, a robust MILP formulation has been employed that accounts for time-varying load profiles and part-load dependent equipment performance as key features for DESS optimization. In the present implementation, a GAMS model is generated that is successfully applied to efficiently solve both retrofit and grassroots synthesis problems. The automated method identifies nontrivial and unexpected solutions with multiple redundant units and complex designs such as trigeneration systems. Furthermore, it allows to conveniently assess the trade-offs between cost and number of redundant units. It is shown that the automated procedure provides an efficient optimization framework for DESS synthesis problems.

Acknowledgments

The authors wish to thank Prof. Petar Varbanov and Zoltán Süle from Centre for Process Integration and Intensification, University of Pannonia, for their courtesy and support on the PNS framework. This study was funded by the German Federal Ministry of Economics and Technology (ref. no.: 0327885A).

Nomenclature

C_t net present value at time t, €

$\boldsymbol{C}$ connectivity matrix, -

i discount rate, -

I_0 investment, €

M constant parameter in cost function, -

n number of redundant units included in a superstructure, -

R_t net cash flow at time t, €

t time, s

Greek symbols

η efficiency

Subscripts and superscripts

N nominal

CF cash flow

Abbreviations

CHP combined heat and power

COP coefficient of performance

DESS distributed energy supply system

References

[1] Farkas T., Rev E., Lelkes Z., Process flowsheet superstructures: Structural multiplicity and redundancy: Part I: Basic GDP and MINLP representations. Computers & Chemical Engineering 2005;29(10):2180-2197.

[2] Frangopoulos C.A., von Spakovsky M.R., Sciubba E.A, Brief review of methods for the design and synthesis optimization of energy systems. Int Journal of Applied Thermodynamics 2002;5(4):151-160.

[3] Biegler L.T., Grossmann E., Retrospective on optimization. Computers & Chemical Engineering 2004;28(8):1169-1192.

[4] Friedler F., Tarjan K., Huang Y.W., Fan L.T., Graph-theoretic approach to process synthesis: axioms and theorems. Chemical Engineering Science 1992;47(8):1972-1988.

[5] Friedler F., Tarjan K., Huang Y.W., Fan L.T., Graph-theoretic approach to process synthesis: polynomial algorithm for maximal structure generation. Computers & Chemical Engineering 1993;17(9):929-942.

[6] Friedler F., Varga J.B., Fehér E., Fan L.T., Combinatorially accelerated branch-and-bound method for solving the MIP model of process network synthesis. In: Floudas, C.A., Pardalos, P.M., editors. State of the Art in Global Optimization. Boston, MA, USA: Kluwer Academic Publishers. 1996. p. 609-626.

[7] Varbanov P.S., Klemeš J.J., Friedler F., Integration of fuel cells and renewables into efficient CHP systems. In: Bojic M., Lior N., Petrovic J., Stefanovic G., Stevanovic V., editors. ECOS 2011: Proceedings of the 24th International Conference on Efficiency, Cost, Optimization, Simulation, and Environmental Impact of Energy Systems; 2011 Jul 3-7; Novi Sad, Serbia. 1021-1033.

[8] Brooke A., Kendrick D., Meeraus A., GAMS: A User's Guide. Tutorial by Rick Rosenthal. GAMS Development Corporation. Washington, DC, USA; 2010.

[9] Yokoyama R., Hasegawa Y., Ito K., A MILP decomposition approach to large scale optimization in structural design of energy supply systems. Energy Conversion and Management 2002;43(6):771-790.

[10] Kasaš M., Kravanja Z., Pintaric Z.N., Suitable modeling for process flow sheet optimization using the correct economic criterion. Industrial & Engineering Chemistry Research 2011;50(6):3356-3370.

[11] Smith R., Chemical Process Design and Integration. Wiley; 2005.

[12] Scheunemann A, Becker M., Kennziffernkatalog – Investitionsvorbereitung in der Energiewirtschaft. Energy Consulting, Gesellschaft für Energiemanagement; 2004. German.

[13] Gebhardt M., Kohl H., Steinrötter T., Preisatlas – Ableitung von Kostenfunktionen für Komponenten der rationellen Energienutzung. Duisburg, Germany: Institute of Energy and Environmental Technology e.V. (IUTA); 2002 Jun. Technical Report No.: S 511.

Characterisation and classification of Solid Recovered Fuels (SRF) and model development of a novel thermal utilization concept through air-gasification

P. Vounatsos[1], K. Atsonios[1],M. Agraniotis[1], K. D. Panopoulos[1], G. Koufodimos[2],P. Grammelis[1], E. Kakaras[1]

1Institute for Solid Fuels Technology and Applications, Centre for Research and Technology Hellas, 4th km. N.R. Ptolemais – Kozani, 50200 Ptolemais, Greece, agraniotis@certh.gr
2EPANA S.A., 25 Ermou Str., 145 64 N. Kifissia, Greece

Abstract:
The need for Solid Recovered Fuels (SRF) standardization becomes gradually essential in European Member States and especially in regions, where the development of a specific market for such fuels is under development. The promotion of standardization practices facilitates their public acceptance, supports the development of quality assurance mechanisms and enhances the marketability of the particular waste streams as fuels with a high biogenic content. In the present work the results of an extensive campaign of sampling and analysis of SRF produced in a material recovery facility (MRF) in AthensGreece are presented. The facility is operated by EPANA S.A. and produces about 15.000 t of SRF per year derived from packaging waste. The particular quantity is currently not thermally utilized in industrial applications, despite its high quality. In this sense the standardization will enhance the fuel's marketability and public acceptance. Sampling and analysis of SRF are carried out according to the standard CEN TC 343. The presented data include the results of six months sampling campaign started in June 2011. Proximate and ultimate analyses of the fuel samples are carried out according to European Norms CEN TC 343. Furthermore the chlorine and heavy metals content is determined. The aforementioned analyses and in particular net calorific value (NCV), Hg and Cl are necessary for the classification of the produced fuel in the as an SRF of a certain class in accordance with CEN TC 343.In order to demonstrate a novel concept for the thermal utilization of the specific waste recovered fuel, a lab scale fluidized bed gasifier is currently being developed. In the present work the results of the process calculations for the design and dimensioning of the gasifier are presented. The aforementioned calculations are based on thermodynamic equilibrium modeling. The analysis of the waste recovered fuel is used as input parameter and the composition and heating value of the produced syngas is then calculated in dependence of several operational parameters, including the operational temperature and the air fraction. Summing up, the development of standardization practices for Solid Recovered Fuels (SRF) is expected to lead to increased acceptability of the particular fuel types and to the development of quality assurance schemes for the certification of their fuel properties. Furthermore, SRF gasification is considered as a beneficial technology for the thermal utilization of waste derived fuels in terms of technical and environmental related aspects. In this framework process modeling is used for the initial design of the process installation.

Keywords:
Solid Recovered Fuels (SRF), fuel analysis, fluidized bed gasification, thermodynamic modeling,

1. Introduction

Municipal Solid Waste (MSW) treatment in Greece and in South-Eastern Europe is still dominated by the least preferable practices according to European waste treatment hierarchy, i.e. land filling instead of materials and energy recovery. This in turn leads to low shares of recycled materials and waste recovered fuels production in comparison with the overall MSW production. Waste recovered fuels- or so called "Refuse Derived Fuels, RDF"-are the remaining fraction of a material recovery process and are produced in Mechanical-Biological Treatment (MBT) plants utilising MSW as inlet materials, as well as in Material Recovery Facilities (MRF) utilising packaging waste as inlet

materials.The promotion of standardization practices for Refused Derived Fuels has led to the adoption of new European Standards according to the work of the CEN Technical Committee 343. Based on this work,waste recovered fuels, which fulfil specific standards regarding fuel parameters (Net Calorific Value, Chlorine content and Mercury concentration) and quality assurance schemes during their production process, can be characterised with the term "Solid Recovered Fuels, SRF". This standardisation process facilitates their public acceptance, supports the development of quality assurance mechanisms and enhances the marketability of the particular fuel streams. As studied by Porteous and Psomopoulos et al. [1,2] waste to energy practices are a successful tool for the utilisation of a considerable energy potential. Furthermore, according to Arena [3], gasification of Refused Derived Fuels (RDF) is a thermal utilization method with promising results as an alternative solution for waste treatment with energy recovery from waste. Moreover, according to a simulation study of Rocca et al. [4] there are promising results regarding a large scale waste gasification application. What is more, gasification and combustion of produced syngas in a boiler may be proven as a technically and economically feasible technology for the thermal utilisation of waste recovered fuels. The requirements for gas cleaning of the produced flue gas after the syngas combustion in the boiler are lower in the proposed concept compared to a conventional concept of incineration of the produced RDF in a grate firing system. Many researchers [5-9] have studied the properties of waste utilization schemes in several different fields of interest. The present study focuses on the characterization of the Refused Derived Fuel produced by EPANA S.A., onthe procedure followed for its standardisation and characterisation as Solid Recovered Fuel (SRF) and on the preliminary calculations for the design and dimensioning of a pilot-scale circulating fluidized bed gasifier for the thermal utilisation of the particular fuel.

2. Methodology

In the following section, the methodology for the sampling procedure of the Refuse Derived Fuel and the gasification modelling are presented.

2.1 Sampling methodology

The sampling procedure was designed and executed by the instructions of European standard EN 15442:2011 [10]. The first step is the definition of sample lot's mass and type. Secondly, the number of increments or sub-samples is defined. The third phase is to define the minimum sample size and the minimum increment size. For this decision there are both analytical mathematical equations and brief methods. In this particular study a brief method was used. The final step is the determination of the effective increment and sample size, which are not necessarily equal to the minimum ones calculated. The following figure presents the decisions made and the parameters defined for the sampling procedure. The decision making sequence is in accordance to the standard:

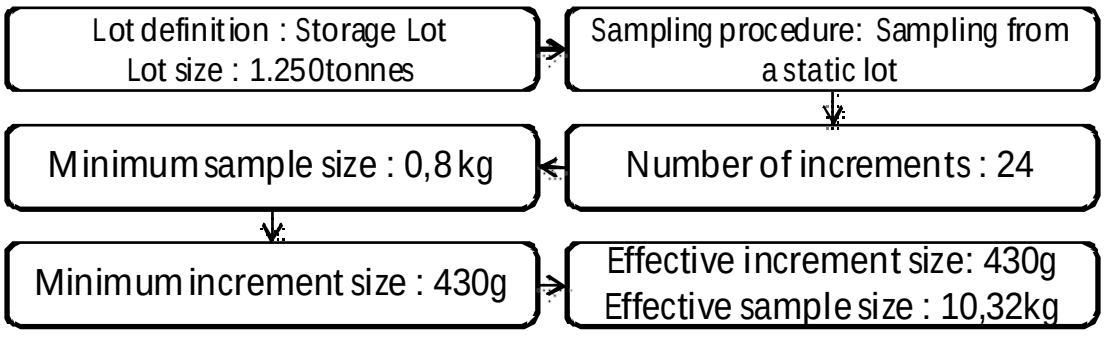

Fig. 1. Diagram of the sampling parameters defined

After the effective quantities are gathered, the final sample for analysis is extracted by consequent divisions.

2.2. Gasification modelling – Process description

Process description

Process modeling is a useful tool towards the design of energy conversion processes. Process simulation employs complicated mechanisms or combinations of simple steps. This is also the case for lab scale RDF/SRF gasifier: the main assumption is the chemical equilibrium corrected by pseudo-kinetic corrections. The gasification of waste recovered fuels (RDF/SRF) undergoes the same sub-process as any kind of biomass.

In the beginning of the heating process moisture is removed (drying). Further heating of RDF causes the volatiles to be released (pyrolysis - devolatilization). The volatile species react in the rich oxygen /steam atmosphere towards the final composition of the product gas. The remaining char (here assumed as solid graphite $C_{(s)}$) continues to react with the available atmosphere, producing more gases [11].

Methodology

Gasification simulation and modelling needs to be energetically consistent. The gasification vessel must take into account any heat losses through the vessel walls. A literature study reveals that most of the studies on gasification modeling at some point extent and employ a chemical equilibrium for some part of the gas. More advanced works combine this with chemical kinetics for some of reaction and species determination [12]. In fluidized bed gasifiers the process can be approached to a large extent as being close to equilibrium [13]. The basic assumptions adopted in this work are:

1. Steady state conditions
2. Zero-dimension approach of the process
3. 2% of the char does not take part to the equilibrium as it remains un-reacted
4. Heat losses from the gasifier ~3% LHVinput fuel
5. No NO_x formation (the only nitrogen product is NH_3)

The required gasification agent - air - is evaluated so as to keep a certain operating temperature of the reactor at which it is assumed phase and chemical equilibrium. The equivalence ratio (ER) is independent from the temperature and the total heat that is resulted from the energy balance of the system determines whether the gasifier is autothermal or not. The definition of equivalent rate is given in Equation 1:

$$\lambda = \frac{\text{oxygen flow in the oxidizing agent (kmol/s)}}{\text{stoichiometric amount of oxygen - oxygen in the fuel (kmol/s)}} \quad (1)$$

Properties Methods

The Equation of State chosen for the gas phase components was the Peng-Robinson with Boston-Mathias alpha function (PR-BM). This combination is suitable for such mixtures at high temperatures [14]. For waste and ash enthalpy and density calculation HCOALGEN and DCOALIGT models are used, respectively [15].

The process flowsheet is shown in figure 2, while the current investigation focuses on the gasification process. The main points investigated are:

- the parameters to achieve autothermal operation,
- the effect of parameters equivalence rate, steam injection, drying on the product gas quality process efficiency

The inlet fuel properties are determined by its Proximate and Ultimate analysis. A first pre drying step can be employed through a "RSTOIC unit operation model". A FORTRAN statement has been set in order to specify the rate of this pre-drying. In the SEPARATOR block that follows, the evaporated water is removed from the main fuel stream.

In the next stage fuel decomposition is modeled by a RYIELD unit operation model. This is used, since the particular fuel is considered as a non-conventional fuel. This model yields elements out of the fuel. With a help of a FORTRAN code these yields are calculated by the exact balance of the elements that are reported in the Ultimate and Proximate analysis of the fuel. As a next step, the main gasification process is modeled by the RGIBBS unit operation model, which is based on the minimization of Gibbs free energy function of defined products.

The Gibbs free energy minimization method for the C-H-O atom blend of the fuel and oxidant mixture is applied for predicting the thermodynamic equilibrium composition of waste gasification in major components: H_2, CO, CH_4, CO_2, H_2O, N_2, as well as char, which is modeled as solid graphite C_s.

The above methodology underestimates methane which derived from the pyrolysis step. Chemical equilibrium under atmospheric pressure does not predict the existence of methane, which plays considerable role on energy balance of the process. This is corrected by taking into account non-equilibrium corrections to bring these product gas components closer to experimental values from fluidized bed gasifiers. The un-reacted char is assumed to consist only of carbon and the considered value is 2% of the total carbon in the fuel [16]. This char (carbon) does not participate in the thermodynamic equilibrium calculations. Similarly, CH_4 content (mostly deriving from the pyrolysis) was assumed to 3% v/v in the final nitrogen free and dry product gas [17]. In the current model, tar formation is neglected.

The equilibrium product, the char and ash as well as the methane is mixed as the gasifier outlet - prior to the separation of solids from gaseous products which modeled with a separating cyclone. The produced raw syngas is cooled down to 525°C before it is combusted in a flare. The cooling medium is the air that is used for gasification and combustion.

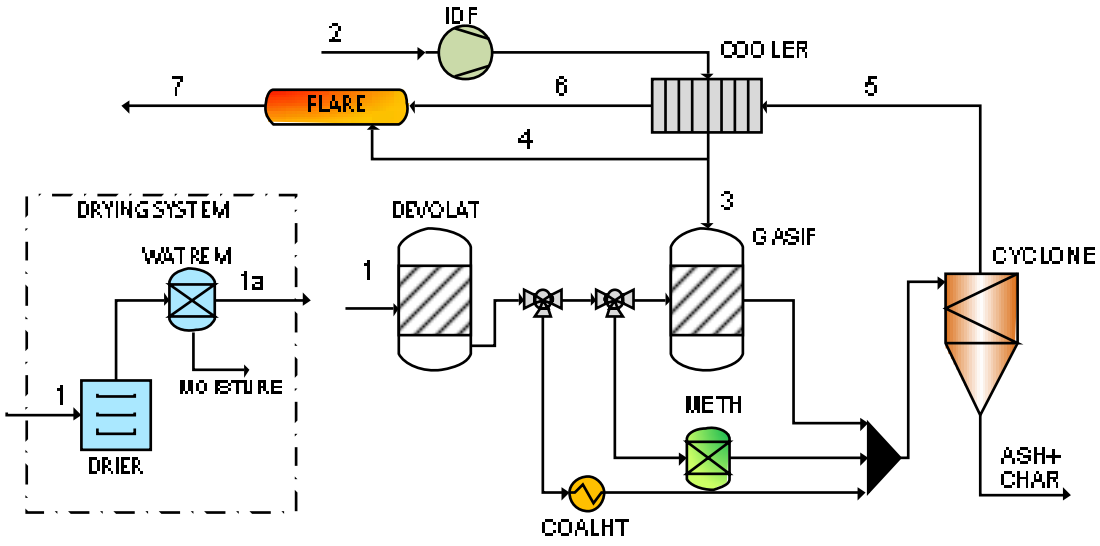

Fig. 2. Flowsheet diagram of the process model

A detailed description of the process modeling blocks used in the particular simulation is presented in Table 1 whereas the corresponding flowsheet diagram is displayed at Figure 2.

Table 1. Description of process modelling blocks used

Block	ASPEN component	Brief description
DRIER	RSTOIC	a fraction of the fuel moisture is evaporated (specified by the user).
WATREM	SEPARATOR	evaporated moisture removal
DEVOLAT	RYIELD	the fuel is decomposed into its constituting components (C, H, O, N, S, Cl)
SEPAR	SEPARATOR	The amount of carbon that is not considered to react is separated from the total fuel
METH	RSTOIC	Production of CH_4 that cannot be predicted by the equilibrium according to real value
GASIF	RGIBBS	The main part of gasification process, where the products prediction is based on minimization of free Gibbs energy.
COALHT	HEATER	In order to be consistent with energy balance in the gasifier, the heating of un-reacted char up to equilibrium temperature should be taken into account
CYCLONE	SEPARATOR	The solids (ash, tars, un-reacted carbon) are separated from the gaseous products
COOLER	MHEATX	A multi- stream heat exchanger where the produced syngas is cooled – heating off the air used for the gasification and combustion
IDF	COMPRESSOR	Delivers air to the gasifier with the required pressurization.
FLARE	RGIBBS	The produced syngas is combusted in a flare: modeled again as minimization of free Gibbs energy.

The gasification efficiency is most commonly expressed as cold gas efficiency, neglecting the sensible heat of the gas and char produced [13]:

$$CGE = \frac{LHV \text{ in cold product gas}}{LHV \text{ in feedstock}} \cdot 100\% \qquad (6)$$

Table 2. RDF composition

Parameters	Fuel A	Fuel B	Fuel C
Proximate analysis (wet basis)			
moisture	26.8	15.0	15.0
fixed carbon	2.4	2.8	4.7
volatiles	64.9	75.4	66.2
ash	5.9	6.9	14.1
Ultimate analysis (dry basis)			
C	45.77	45.77	43.99
H	5.96	5.96	6.36
N	1.16	1.16	1.30
O	38.56	38.56	31.09
S	0.05	0.05	0.58
Cl	0.43	0.43	0.05
calorific values			
HHV (dry) kJ/kg	19281.8	19281.8	17960.9
LHV (raw) kJ/kg	12515.2	14917.7	13720.8

Three representative diverse fuels will be investigated (see Table 2). Fuel A differs from fuel B at the moisture content, whereas the ash content of fuel C is about double than the ash content of fuel A or B.

The specifications of the base case model are exposure at the next table:

Table 3. Base case model assumptions

Parameter	
RDF fuel	fuel A
fuel mass flow rate	30 kg/hr
fuel drying	no
steam injection	no
gasification temperature	800 ^{o}C
pressure	1.01 bar
air preheating	200^{o}C
equivalence ratio	0.31
maximum carbon conversion	98%
methane in dry syngas (v/v)	3%

Under these conditions the operation of the gasifier is autothermal, which means that the gasifier operates without any additional heating or cooling requirement. The issue of defining the nature of the process, as far as the heat release is concerned, is very important. In an endothermic case, if there is a heat source to overbalance the required heat, the whole system shuts down.

3. Results

3.1. Proximate – Ultimate analyses

Through the results of the ultimate analysis the Carbon and Hydrogen contents are determined, which affect the final heating value of the gas, and the produced gas quality. Chlorine is a technological indicator that may influence the operational behaviour through potential corrosion problems. Moreover, the ultimate analysis is required for the determination of the process energy and mass balance.

Through the proximate analysis two significant factors for the operation of the gasifier are determined. The first factor is moisture; that affects the produced gas quality, the thermal energy consumption for the procedure and may influence the behaviour of RDF in the feeding system. The second factor is the ash content of RDF. High ash content, leads to high amounts of leftover ash in the gasifier and may create the following operational issues: i) higher energy losses and difficulty to keep stable operation conditions, due to the removal of preheated ash and ii) operational problems due to ash melting, that may result in agglomerations with the inert material and possible blockages of the gasifier. In the tables bellow, the proximate and ultimate analyses of six months of sampling are given.

Table 4. EPANAs RDF Proximate analysis (% a.r.)

Parameter	RDF 1 – June 2011	RDF 2 – July 2011	RDF 3 – August 2011	RDF 4 – September 2011	RDF 5 – October 2011	RDF 6 – November 2011
Moisture	17.55	24.84	26.76	23.56	39.85	31.74
Ash	12.30	10.99	5.91	8.66	6.03	6.46
Volatiles	63.18	63.41	64.92	63.36	51.13	54.09
Fixed Carbon	6.97	0.77	2.40	4.42	3.00	7.70

Table 5. EPANA's RDF Ultimate analysis (% wt, d.b.)

Parameter	RDF 1 – June 2011	RDF 2 – July 2011	RDF 3 – August 2011	RDF 4 – September 2011	RDF 5 – October 2011	RDF 6 – November 2011
C	40.83	57.02	46.91	50.89	46.95	50.63
H	5.36	8.36	6.22	6.28	6.01	6.63
N	1.18	1.2	1.23	0.51	1.89	1.87
S	0.29	0.48	0.29	0.17	0.11	0.36
O	37.08	17.68	36.85	30.33	34.53	30.80
Cl	0.34	0.64	0.43	0.49	0.49	0.24
Ash	14.92	14.62	8.07	11.33	10.02	9.47
HHV (MJ/kg)	19.150	24.462	19.282	20.391	21.494	23.986
LHV (MJ/kg) (raw)	14.396	16.409	12.474	13.965	11.167	14.610

Assuming that the fuel will be inserted at a constant mass rate, high moisture content in the input fuel leads to reduced low heating value and correspondingly to low thermal input. The increased moisture content leads also to a deterioration of the produced syngas quality. This can be outreached by pre-drying of the input fuel. The air used for the gasification process is preheated in a dedicated heat exchanger by using the heat of the hot syngas that comes out directly from the gasifier and shall be cooled down for the further post treatment step.

Fixed carbon and volatiles represent the part of the fuel that will end up in gaseous form, thus constituting (along with the input air) the mass of the produced syngas.

According to the ultimate analysis of the RDF, carbon and hydrogen measured range from 40.8-57% and 5.3-8.4% respectively. Regarding chlorine, there have been a number of studies by different working teams and different approaches [18-21]. The concentration calculated is believed to originate mainly from PVC, a plastic with high chlorine concentration, while the quantity measured is not expected to cause any significant technical disorders or environmental problems. In comparison with other RDF samples tested EPANAs RDF is considered as a high quality waste recovered fuel [19, 22-25].

3.2. Modelling results

1. Base case study

Similar works regarding gasification of waste or waste recovered fuels can be found in the literature by N. Ramzan et al. [14] and Chen et al. [26], who have studied Municipal Solid Waste (MSW) and by Karellas et al. [27], who have studied the gasification of Refused Derived Fuels (RDF).

Under the aforementioned assumptions the produced syngas has a typical composition (v/v dry basis):

Table 6. Syngas composition (% v/v, dry)

Parameters	wet	dry
H_2O	14.43	-
CO_2	11.62	13.58
CO	16.56	19.36
H_2	21.82	25.50
N_2	32.50	37.99
CH_4	2.57	3.00
H_2S	0.49	0.56
Ar	$3.8 \cdot 10^{-3}$	$4.4 \cdot 10^{-3}$
HCl	$1.0 \cdot 10^{-3}$	$1.1 \cdot 10^{-3}$
LHV (kJ/kg)	5388	6099

The basic streams of the pilot plant with their corresponding characteristics are given in Table 7 (the streams are numbered according to Figure 2):

Table 7. Stream results of the base study (T=800°C; p=1bar; λ=0.30)

		1	2	3	4	5	6	7
mass flow kg/hr		30.0	6.31	1.32	4.99	2.87	2.87	7.22
mole flow kmol/sec		-	0.011	0.011	0.040	0.018	0.018	0.058
Temperature °C		15.0	15.0	174.5	174.5	800.0	525.0	850.0
molar composition %	H_2O	see Table 6	0.010	0.010	0.010	0.083	0.083	0.155
	CO_2		$3.0\cdot10^{-3}$	$3.0\cdot10^{-3}$	$3.0\cdot10^{-3}$	0.080	0.080	0.127
	CO		0	0	0	0.211	0.211	0
	H_2		0	0	0	0.232	0.232	0
	O_2		0.207	0.207	0.207	0	0	0.032
	N_2		0.773	0.773	0.773	0.360	0.360	0.677
	Ar		$9.2\cdot10^{-3}$	$9.2\cdot10^{-3}$	$9.2\cdot10^{-3}$	$4.2\cdot10^{-3}$	$4.2\cdot10^{-3}$	$8.0\cdot10^{-3}$
	CH_4		0	0	0	0.027	0.027	0
	SO_3		0	0	0	0	0	$6.4\cdot10^{-4}$
	HCl		0	0	0	$1.3\cdot10^{-4}$	$1.3\cdot10^{-4}$	$5.0\cdot10^{-5}$
	NH_3		0	0	0	$2.8\cdot10^{-5}$	$2.8\cdot10^{-5}$	0
	COS		0	0	0	$4.5\cdot10^{-5}$	$4.5\cdot10^{-5}$	0
	H_2S		0	0	0	$1.6\cdot10^{-3}$	$1.6\cdot10^{-3}$	0

Table 8 summarizes the energy balance of the pilot plant for the base case study. Fuel heat input is on LHV basis. The negative values in the table correspond to the thermal and electrictiy consumptions of the pilot system. The rest quantity of heat that completes the energy balance of the system is thermal losses at the reactor and sensible heat that hot syngas has at the outlet of the heat exchanger.

Table 8. Energy balance

Parameter	Units	Value
Fuel heat input	kWth	104.3
Syngas heat output	kWth	85.1
Drying	kWth	-5.1
Fan	kWe	-0.4

2. Equivalence rate & drying

The effect of oxidant quantity on syngas composition is shown in the following figure. The trends of each component are similar with corresponding trends of other syngas derived from waste or biomass according to N. Ramzan et al. [14], Chen et al. [26] and Karellas et al. [27].

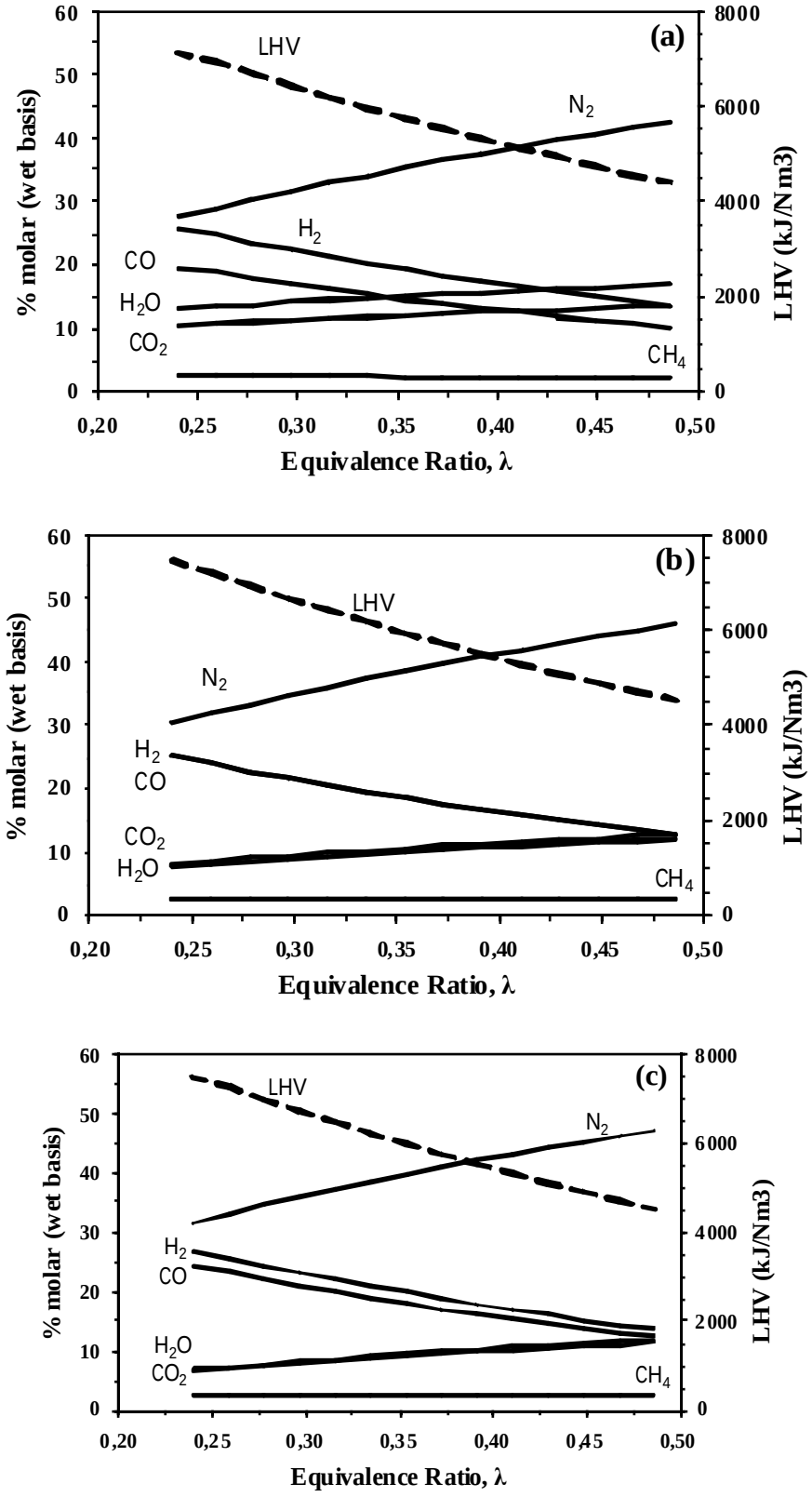

Fig. 3. Effect of air gasification on raw syngas composition for the three fuel types (a: Fuel A, b: fuel B, c: fuel C)

Figure 3 presents the distribution of syngas (wet) composition versus the equivalence ratio. As the oxidizing agent increases, more H_2O and CO_2 are produced from the H_2 and CO oxidation respectively. Hence, the calorific value of the gas is reduced. On the other hand, Figure 4 demonstrates the lower limit of the air requirement for gasification. Values below zero imply the requirement of heat for the proper operation of the gasifier. Values greater than zero imply the

excess of heat production that is rejected to the ambient. For instance, fuel A can be gasified under autothermal conditions at 800°C with an equivalence ratio of 0.31.

The comparison of the curves of fuel A and B shows the effect of drying rate to the process operation. Reducing the moisture content of the fuel, autothermal condition can be met for lower air flow rates (λ=0.275 for fuel B case). In addition, as the quality of the fuel deteriorates (more ash content, less gross calorific value, see Table 2) more oxygen is needed for autothermal operation.

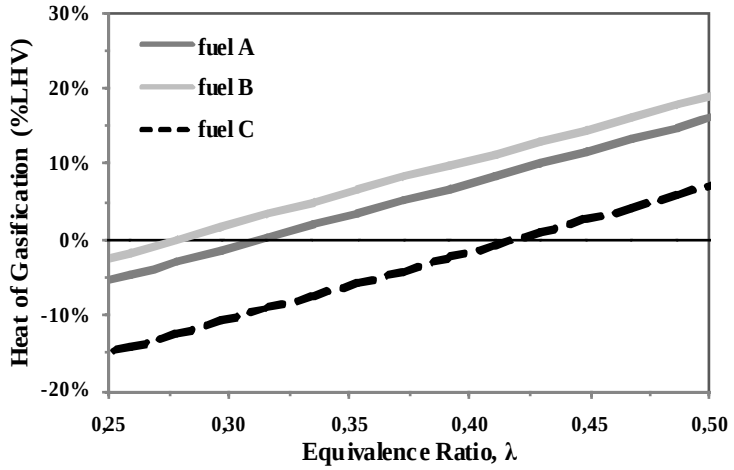

Fig. 4. Surpluss or requirement energy in the form of hypothetical heat exchange between the gasifier and environment for maintaining the operation at 800°C.

Figure 5 correlates what is previously discussed as far as the efficiency is concerned. The bullets indicate the points where there the operation is autothermal. Curves of LHV and CGE for three cases are almost the same. However, for λ=0.31 fuel B is gasified without requiring heat, fuel C need around 10% of total heat input and fuel A yields 5% heat.

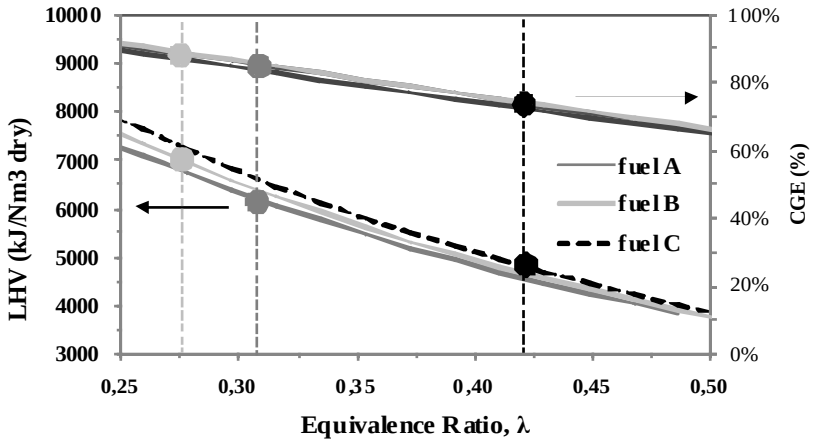

Fig. 5. LHV of dry syngas and cold gas efficiency for three types of fuel (the bullets indicate the points where there is autothermal condition)

3. Temperature effect

Gasification temperature does not have considerable effect on the thermodynamic of syngas composition (figure 6). In that case the validity of assuming a constant methane composition has to be revised and checked. A principle reaction that determines syngas composition is Water Gas Shift reaction:

$$CO + H_2O \Leftrightarrow CO_2 + H_2 \qquad -41\ MJ/kmol \quad \text{(R1)}$$

As the temperature rises the reaction equilibrium shifts at the right side and benefits CO and H_2O production. Hence, heating value increases at elevated temperatures.

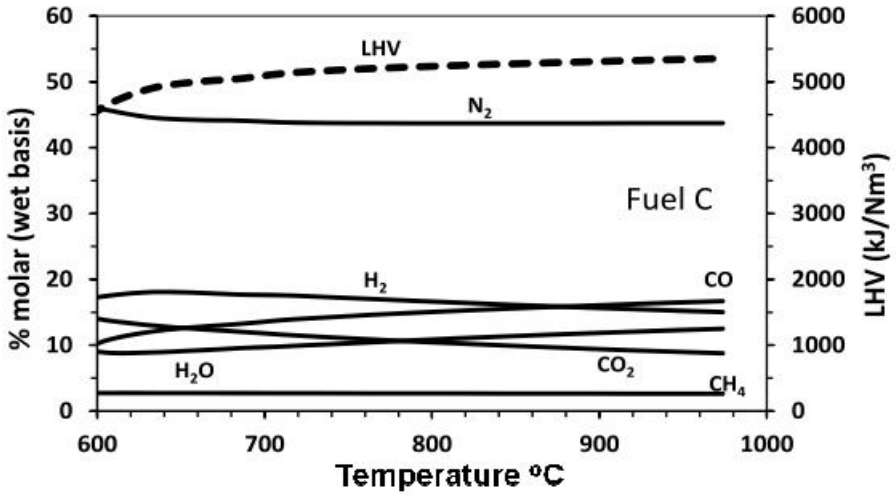

Fig. 6.Effect of temperature of syngas quality (Fuel C, autothermal conditions)

The process efficiency is affected by the operating gasifier temperature. Lowering the reactor temperature, autothermal conditions can be achieved with less oxidant (air) flow rates (Figure 7). However, special attention should be paid for ensuring complete char gasification. Thus, an acceptable range for operational temperature would be 850-900 ^{o}C.

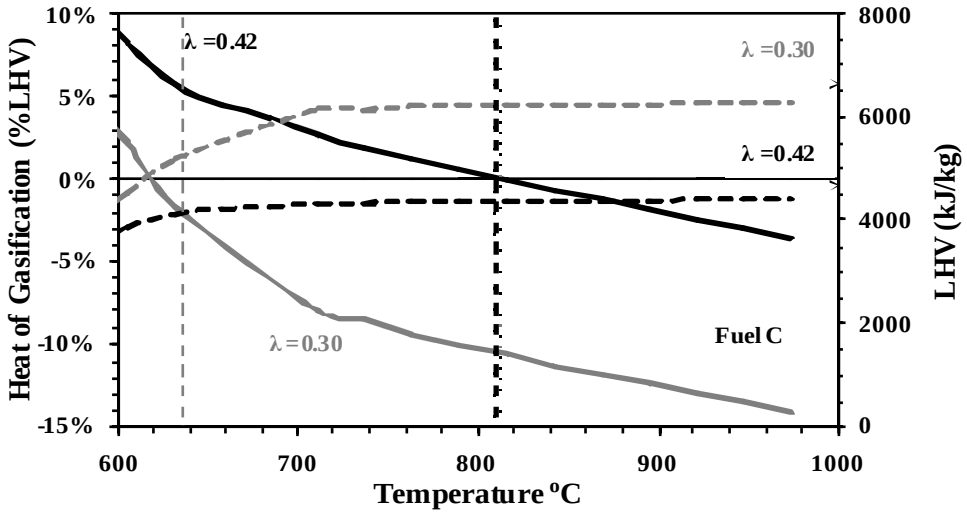

Fig. 7. Heat of gasification (required or rejected and raw syngas LHV (fuel C)

The efficiency of the process is tightly related with the rate of solid carbon conversion i.e. the fixed carbon that is gasified. The major reactions that carbon solids take part are the Boudouard reaction and the reactions with oxygen:

$C+CO_2 \Leftrightarrow 2CO$	+172 MJ/kmol	Boudouard reaction
$C + 0.5 \cdot O_2 \Leftrightarrow CO$	$-111\ MJ/kmol$	partial oxidation
$C + O_2 \Leftrightarrow CO_2$	$+393.8\ MJ/kmol$	total oxidation

(R2)

Figure 8 shows the effect of these low equivalence ratios as well as temperature on the carbon conversion. In case of fuel C, thermodynamic equilibrium predicts that carbon solids can be gasified

for equivalence ratio rates greater than 0.2. Lowering the operational temperature the corresponding critical values reduces, too. However, the demand for autothermal conditions in the reactor pushes this value up. Several other factors also contribute to the solid carbon gasification like kinetic rates, fluid dynamics of the flow, etc. that in this analysis are not taken into account but for assuming maximum carbon conversion efficiency equal to 98%.

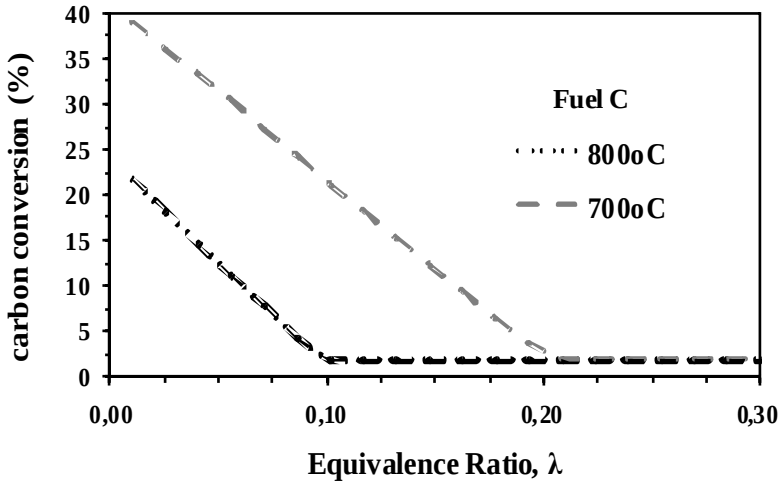

Fig. 8. Effect of temperature on the carbon conversion efficiency (fuel C.

4. Air preheating

Figure 9 shows that air preheating can reduce the required quantity of air for isothermal conditions up to 2%. For constant gasification temperature and provided that maximum of carbon conversion is achieved, the less the oxidizing agent enters to the reactor, the higher the heating value of the produced gas. High preheating rates can be achieved recovering heat from the hot raw syngas. However, assuming constant gasification temperature, the change in air temperature inlet does not have effect on CGE.

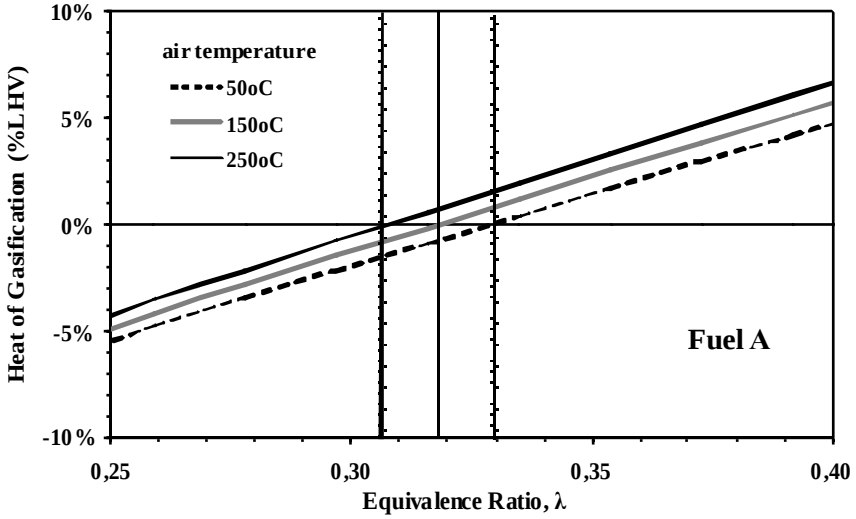

Fig. 9. Effect of air preheating on process operation.

4. Conclusions

Concluding, there are certain points in this study that need to be noted. As seen from the proximate analysis the high moisture content in the input fuel leads to low heating value. In this sense, the operation of the facility shall by supported by external electrical resistances in order to provide the required heat for normal operation. The chlorine (Cl) content calculated is believed to originate mainly from PVC, a plastic with high chlorine concentration. It is not expected that the measured chlorine concentration values may cause technical or operational problems. From the gasification modeling it is concluded that fuel drying has positive effects on the process and therefore the installation of a drying system is considered, in case of utilizing refused derived fuels with increased moisture content. Moreover, fuel quality has considerable effect on process specifications as denoted by the effect of the ash content variation on the mass balance and the required equivalence ratio. The optimal operational temperature, regarding carbon conversion and gasification efficiency should be around 850-900^{o}C based on the process simulation results.

5. Acknowledgments

The support of the European Commission on the Life09 “Energy Waste” project is gratefully acknowledged.

Nomenclature

λ equivalence ratio
CGE Cold Gas Efficiency
LHV Lower Heating Value (MJ/kg)
HHV Higher Heating Value (MJ/kg)
T Temperature (^{o}C)
P Pressure (bar)

References

[1] Porteous A., Why energy from waste incineration is an essential component of environmentally responsible waste management.Waste Management 2005;25: 451–459.

[2] Psomopoulos C.S., BourkaA., ThemelisN.J., Waste-to-energy: a review of the status and benefits in USA.Waste Management 2009;29:1718–1724.

[3] ArenaU., Process and technological aspects of municipal solid waste gasification. A review, Waste management 2011;In press, http://dx.doi.org/10.1016/j.wasman.2011.09.025.

[4] Lombardi L., Carnevale E., Corti A., Analysis of energy recovery potential using innovative technologies of waste gasification.Waste management2011;In press, http://dx.doi.org/10.1016/j.wasman.2011.07.019.

[5] Rocca S., Zomeren A., Costa G., Dijkstra J.J., ComansR.N.J., Lombardi F., Characterization of major component leaching and buffering capacity of RDF incineration and gasification bottom

ash in relation to reuse or disposal scenarios.Waste management 2012;In press, http://dx.doi.org/10.1016/j.wasman.2011.11.018.

[6] Cozzani V., Petarca L., Tognotti L., Devolatilization and pyrolysis of refuse derived fuels: characterization and kinetic modeling by a thermogravimetric and calorimetric approach.Fuel 1995;74:903-912.

[7] PerkoulidisG., PapageorgiouA., KaragiannidisA., KalogirouS., Integrated assessment of a new Waste-to-Energy facility in Central Greece in the context of regional perspectives.Waste Management 2010;30:1395-1406.

[8] He M., Hu Z., Xiao B., Li J., Guo X., Luo S., Yana F., Fena Y., Yana G., Liu S., Hydrogen-rich gas from catalytic steam gasification of municipal solid waste (MSW): Influence of catalyst and temperature on yield and product composition.Hydrogen energy 2009; 34:95-203.

[9] GalvagnoS., CasciaroG., CasuS., MartinoM., MngazziniC., RussoA., PortofinoS., Steam gasification of tyre waste, poplar, and refuse-derived fuel: A comparative analysis.Waste management 2009; 29:678-689.

[10] EN 15442:2011 – Solid recovered fuels - Methods for sampling.

[11] Higman C. and Van Der Burgt M.Coal Gasification, 2nd Edition. Gulf Professional Publishers; 2008.

[12] Puiz-Arnavat M., Bruno J.C., Coronas A., Review and analysis of biomass gasification models.Renewable and Sustainable Energy Reviews 2010; 14:2481-2851.

[13] Higman C. and Van Der Burgt M., Gasification, Gulf Publishing, 2003.

[14] RamzanN., AshrafA., NaveedSh., MalikA., Simulation of hybrid biomass gasification using Aspen Plus: A comparative performance analysis for food, municipal solid and poultry waste.Biomass and Bioenergy 2011; Article in Press, http://dx.doi.org/10.1016/j.biombioe.2011.06.005.

[15] Aspentech, Aspen plus V7 reference manual. Cambridge, MA 02141: Aspen Technology, Inc.; 2009

[16] MoritaH., YoshibaF., WoudstraN., HemmesK.,SpliethoffH., Feasibility study of wood biomass gasification/molten carbonate fuel cell power system—comparative characterization of fuel cell and gas turbine systems.Journalof Power Sources 2004; 138(1-2):31-40.

[17] KakarasE., VourliotisP., PanopoulosK. D., FrydaL., Cotton residue gasification tests in lab scale fluidised bed, Clean Air 2003: Proceedings of theSeventh International Conference on Energy for a Clean Environment;2003 July 7 - 10; Lisbon, Portugal.

[18] Liu G.-Q., ItayaY., YamazakiR., MoriS., YamaguchiM., KondohM., Fundamental study of the behavior of chlorine during the combustion of single RDF.Waste management 2001; 21:427 433.

[19] Wan H.-P., Chang Y.-H., Chien W.-C., Lee H.-T., Huang C.C., Emissions during co-firing of RDF-5 with bituminous coal, paper sludge and waste tires in a commercial circulating fluidized bed co-generation boiler.Fuel 2008; 87:761-767.

[20] HilberTh., ThorwarthH., Stach-LaraV., SchneiderM., MaierJ., ScheffknechtG.,Fate of mercury and chlorine during SRF co-combustion, , Fuel 2007; 86:1935-1946.

[21] Ma W., Hoffmann G., Schirmer M., Chen G., RotterV.S.,Chlorine characterization and thermal behavior in MSW and RDF, Journal of Hazardous Materials 2010; 178:489-498.

[22] CioniM., La MarcaC., RiccardiJ.,RDF Gasification in a Circulating Fluidized Bed Gasifier: Characterization of Syngas and Ashes, , ENEL ProduzioneS.p.A., Research Departement, Via A. Pisano 120, 56122 Pisa, Italy.

[23] Kakaras E., Grammelis P., Agraniotis M.,Solid Recovered Fuels as Coal Substitute in the Electricity Generation Sector, Thermal Science Journal 2005; 9(2):17-30.

[24] Hilber Th., Agraniotis M., Maier J., Scheffknecht G., Grammelis P., Kakaras E., Glorius Th., Becker U., Schiffer H.-P., Derichs W., De Jong M., TorriL.,Advantages and possibilities of Solid Recovered Fuel (SRF) co-combustion in the European Energy Sector , Journal of the Air & Waste Management Association 2007; 57: 1178 – 1189.

[25] Agraniotis M., Grammelis P., KakarasE.,Utilisation of Solid Recovered Fuels (SRF) for energy production", CEMEPE2009: Proceedings of the 2nd International Conference on Environmental Management, Engineering, Planning & Economics; 2009 June 21-26; Myconos.Greece.

[26] Chen C., Jin Y.-Q., Yan J.-H., Chi Y., Simulation of municipal solid waste gasification for syngas production in fixed bed reactors.Applied Physics& Engineering 2010; 11(8): 619-628.

[27] KarellasS., PanopoulosK. D., PanousisG., KakarasE., BoukisI., Energetic and exergetic analysis of energy generation system with integrated gasification of RDF, ECOS 2010: 23rd International Conference on Efficiency, Cost, Optimization, Simulation and Environmental Impact of Energy Systems, 2010 June 14-17; Lausanne, Switzerland.

Design and Modelling of a Novel Compact Power Cycle for Low Temperature Heat Sources

Jorrit Wronski[a], Morten Juel Skovrup[b], Brian Elmegaard[c], Harald Nes Risså[d] and Fredrik Haglind[e]

[a] *Technical University of Denmark, Kgs. Lyngby, Denmark, jowr@mek.dtu.dk, **CA**,*

[b] *IPU, Kgs. Lyngby, Denmark, mjs@ipu.dk,*

[c] *Technical University of Denmark, Kgs. Lyngby, Denmark, be@mek.dtu.dk,*
[d] *Viking Heat Engines, Kristiansand, Norway, hnr@vdg.no,*

[e] *Technical University of Denmark, Kgs. Lyngby, Denmark, frh@mek.dtu.dk*

Abstract:

Power cycles for the efficient use of low temperature heat sources experience increasing attention. This paper describes an alternative cycle design that offers potential advantages in terms of heat source exploitation. A concept for a reciprocating expander is presented that performs both, work extraction and heat addition. Heated by thermal oil, evaporation takes place in two expansion chambers with a transfer of the working fluid at an intermediate pressure level. Using saturated liquid as feed leads to an expansion in the two-phase domain. A dynamic model of this expander is used to determine the state of the working fluid during the process. Based on this model, a first optimisation by means of changed valve timing is conducted and the results of this scenario are shown in this paper. The heat transfer during expansion is investigated and used to establish a representation of the dynamic calculation results for use with a steady state cycle evaluation. An organic Rankine cycle model is developed and used for a comparison. The performance of the expander itself and the different requirements regarding heat source and temperature levels are studied.

Keywords:

Alternative power cycle, two-phase expansion, reciprocating expander, organic Rankine cycle, waste heat recovery, low temperature heat sources.

1. Motivation and background

The world-wide energy demand increases constantly leading to an accelerated consumption of fossil fuels [1]. Rising prices for resources and fuels as well as the political atmosphere abet efforts in energy efficiency and the exploitation of renewable energy sources. Power cycles that convert low-grade heat to valuable electricity can help with both targets mentioned above. The energy efficiency of existing systems can be improved by utilising waste heat streams and several renewable heat supplies like biomass boilers, solar thermal collectors and geothermal sources that meet the requirements of such a cycle.

Organic Rankine cycles (ORC) gain an increasing amount of attention from the scientific and the business community. Plants are being erected and ongoing optimisation efforts increase performance and reliability. However, there is no established solution in the capacity range below 25 kW of electrical output. To circumvent the obstacles faced by turbo machinery at these low capacities, research has turned towards volumetric expanders. There are ongoing efforts to assess the feasibility of for example scroll [2], screw [3] and vane [4] type expansion devices for low capacity applications. By investigating a reciprocating expander, this study contributes information on an additional design.

The proposed cycle was initially sketched by Viking Heat Engines (VHE) and is based on the idea to combine isothermal heat addition and expansion. Excluding evaporation from the primary heat exchanger abets an efficient heat supply while employing compact components. Furthermore, the

system should not rely on a regenerator for efficient operation and offer economic advantages by using a large share of parts from the automotive sector. Pursuing the idea to design a compact power cycle containing a reciprocating expander, a first prototype was designed and set to operation by IPU in a shared workshop located at the Technical University of Denmark (DTU).

To assist with the further optimisation of the prototype, a dynamic model is built that incorporates key features of the existing mechanical design. This model connects two infinitely large reservoirs of design point feed pressure and condensing pressure. The existing prototype has not been operated at these conditions. Yet the characteristics of the simulated pressure curves match with the measured data during operation at lower pressures. This paper introduces the new power cycle and illustrates the concept by presenting first simulation results. In a next step, a steady state representation is developed. Including the expander in a power cycle enables the comparison to a Rankine process with the same fluid and similar operating conditions highlighting differences and similarities of the two power cycles.

2. Design

2.1. Boundary conditions and system layout

The test rig for the experiments, to which this modelling study relates, consists of the classical power cycle components. Condensed working fluid, state 1, coming from a water-cooled plate-type counterflow condenser passes a pump, state 2, and enters the primary heat exchanger. In this second counterflow plate-type device, the pressurised liquid is heated by thermal oil to state 3. It enters the expansion device and is first throttled to state 4 and afterwards expanded to state 5, which corresponds to the condenser inlet conditions. In addition to the basic components of a Rankine cycle, the expander is also connected to the heat supply and delivers thermal energy to the working fluid during the expansion. Figure 1 helps to illustrate the process and clarifies the order in which the working fluid passes the different components.

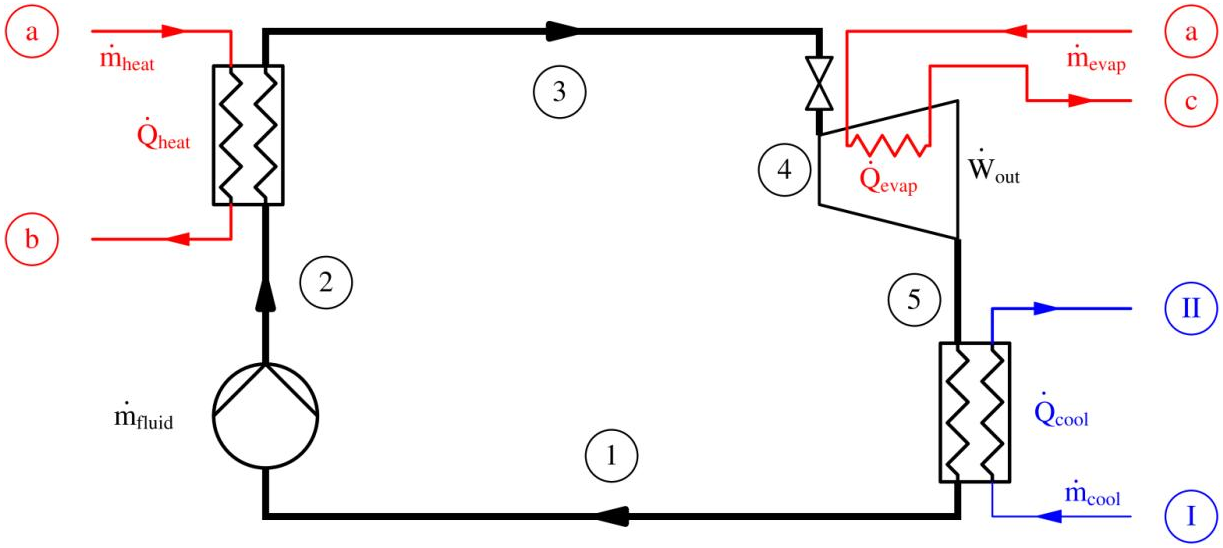

Fig. 1. Layout of the test facilities used in modelling and experiments.

The energy input to the presented heat-to-power conversion system is realised as a loop of thermal oil with a 400 l buffer tank, which is equipped with five temperature controlled electrical heaters giving a total capacity of 60 kW. Due to the large amount of oil and the limited operating time of the test facility, the hot oil is assumed to have a constant temperature of 200 °C. Heat is supplied to the primary heat exchanger and to the expander from the storage tank mentioned above, resulting in

similar inlet conditions, which are denoted with an “a” in Fig. 1. Employing pentane as working fluid enables the test facility to be built from standard components that are certified for pressures up to 35 bar while respecting the expected temperature levels in the components.

2.2. Expander design

Being part of ongoing experimental investigations by IPU and VHE, the calculations in this work are based on a design proposed by these companies. The current concept includes a double-acting piston expander that extracts work from a pressurised fluid by means of a two-stage expansion. The first stage, which is referred to as the high pressure expansion chamber (HPC), contains a built-in heat exchanger that is connected to the hot oil loop and utilises a fixed area for heat transfer to the working fluid during expansion. The same oil line also heats the walls of the low pressure expansion chamber (LPC) before it is fed back into the storage tank. The two stages are connected via a transfer line, which is controlled by a mechanically triggered valve. Injection and exhaust are activated shortly before the volume in HPC and LPC is smallest and largest, respectively. Being confined by the same piston, the bottom dead centre (BDC) for the first stage at 0° crank shaft angle θ coincides with the BDC of the second stage. Since the HPC is located below the piston, its volume is smallest at BDC and largest at top dead centre (TDC). The volume of the second stage changes in the opposite way.

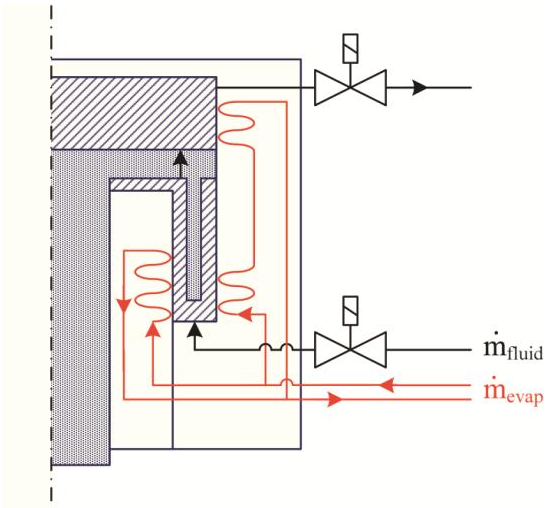

Fig. 2. Cross-sectional cut of the double-acting piston, shown as shaded parts, close to bottom dead centre with sketched heat exchangers, inlet and exhaust valves. Transfer lines and valves inside the piston and are omitted here for simplicity. The volume filled with working fluid is shown with a diagonal pattern.

The sketch of the expander, Fig. 2, illustrates the shape of the device described above. The working fluid enters from the bottom. After injection, it evaporates while receiving heat from the two heated walls of the HPC. Designing the lower chamber as a ring increases the wall area to volume ratio, which is beneficial for the heat exchange process. The additional ring mounted on the bottom side of the piston leads to a decrease in clearance volume and provides a further enhancement of the volume to wall area ratio. The transfer line opens as the piston reaches TDC and the second expansion stage takes place in the two connected volumes.

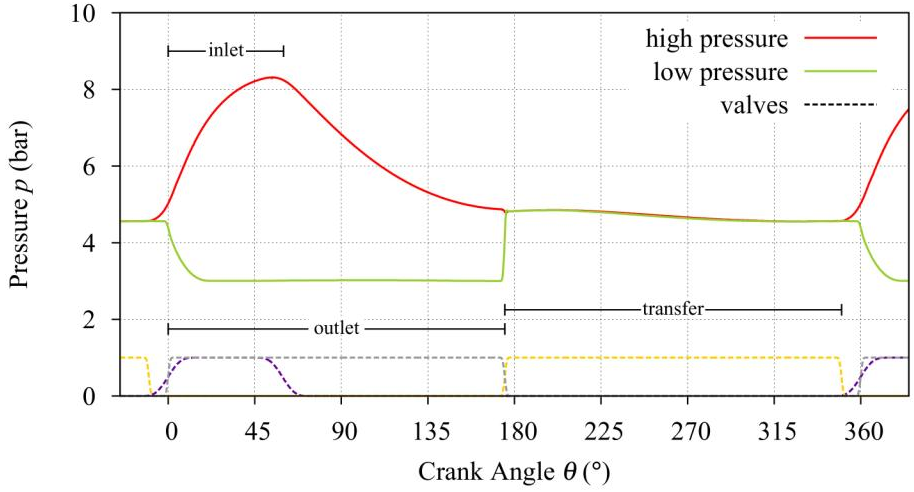

Fig. 3. Pressure in high and low pressure expansion stage, solid lines, and valve states, dashed lines, during one crank shaft revolution.

Following the pressure residing in both expansion volumes for one complete crank shaft rotation gives a good impression of how the two stages are connected and when work can be extracted from the fluid. The series of data shown in Fig. 3 was obtained from a preliminary test run of the model described below, a mixture of liquid and vapour in the supply line and pressures below the intended operating pressures. To clarify the control strategy of the device, the states of the valves for inlet, transfer and exhaust of the fluid are also given as curves alternating between 0 and 1 representing closed and open position, respectively. As mentioned above, high pressure working fluid is injected into the HPC at 0° θ compressing fluid in the clearance volume and elevating the chamber pressure to a maximum at approximately 55° θ. Simultaneously, the exit port of the LPC opens and fluid leaves this part of the device while the pressure becomes similar to the condenser conditions before an isobaric exhaust takes place. Approaching 180° θ, the exit line closes and both chambers get connected via the transfer ports resulting in an almost constant pressure while fluid gets transferred from first to second expansion stage. Due to larger footprint of the LPC, the overall confined volume increases during the transfer of fluid. Hence, the low pressure expansion takes place in both chambers despite the decreasing volume in the HPC. The increased piston surface in the LPC results in a force that successfully counteracts fluid friction in the transfer line.

3. Simulations

3.1. Dynamic expander model

In order to provide assistance regarding the experiments with the custom-built expander, a dynamic model is used to estimate performance and to provide insights in the possible behaviour of the machine. A thermodynamic simulation of the expander's operation was implemented with the software Engineering Equation Solver (EES) [5] using the built-in property functions for pentane originally presented in [6]. The mechanical system of expansion chamber, piston, connection rod, crank arm and crank shaft is considered to operate without friction, lubrication or any deformation. Furthermore, a constant rotational speed is assumed. Hence, only masses of reciprocating parts and the oscillating equivalents of rotating components have to be taken into account.

The basis of the simulation is formed by defining the rate of internally performed work as the product of pressure and instantaneous change in chamber volume

$$\dot{W} = -p \cdot \dot{V} . \qquad (1)$$

Other flows over the systems boundaries occur in terms of heat and mass transfer. The latter also contributes to the exchange of energy by means of enthalpy that enters and leaves the control

volume. The differential expression for internal energy can be used to combine the different influences. Integrating the equation

$$-\frac{dU}{dt} = \frac{dH}{dt} + \dot{Q} + \dot{W} \quad \text{with} \quad \frac{dH}{dt} = \dot{m}_{in} \cdot h_{in} + \dot{m}_{out} \cdot h_{out} \tag{2}$$

yields a way to follow the development of the state of the fluid inside the control volume.

In this work, a heavily idealised simulation is presented that is subject to several simplifications. Compressibility is neglected for the calculation of all flows and the specific mass flow per hydraulic area is expressed by

$$\dot{m}/A = c_d \sqrt{2 \cdot \Delta p \cdot \rho}\,. \tag{3}$$

In (3), Δp is the pressure difference between two connected volumes and ρ denotes the density of the upstream reservoir. The discharge coefficient c_d is always smaller than unity and calculates the pressure drop accounting for the losses in a valve. It is a measure of how much flow develops in comparison to ideal lossless conditions. A second way in which flow resistances are included in the calculations is the available area A. In case of valves, the maximum flow area A_0 is multiplied by a factor to obtain the effective area. This value is modified according to the opening state of the respective port. The switch from opened, 1, to closed, 0, and back is calculated by the function

$$\vartheta_A(\theta) = \frac{-3}{4}\left(\frac{1}{3}\cdot\cos^2\phi\cdot\sin\phi + \frac{2}{3}\sin\phi\right) + \frac{1}{2} \text{ with } \phi = \frac{\theta - \theta_t}{\Delta\theta}\cdot\pi\,, \tag{4}$$

which was initially proposed by [7] and provides a sufficiently smooth transition. The second part of (4) relates the actual crank angle degree θ to the desired switching point θ_t and the length of the transition from one state to the other $\Delta\theta$. Employing different trigger angles and transition durations, (4) is used to generate the alternating functions shown on the bottom part of Fig. 3.

Another important assumption is related to the heat fluxes. It is assumed that heat is only released by the internal heat exchanger and the cylinder walls. Areas in contact with the fluid belonging to the piston and the rest of the housing do not participate in the heat exchange. Furthermore, this heat transfer is of an exclusively convective nature. Neither radiation nor conduction contributes to the energy exchange. Hence, the only equation describing the heat exchange in one chamber is

$$\dot{Q} = \alpha \cdot A_{wall} \cdot \left(T_{wall} - T_{fluid}\right). \tag{5}$$

In order to solve (5) for each of the chambers, the effective surface of heated walls and internal heat exchanger A_{wall} and the temperature difference have to be determined. The first is a function of the geometry only and the latter is the difference between the average fluid temperature and the fixed wall temperature of 180 °C. An additional simplification leads to a value for the heat transfer coefficient α, which is implemented as a function of the vapour content in the chambers.

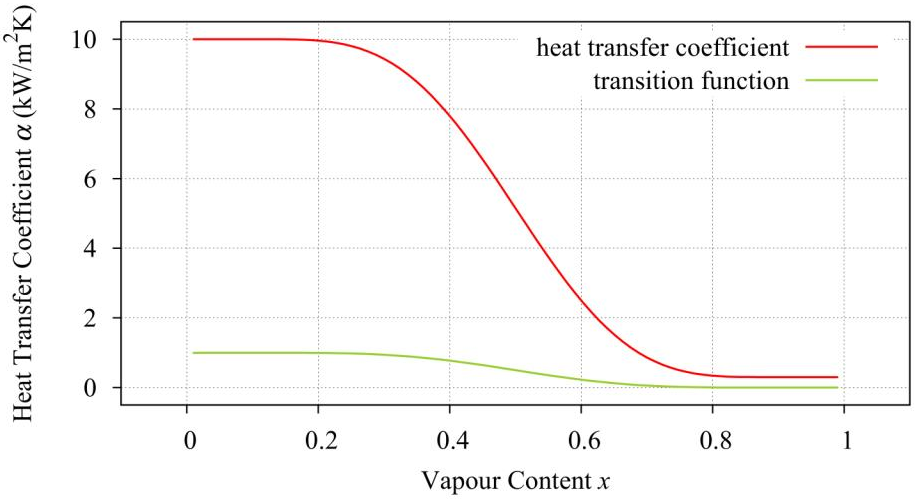

Fig. 4. Heat transfer coefficient as function of vapour content.

To model this variation of the heat transfer properties as shown in Fig. 4, an upper and a lower limit have to be defined. Depending on the superheat at the wall, [8] found that heat transfer coefficients of up to 10 kW/m^{2}K occur in boiling pentane for natural convection in a confined space. This value is used as the upper limit for α. Employing a lower limit of 0.3 kW/m^{2}K and the same general smooth transition equation from [7] as above yields

$$\vartheta_\alpha(x) = \frac{-3}{4}\left(\frac{1}{3}\cdot\cos^2\phi\cdot\sin\phi + \frac{2}{3}\sin\phi\right) + \frac{1}{2} \text{ with } \phi = \frac{x-0.5}{0.8}\cdot\pi\,, \qquad (6)$$

where the centre of the transition process is set to 0.5 and the interval length is defined as 0.8. Thus the heat transfer coefficient is defined as $\alpha/(\mathrm{kW/m^2K}) = \vartheta_\alpha\cdot 10+(1-\vartheta_\alpha)\cdot 0.3$ and depends on the vapour content only. It decreases from 10 kW/m^{2}K for 10% gaseous fluid to the lower limit of 0.3 kW/m^{2}K at 90% vapour.

After defining all the necessary equations to simulate the expander operation, the actual calculation is carried out by means of an integration over crank shaft angle. When steady state operation is reached in the solution, similar results are obtained for every revolution of the crank shaft. To assure such stable conditions, one simulation run comprises at least six crank shaft revolutions and only the last two are used for further data analysis.

The model has been preliminarily validated by comparison to experimental data for the test operation described by Fig. 3. In contrast to these calculations, the simulations presented below were carried out with modified valve timing and design point feed conditions. Closing the exit ports before the end of the stroke leads to an increase of pressure and temperature. This common measure to optimise reciprocating expanders is also used in recent steam engine development [9]. Compressing the remaining fluid in the clearance volumes before admitting a new charge of working fluid minimises losses. The net power output decreases slightly, but there is a valuable gain in efficiency.

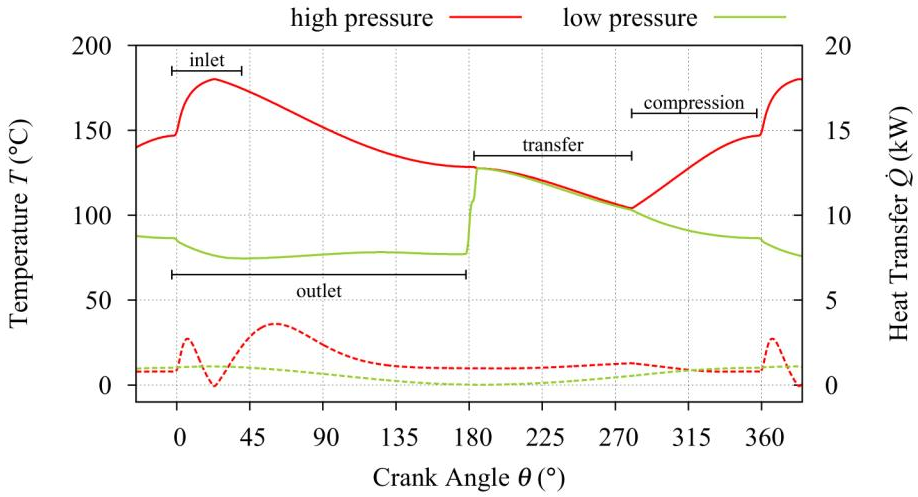

Fig. 5. Temperature, solid lines, and heat uptake, dashed lines, of both expansion chambers.

The temperature variation over crank angle is very much alike the pressure history. Therefore, the result of modifying the valve timing can also be seen on the temperature plot in Fig. 5. Again, admission of high pressure working fluid takes place around BDC at 0° θ. Saturated liquid in the feed line is throttled in the injection system and is sprayed onto the surface of the internal heat exchanger in the HPC. A high liquid fraction yields enhanced heat transfer, as described by (6), leading to an increased heat release from the walls. With progressing evaporation and expansion, temperature and pressure drop in the HPC. The effect of the precompression can be spotted as a two-step rise in temperature in the LPC around TDC at approximately 180° θ and similarly in the HPC during the last 80° θ of the revolution before BDC is reached again.

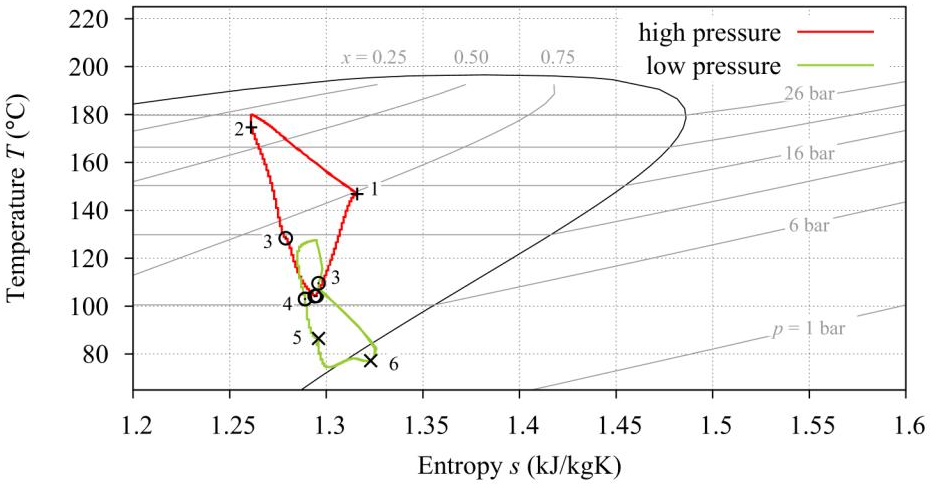

Fig. 6. Dynamic simulation of both expansion chambers, temperature over entropy for one crank shaft revolution.

Depicting the crank shaft revolution shown in Fig. 5 in terms of temperature and entropy, one obtains Fig. 6. The two cycles show the average state of the working fluid in both chambers and have to be read counter-clockwise. The BDC matches the right corner of the graph, 16 bar denote the end of the compression phase. The cross on the right hand side, point 1, is drawn at the opening angle of the inlet valve. During the following admission of working fluid pressure peaks at 26 bar while the average vapour content x in the chamber does not fall below 0.25. Evaporation and expansion start before the second cross, point 2, denotes the closure of the inlet. Reaching 11 bar, the chambers get connected and expansion takes place in the complete volume after an initial pressure increase in the LPC. Circles are drawn on both curves to illustrate the opening and closing of the transfer valves at point 3 and point 4, respectively. The states in the chambers are comparable when the transfer valves close. Both circles are next to each other at around 100 °C and the vapour content in the HPC is above 0.9. Afterwards, precompression elevates temperature and pressure in the high pressure part. Condensation occurs and eventually point 1 is reached. At the same time, expansion continues in the low pressure part of the machine. The two crosses on the graph for the LPC denote a state change of the exhaust valve to open, point 5, and back to closed, point 6. Hence, the final evaporation of the working fluids happens during exhaust and the precompression in the LPC takes place on the right hand side of the lower cycle between cross and circle, from point 6 to point 3 causing condensation of the working fluid.

3.2. Steady state expander model

This part of the paper describes the steady-state operation results based on the dynamic model presented above. By defining a simple and moderately accurate technique to account for the additional heat transfer during expansion, it is possible to compare the alternative expander to an ORC from a system perspective. The approach presented below is based on dividing the expansion into different steps with an isobaric intermediate heat addition.

To identify the temperatures and pressures at which the heat addition should take place, the heating calculated in the dynamic simulations is analysed with a greater level of detail. The average heat transfer rate during expansion $\dot{Q}_{evap}$ is 2 kW at a wall temperature of 180 °C. This number is sensitive to the chosen wall temperature and simulations with 160 °C and 220 °C yield 0.4 kW and 4 kW, respectively. Approximately three quarters of the heat are released in the high pressure chamber as Q_{HPC} and one quarter in the low pressure chamber as Q_{LPC},

$$Q_{LPC} = \frac{1}{4}\dot{Q}_{evap} \cdot \frac{60\ \mathrm{s/min}}{N} \text{ and } Q_{HPC} = \frac{3}{4}\dot{Q}_{evap} \cdot \frac{60\ \mathrm{s/min}}{N}. \qquad (7)$$

Looking for a steady state solution, the crank angle and time domain in Fig. 5 are neglected and the values for one crank shaft revolution are regarded as one set of data. In (7), the average heat transfer rate is divided by the rotational speed N of 1500 min^{-1} to obtain the amount of transferred heat per revolution. Combining the two remaining quantities temperature and heat transfer leads to the temperatures at which the actual heat addition takes place.

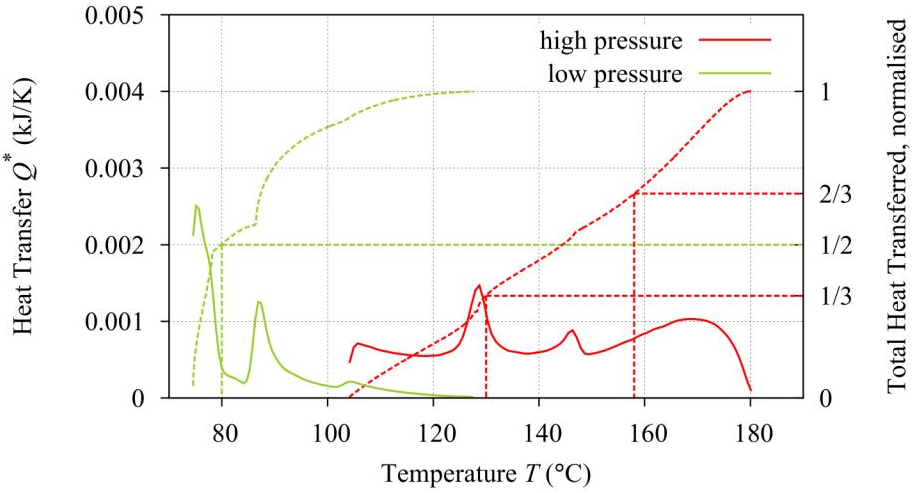

Fig. 7. Heat transfer, solid lines, and the normalised integrated heat transfer, dashed lines, during one crankshaft revolution mapped to bulk fluid temperatures.

The resulting Fig. 7 displays the same data as Fig. 5, but with the heat transfer plotted in relation to the bulk fluid temperature in both chambers. Q^* denotes the sum of all heat added during one crank shaft revolution at a certain temperature and is decoupled from crank angle and time domain. It can be seen that most heat is transferred to the LPC at lower temperatures. Whereas heat input to the HPC takes place in the range between 105 °C and 180 °C, which denote the beginning and the end of the curve for the HPC in Fig. 7. An integration of the heat transfer over temperature gives the total amount of added heat. To define suitable temperatures for the intermediate heating, one has to investigate the integral of the heat transfer per temperature, which is shown as dashed graphs in Fig. 7. For the LPC, all heat release is assumed to take place at the temperature at which the integrated heat transfer reaches half of its final value. Due to the large amount of heat entering the HPC, this heat transfer is split up into two portions that are applied at the temperatures corresponding to one third and two thirds of the integrated heat exchange. As depicted in Fig. 7, three temperatures are chosen for the intermediate heat transfer $T_{heat,3}$ 80 °C, $T_{heat,2}$ 130 °C and $T_{heat,1}$ 158 °C. Summarising the above, the heat uptake during expansion is split up as defined by

$$\frac{1}{2}Q_{LPC} = \int_{70\,^\circ\mathrm{C}}^{T_{heat,3}} Q^*_{LPC}dT;\ \frac{1}{3}Q_{HPC} = \int_{100\,^\circ\mathrm{C}}^{T_{heat,2}} Q^*_{HPC}dT;\ \frac{2}{3}Q_{HPC} = \int_{100\,^\circ\mathrm{C}}^{T_{heat,1}} Q^*_{HPC}dT. \qquad (8)$$

Hence, expansion is divided into four steps between which the amounts of heat given in (8) are added. Each step is considered adiabatic and assumed to have an isentropic efficiency $\eta_{is,exp}$ of 0.825. By defining these temperatures and efficiency, the extracted work matches with the results of the dynamic simulation and the same amount of heat is transferred during the expansion phase.

4. Comparison with an organic Rankine cycle

The presented two-phase expander can be operated in a setup similar to an organic Rankine cycle by adding heat in the preheater only. The same software, EES [5], is also used for the following calculations. For a comparison of the steady state operation, the auxiliary equipment is modelled in a similar manner. Both of the expanders are calculated as part of a comparable cycle consisting of condenser, pump and primary heat exchanger employing pentane as a working fluid. There are no temperature constraints regarding the heat utilisation. The oil loop may be cooled as much as

needed and the supply is of infinite capacity. However, the mass flow of thermal oil is constant and set to 0.15 kg/s for all considered systems. Furthermore, the condenser operates at a constant pressure of 3 bar and there is a subcooling of 1 K at the outlet. The feed pressure for the ORC is adjusted to 13 bar in order to obtain the highest possible power output at the given conditions. Expansion efficiency $\eta_{is,exp}$ is set to 0.825 for the ORC as well as for the adiabatic steps of the two-phase expansion. To account for the initial pressure losses calculated by the dynamic expander model, the feed pressure for the primary heat supply of the two-phase expansion at 30 bar is throttled isenthalpically to a maximum pressure of 25 bar. The ORC is equipped with a regenerator in addition to the two main heat exchangers before and after the pump, which operates with $\eta_{is,pump}$ of 0.5. All considered heat transfer takes place at isobaric conditions, without pressure loss, and with a fixed pinch point temperature difference ΔT of 10 K.

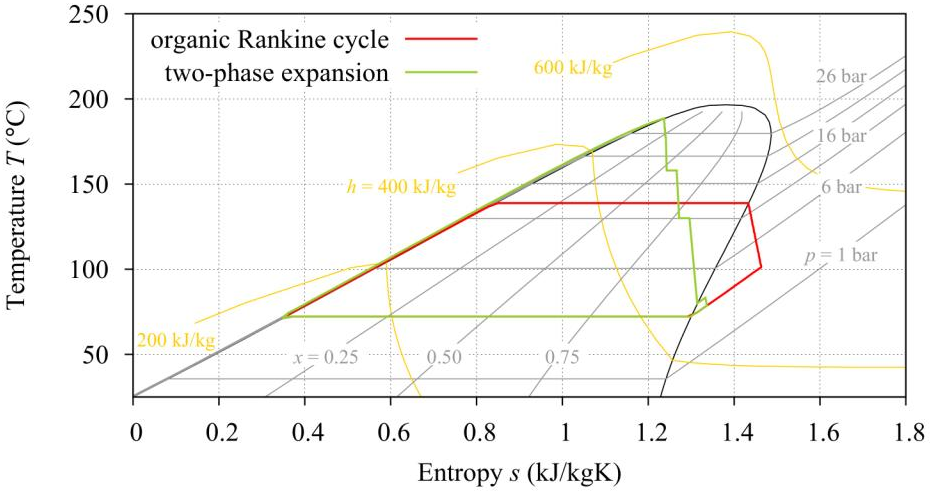

Fig. 8. Steady state simulation of two-phase expansion and organic Rankine cycle.

The resulting process is sketched in a temperature over entropy diagram in Fig. 8. This figure shows the effect of the multi-step expansion and the heat addition and illustrates the effect of the different feed pressures. The working fluid is only slightly superheated after the two-phase expansion process compared to the ORC expander outlet conditions. Defining the minimum temperature difference of 10 K determines the mass flows of working fluid and cooling media in evaporator and condenser as well as the amount of transferred heat in the regenerator. Heat input is modelled by a constant heat supply inlet temperature of 200 °C and a set of equations to approximate the properties of the heat transfer oil.

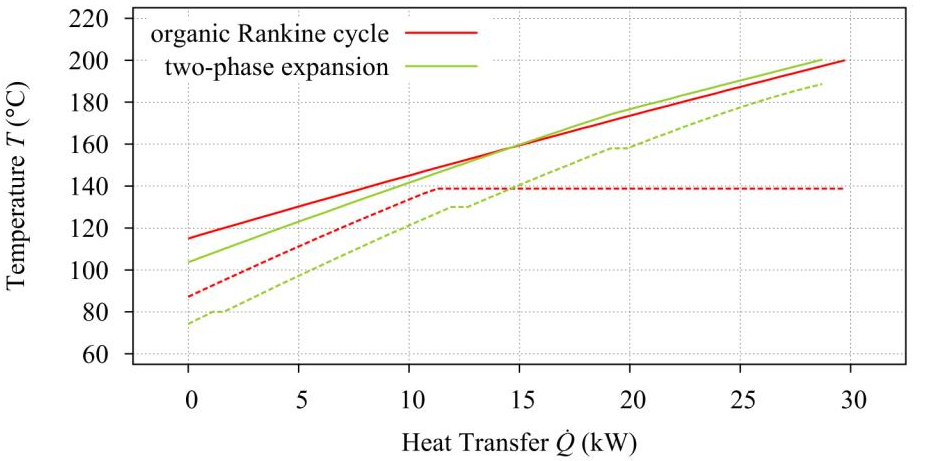

Fig. 9. Heat source, solid line, and working fluid, dashed line, during heat supply to both cycles.

Approximate experimental data provided by the supplier of the oil Texatherm HT22, AB&CO TT Boilers A/S, Greve, Denmark, was used to generate polynomials for the interdependency of heat capacity, density and temperature. On the cold side of the process, water is supplied at 30 °C and 3 bar. The corresponding fluid properties are calculated using equations by [10] and [11], which are already a part of EES. Due to the regeneration, the heat removal from the process looks similar in both configurations.

For the ORC, a working fluid flow of 0.076 kg/s is needed to obtain a suitable inclination of the line representing the heat receiver in Fig. 9 while respecting the defined minimum temperature difference at the given pressure. As a result, there is a large temperature difference of 60 K at the end of the heat transfer. The initial temperature of the working fluid is slightly higher in the ORC system due to the regenerated 3 kW. In total, the two-phase expansion consumes slightly less heat and ends at 26.7 kW of heat transferred from an oil stream of 0.12 kg/s before the expansion. The 2 kW that are supplied to the expansion device are added to the composite curve as horizontal lines at the temperatures calculated in the last section. This heat is provided by 0.03 kg/s of thermal oil that are cooled down to 170 °C. Therefore the inclination of the two-phase expansion heat donation curve in Fig. 9 changes at that temperature and runs parallel to the other one until 200 °C are reached.

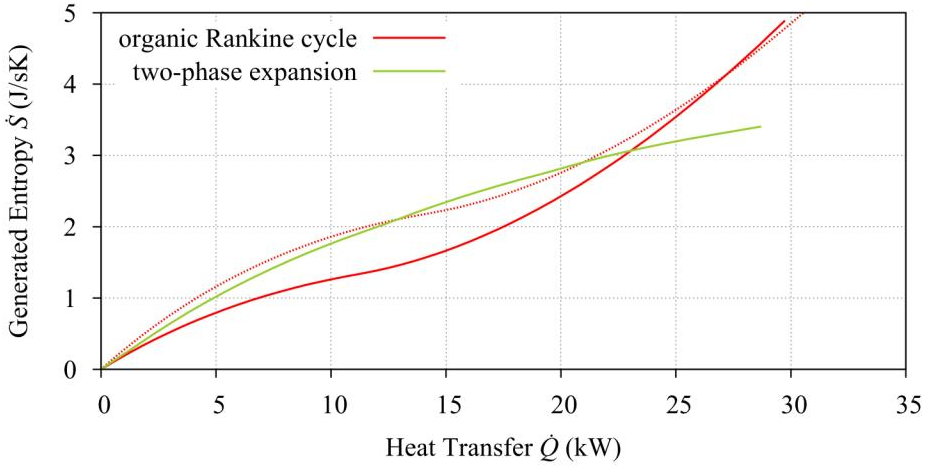

Fig. 10. Entropy generated during heat supply to organic Rankine cycle and two-phase expansion, the red dashed line depicts an organic Rankine cycle without regeneration.

Calculating the entropy generation during the heat exchange illustrates where the initial losses occur. *k* steps in terms of heat transfer are used to follow the working fluid through the heat supply. In Fig. 10, the sum of the generated entropy as given by

$$\dot{S}_{gen,j} = \sum_{i=1}^{j}\left[\left(\frac{1}{T_{mean,\,fluid,i}} - \frac{1}{T_{mean,src,i}}\right)\cdot \dot{Q}_i\right] \forall\ j \in \{1,\ldots,k\} \text{ with } \sum_{i=1}^{k}\dot{Q}_i = \dot{Q}_{in} \qquad (9)$$

is shown. Equation (9) combines the temperature difference between heat donating $T_{mean,src}$ and heat receiving fluid $T_{mean,fluid}$ with the amount of heat $\dot{Q}_{in}$ transferred in the regarded interval. Temperature differences cause irreversibilities. The inclination of the curves in Fig. 10 illustrates that losses occur in the beginning of the heat transfer and, in case of the ORC, also at the end while heating the alternative cycle generates less entropy at larger amounts of transferred heat.

The end points of the three lines in Fig. 10 represent the entropy generated at the end of the heat supply. It can be seen that the improvement from employing a regenerator is limited. Introducing the two-phase expansion decreases the amount of entropy generated due to heat transfer. In total, about a fourth of the entropy production can be avoided at comparable power output.

5. Simulation Results

Despite different pressure levels, results from an adapted ORC and from the steady state representation of the alternative power cycle are comparable. A more efficient heat supply in the primary heat exchanger is combined with irreversibilities from the second heat input leading to a slightly enhanced heat exchanger performance.

To compare both systems on a cycle level, different efficiencies can be calculated. Since the temperatures of the heat source T_{max} and the heat rejection fluid T_{min} are the same, both cases have an ideal efficiency $\eta_{ideal} = 1-(T_{min}/T_{max})$ of 36%. To assess the grade of the energy conversion, first law η_I and second law η_{II} efficiency are obtained from (10). Calculating the first law, or thermal, efficiency is done by comparing the net power output $\dot{W}_{net}$ to the amount of supplied thermal energy $\dot{Q}_{in}$. The first represents the surplus work after the required pump work has been subtracted from the expander output and the latter is the sum of all heat inputs to the system in primary heat exchanger and, if needed, in the expansion device. The second law efficiency of the cycle relates the output of the energy conversion to the corresponding performance of an ideal Carnot cycle η_{ideal}. Hence, the formulae used for first and second law efficiency are

$$\eta_I = \frac{\dot{W}_{net}}{\dot{Q}_{in}} \text{ and } \eta_{II} = \frac{\dot{W}_{net}}{\dot{W}_{ideal}} = \frac{\eta_I}{\eta_{ideal}}. \quad (10)$$

The net power output of all systems is around 3.1 kW, while the pump consumes more than twice the energy in the two-phase cycle. Calculating the efficiencies defined above also yields similar results of slightly more than 10% for thermal efficiency and below 30% for the second law or cycle efficiency. To investigate the potential stored in the working fluid after the heat exchange, a second ideal efficiency is defined that is solely based on the working fluid temperatures only,

$$\eta_{ideal,\,fluid} = 1 - \frac{T_{min,\,fluid}}{T_{max,\,fluid}}. \quad (11)$$

While ORC configurations give values between 16% and 18%, the two-phase cycle has a potential for 25%. This relates to the elevation of 40 K in maximum working fluid temperature. Considering this value, more than half of the potential work in the fluid can be converted to mechanical energy in an ORC. To obtain more information about the losses during the heat to power conversion, the exergy release of the heating fluid is calculated by solving

$$\dot{E}_{in} = \sum_{i=1}^{k}\left[\left(1 - \frac{T_0}{T_{mean,src,i}}\right)\cdot \dot{Q}_i\right] \text{ with } \sum_{i=1}^{k}\dot{Q}_i = \dot{Q}_{in}. \quad (12)$$

The temperature $T_{mean,src}$ denotes the average heating fluid temperature per segment and T_0 is the reference temperature of 25 °C.

Table 1. Performance of two-phase expansion and two organic Rankine cycles.

Parameter	*ORC, no regeneration*	*ORC, regeneration*	*Two-phase expansion*
Mass flow heat carrier (kg/s)	0.15	0.15	0.12+0.03
Mass flow working fluid (kg/s)	0.071	0.076	0.075
Total heat supply (kW)	31.1	29.7	26.7+2
Pump work (kW)	0.28	0.31	0.70
Net power out (kW)	3.1	3.1	3.1
Thermal efficiency, η_I (%)	10.0	10.6	10.8
Cycle efficiency, η_{II} (%)	27.8	29.4	29.9
Ideal efficiency, $\eta_{ideal,fluid}$ (%)	17.6	16.4	25.4
Exergy input (kW)	9.0	8.91	8.66
Exergetic efficiency, η_{ex} (%)	34.4	34.8	35.7

Considering the produced work as being only exergy, the exergetic efficiency η_{ex} is the ratio of power output and exergy input. Also by employing this technique, the alternative cycle performs close to the Rankine cycles. The advantages in terms of primary heat exchange cannot equalise the other losses that occur later in the cycle.

The performance resulting from the operation described above is summarised in Table 1 together with data for an ORC without internal heat recovery. In the column for the two-phase expansion, some rows contain two values. The second number for mass flow of oil and the amount of supplied heat express the contribution of the expansion device whereas the first value is obtained from calculations considering the primary heat exchanger.

6. Conclusion and outlook

The results from a dynamic simulation of a two-stage reciprocating device show that it is possible to design a compact expander that can extract work from working fluid supplied in liquid form. Injecting the working fluid on a fixed surface heat exchanger at simultaneous expansion with accompanying variation of the mean fluid temperature yields an increased heat transfer. This assures a minimum vapour content and minimises the risk of hydraulic locking that might occur during the precompression phase. Calculating three suitable temperatures for bulk heat addition during a step-wise expansion gives an acceptable steady state approximation of this process.

Studying the system performance including the heat supply shows that the presented system layout with the two-phase expansion performs comparable to a Rankine cycle with the same working fluid. The obtained results are sensitive to the constraints arising from the heat source definition and might change when optimising the systems for efficiency instead of power output. Furthermore, this study shows the potential benefits of enhanced heat source exploitation by utilising an unconventional expander that can operate in the two-phase regime.

Due to the number of assumption and simplifications employed in the dynamic and steady state model as well as in the overall boundary conditions, it is desirable to conduct a more detailed analysis of the proposed system. Especially flow and heat transfer calculations in the detailed expander model are sources of uncertainty. Regarding the system, several measures can be taken to generate a more comprehensive study. Among those, auxiliary power consumption and the interaction with a heat source are considered to be of major interest. Investigating the application of low temperature power cycles from a more general point of view, different working fluid should also be compared. A systematic approach on this can contribute performance gains as described by, amongst others, [12] and [13]. Including mixtures [14] and supercritical operation [15] in an efficiency assessment adds even more degrees of freedom to a future study.

Acknowledgments

The authors would like to thank their colleagues Kristian Fredslund Jensen and Nikolas Aulin Paldan at IPU for sharing their expertise regarding energy systems, experimental setups and mechanical details of the expander.

Nomenclature

Abbreviations and Acronyms

BDC bottom dead centre position of the piston

DTU Danmarks Tekniske Universitet (Technical University of Denmark)

HPC high pressure expansion chamber

LPC low pressure expansion chamber

ORC organic Rankine cycle

TDC top dead centre position of the piston

VHE Viking Heat Engines

Letter Symbols

A	area, m^2
c	coefficient
$\dot{E}$	exergy transfer rate, kW
H	enthalpy, kJ
h	specific enthalpy, kJ/kg
k	number of steps in transferred heat
$\dot{m}$	mass flow rate, kg/s
N	rotational speed, min^{-1}
p	pressure, bar
Q	heat, kJ
$\dot{Q}$	heat transfer rate, kW
Q^*	heat transferred at a certain temperature, kJ/K
$\dot{S}$	entropy rate, J/(sK)
s	specific entropy, kJ/(kgK)
T	temperature, °C
t	time, s
U	internal energy, kJ
$\dot{V}$	rate of volume change, m^3/s
$\dot{W}$	work transfer rate, kW
x	vapour content

Greek symbols

α	heat transfer coefficient, $W/(m^2 K)$
Δ	difference
η	efficiency
θ	crank angle, °
ϑ	transition coefficient
π	ratio of circumference to circle diameter
ρ	density, kg/m^3
ϕ	transition position coefficient

Subscripts and superscripts

I	first law
II	second law
0	initial value, reference
cool	cooling
d	discharge
evap	evaporation
ex	exergetic
exp	expansion
fluid	working fluid
heat	heat exchanger
ideal	ideal process

in	input
is	isentropic
max	maximum value over a defined interval
mean	average value over a defined interval
min	minimum value over a defined interval
net	net value
pump	pump
out	output, outlet
src	referring to a heat source
t	transition point
wall	cylinder wall

References

[1] International Energy Agency, Key World Energy Statistics 2011. Paris, France.

[2] Quoilin S., Lemort V., Lebrun J., Experimental study and modeling of an Organic Rankine Cycle using scroll expander. Applied Energy 2010; 87(4):1260-1268.

[3] Grill A., Springer J.-P., Aumann R., Schuster A., Spliethoff H., Simulation and experimental validation of an ORC system for waste heat recovery of exhaust gas. In: Bojić M., Lior N., Petrović J., Stefanović G., Stevanović V., editors. ECOS 2011: Proceedings of the 24th International Conference on Efficiency, Cost, Optimization, Simulation, and Environmental Impact of Energy Systems; 2011 Jul 4-7; Novi Sad, Serbia. University of Niš, Faculty of Mechanical Engineering:840-50.

[4] Daminabo F.F.O., A Novel 2kWe Biomass-Organic Rankine Cycle Micro Cogeneration System [dissertation]. Nottingham, United Kingdom: University of Nottingham; 2009.

[5] Klein S., Alvarado F.L., Engineering Equation Solver (EES) v8.874. Madison, Wisconsin, USA: F-Chart Software; 2011.

[6] Jacobsen R.T., Penoncello S.G., Lemmon E.W., Thermodynamic Properties of Cryogenic Fluids. New York, USA: Plenum Publ. Corp.; 1997.

[7] Richter C.C., Proposal of New Object-Oriented Equation-Based Model Libraries for Thermodynamic Systems [dissertation]. Braunschweig, Germany: Technical University Carolo-Wilhelmina Braunschweig; 2008.

[8] Cardoso E., Passos J., Stutz B., Lallemand M., Confined boiling of n-pentane in a horizontal space. In: EBECEM 2008, Proceedings of the 1st Brazilian Meeting of Boling, Condensation and Multiphase Liquid-Gas Flow; 2008 Apr 28–29; Florianópolis, Brazil. ACBM-UFSC:1-6.

[9] Badami M., Mura M., Preliminary design and controlling strategies of a small-scale wood waste Rankine Cycle (RC) with a reciprocating steam engine (SE). Energy 2009; 34(9):1315–1324.

[10] Saul A., Wagner, W., International Equations for the Saturation Properties of Ordinary Water Substance. Journal of Physical and Chemical Reference Data 1987; 16(4):893–901.

[11] Wagner W., Pruss A., International Equations for the Saturation Properties of Ordinary Water Substance—Revised According to the International Temperature Scale of 1990. Journal of Physical and Chemical Reference Data 1993; 22(3):783–787.

[12] Papadopoulos A.I., Stijepovic M., Linke P., On the systematic design and selection of optimal working fluids for Organic Rankine Cycles. Applied Thermal Engineering 2010; 30(6-7):760-769.

[13] Drescher U., Brüggemann D., Fluid selection for the Organic Rankine Cycle (ORC) in biomass power and heat plants. Applied Thermal Engineering 2007; 27(1):223-228.

[14] Angelino G., Colonna P., Multicomponent working fluids for organic Rankine cycles (ORCs). Energy 1998; 23(6):449–463.

[15] Schuster A., Karellas S., Aumann R., Efficiency optimization potential in supercritical Organic Rankine Cycles. Energy 2010; 35(2):1033-1039.

Dynamic simulation of combined cycles operating in transient conditions: an innovative approach to determine the steam drums life consumption

Stefano Bracco

University of Genova - DIME
Via Montallegro 1, 16145 Genova, Italy
e-mail: stefano.bracco@unige.it, fax: +39-0-1921945104

Abstract:

The present study is relative to the dynamic simulation of heat recovery steam generators. In particular, the study is focused on the development of simulation models able to calculate thermal and mechanical stresses and, as a consequence, the low-cycle fatigue damage of high pressure steam drums in combined cycle systems.

The paper describes the mathematical model that the author has developed to estimate the useful life reduction of the high pressure steam drum belonging to a three pressure levels heat recovery steam generator. The aim of the present study is to propose a detailed calculation procedure useful to electrical energy producers that want to predict the steam drums useful life reduction, due to different transient operating conditions, in order to optimize plant load cycles.

The steam drum life reduction has been evaluated following the guidelines proposed by the EN 13445 Standard, and subjecting the uniaxial equivalent stress to the "rainflow cycle counting method" reported by the ASTM E 1049 Standard. As described in the paper, one of the innovations introduced by the author to apply the EN 13445 Standard is relative to the analytical method proposed to calculate the allowable number of fatigue cycles without using iterative formulas. Furthermore, it is important to say that the calculation tool can be used to estimate the life consumption of any steam drum of a combined cycle power plant; the model is characterized by low run times and high reliability. In fact, it has been successfully tested and validated taking into account experimental data from real power plants; the paper reports some calculation results that refer to typical transient operating conditions.

Keywords:

Combined cycles, Steam drum, Cycling, Life Consumption, Rainflow Method.

1. Introduction

In the liberalized electricity market, combined cycles power plants are subjected to frequent transient operating conditions during their useful life. The market awards power plants characterized by high flexibility and availability; as a consequence, energy companies have to plan their production schedules taking into account both technical and economical aspects, considering that it is profitable to run power plants especially when electricity prices are higher. As reported by Bracco and Trucco in [1], combined cycle power plants are suitable for operating in transient conditions since they are characterized by high flexibility and reduced startup and shutdown times. However, transient operating conditions, also called "cycling", result in high thermal and mechanical stresses in the plant components subjected to high temperature and pressure, such as the gas turbine, the steam turbine and both evaporators and superheaters of heat recovery steam generators (HRSGs); as a consequence, cycling conditions have to be analysed in order to estimate the plant useful life reduction and the relative aging costs, as suggested by Gallestey et al. in [2] and Lefton et al. in [3]. In particular, in [2] the authors describe a decision support system developed to estimate the effect of daily transient operations on the plant life and maintenance costs. It is

important to say that both design and capital costs increase for a power plant characterized by a high degree of cycling flexibility, availability and reliability. Electricity market requirements for flexible power plants are also very strict and they mainly refer to daily start-stop operation, low load operation and high start-up reliability; the goal is that of minimizing start-up duration and shutdown costs, without excessively decreasing the plant efficiency at partial loads.

Lefton et al. in [4] analyse the effect of fatigue on combined-cycle heat recovery steam generators. In particular, they report examples of tube failures in the HRSG and propose fatigue analysis methodologies and recommend cycling countermeasures. Furthermore, as suggested by Pasha et al. in [5] and Lefton et al. in [4] HRSGs manufacturers have to follow innovative design criteria and managing strategies, and to employ materials and welding procedures that can withstand high thermal stresses and, as suggested by Medekshas et al. in [6], great attention must be paid to the estimation of stress concentration factors due to the particular geometrical configuration of heat exchangers and tubes. As a consequence, it is also important to use instrumentation devices and on-line stress calculation tools able to monitoring the health status of the plant critical components.

In literature there are many research studies that report methodologies for predicting fatigue life of mechanical components [7-17]. Fatemi and Yang in [7] analyse the cumulative fatigue damage for homogeneous materials and report several life prediction theories, while Holman and Liaw in [8] describe the stress-life, local-strain and fracture mechanics methods to predict the life under constant or variable amplitude loading conditions. The authors in [8] also analyse the cycle counting methods necessary to estimate the life consumption in complex variable load histories; in particular, they refer to level-crossing counting, peak counting, simple-range counting, range-pair counting and the rainflow method, this last accurately described in the Appendix B of the present paper. Cycle counting methods are also analysed by Nieslony in [9], Langlais et al. in [10], Singh et al. in [11], Amzallag et al. in [12], Downing et al. in [13], and Glinka et al. in [14]. In particular, the ASTM E 1049 Standard [15] has to be taken into account in order to correctly apply the aforementioned techniques.

The present paper has been developed during ongoing research programs focused on innovative methods to control and manage combined cycle power plants operating in the liberalized electricity market. The focus of the research activities is on the dynamic simulation of combined cycles and, in particular, the goal of the study has been that of developing a simulator able to predict the behaviour of a three pressure levels HRSG under transient operating conditions in order to estimate the useful life reduction of the most critical components, such as the high pressure steam drum and superheater. The study is focused on the high pressure steam drum and it describes the model that has been developed in order to calculate the fatigue damage of the component. The model has been tested referring to literature results and taking into account experimental data from a real plant.

The present study derives from several research activities developed by the author since 2005 till today. The first step has been that of creating a dynamic simulation model of a combined cycle power plant characterized by a three pressure levels HRSG; the model, implemented in the Matlab/Simulink environment, is described in [18] by Bracco et al. In particular, in [18] the analysis is centred on the HRSG and its simulation model; the developed tool permits to calculate, as a function of time, the main physical quantities that describe the dynamic behaviour of the HRSG, such as temperature and enthalpy values for both the water/steam and the exhaust gas. The HRSG simulation model is accurately analysed by Bracco in [19] where several simulation results are reported.

The second step of the study has been that of developing a tool in order to estimate thermal and mechanical stresses, due to transient operating conditions, of the high pressure steam drum. In this regard, in [19] the author proposes a mathematical model to calculate the temperature and the thermo-mechanical stress distribution in the metal of steam drum; the relative simulator is illustrated by the author in [20-22].

The third phase of the study has been that of validating and testing the stress simulator using experimental data. Several results of the analysis are reported by Bracco in [19-22].

The forth step is relative to the development of a calculation procedure to estimate the fatigue life consumption of the steam drum metal parts. This work is accurately explained by Bracco in [23]. The life consumption model has been created following both the EN 13445 and the UNI EN 12952 Standards and applied to both the welded and unwelded zones of the component [24-28]. In [23] the author pays the attention to the calculation of stress concentration factors and reports some results for typical transient conditions, such as a warm start-up, a hot start-up, a shutdown and a load variation across the nominal steady state condition.

Finally, during the fifth phase of the study, that is described in the present paper, the author has further improved the steam drum life consumption calculation tool, taking into account two different aspects. First of all, the "rainflow counting method" has been applied in order to accurately identify the fatigue stress cycles to give as input to the life consumption calculation model. Secondarily, the life consumption calculation routine has been modified with the aim of determining the allowable number of fatigue cycles without using iterations; the new algorithm is innovative since it can be easily implemented on real time plant regulators giving as output important information, regarding the component residual life, in order to optimise load cycles without compromising the plant structural integrity.

2. The steam drum simulation model

In [19-22] the author reports the mathematical model that has been implemented in the Matlab/Simulink environment in order to simulate the heat transfer [29-31] through the metal and insulation parts of a high pressure steam drum belonging to a three pressure levels HRSG. More in detail, the mathematical model is based on the discretization of the Fourier's heat transfer equation written in cylindrical coordinates (r, θ, z); furthermore, due to the cylindrical symmetry of the component, the temperature is considered only as a function of radial coordinate and time [32]. The main equations used to calculate the temperature distribution and the thermo-mechanical stresses in the metal part of the steam drum are reported in Appendix A [31, 33-34].

The main inputs of the simulator are: 1) steam drum configuration data (length, inner diameter, metal thickness, insulation thickness), 2) materials data (thermal conductivity, specific heat, density, thermal diffusivity, Young's modulus - E_m, Poisson's ratio - υ, linear coefficient of thermal expansion - α_m), 3) heat transfer coefficients, 4) steam and ambient temperature as a function of time. On the other hand, the main outputs of the simulator are: 1) the temperature distribution inside both the metal and the insulation of the drum, 2) the thermal stresses (due to thermal gradients), 3) the mechanical stresses (due to steam pressure variation).

2.1. The equivalent stress calculation

As reported in [22-23, 33-34], the three principal structural stresses in the metal of the steam drum are calculated by applying the superposition principal to thermal and mechanical stresses (see Appendix A) as follows:

$$\sigma_{struc1} = \sigma_r^p + \sigma_r^T \qquad \sigma_{struc2} = \sigma_\theta^p + \sigma_\theta^T \qquad \sigma_{struc3} = \sigma_z^p + \sigma_z^T \tag{1}$$

The equivalent stress, in accordance with the Tresca's criterion, is then calculated:

$$\sigma_{Tresca} = max\left(\left|S_{12\,max} - S_{12\,min}\right|; \left|S_{23max} - S_{23\,min}\right|; \left|S_{31max} - S_{31min}\right|\right) \tag{2}$$

where the term S_{ij} indicates the difference between the i and j principal stresses reported in (1). It is important to remark that the sign of the maximum principal stress (in modulus) is utilised to give the sign to the Tresca equivalent stress. The simulator verifies, at each calculation time, if the

equivalent stress exceeds the allowable stress, which depends both on the material and the operating temperature.

2.2. The identification of fatigue cycles

Once having determined the signed Tresca equivalent stress, it is necessary to count the fatigue cycles. As explained in Section 1 there are several cycle counting methods; the most important calculation procedures are listed in the ASTM E 1049 Standard [15]. In the present study, the "rainflow counting method" has been chosen since, as suggested by Nieslony in [9], is one of the most popular and widely used algorithms. In particular, the guidelines reported in [15] and in [9] by Nieslony have been followed.

A Matlab model has been developed in order to implement the rainflow algorithm. The main inputs of the model are: 1) the signed Tresca equivalent stress as a function of time, 2) the metal temperature time history. As further explained in the Appendix B, in order to apply the algorithm, the Tresca stress signal is treated to individuate peaks and valleys. It is noted that, in accordance with the ASTM E 1049 Standard [15], a "peak" is a point at which the first derivative of the load-time history changes from a positive to a negative sign, whereas at a "valley" it changes from a negative to a positive sign. The main outputs of the model, for each identified fatigue cycle, are: 1) the stress range $\Delta\sigma$ (algebraic difference between the peak and valley values), 2) the mean value σ_m (algebraic average of the peak and valley values), 3) the value 0.5 if the stress range $\Delta\sigma$ is counted as a half cycle or the value 1 if it is counted as one cycle, 4) the cycle beginning time t_0, 5) the cycle period τ, 6) the average temperature T^* calculated as indicated by the EN 13445 Standard [24] and also reported by Bracco in [23].

3. The life consumption calculation model

The steam drum fatigue life consumption has been evaluated taking as reference the procedure reported by EN 13445 Standard [24] and Zeman et al. in [25], and extensively described by Bracco in [23]. The calculation has been done for both welded and unwelded zones. The results reported in this paper refer to the unwelded zones, that are the metal parts in the proximity of the risers and downcomers connections to the cylindrical part of the steam drum; for the present calculations, a stress concentration factor K_t equal to 3 has been assumed.

The life consumption calculation procedure has been implemented in the Matlab environment and it permits to calculate, for the i^{th} cycle identified by the rainflow counting method, the allowable number of fatigue cycles N_i by applying the following formula:

$$N_i = \left(\frac{46000}{\Delta\sigma_{Ri} - 0.63 \cdot R_m + 11.5} \right)^2 \tag{3}$$

where R_m is the material tensile strength while the stress range $\Delta\sigma_{Ri}$ depends on the stress range $\Delta\sigma_i$, which identifies each cycle, as follows:

$$\Delta\sigma_{Ri} = \frac{\Delta\sigma_f}{f_u} = \frac{K_f\left(K_t, \Delta\sigma_i, k_e, k_v, \Delta\sigma_D\right) \cdot \Delta\sigma_i \cdot k_e \cdot k_v}{f_u\left(N_i\right)} \tag{4}$$

In (4) K_f indicates the effective stress concentration factor; it depends on: the theoretical stress concentration factor K_t, the stress range $\Delta\sigma_i$, the plasticity correction factors k_e and k_v, and the

material endurance limit $\Delta\sigma_D$. The term f_u is an overall correction factor, which depends on: the thickness and roughness of the metal, the average temperature T^* of the ith cycle, and the mean equivalent stress σ_{mean} as defined in the EN 13445 Standard [24]. Furthermore, it is important to remark that, since the factor f_u is a function of the number of allowable cycles, the determination of N_i requires an iterative calculation.

3.1. The calculation of the allowable number of fatigue cycles

As anticipated in Section 1, to improve computational efficiency and to implement the procedure in plant regulators, the N_i calculation has been done developing a non-iterative algorithm. The main goal of the present paragraph is that of describing the steps of the proposed calculation method.

The main inputs of the calculation procedure, for the ith cycle, are: 1) the stress range $\Delta\sigma_i$, 2) the mean equivalent stress σ_{mi}, 3) the material tensile strength R_m evaluated at room temperature, 4) the material roughness R_z, 5) the material thickness e_n, 6) the average temperature T^*, 7) the theoretical stress concentration factor K_t. From these data it is possible to calculate, in accordance with the EN 13445 Standard, the following quantities: the yield strength $R_p=R_p(T^*)$, the endurance limit $\Delta\sigma_D=\Delta\sigma_D(R_m)$, the plasticity correction factors k_e and k_v which depend on $\Delta\sigma_i$ and R_p, the maximum stress $\sigma_{max}=\sigma_{max}(\Delta\sigma_i, \sigma_{mi})$, the correction factor $f_{T^*}=f_{T^*}(T^*)$ and the two terms:

$$F_s = 1 - 0.056 \cdot (ln\, R_z)^{0.64} \cdot ln\, R_m + 0.289 \cdot (ln\, R_z)^{0.53} \qquad F_e = \left(\frac{25}{e_n}\right)^{0.182} \tag{5}$$

which take into account the effects of the material roughness and thickness.

If $\Delta\sigma_i \le 2R_p$ and $-R_p \le \sigma_{mi} \le 0.5\cdot\Delta\sigma_{Ri}/(1+M)$, after some algebra the (3) becomes:

$$A_1 + \frac{B_1}{\sqrt{N_i}} + \frac{C_1}{N_i} - y^{-0.2\,ln\,N_i} = 0 \tag{6}$$

where:

$$\begin{aligned}
A_1 &= \frac{1}{(\Delta\sigma_f)^2 \cdot y^{0.93}} \cdot \left[0.63R_m - 11.5 - \frac{M\cdot(2+M)}{(1+M)} \cdot 2\sigma_{mean}\right] \cdot (f_{T^*})^2 \cdot (0.63R_m - 11.5) \\
B_1 &= \frac{46000}{(\Delta\sigma_f)^2 \cdot y^{0.93}} \cdot \left[2\cdot(0.63R_m - 11.5) - \frac{M\cdot(2+M)}{(1+M)} \cdot 2\sigma_{mean}\right] \cdot (f_{T^*})^2 \\
C_1 &= \frac{2.116\cdot 10^9}{(\Delta\sigma_f)^2 \cdot y^{0.93}} \cdot (f_{T^*})^2 \\
y &= F_s \cdot F_e
\end{aligned} \tag{7}$$

being $M=0.00035\cdot R_m-0.1$ and $\sigma_{mean}=\sigma_{mean}(R_p,\Delta\sigma_i)$.

If $\Delta\sigma_i \le 2R_p$ and $0.5\cdot\Delta\sigma_{Ri}/(1+M) \le \sigma_{mi} \le R_p$ the (3) becomes:

$$A_2 + \frac{B_2}{\sqrt{N_i}} - y^{-0.1\,ln\,N_i} = 0 \tag{8}$$

where:

$$A_2 = \frac{\left[\left(0.63R_m - 11.5\right)\cdot\left(\frac{1+M/3}{1+M}\right) - \frac{M}{3}\cdot 2\sigma_{mean}\right]\cdot f_{T^*}}{\Delta\sigma_f \cdot y^{0.465}} \qquad B_2 = \left(\frac{1+M/3}{1+M}\right)\cdot\frac{46000\cdot f_{T^*}}{\Delta\sigma_f \cdot y^{0.465}} \tag{9}$$

If $\Delta\sigma_i > 2R_p$ the (3) becomes:

$$A_3 + \frac{B_3}{\sqrt{N_i}} - y^{-0.1\ln N i} = 0 \tag{10}$$

where:

$$A_3 = \frac{1}{\Delta\sigma_f \cdot y^{0.465}}\cdot f_{T^*}\cdot\left(0.63R_m - 11.5\right) \qquad B_3 = \frac{1}{\Delta\sigma_f \cdot y^{0.465}}\cdot 46000\cdot f_{T^*} \tag{11}$$

Equations (6), (8) and (10) can be written in the general form:

$$F_j\left(N_i\right) = A_j + \frac{B_j}{\sqrt{N_i}} + \frac{C_j}{N_i} - y^{-\lambda j \ln N i} = 0 \tag{12}$$

having the solution:

$$N_i = \left(-\frac{\alpha_j}{\beta_j}\right)^{1/\gamma j} \tag{13}$$

The terms α_j, β_j and γ_j derive, after a little algebra, from the calculation of the (12) in three different points: x_1 and x_3 chosen by the user and $x_2 = x_1\sqrt{x_3 / x_1}$.

More in detail:

$$\gamma_j = \frac{ln\left[\frac{F_j(x_3) - F_j(x_2)}{F_j(x_2) - F_j(x_1)}\right]}{ln\left(\sqrt{\frac{x_3}{x_1}}\right)} \qquad \beta_j = \frac{F_j(x_3) - F_j(x_1)}{x_3^{\gamma j} - x_1^{\gamma j}} \qquad \alpha_j = F_j(x_2) - \beta_j \cdot x_2^{\gamma j} \tag{14}$$

After having estimated the allowable number of fatigue cycles N_i for the i^{th} cycle, it results that the "cumulative fatigue damage index" D for the examined component can be calculated, as also reported by the author in [23], by applying the Palmgren-Miner rule which suggests to sum the "fatigue damage index" values (LC_i) as follows:

$$D = \sum_{i=1}^{m} LC_i = \sum_{i=1}^{m}\left(\frac{n_i}{N_i}\right) \tag{15}$$

where n_i indicates how many times the i^{th} cycle occurs during the useful life of the component (m being the number of transient conditions taken into account by the fatigue analysis).

4. The analysis of some typical transient conditions

Both the steam drum simulation model and the life consumption calculation procedure, respectively described in Section 2 and 3, have been applied to study some typical transient conditions to which a combined cycle power plant is subjected. In particular, in this paper the author pays the attention on the following three transient conditions: a cold, a warm and a hot start-up; the simulation results refer to a steam drum characterized by: 2 m inner diameter, 13 m length, 0.09 m metal thickness, 122 bar nominal pressure. For each of the aforementioned operating conditions, an accurate analysis has been done in order to calculate: 1) the temperature distribution in the metal and insulation parts of the steam drum, 2) the thermal and mechanical stresses in the metal parts, 3) the Tresca equivalent stress, 4) the life consumption of the component consequent to each load cycle identified by the rainflow counting method applied to the signed Tresca equivalent stress.

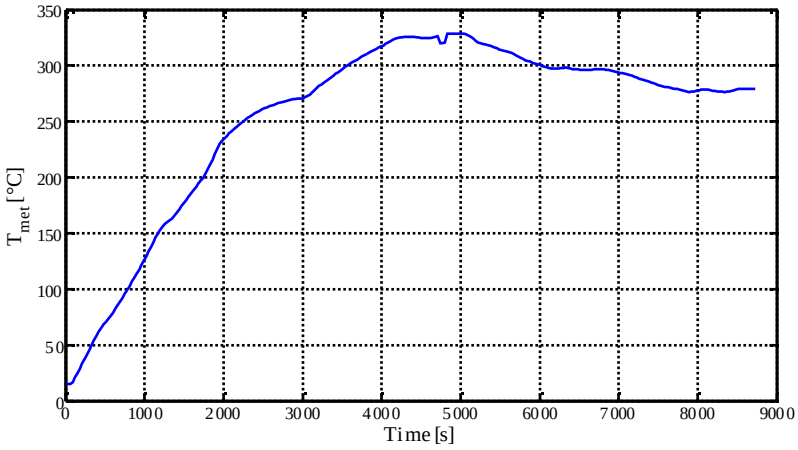

Fig. 1. The metal temperature during the cold start-up.

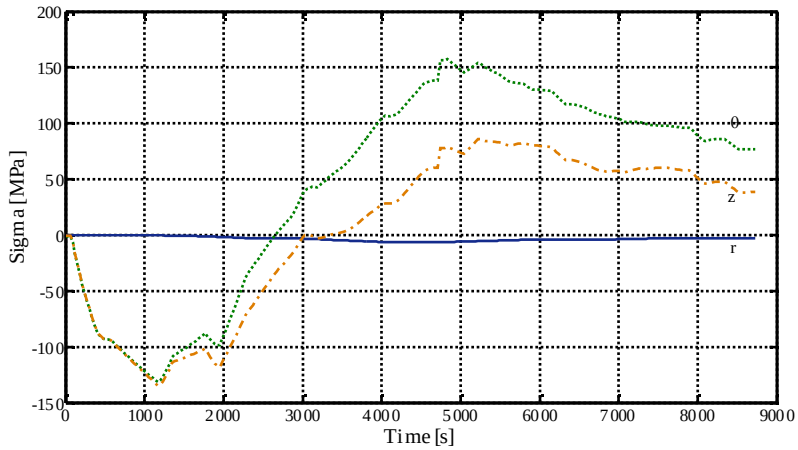

Fig. 2. The principal structural stresses (cold start-up).

In Fig. 1 the temperature of the more stressed metal layer is depicted as a function of time; Fig. 2 shows the three main principal stresses while in Fig. 3 the signed Tresca equivalent stress is represented. The stem plot in Fig. 4 displays the stress range $\Delta\sigma$ values of the cycles counted by the rainflow algorithm, as explained in the Appendix B. The calculation results for the more significant cycles (F1, F2, F3, F4 and F5), characterized by higher $\Delta\sigma$ values, are reported in Tab. 1; it results that only the F4 cycle gives an important contribution to the steam drum life degradation, since it is

characterized by the lower allowable number of fatigue cycles N_i. In Tab. 1 the "fatigue damage index" values (LC_i) are also reported.

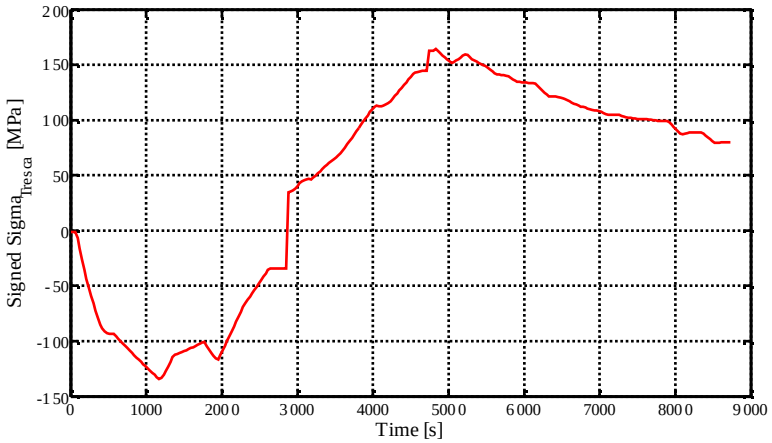

Fig. 3. The signed Tresca equivalent stress (cold start-up).

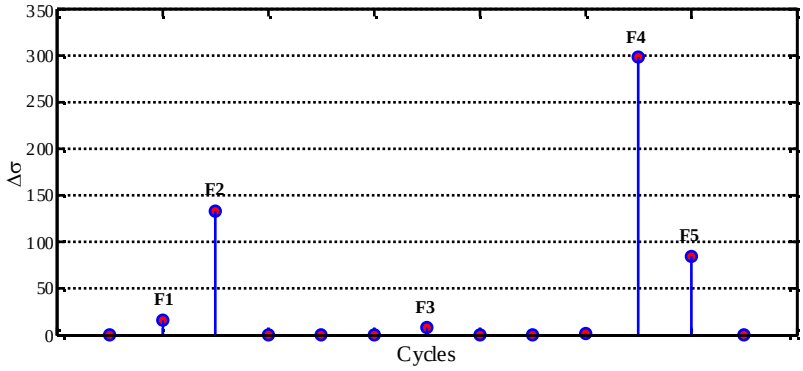

Fig. 4. The stress range $\Delta\sigma$ values of the cycles identified by the rainflow counting algorithm (cold start-up).

Table 1. Results of the rainflow counting method applied to the cold start-up

	F1	F2	F3	F4	F5
$\Delta\sigma$[MPa]	16.2	133.2	8.0	298.6	84.6
σ_m [MPa]	-108.5	-67.9	155.6	14.8	121.8
cycle	1	0.5	1	0.5	0.5
t_0 [s]	1770	60	5040	1170	4830
τ [s]	360	2220	360	7320	7380
T^* [°C]	233.0	116.4	325.8	284.0	315.7
N_i	∞	55800	∞	4670	163000
LC_i	0	1.79E-05	0	2.14E-04	6.1E-06

In Figs. 5 to 6 the metal temperature time history is plotted, respectively for the warm and the hot start-up. The results of the rainflow counting method and fatigue damage evaluation are listed in Tabs. 2 to 3, considering for the two cases the most significant cycles. The hot start-up is the transient condition which determines a lower fatigue damage.

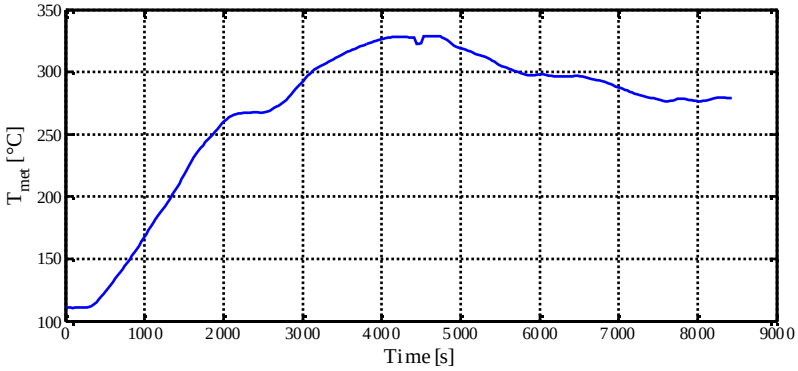

Fig. 5. The metal temperature during the warm start-up.

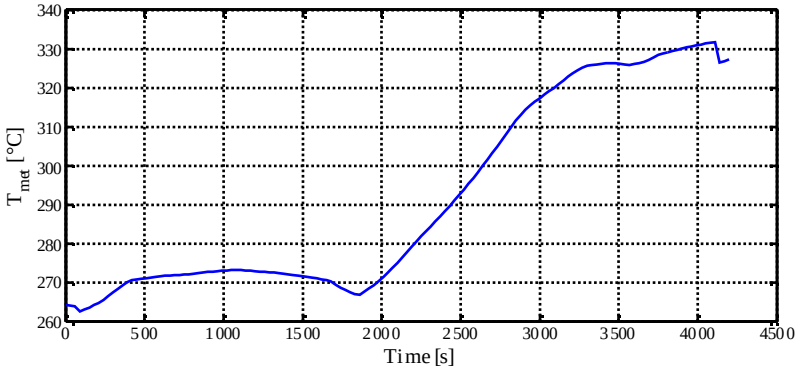

Fig. 6. The metal temperature during the hot start-up.

Table 2. Results of the rainflow counting method applied to the warm start-up

	T1	T2	T3	T4
$\Delta\sigma$ [MPa]	93.2	8.0	255.6	84.6
σ_m [MPa]	-44.9	155.6	36.3	121.8
cycle	0.5	1	0.5	0.5
t_0 [s]	90	4740	1590	4485
τ [s]	3000	360	5790	7470
T^* [°C]	198.6	325.8	303.2	315.7
N_i	393000	∞	5980	163000
LC_i	2.5E-06	0	1.67E-04	6.1E-06

Table 3. Results of the rainflow counting method applied to the hot start-up

	C1	C2	C3	C4
$\Delta\sigma$ [MPa]	5.9	10.5	12.7	106.5
σ_m [MPa]	68.3	66.0	76.9	114.0
cycle	0.5	0.5	1	0.5
t_0 [s]	30	210	1830	420
τ [s]	360	420	720	7500
T^* [°C]	264.2	269.1	288.2	315.5
N_i	∞	∞	∞	50700
LC_i	0	0	0	1.97E-05

Conclusion

In the present paper the topic of the life consumption of combined cycle power plants has been discussed, focusing on high pressure steam drums. A simulation model has been developed and

tested to determine the thermal and mechanical stresses in the metal parts of a steam drum. The paper describes the calculation procedure that has been used to quantify the fatigue damage consequent to transient operating conditions. In order to estimate the consumed life of the component, the EN 13445 Standard has been applied using an innovative approach to determine, without iterative formulas, the allowable number of fatigue cycles; in the developed model the rainflow counting method has been used too, since it has been necessary to reduce the load time history into a set of simple stress cycles each characterized by a certain amplitude.

The life consumption model is characterized by lower run times and it can be used in real time to estimate the residual life of any steam drum.

Acknowledgments

Acknowledgments to Ansaldo Energia SpA for having supplied experimental data.

Appendix A

In the developed mathematical model, a simplified configuration of the steam drum has been adopted: it consists of two coaxial cylinders, the inner for the metal (characterized by internal and external radius respectively equal to r_{int} and r^*) and the outer for the insulation. The Fourier's heat conduction equation has been applied in order to calculate the temperature values inside both the metal and the insulation of the drum:

$$\frac{\partial^2 T}{\partial r^2}+\frac{1}{r}\cdot\frac{\partial T}{\partial r}=\frac{1}{a}\cdot\frac{\partial T}{\partial t} \tag{A.1}$$

where, due to the cylindrical symmetry of the component, the temperature is considered only as a function of the radial coordinate r and time t. A finite differences model has been developed in order to implement the Fourier's equation in the Matlab/Simulink environment; the metal part of the steam drum has been discretized in coaxial cylindrical layers, for each of which the mechanical and the thermal principal stresses (radial, circumferential and axial) have been calculated by means of the formulas respectively reported by (A.2) and (A.3).

$$\begin{aligned}
\sigma_r^p(r_i)&=\frac{p_{\text{int}}\cdot r_{\text{int}}^2-p^*\cdot r^{*2}}{r^{*2}-r_{\text{int}}^2}+\left(p^*-p_{\text{int}}\right)\cdot\frac{r_{\text{int}}^2\cdot r^{*2}}{r_i^2\cdot\left(r^{*2}-r_{\text{int}}^2\right)}\\
\sigma_\theta^p(r_i)&=\frac{p_{\text{int}}\cdot r_{\text{int}}^2-p^*\cdot r^{*2}}{r^{*2}-r_{\text{int}}^2}-\left(p^*-p_{\text{int}}\right)\cdot\frac{r_{\text{int}}^2\cdot r^{*2}}{r_i^2\cdot\left(r^{*2}-r_{\text{int}}^2\right)}\\
\sigma_z^p(r_i)&=\frac{p_{\text{int}}\cdot r_{\text{int}}^2-p^*\cdot r^{*2}}{r^{*2}-r_{\text{int}}^2}
\end{aligned} \tag{A.2}$$

$$\begin{aligned}
\sigma_r^T(r_i)&=\frac{\alpha_m\cdot E_m}{(1-\upsilon)}\cdot\frac{1}{r_i^2}\cdot\left(\frac{r_i^2-r_{\text{int}}^2}{r^{*2}-r_{\text{int}}^2}\cdot\int_{r_{\text{int}}}^{r^*}T\cdot r dr-\int_{r_{\text{int}}}^{r_i}T\cdot r dr\right)\\
\sigma_\theta^T(r_i)&=\frac{\alpha_m\cdot E_m}{(1-\upsilon)}\cdot\frac{1}{r_i^2}\cdot\left(\frac{r_i^2+r_{\text{int}}^2}{r^{*2}-r_{\text{int}}^2}\cdot\int_{r_{\text{int}}}^{r^*}T\cdot r dr+\int_{r_{\text{int}}}^{r_i}T\cdot r dr-T\cdot r_i^2\right)\\
\sigma_z^T(r_i)&=\frac{\alpha_m\cdot E_m}{(1-\upsilon)}\cdot\left(\frac{2}{r^{*2}-r_{\text{int}}^2}\cdot\int_{r_{\text{int}}}^{r^*}T\cdot r dr-T\right)
\end{aligned} \tag{A.3}$$

Appendix B

In order to count the fatigue cycles the "rainflow counting method" has been applied, following the guidelines indicated in the ASTM E 1049 Standard [15]. In Fig. B.1 the rainflow algorithm is schematically described, while in Fig. B.2 an example of the calculation is reported.

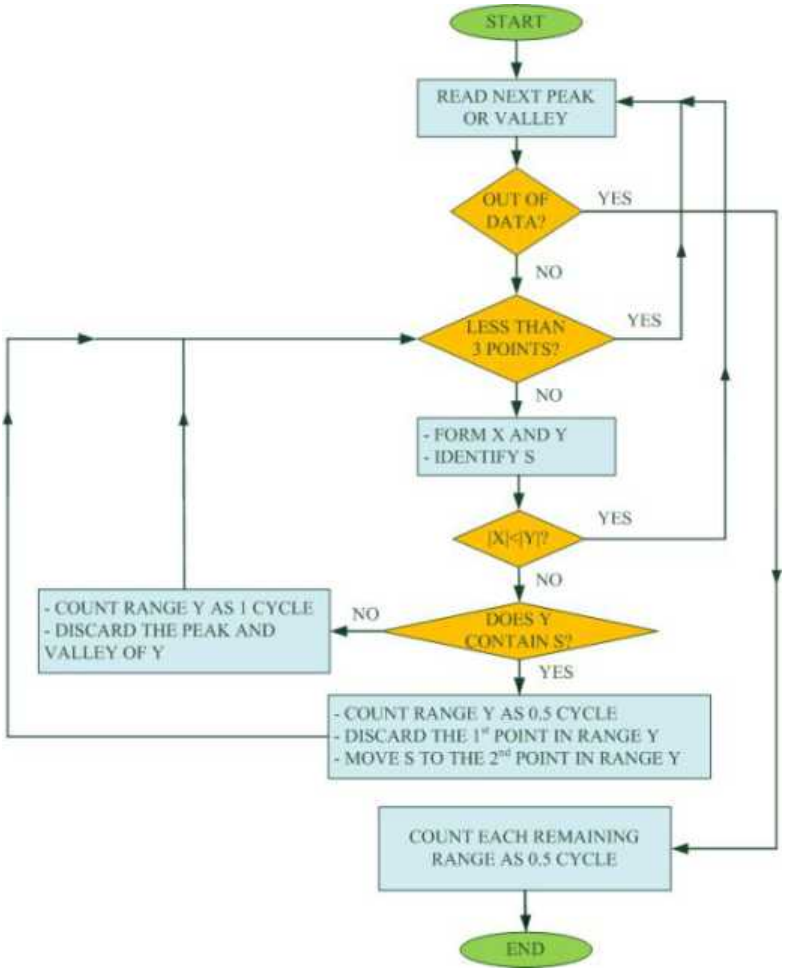

Fig. B.1. The rainflow counting algorithm.

The main input of the rainflow algorithm is the signed Tresca equivalent stress. First of all, the Tresca equivalent stress time history is filtered in order to identify peaks and valleys (points A, B, C, D, E, F, G, H, I in Fig. B.2). Then the algorithm treats three points at a time (e.g. A, B and C at the beginning of the calculation) and it is based on the comparison between two successive stress ranges, denoted respectively by *X* (range under consideration, e.g. B-C segment) and *Y* (previous range adjacent to *X*, e.g. A-B segment); the letter *S* identifies the starting point which moves forward in time (at t=0 *S* coincides with the first point, peak or valley, of the load history). As visible in Fig. B.1, if *Y* is greater than *X* the first in time of the three points is discarded and a new peak or valley is read; on the other hand if *X* is greater than *Y*, this last is counted as a half cycle, in case of *Y* containing *S*, or as one cycle if *Y* does not contain *S*. The algorithm ends by counting as one-half cycle each stress range that has not been previously counted.

In Fig. B.2 the application of the rainflow counting method to a general load history is described. In particular, Fig. B.2.1 shows the load time history, Fig. B.2.2 indicates the identification of peaks and valley, whereas the remaining figures are relative to the cycles counting procedure. As listed in Tab. B.1, the load ranges B-C, G-H and E-F are each counted as one cycle, while the ranges A-D and D-I are each counted as one-half cycle. Furthermore, for each counted cycle the Tab. B.1 also

reports: the stress range, the mean stress, the beginning time t_0 and the period τ.

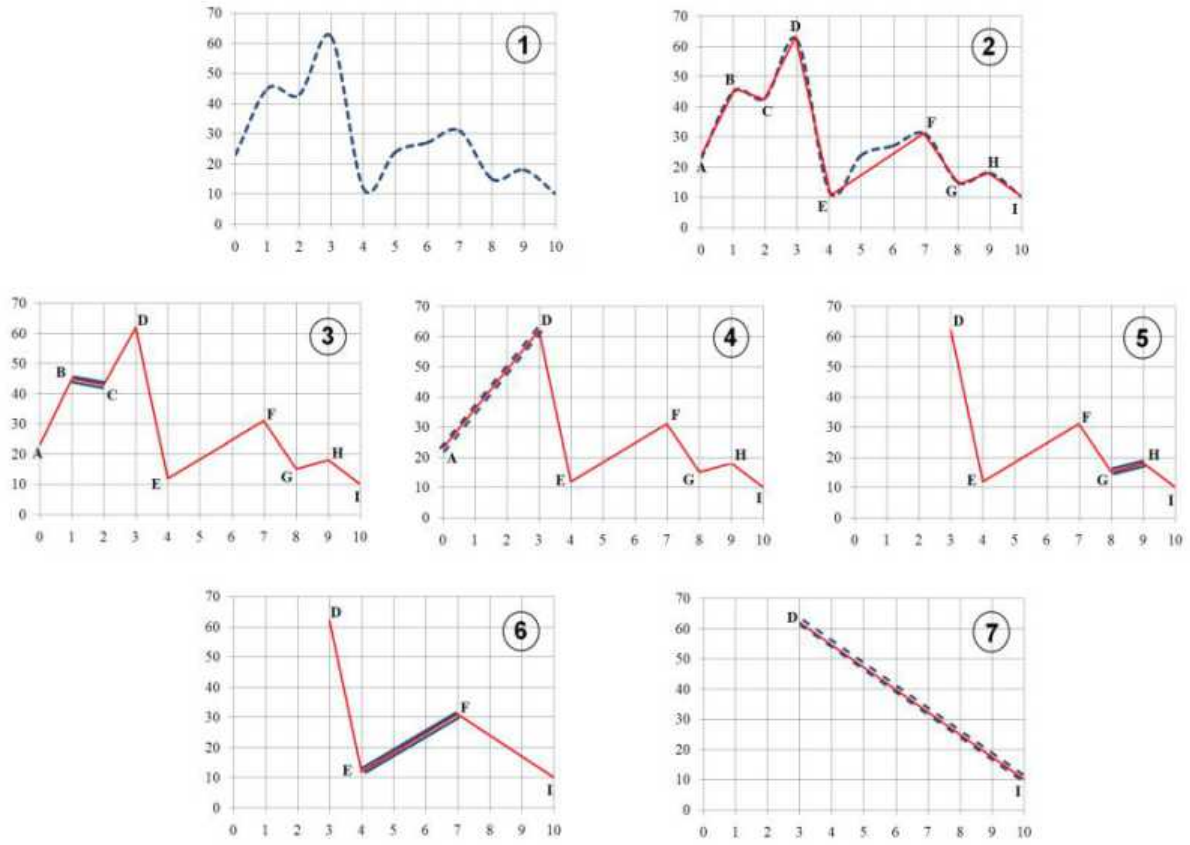

Fig. B.2. The rainflow counting method: an example.

Table B.1. Results of the rainflow counting example

	B-C	A-D	G-H	E-F	D-I
$\Delta\sigma$ [MPa]	2	39	3	19	52
σ_m [MPa]	44	42.5	16.5	21.5	36
cycle	1	0.5	1	1	0.5
t_0 [s]	1	0	8	4	3
τ [s]	2	6	2	6	14

Nomenclature

Symbols:

a	thermal diffusivity, m^2/s
D	cumulative fatigue damage index
E_m	Young's modulus
e_n	thickness, mm
f_{T^*}, f_u	correction factors
K_f, K_t	stress concentration factors
LC	fatigue damage index
N	allowable number of fatigue cycles
n	number of applied stress cycles
p	pressure, MPa

R_m, R_p tensile, yield strength, MPa

R_z material roughness, μm

r radial coordinate, m

T temperature, °C

t time, s

Greek symbols

α_m coefficient of thermal expansion, K^{-1}

σ stress, MPa

$\Delta\sigma$ cycle stress range, MPa

$\Delta\sigma_D$ endurance limit, MPa

$\Delta\sigma_f$ effective equivalent stress range, MPa

$\Delta\sigma_R$ stress range of fatigue curves, MPa

τ period, s

υ Poisson's ratio

Subscripts

r, θ, z radial, circumferential, axial

struc structural

Superscripts

p pressure

T temperature

References

[1] Bracco S., Trucco A., Thermoelectric Power Plants in the Deregulated Electricity Market: Electricity Production Costs and Sales Revenues Evaluation Model. Proceedings of II AIGE Conference; 2008 September 4-5; Pisa, Italy.

[2] Gallestey E., Stothert A., Antoine M., Morton S., Model predictive control and the optimisation of power plant load while considering lifetime consumption. IEEE Transactions on Power Systems 2002; 17(1): 186-191.

[3] Lefton S.A., Besuner P.M., Agan D.D., The real cost of on/off cycling. Modern Power Systems; October 2006: 11-13.

[4] Lefton S.A., Besuner P.M., Grimsrud G.P., Agan D.D., Grover J.L., Analysis of cycling impacts on combined-cycle heat recovery steam generators and evaluating future costs of countermeasures to reduce impacts. ENERGY-TECH.com April 2009; ASME Power Division Special Section: 25-29.

[5] Pasha A., Allen R., Design and Modification of Heat Recovery Steam Generators for Cycling Operations. Vogt-NEM Inc.; 2005.

[6] Medekshas H., Balina V., Assessment of low cycle fatigue strength of notched components. Materials and Design 2006; 27: 132-140.

[7] Fatemi A., Yang L., Cumulative fatigue damage and life prediction theories: a survey of the state of the art for homogeneous materials. Int. J. Fatigue 1998; 20(1): 9-34.

[8] Holman R.K., Liaw P.K., Methodologies for predicting fatigue life. 1997.

[9] Nieslony A., Determination of fragments of multiaxial service loading strongly influencing the fatigue of machine components. Mechanical Systems and Signal Processing 2009; 23: 2712-2721.

[10] Langlais T.E., Vogel J.H., Chase T.R., Multiaxial cycle counting for critical plane methods. Int. J. of Fatigue 2004; 25: 641-647.

[11] Singh K.L., Ranganath V.R., Cycle counting using rainflow algorithm for fatigue analysis.

[12] Amzallag C., Gerey J.P., Robert J.L., Bahuadt J., Standardization of the rainflow counting method for fatigue analysis. Int. J. of Fatigue 1994; 16: 287-293.

[13] Downing S.D., Socie D.F., Simple rainflow algorithm, Int. J. of Fatigue 1982; 4(1): 31-40.

[14] Glinka G., Kam J.C.P., Rainflow counting algorithm for very long stress histories. Int. J. of Fatigue 1987; 9(4): 223-228.

[15] ASTM, E 1049 – 85 Standard Practices for Cycle Counting in Fatigue Analysis. 100 Barr Harbor Dr., West Conshohocken, PA 19428; 1997.

[16] Habib M.A., Al-Zaharnah I., El-Shafei M. et al., Influence of boiler load swing rates on effective stresses of drum boiler riser tubes. Journal of Pressure Vessel Technology 2010; 132.

[17] Cronvall O., Tuurna S., Talja H. at al., Structural Analysis and Lifetime Assessment of Steam Drums. Proc. Baltica VI; 2004; I: 245-259.

[18] Bracco S., Crosa G., Trucco A., Dynamic Simulator of a Combined Cycle Power Plant: Focus on the Heat Recovery Steam Generator. ECOS 2007: Proceedings of the 20th International Conference on Efficiency, Cost, Optimization, Simulation, and Environmental Impact of Energy Systems; 2007 June 25-28; Padova, Italy.

[19] Bracco S., Dynamic Simulation and Useful Life Consumption Evaluation of Combined Cycle Power Plants in the Deregulated Electricity Market [Ph.D. Thesis]. Genova, Italy; 2008.

[20] Bracco S., Simulation models of steam drums based on the heat transfer equations. Applied Mathematical Sciences 2010; 74(4): 3687-3712.

[21] Bracco S., Steady-state and Dynamic Heat Transfer in Steam Drums of Combined Cycle Power Plants: Mathematical and Simulation Model. ICNPAA08: Proceedings of the International Conference on Mathematical Problems in Engineering, Aerospace and Sciences; 2008 June 25-27; Genova, Italy.

[22] Bracco S., Traverso F., Trucco A., The Effects of Thermal Transient Conditions on a Steam Drum in a Heat Recovery Steam. 65° ATI National Congress ; 2010 September 13-17; Italy.

[23] Bracco S., Thermal Stress in Steam Drums: Life Consumption Model. UIT2011: Proceedings of the XXIX UIT Conference on Heat Transfer; 2011 June 20-22; Torino, Italy.

[24] European Committee For Standardization, EN 13445 – Part 3, Unfired Pressure Vessels, Clause 17 (Simplified Assessment of Fatigue Life) and Clause 18 (Detailed Assessment of Fatigue Life); 2002.

[25] Zeman J.L., Pressure Vessel Design – The Direct Route. Elsevier Ltd; 2006.

[26] Fontaine P., Galopin J.F., HRSG optimisation for cycling duty based on Euro Norm EN 12952-3, Proc. of PowerGen Europe, 2007.

[27] European Committee For Standardization, EN 12952 – Part 3, Water Tube Boilers and Auxiliary Installations; December 2001 Edition.

[28] Baylac G., Koplewicz D., EN 13445 Unfired pressure vessels - background to the rules in Part 3 Design, UNM; 2004.

[29] Bohn M., Kreith F., Principles of heat transfer. Thomson Learning College; 2000.

[30] Kern D.Q., Process heat transfer. McGraw-Hill Inc.; 1990.

[31] Annaratone D., Engineering heat transfer. New York: Springer Berlin Heidelberg; 2010.

[32] Kim T.S., Lee D.K., Ro S.T., Analysis of thermal stress evolution in the steam drum during start-up of a heat recovery steam generator. Applied Thermal Engineering 2000; 20: 977–992.

[33] Annaratone D., Pressure vessel design. New York: Springer Berlin Heidelberg; 2007.

[34] Timoshenko S.P., Woinowsky-Krieger S., Theory of plates and shells. International Student Edition; 1959.

Effect of auxiliary electrical power consumptions on Organic Rankine Cycle system with low-temperature waste heat source

Samer Maalouf[a], Elias BouLawz Ksayer[a], Denis Clodic[a]

[a] *Ecole des Mines de Paris, Center for Energy and Processes, 5 rue Leon Blum, Palaiseau, France*
samer.maalouf@mines-paristech.fr
elias.boulawz_ksayer@mines-paristech.fr
denis.clodic@mines-paristech.fr

Abstract:

The valorization of low-temperature waste heat (< 120°C) into electricity within industrial processes undoubtedly plays a crucial role in improving overall energy efficiency of industrial processes. Organic Rankine Cycle (ORC) using organic fluid in converting low-grade energy is investigated in this study. For wet gas heat sources, i.e. high moisture contents ($T_{water\ dew\ point}$ > 50°C), the optimal evaporation temperature at which the overall efficiency is maximal is below the corresponding water dew point temperatures; then a latent heat will be released from the heat source in the boiler leading to high working fluid mass flow rate in the ORC system, involving a high cold water mass flow rate for the condenser. Thus, the overall efficiency of the ORC system will be significantly impacted by the auxiliary electrical power consumptions of the cold water source for the condenser and can be reduced by about a factor 2 when using a cooling tower to cool the water for the condenser. Therefore, the main purpose is to reduce the auxiliary electrical power consumptions by creating a temperature glide in the heat exchangers using an appropriate refrigerant blend as working fluid instead of a pure working fluid. Results show that a refrigerant blend of R-1234yf and R-245fa is the most promising ORC working fluid for the present application. For an ORC using a heat source with an inlet dry temperature of 110°C and water dew point temperature of 60°C for the boiler, and a cooling tower as a cold source for the condenser, an R-1234yf/R-245fa blend at its optimized mole fractions increases the ORC overall efficiency by about 46% compared to R-1234yf (pure working fluid).

Keywords:

Auxiliary electrical power consumptions, Blend working fluid, Low temperature heat source, ORC system, Pure working fluid.

1. Introduction

Many heat sources at low temperature (< 120°C) such as flue gases at cement mill exit are available and wasted into the atmosphere. These heat sources are classified as low-grade heat sources and can be valorized towards electricity production. The investigated conversion cycle is the Organic Rankine Cycle (ORC) technology for its high efficiency at low-temperature heat source. The ORC is a power generation cycle that uses organic fluids instead of water as working fluid and that can be adapted to a large temperature range to produce electricity, primarily for energy at low temperature, e.g. below 120°C. However, generating power from heat sources below 120°C is a challenging task as the thermodynamic maximum represented by the Carnot factor states that efficiency is only 25%. State-of-the-art of current applications of heat valorization have overall electrical efficiencies between 3 and 5%, because of various losses, e.g. heat transfer losses, friction losses, leakage in the turbine, and other losses. Moreover, this

efficiency will be greatly affected by the auxiliary electrical power consumptions, especially when generating power using a wet heat source ($T_{water\ dew\ point} > 50°C$) for the boiler.

Several research studies were mainly focused on low-grade heat ORC. Madhawa et al. [13] based their study on the exergy approach to parameterize properly ORCs for geothermal applications. Wei et al. [15] conducted a performance analysis and optimization of an ORC using R-245fa as working fluid driven by exhaust heat to maximize its recovery in order to improve the system output net power and efficiency. The choice of the working fluid has a significant influence on the system overall efficiency. A number of authors investigated the selection of pure working fluids. Liu et al. [12] analyzed the performance of several working fluids of ORC adapted to waste heat applications. Hung et al. [8] show that the slopes and the shapes of the saturation vapor curve of fluids have a primary effect on the performance and on the architecture of the ORC where the isentropic fluids seem to be the most suitable type of working fluid for recovering low-temperature waste heat. Hung et al. [9] studied the effect of wet and dry fluids on the ORC performance at low-grade temperature. Results indicate that wet fluids with very steep saturated vapor curves in T-s diagram present a better overall performance in energy conversion efficiencies than that of dry fluids.

An interesting approach to optimize the cycle efficiency and electrical power output of the power plant is the use of zeotropic mixtures as working fluids [1]. For those blends, a temperature glide at phase change occurs, which provides a good match of temperature profiles in the condenser and boiler. Heberle et al. [7] detailed simulations of ORC for energy conversion of low-enthalpy geothermal resources using a zeotropic blend as working fluid. It was shown that the use of blends as working fluids leads to an efficiency increase compared to pure fluids, due to a glide match of temperature profiles in the condenser and boiler. Bleim [3] investigated the use of R-114/R-22 for geothermal power generation. The blend shows higher efficiency, between 3% and 8%, compared to R-114.

In this study, the analyzed heat source is characterized by an inlet temperature of 110°C and a water dew point temperature of 60°C. After identifying the exergy potential of the analyzed heat source, the effects of auxiliary electrical power consumptions of the cold water source for the condenser on the ORC parameters are shown. Finally, the effect of using blends as working fluids on the overall system efficiency is studied in order to reduce the auxiliary electrical power consumptions by providing a good match of temperature profiles in the condenser and evaporator.

2. Potential evaluation of low-temperature wet heat sources

The aim of this section is to quantify the energy and exergy potentials, and the ideal efficiencies of the heat source. Analyzing the exergy potential is a good measurement to identify the overall potential for electricity production of a given heat source. The heat source, characterizing the temperature and the available quantity of heat onto a temperature of 20°C, is presented in Fig. 1. This figure shows a breakage shape within the curve at the water dew point. A large amount of heat within the streams is in the form of latent heat and can only be recovered by condensing the water vapor [16]. In order to identify the amount of energy available for conversion into work, the temperature is replaced by the Carnot-Factor. The Carnot-Factor (1) is calculated between the measured temperature and the ambient temperature [4]. Fig. 1 shows the Carnot-Factor vs. the heat load for the studied heat source. The surface under the Carnot-factor curve represents the

available exergy [10]. As the exergy is the work that could be extracted by a perfect cycle, it is a good measurement to identify the overall potentials for electricity production of a heat source.

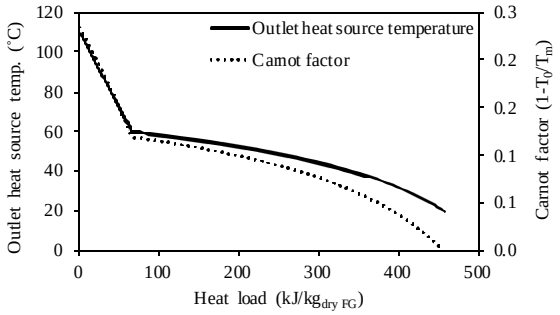

Fig. 1. Outlet heat source temperature and Carnot factor vs. available heat load.

$$Carnot - Factor = 1 - T_o / T_m \qquad (1)$$

Where $T_m = \Delta h / \Delta s$; Δh and Δs are respectively the enthalpy and entropy differences and are calculated for 1-K gas cooling.

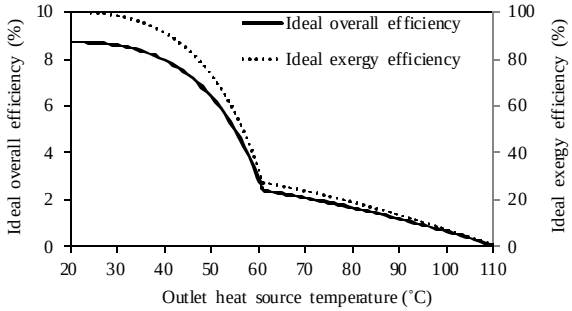

Fig. 2. Ideal overall & exergy efficiencies vs. outlet heat source temperature.

The ideal overall and ideal exergy efficiencies for the studied heat source are shown in Fig. 2. The ideal overall efficiency (2) is the maximal overall efficiency that can be reached into a conversion cycle; it is equal to the amount of energy available for transformation into work (exergy) over the maximal heat load released by the heat source by cooling it down to the ambient temperature. The ideal exergy efficiency (3) is equal to the amount of energy that is available for transformation into work (exergy) over the maximal exergy availability obtained by cooling down the heat source to the ambient temperature. From Fig. 2, a maximal ideal overall efficiency of 8.7% can be reached for the studied heat source.

$$\eta_{overall\ ideal} = Ex_{available,FG} / Q_{\max,FG} \qquad (2)$$

$$\eta_{exergy\ ideal} = Ex_{available,FG} / Ex_{available\ \max,FG} \qquad (3)$$

In (2) and (3), the available exergy, the maximal available exergy, and the maximal heat load released by the heat source are given respectively by:

$$Ex_{available,FG} = m_{FG}\left[(h_{in,FG} - T_o.s_{in,FG}) - (h_{out,FG} - T_o.s_{out,FG})\right] \qquad (4)$$

$$Ex_{available\ \max,FG} = m_{FG}\left[(h_{in,FG} - T_o.s_{in,FG}) - (h_o - T_o.s_o)\right] \quad (5)$$

$$Q_{\max,FG} = m_{FG}(h_{in,FG} - h_o) \quad (6)$$

3. Cooling configurations and process parameters for ORC

Organic Rankine Cycle (ORC) is a power generation cycle that uses organic fluids instead of water as a working fluid. The ORC interest is its ability to adapt to a large temperature range to generate power from heat source at low temperature, e.g. below 120°C.

The evolution of the working fluid into the ORC consists of four operations (Figs 3.a & 3.b). The working fluid, sub-cooled liquid at the condenser outlet (point 1) is compressed by a pump from low to high pressure to enter the boiler (point 2). The high-pressure liquid enters the boiler in liquid phase where it is heated and vaporized at constant pressure by the entering flue gases. The vapor at the boiler exit (point 3) expands through the turbine and generates power. Finally, the vapor enters the condenser (point 4) where it is condensed at constant pressure.

(a) *(b)*

Fig. 3. Simple ORC: a) Schematic diagram, b) (T-s) diagram.

The boiler and condenser capacities are given respectively by:

$$Q_{boiler} = m_r(h_3 - h_2) \quad (7)$$

$$Q_{condenser} = m_r(h_4 - h_1) \quad (8)$$

The turbine and pump powers are expressed respectively by:

$$W_{turbine} = m_r(h_3 - h_4) \quad (9)$$

$$W_{pump} = m_r(h_2 - h_1) \quad (10)$$

The system efficiency is the ratio between the net generated power and the heat capacity transferred in the boiler:

$$\eta_{system} = W_{net}/Q_{boiler} \quad (11)$$

The net generated power is given by:

$$W_{net} = W_{turbine} - W_{pump} - W_{auxiliary\ consumptions} \quad (12)$$

The extraction efficiency of the heat from flue gases (or flue gas efficiency) is defined by:

$$\eta_{FG} = Q_{FG}/Q_{\max,FG} \quad (13)$$

Where in (13), the maximal heat that can be extracted from flue gases is given by (6) and the heat extracted from FG is given by:

$$Q_{FG} = m_{FG}(h_{in,FG} - h_{out,FG}) \quad (14)$$

The overall efficiency is given by:

$$\eta_{overall} = W_{net} / Q_{\max,FG} \quad (15)$$

The overall efficiency can also be written as:

$$\eta_{overall} = \eta_{system} \cdot \eta_{FG} \quad (16)$$

The global exergy efficiency is given by [2]:

$$\eta_{global\ exergy} = W_{net} / Ex_{available\ \max,FG} \quad (17)$$

The thermodynamic properties of the working fluids are calculated using REFPROP 9 developed by the NIST [11].

The auxiliary electrical consumptions generated by the cold source for the condenser are crucial in the evaluation of the optimal operating parameters since the overall efficiency of ORC using heat source below 120°C is relatively low (less than 5%).

Three main configurations for the ORC cold water source are studied (Fig. 4):

- ORC with configuration 1: the cold source for the condenser is not taken into account
- ORC with configuration 2: the cold source for the condenser is either river water or sea water
- ORC with configuration 3: the cold water source for the condenser is a cooling tower

The auxiliary electrical power consumptions include the cold water pump power for ORC with configuration 2, plus the CT blower power for ORC with configuration 3.

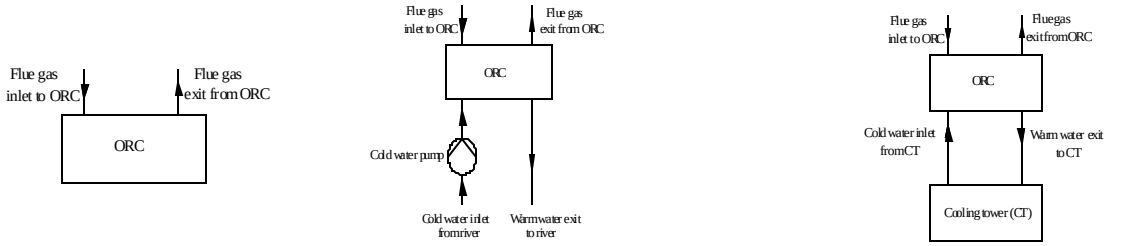

(a) *(b)* *(c)*

Fig. 4. Cold source configurations for ORC system: a) configuration 1, b) configuration 2, c) configuration 3.

The ORC process parameters are listed in Table 1. These parameters are used to evaluate the overall efficiency of the ORC system with the three configurations of the cold water source listed above.

Table 1. ORC process parameters.

Parameters			
Boiler pinch	3 K	$\eta_{is.\ pump}$	80%
Sub-cooled condenser	2 K	$\eta_{is.\ turbine}$	75%
$DP_{condenser}$	20 kPa	$\eta_{CT\ blower}$	60%
$T_{in\ water\ to\ condenser}$	18°C	$DP_{CT\ static}$	200 Pa
$T_{out\ water\ from\ condenser}$	23°C	$DP_{CT\ dynamic}$	100 Pa
$CT_{approach} = T_{out\ cold\ water\ from\ CT} - T_{in\ air\ wet\ bulb\ to\ CT}$	5 K	$DP_{water\ in\ cold\ water\ circuit}$	50 kPa
$T_{in\ water\ to\ CT} - T_{out\ air\ from\ CT}$	3 K	Ambiant air conditions	18°C db, 13°C wb

4. Effect of auxiliary electrical consumptions on optimal operating parameters for ORC

The optimal operating point of the ORC will be evaluated at the maximal overall efficiency instead of the system efficiency, because the latter does not take into account the flue gas extraction efficiency and the final aim is to extract the maximal exergy from the heat source. The overall efficiency is optimized as a function of the thermodynamics parameters for the ORC. Three thermodynamic parameters can be optimized for the ORC system:

- the condensation pressure
- the boiler superheat
- the evaporation pressure

4.1 Condensation pressure

The optimal condensation pressure depends on the auxiliary electrical power consumptions of the cold water source used in the ORC condenser. Fig. 5 shows that the optimal condensation pressure is slightly moved away from the minimal condensation pressure for ORC with configuration 2, due to the electrical power consumption of the cold water pump, whereas a larger deviation exists for ORC with configuration 3 due to the additional blower electrical power consumption. Therefore, for each condenser cooling mode (ORC with configuration 1, 2 or 3), an optimal condensation pressure exists.

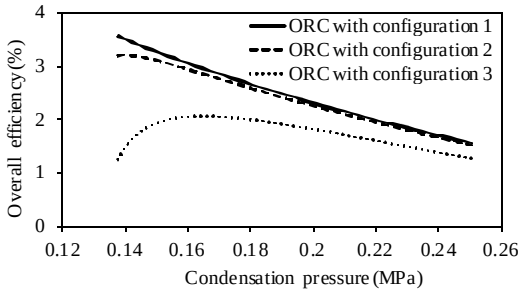

Fig. 5. Overall eff. vs. cond. pressure (P_{evap} = 0.4001 MPa, nil boiler superheat, R-245fa).

4.2 Boiler superheat

The second thermodynamic parameter to be optimized for the ORC system is the boiler superheat.

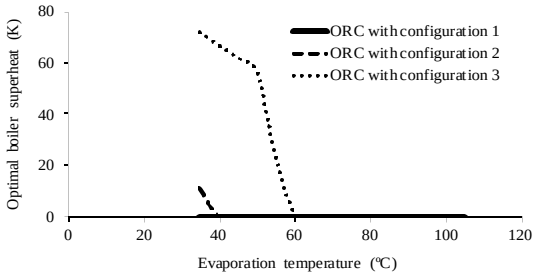

Fig. 6. Optimal boiler superheat vs. evap. temperature at the optimal cond. pressure (R-245fa).

Fig. 6 shows the evolution of the optimal boiler superheat as a function of the evaporation temperature at the optimal condensation pressure for the three ORC configurations using R-245fa as working fluid. From a thermodynamic point of view, the boiler superheat leads to a decrease in the overall efficiency. However, the increase in the boiler superheat leads to a decrease in working fluid and cold water mass flow rates (Fig. 7a), which results in decreasing the auxiliary electrical consumptions. Thus, for ORC with configurations 2 and 3 and at low-temperature evaporation, where the working fluid mass flow rate in the ORC is relatively high (Fig. 7b), the optimal boiler superheat will not be nil (Fig. 6).

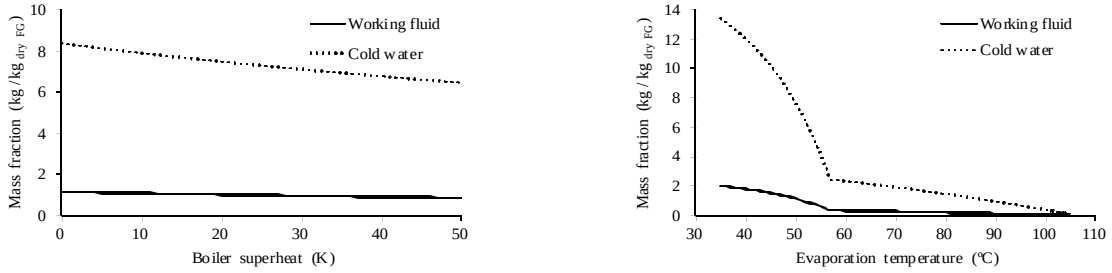

(a) *(b)*

Fig. 7. Mass fractions vs.: a) Boiler superheat (P_{evap} =0.3441 MPa), b) Evap. temperature (optimal boiler superheat) for ORC with configuration 3 (R-245fa).

4.3 Evaporation pressure

The third thermodynamic parameter to be optimized in the ORC system is the evaporation pressure. The evolution of ORC efficiencies, net turbine power and evaporator capacity as a function of the evaporation temperature using R-245fa as working fluid are shown in Fig. 8. The slope change in the flue-gas efficiency curve when crossing the flue-gas dew point temperature leads to two optima for the overall efficiency, exergy efficiency, and turbine power:

- dry optimum: above water dew point temperature ($T_{evap.}$ = 64.2°C)
- wet optimum: below water dew point temperature ($T_{evap.}$ = 45.5°C)

Compared to dry optimum, the turbine power is about 2.5 times higher and the boiler capacity is about 3 times higher at the wet optimum due to the latent heat released below the water dew point temperature.

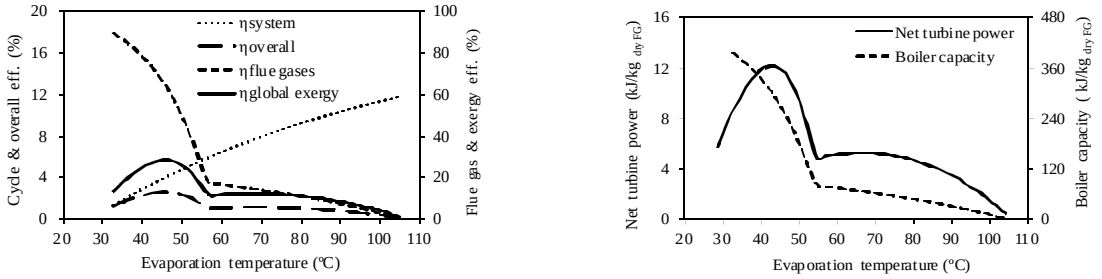

(a) *(b)*

Fig. 8. Evolution of: a) ORC efficiencies, b) Net turbine power and boiler capacity vs. evap. temperature (ORC with configuration 1, R-245fa).

The effect of auxiliary electrical power consumptions on the overall efficiency and net turbine power appears clearly below the water dew point temperature as shown in Fig. 9 where the working fluid mass flow rate in the system is relatively high (refers to Fig. 7b). Compared to ORC with configuration 1, the optimal overall efficiency at wet optimum is reduced by around 10% for ORC with configuration 2 and by 48% for ORC with configuration 3, using R-245fa as working fluid. It should be noted that the optimal evaporation temperature moves slightly away as the auxiliary electrical power consumptions increase.

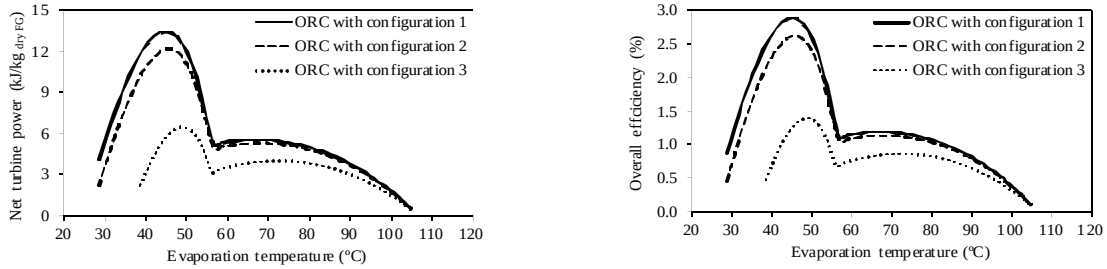

(a) *(b)*

Fig. 9. Effects of ORC cold source configuration on: a) Net turbine power, b) Overall efficiency (R-245fa).

Table 2 shows the effect of ORC cold source configurations on the net turbine power ratio between wet optimum and dry optimum. This ratio varies from 2.42 for ORC with configuration 1 to 1.62 for ORC with configuration 3.

Table 2. Net turbine power ratio between wet optimum and dry optimum.

ORC cold source configuration	$W_{net\ at\ wet\ optimum} / W_{net\ at\ dry\ optimum}$
1	2.42
2	2.30
3	1.62

5. Effect of auxiliary electrical power consumptions on ORC working fluid selection

To identify the most appropriate working fluids of the ORC for the present application, the selection method is based on thermo-physical criteria (high overall efficiency, dry turbine expansion), environmental criteria (GWP < 1000 $kg_{CO2eq.}kg^{-1}$, zero ODP) and safety criteria (no or moderately flammable, non toxic). Basically, working fluids can be classified into three categories: dry, isentropic, and wet depending on the slope of the T-s curve (dT/ds) to be positive, infinite, and negative, respectively and categorized into three flammability classes: 1 for non flammable, 2 for weakly flammable, and 3 for flammable working fluids [6].
The effects of the auxiliary electrical consumptions on the ORC optimal overall efficiency for the possible candidate pure working fluids are shown in Table 3. R-1234yf, R-152a, and ammonia are classified as slightly flammable fluids and belong to class 2 [5]. For wet working fluid, i.e. ammonia and R-152a, the boiler superheat is adjusted to ensure a dry turbine expansion to prevent turbine erosion. However, a vapor quality slightly below one at the turbine exit can be acceptable. As shown in Table 3, the highest overall efficiency is reached using R-1234yf as working fluid for ORC with configuration 1, while it is reached using ammonia for ORC with configuration 3. The results are in good agreement with [8] and [9]. It should be noted that the present study is limited to supercritical case and further investigations would be interesting to study the transcritical and supercritical cases.

Table 3. Effects of auxiliary electrical power consumptions on ORC optimal overall efficiency for the possible pure working fluid candidates

ORC configuration	**1**	**2**	**3**
Pure working fluid	Overall efficiency (%)		
R-1234yf	3.20	2.79	1.58
R-152a	3.12	2.72	1.69
R-245fa	2.89	2.62	1.46
Ammonia	3.15	2.78	1.78

6. Auxiliary electrical consumptions for ORC with refrigerant blend as working fluid

In general, the use of refrigerant blends as working fluids for the present application (T<120°C) will be interesting since the temperature difference between heat source and sink is around 100 K, and it makes sense when taking into account the auxiliary electrical power consumptions (ORC with configurations 2 and 3). In fact, a temperature glide in the condenser reduces the auxiliary electrical power consumptions by reducing the cold water mass flow rate. The temperature glide in the HEXs (boiler and condenser) will be defined according to the auxiliary electrical power consumptions. As the auxiliary electrical power consumptions increase, more temperature glide will be needed in HEXs and vice versa. The thermodynamic properties of the blend working fluids are calculated using REFPROP 9 developed by the NIST [11]. It estimates the interaction between fluids.

In order to define a promising blend as working fluid, a series of binary blend has been tested. Results show that binary blends whose R-1234yf is one of the components are the most promising for the present application and will be presented. The second component of the binary blend has been selected with the aim to increase the critical temperature of R-1234yf (T_{cr} = 94.8°C) by approaching the latter to the inlet heat source temperature on the one hand, and

to give the necessary glide to minimize the auxiliary electrical power consumptions and the exergy losses in HEXs on the other hand. Note that by increasing the critical temperature of R-1234yf, the system efficiency will increase leading to an increase in the overall efficiency [6]. Table 4 lists the most promising binary blends as working fluids at their optimized mole fractions for ORC with configuration 3. A blend between R-245fa and R-1234yf will be selected, because compared to R-1234yf, this blend leads to an increase in the overall efficiency by around 45% on the one hand (Table 4), and adding R-245fa to R-1234yf will reduce the flammability level of this latter on the other hand because R-245fa is classified as non-flammable working fluid [6]. Among hydrocarbon blends with R-1234yf, pentane, isopentane, and neopentane show a good agreement compared to other hydrocarbons including butane, isobutane, hexane, and isohexane, although the flammability remains the main drawback of using such blends [6].

Table 4. Binary blends as working fluid for ORC with configuration 3.

C_1	C_2	Optimal fractions (C_1/C_2, % mol.)	Glide boiler (K)	Glide condenser (K)	$\eta_{overall}$ (%)	RV* (%)
R-1234yf	R-365mfc	85.41/14.32	15.7	19.6	2.26	43.04
R-1234yf	R-245fa	51.12/48.88	13.2	16.8	2.30	45.57
R-1234yf	Butane	52.10/47.90	6.5	7.9	2.14	35.44
R-1234yf	Isobutane	52.40/47.60	4.6	6.6	1.98	22.66
R-1234yf	Pentane	84.44/16.56	17.6	20.5	2.32	46.84
R-1234yf	Isopentane	79.18/20.82	16.4	18.8	2.34	48.10
R-1234yf	Neopentane	53.97/46.03	12.6	14.4	2.35	48.73
R-1234yf	Hexane	97.21/2.79	9.3	12.9	1.97	24.68
R-1234yf	Isohexane	90.98/9.02	19.4	23.5	2.19	38.61

(*) RV denotes relative variation of overall efficiency with respect to R-1234yf

Fig. 10 shows the hot and cold composite curves for R-1234yf and the selected blend between R-1234yf and R-245fa at its optimized mole fractions (Table 4) for ORC with configuration 3. The glides in the HEXs are shown clearly for the selected binary blend (Fig. 10b); the condenser composite curves are almost parallel, similarly to the boiler composite curves below water dew point temperature. The cold water temperature from the condenser exit varies from 26.5°C using R-1234yf as working fluid to 37.5°C using the selected binary blend as working fluid.

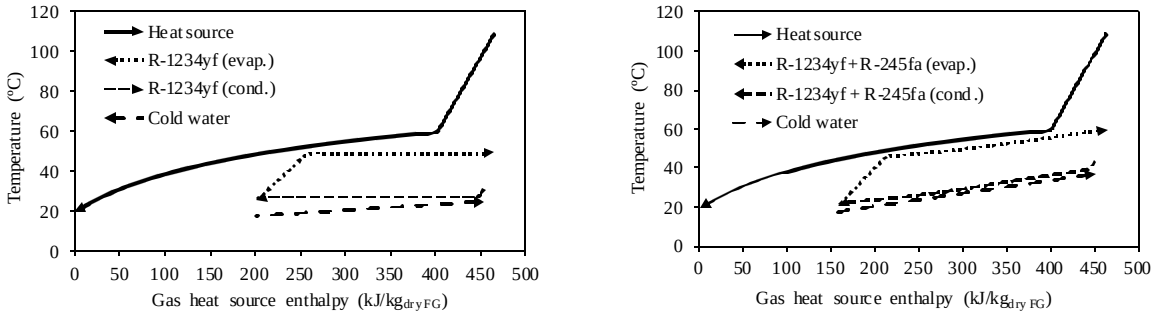

Fig. 10. Hot and cold composite curves for: a) R-1234yf, b) Blend between R-1234yf & R-245fa (51.1/48.9 % mol.) for ORC with configuration 3.

Fig. 11 shows the effect of the selected binary blend on the overall efficiency compared to R-245fa and R-1234yf along an evaporation pressure interval. The optimal overall efficiency of the ORC increases from 1.52% (resp. 1.45%) using R-1234yf (resp. R-245fa) to 2.30% using the defined binary blend. The improvement in the overall efficiency when using a blend instead of a pure working fluid has been reported by [1] which pointed out that the temperature glide using two and three component blends of siloxane at condensation can lead to more than 40% reduction of the cooling tower blower power in comparison to pure fluids.

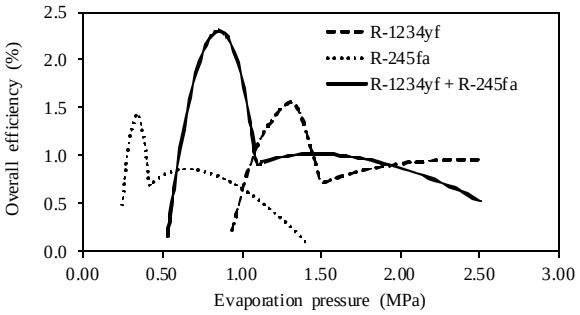

Fig. 11. Overall efficiency vs. evap. pressure for ORC with configuration 3 using R-245fa, R-1234yf and blend between R-1234yf & R-245fa (51.1/48.9 % mol.) as working fluids.

For ORC with configuration 2, the power of the cold water pump is the only auxiliary electrical power consumptions; therefore a little glide in the HEXs will be sufficient (Table 5), and the overall efficiency improvement is 4.67%.

Table 5. Binary blends as working fluid for ORC with configuration 2.

C_1	C_2	Optimal fractions (C_1/C_2, % mol.)	Glide boiler (K)	Glide condenser (K)	$\eta_{overall}$ (%)	RV* (%)
R-1234yf	R-245fa	86.81/13.18	2.8	3.2	2.92	4.67

(*) RV denotes relative variation of overall efficiency with respect to R-1234yf

7. Conclusions

The effect of auxiliary electrical consumptions on ORC generating power from low-temperature heat source was investigated. The studied heat source is characterized by an inlet temperature of 110°C and a water dew point temperature of 60°C. Results show that the auxiliary electrical power consumptions of the cold water source for the condenser affect the ORC optimal thermodynamic parameters (evaporation and condensation pressures, boiler superheat), the working fluid selection and the ORC optimal overall efficiency. In order to reduce these auxiliary consumptions, a defined binary blend between R-1234yf and R-245fa is proposed as working fluid. For an ORC system using a cooling tower as cold water source for the condenser, the proposed binary blend at its optimized mole fractions increases the overall efficiency by around 46% at the optimal operating point compared to R-1234yf (pure working fluid). Further investigations would be interesting to look the effects of varying the inlet and water dew point temperatures of the heat source as well as the condensation temperature on the optimized mole fraction of the selected binary blend. However, techno-economics constraints have to be included in the optimization process. The heat exchangers are the critical components especially for dusty gases cooled below the (acid) dew point in the exhaust and require high quality materials. As

reported by [14], the blend working fluid leads to a reduction of turbine dimension and costs. Nevertheless, as pointed out by [1], depending on fluid blend composition, important design parameters like volume flow rate at the inlet of the turbine vary in a wide range and can affect the turbine costs and material. Thus, a techno-economics analysis is very important after the thermodynamically optimized configuration is set.

Acknowledgments

The research leading to these results has received funding from the European Community's Seventh Framework Program (FP7/2007-2013) under grant agreement n° 256790 ('LOVE').

Nomenclature

C component
CT cooling tower
eff efficiency, %
Ex exergy, W
GWP Global Warming Potential
h specific enthalpy, J/kg
HEX heat exchanger
m mass flow rate, kg/s
mol molar
ODP Ozone Depletion Potential
P pressure, Pa
Q heat capacity, W
s specific entropy, J/(kg K)
T temperature, °C
W power, W

Greek symbols

h efficiency, %

Subscripts

cond condensation
cr critical
db dry bulb
dp dew point
evap evaporation
ex exit
FG flue gases
in inlet
is isentropic
max maximal

nb normal boiling point

o ambient

out outlet

r working fluid

wb wet bulb

References

[1] Angelino G., Colonna di Paliano P., Multicomponent working fluids for Organic Rankine Cycles (ORCs). Energy 1998;23:449-463.

[2] Benelmir Riad., Feidt M., Lallemand, A., Analyse exergétique. Techniques de l'ingénieur, Be8015.

[3] Bliem C., Zeotropic mixtures of halocarbons as working fluids in binary geothermal power generation cycles. Intersociety energy conversion engineering conference; 1987; Portland (USA).

[4] Borel L., Favrat D., Thermodynamique et Energétique. Presses polytechniques et universitaires romandes. CH – 1015 Lausanne ; 2005.

[5] Clodic, D., Low GWP refrigerants and flammability classification. 2010 International Symposium on Next-generation Air Conditioning and Refrigeration Technology; 17-19 February; 2010; Tokyo, Japan

[6] El Chammas, R., Rankine Cycle for hybrid vehicles, simulation and design of a first prototype. Thesis, Centre of Energy and Processes (CEP), Ecole des Mines de Paris, Paris, France, 2005.

[7] Heberle F., Preibinger M., Bruggemann D., Zeotropic mixtures as working fluids in Organic Rankine Cycles for low-enthalpy geothermal resources. Renewable Energy, 2012;37:364-370.

[8] Hung T.C., Shai T.Y., Wang S.K., A review of organic Rankine cycles (ORCs) for the recovery of low-grade waste heat, Energy 1997;22(7):661-667.

[9] Hung T.C., Wang S.K., Kuo C.H., Pei B.S. ,Tsai K.F., A study of organic working fluids on system efficiency of an ORC using low-grade energy sources. Energy 2010;35:1403-1411.

[10] Lallemand A., Bilans entropiques et exergétiques. Techniques de l'ingénieur, Be8008.

[11] Lemmon E.W., Huber M.L., McLinden M.O., Reference Fluid Thermodynamic and Transport Properties. NIST Satndard Reference Database 23, Version 9.0.

[12] Liu B.T., Chien K.H., Wang C.C., Effect of working fluids on organic Rankine cycle for waste heat recovery. Energy 2004;29:1207-1217.

[13] Madhawa H., Golubovic M., Worek W.M., Ikegami Y., Optimum design criteria for an Organic Rankine Cycle using low-temperature geothermal heat sources. Energy 2007; 32:1698–706.

[14] Wang X., Zhao L., Analysis of zeotropic mixtures used in low-temperature solar Rankine cycles for power generation. Solar Energy 2009;83:605-613.

[15] Wei D. , Lu X., Lu Z., Gu J., Performance analysis and optimization of organic Rankine cycle (ORC) for waste heat recovery. Energy conversion and management 2007;48:1113-1119.

[16] Thorn W.F., Waste heat recovery from stacks using direct contact condensing heat exchange. Rocket Research Company. Redmond, Washington; 1969.

Energetic and Exergetic analysis of waste heat recovery systems in the cement industry

S. Karellas[a], A.-D. Leontaritis[a], G. Panousis[a] , E. Bellos [a], E. Kakaras[a]

[a] Laboratory of Steam Boilers and Thermal Plants, National Technical University of Athens, Heroon Polytechniou 9, 15780 Athens, Greece

Abstract:

This paper presents waste heat recovery as a way to gain energy from the exhaust gases in a cement plant. In a typical cement producing procedure, 25% of the total energy used is electricity and 75% is thermal energy. However, the process is characterized by significant heat losses mainly by the flue gases and the ambient air stream used for cooling down the clinker. About 35% - 40% of the process heat is lost by those waste heat streams [8]. Approximately 26% of the heat input to the system is lost by dust, clinker discharge, radiation from the kiln and pre-heater surfaces, and convection from the kiln and pre-heaters. A heat recovery system could be used to increase the efficiency of the cement plant and thus lower the CO_2 emissions. Moreover, it would reduce the amount of waste heat to the environment and lower the temperature of the exhaust gases. Waste heat can be captured from combustion exhaust gases, heated products, or heat losses from systems. This study aims at the identification of a best practice example for energy utilization in an existing commercial cement production plant with a waste heat recovery system as a new component. Two different methods will be examined, using the commercial software IPSEpro™ by Simtech. Firstly, a water-steam Rankine cycle will be analyzed and then an Organic Rankine Cycle (ORC) with an intermediate pressurized water circuit will also be investigated. Another aim of this paper is the optimization of the working fluid, the maximum pressure and temperature of the two cycles as well as the components arrangement, in terms of system efficiency and output power. Finally, an exergetic analysis is done for both cycles.

Keywords:

ORC, waste heat recovery, exergy analysis, cement plant

1. Introduction

The cement industry is one of the major industrial emitters of greenhouse gases, particularly CO_2 [1]. Cement production is an energy-intensive process and each tone of portland cement produced releases approximately 1 tone of CO_2 [2]. The major part of the CO_2 emission from the production of cement is released from the calcination of limestone (50%) and from the combustion of fuels (40%). In addition, the EU has made a commitment to increase the 20 percent emissions target to 30 percent for the post Kyoto period if there are comparable targets from other developed countries and adequate actions by developing countries [3]. This prospect is expected to impose a further burden to the EU industry and the cement industry in particular which, representing more than 10% of the world production [4], is quite vulnerable to the issue of carbon leakage [5].

The cement clinker production sector is a substantially energy intensive industry accounting for 50-60% of the production costs [6] while is currently contributing about 5% to the global anthropogenic emissions [7]. Thermal energy demands depend on the age of the plant and on the specific process but ranges between 3000 and 6500 MJ/tone clinker. The average specific energy consumption is about 2.95 GJ per ton of cement produced for well-equipped advanced kilns, while

in some countries the consumption exceeds 5 GJ/ton. The electric energy demand ranges from 90 to 150 kWh per cement ton [4].

In a typical cement plant, 25% of the total energy used is electricity and 75% is thermal energy. However, the process is characterized by significant heat losses mainly by the flue gases and the ambient air stream used for cooling down the clinker. About 35% - 40% of the process heat is lost by those waste heat streams [8]. Approximately 26% of the heat input to the system is lost by dust, clinker discharge, radiation from the kiln and pre-heater surfaces, and convection from the kiln and pre-heaters [9],[10],[11]. A heat recovery system could be used to increase the efficiency of the cement plant and thus lower the CO_2 emissions. Moreover, it would reduce the amount of waste heat to the environment and lower the temperature of the exhaust gases [12]. Waste heat can be captured from combustion exhaust gases, heated products, or heat losses from systems [13].

Waste heat recovery systems are already in operation in various industries with success. In China, Canada, the Gold Creek Power Plant [14] has a heat recovery system that produces 6.5MW power using ORC technology. In India, the A.P. Cement Works with 4 MW and ORC technology. Another cement industry that uses waste heat recovery is Heidelberger Zement AG Plant in Lengfurt (Germany) [14] with 1.5 MW power and ORC technology. In addition to these industries, a new waste heat recovery system is under construction in Rohrdorf (Germany) [15] with 6.8 MW power and water-steam cycle technology.

This study aims at the identification of a best practice example for energy optimization in an existing commercial cement production plant with waste heat utilization as a new component. Two different methods will be examined in order to find which is more beneficial and more efficient for a Cement industry. Firstly, a water-steam Rankine cycle will be analyzed. The basic characteristics of this cycle are the two drums with 19 bar pressure and a maximum temperature of 350 ºC. The other is an Organic Rankine Cycle (ORC) in an indirect cycle with pressurized water at 30 bar. Part of this study was the evaluation of several organic fluids. It was concluded that isopentane has the optimum performance. Thus, any further analysis was carried out considering isopentane as the organic working fluid of the ORC.

Many parameters were optimized in order to design the optimum thermodynamic cycle, in terms of energetic and exergetic efficiency. Pressure and temperature are the most important parameters regarding the efficiency of those systems. Also changes have been made in the arrangement of the cycle and its different components in order to improve the efficiency and design an optimum system. Aiming to define the cycle with the best performance, energy and exergy analysis will be done in order to find the cycle with the highest thermal and exergetic efficiency.

2. Waste heat recovery

The identification of the waste heat sources in the cement industry is thus of high importance for the improvement of the process efficiency. The two main waste heat sources are:

- The exhaust gases from the rotary kiln, which after passing through the raw material preheater are at a temperature in the range of 380°C
- The waste heat from the clinker cooler, in the form of hot air, at an average temperature of about 360°C.

These waste heat sources can be efficiently used in a waste heat recovery system to produce electricity. Usually, a waste heat recovery boiler is used to produce steam which drives a steam turbine to generate electric power. The plant is then considered as a cogeneration plant, since two products (electricity and cement) are provided through the same process.

The proposed heat recovery system is schematically shown in Fig. 1. As already discussed, there are two waste heat sources that can be used for the production of steam. The exhaust gases from the

rotary kiln (point 1), after preheating and pre-calcinating the raw material are available at a temperature of about 380 ºC This temperature depends on the number of the stages of the preheater. A 4 stage preheater has exhaust gases at 300-380 ºC , whilst a 5-6 stage preheater has exhaust gases at 200-300ºC [16]. After passing through the settling chamber for the necessary dust removal, it enters heat recovery boiler 2 and superheated steam is produced. That is a typical procedure in a cement plant heat recovery system. However, this is not the case with the second heat source. The hot air from the clinker cooler (point 2) is available at an average temperature of about 360 ºC. During the cooling process of the clinker, the air can be taken from different points of the cooler and thus at different temperatures. For example the exit **1a** and **1b** can be at a temperature of 500 and 300 ºC respectively. This offers a number of advantages and can lead to higher system efficiency. The high temperature stream can be used for the superheating of the steam and then it can be mixed with the low temperature stream for the preheating and evaporation of the water. This means that a higher final temperature can be reached and a higher efficiency of the process can be achieved. Having conducted the superheating, stream **1a** can be mixed with stream **1b**. Exit **1c** is used for by-passing the heat exchanger when the heat recovery system is not in operation. The selection of the points that the hot air will be drawn from the cooler as well as the respective mass flows is of great importance for the design of the system. It is expected that the mass flow in exit **1b** will be much higher than in exit **1a**. It is noted that the hot air stream goes through an ESP (Electrostatic Precipitator) system before being released in the atmosphere, in order to remove the particles.

For the current work, the exhaust gases with 96.71 Kg/s mass flow and 380 ºC temperature are investigated as a first heat source. This flow exits the system at a minimum temperature of 270 ºC as it has to be reused in the raw material mill. The other heat source, the hot air from the clinker cooler, has an air mass flow rate of 42.91 Kg/s at a temperature of 360 ºC.

Those aspects will be thoroughly investigated with the help of thermodynamic models and simulations in order to choose the optimum combination and maximize the performance of the system.

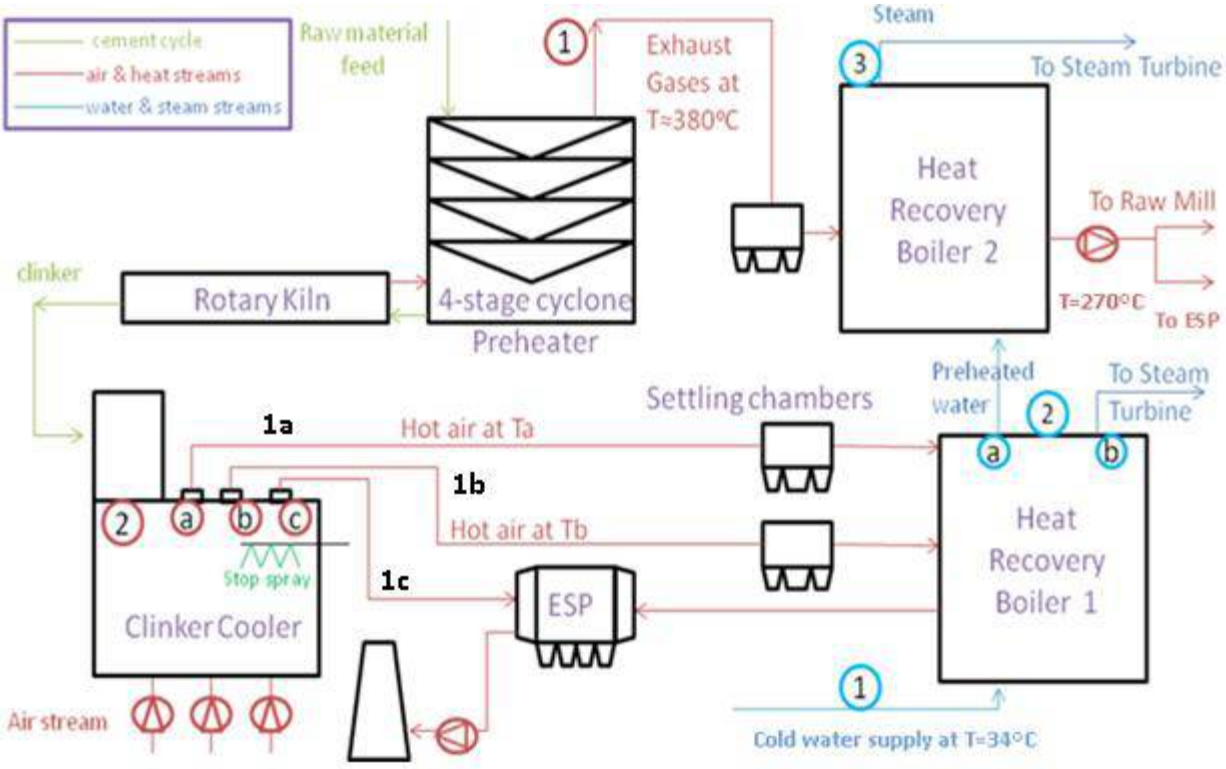

Fig.1. Heat recovery system of a typical cement plant

For analyzing this system, thermal efficiency is defined as:

$$\eta_{th} = \frac{P_{el}}{\dot{Q}_{fluid}}, \quad (1)$$

where P_{el} is the electric power produced by the generator and Q_{fluid} is the heat that the working fluid absorbs from the heat sources.

The efficiency of the heat-exchangers system is defined by the following equation:

$$\eta_{HEx} = \frac{\dot{Q}_{fluid}}{\dot{Q}_{HS}}, \quad (2)$$

where Q_{HS} is the heat source energy.

The heat source consists of the exhaust gas and of the hot air and is calculated as the maximum energy that the heat source can give to the working fluid. This is the sum of the available heat from the exhaust gas and the hot air assuming that both streams in the exit are at ambient temperature. However, this is not the case for the exhaust gas steam, as there is a 270 ºC limit in the exit temperature in order to be reused in the raw material mill. Therefore, the exhaust gas heat is fully utilized taking into account the exit temperatures requirements. So Q_{HS} is calculated as:

$$\dot{Q}_{HS} = \dot{Q}_{gas} + \dot{m}_{air} \cdot \left(h_{in} - h_{ambient}\right), \quad (3)$$

Finally, the system efficiency can be calculated as:

$$\eta_{system} = \eta_{HEx} \cdot \eta_{th}, \quad (4)$$

3. WATER-STEAM CYCLE

The first cycle that will be examined in this paper is a water-steam Rankine cycle in order to recover the waste heat from the cement industry process. The examined system and its specifications are presented in Fig.2. The cycle's maximum pressure is 19 bar at a maximum max temperature of 350 ºC at the inlet of the turbine and 0.06 bar at the exit of the turbine. The exhaust steam of the turbine is condensed in the condenser and then pumped to the deaerator tank. Simultaneously, some of the steam is extracted from the turbine at 1 bar in order to be used in the deaeration process. After that, the condensate goes through the feed pump and enters the air preheater where it is preheated to 200 ºC. From that point, the feed water is separated into two streams. The first stream is preheated, evaporated and superheated utilizing the energy from the cooling air heat source. The other stream follows the same process utilizing the exhaust gas heat source. Each steam generator system consists of a drum and two heat exchangers. Finally, the two streams of superheated steam enter the steam turbine and the process is repeated. The main system characteristics of the water-steam cycle are summarized in Table 1.

Table 1. System characteristics

System parameters	
Turbine isentropic efficiency (%)	85.00
Turbine mechanical efficiency (%)	99.00
Pump isentropic efficiency (%)	70.00
Generator electrical efficiency (%)	98.00
Generator mechanical efficiency (%)	98.00
Environmental temperature (°C)	25.00
Environmental pressure (bar)	1.013

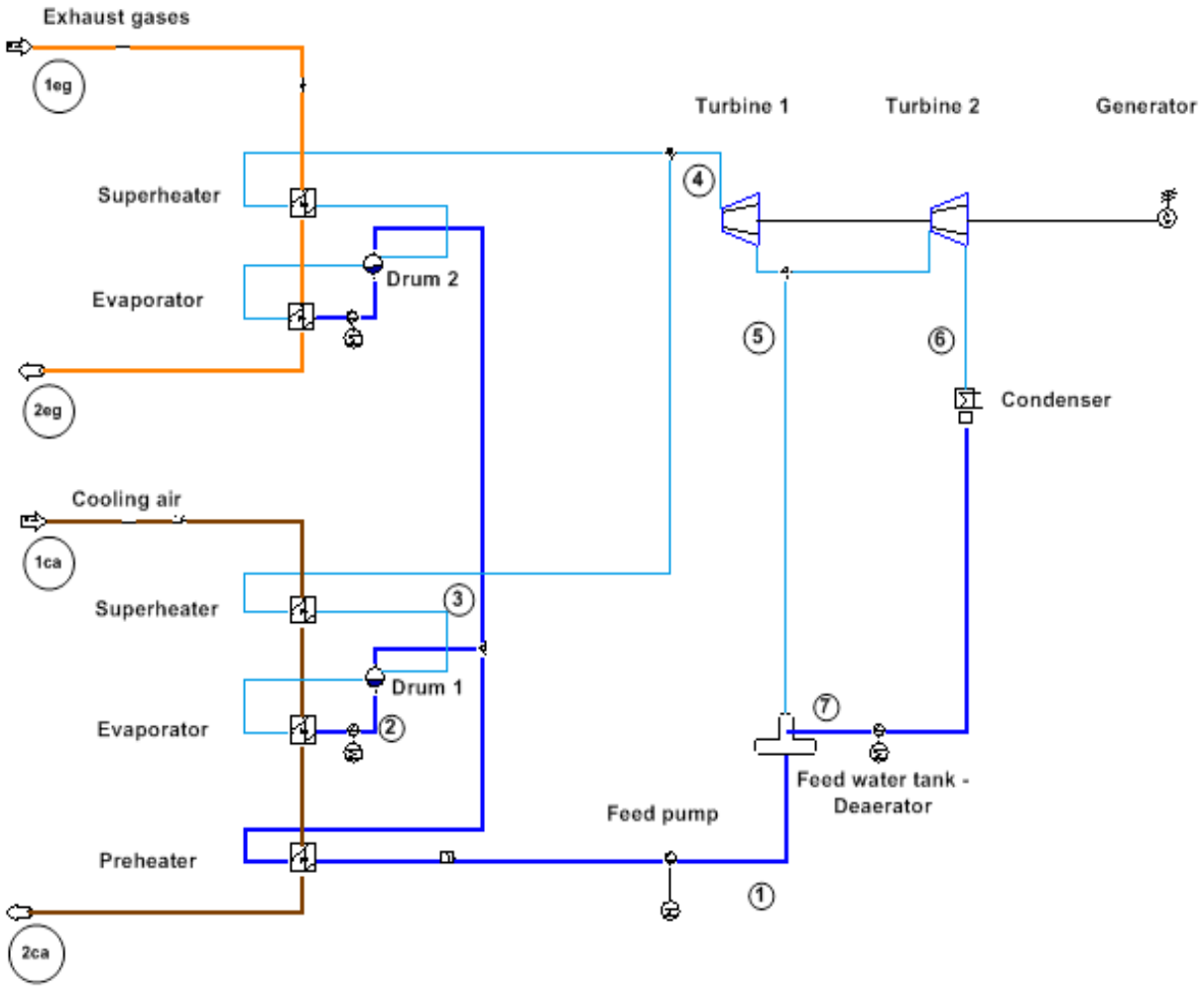

Fig.2. Heat Recovery system with water-steam cycle

At this point, it is necessary to explain the parameters of the Rankine cycle, taking into account that the efficiency of the system increases with the increase of temperature and pressure in the inlet of the turbine. Firstly, the maximum temperature of the superheated steam is set at 350 ºC, 10 ºC lower than the cooling air inlet temperature. The other important parameter, which has a great influence on the efficiency of the system, is the pressure at the inlet of the turbine which is set at 19 bar, taking into consideration the pinch point in the Q-T diagram (Fig. 3).

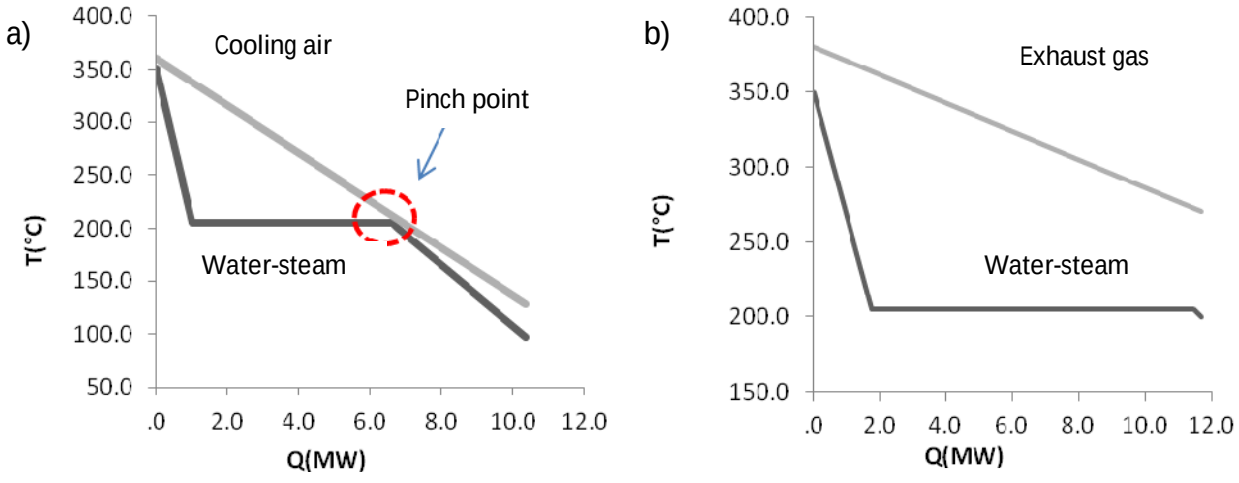

Fig.3. Q-T diagram for the water-steam cycle. a) Drum 1, b) Drum 2

The intermediate pressure of the steam extraction from the turbine is set at 1 bar in order to regulate the temperature of the cooling air at the exit at approximately 130 ºC, which achieves optimum heat recovery. The last pressure, the low pressure, is about 0.06 bar, a low value in order to gain more work from the turbine. Finally it should be noted that the temperature after the air preheater is 200 ºC , 10 ºC lower than the boiling point at 19 bar, which is 210 ºC. The thermodynamic diagram T-S (Fig.4) presents the complete and its parameters are summarized in Table 2.

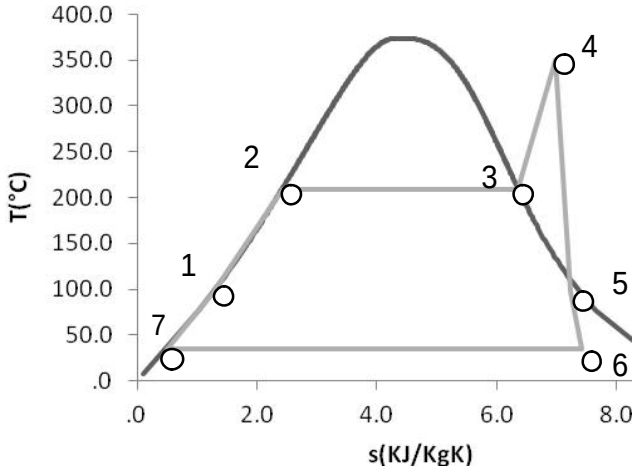

Fig. 4. Water-steam thermodynamic cycle

Table 2: Water-steam cycle points

Point	P (bar)	T (°C)	h (kJ/kg)
1	1.00	99.61	417.40
2	19.00	209.81	896.90
3	19.00	209.81	2797.30
4	19.00	350.00	3139.70
5	1.00	99.61	2626.10
6	0.06	36.20	2286.00
7	0.06	36.20	143.15

4. Organic Rankine Cycle

Another way to recover the waste heat from a cement plant is an indirect ORC. The ORC is used in low-temperature energy sources, because of the low critical point of the organic fluids. In this paper, 4 different organic fluids were examined in order to choose the most appropriate working fluid regarding the thermodynamic performance for the given temperature limits. As it can be seen in Fig.5, isopentane is the working fluid with the maximum system efficiency and thus it was selected as the working fluid for the ORC. Other parameters such as the price of the organic fluid and the energy consumption for its production were not taken into consideration.

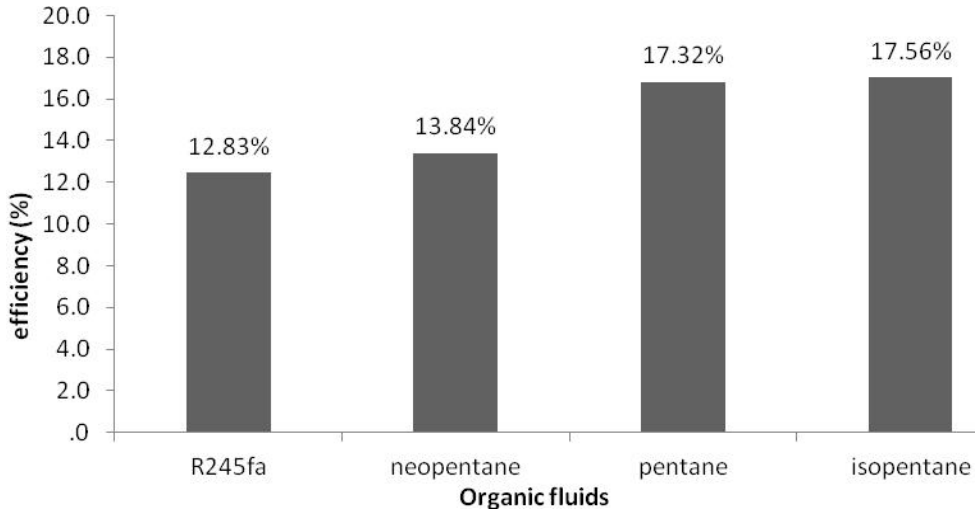

Fig.5. Comparison of different organic fluids

In an ORC heat recovery system there is an intermediate heat transfer fluid in order to transfer the heat from the heat sources to the working fluid through heat exchangers. This is necessary for safety reasons, as many organic fluids are inflammable and in case of failure of the heat exchanger the hot medium of the heat source and the organic fluid would get in contact resulting in an explosion. The heat transfer fluid should remain in liquid state and thus pressurized water at 30 bar is ideal for this use. It is important not to have steam, because steam is not able to transfer the heat to the organic fluid as effectively as water. The system is presented in Fig. 6.

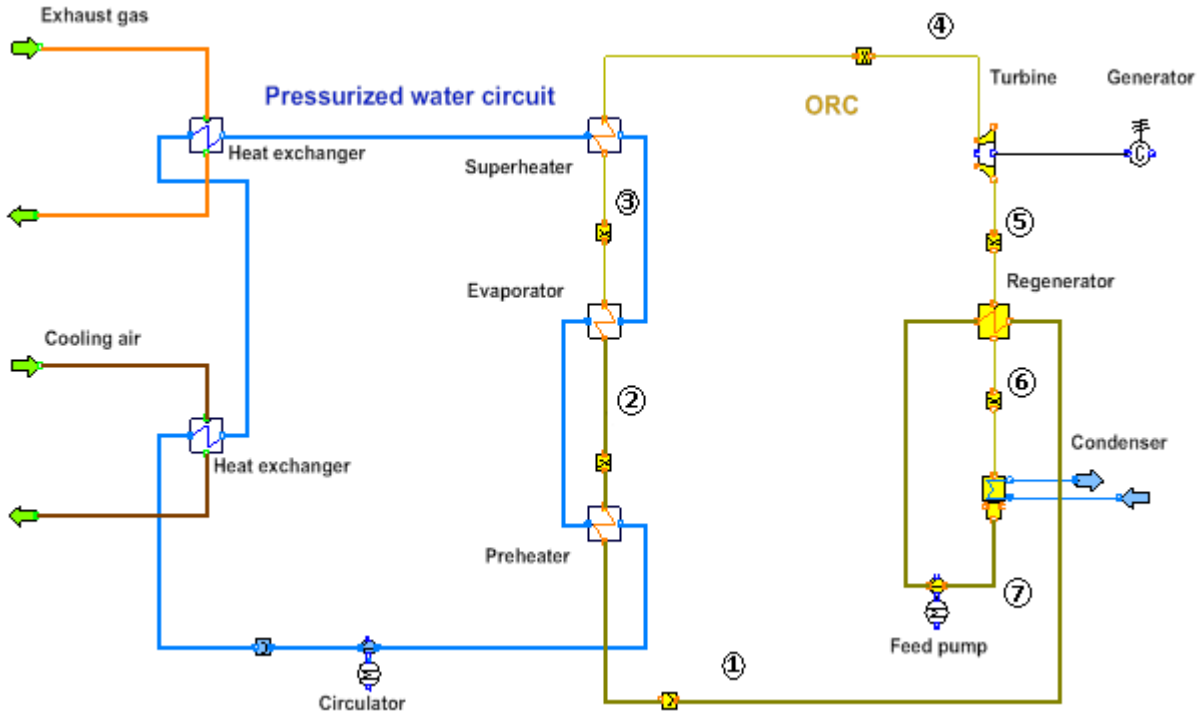

Fig.6. Heat Recovery system with ORC

There are two different circuits, one with pressurized water and one with the working fluid. The first one absorbs heat from the exhaust gas and from the cooling air, with two heat exchangers, in order to transfer this heat to the organic fluid. The water circuit operates between 220 °C and 125 °C, which is lower than the exit of the cooling air in the atmosphere. The energy passes from water to the working fluid through the heat exchangers, which are the preheater, the evaporator and the superheater. At the inlet of the turbine, the organic medium has a maximum temperature and pressure of 185 °C and 30 bar respectively. The turbine exhaust steam goes through the regenerator, before going to the condenser, in order to preheat the working fluid. That way the system rejects less energy to the environment through the condenser. After the regenerator, the working fluid continues to the water heat exchangers and the cycle closes. The system operating parameters, concerning the machinery efficiencies and ambient conditions, remain the same as in water steam cycle (Table 1). These thermodynamic procedures can be seen in the T-s diagram (Fig. 7).

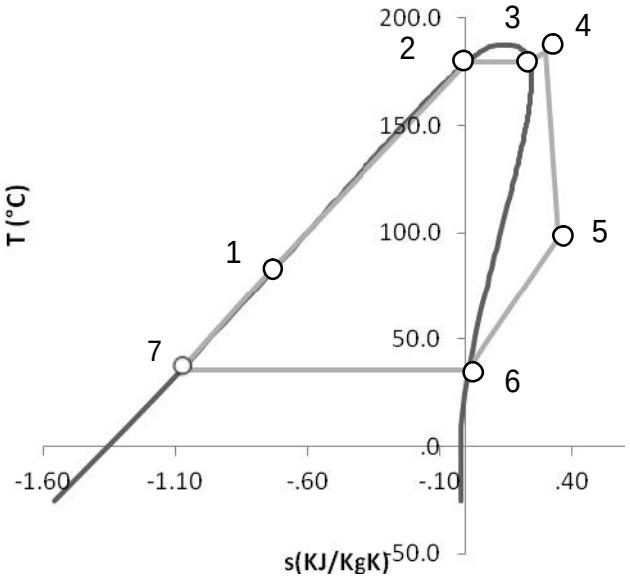

Fig 7. T-S process diagram for isopentane

Table 3. ORC points

Point	P (bar)	T (°C)	h(kJ/kg)
1	30	77.1	-223.0
2	30	179.5	94.9
3	30	179.5	201.4
4	30	184.4	228.0
5	1.4	97.4	127.4
6	1.4	46.9	31.0
7	1.4	35.5	-326.1

The parameters of points 1-7 are given in Table 3. It is important to note that the mass flow rate of the water is 52.67 kg/s and of isopentane 48.71 kg/sec. The Q-T diagram that shows the heat exchange procedure is presented in Fig. 8.

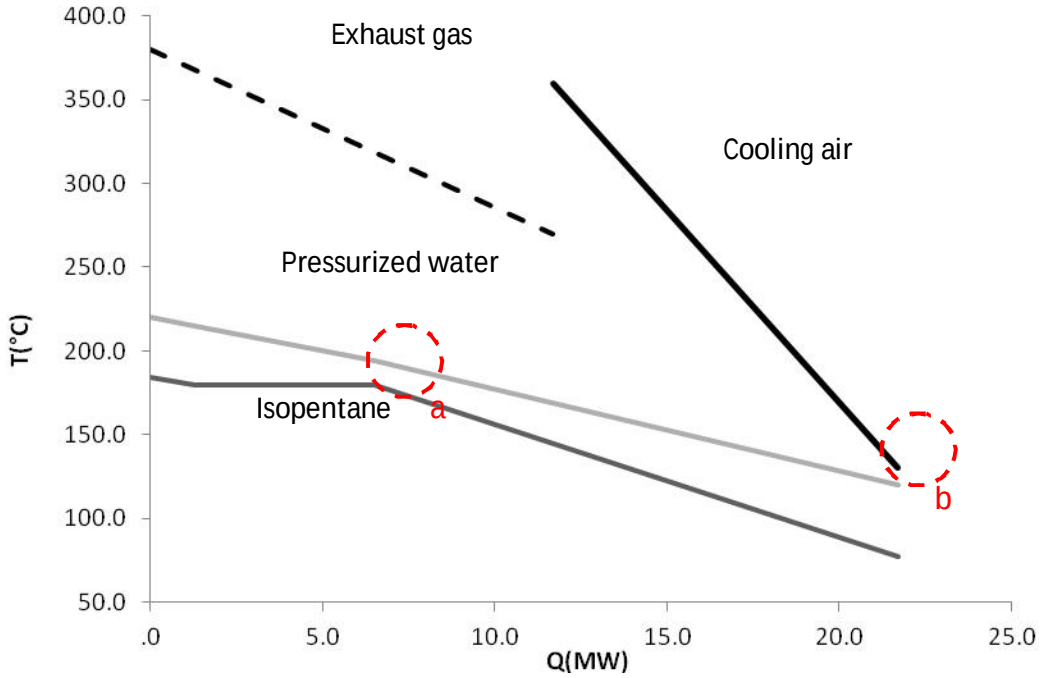

Fig 8. Q-T diagram for the ORC

As it is shown in Fig. 9, there are two pinch points in the Q-T diagram, the first one between pressurized water and isopentane (a) at 15 ºC and the second between pressurized water and cooling

air (b) at 5 ºC. Point b is the most important among them, because it is determines the exit temperature of hot air, which was optimized at 130 ºC.

5. EXERGETIC ANALYSIS

After the energy analysis of the systems, an exergy analysis is the next step in this paper. Exergy analysis is a very useful tool for analyzing thermodynamic systems, as it is possible to determine the maximum performance of the system and to find the components in which exergy loss occurs. So, the performance of the system can be optimized by minimizing the exergy losses [17], taking also into consideration economic factors.

First of all, some theoretical points will be stated. Exergy is the maximum amount of work that can be produced by a system when a heat stream is brought to equilibrium in relation to a reference environment which is at reference conditions (p_0=1.013 bar, T_0=298 K) and consists of reference components. In this paper, the molar physical exergy is considered:

$$E = N \cdot \varepsilon_{ph}, \qquad (5)$$

where N(mol s^{-1}) is the molar flow. Other forms of exergy, such as potential, kinetic and chemical were ignored in this work. The calculation of molar physic energy is a result of the use of 4 thermodynamic properties which are the temperature (T), the pressure (p), the enthalpy (h) and the entropy (s) and the expression that gives the physical exergy is the following:

$$\varepsilon_{ph} = (h - h_o) - T_o(s - s_o), \qquad (6)$$

All the parameters of this equation are calculated for every stream by the simulation program IPSEpro™.

Moreover, the exergy value of power output E^W is equal to the power. The exergy losses due to mechanical and electrical inefficiencies were taken in consideration but the heat losses of the system units were ignored. Both energy losses and exergy destruction have been summed under the term of irreversibilities, symbolized as IR. Taking an exergy balance in a control volume, gives the following expression:

$$\sum E_{i,in} = \sum E_{i,out} + \sum E_{i,losses} + IR, \qquad (7)$$

For the system, an exergetic efficiency can be defined as:

$$\eta_{ex} = \frac{\sum E_{i,out}}{\sum E_{i,in}}, \qquad (8)$$

with $\Sigma E_{i,in}$ and $\Sigma E_{i,out}$ be defined properly for each system describing exactly the amount of exergy that the system consumes to produce useful products. More specifically, $\Sigma E_{i,out}$ in this system concerns only the power of the generator.

6. Results

The two cycles were simulated with IPSEpro™ .The water-steam cycle has a system efficiency of 23.58% producing 6.26 MW electric power, whilst the ORC has a thermal efficiency of 17.56% producing 4.66MW electric power. More specifically, the system with water-steam cycle has the

thermal efficiency and the heat exchangers efficiency 28.53% and 82.7% respectively and for the system with ORC has 21.23% and 82.7%.

The other thermodynamic tool that is used for the comparison of the cycles is the exergy analysis. After the analysis with IPSEpro™, exergy efficiencies were calculated at 32.56% for the water-steam cycle and at 24.00% for the ORC. Once more, it is shown that the water-steam cycle has a better performance in these conditions. The main reason for this result is the higher maximum temperature of the water-steam cycle which results in more work produced by the turbine and the existence of the intermediate pressurized water circuit in the ORC, which causes additional exergy losses.

Another way to determine the most efficient system is to compare the Q-T diagrams (Fig. 3, 8). This can be done by comparing the area between the lines of the heat source and the working fluid. In the ORC, this area is bigger, which means that the exergy destruction is higher and the performance of the system deteriorates. The reasons for this are the use of pressurized water and the lower critical point of the isopentane in comparison to water's.

All the results of the exergy analysis are summarized in Table 4. For the water-steam cycle it is clear that the main exergy loss is the gas exhaust (Table 4a) because of the high exit temperature (270 ºC) of the exhaust gas, which is a restriction imposed by the production process of the cement plant. The next major exergy waste is located in the two heat exchangers that operate as evaporators. For the ORC, the main exergy loss is also located in the gas exhaust (Table 4b) and in the two heat exchangers.

Another useful tool for the exergetic comparison of the two systems is the Grassmann diagrams which are presented in Fig. 9 and 10 for the water-steam and the ORC system respectively. From these diagrams it is clear that the main reason which makes the water-steam system more efficient is the lower exergy losses in the heat exchangers. More specifically, the water-steam system has 21.8% losses compared to 26.7% of the ORC system.

Table 4. Exergy balance for the heat recovery systems a) water-steam cycle, b) ORC

a)Water-steam				**b) ORC**			
Component	**ζ (%)**	**IR (kW)**	**IR (%)**	**Component**	**ζ (%)**	**IR (kW)**	**IR (%)**
Turbine 1	87.6	595	3.10	Turbine 1	87.4	671	3.48
Turbine 2	85.5	428	2.23	Regenerator	71.6	185	0.98
Gas superheater	79.6	259	1.35	Preheater	83.3	834	4.34
Gas evaporator	63.2	2296	11.95	Evaporator	90.7	184	0.97
Air preheater	74.9	274	1.43	Superheater	87.9	64	0.33
Air evaporator	63.3	1317	6.85	Gas heat exchanger	60.7	2765	14.38
Air superheater	77.1	318	1.65	Air heat exchanger	55.8	2373	12.34
Pump	75.3	12	0.06	Pump	70.6	128	0.67
Deaerator		160	0.83	Condenser		670	3.48
Drum 1		25	0.13				
Drum 2		30	0.16				
Condenser		515	2.67				
Exergy losses		**(kW)**	**(%)**	**Exergy losses**		**(kW)**	**(%)**
Gas exhaust		6292	32.74	Gas exhaust		6292	32.74
Air exhaust		440	2.29	Air exhaust		440	2.29
Products exergy		**(kW)**	**(%)**	**Products exergy**		**(kW)**	**(%)**
Power		6258	32.56	Power		4613	24.00
Total		**19219**	**100.00**	**Total**		**19219**	**100.00**

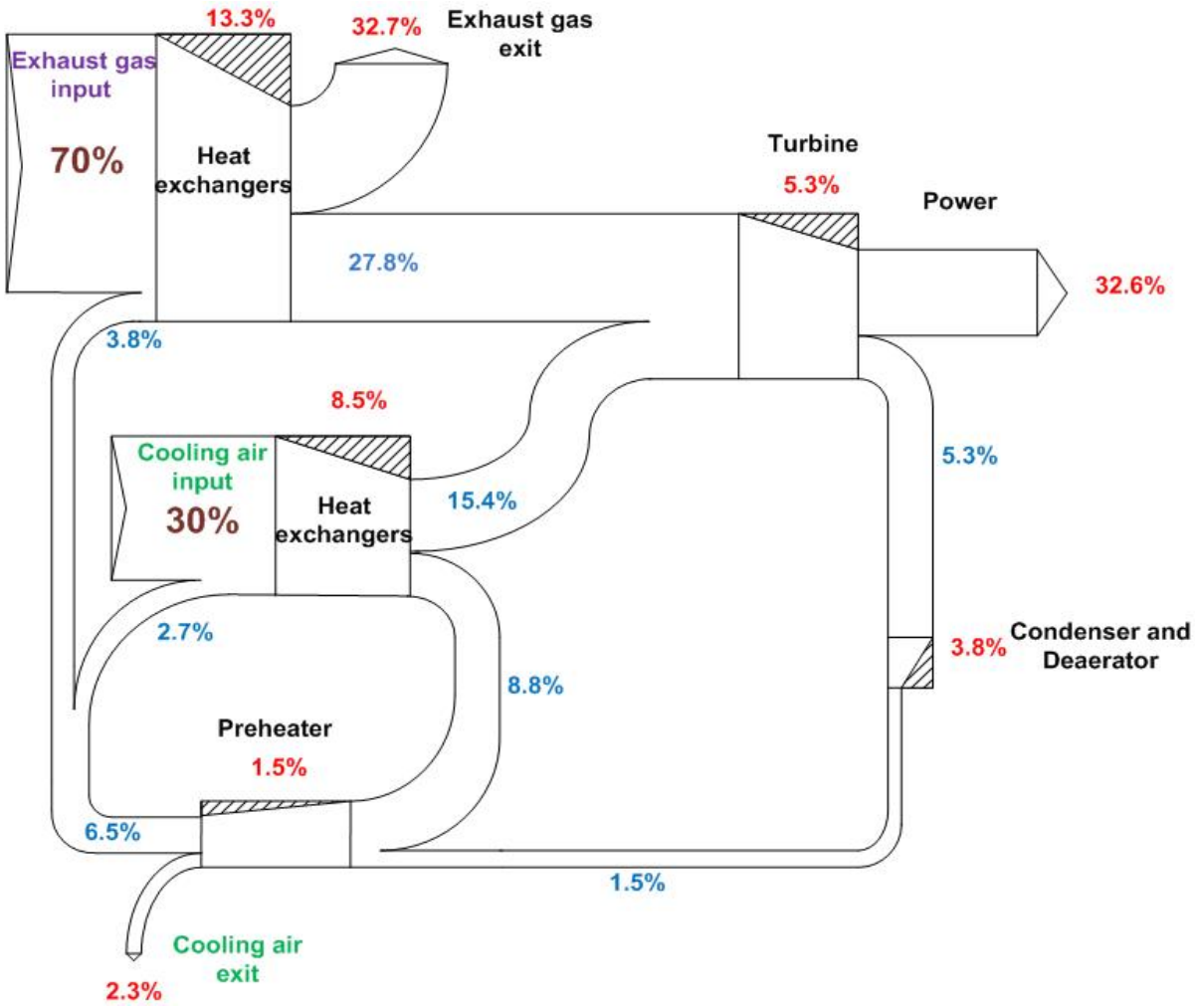

Fig .9.Grassmann diagram for water-steam cycle

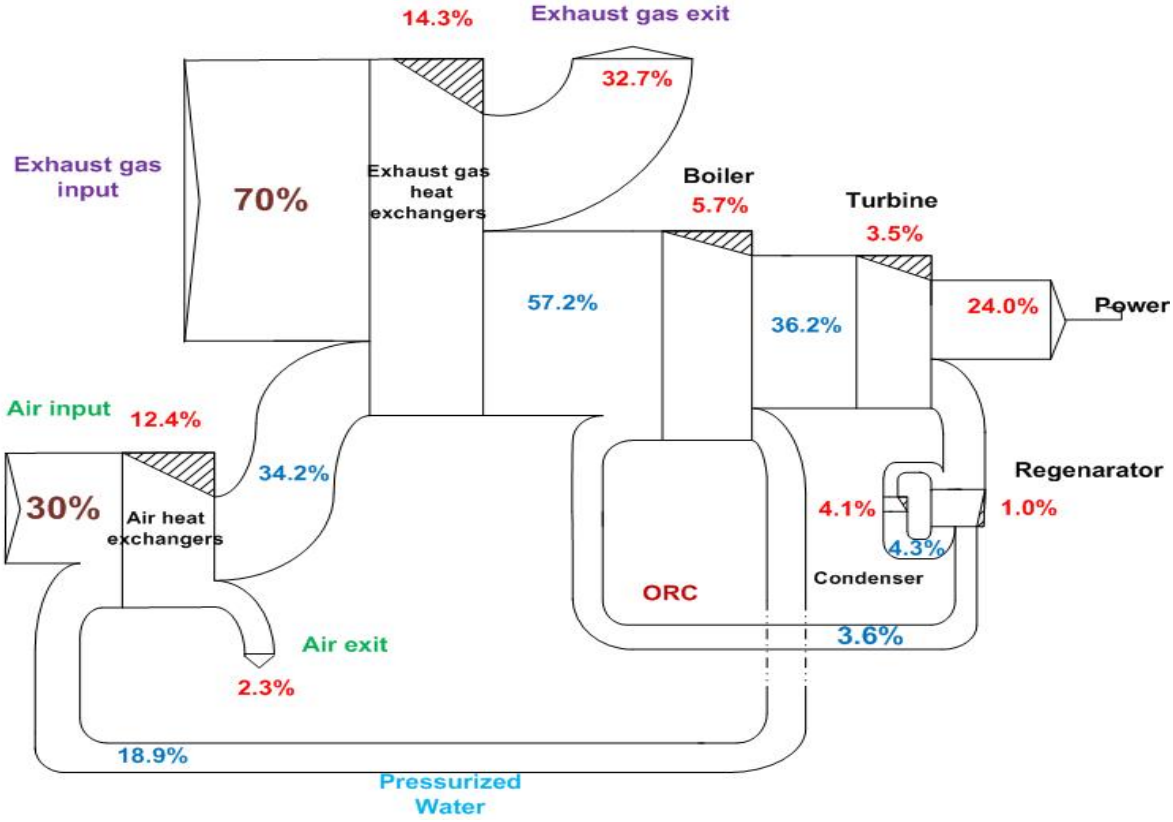

Fig.10. Grassmann diagram for ORC

After the comparison of those two heat recovery systems, it is useful to suggest further possible solutions and changes that could increase the efficiency but may have larger capital cost. For the water-steam cycle, which is the most efficient solution, a further preheating is possible to be done. More specifically, the hot air from point 2ca (Fig. 2) can be utilized to preheat the water in point 7 in order to provide more heat to the system. This change improves the η_{Hex} but reduces the η_{th}. However, the total system efficiency is improved. The comparison of the efficiencies is shown in Fig. 11.

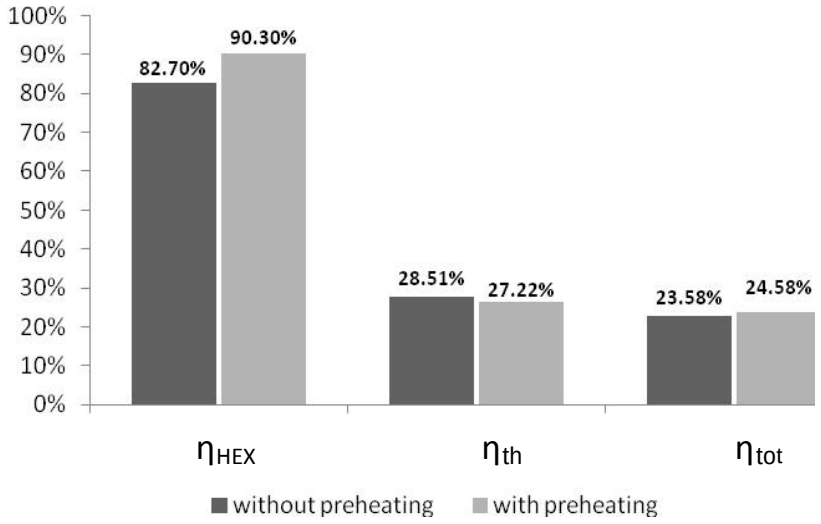

Fig. 11. Comparison of water-steam cycles

After analyzing the performance of the two systems, it is possible to make an estimation of the avoided CO_2 emissions. According to the energy mix of Greece, an average of 0.85 tones of CO_2 are emitted per produced MWhe. In addition it is assumed that the cement plant has an annual operation time of 7000 hours and that all the energy produced by the heat recovery system is either consumed by the plant itself or delivered to the national power grid. The results for the ORC and for the water-steam cycle are shown in Table 5.

Table.5. Avoided annual CO_2 emissions of the two systems

	WATER CYCLE	ORC
POWER (MW)	6.26	4.66
AVOIDED CO_2 (tn/a)	37,247	27,727

It is clear that a significant amount of CO_2 can be annually avoided, for any of the two cases considered.

7. Conclusions

Waste heat recovery is feasible for a cement industry and it can offer about 6MW of electric power for a typical cement plant. The preheater and clinker cooler exhaust gases are the heat sources for the heat recovery systems. Two different cycles were investigated; a water-steam cycle and an ORC with isopentane as working fluid. The energy and exergy analysis proved that the water steam-cycle has better performance with a system efficiency of 23.58% compared to 17.56% of the ORC. Conclusively, the most suitable cycle for a heat source at a temperature greater than 350 ºC is the water steam cycle. By the exergy analysis conducted it is shown that the cycle with the lower

exergy efficiency has the worst performance. The main reason for the lower efficiency of the ORC is its lower maximum temperature compared to the maximum temperature of the water steam-cycle. It is important to recommend that the exergy efficiency is higher than system efficiency. The reason for this is the way that the system efficiency has been determined in this paper. Finally the water – steam cycle can be further improved reaching 24.58% system efficiency by utilizing the high exhaust temperature of the cooling air in order to preheat the condensates before enter the feed tank.

At this point it should be noted that even though there are many existing heat recovery systems that use the ORC technology, this study concludes that the water-steam cycle is the more efficient solution. This is a result of the relatively high temperature level of the heat source which is over 350 ºC. In this case, the higher critical temperature and pressure of water provide increased efficiency compared to organic fluids. In this study, the temperature of the waste heat sources is high due to the low efficiency of the production procedure of the cement plant considered. It is obvious, that in the case of a newer cement plant with higher efficiencies, the ORC may be more advantageous than the water steam recovery cycle. Higher efficient cement plants have lower exhaust gas temperature and a calculation performed has proven that if the exhaust gas temperature is lower than 310 ºC, ORC heat recovery systems are more efficient.

Finally it should be stressed that energy and exergy analysis gives results concerning system efficiency and the presented results will be helpful in further processes development. A techno economic analysis of each process should be implemented in order to provide the most feasible solution also from economical view.

Nomenclature

E	Total exergy of material stream, W
E^W	Work of power output, W
h	Enthalpy of stream, J kg^{-1}
h_0	Standard enthalpy at environmental conditions, J kg^{-1}
IR	Irreversibilities of process, W
m_{air}	Mass flow of cooling air
N	Mole flow rate, mole s^{-1}
P_{el}	Power from generator, W
p	Standard pressure, bar
p_0	Standard pressure, bar
Q_{fluid}	Heat transferred to working fluid, W
Q_{gas}	Heat from the flue gases of the rotary kiln
Q_{HS}	Heat source energy, W
s	Entropy of stream
s_0	Standard entropy at environmental conditions
T	Temperature, K
T_0	Standard temperature, K
x_i	Mole fraction of component i

Greek symbols

ε_{ph}	Specific physical exergy of material stream, J ·mol^{-1}
η_{HEx}	Heat-exchangers efficiency
η_{system}	System efficiency
η_{th}	Thermal efficiency
ζ	Exergy efficiency of component

Subscripts and superscripts

ex	Exergetic
in	Input

out Output

References

[1] Mehta, P.K., 2002. Greening of the concrete industry for sustainable development. Concr. Int. 24 (7), 23–28.

[2] Worrell, E., Price, L., Martin, N., Hendriks, C., Meida, L.O., 2001. Carbon dioxide emissions from the global cement industry. Annu. Rev. Energy Environ. 26, 303–329

[3] Climate Change, Cement and the EU, CEMBUREAU

[4] BAT Reference Document for the Cement, Lime and Magnesium Oxide manufacturing Industries, May 2010, EIPPCB, Seville, Spain

[5] Carbon leakage: European cement industry at risk, Boston Consulting Group, 2008

[6] Exergy analyses and parametric optimizations for different cogeneration power plants in cement industry, J. Wang, Y. Dai, l. Gao, Applied Energy 86 (2009) 941-948]

[7] Cement Technology Roadmap 2009, WBCSD-IEA

[8] N.A. Madloola, R. Saidura,b, M.S. Hossaina, N.A. Rahim, A critical review on energy use and savings in the cement

[9] Hilel Legmann, ORMAT Group, Recovery of industrial heat in the cement industry by means of the ORC processes

[10] Energy balance and cogeneration for a cement plant, Shaleen Khurana, Rangan Banerjee *, Uday Gaitonde, Applied Thermal Engineering 22 (2002) 485–494

[11] Energy Auditing and recovery for dry type cement rotary kiln systems – a case study. T. Engin, V. Ari, Energy Conversion Management 46 (2005) 551-562

[12] P. Saneipoor, G.F. Naterer, I. Dincer. Heat Recovery from a Cement Plant with a Marnoch Heat Engine, Applied Thermal Engineering (2011), doi: 10.1016/j.applthermaleng.2011.02.016

[13] Johnson, I., Choat, B., Dillich, S., “Waste Heat Recovery: Opportunities and Challenges”, Minerals,Metals and Materials Society, EPD Congress, 2008

[14] Lucien Y. Bronicki, Chairman, Organic Rankine Cycle power plant for waste heat recovery

[15] www.siemens.com [accessed 16.1.2012]

[16] European Commission, Integrated Pollution Prevention and Control (IPPC) Reference Document on Best Available Techniques in the Ferrous Metals Processing Industry December 2001

[17] Jiangfeng Wang, Yiping Dai , Lin Gao, 2008, Exergy analyses and parametric optimizations for different cogenerationpower plants in cement industry

[18] Kotas. T.J, 1995, The Exergy Method of Thermal Plant Analysis. Malabar (FL): Krieger Publishing Company

[20] S. Karellas, K. D. Panopoulos , G. Panousis , E. Kakaras, I. Boukis , Energetic and exergetic investigation of integrated RDF gasification energy systems, ECOS 2010: Proccedings the 18th International Conference on Efficiency, Costs, Optimization, Simulation and Environmental Impact of Energy Systems; 2010 Jun 14-17; Lausanne, Switzerland

Energy and Exergy Analysis of Repowering Options for Greek lignite-fired Power Plants

S. Karellas, A. Doukelis, G. Zanni and E. Kakaras

National Technical University of Athens, Lab. of Steam Boilers and Thermal Plants, Athens, Greece, sotokar@mail.ntua.gr

Abstract:

The characteristics of modern society, such as increased consumer needs in combination with important environmental issues concerning the conservation of a healthy standard of living, have resulted in the emergence of new solutions and ideas aiming to a more environmentally friendly energy production. The low efficiency of old electricity generation units in Greece in combination with the low quality and heating value of the Greek lignite can be well suited to the technological concept of repowering. Moreover, the high levels of emissions produced from lignite combustion make the repowering concept even more interesting in order to reduce emissions and comply with the national and international environmental regulations. Several configurations can be applied in order to repower existing power plants to combined cycles. The main idea is to install natural gas-fired gas turbines in parallel operation with existing lignite power plants in order to increase the efficiency and the electricity generation. The paper deals with three basic scenarios. In the first scenario, the exhaust gases of the gas turbine are utilized for preheating the boiler feedwater of the lignite plant. In the second scenario, boiler feedwater is evaporated and superheated from the exhaust gases of the gas turbine in a heat recovery steam generator for further power generation. The third scenario is a combination of the first two scenarios. The performance of these configurations is examined energetically and exergetically under the consideration of enhancing the energy production and reducing lignite consumption. Finally, an economic evaluation of the selected scenarios is presented and discussed.

Keywords:

Repowering, lignite-fired power plants, energy and exergy analysis, economics

1. Introduction

The increased consumer needs required by modern society, along with the environmental restrictions having been set in order to maintain a satisfactory level of living, demand the application of alternative and environmentally friendly energy sources. However, for many decades, most countries have based their electricity generation in fossil fuel power plants. The majority of these plants is still in operation and holds a major role in energy production. Consequently, the need of improving and upgrading the operation and the efficiency of these old power plants is important in order to keep up with the current standards.

More especially, in Greece, a major part of the electricity generation is dependent on lignite power plants. Lignite is the main natural resource in the country. However, the quality and the heating value of the extracted Greek lignite is low, due mainly to the high levels of moisture contained in the fuel. Concerning also the fact that several of the existing power plants are old units that have been in commercial operation for 2-3 decades, the low efficiency of these plants causes important economic losses and environmental issues that have to be solved. Instead of replacing the old power plants before the end of their expected life, repowering of these plants seems to be the most economically viable solution.

The repowering idea is an attractive perspective, not only for increasing the age limit of a power plant, but also for increasing the total energy output of the plant. The main targets of repowering are summarized as follows:

- increasing the efficiency and the power output of the plant
- increasing the age limit of the plant
- increasing the availability and reducing the operating cost of the plant
- increasing the flexibility of the plant
- reducing emissions

The concept of repowering is to set a bottoming cycle (BC) with a topping cycle (TC) in combined cycle operation. In the present paper, a natural gas-fired gas turbine plant is assumed as TC and a lignite power plant as BC. In the literature [1-3], [7, 8], [10], the most commonly used terms of repowering configurations are "fired/fully fired" and "parallel powered/compound". In the fired/fully fired configuration, the GT exhaust is used as oxygen carrier in the burner of the steam-based plant. On the other hand, in "parallel powered/ compound" configuration the energy of the GT exhaust is provided to the water/steam side of the BC.

Many combined cycle configurations are technically feasible and have been proposed and applied throughout the years in existing power plants in order to make them equally productive as a modern plant. In Hemweg, Amsterdam, the natural gas-fired unit 7 was repowered by applying a combination of fully-fired and parallel repowering configuration, achieving an efficiency of 45.6% [23]. In LageWeide (Holland), in the natural gas-fired unit 5, a fully-fired configuration was applied and increased the overall efficiency by 4.7%. In Bilbao (Spain), the Zabalgarbi plant, which is fired with Municipal Solid Waste, was parallel-repowered, achieving an overall efficiency of 41% [15]. In Gersteinwerk (Germany), the brown coal-fired unit K was repowered with a fully-fired configuration. The efficiency was improved from 36.6% to 41% [13]. More case studies for repowering older coal-fired plants have been proposed throughout the years [1], [4-11] and some general presentations of combined cycle plants can be found in [16-18].

This paper presents a thermodynamic performance analysis of two Greek power plants for various combined cycle configurations, including energetic and exergetic calculations. The main goal has been the optimization of the overall performance in terms of electric efficiency and power production of each cycle configuration. All configurations were simulated using the commercial thermodynamic cycle simulation software GateCycle [19]. Furthermore, an economic investigation was carried out concerning the implementation of these configurations in current power plants. The viability of such a project is evaluated under both thermodynamic and economic considerations.

2. Repowering Configurations

The process of repowering is being applied to two Greek lignite power plants. This selection is based on the most important operational characteristics; their age limit and the power production. More specifically, the repowering process should be applied to power plants that are not very close to their predicted age limit, so that there is a remaining life of the plant to enable pay-back of the investment for repowering.

In the present study, the units were selected according to their power output in order to represent an average Greek power plant. In Greece, the vast percentage of the power plants is between 300 and 330MW. Considering these parameters, unit 4 of Megalopoli Power Plant and the Florina Power Plant have been selected as a representative sample of a 300MW and a 330 MW power plant, respectively. Moreover, these units are not close to their age limit since they can stay in operation for at least 15 more years.

From a thermodynamic and operating point of view, these units have similar characteristics with a steam production of 910-956 t/h. The basic steam parameters (Table 1) have been kept similar in all

configurations in order to establish a common basis of comparison. A simplified layout of the selected plants is provided (Reference Case- Fig. 1).

The same gas turbine [4] was selected in all configurations and the main goal was to achieve the lowest possible exhaust gas temperature exiting to the atmosphere (minimum stack temperature 90^{o}C) and in view of having directly comparable economic results. The selected gas turbine has an electric efficiency of 32%, a net power output of 104 MW, an air flow rate of 337.5 kg/s, an exhaust gas flow rate of 400 kg/s and an exhaust gas temperature of 540^{o}C at ISO conditions, in simple cycle mode. Taking into consideration the natural gas availability in Greece, the gas which is used as fuel in the GT has been assumed as a mixture of Algerian and Russian natural gas with a lower heating value of 47,500 kJ/kg.

Table 1. Main parameters of Megalopoli and Florina Power Plant

Parameters	*Values*
Fuel	Lignite
Turbine inlet	540 ^{o}C, 170 bar
Reheat steam	535 ^{o}C, 38 bar
Evaporator pressure	186 bar
Condenser pressure	0.059 bar
Feedwater preheaters	8 (7 + dearator)
Final Feedwater temperature (ECO inlet)	260 ^{o}C
Exhaust gas temperature	156 ^{o}C
Gross electric output	300 MW (Megalopoli), 330 MW (Florina)
Fuel input	192.2 kg/s (Megalopoli), 100.5 kg/s (Florina)
Lower Heating Value of fuel	4200 kJ/kg (Megalopoli), 7980 kJ/kg (Florina)
Net electric efficiency	34% (Megalopoli), 37.2% (Florina)

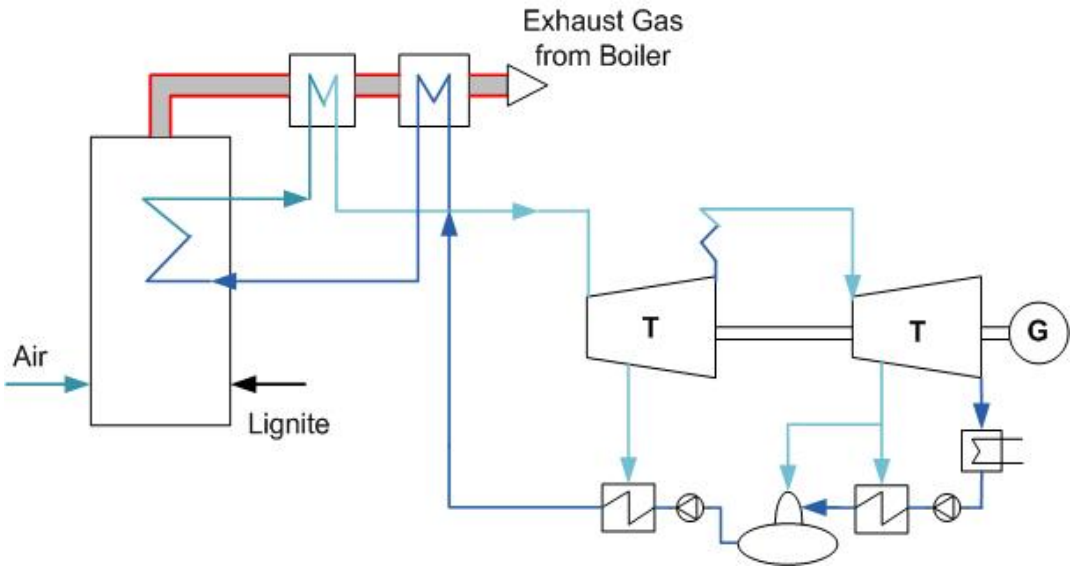

Fig. 1. Simplified schematic of a lignite power plant (Reference Case).

Three different combined cycle configurations were considered (Figs 2-4).

Case 1 refers to parallel repowering of the reference case plant and this method is known as boosting. In this scenario, the GT exhaust gases are utilized in order to substitute all the feedwater steam preheaters. By cutting the steam extractions that were previously used for preheating the

feedwater, it is now possible to exploit the total amount of the produced steam only for power generation purposes, thus increasing the electric power production (Fig. 2).

Case 2, is a parallel repowering configuration. A part of the boiler feedwater is fed to a Heat Recovery Steam Generator (HRSG) section, where it is evaporated and superheated using the waste heat of the GT exhaust. The superheated steam (537 ^{o}C, 38 bar) is mixed with the main steam flow upstream the low pressure steam turbine of the reference plant. The gain from this modification lies in the reduced steam extractions for feedwater preheating and the lower lignite consumption in the boiler (Fig. 3).

Finally, Case 3 is a combination of certain characteristics of Case 1 and Case 2. Taking advantage of the waste heat of the exhaust gases that exit the HRSG section at 200 ^{o}C after having completed the Case 2 scenario, it is possible to further exploit them in preheating the feedwater. In this way, two out of the seven low pressure steam preheaters were substituted and the feedwater is fed to a heat exchanger. The feedwater is heated up to 160^{o}C and the GT gases are exhausted to the atmosphere at 90 ^{o}C (Fig. 4).

Considering that the selected power plants are actually operating and aiming to minimize the cost of the repowering process, the existing steam turbines were considered to remain in use in the repowered plant in order to avoid the extra cost of adding new steam turbines. In this respect, the steam flow through the turbines was kept within the operational limits of the existing turbines by adjusting the lignite combustion in the boiler (boiler operating at part load).

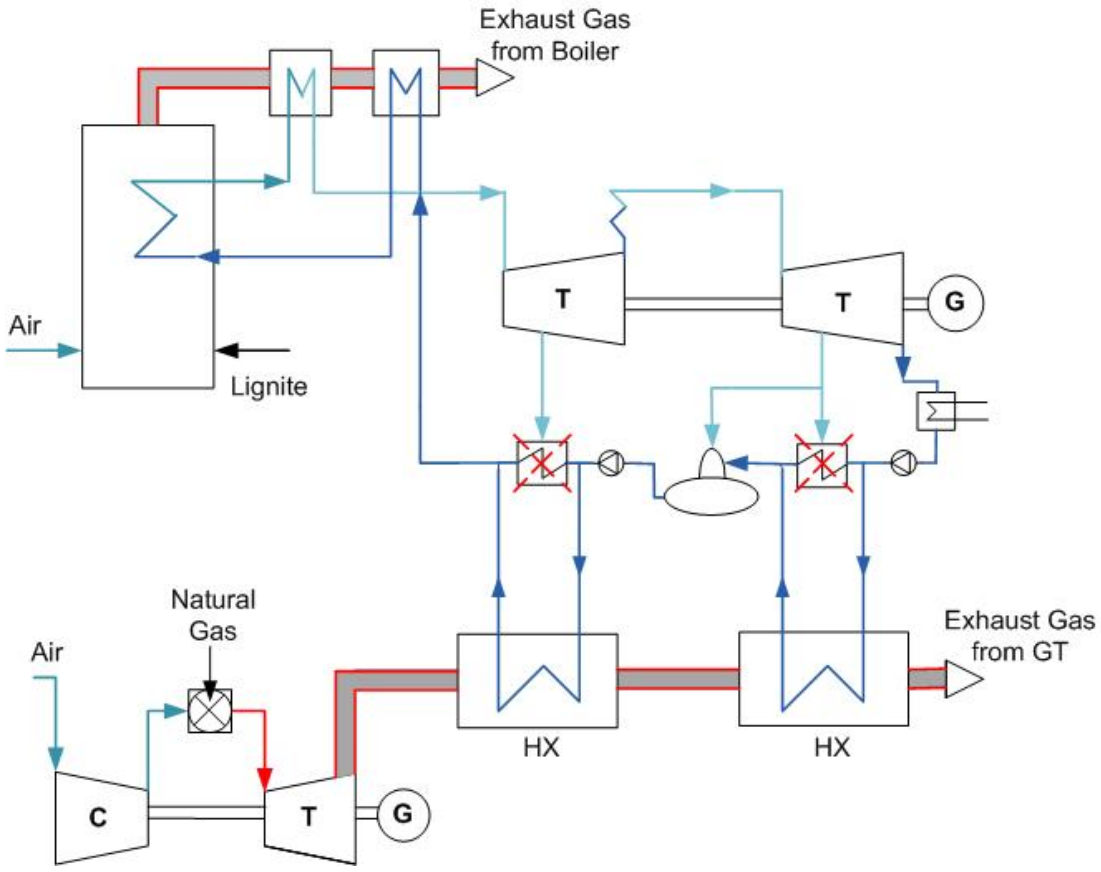

Fig. 2. Simplified schematic of a parallel-repowered combined cycle (boosting) with feedwater preheating from the gas turbine exhaust.

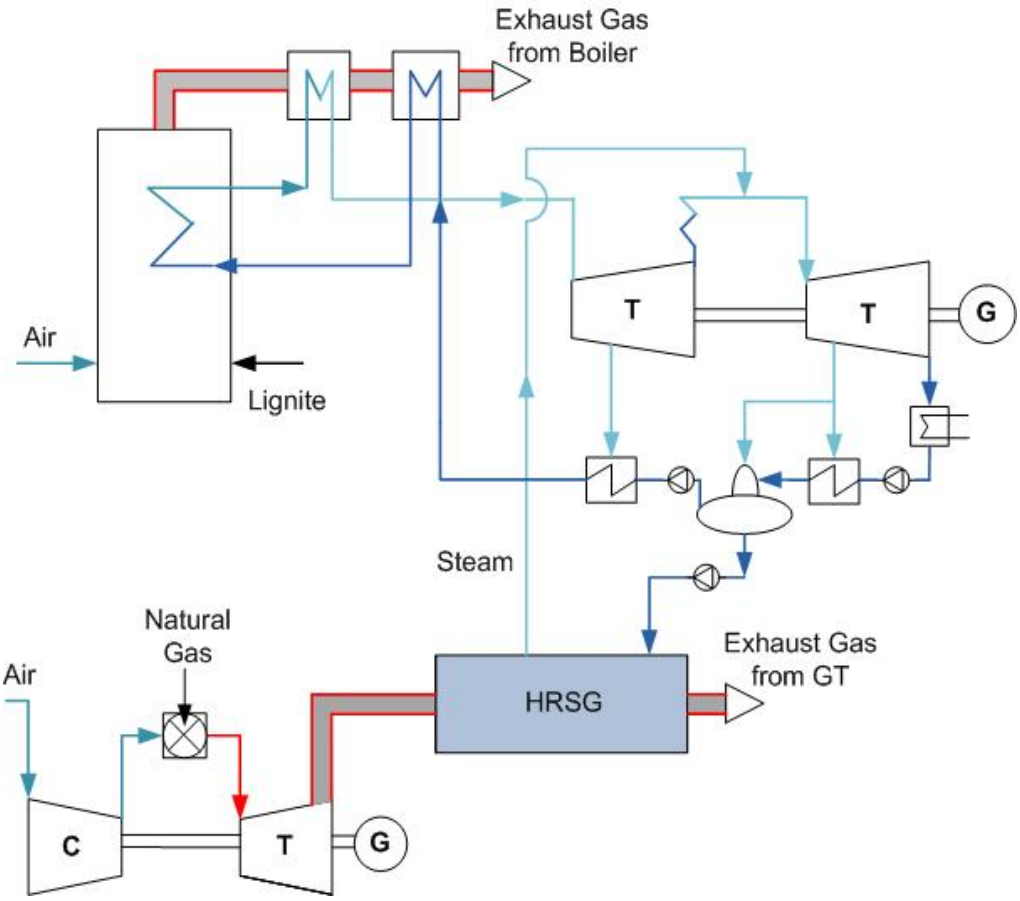

Fig. 3. Simplified schematic of a parallel-repowered combined cycle with parallel steam generation from the gas turbine exhaust (single pressure HRSG section).

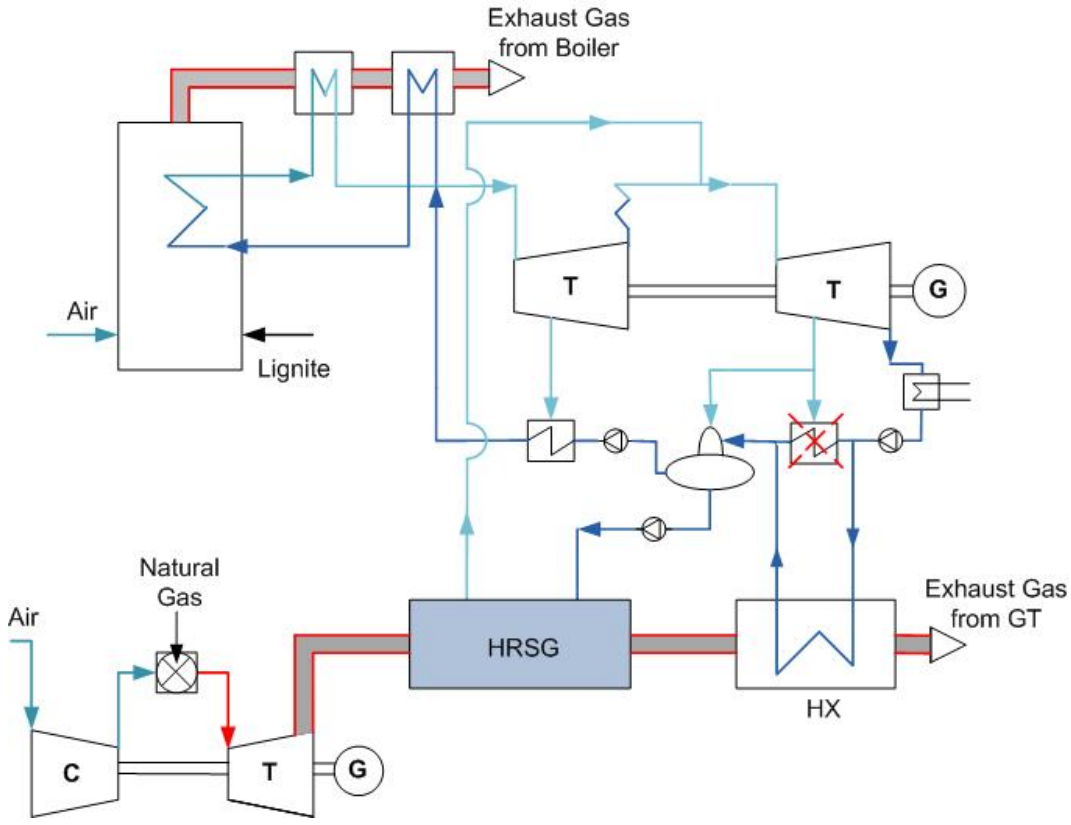

Fig. 4. Simplified schematic of the combination of Case 1 and Case 2. Parallel steam generation (at single pressure level) and feedwater preheating from the gas turbine exhaust.

3. Performance evaluation

3.1 Energetic analysis & results

The results of the proposed configurations are examined in terms of efficiency. Generally, electric efficiency is defined as the ratio of the energy output to the energy input. For a power plant, electric efficiency is defined as the ratio of the net power output to the fuel energy input.

$$\eta_{el} = \frac{P_{el}}{\dot{Q}_{fuel}}, \quad (1)$$

where

$$\dot{Q}_{fuel} = \dot{m}_{lignite} LHV_{lignite} \text{ (W)} \quad (2).$$

In the case of a combined cycle, the electric efficiency is calculated using the equation:

$$\eta_{el} = \frac{P_{TC} + P_{BC}}{\dot{Q}_{TC} + \dot{Q}_{BC}}, \quad (3)$$

where $\dot{Q}_{TC}$, $\dot{Q}_{BC}$ are the fuel energy inputs in the topping and bottoming cycle, respectively. In the current cases, the bottoming cycle refers to the lignite power plant ($\dot{Q}_{BC} = \dot{m}_{lignite} LHV_{lignite}$) and the topping cycle refers to the gas turbine unit, ($\dot{Q}_{TC} = \dot{m}_{NG} LHV_{NG}$). The results showing the fuel input, power output and overall plant efficiencies for each case are presented in Tables 2-3.

The installation of a gas turbine in parallel operation of a lignite power plant enhances significantly the efficiency and the power output of the plant. At the Megalopoli 4 Power Plant, the net efficiency of the combined cycle, based on LHV, was improved from 34% for the reference case to 36.6% for Case 1, to 34.8% for Case 2 and to 35.4% for Case 3. At the Florina Power Plant, the net efficiency is increased from 37.2% for the reference case up to 39.8% for Case 1, to 38.9% for Case 2 and to 39.4% for Case 3. Moreover, in all three cases an increase in the power output of the lignite plants was observed.

Case 1, where the feedwater is preheated using the waste heat of the GT exhaust, seems to be the most effective scenario. Despite the fact that the final power output of Case 2 is the greatest among all three cases, the efficiency has been improved only by 0.8% and 1.7% at the Megalopoli and Florina Power Plant, respectively.

A second approach of studying these configurations [9], [12-14] is to evaluate the bottoming cycles, instead of evaluating the combined cycles, aiming to establish a common base of comparison between the current operation and the repowering estimations. The bottoming cycle and the lignite burner remain unchanged in the repowering process. In this way, a more fair comparison can be conducted in terms of efficiency. The electric efficiency based on the bottoming fuel is given by the following equation:

$$\eta_{BC} = \frac{P_{el}^{TOT} - P_{el}^{GT}}{\dot{Q}_{fuel} + \dot{Q}_{Gas}}, \quad (4)$$

where $\dot{Q}_{fuel}$, $\dot{Q}_{Gas}$ is the energy given to the bottoming cycle through the fuel (lignite) and through the gas turbine exhaust gases ($\dot{Q}_{fuel} = \dot{m}_{lignite} LHV_{lignite}$, $\dot{Q}_{Gas} = \dot{m}_{Gas} c_p \Delta T$). Equation (4) calculates the amount of the power output from the overall combined cycle that corresponds to the bottoming cycle.

Table 2. Summary Results for the Megalopoli Power Plant

	Reference Case	*Case 1*	*Case 2*	*Case 3*
Fuel input (MW)				
Lignite	807.2	546.0	646.9	588.0
Natural Gas	-	318.2	318.2	318.2
Total	807.2	864.2	965.1	906.2
Lignite share (%)	100	63.2	67.0	64.8
Natural Gas share (%)	-	36.8	33.0	35.2
Net Power output (MW)				
Steam Turbine	265	206	231	216
Gas turbine	-	104	104	104
Total	265	310	335	320
Electric Efficiency (%)				
Efficiency of the CC (%)	-	36.6	34.8	35.4
Efficiency of the BC (%)	34.0	29.7	27.1	27.3

Table 3. Summarized Results for the Florina Power Plant

	Reference Case	*Case 1*	*Case 2*	*Case 3*
Fuel input (MW)				
Lignite	804.0	520.0	680.0	640.0
Natural Gas	-	318.2	318.2	318.2
Total	804.0	838.2	998.2	958.2
Lignite share (%)	100.0	63.2	68.1	66.8
Natural Gas share (%)	-	36.8	31.9	33.2
Net Power output (MW)				
Steam Turbine	298	246	286	273
Gas turbine	-	104	104	104
Total	298	350	390	377
Electric Efficiency (%)				
Efficiency of the CC (%)	-	39.8	38.9	39.4
Efficiency of the BC (%)	37.2	36.4	34.3	34.9

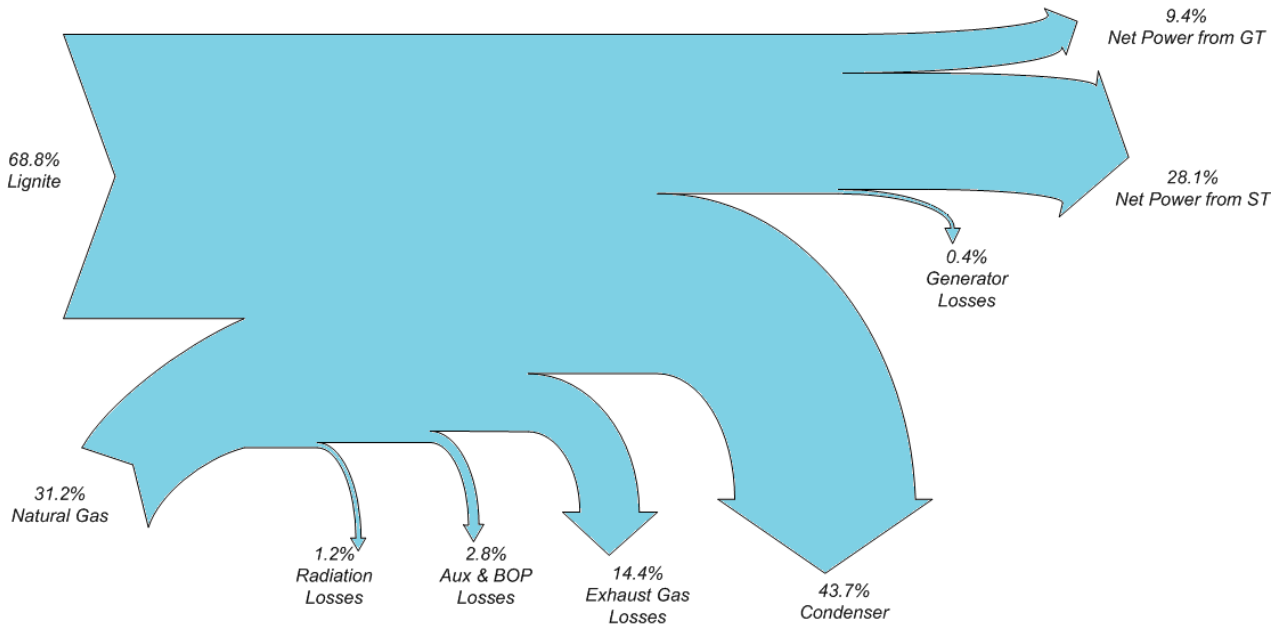

Fig. 5. Sankey diagram of Case 1 for the Megalopoli Power Plant.

All calculated lignite-based efficiencies were reduced compared to the efficiency of the current lignite power plant, which is an expected result because of the part load operation of the boiler. For the more effective scenario, Case 1, a Sankey diagram is provided in Fig. 5 for the Megalopoli Power Plant.

According to Fig. 5, the maximum energy losses are observed in the condenser. Moreover, there is a large amount of energy loss in the stack where the exhaust gases exit to the atmosphere.

3.2 Exergetic analysis

The exergy of a system is the maximum work done by the system during a transformation which brings it into equilibrium with its surroundings. Exergy does not generally follow the law of conservation as energy does, but it is destructed inside the system. Exergy destruction is the measure of irreversibility that is the source of performance loss. Therefore, an exergy analysis assessing the magnitude of exergy destruction identifies the location, the magnitude and the source of thermodynamic inefficiencies in a thermal system. The exergy of a material stream is given as the sum of physical, chemical, kinetic and potential exergy:

$$E = E^{PH} + E^{KN} + E^{PT} + E^{CH} \text{ (W)} \qquad (5).$$

Considering a system at rest, relatively to the environment (p_0= 1,01325bar, T_0=273,15K), E^{KN},E^{PT} are omitted and E^{PH} ,E^{CH} are the maximum theoretical useful work obtainable as the system passes from its initial state (*T, p)* to the zero state (T_0, p_0). The physical exergy of a system at a specific state is given by the expression:

$$E^{PH} = \dot{m}[\,h - h_0 - T_0(s - s_0)] \text{ (W)}, \qquad (6)$$

where enthalpy (kJ/kmol), entropy (kJ/kmol·K), mass flow (kg/s) and temperature (K) are provided from the heat balance software package, GateCycle. For the special case of an ideal gas, physical exergy is calculated with the equation:

$$E^{PH} = \frac{\dot{m}\left(\bar{h} - \bar{h}_0 - T_0(\bar{s} - \bar{s}_0)\right)}{M}, \qquad (7)$$

where M is the molecular weight and $\bar{h}$, $\bar{h}_0$, $\bar{s}$, $\bar{s}_0$ parameters are calculated based on the method that is described in “Thermal Design and optimization” by Adrian Bejan et. al. [22]. Chemical exergy is the exergy component associated with the departure of the chemical composition of a system from the environment. The chemical exergy is obtained when the components of the energy carrier are first converted to reference compounds and then diffuse into the environment, which is in reference state.

For a gaseous stream, the molar chemical exergy is given by the following equation:

$$\bar{e}^{CH} = \sum x_k \bar{e}_k^{CH} + \bar{R}T_0 \sum x_k \ln x_k \text{ (kJ/kmol)}, \qquad (8)$$

where x_k is the mole fraction of k component in the gas mixture, $\bar{e}_k^{CH}$ (kJ/kmol) the standard chemical exergy values for each component k, assuming a reference atmospheric composition given by Kotas [20] and $\bar{R}$ is the ideal gas constant (8.314 kJ·kmol^{-1}·K). The chemical exergy of lignite was calculated with the help of the statistical φ_ξ correlation, proposed by Szargut [21]:

$$\bar{e}^{CH}_{lignite} = (LHV_{lignite} + 2442 \cdot w)\varphi_{\xi} + 9417 \cdot S \quad \text{(kJ/kg)}, \qquad (9)$$

where S is the sulfide included in the fuel.

Considering a system at steady rate, in terms of exergy, the rates at which the fuel is supplied and the product is generated are E_F and E_P. An exergy rate balance for the system is:

$$E_F = E_P + E_D + E_L \text{ (W)}, \qquad (10)$$

where E_D and E_L denote the rates of exergy destruction and exergy loss, respectively. Exergy losses due to mechanical and electrical inefficiencies were taken into account but heat losses of the different units of the systems were neglected.

Exergetic efficiency is defined as:

$$\varepsilon = \frac{E_P}{E_F} = 1 - \frac{E_D + E_L}{E_F} \qquad (11).$$

E_P, E_F are defined properly for each system to describe exactly the amount of exergy that the system consumes to produce useful products. Exergy rate of a power output E^W, equals the power itself. The exergetic efficiency of the combined plants was calculated by the following equation:

$$\varepsilon = \frac{p^{ST} + p^{GT}}{E_{lignite} + E_{NG}} \qquad (12)$$

3.2.1 Exergetic Results

In all the examined scenarios, the exergy analysis has shown an increase in the total exergetic efficiency (Table 4). More specifically, at the Megalopoli Power Plant the total exergetic efficiency was enhanced up to 31-34%. The best exergy result was obtained for Case 1, where efficiency is increased from 28.2% to 33.7%. At the Florina Power Plant, a similar efficiency behavior is observed and the most effective scenario is again Case 1, where the exergetic efficiency is improved significantly compared to the reference case.

Table 4. Exergetic efficiencies for all scenarios

	Reference Case	*Case 1*	*Case 2*	*Case 3*
Megalopoli Power Plant				
ε(%)	28.2	33.7	31.4	31.6
Florina Power Plant				
ε(%)	32.6	36.9	35.8	36.1

For a more detailed overview of the exergy flow and the exergy destruction, Grassmann diagrams for the Megalopoli Power Plant are provided in Figs 6-8.The exergy rates are given as a percentage of the total fuel input.

In Fig. 6 the exergy of the boiler feedwater is increased, utilizing the exergy of the GT exhaust gas. The boiler is fed with a higher exergy than in the reference case. The exergy of the steam, used to preheat the boiler feedwater, improves the power generation achieving a better efficiency of the overall plant.

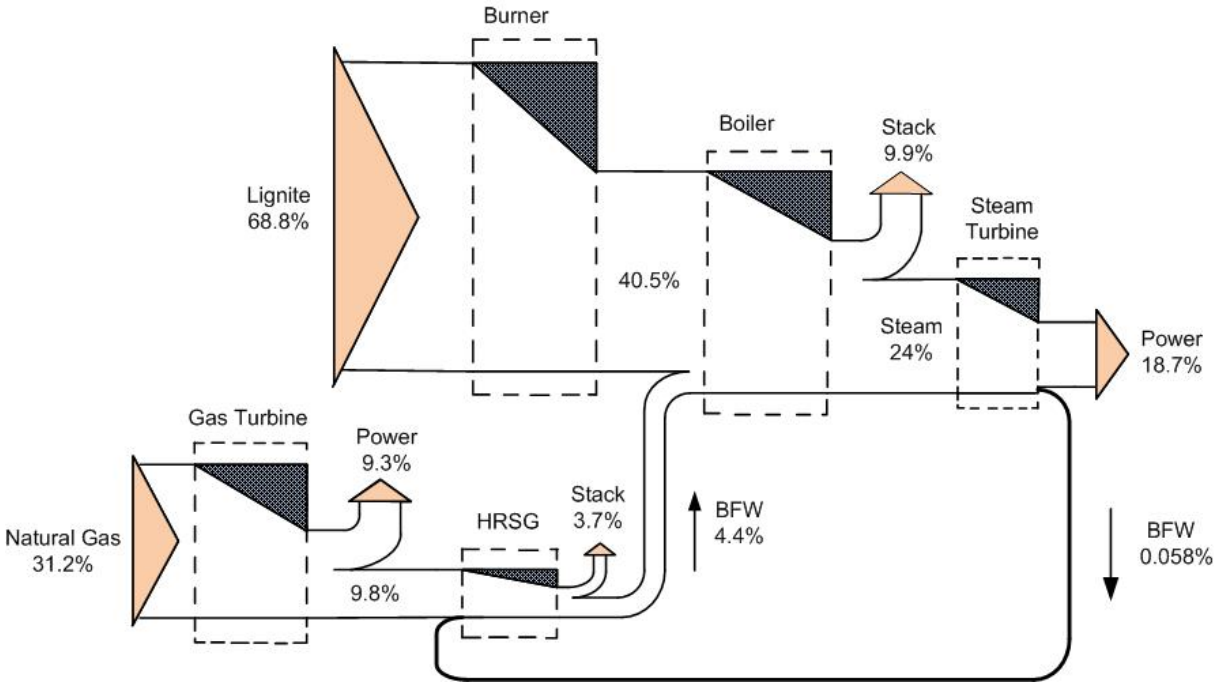

Fig. 6. Grassmann diagram of Case 1 for the Megalopoli Power Plant - parallel repowering (boosting) with feedwater preheating

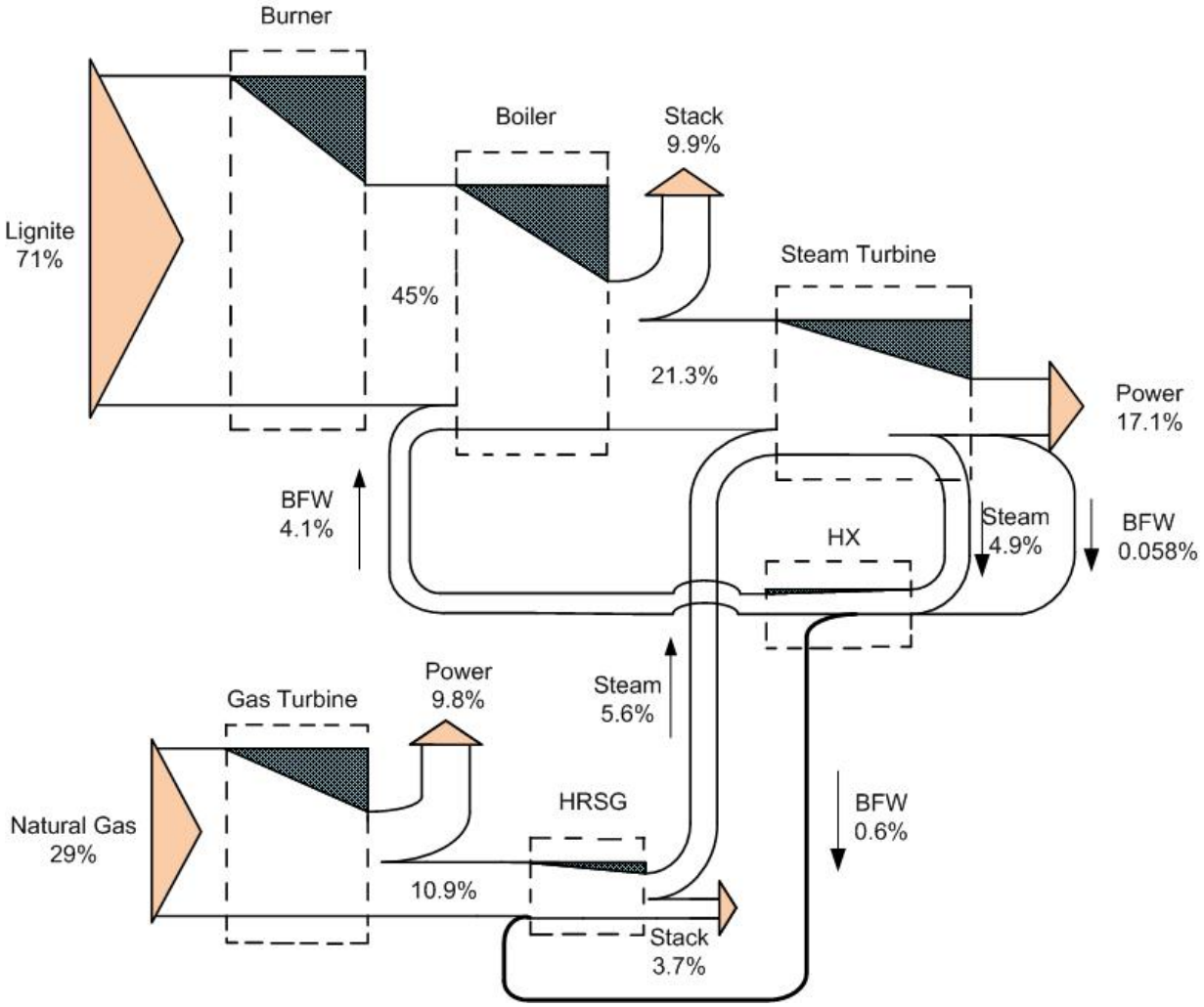

Fig. 7. Grassmann diagram of Case 2 for the Megalopoli Power Plant - parallel repowering with feedwater superheating in a single pressure HRSG.

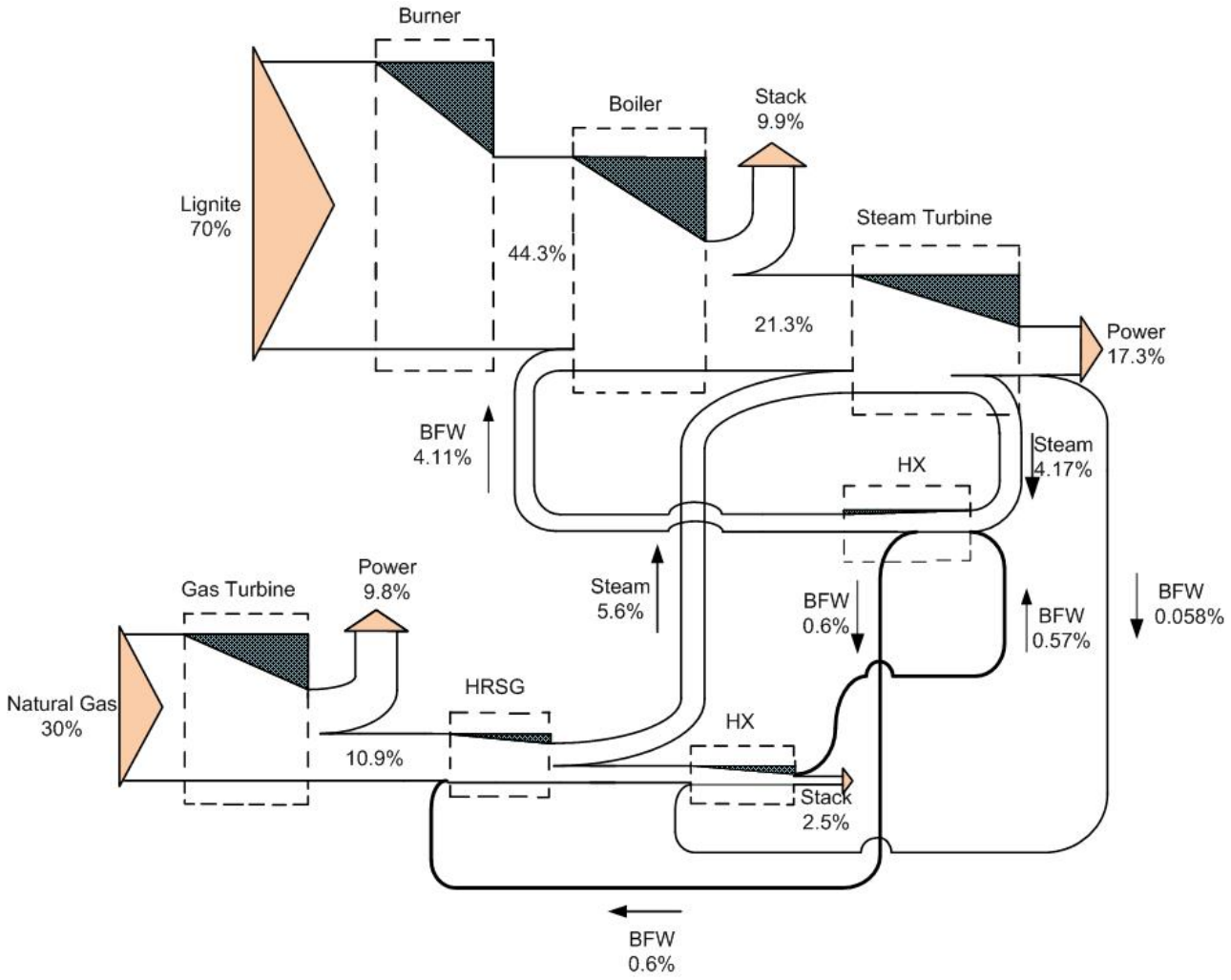

Fig. 8. Grassmann diagram of Case 3 for the Megalopoli Power Plant - combination of Case 1 and 2.

4. Economic evaluation

An economic evaluation of the proposed repowering configurations has also been performed. The investment costs comprise the GT cost, where a specific price of 400 €/kW has been assumed and the cost for the rest of the equipment (heat exchangers, HRSG's and piping). The total investment costs are estimated to 50, 55 and 60 M€ for repowering cases 1, 2 and 3 respectively, both for the Megalopoli and Florina units, for an amortization period of 10 years and an interest of 10%. Lignite costs are assumed 2.4 and 1 €/GJ for the Megalopoli and Florina unit respectively, while natural gas cost is taken as 10 €/GJ. Operating and maintenance variable costs are 1 €/MWh for the lignite power plants and 1.4 €/MWh for the repowered combined cycle plants, while CO_2 emission costs are assumed 10 €/tn. Since unit 4 of the Megalopoli Power Plant is quite old, full depreciation of the lignite plant is assumed, while for the Florina plant, depreciation costs are taken into account for the 20 year period of investment. Finally, it is assumed that both power plants are operated at base load before and after repowering process, for 7,500 hours full-load hours per year. Taking into account the above mentioned economic considerations, Table 5 tabulates analytically the individual costs concluding to the electricity generation costs of the combined cycle for the Megalopoli Power Plant.

Table 5. Cost Analysis for the Megalopoli Power Plant

	Reference Case	*Case 1*	*Case 2*	*Case 3*
Power Generation (MWh)	1,987,500	2,370,000	2,512,500	2,400,000
Lignite Consumption (GJ)	21,795,480	14,742,000	16,783,200	15,876,000
Natural Gas Consumption (GJ)	0	8,592,750	8,592,750	8,592,750
Emissions (tn)	3,040,848	1,958,643	2,178,367	2,063,727
Capital Costs (€)	0	8,137,269	8,950,996	9,764,723
Fuel Costs (€)	52,309,152	121,308,300	126,207,180	124,029,900
O&M Costs (€)	1,987,500	3,318,000	3,517,500	3,360,000
CO_2 Emission Costs (€)	30,408,485	19,586,433	21,783,674	20,637,267
Total Costs (€)	84,705,137	152,350,002	160,459,351	157,791,890
Electricity Generation Costs (€/MWh)	**42.6**	**64.3**	**63.9**	**65.7**

In order to investigate the operation load of the repowering scenarios, a natural gas-fired combined cycle unit has been assumed. Taking into consideration that in Greece the vast percentage of these units are 400-430 MW (gross power output), a 400 MW unit is being selected for further investigation. The total investment costs are estimated to 600 €/KW, natural gas cost to 10 €/GJ and CO_2 emission costs to 10 €/tn, just like in the repowering options. Finally, the operating and maintenance variable costs are considered 1.4 €/MWh for 5,000 operating hours of the combined cycle unit. The final electricity generation costs of a natural gas-fired combined cycle unit are up to 86.6 €/MWh. Simultaneously, for a more analytical economical approach, the variable operational costs for each case are estimated. The estimation of the variable operating costs is based on the operational and maintenance costs, the emission costs and the natural gas costs.

The final electricity generation costs and the variable costs of each repowering option for the Megalopoli and Florina Power Plant and for the natural gas-fired combined cycle unit are provided in Figs 9–10.

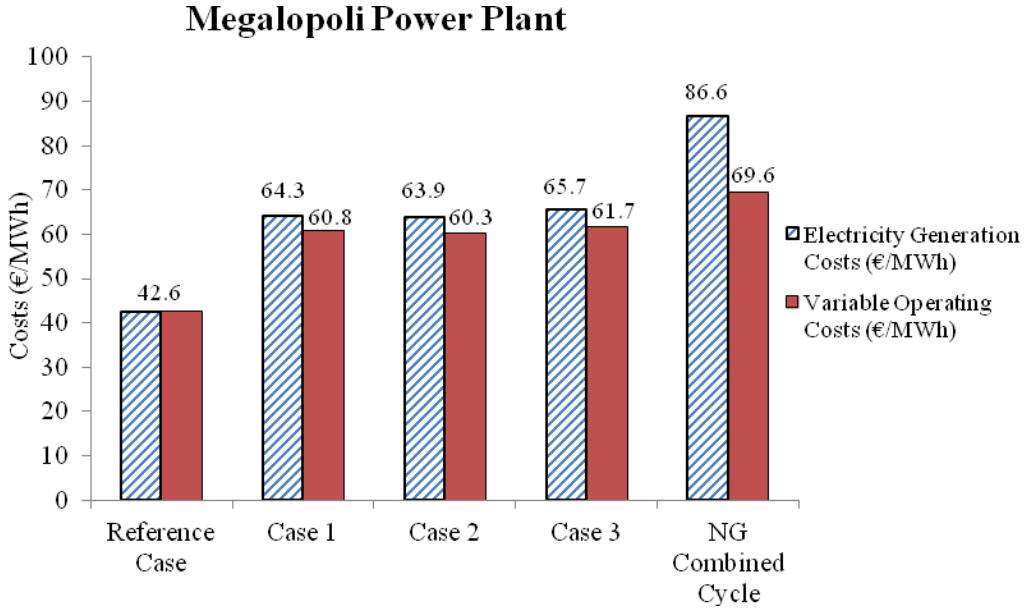

Fig. 9. Electricity Generation & Variable Operating Costs for the Megalopoli Power Plant.

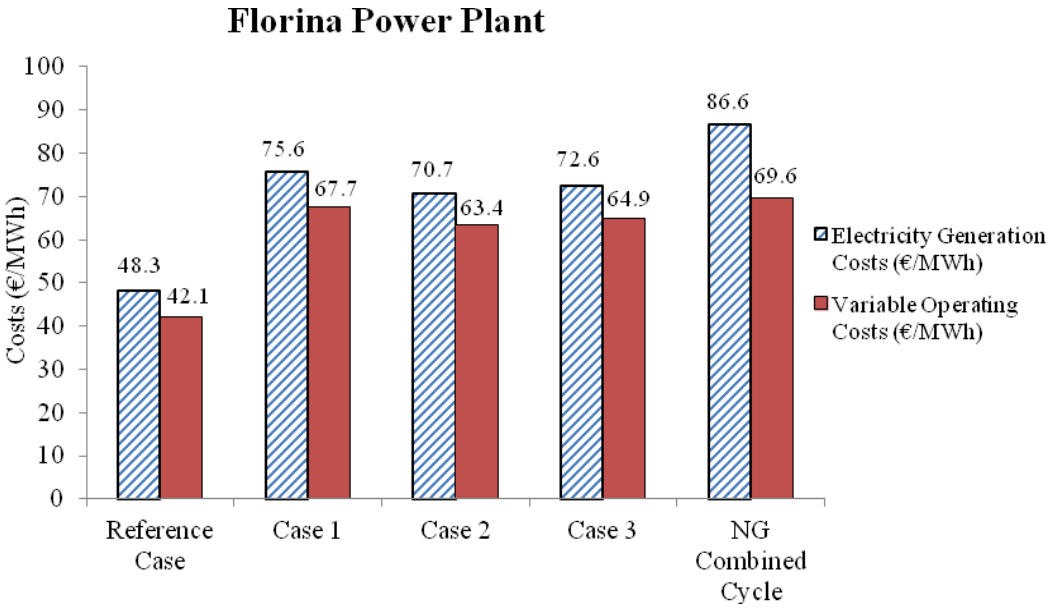

Fig. 10. Electricity Generation & Variable Operating Costs for the Florina Power Plant.

For both power plants, repowering option 2 (Case 2) exhibits the lowest cost of electricity, in spite of the fact that this case has the smallest efficiency among the other options, due to the highest lignite consumption, as has been shown in section 3.1. Given that in all cases, the electricity generation cost is significantly smaller than the cost of high-efficiency natural gas combined cycle units operating in the Greek system (above 86.6 €/MWh), it can be stated that the repowered units incorporating a gas turbine will have priority in entering the grid, displacing natural gas combined cycle units and thus will operate as base load units, as assumed. In order to further establish this fact, a full simulation of the electricity system is required, which is not deemed necessary at this level of analysis. Thus, it is established that repowering option 2 is the best option for the power producer in terms of economic gain, providing the minimum cost of electricity generation and the maximum additional capacity.

5. Conclusions

The current paper has presented a thermodynamic performance analysis of two Greek lignite-fired power plants for various repowering configurations with the utilization of a natural gas fired gas turbine. The main goal has been the optimization of the overall performance in terms of electric efficiency and power production of each cycle configuration and economics.The thermodynamic results have demonstrated that the 1st repowering option, where the feedwater is preheated using the waste heat of the GT exhaust, is the most effective scenario in terms of efficiency, while the 2nd parallel repowering option, where part of the boiler feedwater is fed to a HRSG, to produce superheated steam which is mixed with the main steam flow upstream the low pressure steam turbine of the lignite plant, demonstrates the highest power output. The economic analysis has demonstrated that the examined Case 2 achieves the lowest cost of electricity and is the best option for the power producer in terms of economic gain, providing the minimum cost of electricity and the maximum additional capacity.

NOMENCLATURE

LHV Lower Heating Value (kJ/Kg)

BC	Bottoming Cycle
TC	Topping Cycle
CC	Combined Cycle
$\dot{m}$	Mass flow
P	Power output (MW)
HRSG	Heat Recovery Steam Generator
GT	Gas Turbine
ST	Steam Turbine
$\dot{Q}$	Heat flow (MW)
NG	Natural Gas
E	Exergy flow (MW)
e	Molar exergy (kJ/kmol)
h	Enthalpy (kJ/kmol)
s	Entropy (kJ/kg·K); Sulfur
T	Temperature (K)
M	Molecular weight (kg/kmol)
$\overline{R}$	Ideal gas constant (kJ/kmol·K)
w	Water
BFW	Boiler Feedwater

Greek symbols

η	Electrical efficiency
ε	Exergetic efficiency
φ_ξ	Statistical correlation

Subscripts and superscripts

PH	Physical
KN	Kinetic
PT	Potential
CH	Chemical

References

[1] Bettocchi, R.; Cantore, G.; Galletti, A.; Gusso, R.; Negri di Montenegro, G. (1989) "Comparative Analysis of Gas-Steam Combined Cycles With and Without Supplementary Firing", Quaderni Pignone, Nr.47, June 1989, pp. 5-15.

[2] Fränkle, M.; SRS: the standarized repowering solution for 300 MW steam power plants in Russia. Siemens Power Generation Germany. Report 2006.

[3] Di Pasquale, L.; Torre, A.; Foglino, E.; Macchia, C.; Nicol, W. Converting conventional plants to combined cycles: ENEL, Ansaldo and Siemens experience, POWER-GEN Europe, April 2002.

[4] Brezonick, MJ. (editor); "Diesel and gas turbine worldwide catalog", Diesel and Gas Turbine Publications, vol. 68, Waukesha, WI, USA, 2003.

[5] Bauer, G.; Joyce, J. "The benefits of parallel repowering existing steam turbines with gas turbines", Siemens AG Power Generation Group. Report 1996.

[6] Escosa, Jesús M.; Romeo, Luis M. (2009) "Optimization CO_2 avoided cost by means of repowering'', Applied Energy, Vol. 86, Issue 1, November 2009, pp. 2351-2358.

[7] Brander, J.A.; Chase, D.L. (1991) "Repowering Application Considerations", ASME Paper 91-GT-229, Proceedings of the International Gas Turbine and Aeroengine Congress and Exposition, Orlando FL, USA, June 1991.

[8] Brückner, H.; Bergmann, D.; Termuehlen, H. (1992) "Various Concepts for Topping Steam Plants with Gas Turbines", Proceedings of the 54th Annual Meeting of the American Power Conference, Chicago, Illinois, April 1992, pp. 569-582.

[9] Consonni, Stefano (2000), "Combined Cycles for High Performance, Low Cost, Low Environmental Impact Waste-to-Energy Systems", ASME Paper 2000-GT-24, Proceedings of ASME TURBOEXPO, Munich, Germany, May 2000.

[10] Finckh, H.H.; Pfost, H. (1991), "Development Potential of Combined-Cycle (GUD) Power Plants With and Without Supplementary Firing", ASME Paper 91-GT-227, Proceedings of the International Gas Turbine and Aeroengine Congress and Exposition, Orlando FL, USA, June 1991.

[11] Galletti, Alessandro (1990), "Repowering Power Plants and Cogeneration Stations with Gas Turbines", Quaderni Pignone, Nr.49, December 1990, pp. 29-34.

[12] Kamminga, P. (1987), "Boosting Steam Plant Thermal Efficiency and Power Output by Adding Gas Turbines", Proceedings of the ASME COGEN-TURBO International Symposium, Montreaux, France, 1987, pp. 363-368.

[13] Korobitsyn M. A., Jellema P., Hirs G. G. (1999). Possibilities for Gas Turbine and Waste Incinerator Integration. Energy 24 (9), pp 783-793, Pergamon Press.

[14] Stenhede, T., 2001, "Waste-to-Energy Combined Cycle Plant", Sixth International Conference on Engineering for Profit from Waste, Paper Nr. C598/019/2001, ImechE Conference Transactions, London UK, November 2001, pp. 103-120.

[15] Ribeiro S.G., Kimberlin T. (2010), "High efficiency waste to energy power plant combining municipal solid waste and natural gas or ethanol", Presented at the 18th Annual North American Waste-to-Energy Conference, OrlandoFL, USA, May 2010.

[16] Lowry, William L.; Martin, Charles A. (1990), "Economics of Combined Cycle Waste-to-Energy", Proceedings of the International Joint Power Generation Conference, Boston MA, USA, October 1990, pp. 31-37.

[17] Morikawa, K.; Fukumoto, F.; Kawauchi, A. (1993), "Renewal of Existing Fossil-Fired Plants Incorporating Fully-Fired Combined Cycle", Hitachi Review, Vol. 42, Nr.1, February 1993, pp. 17-24.

[18] Stenzel WC, Sopocy DM, Pace SE. Repowering existing coal fired plants. International Conference on Power Engineering ICOPE-97, Tokyo, July 13–17, 1997.

[19] Gate Cycle User's Guide. Version 5.3, Menlo Park, California, 1995.

[20] Kotas. T.J, 1995, The exergy Method of Thermal Plant Analysis. Malabar (FL): Krieger Publishing Company.

[21] Szargut J, Morris DR, Steward FR. Exergy analysis of thermal, chemical, and metallurgical processes. New York: Hemisphere Publishing, 1988.

[22] Bejan A, Tsatsaronis G, Moran M. Thermal Design and Optimization, John Wiley and Sons, June 1995

[23] Power units Amsterdam cluster, Available at: <http://www.nuon.com/company/core-business/energy-generation/power-stations/Amsterdam-cluster.jsp>[accessed 10.1.2012].

Energy saving by a simple solar collector with reflective panels and boiler

Anna Stoppato [a], ***Renzo Tosato(CA)*** [b]

[a] *D.I.I University of Padova. Padova, Italy, anna.stoppato@unipd.it,*
[b] *D.I.I University of Padova. Padova, Italy, renzo.tosato@unipd.it,*

Abstract:

Solar energy is absorbed by a simple and long-life solar collector set in a garden. The heated water is pumped to a shower directly or through a boiler. This paper focuses on the combination of high efficiency boilers with a simple collector. A tank of water pre-heated by ambient air and solar irradiation and/or a hot water reservoir can be added to the system in order to save fuel and reduce CO_2 emission. The behaviour of the system has been simulated: water temperatures over a day are calculated as a function of the dimensions and the exposure of the pipes and of the surfaces of the reflective panels, of weather data and of water consumption.

The numerical solution of the partial differential equation is obtained by a discrete approximation. The temperature field is approximated by values at discrete points where elements are concentrated.

Numerical results of six different hot water systems with a simple solar collector are presented. The consumption of gas and CO_2 emissions are compared with an instantaneous boiler, a combi-storage boiler and an electric boiler.

Keywords:

Solar Collector, Gas Boiler, Hot Water Service, CO_2 Emissions.

1. Introduction

The use of solar energy for water heating has a long tradition in human history, but at present the need for promoting renewable energy sources and increasing the efficiency in energy systems without decreasing user' welfare, also requires that these systems are properly designed so as to take into account weather conditions and the user demand.

Solar systems aimed at heating water for showers could be an attractive solution in marine places, for example for holiday camps or bathing establishments, where the weather is usually sunny and the user demand is concentrated during the summer. These conditions allow a good exploitation of the solar source. Solar systems could be also interesting in low-income countries, for isolated buildings or communities where the access to fuels is difficult and expensive [1, 2, 3, 4]. For all these kinds of systems the cheapness, the simplicity of installation and of maintenance, the availability and the reliability are more important than the efficiency, so that an analysis aimed at improving them must consider all these aspects.

In order to improve thermal efficiency [4, 5] many authors have studied different solutions for solar collectors systems: they have analysed the thermal regime in the collectors considering weather variations and water temperature [6, 7, 8]. This paper presents a simple method to simulate the operation and/or to forecast the performances of a solar installation for hot water production. Furthermore, this papers takes into account the presence of integrative boilers, a tank where cold water is pre-heated by ambient air and solar radiation, hot water reservoirs and flat and reflective panels for sun radiation concentration on the collector. The method permits the study of energetic efficiency and CO_2 emissions in comparison to those of a boiler during an average year as a function of system geometry and arrangement, solar irradiation, environment temperature and thermal requirement. A simple experimental approach able to determine the exchange coefficients

used in the analysis of the collectors is presented, too. In order to show the potentiality of the method and validate it the paper describes its application to a simple actual shower installation.

2. Description of the experimental apparatus

A simple solar shower [9, 10] has been installed in a seaside place in southern Italy (Calabria). As shown in Fig. 1, as heat exchanger the system uses four series connected pipes for agriculture irrigation; each pipe has a diameter of 6 cm and is 12 m long, with a total length of 52 m, including the connection curves. The pipes form a reservoir containing about 150 liters of water. The heated water gets cold during the night, and it is not stored.

The system was constructed in 1980 in the vicinity of the sea shore. During so long a period none of the important parts (all made of zinc-steel or chromium plated) needed to be replaced. The maintenance of the shower installation consisted mainly in cleaning it from grass and branches.

As a consequence, the costs of construction and maintenance are very low.

It is interesting to note that the thermal dispersions for convection to the ambient are much higher than those in modern thermal solar collectors and that in this simple configuration the pipes in the lowest position are overshadowed by other pipes.

Since in some periods of the year the temperature of water can be too low for shower use a supplementary gas fired boiler, which is series connected with the solar collector, has been added.

An increase in the water temperatures of the pipes has been also obtained by means of flat and reflective panels which concentrate the sun radiation with a higher power (Fig.1).

Data about the ambient and pipes temperatures, water mass flow rate, and solar irradiation have been collected for some months in the past year.

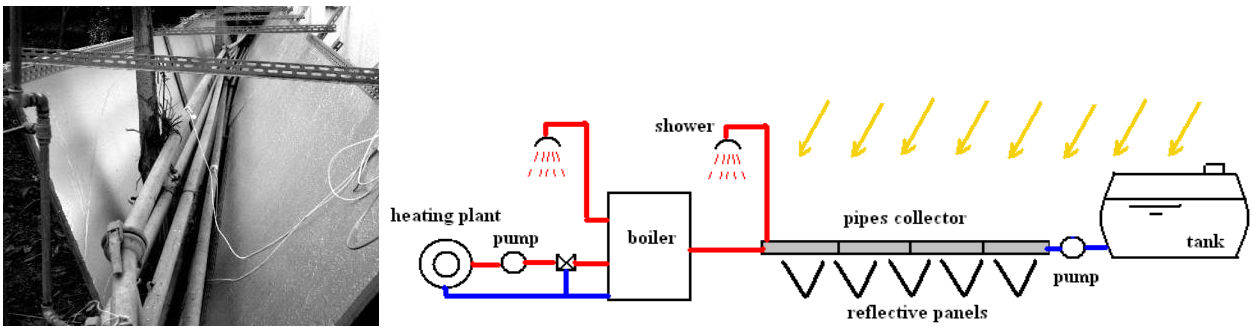

Fig. 1. Solar shower installation in a garden supplemented with flat reflective panels and a combi boiler for Heating and HW services.

2.1 Simulation of the pipe collector

In the model of the plant some components have been considered as concentrated distinct single points, because their temperatures depend mainly on the time.

The pipe collector is composed of 4 tubes, each of which is 12 m long, and has been studied taking into account 4 concentrated points with constant parameters (L=12 m). The simulation program did not give significant differences in numerical results for smaller subdivisions (L=6 m or L=2 m).

Each segment (L=12 m) is subjected to energy exchanges having the following coefficients, which are constant during each interval of time Δt and variable only with time t:

- The convective heat transfer (K coefficient, kW/m^2/K).
- The irradiation to the ambient air (KI coefficient, kW/m^2/K).
- The irradiation of the sun (PSOL, kW/m^2).

- The effects of shadow on solar power absorbed (KS shadow factor).
- The effects of wind on convective heat transfer (KW wind factor).
- The effects of reflective panels on irradiation (KR reflective plates factor).
- The effects of the amount of water W flowed during the interval Δt.

Since the heat conduction in the wall of the pipes and the water side convection are much faster than the heat convection from the surface of pipes towards external air, the temperature gradients inside the water and inside the metal are negligible. As a consequence, the metal temperature is assumed to be equal to that of the water. During the day HWS (Hot Water Service) consumption W, air temperature TA and the other conditions (PSOL, KS, ..), cause continuous water temperature variations T and a new steady state thermal equilibrium is gained at time t+Δt. The numerical simulation of this solar shower is time dependent on the heat transfer.

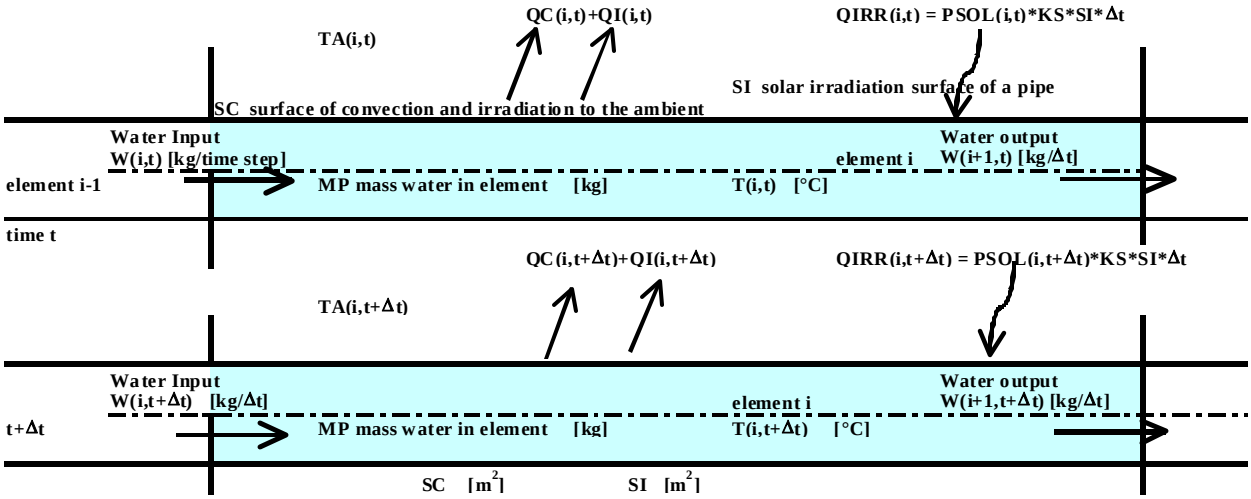

Fig. 2. Schematisation of Heat exchanges in the element i at times t and t+Δt.

The numerical solution of the partial differential equations is obtained by a discrete approximation. The temperature field is approximated by values at discrete points where the elements, long L, are concentrated. Water temperatures T are considered at consecutive time-steps with a time increment Δt.
The increments in x-direction are denoted by points i-1, i and i+1. The length of the collector is divided into few elements and the lengths L are fixed at the start of the calculation.

In fig. 2 the equations for different heat transfer modes of an element i, during a time step Δt, are:

1) Convection and irradiation from the surface SC of the pipe element i to the ambient:

$$QC(i,t) = K \cdot \Delta t \cdot SC \cdot (1+KW) \cdot \left[T(i,t) - TA(i,t)\right] \quad \text{[kWh]} \quad (1)$$

$$QI(i,t) = KI \cdot \Delta t \cdot SC \cdot \left[T(i,t) - TA(i,t)\right] \quad \text{[kWh]} \quad (2)$$

2) Radiation from the sun to the surface SI of the pipe

$$QIRR(i,t) = PSOL(i,t) \cdot \Delta t \cdot SI \cdot KS \cdot KR \quad \text{[kWh]} \quad (3)$$

3) Energy by mass transfer to and from a pipe element

$$QW(i,t) = W(i,t) \cdot \Delta t \cdot cp \cdot \left[T(i-1,t) - T(i,t)\right] \quad \text{[kWh]} \quad (4)$$

In conclusion the equation of energy balance of the pipe element i, during a time step □t, is:

$$QC(i,t) + QI(i,t) + QIRR(i,t) + QW(i,t) = (MP \cdot cp + MM \cdot cpm) \cdot \left[T(i,t+\Delta t) - T(i,t)\right] \text{[kWh]} \quad (5)$$

Air temperature TA, power PSOL, other conditions during a day (KS and KR) as well as water consumption (W) are the main important parameters used to calculate the variation of temperatures T of the water during a day.
The transient problem is solved with the explicit forward differences method: the old temperatures, convection coefficients, … and mass transfer parameters are used to calculate the heat flows during Δt. At time $t+\Delta t$, the new temperature $T(i,t+\Delta t)$ of the element i is calculated by the equation:

$$T(i,t+\Delta t) = T(i,t) + [K \cdot \Delta t \cdot SC \cdot (1+KW) \cdot [T(i,t) - TA(i,t)] + KI \cdot \Delta t \cdot SC \cdot [T(i,t) - TA(i,t)] + \\ + PSOL(i,t) \cdot \Delta t \cdot SI \cdot KS + W(i,t) \cdot \Delta t \cdot cp \cdot [T(i-1,t) - T(i,t)]] / (MP \cdot cp + MM \cdot cpm) \quad [°C] \quad (6)$$

In this equation, temperatures, convection coefficients and the other parameters evaluated at time t are used to calculate the heat transfer during the interval of time Δt.

2.2 Experimental evaluation of K, KS, KR and KW mean coefficients

All the heat coefficients are unknown and variable during a day.

If there is not consumption of water W(i,t), (6) gives the water temperature as:

$$T(i,t+\Delta t) = T(i,t) + [K \cdot \Delta t \cdot SC \cdot (1+KW) \cdot [T(i,t) - TA(i,t)] + KI \cdot \Delta t \cdot SC \cdot [T(i,t) - TA(i,t)] + \\ + PSOL(i,t) \cdot \Delta t \cdot SI \cdot KS] / (MP \cdot cp + MM \cdot cpm) \quad [°C] \quad (7)$$

In order to evaluate K, KW, KI, KS and KR a simple experimental test has been performed. They can be simply considered as constant values during a day and corresponding to their mean values. They have to be assumed as trial values when the program has to calculate step by step the temperatures of the water. If T, TA and PSOL are measured in the experimental plant of Fig. 3 for each pipe and the pipes are differently exposed to air and sun, the unknowns can be determined as the set of values which allows the better fit between the experimental and the calculated trends of T.

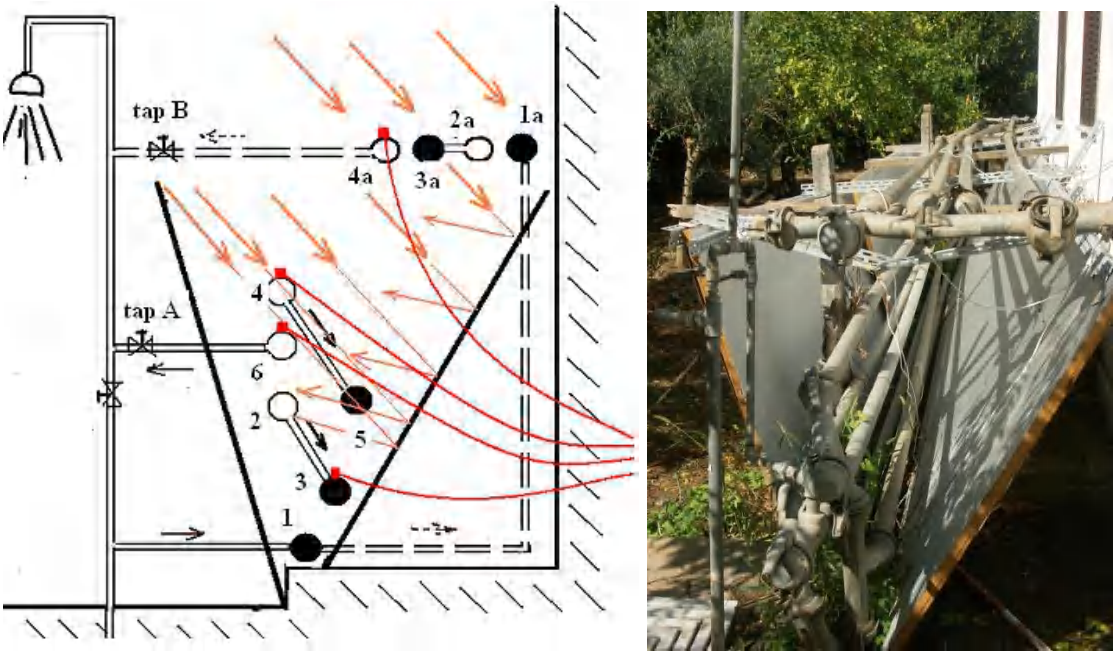

Fig. 3. Test rig with temperature measurement system of pipes 3, 4, 4a and 6 connected to a data logger. Two connections are possible when the shower is open (tap A: pipes 1, 2, 3, 4, 5 and 6 or tap B: pipes 1a, 2a, 3a and 4a)

Different pipes have been put in the experimental solar system, as shown in Fig.3:

- covered (not exposed to the wind) (pipes 1 and 3)
- covered and subject to reflective panels irradiation (pipe 4)
- covered and partially shadowed pipe (pipes 2, 5, 6)
- exposed to the wind (pipes 1a, 2a, 3a, 4a)

Pipes and air temperatures and PSOL have been measured for some months: Figure 4 reports an example of data collected during 7 days in September 2011 in the experimental plant in southern Italy.

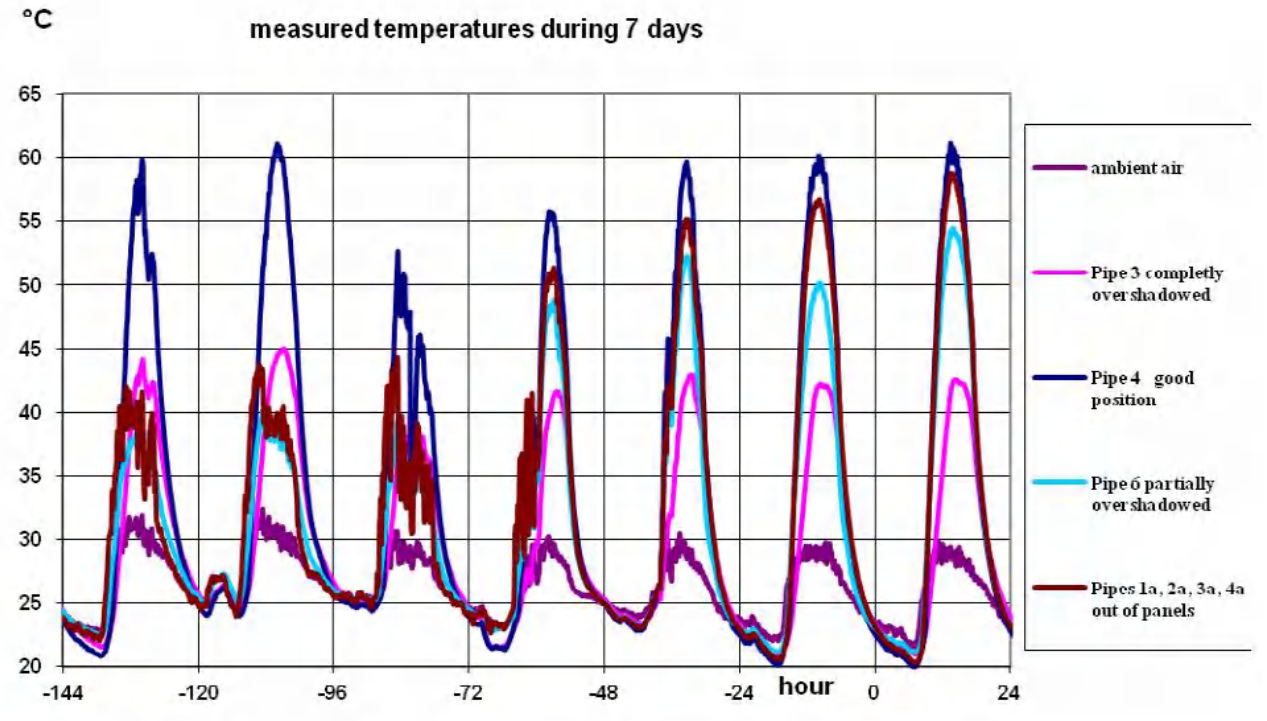

Fig. 4. Air and tubes temperature values collected during 7 summer days.

During the hottest hours (around 2 pm) of the day the temperature of pipe 4, which is exposed to the sun and subject to panels reflections, is above 60°C, while the ambient temperature has a peak value of about 30°C. The highest temperature of a pipe 3, which is very overshadowed, is 45°C. During the night, the temperatures inside all the pipes become equal to that of the ambient air (about 20 °C in the early morning).

Fig. 5 indicates registered and simulated trends of T for a day of pipes 4 and 6. The simulated values have been calculated by means of equation (7), using the coefficients summarized in Table 1. The temperature of the air is TAmin = 21,5 °C at tmin = 5 am and TAmax = 29 °C at tmax = 14 = 2 pm.

During the day TA trend has been simulated as

$$TA = \frac{TA\max + TA\min}{2} - \frac{TA\max - TA\min}{2} * \cos\left(\frac{t - t\min}{t\max - t\min} * \pi\right) = 25{,}25 - 3{,}75 * \cos\left(\frac{t-5}{9} * \pi\right)$$

from tmin = 5,00 until tmax*3/2-tmin/2 = 18,50 = 6:30 pm

While during the evening and the night the temperature TA changes in linear way.

The solar radiation flux is PSOL = -432-1295*cos(t*π/12)) W/m^2, taken only with positive values and equalling zero when this function is negative. The maximum value of PSOL, at 12 am, is

PSOLmax = 865 W/m^2 while duration of solar irradiation is from 7.00 = 7:00 am to 17,00 = 5:00 pm.

Table 1. Values of mean coefficients KS, K, KW and KI during the day of measurements.

11 sept 2011						
	pipe 6	pipe 4	pipe 3	pipes 1a, 2a, 3a, 4a		
PSOLmax	865.0	865.0	865.0	865.0	W/m^2	at 12 am
KS	0.8	1.0	0.5	1.0	-	
KR	1.1	1.1	1.0	1.0		
KR*KS*PSOLmax	713.6	951.5	432.5	865.0	W/m^2	at 12 am
TAmax	29.0	29.0	29.0	29.0	°C	at 2 pm
TAmin	21.5	21.5	21.5	21.5	°C	at 5 am
W	0.0	0.0	0.0	0.0	kg/s	
K	3.5	3.5	3.5	3.5	W/m^2/K	
KW	0.4	0.6	0.2	1.1		
K*(1+KW)	4.9	5.6	4.2	7.4	W/m^2/K	
KI	1.7	1.7	1.7	1.7	W/m^2/K	
K*(1+KW)+KI	6.6	7.3	5.9	9.1	W/m^2/K	
T pipe max	55.0	60.0	41.3	57.2	°C	at 2 pm

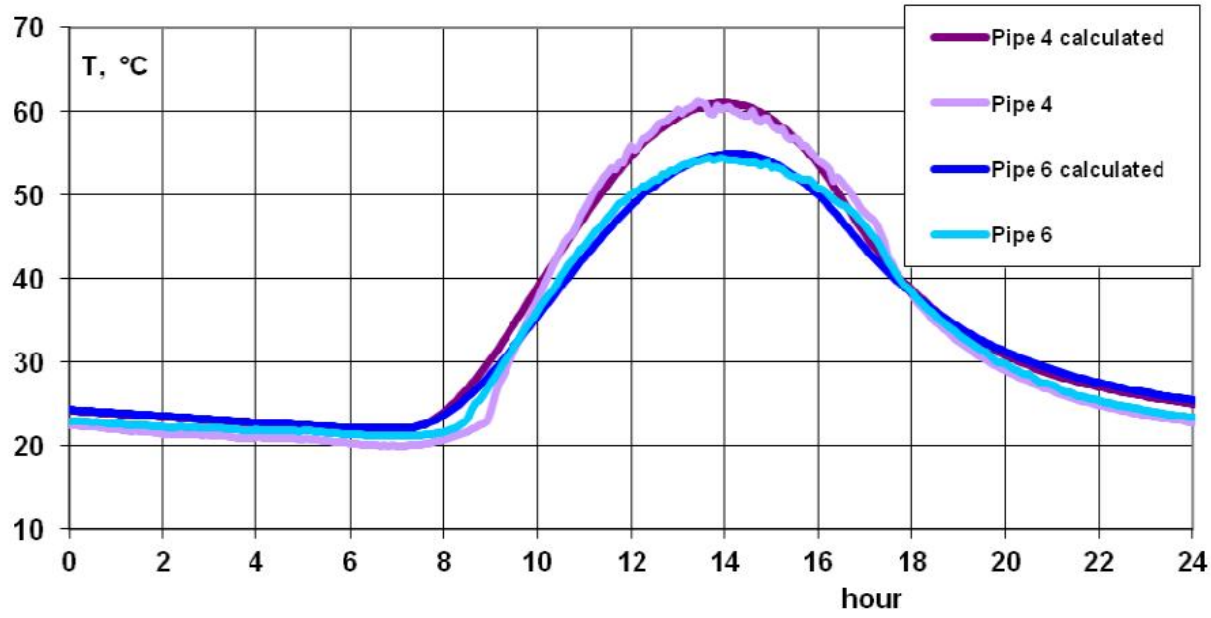

Fig. 5. Comparison between calculated and registered temperatures trend for some pipes of fig. 3.

3. Gas Boilers for Hot Water Service (HWS)

Although in the summer sun-irradiated energy can somewhere be sufficient for some showers without any boiler, the presence of an integrative boiler is often necessary.

For gas boilers working in heating plant in winter cyclical efficiency at partial loads is variable during the day and depends on the characteristics of the boiler, of the plant, of the regulation system, of the weather conditions. For a condensing boiler it can be as the curve of Fig. 6a and can be calculated by using two experimental curves of the boiler: the efficiency at full load (Fig. 6b) and stand-by losses (Fig. 6c) [11, 12].

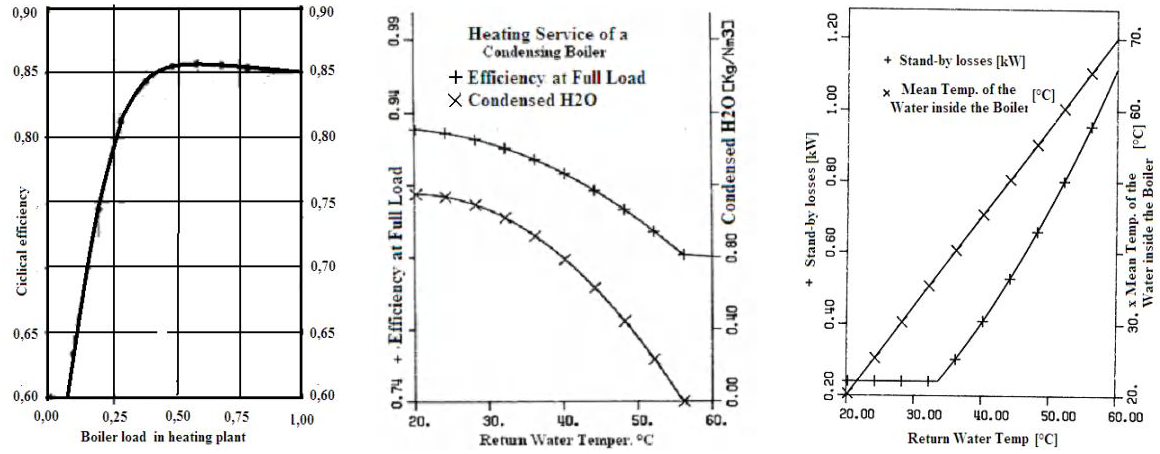

a) b) c)

Fig. 6. Efficiencies of a boiler at partial load in heating plant: a) Condensing boiler connected to a plant by a 3-way mixing valve, b) efficiency at full load as function of return water temperatures, c) stand-by losses as function of mean return water temperatures.

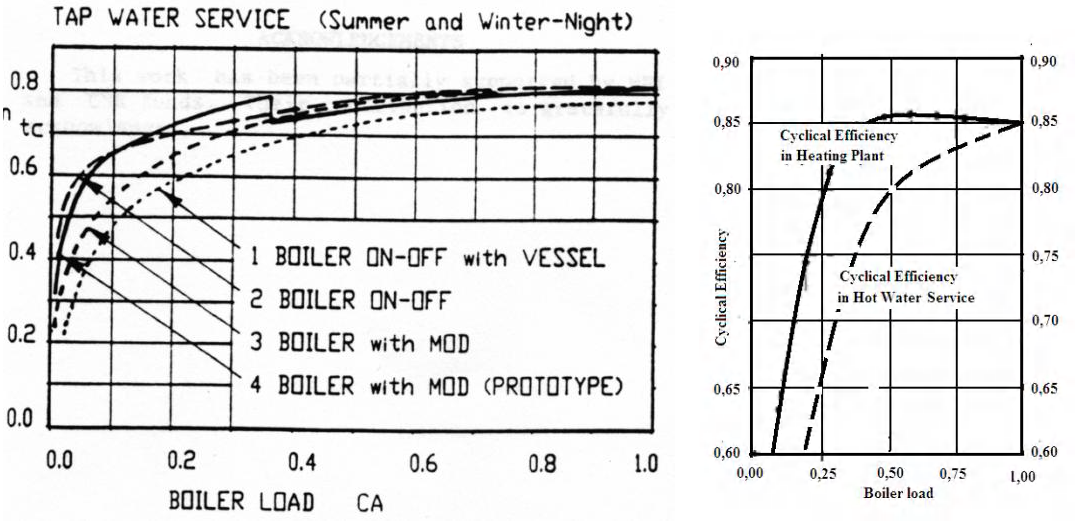

a) b)

Fig. 7. Cyclic efficiency in Hot Water Service (HWS) as function of Boiler Load: a) four combined boilers, b) instantaneous condensing boiler in heating service and HWS.

A combi-instantaneous boiler is widely used for heating plants and for hot sanitary water. Combi boiler is both an efficient water heater and a heating boiler combined within a single unit.

Instantaneous boilers deliver hot water immediately whenever it is needed.

A combi-storage boiler gives better performance through a tank of heated water. At the first tap opening, the storage tank can deliver an abundant water supply and heated water delivery depends upon the size of the tank.

Better efficiency is obtained when HWS and heating service are integrated in a single Combi boiler.

The energy problem of boilers arises from the decrease in the cyclical efficiency when they deliver sanitary hot water [12, 13, 14]. This reduction of efficiency is very large when the boiler is not working for heating plant, for example during the summer and during the night in winter. This depends on the type of boiler and mainly on the flow of Hot Water in comparison with the output of the boiler, as described in fig. 7a. The same condensing boiler of fig. 6 can have the efficiency of fig. 7b.

4. Results

In order to evaluate the simple approach proposed, different solutions able to satisfy the demand of hot water has been simulated and compared. It has been assumed that 1400 kg/day of water at 50°C are required between 8 am and 8 pm. These data correspond to about 30 showers/day. with three peaks in the thermal requirement at 10 am, at 2 pm and at 6 pm. Fig.9 reports user cumulative demand trend (WG).

Six different plants (cases 1- 6) with a simple solar collector have been simulated. All of them are equipped with a high efficiency gas boiler, which guarantees that the temperature of water reaches 50°C, when required. They have been compared also with three more traditional plants equipped with gas boiler (cases 7), with gas boiler and Hot Water Reservoir (case 8) or with an electric boiler (case 9).

The systems differ from each other as:

- Water can be obtained from a well at low temperature (15°C, cases 1, 3 and 5), from the city aqueduct (18°C, cases 7-9) or from a tank at ambient temperature (it has been supposed that its temperature is the mean air temperature of the day, in this case 25°C, cases 2, 4 and 6).
- A hot water reservoir can be present with a capacity of about 300 l (cases 5, 6 and 8). In cases 5 and 6, the water is pumped, by an electronic system, from the solar collector to the reservoir only when its temperature T is higher than that inside the reservoir T_{res}, otherwise it remains inside the tubes. The boiler heats up to 50°C the water required by the users. In case 8, the temperature of the reservoir is kept at 50°C by the combi-storage boiler.
- reflective panels can be present (cases 3-6).
-

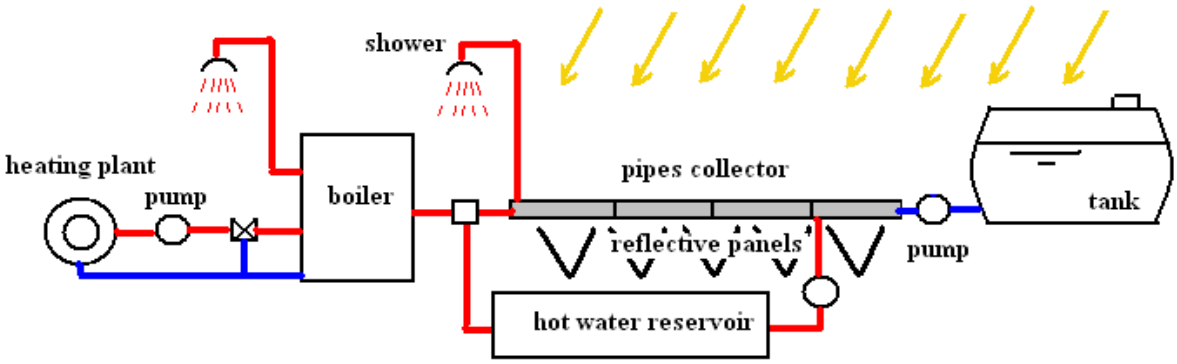

Fig. 8. Configuration of the system in Case 6.

The first 7 columns of Table 2 present a short description of the different systems. For all the 9 cases the following data have been assumed:

- Gas low heating value: 9.72 kWh/m^3 (13.3 kWh/kg).
- Price of the natural gas: 1 €/Nm^3.
- CO_2 emission: 0.2 kg/kWh (1.944 kg/Nm^3_{CH4}).

For all the gas boilers it has been assumed an average efficiency of 0.75, although its value can be lower, as reported previously in section 3. The efficiency of electric boilers is 0.4, which also includes the efficiency of electricity production (in Italy the average value is 0,46).

The most significant results are also reported in Table 2: gas consumption per day, costs per day, CO_2 emissions. The last column presents the gas consumption and CO_2 emissions compared with those of a combi-storage boiler without solar collectors chosen as reference (case 8). All these data have been calculated for a summer day by means of the model described in this paper.

Plant 1, which is the simplest one with solar collector, gives an energy saving of about 30% with respect to the use of a combi-storage boiler. The presence of a cold (at 25°C) tank (case 2) gives an additional saving of 10%. The sole use of reflective panels and a proper configuration of tubes able to avoid the shading (case 3), permits to save about 40% of gas consumption in comparison to plant 1. The best solution is that with a hot reservoir and reflective panels (case 6), with 30% of the consumption compared to reference case 8. The consumption of the electric boiler is more than twice that of the gas boiler.

Table 2. Results of the simulation for 9 different systems.

	A1	A2	A3	A4	A5	A6	A7	A8	A9	A10	A11	A12	A13	A14
Cases	Collector	Wet or Tank	T	Hot water cylinder	Refl.Panels	Gas boiler	Electr boiler	En gas day	Gas per day	Cost per day	CO2 per day	%	Total cost	NPD
			°C			η	η	kWh	Nm3/day	€/day	Nm3/day		€	€
1	x	W	15			0,75		61,085	6	6	12	73	3500	1192
2	x	T	25			0,75		50,233	5	5	10	60	5000	263
3	x	W	15		RF	0,75		37,674	4	4	8	45	4500	1425
4	x	T	25		RF	0,75		26,977	3	3	5	32	6000	488
5	x	W	15	HC	RF	0,75		35,969	4	4	7	43	5500	514
6	x	T	25	HC	RF	0,75		26,202	3	3	5	31	7000	-471
7	no		18			0,75		80,62	8	8	16	96	5000	-1335
8	no		18	HC		0,75		83,721	9	9	17	100	3500	0
9	no		18				0,4	151,16	16	16	30	181	1000	-2376

The column A13 of table 3 shows the total installation cost of the different systems.

Under the hypothesis that the plant works from May to September, the column A14 shows the Net Present Value differences after 10 years of operation between cases 8 and single cases. An annual discount rate of 3 % has been assumed.

The most economical solution is case 3, while despite its better energetic performances the cases 6 is noFig.9 gives an example of the trend of the temperature of the water T at the end of the solar collector (Fig.8), of the temperature of the water T_{res} inside the hot water tank, of gas consumption gas, during a summer day, for a given user demand of WG. These results refer to case 6 for the same day studied in section 2.2. For this solution, the solar system is able to heat the water to a peak value of about 40°C. This value is lower than that of Fig. 5 since the continuous consumption of

water does not permit the same heating. The boiler is used at the three peaks of user requirement, when new colder water is sent to the hot reservoir.

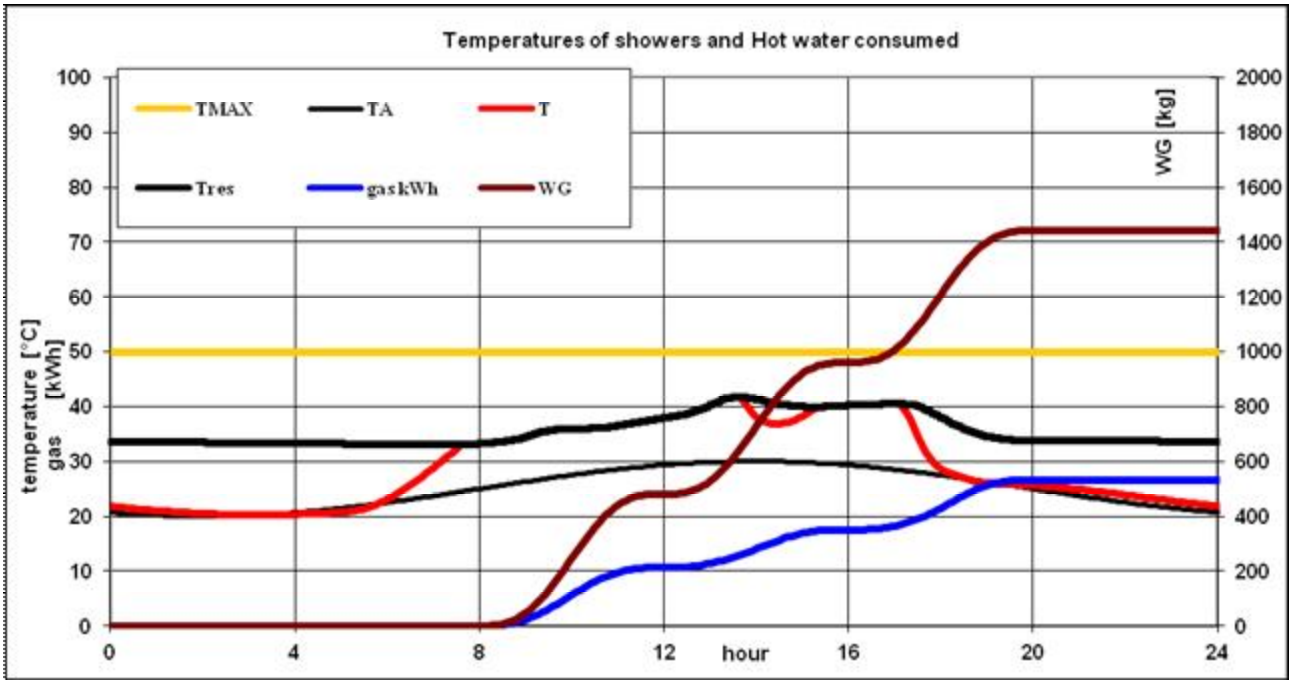

Fig. 9. Main results for Case 6.

5. Conclusion

The simulation of simple solar plants with integrative gas boilers for the hot water service can be a valid instrument to correctly project a solar simple plant able to guarantee the required hot water service during the summer.
By means of a sufficient number of pipes heated by solar irradiation and large and flat reflective panels, a tank of water pre-heated by ambient air and solar irradiation, a hot water reservoir and gas boiler it is possible to save about 70% of gas consumption and CO_2 emission with respect to a gas boiler, and construct a long-life and simple solar collector.

Nomenclature

c_p	specific heat of water, kJ/kg
c_{pm}	specific heat of tube metal, kJ/kg
gas	cumulate consumption of gas during a day, kWh
K	coefficient of convection exchange, W/(m^2 K)
KI	irradiation coefficient to ambient, W/(m^2 K)
KR	reflective plates factor
KW	wind factor
KS	shadow factor
L	length of a pipe element concentrated in a point, m
MM	mass of metal of a pipe element, kg

MP mass of water in a pipe element, kg

PSOL solar irradiance, W/m^2

QC heat transferred for convection to ambient, kW

QI heat transferred for irradiation to ambient, kW

QIRR heat from sun to pipe, kW

QW power related to mass transfer to and from pipe element, kW

SC surface of convection and irradiation to ambient of a pipe element, m^2

SI solar irradiation surface of a pipe element, m^2

T, T(t), T(t+Δt) temperature of the water and of metal of a pipe element, °C

TA, TA(t), TA(t+Δt) temperature of the air, °C

TMAX temperature of the water required by the users (50°C)

T_{res} temperature in the reservoir, °C

t current time, s

W water entering in a pipe element during a time step Δt, kg/s

WG cumulate mass of water during a day, kg

Greek symbols

η overall boiler efficiency

References

[1] Naspolini H.F., Militão H.S.G., Rüther R., The role and benefits of solar water heating in the energy demands of low-income dwellings in Brazil, Energy Conversion and Management 2009; 51(12):2835-2845.

[2] Azad E., Design, installation and operation of a solar thermal public bath in eastern Iran, Energy for Sustainable Development, Available online 23 November 2011.

[3] Veeraboina P., Ratnam G.Y., Analysis of the opportunities and challenges of solar water heating system (SWHS) in India: Estimates from the energy audit surveys & review, Renewable and Sustainable Energy Reviews 2012; 16(1):668-676.

[4] Siqueira D.A., Vieira L.G.M, Damasceno J.J.R., Analysis and performance of a low-cost solar heater, Renewable Energy 2011; 36(9): 2538-2546.

[5] Jaisankar S., Ananth J., Thulasi S., Jayasuthakar S.T., Sheeb K.N., A comprehensive review on solar water heaters, Renewable and Sustainable Energy Reviews 2011; 15(6): 3045-3050.

[6] Muñoz J., Martinez-Val J.M., Ramos A., Thermal regimes in solar-thermal linear collectors Solar Energy 2011; 85(5): 857-870.

[7] Bourke G., Bansal P., New test method for gas boosters with domestic solar water heaters, Solar Energy 2012; 86(1): 78-86.

[8] Andersen E., Furbo S., Theoretical variations of the thermal performance of different solar collectors and solar combi systems as function of the varying yearly weather conditions in Denmark, Solar Energy 2009; 83(4): 552-565.

[9] Tosato R., A simple solar shower: simulation and experimental results. In: Proceedings of EnginSoft International Conference 2010, 21-22 October 2010, Montichiari (BS).

[10] Tosato R. “Simulation of simple solar collector with reflective panels and boiler” STHESCA International Conference July 5-7, 2011 Krakow, Poland.

[11] Tosato R., Testing of a high-efficiency domestic heating system. In: Proceedings of the 24th IECEC, Washington, DC, USA, 1989.

[12] Rosa L., Tosato R., Experimental evaluation of seasonal efficiency of condensing boilers, Energy & Buildings 1990; 14(3): 237-241.

[13] Tosato R., Mathematical models of gas fired boilers. In: 20th EMSS, 2008 European Modeling and Simulation Symposium (Simulation in Industry) September, 17-19, 2008, Campora San Giovanni, Amantea (CS) Italy.

[14] Tosato R., Tests and simulation of gas boilers in domestic heating plants. In: 21th EMSS International Mediterranean Modelling Multiconference, 23-25 September 2009 Tenerife (SP).

[15] Leidl C.M., W. Lubitz W.D., Comparing domestic water heating technologies, Technology in Society 2009; 31(3): 244-256.

Exergetic analysis of biomass fired double-stage Organic Rankine Cycle (ORC)

Markus Preißinger[a], Florian Heberle[a] and Dieter Brüggemann[a]

[a] Lehrstuhl für Technische Thermodynamik und Transportprozesse
Zentrum für Energietechnik, Bayreuth, Germany, lttt@uni-bayreuth.de

Abstract:

Biomass fired double-stage Organic Rankine Cycle (ORC) with net power output of less than 10 kW is studied from exergetic point of view. Focus is laid on appropriate working fluid and pressure level selection. Therefore 21 high temperature fluids and 14 low temperature fluids were under investigation. Analyses show that isopentane gives best efficiency in the low temperature circuit whereas R227ea is least efficient within the chosen boundary conditions. Among the working fluids for the high temperature circuit, maximum thermal efficiency is found to be similar for several working fluids. Irreversibility rates calculated for all heat exchangers enforce these results. As a crucial parameter for high efficiencies the dimensionless heat flow ratio Φ, defined as transmitted heat flux to the low temperature circuit divided by transmitted heat flux to the high temperature circuit is identified and should be around 1.0 for high total efficiency of the cycle. The usage of an internal recuperator is discussed depending on the pressure drop of the gaseous side.

Keywords:

Biomass, Double-stage, Exergy, ORC, Organic Rankine Cycle.

1. Introduction

Organic Rankine Cycle (ORC) has become more and more interesting for the usage of low grade heat sources, waste heat recovery and biomass fired power plants. Comprehensive research on appropriate working fluids for low temperature applications has been carried out by Saleh et al. [1]. They concluded that n-butane shows highest efficiency for ORC operating between 100 °C and 30 °C. According to Lai et al. [2], for high temperature sources (heat carrier inlet temperature up to 350 °C) cyclopentane is the best working fluid concerning thermal efficiency, heat capacity flow rate of the heat carrier and volume flow rates within the turbine. For geothermal power plants Heberle et al. [3,4] investigated pure fluids for combined heat and power production as well as usage of fluid mixtures for low-enthalpy sources. For series circuit high-boiling fluids like isopentane should be used, for parallel circuits and for power production fluid R227ea is preferred. Due to a non-isothermal phase change using zeotropic mixtures like R227ea/R245fa will further increase the efficiency up to 15 %. Waste heat recovery was examined steady-state using genetic algorithm by Dai et al. [5] leading to R236ea as the working fluid with best exergetic efficiency. Quoilin et al. [6] focused on dynamic simulation and appropriate control strategy for part-load operation as well as for start/stop-procedures. Investigations on biomass fired power plants are mostly carried out from an energetic point of view and for single-stage processes [7]. Furthermore, plant net power production is often in the range of up to 1000 kW [8]. In this study a biomass fired double-stage ORC with a net power output of less than 10 kW is studied. Contrary to our previous study [9] focus is laid on optimizing exergetic efficiency by appropriate working fluid and pressure level selection. The results are compared to irreversibility rates of heat exchange equipment, to show potential steps for optimization of double-stage ORC. Lastly, the influence of pressure drop within the internal recuperator is investigated.

2. Methodology

2.1. ORC model

The investigated double-stage ORC consists of a wood pellet heater as a heat source, a thermal oil circuit (TOC), high and low temperature circuit (HTC and LTC, respectively) and a cooling circuit (CC). Thermodynamic analysis is based on certain boundary conditions. The flue gas exits the wood pellet heater at 950 °C, maximum temperatures within TOC and HTC are 340 °C and 320 °C, respectively. Maximum pressure of ORC vapour is set to 20 bar or 70 % of critical pressure of the chosen working fluid. To avoid diffusion of air into the cycle, condensation takes place at 1 bar, however, at least at the corresponding pressure for a condensing temperature of 26.5 °C. Further boundary conditions are given in Table 1, the overall process is shown in Figure 1.

Table 1: Boundary conditions for thermodynamic analysis

Volume flow rate of flue gas	0.06 m³/s
Cooling circuit inlet temperature	15 °C
Temperature rise of cooling water	5 K
ΔT-pinch-point flue gas heat exchangers	30 K
ΔT-pinch-point ORC heat exchangers	10 K
Generator efficiencies	1.0
Isentropic turbine efficiencies	1.0
Isentropic pump efficiencies	0.8
Electro-mechanical pump efficiencies	0.6

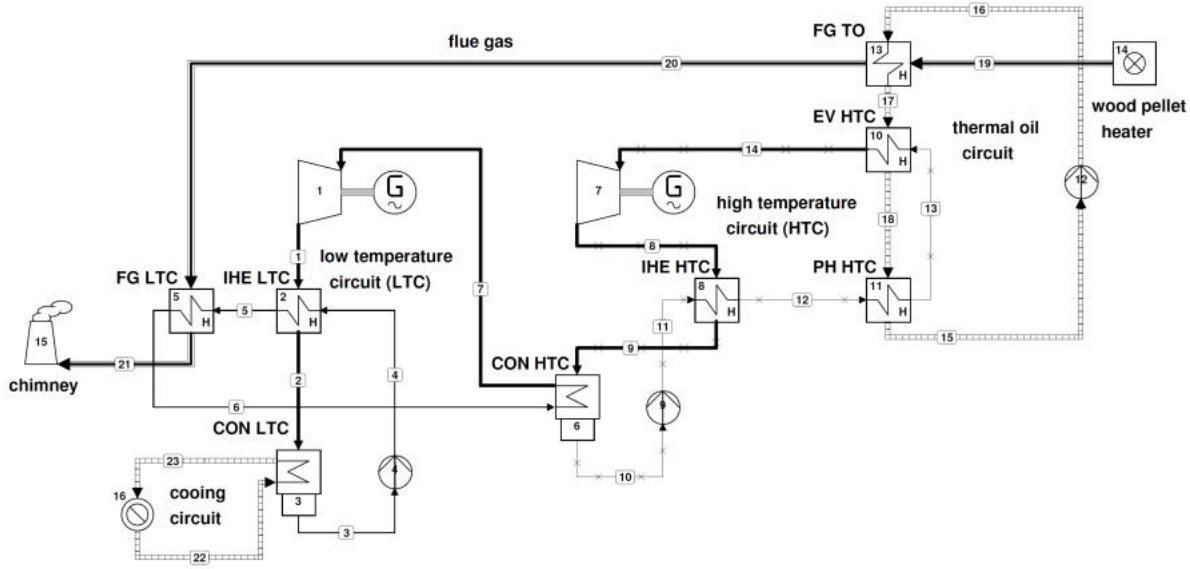

Fig. 1. Biomass fired double-stage Organic Rankine Cycle

2.2. Thermodynamic analysis

The process is simulated using the software Cycle Tempo [10] which is based on the Peng-Robinson equation of state. Taken into account heat exchangers, expansion units and pumps, the process can be characterized by 23 mass and energy equations. Heat exchanger balances can be expressed as

$$\dot{m}_{hot}(h_j - h_i) = \dot{m}_{cold}(h_l - h_k), \qquad (1)$$

isentropic efficiency of pumps are defined as

$$\eta_{i,P} = \frac{h_{j,s} - h_i}{h_j - h_i}, \tag{2}$$

and isentropic efficiency of turbines as

$$\eta_{i,T} = \frac{h_j - h_i}{h_{j,s} - h_i}. \tag{3}$$

Within (1), (2) and (3) indices hot and cold mean the hot stream or the cold stream in the heat exchanger, respectively. Indices j and l are for outlet streams, i and k for inlet streams. Index s declares isentropic expansion or compression in turbines and pumps.

2.3. Exergetic analysis

To allow for an exergetic analysis of the process, the total exergy flow of the heat source is calculated as

$$\dot{E} = \dot{m}e, \tag{4}$$

with e being the specific exergy of the flue gas at the outlet of the wood pellet heater (pipe 19):

$$e = h - h_0 - T_0(s - s_0) \tag{5}$$

Index 0 indicates the dead state with T_0=15 °C and p_0=1 bar.

The exergetic efficiency of the overall process can be written as:

$$\eta_{ex,total} = \frac{\left|P_{P,TOC} + P_{P,HTC} + P_{P,LTC} + P_{EU,HTC} + P_{EU,LTC}\right|}{\dot{E}} \tag{6}$$

Furthermore, within the study irreversibility rates are calculated according to the general approach

$$\dot{I} = T_0 \frac{dS}{dt} = T_0 \dot{m}\left[\sum_{out} s - \sum_{in} s - \sum_i \frac{q_i}{T_i}\right]. \tag{7}$$

Due to the assumption of adiabatic compression and expansion, the term $\sum_i \frac{q_i}{T_i}$ vanishes so that the irreversibility flow rate of the turbines and pumps can be written as:

$$\dot{I}_{T,P} = T_0 \dot{m}\left(s_j - s_i\right) \tag{8}$$

As the internal recuperator is simulated adiabatic to the surrounding, one just has to take internal irreversibility rates of the hot and cold stream into account which lead to:

$$\dot{I}_{IHE} = T_0 \dot{m}\left[\left(s_{j,hot} - s_{i,hot}\right) + \left(s_{j,cold} - s_{i,cold}\right)\right] \tag{9}$$

Same is true for the evaporator in the LTC and HTC as well as for the preheater in the HTC. Just the flue gas/thermal oil heat exchanger, the preheater in the LTC and the condenser interact with the surrounding so that heat transfer has to be taken into account:

$$\dot{I} = T_0 \dot{m}\left[\left(s_j - s_i\right) - \frac{h_j - h_i}{T_m}\right] \tag{10}$$

The characteristic temperature in the right hand term of (10) can be calculated as

$$T_m = \frac{T_{Source,in} - T_{Source,out}}{\ln\left(\frac{T_{Source,in}}{T_{Source,out}}\right)}, \tag{11}$$

whereas source means the thermal oil or cooling water, respectively. Indices *j* and *i* in (10) are ORC outlet and inlet stream.

2.4. Preselection of working fluids

Potential working fluids are selected depending on the temperature level of evaporation and due to literature [1,2,7,8]. LTC operates at temperatures from 26.5 °C to about 150 °C, HTC up to 320 °C. For HTC alkylbenzenes, alkanes, siloxanes and three fluids out of different chemical classes were investigated. Within LTC, short-chain hydrocarbons and refrigerants were analysed. Structural isomerism is taken into account in HTC and LTC. Potential working fluids as well as physico-chemical properties are summarized in Table 2 and Table 3. Therefore one gets 21 potential fluids for HTC and 14 for LTC. As all HTC fluids are combined with each LTC fluid, this leads to a 21x14 matrix of simulated cases.

Table 2: Potential working fluids for high temperature circuit (HTC)

working fluid HTC	T_{crit},°C	p_{crit},bar	M, g/mol
cis-1,2-dimethylcyclohexane	333.00	29.38	112.21
tetramethylpentane	334.35	27.41	128.26
tetraethylsilane	332.85	24.00	144.33
ethylbenzene	344.05	36.06	106.17
p-xylene	343.08	35.11	106.17
1,3,5-trimethylbenzene	364.10	31.27	120.19
1,2,4-trimethylbenzene	375.95	32.32	120.19
n-propylbenzene	365.20	32.00	120.19
m-diethylbenzene	389.85	28.80	134.22
o-diethylbenzene	394.85	28.80	134.22
o-cymene	383.85	29.00	134.22
octane	295.61	24.86	114.22
nonane	321.40	22.81	128.26
decane	344.55	21.03	142.28
undecane	365.85	19.50	156.31
dodecane	384.95	18.17	170.33
hexamethylcyclotrisiloxane	281.05	16.63	222.46
octamethyltrisiloxane	291.25	14.40	236.53
octamethylcyclotetrasiloxane	313.35	13.32	296.62
decamethyltetrasiloxane	326.25	12.27	310.69
decamethylcyclopentasiloxane	346.00	11.60	370.77

Table 3: Potential working fluids for low temperature circuit (LTC)

working fluid LTC	T_{crit},°C	p_{crit},bar	M ,g/mol
n-butene	146.14	40.05	56.11
cis-butene	162.60	42.26	56.11
isobutene	144.94	40.10	56.11
trans-butene	155.46	40.27	56.11
isobutane	134.66	36.29	58.12
isopentane	187.20	33.78	72.15
neopentane	160.59	31.96	72.15
n-pentane	196.55	33.68	72.15
R143 (1,1,2-trifluoroethane)	156.65	52.41	84.04
R245fa (1,1,1,3,3-pentafluoropropane)	154.05	36.40	134.05
R365mfc (1,1,1,3,3-pentafluorobutane)	186.85	32.66	148.07
R236ea (1,1,1,2,3,3-hexafluoropropane)	139.29	35.02	152.04
R236fa (1,1,1,3,3,3-hexafluoropropane)	124.92	32.00	152.04
R227ea (1,1,1,2,3,3,3-heptafluoropropane)	101.75	29.25	170.03
RC318 (octafluorocyclobutane)	115.23	27.78	200.04

3. Results

3.1. Exergetic efficiencies

Figure 2 shows the exergetic efficiency of each HTC and LTC fluid. The average efficiency of a HTC fluid is the mean value of the 14 exergetic efficiencies. The maximum and minimum efficiency displays the most and the least efficient fluid combination, respectively. It can be seen that the relative difference between the most efficient (cis-1,2-dimethylcyclohexane) and the least efficient HTC fluid (decamethylcyclopentasiloxane) is $\Delta\eta_{average} = 21.26\,\%$. Within the LTC the difference between isopentane (most efficient) and R227ea (least efficient) is even higher ($\Delta\eta_{average} = 27.84\,\%$). Therefore, one can deduce that for high exergetic efficiencies, the choice of LTC fluid is more important than the choice of HTC fluid. Explained by thermodynamics one can say that by using a rather inefficient HTC fluid, a high amount of heat is transferred from HTC to LTC in the condenser of the HTC, but still can be converted by a rather efficient LTC fluid. However, the usage of a rather inefficient LTC fluid leads to a high heat flow rate in the condenser of the LTC which cannot be used anymore.

3.2. Irreversibility rates

To explain the interaction between HTC and LTC more detailed, exergetic efficiencies for the following four different fluid combinations are shown in table 3:

- Case 1: Efficient HTC fluid / efficient LTC fluid (1,3,5-trimetylbenzene / isopentane)
- Case 2: Efficient HTC fluid / inefficient LTC fluid (1,3,5-trimetylbenzene / R227ea)
- Case 3: Inefficient HTC fluid / efficient LTC fluid (decamethylcyclopentasiloxane / isopentane)
- Case 4: Inefficient HTC fluid / inefficient LTC fluid (decamethylcyclopentasiloxane / R227ea)

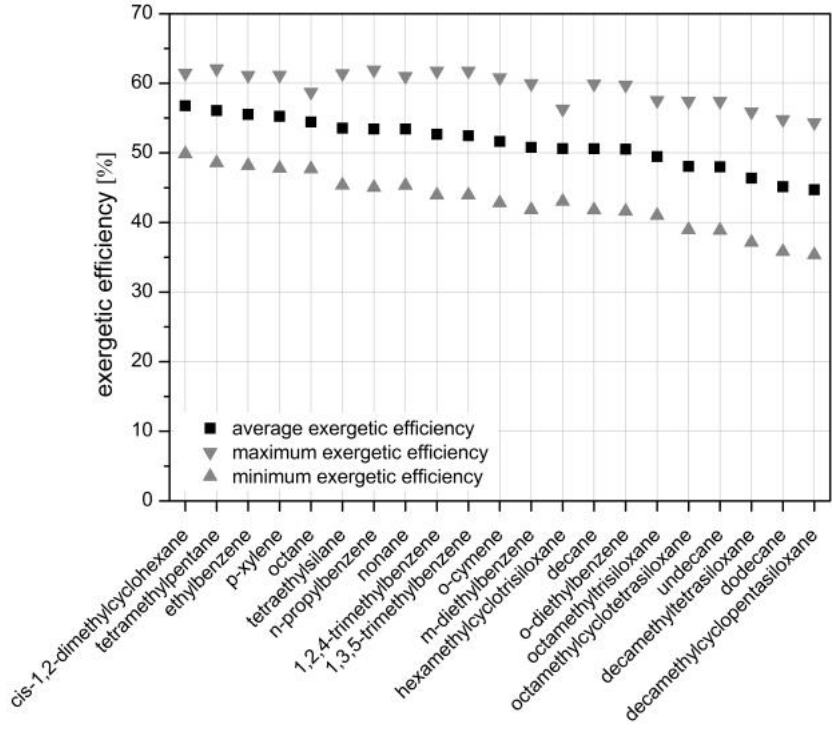

(a)

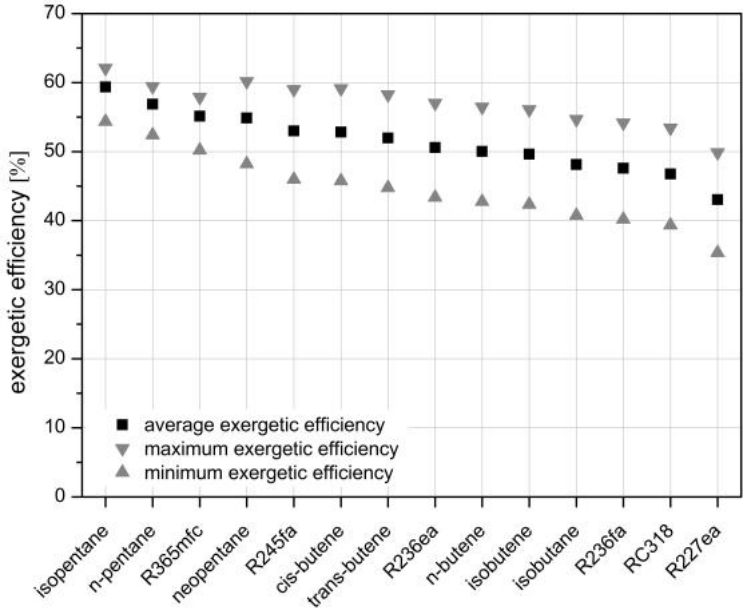

(b)

Fig. 2: Average, maximum and minimum exergetic efficiencies for all investigated HTC fluids (a) and LTC fluids (b), respectively.

Three conclusions can be drawn. Firstly, for 1,3,5-trimethylbenzene the difference between isopentane and R227ea is 28.82 % whereas for decamethylcyclopentasiloxane it is 34.95 %. This denotes that by using an efficient HTC fluid the influence of the LTC fluid is weakened. Secondly, for isopentane the difference between the two HTC fluids is 11.98 %, for R227ea 19.56 %. On that account the aforesaid effect is true for the LTC fluid as well. Using a rather efficient LTC fluid weakens the effect of the choice of HTC fluid. Lastly, the fact that the differences of varying HTC fluid (11.98 % and 19.56 %) are lower than those of varying LTC fluid (28.82 % and 34.95 %) enforces the fact that the choice of the LTC fluid influences the exergetic efficiency more than the HTC fluid.

Table 3: Exergetic efficiency of four different fluid combinations and relative difference (in %)

	1,3,5-trimethylbenzene	decamethylcyclopentasiloxane	$\Delta\eta$
isopentane	61.75	54.35	11.98
R227ea	43.95	35.35	19.56
$\Delta\eta$	28.82	34.95	

In addition to the exergetic analysis, irreversibility rates for all heat exchangers within the process are displayed in table 4. Comparing the irreversibility rates of the evaporator ($\dot{I}_{EV\ HTC}$) and the preheater ($\dot{I}_{PH\ HTC}$) of the HTC, case 3 and 4 in which decamethylcyclopentasiloxane as a HTC working fluid was used give far lower values than case 1 and 2 (using 1,3,5-trimethylbenzene). This can be explained by the steeper slope of the boiling curve within the *T*,*s*-diagram and the resulting temperature match between the thermal oil and the ORC fluid. From that point of view decamethylcyclopentasiloxane should be more efficient than 1,3,5-trimethylbenzene. However, due to the steeper slope of the boiling curve, the irreversibility rate of the flue gas/thermal oil heat exchanger increases as the minimum temperature difference within the heat exchanger has to be maintained. Lastly, irreversibility rates within the internal recuperator and the condenser of the HTC are higher for the siloxane due to the steeper slope of the dew line. A similar effect emerges in the internal recuperator of the LTC in which the irreversibility rate for R227ea as a working fluid is almost zero due to the nearly infinite slope of the dew line. In addition to the higher irreversibility rate in the flue gas/thermal oil heat exchanger, one gets also greater losses within the preheater of the LTC ($\dot{I}_{FG\ LTC}$) and the condenser of the LTC ($\dot{I}_{CON\ LTC}$) using the cyclic siloxane instead of the alkylbenzene. In summary, four conclusions can be drawn:

1. As expected, case 1 gives lowest irreversibility rates (followed by case 3, case 2 and case 4) which correlates with the exergetic efficiencies of table 3.
2. Within one HTC fluid the difference of external losses (for varying LTC fluid) are by far lower than the difference in internal losses due to the almost identical temperature match in the flue gas/thermal oil heat exchanger caused by the slope of the boiling curve.
3. However, within one LTC fluid (and varying HTC fluid) external losses are more important.
4. Lastly, by calculating the difference of the total irreversibility rate between case 2 and case 1 ($\Delta\dot{I}_{21} = 1662.9\ ^{W}/_{K}$) is higher than between case 3 and case 1 ($\Delta\dot{I}_{31} = 688.7\ ^{W}/_{K}$) which shows again the importance of the proper choice of LTC fluid.

Table 4: Irreversibility rates within the heat exchange equipment

Variable	Unit	Case 1	Case 2	Case 3	Case 4
$\dot{I}_{EV\ HTC}$	W/K	454.4	445.8	54.1	54.1
$\dot{I}_{PH\ HTC}$	W/K	903.5	906.8	155.8	155.8
$\dot{I}_{IHE\ HTC}$	W/K	88.9	89.2	173.2	173.2
$\dot{I}_{CON\ HTC}$	W/K	320.5	1609.6	1057.5	2474.2
$\dot{I}_{IHE\ LTC}$	W/K	63.5	0.6	67.8	0.7
$\dot{I}_{TOTAL\ INTERNAL}$	W/K	1830.8	3052.1	1508.4	2858.0
$\dot{I}_{FG\ TO}$	W/K	1004.3	1002.0	1994.0	1994.0
$\dot{I}_{FG\ LTC}$	W/K	912.5	1298.9	912.6	1276.2
$\dot{I}_{CON\ LTC}$	W/K	319.9	377.5	341.3	402.8
$\dot{I}_{TOTAL\ EXTERNAL}$	W/K	2236.7	2678.4	3247.9	3673.0
$\dot{I}_{TOTAL}$	W/K	4067.6	5730.5	4756.3	6531.0

3.3. Dimensionless heat flow ratio

As the previous results show the importance of transferred heat flow to HTC and LTC figure 3 shows the maximum exergetic efficiency of each siloxane depending on the dimensionless heat flow ratio, defined as:

$$\Phi = \frac{\text{heat flow rate LTC}}{\text{heat flow rate HTC}} \qquad (12)$$

Within the HTC, siloxanes are used as working fluids, in LTC isopentane and R227ea were chosen. It can be seen that using a rather inefficient LTC working fluid (R227ea in this case) the exergetic efficiency rises with decreasing heat flow ratio Φ. Though by using a rather efficient LTC fluid (isopentane) the exergetic efficiency first rises with increasing Φ, reaching a maximum around Φ=1 and drops again afterwards. Therefore it can be deduced that the amount of heat transferred to the LTC should be equal to the heat transferred to the HTC to achieve high exergetic efficiencies.

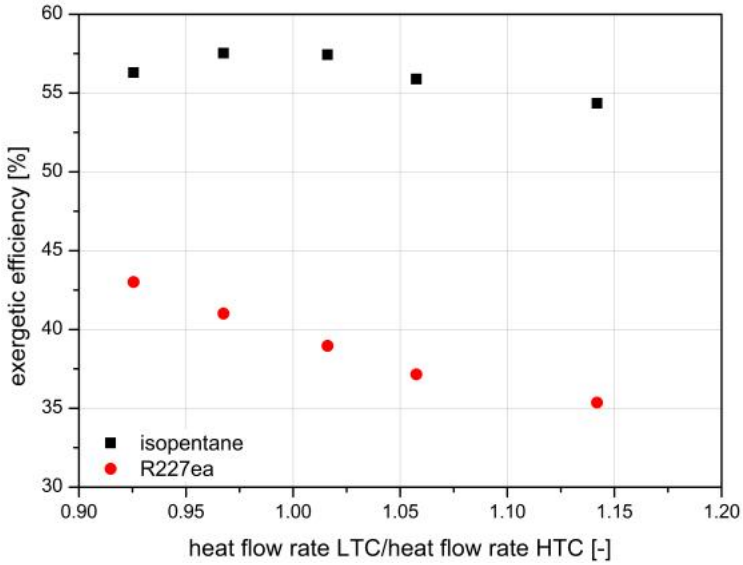

Fig. 3: Exergetic efficiency of five siloxanes depending on the heat flow ratio Φ (LTC fluid isopentane and R227ea, respectively) .

3.4. Internal recuperator

Due to the exergetic analysis of the IR and the fact that isopentane and R227ea show different slopes of the dew line, the effect of pressure drop in the IR (gaseous side) is investigated. In figure 4 the exergetic efficiency of the fluid combinations 1,3,5-trimethylbenzene/isopentane and 1,3,5-trimethylbenzene/R227ea is displayed using the pressure drop in the IR as variable. As expected both curves decrease with increasing pressure drop due to the lower enthalpy difference in the turbine. However, isopentane shows a stronger dependency than R227ea due to the higher slope of the dew line. By calculating the exergetic efficiency of the reference case without IR (isopentane: 57.75 %; R227ea: 43.93 %), one can deduce that an IR should be used for a pressure drop less than 0.5 bar in case of isopentane. Using R227ea as a working fluid, the pressure drop has to be less than 0.02 bar to reach higher efficiencies than the base case without IR. Therefore, the usage of an IR should be reconsidered under economic aspects for each case.

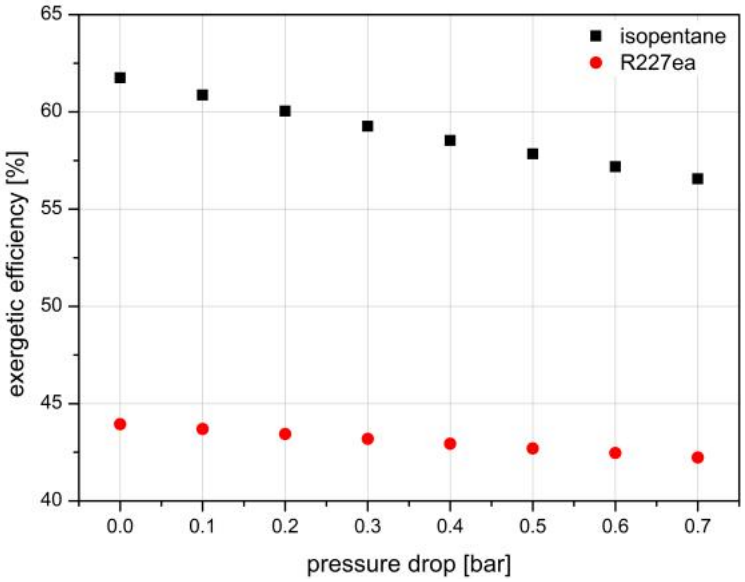

Fig. 4: Exergetic efficiency of trimethylbenzene depending on the pressure drop in the internal recuperator (LTC fluid isopentane and R227ea, respectively)

Conclusion and future work

Biomass fired double-stage ORC using 14 different high temperature and 21 different low temperature fluids was investigated. The results can be summarized as follows:

- Using alkylbenzenes as high temperature fluids in combination with isopentane as low temperature fluid, exergetic efficiencies of more than 60 % can be achieved.
- A case study using 1,3,5-trimethylbenzene and decamethylcyclopentasiloxane in HTC, isopentane and R227ea in LTC shows that the choice of the LTC working fluid influences exergetic efficiency more than the choice of the HTC fluid.
- Calculation of the irreversibility rates within all heat exchangers gives evidence to the above-mentioned dependency.
- For efficient LTC working fluids the dimensionless heat flow ratio Φ, defined as heat flow rate to LTC divided by heat flow rate to HTC should be around 1.0 to reach high exergetic efficiencies. For inefficient LTC working fluids Φ should be as low as possible.
- For dry fluids an internal recuperator should be used from an exergetic point of view, however, for each LTC fluid a specific pressure drop within the IR can be calculated from which exergetic efficiency decreases with the usage of an IR.

In a next step double-stage ORC units will be compared with other advanced ORC concepts (supercritical ORC, fluid-mixtures) from a thermodynamic, exergetic and exergoeconomic point of view. Also two expansion units will be designed by an industrial partner in the range of 5 kW each.

Nomenclature

e	specific exergy, kJ/kg
$\dot{E}$	exergy flow rate, kW
h	specific enthalpy, kJ/kg
$\dot{I}$	irreversibility rate, W/K
$\dot{m}$	mass flow rate, kg/s
M	molar mass, g/mol

P electric power, kW

p pressure, bar

q specific heat, kJ/kg

$\dot{Q}$ heat flux, kW

s specific entropy, kJ/kgK

S entropy, kJ/K

T temperature, K

Greek letters

η efficiency, %

ΔT temperature difference, K

Φ dimensionless heat flow ratio

Subscripts

CON condenser

crit critical

EV evaporator

ex exergetic

FG flue gas

i isentropic

in inlet

out outlet

P pump

PH preheater

T turbine

TO thermal oil

Acronyms

CC cooling circuit

HTC high temperature circuit

IR internal recuperator

LTC low temperature circuit

ORC organic rankine cycle

TOC thermal oil circuit

References

[1] Saleh B., Koglbauer G., Wendland, M.; Fischer, J., Working fluids for low-temperature organic Rankine cycles. Energy 2007;32(7):1210-1221.

[2] Lai N.A., Wendland M., Fischer J., Working fluids for high-temperature organic Rankine cycles. Energy 2011;36(1):199–211.

[3] Heberle F., Brüggemann D., Exergy based fluid selection for a geothermal Organic Rankine Cycle for combined heat and power generation. Applied Thermal Engineering 2010;30(11-12):1326–1332.

[4] Heberle F., Preißinger M., Brüggemann D., Zeotropic mixtures as working fluids in Organic Rankine Cycles for low-enthalpy geothermal resources. Renewable Energy 2012;37(1):364–370.

[5] Dai Y., Wang J., Gao L., Parametric optimization and comparative study of organic Rankine cycle (ORC) for low grade waste heat recovery. Energy Conversion and Management 2009;50(3):576–582.

[6] Quoilin S., Aumann R., Grill A., Schuster A., Lemort V., Spliethoff H., Dynamic modeling and optimal control strategy of waste heat recovery Organic Rankine Cycles. Applied Energy 2011;88(6):2183–2190.

[7] Drescher U., Brüggemann D., Fluid selection for the Organic Rankine Cycle (ORC) in biomass power and heat plants. Applied Thermal Engineering 2007;27(1):223–228.

[8] Angelino G., Colonna P., Multicomponent Working Fluids For Organic Rankine Cycles (ORCs). Energy 1998;23(6):449–463.

[9] Preißinger M., Heberle F., Brüggemann D., Thermodynamic analysis of double stage biomass fired Organic Rankine Cycle for micro-cogeneration. International Journal of Energy Research 2012. Doi:10.1002/er.1952

[10] Woudstra N., van der Stelt T. P., Cycle Tempo, a program for the thermodynamic analysis and optimization of systems for the production of electricity, heat and refrigeration. Release 5.0, Delft University of Technology.

Experimental tests and modelization of a domestic-scale Organic Rankine Cycle

Roberto Bracco[a], Stefano Clemente[b], Diego Micheli[b] and Mauro Reini[b]

[a] *Centro Ricerche FIAT, Orbassano (Torino), Italy, roberto.bracco@crf.it*
[b] *University of Trieste, Trieste, Italy, sclemente@units.it, micheli@units.it, reini@units.it*

Abstract:

The work deals with the realization of a prototype, the experimental testing and the modelization of a small-size Organic Rankine Cycle. The components of the circuit, filled by the refrigerant R245fa, are an inverter-driven diaphragm pump, a plate condenser, an electric boiler and a scroll expander. The latter is a hermetic device, derived from a commercial HVAC compressor, and expected to deliver a power of about 1.5 kW. The rotating speed of the expander, and of the electric generator contained in the same sealed vessel, is free, and the three-phase variable-frequency alternating current is converted into a direct current by a rectifier. The system is controlled regulating the feed pump speed and the vapor temperature at the boiler exit, while the imposed braking torque is varied adjusting the resistance of the electric load connected to the generator.
Some performance parameters of the whole cycle and of the plant components have been investigated with a series of experimental tests, whose results are discussed in the paper. The registered working parameters and efficiencies are comparable with those expected from previous studies and reported in literature, even if the system is not yet optimized.
These results are the basis for the numerical modelization of the cycle, realized with the simulation software LMS Imagine.Lab AMESim®. This has been chosen for its wide libraries of fluid properties and cycle mechanical and electric components and for its capacity to simulate systems also in transient conditions. Such a feature will be needed in the future developments of the work. Once the numerical model has been realized and calibrated on the basis of the experimental measurements, it will be used to achieve a better knowledge of the physical system, to understand which are the main problems to solve in order to achieve better performances, and finally to choose a more suitable control strategy for the prototype.

Keywords:

Organic Rankine Cycle, scroll expander, ORC test bench, ORC dynamic modelization.

1. Introduction

Heat recovery represents one of the most important ways to increase the systems efficiency, to reduce the fossil fuels consumption and therefore to reach the energy sustainability. When the rejected heat is available at high temperatures (e.g. from certain industrial processes, from gas turbine exhaust gases or from concentrating solar panels), electricity can be generated from the thermal power through a number of solutions, like steam Rankine cycles or Stirling engines. However, these technologies are unsuitable to hot source temperature below 500 °C, due to both low efficiencies and technical unfeasibility. According to Bianchi and De Pascale [1], these low temperature sources could be exploited for electric power production through thermo-electric systems or organic Rankine cycles (ORC). While the first technology, based upon the Seebeck-Peltier effect in semiconductors, can be applied only to very small scale systems (below 500 W), the range of power of ORCs is wide, from 1 kW up to 3 MW, so they can be considered for a number of different applications, such as recovery from medium-low temperature industrial wasted heat, biomass-fed cogenerators, low temperature solar cycles or small geothermal plants. For this reason, ORCs have been widely studied in the last 25 years, and interest around this technology is growing: in the first international conference on ORC power systems held in Delft, The Netherlands in 2011, a large number of works, available on the conference website [2], have been presented, covering all the above cited applications. Today several units are available on the market, but most applications are in the medium-high power range (100 kW – 3 MW), while domestic size cycles are not much

commercially exploited [1]. However, small sizes ORCs are suitable for several applications, such as electric generation in remote houses, domestic CHP units or thermally driven heat pumps [3]. For this reason, a number of researches have been conducted in the last years, with the aim of studying an acceptable efficiency and cost effective system suitable for domestic applications. In previous papers, the authors have investigated the performances of a scroll expander [4], of a reciprocating one [5] and of different cycles equipped with these machines [6]. After these experiences, the prototype of ORC presented in this paper has been designed, built and tested, to have at disposal a test bench for achieving a better knowledge of the behavior of the system, in both stationary and transient operating conditions. In particular, the first experimental data acquired on the facility have been used to calibrate and validating in stationary conditions a dynamic model of the system, realized with the simulation software LMS Imagine.Lab AMESim®. The model will be used to define the most suitable control strategy for the ORC, according to the technical requirements of the various heat recovery applications. The strategies will be then applied and tested on the test bench.

2. Description of the ORC prototype

In this section a brief description of the ORC system, reported in Fig. 1, is given, focusing on the peculiar features of the main components. The first design choice has been the selection of the working fluid: on the basis of a preliminary study [6], R245fa has been taken into account, for its thermo-physical, environmental and safety features. Since the goal of this first-phase work is to achieve a general knowledge of the system and to learn how the controllable variables could affect the performances, a simple cycle (without regeneration) has been chosen. In this classical arrangement of a Rankine cycle, the closed loop filled by the working fluid is formed by the feed pump, the vapor generator, the expander and the condenser, in this order, as visible in Fig. 2, which reports a sketch of the components and the different phases on (T,s) diagram.

The chosen pump is an inverter-driven diaphragm unit, because the membrane placed between the fluid chamber and the piston zone ensures both a perfect sealing of the circuit towards environment and the feasibility of high pressure ratio, even pumping a liquid as R245fa that has a very low viscosity and has no lubricant properties. These features make impossible the use of other more common and cheap devices such as gear pumps.

An electric boiler has been chosen to evaporate the fluid: this seemed to be the best solution for an experimental prototype, since it allows setting directly the superheating temperature and reduces the thermal inertia with respect to other boiling systems, therefore decreases the time needed to reach an imposed steady state condition. Moreover, an electrical boiler features a great flexibility in control strategies, allowing simulating also the dynamic behavior of different real heat sources, such as a condensing boiler or a solar panel system.

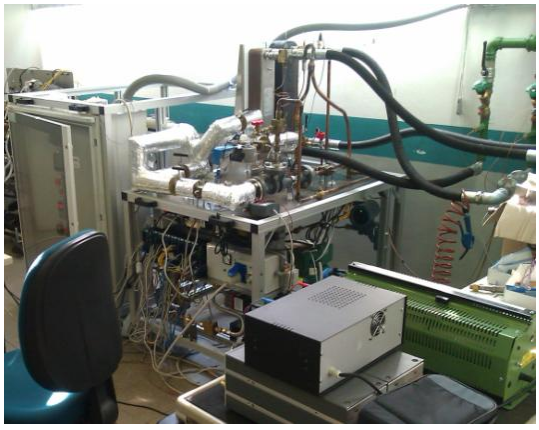

Fig. 1. Experimental ORC setup.

Thanks to the previous works, the expander was the most known component: it has been decided to use a scroll machine, due to its demonstrated high isentropic efficiency, up to 0.65 – 0.70 [7, 8], and its diffusion on the market as HVAC compressor. These devices are commonly hermetic, with the compressor and the electric motor in a unique sealed vessel, and cover a wide range of power and compression ratios, due to the large number of applications in air conditioning and refrigeration.

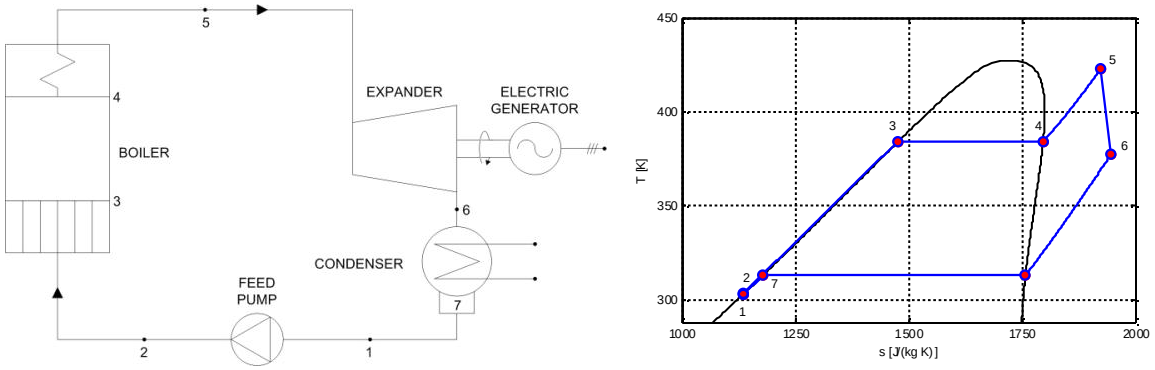

Fig. 2. Main components of an ORC (left) and thermodynamic transformations reported on (T,s) diagram for R245fa as working fluid (right).

Since both the compressor and the electric machine could operate in reverse mode, as an expander and a generator respectively, without major revisions [9], a slightly modified, small sized (in the range of power around 1 kWe) unit has been ordered from the manufacturer and installed in the system. Since the shaft speed of the group is free, the three-phase voltage is generated by the alternator at variable frequency, so it is converted in direct-current by a power conditioning system. Finally, the power is dissipated on a programmable electronic load, capable to measure all the electric variables related to the DC power, while the AC frequency, measured to detect the expander shaft speed, is recorded upstream of the rectifier unit.

A commercial plate heat exchanger has been chosen as the condenser, the last major component of the circuit. In this unit the fluid is de-superheated, condensed and slightly subcooled by industrial water. Then the R245fa flows into the liquid receiver interposed between the condenser and the feed pump.

The test bench has been completed with a series of measurement devices, such as thermocouples, pressure sensors and a Coriolis flow meter at the pump outlet, other than the electric equipment described above.

After the thermal insulation of all the hot parts of the circuit, the latter has been purged with nitrogen, evacuated with a vacuum pump and finally filled by a mixture of R245fa and lubricant, as required by the expander. Since the selected oil ensures the solubility in the refrigerant and since quite high velocities are always reached in the circuit, the circulation of the mixture along all the system is acceptable, avoiding the need of an oil separator downstream of the expander.

3. Experimental tests

The first tests conducted on the system, and described in this paragraph, had the aim of achieving a general knowledge of the prototype, verifying the rough correspondence between measured and expected performances and obtaining the set of data needed to calibrate the developed ORC simulation model.

Further experimental work is required to define properly the potentialities of the system, to optimize its efficiency and to find the best working conditions. These tests will be carried out in the future, after the definition of a suitable control strategy for the cogenerator: this task will be achieved using

the dynamic model already cited in the introduction, so the need of experimental data for the calibration of the code justifies the tests on this un-optimized prototype.

Basically, the data required for the validation of the model are pressures and temperatures of the fluid measured along the circuit, mass flow rates and the values of the electric variables of the generated power. Two global performance indexes are taken into account: the expander isentropic efficiency, $\eta_{exp,is}$, and the cycle electric efficiency, η_{ORC}.

The first one, widely used in literature regarding scroll machines [10], is defined by (1):

$$\eta_{\exp,is} = \frac{P_e}{\dot{m}\left(h_{in} - h_{out,is}\right)} \qquad (1)$$

where P_e is the electric power delivered by the expander, measured as the power dissipated on the electronic load, $\dot{m}$ is the working fluid mass flow rate, h_{in} is the specific enthalpy of the fluid at the expander inlet and $h_{out,is}$ is the specific enthalpy of the fluid after an isentropic expansion from the inlet conditions to the discharge pressure. It must be noted that this is not the classical definition of isentropic efficiency usually adopted in the turbomachinery performance analysis: at the numerator there is the net delivered power (i.e. depurated from mechanical and electric losses), instead of the enthalpy drop of the actual expansion (that in a turbomachinery, but not in a scroll expander, can be considered an adiabatic process, so that the enthalpy drop corresponds to the specific work). The net power is then compared to the work rate of the fluid in an ideal adiabatic expansion, within the hypothesis that kinetic energies in the expander inlet and discharge measurement sections were negligible.

The cycle electric efficiency is defined by (2) as the ratio between the net electric power generated by the system and the heat rate absorbed by the fluid in the boiler:

$$\eta_{ORC} = \frac{P_e - P_p}{\dot{m}\left(h_{VG,out} - h_{VG,in}\right)} \qquad (2)$$

where P_p is the power absorbed by the pump, $h_{VG,out}$ is the specific enthalpy of the fluid at the vapor generator outlet and $h_{VG,in}$ is the specific enthalpy of the fluid at the boiler inlet.

In these preliminary tests, the system has been controlled adjusting three variables: the shaft speed of the pump (therefore the volumetric flow rate flowing through the pump), the temperature of the fluid at the boiler outlet and the resistance of the electronic load (therefore the braking torque applied on the expander). After the variation of one or more of these parameters by the operator, the system reacts and, after a brief transient, reaches a new equilibrium state, operating with different values of the free parameters, such as the working pressures and the expander rotational speed.

In Fig. 3 the superheating degree of the fluid at expander inlet as a function of the expansion ratio (the pressure ratio across the machine) is reported for all the considered pump speeds, ω_{pump} and vapor temperatures, T_{max}. This parameter, defined as the difference between the actual fluid temperature and the saturation temperature at the actual pressure, has been used to carry out some considerations on the ORC control system.

As shown in the diagrams, when the temperature imposed at boiler outlet is relatively low, the degree of superheating remains always around 0 K, i.e. the vapor is produced at saturated or partially saturated conditions. In this situation, the quality of the vapor could not be controlled, since only one parameter of the fluid, the temperature, could be set: for example, the actual regulation system could shut down the electric heaters when the fluid reaches a low degree of vapor saturation, due also to inaccurate temperature measurements linked to thermocouples precision. So the need of a different control system has been demonstrated already after the first tests: in the future layouts of the prototype, a new control strategy will be implemented in the system regulation software, allowing the operator to set the superheating degree instead of the absolute vapor

production temperature and, in case, a flow meter, capable to detect the fluid density, will be installed between boiler and expander.

For the reason explained just above, the recorded measurement points with a degree of superheating near to 0 K has been excluded from successive elaborations. The isentropic efficiency of the expander, defined by (1), is reported in Fig. 4 as a function of the pressure ratio. The trends, slightly decreasing with the expansion ratio, show that the machine is operated in under-expansion (i.e. with a pressure ratio higher than the one defined by the geometry), which is a condition much more preferable than over-expansion, since the latter causes a quick drop of efficiency [4].

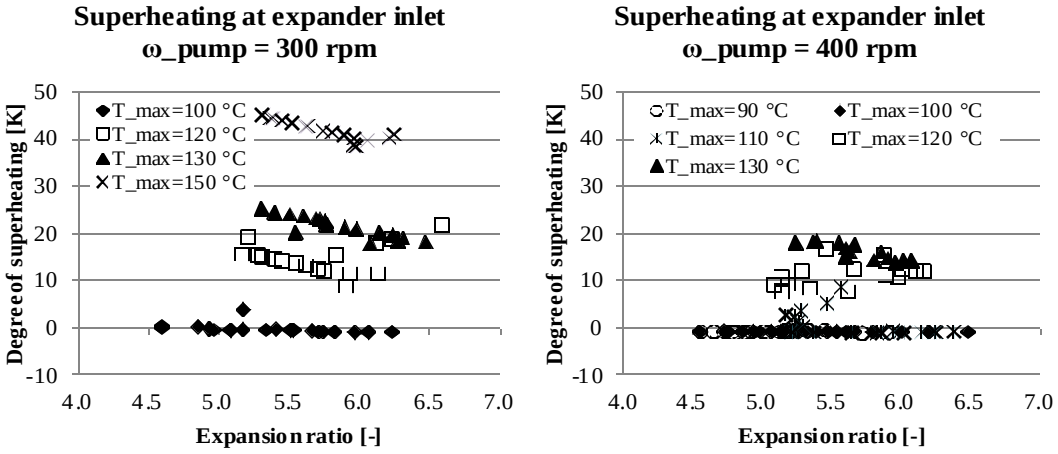

Fig. 3. Degree of superheating of the fluid at the expander inlet as a function of the expansion ratio, at different temperatures of vapor production , for pump shaft speed equal to 300 rpm (left) and 400 rpm (right).

The average values reported in literature for scroll expander isentropic efficiency are usually in the range between 0.60 and 0.65 [9, 11-13], with peaks of 0.68-0.70 [8, 11, 14, 15]. The efficiency achieved by the tested scroll is in a good agreement with these values, as shown in Fig. 4, and this confirm that both the displacement and the built-in volumetric ratio of the machine is suitable for the cycle size, and also that the few modifications made by the manufacturer on the scroll compressor are sufficient to achieve good performances in expander operation mode.

The first law efficiency of the cycle, defined by (2), is reported in Fig. 5 in the same conditions of the previous figures. It can be noted that the efficiency measured on the system, in all the considered working points, is always around 0.08, with only limited variations with the expansion ratio: this last behavior is due to the combination of the scroll efficiency, slightly decreasing with the expansion ratio, as just reported in Fig. 4, and the theoretical cycle efficiency, which increases with the evaporation pressure. The mean calculated value, 0.08, seems to be in good agreement with the results achieved from the numerical simulations of a not regenerative ORC of the same size [6]. It must be underlined once again, however, that these are the performances of a system during its very first tests: after the optimization of the cycle, the improvement of some components such as the thermal insulation and the control system, and the possible installation of an internal recuperator, global efficiencies higher than 0.10 are expected, which can be considered good performances, taking into account the low maximum temperatures of the cycle.

In Fig. 6 the expander shaft speed is reported as a function of the expansion ratio, for different maximum temperatures and feed pump velocities, like the previously analyzed variables. As already written, in this prototype the scroll velocity is free, governed only by the equilibrium between driving and braking torque: when a higher load is applied, the expander slows down, causing a larger chocking effect for the fluid. In this way, a higher pressure ratio is created across the machine (and this explains the trends shown in Fig. 6), so finally a larger driving torque is delivered by the

expander, equilibrating the braking one. As shown in Fig. 6, the speed assumed by the expander during the tests varies between 3000 and 4500 rpm, and the variations in velocity approximately counterbalance the different torque regulations: in fact, as reported in Fig. 7, the delivered power at given values of pump speed and vapor temperature is more or less constant with the expansion ratio, varying from 1100 W (for the lower pump speed and the minimum vapor temperature) to 1500 W (for the higher ones).

It's interesting to note, in Fig. 3 to 7, that the pump speed, and thus the R245fa flow rate, does not influence significantly the performances of the system, with the obvious exception of delivered power, which increases with the mass flow rate.

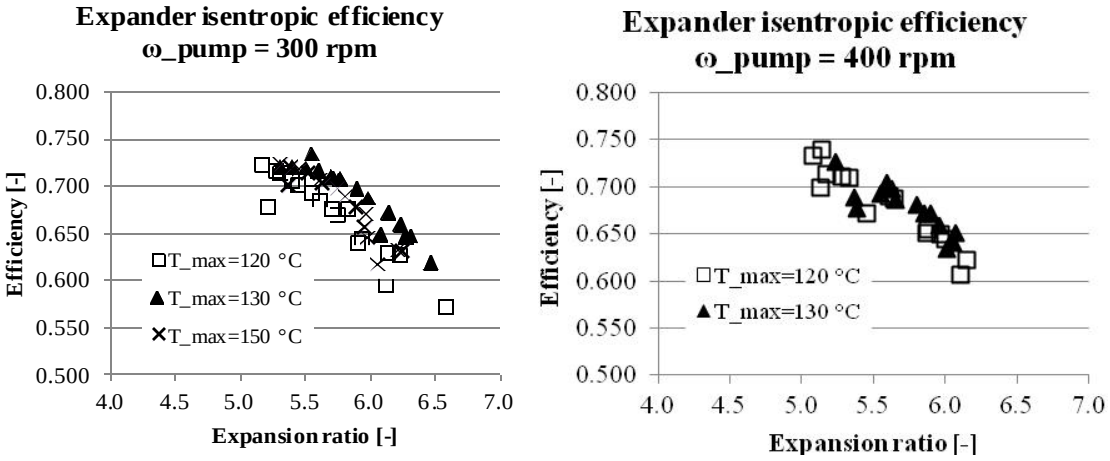

Fig. 4. Isentropic efficiency of the scroll expander as a function of the expansion ratio, at different temperatures of production of vapor, for pump shaft speed equal to 300 rpm (left) and 400 rpm (right).

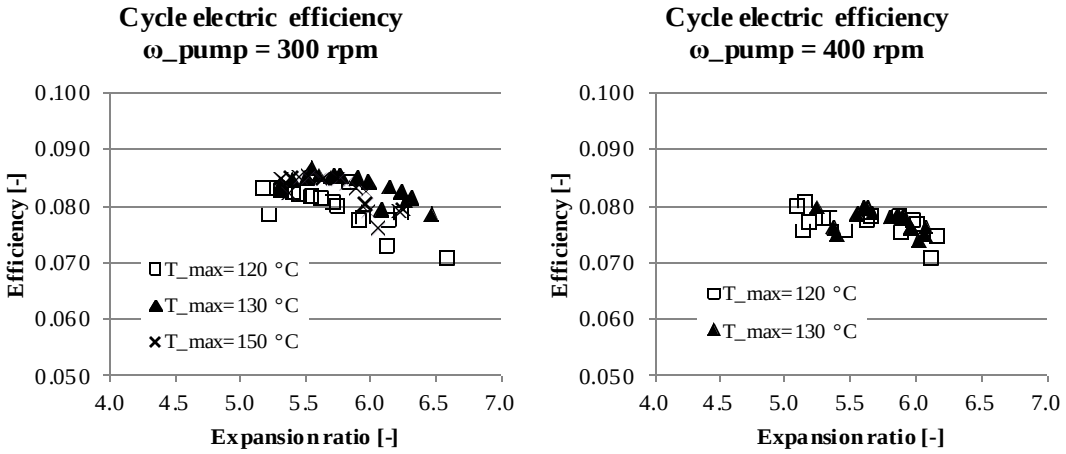

Fig. 5. Electric efficiency of the ORC as a function of the expansion ratio, at different temperatures of production of vapor, for pump shaft speed equal to 300 rpm (left) and 400 rpm (right).

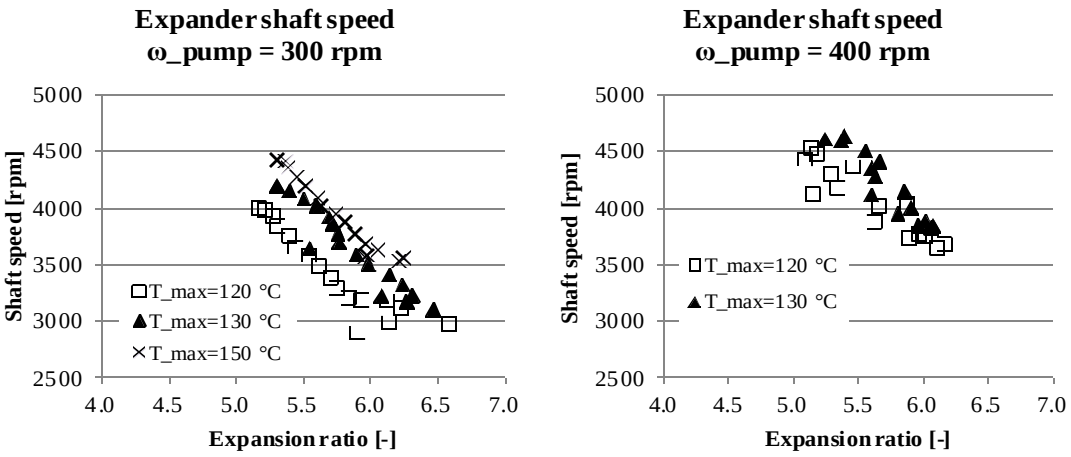

Fig. 6. Expander shaft speed as a function of the expansion ratio, at different temperatures of production of vapor, for pump shaft speed equal to 300 rpm (left) and 400 rpm (right).

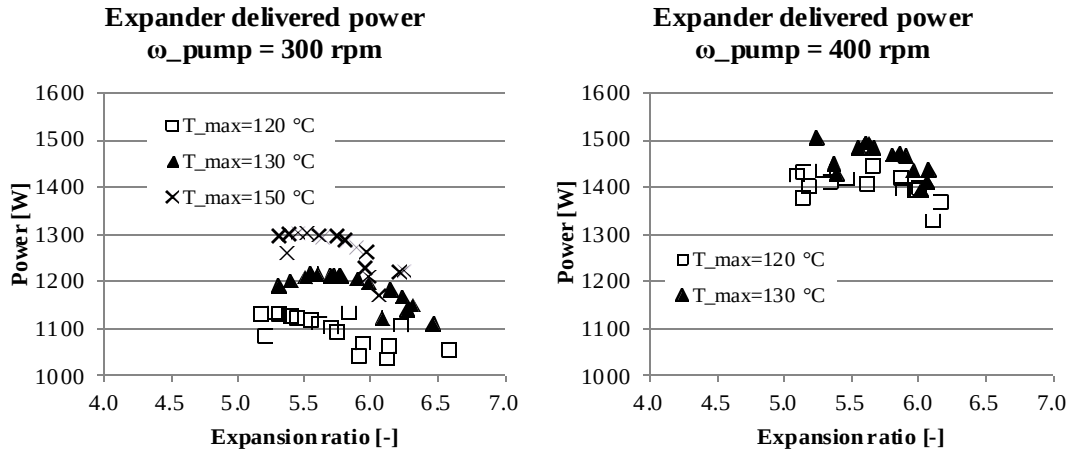

Fig. 7. Power delivered by the expander as a function of the expansion ratio, at different temperatures of production of vapor, for pump shaft speed equal to 300 rpm (left) and 400 rpm (right).

4. Simulation model

The numerical model of the system has been realized with AMESim® (Advanced Modeling Environment for performing Simulations of engineering systems) [16], a simulation software for the modeling and analysis of one-dimensional systems. The package offers a suite of tools to model and analyze multi-domain, intelligent systems and to predict their multi-disciplinary performance. Model components are described taking into account the system's actual hydraulic, pneumatic, mechanic, electrical, thermal and electromechanical behavior. The source code for most of the standard submodels is provided, allowing the user to modify existing models to fit them to his needs. Users can also develop their own submodels, programming in C or in Fortran. AMESim® is particularly suited to the development of dynamic models, so that various control strategies of the modelized system can be tested and transient operating conditions, potentially dangerous, easily simulated. A major difference with standard Simulink is that the variables, shared at the ports between submodels, are physical and operate in both directions.

A sketch of the ORC simulation model is reported in Fig. 8. It comprises the schemes of the ORC circuit assembly, slightly simplified with respect to the real one, and of the alternator, power conditioning system and electric load. The values of the resistance are converted into the braking

torque applied on the expander in the ORC assembly. The resistance values chosen during the experimental tests are taken into account in the validation phase.

Properties of R245fa have been obtained selecting the operating fluid in the software standard “two phase flow” library. The effects of lubricating oil concentration on the thermo physical properties of the oil–refrigerant mixture, which operates as working fluid in the real system, have been neglected. The expander is simulated with the standard TPFTURB00 submodel. The required values of displacement and of isentropic, mechanical and volumetric efficiencies have been obtained on the basis of technical data provided by the scroll manufacturer and the combined use of some experimental results and of a scroll simulation tool, previously developed by the authors [4]. Efficiencies values have been considered constant and the expansion process adiabatic: these assumptions are not quite correct and will be removed with the planned development of an improved expander submodel. The pump is modeled as a standard fixed displacement hydraulic unit with given volumetric and mechanical efficiency, which values have been estimated on the basis of the performance curves reported in a technical data sheet. Condenser is modeled with a small number of standard components, as shown in Fig. 8. Its internal volumes and heat capacities have been obtained on the basis of technical data sheets and direct measurements on the prototype. The mass of refrigerant introduced in the system has been measured during the experimental set up, but due to some leakages of fluid happened during the running in, it has been considered, within a range of reasonable values, as a free validation parameter, together with the internal volume of the vaporizer circuits, which effective value is only approximately known. Other free validation parameters were the gain coefficients of the friction losses in the connecting pipes. Optimization has been carried out with both NLPQL and genetic algorithms, with the objective of minimizing the error on the expander shaft speed, at a reference experimental operating point. This was chosen corresponding to a pump velocity of 300 rpm, vapor superheating temperature of 130°C and resistance set at 70 Ω.

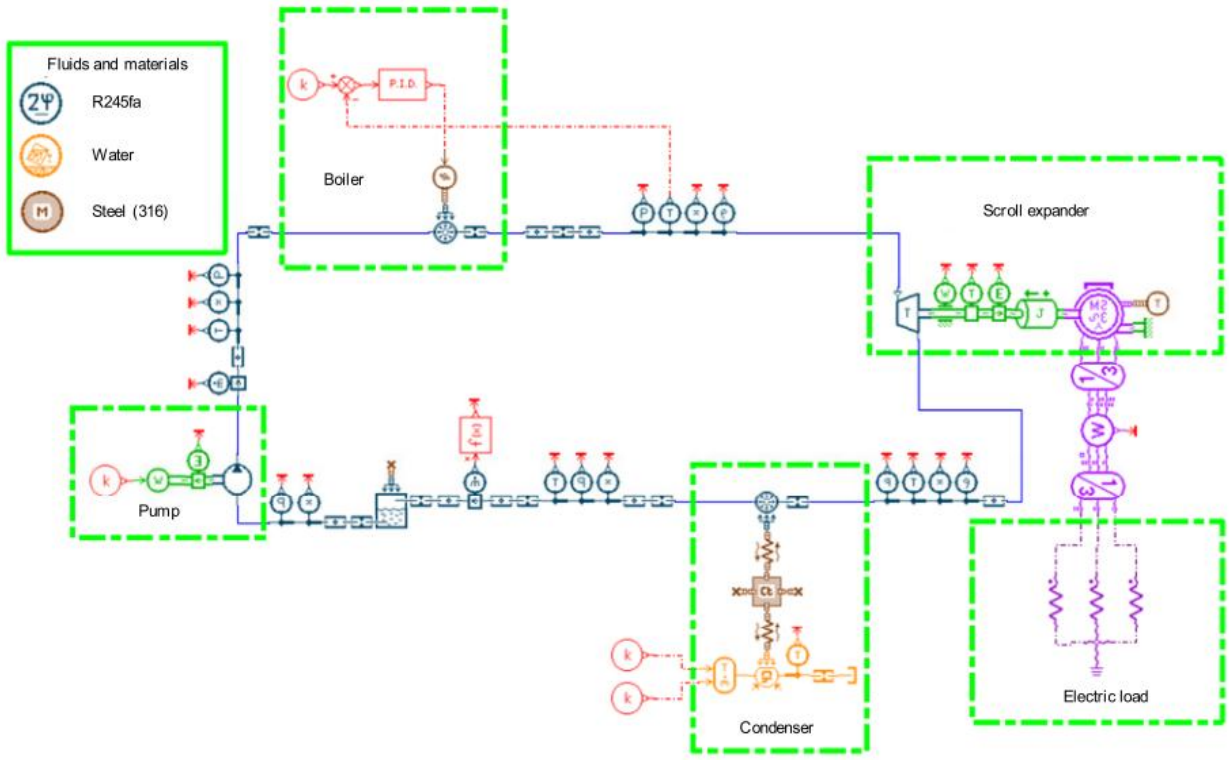

Fig. 8. Sketch of the AMESim® simulation model of the ORC prototype and of the electric load.

5. Comparison between experimental and numerical data

Once the model had been calibrated, its outputs at different working conditions have been compared with experimental measurements, to verify its accuracy. In Fig. 9 several diagrams are reported, which underline the correlation between experimental and numerical results: a perfect correspondence between the two sources of data would result in a point placed on the bisector of the planes.

The first diagram shows the expander shaft speed: a satisfactory correspondence between the two series of data can be noted even if, in some particular working conditions, the model over-estimated the real values. The second diagram reports the voltage supplied by the system after rectification, as representative of all the electric parameters simulated by the model: in this case, the correlation between numerical and experimental data could certainly be considered good, confirming the accuracy in the modelization of the electric devices.

The model exhibited larger difficulties in calculating accurately the fluid properties, in particular the pressures at some sections of the system: for example, in the diagram reporting the pressure at boiler outlet in Fig. 9, a general underestimation by the model is highlighted. The poor correlation can be due to inadequate model calibration, but also to a scarce correspondence of the fluid properties sub-models with the actual operating fluid composition or even to the simplified modelization of some plant component. In fact, the real system is filled by a mixture of R245fa and lubricant, while the simulation is carried out taking into account only the refrigerant as a pure substance. Besides, the expander is modeled as an adiabatic machine with constant efficiency while, in the used scroll device, heat transfer is not negligible and efficiency varies. In the first phase of the research, the approximation given by these simplifying hypotheses is considered sufficient, but the accuracy in calculating the thermodynamic properties of the fluid is surely affected by the cited factors. Another cause of the poor correlation can be, for low temperatures at boiler exit, the already described problems in the control of the system: the presence of fluid with an unknown quality of vapor at the expander inlet results in measurement errors and difficulties in calculating the exact fluid properties. The simulation model achieves a greater accuracy in calculating the pressure at condenser outlet, as reported in the corresponding graph in Fig. 9: in this section, the thermodynamic state is strongly influenced by the temperature of the cooling water, which is a direct calibration parameter for the model, so a better correspondence between experimental and numerical results is reached.

Obviously, due to the problems highlighted in the definition of the thermodynamic states of the fluid, even the calculation of the working parameters of the system based on these states is affected by a relatively low accuracy. For instance, as shown in the corresponding diagram in Fig. 9, the calculated values of the enthalpy drop across the expander lie in a quite large region around the plane bisector. In particular, an underestimation occurs when the vapor production temperature is set on high values, i.e. 150 °C. On the other hand, the global working parameters of the system, i.e. the delivered power and the electric efficiency of the cycle, are only slightly overestimated, as shown in the last two graphs in Fig. 9: in these cases the accuracy is satisfactory, since the scarce precision revealed in the thermodynamic properties estimation is counterbalanced by the good skill of the model to calculate other data such as the fluid flow rate or the electric output. In particular, the mean relative error detected in the numerical estimations of the delivered power is lower than 5%, while the global efficiency is overestimated, on the average, by only one percentage point.

In summary, the comparison between numerical and experimental data highlighted an accuracy of the simulation model which surely has to be improved but, at the moment, it can be considered already sufficient for a tool useful to carry out dynamic simulations having the aim of defining suitable control system strategies.

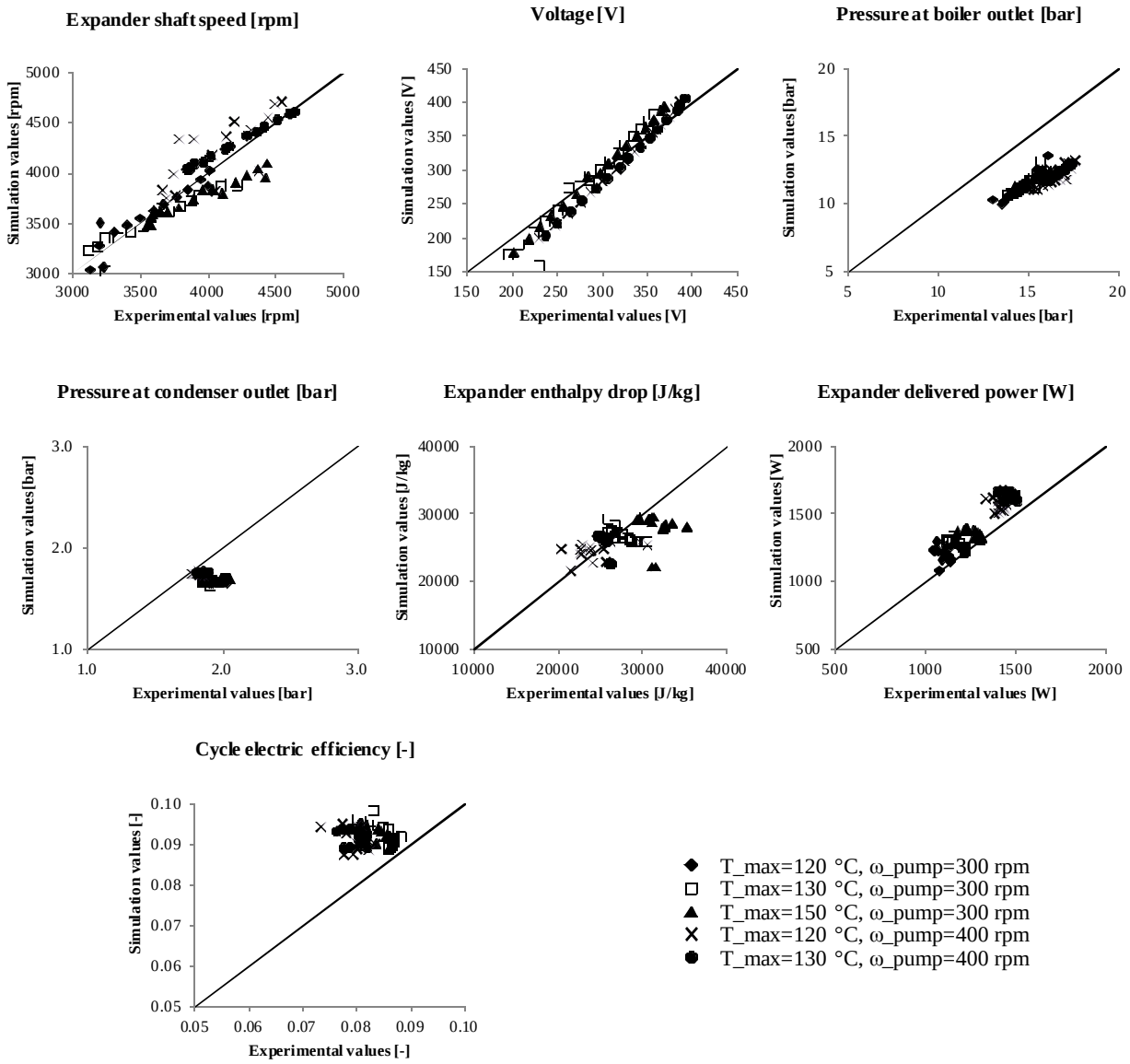

Fig. 9. Comparison between the results of measurements and the model outputs of different working parameters, in the operating conditions reported in the legend.

6. Conclusions

The first part of this paper described an experimental prototype of an ORC-based cogenerator and the first tests conducted on it. The elaboration of the measurement data revealed very promising performances for the system, with a global electric efficiency of about 0.08, even if these has been the very first tests and all the different parts of the cycle need an optimization. However, some malfunctions were detected, mainly related to an unsuitable system of controlling the vapor production temperature, which needs to be modified in the next versions of the prototype.

A dynamic numerical model of the cycle has been realized, using the data recorded after the first sessions of measurements for calibration and validation. The correspondence between experimental and simulation results has been satisfactory in general, so the usefulness of the tool for the study of possible improvements of the system is demonstrated. However, the accuracy of the model is not so good in prediction of the thermodynamic state of the fluid in the different sections of the circuit. This is due to approximations in the calculation of operating fluid properties and to the simplified modelization of the expander, other than to the scarce quality of some data used for calibration. In particular, quality problems regard data relative to the working points featuring a low degree of

superheating, which represent situations not completely governable by the control system actually installed on the prototype. For these reasons, a parallel development of both the test bench and the numeric model is scheduled, using the results obtained from one of them to improve the other.

Acknowledgments

The authors would like to acknowledge Emanuele Crevatin for his collaboration in the numerical modelization of the system and in the execution of the experimental tests, as part of work for his Master's Thesis at University of Trieste.

Nomenclature

CHP	Combined Heat and Power Production
h	specific enthalpy, J/kg
HVAC	Heating, Ventilation and Air Conditioning
$\dot{m}$	mass flow rate, kg/s
ORC	Organic Rankine Cycle
P	power, W

Greek symbols

η	efficiency, -

Subscripts and superscripts

e, exp	expander
in	inlet
is	isentropic
out	outlet
p	pump
VG	vapor generator

References

[1] Bianchi M., De Pascale A., Bottoming cycles for electric energy generation: Parametric investigation of available and innovative solutions for the exploitation of low and medium temperature heat sources. Appl Energy 2011;88:1500-1509.

[2] First International Seminar on ORC Power Systems (ORC2011) – Available at:<http://www.orc2011.nl/> [accessed 13.1.2012].

[3] Demierre J., Henchoz S., Favrat D., Prototype of a thermally driven heat pump based on integrated organic Rankine cycles (ORC). In: ECOS 2010: Proceedings of the 23th International Conference on Efficiency, Cost, Optimization, Simulation and Environmental Impact of Energy Systems; 2010 Jun 14-17; EPFL, Lausanne, Switzerland.

[4] Clemente S., Micheli D., Reini M., Taccani R., Numerical Model and Performance Analysis of a Scroll Machine for ORC Applications. In: ECOS 2010: Proceedings of the 23th International Conference on Efficiency, Cost, Optimization, Simulation and Environmental Impact of Energy Systems; 2010 Jun 14-17; EPFL, Lausanne, Switzerland.

[5] Clemente S., Micheli D., Reini M., Taccani R., Performance Analysis and Modeling of Different Volumetric Expanders for Small-Scale Organic Rankine Cycles. In: ESFuelCell

2011: ASME 2011 5th International Conference on Energy Sustainability and 9th Fuel Cell Science, Engineering and Technology Conference; 2011 Aug 7-10; Washington, DC, USA.

[6] Clemente S., Micheli D., Reini M., Taccani R., Preliminary Design of Organic Rankine Cycles with Scroll Expanders. In: ICAE 2011: 3rd International Conference on Applied Energy; 2011 May 16-18; Perugia, Italy.

[7] Quoilin S., Lemort V., Lebrun J., Experimental study and modeling of an Organic Rankine Cycle using scroll expander. Appl Energy 2010;87:1260-1268.

[8] Kane M., Larrain D., Favrat D., Allani Y., Small hybrid solar power system. Energy 2003;28: 1427-1443.

[9] Zanelli R., Favrat D., Experimental investigation of a hermetic scroll expander-generator. In: 12th Int. Compressor Engineering Conference; 1994 Jul 19-22; Purdue, IN, USA. p. 459-464.

[10] Winandy E., Saavedra C., Lebrun, J., Experimental analysis and simplified modeling of a hermetic scroll refrigeration compressor. Appl Therm Eng 2002;22:107-120.

[11] Lemort V., Teodorese I.V., Lebrun J., Experimental study of the integration of a scroll expander into a heat recovery Rankine cycle. In: 18th International Compressor Engineering Conference; 2006 Jul 15-20; Purdue, IN, USA. p. 1-8.

[12] Yanagisawa T., Fukuta M., Ogo Y., Hikichi, T., Performance of an oil-free scroll-type air expander. Proc IMechE Part C 2001;591/027:167-174.

[13] Saitoh T., Yamada N., Wakashima S.I., Solar Rankine cycle system using scroll expander. J Environ Eng 2007;2(4):708-719.

[14] Hugenroth J., Braun J., Groll E., King G., Experimental investigation of a liquid-flooded Ericsson cycle cooler. Int J Refrig 2008;31:1241-1252.

[15] Lemort V., Quoilin S., Cuevas C., Lebrun J., Testing and modeling of a scroll expander integrated into an Organic Rankine Cycle. Appl Therm Eng 2009;29:3094-3102.

[16] LMS Imagine.Lab AMESim – Available at: <http://www.lmsintl.com/LMS-Imagine-Lab-AMESim> [accessed 2.5.2012].

Model of a small steam engine for renewable domestic CHP system

G. Ferrara[a], G. Manfrida[b], A. Pescioni

Università degli Studi di Firenze, Dipartimento di Energetica "Sergio Stecco", Firenze, Italy,
[a]Giovanni.Ferrara@unifi.it
[b]Giampaolo.Manfrida@unifi.it

Abstract:

A small steam expander is proposed, which can find promising applications in the conversion and utilization of low-grade heat resources of different nature, such as geothermal, solar, and recovery of waste heat. The product to be developed should be able to work with small flow rates and low upper temperature (100-150°C), while rejecting heat at a level still interesting for heating or cooling (with an absorption machine), that is, 50 to 80°C. The efficiency is necessarily low, but electricity can be seen within this views as a by-product with respect to heat. The device should be compact, simple and capable of easy control in order to match electric production and loads, which is a key point in off-grid applications.

Reciprocating engines are a 19th-century tradition for steam expanders; however their technology can be revisited due to advances in materials and in engine control systems, derived from the IC engine sector. Nowadays valve opening/shutoff can be largely controlled by electronic/hydraulic systems, and for small sizes direct DC electricity production, possible at variable speed, can be proposed.

This paper presents a thermodynamic model of the reciprocating engine using real-fluid and real cycle assumptions. It includes a heat transfer model for non-adiabatic compression and expansion, losses through admission/discharge valves, and the effects of dead space. The model applies quasi-stationary modeling of the system: however, its results are successfully compared with those of a dynamic model, working under perfect-gas assumptions. The model allows to calculate and analyze the performance of the system, including its dependence on the main design parameters. The results indicate that the technical solution can be applied and that the performance of the CHP system is competitive with respect to other technologies for renewable energies.

Keywords:

Steam engine, Small Combined Heat and Power Systems, Renewable Energy, Low-Temperature heat Sources.

1. Field of application of small steam engines

The concept of distributed energy conversion and utilization systems is rapidly developing, with a growing attention to off-grid concepts, allowing small houses and/or activities to be independent from services (energy, sewage, information flows) requiring expensive networks of wires and piping. Small steam engines could be devices of relevant interest for the market of combined heat and power (CHP) and distributed electricity production for dwelling applications.

Expanders considered for organic vapours are usually of the scroll or screw type [1, 2, 3, 4, 5]; these expanders have been developed or adapted from compressors used in refrigerating units, and typically cover a range from 10 to 25 kW. The idea is to propose the development of smaller units, in the range from 1 kWe (individual dwellings, possibly connected by a smart grid) to 10 kW (covering the energy needs of small multi-family dwellings). To this end, it was decided to reconsider a well proven technology, that of reciprocating engines. The use of this machine as a steam expander can be traced back to 19th-century tradition, and design methods and technical solutions were advanced considerably in the 20th century [6]; however the technology can be revisited considering advances in materials and in engine control systems, derived from the IC engine sector. Nowadays valve opening/shutoff can be largely controlled by electronic/hydraulic

systems, and for small sizes direct DC electricity production, possible at variable speed, can be proposed; it is even possible to consider adaptation of existing IC engines, or to use existing manufacturing lines for large-scale production.

1.1 - Mode of operation

The reciprocating engine operates with the traditional rod mechanism. The engine is placed between two reservoirs (Figure 1): the steam vessel works as a high-pressure reservoir (HPR) and heat/steam accumulator: it is connected to the external heat source (for example, a field of solar collectors, or a geothermal heat exchanger). A recirculation loop ensures favorable conditions for heat transfer (a low quality of steam). The dry steam is taken from the upper part of the reservoir, and routed to an external super-heater which operates directly on the engine flow rate[1]. The condenser is the low-pressure reservoir (LPR), covering the building heat load[2]: typically it is kept at a temperature of 60 to 70 °C. A small pump makes up for the pressure difference between the reservoirs.

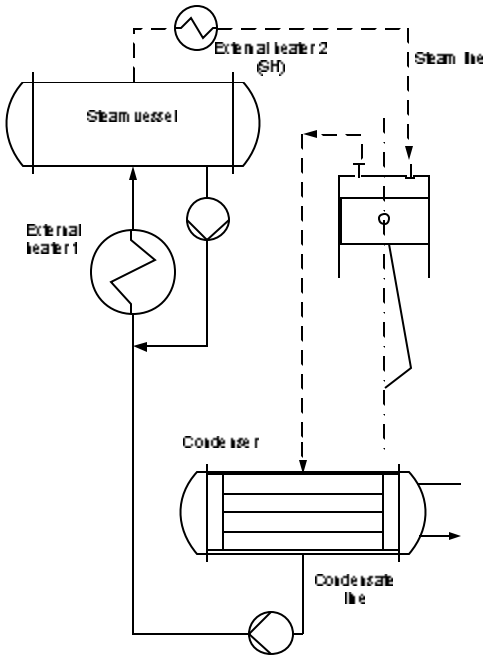

Fig. 1. Schematic of reciprocating steam engine circuit

In practice the engine would be a multi-cylinder unit, of a type similar to what has been developed for heat recovery in IC engines or for biomass applications [5, 6]. With respect to a traditional cycle of an IC engine, the valve timing is completely different. A full cycle is realized in one single turn, following a two-stroke operation mode. The following description applies to the limit cycle (ideal engine, real fluid conditions), which has been previously analyzed [8]. With reference to Figure 2, the Discharge Valve is maintained open to the upper dead end (UDE), so that the compression phase is absent.

[1] The external Heater 2 would typically be using a heat source providing higher temperature, such as a set of parabolic trough solar collectors

[2]During summer it is possible to consider operation of the condenser at higher temperature, and coupling to an absorption cooling loop.

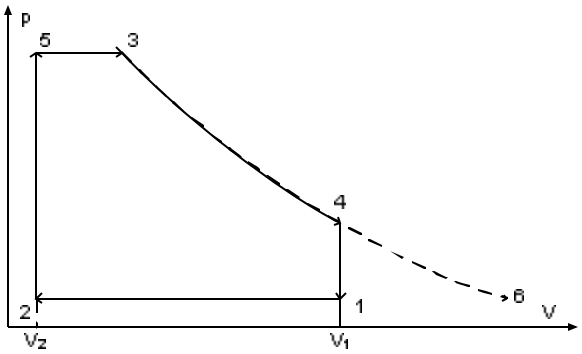

Fig. 2. Steam Reciprocating Engine- Limit cycle

At the UDE the Discharge Valve is closed and the Admission Valve is opened. Steam flows under high pressure difference, rapidly filling the dead space volume (constant-volume admission, 2-5). When the HPR pressure is reached, steam flows inside the cylinder at constant pressure, with increasing volume, until the Admission Valve closes (Constant-pressure admission, 5-3). The expansion phase 3-4 is treated as adiabatic and isentropic (limit cycle). At the Bottom Dead End, the Discharge Valve is opened, and steam exits the cylinder under relevant pressure difference, at constant volume (4-1); when the condenser pressure is reached, discharge of steam continues at constant pressure until reaching the upper dead end (1-2).

1.2 – Engine parameters

In order to have a parametric description of the cycle, the following parameters must be introduced:

Volumetric compression ratio:

$$\rho = \frac{V_1}{V_2} \tag{1}$$

Admission Grade (Cut-off ratio):

$$\sigma = \frac{V_3 - V_5}{V_D} \tag{2}$$

Where V_D is the engine displacement, $V_D = V_1 - V_2$.

The Expansion Grade is defined as:

$$\varepsilon = \frac{\mathbf{V_4}}{\mathbf{V_3}} \tag{3}$$

Defining the non-dimensional dead space as:

$$\mu = \frac{\mathbf{V_2}}{\mathbf{V_D}} \tag{4}$$

it can be shown that:

$$\varepsilon = \frac{1+\mu}{\sigma+\mu} \qquad (5)$$

The problem of determining the mass of fluid operating in the engine was examined and the solution approach was explained in [8] (considering the mass of fluid entrapped in the dead space at the end of the discharge stroke). The method is here generalized to simulation of the real cycle, considering the pressure drops in the discharge and admission valves, that is, calculating the volumetric efficiency of the engine. As in [8], no steam recompression process is considered, that is, the Discharge Valve is kept open until very close to the UDE.

2. Real Cycle Model

With respect to the Limit Cycle [8], the Real Cycle Model adds several complications, which result in the typical cycle diagram looks like in Figure 3, showing a sample calculation.

Basically:

1. the base pressure at point 2 must be iterated from a first guess
2. the mass remaining in the dead space must be iterated (as in the limit case)
3. the admission phase is simulated with a pressure loss model, depending on the admission valve lift
4. the expansion phase includes a heat release model from the expanding fluid to the cylinder walls
5. the discharge phase is simulated with a pressure loss model, depending on the discharge valve lift.

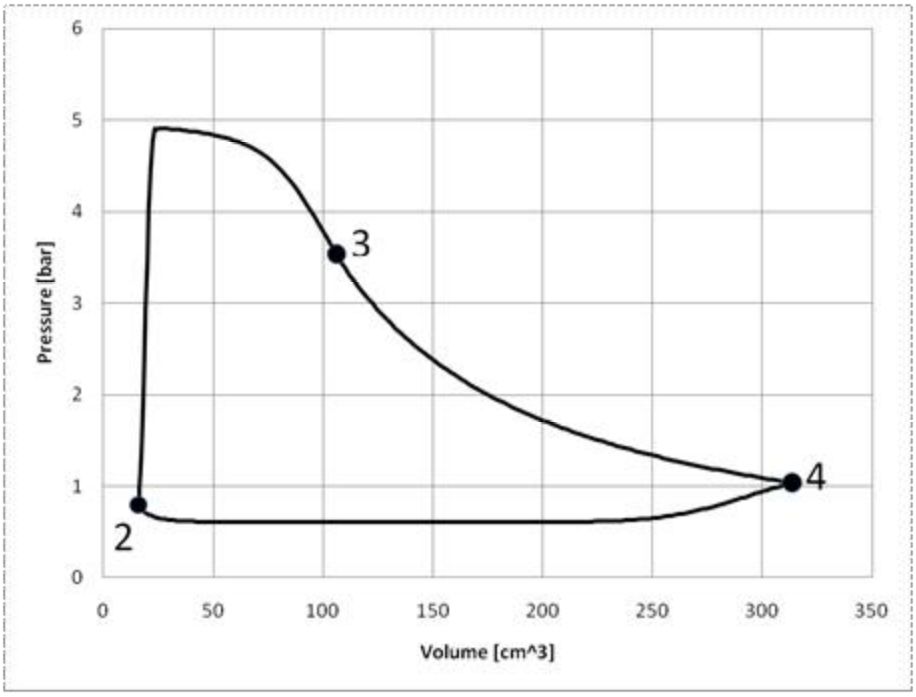

Fig. 3. Steam Reciprocating Engine - Real cycle (Quasi-Stationary model output)

The real cycle model requires a description of the intermediate cycle points, which are calculated from the volume-crank angle relationship:

$$V[\theta] = V_D * \left[\frac{1}{\rho - 1} + 0,5\left(1 + \frac{1}{\lambda} - \cos\theta - \frac{1}{\lambda}\sqrt{1 - \lambda^2 \sin^2\theta}\right)\right] \quad (6)$$

The whole model was implemented using the EES software [7], taking full advantage of the built-in steam properties which allow to consider real fluid properties in all thermo-fluid-dynamics processes.

2.1. Admission phase

The admission phase goes from point 2 (0° crank angle) to point 3 (beginning of expansion phase, determined by the selected Admission Grade); the fluid conditions are solved point by point with a small dθ. Each point between 2 and 3 is solved with a stationary model, which consists of three steps in cascade:

a) steam enters from the AV at constant volume, passing from the HPR to the cylinder
b) steam exits from the DV, always at constant volume (only if this is kept open, DVCD>0)
c) evaluation of the change of volume of the system (valves are still open but no steam enters or exits from the cylinder in this step). Updating of θ for next point.

The valve lift is modelled by a power law in function of θ; from the valve lift as a function of θ, the flow cross section is calculated during step a) (inlet flow) and b) (outlet flow).

During step (a), the upstream conditions are those in the HPR (superheated steam); the ideal mass flow is calculated using perfect-gas assumptions and isentropic flow through a convergent duct, determining if the flow is critical (as is usually at the beginning of admission, with limited lift and cross section) or subsonic. The real mass flow is calculated using a flow coefficient:

$$fc_a = \frac{\dot{m}_r}{\dot{m}_i} = f(lift, D_{AV}) \quad (7)$$

The conditions inside the cylinder are updated assuming that the addition of the real mass flow through the valve takes place with an isenthalpic transformation.

During step (b) (AV, DV open), the mass flow exiting the system is calculated similarly; here, the upstream pressure is that inside the cylinder, while the downstream value is that in the LPR. Differently from step (a), the upstream condition can be of saturated steam: in this case (checked automatically by the model) it is assumed that only the gas phase contributes to the fluid dynamic action; the liquid phase contributes only to the total mass of steam inside the cylinder.

Hence, to calculate the ideal mass flow with saturated steam as upstream condition, the conditions are considered as dry saturated steam at the same temperature.

At the end of step (b) the conditions inside the cylinder are updated with the same assumption done at the end of step a).

During steps(a) and (b) the valve lift is calculated with the following equation

$$lift_a = lift_{a,max}(1 + aa * X^e + bb * X^f + cc * X^g + dd * X^h) \quad (8)$$

with

$$X = \frac{\theta - \frac{OD_A}{2}}{\frac{OD_A}{2}} \quad \text{or} \quad X = \frac{\frac{OD_A}{2} - \theta}{\frac{OD_A}{2}} \quad (9)$$

respectively during closure or opening of the admission valve.

During step c) the system is treated as a closed system, solved simply with conservation of energy and mass. The crank angle θ is updated (with step $d\theta$[3]) as well as the conditions inside the cylinder; the process is then restarted from step (a) with the updated angle, or with expansion phase if the point 3 is reached.

2.2. Expansion phase

The expansion is modelled through a step-by-step closed-system energy balance, starting at $\theta = \theta_3$:

$$u_\theta - u_{\theta-1} = -dW_{r\theta} - dQ_{e\theta} \quad (10)$$

At each step, u = f(V, T) = f(θ, T(θ)). The internal energy is decreasing with increasing expansion, both because of work extraction, and heat release to the cylinder walls. This last can be evaluated as:

$$dQ_{e\theta} = HS(T_{m\theta} - T_p) \quad (11)$$

The cylinder surface T_p is assumed constant; $T_{m\theta}$ is determined as the average between $T_{\theta-1}$ and T_θ (this last is unknown and determined iteratively; the isentropic value is assumed as first guess).

The expansion phase was modelled considering a sequence of at least 100 volume steps. At the end of the expansion, the overall work and heat released to the environment can be calculated summing all dWs and dQs.

2.3. Discharge Phase

The discharge phase is treated similarly to the admission, from point 4 (end of expansion phase) to point 2 (0° crank angle), solved point by point as before. The three steps are:

a) steam enters from the AV at constant volume(only if this is kept open, AVAO>0), passing from the HPR to the cylinder
b) increase of volume of the closed system (valves are still open but no steam enters or exits from cylinder).
c) steam exits from the DV. Updating of θ. If point 2 is reached, check of convergence.

Each single step is treated as in the admission phase. When point 2 is reached, the model checks the convergence comparing the new mass with the one supposed as first guess at the beginning of the cycle. If the convergence is not acceptable (a relative error between successive iterations is used for this check), the mass of point 2 is updated as the average between the old and the new one, to start a new iterative cycle.

2.4. Model Assembly – Calculation of Performance Variables

After the detailed modelling of the admission, expansion and discharge (including overlapping of the three phases as described previously), it is possible to calculate the overall work as:

[3] During the admission and discharge phases, a very small value of $d\theta$ is used, typically $d\theta$ = 1° or 0,1°

$$W_{tot} = W_{D_{tot}} + W_{A_{tot}} + W_{Exp} \quad (12)$$

Where W_{Dtot} is the discharge work (work obtained during the Discharge Phase), W_{Atot} is the admission work (work obtained during the Admission Phase), and W_{Exp} is the expansion work (work obtained with the admission and discharge valves closed).

The first-law balance of the admission transformation allows to calculate the Heat Input:

$$Q_1 = Q_{1v} + Q_{1p} \quad (13)$$

$$Q_{1v} = u[5] - u[2] \quad (14)$$

$$Q_{1p} = h[3] - h[2] + W_{A_{tot}} \quad (15)$$

$$W_{A_{tot}} = p[5] * (V[3] - V[5]) * 100 \quad (16)$$

The cycle efficiency is calculated as:

$$\eta = \frac{W_{tot}}{Q_1} \quad (17)$$

and the Power Output as :

$$P = \frac{W_{tot} * RPM}{60} \quad (18)$$

2.5. Non-Stationary model

The assumption of a quasi-stationary flow is often non–realistic in reciprocating engines. In the present case, the rotational speed is limited and non-stationary effects are expected negligible; however, it was decided to perform a check of the model described at point 2 using a widely-used commercial non-stationary software package developed for IC engines, WAVE [11]. Wave has not been built for such a this application and so it does not allow to consider real fluids, as it applies perfect-gas relationships derived from compressible gas dynamics. However, it is fully capable to calculate wave propagation in ducts, as it solves 1-D Navier-Stokes non-stationary flow equations including, where necessary, heat transfer and pressure losses by using experimental correlations. The model was assembled following the directions of the WAVEBUILD application; a complete description of the inlet/outlet ducts geometry, valve size, lift and timing is necessary for building the model.

As a result of the calculation, a typical cycle diagram is shown in Figure 4:

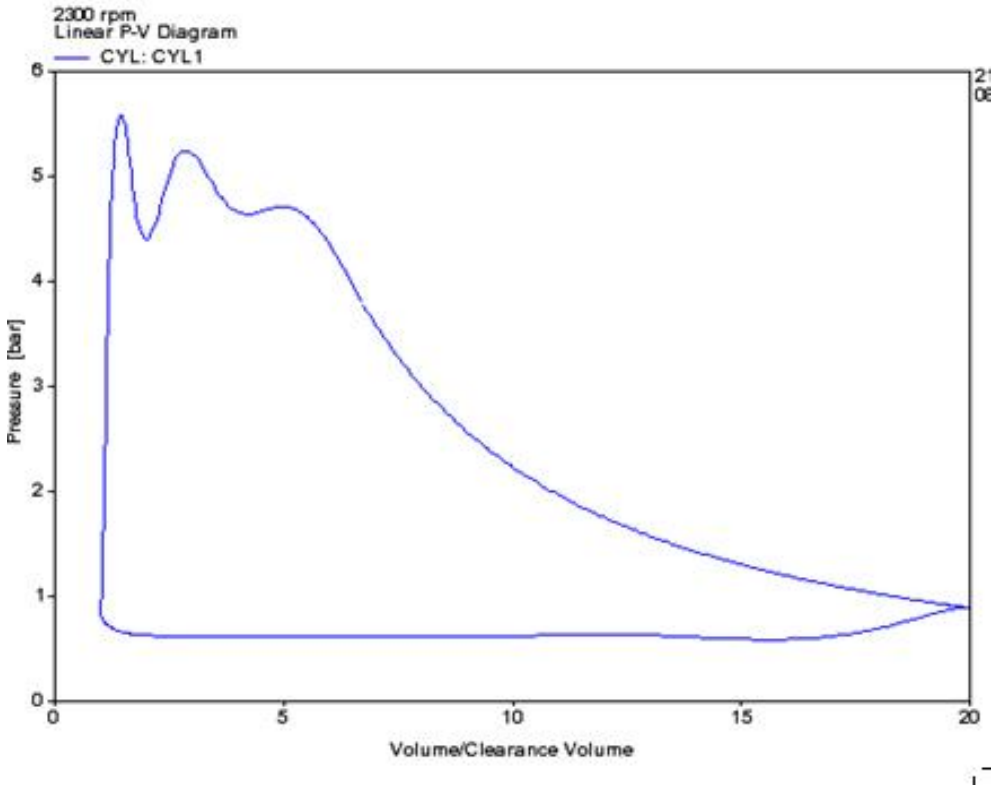

Fig. 4. Steam Reciprocating Engine - Real cycle (Non-Stationary model output)

3. Reference case

As a reference case, the basic data of an experimental engine were considered [9, 10].

- ρ =20
- Displacement =300 cm^3 (Bore x Stroke = 72,6 x 72,6 mm);
- Crank/Rod ratio = 0,27
- Geometrical compression ratio = 20
- Discharge and Admission duct lengths = 100 mm
- Rotational speed =2300 rpm;
- σ=0,30 (Cut-Off, Design Value)
- Admission valve diameter = 30 mm, maximum lift = 4 mm
- Discharge valve diameter = 30 mm, maximum lift = 6 mm

The valve lift trend vs. the crank angle θ is shown in Figure 5. Figure 6 shows the profile of the valve duct flow coefficient. These coefficients have been experimentally evaluated on a real engine head with a geometrical valve-duct configuration consistent with the here-presented reference case.

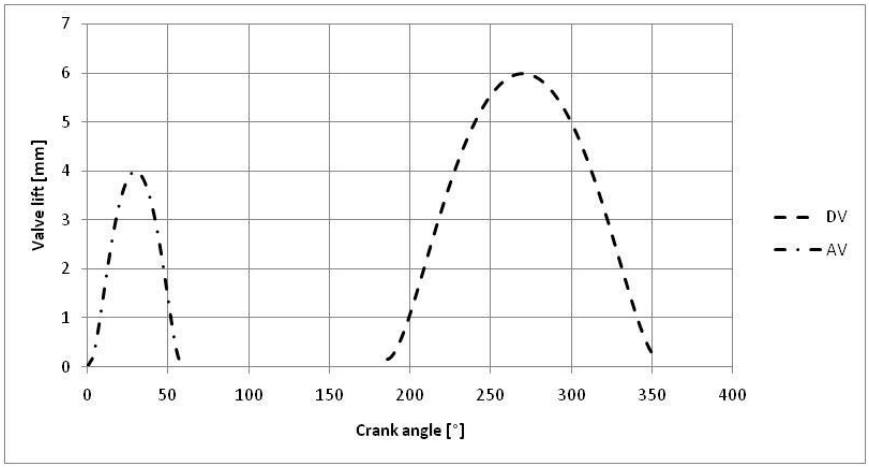

Fig. 5. Admission and discharge valve lift profiles

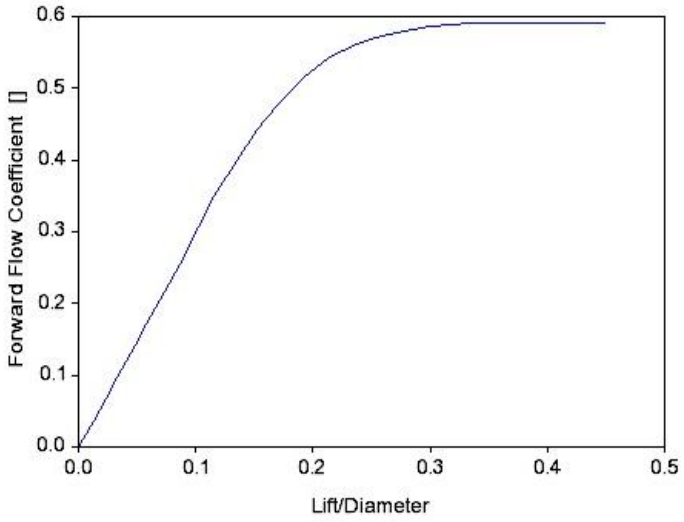

Fig. 6. Valve duct-flow coefficient

The operating conditions were set at values compatible with utilization of low-enthalpy heat sources, such as non-concentrating or low-concentration solar thermal collectors, or low-medium temperature geothermal resources; the LPR was kept at a temperature value compatible with a building heating system, with moderate vacuum conditions at the condenser:

- T_{HPR}=160°C
- P_{HPR}=5 bar
- T_{LPR}=86 °C (Condenser pressure p_{HPR} =0,6 bar)

4. Application of the Cycle Models

4.1. Admission and discharge

Both models are able, through the application of Quasi-Stationary (QS) or non-stationary (NS) flow modelling equations, to calculate the flow conditions across the admission and discharge valve. As

a result, the flow rates can also be calculated, which are shown in Figures 7 (a) and 7 (b) respectively.

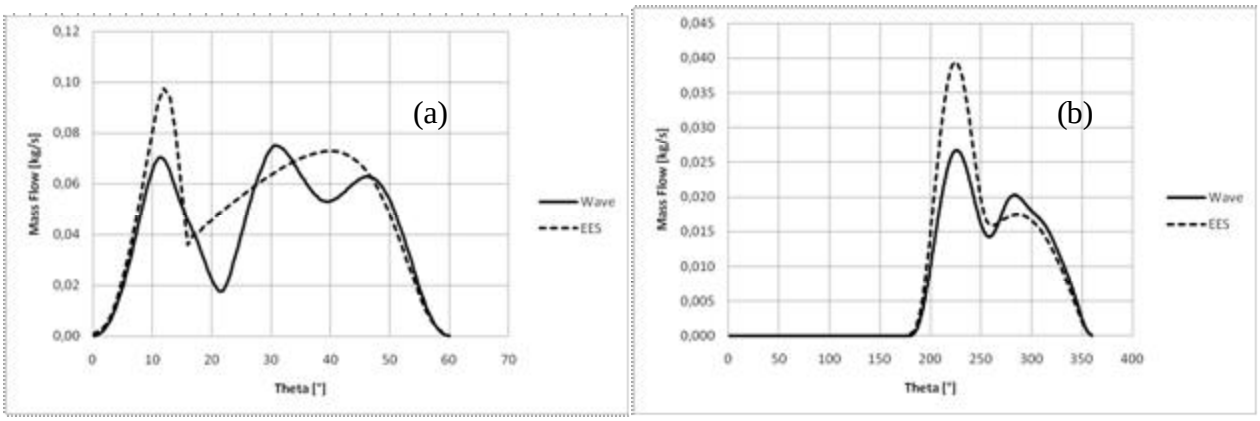

Fig. 7. Flow rate across the Admission (a) or Discharge (b) Valve cross section

NS = Solid Line; QS = Dotted line

It can be seen that the Quasi-Stationary (QS) model is not able to reproduce the strong flow rate oscillations during the short admission phase; in the case of the discharge valve, at least the quality of the time profile is reproduced. For the Quasi-Stationary (QS) model, which is treating real fluid (steam), it is meaningful to examine the Mach Number profiles during the admission and discharge phases, which are shown in Figures 8 a and b respectively.

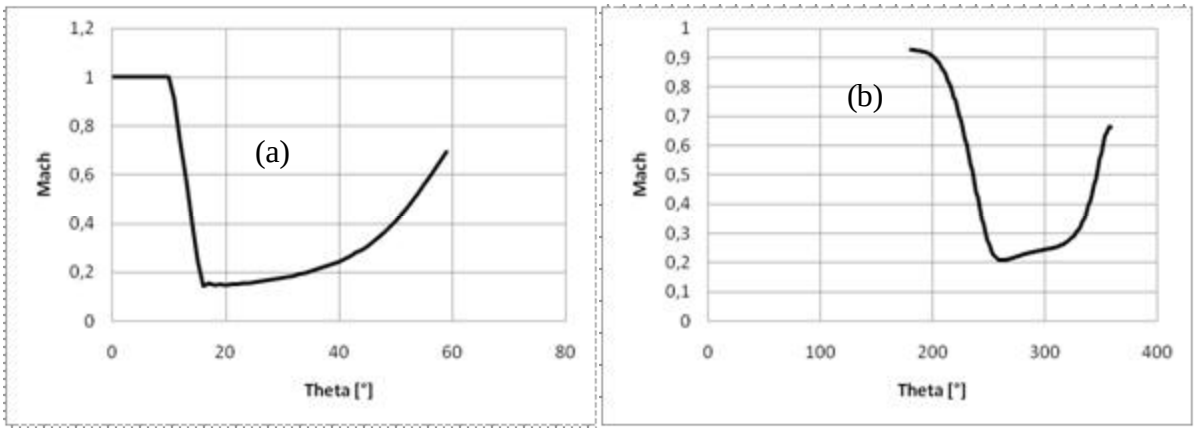

Fig. 8. Mach number across the Admission (a) or Discharge (b) Valve cross section

(Quasi-Stationary model)

As a result of the calculations of the admission and discharge processes, it is possible to calculate the mass present inside the cylinder as a function of the crank angle, which is shown in Figure 9; it can be seen that the two models are providing similar results for this variable.

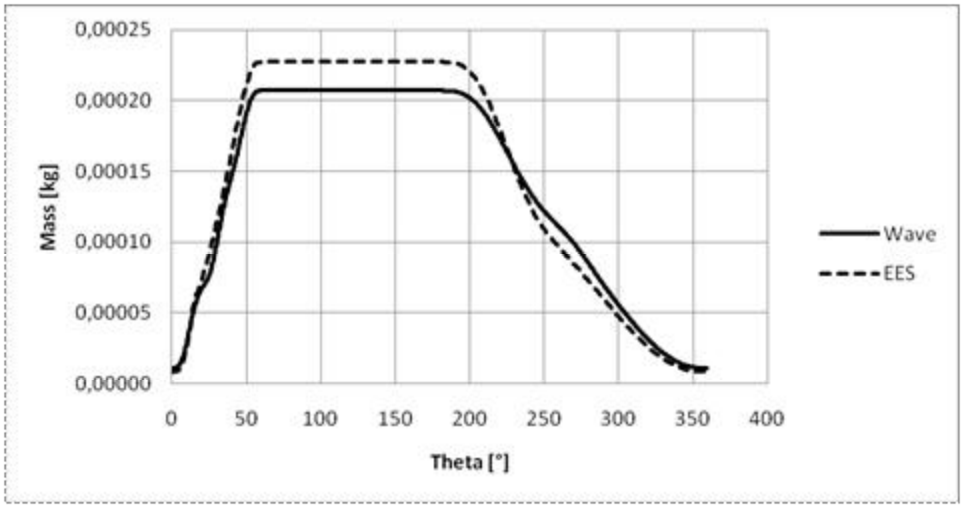

Fig. 9. Steam Reciprocating Engine – Mass inside the cylinder

NS= Solid Line; QS= Dotted line

4.2. Overall performance

The overall results in terms of efficiency, power output and steam consumption are resumed in Table 1:

Table 1- Overall results of cycle calculations

	NS	QS	Limit	Carnot
Efficiency, %	9,7	8,9	10,8	16,2
Power Output, kW	2,1	1,9	3,1	
Steam flow rate, g/s	7,5	8,4	10,3	

For comparison, the results of the limit cycle calculation [8] are also included; and the value of the efficiency of the reversible heat engine (Carnot) operating between the upper and lower temperatures is also included.

5. Parametric Analyses – Sensitivity to design values

After cross-validation of the two models, which was demonstrated at section 4, it is interesting to consider their parametric application to determine:

a) Sensitivity to Cut-Off (Power modulation; Quasi-Stationary model)
b) Sensitivity to rotational speed (Partial-Load operation; Quasi-Stationary model)
c) Sensitivity to heat transfer coefficient (Expansion; Quasi-Stationary model)
d) Sensitivity to rotational speed (Partial-Load operation; Non-Stationary model)

5.1. Sensitivity to Cut-Off (Power Modulation; Quasi-Stationary model)

Variable Cut-Off can be an effective way of adjusting power output to the required electricity load of the local grid. The effects of changing Cut-Off on Efficiency and Power Output are shown in Figures 10 (a) and (b):

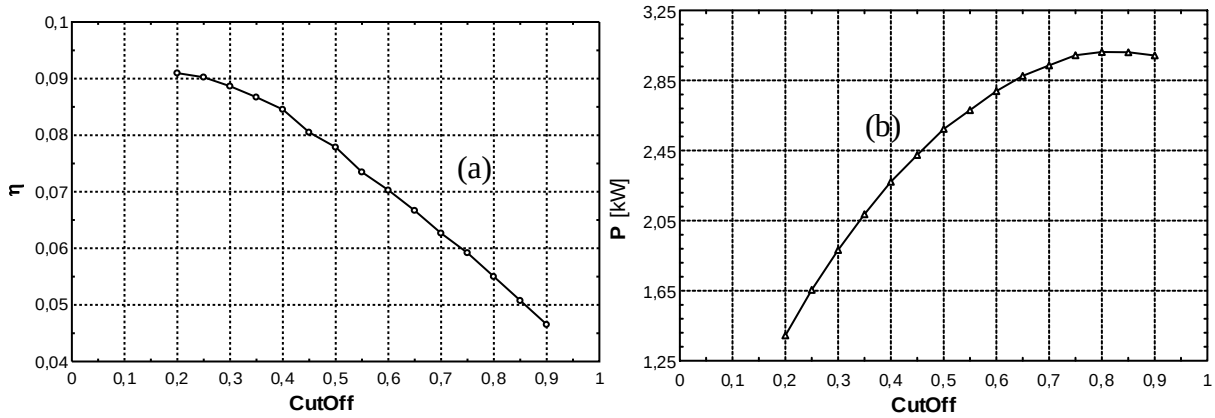

Fig. 10. Efficiency (a) and Power Output (b) with variable Cut-Off (QS model)

Figure 10 shows that it is possible to increase the power output, at the expense of decreasing the engine efficiency. A Maximum Power condition is reached for very large Cut-Off values; however, the efficiency decreases too much under these extra-power conditions.

5.2. Sensitivity to rotational speed (Partial-Load operation; Quasi-Stationary model)

Changing the rotational speed can be an alternative to Variable Cut-Off for power modulation, if the electric generator allows variable-speed operation (in practice, a DC generator with variable-speed AC inverter is needed). The effects of changing the rotational speed on Efficiency and Power Output are shown in Figures 11 (a) and (b):

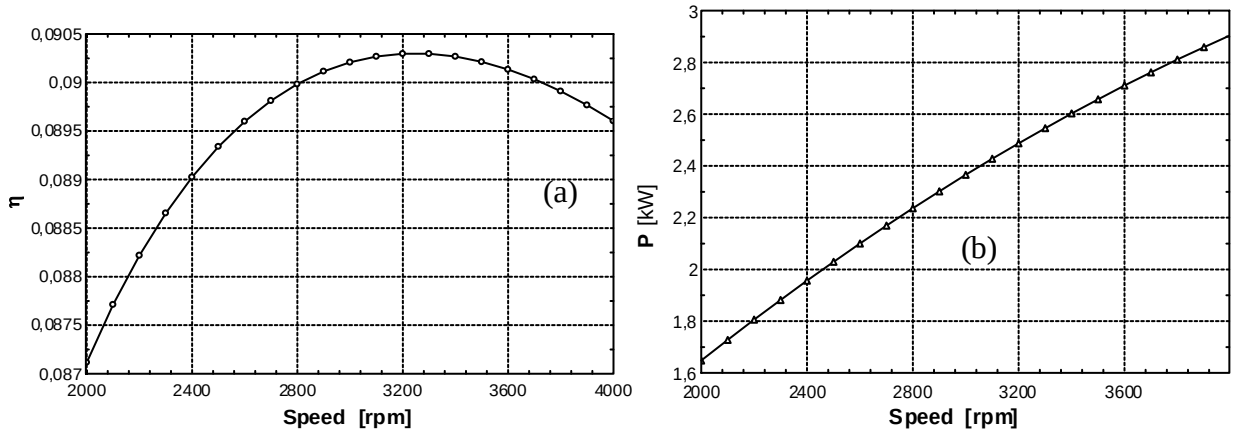

Fig. 11. Efficiency (a) and Power Output (b) with variable speed (QS model)

Figure 11 shows that a maximum condition for efficiency occurs at about 3200 rpm according to the model; power increases rather steadily with increasing rotational speed.

5.3. Sensitivity to cylinder wall heat transfer (Quasi-Stationary model)

The addition of a heat release model during the expansion represents a notable advancement from the limit to real cycle model in IC engines. This happens because the in-cylinder gas temperature can reach values which are much higher than the wall temperatures. In the present case, the real-cycle model includes wall heat transfer from the working fluid (steam) to the cylinder walls, which is modelled under the assumption of a constant overall heat transfer coefficient H. It is important to run a sensitivity analysis in order to confirm what is the influence of assuming different values of H. Figure 12 shows cycle calculations with $0 < H < 5000$ W/(m^2°C). The conclusion is that – as expected under the assumed working conditions - the influence of heat release during the expansion is marginal for the steam reciprocating engine.

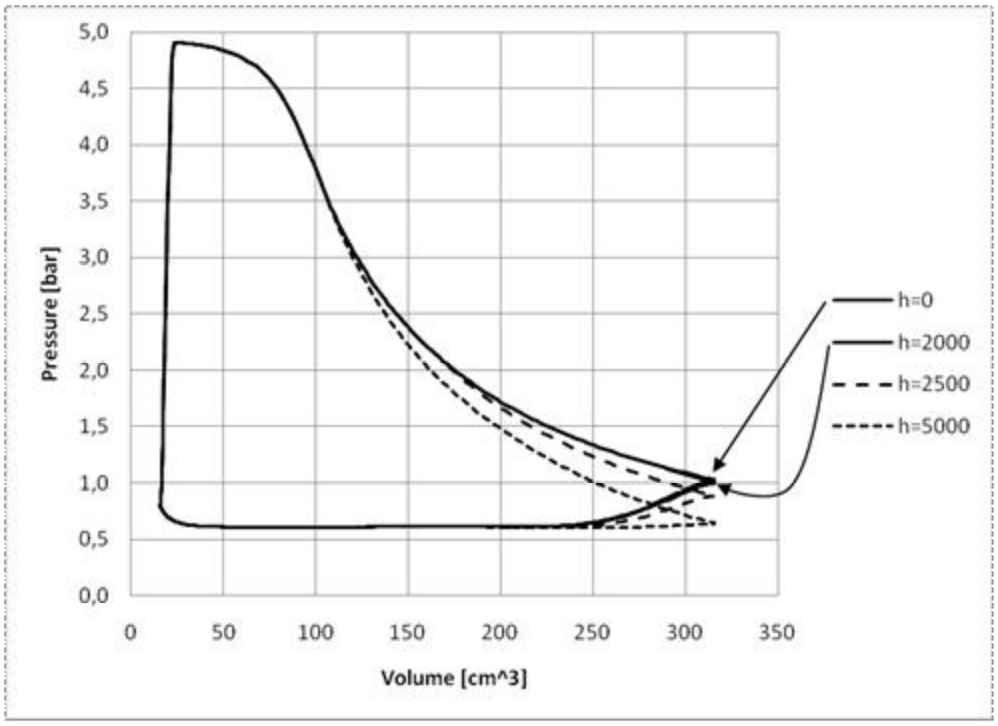

Fig. 12. Real cycle with variable H (W/(m^2°C) (Q-Smodel)

5.4. Sensitivity to rotational speed (Partial-Load operation; Non-Stationary model)

Wave propagation effects can become relevant when the rotational speed is increased, with a negative effect on volumetric efficiency. In case of necessity, these problems can be cured with a careful design of the intake/exhaust system. Before this, it is important to evaluate how much the engine performance would be sensitive to operation at higher speed. Figure 11 shows the cycle diagrams calculated by the non-stationary (NS) model for three different rotational speed values (500, 2000 and 4000 Rpm). The wave oscillation pattern during the admission phase is clearly affected by rotational speed; the main effect – as expected – is a lower cycle area, which confirms the negative effect of increasing rotational speed on the engine volumetric efficiency. The effect can anyway be considered marginal, as the values of RPM should be maintained low in order to minimize problems with engine lubrication, in case that a true engine of this type should be developed.

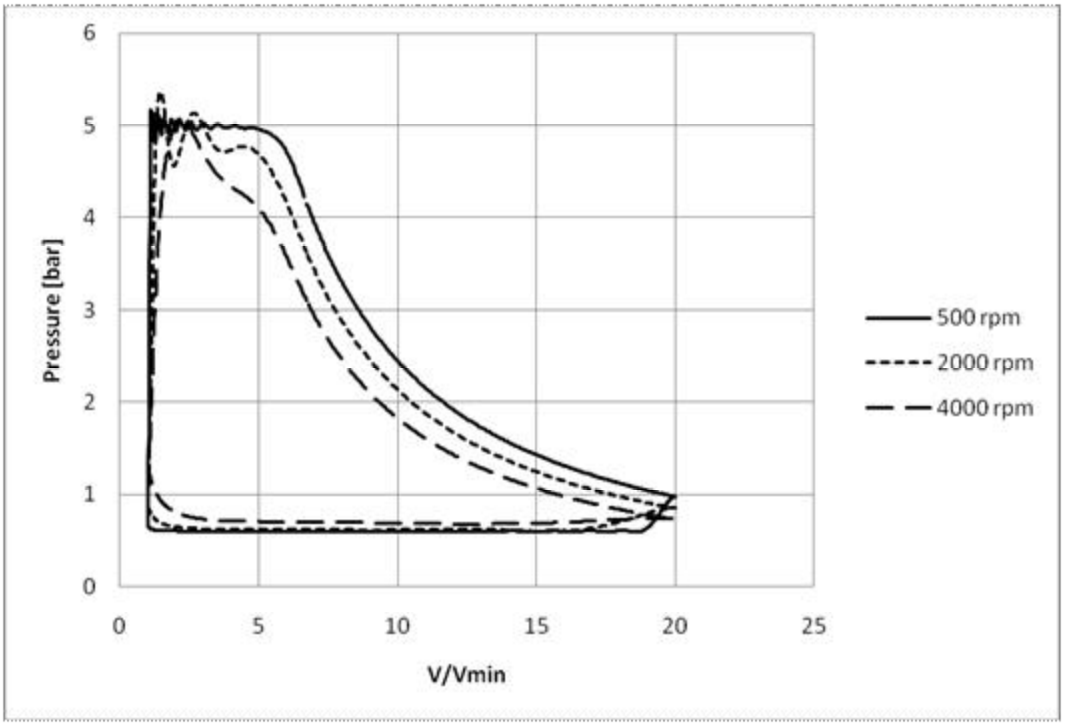

Fig. 13. Cycle diagrams calculated at variable speed (Non-Stationary model)

6. Conclusions

Detailed results have been shown in Sections 4 and 5, consequently the conclusions here reported represent only a synthesis evaluation of the case study.

Engine models represent a precious preliminary tool before developing a true prototype: the model allows a preliminary design and sizing of the engine, and allows to calculate the expected performance; cross-validation among different models can confirm the validity of calculations, and provide solid arguments in the direction of proposing an experimental development.

In the case of reciprocating steam engines, a Quasi-Stationary (QS) real-cycle model considering real fluid (steam) properties was developed; the model allowed simulation of a reciprocating steam engine with "traditional" (poppet) IC engine admission and discharge valve design, verifying that it was thus possible to achieve a reasonable sizing of the admission/discharge system.

A non-stationary model of the engine (NS), assuming perfect-gas fluid behaviour, provided similar results confirming that unsteady flow and wave propagation effects do not alter substantially the results of the Quasi-Stationary model.

The overall performance of the engine, which is conceived for application to low-temperature heat sources (solar, geothermal) and small, distributed CHP applications (e.g., residential buildings, possibly in a smart grid arrangement) was satisfactory both from the point of view of efficiency and power output.

A sensitivity analysis confirmed the possibility of using different solutions for power/load adjustment (variable cut-off or variable speed); and the marginal effects of including in the model cylinder-wall heat transfer, and of the drawbacks of rotational speed on volumetric efficiency, within the expectable operating range.

Nomenclature

aa, bb, cc, dd, e, f, g, h parameters describing the valve lift profile

D Diameter, m

fc Flow Coefficient

h Enthalpy, kJ/cycle

H Heat transfer coefficient, W/(m^2 K)

Lift valve lift, m

$\dot{m}$ mass flow rate, kg/s

p pressure, bar

OD Open Duration of valve (total angle during which the admission valve is opened)

P Power, kW

Q Heat, kJ/cycle

RPM Speed of revolution, rpm

S surface, m^2

T temperature, °C

u internal energy, kJ/cycle

V Volume, m^3

W Work, kJ/cycle

Acronyms

AV AdmissionValve

AVAO Admission Valve Advance Opening

DV Discharge Valve

HPR High Pressure Reservoir

LPR Low Pressure Reservoir

NS Non-Stationary model (WAVE)

QS Quasi-Stationary model (EES)

Greek symbols

ε Expansion Grade

θ Crank angle

λ Crank/Rod length ratio

μ Non-dimensional dead space

ρ Volumetric compression Ratio

σ Admission Grade (Cut-Off)

Subscripts and superscripts

a Air

A Admission

D Discharge

d Displacement

Exp Expansion

max Maximum (lift)

1, 2, 3… Points 1, 2, 3…

References

[1] Quoilin, S., Lemort, V., Lebrun, J., 2010, Experimental study and modeling of an Organic Rankine Cycle using scroll expander, Applied Energy, 87, 1260–1268

[2] Kane, M., Larrain, D., Favrat, D., Allani, Y., 2003, Small hybrid solar power system, Energy 28, 1427–1443

[3] Kim, H.J., Ahn, J. M., Park, I., Rha, P. C., 2007,Scroll expander for power generation from a low-grade steam source, Proc. Inst. Mech. Engrs., Part A: Journal of Power and Energy, 221, 5, 705-712

[4] Smith, I. K. Stosic, N and Aldis, C. A., 1996, Development of the trilateral flash cycle system Part 3: The design of high efficiency two-phase screw expanders. Proc Instn Mech Engrs, Part A: Journal of Power and Energy,210(A2), 75-93

[5] Badr, O., Naik, S., O'Callaghan, P.W., Probert, S.D., 1991, Expansion Machine for a Low Power-Output Steam Rankine-cycle engine, Applied Energy, 39, 93-116.

[6] Acton, O., Caputo, C., Compressori ed espansori Volumetrici, UTET, 1992.

[7] http://www.fchart.com/ees/ees.shtml

[8] Manfrida, G., Marraccini, L., 2010, Model of a Steam/Organic Vapour Volumetric Reciprocating Expander, Proceedings of ECOS 2010, Lausanne.

[9] Badami, M., Mura, M., 2008, Design and performance evaluation of an innovative small scale combined cycle cogeneration system, Energy 33, 1264– 1276

[10] Badami, M., Mura, M., 2009, Preliminary design and controlling strategies of a small-scale wood waste Rankine Cycle (RC) with a reciprocating steam engine (SE) Energy 34, 1315–1324

[11] http://www.ricardo.com/en-GB/What-we-do/Software/Products/WAVE/

Model of vacuum glass heat pipe solar collectors

Daniele Fiaschi, Giampaolo Manfrida

Università degli Studi di Firenze, Dipartimento di Energetica "Sergio Stecco"
Via C. Lombroso 6/17 – 50135 Firenze – Italy
Daniele.fiaschi@unifi.it
Giampaolo.manfrida@unifi.it

Abstract:

Glass heat pipe solar collectors are becoming very popular for heating/sanitary water production. The use of a double glass system, with vacuum in between (Dewar scheme), allows to minimize heat dispersion to the environment, and to reach potentially temperature levels in competition with much more expensive parabolic trough concentrating solar collectors (stagnation temperatures in excess of 200°C are reported). Such high levels of temperature open the use of these devices to solar energy conversion, as they are in line with modern low-temperature ORC technology. This could be an interesting alternative to large SEGS power plants, which suffer from the non-stationary nature of solar energy and require expensive heat storage equipment. However, in the technical literature there is not much information on the design criteria of these collectors, and of models for evaluating absorbed solar radiation and thermo-fluid-dynamics performance.
Starting from the collector's location, tilt angle and some data about the site location, a model to evaluate the absorbed solar radiation is developed. It is based on (I) calculation of the actual angle between solar radiation and the absorbing cylindrical pipe surface; and (II) calculation of the actual absorbed radiation by the heat pipe surface, also including the mutual shading between the different heat pipes is presented and discussed, allowing the estimate of the performance in design conditions. Sensitivity to the main design variables is examined. The model includes modeling of heat transfer (radiation, forced/natural convection, phase transition) in the different sections of the heat pipe.

Keywords:
Heat Pipes, Glass, Organic Rankine Cycle (ORC), Solar Energy Generation Systems (SEGS).

1. Introduction

The glass heat pipe design has become a best-seller in advanced applications of solar energy thermal utilization, with special reference to systems designed for providing heat in regions with low radiation, or during winter; the most performing collectors use a double-pipe design for the absorbing section, with deep vacuum in between, forming a kind of "Dewar" bottle which is very effective in reducing convective heat transfer, and allows thus to reach high absorber temperatures: a typical example of this solution (DGVHP for Double Glass Vacuum Heat Pipe) is shown in Figure 1, while Figure 2 represents two detached heat pipes. Currently, most of these devices are produced in China [1] and are re-branded for worldwide commercialization; their application is limited to hot water production. The idea pursued in this paper is to develop a mathematical model of the DGVHP, in order to be able to modify its design so that it can be adapted to producing a fluid flow at temperature interesting for applying thermodynamic energy conversion to small CHP applications, providing heat and electricity to small, distributed users (residential, commercial, SME industrial production processes). The DGVHP, within such systems [2, 3], represents totally or partially the component dedicated to the conversion of radiation into thermal power, which is then transferred to a suitable working fluid (water/steam, organic or engineered fluid). It has been

demonstrated in previous works [4, 5] that irreversibilities during this specific step of energy conversion are the main source of inefficiency in SEGS systems.

Figure 1 - Example of solar collector using an array of glass heat pipes.

Figure 2 – Detail of two detached heat pipes.

2. Traditional and DGV Heat Pipes

The introductions to the working principles of heat pipes is beyond the purpose of this paper; the reader is referred to the literature [6].

The DGVHP represents a special case of heat pipe: typically, no wick structure is used, and the inner surface where the primary loop working fluid is contained is non-porous glass. The circulation of the working fluid (usually, ethanol) is only controlled by gravity and by the surface tension effects taking place on a flat glass/ liquid interface.

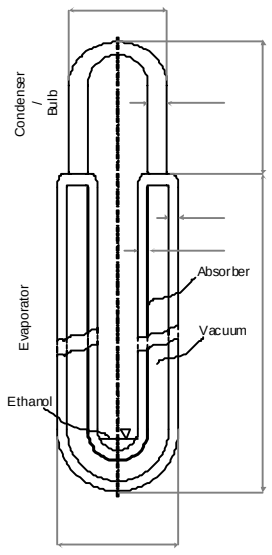

Figure 3 – Schematic of DGVHP

A schematic of a single DGVHP unit is shown in Figure 3.

The evaporator section covers most of the device length (1-2 m typically); it is built as a double glass burette, with vacuum inside (p_V = 0,005 Pa) in order to form a typical Dewar design, effectively suppressing convection and conduction heat transfer. The outer surface of the inner pipe is covered with a sputtered selective coating Al-N/al layer (α = 0,92, ε = 0,08). At the top of the heat pipe, a single-sheet glass bulb forms the condenser, which is connected to a manifold or reservoir (using a gasket, or a conductive metal sealed sheath), where heat is transferred to the (colder) secondary fluid.

This type of design represent the current state of the art, with some notable advantage with respect to the previous versions using copper heat pipes [7, 8], which suffered to a certain extent of the contact resistance between glass Dewar envelope and copper absorber; and of limited size of the condenser/bulb (which is however an advantage from the point of view of sealing). Most applications of this design are for water heating in cold locations, and the potential for producing a higher temperature fluid has not yet attracted attention, even if stagnation temperatures[1] as high as 230°C are reported in the technical literature.

[1] The stagnation conditions for a solar collector are reached when no useful heat is extracted from the collector; under these conditions (no outlet flow), the thermal efficiency falls to zero as all the heat collected by the absorber is lost to the environment

3. Model of DGV Heat Pipes

Although patents have been issued since 1984 [9], and many manufacturers exist [1], very little can be found in the literature about sizing criteria and thermo-physical models for DGVHPs. For the optical characteristics of the double glass layer, and for calculating the heat loss factor, refs. 10 and 11 have been followed. The purpose of the present paper is to develop a model for the prediction of the efficiency curve as could be validated by means of an accepted testing procedure [12] and, eventually, modeling full-day or long-term performance. To this end, the Shah and Furbo model [11] was adopted to evaluate the angle between solar radiation and cylindrical glass surface of collector. It provides an estimation of the fraction of solar collector directly exposed to beam radiation. Successively, the solar absorbed radiation was evaluated following the Perez et al. model [13]. No back reflector was considered, as this component is often incompatible with installation guidelines for many building applications. The model, which is described in the following, was programmed in EES [13]. On the whole, 163 variables are solved with 36 input data (mainly, the geometric data of the collector; data on materials, fluid properties and design operating conditions in terms of radiation, environment temperature, …). The notation follows common solar collector practice [14].

3.1 From radiation to absorber surface

Figure 4 a) shows the three critical angles when the tubes are placed vertically, the collector plane azimuth $\gamma_C=0$ and the solar azimuth γ_S is between 0 and $\pi/2$. Four possible cases of tubes' mutual shading can arise:

1) $\gamma_S < X_1$, there is no shading of the tubes;
2) $X_1 < \gamma_S < X_3$, the tubes are partly shaded;
3) $\gamma_S > X_3$, the tubes are fully shaded;
4) $\gamma_S = X_2$, the tubes are half shaded.

The calculation model to evaluate the angle between solar radiation and cylindrical absorbing surfaces of the evacuated pipes of DGVHP [11] consists of two basic steps:

1) Given the azimuth angle of solar collector and the direction of solar beam radiation (figure 4b), the three critical angles X_1, X_2 and X_3 are calculated (figure 4a); the determination of solar azimuth angle γ_S must be referred to each of the six pies (1 to 6) into which the cross sectional area of the collector pipe has to be ideally divided. They are different depending on the orientation of collector surface: solar azimuth $\gamma_C<>0$ if the collector is oriented toward east or west respectively (figure 4 b).
2) The two initial and final angles (ξ_{start} and ξ_{stop} respectively) which define the actual angle of exposition $q_{\gamma s}$ to beam solar radiation are calculated.

The auxiliary angles X_1, X_2, X_3 are defined for each pie (1 to 6) and each azimuth ($\gamma_C<0$, $\gamma_C>0$). A total of 36 auxiliary angles are defined. For the sake of brevity, only one is here reported for example, i.e. X_1 related to the pie 1 of the case of west oriented solar collector ($\gamma_C>0$). For the detailed description of the model and values of all angles we refer to the Shah and Furbo model [11].

$$X_1 = \arccos[(r_e+r_{abs})/C]-\pi \text{ ; where } r_e=D_e/2;\ r_{abs}=D_{abs}/2 \qquad (1)$$

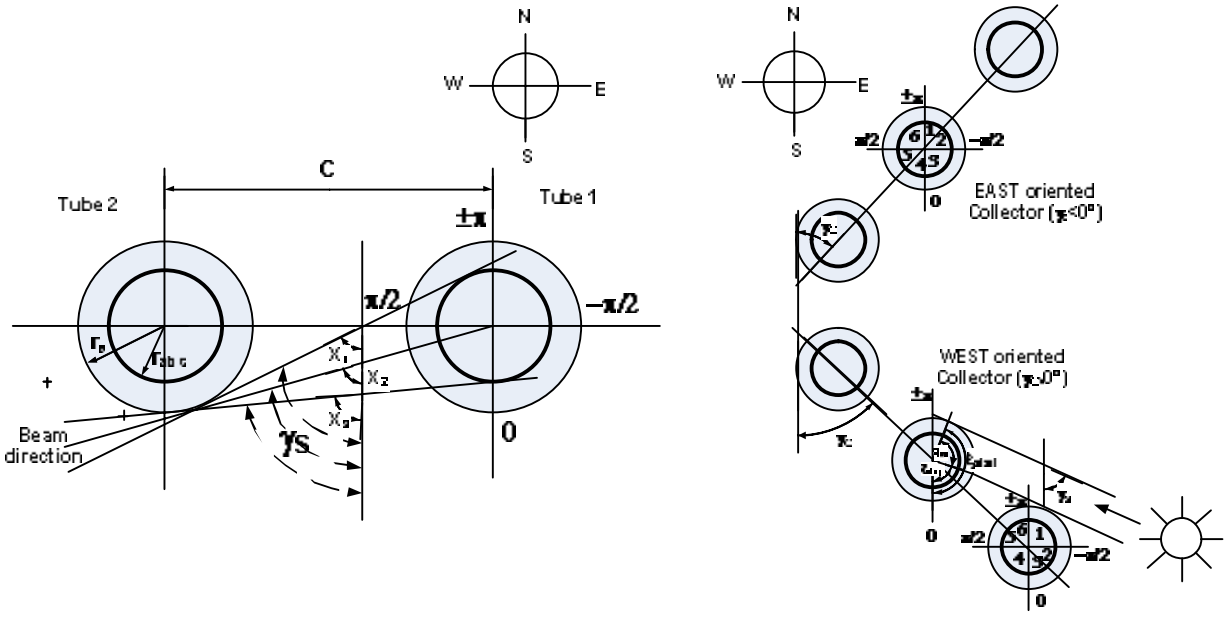

a) Pie division of pipes for different collector orientation

b) critical angles between two different pipes

Figure 4 – pie division of pipes and critical angles

Once obtained the auxiliary angles, according to their value, different formulations to derive the angles of exposure of the absorbing surface $q_{\gamma s}$ are adopted. Once again, one expression only is here reported for example ($\gamma_C>0$, γ_s in pie 1, $X_1<\gamma_s-\gamma_C<X_2$), whereas for the complete calculation formulas the reader is referred to [11]:

$$\xi_{start} = \pi/2-|\gamma_s| - |q_{\gamma s}| \; ; \; \xi_{stop}=\pi/2-|\gamma_s| \; ; \; |q_{\gamma s}| = \pi - \arccos[(C\cos(\gamma_s-\gamma_C+\pi) - r_e)/ r_{abs}] \qquad (2)$$

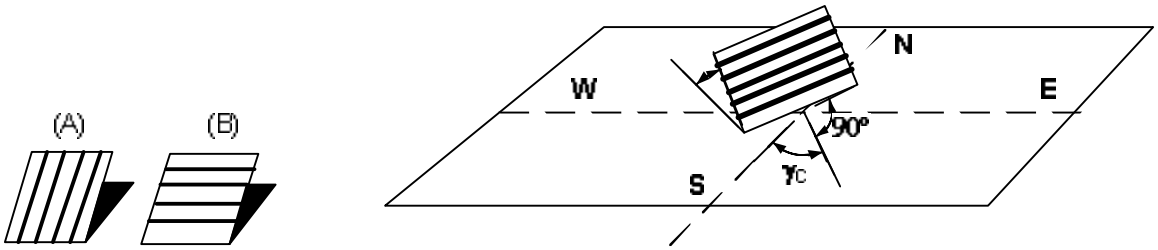

Figure 5 – schematic of pipe arrays mounting on the collector plane

As previously remarked, the actual overall absorbed radiation of the DGVHP has been evaluated referring to Perez et al. model [13]. The model here implemented is referred to the pipe array mounted on free standing plane. Two possible configurations were considered (see figure 5):

1) Pipes are mounted with axis azimuth equal to the plane of pipe array (A);

2) Pipes are mounted horizontally in plane of pipe array (B).

The proposed method allows the calculation of each component of solar radiation (beam, diffuse and ground reflected).

Beam radiation: a tubular surface intercepts exactly so much beam radiation as a solar collector with a flat surface which moves throughout the day (tracking collector), with the same tilt and surface area. Therefore, the problem is reduced to calculate the angle of incidence θpipe referred to a flat plate collector, having equivalent tilt and orientation:

$\cos \theta pipe = \cos \theta 1 / \cos \psi$ (3)

where $\theta 1$ is the angle of incidence of solar beam on the flat equivalent surface and $\psi = atan2(\cos \theta 1, \cos \theta \psi)$. $\theta \psi$ is the angle of solar incidence of a vertical plane containing the axis of pipe and oriented toward east. $\theta pipe$ allows the calculation of the incident radiation coefficient:

$Rb = \cos \theta pipe / \cos \theta z$ (4)

Thus, beam radiation on the pipe surface IbT is given by the beam radiation on the flat surface Ib times Rb:

$IbT = Rb\ Ib$ (5)

Diffused radiation: Perez model has been adopted once again. The effects of circumsolar brilliance and horizon brightness, calculated by the related coefficients f_1 and f_2 respectively, are combined with the basic model of isotropic sky to achieve the following expression of diffused radiation on the tubular surface I_{dT}:

$$I_{dT} = I_d \left[(1 - f_1) \frac{1 + cos\beta}{2} + f_1 \frac{a}{b} + f_2 sin\beta \right] \quad (6)$$

Where:

$a = \max [0, \cos\theta]$; $b = \max [\cos(85°), \cos\theta_z]$

f_1 and f_2 depend on three parameters which characterize the sky conditions: zenith angle θ_z, clearness index *e* and luminosity Δ. The detailed values of brightness coefficients for several ranges of *e* are reported on [13].

Ground reflected radiation: following the Perez model [13], the method is based on the assumption of isotropic ground:

$$I_g = I \rho_g \left(\frac{1 - cos\beta}{2} \right) \quad (7)$$

Finally, the term which takes into account the effect of the mutual passive shading between the different pipes of the DGVHP has to be considered:

$X_P = 1 - \text{Max}[0, (D \cos \theta pipe - Dr \cos \theta 1)/D \cos \theta pipe)(n - 1)/n$ (8)

Where n is the number of pipes.

Starting from the available radiation and following the Shah and Furbo model to determine to the angle between solar radiation and cylindrical absorbing surfaces and Perez et al. model to evaluate actual overall absorbed radiation of the DGVHP, the energy collected by the HP is, on the cylindrical surfaces:

$S = (\tau\alpha)_b I_{bT} + (\tau\alpha)_d I_{dT} + (\tau\alpha)_g I_g$ (9)

$I = I_b + I_d$ (10)

The results achieved by the implemented model have been compared with those obtained from two different models: the Isotropic Sky (ISO) and the Hay, Davies, Klucher, Reindl (HDKR) models, both extensively described on [15] and implemented into the same EES calculation code. For this comparison, the data were referred to a commercial collector described in detail on [16], having 18 heat pipe modules of 1.53 m length, 47 mm absorber diameter and an aperture area of 1.708 m^2. Perez model was applied to the cylindrical surface, whereas ISO and HDKR were applied to the equivalent flat plate collector, having the same surface area. The comparison of results is shown on figure 6 a) and b). The collector tilt β was assumed at 20° with south orientation (γ_S=0). On figure 6 a), the absorbed radiation through the days of the year at midday, referred to a location of Central Italy, is shown. In this location, the beam to total radiation ratio ranges from 60 to 82% in the

middle hours of the days (i.e. from 11 am to 16 pm), practically in all the seasons of the year. The average beam to total radiation ratio along the whole of monthly representative days ranges from 53 (march) to 72% (october). The results of the three models are in agreement and put in evidence the higher absorber radiation of the collector with evacuated pipes, as also remarked on [13].

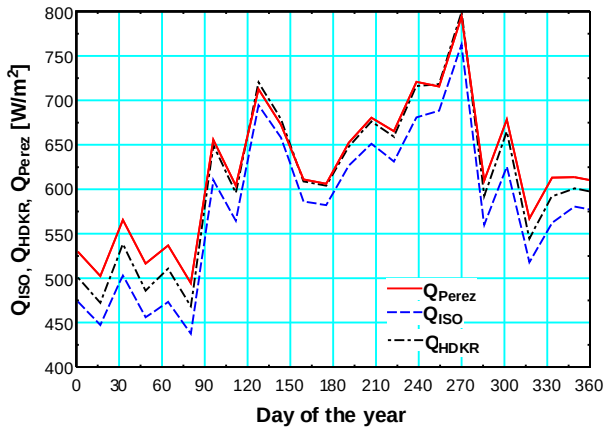

a) absorbed radiation through the year at 12 hrs

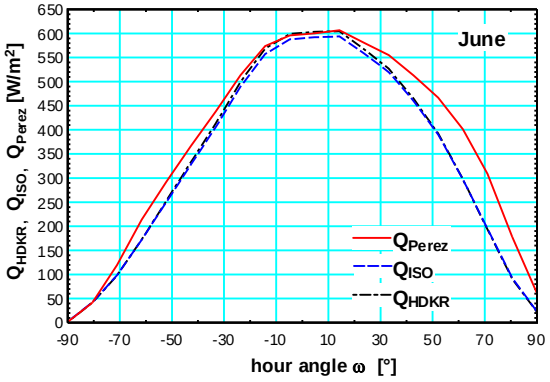

b) absorbed radiation throughout the day in different seasons (June in the example)

Figure 6 – comparison of results of absorbed radiation with Perez, ISO and HDKR models

3.2 Absorber thermal balance

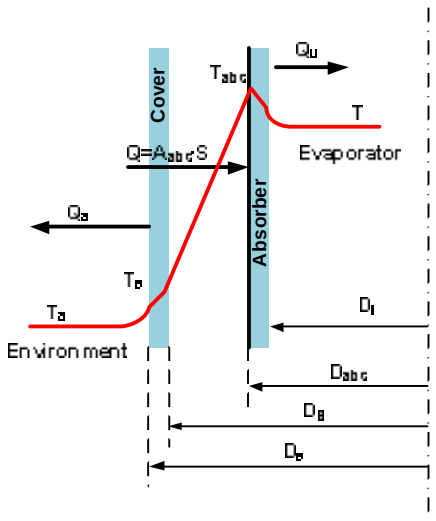

igure 7 – radial temperature profile of the heat pipe

F

The radial temperature profile of the heat pipe is shown on the axial section of figure 7.

The overall heat rate to the absorber is given by:

$$\dot{Q} = A_{abs}\frac{S}{\pi} \qquad (11)$$

with:

$$A_{abs} = \pi\, L\, D_{abs} \qquad (12)$$

and S of the cylindrical absorber given by (9). The collector loss factor is given by:

$$U_l = \frac{1}{\frac{D_{abs}}{D_e\,(h_w + h_{rca})} + \frac{1}{h_{rrc}}} \qquad (13)$$

where:

$$h_{rrc} = \frac{\sigma\left(T_{abs}^{\,2} + T_e^{\,2}\right)\cdot\left(T_{abs} + T_e\right)}{\frac{1-\varepsilon_{abs}}{\varepsilon_{abs}} + \frac{1}{F_{12}} + \frac{D_{abs}}{D_e}\cdot\left(\frac{1-\varepsilon_C}{\varepsilon_C}\right)} \qquad (14)$$

is the equivalent radiation heat transfer coefficient from absorber to the inner surface of the external glass pipe,

$$T_e = \frac{h_{rrc}\,T_{abs} + \frac{D_e}{D_{abs}}\cdot T_a\,(h_{rca} + h_w)}{h_{rrc} + \frac{D_e}{D_{abs}(h_{rca} + h_w)}} \qquad (15)$$

$$h_{rca} = 4\sigma\varepsilon_C T_a^{\ 3} \quad (16)$$

is the equivalent radiation heat transfer coefficient from the external glass cover to the environment , and

$$h_w = \frac{N_{Nus;AIR} \cdot \lambda_{AIR}}{D_e} \quad (17)$$

The value of $N_{Nus;Air}$ is calculated from classic heat transfer correlations (natural/forced convection).

The radiation/heat conversion process proceeds from the absorber transferring heat to the fluid. Following classic solar collector terminology, the useful heat harvested is given by:

$$\dot{Q}_u = F_1 \dot{Q} \tau \alpha_e - A_{abs} U_l (T - T_a) \quad (18)$$

In Equation 18, T is the fluid temperature: considering that the heat pipe should work as a two-phase equilibrium system, this last is considered constant and equal at the pre-set value imposed by the heat pipe internal pressure. This is a notable simplifying assumption, which applies only to design conditions. In practice, the heat pipe is modeled considering always two-phase operation (a discussion about the convenience of this choice flows at point 3.3).

$\dot{Q}_u$ is transferred to the primary circuit fluid, so that the system efficiency is given by:

$$\eta = \frac{\dot{Q}_u}{\dot{Q}} \quad (19)$$

The fraction $1 - \frac{\dot{Q}_u}{\dot{Q}}$ is the heat loss of the collector to the surroundings. Considering stationary operation of the heat pipe, $\dot{Q}_u$ is used to evaporate a primary fluid flow rate given by:

$$\dot{m}_{eva} = \frac{\dot{Q}_{cond}}{\Delta H_{fg}} \quad (20)$$

which is then completely condensed in the condenser/bulb upper section, where:

$$\dot{Q}_{cond} = \dot{Q}_u \quad (21)$$

and, considering the bulb heat transfer (internal convection; conduction; external convection):

$$\dot{Q}_{cond} = h_{c;i} A_{bulb} (T - T_{bi}) \quad (22)$$

$$\dot{Q}_{cond} = \frac{(T_{bi} - T_{be}) \cdot 2 \cdot \pi \cdot \lambda_g \cdot L_{bulb}}{\ln \frac{D_{be}}{D_{bi}}} \quad (23)$$

$$\dot{Q}_{cond} = (T_{be} - T_{water}) \cdot h_{c;e} \cdot A_e \quad (24)$$

3.3 Tuning the heat pipe operating pressure and temperature

The pressure-temperature relation is shown for Ethanol (the most commonly encountered fluid in glass heat pipes) in Figure 8. It is interesting to notice that at standard pressure (101,3 kPa) the operating temperature of the heat pipe is about 80°C; actually most marketed heat pipes for solar

thermal water heating are sealed slightly below ambient pressure, so that the heat pipe is tuned around 50-60°C. Considering the thickness and strength of the glass enclosure, however, it is possible to use internal pressures up to 600-800 kPa, which correspond to tuning the heat pipe to operate around 150°C. In fact, considering an 1.5 mm thickness pipe with an internal pressure of 700 kPa and an outer diameter of 47 mm like the one considered in calculations, the strength of the material is about 11000 kPa, which is less than the maximum allowed tensile stress, even referring to common glass (about 19000 kPa). On the other hand, 1.5 mm thickness glass does not affect its conductance appreciably. The fact that stagnation values exceeding 230 °C have been recorded for marketed collectors means that superheated vapor production has been achieved. In fact, the amount of ethanol used in the heat pipe is very low (1,5 to 3 cc, depending on the heat pipe length), so that pressurization of the system, even when complete evaporation of the liquid is achieved, is very limited.

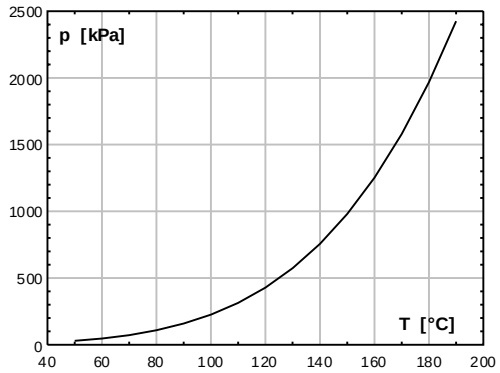

Figure 8 – Saturation pressure vs. temperature (Ethanol)

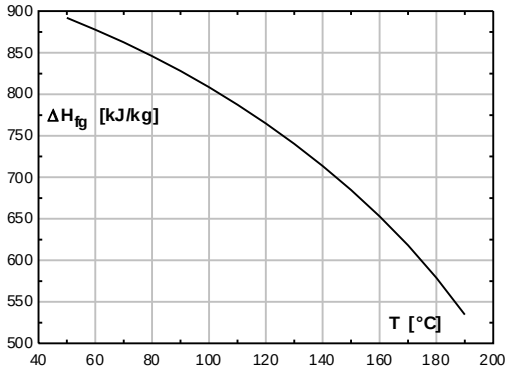

Figure 9 – Heat of transition vs. temperature (Ethanol)

When the incoming radiation is notably larger than its design value, the heat pipe continues its operation with superheated vapor production; this last is anyway condensed in the bulb section; however, when the condensed liquid drips along the evaporator, it is soon completely evaporated, so that the effective heat pipe length is reduced and more complex (three-dimensional, non stationary) thermo-hydraulic regimes are triggered. In practice, it is rather convenient to maintain the heat pipe operating along its full length. This is confirmed by the plot of the heat of phase transition, which is shown in Figure 9. It shows that the heat of transition varies between 850 and 650 kJ/kg when temperature is raised from 80°C to 160°C; on the other hand, when superheating at ambient pressure is considered, the average value of c_p for Ethanol is 2,5 kJ/(kg K); so that a superheating of 80°C (from 80°C to 160°C) is equivalent to a sensible heat of about 200 kJ/kg. This is less than one third of the heat of transition, so that the contribution of super-heating is less attractive than selecting a higher (but technically possible) operating pressure.

When the incoming radiation is notably below design, the heat pipe adjusts its operation circulating lower and lower flow rates $\dot{m}_{eva}$; in practice, however, the reduced flow rate should anyway be able to wet continuously the inner pipe of the evaporator along its full length. These conditions will actually stop to exist for very low radiation, depending on glass roughness and collector inclination.

4. Results

The model can be applied with variable temperature, considering a fixed value of solar radiation, in order to achieve the performance curves; an example is shown in Figure 10, which examines the collector performance curves calculated for I = 800 W/m^2. Performance data available for two commercial collectors are added for comparison [16]. The first one (collector model 1) has an aperture area of 1.708 m^2 and 18 heat pipes modules with L=1.53 m and D_{abs}=47 mm. The second

one (collector model 2) has an aperture area of 1.0 m^2 and 12 heat pipes modules with L=1.524 m and D_{abs}=47 mm. A second-order polynomial was fitted to both data sets, as is usual for solar collector data in order to account for variation of U_l with working conditions (Eq. 9). The comparison of results shows a relatively satisfactory agreement, with the main difference in average curves slope. It appears that the calculation model underestimates the heat losses to the environment. On the other hand, the model slightly underestimates the optical efficiency of the collectors, suggesting a slight overestimation of the shading effects and of the external glazing pipe absorbance. Generally, a better agreement is observed for the collector model 2.

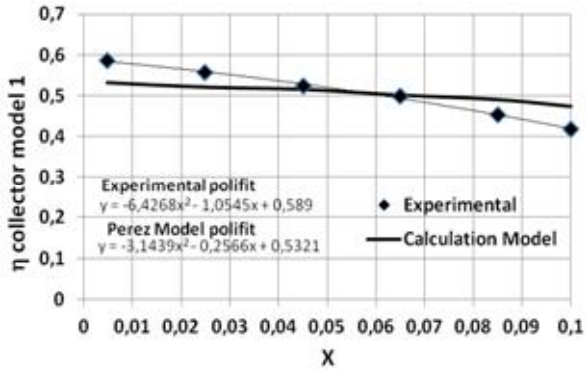

a) collector model 1

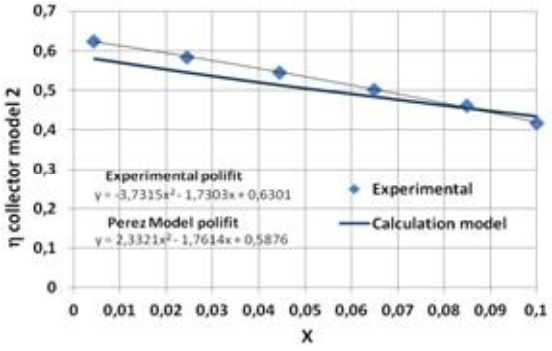

b) collector model 2

Figure 10 – Calculated and experimental performance of a DGVHP solar collector; I=800 W/m^2. X = collector performance parameter, $X = (T - T_a)/I$

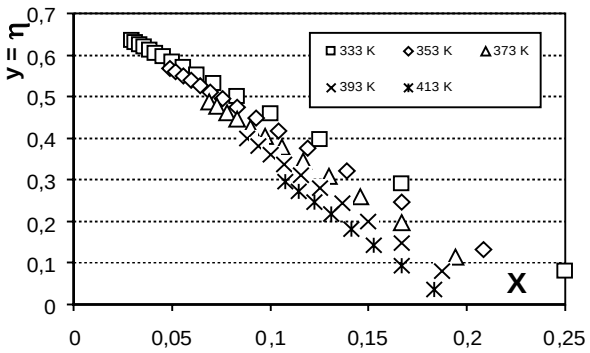

Figure 11 – Calculated performance of a DGVHP solar collector; T = 333 - 413 K.

It is also possible to examine the variation in performance when the heat pipe is operated at different preset temperatures (and pressure, see Figure 9). Figure 11 shows the calculated efficiency for different heat pipe preset temperatures, ranging from 333 to 413 K. At the lower bound (i.e. T = 60 °C), the overall heat loss coefficient U_L is about 0.56 W/(m^2 °C) and increases to about 0.82 W/(m^2 °C) at T = 120 °C. The corresponding overall radiation + convection heat loss increases from 5.6 to 23 W/m^2 respectively.

5. Conclusions

A calculation model of the heat pipes of an evacuated solar collector has been developed. It is based on two fundamental parts: (I) *optical*, to evaluate the actual absorbed solar radiation on the cylindrical absorber, taking into account of sun exposure angle and mutual shading of the pipes; (II) *thermal*, to evaluate the heat balance between absorbed radiation and heat loss to the environment.

The model, even if based on some simplifying assumptions (basically, that the heat pipe is always operating as a two-phase system with no super-heating of vapor or sub-cooling of the liquid), is capable of predicting with an acceptable degree of approximation the actual performance curve of a

DGVHP module. Extrapolation of the model to internally pressurized conditions ("tuned" heat pipe) shows that with increasing preset temperature a somewhat lower performance is obtained. This result is physically acceptable, because the whole system is shifting its operation to larger temperatures, so that also the collector loss coefficient is increased for equal radiation conditions.

The model confirms that it is possible to operate a DGVHP system at temperatures much larger than what is encountered in solar thermal hot water production systems (50 – 70°C); the device appears to be suitable for solar thermal energy conversion, with the DGVHP at the heart of a solar collector system designed for direct production of organic vapor, at temperatures in the range 120 – 140 °C.

From the model results, we conclude that the adopted model can be considered a sufficiently reliable basis to investigate the main design parameters which influence the performance of a DGVHP solar collector. For this reason, once the heat losses parameters are tuned with the necessary experimental tests, it could be adopted as a preliminary design tool, leaving the eventual refining to more detailed CFD codes.

Nomenclature

A area, m^2

c specific heat, J/(kg K)

C axial distance between the heat pipes of the collector, m

D diameter, m

F_1 collector efficiency factor, $F_1 = U_o/U_L$

h heat transfer coefficient, W/(m^2 K)

I radiation, W/m^2

L length of absorber section, m

$\dot{m}$ mass flow rate, kg/s

n number of pipes of collector

N non-dimensional number

p pressure, bar

$q_{\gamma s}$ angles of exposure to sunlight, °

$\dot{Q}$ heat rate, W

R_b ratio of beam radiation on tilted plane to that on the horizontal plane

r radius, m

S absorbed radiation, W/m^2

T temperature, °C

U_o heat loss coefficient, fluid to ambient, W/(m^2 °C)

U_L heat loss coefficient, absorber to ambient, W/(m^2 °C)

X collector performance parameter, $X = (T - T_a)/I$, (K m^2)/W

X_1, X_2, X_3 Auxiliary angles to evaluate the exposure angle, °

X_P factor of mutual passive shading between the different pipes

Greek symbols

α absorptivity

β angle of collector with respect to the ground (tilt)

γ azimuth angle, °

Δ luminosity, cd/m^2

ΔH_{fg} heat of phase transition, J/kg

ε emissivity

ξ_{start} initial angle of exposure of the absorber to sunlight, °

ξ_{stop} final angle of exposure of the absorber to sunlight, °

$\theta 1$ incidence angle of beam radiation on the flat equivalent surface, °

$\theta\psi$ angle of solar incidence of a vertical plane containing the axis of pipe and east oriented, °

$\theta pipe$ incidence angle of beam radiation on tubular surface, °

θz zenith angle of sun, °

η efficiency

λ thermal conductivity, W/(m K)

τ glass cover transmissivity

Subscripts and superscripts

a environmental

abs absorber

AIR air

b beam (normal to collector plane)

be bulb, external wall

bi bulb, internal wall

bT beam on tubular surface

bulb bulb (condenser)

c;i internal convection (bulb)

c cover cylindrical surface

C collector

d diffuse

dT diffuse on tubular surface

eva evaporator

e external

g ground

gl glass

Nus Nusselt

rca radiation, cover-to-ambient

rrc radiation, receiver (absorber)-to-cover

s solar

u useful (transferred to the fluid)

V Vacuum

w wall (bulb, internal)

water collector heated water

wind wind (external convection)

References

[1]http://www.made-in-china.com

[2] Odeh,. S. D., "Unified model of solar thermal electric generation systems", Renewable Energy (2003), 28, 755-767.

[3] Nguyen, V.M., Doherty, P.S., Riffat, S.B., "Development of a prototype low-temperature Rankine cycle electricity generation system", Applied Thermal Engineering 21 (2001) 169±181

[4] Manfrida, G., Kawambwa, S., "Exergy control for a flat-plate Collector/Rankine Cycle Solar Power System", ASME J. of Solar Energy Engineering, 113, 89-93, 1991

[5] Manfrida, G., Gerard, V., "Maximum Exergy Control of a Solar Thermal Plant equipped with Direct Steam Collectors" , Int. Journal of Thermodynamics, 2007, Vol. 11, n. 3, pp.143-149

[6] www.btfsolar.com

[7] http://www.sunflower-solar.com

[8] Ochtebeck, J. R., Heat Pipes. In: Heat Transfer Handbook (Chapt. 16), Editors: Bejan, A., Kraus, A.D.,), pp. 1181-1230, J. Wiley (2004).

[9] US Patent 4474170, http://www.nrel.gov/docs/patents/4560.pdf

[10] Shah,L.J., Furbo, S., "Vertical evacuated tubular-collectors utilizing solar radiation from all directions", Applied Energy 78 (2004), p. 371–395

[11] Theunissen, P.H., Beckman, W.A., "Solar Transmittance Characteristics of Evacuated Tubular Collectors with Diffuse Back Reflectors", Solar Energy, 35 (1985), 4, pp. 311-320.

[12] EN 12975-2 Solar Collectors – Part 2 – Test Methods.

[13] R. Perez, R. Seals, J. Anderson e D. Menicucci, - *Calculating Solar Radiation Received by Tubular Collectors, Journal of Solar Energy Engineering*, November 1995, Vol. 117

[14] http://www.fchart.com/ees/

[15] Duffie, J.A., Beckman, W.A., Solar Engineering of Thermal Processes, Wiley, 2006.

[16] Fabbrica del Sole, private communication, ICARO solar collector, test data report.

[17] Cengel, Y.A., Bowles, Thermodynamics and Heat Transfer, McGraw-Hill, (2002).

Modelling and exergy analysis of a plasma furnace for aluminium melting process

Luis Acevedo[a], Sergio Usón[b], Javier Uche[c] and Patxi Rodríguez[d]

[a]*CIRCE-University of Zaragoza, Zaragoza, Spain, leag@unizar.es*
[b]*CIRCE-University of Zaragoza, Zaragoza, Spain, suson@unizar.es (CA)*
[c]*CIRCE-University of Zaragoza, Zaragoza, Spain, javiuche@unizar.es*
[d]*TECNALIA – Foundry unit, San Sebastián, Spain, patxi.rodriguez@tecnalia.com*

Abstract:
The use of new heating systems like thermal plasma may entail significant improvements in reducing the energy consumption in energy intensive industries as metal foundry sector. In present work, a secondary foundry of aluminium model with two different heating technologies (propane gas combustion and nitrogen plasma) is presented in order to predict its performance. The model was developed to simulate thermal behaviour of a cylindrical crucible furnace in which aluminium is melted. It estimates the temperature of the combustion chamber and the transient heating in furnace walls and aluminium during melting and preheating stages. Equations were solved numerically by means of MATLAB scripts. Energy analysis compared the furnace performance of alternative heating processes (gas fed burner versus plasma). Results showed that thermal plasma is more efficient than a conventional gas burner: specific energy consumption is 52.6% lower. Besides, exergy analysis pointed out that exergy losses are reduced in case of plasma torch since heating is directly oriented into the load (aluminium). The model was validated with a battery test on a pre-commercial pilot plant at Tecnalia facilities. Thus, it could reduce the cost of that industrial laboratory when new design parameters are tested.

Keywords:
Plasma furnace, Aluminium, Energy consumption, Exergy and Efficiency.

1. Introduction

Aluminium is the most abundant metal of the Earth crust. It possesses low density and the ability to resist corrosion. Aluminium industry formally started at 1886 after the discovery of electrolysis as the way to produce it from fused salts. Since that year, its use has grown rapidly and overtaken other metals, such as copper, tin and lead [1], and its cost steadily declined and engineering applications became economically viable [2]. Nowadays, it is the second most widely used metal after steel. Average energy consumption for producing primary aluminium is about 16500 kWh/ton, being the 5.5% (~908 kWh/ton) consumed for melting/casting. The average energy consumption for producing secondary aluminium (melting) is about the 6% of that required for primary aluminium [3].

1.1. Problem description

Industrial furnaces are insulated enclosures that are designed to deliver the heat required to process diverse loads [4]. Current melting furnaces used in the aluminium industry can be classified into three (heating) types: resistance, induction and gas- or oil-fired furnaces [5]. Major problem found during aluminium melting in conventional furnaces is the oxide formation and hydrogen absorption, which could affect the aluminium quality due to the oxide inclusions and higher porosity. As a very energy intensive process, the increasing limitation of raw materials for metallurgy processes, and the serious ecological problems involved, require not only to pay attention to reduce its use, but also in the technology used in its production. For instance, in [6] it was demonstrated that an improved conventional aluminium furnace with preheating and recirculation gas system reduces the fuel

consumption in 38%, while this work will show that fuel savings could reach to the 45% with plasma heating technology.

Main objective of the model is to predict the performance of a crucible heated up by two methods, as well as to calculate some temperature profiles that in practice are difficult to measure. Previous models [6-8] based their analysis on conventional gas burners. Alternatively, the use of plasma in thermal processing was described in [9-11] by means of the complete simulation of the plasma temperature profile and the support of Maxwell and Laplace equations. In [12], apart from the plasma temperature profiles, a complete heat transfer simulation was performed.

In this work, a conventional heating method was analysed and compared with a new heating system (plasma). The cornerstone of this article is to provide a flexible and reliable model that allows to predict the performance of the crucible upon diverse heating systems. To avoid thermal shock, aluminium furnace walls have to be preheated by a gas burner. Then, aluminium could be melted by two alternatives, propane combustion and plasma. The model requires as input data the next list:

- Energy: input energy used during preheating
- Walls and gases: convective and conductive heat transfer coefficients, and irradiative properties.
- Geometry and components of the furnace.
- Load: metal type and thermal properties.

Finally the results of both simulations were compared in order to analyse their efficiency.

1.2. General description of plasma

Thermal plasma is a mix of ions, electrons and neutral particles [13]. It is created by the ionization of a gas provoked by a sustained electric arc supplied between plasma cathode and anode. Elevated density of the electric field forms a high-speed plasma jet. Thermal plasma facilities operate with a D.C. power source. Two arc plasma types are normally found: non-transferred, in which plasma is contained between the cathode and a nozzle anode, and transferred arc type, in which the metallic load acts as the anode closing the circuit. Here, aluminium acts as the anode. Main components of plasma system are described in Fig. 1. Plasma system is fed with nitrogen, which is injected through the cathode.

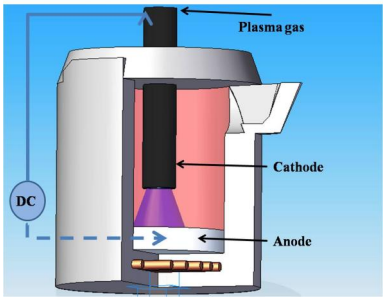

Fig. 1 Transferred arc plasma torch.

2. Furnace numerical simulation

2.1. Gas-fired preheating

Preheating was simulated by considering a high velocity propane gas burner. As it was pointed out by [7, 14], and due to the high recirculation inside of the crucible, a well-stirred model is assumed for combustion gases inside the furnace, and a 1-D model from the inside to outside of the furnace for aluminium load and refractory walls was used to simulate furnace.

The model adopted follows the previous analysis found in [7, 14, 15]. It consists of a governing equation for the combustion chamber, which is described in energy balance (1).

$$\rho \cdot V \cdot cp \cdot dT_g / dt = \dot{Q}_{hi} - \left\{ A_W \cdot \dot{q}_W + \dot{Q}_l + \dot{Q}_{stack} \right\} \quad (1)$$

Equation (1) is an ordinary differential equation that states that the heat provided by combustion gases is consumed in the stack and wall losses (*W*), as well as heating metal (*l*) for further melting. Initial condition for (1) depends on the heating process.

In order to calculate the radiative exchange in furnace, a grey-gas model was taken into account for exhaust gases coming from the burner. Procedure and properties of radiating gases can be found in [16-18]. Shape factors were computed for the furnace geometry distribution [19]. Representation of heat transfer modes can be found in Fig. 2.

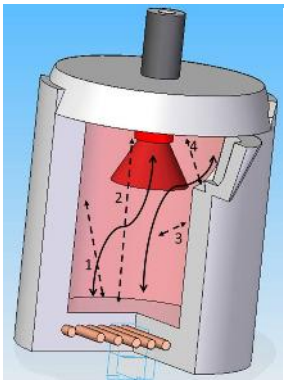

Line	Radiative transfer surfaces
1	wall ↔ bottom
2	cover ↔ bottom
3	wall ↔ wall
4	wall ↔ cover
solid lines	convection

Fig. 2 Heat transfer during preheating.

2.1.2. Computing the temperature profile of the furnace walls

Since its width is much smaller than its radius, walls were treated as a one slab governed by 1-D transient conduction equation:

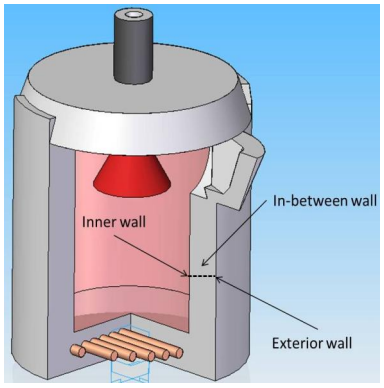

Fig. 3 One dimensional wall analysis.

$$\frac{\partial^2 T}{\partial x^2} + \frac{\dot{e}_{gen}}{k} = \frac{1}{\alpha} \frac{\partial T}{\partial t} \quad (2)$$

Boundary conditions for the walls are heat flux type, in which radiation and convection heat flows are calculated separately. At the beginning of the simulation (preheating stage) all surfaces are assumed to be at ambient temperature: at t=0, T_0=25ºC

$$-k \frac{\partial T}{\partial x} = \frac{\dot{Q}_{total}}{A} \quad (3)$$

$$\frac{\dot{Q}_{total}}{A} = J + \frac{\dot{Q}_{convection}}{A} \qquad (4)$$

Where J is the radiosity calculated following [18] and $Q_{convection}$ was computed following the procedure adopted in [7]. A FDM (finite difference method) was used to analyse and solve (2), by considering a differential wall element Δx. The energy balance on this element in a time interval Δt was expressed as in [7, 18, 20]. The finite difference formulation for an internal node can be expressed as:

$$T_{j-1}^{i} - 2T_{j}^{i} + T_{j+1}^{i} + \frac{\dot{e}_{j}^{i}\Delta x^{2}}{k} = \frac{T_{j}^{i+1} - T_{j}^{i}}{\tau} \qquad (5)$$

Spatial and temporal variations are represented by *j* and *i* respectively. Thermal diffusivity, time interval and differential wall element are related each other by the mesh Fourier number, τ:

$$\tau = \frac{\alpha\Delta t}{\Delta x^{2}} \qquad (6)$$

To complete the equations system of the FDM in refractory wall, equations on the boundary nodes are needed:

$$T_{0}^{i+1} = \left(1 - 2\tau - 2\tau\frac{h\Delta x}{k}\right)T_{0}^{i} + 2\tau T_{1}^{i} + 2\tau\frac{h\Delta x}{k}T_{\infty} + \tau\frac{\dot{e}_{0}^{i}\Delta x^{2}}{k} \qquad (7)$$

Once the system is completed and initial conditions are specified, the solution of transient problem is obtained by (5) and (7).

2.2. Aluminium melting with propane combustion

A 1-D conduction model was also used to estimate the aluminium temperature profile. Fig. 4 shows the new configuration inside of the furnace, as well as the temperature nodes inside of the aluminium layer studied here. Energy coming from exhaust gases or plasma increases the temperature in the upper node; then it is transferred energy by conduction to the lower nodes until the melting process finished.

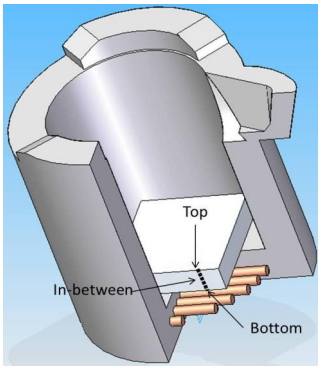

Fig. 4 Load configuration inside the furnace (during gas melting).

Similar equations than those used in refractory walls were implemented to simulate the aluminium melting process. Three different boundary conditions were implemented here:

- Sensible metal heating (liquid and solid): boundary heat flux conditions were defined.
- Phase change (latent heat): constant temperature was established.
- Aluminium in contact with the refractory of furnace bottom: an interface boundary condition was added to the process:

$$k_{Al} A \frac{T_{j-1} - T_j}{\Delta x} + k_{wall} A \frac{T_{j+1} - T_j}{\Delta x} = 0 \quad (8)$$

If aluminum is melted with the propane burner, similar equations are used with respect to preheating, only initial and boundary conditions are changed.

3. Aluminium melting with plasma

In plasma simulation, exhaust gases inside the furnace are almost insignificant and heating is produced by the plasma flame which drives directly into the aluminium. Therefore, gases do not participate in heat transferred by radiation. Plasma heat transferred was simulated with the aid of three consecutive approaches: first, the Elenbass-Heller equation is required to propose a system of equations in which the electric field, temperatures distribution and Joule effect are related [21]. Then, simplifications of a plasma model were taken into account from the Steenbeck and Raizer channel models ("positive column"). Finally, plasma heat transferred to the aluminium is calculated as it is proposed in [22]. Detailed mathematical models are shown below, and the software modules developed to solve the plasma heating process are shown in Fig.5.

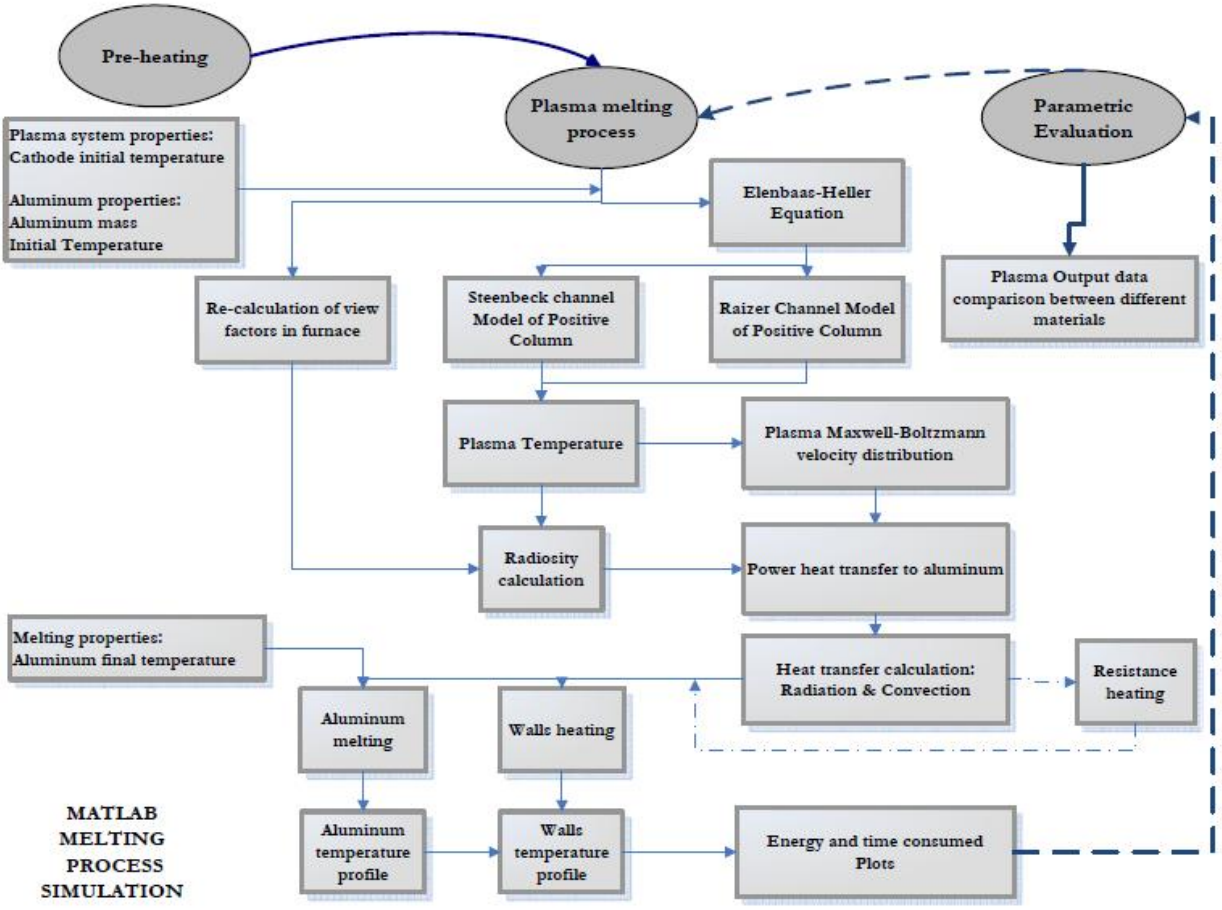

Fig. 5 Simulation architecture of plasma torch melting process.

When the aluminium melting is performed with plasma, the model takes into account several assumptions: it is considered that the current intensity during the whole process is kept constant, whereas the voltage (thus the power) varies (in order to maintain to the arc plasma stability). Radiosity is calculated as the radiant energy exchanged among the surfaces immersed in a transparent medium such as air, and anode effects are neglected. It was also considered that heat

transfer by convection was not relevant with respect to the radiation produced with plasma. Fig. 6 shows different surfaces involved during plasma melting process.

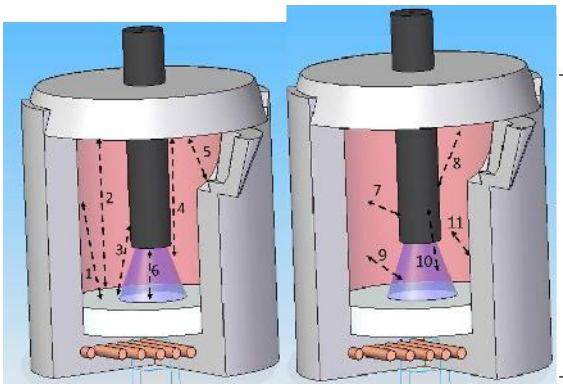

Line	Radiative transfer surfaces
1	wall ↔ aluminum
2	cover ↔ aluminum
3	cathode ↔ aluminum
4	plasma ↔ cover
5	wall ↔ cover
6	plasma ↔ aluminum
7	cathode ↔ wall
8	cathode ↔ cover
9	wall ↔ plasma
10	plasma ↔ cathode
11	wall ↔ wall

Fig. 6 Heat radiation transfer during plasma process

3.1. Simplified plasma equations

The description of the arc "positive column" model requires only the knowledge of the temperature distribution in plasma jet. Such distribution can be found from the Elenbaas-Heller equation [21]. In this equation, the gas pressure is considered a constant value, which is fixed by the experimental conditions:

$$\frac{1}{r}\frac{d}{dr}\left[r\lambda(T)\frac{dT}{dr}\right]+\sigma(T)E'^{2}=0 \qquad (9)$$

The above equation cannot be solved analytically because of the dependence of λ(T) and σ(T). For that reason, a simplified approach to the problem is required. The Steenbeck approach is based on the very strong exponential dependence of electric conductivity on the plasma temperature related in Saha equation [23], which explains the ionization expected in the plasma gas [21]. According to Steenbeck, temperature and electric conductivity can be considered as constant inside of the arc channel, and can be taken equal to their maximum value on the discharge axe. The total electric current of the arc can be expressed as:

$$I = E'\sigma\pi r_0^2 \qquad (10)$$

Application of this principle gives the additional equation of the Steenbeck model in the form that is required:

$$\left(\frac{d\sigma}{dT}\right)_{T=T_m}=\frac{4\pi\lambda\sigma}{w} \qquad (11)$$

To calculate the plasma flame temperature, the Raizer "Channel" Model of Positive Column was used. Key point of this model is the definition of an arc channel as a region where electric conductivity decreases not more than e times with respect to the maximum value at the discharge axe [21]:

$$\sigma(T)=83\exp\left(-\frac{36000}{T}\right) \qquad (12)$$

The electric field *E'* is kept constant along the positive column, so it actually describes the applied voltage.

$$E'=\frac{8\pi\lambda_m T_m^2}{I_i}\frac{1}{I} \qquad (13)$$

In (13) the ionization potential (I_i) is the energy required to remove electrons from gaseous atoms or ions, and the thermal conductivity of plasma jet (λ_m) is estimated constant (1.55 W/m-K), as found in [21, 24]. Thus, electric field is obtained from Steenbeck approach, and temperature was computed by using the Raizer model.

3.2. Plasma heat transfer model

In order to analyse the effect of plasma on the metal, it is necessary to firstly know the flow of plasma particles, and the number of particles per unit area and per unit time hitting the surface given by the product of normal speed to the metal surface [22].

$$v_z = v\cos\theta \tag{14}$$

The number of particles approaching the surface was taken into account and was described in a polar coordinate system as follows: for a small differential volume in velocity space between v and $v+dv$; and θ, and $\theta+d\theta$, ϕ and $\phi+d\phi$:

$$d\Gamma(v,\theta,\phi) = v_z dn(v,\theta,\phi) = \frac{v\cdot f'(v)\sin(\theta)\cos(\theta)d\phi d\theta dv}{4\pi} \tag{15}$$

$$\Gamma = n\left(\frac{2k'T}{\pi m'}\right)^{\frac{1}{2}}\int_0^\infty x^3 e^{-2x}dx = \frac{1}{4}n\left(\frac{8k'T}{\pi m'}\right)^{\frac{1}{2}} \tag{16}$$

In order to know the differential power flux [W/m^2], the differential particle flux must be multiplied by the kinetic energy of each particle.

$$dp(v,\theta,\phi) = \frac{1}{2}m'v^2 d\Gamma(v,\theta,\phi) \tag{17}$$

Substituting (16) in the above equation, the power heat transferred to the metal per unit area is finally obtained [22]:

$$p = \frac{m'}{8}\int_0^\infty v^3 f'(v)dv = \frac{nm'}{2\sqrt{\pi}}\left(\frac{2k'T}{m'}\right)^{3/2}\int_0^\infty x^5 e^{-x^2}dx \tag{18}$$

$$p = \frac{mn'}{2\sqrt{\pi}}\left(\frac{2k'T}{m'}\right)^{\frac{3}{2}} = 2k'T\Gamma \tag{19}$$

With (16), the plasma flow of particles was then computed, and (19) was used to calculate the plasma power delivered to aluminium. This power flux from plasma to the metal is the main parameter to obtain the temperature profile of aluminium. In this case, due to the high plasma temperature (above 8500 ºC) heat transfer by convection can be neglected.

To couple plasma and heat conduction models, equations from section 2.1.2 must be followed as well as boundary conditions from section 2.2. In order to define the link between plasma and heat transfer models, it is necessary to modify the boundary conditions (4).

$$\dot{Q}_{total,Al} = J + p \tag{20}$$

To compute the temperature profile in walls, only radiation was taken into account.

$$\dot{Q}_{total,walls} = J \tag{21}$$

4. Exergy balance of aluminium melting furnace

From previous simulation, mass and energy balances, as well as the furnace energetic efficiency were computed. However, in order to show which are the real potential savings in those complex

heating systems, it is necessary to perform an exergy analysis. The exergy flows are determined by the reference environment definition [25, 26].

The furnace is considered as a set of units consisting of container (made of refractory material) and different heating systems (gas burner or plasma torch). As it was explained before, there are also two heating stages to perform this melting process, see Fig. 7:

- Preheating: In this process, it can be distinguished two exergy inputs (fuel and air), three outputs (exergy of gas combustion, heat losses and the preheated refractory). The last one is not exactly an output flow, but it is considered the productive purpose of this heating stage.
- Aluminium melting: There are three exergy inputs, fuel (propane gas or electricity to activate plasma system), air in case of combustion (or nitrogen in case of plasma) and solid preheated aluminium. Exhausted gases (or ionized nitrogen), heat losses and liquid aluminium (as product) are the outputs of the system.

For a more detailed of exergy analysis, please refer to appendix A.

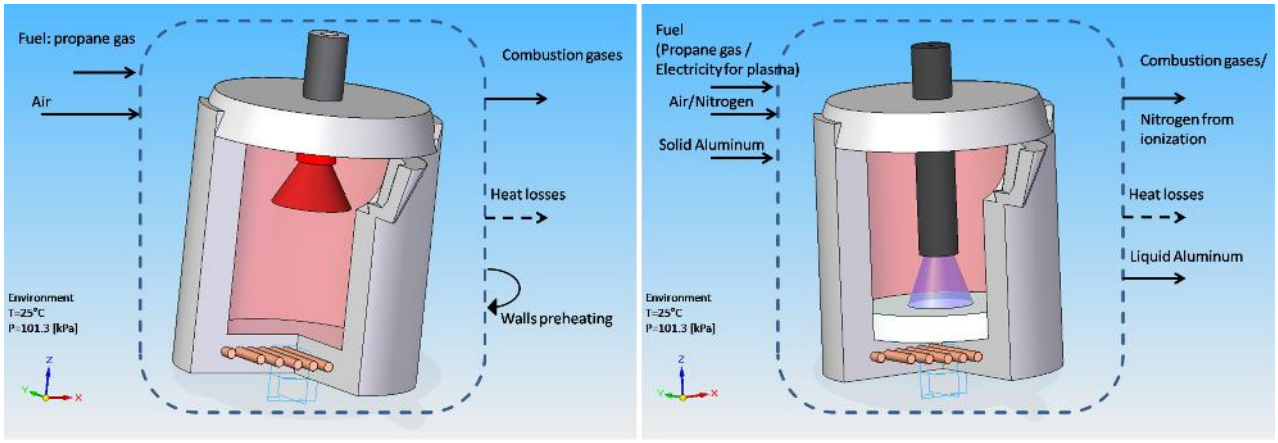

Fig. 7 Exergy balances for preheating (left) and melting (right)

5. Results and discussion

The model was validated with several experimental test performed at Tecnalia facilities. In each case, the temperature profile obtained at the end of the melting process and the energy consumption were compiled and then compared with those simulated. Fig. 8 shows energy consumption results for 5 tests with different aluminium loads and heating patterns: it can be seen that experimental data and simulated results were very similar, and both had the same specific energy ratio.

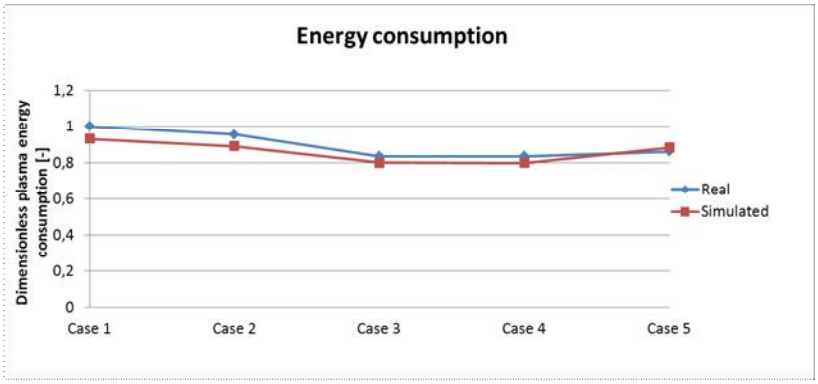

Fig. 8 Dimensionless experimental and simulated energy results

5.1. Energy analysis

Simulation was carried out on Matlab R2011a software. Results for a test including an aluminium load of 20.25 kg heated up to 760 ºC are shown in Table 1, which shows the comparison between the combustion and plasma results for melting. Energy efficiency of plasma without preheating is 67%, while energy consumption is about 0.46 kWh/kg and the furnace overall efficiency (melting and preheating) is 49.74%. Taking into account the energy consumed in the preheating process, the total specific energy consumed by the furnace is 0.95 kWh/kg. As expected, during the heating process, aluminium T-curve presents three different zones: first, temperature rises until the melting point. Here, the temperature is preserved until the energy from plasma equals the energy needed by the aluminium to be totally melted (at around 660ºC). Then, aluminium temperature continues rising until gets to a set-up temperature, as shown in Fig.9.a. Temperatures in furnace cover (T_{w3}) and walls (T_{w1}) are presented in Fig. 9.b: in almost 20 minutes of plasma melting, the temperatures inside the furnace walls get to 900 ºC.

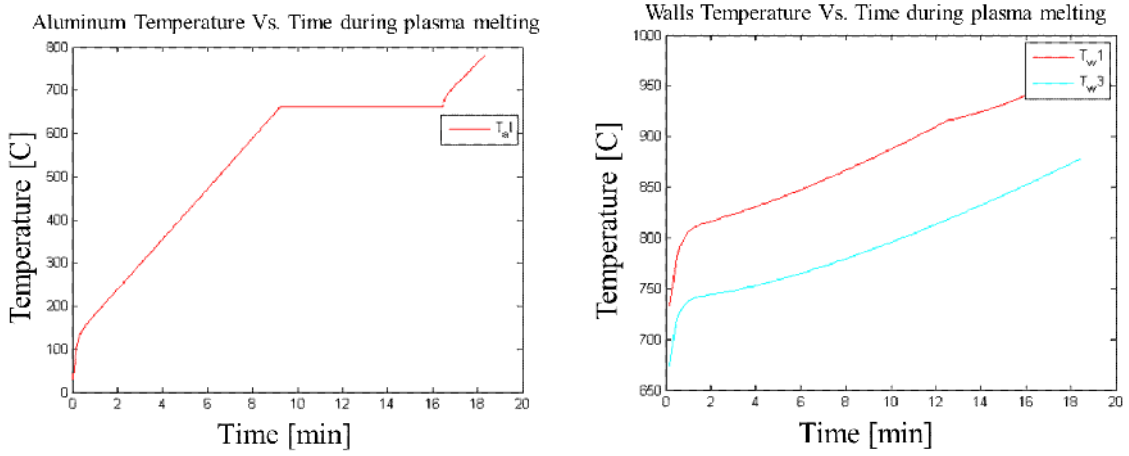

Fig. 9 Temperature evolution: a. Aluminium (left), b. furnace walls (rigth)

Table 1 simulation results for plasma and gas combustion

Parameter	Plasma simulation	Gas simulation	*Δ Plasma-Gas*
Furnace size, kg/h	40	40	0
Current intensity, A	600	-	-
Preheating gas power, kW	10	10	0
Melting power, kW	30	40	-10
Metal mass, kg	20.25	20.25	0
Final metal temp. C	782.63	769.09	13.05
Preheating time, min	60	60	0
Melting time, min	18.43	29.11	-10.68
Preheating energy, kWh	10	10	0
Melting energy, kWh	9.22	19.41	-10.19
Melting speed, kg/h	15.44	13.63	1.80
Melting efficiency, %	66.75	31.71	35.04
Furnace efficiency, %	49.74	32.26	17.47
Total specific energy, kWh/kg	0.95	1.45	-0.50

5.2. Exergy analysis

Annex A presents the main equations to solve exergy balance in the heating process. It can be observed in Table 2 that in plasma melting process, less irreversibilities are produced than in the case of propane gas combustion. For the same aluminium load, gas combustion during melting

consumes almost double of the exergy than in the case of plasma. Main reason is that in plasma furnace, exergy is emitted directly into the aluminium piece: at the end of the process, molten aluminium held the 51% of the input exergy. On the contrary, in propane combustion, heat is spread into walls and metal, therefore the exergy accumulated in molten aluminium is only the 23% of the input fossil fuel exergy. The same could be argued with respect to exergy destruction, in which gas fed furnace destroys three times the exergy destroyed with plasma.

Table 2 Exergy analysis

Parameter	Gas simulation	Gas simulation %	Plasma simulation	Plasma simulation %	Δ Plasma-Gas
Metal mass, kg	20.25		20.25		0
Fuel exergy, kWh	20.93	98.14	9.21	94.10	11.71
Initial metal exergy, kWh	0.5	1.86	0.5	5.9	0
Flue gas exergy, kWh	5.77	27.03	1.46	14.94	4.30
Exergy lost, kWh	1.6	7.51	1.09	11.23	0.50
Final metal exergy, kWh	5.07	23.75	5.07	51.78	0
Destroyed exergy during melting, kWh	8.89	41.70	2.09	21.42	6.79
Total fuel exergy (melting+preheating), kWh/kg	1.59	-	1.02		0.56
Total destroyed exergy, kWh/kg	0.76	-	0.43	-	0.32

5.3. Sensitivity analysis

The model could be also useful to analyze the variation of some design parameters in crucible furnaces. Then, a specific script was created to deal with thermal properties of refractories used in those furnaces. It is important to note that, independently of the heating mode, the highest energy consumption was found during the preheating.

First studied parameter was wall emissivity, often considered as an inherent physical property which usually remains unchanged. The emissivity of furnaces operating at high temperatures is usually about 0.3, but using high emissivity coatings can move to 0.8, thus reducing the fuel consumption by 25 to 45 per cent [27].

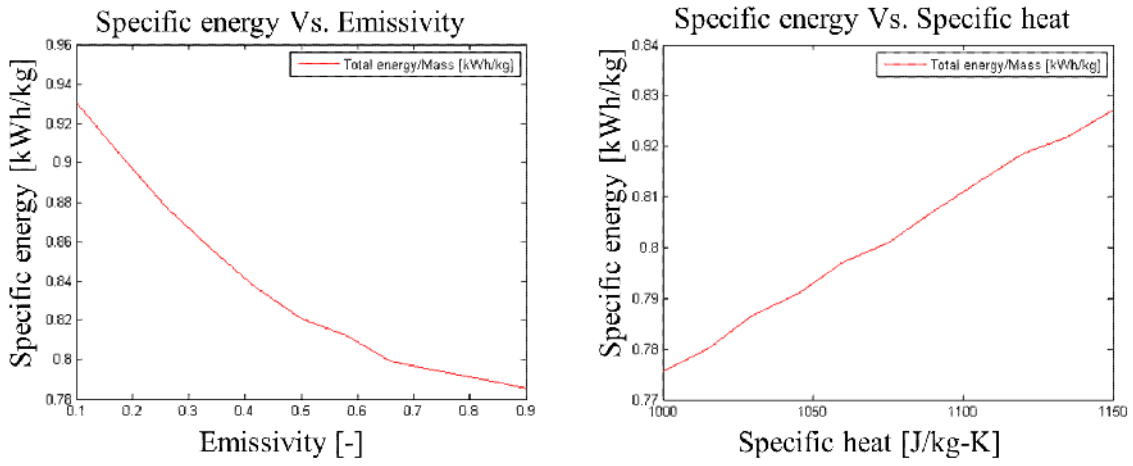

Fig. 10 Parametric simulations, energy consumed when: emissivity (left) and specific heat (right) is varied.

Figure 10 shows that this simulation (plasma case) exactly meets the behaviour described in literature: it can be observed a decrement of almost 30% of the energy consumption when the emissivity rises from 0.3 to 0.85.

Thermal capacity of refractory was also studied by varying the walls specific heat. As expected, the energy consumption mainly increases during the preheating as specific heat increases, because of the difficulty to obtain the desired temperature.

6. Conclusions

In this work, two heating modes for melting aluminium in a secondary crucible furnace were simulated. Both simulations (plasma and propane combustion) were developed in parallel with the aim of performing the automatic comparison. Simulation model was validated with experimental data taken from an industrial pilot plant. In the case of plasma, preheating (by means of a burner) represents the 52% of total energy consumed in the process (20.25 kg of aluminum were melted). In fact, this implies that energy savings can be mainly found in the preheating stage. On the other hand, exergy analysis fairly explained the reasons of the better plasma efficiency: if thermal shock problems are avoided in load and walls, plasma strongly reduces the energy consumption in the process. Taking into account that technical and economic constraints associated to experimental tests are found, it was proved that the model could help in its cost reduction of the design phase of those furnaces, since it is able to predict power consumption and provide some optimization guidelines. To test the feasibility of new heating systems, it could contribute to pave the way to reduce the energy intensity and their associated environmental impacts in this sector.

Appendix A

A.1. Exergy analysis

Considering the whole preheating and melting process, the overall exergy balance of a furnace is expressed as:

$$\sum B_{in} - \sum B_{out} = \sum B_{destroyed} \qquad \text{(A.1)}$$

The previous terms are defined in a different way in the case of preheating and melting.

- Preheating:

$$\sum B_{in} = B_{fuel} + B_{air} \qquad \text{(A.2)}$$

$$\sum B_{out} = B_{walls} + B_{gas} + B_{losses} \qquad \text{(A.3)}$$

- Melting:

$$\sum B_{in} = B_{fuel} + B_{air/N_2} + B_{solid\ Al} \qquad \text{(A.4)}$$

$$\sum B_{out} = B_{liquid\ Al} + B_{gas} + B_{losses} \qquad \text{(A.5)}$$

Where:

$$B_{walls} = m_{wall}\left(c_{wall}\left(T_{w,pre} - T_0\right) - T_0 c_{wall} \ln\frac{T_{wall,pre}}{T_0}\right) \qquad \text{(A.6)}$$

$$B_{gas,ph} = \sum_{i=1}^{nt} \dot{m}_{gas,i} \cdot \Delta t \left(c_{gas,i}\left(T_{gas,i} - T_0\right) - T_0 c_{gas,i} \ln\frac{T_{gas,i}}{T_0}\right) \qquad \text{(A.7)}$$

For each gas, the specific heat is calculated from [28]:

$$c_{gas,i} = a + b \cdot T_{gas,i} + c \cdot T_{gas,i}^2 + d \cdot T_{gas,i}^3 \qquad \text{(A.8)}$$

Since all chemical species of gases are presented in the reference environment, chemical exergy is calculated as in [29]:

$$B_{gas,ch} = \sum_{i=1}^{nt} \dot{m}_{gas,i} \Delta t \left[R_{gas,i} \cdot \sum_{k=1}^{ng} Y_{gas,i}^{k} T_0 \cdot \ln \frac{Y_{gas,i}^{k}}{Y_{0,gas}^{k}} \right] \qquad \text{(A.9)}$$

Total gas exergy is defined by:

$$B_{gas.tot} = B_{gas,ch} + B_{gas,ph} \qquad \text{(A.10)}$$

B_{losses} term represents all the heat losses in the system, this term cannot be computed directly:

$$B_{losses} = Q_{losses} \left(1 - \frac{T_0}{T_{ab}} \right) \qquad \text{(A.11)}$$

$$Q_{losses} = E_{fuel} - E_{product} - E_{gas} \qquad \text{(A.12)}$$

where T_{ab} is the average temperature of the control volume boundary. Equation (A.12) calculates losses from the overall balance of the furnace. In this equation, $E_{product}$ is defined depending on the heating process:

- Preheating: the product is the preheated refractory; $E_{product}$ is the energy stored in walls that avoids thermal shock. For this analysis (A.6) is computed.
- Melting: the product is the molten aluminium and exergy related to temperature variation in walls is included in the losses term. For this analysis, (A.6) is obviously not computed.

In order to compute exergy, it is necessary to firstly know the temperature of the process. This value was calculated as described in sections 2 and 3. Since it is considered that there are not chemical reactions during the melting process only thermo-mechanic exergy component is taken into account:

- Initial aluminium exergy value (during heating of solid aluminium):

$$B_{solid,Al} = m_{Al} \left(c_{Al,s} \left(T_{Al,i} - T_0 \right) - T_0 c_{Al,s} \ln \frac{T_{Al,i}}{T_0} \right) \qquad \text{(A.13)}$$

- Final aluminum exergy value, (during heating of liquid aluminium):

$$B_{liq,Al} = m_{Al} \left(c_{Al,l} \left(T_{Al,i} - T_f \right) - T_0 c_{Al,l} \ln \frac{T_{Al,i}}{T_f} \right) + B_{phasechange,Al} \qquad \text{(A.14)}$$

Where phase change exergy of aluminium is defined as:

$$B_{phasechange,Al} = m_{Al} \left(c_{Al,s} \left(T_{Al,f} - T_0 \right) - T_0 c_{Al,s} \ln \frac{T_{Al,f}}{T_0} \right) + Q_{phasechange} \cdot \Delta t \cdot \left(1 - \frac{T_0}{T_{Al,f}} \right) \qquad \text{(A.15)}$$

Acknowledgments

This work is part of the EDEFU project FP7-NMP-2009-LARGE3 with the grant agreement nº 246335. First author acknowledges the support from the Mexican *Consejo Nacional de Ciencia y Tecnología (CONACYT)* through the scholarship number 25712.

Nomenclature

Thermodynamic symbols

A area, m^2

B exergy, J

c specific heat, J/(kg K)

e internal heat generation, W/m^3

E energy, J

f friction factor

F shape factor

G absorbed energy, W/m^2

h heat transfer coefficient, $W/(m^2 K)$

J radiosity, W/m^2

k thermal conductivity, W/(m K)

k_g absorption coefficient, 1/(m-atm)

m mass, kg

$\dot{m}$ mass flow rate, kg/s

nt number of time steps

ng number of gas components

$\dot{q}$ heat per area, W/m^2

$\dot{Q}$ heat rate, W

Q heat, J

T temperature, K

t time, s

V volume, m^3

Y molar fraction

x differential element

Plasma symbols

E' electric field, V/m

$f'(v)$ maxwellian distribution

I electric current, A

I_i ionization potential, eV

k' Boltzmann constant, J/K

m' electron mass, kg

n density number, particles/m^3

p power flux, W/m^2

r radius, m

v particles velocity, m/s

w joule heat per length, W/m

Thermodynamic Greek symbols

α thermal diffusivity, m^2/s

η efficiency

ρ density, kg/m^3

τ mesh Fourier number

Plasma Greek symbols

Γ Plasma particle flux, particles/(m^2 s)

θ Plasma azimuthal angle

λ Plasma thermal conductivity, W/(m K)

σ Plasma electric conductivity, S/m

ϕ Plasma polar angle

Subscripts and superscripts

0 reference

1 furnace walls

3 furnace cover

ab average boundary

ch chemical

f melting point

g gas

hi fuel

i time interval

j node

k gas component

l Fusion energy

m plasma

ph physical

pr preheating

W *walls*

References

[1] Green, J. Aluminium recycling and processing for energy conservation and sustainability. USA: ASM International, 2007.

[2] Kaufman, J. and L., Elwin. Aluminium Alloy Castings: Properties, Processes, and Applications. USA: ASM International, 2004.

[3] Fu, M., Staples, K. and Sarvepalliis, V. A high-capacity melt furnace for reduced energy consumption and enhanced performance. JOM Journal of the Minerals, Metals and Materials Society, 1998;50(5):42-44.

[4] Trinks, W, et al. Industrial Furnaces, Sixth Edition. USA: John Wiley & Sons, Inc, 2004.

[5] Babos, L. and Martegani, A. D. Energy conservation and recovery in electric arc furnaces dedusting plants. Energy Conversion and Management, 1982;22(4):347-355.

[6] Lee, D. Exergy Analysis and efficiency evaluation for an aluminium melting furnace in a die casting plant [dissertation]. Totronto, Canada: Ryerson University; 2003.

[7] A., Ighodalo O. Development and performance evaluation of a melting furnace for non-ferrous metals. Internal Journal University Epoma-Nigeria, 2010;4:133-138.

[8] Hakan, C. and Arif, H. Exergetic analysis and assessment of industrial furnaces. Journal of Energy Resources Technology, ASME, 2010;132(1):(7 pages).

[9] Mimura K., Komukai T., and Isshiki M. Purification of chromium by hydrogen plasma-arc zone melting. Materials Science and Engineering A 2005;403(1-2):11-16.

[10] Mohebi M., Syedein S. and Reza M. Fluid flow and heat transfer modeling of AC arc in ferrosilicon submerged arc furnace. Journal of iron and steel research, international, 2010;17 (9):14-18.

[11] Wang H., Cheng K., Xhen X. and Pan W. Three dimensional modeling of heat transfer and fluid flow in laminar plasma material re-melting processing. International journal of heat and mass transfer, 2010;49(13-14):2254-2264.

[12] Chu S. and Lian S., Numerical analysis of temperature distribution of plasma arc with molten pool in plasma arc melting. Computational Materials Science, 2004;30(3-4):441-447.

[13] P.V., Ananthapadmanabhan, Venkatramani, N. and Suryanarayana, C. Thermal plasma processing, Pergamon Materials Series. 1999. p. 121-150.

[14] Bui, R. T. and Perron, J. Performance analysis of the Aluminium casting furnace. Metall. Trans. 1988;19(B):171-180.

[15] Davies, I. Master and Gethin, D. J. Numerical modeling of a rotary aluminium recycling furnace. 4th International symposium of recycling of metals and engineered materials.

[16] Tucker, R. J. Gas emissivity. Gas emissivity. 2003. <http://m.safe.mn/3gHI> [accesed 4.26.2011].

[17] Rhine, J. M. and Tucker, R. J. Modelling of gas-fired furnaces and boilers. McGraw-Hill; 1991.

[18] Holman. Heat transfer. McGraw-Hill; 1986.

[19] Howell, J. A catalog of radiation configuration factors. McGraw-Hill; 1982.

[20] Çengel. Heat and Mass transfer. McGraw-Hill; 2007.

[21] Fridman, A. and Kennedy, L. Plasma Physics and Engineering. Taylor and Francis; 2004.

[22] Reece, J. Industrial plasma engineering volume 1: principles.Taylor and Francis; 1995.

[23] Chen, F. Introduction to plasma physics and controlled fusion. Plenum press; 1984.

[24] Dunn, G. and Eagar, T. Calculation of Electrical and Thermal Conductivities of Metallurgical Plasmas. WRC Bulletin. 1990.

[25] Kotas, J. The exergy method of thermal plan analysis. Butterworths; 1985.

[26] Szargut, J. Exergy Method: Technical and Ecological Applications Developments in Heat Transfer, WITpress; 2005.

[27] Energy Efficiency Guide for Industry in Asia. Energy Efficiency Guide for Industry in Asia goverment. <www.energyefficiencyasia.org>[accessed 5.20.2011].

[28] Çengel, Y. A. and A., Boles M. Thermodynamics: An Engineering Approach. McGraw-Hill; 2006.

[29] Moran, M. J. and Shapiro, H. N. Fundamentals of engineering thermodynamics, 3rd ed. Wiley; 2000.

Modelling and experimental validation of a solar cooling installation

G. Anies[a], P. Stouffs[a] and J. Castaing-Lasvignottes[b]

[a] Université de Pau et des Pays de l'Adour, ENSGTI, LaTEP, Rue Jules Ferry, BP 7511, 64075 PAU Cedex, France, guillaume.anies@etud.univ-pau.fr and pascal.stouffs@univ-pau.fr,
[b] Université de la réunion, ESIROI, 117 rue du Général Ailleret, 97430 Le Tampon, Ile de la Réunion, France, jean.castaing-lasvignottes@univ-reunion.fr

Abstract:

In this paper, we deal with a dynamic model of a solar cooling plant. A demonstration device has also been developed, using market-available technologies, the main apparatus being a single-effect absorption chiller of 4.5 kW nominal cooling capacity. A solar collector field supply the plant with hot water. This set has been successfully tested during the summer 2011. The present work is organized as follows. Firstly, we present our installation. Secondly, we show how to develop the model, based on thermodynamic principles. A validation is carried out, thanks to a set of experiments obtained with our plant. Eventually, we use our modelling tool to study design optimization of several parts of the system.

Keywords:

Solar cooling plant, absorption, modelling, simulation, transient, experimental validation, design tool.

1. Introduction

In France, during the summer months, air-conditioning represents an important electricity consumption in both residential and commercial buildings because the thermal comfort demand has not stopped rising since the hot summer of 2003 [1, 2]. In consequence, the distributor must manage these electric demand peaks that are observed and in the same time the global warming continues to increase year by year [3]. To reduce this impact without modifying the thermal comfort, air-conditioning using thermal solar energy has a great potential for saving primary energy because of a good correlation between chilling loads and solar energy resource [4]. The use of tri-thermal refrigeration cycles driven by solar heat energy is an interesting way of research and development. In the world, about 600 solar systems are functioning and among them, 71% are of absorption type [5, 6]. One of these installations is located in Pau, South-West of France. It works with a ROTARTICA Solar 045 machine. Its nominal chilling power is 4.5 kW with a COP of 0.62. It is an innovative absorption technology based on integrated rotating heat exchangers to enhance heat and mass transfer resulting in a potential reduction of size, cost and weight. The heating loop of the generator is fed by 16.6 m² evacuated tube collectors. To reduce the influence of varying conditions (due to clouds for instance), a storage tank of 260 L has been added between the solar field and the chiller. The cooling loop dissipates the heat generated by the absorber and the condenser thanks to an external dry-cooler. The chilling production is used to refrigerate two climatic cells (with controlled chilling load) with two fan coolers.

The main objectives of having built such a pilot are:

- Demonstrating the interest of the absorption system and evaluating its performances,
- Developing a dynamic installation model in order to improve reliability of components, conception, and control strategy.

This paper presents in a first part the installation, i.e. the materiel, the selected configuration and its control strategy. In a second part, thanks to previous work concerning the modelling of the machine alone, the dynamic modelling of the whole system is introduced, taking into account all the elements (solar collectors, storage tank, dry cooler...). In another part, the experimental and simulated results for two typical days (sunny summer day and mean season day with accident) are compared and commented. Finally, the obtained model enables to simulate the installation behaviour with a quite good accuracy.

2. Solar cooling plant description

This section presents the laboratory experimental plant. Figure 1 shows a simplified diagram of the facility with its main components. The unit is located on the University campus of Pau. The city is located in the Pyrénées Atlantiques, in the south west of France (43°18'06" N 0°22'07" W).

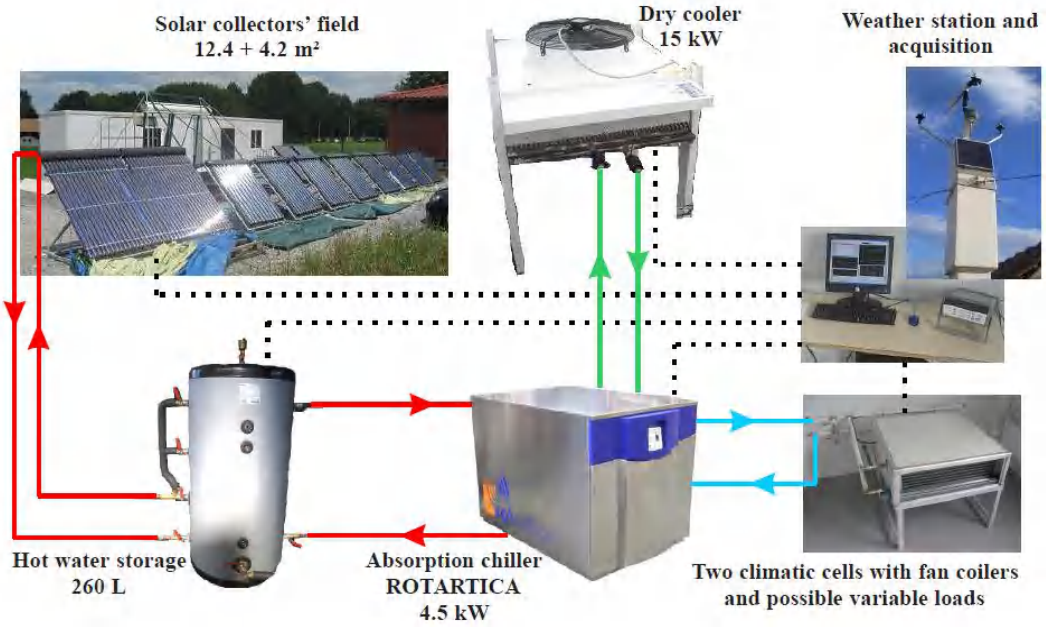

Fig. 1. Simplified diagram of the experimental solar cooling plant and its main components.

2.1. Solar system

In order to supply the heat storage tank and the desorber of the absorption chiller, a 16.6 square meter field of solar thermal collectors was installed on the ground, as can be seen in Figure 1. Two technologies are present: 8 evacuated tubes heat pipes (12.4 m^2) of the Tecnisun brand (10 tubes version) and 2 evacuated tubes direct flow (4.2 m^2) of the Viessmann brand (20 tubes version). All these solar collectors are connected in series. The Tecnisun Technology has a particularity because in this collector there is a heat exchanger inside the panel. This one preheats the heat transfer fluid which enters in the collectors' field and sub cools the heat transfer fluid which exits.

These two devices are depicted in Figure 2.

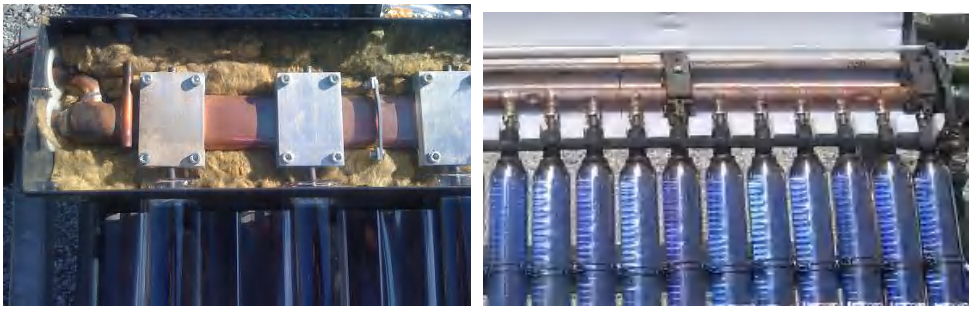

Fig. 2. Pictures of the Tecnisun (left) and Viessmann (right) solar collectors.

2.2. Accumulation system

A hot water tank was installed between the solar collectors' field and the desorber of the absorption chiller. It is used as a buffer tank to allow continuous operation during cloudy periods, for example, during about 10 minutes. The maximum inlet desorber temperature allowed is 5°C.

2.3. Chiller

The absorption chiller Rotartica Solar 045 is the main element of this pilot plant. This is the version without dry cooler. The working fluids are the couple H_2O/LiBr. Its nominal chilling capacity is 4.5 kW for a COP_{th} of 0.62, in the case of the following conditions: 90°C at the desorber entrance, 35°C at the cooling entrance and 12°C at the evaporator outlet. The absorption chiller can operate in the following range: 70°C to 108°C for the hot source (desorber), 30-45°C for the heat removal (absorber and condenser) and 6°C to 20°C for the cold production. This machine uses a rotating system, which allows the solution to mix in each component, the liquid to be distributed over each heat exchanger area and ensure the liquid flow between the different elements. This machine was designed for flow rates of hot water systems, cooling water and cold water, respectively, of 900 L/h, 1980 L/h and 1560 L/h.

2.4. Cooling system

This is a dry cooling tower Contardo, i.e. an air/water heat exchanger. It is installed behind the climatic cells (white buildings visible in Figure 1) in order to be as much as possible in the shade during the day and close to the machine to reduce pressure losses. This component is used to remove the heat liberated by the absorption and condensation process. Air is drawn from the bottom and rejected by the top with a flow rate of 5800 m^3/h.

2.5. Distribution system

Two fan air coilers, connected in parallel, serve to distribute the chilling production to the climatic cells (ALGECO type). They operate with an air flow rate of 1000 m^3/h, which permits to reach a chilling power of 3.2 kW per unit with an input/output temperature range of 8/13°C (for an air at 24°C and 50% humidity in our operating conditions). The chilling load of each cell may be modified so as to analyse the absorption chiller behaviour for different distribution temperature levels.

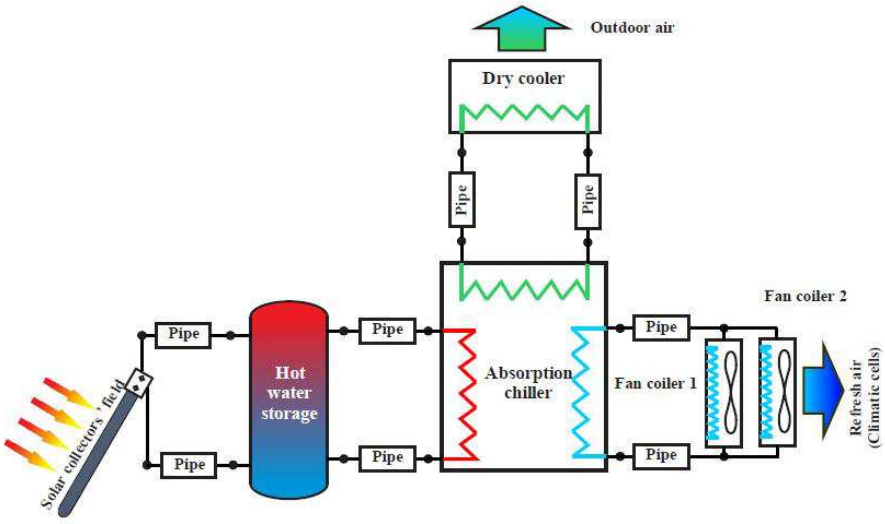

Fig. 3. Sketch of the components interactions of our model.

3. Dynamic model development

Our model consider several elements: 8 pipes, a field of solar collectors, a stratified tank, an absorption chiller, a dry cooler and two fan coilers. These elements connected together by water inputs/outputs, as shown in Figure 3. Each part interacts with its direct neighbours and possibly with the surrounding environment.

The modelling of sub-systems is performed in the Delphi environment, using an explicit Euler time integration. Each sub-model is now considered below.

3.1. Pipes

To evaluate the heat losses on the line, we suppose that we know the inlet/outlet temperatures and the flow rate. External losses are computed through an equivalent thermal resistance. Finally, the inertia of the tube is replaced by an equivalent mass of water.

For example, in the case of a chilling distribution, i.e. considering the connection between the evaporator of the chiller and the fan coiler units, we obtain the following equation:

$$M_{pipe} \cdot \frac{du_{pipe}}{dt} = \dot{Q}_{pipe} + \dot{W}_{pressurelosses} + \dot{m}_{evap} \cdot Cp_{water} \cdot \left(T_{inlet\,pipe} - T_{outlet\,pipe}\right) \quad (1)$$

The thermal resistance of each pipe contains the internal forced convection of the fluid (water), conduction in the tube (copper), conduction in the insulation (ARMAFLEX) and natural convection of the external fluid (air). Consequently, we may deduce the expression of the heat flux exchanged between the heat transfer fluid of each loop and the outside air:

$$\dot{Q}_{pipe} = \frac{T_{pipe} - T_{ext}}{R_{tot}} = \frac{T_{pipe} - T_{ext}}{R_{\text{int}\,conv} + R_{tube\,cond} + R_{insul\,cond} + R_{ext\,conv}} \quad (2)$$

During the flow, the heat transfer fluid exchanges the following work:

$$\dot{W}_{pressurelosses} = \frac{H_m \cdot \rho_{water} \cdot g \cdot \dot{Q}_v}{\eta_{hydrau\,pump}} \quad (3)$$

with H_m is the pressure loose, m, ρ_{water} is the water density, kg/m^3, g is the gravity acceleration, m/s^2, $\dot{Q}_v$ is the volume flow rate, m^3/s and $\eta_{hydrau\,pump}$ is the hydraulic efficiency of the pump.

3.2. Solar collectors' field

Let us first present our basic hypotheses:

- The temperature of the heat transfer fluid is uniform inside the collector pipe,
- The collector tubes are replaced by an equivalent water mass.

Since the Tecnisun's collectors involve a heat exchanger, we have to split the first principle into two parts: one for the upper fluid line (hot), one for the other (cold). If we have a look on the Figure 4, it corresponds to the line between 4 and 3, and 2 and 3 respectively.

Thus, we have:

$$M_{coll\,UP} \cdot \frac{du_{coll\,UP}}{dt} = 0.5 \cdot \eta_{coll} \cdot \Phi_{received} + \dot{Q}_{exchanged} + \dot{W}_{pressure\,losses} + \dot{m}_{coll} \cdot Cp_{water} \cdot \left(T_{inlet} - T_{outlet}\right) \quad (4)$$

$$M_{coll\,DOWN} \cdot \frac{du_{coll\,DOWN}}{dt} = 0.5 \cdot \eta_{coll} \cdot \Phi_{received} - \dot{Q}_{exchanged} + \dot{W}_{pressurelosses} + \dot{m}_{coll} \cdot Cp_{eau} \cdot \left(T_{inlet} - T_{outlet}\right) \quad (5)$$

The thermal power exchanged by the coaxial heat exchanger is:

$$\dot{Q}_{exchanged} = UA_{received} \cdot \left(T_{outletUP} - T_{outlet\,DOWN}\right) \tag{6}$$

As we may see in Figure 5, the heat pipe condenser is in contact with two pipes, that is why we consider that 50% of the solar energy is collected by each pipe.

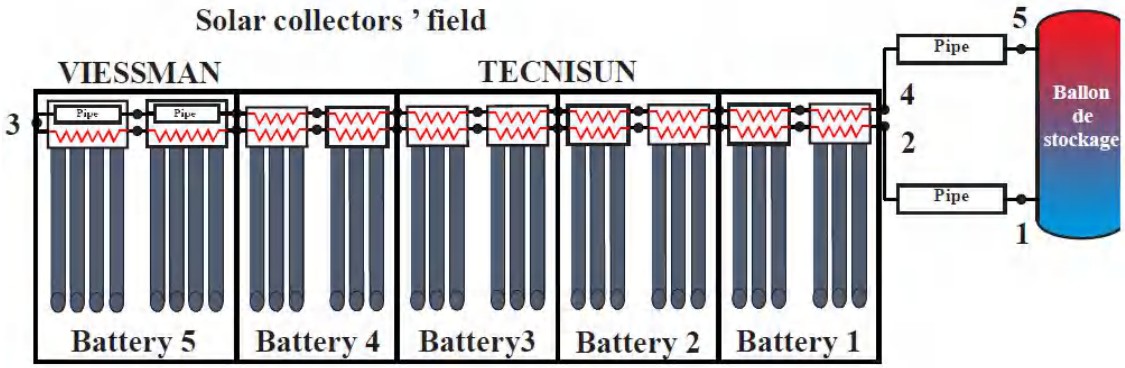

Fig. 4. Schematic representation of the thermal solar collectors' field.

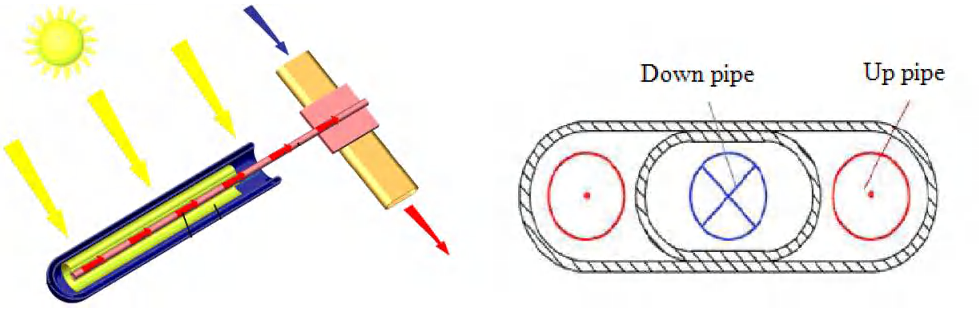

Fig. 5. Scheme of the Tecnisun' collector (left) and section of his coaxial heat exchanger (right).

If we now consider the Viessmann's collector, we have directly:

$$M_{coll\,DOWN} \cdot \frac{du_{coll\,DOWN}}{dt} = \eta_{coll} \cdot \Phi_{received} + \dot{W}_{pressure\,losses} + \dot{m}_{coll} \cdot Cp_{water} \cdot \left(T_{inlet} - T_{outlet}\right) \tag{7}$$

Thermal power received by each solar collector is computed with the efficiency expression of [7]:

$$\eta_{coll} = \eta_0 - a_1 \cdot \frac{T_{fluid} - T_{air\,ext}}{S_{coll} \cdot \Phi_{received}} - a_2 \cdot \frac{\left(T_{fluid} - T_{air\,ext}\right)^2}{S_{coll} \cdot \Phi_{received}} \tag{8}$$

3.3. Hot storage

The model is directly derived from the works of [8]. The hot storage is then divided into several strata, at uniform temperature; we consider in our case four strata.

The physical phenomena considered by the model are:

- The exchange of heat and mass by direct injection and extraction of water,
- The heat transfer by conduction through the different walls of the tank,
- The heat transfer by conduction between each adjacent layers inside the tank,
- The exchange by forced convection inside the storage at each strata.

The model writing is based on the following hypothesis:

- The temperature and density of the fluid in each layer are uniform and constant at each time step,

- The only temperature gradient is in the x-direction.

Consequently, the balance on the first strata gives:

$$Vol_1 \cdot \rho_{water} \cdot Cp_{water} \cdot \frac{dT_1}{dt} = \dot{m}_{coll} \cdot Cp_{eau} \cdot \left(T_{outlet\,coll\ field} - T_1\right) + \dot{m}_{desorb} \cdot Cp_{water} \cdot \left(T_2 - T_1\right) + \frac{\left(k_{water} + \Delta k\right) \cdot S_{stock}}{\Delta x} \cdot \left(T_2 - T_1\right) + UA_1 \cdot \left(T_{ext} - T_1\right) \quad (9)$$

For the two intermediate strata (j=2 and 3), we have:

$$Vol_j \cdot \rho_{water} \cdot Cp_{water} \cdot \frac{dT_j}{dt} = \dot{m}_{coll} \cdot Cp_{water} \cdot \left(T_{j-1} - T_j\right) + \dot{m}_{desorb} \cdot Cp_{water} \cdot \left(T_{j+1} - T_j\right) + \frac{\left(k_{water} + \Delta k\right) \cdot S_{stock}}{\Delta x} \cdot \left(T_{j-1} - T_j\right) + \frac{\left(k_{water} + \Delta k\right) \cdot S_{stock}}{\Delta x} \cdot \left(T_{j+1} - T_j\right) + UA_j \cdot \left(T_{ext} - T_j\right) \quad (10)$$

And finally for the last layer:

$$Vol_4 \cdot \rho_{water} \cdot Cp_{water} \cdot \frac{dT_4}{dt} = \dot{m}_{coll} \cdot Cp_{water} \cdot \left(T_3 - T_4\right) + \dot{m}_{desorb} \cdot Cp_{water} \cdot \left(T_{outlet\,desorb\,loop} - T_4\right) + \frac{\left(k_{water} + \Delta k\right) \cdot S_{stock}}{\Delta x} \cdot \left(T_2 - T_4\right) + UA_4 \cdot \left(T_{ext} - T_4\right) \quad (11)$$

Where Vol is the water volume of a strata, m^3, $\dot{m}_{coll}$ and $\dot{m}_{desorb}$ are respectively the injection and racking between the different strata, kg/s, k_{water} is the water thermal conductivity, W/(m.K), Δk is the correction coefficient of the water thermal conductivity due to the high conductivity of the metal wall, i.e. $k_{water} + \Delta k = k_{effective}$, S_{stock} is the hot storage section, m^2, Δx is the height of a hot storage strata, m, UA_j is the global heat exchange coefficient between the water of the strata j and the environment, W/K.

3.4. Absorption chiller

To simulate varying conditions as well as the startup and shutdown phases, a dynamic model is used. In previous work [9, 10], an unsteady model of H_2O/LiBr absorption chiller has been developed to simulate the transient behavior of a Rotartica machine. Mains hypothesis are as follow: Each component (desorber, absorber, condenser, and evaporator) is divided in two elements that are the vessel (which contains the solution or the refrigerant) and the solution (or the refrigerant). The vessel has generally a double role since it is also the exchange wall between the heat transfer fluid (sources) and the solution (or the refrigerant). Each component is described by its geometric characteristics (volume, exchange area) and by its physical properties (mass, heat capacity, overall heat exchange coefficient). So, there are states variables for each one (temperature, pressure, mass fraction, specific enthalpy…). Therefore, the chiller is described by a coupled non-linear differential equation system which is summarized in the three following balances:

- The energy balance of the system:

$$\frac{dU}{dt} = \sum_i \dot{Q}_i + \sum_i \dot{m}_i \cdot h_i \quad (12)$$

- The liquid solution mass balance:

$$\frac{dM}{dt} = \sum_i \dot{m}_i \quad (13)$$

- The water mass balance:

$$\frac{dM_{H_2O}}{dt} = \sum_i \dot{m}_i \cdot x_i \tag{14}$$

where U is the internal energy, kJ, h_i is the specific enthalpy, kJ/kg, x_i is the mass fraction, M is the mass, kg, m_i are the different mass flow rate, kg/s and $\dot{Q}_i$ represents the thermal exchange of the system, kW.

To access to all the characteristics of the points of the cycle, a properties library based on recent works [11, 12] has been used and covers the working range of the absorption cycles with temperatures from 273 K to 500 K and mass fraction between 0 % and 70 %.

The chiller behaviour is simplified thanks to several hypotheses:

- In the condenser and the evaporator, the refrigerant is composed of pure water,
- The thermodynamic equilibrium is supposed in each component,
- The solution leaving the component is supposed saturated,
- Only convective heat transfer between medium is considered,
- The exchange coefficients are supposed constant,
- The variables (mainly temperature, pressure and composition) are supposed uniform in space,
- The thermal losses are neglected.

For example, if these previous equations are applied to the desorber of the machine represented figure 3, the following equations system is obtained:

$$\begin{cases} \dfrac{dU_{sol}}{dt} = \dot{Q}_{desorb} + \dot{Q}_{desorb\,losses} + \dot{d} \cdot h_5 - \dot{c} \cdot h_6 - \dot{m} \cdot h_7 \\ \dfrac{dM_{sol}}{dt} = \dot{d} - \dot{c} - \dot{m} \\ \dfrac{dM_{H_2O}}{dt} = \dot{d} \cdot X_d - \dot{c} \cdot X_c - \dot{m} \end{cases} \tag{15}$$

$\dot{Q}_{desorb}$ is the heat power exchanged between the solution and the heat exchanger. This latter can be expressed by two equations, one relative to the heat transfer fluid:

$$\dot{Q}_{desorb} = \dot{m}_{desorb} \cdot Cp_{water} \cdot \left(T_{inlet\,desorb} - T_{outlet\,desorb}\right) \tag{16}$$

And the flow of heat from the coolant to the solution:

$$\dot{Q}_{desorb} = UA_{desorb} \cdot \left(T_{outlet\,desorb} - T_{desorb}\right) \tag{17}$$

The thermal losses are directly considered as an energy waste of the solution or the refrigerant contained in each heat exchanger. They are simply estimated by the following equation:

$$\dot{Q}_{desorblosses} = h_{desorb} \cdot S_{ext\ desorb} \cdot \left(T_{desorb} - T_{air}\right) \tag{18}$$

3.5. Dry cooler and fan coilers

To model these components the first principle of the thermodynamic is applied with the following hypotheses:

- The heat transfer fluid outlet temperature is equal to that of water inside the exchanger,
- The equivalent water mass to the mass of the exchanger is added to the heat transfer fluid mass present in it.

We obtain the following equation in the case of the cooling tower:

$$M_{dry} \cdot \frac{du_{dry}}{dt} = \dot{Q}_{dry} + \dot{W}_{pressurelosses} + \dot{m}_{abs/cond} \cdot Cp_{water} \cdot \left(T_{inlet} - T_{outlet}\right) \quad (19)$$

and the next in the case of the fan coil units:

$$M_{fan} \cdot \frac{du_{fan}}{dt} = \dot{Q}_{fan} + \dot{W}_{pressurelosses} + \frac{\dot{m}_{evap}}{2} \cdot Cp_{water} \cdot \left(T_{inlet} - T_{outlet}\right) \quad (20)$$

The effectiveness of an air / water cross flow obeys the relation:

$$\varepsilon_{dry} = \frac{1 - \exp\left(-\frac{\dot{m}_{air} \cdot Cp_{air}}{\dot{m}_{abs/cond} \cdot Cp_{water}} \cdot \left(1 - \exp\left(-\frac{UA}{\dot{m}_{air} \cdot Cp_{air}}\right)\right)\right)}{\frac{\dot{m}_{air} \cdot Cp_{air}}{\dot{m}_{abs/cond} \cdot Cp_{water}}} \quad (21)$$

The method used to estimate the amount of heat transferred by the water/air heat exchangers ($Q_{dry\ cooler}$ and $Q_{fan\ coiler}$) is based on the notion of effectiveness [13]. So, we deduce:

$$\dot{Q}_{dry} = \varepsilon_{dry} \cdot C_{\min} \cdot \left(T_{inlet} - T_{ext}\right) \quad (22)$$

The presented expressions can also be written in the case of fan coil units. Therefore, we conclude that the exchanged heat by each fan coil unit is:

$$\dot{Q}_{fan} = \varepsilon_{fan} \cdot C_{\min} \cdot \left(T_{inlet} - T_{\text{int}}\right) \quad (23)$$

3.6. Coupling model and simulation results

In order to avoid errors compensations between the different modelling, a first study has been done to validate each model of the various components independently from each other. When comparing with the experimental results, i.e the outlet temperatures and associated thermal power, a good agreement was obtained. Then, we may now turn to our main goal: the evaluation of the performances of solar cooling installations based on the absorption cycle. The experimental campaign has been done during summer 2011. We use the July's data for our first validation of each sub-model, and the August's data for the validation of the whole model.

The input data are: the different pumps start/stop orders, the global/diffuse insulations and the outdoor/indoor temperatures of the climatic cells.

For convenience, we present the results for a single day, whose conditions are given in Figure 6. We present the corresponding results in Figure 7.

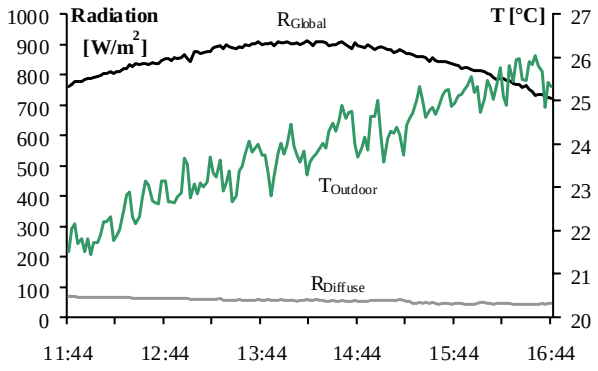

Fig. 6. Weather conditions corresponding to August 10th 2011.

We may note that we have relatively good agreement. Next, as can be seen in Figure 8, the model is able to correctly reproduce the various behaviour of each component. To summarize, we present a quantitative comparison in Table 1.

Eventually, we obtain very good agreement between the experimental results and the simulated ones. Thus, we may now perform a sensitivity analysis of the various parameters.

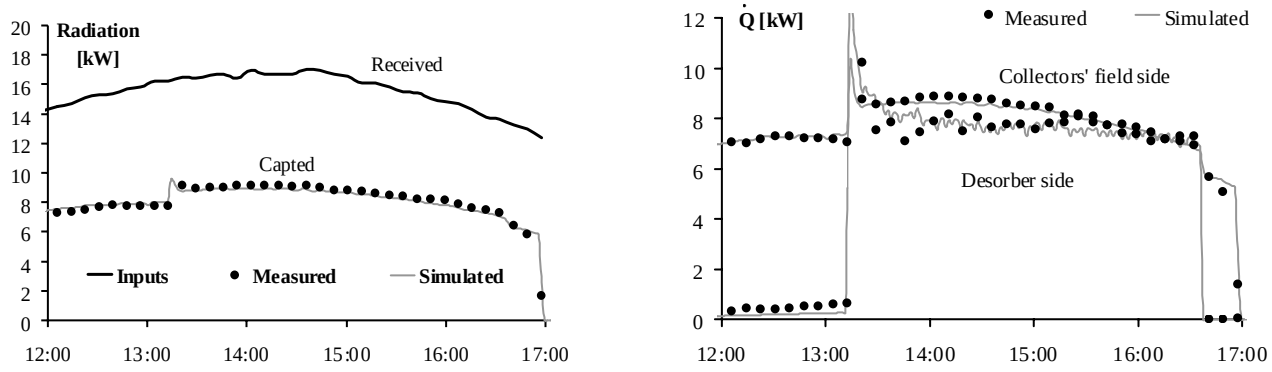

Fig. 7. Comparison of the experimental and numeric collected solar power (left) and thermal power evolution in the hot storage (right).

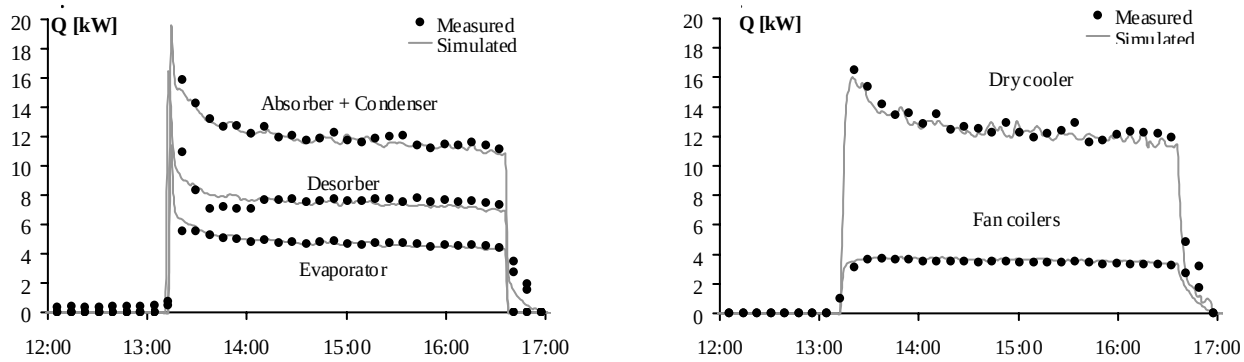

Fig. 8. Comparison between different experimental and simulated powers (August 10th, 2011)

Table 1. Comparison of experimental and simulated performances obtained for August 10th 2011

Performance indicators	Q_{sun}	Q_{coll}	Q_{stock}	Q_{desorb}	$Q_{abs/cond}$	Q_{evap}	η_{coll}	COP_{th}
	kWh	kWh	kWh	kWh	kWh	kWh	-	-
Experimental	96.6	48.3	19.3	26.2	42.2	16.8	0.50	0.64
Simulated	96.6	47.1	20.8	26.3	41.3	16.6	0.49	0.63
Relative differences	-	2%	8%	0%	2%	1%	2%	1%

4. Parametric sensitivity study

Since our model has been validated, it is possible to use it in order to study the system performances in different configurations. The model is used to quantify some improvements on collectors' field, storage tank, fan coil units and cooling tower. The reference configuration is the current experimental pilot. The behavioural changes caused by each studied parameter are compared with the reference configuration through performance indicators.

When analysing the experimental results, an undersized of the collectors' field has been observed. Therefore, we first test an increase of its area, either with only Viessmann technology or with Tecnisun technology. We compare the case of four additional Tecnisun collectors (6.24 m^2) with the case of 3 additional Viessmann collectors (6.33 m^2). Then, we propose to test a variation of the storage volume: increase, reduction and no storage cases are considered. Finally, we show the influence of the cooling tower and fan coilers, by modifying their efficiencies. We thus used a double and an half value for each of them.

The corresponding results are presented together in Figure 9. The addition of Viessmann collectors lead to a better improvement than the Tecnisun collectors, with respectively +43% and +33% of chilling production. In each case, the collectors' field is now well sized. Moreover, the energy stored at the end of the test is also found much higher than the current configuration in the two cases. When using variable hot storage tank, an increase of the volume corresponds logically to an increase in the stored energy but also to a decrease of the chilling production (20%). The opposite effect is observed when reducing the storage's volume. With no storage tank, a raw increase of the chilling production is obtained (60%). Eventually, the cooling tower efficiency has almost no impact (yet we may highlight here this device was over-sized in the reference test case). Concerning the fan coiler, a reduction of its efficiency leads to a decrease of the chilling production.

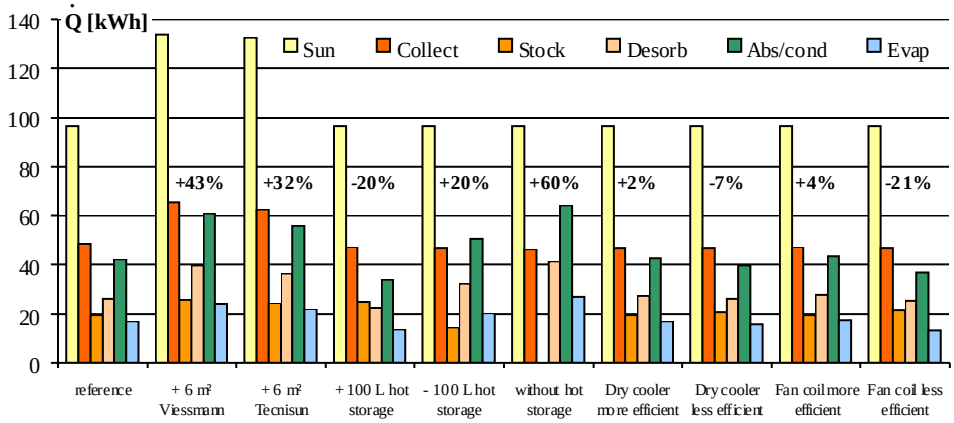

Fig. 9. Synthesis of the parametric sensitivity studies.

5. Conclusion and perspective

In this paper, we present a modelling tool for solar cooling plants. An exhaustive approach has been followed, considering each subsystem: the solar collectors' field, the hot storage tank, the cooling tower, the fan coiler units and the absorption chiller, and all pipelines that connect these components together.

First, each of them has been individually modelled and validated from experimental results obtained in our installation. They all led to conclusive results. Their coupling has been performed in order to develop a tool to assess the performance of an absorption solar cooling system. The simulation results are satisfactory, so a parameters sensitivity analysis was undertaken to identify optimization ways for the experimental installation.

Following the encouraging results obtained with the model, different perspectives were considered to complete the modelling tool of absorption solar cooling units. In the experimental and simulation studies of the installation, the working without hot storage tank has emerged as a powerful solution in sunny weather. The first works will be to study the influence of a regulation on the flow rate of the desorber loop in order to work at part load when the sun is less important and to avoid chiller shutdown with an inlet desorber temperature too low. Then, as it was observed that the performance decreased with the inlet desorber temperature, it was envisaged to study the coupling of a storage tank incorporating phase change materials. If the melting temperature of these materials is close to

the desorber nominal temperature, this storage would reduce its volume and probably increase the installation performance.

Acknowledgments

This work has been funded by the Aquitaine region and by the ADEME in an ANR Project ABCLIMSOL (PREBAT 2007) and ANR Project ORASOL (PREBAT 2006).

Nomenclature

T	temperature, K
P	pressure, Pa
UA	heat exchange characteristic factor, W/K
Q	heating power, W
COP_{th}	coefficient of performance,
m, d, c	mass flow rate of refrigerant, diluted and concentrated solution, kg/s
X	mass concentration in LiBr
Φ	total incident radiation, W/m²

Subscript/superscript

abs	absorber
cond	condenser
desorb	desorber
evap	evaporator
coll	collector
fan	fan coiler
dry	dry cooler
ext	external
int	interior
meas	measured
simul	simulated

References

[1] B. Aebischer, M. Jakob, G. Henderson, G. Catenazzi (2007). Impact of climate change on thermal comfort, heating and cooling energy demand in Europe. Proceedings ECEEE 2007 Summer Study, Saving Energy, Just do it! 4–9 June 2007, La Colle sur Loup, France. ISBN: 978-91-633-0899-4.

[2] Y. Fan, L. Luo, B. Souyri, Review of solar sorption refrigeration technologies: Development and applications, Renewable and Sustainable Energy Reviews 2007;11: 1758–1775.

[3] ADEME, les chiffres clés du bâtiment, énergie, environnement, éditions 2010, available at: < http://www2.ademe.fr/servlet/KBaseShow?sort=-1&cid=96&m=3&catid=12624> [accessed 01-15-2012].

[4] Lamp P. and Ziegler F., European research on solar-assisted air conditioning. International Journal of Refrigeration 1998;21: 89-99.

[5] Henning H.M, Solar air-conditioning and refrigeration - achievements and challenges. EuroSun 2010, International Conference on solar heating, cooling and buildings, Graz – Austria, 2010.

[6] Jakob U., Overview market development and potential for solar cooling with focus on the Mediterranean area. In proceedings of ESTEC conference, Marseille. November 2011.

[7] J. A. Duffie, W. A. Beckman, Solar engineering of thermal process, second editions, Wiley-Interscience Publication, ISBN-10: 0471698679, 1991.

[8] C. A. Cruickshank, S. J. Harrison, Heat loss characteristics for a typical solar domestic hot water storage, Energy and Buildings 2010;42: 1703-1710.

[9] N. Chatagnon, M. Bachmann, G. Anies, J. Castaing-Lasvignottes. Simulation of a domestic absorption chiller. Colloque Francophone sur l'énergie - environnement - economie et thermodynamique. COFRET'10, 5–7 mai 2010, Iaçi – Roumanie.

[10] G. Anies, N. Chatagnon, P. Stouffs, J. Castaing-Lasvignottes. Dynamic simulation of a domestic absorption chiller. International Congress of Refrigeration 2011, 23rd IIR International Congress of Refrigeration, August 21-26, 2011, Prague, Czech Republic.

[11] J. Patek, J. Klomfar, A computationally effective formulation of the thermodynamic properties of LiBr–H2O solutions from 273 to 500 K over full composition range, International Journal of Refrigeration 2006; 29: 566-578.

[12] J. Patek, J. Klomfar, A simple formulation for thermodynamic properties of steam from 273 to 523 K, explicit in temperature and pressure, international journal of refrigeration 2009; 32: 1123-1125.

[13] Jan F. Kreider, Handbook of heating, ventilation and air-conditioning, ISBN 0-8493-9584-4 (alk. paper), 2001.

The influence of operating parameters and occupancy rate of thermoelectric modules on the electricity generation

Camille Favarel[a], Jean-Pierre Bédécarrats[b], Tarik Kousksou[c] and Daniel Champier[d]

[a] Université de Pau et des Pays de l'Adour, LaTEP – EA 1932, Laboratoire de Thermique, Energétique et Procédés, ENSGTI, Rue Jules ferry, BP 7511, Pau, F-64075, France, camille.favarel@univ-pau.fr
*[b] Université de Pau et des Pays de l'Adour, LaTEP – EA 1932, ENSGTI, Rue Jules ferry, BP 7511, Pau, F-64075, France, jean-pierre.bedecarrats@univ-pau.fr, (**CA**)*
[c] Université de Pau et des Pays de l'Adour, Laboratoire des Sciences de l'Ingénieur Appliquées à la Mécanique et au Génie Electrique (SIAME), Hélioparc 2, avenue du Président Angot, 64053 Pau Cedex, France, tarik.kousksou@univ-pau.fr
[d] Université de Pau et des Pays de l'Adour, Laboratoire des Sciences de l'Ingénieur Appliquées à la Mécanique et au Génie Electrique (SIAME), Hélioparc 2, avenue du Président Angot, 64053 Pau Cedex, France, daniel.champier@univ-pau.fr

Abstract:
Thermoelectricity has attracted increasing attention as a "green" and flexible source of electricity able to meet a wide range of power requirements. Thermoelectric modules convert a portion of thermal power into electric power and only require to function the presence of a temperature gradient.
In addition to the improvement of the thermoelectric material and module, the analysis of thermoelectric systems is equally important in designing a high-performance of these ones. The main works consist in predicting the performance of thermoelectric generators with particular configuration of heat exchangers and in studying the effect of fluid flow rates, fluid properties and inlet temperatures on the power supplied by the system.
The electric power generated by thermoelectric modules depends obviously on the nature of the modules but also on heat transfers on both sides of these modules. So the place of the thermoelectric modules in the systems has an influence on the electricity generation.
The purpose of this work is to investigate the electric power extractable from a system equipped with thermoelectric modules and the influence of operating parameters on the electricity generation. A computer model has been developed to simulate the performances of the thermoelectric system. The influence of the occupancy rate of the thermoelectric couples along the system is studied in order to optimize the electrical power. The results obtained for modules made with Bi_2Te_3 from two different data sources and with slightly different thermoelectric properties are also presented in the study. The numerical model shows the importance of the repartition and of the choice of thermoelectric couples. It shows that for each thermoelectric fabrication there is an optimal occupancy rate which can be quite different.

Keywords:
Numerical simulation, Occupancy rate, Power generation, Thermoelectric generator.

1. Introduction

The increasing number of environmental restrictions as well as the growing problems of the availability of energy resources urge the energetic sector not only to develop its technologies but to use them more rationally.

Thermoelectric (TE) devices directly convert thermal to electrical power (Seebeck Effect) and the reverse, electrical to thermal power (Peltier Effect). The phenomena have been known for about 150 years but are anew studied and explored to meet the challenges that arise from these new environmental constraints [1].

Transportation and electricity are the two sectors where the demand for energy will increase the most and are also those that emit the most greenhouse gases.

It is for example the case of the aerospace industry which needs to change its methods of production and consumption of energy to reduce energy costs and reduce its environmental footprint. In addition of oil consumption, the electrical equipments which offer such benefits are now required on board involving additional power generation.

Another example is the case of electricity production in developing countries, where currently about 1.6 billion people lack access to electricity [2].

We focus in our studies on TE generators to produce electricity. Thermoelectricity can be a solution to supply electricity with a significant improvement of the efficiency of a system. Thermoelectric modules convert a portion of thermal power into electric power and only require to function the presence of a temperature gradient. So it is possible to retrieve a part of waste energy to produce electricity.

TE generators are well-known for their advantages such as high reliability, silence and low environmental impact and for their capability of utilizing amounts of waste heat as an energy source in a simple and easy manner. In these cases, TE generators become advantageous as compared to conventional energy technologies even if they have a low energy conversion efficiency of around 2-5% [1].

In a classical thermoelectric generator, a heat exchanger captures the heat from the hot source and transfers this heat to the thermoelectric elements while another heat exchanger evacuates heat with a cold source in order to have a significant temperature gradient between the two faces of the TE elements. Various parameters affect the efficiency of a thermoelectric generator.

The electric power generated by thermoelectric modules depends obviously on the properties of the modules but also on heat transfers on both sides of these modules. So the place of the thermoelectric modules in the systems has an influence on the electricity generation.

The goal of the presented work is to investigate the electric power extractable from a system equipped with thermoelectric modules and the influence of operating parameters on the electricity generation. To understand the factors influencing the TE generator efficiency, we have designed a heat exchanger with a typical configuration. A computer model has been developed to simulate the performances of the designed thermoelectric system under various use conditions.

The influence of the occupancy rate of the thermoelectric couples along the system is studied in order to optimize the electrical power. The results obtained for modules made with Bi_2Te_3 from different data sources and with slightly different thermoelectric properties are also presented in the study.

2. Model

The model has been already described in two of our previous papers [2, 3]. Only the main hypotheses and equations are here presented with a special adaptation to the new configuration. The configuration of the modelled exchanger was selected in order to study experimentally the feasibility of producing electricity with thermoelectric modules. It will be tested in following works.

2.1. Principle of modelling and assumptions

The studied thermoelectric generator, presented in Fig. 1, is mainly composed of a tubular heat exchanger. This exchanger is realized with a pipe of constant rectangular cross section. To increase the inner heat transfer area, fins are added connected to the primary surface. All the parts of the heat exchanger are made with 6063 Aluminium. Hot gas (air) circulates inside this tube.

The thermoelectric modules are placed on the external smooth surface of this tube fin exchanger. The modules are kept pressed against the surface through a second tubular heat exchanger but without fins in which a cold liquid circulates.

Several types of thermoelectric modules can be used.

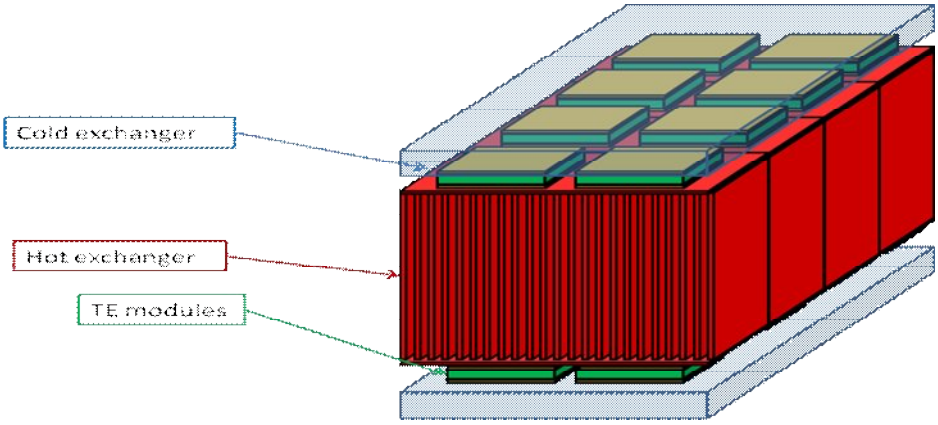

Fig. 1. Schematic diagram of the designed thermoelectric generator.

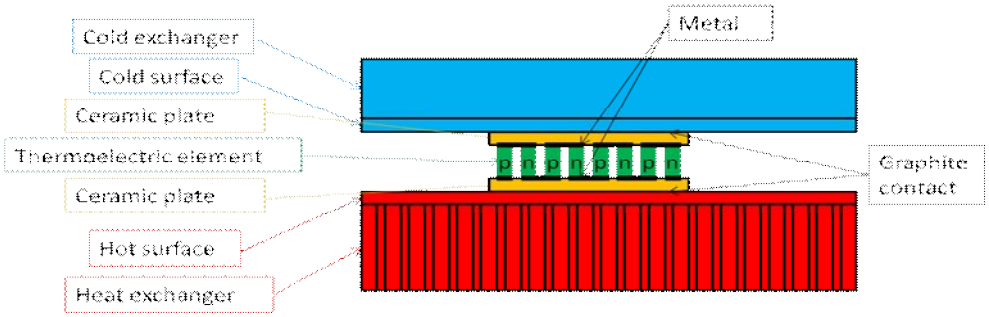

Fig. 2. Cross section of the TE module.

As already mentioned, the thermoelectric (TE) modules are sandwiched between the hot fluid and the cold fluid and they are electrically insulated by ceramic plates (see Fig. 2). A TE module consists of *n* thermocouples composed of two n and p doped semiconductors (Fig. 3b), two ceramic substrates and a graphite layer. The thermocouples are configured so that they are connected electrically in series, but thermally in parallel.

In order to simplify the physical model of the thermoelectric generator, the following assumptions were made:

- Only the steady state case is considered;
- Fluid flows are considered unidirectional;
- Hot and cold fluids flows are incompressible and Newtonian;
- The conduction along the flow direction is negligible;
- All the TE modules are composed by a single layer of p-n junctions as illustrated in Fig. 2;
- The electrical contact resistance between the p and n couples is assumed to be negligible;
- The material properties for the TE couples vary along the length of the exchanger with changes in temperature.

2.2. Heat transfers modelling

Based on these assumptions the energy balance equations at steady state for the hot fluid and the cold fluid are:

$$\rho_H c_{p,H} u_H \frac{\partial T_H}{\partial y} = \frac{-Q_H}{V_H} \qquad (1)$$

$$\rho_C c_{p,C} u_C \frac{\partial T_C}{\partial y} = \frac{Q_C}{V_C} \qquad (2)$$

Where ρ, C_p, u and T respectively represent the density, specific heat capacity, velocity and temperature of the fluid. V is the volume occupied by the fluid. The subscripts C and H correspond to the cold and hot fluid. Q_C is the heat flux transferred between the cold fluid and the TE modules and Q_H the heat flux transferred between the hot fluid and the modules. y corresponds to the position along the heat exchanger (Fig. 3a).

The heat exchanger is cut into four main surfaces where both the occupancy rate and the current of the TE couples are chosen constant. For better accuracy, each principal surface is cut into four secondary surfaces where the equations are solved (Fig. 3a).

The occupancy rate τ is defined for each main surface as the ratio of the area occupied by the TE modules on the area of the heat exchanger (WL/4).

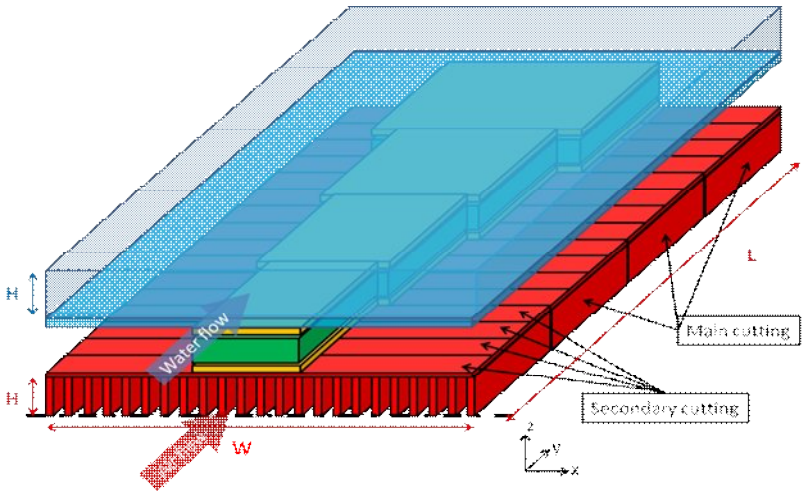

(a)

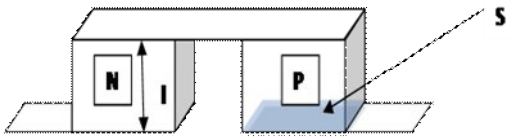

(b)

Fig. 3. (a) Schematic diagram of the global modeled thermoelectric generator (not in scale)

(b) Detailled geometry of a thermoelectric couple.

The geometric characteristics for the modelled exchanger (Fig. 3a) and the TE couples (Fig. 3b) are given in Table 1.

Table 1. Geometric characteristics (Fig. 3)

Symbole	Définition	Value
l	Length of a couple	$1.8\ 10^{-3}$ m
S	Surface of a couple	$(2.6\ 10^{-3})^2$ m²
H	Height	0.059 m
W	Width	33.136 x S m
L	Length	0.224 m

Six temperatures are calculated in each control volume (Fig. 4): the hot and cold fluids temperatures (T_H and T_C), the hot and cold wall surface temperature ($T_{H,w}$ and $T_{C,w}$) and the hot and cold side temperature of the couple ($T_{H,couple}$ and $T_{C,couple}$).

The thermal model through the control volume is given using the various thermal resistances as indicated in Fig. 5, and the associated fluxes.

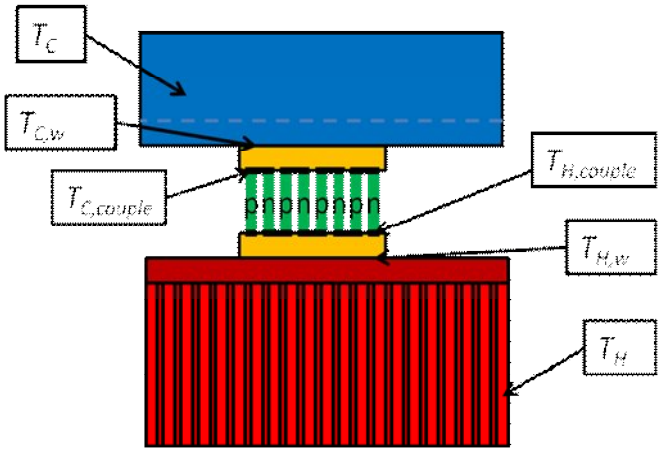

Fig. 4. Geometry of the thermoelectric generator.

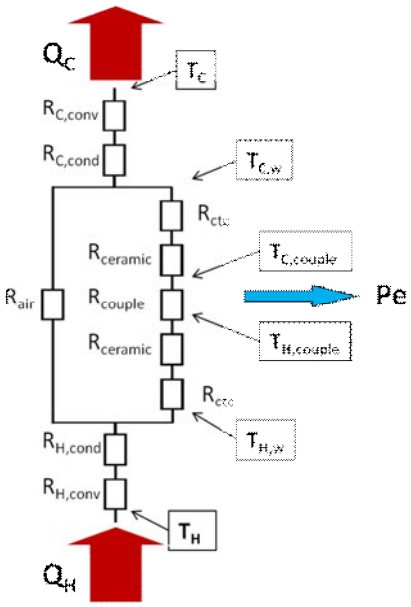

Fig. 5. Thermal resistances model of the thermoelectric generator.

$R_{H,conv}$ and $R_{C,conv}$ are the thermal convective resistances. $R_{H,cond}$ and $R_{C,cond}$ are the thermal conduction resistances of the exchanger. $R_{ceramic}$ is the resistance of the ceramic materials. R_{couple} is the thermal conduction resistance of the TE couples. A thermal contact resistance R_{ctc} exists between the ceramic layer and the heat exchanger material. A constructor datasheet [4], which takes into account the pressure, is used to calculate it.

In order to calculate the thermal convective resistances, the heat exchanger model implements empirical correlations for the hot side (air) and cold side (liquid water with 30% glycol content) convective heat transfers. The different correlations depend on the flow regime (laminar, transient or turbulent). The selected correlations are valid for fully developed pipe flow.

When the Reynolds number $Re < 2300$, the flow is laminar and the Shah and London correlation [5] is used to predict the mean Nusselt number Nu. For the hot fluid flow through the inner tube, $Nu = 7.5$ and for the cold fluid, $Nu = 4.363$.

The Gnielinski correlation [6] is used in the range $2300 \leq Re \leq 5\times10^6$ (transient and turbulent):

$$Nu = \frac{\left(\frac{f}{2}\right)(Re\text{-}1000)\,Pr}{\left[1 + 12.7\left(\frac{f}{2}\right)^{0.5}\left(Pr^{0.66} - 1\right)\right]} \qquad (3)$$

With: $$f = \frac{1}{\left[1.58 \times \ln(Re) - 3.28\right]^2} \qquad (4)$$

the fanning friction factor and Pr the Prandtl number is in the range $0.5 \leq Pr \leq 10^6$.

Because of the rectangular cross section and the presence of fins, we use in each correlation the hydraulic diameter.

The pressure drop of these exchangers is low and is neglected in this work.

2.3. Thermoelectric modelling

The one dimensional model commonly described in literature (1-D heat flow) of a typical TE module made of n thermocouples [1] is used.

These equations are obtained from the study of a single n- or p-type element assuming that all connections between the elements are perfect: no electrical and thermal resistance.

We assume that the TE generator is well insulated (no heat exchange with the ambient).

A simple energy balance around the TE modules yields the following equations for the hot side heat flux into the TEs, the cold side heat flux out of the TEs and the electric power:

$$Q_H = n\left[\alpha I T_{H,couple} - \frac{R_{elec} I^2}{2} - \frac{\left(T_{C,couple} - T_{H,couple}\right)}{R_{couple}}\right] \quad (5)$$

$$Q_C = n\left[\alpha I T_{C,couple} + \frac{R_{elec} I^2}{2} - \frac{\left(T_{C,couple} - T_{H,couple}\right)}{R_{couple}}\right] \quad (6)$$

$$P_e = Q_H - Q_C = n\alpha\left[I(T_{H,couple} - T_{C,couple}) - R_{elec} I^2\right] \quad (7)$$

where I is the current flow through a single thermocouple, α, R_{elec} are respectively, the Seebeck coefficient and electrical resistance of a single thermocouple. In each main surface, the TE couples are wired in serial so they have the same current. This current is the average current optimum of each secondary surface. The next formula is used to calculate the optimum currents:

$$I_{opt} = \frac{\alpha\left(T_{H,couple} - T_{C,couple}\right)}{2R_{elec}} \quad (8)$$

Using the thermal resistance model (Fig. 5), we are able to determine the different temperatures. A Newton Raphson method is used due to the dependence on temperature of the different parameters.

2.4. Optimization algorithm

The optimization problem consists in identifying the number and the position of TE modules that will maximize the electrical output power in the case of a fixed geometry of heat exchanger. The retained optimization strategy is a genetic algorithm (GA) which is a method of stochastic optimization inspired by the biological evolution [7]. The selected genetic algorithm uses real numbers and tournament based selection with elitism.

The algorithm parameters are presented in Table 2:

Table 2. Main parameters used by the GA

Size of the population = 100
Number of generations = 80
Crossover rate =0.5
Mutation rate =0.07

The used crossover operation is the blend crossover operator (BLX-α) and the performed mutation is uniform over the entire domain.

The electrical output power is calculated for each individual in the population. A tournament selection is made: 50% of the population is selected by a criterion corresponding to the best electrical output power and we crossover them to make the other 50% of the next generation. After that the mutation is performed.

3. Results

In the following numerical simulation, the thermoelectric properties of two different types of Bi_2Te_3 TE modules are used [1, 8].

3.1. Hot temperature and air flow parametric analysis

The first optimization that has been performed is the maximization of the electrical output power for different conditions (air flow rate - hot inlet temperature) and for the two different Bi_2Te_3 modules. The cold inlet temperature was set to -10°C and the flow rate to 10 m^3h^{-1}.

Fig. 6 and Fig. 7 present the optimized occupancy rate of the different parts of the exchanger for the two types of TE modules for different inlet temperatures of the hot fluid $T_{H,in}$. τ_1 corresponds to the first main surface at the inlet of the heat exhanger and τ_4 is the last one at the outlet.

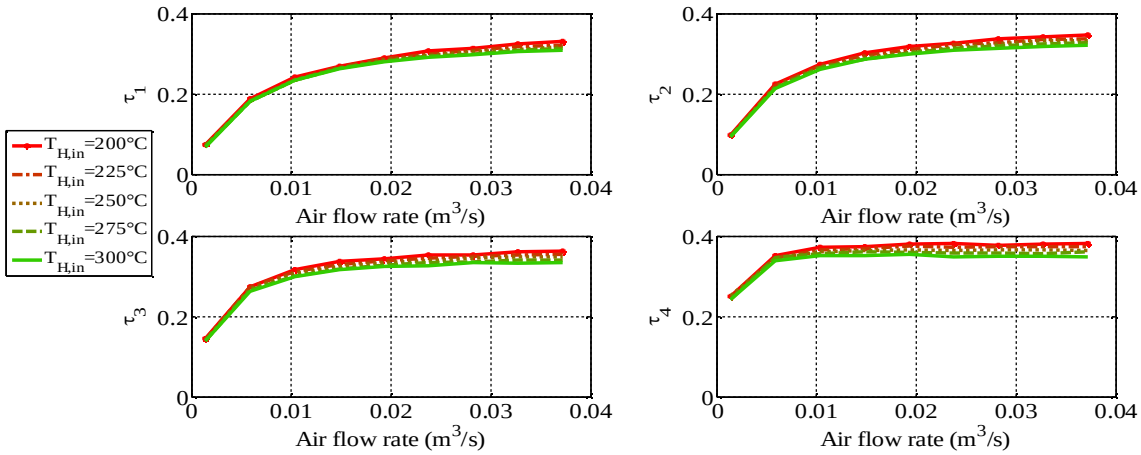

Fig. 6. Optimized occupancy rate for the 4 parts of the exchanger with Bi_2Te_3 [1].

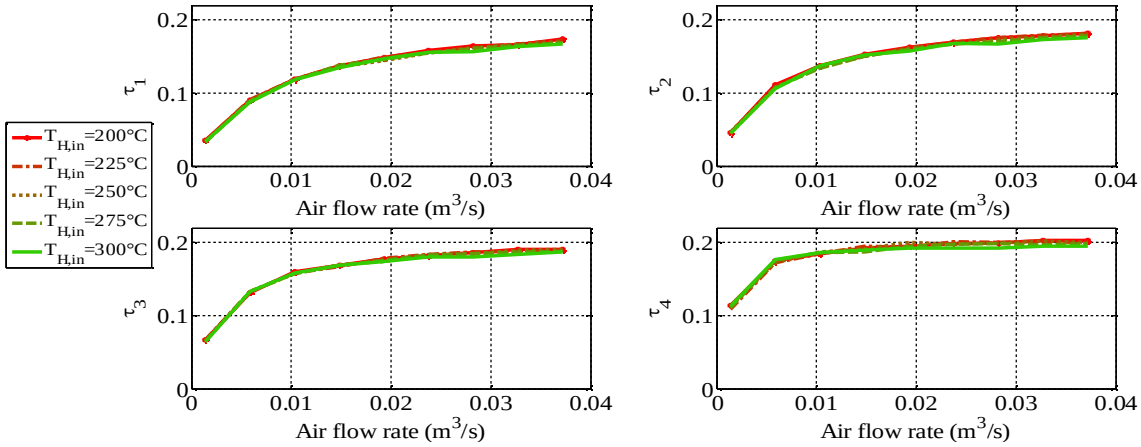

Fig. 7. Optimized occupancy rate for the 4 parts of the exchanger with Bi_2Te_3 [8].

First of all, it appears that the inlet temperature of the hot fluid has a slight influence on the occupancy rate. Moreover, when the heat flow becomes high because of the increase in airflow rate the occupancy rate no longer changes much. For example for Bi_2Te_3 [1], each principal surface seems to converge with a value of the occupancy rate between 30 to 40%. For Bi_2Te_3 of Taihuaxing [8], this value converges between 15 to 20%.

In the two cases, the occupancy rate increases in the direction of the flow rate. To have a higher total electric power, the number of TE modules must be more important at the outlet than at the inlet of the heat exchanger.

These two examples show that for each thermoelectric fabrication there is an optimal occupancy rate which can be quite different and the use of a model seems very pertinent.

Fig. 8 shows the ratio between the optimized electric output power and the output power when the TE modules cover all the area of the exchanger (occupancy rate of 100 %). The results show that the choice of an occupancy rate of 100% is awkward especially for low heat flows. We lose an average of slightly more than 50% of the available electrical output power and we can even lose up to 85% for some.

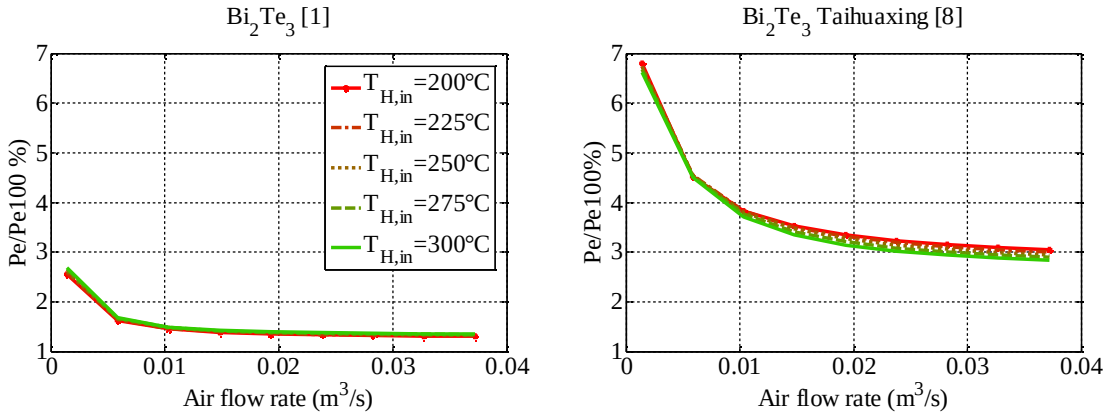

Fig. 8. Increase of the ouput power compared to output power with an occupancy rate of 100 %.

Moreover a maximum occupancy rate of 100% brings the cost to increase because of the number of TE modules.

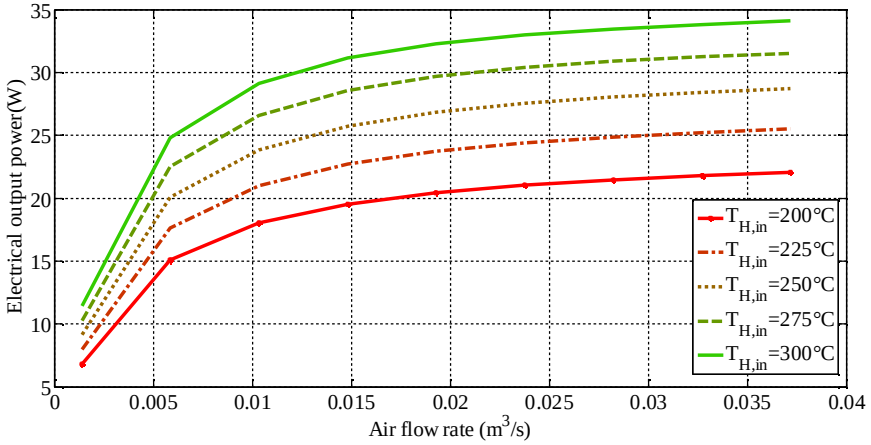

Fig. 9. Optimized electric power Bi_2Te_3 [1] for various inlet temperature.

A typical curve of output power versus the air flow rate is shown in Fig. 9.

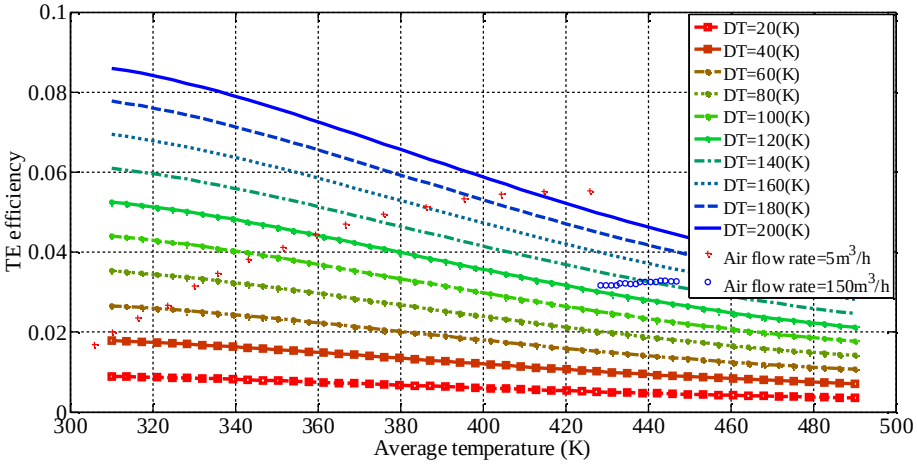

Fig. 10. TE modules efficiency for various temperatures.

For each air flow rate, and $T_{H,in}$, we optimize the occupancy rate and plot the electrical power of the best solution. The output power increases with the air flow rate but evolves slowly after a certain value. Considering the fact that an increase in flow rate of hot air improves the exchange increasing the convective heat transfer coefficient, one wonders why the electrical output power increases so

little. To explain that, it is important to know the characteristic of the Bi_2Te_3 modules and in particular the efficiency versus temperature given in Fig. 10.
The efficiency increases with the temperature difference but decreases with the increase in the average temperature of the TE module. When the air flow rate increases, the heat transfer coefficient increases raising the average temperature of the TE module and bringing down the efficiency.

In the case of a high air flow rate (150 m^3/h), all the temperatures do not change much along the exchanger and therefore T_{avg} and the difference of temperature are almost constant. However in the case of a low flow rate (5 m^3/h), the hot side temperatures vary greatly between the inlet and outlet of the exchanger. We have in this case a greater difference of temperature at the inlet but this difference decreases a lot along this exchanger and a lower average temperature which also decreases. The operating points of the two flows considered were placed on the graph of performance and illustrate these explanations.

The results of the output power versus the air flow rate are shown in Fig. 11 for the other type of modules. The electric power is higher than those obtained in the previous case. These TE modules have a higher ZT value (Fig. 12) so a higher efficiency.

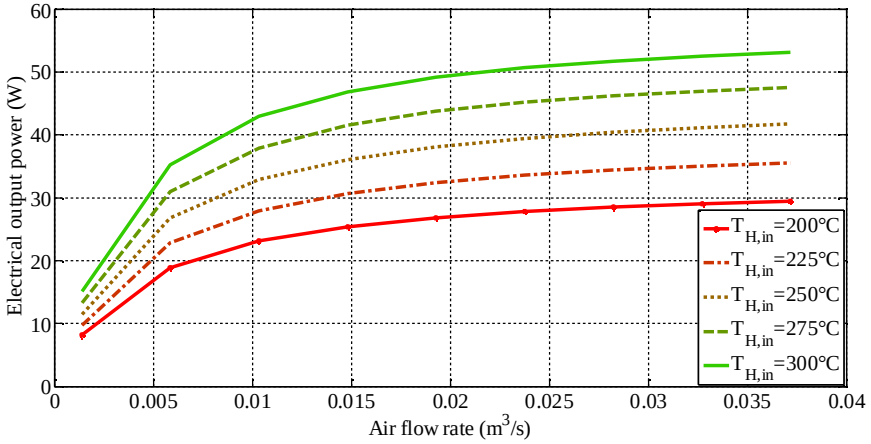

Fig.11. Optimized electric power Bi_2Te_3 Taihuaxing[8] for various temperature.

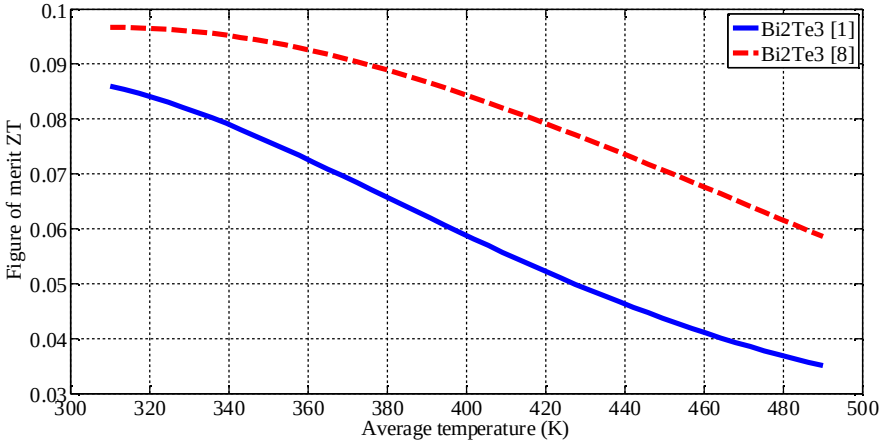

Fig.12. Figure of merit ZT for different Bi_2Te_3 [1],[8].

3.2. Geometric analysis

The influence of the area of the heat exchanger is now studied. The variation of the area (W x L) is made using the W geometric parameter (Fig. 3a). The maximum output power is evaluated choosing the optimized occupancy rate for each exchange surfaces. For this analysis, we set the air flow rate at 5 m^3/h and the inlet temperature of the hot fluid at 250°C. These results are presented in Fig. 13.

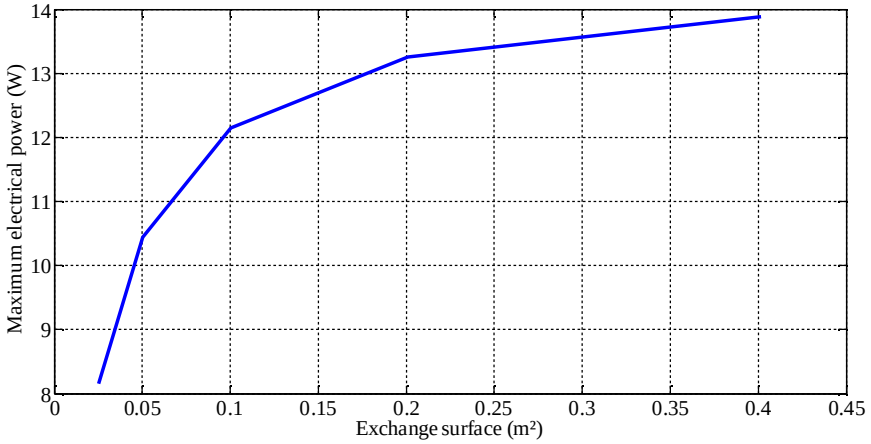

Fig. 13. Evolution of the maximum electrical output power with the exchange surface.

At a fixed air flow rate and hot inlet temperature, the maximum electrical output power increases with the exchange area but does not grow quickly when it exceeds a certain area. If one connects this area to the exchanger size or weight so it will show an optimum in terms of power density or power per mass unit.

The influence on the occupancy rate is shown in Fig. 14.

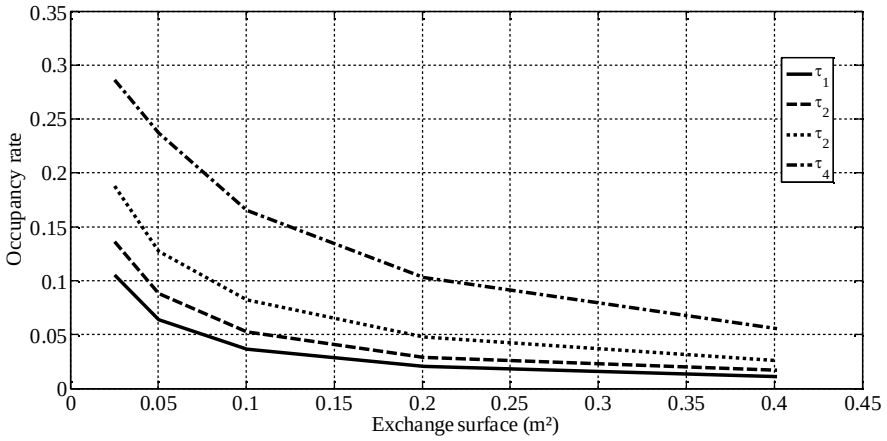

Fig. 14. Evolution of the different occupancies rate with the exchange surface.

When the exchange area increases, the occupancy rates decrease but as Fig. 15 shows, the number of modules increases. The more extensive the area is, the less the number of couple increases.

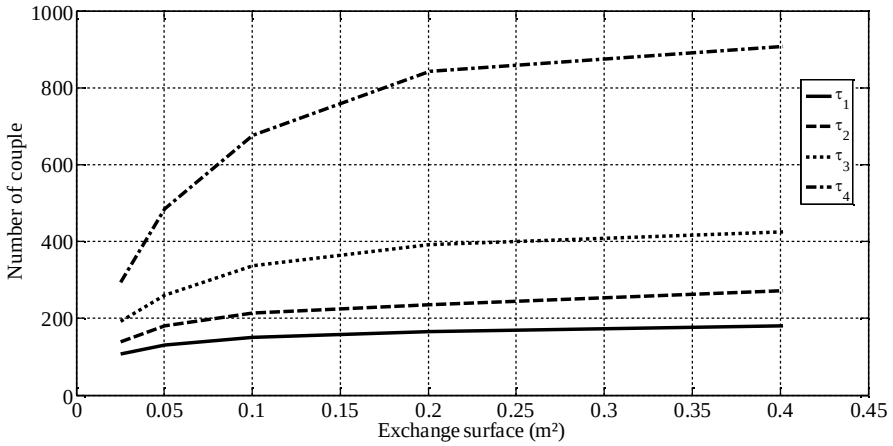

Fig. 15. Evolution of the different number of couples with the exchange area.

4. Conclusion

Current needs for fuel efficient, low emission, power sources for various applications have brought forth a renewed interest in the thermoelectric technology.

The purpose of this work is to investigate numerically the influence of operating parameters on the electricity generation with TE modules. The computer model is based on one-dimensional differential equations representing conservation equations. These equations are restructured and linked to the formulations of thermoelectric modules.

The influence of the occupancy rate of the thermoelectric couples along the system is studied in order to optimize the electrical power. The results obtained for Bi_2Te_3 modules from two different data sources and with slightly different thermoelectric properties show the importance of the repartition. It is found that the output electrical power is sensitive to the number and the place of TE modules on the surface of the heat exchanger.

It is necessary to improve the occupation of the modules because completely cover the heat exchanger surface with TE modules is not the better solution.

These two selected types of modules show that for each thermoelectric fabrication there is an optimal occupancy rate which can be quite different.

So the model which can be applied to various applications is an interesting tool to improve the electric power of TE generators.

Finally, it is important to emphasize that all calculations performed by simulation need an experimental approach to fully validate the results. We already have built the designed TE generator and we project now to carry out experimental studies.

Acknowledgments

This work was carried out within the framework of a project whose objective is to study the feasibility of producing electricity with thermoelectric modules in various applications. It is funded in part by the Regional Council of Aquitaine and the General Council of Aquitaine (France).

Nomenclature

c	specific heat, J/(kg K)
h	heat transfer coefficient, W/(m^2 K)
I	courant (A)
$\dot{m}$	mass flow rate, (kg/s)
n	number of thermocouples

Nu Nusselt number
Pr Prandtl number
P_e power output, (W)
Q the rate of the heat flow, (W)
R_{elec} electrical resistance, (Ω)
Re Reynolds number
R thermal resistance, (K/W)
S area, (m^2)
T température, (K)
u velocity, (m/s)
V volume, (m^3)
y coordinate, m

Greek symbols

α Seebeck coefficient (V/K)
ρ density, (kg/m^3)

Subscripts

avg average
cond conduction
conv convection
ctc contact
C cold fluid
H hot fluid
couple TE couple
w wall

References

[1] Rowe D.M., Thermoelectrics handbook Macro to Nano. CRC Press. 2006

[2] Champier D., Bédécarrats J.P., Kousksou T., Rivaletto M., Strub F., Pignolet P., Study of a TE (thermoelectric) generator incorporated in a multifunction wood stove, Energy 2011; 36:1518-1526.

[3] Kousksou T., Bédécarrats J.P., Champier D., Pignolet P., Brillet C., Numerical study of thermoelectric power generation for an helicopter conical nozzle, Journal of Power Sources 2011; 196:4026-4032.

[4] Technical Data Sheet: eGRAF® HITHERM™ Products – Available at:< http://graftechaet.com/eGRAF/eGRAF-Technical-Documents.aspx > [accessed 30.1.2012].

[5] Rohsenow W.M, Hartnett J.P, Cho Y.I., Handbook of heat transfer, Third Edition, McGraw-Hill, 1998.

[6] Gnielinski, V., New equations for heat and mass transfer in turbulent pipe and channel flow, International Chemical Engineering 1976; 16(2):359-368.

[7] Gosselin L, Tye-Gingras M, Mathieu-Potvin F. Review of genetic algorithms utilization in heat transfer problems. Int J Heat Mass Transfer 2009; 52:2169–88.

[8] Technical Data Sheet: Thermonamic Products – Available at:<http://www.thermonamic.com/pro_view.asp?id=794> [accessed 1.02.2012].

Thermodynamic and Heat Transfer Analysis of Rice Straw Co-firing in a Brazilian Pulverised Coal Boiler

Raphael Miyake [a], Alvaro Restrepo [a], Fábio Kleveston [a], Edson Bazzo [a], Marcelo Bzuneck [b]

[a] Federal University of Santa Catarina, Florianópolis, Brazil
[b] Tractebel Energia S.A., Capivari de Baixo, Brazil

Abstract:

Biomass co-firing is a near term, low cost and low risk alternative for renewable energy production in a coal power plant . A Brazilian experience was proposed in one unit of the Jorge Lacerda thermoelectric complex. The rice straw is used as a biomass option in a 50 MW power plant with up to 10% (thermal basis). This paper presents an thermodynamic and heat transfer analysis in order to evaluate the main boiler changes with the rice straw co-firing. The modeling is based on the boiler equipment characteristics and operational data obtained with the coal burning. The thermodynamic model consists on the mass, species and energy balances of each boiler component (furnace, superheaters, economizer and air heater). A semi-empirical method is used for the furnace heat transfer problem. The modeling is validated with additional coal burning measurements. The rice straw co-firing is simulated, describing the changes in the boiler thermal behavior. The results showed a reduction up to 12% in CO2 and SO2 fossilfuels emissions and an increase up to 5% in gas temperature. The rice straw presents a great potential for co-firing in existing coal-fired boilers. However, there are many technical issues that may be studied for their sustainable use in power generation..

Keywords:
Thermoelectric power plant, Boiler, Co-firing, Coal, Biomass, thermal system modeling.

1. Introduction

The biomass co-firing is the use of a supplementary fuel in a boiler in additional to the primary fuel that it was originally designed. This enables the use of biomass in a existent coal-fired power plant, reducing the required investment in biomass thermal generation [1].

The risks of biomass co-firing are related to the boiler changes caused by the use of a different fuel. Interference in the burners and emission control equipment may occur, reducing the power plant availability. Furthermore, ash deposition and corrosion rates may increase, resulting in higher forced outage rate and maintenance costs [2].

The impact of co-firing in the boiler performance is directly related to the biomass fraction, its moisture at the entrance of the burner and the biomass type used [2]. Biomass has typically lower calorific value than coal, increasing the fuel consumption to maintain the boiler capacity. Cases studies present different results for changes in boiler performance with co-firing, depending on the fuel combination and boiler capacity, as shown in [3], [4], [5] and [6].

More than 288 biomass co-firing projects have been performed, including 50 MW to 700 MW power plants [7]. These experiences have replaced about 3.5 million tons of coal, avoiding the emission of more than 10 Mtons of CO_2 equivalent. In addition, the estimated technical and financial potential for coal replacement is about 30 times larger, as shown in [7]. The main biomass and coal combinations are already evaluated, resulting in different solutions for boiler equipment and biomass transport/processing system.

A pilot test facility is now proposed by Tractebel Energia and Federal University of Santa Catarina (UFSC) for co-firing 10% of rice straw (thermal basis). The project is supported by the Brazilian

Electricity Agency (ANEEL) and it will applied in one unit of the Jorge Lacerda thermoelectric complex, one of the largest thermoelectric power plant in Latin America.

The rice straw option occurs due to the 25,000 ha of rice cultivation in the surroundings of the power plant. In the 2010/2011 harvest, the rice straw production was about 100 thousand tons, ensuring the required provision for this experience. The rice straw is a fibrous material, obtained from the residue of rice harvesting. Nowadays, the rice straw is incorporated to the soil and than, the flooded land enhances the methane formation in the soil. Thus, the rice straw extraction is an option for the reduction of this environmental impact. However, the extraction time, the soil conditions, the different size of the rice straw bales and its low cost hinder the economical and technical viability of the rice straw extraction [8]. Operational conditions were estimated for the rice straw co-firing up to 10%, including air requirements, flue gas composition and boiler efficiency.

The aim of this work is simulate the boiler thermal behavior with the rice straw co-firing. Thus, a thermodynamic and heat transfer analysis is proposed for the retrofitted boiler. The boiler equipments were analyzed in the site, to include the operational boiler configuration in the modeling. Measurements were carried out with coal burning and the data were used as input parameters and in the modeling validation.

Different approaches have been proposed for utility boilers modeling. Stultz and Kitto [9] defines that the two main approaches are: (i) evaluate only the thermal behavior of the system, using thermodynamics, combustion and heat transfer models; (ii) evaluate the fundamental physics of the system, using computational fluid dynamics and chemical reaction models to determine the system behavior.

The first one describes the thermal and heat transfer behavior, using the system characteristics to determine temperature fields and heat losses. These models use flow measures and also semi-empirical and fundamental correlations to analyze the thermal and hydrodynamic boiler behavior. Results are obtained without significantly computational efforts. However, these results are limited to components where the existent correlations are appropriate. Samples of this approach can be found in [10], [11] and [12], [13]. The second type uses fluid dynamics models to simulate the details of the flows inside the boiler. The heat exchangers are modeled in each detail, resulting in the temperature and velocity flow fields and their respective variations. However, this type of simulation has a high complexity level and it can demand high computational requirements [9]. Both approaches have benefits and limitations. The proper use of each one is determined by the objectives of the simulation, the details required by the problem and the available information. In this work, the first approach was used due to the boiler alterations with rice straw co-firing are well defined by this type of modeling.

2. Materials and methods

2.1. Boiler description

A coal-fired boiler was considered for retrofitting into a co-firing pilot plant. The boiler operates in a 50 MWe power plant (UTLA1) located in Capivari de Baixo- SC and it is operated by Tractebel Energia. In operation since 1965, the pulverised coal-fired boiler was designed by MAN. This boiler has a dry bottom radiant furnace and uses balanced draft, with a forced draft air fan at the boiler inlet and an induced draft fan near to the boiler outlet. It is equipped with 16 burners distributed in two rows on an inclined plan, down fired, from which they are fed by 4 coal ball mills. The boiler has one drum, two superheaters and one economizer, without reheater. Two Ljungström air heater are placed in the end of the convection section, fed by two forced fans. Two electrostatic precipitator are used for the flue gas cleaning. The main coal supply is provided by the Southern Santa Catarina's mines, with an approximate consumption of 0.77 t/MWe. The furnace walls has an exchange area of 997 m^2, volume of 784 m^3 and height of 22.5 m between the base of the furnace to their exit plane. Only 12 burners were considered as in the boiler nominal operation.

The furnace pressure was considered equal to 1 bar. The heat exchangers characteristics are shown in Table 1.

Table 1: Heat exchangers characteristics.

	SH2	SH1B	SH1A	ECOA	ECOB
d_i [m]	0.0282	0.04	0.0289	0.0289	0.0289
d_e [m]	0.0318	0.0445	0.0318	0.0318	0.0318
d_h [m]	0.0559	0.0445	0.0318	0.0318	0.0318
$A_i \times 10^4 [m^2]$	6.24	12.6	6.57	6.57	6.57
A_e $[m^2]$	271.3	603.7	529.2	1,189	1,189
l_t [m]	2,715	2,159	5,297	11,902	11.902
n	207	540	216	108	108
s_1	0.354	0.2	0.12	0.1	0.1
s_2	0.296	0.132	0.066	0.128	0.128
s_3	0	0	0	0.066	0.066

2.2. Experimental procedure

The experimental procedure used the ASME PTC 4-2008 [14] to collect the boiler operational data. The data were obtained for 5 hours in 40 MW condition. For any measurement routine, the boiler must operated at steady state and chemical/thermal equilibrium. The data were obtained by the plant supervisor computer system, without specific interference for this procedure. The frequency of observation was 12 s, with a total of 1500 measurements. The fuel analysis was made by Fuller [15]. The procedure for the measurement uncertainty calculation was based on the method described in ASME PTC 4-2008 [14]. The values used in the modeling are shown in table 2 and 3.

Table 2: The boiler main operational data

Superheated steam temperature in SH2 outlet	500±3	°C
Superheated steam pressure in SH2 outlet	88.5±0.6	bar
Atemperation mass flow	4.8±0.3	t/h
Superheated steam mass flow in SH2 outlet	175±10	t/h
Superheated steam temperature in SH1 outlet	430±3	°C
Drum pressure	93.2±0.6	°C
Feedwater pressure	96.4±0.7	bar
Feedwater temperature	203±1	°C
Secondary air temperature	325±2	°C
Primary air temperature	105.0±0.7	°C
Air mass flow in AH	80709±4870	m^3N/h
Air inlet temperature in AH	29±1	°C
Excess air	1.1	-

2.3. Thermodynamic model

The thermodynamic analysis includes a stoichiometric combustion model and the mass and energy conservation equation for each component. The combustion process was considered as the chemical union of a fuel and the oxygen from the air in a controlled manner to produce heat in the performance evaluation and design of utility boilers, as shown in [9]. The energy balance method

was also applied using only the heat losses along the boiler. The modeling equations were based on the demonstrations showed in [16], [17], [18] and [14]. The boiler efficiency was calculated by

$$\eta_b = \left[1 - \frac{\left(\dot{Q}_l - \dot{Q}_{cd}\right)}{\dot{Q}_{in}}\right] \times 100 = \left(1 - \sum L + \sum C\right) \times 100. \quad (1)$$

where

$$\dot{Q}_{in} = \dot{m}_{coal} LHV_{coal} + \dot{m}_{straw} LHV_{straw}; \quad (2)$$

and

$$\sum L = L_{fg} + L_{unb} + L_{rc} + L_{ash}. \quad (3)$$

The heat loss in the flue gas is a sensible heat loss to the environment. This temperature must guarantee that the tube temperature will be higher then the sulfur dew point temperature, avoiding the condensation of sulphur compounds that can corrode elements of low temperature. The dimensionless term L_{fg} was defined by the expression

$$L_{fg} = \frac{\dot{Q}_{fg}}{\dot{m}_{fg} LHV} \cdot 100 = \frac{m_{fg} \bar{c}_{p,fg} \left(T_{fg} - T_{ref}\right)}{LHV} \times 100. \quad (4)$$

Table 3: Fuel analysis [15].

Proximate analysis [%]		
	Brazilian coal	Rice straw
Fixed carbon	38.71 ±0.57	13.8 ± 0.6
Moisture	0.3± 0.07	7.58±0.04
Ash content	41.89±0.6	12.88±0.69
Volatile matter	19.10±0.07	65.70±0.35
Ultimate analysis [%]		
Carbon	46.15±1.36	39.00±0.09
Hydrogen	3.01±0.70	5.33±0.16
Sulphur	1.17±0.13	0.20±0.16
Oxygen	6.64±1.39	34.21±0.20
Nitrogen	0.82±0.04	0.71±0.05
Heating value [kJ/kg]		
HHV	17,775	14,784
LHV	17,162	13,540
Air fuel ratio [kg/kg]		
$(A/F)_s$	5.673	4.684

The loss due to the unburned carbon in residue is related to the fuel burned and the firing system and it was calculated by the expression

$$L_{unb} = \left(\frac{33.830 C_{unb}}{LHV}\right) \times 100. \quad (5)$$

The loss due to the surface radiation and convection was indirectly determined by the boiler average surface conditions and the ambient conditions near it, described by [14] as

$$L_{rc} = \frac{\dot{Q}_{rc}}{\dot{m}_{cb} LHV}; \quad (6)$$

where

$$\dot{Q}_{rc} = (h_r + h_{cv}) A_{sf} (\overline{T}_{sf} - \overline{T}_{ref}); \quad (7)$$

and

$$h_r = 2{,}93 \times 10^{-4} \{0{,}847 + (2{,}367 \times 10^{-3}) \Delta\overline{T}_{sf} + (2{,}94 \times 10^{-6}) \Delta\overline{T}_{sf}^{2} + (1{,}37 \times 10^{-9}) \Delta\overline{T}_{sf}^{3}\}; \quad (8)$$

Equation (8) used the ambient temperature at 25_C and emissivity of 0.8, corresponding to a dirty and oxidized surface. This correlation has considerable uncertainties. As this portion of the loss does not exceed 0.5%, these uncertainties had an insignificant effect in the efficiency overall calculation. For the convection coefficient on the surface, the highest value calculated among the correlations shown in (9) was used.

$$h_{cv} = 2{,}93 \times 10^{-4} 0{,}2 (\overline{T}_{sf} - \overline{T}_{ref})^{0{,}33} \quad \text{ou} \quad h_{cv} = 2{,}93 \times 10^{-4} 0{,}35 (\bar{V}_{ar})^{0.8} \quad (9)$$

Finally, the losses to ashes occur by the loss of sensible heat to the environment and were calculated by

$$L_{ash} = \frac{m_{ash}[(1-\lambda) h_{ash,f} + \lambda h_{ash,b}]}{LHV}; \quad (10)$$

where the enthalpy of fly ash and bottom ash are calculated as shown in [14].

The total credits were calculated based on the auxiliary equipments power and it was equal to 375 kW.

2.4. Heat transfer model

The heat transfer analysis included semi-empirical models for the solution of the radiation and convection heat transfer problem. In the heat exchangers, the ε - NTU method was used to define the heat transfer parameters changes in co-firing operation. Three different methods were used for the furnace exit temperature calculation: an URSS normative method, a method proposed by Strauss [19] and the Hudson-Orrok method.

An URSS normative method was used in the modelling. This method was widely used for oil and coal furnaces, obtaining compatible results to several experimental data as described in detail by Blokh [20]. The method relates the fuel composition, ash characteristics and flue gas and combustion air thermophysical properties. The effective emissivity is the ratio of the incident hemispherical radiation heat flux on the water wall to the hemispherical emissive power of a black body. In this method, the participant medium was considered as a grey body, defining an average value of emissivity for all wavelengths. This was calculated by

$$\varepsilon_f = \frac{\varepsilon_{fl}}{\varepsilon_{fl} + (1 - \varepsilon_{fl}) \psi_{ww}}; \quad (11)$$

where

$$\varepsilon_{fl} = 1 - e^{-\tau_{fl}}; \quad (12)$$

and

$$\tau_{fl} = \alpha_f PE. \quad (13)$$

The effective absorptivity in the furnace depends on the medium absorptivity, composed by the flue gas, char particles and fly ash. Correlations for the experimental absorption coefficients were proposed by Kakaç [18] and expressed as

$$\alpha_f = \alpha_{RO_2} v_{RO_2} + \alpha_{ash}\mu_{ash} + \alpha_{char} x_1 x_2. \quad (14)$$

Where

$$\alpha_{RO_2} = 10\left[\frac{0,78 + 1,6v_{H_2O}}{(10PEv_{RO_2})^{1/2}} - 0,1\right]\left(1 - 0,37\frac{T_{f,e}}{1000}\right); \quad (15)$$

$$\alpha_{ash} = \frac{5990}{(T_{f,e}^2 d_{ash}^2)^{1/3}}; \quad (16)$$

$$\alpha_{char} = 1; \quad (17)$$

Based on experimental data, Blokh [20] shows that the dimensionless temperature ($\theta_f = T_{f;s} / T_{ad}$) is a generalized simple function of the nondimencional group called furnace parameter, expressed as

$$\Pi = \frac{1}{\varepsilon_f}\frac{1}{\psi_{ww}}Bo; \quad (18)$$

This factor relates the energy of the furnace flue gas with its radiation heat transfer rate. The Boltzmann number relates the maximum energy available in the flue gas with to the radiated heat to a black body. It was defined by

$$Bo = \frac{\dot{m}_{fg}\bar{c}_{p,fg}}{\sigma T_{ad}^3 A_{ww}}. \quad (19)$$

Finally, the furnace exit temperature was calculated by

$$\frac{T_{ad} - T_{f,e}}{T_{f,e}} = \frac{M}{\Pi^{0,6}}; \quad (20)$$

where M is an empirical coefficient related to the type of fuel (M = 0.56 – 0.5X for bituminous coal with low volatile and high ash content), where *X* is the height of the highest temperature inside the furnace, defined by

$$X = X_b n / X_f - \Delta X; \quad (21)$$

The water wall thermal efficiency was expressed as

$$\psi_{ww} = \chi\zeta; \quad (22)$$

where χ is an experimental constant related to the slagging (χ = 0.35 – 0.55, for furnaces with coal burners) and ζ is the angular coefficient that relates the dimensions and position of the water wall tubes inside the furnace [18]. In this work, the angular coefficient, ζ was equal to 0.99, and the water wall slagging coefficient, χ , was equal to 0.55, the highest value indicated in the literature. Dubovsky [21, 20] by experimental data determines a correction parameter for Eq. 20) to take account the dependence of the heat transfer rate on the nonuniformity of the flame temperature, expressed by

$$\frac{T_{ad} - T_{fg,f}}{T_{ad}} = 0,96M\left(\frac{1530}{T_{ad}}\right)^{1,2}\left(\frac{1}{\Pi}\right)^{0,6}; \quad (23)$$

Blokh [20] compares this model with experimental data obtained from different boilers with different capacities, burning oil and coal. The results are satisfactory for both cases where the maximum temperature difference between the model and experimental data was about 30°C. Another method for the fumace exit temperature calculation was presented by Strauss [19]. The furnace temperature field was defined as

$$T_{fg} = \sqrt{T_{ad}T_{f,e}}. \quad (24)$$

The method assumes that all heat is transfer by radiation, providing the following furnace temperature definition:

$$\left(\frac{T_{f,e}}{T_{ad}}\right)^2 + Ko\left(\frac{T_{f,e}}{T_{ad}}\right) = \left(\frac{T_{ww}}{T_{ad}}\right)^4 + Ko; \quad (25)$$

where

$$Ko = \frac{\dot{m}_{fg}\bar{c}_{p,fg}}{\beta\varepsilon_f\sigma A_{ww}T_{ad}^3}; \quad (26)$$

The Hudson-Orrok method, described by Annaratone [16], indicates that the heat absorbed by the water walls is a relationship between a burning rate and the relation between the flue gas mass flow and the available energy. Here, the correction proposed by Annaratone [16] is used in the form

$$T_{f,e} = T_{ref} + \frac{1}{\bar{c}_{p,fg}}\left(\frac{1000 + \frac{6.439(1-f_k)h_{fg}}{f_v\sqrt{q_s}}}{\frac{6.439}{f_v\sqrt{q_s}} + \frac{1000}{h_{fg}}}\right) \quad (27)$$

Finally, the ε - NTU method was applied to the secondary superheater, primary superheater and economizer, using the Gnielinsky's and Zukauska's correlations for the internal and external convection.

Here, the heat transfer was divided into three steps: heat transfer from the flue gas to the external tube wall by convection and radiation, heat conduction between the tube wall and deposits (fouling and slagging) and heat transfer by convection from the tube wall to the water/steam. The flue gas radiation considered only the heat radiated from CO_2 and SO_2, using the correlations showed in Annaratone [16]. The modeling uncertainty calculation was made using the EES Professional software, using the method indicated by ASME PTC 4-2008 [14].

3. Results

The simulation is validated comparing the temperature obtained by the model with the boiler operational data in the outlet of each heat exchanger, as shown in Table 4. The results shows that the model reproduces the physical behavior of the boiler operation with coal burning.

Table 4: Comparison between model and measured flue gas temperature with coal operation

	$T_{g,FUR}$ [°C]	$T_{g,SH2}$ [°C]	$T_{g,SH1}$ [°C]	$T_{g,ECO}$ [°C]	$T_{g,AH}$ [°C]
$T_{m,e}$	1011 ±14	828±20	605 ±13	312 ±13	225 ±12
$T_{fg,a}$	1007 ±12	832 ±5	465 ±3	353 ±2	223 ±1
$\lvert T_{m,e} - T_{fg,a}\rvert$	4 (0.4%)	4 (0.5%)	140 (30%)	41 (11.5%)	2 (1%)
$T_{fg,b}$	1020 ±12.2	845 ±5,0	528 ±2	357 ±2	229 ±1
$\lvert T_{m,e} - T_{fg,b}\rvert$	9 (0.9%)	17 (2%)	77 (14.5%)	45 (12.5%)	4 (1.5%)

3.1. Thermodynamic model

The thermodynamic model revealed that the flue gas production should increase with the 10% rice straw co-firing combustion. This behavior occurs due to the increasing of fuel requirement to maintain the boiler thermal load. The simulation estimate a reduction up to 12% of CO_2 and SO_2 concentrations in fossil-fuel emissions, as shown in Fig. 1. Also, the H_2O formation in the flue gas may increase due to the higher hydrogen content of the rice straw, increasing the flue gas losses in the stack.

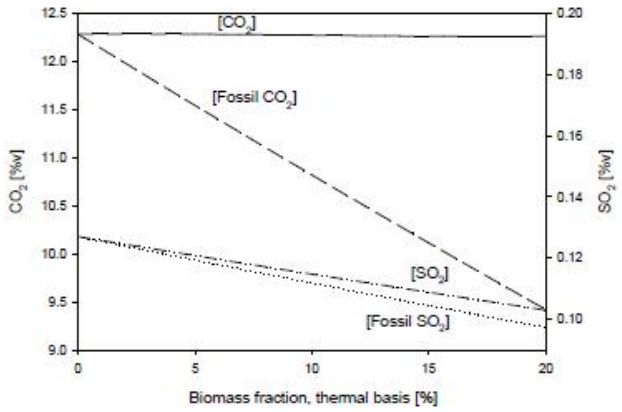

Fig. 1: Estimated variation for CO2 and SO2 emission with co-firing of rice straw
(UCO2 = 0:7% and USO2 = 0:01%)

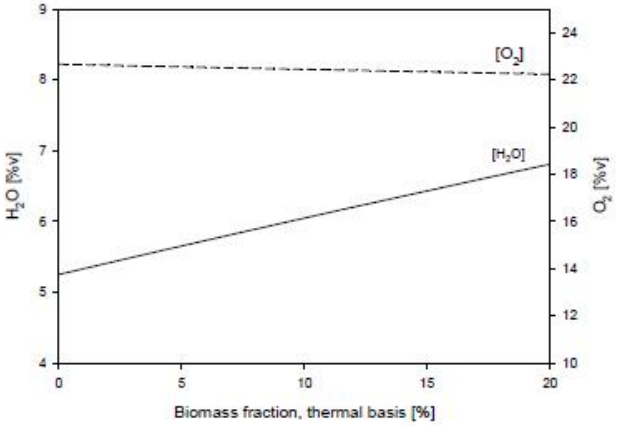

Fig. 2: Estimated variation for H2O and O2 emission with co-firing of rice straw
(UH2O = 1:7% and UO2 = 0:2%)

There is no significantly alteration in calculated boiler efficiency for rice straw co-firing up to 10 %, as shown in Fig. 3 and 4. The losses analysis shows that the flue gases losses increases up to 0.4 %. However, the losses to the unburned carbon also reduces up to 0.4 %. The losses to the ashes slightly reduces and the losses due to the surface convection and radiation remain constant with the rice straw co-firing.

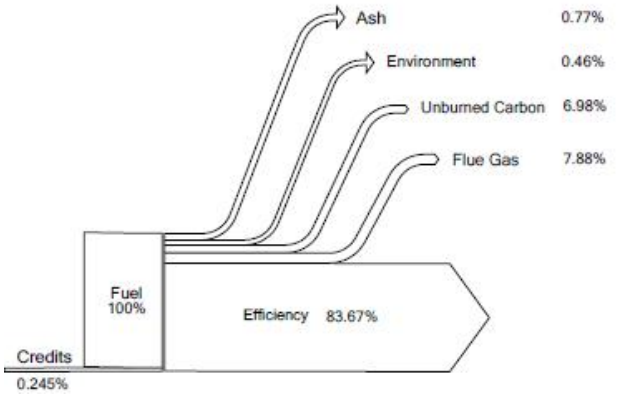

Fig. 3: Calculated boiler losses for 100 % coal operation
(UL f g = 0:5%; ULcnq = 0:4%; ULash = 0:01%; ULamb = 0:01%)

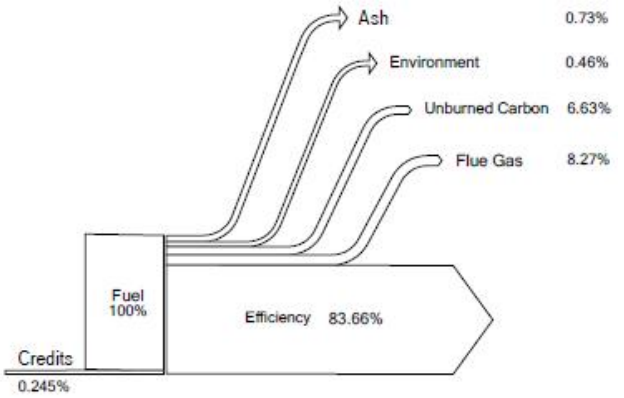

Fig. 4: Calculated boiler losses for 10% rice straw co-firing operation
(UL f g = 0:5%; ULcnq = 0:4%; ULash = 0:01%; ULamb = 0:01%)

3.2. Heat transfer model

Table 5 compares the flue gas temperature in the furnace exit obtained by the Normative method, Strauss method and Hudson-Orrok method with an estimated temperature. This estimated temperature used the closest measured temperature of the flue gas, after the secondary superheater, in a energy balance calculation.

Table 5: Comparison between the flue gas temperature obtained by the described models in furnace exit and an estimated temperature ($T_{fg,a}$ = 1007°C and $T_{fg,b}$ = 1020°C.)

	Normative method	Strauβ	Hudson-Orrok
$T_{m,e}$ [°C]	1011±14	921±12	1069±16
$\lvert T_m - T_{fg,a} \rvert$	4 (0.4%)	86 (8.5%	62 (6.2%)
$\lvert T_m - T_{fg,b} \rvert$	9 (0.9%)	99 (9.7%)	49 (4.8%)

Fig. 5 shows the flue gas temperature in the furnace exit with rice straw co-firing for the three methods. The calculated furnace emissivity increases less than 1% with 10 % rice straw co-firing. Fig. 6 shows the variation of the ashes absorptivity, α_{ash}, and the triatomic gases absorptivity, α_{gt}.

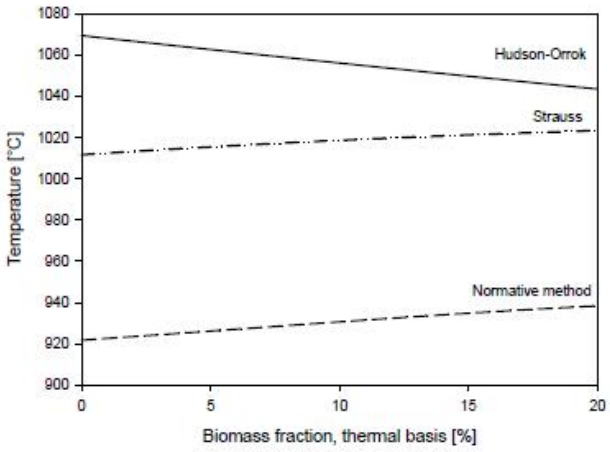

Fig. 5: Calculated flue gas temperature in the furnace exit for rice straw co-firing.

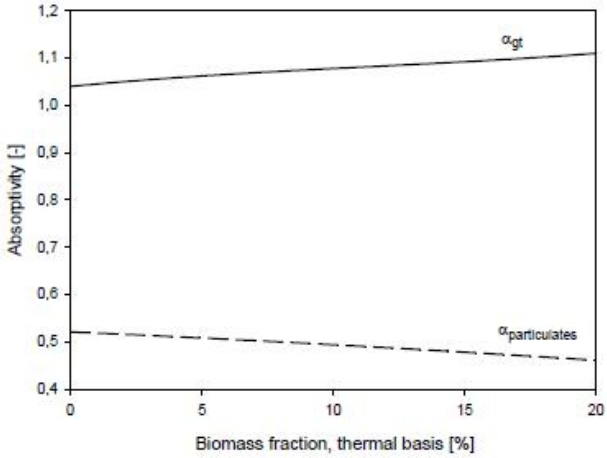

Fig. 6: Variation of the ashes and triatomic gases absorptiveness for rice straw co-firing.

Table 6 shows the main results of the heat exchangers calculation, both for coal burning and 10% rice straw co-firing.

Table 6: Variation of heat transfer properties in each heat exchanger for rice straw co-firing.

	SH2		SH1 B/A		ECO A/B	
	$\theta = 0\%$	$\theta = 10\%$	$\theta = 0\%$	$\theta = 10\%$	$\theta = 0\%$	$\theta = 10\%$
V_{fg} $[m/s]$	7.3	7.6	5.2/4.7	5.4/4.8	4.3/3.6	4.5/3.7
UA $[W/m^2]$	29580	30124	17788/32601	18140/33284	37243/31941	38251/32675
ϵ $[-]$	0.3	0.29	0.2/0.3	0.19/0.33	0.39/0.36	0.37/0.33

4. Discussion and conclusion

The thermodynamic and heat transfer boiler modeling support the estimation of the operational changes with the rice straw co-firing. The boiler modeling process must be carefully conducted for reliable results. Herewith, the evaluated system must be well known through field visits and discussions with the boiler operators for the right choice of the main parameters used in the modeling and the validation process. Also, the information obtained by the control system must be carefully evaluated, tracking the types and locals of the boiler measurement equipments. In this work, the measurements have relatively small uncertainties with high repeatability. These measures respond to the operation requirements, but do not map all the boiler thermal behavior. Thus, the use of assumptions for the calculations was necessary.

The results obtained in the thermodynamic analysis reproduce the thermal behavior of boiler operation with coal-only burning, with differences less than 10% with the measured data. Than, it becomes possible to use it for the assessment in boiler thermal behavior changes for rice straw co-firing. For 10% in thermal base, the modeling suggested that there will be no major changes in boiler behavior.

The combustion calculation indicated that the reduction of CO2 and SO2 in the fossil emissions may be up to 12%. Here, only the CO2 emission reduction in combustion was analyzed. It was not

considering theCO2 captured in biomass harvest and the avoiding emission of rice straw incorporation in soil.

The temperature field along the boiler presented a non-significant change and it may be less than 5 %. Also, the modeling suggested that the boiler efficiency may be slightly reduced due to the increase of flue gas losses. However, the ash sensible losses and unburned carbon losses may be reduced. The unburned carbon proportion was considered constant in both cases. This unburned carbon losses decreased due to the reduction of ash formation in co-firing case.

The normative method better agreed with the furnace estimated temperature, with differences up to 1%. The other two methods also obtain adequate values, with less than 10% of error. However, all these methods do not take account of the flame direct radiation in this section. That can result in indeterminate uncertainties for the furnace modeling. The heat transfer analysis suggests that the 10% co-firing may results in a increase of the flue gas temperature. The reduction of the ash concentration in the flue gas tends to reduce this emissivity. However, the concentration of water vapor in the flue gas is increased and that increases the furnace emissivity, offsetting this reduction. The calculation procedures for flame and medium emissivity are not simple. The grey gas model results in significantly errors due to the temperature gradient inside the flame. The literature shows that the emissivity average value do not well reproduces the variations inside the flame. However, this values are widely used in engineering problems, obtaining satisfactory results in thermal systems design. The calculated furnace effectiveness was equal to 0.59. For 10% of rice straw co-firing, the modelling suggests that there is no significantly changes, since the minimum capacitance increases in proportion to the decrease of the adiabatic flame temperature, resulting in a constant value for the maximum heat transfer rate. For the heat exchangers, the value of heat exchangers effectiveness are lower than other heat exchangers. However, this value is suitable for applications in utility boilers.

The modeling suggests that the fluid dynamic behavior may change less than 2% with rice straw co-firing. Experimental data are needed to confirm this result to ensure the properly boiler operation.

Experimental tests in this boiler will be conducted. Thus, the validation of the co-firing modeling will be possible. In addition, these tests will indicate the main bottlenecks of biomass co-firing in Brazil. Also, the evaluation of fouling and corrosion problems along the boiler will be done. Currently, this is one of the main barriers to the viability of the biomass co-firing in coal power plants. Additional instrumentation will be installed in the boiler to better monitoring the thermal behavior, including temperature, velocity and slagging/fouling probes.

The rice straw logistic and processing are important factors that must be evaluated to the viability of this process in Brazil. The residue logistic is not simple and must be evaluate since the field extraction until the transport to the power plant. The biomass process plant must be analyzed to ensure fuel demand in the project characteristics in an efficiency and safety way.

Acknowledgments

The authors acknowledge the Electrical Energy National Agency and the Tractebel Energia - Suez Group for the financial resources.

Nomenclature

A area, m^2

AH Air heater

Bo Boltzmann number, -

C Credits, -

C_{ung} Unburned carbon, kg/kg
cp specific heat, kJ/(kg-K)
d Diameter, m
E effective thickness of the radiating layer, m
ECO Economizer
fk empirical coefficient related to the volatile matter content in the fuel
fv empirical coefficient related to the slagging
h heat transfer coefficient, W/(m^2 - K)
h_{ash} ash enthalpy, kJ/kg
Ko Konakow number, kW/m^2K^4
l Length, m
L losses, -
LHV Lower heating value, kJ/kg
m mass flow, kg/kg
M empirical coefficient related to the type of fuel
m mass flow rate, kg/s
n Number of tubes, -
P pressure, bar
Q heat per time unit, kW
s1 Parallel distance between the tube center and fluid flow, m
s2 Transversal distance between the tube center and fluid flow, m
s3 Transversal distance between the tube center and fluid flow in partly staggered tubes, m
S H1 primary superheater
S H2 secondary superheater
t temperature, °C
U_x propagated uncertainty, -
v specific volume, m^3/kg
V volume, m^3
X height of the highest temperature inside the furnace, m

Greek Letters

α absorptivity
ε emissivity
η efficiency
λ bottom ash proportion
Π furnace parameter
ψ water wall thermal efficiency
τ optical thickness

Subscripts and superscripts

a air
ad adiabatic
AH Air heater
b boiler
b bottom ash

bn burner
cd credits
cv convection
e external
ECO economizer
f fly ash
f,e flue gas in furnace exit
fg flue gas
f l flame
FUR furnace
i internal
in inlet
h hydraulic
l losses
m model
r radiation
rc radiation and convection
ref reference
RO_2 triatomic gases
sf surface
unb unburned carbon
ww water wall

References

[1] L. Baxter. Biomass-coal co-combustion: Opportunity for affordable renewable energy. Fuel, 84(10):1295–1302, 2005.

[2] J. Koppejan and S. Van Loo. The Handbook of Biomass Combustion and Co-firing. Ear, 2008.

[3] J. Zhang and S.H. Saimbi. Case study of a dedicated biomass firing system at fiddlers ferry power station, uk. In Alstom Annual Conference 2007 Lisbon, 2007.

[4] EPRI. Biomass cofiring: Field test results: Summary of results of the bailly and seward demonstrations.Technical report, EPRI, 1999.

[5] Kate Wieck-Hansen, Peter Overgaard, and Ole Hede Larsen. Cofiring coal and straw in a 150 mwe power boiler experiences. Biomass and Bioenergy, 19(6):395 – 409, 2000. <ce:title>Cofiring Benefits for Coal and Biomass</ce:title>.

[6] Joseph J.Battista Jr, Evan E Hughes, and David A Tillman. Biomass cofiring at seward station. Biomass and Bioenergy, 19(6):419 – 427, 2000.

[7] F. Al-Mansour and J. Zuwala. An evaluation of biomass co-firing in europe. Biomass and Bioenergy, 34:620–629, 2010.

[8] K. Kadam, F. Forrest, and J. Jacobson. Rice straw as a lignocellulosic resource: Collection, processing, transportation, and environmental aspects. Biomass and Bioenergy, 18(5):369–389, 2000.

[9] SC Stultz and JB Kitto. Steam - its generation and use. The Babcock & Wilcox Company, 41a edition, 2009.

[10] V.I. Kouprianov andW. Kaewboonsong. Modeling the effects of operating conditions on fuel and environmental costs for a 310 mw boiler firing fuel oil. Energy Conversion and Management, 45(1):1 – 14, 2004.

[11] V.I Kouprianov. Modeling of thermal characteristics for a furnace of a 500 mw boiler fired with high-ash coal. Energy, 26(9):839 – 853, 2001.

[12] M. Moghari, S. Hosseini, H. Shokouhmand, H. Sharifi, and S. Izadpanah. A numerical study on thermal behavior of a d-type water-cooled steam boiler. Applied Thermal Engineering, 37(0):360 – 372, 2012.

[13] V.I. Kouprianov andW. Kaewboonsong. Modeling the effects of operating conditions on fuel and environmental costs for a 310 mw boiler firing fuel oil. Energy Conversion and Management, 45(1):1 – 14, 2004.

[14] ASME. PTC 4-2008 - Fired Steam Generators - Performance Test Codes. ASME, 2008.

[15] A. Fuller and F. Pereira. Relatório de análise da palha de arroz e do carvão brasileiro (in german). Institut für Feuerungs-und Kraftwerkstechnik - Universität Stuttgart. Stuttgart, 2009.

[16] D. Annaratone. Steam Generators - Description and Des. Springer, 2008.

[17] E. Bazzo. Geração de Vapor. Ed. da UFSC, 1995.

[18] S. Kakaç. Boilers, Evaporators and Condensers. John Wiley & Sons, Inc., 1991.

[19] K. Strauß. Kraftwerkstechnik - zur Nutzung fossiler, nuckerareund regenerativer Energiequellen. Springer, 2006.

[20] A.G. Blokh. Heat Transfer in Steam Boiler Furnaces. Hemisphere Publishing Corp., 1988.

[21] I.E. Dubovsky, V.V. Kompaneets, and P.A. Shemyakin. Concerning the account for the effect of temperature fields in the furnace cross-sections on heat transfer. Teploenergetika, 2:58–61, 1984.

Thermophotovoltaic Generation: A state of the art review

Matteo Bosi[a], Claudio Ferrari[a], Francesco Melino[a], Michele Pinelli[b], Pier Ruggero Spina[b], Mauro Venturini[b]

[a] *IMEM – CNR, Parco Area delle Scienze 37/A, 43124 Parma, Italy*
[b] *ENDIF – Università di Ferrara, Via Saragat, 1, 44122 Ferrara, Italy*

Abstract:

In the last decade thermophotovoltaic (TPV) generator has gained an increasing attention as cogeneration system for the distributed generation sector. Nevertheless, these systems are not fully developed and studied: several aspects need to be further investigated and completely understood.
The aim of this study is to analyze the current state of the art technology for TPV generation; more in details, in this study, the characteristics of a TPV generator are analyzed with a particular attention to the physical relationships which govern the behavior of its main components. Moreover, the current technology regarding the combustor, the emitter, the optical filter and the photovoltaic cells are investigated by taking into account both the role of each component and also their integration in the whole system. Finally, a critical review of the realized prototypes is presented and discussed.

Keywords:

Thermophotovoltaic generator, state of the art, analytical aspects, review.

1. Introduction

A Thermophotovoltaic generator (TPV) is an innovative system able to convert the radiant energy of a combustion into electrical energy. This conversion is realized by using photovoltaic cells. A scheme of a TPV is presented in Figure 1, in which the main components and energy flows are highlighted.
A TPV generator consists of a heat source, an emitter (EM), a filter (F) and an array of photovoltaic cells (PV); the combustion air pre-heating system (HX-A) which uses the combustion products is also sketched in Fig. 1. The thermal production of the TPV is realized by the heat exchangers HX-PV and HX-CP, which respectively recover the heat from the cooling of PV cells and the exhaust combustion products.
The main advantages of this energy system can be found in the (*i*) high fuel utilization factor (close to the unity thanks to the recovery of the most of the thermal losses, making it possible to use the TPV system as a combined heat and power system), (*ii*) low produced noise levels (due to the absence of moving parts), (*iii*) easy maintenance (similar to a common domestic boiler) and (*iv*) great fuel flexibility. In fact, with this regard, it can be observed that the heat source of a TPV system can be provided by various fuel typologies such as fossil fuels (natural gas, oil, coke, etc.) municipal solid wastes, nuclear fuels, etc; concentrated solar radiation can also be used as a TPV heat source [1-3]. A TPV system usually allows very low pollutant emissions (e.g. CO and NOx), since it is often coupled with combustion devices such as domestic boilers.
The main use of a TPV generator can be in the distributed combined heat and power generation, but its application in the automotive sector in case of hybrid vehicles [4], glass [5] or other high temperatures industries [6] has also been analyzed in literature. The TPV system has been proposed for portable generators [7, 8], co-generation systems [9], combined cycle power plants, solar power plants [10], grid connected [11] or independent equipment [12]. Other studies show the integration

of TPV generator with thermoelectric systems [13] or with Organic Rankine Cycles [14]. Further studies were developed in military [15-17] and space [18, 19] sectors.
Even if the first studies [20, 21] about thermophotovoltaic conversion were carried out during the early years of 1960, it was only in the last decade that the research about TPV generation accelerated markedly. The electrical efficiency of the realized prototypes [19, 22-27] ranges from about 0.6 % to slightly less than 11.0 %. Moreover, electrical efficiencies close to 24 % are predicted in literature [28-30], making TPV system very attractive for cogeneration. A comprehensive analysis about the realized TPV generator prototypes will be developed in this work.

2. Electrical performance of a TPV generator

The power balance of a TPV generator is presented in **Figure 2**. The power introduced with the fuel (P_{in}), unless the thermal losses ($P_{fuel,loss}$) of the combustion process, is converted by the emitter and by the optical filter into radiant power ($P'_{GAP} = P_{RAD} - P_{back}$) and thermal power discharged with the gases ($Q_{TH,gas}$ in Figure 2 and sec. F_2 in Figure 1). A fraction of the radiant power (P'_{GAP}), which is in the useful range of wavelengths for the photovoltaic conversion (due to the optical filter selection), can be lost due to the absorption of the optical filter (P_{abs}, even if this term can be usually neglected) and for the view factor between filter and PV cells (P_{loss}, this term can be reduced achieving values very close to zero with a optimal design of the system geometry). The radiant power incident on the photovoltaic cells ($P_U = P_{GAP} - P_{loss} = P'_{GAP} - P_{loss} - P_{abs}$) is then converted into continuous current ($P_{el,dc}$) and thermal power ($Q_{th,pv}$); except for the losses ($P_{el,loss}$) due to the inverter (INV in Figure 1) efficiency, the electrical power ($P_{el,ac}$) can be obtained from the system. On the other hand, the enthalpy content of the gases at the emitter exit ($Q_{TH,gas}$ in Figure 2 and sec. F_2 in Figure 1) can be partially recovered ($Q_{th,cp}$) while the remaining part is discharged into the ambient ($Q_{th,d}$).
The electrical efficiency of a TPV generator can be written as:

$$\eta_{EL,TPV} = \eta_{CC} \cdot \eta_{RAD} \cdot \eta_{GAP} \cdot \eta_F \cdot \eta_{VF} \cdot \eta_{PV} \cdot \eta_{\frac{dc}{ac}} \quad (1)$$

where:
η_{CC}: combustion efficiency; η_{RAD}: radiant efficiency; η_{GAP}: spectral efficiency; η_F: filter efficiency; η_{VF}: view factor efficiency; η_{PV}: cell efficiency $\eta_{\frac{dc}{ac}}$: inverter efficiency.
Each efficiency is separately analyzed and discussed in the following.

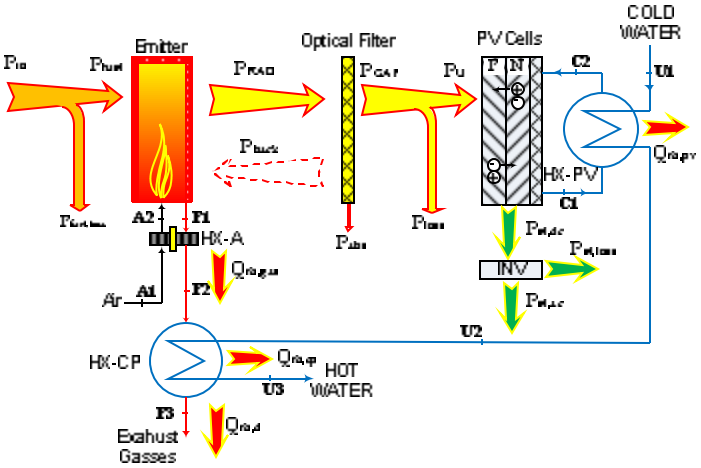

Fig. 1. Scheme of a TPV generator

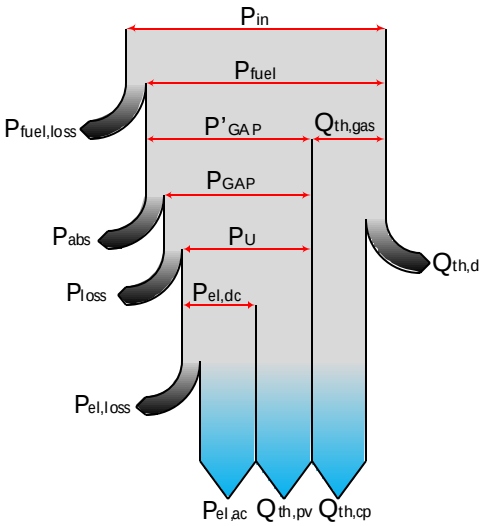

Fig. 2. Power balance of a TPV generator

2.1 Combustion efficiency

With reference to Figure 2, the *combustion efficiency* can be expressed as the ratio between the useful introduced power (P_{fuel}) and the whole power introduced with fuel (P_{in}):

$$\eta_{CC} = \frac{P_{fuel}}{P_{in}} = \frac{P_{fuel}}{\dot{m}_{fuel} \cdot LHV} \quad (2)$$

being $\dot{m}_{fuel}$ and LHV respectively the fuel mass flow rate and its Lower Heating Value (depending on the type of fuel).

From Figure 2, it can be observed that the useful introduced power (P_{fuel}) can only be converted into radiant power ($P'_{GAP} = P_{RAD} - P_{back}$) or discharged with the combustion products ($Q_{TH,gas}$). It results that:

$$P_{fuel} - P'_{GAP} - Q_{TH,gas} = \mathbf{0} \quad (3)$$

This last equation represents the power balance of combustor, emitter and air pre-heater exchanger and shows the important role of the air pre-heater for the thermophotovoltaic conversion.

The thermal power discharged by the system with the combustion products (upstream of the heat recovery exchanger CP-HX) can be written as:

$$Q_{TH,gas} = \dot{m}_{gas} \cdot \boldsymbol{h}_{gas,F2} - \dot{m}_{air} \cdot \boldsymbol{h}_{air,A1} \quad (4)$$

while the thermal power exchanged by air (upstream of the combustor, see Figure 1) and combustion products (downstream of the emitter, see Figure 1) can be written as:

$$Q_{TH,af} = \dot{m}_{gas} \cdot \left(\boldsymbol{h}_{gas,F1} - \boldsymbol{h}_{gas,F2}\right) = \dot{m}_{air} \cdot \left(\boldsymbol{h}_{air,A2} - \boldsymbol{h}_{air,A1}\right) \quad (5)$$

The Eqs. 3 through 5 demonstrate that, by keeping fixed the other factors, the reduction of combustion products temperature (section F2 in Figure 1) and consequently the increase of the air temperature upstream of the combustor (section A2 in Figure 1) allows to enhance the emitted radiant power; this evidence is also confirmed in [31]. The importance of air pre-heater has been also highlighted by Seal et al. [32] and by Christ et al. [33]. In particular, Colangelo et al. [29] developed an air pre-heater by adopting a rotary heat exchanger with a ceramic material which is lighter than metal and has a greater heat capacity to store a high amount of energy. A heat exchanger efficiency greater than 75 % was achieved.

2.2 Radiant efficiency

The *radiant efficiency* can be expressed, with reference to Figure 2, as the ratio between the radiant power from the emitter (P_{RAD}) and the introduced power (P_{fuel}) into the system. It follows:

$$\eta_{RAD} = \frac{P_{RAD}}{P_{fuel}} = \frac{p_{RAD} \cdot S_{em}}{\eta_{CC} \cdot \dot{m}_{fuel} LHV} \quad (6)$$

The radiant power is a function of the radiation power density (p_{RAD}) and of the emitter surface (S_{em}). The radiation efficiency is strictly influenced by several factors: the type of emitter, its dimension and thickness, the combustion mode, the firing rate and, as already noticed, the pre-heating of the air. If the emitter's irradiation spectrum is not known, the power density can be calculated according to the Stefan-Boltzmann's law:

$$P_{RAD} = \epsilon \cdot S_{em} \cdot 2\pi \int_0^{\infty} i(\lambda; T_{em}) d\lambda = \epsilon \cdot S_{em} \cdot 2\pi \int_0^{\infty} \frac{hc^2}{\lambda^5} \left[exp\left(\frac{hc}{\lambda k_B T_{em}}\right) - 1 \right]^{-1} d\lambda \quad (7)$$

where k_B =1.380 x 10^{-23} J K^{-1} and $\boldsymbol{h}$ =6.626 x 10^{-34} J s are the Boltzmann and the Plank constant respectively, c =2,99 x 10^8 m s^{-1} the speed of light, λ the wavelength and ϵ the emissivity of the body. It can be observed that the radiant energy density can be up to 500 kW/m^2 (this value can be obtained by integrating the spectrum of a black body at 1600 °C). This last value is very high if it is considered that the radiant energy density of the sun is equal to 1 kW/m^2 at AM 1.5 condition. The achievement of high temperature is a very important aspect since, according to Planck's law, radiation power density scales with temperature to the fourth power. Therefore, most heat sources used in TPV systems are based on combustion systems; various types of *premixed* and *non-premixed* combustors [34-36] or radiant tube burner [37, 38] have been developed in the last years.

It should be considered that the push towards high temperatures burners is limited by the NOx production.
The radiant energy from the emitter has to be characterized by an emission spectrum suitable for the adopted photovoltaic cells; in fact only the photon energy in a narrow band above the bandgap of the photovoltaic cells can be converted into electrical energy. Therefore, selective emission is required; in order to achieve this goal, a *selective emitter* [39-49] or a *broadband emitter* with a filter can be used. In the first case, the emitter is made with materials such as rare earth oxides which are characterized by an emission spectrum centered on specific wavelength; in the second case, due to their lower energy on the respect of the bandgap of photovoltaic cells, many emitted photons are unusable. It is imperative to send these photons back to the radiator in order to preserve heat and to reduce the fuel consumption needed to achieve the required emitter temperatures.
It should be observed that the material used for the emitter needs to have specific characteristics such as (*i*) thermal stability, (*ii*) corrosion resistance, (*iii*) shock resistance, (*iv*) high thermal conductivity, etc.. Obviously, the high temperatures which are required by the TPV system implies that the emitter's material melting point should be as high as possible. Further, the emitter needs to be thermally stable in the selected atmosphere (i.e. air and/or combustion products) and corrosion high resistant; as an example, graphite (C) has a high-thermal conductivity and a good thermal shock, but it cannot overcome 400 °C in an oxidizing atmosphere [50]. On the contrary, it can operate up to 3000 °C in non-oxidizing atmosphere. The adoption of coatings can improve the corrosion resistance of some materials or a shield, usually made of quartz, can be adopted to protect the emitter from the environment. A high value of thermal conductivity is required in order to have a uniform temperature distribution of the emitter. Lower values of thermal conductivities cause a large temperature gradient inside the emitter which drastically decreases its efficiency. Anyway, in case of a porous emitter, this factor may not be important. Thermal shock resistance is also very important especially in TPV generators with frequent on/off cycles. The sudden change in emitter temperature can cause material failure.
Ceramics selective emitters are based on transition metal oxides such as holmium (Ho), erbium (Er) or ytterbium (Yb); Table 1 provides the main emission peaks of the most common materials adopted for selective emitters [43-49], while Figure 3 shows the emittance (defined as the radiation intensity divided to the corresponding blackbody spectrum) of Er_2O_3 and Yb_2O_3 [17].

Tab. 1. Main emission peaks of the most commons materials adopted for selective emitters

Element	Symbol	Wavelength of the main peak [μm]
Neodymium	Nd	2.5
Samarium	Sm	1.8-5.0
Holmium	Ho	2.0-2.1
Erbium	Er	1.5
Thulium	Tm	1.8
Ytterbium	Yb	1.0

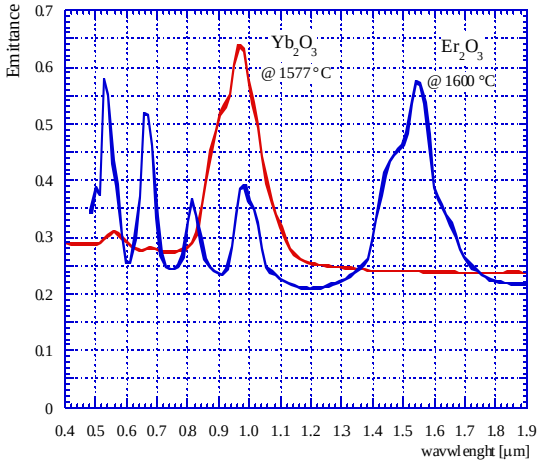

Fig. 3. *Emittance of Er_2O_3 and Yb_2O_3 [17]*

On the other hand, high temperature broadband emitters [51-57] can be divided into (*i*) oxide-based or (*ii*) non oxide-based ceramics. Among oxide-based ceramics, alumina (Al_2O_3) and zirconia (ZrO_2) show a good stability in oxidizing atmosphere and can be used up to 1900 °C or more, if it is considered that their fusion temperatures are 2050 °C and 2600 °C, respectively. Other oxide-based ceramics are magnesia (MgO), silica (SiO_2), beryllia (BeO), hafnia (HfO_2), thoria (ThO_2) and yttria

(Y_2O_3) [51]. Anyway, the major difficult related to the adoption of these materials is the low thermal shock resistance and/or the low emissivity.
A widely used broadband emitter is silicon carbide (SiC), which can operate up to 1650 °C. Silicon carbide has an emissivity close to 0.90 [56] and a very high melting point. Ceramic composites such as SiC/Si and SiC coated ceramic composites fit all the requirements for a TPV emitter [57].

2.3 Spectral efficiency

The *spectral efficiency* is the ratio between the whole radiation from the emitter (P_{RAD}) and the portion which passes through the filter (P'_{GAP})

$$\eta_{GAP} = \frac{P'_{GAP}}{P_{RAD}} \tag{8}$$

The spectral efficiency depends on the adopted filter, used to match the emitter spectral emission to the PV cell; this means that the filter should ideally be able to block all the photons with energy lower than the PV cell bandgap and pass the photons with higher energy. With a simple approach, the P'_{GAP} can be estimated by integrating the radiant intensity $i(\lambda; T_{em})$ in the range of wavelengths (from 0 to λ_{gap}) which passes thought the filter and then can be converted by the photovoltaic cells:

$$P'_{GAP} = \epsilon \cdot S_{em} \int_0^{\lambda_{gap}} I(\lambda; T_{em}) \tau(\lambda) d\lambda = \epsilon \cdot S_{em} \int_0^{\lambda_{gap}} \frac{2\pi h c^2}{\lambda^5} \left[exp\left(\frac{hc}{\lambda k_B T_{em}}\right) - 1 \right]^{-1} \tau(\lambda) d\lambda \tag{9}$$

A more realistic calculation of the filter can be performed by taking into account filter transmissivity $T(\lambda)$ and reflectance $R(\lambda)$.
It follows that the *in band radiant intensity* as a function of the wavelength can be estimated as:

$$P'_{GAP}(\lambda) = T(\lambda) \cdot i(\lambda; T_{em}) \tag{10}$$

The *in band radiant power* (P'_{GAP}) can be calculated by integrating the trend of the $P'_{GAP}(\lambda)$ in Eq. (10) in the range of wavelengths from 0 to ∞.

$$P'_{GAP} = \int_0^{\infty} T(\lambda) \cdot P'_{GAP}(\lambda) d\lambda = \epsilon \cdot S_{em} \int_0^{\infty} T(\lambda) \cdot i(\lambda; T_{em}) \tau(\lambda) d\lambda \tag{11}$$

Anyway, it should be observed that also this approach does not take into account that the filter transmissivity (and therefore its reflectance) is a function of the angle between the incident radiation and the normal to the filter surface. It follows that a complete and realistic filter calculation should be taken into account by using a 3D geometry. In order to consider this issue, another calculation approach (e.g. a Monte Carlo based method) needs to be adopted.
Many types of filters have been developed such as plasma filters, 1-D photonic bandgap filters, 2-D photonic bandgap filters, 3-D photonic bandgap filters, combination of plasma filter and 1-D photonic bandgap filter, dielectric stacks or back-surface reflectors [58-69].
3-D photonic bandgap filters are characterized by an omnidirectional photonic band gaps which means that the propagation of photons is prohibited for arbitrary polarization in any direction [69]; obviously, this characteristic is highly appreciated for TPV generation. Anyway, it should be observed that a well designed 1-D photonic bandgap filter can completely reflect polarized photons at all incident angles showing omnidirectional photonic band gaps [65, 68]. On this regards, filters based on multiple layer of SiO_2 [62-65] have shown promising results for TPV applications.

2.4 Filter efficiency

The *filter efficiency* takes into account the fraction of radiant power which is absorbed by the filter (P_{abs}). The filter efficiency can be written as:

$$\eta_F = \frac{P_{GAP}}{P'_{GAP}} \tag{12}$$

where the balance of the filter is:

$$P_{RAD} - P_{back} = P'_{GAP} = P_{GAP} + P_{abs} \tag{13}$$

The term P_{abs} can be usually neglected with a properly design of the filter and therefore it is possible to assume $\eta_F = 1$ [65].

2.5 View factor efficiency

The *view factor efficiency* is related to the ratio between the radiation (P_U *P*) which is incident on the photovoltaic cells and the value (P_{GAP} *P*).

$$\eta_{VF} = \frac{P_U}{P_{GAP}} \tag{14}$$

The value of view factor can be calculated according to the geometry and to the distance among the surfaces which are involved in the irradiation phenomenon. Many formulations of radiation view factors can be found in literature on the basis of the TPV geometry [71-76].

2.6 PV cells efficiency

The *cells efficiency* can be expressed as follows:

$$\eta_{PV} = \frac{P_{el,dc}}{P_U} = \frac{V_{OC} \cdot J_{SC} \cdot FF}{P_U} \tag{15}$$

which represents the ratio between the electrical power output ($P_{el,dc}$) and the incident power on the cell (P_U); the maximum electrical power produced by a photovoltaic cell can be expressed as a function of short-circuit current (J_{SC}), open-circuit voltage (V_{OC}) and Fill Factor (FF). The radiation efficiency is influenced by many factors such as the cell material, the emitter temperature and the radiation intensity.

Converters for TPV systems are very similar to standard solar cells such as Si and high efficiency GaAs, but they are made of semiconductor materials with lower bandgap, for better spectral matching with the emitter radiation.

Figure 4 shows the relationship between semiconductor lattice constant and energy gap: in order to match the radiation emitted by a 1000-1600 °C black body, few materials and alloys can be adopted, such as Ge, GaSb, InGaAs/GaSb, InGaSb/InP and the quaternary InGaAsSb/GaSb and InGaAsP/InP [77-81]. These materials are not so widely used as Si and GaAs, but their technology is well-assessed for applications such as infrared and near-infrared detectors, lasers and LED. Their main drawback is the high cost of the substrates (Ge, GaSb, InP) with respect to Si. The cost of Ge is comparable to the GaAs, but GaSb and InP cost is from 5 to 8 times the Ge cost. The development of cost-effective cells for TPV should be a compromise between the substrate and processing costs and its overall efficiency in the system.

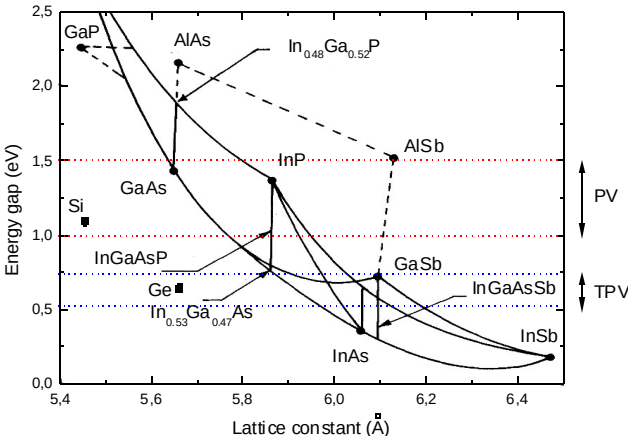

Fig. 4. Relationship between lattice constant and bandgap of standard semiconductors

The heart of a TPV cell is a standard *p-n* (or *n-p*) junction made of one of the semiconductor materials listed above. In the past, only single junction devices were developed for TPV applications: multi-junction designs such as amorphous-Si/crystalline-Si or InGaP/GaAs/Ge were only developed for high efficiency solar photovoltaic applications [82, 83]. The cell structure is made of a *n* or *p* base, usually the semiconductor substrate, and a *p* or *n* doped emitter layer realized

either by diffusion or epitaxy. The emitter layer thickness is in the range 0.2 to 1.0 μm , depending on the minority carriers diffusion length, that should be at least twice the emitter thickness. The complete cell structure also includes other layers such as front and rear metal ohmic contacts, anti-reflection coating (usually realized with MgF_2 and/or ZnO), front surface passivation layer and back surface field to reduce the carrier recombination at the diode interfaces; in Figure 5 the main schemes of TPV cells are presented. The optimal cell structure in term of layers thickness and doping clearly depends on material properties; in any case, the general guidelines are similar to the design of a standard PV cell.

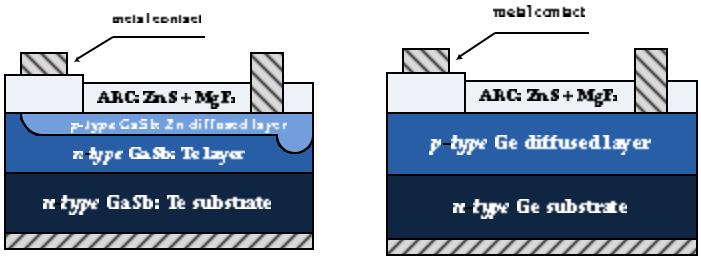

(a) GaSb diffused TPV cell Ge diffused cell

Fig. 5. Scheme of TPV cells

In order to estimate the conversion efficiency of a PV cell, a fundamental parameter is the external quantum efficiency $EQE\ (\lambda)$ which can be defined as the probability that a photon of wavelength λ is absorbed by the cell, generating an electron that will be collected at the terminals: it considers the reflection and absorption of incident photons and the generation/collection of minority carriers, so it describes the behavior of the p-n junction in great detail.

The actual value of the J_{SC} produced by the cell can be calculated from $EQE\ (\lambda)$ of the PV cell and the incident photon flow $\Phi(\lambda)$ is :

$$J_{SC} = e\int_0^{\lambda_{gap}} \Phi(\lambda)\ EQE\ (\lambda)\, d\lambda \tag{16}$$

$EQE\ (\lambda)$ were measured for different semiconductors of choice for TPV and typical behaviors are reported in Fig. 6 [84-88]. It can be noticed that most of the materials used for the TPV cells have high EQE in a large region from near the bandgap to lower wavelength. The EQE drops to very low value for photon wavelength of about 1000 nm, but it should be considered that in this region a standard TPV emitter at 1200-1800 °C has a very low photon emission. For this reason, the TPV cells are usually able to convert the part of the black body radiation that arrives at their surface with a very high efficiency, while the photons with lower energy than the bandgap (i.e. not absorbed), can be effectively redirected towards the emitter by means of appropriate selective filters. This particular characteristic, not possible for solar PV, allows TPV cells to potentially reach very high conversion efficiencies, because the incident radiation could be efficiently coupled with the region where the cell EQE is maximum.

There are two basic techniques to realize *p-n* junctions for TPV: diffusion and epitaxy. Diffusion of a doping element in a semiconductor usually follows Fick's law [89] and it depends on the diffusion coefficients of the selected atoms in a particular material, on their concentration and on process temperature. GaSb and Ge cells realized by diffusion have the advantage of lower cost, since the process is relatively simple, but a better control of the emitter doping concentration and profile can be obtained by using the epitaxial technique, potentially leading to higher efficiency. Ternary and quaternary cells such as InGaAs, InGaSb, InGaAsSb and InGaAsP are realized only by epitaxy, because the alloys need a careful control of the composition.

Diffused emitter in Ge can also be obtained by MOVPE epitaxy by depositing GaAs on n-type or InGaP on p-type Ge substrate. These processes are more expensive, but they allow a better control

of the structure and a surface passivation layers based on lattice matched III-V compounds can also be added [90].
A third way to obtain Ge *p-n* junctions is to epitaxially realize the emitter by depositing a controlled doped epitaxial layer on the Ge substrate: in this case, thickness, doping and interfaces can be better tailored to enhance device performance. Also with this approach, passivation layers can be added to the surface to enhance the conversion efficiency [91, 92].

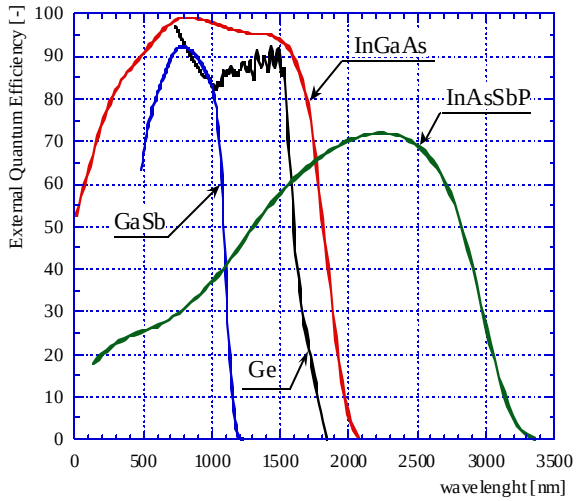

Fig. 6. External quantum efficiency of TPV cells

2.7 Inverter efficiency

Finally, the *inverter efficiency* allows the calculation of the final electrical output of the system. It results:

$$\eta_{\frac{dc}{ac}} = \frac{P_{el,ac}}{P_{el,dc}} \tag{17}$$

Useful information about the efficiency of inverter adopted with PV cells can be found in [93, 95]. In particular it can be observed that the use of transformer usually reduces the conversion efficiency from direct current to alternate current [93].

3 . TPV PROTOTYPES

The TPV prototypes described in the following are grouped by considering the most relevant research groups (i.e. the CANMET Energy Technology Centre, Paul Scherrer Institut, JX Crystals Inc.) who contributed to TPV system experimental development. The progress of each work is analyzed chronologically, to highlight the improvements made and current technological level. Other experiences reported in technical literature are also addressed in a separate section and they are similarly ranked in chronological order.

3.1 CANMET Energy Technology Centre, Ottawa (Canada)

In their first reported experiment [96], Qiu et al. investigated various gas fired radiant radiators and the influence of the combustion processes on radiant power and radiant efficiency. The investigations showed that the major losses in combustion driven TPV systems arose from the limited conversion of fuel to radiant energy, low fraction of in-band radiation and limited photovoltaic conversion. They suggested that conversion of fuel to radiant energy could be increased through the use of selective emitters [97].

In [98], a TPV system with exhaust heat recuperator, made of stainless steel, was investigated. The gas-fired burner in the furnace was fully aerated, and gas and combustion air were entirely premixed before entering the burner. The broadband radiator with reticulated structure was once again made of SiC. The filter used was not ideal and still transmitted a certain amount of non-convertible radiation energy. The PV cells used in this test rig were made of InGaAsSb. The radiant power density and radiant efficiency were determined at different degrees of exhaust heat recuperation. The heat recuperation was observed to have a significant influence on the combustion operation and radiant power output.
Qiu et al. have shown that a radiator with a high conversion level of fuel to radiation energy must be achieved to realize an efficient TPV system. In [99], they investigated different natural gas-fired radiators in order to raise the conversion of fuel energy to thermal radiation.
Finally, Qiu et al. presented in [100] a novel cascaded TPV system with thermoelectric (TE) devices. Both of them convert thermal energy directly into electricity. A prototype cascading TPV and TE generation system was built and tested. This power generation system consisted of a natural gas burner, a SiC porous foam emitter, an optical filter made of ceramic glass with coatings of SiO_2 and TiO_2, GaSb cells, a cell cooling device, PbSnTe-based TE converter and a TE cooling device. In this prototype, the combustion products leaving the thermal emitter flowed through the TE converter, which further converted the residual heat into electricity. With a thermal input of 8260 W, the GaSb TPV cells generated 123.5 W of electricity, whereas the TE converter generated 306.2 W of electricity. The electric efficiency of the TPV system alone was 1.5 %, while the electric efficiency of the cascading system was 5.2 %, which is considerably greater than that of the separate TPV and TE power generation units.

3.2 Paul Scherrer Institut, Villigen PSI (Switzerland)

Durisch et al. presented their first prototype system in [101]. This consisted of a conventional butane burner which was equipped with a spherical mantle emitter made of ytterbia Yb_2O_3. Commercial silicon solar cells, measuring 50 cm^2, with a standard test condition (STC) efficiency of 16 %, were used to fabricate the photocell generator. An infrared radiation-absorbing water layer between the emitter and the photocell-generator was used to protect the photocells from overheating and direct contact with flue gases. This prototype had a thermal power input of 1350 W and an electric power output of 15.2 W, corresponding to an electric efficiency of about 1.1 %.
A second prototype by Durisch et al., based on the same butane burner, was developed in [102] in order to increase the electric output. The emitter material was still Yb_2O_3, but the geometry was changed from spherical to ellipsoidal in order to have a homogeneous irradiation distribution on the photocells. The water filter adopted in [E5] absorbed some of the convertible emitter radiation; in order to reduce these losses, a glass tube replaced the water filter. The glass tube between the emitter and the photocell generator was also necessary to avoid direct contact between the cells and flue gases, and to prevent the condensation of water (contained in the flue gas) onto the cell surface. Durisch et al. used silicon solar cells again, with an efficiency of 16 %, but they used smaller cells (2.4 cm x 9.8 cm), producing lower currents, in order to minimize series resistance losses in the cell circuitry. An electric output of 29 W was obtained with a thermal input of 1905 W, i.e. the electric efficiency was 1.5 %. By using preheated air for combustion at approximately 650 K in the same prototype, 1.8 % electric efficiency was achieved.
In a subsequent step, a third prototype was fabricated, based on the experience gained with the previous prototypes. A cylindrical Yb_2O_3 emitter for more homogeneous illumination of the photocells was adopted. High-efficiency silicon cells (21 % STC-efficiency) were installed. In this generator, the spaces between the cells were minimized, in order to achieve an as high active cell area as possible, while simultaneously reducing radiation losses. Moreover, infrared mirrors (glasses with 1 mm gold coating) at both ends of the glass tube reflected useful emitter radiation back to the photocells. This new system produced an electric output of 48 W with a thermal input of 1985 W, corresponding to an electric efficiency of 2.4 %. An efficiency of 2.8 % was achieved by using preheated air at approximately 620 K.

3.3 JX Crystals Inc., Issaquah (WA, USA)

In [103], Fraas et al. developed their first prototype composed of an AR-coated tungsten emitter, a simple nine layer dielectric filter composed of alternating layers of silicon and silicon dioxide and GaSb cells. The adoption of a tungsten emitter introduced the requirement for operation in an inert gas environment and consequently a need for a tightly sealed enclosure: indeed, tungsten emitter cannot operate in air. The selective AR-coated tungsten emitter was surrounded by a quartz envelope, which was coated by the dielectric filter and the space between the emitter and the quartz was back filled with Argon. The burner had concentric tubes. Fuel and air were mixed and burned in the inner tube; hot combustion gases flowed up through the inner tube, then they turned around and flowed down between the inner tube and the outer emitter support tube. The inner tube was shaped so as to heat the emitter support tube uniformly over the section surrounded by the array. The exhaust gases flowed into a recuperator section at the base of the radiant tube burner, preheating the combustion air. In this system, a thermal input of 4500 W produced an electric output of 500 W, corresponding to an electric efficiency of 11 %.

Subsequently, a new SiC emitter was presented in [104] for a micro-CHP TPV unit designed for households. In addition to the SiC emitter, the TPV unit was equipped with a double quartz shield and GaSb cells with water-cooling. In [105], Fraas et al. brought important modifications to the configuration presented in [104]. The changes were made in the SiC emitter, in order to increase performance and reduce heat dissipation. In the long term, they also suggested the use of the AR coated refractory metal foil IR emitter wrapped around the outer SiC tube as a means to control the IR spectra for maximum conversion efficiency, and use o-ring seals at the top and bottom of the PV array flanges. Thanks to these seals, the space between the PV array and the radiant tube was evacuated and back filled with a noble gas such as krypton. This was done for two reasons: first, it is necessary to protect the emitter foil against oxidation and, second, krypton reduces heat transfer losses to the PV array via thermal conduction.

Fraas et al. also investigated the possibility of designing a mini co-generator *around* a flameless regenerative burner in [106]. The TPV unit is inserted into the hot furnaces to generate electricity and low-grade heat. They used GaSb infrared sensitive photovoltaic cells, antireflection-coated refractory metal emitters and simple dielectric filters. In their experiments, an electric furnace was used with a thermal power of 610 W. An experimental TPV electric efficiency of 10.9 % was obtained for the first time using complete circuits and full size emitters, corresponding to an electric output of 66 W.

3.4 Other experiences

In 1997, a TPV system with Yb_2O_3 emitter and Si PV cells was documented by Kushch et al. in [107]. The TPV system produced 190 W of electricity, with a thermal input of 25 kW, corresponding to an electric efficiency of 0.76 %.

The following year, a TPV system, developed by Becker et al. in [108], once again composed of an Yb_2O_3 emitter and Si PV cells, produced 90 W of electricity, with a thermal input of 5625 W, corresponding to an electric efficiency of 1.6 %.

In the same year (1998), Shukla et al. from NASA presented a report [109], where they fully documented all the steps made and the technical approach followed to develop an experimental TPV test rig. The two laboratory prototype TPV generators were tested extensively. A convertible exitance of 3.7 W/cm^2 was measured at the emitter and, in separate tests of the optical filter, a 50 % convertible radiation fraction was achieved. For the two module prototypes tested without optical filters, a peak power output of 150 W and a gross system efficiency of 1.0 % were measured.

In 2001, Takashi et Masafumi presented the experimental results of two TPV prototypes in [110]. The TPV system consisted of a butane gas burner, a selective emitter and PV cells. One of the TPV generators was composed of GaSb PV cells and erbium-oxide emitter; the second generator had Si PV cells and an ytterbium-oxide emitter. With the same thermal power input of 305 W, the electricity produced by the GaSb system was 0.25 W, while the electricity produced by the Si

system was 0.11 W. The electric efficiencies were extremely low (0.082 % and 0.036 %, respectively). To improve the performance, the authors suggested using a higher number of PV cells to cover the whole mantle and a heat recovery to increase the temperature of the emitter. Indeed, the very high level of exhaust gas loss strongly suggested the necessity of a recuperator to recycle the energy from the exhaust gases.

The TPV system presented in 2002 by Palfinger et al. [111] was built by using a methane burner which should be integrated into a conventional residential heating system. The system was composed of a selective ytterbia emitter (delivering a radiation density of about 100 kW/m^2 at 1800 K with a radiation efficiency of 24 %), a quartz glass tube to prevent the exhaust gas from heating the cells and a 0.2 m^2 water-cooled monocrystalline silicon ASE SH2 cell, with an efficiency of 16 %. The maximum system efficiency was 1.0 %, with a thermal input of 12 kW. Since a crucial parameter for the market penetration of TPV is its electricity production cost, this paper also evaluated the TPV system economic feasibility, by considering retail prices in 2002. It was demonstrated that by passing from the less favorable scenario (system efficiency of existing technology of 1.0 %) to the most favorable scenario (system efficiency of future technology of 5.0 %), the total investment cost could drop from 3000 Euro/kW_{el} to 340 Euro/kW_{el}.

In the following year (2003), a micro-TPV system was presented by Yanga ed al. in [112]. The system used hydrogen as fuel and was capable of delivering power in the order of some watts in a package with a volume of less than 1 cm^3. Hydrogen was chosen as the fuel because of its high heating value, short reaction time and high-flame speed. A micro-cylindrical burner was adopted and a high and uniform temperature was achieved along its walls. Two different types of emitters were used: a broadband emitter made of SiC and a selective emitter with a micro-structure on its surface made of Co/Ni-doped MgO. In such a micro-TPV system, the presence of a filter complicates the fabrication and enlarges the space needed. Therefore, no filter was adopted. However, the selective emitter may have the same function as the filter. Low band gap PV cells GaSb and GaInAsSb were used. The authors concluded that the selective emitter is very useful in improving the performance of micro-TPV systems.

In 2007, a significant paper was published by Basu et al., in order to understand microscale radiation and its role in TPV devices [113]. Though this paper did not report the experimental development of a TPV system, it is included in this review paper since paper [113] outlines several critical issues of TPV systems. Emphasis is given to the development of wavelength-selective emitters and filters and the aspects of microscale heat transfer as applied to TPV systems. In fact, since the most obvious drawbacks of TPV devices are their low conversion efficiency and low throughput due to a large amount of unusable radiation, a possible solution is the application of the principles of microscale radiation to TPV systems. For example, the efficiency can be increased by using micro/nanostructured emitters and filters. On the other hand, the throughput can be enhanced nearly 10-fold by reducing the distance between the emitter and the TPV cell to sub-wavelength dimensions. Since the length scales are comparable to the wavelength, neither the near-field energy enhancement nor the working principles of micro/nanostructured emitters/filters can be comprehensively explained by conventional radiation heat transfer. Hence, paper [113] concludes that a clear understanding of the principles of microscale radiation is required for the further advancement of TPV technology.

Finally, in 2011, Chou et al. [114] developed a micro-combustor suitable for TPV applications, which produces a high and uniform temperature distribution along the wall. The combustor, of 3.5 mm in diameter, was studied thoroughly, to evaluate the effect of backward facing step height on the performance of the system. In fact, a proper step height can facilitate the recirculation of combustion mixture near the wall, enhancing the mixing process of combustion around the rim of the tube and ensuring a complete and stable combustion. For simplicity of fabrication, SiC is employed as the emitter. A novel modular micro-TPV system consisting of a series of planar combustors, emitters, filters and PV cells is under development with the following advantages: (1) the planar design will simplify the fabrication and assembly; (2) the recuperator will not only improve the efficiency of the system, but also make it possible for us to use liquid fuel or liquefied

gas; (3) the modular layout makes it possible to adjust the amount of micro-TPV units according to different power requirements.

3.5 FEATURES OF TPV PROTOTYPES

The electric efficiency of TPV systems is summarized in Figure 7, as a function of electric power. Both measured and predicted values are reported. It can be seen that the electric efficiency increases with TPV system size, as expected. With the exception of very small TPV units, most prototypes have an electric power in the range of 10 – 300 W and the measured electric efficiency ranges from some percentage points up to 7.5 %. Only the JX Crystals Inc. product, with a 66 W electric power, claims a 10.9 % electric efficiency and also envisions a 12.3 % electric efficiency, if the size is increased to 1.5 kW. A calculated target efficiency value of 24.5 % is also reported in [118].
All the data gathered from the bibliographical review is reported in Table 2, for all the main components of the TPV unit (burner, emitter, filter, cells).
Table 1 reports the type of fuel, the emitter material, its type, the surface temperature and the emitter radiation efficiency, the presence or absence of the filter and its material, the type of cells and their efficiency at the Standard Test Condition STC (AM 1.5, 100 mW/cm^2). The subsequent columns report the values of the power introduced with the fuel, the electric power and the consequent electric efficiency. The last column states whether the performance comes from an experimental measurement (experi.) or it is predicted (pre.) by using a numerical model or by envisioning further system improvements. Therefore, Table 1 provides a synoptic view of the state-of-the-art technological level of TPV systems and also highlights possible future pathways for research and development of TPV systems.

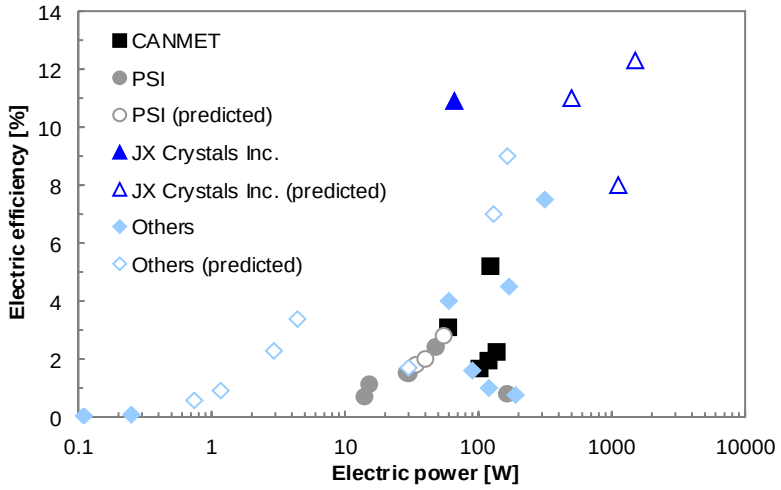

Fig. 7 TPV electric efficiency vs. electric power

4. Concluding remarks

The thermophotovoltaic conversion has gained more and more attention in the last decade. Nevertheless this field of the research is still under development.
This paper wishes to outline the current state-of-the-art of thermophotovoltaic generation under both the analytical and the experimental point of view.
More in details, a deeply investigation of all the analytical aspects which involve the thermophotovoltaic conversion was presented in this study; each term which composes the conversion efficiency between the power introduced with fuel and the produced electric output is

investigated. All the components which compose a TPV generator are investigated in terms of materials and engineering solutions.
A comprehensive review of all the prototypes developed up to present is finally reported and critically analyzed. This analysis showed that present TPV systems present low electric efficiencies (not higher than 5-6 %) compared to other technologies for micro-generation close to a few kW. This can be due primarily to the fact that the effort of many researchers was to develop a "feasible" TPV system, i.e. a TPV system which can be straightforwardly applied and that is economically affordable. This was done by using easy-to-find components (for instance, Si-based PV cells), not too expensive materials or, in some cases, by adapting existing technologies. However, in authors' opinion, this could be the correct approach to make TPV systems penetration faster.
In the future, the possibility of lowering the cost of high efficiency in-band PV cell and exploiting the selective properties of rare earth materials could be the direction to be followed. In particular, the PV cells can highly benefit from the expansion of concentrated photovoltaic technology.
The overall low electrical efficiency can also be due to a lack of component integration and system engineering. In the former case, it can be highlighted that in TPV systems, combining the highest efficiency achievable in a single component (burner, emitter, filter, PV cell) does not necessarily result in a high overall system efficiency. Regarding the latter issue, in many practical cases some features of the engineering phase are sometimes underestimated, such as for instance the use and design of heat exchangers (both for air pre-heating and for PV cell cooling) or the introduction of advanced monitoring and control systems to optimize system operation. As a conclusion, the research in the field of integration and system engineering should be one of the key activities in order to enhance the electrical efficiency. Indeed, it has been yet demonstrated that, by using optimized components and special materials, higher electric efficiencies can be reached, but on the other hand the short term feasibility of these systems could be compromised.

Tab. 2. Summary of TPV prototypes

Reference	Burner fuel	Emitter material	Emitter type	Emitter surface temp.	ς_{rad}	Filter	PV cells	STC* efficiency	P_{fuel}	P_{el}	ς_{el}	Type of result
				[K]	[%]			[%]	[W]	[W]	[%]	
[13]		SiC	porous foam	1558	21.3	coatings of SiO2 and TiO3 on glass	GaSb		8260	123	5.20	experi.
[15]		Yb_2O_3-coated on Al_2O_3	foam ceramic				Si		2000	14	0.70	experi.
[15]		Yb_2O_3	fibrous mantle				Si		2000	30	1.50	experi.
[15]		Yb_2O_3	fibrous mantle			TCO	CuInSe2 thin-film		2000	40	2.00	pre.
[27]	methane	W-coated on SiC				glass tube	GaSb		1800	30	1.70	experi.
[27]	methane	W micro structured				glass tube	GaSb		1800	130	7.00	pre.
[61]	methane	Kanthal					GaSb		1460	60	4.00	experi.
[99]		Sic	coated fiber mat		20.4		GaSb	20.0	6120	102	1.67	experi.
[99]		Sic	honeycomb plaque		22.9		GaSb	20.0	6120	119	1.94	experi.
[99]		SiC	porous foam		26.7		GaSb	20.0	6120	137	2.24	experi.
[99]		(1) Yb_2O_3 fiber felt; (2) ceramic fiber-coated on SiC	Two emitters arranged in tandem		31.0		Si GaSb	36.0 20.0	1920	60	3.09	experi.
[101]	butane	Yb_2O_3	spherical emitter				Si		1350	15	1.13	experi.
[102]	butane	Yb_2O_3				glass tube	Si	16.0	1905	29	1.52	experi.
[102]	butane	Yb_2O_3				glass tube	Si	16.0	1905	34	1.80	pre.
[102]	butane	Yb_2O_3				glass tube	Si	21.1	1985	48	2.41	experi.
[102]	butane	Yb_2O_3				glass tube	Si	21.1	1985	55	2.80	pre.
[103]	diesel	W-coated on SiC		1600			GaSb		4500	500	11.00	pre.
[105]		SiC				double quartz tube	GaSb		14000	1120	8.00	pre.
[105]		W-coated on SiC		1525			GaSb		12200	1500	12.30	pre.
[106]	regenerative burner	Yb_2O_3-coated on Al_2O_3				dielectric filters	GaSb		606	66	10.90	experi.
[107]		Yb_2O_3					Si		25000	190	0.76	experi.
[108]	propane	Yb_2O_3				dielectric filters	Si		5625	90	1.60	experi.
[108]	propane	Yb_2O_3		2100		dielectric filters	Si		1830	165	9.00	pre.
[109]				2000					3778	170	4.50	experi.
[109]				2100					4200	315	7.50	experi.
[110]	butane gas	Yb_2O_3	fibrous mantle			no	Si	10.4	305	0.11	0.04	experi.
[110]	butane gas	Er_2O_3	fibrous mantle			no	GaSb		305	0.25	0.08	experi.
[111]	methane	Yb_2O_3		1800	24.0	quartz tube	Si	16.0	12000	120	1.00	experi.
[112]	hydrogen	SiC		1265		no	GaSb		130	0.74	0.57	pre.
[112]	hydrogen	SiC		1265		no	GaInAsSb		130	1.2	0.91	pre.
[112]	hydrogen	Co/Ni-doped MgO				no	GaInAsSb		130	2.9	2.28	pre.
[112]	hydrogen	Co/Ni-doped MgO				no	GaSb		126	4.4	3.48	pre.
[117]	butane	Yb_2O_3	porous foam	1735		SnO_2 film on quartz	Si		1980	48	2.42	experi.
[118]	diesel	ErAG-coated on SiC		1523		quartz tube	AlGaAs/ GaAs		12157	2976	24.50	pre.

Acknowledgements

The research program on the Thermo -Photo-Voltaic generation developed in *IMEM – CNR* is supported from the project "*Nuove tecnologie e strumenti per l'efficienza energerita e l'utilizzo delle fonti rinnovabili negli usi finali civili*" within the agreement between *Regione Lombardia* and *CNR*.

Nomenclature

Abbreviations

CHP	Combined Heat and Power
INV	Inverter
LHV	Lower Heating Value
TPV	Thermo Photo Voltaic

Symbols

c	speed of light [m/s]
FF	fill factor [-]
h	Plank constant [J·s]
h_{gas}	combustion products specific enthalpy [kJ/kg]
h_{air}	air specific enthalpy [kJ/kg]
k_B	Boltzman constant [J/K]
I	radiant intensity [W/m^2/nm]
$\dot{m}_{air}$	air mass flow rate [kg/s]
$\dot{m}_{fuel}$	fuel mass flow rate [kg/s]
$\dot{m}_{gas}$	combustion products mass flow rate [kg/s]
P	power [kW]
Q_{TH}	thermal Power [kW]
S	surface [m^2]
T	temperature [K or °C]
J_{SC}	short Circuit Current [A]
V_{OC}	open Circuit Voltage [V]
ϵ	grey body emissivity [-]
ε	heat exchange effectiveness [-]
η	efficiency [-]
λ	wavelength [m or nm]

Subscript

ac	alternating current
cc	combustion
dc	direct current
el	electrical
em	emitter
gap	in band (gap)

rad	radiant
TH	thermal
VF	view factor

References

[1] V.M. Andreev, V.A. Grilikhes, V.P. Khvostikov, O.A. Khvostikova, V.D. Rumyantsev, N.A. Sadchikov, and M.Z. Shvarts. *Concentrator PV modules and solar cells for TPV systems*. Solar Energy Materials & Solar Cells, 84:3–17, 2004.

[2] V.M. Andreev, V.P. Khvostikov, O.A. Khvostikova, A.S. Vlasov, P.Y. Gazaryan, N.A. Sadchikov, and V.D. Rumyantsev. *Solar thermophotovoltaic system with high temperature tungsten emitter*. In conference record of the thirty-first IEEE Photovoltaic Specialists Conference, pages 671– 674, 3-7 Jan 2005.

[3] N-P Harder and P Wurfel Theoretical limits of thermophotovoltaic solar energy conversion" Semiconductor Science and Technology, Volume 18, Number 5, May 2003

[4] Morrison O, Seal M Dr, West E, Connelly W 1999 4th NREL Conf. on Thermophotovoltaic Generation of Electricity (AIP Conf. Proc. vol 460) (New York: AIP) p 488

[5] T. Bauer, I. Forbes, R. Penlington, and N. Pearsall. *The potential of thermophotovoltaic heat recovery for the glass industry*. In T.J. Coutts, G. Guazzoni, and J. Luther, editors, proceedings of the 5th Conference Thermophotovoltaic Generation of Electricity, volume 653, pages 101–110, Rome, Italy, 2003.

[6] Coutts T 2001 Clean Electricity from Photovoltaics ed M D Archer and R Hill (London: Imperial College Press) p 482

[7] DeBellis C L, Scotto MV, Fraas L, Samaras J, Waston R C and Scoles S W 1999 *4th NREL Conf. on Thermophotovoltaic Generation of Electricity (AIP Conf. Proc. vol 460)* (New York: AIP) p 362

[8] Becker F E, Doyle E F and Shukla K 1999 *4th NREL Conf. on Thermophotovoltaic Generation of Electricity (AIP Conf. Proc. vol 460)* (New York: AIP) p 394

[9] Fraas L, Ballantyne R, Hui S, Ye S-Z, Gregory S, Keyes J, Avery J, Lamson D and Daniels B 1999 *4th NREL Conf. on Thermophotovoltaic Generation of Electricity (AIP Conf. Proc. vol 460)* (New York: AIP) p 480

[10] Stone K W, Chubb D L, Wilt D M and Wanlass M W 1996 *2nd NREL Conf. on Thermophotovoltaic Generation of Electricity (AIP Conf. Proc. vol 358)* (New York: AIP) p 198

[11] Durisch W, Grob B, Mayor J-C, Panitz J-C and Rosselet A 1999 *4th NREL Conf. on Thermophotovoltaic Generation of Electricity (AIP Conf. Proc. vol 460)* (New York: AIP) p 403

[12] Nelson R E 1996 *2nd NREL Conf. on Thermophotovoltaic Generation of Electricity (AIP Conf. Proc. vol 358)* (New York: AIP) p 221

[13] K. Qiu, A.C.S. Hayden, Development of a novel cascading TPV and TE power generation system, Applied Energy, Volume 91, Issue 1, March 2012, Pages 304-308, ISSN 0306-2619, 10.1016/j.apenergy.2011.09.041.

[14] De Pascale, A., Ferrari, C., Melino, F., Morini, M., Pinelli, M., "Integration between a Thermo-Photo-Voltaic generator and an Organic Rankine Cycle", Applied Energy (2012) – APEN3089 – http://dx.doi.org/10.1016/j.apenergy.2011.12.043

[15] Kruger J S, Guazzoni G and Nawrocki S J 1999 4th NREL Conf. on Thermophotovoltaic Generation of Electricity (AIP Conf. Proc. vol 460) (New York: AIP) p 30

[16] Kittl E and Guazzoni G 1972 Design analysis of TPVgenerator system Proc. 25th Power Sources Symp. pp 106–9

[17] Guazzoni G 1972 High temperature spectral emittance of oxides of erbium, samarium, neodymium and ytterbium Appl. Spectrosc. 26 60–5

[18] Mondt J F and Nesmith B J 1998 STAIF98, January 1098

[19] Kailash Shukla, Edward Doyle, and Frederick Becket "Thermophotovoltaic Energy Development Program Conversion" NASA/CR-- 1998-208512 TR7020-003-98

[20] White D C, Wedlock B D and Blair J 1961 Recent advance in thermal energy conversion *Proc. 15th Power Sources Conf*. pp 125–32

[21] Wedlock B D 1963 Thermo-photo-voltaic conversion *Proc. IEEE* **51** 694–8

[22] Bitnar et al, Se. Sci. Tech. 18, 221, 2003

[23] Fraas et al IV NREL Conf. AIP proc. 460 1999

[24] Fraas et al. Proc 17° EuPV, 2001

[25] W. E. Horne et al., 5° Conf. On TPV, AIP proc. 91, 2002

[26] Qiu et al., 5° Conf. on TPV, AIP proc. 49, 2002

[27] T. Aicher et al 6° Conf. On TPV, 71,2004

[28] European project THEREV Resp. Massimo Mazzer IMEM

[29] G Colangelo, A de Risi and D Laforgia "New approaches to the design of the combustion system for thermophotovoltaic applications" Semicond. Sci. Technol. 18 (2003) S262–S269

[30] Lewis M. Fraas, James E. Avery, Han Xiang Huang "THERMOPHOTOVOLTAICS: HEAT AND ELECTRIC POWER FROM LOW BANDGAP "SOLAR" CELLS AROUND GAS FIRED RADIANT TUBE BURNERS"

[31] K. Qiu, A.C.S. Hayden, Fuel 85 (2006) 1094–1100

[32] Seal M, Christ S, Campbell G, West E and Fraas L 1997 Thermophotovoltaic generation of power for use in a series hybrid vehicle SAE-972648, SAE, Detroit

[33] Christ S and Seal M 1997 Viking 29—a thermophotovoltaic hybrid vehicle designed and built at Western Washington University SAE-972650, SAE, Detroit

[34] T.A. Butcher, J.S. Hammonds, E. Horne, B. Kamath, J. Carpenter, D.R. Woods, Heat transfer and thermophotovoltaic power generation in oil-fired heating systems, Applied Energy, Volume 88, Issue 5, May 2011,

[35] S.K. Chou, W.M. Yang, K.J. Chua, J. Li, K.L. Zhang, Development of micro power generators - A review, Applied Energy, Volume 88, Issue 1, January 2011,

[36] G. Mattarolo. *High Temperature Recuperative Burner*. In 1st Conference for Thermophotovoltaics: Science to Business, 2005.

[37] L.M. Fraas, J.E. Avery, and H. Xiang Huang. *Thermophotovoltaics: heat and electric power from low bandgap "solar" cells around gas fired radiant tube burners*. In conference record of the twenty-ninth IEEE Photovoltaic Specialists Conference, Photovoltaic Specialists Conference, 2002.

[38] L.M. Fraas, J.E. Avery, and H.X. Huang. *Thermophotovoltaic furnacegenerator for home using low bandgap GaSb cells*. Semicond. Sci. Technology, 18:S247–S253, 2003.

[39] G. Torsello, M. Lomascolo, A. Licciulli, D. Diso, S. Tundo, and M. Mazzer. *The origin of highly efficient selective emission in rare-earth oxides for thermophotovoltaic applications*. Nature Materials, 3:632, 2004.

[40] R.E. Nelson. *Thermophotovoltaic Emitter Development*. In proceedings of the 1st NREL/TPV Conference, pages 80–98, 1994.

[41] G.A. Holmquist. *TPV Power source development for an unmanned undersea vehicle*. In proceedings of the 1st NREL/TPV Conference, pages 308–314, 1995.

[42] B. Bitnar, W. Durisch, J.-C. Mayor, H. Sigg, and H.R. Tschudi. *Characterisation of rare earch selective emitters for thermophotovoltaic applications*. Solar Energy Materials & Solar Cells, 73:221–234, 2002.

[43] Gombert A (2003) An overview of TPV emitter technologies. Proceeding of the 5th Conference on thermophotovoltaic generation of electricity, Rome, Italy, 16–19. Sep. 2002, Institute of Physics, pp 123–131

[44] Licciulli A, Diso D, Torsello G, Tundo S, Maffezzoli A, Lomascolo M, Mazzer M (2003) The challenge of high-performance selective emitters for thermophotovoltaic applications. Semicond Sci Technol 18:174–183

[45] Adair PL, Rose MF (1995) Composite emitters for TPV systems. Proceedings of the 1st NREL conference on thermophotovoltaic generation of electricity, Copper Mountain, Colorado, 24–28 July 1994. American Institute of Physics, pp 245–262

[46] Nelson RE (1995) Thermophotovoltaic emitter development. Proceedings of the 1st NREL Conference on thermophotovoltaic generation of electricity, Copper Mountain, Colorado, 24–28 July 1994. American Institute of Physics, pp 80–96

[47] Chubb DL (1990) Reappraisal of solid selective emitters. Proceedings of the 21st IEEE photovoltaic specialists conference, IEEE, pp 1326–1333

[48] Dieke GH (1968) Spectra and energy levels of rare earth ions in crystals. Wiley, Washington 32. Guazzoni GE (1972) High-temperature spectral emittance of oxides of erbium samarium, neodymium and ytterbium. Appl Spectrosc 26:60–65

[49] Touloukian YS, DeWitt DP (1972) Thermophysical properties of matter, Vol. 8, Thermal radiative properties: nonmetallic solids. Plenum Press, New York

[50] Lay LA (1991) Corrosion resistance of technical ceramics. Her Majestys Stationery Office (HMSO)

[51] Thomas Bauer “Thermophotovoltaics Basic Principles and Critical Aspects of System Design” Springer-Verlag Berlin Heidelberg 2011

[52] Richerson DW (1992) Modern ceramic engineering: Properties, Processing and use in design, 2nd edn. Marcel Dekker, New York

[53] Kohl WH (1967) Handbook of materials and techniques for vacuum devices. Reinhold Publishing Corporation, New York

[54] Guyer EC, Brownell DL (1999) Handbook of applied thermal design. Taylor & Francis, London

[55] Noreen DL, Honghua D (1995) High power density thermophotovoltaic energy conversion. Proceedings of the 1st NREL Conference on Thermophotovoltaic generation of electricity. Copper Mountain, Colorado, US, 24–28 July 1994. American Institute of Physics, pp 119–132

[56] U.C. Pernisz, C.K. Saha, “Silicon carbide emitter and burner elements for a TPV converter”, First NREL Conf. Thermophotovoltaic Generation of Electricity, Copper Mountain, CO, 1994, pp.99 -105.

[57] G. Nicholas, P. C. Saxton, Angela L. Moran, Mark J. Harper, Keith W. Lindler, “Thermophotovoltiac Emitter Material Selection and Design”, KAPL Atomic Power Laboratory,KAPL-P-000184,July1997,URL:

[58] T. Coutts. *An overview of thermophotovoltaic generation of electricity*. Solar Energy Materials & Solar Cells, 66:443–452, 2001.

[59] T. D. Rahmlow Jr., D.M. Depoy, P.M. Fourspring, H. Ehsani, J. E. Lazo-Wasem, and E. J. Gratrix. *Development of Front Surface, Spectral Control Filters with greater Temperature Stability for Thermophotovoltaic Energy Conversion*. In proceedings of the 7th conference on

Thermophotovoltaic Generation of Electricity, volume 890, pages 59–67, El Escorial, Spain, September 2006.

[60] T. Nagashima, K. Okumura, and M. Yamaguchi. *A germanium back contact type thermophotovoltaic cell*. In proceedings of the 7 th conference on Thermophotovoltaic Generation of Electricity, volume 890, pages 172–181, El Escorial, Spain, September 2006.

[61] G. Mattarolo, J. Bard, and J. Schmid. *Experimetal Testing and Modelling approach for a TPV Prototype*. In proceedings of the 7 th conference on Thermophotovoltaic Generation of Electricity, volume 890, pages 264–272, El Escorial, Spain, September 2006.

[62] Francis O'Sullivan, Ivan Celanovic, Natalija Jovanovic, John Kassakian "Optical characteristics of one-dimensional Si/SiO2 photonic crystals for thermophotovoltaic applications" JOURNAL OF APPLIED PHYSICS 97, 033529 s 2005 d

[63] Hyun-Yong Lee, Sung-June Cho, Gi-Yeon Nam "Multiple-wavelength-transmission filters based on Si-SiO2 one-dimensional photonic crystals" JOURNAL OF APPLIED PHYSICS 97, 103111 s 2005 d

[64] Francis O'Sullivan, Ivan Celanovic, Natalija Jovanovic, John Kassakian "Optical characteristics of one-dimensional Si/SiO2 photonic crystals for thermophotovoltaic applications" JOURNAL OF APPLIED PHYSICS 97, 033529 s 2005 d

[65] Hyun-Yong Lee, Sung-June Cho, Gi-Yeon Nam "Multiple-wavelength-transmission filters based on Si-SiO2 one-dimensional photonic crystals" JOURNAL OF APPLIED PHYSICS 97, 103111 s 2005 d

[66] DM DePoy, PM Fourspring, PF Baldasaro, JF Beausang, EJ Brown, MW Dashiel, KD Rahner, TD Rahmlow, JE Lazo-Wasem, EJ Gratrix and B Wernsman, " Thermophotovoltaic Spectral Control", LM-04K053, June 9, 2004.

[67] E. Yablonovitch, Phys. Rev. Lett. **58**, 2059 s1987d.

[68] J. D. Joannopoulos, R. Meade, and J. Winn, *Photonic Crystals* sPrinceton University Press, Princeton, 1995d.

[69] J. C. Knight, J. Broeng, T. A. Birks, and P. St. J. Russell, Science **282**, 1476 s1998d.

[70] Lewis Fraas, James Avery, Enrico Malfa, Joachim G. Wuenning, Gary Kovacik, Chris Astle' Thermophotovoltaics for Combined Heat and Power Using Low NOx Gas Fired Radiant Tube Burners - JX Crystals Inc., 1105 12th Ave. NW, Suite A2, Issaquah, WA 98027, USA

[71] Brockmann, H., 1994, "Analytic angle factors for the radiant interchange among the surface elements of two concentric cylinders," *Int. J. Heat Mass Transfer*, vol. 37, no. 7, pp. 1095-1100

[72] Leuenberger, H. and Person, R.A., 1956, "Compilation of radiation shape factors for cylindrical assemblies," *paper no. 56-A-144*, ASME, November.

[73] Hamilton, D.C. and Morgan, W.R., 1952, "Radiant-interchange configuration factors," *NASA TN* 2836.

[74] Alexandrov, V.T., 1965, "Determination of the angular radiation coefficients for a system of two coaxial cylindrical bodies," *Inzh. Fiz. Zh.*, vol. 8, no. 5, pp. 609-612.

[75] Howell, J.R., A Catalog of Radiation Heat Transfer Configuration Factors

[76] Modest, M.F., Radiative Heat Transfer, 2nd Ed., McGraw-Hill, 2003.

[77] M. G. Mauk and V. M. Andreev, Semicond. Sci. Technol. **18** (2003) S191–S201

[78] Michael G. Mauk, Mid-infrared Semiconductor Optoelectronics, Springer Series in Optical Sciences, 2006, Volume 118/2006, 673-738

[79] V.P. Khvostikov, O.A. Khvostikova, P.Y. Gazaryan, S.V. Sorokina, N.S. Potapovich, A.V. Malevskaya, M.Z. Shvarts, N.A. Kaluzhniy, V.M. Andreev, V.D. Rumyantsev, Photoconverters for Solar TPV Systems, Photovoltaic Energy Conversion, Conference Record of the 2006 IEEE 4th World Conference on, Issue Date: May 2006

[80] V. M Andreev, An overview of TPV cell technologies Proceedings of the 5th TPV conference, rome 2002

[81] Minkin TPV HISTORY FROM 1990 TO PRESENT & FUTURE TRENDS Lewis Fraas and Leonid Presented at the 7th World TPV Conference (Thermophotovoltaic Generation of Electricity). El Escorial, Madrid (SPAIN). 25-27 September 2006

[82] M. Taguchi, K. Kawamoto, S. Tsuge, T. Baba, H. Sakata, M. Morizane, K. Uchihashi, N. Nakamura, S. Kiyama, and O. Oota, Prog. Photovoltaics Res. Applic. **8**, 503 (2000),

[83] M. Bosi, C. Pelosi: Progress in Photovoltaics: Research and Applications 15 (2007) 51-68.

[84] M. K. Hudait, M. Brenner, S.A. Ringel, Solid-State Electronics 53 (2009) 102–106

[85] Andreev - Sol.en.mat. sol. cell 84 (2004) 3

[86] W Chan, R. Huang, C. Wang, J. Kassakian, J. Joannopoulos, I. Celanovi, Solar Energy Materials & Solar Cells 94 (2010) 509–514

[87] C. A. Wang,a) H. K. Choi, and S. L. Ransom, G. W. Charache, L. R. Danielson, and D. M. DePoy, Appl. Phys. Lett. 75, 1305 (1999);

[88] Sulima, O.V.; Bett, A.W.; Dutta, P.S.; Mauk, M.G.; Mueller, R.L., Photovoltaic Specialists Conference, 2002. Conference Record of the Twenty-Ninth IEEE , (2002) 892 – 895

[89] S. M. Sze, Physics of semiconductors devices, 2nd ed. John Wiley and Sons Inc.

[90] Khvostikov, V.P.; Khostikov, O.A.; Oliva, E.V.; Rumyantsev, V.D.; Shvarts, M.Z.; Tabarov, T.S.; Andreev, V.M, Photovoltaic Specialists Conference, 2002. Conference Record of the Twenty-Ninth IEEE , vol., no., pp. 943- 946, 19-24 May 2002

[91] M. Bosi, G. Attolini, M. Calicchio, C. Ferrari, C. Frigeri, E. Gombia, A. Motta, F. Rossi, Journal of Crystal Growth 318 (2011) 341

[92] R. Jakomin, G. Beaudoin, N. Gogneau, B. Lamare, L. Largeau, O. Mauguin, I. Sagnes, Thin Solid Films Volume 519, Issue 13, 29 April 2011, Pages 4186–4191)

[93] H. Haeberlin, L. Borgna, M. Kaempfer, U. Zwahlen, Total efficiency – A new quantity for better characterization of grid-connected PV inverters

[94] Frank Vignola, Fotis Mavromatakis, Jim Krumsick, PERFORMANCE OF PV INVERTERS

[95] Dan Ton, Ward Bower, Summary Report on the DOE High-tech Inverter Workshop January 2005

[96] Qiu K, Hayden A C S. Thermophotovoltaic generation of electricity in a gas fired heater: Influence of radiant burner configurations and combustion processes. Energy Convers Manage 2003;44:2779-2789.

[97] Gombert A. An overview of TPV emitter technologies. AIP Conference Proceedings, Volume 653, pp. 123-131 (2003).

[98] Qiu K, Hayden A C S. Performance of low bandgap thermophotovoltaic cells in a small cogeneration system. Solar Energy 2003;74:489-495.

[99] Qiu K, Hayden A C S. Thermophotovoltaic power generation systems using natural gas-fired radiant burners. Solar Energy Materials and Solar Cells 2007;91:588-596.

[100] Qiu K, Hayden A C S. Development of a novel cascading TPV and TE power generation system. Applied Energy 2012;91:304-308.

[101] Durisch W, Grob B, Mayor J C, Panitz J C, Rosselet A. Interfacing a small thermophotovoltaic generator to the grid. Fourth NREL conference on thermophotovoltaic generation of electricity 1999;460:403-416.

[102] Durisch W, Bitnar B, Mayor J C, Fritz von Roth, Sigg H, Tschudi H R, Palfinger G. Small self-powered grid-connected thermophotovoltaic prototype system. Applied Energy 2003;74:149-157.

[103] Fraas L M, Samaras J E, Huang H X, Minkin L M, Avery J E, Daniels W E, Hui S. TPV generators using the radiant tube burner configuration. 2001.

[104] Fraas L M, Avery J E, Huang H X. Thermophotovoltaics: heat and electric power from low bandgap "solar" cells around gas fired radiant tube burners. 2002.

[105] Fraas L M, Avery J E, Malfa E, Wuenning J C, Kovacik G, Astle C. Thermophotovoltaics for combined heat and power using low NOx gas fired radiant tube burner. 2003.

[106] [106] Fraas L M, Avery J E, Daniels W E, Huang H X, Malfa E, Venturino M, Testi G, Mascalzi G, Wuenning J C.TPV tube generators for apartment building and industrial furnace applications. 2003.

[107] Kushch A S, Skinner S M, Brennan R, Sarmiento P A. Development of a cogenerating thermophotovoltaic powered combination hot water heater/hydronic boiler. 1997.

[108] Becker F E, Doyle E F, Shukla K. Operating experience of a portable thermophotovoltaic power supply. 1998.

[109] Shukla K, Doyle E, Becket F. Thermophotovoltaic Energy Development Program Conversion. NASA/CR-- 1998-208512.

[110] Takashi A, Masafumi Y. Analysis of energy balance of electricity and heat generated by TPV generators. Solar Energy Materials and Solar Cells 2001;66:579-583.

[111] Palfinger G, Bitnar B, Durish W, Mayor JC, Grutzmacher D, Gobrecht J. Cost estimates of electricity from a TPV residential heating system. Proc. Of the Fifth Conference on Thermophotovoltaic Generation of Electricity 2002.

[112] Yanga W M, Chou S K , Shu C, Li Z W, Xue H. Research on micro-thermophotovoltaic power generators. Solar Energy Materials and Solar Cells 2003;80:95-104.

[113] Basu S, Chen YB, Zhang ZM. Microscale radiation in thermophotovoltaic devices – a review. Int. J. Energy Res. 2007;31:689-716.

[114] Chou SK, Yang, WM, Chua, KJ, Li, J., Zhang, KL. Development of micro power generators – A review. Applied Energy 2011;88:1-16.

[115] Bitnar B, Durisch W, Fritz von Roth, Palfinger G, Sigg H, Grutzmacher D, Gobrecht J, Meyer E M, Vogt U, Meyer A, Heeb A. Progress in thermophoyovoltaic converters. In: Mart A, Luque A. Next generation photovoltaic, Taylor & Francis; 2003, p. 223-245.

[116] Durisch W, et al. Small self-powered grid-connected thermophotovoltaic prototype system. Applied Energy 2003;75:11-15.

[117] Bitnar B, Mayor J C, Durisch W, Meyer A, Palfinger G, Fritz von Roth, Sigg H. Record electricity-to-gas power efficiency of silicon solar cell based TPV system. Photovoltaic Specialists Conference 2003;653:18-28.

[118] Colangelo G, De Risi A, Laforgia D. Experimental study of a burner with high temperature heat recovery system for TPV applications. Energy Conversion & Management 2006;47:1192-1206.

A DNS method for particle motion to establish boundary conditions in coal gasifiers

Efstathios E. (Stathis) Michaelides[a] and Zhigang Feng[b]

[a] Department of Engineering, Texas Christian University, Fort Worth, TX 76132 USA, E.Michaelides@tcu.edu
[b] Department of Mechanical Engineering, UTSA, San Antonio TX, 78259, USA, zhigang.feng@utsa.edu

Abstract:

Coal gasification is becoming a common method of producing synthetic gas to be used subsequently with reduced pollution products. The coal gasifiers are essentially chemical reactors where the coal particles are fluidized and react chemically with the gas. The modelling of the gasifiers involves both particle flow and heat transfer processes. Direct Numerical Simulation (DNS) methods for particulate flows have been well-developed in the last decade. Following the significant advances in computational power, DNS methods may now be employed to solve relatively complex particulate flow problems and provide us with scientific, reliable and validated information on fluid-particle interactions that will lead to the design optimization of gasifiers. While most of the DNS methods that have been developed pertain to isothermal flows, the effects of heat and mass transfer on the momentum and energy exchanges are very important in all practical applications. This because, for most practical applications of particulate flow – e.g. fluidized bed reactors, gasifiers, coal burners and chemical reactor columns – the heat and mass transfer processes influence significantly the flow and, in addition, are of primary interest to engineers. We have developed a new DNS method, which uses an extension of the Immersed Boundary Method (IBM) to track individual particles and calculate the Lagrangian motion as well as the heat transfer from them. The model enables us to examine the lift of hotter particles due to the buoyancy their temperature field creates; the temperature field around the particles; and the effect of the Reynolds and Grashof numbers on the flow and heat transfer of suspensions. This model is also of use in the determination of the boundary conditions of particles at solid boundaries, conditions that are essential to all two-fluid models. The simulations show that a significant slip exists along the longitudinal direction at the walls of the gasifiers and that the size of the particles is the primary parameter that determines this velocity slip.

Keywords:

Coal gasification, DNS, heat transfer, mass transfer, Immerse Boundary Method, boundary conditions.

1. Introduction

Computer simulations of particulate flows are very important in many engineering applications and natural processes [1-5]. Because of their many applications, particle simulations by different techniques have been developed and are presented in many studies, some of which are described below. Certain numerical techniques [2, 6-8] have taken into consideration the thermal convection that occurs during the heat transfer process. Various studies have been done to describe multiphase flow by two-fluid or Eulerian-Eulerian models [1, 9-13]. In particular, [9] compared the two-fluid model for laminar flow with the direct numerical simulation (DNS) method of bubbly flows and obtained good results with few adjustable constants. Another study [11] presented an Eulerian-Eulerian, or two-fluid model and discussed the limitations of the application of such models. In [14] a similar Eulerian-Eulerian model was introduced, in which the particle inertia and particle settling effects were taken into account.

One of the more recent studies that was done on DNS of two-phase fluid flow with a fictitious domain was implemented in [15], in which spherical and non-spherical particles were investigated. Numerous studies have been done on the implementation of the no-slip boundary conditions [2, 5,

16, 17, 18]. In [16] the boundary conditions are modeled with the use of an external force. In [17] three traditional ways are described in which particle-wall interactions take place: a) Specular reflections, b) Bounce-back reflections, and c) Maxwellian reflections. In most numerical studies with two-fluid models, the no-slip boundary conditions are applied for the two-phase flows at the impermeable wall. The importance of the correct boundary conditions in the two fluid models, in mixture theory and in Computational Fluid Dynamics (CFD) applications was the subject of another study [19], which concluded that the boundary conditions for the solid phase affect significantly the solutions of two-fluid models. For example, the application of an erroneous no-slip condition at the boundary, affects significantly the numerical solution at any boundary layer close to this boundary. Since the boundary layer determines the heat transfer rate, such an erroneous condition will affect significantly calculations on heat or mass transfer at the boundary. Depending on the flow conditions, errors of 30-70% are not uncommon.

In this study, a DNS method is applied to simulate the flow and heat/mass transfer in a coal gasifier. The coal particles are assumed to be spherical with diameters d = 0.6 cm and d = 0.4 cm. The Lagrangian motion of solid particles at and close to the impermeable vertical walls is simulated and studied in order to obtain conditions for the slip of the particle phase at vertical walls. Such simulations and the average behavior of particles assist in prescribing the boundary conditions for the solid phase in two-fluid models, which are increasingly used for the design optimization of fluidized bed reactors and gasifiers. The application of the correct boundary conditions in the two-fluid models will remove a significant cause of the uncertainty in the modeling of these industrial equipment.

2. The DNS Method and Governing Equations

The DNS method that is applied in this study for the modeling of particles is the Immersed Boundary Method (IBM) [5]. While in the previous applications of this method, isothermal flow was assumed, it is feasible to modify the method and include heat and mass transfer from particles [2, 20]. A brief exposition of the method follows in this paper with the presentation of the governing and closure equations that are used in the models. Governing equations are given below in dimensionless form. All variables in the momentum equation are made dimensionless using the following reference quantities:

$$u' = \frac{u}{U_{ref}}, l' = \frac{l}{L_{ref}}, t' = \frac{t}{\frac{L_{ref}}{U_{ref}}}, p' = \frac{p}{\rho_{f0} U_{ref}^2},$$

$$f' = \frac{f L_{ref}}{\rho_{f0} U_{ref}^2} \qquad (1)$$

And for the energy equation we use the following dimensionless variables:

$$\Theta = \frac{T - T_{f0}}{T_{ref}}, q' = \frac{q L_{ref}}{\rho_{f0} c_f T_{ref} U_{ref}}, \lambda' = \frac{\lambda L_{ref}}{\rho_{f0} c_f T_{ref} U_{ref}} \qquad (2)$$

Where u, l, t, p, f, Θ, T, q, λ are velocity, length, time, pressure, body force, dimensionless temperature, temperature, energy source, and energy density, respectively. U_{ref}, L_{ref} and T_{ref} are the reference velocity, length-scale and temperature. The fluid density at the ambient temperature is ρ_{f0} and c_f is the specific heat capacity of the fluid. The convective time-scale (L_{ref}/U_{ref}) is used as the reference time-scale of the problem. T_{f0} is the ambient fluid temperature, and, T_{ref} is chosen to be the initial temperature difference between the particles and the ambient fluid.

The flow is defined by the following dimensionless parameters:

$$\rho_r = \frac{\rho_p}{\rho_{f0}}, c_r = \frac{c_p}{c_f} \quad (3)$$

$$Re = \frac{\rho_f u_{ref} l_{ref}}{\mu_f}, Pr = \frac{\mu_f c_f}{k_f}, Pe = PrRe, \text{ and } Gr = \frac{g\beta L_{ref}}{U_{ref}^2}(T_{p0} - T_{f0})\left(\frac{\rho_f U_{ref} L_{ref}}{\mu_f}\right), \quad (4)$$

where Re is the Reynolds number; Pr is the Prandtl number; Pe is the Peclet number; Gr is the Grashoff number; ρ_p is the particle density; and ρ_f, μ_f, v_f, k_f , β_f are density, dynamic viscosity, kinematic viscosity, thermal conductivity, and thermal expansion coefficient for the fluid. The gravitational constant is denoted as g.

With the introduction of these dimensionless variables, the following set of dimensionless governing equations may be obtained that describe the entire domain Ω of the fluid and the all the particles in the flow system. More details of the derivation of these equations may be found in [2] and [20].

A.) For the velocity field:

$$\frac{\partial \vec{u}}{\partial t} + \vec{u} \cdot \vec{\nabla}\vec{u} = -\vec{\nabla}p + \frac{1}{Re}\nabla^2\vec{u} + \frac{Gr}{Re^2}\vec{e}_g + \vec{f}, \qquad \vec{x} \in \Omega \quad (5)$$

where $\mathbf{e_g}$ is the unit vector in the direction of gravitational acceleration.

B.) For the force density field:

$$\vec{f} = \frac{\partial \vec{u}}{\partial t} + \vec{u} \cdot \vec{\nabla}\vec{u} + \vec{\nabla}p - \frac{1}{Re}\nabla^2\vec{u} - \frac{Gr}{Re^2}\vec{e}_g, \qquad \vec{x} \in \sum S_i \quad (6)$$

C.) Continuity equation:

$$\vec{\nabla} \cdot \vec{u} = 0, \qquad \vec{x} \in \Omega \quad (7)$$

D.) For the velocity field inside the solid particle region:

$$\vec{u} = \vec{U}_p + \vec{\omega}_p \times (\vec{x} - \vec{x}_p) \quad (8)$$

E.) For the temperature field:

Energy equation:

$$\frac{\partial \Theta}{\partial t} + \vec{u} \cdot \vec{\nabla}\Theta = \frac{1}{Pe}\nabla^2\Theta + q + \lambda, \qquad \vec{x} \in \Omega \quad (9)$$

Energy density function:

$$\lambda = \frac{\partial \Theta}{\partial t} + \vec{u} \cdot \vec{\nabla}\Theta - \frac{1}{Pe}\nabla^2\Theta - q, \qquad \vec{x} \in \sum S_i \quad (10)$$

F.) For the motion of the particles:

$$(\rho_r - 1)V_p\frac{d\vec{U}_p}{dt} = \int_s \vec{f}dv + (\rho_r - 1)V_p\frac{gL_{ref}}{U_{ref}^2}\vec{e}_g \quad (11)$$

$$\frac{I_p}{\rho_r}(\rho_r - 1)\frac{d\vec{\omega}_p}{dt} = -\int_s (\vec{x} - \vec{x}_p) \times \vec{f}dv \quad (12)$$

In two dimensions we have the following closure expressions for the volume of particles and for the moment of inertia, where r represents the radius of cylindrical particles:

$$V_p = \pi r^2; I_p = \frac{1}{2}\rho_r \pi r^4 \quad (13)$$

For the particle temperature the energy balance equation for a particle is used:

$$\rho_r V_p c_r \frac{d\Theta_p}{dt} = \frac{1}{Pe}\oint_{\partial s} \vec{\nabla}\Theta \cdot \vec{n} ds + \int_s q_p dv \quad (14)$$

In isothermal flows, the dimensionless temperature, Θ, is zero. The uniformity of temperature in the solid region is enforced by the condition:

$$\Theta = \Theta_p(t) \quad (15)$$

The initial conditions of the above set of equations are:

$$\vec{U}_p(t=0) = \vec{U}_{p0};\ \vec{\omega}_p(t=0) = \omega_{p0};\ \vec{u}(t=0) = \vec{u}_0;\ \Theta(t=0) = \Theta_0;\ \Theta_p(t=0) = \Theta_{p0} \quad (16)$$

The subscript *0* represents the initial value or the initial ambient state.

More details on the method, the derivation of the equations and the numerical procedure may be found in [2] and [20].

3. Numerical Implementation

It is of interest to simulate the motion of particles close to vertical walls and to derive the average velocity of the particles at the plane where the boundary condition of the particles is defined. In the calculations that follow, a small gasifier was chosen with width equal to 15 cm and vertical length 45 cm. A gaseous jet enters at the bottom of the gasifier with variable velocity and a width of 4 cm. The jet fluidizes the particles and exits at the top of the gasifier. The particles are not allowed to exit and rebound from the top. Two sizes of particles were chosen for the simulations that follow: 6 cm and 4 cm. The number of particles in the simulations are N = 264 and 420 respectively. Dimensionless parameters of the flow are: density ratio ρ_r = 2.3, specific heat capacity c_{pr} = 0.01, and thermal gas conductivity k_r = 7.5. The Prandtl number of the fluid is Pr = 0.7. The total time of the simulation is t = 40 s, the time step for the averaging process was chosen as t = 0.02 s and the time used for the simulations of the two-phase mixture is δt = 0.0001.

All the particles have been numbered in a cardinal manner and tracked throughout the computations. In order to see the behavior of particles at the impermeable vertical walls of the gasifier, data for a statistical analysis were selected in regions close to the two vertical walls that are equal to five particle radii. Thus, for the d = 0.6 cm particles these regions were selected from 0.3 cm to 1.5 cm at the left border and from 13.5 cm to 14.7cm at the right border. For the d = 0.4 cm particles the flow regions of interest are 0.2 cm to 1.0 cm at the left border and from 14.0 cm to 14.8 cm at the right border, again 1 to 5 radii from the vertical walls.

Simulations were conducted for a number of c_{ij} values, which is the force scale factor [5]. For every case, the velocity in the y direction was obtained and average data were statistically analyzed. We observed that the resulting statistics were more meaningful when the velocities obtained from the simulations were made dimensionless using the sedimentation velocity (terminal velocity) of the particles in an infinite fluid. The terminal velocity, V_T, of the particles is obtained from the following expression by an iterative method:

$$\frac{1}{2}\rho_f \frac{\pi d^2}{4} V_T C_D = \frac{\pi d^3}{6}(\rho_p - \rho_f)g \quad (17)$$

Where C_D and Re is the drag coefficient and Reynolds number of the particle respectively. The drag coefficient for the solid particles is evaluated from the following expression:

$$C_D = \frac{24}{Re}(1 + 0.15Re^{0.687}) \quad (18)$$

$$Re = \frac{\rho_f V_T d}{\mu_f} \quad (19)$$

The average flow velocity of the fluid in the entire cross-section of the gasifier was defined as follows:

$$V_f = V_{jet}\frac{A_{jet}}{A_{bottom}} \quad (20)$$

where A_{jet} is the jet flow cross sectional area and A_{bottom} is the cross sectional area of the bottom part in the fluidized bed reactor or gasifier.

The dimensionless velocity is evaluated as following:

$$v_a = \frac{v_p - v_f}{V_T} \ . \quad (21)$$

where v_p is the actual particle velocity in the vertical direction. This is obtained from the simulations.

3.1 Collision models and force scale factor

In order to avoid particle overlap and wall penetrations the following two techniques were introduced for the particle-particle interaction and particle-wall interaction:

1) Collisions between particles

When the gap between particles is less than a given threshold, ξ, a repulsive force is applied and that force is added to a total force that particle experiences:

$$F_{ij}^{p} = \begin{cases} 0, & \|x_i - x_j\| > R_i + R_j + \zeta \\ \frac{c_{ij}}{\varepsilon_p}\left(\frac{\|x_i - x_j\| - R_i - R_j - \xi}{\zeta}\right)^2 \left(\frac{x_i - x_j}{\|x_i - x_j\|}\right), & \|x_i - x_j\| \leq R_i + R_j + \zeta \end{cases} \quad (22)$$

where c_{ij} is the force scale factor, ε_p is the stiffness parameter for collisions, R_i and R_j are the radii of the two particles, and ξ defines is the "threshold" or “safe zone” for the two particles.

2) Collisions with the walls

This method is an extension of the interparticle collisions and makes use of a fictitious particle at a symmetric distance from the wall. Hence, the repulsive force between the particle and the wall is as follows:

$$F_{ij}^{w} = \begin{cases} 0, & \|x_i - x_{i,j}\| > 2R_i + \zeta \\ \frac{c_{ij}}{\varepsilon_w}\left(\frac{\|x_i - x_{i,j}\| - 2R_i - \xi}{\zeta}\right)^2 \left(\frac{x_i - x_j}{\|x_i - x_j\|}\right), & \|x_i - x_{i,j}\| \leq 2R_i + \zeta \end{cases} \quad (23)$$

where ε_w is a stiffness parameter; $x_{i,j}$ is the position of fictitious particle $P_{i,j}$, which is located symmetrically on the other side of the wall W_j. The wall restoration force depends on the parameter c_{ij}, which is a force scale factor, as discussed in [4] and [21]. The force scale factor is a measure of the impact of the collisions of the particles with the walls and is necessary in every numerical simulation in order to keep the particles inside the flow domain and to prohibit overlapping of the particles. The force scale factor in this case is of the order of magnitude of the gravity/buoyancy force acting on the particles [21, 4, 5]:

$$c_{ij} \sim \rho_f(\rho_r - 1)V_p g \quad (24)$$

where V_p is the particle volume. While this is a simple way to define the magnitude of this parameter, in general cases the force scale factor may be defined by the user. A full derivation of this collision model and the justification for the use of the pertinent parameters is given in [21].

4. Results and Discussion

We conducted several simulations to analyse the behaviour of particles close to the vertical wall boundaries. From the simulations we also developed several videos that show the motion of the

particles, the effects of the fluid vortices on the particle motion and migration in the flow field and, in general the dynamics of the flow (some of these videos will be shown in the ECOS Conference). We show here some trajectories of the particles and snapshots of the positions and velocities of the particles in the flow domain:

A.) Trajectories

In order to have a visual comprehension of the particulate flow near the vertical boundary, the trajectories of the first 30 particles in the reactor were followed and plotted when they entered the region of five particle radii close to the wall. These trajectories are recorded from t=20 s to t=40 s and are shown in Figure 1. The figure shows the coordinates of the centres of the particles. Because the radii of these particles are 0.3 cm, the centre of a given particle cannot be further than this distance from the wall.

It is observed in this figure that, first, not all the particles come close to the walls, since several particles are missing. Secondly, it is observed that several particles are "reflected" from the wall at distances greater than 0.3 cm. This occurs because of collisions with other particles. Given that the wall is a stagnation region, the concentration of particles at the wall is higher than the rest of the flow domain. Thirdly, it is observed that some particles simply slide downwards along the wall. These particles will interact with other incoming particles and will modify the collisions of the latter with the vertical wall.

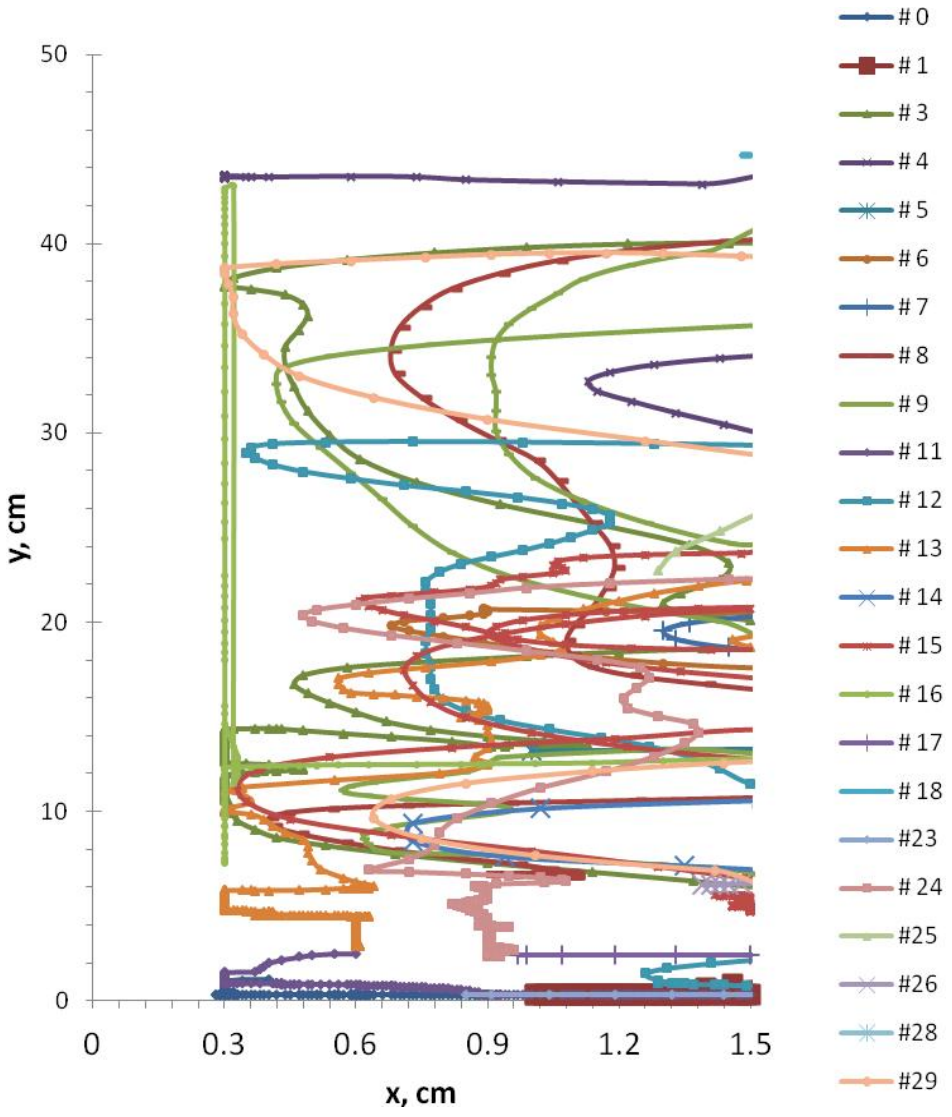

Figure 1: Trajectories of the particles for the first 20 sec of the simulation.

B.) Full domain snapshots

We plotted the vertical component of the velocity of the particles as a function of the particles' position at t=18 s from the inception of the simulations. This is essentially a "snapshot" of the particulate velocities. Figure 2 shows this information, and x is made dimensionless by dividing the horizontal direction with the entire width of the gasifier. As it can be seen, several particles are almost at rest, with their dimensionless velocity, v_a, being equal to 0.36. These are particles that have fallen on the sides of the small gasifier, where the incoming jet velocity is almost zero. It must be noted that these particles move laterally toward the centre of the gasifier, where the upwards gaseous stream lifts them. Hence, these stationary particles are in dynamic equilibrium with the rest of the flow and become fluidized at a later stage of the process.

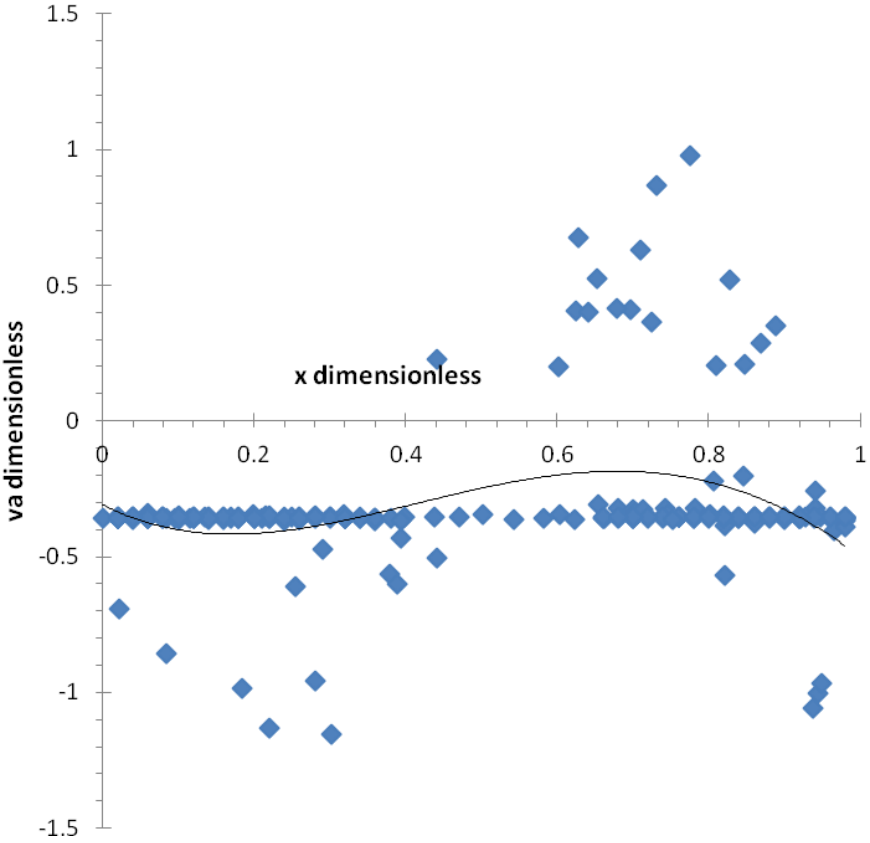

Figure 2: Full domain of the particles d = 0.6 cm at time t=18 sec. The particles with v_a=0.36 are stationary, in dynamic equilibrium with the rest of the flow

C.) Average velocity with all particles

The objective of this study is to obtain the velocity boundary conditions for the particulate flow at the vertical walls of a gasifier. Since the wall is impermeable, the velocity component perpendicular to the wall is equal to zero. However, there is no *a priori* reason for the velocity component parallel to the wall to vanish as well. The finite velocity component parallel to a wall is often referred to as the "slip of the solid phase." In all the simulations, the parameter c_{ij} is an important factor for the behaviour of the particles close to the wall. For this reason, simulations that span a wide range of the factor c_{ij} factors were performed and the vertical components of the velocities of particles were obtained at a distance 0.3 cm from the walls by a statistical method. The data were taken as the averages of the velocities in the time interval 16 s <t < 30 s, a time period when the flow in the small gasifier has been fully developed and the particle behaviour does not depend on the initial configuration of the particles. The data contains the values for all particles that are located close to the borders, and the flow at these times is considered fully developed. The regions of interest, where

the particle velocities were obtained are from 1 to 5 particle radii away from the two vertical walls. Figure 3 shows the average vertical velocity of the particles at the plane boundaries where the velocity boundary condition is defined (d/2 from each wall as explained above). It is observed in this figure that the velocity slip at the wall is finite and that the velocity slip is a very weak function of the force scale factor c_{ij}. Figure 3 implies that the average dimensionless slip in this case is close to 0.4 terminal velocities.

Similar calculations were performed for particles with diameters d = 0.4.The corresponding figure that shows the dependence of the average vertical slip on the force scale factor, $c_{ij,}$ is Figure 4.

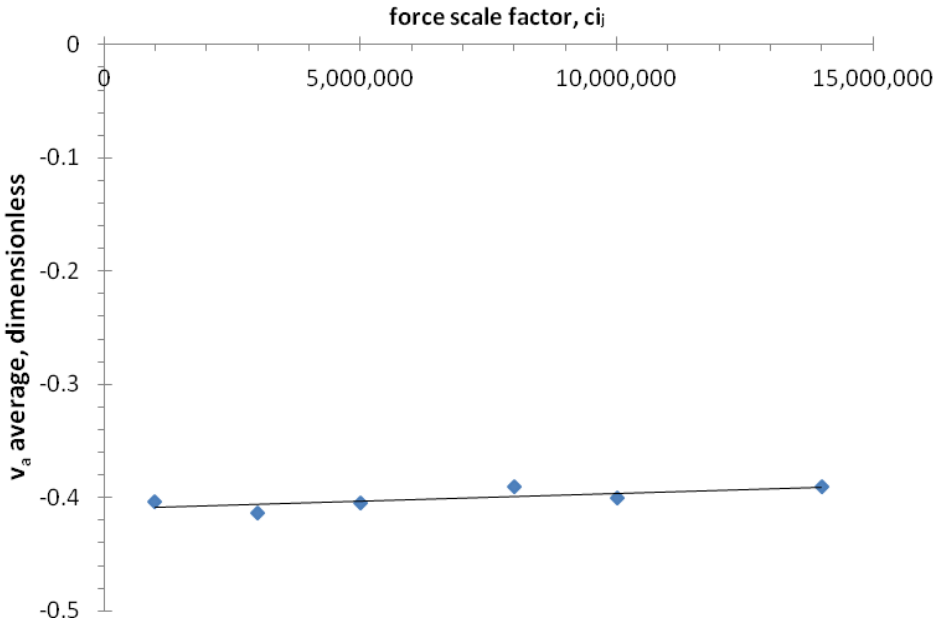

Figure 3: Average dimensionless velocity for all particles of d = 0.6 cm versus the force scale factor, c_{ij}.

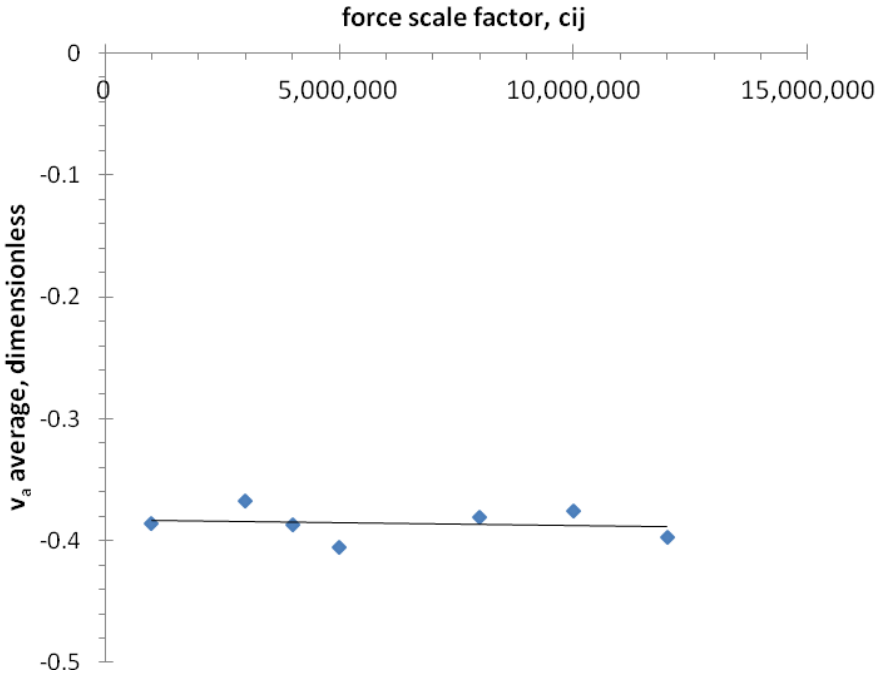

Figure 4: Average dimensionless velocity for all particles of d = 0.4 cm versus the force scale factor, c_{ij}.

A glance in figures 3 and 4 proves that the vertical slip at the wall is almost independent of the magnitude of the force scale factor, c_{ij}. This implies that as long as the collision parameter is scaled with the gravitational force on the particles, the velocity slip will depend on the size of the particles and not on the actual magnitude of the parameter c_{ij}.

D.) Average velocity with suspended particles

Figures 3 and 4 were obtained by including all the particles in the flow domain. However, it was observed in the videos that some of the particles were at rest after having fallen at the sides of the vertical walls. Some of these particles are entrapped in the jet vortices and re-enter the flow field. We obtained results similar to those in the last two figures by excluding the particles that have been settled. We did this by excluding all particles whose velocity vector was below a set limit. We performed the same statistical analysis and obtained the particle velocity slip at the positions where the boundary conditions need to be applied. Figures 5 and 6 show these data for the two sizes of particles examined.

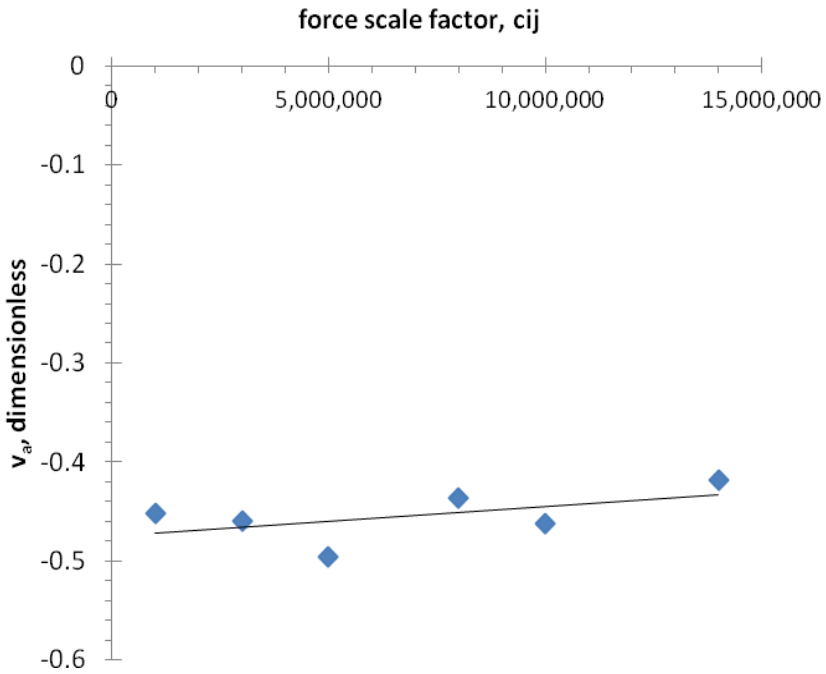

Figure 5: Average dimensionless velocity for suspended particles versus the force scale factor, c_{ij} for particles with d = 0.6 cm.

It is observed in Figures 5 and 6 that the average dimensionless slip velocity at the walls is still a weak function of the interaction force and that (as expected, since we excluded all the stationary particles) the magnitude of the dimensionless slip velocity at the wall is higher than the velocity observed when all particles in the flow field were taken in the computations. Actually it is apparent in these figures that the average value of the velocity of the suspended particles is almost constant and lies in the range 0.46 – 0.47.

5. Conclusions

The behaviour of suspended particles with diameters of d = 0.6 cm and d = 0.4 cm in a coal gasifier close to vertical walls may be studied by numerical simulations. We have conducted several

simulations and obtained the vertical velocity of the particles close to the vertical walls, with the particle size and the force scale factors as parameters. While the actual vertical velocities varied, when these velocities were made dimensionless using their relative value with respect to the fluid and their terminal velocity, it was determined that the average dimensionless vertical velocity slip is a weak function of the size of the particle and of the force scale factor. Actually, the dimensionless slip is close to 0.40 when all the particles are taken into consideration and close to 0.46 when only the suspended particles are counted. Therefore, assuming that there is a no-slip boundary condition for the solid particles at the wall is not an accurate boundary condition and will lead to significant uncertainties and computational errors in the modelling of gas-particle systems. The results of this study show that a slip boundary condition for the solid particles at the walls in the range 0.4 to 0.46 is more accurate and would give more accurate computational results. Numerical simulations with particles of different sizes will establish the form of the particle slip a the vertical walls as a closure equation that may be used as a boundary condition in two-fluid models.

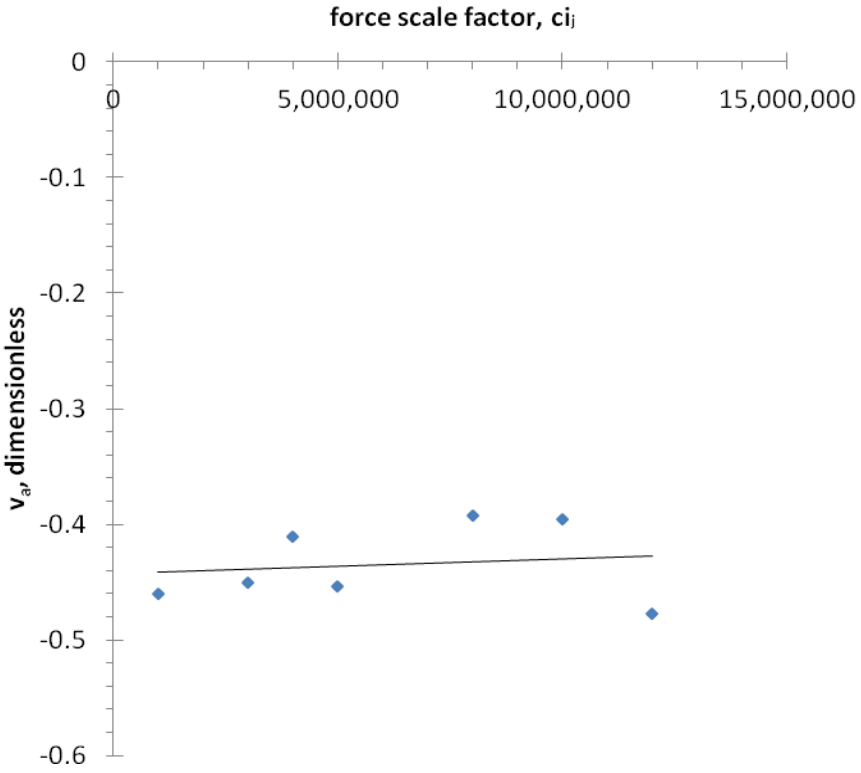

Figure 6: Average dimensionless velocity for suspended particles versus the force scale factor c_{ij} for d = 0.4 cm.

Acknowledgements

This work was partly supported by a grant from the DOE, through the National Energy Technology Laboratory, (DE-NT0008064) Mr. Steven Seachman project manager; by a grant from NSF (HRD-0932339); and by a supplemental grant from the NSF to the SiViRT Center (ENG- 1137764) Dr. Richard Smith, project manager.

Nomenclature

Latin symbols

A	Area
C_D	drag coefficient
c_f	specific heat
c_{ij}	force scale factor
d	diameter
f	body force
Gr	Grashoff number
k	spring constant
k_f	thermal conductivity
l, L	lengths
p	pressure
Pe	Peclet number
Pr	Prandl number
q	energy/heat source
Re	Reynolds number
T	Temperature
u, U	fluid velocity
V, v	particle velocity
x,y,z	coordinates

Greek symbols

β	thermal expansion
ε_d	stiffness scale factor
Θ	dimensionless temperature
λ	energy/heat density
μ,	dynamic viscosity
ν,	kinematic viscosity
ρ	density

superscripts and subscripts

' (prime)	dimensionless
0	ambient
f	fluid
ref	reference
p	particle
T	terminal (sedimentation)

References

[1] Azpitarte, O.E. and Buscaglia, G.C. Analytical and numerical evaluation of two-fluid model solutions for laminar fully developed bubbly two-phase flows, Chem. Eng. Science 58 (2003) 3765–3776.

[2] Feng, Z.G. and Michaelides, E.E. Heat transfer in particulate flows with Direct Numerical Simulation (DNS), Int. J. Heat and Mass Transfer 52 (2009) 777–786.

[3] Uhlmann, M. An immersed boundary method with direct forcing for the simulation of particulate flows, J. Comput. Phys. 2009 (2005) 448–476.

[4] Feng, Z.G. and Michaelides, E.E. The immersed boundary-lattice Boltzmann method for solving fluid–particles interaction problems, J. Comput. Phys. 195 (2004) 602–628.

[5] Feng, Z.G. and Michaelides, E.E. Proteus: a direct forcing method in the simulations of particulate flows, J. Comput. Phys. 202 (2005) 20–51.

[6] Gan, H., Chang, J.Z. and Howard, H.H. Direct numerical simulation of the sedimentation of solid particles with thermal convection, J. Fluid Mech. 481 (2003) 385–411.

[7] Kim, J. and Choi, H. An immersed-boundary finite-volume method for simulations of heat transfer in complex geometries, Korean Soc. Mech. Eng. Int. J. 18 (2004) 1026–1035.

[8] Feng, Z.G. and Michaelides, E.E. Robust treatment of no-slip boundary condition and velocity updating for the lattice-Boltzmann simulation of particulate flows, Computers and Fluids 38 (2009) 370–381.

[9] Biswas, S., Esmaeeli, A. and Tryggvason, G. Comparison of results from DNS of bubbly flows with a two-fluid model for two-dimensional laminar flows, Int. J. Multiphase Flow 31 (2005) 1036–1048.

[10] Liu, S., Wang, Z., Gong, Z. and Peng, Q. Simulation of atmospheric binary mixtures based on two-fluid model, Graphical Models 70 (2008) 117–124.

[11] Chahed, J., Roig, V. and Masbernat, L. Eulerian–Eulerian two-fluid model for turbulent gas–liquid bubbly flows, Int. J. Multiphase Flow 29 (2003) 23–49.

[12] Sokolichin, A., Eigenberger, G., Lapin, A. and Lübbert, A. Dynamic numerical simulation of gas-liquid two-phase flows Euler/Euler versus Euler/Lagrange, Chem. Eng. Science 52 (1997) 611–626.

[13] Wilde, J.D., Vierendeels, J., Heynderickx, G.J. and Marin, G.B. Simultaneous solution algorithms for Eulerian–Eulerian gas–solid flow models: Stability analysis and convergence behaviour of a point and a plane solver, J. Comput. Phys. 207 (2005) 309–353.

[14] Cantero, M.I., Balachandar, S. and García, M.H. An Eulerian–Eulerian model for gravity currents driven by inertial particles, Int. J. Multiphase Flow 34 (2008) 484–501.

[15] Yu, Z. and Shao, X. Direct numerical simulation of particulate flows with a fictitious domain method, Int. J. Multiphase Flow (2009), doi:10.1016/j.ijmultiphaseflow.2009.10.001.

[16] Goldstein, D., Handler, R. and Sirovich, L. Modeling a no-slip boundary with an external force field, J. Comput. Phys. 105 (1993) 354–366.

[17] Wang, L., Ge, W. and Li, J. A new wall boundary condition in particle methods, Computer Phys. Communications 174 (2006) 386–390.

[18] Zhang, Z. and Prosperetti, A. A method for particle simulation, J. Appl. Mech. 70 (2003) 64–74.

[19] Massoudi, M. Boundary conditions in mixture theory and in CFD applications of higher order models, Computers and Mathematics Applications 53 (2007) 156–167.

[20] Feng, Z.G. and Michaelides, E.E. Inclusion of heat transfer computations for particle laden flows, Phys. Fluids 20 (2008) 1–10.

[21] Glowinski, R., Pan, T.-W., Hesla, T.I., Joseph, D.D. and J. Periaux, (2001), "A fictitious domain approach to the direct numerical simulation of incompressible viscous flow past moving rigid bodies: Application to particulate flow," *J. Computational Physics*, vol. 169, pp.363-426.

Effective thermal conductivity with convection and radiation in packed bed

Yusuke Asakuma

University of Hyogo, Himeji, Japan. E-mail: asakuma@eng.u-hyogo.ac.jp

Abstract:

Effective thermal conductivity with convection and radiation is analyzed by the homogenization method. This method can precisely represent the microstructure of a packed bed. In this study, the effects of parameters such as the radiation emissivity, temperature, contact area and particle size of the packed bed on the conductivity have been estimated. For example, heat transfer by radiation does not dominate if the material has voids of less than 1 mm in size**.** Moreover, the effects of contact area and pressure on effective thermal conductivity are negligible for thermal radiation. By considering the microscopic behavior of a packed bed, the homogenization method is thus a powerful tool for estimating the bed's effective thermal conductivity.

Keywords:

effective thermal conductivity, homogenization method, multiscale analysis, microstructure, thermal radiation.

1. Introduction

Packed bed reactors have been used in environmental processes such as reducing harmful exhaust gases (e.g. NO_x and SO_x) and producing new energy sources (e.g. generating hydrogen from methane). In the case of a catalytic reactor, for example, small particles made from a material such as alumina are tightly packed to achieve a large surface area. However, as the particle size is reduced, the superficial velocity decreases, which prevents efficient operation. Moreover, if the reaction is endothermic and heat must be added, heat transfer will be the most important factor of a bed. Accordingly, heat transfer in the bed must be understood and controlled to enhance performance.

Mass transfer and heat transfer in a bed are highly complex. For example, the pressure drop between the inlet and outlet of the bed becomes increasing large as the particle size decreases, which affects reaction rate and gas conductivity. Bed temperatures associated with steam methane reforming typically range from 700 to 1100 °C [1]. Since the reaction is highly endothermic, it is driven by heat conduction from the wall or preheated gas. At higher temperatures, thermal radiation must be considered apart from heat conduction and convection. Moreover, a change in the contact area between the particles and pulverization are caused by thermal expansion. With conventional and empirical models inadequate for considering the various behaviors that occur in beds precisely [2, 3], thermal analysis is required to understand heat transfer due to thermal radiation in a bed and to examine changes in both particle structure and thermal properties. The homogenization method, developed using numerical theory, is proposed in the current study for performing thermal analysis of packed beds, and is considered to be highly useful from the viewpoint that it evaluates precise changes in microstructure, temperature and pressure by employing a three-dimensional finite element method. Owing to these beneficial features, this method has been used for structural analysis [4, 5] and heat transfer analysis of composites and fiber [6-10]. In this study, thermal radiation is added to an existing packed bed model [11, 12], and the effective thermal conductivity (ETC) is calculated in order to study the characteristic behavior of the packed bed during heat transfer at high temperatures.

2. Model

To analyze the packed bed in Fig. 1(a), the simple periodic composite structure in Fig 1(b) is considered. Each cell of this periodic structure consists of two domains: solid, Ω_s, and gas, Ω_g, as shown in Fig. 1(c). In what follows, subscripts *s* and *g* denotes the solid and gas components, respectively, and Γ denotes the interface between their two domains.

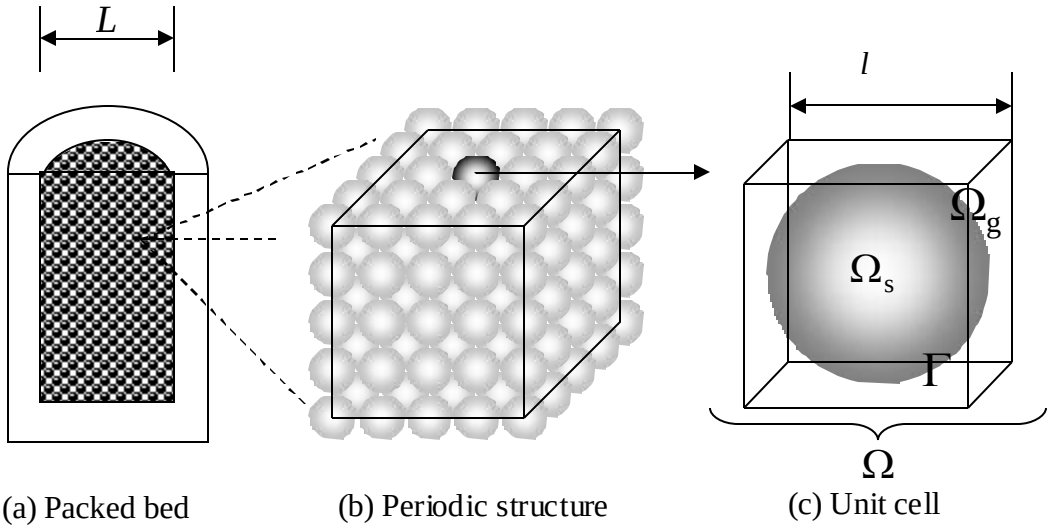

(a) Packed bed (b) Periodic structure (c) Unit cell

Fig. 1 Schematic of model used for homogenization method

The periodic domain Ω is small compared with the characteristic length L at the macroscopic scale:

$$\varepsilon = \frac{l}{L} << 1 \quad , \tag{1}$$

where ε is a scale parameter, and l and L can be understood as the characteristic sizes of the sample at the microscopic and the macroscopic scales, respectively. In this analysis, l is the particle diameter of the packed bed and ε ranges from about 1×10^{-6} to 1×10^{-4}.

The multiscale periodic heat conduction problem under steady-state conditions for the medium described above can hence be mathematically expressed as

$$-\frac{\partial}{\partial x_j^*}\left(\lambda_s \frac{\partial T_s}{\partial x_j^*}\right) = g_s \quad \text{in } \Omega_s, \tag{2}$$

$$-\frac{\partial}{\partial x_j^*}\left(\lambda_g \frac{\partial T_g}{\partial x_j^*}\right) = g_g \quad \text{in } \Omega_g, \tag{3}$$

$$-\lambda_s \frac{\partial T_s}{\partial x_j^*} \boldsymbol{n}_j = -\lambda_g \frac{\partial T_g}{\partial x_j^*} \boldsymbol{n}_j \quad \text{on } \Gamma, \tag{4}$$

$$-\lambda_s \frac{\partial T_s}{\partial x_j^*} \boldsymbol{n}_j = h\left(T_s - T_g\right) \quad \text{on } \Gamma, \tag{5}$$

where λ, T and g are the thermal conductivity, temperature field and volumetric rate of heat generation on a microscopic scale, respectively. Furthermore, $\boldsymbol{n}$ is the outward-pointing unit vector

locally normal to the boundary Γ, and h is the interfacial thermal conductance. Equations (2)–(5) are general expressions, and g_s and g_g become zero in the case that the bed is packed.
By defining the following nondimensionalized quantities,

$$y \equiv \frac{x^*}{l}, \quad \theta \equiv \frac{T}{\Delta T}, \quad \Lambda \equiv \frac{\lambda_g}{\lambda_s}, \tag{6}$$

in which ΔT is the external temperature difference on the macroscopic scale, we can rewrite Eqs. (2)–(5) as

$$-\frac{\partial}{\partial y_j}\left(\frac{\partial \theta_s}{\partial y_j}\right) = G_s \quad \text{in } \Omega_s, \tag{7}$$

$$-\frac{\partial}{\partial y_j}\left(\Lambda \frac{\partial \theta_g}{\partial y_j}\right) = G_g \quad \text{in } \Omega_g, \tag{8}$$

$$-\frac{\partial \theta_s}{\partial y_j}\boldsymbol{n}_j = -\Lambda \frac{\partial \theta_g}{\partial y_j}\boldsymbol{n}_j \quad \text{on } \Gamma, \tag{9}$$

$$-\frac{\partial \theta_s}{\partial y_j}\boldsymbol{n}_j = \mathrm{Bi}\left(\theta_s - \theta_g\right) \quad \text{on } \Gamma. \tag{10}$$

Here, the dimensionless heat generation numbers and the Biot number are given by

$$G_s \equiv g_s \frac{l^2}{\lambda_s \Delta T}, \quad G_g \equiv g_g \frac{l^2}{\lambda_g \Delta T}, \quad \mathrm{Bi} \equiv \frac{hl}{\lambda_s}. \tag{11}$$

Multiplying Eqs. (7) and (8) by a weight function v, integrating over Ω and applying Green's first identity theorem we obtain

$$\int_{\Omega_s} \frac{\partial v_s}{\partial y_j}\frac{\partial \theta_s}{\partial y_j}\,dy - \int_{\Gamma} v_s \frac{\partial \theta_s}{\partial y_j}\boldsymbol{n}_j\,ds = \int_{\Omega_\alpha} G_s v_s\,dy, \tag{12}$$

$$\int_{\Omega_g} \Lambda \frac{\partial v_g}{\partial y_j}\frac{\partial \theta_g}{\partial y_j}\,dy + \int_{\Gamma} \Lambda v_g \frac{\partial \theta_g}{\partial y_j}\boldsymbol{n}_j\,ds = \int_{\Omega_g} G_g v_g\,dy, \tag{13}$$

and we substitute Eqs. (9) and (10) into Eqs. (12) and (13):

$$\int_{\Omega} \alpha \frac{\partial v}{\partial y_j}\frac{\partial \theta}{\partial y_j}\,dy - \int_{\Gamma} \mathrm{Bi}\, v\,\theta\,ds = \int_{\Omega} G v\,dy, \tag{14}$$

where $\alpha = 1$ if $y \in \Omega_s$, and $\alpha = \Lambda$ if $y \in \Omega_g$.
The homogenization method is thus applied to the variational weak form of the multiscale heat conduction problem given in Eq. (14). The method proceeds by using the nondimensionalized temperature field $\theta(x, y)$ as a function of the two spatial variables *x* and *y*, where x is given by

$$x \equiv \frac{x^*}{L}, \tag{15}$$

and we introduce the following multiscale asymptotic expansions:

$$\theta(x, y) = \theta_0(x, y) + \varepsilon\theta_1(x, y) + \varepsilon^2\theta_2(x, y) + \ldots, \tag{16}$$

$$v(x, y) = v_0(x, y) + \varepsilon v_1(x, y) + \varepsilon^2 v_2(x, y) + \ldots, \tag{17}$$

where $\theta_k(x,y)$ and $\nu_k(x,y)$ (k = 1, 2, …) are periodic functions in y. During the computations, we must account for the fact that x and y are considered to be independent variables. To this end, the derivative operator is expressed as

$$\frac{\partial}{\partial y_j} = \frac{\partial}{\partial y_j} + \varepsilon \frac{\partial}{\partial x_j} \quad . \tag{18}$$

The homogenization process, in which $\varepsilon \to 0$, produces a set of equations satisfied by θ_0, and represents the macroscopic behavior of the bed's heat transfer.

Substituting Eqs. (16) and (17) into Eq. (14), and applying the chain rule in Eq. (18), we obtain

$$\begin{aligned} &\int_\Omega \alpha \left(\frac{\partial \nu_0}{\partial y_j} + \varepsilon \frac{\partial \nu_0}{\partial x_j} + \varepsilon \frac{\partial \nu_1}{\partial y_j} + \varepsilon^2 \frac{\partial \nu_1}{\partial x_j} + \varepsilon^2 \frac{\partial \nu_2}{\partial y_j} \right) \left(\frac{\partial \theta_0}{\partial y_j} + \varepsilon \frac{\partial \theta_0}{\partial x_j} + \varepsilon \frac{\partial \theta_1}{\partial y_j} + \varepsilon^2 \frac{\partial \theta_1}{\partial x_j} + \varepsilon^2 \frac{\partial \theta_2}{\partial y_j} \right) dy \\ &+ \int_\Gamma \mathrm{Bi} \left(\nu_0 + \varepsilon \nu_1 + \varepsilon^2 \nu_2 \right) \left(\theta_0 + \varepsilon \theta_1 + \varepsilon^2 \theta_2 \right) ds = \int_\Omega G \left(\nu_0 + \varepsilon \nu_1 + \varepsilon^2 \nu_2 \right) dy \end{aligned} \quad . \tag{19}$$

The final step of the homogenization process is to group the terms associated with each power of ε, which leads to two boundary value problems: one in the homogenized macroscopic region, and the other in each periodic cell [13]. Grouping ε^0 terms, we determine that θ_0 is invariant on the macro-scale. In addition, by assuming that $\mathrm{Bi} = O(\varepsilon^0)$ (i.e., $\varepsilon << \mathrm{Bi} << 1/\varepsilon$) and that $G = O(\varepsilon^2)$, grouping ε^2 terms gives

$$\int_\Omega \alpha \frac{\partial \nu_1}{\partial y_j} \left(\frac{\partial \theta_0}{\partial x_j} + \frac{\partial \theta_1}{\partial y_j} \right) dy + \int_\Gamma \mathrm{Bi}\, \nu_1\, \theta_1\, ds = 0 \quad . \tag{20}$$

We next define the characteristic function $\chi_p(y)$ of arbitrary additive y as follows:

$$\theta_1(x,y) = -\chi_p(y) \frac{\partial \theta_0(x)}{\partial x_p} \quad . \tag{21}$$

$\chi_p(y)$ is a periodic solution of Eq. (20) and corresponds to a unit temperature gradient. Substituting Eq. (21) into Eq. (20) gives

$$\int_\Omega \alpha \left(\delta_{jp} - \frac{\partial \chi_p}{\partial y_j} \right) \frac{\partial \nu_1}{\partial y_j} \frac{\partial \theta_0}{\partial x_p} dy = \int_\Gamma \mathrm{Bi}\, \nu_1\, \chi_p \frac{\partial \theta_0}{\partial x_p} ds \quad , \tag{22}$$

where δ is Kronecker delta, and simplifying Eq. (22) gives

$$\int_\Omega \alpha \frac{\partial \nu_1}{\partial y_j} \frac{\partial \chi_p}{\partial y_j} dy + \int_\Gamma \mathrm{Bi}\, \nu_1\, \chi_p\, ds = \int_\Omega \alpha \frac{\partial \nu_1}{\partial y_p} dy \quad . \tag{23}$$

Equation (23) can then become the cell problem for the characteristic function, $\chi_p(y)$, which is solvable by a finite element method. Here, ETC λ_{eff} is obtained as the homogenized property as follows:

$$\lambda_{\mathrm{eff},\,p} = \frac{1}{\Omega} \int_\Omega \alpha \left(\delta_{pq} - \frac{\partial \chi_q}{\partial y_p} \right) dy \,. \tag{24}$$

Particle and external views of the finite element meshes for the unit cell are shown in Fig. 2, where the number of nodes and elements are 4880 and 4374, respectively. The validity of this model and the mesh number were confirmed through a comparison with the solution of Rocha *et al.* [6].

The Biot number and contact area ratio a [-] (the definition of which is shown in Ref. [11]) are changed as the parameters of λ_{eff}. Heat conduction through both the filling gas and the particle—

that is, the conduction across the neighboring cells—is considered by using periodic boundary conditions [6].

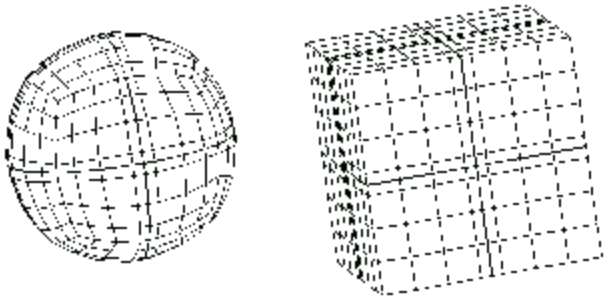

(a) Particle (b) External view

Fig.2 Finite element meshes of unit cell

Generally, the heat flux of thermal radiation q_{rad} is simplified to

$$q_{\mathrm{rad}} = \varepsilon_r \sigma \left(T_s^{\,4} - T_\infty^{\,4}\right) = \varepsilon_r \sigma \left(T_s^{\,2} - T_\infty^{\,2}\right)\left(T_s^{\,2} + T_\infty^{\,2}\right) = h_r \left(T_s - T_{sur}\right), \tag{25}$$

where ε_r, σ, h_{r} T_{sur} and T_∞ are the emissivity, the Stefan-Boltzmann constant, the heat transfer coefficient of the radiation and the temperature of the surroundings and the infinite distance, respectively.

Convection and thermal radiation are considered through the summation of their coefficients (h_{c} and h_{r}, respectively), which form the integrated coefficient h:

$$h = h_c + h_r = h_c + h_{rs} + h_{rv}, \tag{26}$$

$$h_c = \frac{2\lambda_g}{d}\left\{\left(1+\frac{s}{d}\right)\ln\left(1+\frac{s}{\sigma}\right)-1\right\}, \tag{27}$$

$$s = 2\lambda_m \left(2-\gamma\right)/\gamma, \tag{28}$$

where γ is the adaptive coefficient and takes a value of 0.9 for nitrogen [14]. The mean free path λ_m is calculated as in Section 3.2.

Finally, h_{rs} and h_{rv} are the radiation coefficients between particles and between the surface and gas, respectively [15]:

$$h_{rs} = 0.227\frac{\varepsilon_r}{2-\varepsilon_r}\left(\frac{T}{100}\right)^3,$$

$$h_{rv} = \frac{0.227}{1+\dfrac{\nu}{2(1-\nu)}\dfrac{1-\varepsilon_r}{\varepsilon_r}}\left(\frac{T}{100}\right)^3, \tag{29}$$

where particles are simply packed (Fig. 2) and the void fraction, V, is 0.47.

3. Materials

3.1. Solid

Although the conductivity of material varies with temperature, λ_s is set to be constant (λ_s=10) in this study such that the effect of only the radiation can be examined.

3.2. Filling gas

N_2 is considered as the filling gas because the main component of exhaust gas is nitrogen. When the pressure is relatively low, the frequency of collisions between molecules in a micro region increases in importance. In actuality, the thermal conductivity of the gas decreases with pressure because of the increase in the mean free path of the gas molecules (the Smoluchowski effect [2]). The thermal conductivity of the filling gas λ_g is given by

$$\lambda_g = \frac{\lambda_0}{1 + 2b\,\mathrm{Kn}}, \tag{30}$$

$$\mathrm{Kn} = \frac{\lambda_m}{\delta}, \tag{31}$$

where λ_0 is the thermal conductivity of the gas at $p = 1$ bar, b is a constant and Kn is the Knudsen number. Here, δ is defined as the particle diameter, d. The mean free path, λ_m is

$$\lambda_m = \frac{p_0 C_A}{p\left(1 + C_B/T\right)}, \tag{32}$$

where $C_A = 61$ and $C_B = 112$ are gas specific constants and p_0 = 0.00133 bar.

4. Results and discussion

4.1. Effect of contact area ratio on ETC

Changes in temperature and its distribution cause thermal expansion, which is related to the contact area between neighboring particles. In the following calculations, thermal resistance is not considered [12]. Heat is conducted between particles through their contact area, which serves as a pathway for energy diffusion. ETC for various contact area ratios a are shown in Fig. 3 when ε_r = 0.5 bar and p = 1 bar. In the case of a small particle size (d = 0.001 m), heat transfer is controlled by heat conduction only. However, when the particle size is larger (d = 0.1 m) and the temperature increases (T > 800 °C), the effect of a on ETC is reduced because of heat radiation. A contact area ratio of a = 0.00009 is assumed hereinafter.

4.2. Effect of pressure on ETC

Normally, pressure drop is generated between the inlet and outlet of a packed bed. Figure 4 shows the effect of pressure on ETC when T = 400, 800 and 1200 °C and ε_r = 0.5 bar. The solid and broken lines represent the ETC of radiation and convection, respectively. ETC values associated with radiation are constant and independent of the pressure. However, ETC associated with convection increases slightly with pressure because the mean free path is a function of pressure. This behavior is dependent on the Knudsen number, which is a characteristic of the gas from Eqs. (31) and (32). Because packed bed reactors are typically used at high temperatures, the pressure dependence of the gas conductivity is almost negligible for ETC. A packed bed of metal hydride is placed under vacuum in the dehydration reaction process [2], but the temperature is less than 400 °C. Accordingly, the radiation transfer of a metal hydride bed is negligible. A pressure of p = 1 bar is assumed hereinafter.

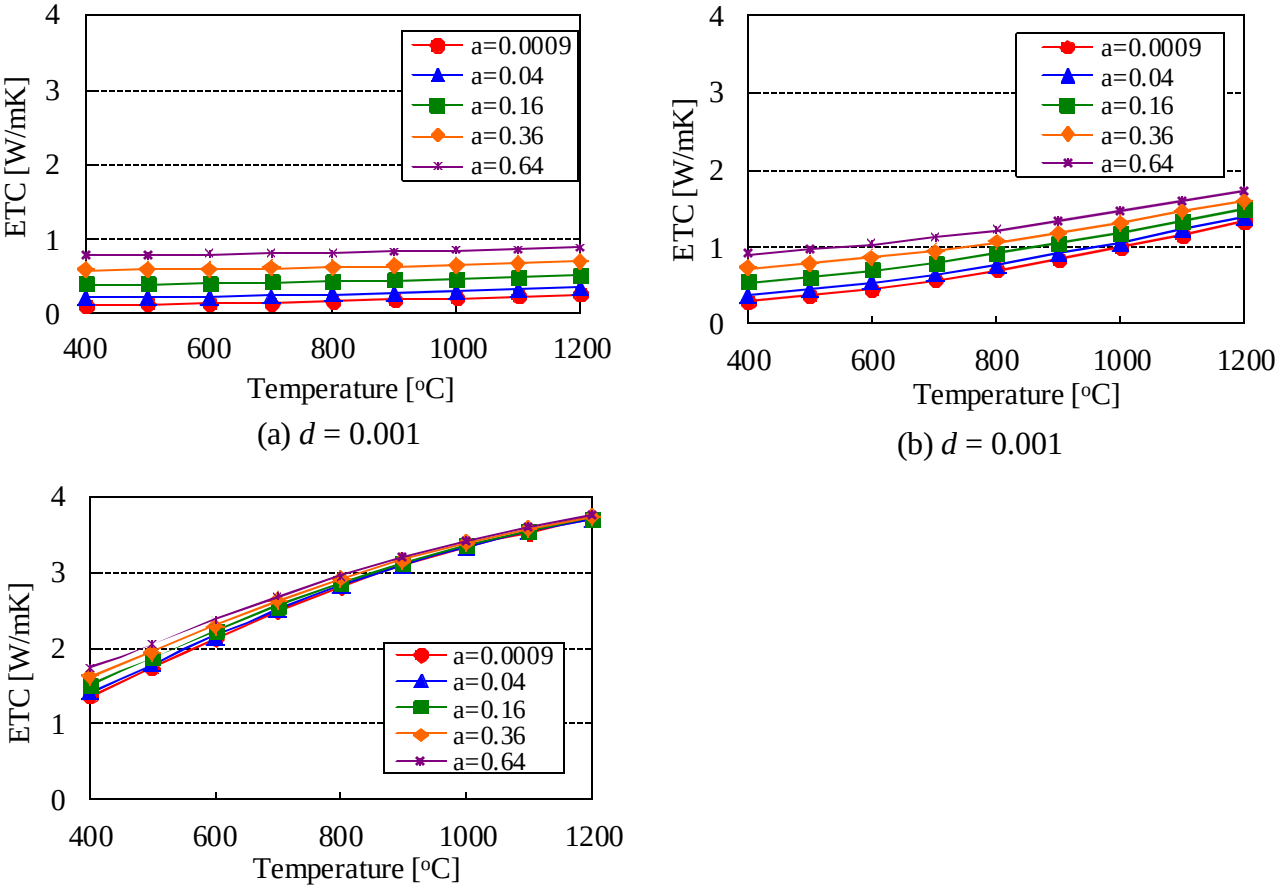

Fig. 3 Effect of contact area on ETC

4.3. Effect of temperature on ETC

The reaction rate in the bed, which is determined by and operating conditions such as the temperature and the pressure, is an essential factor for ensuring the efficiency of the process. Figure 5 shows the effect of temperature on ETC with convection and radiation heat when ε_r = 0.5. If particles are small (d = 0.001 m), radiation transfer in the packed bed is ineffective. As the particle size grows, however, the effect of the radiation increases. In contrast, ETC with only convention is constant. Although the thermal conductivity of gas is controlled by the mean free path, the Knudsen number is small even if d = 0.001 m. Consequently, ETC remains low at even high temperatures. Hence, for ETC with both radiation and convection, the radiation in a packed bed must be considered in cases of high temperatures and large particle sizes.

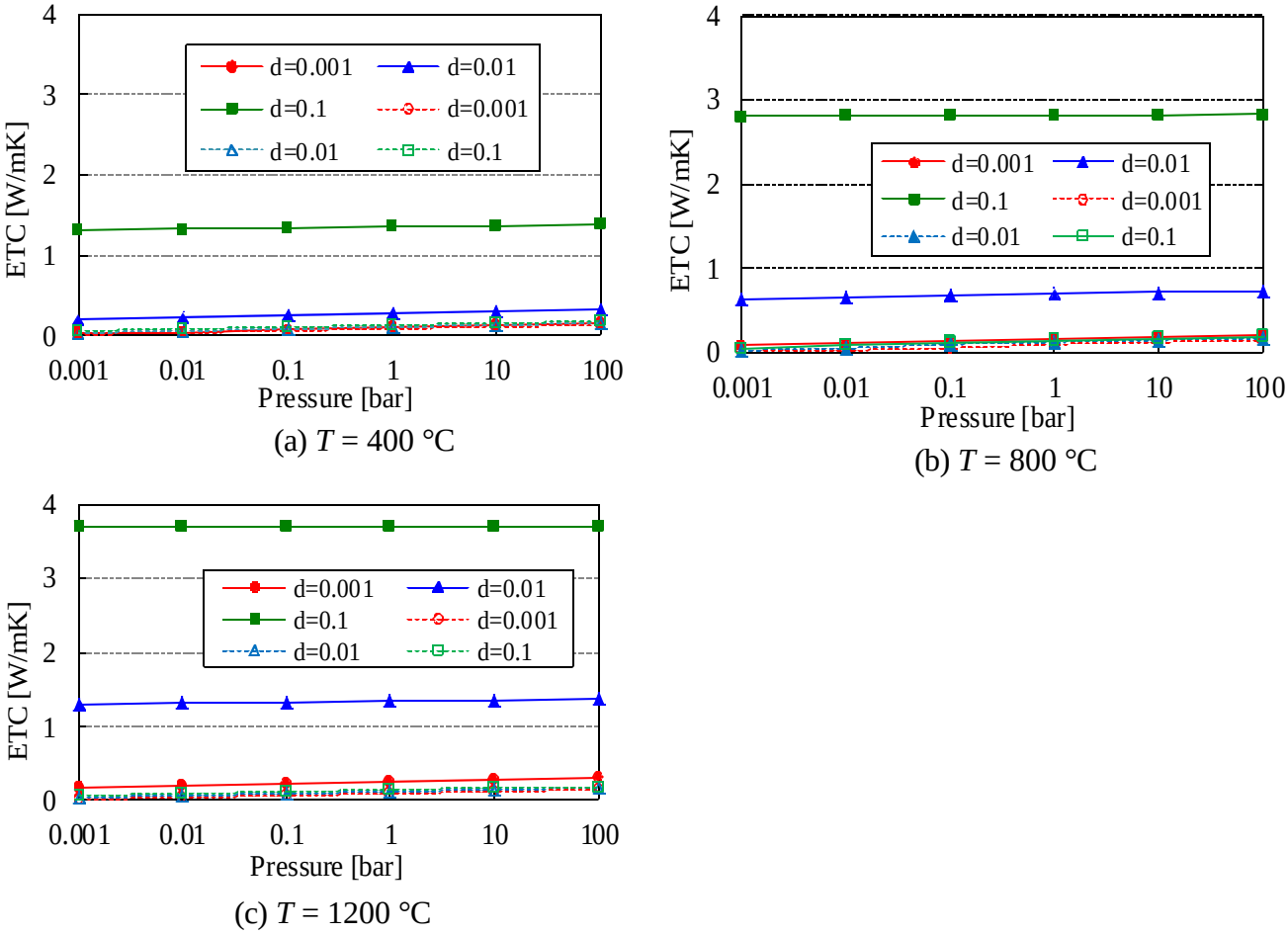

(a) T = 400 °C

(b) T = 800 °C

(c) T = 1200 °C

Fig. 4 Effect of pressure on ETC

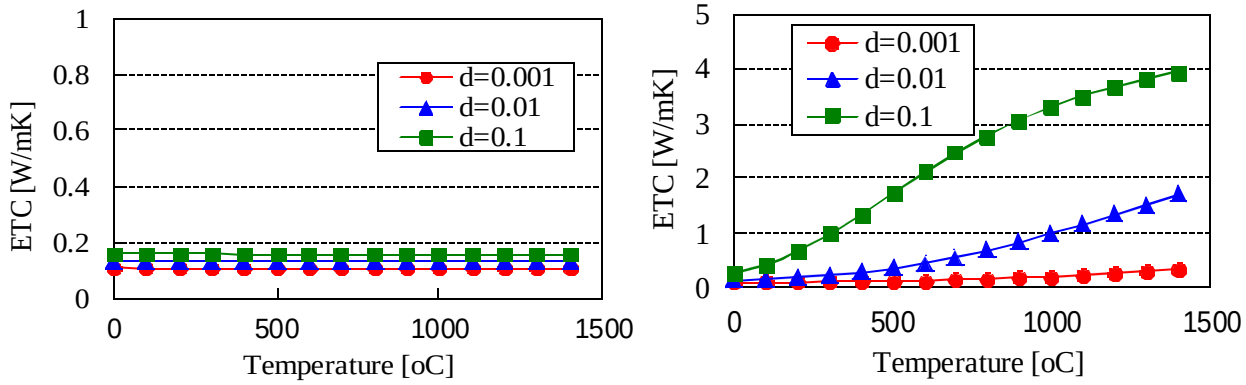

(a) Convection

(b) Radiation

Fig. 5 ETC with convection or radiation for each particle size

4.4. Effect of emissivity on ETC

The emissivity of all bodies generally depends on the wavelength determined by temperature. If we assume that the radiative properties of a gas or a surface are independent of wavelength, this greatly simplifies the radiation transfer equation. For radiative exchange in an enclosure, gray gas and gray body assumptions are generally satisfactory. Under these assumptions, the effect of emissivity on ETC is analyzed for the temperatures and particle sizes shown in Fig. 6. In the small particle case (d = 0.001 m), radiative transfer does not dominate and ETC is independent of the emissivity. At larger particle sizes, the emissivity gradually increases ETC. This method, which is calculated by a finite element method, can also examine the emission angles and the temperature dependence.

5. Conclusion

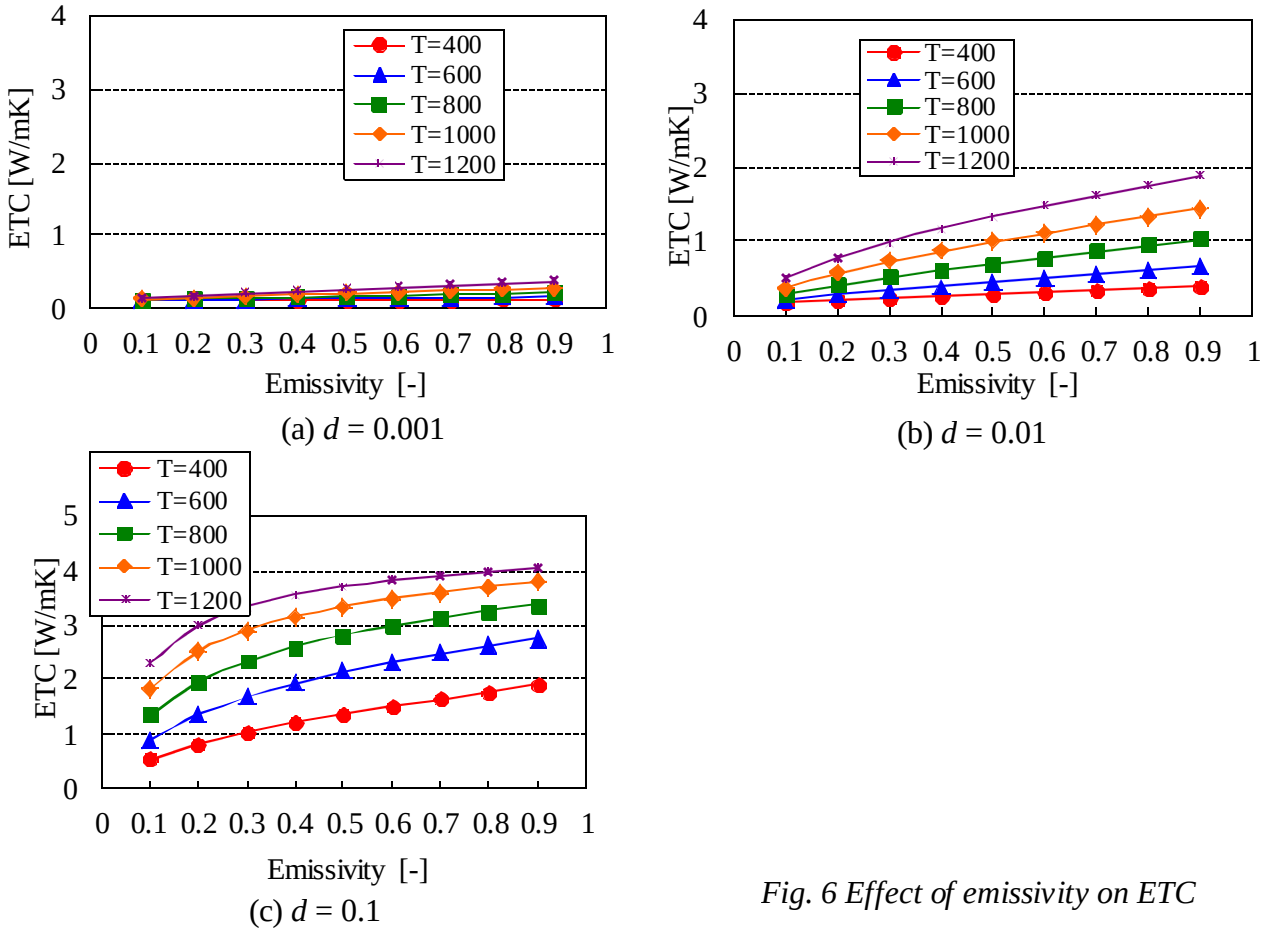

Fig. 6 Effect of emissivity on ETC

A homogenization method was developed for heat transfer with radiation and convection in this study and was applied to a packed bed. Firstly, the pressure dependence of ETC is relatively low. The gas conductivity calculated through the Knudsen number is the factor for determining the pressure dependence of the packed bed at low pressures. Moreover, heat radiation dominates at high temperatures and large particle sizes even though the contact area between particles increases due to thermal expansion. Secondly, if the particle size is less than 0.001 m, radiation transfer is negligible compared with convection transfer. Finally, the importance of emissivity for ETC was indicated quantitatively under gray body and gray gas assumptions. For large particle sizes, the emissivity—which is related to the wavelength, temperature, emission angle and so on—must be considered precisely to provide a more detailed estimation of the heat transfer in the bed. Overall, the proposed method is a useful tool for modeling heat transfer with radiation and convection in a complex system such as a packed bed.

Nomenclature

a Contact area ratio

Bi Biot number

b Constant

C_A Gas specific constant in Eq. (28)

C_B Gas specific constant in Eq. (28)

G Dimensionless heat generation number

g Volumetric rate of heat generation

h Interfacial thermal conductance

h_{c} Heat transfer coefficient of convection

h_{rs} Heat transfer coefficient of radiation among particles

h_{rv} Heat transfer coefficient of radiation between a particle and gas

L Characteristic macroscopic length

l Characteristic microscopic length

Kn Knudsen number

q_{rad} Heat flux of radiation

$\boldsymbol{n}$ Unit normal to Γ

p Pressure

p_0 Reference pressure

s Parameter for calculation of mean free path

T Temperature

ΔT Imposed temperature difference

V Void fraction

x Dimensionless macro-scale variable

x^* Dimensional macro-scale variable

y Dimensionless microscale variable

α Thermal conductivity ratio

γ Adaptive coefficient

χ Particular solution of T

δ Identity matrix

ε Small parameter (l/L)

ε_r Emissivity

Γ Common boundary of the two media

Λ Dimensionless thermal conductivity

λ Dimensional thermal conductivity

λ_m Mean free path

λ_0 Dimensional thermal conductivity at $p=1$

ν Weight function

θ Temperature

Ω Domain

Subscripts

eff Effective

g Gas

p	Number of spatial dimensions
q	Number of spatial dimensions
s	Solid
sur	Surroundings
0, 1, 2	Asymptotic expansion indices

References

[1] S.-K. Ryi,J.-S. Park,D.-K. Kim,T.-H. Kim,S.-H. Kim,Methane steam reforming with a novel catalytic nickel membrane for effective hydrogen production, Journal of Membrane Science, 339 (2009) 189–194

[2] A. Griesinger, K. Spindler and E. Hahne, Measurement and theoretical modelling of the effective thermal conductivity of zeolites, Int. J. Heat and Mass Trans. 42 (1999) 4363-4374

[3] H. Hasselman and L.F. Johnson, Effective Thermal Conductivity of Composites with Interfacial Thermal Barrier Resistance, J. Composite Materials, 21 (1987) 508

[4] H. Sun, S. Di, N. Zhang and W. Changchun, Micromechanics of composite materials using multivariable finite element method and homogenization theory, Int. J. Solids and Structures, 38(17) (2001) 3007-3020

[5] K. Terada, T. Ito and N. Kikuchi, Characterization of the mechanical behaviors of solid-fluid mixture by the homogenization method, Comput. Methods Appl. Mech. Eng., 153 (1998) 223-257

[6] R.P.A. Rocha and M.E. Cruz, Computation of the effective conductivity of unidirectional fibrous composites with an interfacial thermal resistance, Numerical Heat Transfer part A, 39 (2001) 179-203

[7] J.L. Auriault and H.I Ene, Macroscopic modeling of heat transfer in composites with thermal barrier, Int. J. Heat and Mass Trans., 38(18) (1994) 2885-2892

[8] P.W. Chung, and K.K. Tamma, Homogenization of temperature-dependent thermal conductivity in composite materials, J. Thermophysics and Heat Transfer 15(1) (2001) 10-17.

[9] M.B. Taghite, A. Rohmattulla, H. Lanchon-Ducaquis and K. Taous, Homogenization of thermal problem in the plate of a heat exchanger, Comput. Methods Appl. Mech. Eng., 145 (1997) 381-402.

[10] A. Bouddour, J. L. Auriault and M. Mhamdi-Alaoui, Heat and mass transfer in wet porous media in presence of evaporation-condensation, Int. J. Heat and Mass Trans. 41 (1998) 2263-2277.

[11] Y.Asakuma, S.Miyauchi, T.Yamamoto, H.Aoki, T.Miura, Homogenization method for effective thermal conductivity of metal hydride bed International Journal of Hydrogen Energy, 29 (2004) 209-216

[12] K.Ueoka, S.Miyauchi, Y.Asakuma, T.Hirosawa, Y.Morozumi, H.Aoki, T.Miura, An application of a homogenization method to the estimation of effective thermal conductivity of a hydrogen storage alloy bed considering variation of contact conditions between alloy particles, International Journal of Hydrogen Energy, 32 (2007)4225-4232

[13] J. L. Auriault, Heterogeneous medium. Is an equivalent macroscopic description possible?, Int. J. Eng. Sci. 29 (1991) 785-795.

[14] E. U.Schlunder, Waermeubergang an bewegte kugelschutt ungen bei, kurzfristigem kontact, Chemical Engineering Technology 43 (1971) 651-654

[15] S.Yagi, D.Kunii, Studies on effective thermal conductivities in packed beds, AIChE Journal, 3 (1957) 373–381

Experimental and CFD study of a single phase cone-shaped helical coiled heat exchanger: an empirical correlation.

Daniel Flórez-Orrego[a], Walter Arias[a], Diego López[a] and Héctor Velásquez[a]

[a] National University of Colombia, Medellín, Antioquia, daflorezo@unal.edu.co, CA, warias@unal.edu.co, dalopez@unal.edu.co, hivelasq@unal.edu.co

Abstract:

The complex fluid-dynamic inside curved pipe heat exchangers gives them important advantages over the performance of straight tubes in terms of area/volume ratio and enhancing of heat transfer and mass transfer coefficient. In this is work, heat transfer in a non-previously implemented cone-shaped helical prototype with 15cm in maximum diameter, 7.5cm in minimum diameter, 3/8" pitch and 40cm in axial length was studied. An empirical correlation for the determination of average Nusselt number along the duct, with Reynolds ranging between 4300 and 18600 has been developed. The experimental results have been compared with those obtained with the correlation proposed by Seban-McLaughlin and Xin-Ebadian for curved pipes. Also, numerical simulations were performed using ANSYS FLUENT 12.1 software, where the governing equations of mass, momentum and heat transport were solved simultaneously, using realizable k-e two equations turbulence model. The velocity profiles in cross sectional area were obtained and compared with those of conventional helical tube configurations (non-conical). It was found there are similarities in terms of the main flow skewness, but there were slight differences on the path that follows the fluid particles in the secondary flow. Finally, the results for pressure gradient were calculated using Ito and White correlations and were compared with those obtained in computer simulations, obtaining a good agreement.

Keywords:

Single phase, Cone-shaped helical coil, Empirical correlation, Friction factor coefficient, Heat exchanger.

1. Introduction

Complex fluid dynamics occurring in curved tubes have been an invariant issue of research for last few decades [1]. The operating principle of the curved pipes and the benefits attributed to them over the performance of the straight tubes can be summarized as follows: (a) generation of secondary flow in the radial direction; (b) enhanced cross-sectional mixing; (c) reduction in axial dispersion and (d) improved heat-transfer coefficient [1]. Secondary flow is a consequence of the difference in axial momentum between fluids particles in the core and the wall regions. The core fluid experiences a higher centrifugal force than the fluid near the outer wall which is pushed towards the inner wall in two different streams through the pipe walls. Other advantages of the helical tubes are their high heat transfer area per unit volume of space, a good adaptability to cylindrical shapes and an excellent performance in the presence of thermal expansion, behaving as a spring.

In literature, it is suggested that the first investigations of flow in curved geometries can be found in the work of Thompson [2]. Williams et al observed that the location of the maximum axial flow velocity is located in the outermost zone of the tube wall [3] and Eustice demonstrated the existence of a secondary flow by injecting ink into water flowing in a helical tube [4]. Later, Grindley and Gibson studied the effect of the curvature in the flow during experiments on the viscosity of air [5]. Dean [6, 7] was the first to develop an analytical solution for fully developed laminar flow in a curved tube of circular cross section. Jeschke [8] was the first to report the experimental results of heat transfer in two coils for a turbulent condition, developing an empirical correlation. Merkel [9], suggested that the convective heat transfer coefficient in curved

tubes is $(1+3.5(D/D_H))$ greater than in straight pipes, where D and D_H are the tube diameter and the coil diameter, respectively. Heat transfer enhancement in helical coil systems is also reported by Prabhanjan et al. [10].

Seban and McLaughlin [11] developed two correlations for the circumferential average heat transfer coefficient for both laminar and turbulent regimes. They introduced the friction coefficient as a modelling parameter for the Nusselt number. Dravid et al [12] studied the effect of secondary fluid motion on laminar flow heat transfer in helically coiled tubes. They stated that at very short distances from the start of the heat transfer zone, the thermal boundary layer is too thin to be affected by the secondary flow field, which reaches its maximum intensity at some distance away from the tube wall. The authors considered that neglecting that zone would make the design only slightly conservative.

Austen et al [13] carried out the study of laminar flow and heat transfer in helically coiled tubes with substantial pitch. Significant pitch effects were noted in the friction factor and Nusselt number at low Reynolds numbers. These effects are attributed to free convection, and they diminish as Reynolds number increases.

Xin and Ebadian [14] presented an experimental study on heat transfer in helical pipes. The authors explored two values of curvature for Re ranging from 5000 to 1.10^5, and Prandtl ranging from 0.7 to 175. They proposed the following correlation $Nu = 0.00619\,\mathrm{Re}^{0.92}\,\mathrm{Pr}^{0.4}\,(1+3.455\,D/D_H)$.

Cioncolini et al [15] studied the curvature effects on the laminar to turbulent flow transition in diabatic flow through coiled pipes from direct inspection of the experimental Nusselt number profiles. Due to the coil curvature, the turbulence emergence process in the coils tested was found to be much more gradual and smooth than it does in a straight pipe, being the effect enhanced as the coil curvature increases. The coil curvature by inducing the secondary flows acts to increase both the hydraulic resistance and the heat transfer effectiveness, with respect to straight pipe flow.

Jayakumar et al [16] carried out experimental and CFD investigations in a fluid to fluid heat exchanger in order to compare the characteristics inside a helical coil for various boundary conditions. They studied the effect of using constant fluid properties in the computational modelling of heat transfer by contrasting the results with those obtained for constant properties. Standard $\kappa-\varepsilon$ turbulence model was implemented. A correlation in the form $Nu = 0.025 \cdot De^{0.9112}\,\mathrm{Pr}^{0.4}$ was proposed.

Conte et al [17] performed numerical simulations to understand forced laminar fluid flow in rectangular coiled pipes with circular cross-section and characterized by pipe straightness, curvature and torsion. The focus was addressed on exploring the flow pattern and temperature distribution through the pipe. Later, Conte et al [18] investigated the outer convective heat transfer coefficient from conical and helical coils with comparative studies. The results show a better heat transfer performance for the cases of conical coils where much flow turbulence was observed due to an effective flow arrangement. No investigations were made on the inner heat transfer coefficient.

Kumar et al [19] modelled the fluid flow and heat transfer in a tube-in-tube helically coiled heat exchanger for different fluid flow rates in the inner as well as outer tube. The renormalization group (RNG) k– ε model is used to model the turbulent flow and heat transfer in the heat exchanger. New empirical correlations are developed for hydrodynamic and heat-transfer predictions in the outer tube.

Di Piazza et al [20] presented a systematic attempt to assess the applicability of alternative turbulence models to the prediction of pressure drop and heat transfer in coiled tubes. They concluded that the SST $\kappa-\omega$ eddy viscosity/eddy diffusivity model and the second order Reynolds stress $-\omega$ model give comparable results for the friction factor f correlated by Ito [21] and the Nusselt number correlated by Pethukov´s momentum-heat transfer analogy [20].

Various correlations for the pressure drop friction factor, *f*, were proposed by Ito [21], White [22] [23], Hart et al [24] and Mishra and Gupta [25]. The former is the most popular correlation.

An extensive review about the flow and heat transfer characteristics is provided by Naphon and Wongwises [26]. The latest review was published by Vashisth et al [1].
Currently, the various types of curved tube geometries are classified as follows: (a) torus (constant curvature and zero pitch), coiled or helical tube (constant curvature and pitch), serpentine tubes (periodic curved tubes with zero pitch) with bends or elbows, spirals (Archimedean spirals), and twisted tubes. Other different curved chaotic configurations have been developed as a course of technological development [27] [28]. At the author's knowledge, only a work with a cone-shaped helically coiled heat exchanger has been published, and the analysis was focused on the heat transfer in the outer side of the tube [18].
At this work, both experimental and numerical investigations were performed in the purpose of investigating the heat transfer in a cone-shaped helically coiled heat exchanger. The simulation method is concerned with laminar and turbulent flow of incompressible fluid (water) using commercial computational fluid dynamics (CFD) software ANSYS Fluent V 12.1; the velocity profiles are compared with those obtained for non-conical coiled heat exchangers. Experimentally obtained average Nusselt number and pressure drop friction factor *f* are compared with those predicted by the correlations proposed by other authors. Finally, a correlation for the cone-shaped helically coiled heat exchanger used in this study is proposed.

2. Characteristics of cone-shaped helical coil

2.1. Geometrical characteristics

Figure 1 gives the schematic of a cone-shaped helical coil. The pipe has an inner diameter D = 7.904 mm. The coil has big base and small base diameters of D_{MH} = 150 mm and D_{mH} = 75 mm respectively (measured between the centers of the pipe); while the distance between two adjacent turns, called pitch is the sum of inner diameter D plus twice wall thickness e = 0.813 mm. The mean coil diameter is defined as the average diameter between D_{MH} and D_{mH}, namely D_H = 112.5 mm. The ratio of coil diameter to pipe diameter (D_H /D) is called curvature ratio, λ = 14.23. Coil length and pipe length are 400 mm and 12000 mm respectively.

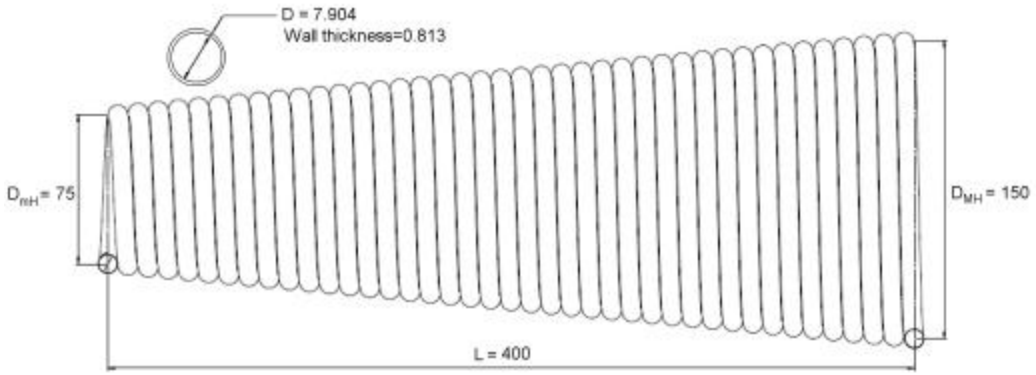

Fig. 1. Coil geometry parameters (Units in milimeters).

2.2. Critical Reynolds number

Similar to Reynolds number (*Re*) for flow in pipes, other parameter used to characterize the flow in a helical pipe is Dean number. The Dean number, *De*, is defined as $De = \mathrm{Re}\sqrt{D/D_H}$. The curvature of

the coil governs the centrifugal force while the pitch influences the torsion to which the fluid is subjected to. The centrifugal force results in the development of secondary flow. Many researchers found that transition from laminar to turbulent flow is delayed because the presence of secondary flow [1]. They correlated the critical Reynolds number as a function of curvature ratio. Ito [21] derived a correlation to calculate the critical Reynolds number at which transition occurs, given by

$$\mathrm{Re}_c = 2000\left[1+13.2\cdot\lambda^{-0.6}\right] \quad (1)$$

and valid in the range $5 \le \lambda \le 2000$. Srinivasan et al [29] proposed the following correlation for the critical Reynolds number in curved pipes

$$\mathrm{Re}_c = 2100\left[1+12\cdot\lambda^{-0.5}\right] \quad (2)$$

valid in the range $7.5 \le \lambda \le 100$. Cioncolini et al [30] found that for low values of the curvature ratio (λ<24), an abrupt transition from laminar to turbulent flow was not observed; the friction coefficient decreased monotonically with Re and transition to turbulence was indicated only by a change in slope of the *f*-Re curve, occurring at a Reynolds number which the authors approximated by the correlation:

$$\mathrm{Re}_c = 30000\lambda^{-0.47} \quad (3)$$

with $7 \le \lambda \le 24$.

3. Experimental set up

3.1. Experimental facility

The material used to construct the cone-shaped helical coil section is copper tubing. Winding was done manually using special wood matrix for the desired maximum and minimum diameters of the coil. Distortion of the cross section was minimized. The cone-shaped helical coil was provided with straight entry and exit hydrodynamic lengths. The entry length, about 21 tube diameters, was used as a hydrodynamic development length, while the exit length was about 40 tube diameters. Both lengths were attached tangentially to the helical coil. Cone-shaped helically coil lies horizontally.

The test section of the helical coil is enclosed in a heat-insulated AISI 430 stainless steel jacket, covered with stone wool. The power heat supply was produced by burning GLP provided from a vessel and controlled by regulating the pressure at the burner inlet. Combustion gases were led through the chamber of the coil and left the chamber trough a chimney. The flame was supposed to uniformly irradiate the surface of the coil, although condensed vapour water and sooting on its surface and a transitional turbulent flame was observed. This can alter the supposition of constant wall heat flux. Due to the method of heating, it was reasonable to assume a linear increase in the bulk temperature across the heated length, which was checked with attached thermocouples to the pipe outer wall.

The cold fluid enters the pipe through the right side connection and the hot fluid leaves the pipe through the left side connection for being discharged in a reservoir. A needle valve regulates the flow to the desired conditions and the rate of flow is measured by a calibrated rotameter at the inlet. The pressure and temperature of the cold fluid and hot fluid are measured with a Bourdon manometer and an immersion type K thermocouple whose values are available on digital displays. Prior to testing, the insulated coil tube-wall thermocouples were calibrated in situ at the water supply temperature. The pipe wall temperature were monitored by six contact thermocouples distributed each 6.7cm along the coil height. The details are given in Fig. 2.

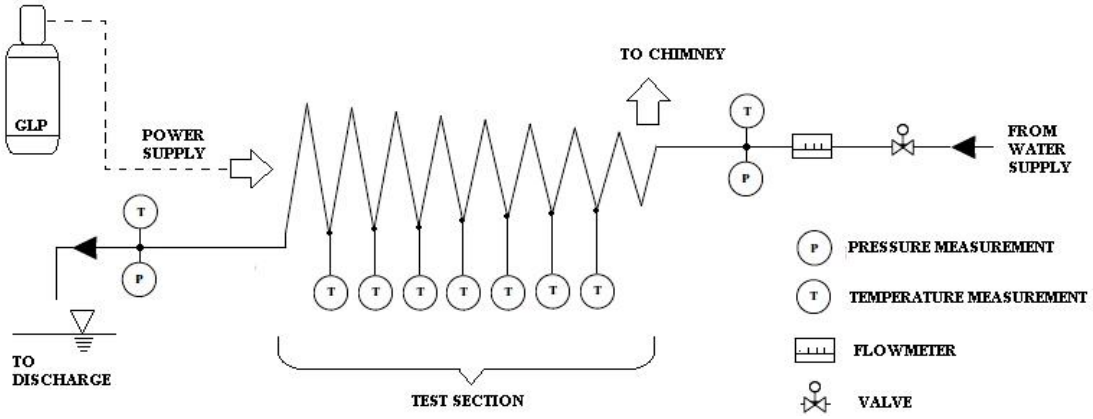

Fig. 2. Scheme of the experimental facility

3.2. Experimental procedure

Experiments were conducted with cold water entering the test section directly from the local water supply service at 295K. In the experiments, the cold water flow rate was increased in small increments for each power heat supply. After that, power supply is increased and new increments of cold water flow rate are carried out, creating so different heat transfer and pressure drop conditions. Before any data were recorded, the system was allowed to approach the steady state. The temperatures and pressure drop at the inlet and outlet zones of the fluid, as well as the temperature at each position in the outer pipe wall were recorded six times and average in the time period. Besides of the rotameter, the mass flow rates were estimated by recording the flow into a graduated vessel (600 ml) from the outlet of the heat exchanger, as an additional measurement source. All the thermodynamic properties of water were calculated using the thermodynamic and transport properties of water and steam software SteamTab™ developed by the Chemicalogic Corporation [31]. In the present experimental work the heat transfer coefficient and heat transfer rates were determined based on the measured pressure, temperatures and flow rates. The heat transferred to the cold water flowing in the heat exchanger was calculated from (4):

$$\dot{Q} = \dot{m}\Delta i = \dot{m}\left(i_2 - i_1\right) = \rho\dot{\forall}\left(i_2 - i_1\right) \tag{4}$$

Where ρ is taken as an average value of the outlet and inlet densities values of the fluid as a function of pressure and temperature. The heat transfer coefficients were calculated with:

$$\bar{h} = \frac{\dot{Q}}{A\Delta T_{avg}} \quad \text{where} \quad \Delta T_{avg} = \frac{\left(T_{w,2} - T_{b,2}\right) + \left(T_{w,1} - T_{b,1}\right)}{2} \tag{5}$$

and *w, b, 2, 1* stands for wall, bulk, outlet and inlet respectively. Average heat transfer coefficients are computed in nondimensional form by means of Nusselt number:

$$\bar{N}u = \frac{\bar{h}D}{k_f} = \frac{\dot{Q}D}{A_w k_f \Delta T_{avg}} \tag{6}$$

Where A_w and k_f are the heat transfer area and the fluid conductivity; the later calculated as an average of the inlet and outlet conductivities values of fluid. The Reynolds and Prandtl numbers were defined in the conventional way as:

$$\bar{\mathrm{Re}} = \frac{4\dot{m}}{\pi D\mu_f} \tag{7}$$

$$\bar{\mathrm{Pr}} = \frac{c_p\mu_f}{k_f} \tag{8}$$

Where μ_f and c_p are the fluid viscosity and heat capacity calculated as an average of the inlet and outlet properties values of fluid.

Either decreasing or increasing the wall heat flux and the mass flow rate, a total of 25 experiments were carried out. Power heat supplies ranged between 5000 - 17000 W and flow rates ranged between 2.50×10^{-5} - 8.17×10^{-5} m^3/s (1.5 - 4.9 l/min). The Reynolds number ranged between 4300 and 18600. The range of Prandtl number in the present experiment is $2 < Pr < 6$.

The following simplifications were assumed: 1) Steady state flow, fully hydrodynamic and thermal developed 2) Uniform wall heat flux, 3) Axial conduction inside the tube and fluid is neglected and 4) Peripheral temperature is uniform [32] [12]. The later assumption is valid if we consider the small tube diameter of the test section. Peripheral differences diminishes even more with high mass flow rates [13].

The difference between the inner and outer wall temperatures can be calculated assuming one-dimensional (radial) conduction within the tube with a uniform rate of heat generation and insulated outer surface. Solving the appropriate conduction equation with the applicable boundary conditions, it can easily be shown that the temperature difference across the wall at any axial location is given by [13]:

$$\bar{T}_{w,o} - \bar{T}_{w,i} = \frac{q'''}{4k_w}\left[2r_o^{\,2}\ln\left(\frac{r_o}{r_i}\right) - \left(r_o^{\,2} - r_i^{\,2}\right)\right] \tag{9}$$

4. Numerical Set up

A CFD methodology has been used to investigate the performance of the cone-shaped helically coil heat exchanger. In this investigation, commercial CFD package ANSYS Fluent v12.1 (double precision, 3D version) was used. A computer with Intel® Core™ i5-2430M Processor (3M Cache, 2.40 GHz) with 4GB RAM was used in these simulations; each run took 12 hours.

4.1. Computational grid

The geometry was created using SOLIDWORKS 2009 design software and later exported as a Parasolid geometric modelling format. The mesh was created using meshing module of the ANSYS FLUENT package. In this model, the pipe wall thickness is not considered and only the fluid control volume is modelled. A structured grid with 5 inflation layers was used to mesh the region near the surface of the control volume. On the other hand, an unstructured mesh was used in the interior volume cells. The grid for the analysis domain, which includes the pipe fluid volume, is shown in Fig. 3.

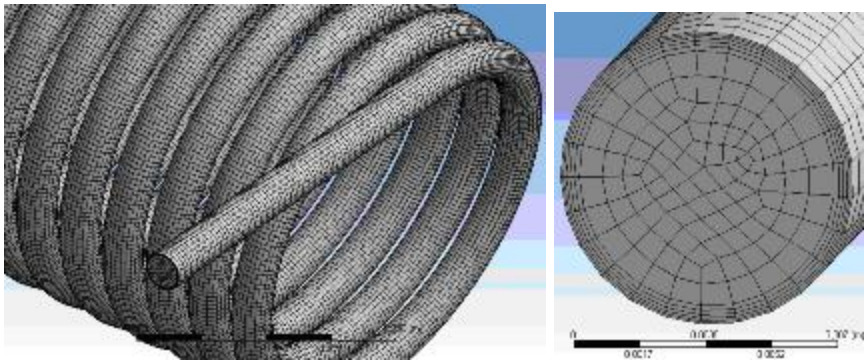

Fig. 3. Grid used in the analysis.

The grid is composed of 3499443 nodes and 3312000 elements. The maximum skewness reported is 0.4852 and the minimum was 0.01121 implying good to excellent cell quality. The grid given in Fig. 3 was chosen because further refinement did not result in reduction of mass and energy errors.

4.2. Boundary conditions and CFD modelling

In this numerical investigation four representative heat transfer conditions were analysed. The steady state, pressure based type solver with an absolute velocity formulation was used. In both laminar and turbulent cases, energy, momentum, and turbulence (if applicable) equations were solved. The operating conditions were defined as 295K and 0 Pascal absolute operating pressure.
For thermal equation, constant wall heat flux boundary condition is stated at the interface between the wall and the fluid (See Fig. 4). For momentum equation, the wall was treated as no-slip adiabatic smooth one. In all the cases, the cold fluid inlet was kept constant at 295K and the analyses were carried out by changing the flow through the cone-shaped helical pipe (see Table 1). At the fluid inlet, velocity inlet boundary condition is specified. For the hot fluid outlet, pressure outlet boundary condition at zero back pressure is specified. The acceleration of gravity is considered as 9.8m/s^2.

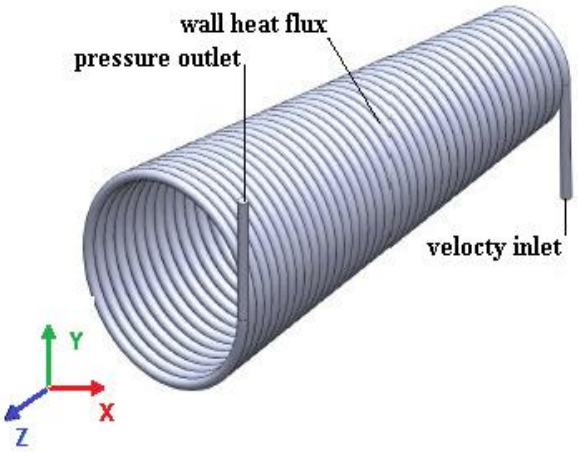

Fig. 4. Specified boundary conditions

For the coil used in this study, the critical Reynolds number at which the transition from laminar to turbulent flow regime occurs is given by the Ito's correlation [21] and equals to $\mathrm{Re}_c = 7679$. Then, only the fourth condition in Table 1 presents a laminar flow regime and in this case the laminar model was considered.
In the turbulent regimes simulations, the Realizable $\kappa-\varepsilon$ turbulence model with Standard wall function was used. An immediate benefit of the realizable $\kappa-\varepsilon$ model is that it is likely to provide superior performance for flows involving rotation, boundary layers under strong adverse pressure gradients, separation, and recirculation. Initial studies have shown that the realizable model provides the best performance of all the $\kappa-\varepsilon$ model versions for several validations of separated flows and flows with complex secondary flow features. Model constants are: $C_{1\varepsilon}=1.44$, $C_2=1.9$, $\sigma_\kappa=1.0$, $\sigma_\varepsilon=1.2$ [33]. For fully-developed turbulent internal flow, the Intensity I and Hydraulic Diameter D specification method was used. The turbulence intensity at the core of a fully-developed duct flow is estimated from the following formula derived from an empirical correlation for pipe flows:

$$I=\frac{u'}{u}=0.16\left(\mathrm{Re}\right)^{-1/8} \tag{10}$$

A turbulence intensity of 1% or less is generally considered low and turbulence intensities greater than 10% are considered high. Turbulent Kinetic energy κ and turbulent dissipation rate ε were calculated as [34]:

$$\kappa = \frac{3}{2}\left(u_{avg} \cdot I\right)^2 \quad (11) \qquad \varepsilon = C_\mu^{3/4} \frac{\kappa^{3/2}}{\ell} \quad (12)$$

Where u_{avg} is the mean velocity inlet, ℓ is the length scale (= 0.07D) and C_μ is an empirical constant specified in the turbulence model (approximately 0.09). The turbulence length scale, ℓ, is a physical quantity related to the size of the large eddies that contain the energy in turbulent flows. In fully-developed duct flows, it is restricted by the size of the duct, since the turbulent eddies cannot be larger than the duct. The factor of 0.07 is based on the maximum value of the mixing length in fully-developed turbulent pipe flow [35]. In all the cases a turbulent length scale of 0.0005533m and a hydraulic diameter of 0.007904m were considered. Turbulence Intensity, Turbulent kinetic energy and Turbulent dissipation rate are shown in Table 1.

Table 1. Boundary and Cell zone conditions.

Condition	Volumetric flow rate m^3/s (l/min)	Mean velocity inlet m/s	Expected outlet temp. K	Wall heat flux W/m^2	Reynolds Number (Flow Regime)	Turbulence intensity %	Turbulent Kinetic energy m^2/s^2	Turbulent dissipation rate m^2/s^3
1	7.50 x 10-5 (4.5)	1.5285	339	37881	17248 (Turb.)	4,73	0,00783	0,20573
2	5.83 x 10-5 (3.5)	1.1888	359	42639	14348 (Turb.)	4,84	0,00496	0,10371
3	4.17 x 10-5 (2.5)	0.8491	358	29992	10220 (Turb)	5,05	0,00275	0,04292
4	2.50 x 10-5 (1.5)	0.5095	358	17996	6132 (Lam.)	---	---	---

At this work, temperature dependent thermal and transport properties of water flowing inside the helical pipe were used, as it was proposed by [36]. For modelling temperature dependent properties, the following polynomial functions ((13)–(16)) were programmed in FLUENT. In CFD code, the governing equations are solved with the fluid properties evaluated at the cell temperatures.

$$\mu(T) = 0.33158 - 0.0037524 \cdot T + 1.6028e-5 \cdot T^2 - 3.055e-8 \cdot T^3 + 2.1897e-11 \cdot T^4 \quad (13)$$

$$\rho(T) = 1227.8 - 3.0726 \cdot T + 0.011778 \cdot T^2 - 1.5629e-5 \cdot T^3 \quad (14)$$

$$k(T) = -1.0294 + 0.010879 \cdot T - 2.261e-5 \cdot T^2 + 1.5362e-8 \cdot T^3 \quad (15)$$

$$C_p(T) = 4631.9 - 1.478 \cdot T - 0.0031078 \cdot T^2 + 1.1105e-5 \cdot T^3 \quad (16)$$

These relationships were obtained by regression analysis using MATLAB. In the above relationships, temperature is specified in K [37]. Pressure velocity coupling was done using the SIMPLEC scheme with skewness correction factor equal to 1. Momentum, Energy, Turbulence kinetic energy and Turbulence dissipation rate equations were discretised using second order upwind scheme. Pressure was discretised using linear scheme. Convergence criterion used was 1.0e−5 for continuity, velocities, *k*, and ε. Convergence criterion for energy balance was 1.0e−07. A mass flow rate surface monitor at pressure outlet boundary condition was used, obtaining convergence at respective mass flow rate at each case. Under relaxation factors was 0.3 for pressure, 1.0 for density, 0.7 for momentum, 1.0 for body force, 0.8 for turbulent kinetic energy and turbulence dissipation rate and 1.0 for energy.

5. Results and Discussion

5.1. Correlation of Experimental Data

Because there is almost no data as in the open literature on the heat transfer and flow characteristics in the cone-shape helically coiled tube, the predicted results are compared with the present experimental data.

5.1.1. Experimental Nusselt number

In our application, the flow is in both laminar and turbulent regimes and the ranges of interest of the Reynolds number and Prandtl number are 4300 and 18600 and 2 to 6, respectively. According to this, Dean number ranges between 1000 and 6000. Based on the nature of the correlations available in the literature, it is proposed that the Nusselt number for the cone-shape helical coil can be represented in the form $Nu = C\,\mathrm{Re}^{m}\,\mathrm{Pr}^{n}$, where C and m are constants to be determined. Index of the Prandtl number, n, is selected to be equal to 0.4. After the linearization of the function, and using linear regression analysis in MATLAB software, the following correlation was generated for estimating the Nusselt number and the averaged heat transfer coefficient, which is applicable to $4300 < \mathrm{Re} < 18600$:

$$Nu = 0.00797 \cdot \mathrm{Re}^{0.82}\,\mathrm{Pr}^{0.4}$$
$$4300 \le \mathrm{Re} \le 18600 \qquad \textbf{(17)}$$
$$2 \le \mathrm{Pr} \le 6$$

Figure 5 show the variation of the average Nusselt number calculated from the present experiment with various water mass flow rates and heat inputs. As expected, the average Nusselt number increases with increasing Reynolds. This is because the Nusselt number depends directly on the heat removal capacity of the cold water.

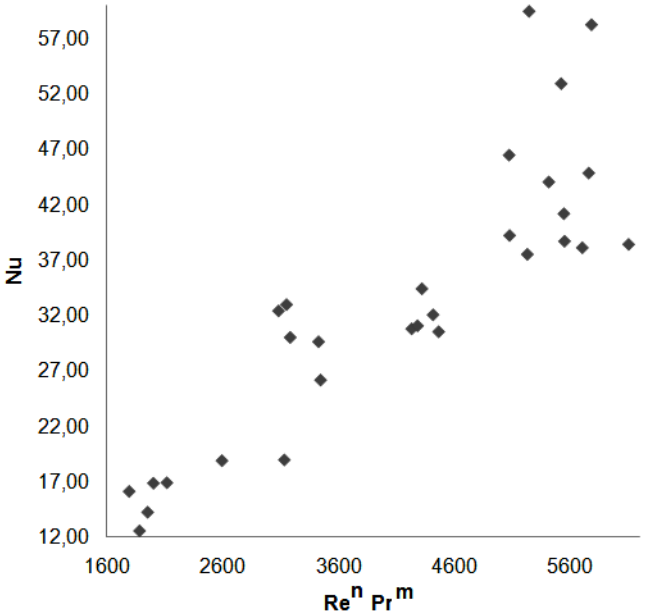

Fig 5. Variation of average Nusselt number with average Reynolds and Prandtl numbers

The methodology for estimation of heat transfer for this cone-shape helically coiled heat exchanger has been successfully validated against experiments. The calculated average Nusselt number from

(17) is plotted versus experimental average Nusselt number in Fig. 6. As shown from this figure the maximum deviation between the experimental data and the correlation is ±23%.

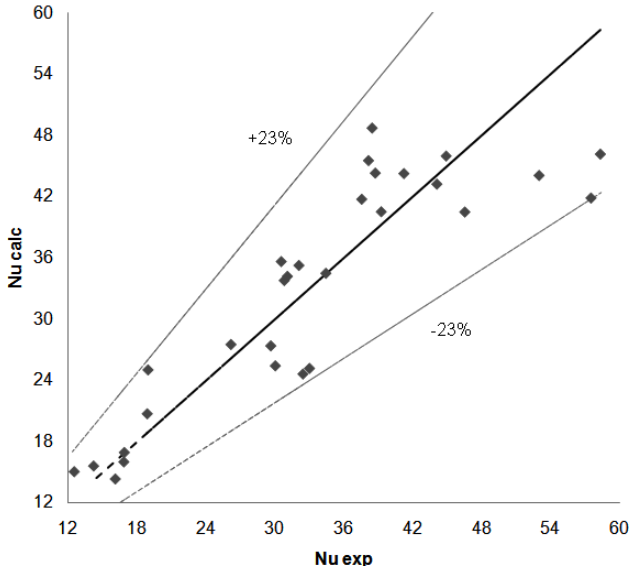

Fig. 6. Calculated Nusselt number against experimental Nusselt number for the cone-shape coil.

5.1.2. Experimental friction factor coefficient

When analyzing the experimentally obtained data for Darcy's friction factor at turbulent regimes and comparing it with those ones calculated with White's [22] and Ito's [21] correlations (See Fig.11), it was found that for low values of Reynolds number, both correlations over-predict (max dev. 6% from Ito's correlation) the friction factor values for the prototype used in this experiment. For Reynolds numbers in the middle the effect is inverse and those correlations under-predict the experimental friction factor (max dev. 9% from White's correlation). Finally, at the high Reynolds numbers, experimental data fall between the predicted values given by the Ito's and White's correlations. Since friction factor is both Reynolds and curvature ratio dependent, the taper effect could be the cause of the deviations, which is not considered in the previous correlations. As it can be seen from Fig. 11 scattering is high and no correlation is proposed at this time for friction factor values.

5.2. Numerical Results

5.2.1. Velocity contours

The contours of velocity magnitude along cold fluid entrance cross sections at several angles (starting from $\theta = 0°$ at the junction of the tangential section of the tube with the first spire of the coil) for 7.50x10-5 m^3/s (4.5 l/min) are shown in Fig. 7. Left and right sides of the Figs 7 and 8 are the inner (***i***) and outer (***o***) walls of the coil respectively. The regime is turbulent. After the last contour no more cross sections are shown, indicating this is the contour reached for fully developed flow.

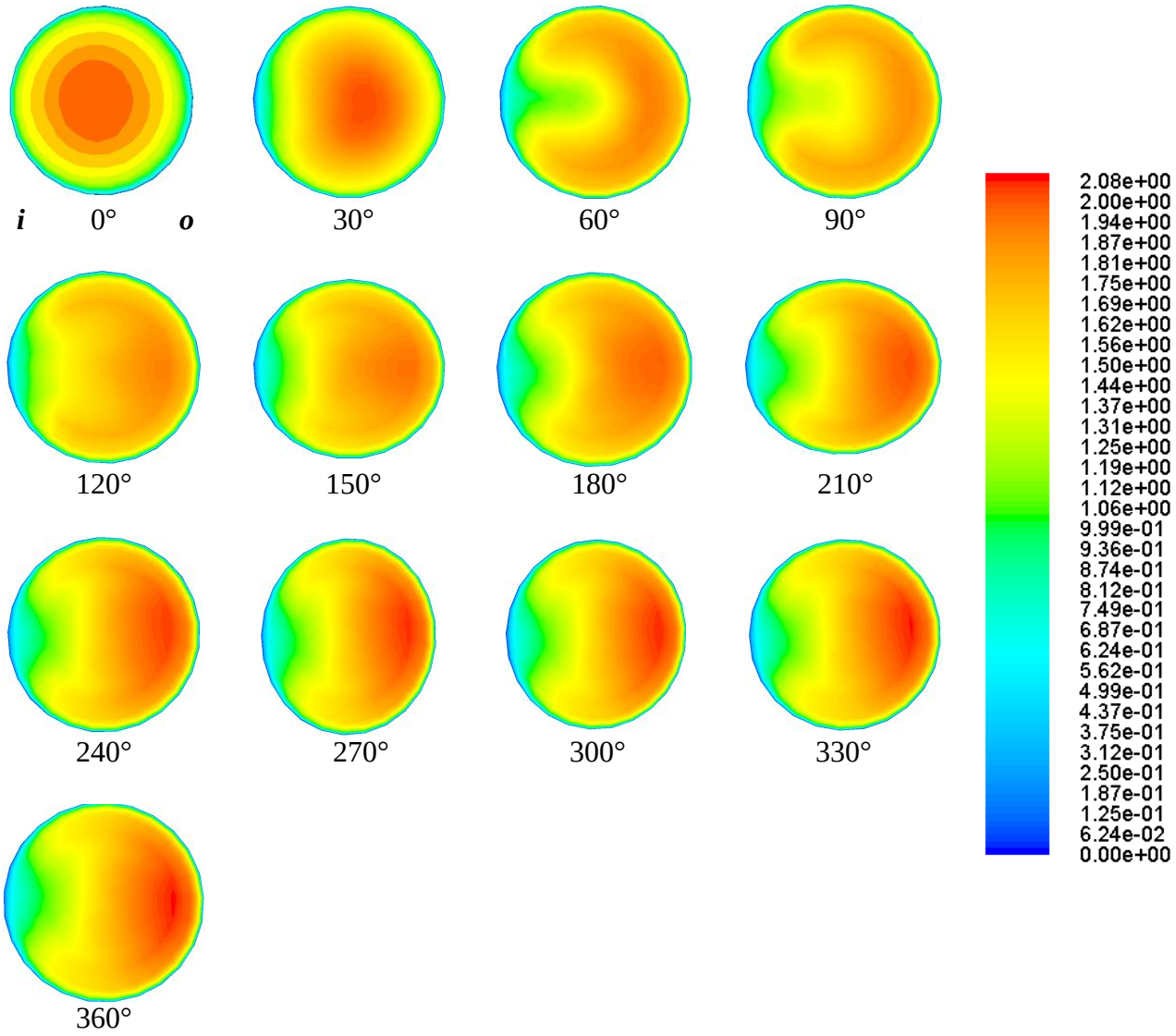

Fig. 7. Contours of velocity magnitude (m/s) at inlet zone for 7.50x10-5 m^3/s (4.5 l/min) flow rate.

As it can be seen in Fig. 7, at $\theta = 0°$ cold fluid enters the coil, and a typical parabolic velocity profile is observed, owed to the developed flow in the inlet straight section. As the fluid flows through the coil, the flow gets developed due to the centrifugal and torsional effects induced by the helical nature of the pipe. Furthermore, as it was expected, velocity on walls is zero because of the nonslip condition. At one complete turn, contours seem to have been complete developed and it can be readily seen that unlike for flow through a straight tube high velocity is on the outer side of the coil.

In Fig. 8, the contours of velocity magnitude along cold fluid entrance cross sections for 2.50×10^{-5} m^3/s (1.5 l/min) are shown. In this case, they correspond to laminar regime.

As it can be seen again, at $\theta = 0°$ cold fluid enters the coil and the typical parabolic velocity profile is observed. As the fluid flows through the coil, the flow gets developed as discussed above. Velocity on walls is zero because of the nonslip condition considered. At one turn, contours seem to have been complete developed and once again it can be seen high velocity is on the outer side.

After the fully developed velocity contour is reached, it is maintained until the fluid reaches the outlet zone. When the flow gets the straight pipe section at the outlet, the centrifugal effect tends to vanishes and once again a parabolic profile is presented.

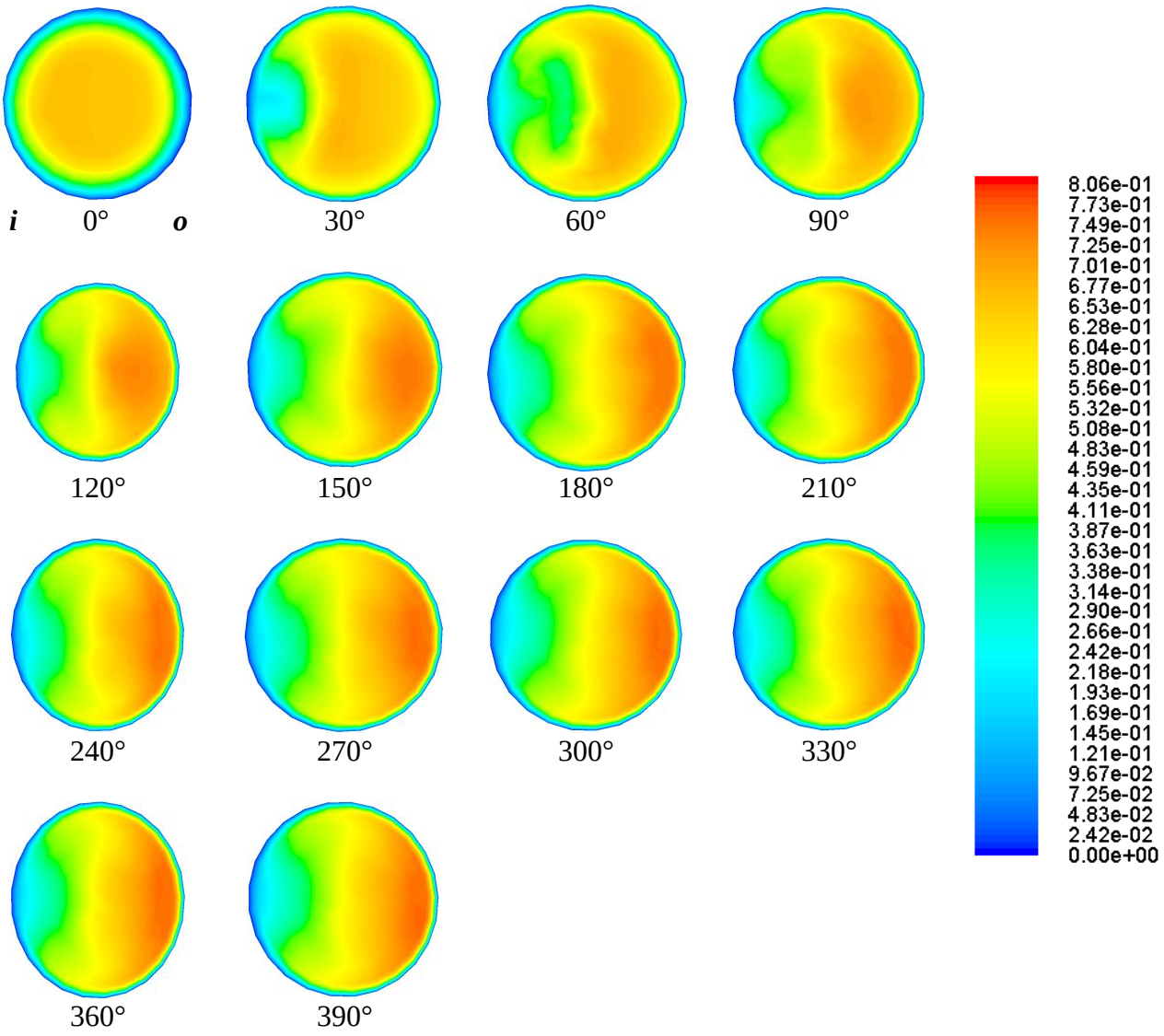

Fig. 8. Contours of velocity magnitude (m/s) at inlet zone for 2.50x10^{-5} m^3/s (1.5 l/min) flow rate.

Results agree with those results reported by other authors [1]: For low Dean numbers, the axial-velocity profile was parabolic and unaltered from the fully developed straight tube flow. As the Dean number is increased, the maximum velocity began to be skewed toward the outer periphery.

In Fig. 9, fully developed flow XZ-velocity vector components are compared for each of the conditions shown in Table 1. The inner (***i***) and outer (***o***) notation follows the convention used in Figs 7 and 8. As it can be seen, the velocity field in the secondary flow is inclined in the same direction that the generatrices of the cone (approximately 46° respect to coil axis), although not with the same angle of inclination of the generatrices (aprox. 5° respect to coil axis). As in straight - non conical- helically coils, where pitch and curvature ratio effects have been widely studied in the literature, in cone-shaped helically coils the effect of taper on the flow must be considered with a parameter counting for instant curvature ratio. In this experiment a single geometry was used and this analysis was not performed.
It is also observed that near the top and the bottom walls of the tube, XZ-velocity vector components are relatively greater compared with the core XZ-velocity vector components, thus indicating a greater influence of the principal flow over the secondary flow at the core of the fluid,

and a lesser effect near the walls. XZ-velocity vector components in the extreme left and right points of the coil are almost negligible; they increase tangentially along to the wall, starting from the left (outer) point, reaching a maximum value at the top point (or bottom point) of the pipe, and decreasing to a negligible value at the inner point. At this point, the flow goes through the core of the pipe, and with a complex oblique path as described above, it reaches the outer point. Finally, it is pointed out that a more disordered secondary flow is presented at the condition of 2.50×10^{-5} m^3/s (1.5 l/min), likely due to the lesser centrifugal force and a relative stronger effect of principal flow.

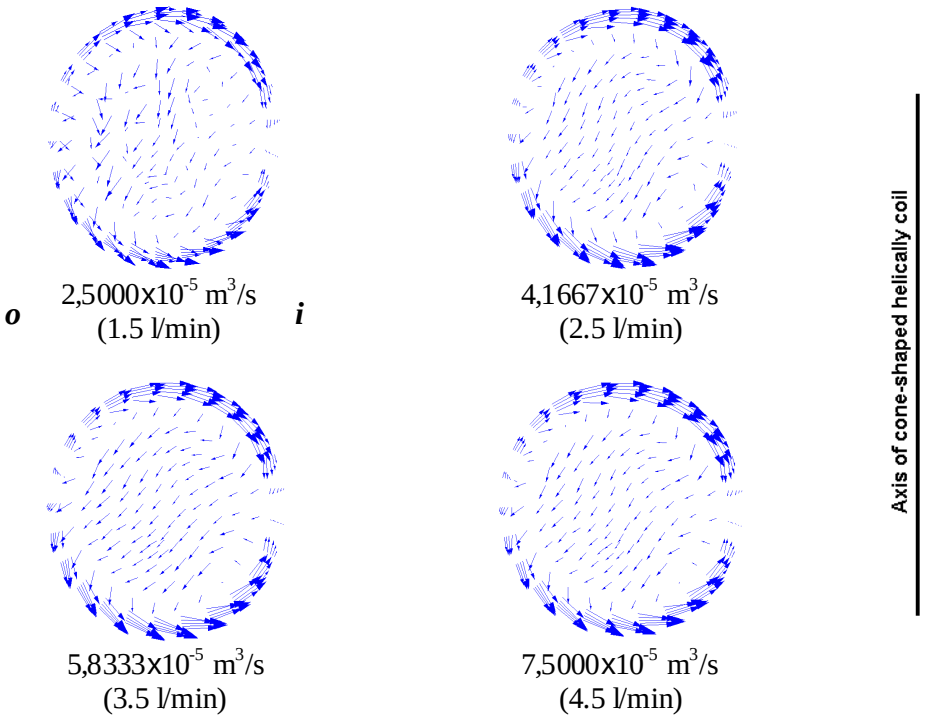

Fig. 9. XZ components of velocity vectors for the different flow conditions presented in Table 1.

5.2.2. Temperature profiles

Temperature profiles along the coil for the cases 1 and 4 described in Table 1 are given in Fig.10. At given cross section, temperatures along the periphery of the tube does not show an appreciable variation, with a maximum of 15°C of difference for laminar regime (condition 4 –Table 1) and 5°C for turbulent regime (conditions 1, 2, 3 - Table 1). Like velocity contours, temperature contours in the cross-section is also skewed, with the inner point of the coil being the hotter zone and the opposite point reporting the lower temperature. Top and bottom points have temperature between the later ones.

Temperature decreasing along the tube axis shows an almost linear tendency, as well the pressure drop along the tube length.

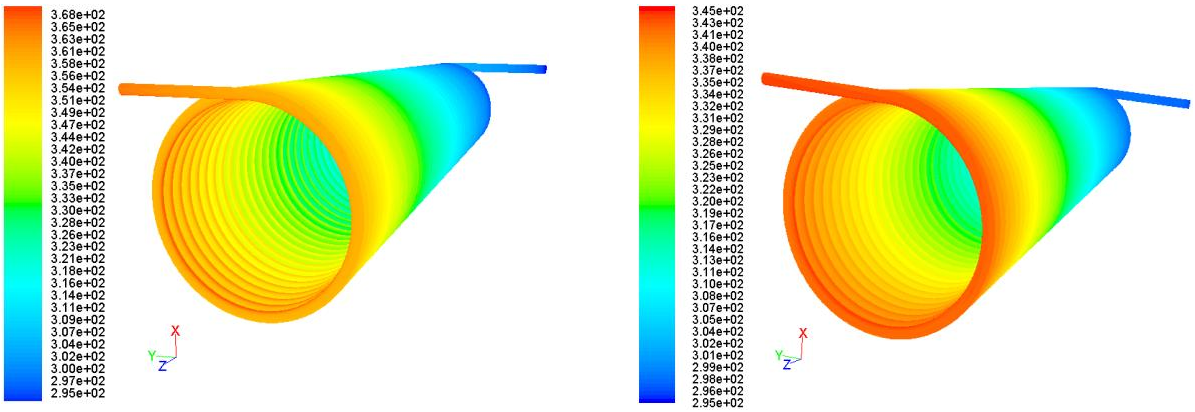

(a) (b)

Fig. 10. Contours of static temperature (K) a) condition 4, Table 1; b) condition 1, Table 1.

5.2.3. Friction factor coefficient

Darcy's friction factor coefficient was calculated as four times the area weighted-average of skin friction coefficient along the pipe (with ρ_{reff} and u_{reff} taken as in the velocity inlet boundary), i.e:

$$f_{Darcy} = 4 \cdot C_f = 4 \cdot \frac{\tau_w}{\left(\frac{1}{2}\rho_{reff} u_{reff}^{\ 2}\right)} \tag{18}$$

Figure 11 shows the comparison between the numerically and experimentally obtained friction factor coefficient with those obtained using Ito's and White's correlations.

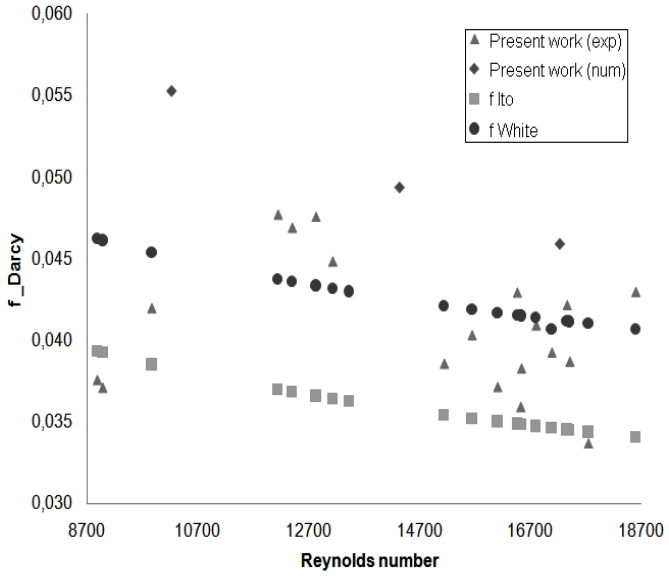

Fig. 11. Comparison of friction factor coefficients (Numerically and experimentally obtained, and calculated by using Ito´s and White's correlation) as a function of Reynolds number.

Although numerically calculated friction factor coefficient tends to over predict the experimentally obtained data at higher Reynolds number, mean deviation was 14% from experimental data. At low turbulent Reynolds number (near 10000) no well agreement was found between numerical and

experimental results. White's correlation attempt to predict the numerical results better than Ito´s correlation. No correlation was proposed at this work for friction factor coefficient.

5.2.4. Numerical Nusselt number

In this section, the results of the analysis of the CFD simulation are used to estimate the overall Nusselt number. Figure 12 gives a comparison of the overall heat transfer coefficients obtained from the experiment and those calculated using the CFD code. A reference temperature of 295 K was taken in the Fluent reference values menu. It is found that the values are well within 30%. The Nusselt numbers obtained from the experimental study slightly over-predict the measured data.

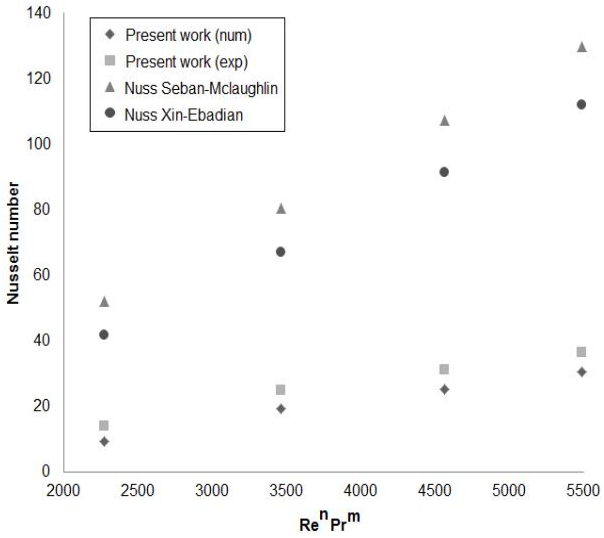

Fig. 12. Comparison of the overall Nusselt number obtained in the present work and other author's correlation.

In Fig. 12, the Nusselt number values obtained in the present work are compared with those predicted by the correlations of Seban and Mclaughlin [11], and Xin and Ebadian [14]. Seban and Mclaughlin's correlation is given by:

$$Nu = 0.023 \cdot \mathrm{Re}^{0.8} \cdot \mathrm{Pr}^{0.4} \left(\mathrm{Re}^{1/20} \left(\frac{D}{D_H} \right)^{1/10} \right) \tag{19}$$

And Xin and Ebadian's correlation is given by:

$$Nu = 0.00619 \cdot \mathrm{Re}^{0.92} \cdot \mathrm{Pr}^{0.4} \left(1 + 3.455 \left(\frac{D}{D_H} \right) \right) \tag{20}$$

Both correlation are valid in the range $5000 \le \mathrm{Re} \le 10^5$ and $\mathrm{Pr} = 5$, and they are used to estimate the "local" Nusselt number in the periphery. The data shown in the Fig. 12 were calculated using average values for the properties at the inlet and the outlet of the pipe, attempting to obtain an average Nusselt number along it. As it can be seen, other author's correlations considerably over predict the experimentally and numerically obtained Nusselt number by at least two and a half times. Since the results obtained by those correlations apply only for straight – non conical – helically coiled heat pipes, (19) and (20) are not appropriate to estimate the Nusselt number in the heat exchanger used at this work. Furthermore, the taper effect and the horizontal position whose effects are not considered if using Seban and Mclaughlin's and Xin and Ebadian's correlations can cause great deviations, as it was validated using the experimental data in the present work.

6. Conclusions

The study of the flow and heat transfer in a cone-shaped helically coiled heat exchanger was carried out in this work. Temperature dependent properties were used in this study and a constant wall heat flux boundary condition was assumed due to the nature of the experiment. An empirical correlation for average Nusselt number was proposed from experimental data and a maximum deviation of 23% was found. Numerical simulations were validated using the experimental results since no information was found for the studied geometry in the literature. It was found that the values were well within 30%. A comparison between the Nusselt number calculated using Seban and Mclaughlin and Xin and Ebadian correlations, and the experimentally obtained data showed that those correlations could overpredict at least three times the experimental values. Concerning the flow field, unlike in the straight helical coils, an appreciable inclination of the velocity vector components in the secondary flow was observed for the cone-shaped helical coils, although velocity contours are similar to the formers, with the particles of the fluid near the outer wall going faster due to the unbalance in centrifugal forces. Frictions factor coefficients were found to be approximately included in the range predicted by Ito's ad White's friction factor correlations, while numerically obtained results slightly overpredict experimental data. Further investigations should be focused in the effect of taper in the local Nusselt number as well as the effect of the pitch, instant curvature ratio and vertical position of the cone-shaped heat exchanger. Part of the deviations and errors can be attributed to the non-uniform flame radiation, sooting and condensed combustion products (due to the use of LPG) which modify the conditions for a constant wall heat flux assumption. Regarding to the differences between the average Nusselt number values obtained in the present work and those calculated using the formulas proposed by other authors, it has to be considered that, as developed for local Nusselt number values, those correlations are not totally reliably when calculating average values. Besides, those correlations do not integrate the effect of the variation of curvature ratio along the coil axis and require local properties values. The taper effect in the heat transfer and fluid flow process, and the conjugate heat transfer using combustion gases shall be further investigated in order to better understand the behavior in cone-shaped helical coil configurations.

Acknowledgments

Authors want to thanks to the National University of Colombia, Medellin, for allowing us to use their facilities and the Research Management Office, campus Medellín -DIME- for financing the building of the prototype. Also, we want to thanks to the technicians at the Laboratories of Heat Machines and Welding for their support in its construction.

Nomenclature

Letter symbol

A Area, m^2

c_p specific heat, J/(kg K)

D Pipe diameter, m

$De = \mathrm{Re}\sqrt{D/D_H}$ Dean number

D_H Mean coil diameter, m

D_{mH} Minimum coil diameter, m

D_{MH} Maximum coil diameter, m

e	Wall thickness, m
f	friction factor coefficient
$\overline{h}$	Average heat transfer coefficient, W/(m^2 K)
I	Turbulence intensity, %
i	specific enthalpy, J/kg
k	conductivity, W/(m K)
ℓ	length scale, m
$\dot{m}$	mass flow rate, kg/s
$\overline{Nu}$	Nusselt number
Pr	Prandtl number
$\dot{Q}$	Heat flow rate, W
r	Radius, m
Re	Reynolds number
ΔT	Temperature difference, °C or K
T	Temperature, °C or K
u	Velocity, m/s
$\dot{\forall}$	Volumetric flow rate, m^3/s

Greek symbols

λ	curvature ratio
μ	dynamic viscosity, Pa s
κ	Turbulent kinetic energy, m^2/s^2
ε	Turbulent dissipation rate, m^2/s^3
ρ	density, kg/m^3
θ	Angle, degrees
τ	Shear stress, Pa

Subscripts and superscripts

2	outlet
1	inlet
avg	average
w	wall
o	outer
b	bulk
i	inner
f	fluid
$reff$	reference

References

[1] Vashisth, S., Nigam, K, Kumar V,, *A review on the potential applications of curved geometries in process industry*. Ind. Eng. Chem. Res., 2008. **47**: p. 3291-3337.
[2] Thompson, J., *On the origin of windings of river and alluvial planes, with remarks on the flow of water round bends in pipes*, Proc. R. Soc. London. Ser. A 1876: p. 5.
[3] Williams, G.S.H., C. W.; Fenkell, G. H, *Experiments at Detroit, Michigan on the effect of curvature on the flow of water pipes*. Trans. Am. Soc. CiV. Eng. , 1902. **47**(1).
[4] Eustice, J., *Experiments of streamline motion in curved pipes*. Proc. R. Soc. London, Ser. A 1911. **85**(119).
[5] Grindley, J.H.G., *On the frictional resistance of air through a pipe*. Proc. R. Soc. London, Ser. A 1908. **80**(114).
[6] Dean, W.R., *Note on the motion of fluid in a curved pipe*. Philos. Mag. , 1927. **4**(208).
[7] Dean, W.R., *The streamline motion of fluid in a curved pipe*. Philos. Mag., 1928. **7**(673).
[8] Jeschke, D., *Heat transfer and pressure loss in coiled pipes*. Ergaenzungsheft Z. Ver. Disch. Ing. , 1925. **68**: p. 24-28.
[9] Merkel, E., *Die grundlagen Der Warmeubertragung*. 1927: p. 51.
[10] Prabhanjan D, R.G., Rennie, T., *Comparison of heat transfer rates between a straight tube heat exchanger and a helically coiled heat exchanger*. Int Commun Heat Mass Transfer, 2002. **29**: p. 185-191.
[11] R.A. Seban, Mclaughlin, E.F., *Heat transfer in tube coils with laminar and turbulent flow*. Int. J. Heat Mass Transf, 1963. **6**: p. 387.
[12] Dravid A, Merrill E, Brian P, *Effect of secondary fluid motion on laminar flow heat transfer in helically coiled tubes*. AiChE Journal, 1971. **27**(5): p. 1114-1122.
[13] Austen, D., Soliman, H., *Laminar Flow and Heat Transfer in Helically Coiled Tubes with Substantial Pitch*. Experimental Thermal and Fluid Science 1988. **1**: p. 183-194.
[14] Xin R.C., *The effects of Prandtl numbers on local and average convective heat transfer characteristics in helical pipes*. J. Heat Transf. , 1997. **119**: p. 467–473.
[15] Cioncolini, A., Santini, L,, *On the laminar to turbulent flow transition in diabatic helically coiled pipe flow*. Experimental Thermal and Fluid Science, 2006. **30**: p. 653–661.
[16] Jayakumar J, M.S., Mandal P, *Experimental and CFD estimations of heat transfer in helically coiled heat exchangers*. CHEMICAL ENGINEERING RESEARCH AND DESIGN, 2008. **86**.
[17] Conté, I., Peng, X, , *Numerical and experimental investigations of heat transfer performance of rectangular coil heat exchangers*. Applied Thermal Engineering, 2009. **29**: p. 1799–1808.
[18] Conté, I., Peng, X, Wang, B, , *Numerical Investigation of Forced Fluid Flow and Heat Transfer from Conically Coiled Pipes*. Numerical Heat Transfer, Part A, 2008. **53**: p. 945–965.
[19] Kumar, V., Faizee B, Mridha, M, Nigam, K, , *Numerical studies of a tube-in-tube helically coiled heat exchanger,*. Chemical Engineering and Processing, 2008. **47**: p. 2287–2295.
[20] Di Piazza, I., Ciofalo, M,, *Numerical prediction of turbulent flow and heat transfer in helically coiled pipes*. International Journal of Thermal Sciences, 2010. **49**: p. 653–663.
[21] Ito, H., *Friction factors for turbulent flow in curved pipes*. J. Basic Eng., 1959. **81**: p. 123–134.
[22] White, C.M., *Fluid friction and its relation to heat transfer*. Trans. Inst. Chem. Eng. , 1932. **10**: p. 66-86.
[23] White, C.M., *Streamline Flow through Curved Pipes*. Proc. R. Soc. Lond. , 1929. **123**: p. 645-663.
[24] Hart, J.E.; Hamersma, P. J, *Single and two-phase flow through helically coiled tubes*. Chem. Eng. Sci. , 1988. **45**(4): p. 775.
[25] P. Mishra, Gupta, S., *Momentum transfer in curved pipes: Newtonian fluids*. Ind. Eng. Chem. Des. Dev. , 1979. **18**: p. 130–137.
[26] Naphon, P., Wongwises,S., *A review of heat transfer and flow characteristics in curved tubes*. Renewbable and sutainable energy reviews, 2006. **10**: p. 463-490.

[27] Charles G. Slominski, W.D.S., and Churchill, W, *Helical and Lemniscate Tubular Reactors.* Ind. Eng. Chem. Res. , 2011. **50**: p. 8842–8850.
[28] Vashisth, S., Nigam, K, *Prediction of flow profiles and interfacial fenomena for two phase flow in coiled tubes.* Chemical Engineering and Process, 2008. **48**(29): p. 452-463.
[29] Srinivasan, S, Holland, *Friction factors for coils.* Trans. Inst. Chem. Eng. , 1970. **48**: p. T156–T161.
[30] A. Cioncolini, L.S., *An experimental investigation regarding the laminar to turbulent flow transition in helically coiled pipes.* Exp. Thermal Fluid Sci, 2006. **30**: p. 367–380.
[31] *Chemicalogic Corporation*. 30/11/2011]; Available from: http://www.chemicalogic.com
[32] Futagami, K., Aoyama, Y, , *Laminar heat transfer in helically coiled tube.* Int. J. Heat Mass Transfer, 1988. **31**(2): p. 387-396.
[33] Shih, H., Liou, W Shabbir, A Yang, Z, Zhu, Y, A, *A New k-e Eddy-Viscosity Model for High Reynolds Number Turbulent Flows - Model Development and Validation.* Computers Fluids, 1995. **24**(3): p. 227-238.
[34] Naphon P, *Effect of curvature ratios on the heat transfer and flow developments in the horizontal spirally coiled tubes.* Journal of Heat and Mass Transfer 2007. **50**: p. 444–451.
[35] *ANSYS FLUENT 12.0/12.1 Documentation*. 11/11/11]; Available from: https://www.sharcnet.ca/Software/Fluent12/index.htm.
[36] Kumar V, Gupta .P., and Nigam K, *Fluid Flow and Heat Transfer in Curved Tubes with Temperature-Dependent Properties.* Ind. Eng. Chem. Res., 2007. **46**: p. 3226-3236.
[37] Jayakumar J, M.S., Mandala J, Iyer K, Vijayanb V, *CFD analysis of single-phase flows inside helically coiled tubes.* Computers and Chemical Engineering, 2010. **34**: p. 430–446.

Thermo-fluid dynamic model for control analysis of latent heat thermal storage system

Adriano Sciacovelli[a], Vittorio Verda[b], Flavio Gagliardi[c]

[a] *Politecnico di Torino, Dipartimento Energia, Torino, Italy, adriano.sciacovelli@polito.it*
[b] *Politecnico di Torino, Dipartimento Energia, Torino, Italy, vittorio.verda@polito.it*
[c] *Politecnico di Torino, Dipartimento Energia, Torino, Italy, flavio.gagliardi@studenti.polito.it*

Abstract:

The present paper describes the application of computational fluid-dynamics (CFD) to the analysis of medium scale LHTES unit for district heating system. The units consists in a shell-and-tube heat exchanger filled PCM and uses water as heat transfer fluid (HTF). The systems has been designed to exchange heat from the primary to the secondary heat district heating network. A paraffin-graphite composite with a 15% graphite volume fraction is considered in order to improve thermal performance of the system. The discharge process of the unit has been studied under several operating conditions characterized by heat requests ranging between 160kW and 260kW. Time evolution of major physical quantities, such as heat fluxes, energy content and HTF outlet temperature, are presented and analyzed. The results show that, under particular operating conditions, the LHTS unit do not operate efficiently and undesirable variations of HTF outlet temperature occurs. For this reason, the paper presents a possible control strategy of the LHTS system based on non-steady-state HTF inlet conditions. The results show that unsteady HTF inlet mass flow rate allows to run the system effectively and for a longer operating time.

Keywords:

Latent energy storage, phase change materials, district heating, CFD

1. Introduction

Thermal energy storage plays a fundamental role in several systems when excess energy is available and that would be wasted if not stored. This is a particularly important problem in renewable and cogeneration systems. Energy storage techniques commonly adopted can be divided in three major categories: sensible, thermo-chemical and latent heat storage. Latent heat thermal energy storage (LHTES) technology has became increasingly attractive and possible applications have been investigated in several fields such as electronics, automobile and solar based power generation. Compared to the other storage techniques, LHTS has some peculiar advantages such as high energy storage density, compactness and uniform temperature during charge and discharge processes, corresponding to the phase transition temperature of the Phase Change Material (PCM). Several reviews on PCMs and their possible applications are available in literature; the interested reader can refer to [1-3].

LHTES units can be classified on the basis of the PCM container configuration [3]. Different geometries have been proposed. For sake of simplicity only the works regarding the cylindrical shell-and-tube design are here considered, since this configuration in the one investigated in this paper. In this configuration the PCM fills the shell while the heat transfer fluid (HTF) flows inside a single tube and therefore heat transfer takes place between the working fluid and the PCM. The shell-and-tube configuration have been experimental studied by several authors: Choi and Kim [4] studied the heat transfer characteristics during solidification of $MgCl_2 \cdot 6H_2O$ in a circular tube unit. Air was used as HTF and the influence of inlet temperature and mass flow rate was determined. Dimaano and Watanabe [5] investigated a vertical cylindrical shell-and-tube latent heat storage system filled with capric and lauric acid mixture as PCM. The temperature distribution inside the PCM was experimentally determinate both for melting and solidification. Heat stored and the heat

released were also measured during the experiments. Hasan [6] experimentally studied palmitic acid as PCM employed in a cylindrical LHTES unit. Detailed measurements of temperatures and melting front propagation were conducted by the author. Hasan [6] also reported the effect of HTF the flow rate on the phase change process. Sari and Kaygusuz [7] investigated the performance of a LHTS unit both in the vertical and horizontal position. In particular the authors observed solid-liquid interface evolution temperature distribution and heat flux. Sari and Kaygusuz [7] concluded that heat transfer is largely influenced by natural convection of liquid PCM. Akgun et al. [8] experimentally analyzed melting and solidification of paraffin in a vertical tube in shell heat exchanger system. The thermophysical properties of the paraffin were obtained through differential scanning calorimeter analysis. Akgun et al. [8] also investigated the effect of the inlet temperature and the mass flow rate of the HTF both on the melting and solidification processes. The temperature profiles obtained by the authors indicated that melting process was strongly affected by buoyancy-driven currents in melted PCM. On the other hand solidification occurs more uniformly in the system since mainly affected by heat conduction. Agynem and co-workers [9] used erythriol as PCM which is particularly suitable for high-temperature applications (117.7°C melting temperature). The authors considered two experimental configurations consisting in a horizontal shell-and-tube with one heat transfer tube and a multitube unit with four pipes. The results show heat transfer extended in the radial and angular directions during the change of phase in both systems, indicating essential two-dimensional heat transfer in the horizontal unit.

A relevant part of the literature is dedicated to the modelling of LHTES units. The modelling of phase change processes is quite challenging due to the coupling of physical problems involved. Further complexity is due to the presence of moving melting front between solid and liquid PCM. The most common methods used are the enthalpy method and the equivalent heat capacity method [3]. The essence of the enthalpy method is based on the inclusion of the latent heat term in the energy equation as a source term which significantly simplifies the numerical treatment of the problem. Moreover, the regions were solid and liquid phases coexists are treated as an equivalent porous medium with the liquid fraction acting as porosity [10]. Lacroix [11] adopted the enthalpy method to developed a 2D numerical model of a shell-and-tube unit. The heat transfer between HTF and PCM was tackled by the author by means of empirical correlations. The results show that shell radius, HTF mass flow rate and inlet temperature are key parameters in order to optimize the performance of the unit. Anica [12] also adopted the enthalpy formulation to solve the energy equation and investigate charging and discharging processes of a shell-and-tube unit. Good agreement was obtained between numerical and experimental data indicating that HTF fluid flow has to be solved to take in account of thermal development regions. Ismail and Melo [13] numerically studied the problem of fusion of PCM in a shell-and-tube unit in the presence of natural convection. The authors employed a 2D model of a meaningful portion of the complete system, however they did not numerically solved the flow field of the HTF. The numerical predictions were compared with available experimental data indicating good agreement. The results illustrates how natural convection strongly enhances the melting rate in the upper portion of the system. Consequently solid-liquid interface presented a typical conical shape.

The equivalent heat capacity method have been also extensively used to investigate phase change problems. When such method is adopted, the apparent specific heat of PCM in the energy equation is given by the sum of the sensible and latent heats [14]. Halliot et al. [15] analyzed a shell-and-tube configuration for a solar water heating system. A graphite-paraffin composite material was considered as PCM. The dynamical behaviour of the system was analyzed by means of a finite element model developed with the aid of COMSOL package. Halliot et al. [15] taken in account of latent heat fusion by means of equivalent heat capacity method. In particular the apparent PCM specific heat was approximated by a Gaussian curve over the melting temperature range. The obtained results showed that the material were able to store daily solar radiation and to reach high level of thermal power during the discharge. Kuravi et al. [16] numerically studied the transient behaviour of a cylindrical tube containing sodium nitrate as phase change material. Equivalent PCM specific heat was modelled by means of a sine curve over the temperature range within which the

phase change takes place. Kuravi et al. [16] performed several simulations to assess the effect Reynolds number and tube diameters on the heat transfer process of the system. It was observed that the propagation of the melt front is directly proportional to the flow rate of the working fluid.

This paper illustrates the application computational fluid dynamics (CFD) for the dynamical modelling of the discharge process in a medium scale shell-and-tube type LHTES unit. The heat transfer problem in the PCM domain is solved using the equivalent heat capacity method and it is coupled to the thermo-fluid-dynamic problem of HTF. The unit is designed to cope with a maximum heat request around 200kW and is used to transfer heat from the primary district heating network working in the 95-65°C temperature range to the secondary user network which works in the 50-30°C temperature range. The charging and discharging process are therefore realized at two different temperature levels, 95°C and 50°C, respectively. The shell contains a paraffin-graphite composite in order to achieve adequate performance of the unit. Dynamical behaviour of relevant physical quantities, such as heat fluxes, HTF and PCM temperatures are illustrated and analyzed. The paper illustrates how effectiveness and operation time of the unit can be increased by varying during time the heat transfer fluid inlet conditions. The novel approach of this work is represented by the characterization of a medium size and temperature LHTES unit, while most of the literature works is dedicated to small-scale PCMs applications. Furthermore, a novel control strategy for the LHTES unit is proposed.

2. LHTES unit description

Figure 1 illustrates The LHTES unit investigated in this paper. It consist in a shell-and-tube unit with a 15×15 matrix of copper pipes. The heat transfer fluid flows through the pipes while PCM fills the gap between the external shell and the tubes. The HTF here considered is water and copper tubes are 2.9 m long with an inner diameter of 12.5 mm. The paraffin wax RT 82 provided by the Rubitherm manufacturer has been adopted as phase change material. Thermo-physical properties of the PCM are reported in Table 1.

Table 1. Thermo-physical properties of the PCM (RT82)[17] and Paraffin-Graphite composite

	Pure Paraffin	**Paraffin-Graphite composite (φ=15%)**
Melting temperature *[K]*	350-358	350-358
Latent heat capacity *[kJ/Kg]*	176	119.0
Thermal conductivity *[W/mK]* (solid-liquid)	0.2-0.2	15.0-15.0
Specific heat *[kJ/kg/K]* (solid-liquid)	1.8-2.4	1.5-1.8
Density *[kg/m^3]* (solid-liquid)	880-780	1090-1000

The main disadvantage of the PCM is represented by its low thermal conductivity. As a consequence charging/discharging process of the unit would take place with low melting/solidification rates. For this reason the application of phase change materials in large scale units is still under investigation and thermal enhancement must be employed. Various techniques have been adopted for enhancing PCM thermal performances such as extended surfaces, thermal conductivity enhancement and micro encapsulation [18]. In the present work a composite of RT82 and graphite is considered in order to improve thermal conductivity of the base PCM. The investigation conducted by Haillot and co-workers **Errore. L'origine riferimento non è stata trovata.** shows that paraffin PCM conductivity can be increased by a factor of 10-300 depending on the density of the graphite matrix adopted. In the present application a volume fraction φ = 15% of natural expanded graphite is chosen in order to achieve a conductivity enhancement factor of 75. Graphite matrix density is 100 kg/m^3 [19].

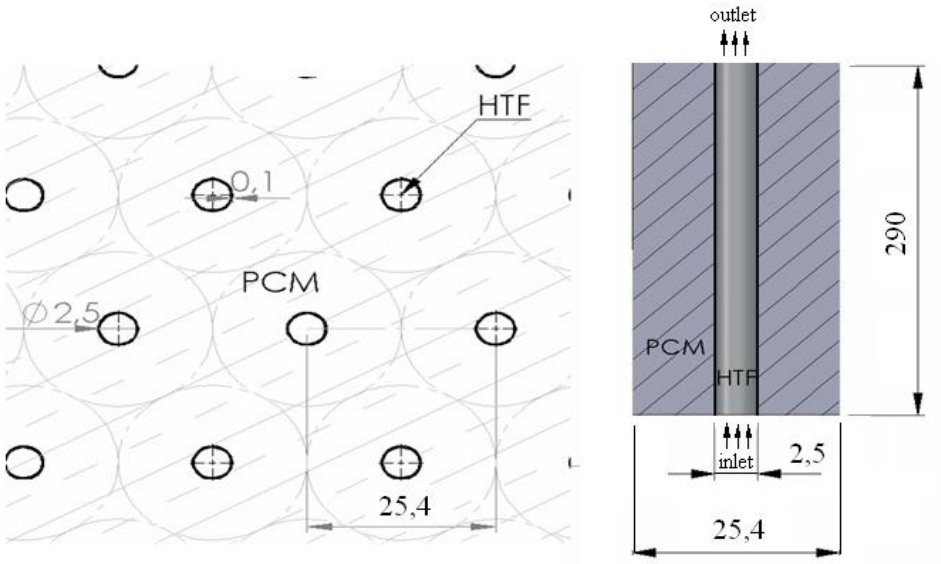

Fig. 1. Left) Cross section of the LHTES unit. Right) Single HFT longitudinal section of a single pipe with PCM (not to scale). Dimensions are expressed in cm.

The composite is treated as continuum media with thermal equilibrium between PCM and graphite, thus thermo-physical properties have been computed as follow [20]:

$$\rho_c = (1-\varphi)\rho_{PCM} + \varphi\rho_g \quad (1)$$

$$(\rho\, c_p)_c = (1-\varphi)(\rho\, c_p)_{PCM} + \varphi(\rho\, c_p)_g \quad (2)$$

$$(\rho\, L)_c = (1-\varphi)(\rho\, L)_{PCM} \quad (3)$$

where ρ is the density, c_p the specific heat, L the latent heat and the subscripts *c*, *PCM* and *g* refer to composite material, pure PCM and expanded natural graphite, respectively. The following thermo-physical properties of the pure graphite have been used: density equal to 2250 kg/m^3 and specific heat equal to 709 J/kg/K [19]. The above referenced equations apply for the PCM both in the liquidus and solidus states.

The LHTES unit here studied is designed to store the heat delivered from the primary district heating network. The temperature range of the primary network is 95-65°C. The unit is charged during night by opening valves P_{in} and P_{out} and closing S_{in} and S_{out}. Heat is transferred from the HTF to the PCM which melts and stores the energy both in terms of sensible and latent forms. Early morning hours are characterized by higher thermal request, thus the LHTS unit is discharged and PCM solidifies. During discharge process S_{in} and S_{out} are open and heat transfer takes place between PCM and the HTF circulating in the secondary user network. In this setup, valves P_{in} and P_{out} are closed. Finally, an auxiliary boiler and the mixing valve S_{mix} are connected to the secondary network. These components are used to regulate the temperature of HTF leaving the LHTES unit. The auxiliary boiler is activated when the temperature of the HTF delivered by the LHTES unit drops below a minimum threshold. The mixing valve S_{mix} is opened water when temperature from the unit exceeds the nominal value required by the end user. Temperature range of secondary network is 50-20°C. In this work the end user at the secondary network is supposed to be an high energy efficiency building. However, the analysis reported in the paper can be repeated for different scenarios, as long as temperature difference between primary and secondary network is at least 10°C.

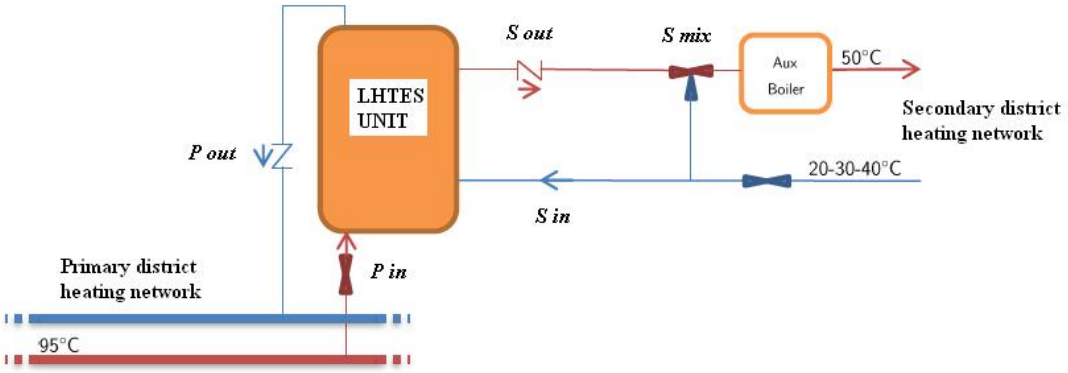

Fig. 2. Schematic of the connections between LHTES unit, primary and secondary district heating networks.

First, three main design conditions have been explored in the present paper. In such scenarios the mass flow rate circulating through the unit is equal to around 2.2 kg/s, 1.6 kg/s and 1.1 kg/s. The corresponding Reynolds number is 900, 650 and 400. In such operating conditions the LHTES unit provides the 100%, 70% and 45% of the maximum thermal request. The discharge process starts with liquid PCM at 95°C corresponding to the hot fluid temperature in the primary district heating network. Water inlet temperature from secondary network ranges between 20°C and 40°C corresponding to Stefan number from 0.7 to 0.9.

Second, the dynamical behaviour of the unit is also investigated when HTF mass flow rate varies during time; thus such operating condition is characterized by a variable *Re* number and it is obtained by regulating the mixing valve S_{in}. In this scenario a constant inlet temperature of 30°C is considered, that is *Ste* = 0.8.

3. Mathematical model

The thermo-fluid dynamic behaviour of the unit has been investigated by considering one HTF pipe and the PCM portion associated with it, as illustrated in Fig. 2. The same approach has been adopted by the vast majority of the numerical studies considered in the literature. The behaviour of HTF has been modelled using the Navier-Stokes equations arranged in axisymmetric fashion. The equivalent heat capacity method has been used to take in account of phase change process. The whole set of partial differential equations is the following one:

Continuity $$\frac{\partial \rho}{\partial t} + \frac{\partial \rho u_i}{\partial x_i} = 0 \qquad (4)$$

Momentum $$\frac{\partial}{\partial t}(\rho u_i) + \frac{\partial}{\partial x_j}(\rho u_j u_i) = \mu \frac{\partial^2 u_i}{\partial x_j \partial x_j} - \frac{\partial p}{\partial x_i} + \rho g_i \qquad (5)$$

Energy $$\rho \cdot c_p \frac{\partial T}{\partial t} + \rho \cdot c_p \cdot u_i \frac{\partial T}{\partial x_i} = \frac{\partial}{\partial x_i}\left(k \frac{\partial T}{\partial x_i}\right) \qquad (6)$$

Where ρ is the fluid density, u the fluid velocity, x the spatial coordinate, t the time coordinate, μ the dynamic viscosity, p the pressure, S the momentum source term and T the temperature. Accordingly to the equivalent heat capacity method, the effective specific heat $c_{p,PCM}$ of the PCM has been described by the following set of equations:

$$c_{p,PCM} = c_{p,s} \qquad \text{if} \quad T < T_s$$

$$c_{p,PCM} = c_{p,s} + \frac{L}{\sigma\sqrt{2\pi}} \exp\left(\frac{-(T - T_{sl})^2}{2\sigma^2}\right) \qquad \text{if} \quad T_s < T < T_l$$

$$c_{p,PCM} = c_{p,l} \qquad \text{if} \quad T > T_l \qquad (7)$$

where T_s and T_l are the solid and liquid temperatures and L is the PCM latent heat of fusion. The equivalent PCM specific heat is thus modelled through a Gauss curve over the melting range temperature $T_s < T < T_l$. The σ parameter allows to set the temperature range within phase change takes place. Outside temperature melting range the ordinary PCM specific heat is used. The HTF and wall material properties are supposed to be independent of the temperature.

Outer boundaries of the computational domain are considered as adiabatic. A velocity boundary condition has been enforced at the HTF inlet, where also the temperature is assumed to be known. A pressure outlet boundary condition has been enforced at the HTF outlet surface. Because of the presence of graphite matrix, natural convection in the liquid phase of the PCM has been neglected. Furthermore, the large aspect ratio and the vertical position of the unit minimize the buoyancy-driven PCM flow [12]. Finally, PCM solidification is mainly affected by heat conduction while natural convection exist only at the beginning of the process [3].

The set of partial differential equations has been solved by using the finite element method. In this particular application a segregated solver has been used to address the Navier–Stokes problem. The fluid has been considered incompressible; Galerkin method has been adopted to solve the weak formulation of Eqs. (4-6) and direct solver has been utilized [21]. An implicit second order Euler scheme has been employed to treat the temporal discretization. Grid independence and the effect of time step size has been also evaluated in order to obtain reliable numerical solutions. Experimental data available from literature have been used to validate the numerical model [22,23].

The mesh is a structured grid of quadrilateral elements as illustrated in Fig. 3. Quadratic lagrangian elements have been adopted in order to properly capture the peculiar features of the solution.

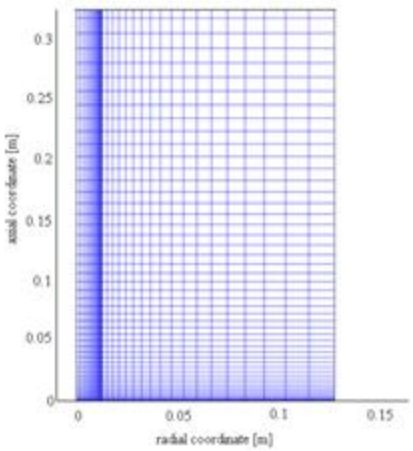

Fig. 3. LHTES meshing pattern.

4. Numerical results

4.1. Dynamical behaviour of the LHTES unit

The dynamical behaviour of the LHTES unit has been investigated by means of several numerical experiments characterized by different operating conditions (i.e. different HTF inlet conditions). For sake of simplicity the peculiar features of the numerical results will be presented for a HTF mass flow rate of 1.6 kg/s (Re = 650) and HTF inlet temperature of 30 °C (Ste = 0.8).

Velocity field of the working fluid is depicted in Figure 4: the profile shows typical features of channel flow such as the development of fluid flow along HTF pipe. Entrance length is around 0.5 m, thus boundary layer is not fully developed along 17% of the HTF pipe length. This can have a significant effect on heat transfer between water and PCM, consequently empirical correlations for heat transfer for fully developed flow conditions may lead to significant errors for the system performance evaluation.

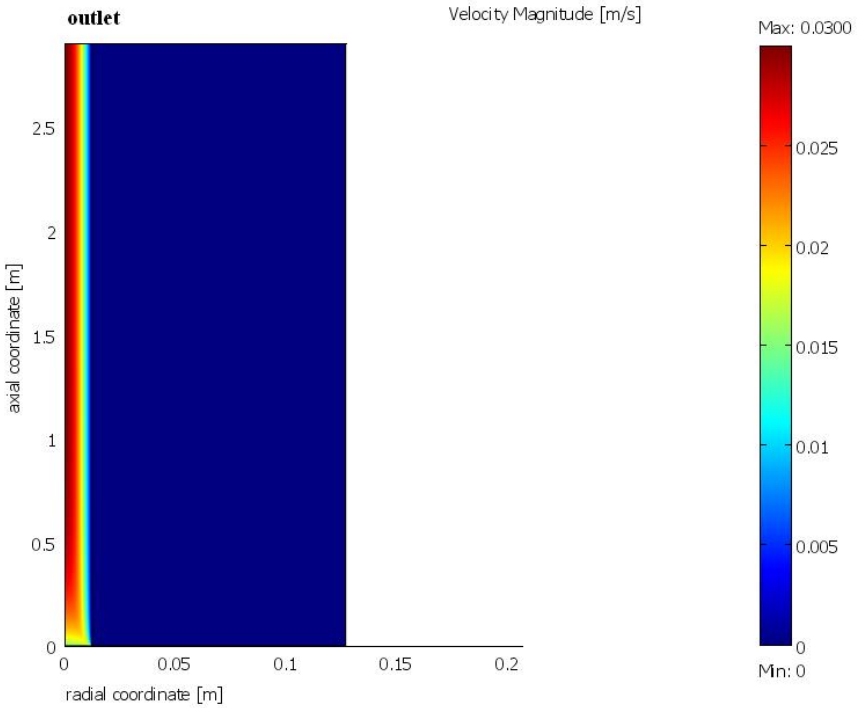

Fig. 4. Velocity profile in the HTF pipe. Re=650; St=0.8. (Not to scale)

Temperature contours for PCM and HTF at different instants of time are illustrated in Fig. 5. The plot illustrates the temperature evolution during the discharge the of LHTES units. It is clear from Fig. 5 that steady state condition are not reached during the process. Furthermore it can be noticed that HTF temperature increases along unit due to the heat flux exchanged with the paraffin-graphite. PCM solidification starts in the lower region of the unit near the HTF inlet and solidification front moves upward during the process. Once solidification is completed sensible heat is exchanged between PCM and working fluid, thus PCM temperature quickly approaches HTF inlet temperature.

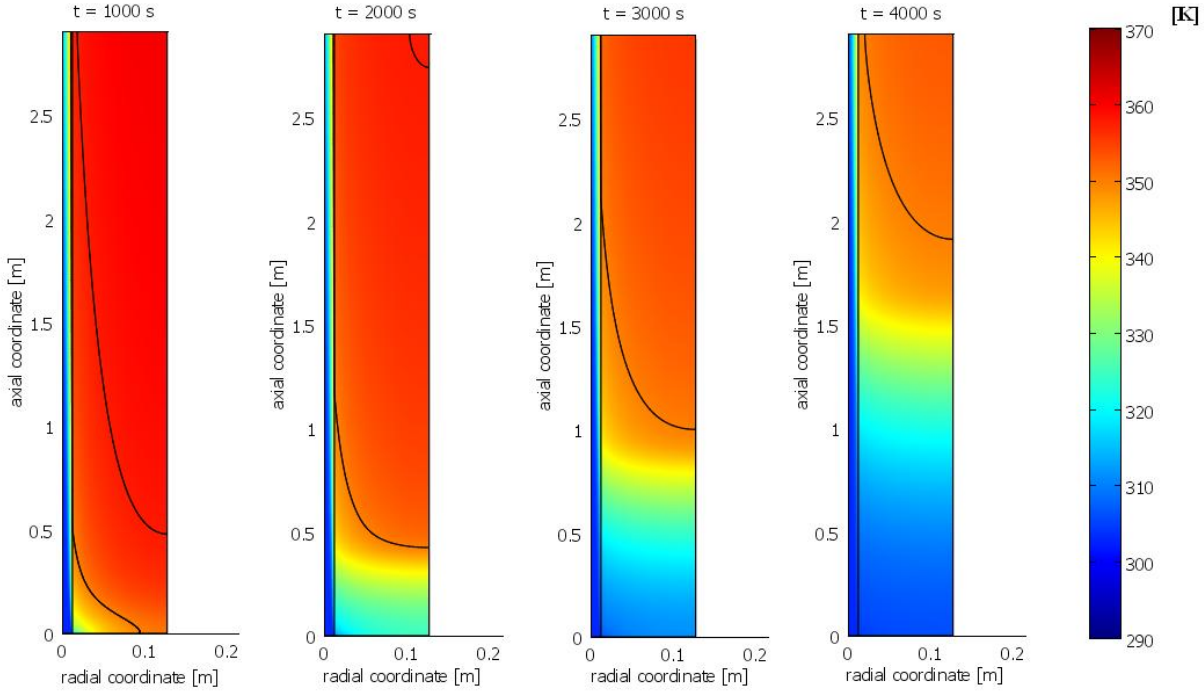

Fig. 5. Temperature distribution in the PCM and in the HTF at four different instant of time. Re=650; St=0.8. (Not to scale)

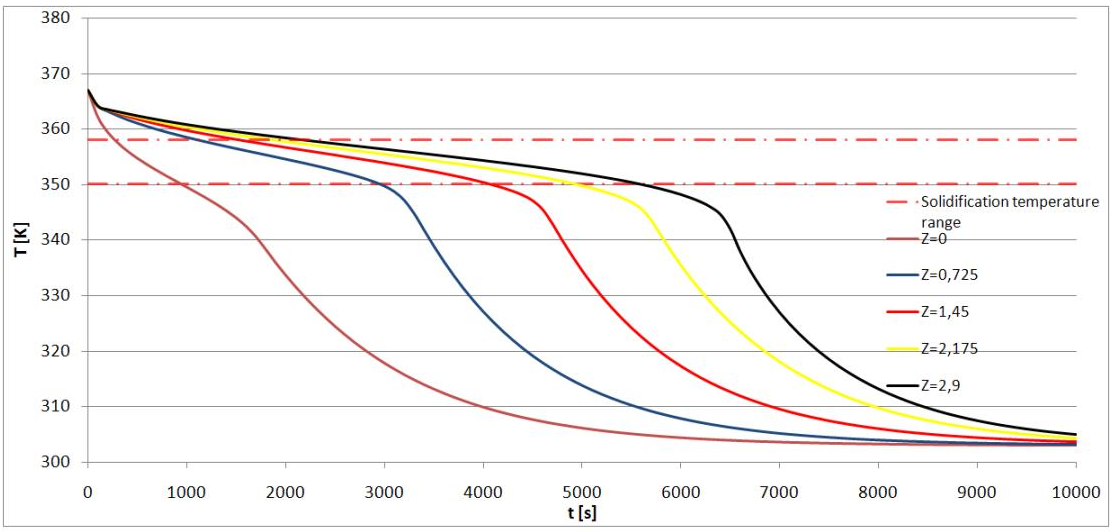

Fig. 6. Temporal evolution of PCM temperature at five different axial positions. Re=650; St=0.8.

PCM temperature evolution at four different axial coordinates is depicted in Figure 6; radial coordinate is equal to 0.127 m for all the plots. As expected within solidification temperature range PCM cooling rate is lower due to higher heat capacity. When solidification is completed heat transfer is dominated by conduction and temperature decreases faster. Near HTF inlet (z = 0 m) discharge process is more efficient (i.e. higher solidification rate): phase change is complete in about 600 s since temperature difference between HTF and PCM is larger. At z = 2.9 m complete solidification requires about 3500 s, which indicates that solidification rate significantly decreases along the axial coordinate of the unit.

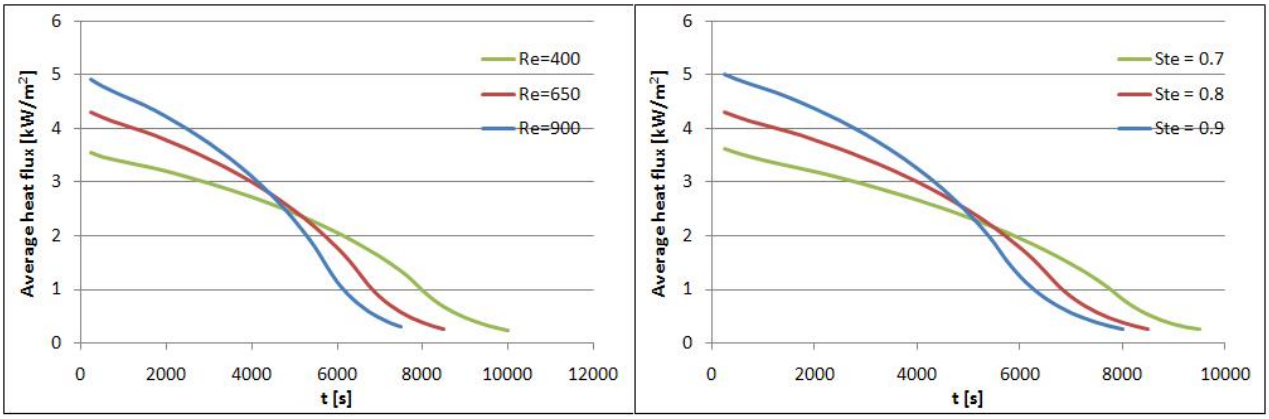

Fig.7. Average heat flux time wise variations. left) Effect of Re number; right) effect of Ste number.

The temporal evolution of average heat flux between water and PCM is illustrated in Fig. 7. These plots emphasize furthermore the unsteadiness of LHTES unit discharge process. The effect of HTF mass flow rate and inlet temperature is also reported in terms of Reynolds and Stefan numbers. Figure 7 shows that larger heat flux can be achieved by increasing the HTF *Re* number. However a more uniform heat flux is obtained when *Re* is decreased, indeed after about 6000 s larger average heat flux is achieved with *Re* = 400. Higher temperature difference between HTF and PCM is achieved by increasing *Ste* number, consequently also a larger heat transfer is established between working fluid and phase change material.

The system is designed in order to deliver water at 50°C (see Fig. 2), thus an important variable that indicates the LHTES unit performance is the HTF outlet temperature. The HTF outlet temperature is shown in Fig. 8 for *Ste* = 0.8 and different Reynolds numbers. It is evident that LHTES unit availability decreases if *Re* increases. For *Re* equal to 900, 650 and 400 the unit can deliver water

with a temperature larger than 50°C for 3000 s, 4500 s and 6500 s, respectively. During such time intervals the unit is able to supply an average thermal power of about 260 kW, 200 kW and 160 kW. From Figure 8 it also clear that in the early stages of discharge process, water outlet temperature significantly exceeds the nominal conditions. This effect is particularly marked for *Re* = 400, indeed HTF outlet temperature initially reaches 70°C while 50°C are requested by the secondary network.

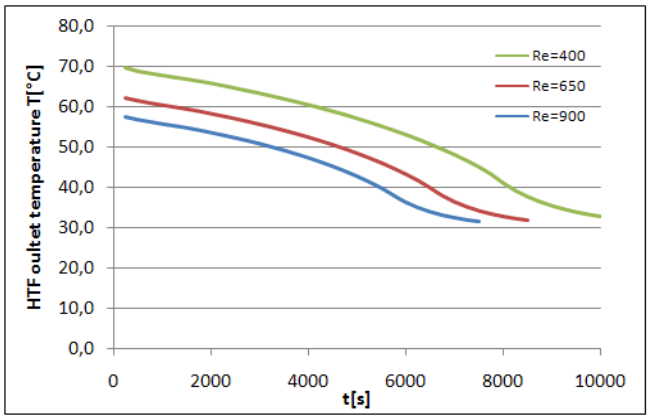

Fig.8. Effect of Re number on HTF outlet temperature. Ste = 0.8.

4.1. Effect of non-steady-state HTF mass flow rate

As illustrated in the previous sections the HTF outlet temperature can largely exceeds the nominal conditions, for this reason in the present work the mixing valve mixing valve S_{mix} (see Fig. 2) is used to control water temperature at the secondary network.

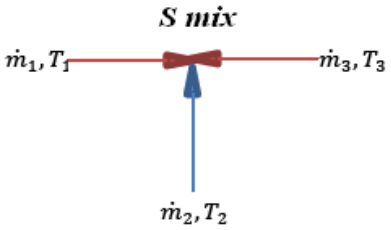

Fig.9. Mixing valve S_{mix}; Definition of temperatures and mass flow rate.

The mixing valve is opened when LHTES outlet temperature T_1 exceeds the nominal value of 50°C. Consequently, due to adiabatic mixing, mass flow rate temperature T_3 at secondary network is decreased and nominal temperature can be achieved. Furthermore when S_{mix} is open, HTF mass flow $\dot{m}_1$ at the LHTES decreases. However, temperature T_1 (see Fig. 9) varies during time, thus the valve S_{mix} must be properly regulated in order to achieve constant temperature T_3 for the entire discharge process. As a result the LHTES unit operates with non-steady-state HTF mass flow rate. In this section dynamic behaviour of the LHTES unit is investigated under unsteady state inlet HTF mass flow rate. Furthermore, optimal operating conditions are individuated to achieve nominal conditions at secondary network for the entire discharge process of the storage unit.

From a simple mass and energy balance is possible to obtain the relation between LHTES unit mass flow rate $\dot{m}_1$ and the secondary network $\dot{m}_3$ when valve S_{mix} is open:

$$\frac{\dot{m}_3}{\dot{m}_1} = \frac{T_1 - T_2}{T_3 - T_2} \qquad (8)$$

the ratio $\dot{m}_3/\dot{m}_1$ is shown in Fig. 10 for T_3 = 50°C and T_2 = 30°C. The reference mass flow rate $\dot{m}_1$ considered in Fig. 10 corresponds to *Re* = 900 while variable HTF outlet temperature T_1 previously obtained by the CFD model has been used to evaluate Eq. (8) for the entire LHTES unit discharge process.

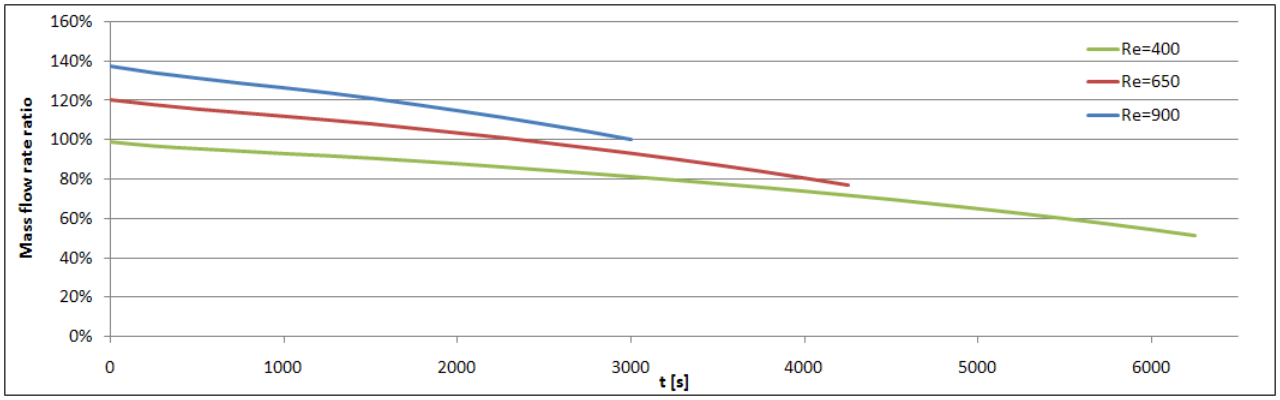

Fig.10. Ratio between secondary mass flow rate and nominal secondary mass flow rate at 50°C.

From Fig. 10 is possible to observe that it is convenient to operate the LHTES unit with lower mass flow rate in order to increase its operation time, even with nominal mass flow rate at the secondary network. From the data reported in Fig. 10 it possible to find a time-dependent LHTS mass flow rate that allows to obtain a constant temperature of 50°C at the secondary network for the longest possible period of time. In the case studied in this paper the function:

$$\dot{m}_1 = 4.762 \cdot 10^{-11} \cdot t^2 + 5.475 \cdot 10^{-7} \cdot t + 0.005 \quad [kg/s] \quad (9)$$

represents the optimal LHTES unit mass flow rate for a single HTF pipe. If such mass flow rate is provided to the unit by means of the S_{mix} valve, a constant temperature can be obtained at the secondary network. Such scenario has been further investigated by means of the CFD model previously described in the paper. Numerical simulations have been performed considering the mass flow rate from Eq. (9) as inlet boundary condition for the HTF. Figure 11 depicts the results obtained.

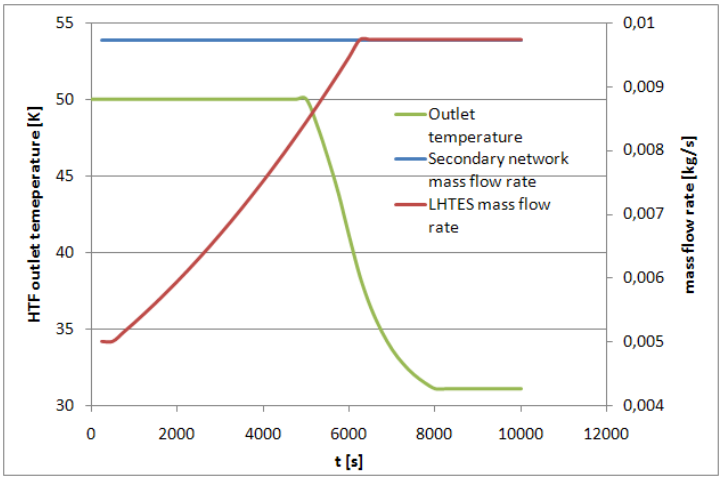

Fig.11. Secondary network temperature (green) for non-steady state LHTES mass flow rate (red). Ste = 0.8.

Significant improvements can be observed by comparing Fig. 8 and Fig. 11: the HTF temperature variations are totally avoided for about 4500s when non-steady-state HTF mass flow rate is adopted. Thus the nominal condition can be met for a significant portion of the discharge process. After t = 4500 s temperature start to decrease since most of the PCM has already solidified.

Therefore, it is necessary to activate the auxiliary boilers to achieve the thermal request of the secondary network. LHTES unit mass flow rate and secondary network mass flow rate for a single HTF pipe are also illustrated in Fig. 11. The red line depicts the mass flow rate described by Eq. (9). At the beginning of the process LHTES mass flow rate is about the 50% of the secondary network mass flow rate. On the other end, when discharge process is completed, i.e. t = 4500 s, 82% of the secondary mass flow rate is provided by the LHTES unit. This means that the valve S_{mix} must be properly regulated for the entire process to realize the mixing and guarantee constant mass flow rate at the secondary network.

Non-steady-state mass flow rate has a significant effect on the heat transfer between PCM and HTF. In Fig. 12 average heat flux is compared for the operating conditions considered in this paper. It can be seen that with variable *Re* number, that is unsteady mass flow rate, the average heat flux is almost constant for until t = 4000 s. When discharge process is nearly completed insufficient energy is stored in the PCM, consequently average heat flux strongly diminish. Variable *Re* number allows to reduce the initial excess of heat flux observed with constant mass flow rate. Moreover, the LHTES unit operating time is larger when unsteady mass flow rate is considered, indeed after 4000 s the average heat flux is appreciably larger than in the cases with constant *Re* number.

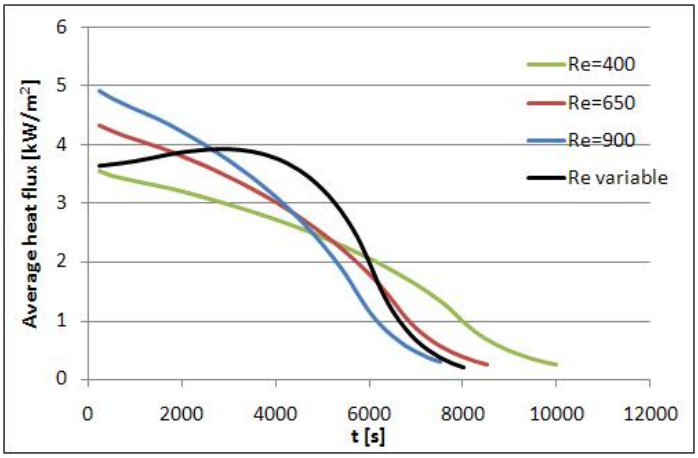

Fig.12. Average heat flux time wise variations. Effect of variable Re number.

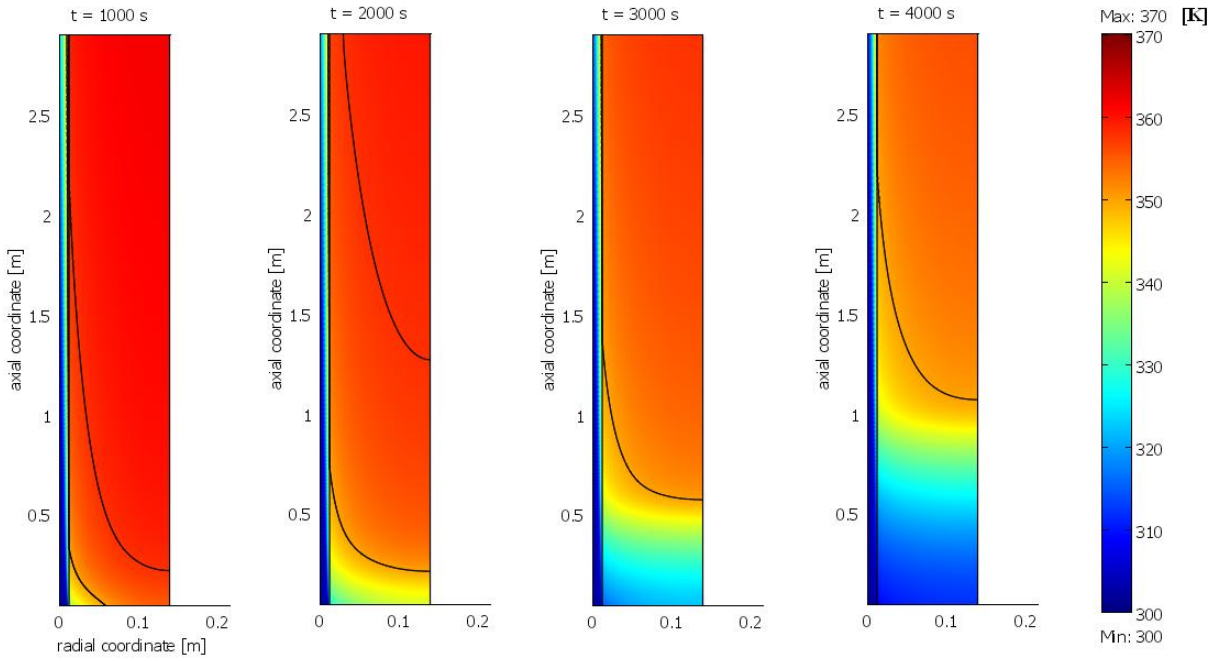

Fig. 12. Temperature distribution in the PCM and in the HTF at four different instant of time. Re=650; St=0.8. (Not to scale).

PCM temperature contours for non-steady-state HTF mass flow rate are reported in Fig. 13 for different instants of time. Significant differences can be observed when Fig. 5 and Fig 13 are compared. In particular it can be appreciated that at each instant of time less PCM is solidified when the LHTES unit operates with a variable mass flow rate. At t = 3000 s solidification front is found at an axial coordinate of about 0.5 m; while at the same instant of time, solid PCM is found at z = 1m if *Re* is constant and equal to 650. Consequently the LHTES unit can potentially operate for a longer time if unsteady mass flow rate is considered.

6. Conclusions

In this paper computational fluid dynamics has been used for the characterization of a medium scale latent heat thermal storage unit. The unit considered is designed to transfer heat between the primary and the secondary network of a district heating system. The unit consists in a cylindrical shell containing a 15x15 matrix of HTF pipes embedded in a paraffin wax. Thermal performance of the PCM are enhanced by means of graphite matrix in order to achieve the required thermal conductivity. Three design operating conditions have been investigated: the CFD analysis shows that the unit is able to supply an average thermal power of about 260 kW, 200 kW and 160 kW. The behaviour of the unit has been further characterized in terms of *Re* and *Ste* numbers. The results show that heat transfer is enhanced when *Re* and *Ste* increase. However HTF outlet temperature is shown to experience unwanted variations during the discharge process. For this reason, it is proposed to dynamically control the LHTES unit by means of non-steady-state HTF mass flow rate. This scenario has been investigated by means of the CFD model: the analysis illustrates that nominal conditions at the secondary network can be achieved when HTF mass flow rate varies during time as a quadratic equation. In particular, a constant temperature of 50°C can be guaranteed at the secondary network for 4500s of the LHTES unit discharge process. Therefore, the analysis shows that the LHTES unit can be operated more effectively when the proposed dynamical control is adopted.

References

[1] Zalba, B., Marin, J.M., Cabeza, L.F., Mehling, H. Review on thermal energy storage with phase change: materials, heat transfer analysis and applications. Appl. Therm. Eng 2003; 23, 251–283.

[2] Farid, M.M., Khudhair, A.M., Razack, S.A.K., Al-Hallaj, S. A review on phase change energy storage: Materials and applications. Energy Convers. Manage. 2004; 45, 1597– 1615.

[3] Agyenim, F., Hewintt, N., Eames, P., Smyth, M. A review of materials, heat transfer and phase change problem formulation for latent heat thermal energy storage systems (LHTESS), Renewable and sustainable Energy Reviews 2010; 14: 615-628

[4] Choi,. J.C., Kim, S.D. Heat-transfer characteristics of a latent heat storage system using $MgCl{\cdot}6H_2O$, Energy 1992; 17(12): 1153-1164.

[5] Dimaano, M.N.R., Watanabe, T., Performance investigation of the capric and lauric acid mixture as latent heat energy storage for a cooling system. Sol. Energy, 2001; 72, 205– 215.

[6] Hasan, A. Phase change material energy storage system employing palmitic acid. Sol. Energy, 1994; 52, 143–154.

[7] Sari, A., Kaygusuz, K. Thermal energy storage system using stearic acid as a phase change material. Sol. Energy, 2001; 71, 365–376.

[8] Akgun, M., Adin, O., Kaygusuz, K. Experimental study on melting/solidification characteristics of a paraffin as PCM. Energy Conversion & Management, 2007; 48: 669-678.

[9] Agyenim F., Eames P., Smyth M. Heat transfer enhancement in medium temperature thermal storage system using a multitube heat transfer array. Renewable Energy, 2010; 35: 198-207.

[10] Voller V.R., Prakash C. A fixed grid numerical modeling methodology for convection-diffusion mushy region phase-change problems. International Journal of Heat and Mass Transfer 1987; 30: 1709-1719.

[11] Lacroix, L. Numerical simulation of a shell-and-tube latent heat thermal energy storage unit. Solar energy, 1993, 50(4): 357-367

[12] Anica T. An experimental and numerical investigation of heat transfer during technical grade paraffin melting and solidification in a shell-and-tube latent thermal energy storage unit. Solar energy 2005; 79: 648-660.

[13] Ismail, K., Abugderah, M. Performance of a thermal storage system of the vertical tube type. Energy Conversion & Management, 2000; 41: 1165-1190

[14] Lamberg, P., Lehtiniemi, R., Henell, A.M. Numerical and experimental investigation of melting and freezing processes in phase change material storage. International Journal of Thermal Sciences, 2004; 43: 277-287.

[15] Haillot D, Py X, Goetz V, Benabdelkarim M. Storage composites for the optimization of solar water heating systems. Chem Eng Res Design 2008; 86:612–7.

[16] Kuravi, S., Tharan, J., Rahman, M., Goswami, D.Y., Stefanakos, E.K. Analysis of transient heat transfer in a thermal energy storage module. Proceedings of IMECE'10: 2010 ASME International Mechanical Engineering Congress & Exposition Vancouver, Canada, November 12 - 18, 2010.

[17] Rubitherm Technologies GmbH. Phase Change Material based on n-Paraffins and Waxes. – Available at: <http:// www.rubitherm.com/> [accessed 26.2.2011].

[18] Jegadheeswaran, S., Sanjay, D. P. Performance enhancement in latent heat thermal storage system: a review. Renewable and Sustainable Energy Reviews 2009; 13: 2225-2244.

[19] Py, X., Olives, R., Mauran, S., Paraffin/porous-graphite-matrix composite as high and constant power thermal storage material. International journal of heat and mass transfer 2001, 44:2727-2737

[20] Kohodadadi, J. M., Hosseinizadeh, S.F., Nanoparticle-enhanced phase change materials (NEFCM) with great potential for improved thermal energy storage. International communications in heat and mass transfer, 2007; 34: 534-543

[21] Quarteroni, A., Valli, A. Numerical approximation of partial differential equations. Springer-Verlag 2008.

[22] Sciacovelli, A., Verda, V. Numerical analysis on melting in a cylindrical heat storage capsule. Second International Conference on Computational Methods For Thermal Problems. September 5 – 7, 2011 Dalian, China.

[23] Sciacovelli, A., Verda, V., Colella, F. Numerical Model for Storage Systems Based on Phase Change Materials. Proceedings of IMECE'11: 2011 ASME International Mechanical Engineering Congress & Exposition Denver, Colorado, November 11 - 17, 2011.

Towards the development of an efficient immersed particle heat exchanger: particles transfer from low to high pressure

Luciano A. Catalano [a], Riccardo Amirante [b], Stefano Copertino [c], Paolo Tamburrano [d], Fabio De Bellis [e]

[a] *Polytechnic of Bari, Italy, catalano@poliba.it*
[b] *Polytechnic of Bari, Italy, amirante@poliba.it*
[c] *Polytechnic of Bari, Italy, stefanocopertino1@alice.it*
[d] *Polytechnic of Bari, Italy, p.tamburrano@poliba.it*
[e] *Polytechnic of Bari, Italy, debellis@imedado.poliba.it*

Abstract:

An innovative heat exchange device has been recently proposed, which employs an intermediate solid medium to transfer heat from a gas flow at low pressure and high temperature to another gas flow at higher pressure but lower temperature, with negligible pressure losses. In this paper, a key component of this innovative heat exchanger is analyzed in deep, namely the pressurization device responsible for the particles transit between the two separate environments. The operation of the proposed pressurization system is described in detail and then modeled as a zero-dimensional time-dependent system to analyze the influence of the related mass and energy losses onto the heat exchanger efficiency. An experimental test rig reproducing the pressurization tank has been also set up: the data collected at different operating conditions confirmed the reliability of the analytical model and the negligible energy losses occurring in the pressurization process.

Keywords:

Gas turbines, external combustion, innovative heat exchanger, pressurization.

1. Introduction

Nowadays, natural gas turbines dominate the field of power generation because of their black start capabilities, high efficiency, lower capital costs, shorter installation times, better emission characteristics and abundance of natural gas supplies. Gas turbines for power generation are employed in both simple and combined cycles: technical improvements such as material advancements and cooling innovations have contributed to enhance their efficiency: accordingly, combined cycle plants are the thermal plants with the highest efficiency (about 60% [1]). However, internal combustion demands the use of clean fuels, which are significantly more expensive than coal or orimulsion or biomass; moreover, their availability is also limited by geo-political aspects. These arguments explain why stand-alone steam power plants using cheaper fuels, in external combustion mode, are still under construction. Their development and maintenance is only slowed down by the introduction of international agreements and taxes aiming at limiting CO_2 emissions and thus at avoiding lower efficiency plants.

Externally fired gas turbines would combine the higher efficiency of a combined cycle plant with the advantages of burning cheaper fuels. However, their development and application is limited by the intrinsic difficulties in realizing gas to gas heat exchangers working at very high temperature and characterized by high thermal efficiency and by a limited pressure drop. Designing and manufacturing high-efficiency heat exchangers is also a limiting factor in the development of gas turbines employing heat recovery Joule-Brayton cycle [2,3,4] .

With respect to the traditional gas to gas heat exchangers, a completely different architecture characterizes the so-called “pebble-bed” devices, which make use of an intermediate medium (a granular ceramic or metallic material) first to recover and then to release heat from one flow to another; this can be achieved either by employing two tanks with large alumina balls where hot and cold air flow alternatively [5] or in a continuous operation mode: to the authors’ knowledge, there are only two examples of the latter architecture, namely, two patents of the 1960s [6,7]. Both of them are made of two heat exchangers: the particles are heated up in the first one and then transfer the heat to a cold flow in the second one; at the same time, the particles are cooled and, thus, are able to repeat the process. The main difference between the two patents lies in the way the particles cross the air flows: one of them [6] is completely gravity-based (particles are simply “injected” and then fall down), while a series of tilted rotating plates drives their path in the other one [7]. Such heat exchangers could have some advantages in comparison with traditional ones: very high efficiency, low pressure drops, and relatively simple construction. However, both proposals did not include detailed fluid-dynamic studies aiming at optimizing the particle trajectories; moreover, they did not mention how hot particles can be injected in the high pressure gas flow without crushing them.

Some of the authors have recently proposed and optimized [8,9,10] an innovative Immersed Particle Heat Exchanger, which employs an intermediate medium with high thermal capacity: small alumina particles fall in a column where hot gas flows from the bottom to the top; the warmed up particles are then collected at the bottom of the column and inserted at the top of a second column where they transfer the accumulated heat to a counterflowing cold gas. The potential of such heat exchange mode was demonstrated, both theoretically and experimentally. An effective one-dimensional model, which allows to compute the column lengths required for achieving the heat exchanger design efficiency, was proposed and validated by means of a test bench, reproducing the upper half of the proposed Immersed Particle Heat Exchanger [8]. Conduction inside the small particles can be neglected, as demonstrated in [10] by means of DNS simulations. The developed test bench was also equipped with a second vertical pipe, used to demonstrate that very fine particles, which could damage turbine blades in a real plant, can be completely eliminated by means of centrifugation. In addition, a tridimensional CFD model, capable of recognizing all 3D geometrical details, was developed with the aim of optimizing some geometric parameters affecting the overall efficiency of the heat exchanger [9].

Application of the Immersed Particle Heat Exchanger to gas turbine plants requires a mechanical system to be interposed between the two columns in order to pressurize the solid intermediate medium; afterwards, the particles can fall in the bottom column for gravity. Such pressurization device must operate without crushing the particles, both to maintain their size constant and to avoid dust [8]. As well, particles collected from the bottom column must be transferred in a lower pressure (atmospheric pressure) environment.

The development of the pressurization system is the subject of this paper: its operating principles are proposed in the next section; in section 3, a design tool is proposed, based on a zero-dimensional model. In section 4, all energy losses related to the operation of the pressurization device are accounted for, so as to estimate its performance. Some experimental tests will be finally presented to validate the analytical models and the effectiveness of the pressurization procedure.

2. Operating principles of the pressurization system

Figure 1 presents a sketch of the Immersed Particle Heat Exchanger. The main components are: two heat exchange modules mainly composed of large vertical ducts, a pressurization system for the solid intermediate medium (interposed between the two columns), a depressurization system (at the bottom of the second column), and a conveyor. Exhaust gas from turbine outlet (heat recovery cycle) or from a separate combustion chamber (external combustion gas turbine) is delivered at the bottom of a vertical cylindrical pipe (top column); a proper flow rate of uniformly distributed cold particles falls from the top and is heated up by the hot gas stream, whose temperature can be ideally

decreased to the particle inlet temperature, before leaving the column at its top. The warmed up particles are then delivered into the bottom column: since the pressure in the bottom column is greater than the pressure in the top column, a pressurization system must increase pressure on the solid particles without damaging them and with minimal energy losses. The bottom column operates in a similar mode: rather cold (compressed) air enters the column at the bottom and flows upwards, in counter-flow with the hot particles falling from the top. Hot air leaves the column at the top, whereas cold particles are collected by means of a depressurization system, and delivered back at the top of the plant by using a conveyor. In this process, heat is absorbed from the hot gas, temporarily stored and then released in the second pipe, where the cold stream is warmed up.

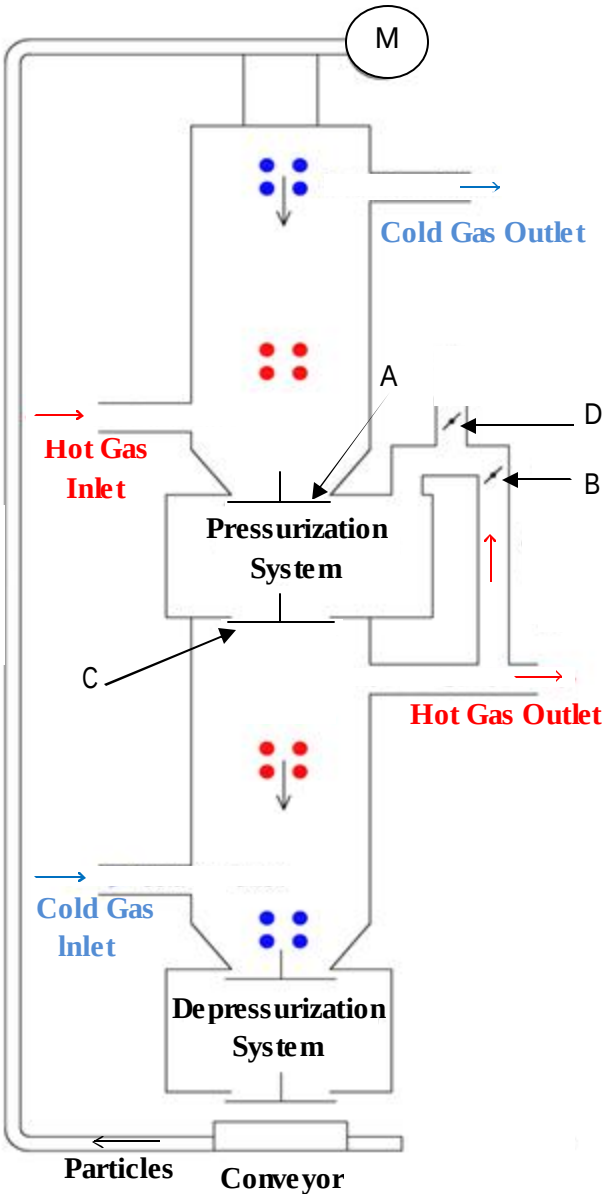

Figure 1- Immersed Particle Heat Exchanger

As shown in Figure 1, the pressurization system proposed in this paper is mainly composed of one pressurization tank placed between the two columns, one duct connecting the pressurization tank with the bottom column and four control valves. The opening and closing of the control valves must automatically be regulated by a proper control system. The following four steps are performed during one pressurization cycle:

1. Tank filling. At the beginning of the cycle, the four valves are in the closed position: the first phase begins when the valve A opens and the solid particles can fall into the pressurization tank.
2. Pressurization. After the particles have entered the tank, the valve A closes and the pressurization phase begins by opening the pressurization valve B: a small amount of compressed gas moves from the bottom column to the tank. As a result, the pressure in the tank increases until it attains the pressure in the bottom column.
3. Particle discharge (from the pressurization tank to the bottom column). This phase starts when the valve C opens and the solid particles can fall down for gravity from the pressurization tank into the bottom column.
4. Depressurization. After the particles have been discharged from the tank, valves B and C are closed and the compressed gas, which remains in the tank, must be ejected in order to return the atmospheric pressure in the pressurization tank and to begin a new cycle. This result is achieved by opening the depressurization valve D.

The following sections proposed a simple design tool for the proposed pressurization device. This zero-dimensional model will be also employed for analyzing its energy losses, related both to the loss of compressed gas discharged into the external environment during the depressurization phase and to the cooling of the hot particles entering the tank, due to the presence of the cold residual gas remaining in the capacity at the end of the depressurization phase.

3. ZERO-DIMENSIONAL MODEL

This section proposes a 0-D model for evaluating the main dimensions of the pressurization tank: the duration of each cycle, denoted with t_c, can be split as:

$$t_c = t_f + t_d + t_x \qquad (1)$$

where t_f is the time interval of the filling phase, t_d is the time interval of the particle discharge phase and t_x amounts the time intervals spent for the pressurization and depressurization phases and for the valves actuation. Furthermore, we assume the equality between the mass flow rates of particles entering the tank and those discharged from the tank to the bottom column: this condition is satisfied if the two valves A and C have the same size, since the mass flow rate of solid particles falling from a reservoir depends only on the size of the orifice and on the diameter of the particles [11]. Equality of inlet and outlet mass flow rates implies that t_f and t_d are equal; accordingly, t_c can be expressed as:

$$t_c = 2t_d + t_x \qquad (2)$$

Assuming that the particles occupy the entire volume of the pressurization tank at the end of the filling phase, the mass flow rate of particles discharged from the pressurization tank into the bottom column can be evaluated as:

$$\dot{m}_p = \frac{\rho_p V_t}{t_d} \qquad (3)$$

where ρ_p is the density of the intermediate medium and V_t is the volume of the tank. The value of $\dot{m}_p$ calculated by means of Equation 3 represents the mass flow rate of particles discharged when the valve C is kept in the open position by the control system, whereas $\dot{m}_p$ is equal to zero in the remaining period of the pressurization cycle. As shown in Figure 2, the particles are discharged intermittently from the tank: indeed $\dot{m}_p$ varies with time from zero to the constant value expressed by Equation 3.

Since the Immersed Particle Heat Exchanger must operate continuously in a real plant, an accumulation grid must be inserted below the pressurization system, in order to achieve a constant mass flow rate of particles in the bottom column. During stationary mode operation, the constant mass flow rate of particles in the bottom column must be equal to the average value of $\dot{m}_p$, which is indicated with $\overline{\dot{m}}_p$ in Figure 2. It is noteworthy that $\overline{\dot{m}}_p$ must be equal to the mass flow rate

required for heating the compressed gas in the bottom column. Since thermal capacities of particles and of gas must be equal for a counterflow heat exchanger, $\overline{\dot{m}}_p$ must be computed as:

$$\overline{\dot{m}}_p = \frac{c_{p,g}\,\dot{m}_g}{c_p} \quad (4)$$

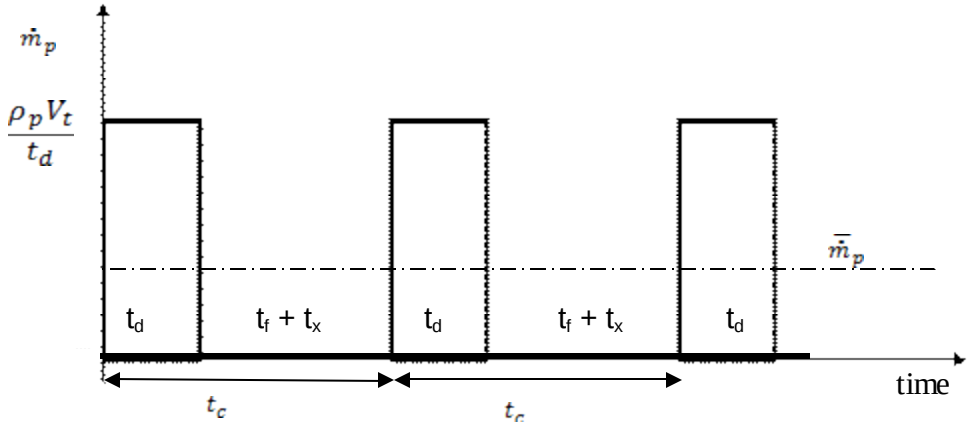

Figure 2- Mass flow rate of particles discharged from the pressurization tank into the bottom column

In equation 4, $c_{p,g}$ is the gas specific heat (supposed constant), c_p is the particle specific heat and $\dot{m}_g$ is the gas mass flow rate flowing through the bottom column. Furthermore, the average mass flow rate of particles discharged from the pressurization tank into the bottom column is related to the tank volume as follows:

$$\overline{\dot{m}}_p = \frac{\rho_p V_t}{t_c} \quad (5)$$

Combining Equations 4 and 5, we obtain Equation 6, which expresses the volume of the pressurization tank depending on the gas mass flow rate, the phisical properties of the particles, and the cycle time (or, equivalently, the number of cycles per seconds, indicated with n) :

$$V_t = \frac{c_{p,g}\dot{m}_g}{\rho_p c_p} t_c = \frac{c_{p,g}\dot{m}_g}{\rho_p c_p}\frac{1}{n} \quad (6)$$

Equation 6 can be manipulated by employing the equation of the gas mass flow rate, that is $\dot{m}_g = \rho_g^c\ v_g\ A$ (A is the sectional area of the bottom column crossed by the compressed gas, ρ_g^c and v_g are respectively the gas density and the gas velocity computed in a cross section of the bottom column near the outlet), by the formula of tank volume $V_t = A_t H_t$ (A_t and H_t are respectively the section and the height of the hopper), and by introducing the parameter $\alpha = A_t/A$. The resulting expression can be used to determine the height of the pressurization tank depending on the geometrical parameter α, the physical properties of the particles (c_p , ρ_p), the velocity and the density of the compressed gas in the bottom column (v_g, ρ_g^c), and the number of cycles n:

$$H_t = \frac{1}{\alpha}\frac{c_{p,g}\,\rho_g^c\ v_g}{\rho_p c_p}\frac{1}{n} \quad (7)$$

In Figure 3, H_t is plotted as a function of n and v_g , for an external combustion gas turbine working at very high turbine inlet temperature (T_g^c = 1400 K) and very high pressure ratio (p_g^c = 30 bar), with the assumption that α = 1 and the particle material is alumina (ρ_p = 3600 kg/m^3 , c_p = 1025 J/(kg K)). The graph shows that, for fixed values of v_g , H_t increases as n decreases. As a consequence, the assumption of low values of n causes large values of H_t: this means that, for a fixed sectional area, the pressurization tank has greater heat exchange surface with the outside and this could imply greater cooling of the hot particles. Therefore, the better choice is to fix high values for n, in order to reduce the effects of the heat exchange with the external environment.

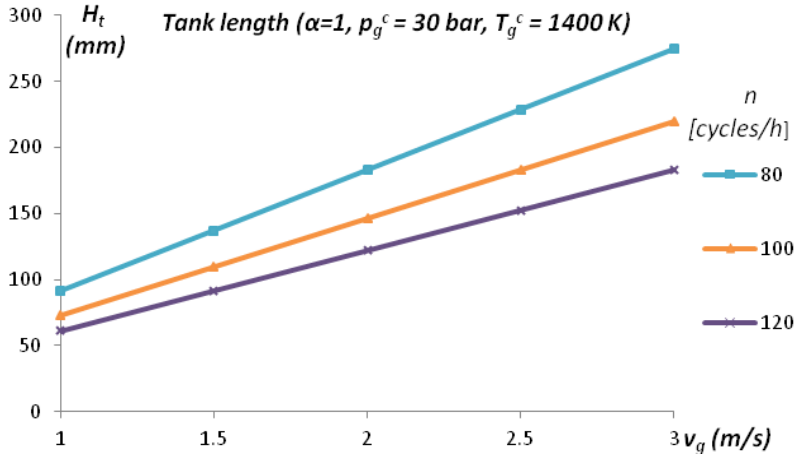

Figure 3- H_t versus v_g for 3 values of n (external combustion gas turbine)

4. Analysis of energy losses

4.1 Energy loss due to the lost compressed gas

During the discharge of the solid particles from the pressurization tank into the bottom column, the connection between the bottom column and the tank is kept open by the pressurization valve (valve B in Figure 1). At the end of this phase, which occurs when all solid particles have been transferred from the pressurization tank into the bottom column, and the valve C and B are closed, the pressurization tank is full of compressed gas. In order to repeat the pressurization cycle, this gas must be ejected to the outside and this is achieved during the last phase of the cycle, by opening the valve D. The compressed gas ejected into the external environment represents an energy loss, which is investigated in this section by means of the quantification of the lost compressed gas flow rate, with respect to the overall gas flow rate flowing through the bottom column.

The mass flow rate of compressed gas discharged into the external environment, $\dot{m}_{lost}$, can be expressed as follows:

$$\dot{m}_{lost} = \frac{m_{lost}}{t_c} \quad (8)$$

where m_{lost} is the mass of compressed gas lost in one cycle: with the worst hypothesis, this amount can be considered equal to the entire mass of gas in the pressurization tank immediately before the opening of the depressurization valve. Therefore, with this hypothesis, Equation 8 can be written as:

$$\dot{m}_{lost} = \frac{\rho_g^c \, V_t}{t_c} \quad (9)$$

Using Equation 9 and the formula of V_t (Equation 6), the ratio $\dot{m}_{lost}/\dot{m}_g$ can be expressed through Equation 10:

$$\frac{\dot{m}_{lost}}{\dot{m}_g} = \frac{\rho_g^c \, V_t}{t_c \, \dot{m}_g} = \frac{c_{p,g} \rho_g^c}{c_p \rho_p} \quad (10)$$

The denominator of Equation 10 is significantly larger than the numerator, since the intermediate medium must be characterized by large values of specific heat and density.

In Figure 4, $\dot{m}_{lost}/\dot{m}_g$ is plotted as a function of T_g^c and p_g^c , assuming that the intermediate medium is alumina.

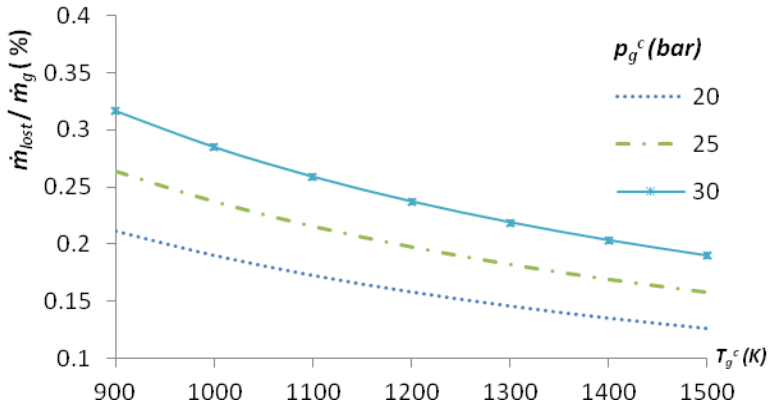

Figure 4 – $\frac{\dot{m}_{lost}}{\dot{m}_g}$ % versus T_g^c for 3 values of p_g^c (external combustion gas turbine)

As shown by the trends of the graph, $\dot{m}_{lost}/\dot{m}_g$% increases both with decreasing T_g^c and with increasing p_g^c, but the maximum value of $\dot{m}_{lost}/\dot{m}_g$% is under 0.35%.

4.2 Cooling of the hot particles in the central tank

After having entered the tank, the hot particles mix with the cold residual gas remained in the capacity at the end of the depressurization phase. The cooling of the hot particles and the related energy loss can be estimated by means of the following numerical analysis.

The first step is to calculate the temperature of the residual gas in the pressurization tank at the end of the depressurization phase. With reference to Figure 5 consider the mass of gas inside the pressurization tank immediately before the opening of the depressurization valve and assume the process to be adiabatic: application of the first law of thermodynamics to this mass leads to

$$L_{ext} = \Delta U \qquad (11)$$

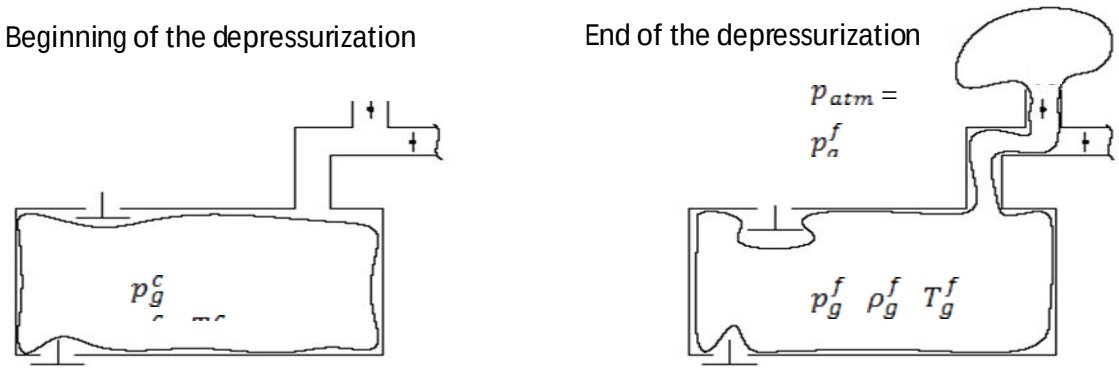

Figure 5- Depressurization phase

In equation 11, L_{ext} is the work done by the gas on the external environment and ΔU is the variation of the internal energy between the final and the initial state. Pressure, temperature and density of the compressed gas in the pressurization tank at the beginning of the depressurization phase can be assumed equal to the values of pressure, temperature and density occurring in the outlet of the bottom column, namely p_g^c, T_g^c and ρ_g^c. Indicating with p_{atm} the atmospheric pressure, with p_g^f, T_g^f, ρ_g^f respectively pressure, temperature and density of gas at the end of the expansion, and assuming constant specific heats $c_{v,g}$ and $c_{p,g}$, one gets:

$$-\left[p_{atm}\left(\frac{1}{\rho_g^f}-\frac{1}{\rho_g^c}\right)\right]=c_{v,g}\left(T_g^f-T_g^c\right) \quad (12)$$

Adding and subtracting the term p_g^c/ρ_g^c to the first member, being $p_{atm}=p_g^f$ and employing the equations $c_{v,g}T_g^f+\frac{p_g^f}{\rho_g^f}=c_{p,g}T_g^f$ and $c_{v,g}T_g^c+\frac{p_g^c}{\rho_g^c}=c_{p,g}T_g^c$, after few steps we obtain the expression of T_g^f:

$$T_g^f=\frac{T_g^c}{k}\left[1+\frac{p_g^f}{p_g^c}(k-1)\right] \quad (13)$$

Equation 13 allows to calculate the temperature of the residual gas in the pressurization tank at the end of the depressurization phase, as well as the temperature of the residual gas when the particles enter the pressurization tank at the beginning of the cycle.

In order to evaluate the cooling of the hot particles entering the pressurization tank when the valve A is kept opened, we can equate the final internal energy with the initial internal energy of the system composed by both the residual gas and the intermediate medium:

$$c_{v,g}\,m_g^f\,T_g^f+c_pm_pT_p^{in}=T_p^{out}\left(c_{v,g}m_g^f+c_pm_p\right) \quad (14)$$

where m_g^f is the mass of residual gas, m_p is the mass of particles contained in the central tank, T_p^{out} is the particle temperature after the cooling, and T_p^{in} is the particle temperature before the cooling, namely the temperature of the particles after the heat exchange in the top column.

Recovering T_p^{out} from Equation 14, and assuming that the volume of the particles contained in the tank is equal to the entire tank volume, after few steps we obtain Equation 15:

$$T_p^{out}=\frac{\frac{c_{p,g}}{k}\rho_g^f\,T_g^f+c_p\rho_pT_p^{in}}{\frac{c_{p,g}}{k}\rho_g^f+c_p\rho_p} \quad (15)$$

Equation 15 can be used to compute the temperature of the solid particles T_p^{out} after the heat exchange with the cold residual gas at the temperature T_g^f, which can be calculated through Equation 13.

Both Equations 13 and 15 allow to evaluate the energy loss due to the cooling of the solid particles in the following manner:

1) For given values of T_g^c and p_g^c, according to the characteristics of the heat exchanger, the temperature T_g^f is calculated through Equation 13;
2) Since the bottom column is a counter-flow heat exchanger, the difference of temperature ΔT between the hot particles and the compressed gas is almost constant over the entire column length, and ΔT depends on the efficiency of the heat exchanger, so it is possible to assign a constant value to ΔT;
3) Once fixed ΔT, T_p^{out} can be calculated through: $T_p^{out}=\Delta T+T_g^c$;
4) By recovering T_p^{in} from Equation 15, one gets the value of T_p^{in} as

$$T_p^{in}=\frac{T_p^{out}\left(\frac{c_{p,g}}{k}\rho_g^f+c_p\rho_p\right)-\frac{c_{p,g}}{k}\rho_g^f\,T_g^f}{c_p\rho_p} \quad (16)$$

5) The energy loss is quantified by means of the difference $T_p^{in}-T_p^{out}$.

Computations from item 1) to item 5) have been repeated for different values of T_g^c , p_g^c, ΔT in order to evaluate the energy loss for several operating conditions. In each case, the energy loss results to be negligible. Here we report two significant cases, for heat recovery cycles and for external combustion gas turbines, with the assumption that the intermediate medium is alumina.

For the heat recovery cycle, typical values are p_g^c = 10 bar, ΔT = 50 K, T_g^c = 1000 K. From these fixed values, computation from item a) to item d) leads to the results T_p^{out} = 1050 K and T_p^{in} = 1050,03 K. The difference $T_p^{in} - T_p^{out}$ and thus the corresponding energy loss is almost null.

For external combustion plant, we report a critical case, occurring at very high pressure ratio and high turbine inlet temperature, i.e. p_g^c = 35 bar and T_g^c = 1500 K. From these fixed values and assuming ΔT = 50 K, the result of computation from item a) to item d) is T_p^{out} = 1550 K and T_p^{in} = 1550,03 K. Also in this case, the energy loss due to the particle cooling is absolutely negligible.

In conclusion, due to the great difference between heat capacities of the intermediate medium and of the residual gas, the hot particles do not undergo any significant cooling before being discharged into the bottom column.

5. Experimental test

An experimental campaign has been carried out in order to test the pressurization system and to evaluate the theoretical model. The developed test rig is shown in Figure 6: it reproduces the pressurization system by means of one central tank which is connected to the top column and to the bottom column by means of two knife gate valves. The upper knife valve has the same function of the valve A in Figure 1, whereas the lower knife valve is the discharge valve (valve C in Figure 1): both knife valves have pneumatic actuator. The blue reservoir is directly connected to the compressed air supply, and it is also connected to the bottom column: a pressure regulator has been inserted between the bottom column and the reservoir in order to fix a constant pressure in the bottom column.

Figure 6 – Test bench

Figure 7 – Panel with the electro-valves, transducers and driver

Figure 7 shows the panel with all components that allow to automate the system. The two valves denoted with "G.1" and "G.2" are 3-way, 2 position electro-valves with pneumatic spring return: they have been employed to drive the knife gate valves. The inlet port of both the two electro-valves is directly connected to the compressed air supply and both outlet ports are connected to the respective knife gate valves in order to control the opening or the closing of the knifes.

The valve indicated with "Press" in Figure 7, is a 3-way, 2 position electro-valve with pneumatic spring return: its inlet port is connected to the compressed air supply, and its outlet port is connected to the piloting of a 2-way, 2 position N.C. pneumatically operated valve. The bottom column and the central pressurization tank are connected to the inlet port and to the outlet port of the 2-2 pneumatically operated valve, respectively: when the solenoid of the "Press" valve is energized, the connection between the tank and the bottom column is opened in order to perform the pressurization phase.

At the same way, the valve indicated with "Depr" in Figure 7, which is a 3-way, 2 position electro-valve with pneumatic spring return, pilots a 3-way, 2 position N.C. pneumatically operated valve. This couple of valves allows to perform the depressurization phase; the inlet port of the 3-2 pneumatically operated valve is directly connected to the central tank: when the solenoid of the "Depr" valve is energized, the compressed gas in the pressurization tank is discharged into the external environment.

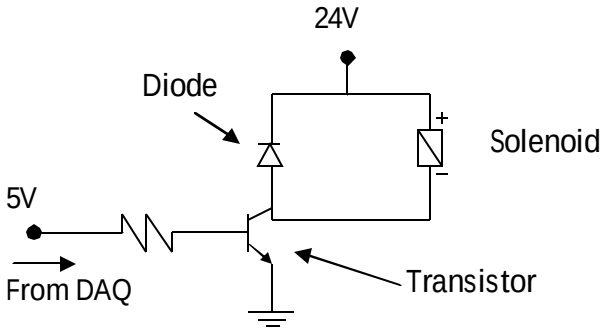

Figure 8 – Driver scheme

The solenoids of the electro-valves have been driven with an external PC by means of a DAQ card: between the data card and the solenoids we have inserted a driver, shown in the bottom right of Figure 7, since the solenoids require 24 Volt power supply with approximately 0.21 A absorbed current to move the internal spool, whereas the maximum current tolerable by the data card is 5 mA. The scheme of the driver is reported in Figure 8, and it consists of one transistor, one diode and

one resistance, connected as in the scheme: with this configuration, the current flowing through the output channel of the data card is different from the current absorbed by the solenoid coils. The panel also reports two strain gauge pressure transducers, allowing to measure pressure in the pressurization tank and in the bottom column, and the linearizer of the thermocouple (accuracy $\pm 1^{o}$C) inserted into the central tank. The pressure transducers are electronically assisted to compensate the temperature variations, with accuracy $< \pm 0.5\%$ of the full scale (10 bar).

Each test starts with the top column filled with alumina under atmospheric pressure, and keeping a constant pressure in the bottom column. The entire pressurization cycle has been performed for several values of pressure in the bottom column, in particular from 2 to 10 bar. At first, the particles are loaded into the pressurization tank by the opening of the upper knife gate valve; then, this valve is closed and the pressurization phase begins when the solenoid of the "Press" valve is energized and it opens the connection between the bottom column and the central tank. After the pressure in the tank has reached the pressure in the bottom column, the lower knife valve is opened and the particles are discharged into the bottom column. At the end, after closing the lower knife valve and the connection between the bottom column and the central tank, the compressed air remained in the tank is discharged into the atmosphere by energizing the solenoid of the "Depr" valve.

The experimental tests have been initially performed in order to evaluate the reliability of the knife gate valves: the tests have shown that the upper valve and the lower valve are capable of regulating the passage of the particles respectively from the top column to the central tank and from the central tank to the bottom column. Many tests have been performed under perfect air tightness condition; however, particle crushing has become significant after such a long operation time: this results in a diminished capability of ensuring total air tightness in the closed position, since some particles were stuck between the knife and the valve seat, causing air leakage. In future works, this drawback will be analyzed in order to find a mechanical solution which ensures total air tightness for a long operation time.

Repeated tests, performed under perfect air tightness condition, have allowed to analyze the losses of the developed system, in particular the mass of compressed air discharged to the atmosphere: the ratio $\dot{m}_{lost}/\dot{m}_g$ has been experimentally determined for several different pressures in the bottom column, and the experimental values have been compared with those achieved by means of the numerical analysis. The graph in Figure 9 reports the comparison between the experimental curve and the theoretical curve, for different pressure levels: the two curves almost overlap each other, and this proves the reliability of the numerical model. Note that each experimental point in Fig. 9 represents the mean value calculated from five independent experiments in order to reduce the effect of random uncertainties.

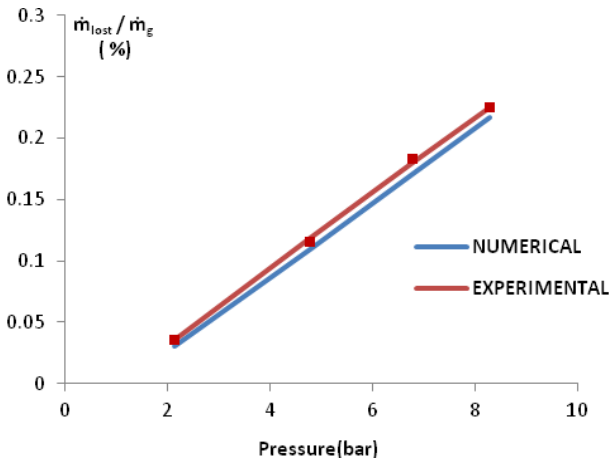

Figure 9 – $\frac{\dot{m}_{lost}}{\dot{m}_g}$ % versus p_g^c (experimental and numerical)

The comparison has been achieved in the following manner. The ratio $\dot{m}_{lost}/\dot{m}_g\%$ can be expressed through equation 17:

$$\frac{\dot{m}_{lost}}{\dot{m}_g}\,\% = \frac{m_{lost}\,n}{v_g\,\rho_g^c A}100\% \quad (17)$$

The mass of lost compressed gas, namely m_{lost} , can be calculated with Equation 18, which expresses the difference between the mass of gas in the tank before the depressurization phase and the mass of gas remaining in the tank at the end of the discharge to the atmosphere:

$$m_{lost} = \left(\frac{p_g^c}{T_g^c} - \frac{p_g^f}{T_g^f}\right)\frac{V_t}{R} \quad (18)$$

The velocity of gas in the bottom column can be recovered from Equation 7 as

$$v_g = \frac{nc_p\rho_p\alpha H_t}{c_{p,g}\rho_g^c} \quad (19)$$

Substituting Equation 19 and Equation 18 into Equation 17 and assuming α = 1, we obtain the expression of $\dot{m}_{lost}/\dot{m}_g$, depending on the physical properties of the particles and on the values of pressure and temperature of the gas within the central tank at the beginning and at the end of the depressurization phase :

$$\frac{\dot{m}_{lost}}{\dot{m}_g}\,\% = \frac{c_{p,g}\left(\frac{p_g^c}{T_g^c} - \frac{p_g^f}{T_g^f}\right)}{\rho_p c_p R}100\% \quad (20)$$

Note that Equation 20 coincides with Equation 10 if we neglect the mass of gas remaining in the pressurization tank at the end of the depressurization phase.

The experimental curve in Figure 9 has been obtained by employing Equation 20, and using the values of pressure and temperature, namely p_g^c , T_g^c , p_g^f , T_g^f , which have been measured during the experimental tests. On the contrary, the numerical curve has been determined, for fixed value of p_g^c , T_g^c and p_g^f , by employing Equation 13 to calculate T_g^f ; the corresponding values have been substituted into Equation 20 to calculate $\dot{m}_{lost}/\dot{m}_g\%$.

As shown in Figure 9, the maximum value of $\dot{m}_{lost}/\dot{m}_g\%$, occurring at the maximum pressure, is under 0.25%. In conclusion, the small values of $\dot{m}_{lost}/\dot{m}_g\%$ make unnecessary to search for solutions aimed at preventing the loss of compressed gas discharged into the external environment.

Conclusions

The aim of this paper has been to develop a pressurization system able to transfer solid particles from a low pressure environment to a high pressure one, without crushing them and with negligible energy loss. The pressurization system is a necessary component of an efficient immersed particle heat exchanger, previously proposed by the authors and currently under full development. The paper has described the operating principle of the pressurization procedure and the mechanical system based on this procedure. A simple zero-dimensional model has been proposed for the evaluation of the size of the pressurization tank in terms of volume and height. A full numerical analysis has been performed: it has shown that the energy losses, related to the proposed mechanical system, are negligible, even in case of very high pressure values. Finally, the entire pressurization procedure has been successfully tested on a test rig: several tests have been performed for different operating conditions in order to experimentally evaluate the main energy loss, specifically that related to the mass of compressed gas discharged into the external environment. The experimental

results have shown that this energy loss is negligible, confirming the results obtained with the analytical model.

Nomenclature

A	Horizontal sectional area of the bottom column [m^2]
A_t	Horizontal sectional area of the pressurization tank [m^2]
$c_{p,g}$	Constant pressure specific heat of gas [J/(kg K)]
c_p	Specific heat of particles [J/(kg K)]
$c_{v,g}$	Constant volume specific heat of gas [J/(kg K)]
g	Acceleration of gravity [m/s^2]
H_t	Tank height [m]
k	Ratio of the specifics heats of the gas
L_{ext}	Work done by the gas on the external environment [J]
$\dot{m}_g$	Mass flow rate of gas flowing through the bottom column [kg/s]
m_g^f	Mass of residual gas after the depressurization phase [kg]
m_{lost}	Mass of lost compressed gas during one pressurization cycle[kg]
$\dot{m}_{lost}$	Mass flow rate of gas discharged to the external environment [kg/s]
m_p	Mass of the particles that fill the pressurization tank[kg]
$\dot{m}_p$	Mass flow rate of particles discharged from the tank into the bottom column [kg/s]
$\overline{\dot{m}}_p$	Average mass flow rate of particles in one cycle[kg/s]
n	Number of cycles [cycles/sec or cycles/h]
p_{atm}	Atmospheric pressure [bar]
p_g^c	Pressure of the compressed gas [bar]
p_g^f	Pressure of the residual gas in the pressurization tank [bar]
R	Gas constant [J/(kg K)]
t_c	Cycle time [s]
t_d	Duration of the particles discharged from the tank into the bottom column [s]
t_f	Filling time [s]
T_g^c	Temperature of the compressed gas in the outlet of the bottom column [K]
T_g^f	Temperature of the residual gas in the pressurization tank[K]
T_p^{in}	Temperature of particles entering the pressurization tank [K]
T_p^{out}	Temperature of particles exiting the pressurization tank [K]
t_x	Interval time occurring for pressurization, depressurization and valve actuation [s]
v_g	Gas velocity in the bottom column[m/s]
V_t	Volume of the pressurization tank[m^3]
α	Ratio between A_t and A
ΔU	Variation of the internal energy [J]
ΔT	Temperature gradient along the bottom column [K]
ρ_g^c	Density of gas in the outlet of the bottom column [kg/m^3]
ρ_g^f	Density of the residual gas in the pressurization tank [kg/m^3]
ρ_p	Particle density [kg/m^3]

References

[1] Correa M. S., Power generation and aeropropulsion gas turbines: From combustion science to combustion technology. International Symposium on Combustion, Volume 27, Issue 2, 1998, Pages 1793–1807.

[2] McDonald, C. F. e Wilson, D. G., The utilization of recuperated and regenerated turbine engine cycles for high-efficiency gas turbine in 21ct century, Applied Thermal Engineering, 1995, Vol. 16, No. 8-9, pp. 635-653.

[3] Rolls Royce Group plc., Annual Report and Accounts, 2008, available at www.rolls-royce.com/reports/2008.

[4] Dallenback, P.A., Improved gas turbine efficiency through alternative regenerator configuration, ASME, Journal of Gas Turbine and Power, 2002.,Vol. 124, pp. 441-446.

[5] Zimmermann, P., Cardenas, A., Hirsch, C., and Sattlemayer, T., Simulation of a Micro Turbine's Dynamic Behavior in a Biomass Incineration Power Plant Based on the Pebble Heater Technology, ASME Paper GT2009-59305, Orlando, FL, USA, 2009.

[6] Brzozowski, W., Dul, J., Yerouchalmi, D., and Jadrowitch, B., Pebble Bed Heat Exchanger, U.S. Patent Office, 1968, U.S. Patent No. 3488402.

[7] Theoclitus, G., Pebble Bed Heat Exchanger, Canadian Intellectual Property Office,1958, CA 557552D.

[8] Catalano L. A., De Bellis F., Amirante R., Rignanese M., An Immersed Particle Heat Exchanger for Externally Fired and Heat Recovery Gas Turbines, Journal of Engineering for Gas Turbine and Power, March 2011, Vol. 133, Issue 3, 032301 (7 pages).

[9] F. De Bellis, L. A. Catalano, "CFD Optimization of an Immersed Particles Heat Exchanger", Third International Conference on Applied Energy - 16-18 May 2011 - Perugia, Italy. Also selected and approved for publication, Applied Sciences – Special Issue: ICAE 2011, APEN-D-11-01319.

[10] L. Nettis, F. De Bellis, L. Catalano, R. Verzicco, "Unsteady Conjugate Heat Transfer Analysis of an Immersed Particle Innovative Heat Exchanger", accepted for publication, Journal of Thermal Science and Engineering Applications, TSEA-11-1057Hilton J. E., Mason L. R., Cleary P. W., The effect of gas dynamics on pressurization tank discharge rate, CSIRO Mathematical and Information Sciences, Clayton, Victoria, Australia, 9-11 December 2009.

[11] Hilton J. E., Mason L. R., Cleary P. W., The effect of gas dynamics on hopper discharge rate, Seventh International Conference on CFD in the Minerals and Process Industries, 2009, CSIRO, Melbourne.

Anthropogenic Heat and Exergy Balance of the Atmosphere

Asfaw Beyene[a], David MacPhee[a], Ron Zevenhoven[b]

[a] Department of Mechanical Engineering, San Diego State University, 5500 Campanile Drive, San Diego, CA 92182, CA, USA, abeyene@rohan.sdsu.edu
[a] Department of Mechanical Engineering, San Diego State University, 5500 Campanile Drive, San Diego, CA 92182, CA, USA, macphee@rohan.sdsu.edu
[b] Department of Chemical Engineering, Thermal and Flow Engineering Laboratory, Åbo Akademi University, Biskopsgatan 8, FI-20500 Åbo/Turku, Finland, rzevenho@abo.fi

Abstract:

Exergy balance of a climate model is discussed from a thermodynamic point of view, using a control volume approach in which the environment and a superficial layer of the earth form the volume, a concentric spherical shell of predominantly gaseous content with a thin layer of the earth. An energy equation that includes anthropogenic heat is suggested based on the mass balance of fossil fuel introduced into the control volume. An exergy balance is also derived for the control volume with this established energy balance. It is argued that the use of temperature as a climate change indicator should be deemphasized since other thermodynamic coordinates including pressure, wind speed, humidity, etc. are equally important. The concept of Equivalent Rate of Evaporation (ERE) is introduced to better estimate the impact of enthalpy of vaporization on climate change. It is argued that both net energy and exergy terms are more accurate representatives of climate change. Exergy is also used as a preferred tool to compare theoretically extractable work from energy resources. For this purpose, we identify source-based exergy components crossing the biosphere, defined as a control volume. The inputs and outputs of energy and mass flows are illustrated to show the net change, with emphasis on anthropogenic exergy destruction. The approach assists in comparing energy reservoirs, defines renewable resources, and provides a more suitable parameter to quantify climate change.

Keywords:

Climate change, thermodynamics, exergy, energy, control volume

1. Introduction

Global atmospheric flow and energy balance are modeled using three differential equations: equation of motion, continuity equation, and the energy equation [1, 2]. The frame of reference in solving these three equations is typically a local Cartesian coordinate system placed on a rotating sphere, with surface temperature as the primary unknown. Invariably, all such climate models assume the earth and its atmosphere to be a unit system with only one enclosing outer boundary separating the earth from the rest of the universe. The coordinate is used to impose conservation laws on the atmosphere's mass and energy and consequently, determine the distribution of heat, vapor, CO_2 and other trace substances. In this approach, no mass exchange takes place with the space outside the boundary, but there is an energy exchange in the long and short wave thermal radiation ranges.

The net energy balance is calculated as what comes into the system less what leaves the control volume. There are three primary energy sources crossing the upper boundary: solar, cosmic, and

gravitational – both lunar and solar. Naturally, these energy sources reach the atmosphere independent of a human activity. All anthropogenic changes in the control volume are as a result of heat and mass introduced to the atmosphere through a lower boundary (Fig. 4). Traditionally, anthropogenic mass introduced to the control volume is ignored because, for a system that defines the earth as part of the control system, no mass crosses the boundary. Out of necessity in accounting for CO_2 impacts, carbon cycle models have introduced this mass as a diffusive constant, but without defining a lower boundary or adopting a control volume approach. The goal of solving the energy equation is to determine the energy absorbed by and reflected from the atmosphere as well as the earth. The net energy balance so determined is scattered unevenly over the entire control volume, i.e., spatial variations have to be accounted for. Accurate determination of this spatial distribution was, and remains to be a serious challenge, and remains outside the scope of this paper.

1.1. Thermodynamic weaknesses of early climate models

Projections of climate change due to increased concentrations of anthropogenic CO_2 are subject to a high degree of uncertainty [3], as a consequence of incomplete and unavailable knowledge [4]. The major uncertainties in the projected ranges of future climate change result from four main areas, [3, 4]:

i) Unpredictable emissions scenarios, influenced by population growth, energy use, economic activity which also remain unpredictable,

ii) Sensitivity of the climate system to greenhouse gas forcing. According to the IPCC, this sensitivity is in the $1.5^{o}C$ - $4.5^{o}C$ range [5], Fig. 1.

iii) Climate system model accuracies, especially long-term variability and chaotic behavior of the models [3], and

iv) Sub-grid scale dynamics and computational limitations to capture smaller spatial scales for full 3-D analytical results.

Due to such uncertainties in the climate model, estimates remain inconclusive and inconsistent [4]. This is compounded by possible non-linear responses of the climate system to anthropogenic forcing, [4, 6].

The 3-D simulation approach has been partly successful due to powerful computational centers built for the sole purpose of climate model calculations. Generally, the impact of feedbacks is primarily segmented, with effects assessed independent of other interrelated factors, and then integrated in global models to revise the results. The net impact of climate feedbacks, their complex interaction, and dynamic synthesis leave misgivings, and there are lingering doubts if they can ever be solved accurately to pass persistent scientific scrutiny. From a thermodynamic point of view, however, all existing systems suffer from two more serious weaknesses:

i) By and large, temperature is selected as an indicator of climate change. However, thermodynamically, the only accurate measure of climate change is the change in the energy balance within the atmosphere and the interaction with earth surface (hydrosphere and terrasphere), not change of temperature. There are processes in which temperature remains constant despite significant change in the energy equilibrium of the system. As such, temperature is just as important as any other thermodynamic coordinate including pressure, wind speed, humidity, etc.

ii) The boundary of the earth-atmosphere system in all the existing climate models is defined only with the top, outer boundary. The grid-scale evolution of this control volume is then determined by equations describing the thermodynamics and fluid dynamics of an ideal gas within the volume.

Energy exchange is allowed across this upper boundary only; no mass enters the control volume from any direction except the insertion of a CO_2 mass as a diffusive constant when carbon cycle analysis is desired. This approach led to addressing anthropogenic consequences of a control volume without proper definition of the control volume.

A control volume modeling the climate of the earth and atmosphere as a spherical shell layer of predominantly gaseous content with a thin layer of the earth (Fig. 2) has been proposed [1]. This leaves a concentric spherical shell volume with two boundaries – one, the traditional boundary at the top of the atmosphere, and the other inner boundary, at some superficial depth of the earth. Only energy crosses the boundary at the top of the atmosphere. However, both energy and mass cross the inner boundary. And yet, energy and mass that cross this "lower" boundary are the only possible causes of anthropogenic climate change. In fact, the lower boundary is appropriate definition of renewable energy resources; - any net mass or net energy that crosses the lower boundary of this control volume cannot be renewable. This implies that climate change is merely the result of using non-renewable energy sources.

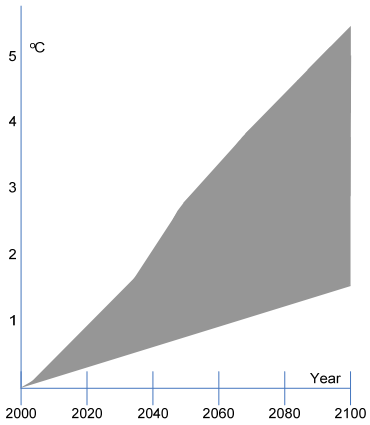

Figure 1: Variations of estimates of temperature change by 2100 depending on emissions scenario [5]

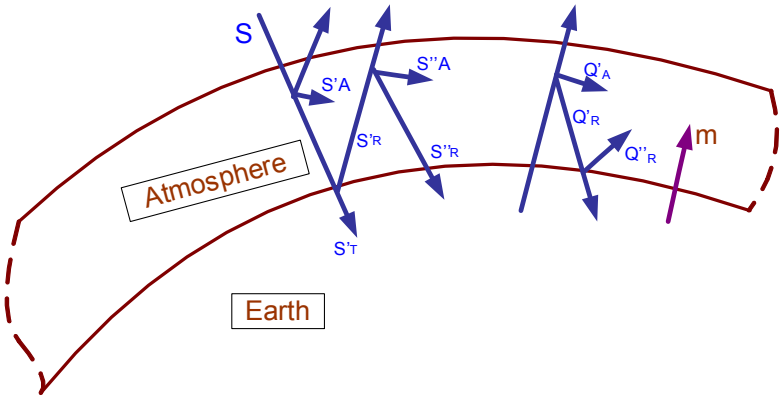

Figure 2: Control volume.

2. The energy equation

The energy equation of a control volume with two boundaries represents the net sum of energy crossing the two boundaries. Energy input crossing the upper boundary of the control volume the sum of solar and cosmic energy absorbed by the atmosphere, (Fig. 3):

$$SA = S - [S\tau(1-\alpha)(1+\alpha R+(\alpha R)^2+\cdots)+\ \alpha S\tau(1-R-A)(1+\alpha R+(\alpha R)^2+\cdots)] \quad (1)$$

which can be rearranged as, [1]

$$SA = S - \frac{S\tau}{1-\alpha R}[1-\alpha R-\alpha A] \quad (2)$$

where SA is the sum of solar and cosmic energy absorbed by the atmosphere, S is the sum of solar and cosmic irradiation, τ is atmospheric transmitivity, A is absorptivity of the atmosphere, α is reflectance of the earth's surface, and R is reflectance of the top of the atmosphere.

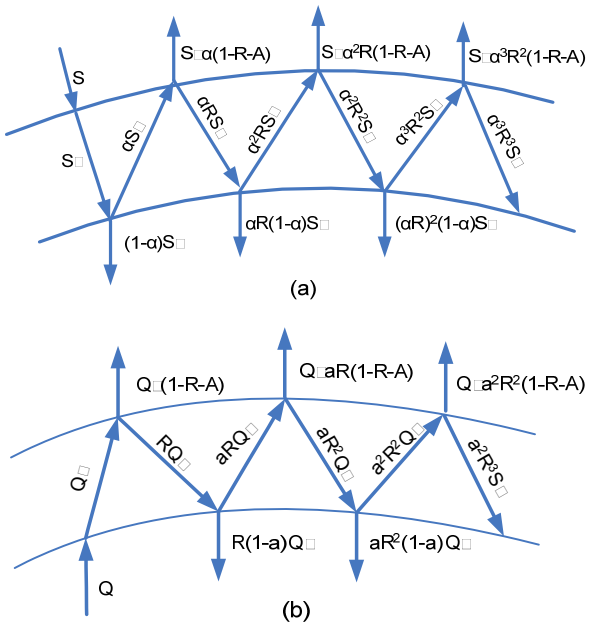

Figure 3: Energy balance (a) solar and cosmic input, (b) fossil fuel input, [1]

The other term of the energy balance equation is the energy that crosses the lower boundary, i.e. the fossil energy absorbed by the atmosphere, QA, [1]:

$$QA = Q - [Q\tau(1-A-R)+\alpha RQ\tau(1-A-R)+\alpha^2R^2Q\tau(1-A-R)+\cdots+RQ\tau(1-\alpha)+\alpha R^2Q\tau(1-\alpha)+\cdots] \quad (3)$$

where Q is the total energy introduced as fossil fuel as well as geothermal. Rearranging,

$$QA = Q - \frac{Q\tau}{1-\alpha R}[1-A-\alpha R] \quad (4)$$

The total energy absorbed by the control volume, EA is the sum of the two sources:

$$EA = SA + QA = S - \frac{S\tau}{1-\alpha R}[1-\alpha R-\alpha A] + Q - \frac{Q\tau}{1-\alpha R}[1-A-\alpha R] \quad (5)$$

This net energy is the only indicator of human-induced climate change, forcing changes in temperature, pressure, wind speed and direction, humidity, etc. EA is resolved by further splitting it into three major components as presented by Pond [7]

$$EA = H_S + H_L + SS \quad (6)$$

where H_S is the sensible heat flux calculated from the energy balance, H_L is the latent heat flux, calculated from net radiation, ground heat flux, and the Bowen ratio, *SS* is subsurface heat flux for the sea and the ground combined [8].

One serious flaw in assuming temperature as a climate change indicator is that such assumption undermines the role of latent heat. And yet, several studies have been made to distinguish and quantify latent and sensible heats in the atmosphere [8]. With a valid presumption that climate feedbacks have not been thoroughly quantified and established in a given scenario, it would be impossible to estimate the net temperature increase in the atmosphere without a serious shortcoming. For example, the impact of clouds as a climate feedback is still unresolved, and in cases where attempts were made to quantify, the results are inconsistent. Most current models predict cloud mass and volume from the instantaneous climatic conditions of a grid box. Alternatively, some models treat clouds as a time-evolving variable. The proposed control volume offers a more convenient approach to determine the amount of vapor added to the atmosphere as a consequence of anthropogenic heat addition. However, it will remain difficult to determine the sequential progression of feedbacks, i.e. the compound effect of clouds and their derivatives on climate change. If one can quantify the latent heat flux, H_L, as well as the Bowen ratio, the vapor addition can be estimated for a simplified scenario where feedbacks and secondary effects are ignored. To better understand the impact of latent heat, the concept of "Equivalent Rate of Evaporation", (ERE) was defined as the total amount of moisture that could be added to the atmosphere if the entire EA were taken as H_L [1].

3. Anthropogenic heat estimate

The anthropogenic heat can be estimated based on the peak extraction method. This assumes that all the thermal energy extracted from the earth is dumped into the atmosphere, independent of the conversion efficiency or thermal storage in the application or in the final products of processes. This is acceptable in as far as the cycle of decomposition of the stored energy in manufactured components is negligible compared to the time scale of the universe.

There are several estimates of when and how much the peak production of oil would be. Laherrere's 1997 estimate predicted the peak would occur around 2010 [9]. Ivanhoe also showed peak production around 2010 [10] whereas Duncan and Youngquist's estimated peak production already for 2005-2007, [11]. EIA predicts that the global conventional oil production peak will occur after 2020, as production was expected to still be growing in 2010, [12, 1]. Once the quantity is known, assuming 5.8 MMBtu/barrel (6.12 GJ/barrel) for oil, we can determine the energy and mass additions to the control volume due to fossil fuels. For 1158 Billion barrels added to the control volume by 2010, i.e., 6716.4 MMBtu (7,086.2 GJ), we project 1808 Billion barrels by 2050, i.e. 10486.4 MMBtu (11,063.74 GJ), [1]. For known enthalpy of vaporization, 2257 kJ/kg = 2.257MJ/kg, the annual ERE for 25 billion barrels/yr (= 1.53×10^{14} MJ) would be 6.78×10^{13} liters of water/yr – which equates to roughly about 62% of the annual flow of the Nile river, [1].

Using a similar approach, we can determine the total energy of natural gas added to the control volume. Knowing the natural gas peak of 90×10^{12} ft^3/yr (2.55×10^{12} m^3/yr), which is equivalent to

90×10^9 MMBtu/yr, 9.50×10^{13} MJ of energy is added to the control volume annually, for an ERE of 4.21×10^{13} liters of water/yr, [1].

We follow a similar procedure as above to determine the peak of 4000 M toe coal use, and 4000 M toe = 1.67×10^{14} MJ of energy added to the volume annually, with an ERE of 7.42×10^{13} liters of water/yr. The sum total of energy at peak for oil, natural gas, and coal is then 4.15×10^{14} MJ/yr, with a peak ERE of 1.84×10^{14} liter/yr, a volumetric flow rate equivalent to 1.7 times that of the Nile River, [1].

Specific humidity can be used to further explain the impact of this anthropogenic heat on climate. Assuming 25°C Dry Bulb Temperature (DBT), relative humidity Φ = 40%, and humidity ratio ω = 8g/kg, for a total of generally accepted atmospheric air mass of 5.15×10^{18} kg, the total mass of vapor in the atmosphere would be 4.12×10^{16} kg – an increase in air humidity of about 0.447% for the year. The impact of this change on pressure gradients and wind velocity are a subject of momentum and continuity equations, [1].

4. Atmospheric Exergy

Exergy as a tool: Exergy that reaches the earth from sources outside of the control volume including the sun is converted into various other forms that sustain life within the control volume. Exergy of an environment as a system measures how far the system deviates from equilibrium with the surrounding environment, the universe in this case. When thermodynamic coordinates as well as chemical potentials stabilize, i.e., become the same for the system and for the reference environment, and the exergy of the system reduces to zero. Conversely, we can deduce that exergy content of the environment is a quantity of exergy needed to produce the environmental condition from the assumed reference, standard condition, i.e., the universe, by a reversible process. This exergy state for our environment renders the control volume livable. However, a livable condition is just another thermodynamic state as non-livable which could be brought about by excessive disruption of the exergy balance, a disruption which can be caused by natural or man-made processes. The processes that take place within the control volume can accelerate or slow down the destruction of exergy. While we have little or no power to impact the natural flow and balance of exergy, we can and should understand the role of human activities, the impact of anthropogenic exergy destruction on the environment. Exergy is a path-independent property, independent of geography or technology. This independence makes it a useful tool for evaluating the quality of energy conversion as well as the magnitude and value of resources.

Exergy balance: The total energy absorbed by the control volume is the sum of the two sources, neglecting cosmic energy, with the addition of the gravitational term if accounted for, $EA = SA + QA + W$. Exergy balance of earth's atmosphere as a control volume in a rate form can be written as:

$$\dot{X}_{SC} + \dot{X}_{w} - \dot{X}_{SR} + \dot{X}_{1E} - \dot{X}_{2E} - \left(T_0 \dot{S}_{gen}\right) = \left(\frac{dX}{dt}\right)_{cv} \quad (7)$$

where $\dot{X}$ is the rate of exergy, $\dot{S}$ is the rate of entropy, T is temperature, and subscripts: sc stands for solar and cosmic, w - work input, 1E – mining input, SR – solar reflected, 2E – earth's discharge, 0 – ambient parameter, and gen – generated, (Fig. 4). The exergy destroyed is quantified by entropy generated. Assuming a steady flow to the control volume, we equate Eq. 7 to zero.

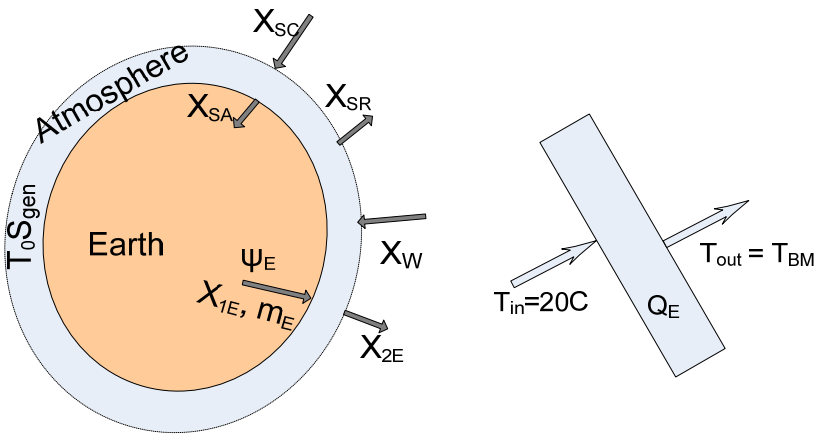

Figure 4: Exergy balance of the environment as a control volume

Regrouping the thermal components, the above equation can also be expressed as:

$$\dot{X}_{EA} + \dot{X}_w + \sum(\dot{m}\Psi)_{in} - \sum(\dot{m}\Psi)_{out} = T_0\dot{S}_{gen} \quad (8)$$

where $\dot{X}_{EA} = \dot{X}_{SC} - \dot{X}_{SR} - \dot{X}_{SA}$ is rate of absorbed net solar and cosmic exergy and $\dot{X}_w$ is rate of exergy input to the control volume due to lunar and solar gravity, Ψ is stream exergy accompanying a mass flow rate of $\dot{m}$ in to the control volume. Subscript EA denotes the net thermal energy input *EA*, defined in (5). For a single stream, ignoring kinetic and potential energy terms, the stream energy is,

$$\Psi_1 - \Psi_2 = (h_1 - h_2) - T_0(s_1 - s_2) \quad (9)$$

Assuming $(\dot{m}\Psi)_{out} = \Psi_2 = 0$; $(\dot{m}\Psi)_{in} = (\dot{m}\Psi)_E = \dot{m}(h_1 - T_{CBM}s_1)$. Equation 8 then attains a form of $\dot{X}_{SC} - \dot{X}_{SR} - \dot{X}_{SA} + \dot{X}_w + \sum(\dot{m}\Psi)_{in} = T_0\dot{S}_{gen}$. The exergy balance for the control volume under consideration yields:

$$\left(1 - \frac{T_{CBM}}{T_{EA}}\right)\bar{Q}_{SC} + \left(1 - \frac{T_{CBM}}{T_{EA}}\right)\bar{Q}_{1E} - \left(1 - \frac{T_{CBM}}{T_{EA}}\right)\bar{Q}_{SR} - \left(1 - \frac{T_{CBM}}{T_{EA}}\right)\bar{Q}_{2E} + \dot{X}_w + \dot{m}(h_1 - T_{CBM}s_1) = T_{CBM}\dot{S}_{gen} \quad (10)$$

Equation 10 represents exergy balance of the atmosphere, assuming *EA* is added at a constant temperature of T_{EA}, while T_{CBM} is the cosmic microwave background temperature of ~ 2.7K. In other words,

$$\dot{X}_{Thermal} = \left(1 - \frac{T_{CBM}}{T_{EA}}\right)\bar{Q}_{SC} + \left(1 - \frac{T_{CBM}}{T_{EA}}\right)\bar{Q}_{1E} - \left(1 - \frac{T_{CBM}}{T_{EA}}\right)\bar{Q}_{SR} - \left(1 - \frac{T_{CBM}}{T_{EA}}\right)\bar{Q}_{2E} \quad (11)$$

As a result of (5), we have:

$$\left(1 - \frac{T_{CBM}}{T_{EA}}\right)[\bar{Q}_{SC} + \bar{Q}_{1E} - \bar{Q}_{SR} - \bar{Q}_{2E}] = \left(1 - \frac{T_{CBM}}{T_{EA}}\right)EA \quad (12)$$

The exergy destruction is proportional to the entropy generated, primarily due to atmospheric irreversibilities such as mixing and heat transfer driven by a finite temperature difference within the atmosphere. Replacing (12) into Eq. 10, we rewrite the exergy balance equation as:

$$\sum\left(1 - \frac{T_{CBM}}{T_{EA}}\right)EA + \dot{X}_w + \dot{m}(h_1 - T_{CBM}s_1) = T_{CBM}\dot{S}_{gen} \quad (13)$$

This net exergy of the control volume is further dissipated into four major components:

$$\dot{X}_S + \dot{X}_L + \dot{X}_{SS} + \dot{X}_w = 0 \quad (14)$$

The sensible exergy flux, $\dot{X}_S$ can be determined from the exergy balance, $\dot{X}_L$ is the latent exergy flux, calculated from net radiation, ground heat flux, and the Bowen ratio, $\dot{X}_{SS}$ is subsurface exergy flux for the sea and the ground combined [8] and $\dot{X}_w$ is known gravitational input. Subscript s stands for the sensible heat flux, L for latent heat flux, and *SS* for subsurface heat flux, and w for gravitational work.

4.1 Solar and cosmic exergy

Solar radiation reaches the Earth with an energy density of about 1368W/m^2 and a spectral composition that can be approximated as blackbody radiation emitted at 5800K [13]. With this assumption the radiation exergy is given as, [14, 15]:

$$\dot{X}_S = E_b[1 - \frac{4T_0}{3T} + \frac{1}{3}(\frac{T_0}{T})^4] \quad (15)$$

where T is the blackbody temperature. For an ambient temperature of 298 K, the ratio of exergy to energy is 0.93 [16].

Incoming non-solar cosmic radiation is composed of several low-energy density spectra that resemble blackbody radiation at various temperatures, reaching the earth with an energy density of about 12.5 μW/m^2 [17]. The average outgoing long-wave energy density varies with location from 100 to 300W/m^2 [18]. The net exergy input to earth due to non-solar cosmic radiation exchange is given by [19]. The average incoming exergy density of cosmic radiation is 132W/m^2. Subtracting the average 11W/m^2 exergy density of the outgoing radiation from the incoming, we get a net average exergy input of 121W/m^2 [16] at the outer boundary of the control volume.

The solar radiation energy density and the ratio of exergy to energy give us X_S = 1272 W/m^2. Adding the net exergy input of cosmic radiation, we get X_{SC} = 1393W/m^2. Note that this value holds for zenith radiation and averaged over the surface of the earth ~70% of an incoming XS + XSC arrives at the earth surface at ~ 130 PW, i.e. 1067×10^6 TWh on an annual basis, which is equal to ~ 40000×10^{14} MJ.

4.2 Tidal exergy

The power of a tidal energy is a function of the gravitational potential of a body of water averaged over significantly large number of tidal cycles. The specific tidal exergy of both rising and falling tides of a body of water depends on the lunar and solar gravities, tidal period, orbit variations, land topology, ocean bathymetry, etc. [20].

An average exergy flow integrated over the height difference between local maxima and minima, and the period between these points can be expressed as [16]

$$\dot{X}_{tidal} = \frac{1}{n}\sum_n \frac{\rho g \int_{z_{n-1}}^{z_n} a_{reservoir}(z)dz}{t_n} \quad (16)$$

where ρ is density, g is gravity, t is the period between local maxima and minima of the tide, a is the area of the water body at height z, and n is the index number for each extreme, maximum or minimum.

Current tidal energy use (which can be combined with the much smaller ocean thermal energy conversion (OTEC) and wave energy) add up to ~ 500 MW electricity production worldwide [21, 22]. On an annual basis this implies 4 TWh exergy (mechanical wave energy) transferred from seawater to waste heat to the surroundings after the electricity was used by customers. (It may be assumed that transfer of wave energy to surroundings-temperature heat by natural friction at shores and beaches will

be much larger.) This is equal to ~14×10^9 MJ/year. Tidal energy contributes to the atmosphere about 0.0059 W/m^2, [23]

4.3 Geothermal exergy

The thermal exergy of a compressible fluid at the wellhead, ignoring subsurface heat transfer losses, can be expressed as:

$$X_{geo} = [h - h_0 - T_0(s - s_0)] \quad (17)$$

A geothermal resource crosses the lower boundary of the control volume, and therefore, according to the definition introduced here, is not considered renewable. Reservoirs will experience a precipitous drop in temperature as well as mass, [24]. Current levels of geothermal energy use are of the order of 70 TWh electricity production [22] which implies, with an assumed thermal efficiency of ~40% for the generation a total energy input of ~ 175 TWh as exergy. This is equal to 1.6×10^{12} MJ/year.

4.4 Exergy of carbon-based fuels

The chemical composition of the fuel is the main source of exergy in fossil fuels. Using Gibbs free energy relations, the chemical exergy of a fuel containing C, H, N, O, S and halogens has been suggested [25, 26]. This approach allows calculating the chemical exergy of a fuel based on its mass fractions. The chemical exergy of a fuel with an empirically determined heat of combustion can be approximated as:

$$X_{fuel} \approx 0.07075[mf_C] - 24.15[mf_H] + 4.328[mf_O] + 7.06[mf_S] - T_0[mf_{ash}]s^o_{ash} - \Delta_R h^0 \quad (18)$$

where the letters in brackets are the mass fractions for each element in the subscript. $\Delta_R h^0$ is specific enthalpy of reaction. A typical value for the entropy of ash is 660 J/kg K [27]. Chemical exergies of carbon-based fuels are approximately equal to the lower heating values, [25]. For conventional petroleum, say, crude oil with a carbon content varying usually from 0.83 to 0.87, (10) gives specific exergy values ranging from 40 to 44MJ/kg, [28].

For example, based on mass fractions from Blacksville bituminous and Absaloka subbituminous coals, specific exergy values of 29.81 MJ/kg bituminous and 19.87 MJ/kg subbituminous are calculated, [29,16]. Exergy of a natural gas is the sum of the chemical exergies of reactions each of the components with oxygen, generally written as:

$$C_aH_b + \left(a + \frac{b}{4}\right)O_2 \rightarrow aCO_2 + \frac{b}{2}H_2O \quad (19)$$

The exergy of such reaction is given by [16]. For a representative composition of natural gas assuming relative humidity of 80%, (12) yields a specific exergy of 50.5MJ/kg, [30, 16].

Exergy of natural gas stored in methane clathrate at near-zero temperature in the permafrost regions of continents or in sediment on the ocean floor, are determined using the Clausius – Clapeyron equation [16, 31]. The average specific exergy of methane clathrate hydrate with about 85% water by mass, for a given location, has been estimated at 4.8 MJ/kg [32]. Natural gas from methane clathrate may or may not be considered renewable depending where the lower boundary of the control volume is placed.

The sum of fossil fuel energy input estimated above as the sum total of energy at peak for oil, natural gas, and coal as 4.15×10^{14} MJ/yr can also be used to determine rough estimate of net exergy.

4.5 Exergy of nuclear resources

Exergy of nuclear materials can be calculated, excluding the neutrino energy [31], assuming the nuclear binding energy release at extreme temperature, as a typical fission reaction. This gives an exergy-to-energy ratio of near unity if the products are approximated as a perfect gas in equilibrium and the reference temperature is 289K [29]. Separation exergy is neglected. For the two isotopes of uranium, U-235 and U-238, found in a ratio of about 1:140 [33], an approximate nuclear exergy of 75 TJ/kg is calculated for U-235. If U-238 is transmuted to Pu-239, the fission of Pu-239 gives a nuclear exergy of about 77 TJ/kg U-238, [16]. Uranium dissolved in seawater gives a nuclear exergy of approximately 260 kJ/kg seawater, [35]. Again, separation exergy is neglected.

Th-232 is another readily available isotope, which, accepts a neutron and transmutes to fissile U-233, releasing energy [35] with an equivalent specific exergy of about 78 TJ/kg thorium, [16].

Furthermore, Lithium has two stable isotopes, Li-6 and Li-7. Tritium can be bred from Li-6 with a slow neutron and a net energy output. However, Li-7 requires a fast neutron and an energy input [33]. The nuclear exergy of lithium combined with deuterium is estimated at 269 TJ/kg equimolar lithium – deuterium mixture for Li-6, and 162 TJ/kg for Li-7. Fusion of solely deuterium if and when the technology allows, has a nuclear exergy of 345 TJ/kg, [16].

Current nuclear fission electricity production is ~ 3000 TWh/yr (data for 2005, [21], which together with ~ twice that amount of energy released to the environment as waste heat (assuming thermal efficiency of ~ 33% for a nuclear fission reactor) means that an exergy stream of ~ 9000 TWh = 9×10^{12} kWh = 0.32×10^{14} MJ/yr is transferred from earth-bound ore to surroundings waste heat. This is one order of magnitude less than the number given in the previous section for carbon-based fuels.

Assuming absorptivity of the atmosphere to solar radiation A = 0.196, is atmospheric transitivity to solar radiation, $\tau = 0.579$, average reflectance of solar energy by the earth's surface back into space, R = 0.06, reflectance of the earth's surface, albedo, $\alpha = 0.15$, [36, 37, 38] we calculate using Eq. 5 EA = 151.5 W/m^2 for which the exergy term becomes about 151.5 W/m^2, as shown in Fig. 5.

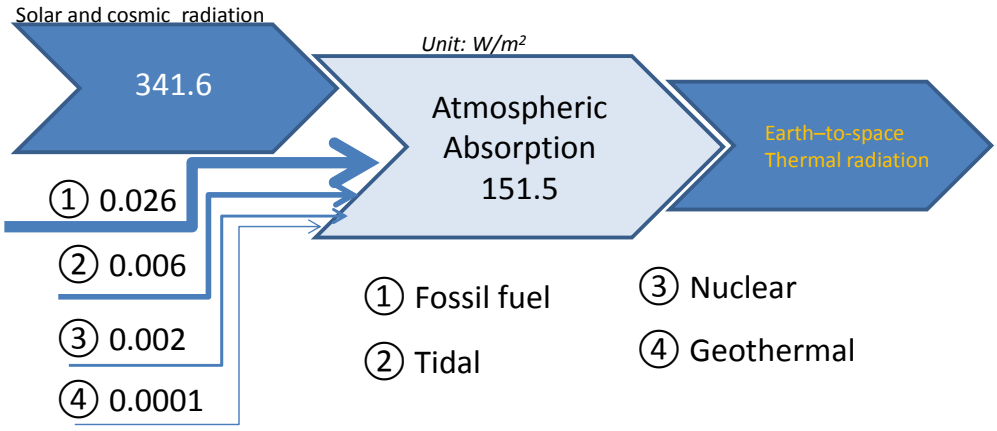

Figure 5: Exergy balance of the atmosphere

5. Conclusion

The longitudinal, latitudinal and depth-wise energy and temperature stratification drive the earth's climate variations, necessitating complex and costly 3-D algorithms to simulate. Current climate

models are resolved by dividing the atmosphere into discrete vertical layers, which are then intersected with a 2-D horizontal grid, producing only a quasi 3-D model, providing results farther from the analytical solution. Furthermore, changes in the energy balance create complex secondary effects, known as feedbacks, with yet unsettled impacts on the primary effects of changes in net energy exchange.

Projections of climate change due to increased concentrations of anthropogenic CO_2 are subject to a high degree of uncertainty. This uncertainty is a consequence of incomplete and unavailable knowledge. From a thermodynamic approach, all existing systems suffer another set of weaknesses. In most cases, temperature is selected as an indicator of climate change. However, thermodynamically, temperature is just another variable. The only accurate measure of climate change should be the change in the atmospheric energy balance, which drives a possible change of temperature. As such, temperature is equally as important as change in any other thermodynamic coordinate including pressure, wind speed, humidity, etc.

At the root of the problems also lies assumption of the boundary of the earth-atmosphere system only at the top of the atmosphere. Energy exchange is allowed across this single boundary; no mass crosses into the control volume. This approach leads to addressing anthropogenic consequences with disregard to anthropogenic sources.

In this paper, a new control volume for climate models is proposed, consisting of a concentric spherical shell with two boundaries – one, the traditional boundary at the top of the atmosphere, and the other, at some superficial depth of the earth. Only energy crosses the top of the atmosphere. However, both energy and mass cross the inner boundaries. To date, no climate model accommodates both the energy, distinguishing also between heat and enthalpy, and mass introduced to the atmosphere from the earth's crust, which is the source and cause of the only anthropogenic climate change.

An energy equation of such a control volume with two boundaries was developed and used to estimate Equivalent Rate of Evaporation (ERE). Based on this approach, it was calculated that the sum total of energy at peak for oil, natural gas, and coal is about 4.15×10^{14} MJ/yr, with ERE at peak of 1.84×10^{14} liter/yr, which is the energy needed to evaporate 1.7 times the annual flow of the river Nile. Assuming 25°C dry bulb temperature, and 40% relative humidity Φ, with humidity ratio ω = 8g/kg, and a total mass of atmospheric air mass generally accepted as 5.15×10^{18} kg, the equivalent total mass of vapor in the atmosphere would be 4.12×10^{16} kg – an increase in air humidity of about 0.447 % for the year.

A comparison of the contributions of fossil-carbon fuel use, nuclear fission electricity production and tidal + geothermal energy shows that the exergy streams passing the boundary given by the earth's surface are primarily (> 92 %) from fossil-carbon fuel use, and 7 % from nuclear fission electricity generation and < 0.5 % form tidal + geothermal energy. At a rate of ~ 4×10^{14} MJ/yr the rate of exergy transfer is ~1/10000 of the incoming solar and cosmic exergy. This can be used to estimate a temperature effect: with a thermal capacity of 3.9×10^{10} TJ/°C for the atmosphere + terrasphere + hydrosphere [39] this readily explains an annual global temperature rise of 0.01°C as a result of the energy input/output imbalance caused.

Nomenclature

A	Absorptivity of the atmosphere
$\mathbf{c_p}$	Specific heat at constant pressure, (J/kg K)
$\mathbf{c_v}$	Specific heat at constant volume, (J/kg K)
DBT	Dry Bulb Temperature, (K)

EA	Total energy absorbed by the atmosphere as a control volume, (J)
EIA	Energy Information Administration
ERE	Equivalent Rate of Evaporation
g	Gravity, (m/s^2)
h	Specific enthalpy, (J/kg)
H	Heat flux, enthalpy, (W/m^2)
IPCC	Intergovernmental Panel on Climate Change
$\dot{m}$	Mass flow rate, (kg/s)
mf	Mass fraction
n	Index number of an extreme
p	Pressure, (Pa)
Q	Heat transfer, energy, (J)
$\bar{Q}$	Heat transfer rate (kW)
QA	Fossil fuel energy absorbed by the atmosphere, (J)
R	Reflectance of the top of the atmosphere
S	Solar and cosmic irradiation, (J, W/m^2)
S	Specific Entropy, (J/kg K)
$\dot{S}$	Rate of entropy (J/kg K s)
SA	Solar energy absorbed by the atmosphere, (J)
SS	Subsurface heat flux for the sea and the ground combined, (W/m^2)
t	Time, period, (s)
T	Temperature, (K)
u	Velocity, (m/s)
u	Specific internal energy (J/kg)
v	Specific volume, (m^3/kg)
W	Work, (J)
X	Exergy, (J/kg)
$\dot{X}$	Rate of exergy, (kW)
z	Height, (m)
3-D	Three dimensional
$\Delta_R \mathbf{h^0}$	Specific enthalpy of reaction, (J/kg)

Greek

α	reflectance of the earth's surface
$\boldsymbol{\rho}$	density, (kg/m3)
$\boldsymbol{\sigma}$	Stefan Boltzmann constant
τ	atmospheric transitivity
Φ	relative humidity
$\boldsymbol{\Psi}$	stream exergy accompanying a mass flow
ω	Specific humidity

Subscript

ARS	arbitrary spectrum radiation
b	blackbody
c	cosmic
CBM	cosmic background temperature
CV	control volume, atmosphere
E	earth
EA	net energy absorbed by the atmosphere
Geo	geothermal

In Inlet
L latent
Out outlet, exit
S sensible, solar
SA Solar energy absorbed
SC solar and cosmic
SR solar reflected
SS subsurface
W work input
0 ambient parameter
Gen generated
1, 2 reference points

Superscript

0 standard reference state

References

[1] Beyene, A., Zevenhoven, R., (2012) Thermodynamics of climate change. Int. J. of Global Warming accepted / in press

[2] Bjerknes KFV (1921) On the Dynamics of the Circular Vortex, *Geofysiske Publikasioner* **2**(4)*: 1-88*

[3] Jones R N (2000) Managing uncertainty in climate change projections – Issues for impact assessment, *Clim. Change* 45, 403–419

[4] Hulme M and Carter TR (1999) Representing uncertainty in climate change scenarios and impact studies pp.11-37 in, Representing uncertainty in climate change scenarios and impact studies Proceedings of the ECLAT-2 Helsinki Workshop, 14-16 April, 1999 (eds.) Carter,T.R., Hulme,M. and Viner,D., Climatic Research Unit, Norwich, UK, 128

[5] IPCC (2001) Impacts, Adaptation, and Vulnerability - Contribution of Working Group II to the IPCC Third Assessment Report, ed. McCarthy JJ, Canziani FO, Leary AN, Dokken JD, White SK. Cambridge: Cambridge University Press

[6] Moss HR and Schneider HS (2000) Uncertainties, In *Guidance Papers on the Cross Cutting Issues of the Third Assessment Report of the IPCC*, edited by R. Pachauri, et al., pp. 33-51. Geneva: Intergovernmental Panel on Climate Change

[7] Pond S (1975) The Exchange of Momentum, Heat, and Moisture at the Ocean-Atmosphere interface, Proceedings of a symposium, Ocean Science Committee of the Ocean Affairs Board, National Academy of Sciences, Durham, New Hampshire, Numerical methods of Ocean Circulation, pp 26

[8] Spittlehouse DL and Black TA (1980) Evaluation of the Bowen Ratio/Energy Balance Method for Determining Forest Evapotranspiration', *Atmos.-Ocean* 18, 98-116

[9] Laherrere JH (1998) Evolution of "development lag" and "development ratio, IEA Oil reserves conference Paris Nov 11 http://dieoff.com/page182.htm or Development ratio evolves as true measures of exploitation, World Oil, Feb, p117-120

[10] French Petroleum Institute (1997) Future Sources of Crude Oil Supply and Quality Considerations, L. F. Ivanhoe's estimate also showed peak production around 2010, "Get Ready For Another Oil Shock," The Futurist, Jan-Feb

[11] Duncan, RC. and Youngquist, W. (1998) Encircling the Peak of World Oil Production: Institute on Energy and Man, Seattle, Washington, p. 32

[12] International Energy Outlook (IEA), Energy Information Administration, Office of Integrated Analysis and Forecasting, U.S. Department of Energy, DOE/EIA-0484(2000), www.eia.doe.gov/oiaf/ieo/index.html, accessed May 2011.
[13] Smil V. Energies, 2nd ed. Cambridge, MA: MIT Press; 1999.
[14] Szargut JT. Anthropogenic and natural exergy losses (exergy balance of the Earth's surface and atmosphere). Energy 2003; 28(11):1047–54.
[15] Shafey HM, Ismail IM. Thermodynamics of the conversion of solar radiation. J Sol Energy Eng 1990; 112(2):140–5.
[16] Hermann A.W., Quantifying global exergy resources, Energy (2006), Volume: 31, Issue: 12, Pages: 1685-1702, DOI: 10.1016/j.energy.2005.09.006
[17] Schlickeiser R. Cosmic ray astrophysics. Berlin: Springer Publishing Corporation; 2002.
[18] NASA. Clouds and the earth's radiant energy system (CERES). Langley, VA: NASA Langley Research Center; 2005 See also: http://asd-www.larc.nasa.gov/ceres/.
[19] Wright SE, Rosen MA, Scott DS, Haddow JB. The exergy flux of radiative heat transfer with an arbitrary spectrum. Exergy, An Int J 2002; 2(2):69–77.
[20] Arbic BK, Garner ST, Hallberg RW, Simmons HL. The accuracy of surface elevations in forward global barotropic and baroclinic
[21] IEA (2008) Energy technology perspectives - Scenarios and strategies to 2050, IEA, Paris
[22] Renewables 2010 Global Status Report (GSR 2010) Available at http://www.ren21.net/REN21Activities/Publications/GlobalStatusReport/tabid/5434/Default.aspx (note: also GSR 2011 is available)
[23] Huddart D, Stott T. Earth Environments: Past, Present and Future, John Wiley & Sons, Oxford, 2010, pp. 26
[24] Flynn T. Geothermal sustainability, heat utilization, and the advanced binary technology solution. Trans-Geotherm Resource Council 1997;21: 489–96.
[25] Stepanov VS. Chemical energies and exergies of fuels. Energy 1995;20(3):235–42.
[26] Sheih JH, Fan LT. Estimation of energy (enthalpy) and exergy (availability) contents in structurally complicated materials. Energy Sourc 1982; 6(1):1–46.
[27] Brouwers HJH, van Eijk RJ. Fly ash reactivity: extension and application of a shrinking core model and thermodynamic approach. J Mater Sci 2002; 37(10):2129–41.
[28] Rudzinski WE, Aminabhavi TM, Sassman S, Watkins LM. Isolation and characterization of the saturate and aromatic fractions of a Maya crude oil. Energy Fuels 2000;14(4):839–44.
[29] Zygarlicke CJ, Galbreath KC, Zhuang Y, Folkedahl BC, Thompson JS, Tibbetts JE, et al. Coal combustion flue gas effects on mercury speciation. Grand Forks, ND: EERC, University of North Dakota; 2002 See also: www.eerc.und.nodak.edu/catm/pdf/CJZ_2002.pdf.
[30] Union Gas. Chemical composition of natural gas. Chatham, Ont: Union Gas Ltd.; 2005 See also: http://www.uniongas.com/aboutus/aboutng/composition.asp.
[31] Durmayaz A, Yavuz H. Exergy analysis of a pressurized-water reactor nuclear-power plant. Appl Energy 2001;69(1):39–57.
[32] Sloan D. Clathrate hydrates of natural gases. New York: Marcel Dekker, Inc.; 1998.
[33] Pruschek VR. Die Exergie der Kernbrennstoffe, The exergy of nuclear fuel. Brennstoff-Warme-Kraft 1970;22(9):429–34 [in German]. tide models. Deep-Sea Res II 2004;51(25-26):3069–70.
[34] Chang J. Table of nuclides. Yusung: Korea Atomic Energy Research Institute (KAERI); 2005 See also: http://sutekh.nd.rl.ac.uk/CoN/.

[35] Nave CR. Hyperphysics. Atlanta: Georgia State University; 2003 See also: http://hyperphysics.phy-astr.gsu.edu/hbase/hph.html

[36] Agami Reddy, Applied data analysis and modeling for energy engineers and scientists, Springer, 2011, pp. 330

[37] Hewitt N. C. and Jackson V. A., (edited by) Atmospheric Science for Environmental Scientists, Vivar Printing, 2009, pp. 56

[38] Park C. Chris, The Environment: Principles and Applications, Routledge, 2001, pp.236

[39] Zevenhoven, R., Beyene, A. The relative contribution of waste heat from power plants to global warming. Energy 2011;363754-3762. doi: 10.1016/j.energy.2010.10.010

Determination of environmental remediation cost of municipal waste in terms of extended exergy

Candeniz SECKIN[a], Ahmet R. BAYULKEN[b]

[a] *Energy Institute, Istanbul Technical University, Istanbul, Turkey, seckin@itu.edu.tr*
[b] *Energy Institute, Istanbul Technical University, Istanbul, Turkey, ahmetbayulken@yahoo.com*

Abstract:

This study focus on determination of environmental remediation cost (EE_{ENV}) of municipal solid waste in terms of extended exergy. In Extended Exergy Accounting methodology (EEA), EE_{ENV} is an indispensable constituent of every flux and can be defined as exergetic expression of the potential environmental impact of an effluent which is represented by the cumulative amount of exergetic resources that must be consumed to attain an ideal, zero-impact disposal of the effluent. To date, in the literature, EE_{ENV} is calculated via conversion of monetary expenses of the considered remediation system into its extended exergy equivalent. This is the first study in the literature that EE_{ENV} of solid waste is obtained in accordance with the original calculation procedure of EEA. The waste treatment procedure includes material recycling, incineration, anaerobic digestion (biogas production) and landfilling. Energy produced from incineration and utilization of biogas in a biorefinery is also included in the study. The considered waste treatment procedure is applied to Turkish municipal waste amount and composition.

Keywords:

Extended exergy accounting, EEA, municipal waste, ecological accounting, solid waste

1. Introduction

Resource availability & use, the environmental consequences of resource exploitation and the relationship between the environment, poverty and economic change have rapidly become very dominant and indispensable concerns in policy making to remedy the present (but clearly non-optimal) situation of resource allocation and exploitation through the world. Researches in these subjects are aimed to determine the boundaries of exploitation of the natural resources and the ways of curing our present situation. The boundaries characterise the balance between levels of development and the use of natural resources, that is, development must be at a level that can be sustained without endangering the "natural environment" or "stock of natural sources". For protection of natural environment, the problem is that many chemicals and materials derived from human activities are not recyclable by natural processes (at least in relatively short time) and additional processing is needed. As such, collection, keeping, treatment and disposal of wastes must be involved in waste management in such a way as to render it harmless to human and animal life, the ecology and the environment generally. As a result, affordable, effective and sustainable waste management system establishment is a cornerstone issue in sustainable development. Hence, in this study, environmental impact of solid waste is determined as resource use equivalent of waste treatment system (in terms of exergy) by means of Extended Exergy Accounting (EEA) methodology.

Extended Exergy Accounting (EEA) is a resource use analysis method which constitutes a substantial generalization of Szargut's "cumulative exergy consumption (CExC)" method: the CExC is the sum of "*all amounts of exergy used in the production of a commodity from the mining of the raw materials to the final distribution and disposal*", and is expressed in purely exergetic terms (J/unit) [1]. Sciubba proposed "Extended Exergy Accounting (EEA) [2,3], which is an entirely resource-based exergy costing method and measures the "cost" of a product or service as the amount of primary exergy resources required to generate it. The method constitutes a substantial generalization of Szargut's "cumulative exergy consumption" method with a novel procedure for

determining the resource equivalent of non-energetic and immaterial quantities: capital, labour and environmental remediation expenditures, in terms of exergy (the attribute "extended" denotes the additional inclusion of previously neglected non-energetic terms) [4]. EEA analysis provides a unified measure for the primary exergy resources consumed in the life cycle of a material or immaterial commodity [5].

The present paper focuses on the determination of "environmental remediation cost (EE_{ENV})" of solid waste. In theoretical structure of EEA methodology, the concept of "environmental remediation cost" relies on the "zero impact" approach which can be described as: bringing the state of effluent streams to the state of thermodynamic equilibrium with the reference state before being discharged into the environment (i.e., the discharged effluent has "zero impact" on the environment) [4]. The essence of this idea is representing the environmental impact of the effluent by the cumulative amount of resources (in terms of exergy) that must be consumed or employed to attain an ideal, zero-impact disposal of the effluent. The cumulative amount of consumed resources is called "environmental remediation cost (EE_{ENV})" in EEA methodology. In brief, EE_{ENV}, which represents the environmental impact of the effluent, is not proportional to the physical exergy of the effluent, but it is equal to the extended exergy (sum of the material exergy and physical exergy, plus exergetic equivalent of externalities -labour and capital required for the installation and operation of the process and also environmental remediation cost of possible effluents from treatment process which must be cleaned) ideally required to cool the effluent to T_0 and break it up into its constituents such that each one of them is in equilibrium conditions with the surroundings [6]. To date, in the literature, EE_{ENV} is calculated via conversion of monetary expenses of the considered remediation system into its extended exergy equivalent [7,8,9]. Although this approach and inserting the CExC of the considered system products are propounded as alternative techniques and applied in one of the articles by the developer of the EEA (E. Sciubba) [10], substituting CExC leads more reasonable results since the values calculated on "monetary cost to exergy" conversion basis are significantly. and uniustifiably. lower [10]. It should be kept in mind that, both of them are just "ersatz" or "substitute" quantities for EE_{ENV}.

In this study, EE_{ENV} of solid waste is obtained in accordance with the original calculation procedure of EEA (a real treatment procedure is analyzed). The analyzed "environmental remediation system" for solid waste consists of material recycling, incineration, anaerobic digestion (biogas production) and landfilling. The approach is applied to the case of municipal solid waste (MSW) generated in domestic (household) sector of Turkey in the year 2006.

2. EEA method and the waste treatment system

In Equation 1, EE (extended exergy) of a commodity is seen [11]:

$$EE = E_M + E_{phys} + EE_L + EE_C + EE_{ENV} \quad (1)$$

where E_M and E_{phys} are exergy of materials and energy carriers, respectively; EE_L and EE_C are total exergetic equivalent of labour and capital, respectively; EE_{ENV} is the exergetic equivalent of environmental remediation cost. Computation of exergetic equivalent of labour and capital is presented in Section 4. Equation for EE_{ENV} is presented in (2):

$$EE_{ENV} = E_{M\text{-}t} + E_{phys\text{-}t} + EE_{L\text{-}t} + EE_{C\text{-}t} + EE_{Env\text{-}t} - E_{P\text{-}t} \quad (2)$$

where $E_{M\text{-}t}$ and $E_{phys\text{-}t}$ are respectively the exergy of material and energy carriers received by the environmental remediation system; $EE_{L\text{-}t}$ and $EE_{C\text{-}t}$ are respectively the exergetic equivalent of labour and capital received by the environmental remediation system, $E_{P\text{-}t}$ is the exergy of the treatment system "possible" product P_t.

The definition of environmental remediation cost is presented in Section 1. Since, in reality, there is no totally "clean" technology [4] or present treatment technologies don't always produce effluents in equilibrium with the surroundings, choosing the minimum environmentally hazardous

technology, i.e., "consciously accepted" level of pollution, is a reasonable approach [12] and applied in this study.

Recycling of MSW can be classified into two parts: 1) heat & energy generation by using the combustible part as a fuel 2) recycling and reusing of the recyclable part.

Most of the combustible components in municipal solid waste are also biodegradable, thus, a combustible gas can be obtained from a biological conversion process [13].

Anaerobic digestion (AD) is the biological decomposition of organic matter under anaerobic conditions (in the absence of oxygen). The products are primarily methane (CH_4) with an accompanying production of other gases (mainly CO_2) [13]. The residue of the AD (digestate) can be composted further to produce "compost" (a kind of fertilizer) which is another product of AD process [14-16].

To sort and process the waste, 2 types of facilities have common use: MRF (Materials Reprocessing Facility) and MBT (Mechanical Biological Treatment). Both of them comprise sorting of waste but in MRF, following procedure after sorting consists of recycling and/or fuel manufacturing (made of waste) and/or preparing the constituents of waste as raw material of different industrial processes [17]. In MBT, the following procedure includes biological treatment of waste constituents (organic part) such as Anaerobic Digestion (AD) or composting [18]. Applied treatment procedure to household sector solid waste in this study can be described as: collected waste is transferred to MRF where the waste is split into its components (organic part is separated from inorganic part as well as the inorganic part is sorted into constituents) and inorganic part is pre-treated and recycled. The organic fraction is mostly made of kitchen garbage while mainly plastics, paper & cardboard, wood, textiles and rubber constitute the inorganic fraction. Non-recyclable part of considered inorganic materials are transferred to an incineration plant where electricity and heat are produced by CHP (combined heat and power system). Remaining materials of recycling process in MRF (sent to recycling but not recycled) and ash produced from incineration of non-recyclables (in incineration plant) are landfilled (see Fig 1). The only discharge to the environment is this landfilled part which has no green house gas emission capacity to the atmosphere after landfilling [19].

The organic fraction is transferred from MRF plant to another plant and undergoes AD process in order to produce biogas (CH_4+CO_2). Afterwards, biogas is upgraded by removing CO_2, H_2S etc. and resulting gas (98% of CH_4 by vol.) is used as a substitute for natural gas. The digestate, i.e., the residue of the anaerobic digestion, is composted and produced compost is taken out of the system as a system product.

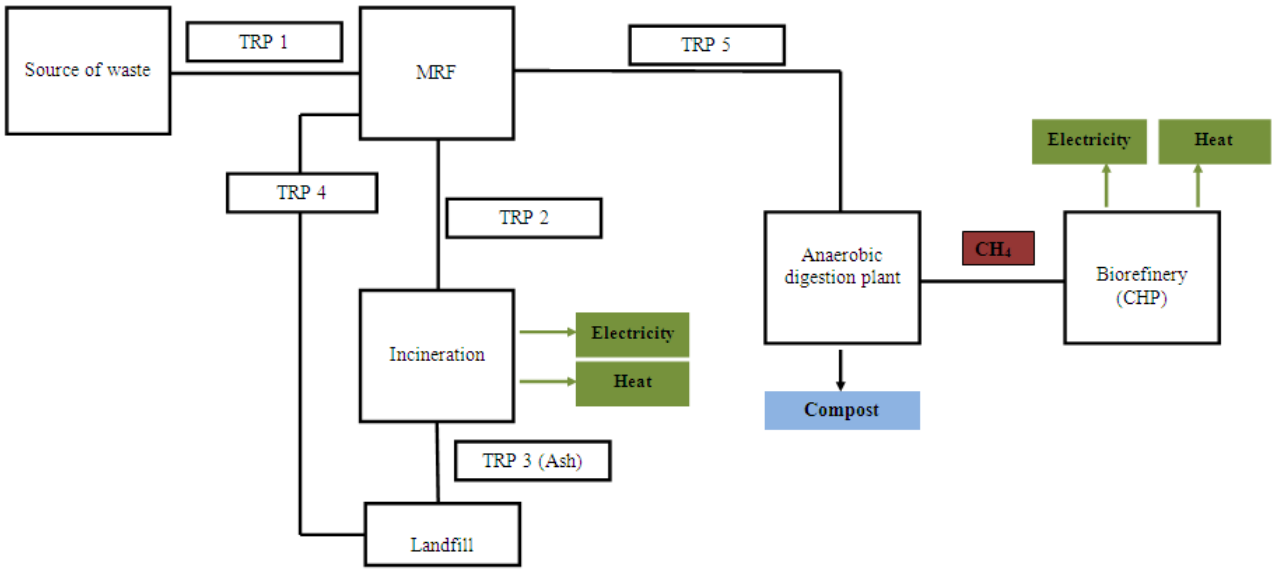

Fig.1. Illustration of household sector solid waste treatment system

3. EEA analysis of the solid waste treatment system

The approach is applied to the case of municipal solid waste (MSW) generated in domestic (DO, household) sector of Turkey in the year 2006. The composition of sectoral solid waste is seen in Table 1 (estimated based on [20]).

Table 1. Composition of DO sector waste

Composition	Percent (% wt.)	Amount (Ton)
Organic	53,92	9385332,68
Paper&Cupboard	8,26	1437953,55
Textile	5,73	997768,57
Plastic	14,90	2593957,59
Diaper	4,23	736988,15
Tetra-pak	0,69	120941,64
Glass	5,80	1009043,08
Metal (Al)	0,47	82670,39
Metal (Fe)	0,69	120464,65
Other metals (Cu)	0,08	13227,99
Wood	0,55	96375,37
Other combustibles	2,26	393026,44
Ash	2,40	417626,62
Total	100	17405376,74

Summarizing tables of DO sector solid waste treatment EEA analysis which report the results of the material, energy carrier, capital and labour inflows into the sector, are seen as Table 2- 6.

The necessary truck numbers for each transportation line and exergetic content of the trucks are presented in Table 2 (exergy of one truck is computed as 0,045 TJ/truck and inserted into the table). In Table 2, TRP lines signify the transportation lines seen in Fig. 1. In calculation of material influxes (except trucks), since no sufficiently reliable data were available on the exact material composition of the used items in the system, and thus an analytical analysis was impossible, the corresponding portion of EE_{ENV} is computed by converting the known monetary cost of the process into exergetic equivalent by means of ee_K (J/$). Computation and numerical value of ee_K is presented in Section 4. The exergy of material flow pertaining to other systems or processes except TRP lines are computed as explained above and presented in Table 3. (Exchange rate between $, € and TL: 1,8 TL= 1 €= 1,26 $ for 2006)

Table 2. Number of trucks and their exergetic content

Transportation line	Number of trucks	Exergy (TJ)
TRP-1	3200	145,51
TRP-2	25	1,13
TRP-3	13	0,59
TRP-4	46	2,09
TRP-5	432	19,64
Total	3716	168,96

Table 3. Material exergy (E_{M-t}) of systems and processes except transportation lines

System/Process	Capital	Ref.	Equivalent exergy (TJ)
MRF plant	100 €/Ton	[17]	20796,22
Incineration plant	64 €/Ton	[17]	4341,06
Anaerobic digestion plant	65 €/Ton	[17]	19601,17
Upgrading of biogas	0,26 €/m^3	[21]	10277,76
Biorefinery	7000 $/$KW_{el}$	[22]	50609,66

Seperation, composting	35 €/Ton	[17]	4221,79
Total			109847,66

[1] The cost of MRF plant includes preliminary sorting, pre-treatment of recyclable materials and recycling
[2] Anaerobic digestion plant includes mixing, sterilization and anaerobic digestion part

In conclusion, exergy of material transfers (E_{M-t}) into the system is the sum of Table 2 and Table 3 which is 110016,62 TJ.

The only exergy inflow of energy carriers (physical exergy) are the diesel fuel consumption of transportation lines. Calculation of diesel fuel consumption for each line is computed based on data presented in [23] and the results are presented in Table 4. (Exergy of diesel fuel is 46366,71 MJ/Ton)

Table 4. Physical exergy (E_{phys-t}) inflow of the environmental remediation system

	Diesel Consumption (Ton)	Exergy of diesel consumption (TJ)
TRP-1	418447,37	19402,03
TRP-2	2664,02	123,52
TRP-3	1332,01	61,76
TRP-4	4723,55	219,02
TRP-5	39479,33	1830,53
Total	466646,28	21636,86

In capital flows, capital investment of the system (Investment cost, IC) is assumed to be supplied by bank credit with annual interest rate of 20% and payback time of 10 years. Annual payment is calculated using the methodology presented by [24] (annual payment is 23.85% of capital investment, calculation is presented in (3) and (4)). Annual "fixed and varying operation costs" (including insurance, wages, maintenance etc., totally abbreviated as "OP") are assumed to be 20% of capital investment. Capital flow of the system is sum of "annualized investment cost plus OP" of each process and system, results are seen in Table 5-7.

$$\text{Annualized cost} = \text{Present value (IC)} \times \left[\frac{r}{1-\left(\frac{1}{(1+r)^n}\right)} \right] \quad (3)$$

where r is the annual interest and n is the number of pay back years.

$$\text{Annualized cost} = \text{Present value (IC)} \times \left[\frac{0,2}{1-\left(\frac{1}{(1+0,2)^{10}}\right)} \right] = 0,239 \quad (4)$$

Table 5. Exergetic equivalent of the capital of processes

System/Process	Capital	Exergetic equivalent of IC (TJ)	Exergetic equivalent of annualized IC (TJ)	Exergetic equivalent of OP (TJ)	Annualized IC+OP (TJ)
MRF plant[1]	100 €/Ton	20796,22	4960,37	4159,24	9119,62
Incineration plant	64 €/Ton	4341,06	1035,44	868,21	1903,65
Anaerobic digestion plant[2]	65 €/Ton	19601,17	4675,33	3920,23	8595,56
Upgrading of biogas	0,26€/m^3	10277,76	2451,48	2055,55	4507,03

Biorefinery	7000 $/$KW_{el}$	55681,13	12071,557	10121,933	22193,49
Separation, composting	35 €/Ton	4221,79	1006,99	844,36	1851,35
Landfilling	10 €/Ton	570,46	114,09	136,07	250,16
Total					48420,86

[1] The cost of MRF plant includes preliminary sorting, pre-treatment of recyclable materials and recycling
[2] Anaerobic digestion plant includes mixing, sterilization and anaerobic digestion part

Use of trucks with an accompanying consumption of diesel fuel brings about capital inputs into the system. The number of trucks and diesel fuel consumption in each TRP line are presented in Table 6 and Table 7, respectively. It is assumed that investment cost of 1 truck is 100000 TL (69930,07 $) as well as annual operation and maintenance cost (OP) is 20% of the investment cost. Density of diesel fuel is taken as 0,835 kg/lt and for the year 2006, the price of diesel fuel is 2,1 TL/l (1,47 $/l) [25]. Diesel fuel cost is accounted in OP cost. As a result, its capital equivalent is not annualized in calculations.

Table 6. Exergetic equivalent of the capital of trucks

Transportation line	Number of trucks	Exergetic equivalent of IC (TJ)	Exergetic equivalent of annualized IC (TJ)	Exergetic equivalent of OP (TJ)	Annualized IC+OP (TJ)
TRP-1	3200	5706,4	1361,11	1141,28	2502,39
TRP-2	25	44,58	10,63	8,91	19,54
TRP-3	13	23,18	5,52	4,64	10,16
TRP-4	46	82,03	19,57	16,4	35,97
TRP-5	432	770,36	183,75	154,07	337,82
Total	3716				2905,88

Table 7. Exergetic equivalent of the capital of diesel fuel consumption

Transportation line	Diesel Consumption (l)	Exergetic equivalent of diesel cost (TJ)
TRP-1	501134572,39	18766,62
TRP-2	3190446,75	119,4767
TRP-3	1595223,37	59,74
TRP-4	5656941,76	211,84
TRP-5	47280631,18	1770,58
Total		20928,25

Due to the lack of data on landfilling, material input coming from landfilling process (tractors, excavators, etc.), energy consumption with accompanying emissions are disregarded in this study.

In conclusion, sum of capital fluxes is the sum of Table 5, 6 and 7 which amounts to 72254,99 TJ.

In the matter of the labour consumption of the system, labour consumed by TRP lines are calculated based on driven distance and average speed of the trucks which are assumed based on [23]. For the left of the system, it is assumed that labour of a CHP system is 200 worker per 1000 MW_{h+el} generated energy, based on data in [26]. Considering the whole system, number of workers is assumed to be 400 worker per 1000 MW_{h+el} with 1800 workhours/year workload for each worker.

Generated electricity and heat power is presented later in Table 14 as 21455,57 TJ_{el} and 25746,68 TJ_h. Generated power is computed as:

$$\text{Generated power}(MW_{el+h}) = \frac{\text{Generated energy}(MJ_{el+h})}{\text{Annual working time}(s)} = \frac{(21455,57 + 25746,68)\text{x}10^6}{340\text{x}24\text{x}60\text{x}60} = 160,83 \quad (5)$$

Hence, labour consumed in the system (excluding transportation) is:

$$\text{Labour}(\text{workhours/year}) = \left[\frac{400 \text{workers}}{1000 \text{MW}}\right] \text{x} \left[\text{Annual work hours}\right] \text{x} \left[\text{Generated power}(MW_{el+h})\right] \quad (6)$$

$$\text{Labour (workhours)} = \left[\frac{400 \text{ (workers)}}{1000 \text{ (MW)}}\right] \text{x} \left[1800 \text{ (hours / year worker)}\right] \text{x} \left[1606,83 \text{ (MW)}\right] \quad (7)$$

$$\text{Labour} = 1156917,94 \text{ hours}$$

The exergetic equivalent of the labour is computed by means of ee_L:

$$EE_L = \text{Labour load (workhours)} \text{ x } ee_L \text{ (MJ/hours)} = 1156917,94 \text{ x } 153,95 = 178110163,51 \text{ MJ} = 178,11 \text{TJ} \quad (8)$$

Resulting labour consumption and exergetic equivalent are presented in Table 8.

Table 8. Labour consumption and exergetic equivalent (EE_L)

Transportation line	Labour (workhours)	Exergetic equivalent of labour (TJ)
TRP-1	10245333,33	1577,29
TRP-2	68000,00	10,47
TRP-3	35360,00	5,44
TRP-4	117300,00	18,06
TRP-5	979200,00	150,75
The left of the system	1156917,94	178,11
Total	12602111,27	1940,12

Environmental remediation cost of the system (EE_{ENV-t}) stems from mainly transportation as well as processes like anaerobic digestion, incineration etc. The emission gasses are obtained based on [27] and presented in Table 9. Due to lack of sufficiently disaggregated data and great variety of emission gasses, three types of greenhouse gasses (CO_2, CH_4, N_2O) are considered in this study.

Table 9. Greenhouse gas emissions from the processes

	Emissions (Ton)		
	CO_2	N_2O	CH_4
TRP-1	1326818,40	69,83	69,83
TRP-2	8447,12	0,44	0,44
TRP-3	4223,56	0,22	0,22
TRP-4	14977,48	0,79	0,79
TRP-5	125181,57	6,59	6,59
Incineration plant	3009323,85	131,27	984,51
Anaerobic digestion	33355,67		13247,55
Upgrading of biogas	1053555,55		8566,75
Biorefinery	1168106,84	2,08	20,82
Composting	495545,57	1126,24	15016,53
Total	7239535,61	1337,47	37914,05

The environmental remediation cost (EE_{ENV}) of considered emission gases are computed as a different study of the same authors. But, since the goal of the present study is determining the environmental remediation cost for solid waste, presenting the computation for gas treatment would be deviation from the subject. Hence, EE_{ENV} of considered gases are inserted into Table 10 to obtain the EE_{ENV-t} for the whole solid waste treatment system.

Table 10. Environmental remediation cost of emission gasses (EE_{ENV})

CO_2 emissions (Ton)	7239535,61
N_2O emission (Ton)	1337,47
CH_4 emission (Ton)	37914,05
CO_2 emission treatment cost (TJ/Ton CO_2)	0,0576
N_2O emission treatment cost (TJ/Ton N_2O)	0,0106
CH_4 emission treatment cost (TJ/Ton CH_4)	0,3224
CO_2 EE_{ENV} (TJ)	417334,19
N_2O EE_{ENV} (TJ)	14,18
CH_4 EE_{ENV} (TJ)	12221,87
Total EE_{ENV} (TJ)	429570,23

As it is seen in Fig.1, the products of the whole treatment system are 1) electricity and heat produced by incineration of non-recyclable part of the inorganic waste and 2) electricity and heat produced in biorefinery 3) recycled materials and 4) compost. The ash generated in considered processes are assumed to have zero exergy. Hence, its exergetic content is not included in exergy of products. The amount of non-recyclables and their energy content are presented in Table 11. The amount of the materials in Table 11 is derived based on data in [28].

Table 11. Low heating value (LHV) of the non- recyclables

	Material (Ton)	LHV (MJ/kg)	Total energy content (TJ)
Paper & Cupboard	202354,27	11,5	2327,07
Textile	74832,64	14,6	1092,56
Plastic	357498,39	31,5	11261,20
Diaper	736988,15	15,41	11353,30
Glass	30271,29	0	0
Metal (Al)	100169,39	0	0
Metal (Fe)	110149,10	0	0
Other metals (Cu)	98764,03	0	0
Wood	6987,21	18,46	128,98
Other combustibles	393026,44	16,93	6653,94
Total	2111040,92		32817,05

Efficiencies of heat and electricity production and produced energy via incineration are seen in Table 12.

Table 12. Properties of incineration process

		Electricity	Heat
Energy of non-recyclables (TJ)	32817,05		
Efficiencies		0,4	0,48
Produced energy (TJ)		13126,82	15752,19

The composition of biogas utilized in the biorefinery involved in the system is 98% CH_4 and 2% CO_2. The biorefinery is a CHP plant and the efficiencies of heat and electricity generation are assumed to be same as those in Table 12. The amount of the biogas utilized in biorefinery and produced energy can be seen in Table 13. LHV (low heating value) of CO_2 is almost zero [21].

Table 13. Properties of biogas utilization

CH_4 (m^3)	617310076,13
CO_2 (m^3)	12598164,82
LHV of CH_4 (MJ/m^3)	33,73

LHV of CO_2 (MJ/m^3)	0
LHV of biogas (TJ)	20821,87
Electricity generation efficiency	0,40
Heat generation efficiency	0,48
Generated electricity (TJ)	8328,75
Generated heat (TJ)	9994,50

As stated earlier, the energy need (both of heat and electricity) is met by the generated energy in the system, i.e., output of biorefinery and incineration process. The energy balance of the environmental treatment system is presented in Table 14. In the Table, it is assumed that produced heat is at the temperature of 100 C.

Table 14. Energy balance of the system

		Consumption		Production	
	Description:	Electricity (TJ)	Heat (TJ)	Electricity (TJ)	Heat (TJ)
MRF plant	preliminary sorting	259,86			
MRF plant	Pre-treatment of recyclable materials and recycling	3397,14	10562,56		
Incineration plant		590,71		13126,82	15752,19
Anaerobic digestion	mixing, sterilization	2027,23			
Anaerobic digestion	anaerobic digestion	333,15	2498,62		
Upgrading of biogas		1353,32	442,90		
Biorefinery		374,79		8328,75	9994,50
Composting	separation, drying, composting	2209,68			
Total		10545,88	13504,09	21455,57	25746,68
Net production				10909,68	12242,59
Exergy of production				10909,68	2460,66

Recycling of the materials is analyzed in accordance with technical details of recycling processes given in [28]. Amount of recycled materials and exergy contents are reported in Table 15. Produced compost from residue of the AD process (digestate) is presented in Table 16.

Table 15. Amount and exergy of recycled materials

	Recycled material (Ton)	Material exergy (MJ/Ton)	Exergy (TJ)
Paper & Cupboard	1305643,53	17000	22195,94
Textile	593672,30	13904,76	8254,87
Plastic	1547691,80	32502,16	50303,33
Glass	948500,50	131,48	124,71
Metal (Al)	80912,59	32928,09	2664,30
Metal (Fe)	90589,42	6740,69	610,63
Other metals (Cu)	11905,19	2112,06	25,14
Wood	82400,94	20658,24	1702,26
Total	4661316,27		85881,19

Table 16. Amount and exergy of produced compost

Amount of produced compost (Ton)	1501653,23
Exergy of compost (MJ/Ton)	18373,31
Exergy of total produced compost (TJ)	27590,33

4. Calculation of the exergy equivalent of externalities

The exergetic equivalent of labor (ee_L) is defined as the exergy used to generate one work-hour and calculated as (9):

$$ee_L = \frac{\alpha \text{ x } E_{in}}{N_{wh}} \quad (9)$$

where, ee_L(MJ/hour), exergetic equivalent of labor; α, the fraction of the primary exergy embodied into labour; E_{in} (MJ/year), global exergy influx and N_{wh}(hours/year), cumulative number of work hours [29].

The unit exergetic equivalent of capital (ee_K) is defined as the equivalent primary exergy resource embodied in one monetary unit and calculated as (10):

$$ee_K = \frac{\alpha \times \beta \times E_{in}}{(M_2 - S)} \quad (10)$$

where, ee_K (MJ/$), exergetic equivalent of capital; β, an amplification factor that accounts for the creation of wealth due to exclusively financial activities [30]; M_2 ($/year), money + quasi-money circulation; S ($/year), global wages and salaries in a country.

Exergetic equivalent of labour and capital is calculated as:

$$EE_L = L \text{ x } ee_L \quad (11)$$

$$EE_C = C \text{ x } ee_K \quad (12)$$

where, L(hours), workhours; C($), capital; EE_L and EE_C are defined in Section 1.

To calculate the econometric factors α and β, (13-16) are occupied:

$$E_{used} = 365 \text{ x } f \text{ x } e_{surv} \text{ x } N_h \quad (13)$$

$$f = \frac{HDI}{HDI_0} \quad (14)$$

$$\alpha = \frac{E_{used}}{E_{in}} \quad (15)$$

$$\beta = \frac{M_2 - S}{S} \quad (16)$$

where, E_{used} (MJ/year), the global exergy used by the society for survival, e_{surv} ($1{,}05 \times 10^7$ J/(person·day)), exergy consumption for survival, [30]; N_h (persons), number of inhabitants; HDI, Human Development Index; HDI_0, Human Development Index of a primitive society, 0,055 [30]. A further discussion is available in [29]. Data for M_2, S, N_h, HDI are obtained from [31],[32],[33] and[34], respectively. Above listed variables and ee_L and ee_K for Turkey are seen in Table 17.

Table 17. Econometric factors, ee_L and ee_K

E_{in} (TJ)	3601655961,68
HDI	0,798
M_2 ($)	208206113706
S ($)	170782627832
N_{wh}	28266496268,07

N_h	78259264
α	0,001208
β	0,219
ee_L (MJ/hours)	153,952
ee_K (MJ/$)	25,5

5. Results

The formulation of EE_{ENV} is presented in (1). The necessary terms of the equation (E_{M-t}, E_{phys-t}, EE_{L-t}, EE_{C-t}, EE_{ENV-t}) and resulting EE_{ENV} for DO sector solid waste are presented in Table 18.

Table 18. EE_{ENV} for DO sector solid waste

	Exergetic equivalent (TJ)
E_{M-t}	110016,62
E_{phys-t}	21636,86
EE_{L-t}	1940,12
EE_{C-t}	72254,99
EE_{Env-t}	429570,23
E_{P-t}	126841,87
EE_{Env}	508576,96

6. Conclusion

As it is seen in previous sections, EE_{Env} is directly related to the composition of solid waste and type of waste treatment processes. It must be noticed that, in this study, solid waste remediation extended exergetic costs (EE_{Env}) are computed on a defined disposal process chain. However, it is well known that different effluent remediation technologies carry different costs, and their EE_{Env} values may differ. Hence, the most important consequence of the present study is the necessity of further examination of different handling and treatment routes to determine the lowest extended exergetic cost of EE_{ENV} for MSW. But, this study proposes numerical results for state-of-the-art industrial treatment technologies and has the corresponding importance.

As it is seen in Table 14, energy consumption of waste sorting (preliminary sorting) has a little fraction in total energy consumption. Therefore, source sorting of MSW is not determining on energy consumption. Extended exergetic inputs to the above mentioned processes are reported in Table 19. As a result of disallocation of labour fluxes through the processes, labour is not inserted into Table 19 except transportation. But, as it seen in Table 8, total exergetic equivalent of labour of all processes is almost 1/10 of the labour consumed in the transportation. Hence, it doesn't dominate the results. Since the material influxes (except transportation lines) are computed via converting capital into its exergetic equivalent, results are not very accurate. However, it is seen that, transportation lines cause high resource consumption mainly stems from high greenhouse gas emission (mainly CO_2) and consumption of diesel fuel (which has high exergetic content as a fossil fuel). This conclusion concurs with the results of some studies in the literature [15,18].

Table 19. Exergy of input fluxes into the processes

	MRF	Incineration	AD	Upgrading	Composting	Biorefinery	Transportation
Material (TJ)	20796,22	4341,06	19601,17	10277,76	4221,79	50609,66	168,96
Physical exergy (TJ)							21636,86
Capital (TJ)	9119,62	1903,65	8595,56	4507,03	1851,35	22193,49	2905,88
Labour (TJ)							1762,01
Environmental remediation (TJ)		173795,87	6193,28	63495,39	33419,11	67344,05	85322,53
Total EE consumption (TJ)	29915,84	180040,57	34390,01	78280,18	39492,25	140147,21	111796,23
Products (TJ)	85881,2	16292,88			27590,3	10337,56	

As it is seen in Table 1, organic fraction is 54% of the sectoral solid waste composition and AD process has an essential part of the system. In the case of comparison, incineration of only "non-recyclable part" of inorganic waste produces more heat and electricity than those produced in biorefinery (see Table 14). It is seen that incineration is more efficient in energy production but total EE consumption and environmental remediation cost is almost the same as sum of (AD+ upgrading+composting+biorefinery). Considering the difference in mass of processed materials in this study (much less mass processed in incineration plant), it can be estimated that if organic waste is directly incinerated, produced energy would be more but total resource exergy consumption (EE) would be much higher for organic waste treatment. As a result, AD process is much more preferable for organic waste treatment, on the resource consumption side of the issue.

Nomenclature

AD anaerobic digestion

CExC cumulative exergy consumption, J

CHP combined heat and power

DO domestic sector

E exergy, J

EE extended exergy, J

ee specific extended exergy, J/(hour, mass, $,...)

EEA extended exergy accounting

EE_{ENV} environmental remediation cost, J

E_{in} global exergy influx, J/year

E_{used} the global exergy used by the society for survival (J/year)

HDI human development index

IC investment cost, $

LHV low heating value, J

M_2 money + quasi-money circulation, $/year

MSW municipal solid waste

N_h population

N_{wh} cumulative number of work hours, hours

OP operation and maintenance cost, $

P product

S global wages and salaries in a country, $/year

T_0 ambient temperature, °C

TRP transportation line

Greek symbols

$ dollar

€ euro

β an amplification factor represents the creation of wealth due to exclusively financial activities

α fraction of the primary exergy embodied into labour

Subscripts and superscripts

C capital

el electrical

ENV environmental remediation

h heat
L labour
M material
phys physical
t for treatment system

References

[1] Sciubba E., Exergy-based Ecological Indicators: a necessary tool for Resource Use assessment studies. In: Keynote address to IEEES 2009 , A.U.S., Sharjah, UAE.

[2] Sciubba E., Extended exergy accounting: towards an exergetic theory of value. In: Proceedings of the ECOS '99, Tokyo, Japan, 1999. ECOS: 85–94

[3] Sciubba E., Beyond thermoeconomics? The concept of extended exergy accounting and its application to the analysis and design of thermal systems. The International Journal of Exergy, 2001;1(2):68-84.

[4] Sciubba E., Extended exergy accounting applied to energy recovery from waste: The concept of total recycling. Energy 2003; 28(13):1315-1334

[5] Milia D., Sciubba E., Exergy-based lumped simulation of complex systems: An interactive analysis tool. Energy 2006;31:100–11

[6] Sciubba E., Exergo-economics: thermodynamic foundation for a more rational resource use, Int. J. Energy Res. 2005;29:613–636.

[7] Chen GQ, Chen B. Extended-exergy analysis of the Chinese society. Energy 2009;34:1127-44.

[8] Ptasinski KJ, Koymans MN, Verspagen HHG. Performance of the Dutch energy sector based on energy, exergy and extended exergy accounting. Energy 2006;31:3135-44.

[9] Sciubba E, Bastianoni S, Tiezzi E. Exergy and extended exergy accounting of very large complex systems with an application to the province of Siena, Italy. Journal of Environmental Management 2008;86:372-82.

[10] Corrado A, Fiorini P, Sciubba E. Environmental assessment and extended exergy analysis of a ''zero CO2 emission'' high-efficiency steam power plant. Energy 2006;31:3186-98.

[11] Sciubba E., Cost analysis of energy conversion systems via a novel resource-based quantifier. Energy 2003;28:457–477

[12] Sciubba, E. Using exergy to evaluate environmental externalities. In Proceedings of the IV NTVA Seminar of Industrial Ecology, Trondheim, Norway, June 14, 2001.

[13] United Nations Environment Programme (UNEP), 2005. Solid Waste Management. - Available at:<http://www.unep.or.jp/ietc/publications/spc/solid_waste_management/index.asp> [accessed 12.10.2011].

[14] Midwest Rural Energy Council (MREC), 2003. Anaerobic digestion of farm and food processing residues, Good Practice Guidelines. - Available at:<http://www.mrec.org/biogas/adgpg.pdf> [accessed 12.10.2011].

[15] European Environment Agency (EPA). Biodegradable municipal waste management in Europe, Part 3: Technology and market issues. - Available at:<http://scp.eionet.europa.eu/publications/topic15_2001> [accessed 12.10.2011].

[16] Poschl M., Ward S., Owende P., Evaluation of energy efficiency of various biogas production and utilization pathways. Applied Energy 2010;87:3305–3321.

[17] Smith A., Brown K., Steve O., Kathryn R., Bates J. Waste Management Options and Climate Change Final report to the European Commission. - Available at:<http://ec.europa.eu/environment/waste/studies/pdf/climate_change.pdf> [accessed 12.10.2011].

[18] Glasgow City Council, 2010. Waste Awareness Sustainability Technology Environment Strategy, 2009. Available at:< http://www.glasgow.gov.uk/NR/rdonlyres/FC2FE19A-3FAE-44EF-9ACE-9333DD882DF4/0/WasteStrategy101Jpublishedversion.pdf >[accessed 12.03.2012].

[19] Chen T.C., Cheng F.L. Greenhouse gases emissions from waste management practices using Life Cycle Inventory model. Journal of Hazardous Materials 2008;155:23–31

[20] Kanat G., Municipal solid-waste management in Istanbul. Waste Management 2010;30:1737–45

[21] De Hullu J., Maassen J.I.W., Van Meel P.A., Shazad S., Comparing different biogas upgrading techniques. Final report, 2008. - Available at:<http://students.chem.tue.nl/ifp24/BiogasPublic.pdf> [accessed 12.10.2011].

[22] EIA (U.S. Energy Information Administration), Updated Capital Cost Estimates for Electricity Generation Plants, 2010. - Available at:<http://www.mit.edu/~jparsons/current%20downloads/EIA%202010%20updated%20capital%20costs.pdf>[accessed 12.10.2011].

[23] Berglund M., Borjesson P., Assessment of energy performance in the life-cycle of biogas production. Biomass and Bioenergy 2006;30:254-266

[24] Bejan A, Tsatsaronis G Moran M., Thermal Design and Optimization. New York:John Wiley & Sons;1996.

[25] Turkish Energy News. - Available at:<http://www.turkishenergynews.com/haber/hangi-yakit-daha-ekonomik-103.htm>[accessed 12.10.2011].

[26] Bezdek R.H., Wendling R.M., Establishing benchmarks for environmental comparison 2008. - Available at:<http://www.misi-net.com/publications/ModernPowerSystems-1206.pdf>[accessed 12.10.2011].

[27] Eggleston, S., Buendia, L., Miwa, K., Ngara, T., Tanabe, K., 2006. IPCC Guidelines for National Greenhouse Gas Inventories. IPCC National Greenhouse Gas Inventories Programme, Institute for Global Environmental Strategies, Hayama, Kanagawa, Japan. - Available at:<http://www.ipcc-nggip.iges.or.jp/public/2006gl/index.html>[accessed 12.10.2011].

[28] Rigamonti L., Grosso M., Giugliano M., Life cycle assessment for optimising the level of separated collection in integrated MSW management systems. Waste Management 2009;29:934–944

[29] Sciubba E., A revised calculation of the econometric factors α- and β for the Extended Exergy Accounting method. Ecological Modelling 2011; 222(4):1060-66

[30] TalensPeiró L., Villalba Méndez G., Sciubba E., Gabarrelli Durany X., Extended exergy accounting applied to biodiesel production. Energy 2010;35:2861-69

[31] Turkish Statistical Institute, Statistical Indicators 1923-2007, Ankara, Turkey: Turkish Statistical Institute: 2010

[32] Turkish Statistical Institute. Annual Industry and Service Statistics 2006. Ankara, Turkey: Turkish Statistical Institute; 2009

[33] Turkish Ministry of the Interior Affairs - Available at < http://www.nvi.gov.tr/>[accessed 12.10.2011].

[34] United Nations Development Programme (UNDP), Human development indices report 2008, - Available at <http://hdr.undp.org/en/media/HDI_2008_EN_Tables.pdf>[accessed 12.10.2011].

Development of Product Category Rules for the application of Life Cycle Assessment to Carbon Capture and Storage

Carlo Strazza[a], Adriana Del Borghi[a], Michela Gallo[a]

[a] CE.Si.S.P. (Centre for the Development of Product Sustainability), University of Genoa, Via all'Opera Pia 15 – 16145 Genova, Italy, carlo.strazza@unige.it (CA)

Abstract:

In order to develop a Life Cycle Assessment (LCA) study with the aim of communicating its results, precise methodological considerations are required, whose common and harmonised definition must consider and guarantee the comparability among different studies within the same service group.
This paper describes the reasons leading to each choice in the development of specific rules, i.e. Product Category Rules (PCR), for the application of Life Cycle Assessment (LCA) to Carbon Capture and Storage (CCS). CCS is a very innovative and promising approach for greenhouse gases (GHG) reduction, i.e. capturing carbon dioxide (CO_2) at its source and storing it indefinitely to avoid its release to the atmosphere.
A robust environmental management tool such as LCA, based on ISO 14040 standard, can play a vital role in assessing CCS techniques in a holistic way that enables the identification of critical processes and the potential improvements of the system.
In a communication perspective, the specific rules defined in this study have been developed coherently with the requirements of a type III environment label scheme, the International EPD® System, according to ISO 14025 standard. The following LCA-based information are addressed in this work: definition of service type, definition of functional unit, choice and description of system boundaries, choice of allocation rules, choice of selected Life Cycle Inventory (LCI) results or other selected parameters for description of environmental performance to be communicated, additional environmental information.

Keywords:

PCR, LCA, CCS, Carbon dioxide, EPD.

1. Introduction

The world is facing a climate challenge, and this fight is nowadays one of the main topics of international debate. Although there is not universal agreement, the major cause of global climate change has been identified as the anthropogenic emission of greenhouse gases (GHG) into the atmosphere [1]. As reported by the International Energy Agency (IEA), electricity sourced from fossil fuels accounts for more than 40 per cent of the world's energy-related carbon dioxide (CO_2) emissions. Another 25 per cent comes from large-scale industrial processes such as iron and steel production, cement making, natural gas processing and petroleum refining. In this context, demand for fossil fuels is still rising, especially in developing countries. Trends in CO_2 emissions from fuel combustion illustrate the need for all countries to shape a more sustainable energy future [2].

According to IPPC, the average temperature rise must be capped to 2 degrees Celsius relatively to pre-industrial times. A revolutionary scale of mitigation may see the contribution of Carbon Capture and Storage (CCS) technologies ranging between 15 per cent and 55 per cent of the required abatement to the year 2100 [3]. CCS is an integrated suite of technologies that are able to prevent large quantities of carbon dioxide from being released into the atmosphere. As the name implies, the technology captures the CO_2, typically from large industrial processes, before it is emitted into the atmosphere; then the CO_2 is transported to a carefully selected and safe storage site, where it can remain permanently stored away from the atmosphere.

Technologies that prevent or minimise CO_2 being emitted into the atmosphere from the production or use of fossil fuels can potentially play a major role in overall efforts to limit GHG emissions. Therefore, significant effort is being put into research and development of CCS technologies, and governments around the world have committed funds to demonstrating projects at large scale. In fact, CCS technologies are a viable option - and in some cases, the only viable option - for reducing emissions from large-scale point sources and have the potential to help reduce to almost zero the emissions to atmosphere from power plants and factories [4].

IEA concluded that, in order to achieve the required emissions reductions in the most cost-effective manner, carbon capture and storage will need to contribute around one-fifth of total reductions in emissions by 2050. With this target, it would be necessary to deploy around 100 CCS projects by 2020, and over 3000 projects by 2050 [5-6]. Such rapid expansion and scale-up of these technologies raises a number of assessment issues that must be addressed in parallel with ongoing efforts to demonstrate the technical, safety and environmental viability of industrial-scale CCS projects. With regard to this, the implementation of appropriate regulatory frameworks for CCS is required to underpin performance and associated incentive schemes, support commercial transactions relating to CCS operations, build public confidence in the technology and public acceptance [7].

Table 1. Aspects covered by LCA studies for CCS systems

Study	Year	Capture			Transport	Storage
		post-combustion	*pre-combustion*	*oxyfuel*		
Waku et al. [26]	1995	✓	✓		✓	✓
Aycaguer et al. [17]	2001					✓
Doctor et al. [10]	2001		✓			
Rao and Rubin [11]	2002	✓				
Lombardi [14]	2003	✓	✓	✓		
Benetto et al. [12]	2004	✓				
Spath and Mann [19]	2004	✓			✓	✓
IEA [15]	2006	✓	✓			
Khoo and Tan [20]	2006	✓				✓
Khoo and Tan [21]	2006					✓
Suebsiri et al. [18]	2006					✓
Viebahn et al. [27]	2007	✓	✓	✓	✓	✓
Hertwich et al. [22]	2008	✓			✓	✓
Koorneef et al. [23]	2008	✓			✓	✓
Odeh and Cockerill [16]	2008	✓	✓			
Bouvart and Prieur [28]	2009	✓	✓		✓	✓
Korre et al. [13]	2009	✓				
Pehnt and Henkel [29]	2009	✓	✓	✓	✓	✓
Schreiber et al. [24]	2009	✓			✓	✓
Modahl et al. [25]	2011	✓			✓	✓
Nagashima et al. [32]	2011	✓			✓	✓
Nie et al. [30]	2011	✓		✓	✓	✓
Singh et al. [31]	2011	✓	✓	✓	✓	✓

In this context, the need of reporting the environmental performance of such mitigation systems in a transparent manner is emerging. Lack of knowledge on environmental impacts may postpone the actual implementation of CCS projects; at the same time, vagueness in the reporting methodology for the communication of results may spoil public understanding and confidence. A series of key issues regarding the assessment of CCS activities have been summarized in literature [8], highlighting the need of identifying a set of significant environmental indicators. A life cycle approach is able to provide comprehensive evaluation of all environmental effects of the considered

technologies “from cradle to grave” along the whole system, thus Life Cycle Assessment (LCA) has been proved to be a helpful tool to investigate the environmental consequences related to the introduction of CCS [9].

In the last years an increasing number of LCA applications for these technologies were registered, but the focus of the work were is very fragmented and often not easily comparable (Table 1). Many of these studies have only focused on the capture process, either concentrating on one specific CCS technology [10-13], or comparing different technological options [14-16]. Few studies have covered the storage phase only, investigating CO_2 enhanced oil recovery (EOR) [17,18]. Most of the assessments particularly regarded the effects of the integration of post-combustion capture in fossil fuel power plants, coupled with different transport and storage scenarios [19-25]. Nevertheless, this capture option was compared with pre-combustion and oxyfuel solutions within a wide range of transport and storage scenarios [26-31]. Only a single study [32] performs an analysis of model cases that include further CO_2 generation sources than thermal power stations such as ironworks, paper mill and oil refinery, where the results are reported per ton of CO_2 rather than per kWh produced. In fact, the use of kWh as a functional unit is useful for understanding the implications at a power plant level, but it is not fruitful for considering large scale effects and for indicating the output of the overall system. A recent study [33] highlights the need of setting a methodological framework in order to address this and further issues that LCA practitioners might face when analyzing CCS systems. The aim of the present study is to describe the reasons leading to the key choices in the development of a robust and objective methodology, i.e. Product Category Rules (PCR) according to ISO 14025 standard [34], for the application of LCA to CCS and reporting and disseminating the results to the scientific community and stakeholders, in a communication perspective such as Type III environmental declaration framework.

2. Methodology

2.1. Life Cycle Assessment

In the field of environmental sustainability, Life Cycle Assessment (LCA) represents an environmental management tool that is widely recognized by the scientific community for objectively measuring the evaluating the effects of a product or a service on the environment. Widening the perspective in designing activities permits to consider all the environmental aspects along the entire product/service life cycle, without transferring the impacts from one phase to the successive ones.

LCA methodology is in fact an objective assessment process of the environmental burdens related with a product or a service, through the identification and quantification of energy and material inputs and outputs over the entire period of its life: from the extraction and processing of the raw materials from which it is made, through the manufacturing, packaging and marketing processes, the use, re-use and maintenance of the product, and on to its eventual re-use, recycling and/or disposal as waste at the end of its useful life. Emissions and consumption of resources are evaluated at every stage of the life cycle, in order to address the environmental impacts from the entire life cycle of products and services.

The elaboration of a LCA study, as stated in ISO 14040 standard [35] and illustrated in Fig. 1, is based on the evaluation of four phases:

1. Goal and scope definition: identification of the purpose of the study (e.g. a comparative evaluation of systems that are functionally equivalent), the functional unit (i.e. a measure of the function of the studied system, that provides a reference to which the inputs and outputs can be related) and the system boundaries;
2. Inventory analysis: data collection, assessment of the procedures for the calculation of the inlet/outlet fluxes from/to the system, including the resource utilization and air emissions, waterborne effluents and solid waste;

3. Impact assessment: procedure to evaluate the effects of the compounds identified in the inventory phase on specific impact categories, such as global warming, ozone layer depletion, acidification, ground-level ozone creation, eutrophication;
4. Interpretation: combination of the results obtained in the inventory phase and in the impact assessment phase, in order to draw conclusions and formulate recommendations.

LCA allows designers to identify possible areas where a good or service could be improved by lowering its environmental impact and reducing resource consumption throughout its life cycle. Besides, LCA represents a key stepping stone on the path to sustainable growth in Europe. By providing clear and verifiable information to policy-makers, LCA is able to help shape sustainable consumption and production policies. In its Communication on Integrated Product Policy (COM (2003)302) [36], the European Commission concluded that Life Cycle Assessments provide the best framework for assessing the potential environmental impacts of products currently available. Information from LCA can also support eco-design criteria setting, such as contributing to performance targets within the Environmental Technology Action Plan (EcoAP) [37] and providing the methodological basis for Type III environmental declarations.

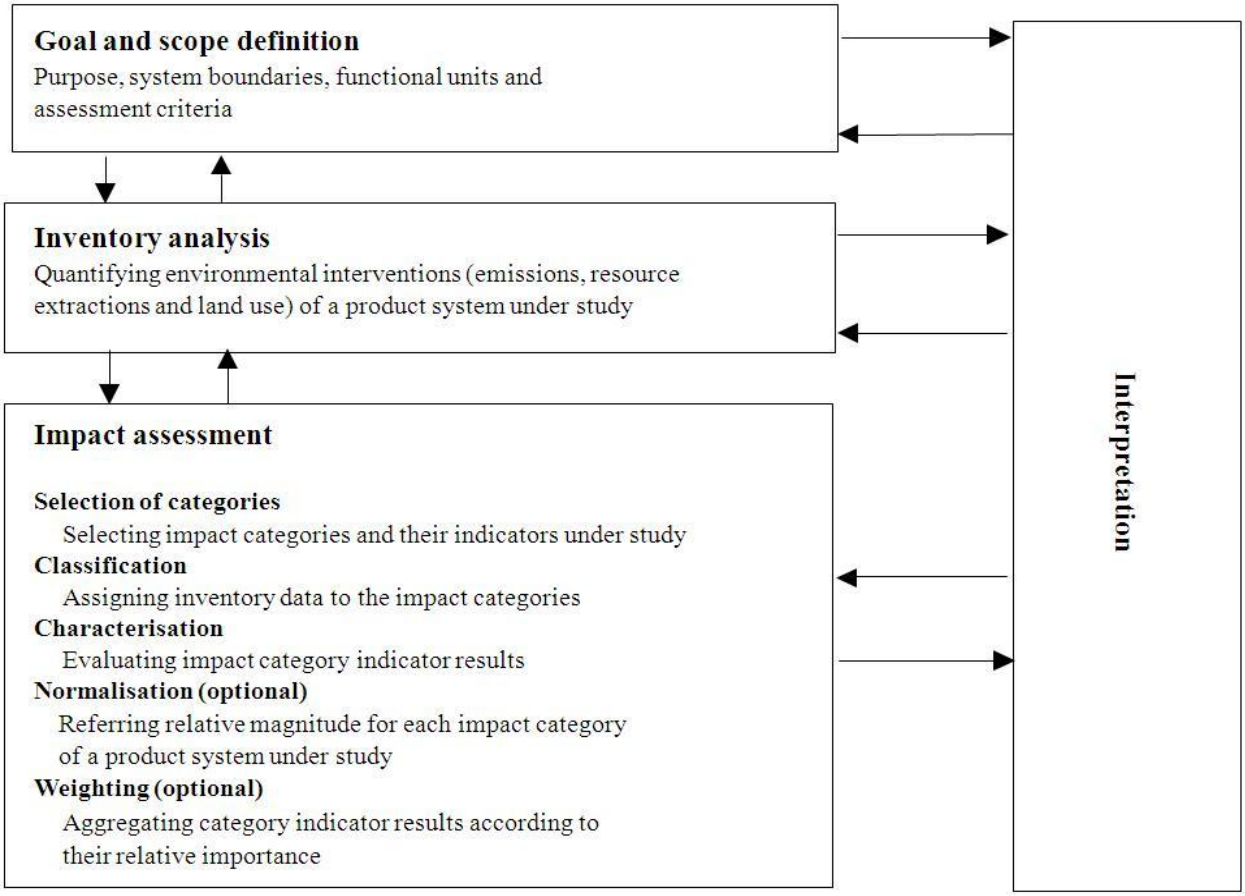

Fig. 1. LCA phases according to ISO 14040.

2.2. Type III environmental declarations

Type III environmental declarations, as the Environmental Product Declaration (EPD), are communication tools providing environmental data on products and services using pre-determined parameters based on the ISO 14040 standard and, where relevant, additional environmental information. They are developed in accordance with the ISO 14025 standard.

Systems for ISO 14025 Type III environmental declarations are gradually becoming more known and operational on the market. The so-called International EPD® system is one of these programmes operating on the market in several countries, which has considerably gained importance during the last decade. As stated in its General Programme Instructions (GPI) [38], he main objective of the system is to support organisations in any country to disseminate verified product-related information for a number of market applications. With this purpose, the International EPD® system is supporting other environmental declaration programmes (i.e. national, sectorial etc.) in seeking cooperation and harmonisation and helping organisations to broaden the use of their environmental declarations on an international market.

One of the main purposes of an EPD is to provide the basis for a fair comparison between goods and services having the same principal function based on their inherent environmental performance. Moreover, EPDs can communicate and add up relevant environmental information along a product's supply chain as well as to reflect the continuous environmental improvement of products and services over time. With this perspective, the system is based on so-called attributional LCA studies, describing the environmentally relevant physical flows to and from one product system and its subsystems. Although sometimes the underlying data for upstream and manufacturing processes are referred to "historic data", they have the form of a "book-keeping system" being traceable and documented, and representative to reflect the present situation to the best extent possible. Besides, in case of downstream processes (especially end-of-life), data often reflect future scenarios, depending also on product life span and the modelling assumptions. This approach is aimed to meet specified data quality assurance criteria, that are especially important for a credible updating and verification process [39].

2.3. Product Category Rules

As an EPD is aimed to ensure objectivity, comparability and credibility in communicating the environmental performance within clearly defined and classified product categories and service types, it has to meet and comply with specific and strict methodological prerequisites. ISO 14025 describes the procedure necessary for preparing the declarations, how to develop consistent and comparable data sets [40], according to common rules, i.e. Product Category Rules (PCR) [41].

As defined in the GPI of the International EPD® system [38], the PCR shall define the criteria according to assigning a product to a specific category, which parameters are set out to prepare the EPDs, the data quality requirements and the collection and calculation rules for data to be included in the EPD, as well as what kind of information suitable to convey to the primary audience of the EPD.

A hierarchic approach is followed in order to structure the documents in modules according to an UN-based product classification scheme, i.e. Central Product Classification (CPC) [42]. The CPC classification scheme facilitates a well-structured and easy to communicate product identification. Thus it is helpful for outlining general and common LCA-based calculation rules for cradle-to-gate and gate-to-gate data to be valid to the maximum extend in as many PCR documents as possible.

3. Results and discussion

The following sections summarize five key issues that must be rigorously considered by practitioners when assessing of the environmental performance of Carbon Capture and Storage (CCS) through LCA methodology in a communication perspective such as the EPD framework. These issues have been identified during the preparation phase of PCR for CCS according to ISO 14025 standard and shall be integrated in the classic structure of Product Category Rules (PCR) within the aforementioned International EPD® system.

3.1. Specification of the service

Within goal and scope definition phase, a unequivocal identification of the service must be assured when starting the activities of assessment and when reporting the results in the declaration format.

This issue represented a fundamental element in the development of the methodology, since the details of this definition unequivocally orient the focus of entire procedure. Since the aim of the developed PCR is to assure the widest applicability in the whole spectrum of technological scenarios, CCS was here considered as a end-of-life process, so that it can be integrated to whatever industrial plant that is an anthropogenic source of carbon dioxide. On the other side, when analyzing the effect of CCS on integrated systems such as combustion technologies based on fossil and renewable fuels and peat equipped with CCS, the specific PCR for electrical energy, steam and hot water [43] shall be considered.

The product category was therefore defined under ISIC – CPC's classification:

- Section: 9 - Community, social and personal services
- Division: 94 - Sewage and waste collection, treatment and disposal and other environmental protection services
- Group: 949 - Other environmental protection services n.e.c.

As the methodology must cover the whole CCS process chain with a modular structure, the product category was defined as a system of technologies that integrates three stages: carbon dioxide (CO_2) capture, transport and storage services. The definition of the three stages was drawn up in order to cover every feasible management option:

- *Capture* is based on capturing carbon dioxide from large point sources, such as large fossil fuel or biomass energy facilities, industries with major CO_2 emissions, natural gas processing, synthetic fuel plants and fossil fuel-based hydrogen production plants, by three different types of technologies: post-combustion, pre-combustion, and oxyfuel;
- *Transport* includes the operation of CO_2 captured transfer to suitable storage sites by high-pressure pipeline networks or by other means;
- *Storage* includes geological storage (gaseous storage in various deep geological formations, including saline formations, oil and gas reservoirs and deep unminable coal seams), mineral storage (solid storage by reaction of CO_2 with metal oxides to produce stable carbonates) and biological storage (e.g. carbon dioxide storage using micro-algal systems).

The storage process involves a series of particular investigation elements. Firstly, it was stated that leakage of stored CO_2 has to be taken into consideration. Moreover, a clear definition of geological storage was necessary [44-46]. It is important to note that this PCR does not apply to afforestation/reforestation process, since considered to be out of the scope, and neither to ocean storage (i.e. liquid storage in the ocean), since the chronic effects of direct CO_2 injection into the ocean on ecosystems over large ocean areas and long time scales have not yet been studied [3].

3.2. Functional unit

In Life Cycle Assessment, the functional unit is defined as the reference unit used to quantify the performance of a product system [35]. In fact, its main purpose is to provide a reference to which the inputs and outputs can be linked. The functional unit is important as a basis for collection, handling and calculation of LCA data, aimed to ensure the possibility to add up information from EPDs in the supply chain and to be able to compare EPDs within a given product category.

As concerns assessments of services, the basic rule is to declare the expected functional outcome of the service provided. End-of-life systems, such as waste treatment systems, usually consider the disposal as function, so that the functional unit is the quantity entering into the treatment system [47, 48]. Nevertheless, in CCS case the function is to capture *in order to store*. The captured quantities that are not stored are out of the system purpose. Therefore the functional unit was defined as the *storage* of 1000 kg (1 ton) of *captured* carbon dioxide (CO_2).

As a corollary, considerations about leakage were included in the rules, according to the current regulatory framework. CO_2 leakage, associated with capturing 1000 kg of carbon dioxide, shall be

modeled for a time period of 20 years since site closure, in accordance with article 18 of EU CCS Directive [44].

3.3. System boundaries

The definition of the system boundaries is a particularly delicate point of investigation as it determines the unit processes to be included in the study and what type of upstream data and downstream data that could be omitted.

The international EPD® system has adopted a LCA procedure which is separated into three different life cycle stages: *upstream module*, *core module* and *downstream module*. This separation is based on a modularity approach; moreover, in this way it is possible to differently perform the LCA-based calculations for the separate LCA stages due to various types of background assumptions, different data availability, different accuracies of the calculated data and different needs for data representativeness and quality.

For EPDs of goods, the core module is usually equal to the manufacturing processes, while as concerns EPDs of services, the "production of the service" is regarded as the core module. In the case of CCS, coherently with the final target of the service and the choice of functional unit, the core module covers CO_2 transport and storage phases. Capture phase is consequently considered to be the necessary upstream process, while leakage represents the downstream phase. The lifecycle boundaries that were defined for CCS are described in Fig. 2.

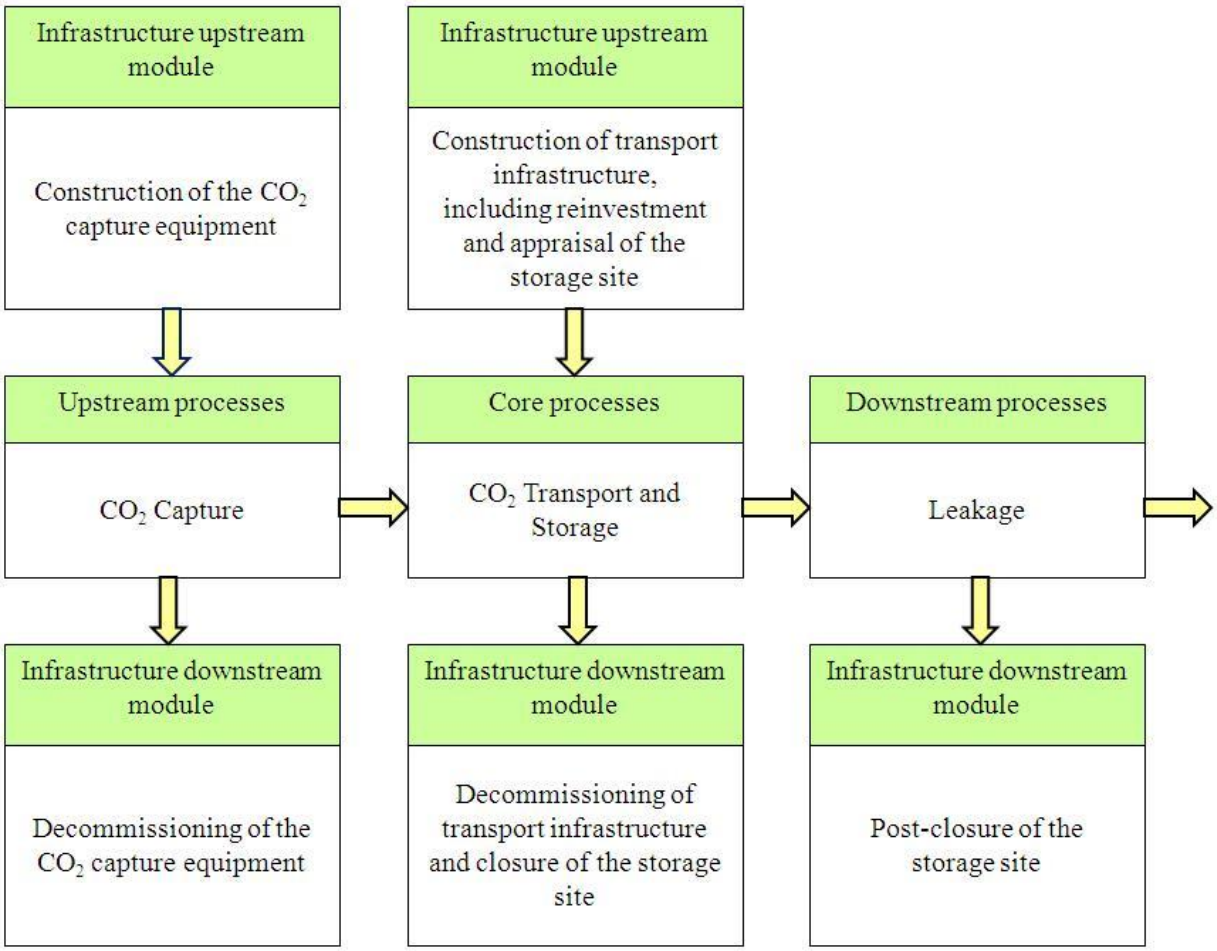

Fig. 2. System boundaries.

3.3.1. Core module

The processes that were considered to be compulsory included as core processes are listed below:

- CO_2 transport through pipelines or mobile transport facilities

- Operation stage (including CO_2 injection, site monitoring, CO_2 reaction with metal oxides)
- Handling/treatment/storage of process-related emissions and waste (including CO_2 leakage during transport and operation stage).

As concerns the infrastructures, the methodological approach opted for only including those facilities that are specifically linked to transport and storage processes. This selection included the following operations:

- Construction of new and dedicated infrastructure such as CO_2 pipelines systems, road, railways or modification of existing infrastructure, such as oil and gas pipeline (including main transports and reinvestment). As mobile transport facilities are often used not only for the purpose of CO_2 transport, the construction of the means of transport might be negligible with respect to resource use during the lifecycle and shall be included only if they are exclusively dedicated to CO_2 transport
- Storage site appraisal (e.g. well drilling and completion)
- Construction of injection station or other facilities such as platforms, etc.
- Dismantling of dedicated transport infrastructure (dedicated CO_2 pipelines, roads, railways) Dismantling of transport facilities shall be included only if they are exclusively dedicated to CO_2 transport
- Site closure (including infrastructure removing, wells plugging and main transports).

Some considerations about boundaries towards risk assessment must be added. Environmental impacts due to accidents and undesired events are not part of the LCA but part of the environmental risk assessment that may be reported under the additional environmental information. Anyway, due to the process technological peculiarities, it has been established that the site selection criteria adopted, including criteria of the risk and safety assessment of the CO_2 storage sites, shall be declared.

3.3.2. Upstream module

After a screening of the currently feasible technological options for carbon capture, the processes that were considered to be compulsory included are listed below:

- CO_2 capture (taking into account CO_2 formation and capture efficiency) by:
  - Post-combustion capture technology (including CO_2 separation from flue gas stream through amine-based solvents, membrane separation, chemical looping and solid adsorption processes)
  - Pre-combustion capture technology (including IGCC - Integrated Gasification Combined Cycle plants, involving the partial oxidation of solid fuel feedstock in a gasifier to produce a mixture of hydrogen and carbon monoxide, then treated in a shift converter and a physical adsorption unit)
  - Oxyfuel (combusting fossil fuels in recycled flue gas enriched with oxygen)
- CO_2 purification/separation
- CO_2 compression to high-pressure supercritical conditions.

The upstream infrastructures that were listed in the selection included specific equipments such as CO_2 absorber, air separator, compressor, etc.

It is important to higlight that plants modifications (e.g. retrofitting of existing plant) and power plants efficiency losses have to be taken into account in the calculations. For combustion technologies based on fossil and renewable fuels and peat equipped with CCS, the related PCR [43] shall be considered.

3.3.2. Downstream module

According to the modular approach undertaken, the following items shall be included in the LCA calculations for downstream processes:

- Site post-closure (including site management, remediation and main transports)
- Data about CO_2 leakage.

As described when discussing the functional unit, CO_2 leakage shall be modelled for a time period of 20 years since site closure, in accordance to EU CCS Directive [44].

3.4. Allocation rules

Allocation is the partitioning of input or output flows of a process or other product systems to the product system under study [35]. Thus, the inputs and outputs shall be allocated to the different products according to clearly stated procedures. As a general rule, allocation between different products and co-products shall be based on physical relationships. If physical relationships cannot be established or used, allocation can be based on other relationships, e.g. economical allocation.

Allocation always implies valuation and the main goal for the allocation choices made for this product category is to keep the allocation methodology rather simple but transparent and maintain comparability between EPDs. Other allocation choices than the mandatory one listed below may be reported and discussed in the EPD under the section of additional environmental information.

In fact the studied system is a multi-output process that delivers CO_2 treatment services (CCS) together with steam, hot water and/or electricity production. The allocation between service and products follows the International EPD® system instructions regarding waste treatment [49]. The burdens of equipment and processes needed to produce heat, process steam or electricity shall be declared in the EPD per kWh of these products, whereas the CO_2 capturing, transport and storage processes shall be allocated to the CO_2 treatment service and be declared per ton of CO_2 captured. This approach is based on the application of the Polluter-Pays (PP) allocation method [50], that separates interlinked product systems at the pointing in the life cycle where they have their lowest market value.

3.5. Environmental performance

The environmental performance-related part of the EPD, representing the LCA-based information, always includes information about the use of resources, energy consumption, polluting emissions from the life cycle inventory work (when relevant) and the resulting potential environmental impacts.

According to the GPI of the International EPD® system [38], the following parameters were identified: use of non-renewable/renewable material and energy resources; water and electricity consumption; potential environmental impacts as global warming, acidification, ozone depletion, photochemical oxidant formation, eutrophication; waste generation, land use and toxic emissions.

In addition to the identified standard parameters, the following specific ones were added:

- LCI emissions of CO_2 captured
- LCI emissions of CO_2 leakage
- Ratio between the CO_2 permanently stored and the CO_2 emitted from the considered source.

In this way the methodology permits the direct monitoring of capture and storage activities in terms of inventory data, and the direct measuring of the yield of the entire process.

Moreover, further information that is not part of the LCA but identified as an important environmental aspect of the product or information asked for by customers and other stakeholders, were identified to be declared. The following issues (if pertinent) shall be addressed:

- Soil pollutions
- Acidification
- Impacts on biodiversity: direct regional impacts concerning nature conservation issues like biodiversity and visual impact connected to land use

- Risk and safety assessment: assessment of the risks and safety of the development and operation of the full CCS chain (including impacts of any CO_2 seepage, e.g. CO_2 infiltration into other resources or leakage to surface; any secondary impacts of CO_2 storage, e.g. brine migration, etc.).

As concerns the verification procedure of these integrations, any literature reference or methodology used to acquire and describe additional environmental information shall be openly accessible and made available to the verifier.

4. Conclusions

Because of the significant emission reductions CCS can achieve, it is considered a key option within the portfolio of approaches required to reduce emissions. Today, there is a growing demand for science-based, verified and comparable information about the environmental performance of these systems. Despite the rather challenging task to describe such complex, emerging processes in the environment, LCA represents an effective and objective evaluation tool that enables its use in communication on a wide international scale.

In order to meet this demand, a type III environmental declaration such as EPD is able to add up LCA-based information in the supply chain and allow the comparison between different declaration within the same service group. To achieve this goal, common and harmonized calculation rules have to be established to ensure that similar procedures are used when assessing CCS systems. Outlining a profile of the environmental performances of the service, including objective, comparable and credible data, entails a particularly rigorous definition of an appropriate methodology.

Here we have identified and discussed a set of key issues that are fundamental in the development of a robust methodological framework, i.e. Product Category Rules (PCR), for the application of LCA to CCS and the reporting of the results. Firstly it has been highlighted that the service must be considered as end-of-life process, allowing its integration to every feasible CO_2 generation source. Consequently, the definition of functional unit shall be coherent with objective of the overall system. The quantification of the results on a CO_2 basis permits to give indication on the specific output of CCS, allowing users to draw a direct connection between the environmental impacts and the emission reductions. Besides, the selection of the system boundaries has been analyzed, with the aim of including the whole technological spectrum that may be involved in such differentiated processes. The importance of considering CO_2 leakage has been strengthened. Moreover, allocation choices have been discussed, stressing the adherence with Polluter-Pays (PP) method and addressing the impacts of electricity generation to its specific set of rules. Finally, a set of suitable and clearly significant environmental indicators have been selected in order to give specific useful information to users when reporting the environmental performance of the system. No value-based judgements are included, as it is up to the users to make their evaluation of the environmental performance based on the information that are made available.

The dissemination of the LCA-based information compiled through such a strict methodology may allow organizations to communicate the environmental performance of any CCS systems to a diverse group of audiences, being both related to business-to-business (B2B), business-to-public authorities (B2P) and business-to-consumers (B2C).

References

[1] Solomon S., Qin D., Manning M., Chen Z., Marquis M., Averyt K.B., Tignor M., Miller H.L., Climate Change 2007: The Physical Science Basis. Contribution of Working Group I to the Fourth Assessment Report of the Intergovernmental Panel on Climate Change. Cambridge, UK and New York, NY, USA: Cambridge University Press; 2007.

[2] International Energy Agency (IEA), CO_2 emissions from fuel combustion highlights (2011 Edition). Paris, France: OECD/IEA; 2011.

[3] Metz B., Davidson O., de Coninck H.C., Loos M, Meyer L.A., IPCC special report on carbon dioxide capture and storage, prepared by Working Group III of the Intergovernmental Panel on Climate Change. Cambridge, UK and New York, NY, USA: Cambridge University Press; 2005.

[4] Global CCS Institute, The global status of CCS. Canberra, Australia; 2011.

[5] International Energy Agency (IEA), Energy Technology Perspectives 2010, Part 1: Technology and the global energy economy to 2050. Paris, France: OECD/IEA; 2010.

[6] International Energy Agency (IEA), Energy Technology Perspectives 2010, Part 2: The transition from present to 2050. Paris, France: OECD/IEA; 2010.

[7] International Energy Agency (IEA), CCS Model Regulatory Framework. Paris, France: OECD/IEA; 2010.

[8] Koornneef J., Ramírez A., Turkenburg W., Faaij A., The environmental impact and risk assessment of CO_2 capture, transport and storage - An evaluation of the knowledge base. Prog Energ Combust 2012;38:62-86.

[9] Marx J., Schreiber A., Zapp P., Haines M., Hake J.-Fr., Gale J., Environmental evaluation of CCS using life cycle assessment - a synthesis report. Energy Procedia 2011;4:2448-56.

[10] Doctor R.D., Molburg J.C., Brockmeier N.F., Lynn M., Victor G., Massood R., Life-Cycle Analysis of a Shell Gasification-Based Multi- Product System with CO_2 Recovery. In: Proceedings of the First National Conference on Carbon Sequestration; Washington, D.C., USA; 2001.

[11] Rao A.B., Rubin E.S., A technical, economic, and environmental assessment of amine-based CO_2 capture technology for power plant greenhouse gas control. Environ Sci Technol 2002,36: 4467-75.

[12] Benetto E., Popovici E.C., Rousseaux P., Blondin J., Life cycle assessment of fossil CO_2 emissions reduction scenarios in coal-biomass based electricity production. Energy Convers Manage 2004;45:3053-74.

[13] Korre A., Nie Z., Durucan S., Life cycle modelling of fossil fuel power generation with post combustion. Energy Procedia 2009;1:3771-8.

[14] Lombardi L., Life cycle assessment comparison of technical solutions for CO_2 emissions reduction in power generation. Energy Convers Manage 2003;44:93-108.

[15] International Energy Agency (IEA), Environmental Impact of Solvent Scrubbing of CO_2. Stoke Orchard, UK: IEA Greenhouse Gas R&D Programme (IEAGHG); 2006 Oct. Technical Report No.:2006/14.

[16] Odeh N.A., Cockerill T.T., Life cycle GHG assessment of fossil fuel power plants with carbon capture and storage. Energy Policy 2008;36(1):367-80.

[17] Aycaguer A.C., Lev-On M., Winer A.M., Reducing carbon dioxide emissions with enhanced oil recovery projects: A life cycle assessment approach. Energy Fuels 2001;15:303-8.

[18] Suebsiri J., Wilson M., Tontiwachwuthikul P., Life-cycle analysis of CO_2 EOR on EOR and geological storage through economic optimization and sensitivity analysis using the weyburn unit as a case study. Ind Eng Chem Res 2006;45:2483-8.

[19] Spath P., Mann M., Biomass power and conventional fossil systems with and without CO_2 sequestration comparing the energy balance, greenhouse gas emissions and economics. Golden, Colorado (USA): National Renewable Energy Laboratory. 2004, Jan. Report No.: BB04.4010.

[20] Khoo H.H., Tan R.B.H., Life cycle investigation of CO_2 recovery and sequestration. Environ Sci Technol 2006;40:4016-24.

[21] Khoo H.H., Tan, R.B.H., Environmental impact evaluation of conventional fossil fuel production (oil and natural gas) and enhanced resource recovery with potential CO_2 sequestration. Energy Fuels 2006;20:1914-24.

[22] Hertwich E.G., Aaberg M., Singh B., Strømman A.H., Life-cycle Assessment of Carbon Dioxide Capture for Enhanced Oil Recovery. Chinese J Chem Eng 2008;16(3):343-53.

[23] Koornneef J., van Keulen T., Faaij A., Turkenburg W., Life cycle assessment of a pulverized coal power plant with post-combustion capture, transport and storage of CO_2. Int J Greenhouse Gas Control 2008;2(4):448-67.

[24] Schreiber A., Zapp P., Kuckshinrichs W., Environmental Assessment of German Electricity Production from Coal-fired Power Plants with Amine-based Carbon Capture. Int. J Life Cycle Assessment 2009;14:547-59.

[25] Modahl I.S., Nyland C.A., Raadal H.L., Kårstad O., Torp T.A., Hagemann R., Life cycle assessment of gas power with CCS - a study showing the environmental benefits of system integration. Energy Procedia 2011;4:2470-7.

[26] Waku H., Tamura I., Inoue M., Akai M., Life cycle analysis of fossil power plant with CO_2 recovery and sequestering system, Energy Convers Manage 1995;36:877-80.

[27] Viebahn P., Nitsch J., Fischedick M., Esken A., Schuwer D., Nikolaus S., Zuberbuhler U., Edenhofer O., Comparison of carbon capture and storage with renewable energy technologies regarding structural, economic, and ecological aspects. Int J Greenhouse Gas Control 2007;1: 121-33.

[28] Bouvart F., Prieur A., Comparison of Life Cycle GHG Emissions and Energy Consumption of combined Electricity and H_2 production pathways with CCS : Selection of technologies with Natural Gas, Coal and Lignite as fuel for the European HYPOGEN Programme. Energy Procedia 2009;1:3779-86.

[29] Pehnt M., Henkel J., Life cycle assessment of carbon dioxide capture and storage from lignite power plants. Int J Greenhouse Gas Control 2009;3(1):49-66.

[30] Nie Z., Korre A., Durucan S., Life cycle modelling and comparative assessment of the environmental impacts of oxy-fuel and post-combustion CO_2 capture, transport and injection processes. Energy Procedia 2011;4:2510-7.

[31] Singh B., Strømman A.H., Hertwich E.G., Comparative life cycle environmental assessment of CCS technologies. Int J Greenhouse Gas Control 2011;5.911-21.

[32] Nagashima S., Miyagawa T., Matsumoto M., Suzuki S., Komaki H., Takagi M., Murai S., Life Cycle Assessment Performed on a CCS Model Case in Japan and Evaluation of Improvement Facilitated by Heat Integration. Energy Procedia 2011;4:2457-64.

[33] Sathre R., Chester M., Cain J., Masanet E., A framework for environmental assessment of CO_2 capture and storage systems. Energy 2012;37:540-8.

[34] International Organization for Standardization (ISO), Environmental labels and declarations, Type III environmental declarations, Principles and procedures. European Standard ISO 14025.

[35] International Organization for Standardization (ISO), Environmental management, life cycle assessment. European Standard ISO14040; 2006.

[36] Commission of the European Communities, Integrated Product Policy Building on Environmental Life-Cycle Thinking. Brussels, Belgium: Communication from the Commission to the Council and the European Parliament; 2003 Jun. No.: COM(2003) 302 final.

[37] European Commission – Environment – ETAP Environmental Technologies Action Plan – Available at:http://ec.europa.eu/environment/etap/ [accessed 26.1.2012].

[38] The International EPD Cooperation (IEC). General Programme Instructions for Environmental Product Declarations, EPD. - Available at: <http://www.environdec.com/documents/pdf/EPD_instructions_080229.pdf> [accessed 26.4.2008].

[39] The International EPD Cooperation (IEC). Introduction, Intended Uses and Key Programme Elements for Environmental Product Declarations, EPD. - Available at:

<http://www.environdec.com/documents/pdf/EPD_introduction_ 080229. pdf> [accessed 26.4.2008].

[40] Grahl B., Schmincke E., The part of LCA in ISO type III environmental declarations. Int J Life Cycle Assessment 2007;Spec Issue12(1):38-45.

[41] Fet A.M., Skaar C., Eco-labeling, product category rules and certification procedures based on ISO 14025 requirements. Int J Life Cycle Assessment 2006;11(1):49-54.

[42] United Nations Statistic Division. - Available at: <http://unstats.un.org/unsd/default.htm> [accessed 26.11.2011].

[43] The International EPD® system. Product Category Rules CPC 171 Electrical energy and CPC 173 Steam and hot water. PCR 2007:08. Version 2.01. - Available at: http://www.environdec.com/en/Product-Category-Rules/Detail/?Pcr=5802[accessed 26.1.2012].

[44] EUROPA- the official web site of the European Union. Official Journal of the European Union. Directive 2009/31/EC of the European Parliament and of the Council of 23 April 2009 on the geological storage of carbon dioxide. – Available at: http://eur-lex.europa.eu/LexUriServ/LexUriServ.do?uri=OJ:L:2009:140:0114:0135:EN:PDF [accessed 26.1.2012].

[45] Authenticated U.S. Government Information GPO. Environmental Protection Agency. Federal Requirements under the Underground Injection Control (UIC) Program for Carbon Dioxide (CO_2) Geologic Sequestration (GS) Wells, Final Rule, 75 Fed. Reg. 77230. Dec. 10, 2010. – Available at: <http://www.gpo.gov/fdsys/pkg/FR-2010-12-10/pdf/2010-29954.pdf> [accessed 26.1.2012].

[46] Authenticated U.S. Government Information GPO. Environmental Protection Agency, Mandatory Reporting of Greenhouse Gases: Injection and Geologic Sequestration of Carbon Dioxide, Final Rule, 75 Fed. Reg. 75060 Dec. 1, 2010. – Available at: <http://www.gpo.gov/fdsys/pkg/FR-2010-12-01/pdf/2010-29934.pdf> [accessed 26.1.2012].

[47] Del Borghi A., Analisi Del Ciclo Di Vita Applicata ai Rifiuti: uno Strumento per la Progettazione Ecosostenibile. Milano, Italy: Quaderno di Ingegneria Ambientale n°37. C.I.P.A. S.r.l. Editore; 2003.

[48] Del Borghi A., Gallo M., Del Borghi M., A survey of life-cycle thinking integrated into waste management. Int. J Life Cycle Assessment 2009;14(7):597-610.

[49] The International EPD Cooperation (IEC). Supporting Annexes for Environmental Product Declarations, EPD. - Available at: <http://www.environdec.com/documents/pdf/EPD_annexes_080229.pdf> [accessed 26.4.2008].

[50] Organisation for Economic Co-Operation and Development (OECD). Recommendation of the Council on Guiding Principles concerning International Economic Aspects of Environmental Policies. Recommendation C(72)128. Adopted May 26, 1972. - Available at: < http://acts.oecd.org/Instruments/ShowInstrumentView.aspx?InstrumentID=4&InstrumentPID=255&Lang=en&Book=False> [accessed 26.4.2008].

Electricity production from renewable and non-renewable energy sources: a comparison of environmental, economic and social sustainability indicators with exergy losses throughout the supply chain

Lydia Stougie[a], Hedzer van der Kooi[b] and Rob Stikkelman[c]

[a] Delft University of Technology, Delft, The Netherlands, l.stougie@tudelft.nl,
[b] Delft University of Technology, Delft, The Netherlands, jvdkooi@casema.nl,
[c] Delft University of Technology, Delft, The Netherlands, r.m.stikkelman@tudelft.nl

Abstract:

The worldwide demand for electricity is growing and attempts are being made to make the production of electricity more sustainable. It is difficult to determine which energy supply option is preferred when all three aspects of sustainability, i.e. the environmental, economic and social aspects, are taken into account. According to literature a relation exists between sustainability and exergy. Exergy is a measure of the quality of energy and equals the amount of work that can be obtained from an amount of energy.
This research investigates whether exergy analysis can be helpful in choosing between different energy supply options. The case study presented here comprises the following renewable and non-renewable energy sources for the production of electricity in the Netherlands: co-firing of wood pellets originating from Georgia (USA) in the 'Amercentrale' power plant located in Geertruidenberg, a wind farm based upon the plan to build 86 windmills in the 'Noordoostpolder' area, and the production of bioethanol, fibres and proteins from grass by fermentation, followed by combustion of this bioethanol in a combined-cycle power plant.
The method called Cumulative Exergy Loss (CExL) is introduced to determine the exergetic sustainability of the exergy supply options. This method comprises the calculation of the internal exergy losses, the exergy losses accompanied with the abatement of the process emissions to an acceptable level, and the exergy losses related to the land occupied by the installations. From the comparison of the CExL with the results of the environmental, economic and social sustainability assessments it is concluded that CExL could be an indicator that helps in achieving a more sustainable society via selecting preferred energy supply options. On the basis of the indicative results of the analyses it is concluded that the wind farm option is preferred, except for the economic indicator called present worth ratio.

Keywords:

Electricity Production; Environmental, Economic and Social Sustainability; Exergy; Renewable Energy.

1. Introduction

Electricity plays a major role in our society. The increase in the use of consumer electronics like mobile phones, tablet computers, televisions, electric vehicles and other electricity powered devices results in a growing demand for electricity. At the same time, it is unclear which technology and feedstock for power generation are the most sustainable. When striving for sustainability, the environmental as well as the economic and social aspects of sustainability should be taken into account [1]. According to literature, e.g. [2], a relation exists between sustainability and exergy, but a careful underpinning of this relation has not yet been found [3]. Exergy is a measure of the quality of energy and equals the maximum amount of work that can be obtained from an amount of energy. In literature many methods of exergy analysis are described, like Cumulative Exergy Consumption [4], Exergetic Life Cycle Analysis [5], Life Cycle Exergy Analysis [6], Extended Exergy Accounting [7], Exergoenvironmental analysis [8], but until now no method has been found that fully takes into account the three aforementioned aspects of sustainability. Particularly the social

aspect of sustainability is not, or just minimally, taken into account in these methods. This research considers all three aspects of sustainability.

The case study presented in this paper is part of a larger research project about the potential benefits of exergy analysis in achieving a more sustainable society. It is investigated how the environmental, economic and social sustainability of an energy supply system are influenced by involving exergy analysis in the choice between possible energy supply options. The three energy supply options compared in this case study are the following: co-firing of wood pellets originating from Georgia (USA) in the 'Amercentrale' power plant located in Geertruidenberg, The Netherlands, a wind farm based upon the plan to build 86 windmills in the Dutch 'Noordoostpolder' area, and finally the production of bioethanol, fibres and proteins from verge grass by fermentation, followed by combustion of the bioethanol in a combined cycle power plant, located in the Netherlands as well.

In a previous paper [9], a case study was presented in which three options for LNG evaporation were compared by comparing the results of environmental life cycle assessment (E-LCA), life cycle costing (LCC) and social life cycle assessment (S-LCA) with the results of applying the exergetic type of LCA called Cumulative Exergy Extraction from the Natural Environment (CEENE [10]). During the current research a tailor-made extended exergy analysis method called Cumulative Exergy Loss (CExL) is applied. This method comprises the calculation of the internal exergy losses, the exergy losses accompanied with the abatement of the process emissions to an acceptable level, and the exergy losses related to the surface area needed for the installations (in short: 'land use' or 'land occupation').

2. Research approach

The influence of involving exergy analysis on the sustainability of an energy supply system is investigated by conducting a number of case studies. Each case study comprises several possibilities for fulfilling the demand for energy carriers, called options, that can be compared. This paper presents the results of the case study in which electricity production from renewable and non-renewable energy sources is considered.

On the basis of the results of the assessments it can be concluded which option is preferred from an environmental point of view, which option is preferred from an economic point of view, etcetera. It can also be concluded what the consequences are for the environmental, economic and social sustainability of the case study when the option is chosen that is preferred from an exergetic point of view. Sections 2.1 and 2.2 describe the four methods of assessment that have been applied.

2.1. Determining the environmental, economic and social sustainability

2.1.1. Environmental sustainability

The Endpoint indicator approach of ReCiPe [11] has been chosen to analyse the environmental sustainability (E-LCA). This has been done because ReCiPe is the result of a thorough cooperation between experts in the field of LCA, it is the most recent development in this field and it offers the possibility to express the environmental sustainability as one number. The software tool SimaPro [12] in combination with the Ecoinvent database [13] has been used to calculate the ReCiPe Endpoint indicators.

2.1.2. Economic sustainability

Several methods for calculating the life cycle costs exist [14]. The method that is recommended by [14] is the calculation of the steady state costs (SSC), also called average yearly costs (AYC), because this method is in accordance with the steady-state nature of life cycle assessments. The SSC can be calculated from the costs in year t (C_t) and the functional number of years of the system (fn) by applying (1):

$$SSC = AYC = \frac{\sum_{t=1}^{t=n} C_t}{fn}. \qquad (1)$$

In addition to the SSC also the Net Present Value (NPV) is calculated because it is well-known and has already been used in assessing the sustainability of energy systems [15]. The NPV is calculated from the net cash flow in year t (C_t) and the discount rate r (2):

$$NPV = \sum_{t=0}^{t=n} \frac{C_t}{(1+r)^t} \qquad (2)$$

The NPV can be used to calculate the Present Worth Ratio (PWR). This PWR is equal to the NPV divided by the investment costs, and can be used to compare options. The higher the PWR is, the more likely the investment will be.

2.1.3. Social sustainability

A standard method of social life cycle assessment (S-LCA) is under development [16-17]. One of the difficulties in determining the social sustainability is the type (qualitative, semi-quantitative or quantitative) and availability of data [18]. It would be too time-consuming and costly to gather site-specific social data, therefore it was decided to take into account the social aspect of sustainability by means of the Inequality-adjusted Human Development Index (IHDI) as reported by [19]. The Human Development Index (HDI), which was launched in 1990, is based upon the average achievements in a country in the fields of 'a long and healthy life', 'access to knowledge' and 'a decent standard of living'. The IHDI has been developed by the UNDP to correct for inequalities in human development across the population of a country. The method to calculate the overall IHDI of a supply chain was introduced by [9]. The method starts with determining the number of man-hours of the different stages of the production chains (e.g. exploration, conversion, transport) and dividing these man-hours between the countries the employees originate from. This is followed by aggregating the number of man-hours per country over the whole production chain. Finally, the overall IHDI ($IHDI_{overall}$) can be calculated by summing the products of the percentage of man-hours per country ($perc.man.hrs_i$) and the IHDI of that country ($IHDI_i$) over all countries (3):

$$IHDI_{overall} = \frac{\sum_{i=1}^{i=n} (perc.man.hrs_i \cdot IHDI_i)}{100} \qquad (3)$$

2.2. Designing the method of exergy analysis

In literature no exergy analysis method has been found that takes into account all relevant aspects of the life cycle of a process or product. E.g. the CExC method [4] does not take into account land use, the CEENE method [10] disregards the emissions caused by a process and the ELCA method [5] neglects the environmental impact due to land use, and so on. Therefore it was decided to design a tailor-made method of exergy analysis that takes into account all relevant aspects. This exergy analysis method is called Cumulative Exergy Loss (CExL) and comprises the calculation of the internal exergy losses throughout the supply chain, the exergy losses accompanied with the abatement of emissions to an acceptable level, and the exergy losses related to the land occupied by the installations.

2.2.1. CExL: Internal exergy loss and abatement exergy

The internal exergy loss, also called exergy destruction [20], is equal to the amount of exergy entering the system under consideration minus the amount of exergy exiting this system. This internal exergy loss cannot be made visible through energy analysis and is a consequence of the irreversibility of all processes in real life. The exiting flows of a system consist of a product and

usually one or more waste flows and emissions, in short 'emissions'. These emissions can cause environmental effects because of the work potential they represent. The external exergy loss caused by `throwing away' emissions is no measure of their environmental impact, e.g. their toxicity. Instead of taking into account the external exergy loss it was decided to assess the emissions by considering the exergy losses accompanied with the abatement of the emissions until the effects of these emissions on the environment are negligible, the so-called abatement exergy. This abatement exergy is added to the internal exergy loss. Summing the internal exergy losses throughout the supply chain and the abatement exergy is comparable with the extension of system boundaries of the supply chain to include these abatement technologies as well. This summation differs from the Cumulative Exergy Consumption for Construction and Abatement (CExCA) [21] in that here the internal exergy loss is taken into account while the CExCA considers the CExC.

The distinction between the use of renewable and non-renewable resources can be made via the exergy loss caused by abatement of emissions. CO_2 and other emissions that originate from renewable resources are not regarded as a problem because these are short-cycle emissions. The abatement of emissions originating from renewable resources is not taken into account.

2.2.2. CExL: Land use

Another aspect of the tailor-made exergy analyis is that the role of ecosystem goods and services (in short: ecosystem services) is taken into account. Examples of ecosystem goods and services are fossil and biomass fuels, water purification, pollination and photosynthesis [22]. The role of ecosystem services is taken into account by considering the amount of solar exergy that becomes unavailable to the ecosystem because of land occupied by the installations of the supply chain. When this land is not occupied by installations, the ecosystem can capture the solar energy radiated on the land via photosynthesis, therefore in analogy with [10] the exergy loss through land occupation is calculated from the average solar irradiation (IRR_{solar}) on the area, the exergy/energy factor of 0.9327 of solar irradiation and the efficiency of converting solar energy into biomass ($\eta_{photosynthesis}$) as follows (4):

$$Ex_{loss,land\cdot use} = IRR_{solar} \cdot 0.9327 \cdot \eta_{photosynthesis} \quad (4)$$

with IRR_{solar} = average solar irradiation [GJ/(ha.a)]

3. Brief description of the compared options

3.1. Co-firing of coal and wood pellets

The Co-firing option is depicted in Fig. 1. This option is based upon the current situation in the Netherlands, i.e. the 'Amercentrale' power plant located in Geertruidenberg [23], The Netherlands. This power plant has a capacity of 1,245 MW_e and 600 MW_{th}. The power plant co-fires about 30 mass percent biofuels and adaptations are being made to increase this number to 50 mass percent in 2015 and even further. Apart from wood pellets from the Georgia Biomass plant [24] in Waycross, Georgia (USA), which is the main source of biomass, also other sources of biomass like biocoal are co-fired in the Amercentrale power plant. In this case study it is assumed that all biomass consists of wood pellets originating from the Georgia Biomass plant. The Georgia Biomass plant has an annual capacity of approximately 750,000 tons of wood pellets and was commissioned by the owner of the Amercentrale power plant because of the limited availability of biofuels in Europe.

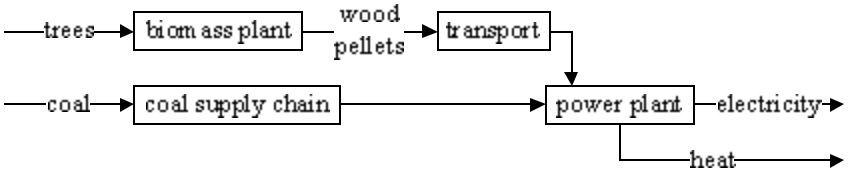

Fig. 1. Co-firing of coal and wood pellets (Co-firing option).

3.2. Wind farm

The wind farm option is based upon the plans to realise a wind farm in the 'Noordoostpolder' area in the Netherlands [25,26]. The wind farm is planned to be operational in 2014 and is expected to produce about 1.4 billion kWh of electricity a year. The planned wind farm consists of 38 onshore wind turbines with a capacity of 7.5 MW (type Enercon E126) and 48 offshore wind turbines with a capacity of 3 or 3.6 MW (type Siemens SWT3.0 or Siemens SWT3.6). In this study it is assumed that the offshore wind turbines are of type SWT3.6.

3.3. Combustion of bioethanol from verge grass

The third option (Fig. 2) is based upon the research conducted by De Vries [27]. In this option verge grass is fermented into bioethanol (96 mass percent in water) with fibres and proteins as by-products, followed by combustion of the bioethanol in a combined-cycle power plant. The capacity of this power plant is about 30 MW.

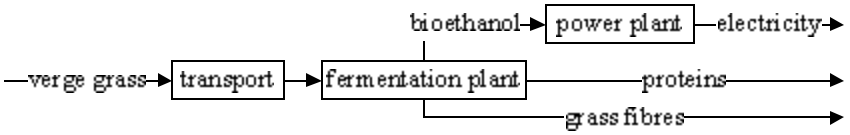

Fig. 2. Combustion of bioethanol from verge grass (Bioethanol option).

4. Analysis

4.1. Functional unit, allocation and system boundaries

The functional unit used in the life cycle assessment has been set at the production of a net amount of 1 PJ of electricity. Reasons for choosing 1 PJ of electricity are that electricity is the main product of the three options, all three options can produce this amount of electricity and because it is a practical unit to use when comparing with other options in the future. In case of production of by-products, like heat in the Co-firing option and grass fibres and proteins in the bioethanol option, only the inputs and emissions of the process or processes have been taken into account that were allocated to the main product electricity. This allocation was done on an exergy basis, i.e. the inputs and emissions were multiplied by the amount of exergy represented by the main product over the total amount of exergy of all products.

The analysis includes the extraction, processing and transport of coal, the growing and thinning of trees till wood pellets arrived in the Netherlands, the mowing and transport of verge grass and so on, like schematically shown in Figs 1 and 2.

The ashes resulting from the Amercentrale power plant are regarded as by-products without an economic value. The use of river water for cooling purposes and all other auxiliary substances not mentioned in this paper have not been taken into account, because it is assumed that the effects thereof are negligible compared to the other effects.

The E-LCA has been carried out with and without the construction of the installations and their disposal. According to [28] it takes only a few months for a modern power plant to produce enough electricity to compensate for the exergy used for its construction, maintenance and disposal. Furthermore only 5 to 10 per cent of the cumulative exergy consumption of a product chain is caused by the production of machines and installations [4]. Therefore the construction of the installations has been neglected in the social and exergetic assessment. The same holds for the costs of disposal of the installations in the economic, social and exergetic assessments.

The investment costs of the installations and the amount of land that is occupied by these installations have been calculated in accordance with the method applied in E-LCA, which means that only a fraction of the investment costs and land occupied is taken into account. This fraction is equal to the amount of product related to the functional unit divided by the total production of that

installation or piece of land during the assumed lifetime. The costs of carbon dioxide emissions of fossil origin have not been taken into account.

4.2. Data

This research is based upon a large number of data from various data sources, completed with additional calculations and educated guesses by the authors. When possible the data and estimates have been checked with other data sources. It is impossible to present all data in this publication, therefore only the most important data are presented in the following subsections.

4.2.1. Environmental sustainability

The Co-firing option was modelled on the basis of data about the Amercentrale [29-34], the Georgia Biomass plant [23,35,36] and several unit processes from the Ecoinvent database v2.2 [13]. The coal consumption was modelled by selecting the Ecoinvent unit process 'Hard coal supply mix/NL'. One cubic meter of wood used for producing pellets in Georgia (in short: Georgia wood) was assumed to consist of the following Ecoinvent unit processes: 0.65 m^3 of 'Round wood, softwood, under bark, u=70% at forest road/RER', 0.235 m^3 of 'Industrial wood, softwood, under bark, u=140%, at forest road/RER' and 0.115 m^3 of 'Residual wood, softwood, under bark, u=140%, at forest road/RER'. The production of wood pellets from wood was based upon the unit process 'Wood pellets, u=10%, at storehouse/RER' and the Ecoinvent processes that connect this process with the aforementioned 'Georgia wood'. As much as possible the unit processes have been adapted to the situation in the USA, e.g. the transport distances and ways of transport.

The wind turbines are modifications of the largest onshore and offshore wind turbines modelled in the Ecoinvent database, i.e. 'Electricity, at wind power plant 800kW/RER U' and 'Electricity, at wind power plant 2MW, offshore/OCE U'. The capacity and size of the turbines was adapted on the basis of several information sources [37-41]. It is assumed that the material composition of the moving and fixed parts of the wind turbines is the same as in the Ecoinvent unit processes. The capacity factor of the wind turbines was assumed to be 0.45 on average, based upon an average wind speed of 8.3 to 8.7 m/s [37,38,41].

The fermentation plant of the bioethanol option is based upon the Ecoinvent unit process 'Ethanol, 95% in H_2O, from grass, at fermentation plant/CH' in which verge grass instead of grass from meadows is used as a feedstock. The data for modelling the combined cycle power plant originate from [27].

Table 1 presents an overview of the main inputs and outputs of the three options.

Table 1. Overview of the main inputs and outputs of the three options (indicative numbers). The inputs and outputs of the Co-firing and Bioethanol options are the amounts allocated to electricity.

Per year	Co-firing	Wind	Bioethanol
INPUTS			
Coal [Mton]	0.11		
Wood [Mton]	0.049		
Wind [PJ]		2.4	
Verge grass [Mton]			0.49
OUTPUTS			
Electricity [PJ]	1	1	1
Flue gases			
CO_2 fossil [Mton]	0.16	0	0.029
CO_2 biogenic [Mton]	0.042	0	0.17
NO_x [kton]	0.32	0	0.30
SO_2 [kton]	0.19	0	0.0023
Ashes [kton]	15	0	0

The inputs and outputs of the Co-firing and Bioethanol options have been allocated to the amount of electricity produced. The overall Co-firing option delivers 0.17 PJ of heat by-product per PJ of electricity. The overall bioethanol option results in 0.14 Mton of grass fibres and 0.17 Mton of proteins per PJ of electricity.

4.2.2. Economic sustainability

The investment costs of the wood pellet and coal power plants are calculated at 137 Million euro [24] and 1100 Million euro [42] respectively. The investment costs of the Wind turbines are 1 Billion euro [25] and the investment costs of the fermentation and power plant of the Bioethanol option amount to 80 Million euro [27].

The lifetime of the three options (fn) is assumed to be 20 years and the discount rate (r) was specified at 10 per cent. It was assumed that it takes 3 years to build the installations and that the operation and management costs are about 4 per cent of the investment costs. The cost price of coal is assumed at 2.65 euro/GJ [43] and the costs of the trees originate from the feedstock costs of the wood pellet plant [24]. The disposal of verge grass costs about 20 euro per ton [44], therefore the costs of fuels/feedstocks in the bioethanol option is a negative number. It was assumed that 75% of the disposal costs, i.e. 15 euro per ton of verge grass, is received in the Bioethanol option. Table 2 presents an overview of the investment costs allocated to 1 PJ of electricity, the operation and management costs and the costs and revenues of fuels, feedstocks and products.

Table 2. Overview of the economic data of the three options (indicative numbers). The investment costs are allocated to the production of 1 PJ of electricity.

Per year	Co-firing	Wind	Bioethanol
Investment costs [M€]			
Wood pellet plant	0.34		
Coal power plant	2.0		
Wind turbines		9.9	
Fermentation & power plant			4.6
Total investment costs	2.3	9.9	4.6
O&M costs [M€/year]	0.095	0.40	0.23
Costs of fuels/feedstocks [M€/year]	6.8		-7.4
Revenues of electricity [M€/year]	17	17	17

4.2.3. Social sustainability

The man-hours per stage of the co-firing production chain (Table 3) were calculated on the basis of many references [24,45-49], completed with estimates by the authors. The man-hours needed for loading/unloading and storage of coal have been neglected. The man-hours of the wind and bioethanol options have not been calculated because the supply chains of these options are located in the Netherlands, which means that the IHDI of the Netherlands is applicable in both options. The man-hours spent abroad for activities related to the construction, e.g. exploring, processing and transport of materials, and disposal of the installations have not been considered.

Table 3. Overview of man-hours in the production chain of the Co-firing option (indicative numbers).

Man-hours/Mton	Coal	Wood pellets
Exploration/processing	$2 \cdot 10^2$	
Wood pellet plant		$2 \cdot 10^2$
Deep sea transport	$1 \cdot 10^2$	$3 \cdot 10^2$
Coal power plant	$1 \cdot 10^1$	

4.2.4. Exergetic sustainability

As explained in Section 2.2, the exergetic sustainability assessment consists of the calculation of the internal exergy losses throughout the supply chain, the exergy losses accompanied with abatement of emissions and the exergy losses related to land use. The calculation of the exergy losses is based upon the mass and energy flows resulting from the environmental assessment. These data have been used to compose an overall process with the feedstocks of the supply chain and energy carriers needed throughout the supply chain for transport, mowing of grass etcetera as inputs and the main product of the supply chain and the emissions related to combustion of the intermediate energy carriers as outputs. In the exergy calculations it was assumed that all coal needed in the Co-firing option originates from South Africa. The production of the intermediate energy carriers from primary energy sources has been neglected in the exergetic assessment. The same holds for the construction and disposal of the installations (Section 4.1).

In this paper abatement exergy vales from literature [5,50,51] as presented in Table 4 have been applied. During future research, abatement exergy values based upon the newest abatement technologies will be calculated as well as abatement exergy values of other emissions.

Table 4. Overview of the abatement exergy of some emissions [5,50,51].

Emission	CO_2	SO_2	NO_x
Abatement exergy [MJ/kg]	5.86	57	16

In calculating the exergy loss caused by land use, not yet a distinction has been made between the locations of the installations. In analogy with [10] the average solar irradiation in Western Europa has been applied, which is about 2.78 kWh/m^2·day [52].

According to [53] the exergy efficiency of the photosynthesis process itself equals 41% at a 680 to 700 nm wavelength of the photons, but the average overall efficiency of the capturing of solar energy by plants during a year is much lower. This efficiency strongly depends on the amount of solar radiation, its wavelength and the temperature on earth. In the CEENE method [10] the amount of exergy withdrawn from the ecosystem by 1 year of land use is assumed to be 2% of the average solar irradiation on that area. According to [54-56] the maximum efficiency during a short time can be 5%, but on average a value between 0.5 and 1 percent is more realistic. It was therefore decided to assume that the efficiency of capturing solar energy via photosynthesis equals 0.75%.

This results (4) in an exergy loss due to land use of 256 GJ exergy/ha·year.

5. Results

5.1. Environmental sustainability

The software tool SimaPro version 7.2.4 [12] has been used to calculate the ReCiPe endpoint indicators (Section 2.1.1) by applying ReCiPe's default endpoint method and normalisation/weighting set, i.e. 'ReCiPe Endpoint (H) V1.04' and 'Europe ReCiPe H/A'. The 'Hierarchist' (H) perspective is a consensus model between the two other perspectives called 'Individualist' (I) and 'Egalitarian' (E), and was selected because there was no reason to deviate from the default method. The 'Europe ReCiPe H/A' refers to the normalisation values of Europe with the average weighting set and was chosen because it is recommended by the developers of SimaPro. The results of the environmental assessment are presented in Table 5. This table presents the ReCiPe scores with and without the infrastructure processes, i.e. with and without considering the construction and disposal of plants, machinery etc.

Table 5. ReCiPe scores of the three options including and excluding infrastructure (indicative numbers) with the scores excluding infrastructures between brackets.

	Co-firing	Wind farm	Bioethanol
Human Health	7.2 (7.0)	0.27 (0.0019)	3.1 (2.7)
Ecosystems	5.5 (5.2)	0.10 (0.0011)	1.6 (1.4)
Resources	6.3 (6.2)	0.17 (0.0030)	2.8 (2.4)
Total	19 (18)	0.54 (0.0059)	7.6 (6.5)

From Table 5 it can be concluded that the Co-firing option has the highest environmental impact of the three options, and that infrastructure processes play a major role in the Windfarm option but that the ReCiPe score of this option is very small compared to the other two options. The ReCiPe scores including infrastructure will be used in the comparison of the results of the four methods of analysis because of the life cycle perspective of this study. The influence of the origin of the grass used in the Bioethanol option has been investigated by calculating the ReCiPe score of this option when grass from meadows is used instead of verge grass. With grass from meadows the total ReCiPe score of the Bioethanol option increases to 17 and 15 Million points including and excluding infrastructure processes respectively. In this study it is assumed that verge grass is used in the Bioethanol option.

5.2. Economic sustainability

Table 6 presents the average yearly costs (AYC), and the net present value (NPV) of the three options, both allocated to 1 PJ of electricity.

Table 6. Life Cycle Costs of the three options allocated to 1 PJ of electricity (indicative numbers).

Life Cycle Costs	Co-firing	Wind farm*	Bioethanol
AYC** [M€]	9.6	16	24
NPV [M€]	66	105	163

* Without taking into account subsidy.
** A positive value indicates a profit.

The influence of the (negative) price of verge grass has been investigated by calculating the life cycle costs of the Bioethanol option when the revenues of processing verge grass are 7.5 instead of 15 euro per ton. In that case the AYC equals 20 million euro, which means that the Bioethanol option is still preferred but that the difference with the other two options becomes smaller. I.e. the AYC and NPV of the Bioethanol option are a little higher than the values of the Wind farm option and the PWR is a little higher than the Co-firing option. In this paper it is assumed that the revenues of processing verge grass equal 15 euro per ton.

5.3. Social sustainability

The Wind farm and bioethanol options have the IHDI of the Netherlands as these options take place in the Netherlands and possible man-hours spent abroad related to construction and disposal of the installations have not been taken into account. Table 7 presents the $IHDI_{overall}$ of the three options. For comparison, the country with the highest IHDI, 0.89, is Norway and the HDIs of Norway and the Netherlands are 0.943 and 0.91 respectively [18]. The percentage of man-hours by country of the Co-firing option is presented in Fig. 3. All man-hours of the Wind farm and Bioethanol options are assumed to be spent in the Netherlands.

Table 7. Results of the social LCA of the three options (indicative numbers).

	Co-firing	Wind farm	Bioethanol
$IHDI_{overall}$	0.61	0.85	0.85

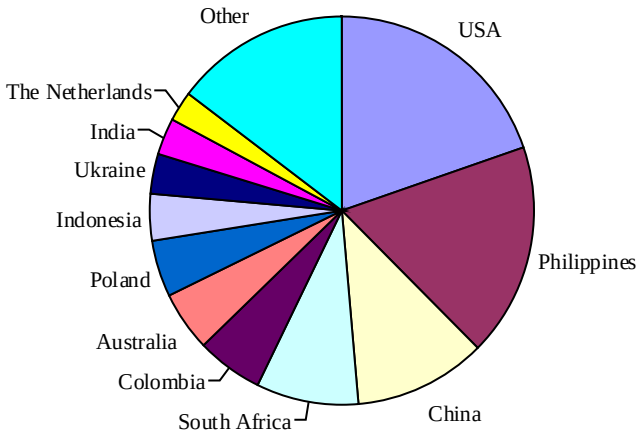

Fig. 3. Overview of the man-hours by country of the Co-firing option (indicative numbers).

5.4. Exergetic sustainability

The results of the exergetic sustainability assessment are presented in Table 8. From Table 8 it becomes clear that most of the exergy loss is caused by internal exergy losses and that the exergy loss caused by land use is negligible. The exergy loss caused by land use strongly depends on the percentage used in (4) for the efficiency of capturing solar energy via photosynthesis, but even if this percentage is increased from 0.75 to the maximum efficiency of 5 per cent that can be reached during a short time, the amount of exergy loss through land use is negligible.

Table 8. Cumulative Exergy Loss caused by the three options (indicative numbers).

PJ/year	Co-firing	Wind farm	Bioethanol
Internal exergy loss	3.0	1.4	3.6
Abatement exergy	0.94	0	0.17
Exergy loss land use	0.015	0.000062	0.00047
Cumulative Exergy Loss	3.9	1.4	3.7

When calculating the internal exergy loss no distinction has been made between the renewable (wood pellets, wind, grass) and non-renewable inputs (coal), i.e. in both cases the exergy equivalent of the amounts of wood pellets etc was regarded as an input. The distinction between these two types of inputs has been made in the CExL method by only considering the abatement exergy of emissions originating from non-renewable inputs.

5.5. Comparison of the results

The results of the environmental (ReCiPe), economic (AYC) and social (IHDI) sustainability assessments as well as the results of the exergetic life cycle assessment are presented in Table 9.

Table 9. Overview of the results of the sustainability assessments (indicative numbers).

	Co-firing	Wind farm*	Bioethanol
ReCiPe incl. infra [MPt]	19	0.54	7.6
AYC** [M€/year]	9.6	16	24
IHDI [-]	0.61	0.85	0.85
Cumulative Exergy Loss [PJ/year]	3.9	1.4	3.7

* Without taking into account subsidy.
** A positive value indicates a profit.

From the results in Table 9 it can be concluded that the Wind farm option is preferred from an environmental, social and exergetic point of view and that the Bioethanol option is preferred from

an economic point of view. The profitability of the Bioethanol option is to a large extent caused by the disposal costs of the 20 euro per ton of verge grass. As already mentioned in Section 5.2 the AYC of this option decrease to 20 million euro per year when the disposal costs are cut in half, making the distinction between the AYC of the Wind farm and Bioethanol options relatively small. Table 10 presents an overview of the grading of the options. If two options have the same score, they are rated the same.

From the comparison of the results of the four sustainability assessments in Tables 9 and 10 it is learnt that the Co-firing option is the least preferred option. The option that is preferred from an exergetic point of view is the Wind farm. This option is also preferred from the environmental point of view. The preference for the Bioethanol option in the economic assessment is mainly caused by the disposal costs of verge grass. When these costs are neglected, the results of the economic assessment of the Wind farm and Bioethanol options are comparable. The Wind farm and Bioethanol options are equally rated from the social assessment point of view.

Table 10. Grading the options according to the sustainability assessments. The preferred option per assessment is assigned the value '1', the second best '2' etc.

	Co-firing	Wind farm	Bioethanol
Environmental	3	1	2
Economic	3	2 (1)*	1
Social	3	1	1
Exergetic	3	1	2

* When the disposal costs of verge grass are assumed to be cut in half, the economic sustainability of the Wind farm and Bioethanol options are comparable.

Apart from the AYC also other indicators of the economic sustainability have been calculated. The problem with comparing the NPVs presented in Table 6 is that NPVs are no measure of the likeliness that an investment will be made. Instead of the NPV, the PWR is used to make decisions about investments. The PWR is calculated from the NPV of the installation as a whole, thus not allocated to the functional unit of 1 PJ of electricity, and the investment costs (Table 11).

Table 11. Life Cycle Costs of the three options, whole installation (indicative numbers).

	Co-firing	Wind farm*	Bioethanol
Investment costs [M€]	1237	1000	80
NPV [M€]	288	-690	46
PWR [-]	0.23	-0.69	0.58

* Without taking into account subsidy.

According to the PWR values of Table 11 the Bioethanol option is preferred and the Wind farm option is not profitable without subsidy. The PWR of the Bioethanol option strongly depends on the disposal costs of verge grass. When these costs are cut in half, the PWR becomes 0.29.

6. Discussion and conclusions

On the basis of the assessments it is concluded that the Wind farm option is preferred, except for the economic indicator called present worth ratio (PWR). To be able to make a more precise economic comparison of the three options, the possible subsidy of the Wind farm option as well as the costs related to carbon dioxide emissions of fossil origin have to be taken into account. Another aspect that has not yet been considered is the discontinuity in electricity production caused by too low or too high wind speeds.

The social LCA has been based upon the Inequality-adjusted Human Development Indices as reported by the UNDP because of lack of site-specific social data. Maybe in the future enough data will be available to conduct a more detailed analysis.

The abatement exergy values of only a few emissions have been taken into account as data about other emissions were not yet available.

The exergy losses caused by land use are small compared to the other exergy losses that contribute to the Cumulative Exergy Loss (CExL), therefore calculation of exergy loss caused by land use and its inclusion in the CExL needs to be reconsidered.

The comparison of the environmental, economic and social sustainability indicators with the Cumulative Exergy Loss throughout the supply chain learnt that the option that is preferred from an exergetic point of view is also preferred from the environmental and social points of view. This option is rated as second best based upon the average yearly costs (AYC) of the three options, but becomes comparable to the preferred option when the disposal costs of verge grass are assumed to be cut in half.

On the basis of the indicative results presented in this paper it is concluded that the Cumulative Exergy Loss could be an indicator that helps in achieving a more sustainable society via selecting preferred energy supply options, but that more research is needed.

7. Future research

In the future, a more detailed investigation and analysis will be carried out of the options described in this paper. Also the method of calculating the Cumulative Exergy Loss (CExL) will be improved by updating the abatement exergy of emissions and providing abatement exergy values of other emissions as well and reconsidering the exergy loss caused by land use.

It will also be investigated which method can best be used for a systematic comparison of the results.

References

[1] Dos Santos M., Park S., Exergy and sustainable development for chemical industry revisited. Computer Aided Chemical Engineering 2009;27(C):1923-28.

[2] Dincer I., Rosen M., Exergy: energy, environment and sustainable development. Oxford, UK: Elsevier; 2007.

[3] Stougie L., Van der Kooi H., The relation between exergy and sustainability according to literature. In: Koroneos C.J., Rovas D., Dompros A.T., editors. ELCAS 2011: Proceedings of the 2nd International Exergy, Life Cycle Assessment, and Sustainability Workshop & Symposium; 2011 Jun 19-21; Nisyros, Greece. European Cooperation in Science and Technology (COST), COSTeXergy:590-597.

[4] Szargut J., Morris D., Steward F., Exergy Analysis of Thermal, Chemical, and Metallurgical Processes. New York: Hemisphere Publ. Corp; 1988.

[5] Cornelissen R.L., Thermodynamics and sustainable development; the use of exergy analysis and the reduction of irreversibility [dissertation]. Enschede, The Netherlands: Twente University; 1997.

[6] Gong M., Using exergy and optimization models to improve industrial energy systems towards sustainability [dissertation]. Linkping, Sweden: Linkping University; 2004.

[7] Sciubba E., Beyond thermoeconomics? The concept of extended exergy accounting and its application to the analysis and design of thermal systems. Exergy, an International Journal 2001;1(2): 68-84.

[8] Meyer L., Tsatsaronis G., Buchgeister J., Schebek L., Exergoenvironmental analysis for evaluation of the environmental impact of energy conversion systems. Energy 2009;34(1):75-89.

[9] Stougie L., Van der Kooi, H., The sustainability of LNG evaporation. In: Bojić M., Lior N., Petrović J., Stefanović G., Stevanović V., editors. ECOS 2011: Proceedings of the 24th

International Conference on Efficiency, Cost, Optimization, Simulation, and Environmental Impact of Energy Systems; 2011 Jul 4-7; Novi Sad, Serbia. University of Niš:3157-70.

[10] Dewulf J., Bösch M., De Meester B., Van der Vorst G., Van Langenhove H., Hellweg S., Huijbregts M., Cumulative exergy extraction from the natural environment (CEENE): a comprehensive life cycle impact assessment method for resource accounting. Environmental Science & Technology 2007;41(24):8477-83.

[11] Goedkoop M., Heijungs R., Huijbregts M., De Schryver A., Struijs J., Van Zelm R., ReCiPe 2008, A life cycle impact assessment method which comprises harmonised category indicators at the midpoint and the endpoint level, Report I: Characterisation. The Hague, The Netherlands: Ministry of Housing, Spatial Planning and Environment; 2009.

[12] Pré Consultants, Amersfoort, The Netherlands. SimaPro LCA software – Available at: <http://pre.nl/content/simapro-lca-software> [accessed 26.1.2011].

[13] Ecoinvent Centre (Swiss Centre for Life-Cycle Inventories) St-Gallen, Switzerland. Ecoinvent database – Available at: <http://www.ecoinvent.org> [accessed 26.1.2011].

[14] Huppes G., Van Rooijen M., Kleijn R., Heijungs R., De Koning A., Van Oers L., Life Cycle Costing and the Environment. Leiden, The Netherlands: CML; 2004. Technical Report No.: 200307074.

[15] Frangopoulos C.A., Keramioti D.E., Multi-Criteria Evaluation of Energy Systems with Sustainability Considerations. Entropy. 2010;12(5):1006-20.

[16] Benoît C., Mazijn B., Guidelines for social life cycle assessment of products. UNEP/SETAC Life Cycle Initiative; 2009.

[17] Benoît C., Norris G., Valdivia S., Ciroth A., Moberg A., Bos U., Prakash S., Ugaya C., Beck T., The guidelines for social life cycle assessment of products: just in time!. The International Journal of Life Cycle Assessment 2010;15(2):156-63.

[18] Udo de Haes, H., The Scientific Basis for SLCA. The International Journal of Life Cycle Assessment 2008;13(2):95.

[19] Klugman J., Human Development Report 2011 - Sustainability and Equity: A Better Future for All. United Nations Development Programme; 2011.

[20] Tsatsaronis G., Recent developments in exergy analysis and exergoeconomics. International Journal of Exergy 2008;5(5):489-99.

[21] Dewulf J., Van Langenhove H., Dirckx J., Exergy analysis in the assessment of the sustainability of waste gas treatment systems. Science of the Total Environment 2001;273(1-3):41-52.

[22] Zhang Y., Singh S., Bakshi B., Accounting for ecosystem services in life cycle assessment part I: A critical review. Environmental Science & Technology 2010;44(7):2232-42.

[23] Essent N.V., Amercentrale – Available at: <http://www.essent.nl/content/Images/26746_Amercentrale_26-32384.pdf> [accessed 20.12.2011].

[24] Georgia Biomass, LLC. Website – Available at: <http://www.gabiomass.com> [accessed 21.9.2011].

[25] Koepel Windenergie Noordoostpolder. Website – Available at: <http://www.windkoepel-nop.nl> [accessed 8.9.2011].

[26] Stuurgroep Windenergie Noordoostpolder. Website – Available at: <http://windpark-noordoostpolder.nl> [accessed 8.9.2011].

[27] Vries S.S. de, Thermodynamic and Economic Principles and the Assessment of Bioenergy [dissertation]. Delft, The Netherlands: Delft University of Technology; 1999.

[28] Gong M., Wall G., On exergy and sustainable development - Part 2: Indicators and methods. Exergy, An International Journal 2001;1(4):217-33.

[29] Essent N.V., Productie- en emissieoverzicht Essent 2010 – Available at: <http://www.essent.nl/content/Images/87037_86028_Productie-en-emissies-Essent-v2.pdf> [accessed 26.9.2011].

[30] Boudewijn R., Koopmans W.F., Milieu-effectrapport Mee- en/of bijstoken van secundaire brandstoffen op het Amercentralecomplex te Geertruidenberg. Nijmegen, The Netherlands: Royal Haskoning; 2001.

[31] Didde R., Amercentrale verstookt als eerste getorrefacteerde biomassa, C2W, 2 oktober 2010. Available at: <http://www.c2w.nl/amercentrale-verstookt-als-eerste.108777.lynkx> [accessed 21.9.2011].

[32] Arthers C. et al., Ambitie Verantwoord, CR Report 2010, Essent N.V. - Available at: <http://www.essent.nl/content/Images/86718_MVO%20Jaarverslag%202010.pdf> [accessed26:9:2011].

[33] Essent N.V., Amercentrale Essent zet historische stap richting biomassacentrale. Press release. 28 June 2010, Available at: <http://www.essent.nl/content/overessent/actueel/archief/2010/Amercentrale_zet_historische_stap_richting_biomassacentrale.html> [accessed 26.9.2011].

[34] Essent N.V., Techniek. Available at : <http://www.essent.nl/content/grootzakelijk/producten/warmte/warmtenet/techniek.html> [accessed 20.12.2011].

[35] Van der Voet E., Van Oers L., Davis C., Nelis R., Cok B., Heijungs R., Chappin E., Guinée J.B., Greenhouse Gas Calculator for Electricity and Heat from Biomass. Leiden, The Netherlands: Leiden University, CML Institute of Environmental Sciences; 2008. Technical Report No.: CML-report 179.

[36] Sims R.E.H., The brilliance of bioenergy in business and in practice. James & James (Science Publishers) Ltd; 2002.

[37] Enercon GmbH, Wind energy converters Product overview, July 2010 – Available at: <http://www.enercon.de/p/downloads/EN_Productoverview_0710.pdf>? [accessed 15.9.2011].

[38] Siemens AG, Thoroughly tested, utterly reliable Siemens Wind Turbine SWT-3.6-120 – Available at: <http://www.energy.siemens.com/br/pool/hq/power-generation/wind-power/E50001-W310-A169-X-4A00_WS_SWT_3-6_120_US.pdf> [accessed 15.9.2011].

[39] Erneuerbare Energie Nachrichten, 1.2.2010, Größte Windkraftanlage der Welt – die E-126. - Available at: <http://www.energieblog24.de/e126/> [accessed 8.12.2011].

[40] Anonymous, Milieu Effect Rapport Windpark Noordoostpolder - Algemeen Deel. Hengelo, The Netherlands: Pondera Consult; 2009. Technical Report No.: 707016.

[41] Van Grinsven L., Onderzoek naar slagschaduwhinder van vijf windparken in de Noordoostpolder. Nuland, The Netherlands: Van Grinsven Advies; 2009.

[42] Croezen H.J., Vroonhof J.T.W., Rooijers, F.J., Welke nieuwe energiecentrale in Nederland? Vernieuwd CE-model. Delft, The Netherlands: CE Delft; 2006, Technical Report No.: 06.3113.45.

[43] Anonymous. Overview of coal prices. The Hague, The Netherlands: Statistics Netherlands - Available at: <http://statline.cbs.nl/StatWeb/publication/?DM=SLNL&PA=37215&D1=a&D2=13847&HDR=T&STB=G1&VW=T> [accessed 10.1.2012].

[44] Huizing H.J. et al., Grasol - Een haalbaarheidsstudie. InnovatieNetwerk Groene Ruimte en Agrocluster; 2005. Technical Report No.: 05.2.105.

[45] United States Department of Labor, Career Guide to Industries, 2010-11 Edition, 17.12.2009 – Available at: <http://www.bls.gov/oco/cg/cgs004.htm> [accessed 23.1.2012].

[46] Alderton T., Lane T., Bulk Carrier Vessels - An analysis of crew composition and performance; vessel safety and voyage cycles. Cardiff, UK: Cardiff University; 2001.

[47] EIA. Annual Coal Report 2009. Washington, USA: U.S. Energy Information Administration; 2010. Technical Report No.: DOE/EIA-0584 (2009).

[48] Anonymous, Dry Bulk Ships Segments. Copenhagen, Denmark: Danish Ship Finance – Available at: <http://www.skibskredit.dk/Shipping-Research/Dry-Bulk-Ships/ Segments.aspx> [accessed 26.3.2011].

[49] Anonymous. Recruitment of employees power plant Eemshaven completed (in Dutch). Groningen, The Netherlands, RTV Noord – Available at: <http://www.rtvnoord.nl/nieuws/nieuws.asp?pid=88747> [accessed 26.3.2011].

[50] Dewulf J., Van Langenhove H., Mulder J., Van den Berg M.M.D., Van der Kooi H.J., De Swaan Arons, J., Illustrations towards quantifying the sustainability of technology, Green Chemistry 2000;2:108-14.

[51] Van der Vorst G., Dewulf J., Van Langenhove H., Developing Sustainable Technology: Metrics From Thermodynamics. In: Bakshi B.R., Gutowski, T., Sekulic, D, editors. Thermodynamics and the Destruction of Resources. Cambridge: Cambridge University Press. 2011. p. 249-64.

[52] University of Massachusetts Lowell, UMass Lowell Solar Energy Engineering – Available at: <http://energy.caeds.eng> [accessed 24.8.2011].

[53] Lems S., Thermodynamic explorations into sustainable energy conversion - Learning from living systems [dissertation]. Delft, The Netherlands, Delft University of Technology; 2009.

[54] Turkenburg W., Renewable energy technologies. In: World Energy Assessment - Energy and the challenge of sustainability. 2000 p. 219-72.

[55] Archer M.D., Barber J., Photosynthesis and photoconversion. In: Archer M.D., Barber J, editors. Molecular to Global Photosynthesis. London: Imperial College Press. 2004. p. 1-41.

[56] Schiermeier Q., Tollefson J., Scully T., Witze A., Morton O., Energy alternatives: Electricity without carbon. Nature 2008;454:816-23.

Exergy analysis of the industrial symbiosis model in Kalundborg

Alicia Valero, Sergio Usón and Jorge Costa

CIRCE, Research Centre for Energy Resources and Consumption, University of Zaragoza, Zaragoza, Spain, email: aliciavd@unizar.es

Abstract

In this paper, the first exergy analysis of the main energy and material flows interchanged in the ecoindustrial park of Kalundborg is carried out. Being the Asnaes power plant the "heart of the industrial symbiosis", the main flows coming in and out of it are considered. These are the following: waste gas from Statoil refinery used by Asnaes, steam from Asnaes used by Statoil and the pharmaceutical company Novo group, district heating steam from Asnaes used in the municipality of Kalundborg, hot water from Asnaes used for a fishing farm, ashes from Asnaes used by Portland cement and gypsum from the desulphurization process of Asnaes for the gypsum board company Gyproc.

The exergy analysis allows a physical and hence rigorous characterization of each of the interchanged flows studied. Furthermore, it constitutes the first step for a later exergy input-output analysis based on Thermoeconomics.

Keywords:

Exergy, Material Flow Analysis, Eco-industrial park, Industrial Symbiosis, Kalundborg.

1. Introduction

Natural ecosystems do not produce waste. In a cyclic way, wastes produced by a living system are used as feedstock for another one. All resources are used in an optimal and sustainable way, with the sun as ultimate energy source. Those are the premises of Industrial Ecology: to imitate Nature for reducing the resources inputs, wastes and emissions of the industry, by closing the energy and material's cycle. This innovative alternative to the traditional industrial development emerged at the end of the 20th century.

Industrial ecology is materialized in the form of Eco-industrial parks. The main objective of the latter is that the companies situated in the park obtain important economic savings and minimize environmental pollution by interchanging resources and wastes. The result is what is called "industrial symbiosis". The latter refers to a network of exchange of wastes and by-products among different industries. For that purpose, it is imperative to overcome the traditional concept of industrial park where the establishment of industries does not follow any organizational criterion and all facilities follow linear input-output schemes. An eco-industrial park needs to be diversified, so that the different industries are able to use as feedstock, the wastes of other neighboring companies. This evolution requires cooperation and a long-term planning between companies.

The Industrial Symbiosis model of Kalundborg [1] is probably the best known eco-industrial park in the world. It is based essentially in physically connecting neighbouring companies so as to interchange water, materials (in the form of wastes as feedstocks) and energy, resulting in the minimization of production costs and waste treatment. The Kalundborg park was created in a natural and gradual way, as a result of a common will of optimizing the use of resources. Since its first establishment in the sixties, this park has saved yearly many tons of raw-materials, cubic meters of water and gigajoules of energy. Kalundborg constitutes nowadays the best model of eco-industrial park to follow.

Unfortunately, the replication of Kalundborg elsewhere is not an easy task. There are not few barriers to overcome. Facilities need to be close in proximity except for high-value by-products. Generally, a big plant such as a power plant or a refinery should be present, constituting the "heart" of the eco-industrial park. For instance, the presence of a power plant acting in cogeneration can help to reduce the total energy consumption. Security of supply is also a key issue. It is important to achieve sufficient scale in by-products. Moreover, new technologies are usually required for their valorization. Additionally, the law requires that by-products be matched to specific mandatory protocols through a very extensive set of rules that leaves little room for innovation. However, regulatory actions can also encourage industrial symbiosis.

But probably, the most important barrier to overcome is the willingness of the different companies to collaborate. It is not infrequent to bump into confidential issues. Although private actors need not be the initiators, they clearly must be committed to the implementation of industrial symbiosis. Companies will do what is in their economic interest. If they can eliminate waste in a cost-effective manner, they will do so. That is the reason why a good design of the network and a rigorous savings assessment is imperative.

In this aspect, the exergy analysis and particularly Thermoeconomics, can constitute very useful tools for assessing objectively the real costs appearing in the park, independently of their economic value. The idea that exergy can help quantifying the benefits of industrial ecology was stated by a number of authors [2-7]. The further use of Thermoeconomics in the cost assessment was also stated in [8].

This paper makes the first exergy assessment of the main energy flows interchanged in Kalundborg. It should serve as the starting point for the thermoeconomic cost evaluation described in the second part of this paper[1]. The aim is to show over a real case study, the usefulness of the exergy and thermoeconomic cost assessment.

As stated before, the industrial symbiosis model of Kalundborg appeared in a rather spontaneous way favoured by resources scarcity problems but also by the mutual trust among the leaders of the facilities in the network. It has worked so well, that no complicated planning has been required during its transformation. This is the reason why very little detailed information of the exchanged fluxes is available. The information found in the literature is qualitative rather than quantitative. Hence, different assumptions need to be carried out in our particular model.

2. Description of the Park

Currently the Kalundborg Industrial Symbiosis model is made up mainly of five facilities: Asnaes DONG Energy (power plant), Statoil (refinery), Gyproc (plasterboard manufacturer), Novo Group (pharmaceutical and biotechnology company) and the municipality of Kalundborg. Additionally, the park includes another ten industrial facilities.

The industrial symbiosis started when Gyproc decided to install its plasterboard factory in Kalundborg[2], in order to reduce their production costs through the exploitation of surplus gas that Statoil was burning unprofitably. From this moment on, neighboring companies started to see the economic and environmental benefits of such exchanges.

Due to underground water shortages, Asnaes changed its water supply system through a combination of water from Lake Tisso with cooling water and wastewater from the Statoil refinery

[1] Sergio Usón, Antonio Valero, César Torres and Alicia Valero. Thermoeconomic Fuel Impact Approach for Assessing Resources Savings in Industrial Symbiosis. Application to Kalundborg Eco-Industrial Park. Paper accepted for publication at the ECOS 2012 conference. June 26-29 (2012), Perugia, Italy.

[2] Source: www.symbiosis.dk

in 1976. Additionally, Asnaes began to reuse its own wastewater, avoiding a 100% use of underground water.

The municipality of Kalundborg profits from the energy surplus of the power plant. The latter provides energy for the district heating system which replaces around 3,500 individual heating systems. This has allowed reducing by 80% the waste energy of the power plant, producing a cost-effective energy alternative to the community.

Asnaes also distributes several thousand tons of steam to Statoil and Novo Nordisk. This industry also built a fish farm in which water is heated with waste energy.

The ashes and the gypsum produced in the desulphurization process in the power plant are reused to make cement by Aalborg Portland and for plasterboards by Gyproc, respectively. Finally, Asnaes receives surplus gas from the refinery, reducing its coal consumption and hence lowering the emissions of greenhouse gases.

On the other hand, the insulin and enzymes manufacturer Novo Nordisk recovers the sludge rich in phosphorous and nitrogen from the fermentation process and converts it into fertilizers, which are distributed free of charge to local farmers.

It should be stated that each of the interchanged byproducts have been subjected to a separate and confidential negotiation, giving rise to different transaction options: trade, barter, get a good price in exchange of constructing the transport infrastructure, etc. Since the facilities are close to one another, the byproduct prices can be traded at convenient low prices.

Fig.1 shows in a schematic way the main flows exchanged in the park currently found.

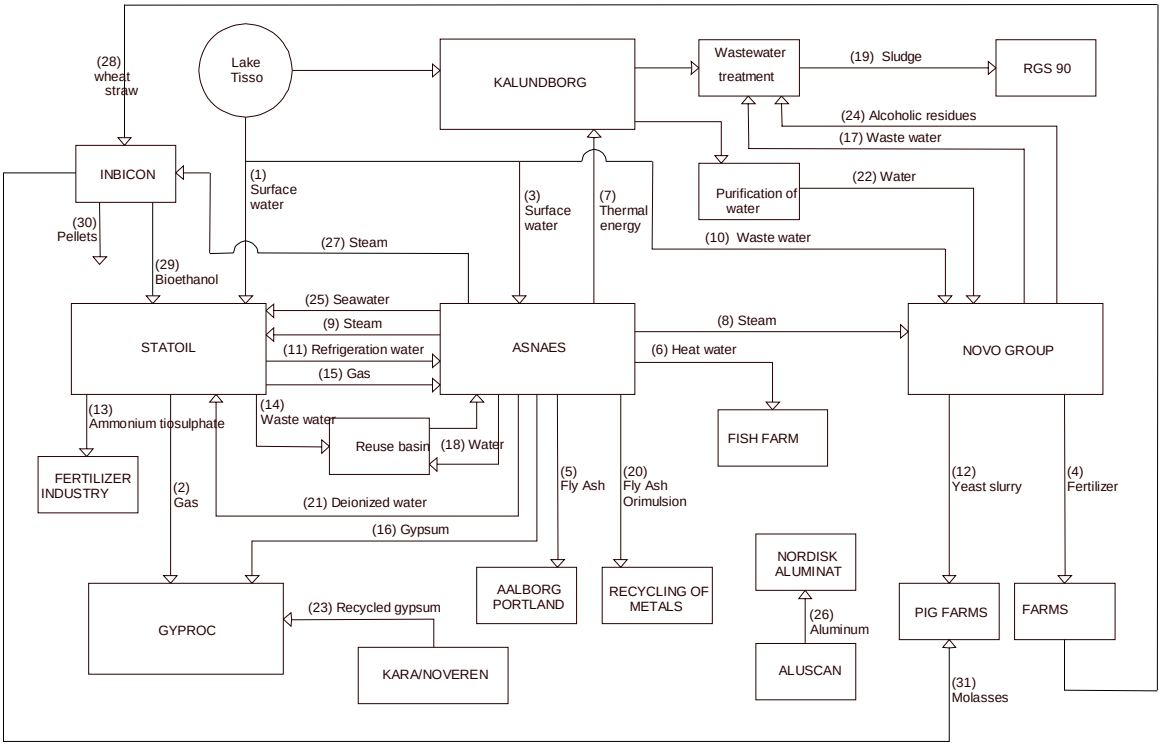

Fig. 1. State of the Industrial Symbiosis in Kalundborg in year 2011. Source: adapted from Andersen [9].

The network between different the participants of the Industrial Symbiosis is constituted by 31 flows, which can be classified into three categories: water, energy and byproducts.

Table 1 summarizes the data collected of the exchange network, obtained through an extensive search in different bibliographical sources. It should be pointed out that different values have been found for the same flow from different information sources in the literature. This could be due to changes in the production volume or production process. This fact makes the data collection task even more difficult.

Table 1. Description of the flows of the Industrial Symbiosis

Nº	Flow	Type	Quantity/year	Source
1	Superficial water	Water	1.600.000 m^3	[10]
2	Gas	Energy	8.000 t	[11]
3	Superficial water	Water	686.000 m^3	[10]
4	Fertilizer	Byproduct	150.000 t	www.symbiosis.dk
5	Fly ash	Byproduct	200.000 t	[11]
6	Heat wáter	Energy	390.000 GJ	[10]
7	Thermal energy	Energy	931 TJ	[10]
8	Steam	Energy	1.500 TJ	www.symbiosis.dk
9	Steam	Energy		
10	Superficial water	Water	491.000 m^3	[10]
11	Cooling wáter	Water	483.000 m^3	[10]
12	Yeast slurry	Byproduct	92.000 m^3	www.novonordisk.com
13	Ammonium thiosulphate	Byproduct	2.800 t	[11]
14	Wastewater	Water	9.000 m^3	[10]
15	Gas	Energy	60.000 t	[11]
16	Gypsum	Byproduct	80.000 t	[11]
17	Waste wáter	Water	2.300.000 m^3	[10]
18	Water	Water	200.000 m^3	[10]
19	Slurry	Byproduct	-	-
20	Orimulsion ashes	Byproduct	-	-
21	Deionized wáter	Water	50.000 m^3	[10]
22	Purified wáter	Water	-	-
23	Recycled gypsum	Byproduct	8.000 t	[12]
24	Alcoholic residues	Water	-	-
25	Seawater	Water	-	-
26	Aluminium	Byproduct	-	-
27	Steam	Energy	-	-
28	Wheat Straw	Byproduct	30.000 t	www.inbicon.com
29	Bioethanol	Energy	4.300 t	www.inbicon.com
30	Pellets	Byproduct	8.250 t	www.inbicon.com
31	Molasses	Byproduct	11.100 t	www.inbicon.com

3. Case study

Our case study includes the most representative flows of the Industrial Symbiosis in Kalundborg. It focuses on the power station, as Asnaes represents the heart of the Industrial Symbiosis. The integrations considered are the following: (1) surplus gas from the refinery used in the boiler of the power plant, substituting part of the feeding coal; (2) process steam from the power plants turbines for its use in companies Novo Group and Statoil; (3) steam from the Asnae's turbines used for feeding the District Heating system of Kalundborg municipality; (4) seawater heated at low temperature from the condenser used for the fish farm; (5) fly ashes generated in the burning of coal, substituting clinker for the production of cement; (6) use of the gypsum generated in the desulphurization process of the power plant's waste gases as raw material for the manufacturing of plaster boards and as a substitute of natural gypsum imported from Spain.

In order to assess the effect of the Industrial Symbiosis on resources saving, the case study is divided into the base case and the alternative case study. The base case study simulates the symbiosis with the six considered integrations (Fig. 2-a). The alternative case study simulates a fictitious situation where no integration among the facilities exist. Accordingly, the symbiotic flows are substituted by conventional processes. This way, the surplus gas from Statoil is burnt in a torch leading to an additional coal consumption in the power plant; water and steam integrations are replaced by natural gas boilers; fly ashes are substituted by clinker produced in a kiln and the gypsum is shipped from Spain (Fig. 2-b).

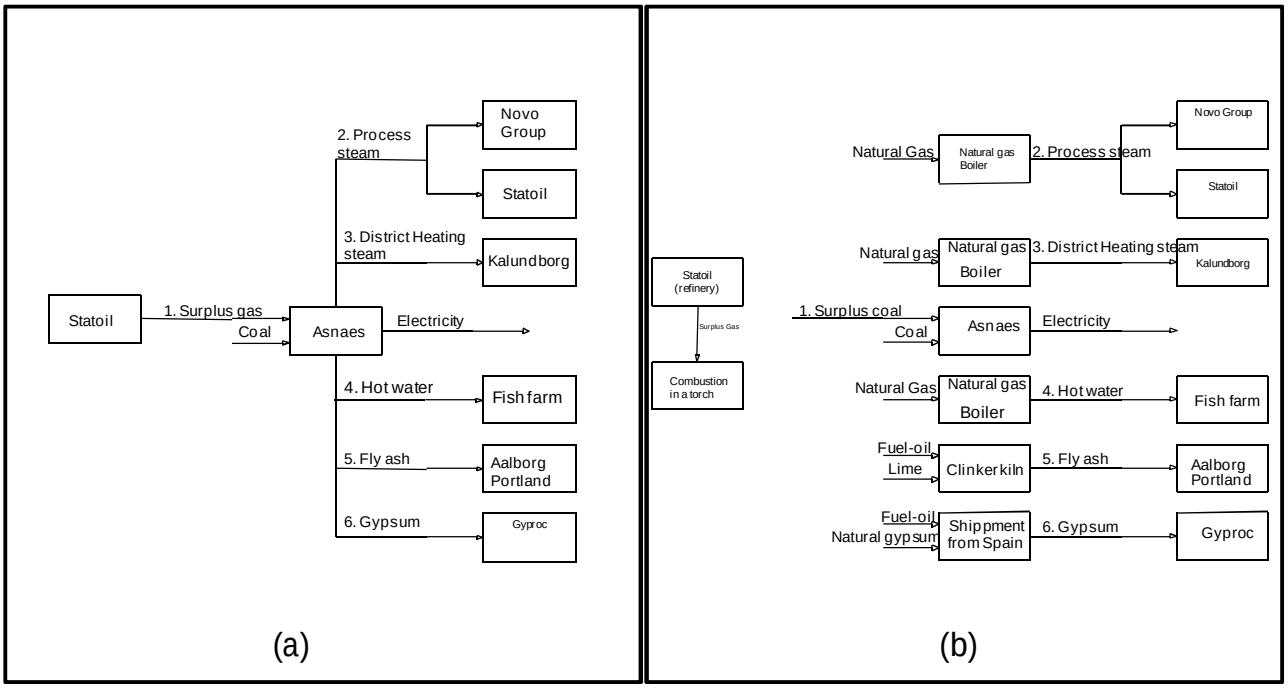

Fig. 2. Base case study with symbiosis (a) and alternative case study without symbiosis (b)

4. Thermodynamic model

In this section, the exergy analysis of the case studies described previously, are done. Due to the lack of detailed information for some of the integrations considered, similar alternative processes found in the literature have been used for obtaining technical data and adopting reasonable assumptions.

4.1 Base case with symbiosis

Coal and surplus gas

It has been assumed that the coal composition used in Asnaes power station is the one given by Larson et al. [13]. The exergy content of the flux is assumed as being equivalent to its HHV. For the refinery surplus gas, it has been assumed that it is in the form of natural gas with an exergy content of 50.500 kJ/kg [14].

Fly ash

It has been assumed that the composition of fly ash is 49% SiO_2, 26% Al_2O_3, 15% CaO y 10% Fe_2O_3, and its specific exergy, $b_{fly\ ash}$, is equal to 454 kJ/kg [8]. The mass flow of fly ash is obtained from the composition of coal mentioned before.

Flows for the desulphurization plant

The desulphurization plant is based on wet technology with limestone and forces oxidation. This process gives as byproduct gypsum from the SO_2 contained in the combustion gases. The SO_2 production can be obtained from the coal composition and consumption. Accordingly, with the stochiometric reaction and considering a 5% lime surplus, the production of gypsum, water and limestone required can be obtained. The chemical exergy of the different flows are calculated with the well known formula proposed by Szargut and Morris [15].

The required energy used for the desulphurization process is unknown. However, it has been assumed that this energy is around 4.000 kW, which is equivalent to that of the Lada power plant in Asturias [16].

Process steam

For the process steam generated in the power station and delivered to Statoil and Novo Group, it has been considered pressure and temperature conditions of 8,5 bar and 300 °C, which have been fixed with the conditions of steam at the exit of a medium pressure turbine of a similar power plant [8]. It has been also assumed that all steam is returned at 180ºC with no pressure losses.

District heating steam

At the exit of the medium pressure turbine, the steam is distributed into the low pressure turbine and the heat exchangers for the district heating system. In the latter, water is heated at 100-120 °C and is pumped into the district heating system[3]. It is assumed that the supply system is at 25 bar and 120ºC and the return is at 60ºC [16]. No pressure losses are assumed. The water flow is obtained from the thermal power delivered to the district heating system.

Fish farm water

Seawater increases its temperature 8°C in the condenser of the power plant. Around 23.000.000 m^3/year are delivered to the fish farm [10]. The exergy of this water is calculated assuming an average water temperature of the Baltic sea of 15°C [18].

Turbine steam

The thermodynamic model is closed by calculating the exergy of the superheated steam used for the electricity production in the turbine. Unfortunately this information is not available. It has been assumed that 60% of the fuel exergy (coal plus gas) is destroyed in the boiler.

Fig. 3 shows a schematic diagram of the base case and alternative case. The dashed lines represent the flows exchanged only in the base case (with integration). They would disappear in the alternative case (with no integration).

[3] Source: www.dongenergy.com.

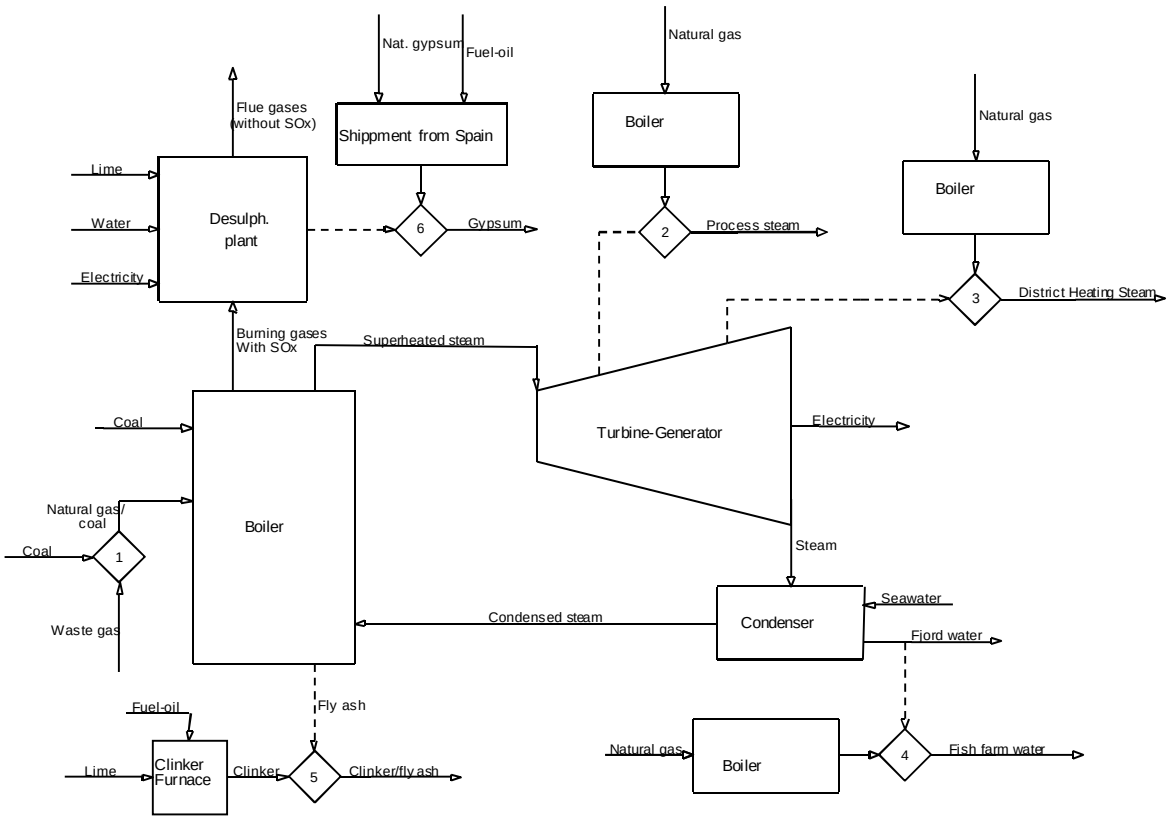

Fig. 3. Physical structure of the base and alternative case study

4.2 Alternative case without symbiosis

In the alternative case there is no integration among the different industries of the Industrial Symbiosis. This means that each facility operates independently, so that the integrations of the base case disappear (the flows represented by the dash lines of Fig. 3 do not exist).

Coal

The surplus gas of the refinery is replaced by a greater coal consumption in the power plant. However, as there is no district heating supply, not so much fuel is required. Both factors need to be taken into account.

Since the mass flow of coal increases with respect of the base case, more ashes, SO_2, lime, water and gypsum are produced/needed.

Natural gas

The energy supply from the power plant in the integrated case is now substituted by individual natural gas boilers with a 90% efficiency. They will be used for process steam, the District Heating network and the fish farm.

Flows for the production of clinker

The use of fly ash in the cement factory is substituted by a greater clinker production. The clinker flow mass produced in the furnace is equal to the fly ash generated in the power plant. The specific exergy of clinker assumed is 1.240 kJ/kg [8].

On the other hand, the kiln where the clinker is produced is fed with limestone as rawmaterial, requiring 1,54 kg of limestone per kg of clinker [8]. Additionally, an extra 4.195 kJ of fuel per kg of Clinker needs to be accounted for [8]. It is assumed that the fuel used has a HHV of 35,71 MJ/kg.

Fuel-oil for gypsum shipment

The supply of gypsum to Gyproc from the power plant is replaced by the import of natural gypsum from Spain. Hence, we need to consider the additional fuel used in the shipment. The required data

are the energy intensity in sea transport, assumed to be 0,2 kJ/kg·km [19], the sea distance considered (from Algeciras to Odense), which is 3.180 km and the load to be transported, corresponding to the gypsum produced in the desulphurization plant. The latter values give an exergy demand of 1,565 MW.

The exergy results of the thermodynamic model for both studies are shown in Table 2.

Table. 2. Yearly exergy demand of the case studies

	$B\left[GWh/_{year}\right]$	
Flow	With symbiosis	w/o symbiosis
Coal	10.376	10.591
Surplus gas*	841,7	841,7
Electricity	3.968	3.968
Fly ash*	21,79	22,24
SO2	25,98	26,51
Desulfurization lime	1,933	1,973
Desulfurization water	4,51	4,604
Gypsum*	2,036	2,078
Desulfurization electricity	24,8	24,8
Process steam	193,4	193,4
District Heating Steam	63,8	63,8
Fish farm water*	14	14
Turbine steam	4.487	4.487
Process natural gas	-	495,8
District Heating natural gas	-	307,7
Fish farm natural gas	-	254,4
Clinker limestone	-	16,2
Clinker Fuel oil	-	213,4
Clinker	-	59,5
Natural gypsum	-	2,0
Fuel-oil for gypsum transport	-	9,7

The flows with an asterisk represent those which are wasted in the alternative case (without symbiosis) since they cannot be avoided. We have only considered the dissipation process of the refinery surplus gas through a torch, since this flux could not be omitted due to its elevated exergy content.

Additionally, applying the exergy analysis, we can obtain the irreversibilities generated in each of the components analyzed, as the exergy difference between the integrated case and the alternative case (Table 3).

Table. 3. Analysis of the irreversibilities of the case studies (with and without integration)

Component	ΔI, GWh/year
Separation unit+desulph.	-25
Boiler	357
Turbine	0
Process steam boiler	-302
District heating boiler	-244
Fishing farm boiler	-240
Clinker kiln	-170
Gypsum transport	-10
Torch	-842
TOTAL	-1476

As can be seen in Table 3, the symbiosis network constitutes an irreversibilities reduction of 1,476 GWh/year. The fuel saved with the integration is equal to 1,514 GWh/year. The difference of both figures relies on the fact that the quantity of clinker substituted by fly ash was carried out in mass terms and not in exergy terms.

Table 3 also shows that all components show an improvement in their performance except for the boiler in the power plant. This is not due to the fact that the boiler is working deficiently in the integrated case. The reason is because the boiler needs to produce more steam for feeding the district heating system, the fish farm and the production of process steam. Hence, we can observe that exergy alone does not provide enough information. If we want to find out the real contribution of each component to the savings obtained, we should resort to the thermoeconomic analysis, which is explained in the second part of this paper.

However, property exergy gives also important insights to the analysis. We were able to estimate with a single unit, the savings achieved. This cannot be done, if the accounting property is with mass. Moreover, it constitutes the starting point of the thermoeconomic analysis. With the latter, the physical costs of the interchanged products can eventually be rigorously assessed and “fair” prices to by-products can be calculated.

5. Conclusions

In this paper the first exergy analysis of the Industrial Symbiosis model of Kalundborg has been carried out. The analysis has been focused on the main energy flows exchanged between the “heart” of the symbiosis which is the power plant and the rest of the neighbouring facilities. The analysis could be done after a careful and comprehensive data collection which was not always available. Hence, for those cases were data was lacking, reasonable assumptions were done.

The results obtained are therefore approximations and should not be taken as definitive. They should rather show an order of magnitude of the exchanges present in the park and moreover they

are the basis for a further thermoeconomic analysis of Kalundborg eco-industrial park. The final aim is to show the applicability of Thermoeconomics for the analysis, optimization and rigourous cost-assessment of eco-industrial parks. Thermoeconomics could eventually serve as a powerful tool for helping decision makers in the establishment of Industrial Ecology world-wide.

Acknowledgments

Authors would like to acknowledge ARAID and IberCaja for its support within the project "Thermoeconomics and Industrial Ecology. Application to Teruel coalfield", Young researchers program, 2010.

References

[1] Chertow, M. "Uncovering" Industrial Symbiosis Journal of Industrial Ecology, 2007, 11, 11-30

[2] Ayres, R. and Ayres, L. *Industrial Ecology. Towards closing the material cycle*; Edward Elgar Publishing: 1996.

[3] Connelly, L.; Coshland, C. Exergy and industrial ecology. Part 2: A non-dimensional analysis of means to reduce resource depletion. *Exergy Int. J.*, 2001, *1*, 234-255.

[4] Finnveden, G.; Ostland, P. Exergies of natural resources in life-cycle assessment and other applications. *Energy*, 1997, 22, 923-931.

[5] Cornelissen, R. L.; Hirs, G. G. The value of the exergetic life cycle assessment besides the LCA *Energy Conversion and Management*, 2002, 43, 1417-1424.

[6] Dewulf, J.; Langenhove, H. V. Assessment of the Sustainability of Technology by Means of a Thermodynamically Based Life Cycle Analysis ESPR. *Environ Sci & Pollut Res*, 2002, 9, 267-273.

[7] Dewulf, J.; Langenhove, H. V. Integrating industrial ecology principles into a set of environmental sustainability indicators for technology assessment. *Resources, Conservation and Recycling*, 2005, 43, 419-432.

[8] Valero, A.; Usón, S; Torres, C.; Valero, A. Application of Thermoeconomics to Indsutrial Ecology. Entropy, 2010, 12, 591-612.

[9] Andersen, M. *"Kalundborg Industrial Symbiosis"*. Resource Efficiency, Green Week, Brussels, 2011.

[10] Jacobsen, N.B. "Industrial Symbiosis in Kalundborg, Denmark. A Quantitative Assesment of Economic and Environmental Aspects". Journal of Industrial Ecology, vol. 10, nº 1-2, pp.239-255, 2006.

[11] Lowe, E.A. "Eco-industrial Park Handbook for Asian Developing Countries. A Report to Asian Development Bank". Environment Department, Indigo Development, Oakland, CA, 2001.

[12] Grann, H. "The Industrial Symbiosis at Kalundborg, Denmark". The Industrial Green Game, pp. 117-123. National Academies Press, 1997.

[13] Larsen, M.; Bech, M.; Bidstrup, T.; Christensen, N.P.; Vangkilde-Pedersen, T.; Biede, O. "Kalundborg case study, a feasibility study of CO2 storage in onshore saline aquifers". Geological Survey of Denmark and Greenland, Ministry of the Environment, 2007.

[14] Hermann, W.A. *"Quantifying global exergy resources"*. Energy, 31(12), pp. 1685-1702, 2005.

[15] Szargut, J. & Morris, D. Calculation of standard chemical exergy of some elements and their compounds based upon seawater as the datum level substance *Bulletin of the Polish Academy of Sciences. Techical Sciences.*, 1985, *33*, 293-305

[16] Consejería de Medio Ambiente, Ordenación del Territorio e Infraestructuras. "Resolución de 9 de marzo de 2009, por la que se modifica la Autorización Ambiental Integrada de la instalación industrial Central Térmica de Lada con emplazamiento en Langreo, promovida por la empresa Iberdrola Generación, S.A.U., al objeto de incluir la Planta de Desulfuración del Grupo IV". Boletín Oficial del Principado de Asturias nº 195, 2009.

[17] Renedo, C.J. *"Sistemas a escala urbana: District Heating y District Cooling"*. Curso de Postgrado Construcción Sostenible, UPV-EHU, 2007.

[18] European Environmental Agency. www.eea.europa.eu

[19] UNCTAD. *"Review of maritime transport 2005"*. United Nations Conference on Trade and Development, 2006.

GLOBAL GOLD MINING: Is technological learning overcoming the declining in ore grades?

Adriana Domínguez and Alicia Valero

CIRCE, Centre of Research for Energy Resources and Consumptions, Universidad de Zaragoza, Zaragoza, Spain, adrianad@unizar.es, aliciavd@unizar.es

Abstract:

Future availability of mineral resources is influenced by two opposed facts. On the one hand, general trends suggest a long-term decline in ore grade, which increases energy consumption in mining industry. But on the other hand there have been technological transitions that might avert rises in energy consumption. The aim of this paper is to become acquainted if technological breakthroughs that have occurred can preclude the rising energy demand for the gold mining industry. As experience is acquired, material and energy efficiency increase and technical changes can be expressed through the so called learning curves. For this purpose, the learning curve approach is applied to several data sets of 17 major gold producing countries. Our results show that technological learning is as dependent on ore grade as it is on mining operation and recovery processes. Applying the learning curve method we obtain average progress ratios varying from +20% to -22%. This survey allows us to have a better understanding of the mining sector and the outcomes of technology evolution together with ore grade declining by means of identifying best mining practices around the world.

Keywords:

Gold mining, technological learning, declining ore grades, learning curves.

1. Introduction

The mining industry is experiencing groundbreaking changes such as commodity price fluctuating, rising energy demand, water and cyanide consumption, increasing costs, declining ore grades, greenhouse gas emissions, increasing waste volumes and the challenge to achieve sustainable industry. Thence, sustainability[1] practices have become important for most major mining companies in order to reach a balance between socio-political, economic and environmental issues.

Otherwise, there is a debate about the availability of commodities in the future. Although there is evidence supporting the long-term decline in gold ore grades, there also exists the possibility that technological learning will overwhelm this fact. Hence, this paper analyzes the relationship between two issues: the decline in ore grades and the rising in energy consumption per ton of metal extracted.

The analysis of data set on historic gold mining in the main gold producing countries was carried out by means of linking resource extraction with energy use through the learning curves approach. Learning curves were originally developed to evaluate the effect of learning by doing in manufacturing. However, there are new applications such as analysis innovation and technical change in energy technology.

[1] For Placer Dome Inc. [1] which is one of the world's largest gold producers "sustainability means the exploration, design, construction, operation and closure of mines in a manner that respects and responds to the social, environmental and economic needs of present generations and anticipates those of future generations in the communities and countries where it works".

This paper looks over energy data on gold mining for Australia, North America, Africa and the Asia-Pacific compiled by Mudd [2-3], who pointed out the critical aspects of mineral resource sustainability such as resource intensity linked to technology.

1.1. Gold Mining Issues

1.1.1. Production and Reserves

The world gold production during 2010 was produced in the following countries: China (13.8%), Australia (10.2%), USA (9.2%), South Africa (7.6%), Russia (7.6%), Peru (6.8%), Indonesia (4.8%), Ghana (4%), Canada (3.6%), Uzbekistan (3.6%), Brazil (2.6%), Papua New Guinea (2.4%), Mexico (2.4%), Chile (1.6%) and other countries (19.7%). The major reserves are located in Australia (14.4%), South Africa (11.84%), Russia (9.86%) and Chile (6.71%). Reserves data are dynamic because they may be reduced as ores are mined and/or the extraction feasibility decreases, or more commonly, they may continue to increase as further deposits (known or recently discovered) are developed, or currently exploited deposits are more completely explored and/or new technology or economic variables enhance their economic feasibility [4]. Hence, reserves data are a major issue because they betray where the largest resources are, allowing us to be aware of the countries that must improve its mining methods in order to extract in the best possible way.

1.1.2. Energy consumption

Gold production is one of the processes with the greatest energy requirements in the mining industry. Energy consumption is dependent on several factors such as the recovery process and the kinds of mining operations analysed in this paper. For instance, energy consumed in open pit (OP) mining usually is greater than the energy required in underground (UG) mining because ore grades in open pit mines are smaller than those presented in underground mines. For open pit mines the average energy requirement is 170,000 GJ/t whilst for underground mining is 127,000 GJ/t of gold produced. The energy required to separate the gold from the mine increases abruptly when the concentration of the ore in a deposit tends to zero.

1.2. Learning Curves Theory

Learning curves come out as an empirical method to assess the effect of learning on technical change. As experience is acquired, efficiency and quality upgrade, mining costs decline and wastes are reduced. Technical change is a gradual process that entails technical knowledge and investment, but also an increase in material and energy efficiency. Both material and energy efficiency increase independently and changes can be leaded to the learning by doing concept [5]. Technical change is introduced by implementing technology learning rates, which specify the quantitative relationship between the cumulative experiences of the technology and cost reductions [6].

There is a widespread use of learning curves because of their usefulness to quantify the impact of increased experience and learning of a given technology. This allows obtaining a representation of technical change with a variety of different indicators of technological performance.

A good number of studies based on the learning curves theory have been carried out. For instance, Soderholm [6] used learning curves for assessing the economic outlook of renewable energy technologies to link future cost developments to current investment in new technology. Other studies [7,8] about the impact of quality on learning, suggest that learning is the link between quality improvement and productivity increase.

The simplest and most frequently representation of learning curves in energy technology studies is the Wright's log-linear model [9]:

$$Y_x = Y_0 x^b \quad (1)$$

Where Y_x represents the energy required to produce the x^{th} unit, Y_0 is the theoretical energy of the first production unit, x is the sequential number of the unit for which the energy is to be computed and b is a constant reflecting the rate energy decrease from year to year (learning index) and is calculated as:

$$b = \frac{\ln S}{\ln 2} \quad (2)$$

Where S is the energy slope expressed as a decimal value (learning rate), while $(1\text{-}S)$ is defined as the progress ratio (PR) which expresses the fraction to which energy requirements are reduced with cumulated production.

Nonetheless, there is a limit on the energy use to ore production that cannot be exceeded with increasing experience and in this case it is the minimum theoretical energy required to concentrate a substance from an ideal mixture of components [10] and is given by the following expression:

$$b_c = -RT_0\left[\ln(x_i) + \frac{1-x_i}{x_i}\ln(1-x_i)\right] \quad (3)$$

Where x_i is the concentration of substance i, R is the gas constant ($8.3145\ J/molK$) and T_0 is the reference temperature ($298.15\ K$).

Considering the energy limiting value, the learning curve can be expressed as:

$$Y - b_c = Y_0 x^b \quad (4)$$

Equation (4) integrates thermodynamic concepts to the learning curve analysis.

In this case technology learning rates state the correspondence between the cumulative experience of the technology and the energy requirement reductions.

Energy requirement reductions are the result of learning by doing. For instance, performance improves as new technologies and mining methods are implemented. Accordingly, learning curves will be used to empirically quantify the impact of accomplishing new mining practices on the energy consumptions of ore mining.

There is an enhancement for the simplest learning curve by applying a factor related with research and development. This extended formulation is known as the two factor learning curve (TFLC) expressed as the following:

$$Y(x, KS) = Y_0 x^b \cdot KS^c \quad (5)$$

Where KS is the knowledge stock and c is the elasticity of learning by researching [11]. Both types of learning curves are the most commonly used to assess technology learning rates in the energy sector [6]. Multiple-factor learning curves that account for other independent variables besides cumulative production represent an approach to get a better understanding of technological learning by enhancing the knowledge base [12,13].

Learning rates depend on the data points that are chosen. Previous surveys reveal significant variability

in estimated rates between different energy technologies, which ranges from 1% to 41.5% [11]. On the other hand, the study developed by McDonald shows that the average value of learning rates for energy technologies is 16-17% and learning rates for manufacturing is 19-20% [14]. Negative learning rates can be interpreted as a consequence of experience depreciation, if no important external factors (such as declining ore grades in mining technologies) are influencing the production process.

The estimation of learning curves has some highlights. For instance, the need to explore the effect of detaching single observations especially outliers that may affect the learning rate estimate.

2. Learning Curves applied to Global Gold Mining

Learning rates and progress ratios were calculated for each mine using Eq. (2) and Eq. (4). The information was grouped according to the different mining technologies used, because learning by doing will differ between mines, countries and technologies.

Progress ratios are different for each country and even for each mine although they use the same recovery process technology. This is due to inherent factors to each mine such as project age, depth, ore types, etc. Results of the analysis performed for different mining operations and recovery processes are shown in Table 1.

The assorted configurations of gold mines like open pit (OP), underground (UG) or mixed (MIX), as well as the energy source (diesel, coal, hydro, gas or any mix among them) are factors that influenced the progress ratio.

Recovery process technologies show average progress ratios around ±25% as shown in figure 1. Open pit operations with heap leach technology (HL) as recovery process as well as underground operations using carbon in pulp (CIP)[2] technology are the mining options with the greatest progress ratios.

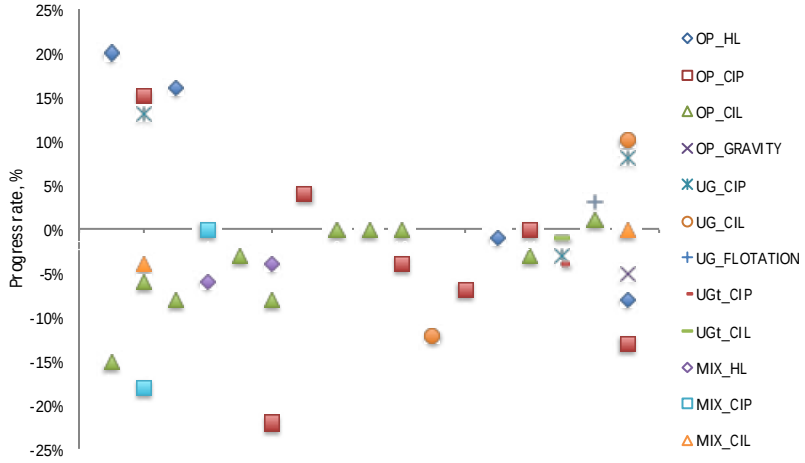

Fig. 1. Distribution of average progress ratios for gold mining industry.

Negative progress ratios convey that technological learning has been unable to overcome the increase in energy consumption during mining operations due to the declining in ore grade. On the

[2] The difference between carbon-in-pulp and carbon-in-leach processes is that for the first one the adsorption occurs after the leaching cascade section of the plant, whilst for the second one leaching and adsorption occur simultaneously [15].

other side, positive progress ratios imply that mining recovery processes have achieved to maintain or decrease the energy consumption during mining operations through time. Then, progress ratio becomes an indicator to identify those mines where mining practices are successful when saving energy.

Table 1. Progress ratio for global gold mining.

Country	Mines	Operation	Recovery process	Energy consumption (GJ/t Au)	Average ore grade (g/t Au)	Progress ratio by mine (%)
Argentina	Veladero	OP	HL	476,295	1.2	20%
	Cerro Vanguardia	OP	CIL	57,568	7.4	-15%
Australia	Granny Smith	OP	CIP	48,010	12.0	-1%
	Kidston	OP	CIP	95,494	10.5	-7%
	Henty	UG	CIL	91,984	5.6	-31%
	Kalgoorlie West	MIX	CIL	88,191	39.3	-8%
	Agnew	MIX	CIP	171,934	21.6	-22%
	Hill 50	MIX	CIL	76,790	12.2	-6%
	St Ives	MIX	CIP, HL	47,554	12.9	4%
	Central Norseman	MIX	CIL	148,309	8.4	1%
	Plutonic	UG	CIP, HL	155,778	3.5	2%
	Darlot	UG	CIL	181,927	1.5	14%
	Lawlers	UG	CIL	168,441	2.0	4%
	SuperPit	OP	CIL	141,350	2.1	-4%
	Mt Leyshon	OP	CIP	117,687	2.9	5%
	Tanami-Granites	MIX	CIP/CIL	174,270	1.6	-30%
	Boddington	OP	CIL	498,021	1.1	-14%
	Pajingo	UG	CIP	112,653	4.3	24%
	Bronzewing	MIX	CIL	63,504	7.5	4%
	Jundee	MIX	CIL	144,078	3.9	-19%
	Sunrise Dam	OP	CIL	180,196	0.4	1%
	Challenger	MIX	CIP	210,419	0.5	-26%
	Ravenswood	OP	CIP	236,498	1.5	18%
	Stawell	UG	CIL	87,669	1.1	-4%
	Fosterville	OP	BIOX, CIL	167,234	1.2	-5%
	Peak (NSW)	MIX	CIL	162,455	3.3	6%
Brazil	Mineracao	OP	HL	73,567	6.9	-4%
	Serra Grande	OP	CIL	64,707	6.3	-23%
	Amapari	OP	HL	208,293	2.4	29%
	Morro do Ouro	OP	CIL	176,444	0.5	1%
	Paracatu	OP	CIL	191,369	0.3	-2%
	Maricunga	OP	HL	163,089	0.4	24%
Canada	Dome-Porcupine	MIX	CIP	113,562	2.9	0%
	Hemlo	MIX	HL	102,457	4.6	-6%
	Musselwhite	UG	CIP	91,984	5.6	-16%
	Campbell	UG	CIL/CIP	67,688	16.8	-2%
	Eskay Creek	UG		88,191	39.3	-16%
	Red Lake	UG	CIP	22,401	79.7	0%
Chile	La Coipa	OP	CIL	385,254	1.1	-3%

Ghana	Tarkwa	OP	CIL	110,248	1.0	-4%
	Damang	OP	CIL	166,186	1.4	-11%
	Iduapriem	OP	CIP	130,283	1.8	-22%
	Obuasi	MIX	HL	192,560	2.1	-4%
Guinea	Siguiri	OP	CIP	189,244	1.1	4%
Indonesia	Kelian	OP	CIL	190,161	2.4	0%
Laos	Sepon Au	OP	CIL	217,951	2.4	0%
Mali	Sadiola	OP	CIP	102,837	2.9	-9%
	Yatela	OP	CIP	56,497	3.5	1%
	Morila	OP	CIL	125,031	4.2	0%
Mexico	San Dimas	UG	CIL/CIP	59,814	7.3	-12%
Namibia	Navachab	OP	CIP	110,056	1.8	-7%
Peru	Pierina	OP	HL	64,597	1.9	-9%
	Lagunas Norte	OP	HL, CIP/CIL	37,261	2.2	7%
PNG	Misima	OP	CIP	352,899	1.1	-2%
	Porgera	OP	CIP	431,600	5.2	2%
	Lihir	OP	CIL	374,258	5.4	-3%
South Africa	Harmony Group	UG-tails	CIP/CIL	205,291	5.0	-4%
	Beatrix	UG-tails	CIL	195,083	4.5	-1%
	Driefontein	UG-tails	CIP	204,009	5.1	-1%
	Kloof	UG-tails	CIP	229,860	7.0	-12%
	West Wits Field	UG-tails	CIP	175,272	8.5	0%
	South Deep	UG	CIP	424,041	6.5	-3%
	Vaal River	UG-tails	CIP, CIL	170,913	3.4	-2%
Tanzania	Geita	OP	CIL	257,028	2.3	-18%
	North Mara	OP	CIL	201,729	3.5	12%
	Tulawaka	OP	CIL	178,024	10.7	11%
	Bulyanhulu	UG	FLOTATION	78,621	12.0	3%
United States	Round Mountain	OP	GRAVITY	151,530	0.6	-5%
	Marigold	OP	HL	157,725	0.7	-5%
	Bald Mountain	OP	HL	129,211	1.1	-33%
	Cripple Creek-Victor JV	OP	HL	148,190	0.6	-3%
	Golden Sunlight	OP	CIP	131,676	2.6	-13%
	Cortez	OP	CIL	124,621	2.5	-5%
	Fort Knox	OP	HL	187,460	0.8	1%
	Wharf	OP	HL	146,938	1.0	-1%
	Goldstrike	MIX	CIL	138,706	6.8	0%
	Turquoise Ridge	UG	CIL	49,936	14.9	10%
	Pogo	UG	CIP	111,056	14.6	8%

In the coming sections, the key aspects of gold mining in the largest gold producer countries are briefly analyzed.

2.1. Argentina

Gold is produced in two open pit mines; Veladero and Cerro Vanguardia. There is another important mine in Argentina named Bajo la Alumbrera in which gold and copper are produced.

The Veladero mine [16] with typical ore grades under 2.5 g/t Au started its production on 2005 so it is a new mine that has been increasing its production with lower energy requirements. Hence

positive learning rates are obtained when applying the learning curve approach. Otherwise, Cerro Vanguardia mine with ore grades between 7 and 8 g/t Au has been dispalying a decline in its ore grade. Although cumulative production has grown, the energy per unit of gold produced has also increased and thereby negative progress ratios are presented. Available data: from 2005 through 2007.

2.2. Australia

Gold is produced in almost 30 mines, including open pit, underground and mixed. A previous work accomplished by Valero et. al. [17] analyzed the influence of technical development and declining ore grades on the availability of Australian gold resources. Obtained results suggests that although progress in technology has been made, in most cases energy requirements are increasing, because the main variable is the ore grade. Progress ratios represent the amount of improvement in mining technologies for several mines in Australia, such as Kidston [18], Henty [19], Kalgoorlie [20], Agnew [21], St Ives [22], Plutonic [23], Darlot [15], Lawers [15], Superpit [23], Mt. Leyshon [24], Tanami [25], Boddington [23], Pajingo [26], Sunrise Dam [27], Challenger [23], Ravenswood [28], Peak [29]. Available data: from 1990 through 2008.

2.3. Brazil

There are two mines in which gold is extracted with an ore grade range less than 0.35 g/t Au, Maricunga and Paracatu [30]. Maricunga mills only 35% of the total ore milled in Paracatu. In that case, the energy consumption in mining is related with quantity (cumulative production) and quality (ore grade) resulting a positive PR of 24% for Maricunga but not for Paracatu, which has a negative PR. Amapari mine [31] shows an improvement from 2005 to 2006 when it reduces its energy requirement almost 60% even though ore grade decreases. Hence, it presents the highest progress ratio of all mines analyzed. Available data: from 2001 through 2007.

2.4. Canada

Dome-Porcupine mine belongs to Goldcorp Company [32], these mine does not show variation in progress ratios although three situations were identified: 1) with the same ore grade in 1997 and 2005, an increment in energy consumption was presented, this can imply that there was no improvement in the process and that this increase can be caused by the deterioration in the mining equipment, 2) energy consumption can diminish although ore grade declines; for instance from 1997 to 1998, where energy reduction was influenced by the increase in the tons of ore milled, leading to a positive learning rate, and 3) the expected behavior of when ore grades decrease energy consumption increase and vice verse.

Hemlo [15], Musselwhite [32] and Campbell [23] mines show negative progress ratios as a result of ore grade declining, as well as the increment in energy consumption although ore grade remains constant.

Eskay Creek Mine belongs to Barrick's Company. This mine is a clear example of ore grade declining trend insomuch as ore grade in 2001 was 53.14 g/t Au and then in 2007 it was of 20.91 g/t Au. This situation have an effect on the energy consumption because in 2001 the energy required was 35.09 MJ/kg Au while in 2007 it reached 203.378 MJ/kg Au. Accordingly, negative progress ratios are presented. For values of ore grade between 40 and 90 g/t Au, besides Eskay Creek, there is another mine Red Lake from Goldcorp. Inc. [32]. Available data: from 1997 through 2007.

2.5. Chile

Coipa mine [33] uses conventional open pit mining methods and crushing, grinding and leaching operations to process gold. Energy consumption has been increasing over time, leading to negative progress ratios. Available data: from 2003 through 2004.

2.6. Ghana

The main gold producing country in West Africa is Ghana. For ore grades below 1.5 g/t Au, there are two mines from Gold Fields Co.: Tarkwa Gold Mine [34] and Damang Gold Mine [34]. The first one consists of six open pits, two heap leach facilities, and a CIL plant. The operation is currently mining multiple-reef horizons from open pits and there is potential for underground mining in the future. Tarkwa has mineral resources equal to 433.75 gold tons and a mineral reserve of 280.6 tons. The second one is composed of multiple open pits, surface stockpile sources and a CIL plant, with a mineral resource of 133.2 gold tons and a mineral reserve of 59.5 tons.

In accordance with the above information, it is reasonable that Damang mine has energy consumptions greater than Tarkwa mine for the same ore grade, leading to lower PR values. Furthermore, both mines show an increasing energy consumption trend under two conditions, when ore grades decrease and when cumulative production increase. Consequently, both mines have negative progress ratios, because under any circumstances there is an increase in energy consumption.

AngloGold Ashanti has two mines in Ghana: Iduapriem [27] and Obuasi [23]. The decrease in ore grade together with the rising energy consumption, result in negative progress ratios for both.

Available data: from 2004 through 2008.

2.7. Guinea

Siguiri gold mine belongs to AngloGold Ashanti Co. [23]. The annual production is 7.9 gold tons. It has a mineral resource of 138.9 gold tons and a mineral reserve of 73.7 tons. This mine fulfills the learning curve theory, since energy consumption decreases as cumulative production increases despite the ore grade is declining. Then, positive progress ratios are presented. Available data: from 2005 through 2007.

2.8. Indonesia

Kelian Equatorial Mining [35] is 90% owned by Rio Tinto. This open pit mine started its production in 1992 and finished it in 2004. The gold recovery process uses SAG and Ball Mills followed by gravity separation and carbon in leach (CIL) cyanidation. This mine shows a neutral PR. Available data: from 2002 through 2004.

2.9. Laos

MMG owns Seapon mine [36] which has gold and copper operations. Gold has been produced since 2002. In early 2005, an expansion of the original gold processing facility was completed doubling the capacity of the gold processing plant to 2.5Mt/year, with a new crusher and mill allowing more flexibility and efficiency in the treatment of Sepon ore. The mine has a mineral resource of 93.5 gold tons and a mineral reserve of 5.1 tons. The Seapon gold mine is expected to be operational until 2012. There is not enough data to establish a trend in its energy consumption, then its PR is zero. Available data: 2003 and 2005.

2.10. Mali

Sadiola Gold Mine [37] is operated by AngloGold Ashanti. Yatela Gold Mine performs the elution and smelting processes at the nearby Sadiola Gold mine. Morila Gold Mine [38] is a joint venture company between Randgold (40%), AngloGold Ashanti Ltd (40%) and the State of Mali (20%). During the first quarter of 2009, a successful transition was made from open pit mining to stockpile treatment. The operation is expected to come to an end in 2013 although the mine is currently investigating the opportunity to retreat the Tailings Storage Facility (TSF) material, which would extend the mine life by approximately five years. For ore grades under 3 g/t Au, energy

consumption increases as cumulative production rises, leading to negative progress ratios. The positive progress ratio is due to the increment in ore grade. For the ore grades ranging between 3 and 6 g/t Au energy consumptions vary for each mine, but the general trend is a decreasing in energy consumption when cumulative production grows. Consequently, a null progress ratio is presented. Available data: from 2005 through 2007.

2.11. Mexico

San Dimas Mine [39] consists of five ore zones or blocks where underground gold and silver mining operations are carried out using mechanized cut-and-fill mining methods, with LHD equipment feeding either truck or rail haul to the mills. After milling, cyanidation, zinc precipitation and smelting, dore bars are poured and then transported to refineries in the United States. Over the last ten years investments have been made to significantly upgraded tailings management, increasing production and achieving a lower cost structure in the future. Besides, in 2005, crushing capacity was increased, as well as improvements to the chemical treatment and leaching area. Energy consumption increases although cumulative production grows and ore grade increases, but there is a change in 2005 where a reduction in energy requirements is presented despite the fact that ore grade decreases due to the improvement in the processes indicated above. Nevertheless, a negative progress ratio is presented. Available data: from 2004 through 2006.

2.12. Namibia

Navachab gold mine [40] recovers 85% of gold. After CIP extraction, elution and smelting, the unrefined bullion is sent to Switzerland, where it is refined. Energy consumption increase through the time due to the decline in ore grades, leading to a negative progress ratio. Available data: from 2005 through 2007.

2.13. Peru

Pierina [15] is an open-pit mine, with truck and loader operations. Ore is crushed and transported through an overland conveyor to the leach pad area. Run-of-mine ore is trucked directly to a classic valley-fill type of leach pad. Pierina is currently engaged in energy efficiency optimization efforts which lead to decreasing energy consumptions or increasing energy efficiencies as well as reducing greenhouse gas emissions [41]. Over the last decade, improvements in the leach pad system as well as in the surface water management system have been made [42]. Despite the improvements made in the mine, energy consumptions continue growing due to the ore grade declining, leading to negative progress ratios. This can imply that technological efforts adopted by the mine aren't enough to bring down the energy increasing trend.

Yanacocha Gold Mine is the largest and most profitable gold mine in Latin America. It operates a complex of six open pit gold mines, five leach pads and two processing facilities. Gold is extracted from ore through a cyanide heap leach process, then the solution is treated by the Merrill Crowe process. After recovery, the contained metal is smelted and casted as bars containing 75% gold and 20% silver [23]. Everything about Yanacocha facilities are enormous as well as its wealth, then this mine has the largest gold production with very low energy consumption.

Lagunas Norte mine is owned by Barrick Co. [33]. In 2006 began the development of a high grade area with a longer hauling cycle. Gold and silver are recovered in a conventional clarification and zinc precipitation circuit, using the Merrill- Crowe process. For this reason, a decrement in energy consumption from 2006 is observed, leading to a positive progress ratio, regardless the ore grade declining.

Available data: from 2001 through 2007.

2.14. Papua New Guinea

Misima gold/silver mine [23] ends its operation in 2001 with stockpile milling anticipated to continue into 2004. Gold recovery uses a standard crushing, grinding and carbon-in-pulp (CIP) flowsheet. All data analyzed for this mine indicates that both cumulative production and energy consumption increase. Besides, ore grades are declining, resulting in negative progress ratios.

For ore grades varying between 3 and 5 g/t Au, there are two mines that are mined: Porgera and Lihir mines. Almost all data for this range is from Porgera mine, the energy consumption grows as cumulative production does, whilst progress ratios vary according to the ore grade changes. For the interval within 5 and 6 g/t Au of ore grade, Porgera mine reveals a slightly trend of ore grade decrease, whilst cumulative production increase. The result is a decreasing tendency of energy consumption prompting a positive progress ratio.

The Porgera gold mine [23] is operated by a Barrick subsidiary. Both open-pit and underground mining methods are employed because it was initially an underground operation until 1997, but was resumed in 2002. Additionally an open-pit mining became increasingly important from 1993. A lot of changes have been made into the mining processes. For instance, the open pit has been mined in five stages, with final-stage overburden removal taking place during 2001. The open-pit truck and shovel fleet was expanded in 1995 and 1997. Besides, in 1999 a flotation expansion was installed as well as and additional oxygen capacity to increase autoclave throughput. Run-of-mine ore is crushed and ground, then gold is recovered in a gravity circuit and flotation is used to recover a sulphide concentrate before the applying of CIP cyanide leaching process. The final step is the electrowinning process that produces bars of 88% gold average.

The Lihir gold mine [33] is an open-pit mine consisting of two adjacent overlapping pits. Its operations include; crusher, SAG and ball mill circuit, flotation circuit, pressure oxidation and CIL processing facilities, and electrowinning and smelting facilities to produce gold doré.

Available data: from 1997 through 2007.

2.15. South Africa

In South Africa the data are from the following mines: Harmony Group, Vaal River, Beatrix, Driefontein, South Deep, Kloof and West Field. Gold Fields company owns Beatrix, Driefontein, South Deep and Kloof.

Beatrix Gold Mine [34] consists of four surface operating shafts that mine various gold bearing reefs from open ground and pillars. Ore is processed at two metallurgical plants, where milling, CIL process, elution and gravity circuits, electrowinning and smelting operations are carried out.

Driefontein Gold Mine [34] includes eight shaft systems that mine various gold bearing reefs from open ground and pillars. Ore extracted from the bearing reefs is processed at three metallurgical plants. It has a centralized elution and carbon treatment facility since 2001. The mineral processing technology was based on SAG milling circuit following by a cyanide leaching until the year 2003, when these processes were replaced by the CIP plant.

Kloof Gold Mine [34] is composed of five shaft systems and two gold plants, the gold is produced from a combination of underground mining and processing of surface waste rock dump material. For the mineral processing, two operational metallurgical facilities are used, including a central elution and smelting facility. In 2001 and ACC Pump Cell CIP circuit was installed to replace the less efficient drum filtration and zinc precipitation. Also, the upgrade included the installation of continuous electrowinning sludge reactors.

South Deep Gold Mine [34] incorporates two shaft systems that mine various auriferous conglomerates from open ground and pillars. The ore is processed at a central metallurgical plant. The mineral processing includes a milling circuit SAG, a CIP circuit, an elution system to finally recover gold by electrowinning and smelting processes.

Great Noligwa underground gold mine [23] is situated close to the Vaal River, it comprises four gold plants, one uranium plant and a sulphuric acid plant. Great Noligwa has its own milling and treatment plant which applies conventional crushing, screening, grinding and CIL processes to threat the ore and extract the gold.

Harmony Group in South Africa include the next mines: Bambanani, Doornkop, Kusasalethu, Evander, Joel, Kalgold, Masimong, Phakisa, Phoenix, Target, Tshepong and Virginia [43]. Sometimes the value of ore milled is too large compared with the values of other mines in the same ore grade scope. Therefore, it is probably that these data are referred to several mines. West Wits Operations include Driefontein, Kloof and South Deep Gold Mines [34].

Harmony Group reports the highest energy consumption value, leading to a negative progress ratio. For ore grades from 6 to 7 g/t Au, the only existing mine is Kloof, which shows an increase in the energy consumption for the same ore grade value from 2004 to 2008, therefore a negative progress ratio is shown. Data in the span between 8 and 9 g/t Au is from West Wits Field, eventhoug ore grade decrease, energy consumption decrease too, leading to a null positive progress ratio. Available data: from 2003 through 2008.

2.16. Tanzania

North Mara gold mine consists of three open pit deposits and belongs to Placer Dome Company. AngloGold Ashanti Ltd owns Geita gold mine, which began production in 2000. Geita [27] is a multiple open-pit operation with underground potential. For ore grades between 3 and 5 g/t Au, most of the data is from North Mara, during 2003 and 2004 the ore grade is the same but the energy consumption differ greatly, almost by a 50%, the same situation is repeated for years 2005 and 2007, despite of these observations, there is a declining trend in energy consumption, resulting in a positive progress ratio of 12%.

Tulawaka Gold mine [33] consists of a completed open pit mine with an underground access ramp, an ore stockpile area and crushing plant, a processing plant. The ore processing method includes SAG, gravity recovery and CIL. It is the only mine which report data in the span of 9 and 14 g/t Au, within this large ore grades the energy consumption falls as cumulative production increase, hence a positive progress ratio of 11% is shown.

Bulyanhulu Mine [44] is owned by Barrick Gold Corp. Bulyanhulu is an underground trackless operation using long hole and drift and fill as its principal toping methods, it shows a clear downtrend in ore grade that results in an energy consumption increase as cumulative production rises. However, due to the fact that ore grade vary from one year to another without a clear trend of increase or decrease and this variation is not significant, the progress ratio is positive.

Available data: from 2001 through 2007.

2.16. United States

Barrick Company [15] in USA owns several mines. Bald Mountain mine is an open pit, run-of mine with conventional heap leaching technology and carbon absorption for ore treatment.

Cortez mine is mined by conventional open-pit methods. It employs three different metallurgical processes to recover gold. Lower-grade oxide ore is heap leached, while higher grade ore is treated

in a conventional mill using cyanidation and a CIL process. Heap leached ore is hauled directly to leach pads for gold recovery.

Golden Sunlight mine is mined by conventional open-pit methods. The ore treatment plant uses conventional CIP technology as well as San Tailing Retreatment (SRT). Goldstrike complex includes an open pit mine and two underground mines. The open pit is a truck and shovel operation using large electric shovels. While one of the underground mines is a high grade ore body which is mined by transverse longhole stoping, underhand drift and fill mining methods, while the other is a trackless operation, using two different underground mining methods: long-hole open stoping and drift and fill. Also, it consists of two processing facilities that are used for both the surface and underground operations: (1) an autoclave circuit and (2) the roaster.

Marigold mine is an open-pit operation that uses heap-leaching to process its ore.

Round Mountain mine is a conventional open-pit operation that uses multiple processing methods including crushed ore leaching, run of mine ore leaching, milling of higher grade ore and the gravity concentration circuit.

Turquoise Ridge mine uses underhand cut and fill mining methods. Ore is transported to an external mill for processing. The refractory gold ore is treated by pressure oxidation technology and gold is recovered using conventional CIL technology.

Cripple Creek Victor JV gold mine [23] is a low-grade, open pit operation. The ore is treated using a valley-type, heap leach process with activated carbon used to recover the gold. The resulting doré buttons are shipped to a refinery for final processing.

Fort Knox mine [30] is an open pit mine, that uses as processing methods CIP mill, heap leach and gravity. Production from heap leach began in late 2009. Ridgeway underground mine [23] produces gold and copper. It is in the process of transitioning from the sub-level cave to a block cave beneath the existing mine. Crushed ore from the underground is delivered by conveyor to a surface stockpile; then, gold and copper are recovered in a conventional floatation circuit to produce a copper concentrate containing elevated gold levels. The next step is to pump to the filtration plant where it is dewatered prior to being transported to export to smelters throughout East Asia.

Wharf [32] is an open pit and heap leach mine that has been in operation since 1983.

Barneys Canyon gold mine [33] is an open pit mine that started production in 1989. Mining and milling ended in 2001. Gold production from stockpiles continued until 2005.

Kettle River-Buckhorn gold mine [30], was originally conceived as an open pit mine, but then it was redesigned and developed as an underground mine. The primary mining method employed is cut and fill. Its ore is processed through milling, flotation and CIP processes.

Pogo gold mine [33] is an underground mine that utilizes a cut and fill drift method. The milling operation includes grinding, sulfide flotation, paste thickening, leach/CIP, cyanide detoxification, tailings filtration and gravity recovery.

Open pit mining in USA is characterized by negative progress ratios, but underground mining using CIL and CIP shows positive progress ratios. Available data: from 2002 through 2007.

3. Summary of the results

Assuming that all mines of the same kind of operation as well as recovery process for a specific country are comparable, progress ratios can be presented as figure 2 displays.

For instance, Australia has an excellent progress ratio when CIP technology is used either in open pit or underground mines. This can imply that gold mining industry in Australia has overcome the declining in ore grades through technological learning. A compilation of the best practices and all mining process in general would be very useful for mines using the same recovery process around the world. The sharing of operational and technical experiences, with countries such as Papua New Guinea would be an excellent way to improve the efficiency in the gold mining sector.

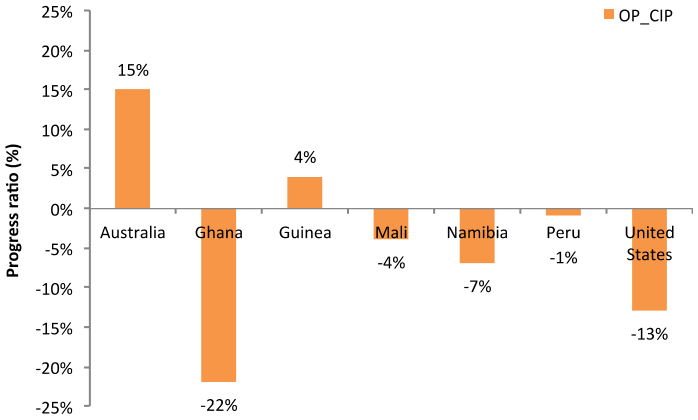

(a)

(b)

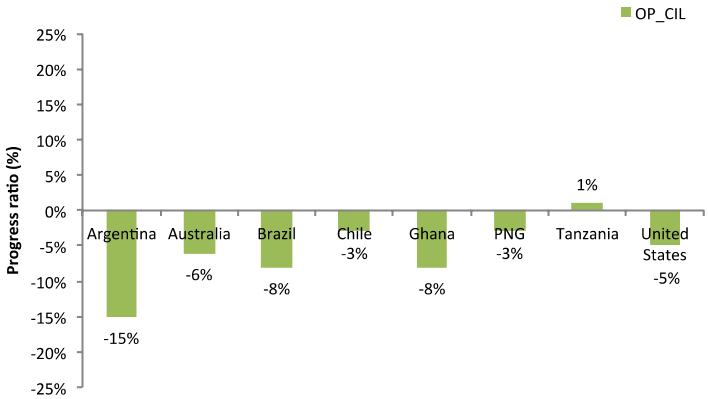

(c)

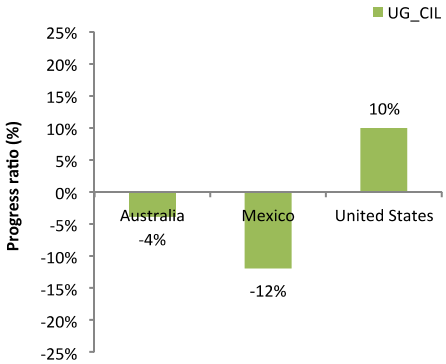

(d)

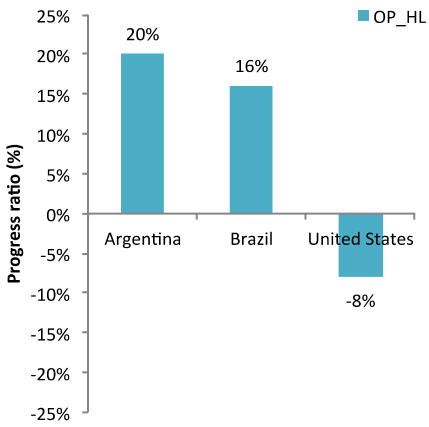

(e)

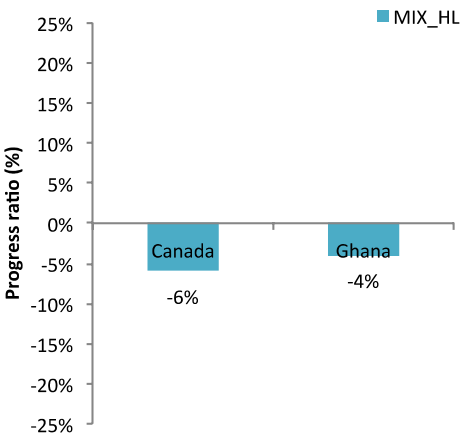

(f)

Fig. 2. Progress ratio for different recovery process and countries in gold mining industry.

For the United States, positive progress ratios can be observed when underground mining is performed (either when CIP or CIL process are applied). Hence, the relevant fact here is the kind of mining operation used: underground. Performance benchmarking of gold mines in Canada can be a worthwhile action to improve practices in the gold mining industry.

In South America, countries like Argentina and Brazil show great positive progress ratio when operations in open pit mines with heap in leach technology as recovery process is employed. Again, it would be very useful an extended compilation of their best practices in order to share this information with countries that have mines with the same geological and technological characteristics, such as mines in Peru.

4. Conclusions

This paper has studied the influence of technical development and declining ore grades on the availability of world gold resources, applying the learning curves approach and estimating progress ratios for each country. The latter allowed us to identify mines in which mining operations have proved to be successful when the goal is to save energy. Therefore these estimates can be used to point out best mining practices and serve as a reference for other mines with similar conditions.

Average progress ratios obtained between different operation and recovery processes ranged from + 20% to – 22%. The learning effect is measured in terms of reduction in the energy requirements of mining operations.

It should be pointed out, that the improvement in mining technologies, represented in this paper by the progress ratios calculated for different countries, mines operations and recovery processes are not related to time or cumulative production as it happens to conventional applications (such as manufacturing) when the theory of learning curves is applied. In the mining sector, an additional factor needs to be taken into account, and that is the key variable ore grade change. This way, an improvement in the energy efficiency of the processes does not necessarily imply an overall energy reduction, since the decrease in the ore grade may dominate.

General results suggest that although progress in technology has been made, in most cases energy requirements are increasing, because the main variable is the ore grade. Therefore, it can be asserted that technology cannot in general avert the rising energy demand for gold mining in the future if no major changes are performed in gold mines around the world.

It is crucial to analyze carefully those countries that are and will be the major gold producers such as Australia, South Africa, Russia, Chile, United States and Indonesia. The data analyzed reveals that South Africa and Australia show the greatest energy consumptions and hence should increase their efforts in improving their mining practices. Additionally, due to the strategic position of China in the gold mining industry, analyzing its data sets in energy consumptions and ore grades would be also very interesting and profitable.

This survey has been carried out for gold, but future studies will be accomplished to other important commodities. This will allow us to have a more suitable understanding of the mining sector and the outcomes of technology evolution together with ore grade declining. Furthermore, this analysis lets us understand the general trends in resource consumption in the mining industry.

Nomenclature

b Constant reflecting the rate energy decrease from year to year (learning index)

c Elasticity of learning by researching

KS Knowledge stock

R Gas constant (8.3145 J/molK)

S Energy slope expressed as a decimal value (learning rate)

T_0 Reference Temperature (298.15 K)

x Sequential number of the unit for which the energy is to be computed

X_c Ore grade

x_i Molar concentration of substance i

Y_0 Theoretical energy of the first production unit

Y_x Energy required to produce the x^{th} unit

Abbreviations

CIP Circuit in Pulp

CIL Circuit in Leach

HL Heap Leach

MIX Mixed (open pit and underground)

OP Open Pit

PR Progress ratio

UG Underground

UGt Underground tailings

Acknowledgements

This paper has been financed by the IDERE II project from the Spanish Ministry of Industry and Science. We thank Dr. Gavin Mudd for sharing with us his comprehensive and useful data set of global gold mining.

References

[1] Placer Dome Asia Pacific; 1998 Porgera Mine Sustainable Report. PDAP, Milton.

[2] Mudd G., Global Trends in Gold Mining: Towards Quantifying Environmental and Resource Sustainability?. Resources Policy 2007; 32:42–56.

[3] Mudd G., Gold Mining in Australia: Linking Historical Trends and Environmental and Resource Sustainability. Environmental science & policy 2007; 10:629–644.

[4] U.S. Geological Survey. USGS. Mineral Commodities Summaries 2011. U.S. Department of the Interior. Available at: < http://minerals.usgs.gov/minerals/pubs/mcs/2011/mcs2011.pdf > [accessed 18.1.2012].

[5] Ruth M., Integrating Economics, Ecology and Thermodynamics. The Netherlands, Kluwer Academic Publishers; 1993.

[6] Soderholm P., Sundqvist T., Empirical Challenges in the Use of Learning Curves for Assessing the Economic Prospects of Renewable Energy Technologies. Renewable Energy 2007; 32: 2559–2578.

[7] Giurco D., Prior T., Mudd G., Mason L., and Behrisch J., Peak Minerals in Australia: A Review of Changing Impacts and Benefits; 2010 Technical Report, Institute for Sustainable Futures University of Technology, Sydney and Department of Civil Engineering Monash University, Australia.

[8] U. S. Geological Survey. USGS. Minerals Yearbook Gold; 2011 Technical Report.

[9] Yelle L., The Learning Curve: Historical Review and Comprehensive Survey. University of Lowell, 1979; 10:302–328.

[10] Ruth M., Thermodynamic Constraints on Optimal Depletion of Copper and Aluminum in the United States: A Dynamic Model of Substitution and Technical Change. Ecological Economics, 1995; 15: 197–213.

[11] Kahouli-Brahmi S., Technological Learning in Energy Environmental Economy Modelling: A survey. Energy Policy, 2008; 36:138–162.

[12] Weiss M., Junginger M., Patel M., Blok K., A Review of Experience Curve Analyses for Energy Demand Technologies. Technological Forecasting & Social Change, 2010; 77: 411–428.

[13] Jamasb T., Kohler J., Learning Curves for Energy Technology and Policy Analysis: A Critical Assessment. 2007, University of Cambridge, UK.

[14] McDonald A., Schrattenholzer L., Learning Rates for Energy Technologies. Energy Policy, 2001; 29: 255–261.

[15] De Andrade L., Dynamic simulation of the carbon-in-pulp and carbon-in-leach processes. Brazilian Journal of Chemical Engineering, 2007; 24 (04): 623 - 635.

[16] Barrick Company. Available at: < http://www.barrick.com/GlobalOperations > [accessed 18.1.2012].

[17] Valero Al., Valero A., Domínguez A., Influence of technical development and declining ore grades on the availability of gold resources. SDEWES 2011. Proceedings of the 6th Dubrovnik Conference on Sustainable Development of Energy, Water and Environment Systems; 2011 Sept 25-29; Dubrovnik, Croatia.

[18] Mulligan D., Environmental management in the Australian minerals and energy industries. Principles and practices. Australia: University of New South Wales Press; 1996. Australia.

[19] Unity Mining Limited. Available at: < http://www.unitymining.com.au/ > [accessed 7.5.2012].

[20] The Superpit. Available at: < http://www.superpit.com.au/Production/MineralProcessing > [accessed 7.5.2012].

[21] Gold Fields; 2011 Agnew Gold Mine Technical Short Form Report. Available at: < http://www.goldfields.co.za/pdfs/technical_short_forms_2011/agnew_mine.pdf > [accessed 7.5.2012].

[22] Gold Fields; 2011 St Ives Gold Mine Technical Short Form Report. Available at: < http://www.goldfields.co.za/pdfs/technical_short_forms_2011/st_ives_mine.pdf > [accessed 7.5.2012].

[23] Mining Technology. Available at: < http://www.mining-technology.com/projects/ > [accessed 18.1.2012].

[24] Normandy Mining Limited; 1998 Environment Report. Mt Leyshon Operations. Available at: < http://www.corporateregister.com/a10723/nml-ml98-se-az.pdf > [accessed 18.1.2012].

[25] Normandy Mining Limited; 1998 Environment Report. Tanami Operations. Available at: < http://www.corporateregister.com/a10723/nml-tan98-se-az.pdf > [accessed 18.1.2012].

[26] Evolution Mining. Available at: < http://www.evolutionmining.com.au/ > [accessed 18.1.2012].

[27] AngloGold Ashanti. Available at: < http://www.anglogold.co.za/Home > [accessed 18.1.2012].

[28] Minesite. Available at: < http://minesite.com/ > [accessed 18.1.2012].

[29] Lloyd P., Berthelsen R., Strom E., Australia: New South Wales; 2009 Technical Report on Peak Gold Mines.

[30] Kinross. Available at: < http://www.kinross.com/ > [accessed 18.1.2012].

[31] Newgold. Available at: < http://newgold.com/ > [accessed 18.1.2012].

[32] Goldcorp. Available at: < http://www.goldcorp.com > [accessed 18.1.2012].

[33] Global Infomine. Available at: < http://www.infomine.com/minesite/ > [accessed 18.1.2012].

[34] Gold Fields. Available at: < http://www.goldfields.co.za/ > [accessed 18.1.2012].

[35] McGuire, G., Managing Mine Closure Risks in Developing Communities — A Case Study, Kelian Equatorial Mining, Indonesia. Mining Risk Management Conference; 2003 Sept 9-12; Sydney, NSW.

[36] Minmetals Resources Limited. Available at: < http://www.mmg.com/pages/828.aspx > [accessed 18.1.2012].

[37] IamGold Corporation. Available at: < http://www.iamgold.com/English/Operations/default.aspx > [accessed 18.1.2012].

[38] RandGold Resources. Available at: < http://www.randgoldresources.com/randgold/content/en/2009/randgold-home > [accessed 18.1.2012].

[39] Primero Mining. Available at: < http://www.primeromining.com/Operations/San-Dimas-Mine/default.aspx > [accessed 18.1.2012].

[40] AditNow. Available at: < http://www.aditnow.co.uk/ > [accessed 18.1.2012].

[41] Barrick Company. Available at: < http://www.barrick.com/Theme/Barrick/files/docs_presentations/pr11_12_2003_weauau.pdf > [accessed 7.5.2012].

[42] Ausenco. Available at: < http://www.ausenco.com/page/Our_Projects/Pierina_Gold_Mine/ > [accessed 18.1.2012].

[43] Harmony. Available at: < http://www.harmony.co.za/ > [accessed 18.1.2012].

[44] Gold mining in Tanzania. Available at: < http://www.tanzaniagold.com/ > [accessed 18.1.2012].

Personal Transportation Energy Consumption

Matteo Muratori[a], Emmanuele Serra[b], Vincenzo Marano[c], Michael Moran[d]

[a] Mechanical Engineering Department and Center for Automotive Research (CAR), The Ohio State University, 930 Kinnear Rd, Columbus, OH 43212, USA (muratori.2@osu.edu)

[b] Center for Automotive Research (CAR), The Ohio State University, 930 Kinnear Rd, Columbus, OH 43212, USA (serra.17@osu.edu)

[c] Center for Automotive Research (CAR), The Ohio State University, 930 Kinnear Rd, Columbus, OH 43212, USA (marano.8@osu.edu)

[d] Mechanical Engineering Department, The Ohio State University, E407 Scott Laboratory 201 W 19th Ave, Columbus, OH 43210, USA (moran.4@osu.edu)

Abstract:

This paper centers on the estimation of the total energy consumption for personal transportation in the United States, to include fossil fuel and/or electricity consumption, depending on vehicle type. The bottom-up sector-based estimation method introduced here contributes to a computational tool under development at The Ohio State University for assisting decision making in energy policy, pricing, and investment.

In this work, driving patterns are classified into two categories: commuting to work, and driving for leisure and shopping. For commuting, distribution of distance data is available in the literature. Leisure/shopping driving durations are estimated using activity patterns for a driving population, modeled using a heterogeneous Markov chain. A backward vehicle dynamic simulator is used to compute energy consumption for different vehicle types.

Key findings of the current study include: (i) Independent of the total number of miles driven annually, the higher the vehicle electrification the lower the total primary energy consumption. (ii) With the modeling in this work, the percentage of trips that purely electric vehicles are unable to complete varies from 7% to 13% for driving distances up to 20000 miles per year. The percentage increases significantly for driving distances over that threshold, owing to intrinsic limitations of the battery.

Keywords:

Transportation Sector, Personal Energy Consumption, Bottom-up Modelling, Electric Vehicles, Fuel Saving, Oil Dependency.

1. Introduction

At The Ohio State University a new computational tool, called *Integrated Computational System for Energy Pricing and Policy* (ICS-EPP), is currently under development to assist the formulation of energy policy, pricing, and investment decisions. The ICS-EPP will include multiple interacting sub-models of: (a) the behavior of individuals; (b) the electric power grid with distributed and stochastic power generation and consumption; (c) the energy profile of individual vehicles based on driving patterns; (d) long-term investment decisions; and (e) economic policy. Such sub-models are sufficiently robust to be applicable to the major power grids in the United States.

In particular this paper focuses on estimating the total primary energy consumption for personal transportation in the United States, including fossil fuel consumption and/or electricity consumption in the case of Plug-in Electric Vehicles (PEVs), which include Plug-in Hybrid Electric Vehicles (PHEVs) and purely Electric Vehicles (EVs). Personal transportation represents all travel by individuals, including private trips for shopping and leisure as well as commuting to work. Personal transportation does not include commercial and industrial activities.

To give an idea of the dimensions of the problem:

- The U.S. is responsible for about 20% of the world primary energy consumption and 22% of the oil burned world-wide [***1***];
- The transportation sector represents one third of U.S. primary energy consumption, totaling 27507 Trillion BTU ($2.9 \cdot 10^{19}$ J) in 2010 [***2***];
- Personal transportation accounts for over 65% of the U.S. transportation sector (accounting for 8.9 million barrels of oil per day out of a total 13.5 million barrels consumed, [***2***]).

Nearly all energy consumed in the transportation sector comes from petroleum, most of which is imported from other countries.

This work centers on personal energy transportation, namely the energy consumed when private citizens drive their personal vehicles. The paper is structured as follows: Section 2 presents an overview of the state-of-the-art of energy demand modeling techniques. Section 3 reports the development of the proposed model. Results are presented in Section 4. Finally, concluding remarks can be found in Section 5.

2. Modeling Approach

In this paper, a bottom-up sector-based estimation technique is adopted to compute personal transportation energy consumption.

When estimating energy demand of a population, both top-down or bottom-up approaches can be exploited. Top-down models use regression analysis and historical data to determine the relationship between the demand and macro variables, including Gross Domestic Product (GDP), Human Development Index (HDI), weather, price of fuels, rate of population and economic growth. Such models provide useful macro-level results in the form of aggregated data but they present a low level of resolution. The data are usually obtained through surveys conducted on a representative statistical sample of the population by federal agencies (i.e. [***1***], [***3***], [***4***]). Besides the lack of coarseness of the data, the main drawback of this approach is the absence of a prediction model able to characterize the time-dependence of the demand.

Bottom-up approaches, instead, exploit available statistical data to calibrate a consumption model, while aggregated statistical data are used for its validation by means of large-scale simulations (i.e. see [***5***] and [***6***]). In particular, the energy consumption of the whole population can be computed by aggregation of a group of individuals representing the population characteristics.

Bottom-up models provide high-resolution data (at a defined time-step level) without relying on historical data, providing the ability to model the impact of different technologies and allowing the implementation of energy optimization techniques. The versatility of the output in the bottom-up approaches comes at a price: the model complexity increases and its calibration process typically requires more effort than the top-down technique.

Estimation models can also be categorized according to consumption data. Following this approach, energy demand models can be classified as sector-based or consumer-oriented. The former approach – largely used – divides the total energy demand among several sectors (typically residential, commercial, industrial, and transportation). Consumer-oriented approaches, instead, try to estimate the same energy demand by only accounting for the role of different consumers, and their consumption patterns ([***6***] and [*7*]).

For instance, in the sector-based approach the energy consumption for the production of an asset is taken into account as a direct industrial cost, whereas in the consumer-oriented paradigm that same energy consumption is seen as an indirect cost allocated to the consumer buying that specific asset. The advantage of the consumer-oriented approach over the sector-based consists in the ability to capture the total impact of consumer activities, accounting for both direct and indirect consumptions.

Characterization of both direct and indirect energy use – and associated emissions – can be useful in designing more effective energy policies and incentives. In [***6***], the authors claim sector-based models are limited in their capacity to mirror the total impacts of consumer activities on energy use. However, sector-based approaches offer a sector by sector overview of the energy demand and thus allow allocation of the energy demand among the various sectors according to their final use. A summary of the advantages and disadvantages of the energy demand estimation models is provided in *Table 1*.

Table 1. Summary of energy demand modeling techniques.

	sector-based	***consumer-oriented***
bottom-up	+ high resolution + model available + differentiation based on energy final-use – difficult calibration process	+ high resolution + model available + account for direct and indirect use – difficult calibration process
top-down	+ data collection through surveys + differentiation based on energy final-use – low resolution aggregate data – model not available	+ data collection through surveys + + account for direct and indirect use – low resolution aggregated data – model not available

3. Model Development

The aim of the bottom-up, sector-based model introduced in this paper is to compute personal transportation primary energy consumption of U.S. citizens, providing as output a highly resolved consumption profile, including fossil fuel and and/or electricity consumption (in case of PEVs).

These consumption profiles include information on how much energy is consumed per each trip and when in time this consumption occurs. The information is stored in a five-dimensional array, with length equal to the total number of trips per year. The five dimensions include liquid fuel consumption, electricity consumption, starting and ending time of each trip, and final State of Charge (SOC) of the battery.

As shown in *Figure 1*, the personal transportation energy consumption has been divided into two main categories, according to driving purpose:

1. Commuting to work.
2. Driving for leisure and shopping.

Once the length of each trip is known, a statistical model (*Velocity Profile Generator,* presented in Section 3.4) is used to generate velocity profiles for each trip. These profiles are fed to a backward vehicle dynamic simulator able to compute the fuel consumption and/or electricity consumption for PEVs, including charging time and duration.

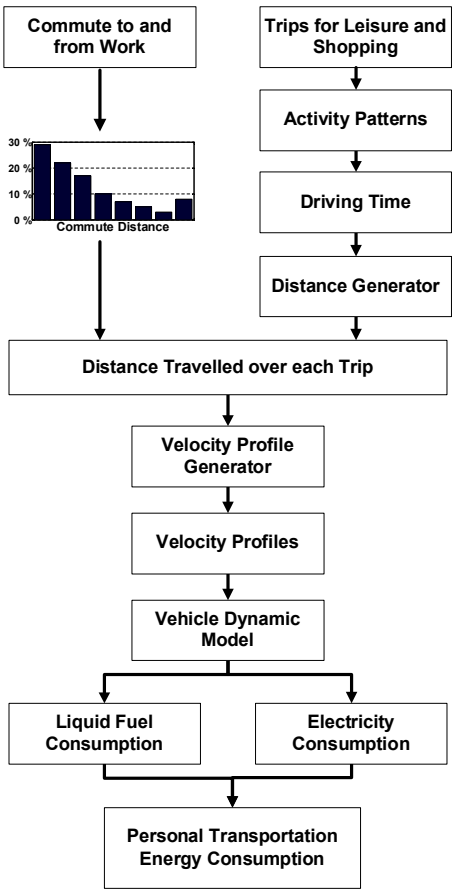

Figure 1. Model scheme.

3.1. Commuting to and from Work

The energy consumed for daily commutes to and from work is computed starting from the data shown in *Figure 2*.

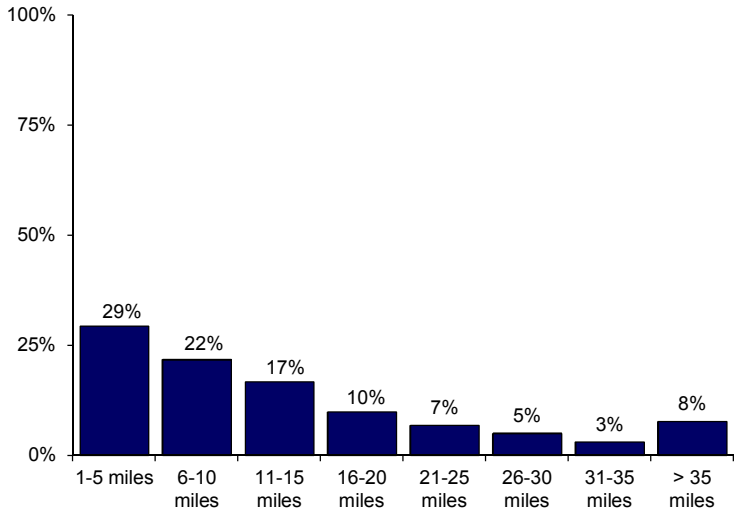

***Figure 2. Typical one-way commute to work statistics for the U.S. From* [*3*].**

These data report statistics of one-way commute-to-work distance in the United States, collected by U.S. Department of Transportation as part of the *Omnibus Household Survey,* a monthly household survey where at least one thousand interviews are completed each month. The *Omnibus Household Survey* collects data on core questions about general travel experiences, satisfaction with the system, and some demographic data. Data presented in *OmniStats,* [*3*], are taken from several issues

of the 2003 *Omnibus Household Survey* (covering activities in the months prior to the survey). The target population for the survey are current adults (18 years or older). Results are based on completed bi-monthly samples that are randomly selected using a list-assisted random digit dialing (RDD) methodology. An implicit stratification on the telephone prefixes is imposed to ensure that the sample is representative of the entire Country.

As reported in [***3***], to reach the workplace the average commuter travels approximately 15 miles, one way. Two out of three commuters (68%) reported a one-way commute of 15 miles or less, 22% traveled between 16 and 30 miles and 11% traveled more than 30 miles. The majority of commuters (81%) used only their personal vehicle to complete their commute and most personal vehicle users (86%) drove alone [***3***].

For each person considered in the simulation a commute distance is drawn from the distribution shown in *Figure 2* and two one-way trips are considered for every working day. The first trip (morning commute to work) occurs randomly between 7 am and 10 am while the second trip (evening commute from work) occurs randomly between 3 pm and 8 pm.

Commute-to-work distances are converted into velocity profiles by means of a *Velocity Profile Generator* and these profiles are fed to a backward vehicle dynamic simulator to compute the final energy consumption, in terms of fossil fuel and/or electricity.

3.2. Leisure and Shopping Trips

For the second category of trips considered: driving for leisure and shopping, synthetic activity patterns for each individual included in the simulation are generated using a heterogeneous Markov-chain approach. This stochastic model has been tuned using time-use data collected in *The American Time Use Survey* (ATUS) [***8***]. These profiles are a representation of the time-sequence of activities performed by typical U.S. drivers. Each individual is in one of several possible states in every discrete time step (i.e. *sleeping, working, cooking*, etc.).

One of the possible states is classified as *Away-not-working* (for further details refer to [***9***]). When an individual is in this state it is assumed that he/she can drive for a period of time that is no more than half of the time spent in the *Away-not-working* state. The exact driving duration is computed as:

$$t_{Driving} = \alpha \cdot t_{Away-not-working} \tag{1}$$

In the current study, α is drawn from a random variable uniformly distributed in the interval [0, 0.5]. With this interval, the calculated average mileage driven matches real data. Once the driving duration is known (and precisely defined in time) a stochastic model (*Distance Generator*) is used to find the distance traveled per each trip. Again, the distance travelled is converted to a velocity profile that is then fed to a vehicle model to compute energy consumption.

3.3. Distance Generator

The *Distance Generator* is a stochastic model based on historical data that converts a driving time to a corresponding driving distance.

In general, the relationship between driving time and driving distance of individuals is dependent on a very large set of personal and physical factors, such as driving style, weather, vehicle performance, road conditions and others. The *Distance Generator* has been calibrated using data collected from a PEV fleet composed of nine different vehicles for a total of over 100000 miles of real driving profiles. These data capture the driving styles of different drivers for a variety of alternative situations. The data are used to generate a probability distribution function relating trip distance and driving duration. Using a specified time as an input, different distances may be

generated as an output, capturing the effects of several factors, including use of highways versus streets, congestion phenomena, and other factors influencing the relationship between driving time and distance.

In this work it has been assumed that, for passenger vehicles, the relationship between duration and distance for a particular trip does not depend on the particular type of vehicle. Therefore the results can be applied to all classes of vehicles.

The raw trip distance and trip duration data have been aggregated into classes of coarseness with intervals of 5 kilometers and 5 minutes, respectively. Based on the trips present in each class, a trip distance probability distribution is derived. This is shown in *Figure 3*, where the color-coding indicates trip durations. *Figure 4* is a slice from *Figure 3* that reports the trip distance distribution for a trip duration of 50 minutes. This probability distribution matrix is then used to generate a realistic trip distance corresponding to a given trip duration.

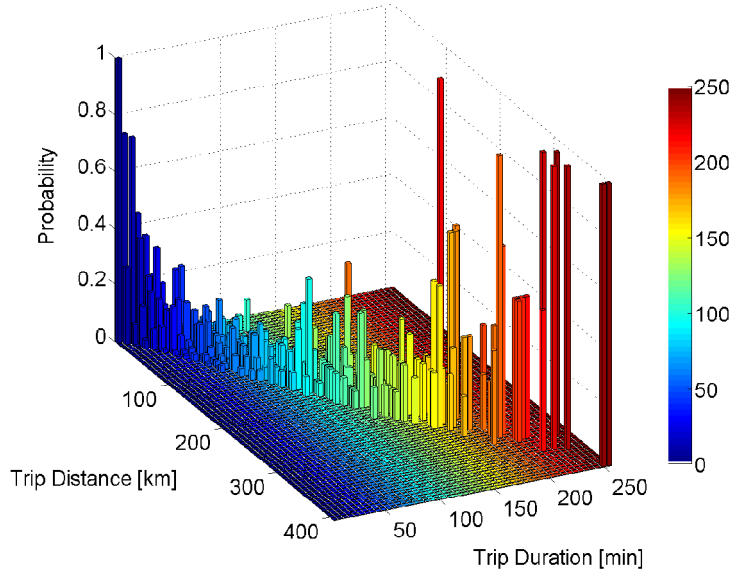

Figure 3. Trip distance probability distribution with respect to the trip duration.

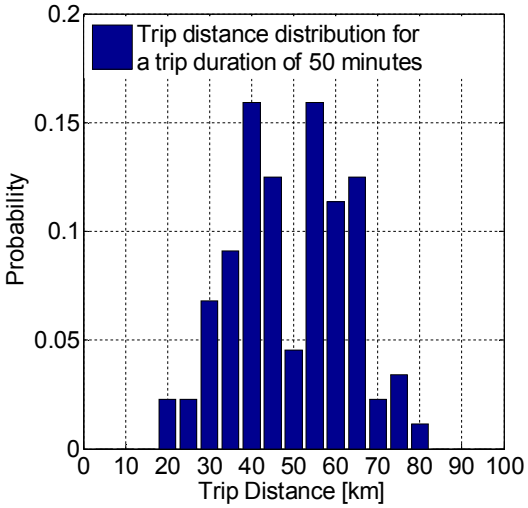

Figure 4. Trip distance distribution for a trip duration of 50 minutes.

The data used were collected as part of the SMART@CAR research program at The Ohio State University - Center for Automotive Research (CAR). This database includes detailed fleet data, including charging and duty cycles. More details can be found in [***10***] and [***11***].

3.4. Velocity Profile Generator

The *Velocity Profile Generator* is a simulation tool that generates vehicle velocity profiles based on the total trip distance and highway ratio[1]. Velocity profiles are generated using a Markov chain model whose probability transition matrixes have been identified using historical data.

To generate the velocity profile, the velocity v has been assumed to take on a finite number of values: $v \in \{v^1, v^2, \ldots, v^N\}$. Starting from the velocity, acceleration values, a, can be computed, which are also discretized into a finite set of values: $a \in \{a^1, a^2, \ldots, a^M\}$. All data have been clustered into one of the two classes of driving patterns considered, namely urban and highway.

The state vector of the Markov chain model is defined as: $x_k = (v_k, a_k)$, and its dynamics can be expressed by $x_{k+1} = w_k$. Since the transition of a_k is a deterministic process, the two-dimensional Markov chain describing the probability distribution of w_k can be reduced to a one-dimensional Markov chain:

[1] The highway ratio is defined as the proportion of the trip occurring on highways with respect to the total length of the trip, and it is determined starting from the probability distribution of collected data [HYPERLINK \l "QGo12" ***11***].

$$Pr\{w_k = (v^i, a^l) \mid w_{k-1} = (v^j, a^l)\} = p_{i,j}^l$$
$$i, j \in \{1,2,\dots,N\}, \qquad l \in \{1,2,\dots,M\} \tag{2}$$

where $\sum_{j=1}^{N} p_{i,j}^l = 1, \ \forall l \in \{1,2,\dots,M\}$ represents the one-step transition probability associated with the acceleration a^l. As described in Equation (2), the acceleration has been assumed to be constant during each transition. Starting from the empirical time-synchronized velocity and acceleration data collected for a set of vehicles, nearest-neighbour quantization is used to map the sequence of continuous observations (v, a) into a sequence of quantized states (v^i, a^l) [*12*]. The transition probabilities can then be estimated by means of the maximum likelihood estimator, which counts the observation data as:

$$\hat{p}_{i,j}^l = \frac{m_{i,j}^l}{m_i^l} \tag{3}$$

where $m_{i,j}^l$ is the number of times that a transition has occurred from v^i to v^j given that the acceleration was in the state a^l, and $m_i^l = \sum_{j=1}^{N} m_{i,j}^l$ is the total number of times that a transition has occurred from v^i when the acceleration was a^l. The procedure is repeated to calibrate a transition probability matrix for both the urban and highway portions of the trip. Accordingly, the data from the two classes of driving patterns have been exploited.

In this work, the velocity profile of a complete trip is obtained by composing three segments: each trip starts with an urban portion, followed by a highway portion and a second urban portion. This approach has been chosen to reproduce realistic driving conditions. The proportion of highway-to-urban driving is dictated by the highway ratio, while the proportion of the first urban portion (segment 1) to the second urban portion (segment 3) is drawn from a standard uniform distribution.

Again, note that the *Velocity Profile Generator* has been calibrated using historical data from a PEV fleet but it can be assumed that the relationships between trip duration and corresponding velocity profile do not depend on the type of vehicle. Velocity profiles generated can thus be used for all classes of vehicles.

3.5. Vehicle Dynamic Models

The driving profiles generated by the model discussed in Section 3 are used in a backward dynamic simulator developed in the Simulink-MATLAB® environment. The vehicle's longitudinal dynamics are given by [*13*]:

$$\dot{W}(t) = \left[m\dot{v}(t) + mg\cos(\theta)[r_0 + r_1 v(t)] + \frac{1}{2}\rho_{air} C_D v^2(t) + mg\sin(\theta)\right] v(t) \tag{4}$$

where $\dot{W}$ represents the power required at the wheels to move the vehicle at the desired velocity v, m is the mass of the vehicle, r_0 and r_1 are rolling resistance coefficients, ρ_{air} is the air density, C_D is the aerodynamic drag coefficient, and θ is the road grade.

The simulator has been used to model electricity and fossil fuel used by a set of four different vehicles:

1. Gasoline-fueled spark ignition vehicle (Conventional Vehicle)
2. Hybrid Electric Vehicle (HEV)
3. Plug-in Hybrid Electric Vehicle (PHEV)
4. Electric Vehicle (EV)

Table 2. Vehicles data.

	Vehicle	Curb Weight [kg]	Battery Capacity [kWh]	Electric Motor [kW]	ICE
	Conventional	1450	-	-	L4 – 2.2 liters
	HEV	1550	1.3	100	L4 – 1.6 liters
PEV	PHEV[1]	1700	16	110	L4 - 1.6 liters
PEV	EV[2]	1500	24	80	-

[1]40 miles all-electric range, [2]100 miles range.

Table 2 reports the main specifications of the four vehicle classes considered. Note that the values of these parameters can be adjusted depending on the specific vehicle being modeled. Here average parameters representative of the four types considered have been chosen, starting from characteristics of vehicles currently available on the market.
The model takes as input the velocity profile, $v(t)$, and computes liquid fuel consumption (in liters of fossil fuel), electricity drawn from the battery (in kWh) and final state of charge (SOC) of the battery. The output of the four vehicle models are presented in the next figures.

In conventional vehicles the amount of gasoline burned in the internal combustion engine represent the only contribution to the energy consumption, as shown in *Figure 5*.

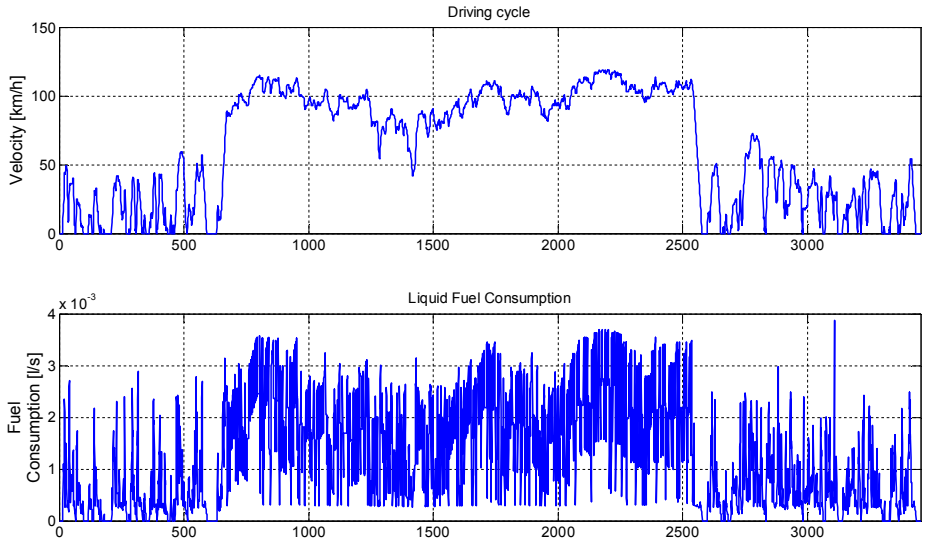

Figure 5. Conventional vehicle model output

In hybrid vehicles (HEVs and PHEV), both an internal combustion engine (ICE) and an electric motor (EM) are present on board. Thus, an energy split strategy is implemented to optimize the fuel consumption and battery depletion while coping with vehicle performance requirements.

The HEV control strategy is aimed at maintaining the battery state of charge within a pre-determined range – 62% to 68% – operating the vehicle in *charge-sustaining mode* (see Figure 6). The electric motor is used to assist the internal combustion engine in sudden accelerations. Also, the presence of the battery allows for regenerative breaking. Again, in this class of vehicles, fossil fuel is the only contributor to the energy consumption, since the battery cannot be charged via an external source.

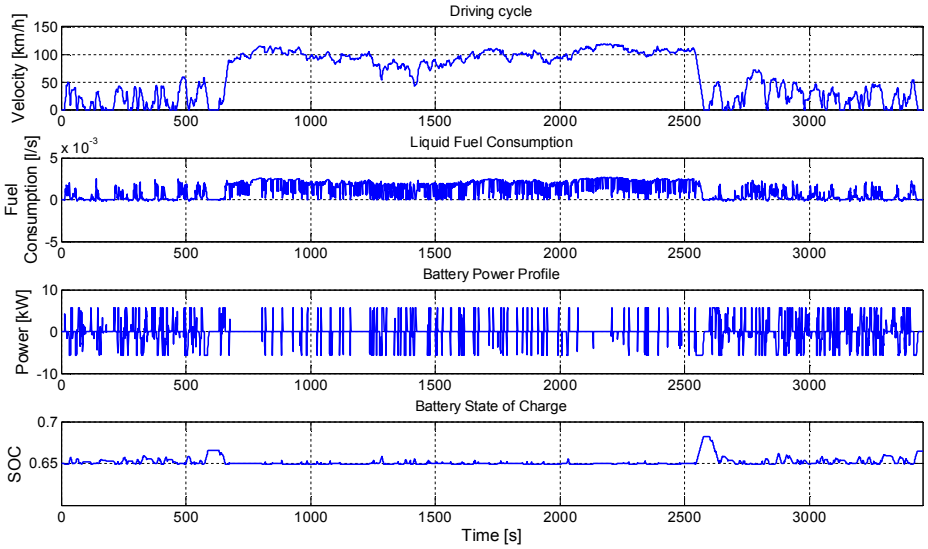

Figure 6. HEV vehicle model output

In PHEVs the energy splitting strategy is a combination of an initial *charge-depleting mode* followed by a *charge-sustaining mode* once the state of charge of the battery reaches 25% (see *Figure 7*). After the first portion of the trip, where the vehicle works as a pure EV, the PHEV behaves like an HEV and the internal combustion engine allows for an indefinitely long range (assuming availability of refueling stations).

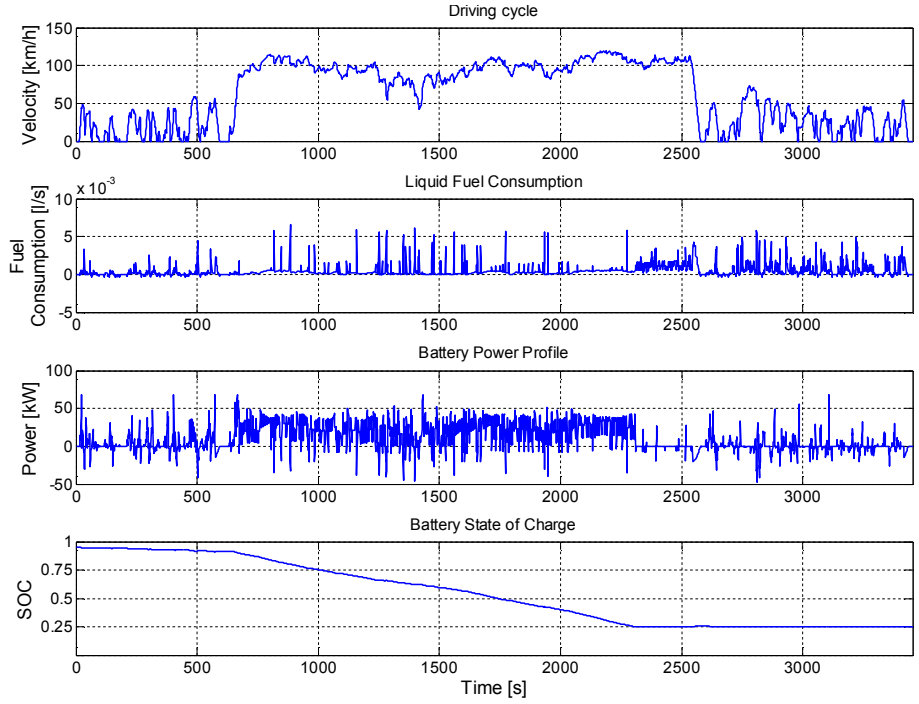

Figure 7. PHEV vehicle model output.

The PHEV has an *all-electric range,* namely the distance that can be covered in *charge-depleting mode,* which is directly proportional to the capacity of the battery. Typical values range from 10 to 40 miles. In PHEVs, both fossil fuel and electricity consumption are present since the battery can be recharged when the vehicle in connected to the grid.

Figure 8 shows the output of the EV model. For pure electric vehicles (EVs), electricity drawn from the grid is the only energy source and once the state of charge of the battery achieves a lower value (here assumed to be 20%) the vehicle shuts down, limiting the total range of the vehicle. Typical electric vehicles have a range of 100 to 180 miles, depending on the size of the battery installed (and in turn influencing the cost of the vehicle).

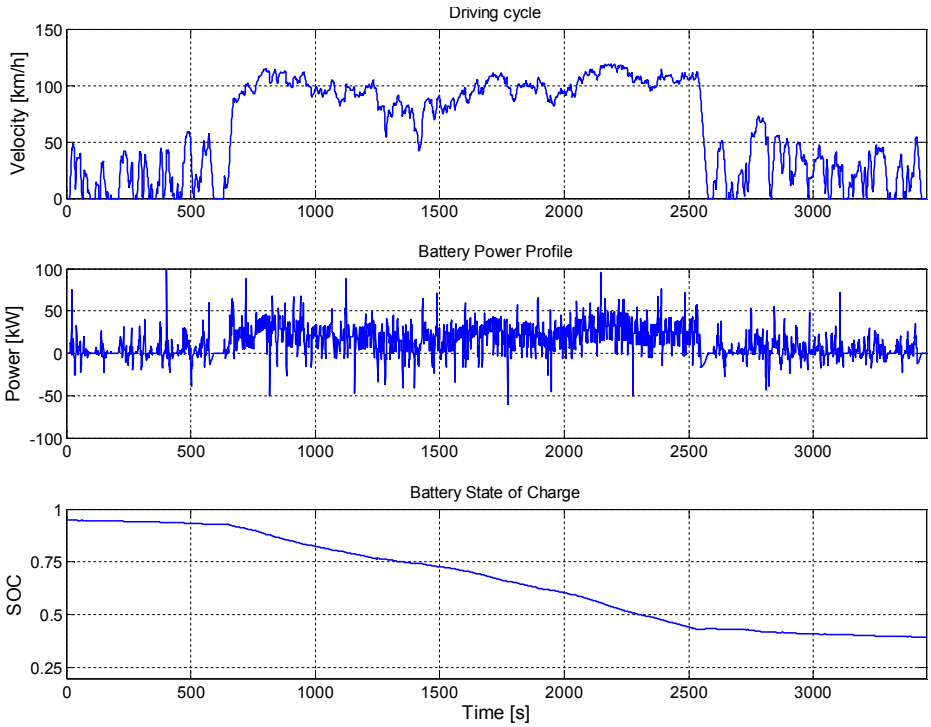

Figure 8. EV vehicle model output

4. Results

For the purpose of this work, a population of 100 individuals is used to represent the actual U.S. driving population. The representative population is composed by considering both the sex ratio (0.97 male/female, from [***14***]), and the labor force participation (73% for males and 60% for females, according to [***15***]). Hence, the population considered is:

- 36% working males;
- 31% working females;
- 20% non-working females;
- 13% non-working males.

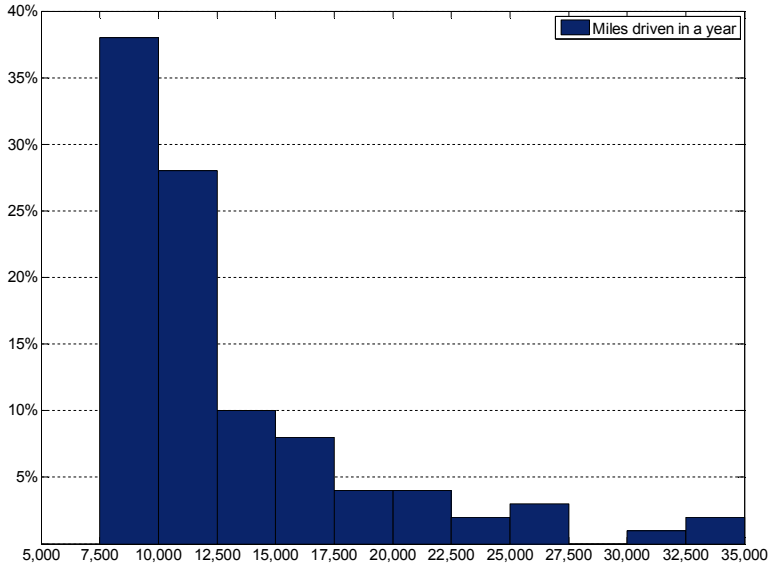

Figure 9. Annual traveled distance distribution, in miles, for the simulated population.

Figure 9 reports the distribution (in miles) of the total distance traveled by the individuals in the representative population, including both leisure trips and commuting to work. The simulated average distance traveled is 13057 miles. In [***16***], the average annual miles per driver in the U.S. is reported to be 13476, validating the procedure used in this work to generate the distances travelled over a year by the individuals composing the representative population.

The energy consumption of the four categories of vehicles comes from two different energy sources: gasoline burned in the engine and electricity used to charge the battery (produced off-board). In order to compare the performance in terms of total energy consumption, the electricity is converted to equivalent liters of gasoline on the basis of exergy. Accounting for the exergy efficiencies of the system components, kWh of electricity is converted into equivalent liters of gasoline as:

$$Q_{eq} = E \cdot \left(\frac{\varepsilon_{electricity} \cdot \varepsilon_{battery} \cdot \varepsilon_{EM}}{\varepsilon_{ICE} \cdot \varepsilon_{gasoline}} \right) \cdot \frac{3600}{LHV_{gasoline} \cdot \rho_{gasoline}} \tag{5}$$

Where Q_{eq} represents the equivalent liters of gasoline, E is the electricity consumption, in kWh, $\varepsilon_{electricity}$ is a term accounting for electricity generation efficiency and transmission losses, $\varepsilon_{battery}$ is the exergetic efficiency of the battery, ε_{EM} is the efficiency of the electric motor, $\varepsilon_{gasoline}$ represents the exergetic efficiency of gasoline production, and ε_{ICE} is the average efficiency of the internal combustion engine. LHV is the higher heating value of the gasoline, namely $44400\ kJ/kg$, $\rho_{gasoline}$ is $0.74\ kg/l$, and 3600 is a unit conversion factor.

Here the system boundaries have been considered to include the vehicle and related sources of exergy. Thus the power plant producing electricity and the plant for producing the gasoline, namely the refinery, appear inside the system considered. Electricity transmission and distribution losses have been considered while the gasoline distribution losses to reach the gasoline pump are assumed negligible [***17***]. The second term on the right side of Equation (5) is the ratio of the chain of efficiencies of the electric system to the efficiency of the internal combustion engine multiplied by the gasoline production efficiency.

In this work average exergetic efficiencies have been assumed to be:

- $\varepsilon_{electricity} = 0.34 \cdot 0.97 = 0.33$
- $\varepsilon_{battery} = 0.99$ [***18***]
- $\varepsilon_{EM} = 0.9$ [***19***]
- $\varepsilon_{ICE} = 0.21$
- $\varepsilon_{gasoline} = 0.9$ [***20***]

$\varepsilon_{electricity}$ has been computed using data from [***21***] and [***22***] for generation and transmission, respectively. For ε_{ICE}, 0.21 is the average value of the efficiency of the engine for the conventional vehicle presented in Table 2. This term is reported to vary up to 0.35, [***23***]

Table 3 gives a summary of the average energy consumption for the four classes of vehicles, expressed in terms of fuel or equivalent fuel consumption and normalized with respect to the conventional vehicle consumption. The results show that total energy consumption decreases as the electrification of the vehicle increases.

On average, for PHEV vehicles the equivalent electricity consumption is higher than the fossil fuel consumption. The proportion of these two terms is strongly affected by the charging strategy and availability of charging stations. In these simulations two recharges per day were allowed.

Table 3. Simulation results.

	Vehicle	Average Annual Traveled Distance [km]	Average Fossil Fuel Consumption	Average Equivalent Electricity Consumption
	Conventional	21013	100%	-
	HEV	21013	86%	-
PEV	PHEV[1]	21013	24%	29%
PEV	EV[2]	21013	-	37%

[1]40 miles all-electric range, [2]100 miles range.

Figure 10 shows the average simulated energy consumption, namely the sum of fossil fuel and equivalent electricity calculated as in Equation 5. The results for the 100 people simulated are aggregated into four classes with respect to the total miles driven in the year. Among each class the results are normalized with respect to the average conventional vehicle energy consumption for that specific class, to remove the influence of the total miles driven.

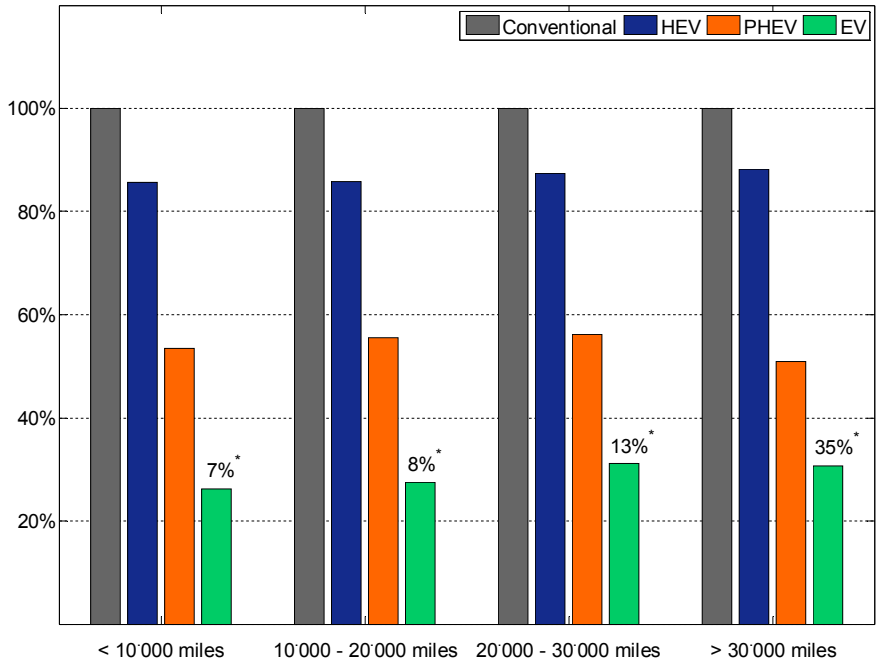

Figure 10. Normalized average energy consumption for vehicle types per yearly distance-driven classes. *Percentage of trips not completed due to limited range.

These results show that, independent of the miles driven annually, the higher the electrification of the vehicle, the lower the total primary energy consumption. This indicates that vehicle electrification would achieve the same relative energy savings for every kind of driver, spanning from those who rarely drive to those who drive over 30000 miles per year.

On the other hand, at the extreme of vehicle electrification, EVs exhibit a significant range issue. In *Figure 10*, the percentages of trips purely electric vehicles are unable to complete owing to intrinsic limitations of the battery are reported by *. The percentage varies from 7% to 13% for driving distances up to 20000 miles per year, but increases dramatically for driving distances over that threshold. These results are valid for the modeling used to simulate an EV: 100 miles of all-electric range with charging twice daily.

It is worth noting that the last two classes, including individuals driving more than 20000 miles per year, are composed solely by those who are classified as working, while non-working people are concentrated in the first two classes.

5. Conclusions

In this work a modeling approach to compute the total primary energy consumption for personal transportation in the United States has been presented. Realistic driving patterns for different individuals and highly resolved consumption patterns have been computed for four different vehicle types. For conventional vehicles and HEVs these consumption patterns include only fossil fuel, while electricity consumption is also considered in case of PHEVs and EVs.

The simulations performed in this work report a quantitative comparison of the four vehicles in terms of total primary energy consumption. Moreover, a numeric evaluation of the percentage of trips that purely electric vehicles are unable to complete is assessed.

The results obtained indicate that the higher the electrification of the vehicle the higher the primary energy savings. But we should qualify this by noting that the number of uncompleted trips by fully electric vehicles increases dramatically with the total mileage driven. Still, a better charging infrastructure, batteries with higher capacity, or a different charging technology (e.g. high voltage direct current or battery swapping) would alleviate the range issue of all-electric vehicles.

Finally, the results obtained indicate that the total primary energy consumption for all vehicle types is essentially independent of the total mileage driven during the year.

This modeling methodology can serve as a tool for:

- Generating realistic driving patterns for different individuals (e.g. useful in performing statistical analysis, evaluation and comparison of different vehicles, or in deciding preferred dwelling locations relative to workplace).
- Developing demographic considerations on transportation energy consumption for different classes of drivers (e.g. working people versus people not included in the labor force).
- Evaluating the impact of PEVs on the electric grid – especially at the distribution level. For this, precise information on charging time and duration of PHEVs and EVs is crucial.
- Assisting policy-makers in evaluating incentives in the transportation sector, such as automaker-discounts for PEVs and tax discounts for owing high-efficiency vehicles.
- Assisting policy-makers in estimating impact of PEV market penetration on primary energy and crude oil consumption.
- Comparing the initial cost of different vehicles and their expected energy-use operating cost.

Acknowledgments

This work has been supported in part by the National Science Foundation through grant CBET-1029337 and in part by the SMART@CAR Program (a multi-industry and academic R&D collaborative focused on plug-in electric vehicles and intelligent charging) at The Ohio State University - Center for Automotive Research. Any opinions and conclusions expressed in this paper are those of the authors and do not necessarily represent those of SMART@CAR members.

References

[1] U.S. Energy Information Administration. (2010) International Energy Statistics. [Online]. http://www.eia.gov/cfapps/ipdbproject/IEDIndex3.cfm

[2] U.S. Energy Information Administration, "Annual Energy Review 2009," DOE/EIA-0384, August 2010.

[3] Research and Innovative Technology Administration (RITA), "Omnibus Household Survey," U.S. Department of Transportation, Bureau of Transportation Statistics, Vol. 3, Issue 4 2003.

[4] U.S. Department of Transportation, Federal Highway Administration, "National Household Travel Survey," http://nhts.ornl.gov, 2009.

[5] A. Capasso, W. Grattier, R. Lamedica, and A. Prudenzi, "A bottom-up approach to residential load modeling," IEEE Trans Power Syst, vol. 9, pp. 957–64., 1994.
[6] Shui Bin and Hadi Dowlatabadi, "Consumer lifestyle approach to US energy use and the related CO2 emissions," Energy Policy, vol. 33, no. 2, pp. 197-208, 2005.
[7] C. Weber and A. Perrels, "Modeling lifestyle effects on energy demand and related emissions," Energy Policy, vol. 28, pp. 549-566, 2000.
[8] U.S. Bureau of Labor Statistics. (2010, June) American Time Use Survey. [Online]. http://www.bls.gov/tus/home.htm
[9] Matteo Muratori, Vincenzo Marano, Ramteen Sioshansi, and Matthew Roberts, "Residential Power Demand Prediction and Modelling," in The 24th International Conference on Efficiency, Cost, Optimization, Simulation and Environmental Impact of Energy Systems, Novi Sad, Serbia, July 4-7, 2011.
[10] Q. Gong, S. Midlam-Mohler, V. Marano, and G Rizzoni, "An Iterative Markov Chain Approach for Generating Vehicle Drive Cycles," SAE International Journal on Engines, vol. 4, no. 1, pp. 1035-1045, 2011.
[11] Q. Gong, S. Midlam-Mohler, V. Marano, and G Rizzoni, "Virtual PHEV Fleet Study Based on Monte Carlo Simulation," International Journal of Vehicle Design (IJVD), vol. [in press], 2012.
[12] C.-C. Lin, H. Peng, and J.W. Grizzle, "A Stochastic Control Strategy for Hybrid Electric Vehicles," in 2004 American Control Conference, Boston, MA. USA., 2004.
[13] G. Nakhaie Jazar, Vehicle Dynamics: Theory and Application, 120083rd ed.: Springer.
[14] Central Intelligence Agency, "The World Factbook 2009," Washington, DC, 2009.
[15] Marlene A. Lee and Mark Mather, "U.S. Labor Force Trends," Population Bulletin, vol. 63, no. 2, June 2008.
[16] Federal Highway Administration - Office of Highway Policy Information, "Our Nation's Highways," U.S. Department of Transportation, FHWA-PL-01-1012, 2011. [Online]. http://www.fhwa.dot.gov/ohim/onh00/bar8.htm
[17] Michael Wang, "Well-to-Wheels Energy and Emission Impacts of Vehicle/Fuel Systems," Center for Transportation Research - Argonne National Laboratory, 2003.
[18] A. J. Smith, J. C. Burns, and J. R. Dahn, "A High Precision Study of the Coulombic Efficiency of Li-Ion Batteries," Electrochemical and Solid-State Letters, vol. 13, no. 12, pp. A177–A179, 2010. [19] H. Auinger and Erlangen, Germany Siemens AG, "Efficiency of electric motors under practical conditions," Power Engineering Journal, vol. 15, no. 3, pp. 163 - 167 , June 2001.
[20] Ignasi Palou-Rivera and Michael Wang, "Updated Estimation of Energy Efficiencies of U.S. Petroleum Refineries," Center for Transportation Research - Argonne National Laboratory, July 2010.
[21] U.S. Energy Information Administration, "Power Plant Operations Report," Form EIA-923, 2011.
[22] U.S. Energy Information Administration, "Annual Energy Outlook 2012 Early Release," January 2012.
[23] Richard Van Basshuysen and Fred Schafer, Internal Combustion Engine Handbook. Warrendale, Pa., USA: SAE International, 2004.

Resource Use Evaluation of Turkish transportation Sector via the Extended Exergy Accounting Method

Candeniz SECKIN[a], Enrico Sciubba[b] Ahmet R. BAYULKEN[c]

[a] *Energy Institute, Istanbul Technical University, Istanbul, Turkey, seckin@itu.edu.tr*
[b] *Department of Mechanical and Aerospace Engineering, University of Roma La Sapienza, Rome, Italy, enrico.sciubba@uniroma1.it*
[c] *Energy Institute, Istanbul Technical University, Istanbul, Turkey, ahmetbayulken@yahoo.com*

Abstract:

The purpose of this work is to apply the Extended Exergy Accounting (EEA) method to the different modes of the Turkish transportation sector (TR) for the year 2006. To evaluate the sectoral resource use, the extended exergetic efficiency (EEA_{eff}) is calculated, which requires the consideration of all commercial and private transportation services (passengers and goods) and also of all services directly related to transportation (post, cargo, etc.). As a result of the current unsustainable transportation strategy that relies on road transportation - which causes high fossil fuel consumption and destruction of high percentage of the incoming exergy into the sector – the resulting EEA_{eff} of the sector is rather low. Another result of the high fossil fuel consumption is the substantial amount of CO_2-equivalent emissions that demand for a high environmental remediation cost (EE_{ENV}) which contributes to the low EEA_{eff} of the sector.

Keywords:

Extended exergy accounting, EEA, transportation, ecological accounting, Turkey

1. Introduction

In the last decades, scientists, researchers and engineers paid a great attention to the concept of exergy and routinely applied exergy analysis to various industrial processes. **"**Exergy" (available energy) is defined as the maximal amount of work that can be extracted from the system in the process of reaching equilibrium with the environment (dead state) [41]. This definition underlines the impossibility of obtaining further work from a system which is in equilibrium with the dead state. Hence, Exergy can be regarded as the part of the physical resource base used (consumed) in all types of anthropic activities and serves as a rationally unified measure of utility and scarcity. The exergy content of a natural resource characterizes "the measure for potential usefulness" (in other words, quality), i.e., its ability to perform "useful work" [1]. The main advantage of an exergy based analysis compared with the more traditional energy analysis is the identification and quantitative assessment of global and local irreversibilities, which result in a measure of resource degradation in the processes. Besides, the exergy concept provides a unified quantifier which can be used in the evaluation of resource quality (material or immaterial). Exergy is not a direct measure of pollution [37] but indicates the potential to cause change in the environment since it is also a measure of distance between a released substance and the environmentally neutral (pseudo-equilibrium) state. It ought to be noticed that exergy does not directly measure, for instance, toxicity [37, 55].

Society exergy analysis can be defined as an accounting of resource exergy use through the society. It answers the question of how effective the exergetic resources have been consumed in sectoral processes and how much exergy is destroyed within each societal sector. Hence, it contributes to establishing the energy and environmental policies of a society. As a result, exergy based studies in the scientific literature have been proposed as an auxiliary tool for Energy Managers and policymakers [54, 55].

Classical energy and exergy analysis and also some enhanced methodologies derived from them (like Cumulative Exergy Analysis, Embodied Energy Analysis, Thermoeconomics, Emergy Analysis, Exergy Life-Cycle Analysis etc.) do not rationally address the problem of converting non-energetic/immaterial expenditures into resource consumption. Extended Exergy Accounting (EEA) has incorporated some elements of aforementioned methods [33,34] and can be considered as a synthesis of the pre-existing theories but with a novelty: providing a calculation route to obtain the exergetic equivalent of non-energetic expenditures "invested" in labour, capital and environmental impact (the apposition "extended" refers in fact to the enhanced capabilities of the method). EEA is a totally resource-based exergy costing method and determines the exergetic cost as the "amount of primary exergy resources" required to generate a product or a service. The exergetic equivalent of labour and capital is the sum of all direct and indirect exergy expenditures necessary to generate them. Environmental impact is represented by the total exergetic resource consumption in the environmental remediation processes needed to treat the considered emissions. Thus, EEA provides a direct quantitative comparison of energetic and/or material quantities with non-energetic and/or immaterial quantities [33].

As implied in the title, this study is primarily about resource consumption of the Turkish transportation sector by means of EEA method (on a year 2006 database). The transportation sector provides many benefits to the society: it is indispensable, for instance, for business to link different locations and to enable physical access to markets, and for inhabitants to access labour markets, to support economy and socialization [8]. The sector is also crucial in the global national resource use (especially energy use) in development and developing countries, and it also has a very special importance as one of the major sources of air pollution (it accounts for more than 15% of the greenhouse gas emission in Turkey [45]). Hence, it is worthy to analyze the sector from a resource consumption point of view [21, 40]. To examine sectoral resource use, classical exergy analyses applications of Turkish transportation sector are available in the literature [8,54], as well as those for other countries [9, 2, 7, 56, 31, 20, 12]: calculations of the EEA efficiency of the TR sector are presented in the studies of societal EEA analyses of Norway [10], Italy [24], UK [14] and China [6] and also for province of Siena in Italy [32]. Since the environmental remediation costs (EE_{ENV}) of sectoral solid waste and gas emissions are explicitly calculated by means of real treatment processes, in accordance with the original specifications of the EEA method [38] (avoiding the somewhat artificial conversion of monetary expenses related to environmental treatment systems into exergetic costs), the present study is different from earlier EEA analyses and contributes to the development of EEA method and its future applications.

The present paper focuses also on the determination of "environmental remediation cost (EE_{ENV})" of the solid waste originated in TR. The concept of "environmental remediation cost" relies on the "zero impact" approach which can be described as bringing the state of the effluent streams to thermodynamic equilibrium with the reference state before being discharged into the environment (i.e., the discharged effluent has "zero impact" on the environment) [38]. The cumulative amount of resources (each one of them measured by its exergy) "used up" in environmental remediation processes to attain a zero-impact disposal represents the "EE_{ENV}" of the considered effluent.

2. The EEA method

In EEA, the cost of a product is the sum of energy carriers, materials, capital and labor transferred to the system, plus the primary resource equivalent to avoid the environmental impact of effluents and pollutants. This sum represents the "extended exergy (EE)" of the system products.

The EE (extended exergy) of a commodity is [34]:

$$EE = E_M + E_{phys} + EE_L + EE_C + EE_{ENV} \quad (1)$$

where E_M (material exergy) is the sum of the raw materials' exergy used in the production of the commodity; E_{phys} (physical exergy) indicates the algebraic sum of the exergy of energy flows used in the production of the commodity (heat, electrical energy, etc.); EE_C (capital equivalent exergy) is

the exergetic equivalent of the total net monetary influx into production; EE_L (labour equivalent exergy) is the exergetic equivalent of the sum of the labour contributions; EE_{ENV} is the exergetic equivalent of the environmental remediation cost. The computation of the exergetic equivalent of labour and capital is presented in Appendix A.

The EE_{ENV} is:

$$EE_{ENV} = E_{M-t} + E_{phys-t} + EE_{L-t} + EE_{C-t} + EE_{ENV-t} - E_{P-t} \quad (2)$$

where E_{M-t}, E_{phys-t}, EE_{L-t} and EE_{C-t} are respectively the net exergy of material, energy carriers, labour and capital received by the environmental remediation system; E_{P-t} is the exergy of the environmental remediation system "possible" product (P_t).

3. EEA analysis of transportation sector

3.1. Energy Carriers

Table 1 presents the total transferred energy carriers consumed by the TR sector and the total exergy use: the sum of exergy consumptions via energy carriers amounts to 663682,24 TJ (based on [17] and [44]).

Table 1. TR Sector energy consumption

	LPG[1]	Motor Gasoline[1]	Aviation Fuel[1]	Diesel[1]	Heavy Fuel Oil[1]	Liquid Biomass[1]	Natural Gas[2]	Electricity[2]
Rail	0	0	0	214	0	0	0	810
Air	0	0	1723	0	0	0	0	0
Marine	0	0	0	345	112	0	0	0
Road	1570	2702	0	7661	0	2	165	0
Pipeline transport	0	0	0	0	0	0	5227	522
Non-specified	0	0	0	0	0	0	0	1512
Consumption	1570	2702	1723	8220	112	2	5392	2844
Exergy (MJ/Ton)	46837,75	44350,77	44589,42	46366,72	39791,35	43961,40		
Total Exergy (TJ)	73535,28	119835,79	76827,57	381134,41	4456,63	87,92	4960,64	2844,00

[1] 1000 Ton

[2] TJ

3.2. Materials

To determine the exergy of materials (E_M) transferred to the TR sector (industrial products and imported commodities), exact data of material transfers between Turkish sectors are necessary. Unfortunately, such data are unavailable for Turkey. As an alternative, in this study, it is assumed that the exergy of industrial products is distributed through the sectors proportionally to the sectoral "fixed capital investment + purchases of goods and services" for which accurate data exist [45, 46]. The TR share is 7,25% of the sum of the industrial and net "import-export" flows. Details are presented in Table 2.

Table 2. TR sector material consumption

Industrial products exergy (TJ)[a]	5.521.069
Industrial "Import-Export" products exergy (TJ)[b]	17.626.763
Material transfer received by TR (TJ)	1.678.879

3.3. Exergy equivalent of externalities

In Appendix A, ee_L (primary resource exergy embodied in one workhour) and ee_K (primary resource exergy embodied in one monetary unit) are calculated and results for the Turkish society 2006 are presented. Details of the calculation route and detailed explanations are available in [34,35].

The definition of environmental remediation cost is presented in Section 1. Since, in reality, there is no totally "clean" technology [38] and most current treatment technologies do not always produce

effluents in equilibrium with the surroundings, choosing the minimum environmentally hazardous technology is a reasonable approach [36] and is adopted in this study.

3.3.1. Labour

The annual labour received by TR and its exergetic equivalent are presented in Table 3. Workhours for regular and part-time, seasonal and occasional employees are extracted from [47,49]. Due to the lack of accurate data for self-employed workers, it is assumed that their average work load is 35 hours/week. Multiplying the total sectoral workhours by ee_L provides the exergetic equivalent of labour (ee_L for Turkey is presented in Appendix A)

Table 3. Embodied exergy of labour (EE_L) consumed in TR

	Workhours	Exergy of labour (TJ)
Regular&occasional employees	2.269.391.832	349.378
Self employed	340.949.840	52.490
Employers	66.322.730	10.211
Unpaid family workers	20.429.020	3.145
TOTAL	2.697.093.422	415.224

3.3.2. Capital

The exergy embodied in capital is obtained by multiplying the corresponding monetary flux by the unit exergetic equivalent of capital (ee_K) which is presented in Appendix A. Monetary and exergetic capital fluxes are shown in Table 4.

Table 4. Embodied Exergy of Capital (EE_C) consumed in TR

	Monetary flux ($)	EE_C (TJ)
Input	$150{,}928 \times 10^9$	3.848.726
Output	$127{,}558 \times 10^9$	3.252.783

3.3.3. Environmental remediation

In the assessment of the environmental impact of TR effluents (which consist of solid waste and gas emissions), alternative treatment technologies can be also considered [11] but the technologies used in this study are mainly well-established and commercially mature systems. Sectoral solid and gas effluents display a broad diversity and it is impossible to deal with all of them in detail in a single global study. The solid waste considered here pertains therefore only to the road transportation subsector, known to be by far the strongest contributor to the total sectoral solid waste, since Turkey's transportation infrastructure mainly relies on road transportation. Due to lack of reliable data, recycled batteries, motor oil and other fluids are not included in this study. For sectoral gas emissions, the CO_2 equivalent is considered.

3.3.3.1. Solid waste

The system (chain of processes) employed in this study to remedy the TR solid waste is presented in Fig. 1. In this study, ELVs (end of life vehicles) undergo dismantling, shredding and recycling in MRF (mechanical recycling facilities). Shredded tires are dispatched to a nearby CHP (combined heat and power plant) for energy production (i.e. tire incineration). Produced ash from recycling and incineration is landfilled. In the figure, TRP 1, 2, 3 and 4 refer to number of necessary transportation lines in the system.

Details of waste generation estimations are presented in Appendix B. Solid waste generation from the TR sector is estimated to amount to 176832 Ton materials extracted from ELVs and 109326 Ton of tires. ELV's are assumed to be self-driven to the MRF plant. Waste tires from operating

(IUV) are collected by 16 tons trucks. The number of trucks and their energy consumption is calculated based on data adapted from [3].

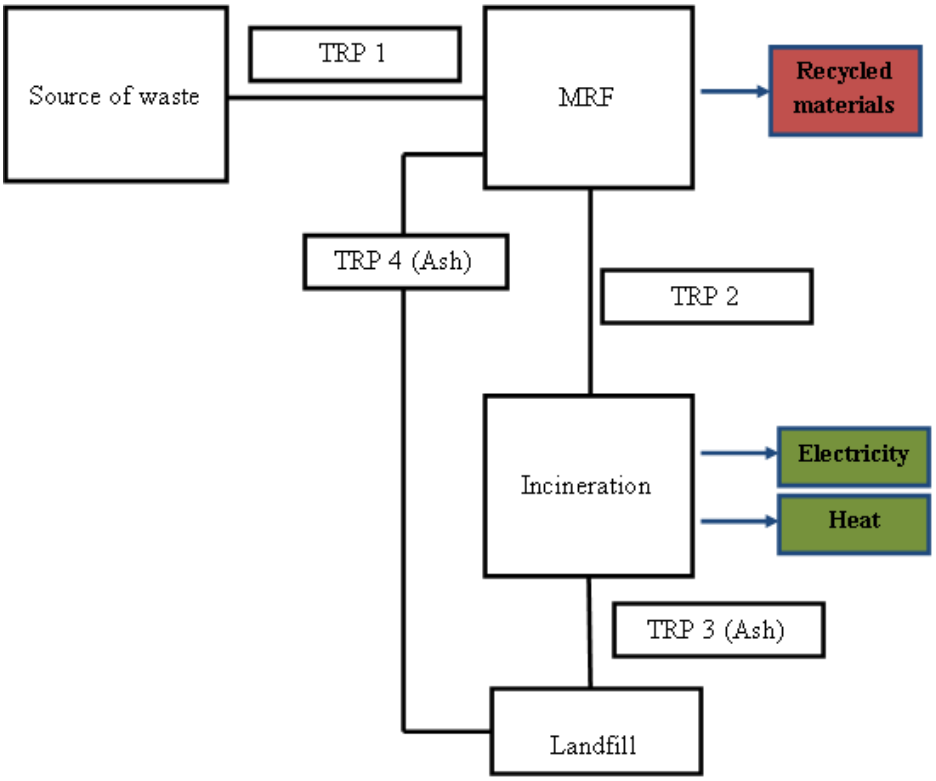

Fig. 1. Flowchart of TR sector solid waste treatment

An exact analytical analysis is impossible due to lack of sufficiently disaggregated data on the material composition of several items in the system. As a result, the exergy of tools and materials in the whole system (material exergy) is computed by converting the known monetary cost of the processes into its exergetic equivalent by means of ee_K (Appendix A) and presented in Table 5.

As for the capital flows, capital investment in the system is assumed to be supplied by bank loans at an annual interest rate of 20% and payback time of 10 years: the resulting annual payment is 23,85% of the capital investment. Annual "fixed and varying operation costs" are assumed to be 20% of capital investment and referred as "OP" in Table 6. Diesel fuel price in $Turkey_{2006}$ was 1,47 $/l [51]. Due to the lack of disaggregated data for landfilling, total resource consumption of the process is taken to be the exergetic equivalent of the landfilling price (10€/ton [42] in this study**)** and are shown in Table 6- Table 8. Their total amount is 4152,27 TJ.

Table 5. Exergy of material fluxes (E_{M-t})

Part of the system	Unit cost	Material Exergy (TJ)
Dismantling of ELVs	6,6 $/ton[1]	30,48
Shredding of ELVs	124,15 $/ton[1]	529,82
Shredding of tires	12 $/ton[2]	33,45
Recycling	100 $/ton[3]	537,6972
CHP	7000 $/$KW_{el}$	7706,11
TRP1 trucks		1,82
TRP2 trucks		0,45
TRP3 trucks		0,45
TRP4 trucks		0,45
Total		8840,74

[1] [13]

[2] [26]
[3] [39]

Table 6. Exergetic equivalent of capital

System/Process		Capital	Exergetic equivalent of IC (TJ)	Exergetic equivalent of annualized IC (TJ)	Exergetic equivalent of OP (TJ)	Annualized IC+OP (TJ)
MRF plant:						
	Dismantling of ELVs	6,6 $/ton	30,48	7,27	6,10	13,37
	Shredding of ELVs	124,15 $/ton	529,82	126,37	105,96	232,34
	Shredding of tires	12 $/ton	33,45	7,98	6,69	14,67
	Recycling	100 $/ton	537,70	128,25	107,54	235,79
Incineration plant		7000 $/$KW_{el}$	7706,11	1838,08	1541,222	3379,30
Landfilling		10 €/Ton	12,81	3,06	2,56	5,62
Total						3881,09

Table 7. Exergetic equivalent of the capital of trucks

Transportation line	Number of trucks	Exergetic equivalent of IC (TJ)	Exergetic equivalent of annualized IC (TJ)	Exergetic equivalent of OP (TJ)	Annualized IC+OP (TJ)
TRP-1	39	69,55	16,59	13,91	30,50
TRP-2	1	1,78	0,43	0,36	0,78
TRP-3	1	1,78	0,43	0,36	0,78
TRP-4	1	1,78	0,43	0,36	0,78
Total	42				32,84

Table 8. Exergetic equivalent of the capital of diesel fuel consumption

Transportation line	Diesel Consumption (lt)	Exergetic equivalent of diesel cost (TJ)
TRP-1	6059879,17	226,93
TRP-2	165225,97	6,19
TRP-3	82612,99	3,09
TRP-4	56820,87	2,13
Total		238,34

The only energy carrier input to the system is diesel fuel consumption of the TRP lines (T1-4 in Fig.1**)** and is presented in Table 9 (calculations based on data from [3]**)**. The trucks are assumed to have 16 tons carrying capacity and to travel empty on their respective return routes.

Table 9. Exergy of energy carrier fluxes ($E_{phys\text{-}t}$)

	Diesel Consumption (Ton)	Exergy of diesel consumption (TJ)
TRP-1	5060,00	234,62
TRP-2	137,96	6,40
TRP-3	68,98	3,20
TRP-4	47,45	2,20
Total		246,41

For labour flows, it is assumed that the system is manned for 340 days a year/24 hours a day (including annual shutdowns for maintenance). Based on data in [4], the labour force of the CHP plant is assumed to consist of 200 worker/1000 MW_{h+el}. For the whole system, the number of workers is assumed to be 300 worker/1000 MW_{h+el} with 1800 workhours/year for each worker. For transportation, labour is calculated based on the total number of truck missions. For T1, the average speed of trucks is assumed to be 40 km/h (including collection of waste-urban transportation) and for T2, T3 and T4, 60 km/h (rural transportation). Other details about the TRP lines can be derived from [3] and labour consumption of the system is shown in Table 10.

Table 10. Exergy of labour fluxes (EE_{L-t})

Transportation line	Labour (workhours)	Exergetic equivalent of labour (TJ)
TRP-1	124865	19,22
TRP-2	2720	0,42
TRP-3	1760	0,27
TRP-4	1200	0,18
System excluding transportation	50121,15	7,72
Total		27,81

The need for environmental remediation of the system is originated by the emissions of transportation and by the incineration of tires. Emissions from diesel fuel use and tire incineration are taken from [18] and [5] respectively and presented in Table 11. Total diesel consumption and total weight of incinerated tires are reported in Table 9 and Table B1, respectively. System CO_2 emissions and corresponding EE_{ENV-t} are shown in Table 12 (EE_{ENV-t} for CO_2 is computed in Section 3.3.3.2)

Table 11. Emission factors

	CO_2 (kg/TJ)
Diesel use	74100
Tire incineration	85303,20

Table 12. System emissions and treatment cost (EE_{ENV-t})

Diesel consumption (Ton)	5.314,39
Incinerated tires (Ton)	109.326
Diesel Energy (MJ/Ton)	42.791
Tire Energy (MJ/Ton)	29.000
CO_2 emissions (Ton)	287.300
CO_2 emission treatment cost (TJ/Ton CO_2)	0,0576
CO_2 EE_{ENV} (TJ)	16.561,89

In Table 13, recycled materials in MRF and their exergy content are presented. Data for energy use and efficiency in recycling processes are obtained from [29]. Heat and electricity consumption of the system are supplied from the CHP plant. Net electricity and heat output of the system are presented in Table 14. (It is assumed that the CHP plant produces useful heat at an average temperature of 100°C).

The total exergy of the system products (E_{P-t} in (2)) is calculated as:

$$E_{P-t} = E_{el-net} + E_{h-net} + E_{rcy} \quad (3)$$

where E_{el-net}, E_{h-net} and E_{rcy} are the exergy of generated net electricity, net heat and recycled materials respectively. E_{el-net}, E_{h-net} and E_{rcy} are presented in Table 13 and 14. The total exergy (E_{P-t}) is 2762,34 TJ.

Table 13. Recycled material products

	Recycled material (Ton)	Exergy[1] (MJ/Ton)	Total Exergy (TJ)
Ferrous metal	129.043,62	6800	877,50
Rubber	4.055,89	32.502,16	131,83
Magnesium, Zinc	2.524,08	15.628,64	39,45
Copper	2.297,45	2.112,06	4,85
Aluminum	5.695,85	32.928,09	187,55
Glass	5.080,79	131,48	0,67
Plastic	6.117,35	32.502,16	198,83
Total			1.440,67

[1] [41]

Table 14. Products of the treatment system of TR sector solid waste

Products	Energy (TJ)	Exergy (TJ)
Electricity	1079,72	1079,72
Heat	1203,77	241,95
Recycled materials		1440,67
Total		2762,34

$E_{M\text{-}t}$, $E_{phys\text{-}t}$, $EE_{L\text{-}t}$, $EE_{C\text{-}t,}$ $EE_{ENV\text{-}t}$ for solid waste treatment system is presented above. Accordingly, environmental remediation cost (EE_{ENV}) for solid waste of TR sector is obtained from equation (2) and amounts to 27066,78 TJ

3.3.3.2. Gas emissions

The schematic representation of the Ca-based CO_2 capture system is shown in Fig. 2 for 1 kg CO_2/year. In the "CO_2 removal part", a "carbonization reaction" occurs (equation (4)) at high temperatures (~600–750 °C) and atmospheric pressure [16]:

$$CaO(s) + CO_2(g) \longrightarrow CaCO_3(s) \qquad \Delta H = -177 \text{ kJ/mole} \qquad (4)$$

The system used in this study is based on a process description given in [30]. System CO_2 capture efficiency is 85%. The incoming CO_2 is at the annual average temperature of Turkey (14°C) and atmospheric pressure. Details of the system are provided in [30]. Heating of CO_2 is done by a natural gas fueled heater (80% efficiency, natural gas high heating value: 38,73 MJ/m^3) whose natural gas consumption is given in Fig. 2. Heat released from the carbonization reaction and from the cooling of $CaCO_3$, CaO and CO_2 is used for electricity generation (Fig 2). CaO and $CaCO_3$ are landfilled as system products. System products (P_t) are: electricity, CaO and $CaCO_3$. A mass balance of the system is shown in Fig. 2. The electricity generation unit has an efficiency of 35% and the plant self-consumption amounts to 4,5% of the generated power [27]. $E_{M\text{-}t}$, $E_{phys\text{-}t}$, $EE_{L\text{-}t}$, $EE_{C\text{-}t,}$ flows are shown in Table 15. For material flows, the same calculation route described in Section 3.3.3.1 is applied.

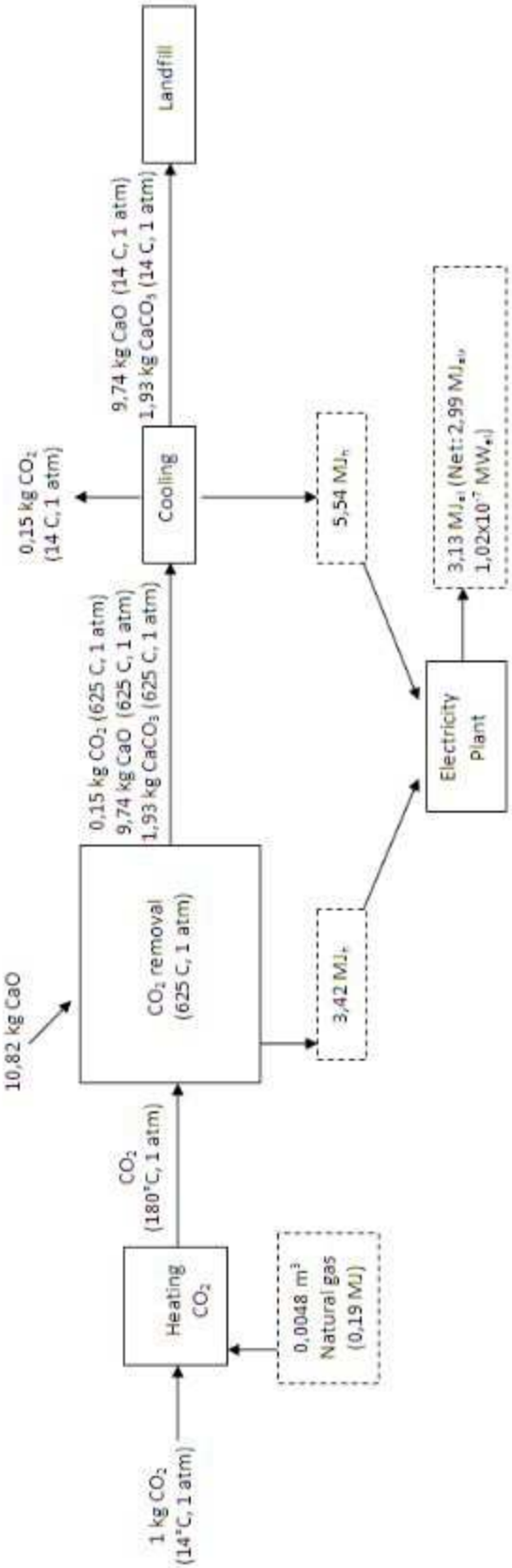

Fig 2. Flowchart of the CO_2 treatment system

Table 15. E_{M-t}, E_{phys-t}, EE_{L-t}, EE_{C-t} fluxes into CO_2 treatment system

	Unit cost	Capital Cost (MJ)	Annualized capital cost (MJ)	OP Cost (MJ)	EE_L (MJ)	Exergy (MJ)
Material input (E_{M-t})						
CaO [a]						21,294
Natural gas heater	5 $/KW	$8,0x10^{-4}$				$8,0 x10^{-4}$
Electricity plant	5000$/$KW_{el}$	13,62				13,62
Trucks for transportation						0,01
Energy Carrier (E_{phys-t})						
Natural gas						0,17
Diesel for transportation						1,37
Capital Input (EE_{C-t})						
CaO	0,063 $/kg			17,37		17,37
Natural gas heater	5 $/KW		$1,94 x10^{-4}$	$1,63 x10^{-4}$		$3,575 x10^{-4}$
Natural gas	0,335 $/$m^3$			0,04		0,04
Electricity plant	5000$/$KW_{el}$		3,25	2,72		5,97
Truck for transportation			0,11	0,10		0,21
Diesel fuel cost	1,47 $/l			1,32		1,32
Landfill	12,6 $/Ton	3,75				3,75
Labour (EE_{L-t})						
System (except transportation)	250 workers/1000 $MW_{(el+h)}$				0,0098	0,0098
Transportation					0,11	0,11
$E_{M-t}+E_{phys-t}+EE_{C-t}+EE_{L-t}$:						65,25

Natural gas heating, transportation emissions and system CO_2 loss (untreated CO_2) are the effluents from the CO_2 environmental remediation system. The transportation system is the same as presented in Section 3.3.3.1. Emission factors are extracted from [18, 19] and presented in Table 16 (based on LHV of the respective fuels). E_p (sum of products exergy) is listed in Table 17 (based on [41]).

Table 16. CO_2 emissions from the system

	CO_2
Diesel	
Emission factor (kg/TJ)	74100
Emissions (kg)	0,09
Natural Gas	
Emission factor (kg/TJ)	56100
Emissions (kg)	$9,59x10^{-3}$
Untreated CO_2 (kg)	0,15
Total Emissions (kg)	0,25

Table 17. CO_2 treatment system products

	Amount (kg)	Exergy (MJ)
Electricity		2,99
CaO	9,74	19,16
$CaCO_3$	1,93	0,019
Total (E_p)		22,169

As shown in Table 16, the treated portion of each kg of CO_2 entering the system is (1-0,25=0,75) kg. The cleaning cost of CO_2 is also considered:

$$ee_{ENV} = \frac{E_{M\text{-}t} + E_{phys\text{-}t} + EE_{C\text{-}t} + EE_{L\text{-}t} - E_{P\text{-}t}}{\text{treated } CO_2} = \frac{65{,}25 - 22{,}17}{0{,}75} = 57{,}44\,MJ/kg\,CO_2 \quad (5)$$

$$= 0{,}057\,TJ/Ton\,CO_2$$

The CO_2 emission of Turkish TR sector is therefore 43.738.000 Ton, with a resulting EE_{ENV} for CO_2 emission of:

$$EE_{ENV} = 0{,}057 \text{ x } 43738000 = 2521344{,}41\ TJ \quad (6)$$

4. Output

Exergy transfer by work interaction is associated with shaft power which is directly equal to exergy. Shaft work output is calculated from (7) and (8) for electrically and fossil fuel propelled vehicles, respectively. Further discussion is available in [31, 22].

$$W = \eta \text{ x } En_{el} \quad (7)$$

$$W = \eta \text{ x } LHV \text{ x } m_F \quad (8)$$

where η is the first law efficiency; W (J) the shaft work; En_{el} (J) the electrical energy; LHV (J/ton) is the low heating value of the fuel; m_F (ton/year) is the fuel consumption.

The efficiency (η) of road, marine, air, rail [25] and pipeline [23] are seen in Table 18. For non-specified transportation, the efficiency is assumed to be 75%. The exergetic outputs of different transportation modes are presented in Table 19.

Table 18. Efficiencies of transportation modes

Transportation mode	Efficiency (η) (%)
Rail	
Electricity	75,8
Diesel	25
Air	26
Marine	31
Road	12
Pipeline transport	
Electricity	90
Natural Gas	29
Unspecified	75

Table 19. Exergetic output (E_P) of TR sector

	Output (E_P) (TJ)
Rail	2.903,30
Air	19.725,15
Marine	5.911,69
Road	62.045,06
Pipeline transport	1.849,21
Non specified	1.134
Total	93.568,40

5. Results and discussion

Based on Fig. 1 and 2, the extended exergetic efficiency (EEA_{eff}) as:

$$EEA_{eff} = \frac{\sum \text{Output fluxes}}{\sum \text{Input fluxes}} = \frac{\sum_{output} E_p + EE_C}{\sum_{input} E_m + E_{phys} + EE_L + EE_C + EE_{ENV}} \quad (9)$$

In Eq .9, the output exergy fluxes are seen as product (E_P) and capital (EE_C) since these are the only outputs of the sector. A summary of the EEA fluxes in the TR sector is given in Table 20. As discussed in Section 3.3.3, the only effluents included in the environmental remediation cost (EE_{ENV}) are solid waste and sectoral CO_2 emission which have 27.066,78 TJ and 2.521.344,41 TJ extended exergetic cost, respectively. The sum of these 2 constituents of EE_{ENV} amounts to 2.548.411,19 TJ (Table 20).

EEA efficiency of TR is 0,43 and the first and second exergetically highest input flows are EE_C and EE_{ENV}, and the third one is EE_M. This result shows the advantage of EEA methodology which is capable of indicating the dominant role of capital and material consumption in total resource consumption of the sector (in terms of exergy). The result is very interesting especially for a sector like TR, since the fossil fuel consumption is high (E_{phys} is high) and it may be expected that this much fossil fuel consumption can be high enough to dominate the E_{in} but the reality is E_{phys} is the fourth highest resource consumption flow of the sector. As a result of the fact that it takes a detailed structural analysis to evaluate the reasons and also to make suggestions to reduce EE_C and EE_M, these flows are not analyzed in this study.

As for EE_{ENV}, the difference between EE_{ENV} caused by solid waste and CO_2 shows that one of the main lowering factor of EEA_{eff} is the high sectoral CO_2 emission. It should be noted that, in this study, gas emissions are restricted to CO_2. Thus, one of the welcome consequences here is the necessity of widening the scope of analysis and determining the "extended exergetic cost" of other emission gases to be used in future EEA analyses. Furthermore, it must be noticed that different effluent remediation technologies for solid waste and gas treatment may carry different EE_{ENV} values. It is worthy to examine the different technologies to identify the exergetically cheapest route of environmental remediation.

Table 20. EEA fluxes of TR sector

Fluxes	Exergy (TJ)
INPUT:	
E_M	1.678.879
E_{phys}	663.682,24
$EE_{C\text{-input}}$	3.848.726
EE_L	415.224
EE_{ENV}	2.548.411,19
Total EE_{input}	9.154.922,43
OUTPUT:	
E_P	93.568,4
$EE_{C\text{-output}}$	3.848.726
Total EE_{output}	3.942.294,4
EEA_{eff}	0,43

Appendix A

The exergetic equivalent of labor (ee_L) is defined as the exergy cumulatively used to generate one work-hour and is calculated as:

$$ee_L = \frac{\alpha \text{ x } E_{in}}{N_{wh}} \quad (A1)$$

where ee_L (MJ/hour) is the exergetic equivalent of labor; α the fraction of primary exergy embodied into labour; E_{in} (MJ/year) the global exergy influx and N_{wh} (hours/year) the cumulative number of work hours [35].

The unit exergetic equivalent of capital (ee_K) is defined as the equivalent primary exergy resource embodied in one monetary unit and is calculated as:

$$ee_K = \frac{\alpha \times \beta \times E_{in}}{(M_2 - S)} \quad \text{(A2)}$$

where, ee_K (MJ/$) is the exergetic equivalent of capital; β an amplification factor that accounts for the creation of wealth due to exclusively financial activities [35]; M_2 ($/year) is a monetary indicator usually referred to as "money + quasi-money circulation"; S ($/year) is the yearly total of wages and salaries in a country.

The exergetic equivalents of a certain number of workhours L and of a certain amount of capital C are therefore calculated as:

$$EE_L = L \times ee_L \quad \text{(A3)}$$

$$EE_C = C \times ee_K \quad \text{(A4)}$$

With L in workhours and C in $; EE_L and EE_C are defined in Section 1.

To calculate the econometric factors α and β, the procedure suggested in [35] has been used here:

$E_{used} = E_{cons}$, if sufficient statistical data exist to calculate $E_{consumed}$

$E_{used} = 365 \times f \times e_{surv} \times N_h$ otherwise, with $f = \frac{HDI}{HDI_0}$.

$$\alpha = \frac{E_{used}}{E_{in}} \quad \text{(A5)}$$

$$\beta = \frac{M_2 - S}{S} \quad \text{(A6)}$$

where E_{used} and $E_{consumed}$(MJ/year) are the global exergy used by the society; e_{surv} ($1{,}05 \times 10^7$ J/(person·day)) is a conventional level of exergy consumption for survival [42]; N_h (persons) is the number of inhabitants; HDI is the Human Development Index and HDI_0 its value for of a primitive society, assumed equal to 0.055 in [42]. A detailed discussion is available in [35]. Data for M_2, S, N_h, HDI are obtained from [45],[46],[43] and [53], respectively. A list of the quantities described in this Appendix, plus ee_L and ee_K for $Turkey_{2006}$ are seen in Table A1.

Table A1. Econometric factors, ee_L and ee_K

E_{in} (TJ)	3.601.655.961,68
HDI	0,798
M_2 ($)	208.206.113.706
S ($)	170.782.627.832
N_{wh}	28.266.496.268,07
N_h	78.259.264
α	0,0022
β	0,219
ee_L (MJ/hours)	153,952
ee_K (MJ/$)	25,5

Appendix B

Table B1. Weight of tires (IUV+ELV)

	Car	Minibus	Bus	Light truck	Truck	Motorcycle
Average tire weight[1] (kg)	5,91	10,58	13,5	10,58	52,67	4,1
Number of ELVs[2]	28295	3712	3580	9257	12416	7738
Number of IUVs[2]	6140992	357523	175949	1695624	709535	1822831
Total number of tires	6254172	372371	190269	1732652	759199	1838307
Total tire weight (Ton)	36962,16	3939,69	2568,63	18331,46	39987,01	7537,06

[1] [12]
[2] [45], [51]

Table B2. Constituting materials in ELV (excluding tires)[3]

	Car	Minibus	Bus	Light truck	Truck	Motorcycle	Total
Ferrous metal (Ton)	27878,27	9322,82	30892,54	15658,55	52244,84	1283,42	137280,44
Rubber (Ton)	1524,03	448,99	1631,41	564,27	1306,09	58,50	5533,28
Magnesium&Zinc (Ton)	721,52	259,84	859,20	185,14	620,80	38,69	2685,19
Copper (Ton)	594,20	194,88	644,40	185,14	620,80	58,04	2297,45
Aluminum (Ton)	3055,86	324,80	1074,00	370,28	1241,60	58,04	6124,58
Glass (Ton)	1230,83	519,68	1718,40	370,28	1241,60	0,00	5080,79
Others (Fluids and lubricants) (Ton)	3585,71	984,38	3369,14	418,31	946,87	180,91	9485,32
Plastic (Ton)	3183,19	779,52	2577,60	370,28	1241,60	193,45	8345,64
Total (Ton)	41773,61	12834,91	42766,68	18122,24	59464,20	1871,05	176832,68

[3] Compositions of vehicles are extracted from [15], average vehicle weights are extracted from [28].

Nomenclature

MRF	Materials recovery facility
CHP	combined heat and power
TR	transportation sector
E	exergy, J
EE	exergetic equivalent, J
ee	specific extended exergy, J/(hour, mass, $,...)
EEA	extended exergy accounting
EE_{ENV}	environmental remediation cost, J
E_{in}	global exergy influx in to the country, J/year
E_{used}	the global exergy used by the society for survival (J/year)
HDI	Human Development Index
IC	investment cost, $
LHV	low heating value, J
M_2	money + quasi-money circulation in the country, $/year
N_h	population
N_{wh}	cumulative number of work hours, hours
OP	operation and maintenance cost, $
P	product
S	global wages and salaries in a country, $/year
TRP	transportation line
EEA_{eff}	extended exergetic efficiency

ELV end of life vehicle

IUV in use vehicle

m mass, Ton

En energy, J

W shaft work, J

Greek symbols

η first law efficiency

$ dollar

€ euro

β an amplification factor that accounts for the creation of wealth due to exclusively financial activities

α fraction of the primary exergy embodied into labour

Subscripts and superscripts

C capital

el electrical

ENV environmental remediation

h heat

L labour

M material

phys physical

t for treatment system

ryc recycled

net net

cons consumed

References

[1] Ayres RU., Ayres LW.: Accounting for resources 2: The life cycle of materials. Cheltenham, UK, 1999.

[2] Ayres R.U., Ayres LW., Warr B.: Exergy, power and work in the US economy, 1900–1998. Energy 2003; 28: 219–73.

[3] Berglund M., Borjesson P.: Assessment of energy performance in the life-cycle of biogas production. Biomass Bioenerg 2006; 30: 254–266

[4] Bezdek, R.H., Wendling, R.M.: Establishing benchmarks for environmental comparison. - Available at:<http://www.misi-net.com/publications/ModernPowerSystems-1206.pdf>, [accessed June 2011]

[5] California Air Resources Board: Instructional Guidance for Mandatory GHG Emissions Reporting, Chapter 13. - Available at:<http://www.arb.ca.gov/cc/reporting/ghg-rep/ghg-rep-guid/13_CommonMeths.pdf>, [accessed June 2010]

[6] Chen G-Q., Chen B.: Extended-exergy analysis of the Chinese society. Energy 2009; 34:1127–44

[7] Dincer I., Hussain MM., Al-Zaharnah I.: Energy and exergy utilization in transportation sector of Saudi Arabia. Appl Therm Eng 2004; 24: 525–38.

[8] Ediger V.S., Camdalı U.: Energy and exergy efficiencies in Turkish transportation sector, 1988–2004. Energy Policy 2007; 35:1238–1244

[9] Ertesvag I.S.: Society exergy analysis: a comparison of different societies. Energy 2001; 26: 253–70.

[10] Ertesvag IS.: Energy, exergy, and extended-exergy analysis of the Norwegian society 2000. Energy 2005; 30: 649–75

[11] European Commission Environmental Department: A study to examine the benefits of the End of Life Vehicles Directive and the costs and benefits of a revision of the 2015 targets for recycling, re-use and recovery under the ELV Directive 2006. – Available at: <http://ec.europa.eu/environment/waste/elv_index.htm> [accessed June 2011]

[12] Federici M., Ulgiati S., Verdesca D., Basosi R.: Efficiency and sustainability indicators for passenger and commodities transportation system: the case of Siena, Italy. Ecol Indic 2003; 3: 155–69.

[13] Ferrao P, Amaral J.: Assessing the economics of auto recycling activities in relation to European Union Directive on end of life vehicles. Technol Forecast Soc 2006;73:277–89

[14] Gasparatos A., El-Haram M., Horner M.: Assessing the sustainability of the UK society using thermodynamic concepts: Part 2. Renew Sust Energ Rev 2009; 13: 1074-81

[15] Giannouli M., Haan P., Keller M., Samaras Z.: Waste from road transport: development of a model to predict waste from end-of-life and operation phases of road vehicles in Europe. Journal Clean Prod 2007; 15: 1169-82

[16] Hughes R.W., Lu DY., Anthony EJ., Macchi, A.: Design, process simulation and construction of an atmospheric dual fluidized bed combustion system for in situ CO_2 capture using high-temperature sorbents , Fuel Process Technol 2005; 86: 1523–31

[17] IEA (International Energy Agency): Energy Statistics of OECD Countries. IEA: Paris, 2008

[18] IPCC National Greenhouse Gas Inventories Programme: 2006 IPCC Guidelines for National Greenhouse Gas Inventories, Chapter 3: Mobile Combustion. - Available at:<**Errore. Riferimento a collegamento ipertestuale non valido.**>, [accessed December 2011]

[19] IPCC National Greenhouse Gas Inventories Programme: 2006 IPCC Guidelines for National Greenhouse Gas Inventories, Chapter 2: Stationary Combustion. - Available at:< http://www.ipcc-nggip.iges.or.jp/public/2006gl/pdf/2_Volume2/V2_2_Ch2_Stationary_Combustion.pdf, [accessed December 2011

[20] Jaber JO, Al-Ghandoor A., Sawalha SA.: Energy analysis and exergy utilization in the transportation sector of Jordan. Energy Policy 2008; 36: 2995-3000

[21] Ji X., Chen G.Q., Chen B., Jiang M.M.: Exergy-based assessment for waste gas emissions from Chinese transportation. Energy Policy 2009; 37: 2231–40

[22] Ji X., Chen G.Q.: Exergy analysis of energy utilization in the transportation sector in China. Energy Policy 2006; 34: 1709-19

[23] Johnson, A.: A Discussion of Natural Gas Pipeline System Efficiency. - Available at:<http://www.gaselectricpartnership.com/BBPipeline%20Efficiency%20ATJ.pdf>, [accessed January 2011]

[24] Milia D., Sciubba E.: Exergy-based lumped simulation of complex systems: An interactive analysis tool. Energy 2006; 31:100–11

[25] Nakicenovic N., Gilli PV., Kurz, R.: Regional and global exergy and energy efficiencies. Energy 1996; 21: 323–37.

[26] Pehlken A, Essadiqi E.: Scrap Tire Recycling in Canada. – Available at: <http://www.nrcan.gc.ca/sites/www.nrcan.gc.ca.minerals-metals/files/pdf/mms-smm/busi-indu/rad-rad/pdf/scr-tir-rec-peh-eng.pdf> [accessed June 2011]

[27] Poschl M., Ward S., Owende P.: Evaluation of energy efficiency of various biogas production and utilization pathways. Applied Energy 2010; 87: 3305–21

[28] Recycling Council of Ontario: Measuring energy savings and greenhouse gas (GHG) emission reductions benefits resulting from recycling in Canada. 2010 - Available at < https://www.rco.on.ca/uploads/File/projects/completed/GreenhouseGasAndRecycling/RC_Projects-GHG-Fact_Sheet.pdf>[accessed 12.10.2011].

[29] Rigamonti L., Grosso M., Giugliano M.: Life cycle assessment for optimising the level of separated collection in integrated MSW management systems, Waste Manag. 2009; 29: 934–944

[30] Romeo L.M., Uson S., Valero A., Escosa J.M.: Exergy analysis as a tool for the integration of very complex energy systems: The case of carbonation/calcination CO_2 systems in existing coal power plants. Int J Greenh Gas Con 2010; 4: 647–54

[31] Saidur R., Sattar MA., Masjuki HH., Ahmed S., Hashim U.: An estimation of the energy and exergy efficiencies for the energy resources consumption in the transportation sector in Malaysia. Energy Policy 2007; 35: 4018–26

[32] Sciubba E., Bastianoni S., Tiezzi E.: Exergy and extended exergy accounting of very large complex systems with an application to the province of Siena, Italy. J Environ Manage 2008; 86: 372–382

[33] Sciubba E.: Beyond thermoeconomics? The concept of Extended Exergy Accounting and its application to the analysis and design of thermal systems. Exergy 2001; 1(2): 68-84

[34] Sciubba E.: Cost analysis of energy conversion systems via a novel resource-based quantifier. Energy 2003; 28: 457-477

[35] Sciubba, E.: A revised calculation of the econometric factors α and β for the Extended Exergy Accounting method. Ecol Model 2011; 222:1060-66

[36] Sciubba, E.: Using exergy to evaluate environmental externalities. In Proceedings of the IV NTVA Seminar of Industrial Ecology, Trondheim, Norway, June 14, 2001.

[37] Sciubba, E.: Exergy-based Ecological Indicators: a necessary tool for Resource Use assessment studies. In: Keynote address to IEEES 2009 , A.U.S., Sharjah, UAE..

[38] Sciubba, E,: Extended exergy accounting applied to energy recovery from waste: The concept of total recycling. Energy 2003;28:1315–1334

[39] Smith A., Brown K., Steve O., Kathryn R., Bates J.: Waste Management Options and Climate Change Final report to the European Commission. - Available at: <http://ec.europa.eu/environment/waste/studies/pdf/climate_change.pdf> [accessed 12.10.2011].

[40] Soylu S.: Estimation of Turkish road transport emissions. Energy Policy 2007; 35: 4088–94

[41] Szargut, J., Morris, D.R. and Steward, F.R.: Exergy Analysis of Thermal, Chemical and Metallurgical Processes. Hemisphere Pub., New York, USA, 1988

[42] TalensPeiró L., Villalba Méndez G., Sciubba E., Gabarrell y Durany X.: Extended exergy accounting applied to biodiesel production. Energy 2010;35:2861-69

[43] Turkish Ministry of the Interior Affairs: Available at < http://www.nvi.gov.tr/>[accessed 12.10.2011

[44] Turkish Republic Ministry of Energy and Natural Resources, 2007. Energy balance table of Turkey (2006). – Available at: <http://www.enerji.gov.tr/index.php?dil=tr&sf=webpages&b=y_istatistik&bn=244&hn=244&id=398> [accessed March 2011]

[45] Turkstat (Turkish Statistical Institute): Statistical Indicators 1923-2007, Ankara, 2010

[46] Turkstat (Turkish Statistical Institute): Annual Industry and Service Statistics 2006. Ankara, 2009

[47] Turkstat (Turkish Statistical Institute): Labour Cost Survey 2004-2008. Ankara, 2009.

[49] Turkstat (Turkish Statistical Institute): Household Labour Force Statistics 2006. Ankara, 2007

[51] Turkstat (Turkish Statistical Institute): Turkey's Statistical Yearbook 2008. Ankara, 2009.

[52] Ultu Z, Hepbasli A.: A review on analyzing and evaluating the energy utilization efficiency of countries. Renew Sust Energ Rev 2007;11:1–29.

[53] United Nations Development Programme (UNDP): Human development indices report 2008, Available at <http://hdr.undp.org/en/media/HDI_2008_EN_Tables.pdf>[accessed 12.10.2011].

[54] Utlu Z., Hepbasli A.: Assessment of the energy utilization efficiency in the Turkish transportation sector between 2000 and 2020 using energy and exergy analysis method. Energy Policy 2006; 34: 1611–18

[55] Zhang B, Chen GQ.: Physical sustainability assessment for the China society. Renewable and Sustainable Energy Reviews 2010;14:1527-45

[56] Zhang M., Li G., Mu HL., Ning YD.: Energy and exergy efficiencies in the Chinese transportation sector, 1980-2009. Energy 2011; 36: 770-76

The impact of higher energy prices on socio-economic inequalities of German social groups

Holger Schlör[a], Wolfgang Fischer[a], Jürgen-Friedrich Hake[a]

[a] *Forschungszentrum Jülich, Institute of Energy and Climate Research (IEK-STE), Jülich, Germany, h.schloer@fz-juelich.del*

Abstract:

The Stiglitz-Sen study "Commission on the Measurement of Economic Performance and Social Progress" recommended a shift from measuring economic production to measuring people's well-being and the trends in well-being should be gauged by "measures of household income and consumption". We take up the suggestions of the Stiglitz-Sen Commission and use the Atkinson index to estimate the distributional effects of increasing energy prices on income and energy consumption.

The Atkinson index is an inequality measure based on a social welfare function. The Atkinson index is widely employed by economists to analyse income distribution. However, up to now, it has not been used in energy analysis. It provides a new tool not only to measure the distribution of income but also to estimate the distributional dimensions of energy consumption. The Atkinson index has a specific feature for the calculation of distribution. The index uses the epsilon parameter to explicitly reveal the inequality aversion of society. Epsilon defines how sensitively the Atkinson index should react to income inequalities.

Within the scope of our energy price scenario, we analyse a reference scenario and two price scenarios derived from the development of energy prices (2004 to 2008) before the financial crises. Our findings can be summarized as follows: In the first price scenario I we see a small rise in equality in all social groups, but in the second energy price scenario we detect a significant rise in inequality. All households could cope with the first rise of the energy prices in scenario I by using their savings, but a further increase in energy prices in scenario II could not be covered by the households' savings and hence we see a sharp increase of inequality among the German social groups measured by the Atkinson index. The distributional effects of the analysed price scenarios could make a significant contribution to science and policy debates on the consequences of higher energy prices during the transition of the current energy system.

Keywords:

Energy Prices, Inequality, Atkinson Index.

1. Introduction

The German Federal Statistical Office determined that expenditure for energy of German private households rose by approximately 55% between 2002 and 2008, and that fuel oil prices almost doubled from 2004 to 2008. In the following, we use the Atkinson index to analyse the distributional effects of this price increase on German private households. The Atkinson index enables us to calculate how society implicitly assesses the distribution of income and consumption between the different income groups within the German social groups. We chose the Atkinson index because "Kolm and Atkinson laid the basis for the field of distributional analysis as we know it today (Cowell and Kanbur 2011)." They "inspired the work on the nature of economic inequality, on the role of social values and moral intuition in the assessment of income distributions and on the structure of several classes of related measurement problems in poverty, mobility, polarization and other fields" (Cowell and Kanbur 2011).

Taking the example of Germany, we analyse the distribution of income, of entire consumption and of energetic consumption in a reference scenario for the year 2003. In two energy price scenarios, we examine the distributional effects of rising energy prices. In scenario I, we assume an energy price increase of 55% and in scenario II an increase of 100%. We focus on energy expenditure,

because energy is the "universal currency" (Smil 1994) for the improvement of people's living conditions and the foundation of every civilization (Sieferle 2001; Smil 1994; White 1943). Hence the availability of energy is, like income, a central defining element for the quality of life of any society and can be seen as a benchmark for improvements of living conditions and well-being (Smil 1994). In our analysis, we take up the recommendation of the Stiglitz-Sen study "Commission on the Measurement of Economic Performance and Social Progress" (Stiglitz et al. 2009), who recommended a shift from measuring economic production to measuring people's well-being and that trends in well-being should be gauged by "measures of household income and consumption (Stiglitz et al. 2009)". We take up this suggestion and use the Atkinson index (Atkinson 1970) to estimate the distributional effects of increasing energy prices.

2. The Atkinson Index – Measuring Inequality

The Atkinson index (AI) is an inequality measure based on the social welfare function (Atkinson 1970, 1973, 1975, 1983; Cowell 2000a; Cowell 1977; Sen 1973; Dalton 1920; Sen 1998). It defines maximum inequality with 1 and maximum equality with 0. Y_i is the income of individuals in the ith income range (N ranges altogether), f_i is the proportion of the population with income in the ith range, $\overline{Y}$ is the mean household income (Atkinson 1970), resulting in the following Atkinson equation (Atkinson 1983, 1975):

$$AI = 1 - \left[\sum_{i=1}^{n} \left(\frac{Y_i}{\overline{Y}} \right)^{1-\varepsilon} f_i \right]^{\frac{1}{1-\varepsilon}}, \text{ if } \varepsilon \neq 1.$$

$$AI = 1 - \exp\left[\sum_{i=1}^{n} f_i \log_e \frac{Y_i}{\overline{Y}} \right], \text{ if } \varepsilon = 1.$$ [1]

Several authors have demonstrated that the Atkinson index fulfils six axioms for inequality measures, therefore allowing inequality to be measured (Lüthi 1981; Litchfield 1999; Cowell 2000a; Seidl 2001; Cowell 2000b). The Atkinson index fulfils

- the Bresciani-Turroni condition[2] (income scale independence),
- the criterion of the independence of the population size[3] (principle of population),
- the anonymity condition[4],
- the Pigou-Dalton transfer principle[5],
- the operationality condition[6],
- and the decomposability condition[7].

[1] The special case of Atkinson index $\varepsilon = 1$ is also known as the measure of Champernowne (Champernowne 1974). It corresponds to the hypothesis of Bernoulli that the marginal utility of the income is inversely proportional to the income level (Lüthi 1981).

[2] The Bresciani-Turroni condition (income scale independence (Cowell 2000b; Cowell 2000a) says that a doubling of all incomes should not influence the index value (Diekmann 1981; Mosler and Muliere 1996; Bresciani-Turroni 1937).

[3] The population principle says "that an income distribution is to be regarded as distributionally equivalent to a distribution formed by replications of it (Cowell 2000b)."

[4] The anonymity condition says that the inequality measure should "be independent of any characteristics of individuals other than their income (Litchfield 1999)."

[5] The Pigou-Dalton criterion says (Seidl 2001; Eichhorn 1988) that the transfer of one monetary unit from a poorer household to a relatively richer household raises the value of an inequality measure (Amiel and Cowell 1999; Litchfield 1999). The inequality increases (Lüthi 1981).

[6] The criterion of operationality says that the inequality measure should be easy to handle (Lüthi 1981). The Atkinson index also fulfils the decomposability condition.

[7] "Other measures, such as the Atkinson set of inequality measures, can be decomposed but the two components of within- and between-group inequality do not sum to total inequality (Litchfield 1999)."

Based on these six axioms, the Atkinson Index enables us to measure the distribution of welfare which is determined decisively by the income and consumption of households (Barr 1993; Atkinson 1970, 1973, 1975, 1983; Foster and Sen 1997). Rising net income also implies rising welfare.

The Atkinson index has a specific feature for calculating distribution, namely the parameter epsilon ε. "This parameter represents the weight attached by society to inequality in the distribution (Atkinson 1983)." With the parameter epsilon ε, the size of the welfare difference of additional income can be fixed between a person with a high income and a person with a low income. Epsilon ε "is clearly a measure of the degree of inequality-aversion – or the relative sensitivity to transfer at different income levels. As ε rises, we attach more weight to transfers at the lower end of the distribution and less weight to transfers at the top (Atkinson 1970)."

The epsilon parameter defines how sensitively the Atkinson index should react to income inequalities. The larger epsilon is, the stronger the Atkinson index reacts to inequalities. Epsilon therefore represents the inequality aversion of society. Epsilon confronts a society with its self-assessment as a just and fair society. The value could range from zero, if society is totally indifferent to the distribution of income, to infinity, if society only looks after the position of the lowest income group.[8]

The distribution of income between members of society is an important aspect of social well-being. In 1971, it was defined as a public good (Thurow 1971) because every individual is confronted with the current distribution of income. No individual can be excluded from the disadvantages and advantages of a certain distribution of income and there is also a non-rivalry of the consumption of the advantages of a certain distribution of income (Thurow 1971). Samuelson and Nordhaus support Thurow's interpretation of equality as a public good (Samuelson and Nordhaus 2007; Okun 1975) where the value of the epsilon parameter expresses the price society is willing to pay for the realization of equality. This refers to a basic problem within democratic affluent societies: where the constitution guarantees political equality of the citizens, they are confronted with economic inequality, measured in income and consumption, as a result of market forces (Gordon 1975).

Gordon concluded that this "mixture of the same rights and unequal income generates social tensions between the political principles of society and the economic principles of capitalism (Gordon 1975; Bell 1996 (1976))." But there is no simple solution for welfare economics and politics due to a conflict between equality and efficiency. "At some points along the way, society confronts choices that offer somewhat more equality at the expense of efficiency or somewhat more efficiency at the expense of equality. In the idiom of the economist, a trade-off emerges between equality and efficiency (Gordon 1975)." If the distribution of income is perceived as a public good (Thurow), then the trade-off between political equality and economic efficiency could be shaped by political decision making and the Atkinson index (epsilon parameter) is the instrument for this.

Hence we see epsilon in the context of Gordon as a value that represents the social trade-off between social equality and economic efficiency. With the Atkinson parameter, a normative dimension is incorporated into the inequality analysis, which allows inequality aversion to be introduced into the inequality analysis. We refer to this as "normative" because government and society can discuss and determine what the trade-off looks like. Society can define a particular epsilon as a social objective.

The advantage of the Atkinson index is that the epsilon parameter can be varied in such a way that the welfare of the lower income groups is weighted strongly or weakly in the welfare measurement.

The epsilon parameter of the Atkinson index reveals both the values of society for distributional justice and for economic efficiency and expresses the willingness of society to accept transfer costs to achieve distributional justice.

[8] This analytical view is based on Rawls' theory of justice, where inequality is determined by the "position of the least advantaged members of society. Where epsilon lies between these extremes depends on the importance attached to redistribution towards the bottom (Atkinson 1983)."

According to Okun, the question of the socially acceptable epsilon value can be answered from two different perspectives: whether the main focus is on social equality in the sense of Rawls or on economic efficiency in the sense of Milton Friedman (Okun 1975; Rawls 1971; Friedman 1962). He explained in his book "Free to Choose" his view on justice and social equality in the following way: "Life is not fair. It is tempting to believe that government can rectify what nature has spawned (Friedman 1990)." John Rawls responded to Milton Friedman and his view on natural distribution: "The natural distribution is neither just nor unjust; nor is it unjust that persons are born into society at some particular positions. These are simply facts. What is just or unjust is the way that institutions deal with these facts (Rawls 1971)." The social institutions can adjust the epsilon parameter based on the two different views of the nature of society and the need for social adjustments of the natural distribution.

Epsilon indicates how high the welfare difference can be between the lower and higher income groups from society's viewpoint. The epsilon parameter represents a connection between the universal equal political rights of the citizens and the efficiency criterion of the economy, and it defines fairness from the perspective of society.

Finally, it has to be pointed out that no objective, statistically neutral inequality measures exist. Every measure contains implicit evaluations about a desirable distribution of income. The degree of inequality cannot be measured without taking social judgments into consideration. "Measures such as the Gini coefficient are not purely 'statistical' and they embody implicit judgments about the weight to be attached to the inequality at different points on the income scale (Atkinson 1983)." If the Gini coefficient indicates a decrease in inequality, then not everyone must agree with that judgment (Hauser 1996). Due to the fact that inequality measures contain implicit judgments about a certain distribution, it is sensible to use inequality measures that reveal this judgment explicitly. This is the case with the Atkinson index, because the distribution parameter epsilon can be chosen freely (Atkinson 1975). The index makes clear "just what distributional objectives are being incorporated (Atkinson 1983)" in the distribution analysis and reveal this normative assumption explicitly to the public. Inequality measures such as the Gini coefficient, Dalton's inequality measure and the Theil measure do not explicitly reveal the inequality aversion of the author/researcher to the public (Cowell 2000b).

We will carry out our distribution analysis on the basis of the German household expenditure survey data (EVS) 2003 of the German Federal Statistical Office (Statistisches Bundesamt 2008a, 2008b).

3. Data Basis - German Household Expenditures and Income

The German Household Expenditure Survey data (EVS) provide information on German economic life and the consumer behaviour of private households (Statistisches Bundesamt (Federal Statistical Office) 2005b), offering a basis for estimating the effects of economic policy. The EVS is constructed according to the methodological Eurostat[9] recommendations "Household Budget Surveys in the EU. Methodology and Recommendations for Harmonisation – 2003" (Statistisches Bundesamt (Federal Statistical Office) 2005b)."

Every five years, a selection of German households (0.2% of all German households) is questioned as part of a household expenditure survey about their income, expenditures, assets, consumer goods and residential situation. The 2003 survey was the ninth survey, following surveys in 1962/63, 1969, 1973, 1978, 1983, 1988, 1993, 1998, 2003, and 2008. (Statistisches Bundesamt (Federal Statistical Office) 2005a; Jung 2001). The EVS of 2008 was published in 2011 and has not yet been fully analysed, hence we use the EVS of 2003 to analyse developments before the financial crises. We will use the EVS of 2008 and 2003 for a time series analysis the distributional effects of energy.

9 http://epp.eurostat.ec.europa.eu/statistics_explained/index.php/Household_budget_survey_%28HBS%29

The main focus of the survey is collecting households` income and expenditure data which are necessary to assess the income situation, standard of living and the expenditure behaviour of the whole population and its different social groups (Statistisches Bundesamt (Federal Statistical Office) 2005b). The EVS delivers detailed data on the distribution of household income and consumption. Therefore, based on the data, it is possible to assess the consequences of income changes, tax alterations, changes in consumer prices and social security contributions for, firstly, the consumption behaviour of households and, secondly, for a country's economic development (Statistisches Bundesamt (Federal Statistical Office) 2005b). The EVS reveals indirectly the preference ordering of German households.

A private household is an individual living alone, a group of related or linked (not necessarily family-related) persons, who belong together in terms of income and consumption. A household must dispose together over one or several incomes or over income shares and it must be supplied completely or predominantly within the scope of the household (Statistisches Bundesamt (Federal Statistical Office) 2005b). The key statistical issue in EVS is the income and expenditure of private households, based on the market concept (Statistisches Bundesamt (Federal Statistical Office) 2005b; Burghardt 2000; Münich 2000).

Our analysis focuses on the following household types:

1. self-employed persons
2. civil servants
3. white-collar workers
4. blue-collar workers
5. all households

The following table shows how German households are distributed among social groups and income groups. We analysed 10 income classes and the class of all households, as shown in the following table.

Table 1: Distribution of the German households to the different social groups in 2003

Distribution of the households to the different social groups in 2003											
	Total	900 -1300	1300 - 1500	1500 - 1700	1700 - 2000	2000 - 2600	2600 - 3600	3600 - 5000	5000 - 7500	7500 - 10000	10000 - 18000
					Number of households in 1000						
Self-employed	2211	102	59	52	127	266	403	435	428	158	116
Civil servant	1649	59	18	22	62	134	294	488	459	85	27
White-collar worker	11290	704	596	560	871	1504	2484	2259	1591	334	139
Blue-collar worker	6453	546	311	349	476	1118	1841	1208	292	18	10
Unemployed	2083	516	178	133	159	207	187	69	25	15	8
Not being employed	14423	2742	1158	1095	1393	2379	2113	1082	469	102	45
All households	38109	4669	2320	2211	3088	5608	7322	5541	3264	712	345
					Share of the social group on all households						
Self-employed	5.8	2.2	2.5	2.4	4.1	4.7	5.5	7.9	13.1	22.2	33.6
Civil servant	4.3	1.3	0.8	1.0	2.0	2.4	4.0	8.8	14.1	11.9	7.8
Whitel-collar worker	29.6	15.1	25.7	25.3	28.2	26.8	33.9	40.8	48.7	46.9	40.3
Blue-collar worker	16.9	11.7	13.4	15.8	15.4	19.9	25.1	21.8	8.9	2.5	2.9
Unemployed	5.5	11.1	7.7	6.0	5.1	3.7	2.6	1.2	0.8	2.1	2.3
Not being employed	37.8	58.7	49.9	49.5	45.1	42.4	28.9	19.5	14.4	14.3	13.0
All households	100	100	100	100	100	100	100	100	100	100	100
					Distribution of the social groups over the income classes						
Self-employed	100	4.6	2.7	2.4	5.7	12.0	18.2	19.7	19.4	7.1	5.2
Civil servant	100	3.6	1.1	1.3	3.8	8.1	17.8	29.6	27.8	5.2	1.6
White-collar worker	100	6.2	5.3	5.0	7.7	13.3	22.0	20.0	14.1	3.0	1.2
Blue-collar worker	100	8.5	4.8	5.4	7.4	17.3	28.5	18.7	4.5	0.3	0.2
Unemployed	100	24.8	8.5	6.4	7.6	9.9	9.0	3.3	1.2	0.7	0.4
Not being employed	100	19.0	8.0	7.6	9.7	16.5	14.7	7.5	3.3	0.7	0.3
All households	100	12.3	6.1	5.8	8.1	14.7	19.2	14.5	8.6	1.9	0.9

Source: German Federal Statistical Office, 2006 and own calculation IEK-STE 2012

The EVS covers approx. 38.109 million households of which 14.4 million (37.8%) are not employed, 11.3 million are defined as white-collar households (30%), and 6.4 million are blue-collar (17%) households. When taken together, the 2.2 million self-employed, 2.08 million unemployed and 1.6 million civil servant households account for 15.3% of all households. With respect to the distribution of households over the 10 income classes, the table shows that in the social group of the overall households 19.2% of households belong to the income class € 2600-3600. Within the social group of the not-being employed and the unemployed households, in contrast, the largest portion belongs to the income class € 900-1300. Within the blue-collar and the white-collar households, the largest portion belongs to the income class € 2600-3600, while the self-employed and civil servant households have their biggest share in the income class of € 3000-5000. Based on this statistical sample, we measured the socio-economic inequalities.

4. Socio-Economic Inequalities in Germany

4.1. Inequality of income and consumption of social subgroups

We use the Atkinson index (Atkinson 1983) to determine the distributional effect of income and energy. In order to calculate the distribution of income, consumption and energy expenditures for the different social groups, we use the modified Atkinson index (AI_m):

$$AI_m = 1 - \left[\sum_{i=1}^{n} \left(\frac{X_{i,g}}{\overline{X_g}} \right)^{1-\varepsilon} f_{i,g} \right]^{\frac{1}{1-\varepsilon}}, \quad X = Y^G, Y^N, K, E, EK, EW, \text{ for } \varepsilon \neq 1 .$$

$$AI_m = 1 - \exp\left[\sum_{i=1}^{n} f_{i,g} \log_e \frac{X_{i,g}}{\overline{X_g}} \right], \quad X = Y^G, Y^N, K, E, EK, EW, \text{ for } \varepsilon = 1 .$$

$Y_{i,g}^{G,N}$ represents the gross and net income of individuals, $K_{i,g}$ represents the consumption expenditures, $E_{i,g}$ the energy consumption expenditures, $EW_{i,g}$ the residential energy consumption expenditures, $EK_{i,g}$ the car energy consumption expenditures in the ith income range (n sum of the income classes) in the g social groups (overall households, self-employed, civil servant, white-collar, blue-collar households), $f_{i,g}$ is the proportion of the population in the social groups with income in the ith income range, $\overline{X}_g$ is the mean household value of six income and expenditure issues (YG, YN, K, E, EK, EW) of the social groups, and the epsilon parameter is equal for all groups.

The following table shows the results of our calculations using the various Atkinson indices.

Table 2: Distribution of income and consumption in Germany

Atkinson Index of selected social household groups 2003

Atkinson Epsilon	Gross income (AIY^G)	Net income (AIY^N)	Private consumption (AIK)	Energy (AIE)	Residential energy (AIEW)	Car energy* (AIEK)
			Self-employed			
0.5	0.07	0.06	0.02	0.01	0.01	0.01
1.0	0.15	0.14	0.06	0.03	0.02	0.03
1.5	0.22	0.21	0.10	0.05	0.04	0.06
2.0	0.29	0.28	0.13	0.07	0.06	0.09
			Civil servant			
0.5	0.05	0.05	0.03	0.02	0.03	0.02
1.0	0.10	0.10	0.07	0.05	0.05	0.04
1.5	0.16	0.16	0.10	0.07	0.08	0.06
2.0	0.23	0.21	0.14	0.10	0.11	0.09
			White-Collar worker			
0.5	0.05	0.05	0.02	0.01	0.01	0.01
1.0	0.11	0.12	0.05	0.03	0.03	0.03
1.5	0.17	0.18	0.09	0.05	0.05	0.06
2.0	0.22	0.24	0.12	0.07	0.07	0.08
			Blue-Collar worker			
0.5	0.01	0.01	0.00	0.0	0.0	0.0
1.0	0.05	0.05	0.03	0.01	0.01	0.02
1.5	0.09	0.10	0.05	0.03	0.02	0.05
2.0	0.13	0.14	0.08	0.06	0.04	0.08
			All households			
0.5	0.02	0.09	0.05	0.00	0.00	0.00
1.0	0.10	0.19	0.10	0.01	0.01	0.04
1.5	0.17	0.24	0.13	0.04	0.02	0.10
2.0	0.24	0.30	0.17	0.07	0.04	0.16

*) car energy = fuel and lubricant

Source: Own calculations IEK-STE 2012

Table 2 shows that the value of the Atkinson index increases when society attaches a higher weight to the lower income groups with rising epsilon. This development is independent of the chosen household type and the object of investigation (income, consumption), i.e. inequality increases with the rising inequality aversion of society.

Gross income

If the epsilon parameter rises from 0.5 to 2.0, the Atkinson index for the distribution of gross income increases for all households from 0.02 to 0.24. The analysis of the gross income distribution of the four social groups reveals a greater inequality split for self-employed households in relation to blue-collar workers. By raising epsilon the inequality increases for the self-employed from 0.07 to 0.29 while for blue-collar workers the inequality only increases from 0.01 to 0.13. The gross

income is more equally distributed in the blue-collar group than in self-employed households. The civil servants (0.05-0.23) and the white-collar workers (0.05-0.22) have a similar gross income distribution.

Net income

In the case of net income, we see a differentiated picture of the spread by raising epsilon. For the group of all households, inequality rises significantly from 0.09 to 0.3. The inequality of the distribution of the net income rises for blue-collar-workers from a nearly equally distributed income with an Atkinson index of 0.01 to 0.14. For white-collar-workers, this ranges, from 0.05 to 0.24, 0.05-0.21 for civil servants and 0.06-0.28 for self-employed households.

Private consumption

The analysis shows that private consumption is more equally distributed among households independent of the chosen social group. The split of the Atkinson-index of the various social groups ranges from 0.0 to 0.17. For the group of all households, the inequality increases by raising the epsilon parameter from 0.05 to 0.17. In the social group of blue-collar workers, consumption is equally distributed among the households. The Atkinson index only increases from 0.0 – 0.08 by raising the value of the epsilon parameter. Blue-collar workers have the smallest increase of inequality among all social groups with respect to private consumption. White-collar workers (0.02-0.12), civil servants (0.03-0.14) and the self-employed (0.02-0.13) show nearly the same distribution of private consumption among the income groups. The Atkinson index increases for these three groups in the range of 0.02 to 0.14 by raising the value of the epsilon parameter from 0.5-2.0.

Energy consumption

Table 1 also shows that energy consumption is more equally distributed than consumption expenditure in general. In the case of the distribution of energy consumption between the income groups of the social groups, the social groups can be summarized in two major subgroups. The group of all households (0.00-0.07), the self-employed (0.01-0.07), white-collar workers (0.01-0.07) and blue-collar workers (0.0-0.06) display nearly the same distribution by raising the epsilon parameter, whereas in the group of civil servants (0.02-0.10) the Atkinson index is slightly higher.

Residential energy is nearly equally distributed between the income groups in all social groups. The Atkinson index ranges from 0.00-0.11. In the case of car energy consumption, we see a slightly different picture. The self-employed, white-collar workers, blue-collar workers and civil servants show nearly the same distribution of car energy consumption (0.0-0.09). Only the group of all households (0.00-0.16) shows a different distribution. Especially in the group of all households, we recognize a broader range of distribution of car energy consumption expenditure.

To summarize: Private consumption is more equally distributed than income, and the expenditures for energy consumption are more equally distributed than private consumption in general. The income and consumption of blue-collar-workers are more evenly distributed than in the other social groups. In the group of white-collar workers, both income and consumption are more equally distributed than in self-employed and civil servant households. For the self-employed and civil servants, we obtain a differentiated picture. The income distribution is more unequal with respect to the self-employed, but in the case of consumption the distribution is more unequal in the civil servant households.

Table 1 also makes clear that energy expenditures are distributed almost equally between the households. We can conclude that the universal currency is almost equally distributed between the overall households and the four social groups. Hence energy is not only a universal currency but also a universal consumer good. In the following, we will analyse the effects of higher energy prices on the distribution of energy welfare.

4.2. Energy price scenario and distributional effects

Within the scope of our energy price scenario, we analysed a reference scenario and two price scenarios. In the first price scenario, we examine the distribution effect of the energy price rise determined by the German Federal Statistical Office for the period from 2002-2008 for private households (Statistisches Bundesamt (Federal Statistical Office) 2008). In this period, household expenses rose for energy expenses in total, for residential energy and fuels by approx. 55% (scenario 1.55). In the second price scenario, we supposed that energy prices rise by 100% and we examined what distributional effects such an increase will have (scenario 2.0). The starting point for this scenario was the price development on the German fuel oil market. Fuel oil prices almost doubled within 4 years from 2004 to 2008. In the same period, the crude oil price more than doubled (Energieagentur NRW 2010).[10] The energy price scenarios are interpreted as exogenous shocks *(Stobbe 1991; Dornbusch et al. 2011; Blanchard and Illing 2009* under ceteris paribus conditions. Moreover, an exogenous shock defines a sudden change of exogenous variables which cannot be anticipated by the economic subjects, as for example the oil crises of 1973 (Alpanda and Peralta-Alva 2010) and the current rise of the rare earth elements[11,12]. We analysed the distributional effects for consumer energy prices only. We did not analyse the consequences of increasing energy prices on the other energy sectors or on other markets in order to keep our analysis focused on distributional effects.

In our analysis, we differentiated between the long and short run in the preference order of households (Schefczyk 1998). We assumed that the preference order is relatively stable in the short run and that it can be changed in the long run if the consumers get the impression of constantly growing energy prices. We assumed that current preferences are more stable than restrictions affecting the realization of the preferences of the consumer. In our case, the preferences of the consumers were restricted by the volatility of the energy prices. We did not question the preference order of the German consumers expressed in the EVS.[13]

So we assumed that the households have in the short run a stable preference order and these savings are the share of the budget which can be used for rising energy expenses, without reducing the present consumption of other goods. That is to say, the capital reserves for future consumption are sacrificed for today's consumption. We assumed, furthermore, that households with negative savings will limit their energy consumption and will not reduce their other consumption expenses.

Against the background of these assumptions, we obtain the following picture of the distributional effects of higher energy prices.

[10] http://www.energieagentur.nrw.de/infografik/grafik.asp?TopCatID=3106&CatID=3106&RubrikID=3153

[11] http://www.nytimes.com/2011/05/03/business/03rare.html?pagewanted=all,

[12] http://www.bloomberg.com/news/2011-06-17/rare-earth-prices-double-on-china-industrial-minerals.html

[13] Further research has to be done on the issue of changing preference order caused by constantly increasing energy prices. This research can be done on the basis of a time-series analysis.

Table 3: Energy price scenarios and distribution

Energy Price Scenario and Distribution			
Atkinson Epsilon	Energy (IE_g) - Reference Scenario	Increase Energy Costs 2002 - 2008 Scenario (1.55)	Doubling Energy Costs Scenario (2.0)
	Self-employed		
0.5	0.01	0.10	0.15
1.0	0.03	0.14	0.20
1.5	0.05	0.19	0.27
2.0	0.07	0.24	0.34
	Civil servant		
0.5	0.02	0.04	0.22
1.0	0.05	0.07	0.27
1.5	0.07	0.10	0.32
2.0	0.10	0.15	0.36
	White-Collar worker		
0.5	0.01	0.03	0.08
1.0	0.03	0.07	0.12
1.5	0.05	0.10	0.17
2.0	0.07	0.14	0.23
	Blue-Collar worker		
0.5	0.0	0.04	0.11
1.0	0.01	0.07	0.15
1.5	0.03	0.11	0.20
2.0	0.06	0.14	0.24
	All households		
0.5	0.00	0.06	0.16
1.0	0.01	0.12	0.23
1.5	0.04	0.18	0.30
2.0	0.07	0.24	0.37
*) car energy = fuel and lubricant			
Source: Own calculations			IEK-STE 2012

Table 3 shows the results for the reference scenario and the two price scenarios.

For the social group of all households, the inequality of energy consumption increases with rising energy prices. For this group, the distribution changes from a nearly equal distribution of energy consumption (0.04-0.07) in the reference energy scenario to a more unequal distribution in the first energy scenario. The inequality increases in the range of 0.06-0.24 and in the second scenario we recognize a further rise in inequality. The Atkinson index ranges from 0.16 for an epsilon of 0.5 to 0.37 for an epsilon value of 2.0.

The distribution of energy consumption changes significantly in the social group of the blue-collar workers. The Atkinson index rises sharply from a more or less equal distribution (Atkinson index 0.0 to 0.06) in the reference scenario to a more unequal distribution with an Atkinson index between 0.04 and 0.14 for scenario I and 0.11 and 0.24 for scenario II. This is a sharp increase of inequality caused by increasing energy prices.

In the case of the white-collar households, the distribution increases slightly from a nearly equal distribution of energy consumption in the reference scenario (0.01-0.07) to a growing inequality in scenario I (0.03-0.14). In scenario II (0.08–0.23), we see a significant rise in the inequality of the distribution of energy consumption. Also for civil servants, we see an increase of the inequalities. In the reference scenario, we see a relatively equal distribution of energy consumption in the group of civil servants, but in scenario I we see a small increase of inequality. However, in scenario II we see a considerable increase of inequality. The Atkinson index rises to values between 0.15-0.36 depending on the chosen epsilon parameter.

A similar picture is obtained by analysing the self-employed households. We see a nearly equal distribution of energy expenditures in the reference scenario. By raising the energy prices by about 55% in the first scenario, we can detect a rise of inequality (0.1-0.24) and a significant increase of inequality in the second scenario (0.15-0.34).

We can therefore summarize that in all social groups we see a small rise in inequality in scenario I, but in the second energy price scenario we detected a significant rise of inequality. The first rise of the energy prices in scenario I could be managed by all households by using their savings, but a further increase in energy prices in scenario II could not be covered by household savings. Some households could not increase their energy expenditures, which results in an increase of the Atkinson index. The perception of the distribution of the energy consumption by society is becoming more unequal due to rising energy prices.

5. Outlook

The Atkinson index provides a meaningful tool not only to measure the distribution of income but also to estimate the distributional dimensions of energy consumption. A distribution analysis based on the Atkinson index can make an important contribution to the social debate about the distributional justice of income, consumption, and energy expenditures. With the epsilon parameter, the Atkinson index explicitly reveals the implicit inequality aversion of society, and it enables us to define how sensitively the Atkinson index should react to inequalities. Our inequality research contributes to the IEK-STE multi-sectoral energy model, which analyses the macroeconomic and energy effects of the transformation of the German energy sector and explicitly considers the distributional effects of increasing energy prices not only on the German households but on all sectors of the German economy (Kronenberg et al. 2010; Kronenberg 2010).

Our analysis represents a contribution to implementing the recommendations of the Stiglitz Commission to develop better welfare measures, and deliver data for politicians and decision-makers about the distributional effects of the current energy expenditures and of higher energy prices. We developed a method to specify Gordon's trade-off between political equality and economic efficiency. We tried to ensure that the recommendations of the Stiglitz-Commission could be used to develop better measures and deliver data for politicians and decision-makers on the distributional effects of the current energy expenditure and of higher energy prices. The analysis using the Atkinson index allowed a deeper look at the self-perception of society and society's judgement of Gordon's trade-off. These research results can be used to support politics in the expensive transformation of energy systems into "sustainable energy systems" based on renewables which is currently taking place in particular in Germany after Fukushima (Ethics Commission for a Safe Energy Supply 2011; Bundesministerium für Umwelt Naturschutz und Reaktorsicherheit (BMU) 2012; Röttgen 2011). Energy prices, in particular the tariffs for electricity, are steadily increasing. However, as our paper has demonstrated, the impact of price increases on income

groups varies considerably. Therefore, energy policy should not only focus on the price increase for an abstract "average" citizen. Instead, policy should take into account the negative social impact of rising prices on the low and lowest income groups. In Germany, more than 200,000 people with a low income or dependency on social security are unable to pay for the electricity bill, and this number is increasing fast.[14] Therefore, the transformation of energy systems should be accompanied by efforts to support or compensate these groups financially (Federal Ministry for the Environment Nature Conservation and Nuclear Safety 2011; Ethics Commission for a Safe Energy Supply 2011; Bundesministerium für Umwelt Naturschutz und Reaktorsicherheit (BMU) 2012). Otherwise, economic and social inequality may lead to social divisions, and social divisions may destroy relationships between individuals and could become a driving force for the destabilization of societies. (Wilkinson and Pickett 2009) take the view that equality is better for a society and its citizens – a thesis which is disputed (O'Connell 2010) because inequality and freedom must be balanced. Therefore, information and knowledge about status, development and the implication of inequality is necessary both from the perspective of science (Cowell and Kanbur 2011) and policy (Diezinger and Mayr-Kleffel 2009).

6. References

Alpanda, S. and A. Peralta-Alva. 2010. Oil crisis, energy-saving technological change and the stock market crash of 1973–74. *Review of Economic Dynamics* 13(4): 824-842.

Amiel, Y. and F. A. Cowell. 1999. *Thinking about Inequality*. Cambridge: Cambridge University Press.

Atkinson, A. B. 1970. On the measurement of inequality. *Journal of Economic Theory* 2(3): 244-263.

Atkinson, A. B. 1973. *Wealth, Income and Inequality* London: Penguin.

Atkinson, A. B. 1975. *On the Measurement of Inequality*. Oxford: Oxford University Press.

Atkinson, A. B. 1983. *The Economics of Inequality*. 2 ed. Oxford: Clarendon Press.

Barr, N. 1993. *The Economics of the Welfare State*. 2 ed. Stanford: Stanford University Press.

Bell, D. 1996 (1976). *The cultural contradictions of capitalism*. 1996 edition ed. New York: Basic Books.

Bresciani-Turroni, C. 1937. Annual Survey of Statistical Data: Pareto's Law and the Index of Inequality of Incomes. *Econometrica* 7(2): 107-133.

Bundesministerium für Umwelt Naturschutz und Reaktorsicherheit (BMU). 2012. Energiewende, edited by R. Ö. BMU: Bundesministerium für Umwelt, Naturschutz und Reaktorsicherheit (BMU).

[14] http://www.spiegel.de/politik/deutschland/200-000-hartz-iv-empfaenger-koennen-ihre-stromrechnung-nicht-bezahlen-a-835832.html

Burghardt, M. 2000. Zur Revision der privaten Konsumausgaben im Rahmen der Volkswirtschaftlichen Gesamtrechnungen 2005. *Wirtschaft & Statistik* 2000(3): 136-144.

Champernowne, D. G. 1974. A comparison of Measures of Inequality of Income Distribution. *Economic]ournal* 84(336): 787-816.

Cowell, F. and R. Kanbur. 2011. Introduction to the symposium on "Inequality: new directions". *Journal of Economic Inequality* 9(3): 315-318.

Cowell, F. A. 1977. *Measuring inequality*. New York: Halsted Press.

Cowell, F. A. 2000a. Measuring Inequality. http://eclass.yonsei.ac.kr/hoskim/lectures/public/Measuring%20Inequality%20%28Cowell%29.pdf. Accessed.

Cowell, F. A. 2000b. Measurement of Inequality. In *Handbook of Income Distribution, Vol. 1*, edited by A. B. Atkinson and F. Bourguignon. Amsterdam: Elsevier.

Dalton, H. 1920. The measurement of the inequality of incomes. *Economic Journal* 30(119): 348-361.

Diekmann, A. 1981. *Sozialindikatoren der Ungleichheit, Chancenungleichheit und Diskriminierung*. Vienna: Insitut für Höhere Studien.

Diezinger, A. and V. Mayr-Kleffel, eds. 2009 *Soziale Ungleichheit (Social inequality)*: Freiburg, Lambertus-Verlag.

Eichhorn, W. 1988. On a class of inequality measures. *Social Choice and Welfare* 5(2-3): 171-177.

Energieagentur NRW. 2010. Energiepreise: Energieagentur NRW.

Ethics Commission for a Safe Energy Supply. 2011. *Germany's energy transition – A collective project for the future Federal Ministry for the Environment, Nature Conservation and Nuclear Safety,*. Berlin.

Federal Ministry for the Environment Nature Conservation and Nuclear Safety. 2011. *The Federal Government's energy concept of 2010 and the transformation of the energy system of 2011 (publised in German)*. Berlin (Germany): Federal Ministry for the Environment Nature Conservation and Nuclear Safety.

Foster, J. and A. Sen. 1997. Annexe "On Economic Inequality after a Quarter Century". In *On Economic Inequality*, edited by A. Sen. Oxford: Clarendon Press.

Friedman, M. 1962. *Capitalism and Freedom*. Chicago: University of Chicago Press.

Friedman, M. 1990. *Free to Choose: A Personal Statemen*. San Diego: Harvest Books.

Gordon, K. 1975. Foreword. In *Equality and Efficiency: The Big Tradeoff*, edited by A. M. Okun. Washington D.C: The Brookings Institution.

Hauser, R. 1996. Zur Messung individueller Wohlfahrt und ihrer Verteilung. In *Wohlfahrtsmessung - Aufgabe der Statistik im gesellschaftlichen Wandel*, edited by J. Chlumsky and R. Wiegert. Wiesbaden: Statistisches Bundesamt.

Jung, S. 2001. *Privater Verbrauch in Deutschland*. Wiesbaden: DUV.

Kronenberg, T. 2010. A Post-Keynesian Input-Output Model for Sustainability Studies In *18th International Input-Output Conference*. Sydney, Australia.

Kronenberg, T., W. Kuckshinrichs, and K. Weber. 2010. Feedbacks between the energy sector and the economy – a fully integrated energy-economic model for Germany. In *11th biennial conference of the International Society for Ecological Economics*. Bremen, Oldenburg, Germany.

Litchfield, J. A. 1999. *Inequality: Methods and Tools*. Washington: World Bank.

Lüthi, A. P. 1981. *Messung wirtschaftlicher Ungleichheit, Lecture Notes in Economics and Mathematical Systems*. Berlin, Heidelberg: Springer-Verlag.

Mosler, K. and P. Muliere. 1996. Inequality indices and the starshaped principle of transfers. *Statistical Papers* 37(4): 343-364.

Münich, M. 2000. Zur Höhe und Struktur der Ausgaben privater Haushalte. *Wirtschaft & Statistik* 2000(11): 853.

O'Connell, M. 2010. *Title Affluence versus Equality? A critique of Wilkinson and Pickett*. Working Paper, University Collge Dublin, http://irserver.ucd.ie/dspace/bitstream/10197/2475/3/spirit%20level%20summary%20critique.pdf.

Okun, A. M. 1975. *Equality and Efficiency: The Big Tradeoff*. Washington D.C: The Brookings Institution.

Rawls, J. 1971. *A Theory of Justice*. Cambridge, MA: Harvard University Press.

Röttgen, N. 2011. Aufbruch in ein neues Energiezeitalter. Gemeinsam auf dem Weg in eine nachhaltige Moderne, edited by R. Öffentlichkeitsarbeit. Berlin: Bundesministerium für Umwelt, Naturschutz und Reaktorsicherheit (BMU).

Samuelson, P. A. and W. D. Nordhaus. 2007. *Volkswirtschaftslehre*. 3 ed. Landsberg am Lech: mi-Fachverlag.

Schefczyk, M. 1998. *Personen und Präferenzen*. Marburg: Metropolis.

Seidl, C. 2001. Inequality measurement and the leaky−bucket paradox. *Economics Bulletin* 4(6): 1-7.

Sen, A. 1973. *On Economic Inequality*. 1 ed, *Proceedings-of-the-International-Conference-on-Systems-Science*. New York: Norton.

Sen, A. K. 1998. *Choice, Welfare and Measurement*. 2 ed. Cambridge: Harvard University Press.

Sieferle, R. P. 2001. *Subterranean Forest: Energy Systems and the Industrial Revolution* Cambridge: White Horse Press.

Smil, V. 1994. *Energy in World History*. Boulder: Westview.

Statistisches Bundesamt. 2008a. *Einkommens- und Verbrauchsstichprobe -Einnahmen und Ausgaben privater Haushalte 2003*. Wiesbaden:

Statistisches Bundesamt. 2008b. *Einkommens- und Verbrauchsstichprobe - Einkommensverteilung in Deutschland 2003*. Wiesbaden:

Statistisches Bundesamt (Federal Statistical Office). 2005a. Einkommens- und Verbrauchsstichprobe - Einnahmen und Ausgaben privater Haushalte 2003. *Fachserie Wirtschaftsrechnungen* 15(4).

Statistisches Bundesamt (Federal Statistical Office). 2005b. Einkommens- und Verbrauchsstichprobe - Aufgabe, Methode und Durchführung der EVS. *Fachserie Wirtschaftsrechnungen* 15(7).

Statistisches Bundesamt (Federal Statistical Office). 2008. Energieausgaben privater Haushalte. Wiesbaden: Statistisches Bundesamt,.

Stiglitz, J. E., A. Sen, and J.-P. Fitoussi. 2009. *Report by the Commission on the Measurement of Economic Performance and Social Progress*. Paris:

Thurow, L. C. 1971. The Income Distribution as a Pure Public Good. *The Quarterly Journal of Economics* 85(2): 327-336.

White, L. A. 1943. Energy and the Evolution of Culture. *American Anthropologist* 45(3): 335-356.

Wilkinson, R. and K. Pickett. 2009. *The Spirit Level: Why Equality is Better for Everyone*. London: Penguin.

ECOS 2012

The 25th International Conference on Efficiency, Cost, Optimization and Simulation of Energy Conversion Systems and Processes

(Perugia, June 26th-June 29th, 2012)

edited by
Umberto Desideri, Giampaolo Manfrida,
Enrico Sciubba

firenze university press
2012

ECOS 2012 : the 25th International Conference on Efficiency, Cost, Optimization and Simulation of Energy Conversion Systems and Processes (Perugia, June 26th-June 29th, 2012) / edited by Umberto Desideri, Giampaolo Manfrida, Enrico Sciubba. – Firenze : Firenze University Press, 2012.
(Proceedings e report ; 90)

http://digital.casalini.it/9788866553229

ISBN 978-88-6655-322-9 (online)

Progetto grafico di copertina Alberto Pizarro, Pagina Maestra snc
Immagine di copertina: © Kts | Dreamstime.com

Peer Review Process
All publications are submitted to an external refereeing process under the responsibility of the FUP Editorial Board and the Scientific Committees of the individual series. The works published in the FUP catalogue are evaluated and approved by the Editorial Board of the publishing house. For a more detailed description of the refereeing process we refer to the official documents published on the website and in the online catalogue of the FUP (http://www.fupress.com).

Firenze University Press Editorial Board
G. Nigro (Co-ordinator), M.T. Bartoli, M. Boddi, F. Cambi, R. Casalbuoni, C. Ciappei, R. Del Punta, A. Dolfi, V. Fargion, S. Ferrone, M. Garzaniti, P. Guarnieri, G. Mari, M. Marini, M. Verga, A. Zorzi.

© 2012 Firenze University Press
Università degli Studi di Firenze
Firenze University Press
Borgo Albizi, 28, 50122 Firenze, Italy
http://www.fupress.com/
Printed in Italy

ECOS 2012

The 25th International Conference on

Efficiency, Cost, Optimization and Simulation
of Energy Conversion Systems and Processes

Perugia, June 26th-June 29th, 2012

Book of Proceedings - Volume II

Edited by:
Umberto Desideri, Università degli Studi di Perugia
Giampaolo Manfrida, Università degli Studi di Firenze
Enrico Sciubba, Università degli Studi di Roma "Sapienza"

ECOS 2012 - THE 25TH INTERNATIONAL CONFERENCE ON
EFFICIENCY, COST, OPTIMIZATION, SIMULATION AND ENVIRONMENTAL IMPACT OF ENERGY SYSTEMS
JUNE 26-29, 2012, PERUGIA, ITALY
EDITED BY UMBERTO DESIDERI, GIAMPAOLO MANFRIDA, ENRICO SCIUBBA
FIRENZE UNIVERSITY PRESS, 2012, ISBN ONLINE : 978-88-6655-322-9

Advisory Committee (Track Organizers)

Building, Urban and Complex Energy Systems
V. Ismet Ugursal
Dalhousie University, Nova Scotia, Canada

Combustion, Chemical Reactors, Carbon Capture and Sequestration
Giuseppe Girardi
ENEA-Casaccia, Italy

Energy Systems: Environmental and Sustainability Issues
Christos A. Frangopoulos
National Technical University of Athens, Greece

Exergy Analysis and Second Law Analysis
Silvio de Oliveira Junior
Polytechnical University of Sao Paulo, Sao Paulo, Brazil

Fluid Dynamics and Power Plant Components
Sotirios Karellas
National Technical University of Athens, Athens, Greece

Fuel Cells
Umberto Desideri
University of Perugia, Perugia, Italy

Heat and Mass Transfer
Francesco Asdrubali, **Cinzia Buratti**
University of Perugia, Perugia, Italy

Industrial Ecology
Stefan Goessling-Reisemann
University of Bremen, Germany

Poster Session
Enrico Sciubba
University Roma 1 “Sapienza”, Italy

Process Integration and Heat Exchanger Networks
Francois Marechal
EPFL, Lausanne, *Switzerland*

Renewable Energy Conversion Systems
David Chiaramonti
University of Firenze, Firenze, Italy

Simulation of Energy Conversion Systems
Marcin Liszka
Polytechnica Slaska, Gliwice, Poland

System Operation, Control, Diagnosis and Prognosis
Vittorio Verda
Politecnico di Torino, Italy

Thermodynamics
A. Özer Arnas
United States Military Academy at West Point, U.S.A.

Thermo-Economic Analysis and Optimisation
Andrea Lazzaretto
University of Padova, Padova, Italy

Water Desalination and Use of Water Resources
Corrado Sommariva
ILF Consulting M.E., U.K

Scientific Committee

Riccardo Basosi, University of Siena, Italy
Gino Bella, University of Roma Tor Vergata, Italy
Asfaw Beyene, San Diego State University, United States
Ryszard Bialecki, Silesian Institute of Tecnology, Poland
Gianni Bidini, University of Perugia, Italy
Ana M. Blanco-Marigorta, University of Las Palmas de Gran Canaria, Spain
Olav Bolland, University of Science and Technology (NTNU), Norway
Renè Cornelissen, Cornelissen Consulting, The Netherlands
Franco Cotana, University of Perugia, Italy
Alexandru Dobrovicescu, Polytechnical University of Bucharest, Romania
Gheorghe Dumitrascu, Technical University of Iasi, Romania
Brian Elmegaard, Technical University of Denmark , Denmark
Daniel Favrat, EPFL, Switzerland
Michel Feidt, ENSEM - LEMTA University Henri Poincaré, France
Daniele Fiaschi, University of Florence, Italy
Marco Frey, Scuola Superiore S. Anna, Italy
Richard A Gaggioli, Marquette University, USA
Carlo N. Grimaldi, University of Perugia, Italy
Simon Harvey, Chalmers University of Technology, Sweden
Hasan Heperkan, Yildiz Technical University, Turkey
Abel Abel Hernandez-Guerrero, University of Guanajuato, Mexico
Jiri Jaromir Klemeš, University of Pannonia, Hungary
Zornitza V. Kirova-Yordanova, University "Prof. Assen Zlatarov", Bulgaria
Noam Lior, University of Pennsylvania, United States
Francesco Martelli, University of Florence, Italy
Aristide Massardo, University of Genova, Italy
Jim McGovern, Dublin Institute of Technology, Ireland
Alberto Mirandola, University of Padova, Italy
Michael J. Moran, The Ohio State University, United States
Tatiana Morosuk, Technical University of Berlin, Germany
Pericles Pilidis, University of Cranfield, United Kingdom
Constantine D. Rakopoulos, National Technical University of Athens, Greece
Predrag Raskovic, University of Nis, Serbia and Montenegro
Mauro Reini, University of Trieste, Italy
Gianfranco Rizzo, University of Salerno, Italy
Marc A. Rosen, University of Ontario, Canada
Luis M. Serra, University of Zaragoza, Spain
Gordana Stefanovic, University of Nis, Serbia and Montenegro
Andrea Toffolo, Luleå University of Technology, Sweden
Wojciech Stanek, Silesian University of Technology, Poland
George Tsatsaronis, Technical University Berlin, Germany
Antonio Valero, University of Zaragoza, Spain
Michael R. von Spakovsky, Virginia Tech, USA
Stefano Ubertini, Parthenope University of Naples, Italy
Sergio Ulgiati, Parthenope University of Naples, Italy
Sergio Usón, Universidad de Zaragoza, Spain
Roman Weber, Clausthal University of Technology, Germany
Ryohei Yokoyama, Osaka Prefecture University, Japan
Na Zhang, Institute of Engineering Thermophysics, Chinese Academy of Sciences, China

The 25th ECOS Conference 1987-2012: leaving a mark

The introduction to the ECOS series of Conferences states that "ECOS is a series of international conferences that focus on all aspects of Thermal Sciences, with particular emphasis on Thermodynamics and its applications in energy conversion systems and processes". Well, ECOS is much more than that, and its history proves it!

The idea of starting a series of such conferences was put forth at an informal meeting of the Advanced Energy Systems Division of the American Society of Mechanical Engineers (ASME) at the November 1985 Winter Annual Meeting (WAM), in Miami Beach, Florida, then chaired by Richard Gaggioli. The resolution was to organize an annual Symposium on the Analysis and Design of Thermal Systems at each ASME WAM, and to try to involve a larger number of scientists and engineers worldwide by organizing conferences outside of the United States. Besides Rich other participants were Ozer Arnas, Adrian Bejan, Yehia El-Sayed, Robert Evans, Francis Huang, Mike Moran, Gordon Reistad, Enrico Sciubba and George Tsatsaronis.

Ever since 1985, a Symposium of 8-16 sessions has been organized by the Systems Analysis Technical Committee every year, at the ASME Winter Annual Meeting (now ASME-IMECE). The first overseas conference took place in Rome, twenty-five years ago (in July 1987), with the support of the U.S. National Science Foundation and of the Italian National Research Council. In that occasion, Christos Frangopoulos, Yalcin Gogus, Elias Gyftopoulos, Dominick Sama, Sergio Stecco, Antonio Valero, and many others, already active at the ASME meetings, joined the core-group.

The name ECOS was used for the first time in Zaragoza, in 1992: it is an acronym for **Efficiency, Cost, Optimization and Simulation** (of energy conversion systems and processes), keywords that best describe the contents of the presentations and discussions taking place in these conferences. Some years ago, Christos Frangopoulos inserted in the official website the note that "ècos" ('οικος) means "home" in Greek and it ought to be attributed the very same meaning as the prefix "Eco-" in environmental sciences.
The last 25 years have witnessed an almost incredible growth of the ECOS community: more and more Colleagues are actively participating in our meetings, several international Journals routinely publish selected papers from our Proceedings, fruitful interdisciplinary and international cooperation projects have blossomed from our meetings. Meetings that have spanned three continents (Africa and Australia ought to be our next targets, perhaps!) and influenced in a way or another much of modern Engineering Thermodynamics.
After 25 years, if we do not want to become embalmed in our own success and lose momentum, it is mandatory to aim our efforts in two directions: first, encourage the participation of younger academicians to our meetings, and second, stimulate creative and useful discussions in our sessions. Looking at this years' registration roster (250 papers of which 50 authored or co-authored by junior Authors), the first objective seems to have been attained, and thus we have just to continue in that direction; the second one involves allowing space to "voices that sing out of the choir", fostering new methods and approaches, and establishing or reinforcing connections to other scientific communities. It is important that our technical sessions represent a place of active confrontation, rather than academic "lecturing".
In this spirit, we welcome you in Perugia, and wish you a scientifically stimulating, touristically interesting, and culinarily rewarding experience. In line with our 25 years old scientific excellency and friendship!

Umberto Desideri, Giampaolo Manfrida, Enrico Sciubba

CONTENT MANAGEMENT

The index lists all the papers contained all the eight volumes of the Proceedings of the ECOS 2012 International Conference.
Page numbers are listed only for papers within the Volume you are looking at. The ID code allows to trace back the identification number assigned to the paper within the Conference submission, review and track organization processes.

CONTENT

VOLUME II

II . 1 – EXERGY ANALYSIS AND 2ND LAW ANALYSIS

» A comparative analysis of cryogenic recuperative heat exchangers based on exergy destruction (ID 129) ……..... *Pag. 1*
Adina Teodora Gheorghian, Alexandru Dobrovicescu, Lavinia Grosu, Bogdan Popescu, Claudia Ionita

» A critical exploration of the usefulness of rational efficiency as a performance parameter for heat exchangers (ID 307) ……..... *Pag. 13*
Jim McGovern, Georgiana Tirca-Dragomirescu, Michel Feidt, Alexandru Dobrovicescu

» A new procedure for the design of LNG processes by combining exergy and pinch analyses (ID 238) ……..... *Pag. 24*
Danahe Marmolejo-Correa, Truls Gundersen

» Advances in the distribution of environmental cost of water bodies through the exergy concept in the Ebro river (ID 258) ……..... *Pag. 40*
Javier Uche Marcuello, Amaya Martínez Gracia, Beatriz Carrasquer Álvarez, Antonio Valero Capilla

» Application of the entropy generation minimization method to a solar heat exchanger: a pseudo-optimization design process based on the analysis of the local entropy generation maps (ID 357) ……..... *Pag. 58*
Giorgio Giangaspero, Enrico Sciubba

» Comparative analysis of ammonia and carbon dioxide two-stage cycles for simultaneous cooling and heating (ID 84) ……..... *Pag. 79*
Alexandru Dobrovicescu, Ciprian Filipoiu, Emilia Cerna Mladin, Valentin Apostol, Liviu Drughean

» Comparison between traditional methodologies and advanced exergy analyses for evaluating efficiency and externalities of energy systems (ID 515) ……..... *Pag. 90*
Gabriele Cassetti, Emanuela Colombo

» Comparison of entropy generation figures using entropy maps and entropy transport equation for an air cooled gas turbine blade (ID 468) ……..... *Pag. 107*
Omer Emre Orhan, Oguz Uzol

» Conventional and advanced exergetic evaluation of a supercritical coal-fired power plant (ID 377) ……..... *Pag. 115*
Ligang Wang, Yongping Yang, Tatiana Morosuk, George Tsatsaronis

» Energy and exergy analyses of the charging process in encapsulted ice thermal energy storage (ID 164) ……..... *Pag. 127*
David MacPhee, Ibrahim Dincer, Asfaw Beyene

» Energy integration and cogeneration in nitrogen fertilizers industry: thermodynamic estimation of the efficiency, potentials, limitations and environmental impact. Part 1: energy integration in ammonia production plants (ID 303) ……..... *Pag. 138*
Zornitza Vassileva Kirova-Yordanova

» Evaluation of the oil and gas processing at a real production day on a North Sea oil platform using exergy analysis (ID 260) ……..... *Pag. 153*
Mari Voldsund, Wei He, Audun Røsjorde, Ivar Ståle Ertesvåg, Signe Kjelstrup

FIRENZE UNIVERSITY PRESS, 2012, ISBN ONLINE : 978-88-6655-322-9

» Exergetic and economic analysis of Kalina cycle for low temperature geothermal sources in Brazil (ID 345) ……..... *Pag. 167*
Carlos Eymel Campos Rodriguez, José Carlos Escobar Palacios, Cesar Adolfo Rodríguez Sotomonte, Marcio Leme, Osvaldo José Venturini, Electo Eduardo Silva Lora, Vladimir Melián Cobasa, Daniel Marques dos Santos, Fábio R. Lofrano Dotto, Vernei Gialluca

» Exergy analysis and comparison of CO2 heat pumps (ID 242) ……..... *Pag. 180*
Argyro Papadaki, Athina Stegou - Sagia

» Exergy analysis of a CO2 Recovery plant for a brewery (ID 72) ……..... *Pag. 192*
Daniel Rønne Nielsen, Brian Elmegaard, C. Bang-Møller

» Exergy analysis of the silicon production process (ID 118) ……..... *Pag. 203*
Marit Takla, Leiv Kolbeinsen, Halvard Tveit, Signe Kjelstrup

» Exergy based indicators for cardiopulmonary exercise test evaluation (ID 159) ……..... *Pag.215*
Carlos Eduardo Keutenedjian Mady, Cyro Albuquerque Neto, Tiago Lazzaretti Fernandes, Arnaldo Jose Hernandez, Paulo Hilário Nascimento Saldiva, Jurandir Itizo Yanagihara, Silvio de Oliveira Junior

» Exergy disaggregation as an alternative for system disaggregation in thermoeconomics (ID 483) ……..... *Pag. 226*
José Joaquim Conceição Soares Santos, Atilio Lourenço, Julio Mendes da Silva, João Donatelli,
José Escobar Palacio

» Exergy intensity of petroleum derived fuels (ID 117) ……..... *Pag. 240*
Julio Augusto Mendes da Silva, Maurício Sugiyama, Claudio Rucker, Silvio de Oliveira Junior

» Exergy-based sustainability evaluation of a wind power generation system (ID 542) ……..... *Pag. 263*
Jin Yang, B. Chen, Enrico Sciubba

» Human body exergy metabolism (ID 160) ……..... *Pag. 271*
Carlos Eduardo Keutenedjian Mady, Silvio de Oliveira Junior

» Integrating an ORC into a natural gas expansion plant supplied with a co-generation unit (ID 273) ……..... *Pag. 284*
Sergio Usón, Wojciech Juliusz Kostowski

» One-dimensional model of an optimal ejector and parametric study of ejector efficiency (ID 323) ……..... *Pag. 303*
Ronan Killian McGovern, Kartik Bulusu, Mohammed Antar, John H. Lienhard

» Optimization and design of pin-fin heat sinks based on minimum entropy generation (ID 6) ……..... *Pag. 314*
Jose-Luis Zuniga-Cerroblanco, Abel Hernandez-Guerrero, Carlos A. Rubio-Jimenez, Cuauhtemoc Rubio-Arana, Sosimo E. Diaz-Mendez

» Performance analysis of a district heating system (ID 271) ……..... *Pag. 325*
Andrej Ljubenko, Alojz Poredoš, Tatiana Morosuk, George Tsatsaronis

» System analysis of exergy losses in an integrated oxy-fuel combustion power plant (ID 64) ……..... *Pag. 338*
Andrzej Ziębik, Paweł Gładysz

» What is the cost of losing irreversibly the mineral capital on Earth? (ID 220) ……..... *Pag. 352*
Alicia Valero Delgado, Antonio Valero

II . 2 – THERMODYNAMICS

» A new polygeneration system for methanol and power based on coke oven gas and coal gas (ID 252) ……..... *Pag. 364*
Hu Lin, Hongguang Jin, Lin Gao, Rumou Li

» Argon-Water closed gas cycle (ID 67)
Federico Fionelli, Giovanni Molinari ……..... *Pag. 373*

» Binary alkane mixtures as fluids in Rankine cycles (ID 246) ……..... *Pag. 388*
M. Aslam Siddiqi, Burak Atakan

» Excess enthalpies of second generation biofuels (ID 308) ……..... *Pag. 405*
Alejandro Moreau, José Juan Segovia, M. Carmen Martín, Miguel Ángel Villamañán, César R. Chamorro, Rosa M. Villamañán

» Local stability analysis of a Curzon-Ahlborn engine considering the Van der Waals equation state in the maximum ecological regime (ID 281) ……..... *Pag. 411*
Ricardo Richard Páez-Hernández, Pedro Portillo-Díaz, Delfino Ladino-Luna, Marco Antonio Barranco-Jiménez

» Some remarks on the Carnot's theorem (ID 325) ……..... *Pag. 422*
Julian Gonzalez Ayala, Fernando Angulo-Brown

» The Dead State (ID 340) ……..... *Pag. 435*
Richard A. Gaggioli

» The magnetocaloric energy conversion (ID 97) ……..... *Pag. 448*
Andrej Kitanovski, Jaka Tusek, Alojz Poredos

CONTENTS OF ALL THE VOLUMES

VOLUME I

I . 1 – SIMULATION OF ENERGY CONVERSION SYSTEMS

» A novel hybrid-fuel compressed air energy storage system for China's situation (ID 531)
Wenyi Liu, Yongping Yang, Weide Zhang, Gang Xu,and Ying Wu

» A review of Stirling engine technologies applied to micro-cogeneration systems (ID 338)
Ana C Ferreira, Manuel L Nunes, Luís B Martins, Senhorinha F Teixeira

» An organic Rankine cycle off-design model for the search of the optimal control strategy (ID 295)
Andrea Toffolo, Andrea Lazzaretto, Giovanni Manente, Marco Paci

» Automated superstructure generation and optimization of distributed energy supply systems (ID 518)
Philip Voll, Carsten Klaffke, Maike Hennen, André Bardow

» Characterisation and classification of solid recovered fuels (SRF) and model development of a novel thermal utilization concept through air- gasification (ID 506)
Panagiotis Vounatsos, Konstantinos Atsonios, Mihalis Agraniotis, Kyriakos D. Panopoulos, George Koufodimos,Panagiotis Grammelis, Emmanuel Kakaras

» Design and modelling of a novel compact power cycle for low temperature heat sources (ID 177)
Jorrit Wronski, Morten Juel Skovrup, Brian Elmegaard, Harald Nes Rislå, Fredrik Haglind

» Dynamic simulation of combined cycles operating in transient conditions: an innovative approach to determine the steam drums life consumption (ID 439)
Stefano Bracco

» Effect of auxiliary electrical power consumptions on organic Rankine cycle system with low-temperature waste heat source (ID 235)
Samer Maalouf, Elias Boulawz Ksayer, Denis Clodic

» Energetic and exergetic analysis of waste heat recovery systems in the cement industry (ID 228)
Sotirios Karellas, Aris Dimitrios Leontaritis, Georgios Panousis, Evangelos Bellos, Emmanuel Kakaras

» Energy and exergy analysis of repowering options for Greek lignite-fired power plants (ID 230)
Sotirios Karellas, Aggelos Doukelis, Grammatiki Zanni, Emmanuel Kakaras

» Energy saving by a simple solar collector with reflective panels and boiler (ID 366)
Anna Stoppato, Renzo Tosato

» Exergetic analysis of biomass fired double-stage Organic Rankine Cycle (ORC) (ID 37)
Markus Preißinger, Florian Heberle, Dieter Brüggemann

» Experimental tests and modelization of a domestic-scale organic Rankine cycle (ID 156)
Roberto Bracco, Stefano Clemente, Diego Micheli, Mauro Reini

» Model of a small steam engine for renewable domestic CHP system (ID 31)
Giampaolo Manfrida, Giovanni Ferrara, Alessandro Pescioni

» Model of vacuum glass heat pipe solar collectors (ID 312)
Daniele Fiaschi, Giampaolo Manfrida

» Modelling and exergy analysis of a plasma furnace for aluminum melting process (ID 254)
Luis Enrique Acevedo, Sergio Usón, Javier Uche, Patxi Rodríguez

» Modelling and experimental validation of a solar cooling installation (ID 296)
Guillaume Anies, Pascal Stouffs, Jean Castaing-Lasvignottes

» The influence of operating parameters and occupancy rate of thermoelectric modules on the electricity generation (ID 314)
Camille Favarel, Jean-Pierre Bédécarrats, Tarik Kousksou, Daniel Champier

» Thermodynamic and heat transfer analysis of rice straw co-firing in a Brazilian pulverised coal boiler (ID 236)
Raphael Miyake, Alvaro Restrepo, Fábio Kleveston Edson Bazzo, Marcelo Bzuneck

» Thermophotovoltaic generation: A state of the art review (ID 88)
Matteo Bosi, Claudio Ferrari, Francesco Melino, Michele Pinelli, Pier Ruggero Spina, Mauro Venturini

I . 2 – HEAT AND MASS TRANSFER

» A DNS method for particle motion to establish boundary conditions in coal gasifiers (ID 49)
Efstathios E Michaelides, Zhigang Feng

» Effective thermal conductivity with convection and radiation in packed bed (ID 60)
Yusuke Asakuma

» Experimental and CFD study of a single phase cone-shaped helical coiled heat exchanger: an empirical correlation (ID 375)
Daniel Flórez-Orrego, Walter Arias, Diego López, Héctor Velásquez

» Thermofluiddynamic model for control analysis of latent heat thermal storage system (ID 207)
Adriano Sciacovelli, Vittorio Verda, Flavio Gagliardi

» Towards the development of an efficient immersed particle heat exchanger: particle transfer from low to high pressure (ID 202)
Luciano A. Catalano, Riccardo Amirante, Stefano Copertino, Paolo Tamburrano, Fabio De Bellis

I . 3 – INDUSTRIAL ECOLOGY

» Anthropogenic heat and exergy balance of the atmosphere (ID 122)
Asfaw Beyene, David MacPhee, Ron Zevenhoven

» Determination of environmental remediation cost of municipal waste in terms of extended exergy (ID 63)
Candeniz Seckin, Ahmet R. Bayulken

» Development of product category rules for the application of life cycle assessment to carbon capture and storage (537)
Carlo Strazza, Adriana Del Borghi, Michela Gallo

» Electricity production from renewable and non-renewable energy sources: a comparison of environmental, economic and social sustainability indicators with exergy losses throughout the supply chain (ID 247)
Lydia Stougie, Hedzer van der Kooi, Rob Stikkelman
» Exergy analysis of the industrial symbiosis model in Kalundborg (ID 218)
Alicia Valero Delgado, Sergio Usón, Jorge Costa

» Global gold mining: is technological learning overcoming the declining in ore grades? (ID 277)
Adriana Domínguez, Alicia Valero

» Personal transportation energy consumption (ID305)
Matteo Muratori, Emmanuele Serra, Vincenzo Marano, Michael Moran

» Resource use evaluation of Turkish transportation sector via the extended exergy accounting method (ID 43)
Candeniz Seckin, Enrico Sciubba, Ahmet R. Bayulken

» The impact of higher energy prices on socio-economic inequalities of German social groups (ID 80)
Holger Schlör, Wolfgang Fischer, Jürgen-Friedrich Hake

VOLUME III

THERMO-ECONOMIC ANALYSIS AND OPTIMIZATION

» A comparison of optimal operation of residential energy systems using clustered demand patterns based on Kullback-Leibler divergence (ID 142)
Akira Yoshida, Yoshiharu Amano, Noboru Murata, Koichi Ito, Takumi Hashizume

» A Model for Simulation and Optimal Design of a Solar Heating System with Seasonal Storage (ID 51)
Gianfranco Rizzo

» A thermodynamic and economic comparative analysis of combined gas-steam and gas turbine air bottoming cycle (ID 232)
Tadeusz Chmielniak, Daniel Czaja, Sebastian Lepszy

» Application of an alternative thermoeconomic approach to a two-stage vapor compression refrigeration cycle with intercooling (ID 135)
Atilio Barbosa Lourenço, José Joaquim Conceição Soares Santos, João Luiz Marcon Donatelli

» Comparative performance of advanced power cycles for low temperature heat sources (ID 109)
Guillaume Becquin, Sebastian Freund

» Comparison of nuclear steam power plant and conventional steam power plant through energy level and thermoeconomic analysis (ID 251)
S. Khamis Abadi, Mohammad Hasan Khoshgoftar Manesh, M. Baghestani, H. Ghalami, Majid Amidpour

» Economic and exergoeconomic analysis of micro GT and ORC cogeneration systems (ID 87)
Audrius Bagdanavicius, Robert Sansom, Nick Jenkins, Goran Strbac

» Exergoeconomic comparison of wet and dry cooling technologies for the Rankine cycle of a solar thermal power plant (ID 300)
Philipp Habl, Ana M. Blanco-Marigorta, Berit Erlach

» Influence of renewable generators on the thermo-economic multi-level optimization of a poly-generation smart grid (101)
Massimo Rivarolo, Andrea Greco, Francesca Travi, Aristide F. Massardo

» Local stability analysis of a thermoeconomic model of an irreversible heat engine working at different criteria of performance (ID 289)
Marco A. Barranco-Jiménez, Norma Sánchez-Salas, Israel Reyes-Ramírez, Lev Guzmán-Vargas

» Multicriteria optimization of a distributed trigeneration system in an industrial area (ID 154)
Dario Buoro, Melchiorre Casisi, Alberto de Nardi, Piero Pinamonti, Mauro Reini

» On the effect of eco-indicator selection on the conclusions obtained from an exergoenvironmental analysis (ID 275)
Tatiana Morosuk, George Tsatsaronis, Christopher Koroneos

» Optimisation of supply temperature and mass flow rate for a district heating network (ID 104)
Marouf Pirouti, Audrius Bagdanavicius, Jianzhong Wu, Janaka Ekanayake

» Optimization of energy supply systems in consideration of hierarchical relationship between design and operation (ID 389)
Ryohei Yokoyama, Shuhei Ose

» The fuel impact formula revisited (ID 279)
Cesar Torres, Antonio Valero

» The introduction of exergy analysis to the thermo-economic modelling and optimisation of a marine combined cycle system (ID 61)
George G. Dimopoulos, Chariklia A. Georgopoulou, Nikolaos M.P. Kakalis

» The relationship between costs and environmental impacts in power plants: an exergy-based study (ID 272)
Fontina Petrakopoulou, Yolanda Lara, Tatiana Morosuk, Alicia Boyano, George Tsatsaronis

» Thermo-ecological evaluation of biomass integrated gasification gas turbine based cogeneration technology (ID 441)
Wojciech Stanek, Lucyna Czarnowska, Jacek Kalina

» Thermo-ecological optimization of a heat exchanger through empirical modeling (ID 501)
Ireneusz Szczygieł, Wojciech Stanek, Lucyna Czarnowska, Marek Rojczyk

» Thermoeconomic analysis and optimization in a combined cycle power plant including a heat transformer for energy saving (ID 399)
Elizabeth Cortés Rodríguez, José Luis Castilla Carrillo, Claudia A. Ruiz Mercado, Wilfrido Rivera Gómez-Franco

» Thermoeconomic analysis and optimization of a hybrid solar-electric heating in a fluidized bed dryer (ID 400)
Elizabeth Cortés Rodríguez, Felipe de Jesús Ojeda Cámara, Isaac Pilatowsky Figueroa

» Thermoeconomic approach for the analysis of low temperature district heating systems (ID 208)
Vittorio Verda, Albana Kona

» Thermo-economic assessment of a micro CHP systems fuelled by geothermal and solar energy (ID 166)
Duccio Tempesti, Daniele Fiaschi, Filippo Gabuzzini

» **Thermo-economic evaluation and optimization of the thermo-chemical conversion of biomass into methanol (ID 194)**
Emanuela Peduzzi, Laurence Tock, Guillaume Boissonnet, François Marechal

» **Thermoeconomic fuel impact approach for assessing resources savings in industrial symbiosis: application to Kalundborg Eco-industrial Park (ID 256)**
Sergio Usón, Antonio Valero, Alicia Valero, Jorge Costa

» **Thermoeconomics of a ground-based CAES plant for peak-load energy production system (ID 32)**
Simon Kemble, Giampaolo Manfrida, Adriano Milazzo, Francesco Buffa

VOLUME IV

IV . 1 – FLUID DYNAMICS AND POWER PLANT COMPONENTS

» **A control oriented simulation model of a multistage axial compressor (ID 444)**
Lorenzo Damiani, Giampaolo Crosa, Angela Trucco

» **A flexible and simple device for in-cylinder flow measurements: experimental and numerical validation (ID 181)**
Andrea Dai Zotti, Massimo Masi, Marco Antonello

» **CFD Simulation of Entropy Generation in Pipeline for Steam Transport in Real Industrial Plant (ID 543)**
Goran Vučković, Gradimir Ilić, Mića Vukić, Milan Banić, Gordana Stefanović

» **Feasibility Study of Turbo expander Installation in City Gate Station (ID 168)**
Navid Zehtabiyan Rezaie, Majid Saffar-Avval

» **GTL and RME combustion analysis in a transparent CI engine by means of IR digital imaging (ID 460)**
Ezio Mancaruso, Luigi Sequino, Bianca Maria Vaglieco

» **Some aspects concerning fluid flow and turbulence modeling in 4-valve engines (ID 116)**
Zoran Stevan Jovanovic, Zoran Masonicic, Miroljub Tomic

IV . 2 – SYSTEM OPERATION CONTROL DIAGNOSIS AND PROGNOSIS

» **Adapting the operation regimes of trigeneration systems to renewable energy systems integration (ID 188)**
Liviu Ruieneanu, Mihai Paul Mircea

» **Advanced electromagnetic sensors for sustainable monitoring of industrial processes (ID 145)**
Uroš Puc, Andreja Abina, Anton Jeglič, Pavel Cevc, Aleksander Zidanšek

» **Assessment of stresses and residual life of plant components in view of life-time extension of power plants (ID 453)**
Anna Stoppato, Alberto Benato and Alberto Mirandola

» **Control strategy for minimizing the electric power consumption of hybrid ground source heat pump system (ID 244)**
Zoi Sagia, Constantinos Rakopoulos

» **Exergetic evaluation of heat pump booster configurations in a low temperature district heating network (ID 148)**
Torben Ommen, Brian Elmegaard

» **Exergoeconomic diagnosis: a thermo-characterization method by using irreversibility analysis (ID 523)**
Abraham Olivares-Arriaga, Alejandro Zaleta-Aguilar, Rangel-Hernández V. H, Juan Manuel Belman-Flores

» Optimal structural design of residential cogeneration systems considering their operational restrictions (ID 224)
Tetsuya Wakui, Ryohei Yokoyama

» Performance estimation and optimal operation of a CO2 heat pump water heating system (ID 344)
Ryohei Yokoyama, Ryosuke Kato, Tetsuya Wakui, Kazuhisa Takemura

» Performances of a common-rail Diesel engine fuelled with rapeseed and waste cooking oils (ID 213)
Alessandro Corsini, Valerio Giovannoni, Stefano Nardecchia, Franco Rispoli, Fabrizio Sciulli, Paolo Venturini

» Reduced energy cost through the furnace pressure control in power plants (ID 367)
Vojislav Filipović, Novak Nedić, Saša Prodanović

» Short-term scheduling model for a wind-hydro-thermal electricity system (ID 464)
Sérgio Pereira, Paula Ferreira, A. Ismael Freitas Vaz

VOLUME V

V . 1 - RENEWABLE ENERGY CONVERSION SYSTEMS

» A co-powered concentrated solar power Rankine cycle concept for small size combined heat and power (ID 276)
Alessandro Corsini, Domenico Borello, Franco Rispoli, Eileen Tortora

» A novel non-tracking solar collector for high temperature application (ID 466)
Wattana Ratismith, Anusorn Inthongkhum

» Absorption heat transformers (AHT) as a way to enhance low enthalpy geothermal resources (ID 311)
Daniele Fiaschi, Duccio Tempesti, Giampaolo Manfrida, Daniele Di Rosa

» Alternative feedstock for the biodiesel and energy production: the OVEST project (ID 98)
Matteo Prussi, David Chiaramonti, Lucia Recchia, Francesco Martelli, Fabio Guidotti

» Assessing repowering and update scenarios for wind energy converters (ID 158)
Till Zimmermann

» Biogas from mechanical pulping industry – potential improvement for increased biomass vehicle fuels (ID 54)
Mimmi Magnusson, Per Alvfors

» Biogas or electricity as vehicle fuels derived from food waste - the case of Stockholm (ID 27)
Martina Wikström, Per Alvfors

» Compressibility factor as evaluation parameter of expansion processes in organic Rankine cycles (ID 292)
Giovanni Manente, Andrea Lazzaretto

» Design of solar heating system for methane generation (ID 445)
Lucía Mónica Gutiérrez, P. Quinto Diez, L. R. Tovar Gálvez

» Economic feasibility of PV systems in hotels in Mexico (ID 346)
Augusto Sanchez, Sergio Quezada

» Effect of a back surface roughness on annual performance of an air-cooled PV module (ID 193)
Riccardo Secchi, Duccio Tempesti, Jacek Smolka

» Energy and exergy analysis of the first hybrid solar-gas power plant in Algeria (ID 176)
Fouad Khaldi

» Energy recovery from MSW treatment by gasification and melting technology (ID 393)
Fabrizio Strobino, Alessandro Pini Prato, Diego Ventura, Marco Damonte

» Ethanol production by enzymatic hydrolysis process from sugarcane biomass - the integration with the conventional process (ID 189)
Reynaldo Palacios-Bereche, Adriano Ensinas, Marcelo Modesto, Silvia Azucena Nebra

» Evaluation of gas in an industrial anaerobic digester by means of biochemical methane potential of organic municipal solid waste components (ID 57)
Isabella Pecorini, Tommaso Olivieri, Donata Bacchi, Alessandro Paradisi, Lidia Lombardi, Andrea Corti, Ennio Carnevale

» Exergy analysis and genetic algorithms for the optimization of flat-plate solar collectors (ID 423)
Soteris A. Kalogirou

» Experimental study of tar and particles content of the produced gas in a double stage downdraft gasifier (ID 487)
Ana Lisbeth Galindo Noguera, Sandra Yamile Giraldo, Rene Lesme-Jaén, Vladimir Melian Cobas, Rubenildo Viera Andrade, Electo Silva Lora

» Feasibility study to realize an anaerobic digester fed with vegetables matrices in central Italy (ID 425)
Umberto Desideri, Francesco Zepparelli, Livia Arcioni, Ornella Calderini, Francesco Panara, Matteo Todini

» Investigations on the use of biogas for small scale decentralized CHP applications with a focus on stability and emissions (ID 140)
Steven MacLean, Eren Tali, Anne Giese, Jörg Leicher

» Kinetic energy recovery system for sailing yachts (ID 427)
Giuseppe Leo Guizzi, Michele Manno

» Mirrors in the sky: status and some supporting materials experiments (ID 184)
Noam Lior

» Numerical parametric study for different cold storage designs and strategies of a solar driven thermoacoustic cooler system (ID 284)
Maxime Perier-Muzet, Pascal Stouffs, Jean-Pierre Bedecarrats, Jean Castaing-Lasvignottes

» Parabolic trough photovoltaic/thermal collectors. Part I: design and simulation model (ID 102)
Francesco Calise, Laura Vanoli

» Parabolic trough photovoltaic/thermal collectors. Part II: dynamic simulation of a solar trigeneration system (ID 488)
Francesco Calise, Laura Vanoli

» Performance analysis of downdraft gasifier - reciprocating engine biomass fired small-scale cogeneration system (ID 368)
Jacek Kalina

» Proposing offshore photovoltaic (PV) technology to the energy mix of the Maltese islands (ID 262)
Kim Trapani, Dean Lee Millar

» Research of integrated biomass gasification system with a piston engine (ID 414)
Janusz Kotowicz, Aleksander Sobolewski, Tomasz Iluk

» Start up of a pre-industrial scale solid state anaerobic digestion cell for the co-treatment of animal and agricultural residues (ID 34)
Francesco Di Maria, Giovanni Gigliotti, Alessio Sordi, Caterina Micale, Luisa Massaccesi

» The role of biomass in the renewable energy system (ID 390)
Ruben Laleman, Ludovico Balduccio, Johan Albrecht

» Vegetable oils of soybean, sunflower and tung as alternative fuels for compression ignition engines (ID 500)
Ricardo Morel Hartmann, Nury Nieto Garzón, Eduardo Morel Hartmann, Amir Antonio Martins Oliveira Jr, Edson Bazzo, Bruno Okuda, Joselia Piluski
» Wind energy conversion performance and atmosphere stability (ID 283)
Francesco Castellani, Emanuele Piccioni, Lorenzo Biondi, Marcello Marconi

V. 2 – FUEL CELLS

» Comparison study on different SOFC hybrid systems with zero-CO2 emission (ID 196)
Liqiang Duan, Kexin Huang, Xiaoyuan Zhang and Yongping Yang

» Exergy analysis and optimisation of a steam methane pre-reforming system (ID 62)
George G. Dimopoulos, Iason C. Stefanatos, Nikolaos M.P. Kakalis

» Modelling of a CHP SOFC power system fed with biogas from anaerobic digestion of municipal wastes integrated with a solar collector and storage units (ID 491)
Domenico Borello, Sara Evangelisti, Eileen Tortora

VOLUME VI

VI . 1 – CARBON CAPTURE AND SEQUESTRATION

» A novel coal-based polygeneration system cogenerating power, natural gas and liquid fuel with CO2 capture (ID 96)
Sheng Li, Hongguang Jin, Lin Gao

» Analysis and optimization of CO2 capture in a China's existing coal-fired power plant (ID 532)
Gang Xu, Yongping Yang, Shoucheng Li, Wenyi Liu and Ying Wu

» Analysys of four-end high temperature membrane air separator in a supercritical power plant with oxy-type pulverized fuel boiler (ID 442)
Janusz Kotowicz, Sebastian Stanisław Michalski

» Analysis of potential improvements to the lignite-fired oxy-fuel power unit (ID 413)
Marcin Liszka, Jakub Tuka, Grzegorz Nowak, Grzegorz Szapajko
» Biogas Upgrading: Global Warming Potential of Conventional and Innovative Technologies (ID 240)
Katherine Starr, Xavier Gabarrell Durany, Gara Villalba Mendez, Laura Talens Peiro, Lidia Lombardi

» Capture of carbon dioxide using gas hydrate technology (ID 103)
Beatrice Castellani, Mirko Filipponi, Sara Rinaldi, Federico Rossi

» Carbon dioxide mineralisation and integration with flue gas desulphurisation applied to a modern coal-fired power plant (ID 179)
Ron Zevenhoven, Johan Fagerlund, Thomas Björklöf, Magdalena Mäkelä, Olav Eklund

» Carbon dioxide storage by mineralisation applied to a lime kiln (ID 226)
Inês Sofia Soares Romão, Matias Eriksson, Experience Nduagu, Johan Fagerlund, Licínio Manuel Gando-Ferreira, Ron Zevenhoven

» Comparison of IGCC and CFB cogeneration plants equipped with CO2 removal (ID 380)
Marcin Liszka, Tomasz Malik, Michał Budnik, Andrzej Ziębik

» Concept of a "capture ready" combined heat and power plant (ID 231)
Piotr Henryk Lukowicz, Lukasz Bartela

» Cryogenic method for H2 and CH4 recovery from a rich CO2 stream in pre-combustion CCS schemes (ID 508)
Konstantinos Atsonios, Kyriakos D. Panopoulos, Angelos Doukelis, Antonis Koumanakos, Emmanuel Kakaras

» Design and optimization of ITM oxy-combustion power plant (ID 495)
Surekha Gunasekaran, Nicholas David Mancini, Alexander Mitsos

» Implementation of a CCS technology: the ZECOMIX experimental platform (ID 222)
Antonio Calabrò, Stefano Cassani, Leandro Pagliari, Stefano Stendardo

» Influence of regeneration condition on cyclic CO2 capture using pre-treated dispersed CaO as high temperature sorbent (ID 221)
Stefano Stendardo, Antonio Calabrò

» Investigation of an innovative process for biogas up-grading – pilot plant preliminary results (ID 56)
Lidia Lombardi, Renato Baciocchi, Ennio Antonio Carnevale, Andrea Corti, Giulia Costa, Tommaso Olivieri, Alessandro Paradisi, Daniela Zingaretti

» Method of increasing the efficiency of a supercritical lignite-fired oxy-type fluidized bed boiler and high-temperature three - end membrane for air separation (ID 438)
Janusz Kotowicz, Adrian Balicki

» Monitoring of carbon dioxide uptake in accelerated carbonation processes applied to air pollution control residues (ID 539)
Felice Alfieri, Peter J Gunning, Michela Gallo, Adriana Del Borghi, Colin D Hills

» Process efficiency and optimization of precipitated calcium carbonate (PCC) production from steel converter slag (ID 114)
Hannu-Petteri Mattila, Inga Grigaliūnaitė, Arshe Said, Sami Filppula, Carl-Johan Fogelholm, Ron Zevenhoven

» Production of Mg(OH)2 for CO2 Emissions Removal Applications: Parametric and Process Evaluation (ID 245)
Experience Ikechukwu Nduagu, Inês Romão, Ron Zevenhoven

» Thermodynamic analysis of a supercritical power plant with oxy type pulverized fuel boiler, carbon dioxide capture system (CC) and four-end high temperature membrane air seprator (ID 411)
Janusz Kotowicz, Sebastian Stanisław Michalski

VI . 2 – PROCESS INTEGRATION AND HEAT EXCHANGER NETWORKS

» A multi-objective optimization technique for co- processing in the cement production (ID 42)
Maria Luiza Grillo Renó, Rogério José da Silva, Mirian de Lourdes Noronha Motta Melo, José Joaquim Conceição Soares Santos

» Comparison of options for debottlenecking the recovery boiler at kraft pulp mills – Economic performance and CO2 emissions (ID 449)
Johanna Jönsson, Karin Pettersson, Simon Harvey, Thore Berntsson

» Demonstrating an integral approach for industrial energy saving (ID 541)
René Cornelissen, Geert van Rens, Jos Sentjens, Henk Akse, Ton Backx, Arjan van der Weiden, Jo Vandenbroucke

» Maximising the use of renewables with variable availability (ID 494)
Andreja Nemet, Jiri Jaromír Klemeš, Petar Sabev Varbanov, Zdravko Kravanja

» Methodology for the improvement of large district heating networks (ID 46)
Anna Volkova, Vladislav Mashatin, Aleksander Hlebnikov, Andres Siirde

» Optimal mine site energy supply (ID 306)
Monica Carvalho, Dean Lee Millar

» Simulation of synthesis gas production from steam oxygen gasification of Colombian bituminous coal using Aspen Plus® (ID 395)
John Jairo Ortiz, Juan Camilo González, Jorge Enrique Preciado, Rocío Sierra, Gerardo Gordillo

VOLUME VII

VII . 1 - BUILDING, URBAN AND COMPLEX ENERGY SYSTEMS

» A linear programming model for the optimal assessment of sustainable energy action plans (ID 398)
Gianfranco Rizzo, Giancarlo Savino

» A natural gas fuelled 10 kW electric power unit based on a Diesel automotive internal combustion engine and suitable for cogeneration (ID 477)
Pietro Capaldi

» Adjustment of envelopes characteristics to climatic conditions for saving heating and cooling energy in buildings (ID 430)
Christos Tzivanidis, Kimon Antonopoulos, Foteini Gioti

» An exergy based method for the optimal integration of a building and its heating plant. Part 1: comparison of domestic heating systems based on renewable sources (ID 81)
Marta Cianfrini, Enrico Sciubba, Claudia Toro

» Analysis of different typologies of natural insulation materials with economic and performances evaluation of the same buildings (ID 28)
Umberto Desideri, Daniela Leonardi, Livia Arcioni

» Complex networks approach to the Italian photovoltaic energy distribution system (ID 470)
Luca Valori, Giovanni Luca Giannuzzi, Tiziano Squartini, Diego Garlaschelli, Riccardo Basosi

» Design of a multi-purpose building "to zero energy consumption" according to European Directive 2010/31/CE: Architectural and plant solutions (ID 29)
Umberto Desideri, Livia Arcioni, Daniela Leonardi, Luca Cesaretti ,Perla Perugini, Elena Agabitini, Nicola Evangelisti

» Effect of initial systems on the renewal planning of energy supply systems for a hospital (ID 107)
Shu Yoshida, Koichi Ito, Yoshiharu Amano, Shintaro Ishikawa, Takahiro Sushi, Takumi Hashizume

» Effects of insulation and phase change materials (PCM) combinations on the energy consumption for buildings indoor thermal comfort (ID 387)
Christos Tzivanidis, Kimon Antonopoulos, Eleutherios Kravvaritis

» Energetic evaluation of a smart controlled greenhouse for tomato cultivation (ID 150)
Nickey Van den Bulck, Mathias Coomans, Lieve Wittemans, Kris Goen, Jochen Hanssens, Kathy Steppe, Herman Marien, Johan Desmedt

» Energy networks in sustainable cities: temperature and energy consumption monitoring in urban area (ID 190)
Luca Giaccone, Alessandra Guerrisi, Paolo Lazzeroni and Michele Tartaglia

» Extended exergy analysis of the economy of Nova Scotia, Canada (ID 215)
David C Bligh, V.Ismet Ugursal

» Feasibility study and design of a low-energy residential unit in Sagarmatha Park (Nepal) for envirnomental impact reduction of high altitude buildings (ID 223)
Umberto Desideri, Stefania Proietti, Paolo Sdringola, Elisa Vuillermoz

» Fire and smoke spread in low-income housing in Mexico (ID 379)
Raul R. Flores-Rodriguez, Abel Hernandez-Guerrero, Cuauhtemoc Rubio-Arana, Consuelo A. Caldera-Briseño

» Optimal lighting control strategies in supermarkets for energy efficiency applications via digital dimmable technology (ID 136)
Salvador Acha, Nilay Shah, Jon Ashford, David Penfold

» Optimising the arrangement of finance towards large scale refurbishment of housing stock using mathematical programming and optimisationg (ID 127)
Mark Gerard Jennings, Nilay Shah, David Fisk

» Optimization of thermal insulation to save energy in buildings (ID 174)
Milorad Bojić, Marko Miletić, Vesna Marjanović, Danijela Nikolić, Jasmina Skerlić

» Residential solar-based seasonal thermal storage system in cold climate: building envelope and thermal storage (ID 342)
Alexandre Hugo and Radu Zmeureanu

» Simultaneous production of domestic hot water and space cooling with a heat pump in a Swedish Passive House (ID 55)
Johannes Persson, Mats Westermark

» SOFC micro-CHP integration in residential buildings (ID 201)
Umberto Desideri, Giovanni Cinti, Gabriele Discepoli, Elena Sisani, Daniele Penchini

» The effect of shading of building integrated photovoltaics on roof surface temperature and heat transfer in buildings (ID 83)
Eftychios Vardoulakis, Dimitrios Karamanis

» The influence of glazing systems on energy performance and thermal comfort in non-residential buildings (ID 206)
Cinzia Buratti, Elisa Moretti, Elisa Belloni

» Thermal analysis of a greenhouse heated by solar energy and seasonal thermal energy storage in soil (ID 405)
Yong Li, Jin Xu, Ru-Zhu Wang

» Thermodynamic analysis of a combined cooling, heating and power system under part load condition (ID 476)
Qiang Chen, Jianjiao Zheng, Wei Han, Jun Sui, Hong-guang Jin

VII . 2 – COMBUSTION, CHEMICAL REACTORS

» Baffle as a cost-effective design improvement for volatile combustion rate increase in biomass boilers of simple construction (ID 233)
Borivoj Stepanov, Ivan Pešenjanski, Biljana Miljković

» Characterization of CH4-H2-air mixtures in the high-pressure DHARMA reactor (ID 287)
Vincenzo Moccia, Jacopo D'Alessio

» Development of a concept for efficiency improvement and decreased NOx production for natural gas-fired glass melting furnaces by switching to a propane exhaust gas fired process (ID 146)
Jörn Benthin, Anne Giese

» Experimental analysis of inhibition phenomenon management for Solid Anaerobic Digestion Batch process (ID 348)
Francesco Di Maria, Giovanni Gigliotti, Alessio Sordi, Caterina Micale, Claudia Zadra, Luisa Massaccesi

» Experimental investigations of the combustion process of n-butanol/diesel blend in an optical high swirl CI engine (ID 85)
Simona Silvia Merola, G. Valentino, C. Tornatore, L. Marchitto , F. E. Corcione

» Flameless oxidation as a means to reduce NOx emissions in glass melting furnaces (ID 141)
Jörg Leicher, Anne Giese

» Mechanism of damage by high temperature of the tubes, exposed to the atmosphere characteristic of a furnace of pyrolysis of ethane for ethylene production in the petrochemical industry (ID 65)
Jaqueline Saavedra Rueda, Francisco Javier Perez Trujillo, Lourdes Isabel Meriño Stand, Harbey Alexi Escobar, Luis Eduardo Navas, Juan Carlos Amezquita

» Steam reforming of methane over Pt/Rh based wire mesh catalyst in single channel reformer for small scale syngas production (ID 317)
Haftor Orn Sigurdsson, Søren Knudsen Kær

VOLUME VIII

VIII . 1 – ENERGY SYSTEMS : ENVIRONMENTAL AND SUSTAINABILITY ISSUES

» A multi-criteria decision analysis tool to support electricity planning (ID 467)
Fernando Ribeiro, Paula Ferreira, Madalena Araújo

» Comparison of sophisticated life cycle impact assessment methods for assessing environmental impacts in a LCA study of electricity production (ID 259)
Jens Buchgeister

» Defossilisation assessment of biodiesel life cycle production using the ExROI indicator (ID 304)
Emilio Font de Mora, César Torres, Antonio Valero, David Zambrana

» Design strategy of geothermal plants for water dominant medium-low temperature reservoirs based on sustainability issues (ID 99)
Alessandro Franco, Maurizio Vaccaro

» Energetic and environmental benefits from waste management: experimental analysis of the sustainable landfill (ID 33)
Francesco Di Maria, Alessandro Canovai, Federico Valentini, Alessio Sordi, Caterina Micale

» Environmental assessment of energy recovery technologies for the treatment and disposal of municipal solid waste using life cycle assessment (LCA): a case study of Brazil (ID 512)
Marcio Montagnana Vicente Leme, Mateus Henrique Rocha, Electo Eduardo Silva Lora,Osvaldo José Venturini, Bruno Marciano Lopes, Claudio Homero Ferreira

» How will renewable power generation be affected by climate change? – The case of a metropolitan region in Northwest Germany (ID 503)
Jakob Wachsmuth, Andrew Blohm, Stefan Gößling-Reisemann, Tobias Eickemeier, Rebecca Gasper, Matthias Ruth, Sönke Stührmann

» Impact of nuclear power plant on Thailand power development plan (ID 474)
Raksanai Nidhiritdhikrai, Bundhit Eua-arporn

» Improving sustainability of maritime transport through utilization of liquefied natural gas (LNG) for propulsion (ID 496)
Fabio Burel, Rodolfo Taccani, Nicola Zuliani

» Life cycle assessment of thin film non conventional photovoltaics: the case of dye sensitized solar cells (ID 471)
Maria Laura Parisi, Adalgisa Sinicropi, Riccardo Basosi

» Low CO2 emission hybrid solar CC power system (ID 175)
Yuanyuan Li, Na Zhang, Ruixian Cai

» Low exergy solutions as a contribution to climate adapted and resilient power supply (ID 489)
Stefan Goessling-Reisemann, Thomas Bloethe

» On the use of MPT to derive optimal RES electricity generation mixes (ID 459)
Paula Ferreira, Jorge Cunha

» Stability and limit cycles in an exergy-based model of population dynamics (ID 128)
Enrico Sciubba, Federico Zullo

» The influence of primary measures for reducing NOx emissions on energy steam boiler efficiency (ID 125)
Goran Stupar, Dragan Tucaković, Titoslav Živanović, Miloš Banjac, Srđan Belošević,Vladimir Beljanski, Ivan Tomanović, Nenad Crnomarković, Miroslav Sijerčić

» The Lethe city car of the University of Roma 1: final proposed configuration (ID 45)
Roberto Capata, Enrico Sciubba

VIII . 2 - POSTER SESSION

» A variational optimization of a finite-time thermal cycle with a Stefan-Boltzmann heat transfer law (ID 333)
Juan C.Chimal-Eguia, Norma Sanchez-Salas

» Modeling and simulation of a boiler unit for steam power plants (ID 545)
Luca Moliterno, Claudia Toro

» Numerical Modelling of straw combustion in a moving bed combustor (ID 412)
Biljana Miljkoviü, Ivan Pešenjanski, Borivoj Stepanov, Vladimir Milosavljeviü, Vladimir Rajs

» Physicochemical evaluation of the properties of the coke formed at radiation area of light hydrocarbons pyrolysis furnace in petrochemical industry (ID 10)
Jaqueline Saavedra Rueda , Angélica María Carreño Parra, María del Rosario Pérez Trejos, Dionisio Laverde Cataño, Diego Bonilla Duarte, Jorge Leonardo Rodríguez Jiménez, Laura María Díaz Burgos

» Rotor TG cooled (ID 121)
Chiara Durastante, Paolo Petroni, Michela Spagnoli, Vincenzo Rizzica, Jörg Helge Wirfs

» Study of the phase change in binary alloy (ID 534)
Aroussia Jaouahdou, Mohamed J. Safi, Herve Muhr

» Technip initiatives in renewable energies and sustainable technologies (ID 527)
Pierfrancesco Palazzo, Corrado Pigna

ECOS 2012

VOLUME II

A comparative analysis of cryogenic recuperative heat exchangers based on exergy destruction

Adina Gheorghian[a], Alexandru Dobrovicescu[b], Lavinia Grosu[c], Bogdan Popescu[d] and Claudia Ionita[e]

[a] *"Politehnica" University of Bucharest, Romania, adina_gheorghian@yahoo.com*
[b] *"Politehnica" University of Bucharest, Romania, adobrovicescu@yahoo.com (CA)*
[c] *University Paris Ouest Nanterre La Défense, France, mgrosu@u-paris10.fr*
[d] *"Politehnica" University of Bucharest, Romania, pbogdan1990@gmail.com*
[e] *"Politehnica" University of Bucharest, Romania, claudia_c_ionita@yahoo.com*

Abstract:
The paper deals with the possibility of optimizing the recuperative heat exchanger for a cryogenic system. The effect of the pressure drop, the heat transfer across a finite temperature difference and the imperfect insulation of the cryogenic recuperative heat exchanger is estimated by a unique measure, which is the exergy destruction. The analysis takes into account the heat exchanger and heat transfer surface type, the flow velocity of the cryogenic agent, the value of the state parameters of the working agent and the outside size of the heat exchanger insulation. The different types of recuperative heat exchangers have equipped a cryogenic refrigeration plant working with air. The simulation program developed for this case calculates for each type of cryogenic recuperative heat exchanger the size of the heat transfer surfaces, the volume, weight and cool-down time. Two different types of heat exchangers, a helically coiled heat exchanger and a plate-fin heat exchanger were analysed considering exergy destruction.

Keywords:
Exergy destruction, Recuperative heat exchanger, Optimization.

1. Introduction

Exergy analysis is an essential tool in technical and economical optimization of thermal systems, during both operation and design phase.

Thermal equipment most frequently used in industrial applications are heat exchangers. A heat exchanger is the typical example of exergy destruction due to heat exchange at finite difference of temperature and pressure drop. A significant number of studies can be found in literature attempting optimization of various types of heat exchangers through minimization of entropy generation.

Ogulata and Doba [1] carried out and experimental and analytical investigation atempting to minimize the entropy generation in a recuperative cross-flow air-air heat exchanger. The concept of path flow length given by the ratio 4L/D was introduced and its influence on the exergy efficiency of the heat exchanger was assesed. The optimum value of the path flow length resulting in the lowest value of the number of entropy generation units was determined analytically. The existence of an optimum value for the flow path length is intuitivelly explained by the two contradictory effects resulting from its increase: the positive effect is the increase in the heat exchanger efficiency, while the negative effect is an increase in the irreversibility due to friction.

Narayan et al [2] investigated analytically the entropy generation optimization for devices with heat and mass transfer (air deumidifiers, cooling towers, etc.). A non-dimensional parameter was defined as the ration between maximum enthalpy increase of the cold fluid and maximum decrease of enthalpy of the hot fluid (considering also enthalpy variation due to mass transfer). It was shown

that an optimum value of this parameter exists for which entropy generation in devices with combined heat and mass transfer exists and its value was determined analitically.

Lerou et al [3] carried out a study attempting to optimize the geometry of a counter-flow heat exchanger using the entropy generation minimization criteria. Unlike conventional design approaches, which take into account estimations of various losses, resulting in a geometry with a certain degree of arbitrary, the analytical study carried out by Lerou et al considered all losses as entropy generation sources. Such an approach made possible to compare and to summ up various types of losses (thermal and friction). By modifying some geometrical parameters of the heat exchangers it was possible to identify those values for which entropy generation reaches the minimum value.

The number of entropy generation units is a fundamental concept in exergy analysis of thermal systems introduced by Bejan [4]. Based on the number of entropy generation units, Sarangi and Chowdhury [5] carried out an analytical investigation of entropy generation in a counter-flow heat exchanger. It was shown that a critical value of the heat exchanger efficiency exists for which the number of entropy generation units reaches a maximum value. The effect of the heat capacity ratio on the critical value of the heat exchanger efficiency was also assesed.

Cornelissen and Hirs [6] integrated life cycle analysis study in the design of a heat exchanger. The concept of life cycle irreversibility was introduced and a design approach was presented, in the aim of using with the highest possible efficiency the exergy of natural resources.

2. The schematic of the gaseous cryogenic refrigeration cycle

The analysis is focused on the recuperative heat exchanger of a gaseous cryogenic refrigeration system. The cryogenic system operates under the following conditions: the temperature level of the cold chamber is Tc = 180 K; the minimum temperature difference between the refrigerant (air) and the cold chamber is ΔTc = 3 K; the temperature of the environment is T_0 = 300 K; the temperature difference at the warm end of the recuperative heat exchanger is ΔT_h = 6 K; the pressure of the forward gas stream is p_2 = 4 MPa; the pressure of the return gas stream is p4 = 0.15 MPa; the pressure drop in the low temperature chamber (LTC) is Δp_{LTC} = 0.1 MPa; the isentropic efficiency of the expander is η_s = 0.8; the mechanical efficiency of the expander (the fraction of the compression work returned to the cycle) is η_m = 0.8 and the isothermal efficiency of the compressor is η_T = 0.6; the heat insulation of the recuperative heat exchanger has a medium thermal conductivity λ_i= 0.033 W/(m^{2}K), the convective heat transfer coefficient on the external side of the insulation is λ_e = 10.5 W/(m^{2}K).

The flow chart and the representation of the cycle in the T-S diagram are presented in Fig. 1.

A simple gas expander cycle includes the refrigeration cycles or systems in which expanders are located at the lower temperature level. The refrigerant used in this cycle is air. On being compressed in a compressor *K*, the gas is cooled in a cooler *C* to a temperature T_2 and admitted to a heat exchanger *HX*. The work performed by the compressor is w_k and the heat rejected is $q_{k'}$. The heat absorbed in the cooler is $q_{k''}$. After the heat exchanger, the gas is admitted to an expander, *E*, where it expands to a low pressure and goes to a low temperature chamber, *LTC*. In the low temperature chamber, the gas absorbs the heat q_c, and is raised in temperature from T_4 to T_5. Then, the return stream is heated in the heat exchanger by absorbing the heat from the compressed gas (the forward stream). At the warm (high temperature) end of the heat exchanger, the difference in temperature between the forward and return gas streams is ΔT_h. The heat exchanger, expander, and low temperature chamber are insulated from the surroundings.

Different types of heat transfer surfaces have been compared from the point of view of conceiving the available energy during the working processes.

The heat transfer process that occurs in the recuperative heat exchanger of a cryogenic system is accompanied by losses due to gas dynamic resistance at the passing of the forward and return flow gas, heat transfer at variable finite difference of temperature and imperfect thermal insulation.

Noticing that the pressure drops, the destructions due to heat transfer at a variable finite difference of temperature and imperfect thermal insulation are brought about by internal and external irreversibility, the performance of the recuperative heat exchanger has been estimated by an unique amount – the growth rate of the whole exergy loss and destruction of the working processes, $\dot{I}_{HX}$.

The heat transfer surface types analyzed and compared from the point of view of conserving the available energy during the working processes have equipped a gaseous air refrigeration plant.

For studying a various number of cryogenic heat exchanger types, a computer program has been conceived, which also calculates the heat transfer surfaces size, volume, weight and cool-down time of these devices based on the Fourier equation [7].

The analysis has been performed under real conditions on a computer program based on the state equation developed by Baehr and Schwier [12] and the thermal and caloric properties of the working agent [8].

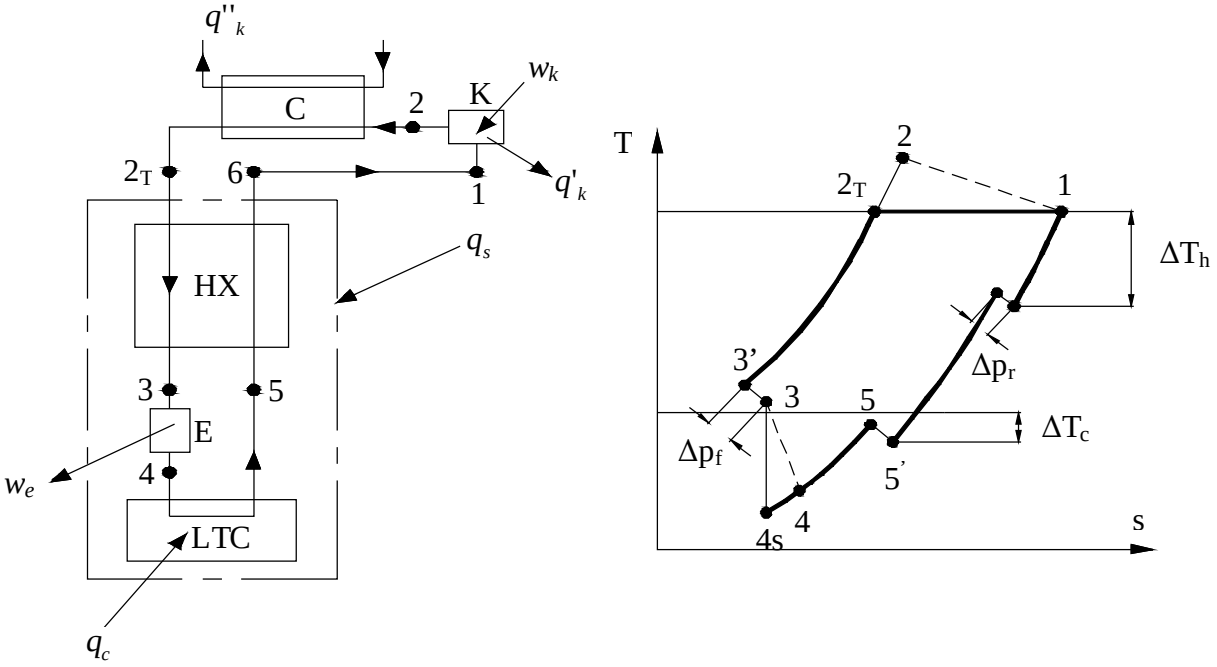

Fig. 1 Refrigeration cycle: (a) flow diagram; (b) T-s diagram.

3. Exergy Analysis

In general, in the case of a surface heat exchanger, if the heat flux and the inlet states of the two agents are specified, an increase in the heat transfer surface obviously leads not only to a reduction in the temperature difference between the two fluids, but also to a corresponding growth of the pressure drops and heat leaks due to imperfect thermal insulation. In cryogenic systems, on the other hand, due to the functional interdependence between the different parts, the working parameters of recuperative heat exchangers depend on their own design and conduct.

For cryogenic heat exchangers, the demand for high-level performance from the point of view of efficiency, compactness and heat transfer coefficients together with the concern for low pressure drops has determined their large number of design solutions and analyzing methods.

The great variety of heat transfer augmentation techniques used in the aim of reducing the apparatus size causes the rise in friction coefficients.

At the design stage, it is important to be able to predict if, by using a certain heat transfer augmentation technique, the overall effectiveness of the heat exchanger will be improved or not.

The overall exergy destruction and loss due to the internal and external irreversibility of the working processes in the recuperative heat exchanger is:

$$\dot{I}_{HX} = \dot{I}_{\Delta T} + \dot{I}_{\Delta p_f} + \dot{I}_{\Delta p_r} + \dot{I}_{q_s}, \qquad (1)$$

where the terms from the right side represent, in order, the destruction exergy rates due to the irreversibility of the heat transfer at a finite difference of temperature - $I_{\Delta T}$, throttling corresponding to the pressure drops of the forward - $I_{\Delta p_f}$ and return flow - $I_{\Delta p_r}$ and the exergy loss due to the imperfect thermal insulation - I_{q_s}.

These destructions and losses are not independent, there is a straight connection between the resistance to flow, the temperature difference between the forward and return streams, the heat exchanger type, the heat transfer surface geometry, the flow velocity and the value of the state parameters of the working agent.

Taking into account the Gouy-Stodola theorem, the exergy destruction due to internal irreversibility in the recuperative heat exchanger may be calculated such as:

$$\dot{\mathrm{I}}_{\Delta \mathrm{T}} = T_0 \cdot \dot{S}_{\Delta T}^{gen} = T_0 \cdot \left|\dot{Q}\right| \left(\frac{1}{T_{m_r}} - \frac{1}{T_{m_f}} \right). \qquad (2)$$

$$I_{\Delta p_f} = T_0 \cdot \dot{S}_{\Delta p_f}^{gen} = T_0 \cdot \frac{\dot{Q}_{f_f}}{T_{m_f}}, \qquad (3)$$

where $\dot{Q}_f$ represents the thermal effect due to friction in the forward gas stream; considering that the specific shaft work wasted to overcome the friction forces is entirely transformed into thermal energy, namely $q_{f_f} = \left| w_{f_f} \right|$, (3) becomes:

$$\dot{I}_{\Delta p_f} = T_0 \cdot \dot{m} \frac{\left| w_{f_f} \right|}{T_{m_f}}, \qquad (4)$$

and finally

$$\dot{I}_{\Delta p_f} = T_0 \cdot \dot{m} \frac{v_{m_f} \left| \Delta p_f \right|}{T_{m_f}}. \qquad (5)$$

The loss from imperfect insulation is equal to the absolute value of the heat exergy income from the surroundings:

$$\dot{I}_{q_s} = \left| \dot{E}x_{q_s} \right|. \qquad (6)$$

Depending on the gas dynamic and heat transfer characteristics, the pressure drops in the forward and return flow may be calculated, for instance, using the following relationship [9]:

$$\Delta p = \frac{u^2}{2} v_i \left(\left(K_c + 1 - \sigma^2 \right) + 2 \left(\frac{v_o}{v_i} - 1 \right) + f \frac{A}{A_c} \cdot \frac{v_m}{v_i} - \left(1 - \sigma^2 - K_e \right) \frac{v_o}{v_i} \right), \qquad (7)$$

where the terms in brackets take into account, in order: the heat exchanger entrance effect, the flow acceleration, the core friction and the leaving effect.

In order to avoid the difficulties coming out at the calculation of the medium difference of temperature between the forward and return streams, the heat transfer study is accomplished by the NTU - ε approach [9].

The total heat transfer area on one side of the heat exchanger may be calculated using the following relationship:

$$A = \frac{NTU \cdot C_{\min}}{k_t}. \qquad (8)$$

Considering a uniform distribution of the fluid stream on the free flow area, it results:

$$A_c = \frac{\dot{m}}{u}. \qquad (9)$$

Taking into account (8) and (9), (7) becomes:

$$\Delta p = \frac{u^2}{2} v_i \left(\left(K_c + 1 - \sigma^2 \right) + 2\left(\frac{v_o}{v_i} - 1 \right) + f \frac{NTU \cdot c_{\min} \cdot u}{k_t} \cdot \frac{v_m}{v_i} - \left(1 - \sigma^2 - K_e \right) \frac{v_o}{v_i} \right). \qquad (10)$$

The determination of the friction factors and the heat transfer convective coefficients on the forward or return flow side is performed on the basis of the heat transfer surfaces criterial equations.

4. A comparative analysis of the heat exchanger surfaces performance

Two heat transfer surfaces corresponding to two different types of heat exchangers have been analyzed from the point of view of the overall exergy destruction.

In Fig. 2 a copper coiled tubular heat exchanger with smooth inside surface, characterized by the following design and operating parameters [10,11] is presented: smooth outside surface, compact winding, diameter of the mandrel (central body), d_c = 150 mm, transverse tube spacing x_1 = 11.5 mm, longitudinal tube spacing x_2 = 10 mm, tube outside diameter d_o = 10 mm, tube inside diameter d_i = 6 mm, the heat transfer and pressure drops are given by the criterial relationships $Nu_r = 0.0185\,\mathrm{Re}_r^{0.95}$ and $\left(Eu/n\right)_r = 8.1\,\mathrm{Re}_r^{-0.21}$ [10].

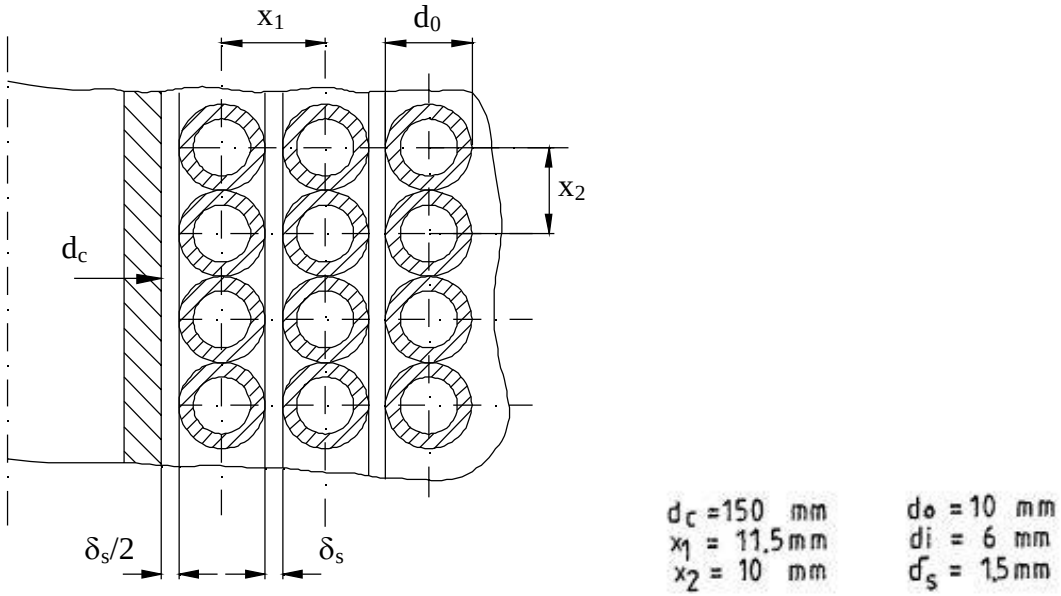

Fig. 2 Coiled tubular heat exchanger with smooth outside surface.

It has been noticed that, in the specified study conditions, at the variation of the flowing pattern from the forward and return streams, the overall loss $\dot{I}_{HX}$ is practically influenced only by the irreversibility of throttling at the gas passing through the heat exchanger and the incoming heat from imperfect insulation.

Obviously, the rise in Re_r and Re_f leads to a rapid decrease of the heat transfer surface and the cool down time of the heat exchanger (Figs 3. b, 3. c).

At the increase of Re_r, the rising effect of both friction factor and mass velocity, from the return stream, more important than the heat transfer surface reduction, involves a quick increase in the overall loss $\dot{I}_{HX}$ (Fig. 3. a).

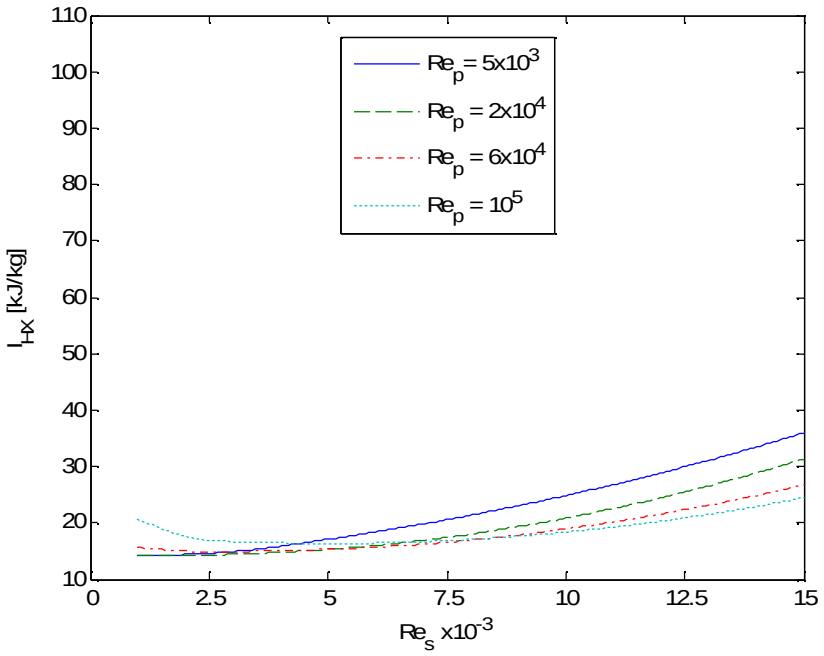

Fig. 3. a Variation of exergy destruction rate at the increase of Re_s with Re_p as curve parameter.

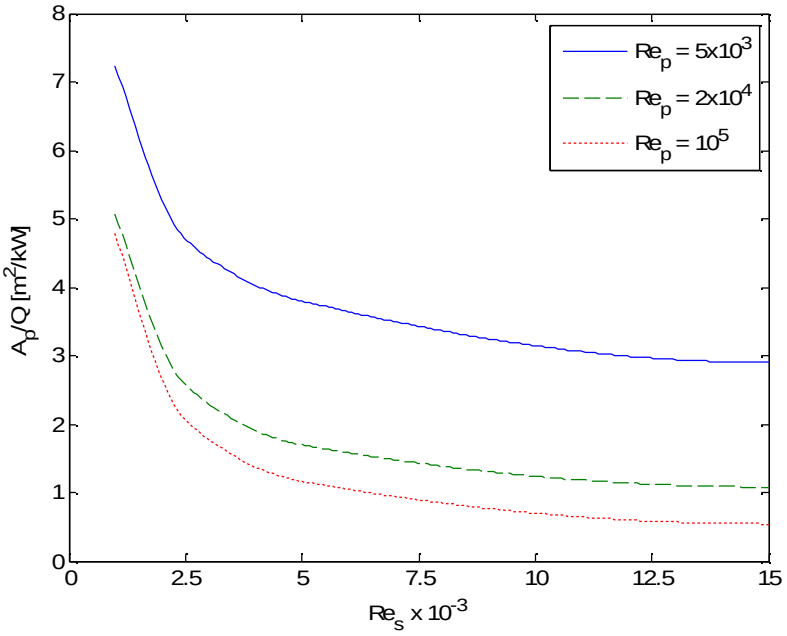

Fig. 3. b Variation of heat transfer surface area at the increase of Re_s with Re_p as curve parameter.

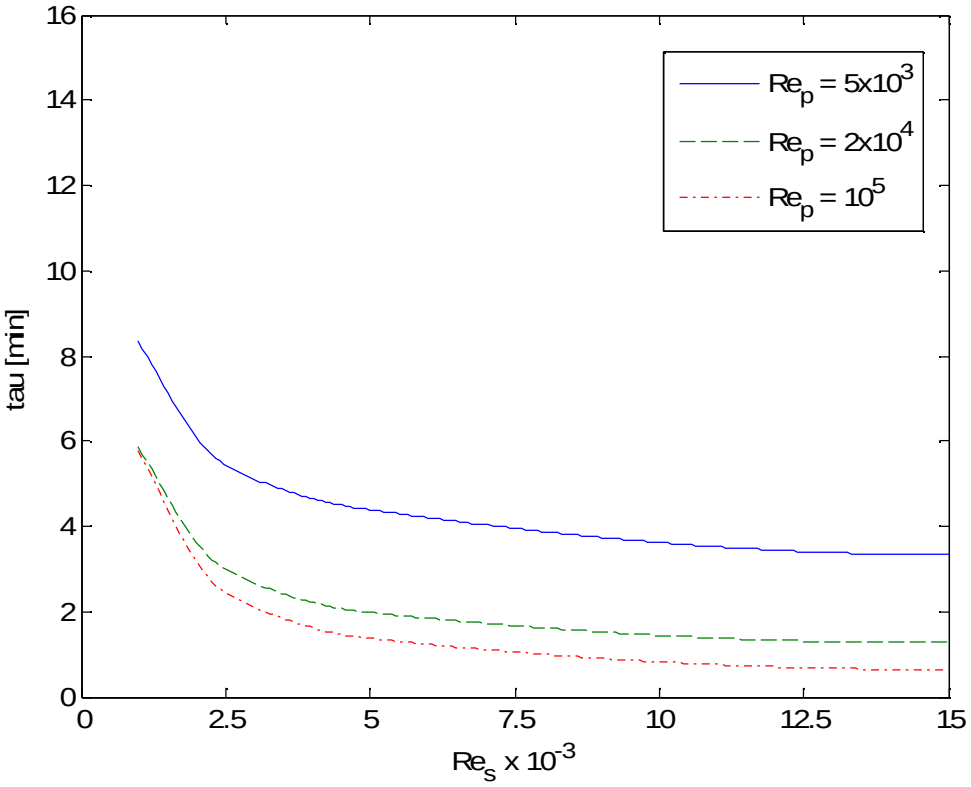

Fig. 3. c Variation of cooling down time at the increase of Re_s with Re_p as curve parameter.

From a certain flow pattern of the return stream, the increase in Re_f leads to a reduction of the heat transfer surface at a higher rate than that of the forward stream friction factor rising, finally involving the decrease in $\dot{I}_{HX}$.

In Fig. 4 is presented the conduct, at the variation of the flowing pattern from the forward and return streams of a plate-fin heat transfer surface defined by the following design and operating parameters: the heat transfer surface on the forward stream side has lowered plate-fin being of 3/16-11.1 [9] type for which the heat transfer and the resistance to flow are described by relationships $j_f = St_f \cdot Pr_f^{2/3} = 0.1922\, Re_f^{-0.383}$ and respectively $f_f = 1.03\, Re_f^{-0.3968}$; the heat transfer surface on the return gas flow has wavy-fin plate-fin being of 11.44-3/8w [9] type for which $j_r = 0.2285\, Re_r^{-0.387}$ and $f_r = 1.197\, Re_r^{-0.389}$.

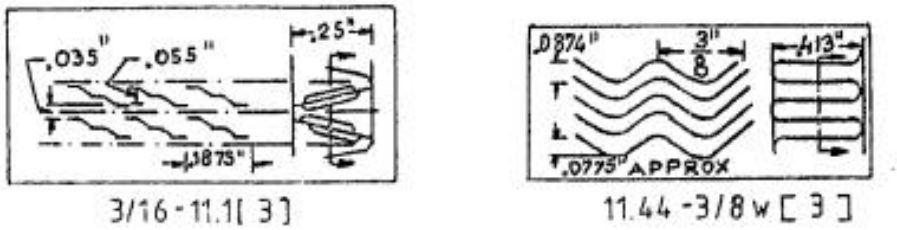

Fig. 4 Plate-fin heat exchanger.

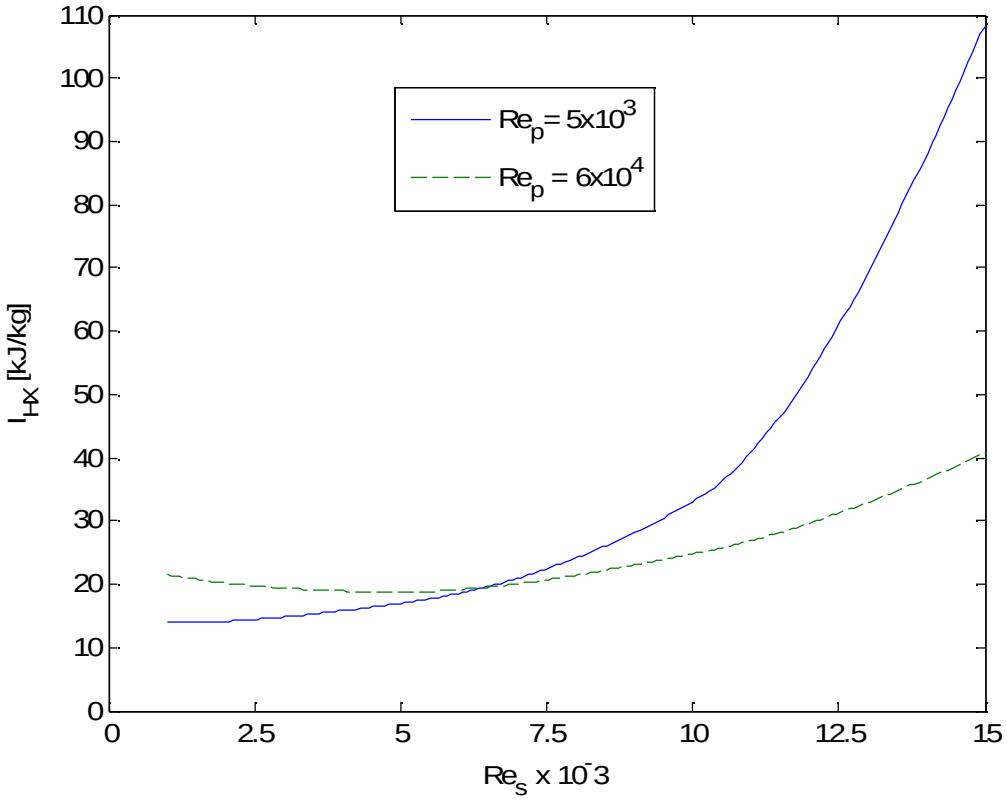

Fig. 5. a Variation of exergy destruction rate at the increase of Re_s with Re_p as curve parameter.

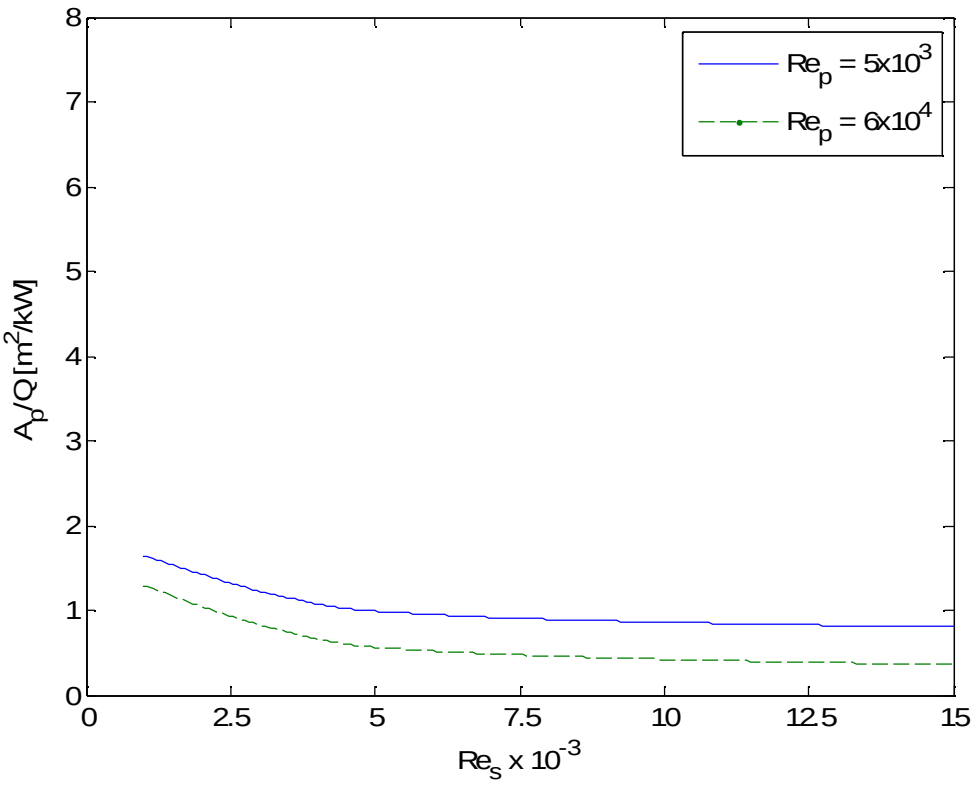

Fig. 5. b Variation of heat transfer surface area at the increase of Re_s with Re_p as curve parameter.

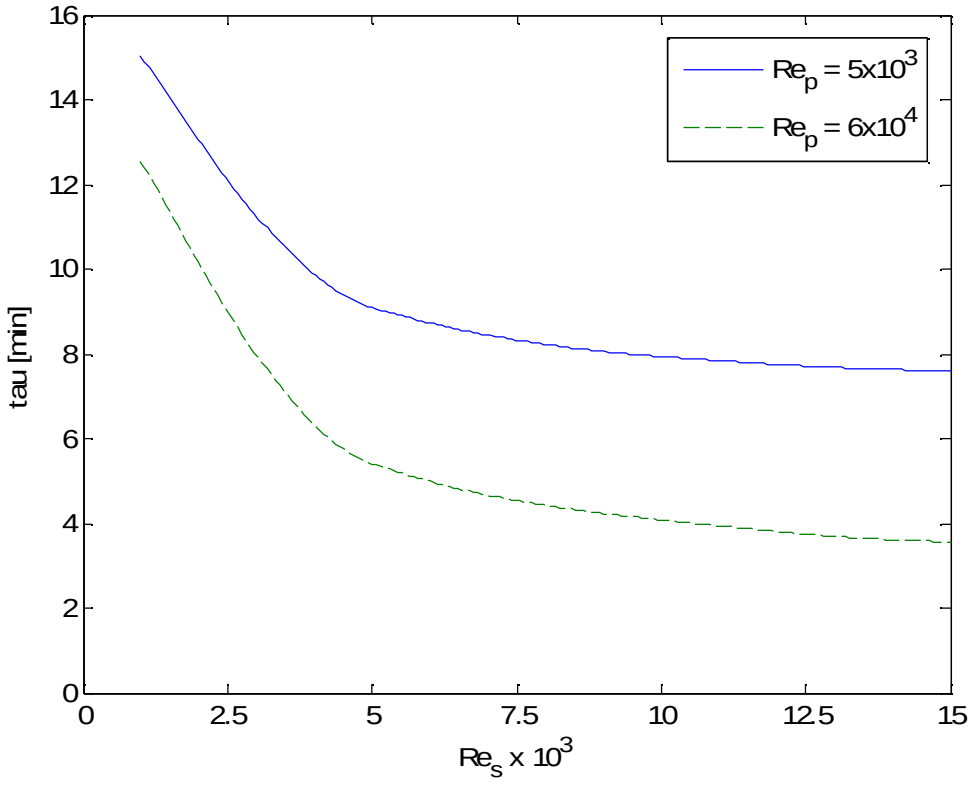

Fig. 5. c Variation of cooling down time at the increase of Re_s with Re_p as curve parameter.

It can be noticed for the plate-fin type heat exchanger has the smallest surface and much reduced thermal inertia. The lowest exergy destruction and losses are registered for the copper coiled tubular heat exchanger with smooth outside surface case, phenomena accompanied by the largest heat transfer surface and longest cool down times (Figs 2 and 4).

Obviously, beside this thermodynamic analysis, a thermo-economic one will provide more information concerning the proper choose of the cryogenic heat exchanger.

5. Conclusions

The large variety of heat transfer surfaces and types of heat exchangers require a procedure for rating their performance.

Noticing that the pressure drops, losses due to heat transfer across a finite temperature difference and heat inlets from the surroundings are due to internal and external irreversibility, in this paper is evaluated the thermodynamic performance of the heat exchanger based on a unique measure – the total exergy destruction and loss.

The heat exchanger has been analyzed operating in a gaseous cryogenic refrigeration system.

For identical values of Re_s and constant values of Re_p, I_{HX} value for the plate-fin heat exchanger (fig. 5. a) is higher than the one for the coiled tubular heat exchanger (fig. 3. a).

The situation is reversed for the parameter A_p/Q, in the sense that the specific area requirements for the plate-fin heat exchanger (fig. 5. b) is lower than for the coiled tubular heat exchanger (fig. 3. b).

From the stationary operating point of view, the coiled tubular heat exchanger with smooth inside and outside surfaces is the most economic one, being characterized by the smallest exergy destruction.

The plate heat exchanger is the most compact one, with the lowest time to get into a stationary regime.

The exergoeconomic analysis, which takes into account both the operating cost and the capital amortization rate, will offer more information concerning the proper choice of the cryogenic heat exchanger.

Acknowledgments

This work was supported by the the strategic grant *POSDRU/107/1.5/S/76909, Project ID 76909,* co-financed by the European Social Fund – Investing in People, within the Sectoral Operational Programme Human Resources Development 2007-2013.

Nomenclature

Latin symbols

A exchanger total heat transfer area on one side, m^2

A_C exchanger minimum free-flow area, m^2

A_{fr} exchanger total frontal area, m^2

C cooler

$C_{\min}$ minimum flow stream capacity rate, W/K

$c_{\min}$ minimum specific heat, $J/(kgK)$

d_c heat exchanger's central body diameter, m

D_f outside fin diameter, m

d_i tube inside diameter, m

d_0 tube outside diameter, m

f friction factor

E expander

$\dot{E}x$ exergy flux, W

Eu Euler number

HX heat exchanger

$j = St \cdot Pr^{2/3}$ generalized heat transfer grouping

K compressor

K_c contraction coefficient

K_e expansion coefficient

k_t overall heat transfer coefficient, $W/\left(m^2 K\right)$

LTC low-temperature chamber

$\dot{m}$ mass flow, kg/s

NTU number of heat transfer units

Pr Prandlt number

p pressure N/m^2, fin pitch

Q heat, J

$\dot{Q}$ heat flux, W

q heat per unit mass, J/kg

$\dot{Q}_f$ Friction heat flux, W

q_s heat inleak from the surroundings, J/kg

Re Reynolds number

St Stanton number

S entropy, J/K

$\dot{S}$ entropy rise rate, W/K

T absolute temperature, K

T_m mean thermodynamic temperature, K

u mass velocity, $kg/(m^2 s)$

v specific volume, m^3/kg

w_S specific shaft work, J/kg

x_1 transverse tube spacing, m

x_2 longitudinal tube spacing, m

Greek symbols

α convective heat transfer coefficient, $W/(m^2 K)$

δ fin thickness, m

δ_S intermediate shell thickness, m

ε exchanger effectiveness

η_m mechanical efficiency of the expander (the fraction of the compression work returned to the cycle)

η_S isentropic efficiency of the expander

η_τ isothermal efficiency of the compressor

λ thermal conductivity, $W/(mK)$

Π loss due to irreversibility, J

π specific exergetic loss, J/kg

$\dot{\Pi}$ exergetic loss flux, W

$\sigma = A_c/A_{fr}$ ratio of free-flow area to frontal area

τ cool down time, s

$\varphi = A_r/A_f$ ratio of the outside heat transfer area to inside area

Subscripts and superscripts

c cold

e external

f forward gas stream, friction

gen generated

h hot

HX heat exchanger

i inlet, insulation

m	medium
min	minimum
o	outlet
p	high pressure gas
r	return gas stream
0	environment
Δp	pressure drop
q_S	heat inleak
s	low pressure gas
ΔT	temperature difference

References

[1] Ogulata, R. T., Doba, F., Experiments and entropy generation minimization analysis of a cross-flow heat exchanger, Int. J. Heat Mass Transfer, Vol. 41, No. 2; 1998. p. 373-381.

[2] Narayan, P. G., Lienhard, Zubair, J. H., S. M., Entropy generation minimization of combined heat and mass transfer devices, International Journal of Thermal Sciences, 49; 2010. p. 2057-2066.

[3] Lerou, P.P.P.M., Veenstra, T.T., Burger, J.F., ter Brake, H.J.M., Rogalla, H., Optimization of counterflow heat exchanger geometry through minimization of entropy generation, Cryogenics 45; 2005. p. 659–669.

[4] Bejan, A., The concept of irreversibility in heat exchanger design: counterflow heat exchangers for gas-to-gas applications, J Heat Transfer 99C 3, 374; 1977.

[5] Sarangi, S., Chowdhury, K., On the generation of entropy in a counterflow heat exchanger, Cryogenics; February 1982. p. 63-65.

[6] Cornelissen, R., L., Hirs, G., G., Exergetic optimization of a heat exchanger, Journal of Energy Conversion and Management, Vol. 38, No. 15-17 ; 1997. p. 1567-1676.

[7] Gifford, W.E., A New Performance Parameter for Heat Exchangers in Transient Operation, Proceedings of the XIIIth International Congress of Refrigeration, Vol. II. USA: Washington; 1971. p. 220-230.

[8] Dobrovicescu, Al., Radcenco, Vs., Rãducanu, P., A Computer Package for the Thermodynamic and Thermophysical Properties for Air. Numerical Methods in Thermal Problems, SIAC Meeting, Vol. 1, Nov. 15-16. Bucharest; 1990. p. 1-5.

[9] Kays, W.M., London, A.L., Compact Heat-Exchangers, McGraw-Hill; 1964.

[10] Usyukin, I.P., Cryogenic Plants, Machines and Apparatus, Pishchevaya Promyshlennost. Moscow; 1976.

[11] Krasnikova, O.K., Usanov, V.V., Mishchenko, T.S., Orekhov, A.M., Kondrateva, G.A., Tubular Heat Exchanger for Helium Refrigeration Systems, Khimicheskoe i neftyance mashinostroenie, 5; 1975. p. 17-20.

[12] Baehr, H.D., Schwier, K, Die thermodynamischen Eigenschaften der Luft im Temperaturbereich zwischen -210^{0}C und +1250^{0}C bis zu Drucken von 4500 bar, Springer-Verlag, Berlin; 1961.

A Critical Exploration of the Usefulness of Rational Efficiency as a Performance Parameter for Heat Exchangers

Jim McGovern[a], Georgiana Tirca-Dragomirescu[b], Michel Feidt[c] and Alexandru Dobrovicescu[d]

[a] *Dublin Institute of Technology, Ireland, jim.mcgovern@dit.ie*
[b] *University Politehnica of Bucharest, Romania, georgianatirca@gmail.com*
[c] *L.E.M.T.A., Nancy, France, michel.feidt@ensem.inpl-nancy.fr*
[d] *University Politehnica of Bucharest, Romania, adobrovicescu@yahoo.com*

Abstract:

This paper examines and critically explores the possible usefulness of rational efficiencies of heat exchangers, based on the theoretical principles of exergy analysis. The rational efficiency is described first for the simplest possible heat exchanger, consisting of a flat conducting layer between two isothermal reservoirs. Secondly, a rational efficiency is defined for a simple compound heat exchanger with multiple isothermal heat sources and sinks. The concept is then expanded to include heat exchangers wherein heat transfer occurs from one fluid stream to another through a separating wall, with each stream experiencing a pressure loss due to fluid friction that depends on the flow rate of the fluid. The mathematical form of the rational efficiency in terms of the temperatures at which heat transfer occurs and of the environment is investigated. The manner of involvement of heat transfer and fluid friction effects in the rational efficiency is critically examined. Lastly, the relationship of the rational efficiency of a heat exchanger to the overall rational efficiency of a complete plant is considered. Based on the critical and analytical exploration, the authors conclude that rational efficiency is a useful performance parameter for heat exchangers that do not exchange heat directly with the exergetic reference environment.

Keywords:

Exergy, Fluid Friction, Heat Exchanger, Performance Parameter, Rational Efficiency.

1. Introduction

It is not common practice for engineers to make use of a rational or exergetic efficiency of heat exchangers for design or performance characterization purposes. For instance, heat transfer textbooks [1] and [2] make no reference to such an efficiency. However, the concept of exergetic or rational efficiency for heat exchangers is not new and [3] provides some useful insights, as well as referring to a definition from Andreev and Kostenko (paper in Russian), 1965, in which the exergetic input and output are based on the exergy changes of the hot and cold streams respectively. The work described in the present paper was undertaken to explore and clarify the possible usefulness of the concept of heat exchanger rational efficiency.

2. Rational Efficiency of Steady State Systems

The rational efficiency of a steady state system with exergy flows in and out, based on the boundary that encloses it, can be defined as the rate of exergy output divided by the rate of exergy input, (1).

$$\psi = \frac{\dot{\Xi}_{\text{out}}}{\dot{\Xi}_{\text{in}}} \qquad (1)$$

Certain exergetic inputs or outputs are constrained in such a way that a net exergy input cannot be represented as separate input and output components. For example, the pumping work for a flow

stream cannot be represented as an exergy input associated with **flow work** and an exergy output associated with flow work because of a **flow constraint**. Conceptual devices that can be used to explain and visualize such flow constraints are provided in [4]. A flow constraint arises because a stream of fluid that passes through, for example, one side of a heat exchanger is contained by an impermeable, rigid boundary that ensures the fluid's separation from the remainder of the system and, in steady state, that there is no net mass or substance transfer to the system from the stream. For fixed entry and exit states of the flow stream, the net flow work transfer (which has a corresponding net exergy transfer) is fully determined. An approach to applying (1) to a heat exchanger is included in [5,6]. The nature of irreversibility and entropy generation within a heat exchanger has been understood for a long time, e.g. [7,8], and it is straightforward to express the rational efficiency in terms of these quantities and the rate of exergy input, as in (2).

$$\psi = \frac{\dot{\Xi}_{\text{in}} - \dot{I}}{\dot{\Xi}_{\text{in}}} = \frac{\dot{\Xi}_{\text{in}} - T_0 \dot{S}_{\text{gen}}}{\dot{\Xi}_{\text{in}}} \qquad (2)$$

3. The Simplest Heat Exchanger

The simplest heat exchanger might be a flat conducting layer of uniform thickness that separates a thermal reservoir at a constant temperature T_{H} from a thermal reservoir at a lower constant temperature T_{L}. The heat transfer within the plate is assumed to be one-dimensional and so the heat flux is given by (3).

$$\phi = \frac{\dot{Q}}{A} = \frac{k(T_{\text{H}} - T_{\text{L}})}{l} = U(T_{\text{H}} - T_{\text{L}}) \qquad (3)$$

3.1. Description of the simplest heat exchanger in exergetic terms

For the purposes of exergy analysis the heat exchanger is assumed to exist in the context of an all-enclosing infinite environment that has a uniform temperature T_0, as shown in Fig. 1. For compactness in some of the expressions that follow, it is convenient to define the dimensionless temperature ratios $\theta_{\text{H}} = T_{\text{H}} / T_0$ and $\theta_{\text{L}} = T_{\text{L}} / T_0$.

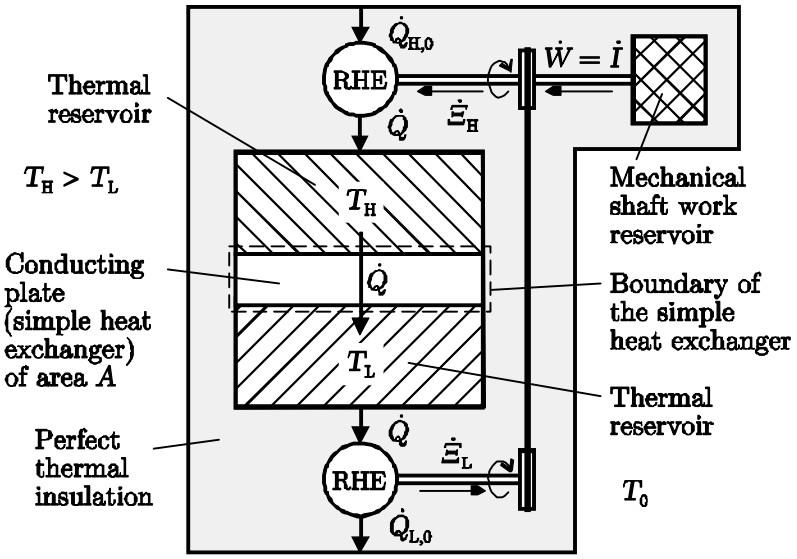

Fig. 1. Schematic representation of the simplest heat exchanger for exergy analysis purposes. The perfect thermal insulation shown is for the exclusion of any incidental heat losses or gains.

By imagining a boundary around the heat exchanger, the exergy flows into and out of the 'system' are easily identified as

$$\dot{\Xi}_{\mathrm{H}} = \dot{Q}\frac{T_{\mathrm{H}} - T_0}{T_{\mathrm{H}}} = \phi A \frac{T_{\mathrm{H}} - T_0}{T_{\mathrm{H}}} = \phi A(\theta_{\mathrm{H}} - 1)/\theta_{\mathrm{H}} \tag{4}$$

and

$$\dot{\Xi}_{\mathrm{L}} = \dot{Q}\frac{T_{\mathrm{L}} - T_0}{T_{\mathrm{L}}} = \phi A \frac{T_{\mathrm{L}} - T_0}{T_{\mathrm{L}}} = \phi A(\theta_{\mathrm{L}} - 1)/\theta_{\mathrm{L}}. \tag{5}$$

In exergetic terms, the simplest heat exchanger can be described as a system that accepts heat transfer at temperature T_{H} and provides the same amount of heat transfer at temperature T_{L}. The heat transfer at T_{H} is associated with an exergy input if $T_{\mathrm{H}} > T_0$, while the heat rejection at T_{L} is associated with an exergy output if $T_{\mathrm{L}} > T_0$. From (4) and (5), if either T_{H} or T_{L} equals T_0 then the corresponding exergy flow is zero. The rate of exergy destruction in the simple heat exchanger is given by (6) and the rate of entropy generation by (7).

$$\dot{I} = \dot{\Xi}_{\mathrm{H}} - \dot{\Xi}_{\mathrm{L}} = \dot{Q}T_0 \frac{T_{\mathrm{H}} - T_{\mathrm{L}}}{T_{\mathrm{H}}T_{\mathrm{L}}} = \phi A \frac{\theta_{\mathrm{H}} - \theta_{\mathrm{L}}}{\theta_{\mathrm{H}}\theta_{\mathrm{L}}} \tag{6}$$

$$\dot{S}_{\mathrm{gen}} = \frac{\dot{I}}{T_0} = \dot{Q}\frac{T_{\mathrm{H}} - T_{\mathrm{L}}}{T_{\mathrm{H}}T_{\mathrm{L}}} = \frac{\phi A}{T_0}\frac{(\theta_{\mathrm{H}} - \theta_{\mathrm{L}})}{\theta_{\mathrm{H}}\theta_{\mathrm{L}}} \tag{7}$$

3.2. The rational efficiency of the simplest heat exchanger

Equation (1) can be applied to the simplest steady state heat exchanger, yielding (8) to (10).

$$\psi = \left.\frac{(T_{\mathrm{L}} - T_0)/T_{\mathrm{L}}}{(T_{\mathrm{H}} - T_0)/T_{\mathrm{H}}}\right|_{T_{\mathrm{L}} > T_0} = \left.\frac{(\theta_{\mathrm{L}} - 1)/\theta_{\mathrm{L}}}{(\theta_{\mathrm{H}} - 1)/\theta_{\mathrm{H}}}\right|_{\theta_{\mathrm{L}} > 1} \tag{8}$$

$$\psi = \left.\frac{(T_{\mathrm{H}} - T_0)/T_{\mathrm{H}}}{(T_{\mathrm{L}} - T_0)/T_{\mathrm{L}}}\right|_{T_{\mathrm{H}} < T_0} = \left.\frac{(\theta_{\mathrm{H}} - 1)/\theta_{\mathrm{H}}}{(\theta_{\mathrm{L}} - 1)/\theta_{\mathrm{L}}}\right|_{\theta_{\mathrm{H}} < 1} \tag{9}$$

$$\psi = 0\big|_{T_{\mathrm{L}} < T_0 < T_{\mathrm{H}}} = 0\big|_{\theta_{\mathrm{L}} < 1 < \theta_{\mathrm{H}}} \tag{10}$$

Given that $T_{\mathrm{L}} < T_{\mathrm{H}}$, there is a range of values of T_{L}, defined by the inequality $T_{\mathrm{L}} \le T_0 \le T_{\mathrm{H}}$, for which the rate of exergy output is zero while there is a positive rate of exergy input. Of particular note are the cases where either T_{H} or T_{L} equals T_0, where there is one exergy input only. It is important to

note too that, in accordance with (5), the rate of exergy output at T_L is negative when T_L is less than T_0, i.e. the direction of the exergy flow associated with the heat rejection is into the simple heat exchanger. Similarly, the rate of exergy input at T_H is negative if T_H is less than T_0. Where both T_H and T_L are below T_0, there is a flow of exergy from the heat sink to the heat source and the rates of exergy transfer at both T_H and T_L have the opposite direction to the heat transfer rate.

3.2.1. Dependence of rational efficiency on T_0 for the simplest heat exchanger

Perhaps the strongest objection to the use of rational efficiency as a performance parameter for heat exchangers is the dependence of the rational efficiency on the temperature of the all-enclosing equilibrium environment. As illustrated by (8) to (10), for a given heat exchanger operating between given constant temperature thermal reservoirs with a given rate of heat transfer there are two distinct ranges of T_0 for which the rational efficiency has positive values and one range of values of T_0 for which the rational efficiency is zero. However, as has been shown in these equations, a certain simplification can be achieved by using dimensionless temperatures in place of the actual temperatures. In exergetic terms, the dependence of the performance of the simple heat exchanger on the reference temperature is inescapable.

3.2.2. Usefulness of ψ as a performance parameter for the simplest heat exchanger

The simplest heat exchanger, as described thus far, can be regarded as having an energy-based efficiency of 100%, as the energy input from the source thermal reservoir at T_H equals the energy output to the sink thermal reservoir at T_L. For simplicity, any incidental heat losses or gains are excluded here. The commonly-used concept of heat exchanger effectiveness is not directly applicable to the simple heat exchanger, as neither thermal reservoir involves a temperature glide. In contrast, the rational efficiency is a meaningful performance parameter. In 'pure' thermodynamics an ideal heat exchanger would be a compound heat engine, requiring access to the reference environment, but in finite dimensional thermodynamics the rational efficiency quantifies the goodness of a compromise device, not requiring access to the reference environment, for which the irreversibility rate, or the rate of entropy generation, can be minimized or optimized. The economic optimum may not correspond to the thermodynamic goal of irreversibility rate minimization.

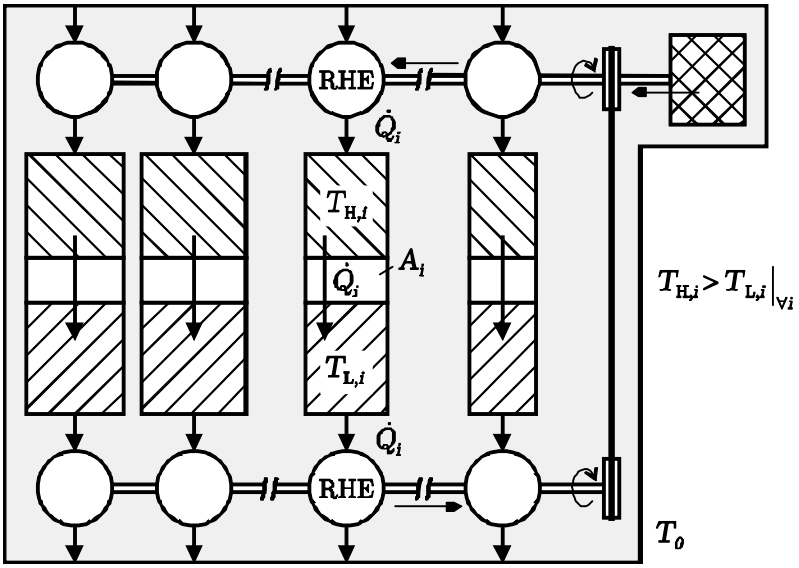

Fig. 2. Schematic representation of a simple compound heat exchanger for exergy analysis purposes.

4. Simple Compound Heat Exchanger

Fig. 2 represents a simple compound heat exchanger consisting of n simple heat exchangers. There are multiple heat source thermal reservoirs at temperatures $T_{H,i}$ and each of these has a corresponding heat sink thermal reservoir at temperatures $T_{L,i}$. Fig. 3 is a diagram of temperature versus cumulative heat transfer rate for this simple compound heat exchanger.

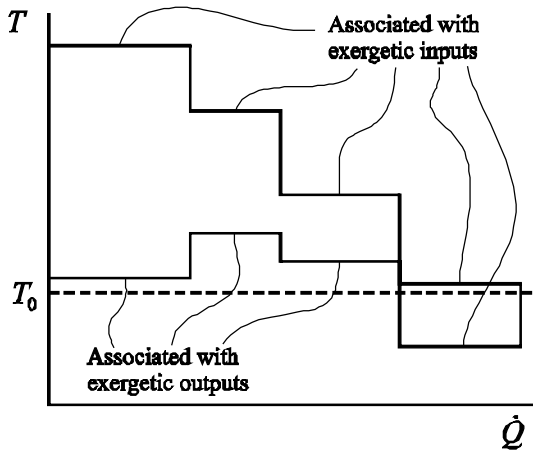

Fig. 3. Plot of temperature versus cumulative heat transfer rate for a simple compound heat exchanger.

4.1. Rational efficiency of the simple compound heat exchanger

The rational efficiency of the simple compound heat exchanger can be expressed by inserting the appropriate expressions for $\dot{\Xi}_{\text{in}}$ and $\dot{\Xi}_{\text{out}}$ into (1), yielding (11), which contains four conditional summation terms.

$$\psi = \frac{\displaystyle\sum_{i,\,\text{iff}\ \theta_{\text{L},i}>1} \dot{Q}_i \frac{\theta_{\text{L},i}-1}{\theta_{\text{L},i}} + \sum_{i,\,\text{iff}\ \theta_{\text{H},i}<1} \dot{Q}_i \frac{\theta_{\text{H},i}-1}{\theta_{\text{H},i}}}{\displaystyle\sum_{i,\,\text{iff}\ \theta_{\text{L},i}<1} \dot{Q}_i \frac{\theta_{\text{L},i}-1}{\theta_{\text{L},i}} + \sum_{i,\,\text{iff}\ \theta_{\text{H},i}>1} \dot{Q}_i \frac{\theta_{\text{H},i}-1}{\theta_{\text{H},i}}} \qquad (11)$$

By way of clarifying the notation for $\dot{Q}_i$ in (11) and $\dot{Q}$ in (12), these terms are all positive in the direction from higher to lower temperature.

5. Simple Heat Exchangers with a Temperature Glide

By extension of the concept represented in Fig. 2 it is possible to imagine a composite heat source and a composite heat sink that each involve a continuous temperature range. A heat exchanger consisting of a conducting medium is envisaged. A diagram of temperature versus cumulative heat transfer rate for this type of simple heat exchanger is represented in Fig. 4. The corresponding expression for rational efficiency is (12).

$$\psi = \frac{\displaystyle\int_{\forall\,\theta_{\text{L}}>1} \frac{\theta_{\text{L}}-1}{\theta_{\text{L}}}\,\mathrm{d}\dot{Q} + \int_{\forall\,\theta_{\text{H}}<1} \frac{\theta_{\text{H}}-1}{\theta_{\text{H}}}\,\mathrm{d}\dot{Q}}{\displaystyle\int_{\forall\,\theta_{\text{L}}<1} \frac{\theta_{\text{L}}-1}{\theta_{\text{L}}}\,\mathrm{d}\dot{Q} + \int_{\forall\,\theta_{\text{H}}>1} \frac{\theta_{\text{H}}-1}{\theta_{\text{H}}}\,\mathrm{d}\dot{Q}} \qquad (12)$$

6. Heat Exchangers with Two Fluid Streams

Actual heat exchangers with two fluid streams are usually insulated externally so that extraneous heat losses or heat gains are kept small or negligible. These effects can be accounted for readily in the rational efficiency, but, for brevity are not addressed in the present paper.

The principal causes of irreversibility are the heat transfer that occurs from one fluid to the other over finite temperature differences and fluid friction within each fluid stream within the heat exchanger. Another, usually relatively minor, mechanism of irreversibility is due to heat fluxes within the fluid streams or within the material of the heat exchanger that are not part of the overall heat transfer from one stream to the other. In traditional calculations for heat exchangers a continuously varying quasi-equilibrium state is assumed for the bulk fluid of each stream as it moves through the heat exchanger. The use of this same assumed quasi-equilibrium state is also useful, as a practical approximation, in exergy analysis.

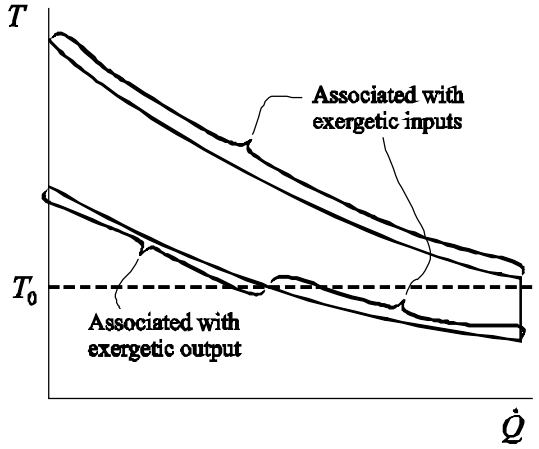

Fig. 4. Plot of temperature versus cumulative heat transfer rate for a simple heat exchanger wherein there is a temperature glide within the heat source and within the heat sink. In this particular case T_0, the temperature of the environment, happens to lie between the maximum temperature of the heat source and the minimum temperature of the heat sink.

6.1. Incorporating convective heat transfer irreversibility into the rational efficiency

Fig. 5 illustrates how the convection temperature differences for heat transfer within a two-fluid counter flow heat exchanger can be represented on a diagram of the same type as Figs 3 and 4. The temperature curves can be established from the standard techniques for heat exchanger analysis and a rational efficiency for convection and conduction between the fluid streams can be calculated using (12).

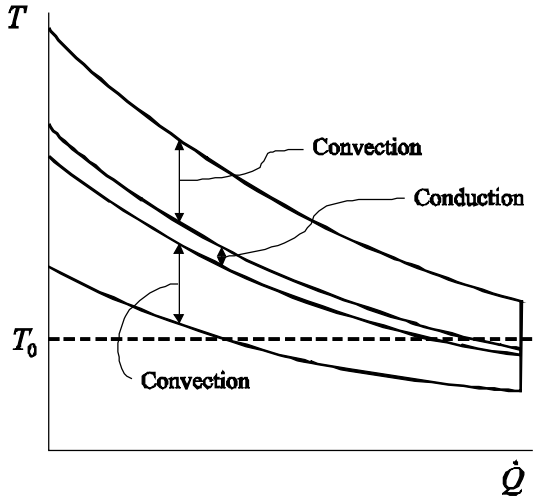

Fig. 5. Plot of temperature versus cumulative heat transfer rate for a two-fluid heat exchanger wherein there is a temperature glide of each fluid. The uppermost and lowermost curves represent the quasi-equilibrium bulk fluid temperatures.

6.2. Incorporating fluid friction irreversibility into the rational efficiency

Traditional approaches can be used to establish the quasi-equilibrium thermodynamic states at the positions where each fluid stream enters or leaves a heat exchanger, e.g. positions 2, 7, 4 and 8 for recuperator R in Fig. 6, allowing for the pressure losses within each fluid stream. The net rate of exergy input to a heat exchanger from a flow stream that passes through it is

$$\begin{aligned}\dot{\Xi}_{\text{in}} &= \dot{m}(\beta_{\text{i}} - \beta_{\text{o}}) \\ &= \dot{m}[(h_{\text{i}} - T_0 s_{\text{i}}) - (h_{\text{o}} - T_0 s_{\text{o}})].\end{aligned} \qquad (13)$$

If the rate of exergy input (13) is negative then the exergetic interaction is an output. Thus (13) can be used to evaluate the numerator and the denominator for (1) to calculate the overall rational efficiency of the heat exchanger to include all irreversibilities.

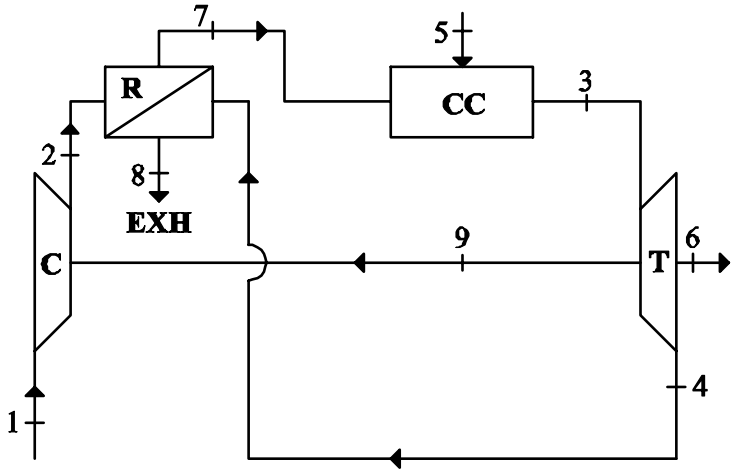

Fig. 6. Schematic representation of a gas turbine installation with recuperation of heat.

7. Numerical Example

In order to better illustrate the usefulness of the rational efficiency, the case of a gas turbine with recuperation of heat will be analysed, Fig. 6. The heat exchanger of the system is a gas-to-gas plate and fin heat exchanger, Fig. 7, and its purpose is to preheat the compressed air before it enters the combustion chamber using the residual heat of the exhaust gases from the turbine.

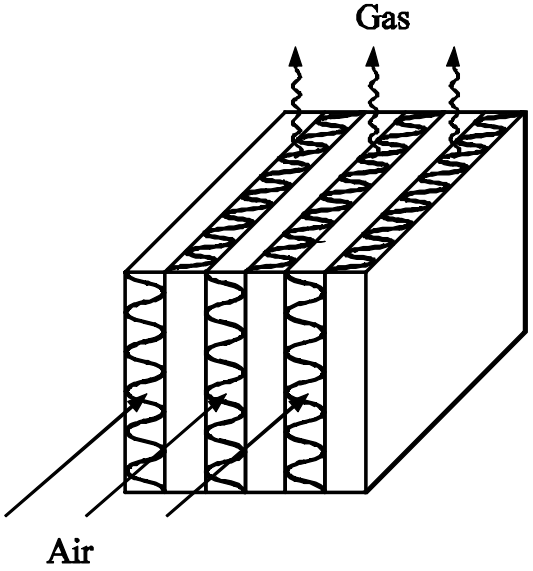

Fig. 7. Schematic representation of the plate and fin heat exchanger used in the gas turbine installation.

In order to analyse the system, fixed parameters for the environment were chosen, namely T_0 = 300 K and p_0 = 1.013 bar. The maximum temperature of the cycle was set at T_3 = 1,500 K. The pressure ratio was taken as r_p = 10. Table 1 shows the main imposed parameters for the analysis. The simulation was performed using Engineering Equation Solver.

Table 1. Imposed parameters for the analysis.

Parameter	Value
Isentropic efficiency of the compressor	$\eta_C = 86\%$
Isentropic efficiency of the turbine	$\eta_T = 87\%$
Combustion efficiency	$\eta_{comb} = 98\%$
Mechanical efficiency of the system	$\eta_M = 99.8\%$
Flow stream mass velocity on the air side of the heat exchanger	$G_a = 25$ kg/(m^{2}s)
Flow stream mass velocity on the gas side of the heat exchanger	$G_g = 12$ kg/(m^{2}s)

The calculated thermal efficiency of the entire plant, taking into account all the irreversibilities due to pressure losses and temperature differences, is η = 38.19%.

Using (1), the rational efficiency of the plant is:

$$\psi = \frac{\dot{\Xi}_{\text{out}}}{\dot{\Xi}_{\text{in}}} = \frac{\dot{\Xi}_6}{\dot{\Xi}_{\text{fuel}}} = 31.8\%.$$

According to (13) and (1), the rational efficiency of heat exchanger R is 78.1%. The dependence of this rational efficiency on the ambient temperature is plotted in Fig. 8 for values of T_0 from 273 K to 313 K.

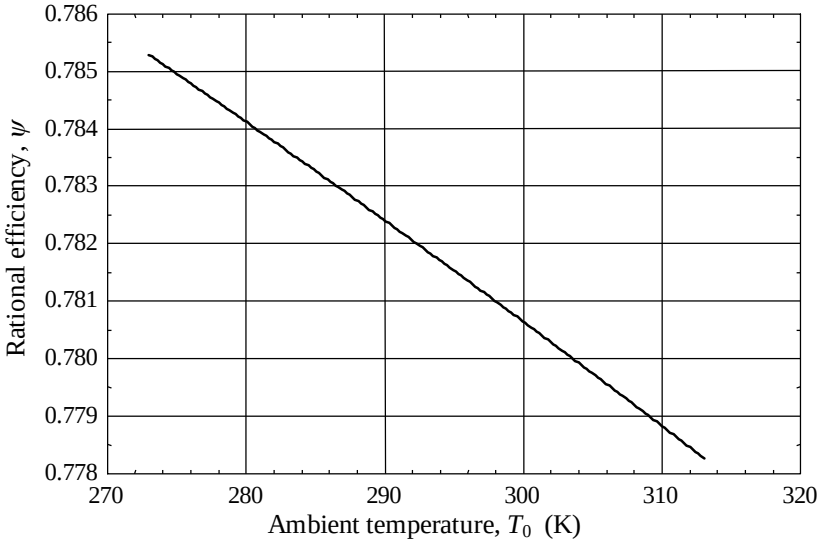

Fig. 8. Heat exchanger rational efficiency as a function of the ambient temperature T_0.

The approach of [6] for evaluating sub-rational efficiency values for heat transfer and fluid friction yields the following:

$\psi_Q = 87.2\%$ Rational efficiency value for heat transfer

$\psi_{F,A} = 95.8\%$, $\psi_{F,B} = 93.5\%$ Rational efficiency values for fluid friction

$\psi = 78.1\%$.

8. Heat Exchanger Rational Efficiency in the Overall Context

Using the approach of [9,10], the exergy interaction rate diagram, Fig. 9, is drawn. Without regenerator R the exergy input with the fuel $\dot{\Xi}_{\text{fuel}}$ would be increased significantly and the exergy destruction in the exhaust discharge region $\dot{\Xi}_{0,\text{EXH}}$ would be greater. Thus, the regenerator allows recovery of part of the exergy that would be wasted with the exhaust. A high rational efficiency ψ_{R} for the regenerator has a calculable influence on the rational efficiency of the entire plant. It can be seen from Fig. 9 that this is somewhat analogous to the way in which the rational efficiency of the turbine or that of the compressor has a calculable influence on the overall rational efficiency.

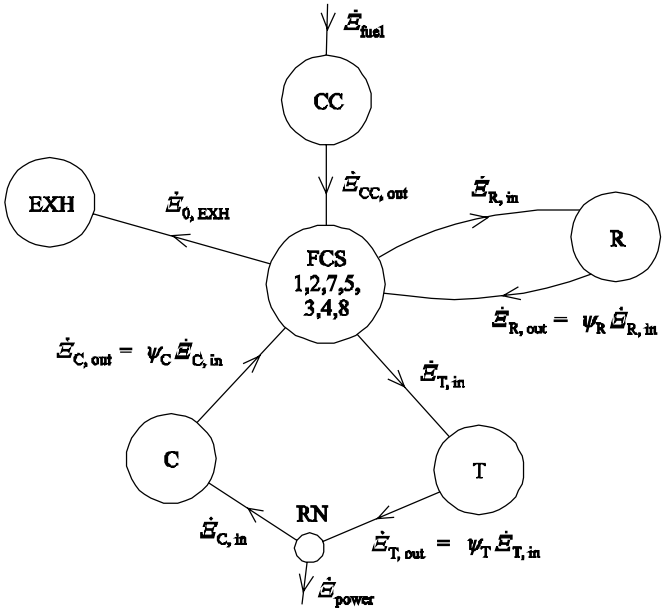

Fig. 9. Exergy interaction diagram for the gas turbine plant.

Conclusions

On the basis of the considerations presented in this paper the authors believe that rational efficiency has a useful role as a performance parameter for heat exchangers wherever they do not interact directly with the exergetic reference environment. This performance parameter can be useful in the process of design optimization in the same way as the efficiency of an electric motor or generator can be useful: in the optimum design the efficiency will be maximized subject to constraints. The rational efficiency of a heat exchanger (provided it is non-zero) has a calculable influence on the rational efficiency of the entire plant. Thus, the heat exchanger rational efficiency can also be useful in following the trail of exergy currents in exergoeconomics. Where a heat exchanger interacts directly with the environment, to reject or accept heat, it is an exergy destruction sink and has a rational efficiency of zero.

Acknowledgments

The work has been funded in part by the Sectorial Operational Program, Human Resources Development 2007-2013, of the Romanian Ministry of Labour, Family and Social Protection through the Financial Agreement POSDRU/88/1.5/S/61178.

Nomenclature

A area, m^2

C compressor

CC combustion chamber

EXH exhaust discharge region

FCS flow constraint system

G mass velocity, $kg/(m^2s)$

h specific enthalpy, J/kg

$\dot{I}$ irreversibility rate, W

k thermal conductivity, W/(mK)

l length, m

n number of heat exchanger elements

p pressure, Pa

$\dot{Q}$ rate of heat transfer, W

R regenerator

RHE reversible heat engine

RN reversible node

r_p pressure ratio

s specific entropy, J/(kgK)

$\dot{S}_{gen}$ rate of entropy generation, W/K

T turbine

T, T_H absolute temperature, K

T_L absolute temperature, lower than T_H, K

T_0 absolute temperature of the environment, K

U overall heat transfer coefficient, W/(m^{2}K)

$\dot{W}$ rate of work, W

Greek symbols

β specific flow exergy function, J/kg

θ temperature ratio

$\dot{\Xi}$ rate of exergy transfer, W

ϕ heat flux, W/m^2

η efficiency

ψ rational efficiency

Subscripts and superscripts

0 reference environment

A, B fluid streams

a air

comb combustion

F fluid friction

fuel associated with the fuel

g gas

gen generation

H high

in into a specified system

i inlet

i index of a heat exchanger element

L low

M mechanical

o outlet

out out of a specified system

Q relates to heat transfer

References

[1] Incropera FP., DeWitt DP., Bergman TL. and Lavine AS. Fundamentals of heat and mass transfer. John Wiley & Sons; 2007.

[2] Kays WM., London AL., Compact heat exchangers, 3rd edition. Krieger Publishing Company, 1998.

[3] Evenko VI., Exergetic efficiency of heat exchangers. Chemical and Petroleum Engineering, 32(1):37-42, 1996.

[4] O'Toole F., McGovern JA., Some concepts and conceptual devices for exergy analysis. Proceedings of the Institution of Mechanical Engineers, Part C: Journal of Mechanical Engineering Science, 204(53):329-340, June 1990.

[5] Smyth B., The exergy analysis of a multi-effect evaporation unit for seawater desalination. Master's thesis, Trinity College, Dublin, Thesis 5540, 1997.

[6] McGovern J., Smyth BP., Rational efficiency of a heat exchanger, October 2011. Available at <http://arrow.dit.ie/engschmecart/27/> [accessed 22.1.2012].

[7] Bejan A., The concept of irreversibility in heat exchanger design: counterflow heat exchangers for gas-to-gas applications. Joumal of Heat Transfer, 99(3):374-380, 1977.

[8] Bejan A. General criterion for rating heat-exchanger performance. International Journal of Heat and Mass Transfer, 21(5):655-658, 1978.

[9] McGovern JA., O'Toole F., A virtual-system concept for exergy analysis of flow network plant; Part I: Principles, in ECOS'92, Proceedings of the international symposium on efficiency, costs, optimization and simulation of energy systems, Zaragoza, Spain, ed. Valero, A. and Tsatsaronis, G., American Society of Mechanical Engineers, June 15-18, 1992, pp. 155-160. <http://arrow.dit.ie/engschmeccon/48/> [accessed 23.1.2012].

[10] McGovern JA., O'Toole F., A virtual-system concept for exergy analysis of flow network plant; Part II: Exergetic and exergoeconomic analysis illustration, in ECOS'92, Proceedings of the international symposium on efficiency, costs, optimization and simulation of energy systems, Zaragoza, Spain, ed. Valero, A. and Tsatsaronis, G., American Society of Mechanical Engineers, June 15-18, 1992, pp. 161-166. <http://arrow.dit.ie/engschmeccon/49/> [accessed 23.1.2012].

A new procedure for the design of LNG processes by combining Exergy and Pinch Analyses

Danahe Marmolejo-Correa, Truls Gundersen

Department of Energy and Process Engineering, Norwegian University of Science and Technology, Trondheim, Norway, danahe.m.correa@ntnu.no; danahe.marmolejo@gmail.com. (CA), truls.gundersen@ntnu.no

Abstract:

This paper presents an alternative design procedure for LNG processes. The procedure combines Pinch and Exergy Analyses and uses a new graphical representation of exergy. In the literature, there are several approaches using the pinch method and exergy analysis in combination for process design; however, most of them use exergy analysis as a post design tool. One goal of this work is to illustrate the inclusion of exergy calculations in the early stages of design, such as in energy (and exergy) targeting. The paper introduces a novel diagram for exergy and energy targeting which utilizes a new energy quality parameter called exergetic temperature. This quality parameter can be used to manipulate exergy changes caused by pressure adjustments. The main objective of the pressure manipulations is to reduce both heat and power requirements. The Reverse Brayton process is used as a case study for illustrating both the novel diagram and the proposed methodology.

Keywords:

Exergy Analysis, LNG, Low Temperature Processes, Pinch Analysis, Process Design.

1. Introduction

The simultaneous use of Pinch Analysis (PA) and Exergy Analysis (EA) is not a new idea. Actually, PA is based on the Second Law of Thermodynamics [1] (by matching hot and cold streams with corresponding level of energy; highest hot stream temperature with highest cold stream temperature and vice versa for the cold end). PA has proven to be a powerful tool for designing Heat Recovery Systems (HRSs). By decomposing an HRS into two independent systems, one above pinch and the other below pinch, the PA method provides a set of designs with minimum heating and cooling requirements. However, PA is rather limited in the sense that it only uses temperature as the main design variable. For an HRS operating below ambient temperature (T_0), where expansion and/or compression of streams are required, pressure is also an important variable. Moreover in HRSs, if pressure is manipulated, the utility requirements may be reduced in comparison to those obtained with the *traditional* PA. Exergy Analysis (EA) is a good alternative for measuring the minimum exergy required or rejected by the HRS. Conveniently, temperature, pressure and composition are the main process variables utilized in the calculation of exergy content in process streams. However, EA can be used only to evaluate design decisions but not to guide them, thus it does not give conclusive information with respect to the design [2]. For process analysis of HRSs operating below or across ambient temperature, using PA and EA in combination can be beneficial due to the large amount of energy in form of shaftwork required for compression in the utility system (refrigeration cycles). In addition, for processes operating below ambient temperature where external cooling is provided by compression, there is an intimate relationship between thermal energy and mechanical energy, thus both temperature and pressure are important design variables. In this paper, the Reverse Brayton process for the liquefaction of natural gas is used as a case study to illustrate the use of the new energy quality parameter and the new graphical diagram.

Typically for processes with operating conditions below ambient temperature, the most important objective is to supply the cooling demand i.e. refrigeration load. Because refrigeration is expensive

and its demand increases significantly as temperature is reduced, such processes tend to become rather complicated. The temperature differences inside heat exchangers can be very small, (i.e. less than 5 K) hence the heat transfer area is quite large causing other problems related to material stresses and two-phase flow distribution. In conclusion, the design of such processes is not a simple task and should be done in a systematic way by utilizing the energy resources available in the best possible way.

1.1 Background

Many attempts have been made for combining PA and EA [1, 3-10]. In 1979, Umeda et al. [3] presented the so-called *energy availability* diagram where the Carnot factor is used as ordinate and enthalpy as abscissa. Here, the hot and cold streams of an HRS are plotted in a composite manner generating two curves: a total hot curve and a total cold curve. Later, Linnhoff [1] and Linnhoff and Dhole [4] re-named this diagram as the *Exergy Composite Curves* (ECCs). An example diagram of the ECCs is shown in Fig. 1*a*. The area between the hot and the cold ECC provides a quantitative measure of the exergy losses due to heat transfer since the axes are enthalpy and Carnot factor. There is also a corresponding *Exergy Grand Composite Curve* (EGCC) that shows the exergy loses related to the heat transfer between the process and the utility system. The EGCC can be used for appropriate placement of heat engines, heat pumps and refrigeration cycles (load, level and number of cycles)

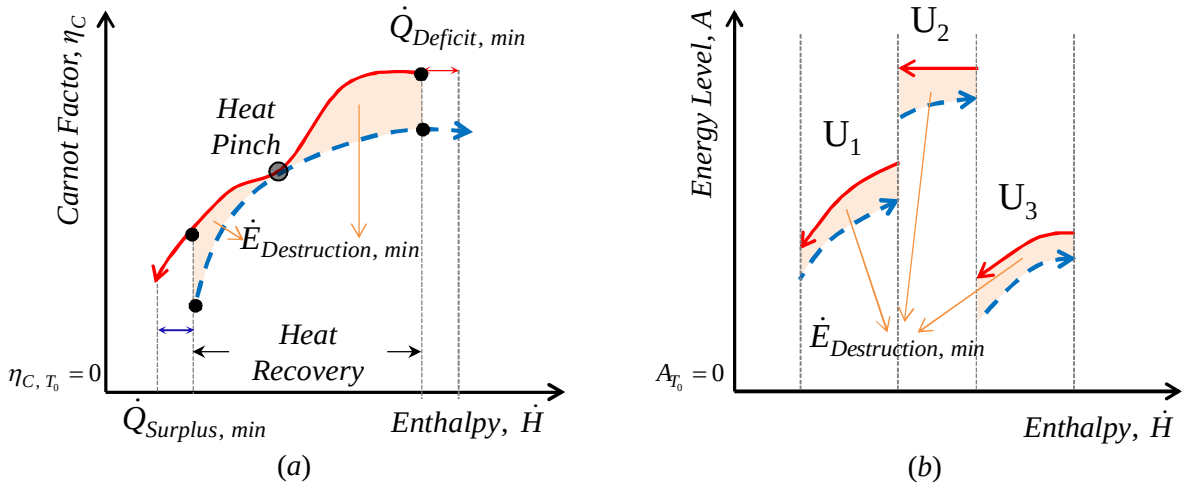

Fig. 1 a) Exergy Composite Curves (ECCs), b) Energy Utilization Diagram (EUD)

In 1993, Staine and Favrat [5] extended the ECCs diagram for representing the exergy losses not only due to process-to-process heat transfer (exergy destruction), but also those caused by dissipation (pressure drop) and the losses during the fabrication of the heat exchanger. In addition, they introduced an alternative diagram for representing exergy losses in mechanical equipment (pumps, fans, compressors). Later, Sorin and Paris [6, 8] used the so-called *exergy load distribution approach* (introduced by Sorin and Brodyansky [11]) and minimum energy requirements obtained from the *traditional* PA. They used their approach for improving a hydrogen production process [6] and found that the number of unit operations was reduced and the yield increased by 2%. In 1997, Feng and Zhu [7] presented the referred to as *energy level – enthalpy* diagram where they combined the exergy loss representations of HRSs and mechanical equipment. The *energy level* concept was first suggested by Rant [12] with his *Exergy/Energy ratio* which can be directly applied to energy streams. For material streams with change in state conditions from state 1 to state 2, Ishida and Kawamura [13] introduced the *energy level* factor (*A*) as shown in Eq. (1).

$$A=\frac{\dot{E}_2-\dot{E}_1}{\dot{H}_2-\dot{H}_1}=\frac{\Delta\dot{E}}{\Delta\dot{H}} \tag{1}$$

The Energy Utilization Diagram (EUD) was also introduced by Ishida and Kawamura [13]. Fig. 1*b* shows the EUD for three unit operations: U_1 (first heat exchanger), U_2 (compressor) and U_3 (second heat exchanger). Here, the so-called energy donors (top curves) and energy acceptors (bottom curves) are plotted for all unit operations, not only the HRS. The *energy level* is plotted on the *y* axis while enthalpy is plotted on the *x* axis. Both the EUD and the diagram presented by Feng and Zhu [7] illustrate the irreversibilities in all unit operations. The difference between these two diagrams is that the first (EUD) plots the energy donors and acceptors of all unit operations in a consecutive manner according to the process flow. Intermediate state conditions are calculated for a more accurate shape of the energy donor and acceptor curves. In contrast, the diagram developed by Feng and Zhu [7] is focused on illustrating the exergy losses without considering the order in which the unit operations are plotted, and without calculating intermediate states for other units than heat exchangers.

In our research group, efforts have been placed on developing new process design methodologies that combine PA and EA. Anantharaman et al. [9] used the *energy level* parameter in the construction of a set of energy donor and energy acceptor composite curves for complete processes. In contrast to the EUD and the diagram proposed by Feng and Zhu [7], Anantharaman et al. [9] constructed the so-called *energy level composite curves* by sorting, in descending order, the energy level of the streams without taking into consideration the order in which the streams appear in the process flow diagram or the corresponding unit operations. Thus, with the *energy level composite curves*, one can clearly visualize where in the process the most energy demanding streams are. However, in terms of process integration, this diagram does not indicate which streams should be coupled. Aspelund et al. [10] proposed the *Extended Pinch Analysis and Design (ExPAnD)* procedure. One objective of the ExPAnD methodology is to maximize the utilization of the exergy obtained by pressure changes and to minimize work consumption (or maximize work production) while maximizing heat recovery. The ExPAnD method utilizes ten heuristic rules to achieve this goal. At present, the ExPAnD method has only been applied in processes operating below ambient.

1.2 Scope

This paper is focused on demonstrating the use of a new representation of exergy for the design of Heat Recovery Systems where both temperature and pressure are important design variables. A extended problem definition for such systems has been proposed by Aspelund et al. [10].

"*Given a set of process streams with a supply state (temperature, pressure, and resulting phase) and a target state, as well as utilities for power, heating, and cooling; design a system of heat exchangers, expanders, compressors, pumps and valves in such a way that the irreversibilites are minimized*"

Examples of such systems are low temperature processes e.g. refrigeration and liquefaction processes. The graphical representation described here fits very well in HRSs where the streams have near-constant heat capacity and that may or not require a change in pressure from their supply to target conditions. In the case that process streams require pressure modifications; these streams should be preferable in gas phase and with a behavior close to an ideal gas. One could use this graphical representation for real gases for a first and quick estimation; however, the results should be contrasted with those from rigorous calculations.

For the design of the extended HRSs, a similar procedure to the one described by Linhoff et al. [14] for the design of HRS is proposed. The extended procedure is decomposed into several stages: Data Extraction, Exergy Calculations, Exergy Targeting, Process Modifications, Design and Optimization. The new diagram is proposed to be used for exergy targeting e.g. for obtaining the minimum exergy requirement (minimum theoretical work required) in HRSs, as well as in the process modification stage. This diagram can be used as alternative to the ECCs introduced by Linnhoff and Dhole [4].

2. Exergy Analysis of Heat Recovery Systems

In HRSs, two classes of exergy are included for EA calculations: the thermo-mechanical exergy of process streams and the exergy of heat. In the literature, the thermo-mechanical exergy [15] is also referred to as physical exergy [16] and its components are also known as thermal and mechanical exergies [17, 18]. In other publications [19, 20], the sum of the thermo-mechanical (physical) and chemical exergy is referred to as thermal exergy. Petela [20] calls mechanical exergy to the sum of the potential and thermo-mechanical (physical) exergy. Thus, in order to have a homogeneous nomenclature in this paper, the authors decided to use self-explanatory names for the exergy of material streams and its components. Thus for a material stream, the exergy content given by its temperature and pressure is referred to as thermo-mechanical exergy and its components are named as temperature based exergy and pressure based exergy.

2.1 Exergy of process streams

The exergy of process streams is equal to the sum of thermo-mechanical and chemical exergies. If the process stream is under a change of state from (T_1, p_1) to (T_2, p_2) and there is no chemical reaction, separation or mixing, then the chemical exergy of the stream can be omitted in the exergy calculations. The thermo-mechanical exergy is given by (2).

$$\dot{E}^{TM}(T,p)=\dot{H}(T,p)-\dot{H}(T_0,p_0)-T_0\left[\dot{S}(T,p)-\dot{S}(T_0,p_0)\right] \tag{2}$$

$$\dot{E}^{T}(T,p)=\dot{H}(T,p)-\dot{H}(T_0,p)-T_0\left[\dot{S}(T,p)-\dot{S}(T_0,p)\right] \tag{3}$$

$$\dot{E}^{p}(T,p)=\dot{H}(T_0,p)-\dot{H}(T_0,p_0)-T_0\left[\dot{S}(T_0,p)-\dot{S}(T_0,p_0)\right] \tag{4}$$

The thermo-mechanical exergy ($\dot{E}^{TM}$) can be further decomposed into temperature based exergy ($\dot{E}^{T}$) and pressure based exergy ($\dot{E}^{p}$). While this decomposition is not unique and thus has no fundamental meaning, commonly accepted definitions for $\dot{E}^{T}$ and $\dot{E}^{p}$ are given in (3) and (4). Fig. 2*a* shows this exergy decomposition graphically. Despite the arbitrariness of this decomposition, it is used for a better understanding of the temperature and pressure based exergy contributions in various processes.

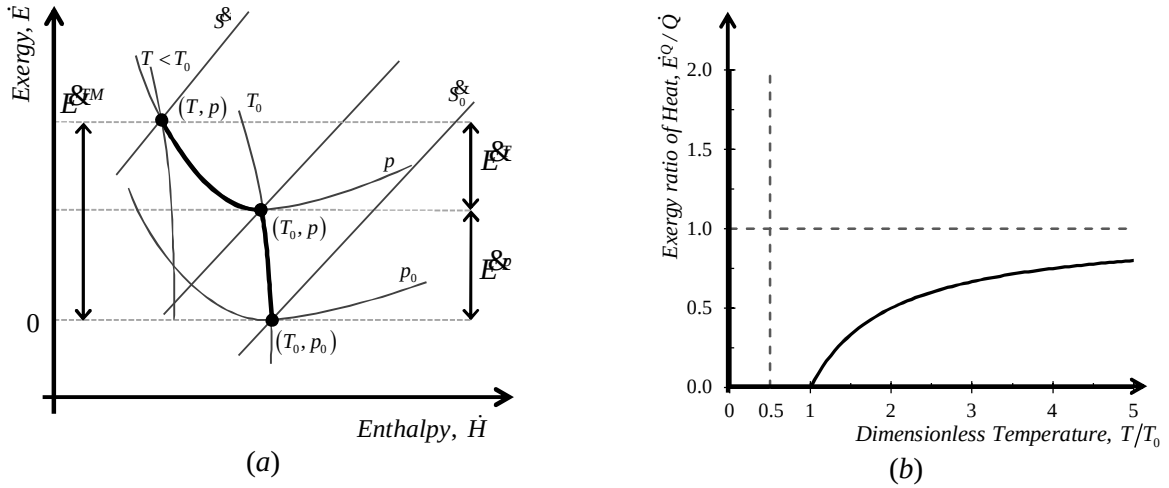

Fig. 2 (a) $\dot{E}-\dot{H}$ diagram and decomposition of $\dot{E}^{TM}$ into $\dot{E}^{T}$ and $\dot{E}^{p}$, and (b) $\dot{E}^{Q}-T$ diagram

2.2 Exergy of heat

The exergy accompanying heat also depends on temperature. In Fig. 2*b*, it is shown that the exergy of heat (energy stream) above T_0 is horizontally asymptotic to $\dot{Q}$ (5); the maximum work produced

even by an ideal (reversible) heat engine will always be less than the energy supplied by the heat reservoir $(\dot{Q})$. Below T_0, the exergy of heat is vertically asymptotic to zero (6); the minimum work required to take $\dot{Q}$ from T_0 to lower temperatures can be equal or larger than $\dot{Q}$ (at T = 0 K, an infinite amount of work is required). Actually, for temperatures below half of T_0, the ratio between $\dot{E}^Q$ and $\dot{Q}$ is larger than one (see Fig. 1*b*), meaning that heat (cooling) is more valuable than work.

$$\dot{E}^Q = \dot{Q}\left(1-\frac{T_0}{T}\right) \quad \text{for} \quad T \geq T_0 \tag{5}$$

$$\dot{E}^Q = \dot{Q}\left(\frac{T_0}{T}-1\right) \quad \text{for} \quad T \leq T_0 \tag{6}$$

3. A novel energy quality parameter

As discussed earlier in the paper, the established energy quality parameters such as *Carnot factor* and the so-called *energy level* introduced in different forms have limitations when used in graphical representations and for exergy targeting. This section introduces a new energy quality parameter that enables new graphical diagrams that are easy to construct and that can be used explicitly for exergy targeting.

3.1 Exergetic temperatures

If the specific heat capacity is assumed constant with respect to temperature in the range from T to T_0, Equation (3) can be rewritten as (7). In addition, if ideal gas conditions are valid, then (4) can be simplified as shown in (8). Notice that in (7) and (8), the factors inside the square brackets have temperature dimension and absolute temperature units (K). These factors are the so-called *exergetic temperatures*. For $\dot{E}^T$, the exergetic temperature (T^{E^T}) is only a function of temperature, and for $\dot{E}^p$, the corresponding exergetic temperature (T^{E^p}) is only a function of pressure. The procedure for obtaining (7) and (8) from (3) and (4) is straightforward using the correct thermodynamic relations for the abovementioned assumptions. Several text books have derived (7) and (8) in a very comprehensive manner [15, 16, 19, 21], thus the mathematical development for these equations is left to the reader. One should notice that the assumption of ideal gas conditions only has an effect in (8) and not in (7).

$$\dot{E}^T = \dot{m}c_p\left[T_0\left(\frac{T}{T_0}-\ln\frac{T}{T_0}-1\right)\right] = \dot{m}c_p T^{E^T} \tag{7}$$

$$\dot{E}^p = \dot{m}c_p\left[T_0 \ln\left(\frac{p}{p_0}\right)^{\frac{\kappa-1}{\kappa}}\right] = \dot{m}c_p T^{E^p} \tag{8}$$

Notice that the simplified equations for $\dot{E}^T$ and $\dot{E}^p$ in (7) and (8) exhibit a linear relation between the exergetic temperatures and the corresponding exergy components. This linear relationship is of course also present between the changes in exergetic temperatures and the corresponding changes in exergy components as shown in (9) and (10).

$$\Delta\dot{E}^T_{1\to 2} = \dot{m}c_p\left[T_0\left(\frac{T_2-T_1}{T_0}-\ln\frac{T_2}{T_1}\right)\right] = \dot{m}c_p\Delta T^{E^T}_{1\to 2} \tag{9}$$

$$\Delta\dot{E}^p_{1\to 2} = \dot{m}c_p\left[T_0 \ln\left(\frac{p_2}{p_1}\right)^{\frac{\kappa-1}{\kappa}}\right] = \dot{m}c_p\Delta T^{E^p}_{1\to 2} \tag{10}$$

3.2 Relationship between ΔT^{E^T} and ΔT^{E^p}

For a given state (T, p), T^{E^T} and T^{E^p} are independent variables (the first is only a function of temperature and the second is only a function of pressure). For a process where the pressure of a stream changes from p_1 to p_2 (i.e. compression or expansion), there will be a corresponding change in temperature from T_1 to T_2^{ise} unless an isothermal process is assumed. While the pressure p_2 after the process can be regarded as a specification (fixed by some process needs), the corresponding temperature T_2^{ise} is a function of the initial temperature T_1 and the pressure ratio (p_2/p_1). Considering the definitions of the changes in exergetic temperatures in (9) and (10), it is clear that for such processes, while $T_2^{E^p}$ only depends on p_2 which is specified, $T_2^{E^T}$ depends on T_2^{ise}; which in turn depends on T_1 and the ratio p_2/p_1. This means that $T_2^{E^T}$ depends on both $T_1^{E^T}$ and p_2/p_1 (or $\Delta T_{1\to 2}^{E^p}$). If the change in pressure follows an isentropic path, Equations (11) and (12) are valid for ideal gases. If (11) is substituted into (10), then the change in pressure based exergy for an isentropic operation is shown in (13). The resulting change in temperature based exergy is given by (14). Thus, the change in T^{E^T} is defined as in (15)

$$\frac{T_2^{ise}}{T_1}=\left(\frac{p_2}{p_1}\right)^{\frac{\kappa-1}{\kappa}} \tag{11}$$

$$-\dot{W}_{ise}=\dot{m}c_p\left(T_2^{ise}-T_1\right) \tag{12}$$

$$\Delta\dot{E}_{ise}^{p}=\dot{m}c_p\left[T_0\ln\left(\frac{p_2}{p_1}\right)^{\frac{\kappa-1}{\kappa}}\right]=\dot{m}c_p\left[T_0\ln\left(\frac{T_2^{ise}}{T_1}\right)\right]_{p_1\to p_2}=\dot{m}c_p\,\Delta T_{ise}^{E^p}\Big|_{p_1\to p_2} \tag{13}$$

$$\Delta\dot{E}_{ise}^{T}=\dot{m}c_p\underbrace{\left[\left(T_2^{ise}-T_1\right)-T_0\ln\left(\frac{T_2^{ise}}{T_1}\right)\right]_{p_1\to p_2}}_{\Delta T_{ise}-\Delta T_{ise}^{E^p}}=\dot{m}c_p\,\Delta T_{ise}^{E^T}\Big|_{p_1\to p_2} \tag{14}$$

$$\Delta T_{ise}^{E^T}=\underbrace{T_1\left[\left(\frac{p_2}{p_1}\right)^{\frac{\kappa-1}{\kappa}}-1\right]}_{\Delta T_{ise}}-\underbrace{T_0\ln\left[\left(\frac{p_2}{p_1}\right)^{\frac{\kappa-1}{\kappa}}\right]}_{\Delta T_{ise}^{E^p}} \tag{15}$$

By substituting (13) into (14) and realizing that $T_2^{ise}-T_1=\Delta T_{ise}$, the relationship between the changes in exergetic temperatures reduces to the very simple form given in (16). Equation (17) is the equivalent relation for exergy components and shaft-work for isentropic changes of pressure.

$$\Delta T_{ise}=\Delta T_{ise}^{E^T}+\Delta T_{ise}^{E^p} \tag{16}$$

$$-\dot{W}_{ise}=\Delta\dot{E}_{ise}^{T}+\Delta\dot{E}_{ise}^{p} \tag{17}$$

Notice that the changes for the variables in (16) and (17) can be positive or negative. The sign of the changes is determined by two things: (*i*) the temperature level of the streams (i.e. whether the operation is carried out above or below ambient temperature), and (*ii*) the type of operation

performed (i.e. compression or expansion). Here, the sign convention adopted is the one used by Moran and Shapiro [22]; for a control volume, all heat flow inlets and generated work are positive entities while heat outlets and consumed work are negative. Table 1 shows the combinatorial scenarios for (16) and (17).

Table 1. Combinatorial scenarios for the relationship between ΔT^{E^T} *and* ΔT^{E^p}

		$\Delta T_{ise}^{E^T}$ $\left[\Delta \dot{E}_{ise}^{T}\right]$	$\Delta T_{ise}^{E^p}$ $\left[\Delta \dot{E}_{ise}^{p}\right]$	ΔT_{ise} $\left[-\dot{W}_{ise}\right]$	Description
Above T_0	**Compression**	+	+	+	The shaftwork input increases both exergy components.
	Expansion	−	−	−	Reductions in both exergy components contribute to generate shaftwork.
Below T_0	**Compression**	−	+	+	Both shaftwork input and reduction in $\dot{E}^T$ increases $\dot{E}^p$.
	Expansion	+	−	−	The reduction in $\dot{E}^p$ generates both shaftwork and an increase in $\dot{E}^T$.

If the changes in pressure are performed with an isentropic efficiency (η) less than unity, then (18a) and (18b) need to be introduced in the analysis. The isentropic efficiency factor (f_{is-eff}) is equal to the inverse of the isentropic efficiency for compressors $(1/\eta_{compressor})$ while for expanders it is equal to the isentropic efficiency $(\eta_{expander})$. Thus, the corresponding power and the changes in pressure and temperature based exergies are calculated with (19), (20) and (21). The change in pressure based exergy is not affected by the isentropic efficiency as shown in (20). Equation (22a) shows in a similar way to which it was demonstrated in (15), that the change in T^{E^T} is a function of T_1, pressure ratio and, in this case, also of f_{is-eff}. The relation between the changes in exergetic temperatures shown in (23) is observed after (22a) is rearranged into (22b). Notice that the exergy balance shown in (17) has now changed into (24) by including the exergy destruction rate $\left(\dot{E}^{D^p}\right)$.

$$T_2^{\eta<1} - T_1 = f_{is-eff}\left(T_2^{ise} - T_1\right) \tag{18a}$$

$$\frac{T_2^{\eta<1}}{T_1} - 1 = f_{is-eff}\left[\left(\frac{p_2}{p_1}\right)^{\frac{\kappa-1}{\kappa}} - 1\right] \tag{18b}$$

$$-\dot{W}_{\eta<1} = \dot{m} c_p f_{is-eff}\left(T_2^{ise} - T_1\right) \tag{19}$$

$$\Delta \dot{E}_{\eta<1}^{p} = \dot{m} c_p \left[T_0 \ln\left(\frac{p_2}{p_1}\right)^{\frac{\kappa-1}{\kappa}}\right] = \dot{m} c_p \left[T_0 \ln\left(\frac{T_2^{ise}}{T_1}\right)\right]_{p_1 \to p_2} \tag{20}$$

$$\Delta \dot{E}^{T}_{\eta<1} = \dot{m}c_p \left\{ f_{is-eff}\left(T_2^{ise} - T_1\right) - T_0 \ln\left[1 + f_{is-eff}\left(\frac{T_2^{ise}}{T_1} - 1\right)\right]\right\}_{p_1 \to p_2} \quad (21)$$

$$\Delta T^{E^T}_{\eta<1} = f_{is-eff} T_1 \left[\left(\frac{p_2}{p_1}\right)^{\frac{\kappa-1}{\kappa}} - 1\right] - T_0 \ln\left\{1 + f_{is-eff}\left[\left(\frac{p_2}{p_1}\right)^{\frac{\kappa-1}{\kappa}} - 1\right]\right\} \quad (22a)$$

$$\Delta T^{E^T}_{\eta<1} = \underbrace{f_{is-eff} T_1 \left[\left(\frac{p_2}{p_1}\right)^{\frac{\kappa-1}{\kappa}} - 1\right]}_{\Delta T_{\eta<1}} \underbrace{- T_0 \ln\left[\left(\frac{p_2}{p_1}\right)^{\frac{\kappa-1}{\kappa}}\right]}_{\Delta T^{E^P}_{\eta-1}} \underbrace{- T_0 \ln\left\{\left(\frac{p_2}{p_1}\right)^{\frac{1-\kappa}{\kappa}}\left[1 + f_{is-eff}\left(\left(\frac{p_2}{p_1}\right)^{\frac{\kappa-1}{\kappa}} - 1\right)\right]\right\}}_{\frac{\dot{E}^D}{\dot{m}cp}} \quad (22b)$$

$$\Delta T_{\eta<1} = \Delta T^{E^T}_{\eta<1} + \Delta T^{E^P}_{\eta-1} + \frac{\dot{E}^D}{\dot{m}cp} \quad (23)$$

$$-\dot{W}_{\eta<1} = \Delta \dot{E}^{T}_{\eta<1} + \Delta \dot{E}^{P}_{\eta-1} + \dot{E}^{D} \quad (24)$$

4. A novel diagram for exergy targeting

In the Composite Curves of Pinch Analysis, due to the assumption of constant mc_p or piecewise linear enthalpy/temperature relationship, the construction of the diagram is very simple and only needs the supply and target temperatures of the streams. In exergy based diagrams (such as ECCs and EGCC), there is a non-linearity introduced since exergy is a non-linear function of temperature even when the heat capacity flowrate is constant (e.g. through the Carnot factor). The introduction of exergetic temperatures is motivated by the resulting linear behavior, which again means that by only using the supply and target conditions of the streams, in the form of exergetic temperatures one does not have to do multiple simulations/calculations to get points along a non-linear curve. The proposed diagram plots exergy sources and exergy sinks as linear composite curves in a $T^{E^T} - \dot{E}^T$ diagram (Figs 3*a* and 3*b*). For HRSs above T_0, the exergy sources are the hot streams and the exergy sinks are the cold streams, while for HRSs below T_0 the cold streams are the exergy sources and the hot streams are the exergy sinks. It is important to notice that below T_0, exergy and heat flows have opposite directions.

Some characteristics of the new diagram are:

- The minimum value of T^{E^T} (zero) is at ambient temperature. Thus, T^{E^T} is positive for the complete temperature range, which is in contrast to the Carnot factor in the ECCs. The stream with the condition that has the highest exergy value is always placed at the top of the curves while the lowest (closest to T_0) is at the bottom. *Notice that for streams below T_0, the coldest temperature corresponds to the highest exergy content and the largest exergetic temperature.*
- When the minimum approach temperature (ΔT_{min}) between the CCs is fixed, then a corresponding minimum exergetic approach temperature ($\Delta T^{E^T}_{min}$) is obtained. As a consequence:
  - The exergy deficit and surplus are calculated ahead of any design actions from the exergy cascade by only using the stream data, similar to how minimum external heating and cooling demands are obtained from the traditional heat cascade. The exergy cascade is described in Section 5.
  - The *heat pinch* and *exergy pinch* are placed in corresponding enthalpy and exergy intervals, thus if the pinch rules are followed, exergy is neither imported below pinch nor exported above pinch, and exergy is not transferred across pinch.

- The exergy destruction is graphically shown by transforming the boundary temperatures of the overlapping region obtained in *the traditional CCs* into exergetic temperatures (squares and circles in Figs. 3*a* and 3*b*).

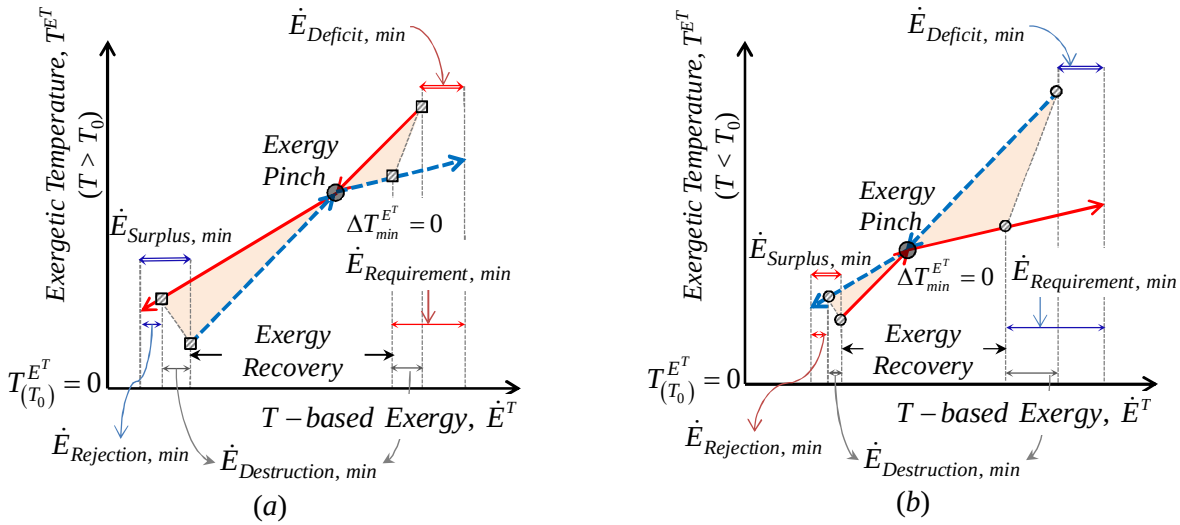

Fig. 3 $T^{E^T} - \dot{E}^T$ diagram (a) above T_0, and (b) below T_0

- The maximum exergy recovery for a given ΔT_{min} is the maximum amount of exergy that the exergy sink curve can accept in the overlapping region, and the minimum process-to-process exergy destruction is the difference between the process-to-process exergy transferred from the exergy source curve and the maximum exergy recovered. The calculation of exergy targets is given by (25) and (26).

Above exergy pinch: $$\dot{E}_{Requirement,\,min} = \dot{E}_{Deficit,\,min} + \dot{E}_{Destruction,\,min} \tag{25}$$

Below exergy pinch: $$\dot{E}_{Rejection,\,min} = \dot{E}_{Surplus,\,min} - \dot{E}_{Destruction,\,min} \tag{26}$$

5. Heat and Exergy cascades

The algorithm used for the calculation of the minimum exergy deficit and surplus is similar to the one used for obtaining the minimum heat deficit and surplus. Following the analogy made by Papoulias and Grossmann [23] with the transshipment model for heat recovery problems, one could represent the transportation of exergy from exergy sources to exergy sinks. Fig. 4*a* shows the heat and exergy patterns for the k^{th} temperature interval both heat and exergy cascades. The regular temperature intervals are calculated using the method proposed by Linnhoff and Flowers [24] for a given minimum temperature difference ΔT_{min}. The exergetic temperature intervals can be calculated from the regular temperature intervals or by means of the corresponding minimum exergetic temperature difference $\Delta T_{min,k}^{E^T}$ described in (27*a*) and (27*b*).

$$\Delta T_{min,k}^{E^T} = \Delta T_{min} - T_0 \ln\left(\frac{T_{i,k}}{T_{j,k}}\right) \tag{27a}$$

$$\Delta T_{min,k}^{E^T} = -\Delta T_{min} + T_0 \ln\left(\frac{T_{j,k}}{T_{i,k}}\right) \tag{27b}$$

It should be mentioned that Fig 4*a* and (27*a*) are valid for HRSs operating above ambient temperature. For systems operating below T_0, the heat sources are exergy sinks and vice versa, thus the corresponding identification of the streams identity should be made and (27*b*) be used instead of (27*a*).

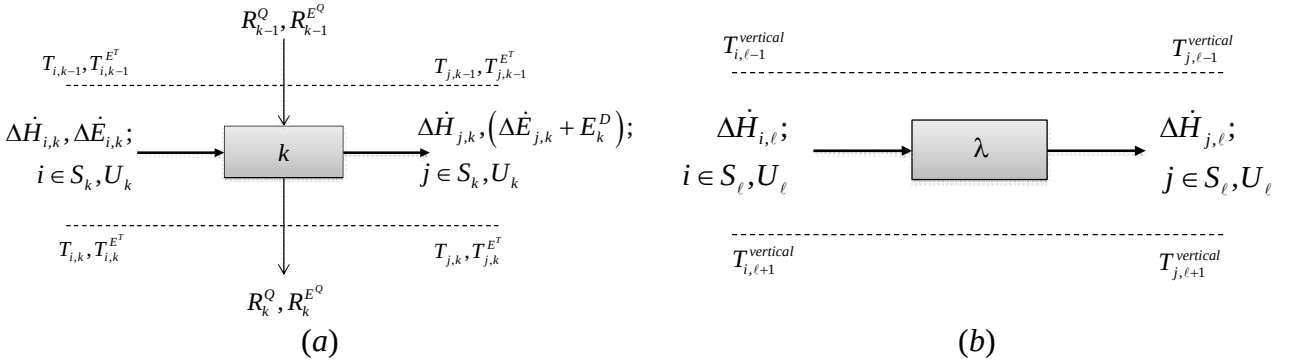

Fig.4 (a) Heat and exergy flow pattern in each Temperature Interval (TI) and (b) heat flow pattern in each Enthalpy Interval (EI)

Notice that the exergy destruction of the k^{th} Temperature Interval (TI) is lumped in the exergy sinks. Then, it is obvious that the heat cascade fails in illustrating clearly the exergy destruction in each TI, however, the information given by the exergy cascade is valuable. The obtained exergy deficit or exergy surplus in each TI assumes that all the exergy from the exergy sources is transferred to the exergy sink without exergy *losses*. In order to calculate the minimum exergy destruction (irreversibilities) one should shift from TI to Enthalpy Intervals (EI) by means of *vertical* heat exchange. In practice, a strict *vertical* exchange will lead to the so-called *Spaghetti design* which should not be used in actual HEN designs (i.e. it will need a large number of units), however, for targeting purposes, *vertical* heat exchange may aid in the calculation of the HEN minimum area [25]. Pure countercurrent (strict *vertical*) heat exchange will indubitably be using the driving forces more efficiently than any other heat exchange arrangement i.e. concurrent or criss-cross; even when it cannot always ensure the HEN minimum area. Exergy destruction due to heat exchange on the other hand, is only a function of the temperature differences of the streams, thus *vertical* heat exchange will always lead to the minimum exergy destruction of the HEN. Fig. 4*a* illustrates the heat flow pattern in each λ^{th} EI where $\Delta\dot{H}_{i,\ell} \equiv \Delta\dot{H}_{j,\ell}$.

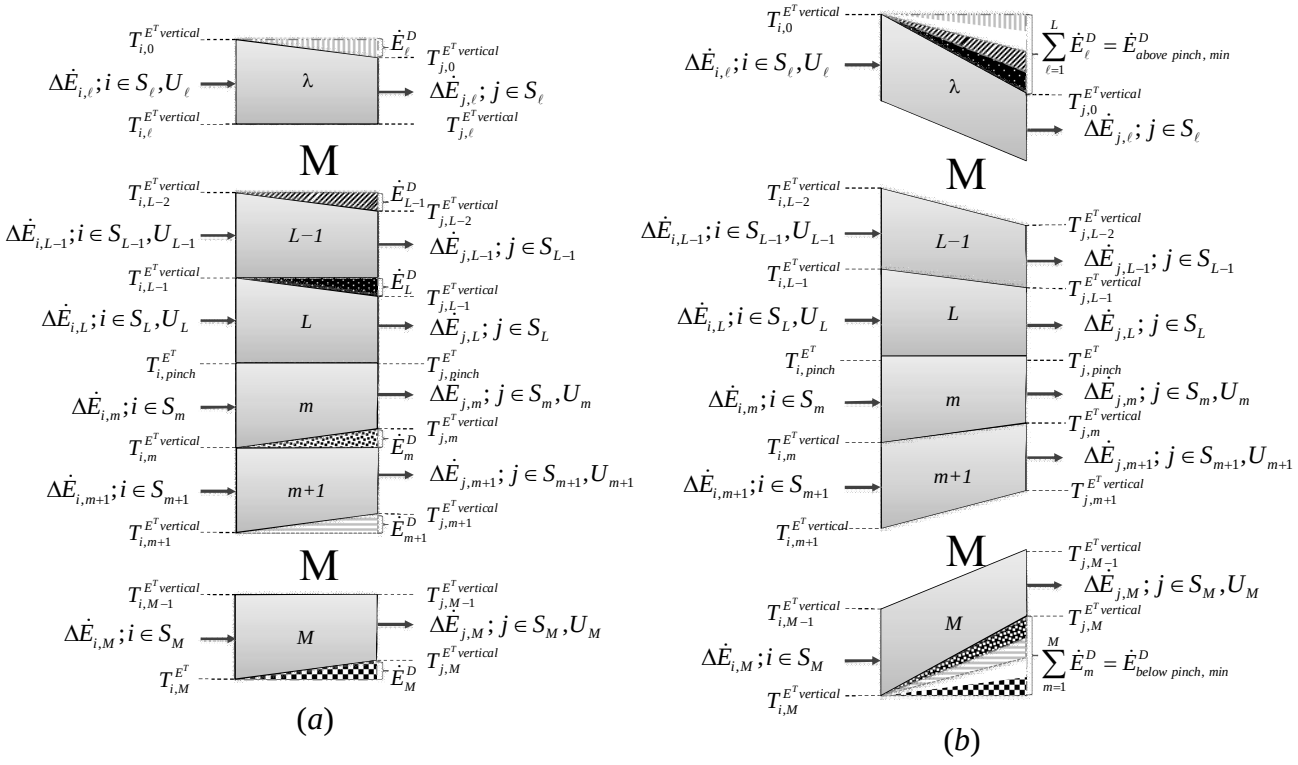

Fig. 5 Exergy flow patterns for HRSs with L+M EIs in (a) discontiluos and (b) continuos exergy exchange representations.

Gundersen and Grossman [26] proposed the *vertical* transshipment model as an extension of the heat cascade. In their analysis, they combined the *vertical* heat exchange with the heat cascade in a transshipment model with the intention of automatizing the Heat Exchange Network Synthesis (HENS). For calculating the exergy targets, the coupling of these two models is not needed. Figs 5*a* and 5*b* show the exergy flow pattern for *vertical* heat exchange in a *balanced* HRS. If the pinch rules abovementioned are followed, then utility streams can only supply exergy in the above pinch EIs (λ) and exergy can only be rejected from below pinch EIs (*m*). Fig. 5*a* shows the actual exergy balance of each (L+M) EIs including the exergy destruction. Because the CCs and the curves in the $T^{E^T} - \dot{E}^T$ diagram are continuous, Fig. 5*b* shows a better representation of the exergy exchange in HRS. The exergetic temperature intervals in Figs. 5*a* and 5*b* are calculated from the regular temperatures.

6. Case study: Design of an LNG process

The liquefaction of natural gas is used as case study. The main purpose of this example is to illustrate the application of the new thermodynamic diagram by providing the information when changes in pressure are introduced.

6.1 Stream data for the process

The design starts with basic stream data only. Table 2 shows the stream data for 2 hot streams (natural gas and nitrogen) and one cold stream (nitrogen). The natural gas is mainly composed by methane (> 85% mole) and has an average compressibility factor of 0.8 from 25°C to its dew point (≈−50°C) at 65 bar. At supply conditions, the natural gas can be regarded as close to ideal gas while at target conditions is in liquid state. On the other hand, both nitrogen streams can be considered as ideal gases at both supply and target conditions, even at very high pressure. The heat capacity flowrate of the natural gas stream is varying with temperature, and this is also the case with the value of κ. The natural gas stream is divided into segments with constant heat capacity flowrates.

Table 2. Initial stream data

	T_s (°C)	T_t (°C)	P_s (bar)	P_t (bar)	$\dot{m}c_p$ (kW/°C)	κ	$\Delta\dot{H}$ (MW)
NG	25.0	−168.0	65.0	1.0	varying	varying	−13.84
$N2_a$	25.0	−168.0	120.0	6.3	121.6	1.48	23.46
$N2_b$	−168.0	25.0	6.3	120.0	121.6	1.48	23.46

6.2 Changes in exergy components and construction of diagrams

Table 3 shows the exergetic temperatures and the changes in the exergy components. The calculations have been carried out with (9) and (10). The ambient conditions are 25°C and 1 bar. Notice that the pressure based exergy of the natural gas is decreased to zero from supply to target pressure (1 bar), and therefore $\Delta\dot{E}^p = \dot{E}_s^p$.

Table 3. Exergetic temperatures and changes in exergy components

	$T_s^{E^T}$ (K)	$T_t^{E^T}$ (K)	$T_s^{E^p}$ (K)	$T_t^{E^p}$ (K)	$\Delta\dot{E}^T$ (MW)	$\Delta\dot{E}^p$ (MW)
NG	0.00	117.73	555.33	0.00	8.13	−27.21
$N2_a$	0.00	117.73	462.94	177.98	14.32	−34.65
$N2_b$	117.73	0.00	177.98	462.94	−14.32	34.65

Figs. 6*a* and 6*b* show the CCs and the $T^{E^T} - \dot{E}^T$ diagram without considering changes in the stream pressures. The *heat* and *exergy* pinches are at 25°C and 0 K respectively, and the minimum temperature approaches both in *regular* and *exergetic* temperatures are zero. There is no heating requirement but 13.8 MW of cooling is necessary. In terms of exergy, the deficit is 8.1 MW (22.4 – 14.3), while the exergy destruction is 7.5 MW (14.3 − 6.8). The exergy requirement is then 15.6 (8.1 + 7.5). Notice that all stream conditions are at or below ambient temperature.

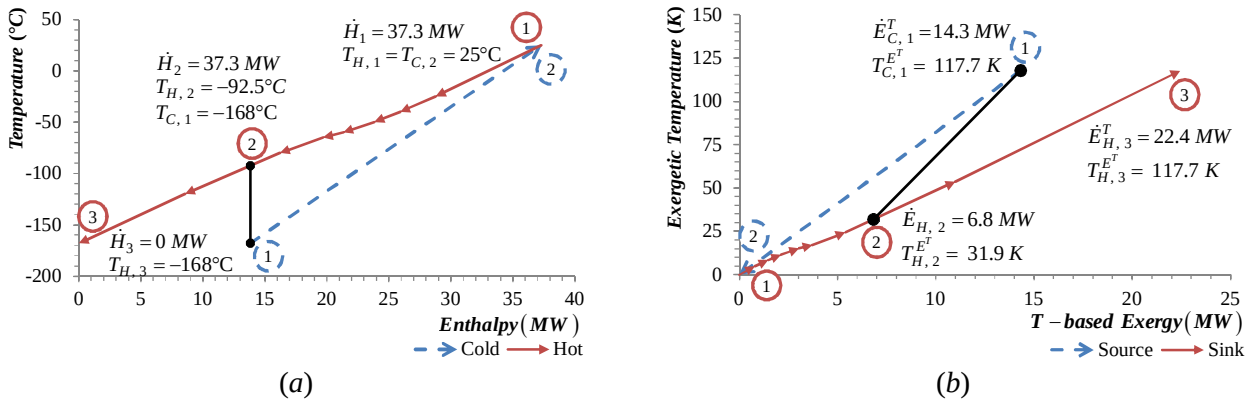

Fig. 6 Diagrams before including pressure changes: (a) CCs and (b) $T^{E^T} - \dot{E}^T$

From Figs. 6*a* and 6*b* and according to the plus-minus principle for modifications forHRS design [14] one have two options for reducing the cooling or exergy requirement. These options are: *a*) to increase the heat sinks (exergy sources) and *b)* to reduce the heat sources (exergy sinks). If the first one is chosen, one would need to include a cold utility i.e. an external exergy source such as refrigeration, in addition to the compression work needed for taking the cold nitrogen stream from 6.3 to 120 bar. Thus, the second option for reducing the exergy requirement seems to be the solution. If one forces the hot nitrogen stream to reach both target conditions simultaneously, by means of an expansion, then the cooling demand of this steam is reduced and most of the total cooling demand of the system will come from the natural gas steam.

6.3 Introducing pressure manipulations

For this exercise, the expansion of the natural gas is left at the end of the liquefaction process. This means that the natural gas streams will be cooled, liquefied and subcooled at constant pressure. Later, by using a liquid expander, the LNG will be expanded until 1 bar. This is typically done by most of the industrialized liquefaction processes. Because the expansion of the LNG is done in liquid phase, the equations described in Section 3 are not valid; however, the temperature decrease in the the expansion is typically very small (>5 K). Assuming that after the liquid expander, the temperature of natural gas decreases only 3°C, the inlet temperature to the expander is −165°C. In this way, the minimum temperature difference in the cold end of the CCs is 3 K. The cooling and exergy requirements for the liquefaction of the natural gas are 13.66 MW and 7.82 MW, respectively. According to the discussion at the end of Section 6.2, the hot nitrogen stream will reach both target conditions (temperature and pressure) simultaneously after the expansion. By using either (18*a*) or (18*b*), one can calculate the inlet temperature in the nitrogen expander which is equal to −52.64°C. Thus for this stream, the cooling and exergy requirements have been reduced from 23.46 MW and 14.32 MW to 9.44 MW and 1.50 MW. The total cooling and exergy requirements are then 23.1 MW and 9.32 MW. Finally, for cold nitrogen stream is decided that the compression is done after heat has been exchanged with both hot streams. Then, the outlet temperature of the cold nitrogen stream is close to 22°C. The compression takes place in 6 stages of equal pressure ratio and cooling water is used in the intercoolers. The isentropic efficiencies for the compressor stages and expander are 80% and 85%, respectively. The modified stream data shown in Table 4 and 5 includes the effects of the changes in pressure.

Table 4. Modified stream data for heat exchanges (Δp=0)

	T_s (°C)	T_t (°C)	$\Delta\dot{H}$ (MW)	$T_s^{E^T}$ (K)	$T_t^{E^T}$ (K)	$\Delta\dot{E}^T$ (MW)
NG	25.00	−165.00	−13.66	0.00	112.35	7.82
$N2_c$	25.00	−52.64	−9.44	0.00	12.30	1.50
$N2_d$	−168.00	22.00	23.11	117.73	0.02	−14.32
$N2_e$	85.71	25.00	−46.96*	6.08	0.00	−4.44**

* Total requirement of cold thermal energy for the five intercoolers and the aftercooler.
** Total exergy rejection for the five intercoolers and the aftercooler.

One should notice that the compression stages operate above ambient temperature while the rest of the unit operations operate below T_0. The total cooling and power requirements are reported in both tables.

Table 5. Modified stream data for expanders and compression stages

	T_s (°C)	T_t (°C)	P_s (bar)	P_t (bar)	$\Delta\dot{E}^T$ (MW)	$-\dot{W}$ (MW)	$\Delta\dot{E}^p$ (MW)
NG	−165.00	−168.00	65.0	1.0	0.31	−0.17	−27.21
$N2_f$	−52.64	−168.00	120.0	6.3	12.82	−14.03	−34.65
$N2_g$	22.00	85.71	6.3*	120.0*	4.36	46.88**	34.65

* The compression is done in six stages with intercooling.
** Total power requirement for the six compression stages.

The CCs and the $T^{E^T} - \dot{E}^T$ diagram with pressure changes included are shown in Figs 7*a* and 7*b*. One important feature of the $T^{E^T} - \dot{E}^T$ diagram is shown in Fig. 7*b*. One can clearly see that the exergy source curve has a discontinuous slope change at the point (4.4; 0.0). Here, the representation of two exergy sources (one above T_0 and the other below T_0) meet close to ambient temperature. These exergy sources are the streams exiting the compression stages (above T_0) and the nitrogen stream from 5 to 1 (below T_0). Hence, the HRS should be decomposed into two subsystems; one above T_0 and the other below T_0. Below ambient temperature, the cooling (refrigeration load) and heating requirements are zero (see left-hand-side of Fig. 7*a*). The exergy requirement and rejection are both zero, while the process-to-process exergy destruction due to driving forces is around 5.0 MW (quite large).

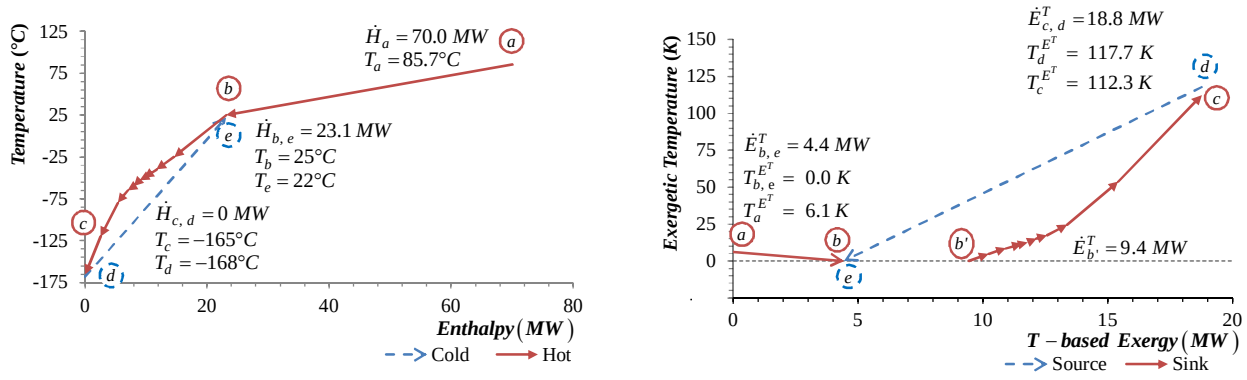

Fig. 7 Diagrams with compression and expansion operations included: (a) CCs and (b) $T^{E^T} - \dot{E}^T$

Below T_0, close to 35% of the exergy available in the exergy source (i.e. 18.8 − 4.4 = 14.4 MW) is destroyed (5.0 kW). Above T_0, there is both heat and exergy surplus of 46.96 MW and 4.44 MW, respectively. Notice that there are two *heat pinches*: 25°C/22°C and -165°C/-168°C (ΔT_{min} = 3 K), while there is only one *exergy pinch* at 117.73 K for the exergy source curve and 112.35 K for the exergy sink curve. The $\Delta T_{min}^{E^T}$ is calculated by (19.*b*) to be 5.38 K. The power produced by the turbine and the liquid expander (14.2 MW) is not enough to overcome the power required by the compressor stages (46.88 MW). The exergy destructions in the compressor stages, turbine and liquid expander are calculated by (21) to be 7.87 MW, 7.80 MW and 26.73 MW, respectively.

The flow diagram for the complete process is shown in Fig. 8. Actually, the flowsheet in Fig.8 as well as the CCs in Fig. 7*a* and the exergy based curves in Fig. 7*b* correspond to the Reversed Brayton (RB) process for producing LNG.

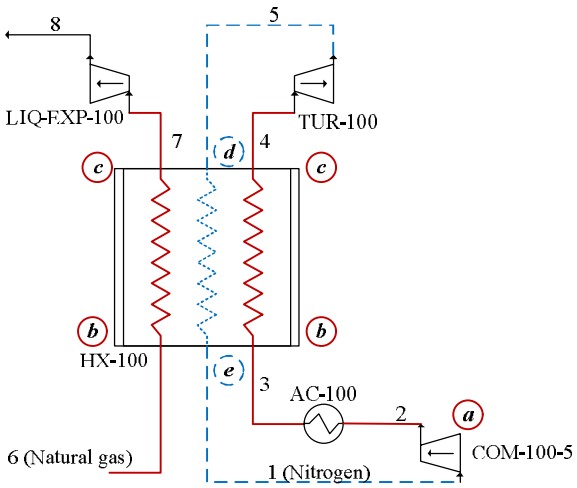

Fig. 8 Flowsheet of the Reverse Brayton process

This is not a big surprise since this exercise was meant to illustrate the application of the new thermodynamic diagram by showing how one could develop the well-known RB process. In the RB process, the natural gas is liquefied with cold nitrogen (refrigerant) which is in gas phase in the entire cycle. The nitrogen cycle consists of: (*i*) one compression service consisting of four to eight compression stages with intercooling (COM-100-5), (*ii*) one aftercooler (AC-100) that will condition the nitrogen before the main heat exchanger, (*iii*) one turbine for expanding and cooling the nitrogen stream (TUR-100), and (*iv*) a main heat exchanger (HX-100) where nitrogen liquefies the natural gas stream. The main heat exchanger also acts as an economizer for the nitrogen stream coming from the aftercooler.

7. Conclusions

A new diagram for exergy targeting of Heat Recovery Systems (HRSs) where pressure is an important design variable has been proposed. The method is particularly suited for low temperature systems and could be used for designing LNG processes. The diagram uses a new energy quality parameter called *exergetic temperature*. These exergetic temperatures are used due to their linear relationship with exergy and for calculating exergy targets such as the minimum values for exergy requirement, exergy rejection and exergy destruction. An alternative exergy cascade that uses the transshipment model is proposed for finding the minimum exergy deficit and exergy surplus of the HRS. For the calculation of the minimum exergy destruction, the *vertical* heat transfer model is used. The Reverse Brayton process for the liquefaction of natural gas is used as a case study, where it was possible to illustrate the use of the alternative diagram for exergy targeting. It is worth mentioning that this representation can be intimately linked with the Extended Pinch Analysis and Design (ExPAnD) method under development in our research group.

Nomenclature

A	energy level
$\dot{E}$	exergy flow, MW
$f_{is\text{-}eff}$	isentropic efficiency factor
$\dot{H}$	enthalpy flow, MW
p	pressure, bar
$\dot{Q}$	heat flow, MW
$\dot{m}c_p$	heat capacity flowrate, MW/°C
R	heat or exergy residual in the heat or exergy cascade
$\dot{S}$	entropy rate, MW/°C
S	process streams
T	temperature, °C [or K]
U	utility streams
$\dot{W}$	power, MW

Greek symbols

η	isentropic efficiency
κ	heat capacity ratio for ideal gas

Subscripts and superscripts

0	ambient conditions
D	exergy destruction
i	heat or exergy source streams
ise	isentropic process
j	heat or exergy sink streams
k	temperature interval
λ, m	enthalpy intervals for above and below ambient temperature
p	pressure based exergy
T	temperature based exergy
TM	thermo-mechanical exergy
Q	exergy of heat

References

[1] Linnhoff, B., *Pinch technology for the synthesis of optimal heat and power systems.* Journal of Energy Resources Technology, 1989. 111(3): p. 137-147.

[2] Linnhoff, B. *Pinch analysis and exergy - A comparison. in:* J. Szargut, G. Tsatsaronis, Z. Kolenda, and A. Ziebik, eds. *ENSEC ´93: Energy Systems and Ecology, International Conference*. 1993. Cracow, Poland.

[3] Umeda, T., T. Harada, and K. Shiroko, *A thermodynamic approach to the synthesis of heat integration systems in chemical processes.* Computers & Chemical Engineering, 1979. 3(1-4): p. 273-282.

[4] Linnhoff, B. and V.R. Dhole, *Shaftwork targets for low-temperature process design.* Chemical Engineering Science, 1992. 47(8): p. 2081-2091.

[5] Staine, F. and D. Favrat, *Energy integration of industrial processes based on the pinch analysis method extended to include exergy factors.* Applied Thermal Engineering, 1996. 16(6): p. 497-507.

[6] Sorin, M. and J. Paris, *Combined exergy and pinch approach to process analysis.* Computers & Chemical Engineering, 1997. 21 Suplement: p. S23-S28.
[7] Feng, X. and X.X. Zhu, *Combining pinch and exergy analysis for process modifications.* Applied Thermal Engineering, 1997. 17(3): p. 249-261.
[8] Sorin, M. and J. Paris, *Integrated exergy load distribution method and pinch analysis.* Computers & Chemical Engineering, 1999. 23(4-5): p. 497-507.
[9] Anantharaman, R., O.S. Abbas, and T. Gundersen, *Energy level composite curves - A new graphical methodology for the integration of energy intensive processes.* Applied Thermal Engineering, 2006. 26(13): p. 1378-1384.
[10] Aspelund, A., D.O. Berstad, and T. Gundersen, *An extended pinch analysis and design procedure utilizing pressure based exergy for subambient cooling.* Applied Thermal Engineering, 2007. 27(16): p. 2633-2649.
[11] Sorin, M. and V.M. Brodyansky, *A method for thermodynamic optimization - I Theory and application to an ammonia synthesis plant.* Energy, 1992. 17(11): p. 1019-1031.
[12] Rant, Z., *The influence of preheated air on the combustion irreversibilities.* Brennstoff-Wärme-Kraft 1961. 13(11): p. 496-500. (in German).
[13] Ishida, M. and K. Kawamura, *Energy and exergy analysis of a chemical process system with distributed parameters based on the enthalpy-direction factor diagram.* Industrial & Engineering Chemistry Process Design and Development, 1982. 21(4): p. 690-695.
[14] Linnhoff, B., D.W. Townsend, D. Bolland, G.F. Hewitt, A.R. Guy, and R.H. Marsland, *A user guide on process integration for the efficient use of energy* 1982, London: IChemE.
[15] Brodyansky, V.M., M.V. Sorin, and P. Le Goff, *The Efficiency of Industrial Processes: Exergy Analysis and Optimization* 1994, Amsterdam: Elsevier.
[16] Kotas, T.J., *The exergy method of thermal plant analysis*. Second ed. 1995, Malabar, Florida: Krieger Publishing.
[17] Morosuk, T. and G. Tsatsaronis. *Graphical models for splitting physical exergy*. *in:* S. Kjelstrup, E. Hustad, T. Gundersen, A. Røsjorde, and G. Tsatsaronis, eds. *ECOS 2005: Proceedings of the 18th International Conference on Efficiency, Cost, Optimization, Simulation and Environmental Impact of Energy Systems*. 2005. Trondheim, Norway: Tapir Academic Press. p. 377-384.
[18] Palazzo, P. *Thermal and mechanical aspect of entropy-exergy reletionship*. *in:* M. Bojić, N. Lior, J. Petrović, G. Stefanović, and V. Stevanović, eds. *ECOS 2011:- Proceedings of the 24th International Conference on Efficiency, Cost, Optimization, Simulation and Environmental Impact of Energy Systems*. 2011. Novi Sad, Serbia. p. 280-292.
[19] Szargut, J., D.R. Morris, and F.R. Steward, *Exergy analysis of thermal, chemical, and metallurgical processes* 1988, New York: Hemisphere Publishing Corporation.
[20] Petela, R., *Influence of gravity on the exergy of substance.* International Journal of Exergy, 2008. 5(1): p. 1-17.
[21] Tsatsaronis, G., *Thermoeconomic analysis and optimization of energy systems.* Progress in Energy and Combustion Science, 1993. 19(3): p. 227-257.
[22] Moran, M.J. and H.N. Shapiro, *Fundamentals of engineering thermodynamics*. Fifth ed. 2006, Chichester: John Wiley & Sons, Inc.
[23] Papoulias, S.A. and I.E. Grossmann, *A structural optimization approach in process synthesis—II: Heat recovery networks.* Computers & Chemical Engineering, 1983. 7(6): p. 707-721.
[24] Linnhoff, B. and J.R. Flower, *Synthesis of heat exchanger networks: I. Systematic generation of energy optimal networks.* AIChE Journal, 1978. 24(4): p. 633-642.
[25] Townsend, D.W. and B. Linnhoff, *Surface area targets for heat exchanger networks*, in *IChemE Annl Res. Mtg.* 1984: Bath, UK.
[26] Gundersen, T. and I.E. Grossmann, *Improved optimization strategies for automated heat exchanger network synthesis through physical insights.* Computers & Chemical Engineering, 1990. 14(9): p. 925-944.

Advances in the distribution of environmental cost of water bodies through the Exergy concept in the Ebro river

Javier Uche Marcuello[a], Amaya Martínez Gracia [b], Beatriz Carrasquer Álvarez [c] Antonio Valero Capilla [d]

[a] *CIRCE, Centro de Investigación de Recursos y Consumos energéticos. Universidad de Zaragoza. Spain. javiuche @unizar.es*
[b] *CIRCE, Centro de Investigación de Recursos y Consumos energéticos. Universidad de Zaragoza. Spain. amayamg@unizar.es*
[c] *CIRCE, Centro de Investigación de Recursos y Consumos energéticos. Universidad de Zaragoza. Spain. becarras@unizar.es* ***(CA)***
[c] *CIRCE, Centro de Investigación de Recursos y Consumos energéticos. Universidad de Zaragoza. Spain. valero@unizar.es*

Abstract:

The Physical Hydronomics (PH) methodology is a tool to properly calculate restoration cost of water masses in exergy terms, in the framework of the Second Law of Thermodynamics. This methodology makes possible to assess the quality degradation of water as well as the water consumption. An opportunity which that methodology brings up is the development of River exergy profiles which can be represented along the length of the river, for different periods and degradation statuses. Focussing on the Water Framework Directive milestones, fist novelty presented here consist on developing an hypothetical scenario corresponding to the state reached by applying the restoration Plan of Measures, therefore making possible to test their suitability by comparing that scenario with the Environmental Objectives, pursued by the Directive. Together with it, the second most relevant contribution which is presented here is the assessment of restoration cost among diverse water polluters, from physico-chemical parameters of the river according to the exergy degradation provoked individually by each of them.

The case study which is developed is the Ebro basin, an Spanish very representative river which flows into the Mediterranean sea. Important differences within the average rainfall values among the diverse areas of the Ebro and changing natural average total water resources are typical from this river. Results shown that quality restoration costs found in the agriculture user resulted to be the highest, in dry years, but quite similar to the ones fund in the urban user in wet years. On the other hand, degradation provoked by the hydroelectric user, never taken into account before in the PH spectrum, resulted to be the lowest, but increases in wet years. Considering changes in flow downstream dams due to their storing and delivering effect, it ranges during hydrologic periods, but it reaches maximum values during wet years.

The Plan of Measures proposed by 2015 is enough to fulfil with environmental objectives pursued by the Ebro river Environmental Authorities. Only punctual non-compliances were found during the simulated period. Reposition Cost varied among hydrological years: the more dry the year is, the higher reposition costs. In any case, the total investment cost to put into practice the measures projected in the draft version of the Ebro river management Plan seems to be enough to fulfil the already mentioned Environmental Objectives.

Keywords:

Exergy analysis, Ebro river, Restoration (environmental) costs.

1. Background

Methods, procedures and indicator parameters necessary for characterising the condition of water, as well as the strategies and instruments needed to protect this condition and to regenerate it (if necessary) were defined in the Water Framework Directive [1] which came into force in 2000.

The effective milestones pursued by this European Directive are focussed mainly on evaluating the condition of all water bodies, as well as determining their ecological status by using quantitative

and qualitative parameters. The associated pressures, impacts and risks conditioning that status should be properly identified. Article 11 of the Directive bounds to the Member States to draw up river basin water plans including the programmes of measures to achieve the Environmental Objectives pursued for each water body of a given basin by 2015, and all the exceptions or difficulties to get the compliance [1].

Directive also emphasises on cost recovery. Its Article 9 states that EU countries "*shall take account of the principle of recovery of the costs of water services*". Economic analyses should be carried out to ensure adequate contributions by different classes of users. The article does, however, note that Member States can take into account "social, environmental and economic effects" of cost recovery.

In this sense, focussing on the above mentioned milestones of the Directive, some improvements were introduced in the Physical Hydronomics methodology through the development of this work.

As it was stated in [2], any river state can be characterized by its exergy value (B, given in kWh), defined as the product of its flow (Q, given in m^3/s) and its specific exergy (b, given in kJ/kg of water). On the one hand, the flow increases linearly from approximately cero, in the point were the river springs, until its maximum value, were the river dies. On the other hand, the specific exergy, that expresses the quality of the river (accounted by physical interactions taking place along the river course), decreases from its maximum value in the point were the river has its source, to the mouth, were its value is lower. Nevertheless, it still remains positive until the end of river course mainly due to the kinetic component of the exergy. The theoretical representation of the Q and b product should be a Gauss bell. However, in real case studies, the contribution of flow resulted to be much bigger (see Fig. 1). That is the reason why B and Q representations have similar shapes.

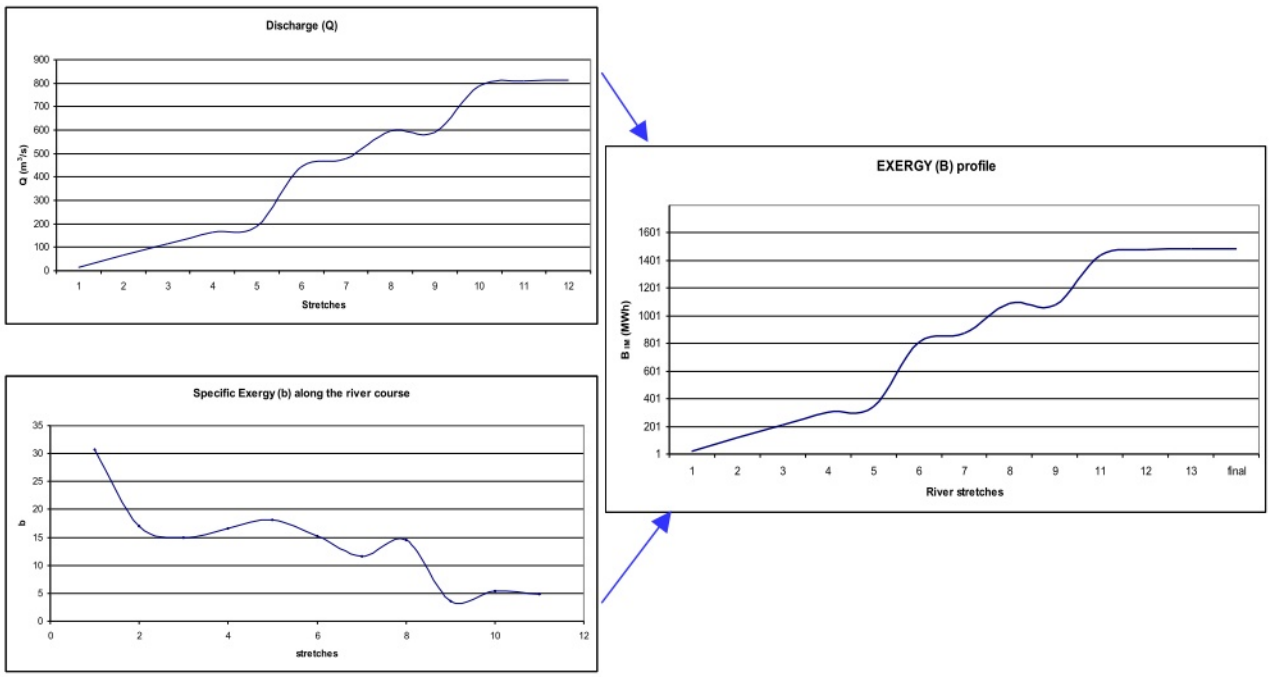

Fig. 1. Representation of Exergy along the river course, real sample (Own elaboration)

Furthermore, Valero et al [3] showed that an Exergy gap between two states, 1 and 2, can be accounted and disaggregated in the corresponding quantity and quality terms as well, as indicated in (1)

$$\Delta B_{2-1} = B_2 - B_1 = b_1 \Delta Q + Q_2 \Delta b = \Delta B_m + \Delta B_q \quad (1)$$

Where ΔQ and Δb are the flow and specific exergy gaps between two exergy states (states 1 and 2), and *m* and *q* stands for quantity and quality exergy components, respectively.

The addition of all exergy components (potential, inorganic, organic, etc) expresses the total exergy of the given water resource. That reasoning was fruitfully applied in [4].

Then, PH brings up the opportunity to development different River exergy profiles which can be represented along the length of the river, for different periods and degradation statuses. First novelty presented here consist on developing an hypothetical scenario corresponding to the state reached by applying the already mentioned restoration Plan of Measures, therefore testing their suitability by comparing that scenario with the Environmental Objectives, pursued by the Directive. Additionally, individual scenarios for each user, could be also simulated and confronted to account the environmental cost of water, as well as fairly distribute this cost among different users. Both constitute key objectives of this work being a really important consequence of the river simulation.

In order to illustrate the applicability of the methodology proposed here, the Ebro River basin (described in section 3) was analysed. It was simulated with the help of a comprehensive hydrologic model, giving a complete vision of the basin. Discharge, composition and physical characteristics of water flows were compiled trough the Aquatool hydrographical simulation software [5] thus making possible not only to test the already mentioned Plan of Measures, but also to assess the degradation provoke for each user of the basin, individually.

2. Methodology

Quantity and quality data should be accurately provided for every stretch of the river in order to obtain the precise river profiles. As mentioned, these profiles are required to assess the cost necessary to bridge the gap between two given degradation states.

Then, the methodology followed in this work to develop the already mentioned milestones (to test the programme of measures and to allocate restoration costs among users) is developed in the first part of the section. For the sake of completeness, a table summarizing the accounting of the parameters to develop river scenarios is presented in Appendix A (Table A.1). Secondly, it was also mentioned that an hydrographical simulation tool is necessary to apply the methodology to real case study. The followed simulation process is deeply explained in the second part of this section.

2.1. Definition of river scenarios.

2.1.1. Testing the Measures Plan

With the aim of reaching the Ecological Status defined in the WFD some measures should be applied for each water body of a given basin when required. Therefore, a great opportunity given by the Aquatool model emerges since it allows simulating any defined state of the river. Traditionally, the environmental cost (EC) has been the main cost considered by PH. It is defined as the cost the reach the Environmental Objectives from the Present State of the river in future scenario (2015). Complementary, in this work, a new a hypothetic Measures State (MS) in which the potential measures conceived in Hydrologic Basin Plans are included is defined. It will make possible to asses the gaps between the Present State by 2015 (FS) and the Measures State, and between Measure State and Objective State (OS), respectively. The effectiveness of such a Plan could be also easily tested, as well as the additional cost of non compliance of the PM initially though up in case of those measures were not enough to reach the Good Ecological State.

In this sense, the new defined river state (MS) makes possible to assess two additional costs:

- The Measures Costs (MC). It can be defined as the necessary cost to implement the PM presented by the competent authority, that is, the difference between the FS of the river and the MS.
- The non-compliance cost (NCC) which asses the gap between MS and OS. It informs about the accuracy of the implemented measures in the water body.

Following the guidelines of equation (1), the MC and NCC are determined by the difference between the FS and MS, and the OS and the MS, respectively, according to (2) and (3).

$$MC = \Delta B_{MS-FS} = B_{MS} - B_{FS} = b_{FS}\Delta Q + Q_{MS}\Delta b \quad (2)$$

$$NCC = \Delta B_{OS-MS} = B_{OS} - B_{MS} = b_{MS}\Delta Q + Q_{OS}\Delta b \quad (3)$$

These previously mentioned exergy states and costs are summarized graphically in Fig.2.

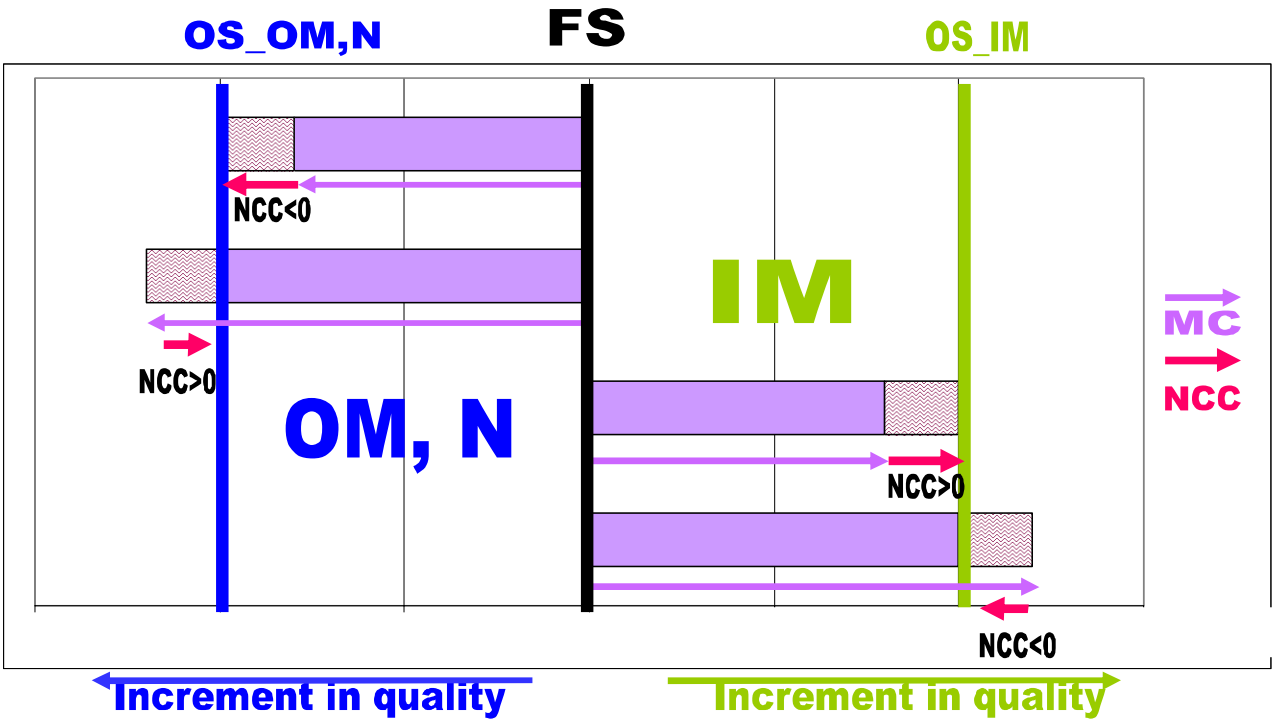

Fig. 2. MC and NCC interpretation for different exergy components

It is interesting to be underlined in this point that by working with monthly simulated data, the temporal variability of results should be taking in mind, making possible to obtain positive NCC results in some months and negative in other months. Consequently, this accounting procedure, already presented and also tested in some study examples [6], gives valuable information and it could be used in forecast and planning management. By working with monthly simulated data, the temporal variability of results should be taking in mind. It makes possible to evaluate results to conclude the months where the PM was over or under sized, to propose some alternatives to the current PM, in case they where necessary.

Considering separately different exergy components, MC and NCC results should be accurately interpreted.

On the one hand, the quality of the river regarding to Inorganic Matter (IM) is lower when values of exergy are lower. The Inorganic Matter exergy component tends to decrease along the river due to human uses. That also implies an increase in salinity. Therefore, positive values of MC and NCC for the IM component implies the reduction of salinity by applying some measures, but also show the remaining necessity to bridge the gap between MS and OS by putting into practice additional measures. In this sense, a positive value of the NCC indicates that the PM within the watershed is not good enough because the OS has not been reached. On the other hand, a negative value, however, leads to the conclusion that the PM projected to that river has been oversized.

On the other hand, organic matter (OM) or Nitrogen (N) exergy components increase with concentration. Therefore, higher values imply lower quality. It can be assumed that, in that case, a negative value of organic matter component of the MS implies a reduction in the concentration, and a lower exergy value. Then, measures reduce the OM concentration of FS. That analysis is summarized in Table 1.

Table 1. MC and NCC analysis

		IM	OM, N	Interpretation
MC		> 0	< 0	Measures improve the quality of river
		< 0	> 0	Measures diminish the quality of river
NCC	**a**	> 0	< 0	Measures are not good enough
	b	< 0	> 0	Measures have been oversized

2.1.2. Distribution of costs among users

The PH methodology makes possible not only to calculate restoration costs of water bodies, but also to allocate them among different users. To do that, different statuses of the river were developed, with the aim of studying separately the pollution charges of each use of the basin. Those statuses were used to account and allocate the Restoration Cost for each water user.

The first step consisted on defining different individual scenarios for each user. The developed statuses were:

- Without Users State (WUS) of the river is understood as the state of the river without any demand. It is similar to the natural state of the river.
- Urban Users State (UUS) is the state in which only urban demands are considered.
- Agriculture Users State (AUS) is defined as the resulting state by taking into account only the agriculture demands.
- Hydroelectric Users State (HUS) is the state in which only the hydroelectric facilities are taken into consideration. Its reposition cost comes from the energy necessary to restore the power generated by them.
- Dams State (DS). It is a state without uses but with the presence of dams. It was defined in order to separately calculate the affection (ΔB) due to the presence of these infrastructures, necessary to cover different demands. Dams change the available flow along time and space, since they manage the flow coming from the river to be stored or delivered. That lies in a changing gap of flow, and, therefore, in a quantitative degradation of water, that could be negative or positive considering the monthly balance of input and output flows.

Exergy gap between a scenario only with Dams (DS) and the scenarios reached by each of these users individually IUS were represented by ΔB_i and calculated by applying (4).

$$\Delta B_i = \Delta B_{DS-IUS} = B_{DS} - B_{IUS} = b_{IUS}\Delta Q + Q_{DS}\Delta b = \Delta B_m + \Delta B_q \quad (4)$$

Additionally, the dams storing effect (ΔB_{dams}) was assessed as the exergy gap between a scenario DS, and the WUS scenario, by applying (5).

$$\Delta B_{dams} = \Delta B_{WUS-DS} = B_{WUS} - B_{DS} = b_{DS}\Delta Q + Q_{WUS}\Delta b = \Delta B_m + \Delta B_q \quad (5)$$

The exergy gap between the state without users and the real present state, the total restoration exergy gap (ΔB_{TOTAL}) it should be tested to be approximately equal to the addition of individual gaps (ΔB_{uses}) presented above (according to 6) as summarized next in an application example.

$$\Delta B_{TOTAL} \approx \Delta B_{uses} = \sum \Delta B_i + \Delta B_{dams} \quad (6)$$

Figure 3 summarizes that methodology.

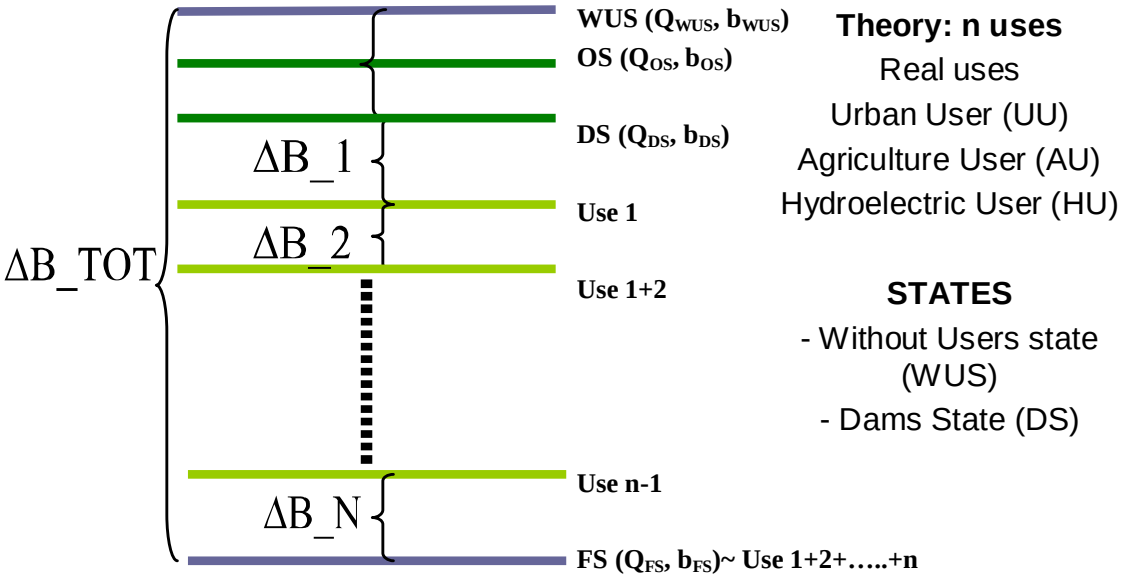

Fig. 3. Distribution of restoration costs among users

Urban and irrigation users provoke a gap in the quality exergy component due to changes in water composition (inorganic, organic, or nitrogen and phosphorous content are affected by them).

On the other hand, changes in quality exergy due to the hydroelectric uses are found in the potential component. Potential component depends on the height gap (ΔH) in each river stretch. Since this exergy gap varies depending on the kind of hydroelectric technology, an accurate analysis of the main hydroelectric facilities located in the case study, was carried out with the help of monthly data from Endesa [7]. They were considered to asses the degradation provoked by this user.

2.1.2.1. Application example

In order to verify the methodology, it was necessary to test if the total restoration exergy gap (ΔB_{TOT}) was equal to the addition of individual gaps defined for the previously mentioned individual scenarios ($\Sigma\Delta B_{USES}$). Data from the hydrologic period (2002-2006), from a simple real case study located in the Segre river, a main tributary of the Ebro river, were considered to carry out that test. Input data where calculated from the watershed organism *"Confederación Hidrográfica del Ebro"* [8]. The river characterization scheme includes a reservoir, and downstream, firstly, a gravity hydropower plant, and then, agriculture and urban plus industry demands. All the above mentioned states were considered in that simulation. More over, both quantity and quality flow data were obtained, in a monthly basis and for each simulated year and stretch. Quantity and quality components for each user could be studied individually. Table 2 includes final results for a representative hydrologic year (here, 2005-2006), for quantity and quality contributions to the total exergy gap, for OM, IM, and Nitrogen components, and for different users.

Table 2. Contribution to the quality and quantity exergy gaps, due to different uses

% to the total exergy gap	Urban	Agric.	Hidro.	Dams
Quality exergy gap □□ΔB_q	68.98	19.02	11.93	0.00
Quantity exergy gap, ΔB_m	2.46	34.39	0.00	63.15

It was tested that the ratios between the total exergy gap (ΔB_{TOT}) and the addition of individual uses exergy gaps ($\Sigma\Delta B_{USES}$) are higher but similar than one (see Table 3). Consequently, when many users are included simultaneously in the scheme, degradation results to be a little higher than the

addition of degradation scenarios assessed individually for each user. That is due to the non-linear behaviour of exergy in liquid solutions.

Obtained ratios for quality and quantity components are summarized in Table 3.

Table 3. Ratios between PS exergy degradation and the addition of individual users states exergy gaps. Application example.

COMPONENT	q_{OM}	q_{NP}	q_{IM}	**m**	**q,p**
$\Delta B_{PS}/(\Delta B_{USES})$	1.02	1.01	1.12	1.03	1.00

2.2. Modelling process

The relationships between waste loads and the resulting water qualities are always better described with mathematical models than only from the available data given by the River Basin Authorities. An adequate hydrological simulation tool could provide of enough compiled river data to characterize the river as exactly as the user wants, during a period of time and almost in every desired point, especially in those points where no data are available. Depending on how specific are its discrete simulation units, it can be really useful to complete the sometimes discontinuous or insufficient available data for a given case study. More over, hydrographical simulation tools can be a great operational support to analyze the river when simulations do not correspond to actual measurable situations.

With the help of the Aquatool software it was possible to generate different states, so obtaining enough physical and chemical data to correctly characterize each stretched of the river. Thus, it makes possible the representation of the river exergy profiles for different degradation states.

Input monthly flows data for the case study presented in next section (the Ebro river) for each simulated year within the 2002-2007 period were introduced in the Aquatool-GESCAL interface [5]. Point pollution discharges coming from the industry were also included to calibrate the simulation results (by comparing them with real data available from quality data stations). In particular, the modelled quality inputs parameters were sulphates, alkalinity, calcium, sodium, magnesium, chlorine, organic matter, nitrates, ammonium, and conductivity. Mass balances were previously carried out with the different water flows, by using the SIMGES program module, which deals with water flows (see Annex A for details).

Quality data given by quality control stations along the river course [8] were used to estimate the quality water inflows in river stretches. Water deterioration provoked by uses was calculated from the common return ratios applied for the Ebro, corresponding to different uses, 80 and 20 % for urban and agriculture, respectively, according to [9]. Thypical elimination ratios of existing Wastewater Treatment Plants from [9] and pollution rates for different users found in [10] where considered. Additionally, monthly evolution of temperature, and dam related data, as evapo-transpiration and level-capacity curves were obtained from [8].

Finally, quantity and quality flow data were then obtained, per month of each simulated year and stretch. Therefore, exergy profiles could be calculated for the simulated users-related states, as it was previously done for the current state of the river (FS). Then quantity and quality components for each user could be studied individually. Figures, divided by components and stretches can be shown in graphics, tables, or can be exported to operate in Excel dynamic tables (see Fig. 4).

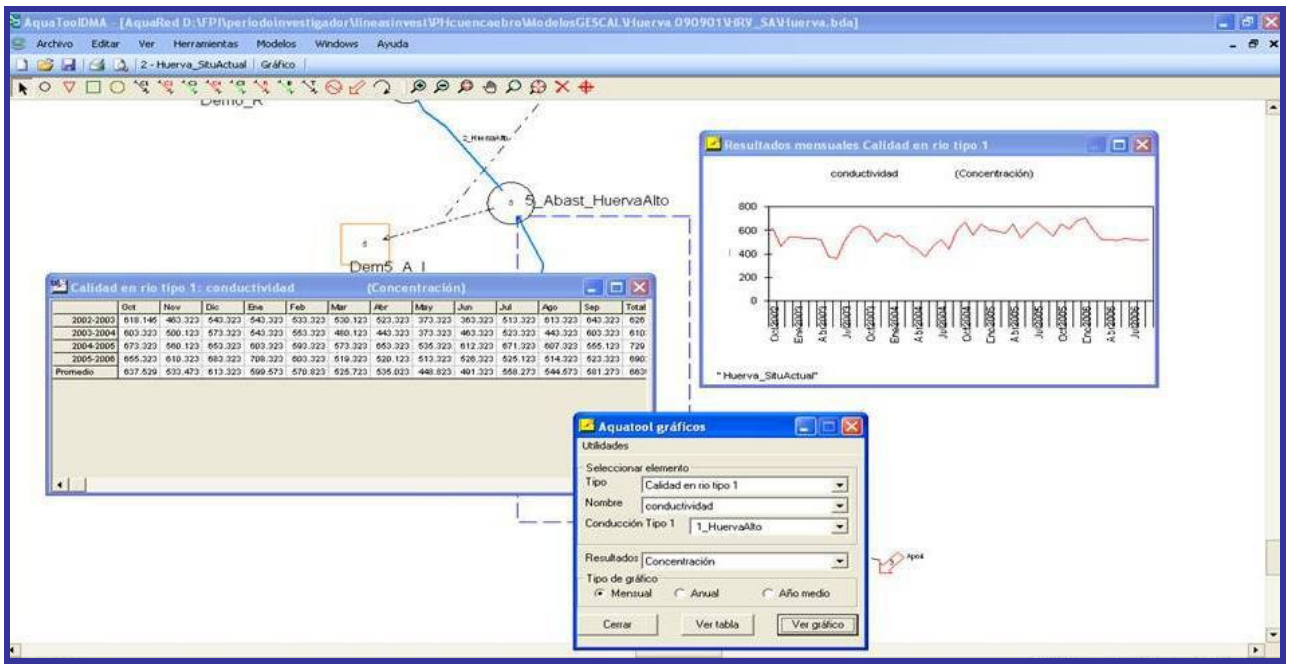

Fig. 4. Aquatool software results

3. The Ebro river basin: case study

This section includes a description of the Ebro River Basin, and also summarizes the main water uses in the basin, as well as the Plan of Measures projected by the Ebro river Basin water Authority (Confederación Hidrográfica del Ebro). It also covers the modelling process of this river basin with Aquatool.

3.1. Description

The Ebro river basin (see Fig. 5) is located in the north-east of Spain. It springs in Fontibre (Cantabria, 2000 meters high) and flows into the Mediterranean sea, in a Delta located in Amposta (Tarragona, Catalonian region). The Ebro river has a surface of 85500 km^2, with about 8000 km^2 of irrigated land. Most of this surface belongs to Spain. Only 506 km^2 are French and 444 km^2 belong to Andorra [11] The Confederación Hidrográfica del Ebro is its management organism, framed within the Spanish Ministry of Environment, Farming and Agriculture. Its average rainfall is about 620 mm and its length is close to 930 km. There are important differences within the average rainfall values in the different Ebro areas. The highest values (more than 1500 mm) are found in the north area, but the central area of the basin has a rainfall around the 400 mm. The natural average total water resources there are 18200 hm3/year (Average interannual), ranging between 29700 (máx.) and 8400 (mín) hm3/year [12, 13].

Fig. 5. The Ebro river basin

3.2. Water uses in the Ebro river

The population of the area is approximately 3 million of people, with a gross domestic product (GDP) per capita around 25000 €/inhabitant and year. More that the 50 % of the income and the 50% of the total number of jobs correspond to the services sector [10].

The next most important sector is the industrial one. Around 3 million of people within the basin and nearly 1.5 million out of the basin (transfers) are supplied. That implies 550 hm^3/year of the urban water needs. The industrial water needs are 414 hm^3/year, and the supply guarantee, close to the 100%. Energy uses are characterized for being not water consumptive or return a high percentage of supplied water [11].

Regarding to agriculture uses, the irrigated surface under concession is close to the 800,000 ha [12]. Total water needs are around 6000 hm^3/year. The supply guarantee is limited, dependent on precipitations regime. Water sources are mainly coming from surface water bodies (91 %) and also from groundwater bodies (8%).

Main data related to high capacity infrastructures to supply water services (water reservoirs) are summarized in Table 4.

Table 4. Water service: high capacity infrastructures (Adapted from [12])

	Total	**Goverment (CHE)**
Number of dams > 1 hm^3	107	45
Flooded surface (has)	41634	22911
% on basin surface	0.49	0.27
Total water stock capacity (hm^3)	7580	4055
stock capacity/natural resources	41.89	22.26

Since WFD is focussed on biological quality, it is important to remark the physico-chemical quality on surface water. It is summarized in Table 5. It also includes the characteristics of each quality category.

Table 5. Physico-chemical quality on surface water (Adapted from [12])

AVERAGE QUALITY	CHARACTERISTICS	% of control points
A1-A2	Simple or normal treatment + disinfection	78
A3	Intensive treatment +disinfection	17
<A3	Not allowed as input for drinkable water	2

3.3. The Programme of Measures proposed by the Ebro River water management authorities

According to the Ebro river draft Management Plan, total projected budgets for the 2015 scenario ranges from 6000 to 10000 M€. Largest budgets to apply the actions considered in the program of measures for the period 2010-2015 in the Ebro river basin are the modernization of irrigation systems (30% of the total modernization budgets), water and sewage treatment accounts (10%) and water supply projects (7.4 %). The budgets in new irrigation (20%) and operational infrastructures associated with them (10%) are also important [14]. Its total demand is around 2022 hm^3 per year, and the total surface of new modernized and low water consumption irrigated areas is 425000 hectares. In this sense, an intensive debate can be expected in society on the need to carry out the proposed irrigation. In Spanish basins with a more intensive water use, new irrigated are not included in the water plans. However, since the majority of the Ebro river basin population are in favour of the new irrigation, the moratorium called by some environmental groups has not had much effect on society, as long as the new irrigation complies with the objectives of environmental quality.

3.4. Modelling process

Figure 6 shows the Ebro river basin scheme as it was prepared to be used in the Aquatool software. The area where Mequinenza and Ribarroja dams are located is shown, in detail. In spite of the main course of the river considered here, the complete Ebro river basin simulated in Aquatool accounts for 27 dams, 72 river stretches, 45 water inputs, 111 catchments and 59 returns.

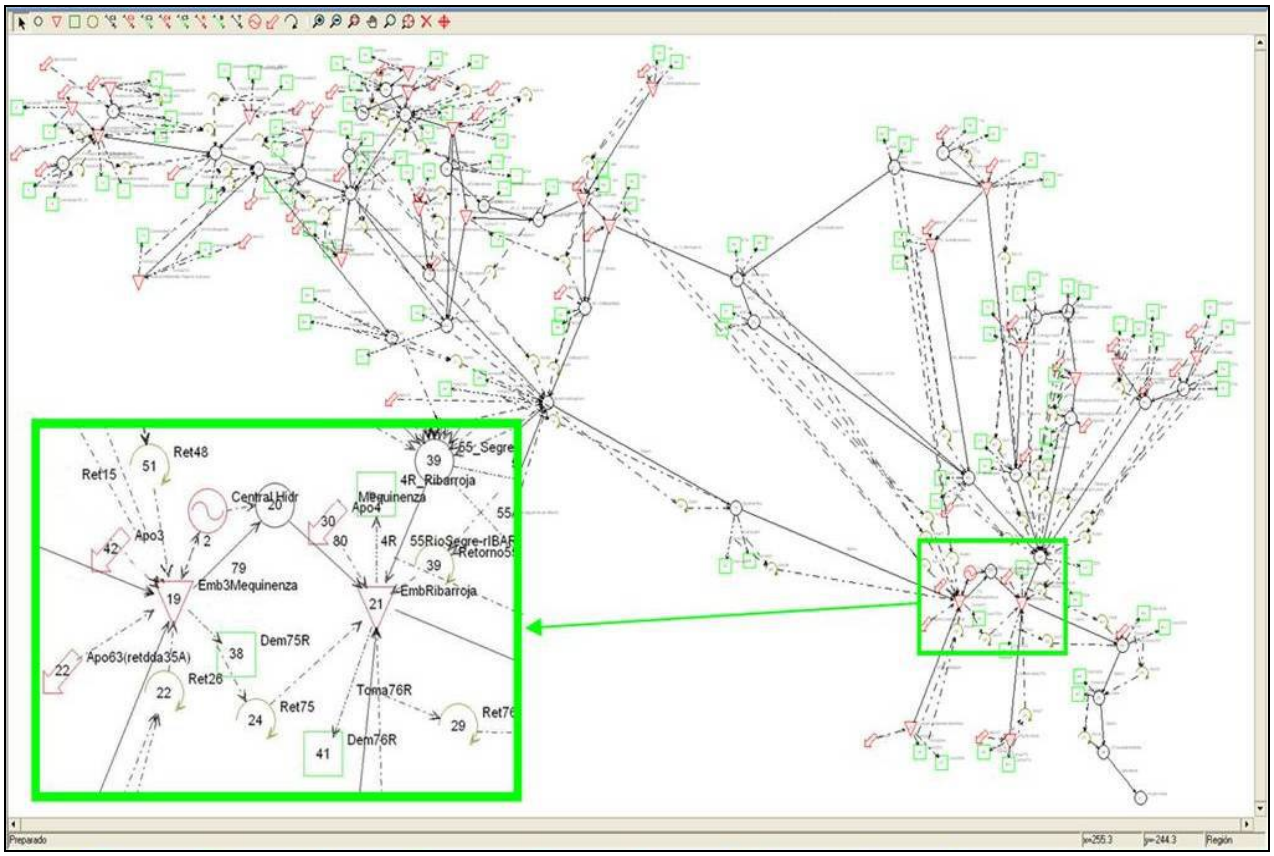

Fig. 6. The Ebro river basin in Aquatool software, and zoom of the lower area of the river

Present, measures, and individual scenarios for each user, where simulated. Quantity and quality contributions, for each chemical component where considered. Inorganic Matter (IM), which stands for inorganic salts and water; the Nitrogen (N) component, which accounts for nitrates, nitrites, ammonia contained in water, as well as organic matter (OM), thermal and potential components were calculated.

3.4.1. Calibration

Aquatool-DMA was chosen by the Ebro river Basin Authority as a support to test the fulfilment of the WFD and a help to write the Ebro river Management Plan. Since this work is somehow conceptually linked to the Confederación Hidrográfica del Ebro (CHE), it was considered other important advantage to choose Aquatool over the other softwares. It was decided that the simulated period should be the last four hydrologic years (October 2002- September 2006) from which enough complete and calibrate monthly data of flows could be facilitated by the Ebro river Basin Authority. The adequate calibrated flows given personally by the CHE staff which represented a great support to start with the development of the case study. Nevertheless, it is interesting to bring in this point the idea that the Management organism is used to the quantity model, but not to the quality model. That is the main reason why it was necessary to calibrate the model making possible to correctly work with quality data.

In this sense, it was necessary not only complete and improve the quantity model SIMGES by introducing more precise data such as the ones related with dams, to accurately obtain proper quantity results. It was also necessary to develop the GESCAL (quality model) with all requirements to be adequately compiled. Inputs, returns, point and non-point contamination, where monthly calibrated for the simulated period 2002-2006, for main stretches of the whole river and for each main component forming part of the water flow. Main components which were considered stand for organic matter, sulphates and nitrates.

An iterative process was required to attain optimal agreement between model output and field measurements. Calibration parameters had to be modified, running the program several times, by a manual trial-and-error process. SIMGES and GESCAL modules should be absolutely coherent. Then, if quantity simulation results change, it is necessary to run the quality module again to obtain proper results. Calibration parameters stand for different quantity and quality model data, in special punctual pollution inflows (simulating industrial pollution), returns, and non-point pollution. A quality control station was accurately selected in each stretch. Several punctual inputs were added in the model to simulate inflows from industry, along the basin. Average and maximum errors, and standard deviation were calculated in each point for different water components. Obtained average error between simulated and data taken from real stations resulted to be not higher than 10%.

4. Review and analysis of results

The most representative obtained figures are summarized next. As it was expected, the flow increases in the low Ebro. It can be also appreciated that it decreases along the simulated temporal period (see Figure 7). It was also checked that Natural State remains always higher than the other states, as expected.

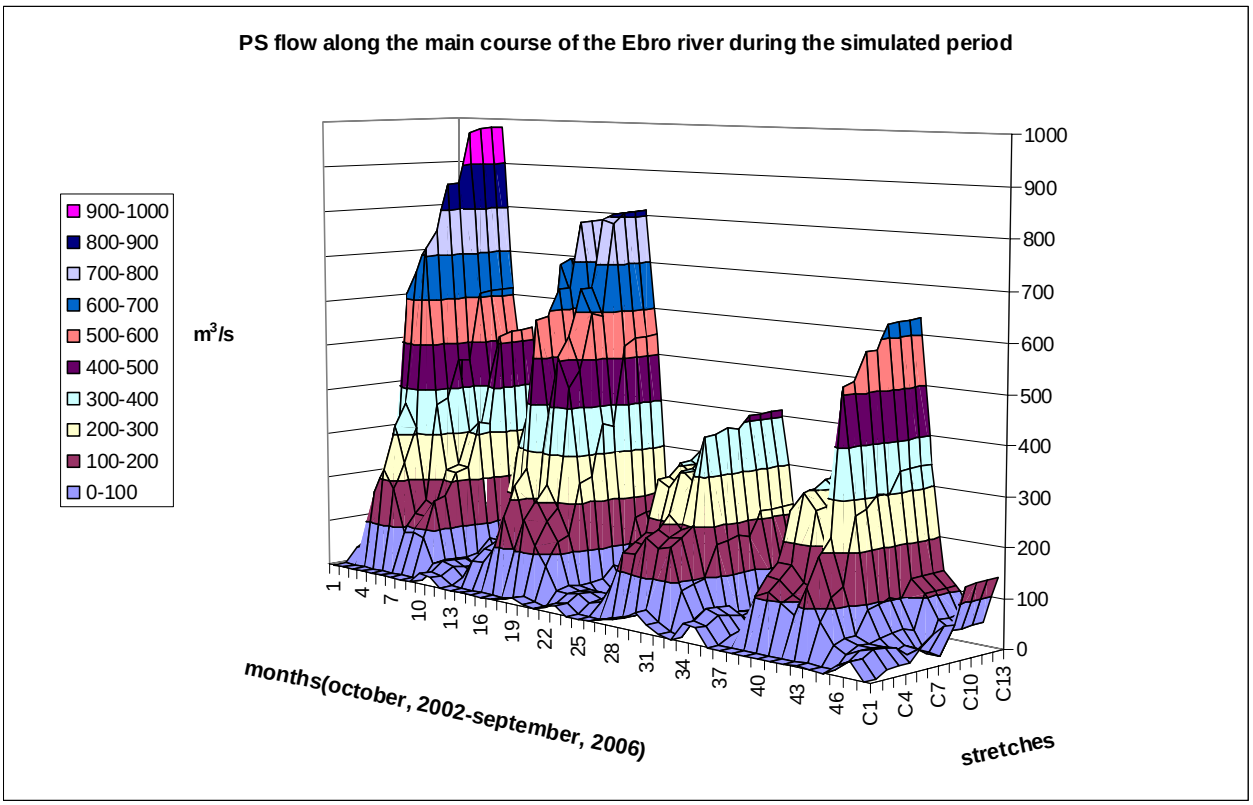

Fig. 7. Present State flow along the Ebro river

Regarding to composition, the sulphates concentration is quite high (280 ppm) at the end of the upper river, but reaches its maximum value in the medium Ebro (380 ppm). It is also noticed also an increment in the salinity at the end of the river, close to the delta. According to the Organic matter,

in the upper Ebro values close to 4 ppm were found, and close to 6 ppm (maximum value) in the medium course (after industrial parks, and polluter tributaries). The nitrates concentration presents also maximum before the medium course of the river (12 ppm), and increases until 30 ppm in the medium Ebro, due to importance of irrigation in this area. The last significant increment is found at the end of the river, where the nitrates coming from the agriculture returns make the concentration rises until close to 14 ppm. These results are similar to the theoretical description of the basin (see Case Study section).

It can be concluded that proposed Measures are enough to fulfil the Ecological Objectives during the simulated period 2002-2006. Table 6 summarized the only 6 months of non-compliance in the Ebro. They are found mainly in September and November, in sulphates and Nitrates.

Table 6. Non-compliance in the Ebro river for the period 2002-2006

		Stretches	6	7	8	9
2003-2004	**Sulphates**	**November**			X	X
		September		X		
	Nitrates	**November**			X	X
		September		X		
2005-2006	**Sulphates**	**September**	X	X	X	X
	Nitrates	**September**	X	X	X	X

As an example, the difference between sulphates concentration in Measures and Objective States is represented in Figure 8, along the river for each simulated month. Non-compliances of table 5 are confirmed there. Some punctual positive results (which imply a concentration in MS higher than the maximum allowed concentration in OS) are found in stretches 6 to 9, during November and September.

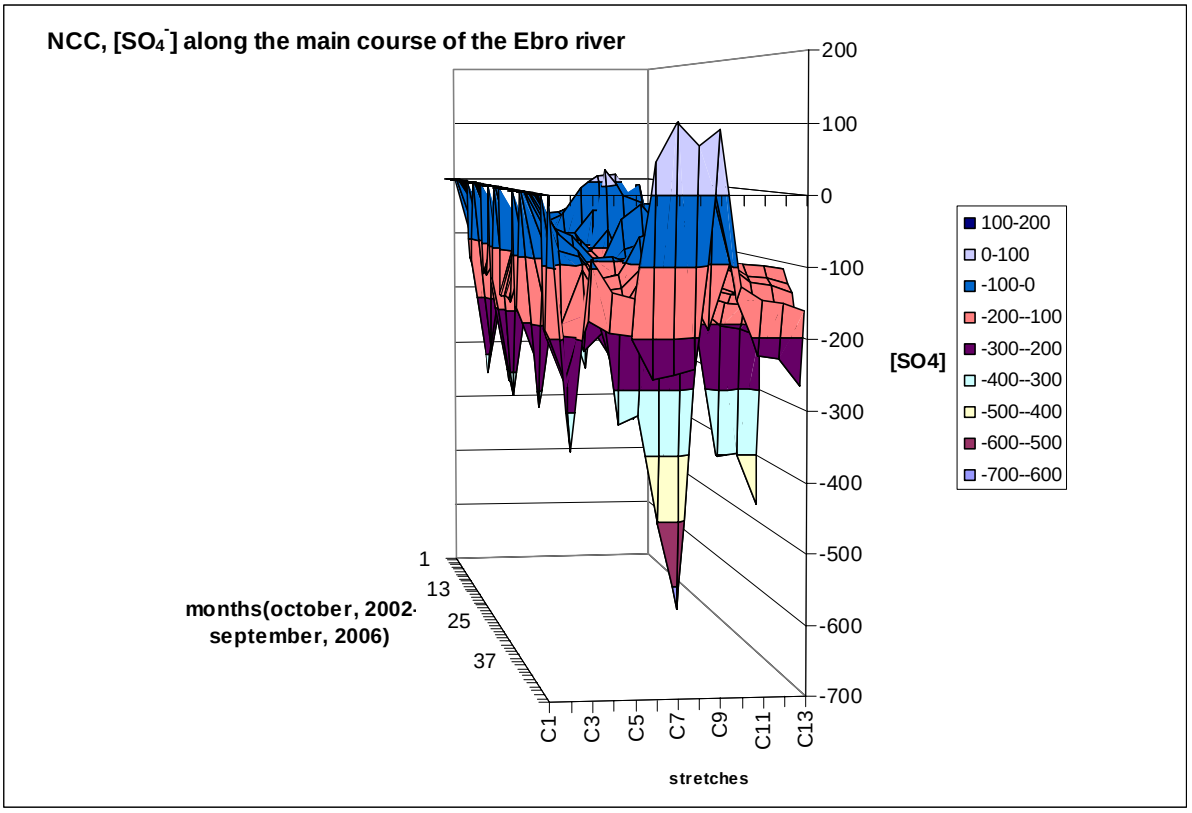

Fig. 8. Sulphates non-compliance along the Ebro river

Exergy costs for each component and user were calculated, month by month, and aggregated by hydrologic year. For the sake of clearness, results for the representative dry year, 2005-2006 are summarized in Table 7. Restoration costs for quantitative (ΔB_m) and qualitative (ΔB_q) degradation were considered to share out degradation rates among users. The relative percentages from the total reposition cost, for different users, and for quantity (m) and quality (q) components were also assessed.

Table 7. Exergy components for different users. Total Restoration costs in the Ebro river. Dry hydrologic year 2005-2006.

Degrad (ΔB)	% Urban	% Agric	% Hidro	% Dams	TOTAL (ΔB, GWh/year)
$\Delta B_{OM,q}$	30.85	69.15	0.00		9894
$\Delta B_{IM,q}$	8.06	91.94	0.00		758
$\Delta B_{NP,q}$	75.55	24.45	0.00		693
$\Delta B_{p,q}$	0.00	0.00	100.00		911
ΔB_q	29.68	62.89	7.43		12256
ΔB_m	28.53	73.96	0.00	-2.49	55213

The highest total values of quality components gap is found in the agriculture user. On the other hand, the contribution of hydroelectric is the lowest. Regarding to the dams storage, as it was explained previously, it was considered an exergy gap due to the variation of flow downstream reservoirs. That variation can be negative or positive by considering a monthly balance of flows. During the hydrologic period 2005-2006, total monthly balance of water storage results to be negative: the users demands increased the natural discharge from dams.

Previous results are compared next with the ones obtained for a wet hydrologic year (2002-2003). It is shown that the effect of dams increases, but, on the other hand, total reposition cost diminishes (see Table 8). Previous results consider both storing and delivering effects in the accounting (that is, not only the months when negative but also the months with positive net flow balances exist). In case of dry hydrologic years (2005-2006), the yearly balance results to be negative, that means, more water is delivered than received by the dam. In case of wet hydrologic analyzed years (2002-2003), the balance result to be positive.

Table 8. Exergy components for different users. Wet hydrologic year 2002-2003

Degrad (ΔB)	**% Urban**	**% Agric**	**% Hidro**	**% Dams**	**TOTAL (ΔB, GWh/year)**
$\mathbf{\Delta B_{OM,q}}$	66.93	33.07	0.00		2444
$\mathbf{\Delta B_{IM,q}}$	31.65	68.35	0.00		330
$\mathbf{\Delta B_{N,q}}$	35.99	64.01	0.00		1203
$\mathbf{\Delta B_{p,q}}$	0.00	0.00	100.00		1276
$\mathbf{\Delta B_q}$	41.37	34.33	24.29		5253
$\mathbf{\Delta B_m}$	13.58	73.46	0.00	12.97	13845

The ratios between the total exergy gap (ΔB_{TOT}) and the addition of individual uses exergy gaps ($\Sigma\Delta B_{USES}$) are summarized in Table 9. It was stated previously that these ratios should be a little higher than one. Then, in spite of the computational effort, results seemed to be coherent, in mathematical terms.

Table 9. Ratios between PS exergy degradation and the addition of individual users states exergy gaps. Ebro river (hydrologic years 2002-2003 and 2005-2006)

$\Delta B_{PS}/(\Delta B_{USES})$	$B_{q,OM}$	$B_{q,NP}$	$B_{q,IM}$	B_m	$B_{q,p}$
2002–2003	1.50	1.30	1.20	1.18	1.00
2005–2006	1.22	1.10	1.33	1.05	1.00

Total monetary restoration costs (TRC), and also the costs for each component, given in M€/year, are included in Table 10. In this sense, it was explained that PH assesses reposition costs considering an Objective State, according to the WFD milestones. Therefore, regarding to Dams effect, it is not possible to calculate the restoration economic costs, since the gap provoke by dams is compared with the Natural state of the river. Moreover, there is not a need to restore water flow variation due to dams: dams only provoke a displacement of flow availability during different hydrological periods, but not so much water losses (evaporation) occur. That is the reason why their effect is not included in Table 10 (restoration costs).

Table 10. Monetary restoration costs for different users (M€/year).

YEAR	TRC (M€/year)	TOTAL	Urban	Agric	Hidro
2005-2006	Quantity	981	237	708	0
	Quality	3198	949	2011	238
	TOTAL	4179	1181	2925	73
2002-2003	Quantity	420	66	354	0
	Quality	964	399	331	234
	TOTAL	1384	324	958	102

Total environmental costs, defined by the WFD as the gap between present and Objective states were also calculated in order to furtherly distribute among diverse water users. To define the objective state, data of composition found in [15] were taken into account. They resulted to be around the 20% of total reposition costs already presented. The important gap between both costs stands for the Remaining Resource Cost (RRC), related to the difference between Objective and Natural states. Results regarding to the hydrologic year 2005-2006 are summarized next in Table 11.

Table11. RRC in the Ebro river. Comparison with Total restoration cost. Year 2005-2006.

% Urban	% Agriculture	% Hydroelectric	Environmental Costs(M€/year)	RRC (M€/year)
30	63	7	981	4201

Any comparison of the results obtained here with existing published official economic figures is somehow complicated, since PH gives operating costs, and only investment cost could be found in the draft version of the new Basin Plan [15].

Checking the Ebro River Water Treatment Plans (WWTP) installed in last 20 years [8], and considering the WWTP operation cost given in [16], the yearly water treatment operation cost during that period was calculated.

Then, the ratio between cost of operation and cost of investment given by the "Aragonian Water Institute" in [17], was used to calculate investment in WWTP during last twenty years. It was concluded that that investment was approximately 2700 M€.

According to the draft version of the Ebro management Plan [15], yearly Waste Water treatment cost are around 103 M€ per year. Then, the same ratio between investment and WWTP yearly exploitation cost already mentioned (which was found in [17]) was considered to calculate exploitation costs from the investment for 2015 given by CHE in [15]. These exploitation costs

resulted to be around 900 M€ per year, similar to the restoration cost due to changes in water composition (chemical component) according to results shown in this work.

5. Conclusions

This work was focussed on the assessment of restoration costs to fulfil with the Environmental Objetives pursued by the WFD. The PH methodology, based on a thermodynamic property named Exergy made possible to calculate these costs. Exergy depends on the physico-chemical characteristics of the studied resource. In this sense, PH made possible to analyze the seasonability of results, assessing not only the contamination rate of water bodies, but also its consumption. It makes also possible to assess water cost upon a physical objectives but after it also includes economic aspects.

The main contribution of this work lies not only in testing the Plan of Measures projected by the CHE in the Ebro river management plan, but also in the successful share of water uses degradation among the economic agents. Both constitute key milestones of this work. The improvements introduced in the PH methodology were mathematically tested with a sample real case, to be then applied to the whole Ebro river. That river basin was simulated with the Aquatool-DMA software, for different hypothetic states of the river. Therefore, the costs between them were accounted by comparison of its exergy profiles.

Results shown that total restoration costs found in the quality component of the agriculture user resulted to be the highest in analyzed dry years, but values for both users are quite similar in wet years. Focussing on quantitative figures, the highest restoration cost is found in the agriculture user. On the other hand, degradation provoked by the hydroelectric user resulted to be the lowest, but increases in wet years. The introduction of that user in the PH spectrum also constitutes an important novelty of this work.

The cost to restore the dams storage provokes a diminution of downstream river flows in some months and an increase in some others. The net yearly effect is shown for both dry and wet years, ranging from negative to positive balances, respectively.

According to the Aquatool-DMA results, the Plan of Measures (PM) proposed by 2015 is enough to fulfil with environmental objectives pursued by the Environmental Authorities, since only punctual non-compliances were found during the simulated period. More over, the total investment cost to put into practice the projected measures in the Ebro river by 2015 seems to be enough to fulfil the environmental objectives, according to obtained results.

Acknowledgments

The authors greatly acknowledge the financial support given to carry out this work, which is under the framework of the project ENE2010-18934 financed by the Spanish Ministry of Education and Science.

Appendix A

Table A.1. Assessment of flow and specific exergy in different river scenarios

		River States	Starting Sources	Input parameters (results compilation)*	Compil. Tool	Considerations
Q	FLOW (Q)	PS	Flow data from real gauging stations	Input flows, demands, returns, dams data	SIMGES	the river in the PS, with every inputs, demands and returns
		FS	PS Aquatool simulation	Input flows, demands, returns, dams data	SIMGES	5% of water diminution (because of the Climate change), and higher demands
		MS	FS Aquatool simulation, PHEBro proposed Measures	Input flows, demands, returns, dams data	SIMGES	MEASURES (PHEbro)*
		OS	PHEBro proposed Env.flows, FS Aquatool simulation	-	-	PH Ebro, proposed env. Flows-Future State
		NS	PS Aquatool simulation	Input flows	SIMGES	Modification of PS Aquatool scheme, only input flows
		UUS	PS Aquatool simulation	Input flows, demands, returns, dams data	SIMGES	Modification of PS Aquatool scheme, only urban demands
		AUS	PS Aquatool simulation	Input flows, demands, returns, dams data	SIMGES	Modification of PS Aquatool scheme, only irrigation demands
		HUS	PS Aquatool simulation	Input flows, demands, returns, dams data	SIMGES	Modification of PS Aquatool schemme, only hydroelectric demands
		DS	PS Aquatool simulation	Input flows, demands, returns, dams data	SIMGES	Returns: 100% of demands, with the same composition than catchments
b * **	composit.	PS	Quality data from real gauging stations	Input composition, returns composition, punctual and non-point pollution	GESCAL	the river in the PS, with every demands
		FS	PS Aquatool simulation	Input composition, returns composition, punctual and non-point pollution	GESCAL	5% of water diminution (because of the Climate change), and higher demands
		MS	FS Aquatool simulation, PHEBro proposed Measures	Input composition, returns composition, punctual and non-point pollution	GESCAL	MEASURES (PHEbro)**
		OS	PHEBro proposed Obj, compositions	-	-	PH Ebro, proposed composition for different water components
		NS	PS Aquatool simulation	Input composition, non-point pollution	GESCAL	Modification of PS Aquatool scheme, only input flows
		UUS	PS Aquatool simulation	Input composition, returns composition, punctual OM and non-point pollution	GESCAL	Modification of PS Aquatool scheme, only urban demands
		AUS	PS Aquatool simulation	Input composition, returns composition, puntual SO4 and NO3, and non-point pollution	GESCAL	Modification of PS Aquatool scheme, only irrigation demands
		HUS	PS Aquatool simulation	Input composition, returns composition, non-point pollution, hidro-facilities data	GESCAL	Modification of PS Aquatool scheme, only hydroelectric demands
		DS	PS Aquatool simulation	Input composition, returns composition, non-point pollution	GESCAL	Returns: 100% of demands, with the same composition than catchments
	physical paramet.	every state	CHE website, CHE quality stations reports	Temperature, lenght, high (every stretch)	-	

* Monthly values

** Lower and more concentrated returns (modernization), water treatment improvements

*** Final monthly values of each component of b , for different degradation states, were calculated from the Q, composition and physical parameters data in every stretch of the river, by using an specific equations solver software

Nomenclature

AUS: Agriculture Users State

b: Specific exergy (kJ/kg water)

B: Exergy (KWh)

CHE: Confederación Hidrográfica del Ebro (Ebro River Basin Authority)

DS: Dams State

EC: Environmental Costs

FS: Future State

GDP: Gross Domestic Product

HUS: Hydroelectric Users State

MC: Measures Costs

MS: Measures State

OS: Objective State

PH: Physical Hydronomics

PM: Plan of Measures

PS: Present State

RRC: Remaining Resource Costs

TRC: Total Restoration Costs

UUS: Urban Users State

WFD: Water Framework Directive

WUS: Without Users State

WWTP: Waste Water Treatment Plant

Subscripts and superscripts

IM: Inorganic matter

m: quantity component

N: Nitrogen-based components

OM: Organic Matter

p: potential

q: quality component

References

[1] D.O.C.E. *Directiva 2000/60/CE del Parlamento Europeo y del Consejo de 23 de Octubre del 2000 por la que se establece un Marco Comunitario de actuación en el ámbito de la política de aguas*. D.O.C.E. 2000. L 327 de 22.12.00 69 pp. [in Spanish].

[2] Valero, A.; Uche, J.; Valero, A. and Martínez A., (2009). *Physical Hydronomics: Application of the exergy analysis to the assessment of environmental costs of water bodies. The case of the inland basins of Catalonia*. Energy 34 (12), pp. 2101-2107.

[3] Valero, A.; Lozano, M. and Muñoz, M. A., (1986). *A general theory of exergy saving I. On the exergy costs*. AES Congress, vol. 2-3, ASME Book H0341C, New York.

[4] Zaleta-Aguilar, A.; Ranz, L. and Valero, A., (1998). *Towards a Unified measure of renewable resources availability: The exergy method applied to the water of a river*. Energy Conversion Management. Vol. 39 nº 16-18 pp. 1911-1917.

[5] Aquatool-DMA, *(Quantity and quality water masses simulation software),* (2009). Software Package. Universidad Politécnica de Valencia. IIAMA. Spain.

[6] Carrasquer, B.; Uche, J.; Martínez, A. and Valero, A., (2010). *Testing the compliance of the European Water Framework Directive in the Huerva river from the exergy approach*. Proceedings of the 23th conference on Efficiency, Cost, Optimization and Simulation and Environmental Impact of Energy Systems. 14-17 June 2010, Laussane.

[7] Endesa, (2007). *Presas en el mundo. Centrales hidráulicas en España*. Endesa ediciones. Madrid. [in spanish].

[8] Confederación Hidrográfica del Ebro, (2011). *Datos de la Oficina de Planificación Hidrológica*, Ministerio de Medio Ambiente y Medio Rural y Marino. Gobierno de España [available online] <http://oph.chebro.es/> [accesed 10.1.2012]

[9] Hernández, A., (2001). *Saneamiento y alcantarillado. Vertidos Residuales*. Colegio de Ingenieros de Caminos, Canales y Puertos, Universidad de Zaragoza. Zaragoza, Spain [in Spanish].

[10] Instituto Nacional de Estadística (INE), *Datos de Aragón. Instituto Nacional de Estadística*. Madrid, Spain. [available online] <http://www.ine.es/> [accesed in 10.1.2012] [in Spanish].

[11] River Net, *The Ebro river basin*. The European Rivers Network. [available online] <http://www.rivernet.org/ebro/basic.htm>. [accesed in 10.1.2012].

[12] De Lucas Martín, A. (2012). *Ebro River Basin Organization. Ebro Hydrographic Confederation* Oficina de Planificación Hidrológica. Ministerio de Medio Ambiente y Medio Rural y Marino. Gobierno de España [available online] <http://www.tecniberia.es/>. [accesed in 10.1.2012].

[13] Del Valle, J., el at, (2009). *Atlas de los ríos en Aragón*. Prames Ediciones. Gobierno de Aragón, Zaragoza, Spain [in Spanish].

[14] García Vera, A and Galván Plaza, R., (2010). *Water scarcity and drought Management*. Confederación Hidrográfica del Ebro. Ministerio de Medio Ambiente y Medio Rural y Marino. Gobierno de España. International Symposium in Water scarcity and drought in Spain. Riverside. March, 23.25th.

[15] Confederación Hidrográfica del Ebro, (2010). *Proyecto de plan Hidrológico de la Cuenca del Ebro. Documento borrador*. Technical Report. Ministerio de de Medio Ambiente y Medio Rural y Marino. Gobierno de España. Confederación Hidrográfica del Ebro. [In Spanish].

[16] IDAE, (2010). *Estudio de prospectiva. Consumo energético en el sector del agua*. Fundación OPTI, Gobierno de España. Ministerio de Industria, turismo y comercio. Instituto para la diversificación y ahorro de la Energía, 2010 [In Spanish]

[17] Instituto Aragonés del Agua, (2008). *Plan especial de depuración de aguas residuales en Aragón*, Gobierno de Aragón, Instituto Aragonés del Agua, Sodemasa. Zaragoza. In Spanish.

Application of the entropy generation minimization method to a solar heat exchanger: a pseudo-optimization design process based on the analysis of the local entropy generation maps

Giorgio Giangaspero[a]✉, Enrico Sciubba[b]

[a] *Department of Engineering and Fluid Dynamics, University of Twente, Enschede, Netherlands, g.giangaspero@utwente.nl, CA.*
[b] *Department of Mechanical and Aerospace Engineering, University of Roma 1 "La Sapienza", Roma, Italy, enrico.sciubba@uniroma1.it.*

Abstract:
This paper presents an application of the entropy generation minimization method to the pseudo-optimization of the configuration of the heat exchange surfaces in a Solar Roof Tile. An initial "standard" commercial configuration is successively improved by introducing design changes aimed at the reduction of the thermodynamic losses due to heat transfer and fluid friction. Different geometries (pins, fins and others) are analysed with a commercial CFD code that also computes the local entropy generation rate. The design improvement process is carried out on the basis of a careful analysis of the local entropy generation maps and the rationale behind each step of the process is discussed in this perspective. The results are compared with other entropy generation minimization techniques available in the recent technical literature. It is found that the geometry with pin-fins has the best performance among the tested ones, and that the optimal pin array shape parameters (pitch and span) can be determined by a critical analysis of the integrated and local entropy maps and of the temperature contours.

Keywords:
CFD, thermal convection, entropy, solar heat-exchanger, EGM.

1. Introduction

A fundamental thermodynamic theorem states that for whatever open process whose evolution can be approximated as a succession of quasi-equilibrium states and working in thermal contact with an ambient at T_0, the lost available power $\left|\dot{W}_{rev} - \dot{W}\right|$, i.e., the difference between the ideally produced power and the one really extracted, is proportional to the global rate of entropy generation $\dot{S}_{gen}$: $\dot{W}_{rev} - \dot{W} = T_0 \cdot \dot{S}_{gen}$ [1]. The lost power ($\dot{W}_{rev} - \dot{W}$) is always positive, regardless of whether the system is a power producer (e.g., an expander) or a power user (e.g., a compressor). Although not often exploited in real design applications, this theorem is of the utmost importance for the designer, in that it allows for a direct comparison of different configurations ("design options") that either produce the same output with less irreversible losses or use the same amount of resource input to generate a larger output; both cases corresponding of course to a higher resource-to-end use efficiency. Naturally, the minimization of the entropy generation is not an easy task in practical cases, especially when complicated boundary conditions apply and/or when the operating point is varying in time. During the last three decades the Entropy Generation Minimization (EGM) method has become a well-established procedure in thermal science and engineering: it relies on the simultaneous application of the heat transfer and engineering thermodynamics principles, in pursuit of realistic models for heat transfer processes, devices and installations. The overwhelming majority of applications of the method for heat transfer problems employs lumped-sum parameter models:

✉ Corresponding Author

the global rate of entropy generation ($\dot{S}_{gen}$ [W/K]) is analytically expressed as a function of the topology and physical characteristics of the system (critical dimension, materials...) using correlations for average heat transfer rates and fluid friction available in literature. Then, by varying one or more of the design variables which $\dot{S}_{gen}$ depends upon, a minimum of the entropy generation rate is sought after; thence, an optimal geometry is determined. Many examples of this lumped-sum parameter model technique applied to fundamental heat transfer problems are presented in [1–5]. Pin-fins geometries are optimized with this method in [6,7], while plate-fins heat sinks are optimized in [8,9]. The key point of this *deterministic* approach is the analytical definition of $\dot{S}_{gen}$ as a function of critical design parameters, like geometry and working conditions. This function has to be inferred with the simultaneous application of principles of heat and mass transfer, fluid mechanics and engineering thermodynamics. Its ability to well describe the inherent irreversibility of the engineering system is closely linked to the "quality" of the correlations on which it relies. But, once we are able to actually write a semi-empirical analytic functional for $\dot{S}_{gen}$, finding its minimum is more a mathematical than a physical problem. One of the aims of the present work is to describe a different, *heuristic*, approach: the initial configuration is successively improved by introducing design changes based on a careful analysis of the local entropy generation maps obtained by means of CFD simulations. One of the advantages of this approach is that the rationale behind each step of the design process can be justified on a physical basis. This approach is particularly well suited for problems where a CFD simulation has to be carried out anyway (not explicitly for the purpose of a second-law analysis) and no reliable and explicit correlations for the mean heat transfer and fluid friction are available. Typical examples are turbomachinery and (convective) heat exchangers design problems. While this approach has been already adopted in some turbomachinery problems ([10,11]), examples for heat exchangers like the one covered in this work appear quite rarely in the archival literature. One example can be found in [12]. This approach consists in focusing the attention first on the local entropy generation rates $\dot{s}_T$, $\dot{s}_V$ and in considering the global one $\dot{S}_{gen}$ only after having carefully studied the implications of the local irreversibility on the overall design. It must be noted that, while $\dot{S}_{gen}$ cannot directly reflect the specific local features of the flow that are necessary for its phenomenological interpretation, it is nevertheless the global quantifier that allows us to identify which one of two different configurations is the better performer from a second-law perspective: if systems A and B have the same input and operate so that $\dot{S}_{gen,A} > \dot{S}_{gen,B}$, it can be inferred that system A operates more irreversibly than system B, therefore -*ceteris paribus*- B should be preferred. In order to calculate these local rates, both the velocity and temperature field have to be completely resolved, and therefore a CFD solver, i.e., a distributed-parameter model, is needed. Once the entropy rates are known, thanks to the visualization tool of the solver, we can display the maps of and $\dot{s}_T, \dot{s}_V$ so that the designer is able to literally see where the entropy is produced at higher rates and therefore where exergy is destroyed at a higher rate; it is possible to pinpoint the areas where we should focus our attention on.

2. Strategy for probing the solution space and description of the heuristic procedure

The entropy generation rate can be shown, for the case in study (i.e. in the absence of phase changes and chemical reactions), to consist of two parts [1]: one, called "*viscous*" ($\dot{s}_V$), that depends on the physical viscosity, on the local temperature of the fluid and on the second power of the local velocity gradient, and another, called "*thermal*" ($\dot{s}_T$), that depends on the physical conductivity, on the square of the local temperature of the fluid and on the second power of the local temperature gradient:

$$\dot{s}_{gen} = \dot{s}_T + \dot{s}_V = \frac{k}{T^2}\left[\left(\frac{\partial T}{\partial x}\right)^2 + \left(\frac{\partial T}{\partial y}\right)^2 + \left(\frac{\partial T}{\partial z}\right)^2\right] + \frac{\phi}{T} \qquad (1)$$

ϕ being the rate of *viscous dissipation* per unit volume. Note that the entropy generation rate expressed in (1) is per unit volume (W/(K m^3)). The global entropy generation rate $\dot{S}_{gen}$ of the entire domain (W/K) is computed as the integral of the local rates over the entire volume V:

$$\dot{S}_{gen} = \int_V \dot{s}_{gen} dV = \int_V (\dot{s}_T + \dot{s}_V) dV = \dot{S}_T + \dot{S}_V \qquad (2)$$

As mentioned above, the approach adopted in this work consists in focusing the attention first on the local entropy generation rates $\dot{s}_T$, $\dot{s}_V$ and in considering the global one $\dot{S}_{gen}$ only after having carefully studied the implications of the local irreversible losses. In particular, the procedure for 'optimising' a design by means of an entropy generation analysis is the following:

1. Define a starting geometry or a family of starting geometries.
2. Acquire the geometries and create the computational grid to be imported into the CFD solver.
3. Compute the temperature and the velocity fields.
4. Compute and display the maps of $\dot{s}_T$, $\dot{s}_V$.
5. Integrate the local values to obtain the global entropy generation rate $\dot{S}_{gen}$.
6. Modify the design as suggested by a critical inspection of the local entropy maps.
7. Repeat the computation, and iterate until a feasible and acceptable "minimum" of $\dot{S}_{gen}$ is obtained.

It is now clear that the process described above is not an optimization proper, but rather a heuristic design approach, essentially based on a thermodynamically sound trial-and-error procedure. Nevertheless, the amount of phenomenological information contained in the local entropy generation maps is so high that a convergence towards a better design is almost guaranteed ([10]).

3. The Solar Roof tile

3.1 The TAK plant

The object of this study is the solar roof tile, called TAK, which is part of a complex system (the TAK plant) to provide the heating and cooling of a house (Fig. 1). The TAK plant can be divided in four main sub-systems:

- **TAK sub-system**: consisting of south-facing roof-tiles through which a secondary fluid flows, XEN, whose physical properties are given in Tab. 1. A pump (P1 in Fig. 1) provides fluid circulation.
- **Heat Pump sub-system:** a first heat exchanger (EX1) allows connecting the TAK sub-system with a Heat Pump sub-system through the heat exchange between secondary and primary fluid. The primary fluid, flowing through the heat pump cycle, is refrigerant 407C. A second heat exchanger (EX2) is necessary for the heat transfer to the Domestic Water Heating sub-system. An expansion valve is inserted to complete the cycle of the heat pump.
- **House Heating/Cooling sub-system**: this is the sub-system that interacts with the internal space; it includes radiators, fan coils or radiant panels with all their respective customary auxiliary components (pumps, valves, exc.).
- **Domestic Water Heating sub-system:** a boiler (B1) contains the water necessary for domestic use. This water receives heat from water circulating through the coil, which is then channelled into the heat exchanger EX2 of the Heat Pump sub-system. Another boiler is connected to a valve that allows the mixing of hot water with cold water.

The aim of this study is to optimize the geometry of the roof tile in winter conditions. In this season, during the hours of sun irradiation, the secondary fluid, XEN, is pumped (P1) through the south-side tiles. The XEN is heated in the row of tiles and then flows into the evaporator (EX1) of the Heat-Pump where it is cooled again to repeat the cycle (1S-8S in Fig. 1). The primary fluid, the refrigerant R407C, is heated by the secondary fluid in the evaporator, compressed (C) and channelled into the condenser (EX2) where it condensates, heating the water flowing in the Heating sub-system (streams 1W to 9W). The hot water is first used to heat the domestic water (in the boiler B1) and then flows into the inertial tank (T1) that feeds the Heating System. If the inertial tank temperature is lower than the temperature of water leaving B1 (Stream 5W), the hot water by-passes the tank (5cW) and it is used directly by the Heating Systems.

3.2 The solar roof tile

The TAK roof tile consists of a lower part made of a suitable polymeric material with a sealed aluminium slab on top of it (Fig. 2). The aluminium slab has dimensions 378.5x157.3x0.5*mm* while the height of the fluid channel is 3.5*mm*, as shown in Fig. 3. It should be mentioned that, as we shall see later, many other geometries were proposed and analysed, but in the optimization process the dimensions just given and the peripheral edges and faces of the fluid channel were kept constant.

3.2.1 Working conditions

On the basis of the sizing and simulations of the complex system described above, the mass flow and inlet temperature of the first line of the roof tile have been determined to be:

$$\dot{m} = 0.0044 kg/s \qquad (3)$$

$$T_{in} = 30°C \qquad (4)$$

As representative working conditions, the following values for the sun irradiation $\dot{q}_{sun}$ and external temperature T_{ext} are chosen[1]:

$$\dot{q} = 400 W/m^2, \qquad (5)$$

$$T_{ext} = 10°C, \qquad (6)$$

As mentioned above, this work presents an application of the entropy generation minimization method to the pseudo-optimization of the configuration of the heat exchange surfaces in this solar roof tile. A group of initial "standard" geometries is first presented and analyzed (see Section 3.2.2). Then two of them are successively modified by introducing design changes aiming at the reduction of the thermodynamic losses due to heat transfer and fluid friction. The different geometries (featuring pins, fins and others) are simulated with a commercial CFD code that also computes the local entropy generation rate. The design improvement process is carried out on the basis of a careful analysis of the local entropy generation maps and the rationale behind each step of the process is discussed in this perspective.

Table 1. XEN fluid data.

Property	symbol	value	units
Density	ρ	1106	kg/m^3
Viscosity	μ	0.003	*Pa s*
Specific Heat	c_p	2698	*J/(kg K)*
Thermal conductivity	*k*	0.29	*W/(m K)*
Prandtl number	*Pr*	27.9	

[1] Average winter values in a city like Rome (latitude ≈ 42° N), at noon on a roof with a tilt angle of 30° [13].

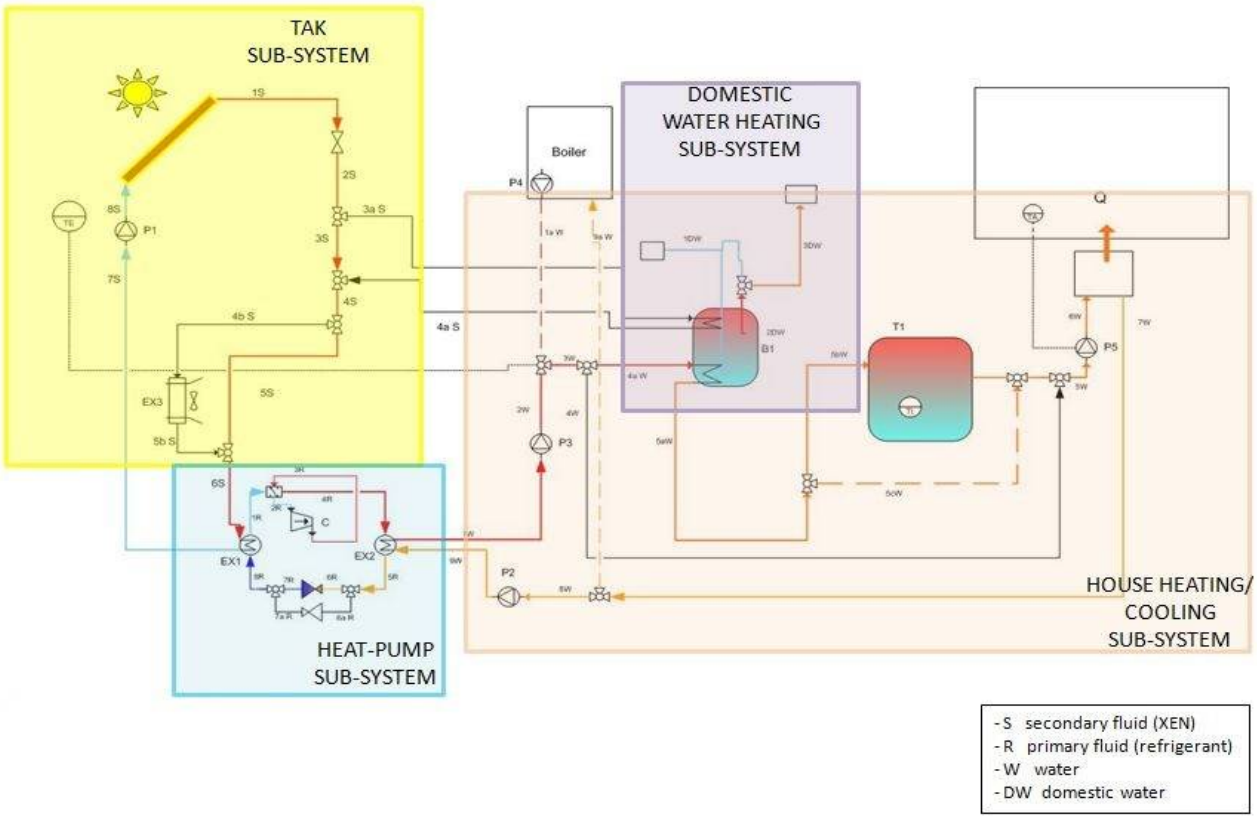

Fig 1. TAK plant flow chart..

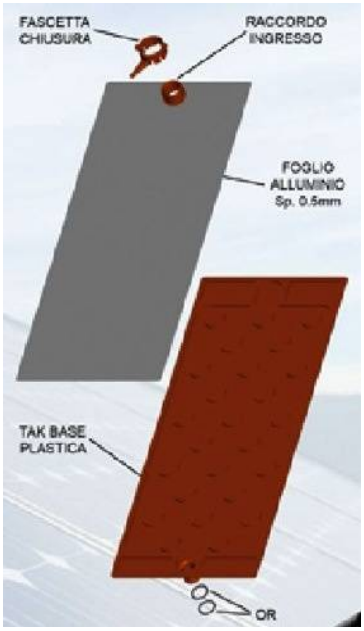

Fig. 2. Exploded view of the TAK roof tile.

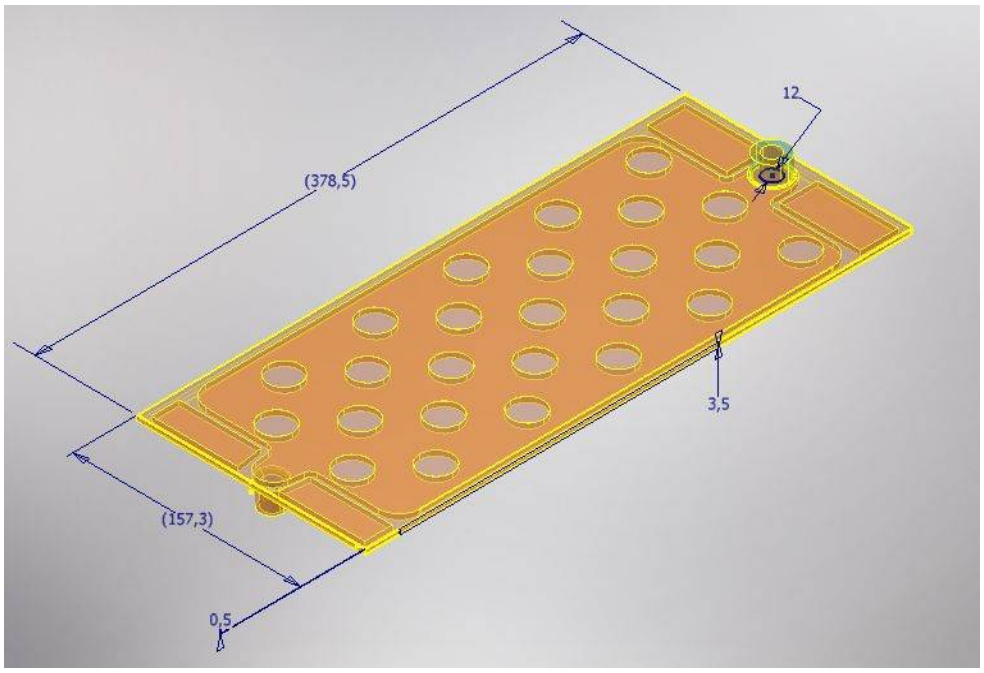

Fig. 3. TAK main dimensions in mm.

3.2.2 The Initial geometries

The starting geometries, proposed by the original patent holder, GreenMind Company, are reported in Fig. 4(a). Geometry A.0 presents 24 plastic pin-fins with a diameter of D = 2.24*cm*. To this group of starting geometries we added Geometry E.0 (Fig. 4(b)), in which the heat transfer is enhanced by four aluminium plate-fins cold rolled on the slab. The fins are 1*mm* thick, 3.5*mm* high, their length is *L*=28*cm* and their distance in the span-wise directions is *δ=30mm*.

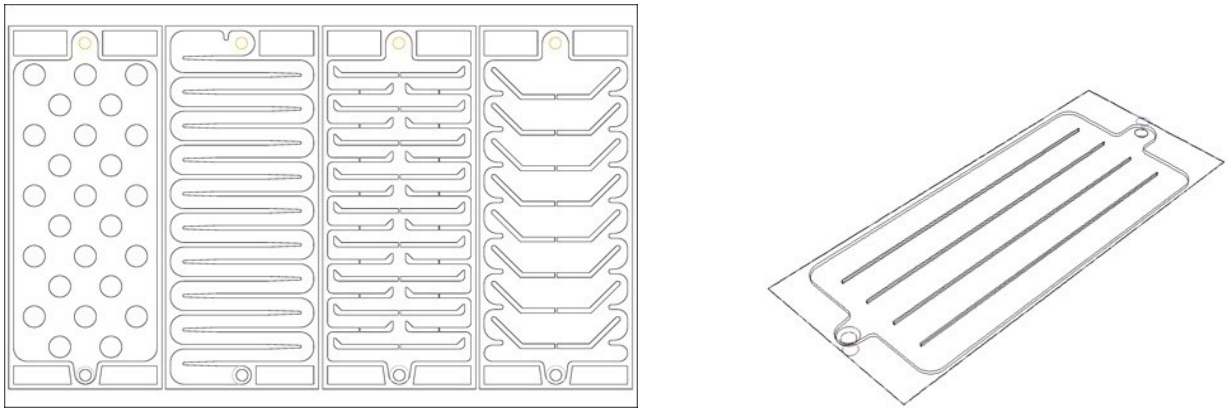

(a) *(b)*

Fig. 4. Top view of: (a) geometry A.0, B, C, D; (b) geometry E.0.

The main results of the simulations of the starting geometries are reported in Table 2 (for the simulation details, see Section 5), from which the following general considerations can be made:

- $\dot{S}_V$ is one or two orders of magnitude smaller than $\dot{S}_T$;
- $\dot{S}_V$ is proportional to the pressure losses (Δp); the higher $\dot{S}_V$, the higher Δp;

- as $\dot{S}_T$ decreases, the average temperature of the aluminium slab, $T_{av,slab}$ decreases as well; lower $T_{av,slab}$ means lower heat losses and therefore a higher heat transfer rate $\dot{Q} = \dot{m} \cdot c_p \cdot \Delta T$ to the fluid.

Furthermore, it can be seen that geometry B presents the lowest $\dot{S}_T$ and the highest value of $\dot{S}_V$. In fact, the flow is confined to a relatively small area so the velocity is high and this ensures high heat transfer coefficients. At the same time, the high mean velocity, combined with the presence of many sharp curves, causes a quite high value of pressure losses and therefore of viscous dissipation. Geometry B is also the best performer from a thermodynamic point of view, nevertheless the relatively high pressure losses are a big drawback. Geometries C and D do not appear to have a big "potential" for an optimization process. For these reasons, the geometries chosen to apply to the optimization process described in Sections 1 and 2 are A and E.

Tab. 2. Simulation results for the starting geometries. $T_{av,slab}$ the average temperature of the upper surface of aluminium slab; $\dot{Q} = \dot{m} \cdot c_p \cdot \Delta T$ represents the heat transfer rate to the fluid and Δp is the pressure drop across the solar roof tile.

	$T_{av,slab}$ [K]	$\dot{Q}$ [W]	ΔT	Δp [Pa]	$\dot{S}_T$ [W/K]	$\dot{S}_V$ [W/K]	$\dot{S}_{gen}$
A.0	304.91	10.665	0.91	25	1.39E-04	2.85E-07	1.39E-04
B	304.30	10.898	0.92	961	7.78E-05	1.10E-05	8.88E-05
C	304.43	10.841	0.91	278	9.80E-05	2.13E-06	1.01E-04
D	304.92	10.658	0.9	77	1.26E-04	1.39E-06	1.27E-04
E.0	304.32	10.777	0.91	19	1.11E-04	2.18E-07	1.11E-04

4. Alternative geometries

As stated before, the ("family" of) geometries chosen for further development are geometry A and E. In the next paragraphs the variations on each of these two families are presented. In section 6, the results and the rationale behind each design change is discussed.

4.1 Geometries of type E

Geometry E.1 presents 9 plate-fins 1*mm* thick, 2*mm* high, *L*=28*cm* long and distanced δ=15*mm* in the spanwise direction (Fig. 5(a)). Instead, Geometry E.2 features 10 "split-entry-length", 7.5*cm* long, fins, along with the 9 plate-fins of geometry E.1 (see Fig. 5(b)).

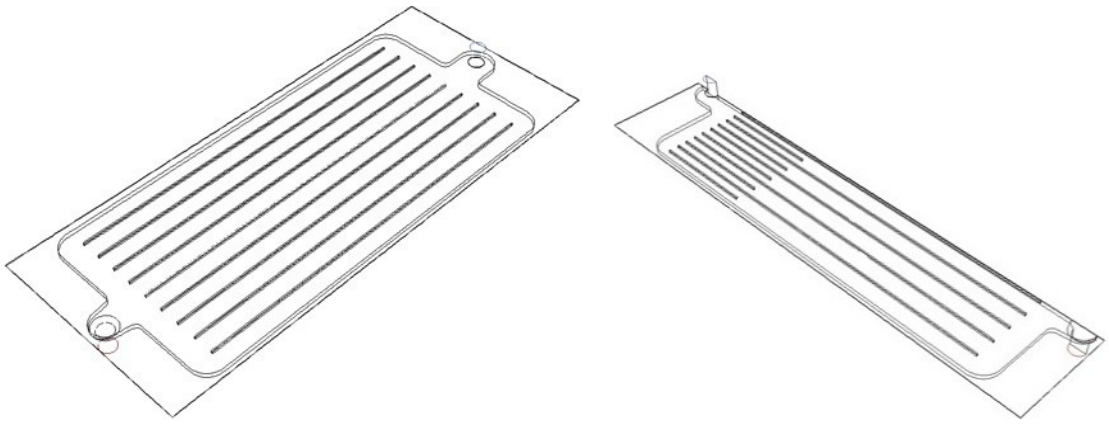

(a) (b)

Fig. 5. Geometry E.1 (a) and half of geometry E.2 (b).

For comparison, geometry E.3 (not shown) has been also designed and simulated. This geometry has 19 fins 28*cm* long, 2*mm* high and 1*mm* thick. The only difference with geometry E.2 is that all the 19 (9+10) fins are 28*cm* long.

4.2 Geometries of type A

The starting geometry of the A family presents 24 pin-fins with a diameter of D = 2.24*cm* made of plastic material. As a first design modification, the plastic fins are substituted with aluminium ones impressed with the slab, geometry A.1. This simple modification leads to a 15% improvement of the global entropy generation rate. For this geometry, the dimensionless pitches are $P^*_T=P_T/D=2.34$ and $P^*_L=P_L/D=1.41$, where P_T and P_L are the transverse (spanwise) and the longitudinal (streamwise) pitch, respectively.

In order to enhance heat transfer, it was decided to design a new geometry, A.2, with fins half the diameter of the current ones but keeping the same array geometry, i.e. same P^*_T and P^*_L. Therefore, geometry A.2 presents 104 fins with a diameter of D=1.12*cm*, height of 3.5*mm*, P^*_T =2.34 and P^*_L=1.41, as can be seen in Fig. 6. As will be seen later, at the bottom of the channel the fins are not effective; therefore, in geometry A.3, it is decided to limit the height of the fins to 2*mm*.

Geometry A.4 features pins of different diameters placed in "strategic" positions determined by a careful analysis of the local entropy maps (see Section 6). As shown in Fig. 7, smaller fins are placed in between the columns and row of the original array.

Geometry A.5 (shown in Section 6), is obtained by simply inserting in A.3 another column of pin fins. Pins now become 161 (57 more than geometry A.3) and the characteristics parameters of the array are P^*_T=1.46 and P^*_L =1.41.

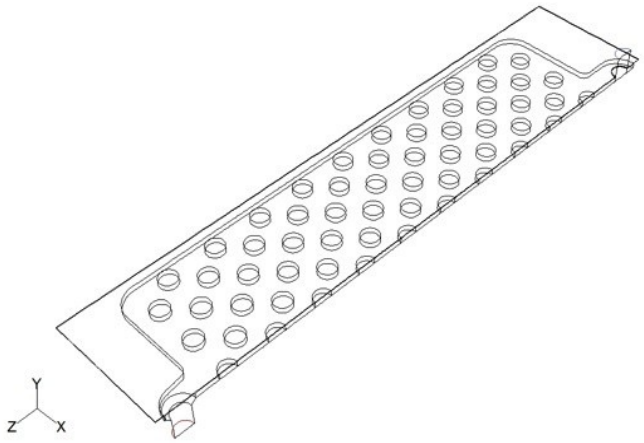

Fig. 6. Geometry A.2 (half).

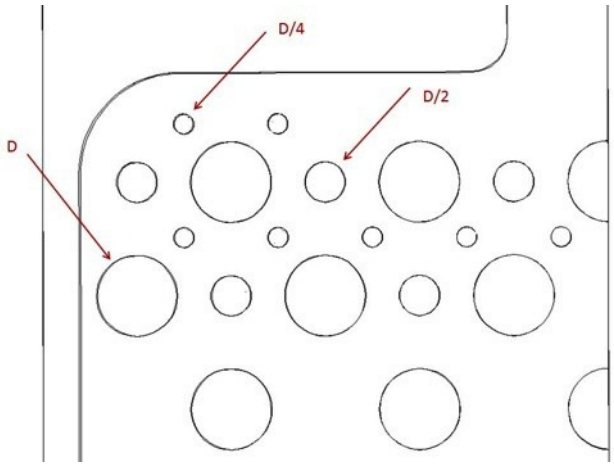

Fig. 7. Detail of geometry A.4.

5. The numerical simulations

5.1 Meshing

Four starting geometries (A.0, B, C, D in Fig. 4(a)) were made available by the GreenMind Company which provided the relative IGES files. Once imported into GAMBIT, the mesh generator, all of the geometric features of the TAK deemed inessential for the goals of the present simulations were removed: only the fluid channel, the inlet and outlet ducts and the aluminium slab are retained. The obvious symmetry of the design, and with the exception of geometry B, only half of the TAK was modelled, discretized and simulated. As mentioned above, many other geometries were designed and tested (see Section 3) but are not reported here. The control volume of all geometries is always created starting from the "base" volume shown in Fig. 8.

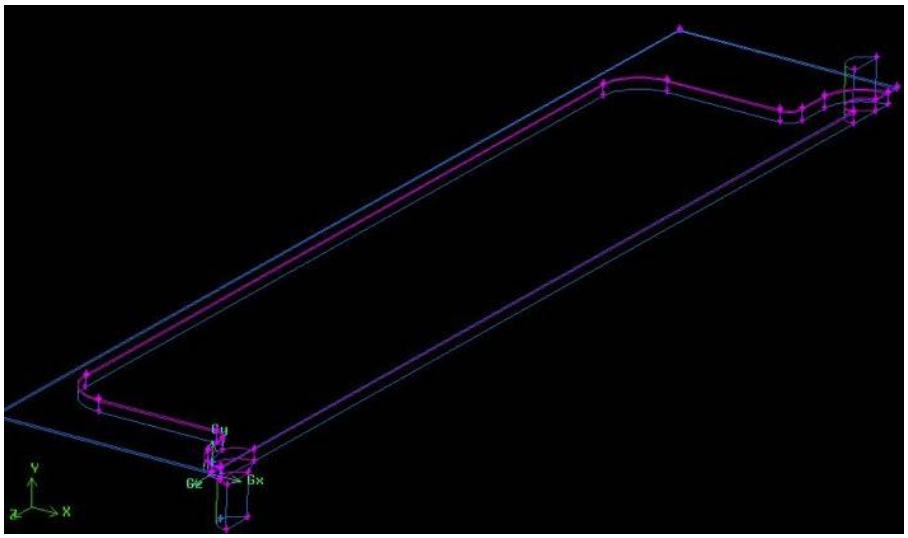

Fig. 8. Base geometry used in the optimization process.

The following general procedure is applied to all geometries:

- The control volume is split in several smaller sub-volumes, as indicated in Fig. 9 for one representative geometry. This step produces a decomposition of the control volume necessary to successfully apply the Cooper meshing scheme.
- Each edge is meshed using an element size specific of the single volume given in Tab. 3 with the only exception of the fluid channel height, which is meshed with 16 elements.
- If the geometry features pins, a boundary layer with 10 rows is attached to the solid wall.
- The bottom surface of the fluid channel is meshed using a "paved" scheme, which allows meshing such a complex surface without further subdividing it. The drawback, of course, is the generation of an unstructured mesh, in which the regularity of the internal gridpoint is lost.
- The fluid channel volume is meshed with the Cooper scheme (GAMBIT automatically selects the source surfaces).
- The remaining volumes are meshed using again the Cooper scheme.

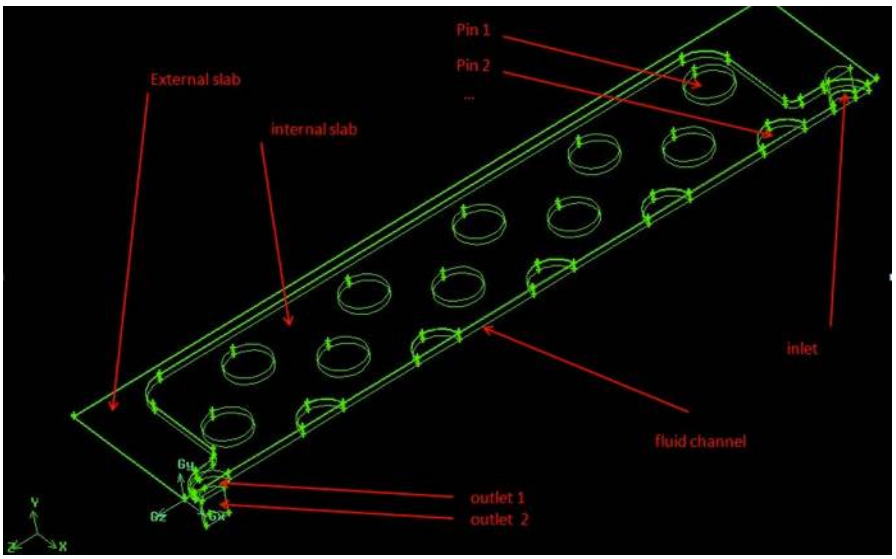

Fig. 9. Definition of the sub-volumes.

This procedure leads to a very high quality mesh; usually more than 98% of the cells have an Equisize skew < 0.55. The number of elements is highly dependent on the fin diameter D: it goes from 231761 to 1327432 for D = 2.24 cm and D = 0.56 cm, respectively. The meshes of finless geometries are usually composed by no more than 400000 elements. All meshes consist only of hexahedral or wedge elements. Thus the mesh can be directly read by the parallel solver and all the cells are eligible for grid adaption.

Tab. 3. Mesh element size for the edges of the indicated sub-volumes.

Volumes:	Element size [mm]
Fluid channel	11
Inlet	1
Outlet	1
Pins	D/24
Internal slab	1
External slab	5

5.2 Boundary conditions and parameters setting

All simulations have been processed by means of the CFD code FLUENT in Parallel mode, with 2 processors. After performing the grid check, the mesh has been scaled. Then the *Pressure Based* solver with the *Green-Gauss Node Based gradient* option at *steady state* has been chosen, and the energy equation enabled. The *Laminar* viscous model was selected, since the Reynolds number in all cases is well below the transition regime. In the *Materials Panel* a custom fluid, with the properties of the XEN fluid given above, is created.

The boundary conditions are imposed as follows:

- Inlet: constant mass flow, equal to 1/2 of the valued given in (3), i.e. 0.0022 kg/s, and constant temperature T_{inlet}*=30°C.*
- Outlet: constant atmospheric pressure.
- Symmetry planes: zero gradients of all variables.
- External surface of the aluminium slab: this *Wall* surface receives the solar irradiation. In order to take into account the presence of a glass and an air gap (5 *mm* thick) on top of the slab, a *convective boundary condition* is used. The Heat Transfer Coefficient and the Free Stream Temperature are 6.29 W/(m^2 K) and 60.29 °C, respectively. These values represent the overall

heat transfer coefficient and the so called “solar air temperature”, respectively. They are based on the values given in (5) and (6).

- Fluid and Solid: these boundary conditions allow the definition of the fluid evolving through the roof tile as well as the material of the solid volumes. In this problem, the previously defined XEN is selected for the fluid volume, while the default material, aluminium, is retained for the solid parts.

For all remaining wall surfaces the default settings have not been modified so that adiabaticity, impermeability and no slip conditions are imposed.

All simulations are initially started with a first order discretization scheme, then, when convergence is obtained, the second order scheme is enabled and the iteration restarted until convergence is attained (all the scaled residuals below 10^{-3}, except for the energy equation for with the threshold is set to 10^{-6}).

5.3 Mesh refinement

The next step involves a critical process: the grid sensitivity analysis. Goal of the mesh refinement is to demonstrate the mesh ability to capture the smallest (modelled) scales of the fluid dynamics phenomena involved in the simulation. An improved grid should be able to better describe the fluid behaviour and in order to determine the grid “quality” enhancement a cornerstone function field is needed for a performance comparison: the cornerstone function adopted in this work is the thermal entropy generation rate, since in this case it is one or two order of magnitude larger than the viscous one. The adaption tool available in the solver permits to change the number of cells belonging to a grid, both by coarsening and refinement. Excluding a priori any possibility of coarsening that will lead to a worse grid, the refinement can be operated with a criterion based on the gradient magnitude of the objective function. This “gradient” is the difference of the values of the selected field function between two adjacent cells; therefore a large gradient indicates a potentially inaccurate numerical solution. The grid refinement should deliver a more efficient control volume, and to result in a better evaluation of the entropy generation rates. In fact, to increase the number of cells is tantamount to increase the numerical solver aptitude to capture the small-scale dissipative phenomena, which are reflected in the value of the entropy generation rates. In this perspective, a critical analysis on the magnitude distribution across the control volume of the gradient of the entropy generation rates was performed. In the refinement of the grid, the *Refine Threshold* has been set to approximately 5% of the values reported in the Max field (i.e. the maximum value of the adaption function). As suggested in [14], the adaption threshold value has not been changed during the successive mesh adaptions which were repeated until the variation in the entropy rates lower than a 4% was reached.

6. RESULTS AND DISCUSSION

6.1 Geometry E

The central idea is that we expect low values of the local entropy rates in areas where similar boundary layers merge. The word “similar” means that the two boundary layers must draw origin from the same boundary conditions: that is the same surface geometry and the same ΔT. On the contrary, we expect high values of $\dot{s}_T$ and $\dot{s}_V$ inside the boundary layers, since these are zones where velocities and temperatures change rapidly; so, from a thermodynamic perspective, we would like to reduce them. Nevertheless, boundary layers are “necessary”: by definition, convective heat transfer is the energy transfer between a surface and a fluid moving over the surface. If we limit the surface area and thus the boundary layer, we also decrease the heat transfer to the fluid. A compromise is needed. A possible solution was found in the insertion of another plate in the middle of the channel, parallel to the mean flow direction and long enough to generate a thermal boundary layer which merges with the ones generated by the other plates at its end (Fig. 10). This “new”

boundary layer will cause a local increment of $\dot{s}_T$ and $\dot{s}_V$ at the entrance of the channel, but will reduce $\dot{s}_T = k\,(\Delta T)^2/T^2$ downstream. In fact, the velocity profile becomes smoother and the presence of another heat transfer surface causes a local increment of the mean fluid temperature T. As we shall see later, the overall balance is favourable: the introduction of the middle plate causes a reduction of the total entropy $\dot{S}_{gen}$ generated in the system.

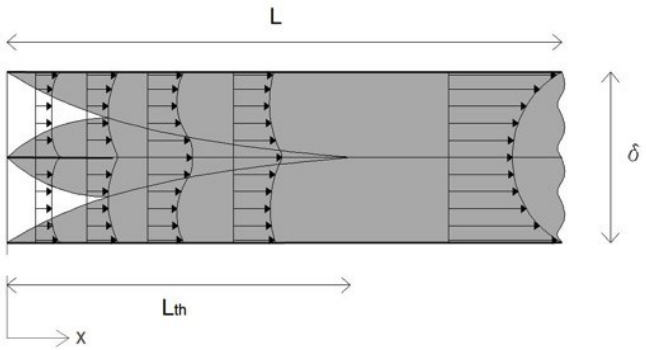

Fig. 10. Growth of the thermal boundary layer between two parallel plates with a "split-entry length"($T_{plate} > T_{fluid}$).

In geometry E.0 of Fig. 4, the distance between the fins δ has been originally chosen by solving the thermal entry length problem so that the thermal boundary layers would merge right at the end of the fins, that is after a distance $L=L_{th}$ in the streamwise direction. The thermal entrance length L_{th} is conventionally defined as the duct length required to achieve a value of the local Nusselt number Nu_x equal to $1.05Nu$ for fully developed flow (see [15]). A fully developed temperature profile starts where the thermal boundary layers merge. The dimensionless thermal entrance length is expressed as:

$$L_{th}^{*} = \frac{L_{th}}{D_h \cdot \mathrm{Re} \cdot \mathrm{Pr}}, \qquad (7)$$

where D_h is the duct hydraulic diameter, *Re* is the duct Reynolds number and *Pr* is the Prandtl fluid number. Fig.11 represents the plot of the temperature profile at a constant height $y = 1.75mm$ at four different sections (*z1*,*z2*,*z3*,*z4*) in the streamwise direction *z*; these four sections are defined as $z1 = 0$, $z2 = L/3$, $z3 = 2L/3$and $z4 = L$, *L* being the length of the fin. The thermal boundary layer starts growing at *z1* and reaches its maximum thickness at *z4*.

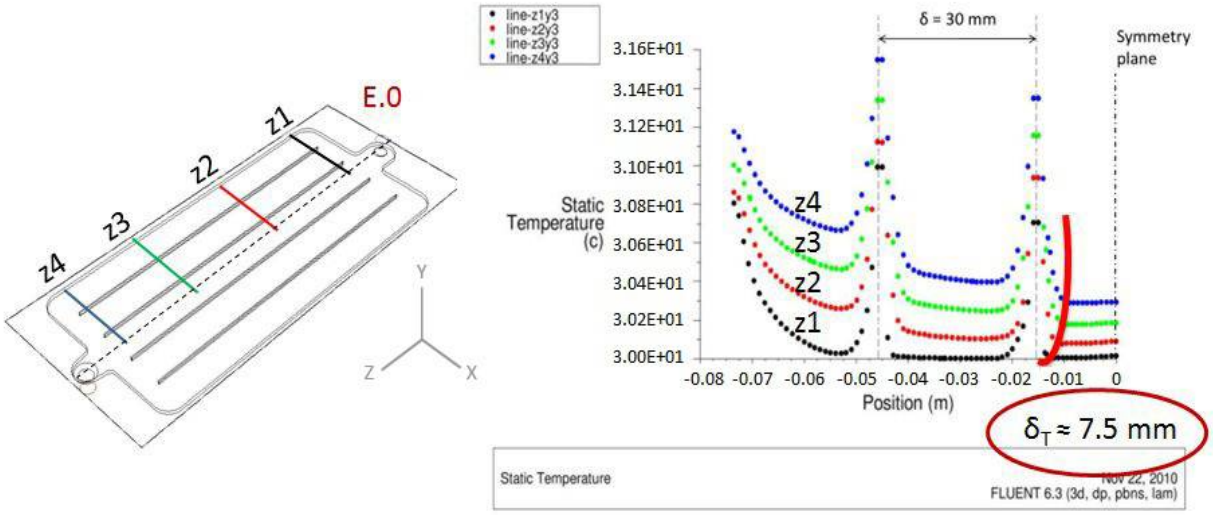

Fig. 11. Temperature profile in the mid plane at different sections downstream (geometry E.0).

From Fig. 11 we find that the thermal boundary layer thickness δ_{th} at the end of the fin, *z4*, is $\delta_{th}\approx 7.5mm$. Therefore, since we want the thermal boundary layer to merge right at the end of the fins, the distance between them should be $\delta=2\ \delta_{th}=15\ mm$, which was therefore selected as the distance between the fins of geometry E.1. Once we know the dimensionless thermal entry length of the problem, it is possible to calculate the split-entry length fin of Fig. 10, which turns out to be 7.5*cm* long. Accordingly, the ten intermediate fins of geometry E.2 (Fig. 5(b)) are 7.5*cm* long.

Fig. 12 shows the contours of $\dot{s}_T$ at $y=2\ mm$ for geometry E.1 and E.2. It can be seen how the presence of the middle fins causes a reduction of the local thermal entropy generation rate.

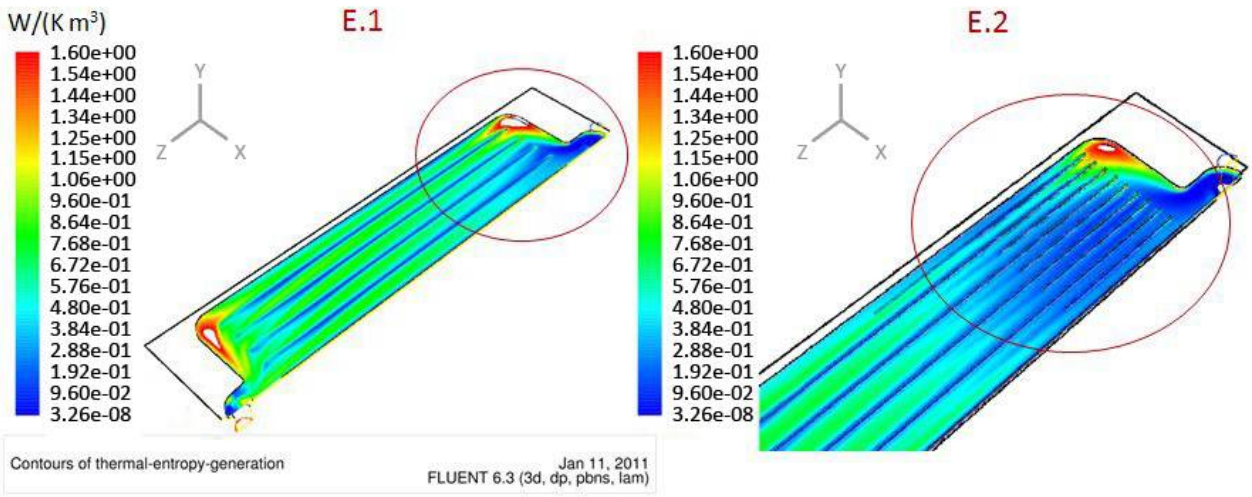

(a) (b)

Fig. 12. Contours of $\dot{s}_T$ at y = 2mm for geometry E.1 (a) and E.2 (b).

The simulation results, for all the E-type geometries, are reported in Tab. 4. As shown in Tab. 4, even though the heat transfer area is significantly different, no appreciable variation of Q, and therefore of ΔT, is obtained (at least in this first roof tile). Instead, the generated entropy appears to be more sensible to the variation of the heat transfer area. In fact, $\dot{S}_{gen}$ in E.2 is 11% less than in E.1 while E.3 produces 14% less entropy than E.1. The variation of the heat transfer area, though, is not proportional: only 5% in the first case and 14% in the second. Hence, it could be inferred that the shorter (interstitial) fins are more effective from a thermodynamic perspective.

Table 4. Comparison between the main results obtained for geometries E.1, E.2 and E.3. $\Delta E2-1$ represents the percentile variation of the indicated quantities between E.1 and E.2; $\Delta E3-2$ represents the percentile variation of the indicated quantities between E.2 and E.3.

	E.1	E.2	E.3	ΔE_{2-3}	ΔE_{2-3}
Heat transfer area [cm^2]	573.57	603.97	685.97	5%	14%
$T_{av,slab}$ [K]	304.60	304.52	304.43	-0.03%	-0.03%
$\dot{Q}$ [W]	10.777	10.811	10.842	0.32%	0.29%
ΔT	0.909	0.911	0.913	0.24%	0.22%
Δp [Pa]	19	20	22	3%	9%
$\dot{S}_T$ [W/K]	1.11E-04	9.83E-05	8.43E-05	-11%	-14%
$\dot{S}_V$ [W/K]	2.87E-07	2.26E-07	2.43E-07	4%	7%
$\dot{S}_{gen}$	1.11E-04	9.86E-05	8.45E-05	-11%	-14%

6.2 Geometry A

Fig.13-14, represent the contour of thermal entropy generation and temperature, respectively, at different height of the channel. $\dot{s}_T$ decreases towards the bottom of the channel (lower *y*), except in very small zones in the proximity of the fins where it remains high. In these zones of high temperature gradients, the local heat transfer coefficients are low and the fins are not effective. Therefore, it was decided to limit the height of the fins in geometry A.3 to 2*mm*; this modification leads to an improvement in the fin effectiveness and in the global entropy generation which is reduced by 6% (Tab. 5). As shown in Fig. 13, $\dot{s}_T$ assumes the highest values in proximity of the lateral boundaries where the heat absorbed by the corners of the slab is exchanged with an almost stagnant fluid. Moreover, near the outlet, the entropy production is increased also by the mixing of the upper, hotter, fluid with the lower and colder part of the stream. High values of $\dot{s}_T$ are also found in between columns of fins, forming a sort of "entropy rivers" flowing along the roof tile.

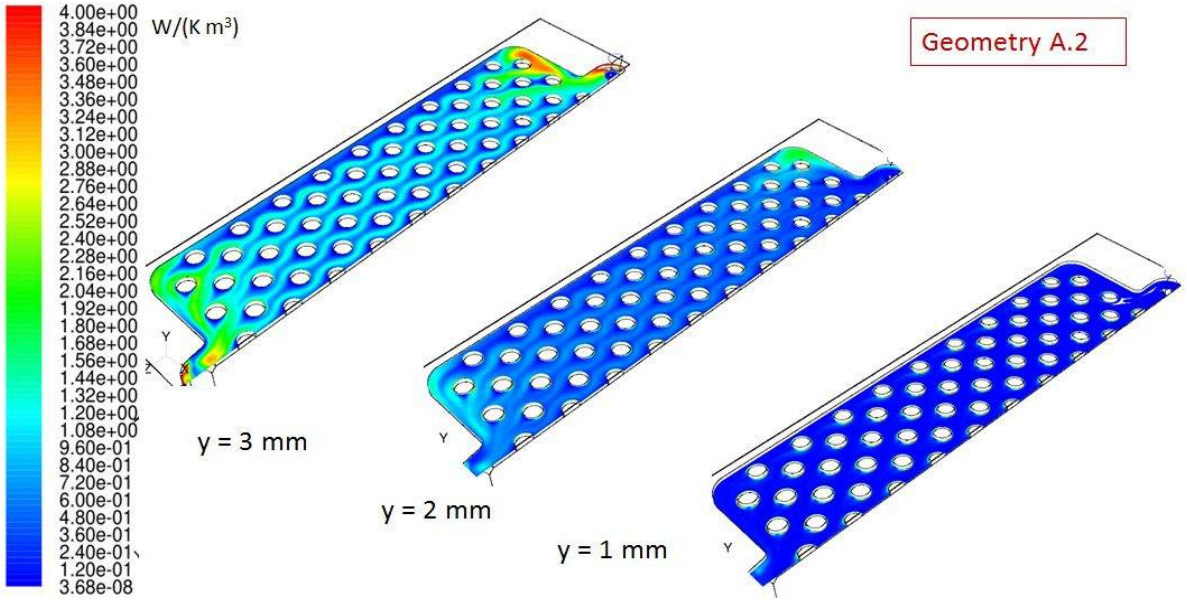

Fig. 13. Contours of Thermal Entropy generation for Geometry A.2 at different height of the channel.

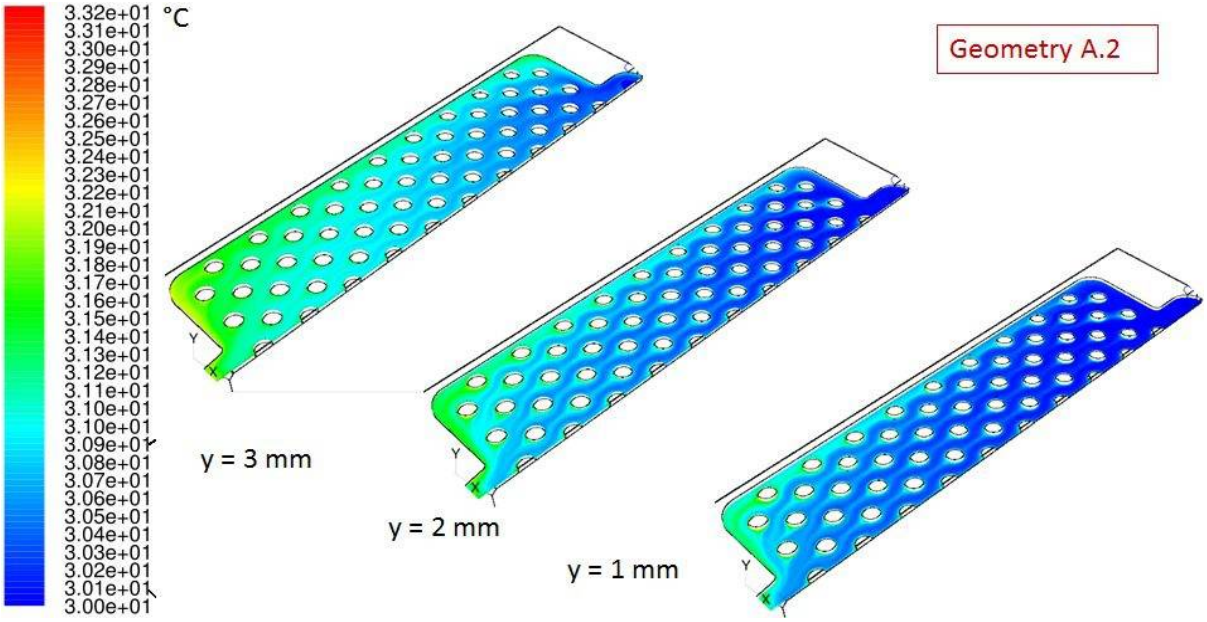

Fig. 14. Contours of Temperature for Geometry A.2 at different height of the channel.

Looking at the temperatures contours, Fig. 14, it can be seen that the thermal boundary layers generated by one row of fins do not merge with the thermal wake generated by the very next row. On the basis of these considerations, it was argued that an “optimal” (in a second law perspective) geometry, should feature a gradual increment of the transverse pitch P^*_T along the streamwise direction. In addition, the diameter of the fins should increase moving towards the bottom of the channel. In fact, the maximum thickness of the boundary layer increases in the streamwise direction as well as along *y*. A fin of such geometry, however, would imply important technological issues and increased costs.
Two more configurations were devised: A.4 was designed to counteract the entropy generation due to the boundary effects, and A.5 to eliminate the entropic rivers.

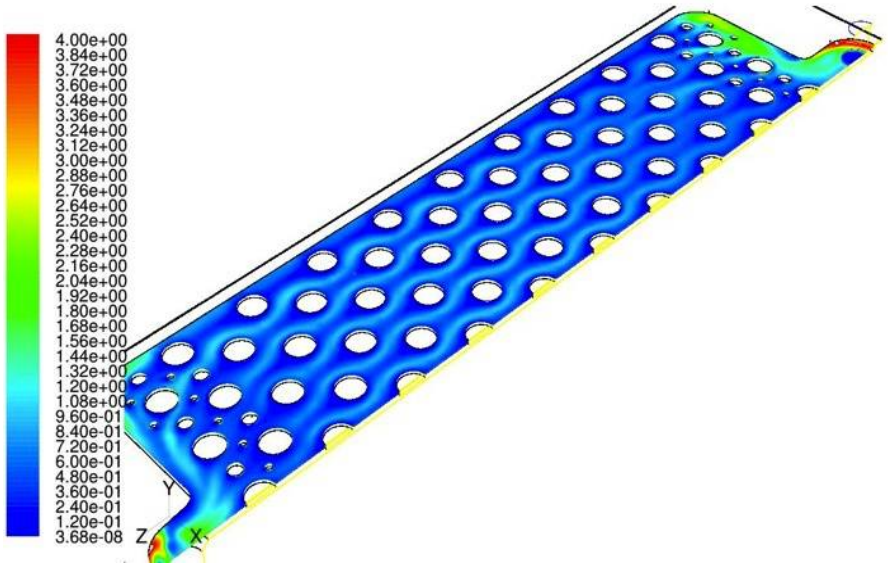

Fig. 15. Contours of the local Thermal Entropy Generation for Geometry A.4 at y=3mm.

As can be seen comparing Fig. 13 and 15, the boundary effects have been limited but areas of high $\dot{s}_T$ still persist. Geometry A.4 produces 9% less entropy than geometry A.3 (Tab. 5). As stated before, Geometry A.5, instead, is obtained by A.3 simply by inserting another column of pin fins. This design modification leads to a substantial improvement in the rate of entropy production which decays by 20% with respect to geometry A.3. In fact, looking at Fig. 16 and 17, the entropic rivers are no longer present and the individual thermal boundary layers originated on a single fin are actually no longer distinguishable since they all merge.

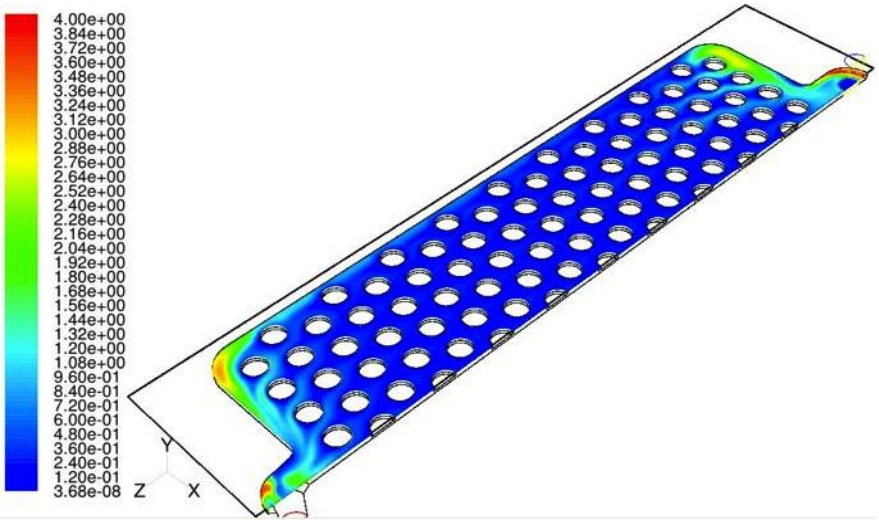

Fig. 16. Contours of the local Thermal Entropy Generation for Geometry A.5at y=3mm.

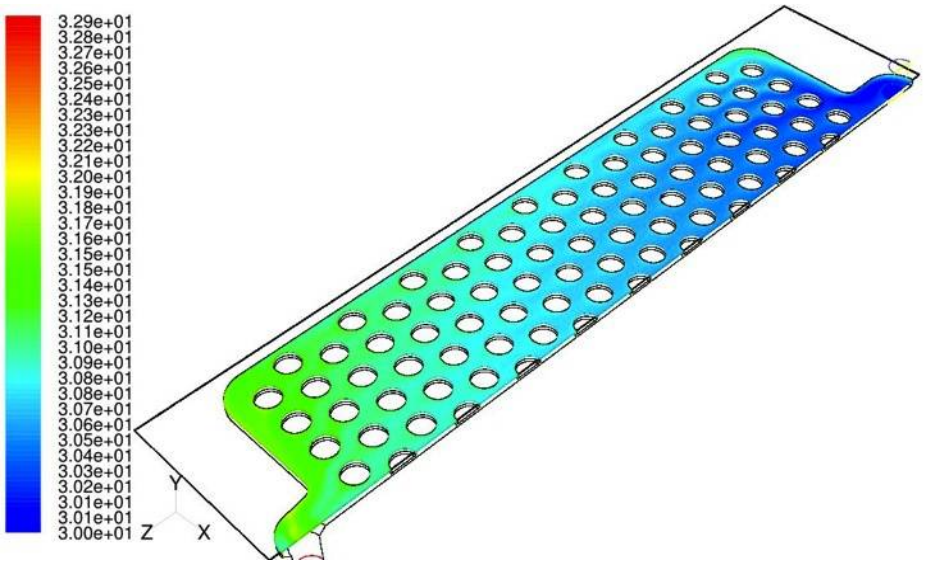

Fig. 17. Contours of Temperature for Geometry A.5at y=3mm.

Comparing the results obtained for geometries A.3, A.4 and A.5, it seems that the entropic rivers, i.e. the entropy generated by a sub-optimal choice of the transverse pitch P^*_T, have more influence on $\dot{S}_{gen}$ than the local entropy production due to boundary effects, which, however, appear difficult to counteract.

Tab. 5. Simulation results for all the A-family geometries.

	$T_{av,slab}$ [K]	$\dot{Q}$ [W]	ΔT	Δp [Pa]	$\dot{S}_T$ [W/K]	$\dot{S}_V$ [W/K]	$\dot{S}_{gen}$
A.0	304.91	10.665	0.91	25	1.39E-04	2.85E-07	1.39E-04
A.1	304.76	10.720	0.91	25	1.18E-04	2.85E-07	1.18E-04
A.2	304.56	10.795	0.91	26	9.92E-05	3.03E-07	9.95E-05
A.3	304.47	10.827	0.91	25	9.35E-05	2.90E-07	9.38E-05
A.4	304.40	10.854	0.91	26	8.55E-05	3.03E-07	8.58E-05
A.5	304.29	10.894	0.92	32	7.46E-05	3.82E-07	7.50E-05

6.3 Integrating the heuristic and the deterministic approach

Clearly, the optimization process described above can be applied, mostly, to a limited number of values of the fin diameter *D*: the heuristic approach, though powerful, has intrinsic limitations. However, a further study about the influence of the pin-fin array on the thermodynamic performance of the roof tile can be developed. Hence a deterministic approach was adopted. Following a procedure employed by many authors[2], a lumped-sum parameter model was developed to analytically express $\dot{S}_{gen}$ only in terms of the dimensionless transverse pitch P^*_T and the fin diameter *D*. Details are given in [16].

The entropy generation model can be developed by considering the control volume CV shown in Fig. 18. The CV includes the pin fin array and a base plate. The side surfaces AEFG and BCJI and the top surface CJFE of this CV are regarded as impermeable and adiabatic. The incompressible fluid of density ρ enters the volume at temperature T_{in} and velocity U_{in}. T_{base} and T_{fin} are the average temperatures of the base plate and the fins, respectively. The total heat transfer rate over the boundary of the CV is

$$\dot{Q} = \dot{Q}_{fins} + \dot{Q}_{base}. \qquad (8)$$

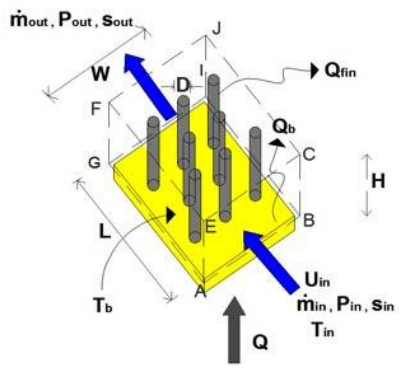

Fig. 18. Control volume for calculating $\dot{S}_{gen}$ for a pin fin array

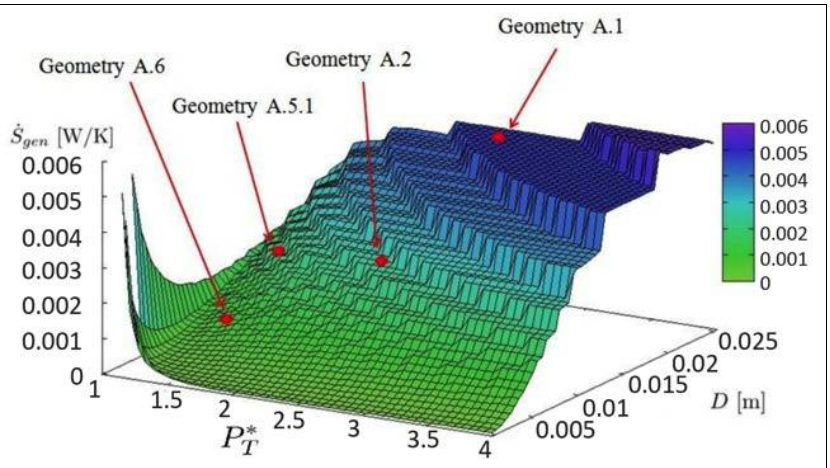

Fig. 19. 3D plot of the function $\dot{S}_{gen}$ for the control volume. Representative points of the indicated geometries are also shown.

Assuming $T_{base} \approx T_{fin} \approx T_{wall}$, the global entropy generation in the CV can be written as ([1]):

$$\dot{S}_{gen} = \dot{S}_T + \dot{S}_V = \frac{\dot{Q} \cdot \Delta T}{T^2_{in}} + \frac{\dot{m} \cdot \Delta p}{\rho T_{in}}, \qquad (9)$$

where $\Delta T = T_{wall} - T_{in}$ and $\Delta p = p_{in} - p_{out}$ is the pressure difference experienced by the fluid across the CV. As shown in Fig.19, the global entropy generation reaches its maximum for both high P^*_T and

[2] See the already cited [1-2] and [6-9].

D; it tends to infinity for $P^*_T \rightarrow 1$ for any diameter due to a very steep increase of the viscous entropy. Moreover, the plot shows the existence of an optimal value of P^*_T for each diameter, as found in [17] and [18]. However, the dependence of $\dot{S}_{gen}$ on the geometry parameter P^*_T appears to be less pronounced for smaller values of *D*. In order to compare the results obtained with the above discussed simulations with those given by the model, two new geometries were designed and simulated. Geometry A.5.1 is simply geometry A.5 but the fin height is 3.5*mm* instead of 2*mm*. Geometry A.6 features the same $P^*_T = 1.46$ and height as geometry A.5.1 but the fin diameter is *D* = 0.56*cm* instead of 1.12*cm*. With these values, the pins of geometry A.6 become 374, leading to a 20% increase of the heat transfer area. The simulations results are given in Tab. 6.

Tab. 6. Simulation results for geometry A.5.1 and A.6.

	$T_{av,slab}$ [K]	$\dot{Q}$ [W]	ΔT	Δp [Pa]	$\dot{S}_T$ [W/K]	$\dot{S}_V$ [W/K]	$\dot{S}_{gen}$
A.5.1	304.36	10.868	0.92	40	8.15E-05	4.62E-07	8.19E-05
A.6	304.09	10.869	0.93	62	5.09E-05	5.92E-07	5.15E-05

Tab. 7. Comparison of the values of $\dot{S}_{gen}$ *obtained with the simulations and the lumped-sum parameter model.*

	simulations	model	$\Delta \dot{S}_{gen}$
A.1	1.18E-04	4.78E-04	-304%
A.2	9.95E-05	2.60E-04	-161%
A.5.1	8.19E-05	1.71E-04	-109%
A.6	5.15E-05	5.22E-05	-1%

Tab. 8. Variation of $\dot{S}_{gen}$ *between the indicated geometries on the basis of the two different groups of results.*

	simulations	model
A.1/A.2	16%	46%
A.2/A.5.1	18%	34%
A.6/A.5.1	37%	70%

Tab.7 and 8 show the comparison between the simulations results and those given by the model of Eq. (9). As shown in Tab. 7, the lumped-sum parameter model overpredicts $\dot{S}_{gen}$ but the differences between the two groups of results become negligible if we consider geometries with lower entropy generation rates. For geometry A.6, almost the same values are obtained. Moreover, the trends are similar even though the model predicts entropy rate differences (between two "geometrically close" configurations) roughly double than those obtained with the simulations (see Tab. 8). A possible interpretation of this behavior is that the boundary effects introduce a sort of damping in the thermodynamic performance of the tile, limiting the differences of $\dot{S}_{gen}$ from one geometry to the other. In conclusion, the model seems to represent well the global trend of $\dot{S}_{gen}$. In fact, recalling Fig. 19, the model predicts almost the same optimal P^*_T for D=1,12cm that was found analyzing the local entropy maps. However, large numerical differences with the simulations results are found. In addition, these differences vary greatly as they depend on the values of the two independent variables P^*_T and D. Therefore, it is very difficult to assess if and to what extent they are caused by the influence of the boundary effects (not considered in the lumped model), or by the approximations intrinsic in the correlations the model relies on. As mentioned in Section 1, a deterministic approach also has its limitations. This doesn't mean that the two approaches cannot be integrated. In fact, a possible procedure is to first select a pair (P^*_T, D) on the basis of the plot of $\dot{S}_{gen}$ given by the model; then, to use the heuristic approach for the "fine tuning". For example, as shown above, a careful analysis of the local entropy maps guides the designer in the choice of the optimal height of the fin, which is something the model cannot "see".

This said, further developments cannot ignore any longer the technological issues affecting the realization of the aluminum slab and fins. In order to have a complete picture of the problem, in fact, it would be necessary to estimate the costs associated with each configuration; in particular, the influence of the fin diameter, height and number. In this context, the exergy of the production process ought to be considered in the overall balance as well. Only after these factors have been considered and a selection criterion adopted, it would be possible to choose the final design of the Roof tile. Such analysis, however, is beyond the scope of this work.

7. CONCLUSIONS AND SUGGESTIONS

A careful and detailed description of the steps of the heuristic optimization of a particular type of heat exchanger has been presented. The thermodynamic fields, in all simulations, have been evaluated on a satisfactorily refined grid, using the thermal or the total entropy generation rate as an objective function. In this way, a sufficiently large and reliable database of "numerical experimental data" has been obtained. The pseudo-optimization process described in this work is an effective tool in the hands of an expert designer. In fact, it led here to a significant improvement of the thermodynamic performance. The adopted procedure for "optimizing" a design by means of an entropy generation analysis is not an optimization proper, but rather a heuristic design approach, essentially based on a thermodynamically sound trial-and-error procedure. It results from the direct

scanning of a finite (and in fact quite small) solution set and is similar to a (single or multiple parameter) sensitivity study. Nevertheless, the amount of phenomenological information contained in the local entropy generation maps is so high that a better design invariably emerges.

Among all the examined configurations, A.5 had the best performance from the point of view of both First and Second Law, quite superior to that of geometry B (the "best" among the starting ones). For the same $\Delta T = 0.92$, A.5 displayed pressure losses more than one order of magnitude lower than B (40 against 960 Pa). The calculated total entropy production was 10% lower.

The results of this study have quite general implications on the development of a general optimization criterion to be adopted in heat transfer problems. While it is well known that the optimal pin array shape parameters (pitch and span) can be determined by a critical analysis of the temperature contours, an optimization based on the integrated and local entropy maps shows that "optimal" arrays (i.e., those with optimal pitch and span) generate a flow path in which the individual thermal boundary layers originated on a single fin cannot be distinguished any longer because they all merge. Similar results emerged in the optimization process of geometry E. Another lesson can be learned from this latter case: even though the idea behind the development of this geometry originated from a simple 2-D physical reasoning, the introduction of the "split entry length" between two parallel fins proved to be an effective design modification aimed at the reduction of the entropy rate, and, at the same time, a possible way to optimize the heat transfer area.

Nomenclature

$Be = \frac{\dot{s}_T}{\dot{s}_T + \dot{s}_V}$	Bejan number
c	specific heat, J/(kg K)
D	fin diameter, mm
h	heat transfer coefficient, W/(m^2 K)
$\dot{m}$	mass flow rate, kg/s
L	length, cm
p	pressure, Pa
P	pitch, cm
$\dot{q}$	solar irradiation, W/m^2
$\dot{Q}$	heat transfer rate to the fluid, W
$\dot{S}_{gen}$	global entropy generation rate, W/K
$\dot{s}$	local entropy generation rate, W/(K m^3)
T	temperature, K
W	width, cm
v	velocity, m/s

Greek symbols

δ	distance between fins, mm
η	efficiency
μ	dynamic viscosity, Pa s
ρ	density, kg/m^3
ϕ	rate of viscous dissipation, W/(m^3)

Subscripts and superscripts

*	dimensionless
av	average
ext	external ambient air temperature
L	longitudinal
in	inlet
slab	aluminium slab
th	thermal entry length
T	thermal entropy generation
V	viscous entropy generation

References

[1] Bejan A. Entropy generation through heat and fluid flow. New York, NY: Wiley; 1982

[2] Bejan A. A study of entropy generation in fundamental convective heat transfer. Journal of Heat Transfer 1979;101(4):718–725.

[3] Benedetti P, Sciubba E. Numerical calculation of the local rate of entropy generation around a heated finned-tube. The 1993 ASME Winter Annual Meeting;1993 Nov 11-Dec 3; New Orleans, AL, USA. 81-91.

[4] Natalini G, Sciubba E. Minimization of the local rates of entropy production in the design of air-cooled gas turbine blades. Journal of Engineering for Gas Turbines and Power 1999;121(3):466–475.

[5] Robbe M, Sciubba E. A CFD-aided design procedure for compact heat exchangers. Numerical Heat Transfer 2005;48.

[6] Lee D J, Lin W W. Second-law analysis on a pin-fin array under cross flow. International Journal of Heat and Mass Transfer 1997;40(8):1937–1945.

[7] Culham J, Khan W, Yovanovich M. Optimization of pin-fin heat sinks using entropy generation minimization. Components and Packaging Technologies, IEEE Transactions on 2005;28(2):247–254.

[8] Culham J, Muzychka Y. Optimization of plate fin heat sinks using entropy generation minimization. Components and Packaging Technologies, IEEE Transactions on 2001;24(2):159–165.

[9] Liu G, Shih C. Optimal design methodology of plate-fin heat sinks for electronic cooling using entropy generation strategy. Components and Packaging Technologies, IEEE Transactions on 2004;27(3):551-559.

[10] Iandoli C, Sciubba E, Zeoli N. The computation of the entropy generation rate for turbomachinery design applications: some theoretical remarks and practical examples. International Journal of Energy Technology and Policy 2008;6(32):64–95.

[11] Iandoli C, Sciubba E. 3-D numerical calculation of the local entropy generation rates in a radial compressor stage. International Journal of Thermodynamics 2010;8(2).

[12] Giangaspero G, Sciubba E. Application of the entropy generation minimization method to a LED based spotlight: a constrained pseudo-optimization design process based on the analysis of the local entropy generation maps. ECOS 2011: Proceedings of the 24th International Conference on Efficiency, Cost, Optimization, Simulation, and Environmental Impact of Energy Systems; 2011 July 4-7; Novi Sad, Serbia. 1024-1441.

[13] E.C. Joint Research Centre – Available at: <http://re.jrc.ec.europa.eu/pvgis/index.htm.> [accessed 10.8.2010].

[14] Fluent. User's Guide ver. 6.3 2006. Fluent Inc., Lebanon, New Hampshire.

[15] Shah R, London A. Laminar flow forced convection in ducts: a source book for compact heat exchangers analytical data. Advances in heat transfer: Supplement. Academic Press, 1978.

[16] Giangaspero G. Application of the entropy generation minimization method to industrial heat transfer problems [dissertation]. Roma, Italy: Università di Roma 1 "La Sapienza"; 2011.

[17] Bejan A. The optimal spacing for cylinders in crossflow forced convection. Journal of Heat Transfer 1985:767-770(117).

[18] Bejan A, Morega A. Optimal arrays of pin fins and plate fins in laminar forced convection. Journal of Heat Transfer 1993:75-81(115).

COMPARATIVE ANALYSIS OF AMMONIA AND CARBON DIOXIDE TWO-STAGE CYCLES FOR SIMULTANEOUS COOLING AND HEATING

Alexandru Dobrovicescu [a], Ciprian Filipoiu[b], Emilia Cerna Mladin[c] Valentin Apostol[d] and Liviu Drughean[e]

[a] University Politehnica of Bucharest , Romania, adobrovicescu@yahoo.com (CA)
[b] University Politehnica of Bucharest, Romania, ciprian.filipoiu@prorefrigeration.ro
[c] University Politehnica of Bucharest, Romania, cerna_mladin@yahoo.fr
[d] University Politehnica of Bucharest, Romania, apostol@marco-alex.ro
[e]Technical University of Civil Engineering, Bucharest, Romania, ldrughean@gmail.com

Abstract:

The paper deals with the comparative analysis of the performance of cooling and heating systems operating with NH_3 (ammonia) or CO_2 (carbon dioxide), both natural refrigerants.
The study is based on the exergetic analysis that points out the location and the magnitude of a system malfunction. Both systems, with NH_3 or CO_2 operate in two stages. The exergetic analysis gives the direction of the structural optimization. The exergetic analysis has shown that the best structural schematic is not the same for the two agents. The exergetic analysis points out that the largest exergy destruction in the CO_2 cycle is due to the throttling process and offers solutions to diminish it.

Keywords:
Exergtic Analysis, Cooling and heating systems, Two stage refrigeration system, Structural optimization.

1. Introduction

Concerns for limiting the global warming phenomenon and the ozone depletion turned back the interest of the refrigeration industry towards the natural refrigerants NH_3 and CO_2 [1]. If ammonia, in spite of its very good thermodynamic properties does not match the requirements of safe refrigerant caused by toxicity and/or flammability, CO_2 keeps the standard of safety refrigerant.

Ammonia has by far the highest COP (Table 1) but for safety reasons Carbon dioxide is preferred in commercial and large transport refrigeration.

Table 1. Thermodynamic properties of the natural refrigerants NH_3 and CO_2

Substance	Refrigerant	Normal Boiling Temperature [^oC]	Critical Point [^oC]	ODP	GWP	COP -15/30[^oC]
Carbon dioxide	R-744	-55.6	31.0	0	1	2.56
Ammonia	R-717	-33.3	135.0	0	0	4.76

The problem of low critical temperature of Carbone dioxide is overcome by operating the system in the transcritical region. Many researches reveal the good efficiency of CO2 when used in heat pumps for hot water heating [2,3].

Carbon dioxide is characterized by environment friendliness, low price, easy availability, non-flammability, non-toxicity, compatibility with various common materials and compactness due to high operating pressures.

This paper attempts to give some answers about the conduct of CO_2 as refrigerant in systems for simultaneous cooling and heating in the aim of finding the best structure of the cycle.

To reveal the weaknesses of the CO_2 systems comparatively with the ones operating with NH_3, an exergetic analysis was carried on. The exergetic analysis is the only one capable to point out a malfunction intrinsically connected to a specific process. Moreover the systems used for both refrigeration and heating offer two products represented by two quantities of heat – one received from the cold chamber and the other one transferred to the hot carrying agent. The two thermal energies have different temperature levels. Only the exergetic analysis that accounts for both the quantity of heat transferred and its temperature level in correlation with the ambient temperature can give the real measure of the system performance [4-6].

The comparative analysis of the exergy destruction and losses of the key pieces of the cooling and heating systems operating with NH_3 and CO_2 has revealed the weakness of each process due to the peculiar conduct of each one of the two refrigerants. Such a study done by Cavallini and Neksa [7] on a refrigeration system with CO_2 clearly shows that for this agent throttling is the most penalizing process.

In the present paper three schematics of two-stage refrigeration cycles have been analysed: a two-stage system with intermediary cooling performed by the environmental medium, a two – stage system with intercooling by the injection of a cold stream and a two-stage system with flash intercooling.

The comparative exergetic analysis performed on these different two-stage refrigeration cycles operating with CO_2 and NH_3 has shown that the best structural schematic is not the same for the two agents.

2. Schematic of a two-stage system with incomplete intermediary cooling

The constructive and operating characteristics of the system (Fig. 1) are: the cold carrying agent is water that is cooled in the evaporator from $t_{v,wi}$ = 15°C to $t_{v,wo}$ = 8°C, the heat carrying agent is water whose temperature increases in the condenser from $t_{c,wi}$ = 45°C to $t_{c,wo}$ = 55°C, the ambient temperature is t_0 = 25°C, the isentropic, mechanic and electric efficiencies of compressors and water pumps for NH3 are respectively η_s = 0.8, η_m = 0.83 and η_{el} = 0.9. For CO_2 the isentropic efficiency of the compression process has been calculated with the correlation $\eta_{s,cp} = 0.9343 - 0.04478 \cdot \pi_{st}$ [8].

The NH_3 system is provided with a flash evaporator (Fig. 1a) while the CO_2 one operates with direct expansion evaporator and an internal subcooler-superheater (Fig. 1b).

2.1 Exergetic analysis

The two-stage refrigeration system offers to the customers two products – the exergy of the refrigerating power at the temperature level of the cold carrying agent $\left|\dot{E}x_{Qv}^{T_{v,w}}\right|$ and the exergy of the thermal power at the temperature level of the heat carrying agent $\left|\dot{E}x_{Qc}^{T_{c,w}}\right|$.

For the cooling process realized in the evaporator the Product and the Fuel of this operating zone are respectively (Fig. 1a):

$$\dot{P}_v = \dot{E}x_9^T - \dot{E}x_8^T = \dot{m}_{v,w} \cdot c_{v,w}\left[(t_9 - t_8) - T_0 \ln\frac{T_9}{T_8}\right] \qquad (1)$$

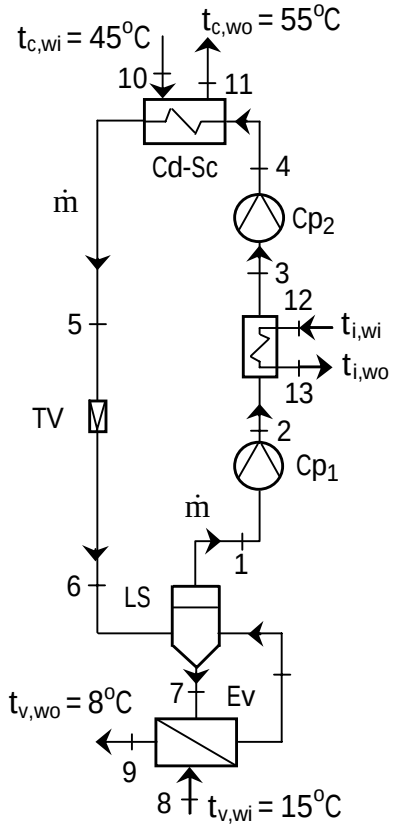

Fig. 1.a NH_3 system with intermediary cooling performed by the environmental medium

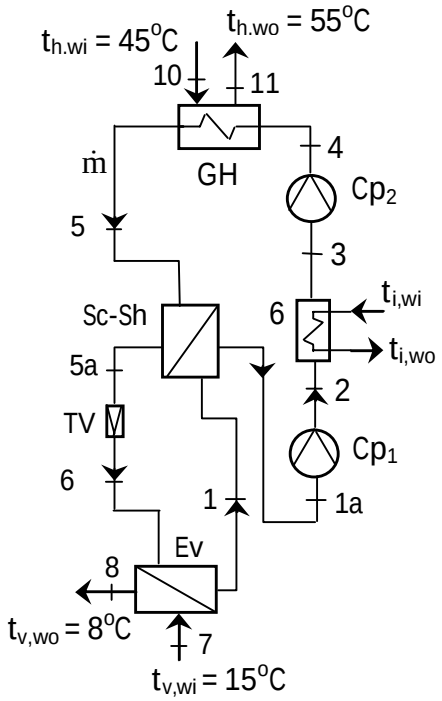

Fig. 1.b CO_2 system with intermediary cooling performed by the environmental medium

$$\dot{F}_v = \left(\dot{E}x_6^{TOT} - \dot{E}x_1^{TOT}\right) + \left(\dot{E}x_8^{M} - \dot{E}x_9^{M}\right) = \dot{m}\left[h_6 - h_1 - T_0\left(s_6 - s_1\right)\right] + \frac{\dot{m}_{v,w} \cdot v_{v,w} \cdot \left|\Delta p_v\right|}{\eta_s \cdot \eta_m \cdot \eta_{el}}. \qquad (2)$$

The fuel consists of the total exergy ($\dot{E}x^{TOT}$) consumed on the refrigerant side (NH_3 or CO_2) to which the mechanical exergy consumed by the pump that runs the cold carrying agent is added [9].

For the evaporator, besides the fact that nothing from the power consumed by the pump to run the cold carrying agent is recovered, in addition, the heat generated by friction and taken away by the cold carrying agent represents a destruction that the compressors of the system have to supplementary compensate.

The exergy destruction due to pressure loss in the evaporator is:

$$\dot{I}_{v,f} = \frac{\dot{m}_{v,w} \cdot v_{v,w} \cdot \left|\Delta p_v\right|}{\eta_s} + \frac{\dot{m}_{v,w} \cdot v_{v,w} \cdot \left|\Delta p_v\right|}{\eta_s}\left(\frac{T_0}{T_{v,w}} - 1\right). \qquad (3)$$

The irreversibility of the heat transfer at a finite temperature difference in the evaporator leads to the exergy destruction:

$$\dot{I}_{v,\Delta T} = \dot{Q}_{01} \cdot T_0 \frac{T_{v,w} - T_v}{T_{v,w} \cdot T_v}. \qquad (4)$$

For the heater (condenser for NH_3) the Product is represented by the increase in the thermal exergy of the heat carrying agent (Fig.1.a):

$$\dot{P}_{cd} = \dot{E}x_{11}^{T} - \dot{E}x_{10}^{T} = \dot{m}_{c,w} \cdot c_{c,w}\left[(t_{11} - t_{10}) - T_0 \ln\frac{T_{11}}{T_{10}}\right]. \qquad (5)$$

$$\dot{F}_{cd} = \left(\dot{E}x_4^{TOT} - \dot{E}x_5^{TOT}\right) + \left(\dot{E}x_{10}^{M} - \dot{E}x_{11}^{M}\right) = \dot{m}_2\left[h_4 - h_5 - T_0(s_4 - s_5)\right] + \dot{m}_{c,w}\frac{v_{c,w} \cdot |\Delta p_c|}{\eta_s \cdot \eta_m \cdot \eta_{el}} \qquad (6)$$

The exergy destruction in the heater is represented by :

$$\dot{I}_{cd} = \dot{I}_{cd,f} + \dot{I}_{cd,\Delta T}, \qquad (7)$$

where

$$\dot{I}_{cd,f} = T_0 \frac{\dot{m}_{c,w} \cdot v_{c,w} \cdot |\Delta p_h|}{\eta_s \cdot T_{c,w}}, \qquad (8)$$

and

$$\dot{I}_{cd,\Delta T} = \dot{Q}_{cd} \cdot T_0 \frac{T_c - T_{c,w}}{T_c \cdot T_{c,w}}. \qquad (9)$$

Denoting by $\dot{W}_{cp,t}$ and $\dot{W}_{P,t}$ the mechanical powers consumed by the system compressors and pumps – the exergetic balance equation on the customer side becomes (Fig. 1.a):

$$\left|\dot{W}_{cp1,t}\right| + \left|\dot{W}_{cp2,t}\right| + \left|\dot{W}_{P1,t}\right| + \left|\dot{W}_{P2,t}\right| = \left(\dot{E}x_9^{T} - \dot{E}x_8^{T}\right) + \left(\dot{E}x_{11}^{T} - \dot{E}x_{10}^{T}\right) + \\ + \dot{I}_{cp1} + \dot{L}_{cp1,m,el} + \dot{I}_{cp2} + \dot{L}_{cp2,m,el} + \dot{I}_{cd,f} + \dot{I}_{cd,\Delta T} + \dot{L}_{cd,P} + \dot{I}_{t1} + \dot{I}_{v,\Delta T} + \dot{I}_{v,f} + \dot{L}_{v,P} \qquad (10)$$

The exergetic efficiency is:

$$\eta_{ex} = \frac{\Delta\dot{E}x_v^{T} + \Delta\dot{E}x_c^{T}}{\sum\dot{W}_t}; \ \eta_{ex,ev} = \frac{\dot{P}_v}{\dot{F}_v}; \ \eta_{ex,cd(gh)} = \frac{\dot{P}_{cd}}{\dot{F}_{cd}} \qquad (11)$$

2.2 Influence of the variation of the operating parameters

The project states the refrigeration power and the temperature levels at which cold and heat are supplied to the customers.

The intermediary pressure of the two-stage system will be stated based on the maximum efficiency criterion.

For the refrigeration and heat pump systems presented in Fig. 1.a,b the temperatures in the key states of the cycles, the mass flow rates and the energy rates per 1 kW of cold are shown in Tables 2 and 3.

Table 2. NH_3 system. Temperatures, mass flow rates and energy rates per 1 kW of cold (*Fig. 1a*)

p_{int} [bar]	$\dot{m} \cdot 10^3$ [(kg/s)/kWcold]	$\dot{W}_{cp,t}$ [kW/kW cold]	$\dot{Q}_{cd} + \dot{Q}_{int\,c}$ [kW/kW cold]	t_2 [°C]	t_4 [°C]
10	1.0002	0.4063	1.4063	60.53	130.2
12	1.0002	0.4112	1.4112	76.87	131.7
14	1.0002	0.4144	1.4144	91.17	132.57

Table 3. CO_2 system. Temperatures, mass flow rates and energy rates per 1 kW of cold (*Fig. 1b*)

p_{int} [bar]	$\dot{m} \cdot 10^3$ [(kg/s)/kWcold]	$\dot{W}_{cp,t}$ [kW/kW cold]	$\dot{Q}_h + \dot{Q}_{int\,c}$ [kW/kW cold]	t_2 [^oC]	t_4 [^oC]
65	8.511	0.7573	1.7573	75.2	114.4
70	8.511	0.7652	1.7652	82.03	114.9
75	8.511	0.7738	1.7738	88.52	115.3

For both NH_3 and CO_2 cycles, temperature t_2 at the discharge from the first stage compressor strongly recommend using the intercooler as well, for heating the thermal agent. The overall efficiency of the cycle increases in this way.

While for CO_2 temperatures at the discharge from compressors cause no problem, for NH_3 the second stage compressor operates at the highest avoidable temperature limit.

In Fig. 2 are presented the variation of the overall exergy efficiency and of the compression ratio in the first stage against the intermediary pressure for the two compared refrigeration systems.

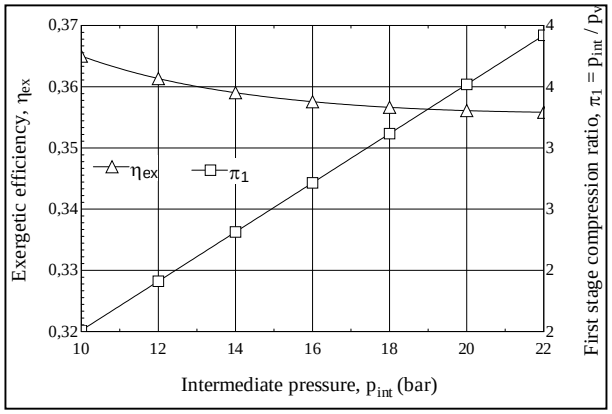

Fig 2.a, NH_3 System. Variation of the exergetic efficiency and of the first stage compression ratio against the intermediary pressure for schematic Fig. 1.a

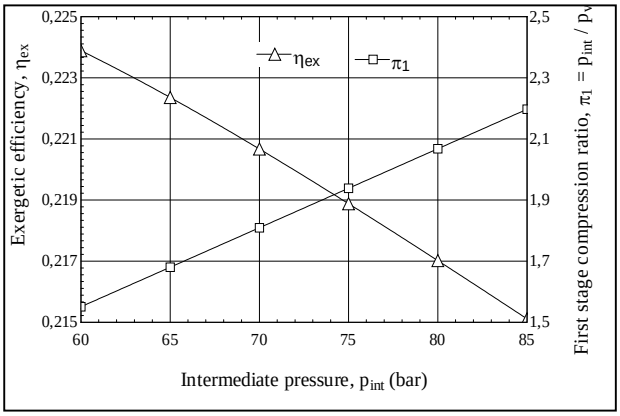

Fig 2.b, CO_2 System. Variation of the exergetic efficiency and of the first stage compression ratio against the intermediary pressure for schematic Fig. 1.b

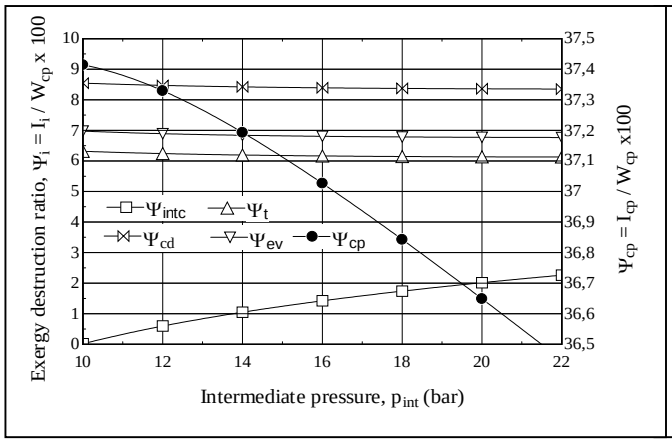

Fig.3.a, NH_3 System. Exergy destruction ratio related to the exergy of the total plant fuel against the intermediary pressure for schematic Fig. 1.a

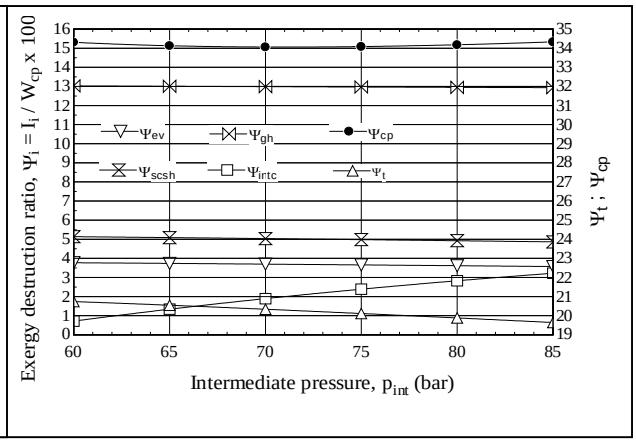

Fig.3.b, CO_2 System. Exergy destruction ratio related to the exergy of the total plant fuel against the intermediary pressure for schematic Fig. 1.b

In both cases, the lower is the intermediary pressure, with respect to the NH_3 system for the temperature limit in the discharge of the second stage compressor, the higher is the exergetic efficiency. In spite of the large operating pressures for the CO_2 system, the first stage compression ratio is approximately twice lower than for the NH_3 system leading for CO_2 to low mechanical work input.

The lower exergetic efficiency for CO_2 compared to the NH_3 system is due to higher exergy destructions.

The comparative analysis for the NH_3 and CO_2 systems (Figs 3.a,b) reveales a three times higher exergy destruction ratio with throttling for CO_2. The large exergy destruction with throttling explains the lower exergetic efficiency for the CO_2 system compared with the NH_3 one.

Another larger exergy destruction ratio that leads to lower exergetic efficiency for CO_2 than NH_3 is in the gas heater. This characteristic recommends CO_2 for heating at higher temperatures i.e. hot water.

As expected, the lower compression ratio in the first stage for CO_2 is accompanied by the lower exergy destruction ratio in the compressor, compared to NH_3 (Figs 3.a,b).

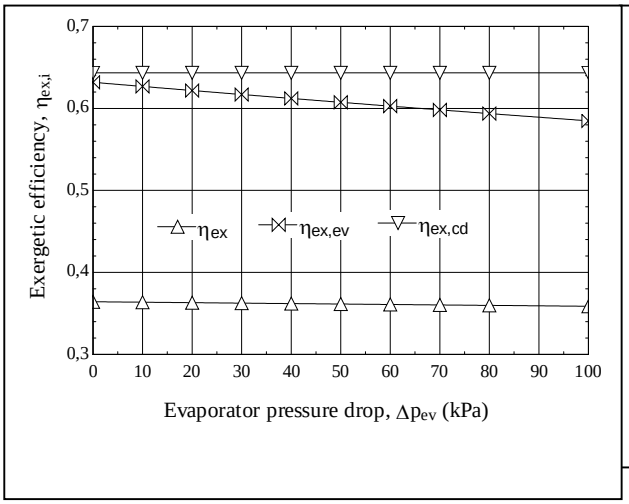

Fig. 4.a, NH_3 System. Variation of the exergetic efficiency against the pressure drop in the evaporator Fig.1.a

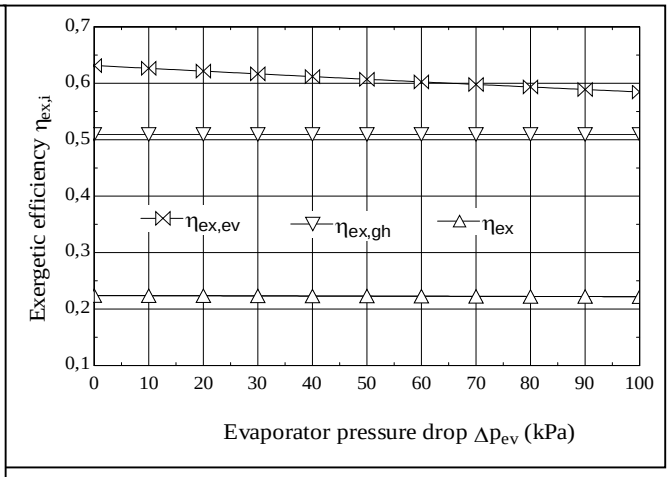

Fig. 4.a, NH_3 System. Variation of the exergetic efficiency against the pressure drop in the evaporator Fig. 1.b

In figures 4a,b the behaviour of the exergetic efficiency of the overall cycle, of the evaporate and of the condenser or gas heater is presented at the variation of the evaporator pressure drop.

For both systems the pressure drop in the evaporator has the same influence on the exergetic efficiency of the evaporator (Figs 4.a,b).

3. Schematic of a two-stage system with intermediary cooling performed by the injection of a cold stream in the first stage discharged gas

To diminish the temperature of the gas at the discharge from the high pressure compressor and to reduce in this way the accompanying exergy destruction due to heat transfer at a high temperature difference in the heater, the intermediary cooling is performed by the injection of a cold stream in the compressed gas between the two stages (Figs. 5. a,b).

For the flow charts presented in Figs. 5. a,b the temperatures in the key states of the cycles, the mass flow rates and the energy rates per 1 kW of cold are shown in Tables 4 and 5.

Table 4. NH_3 system. Temperatures, mass flow rates and energy rates per 1 kW of cold (*Fig. 5a*)

p_{int} [bar]	$\dot{m}_1 \cdot 10^3$ [(kg/s)/kWcold]	$\dot{m}_2 \cdot 10^3$ [(kg/s)/kWcold]	$\dot{W}_{cp,t}$ [kW/kW cold]	$\dot{Q}_{cd}$ [kW/kW cold]	t_2 [^oC]	t_4 [^oC]
10	1.0002	1.083	0.413	1.413	60.53	115,90
12	1.0002	1.111	0.4112	1.412	76.87	105,02
14	1.0002	1.137	0.4144	1.412	91.17	96.23

Table 5. CO_2 system. Temperatures, mass flow rates and energy rates per 1 kW of cold (*Fig. 5b*)

p_{int} [bar]	$\dot{m}_1 \cdot 10^3$ [(kg/s)/kWcold]	$\dot{m}_2 \cdot 10^3$ [(kg/s)/kWcold]	$\dot{W}_{cp,t}$ [kW/kW cold]	$\dot{Q}_h$ [kW/kW cold]	t_2 [oC]	t_4 [oC]
60	11.77	17.69	1.068	2.068	43.31	85.52
65	11.77	19.72	1.090	2.090	50.01	81.31
70	11.77	22.23	1.115	2.115	56.34	77.49

The intermediary cooling performed by the injection of a cold stream leads for both agents to a decrease in the discharge temperature from the second stage compressor. For both agents the exergy destruction due to heat transfer at a finite temperature difference in the heater is expected to diminish. For CO_2 the quantity of heat transferred to the thermal agent increases (Tables 5 a,b)

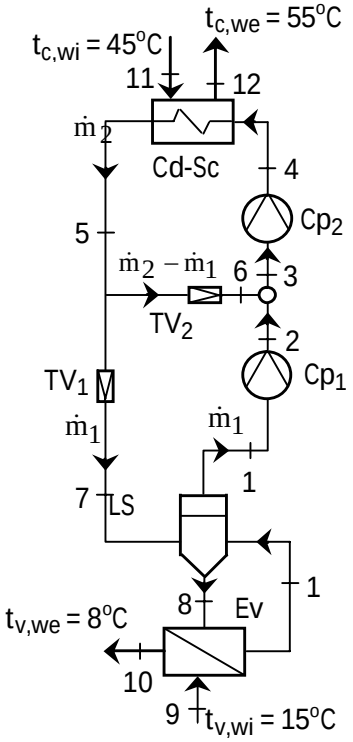

Fig.5.a NH_3 System with intermediary cooling achieved by the injection of a cold stream

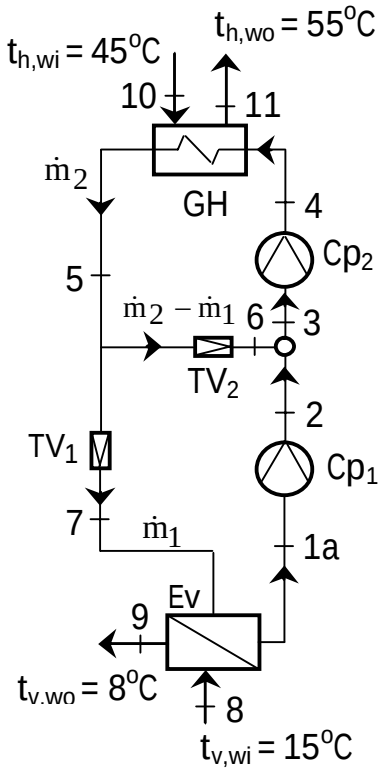

Fig.5.b CO_2 System with intermediary cooling achieved by the injection of a cold stream

For NH_3, the overall exergy efficiency remains practically unchanged, while for CO_2, it decreases (Fig. 6. a,b).

The exergy destructions related to the total input power are presented in figures 7a,b. The decrease in the exergetic efficiency of the CO_2 cycle is due to the rapid increase in the exergy destruction ratio of the throttling process (Fig. 7.b).

Compared to the schematic given in Fig. 1 characterized by a single throttling process, in the present case (Fig. 5.b) the cycle operates with two throttlings.

As expected, for CO_2, the exergy destruction ratio in the heater due to the intermediary cooling by the injection of a cold stream (Figs 5.b) is lower than the one corresponding to schematic presented in Figure 1 (Fig. 7.b).

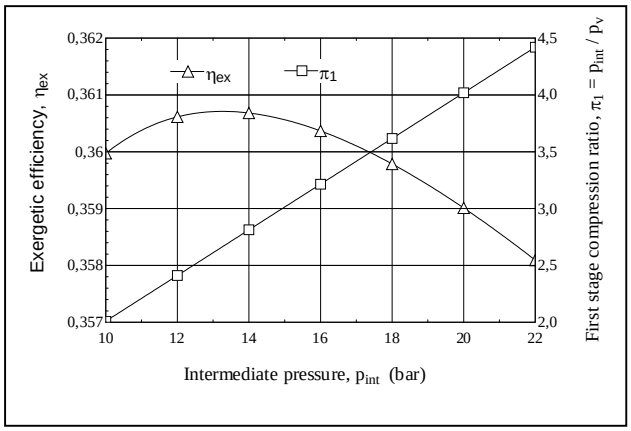

Fig. 6.a, NH_3 System. Variation of the exergetic efficiency and of the first stage compression ratio against the intermediary pressure for schematic Fig. 5.a

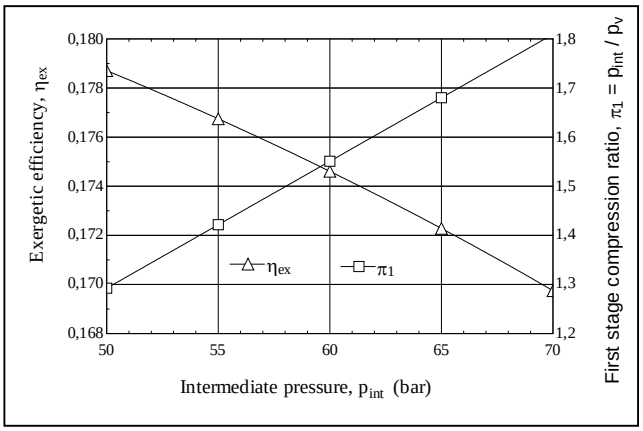

Fig. 6.b, CO_2 System. Variation of the exergetic efficiency and of the first stage compression ratio against the intermediary pressure for schematic Fig. 5.b

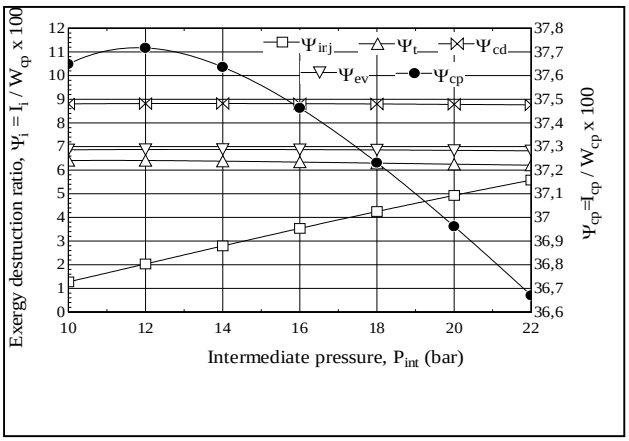

Fig. 7.a, NH_3 System. Exergy destruction ratio related to the exergy of the total plant fuel against the intermediary pressure for schematic Fig. 5.a

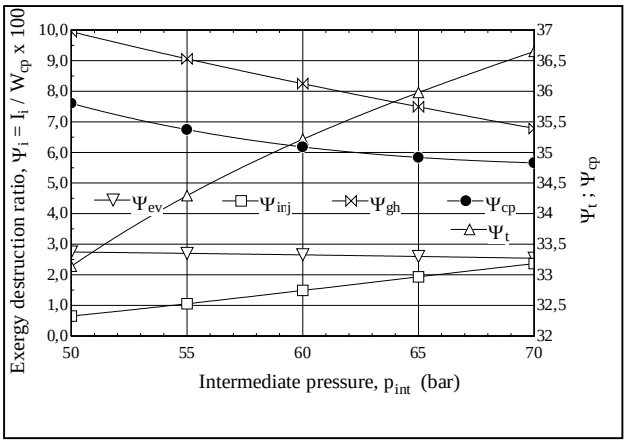

Fig. 7.b, CO_2 System. Exergy destruction ratio related to the exergy of the total plant fuel against the intermediary pressure for schematic Fig. 5.b

4. Schematic of a two-stage system with flash intercooling

To continue to diminish the exergy destruction a schematic with flash intercooling is proposed (Figure 8.a,b).

For the flow charts presented in Figs. 8. a,b the temperatures in the key states of the cycles, the mass flow rates and the energy rates per 1 kW of cold are shown in Tables 6 and 7.

Table6. NH_3 system. Temperatures, mass flow rates and energy rates per 1 kW of cold (*Fig. 8a*)

p_{int} [bar]	$\dot{m}_1 \cdot 10^3$ [(kg/s)/kWcold]	$\dot{m}_2 \cdot 10^3$ [(kg/s)/kWcold]	$\dot{W}_{cp,t}$ [kW/kW cold]	$\dot{Q}_{cd}$ [kW/kW cold]	t_2 [^oC]	t_4 [^oC]
10	0.87	1.084	0.386	1.386	60.52	108.88
12	0.89	1.113	0.385	1.385	76.87	98.37
14	0.91	1.14	0.387	1.387	91.17	89.91

Table 7. CO_2 system. Temperatures, mass flow rates and energy rates per 1 kW of cold (*Fig. 8b*)

p_{int} [bar]	$\dot{m}_1 \cdot 10^3$ [(kg/s)/kWcold]	$\dot{m}_2 \cdot 10^3$ [(kg/s)/kWcold]	$\dot{W}_{cp,t}$ [kW/kW cold]	$\dot{Q}_h$ [kW/kW cold]	t_2 [oC]	t_4 [oC]
60	5.71	22.04	1.068	1.97	43.31	75.92
65	6.19	28.65	1.090	2.061	50.01	70.56
70	6.9	48.62	1.115	2.397	56.34	64.66

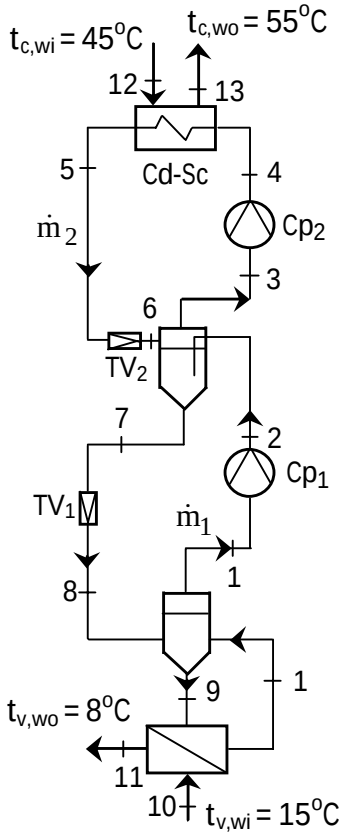

Fig. 8.a NH_3 System with flash intercooling

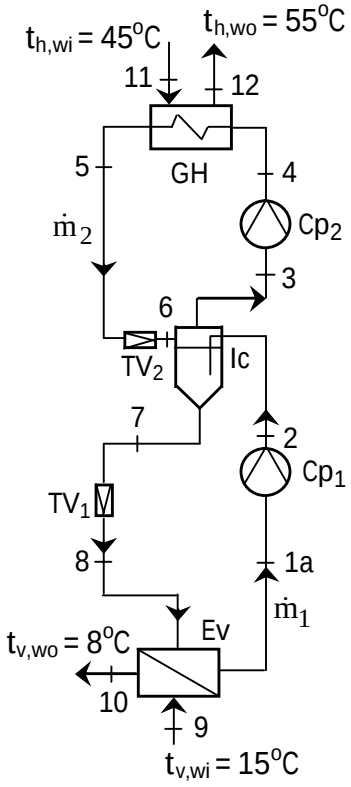

Fig. 8.b CO_2 System with flash intercooling

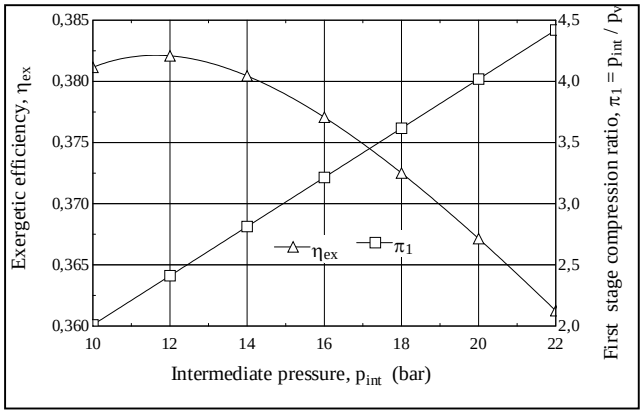

Fig 9.a, NH_3 System. Variation of the exergetic efficiency and of the first stage compression ratio against the intermediary pressure for schematic Fig. 8.a

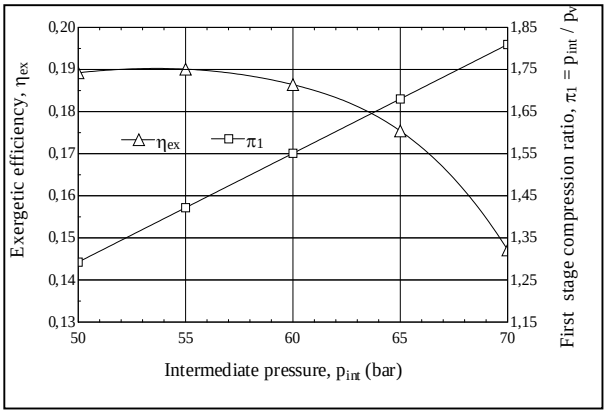

Fig 9.b, CO_2 System. Variation of the exergetic efficiency and of the first stage compression ratio against the intermediary pressure for schematic Fig. 8.b

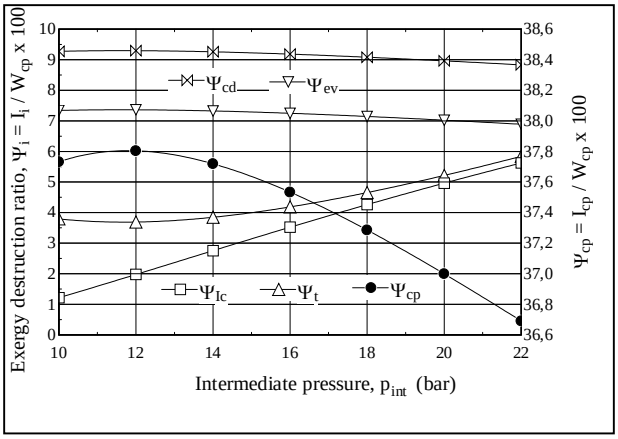

Fig. 10.a, NH_3 System. Exergy destruction ratio related to the exergy of the total plant fuel against the intermediary pressure for schematic Fig. 8.a

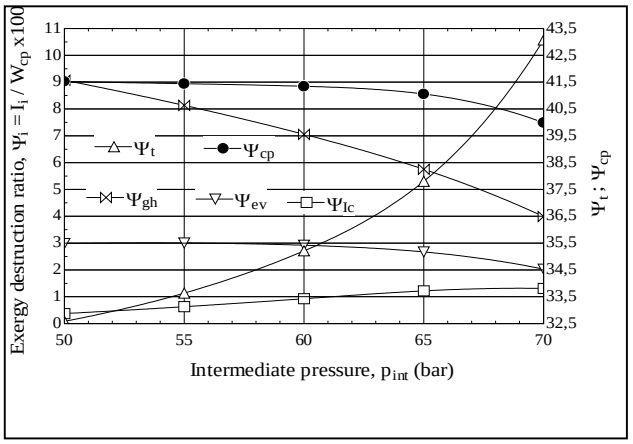

Fig. 10.b, CO_2 System. Exergy destruction ratio related to the exergy of the total plant fuel against the intermediary pressure for schematic Fig. 8.b

For NH_3 the exergetic efficiency has incresed substantially (Fig. 9.a). This fact is due to the decrease in the total exergy destruction associated with throttling (Fig. 10.a).

For CO_2 the overall exergetic efficiency increases comparatively with the flash gas by-pass intercooling (Figs 6.b, 9.b) but remains inferior to the efficiency corresponding to the incomplete intermediary cooling (Figs 3.b, 9.b). The slight increase in the exergetic efficiency is mainly due to the decrease in the exergy destruction in the gas heater (Figs 7.b, 10.b).

5. Conclusion

The exergetic analysis is the only method capable to rate the performance of a system operating with thermal energies at different levels of temperature.

The exergetic analysis finds the location and the magnitude of a malfunction that occures inside the borders of a system and is capable to give solutions for improvement.

The exergy destruction associated with throttling is responsible for the lower exergetic efficiency of the CO_2 system compared to the one that operates with NH_3. For CO_2 the lower is the throttling process the higher is the overall efficiency. All the attempts to reduce the exergy destructions in the

gas heater or intermediary cooling processes have had no benefit as long as throttling has been increased.

The schematic from Fig. 1.b with the incomplete intermediary cooling has the lower throttling and consequently the higher overall exergetic efficiency.

For NH_3 the structural changes brought to the system in the aim to reduce the exergetic destruction associated with the intermediary cooling and heat transfer in the condenser have improved the performance of the cooling and heating system.

Nomenclature

Cd-Sc condenser-subcooler

Cp compressor

Ev evaporator

$\dot{E}x$ exergy current, kW

$\dot{E}x^M$ current of mechanical exergy, kW

$\dot{E}x^T$ current of thermal exergy, kW

$\dot{E}x_Q^T$ exergy of the heat current $\dot{Q}$ at the average thermodynamic temperature T, kW

$\dot{F}$ fuel, kW exergy

h specific enthalpy, kJ/(kg K)

$\dot{I}$ exergy destruction due to internal irreversibility, kW

LS liquid separator

$\dot{m}$ mass flow rate, kg/s

p pressure, kPa

$\dot{P}$ product, kW exergy, EU/yr

$\dot{Q}$ heat current, kW

$\dot{Q}_0$ cooling charge, kW

s specific entropy, kJ/(kg K)

t temperature, ^oC

T temperature, K, average thermodynamic temperature, K

TV throttling valve

v specific volume, m^3/kg

$\dot{W}$ mechanical power, kW

Subscripts and superscripts

c condenser

cp compressor

el electrical

f friction

h heater

i intermediary, inlet

m mechanical

o outlet

P pump

t total, throttling
v evaporator
w water
wi water inlet
wo water outlet
0 ambient parameter
1 first stage
2 second stage

References

[1] Lorenzen G., Revival of carbon dioxide as a refrigerant, Int.J.Refrig. 17 (1994) 292-300.

[2] Yokoyama, R., Shimizu, T., Ho, K., Takemura, K., Influence of ambient temperatures on performance of a CO_2 heat pump water heating system, Energy, 32(2007), 388-398.

[3] .Neska, P., CO2 heat pump systems, Int.J.Refrig. 25(2002) 421-427

[4] Yumrutas, R., Kundus, M., Kanoglu, M., Exergy analysis of vapor compression refrigeration systems, Exergy, An Int. J. 2002, 2(4). p. 266-72.

[5] Bilgen, E., Takahashi, H., Exergy analysis and experimental study of heat pump system, Exergy, An Int. J. 2002, 2(4). p. 259-65.

[6] Sarkar, J., Souvik, Bhattacharyya, Gopal, M.R., Transcritical CO_2 heat pump systems: exergy analysis including heat transfer and fluid flow effects, Energy Conversion and Management 46 (2005). p. 2053-2067.

[7] Cavallini, A., Neksa, P., prospects for the return of CO_2 as a refrigerant, CIAR 2001, Buenos Aires, Argentina 2001. p. 761-790 (**http://www.aafrio.org.ar/tema_congressos/ciar-2001/ciar_2001.htm**)

[8] Brown, J.S., Yana-Motta, S.F., Domanski, P.A., Comparative analysis of automotive air conditioning systems operating with CO_2 and R134a, Int. J. Refrig., 2002, 25. p. 19-32.

[9] Dobrovicescu, A., Tsatsaronis, G., Exergy destruction due to friction in heat exchangers – A refrigeration system case study, ECOS 2006, p. 165-173

Comparison between Traditional Methodologies and Advanced Exergy Analyses for Evaluating Efficiency and Externalities of Energy Systems

Gabriele Cassetti [a]***, Emanuela Colombo*** [a]

[a]*Politecnico di Milano, Department of Energy, Milan, Italy*

Abstract:

The majority of the studies available in Oil and Gas Industry literature isoften related to the downstream impact of the process chain, while less attention is given to the upstream side.
In this frame, efficiency improvements in the sector would provide relevant contributions to the issue of the impact of the oil chain on environment and society. In industrial sector, environmental impact and efficiency of energy systems are assessed through traditional methodologies (Environmental Impact Assessment, Life Cycle Assessment, Risk Analysis).Several innovative methodologies of analysis have been developed to evaluate the overall impacts of complex systems in terms of exergy consumption. These methodologies underline the tendency to extend the evaluation of the impact including the life time of the energy systemby considering the exploitation of the involved resources (Cumulative Exergy Consumption, Exergetic Life Cycle Assessment), and including the interaction with the space around the system, by assessing the externalities from the environmental and the economic point of view (Thermoeconomics, Extended ExergyAccounting).
The purpose of this paper is to compare the different methodologies commonly used in the industrial sector to assess the environmental impact and the efficiency related to oil and gas sector with the methodologies based on advanced exergy analysis. To perform the comparison a decision model from multi-attribute methodsis developed and a hierarchical analysis based on the Analytic Hierarchy Process is performed.
Methodologies are compared through a range of criteria based on input-output approach and declined in thirteen indicators concerning integrated assessment and environmental assessment.
This paper is part of a wider work aiming to develop a new approach to integrate the different peculiarities of the methodologies to reduce the environmental impact while increasing the technical and economic efficiency of the upstream chain of Oil and Gas sector, by analysing energy and exergy flows, material and waste flows and externalities of the global system.

Keywords:

Exergy, Upstream, Oil and Gas, Energy, Environmental Impact, Efficiency.

1. Introduction

Environmental impact of energy systems is one of the main issues for developing technologies, policies and programs in industrial sector.

A major challenge in the evaluation of the impact related to processes in energy systems is to include the overall externalities, as suggested by International Energy Agency(IEA) [1].

In industrial sector, externalities of energy systems are assessed through traditional methodologies (Environmental Impact Assessment [2], Life Cycle Assessment[3], Risk Analysis [4]). Several advanced methodologies of analysis have been developed to evaluate the overall impacts of complex systems in terms of exergy consumption. These methodologies underline the tendency to extend the evaluation of the impact of energy systems through time, by considering the exploitation of resources involved in the construction of the system ([5],[6]), and space, by assessing the externalities, environmental and economic concerns ([7],[8],[9]).

Purpose of this paper is to assess which methodology may be preferable to assess the environmental impact of Oil and Gas sector (O&G).Available methodologies are defined through an analysis of

the literature showing relevant dimensions of the issue, and a decision model based on a hierarchical analysis is developed.

2. Relevance and Environmental impact of Oil and Gas sector

In 2009, Oil and Gas represented the 52,7 % of the World Total Primary Energy Supply (TPES) (79,5% considering globally fossil fuels with coal) for a total of 6403 Mtoe [1]. Despite the growing contribution of renewable technologies, IEA stats [10] that the contribution of oil and gas in 2035 will still cover the 52,2 % of TPES in the Current Policy Scenario (CPS), and the 45,6% in the 450 Policy Scenario (450 PS). In CPS 2035, relative contribution of renewable technologies will slightly differ from today values (11%), because of the contemporary foreseen growing of the TPES from 12150 Mtoe in 2009 to 18048 Mtoe in 2035. The 450 PS 2035, on the other hand, foresees an increase of TPES up to 14920 Mtoe, with a consequently increase of renewables contribution to 18% [10].

These numbers lead to two important considerations: the first is that worldwide economic development requires more and more energy, and, the second, that the socio-economic and technical development path will strongly affect emissions in the environment since the share of fossil fuel (mainly Oil and Gas) in the energy supply is due to remain high [11].

CO_2 from energy represents indeed the 65% of global anthropogenic greenhouse-gas emissions (81% in Annex I countries, figure 1), and consequently fossil fuels contribution is relevant.

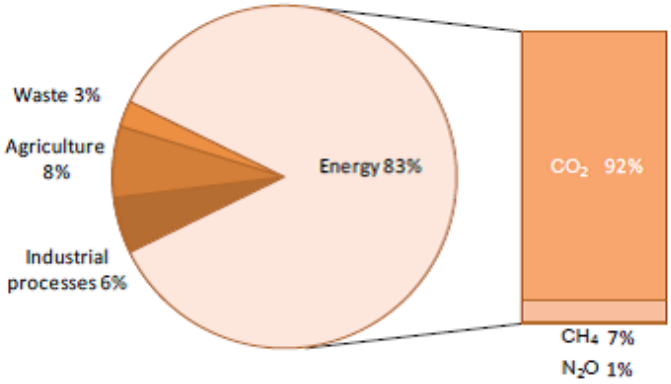

Fig.1 Shares of anthropogenic greenhouse-gas emissions in Annex I countries, in 2009. Source: IEA, CO2 Emissions from Fuel Combustion – Highlights, 2011

Environmental impact of O&G sector has high relevance at global, regional and local. At the global scale, O&G impact is related to greenhouse-gas emissions (mainly $CO_2$and CH_4) thus contributing to the anthropogenic share.In figure 2 the share by fuel in 2009 of TPES and CO_2 emissions is represented.

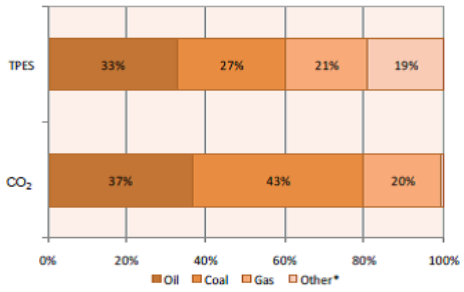

*Fig.2Percent shares of World Total Primary Energy Supply and CO_2 emissions in 2009. (*Other includes nuclear, hydro, geothermal, solar, tide, wind, biofuels and waste). Source: IEA, CO2 Emissions from Fuel Combustion – Highlights, 2011*

At local and regional scale, O&G impact concerns chemical pollution due to combustion processes and waste emissions: oxides of sulphur, nitrogen and carbon, organic compounds, such as hydrocarbons (fuel vapours and solvents), particulate matter, such as smoke and dust, metal oxides, especially those of lead, cadmium, copper and iron, hazardous air pollutants (HAP), persistent organic pollutants (POPs), odours. These pollutant has high effect on human health, materials and ecosystems as well as on acidification and eutrophication of waterbodies.

In this frame, efficiency improvements in the sector of O&G would provide relevant contributions to the issue of the impact on environment and society.

Moreover, the majority of the studies available in O&G industry literature is related to the downstream impact of the process chain, while less attention is given to the upstream side, but the contribution of the latter in the balance of global impact is much more relevant than the former [12].In figure 3, O&G operations and relative emissions of CO_2 equivalent (CO_2e) are shown.

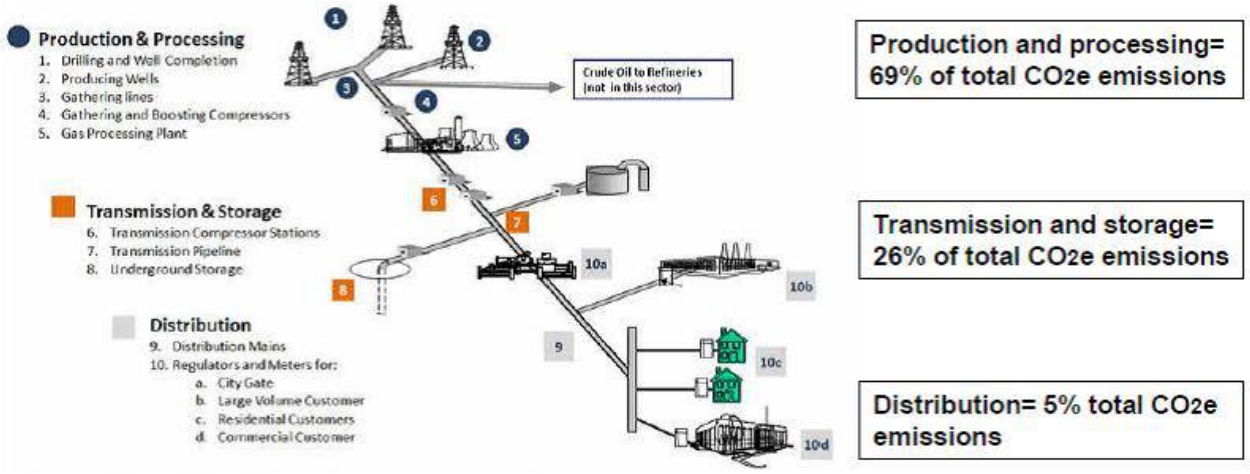

Fig.3 Oil and Gas Operations and relative CO_2e. Data: DBCCA-EPA

3. Methodologies

The objective of the comparison between methodologies is to evaluate how the environmental impact of O&G sector may be assessed by different methodologies.The selected methodologies are: Environmental Impact Assessment (EIA), Life Cycle Assessment (LCA) and Risk Assessment (RA) in industrial sector; Cumulative Exergy Consumption (CExC), Exergoenvironmental Analysis and Extended Exergy Accounting (EEA) for those based on exergy analysis.

EIA, LCA and RA have been selected according to their wide diffusion in industrial sector and because the approach is standardized in policy framework.CexC, Exergoenvironmental Analysis and EEA have been selected on the base of a literature review on advanced exergy analyses of energy systems. Exergy based methodologies analysed belong to a wider ensemble of methodologies, among them it is worth to mention Exergetic Life Cycle Assessment by Cornelissen [6], Environomic method by Frangopoulos [15] and Exergoecological analysis by Valero [16].

The approach of the different methodologies will be described in detail in this paragraphs, where a specific attention is given to the exergy-based methodologies.

Indeed exergy is widely recognized to be appropriate to assess environmental impact of energy systems [5,6,7,8,9,13], for two main properties: (1) it allows to convert everything in a homogeneous unit, and (2) it allows to include the externalities of the process into the global evaluation [14,15].

Despite exergy allows to measure the quality of energy transformations occurring in a process as well as the quantity, exergy analysis has still low appeal in legislators and decision makers, probably due to the its very technical origin and the technical result that it supplies [9].

In terms of environmental impact there is still anopen question in the literature related to theproper approach to follow for measuring theexergy destruction generated by the system into the environment.This means to define the transfer function between the exergy content and the pollutant concentration of a flow [5,9,15].

Environmental Impact Assessment (EIA)

EIA is the instrument based on the Directive 85/337/EEC of the European Commission, and ensures an ex ante environmental evaluation of projects [18], with the aim of preventing and mitigating impacts.EIA is performed for those projects considered having significant impact. The approach of EIA in evaluating impacts is essentially output-oriented and descriptive of the typology and quantity of waste generated by the system during its operating life. It includes also the description of the principal alternatives of impact scenario.EIA assesses the components of the environment potentially subject to impacts and describes the possible effects generated. The major criticisms of EIA are: 1) a limited consideration of alternatives, and 2) insufficient consideration of externalities derived from effects. EIA may represent an appropriatetool for assessing a single system, but it is not properly designed for evaluating the externalities.EIA Directive is usually implemented together with other two Directives aiming at managing the environmental strategies and reducing the impact of projects, the Strategic Environmental Assessment (SEA, Directive 2001/42/EC) and the IPPC Directive (Directive 2008/1/EEC) on the pollution of existing projects in the industrial sector.A limit highlighted in the Commission Report on the application and effectiveness of EIA [19] is the approach "*compliance a commitment*", from which emerges that EIA is not well satisfactory in improving the environmental performances of a project.

Life Cycle Assessment (LCA)

LCA is a tool for the systematic evaluation of the environmental issue of a system through all stages of its life cycle.LCA derives from the approach of Life Cycle Thinking and it is an evolution of classical energy analyses. LCA tries to identify the overall impact through an input-output approach.The logic of this approach consists in the assessment of the energy and material inputs and outputs across the processes of a system. The main advantage of this approach is given by the holistic vision that carries out, so that it can be used to highlight the inter-linkages of environmental aspects. International Organization for Standardization (ISO) developed a standardset for guidelines (ISO14040[20]) for conducting LCA studies.LCA takes into consideration only the energy and environmental dimensions of the impact, and manages them separately [21].LCA classifies the energy entering in the system in five main categories:

- *capital energy,* linked to the construction of machineries,
- *energy content of delivered fuel* E_c, necessary to the operations and processes,
- *production and delivery energy* E_p, to produce and transform energy and materials,
- *feedstock energy,* that is the energy content of input material that can be still used by the products,
- *energy consumed by labour,* divided in the daily energy supply needed by one person (10MJ/d) and the energy needed for their transportation.

Critical point of LCA is the allocation of loads. Allocation consists in relating the energetic and environmental loads of processes to specific co-products and sub-productsas well as the fuel consumption of single components [21].Other critics about LCA lie in impact assessment, in particular in the normalization of theimpacts over the relative effects of processes. There are several normalizing methods, but none of them solves the intrinsic subjectivity of LCA:

- Proxy Approach (mandatory approach);
- Monetization of effects;

- Distance to target;
- Panel Approach (panel of scientists);
- Eco-indicator: weights the impact of process through the Triangle Method: Human Health, Ecosystem Quality, Resources.

Risk Assessment (RA)

RA is a very well recognized approach to identify risks and uncertainties related to industrial processes and activities [23].RA typically involves measuring two quantities of risk: the magnitude of the potential event and the probability of occurrence. The concept of magnitude of a potential event is linked to the intensity of the caused effects and the vulnerability of the people and the environment exposed.RA covers an extremely wide number of activities and sectors, and its complexity is elevated. For the same reason, there is a wide number of standards related to RA. The most important European legislation relevant to RA is the Framework Directive 89/391/EEC [4].

Many different tools and techniques can be adapted to the specific situation, e.g calculation of complex event probability, risk mapping, probabilistic cost estimating.The principal target of RA isHuman Health and the objective is the minimization of probability of occurrence of uncontrolled events. For this reason, RA is often related to the complementary practice of Health, Safety and Environment (HSE), that actively monitors any potential risk issue regarding safety, security and environment.The first step of a RA consists in the identification of all the sources of risk related to an activity or a process, since thelack of knowledge of all the possible risks can lead to an insufficient level of safety.The identification of risk requires the utilization of adequate methodologies, e.g historic analysis, control lists, what-if analysis, HAZOP, etc, that must guarantee all possible sources of risk and danger to be identified.The principal result of a RA is a hierarchy of all the possible undesired events related to their associated risk and a systemic knowledge of the cause-effect relations involving the processes.RA can be approached with a Plan – Do – Check – Act method.Finally, RA represents an instrument to put in place pro-active policies of intervention in the system.

Cumulative ExergyConsumption (CExC)

The objective of CExC is the assessment of the exergy of natural resources, renewable and non-renewable, absorbed by all the subsystems of the productive chain of a given product.The relevant aspect of cumulative exergy analysis rather than cumulative energy is the capability to determine the influence of non-ideality of processes in the final result, so to localize e quantify inefficiencies along the chain of processes and set the improvements. On the other hand, the calculation of cumulative energy consumption requires much less information, as far as CExC requires the knowledge of the exergy content of primary resources extracted from environment [26].The cumulative consumption of exergy of non-renewable resources is defined thermo-ecological cost, and expresses the consumption of non-renewable exergy involved in the production of a final product.The statement at the bases of thermo-ecological cost is that the final cost of a product results from the sum of thermo-ecological costof delivered materials, semi-finished products and energy carriers.Performing the analysis of a system relatively to a given region, the specific thermo-ecological cost $(_i k$ of a general waste *k* generated by the system has the following expression[26]:

$$(_i k = (B\sigma_i k)/(DCP + \Sigma_i k \in [P_i k\, \sigma_i k \,]\,) \quad (1)$$

where B is the annual domestic consumption of non-renewable exergy, DCP the domesticconsumption product in monetary units, σ_k is the monetary index of harmfulness of *k*-th waste and P_k is the annual production of the *k*-thaggressive component of waste products rejected to theenvironment in the considered region.CExC may be finally performed to minimize the non-renewable exergy depletion in a chain of processes. The expression of the objective function

representing the non-renewable exergy depletion on annual basis, assuming a singular output of the given process, has the form:

$$P_A = \tau_n \left(\sum_j \left[\dot{G}_j \rho_j\right] + \sum_k \left[\dot{P}_k (_k)\right] + 1/\tau \left[\sum_m \left[G_m \rho_m (1 - u_m)\right] + \sum_r \left[G_r \rho_r\right]\right] \quad (2)$$

where $\dot{G}_j$, ρ_j are the nominal flow rate and specific thermo-ecological cost of the *j*th rawmaterial, semi-finished product or energy carrier supplied to the production process, $\dot{P}_k$, $(_k$ are the nominal flow rate and index of the specific thermo-ecological cost of the *k*thdeleteriouswaste product generated in the considered process and rejected to the environment, τ_n is theannual operation time withnominal capacity, τ the nominal life time of the installation expressedin years, u_m is the expected recovery factor of the *m*thmaterial, G_m, ρ_m are the consumption andspecific thermo-ecological cost of the *m*thmaterial or energy carrier used for the construction ofthe installation, G_r, ρ_r are the predicted consumption and specific thermo-ecological cost of ther*r*thmaterials or energy carrier used in repairs.

Exergoenvironmental Analysis

The approach of Exergoenvironmental Analysis derives from Exergoeconomics [27] and has the objective to combine an exergy analysis with an environmental assessment method as the LCA [21].Aim of the analysis is mainly to overcome the limitations affecting LCA: allocation of environmental loads and energy consumption for each component.Exergoenvironmental Analysis consists of three main steps: the first is an exergy analysis of the energy conversion system, the second is a LCA of the relevant components and the relevant input streams of system and finally an environmental impact is assigned to each exergy stream and each component of the system.The environmental impact is expressed by a quantitative indicator: the Eco Indicator 99 [21] or the Recipe indicator [30]. These indicators are internationally recognized as instruments for environmental assessment [29,30] and decline the environmental impact in three damage categories: Human Health, Ecosystem Quality and Resources. The final indicator represents the synthesis of the three categories and the impact is expressed in terms of points (Pts).The environmental impact is assigned to the exergy streams involved in the process through the SPECO approach [27] in order to obtain the environmental impact rate $\dot{B}_j$ for each stream (expressed in Pts/s). $\dot{B}_j$ is calculated as the product of the specific environmental impact b_j, the average environmental impact associated with the production of *j*th stream per exergy unit of the same stream (Pts/GJ exergy), times the exergy rate $\dot{E}_j$:

$$\dot{B}_j = b_j \dot{E}_j \quad (3)$$

In addition to the impact associated to each exergy stream, the component-related impact $\dot{Y}_k$ associated to the *k*th over its lifecycle is considered: $\dot{Y}_k = \dot{Y}_k^{CO} + \dot{Y}_k^{OM} + \dot{Y}_k^{DI}$ (4), where $\dot{Y}_k^{CO}$, $\dot{Y}_k^{OM}$ and $\dot{Y}_k^{DI}$ are the impact related to the construction (including manufacturing, transport and installation), operating and maintenance (including pollution formation) and disposal of the *k*th component, respectively.The assessment of the environmental impact at component level aims at developing improved design options.The final step of the analysis is the identification of the environmental relevant components and the sources of impacts in the system.

Extended Exergy Accounting (EEA)

EEA is a methodology that has the objective to assess the overall amount of resources, expressed in terms of exergy, globally absorbed by a system over its life cycle span.The originality of EEA is represented by the improved concept of primary resource, since it is extended to all the externalities generated by system, not only material and energy streams: also capitals, labor (in terms of workhours) and environmental costs are converted in equivalent exergy. This peculiarity simplifies

the operation of comparison among systems of different nature, since all non-homogenous measures are converted in a homogeneous unit.EEA includes the principal characteristics of CExC, as the cumulative exergy absorbed in the productive chain of a product, and Exergoeconomics, since also economic issue is included.Unlike Exergoeconomics, capitals in EEA are converted in equivalent exergy through the econometric factor β, defined as $\beta = \frac{M2}{S}$, where M2 is a monetary indicator that expresses the amount of circulating money in a given society at a given period, and S is the cumulative salary of labor in the same period.As consequence, the extended exergy of a system may differ in function of the place where the system is built and the result being strictly related to local context and this may represent a limitation mainly when more than one country are involved within the supply chain of a product or a process.

EEA is indeed based on the assumption that the global input of exergy resources in the system has the objective to maintain the labor, assumed as product of the society.The equivalent exergy of capitals $\mathbf{E_K}$ involved in the system is then expressed as:

$$\mathbf{E_K} = \beta \cdot \mathbf{E}_L \tag{5}$$

where $\mathbf{E}_L$ is the equivalent exergy of labor and it is defined as:

$$\mathbf{E_L} = f \cdot \mathbf{e_{surv}} \cdot N \tag{6}$$

where $f, \mathbf{e_{surv}}$ and Nare the amplification factors of exergy consumption from the society, the minimum exergy necessary to human survival, equal to $1{,}05 \cdot 10^7 \frac{J}{(person \cdot day)}$[31] and population respectively.Avoided impact, or zero impact [9], approach is used by EEA for assessing environmental impact of systems.Environmental impact of an output stream from the system is defined as an exergy flow non in equilibrium with the environment reference state and the exergetic cost $\mathbf{E_{ENV}}$ of all the abatement systems required to the zero impact is calculated. Also abatement systems are expressed in terms of extended exergy.The global extended exergy consumed by the *k*th system is finally:

$$EE_k = EE_k^{CO} + EE_k^{OM} + EE_k^{DI} \tag{7}$$

where $EE_k^{CO,OM,DI}$ is the extended exergy of construction, operation and maintenance, and dismantling of system, respectively. Each component of (7) is defined as:

$$EE_k^j = \sum_j CExC + E_L^j + E_K^j + E_{ENV}^j \tag{8}$$

where *j*is equal to CO,OM,DI alternatively.

Finally, it is worth mentioning that extended exergy do not include a number of impacts which may affect the overall consumption of resources by the system. In particular biodiversity loss of an ecosystem is not considered and also and the social impact on the quality of life, or the human capital are at the moment not included within the extended exergy concept. This limitations must be kept into account when using information coming form an extended exergy evaluation.

4. Methodology of the comparison

The approach used to develop the comparison between the methodologies derives frommulti-attribute decision methods. Taking into account the goal of the analysis (environmental impact of O&G upstream chain), the Analytic Hierarchy Process (AHP), developed by Saaty [32] and based on hierarchical analysis, is selected as investigating method.

The choice of the AHP model isbased onits key characteristics that make it suitable for the application to the case under study:

- a hierarchical analysis, defined around a specific goal, carries out a general cost-benefit analysis not requiring an initial knowledge of specific indicators;
- the construction of a hierarchy makes possible to break down in simpler sub-problem any complex problem and thedefinition of a set of indicators (qualitative and/or quantitative) becomes more feasible. The pairwise comparison makes the procedure more user-friendly;
- the result of AHP model is a vector that represents the level of preference to attribute to each alternative.

To apply the AHP to a defined problem a step by step procedure is followed.

First, the specific goal is divided in three sub-problems, corresponding to three different criteria, so thatthe combination of the three criteria produces the solution for the goal.After the definition of the criteria, a series of indicators, related to each criterion is defined. Indicators are used to evaluate each alternative (in this case, each methodology) in pairwise comparisons.

In order to rank the alternatives in function of their performance related to the goal, the Saaty scale [35], defined for the specific problem, is used.

Definition of the hierarchyof a specific goal

The specific goal of the study, as previously underlined, is the evaluation of the best methodology to analyse the environmental impact of the Oil & Gas chain.

Accordingly to the literature [36,37,38], the most appropriate methodology to achieve the given goal should be able to

- to evaluate impact at the global and local level,
- to evaluate the process from the perspective ofthe overall system,
- to extend the analysis to the life cycle,
- to consider cumulative processes,
- to evaluate the impact over the different dimensions of environment: air, soil and water,
- to require a consistent, but not too wide data set as input,
- to allow homogeneous comparison between technical, environmental and economic elements,
- to assure data to be available,
- to be more general as possible compared to the context,
- to estimate alternative scenarios,
- to optimise the processefficiency,
- to allow a comprehensive evaluation of resource consumptions,
- to evaluate externalities.

The above statementshave been aggregatedin three criteria representing the main dimensions of relevance forachieving the specific goal, and thirteen indicators have been carried out. This structure has been proposed by the Authors and its subjectivity, although supported by literature review,may affects the final solution. Therefore , a sensitivity analysis of the relative weights of criteria and indicators have been performed:

- *Criterion Strategy*, expressing the insights and peculiarities of the methodology. The indicators for this criterion are:
  - Scale, aiming at investigating if the environmental impact is evaluated at local or global or both scales;
  - Level, aiming at investigating if the environmental impact is considered at the level of the single component (or partial portion of the system) or at the level of the overall system;

- Time Frame, same question as above related to the temporal frame (operating life or lifecycle);
- Spatial Frame: same question as above related to the capability of predicting cumulative processes of productive chains or simply to evaluate current processes;
- Environmental dimensions, aiming at considering the impact over the whole set of environmental dimensions: air , water and soil.

- *Criterion Input, defining the typology of input that the methodology requires for being applied.It has four indicators:*
  - Data set extension, aiming at investigating the amount of the data required for the methodology to be applied,
  - Data set availability, aiming at investigating the availability of the data,
  - Data set homogeneity, aiming at providing a uniform unit of measure for the technical, environmental and economic elements,
  - Context: aiming at evaluating the context-dependency of the methodology or its general applicability.
- *Criterion Output, defining the typology of output that the methodology is able to provide, has four indicators:*
  - Alternative Scenarios: aiming at investigating if alternative scenarios are generated by the methodology,
  - Efficiency: aiming at investigating if the methodology allows efficiency optimization or at least efficiency assessment or does not consider this element,
  - Resource consumption: aiming at investigating if the methodology assesses the overall resource consumption of the system,
  - Externalities, aiming at evaluating if the model is able to account for the externalities generated by the system.

According with this assumption the hierarchy developed for this goal, is proposed in figure 4.

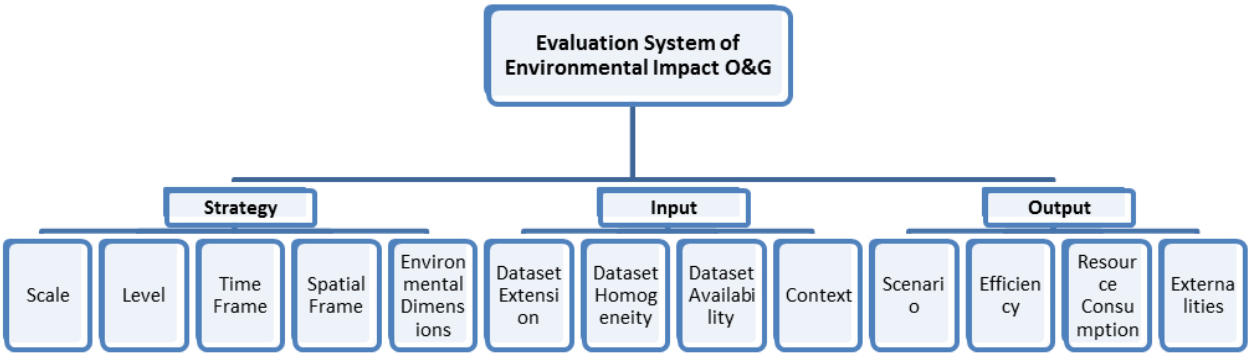

Fig. 4 Hierarchy for O&G impact assessment. First row: the goal; second raw: the criteria; third raw: the indicators

The hierarchy gathers indicators selected from integrated assessment and environmental evaluation literature. The criterion Strategy reflects the issues mostly involved in Risk Assessment [39] and regulatory frameworks, as EPA [40]. Indeed, environmental laws and regulation stress the evaluation of impacts over all the compounds of environment: atmosphere, lithosphere and hydrosphere.

Input and Output criteria are developed on the basis of integrated assessment literature [22,41,42]. In particular, Input indicators have the objective to assess the computational effort needed to gather the necessary information required by the single methodology. This indicator may appear less relevant than the other two, but it reflects an essential phase in any kind of analysis, the data

collection. The complexity and the completeness of this phase is crucial for all the other phases of the analysis as well as the quality of the output.

Output indicators follow the approach of the International Atomic Energy Agency (IAEA) in assessing the different dimensions of sustainable development [43].

It is worth mentioning the absence of indicators referring directly to exergy: indeed, exergy may be seen as an instrument able to improve the performances of a methodology, but the peculiarity of using exergy is not relevant for the goal of the analysis.

The thirteen indicators are qualitative indicators, therefore it is possible to compare each alternative through qualitative pairwise comparisons using the AHP.

Weight assignment to all the elements of each level of the hierarchy

To build up the hierarchy, the weights of the indicators referred to the relative criterion are equal, as well as the weight of each criterion referred to the goal. On the consequence, defining the weight of a general criterion as w_c, and the weight of a general indicator w_i, the model assigns a weight to each criterion of w_c = 1/3= 0,333, and to each indicator, $w_{i_{str}}$ = 1/5 = 0,20, $w_{i_{inp}}$ = 1/4 = 0,25, $w_{i_{inp}}$ = 1/4 = 0,25. It is clear that the choice to maintain the same w_c for each criterion leads to different w_i, only due to the different number of indicators defined for each criterion. In the sensitivity analysis performed, indeed, the weight w_i will be set equal for each indicator.

Pairwise comparisons and priority vector.

To perform the pairwise comparison between alternatives, the Saaty ranking scale is used (table 2).

Table.2 Saaty Scale of absolute numbers

Intensity of importance	Definition	Explanation
1	Equal importance	Two factors contribute equally to the objective
3	Somewhat more important	Experience and judgement slightly favour one over the other
5	Much more important	Experience and judgement strongly favour one over the other
7	Very much more important	Experience and judgement very strongly favour one over the other. Its importance is demonstrated in practice.
9	Absolutely more important	The evidence favouring one over the other is of the highest possible validity
2,4,6,8	Intermediate values	When compromise is needed

According to the literary review of each methodology [5,6,7,8,9,13,14,15,16,18,19,20,21,23,24,25,26,27,28], values of Saaty scale have then been associated tooil and gas characteristics as previously stated [36,37,38].

In table 3, the corresponding Saaty scale for oil and gas sector is shown.According to the explanation of Saaty scale values, the value of 1, corresponding to “Equal Importance” is assigned if the two alternatives *a* and *b* compared present the same performance on the indicator, and a value of 9, corresponding to “Absolutely more important”, if the performance between the two alternatives is relevant. For those indicators having a middle scale value, a value of 5, corresponding to “Much more important” is set.

Taking as example the indicator “Scale”, we will assign the value 1 if both methodologies *a* and *b* analyse the system at the local scale (or both at the global, or global *and* local). The value 5 will be assigned to *a* if *a* analyses the system at the global scale while *b* only at the local scale (or if *a* analyses the global *and* local scale, while *b* only the global). Finally, we will assign the value 9 to *a* if *a* analyses the global *and* local scale, while *b* only the local scale.

Once the assignment has been set, the *Super Decisions* Software, developed by *Creative Decision Foundation* [44] was used.

Table 3. Saaty scale values for O&G Impact Evaluation

STRATEGY	Scale	1	Local
		5	Global
		9	Local and Global
	Level	1	Component
		5	System
		9	Component and System
	Time Frame	1	Operating Life or Partial Cycle
		9	Lifecycle
	Spatial Frame	1	Single Process
		9	Cumulative Processes
	Environmental Dimensions	1	Single Environmental Dimension
		5	Full Environmental Dimensions
INPUT	Dataset Extension	1	Wide Input Dataset required
		9	Reduced Input Dataset required
	Dataset Homogeneity	1	Non homogeneous Input Dataset
		9	Homogeneous Input Dataset
	Dataset Availability	1	Scarce Availability of Input Dataset
		9	High Availability of Input Dataset
	Context	1	Relevant affection
		9	Non relevant affection
OUTPUT	Scenario	1	Single Scenario
		9	Multiple Scenario
	Efficiency	1	Non assessment
		5	Assessment
		9	Optimization
	Externalities	1	Environmental Focus
		5	Environm. and Economic or Social Focus
		9	Environm., Economic and Social Focus
	Resource consumption	1	Non assessment
		9	Assessment

5. Results and discussion

The result of the calculation is the priority vector representing the ranking of the alternatives from the one which has the closest performance to satisfy the goal, to the least.Alternatives are ranked on descending order.

The priority vector, normalised to the best alternative, is reported in histogram form in figure 5. The preferable methodology to better reach the goal according to the decision model presented, seems to be the Exergoenvironmental Analysis. EEA and LCA are second and third priority, respectively.The results may be better understood by breaking down the evaluation into the three criteria. To do this, the priority vector of a single criterion is considered. The software allows to evaluate the contribution of each indicator *i* on the criteria *c* referred to each alternative *a* (figures 6,7,8).

Exergoenvironmental Analysis is globally preferred, mainly due to criterionInput (figure 6) with respect to EEA. On the other side, while EEA seems more appropriate for the criterion Output

(figure 7) and Strategy (figure 8), the effect does not compensate the associated penalty to criterion Input. Under the criterion Strategy, EEA seems to be preferred since it allows an approach to the problem which is based on an holistic view of the system, oriented to a global scale, at the level of the overall system, considering lifecycle and cumulative processes. Exergoenvironmental analysis has a weak performance in this indicator since it is more focused on the single component (rather than on a system) evaluated over the operating life (rather than the lifecycle).

In criterion Output, the preferred methodology results to be again EEA mainly because of its capability to account for overall externalities. Exergoenvironmental analysis follows with a high score where the reduced value in predicting externalities is balanced by the increased value attributed to efficiency optimisation.

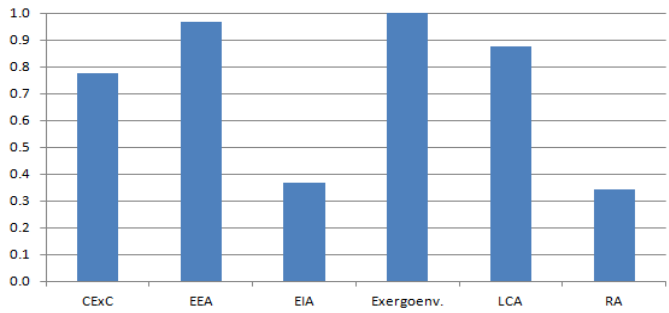

Fig. 5Normalised Priority Vector in graphical form for alternatives

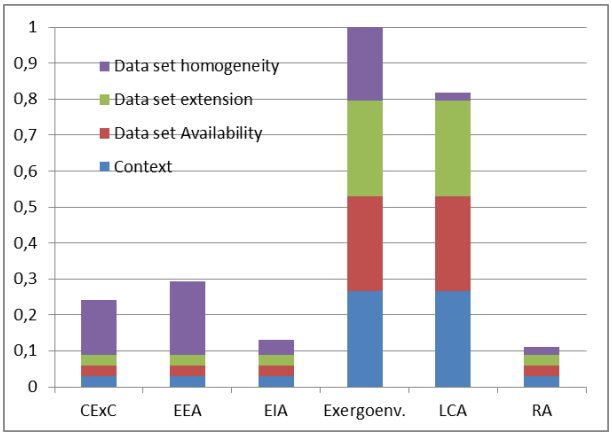

Fig. 6Criterion Input (normalised to the "best in class" alternative) alternatives evaluation

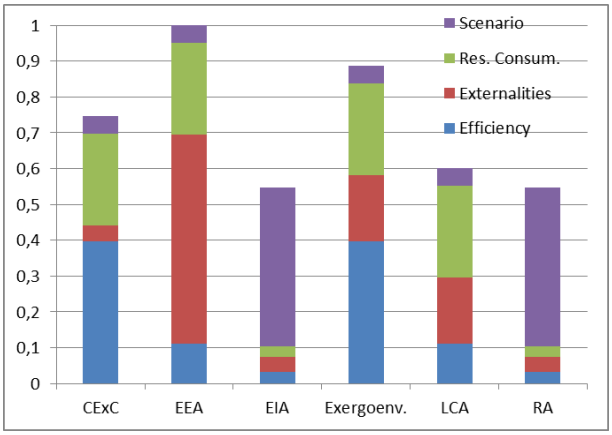

Fig. 7Criterion Output(normalised to the "best in class" alternative) alternatives evaluation

Under the criterion Input, the ideal methodology is Exergoenvironmental analysis, followed by LCA. This result is due to the high level of standardization nowadays reached by LCA database in industrial sector, which is also used by Exergoenvironmental analysis.The latter is able to provide the data in more homogeneous framework by using exergy-based indicators. Under this criterion EEA is affected by a penalty mainly due to the very extended dataset required and the current scarce availability of necessary data.

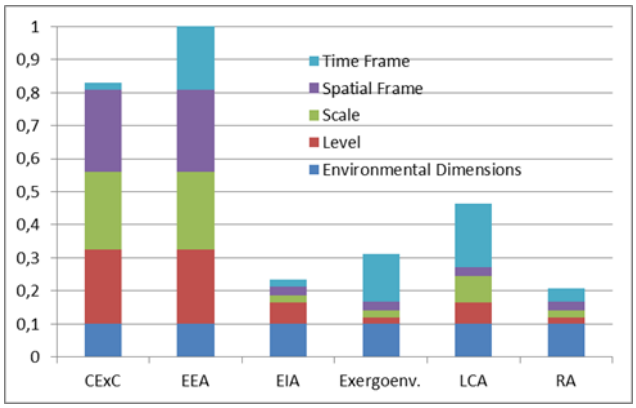

Fig. 8Criterion Strategy (normalised to the best in class alternatives) alternatives evaluation

Anyway it is relevant to observe that Exergoenvironmental analysis and EEA are very close in the priority vector, thus demonstrating that they may be valid alternatives which can be used accordingly to the different relevance that the decision maker gives to each single indicator and/or criterion.

Even LCA performs very well being slightly penalised by the criterion output where it is affected by low score in efficiency optimisation and externalities, both considered of high relevance for the goal.

The result of analysis confirms, as anticipated by the literature review in paragraph 3, the high potential ofexergy-based methodologies in criterion Output, since from the output of the analysis depend the actions that the decision maker may subsequently operate to reduce the impact of the Oil&Gas sector. This consideration, due to the capability of these methodologiesto convert all the externalities generated in exergy flows, represent effective tools able to supply a more profitable and complete information to manage the environmental issue.

As initially mentioned, a sensitivity analysis on the relative weights of criteria w_c can be performed. By assigning a w_c proportional to the number of indicator for each criterion, the singular w_i assumes the value w_i = 1/13 = 0,08 , while $w_{c_{str}}$ = 5/13 = 0,385, $w_{c_{inp}}$ = 4/13 = 0,308 and $w_{c_{out}}$ = 4/13 = 0,308, respectively.

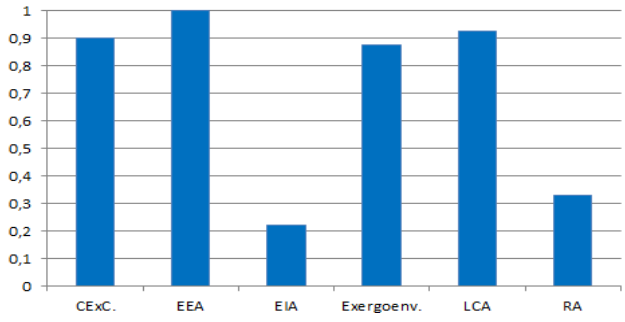

Fig. 9 Normalized priority vector with proportional w_c

As we may see, the result of the sensitivity analysis presents a rank reversal in the priority vector, in favour of EEA. Exergoenvironmental Analysis maintains however a good performance, as well as LCA and CExC. The result so confirms the utility represented by exergy based analysis. Indeed, they are still considered globally preferable to analyse the specific problem analysed with respect to traditional methodologies, for the characteristics previously mentioned.

6. Conclusion

The objective of the present work is to define the most appropriate methodology to evaluate the environmental impact of Oil and Gas sector. A comparison between methodologies from industrial sector (Life Cycle Assessment, Environmental Impact Analysis, Risk Assessment) and exergy based methodologies (Cumulative Exergy Consumption, Extended Exergy Accounting and Exergoenvironmental Analysis) is developed by using a decision model based on Analytic Hierarchy Process. The problem is broken in three main criteria: Strategy, Input and Output, equally weighted, and thirteen indicators are used. For attributing values to these qualitative indicators a sensitivity analysis has also been performed to reduce subjectivity.

The application of AHP in the selection of the methodologies in the case analysed leads to results consistent with the literature on the subject and represents an effective tool in the end of the analysis for avoiding a priory choices.

In particular, results show that Exergoenvironmental analysis and EEA represent very useful tools for assessing externalities, consumptions and efficienciesand provide an objective and compact final indicator, while LCA is well appreciated being the best trade-off among computational load and effectiveness of results provided.

The analysis confirms the relevance of exegy-based methodologies to provide proper indication to decision makers, since they synthetize distributed information and help to reduce the range of subjectivity in operating actions.Also by modifying the weight of criteria w_c in the model, results show that exergy based methodologies are still highly competitive with traditional analysis.

It is necessary to mention that exergy is a useful tool to *integrate* an analysis, but it cannot be the exclusive tool on which the analysis should be based. Indeed exergy and the logic of extensionto externalities are at the moment not able yet to include some aspects that the decision maker must take into consideration as, for example, the safety of the workers and the population around the system or the biodiversity loss that it can generate in the environment.

Finally, it is worth mentioning that some subjectivities, intrinsic of the model, are still affecting the evaluation but it is shifted from the choice of the methodologies to the definition of the hierarchy of the problem, thus making it more explicit and therefore more manageable, arguable, defendable or not.

7. References

[1]. International Energy Agency, 25 Energy Efficiency Policy Recommendations. 2011, Technical Report.

[2]. EU, Directive 85/337/EEC.

[3]. UNI EN ISO 14001, Environmental Management System Requirements and Guidelines

[4]. EU,Directive 89/391/EEC.

[5]. Szargut J.,Exergy method: technical and ecological applications.Southampton, Boston: WIT Press, 2005.

[6]. Cornelissen, R.L., Hirs, G.G., The value of the exergetic life cycle assessment besides the LCA". Energy Conversion and Management 2002; vol. 43, no. 9–12, pp. 1417-1424.

[7]. Bejan A., Moran M., Tsatsaronis G., Thermal design and optimization. New York: John Wiley & Sons, 1996.

[8]. Enrico, S., Beyond thermoeconomics? The concept of Extended Exergy Accounting and its application to the analysis and design of thermal systems.Exergy; An International Journal 2001; vol. 1, no. 2, pp. 68-84.

[9]. Enrico, S. 2003, Extended exergy accounting applied to energy recovery from waste: The concept of total recycling", Energy 2003; vol. 28, no. 13, pp. 1315-1334.

[10]. International Energy Agency, KeyWorld Energy Statistics. 2011, Technical Report.

[11]. International Energy Agency, CO2 Emissions from Fuel Combustion – Highlights. 2011, Technical Report.

[12]. DB Climate Change Advisors, DBCCA, Comparing Life Cycle Greenhouse Gas Emissions from Natural Gas and Coal. 2011, Technical Report.

[13]. Sciubba E., Wall G., A brief commented history of exergy from the beginnings to 2004.International Journal of Thermodynamics2007;vol. 10, no. 1, pp. 1-26.

[14]. Simpson A.P., Edwards C.F., An exergy-based framework for evaluating environmental impact, Energy 2011; vol. 36, no. 3, pp. 1442-1459.

[15]. Frangopoulos C.A., Caralis Y.C.,A method for taking into account environmental impacts in the economic evaluation of energy systems.Energy Conversion and Management1997;vol. 38, no. 15-17, pp. 1751-1763.

[16]. Valero A., Valero A., Exergoecology: A thermodynamic approach for accounting the Earth's mineral capital. The case of bauxite–aluminium and limestone–lime chains. Energy2010; vol. 35, no. 1, pp. 229-238.

[17]. EU, Directive 85/337/EEC.

[18]. EU, Commission Report on the application andeffectiveness of EIA Directive. 2009, Technical Report.

[19]. ISO 14040:2006, Environmental Management – Life Cycle Assessment – Principle and Framework.

[20]. Baldo G., Marino M., Analisi del Ciclo di Vita LCA. Italy: EdizioniAmbiente, 2008.

[21]. Meyer L., Tsatsaronis G., Buchgeister J., Schebek L.,Exergoenvironmental analysis for evaluation of the environmental impact of energy conversion systems.Energy2009;vol. 34, no. 1, pp. 75-89.

[22]. Thabrewa L., Wiek A., Ries R., Environmental decision making in multi-stakeholder contexts: applicability of life cycle thinking in development planning and implementation.Journal of Cleaner Production 2009; vol.17 pp.67-79.

[23]. Rota R., Nano G., Introduzione alla Affidabilità e Sicurezza nell'industria di processo.Italy: Pitagora, 2007.

[24]. Szargut J., Morris D.R.,Cumulative exergy consumption and cumulative degree of perfection of chemical processes. International Journal of Energy Research1987: vol. 11; no. 2, pp. 245-261.

[25]. Szargut J., Ziębik A., Stanek W.Depletion of the non-renewable natural exergy resources as a measure of the ecological cost. Energy Conversion and Management2002: vol; 43, no. 9-12, pp. 1149-1163.

[26]. SzargutJ. Optimization of the design parameters aiming at the minimization of the depletion of non-renewable resources. Energy 2004: vol. 29; no. 12-15, pp. 2161-2169.

[27]. Lazzaretto A., Tsatsaronis G.,SPECO: A systematic and general methodology for calculating efficiencies and costs in thermal systems. Energy2006: vol. 31; no. 8-9, pp. 1257-1289.

[28]. Banerjee A., Tierney M., Comparison of five exergoenvironmental methods applied to candidate energy systems for rural villages in developing countries. Energy2011: vol. 36; no. 5, pp. 2650-2661.

[29]. Goedkoop M., Spriensma R., The Eco Indicator 99 - A damage oriented method for Life Cycle Impact Assessment, Methodology Report. 2001, Technical Report.

[30]. Goedkoop M. et al.,ReCiPe2008, A life cycle impact assessment method which comprises harmonised category indicators at the midpoint and the endpoint level. First edition. 2009, Technical Report.

[31]. Sciubba E., Modeling the energetic and exergetic self-sustainability of societies with different structures. Journal of energy resources technology 1995: 117 (2), pp. 75-86.

[32]. Saaty T.L., How to make a decision: the Analytic Hierarchy Process. Interfaces 1994: Vol. 24; No. 6, pp.19-43,1994

[33]. Tversky A., Kahneman D., The Framing of Decision and the Psychology of Choice. Science, New Series, Volume 211, Issue 4481 (1981), 453-458.

[34]. Superdecisions Software available at: http://www.superdecisions.com.[accessed 25/01/12]

[35]. Saaty T.L., Decision making with the analytic hierarchy process, Int. J. Services Sciences 2008: Vol. 1, No.1, 2008.

[36]. Cleveland C.J. Net energy from the extraction of oil and gas in the United States.Energy 2005;30(5):769-782.

[37]. Riva A., D'Angelosante S. and Trebeschi C. Natural gas and the environmental results of life cycle assessment.Energy 2006;31(1 SPEC. ISS.):138-148.

[38]. Salter E. and Ford J. Holistic environmental assessment and offshore oil field exploration and production. Mar.Pollut.Bull. 2001;42(1):45-58.

[39]. Bruce K. H. An examination of ecological risk assessment and management practices. Environ Int 2006;32:983-95.

[40]. EPA Laws and Regulations available at: http://www.epa.gov/lawsregs/.[accessed 27/02/12].

[41]. SETAC Technical Issue Paper, 2004.

[42]. UNEP Initiative on Capacity Building for Integrated Assessment and Planning for Sustainable Development, 2003.

[43]. International Atomic Energy Agency, Energy Indicators for Sustainable Development, 2005.

[44]. Tsoukias A., From decision theory to decision aiding methodology.European Journal of Operational Research 2008: 187 (2008) 138–161.

Comparison of entropy generation figures using entropy maps and entropy transport equation for an air cooled gas turbine blade

Ömer Emre Orhan[a], Oguz Uzol[b],

[a] *METU,Ankara,Turkey,omer.emreorhan@gmail.com*
[b] *METU,Ankara,Turkey,uzol@.metu.edu.tr*

Abstract:

In the design and analysis of turbomachinery components, there are studies for the application of Second Law based methods. Since entropy generation can be considered as one of the most important parameters affecting the performance of turbomachinery, accurate calculation of entropy may be utilized as a design parameter. Therefore, an improvement in such a design parameter may as well increase the efficiency of the whole system which is the desired aim of the overall design procedure.
There are several methods available for the calculation of entropy generation. One method could be possible if complete quantitative descriptions of velocity and temperature fields are available. Field distributions of viscous and thermal entropy rates can be computed by post processing the available velocity and temperature data using positive definite entropy equation. There are several studies about this method in the literature one of them being about an air cooled gas turbine stator blade by Natalini and Sciubba [1].
In this study, results obtained in [1] are compared with the results obtained through direct solution of entropy transport equation. Entropy transport equation has been implemented to a commercial CFD software as a User Defined Scalar (UDS) and solved as an additional equation to continuity and Navier-Stokes equations. Results are then compared for both solutions. It is concluded that such an approach could offer significant improvements in loss and entropy production in turbomachinery flows.
It is seen that the direct calculation of entropy production as a part of the solution process produces a much smoother variation emphasizing the entropy generation within the blade boundary layers and wakes and the diffusion of the generated entropy within the blade passage that is mainly generated due to the temperature differences between the blade surface and the gas

Keywords:

Entropy; Turbomachinery; Second Law; CFD; Gas Turbine; Efficiency

1. Introduction

Loss predictions in turbomachinery could be based on the direct solution of the entropy generation equation. The entropy production actually can be used as a performance parameter if it can be calculated accurately as a part of the flow solution. One of the first ideas of utilizing the so called Entropy Generation Minimization (EGM) technique was developed by Bejan [1]. Bejan indicates that EGM, in addition to the importance of the first law of thermodynamics, shall have an important role in the analysis of systems involving heat transfer and viscous dissipation phenomena, which are dominant in turbomachinery flows demonstrating the necessity of entropy generation calculation.

In the design and analysis of turbomachinery components, the performance deterioration due to various real flow effects such as secondary flows, profile losses or tip-leakage losses is generally represented through semi-empirical loss coefficients. Instead of relying on these coefficients one can use entropy generation rates as a consistent and quantitative measure of lost work due to irreversibilities, which can be calculated globally using the inlet and exit values of calculated pressures and temperatures of a system. However, if complete quantitative descriptions of velocity and temperature fields are available, one can compute field distributions of local viscous and

thermal entropy generation rates by post-processing the available data. One such example for an air-cooled gas turbine stator blade can be found in Natalini and Sciubba [2]. The effective loss of work or destruction of exergy (Sciubba [3]) is related to the entropy generation through the Gouy-Stodola theorem as explained in Bejan [1] and Natalini and Sciubba [2].

Drost and White [4] realized the lack of entropy generation applications to complex problems and pointed out that up to that time there was no integration of the entropy generation equations with the CFD codes. They emphasized that since no analytical formulations of local entropy generation in turbulent flows exist in open literature, that part of the calculation could not be benchmarked for turbulent flows. Kock and Herwig [5], calculated the entropy generation for a heated pipe. In the study, the entropy production mechanisms were divided into four different groups such as the ones due to mean and fluctuating velocity fields and heat flux. The study concluded that the entropy production can be a parameter to define the efficiency of the system analyzed. McEligot et al. [6], on the other hand, performed a calculation of entropy production using the already available DNS data by Abe et al [7] instead of using a CFD code. Their study was mainly concentrated on the near wall region where they compared two different approaches about pointwise calculation of entropy generation.

All of the above mentioned studies reveal the importance of calculating the entropy generation as a performance parameter. However, all of them are based on a calculation that requires the solution of the velocity and temperature fields. Adeyinka and Naterer [8] proposed a more direct approach which involves including the Reynolds Averaged Entropy Transport equations, known as the Reynolds Averaged Clausius-Duhem equality, as a part of the solution process in turbulent flows. This technique of course involves a closure problem, similar to the closure of Reynolds stresses in the momentum equation, related to the calculation of mean entropy generation in terms of other mean flow quantities. A closure model was proposed by Adeyinka and Naterer [8] and tested in a turbulent channel flow between two parallel plates using Direct Numerical Simulation (DNS) data obtained by Moser et al. [9].

This paper presents an implementation of this approach to the 2D gas turbine blade section problem given in Natalini and Sciubba [2]. The Reynolds Averaged Entropy Transport and the necessary modeling equations are implemented to Ansys Fluent v14.0 [10] as User Defined Scalar (UDS). The model is applied to the air-cooled gas turbine blade configuration. The results are compared with those obtained by post-processing the temperature and velocity fields obtained by solving full Navier-Stokes equations using a Reynolds stress closure.

2. Entropy Production Modelling

For the formulation of entropy generation there are several methods available in the literature. One is the so called positive definite entropy generation equation as given below and in [8]:

$$\dot{P}_s = \frac{k}{T^2}\left(\frac{\partial T}{\partial x_i}\right)^2 + \frac{\tau_{ij}}{T}\frac{\partial u_i}{\partial x_j} \qquad (1)$$

where $\dot{P}_s$ is the rate of entropy production and stress tensor τ_{ij} can be stated as:

$$\frac{\tau_{ij}}{T} = \mu\left(\frac{\partial u_i}{\partial x_j} + \frac{\partial u_j}{\partial x_i}\right) \qquad (2)$$

The first term on the right hand side of Eq. (1) represents the entropy generation due to thermal effects whereas the second term is for the viscous entropy generation.

Using Eq. (1) together with Eq. (2), it is possible to obtain the total entropy generation rate. However, as can be seen from the components of Eq. (1) and (2), it requires the computation of the

flow fields for temperature and velocity. This is of course possible through the computation of Reynolds Averaged Navier-Stokes equations.

The other possible method is the use of entropy transport equation given as:

$$\frac{\partial S}{\partial t} + \frac{\partial F_i}{\partial x_j} \equiv \dot{P}_s \tag{3}$$

where S and F_i are the entropy per unit volume and flux of entropy respectively.

After Reynolds averaging Eq. (3) and several manipulations using Eq. (1) it is possible to obtain the transport equation for the rate of entropy generation [2]:

$$\frac{\partial(\rho\bar{s})}{\partial t} + \frac{\partial}{\partial x_i}\left[\rho\overline{u_i s} + \frac{\rho C_V}{\bar{T}}\overline{u_i{}'T'} - \frac{k}{\bar{T}}\frac{\partial \bar{T}}{\partial x_i}\right] = \frac{k}{\bar{T}^2}\left(\frac{\partial \bar{T}}{\partial x_i}\right)^2 + \rho\overline{u_i{}'T'}\frac{\partial s}{\partial x_i} + \frac{\overline{\tau_{ij}}}{\bar{T}}\frac{\overline{\partial u_i}}{\partial x_j} + \frac{\bar{\epsilon}}{\bar{T}} + \left\{\frac{k}{\bar{T}^2}\left(\frac{\partial T'}{\partial x_i}\right)^2 + \right.$$

$$\left.\frac{k}{2}\frac{\partial}{\partial x_i}\left(\frac{1}{\bar{T}}\right)\frac{\partial}{\partial x_i}(\overline{T'})^2 - \frac{\rho C_V}{\bar{T}}\left[\frac{\partial}{\partial x_i}\left(\frac{\overline{u_i{}'T'^2}}{\bar{T}}\right) + \bar{u}_i\frac{\partial}{\partial x_i}\left(\frac{T'^2}{\bar{T}}\right)\right] + \frac{\rho C_V}{2\bar{T}^2}\left[\frac{\partial}{\partial x_i}\left(\overline{u_i{}'T'^2}\right) + \bar{u}_i\frac{\partial}{\partial x_i}\left(\overline{T'^2}\right)\right]\right\} \tag{4}$$

The left hand side of Eq. (4) is the entropy production rate, $\dot{P}_s$. The first four terms on the right hand side are entropy generation rates due to molecular diffusion of the temperature field, diffusive entropy transport due to fluctuating velocity, viscous dissipation of the mean velocity field and dissipation of turbulent kinetic energy, respectively. The terms in braces are responsible for entropy production due to irreversible fluctuating velocity and fluctuating temperature fields [8].

Inclusion of Eq. (4) in the solution process is a more direct way of calculating the entropy generation rates in turbulent flows, though obviously it requires modelling effort related to the closure problem.

3. Methodology

Equation (4) can be written as:

$$\frac{\partial\overline{\rho(s)}}{\partial t} + \frac{\partial}{\partial x_i}\left[\rho\overline{u_i s} + \frac{\rho C_V}{\bar{T}}\overline{u_i{}'T'} - \frac{k}{\bar{T}}\frac{\partial \bar{T}}{\partial x_i}\right] = Source\ terms \tag{5}$$

Since the flows considered in this study are steady, first component on the left hand side is equal to zero.

The gradient of entropy can be defined as:

$$\frac{\partial \bar{s}}{\partial x_i} = \frac{C_V}{\bar{T}}\frac{\partial \bar{T}}{\partial x_i} \tag{6}$$

Substituting Equations (6) and (7) into Eq. (5) gives:

$$\frac{\partial}{\partial x_i}\left[\rho\overline{u_i s} + \frac{\rho C_V}{\bar{T}}\overline{u_i{}'T'} - \frac{k}{\bar{T}}\frac{\partial \bar{T}}{\partial x_i}\right] = Source\ terms \tag{7}$$

where,

$$Source\ terms = \frac{k}{\bar{T}^2}\left(\frac{\partial \bar{T}}{\partial x_i}\right)^2 + \rho\overline{u_i{}'T'}\frac{\partial s}{\partial x_i} + \frac{\overline{\tau_{ij}}}{\bar{T}}\frac{\overline{\partial u_i}}{\partial x_j} + \frac{\bar{\epsilon}}{\bar{T}} + \left\{\frac{k}{\bar{T}^2}\left(\frac{\partial\overline{T'^2}}{\partial x_i}\right) + \frac{k}{2}\frac{\partial}{\partial x_i}\left(\frac{1}{\bar{T}}\right)\frac{\partial}{\partial x_i}\partial(\overline{T'^2}) - \right.$$

$$\left.\frac{\rho C_V}{\bar{T}}\left[\frac{\partial}{\partial x_i}\left(\frac{\overline{u_i{}'T'^2}}{\bar{T}}\right) + \bar{u}_i\frac{\partial}{\partial x_i}\left(\frac{\overline{T'^2}}{\bar{T}}\right)\right] + \frac{\rho C_V}{2\bar{T}^2}\left[\frac{\partial}{\partial x_i}\left(\overline{u_i{}'T'^2}\right) + \bar{u}_i\frac{\partial}{\partial x_i}\left(\overline{T'^2}\right)\right]\right\} \tag{8}$$

The right hand side of Eq. (8) requires heavy modelling effort and these models are mostly non-existent in the open literature. The terms other than the first four, involve temperature fluctuations, could either be modeled using the STTAss (Small Thermal Turbulence Assumption) as given in

Kramer-Bevan [11] or additional transport equations could be solved as explained [12]. STTAss model assumes the fluctuating part of temperature is small compared to the mean temperature and Taylor series expansions can be used to model the fluctuating temperature by including only the linear terms

The terms that need modelling are $\overline{u_i'T'}$, $\overline{T'^2}$ and $\overline{u_i'T'^2}$. Some model equations are proposed by Hanjalic and Jakirlic [12] for the first two terms but no model equation has been encountered for the last term. In our future studies we will investigate the effects of modeling these terms in detail using either one of these approaches.

The model equation for $\overline{u_i'T'}$ is given as [12]:

$$\frac{D\overline{(T'u_i')}}{Dt} = -\overline{u_i'u_k'}\frac{\partial\bar{T}}{\partial x_k} - (1-C_{2T})\overline{(T'u_k')}\frac{\partial\bar{U}_i}{\partial x_k} - (1-C_{3T})\beta g_i\overline{T'^2} - C_{1T}\frac{\overline{(T'u_i')}}{k}\varepsilon + C_T\frac{\partial}{\partial x_k}\left(\overline{u_k'u_l'}\frac{k}{\varepsilon}\frac{\partial\overline{(T'u_i')}}{\partial x_l}\right) \quad (9)$$

and the model equation for $\overline{T'^2}$ is:

$$\frac{D\overline{T'^2}}{Dt} = -\frac{2\overline{(T'u_i')}\left(\partial\overline{T}\right)}{\partial x_i} - \frac{1}{2R}\frac{\overline{T'^2}}{2k}\varepsilon + C_{T^2}\frac{\partial}{(\partial x_j)\left(\frac{\overline{u_i'u_j'}k}{\varepsilon}\frac{\partial\overline{T'^2}}{\partial x_i}\right)} \quad (10)$$

For which the recommended coefficients are given in Table 1

Table 1. Recommended Coefficients for the model equations [12]

C_{T^2}	C_T	C_{1T}	C_{2T}	C_{3T}	R
0.2	*0.15*	*3.5*	*0.55*	*0.55*	*0.5*

Eq. (8), (9) and (10) are implemented in Fluent, using the UDS feature, which enables the solution of an additional scalar transport equation. There are two main parameters for the implementation of Eq. (8); diffusivity and source terms. After these terms are defined and a converged solution is obtained, it is possible to postprocess the results to obtain the distributions of the solved scalar, in this case the entropy.

4. Results

The methodology is applied to the two-dimensional cascade problem given in Natalini and Sciubba [2]. This is an air-cooled turbine stator cascade. For the purpose of this study, the air cooling holes inside blade have not been modeled, but the blade surface is kept at constant temperature. The boundary conditions are applied as given in [2] such as the blade surface and the air temperatures are 1118 K and 1300 K, respectively. The inlet velocity is V_g=103 m/s. The inlet conditions for turbulence are k_g=0.01 V_g^2 and ϵ_g=0.006 V_g^2 for the turbulent kinetic energy and dissipation rate of turbulent kinetic energy, respectively.

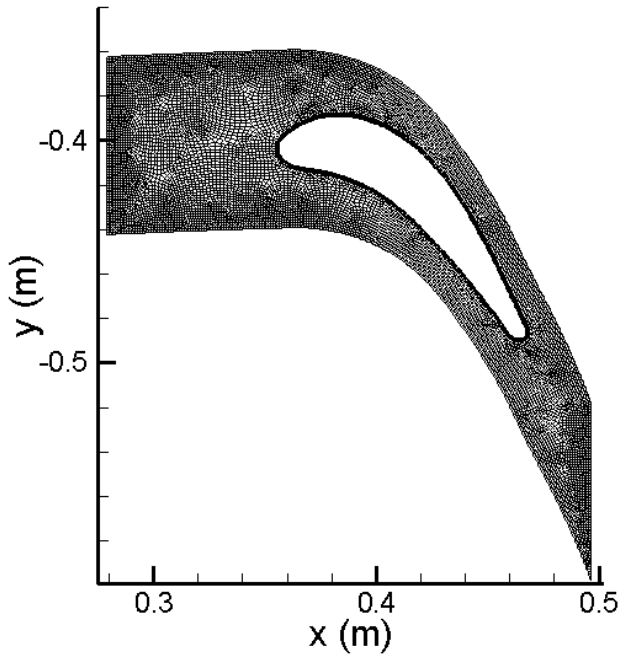

Figure 1 Geometry and the computational grid used in the gas turbine stator blade simulations.

Velocity inlet boundary condition has been applied as inlet boundary condition and pressure outlet as the outlet boundary condition. Upper and lower surfaces have been selected as periodic. They are half pitch distance away from the chord representing surfaces exposed to the flow conditions.

In order to obtain a wall y^+ value around 1, a boundary of 40 layers is attached for the accurate calculation of especially the viscous phenomena. A total of 25000 elements are used. The number of grid points is decided after a grid convergence study up to about 50000 elements, which showed that the calculated total entropy generation rate values do not change much after about 25000 elements. The details of the geometry and the mesh can be seen in Figure 1.

The calculated entropy generation rates within the cascade are presented in Figure 2. The distribution obtained through solving Reynolds-Averaged Entropy Transport equation (Equations (7) and (8)) as a part of the CFD solution is given in Figure 2. Figures 5b and 5c present the viscous and thermal entropy generation rate values, respectively, obtained through post-processing the obtained velocity and temperature field data. Equations (11) and (12) given below are used for this purpose:

$$s_V = \frac{2}{T}\mu\left\{\left(\frac{\partial u}{\partial x}\right)^2 + \left(\frac{\partial v}{\partial y}\right)^2 + \frac{1}{2}\left(\frac{\partial u}{\partial y} + \frac{\partial v}{\partial x}\right)^2\right\} \tag{11}$$

$$s_T = \frac{k_{air}}{T^2\left\{\left(\frac{\partial T}{\partial x}\right)^2 + \left(\frac{\partial T}{\partial y}\right)^2\right\}} \tag{12}$$

It is seen that the direct calculation of entropy production as a part of the solution process produces a much smoother variation emphasizing the entropy generation within the blade boundary layers and wakes and the diffusion of the generated entropy within the blade passage that is mainly generated due to the temperature differences between the blade surface and the gas. The results obtained through equations (11) and (12) show that viscous entropy production is much larger than the thermal one, the high entropy regions are confined to the very near wall and the leading and trailing edge zones (consistent with the distributions given in Natalini and Sciubba [2]). In addition, the diffusion characteristics of entropy are not captured as well as the one presented in Figure 5a. Figure 5d shows the spatial distribution of the absolute value of the difference between the results

presented in 5a and the sum of the distributions given in 5b and 5c. As is evident, main differences occur near the leading and trailing edge zones as well as within the wake regions of the blades. Since the diffusion characteristics of entropy generation are not captured by using equations (11) and (12), these show up as elevated levels of the difference value within the passage, mostly after the mid-chord position. Of course one needs more detailed comparisons with experimental data, and the effects of ignoring the temperature fluctuation related terms in equation (9) have to be investigated.

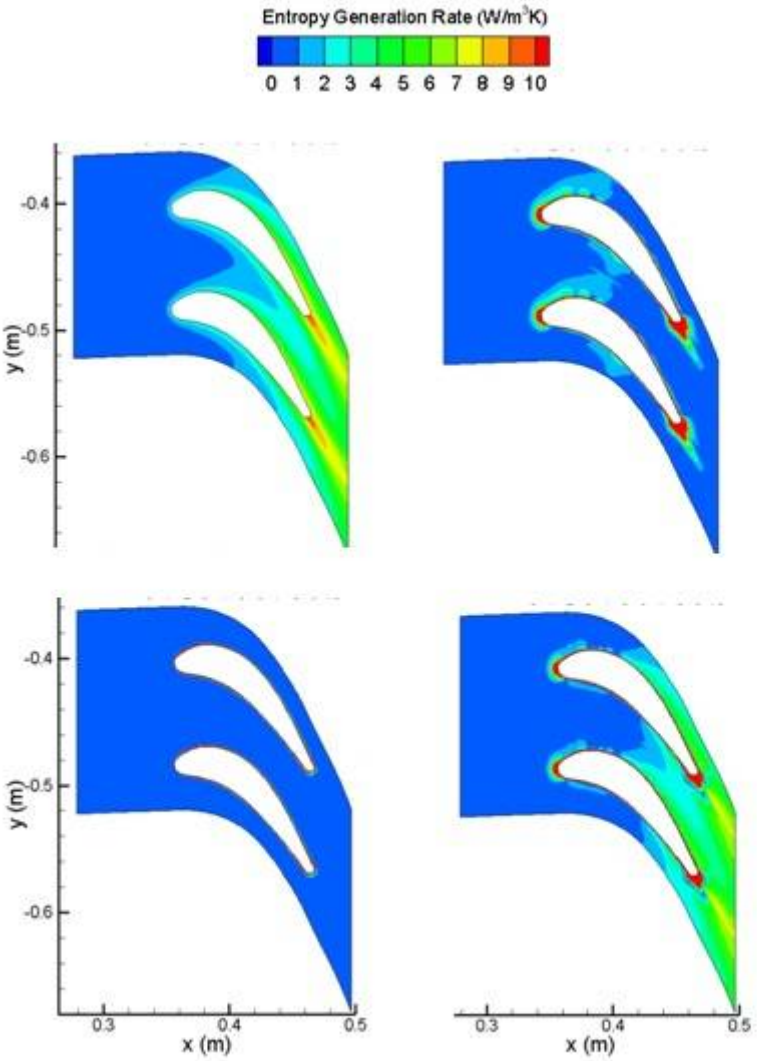

Figure 2. (a) Calculated total entropy generation rate through solving equations (8) and (9); (b) and (c) viscous and thermal entropy generation rates, respectively, as calculated using equations (11) and (12) by post-processing the calculated velocity and temperature fields; (d) the absolute value of the difference between the distribution presented in (a) and the sum of the distributions presented in (b) and (c).

In addition to Figure 2, further analysis has been conducted using the modelling approaches for the equations (9) and (10). However, the implementation of these terms into Fluent requires the solution of four additional transport equations. Several solutions have been obtained but the validity of these results is not presented in this study at the moment.

5. Conclusions

The effect of calculating the entropy generation rate directly using the Reynolds-Averaged Entropy Transport equation is demonstrated by comparing the obtained results with the ones that are calculated by post-processing the velocity and temperature fields for a two-dimensional turbine cascade configuration. Results show that there could be significant differences especially in the spatial distributions of entropy fields. This type of approach could offer significant improvements in entropy and loss prediction in turbomachinery flows. In the meantime, this may require more time budgets. This will be understood when more detailed test cases are studied. However, this approach needs more studies especially for accurate modeling of temperature fluctuations and temperature-velocity correlations in the entropy transport equation. Accurate modelling techniques are available in the literature but it was observed that the application of such techniques is very tedious but will be conducted in the future studies.

6. Acknowledgements

It is greatly acknowledged the support of Prof. Sciubba and Giorgio Giangaspero from University of Rome 'La Sapienza' and Dr. Derek Baker from Middle East Technical University. They put great value on the publication of this paper.

7. Nomenclature

$\dot{P}_s$	entropy generation rate,	W/m^3 K
k	thermal conductivity,	W/m K
T	temperature	K
x	cartesian coordinate	
u	velocity	m/s
S	entropy per unit volume	
F_i	flux of entropy	
k_t	turbulent thermal conductivity	W/m K
C_v	specific heat	J/kg K

Greek symbols

τ_{ij}	stress tensor	
μ	dynamic viscosity	kg/m s
$\bar{\epsilon}$	dissipation of turbulent	m^2/s^3

kinetic energy

γ	ratio of specific heats	
ρ	density	kg/ m^3

8. References

[1] A. Bejan, "Entropy Generation Through Heat and Fluid Flow", John Wiley and Sons, 1982.

[2] G. Natalini, E.Sciubba, "Minimization of the Local Rates of Entropy Production in the Design of Air Cooled Gas Turbine Blades", Journal of Engineering for Gas Turbines and Power, pp. 466-475, vol. 121, November 1999.

[3] E. Sciubba, "Numerical Calculation of Local Irreversibilities in Compact Heat Exchangers ", Proceedings NATO-TIBTD Workshop on 2nd Law, Erciyes University, Kayseri, Turkey, 1990.

[4] M.K. Drost, M.D. White, “Numerical Prodictions of Local Entropy Generation in an Impinging Jet”, Journal of Heat Transfer, pp. 823-829, vol. 113, November 1991.

[5] F. Kock,H. Herwig, “Entropy Production Calculation for Turbulent Shear Flows and Their Implementation in CFD codes”, International Journal of Heat and Fluid Flow, pp. 672-680, vol. 26, June 2005.

[6] D. M. McEligot, E.J. Walsh, E. Laurien “Entropy Generation in the Viscous Layer of a Turbulent Channel Flow”, 5th International Symposium on Turbulence, Heat and Mass Transfer, September 2006.

[7] H. Abe, H. Kawamura, Y. Matsuo, “Direct Numerical Simulation of a Fully Developed Turbulent Channel Flow With Respect to the Reynolds Number Dependence”, Journal of Fluids Engineering, pp. 382-393, February 2001.

[8] O.B. Adeyinka, G.F. Naterer, “Modeling of Entropy Generation in Turbulent Flows”, Journal of Fluids Engineering, pp. 893-899, vol. 126, November 2004.

[9] R. D. Moser, J. Kim, N.N. Mansour “Direct Numerical Simulation of Turbulent Channel Flow up to Re_T =590”, Physics of Fluids, pp. 943-945, December 1998.

[10] http://www.ansys.com, 2012

[11] J.S. Kramer-Bevan, “A Tool for Analyzing Fluid Flow Losses”, M. Sc. Thesis, University of Waterloo, Canada, 1992.

[12] Hanjalic, K., and Jakirlic, S “Closure Strategies for Turbulent and Transitional Flows”, Cambridge University, Cambridge 2002.

[13] F. M. White, “Viscous Fluid Flow”, Mc Graw-Hill Education, 2005.

Conventional and advanced exergetic evaluation of a supercritical coal-fired power plant

Ligang Wang[a], YongpingYang[b,CA], Tatiana Morosuk[c], George Tsatsaronis[d]

a North China Electric Power University, Beijing, China, lg_lglq@163.com
b North China Electric Power University, Beijing, China, yyp@ncepu.edu.cn
c Technische Universitat Berlin, Berlin, Germany, morozyuk@iet.tu-berlin.de
d Technische Universitat Berlin, Berlin, Germany, tsatsaronis@iet.tu-berlin.de

Abstract:

A conventional exergy analysis can highlight the main components having high thermodynamic inefficiencies, but cannot consider the interactions among components or the true potential for the improvement of each component. By splitting the exergy destruction into endogenous/exogenous and avoidable/unavoidable parts, the advanced exergy analysis is capable of providing additional information to conventional exergy analysis for improving the design and operation of energy conversion systems. This paper presents the application of both a conventional and an advanced exergy analysis to a supercritical coal-fired power plant to quantify the interactions among components of the overall system and to reveal the potential for the performance enhancement of a system component.

The results show that the ratio of exogenous exergy destruction differs quite a lot from component to component. In general, almost 90% of the total exergy destruction within turbines comes from their endogenous parts, while that of feedwater preheaters contributes more or less 70% to their total exergy destruction. Moreover, the boiler subsystem is proven to have a large amount of exergy destruction caused by the irreversibilities within the remaining components of the overall system.

It is also found that the boiler subsystem still has the largest avoidable exergy destruction; however, the enhancement efforts should focus not only on its inherent irreversibilities but also on the inefficiencies within the remaining components. A large part of the avoidable exergy destruction within feedwater preheaters is exogenous; while that of the remaining components is mostly endogenous indicating that the improvements mainly depend on advances in design and operation of the component itself.

Keywords:

Supercritical Power Plant, Advanced Exergy Analysis, Improvement Strategy

1. Introduction

Nearly 45% of global electricity generation is derived from coal while natural gas and nuclear energy make up about 20% and 15%, respectively [1,2]. Despite the rapid growth of cleaner sustainable energies, the heavily dependence of world energy on coal is expected to continue for decades. It has been well known that the supercritical coal-fired power plants are energy systems with high fuel consumption, low efficiency, and relatively large amounts of pollutants and greenhouse gas emissions. Consequently, efficiency improvements of both existing units and plants under construction are of particular importance.

Exergy analysis can identify the location, the magnitude, and the sources of thermodynamic inefficiencies in a thermal system [3], and thus provide information for improving the overall efficiency and the cost effectiveness of a system or for comparing the performance of various systems [4]. Throughout the last decades, this conventional exergy analysis has been discussed and applied to a wide variety of coal-fired power plants, for example, see Refs. [5-9]. However, conventional exergy analysis is always used to evaluate the performance of an individual component at certain operation conditions, without considering the interactions among components or the actual achievable best behavior of the component under investigation.

The advanced exergy analysis was proposed and developed in [10-18] to evaluate energy conversion systems by splitting the exergy destruction into endogenous/exogenous and

avoidable/unavoidable parts, which are crucial for improving complex systems. Therefore, more comprehensive, practical and not just rigorous information on how and to what extend the components can be improved is provided by an advanced exergy analysis to explicitly develop strategies for system performance enhancement. In the last years, advanced exergy analyses have been successfully applied to many energy conversion systems including simple and complex systems. At first, systems such as a simple gas-turbine-based cogeneration system [11], a simple vapor-compression refrigeration machine [15], and a novel cogeneration system for vaporizing liquefied natural gas [17] were used for demonstrating the theory development and applications. Later applications include more complex systems such as a cogeneration power plant based on gas turbine [12], and a three-pressure level combined cycle [18]. The results of these applications show that considering the interactions among components and the energy-saving potentials makes the approach a promising and powerful tool for effectively improving complex energy systems, such as coal-fired power plants.

However, until now no supercritical coal-fired power plant has been analyzed and evaluated using this method. Hence in this paper both conventional and advanced exergy analyses were performed to an existing modern supercritical pulverized-coal power-generation unit, in order to formulate some recommendations for system improvement.

2. Methodology

2.1. Conventional exergy analysis

It is assumed that the system boundaries are at the temperature T_0 of the reference environment, and therefore, there are no exergy losses associated with the kth component [19]. As a consequence, the exergy loss term actually only appears at the level of the overall system. Hence, the exergy balance of the *k*th component is expressed as

$$\dot{E}_{F,k} = \dot{E}_{P,k} + \dot{E}_{D,k} . \tag{1}$$

For the overall system, it becomes

$$\dot{E}_{F,tot} = \dot{E}_{P,tot} + \sum_{k} \dot{E}_{D,k} + \dot{E}_{L,tot} \tag{2}$$

The exergetic efficiency of the *k*th component is written as

$$\varepsilon_k = \frac{\dot{E}_{P,k}}{\dot{E}_{F,k}} = 1 - \frac{\dot{E}_{D,k}}{\dot{E}_{F,k}} \tag{3}$$

To identify the part of total fuel exergy input destroyed within the kth component, the exergy destruction ratio is defined as

$$y_{D,k} = \frac{\dot{E}_{D,k}}{\dot{E}_{F,tot}} \tag{4}$$

2.2. Advanced exergy analysis

In an advanced exergy analysis, the exergy destruction within each component is split to better reveal its sources (endogenous/exogenous) and its potential for reduction (avoidable/unavoidable) [18]. The endogenous part is the exergy destruction obtained when all other components operate ideally and the component being considered operates with its real efficiency. The exogenous part of the exergy destruction within the considered component, is caused by irreversibilities in the remaining components and by the structure of the overall system, and is the difference between total exergy destruction of the component at real conditions and the endogenous part. The unavoidable part is the part that cannot be eliminated, even if the best available technology in the near future

would be applied. Finally the avoidable part is the difference between the total exergy destruction within the component in the real plant and the unavoidable part of exergy destruction. [15].

2.2.1. Endogenous/exogenous exergy destruction

To consider the interactions among components, the exergy destruction within the *k*th component is expressed, as equation (5) shows, as the sum of endogenous and exogenous exergy destruction:

$$\dot{E}_{D,k} = \dot{E}_{D,k}^{EN} + \dot{E}_{D,k}^{EX} \tag{5}$$

Since it is also important, how and to what extend one component affects another component[17], the exogenous exergy destruction can be further split as

$$\dot{E}_{D,k}^{EX} = \sum_{\substack{r=1 \\ r\neq k}}^{n} \dot{E}_{D,k}^{EX,r} + \dot{E}_{D,k}^{MX} \tag{6}$$

where $\dot{E}_{D,k}^{EX,r}$ is the effect of exergy destruction within the *r*th component caused by the exergy destruction of the *k*th component. It can be seen that the total exogenous exergy destruction is comprised of two terms, a sum term and a term called mexogenous exergy destruction $E_{D,k}^{MX}$ due to the simultaneous interactions of all (*n-1*) components.

2.2.2. Avoidable/unavoidable exergy destruction

Due to technical and economic limitations and manufacturing methods, each component has an unapproachable best thermodynamic behavior in the near future that determines the unavoidable part of exergy destruction. When each component operates with its best possible conditions, the unavoidable process is established, to obtain the ratio $(\dot{E}_D / \dot{E}_P)_k^{UN}$ for the component. This ratio is the key parameter for calculating the unavoidable part of exergy destruction of individual components in a real process. Therefore, the exergy destruction of the *k*th component can also be written as

$$\dot{E}_{D,k} = \dot{E}_{D,k}^{UN} + \dot{E}_{D,k}^{AV}, \tag{7}$$

where the unavoidable part can be calculated by

$$\dot{E}_{D,k}^{UN} = \dot{E}_{P,k} \cdot (\dot{E}_D / \dot{E}_P)_k^{UN} \tag{8}$$

2.2.3. Combination of the splitting

By further combining the two splitting concepts, the avoidable-endogenous/avoidable-exogenous and unavoidable-endogenous/unavoidable-exogenous terms can be obtained by

$$\dot{E}_{D,k}^{UN,EN} = \dot{E}_{P,k}^{EN} \cdot (\dot{E}_D / \dot{E}_P)_k^{UN} \tag{9a}$$

$$\dot{E}_{D,k}^{UN,EX} = \dot{E}_{D,k}^{UN} - \dot{E}_{D,k}^{UN,EN} \tag{9b}$$

$$\dot{E}_{D,k}^{AV,EN} = \dot{E}_{D,k}^{EN} - \dot{E}_{D,k}^{UN,EN} \tag{9c}$$

$$\dot{E}_{D,k}^{AV,EX} = \dot{E}_{D,k}^{EX} - \dot{E}_{D,k}^{UN,EX} \tag{9d}$$

In order to calculate each part of the exergy destruction within all components, five sorts of processes including real, theoretical, hybrid I, hybrid II and unavoidable processes should be considered and simulated. In a theoretical process, all components operate under their theoretical conditions, while in a hybrid I process only the component being considered is set at its real condition to compute its endogenous exergy destruction. Simulations of totally $(C_n^2 - n)$ hybrid II

processes enable us to quantify the interaction between any two components operating under their real conditions with *n* being the total number of components. The unavoidable process where each component operates under its unavoidable conditions is simulated for obtaining the unavoidable ratios of all components.

3. Plant descriptions

The supercritical power plant, as shown in Fig.1, has a total installed power capacity of 671MW, consisting of a boiler subsystem and a turbine subsystem and an electrical generator. The properties of bituminous coal are listed in Table 1.

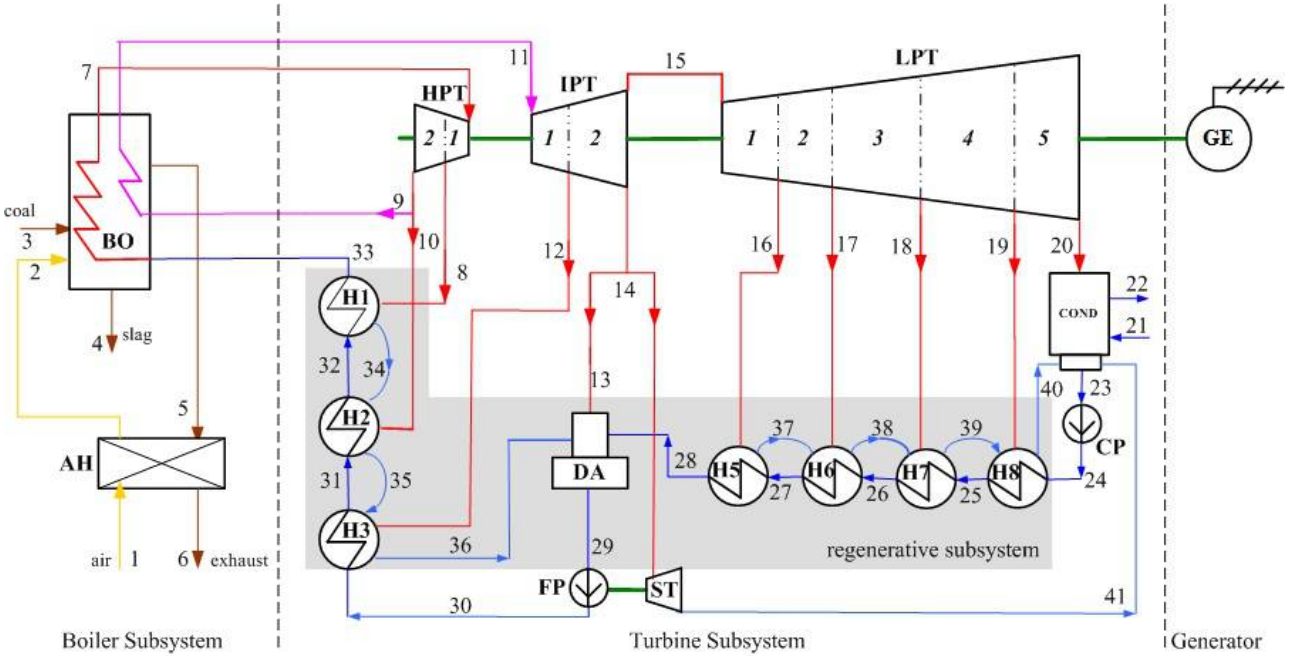

Fig. 1. Schematic diagram of the overall supercritical power generation unit

Table 1. Approximate analysis of coal (wt. %; as received)

Item	*value*	*Item*	*value*	*Item*	*value*	*Item*	*value*
Moisture	2.10%	Carbon	57.52%	Oxygen	2.78%	Sulphur	2.00%
Ash	23.70%	Hydrogen	3.11%	Nitrogen	0.99%	LHV	21981kJ/kg

The boiler subsystem with dry ash extraction and single reheat is simulated by two components: boiler and air preheater. The coal combustion process and the heat transfer between flue gas and working fluid occur in the boiler. In this way, the theoretical condition of boiler subsystem can be readily specified.

The main steam is expanded in the high-pressure turbine and then the steam is reheated and expanded through the stages of intermediate-pressure and low-pressure turbines. The intermediate-pressure turbine (IPT) is considered in two parts: from the inlet to steam extraction (IPT1) and from steam extraction to outlet (IPT2). Similarly, the low-pressure turbine (LPT) is considered in five parts (LPT 1 through LPT5). A surface condenser is used to remove to the environment heat from exhausted steam. To increase the thermodynamic average temperature of the working fluid in the boiler, a feedwater regenerative system with three high-pressure heaters, four low-pressure heaters and a deaerator is configured. The condensate and feedwater pumps are driven by electric motors and a secondary steam turbine with the same steam supply as for the deaerator.

Table 2. Thermodynamic properties of all material flows

No	*m, kg/s*	*T, ℃*	*p, bar*	E_{tot}*, MW*	*No*	*m, kg/s*	*T, ℃*	*p, bar*	E_{tot}*, MW*
1	619.385	25.00	1.002	0.85	22	29813.6	30.79	1.000	81.39
2	619.385	330.41	1.000	61.40	23	395.497	35.79	0.059	1.27
3	68.802	25.00	1.000	1603.07	24	395.497	35.94	17.24	1.96
4	15.980	600.00	1.000	15.97	25	395.497	58.16	15.84	4.41
5	670.831	394.00	0.998	133.39	26	395.497	85.41	14.54	10.46
6	670.831	127.00	0.978	48.85	27	395.497	105.06	12.94	16.63
7	522.217	571.00	254.0	806.90	28	395.497	143.24	11.44	32.57
8	39.407	364.23	67.97	46.81	29	522.217	180.06	10.04	69.16
9	438.914	304.98	43.00	474.94	30	522.217	185.59	308.7	87.76
10	43.896	304.98	43.00	47.50	31	522.217	211.95	303.7	109.57
11	438.914	569.00	41.10	632.49	32	522.217	253.27	298.4	149.16
12	19.400	459.68	20.58	23.45	33	522.217	284.05	293.5	183.29
13	24.018	362.68	10.44	24.20	34	39.407	258.82	64.97	11.05
14	28.702	362.68	10.44	28.92	35	83.303	217.50	41.00	16.41
15	366.794	362.68	10.44	369.52	36	102.702	191.14	19.08	15.45
16	25.599	253.53	4.374	20.12	37	25.599	110.61	4.174	1.19
17	12.993	128.72	1.333	7.01	38	38.592	90.96	1.333	1.13
18	17.286	88.19	0.655	7.27	39	55.878	63.71	0.655	0.68
19	13.574	60.94	0.208	3.41	40	69.452	41.49	0.208	0.30
20	297.343	35.79	0.059	23.80	41	28.702	39.68	0.073	3.20
21	29813.6	25.00	1.000	74.47					

The simulation of the supercritical coal-fired power plant was conducted with the help of the software EBSILONProfessional and the main thermodynamic parameters of each flow are listed in Table 2.

4. Simulations for the advanced exergy analysis

Defining the theoretical and unavoidable conditions of each component is the most important task for the calculation of different parts of exergy destruction. In this section, the theoretical and unavoidable conditions of different components of the energy system are discussed.

4.1. Theoretical conditions

The theoretical operation conditions for each component should follow the assumptions: $E_D=0$, (if possible), or otherwise $E_D=min$.

With regards to the features of the power plant, many parameters in the theoretical process are the same as in the real process: for example, temperature and pressure of superheated steam, temperature of reheated steam, pressure levels of steam extractions, back pressure of turbine, and the inlet temperature of cooling water flowing into condenser remain unchanged when a component is under theoretical conditions. However, the temperature and pressure of feedwater into boiler, the pressure of reheated steam, the temperature of steam extraction as well as the outlet temperature of cooling water flowing out of the condenser always vary with the conditions assumed for the corresponding component.

For turbines, fans and pumps, both the isentropic efficiency and the mechanical efficiencies should equal to *1* to guarantee no exergy destruction during the corresponding process.

For heat exchangers, it is apparent that the working condition with no entropy generation is normally unachievable due to the existence of a pinch point. Only the state where the exergy destruction is minimal can be achieved by assuming no pressure drop and zero temperature difference at the pinch point.

The combustion process in this case is not considered separately but is integrated into the component boiler with the heat transfer process. However, there are still some assumptions referring to the combustion process for defining the theoretical conditions of the boiler. The chemical composition of flue gas should be kept the same as in the real conditions to make sure that the excess air/fuel ratio is equal to that of the real process. In addition, no pressure drop occurs to satisfy the theoretical conditions of combustion process. Detailed explanations are given in [13].

4.2. Unavoidable conditions

The unavoidable conditions refer to the best unapproachable working conditions associated with the technical and economic limits related to the considered component. In general, it would be better if the best performance characteristics can be derived in conjunction with some kind of investment-efficiency curves or the best practice of the same type components under operation. If no such resources are available, the best behavior is determined more than less arbitrarily, depending highly on the understanding and practical experience of the analyzer. In this paper the unavoidable conditions of each component are chosen as listed in Table 3.

Table 3. Assumptions of theoretical and unavoidable conditions

Comp.	*Real Process*	*Unavoidable Process*	*Comp.*	*Real Process*	*Unavoidable Process*
HPT1	η_s=0.89, η_m=0.998	η_s=0.92, η_m=1	H7	$\triangle T_p$=2.9, $\triangle T_p$=5.5	$\triangle T_p$=1.5, $\triangle T_p$=3.0
HPT2	η_s=0.88, η_m=0.998	η_s=0.92, η_m=1	H6	$\triangle T_p$=3.1, $\triangle T_p$=5.5	$\triangle T_p$=1.5, $\triangle T_p$=3.0
IPT1	η_s=0.92, η_m=0.998	η_s=0.96, η_m=1	H5	$\triangle T_p$=6.3, $\triangle T_p$=5.5	$\triangle T_p$=3.0, $\triangle T_p$=3.0
IPT2	η_s=0.93, η_m=0.998	η_s=0.96, η_m=1	DA	$\triangle p$=0.4	$\triangle p$=0.1
LPT1	η_s=0.94, η_m=0.998	η_s=0.96, η_m=1	FP	η_s=0.84, η_m=0.998	η_s=0.87, η_m=1
LPT2	η_s=0.96, η_m=0.998	η_s=0.97, η_m=1	H3	$\triangle T_p$=4.9, $\triangle T_p$=5.5	$\triangle T_p$=3.0, $\triangle T_p$=3.0
LPT3	η_s=0.92, η_m=0.998	η_s=0.94, η_m=1	H2	$\triangle T_p$=3.0, $\triangle T_p$=5.5	$\triangle T_p$=1.5, $\triangle T_p$=3.0
LPT4	η_s=0.74, η_m=0.998	η_s=0.85, η_m=1	H1	$\triangle T_p$=2.8, $\triangle T_p$=5.5	$\triangle T_p$=1.5, $\triangle T_p$=3.0
LPT5	η_s=0.82, η_m=0.998	η_s=0.85, η_m=1	ST	η_s=0.80, η_m=0.998	η_s=0.87, η_m=1
COND	$\triangle T_p$=5	$\triangle T_p$=3	GT	η_m=0.986	η_m=0.998
CP	η_s=0.80, η_m=0.998	η_s=0.87, η_m=1	BO	η_c=0.980, $\triangle p_{sh}$=40.5 $\triangle p_{rh}$=1.90, α=1.2	η_c=0.995, $\triangle p_{sh}$=20 $\triangle p_{rh}$=0.50, α=1.03
H8	$\triangle T_p$=2.9, $\triangle T_p$=5.5	$\triangle T_p$=1.5, $\triangle T_p$=3.0	AH	T_{ex}=127	T_{ex}=90

Table 4. Results from the conventional exergy analysis at the component level

Comp.	E_F,*MW*	E_P, *MW*	y_D, %	ε , %	*Comp.*	E_F,*MW*	E_P, *MW*	y_D, %	ε , %
HPT1	186.55	175.69	0.72	94.2	H7	7.72	6.05	0.11	78.4
HPT2	51.10	47.63	0.23	93.2	H6	7.07	6.17	0.06	87.2
IPT1	101.99	98.2	0.25	96.3	H5	18.93	15.93	0.20	84.2
IPT2	84.41	81.36	0.20	96.4	DA	22.86	19.81	0.20	86.7
LPT1	81.28	78.22	0.20	96.2	FP	20.80	18.6	0.15	89.4
LPT2	83.93	81.56	0.16	97.2	H3	24.41	21.81	0.17	89.4
LPT3	39.13	36.5	0.17	93.3	H2	42.14	39.6	0.17	94.0
LPT4	52.63	39.89	0.85	75.8	H1	35.76	34.13	0.11	95.4
LPT5	50.94	41.95	0.60	82.4	ST	25.72	20.8	0.33	80.9
COND	26.03	-	1.27	-	GT	681.00	671.21	0.65	98.6
CP	0.86	0.69	0.01	80.5	BO	1483.04	781.16	46.57	52.7
H8	3.79	2.46	0.09	64.8	AH	84.54	60.55	1.59	71.6

5. Results and discussions

The results from the conventional and the advanced exergy analysis at the component level are summarized in Tables 4 and 5.

Table 5. Results of advanced exergetic analysis at the component level (Unit: MW)

Comp Name	$\dot{E}_{D,k}^{EN}$, MW	$\dot{E}_{D,k}^{EX}$, MW	$\dot{E}_{D,k}^{UN}$, MW	$\dot{E}_{D,k}^{AV}$, MW	$\dot{E}_{D,k}^{EN}$, MW		$\dot{E}_{D,k}^{EX}$, MW	
					$\dot{E}_{D,k}^{UN,EN}$	$\dot{E}_{D,k}^{AV,EN}$	$\dot{E}_{D,k}^{AV,EX}$	$\dot{E}_{D,k}^{UN,EX}$
HPT1	9.90	0.96	7.25	3.61	6.67	3.23	0.38	0.58
HPT2	3.05	0.42	2.16	1.31	1.87	1.18	0.13	0.29
IPT1	3.64	0.16	2.59	1.21	2.47	1.17	0.04	0.12
IPT2	2.69	0.37	2.04	1.01	1.77	0.92	0.09	0.28
LPT1	2.78	0.28	2.38	0.68	2.10	0.68	0.00	0.28
LPT2	2.13	0.24	1.92	0.46	1.65	0.48	-0.02	0.26
LPT3	2.31	0.31	1.92	0.70	1.72	0.59	0.11	0.20
LPT4	11.46	1.29	6.28	6.46	5.72	5.74	0.72	0.56
LPT5	7.84	1.15	7.15	1.84	6.23	1.61	0.23	0.92
COND	15.30	3.81	-	-	-	-	-	-
CP	0.15	0.02	0.12	0.05	0.10	0.04	0.01	0.01
H8	1.18	0.16	1.12	0.21	0.99	0.19	0.03	0.13
H7	1.21	0.46	1.41	0.26	1.15	0.06	0.20	0.26
H6	0.61	0.29	0.71	0.19	0.54	0.07	0.12	0.17
H5	2.17	0.83	2.47	0.53	2.02	0.15	0.38	0.45
DA	2.03	1.02	2.89	0.16	2.12	-0.09	0.25	0.78
FP	1.70	0.50	1.72	0.49	1.34	0.37	0.12	0.38
H3	2.28	0.32	2.16	0.44	1.96	0.33	0.11	0.20
H2	1.58	0.96	1.99	0.55	1.45	0.13	0.42	0.54
H1	1.15	0.49	1.25	0.38	1.00	0.15	0.24	0.25
ST	3.20	1.72	3.50	1.42	2.31	0.89	0.53	1.19
GT	9.79	0.00	1.35	8.45	1.35	8.45	0.00	0.00
BO	615.20	86.68	676.29	25.60	608.98	6.23	19.37	67.31
AH	16.91	7.09	11.46	12.53	11.56	5.34	7.19	-0.10

5.1. Conventional analysis

It is very clear from Table 4 that 45% of the total input fuel exergy is destroyed in the boiler due to coal combustion and heat transfer under high temperature differences. The air preheater, turbines and condenser follow with much lower values of exergy destruction. The regenerative subsystem has little exergy destruction, whereas the secondary turbine and the generator have relatively large exergy destruction value.

From the perspective of the conventional analysis, the greater the irreversibility in a component, the higher the priority for improvement must be for increasing the efficiency of the overall system. Hence, the boiler should be given the first priority for the reduction of total inefficiencies. Then, the air preheater, the first and the last two stages of turbine have relatively high priorities, because these components have large operational exergy destruction.

5.2. Advanced analysis

5.2.1. Interactions among components

To investigate how and to what extend one component exerts impact on another, each $\dot{E}_{D,k}^{EX,r}$ is calculated and listed in Table 6, which also contains the endogenous exergy destruction of each component. It is apparent that the interactions between different components can be positive or negative. The former indicates that the exergy destruction in the *k*th component increases with the introduction of additional irreversibilities in the *r*th component. On the contrary, the latter means that adding inefficiencies in the *r*th component contributes to a reduction of the exergy destroyed in the *k*th component. These two distinct impacts can be the results of mass flow changes or thermodynamic property variation of material flows flowing through the *k*th component due to the introduction of additional irreversibility in the *r*th component. For example, when evaluating the interaction between components IPT1 and H3, introducing irreversibility in H3 reduces the outlet temperature of feedwater. This requires more steam extraction in the following feedwater preheater H2. Since the total mass flow rate is kept almost unchanged, the mass flow of steam through IPT1 is reduced. However, the impact of thermodynamic inefficiency in boiler on IPT1 results from large flow property changes. For example, we can assume that the irreversibilities in the boiler increase because of an increase in the pressure drop in the reheater. If the pressure at the outlet of the first part of the intermediate-pressure turbine (IPT1) remains constant, then the steam temperature at that point will increase, leading to a reduction in the exergy destruction within IPT1. Thus, increasing the exergy destruction in the boiler (component *r*) leads to a reduction in the exergy destruction within the IPT1 (component *k*). This explains the negative sign related to the interaction between these two components (see Table 6, third row and second to last column).

The exergy destruction within each turbine stage is mainly affected by the other stages, especially the stages with large irreversibility, the directly-connected feedwater preheater as well as the electrical generator. The irreversibilities in other turbine stages all have contributions to the exergy destruction in the considered turbine stage, whereas the inefficiencies of its corresponding feedwater preheater have a negative influence (negative sign in Table 6) on it due to the change of mass flow rate. In addition, the generator greatly affects the exergy destruction of each turbine stage, when the total generated power, as assumed here, remains constant.

With its constant pressure, the condenser has no effect on other components but its own exergy destruction greatly depends on other components, especially the turbine, secondary turbine, generator and the boiler. Good performance of these components can reduce the mass flow of main steam.

The pumps, condensate and feedwater pumps, are almost independent of all other components with the exception of the interaction between feedwater pump and boiler, since the pressure drop in boiler directly determines the pressure head provided by feedwater pump.

Although the regenerative subsystem is affected by the irreversibilities in turbine, the effects tend to be rather small. The performance of each feedwater preheater mostly relies on its preceding component. Hence, performance the enhancement of the feedwater heating system requires the best possible better operation conditions of all preheaters.

The components secondary turbine, feedwater pump, turbine, feedwater preheater and air preheater have a large effect on the boiler. The interaction between boiler and air preheater is intensive, thus, these components should be optimized as one unit.

5.2.2. Endogenous/exogenous exergy destruction

Table 5 shows that a large part of the exergy destruction in all components is endogenous. However, for different types of components, the proportions of exogenous part differ significantly. All the exergy destruction in generator is endogenous. Nearly 10% of exergy destructions of turbine stages are considered as exogenous, while the average ratio of exogenous part in the regenerative system almost reaches 30%, which indicates that the effect of system topology contributes largely

to their exergy destruction. The boiler, air preheater and condenser are the three components with the largest absolute exogenous destruction values, especially that of boiler reaching 86MW. In addition, all the exogenous exergy destructions are positive which means that the performance of any component improves with the performance enhancement of the remaining system components.

5.2.3. Unavoidable/avoidable exergy destruction

The real potential for improving a component is not fully revealed by its total exergy destruction but by its avoidable part. With the exception of boiler, 20%-40% of exergy destruction of the most components can be generally avoided with that part of the exergy destruction of generator and air preheater reaching 86% and 50%, respectively. The energy-savings potential from the generator also should call for attention, since the work saved is pure exergy and even a slight change of its efficiency contributes largely to total fuel consumption. Moreover, if the combustion process is stable and fulfils a much higher burnout rate under even lower oxygen ratio, and the temperature of flue gas exhaust would further decline to around 90ºC, which is now allowed due to the development of acid-resistant materials, up to 38MW of exergy could be saved just in the boiler. Finally, the potential in other components such as the secondary turbine should also be emphasized.

5.2.4. Combined analysis

The boiler subsystem has the largest avoidable exergy destruction; however, most of it is exogenous. For boiler the avoidable/endogenous part is slightly less than 25% of total avoidable part, while that of air preheater achieves nearly 45%. This indicates that the strategy for reducing the exergy destruction within the boiler should focus more on the components with a large effect on the boiler, such as turbine, secondary turbine and the last feedwater preheater. The irreversibilities occurring in air preheater itself and boiler have a similar contribution to the total avoidable exergy destruction within air preheater. To improve the air preheater, the entire boiler subsystem should be considered.

The generator also has a large amount of avoidable/endogenous exergy destruction, reaching almost 9MW. The performance enhancement of this component in isolation can have great benefits to the reduction of overall fuel consumption. More or less 90% of avoidable exergy destruction of turbines is endogenous, which indicates the improvement measurements for turbines should be concentrated on the components themselves.

5.3. Improvement strategy

Considering both the interactions among components and the potential for improving components, more effective and efficient improvement priorities can be proposed. The generator should be the first component to be enhanced in a separate way. Then, the turbines with high endogenous avoidable exergy destruction should also be improved separately. Subsequently, the measurements for enhancing feedwater regeneration subsystem with high proportion of exogenous avoidable exergy destruction should be concentrated on its subsystem level, since each individual preheater is mainly affected by its preceding one. The separate enhancement of only one feedwater preheater actually contributes little to the reduction of overall subsystem energy consumption. Finally, the boiler and air preheater can be improved by reducing both their inherent irreversibilities and the inefficiencies in the components with large contribution to their total exergy destruction, mainly the generator, turbines, last high-pressure feedwater preheater as well as feedwater pump. Given the combustion mode and boiler configuration, the effective approach for reducing fuel consumption is the combustion optimization with low air ratio and a further decrease of the exhaust gas temperature but not the rearrangement of heating surface configuration.

6. Conclusions

Exergy destruction in each component calculated in conventional exergy analysis is split, according to the sources and controllability. Considering detailed interactions among components and real potentials for improving components, the following conclusions can be obtained:

Table 6. Endogenous exergy of component k and the exogenous part caused by component r

k \ *r*	HPT1	HPT2	IPT1	IPT2	LPT1	LPT2	LPT3	LPT4	LPT5	COND	CP	H8	H7	H6	H5	DA	FP	H3	H2	H1	ST	GE	BO	AH
HPT1	9.90	0.08	0.06	0.04	0.04	0.03	0.04	0.18	0.12	0.00	0.00	0.01	0.00	0.01	0.01	0.00	0.03	0.04	0.03	-0.09	0.06	0.15	0.05	0.00
HPT2	0.14	3.05	0.02	0.01	0.01	0.01	0.01	0.05	0.04	0.00	0.00	0.00	0.00	0.00	0.00	0.00	0.01	0.02	-0.03	0.00	0.02	0.04	0.02	0.00
IPT1	0.10	0.03	3.64	0.02	0.02	0.01	0.01	0.07	0.05	0.00	0.00	0.00	0.00	0.00	0.00	0.00	0.01	-0.05	-0.01	0.01	0.02	0.05	-0.21	0.00
IPT2	0.08	0.02	0.02	2.69	0.01	0.01	0.01	0.05	0.03	0.00	0.00	0.00	0.00	0.00	0.00	-0.01	0.01	0.00	0.00	0.01	0.01	0.04	0.02	0.00
LPT1	0.08	0.02	0.03	0.02	2.78	0.01	0.01	0.05	0.03	0.00	0.00	0.00	0.00	0.00	-0.03	0.00	-0.01	0.00	0.00	0.01	-0.02	0.04	0.01	0.00
LPT2	0.06	0.02	0.03	0.02	0.02	2.13	0.01	0.04	0.03	0.00	0.00	0.00	0.00	-0.01	0.00	0.00	-0.01	0.00	0.00	0.01	-0.02	0.03	0.01	0.00
LPT3	0.07	0.02	0.03	0.02	0.02	0.02	2.31	0.04	0.03	0.00	0.00	0.00	-0.01	0.00	0.01	0.00	-0.01	0.00	0.00	0.01	-0.02	0.03	0.01	0.00
LPT4	0.33	0.10	0.15	0.11	0.11	0.08	0.09	11.46	0.14	0.00	0.00	-0.06	-0.01	0.01	0.03	0.01	-0.06	0.02	0.01	0.04	-0.10	0.17	0.06	0.00
LPT5	0.23	0.07	0.10	0.08	0.07	0.06	0.06	0.31	7.84	0.00	0.00	-0.01	0.01	0.01	0.02	0.00	-0.04	0.01	0.00	0.03	-0.07	0.11	0.04	0.00
COND	0.43	0.13	0.18	0.13	0.14	0.10	0.11	0.57	0.39	15.30	0.00	0.03	0.01	0.02	0.03	0.01	0.16	0.03	0.01	0.03	0.30	0.22	0.24	0.00
CP	0.00	0.00	0.00	0.00	0.00	0.00	0.00	0.00	0.00	0.00	0.15	0.00	0.00	0.00	0.00	0.00	0.00	0.00	0.00	0.00	0.00	0.00	0.00	0.00
H8	0.03	0.01	0.01	0.01	0.01	0.01	0.01	0.02	0.02	0.00	-0.01	1.18	0.00	0.00	0.00	0.00	0.01	0.00	0.00	0.00	0.01	0.02	0.01	0.00
H7	0.04	0.01	0.01	0.01	0.01	0.00	0.01	0.02	0.02	0.00	0.00	0.25	1.21	0.00	0.00	0.00	0.01	0.00	0.00	0.00	0.01	0.02	0.01	0.00
H6	0.02	0.01	0.01	0.00	0.00	0.00	0.00	0.01	0.01	0.00	0.00	0.00	0.17	0.61	0.00	0.00	0.00	0.00	0.00	0.00	0.00	0.01	0.01	0.00
H5	0.06	0.02	0.05	0.04	0.04	0.00	0.01	0.04	0.03	0.00	0.00	0.00	0.00	0.30	2.17	0.00	0.01	0.00	0.00	0.01	0.01	0.03	0.04	0.00
DA	0.06	0.02	0.04	0.03	-0.01	0.01	0.01	0.04	0.02	0.00	0.00	-0.04	-0.03	-0.06	0.62	2.03	0.00	-0.02	0.00	0.00	0.01	0.03	0.04	0.00
FP	0.05	0.01	0.01	0.01	0.01	0.01	0.01	0.03	0.02	0.00	0.00	0.00	0.00	0.00	0.00	0.01	1.70	0.01	0.00	-0.01	0.01	0.02	0.27	0.00
H3	0.06	0.02	0.08	0.01	0.01	0.01	0.01	0.04	0.03	0.00	0.00	0.00	0.00	0.00	0.00	0.18	-0.12	2.28	-0.05	-0.01	0.01	0.03	0.00	0.00
H2	0.09	0.03	-0.01	0.01	0.01	0.01	0.01	0.03	0.02	0.00	0.00	0.00	0.00	0.00	0.00	-0.03	0.02	0.61	1.58	-0.03	0.01	0.02	-0.01	0.00
H1	0.07	0.00	0.01	0.01	0.01	0.00	0.00	0.02	0.01	0.00	0.00	0.00	0.00	0.00	0.00	0.00	0.00	-0.02	0.22	1.15	0.01	0.02	0.00	0.00
ST	0.09	0.03	0.02	0.01	0.01	0.01	0.01	0.06	0.04	0.00	0.00	0.00	0.00	0.00	0.00	0.00	0.63	0.01	0.01	-0.03	3.20	0.05	0.50	0.00
GE	0.00	0.00	0.00	0.00	0.00	0.00	0.00	0.00	0.00	0.00	0.00	0.00	0.00	0.00	0.00	0.00	0.00	0.00	0.00	0.00	0.00	9.79	0.00	0.00
BO	7.00	2.11	3.39	2.63	2.66	2.03	2.21	10.93	7.48	0.00	-0.01	0.33	0.23	0.30	0.64	0.12	1.84	0.32	-0.04	1.37	3.67	8.98	615.20	19.25
AH	0.26	0.07	0.10	0.07	0.07	0.06	0.06	0.30	0.21	0.00	0.00	0.01	0.01	0.01	0.02	0.00	0.04	0.01	0.03	-0.20	0.09	0.25	4.74	16.91

1. The ratio of exogenous exergy destruction differs quite a lot from component to component. In general, inherent irreversibilities in turbines contribute more or less 90% to their total exergy destruction, while this proportion drops down to 70% when it comes to feedwater preheaters. The boiler subsystem also has a large amount of exergy destruction caused by the inefficiencies in other components.
2. The boiler subsystem still has the largest avoidable exergy destruction; however, the enhancement efforts should be made not only to its inherent irreversibilities but also to inefficiencies of the remaining components. Moreover, around 60% of the avoidable exergy destruction of feedwater preheaters is exogenous. For the remaining components efforts should mainly focus on improving the components themselves.
3. Due to the interactions among components, the improvement priorities refer not only to the components that should be modified, but also to the sequence for optimization. We believe that the improvement of the boiler subsystem will be more meaningful if the remaining important components are improved first and can provide persuading good performances.

Acknowledgement

Ligang Wang and Yongping Yang would like to thank China 973 Project 'Tempo-Spatial Distribution of Energy Consumption, Evaluation Method and System Integration for Large-scale Coal-fired Power Generation Unit' (2009CB219801), National Science Fund for Distinguished Young Scholars (51025624) and National nature Science Fund of China (51006034) for the financial supports.

Nomenclature

$\dot{E}$ exergy rate, MW
$\dot{m}$ mass flow rate, kg/s
h enthalpy, kJ/kg
p pressure, bar
$T(t)$ temperature, K (ºC)
y exergy destruction ratio, %
n number of components

Greek symbols

Δ difference
η energy efficiency
ε exergy efficiency
γ ratio
α air/fuel ratio

Subscripts

0 thermodynamic environment
c combustion
D destruction
d drainage
ex exhaust
F fuel
k *k*th component
L loss
sh superheated steam
m mechanical
P product
p pinch point
rh reheated steam
s isentropic
T theoretical
tot overall system

Superscripts

AV avoidable
EN endogenous
EX exogenous
MX mexogenous
r *r*th component
UN unavoidable

Abbreviations

AH air preheater
BO boiler
COND condenser
CP condensate pump
DA deaerator
FP feedwater pump
GE generator
H heater
HPT high-pressure stage group
IPT intermediate-pressure group
LHV lower heating value
LPT low-pressure group
ST secondary turbine

References

[1] Energy information administration (EIA), International energy annual – Available at: <www.eia.doe.gov/iea> [accessd 10.09.2011].
[2] Som SK., Datta A., Thermodynamic irreversibilities and exergy balance in combustion processes. Prog Energy Combut Sci 2008; 34(3): 351–376.
[3] Tsatsaronis G., Cziesla F., Thermoeconomics. In: Robert A Meyers, Editor. Encyclopedia of Physical Science and Technology, New York: Academic Press. 2001. p. 659-680.
[4] Bejan A., Tsatsaronis G., Moran M., Thermal design and optimization. New York, USA: Wiley; 1996.
[5] Rosen MA., Energy and exergy-based comparison of coal-fired and nuclear steam power plants. Exergy Int J 2001; 1 (3): 180-192.
[6] Sengupta S., Datta A., Duttagupta S., Exergy analysis of a coal-based 210 MW thermal power plant. Int J Energy Res 2007; 31(1): 14-28.
[7] Aljundi IH., Energy and exergy analysis of a steam power plant in Jordan. Appl Therm Eng 2009; 29(2-3): 324-328.
[8] Ameri M., Ahmadi P., Hamidi A., Energy, exergy and exergoeconomic analysis of a steam power plant: a case study. Int J of Energy Res 2009; 33(5): 499-512.
[9] Regulagadda P., Dincer I., Naterer GF., Exergy analysis of a thermal power plant with measured boiler and turbine losses. Appl Therm Eng 2010; 30(8-9): 970-976.
[10] Tsatsaronis G., Morosuk T., A general exergy-based method for combining a cost analysis with an environmental impact analysis, part I – theoretical development. Proceedings of ASME 2008 International Mechanical Engineering Congress and Exposition (IMECE 2008), November 2-6, 2008, Boston, Massachusetts, USA.
[11] Tsatsaronis G., Morosuk T., A general exergy-based method for combining a cost analysis with an environmental impact analysis, part II – application to a cogeneration system. Proceedings of ASME 2008 International Mechanical Engineering Congress and Exposition (IMECE 2008), November 2-6, 2008, Boston, Massachusetts, USA.
[12] Kelly S., Energy system improvements based on endogenous and exogenous exergy destruction [dissertation]. Berlin, Germany: Technische Universitat Berlin, 2008.
[13] Morosuk T., Tsatsaronis G., Advanced exergy analysis for chemically reacting systems – application to a simple open gas-turbine system. International Journal of Thermodynamics 2009; 12(3): 105-111.
[14] Kelly S., Tsatsaronis G., Morosuk T., Advanced exergetic analysis: Approaches for splitting the exergy destruction into endogenous and exogenous parts. Energy 2009; 34: 384-391.
[15] Morosuk T., Tsatsaronis G., Advanced exergetic evaluation of refrigeration machines using different working fluids. Energy 2009; 34: 2248-2258.
[16] Petrakopoulou F., Tsatsaronis G., Morosuk T., Conventional and advanced exergetic analysis applied to a combined cycle power plant. Proceedings of 2010 International Conference on Efficiency, Cost, Optimization, Simulation and Environmental Impact of Energy Systems (ECOS 2010), Lausanne, Switzerland.
[17] Tsatsaronis G., Morosuk T., Advanced exergetic analysis of a novel system for generating electricity and vaporizing liquefied natural gas. Energy 2010; 35: 820-829.
[18] Petrakopoulou F., Tsatsaronis G., Morosuk T., Carassai A., Advanced exergoeconomic analysis: applied to a complex energy conversion system. Proceedings of ASME 2010 International Mechanical Engineering Congress and Exposition (IMECE 2010), November 12-18, 2010, Vancouver, British Columbia.
[19] Tsatsaronis G., Design optimization using exergoeconomic. In: Bejan A, Mamut E, editors. Thermodynamic optimization of complex energy systems. Dordrecht: Kluwer Academic Publishers 1999: 101-117.

Energy and exergy analyses of charging process in Encapsulated Ice Thermal Energy Storage systems

David MacPhee[a], Ibrahim Dincer[b] and Asfaw Beyene[c]
[a] *San Diego State University, San Diego, CA, USA, macphee@rohan.sdsu.edu*
[b] *University of Ontario Institute of Technology, Oshawa, ON, Canada, ibrahim.dincer@uoit.ca*
[c] *San Diego State University, San Diego, CA, USA, abeyene@rohan.sdsu.edu*

Abstract:
Encapsulated ice Thermal Energy Storage (TES) is an effective means to conserve energy and costs for warmer climates. In this strategy, water is encased in a capsule and placed in a large storage tank. During off-peak hours, a vapor compression refrigeration cycle is used to chill the brine solution for freezing the encapsulated water. During peak hours, this ice is used as a heat sink for space cooling purposes, and can save considerable amounts of money, as well as help lower peak electricity demand. In this paper, we numerically investigate the solidification process of a capsule in the storage tank. Using FLUENT software, we simulate the freezing process and evaluate system performance based on inlet Heat Transfer Fluid (HTF) temperature and flow rate, as well as capsule geometry. In all, 105 test cases are compared; seven capsule shapes, five inlet HTF temperatures and three inlet HTF flow rates. The results were assessed thermodynamically in terms of energy efficiency, exergy efficiency and entropy generation. It is found that the energy efficiencies are not indicative of overall system performance, since in all cases they are found to be above 99.96%, as viscous dissipation is the only mode of loss. However, exergy efficiencies range from 78% to 92% and provide much better insight into system performance. It is found that the most effective way to increase efficiency of the solidification process is to increase inlet HTF temperature to closer to that of the freezing point of water. This is due to the fact that surprisingly, viscous dissipation has very little effect on entropy generation, and hence, exergy efficiency, when compared to other modes of losses. As a result, the actual capsule geometry is relatively inconsequential to system performance. These findings indicate that encapsulated ice TES designers could increase flow rates considerably during charging processes and as a result realize energy and cost savings.

Keywords:
Energy, Exergy, Thermal Energy Storage, Efficiency.

1. Introduction

With urban population density increasing in many temperate, tropical and subtropical cities, the demand for space heating and cooling increases along with it. There are many strategies which deal with increasing building efficiency, for example Combined Heat and Power (CHP) and Combined Cooling, Heat and Power (CCHP) scenarios, each with its own set of challenges. However, for the vast majority of cases, producing power on-site is not an option, so many opt for Thermal Energy Storage (TES) system in order to alleviate costs associated with space cooling on a daily basis.

One of the main advantages of TES for cooling purposes is its ability to help better match power supply with demand. This is done through loading the chiller to produce a cold storage during low demand (night) ties, which can be used during high demand (day) times. This helps not only to reduce operational costs, but it reduces peak electricity usage on the local grid, ultimately helping to lower Green House Gas (GHG) emissions.

There are many types of cold TES forms, and all fall into either latent or sensible storage. Although sensible cold TES storage is receiving interest as of late, for example in chilled water systems, latent systems are becoming more popular due to the high specific latent energy stored in water. Though many types of ice storage systems are popular, most fall under either the ice-on-coil [1-3] or encapsulated ice [4-7] types.

Encapsulated ice systems utilize a latent medium (de-ionized water) which is contained within a capsule, usually made of plastic. Such capsules are placed in a storage tank, and a Heat Transfer Fluid (HTF) is used to transfer heat to and from the thermal storage tank. Advantages of this type of system are that it is usually less costly, due to the mass production of capsules (for example, [8]), and is easier to operate and maintain.

Concerning encapsulated ice TES systems, very few studies have been performed to investigate the efficiency of such systems according to capsule geometry and/or Heat Transfer Fluid (HTF) characteristics. The authors have completed a number of investigations (for example [9-12]) investigating thermodynamic performance of encapsulated ice TES systems. In particular, the authors investigated in [12] a cold TES discharging process in which other geometries besides spheres [8] are considered. This study is a continuation of the aforementioned work, and is concerned with the charging process. There are very few works which investigate such a process – none which numerically investigate the charging (freezing) process while taking into consideration geometrical and HTF properties. In this paper, we vary the inlet HTF temperature and flow rate, capsule geometry (rectangular, spherical and cylindrical) in order to determine what effects they have on overall energy and exergy efficiency.

2. Mathematical Modeling

This study is concerned with numerical simulation of the charging (freezing) process of a capsule filled with de-ionized water, by using thermodynamic relations. In order to facilitate this, we use Fluent 6.3 software to obtain the required data for thermodynamic post-processing. However, before continuing with the mathematical modelling inherent in Fluent software, we make known the assumptions used as follows:

- Capsules will have a wall thickness of 5mm and inner volume 268ml.
- HTF and Phase Change Material (PCM) will have piecewise constant thermo physical properties.
- Heat penetration from storage tank wall is negligible.
- Density change during solidification is negligible.

Since this is a continuation from the study in [12], material properties will then be identical, and are shown in Table 1. The PCM is assumed to be water, the HTF to be ethylene glycol (30% by mass) [13], and the capsule is assumed to be polyvinyl chloride (PVC).

Table 1: Material properties used in the analysis (modified from [12]).

Material	ρ [kg/m^3]	C [kJ/kg·K]	μ [kPa·s]	k [W/m·K]
Capsule	1380	9.00	N/A	0.160
PCM (solid)	917.4	2.11	N/A	2.108
HTF	1053	3.57	5.03	0.422
PCM (liquid)	1000	4.20	1.52	0.558

2.1. Heat Transfer and Fluid Flow

In order to facilitate the presentation of equations, Figure 1 shows a simplification of the domain in question. The left side shows the basic concept for simulation: here the capsule is immersed in a sub-cooled, flowing HTF, which initiates freezing of the capsule. The right side shows a further simplification by describing the simulation as three domains of interest Ω_i and subsequent boundaries Γ_i, where i = {1,2,3}, in order to facilitate the presentation of governing equations in a Cartesian coordinate system. All simulations are performed in three dimensions using a Cartesian coordinate system. Figure 2 should be consulted for a more detailed view of the geometries simulated.

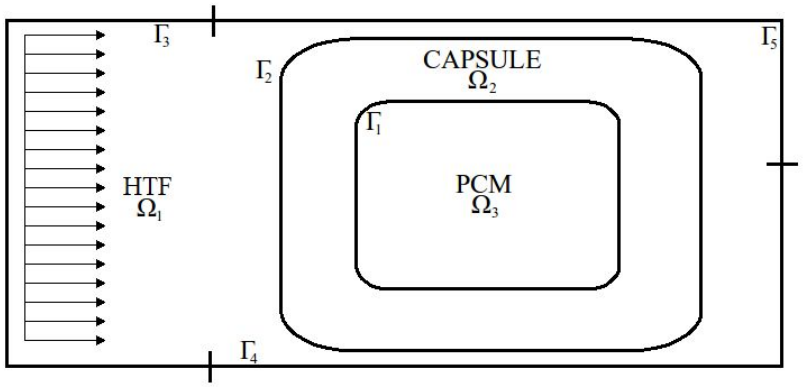

Figure 1: Simplification of domain description used in this study.

The momentum, continuity and energy equations govern the HTF, occupying Ω_1:

$$\rho\left(\frac{\partial u_i}{\partial t}+u_j\frac{\partial u_i}{\partial x_j}\right)=-\frac{\partial p}{\partial x_i}+\mu\frac{\partial^2 u_i}{\partial x_j^2}\quad \text{in } \Omega_1 \tag{1}$$

$$\frac{\partial u_i}{\partial x_i}=0\quad \text{in } \Omega_1 \tag{2}$$

$$\rho\frac{Dh}{Dt}=\frac{Dp}{Dt}+k\frac{\partial^2 T}{\partial x_i^2}+\Phi\quad \text{in } \Omega_1 \tag{3}$$

which uses the material derivative and viscous dissipation function, respectively:

$$\frac{D}{Dt}=\frac{\partial}{\partial t}+u_j\frac{\partial}{\partial x_j} \tag{4}$$

$$\Phi=\mu\left[2\left(\frac{\partial u_i}{\partial x_i}\right)^2+\left(\frac{\partial u_1}{\partial x_2}+\frac{\partial u_2}{\partial x_1}\right)^2+\left(\frac{\partial u_2}{\partial x_3}+\frac{\partial u_3}{\partial x_2}\right)^2+\left(\frac{\partial u_3}{\partial x_1}+\frac{\partial u_1}{\partial x_3}\right)^2\right] \tag{5}$$

In the PVC capsule, domain Ω_2, we must solve only the sensible energy equation:

$$\rho\frac{Dh}{Dt}=k\frac{\partial^2 T}{\partial x_i^2}\quad \text{in } \Omega_2 \tag{6}$$

The PCM domain Ω_3 again uses only the energy equation, but with a slight complication due to latent heat presence:

$$\rho\frac{DH}{Dt}=k\frac{\partial^2 T}{\partial x_i^2}\quad \text{in } \Omega_3 \tag{7}$$

where *H* and *h* are functions of temperature:

$$H(T)=h_o+C(T-T_o)+H_l \tag{8}$$

$$h(T)=h_o+C(T-T_o) \tag{9}$$

The latent heat term H_l is evaluated according to the process in [14-16], and depends on the liquid fraction β of each cell:

$$H_l = \beta L \tag{10}$$

β takes on a value between 0 and 1 (completely solid and completely liquid, respectively).

In order to simulate the computational domain, the boundary value problem needs the necessary boundary and initial conditions. To begin with, all domains are initialized at a temperature T_{ini}, where $T_{ini} > T_{sf}$:

$$T(t=0) = T_{ini} \quad \text{in } \Omega_1, \Omega_2, \Omega_3 \tag{11}$$

Additionally, at the beginning of each simulation, all cells are initialized with zero velocity:

$$u_i(t=0) = 0 \text{ in } \Omega_1, \Omega_2, \Omega_3 \tag{12}$$

As far as boundary conditions are concerned, we have the no-slip boundary between capsule and PCM:

$$u_i = 0 \text{ on } \Gamma_2 \tag{13}$$

We also require the temperature and velocity at the inlet, Γ_3,

$$T = T_{in}, \quad u_i = -Q/An_i \quad \text{on } \Gamma_3 \tag{14}$$

where n is the outward pointing unit normal. At the outlet, Γ_4, we impose fully developed conditions in both temperature and velocity:

$$\frac{\partial T}{\partial n_i} = \frac{\partial u_1}{\partial n_i} = \frac{\partial u_2}{\partial n_i} = \frac{\partial u_3}{\partial n_i} = 0 \quad \text{on } \Gamma_4 \tag{15}$$

Γ_5 is included for symmetry purposes, and serves to lessen the computational cost. This boundary is considered a slip boundary condition and is fully developed in the direction of symmetry:

$$\frac{\partial T}{\partial n_i} = 0, \quad u_i \cdot n_i = 0 \quad \text{on } \Gamma_5 \tag{16}$$

2.2. System Thermodynamics

In order to evaluate the performance of the charging processes, we are interested in the energy and exergy efficiencies, as well as entropy generation. Since this study is a continuation of [12] and uses the same thermodynamic evaluation process as in [11], we will omit much of the derivation of the governing thermodynamic equations. It should also be noted that this study omits the thermodynamic treatment of the refrigeration system used to charge the capsules, instead treating only the output of such systems, i.e. the cold HTF, as the only input to the control volume in this analysis. For the energy efficiencies, we first present the energy balance on our control volume:

$$\Delta E_{sys} = E_{in} - E_{out} \tag{17}$$

Here, the total change in energy of the system can be accounted for by considering the energy change in material 1, 2 and 3 (corresponding to domains Ω_1, Ω_2 and Ω_3, respectively) and the difference in total energy in and out is accounted for through analysis of the total enthalpy H, total volume flow X and average inlet and outlet pressure, P_{in} and P_{out}, respectively. Then, as in [11], the energy efficiency is calculated as follows:

$$\eta = \frac{\Delta E_1 + \Delta E_2 + \Delta E_3}{\Delta E_1 + \Delta E_2 + \Delta E_3 - X\left(P_{in} - P_{out}\right)} \tag{18}$$

where the energy changes in each domain are calculated as follows:

$$\Delta E_1 = m_1 C_1 \left(\overline{T}_{f,1} - T_{ini}\right) \tag{19}$$

$$\Delta E_2 = m_2 C_2 \left(\overline{T}_{f,2} - T_{ini}\right) \tag{20}$$

$$\Delta E_3 = m_3 \left[C_{fl}\left(T_{sf} - T_{ini}\right) + C_s\left(\overline{T}_{f,3} - T_{sf}\right) - L\right] \tag{21}$$

Here, the subscripts *fl* and *s* refer to the PCM in liquid and solid states, respectively, and *sf* refers to the solidification temperature. Volume weighted average temperatures are recorded and used to evaluate the temperature terms in the above equations, while area weighted average pressures are used to record incoming and outgoing total pressures.

For the exergy efficiencies, we proceed in the same way, by first writing the exergy balance equation:

$$\Delta \Xi_{sys} = \Xi_{in} - \Xi_{out} - \Xi_d \tag{22}$$

$$\psi = \frac{\Delta \Xi_1 + \Delta \Xi_2 + \Delta \Xi_3}{\Delta \Xi_1 + \Delta \Xi_2 + \Delta \Xi_3 + \Delta \Xi_d} \tag{23}$$

where the exergy differences in each domain over the course of the simulation can be calculated as:

$$\Delta \Xi_1 = m_1 C_1 \left(\overline{T}_{f,1} - T_{ini} - T_o \ln \frac{\overline{T}_{f,1}}{T_{ini}} \right) \tag{24}$$

$$\Delta \Xi_2 = m_2 C_2 \left(\overline{T}_{f,2} - T_{ini} - T_o \ln \frac{\overline{T}_{f,2}}{T_{ini}} \right) \tag{25}$$

$$\Delta \Xi_3 = m_3 \left[C_{fl} \left(T_{sf} - T_{ini} - T_o \ln \frac{T_{sf}}{T_{ini}} \right) + C_s \left(\overline{T}_{f,3} - T_{sf} - T_o \ln \frac{\overline{T}_{f,3}}{T_{sf}} \right) + L \left(\frac{T_o}{T_{sf}} - 1 \right) \right] \tag{26}$$

The destroyed exergy must also be calculated, and is a result of generated entropy as

$$\Xi_d = T_o S_{gen} \tag{27}$$

In order to calculate S_{gen}, we must write the entropy balance equation as

$$\Delta S_{sys} = \Delta S_1 + \Delta S_2 + \Delta S_3 = S_{in} - S_{out} + S_{gen} \tag{28}$$

where the individual components are evaluated as

$$\Delta S_1 = m_1 C_1 \ln \frac{\overline{T}_{f,1}}{T_{ini}} \tag{29}$$

$$\Delta S_2 = m_2 C_2 \ln \frac{\overline{T}_{f,2}}{T_{ini}} \tag{30}$$

$$\Delta S_3 = m_3\left[C_{fl} \ln \frac{T_{sf}}{T_{ini}} + C_s \ln \frac{\overline{T}_{f,3}}{T_{sf}} - \frac{L}{T_{sf}} \right] \tag{31}$$

$$S_{in} - S_{out} = MC_1 \ln \frac{\overline{T}_{out}}{T_{in}} \tag{32}$$

Here, we use the total mass M of HTF used to charge the capsules, as well as the average outlet temperature. It is interesting to discuss the amount of entropy generated solely as a function of viscous dissipation within the fluid, assuming a bulk temperature as the average HTF temperature within the domain:

$$S_{gen,diss} = \frac{M\left(\overline{P}_{in} - \overline{P}_{out}\right)}{\rho_3 T_b} \tag{33}$$

$$T_b = T_{in} + \frac{\Delta E_{sys}}{2MC_3} \tag{34}$$

3. Simulation Description

The present work involved the simulation of seven different geometries, listed in Table 2. All capsules were chosen to have equal inner volume, corresponding to that of geometry "A". In addition, Table 2 lists only inner dimensions, noting that we use a 5mm capsule shell thickness for the computational geometries.

Table 2: Capsule geometry descriptions (AR denotes Aspect Ratio).

Geometry	Type	Aspect Ratio	Inner Dimensions
A	Spherical	N/A	Radius 4.0cm
B	Slab	2	8.1cm × 8.1cm × 4.1cm
C	Slab	5	11.0cm × 11.0cm × 2.2cm
D	Slab	8	12.9cm × 12.9cm × 1.6cm
E	Cylindrical	2	Radius 2.7cm; length 11.1cm
F	Cylindrical	5	Radius 2.0cm; length 20.4cm
G	Cylindrical	8	Radius 1.7cm; length 28.0cm

More discussion is warranted in order to describe the computational domains, since they have not been explicitly defined thus far. In order to save computational costs, only one capsule is simulated in a bed of identical capsules, and the simulation domains are taken similar to that seen in Fig. 2. It should be noted that entrance and far-field effects, model validations, grid size and time step effects have been avoided through the same process described in [12].

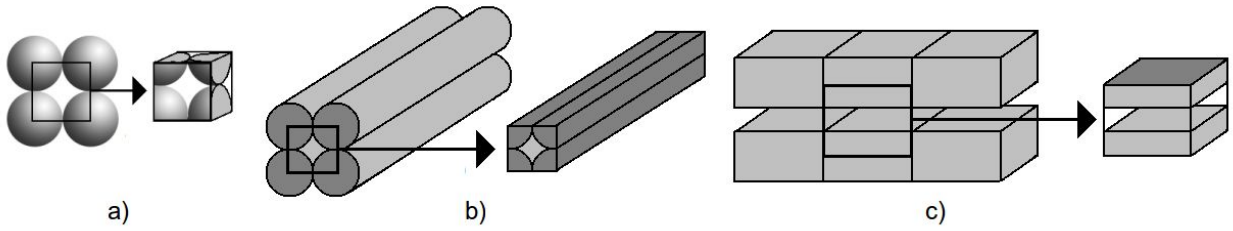

Figure 2: Simplification of domains for a) spherical, b) cylindrical and c) rectangular capsule geometries.

In addition to a variable capsule geometry, we also choose three flow rates: Q_1 = 0.87 l/s, Q_2 = 1.74 l/s and Q_3 = 2.61 l/s, which are chosen to be similar to that experienced by a moderately sized storage tank for encapsulated ice TES. We also vary inlet temperatures from 267K to 271K in increments of 1K, meaning that we perform 105 total simulations to gain insight into what combinations of geometry and HTF characteristics give the best efficiency. As mentioned earlier, the PCM is assumed to be deionized water, with a solidification temperature of T_{sf} = 273K, latent heat L = 334kJ/kg, and initial temperature of T_{ini} = 275K. Residual tolerances for velocity and energy are set to$1e^{-3}$ and $1e^{-6}$, respectively, and all simulations concluded once a complete solidification of the capsule was reached. The reference temperature is T_o = 298K.

4. Results and Discussion

The most important results to discuss are the charging times, energy efficiencies, and exergy efficiencies, accompanied by a discussion of the exergy losses (which are directly related to entropy generation). Firstly, we present the charting times for all simulations as seen in Table 3. When compared across geometries, the fastest geometries to charge/freeze were the cylindrical and rectangular capsules with highest aspect ratios. This is due to the higher surface areas which enhance heat transfer.

Not surprisingly, those simulations conducted with lower HTF temperatures realized lower charging times, and there was a small amount of difference in charging times when compared by HTF flow rate.

Table 3: Charging times (in seconds) for all simulations.

Flow Rate [l/s]	**T_{in} [K]**	**A**	**B**	**C**	**D**	**E**	**F**	**G**
Q_3 [2.61]	267	1035	1264	662	661	1051	728	591
	268	1156	1455	760	760	1189	822	667
	269	1326	1729	900	893	1384	957	775
	270	1586	2155	1113	1104	1686	1163	942
	271	2045	2877	1472	1469	2214	1522	1231
Q_2 [1.74]	267	1039	1274	668	667	1079	748	608
	268	1160	1468	767	768	1221	846	687
	269	1332	1744	908	901	1422	985	799
	270	1594	2170	1121	1114	1734	1198	972
	271	2055	2902	1485	1483	2278	1569	1271
Q_1 [0.87]	267	1051	1298	682	681	1130	788	642
	268	1174	1494	783	780	1280	893	727
	269	1348	1774	925	919	1493	1041	846
	270	1613	2215	1136	1140	1822	1268	1029
	271	2082	2955	1512	1514	2397	1662	1349

We next discuss the energy efficiency η from (18). From (18), it is apparent that the only losses in the system are a result of viscous dissipation, which results in a lowered pressure at the outlet. It was found that these losses are inconsequential to the energy efficiency, and all energy efficiencies were calculated to be above 99.9%. This solidifies the notion that second law (exergy) efficiency is required in order to properly address the actual performance of the charging process.

These exergy efficiencies are shown in Table 4, and range from 78-92%. The scenarios which achieved the highest exergy efficiencies were those with an inlet HTF temperature closer to that of the solidification temperature. Exergy efficiencies did not appear to vary much across geometry type and even flow rate. This suggests that the temperature of the inlet HTF is the most important factor in charging an encapsulated ice TES storage tank. It also suggests that viscous dissipation, discussed next, does not markedly affect performance of the charging of capsules.

Table 4: Exergy efficiency (in percent) for all case studies

Flow Rate [l/s]	T_{in} [K]	A	B	C	D	E	F	G
Q_3 [2.61]	267	78.98	78.91	79.01	79.01	78.94	78.94	78.93
	268	81.88	81.83	81.91	81.91	81.84	81.83	81.80
	269	84.98	84.94	85.02	85.02	84.94	84.91	84.86
	270	88.30	88.28	88.34	88.34	88.26	88.20	88.11
	271	91.86	91.86	91.91	91.90	91.82	91.70	91.56
Q_2 [1.74]	267	79.05	78.96	79.10	79.11	79.01	79.07	79.11
	268	81.95	81.87	82.00	82.01	81.91	81.96	81.99
	269	85.05	84.99	85.10	85.10	85.01	85.05	85.06
	270	88.37	88.32	88.42	88.41	88.33	88.35	88.35
	271	91.93	91.90	91.97	91.97	91.90	91.88	91.85
Q_1 [0.87]	267	79.24	79.11	79.39	79.39	79.18	79.33	79.44
	268	82.13	82.01	82.27	82.27	82.07	82.21	82.31
	269	85.22	85.11	85.34	85.34	85.17	85.29	85.38
	270	88.52	88.43	88.63	88.62	88.47	88.58	88.65
	271	92.06	91.98	92.14	92.14	92.02	92.10	92.15

In order to properly address the affect of viscous dissipation, we calculate the total entropy generated in each simulation, and compare that with the entropy generated through viscous dissipation. Table 5 gives this information by means of the calculated total percent of generated entropy through viscous dissipation. It is immediately apparent that viscous dissipation, although important in sizing such equipment as pumps and piping, is not detrimental to the charging of capsules.

Table 5: Entropy generated, both total and through viscous dissipation.

Flow Rate [l/s]	T_{in} [K]	S_{gen} [J/K]							$S_{gen,diss}$ / S_{gen} × 100 [%]						
		A	B	C	D	E	F	G	A	B	C	D	E	F	G
Q_3 [2.61]	267	7.4	7.3	7.3	7.3	7.3	7.4	7.4	0.1	0.0	0.0	0.0	0.2	0.5	0.8
	268	6.1	6.1	6.0	6.1	6.1	6.1	6.1	0.1	0.0	0.0	0.1	0.2	0.6	1.1
	269	4.9	4.8	4.8	4.8	4.9	4.9	4.9	0.2	0.0	0.1	0.1	0.3	0.9	1.6
	270	3.6	3.6	3.6	3.6	3.6	3.7	3.7	0.3	0.1	0.1	0.1	0.5	1.5	2.6
	271	2.4	2.4	2.4	2.4	2.4	2.5	2.5	0.5	0.1	0.2	0.3	1.0	2.9	5.0
Q_2 [1.74]	267	7.3	7.3	7.2	7.3	7.3	7.3	7.3	0.0	0.0	0.0	0.0	0.1	0.2	0.3
	268	6.1	6.0	6.0	6.0	6.1	6.1	6.0	0.0	0.0	0.0	0.0	0.1	0.3	0.5
	269	4.8	4.8	4.8	4.8	4.8	4.8	4.8	0.1	0.0	0.0	0.0	0.1	0.4	0.7
	270	3.6	3.6	3.6	3.6	3.6	3.6	3.6	0.1	0.0	0.0	0.1	0.2	0.6	1.1
	271	2.4	2.4	2.4	2.4	2.4	2.4	2.4	0.2	0.1	0.1	0.1	0.4	1.2	2.1
Q_1 [0.87]	267	7.2	7.2	7.1	7.1	7.2	7.2	7.1	0.0	0.0	0.0	0.0	0.0	0.0	0.1
	268	6.0	6.0	5.9	5.9	6.0	5.9	5.9	0.0	0.0	0.0	0.0	0.0	0.1	0.1
	269	4.8	4.8	4.7	4.7	4.8	4.7	4.7	0.0	0.0	0.0	0.0	0.0	0.1	0.2
	270	3.5	3.6	3.5	3.5	3.6	3.5	3.5	0.0	0.0	0.0	0.0	0.0	0.1	0.3
	271	2.4	2.4	2.3	2.3	2.4	2.3	2.3	0.0	0.0	0.0	0.0	0.1	0.3	0.5

To gain a better understanding of the effects that each variable (geometry, inlet HTF temperature and HTF flow rate) has on the exergy efficiency, Figure 3 shows the average ψ holding only one of the three variables constant.

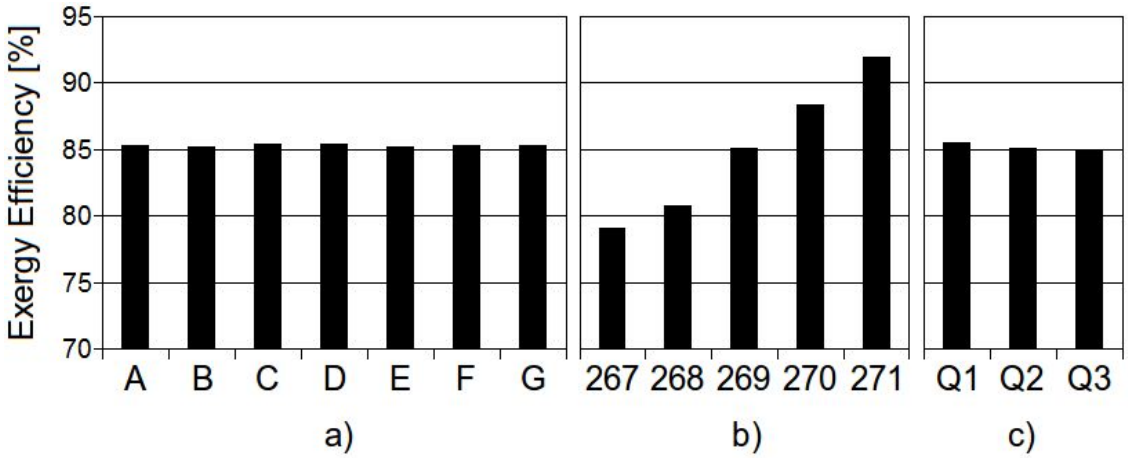

Figure 3: Average exergy efficiencies holding a) capsule geometry, b) inlet HTF temperature and c) HTF flow rate constant.

Here, we can plainly see that the inlet HTF temperature has the biggest impact on the exergy efficiency.

5. Conclusions

The solidification process for an encapsulated ice TES system is investigated herein, using Fluent software. In all, 105 simulations were run, varying capsule geometry, HTF flow rate and HTF temperature. In all cases, the energy efficiency, exergy efficiency and entropy generated were calculated, as well as entropy generated through viscous dissipation.

The first main finding of the study was that the energy efficiency was unrealistically high in all cases. Due to the assumptions used in the study, heat penetration and wall effects from the storage tank walls were ignored, thus the only source of energy loss was due to viscous dissipation. However, when compared to the thermal energy stored in each capsule, these losses were extremely small, and resulted in energy efficiencies of over 99.9% in all cases. For this reason, second law (exergy) efficiencies were sought, in order to gain better insight into the actual performance of the charging process.

Exergy efficiencies were much more reasonable, and varied from 78-92%. It was found that, most interestingly, the variable with the most impact on exergy efficiencies was the inlet HTF temperature, with those temperatures closer to the solidification temperature experiencing the highest efficiency. Another interesting finding was the relatively little effect viscous dissipation had on exergy efficiency, as well as entropy generated. In contrast, during calculation of energy efficiency equation viscous dissipation was the only mode of loss.

The findings illustrate two main points. Firstly, that energy analyses alone are not sufficient in analyzing the performance of cold TES systems. Secondly, the results show that although pressure loss developed in a storage tank is important in terms of equipment sizing, of much more importance is the temperature of the HTF used to charge the tank. In other words, much more thought must be given in order to size the HTF chiller than the method of moving the HTF.

Acknowledgements

The authors acknowledge support from the National Sciences and Engineering Research Council of Canada.

Nomenclature

A Area [m^2]

C Specific heat [J/kg·K]

E Energy [J]
H Enthalpy [J]
h Specific Enthalpy [J/kg]
k Thermal conductivity [W/m·K]
L Latent heat [J/kg]
M Total Mass [kg]
m mass [kg]
n Outward pointing unit normal [m]
P Average Pressure [pa]
p Pressure [pa]
Q Flow rate [m^3/s]
S Entropy [J/K]
T Temperature [K]
t Time [s]
u Velocity [m/s]
X Volume [m^3]
x Spatial Coordinate [m]

Greek symbols

β Liquid fraction
Γ Boundary
Δ Change in
η Energy efficiency
μ Dynamic viscosity [Pa·s]
Ξ Exergy [J]
ρ Density [kg/m^3]
ψ Exergy efficiency
Ω Domain

Subscripts and superscripts

b bulk
f Final
fl fluid
gen Generated
i Dummy index
in Inlet
ini Initial
l Latent
o Reference state
out Outlet
s solid
sf Solidification
sys system

Acronyms

AR Aspect ratio

HTF Heat transfer fluid

PCM Phase change material

TES Thermal energy storage

References

[1] Lee, A. and Jones, J., 1996. Modeling of an ice-on-coil thermal energy storage system. Energy Convers. Mgmt 37 (10), pp. 1493-1507.

[2] Soltan, B. and Ardehali, M., 2003. Numerical simulation of water solidification phenomenon for ice-on-coil thermal energy storage application. Energy Conversion and Management 44, pp. 85-92.

[3] Zhu, Y. and Zhang, Y., 2001. Modeling of thermal processes for internal melt ice-on-coil tank including ice-water density difference. Energy and Buildings 33, pp. 363-370.

[4] Dincer, I., 2002. On thermal energy storage systems and applications in buildings. Energy and Buildings 34, p. 377-388.

[5] Saito, A., 2002. Recent advances in research on cold thermal energy storage. International Journal of Refrigeration 25, pp. 177-189.

[6] Dincer, I. and Rosen, A., 2010. Thermal Energy Storage, Systems and Applications, second edition. John Wiley & Sons, Chichester, England.

[7] Kousksou, T., Bedecarrats, J., Dumas, J. and Mimet, A., 2005. Dynamic modeling of the storage of an encapsulated ice tank. Applied Thermal Engineering 25, pp. 1534-1548.

[8] Lenotre, C., 2003. Sub-zero thermal energy storage for process cooling. Kansas City Technical Program (Seminar 16: Emerging Technologies in the Refrigeration Industry), Cristopia Thermal Energy Storage, Inc., San Dimas, CA.

[9] MacPhee, D. and Dincer, I., 2009. Thermal modeling of a packed bed thermal energy storage system during charging. Applied Thermal Engineering 29, pp. 695-705.

[10] Erek, A. and Dincer, I., 2008. Numerical heat transfer analysis of encapsulated ice thermal energy storage system with variable heat transfer coefficient in downstream. International Journal of Heat and Mass Transfer 52, pp. 851-859.

[11] MacPhee, D. and Dincer, I., 2009. Thermodynamic analysis of freezing and melting processes in a bed of spherical PCM capsules. ASME Journal of Energy Engineering 131 (3). 031017 (11 pages).

[12] MacPhee, D. and Dincer, I., 2009. Heat transfer and thermodynamic analyses of some typical encapsulated ice geometries during discharging process. ASME Journal of Heat Transfer 131 (8). 082301 (15 pages).

[13] ASHRAE, 1997. ASHRAE Fundamentals Handbook, American Society of Heating, Refrigeration and Air-conditioning Engineers, Inc., Atlanta, GA, Chap. 20.

[14] Voller, V., and Prakash, C., 1987. A fixed-grid numerical modeling methodology for convection-diffusion mushy region phase-change problems. International Journal of Heat and Mass Transfer 30, pp. 1709-1720.

[15] Voller, V., 1987. Modeling solidification processes. Technical Report, Mathematical Modeling of Metals Processing Operations Conference, American Metallurgical Society, Palm Desert, CA.

[16] Voller, V., Brent, A., and Reid, K., 1987. A computational modeling framework for the analysis of metallurgical solidification process and phenomena. Conference for Solidification Processing.

Energy Integration and Cogeneration in Nitrogen Fertilizers Industry: Thermodynamic Estimation of the Efficiency, Potentials, Limitations and Environmental Impact. Part 1: Energy Integration in Ammonia Production Plants

Zornitza Kirova - Yordanova

Department of Inorganic Technology, University "Prof. Assen Zlatarov", 8010 Bourgas, Bulgaria
e-mail: zkirova@btu.bg, zornitzakirova@yahoo.co.uk

Abstract:

The nitrogen fertilizers production is an energy intensive industry branch. However, from a thermodynamic point of view, the basic reactions of the nitrogen fertilizers production processes are exothermic and the overall reactions of both process routes (ammonium nitrate and urea production routes) are also exothermic. This means that, if all these reactions could be performed in a thermodynamically ideal way and at the reference conditions, some heat and/or power could be obtained from these reactions, rather than consumed. However, most of the reaction stages are limited by the chemical equilibrium and reaction's kinetics, which require high pressures and temperatures, hence, big quantities of shaft power and heat (steam) have to be consumed. In modern energy-integrated ammonia and nitric acid plants the heat of the exothermic chemical reactions is used to generate mechanical work (by a steam cycle or/and by a gas turbine cycle) to drive compressors and other machinery. If needed, an extra amount of fuel is burned to satisfy all the requirements of energy in the plant itself and/or in the overall fertilizers production complex. The problem is whether it would be more effective to burn some quantity of fuel to provide a chemical plant with power and/or steam in the energy-integrated chemical plant itself; in an utility boiler or in a CHP plant at the same industrial site.
The goal of this work is to analyse the efficiency of the energy integration in a nitrogen fertilizers production site, including ammonia and nitric acid plants. The main issue is how to distinguish the technological and energy conversion processes in order to estimate their efficiencies separately despite the strong integration of these processes and the complexity of modern energy-integrated chemical plants.
The approach presented in this work is to define a model of the ammonia production process that enables specifying separately the theoretical minimum of energy and feedstock consumption in the chemical process and in the energy conversion processes (especially shaft work generation). Then, using real data for efficiency indices of both groups of processes, the next step is to examine the influence of these indices on the energy (and exergy) consumption and to specify the sets of parameters corresponding to the more efficient kind of plant, energy integrated or non-integrated, respectively. In Part 1 of this work, ammonia production plants are selected as a subject of analysis.

Keywords:

Energy integration, Cogeneration, Ammonia, Efficiency, Environmental impact

1. Introduction

In power industry the Combined Heat and Power (CHP) is defined as a simultaneous generation of usable heat and power (electricity or mechanical energy) in a single process. CHP is also referred to as cogeneration [1].
For many years the CHP generation has been applied predominantly in the chemical industry, petroleum refineries and other large industrial sites. In 2005 about 50% of the steam and hot water demand in EU27 industry was satisfied by CHP [1].

In chemical industry an energy-integrated chemical plant is a well-fitted combination of a chemical and a power plant. The waste heat of the exothermic chemical reactions is used to generate mechanical energy (by a steam cycle or/and by a gas turbine cycle) to drive compressors, pumps, fans, etc. In some cases the term "cogeneration" is also used [2], but only if electricity is produced [3]. The energy-integration concept enables the chemical plants to be energetically self-sufficient and to consume only feedstock and fuel and rather less electricity.

A vigorous growth of cogeneration in the chemical industry began since the first large single-train energy-integrated ammonia plant was put into operation in 1965 [4]. For the last five decades the energy-integrated chemical plants have been commonly used in the bulk chemicals industry. Nearly all modern ammonia, methanol and ethylene plants over the world are energy-integrated [4,5]. The developing of high-pressure (up to 30 MPa) multi-stage centrifugal compressors enabled the use of steam- and gas-turbines to drive all machinery, which in turn enabled designing large capacity plants as single-train units.

However, in some integrated plants the available heat of reactions cannot satisfy all demands and its temperature is relatively low. To solve this problem, in earlier designs an extra amount of fuel was burned in an auxiliary boiler (or in the process furnace itself) to satisfy all the requirements for power and steam in the plant.

The main question that should be answered is whether it would be more effective to burn some quantity of fuel to provide a chemical plant with power and/or steam in the energy-integrated chemical plant itself, in a utility boiler or in a CHP plant at the same industrial site.

In many cases the answer depends mainly on the demand of steam and power in the overall production site, on the export / import opportunities of electric power, etc.

The relative efficiencies of energy-integrated and non-integrated plants depend strongly on the sign of the reaction heat of the main chemical processes. According to this, three kinds of chemical plants could be distinguished:

- main reactions are exothermic, i.e., the plant is an energy source; examples are nitric acid and sulphuric acid plants;
- main reactions are endothermic, i.e., the plant is an energy sink; examples are ethylene plants;
- some of the main reactions are exothermic and some are endothermic; the overall effect is near neutral, examples are ammonia and methanol plants.

The nitrogen fertilizers production is selected as an appropriate subject of analysis, as it includes two different kinds of plants: ammonia and nitric acid production processes, both existing in energy-integrated and non-integrated versions.

The goal of the present work is to analyse the efficiency of the energy integration in a nitrogen fertilizers production site, including production of intermediates: (ammonia and nitric acid) and final product (ammonium nitrate). The subject of the first part of the analysis is the energy integration in ammonia production plants.

The exergy method [8] is used in both parts of this work in order to compare the efficiency of energy-integrated and non-integrated ammonia and nitric acid plants, as well as to estimate the overall efficiency of a whole nitrogen fertilizers production site.

In some previous works [9-11] we have compared the efficiencies of energy integrated and non-integrated ammonia plants [9] and nitric acid plants [10] using some Second Law-based (exergy and cumulative exergy) indices and operational data from real plants. The results showed that non-integrated ammonia plants are definitely more efficient than energy integrated; the results for nitric acid plants are opposite. A generalized conclusion was made that the energy integration is more advantageous in the case when the efficiency of the energy conversion process (shaft work generation) is higher than the efficiency of the chemical process and vice versa. However, these results could be questionable to some extent because they were obtained by processing data for similar, but yet different plants, and the difference of some of the process parameters in the compared plants might have an effect on these results. The considerable recent achievements both in chemical technology and in energy conversion processes and machinery, which undoubtedly influence the efficiency of the energy integration, also motivated the present study.

The main problem is how to distinguish the technological and energy conversion processes in order to estimate their efficiencies separately despite the strong integration of these processes and the complexity of modern energy-integrated chemical plants. Hence, we need to define a model of the ammonia production process that enables specifying separately the theoretical minimum of energy and feedstock consumption in the chemical process and in the energy conversion processes (especially shaft work generation). Then, using real data about heat and exergy losses and efficiency indices of both groups of processes, the next step is to examine the influence of these indices on the energy and exergy consumption and to specify the sets of parameters corresponding to the more efficient kind of plant, energy integrated or non-integrated, respectively.

2. Ammonia production background: basic reactions and heat effects

The commercial manufacture of ammonia since its beginning in 1913 is based on the catalytic synthesis of ammonia from a highly purified mixture of hydrogen and nitrogen. Although the synthesis of ammonia is an exothermic reaction, to obtain this mixture, especially hydrogen, a lot of energy is necessary to split a molecule of water, which is the main hydrogen-containing source. If a part of the hydrogen is supplied by another hydrogen-containing feedstock, like hydrocarbons, energy requirements are lower. Thus the most favourable feedstock for ammonia production is the natural gas (CH_4) because in this case only a half of the hydrogen is obtained from water.
However, the hydrogen production from hydrocarbons and water is a strongly endothermic process, hence a considerable amount of high temperature heat is necessary to be introduced into the process, usually obtained by burning of some quantity of fuel with air.
The combination of both steam reforming and burning processes enables to obtain the hydrogen-nitrogen mixture directly, avoiding the air separation as a preliminary step. Thus the two-step steam and air reforming of hydrocarbons became the best industrial process of the hydrogen-nitrogen mixture preparing for more than 60 years [4,5].
Assuming approximately the oxygen and nitrogen content in air as 20% and 80 % respectively, the following basic reactions of ammonia production from natural gas (CH_4) could be written:

$$3/8\ CH_{4(g)} + 3/8\ H_2O_{(g)} = 3/8\ CO_{(g)} + 9/8\ H_{2(g)} - 77.3\ kJ \quad (1)$$

$$3/8\ CO_{(g)} + 3/8\ H_2O_{(g)} = 3/8\ CO_{2(g)} + 3/8\ H_{2(g)} + 15.5\ kJ \quad (2)$$

$$1/8O_2 + 4/8N_2 + 1/16CH_4 = 1/16CO_2 + 1/8H_2O + 4/8N_2 + 50.1k\ J \quad (3)$$

$$12/8\ H_2 + 4/8\ N_2 = NH_3 + 46.2\ kJ \quad (4)$$

Summarising reactions (1), (2), (3) and (4), the total ammonia production process could be expressed by the formal reaction:

$$3.5/8CH_{4(g)} + 5/8H_2O_{(g)} + 1/8O_2 + 4/8N_2 = NH_{3(g)} + 3.5/8CO_{2(g)} + 34.5\ kJ \quad (5)$$

Thus the overall heat of reactions in ammonia production is slightly positive.
But if water enters into the process as a liquid, the overall reaction is near thermally neutral:

$$3.5/8CH_{4(g)} + 5/8H_2O_{(l)} + 1/8O_2 + 4/8N_2 = NH_{3(g)} + 3.5/8CO_{2(g)} + 6.98\ kJ \quad (6)$$

The theoretical minimum energy consumption in natural gas-based production of ammonia calculated on the basis of the reactions (1) – (6) is shown in Table 1. No heat losses are included.

3. Energy integration in ammonia plants

3.1. Theoretical and actual minimum energy consumption in ammonia production – the model of the chemical processes, methodology and calculations

As was shown in section 2, the overall heat of reactions of methane-based ammonia production is slightly positive, i.e., a small surplus of heat exists.

However, this is a mere theoretical thermochemical calculation, First Law-based, using the heat quantities only, not the heat potential (exergy).
As it is shown in Table 1, the heat of the exothermic reactions (2) and (4) is released at relatively medium and low temperatures, but the heat consumed by the endothermic reaction (1) must be put into the process at very high temperature, which can be only obtained by burning of some kind of fuel. Thus two separate heat balances must be fitted: a high temperature (HT) heat balance (Table 2) and a balance of the middle- and low-temperature (MT&LT) heat (Table 3).
Table 2 shows that the balance of the high-temperature heat sources and sinks is not fitted. The heat released from the exothermic reaction of methane burning (3) by the process air is not sufficient to supply all the heat necessary for the endothermic steam reforming of methane by reaction (1). **Thus an additional quantity of methane must be burnt in order to fit the high temperature heat balance of the process** no matter if the released heat is introduced directly or indirectly in the steam reforming process. The problem is where this methane could be burnt without introducing some additional nitrogen into the reaction mixture.
In the commercial ammonia technology, the reaction (1) is partly (up to 50%) going simultaneously with the reaction (3) in an autothermal reactor as a second step (known as "secondary reforming") of the hydrogen-nitrogen mixture generation process (Fig. 1).
The first step (steam reforming of methane, or "primary reforming") is carried out in a reactor of heat exchanger type, heated indirectly either by the hot effluent (up to 1000^0C) of the second step autothermal reactor or by combustion of natural gas in a "reforming furnace". The former case is the relatively new design known as "gas-heated-reactor" or GHR, but the latter is the traditional and still the most common design. In this case the natural gas burned in the reforming furnace, is much more than the theoretical quantity, shown in Table 1, calculated to meet the heat balance of the process. After the radiation heat transfer in the furnace, the remainder flue gas heat is used partly for HP steam generation and superheating and then for preheating of the process flows (natural gas, steam and air) in the convection section.
The advantage of the GHR steam reforming design is the elimination of the furnace and combustion process, but the major problem of the ammonia plants with GHR is how to meet the high temperature heat balance of the reforming and of the overall ammonia production process. Although various designs are approved, the common approach is the rejection of the basic principle of modern ammonia technology to produce ammonia using stoichiometric air quantity, without any form of air separation. The most used approach is to burn the additional methane using surplus of air in the second step autothermal reforming reactor and obtain a non-stoichiometric hydrogen-nitrogen mixture. Then a new problem arises how to remove the surplus nitrogen from the mixture. The alternative is to add some oxygen to the air, but the air separation is a highly energy intensive process.
As it is clear from Table 2, **the theoretical minimum of energy consumption for the process itself (represented by LHV of methane) is 22.2 GJ/t NH_3,** corresponding to 620 Nm^3 CH_4/t NH_3.
Not all real stages of the modern ammonia technology are included in this model. Nevertheless, reactions (1) – (6) are quite enough to present the ammonia production process.
The methanation reactions of CO and CO_2 are combinations of the reverse steam reforming (1) and CO conversion (3) reactions, hence they are included in the model indirectly. The average methane concentration in the make-up hydrogen-nitrogen mixture is 0.6-0.8%, corresponding to about 4% of the methane feedstock entering the steam reforming. As all this methane is recovered and returns back to the reforming furnace, but as a fuel, the overall heat balance (Table 1) remains unchanged and the total methane consumption is nearly the same, only its distribution between feedstock and fuel is slightly changed. Really, the total methane consumption is slightly higher, as the high temperature heat balance requires 4% more heat to be put into the reforming furnace; simultaneously the methanation reactions ($250\text{-}300^0$C) increase the heat supply into the medium and low temperature heat balance.
Another process, included indirectly in the model, is the CO_2 removal, which is an energy consuming process. The theoretical minimum separation energy consumption depends on the

concentrations of the components only. Thus, the theoretical (isothermal) work consumption for the separation of an ideal mixture of CO_2 and hydrogen/nitrogen mixture (known as synthesis or make-up gas), based on the stoichiometric concentrations of the products of the reactions (1), (2) and (3), is included in the theoretical heat and work balance of the ammonia production, shown in Table 1. The real energy consumption in separation processes is much higher than the theoretical work consumption. However, the exergy consumption is not so high, because in the most used CO_2 separation processes the energy input is as medium or low temperature heat. The actual heat consumption for CO_2 separation in ammonia plants dropped dramatically in the last 30 years from about 5000 kJ/Nm^3 to about 1200 -1400 kJ/Nm^3CO_2.

Table 1. Overall balance of exothermic and endothermic heat of reactions in ammonia production

Production process	Standard heat of reaction (-ΔH, 25^{0}C, 101325 Pa)			CH_4 consumed		Average reaction tempera-ture, ^{0}C	Exergy of heat GJ/t NH_3
	kJ/mol product of reaction	kJ/mol NH_3	GJ/t NH_3	GJ/t NH_3 (LHV)	Nm^3/t NH_3		
Exothermic reactions – available heat							
Water gas shift reaction (2)	41.17	15.44	0.907	-	-	370-220	0.428
Methane burning reaction (3)	802.34	50.15	2.945	2.945	82.2	1000	2.255
Ammonia synthesis reaction (4)	46.19	46.19	2.712	-	-	425	1.554
Total heat from exothermic reactions	**-**	**111.78**	**6.564**	**2.945**	**82.2**	**-**	**4.237**
Endothermic reactions – consumed heat							
Steam reforming of methane (1)	206.10	77.29	4.539	-	-	850	3.334
Water (stoichiometric) evaporation heat	44.01	27.51	1.615	-	-	235	0.668
Total heat for endothermic processes	**-**	**104.80**	**6.154**	**-**	**-**	**-**	**4.002**
Theoretical work consumption for CO_2 removal from H_2/N_2 mixture	-	2.84	0.167	-	-	-	0.167
Total heat and work consumption	**-**	**107.64**	**6.321**	**-**	**-**	**-**	**4.169**
Surplus total	**-**	**4.14**	**0.243**	**-**	**-**	**-**	**0.068**
Methane consumption as feedstock in steam reforming by reaction (1)				**17.667**	**493.3**		**18.595***
Total theoretical minimum methane consumption (feedstock and fuel)				**20.612**	**575.5**		**21.690***

*Exergy of consumed CH_4 (25^{0}C, 3.0 MPa)

Table 2. Theoretical high temperature (>8000C) heat balance: available and consumed heat of reactions

Production process	Standard heat of reaction (-ΔH, 25^{0}C, 101325 Pa)			CH_4 consumed		Average reaction tempera-ture, ^{0}C	Exergy of heat GJ/t NH_3
	kJ/mol product of reaction	kJ/mol NH_3	GJ/t NH_3	GJ/t NH_3 (LHV)	Nm^3/t NH_3		
Endothermic reactions – consumed heat							
High temperature heat consumption Steam reforming of methane by reaction (1)	**206.10**	**77.29**	**4.539**	**-**	**-**	**850**	**3.334**
Exothermic reactions – available heat							
High temperature heat available Methane burning by reaction (3)	802.34	50.15	2.945	2.945	82.2	1000	2.255
Heat supply by additional methane burning	802.34	27.14	1.594	1.594	44.5	1000	1.221
Total heat supply by methane burning	802.34	**77.29**	**4.539**	**4.539**	**126.7**	**1000**	**3.476**
Surplus total	**-**	**0.0**	**0.0**	**-**	**-**	**-**	**0.142**
Methane consumption as feedstock in steam reforming by reaction (1)				**17.667**	**493.3**		**18.595***
Total theoretical minimum methane consumption (feedstock and fuel)				**22.206**	**620.0**		**23.367***

*Exergy of consumed CH_4 (25^{0}C, 3.0 MPa)

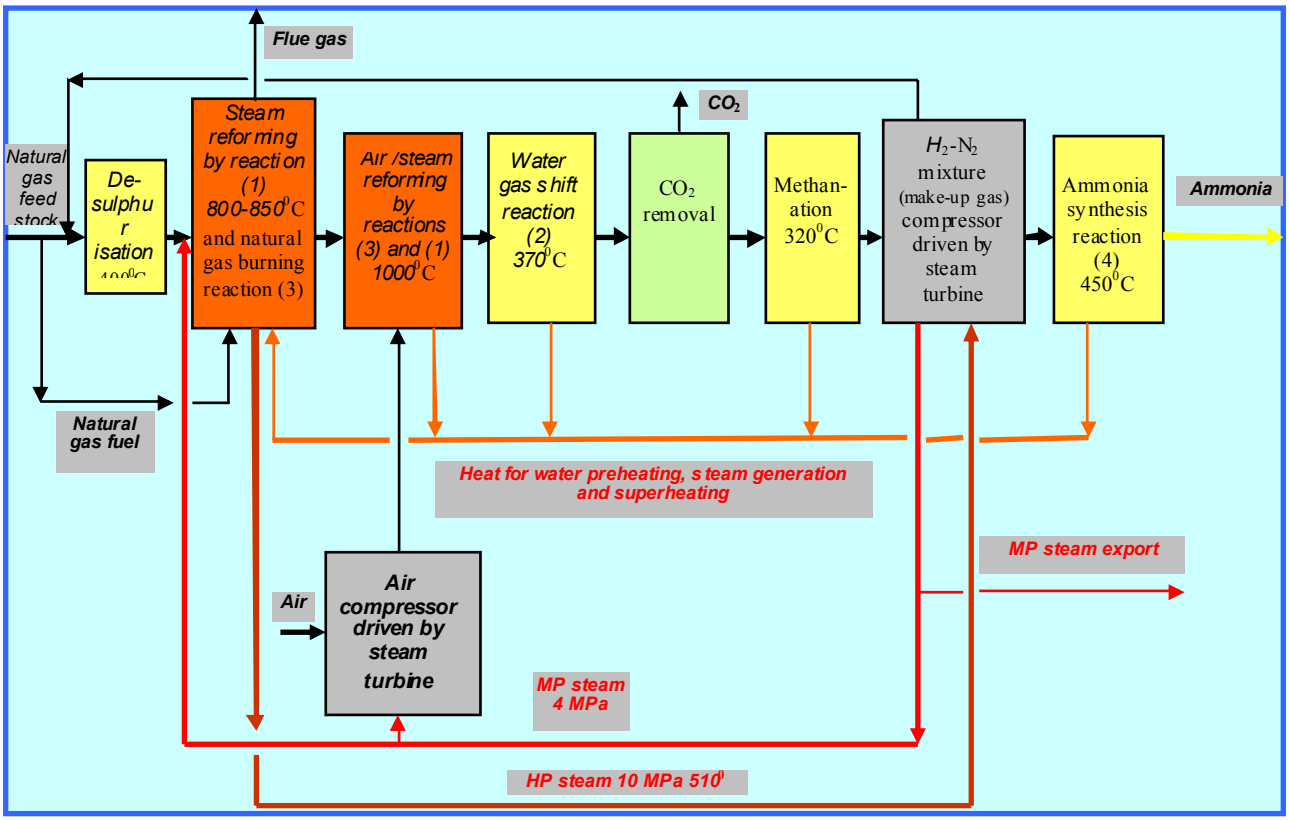

Fig. 1. Flowsheet of an energy integrated ammonia production plant

Table 3. Medium and low temperature (MT&LT) heat balance: available and consumed heat

Production process	Standard heat of reaction (-ΔH, 25°C, 101325 Pa)			CH_4 consumed		Average reaction tempera-ture, °C	Exergy of heat GJ/t NH_3
	kJ/mol product of reaction	kJ/mol NH_3	GJ/t NH_3	GJ/t NH_3 (LHV)	Nm^3/t NH_3		
Endothermic processes – consumed heat							
MT&LT heat consumption in process steam generation for reactions:							
• Stoichiometric for reactions (1) and (2)	44.01	27.51	1.615	-	-	235	0.668
• Excess steam (over stoichiometric)	44.01	16.50	0.969			235	0.401
Total for process steam generation	-	**44.02**	**2.588**			-	**1.069**
Minimum actual MT&LT heat consumption for CO_2 removal from H_2/N_2 mixture	-	12.24	0.719	-	-	160	0.224
Total MT&LT heat consumption	**-**	**56.25**	**3.307**	**-**	**-**	**-**	**1.293**
Heat losses 10% from heat supply	-	7.81	0.459				0.220
Total actual MT&LT heat consumption	**-**	**64.06**	**3.766**	**-**	**-**	**-**	**1.513**
Exothermic reactions – available heat							
Water gas shift reaction (2)	41.17	15.44	0.907	-	-	370-220	0.428
Ammonia synthesis reaction (4)	46.19	46.19	2.712	-	-	425	1.554
Total MT&LT heat supply from exothermic reactions	**-**	**61.63**	**3.619**	**-**	**-**	**-**	**1.982**
Excess steam condensation heat	-	16.50	0.969	-	-	170- 60	0.220
Total MT&LT heat supply	**-**	**78.13**	**4.588**	**-**	**-**	**-**	**2.202**
MT&LT heat surplus for export steam generation	**-**	**14.07**	**0.822**	**-**	**-**	**-**	**0.689**

Thus, in Table 3 the value 1250 kJ/Nm^3CO_2 is used, as typical in modern low energy ammonia plants [4]. The preferable temperature range of the heat sources is rather narrow for many reasons,

typically 170-140^{0}C, hence, the heat available from the excess steam condensation and other low temperature sources is used mainly for this purpose.

In the real reforming process not liquid water, but steam is used as a reagent in reactions (1) and (2). Thus some heat is necessary to evaporate the water and this heat must be included in the balance [4]. Moreover, the steam reforming of methane by reactions (1) and (2) requires some surplus of steam above the stoichiometric ratio in order to obtain higher methane and CO conversion and to prevent carbon formation [4,5]. A 50 to 100% surplus is commonly used with a trend towards the minimum of 50% surplus in new plants. Thus, the total heat necessary for the water evaporation is about 2.6 GJ/t NH_3. A part of the available middle- and low-temperature heat from reactions (2) and (4) is consumed to evaporate the water for the process (Table 3). Indeed, the heat consumed for the evaporation of the overstoichiometric water is recovered back as the excess steam is condensed in the next stages of the process. But the exergy of this heat is much lower, because the condensation proceeds at gradually decreasing temperature from about 170^0 down to ambient temperature and this heat can't be entirely used.

It is clear that some heat losses are present in all thermal processes. In the most common design, the heat of the flue gas released into the atmosphere from the convection section of the reforming furnace, is the major source of the losses; in the newest GHR design these losses are eliminated. Some heat losses through the insulation and in the end coolers are unavoidable. The industrial practice shows that, depending on the design, the heat losses in modern ammonia plants are in the interval 10-15%, i.e., a thermal efficiency 85-90% could be reasonable. Assuming a minimum heat losses value equal to 10% of the exothermic reactions heat, this means that 10% more methane has to be burnt to close the high temperature heat balance.

Thus, the **actual minimum energy consumption for the ammonia process itself could be estimated as 22.7 GJ/t NH_3,** corresponding to 634 Nm^3 CH_4/t NH_3, including the minimum feedstock (17.7 GJ/t) and fuel (5.0 GJ/t) consumption, respectively (Table 4).

Table 4. Actual high temperature (>800^{0}C) heat balance: available and consumed heat of reactions

Production process	Standard heat of reaction (-ΔH, 25^{0}C, 101325 Pa)			CH_4 consumed		Average reaction tempera-ture, ^{0}C	Exergy of heat GJ/t NH_3
	kJ/mol product of reaction	kJ/mol NH_3	GJ/t NH_3	GJ/t NH_3 (LHV)	Nm^3/t NH_3		
Endothermic reactions – consumed heat							
Steam reforming of methane by reaction (1)	206.10	77.29	4.539	-	-	850	3.334
Heat losses 10% from heat supply	-	8.59	0.504	-	-	850	0.370
Total high temperature heat consumption	**-**	**85.88**	**5.043**	**-**	**-**		**3.704**
Exothermic reactions – available heat							
High temperature heat available Methane burning in the process by reaction (3)	802.34	50.15	2.945	2.945	82.2	1000	2.255
Heat supply by additional methane burning	802.34	27.14	2.098	2.098	58.6	1000	1.607
Total heat supply by methane burning	802.34	**77.29**	**5.043**	**5.043**	**140.8**	**1000**	**3.832**
Surplus total	**-**	**0.0**	**0.0**	**-**	**-**	**-**	**0.128**
Methane consumption as feedstock in steam reforming by reaction (1)				**17.667**	**493.3**	**-**	**18.595***
Total minimum methane consumption (feedstock and fuel)				**22.710**	**634.1**	**-**	**23.902***

*Exergy of consumed CH_4 (25^{0}C, 3.0 MPa)

Note: In most ammonia plants, the typical **real methane consumption,** marked as ***feedstock only,*** is very close to the value 22.7 GJ/t [4]. Indeed, this value includes, except the methane, converted by reaction (1), also the methane burned in the secondary air reforming by reaction (3).

3.2. Theoretical and actual energy consumption for shaft work generation in ammonia production plants

In some references, values about 22 GJ/t are specified as the practical minimum methane consumption for ammonia production, in contrast to the value 17 GJ/t (LHV of ammonia), marked as a theoretical minimum [4].

However, the theoretical (22.2 GJ/t) and practical (22.7 GJ/t) minimum energy consumption values, shown in Tables (2) and (4), include the methane consumed in reactions (1) – (6), if they are performed at atmospheric pressure. Energy for the reagents compression is not taken into account.

As the ammonia synthesis equilibrium is unfavourable at low pressure and the degree of conversion of the hydrogen-nitrogen mixture to ammonia is low even at high pressures, significant additional energy is required to compress the hydrogen-nitrogen mixture (synthesis gas) to high pressure (8 – 30 MPa), to drive the recirculation compressor and also to remove ammonia from the unreacted gaseous mixture.

Thus, the value 22.7 GJ/t can't be seen as a practical minimum energy consumption measure.

In the old non-integrated and multiple-trains ammonia plants, designed before 1965, electric motors were used to drive the reciprocating compressors used at the time. In most modern single-train energy integrated ammonia plants, both make-up synthesis gas and air compressors are driven by steam turbines. In plants designed in the 60-ties and 70-ties nearly all pumps and fans are also turbine – driven. The complicated HP (10 – 14 MPa) steam generation system is precisely fitted to the chemical processes in order to use most effectively the heat of all reactions. However, as the reactions heat is not sufficient, significant quantities of fuel were burned in these plants for HP steam generation and superheating.

The fuel consumption depends strongly on the compressors and turbines efficiency (Table 5, Figure 2). As the efficiency of the first generation high pressure 3 or 4 cases centrifugal compressors was rather low, the steam and, accordingly, the fuel consumption, were rather high. In these plants about 2/3 of the natural gas was used as feedstock and 1/3 and even more – as fuel. Auxiliary boilers were included in ammonia plants in order to generate huge quantities of HP steam, about 5 to 7 times the produced ammonia and the total natural gas consumption was about 40 GJ/t ammonia. *Ammonia plants from that epoch are facetiously described amongst professionals as "a steam power plant, which produces also some ammonia as a by-product"[4]*.

After 1973, the growing energy prices pressure stimulated the energy saving in ammonia plants in the next 20 years, mainly by reduction of the fuel burning, having as a result a total energy consumption drop down to 28 – 29 GJ/t.

Besides the substantially improving of the technological processes, some return back to the electric motors, especially for driving pumps and fans, contributed slightly to the energy saving, due to the low efficiency of small steam turbines. However, in most modern plants both compressors are still driven by steam turbines. Various options were tested in last 20 years: to drive the air compressor by a gas turbine or the make-up syngas compressor by an electric motor. Some attempts are made to integrate ammonia and CHP power plants in the same site by shifting the superheating the HP steam (generated in the ammonia plant) to the CHP plant.

However, last year's industrial experience shows no substantial advantages for any of these versions. It is clear, that the situation is changing over the years due to the improving of the compressors, turbines, as well as the electricity generation in power plants (Fig. 2). Thus the minimum energy consumption point is gradually shifting across the parameters space roaming between electrical motors and steam turbines driving (Fig. 2 - 4).

The steam generation system structure and the basic steam system parameters of all single-train ammonia plants are nearly the same: HP steam 10-14 MPa, superheated to 510 ± 20^0C; MP steam extraction for process at 4-4.5 MPa [4].

Hence, specifying a set of basic parameters of the technological process, it is possible to calculate the minimum value of total feedstock and energy (heat and shaft work) consumption, then to add

the values of the heat and/or exergy losses and thus to approximate step by step the real consumption values. As a result we obtain the real values of the shaft work, necessary to drive the production process and the primary energy (methane) consumed for the shaft work generation. Then the dependence of the methane consumption for shaft work generation on the basic parameters can be examined and compared with the fuel consumption in a power plant. The goal of the comparison is to specify the set of parameters where the steam turbine drivers are more preferable than electric motors and vice versa.

To estimate a minimum of the shaft work needed for an ammonia production plant, at least two major gas compression processes have to be taken into consideration: compression of the process air from atmospheric pressure to the pressure in the reforming process, which is about 3.0 MPa, and compression of the purified hydrogen-nitrogen gaseous mixture (make-up gas) from the reforming pressure to the ammonia synthesis pressure, which in modern plants is specified in a rather wide interval. The lowest value, used in commercial designs, is 8.0 MPa, the highest about 30.0 MPa, but the most used in modern designs are synthesis pressures between 12 to 22 MPa, which represent a flat optimum of total energy consumption [12]. To explain the existence of this optimum, two other compression processes have also to be considered: the circulation (recycle) compressor, and the refrigeration compressor, both related to the ammonia synthesis section of the plant. The shaft work consumption for refrigeration and circulation is much lower than for the make-up gas compression and depends conversely on the synthesis pressure. Thus the sum of the shaft work consumption of the three compressors is nearly constant in the optimum pressures interval [12].

At the upper limit of this interval, the work, consumed by the circulation and refrigeration compressors, is rather low and only shaft work consumed by the make-up gas and air compressors could be included in the model.

Table 5. Shaft work consumption in ammonia production plants

Process	**Shaft work**	
	GJ/t NH_3	kWh/t NH_3
Theoretical shaft work (isothermal) for driving:		
• H_2/N_2 compressor 3 –20 MPa	0.553	153.6
• Air compressor 0.1-3 MPa	0.309	85.8
• Ammonia synthesis recycle compressor 19-20 MPa	0.076	21.1
Total theoretical shaft work generated in steam turbines	**0.938**	**260.5**
• Refrigeration compressor	0.030	8.3
• Others (BFW pump, CO_2 removal solution pumps, fans, etc.)	0.070	19.5
Total theoretical shaft work (isothermal)	**1.038**	**288.3**
Minimum actual shaft work ($\eta_{isoth} = 0.7$) for driving:		
• H_2/N_2 compressor 3 –20 MPa	0.789	219.4
• Air compressor 0.1-3 MPa	0.442	122.6
• Ammonia synthesis circulation compressor 19-20 MPa	0.109	30.3
Total minimum actual shaft work generated in steam turbines	**1.340**	**372.3**
• Refrigeration compressor	0.043	11.9
• Others (BFW pump, CO_2 removal solution pumps, fans, etc.)	0.100	27.8
Total minimum actual shaft work consumed	**1.483**	**412.0**
Maximum actual shaft work ($\eta_{isoth} = 0.4$) for driving:		
• H_2/N_2 compressor 3 –20 MPa	1.383	384.2
• Air compressor 0.1-3 MPa	0.772	214.4
• Ammonia synthesis circulation compressor 19-20 MPa	0.190	52.8
Total maximum actual shaft work generated in steam turbines	**2.345**	**651.3**
• Refrigeration compressor	0.075	20.8
• Others (BFW pump, CO_2 removal solution pumps, fans, etc.)	0.175	48.6
Total maximum actual shaft work consumed	**2.595**	**720.8**

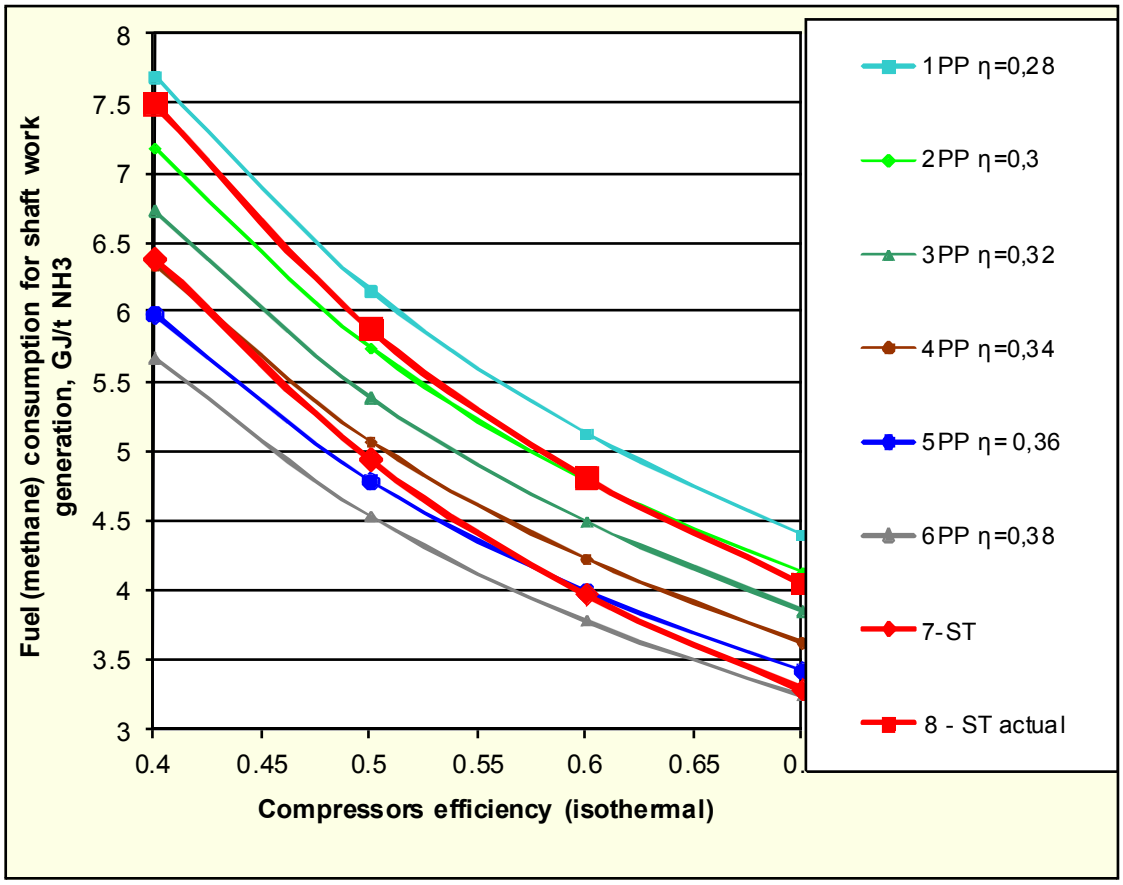

Fig. 2. Dependence of the fuel consumption for shaft work generation on the efficiency of the main compressors in ammonia plants and energy efficiency of power plants (PP). 1- 6 - compressors driven by electric motors; 7- 8 – compressors driven by steam turbines (ST), steam generated in ammonia plant.

However, in all energy integrated modern ammonia plants, the circulation and make-up gas compressors are fitted together and driven by a joint driver (steam turbine). The air compressor is driven also by a steam turbine. The refrigeration compressor and other machinery (pumps, fans, etc.) could be driven by small steam turbines or by electric motors. In most modern plants electric motors are preferable as drivers of small machines, due to the relatively low efficiency of small steam turbines. So, in this work the main three compressors are assumed to be driven by steam turbines, other machinery – by electric motors.

The isothermal shaft work values shown in Table 5, represent the theoretical minimum work necessary to run the ammonia synthesis reaction at 20 MPa. In order to have actual values, the efficiency of the compressors should be known. In Tables 5 and 8 two examples are shown, representing the minimum and maximum actual shaft work consumed by the compressors at boundary values of the isothermal efficiency (0.7 and 0.4, respectively). For the first example, the heat balances and overall methane consumption in ammonia plants with steam-turbines driven and with electric motors-driven main compressors are shown in Tables 6 and 7, respectively.

A comparison of the fuel (methane) consumption for shaft work generation in ammonia plants (without and with heat losses in the steam system) and in power plants (First Law efficiencies from 0.28 to 0.38) at isothermal efficiencies of the main compressors from 0.4 to 0.7, is shown in Figure 2. The dependence of the fuel (methane) consumption for shaft work generation on the efficiency of the compressors in ammonia plants and energy efficiency of power plants is shown in Figure 3. The

Figure 4 presents the influence of the heat losses in the steam generation system of ammonia plants over the fuel (methane) consumption for shaft work generation.
The results show that the fuel consumption values for the shaft work generation in ammonia and power plants are comparable and depends strongly on the machinery efficiency in ammonia plants and on the energy efficiency of power plants, respectively. Due to the utilization of a part of the available MT&LT heat from the chemical processes in the steam cycle, the fuel consumption for the work generation in ammonia plants is lower than in power plants working at equal steam parameters.

Table 6. Heat and fuel (methane) consumption for shaft work generation in ammonia production (Main compressors driven by steam turbines)

Process	**Shaft work** GJ/t NH_3	Steam kg/t NH_3	**CH_4 consumed**		Exergy of work or heat GJ/t NH_3	Exergy of CH_4 GJ/t NH_3
			LHV GJ/t NH_3	Nm^3/t NH_3		
Shaft work to be generated in ammonia plant – main compressors driven by steam turbines						
Total minimum actual theoretical shaft work generated in steam turbines η_{ad}=0.7						
• HP steam (10 MPa, 500^0C) to MP steam 4MPa	0.422	2244	-	-	0.422	-
• MP steam (4 MPa) to condensation	0.918	1183			0.918	
Total shaft work generated	**1.340**	-			**1.340**	
Heat consumption for HP steam generation in ammonia plant						
Heat consumption for HP steam generation:						
• Steam superheating	1.458				0.759	
• Water evaporation	2.953	2244	-	-	1.372	-
• BF water preheating	2.857				0.854	
Total heat for HP steam generation	**7.268**				**2.985**	
Actual medium and low temperature (MT&LT) heat balance						
Total MT&LT heat available from reactions (2) and (4)	**3.619**	-	-	-	**1.982**	-
Excess steam condensation heat	0.969	-	-		0.220	
Total MT&LT heat supply	**4.588**	-	-		**2.202**	
Minimum actual MT&LT heat consumption for CO_2 removal from H_2/N_2 mixture	0.719	-	-	-	0.224	-
Heat losses (10% from heat supply)	0.459				0.220	
MT&LT heat available for BF water preheating and water evaporation	**3.410**	-	-	-	**1.758**	-
High temperature (HT) heat balance						
HT heat consumption for HP steam generation:						
• Steam superheating	1.458	2244	1.458	40.7	0.759	1.534
• Water evaporation	2.400		2.400	67.0	1.040	3.110
Total HT heat consumed for HP steam generation	**3.858**	**2244**	**3.858**	**107.7**	**1.799**	**4.060**
Heat losses (10% from methane burning heat)	0.429	-	0.429	12.0	-	0.452
Total HT heat supply by additional methane burning	**4.287**	-	**4.287**	**119.7**	**1.799**	**4.512**
Total actual minimum methane consumption in ammonia plant						
Actual minimum methane consumption as feedstock and fuel for process (from Table 4)	-	-	**22.711**	**634.1**	-	**23.902**
Total actual minimum methane consumption for HP steam generation	-	-	**4.287**	**119.7**	**1.799**	**4.512**
Total actual minimum methane consumption in ammonia plant	-	-	**26.998**	**753.8**	-	**28.415**
Electricity from power plant for driving other machinery	0.143	-			0.143	
Fuel (methane) consumption in power plant for electricity generation (η=0.32)			0.447	12.5	-	0.472
Total actual minimum methane consumption in ammonia plant (incl. electricity generation)	-	-	**27.445**	**766.3**	-	**28.886**

Table 7. Total methane consumption in ammonia plant and for electricity production in power plant (All compressors in ammonia plant driven by electric motors)

Process	Shaft work GJ/t NH_3	CH_4 consumed		Exergy of CH_4 GJ/t NH_3
		LHV GJ/t NH_3	Nm^3/t NH_3	
Actual minimum methane consumption as feedstock and fuel for process (from Table 4)	-	**22.711**	**634.1**	**23.902**
Minimum electricity from power plant for driving all machinery	1.483	-	-	-
Minimum fuel (methane) consumption in power plant for electricity generation (η=0.32 [4])	-	4.634	129.4	4.877
Total minimum methane consumption in ammonia and power plants	**-**	**27.345**	**763.5**	**28.779**
Maximum electricity from power plant for driving all machinery	2.595	-	-	-
Maximum fuel (methane) consumption in power plant for electricity generation (η=0.32 [4])	-	8.109	226.4	8.534
Total maximum methane consumption in ammonia and power plants	**-**	**30.820**	**860.5**	**32.436**

Table 8. Theoretical and actual energy consumption and CO_2 emissions in natural gas-based production of ammonia

Methane consumption and CO_2 emissions in ammonia production plants	Methane consumption				CO_2 emissions kg/ t NH_3	
	GJ/t NH_3		Nm^3 /t NH_3			
	min	max	min	max	min	Max
Methane as feedstock for steam reforming reaction (1)	17.667		493.3		969	
Methane burning reaction (3)	2.945		82.2		162	
Additional methane burning	1.594		44.5		87	
Theoretical minimum consumption for chemical process	**22.206**		**620.0**		**1218**	
Heat losses in methane burning (10%)	0.505		14.1		28	
Actual minimum consumption for chemical process	**22.711**		**634.1**		**1246**	
Actual consumption for work generation: • in ammonia plants • in power plants	4.287 0.447	8.031 0.781	119.7 12.5	224.2 21.8	212 24	440 43
Total actual consumption in BAT new plants: Main compressors driven by steam turbines	**27.445**	**31.523**	**766.3**	**880.1**	**1505**	**1729**
Total actual consumption in BAT new plants: All machinery driven by electric motors	**27.345**	**30.820**	**763.5**	**860.5**	**1500**	**1690**
CO_2 benchmark allowances for ammonia production for 2013-2014; carbon leakage exposure is in consideration (EC Decision 27.4.2011, [13])	29.522		824.2		**1619**	
CO_2 benchmark allowances for ammonia production for 2020 if carbon leakage exposure would be not in consideration (factor 0.8 for 2013 down to 0.3 for 2020).	11.071		309.1		**607.1**	

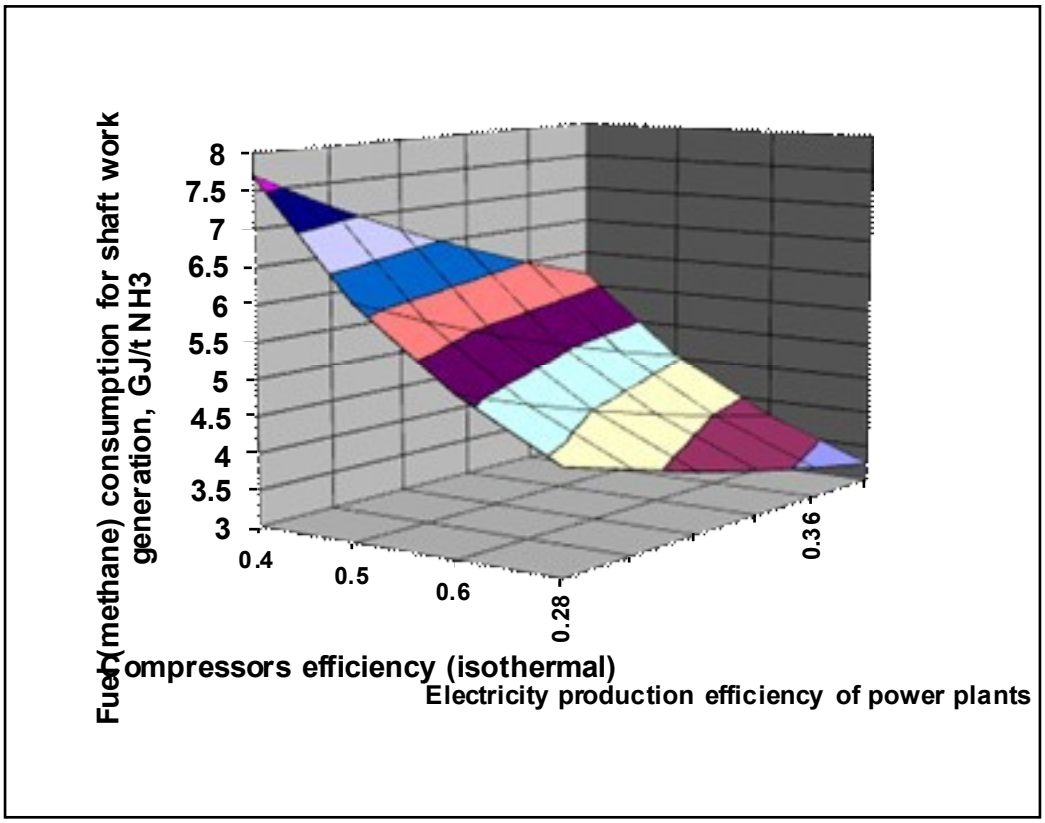

Fig. 3. Dependence of the fuel (methane) consumption for shaft work generation on the efficiency of the compressors in ammonia plants and energy efficiency of power plants.

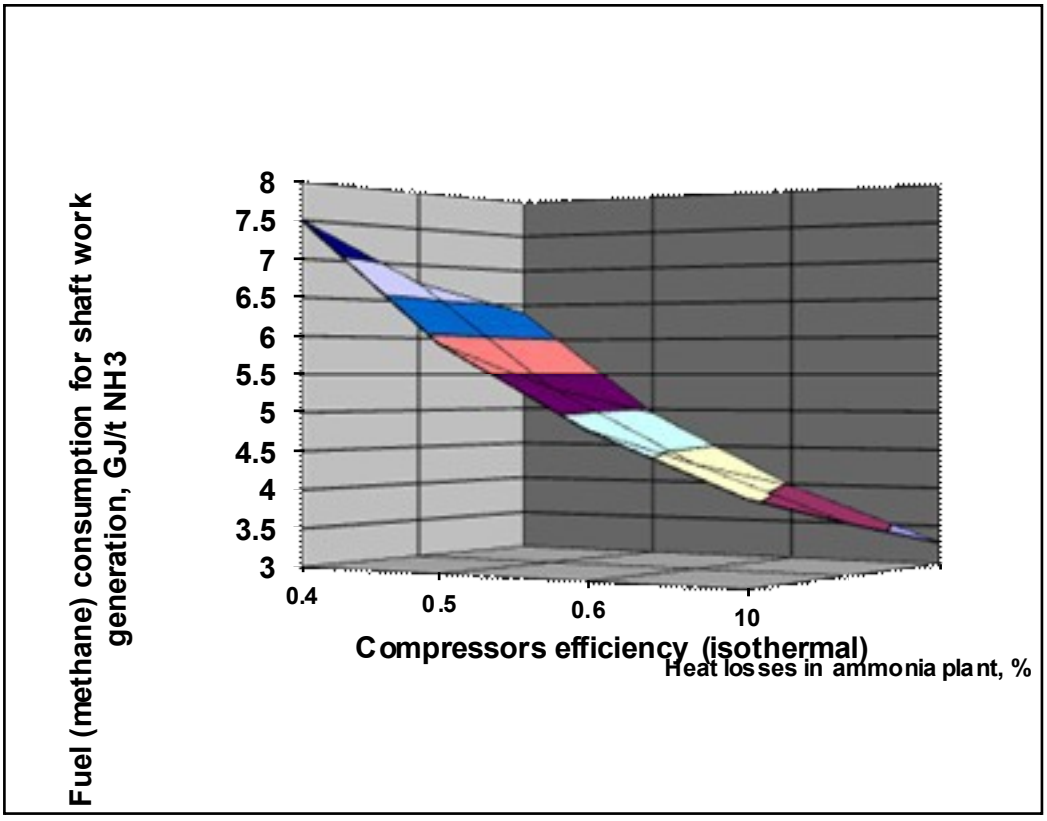

Fig. 4. Dependence of the fuel (methane) consumption for shaft work generation on the efficiency of the compressors and heat losses in ammonia plants.

3.3. Theoretical and actual minimum CO2 emissions estimation

The proposed model of the ammonia production process enables specifying separately also the theoretical and actual CO_2 emissions from the chemical process itself and from the shaft work generation. The first conclusion is that the CO_2 emissions couldn't be made lower than 1218 kg/t, corresponding to the theoretical minimum methane consumption for the chemical process (Table 8).

Moreover, extra emissions must be added from the shaft work generation processes in the ammonia plant or in a power plant. In case the main compressors are driven by steam turbines (HP steam generated in the ammonia plant), the CO_2 emissions would be in the range from 236 to 483 kg/t, depending on the turbines and compressors efficiency. In this case the total actual minimum of the CO_2 emissions would be from 1482 to 1729 kg/t (Table 8). In case the main compressors are driven by electric motors, the total actual minimum of the CO_2 emissions would be from 1500 to 1690 kg/t, depending on the power plant efficiency.

The comparison of these values with the CO_2 benchmark allowances for ammonia production, established by the European Commission [13] for years 2012 and 2013, shows that the value 1619 kg/t is within the range of the actual minimum values for both shaft work generation options. The fulfilment of this regulation requires the application of the best available ammonia technology as well as the high efficient compressors and turbines.

However, if the proposed in the same EC decision [13] further CO_2 emissions reduction (linear decrease by factor of 0.8 for 2013 down to 0.3 for 2020) would be implemented for ammonia plants as well, the corresponding value of 607 kg/t would be unfeasible since it would be twice lower even than the theoretical minimum of 1218 kg/t for the chemical process only.

4. CONCLUSIONS

- A simplified, but generalized model of the overall ammonia production process, presented by reactions (1) – (6), is used to distinguish the methane consumption for the chemical process and for the energy transformation processes (shaft work generation). The model is applicable to all types of modern ammonia plants with conventional reforming, advanced reforming and gas-heated reforming, as the model parameters for methane consumption and heat balance of the plant are independent from the features of the specific plant design. The model is used to find the theoretical minimum and actual methane consumption of the chemical processes in ammonia production. The dependence of the actual consumption on the heat losses is examined.
- The dependence of the additional fuel consumption for shaft work generation in ammonia plants on the isothermal efficiency of the compressors and thermal efficiency of the steam generation is investigated and compared with the fuel consumption in power plants with different energy efficiencies.
- The results show that the fuel consumption values for the shaft work generation in ammonia and power plants are comparable and depends strongly on the machinery efficiency in ammonia plants and on the energy efficiency of power plants, respectively. Due to the utilization of a part of the available MT&LT heat from the chemical processes in the steam cycle, the fuel consumption for the work generation in ammonia plants is lower than in power plants working at equal steam parameters.
- At higher machinery and thermal efficiencies, the generation of the shaft work in the ammonia plants itself is preferable than in old power plants with typically lower efficiencies. However, as the power plants offer more opportunities for improvements than ammonia plants, in the future electric motors could become again preferable for compressors driving.
- The theoretical and the actual minimum of the CO_2 emissions from the chemical process itself and from the shaft work generation are specified and compared for both cases of the main compressors drivers: steam turbines and electric motors.

Nomenclature

BFW Boiler Feed Water
CHP Combined Heat and Power
GHR Gas-Heated Reforming
HP High Pressure, MPa
HHV High Heating Value, kJ
LHV Low Heating Value, kJ
LP Low Pressure, MPa
LT Low temperature, ^{0}C
MP Middle Pressure, MPa
MT Middle Temperature, ^{0}C
η efficiency

References

[1]Sectoral Emission Reduction Potentials and Economic Costs for Climate Change (SERPEC-CC) Industry & Refineries Sectors October 2009, Ecofys, JRC-IPTS. Available at: http://www.ecofys.com/com/publications/documents/SERPEC_industryrefineries_report.pdf

[2]Kovacik J.M., Franklin J.C. Cogeneration in Large Complexes, CEP 1982; February: 58-64

[3]Strait R, Fischbach M. Cut Energy Costs with Cogeneration. Hydrocarbon Processing 1986; October: 55-57.

[4]Appl M. Ammonia: Principles and Industrial Practice. New York:Wiley-VCH Verlag; 1999.

[5]Appl M. The Haber Bosch Heritage: The Ammonia Production Technology, 50 Anniversary of the IFA Technical Conference, September 25-26 1997, Sevilla, Spain.

[6]Integrated Pollution Prevention and Control. Reference Document on Best Available Techniques in the Large Volume Inorganic Chemicals, Ammonia, Acids and Fertilizers Industries, European Commission, Directorate-General JRC; 2007 August. Available at: ftp://ftp.jrc.es/pub/eippcb/doc/lvic_bref_0907.pdf

[7]Best Available Techniques for Pollution Prevention and Control in the European Fertilizer Industry: Booklet N 1: Production of Ammonia; 2000, EFMA, Brussels, Belgium. Available at: http://www.efma.org/subcontent.asp?id=6&sid=31&ssid=31

[8]Szargut J., Morris D.R., Steward F.R., Exergy analysis of thermal, chemical and metallurgical processes. New York: Hemisphere Publ. Corp; 1988.

[9]Kirova-Yordanova Z, Hrusulev G, Atanasova L. Exergy Analysis of Ammonia Plants: A Comparison of Energy-Integrated and Non-Integrated Plants. In: Gogus YA, Ozturk A, Tsatsaronis G, editors. ECOS 1995: Proceedings of the ASME International Conference ECOS'95 on Efficiency, Costs, Optimization, Simulation and Environmental Impact of Energy Systems; 1995 July 11-14; Istanbul, Turkey. Vol.1: 237-242.

[10] Kirova - Yordanova Z, Barakov Y, Koleva D. Exergy Analysis of Nitric Acid Plants: a Case Study, In: Carnevale E, Manfrida G, Martelli Fr, editors. Proceedings of the Florence World Energy Research Symposium "Energy for the 21st Century"; 1994 July 6-8; Florence, Italy: 931-939.

[11] Kirova-Yordanova Z., Energy Integration in Chemical Plants: The Pros and Cons. A Second Law-Based Evaluation of Industrial Experience, Proceedings of The Int. Conference on Process Integration PI'99; 1999 March 7-10; Copenhagen, Denmark: Vol. 2: 78-80.

[12] Kirova-Yordanova Z, Simeonova A. and Atanasova L. Exergy Analysis of Industrial Ammonia Synthesis at Various Process Pressures. Proceedings of the 16th Int. Conference ECOS 2003, Copenhagen, Denmark, June 30 - July 2, 2003, Vol. II, 767 - 775.

[13] European Commission Decision, Brussels, 27.04.2011EC, C(2011) 2772 final, 27.04.2011.

Evaluation of the Oil and Gas Processing at a Real Production day on a North Sea Oil Platform Using Exergy Analysis

Mari Voldsund[a], Wei He[b], Audun Røsjorde[c], Ivar S. Ertesvåg[d] and Signe Kjelstrup[e]

[a] *Norwegian University of Science and Technology, Norway, mari.voldsund@chem.ntnu.no, **CA***
[b] *Statoil ASA, Norway, weih@statoil.com*
[c] *Statoil ASA, Oslo, audr@statoil.com*
[d] *Norwegian University of Science and Technology, Norway, ivar.s.ertesvag@ntnu.no*
[e] *Norwegian University of Science and Technology, Norway, signe.kjelstrup@chem.ntnu.no*

Abstract:
Industry may benefit from knowledge about the 2nd law of thermodynamics and exergy analysis. The motivation for this study is to explore the applicability of exergy analysis as an evaluation and monitoring tool for an offshore platform. A particular oil producing platform located in the North Sea is analysed. We use exergy analysis to indicate the potential for reduction in power consumption of the oil and gas processes on the platform, and present the exergetic efficiency as a useful performance parameter. The exergetic efficiency says something about improvement potential, while current performance parameters only focus on power consumption. We analyse the oil and gas processing at the particular platform for a real production day. A mix of water and reservoir petroleum is separated into oil, gas and water. The produced oil is stabilized and pumped 18 km to a nearby platform, the water is treated and discharged to the sea and the produced gas is compressed and reinjected into the reservoir. The oil and gas processing is driven by gas turbines, and produced gas that is treated in the fuel gas system is used as fuel. The oil and gas processing can be divided into five sub-processes; the separation train, the recompression train, the reinjection train, the export oil pumping section and the fuel gas section. A flowsheet for these processes is simulated using measured process data, and the exergy loss in each process unit is calculated. In addition to a real production day (Case 1), we have looked at the same data but with all adiabatic compressor efficiencies increased by 2 percentage points (Case 2) as well as absence of anti-surge recycling (Case 3). In Case 1 the specific power consumption was 180 kWh/Sm3 while the exergetic efficiency was 0.32. The highest losses were related to compression of gas. In Case 2 the specific power consumption was reduced with 3 % while the exergetic efficiency of the process increased to 0.33. In Case 3 the specific power consumption was reduced with 15 % and the exergetic efficiency increased to 0.38. Clearly, efficient gas compression is important. We see the advantage of considering destructed exergy and exergetic efficiency in addition to the industry's own measures of performance, as these parameters show different features of the processes.

Keywords:
Exergy, Efficiency, Compressor Efficiency, Anti-Surge Control, Oil Platform.

1. Introduction

In 2008, gas turbines and diesel engines on oil and gas platforms were responsible for 21 % of Norway's total CO_2-emissions [1]. Most platforms generate their own power with gas turbines, and the typical power consumption at a Norwegian continental shelf platform is between 10 MW and several 100 MW. There is a general agreement that the world's CO_2 emissions should be reduced and that the worlds resources should be utilised in sustainable way. Improvement of energy efficiency is a challenge in the petroleum sector, as in the industry in general. The sector is therefore in need for a tool to monitor the energy performance of the platform processes.

Today, specific CO_2 emissions (CO_2 emission per barrel produced oil) is often used as a performance parameter by the oil and gas industry. This parameter reflects the aim of reducing the world's CO_2 emissions - it encourages energy efficiency and use of renewable energy sources. However, it does not account for the varying operating conditions for different platforms.

Obtaining a sustainable resource management in the petroleum sector can be complex. In Norway, as well as in a number of other countries, the industry has to pay tax for CO_2 and NO_x emissions. At the same time increased recovery and extended lifetimes in mature fields is encouraged. However, measures designed to improve recovery often require significant amounts of energy and may entail additional emissions to air [2]. The taxes do then punish measures that are encouraged by the authorities [3].

We want to explore the use of exergy analysis as a tool for platform performance benchmarking and as an everyday tool to evaluate performance. The exergetic efficiency compares the work used in a process with the work needed for the same process if it were reversible. We also want to calculate the destructed exergy in different parts of the process to indicate possibilities for improvement. We therefore analyse the oil and gas separation processes on a specific North Sea oil platform. Exergy analysis is a thermodynamic method which is not yet systematically used by the oil and gas industry.

The oil and gas produced at the platform are subject to certain specifications. The oil must meet the pressure required for 18 km transportation through a pipeline, and it must have a specified vapor pressure. The gas must meet the pressure required to be injected into the reservoir for pressure maintenance.

Specific CO_2 emissions accounts for both fuel gas consumption and flaring. The CO_2 emissions associated with the part of the platform studied is proportional to the fuel gas consumption, and thus the power consumption. We choose to look at specific power consumption when we compare with exergy analysis in the rest of this paper.

Oliveira et al [4] did in 1997 an exergy analysis of the petroleum separation processes on a Brazilian offshore platform. On this platform exergy is consumed in order to heat petroleum before separation, to compress natural gas and to pump oil to the coast. There is recovery of exhaust gases for heating purposes. The analysis showed that exergy destruction on this platform is dominated by heating of oil, despite the heat recovery system, and by compression of gas.

This paper is a continuation of a work presented earlier [5], where an exergy analysis was performed using a process flowsheet that was considered representative for the processes on the platform we look at. Adiabatic efficiencies were assumed to be 75 % in all compressors and pumps. It was pointed out that the highest losses took place in the reinjection trains where gas is compressed before it is reinjected into the reservoir. The calculated destructed exergy at the process plant was 12 MW and the exergetic efficiency 0.36.

In the current work we analyse a real production day for the same platform. However, the process flowsheet has now been established using measured temperatures, pressures, flow rates and power consumption throughout the process for a specific production day. We have also included fuel gas treatment, and recycling of gas due to anti-surge protection of the compressors. This will give results that are more realistic - especially for the gas compression processes. We have done a case-study where in addition to the real production day (Case 1), we have looked at the same day, but with all adiabatic compressor efficiencies increased with 2 pp (percentage points) (Case 2) and the same day but without need for anti-surge recycling (Case 3).

2. Theoretical background

2.1. Exergy

The basic principles of exergy and exergy relations relevant for this study are presented. For a comprehensive introduction to exergy analysis, see [6] or [7]. The exergy of a system is defined as the maximum theoretical work obtainable when the system interacts with the environment to equilibrium [7]. This maximum theoretical work is obtained when all processes involved are reversible. In all real processes some exergy will be destructed. In an exergy analysis of a process,

thermodynamic inefficiencies can be identified. Important quantities in exergy analysis are defined by [8] as follows:

- The *product exergy*, E_P, represents the desired result expressed in terms of exergy.
- The *fuel exergy*, E_F, represents the resources in terms of exergy used to provide the product exergy.
- *Exergy loss*, E_L, represents thermodynamic inefficiencies of a system associated with the transfer of exergy with energy and material streams to the surroundings.
- *Exergy destruction*, E_D, represents thermodynamic inefficiencies of a system associated with the irreversibilities (entropy generation) within the system boundaries.

For a system in steady state the destructed exergy, E_D, for a certain time period is the exergy entering the system minus the exergy leaving the system:

$$E_D = W + \sum_k \int_{T_k} \left(1 - \frac{T_0}{T_k}\right) \delta Q_k + \sum_j n_j e_j \,, \qquad (1)$$

where W is work added, Q is heat transferred at temperature T_k, T_0 is the temperature of the environment, n is number of moles in a material stream, and e is molar exergy. Subscript j denotes material stream j. Some of the terms in (1) will correspond to fuel exergy rate, some will correspond to product exergy rate and some will correspond to rate of exergy loss, depending on the system considered:

$$E_D = E_F - E_P - E_L \,. \qquad (2)$$

2.2. Process performance parameters

There exists a variety of ways to define performance parameters for industrial processes based on energy and exergy. We present some parameters that are useful for oil and gas processing:

- The *specific power consumption* we define as consumed power per oil produced. As long as all power comes from the same fossil power source, this is proportional to specific CO_2.
- The *exergetic efficiency*, ε, as defined in [8]:

  $$\varepsilon = \frac{E_P}{E_F} \,. \qquad (3)$$

  This parameter takes into account the minimum theoretical work that has to be done for the given process.
- The *efficiency defect*, δ_i, of subsystem i, presented in [6] as the fraction of the input exergy to the whole system which is lost through irreversibilities in the subsystem. In our notation:

  $$\delta_i = \frac{E_{D,i}}{E_F} \,. \qquad (4)$$

  This parameter shows how different subsystems contribute to reduction in the exergetic efficiency.

3. System description

3.1. Process overview

A schematic overview of the oil and gas processing at the studied platform is given in Fig. 1. Details for the simulated process flowsheet for the processes are given in Appendix A with set-up of the process units, compositions of feed streams and temperatures, pressures, efficiencies and flow rates throughout the process.

The feed stream of the process consists of reservoir fluids with 78 mol% gas. It comes from a production manifold and enters a separation train. Here gas and water are separated from the crude oil using gravitational separators and an electrostatic coalescer. The train consists of three stages where in the first two stages there are three-phase separators, and in the third stage there are a two-phase separator and an electrostatic coalescer. For each separator, the pressure is reduced, so that more gas is released from the oil. The oil shall meet specifications of basic sediment content, water content and vapour pressure, which is why the separation process is performed in several stages at different pressures. In total the pressure is reduced from 71 to 2.8 bar during this section. Fuel gas for the gas turbines is supplied from high pressure gas from the 1st-stage separator. Oily water from the separators is sent to a water treatment process where traces of oil are removed. The water treatment process is neglected here. A water pump pumps water from the electrostatic coalescer back to the 2nd separator.

The remaining, stabilised oil is pumped 12 km to a nearby platform via two pumps with cooling of the oil in between. A minimum flow is required through the pumps, and to achieve this, some of the oil is recycled back right after the 2nd-stage separator.

The gas that is released in each stage in the separation train is sent to a recompression train. The train consists of three stages, each with a cooler, a scrubber and a compressor. The cooler cools the gas in order to get a low inlet temperature for the compressor and by this way get a more efficient compression. The scrubber is a separator that removes small amounts of condensed liquid. Scrubbing of the gas protects the compressor and allows more optimal compression. In each stage, the gas is compressed to the pressure of the previous stage of separation. A minimum flow of gas is required through the compressors to prevent compressor surging, and to achieve this some of the gas is recycled around each stage (anti-surge recycling). Approximately $15 \cdot 10^3$ Sm^3/h, $21 \cdot 10^3$ Sm^3/h and $22 \cdot 10^3$ Sm^3/h is recycled in the 1st, 2nd and 3rd recompression stages, respectively. In the end, the pressure has reached the 1st-stage separation pressure.

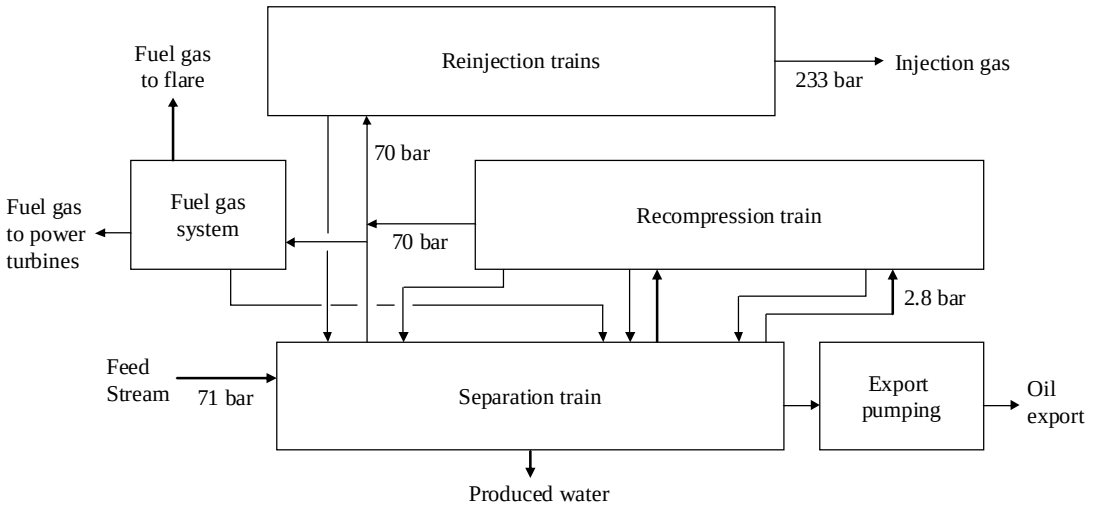

Fig. 1. Schematic overview of the mass streams in the oil and gas processing. First the feed stream enters the separation train where it is separated into gas, oil and water. The water is sent out of the process, the oil is sent to the export pumping section where it is pumped for export, high pressure gas is sent to the reinjection trains and low pressure gas is sent to the recompression train where it is compressed before it is sent to the reinjection train. In the reinjection train the gas is further compressed before it is reinjected into the reservoir. Fuel gas is taken from the high pressure gas from the separation train, and treated in the fuel gas system. It is used in the power turbines and in pilot flames in the flare. There is a drain system where small amounts of liquid from the different sub-processes are collected and pumped back to the separation train. It consists of several units, but for simplicity it is represented by only mass streams in the figure. The pressure of some of the process streams are given to show the pressure variations through the process.

After the recompression, the gas enters three parallel reinjection trains. Here it is compressed up to injection well pressure, which is 233 bar. In each of these trains there are two stages, each with a cooler, a scrubber and a compressor, the same way as in the recompression train. The train is run at maximum capacity, so there is no need for anti-surge recycling. The resulting high pressure gas is injected back into the reservoir.

Fuel gas drawn from the 1st-stage separator is cooled and fed through a pressure reducing control valve to a scrubber for liquid removal. After the scrubber, the gas is heated with an electrical heater before a last chance liquid removal and then sent to the power turbines. Gas for a pilot flame at the flare is also taken from this section. For normal process conditions, the amount of gas to the flare from other parts of the processes is negligible.

Condensate from scrubbers throughout the processes is sent back to the 2nd separation stage, either directly or through a drain system.

3.2. Process characteristics – the real production day

The real production day we consider, is one out of a series of days from 2009 to 2011 with available measured process data. The selected day is *normal* in the sense that it is among the 85 % of the days that give values closest to the median for selected process variables like pressures and temperatures in process streams. The process conditions were *stable* throughout the day: The standard deviation in measured produced oil flow rate is less than 10 Sm^3/h (for an average flow rate of 132.5 Sm^3/h) and the injected gas rate measured in each of the in total 5 injection wells is less than 10^3 Sm^3/h (for an average total flow rate of $370 \cdot 10^3$ Sm^3/h).

There are several parameters that vary from day to day, which are important for the performance of the oil platform. These parameters and process characteristics for the selected real production day are summarised in Table 1.

Table 1: Variation in process parameters important for the performance of the oil platform for all normal production days, together with process characteristics for the real production day analysed.

Process parameter	Variation	Real production day analysed	
Gas injection flow rate, 10^3 Sm^3/h	332 – 391	370	(Median)
Oil production, Sm^3/h	121.6 – 302.6	132.5	(Low)
Gas injection pressure, bar	210 – 240	233	(High)

The adiabatic efficiencies calculated from measured inlet and outlet temperature and pressure for the real production day are given in Table 2.

Table 2: Adiabatic efficiencies for the compressors for the real production day analysed.

Compressor	Adiabatic efficiency	Compressor	Adiabatic efficiency
Recompression		*Reinjection B*	
1st stage	47 %	1st stage	64 %
2nd stage	69 %	2nd stage	57 %
3rd stage	56 %		
Reinjection A		*Reinjection C*	
1st stage	64 %	1st stage	69 %
2nd stage	54 %	2nd stage	64 %

For the selected real production day, we studied three cases:

- *Case 1: Real production day.* Temperatures, pressures and flow rates throughout the process based on historical data.
- *Case 2: Increased compressor efficiencies.* The same process flowsheet as in Case 1 was used, except for that adiabatic efficiencies were increased with 2 pp for all gas compressors.

- *Case 3: No anti-surge recycling*. The same process flowsheet as in Case 1 was used, except for that all anti-surge flows around compressors in the recompression section were set to zero.

4. Methodology

4.1 Simulation of the process flowsheet

The platform processes were simulated using Aspen HYSYS [9]. We chose to use the Peng-Robinson property package, where the Peng-Robinson (PR) equation of state is used to calculate thermodynamic properties. This package is the recommended property package for oil and gas applications [10]. Liquid densities were calculated with the COSTALD method, since this generally gives better results than the equation of state. The HYSYS PR option was chosen. This option has several enhancements to the original PR equation [10]. Interaction coefficients were set to values from the HYSYS library and the interaction parameters unavailable from the library were set as estimated by HYSYS. Hypothetical components were used to simulate the heavy oil fractions. Details about the hypothetical components used, together with the composition of the feed streams, and process variables set throughout the process for Case 1 are given in Appendix A. For Case 2 and 3 the same simulated process flowsheet were used, except for the modifications described in Section 3.2.

4.2 Exergy analysis

The exergy destruction in each process unit was found from the exergy balance of the unit. Thermodynamic properties like enthalpy and entropy were taken as calculated by HYSYS. Contributions to the exergy from kinetic energy were neglected, while a contribution from potential energy was included once where height difference lead to a pressure increase in an oil stream. This was taken into account by introducing a dummy pump that increased the pressure in the simulated process flowsheet.

We chose to define E_P as the exergy difference between process streams leaving and entering the system and E_F as power delivered to the process units (after electrical losses and mechanical losses in gears etc.). The simulated power delivered to the dummy pressure increase pump was not included in the fuel exergy, as this exergy was not delivered by the power turbines.

Exergy lost with cooling water is mixed irreversibly with the sea, and this was therefore regarded as destructed exergy, E_D. This means in practice that the control volume boundaries around these units were extended and drawn around the points where cooling water and sea water are mixed. There are no other streams considered as exergy loss, giving $E_L = 0$.

5. Results and discussion

In Table 3 the efficiency defects for each sub-process for the three cases studied are presented. The destructed exergy in each subsystem distributed over type of process unit is presented for each case in Fig. 2, while performance parameters are presented for the three cases in Table 4.

Table 3. Efficiency defect for each sub-process in the oil and gas processing at the platform for the three cases analysed.

Sub-process	Case 1: Real production day	Case 2: Increased compressor efficiencies	Case 3: No anti-surge recycling
Separation train	0.04	0.04	0.05
Export section	0.01	0.01	0.01
Recompression train	0.17	0.17	0.03
Reinjection trains	0.44	0.43	0.51
Fuel gas system	0.02	0.02	0.03

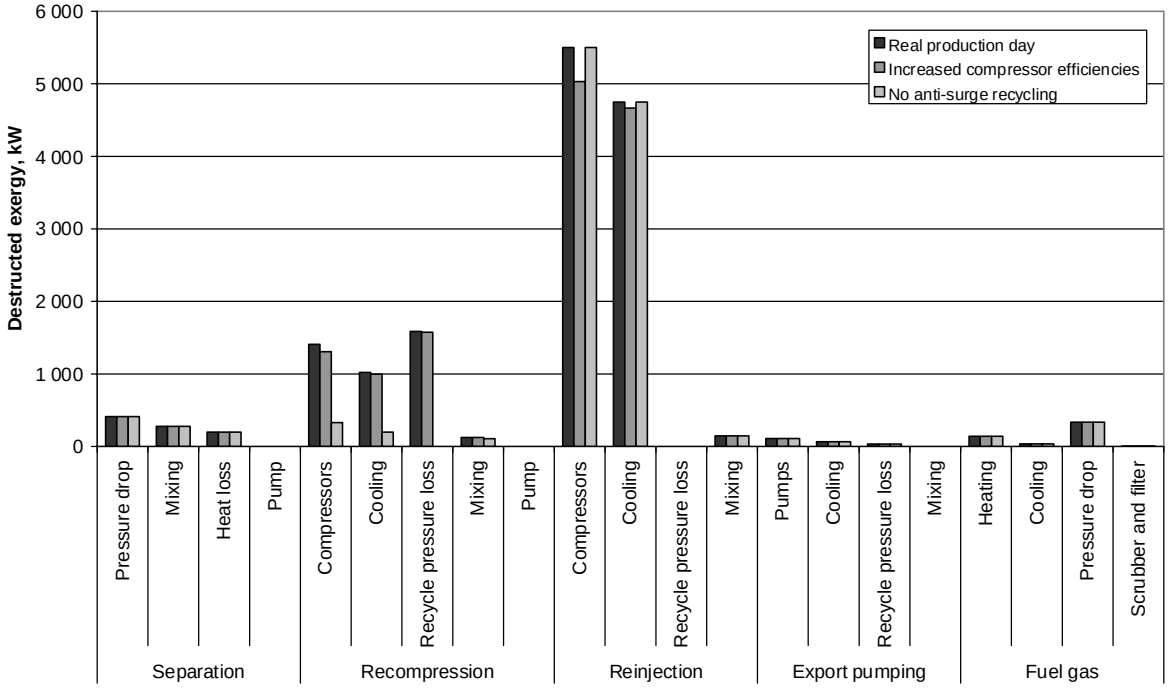

Fig. 2. Destructed exergy distributed on type of process unit in the different sub-processes of the oil and gas processing at the platform, for a real production day, for the same day but with all adiabatic compressor efficiencies increased with 2 pp and for the same day but without anti-surge recycling.

Table 4. Performance parameters for the oil and gas processing at the platform for the three cases analysed. 'Power consumption' is power added to the process units, after electric losses and mechanical losses in gears etc.

Parameter	Case 1: Real production day	Case 2: Increased compressor efficiencies	Case 3: No anti-surge recycling
Power consumption (E_F), MW	23.9	23.1	20.3
Destructed exergy (E_D), MW	16.1	15.5	12.6
Product exergy (E_P), MW	7.7	7.7	7.7
Specific power consumption, kWh/Sm^3	180	174	154
Exergetic efficiency	0.32	0.33	0.38

5.1. Case 1: Real production day

In Table 3 we see that losses take place mainly in the reinjection trains and the recompression train, which have efficiency defects of 0.44 and 0.17 respectively. The pressure is raised significantly in these sections, and this is where the largest part of the power is consumed. Figure 2 shows that the losses in the reinjection trains consist almost exclusively of losses in compressors and losses with the cooling water. The losses in the recompression train consist of losses in the compressors, losses with the cooling water and losses due to anti-surge recycling of gas around the compression stages. It is clear that to improve the exergy efficiency and reduce the power consumption of the process one should focus on the gas compression, which is as expected.

The current result shows considerably more losses associated with gas compression compared to results in [5]. The results in the previous paper correspond to efficiency defects of 0.24 and 0.04, for the reinjection and recompression trains, respectively. The large difference is mainly due to the use of adiabatic efficiencies of 75 % in the previous paper, while the efficiencies simulated based on

measured inlet and outlet temperatures and pressures were lower. Furthermore, anti-surge recycling was not taken into account in the previous paper.

5.2. Case 2: Increased compressor efficiencies

With 2 pp higher adiabatic efficiencies in all gas compressors, we see a reduction in destructed exergy of 0.5 MW in the compressors in the reinjection train, 0.1 MW in the coolers in the reinjection train and 0.1 MW in the compressors in the recompression train. Reduction of exergy destruction in the compressors is a direct effect of the increased efficiencies. The reduction of exergy destruction in coolers is due to a lower outlet temperature from the compressors, so that less heat has to be removed with the cooling water in the following cooler. The improvements result in a specific power consumption reduced with 3 % (cf. Table 4). We see that the efficiency defect in the reinjection trains is reduced. Since less power is now needed for the whole process, other efficiency defects are slightly increased, which is observed for the separation train. The exergetic efficiency of the whole process increases from 0.32 to 0.33.

5.3. Case 3: No anti-surge recycling

Without anti-surge recycle flow around the compressors in the recompression train, the destructed exergy of 1.6 MW due to pressure loss in recycle streams is eliminated. We also obtain a reduction in destructed exergy of 1.1 MW in the compressors and 0.8 MW in the coolers. This is due to a lower amount of gas compressed and cooled. The efficiency defect of the recompression train is reduced from 0.17 to 0.03. The improvements reduce the specific power consumption with 15 % (cf. Table 4). Since no exergy is saved in the other sections and the total power consumption is reduced, the efficiency defects in the other sections are increased. The exergetic efficiency of the whole process increases from 0.32 to 0.38.

5.4. Perspectives on exergy analysis in the oil industry

The oil and gas industry is well aware of the large losses related to gas compression. Furthermore it is well known that a lot of thermal energy is released with the cooling water to the sea. The thermal energy discharge cannot however well represent the thermodynamic losses, as the temperatures of the discharges are relatively low compared to the ambient temperatures. Exergy analysis is a systematic approach that localises thermodynamic losses and quantifies theoretical saving potential. It makes it possible to compare the magnitude of different types of losses. This is more useful, the more complex the system is.

The destructed exergy is for our system equal to the power consumption minus the theoretical minimum work needed for the process. This is valuable information and gives a wider picture of the situation. The exergetic efficiency is the ratio between this minimum work and the power consumption. Both these parameters can add to the industry's own measures of performance, like the specific CO_2 emissions. The exergetic efficiency can be used to both quantify as well as justify best practices. It can also be used by the public sector to set standards for performance, that all should adhere to. Such standards may eventually lead to developments of more energy efficient technologies and to the best operation of these.

Under the introduction of other power sources for offshore platforms, for instance electric power from land or power from offshore windmills [11], specific CO_2 emissions is no longer proportional to specific power consumption. Specific CO_2 emissions encourages the use of renewable power sources, but once such a source is taken into use, this parameter do not say anything about the performance of the process anymore. Exergetic efficiency, however, will always evaluate the process.

We have now only looked at the oil and gas processing at one platform. We propose that more platforms should be analysed, to explore the applicability of exergy analysis when comparing different platforms. We also propose that one platform should be monitored over time, to see how

exergy analysis can be used to evaluate efforts on adapting to changing process conditions or on increasing the process efficiency.

6. Conclusion

An exergy analysis has been performed for a real production day on a North Sea oil platform. The specific power consumption was 180 kWh/Sm^3 while the exergetic efficiency was 0.32. The highest losses were related to compression of gas. By increasing all adiabatic compressor efficiencies with 2 pp the specific power consumption was reduced with 3 % while the exergetic efficiency of the process increased to 0.33. By eliminating need for anti-surge recycling of gas, the specific power consumption was reduced with 15 % and the exergetic efficiency increased to 0.38. It has been shown that exergy analysis is useful for the oil industry both for location and quantification of thermodynamic losses. Destructed exergy and exergetic efficiency give useful information in addition to the industry's own measures of performance.

Appendix A

We present the set-up of the flowsheet that was simulated for the real production day using HYSYS in Section A.1. In Section A.2 we give the process variables and the feed streams set in the simulation.

A.1. Set-up for process flowsheet

Figs. A.1 – A.6 show the set-up for each sub-process. A short overview of the whole system is already given in Section 3.

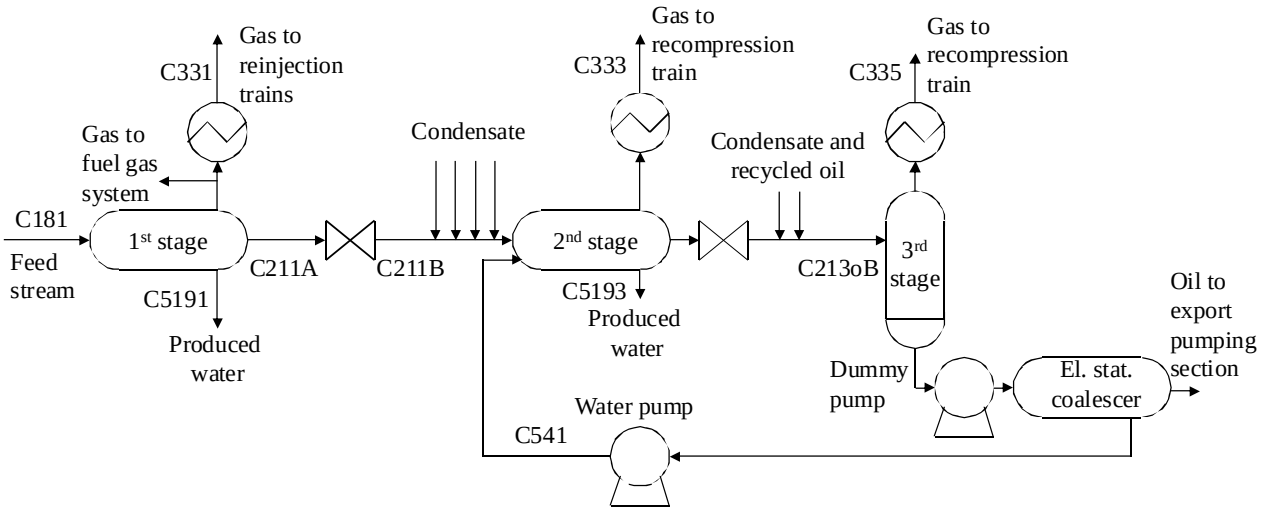

Fig. A.1. Simulated process flowsheet for the separation train. The separation train has three separation stages. In the 1st stage there are two three-phase separators; one normal and one test-separator (both are continuously in use). For simplicity they are merged into one separator in the simulated process flowsheet. In the 2nd stage there is one three-phase separator. In the 3rd separation stage there are one two-phase separator and one electrostatic coalescer. The feed stream enters the 1st separation stage. The pressure is reduced between each stage. A water pump pumps water from the electrostatic coalescer back to the 2nd three-phase separator. Coolers are added on the gas streams to simulate heat losses to the environment. A dummy pump is included after the two-phase separator to simulate pressure increase due to height difference in the liquid stream.

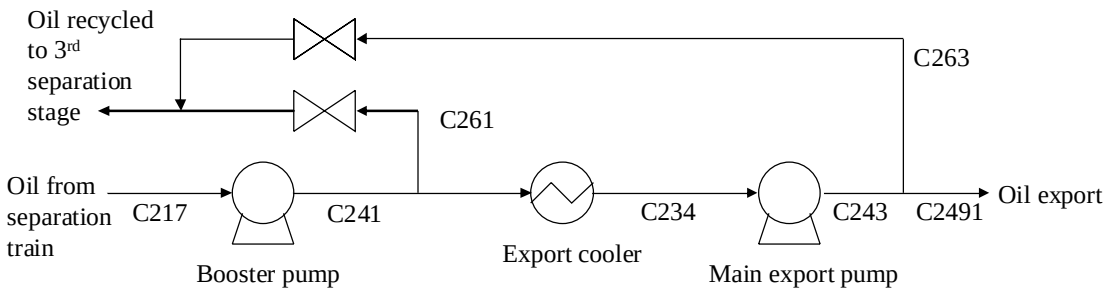

Fig. A.2. Simulated process flowsheet for the export pumping section. The oil is first pumped in a booster pump, then cooled, and then pumped in a main export pump. To ensure a minimum flow in the pumps, there are liquid recycle streams that recycle oil to the separation train. Parallel stand-by pumps and coolers are not included in the simulation.

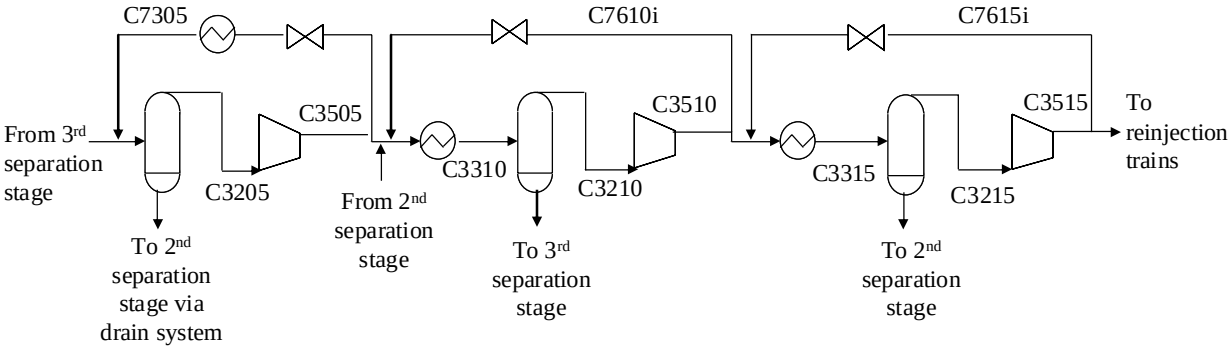

Fig. A.3. Simulated process flowsheet for the recompression train. The gas is compressed in three stages, with a cooler, a scrubber and a compressor in each stage. Gas is recycled around each stage to keep a minimum flow through the compressors.

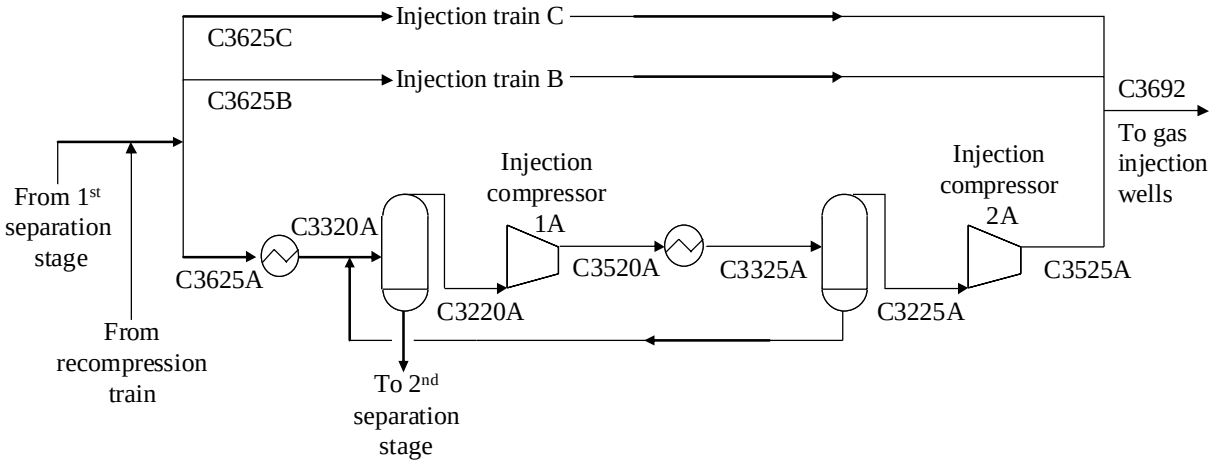

Fig. A.4. Simulated process flowsheet for the reinjection trains. The gas is compressed in three parallel trains with two stages each. Each stage consists of a cooler, a scrubber and a compressor. Only train A is shown in detail, since the three trains have the same set-up. The mass streams of train B and C have the same numbers as shown in train A, but the numbers end with B and C instead of A.

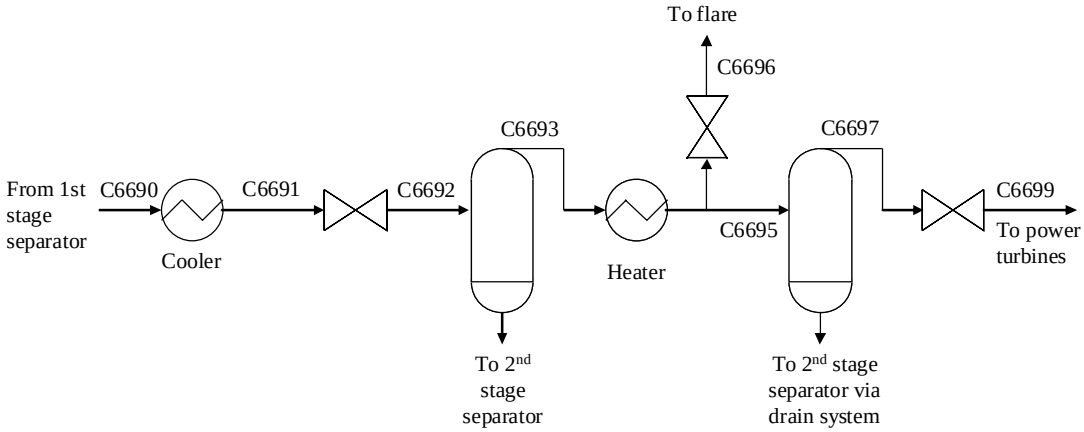

Fig. A.5. Simulated process flowsheet for the fuel gas system. The gas is cooled and depressurised, before it is scrubbed and heated. Some gas is split off to the pilot flames in the flares, and the rest is split into two, scrubbed, filtered and depressurised before it is sent to the power turbines. In the simulated flowsheet, the last two scrubbers and filters are merged into one scrubber.

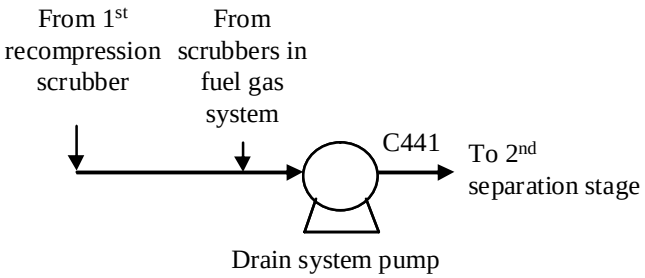

Fig. A.6. Simulated process flowsheet for the drain system. In the drain system small amounts of liquid from knock out drums in the flare system and from scrubbers with low liquid flow rates in the oil and gas processes are collected in a reclaimed oil sump. When the liquid in the reclaimed oil sump reaches a certain level, it is pumped to the 2nd separation stage. For simplicity this is replaced by a small pump that continuously pumps liquid from scrubbers to the 2nd separation stage in the simulated process flowsheet. Since we look at a normal production day with a stable production, liquid from the flare system is neglected.

A.2.1. Temperatures, pressures and efficiencies

Temperatures and pressures throughout the system were set to the average measured value for the real production day (24 h), see Table A.1. For some process units efficiency and pressure drop were set to values found in documentation from the contractors of the equipment, see Table A.2. For some small pumps efficiencies were assumed, see Table A.3.

Table A.1. Process variables set as average measured value in process streams for the real production day (24 h). The measured pressures, P, have uncertainties of 1 % while the temperatures, T, have 1.0 ºC where the uncertainties are expressed as 95 % confidence intervals.

Sub-process and stream number	Variable	Value	Sub-process and stream number	Variable	Value
Separation			C234	*P*, bar	12.81
C181	*P*, bar	70.4♣	C243	*P*, bar	32.1
C211B	*P*, bar	8.50	C234	*T*, ºC	48.1
C213oB	*P*, bar	2.80	*Reinjection A*		
C541	*P*, bar	8.77	C3220A	*P*, bar	68.8
C181	*T*, ºC	76.5♪	C3520A	*P*, bar	137.4
C331	*T*, ºC	73.6♣	C3225A	*P*, bar	137.4♠
C333	*T*, ºC	59.2	C3525A	*P*, bar	236
C335	*T*, ºC	46.9	C3320A	*T*, ºC	28.0♦
Recompression			C3520A	*T*, ºC	94.0
C3205	*P*, bar	2.41	C3325A	*T*, ºC	28.0
C3505	*P*, bar	5.72	C3525A	*T*, ºC	77.1
C3210	*P*, bar	5.20	*Reinjection B*		
C3510	*P*, bar	18.75	C3220B	*P*, bar	68.9
C3215	*P*, bar	18.29	C3520B	*P*, bar	139.8
C3515	*P*, bar	70.0	C3225B	*P*, bar	139.1
C7305	*T*, ºC	39.9	C3525B	*P*, bar	236
C3505	*T*, ºC	104.9	C3320B	*T*, ºC	28.0
C3310	*T*, ºC	21.0	C3520B	*T*, ºC	95.6
C3510	*T*, ºC	111.8	C3325B	*T*, ºC	28.0
C3315	*T*, ºC	24.0	C3525B	*T*, ºC	74.4
C3515	*T*, ºC	146.5	*Reinjection C*		
Fuel gas system			C3220C	*P*, bar	66.1
C6692	*P*, bar	38.8	C3520C	*P*, bar	131.9
C6695	*P*, bar	38.4	C3225C	*P*, bar	129.2
C6697	*P*, bar	38.0	C3525C	*P*, bar	236
C6696	*P*, bar	9.3	C3320C	*T*, ºC	30.0♥
C6699	*P*, bar	18.25	C3520C	*T*, ºC	93.4
C6693	*T*, ºC	35.0	C3325C	*T*, ºC	30.0♥
C6695	*T*, ºC	63.0	C3525C	*T*, ºC	80.7
Export pumping			*Drain system*		
C217	*P*, bar	4.25	C441	*P*, bar	8.52♫
C241	*P*, bar	13.30			

♣The weighted mean based on mass flow rate for the measured values in the gas flow from the two separators that in the simulated flowsheet is merged into one, see Fig. A.1.
♪Temperature is assumed to be as measured in test manifold.
♠The measured pressure is 137.5 bar, but since it cannot be higher than the pressure in C3528A, it is set to 137.4 bar.
♦ This temperature is not measured for the real production day, so the set point for the cooler upstream is used.
♥ This temperature is not measured for the real production day, and the set point for the cooler upstream is not known for the specific day, so the set point a few weeks earlier is used.
♫The pressure is set to the highest measured pressure in the closest pumping period.

Table A.2. Efficiencies, η, and pressure drop, ΔP, given for process equipment in documentation from the contractors.

Sub-process	Process unit	Variable	Value
Export pumping	Booster pump	η, %	55
	Main export pump	η, %	48
Fuel gas system	Fuel gas cooler	ΔP, bar	0.50

Table A.3. Assumed efficiencies, η, for small pumps. The efficiency for the dummy pump has no practical meaning.

Sub-process	Process unit	Variable	Value
Separation	Water pump	η, %	75
	Dummy pump	η, %	100
Drain system	Drain system pump	η, %	75

A.2.2. Feed streams and flow rates

The feed entering the system consists of fluid coming from two different parts of the reservoir. The compositions of the gas, oil and water phases from each of the two feed types are set as predicted by the operator for 2009. It is assumed that they are unchanged until the day we look at, which is in 2011. The heavy oil fractions are simulated using hypothetical components in HYSYS. They are defined by setting molecular weight, normal boiling point and ideal liquid density, see Table A.4. Other properties are estimated by HYSYS. The hypothetical components are developed by the operator, and are representative for the well streams at this specific platform.

The flow rates of oil, gas and water vary from day to day. The flow rates of the feed streams are set to fit the simulated flow rates of exported oil, injected gas and produced water with measurements, see Table A.5. For each phase, it is assumed that the ratio between flow rates from the two reservoir parts is the same as the ratio between the flow rates that were predicted for 2011 in 2007 for the two parts. The resulting molar flow rate for each component in the feed is given in Table A.6.

Molar flow rates for streams that are split off from the main stream throughout the process are given in Table A.7. They are set to fit with measured volumetric flow rates. In the reinjection trains the volumetric flow rates are measured several places. Then the molar flow rate of each of the train is set to make the simulation fit as good as possible with all the measurements and so that the simulated volumetric flow rates are within the uncertainty limits (95 % confidence interval) of the measured values.

Table A.4. Molecular weight, M, normal boiling point, T_b, and ideal liquid density, $\rho_{id.liq.}$, for the hypothetical components used to describe the heavy oil fractions.

Name	*M*, g/mol	T_b, ºC	$\rho_{id.liq.}$, kg/m^3	Name	*M*, g/mol	T_b, ºC	$\rho_{id.liq.}$, kg/m^3
HypoA-1	81	73	721.2	HypoC-1	94	69	707.5
HypoA-2	108	99	740.1	HypoC-2	119	133	781.7
HypoA-3	125	152	774.6	HypoC-3	172	215	821.3
HypoA-4	171	230	817.1	HypoC-4	238	293	860.3
HypoA-5	247	316	859.3	HypoC-5	383	405	900.7
HypoA-6	388	437	906.2	HypoC-6	636	567	963.7
HypoA-7	640	618	988.5				

Table A.5. Measured flow rates in process streams leaving the platform.

Produced fluid	Stream number	Flow rate, Sm^3/h
Oil export	C2491	132.5 ± 0.4
Injection gas	C3692	$370 \cdot 10^3 \pm 40 \cdot 10^3$
Produced water	C5191 + C5193	67 ± 5

Table A.6. Molar flow rates for each component in the feed stream of the simulated process flowsheet.

Component	Molar flow rate kmol/h	Component	Molar flow rate kmol/h	Component	Molar flow rate, kmol/h
CO_2	151.67	H_2O	3777.38	HypoA-7	25.03
Methane	13608.28	N_2	148.82	HypoC-1	3.96
Ethane	1117.99	HypoA-1	181.30	HypoC-2	2.35
Propane	615.70	HypoA-2	117.12	HypoC-3	1.68
i-Butane	94.71	HypoA-3	114.99	HypoC-4	1.70
n-Butane	221.74	HypoA-4	90.01	HypoC-5	1.10
i-Pentane	72.66	HypoA-5	65.67	HypoC-6	0.71
n-Pentane	94.61	HypoA-6	38.06		

Table A.7. Molar flow rates for streams that are split off from main stream throughout the process. They are set to fit with measured volumetric flow rates.

Sub-process and stream number	Molar flow rate, kmol/h	Sub-process and stream number	Molar flow rate, kmol/h
Export pumping		*Reinjection*	
C261	270.5	C3625B	4366
C263	203.0	C3625C	7631
Recompression		*Fuel gas system*	
C7605i	623.7	C6690	428.1
C7610i	879.2	C6696	14.2
C7615i	922.5		

References

[1] Statistics Norway, Statistisk Sentralbyrå. Emissions of greenhouse gases. 1990-2008*. http://www.ssb.no/emner/01/04/10/klimagassn/ [29.04.10]

[2] The Ministry of Petroleum and Energy and The Norwegian Petroleum Directorate. Facts 2011 – The Norwegian petroleum sector. June 2011.

[3] Ole Ketil Helgesen. Klimameldingen kan gi mindre utvinning. Teknisk Ukeblad. 3 May 2012: 14

[4] Oliveira Jr S., van Hombeeck M., Exergy analysis of petroleum separation processes in offshore platforms. Energy Convers Manage 1997;38(15-17):1577-1584.

[5] Voldsund M., et al, Exergy Analysis of the Oil and Gas Separation Processes on a North Sea Oil Platform. In: Favrat D., et al, editors. ECOS 2010: Proceedings of the 23rd International Conference on Efficiency, Cost, Optimization, Simulation, and Environmental Impact of Energy Systems; 2010 Jun 14-17; Lausanne, Switzerland.

[6] Kotas T.J., The Exergy Method of Thermal Plant Analysis. Malabar, Florida: Krieger Publishing Company; 1995.

[7] Moran M. J., Shapiro H. N., Fundamentals of Engineering Thermodynamics. USA: John Wiley & Sons, Inc; 2004.

[8] Tsatsaronis G., Definitions and nomenclature in exergy analysis and exergoeconomics. Energy 2007;32(4):249-253.

[9] Aspen HYSYS, 2009. Software package, Ver. 7.1, Aspen Technology Inc.

[10] Aspen Hysys 7.2 Documentation. Simulation Basis. Aspen Technology, Inc; 2010.

[11] He, W., et al, The Potential of Integrating Wind Power with Offshore Oil and Gas Platforms. Wind Engineering 2010;34(2):125-138.

Exergetic and economic analysis of Kalina cycle for low temperature geothermal sources in Brazil

Carlos Eymel Campos Rodríguez[a], José Carlos Escobar Palacio[a], César Rodríguez Sotomonte[a], Marcio Leme[a], Osvaldo J. Venturini[a], Electo E. Silva Lora[a], Vladimir Melián Cobas[a], Daniel Marques dos Santos[b], Fábio R. Lofrano Dotto[c], Vernei Gialluca[d]

[a] *Federal University of Itajuba (UNIFEI).* Mechanical Engineering Institute – IEM. Excellence Group in Thermal Power and Distributed Generation (NEST). *Minas Gerais. Brazil;* eymelcampos@hotmail.com
[b] AES Tietê; Bauru, São Paulo – Brazil; danielmarques.Santos@aes.com
[c] ***FAROL Pesquisa, Desenvolvimento e Consultoria;*** *fabio@farolconsultoria.com.br*
[d] *Gênera Serviços e Comércio LTDA; vernei@generatech.com.br*

Abstract:

This paper deals with the thermodynamic analysis (of both the first and second law of thermodynamic) of the Kalina cycle to find the optimum ammonia-water concentration and evaporation pressure at turbine inlet for different low temperatures geothermal sources on the basis of an exergy analysis. In this work, the Aspen-HYSYS software was used to simulate the Kalina cycle and to calculate the thermodynamic properties based on Soave-Redlich-Kwong (SRK) Equation of State (EoS). The influence of these parameters over the power generation and over the first and second efficiency laws, were calculated. The exergy losses of each component were also studied, pointing the ammonia-water concentration and pressure influence over the power generation and cycle efficiency. Finally the size of the component for the different configurations of the plant and the costs of heat exchanger, turbine and pump were evaluated for the condition of the real geothermal source in Brazil. Lower values of US$/kW (888 US$/kW) were obtained for the configuration of 84% of ammonia and 16% of water mass fraction in the composition of the working fluid at an evaporation pressure of 2500 kPa, producing 923.98 kW with 5.86% of thermal efficiency.

Keywords:

Thermodynamic analysis, Kalina cycle, ammonia-water mixture, equation of state, exergy, costs of investment, energy output, geothermal energy.

Introduction

One of the pillars for sustainable development is based on the use of renewable energy sources. In Brazil, during the last years the demand for energy has increased significantly, and this growth trend will be maintained in the coming years. So it is essential that reliable sources of renewable energy are included in the national energy matrix. However, the use of alternative energy sources is always complementary to the use of traditional fossil sources. Currently some alternative renewable energy sources are already technical and economically feasible. The processes and equipment used have a significant degree of efficiency and reliability. The new renewable energy also increases the diversity of the energy supply, ensures the sustainability of the energy generation. In the long terms, reduces atmospheric emissions of greenhouse gases and air pollutants, creates new employment opportunities in remote rural areas and promotes stability and reliability of the energy system. More traditional renewable energy sources are: solar, wind, geothermal, hydropower and biomass.

Renewable energy sources such as solar, low-enthalpy geothermal sources and large amounts of heat from the industrial wastes are potentially promising sources of energy, able to supply a large share of global electric energy demand. However, low and moderate temperatures of these sources cannot be efficiently converted into electricity through conventional power generation, which is why a lot of this energy is simply wasted.

Nomenclature

P pressure, (kPa)
T (absolute) temperature, (K)
t temperature, (^{o}C)
R gas constant, (J/kg K)
V specific volume, (m^3/kg)
w acentric factor of the working fluid
a coefficient of the Soave-Redlich-Kwong equation of state (J/kg)
b coefficient of the Soave-Redlich-Kwong equation of state (J/kg)
U global heat transfer coefficient, (W/m^{2}K)
A area (m^2)
C cost (US$)
$\dot{m}$ mass flow rate (kg/s)
$\dot{Q}$ heat rate (kW)
$\dot{W}$ power rate (kW)
h enthalpy (kJ/kg)
e specific exergy (kJ/kg)
s entropy (kJ/kg K)
$\dot{E}$ exergy (kW)
η efficiency (%)
q total heat transfer

Subscripts
c critical
r reduced temperature $\left(T_r = \frac{T}{T_c}\right)$
in inlet
out outlet
0 dead state
t turbine
p pump
d destruction
w geothermal fluid
th thermal
e exergy
eq equipment
h hot
c cold

Abbreviations
HT high temperature
LT low temperature

For low-temperature geothermal reservoirs, the common type of plants used for the conversion of heat into electrical energy, are binary plants. Up to December 2010, there was not an installed capacity of electricity generation from geothermal energy reported in Brazil. Right now, the main use of geothermal resources in Brazil is in direct use as spas and heating.

The Kalina cycle, originally conceived by Kalina [1] is potentially viable for efficiently generating energy from low temperature sources. The first geothermal plant of this type was built in Husavik, Iceland [2]. Currently, the Kalina cycle is of great interest in different applications [3-6]. Indeed, there are several different configurations of the Kalina cycle, depending, essentially, on the characteristics of the heat source. Various studies had been published about the thermodynamic properties of ammonia-water mixtures [7-10]. The design studies for the use of Kalina cycle, for electric generation from geothermal resources with low temperature indicate different compositions of ammonia-water mixtures, being the most common one about 70 % ammonia – 30 % water [11-13].

Water-Ammonia mixture

The ammonia-water mixture is non-azeotropic. The characteristic of nonazeotropic mixtures is that the composition and temperature changes during boiling for all possible compositions of the mixture. Ammonia-water mixture differ of pure water or pure ammonia, the four main differences of the mixture and pure water are listed below.

1. The ammonia-water mixtures have variable boiling and condensation temperatures. Conversely, pure ammonia and pure water have constant boiling and condensation temperatures.
2. The physical properties of the mixture can be altered by changing the concentration of ammonia. Since the thermophysical properties remain constants.

3. These mixtures have thermophysical properties that lead to increases or decreases the fluid temperature without changing its energy content.
4. Another important characteristic is about the freezing point of the fluid. The pure water freezes at (0 °C), pure at (-78 °C). Solutions of ammonia and water have lower freezing temperature.

Because of the above points, the ammonia-water solutions are appropriate to be used in Kalina cycle applications for low temperatures geothermal electric generation systems.

Phase diagram

Ammonia has a lower boiling temperature compared with water, and so is the most volatile component of the ammonia-water solution. This means that when the temperature of the mixture increases, the ammonia will boil first. Contrary, when the mixture is cooled, water will condense first. This unique feature is shown in Fig 1. This diagram plots the temperature versus the concentration of ammonia in the mixture at 550 kPa.

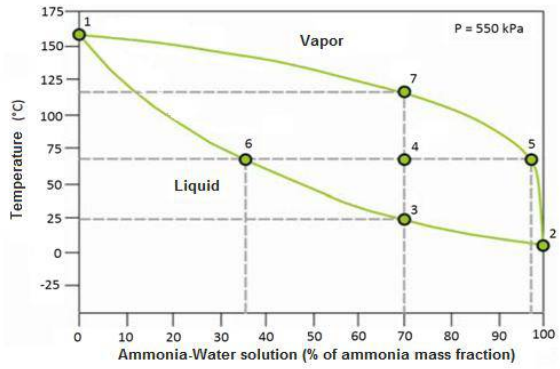

Figure 1: Equilibrium temperature-concentration curve for NH_3- H_2O at constant pressure.

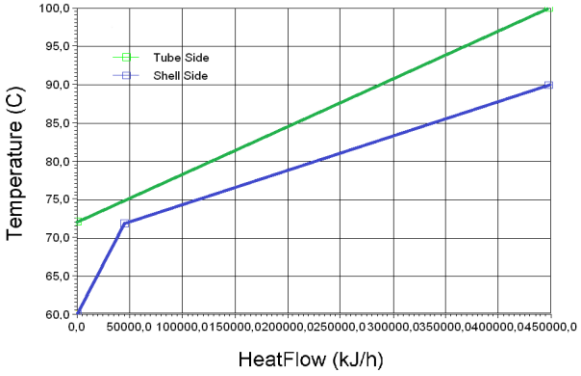

Figure 2. Evaporation process in a Kalina Cycle

In figure 1, the lower curve is the curve of saturated liquid, which happen the start of boiling when the mixture is heated or complete condensation occurs when cooling. While, the upper curve shows the saturated vapour line, or point where there is the complete vaporization of the mixture or the onset of condensation.

When a mixture of ammonia-water is vaporized, a phase diagram conveys much information about the process. For example, when the mixture begins to boil at the boiling point temperature, given by point 3, the % of ammonia in mass is 70% and 30% of water.

As the mixture continues boiling, the temperature increases and point 4 is achieved, wherein the concentration of the remaining liquid and the vapour formed are given by points 6 and 5 respectively. Eventually, the line 7 is reached, where the mixture is saturated vapour at a temperature above the dew point and the vapour concentration is the same as the concentration of the liquid to the beginning of the evaporation process.

In figure 2 is shown an evaporation process in a Kalina Cycle. This non-constant temperature in an evaporation/condensation process permits, if comparing whit pure working fluids cycles, lower values of irreversibilities and higher power output of the cycle.

Kalina cycle modelling

In the process flow diagram given in Fig 3, the main components of the Kalina cycle plant are: evaporator, separators, low and high temperature recuperator, circulation pump, condenser and

turbine-generator. The ammonia-water mixture is heated in the high-temperature recuperator and evaporator; ammonia-rich vapor is separated in the separator and sent to the turbine-generator. After passing through the turbine-generator, the expanded ammonia-rich liquid is mixed in the low-temperature recuperator with the cool ammonia-poor liquid from the separator and sent to the condenser, whence it is recirculated to the evaporator to complete the cycle.

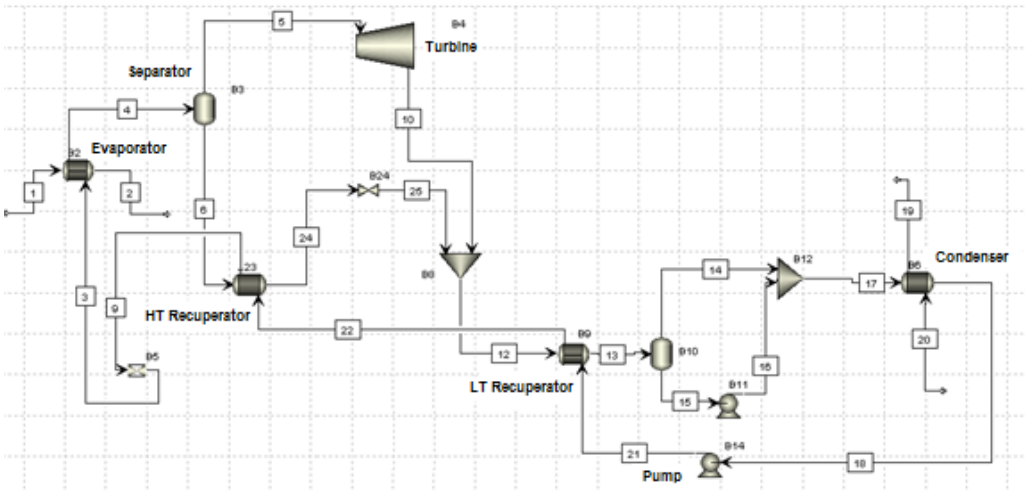

Figure 3. Schematic representation of Kalina cycle with AspenPlus software

Method

The study of the Kalina cycle requires knowing the thermodynamic properties of the ammonia-water mixture which acts as the working fluid.

The property packages available in Aspen-HYSYS allow you to predict properties of mixtures ranging from well defined light hydrocarbon systems to complex oil mixtures and highly non-ideal (non-electrolyte) chemical systems.

These properties can be obtained from cubic equations of state (*EoS*). The cubic equations of estate SRK (Soave-Redlich-Kwong) packages contain enhanced binary interaction parameters for all library hydrocarbon-hydrocarbon pairs (a combination of fitted and generated interaction parameters), as well as for most hydrocarbon-nonhydrocarbon binaries.

$$P = \frac{RT}{V-b} - \frac{\alpha a}{V(V+b)} \qquad (1)$$

The parameters of the SRK EOS are calculated from the following equations:

$$a = 0.42747 \frac{R^2 T_c^{\,2}}{P_c} \qquad (2)$$

$$b = 0.08664 \frac{RT_c}{P_c} \qquad (3)$$

$$\alpha = \left[1 + m\left(1 - \sqrt{T_r}\right)\right]^2 \qquad (4)$$

$$m = 0.48508 + 1.55171w - 0.1561w^2 \qquad (5)$$

Assumptions used in the analysis

1. Pressure drop and heat loss in pipe lines are neglected.
2. Ambient temperature 25 °C.
3. The ammonia-water mixture at the turbine inlet is saturated vapour.
4. The condensing temperature, lower temperature of the system was set at 36 °C.
5. The isentropic efficiency of the turbine is 85%.
6. The pump efficiency is assumed to be 55%.
7. The pinch point was set at 3 ^{o}C at the evaporation start, (see fig. 2)
8. The terminal temperature differential (TTD), between inlet geothermal source temperature and outlet working fluid temperature in evaporator was set in 10 °C, (see fig. 2).

Thermodynamics analysis

Mass and energy balances for each component of the heating system can be calculated using equations (6-7).

$$\sum \dot{m}_{in} = \sum \dot{m}_{out} \qquad (6)$$

$$\dot{Q} - \dot{W} = \sum \dot{m}_{in} h_{in} - \sum \dot{m}_{out} h_{out} \qquad (7)$$

The objective of the exergy analysis is to determine the operating conditions of a system which destroys the least available work. The exergy of the ammonia-water mixture can be calculated from the following relation:

$$e = ((h - h_0) - T_0(s - s_0)) \qquad (8)$$

Where the properties in the dead state are evaluated at T_0 and P_0. When the fluid is in the liquid phase at the dead-state conditions, it is sufficiently accurate to take the dead-state enthalpy and entropy values as if the fluid were a saturated liquid at the dead-state temperature, for this case, 25 ^{o}C.

The exergy destruction rate can be calculated for each component of the cycle from the following exergy balance equation:

$$\dot{E}_d = \sum \dot{m}_{in} e_{in} - \sum \dot{m}_{out} \dot{e}_{out} - W \qquad (9)$$

Finally, the previous energy and exergy analysis makes it possible to calculate the respectively thermal and exergetic efficiency of the cycle from the followings equations:

$$\eta_{th} = \frac{\dot{W}_t - \dot{W}_p}{\dot{Q}_{in}} \cdot 100 \qquad (10)$$

$$\eta_e = \frac{\dot{W}_t - \dot{W}_p}{\dot{m}_w e_{w_{in}}} \cdot 100 \qquad (11)$$

Based on (6–9), the balance of first and second law of the thermodynamic of the most important cycle components has been developed.

Results and discussion

The following analysis was performed for 1 Kg/s and temperature between 90 °C to 140 °C of a geothermal source. In order to obtain the optimum performance for the Brazilian conditions of the cycle the concentrations of ammonia-water and the operation pressure were varied.

First, the optimum working pressure was evaluated, in order to obtain a maximum power output, at saturated conditions in the turbine inlet at different composition of the working fluid, that vary from ammonia 65% - water 35%, ammonia 75% - water 25%, to 84% ammonia – water 16% as shown in Figure 4. It can be observed that the power output varies with the working pressure, temperature and composition of the ammonia-water mixture. At each concentration and temperature, we obtain a maximum power output under a determinate working pressure.

For Brazilians condition, where the condensation temperature of the cycle is approximately 36 °C due to the ambient temperature of 25 °C, different condensation pressure is required for the different composition of the working fluid. At lower condensation pressures, which theoretically would render higher values of power output and efficiency, is not possible to work at, because the fluid will not get totally condensed at the end of the condenser and would cause damages to the circulation pump. Moreover, to vary the condensation pressure of the cycle by decreasing the concentration of ammonia in the working mixture was also analyzed and shown in Figure 4, where the evaporation pressure was plotted against the power output at different temperature and composition of the working mixture. Different condensation pressure was assumed for each ammonia-water composition in order to reach maximum power output and cycle efficiency. Condensation pressure of 800 kPa was used for 65%-35% of ammonia-water solution, 1000 kPa for 75%-35% and 1200 kPa for 84%-16%.

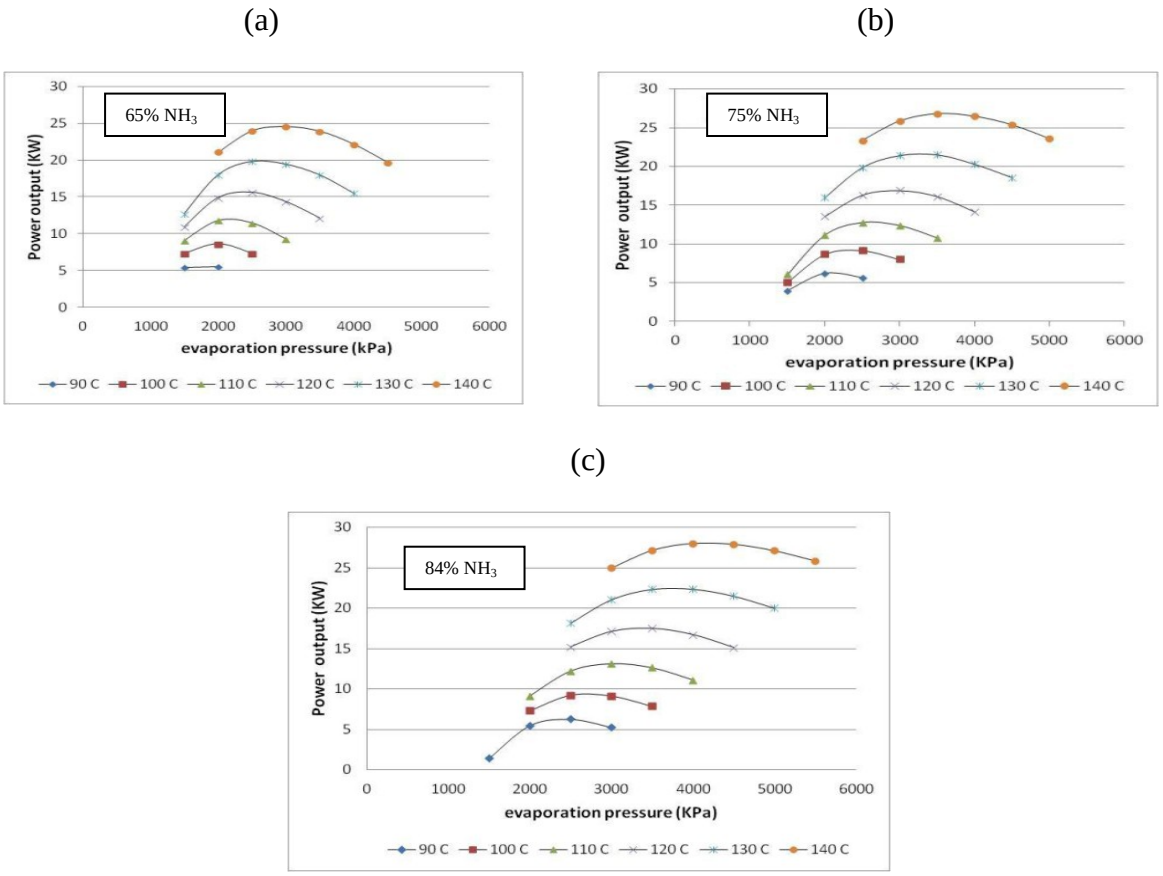

Figure 4. Cycle maximum power achieved for different temperatures of the geothermal source and evaporation pressures. (a) 65% of ammonia fraction (b) 75% of ammonia fraction (c) 84% of ammonia fraction.

(a) (b)

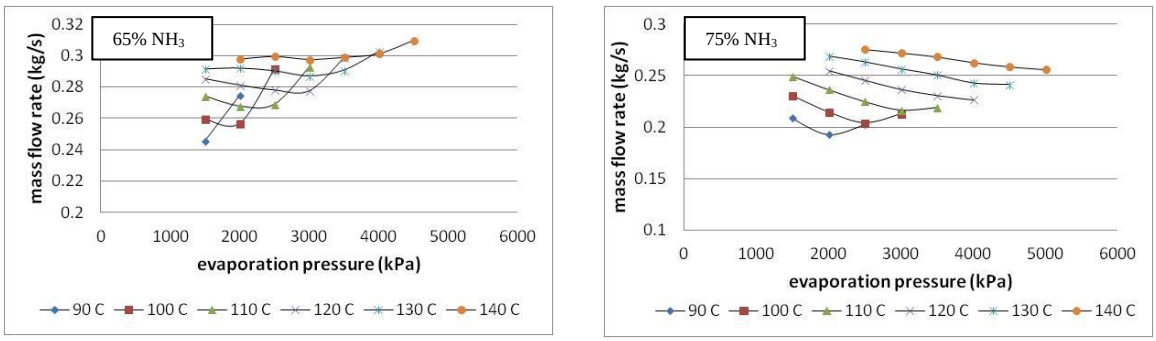

(c)

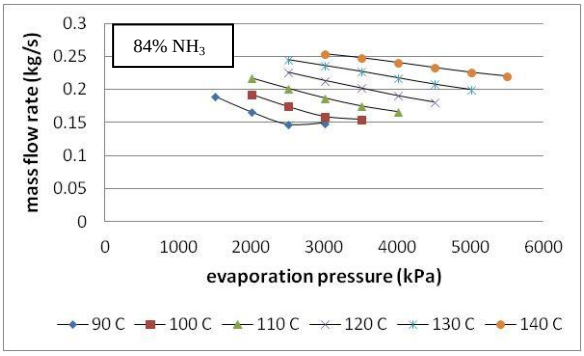

Figure 5. Mass flow rate for different temperatures of the geothermal source and evaporation pressures. (a) 65% of ammonia fraction (b) 75% of ammonia fraction (c) 84% of ammonia fraction.

(a) (b)

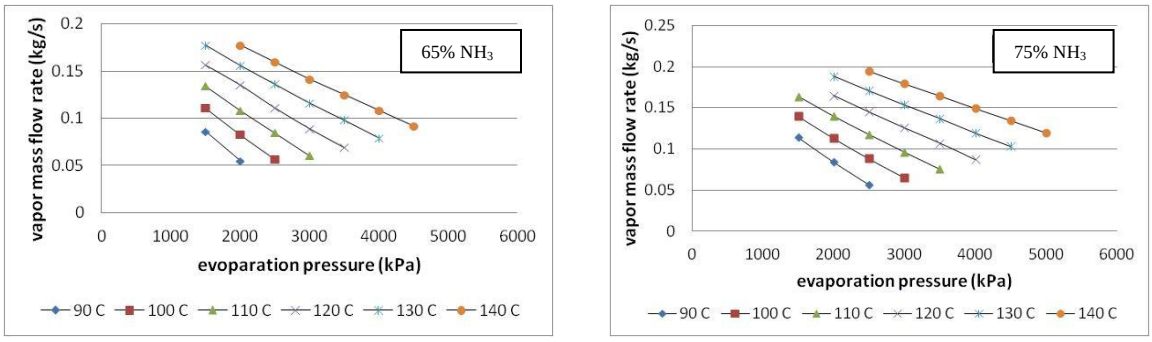

(c)

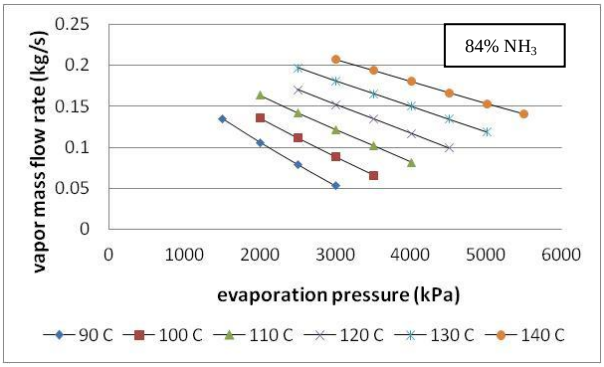

Figure 6. Vapor mass flow rate for different temperatures of the geothermal source and evaporation pressures. (a) 65% of ammonia fraction (b) 75% of ammonia fraction (c) 84% of ammonia fraction.

From figure 4, 5 and 6, it can be conclude that exist a value of pressure in which power output is greatest, pressure below this optimal value the cycle is able to evaporate more working fluid but the variation of the enthalpy in the turbine is lower, that result in lower power output of the cycle. By other hand, higher pressure than optimal produce higher variation of enthalpy in the turbine, but the cycle is able to evaporate less mass flow rate, that result in lower power output too. Then, is possible to determine, what is the evaporation pressure of the Kalina Cycle for a given mass flow rate and temperature of the geothermal source in which is obtained higher cycle performance.

The energy efficiencies of the Kalina cycle plants vary between 5.5 and 10.6% while the exergetic efficiency vary from 32.3 to 46.7%. The variations of thermal and exergetic efficiency are shown in Fig. 7. The maximum thermal efficiency is 10.6%, when geothermal fluid temperature is 140 °C and 84% of ammonia mass fraction in the composition of the working fluid mixture. Higher values of exergy efficiency were obtained under the same working conditions.
In practice, 90% ammonia fraction is the break point of this curve beyond which efficiency start to decrease sharply as the plant approaches a standard binary cycle [2].

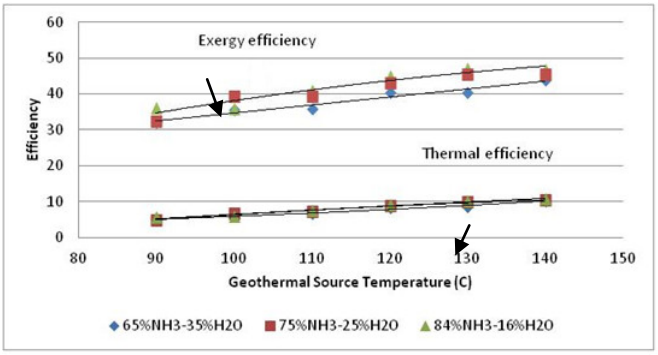

Figure 7. Influence of the temperature of the geothermal source and ammonia-water composition over the thermal and exergetic efficiency of the cycle.

In figure 8 is shown the exergy destruction of each component of the cycle for the different ammonia-water composition as a working fluid. The exergy destruction in the cycle behaves as fallow: the condenser is responsible for the biggest irreversibility, following by the evaporator, turbine HT and LT recuperator and finally the pump.

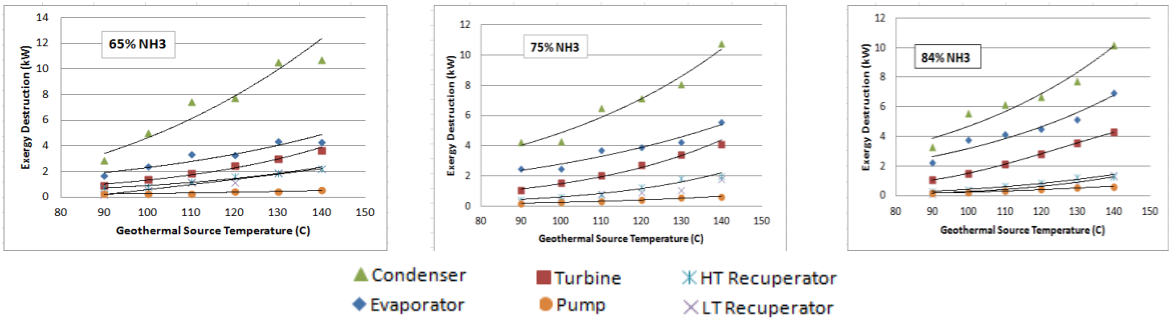

Figure 8. Exergy destruction by components of the Kalina Cycle.

Economic Evaluation

Table 1 is shown some operation parameters for a Kalina Cycle of the geothermal source found in Brazil [17], (100 °C and 100 kg/s of geothermal water), working at different composition of the working fluid.

An economic evaluation to find a lower cost per kW was carried out for the different percent of ammonia in mass in the composition of the working fluid, taking to account the costs of the components of the cycle.

Table 1. Operation parameters of the cycle at different ammonia-water compositions of the working fluid.

Operation parameters			
% of ammonia mass fraction	65	75	84
Power output (kW)	861.62	914.81	923.98
Evaporator heat consumption (kW)	13071.11	12447.78	14666.94
Circulation pump (kW)	79.86	83.48	64.8
Thermal efficiency (%)	5.98	6.68	5.86
Exergetic efficiency (%)	35.52	39.29	35.67
Evaporation pressure (kPa)	2000	2500	2500
Condensation pressure (kPa)	800	1000	1200
Mass flow rate (kg/s)	25.71	20.4	15.81
Vapor mass flow rate (kg/s)	8.27	8.8	8.91
Cooling water temperature (^{o}C)	25	25	25
Turbine efficiency (%)	85	85	85
Pump efficiency (%)	55	55	55

Size of the Components and Operations Cost Estimation

Can be consider that the total cost of the equipments of the cycle (evaporator, pump, generator and condenser) contributes largely to the total system cost in a low-temperature geothermal power plant and is assumed to be representative of the complete system cost.

Heat exchanger sizing

The size of the main components (heat exchangers, pumps and turbine) can be estimated for the four different options fixed for the Kalina cycle. Basically, the size of the heat exchanger can be calculated using the LMTD methods (log Mean Temperature Difference), [20]

The total heat transfer rate per unit of time (q), can be expressed in the following equations:

$$q = UA\Delta T_m = UA\left[\frac{(T_{h2} - T_{c2}) - (T_{h1} - T_{c1})}{ln\left[\frac{T_{h2} - T_{c2}}{T_{h1} - T_{c1}}\right]}\right] \quad (12)$$

The determination of the overall heat transfer coefficient (*U)* is often tedious and needs data not yet available at the preliminary stages of the design. As a first approximation, for preliminary

calculations, the values shown below were used. Since the heat exchangers can be built according to varies geometrical design, there are corrections factors that must be used with the equations (12) depending on the configuration [22].

Therefore, typical values of *U* are useful for quickly estimating the required exchange area [18, 21, 22]. Thus, *U* is given as a conventional value of 1 kW/m^2 K to estimate the sizes of the HT and LT recuperators. Values of 0.9 and 1.1 kW/m^2 K were used for size estimation of the vaporizer and the condenser. The value for the vaporizer is the lowest one, for a steam in the shell and liquid in the tubes of the heat exchanger, running under forced circulation. The value for the condenser is based on ammonia in the shell and cooling water in the tubes.

Estimated heat transfer areas of the heat exchangers in the Kalina cycle are listed in Table 2 for the different configurations.

Table 2: Estimated sizes of the heat exchangers for different ammonia fractions in Kalina Cycle.

	% of ammonia mass fraction		
Components	65	75	84
	Size (m^2)		
Vaporizer	490.4	478.55	455.14
Condenser	860.68	878.22	940.18
HT recuperator	104.63	76.72	50.45
LT recuperator	223.86	187.04	144.65
Total	**1679.57**	**1620.53**	**1590.37**

Costs estimation of the equipments

To determine the purchase costs of the equipments an approach estimation of the costs was used, based on costs values from past purchase orders, and quotations from experienced professional of cost estimations [18-19].

In the estimation of the purchase cost of the heat exchangers, the base cost C_o=588 US$ per square meter of heat transfer surface area was used. Thus:

$$C_{eq} = C_o(Eq_{size})^n \qquad (13)$$

Where the exponent *n* is a constant decimal number, in this case 0.8, and Eq_{size} stands for the heat transfer surface area of the heat exchanger, available in table 2 for the different configurations. Using these data the costs of the heat exchangers have been estimated by the relationship in Equation 13 and are presented in Table 3.

Table 3: Costs estimation of the heat exchangers for different ammonia fractions in Kalina Cycle

Components	% of ammonia mass fraction		
	65	75	84
	Cost, US$		
Vaporizer	83,525.23	81,906.65	78,685.25
Condenser	130,993.79	133,125.11	140,587.31
HT recuperator	24,271.82	18,936.7	13,541.48
LT recuperator	44,602.43	38,630.02	31,450.83
Total	**283,393.27**	**272,598.48**	**264,264.87**

The cost for the other main components (turbine and pump) has been estimated. Considering in these cases, the power capacity of each component:

$$C_{eq} = C_o(Power)^n \quad (14)$$

where the base cost, C_o, for the pump is 1120 US$/kW, and for the turbine 4405 US$/kW. The exponents 0.8 and 0.7 were used for size estimation of the pump and turbine. Estimated values of purchased equipment cost for the turbine and the pump are listed in Table 4.

Table 4: Capacities and costs of the turbine and pump for different ammonia fractions in Kalina Cycle

Components	% of ammonia mass fraction					
	65		75		84	
	Capacity (kW)	Cost, US$	Capacity (kW)	Cost, US$	Capacity (kW)	Cost, US$
Turbine	861.62	499,651.22	914.81	521,047.77	923.98	524,698.37
Pump	79.86	37,246.16	83.48	38,590.82	64.8	31,512.15

So, in figure 9, the increase of the total costs of the equipment was plotted with the power output of the turbine and the ammonia-water solution of the working fluid. Just taking to account the capital cost of equipment of the cycle, was obtain a rate of US$/kW of power output of the plant as shown in figure 10.

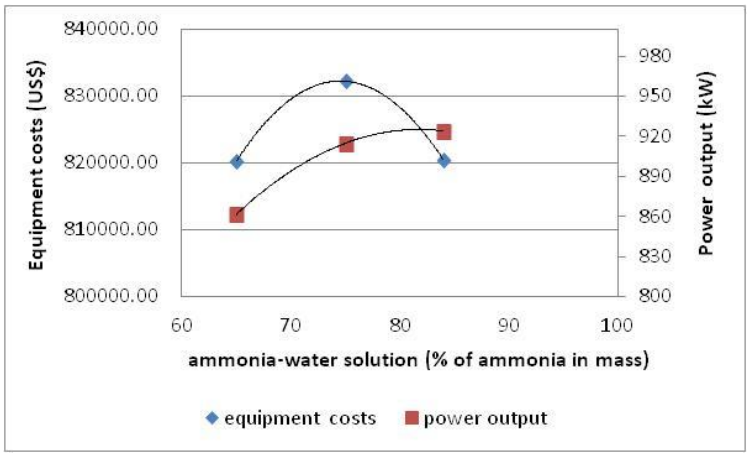

Figure 9. Increase of the total purchase costs of equipment with the power output for different ammonia-water solution of the working fluid.

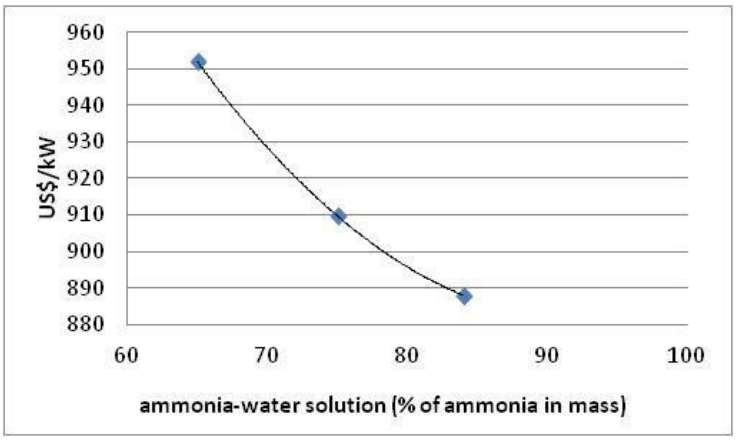

Figure 10. Variation of the costs of a kW with the total purchase cost of equipment for different ammonia-water solution of the working fluid.

Conclusions

The present study analyze the Kalina cycle from the point of view of the first and second law of thermodynamic and the costs of the kW produced, taking to account the equipment costs of the system. Considering the key parameters, which affect the cycle as a whole, and they were identified for this analyze as: the ammonia-water composition, the evaporation/condensation pressures and the temperature of the heat source, identifying the operation point where the plant provides higher power output with the best efficiency.

1. The maximum performance of the cycle, for the analyzed conditions, is reached with 84% of ammonia mass fraction.
2. When increasing the percent of ammonia mass fraction in the composition of the working fluid, the mass flow rate decrease and increases the percentage of mass that can be evaporated. It impact in lower size of heat exchangers and higher power output of the cycle for this composition of the mixture.
3. The lower value of 888 US$/kW of the investment was obtained at 84% of ammonia mass fraction and a power output of 923.98 kW.

Acknowledgments

The authors want to thanks the Coordination of Improvement of Higher Education (CAPES), The National Council of Technological and Scientific Development (CNPq) and The Foundation for Research Support of Minas Gerais State (FAPEMIG) for their collaboration and financial support in the development of the research work. Also want to thanks AES Tietê Company for funding the Project: "Technological Alternatives for the Implantation of Hybrid Geothermal Energy in Brazil from Low-Temperature Sources".

References

[1] I. Kalina, Combined cycle system with novel bottoming cycle. ASME Journal of Engineering for Gas Turbine and Power 106 (1984) 737 e 742A.

[2] H. Leibowitz, H. Micak, Design of 2 MW cycle binary module for installation in Husavik, Iceland, Geothermal Resourses Council Transaction 23 (1999) 17-20

[3] E. Olsson, U. Desideri, S. S. Stecco, G. Svedberg, An Integrated Gas Turbine Kaline Cycle for Cogeneration. ASME Paper 91-GT-202, 1991.

[4] E. Thorin, Power cycles with ammonia-water mixture as working fluid. Analysis of different applications and the Influence of thermophysical properties. Doctoral thesis. Department of Chemical Engineering and Technology. Energy Processes. Royal Institute of Technology. Stockholm. Sweden. (2000).

[5] D. A. Jones, A Study of the Kalina Cycle System 11 for the Recovery of Industrial Waste Heat with Heat Pump Augmentation. MSc Thesis. Faculty of Auburn University. Alabama, 2011.

[6] P. Bombarda, C. M. Invernizzi, C. Pietra, Heat recovery from Diesel engines: A thermodynamic comparison between Kalina and ORC cycles. Applied Thermal Engineering 30 (2010) 212-219.

[7] B. Ziegler, C. H. Trepp, Equation of State for Ammonia-Water mixtures. Refrig., 7 (1984) 101-106

[8] M. Barhoumi, A. Snoussi, E. N. Ben, K. Mejbri, A Bellagi, Modeling of the Thermodynamic properties of the Ammonia/Water mixture. Int. J. Refrig., 27 (2004) 271-283

[9] R. Senthil, P. M. V. Murugan, Subbarao, Thermodinamic Analysis of Rankine-Kalina Combined Cycle. Int. J. Thermodynamic. 11 (2008) 133-141

[10] N. S. Ganesh, T. Srinivas, Evaluation of thermodynamic properties of ammonia-water mixture up to 100 bar for power application systems. Journal of Mechanical Engineering Research Vol. 3. (1), pp. 25-39, January, 2011.

[11] U. Desideri, G. Bidini, Study of possible optimization criteria for geothermal power plants. Energy Conservation and Management 38 (1997) 1681-1691

[12] H. A. Mlcak, Kalina Cycle Concepts for low temperature geothermal. Geothermal Resourses Council Transactions 26 (2002) 707-713

[13] P. Valdimarsson, L. Eliasson, Factors Influencing the Economics of Kalina Power Cycle and Situations of Superior Performance. Proceedings of International Geothermal Conference, Reykjavik (2003) 31-39

[14] P. K. Nag, A. V. S. S. K. S. Gupta, Exergy Analysis of the Kalina cycle. Applied Thermal Engineering Vol. 18, No. 6, pp. 427-439, 1998.

[15] P. Roy, M. Désilets, N. Galanis, H. Nesreddine, E. Cayer, Thermodynamic analysis of a power cycle using a low-temperature source and a binary NH_3-H_2O mixture as working fluid. International Journal of Thermal Sciences 49 (2010) 48-58.

[16] O. Arslan, Exergoeconomic evaluation of electricity generation by the medium temperature geothermal resources using Kalina cycle: Simav case study. International Journal of Thermal Science 49 (2010) 1866-1873.

[17] V. M. Hamza, R. R. Cardoso, A. J. L. Gomes, C. H. Alexandrino, Brazil: Country Update. Proceedings World Geothermal Congress 2010.

[18] P. Dorj, Thermoeconomic Analysis of a New Geothermal Utilization CHP Plant in Tsetserleg, Mongolia. MSc thesis, Department of Mechanical and Industrial Engineering. University of Iceland. ISBN 9979-68-166-7, 2005.

[19] A. Bejan, G. Tsatsaronis, M. Moran, *Thermal design and optimization*. John Wiley & Sons, Inc. The United States of America, 533 pp. 1996

[20] J.P. Holman, Heat transfer. McGraw-Hill Companies, 665 pp. 2002

[21] R. DiPippo, Geothermal Power Plants: Principles, Applications and Case Studies, Elsevier, Oxford UK, 2005. p. 183. (Chapter 8).

[22] F. P. Incropera and D. P. DeWitt, Fundamentals of Heat and Mass Transfer, 4^{th} ed., John Wiley & Sons, New York, 1996

Exergy analysis and comparison of CO_2 heat pumps

A. Papadaki [a], A. Stegou-Sagia[b]

[a] National Technical University of Athens, Greece, e-mail: apapadaki@gmail.com
[b] National Technical University of Athens, Greece, e-mail: asagia@central.ntua.gr

Abstract:
Carbon dioxide (CO2, R744), being a natural refrigerant with extraordinary beneficial properties found everywhere in our ambiance, can provide answer to the environmental problems caused by the use of other refrigerants. The intention of this work is to outline the variation of exergy efficiency factor, COP and exergy flow related to the use of carbon dioxide in two stage and single stage CO2 cycle heat pumps. To conjure up the relevant mathematical models for the thermodynamic cycles were developed and an attempt was made for our efficiency and exergy losses results to be displayed. Moreover, fundamental process and system design issues of the applicable CO2 heat pumps cycles were inaugurated, along with their properties and characteristics comparing CO2 use to that of R22 and its substitutes R407C and R410A applied to relevant conditions. Since exergy analysis is of importance to provide theoretical basis for optimization of the systems operation and the minimization of losses, the results of this paper will advance the systems' design and performance. For some conditions R744 may seem to fall short in comparison to the rest refrigerants, nevertheless it signifies a more eco-friendly epoch for the field. The downside of the very high discharge pressure associated with transcritical cycles is counterbalanced by adopting staging in compression. There is a significant increase in COP for the two-stage R744 system compared to the single stage one, with the COP ranging between 3.40 and 2.70 depending on the temperature ratio, that is the gas cooler outlet temperature to the evaporator temperature.

Keywords:
Exergy, Carbon Dioxide, Heat pumps, Exergy Analysis, Single Stage Cycle, Two Stage Cycle.

1. Introduction

Carbon dioxide is one of the most feasible answers to the contribution of the fluorocarbon refrigerants to global warming and ozone depletion, being a natural refrigerant with zero ODP (Ozone depletion potential), negligible GWP (Global warming potential), and very low cost. Global warming effect is considered to be the most prominent problem of the world climate. Refrigerants that are utilized in the heat and cooling systems have quite higher GWP than CO_2. Even refrigerants that were considered ozone layer friendly, such as HFC-134a, have GWP of many times greater than CO_2's (in HFC-134a is 1300 times)[1, 2]. In addition carbon dioxide (CO_2) is not toxic, flammable or corrosive. It is inexpensive and readily available. After the Montreal Protocol the interest for CO_2 cycles was so great that a large number of research developments have been commenced for the production of carbon dioxide's refrigeration system components.

1.1 - CO_2 Properties

Carbon dioxide furthermore has two exceptional properties, its most remarkable one being its low critical temperature T_{crit}, of 31.1◦C, compared to conventional refrigerants and working close or even above the critical pressure P_{crit} of 73.8 bar in vapour compression systems functioning in normal ambient temperatures [3, 4].

In a subcritical heat pump cycle, such low critical temperature is considered an inconvenience as heat cannot be delivered at temperatures greater than the critical temperature limiting consequently

the operating temperature range. Additionally, heating capacity and the performance of the system are relegated at temperatures inferior but close to T_{crit}, since the enthalpy of vaporization then is reduced [5], making the operation of a conventional heat pump avoidable at a heat rejection temperature near T_{crit}. Carbon dioxide's low critical temperature provides the opportunity to operate in a transcritical manner. In a transcritical heat pump, heat rejection (gas cooler) is operated above the critical pressure, heat delivery temperatures are no longer limited by T_{crit} and the evaporator is operated below that and for this reason the cycle is identified as transcritical.

The other unique property of CO_2 is the high working pressure required to use under typical heat pump conditions. Heat pump systems, both sub and transcritical, using CO_2, work at greater pressures than with the majority of other refrigerants. The operational pressures of subcritical CO_2 heat pumps reach as high as 60–70 bar, whereas for the transcritical pressures vary from 80 to 110 bar or even more. Although high pressure defies compressors' capability and components' robustness, it presents some benefits as well, providing to CO_2 a relatively high vapor density and an equally high volumetric heating capacity. This attribution offers the option for CO_2 to have a smaller working volume cycled in order to attain the same heating demand which permit the use of smaller components and more compact systems [3].

Nevertheless, the most important disadvantage of CO_2 cycle is that owing to huge expansion loss compared to conventional refrigerants' cycle it presents lower COP making the modifications of the cycle crucial [6]. Lorentzen [4] described more than a few customized cycles comprising of two-stage internal 'subcooling' and expansion options. By modifying the basic single-stage transcritical cycle a lot can be achieved. Some adaptations that are promising are dividing of flows, expansion via work generation instead of throttling, staging compression and expansion and the use of internal heat exchange. Trying to obtain higher efficiency values, we will employ the modification of the two-stage compression of the CO_2 with intercooling. Then we will compare these results to the equivalents of the single stage CO_2 and conventional vapour compression cycles. In order to model the total systems, and thereby investigate the possible operating conditions with replacement refrigerant mixtures, a computer code was created.

1.2 - First and Second Law analysis

Studying the inefficiencies of existing systems our work focuses on the understanding of heat pumps cycles, their efficiencies and potentials for improvement, based on First and Second Laws of Thermodynamics. COP is used to evaluate performance of air-conditioning or heat pump from the viewpoint of the First Law of Thermodynamics. Exergy, being presented in an amount of works [7-13] corresponds quantitatively to the useful part of energy, the maximum possible amount of work a system, a flow of matter or energy can produce as it comes to equilibrium with an appointed reference environment. Exergy analysis combines the conservation of mass and energy principles with the second law of thermodynamics for the design of more efficient and environmental friendly systems. While efficiencies using energy are ambiguous for not being measures of "an approach to an ideal", exergy efficiencies are considered as such, measuring, in a way, the potential of the system for improvement [11].

2. Modelling of Operation

2.1- Conventional Heat pump's model

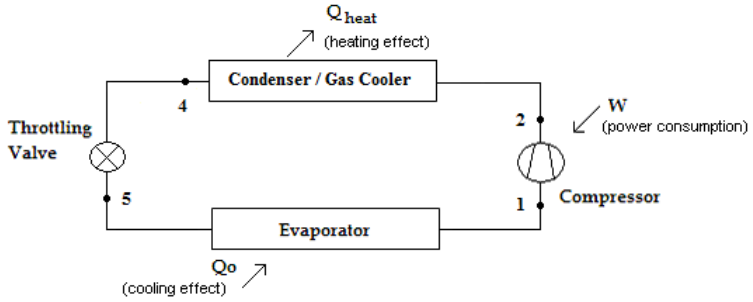

Fig. 1. Schematic diagram of the single stage heat pump cycle.

Figure 1 shows the heat pump's vapour / transcritical CO_2 compression cycle flow chart. The working fluid moves from the evaporator, which is connected to the low-temperature heat source into the compressor as a superheated vapour. Following, the compressed vapour, flows into the condenser which is connected to the high-temperature heat sink and respectively to the gas cooler for the CO_2. Here it condenses and afterwards, as a liquid, it undergoes expansion in the throttling valve. The throttled two-phase mixture, which is liquid for the most part, moves into the evaporator from which ensues the vapour that is then superheated and directed to the compressor to complete the flow cycle.

2.2 - Transcritical two-stage CO_2 cycle with intercooling.

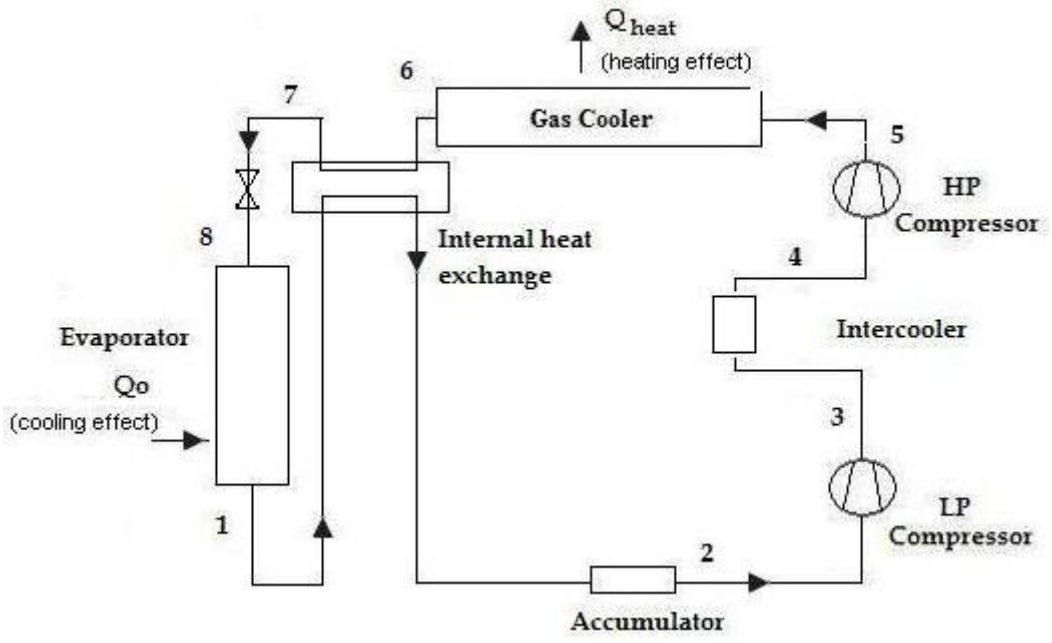

Fig.2 Schematic diagram of the two stage heat pump cycle with intercooling.

Figure 2 shows the two stage CO_2 transcritical heat pump cycle with intercooling used. Here the saturated working fluid of state 2 moves from the evaporator into the low pressure (LP) compressor where it's compressed to state 3 before it enters the intercooler. There takes place the cooling, by external fluid, of the vapour which increases the mass of CO_2 vapour entering the high pressure

(HP) compressor. Ambient air is taken as the external fluid. The saturated vapour from the intercooler at state 4 is compressed to state 5 and afterwards the super-critical vapour is cooled in the gas cooler to state 6. CO_2 vapour is further cooled in the internal heat exchanger to state 7. CO_2 then expands in the expansion device to state 8 and evaporates to state 1 producing cooling effect. The internal exchanger in the system exists for system thermal efficiency improvement [14].

2.3 - Thermodynamic analysis

2.3.1 - Single stage cycle

Based on the known equations for the exergy and energy analysis [16-18] of a heat pump cycle, as the one shown in Figure 1, we have:

The exergy efficiency factor is

$$\zeta = COP.\left(\frac{T_w - T_a}{T_w}\right). \quad (1)$$

with the coefficient of performance (COP) of the system being

$$COP = \frac{q}{\Delta e_{abs} + \sum \Delta e_{loss}} = \frac{(h_2 - h_4)}{(h_2 - h_4)\left(1 - \frac{T_a}{T_w}\right) + \sum \Delta e_{loss}} \quad (2)$$

Exergy losses, for each component of the system are:

o Compression losses:

$$\Delta e_{comp} = T_a (s_2 - s_1) \quad (3).$$

Additional losses due to the compressor motor:

$$\Delta e_{mot} = w \frac{1 - \eta_{mot}}{\eta_{mot}} \frac{T_a}{T_w}, \quad (4)$$

where η_{mot} is the compressor motor efficiency factor, w the specific compression power demand (h_2-h_1) and the heat from the heat pump motor absorbed by the heated substance [17].

♣ Condensation / gas cooler losses:

$$\Delta e_{cond} = (h_2 - h_4)\frac{T_a}{T_w} - T_a (s_2 - s_4). \quad (5)$$

♣ Evaporation losses:

$$\Delta e_{evap} = T_a (s_1 - s_5) - (h_1 - h_5). \quad (6)$$

♣ Throttling (isenthalpic process) losses:

$$\Delta e_{thr} = T_a (s_5 - s_4). \quad (7)$$

Therefore, summing up we obtain the total exergy loss:

$$\sum \Delta e_{\text{loss}} = \Delta e_{\text{comp}} + \Delta e_{\text{mot}} + \Delta e_{\text{cond}} + \Delta e_{\text{evap}} + \Delta e_{\text{thr}} = (h_5 - h_1) + \left[(h_2 - h_4) + (h_2 - h_1) \frac{1-\eta_{\text{mot}}}{\eta_{\text{mot}}} \right] \frac{T_a}{T_w} \qquad (8)$$

The exergy efficiency factor is consequently given by the equation (1):

$$\zeta = \frac{(h_2 - h_4)(1 - \frac{T_a}{T_w})}{(h_2 - h_1)\left(1 + \frac{1-\eta_{\text{mot}}}{\eta_{\text{mot}}} \frac{T_a}{T_w}\right)}. \qquad (9)$$

The refrigerants compared to R74 are R407C and R410A and R22.

A variety of sources were used [19-25] to ensure the consistent application of property. The differences observed were minimal. It is taken into consideration in all relevant calculations the fact that R407C and R410A are non-azeotropic, since they show a different behaviour from pure substances as it is presented by Smith and Van Ness [26].

Firstly, due to different evaporator and condenser inlet/outlet temperatures, we have to select condenser inlet temperature in opposition to the warm space temperature taking care of the condenser inlet and outlet temperatures to be sufficient so as to reject heat and finally liquid enthalpy at the expansion device and related property data being in position to achieve the suitable evaporator inlet temperature. The fluid behaves normally in all other points. Undeterred by the fact that this method of evaluation occupied in this study is not fully representative of a dynamic operation of a heat pump system, yet it sets up the foundations for understanding its thermodynamic performance.

3.2.2 - Two stage cycle

The two-stage CO2 transcritical heat pump cycle with intercooling is modelled modularly incorporating each individual process of the cycle. The state points in Figure 2 are defined as the conditions of the refrigerant characterized by its temperature, mass flow rate and quality.

Exergy losses, for each component of the system are:

♣ Compression losses:

$$\Delta e_{\text{comp}} = \Delta e_{\text{comp1}} + \Delta e_{\text{comp2}} = T_a (s_3 + s_5 - s_2 - s_4) \qquad (10).$$

Additional losses due to the compressors motors:

$$\Delta e_{\text{mot}} = w \frac{1-\eta_{\text{mot}}}{\eta_{\text{mot}}} \frac{T_a}{T_w}, \qquad (11)$$

where η_{mot} is the compressors motor efficiency factor, *w* the specific compression power demand (h_5- h_4+h_3-h_2) and the heat from the heat pump motor absorbed by the heated substance.

♣ Intercooler losses

$$\Delta e_{\text{ic}} = (h_3 - h_4) \frac{T_a}{T_w} - T_a (s_3 - s_4). \qquad (12)$$

♣ Gas cooler losses:

$$\Delta e_{\text{gc}} = (h_5 - h_6) \frac{T_a}{T_w} - T_a (s_5 - s_6). \qquad (13)$$

♣ Evaporation losses:

$$\Delta e_{\text{evap}} = T_{\text{a}}(s_1 - s_8) - (h_1 - h_8). \qquad (14)$$

♣ Expander valve (isenthalpic process) losses:

$$\Delta e_{\text{ex}} = T_{\text{a}}(s_8 - s_7). \qquad (15)$$

♣ Internal heat exchanger:

$$\Delta e_{\text{ihe}} = T_{\text{a}}[(s_7 - s_6) - (s_1 - s_2)]. \qquad (16)$$

Therefore, summing up we obtain the total exergy loss:

$$\sum \Delta e_{\text{loss}} = \Delta e_{\text{comp}} + \Delta e_{\text{mot}} + \Delta e_{\text{gc}} + \Delta e_{\text{evap}} + \Delta e_{\text{ihe}} = (h_8 - h_1) + \left[(h_3 - h_4 + h_5 - h_6) + (h_5 - h_4 + h_3 - h_2) \frac{1 - \eta_{\text{mot}}}{\eta_{\text{mot}}} \right] \frac{T_{\text{a}}}{T_{\text{w}}} \qquad (17)$$

The exergy efficiency factor is consequently given by the equation (1):

$$\zeta = \frac{(h_3 - h_4 + h_5 - h_6)(1 - \frac{T_{\text{a}}}{T_{\text{w}}})}{(h_5 - h_4 + h_3 - h_2)\left(1 + \frac{1 - \eta_{\text{mot}}}{\eta_{\text{mot}}} \frac{T_{\text{a}}}{T_{\text{w}}}\right)}. \qquad (18)$$

2.4 - Assumptions

It is renowned that CO2 refrigeration and air conditioning systems shows cooling COP more sensitive to ambient temperature variation than conventional systems, being therefore superior at sensible and low ambient temperature, and to some extent poorer at very high temperature. Consequently, it would be deceptive to base a comparison of CO2 with the other refrigerants on design point conditions, which typically are at an extreme ambient temperature while the use of average seasonal conditions is wiser [27].

Our exergy efficiency, COP and exergy losses diagrams of the mixtures under consideration are schematized in comparison with the CO2 and are plotted based on calculations, having taken into consideration the following assumptions:

The environmental temperature (Ta) is equal to 273 K [17, 28], while the temperature of the warm place (Tw) is considered 308 K [29]. The temperatures Tcon and Te are taken: Tcon at the inlet of the condenser at the vapour saturation curve for R22, R407C and R410A and at the inlet of the gas cooler for R744, while Te at the exit of the evaporator in the superheat region. Pressure drops in evaporator are for R22 [30] and R407C [31, 32] 135 kPa, for R410A [33] 85 kPa and for R744 [34] 100kPa, while during condensation the pressure drop varies for R22 [30] from 46 to 52 kPa, for R407C [31,32] from 40 to 46 kPa and for R410A [32, 33] from 32 to 35 kPa, lessening with increasing condensation temperature; whereas correspondingly for R744 [29, 35] the already small (1 to 3 kPa as shown in [36]) pressure drop during cooling process of supercritical CO2 decreases as inlet pressure of gas cooler increases having a temperature glide of approximately 61K [29]. In addition the isentropic compressor efficiency factor is chosen as 0,75 and the compressor motor efficiency factor as 0,85 in a endeavor to maintain a logical price for the evaluation.

The evaporator temperature (Te) is taken as 263K for all condensing temperatures whilst condensation temperature (Tcon) for the mixtures and the outlet temperature of the CO2 gas cooler is ranging from 313 to 328 K. Accordingly the temperature ratio τ = (Tcon/Te) or τ = (Tgc/Te) varies within the range of 1.19 to 1.25.

The featured two-stage CO2 transcritical cycle configuration is solely a theoretical one to present the basis for performance comparison with other refrigerants. It is simulated and its performance is evaluated on the basis of maximum combined COP to obtain the optimum gas cooler and in-between pressures. These values are obtained for various operating conditions along with simultaneous variation of the compressors discharge pressure and intermediate pressure having a step size of 0.5 bar for each. The performance is evaluated on various evaporator temperatures Te from 223 K to 243 K) and gas cooler outlet temperatures Tgc (308 K to 333 K) [37].

3. Results and discussion

The results attained in this analysis are comparison of refrigerants for exergy efficiency, COP and exergy losses (Figures 3 to 5). Properties of R22 are illustrated in plots by bold continuous lines, while R407C by thin discontinuous lines, R410A by thin continuous lines, R744 (single stage) by dotted lines and R744 (two stage) bold dotted lines.

Figure 3 shows the exergy efficiency factor as a function of temperature ratio τ. Exergy efficiency decreases when the temperature ratio τ increases. The curves' hollows are facing upwards.

The single stage heat pump working with R744 has the least favourable exergy behaviour with an exergy efficiency of 13% at the temperature ratio of τ = 1.25 and 28% at the temperature ratio of τ = 1.19. While the R744 of the two-stage transcritical heat pump features far better exergy performance compared to the latter, with an exergy efficiency of 31% at a temperature ratio of τ = 1.25 and 38% at a temperature ratio of τ = 1.19, demonstrating less variation on its performance with the change of temperature ratio.

R22, on the other hand, presents the best exergy behaviour of all with an exergy efficiency of 42% at a temperature ratio of τ=1.19 and 33% at τ=1.25, followed by R407C (ζ = 41% at τ=1.19 and ζ = 32% at τ=1.25) and R410A (ζ= 40% at τ=1.19 and ζ = 29.5% at τ=1.25).

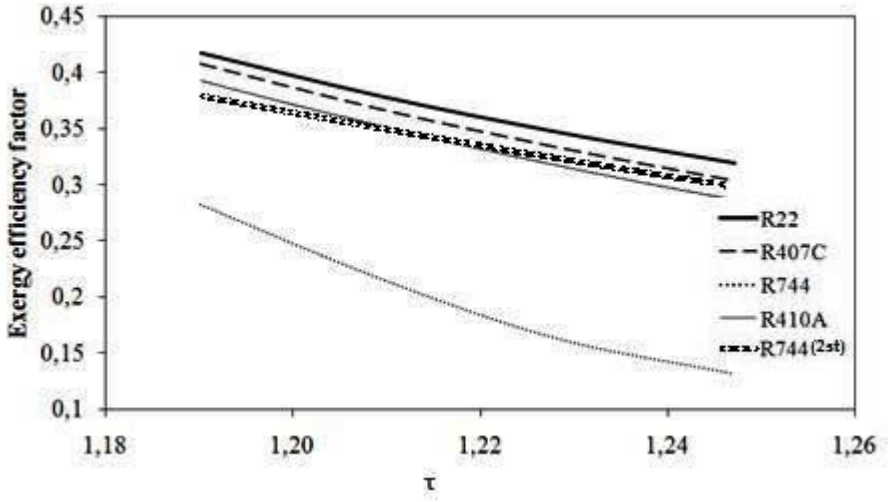

Fig.3 Variation of exergy efficiency factor for various temperature ratios

Figure 4 shows the disparity of COP of the heat pump system for each working refrigerant related to the temperature ratio τ, decreasing while the latter lifting as exergy efficiency factor does. COP ranges from 1.05 at temperature ratio of τ=1.19 (for R744) to 3.77 (for R22) at τ=1.19. There is a pointed increase in COP for the two-stage R744 system compared to the single stage one. Here, the single stage working R744 has likewise the worst behaviour, with COP to vary between 2.48 (at τ=1.19) and 1.15 (at τ=1.25), whilst the R744 of the two-stage transcritical heat pump features once more better comportment, with COP fluctuating amid 3.40 (at τ=1.19) and 2.70 (at τ=1.25).

The optimum performance is displayed yet again by R22, with COP of 3.67 at a temperature ratio of τ=1.19 and 2.88 at τ=1.25, followed by R407C with COP of 3.70 at a temperature ratio of τ=1.19

and 2.74 at τ=1.25 and R410A with COP of 3.57 at a temperature ratio of τ=1.19 and 2.58 at τ=1.25. R22 may seem more attractive to use from the efficiency aspect, however we have to bear in mind that it constitutes a harmful effect on the ozone layer with the result of extreme UV levels conducing to further environmental damage and several deadlines have been arranged depending on the country for complete R22 replacement in accordance to the terms established by the Montreal Protocol meetings.

The prices for COP and exergy efficiency factor are in agreement with those of Robinson and Groll E.M. [39] at the equivalent conditions' region.

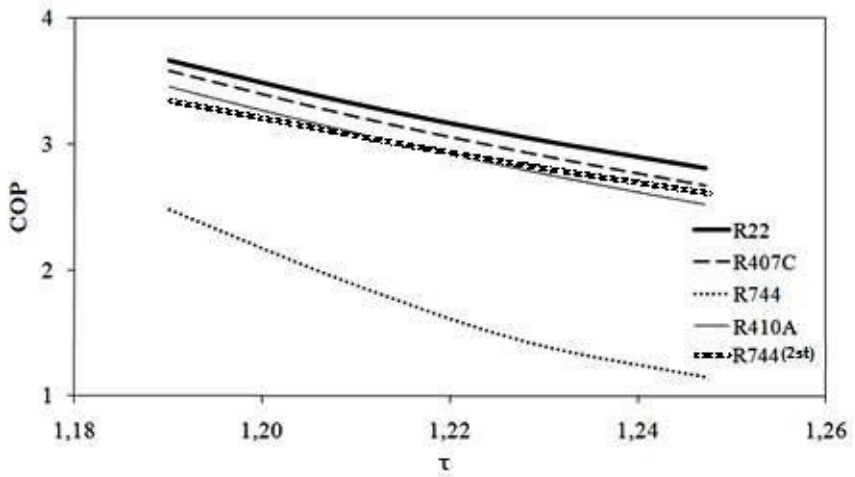

Fig.4 Variation of COP for various temperature ratios

Figure 5 presents the percentage of the major exergy losses for the two CO_2 systems. These are of the gas cooler and of the compressor and we can conclude that for the two stage CO_2 transcritical cycle the losses lessen dramatically. For the single stage heat pump working with R744 the compressor accounts for approximately 49% of the total cycle irreversibility and the gas cooler for the 25%, while respectively the percentage of exergy losses in the two-stage transcritical heat pump is 32% for the compressor and 20% for the gas cooler.

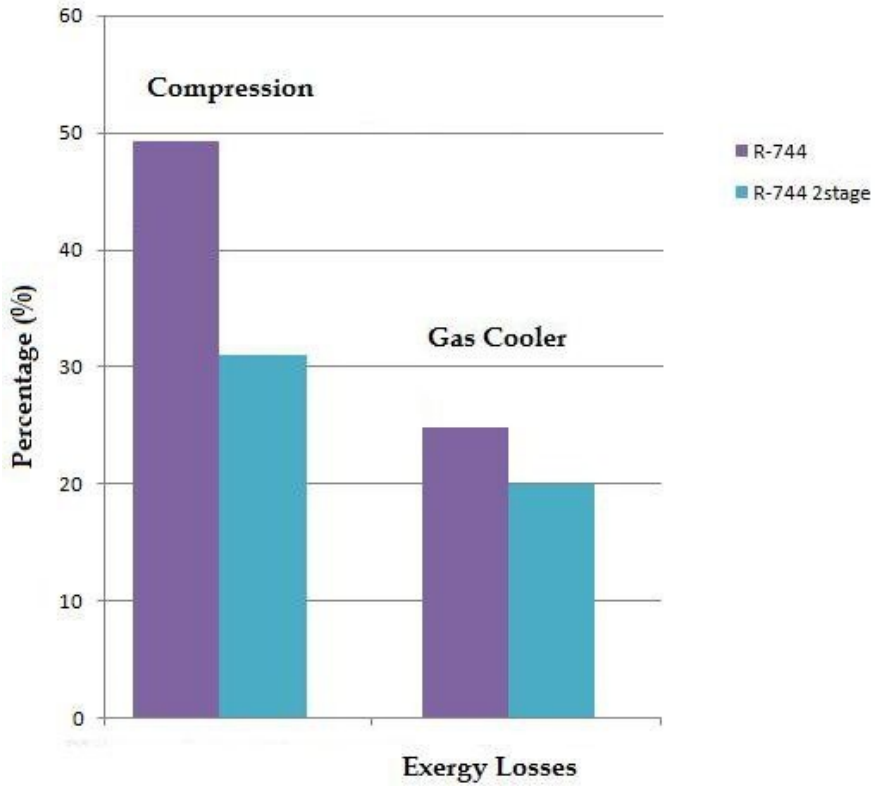

Fig.5 Exergy losses of the systems' components

As pointed out by Dincer and Rosen [15] "Exergy efficiency weights energy flows by accounting for each in terms of availability. It stresses that both losses and internal irreversibilities need to be dealt with to improve performance" and by Moran and Shapiro [38] "Exergy analysis is particularly suited for furthering the goal of more efficient energy use, since it enables the locations, types, and true magnitudes of waste and lost to be determined". Following the above described study the behaviour of the system can be improved, minimising individual exergy loss of each component and maximising efficiencies. Compressor efficiency is a major factor in enhancing the performance of the system, the smaller the compressor, the more prominent the compression losses. Generally speaking throttling losses can be reduced minimising the temperature difference before and after the throttling valve, as well as by decreasing the temperature differences in evaporator and condenser. This would also produce lower compression losses.

4. Conclusions

In this report we have made an effort to elucidate the diversity of the alternatively used refrigerant mixtures R407C and R410A replacing R22, and R744 replacing all of them in the field of exergy efficiency, COP and exergy losses depending on temperature ratio τ, for constant warm place temperature. The best exergy behaviour of all is presented by R22, with an exergy efficiency of 42% at a temperature ratio of τ=1.19. R744 may seem to fall short in comparison to the rest refrigerants for some conditions, nevertheless it is the most environment friendly of all and based on that and on its beneficial potentialities its use signifies a "new" ecological era for the field. As stated before, one of the downsides associated with transcritical cycles is that the system operates at a very high discharge pressure. There is a sharp reduction in optimum discharge pressure by adopting staging in compression. Inter-stage pressure is one of the most critical parameters for optimizing COP values. Moreover, by using highly efficient system components, the transcritical two-stage CO2 systems can be used more effectively. Two-stage transcritical heat pump working with R744 features far better exergy performance compared to the single stage cycle with a pointed increase in

COP for the two-stage R744 system. Furthermore for the two stage R744 transcritical cycle the losses lessen dramatically.

The evolution of exergy efficiency factor and COP are illustrated and collated in diagrams so as to clarify the differences of alternative refrigerants more accurately.

Nomenclature

C_p	Specific heat at constant pressure	($kJ.kg^{-1}.K^{-1}$)
e	Specific exergy	($kJ.kg^{-1}$)
h	Enthalpy	($kJ.kg^{-1}$)
P	Pressure	(kPa)
q	Specific heating capacity	($kJ.kg^{-1}$)
R	Gas constant	($kJ.kg^{-1}.K^{-1}$)
s	Specific entropy	($kJ.kg^{-1}.K^{-1}$)
T	Temperature	(K, ^oC)
w	Specific compression power demand	($kJ.kg^{-1}$)

Greek symbols

Δ	Differentiation	
ζ	Exergy efficiency factor	(%)
η_{mot}	Compressor motor efficiency factor	(%)
τ	T_{con}/T_e, Temperature ratio	*(-)*

Superscripts

a	Ambient conditions
abs	Absorbed
c	Critical point
co	Cold space
con	Condenser
e	Evaporator
ex	Expander
gc	Gas cooler
ihe	Internal Heat Exchange
loss	Losses
w	Warm space

References

[1] Bellstedt, M., Elefsen, F., Jensen, S.S; Application of CO2 (R744) refrigerant in industrial cold storage plant. EcoLibrium 2002; 1(5):25-30.

[2] Laipradit P, Tiansuwan J, Kiatsiriroat T, Aye L. Theoretical performance analysis of heat pump water heaters using carbon dioxide as refrigerant. International Journal of Energy Research 2008; 32(4): 356–366.

[3] Cavallini A., Cecchinato L., Corradi M., Fornasieri E., Zilio C., Two-stage transcritical carbon dioxide cycle optimisation: A theoretical and experimental analysis. International Journal of Refrigeration 2005; 28: 1274–1283.

[4] Lorentzen G., Revival of carbon dioxide as a refrigerant. Int J Refrigeration 1994; 17(5): 292–301.

[5] Kim, M.H., Pettersen, J. and Bullard C.W. , Fundamental process and system design issues in CO2 vapor compression systems. Progress Energy Combustion Science 2004; 30(2): 119-174.

[6] Sarkar, J., Bhattacharyya, S. and Ramgopal, M., Transcritical CO2 heat pump systems: Exergy analysis including heat transfer and fluid flow effects. Energy Conversion Management 2005; 46(13-14): 2053-2067.

[7] Bejan A., Fundamentals of exergy analysis, entropy generation minimization, and the generation of flow architecture. Int. Journal of Energy Research 2002; 26: 545-565.

[8] Dincer I., The role of exergy in energy policy making, Energy Policy 2002; 30: 137-149.

[9] Kotas T.J., The Exergy Method of Thermal Plant Analysis. Reprint edition, Malabar, FL: Krieger; 1995.

[10] Moran M.J., Sciubba E, Exergy analysis: principles and practice. Journal of Engineering for Gas Turbines and Power 1994; 116: 285–290.

[11] Rosen M.A., Clarifying thermodynamic efficiencies and losses via exergy. Exergy, an International Journal 2002; 2: 3-5.

[12] Szargut J., Component efficiencies of a vapour-compression heat pump. Exergy, an International Journal 2002; 2: 99-104.

[13] Frangopoulos C. A., Exergy, Energy System Analysis, and Optimization: v. 1. EOLSS Publishers Co Ltd, Ramsey/Is; 2009.

[14] Chen Y, Gu J. The optimum high pressure for CO2 transcritical refrigeration systems with internal heat exchangers. International Journal of Refrigeration 2005; 28: 1238–1249.

[15] Dincer I., Rosen M.A., Thermodynamic aspects of renewable and sustainable development. Renewable and Sustainable Energy Reviews 2005; 9: 169-189.

[16] Baehr H.D., Thermodynamik. Siebente Auflage, Berlin/Heidelberg: Springer-Verlag; 1989.

[17] IIR., Compression Cycles For Environmentally Acceptable Refrigeration, Air Conditioning and Heat Pump Systems; 1992.

[18] Stegou-Sagia A., Papadaki A, Exergy modelling of vapour compression heat pumps using refrigerant mixtures. International Journal of Exergy 2006; 3(3): 304-321.

[19] ASHRAE, Fundamentals handbook, New York: American Society of Heating Refrigerating and Air-conditioning Engineers; 2001.

[20] Lemmon, E.W., McLinden, M.O., Huber M.L. NIST Reference Fluids Thermodynamic Properties - REFPROP, Ver. 7.0, NIST Standard Reference Database 23, Gaithersburg, ML, U.S.A.: NIST; 2002

[21] Span R., Wagner W. A new aquetion of state for carbon dioxide covering the fluid region from the triple point temperature to 1100 K at pressures up to 800 MPa. Journal of Physical and Chemical Reference Data 1996; 25(6): 1509-1596.

[22] Stegou-Sagia A. Thermodynamic property formulations and heat transfer aspects for replacement refrigerants R123 and R134a. Int. Journal of Energy Research 1997; 21: 871-884.

[23] Desideri, U. , Sorbi, N., Arcioni, L., Leonardi, D. Feasibility study and numerical simulation of a ground source heat pump plant, applied to a residential building. Applied Thermal Engineering 2011; 31(16) : 3500-3511.

[24] Stegou-Sagia A., Damanakis M. Thermophysical property formulations for R32/R134a mixtures. Int. Journal of Applied Thermodynamics 1999; 2(3): 139-143.

[25] Stegou-Sagia A., Damanakis M. Binary and ternary blends of R134a as alternative refrigerants to R-22. Int. Journal of Energy Conversion and Management 2000; 41: 1345-1359

[26] Smith J.M., Van Ness H.C. Introduction to chemical engineering thermodynamics, third edition, Chemical Engineering Series, New York: McGraw-Hill.; 1975.

[27] Neksa P., CO_2 as a refrigerant for systems in transcritical operation: principles and technology. EcoLibrium 2004; 3(9): 26-31.

[28] Lorentzen G., Heat pumps - where are improvements possible? An exercise in exergy. Rev. Int. Froid 1986; 9: 105-107.

[29] Brown J.S., Kim Y., Domanski P.A., Evaluation of carbon dioxide as R-22 substitute for residential air-conditioning. ASHRAE Trans 2002; 108(2): 3–13; HI-02-13-3.

[30] Judge J., Hwang Y., Radermacher, R. A Transient and Steady State Study of Pure and Mixed Refrigerants in a Residential Heat Pump, Prepared for the U.S. Environmental Protection Agency Office of Research and Development, Washington, D.C., EPA; 2001.

[31] Choi J.Y., Kedzierski M.A., Domanski P.A. A Generalized Pressure Drop Correlation for Evaporation and Condensation of Alternative Refrigerants in Smooth and Micro-fin Tubes. NISTIR 6333; 1999.

[32] Spatz M.W., Yana Motta S.F.An evaluation of options for replacing HCFC-22 in medium temperature refrigeration systems. International Journal of Refrigeration 2004; 27: 475-483.

[33] Hsieh Y.Y., Lin T.F. Evaporation heat transfer and pressure drop of refrigerant R-410A flow in a vertical plate heat exchanger, ASME Trans. Journal of Heat Transfer 2003; 125(October): 852-857.

[34] Yin J.M., Bullard C.W., Hrnjak P.S. R744 gas cooler model development and validation. International Journal of Refrigeration 2001; 24: 692-701.

[35] Petrov N.E., Popov V.N. Heat transfer and resistance of carbon being cooled in the supercritical region, Therm Eng 1985; **32**(3):131–134.

[36] Yoon S. H., Kim J. H., Hwang Y.W., Kim M. S., Min K., Kim Y. Heat transfer and pressure drop characteristics during the in-tube cooling process of carbon dioxide in the supercritical region. International Journal of Refrigeration 2003; 26: 857–864.

[37] W.F. Stoecker, Industrial Refrigeration Handbook, McGraw-Hill International Edition; 1998.

[38] Moran M.J., Shapiro, H.N. Fundamentals of Engineering Thermodynamics, 4th edition, New York: Wiley; 2000.

[39] Robinson D.M., Groll E.M. Efficiencies of transcritical CO_2 cycles with and without an expansion turbine, International Journal of Refrigeration 1998; 21(7): 577-589.

Exergy Analysis of a CO2 Recovery Plant for a Brewery

D. R. Nielsen[a], B. Elmegaard[b], C. Bang-Møller[3]
[a] *Technical University of Denmark, Kgs. Lyngby, Denmark, drni@alectia.com*
[b] *Technical University of Denmark, Kgs. Lyngby, Denmark, be@mek.dtu.dk*
[c]*Technical University of Denmark, Kgs. Lyngby, Denmark, cbm@mek.dtu.dk*

Abstract:
A large number of new and old breweries around the world experience increasing energy cost associated with the production of beer. Large heating and cooling demands in the brewing process and a wide use of utilities for assisting the processes necessitate a detailed analysis of individual efficiencies for processes and the different utility plants.
One considerable utility plant is the CO2 recovery plant, which purifies/purges the CO2 generated in the fermentation process in order to reuse it in the brewery site or sell it to customers who demand high quality CO2.
In the paper a detailed model of a 2000kg/h CO2 recovery plant for a brewery is presented, which is a typical plant capacity for a large CO2 self-sufficient brewery. The model includes all significant unit operation in the CO2 plant and a complete mass and energy balance of it.
In order to prevent hidden loads and misleading analysis; the system is modeled as a final supplier solution, which is initially considered without heat and recovery integration even though this is commonly used.
The following steps are presented. First step introduces the process and the component appearance followed by the energy requirements and corresponding loads. Consumptions and loads are compared with an existing plant at a corresponding capacity and are validated.
Energy and exergy analysis are used in order to illustrate the performance of each individual system component of the CO2 recovery plant.
A schematic overview of all exergy flows including destruction is presented and proves a clear understanding of the exergy inefficiencies associated with the plant.
The highly detailed and validated model enables and prepares different holistic methodologies and analyses to be used, including thermoeconomic diagnosis and optimization of plant set points.

Keywords:
Exergy analysis, Grassmann diagram, CO2 recovery plant, utility plant.

1. Introduction

Many breweries all over the world contain a CO2 recovery system in order to collect the generated CO2 from the fermentation process and exploit it for the process use. Energy requirements have been investigated in several breweries in order to determine overall electric and thermal demands, e.g. using pinch analysis in order to design the optimal heat exchanger network [1]. Even manual power, such as physical human work has been converted into exergy and included in the analyses [2]. Further evaluations have presented data for exergetic inefficiencies in the various parts of the production lines and comparison with other production sites [1].

1.1 Process description

This study examines a CO_2 recovery plant in the application of a brewery. The plant capacity is 2000 kg CO_2 per hour, designed for a typical brewery in the size of 4 million hectoliter of beer per year.

The recovery process is composed of three parts: (1) compression and purification processes, (2) stripping and condensing process finally followed by (3) a pressure storage and evaporation of the CO_2 for use in the production. A cooling facility is assisting the CO_2 plant.

1.1.1 Compression and purification processes

A schematic diagram is shown in Figure 1. CO_2 is produced during fermentation of the beer and with a small overpressure it reaches the recovery plant first arriving in the foam trap which discards possible visible gas impurities such as foam generated during fermentation. Water soluble impurities (mainly alcohol) are removed in the water scrubber and the CO_2 is lead to the balloon as a buffer supplying the following two-step-compressors containing inter- and after cooler and dehumidifier. Here the CO_2 has reached a relatively high pressure close to 20bar. After the compression odours are removed in the carbon filters followed by drying the CO_2 to a dew point of -60C in the dehydrator. The carbon filters and dehydrators are regenerated by an electric heating element and by CO_2 purge gas or air.

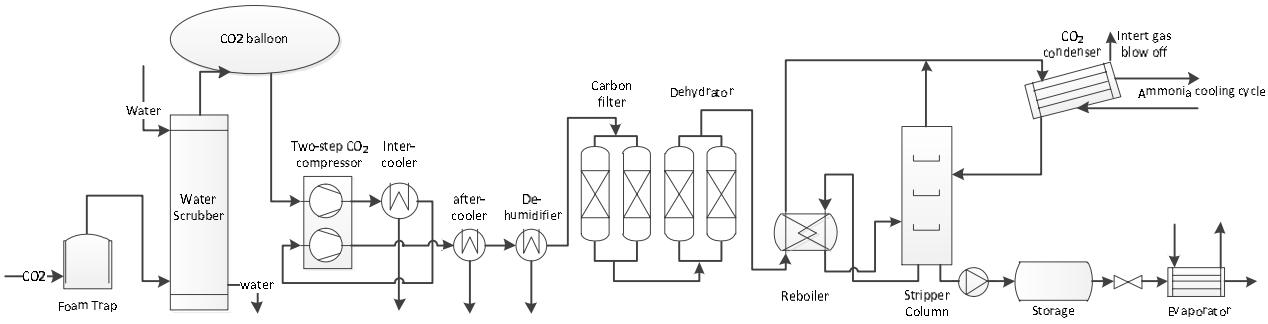

Figure 1: CO_2 compression and purification processes followed by stripping and liquefaction.

1.1.2 Stripping and liquefaction process

Purified CO_2 enters the reboiler for the stripping column in which it is precooled before liquefaction in the CO_2 condenser at temperature down to -25°C. Here the CO_2 is condensed to the reflux tank and inert gas is separated and discharged to the surroundings.

Liquid CO_2 is pumped to the top of the stripping column, where further reduction of oxygen and inert gas is obtained. From the bottom of the column liquid CO_2 is partly pumped to the storage tank and partly circulated through the reboiler which heats the column and herby ensure continuous evaporation. For the simplest plant setup the CO_2 is finally led through a steam heated evaporator before entering the production site, which means that the cooling potential is not utilized due to time constraints.

1.1.3 Low temperature cooling facility

Figure 2 shows how the cooling demand is supplied to the CO_2 plant. An ammonia cycle supplies the CO_2 condenser and dehumidifier with cooling at two different stages, which are separated in an economizer. Heat removal from the ammonia condenser is done by a water cycle assisted with a cooling tower that furthermore supplies the inter cooler and after cooler with cooling.

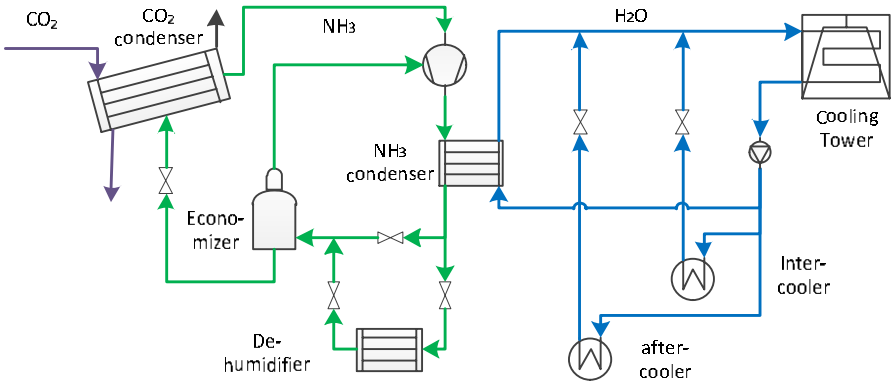

Figure 2: Cooling facility for the CO_2 liquefaction.

CO2 process:		
After component:	p [bar]	T [C]
Balloon	1,028	34,2
CO2 compressor step 1	4,7	192
Inter cooler	4,5	40
CO2 compressor step 2	18,4	186
after cooler	18,2	35
Dehumidifier	18	20
Dehydrator	17,6	19,5
Reboiler	17,6	-15
CO2 condenser	17,6	-23,6
Stripper column	17,6	-23,6
Storage pump	18,5	23,6
CO2 expansion	5	-56,5
CO2 evaporator	5	2

NH3 cycle:		
After component:	p [bar]	T [C]
Economizer	3	-12
CO2 condenser	0,95	-34,6
NH3 compresser	14	227
NH3 condenser	13	35
Dehumidifier	4	0,7

Water cycle:		
After component:	p [bar]	T [C]
Pump	3	30
NH3 condenser	3	33
Inter cooler	3	40
After cooler	3	40
Mixing (before cooling tower)	3	34,1

Tabel 1: Oparation states for the CO_2 recovery plant.

2. Methodology

An exergy analysis has been performed on a CO_2 recovery plant. The process setup is shown in Figure 1, while states throughout the process is shown in Tabel 1.

Assumptions

The following studies have been done on basis of the following assumptions:

- The system operates steady state at maximum capacity.
- Electricity consumed due to regeneration of filters is included due to a time average approach.
- Component efficiencies and heat transfer coefficients do not vary with pressure, temperature or mass flow.
- Only pressure drops in heat exchangers and filters are taken into account, while remaining pressure drops and thermal losses are neglected. E.g. heat transfer to the storage tank is neglected. This loss will cause an extra load in the CO_2 condenser, due to the fact that CO_2 gas is rejected from the tank to the condenser supply line.
- All compressors are cooled by cooling water from the same stream as for the following coolers (inter cooler, after cooler, NH3 condenser).
- The stripping column is regenerative. It is therefore assumed that the stream out of the reboiler is pure gas and corresponds (due to mass and state) to the evaporation from the stripping column.

- ♣ It is estimated that the incoming CO_2 contains 4.2% gaseous water. Chemical exergy in the CO_2 is neglected due to the fact that its impact is less than 0.1%.

Data validation and solution procedure

Simulations have been made in DNA [3] (Dynamic Network Analysis) which is an open source simulation software [4]. It contains a list of standard components that in this case fulfills the modeling requirements.

Operating parameters, such as compressor isentropic and mechanical efficiencies, pressure drop in heat exchangers, operating states (temperatures and pressures) is all data from a specific plant setup.

The simulation has been split into three parts. First part presents CO_2 containing water as a real gas in order to model the compression and condensing of water in the gaseous CO_2. Second part is a model for CO_2 as cooling media (R744) and it handles the condensing-, stripping- and evaporation process. Finally the cooling facility is modeled as an ammonia refrigeration cycle connected with a water cycle.

The stripping column is regenerative (not external heated), and therefore calculations are based on input and output data which is verified.

Exergy analysis and entropy generation

Exergy has the advantage that it valorizes energy as potential work and not only consider the mounts of energy available. An exergy analysis of the system will reveal component irreversibilities, which is an expression of entropy generation. This encourages determination of lost available work (or exergy destruction) for each component in the system and mapping of the disappearance of the work added to the system. This analysis provides a reasonable basis for optimizing the system design trough for example a thermoeconomic analysis [5].

For a system or a component only a given amount of work can be transferred to the output stream [6]. This originates in the entropy generation, of which the transferred work is given (1):

$$\dot{W} = \dot{W}_{rev} - T_0 \dot{S}_{gen} \qquad (1)$$

which leads to the relation of lost work (2) (the Guoy-Stodola Theorem) [6]:

$$\dot{W}_{lost} = T_0 \dot{S}_{gen} \qquad (2)$$

Entropy generation may in some cases appear a bit abstract in order to understand and present lost work. The following representation of exergy is therefore used during the execution of an exergy analysis.

Methodology for exergy analysis

All exergy transfers in inlets and outlets, E_i and E_e are calculated in the model. The exergy of the given stream refer to the maximum theoretical work that can be obtained by bringing the stream to the dead state or environmental state (T_0, p_0). Exergy flow is determined on basis of the unit-of-mass exergy [kJ/kg], so called specific exergy (3) [5]. In the case we decide to neglect chemical exergy, because of its neglectable impact, this only represents the phisycal exergy.

$$e^{ph} = (h - h_0) - T_0(s - s_0) \qquad (3)$$

Destruction of exergy is calculated by the exergy balance (4):

$$\dot{E}_i = \dot{E}_e + \dot{E}_L + \dot{E}_D \qquad (4)$$

In which E_L and E_D describes the loss and destruction respectively. For the major part of the components in the respective model, lost streams are not utilized and therefore included as a part of the destruction according to the system.
Destruction will be considered for each component and can be expressed in different ratios. One useful ratio is of the total destruction in the plant (5):

$$y_D^{\bullet} = \frac{\dot{E}_D}{\dot{E}_{D,tot}} \quad (5)$$

Another representation of the destruction, which is used in this paper, is destruction as a ratio of total fuel input (6):

$$y_D = \frac{\dot{E}_D}{\dot{E}_{F,tot}} \quad (6)$$

This is in order to have the same reference when comparing with exergy streams relatively. For example exergy losses are likewise determined as a rate of the total fuel input (7).

$$y_L = \frac{\dot{E}_L}{\dot{E}_{F,tot}} \quad (7)$$

The final product leaves the plant as requested in the production site. The exergy content of the product stream leads to determine the overall exergy efficiency for the plant (8).

$$\eta_{II} = \frac{\dot{E}_{product}}{\dot{E}_{F,tot}} \quad (8)$$

In cases where the exergy of the final product is equal to the ambient, it may be more evident to focus on the destruction in each component in order to reduce the overall efficiency.

Grassmann diagram for CO_2 recovery plant
A Grassmann diagram shows a graphical representation of the exergy development throughout the process. The so called exergy diagram illustrates all exergetic inputs and outputs for the entire plant – both the CO_2 recovery process and cooling facility.
Exergy inputs and outputs related to the product streams, power inputs, waste streams and exergy interactions due to heat exchangers determines the destructions. All these are shown for each incorporated component in the diagram.
This exergy flow representation provides a valuable overview of the plant details which energy considerations alone cannot accommodate. It locates/pinpoint destruction of exergy and may provide better knowledge in order to improve the overall performance in a CO_2 recovery plant [7].
A Grassmann diagram of the investigated CO_2 recovery plant is shown in Figure 7.

3. Results

Energy demand for the isolated CO_2 recovery process
Figure 1 shows the energy demands for the isolated CO_2 recovery process, i.e. without the cooling facility. It appears that the total energy consumption is 767kW, contributed by cooling, heating and electricity with a share of 51.6%, 24.6% and 23.8% respectively.
The majority of electricity is consumed in the CO_2 compressors, while a minor part is consumed due to pumps and regeneration of filters.
A little more than half of the consumption is related to a cooling demand. Apparent is the cooling needed for CO_2 condensing, which contributes with 25% of the total consumption. A similar

amount of cooling demand is needed in order to remove the heat generated due to the compression stages. Out of these 205kW it appears that 15% are expended on condensing water due to humidity. After the recovery process the CO_2 is delivered to the production as gas at a reduced pressure. This expansion generates a cooling effect that has to be removed corresponding to another 25% of the total energy demand.

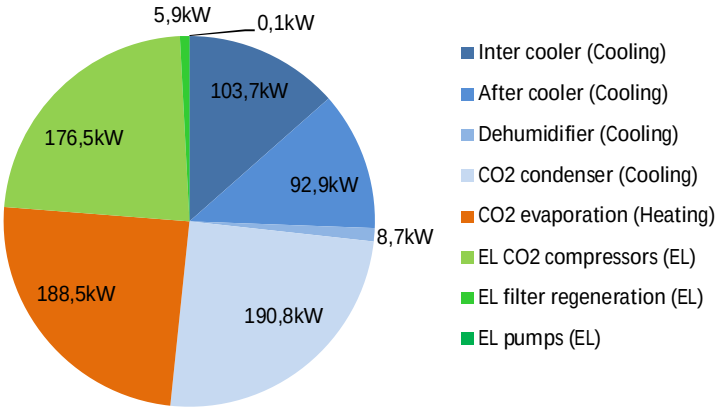

Figure 3: Energy demands for the isolated CO_2 recovery process.

Exergy expenditure in the isolated CO_2 recovery process
Converting the previous energy demand analysis into an exergy consideration of input and output exergy streams (cf. Figure 4), the following is observed:

- Total exergy input/output is 220kW.
- Electricity consumption remain unchanged, thus its share of the total consumption increases.
- The large cooling consumption for the CO_2 condenser (190.8kW) is strongly reduced to 20% (37.3kW) due to the exergy perspective.
- Cooling in the inter cooler, after cooler and dehumidifier are all above ambient temperature, which in the exergy perspective has been added to the output as a hot waste stream. Accordingly the energy flow (205kW) reduces to 9.6% (19.7kW) exergy.
- Evaporation of CO_2 is added as an output stream because of its cooling potential. This stream is also reduced (from 188.5kW energy) to 36% (67.3kW) when based on exergy.
- The CO_2 product appears to leave the plant containing 23.1% of the total exergy.
- Finally the exergy destruction occurs due to lost streams and other thermal irreversibilities. This share represent 58.9kW corresponding to 26.7% of the total output exergy.

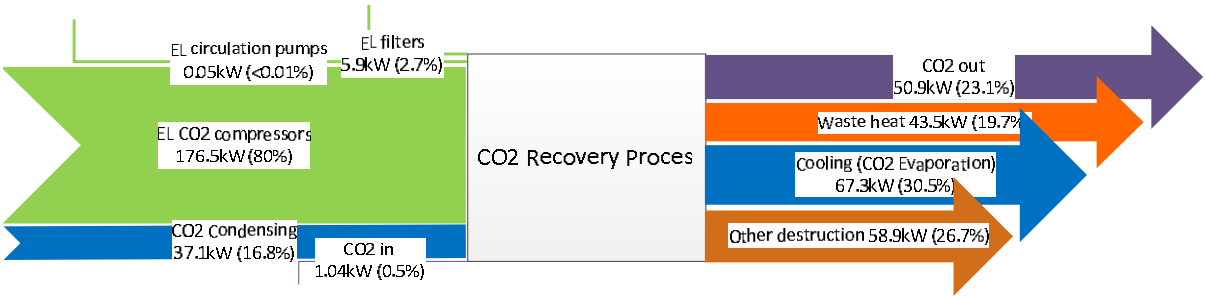

Figure 4: Exergy expenditure in the isolated CO_2 recovery process.

Energy demand for the entire CO_2 recovery plant

Considering the demand in the existing CO_2 recovery plant setup (Figure 5) the supply of cooling facility increases the consumption by 30% which results in a total energy consumption of 991kW. The heating demand remains constant while the electricity consumption is extended by an ammonia compressor of 110kW. The cooling demand keeps its share of 51%. All 507kW cooling of the plant is placed in a cooling tower.

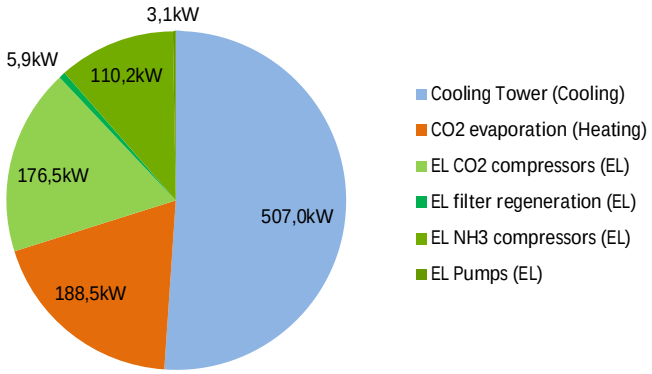

Figure 5: Energy demands for the entire CO_2 recovery plant.

Exergy expenditure for the entire CO_2 recovery plant
Figure 6 shows the input and output exergy streams for the entire plant and the following can be observed:

- ♣ Total exergy input/output is 358kW.
- ♣ Electricity still remains unchanged, but as a major part, 83% of the exergy input, while the heating demand (of 188.5kW) is replaced by steam consumption reduced to 32% (61.2kW) exergy
- ♣ The exergy output of CO_2 remains unchanged and has a share of 14.2%.
- ♣ Cooling demand of 507kW is all rejected in the cooling tower as heat just above the ambient temperature, which reduces to 2.2% (7.7kW) exergy of waste heat and becomes a part of the exergy destruction.
- ♣ Due to the steam input a small amount of 2% exergy is leaving as return condensate.
- ♣ As much as 82.6% of the exergy output disappears as thermal irreversibilities and streams that are being discharged to the environments.

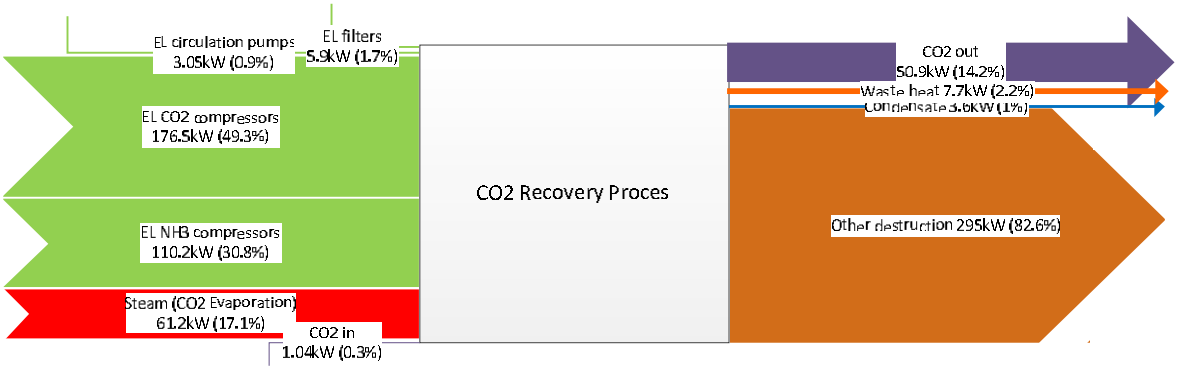

Figure 6: Exergy expenditure in the entire CO_2 recovery plant.

The consumption of the pressurized CO_2 in the production site and return of condensate to a given boiler results in an overall exergy efficiency for the CO_2 recovery plant of 0.15. However utilization of the cooling potential due to the CO_2 evaporation would increase the exergy efficiency to 0.5.

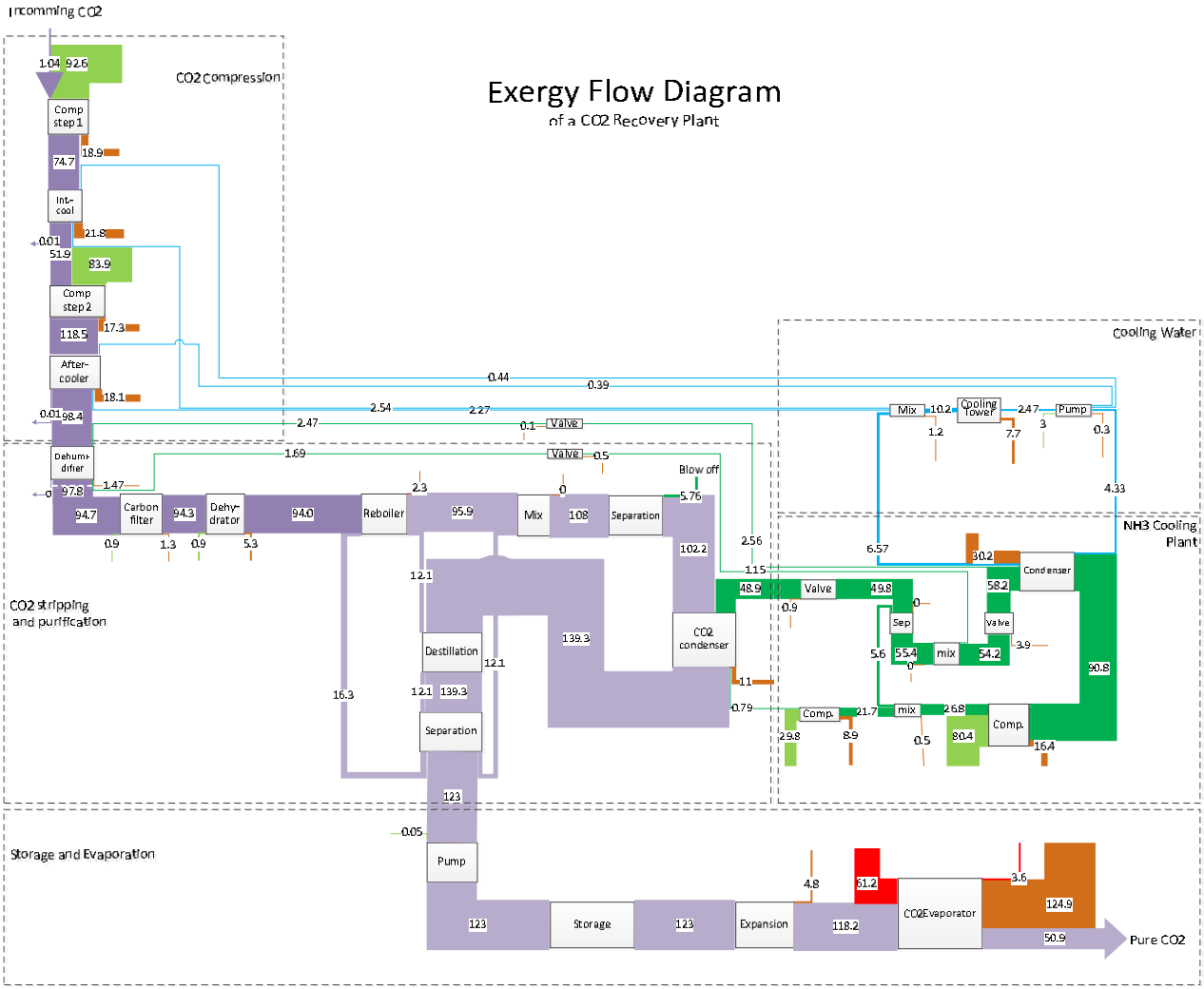

Figure 7: Grassmann diagram of the exergy flows in a CO_2 recovery plant complemented by cooling facilities.

Exergy appearance in CO_2 recovery plant in details

Figure 7 shows the exergy formation throughout the recovery plant and Figure 8 describes the exergy destruction in each single component as a ratio of the total fuel input. The following observations are made:

CO_2 process

- ♣ As long as the cooling potential due to CO2 evaporation and the waste heat streams are not utilized, the total exergy destruction associated with the recovery plant becomes 85% (303kW), of the total fuel exergy input of 357kW.
- ♣ 35% of the input exergy is destroyed due to the CO2 evaporation, which is a result of using steam containing a high exergy value in order to heat the low temperature CO2 that also has high exergy content as cooling potential.

- ♣ Due to the compressor inefficiencies 10.1% of the total exergy input is destroyed.
- ♣ Waste heat after the two compression steps is generated, even though 11.2% of the exergy input is disposed by cooling water. The following dehumidifier causes another 0.4% of destruction.
- ♣ Temperature difference between NH3 and CO_2 in the CO_2 condenser carries 3% destruction of the input exergy.
- ♣ Minor exergy destruction is the CO_2 expansion of 1.4%. Regeneration of carbon filter and dehydrator entails 1.9% and the reboiler 0.6%. Finally to be mentioned is the blow off loss stream that carry another 1.6% of the input exergy.

Cooling facility

- ♣ Inefficiencies in NH3 compressor induces 7% destruction, while the heat generated and disposed in the NH3 condenser carries 8.4% of the total exergy input.
- ♣ Only 2.1% is destroyed in the cooling tower in spite of the relatively large heat disposal (Figure 5). The exergy destruction connected to this large amount of energy is placed in the local heat exchange such as NH3 condenser, inter cooler and after coolers.
- ♣ Finally some minor destructions are found due to expansion valves, pump inefficiencies and mixing of medias containing different temperature levels.

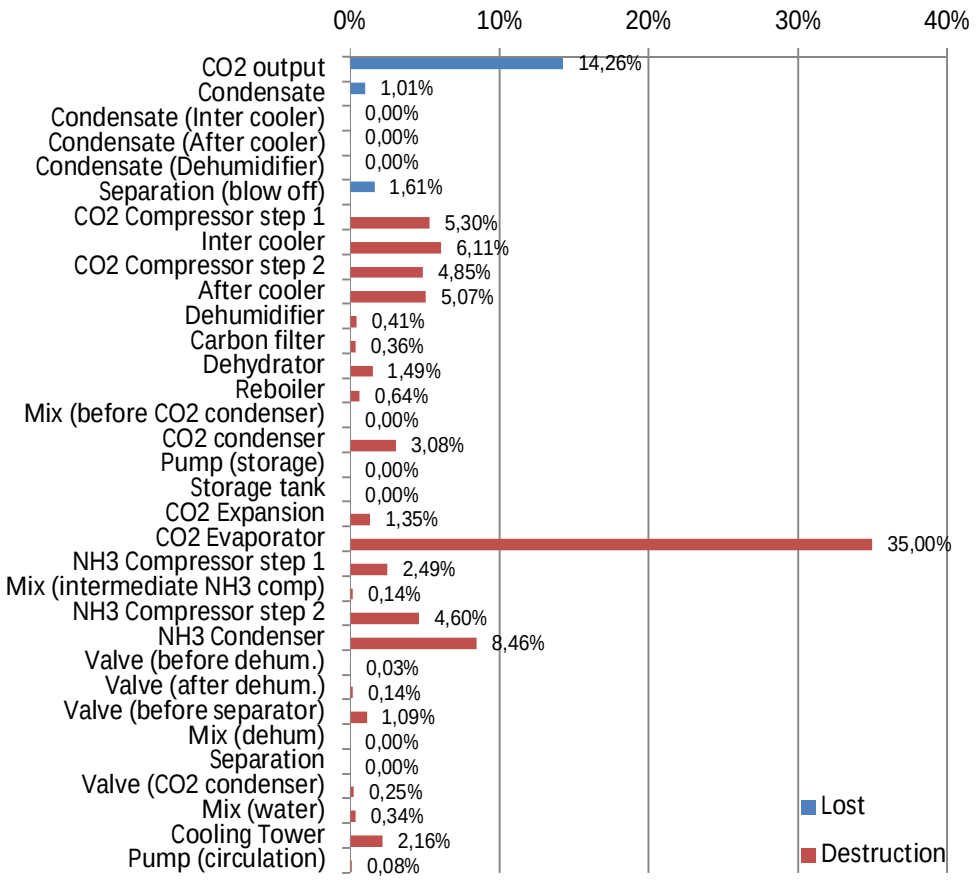

Figure 8: Exergy destruction in each component as a ratio of the total fuel input.

Evaluation of the cooling plant shows that the ammonia refrigeration cycle contributes with 200kW cooling of energy, in which 191kW and 9kW is located in the CO_2 condenser and dehumidifier respectively.

The total electricity input is 110kW which gives a COP of 1.81. Reconfiguration of temperatures may lead to less exergy destruction and therefore higher energy efficiency. By increasing the evaporation temperature both COP will increase and less exergy destruction in the evaporator (CO_2 condenser) is obtained.
The total cooling load of the entire cooling system (including the water cycle) is 396kW of energy which lead to a COP of 3.5. What is relevant to notice is the introduction of circulation of water, which transports and disposes heat from above ambient temperature to the ambient trough a cooling tower.
In order to reduce the exergy destruction the operating temperatures in the NH3 cycle may be analyzed.

4. Discussion

The major sinner of the plant turns out to be the CO_2 evaporator that destroys 35% of the total exergy input. CO2 should obviously not be evaporated by steam (according to an energy/exergy perspective). Apparently, the cooling potential associated with the CO_2 expansion has to be utilized. In order to exploit most of the refrigeration potential as possible, it is necessary to locate low temperature cooling demands. Since the condensing of the CO_2 involves the lowest temperature demands in the brewery the evaporation may be utilized in order to cool the CO_2 condenser – directly or indirectly. Due to time constraints between production and consumption of CO_2, it may be necessary to introduce thermal heat storage (sensible or latent).
Almost 10% of the total exergy input is destroyed due to thermal degradation in the ammonia condenser. A reduction of the condensing temperature or an exploitation of this excess heat may therefore be important in order to obtain a reduction in the total energy consumption of a brewery. Moreover, excess heat corresponding to 11.1% of the exergy input is destroyed in inter- and after cooler, of which 15% is due to condensing of water. A reduction of the water content in the incoming CO_2 will accordingly contribute in the reduction of cooling demand.
Compressor inefficiencies represent 17.1% destruction of the total exergy input, which encourage investigating the technical and economic feasibility in using more efficient compressors.
The analysis performed enables a thermoeconomic analysis on the system design and further evaluation of optimal operating set points.

5. Conclusion

An analysis of energy demands for the CO_2 recovery process has been made, which gives a good foundation for determining capacities/plant dimensions for cooling facilities, heat- and power supply. The analysis has been extended by an exergy analysis in which it turns out to be more representable to illustrate some demands, such as the waste heat and cooling potential (CO_2 expansion) as output streams rather than input streams. This enables a more detailed analysis of the energy consumption and utilization through the plant.
The same has been concluded in a corresponding analysis for the entire plant setup.
An exergy analysis has been performed on a complete CO_2 recovery plant setup and presented in a Grassmann diagram in which amounts of input and output exergies are shown graphically. This presentation improves the understanding of the exergy (or value of energy) appearance in the process.
A schematic overview of all exergy output including destructions has been presented as a ratio of the total exergy input. This provides a clear understanding of the exergy inefficiencies associated with the plant – in other words a description of where the valuable energy disappear in the system.

The major contributors to the exergy destruction constitutes of the CO_2 evaporation (35% of the total exergy input), followed by the temperature degradation of generated heat due to compression of CO_2 and NH_3 and destruction associated with compression irreversibilies.

Acknowledgement

Union Engineering is acknowledged for sharing data for plant setup and operational states.

Nomenclature

$\dot{e}^{ph}$ physical specific exergy

$\dot{E}_D$ Exergy destruction

$\dot{E}_{D,tot}$ Total exergy destruction

$\dot{E}_e$ Exergy output

$\dot{E}_{F,tot}$ Total fuel exergy input

$\dot{E}_i$ Exergy input

$\dot{E}_L$ Exergy loss

$\dot{E}_{product}$ Exergy in product

$\dot{S}_{gen}$ Entropy generation

$\dot{W}$ Work

$\dot{W}_{rev}$ Reversible work

$\dot{W}_{lost}$ Lost work

y_D Destruction ratio of the total input

y_D^* Destruction ratio of the total exergy destruction

y_L Exergy loss as ratio of the total exergy input

η_{II} Second law efficiency

References

[1] Muster-Slawitsch B, Brunner C, De Lima DR, Schnitzer H, Muster-Slawitsch B, Brunner C. The Green Brewery concept - Energy efficiency and the use of renewable energy sources in breweries. Chem Eng Trans 2010;21:649-54.

[2] Fadare DA, Nkpubre DO, Oni AO, Falana A, Waheed MA, Bamiro OA. Energy and exergy analyses of malt drink production in Nigeria. Energy 2010;35:5336-46.

[3] B. Elmegaard NH. DNA - A Thermal Energy System Simulator http://orbit.dtu.dk/RecordLinkPage.external?sp=recid&sp=231251. 2009.

[4] Elmegaard B, Houbak N. Software for the Simulation of Power Plant Processes. Proceedings of ECOS 2002 2002.

[5] Bejan A, Tsatsaronis G, Moran M. Thermal design and optimization. New York: Wiley-Interscience, 1996.

[6] Bejan A. Advanced engineering thermodynamics. Hoboken,N.J.: Wiley, 2006.

[7] Thomas RJ, Ghosh P, Chowdhury K. Application of exergy analysis in designing helium liquefiers. Energy 2012;37:207-19.

Exergy analysis of the silicon production process

Marit Takla[a], Leiv Kolbeinsen[b], Halvard Tveit[c], Signe Kjelstrup[d]

[a]*The Norwegian University of Science and Technology, Trondheim, Norway,*
marit.takla@chem.ntnu.no ***(CA)***
[b]*The Norwegian University of Science and Technology,Trondheim, Norway, leiv.kolbeinsen@sintef.no*
[c] *Elkem Silicon, Trondheim, Norway, halvard.tveit@elkem.no*
[d] *The Norwegian University of Science and Technology, Trondheim, Norway,*
signe.kjelstrup@chem.ntnu.no

Abstract:

We present an exergy analysis of the theoretical silicon production process and for two cases of an industrial process. The theoretical process is a first effort to establish a reference case for the silicon production process.
In the theoretical process we consider the process with pure reactants and stoichiometric reactions. The industrial process is evaluated for the case of no power production and power production using a steam turbine and generator equipment in the off-gas system. For the theoretical process we find that the exergetic efficiency is 47.5 % for a silicon yield of 1 while utilization of thermal exergy in the off-gas increases the exergetic efficiency to 58.6 % and 67.4 % for off-gas temperatures of 300 ºC and 800 ºC, respectively. The exergetic efficiency for the industrial process is estimated to 30.8 % and 38.9 % for the case of no power production and power production, respectively.

Keywords:

Exergy analysis, Exergetic efficiency, Silicon production process.

1. Introduction

According to the International Energy Agency [1], the industrial sector accounted for 40 % of the total global power consumption in 2009. To increase the efficiency of resource utilization in industrial processes is thus a benign and substantial route to address environmental concerns and energy security.

Exergy analysis of a process as it is operated today is a first step towards a resource efficient process. The exergy analysis method combines the first law (conservation of energy) and second law of thermodynamics (degradation of energy) in the analysis of thermal, mechanical and chemical systems. It determines the locations, types and magnitudes of waste and losses and therefore it is particularly well suited for evaluating a process in terms of resource utilization. The exergy analysis method is an established method described in several text books, see e.g. [2, 3].

Silicon and its alloys (high in silicon content) are produced by carbothermic reactions in submerged arc furnaces which require high temperatures. Such are reached by adding large amounts of electric energy. Most plants use 11-13 kWh per kilogram of silicon metal produced [4]. An exergy analysis of a ferrosilicon furnace at an Elkem plant on Iceland published in 2009 [5] showed that 70 % of the total exergy put into the furnace is lost. Thus, the *exergetic efficiency*, defined as the ratio of the exergy in the product and the exergy used in the process, was 30 %. The analysis showed that almost half of the total exergy input is lost in the furnace. Around one fifth is lost with the off-gas.

The theoretical upper limit for the exergetic efficiency is unity. In practice, lower limits apply as all real processes are associated with irreversibilities, e.g. uncontrolled chemical reactions. To explore

a practical limit of a process is of interest as it gives a more realistic figure on the real potential for process improvements.

We present an exergy analysis of the theoretical silicon production process and for two cases of an industrial process. The theoretical process is the process with pure reactants and stoichiometric reactions; it covers the main features of an industrial process and it is a first effort to establish a reference case for exergy analysis of the industrial process.

1.1 Production of silicon

Silicon is commercially prepared by reduction of silicon dioxide with carbon in a submerged arc furnace (SAF); a schematic drawing illustrating the process is given in Fig. 1. The illustration shows the furnace surrounded by raw material - and power supply system, off-gas removal - and heat recovery equipment, tapping, casting and crushing.

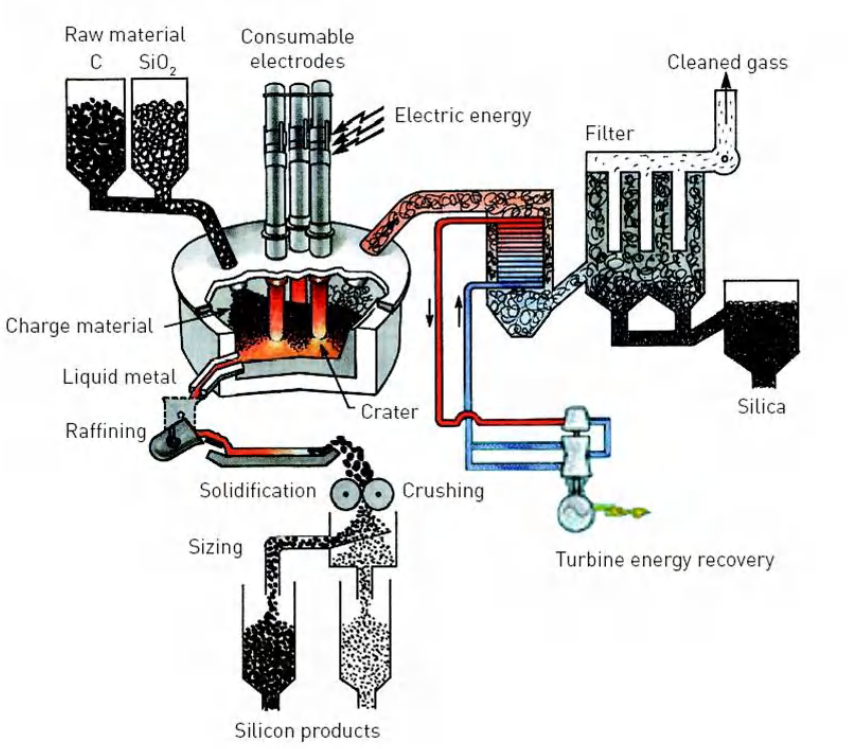

Fig. 1. Schematic drawing illustrating a typical silicon production process [6]. Silicon is commercially prepared by reduction of silicon dioxide with carbon in a submerged arc furnace (SAF). The illustration shows the SAF surrounded by raw material and electrical power supply systems, off-gas and heat recovery equipment, tapping, casting and crushing of the product.

The SAF is the heart of the silicon plant. The size of the furnace is characterized by the electrical power needed, which can be in the range from less than 10 MW to 45 MW. The raw materials, quartz and carbonaceous reduction materials (coke, coal, charcoal and woodchips), are fed to the furnace at the top, and are referred to as the charge material.

Production of silicon is an energy intensive process, requiring temperatures above 1800 °C. These temperatures are achieved by adding large amounts of electric energy. Liquid silicon is tapped from the bottom of the furnace. After tapping, the liquid is refined by slag treatment or gas purging. Then the liquid silicon is poured into suitable moulds, allowed to cool down and then crushed to the desired particle sizes.

The off-gas from the furnace reaction (SiO+CO) is mixed with excess air under the furnace hood and burned, captured into the gas-cleaning system and filtered. The off-gas temperature is controlled by the excess of air. Sometimes this parameter is shown as the ratio of the total off-gas volume and the furnace load ((Nm^3/s)/MW load). The dust in the filter consists mainly of SiO_2 particles, also referred to as condensed silica fume, which can be used as filler material in concrete, ceramics, rubber etc. Since the off-gas escapes from the furnace hood at high temperatures (200 - 700 °C), it is suitable for electric energy production using a steam turbine and generator system.

2. Theory

2.2 Energy analysis

The energy balance for a control volume, assuming steady state and neglecting the contribution from kinetic and potential energy can be written as

$$0 = \dot{Q}_{\mathrm{CV}} + \dot{W}_{\mathrm{CV}} + \sum_{\mathrm{i}} \dot{m}_{\mathrm{i}} h_{\mathrm{i}} - \sum_{\mathrm{e}} \dot{m}_{\mathrm{e}} h_{\mathrm{e}} \tag{1}$$

The first two terms on the right hand side is the heat and work added to the control volume and h is the specific enthalpy of the material stream m. Subscripts i and e refer to inlet and outlet streams, respectively.

2.2 Exergy analysis

The exergy of a system is defined as the maximum work obtainable from the interaction between the system and an idealized system called the reference environment [3]. In this work, the reference environment takes the temperature and pressure T_0 = 25 ºC and p_0 = 1 atm respectively. When doing an exergy analysis of a process, all energy streams entering and leaving the system are evaluated in terms of its exergy. The exergy balance for a control volume assuming steady state is

$$0 = \sum_{j} \left(1 - \frac{T_0}{T_j} \right) \dot{Q}_j + \dot{W}_{\mathrm{CV}} + \sum_{i} m_i e_i - \sum_{e} m_{\mathrm{e}} e_{\mathrm{e}} - \dot{E}_D \tag{2}$$

The first term on the right hand side can be interpreted as exergy accompanying transfer of thermal energy. The second term can be interpreted as exergy accompanying work. Further, e is the specific exergy of the stream of material m and $\dot{E}_{\mathrm{D}}$ is the exergy destruction.

The specific exergy of a stream of material (neglecting contributions from kinetic and potential energy) can be written as the sum of the physical and chemical exergy

$$e = e^{PH} + e^{CH} \tag{3}$$

The physical exergy is the maximum work obtainable as the system passes from its initial temperature and pressure, T and p, to the temperature and pressure of the reference environment, T_0 and p_0. At T_0 and p_0, the system is said to be in the restricted dead state. The physical exergy is given by the expression

$$e^{PH} = \left(h - h_0 \right) - T_0 \left(s - s_0 \right) \tag{4}$$

Here, h and s are the specific enthalpy and entropy at the system temperature and pressure, while $h_0 = h(T_0, p_0)$ and $s_0 = s(T_0, p_0)$.

The chemical exergy is the maximum work obtainable as the system at T_0 and p_0 comes into total equilibrium with the reference environment. The system is then said to be in the dead state.

Standard chemical exergy values based on standard exergy reference environment is tabulated, see e.g. [2]. The chemical exergy of a substance can be determined from:

$$\bar{e}^{CH} = -\Delta G_0 + \sum_P n\bar{e}^{CH} - \sum_R n\bar{e}^{CH} \quad (5)$$

Here ΔG_0 is the change in the Gibbs energy for the reaction forming a substance from the reference substances at temperature T_0 and pressure p_0 and $\bar{e}$ is the molar chemical exergy. The last two terms in (5) are evaluated from known standard chemical exergies. P and R refer to the products and reactants, respectively, and n is the number of moles.

The chemical exergy of an ideal mixture is determined from

$$\bar{e}_{mix}^{CH} = \sum x_i \bar{e}_i^{CH} + RT_0 \sum x_i \ln x_i \quad (6)$$

Here, x_i is the mole fraction of component i in the solution and R is the universal gas constant.

The exergetic efficiency, ε, is used as a parameter for evaluating thermodynamic performance for the system [3]:

$$\varepsilon = \frac{\text{exergy in product}}{\text{exergy used in the process}} \quad (7)$$

3. Case studies

3.1 The theoretical silicon production process

The theoretical silicon production process is the process with pure reactants and stoichiometric reactions. It is described by Schei et.al in [4]. This simplified description covers the main features of the process as it is operated today. Therefore, it may be suitable as a reference case for the industrial process.

In the theoretical process, the overall process is divided into three subsystems; the submerged arc furnace, the gas treatment section and the product treatment section, see Fig. 2.

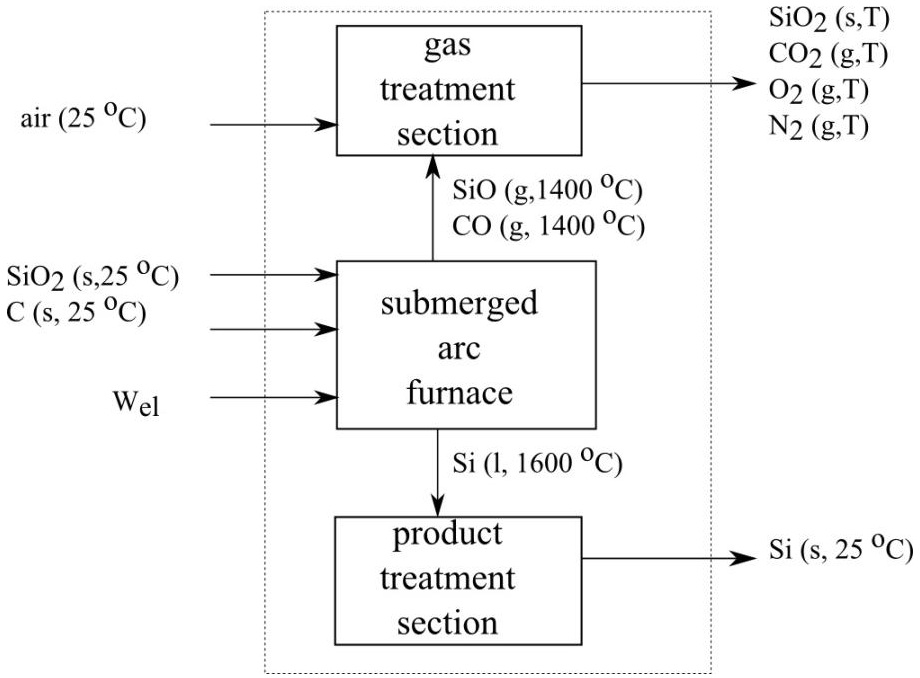

Fig. 2. A schematic diagram of the theoretical silicon production process showing the material and energy flows in the system. The theoretical silicon production process is described by Schei et.al in [4].

The submerged arc furnace:

Pure silicon dioxide and carbon (graphite) are added to the furnace together with electrical energy. The furnace reaction is described by the following equation

$$(1+x)\,\mathrm{SiO_2} + (2+x)\,\mathrm{C} = \mathrm{Si} + x\,\mathrm{SiO} + (2+x)\,\mathrm{CO} \tag{8}$$

The enthalpy and the entropy of this reaction are positive. The theoretical amount of electrical energy needed to produce one mole of silicon is determined from the enthalpy of the furnace reaction. The amount of electrical energy added to the furnace is referred to as the furnace load. There are no losses in the electrical supply system or thermal energy losses from the furnace to the surroundings. The gas leaving the top of the furnace consists of SiO and CO and it has a measured temperature of 1400 °C. Liquid silicon leaves the bottom of the furnace at a temperature of 1600 °C.

The silicon yield S, where $0 \leq S \leq 1$, is the amount of silicon in the quartz that goes to the silicon. It relates to the parameter x as

$$S = \frac{1}{1+x} \tag{9}$$

Gas treatment section

The gas leaving the top of the furnace enters the gas treatment section where it is burned in excess air. The gas treatment section corresponds to the area under the furnace hood in a real furnace. The reaction in the gas treatment section can be described as

$$x\,\mathrm{SiO} + (2+x)\,\mathrm{CO} + m\,\mathrm{O_2} + 4m\,\mathrm{N_2} = x\,\mathrm{SiO_2} + (2+x)\,\mathrm{CO_2} + (m-x-1)\,\mathrm{O_2} + 4m\,\mathrm{N_2} \tag{10}$$

Here, m is the amount of oxygen introduced with air. The amount of excess air determines the temperature of the off-gas leaving the gas treatment section.

Product treatment section

In the product treatment section, liquid silicon at a temperature of 1600 °C and $p = p_0$ solidifies and cools down to 25 °C. Silicon leaves the process at $p = p_0$ and $T_0 = 25$ °C.

3.2 A submerged arc furnace operated at a Norwegian silicon plant

The industrial process is a 45 MW furnace operated at an Elkem Silicon plant in Norway. In 2010, Kamfjord et al. [7] published an energy balance for this furnace. We use their input data [8], scaled to a 10 MW furnace, to establish the energy balance (1) which we use to characterize the furnace. For this furnace, the control volume includes the furnace and the area under the furnace hood which is equivalent to the furnace and the gas treatment section for the theoretical process described above.

Energy enters the process as electrical energy and as enthalpy in the raw materials which is a mixture of coke, coal, charcoal, woodchips and quartz. Energy leaves the process as enthalpy in the product, cooling water and off-gas and by radiation and convection from the furnace, cf. (1). Typical composition of carbonaceous raw materials used in silicon production is given in Table 1.

In the calculations, we neglect the contributions from moisture and ash in the carbonaceous raw material and only take into account the contribution from fixed carbon, which is a measure of the solid combustion material in carbonaceous materials, and the volatile matter. The fixed carbon is pure graphite and we make a distinction between volatile matter contained in coke/coal/charcoal and woodchips. The product is taken to be pure silicon. Table 2 shows the amount of fixed carbon, volatile matter and silicon for the furnace evaluated.

Table 1. Typical composition of carbonaceous materials used as raw materials in the silicon production process, given on a wet basis [4].

Type	Fixed Carbon (%)	Volatile (%)	Moisture (%)	Ash (%)
Coke	75	4	16	4
Coal	51	35	12	2
Charcoal	46	8	39	6
Woodchips	12	35	52	1

The enthalpy in the cooling water is determined from measured values of flow and the difference between inlet and outlet temperature. We estimate the heat lost by radiation and convection to be 5 % [4] of the total energy put into the process. The enthalpy in the off-gas is taken from difference between the total energy put into the process and the enthalpy in cooling water, heat lost by radiation and convection and enthalpy in the product, cf. (1).

Table 2. Material entering and leaving the submerged arc furnace operating at one silicon plant in Norway [8]. The numbers given refer to one hour of production in a 10 MW furnace. Volatile Matter (VM) type 1 refers to VM contained in coke, coal and charcoal while type 2 refers to VM contained in woodchips.

Material	Amount (kg)
Fixed carbon	855
Volatile Matter type 1	235
Volatile Matter type 2	158
Si- metal	855

3.2.1 Case I: No energy recovery

The energy balance for the furnace, established using (1) and the same input data as Kamfjord et al. [7], is presented in Fig. 3. The numbers refer to a 10 MW furnace. Thermal losses include thermal energy lost to the surroundings from the furnace, by radiation and convection, and from the product during cooling and solidification. The enthalpy in the off-gas is lost as thermal energy to the surroundings. Hot cooling water from this furnace is used for heating purposes [7]. This is not taken into consideration in this work. All energy streams leaving the furnace, except the product stream, represent thermal energy losses to the surroundings.

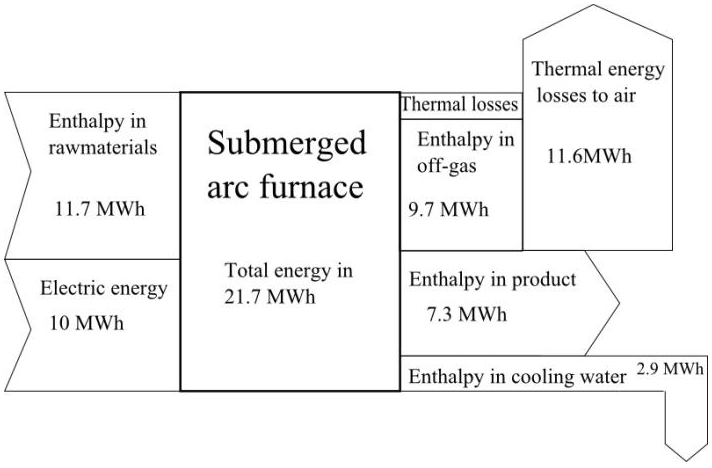

Fig. 3. Energy balance for one submerged arc furnace operated at a Norwegian silicon plant. The energy balance is established using the same input data as Kamfjord et al. [7]. The numbers are given on a basis of one hour production in a 10 MW furnace.

3.2.2 Case II: Energy recovery

To investigate the potential for energy recovery of thermal energy in the off-gas for this furnace, Kamfjord et al. [7] used data from [9] to recalculate new energy flows for the case of energy recovery. Using the energy balance given in Fig. 3, and data from [9] we recalculate new energy flows for the case when energy recovery equipment is installed in the off-gas system, see Fig. 4. All energy streams leaving the process, except the product and the power produced, represent thermal energy losses to the surroundings.

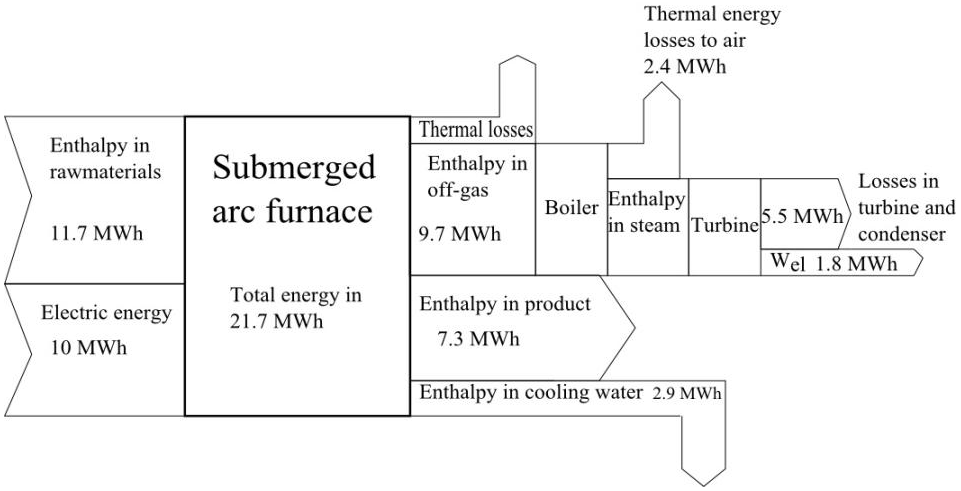

Fig. 4. Energy balance for one submerged arc furnace operated at a silicon plant in Norway with energy recovery equipment installed in the furnace off-gas system. The energy balance is established using the same input data as [7] and numbers in [9]. The numbers are given on a basis of one hour production in a 10 MW furnace.

3.3 Differences between the theoretical and the industrial process

The industrial process has thermal energy losses from the furnace, losses in the electric supply system, loss of carbon to the off-gas system and use of non-pure raw materials in addition to other minor deviations from the theoretical process [4]. The main differences between the theoretical and the industrial silicon process are summarized in Table 3.

Table 3. Main differences between the theoretical silicon production process and the industrial silicon production process [4].

	Theoretical process	Industrial process
Raw materials:	pure	Non-pure
SiO_2	100 %	< 100 %
reductants	100 % carbon	fixed carbon, volatile matter, moisture, trace elements
Product	100 % Si	< 100 % Si
Silicon yield	Can be 100 %	Less than 100 %
Thermal energy loss to surroundings:		
Radiation and convection from furnace	NO	YES
Thermal energy cooling water	NO	YES

4. Calculation details

4.1 Theoretical silicon production process

We calculated the material streams for several silicon yields (9) for a furnace load of 10 MW.

We take the off-gas temperatures to be 300 °C and 800 ºC and determine the amount of air flow into the gas treatment section from the energy balance (1) by assuming the gas treatment section to be adiabatic. This calculation is performed using the thermochemical software HSC Chemistry® 6.1 from Outotec [10]. This software is chosen because it is commonly used by the ferroalloy producers and researchers within this field. The air consists of 20 % O_2 and 80 % N_2. All gas streams are assumed to behave ideally.

4.2 A submerged arc furnace operated at a Norwegian silicon plant

Operating data were supplied for the furnace operating at an Elkem silicon plant in Norway [8]. In calculating the exergy input to the furnace, we considered the amount of fixed carbon and volatile matter supplied to the process, cf. Table 2. When calculating the exergy in the product, we assumed the product to be pure silicon. The environmental temperature and pressure were taken to be T_0 = 25 ºC and p_0 = 1 atm.

4.3 Thermodynamic data

We used standard chemical exergies given by Kotas [2] for all components except SiO(g) and the volatile matter in the carbon materials. Kotas gives the standard chemical exergies for a standard state of T_0 = 25 °C and p_0 = 1 atm for a reference environment originally developed by Szargut and co-workers.

The chemical exergy of SiO(g) was calculated by (5), using O_2 as the reactant component and SiO_2 as the product. Value for the Gibbs energy (ΔG_0) together with values for the enthalpy and entropy differences needed in the calculation of the physical exergies (4) were found from HSC Chemistry® [10]. HSC uses 1 bar as reference pressure for thermodynamic data which is slightly different from the environmental pressure of 1 atm. This difference is neglected in the calculations. As a crude first estimate for the exergy of the volatile matter in the reduction materials, we use the enthalpy for the exergy of the volatile matter. These are estimated values given in [11].

5. Results and discussion

5.1 Theoretical silicon production process

The exergy flow for the theoretical process will naturally depend upon the silicon yield as well as the off-gas temperature. The purpose of the simple Grassman diagram given in Fig. 5 is to illustrate the characteristics of the exergy flow for the theoretical silicon production process. The amount of exergy in a stream is represented by the width of the stream in the diagram. We observe that the exergy content in the gas stream and the product stream leaving the furnace are both large. The SiO(g) and CO(g) are burned in excess of air in the gas treatment section, the exergy in the off-gas leaving this section is mainly thermal exergy and depends upon the temperature which is controlled by the excess of air inlet. The off-gas exergy represents the potential for power production by installation of energy recovery equipment in the off-gas system. The difference between the exergy in the product stream in and out of the product treatment section is due to the thermal exergy loss from the product during cooling and solidification.

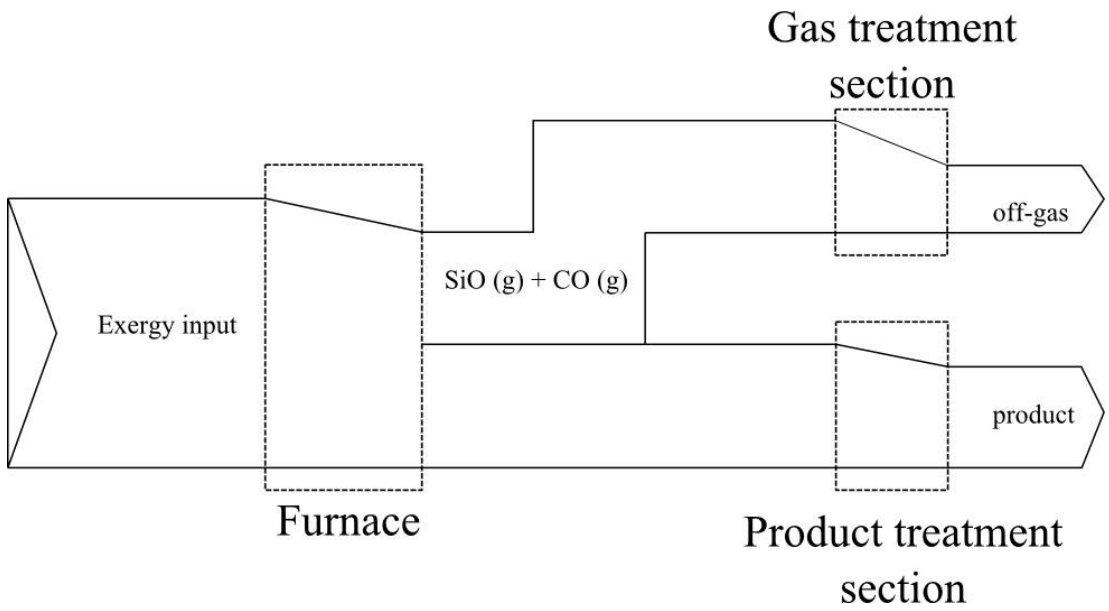

Fig. 5. A Grassman diagram illustrating the characteristics of the exergy flow in the theoretical silicon production process. The width of the streams represents the amount of exergy in the stream.

The overall exergy input, exergy in the product and the total exergy losses for the theoretical process are given in Table 4 for several silicon yields. The total exergy losses in the process amounts to 52.5 % of the total exergy input to the process for a silicon yield of 1.0 and increases to 63.6 % for a silicon yield of 0.7.

Table 4. The total exergy in and out and the total exergy losses of the theoretical silicon production process. The numbers refer to one hour of production in a furnace with 10 MW electric load.

Silicon yield	1.0	0.9	0.8	0.7
Exergy into process (MWh)	19.45	19.06	18.67	18.26
Exergy in product (MWh)	9.23	8.38	7.52	6.64
Exergy losses (MWh)	10.22	10.68	11.15	11.62
Exergy losses as % of exergy into the process	52.5	56.0	59.7	63.6

Table 5 shows the distribution of the total exergy losses over the three subsystems and the exergy lost with the furnace off-gas for a silicon yield of 0.8 and for off-gas temperatures of 300 ºC and 800 ºC for the theoretical process. Table 5 shows that the furnace accounts for about 20 % of total losses and the product treatment for around 6 % while exergy loss in the gas treatment section and the non-utilized exergy in the off-gas accounts for about 70 % in total. The gas treatment section has the largest contribution to the exergy losses for an off-gas temperature of 300 ºC; almost half of the total exergy loss is located here while the exergy lost with the off-gas amounts to around one quarter of the total losses. The exergy content of the gas stream entering the gas treatment section is large and is almost exclusively chemical exergy. Combustion reactions are associated with large exergy losses [12], and a big fraction of the exergy entering the gas treatment section is destroyed due to this. The large exergy loss associated with burning of CO(g) is well known, and there have been attempts in designing closed silicon furnaces [13] with no success so far.

Table 5 shows that increasing the off-gas temperature to 800 ºC, by reducing the excess of air inlet, reduces the exergy loss in the gas treatment section and increases the exergy in the off-gas; the exergy loss in the gas treatment section then accounts for about 30 % of total exergy losses while exergy lost with the off-gas accounts for about 45 % of total losses. Thermal exergy is the largest contribution to the exergy in the off-gas leaving the gas treatment section and utilization of this will

reduce the total exergy loss in the process. Furthermore, increasing the off-gas temperature enhances the potential for increasing the overall resource utilization. This is a well-known measure [4, 5, 9, 14] and several plants have installed an energy recovery system in the off-gas system today.

Table 5. Distribution of the exergy loss over the sub-systems and exergy lost with the off-gas for a silicon yield S = 0.8 for the theoretical silicon production process.

Exergy losses	Exergy (MWh)	% of total losses
Off-gas temperature is 300 ºC:		
In furnace	2.34	21.0
In gas treatment section	5.24	47.0
With off-gas	2.93	26.3
In product treatment section	0.64	5.7
SUM	11.15	100
Off-gas temperature is 800 ºC:		
In furnace	2.34	21.0
In gas treatment section	3.28	29.4
With off-gas	4.89	43.9
In product treatment section	0.64	5.7
SUM	11.15	100

The exergy analysis put numbers on the quality of energy, in contrast to the energy analysis which put numbers on the quantity of energy, cf. Fig. 3 and Fig. 4. Quality is the potential to do work, and is the theoretical amount of work you can achieve from a given quantity of energy. Thus, the exergy analysis put numbers on the potential for process improvements in terms of resource utilization.

5.2 A submerged arc furnace operated at a Norwegian silicon plant

Table 6 shows the exergy input, exergy in product and exergy losses for the two cases of the furnace operating at a silicon plant in Norway. The exergy in the product for the case of no energy recovery system amounts to about 30 % of the exergy input which means that 70 % of the total exergy input is lost. These numbers correspond to the numbers in [5] for a ferrosilicon furnace at an Elkem plant on Iceland. The furnace load for the furnace in [5] is about 40 MW while it is about 45 MW for the furnace in this study. Therefore, we may assume that the distribution of the losses for the furnace studied in this work follow the same trend as the distribution given in [5] which shows that 47.4 % of the total exergy input is lost in the furnace, which includes the furnace and the gas treatment section in the theoretical process, 18.7 % is lost with the off-gas while about 4 % is lost with heat from furnace, in cooling water and as thermal energy from the product. However, as discussed above, the exergy in the off-gas and the exergy loss in the gas treatment section will depend upon the off-gas temperature and there might be a deviation between the furnace studied in this work and the one in [5].

From Table 6, we see that the exergy loss in the process may be reduced to about 60 % of total exergy input, which is a reduction of about 12 %, by installing energy recovery equipment in the off-gas system. Even though numbers have uncertainties they demonstrate that this effort will improve the exergetic efficiency significantly.

Table 6. Estimated exergy input, exergy in the product and the exergy loss for the two cases of no recovery and recovery of thermal exergy from the furnace off-gas for one furnace operating at a silicon plant in Norway. The numbers are given on a basis of one hour production in a 10 MW furnace. For the case of energy recovery system installed; product includes both the silicon and electric power delivered from the energy recovery system.

	No energy recovery system		Energy recovery system	
	Exergy (MWh)	% of input	Exergy (MWh)	% of input
Exergy input	22.1	100	22.1	100
Exergy in product	6.8	30.8	8.6	38.9
Exergy loss	15.3	69.2	13.5	61.1

5.3 Comparing the exergetic efficiencies for the theoretical and the industrial process

In evaluating industrial processes, it is useful and necessary to know the practical limit for the resource utilization. The theoretical process serves to give this limit for the silicon production process. Table 7 shows the exergetic efficiencies for several cases for the theoretical process and for the furnace operated at a Norwegian silicon plant. The case of energy recovery for the theoretical process means that all thermal exergy in the off-gas is utilized.

From Table 7 we observe that with no utilization of the thermal exergy in the off-gas for the theoretical process, the exergetic efficiency for a silicon yield of 1.0 is nearly 50 % and that it is reduced to about 40 % for a silicon yield of 0.8. In comparison, the exergetic efficiency for the industrial process with no energy recovery is about 30 %. Utilization of the thermal exergy in the off-gas enhances the exergetic efficiency for the theoretical process to roughly 65 % for an off-gas temperature of 800 ºC and silicon yield of 0.8. The exergetic efficiency of the industrial process increases to around 40 % with energy recovery.

Table 7. Comparing the exergetic efficiencies for several cases of the theoretical silicon production process and for the furnace operated at a Norwegian silicon plant denoted the industrial process in the table. Energy recovery means recovery of thermal exergy in the off-gas.

	Exergetic efficiency, ε (%)
Theoretical process: No Energy Recovery:	
Silicon yield is 1.0	47.5
Silicon yield is 0.8	40.3
Theoretical process: Energy Recovery (silicon yield 1.0):	
Off-gas temperature is 300 ºC	58.6
Off-gas temperature is 800 ºC	67.4
Theoretical process: Energy Recovery (silicon yield 0.8):	
Off-gas temperature is 300 ºC	54.2
Off-gas temperature is 800 ºC	64.6
Industrial process:	
No energy recovery	30.8
Energy recovery	38.9

6. Conclusions

The theoretical silicon production process is established as a first reference case for the silicon production process. For the theoretical process, we have calculated exergetic efficiencies of 47.5 % and 40.3 % for a silicon yield of 1.0 and 0.8, respectively. Utilization of thermal exergy in the off-gas increased the exergetic efficiency to 58.6 % and 67.4 % for off-gas temperatures of 300 ºC and 800 ºC, respectively, for a silicon yield of 1.0.

For the industrial process, the exergetic efficiency was estimated to be 30.8 % and 38.9 % with no recovery and recovery of thermal exergy in the off-gas, respectively. This shows, as expected, that it is rather beneficial to recover thermal exergy in the off-gas and that it is still a potential for process improvements.

Acknowledgement

This work is financed by the Research Council of Norway and the Norwegian Ferroally Producers Research Association through the FUME (Fugitive emissions of Materials and Energy) project.

Elkem is acknowledged for providing data.

References

[1] Key World Energy Statistics 2011, Technical report, International Energy Agency, 2011

[2] Kotas, T.J., The exergy method of thermal plant analysis. Florida: Krieger Pub.; 1985

[3] Bejan, A., Tsatsaronis, G. and Moran, M., Thermal Design and Opimization, USA, John Wiley and Sons; 1996

[4] Schei, T., Tuset, J.K. and Tveit, H., Production of High Silicon Alloys. Trondheim: Norway:Tapir; 1998

[5] Hjartarson, H., Waste Heat Utilization at Elkem Ferrosilicon Plant in Iceland [dissertation]. Iceland: University of Iceland; 2009

[6] Tveit, H., Personal communication, 2012

[7] Kamfjord, N.E, Myrhaug, E.H., Tveit, H. and Wittgens, B., Energy balance of a 45 MW (ferro-) silicon submerged arc furnace, INFACON XII; In Proceedeings of the Twelfth International Ferro Alloy Congress; 2010 Jun 6-9; Helsinki, Finland;2010

[8] Kamfjord, N.E., Personal communication, 2011

[9] Almås, K. Delbeck, H.K., Halland, T., Rong, H.M. and Tveit, H., Improved Environmental and Energy Recovery Performance with New furnace hood Design at Elkem Thamshavn., In Proceedings of Silicon for the Chemical Industry VI; Loen, Norway; 2002

[10] Roine, A., HSC Chemistry® 6.0 User's Guide, 2006

[11] Grønli, M. and Tveit, H., Bruk av Biokarbon i Norsk Ferroleferingsindustri. Trondheim:Norway: SINTEF technical report (in Norwegian); 1997

[12] Kjelstrup, S. Bedeaux, B., Johannesen E., and Gross, J., Non-Equilibrium Thermodynamics for Engineers. Singapore: World Scientific; 2010

[13] Dosaj, V.D., May, J.B. and Arvidson, A. N., Direct Current, Closed Furnace Silicon Technology, In Proceedings of Silicon for the Chemical Industry II, Loen, Norway, 1994

[14] Kolbeinsen, L., Lindstad, L., Tveit, H., Bruno, M. and Nygaard, L., Energy Recovery in the Norwegian Ferro Alloy Industry, In: Tuset, J.K., Tveit, H. and Page, I.G editors INFACON 7: Proceedings of the 7th International Ferro Alloy Congress;1995 Jun 11-14; Trondheim; 165-177

Exergy based indicators for cardiopulmonary exercise test evaluation

Carlos Eduardo Keutenedjian Mady[a], Cyro Albuquerque-Neto[b], Tiago Lazzaretti Fernandes[c], Arnaldo Jose Hernandez[d], Paulo Hilário Nascimento Saldiva[e], Jurandir Itizo Yanagihara[f], Silvio de Oliveira Junior[g]

*[a,f,g] Department of Mechanical Engineering, Polytechnic School of University of São Paulo, São Paulo, Brazil, cekm@usp.br[a] (**CA**), jiy@usp.br[f], soj@usp.br[g]*
[b]Department of Mechanical Engineering, Centro Universitário da FEI, São Bernardo do Campo, Brazil, cyroan@fei.edu.br
[c,d] Sports Medicine Group of the Department of Orthopedics and Traumatology, University of São Paulo Medical School, São Paulo, Brazil, tiago.lazzaretti@usp.br
[e]Department of Pathology,University of São Paulo Medical School, São Paulo, Brazil, pepino@usp.br[e]

Abstract:

The cardiopulmonary exercise test is one of the most used tests to assess the functional capacity of individuals with varying degrees of physical training. One of the indices that are used for these analyses is the maximum oxygen consumption (maximum capacity of the body to transfer and transport oxygen to tissues). Lactate threshold is another metabolic parameter used to identify the state of the aerobic training. During the experimental procedure, the individuals are submitted to increasing levels of velocities, which is suitable for the obtainment of the blood lactate concentration. The aim of this work is the development of performance indicators for individuals under physical activity based on the concepts of exergy destroyed rate and exergy efficiency. To perform the exergy analysis, it was necessary to calculate heat and mass flow rates, associated with radiation, convection, vaporization and respiration, determined from the measurements and some relations found in the literature. The energy balance allowed the determination of the internal temperature over time. Those information were used to obtain the exergy variation of the body along the experiment. Eventually, it was possible to calculate the destroyed exergy and the exergy efficiency from the exergy analysis. During the tests the following measurements were made: the skin temperature of the trunk, legs and arms, the tympanic temperature, the respiratory gas exchanges, the blood lactate concentration, and some anthropometric parameters. The exergy rates and flow rates are dependent of the exercise level and the body metabolism. The results show that the relation between the destroyed exergy and the metabolism is almost constant during the test; furthermore its value has a great dependence of the subject age. Moreover, the exergy efficiency has a different behavior between the low trained subjects and the others.

Keywords:

Exergy Analysis, Exergy Efficiency, Treadmill Running, Aerobic Threshold.

1. Introduction

Exergy analysis is applied to assess the energy conversion processes that take place in the human body during physical exercise, aiming at developing indicators of performance based on the concepts of exergy destroyed rate and exergy efficiency. The Second Law of Thermodynamics was applied to the human body by several authors [1-15].

Initially the Second Law was applied to biological systems to study the Prigogine and Wiame [1] theory, which states that the entropy production tends to decrease over lifespan. Several authors confirmed this principle [1-7,15].

Batato at al. [8] proposed a pioneer model to perform the exergy analysis to the human body. Later, Prek [9,10], Prek and Butala [11] and Simone et al. [12] performed the exergy analysis for the human body to obtain relations of destroyed exergy with thermal comfort and thermal sensation conditions.

A few authors applied the exergy analysis [14], or the Second Law analysis [5-7] to the human body during physical exercise. Results of Rahman [5] indicate that the entropy generation rate increases with the increment of the exercise level. Silva and Annamalai [6,7] compared the entropy generation and lifespan for individuals under basal conditions, for different content of diets and different levels of physical activities; the authors suggested that physical activities should be kept in a "healthy minimum" if the entropy generations is to be minimized.

Albuquerque-Neto et al. [14] suggested a model of the respiratory and of the thermal system to perform the exergy analysis of the human body under physical activities. According to the exergy analysis, the internal respiration is more effective under physical activity than the external respiration.

The majority of energy analyses of the whole human body under physical exercise are based on the evaluation of the performed work and its efficiency. In the most common approach, the work of walking or running is determined from the dynamic of the mass center and limbs [16,17].

Two efficiencies are normally used in exercise physiology. One is the net efficiency, defined as the relation between the work and the net energy expenditure (the difference between the total and basal metabolism). The other is the delta efficiency, defined as the relation between the increase of the work and the increase of the energy expenditure. According to Kaneko[18], the net efficiency of running decreases while the speed increases, from about 60 to 15% between 3.9 to 9.4 m/s. Ito et al. [19] found that the net efficiency remains approximately the same (55 ± 12.7%);Williams and Cavanagh [20] found the net efficiency of 44% for running at 3.6 m/s; and Bijker et al. [21] found the value of 48% for the delta efficiency running at 2.2 m/s over an inclined treadmill. Those controversial results are mainly due to the calculation of the net energy expenditure, which may be inaccurate during the anaerobic exercise [18], and due to the method used to obtain the work – values from 343 to 1650 W for speeds between 3.6 and 3.9 m/s are found in the literature [20].

The lactate threshold (LT) is nowadays one of the most reliable indicators of functional capacity. It indicates the moment when the anaerobic threshold overtakes the aerobic threshold, which is characterized by the abruptly increase in the lactate concentration. A common experimental protocol used for its determination is the treadmill incremental running test. The subject must stay in the same speed for a time long enough to the lactate level in the blood become stabilized. The lactate threshold is obtained directly from blood analysis.

In the present work, exergy analysis is applied to the human body under treadmill incremental running tests. The analyses are based on experimental results and on the energy and exergy balances.

2. Methods

2.1. Energy analysis

The energy and exergy analysis proposed in the present work is based on a previous study by Mady et al [15]. The heat transfer rate and mass flow rates to the environment were obtained from a procedure described by [23] and by [24].

The total internal energy variation of the body was assumed to be as indicated in (1). Accordingly, it is a sum of the metabolic internal energy (M) and the internal energy variation of the body over time due to the transient environment conditions ($dU/dt\big|_{\Delta T}$). In the following equation, m is the subject mass, c is the body specific heat, and T_b is the representative of the internal temperature of the body.

$$\frac{dU}{dt} = -M + \left.\frac{dU}{dt}\right|_{\Delta T} = -M + mc\frac{dT_b}{dt}, \quad (1)$$

The First Law of Thermodynamics (2) can be applied to the subject under physical activity to obtain $dU/dt\big|_{\Delta T}$ and, therefore, the body temperature variation over time:

$$\left.\frac{dU}{dt}\right|_{\Delta T} = M - \left(Q_c + Q_r + H_e + \Delta H_{res}\right) - W, \qquad (2)$$

In (2) Q_c is the convective heat transfer rate, Q_r is the radiative heat transfer rate, H_e is the vaporization flow rate through skin; ΔH_{res} is the enthalpy flow rate variation due to the respiration and W is the performed power.

It is important to highlight that the convection heat transfer coefficient was correlated with the leg speed through relations found in [25]. Moreover, the convection and vaporization coefficients were adjusted so that the calculated internal temperature and the water loss are in accordance with the measured data.

The performed work by the subject used in the present analysis is the external performed work defined by [17] as a function of mass and speed. This choice was based on a discussion present in Ward-Smith [26] about the energy exchanges during running. Besides, this definition provides coherent results for the internal temperature and the net efficiency.

The net efficiency is defined as the relation between the work and the net energy expenditure (the difference between the total and the basal metabolism) as proposed by Kaneko [18]:

$$\eta_{en,net} = \frac{W}{M - M_0}, \qquad (3)$$

where M_0 is the metabolism at basal condition. In the present work, it is considered as the mean metabolism of the initial 5 minutes standing in the treadmill.

2.2. Exergy analysis

The Exergy analysis is applied to each subject, with a given environment/reference condition, such as temperature ($T_0 = T_a$), pressure ($P_0 = P_a$) and relative humidity ($\phi_0 = \phi_a$). Thus, (4) indicates a general equation of the exergy balance.

$$\frac{dB}{dt} = \sum B_{in} - \sum B_{out} + \sum_k Q_k \left(1 - \frac{T_0}{T_k}\right) - W - B_{dest}, \qquad (4)$$

Similar to the internal energy variation over time, the metabolic exergy (B_M) constitutes a part of $d\mathbf{B}/dt$ indicated in (5), neglecting the body volume variation over time:

$$\frac{d\mathbf{B}}{dt} = -B_M + \left.\frac{d\mathbf{B}}{dt}\right|_{\Delta T} = -B_M + \left(\left.\frac{dU}{dt}\right|_{\Delta T} - T_0 \left.\frac{dS}{dt}\right|_{\Delta T}\right), \qquad (5)$$

where, $\mathbf{B}$ is the body exergy, $d\mathbf{B}/dt|_{\Delta T}$ is the exergy variation of the body due to a variation in environmental conditions.

Batato et al. [14] achieved that the metabolic internal energy and the metabolic exergy are very close; therefore, the approximation $B_M \approx M$ might be used. The term $dU/dt|_{\Delta T}$ is calculated from the energy balance (2) and $dS/dt|_{\Delta T}$ is calculated from (6):

$$\left.\frac{dS}{dt}\right|_{\Delta T} = mc \ln\left(\frac{T_b^{i+1}}{T_b^i}\right), \qquad (6)$$

where, T_b^i is the body temperature at instant i and m is the body mass.

Equation (7) indicates the exergy balance applied to the human body:

$$B_{dest} = B_M - \left(B_c + B_r + B_e + \Delta B_{res}\right) - \left.\frac{d\mathrm{B}}{dt}\right|_{\Delta T} - W, \qquad (7)$$

where the exergy rate and flow rates B_c, B_r, B_e and $\Delta B_{res}=(B_{ex} - B_a)$ are the exergy associated with convection, radiation, vaporization and respiration, as considered by [15].

The exergy efficiency is defined in (8):

$$\eta_b = 1 - \frac{B_{dest}}{\left| -B_M + dB/dt\big|_{\Delta T} \right|}, \qquad (8)$$

2.3. Experimental procedure

Eleven male subjects participated in this study. The mean age was 31.4 ±10.1 (mean ± standard deviation); the mean mass was 73.3 ± 7.8 kg; the mean height was 1.76 ± 0.07 m; and the mean surface area was 1.89 ± 0.11 m^2. The subjects were all runners with different levels of training; seven of them trained four or more times a week, and four trained less than four times a week.

After the connection of the subject with the measurement system, 5 minutes of data were collected for control, with the subject standing over the treadmill. Then the subject ran for 3 minutes to warm-up with 30% of his long distance training speed. After that the speed was set to 70% of the training speed. The speed was incremented by 1 km/h every 4 minutes until the subject becomes exhausted. During the experiment, the treadmill was set to 1% of inclination, so that the energy expenditure is equivalent to an outdoor running [22]. The experimental procedure was approved by the Ethics Committee for Analysis of Research Projects (CAPPesq).

A calorimetric system (TruMax 2400 Metabolic Measurement System, Consentius Technologies) was used to measure the ventilation and the oxygen and carbon dioxide concentration in the expired gas. Those data were used to calculate the O_2 consumption, the CO_2 production and the energy expenditure (metabolism).

In order to obtain the lactate concentration, a blood sample was collected from the fingertip after 3.5 minutes at each speed and analyzed with the Accutrend® Lactate (Roche, type 3012522). Three methods were used to obtain the speed in which the lactate threshold happens: when the difference from the last value was larger than 1 mmol/L; when the absolute value was 4 mmol/L; and by graphical analysis with a logarithmic scale. The mean value of these three methods was used in the analysis.

The skin temperatures were measured with an infrared thermometer (MX2, Raytek) in three locations: center of back, posterior right arm, and posterior right leg. Those measurements were made in the last two minutes of each test speed. The tympanic temperature (representative of the body temperature) was measured before and after the exercise with an ear thermometer (G-Tech).

The internal environmental conditions were measured just before the beginning of each experiment. The mean air temperature was 23.6 ± 1.5 °C; the mean radiant temperature was 22.8 ± 1.5 °C; and the mean relative humidity was 56.6 ± 8.5 %. The barometric pressure of the laboratory was 688 mmHg. The tests were carried out in three different days.

3. Results

Figures 1 to 6 show the main measured and calculated results of the present work for all the subjects. They are separated into three groups, based on the speed in which the lactate threshold (LT) was achieved. The first group (low LT) includes four subjects with the LT speed ≤ 3.1m/s. The second group (medium LT) includes three subjects with 3.1< LT speed <3.5 m/s. The last group (high LT) includes four subjects with the LT speed ≥ 3.5 m/s. The mean LT speeds for the groups are 2.8 ± 0.3, 3.3 ± 0.1, and 3.8 ± 0.4m/s.

The graphs of Figs. 1 to 5 show relations between a calculated or measured variable as a function of the treadmill speed. The dots are mean values for the last minute of each speed level (the lines between the dots are only for the identification of each subject). This is a period sufficient for stabilization of several physiological variables. In order to improve the clearness of the graphs, the periods that are not used to obtain the performance indicators (control, warm-up and recovery periods) were not included. The most trained subject that participated in the tests is the only one that

reached a speed greater than 5 m/s. The least trained subject is the one that reached a maximum speed lower than 3 m/s.

In Figure 1a it is indicated the increase of the metabolism (by subject mass) with the treadmill speed for each subject (from lowest, 1; to highest LT, 11,). Their relation is approximately linear. The subjects have metabolisms very close for the same speed, independent of the lactate threshold. The largest discrepancy is found in the subject 1 for which the metabolism is clearly greater than the others for the same speed. This subject is the one with the lowest lactate threshold, which may indicate that he is not adapted to run in an efficiency way, in other words, he probably uses more nutrients to develop the same speed. The net efficiencies of the subjects are indicated in Fig. 1b. The subject 1 is the one that reachs the smallest net efficiency. However, this result is not observed in the other subjects with low LT. In fact, the other subjects of the low lactate threshold group reached the largest values of efficiency in low speeds, which were not run by the most trained subjects. The results do not show expressive differences between the groups. The net efficiency for each subject decreases with speed. This result is in agreement with [18] for a large range of speeds.

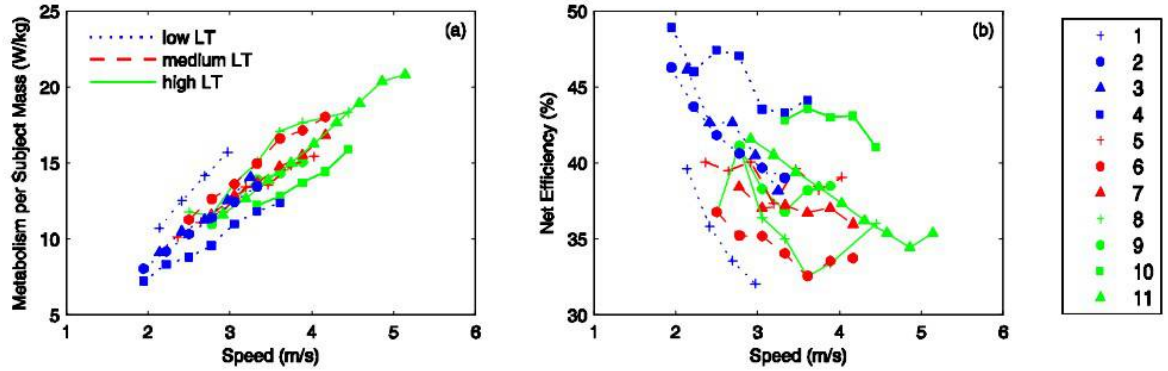

Fig. 1. a) Metabolism and b) energetic net efficiency for each subject (1-11).

Figure 2a shows the calculated internal body temperature. The curves have similar trends for all the subjects. In the beginning of the running test, the internal temperature starts to increase in a high rate, but with a tendency to stabilize in a maximum value. However, during the last third of the test, the internal temperature returns to increase in a high rate, which is a consequence of the skin saturation by water due to the sweating regulatory mechanism.

Figure 2b shows the measured mean skin temperature, weighted by the limb surface area. The skin temperature depends mostly of the environment conditions. It is observed in the graph a small variation due to the increase in the physical activity (with exception of one subject from the low LT group whom the skin temperature raised from 29 to almost 33 °C). This happens because the effect of the metabolism increase is compensated by the increase of the convection heat transfer and the evaporation. Moreover, the subject 1 reached the highest skin temperatures is the one with the highest relation between metabolism and speed, as discussed above.

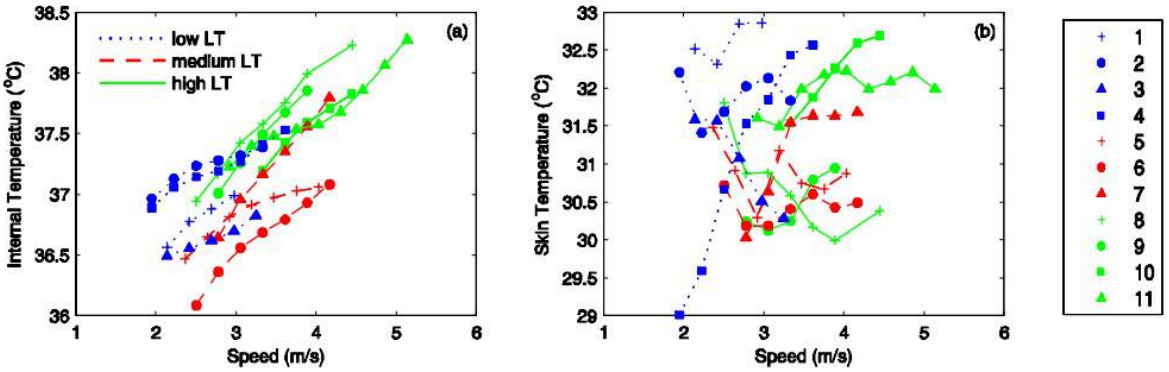

Fig. 2. a) Internal temperature, and b) mean skin temperature.

In Fig. 3a it is indicated the calculated total energy transfer rate (per surface area) to the environment through the skin (by convection, radiation and evaporation) and the respiratory entalphy variation through the ventilation. The energy transfer increases fast in the beginning of the exercise due to the increase in the convection, evaporation and ventilation. The main reasons of the increase in the energy transfer by those mechanisms is the increase of the limb movements (which increase the heat transfer coeficient), the wet surface,and the respiratory tract flow. The saturation of the skin by sweat diminishes the increase of the total energy transfer with the environment, which is clearly observed in the graph.

Figure 3b shows the total exergy transfer rate (by surface area) with the environment. The main mechanisms of exergy transfer with the environment are related with mass transfer. For all subjects, the maximum exergy transfered by convection is 2.1 W/m^2, the maximum exergy transfered by radiation is 1.8 W/m^2, and the maximum exergy variation by the pulmonary ventilation is 3.0 W/m^2. The evaporation through the skin is indicated in Fig. 3c. The exergy transfer reachs a maximum value after the skin gets saturated by the sweat. The subject 1 has a distinct exergy transfer value from the others, as a result of its higher relation between the air temperature and the skin temperature. As indicated by [8,15] for basal conditions, the contributions of heat transfer rate and mass flow rates to the environment during exercise are an order of magnitude higher than their exergy contribution.

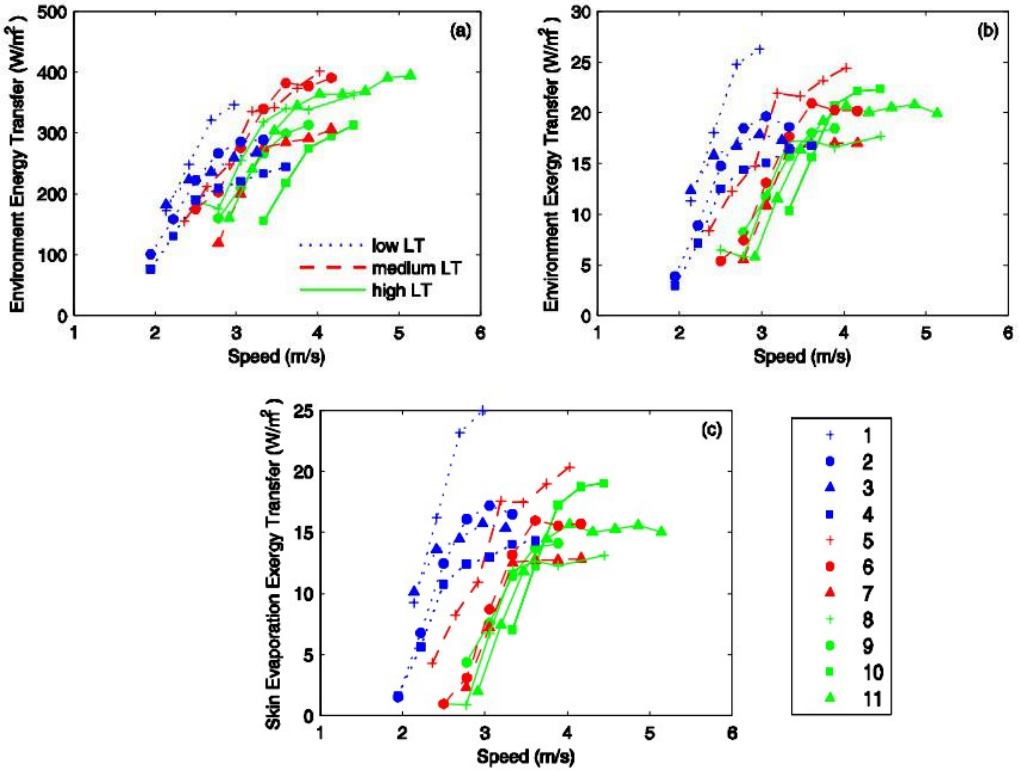

Fig. 3 a) Total energy transfer rate to the environment through skin, b) total exergy transfer to the environment, c) evaporative exergy transfer to the environment.

Figure 4a shows the increase in the destroyed exergy (per unit of mass) with the speed, which confirms previous results found on literature [5-7]. The increase for each subject is similar to the increase of the metabolism, but with lower values. For all subjects the trend is similar. Figure 4b indicates the ratio of destroyed exergy and metabolism, which ranged from 56 to 70%. The subject 1 was the one with highest ratio, hence it follows that this subject destroy more exergy than the others for the same speed.

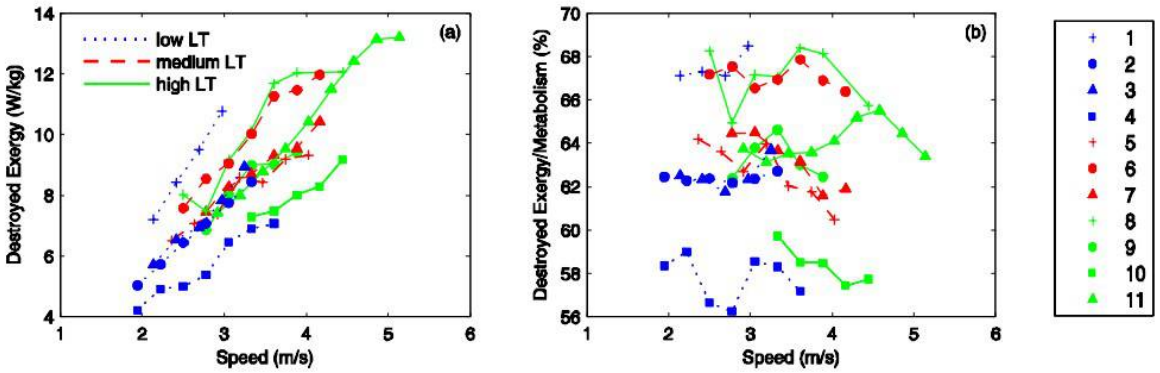

Fig. 4. a) Destroyed exergy rate; b) relation between destroyed exergy and exergy metabolism (in exergy basis).

In Fig. 5a, the exergy efficiency is indicated as a function of treadmill speed, where the values ranged between 30 to 44%. An unexpected result is that the subjects with low LT have higher exergy efficiency for the same speed, and their maximum is earlier than others. This last result is justified by the exergy transfer to the environment (mostly evaporative). The exercise for this group began in a lower speed, hence their skin get saturated with sweat earlier. A comparison between the other groups does not show a clear trend. Figure 6b indicates the ratio of exergy efficiency and net energy efficiency, where there is a point of inflection for most subjects.

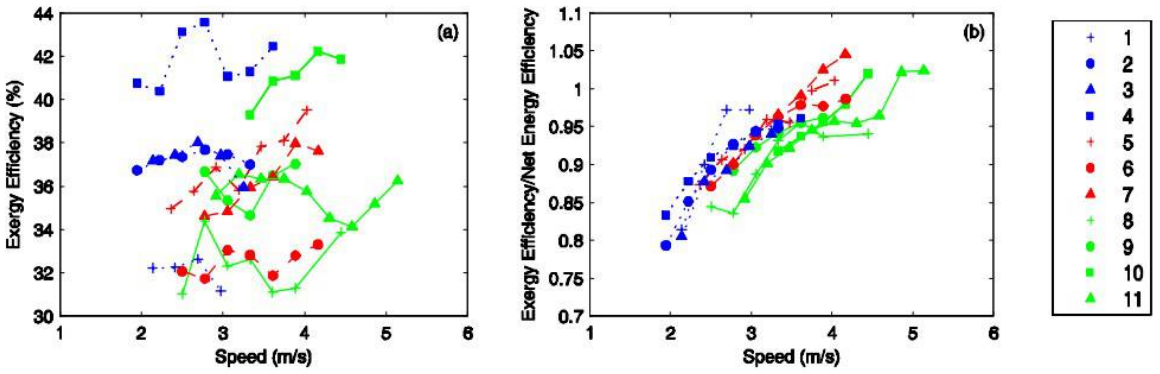

Fig. 5. a) Exergy efficiency and b) ratio of exergy efficiency and net efficiency as a function of treadmill speed

Table 1 indicates the values of the exergy balance (per unity of mass) integrated over time, for each subject. A comparison with results of basal conditions obtained in [8,15] indicates that the exergy efficiency during physical activities may reach values of 45%, whereas in basal conditions the efficiency is lower than 5% [15] or neglegitable [8] .The exergy variation of the body does not correspond to more than 1% of the total metabolic exergy; and the exergy lost to the environment during test does not correpond to more than 5% of the total metabolic exergy.

Table 1. Values of exergy balance (per unity of mass) integrated over time and calculated exergy efficiency for each subject

Subject	Test Duration (min)	Δb (J/kg)	$\int b_M dt$ (J/kg)	$\int b_d dt$ (J/kg)	$\int b_{env} dt$ (J/kg)	$\int w dt$ (J/kg)	η_b (%)
1	29.5	57	16890	11194	769	4870	34
2	34	72	17819	10797	588	6363	40
3	29	68	15752	9884	569	5232	38
4	36	117	17220	9674	474	6956	44
5	43.5	103	27248	17750	1014	8381	35
6	42.5	89	30746	20286	937	9435	34
7	41.5	125	25310	15838	763	8584	38
8	42.5	101	30249	19855	865	9428	35
9	37	223	22959	15052	683	7001	35
10	35	169	20927	12757	772	7229	40
11	52.5	146	42761	27971	1366	13277	35

The results of Figure 6 indicate the ratio of the destroyed exergy with the metabolic exergy (Fig. 6a) and the exergy efficiency (Fig. 6b) as a function of subject age. The ratio of the destroyed exergy with the exergy metabolism tends to decrease as a function of age, which confirms the results of basal conditions [1-7,15]. Finally, the exergy efficiency increases as a function of age, which differ from the basal conditions result [15], where the exergy efficiency decreases as a function of age (basal conditions).

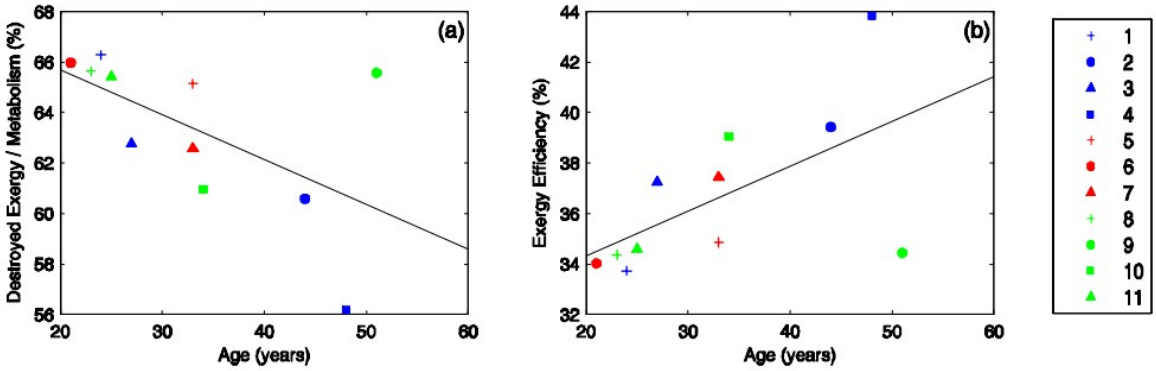

Fig 6. (a) Ratio of the destroyed exergy and metabolism (in exergy basis) and (b) exergy efficiency as a function of the subject age

4. Conclusion

The destroyed exergy and exergy efficiency were determined for the human body for the cardiopulmonary exercise test evaluation. From the analyzed range of parameters, it was possible to conclude that:

- metabolism increases with the increment of treadmill speed, while the net efficiency tends to decrease;
- the body temperature tends to increase as a function of treadmill speed while the skin temperature remains almost constant;
- when the subject is under physical exercise, the heat transfer rate and the mass flow rates are order of magnitude larger that the exergy rates and flow rates, similar to basal conditions [8,15];

- the exergy efficiency has a different trend between the low LT group and the medium and high LT groups. Moreover, it is higher for the low LT group. Values of exergy efficiency ranged between 30 to 44%, whereas in basal conditions the exergy efficiency was lower than 5%.
- the destroyed exergy rate increases as a function of speed, as previously obtained in the literature, but for entropy production [5-7];
- the ratio of the destroyed exergy and metabolic exergy remains almost constant independently of the level of exercise, but it tends to decrease as a function of the subject age, as occur for basal conditions [1-7,15]. The exergy efficiency tends to increase with age, which differs from the basal conditions results [15].

Acknowledgments

The authors acknowledge FAPESP (the State of São Paulo Research Foundation) and CNPq (National Research Council) for the financial support. The authors are also grateful to Paulo Roberto Santos Silva, Larissa Souza and Andrea Baptista for their support in the experimental procedure.

Nomenclature

B	exergy rate and flow rate, W
$\mathbf{B}$	body exergy, J
b	specific exergy, W/kg
$\mathbf{b}$	body specific exergy, J/kg
c	heat capacity, W/(kg.K)
H	enthalpy flow rate, W
LT	lactate threshold, mmol/L
M	metabolism, W
m	body mass, kg
Q	heat transfer rate, W
P	pressure, Pa
S	entropy rate, W/K
T	temperature, °C or K
t	time, s
U	internal energy, J
W	performed work, W
w	specific performed work, W/kg

Greek symbols

η	efficiency
ϕ	relative humidity, %

Subscripts and superscripts

0	reference
a	environment air
b	body
b	exergy
c	convective
dest	destroyed
e	evaporative

en energy
ex expired
in inflow
M metabolic
out outflow
r radiative
res respiration
ΔT due to body temperature variation

References

[1] Prigogine I., Wiame J., Biologie et Thermodynamique des phenomenes irreversibles. Experimentia 1946;2(11):451-453.

[2] Zotin A.I., Zotina R.S.. Thermodynamics aspects of developmental biology. Journal of Theoretical Biology 1967;17(1):57-75.

[3] Balmer R.T., Entropy and aging in biological systems. Chemical Engineering Communications 1984;17(1):171-181.

[4] Aoki I., Entropy principle for human development, growth and aging. Journal of Theoretical Biology 1991;150(2):215-223.

[5] Rahman M.A., A novel method for estimating entropy generation rate in human body. Thermal Science 2007;11(1):75-92.

[6] Silva C., Annamalai K., Entropy generation and human aging: lifespan entropy and effect of Physical Activity Level. Entropy 2008;10(2):100-123.

[7] Silva C., Annamalai K., Entropy generation and human aging: lifespan entropy and effect of diet composition and caloric restriction diets. Journal of Thermodynamics 2009;2009:1-10.

[8] Batato M., Borel L., Deriaz O., Jequier, E., Analyse exergétique théorique et expérimentale du corps humain. Entropie 1990;26(153-154):120-130.

[9] Prek M., Thermodynamic analysis of human heat and mass transfer and their impact on thermal comfort. International Journal of Heat and Mass Transfer 2005;48(3-4):731-739.

[10] Prek M., Thermodynamical analysis of human thermal comfort. Energy 2006;31(5):732-743.

[11] Prek M., Butala, V., Principles of exergy analysis of human heat and mass exchange with the indoor environment. International Journal of Heat and Mass Transfer 2010;48(25-26):731-739.

[12] Simone A., Kolarik J., Iwamatsu T., Asada H., Dovjak M., Schellen L., Shukuya M., Olesen B.W., A relation between calculated human body exergy consumption rate and subjectively assessed thermal sensation. Energy and Buildings 2011;43(1):1-9.

[13] Lems S., Thermodynamic explorations into sustainable energy conversion - Learning from living systems [dissertation]. Delft, Netherlands, Technische Universiteit Delft; 2009.

[14] Albuquerque-Neto C., Pellegrini L.F., Ferreira M.S., Oliveira Jr S., Yanagihara J.I., Exergy analysis of human respiration under physical activity. International Journal of Thermodynamics 2010;13(3):105-109.

[15] Mady C.E.K., Ferreira M.S., Yanagihara J.I., Saldiva P.H.N., Oliveira Jr S., Modeling the exergy behavior of human body. In: Bojić M., Lior N., Petrović J., Stefanović, G. Stevanović, V., editors. ECOS 2011: Proceedings of the 24th International Conference on Efficiency, Cost, Optimization, Simulation, and Environmental Impact of Energy Systems; 2011 Jul 4-7; Novi Sad, Serbia. 245-257.

[16] Feen W.O., Work against gravity and work due to velocity changes in running: movements of the center of gravity within the body and foot pressure on the ground. American Journal of Physiology 1930;93(2):433-462.

[17] Cavagna G.A., Kaneko, M., Mechanical work and efficiency in level walking and running. Journal of Physiology 1977;268(2):467-481.

[18] Kaneko M., Mechanics and energetics in running with special reference to efficiency. Journal of Biomechanics 1990;23(1):57-63.

[19] Ito A., Komi P.V., Sjödin B., Bosco C., Karlsson J., Mechanical efficiency of positive work in running at different speeds. Medicine and Science in Sports and Exercise 1983;15(4):299-308.

[20] Williams K.R., Cavanagh P.R., A model for the calculation of mechanical power during distance running. Journal of Biomechanics 1983;16(2):115-128.

[21] Bijker K.E., de Groot G., Hollander A.P., Delta efficiencies of running and cycling. Medicine and Science in Sports and Exercise 2001;33(9):1546-1551.

[22] Jones A.M., Doust J.H., A 1% treadmill grade most accurately reflects the energetic cost of outdoor running 1996;14(4):321-327.

[23] ASHRAE: American Society of Heating, Refrigerating and Air-Conditioning Engineers, Thermal comfort. In: Handbook of Fundamentals. Atlanta, USA.2009, p.9.1–9.29.

[24] Ferreira M.S., Yanagihara J.I., A transient three-dimensional heat transfer model of the human body. International Communications in Heat and Mass Transfer 2009;36(7):718–724.

[25] Incropera F.P., DeWitt D.P., Bergman T.L., Lavine A.S., Fundamentals of heat and mass transfer. New York, USA: John Wiley & Sons; 2006.

[26] Ward-Smith, A.J., Air resistance and its influence on the biomechanics and energetics of sprinting at sea level and at altitude. Journal of Biomechanics 1984;17(5):339-347.

Exergy Disaggregation as an Alternative for System Disaggregation in Thermoeconomics

José J. Santos[a], Atílio B. Lourenço[b], Júlio A. Mendes da Silva[c], João L. Donatelli[d] and José C. Escobar Palacio[e]

[a] *Federal University of Espírito Santo, Vitória-ES, Brazil, jjcsssantos@yahoo.com.br* ***(CA)***
[b] *Federal University of Espírito Santo, Vitória-ES, Brazil, atiliobl@gmail.com*
[c] *University of São Paulo, São Paulo-SP, Brazil, jams_mendes@yahoo.com.br*
[d] *Federal University of Espírito Santo, Vitória-ES, Brazil, donatelliufes@gmail.com*
[e] *Federal University of Itajubá, Itajubá-MG, Brazil, jocescobar@gmail.com*

Abstract

Sometimes, under a thermoeconomic analysis point of view, it is necessary to consider a system as a group of subsystem. The disaggregation of the exergy flows may be also required, and it is usually performed by splitting these flows in several components, for example thermal, mechanical or chemical exergy or even including the fictitious flow called negentropy. In order to disaggregate a system we need to define the product and the fuel of each subsystem. Therefore, the introduction of the negentropy in thermoeconomics represented a great advance in the discipline, since this magnitude allows quantifying the condenser product, which was not possible before because the condenser is a dissipative component, whose product cannot be expressed neither in terms of total exergy nor in terms of thermal, mechanical or chemical exergy. Recently, it was shown that the disaggregation of physical exergy into its enthalpic term ($H-H_0$) and its entropic term ($T_0S-T_0S_0$) is a consistent alternative to quantify the condenser product. This approach is called H&S Model. However, neither the inclusion of negentropy itself nor the disaggregation of exergy into enthalpic and entropic terms does not allow defining the product of valves. A more recent approach overcame such limitation by proposing the disaggregation of the physical exergy into three terms, namely internal energy ($U-U_0$), flow work ($pV-p_0V_0$) and the entropic term ($T_0S-T_0S_0$). This approach is called UFS Model. This paper shows that exergy disaggregation is a consistent alternative for total disaggregation of systems in thermoeconomic modeling. Both exergy disaggregation level (H&S and UFS Model) can be used in order to quantify irreversibilities as well as the conventional exergy analysis. Furthermore, the results obtained, by aplying theses aproaches, show that the product-fuel ratios of each isolated components of the productive structure vary from zero (for totally irreversible processes) to one (for totally reversible ones).

Keywords

Exergy Disaggregation, Dissipative Components, System Disaggregation, Thermoeconomics.

1. Introduction

Thermoeconomics can be considered a new science which, by connecting Thermodynamics and Economics, provides tools to solve problems in complex energy systems that can hardly or not be solved using conventional energy analysis techniques based on First Law of Thermodynamics (mass and energy balance), as for instance a rational price assessment to the products of a plant based on physical criteria [1].

Most analysts agree that exergy, instead of enthalpy only, is the most adequate thermodynamic property to associate with cost (originally an economic property) since it contains information from the second law of thermodynamics and accounts for energy quality. An exergy analysis locates and quantifies the irreversibilities [2].

Depending on the type of analysis, different levels of accuracy of the results are required, i.e., each thermoeconomic analysis requires a specific aggregation level of the components, and of the flows of the plant. During the local optimization and diagnosis, for instance, the total disaggregation of the components of the system is generally required.

According to Torres et al. [3], sometimes, under a thermoeconomic analysis point of view, it is necessary to consider a component as a group of subsystems (made up of a group of subsystems) or a mass or an energy flow rate consisting of several components, for example thermal, mechanical or chemical exergy, or even including fictitious flow streams (negentropy) without a physical existence in the flow sheet of the plant.

In order to disaggregate the components of the systems we need to define the product and the fuel of each of them. Thus, the introduction of the negentropy in thermoeconomics represented a great advance in the discipline, since this magnitude allows quantifying the condenser product, which was not possible before because the condenser is a dissipative component, whose product cannot be expressed in terms of exergy only.

Valero et al. [2] stated that, although the magnitudes applied by most thermoeconomic approaches are exergy, negentropy and money, other magnitudes, like enthalpy and entropy, can also be used. According to Valero et al. [4], the fuels and the products (productive structure) of a system must be defined based in the trajectories that the flows describe in the h,s plane when they work for the specific purpose of the plant. Bearing this in mind, recently, Santos et al. [5] showed that the disaggregation of physical exergy into its enthalpic term ($H-H_0$) and its entropic term ($T_0S-T_0S_0$) is a consistent alternative to quantify the condenser product in a Rankine cycle. This approach is called H&S Model.

However, neither the disaggregation of exergy into its enthalpic and entropic terms nor the inclusion of negentropy itself allows defining the product of the valves in a refrigeration or heat pump cycles, which is also a dissipative component.

A more recent approach, proposed by Lourenço et al. [6], overcame such limitation by proposing the disaggregation of the physical exergy into three terms, namely internal energy ($U-U_0$), flow work ($pV-p_0V_0$) and the entropic term ($T_0S-T_0S_0$). This approach is called UFS Model.

This paper shows that both exergy disaggregation level (H&S Model and UFS Model) can be used in order to quantify local irreversibility as well as the conventional exergy analysis, and also the product-fuel ratios of each components of the productive structure vary from zero (for totally irreversible processes) to one (for totally reversible ones). Consequently, this paper shows that the UFS Model is an extension of the H&S Model and its application only could be justified if there is a valve in the flow sheet of the plant, because of the increasing complexity and computational efforts.

2. Physical Exergy Disaggregation

According to Torres et al. [3], the disaggregation of physical exergy in thermoeconomics was proposed by Tsatsaronis in 1990. Tsatsaronis and Pisa [7] defined the fuels and the products of the components by using the physical exergy disaggregated into thermal and mechanical components. But, this kind of disaggregation itself does not allow the isolation of dissipative components. In agreement with Lazzaretto and Tsatsaronis [8], although by considering separate exergy forms improve the accuracy of the results, this splitting might not be always meaningful because of the arbitrariness that might be involved in the separate calculation of mechanical and thermal exergies, particularly when working fluids that can change phases are used in the process being considered.

This arbitrariness does not occur when the physical exergy (1) is disaggregated into its enthalpic (2) and entropic (3) terms during the application of the H&S Model proposed by Santos et al. [5].

$$E_{i:0} = m_i \cdot \left[(h_i - h_0) - T_0 \cdot (s_i - s_0)\right] \tag{1}$$

$$S_{i:0} = m_i \cdot T_0 \cdot (s_i - s_0) \tag{2}$$

$$H_{i:0} = m_i \cdot (h_i - h_0) \tag{3}$$

Once that the enthalpy can be defined in terms of internal energy and flow work, the physical exergy (4) can be defined into three terms: internal energy (5), flow work (6) and entropic term (7).

$$E_{i:0} = m_i \cdot \left[(u_i - u_0) + (p_i \cdot v_i - p_0 \cdot v_0) - T_0 \cdot (s_i - s_0)\right] \quad (4)$$

$$U_{i:0} = m_i \cdot (u_i - u_0) \quad (5)$$

$$F_{i:0} = m_i \cdot (p_i \cdot v_i - p_0 \cdot v_0) \quad (6)$$

$$S_{i:0} = m_i \cdot T_0 \cdot (s_i - s_0) \quad (7)$$

This kind of disaggregation was the basis for the application of UFS Model by Lourenço et al. [6].

3. Definitions: fuel, product, irreversibility and efficiency

In agreement with Torres et al. [3], all thermoeconomic methodologies need to define a function or a productive purpose to each component of the plant. This is a key factor to know the process of cost formation and to know the causes that generate the cost in complex power plants. The causal of productive interaction between components determines the productive structure. According to Valero et al. [2], irreversibility is the physical magnitude generating the cost. Çengel and Boles [9] defines efficiency as the ratio of desired result for an event to the input required to accomplish the event. Moran and Shapiro [10] stated that efficiency gauges how effectively the input is converted to the product. Thus, we conclude that in thermoeconomics the concept of fuel (*Fu*), product (*Pr*), irreversibility (*Ir*) and efficiency (η) are not independents, as shown in (8) and (9).

$$Fu - \mathrm{Pr} = Ir + Lo \quad (8)$$

$$\eta = \frac{\mathrm{Pr}}{Fu} \quad (9)$$

Thus, in agreement with Çengel and Boles [9], we recognize that there is some disagreement on a general definition of the second-law efficiency, and thus a person may encounter different definitions for the same device. But, the thermodynamicists [9,10] agree that the second-law efficiency serves as a measure of approximation to reversible operation, and thus its value should range from zero in the worst case (totally irreversible process) to one in the best case (totally reversible process). According to Moran and Shapiro [10], it is important to recognize that the limit of 100% second-law efficiency should not be regarded as a practical objective. This theoretical limit could be attained only if there were no irreversibility (*Ir*) or losses (*Lo*).

With this in mind, during the definition of the productive structure for application of the H&S Model and UFS Model, the fuel and the product of the subsystems must be defined by taking into account that the second-law efficiency ranges from zero (for a totally irreversible process) to 100 percent (for a totally reversible process).

In the H&S Model the physical exergy is disaggregated into its enthalpic and entropic terms, thus, efficiency, cost and behaviour of the system are based in the trajectory in the h,s plane any flow performs when it works for the specific purpose of the plant. The products and the fuels of each subsystem, in terms of the enthalpic term, are defined based on the quantity of enthalpy added to and removed from the working fluid, respectively. On the other hand, because the entropic term has

a negative contribution to de physical exergy, as we can see in (1), this term is the products of the subsystems that decrease the working fluid entropy, and the subsystems that increase the working fluid entropy have the entropic term as fuel. This consideration allows one to define the fuels and the products of the productive component and condensers (dissipative component). However, this way, we can not define de product of the valves in which we consider that enthalpy does not vary.

Using the UFS Model, in which the enthalpic term is disaggregated into internal energy term and flow work term allows one solving this limitation of the H&S Models. As shown in (4), these two new terms have positive contribution to the physical exergy. Thus, in UFS Model, products and fuels of each subsystem, in terms of the internal energy term and flow work term, are defined based on the quantity of these magnitudes added to and removed from the working fluid, respectively. In a valve of a refrigeration or heat pump cycle the internal flow and the flow work of the working fluid vary: the internal energy decreases (fuel) and the flow work increases (product).

4. Application Examples

The beauty of a theory is usually shown in the simplicity of its forms and the generality of its message, but its power resides in its capacity to solve practical cases [11]. Thus, two simple examples of thermal systems are used, in this paper, to illustrate the application of the H&S Model and UFS Model, respectively: a Rankine cycle power plant and a heat pump cycle. By using these plants, this paper shows the capacity and the limitation of the H&S Model and UFS Model to treat two different kind of dissipative components in thermoeconomics: condensers and valves. In order to show the consistency these two models, actual, ideals and reversible cycles are used in this paper.

4.1. Rankine Cycle

4.1.1. Actual Cycle

The physical structure of the Rankine cycle power plant represented in Fig. 1 essentially coincides with the one used by [11] and [12]. The plant is considered made up of four components: boiler (B), turbine and generator (T-G), condenser and cooling water pump (C), and boiler feeding pump (P).

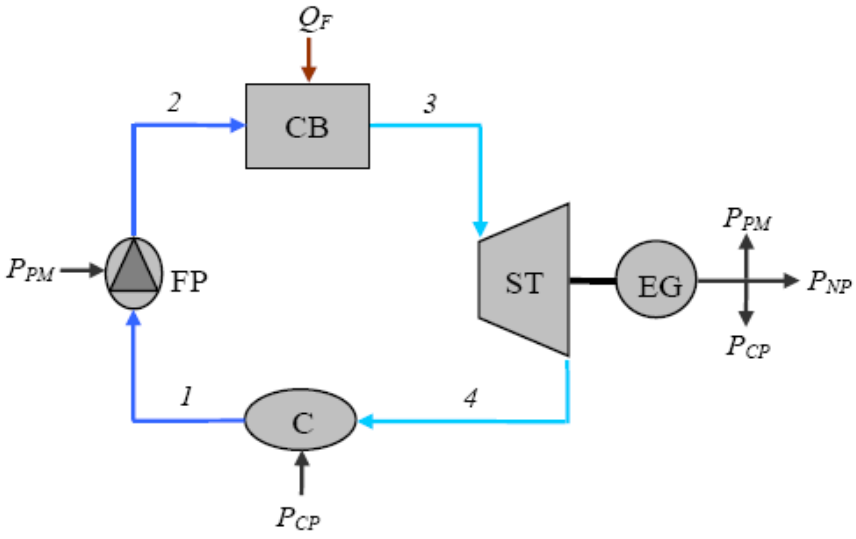

Fig. 1. Physical Structure of the Actual Steam Power Cycle

The external exergy consumption (Q_F) is 70.000 kW and the net power (P_{NP}) is 20.000 kW. The feeding and the cooling pump consume 155 kW (P_{PM}) and 75 kW (P_{CP}), respectively. Table 1 shows the main physical flow parameters.

The functional diagram is shown in Fig. 2. The enthalpy of the working fluid is increased as much in the pump as in the boiler. The turbine consumes part of this enthalpy. The operation of these

productive units (pump, boiler and turbine) increases the entropy of the working fluid. The condenser consumes the remaining part of enthalpy while it decreases the entropy of the working fluid. In other words, the condenser product is the entropic term and its fuel is the enthalpic term.

Table 1. Main Parameters of the Main Physical Flows of the Actual Steam Power Cycle

PHYSICAL FLOW		m [kg/s]	p [kPa]	T [°C]
N°	Description			
1	Water	19.5	7	39.04
2	Water	19.5	6300	39.50
3	Steam	19.5	6000	500.0
4	Moisture (x = 0,9)	19.5	7	39.04

The functional diagram represents graphically the cost formation process of the system. The rectangles are the real units (or subsystems) that represent the actual equipments of the system. The rhombus and the circles are fictitious units called junction and bifurcations, respectively.

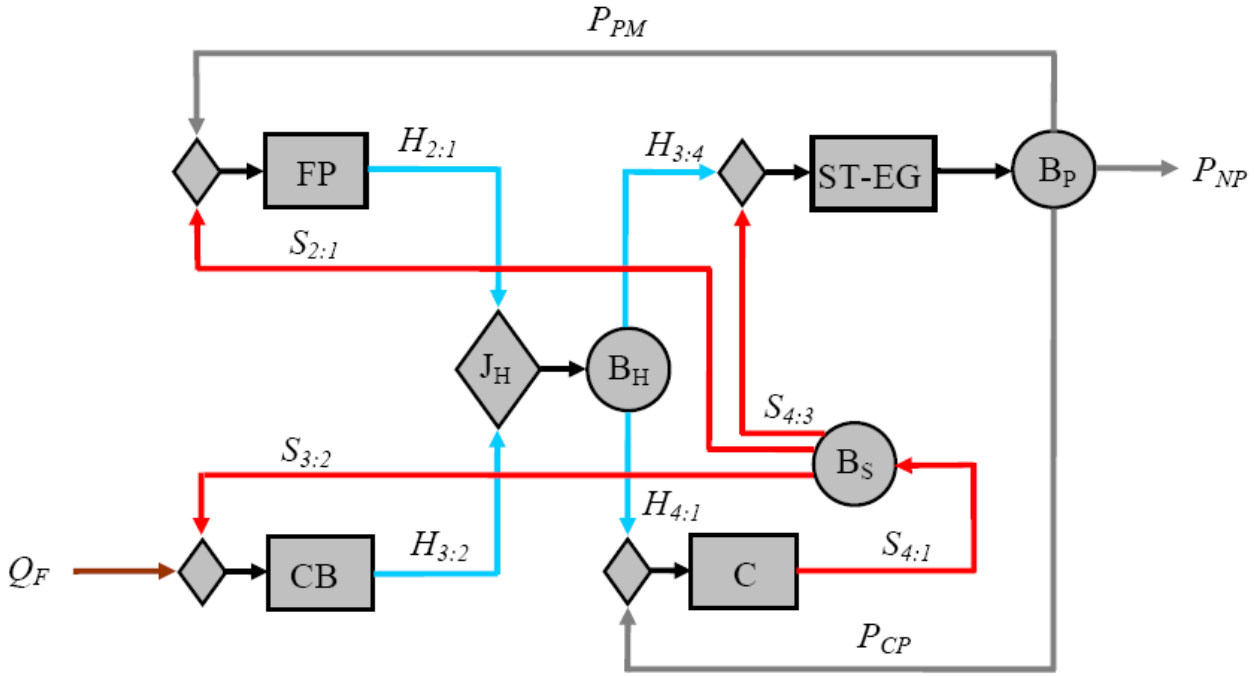

Fig. 2. Productive Diagram of the Actual Steam Power Cycle according to the H&S Model

Each productive units has inlet and outlet arrows, that represent its fuel (or resource) and products, respectively. There are productive units that have small junction to indicate that they have more than one fuel, and/or a small bifurcation to indicate that they have more than one product.

The flows of the functional diagram are productive flows. The only limitation which must be imposed is that it must be possible to evaluate all these flows in relation to the state of the plant as defined by the physical structure.

The productive flows that represent power (P_{PM}, P_{NP} and P_{CP}) and external fuel (Q) are the same flows presented in the physical structure. These flows are total exergy. The remaining productive flows are the variation of an exergy term between two different states (j and k) of the physical structure. The productive flows representing the enthalpic ($H_{j:k}$) and the entropic ($S_{j:k}$) terms of the physical exergy are calculated using (10) and (11), respectively.

$$H_{j:k} = m_j \cdot (h_j - h_k) \tag{10}$$

$$S_{j:k} = m_j \cdot T_0 \cdot (s_j - s_k) \tag{11}$$

The mathematical model for cost allocation is obtained by formulating the cost equations balance in each actual and fictitious units of the functional diagram, as shown in (12), where *c* is the monetary unit cost of each flow of the productive structure (unknown variable) and *Y* is a generical way to represent the flows of the functional diagram, which can be power (*P*) and external fuel (*Q*), or enthalpic (*H*) or entropic (*S*) terms of physical exergy added to and removed from the working fluid. The monetary unit cost of a flow is the amount of monetary unit required to obtain one unit of this flow. The variable *Z* is the hourly cost of each unit due to the capital cost, operation and maintenance. Note that the monetary unit cost of the external fuel is a known variable.

$$c_{ufd} \cdot \sum Y_{out} - \sum (c_{in} \cdot Y_{in}) = Z \tag{12}$$

As shown in (12), the H&S Model attributes the same monetary unit cost (c_{ufd}) to all of the flows leaving the same productive unit or leaving the same bifurcation (Y_{out}). By modifying (12) in order to formulate the cost balances to provide the exergetic unit cost (*k*) of each flow of the productive structure, we obtain (13). The exergetic unit cost of a flow is the amount of exergy required to obtain one unit of this flow. This cost is a measure of the thermodynamic efficiency of the production process generating this flow [2]. In this case, the hourly cost of the subsystem due to the capital cost, operation and maintenance must be equals zero ($Z = 0$) and the monetary unit cost of the external fuel is replaced by the exergetic unit cost of an external resource, which is equal 1.00 kW/kW, because there is no exergy destruction before the productive process is performed [2]. The auxiliary equations are the same as used to obtain the monetary unit cost.

$$k_{ufd} \cdot \sum Y_{out} - \sum (k_{in} \cdot Y_{in}) = 0 \tag{13}$$

The solution of the sets of cost equations obtained by applying (12) and (13) in each device of the productive structure allows the attainment of the monetary and exergetic unit cost of each internal flow and final product, respectively. In this paper, only the exergetic unit costs are obtained. Table 2 shows the productive flows, its exergy values and its respective exergetic unit costs.

Table 2. Exergetic Unit Cost of the Productive Flows of the Actual Steam Cycle by H&S Model

FLOW	VALUE [kW]	EXERGETIC UNIT COST [kW/kW]
$H_{2:1}$	146.22	4.150
$H_{3:2}$	63,406.09	2.820
$H_{3:4}$	21,304.58	2.824
$H_{4:1}$	42,247.73	2.824
$S_{2:1}$	21.70	2.963
$S_{3:2}$	36,731.52	2.963
$S_{4:3}$	3,594.51	2.963
$S_{4:1}$	40,347.73	2.963
P_{PM}	155.00	3.500
P_{CP}	75.00	3.500
P_{NP}	20,000.00	3.500

According to Valero et al. [2], irreversibility is the magnitude generating the costs. Consequently, in any irreversible (actual) cycle plant, the exergetic unit cost should be increased along the productive structure. Bearing this in mind, the exergetic unit costs of the internal flows and final products obtained by the H&S Model are consistent because they are greater than one, once that the exergetic unit cost of the external fuel is equals one.

In H&S Model, the fuels and products used in the functional diagram in order to calculate the costs coincide with the fuels and product which can be used for calculating efficiency (performance) for both productive and dissipative units, as shown in (14). This equation under any condition, for any subsystem, can be interpreted as, or coincide with the classical and well-known product-fuel definition of efficiency, because it value is less than one for any actual (irreversible) cycle.

$$\eta_{ufd} = \frac{\sum Y_{out}}{\sum Y_{in}} \tag{14}$$

The formulas and the values of efficiency (product-fuel ratio) for each unit or subsystem of the functional diagram are shown in Table 3. The product-fuel ratio value (the efficiency) of the turbine and generator was calculated as a single unit, but the efficiencies of the turbine and generator, separately, are 85.56% and 94.96%, respectively. We can see that the efficiency of each unit (subsystem or component) is lower than 100%, including that of the dissipative ones.

Table 3. Product-Fuel Ratio (Efficiency) of the Productive Units of the Actual Steam Cycle

PRODUCTIVE UNIT	EFFICIENCY	
	Formula	Value (%)
Pump (P)	$\frac{H_{2:1}}{S_{2:1} + P_P}$	82.75
Boiler (B)	$\frac{H_{3:2}}{S_{3:2} + Q_F}$	59.41
Turbine and Generator (T-G)	$\frac{P_N + P_P + P_C}{H_{3:4} + S_{4:3}}$	81.25
Condenser and pump (C)	$\frac{S_{4:1}}{H_{4:1} + P_C}$	95.33
Power Plant (ASC)	$\frac{P_N}{Q_F}$	28.57

The efficiency of the condenser and cooling water pump (Table 3) is 95.33%, but the efficiency of the condenser, alone, is 95.50%. By using the H&S Model, the condenser efficiency in an actual steam power cycle will always be less than 100%, and this efficiency would only be 100% in case it were possible to transfer heat in the condenser at the same temperature, i. e., if the condensation temperature and the reference temperature were the same. In other words, by using the H&S Model, the product-fuel ratio of each component (including the dissipative one, such as the condenser) ranges from zero (for a totally irreversible process) to one (for a totally reversible process).

4.1.2. Reversible Cycle

Although reversible steam cycle cannot actually exist, it can be imagined as the limiting case as irreversibilities are reduced further and further. The physical structure of the reversible steam power cycle, in Fig. 3, is defined by imagining the limit of perfection of the steam cycle used above in Fig. 1. The condensation temperature is equal to the reference temperature and there is no pressure drop in the condenser. Thus, the cooling water pump is neglected. The external exergy consumption (Q_F)

is equal to the exergy transferred to the working fluid in the boiler. Both compression and expansion processes are isentropic. All the conversion processes that involve the working fluid of the reversible steam cycle are considered as prefect. Furthermore, there are no power losses in the electric generator nor in the electric motor of the boiler feed water pump. Table 4 shows the stream parameters and Fig. 4 shows the productive diagram of the reversible steam power cycle.

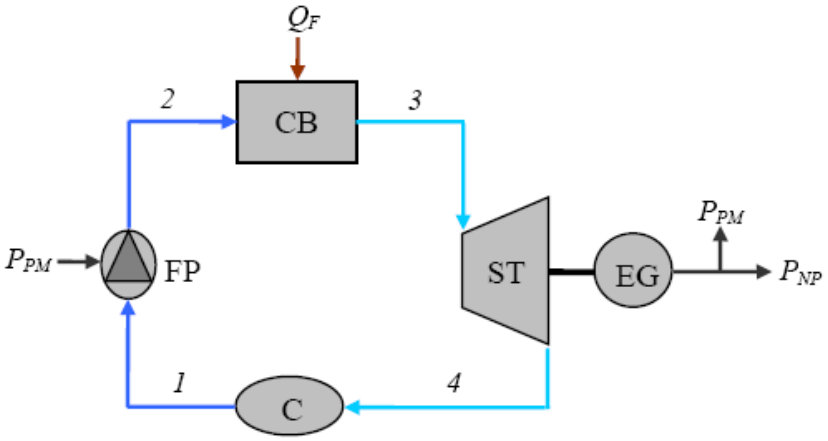

Fig. 3. Physical Structure of the Reversible Steam Power Cycle

Table 4. Main Parameters of the Main Physical Flows of the Reversible Steam Power Cycle

PHYSICAL FLOW		*m* [kg/s]	*p* [kPa]	*T* [°C]
N°	Description			
1	Moisture (x = 0, 325)	19.5	3.2	25.0
2	Saturated Water	19.5	6000	275.6
3	Saturated Steam	19.5	6000	275.6
4	Moisture (x = 0, 674)	19.5	3.2	25.0

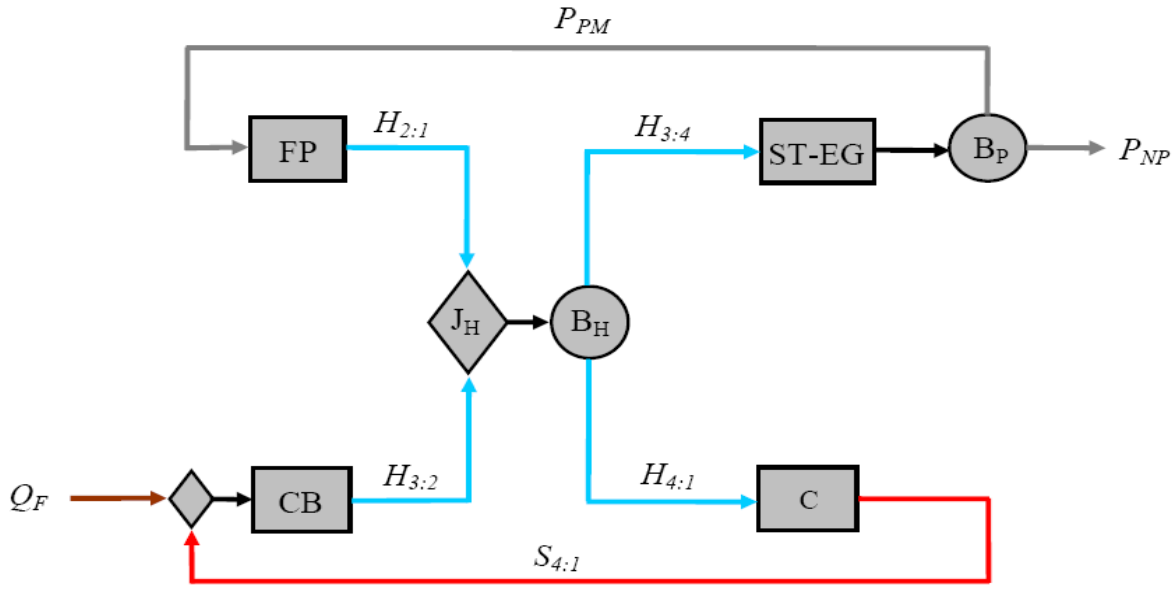

Fig. 4. Productive Diagram of the Reversible Steam Power Cycle

Because both the compression process and the expansion process are isentropic, the condenser product is charged to the boiler, which is the only subsystem that increases the working fluid

entropy. Table 5 shows the values of the productive flows present in the productive diagram of the reversible steam power cycle and the respective exergetic unit cost by applying the H&S Model.

Table 5. Exergetic Unit Cost of the Productive Flows of the Reversible Steam Cycle

FLOW	VALUE [kW]	EXERGETIC UNIT COST [kW/kW]
$H_{2:1}$	6,154.82	1.000
$H_{3:2}$	30,628.67	1.000
$H_{3:4}$	20,142.77	1.000
$H_{4:1}$	16,640.72	1.000
$S_{4:1}$	16,640.72	1.000
P_{PM}	6,154.82	1.000
P_{NP}	13,987.95	1.000

Table 5 confirms that H&S Model is a consistent approach, because the productive diagram is defined by isolating the four conversion processes of the reversible steam cycle, the fuel value of each equipment is equal to its product, and consequently, the exergetic unit cost of each productive flow is equal to one, and the efficiency is equal to one too, because there are no irreversiblities.

4.2. Heat Pump Cycle

4.2.1. Actual Cycle

The physical structure of the Heat Pump cycle represented in Fig. 5 essentially coincides with the one analysed by Lourenço et al. [6]. The plant is considered made up of four components: the compressor (cmp), the condenser (cnd), the expansion valve (vlv) and the evaporator (evp).

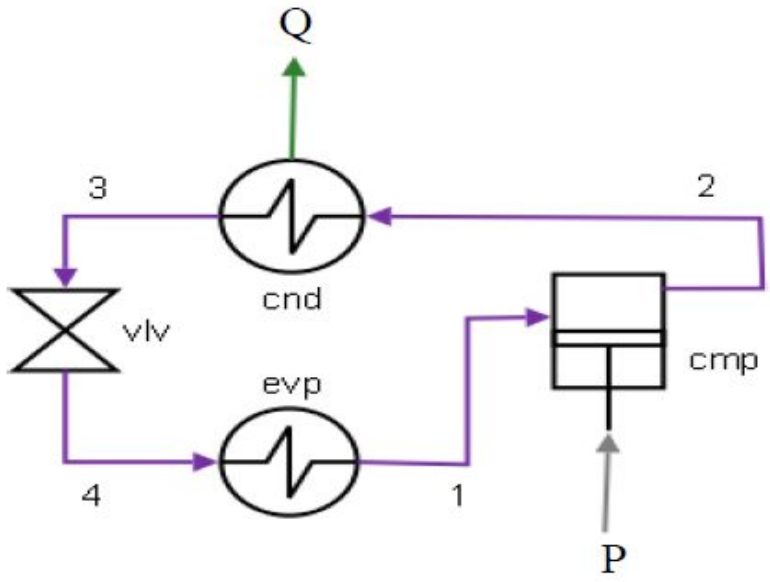

Fig. 5. Physical Structure of the Actual Heat Pump Cycle

The power consumption is 15.65 kW and the heat supplied exergy is 7.93 kW. The temperature difference between the state 3 and the room that receives the heat supplied is 5 K and the temperature difference between the environment (ref) and the state 4 is 5 K. The refrigerant is Freon R-134a, which mass flow is equal to 0.8 kg/s. Table 6 shows the main physical flow parameters.

Table 6. Main Parameters of the Main Physical Flows of the Actual Heat Pump Cycle

PHYSICAL FLOW		*p* [kPa]	*T* [°C]
N°	Description		
1	Vapor (*x = 1*)	293.01	0.00
2	Vapor	685.84	31.19
3	Liquid (*x = 0*)	685.84	26.00
4	Mixture (*x = 0.181*)	293.01	0.00

The functional diagram is shown in Fig. 6. The internal energy of the working fluid is increased in the evaporator and in the compressor (products). The condenser and the valve decrease the internal energy (fuels). The flow work of the working fluid is decreased in the condenser only (fuel). The remaining components increase the flow work (products). The operations of the productive units (compressor and evaporator) and of the valve increase the entropy of the working fluid (fuels). The condenser decrease the working fluid entropy, i.e., the entropic term is a condenser product.

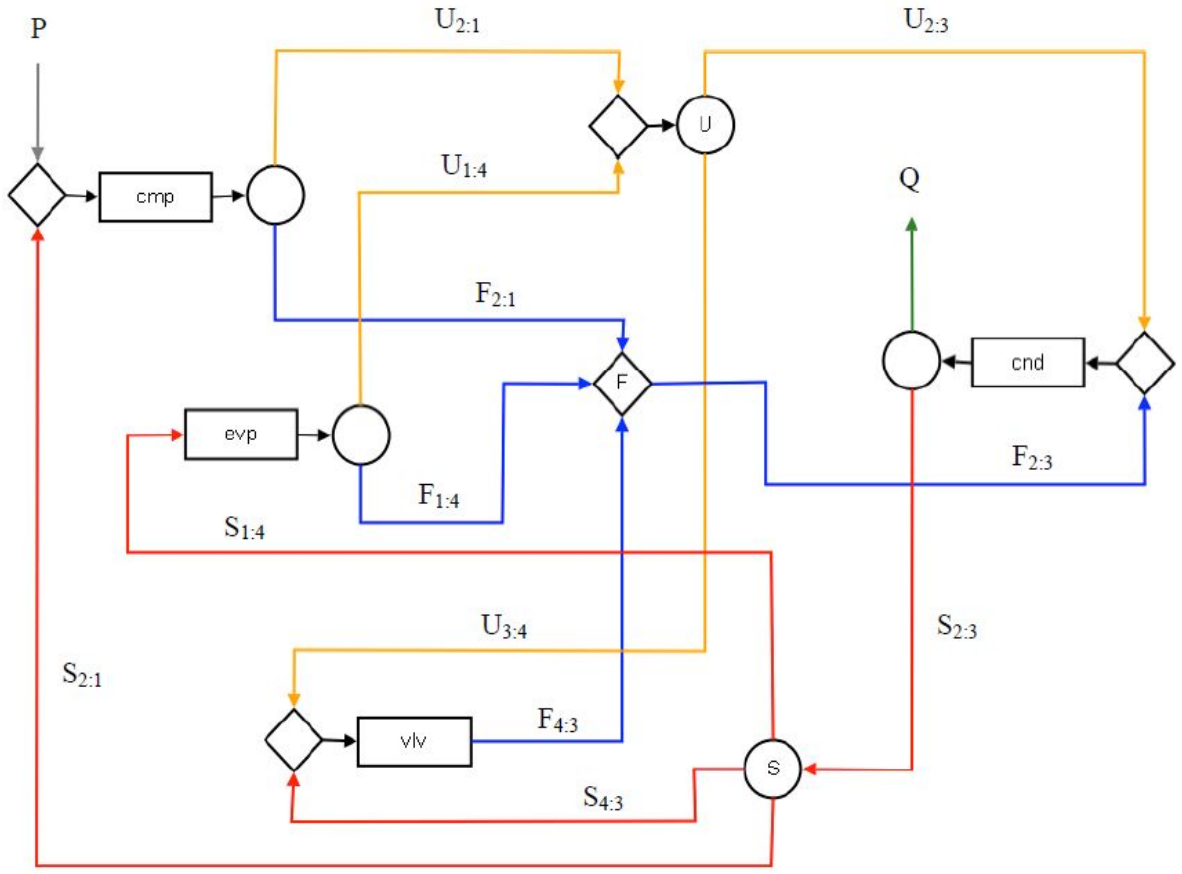

Fig. 6. Productive Diagram of the Actual Heat Pump Cycle according to the UFS Model

The productive flows representing the variation of the internal energy ($U_{j:k}$), flow work ($F_{j:k}$) and entropic ($S_{j:k}$) terms of the physical exergy are calculated using (14), (15) and (11), respectively. Table 7 shows the productive flows, its exergy values and its respective exergetic unit costs.

$$U_{j:k} = m_j \cdot (u_j - u_k) \tag{14}$$

$$F_{j:k} = m_j \cdot (p_j \cdot v_j - p_k \cdot v_k) \tag{15}$$

Table 7. Exergetic Unit Cost of the Productive Flows of the Actual Heat Pump by UFS Model

FLOW	VALUE [kW]	EXERGETIC UNIT COST [kW/kW]
$U_{2:1}$	14.91	1.181
$U_{2:3}$	129.93	1.916
$U_{3:4}$	2.63	1.916
$U_{1:4}$	116.95	2.010
$F_{2:1}$	0.74	1.181
$F_{2:3}$	16.51	2.145
$F_{4:3}$	2.63	3.091
$F_{1:4}$	13.14	2.010
$S_{2:1}$	1.44	1.974
$S_{2:3}$	135.47	1.974
$S_{4:3}$	1.57	1.974
$S_{1:4}$	132.47	1.974
P	15.65	1.000
Q	7.93	1.974

The exergetic unit costs of the internal flows and final product obtained by the UFS Model are consistent too because they are greater than one. The formulas and the values of efficiency (product-fuel ratio) for each unit or subsystem of the functional diagram are shown in Table 8.

Table 8. Product-Fuel Ratio (Efficiency) of the Productive Units of the Actual Heat Pump

PRODUCTIVE UNIT	EFFICIENCY	
	Formula	Value (%)
Compressor (cmp)	$\frac{U_{2:1} + F_{2:1}}{P + S_{2:1}}$	91.60
Condenser (cnd)	$\frac{Q + S_{2:3}}{U_{2:3} + F_{2:3}}$	98.39
Valve (vlv)	$\frac{F_{4:3}}{U_{3:4} + S_{4:3}}$	62.68
Evaporator (evp)	$\frac{U_{1:4} + F_{1:4}}{S_{1:4}}$	98.21
Heat Pump (hp)	$\frac{Q}{P}$	50.67

The results in Table 8 show that the efficiency, obtained by the product-fuel ratio of each unit, subsystem or component, is less than 100%, including that of the dissipative ones.

4.2.2. Ideal Cycle

In this case, we cannot imagine a reversible cycle because of the expansion valve where unavoidably irreversibility occurs. But, it is possible to analyze an ideal heat pump in which: (i) the compression process is isentropic; (ii) there is no difference between the constant condensation temperature in the condenser and the room temperature, and (iii) the constant evaporation temperature in the evaporator is equal to the environment temperature. In other words, the processes of heat transfer in the condenser and in the evaporator are totally reversible. The refrigerant is Freon R-134a, which mass flow is equal to 0.8 kg/s. Table 9 shows the main physical flow parameters.

Table 9. Main Parameters of the Main Physical Flows of the Ideal Heat Pump Cycle

PHYSICAL FLOW		p [kPa]	T [°C]
N°	Description		
1	Mixture ($x = 0.9846$)	293.01	0.00
2	Vapor ($x = 1$)	685.84	26.00
3	Liquid ($x = 0$)	685.84	26.00
4	Mixture ($x = 0.1811$)	293.01	0.00

Table 10 shows the productive flows, its exergy values and its respective exergetic unit costs. We can see that, in this case, the exergetic unit costs of the internal flows and final product are not equal one. But, they are consistent too because they are not less than one. These values would be equal to one if all processes were totally reversible, including that of the expansion (valve). The formulas and the values of efficiency (product-fuel ratio) for each unit or subsystem are shown in Table 11, in which we can see that, except the expansion valve, all components are totally reversible.

Table 10. Exergetic Unit Cost of the Productive Flows of the Ideal Heat Pump by UFS Model

FLOW	VALUE [kW]	EXERGETIC UNIT COST [kW/kW]
$U_{2:1}$	13.37	1.000
$U_{2:3}$	125.49	1.112
$U_{3:4}$	2.63	1.112
$U_{1:4}$	114.75	1.125
$F_{2:1}$	0.46	1.000
$F_{2:3}$	15.99	1.228
$F_{4:3}$	2.63	1.770
$F_{1:4}$	12.90	1.125
$S_{2:1}$	0.00	0.000
$S_{2:3}$	129.18	1.125
$S_{4:3}$	1.54	1.125
$S_{1:4}$	127.64	1.125
P	13.84	1.000
Q	12.30	1.125

Table 11. Product-Fuel Ratio (Efficiency) of the Productive Units of the Ideal Heat Pump

PRODUCTIVE UNIT	EFFICIENCY	
	Formula	Value (%)
Compressor (cmp)	$\frac{U_{2:1} + F_{2:1}}{P + S_{2:1}}$	100
Condenser (cnd)	$\frac{Q + S_{2:3}}{U_{2:3} + F_{2:3}}$	100
Valve (vlv)	$\frac{F_{4:3}}{U_{3:4} + S_{4:3}}$	63.1
Evaporator (evp)	$\frac{U_{1:4} + F_{1:4}}{S_{1:4}}$	100
Heat Pump (hp)	$\frac{Q}{P}$	88.9

5. Conclusions

This paper showed that exergy disaggregation is a consistent alternative for total disaggregation of systems in thermoeconomic modelling, particularly when there are dissipative components in the system being analysed. Two different approaches based on two different levels of physical exergy disaggregation were presented and applied. The first one is the H&S Model based on the disaggregation into enthalpic and entropic terms. The second is the UFS Model, in which the physical exergy is disaggregated into internal energy, flow work and entropic terms. The first one allows defining de product of one kind of dissipative component (condensers) but it does not work for the valves, which are another kind of dissipative component. The UFS Model overcame this limitation because it allows defining the product of both kinds of dissipative component.

Both exergy disaggregation level (H&S Model and UFS Model) can be used in order to quantify irreversibilities as well as the conventional exergy analysis. The results show that the product-fuel ratios of each components of the productive structure vary from zero (for totally irreversible processes) to one (for totally reversible ones). Thus, in these approaches, the product-fuel ratios can be used in order to quantify the performance of both productive and dissipative components, by establishing a general and systematic link between efficiency and cost in thermoeconomics.

This paper shows that the UFS Model is an extension of the H&S Model, keeping the same characteristics. However, the application of the former only could be justified if there is a valve in the structure of the system, due to its increasing modelling complexity and required computational efforts. However, it is very important to say that this is not a competition among all the thermoeconomics approaches, because we recognize that each methodology has specific fields of application for which it provide proven and efficient solutions. This paper aimed at show that the exergy disaggregation is a coherent and consistent alternative in order to solve this difficult problem in thermoeconomics related to the treatment of the so-called dissipative components.

Acknowledgments

The authors would like to tank ANP, Capes and CNPq for the financial supports.

Nomenclature

c monetary unit cost, $/kWh
E physical exergy flow, kW
F flow work term flow, kW
Fu component or control volume fuel, kW
h specific enthalpy, kJ/kg
H enthalpic term flow, kW
Ir component or control volume irreversibility, kW
k exergetic unit cost, kW/kW
Lo component or control volume loss, kW
m mass flow, kg/s
p pressure, kPa
Pr component or control volume product, kW
s specific entropy, kJ/(kg.K)
S entropic term flow, kW
T temperature, K
u specific internal energy, kJ/kg
U internal energy term flow, kW
v specific volume, m^3/kg
Y generic productive flow, kW

Z hourly cost of the subsystem, \$/h

Greek symbols

η efficiency

Subscripts

in inlet flow

i physical stream

j:k from stream *k* to stream *j*

o environment or reference

out outlet flow

ufd subsystem or unit of the functional diagram

References

[1] Erlach, B., Serra, L. and Valero, A., Structural Theory as Standard for Thermoeconomics. Energy Conversion and Management 1999;40:1627-1649.

[2] Valero, A., Serra, L. and Uche, J., Fundamentals of Exergy Cost Accounting and Thermoeconomics. Part I: Theory. Journal of Energy Resources Technology 2006;128:1-8.

[3] Torres, C., Serra, L., Valero, A. and Lozano, M.A., The Productive Structure and Thermoeconomic Theories of System Optimization. ME'96: International Mechanical Engineering Congress & Exposition 1996 (ASME WAM' 96).

[4] Valero, A., Royo, J. and Lozano, M. A., The Characteristic Equation and Second Law Efficiency of Thermal Energy Systems. International Conference Second Law Analysis of Energy Systems 1995: Towards the 21st Century, Eds. E. Sciubba, M.J. Moran. Roma "La Sapienza": 99-112.

[5] Santos J., Nascimento N., Lora E., Reyes A.M., On the Negentropy Application in Thermoeconomics: A Fictitious or an Exergy Component Flow?. International Journal of Thermodynamics 2009;12(4):176-163.

[6] Lourenço A.B., Santos J.J., Donatelli J.L., Thermoeconomic Modeling of a Simple Heat Pump Cycle: An Alternative Approach for Valve Isolation. In: Mitrović D., Laković M., editors. SimTerm 2011: Proceedings of the Fifteenth Symposium on Thermal Science and Engineering of Serbia; 2011 Oct 18-21; Sokobanja, Serbia. 453-446.

[7] Tsatsaronis, G. and Pisa, J., Exergoeconomic Evaluation and Optimization of Energy System - Application to the CGAM Problem. Energy 1994;19(3):287-321.

[8] Lazzaretto, A. and Tsatsaronis, G., SPECO: Systematic and General Methodology for Calculating Efficiencies and Costs in Thermal Systems. Energy 2006;31:1257-1289.

[9] Çengel, Y. A. and Boles, M. A., Thermodynamics: An Engineering Approach, 5th ed, McGraw-Hill; 2006.

[10] Moran M. J. and Shapiro, H. N., Fundamentals of Engineering Thermodynamics, 5th ed, John Wiley & Sons, New York; 2004.

[11] Lozano, M.A., Valero, A., Serra, L., Theory of Exergetic Cost and Thermoeconomic Optimization, Energy Systems and Ecology; 1993, Eds. J. Szargut, Z. Kolenda, G. Tsatsaronis and A. Ziebik. Vol. 1, pp. 339-350, July 5-9, Cracow, Poland.

[12] Frangopoulos C.A., Thermo-Economic Functional Analysis and Optimization. Energy 1987; 12(7):571-563.

Exergy Intensity of Petroleum Derived Fuels

Julio A. M. Silva [a], Maurício Sugiyama [b], Cláudio Rucker,[c] Silvio de Oliveira Junior [d]

*[a] Polytechnic School - University of São Paulo, São Paulo, Brazil, jams@usp.br **(CA)***
[b] Petrobras, São Paulo, Brazil, mauricio.sugiyama@petrobras.com.br
[c] Petrobras, Rio de Janeiro, Brazil, rucker@petrobras.com.br
[d] Polytechnic School -University of São Paulo, São Paulo, Brazil, soj@usp.br

Abstract:

In view of the continuous yet finite exergy supply to Earth, in addition to the inability to complete recycle this exergy, imposed by the Second Law of Thermodynamics, the proper comparison between different fuels as well as the actual exergy costs necessary for environmental evaluation of any produced good is of great importance. The exergy cost of any product lies on the calculation of the exergy intensity of the used fuels. The calculation of the exergy intensity for petroleum derived fuels is performed by solving the set of linear equations used to describe the cost formation process of these fuels. The production process of petroleum derived fuels is a complex series of processes including primary separation, transportation, atmospheric and vacuum distillation, delayed coking, fluidized catalytic cracking, hydrotreating, hydrogen generation, as well as residues treatment, such as sulphur recovery and sour water treatment. Exergoeconomy analysis provides the rational tool for partitioning the exergy consumed in both: production processes and residues treatment processes among the produced fuels. Furthermore, it provides the exergy efficiency of the utilities produced by refinery utilities plant. Exergy and exergoeconomy analysis were performed in a 415,000 bpd refinery which processes a 28 API crude mixture, mainly from Campos basin in Rio de Janeiro Brazil. The unit exergy cost determined for FCC LPG and gasoline is: 1.08 kJ/kJ while for hydrotreated diesel, which requires more processing steps, is 1.11 kJ/kJ. The exergy intensity obtained for these petroleum derived fuel are: 52.89 MJ/kg, 50.71 MJ/kg and 50.19 MJ/kg, respectively, while values reported for typical sugar cane Brazilian ethanol (a well know renewable fuel) are 3.4 kJ/kJ and 92.56 MJ/kg.

Keywords:

Exergy, Exergoeconomy, Fuels unit exergy cost, Fuels exergy intensity, Petroleum refinery.

1. Introduction

The exergy expenditure for petroleum extraction, transportation and refining and its rational partition among the produced substances can be used to evaluate the exergy intensity of an enormous quantity of goods produced from petroleum derived matter. It can also help fuel polices since it informs the work capacity spent to obtain each petroleum derived fuel which is an important information for comparison between petroleum derived fuels and renewable fuels and among the different fuels produced in a refinery as proposed in [1]. In addition to this, exergy analysis pinpoints the processes responsible for main exergy destructions, properly evaluates the waste heat and waste of mechanical exergy (pressure drop in valves), both present in large scale in petroleum industry. The refining processes are complex and highly integrated, thus thermoeconomy theories [2-7] are of great use to indicate the actual efficiency of production of the several fuels and utilities as well as the exergy destroyed for their production. Although the importance of the subject, few works are found in literature: Dinçer [8] applied exergy analysis to a petroleum refinery and an overall availability efficiency of 5.9% was reported. Rivero [9] conducted an exergy analysis to optimize a 150,000 barrels per day (bpd) refinery. In this analysis the main exergy destruction was present in the utilities plant followed by catalytic cracking unit and combined distillation. Several modifications were performed and new systems were implemented: retrofit of heat exchangers network by the Pinch method, pre-heating air systems, CO steam generators[1] and water pre-heaters.

[1] This steam generator re-burns the hot CO rich gas exhausted by catalytic cracking unit during catalyst regeneration.

A reduction of 26% of total degraded energy was observed. Some works using exergy analysis were performed in single distillation processes such as [10], [11] and [12]. Exergoeconomy analysis were usually applied for utilities plant alone as in [13] and [14], in the latter a critical point of view is presented. Rivero et al. [15] applied exergoeconomy to a combined distillation unit. Other important works were carried out, however without the direct use of the Second Law of Thermodynamics: a reduction of 31% in energy consumption per barrel processed was reported by [16], due to the modernization of a refinery. The reported modernization may include: CO boiler, increase heat exchange between streams and units, hotter feeds between processes units, more efficient equipment, inclusion of combined cycles in utilities plant, among other typical improvements. The increase in energy consumption and CO_2 emission due to increase in the production of hydrotreated fuels[2] was highlighted by [17]. None of these works however, performed an exergoeconomy analysis of the entire refinery including processes units such as: combined distillation, fluidized catalytic cracking (FCC), delayed coking and hydrotreating, utilities plant and treatment units such as: sulphur recovery and sour water treatment. In this work exergoeconomy analysis is performed for the whole petroleum sector, Fig.1. It uses the unit exergy cost of natural gas and petroleum from a production plant (offshore platform), adds the exergy spent during transportation, and uses exergoeconomy to distribute the refinery exergy income among its products. Thus, it is possible to quantify the exergy destroyed to produce each one of the petroleum derived fuels in a thermodynamic rational basis. Furthermore the exergy analysis is applied to the refining process, in which the highest exergy destructions take place, in order to highlight the processes more representative for exergy saving in the sector.

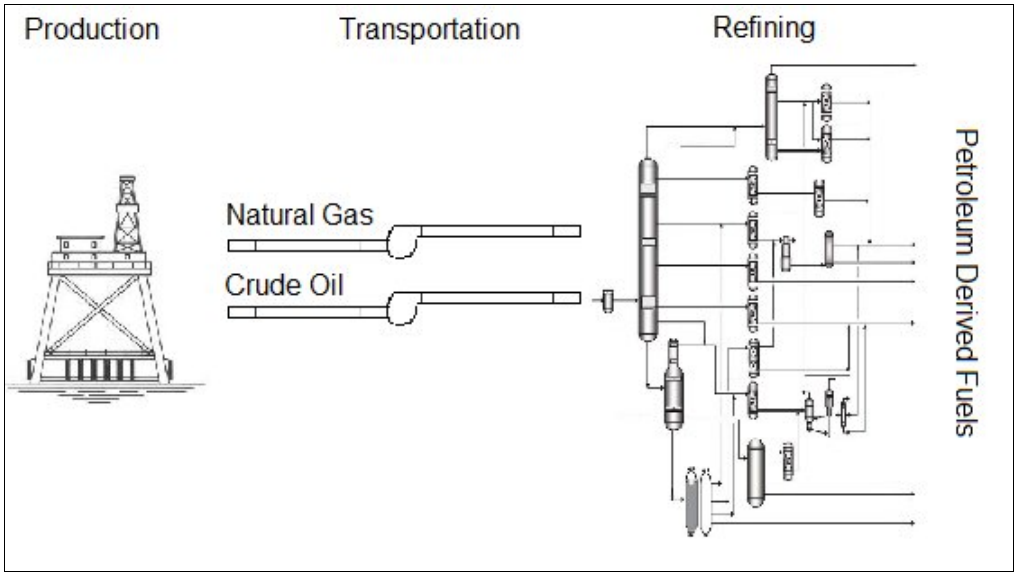

Fig. 1. Petroleum sector composed by production, transportation and refining

The paper is organised as follows: Section 2 presents the refining process analysed, which is the main exergy consumer in petroleum sector; Section 3 describes the methodology used for refinery exergy and exergoeconomy analysis; Section 4 presents the considerations used to take into account the production and transportation in the exergoeconomy analysis as well as its overall results; Section 5 presents the main conclusions.

[2] Fuels with low sulphur content (< 50 ppm).

2. Refinery description

Exergy and exergoeconomy analysis were performed in a 415,000 bpd refinery which processes a 28 API crude mixture, mainly from Campos basin in Rio de Janeiro Brazil. This refinery is composed of the following process units: combined distillation, FCC, delayed coking, hydrogen generation, hydrotreating, sulphur recovery and sour water treatment. A utilities plant is used to provide steam at three different grades, electricity, mechanical power and water at different pressure levels to the process units.

2.1. Refining scheme

A mixture of crude oils from primary separation units enters in the combined distillation unit. In combined distillation the oil is desalted using rectified water and then it goes to atmospheric distillation. The residue of atmospheric distillation is sent to vacuum distillation in which it distillates at moderate temperatures. The residue of vacuum distillation is sent to delayed coking unit in which lighter products and coke are produced. The feed of FCC unit is a mixture of naphtha and gasoil produced in delayed coking and combined distillation. Products such as gasoline, liquefied petroleum gas (LPG), light cycle oil (LCO) and decanted oil (DECO) are produced in FCC. The hydrogen generation unit receives natural gas in order to provide the hydrogen necessary for hydrotreating process. In hydrotreating process streams in diesel range are treated to produce hydrotreated diesel. The refining scheme together with utilities and residues streams are depicted in Fig.2.

2.2. Combined distillation (CD)

The control volume considered for combined distillation consists of three processes: desalting, atmospheric distillation and vacuum distillation. The desalting process is the first process in combined distillation, it mixtures dilution water in the crude oil in order to dissolve the salts remaining from primary separation[3], then the salty water is separated by electrostatic separators. After desalting and pre-heating by the products leaving the unit the petroleum is sent to a pre-flash column, where the light fractions are removed so that the main column and furnace can be designed for the heavier fractions only. After leaving the pre-flash column the heavier fractions are sent to the furnace and are heated to temperatures close to 400ºC. Steam is also injected in the tower to strip the residue and to reduce the components partial pressure. The residue of atmospheric distillation is then sent to a vacuum distillation tower in which it is evaporated at temperatures close to 415ºC and sub atmospheric pressures between 30 and 100 (mbar), provided by steam ejectors.

2.3. Fluidized catalytic cracking (FCC)

The fluidized catalytic cracking is a chemical conversion process that uses a zeolite type catalyst. The feed of this process is a mixture of gasoil and naphtha produced by combined distillation and delayed coking processes while the products are high value streams such as: gasoline (GLN) and liquefied petroleum gas (LPG). The catalyst regeneration process is the main energy source for the endothermic reactions present in the process. The catalyst is regenerated by burning the coke that adhere to catalyst surface, thus the hot regenerated catalyst, at temperatures close to 700ºC, and the feed are mixed at the bottom of the riser. The exhausting gas from the catalyst regeneration process is a hot gas rich in carbon monoxide, usually called CO gas, used in a recovery boiler to generate steam. This CO gas represents an important fraction of the energy consumed in the refinery.

[3] BSW - Basic Sediments and Water is usually below 1%.

2.4. Delayed coking (DC)

The delayed coking is a thermal cracking process. The vacuum residue is pre-heated at temperatures around 350ºC so that the lighter fraction can bypass the main furnace. The heavier fraction passes through the main furnace and leaves at temperatures close to 500ºC. The not evaporated feed is then sent to the coking drums where it stays for a certain period necessary for coking. The quantity of coke produced is function of the Conradson Carbon Residue (CCR) of the feed. Since it is an intermittent process, several drums are used in parallel so that while one is coking the others can be filled. As the coke has a very low H/C ratio the other streams leaving the delayed coking have a higher H/C ratio, thus the main function of the delayed coking unit is to increase the yield of light fractions by removing coke.

2.5. Hydrogen generation (HG)

Hydrogen is generated by natural gas steam reforming process. This is a catalytic process usually represented by two chemical reactions: (R1) and (R2). The former is an endothermic reaction that forms syngas (CO and H_2), and the later is an exothermic reaction known as shift reaction and used to convert the remaining CO in more H_2 and CO_2.

$$C_nH_m + nH_2O \Rightarrow nCO + (n + m/2)H_2 \quad \text{(R1)}$$

$$CO + H_2O \Rightarrow CO_2 + H_2 \quad \text{(R2)}$$

After the reactions take place the hydrogen purification is performed by a pressure swing adsorption system (PSA) that allows a 99.9% purity.

2.6. Diesel hydrotreating (HDT)

This process is a catalytic process using a Co-Mo in alumina base catalyst. It aims to remove contaminants, mainly sulphur, (R3), from diesel range streams. It also increases the cetane[4] number of diesel since double bonds are broken to form single bonds.

$$RSH + H_2 \rightarrow RH + H_2S \quad \text{(R3)}$$

The diesel feed and the hydrogen are mixed and heated in a furnace. The mixture is sent to a reactor where the reactions occur. The products go to a separator where the gaseous fraction is separated. The gaseous stream is directed to an amine scrubber where the sour gas is separated and sent to a sulphur recovery unit while the remaining H_2 is recycled.

2.7. Utilities plant

For the sake of simplicity similar components of the utilities plant were aggregated. The synthesis plant is then composed of a gas turbine, a heat recovery steam generator (HRSG) that also burns fuel gas (FG), a CO and fuel gas boiler, a fuel gas and fuel oil (FO) boiler, an extraction and condensation steam turbine for electric power generation, four steam turbines for mechanical power generation, an air compressor, a deaerator, three pumps, a pre-heater, a cooling tower and a water treatment process. The utilities synthesis plant can be seen in Fig.3.

[4] The cetane number indicates the explosion resistance to pressure of a fuel.

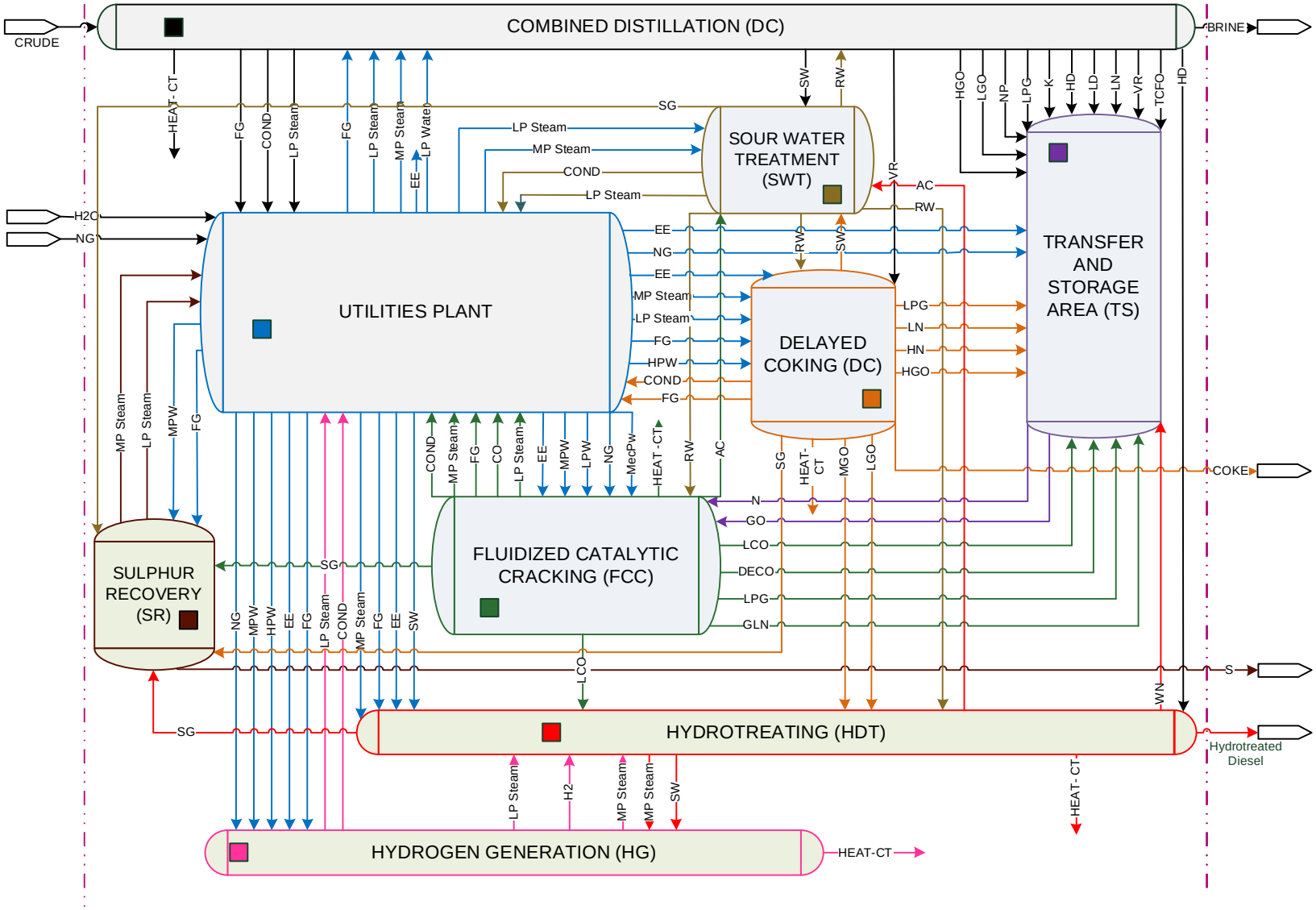

Fig. 2. Refinery configuration

2.8. Sulphur recovery (SR)

All sour gas produced in the refinery is treated in the sulphur recovery unit. The process consists of a series of chemical reactions and it is usually called Claus process. The first step: (R4) and (R5) is a thermal and very exothermic step, occurring at temperatures above 850ºC. This thermal step is responsible for 60% to 70% of conversion of H_2S into elementary sulphur. In the catalytic converter chemical step, (R6) is conducted. The steps can be continually repeated, always with the entrance temperature decreased. The remaining H_2S, after last chemical step, is incinerated. As the reactions present in this process are exothermic, their heat of reaction are used for steam generation.

$$2H_2S + O_2 \rightarrow 2S + 2H_2O \quad \text{(R4)}$$

$$2H_2S + 3O_2 \rightarrow 2SO_2 + 2H_2O \quad \text{(R5)}$$

$$2H_2S + SO_2 \rightarrow 3S + 2H_2O \quad \text{(R6)}$$

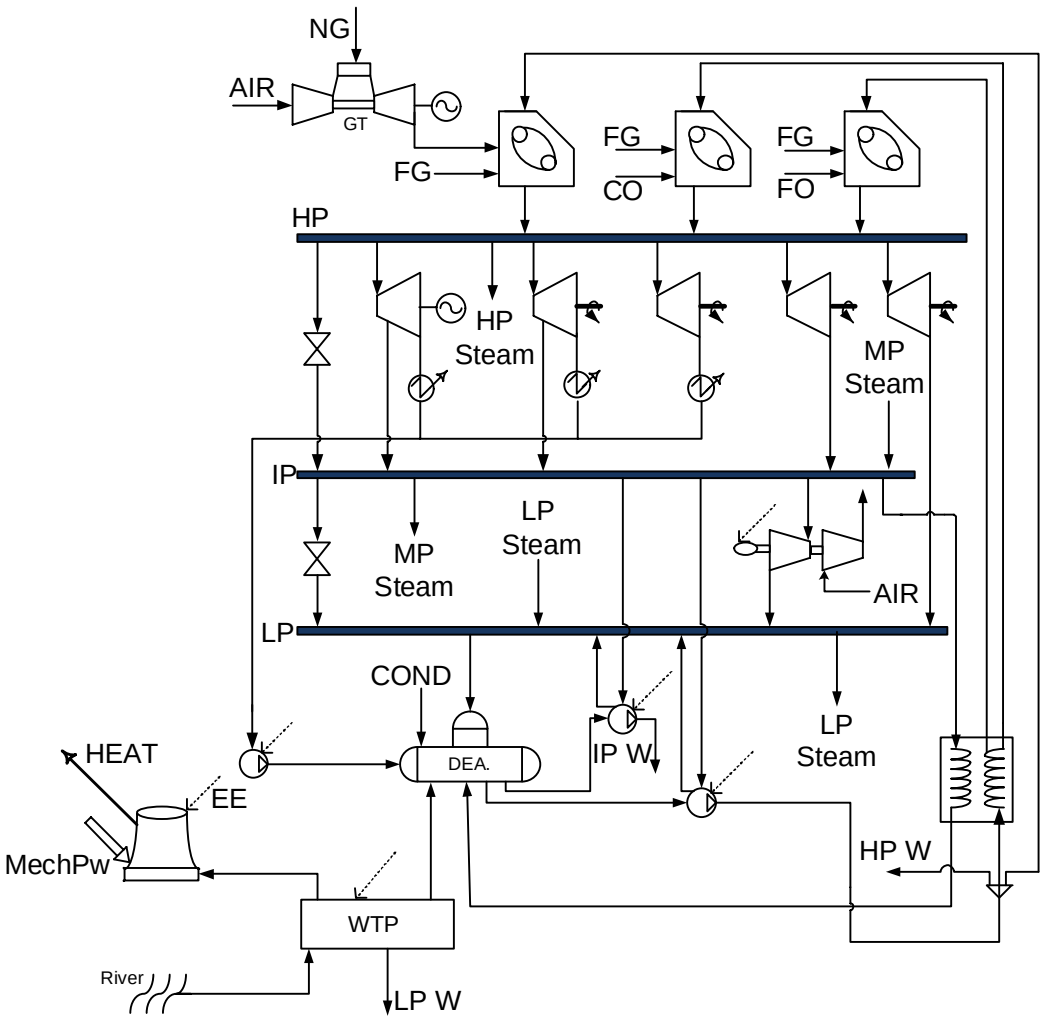

Fig. 3. Utilities plant configuration

2.9. Sour water treatment (SWT)

Sour water is mainly produced by contact with hydrocarbons since steam is extensively used to decrease the partial pressure of the hydrocarbon components. Water is also used in cleaning and decoking, thus large quantities of sour water are produced. Although called "sour water" this water has a pH around 9 and it is called sour because of its characteristic smell. This sour water is sent to a rectifying tower where it is mixed with steam and the contaminants are removed in sour gas form and finally treated in sulphur recovery process. Further information about refining process units can be found in [18] and [19].

3. Methodology

In the analysed refinery all the processes are duplicated, thus only one half of the refinery was studied. A hybrid method composed of real plant data and simulated data was used. The mass flow, elementary composition and lower heating value of each stream were provided by Petro-SIM software for the given feeds of a given unit process. The feed is characterized by its distillation curve: TBP (ASTM-2892), ASTM-86, ASTM-D2887 or ASTM-D1160, when available the feed API gravity and viscosity are used to provide more accurate data. The temperature of the streams connecting the process units is the average of the values collected from plant information system (PI) during a typical operation day. This average temperature takes into consideration all heat changed before the stream leaves the control volume of the unit. The feeds mass flow and utilities consumption are also collected from PI. The utilities plant as well as both treatment process: sulphur recovery and sour water treatment have their products and feed according to the other units requirements, keeping the real production rates and efficiencies constant.

3.1. Exergy calculation

The total specific exergy is calculated as in Szargut [20], as the sum of physical and chemical exergy, (1).

$$b_{Total} = b_{Physic} + b_{chemical} \tag{1}$$

The physical exergy was calculated according to (2), using Petro-SIM [21] software to calculate enthalpy and entropy. The reference temperature considered was 25ºC. The Petro-SIM uses correlations such as those explained in Riazi [22], using a proper equation of state and residual properties or an activity model to calculate enthalpy and entropy.

$$b_{Physic} = \left(h - h_0\right) - T_0 \cdot \left(s - s_0\right) \tag{2}$$

The chemical exergy is calculated as in (3), using Rivero et al. [23] correlation (4) that differently from Szargut et al. [20] and Kotas [24] also takes the sulphur concentration into account.

$$b_{Chemical} = \varphi \cdot LHV \tag{3}$$

$$\varphi = 1.041 + 0.1728 \cdot \left(\frac{X_{H_2}}{X_C}\right) + 0.0432 \cdot \left(\frac{X_{O_2}}{X_C}\right) + 0.2169 \cdot \left(\frac{X_S}{X_C}\right) \cdot \left(1 - 2.0628 \cdot \left(\frac{X_{H_2}}{X_C}\right)\right) + 0.0428 \cdot \left(\frac{X_{N_2}}{X_C}\right) \tag{4}$$

The factor φ used for coke, solid fuel, was 1.05 provided by Kotas [24].

3.2. Exergy efficiency

3.2.1. Utilities plant

The energy and exergy efficiency equations used for the components of the utilities plant are shown in Table 1. Note that these equations drive the exergoeconomy equations for the respective components. Also note that in gas turbines the exhausting gas exergy was subtracted from the fuel exergy since it is used in heat recovery boilers. The *x* coefficient is used in steam turbine to include the energy and exergy expenses due to the use of cooling towers: make up water, electric and mechanic power. The quantity of energy in heat form sent to the cooling water was the weighting factor used. All boilers use two fuels, the function of the heat exchangers is to heat the cold fluid, the air compressors and pumps efficiency are for a group of equipment driven by steam and electricity.

3.2.2. Process units

The function of the units of thermal and chemical separation is to increase the chemical exergy of feed, since a mixture is separated into its components. Thus the most adequate efficiency seems to be (5).

$$\eta_b = \frac{\sum B_{PRODUCTS} - \sum B_{FEED}}{\sum B_{CONSUMED}} \tag{5}$$

However, the substantial difference in the exergy magnitude of the products and feed in relation to the consumed exergy prevents this calculation. In the analysed processes the consumed exergy is no more than 2.2% of the feed exergy while the accuracy of the in LHV calculation is near 1,45% [25], the accuracy in φ calculation is around 0,38% [24] and considerable errors are expected in the enthalpy and entropy calculations since they are given by a series of correlations [22]. Therefore the exergy efficiency indicator used was given by (6) for all process units.

$$\eta_b = \frac{\sum B_{OUT}}{\sum B_{IN}} \tag{6}$$

Furthermore, the process units were considered responsible for the use of treatment units: sour water treatment and sulphur recovery as well as for cooling water system (cooling towers). Consequently all exergy fluxes consumed and produced by cooling towers and by these treatment units were allocated to the units that produce residues and dissipate exergy through cooling water circuit.

Table 1. Equations used for energy and exergy performance evaluation of utilities plant components

Component	Energy performance parameter	Exergy efficiency
Gas turbines	$\eta_e = \frac{\dot{W}_{Electric}}{\dot{m}_{Fuel} \cdot LHV}$	$\eta_b = \frac{\dot{W}_{Electric}}{\dot{m}_{Fuel} \cdot b_{Fuel} - \dot{m}_{Exhausting} \cdot b_{Exhausting}}$
Steam turbines	$\eta_e = \frac{\dot{W}_{Electric/Mechanic}}{\dot{H}_{Steam} - \dot{H}_{Extraction} - \dot{H}_{Condensate} + x \cdot (\dot{H}_{H_2O} + \dot{W}_{Electric} + \dot{W}_{Mechanic})}$	$\eta_b = \frac{\dot{W}_{Electric\,/\,Mechanic}}{\dot{B}_{Steam} - \dot{B}_{Extraction} - \dot{B}_{Condensate} + x \cdot (\dot{B}_{H_2O} + \dot{W}_{Electric} + \dot{W}_{Mechanic})}$
Pumps	$\eta_e = \frac{\sum\left(\frac{\dot{m}_{Water} \cdot \Delta P_{Water}}{\rho_{Water}}\right)}{\sum\left[\dot{W}_{Electric} + \left(\dot{H}_{Steam_in} - \dot{H}_{Steam_our}\right)\right]}$	$\eta_b = \frac{\sum\left(\dot{B}_{Water_out} - \dot{B}_{Water_in}\right)}{\sum\left[\dot{W}_{Electric} + \left(\dot{B}_{Steam_in} - \dot{B}_{Steam_out}\right)\right]}$
Steam generators	$\eta_e = \frac{\dot{H}_{Steam} - \dot{H}_{Water}}{\dot{m}_{Fuel1} \cdot LHV_{Fuel1} + \dot{m}_{Fuel2} \cdot LHV_{Fuel2}}$	$\eta_b = \frac{\dot{B}_{Steam} - \dot{B}_{Water}}{\dot{m}_{Fuel1} \cdot b_{Fuel1} + \dot{m}_{Fuel2} \cdot b_{Fuel2}}$
Heat exchangers	$\varepsilon = \frac{C_{Cold}(T_{Cold_in} - T_{Cold_out})}{C_{Cold=\min}(T_{Hot_in} - T_{Cold_in})}$	$\eta_b = \frac{\dot{B}_{Cold_out} - \dot{B}_{Cold_in}}{\dot{B}_{Hot_in} - \dot{B}_{Hot_out}}$
Valves	$\eta_e = \frac{\dot{H}_{Out}}{\dot{H}_{In}}$	$\eta_b = \frac{\dot{B}_{Out}}{\dot{B}_{In}}$
Deaerators	$\eta_e = \frac{\sum \dot{H}_{Out}}{\sum \dot{H}_{In}}$	$\eta_b = \frac{\sum \dot{B}_{Out}}{\sum \dot{B}_{In}}$
Air compressors	$\eta_{IsoThermic} = \frac{\sum\left[\dot{m} \cdot R \cdot T_0 \cdot \ln\left(\frac{P_{Air_out}}{P_0}\right)\right]}{\sum\left[\dot{W}_{Electric} + \left(\dot{H}_{Steam_in} - \dot{H}_{Steam_out}\right)\right]}$	$\eta_b = \frac{\sum\left(\dot{B}_{Air_out} - \dot{B}_{Air_in}\right)}{\sum\left[\dot{W}_{Electric} + \left(\dot{B}_{Steam_in} - \dot{B}_{Steam_out}\right)\right]}$
Water treatment	$\eta_e = \frac{\dot{H}_{Water_out} - \dot{H}_{Water_in}}{\dot{W}_{Electric}}$	$\eta_b = \frac{\dot{B}_{Water_out} - \dot{B}_{Water_in}}{\dot{W}_{Electric}}$

3.3. Exergoeconomy

The principles used for exergoeconomy formulation are in general the ones proposed by Lazzareto and Tsatsaronis [2]. The set of exergoeconomy equations for utilities plant components were driven by the exergy efficiencies given in Table 1. The exergoeconomy formulation for process units, (7), considers that each process unit has its own unit for sour water treatment (SWT) and sulphur recovery (SR) as well as its own cooling water circuit as shown in Fig.4. The coefficients x_1, x_2 and x_3 are used to weight, using mass flow and heat, the exergy input and output of the given process due to the use of auxiliary process, see (8), (9) and (10). In the following equations *i* represents the analysed process unit and *m* the auxiliary units.

$$\begin{aligned}&\sum_i\left(c_{PRODUCTS}\cdot\dot{B}_{PRODUCTS}\right)_i+c_{MP_Steam}\cdot\dot{B}_{MP_Steam}+c_{LP_Steam}\cdot\dot{B}_{LP_Steam}+c_{RW}\cdot\dot{B}_{RW}+c_S\cdot\dot{B}_S-c_{Cond}\cdot\dot{B}_{Cond}=\\&x_1\cdot\sum_m\left(c_{B_in_SWT}\cdot\dot{B}_{in_SWT}\right)_m+x_2\cdot\sum_m\left(c_{\text{B_in SR}}\cdot\dot{B}_{\text{in SR}}\right)_m+\\&x_3\cdot\sum_m\left(c_{\text{B_in Tower}}\cdot\dot{B}_{\text{in Tower}}\right)_m+\sum_i\left(c_{FEED}\cdot\dot{B}_{FEED}\right)_i+\sum_i\left(c_{\text{B_in_unit}}\cdot\dot{B}_{\text{in Unit}}\right)_i\end{aligned}\tag{7}$$

$$x_1=\frac{\dot{m}_{SW_i}}{\sum_m\dot{m}_{SW_m}}\tag{8}$$

$$x_1=\frac{\dot{m}_{SG_i}}{\sum_m\dot{m}_{SG_m}}\tag{9}$$

$$x_3=\frac{\dot{Q}_i\cdot\left(1-\frac{T_0}{T_{Ci}}\right)}{\left(1-\frac{T_0}{T_{CW}}\right)\cdot\sum_m\dot{Q}_m}\cong\frac{\dot{Q}_i}{\sum_m\dot{Q}_m}\tag{10}$$

The approximation in (10) is feasible since the temperature in which the heat is sent to cooling water, T_{Ci}, is close to all processes and it is also close to the temperature in which the heat is dissipated by cooling tower, T_{CW} .

All the fluxes that leave the control volume of Fig.4 except for the heat sent to the environment and the condensed steam are considered as products of the process unit and have the same unit exergy cost, as shown in (11).

$$c_{PRODUCT_i}=c_{MP_Steam}=c_{LP_Steam}=c_{RW}=c_S\tag{11}$$

The cost of the condensed steam is provided by (12) since it comes from medium and low pressure steam used as energy source in the unit.

$$\frac{\sum_i\left(c_{MP_Steam}\cdot\dot{B}_{MP_Steam}\right)_i+\sum_i\left(c_{LP_Steam}\cdot\dot{B}_{LP_Steam}\right)_i}{\sum_i\dot{B}_{MP_Steam_i}+\sum_i\dot{B}_{LP_Steam_i}}=c_{Cond}\tag{12}$$

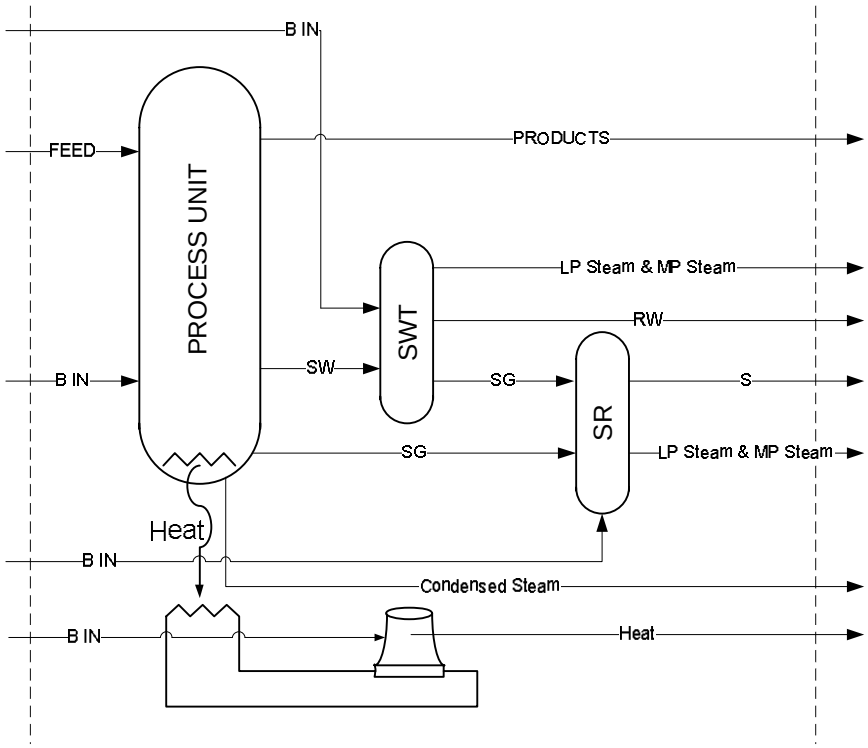

Fig. 4. Control volume used to determine exergoeconomy equations for process units

In order to calculate the unit exergy cost of the refinery streams, the exergoeconomy equations for process units together with the exergoeconomy equations for utilities plant components, derived from the efficiencies presented in Table 1, were solved using Engineering Equation Solver (EES) [26].

4. Results

4.1. Exergy analysis results

The exergy efficiency and exergy destroyed in each process unit were calculated. The exergy spent in residue treatment is allocated to the process units responsible for the residue production using the residue mass flow as the weight factor. This approach is also used to distribute the exergy costs related with cooling water circuit (cooling towers), however the weight factor used was the quantity of heat sent to the cooling water. The products of the treatment processes: rectified water, elementary sulphur and steam were distributed to process units using the same criteria.

4.1.1. Combined Distillation

The Grassmann diagram in Fig.5 shows the direct exergy input and output of combined distillation. The combined distillation is responsible for 43.7% of all heat sent to the cooling water circuit and by 24.9% of total sour water produced. Therefore 12.1 MW were added as exergy input to represent the exergy consumed in auxiliary unit and more 3.6 MW were added to products, in order to represent the auxiliary units products: rectified water, elementary sulphur and steam.

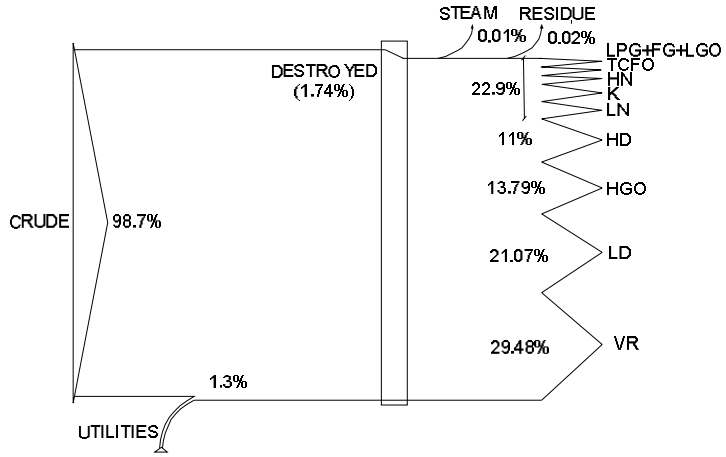

Fig. 5. Grassmann diagram of combined distillation

As result an exergy efficiency of 98.18% is observed. Approximately 1 kg of brine is produced for 10 kg of processed crude. Despite of high exergy efficiency, 264 MW of exergy are destroyed.

4.1.2. Fluidized Catalytic Cracking

Besides the direct exergy flows rates shown in Fig.6, more 14.8 MW are added as exergy input in FCC control volume since it is responsible for 43% of sour water production and 38% of the total heat sent to cooling water circuit. Also 13.7 MW are added as products since rectified water, elementary sulphur and steam are additionally produced in the auxiliary units.

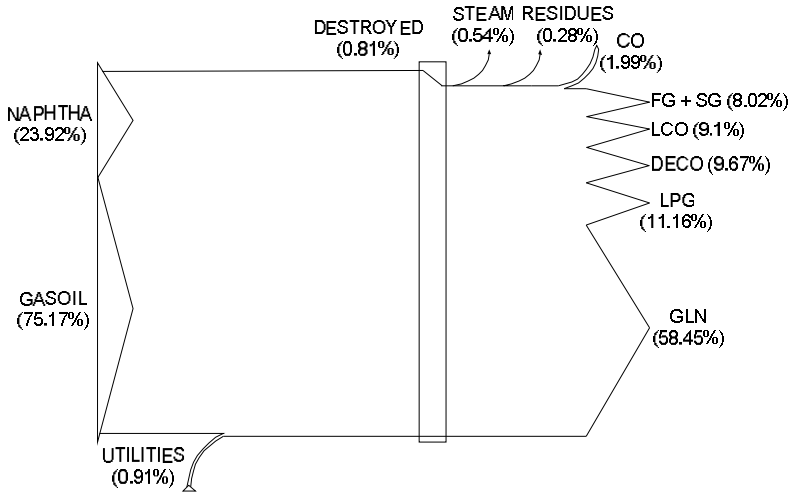

Fig. 6. Grassmann diagram of fluidized catalytic cracking

The exergy efficiency of FCC unit is 98.93%. This high efficiency results from the use of CO gas in CO boilers, thus it is considered as a product, and from the use of heated catalyst from regeneration process as the main exergy input.

4.1.3. Delayed coking

In addition to the direct exergy input and output shown in Fig.7 more 3.9 MW are added as input and more 4.1 MW are added as product due to sour water and sour gas production and heat sent to cooling water. More exergy is added to the products than to input since the sulphur recovery process makes use of the exergy present in the sour gas to produce the elementary sulphur, thus this process has a positive impact in all process units that produce sour gas.

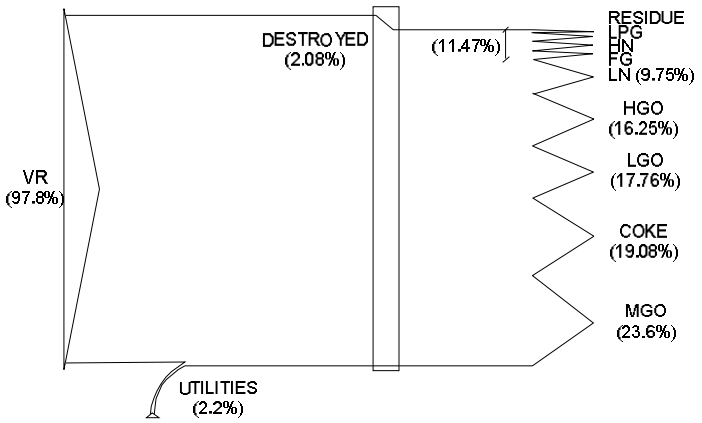

Fig. 7. Grassmann diagram of delayed coking unit

The total exergy efficiency observed was 98%. 61.8 MW of exergy is destroyed.

4.1.4. Hydrogen generation

The process of hydrogen generation produces neither sour gas nor sour water. It sends a very small quantity of heat to cooling water circuit, been penalised by only 12,6 kW.

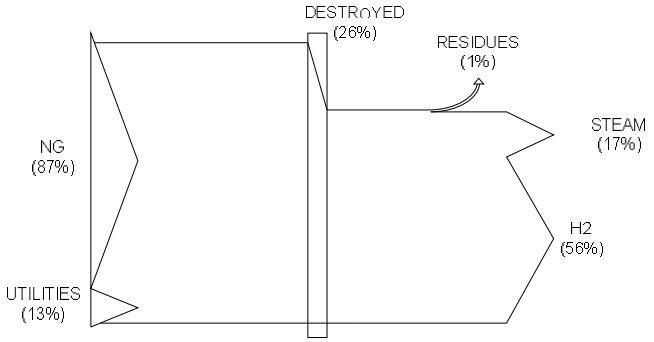

Fig. 8. Grassmann diagram of hydrogen generation unit

The process exergy efficiency for hydrogen generation unit is 73,6%, see Fig.8. The total exergy destroyed is 36.7 MW. Note that the steam generated has a significant role in this process.

4.1.5. Hydrotreating

Since the function of hydrotreating unit is to remove sulphur compounds, a great quantity of sour gas is produced (46% of total). Besides sour gas, sour water is also produced and heat is sent to cooling water circuit. Therefore 5.5 MW of exergy is added to the exergy input and 19.6 MW is added to the products.

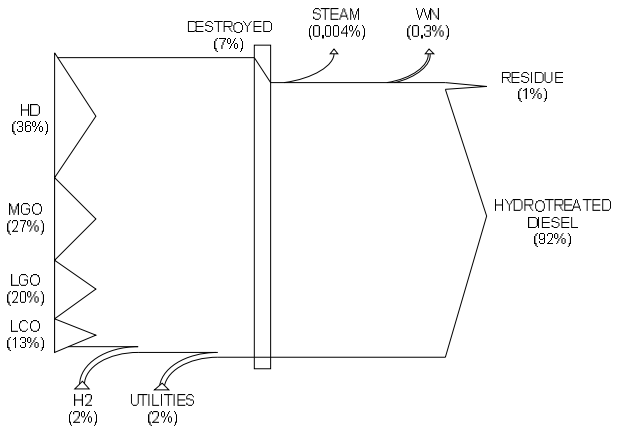

Fig. 9. Grassmann diagram of hydrotreating unit

The hydrotreating exergy efficiency is 92.88%, 192.1 MW of exergy is destroyed, Fig.9. Note that the hydrogen is responsible for only 2% of exergy input.

4.1.6. Utilities plant

For utilities plant an exergy efficiency of 30% was observed. The energy and exergy efficiency given by the equations described in Table 1. for each plant component, can be seen in Fig. 10. The exergy efficiency is higher than energy efficiency for gas turbine (GT) since the exergy of exhausting gas was subtracted from the exergy of the fuel. The recovery boiler (RB) and the conventional boiler (B1, B2) presented an exergy efficiency of 39%, 49% and 40%, respectively. The steam turbines (T) presented a large variation in exergy efficiency: 38% up to 76% highlighting some possible problems. The water treatment process (WTP) has a very low efficiency since it is not and energy conversion process.

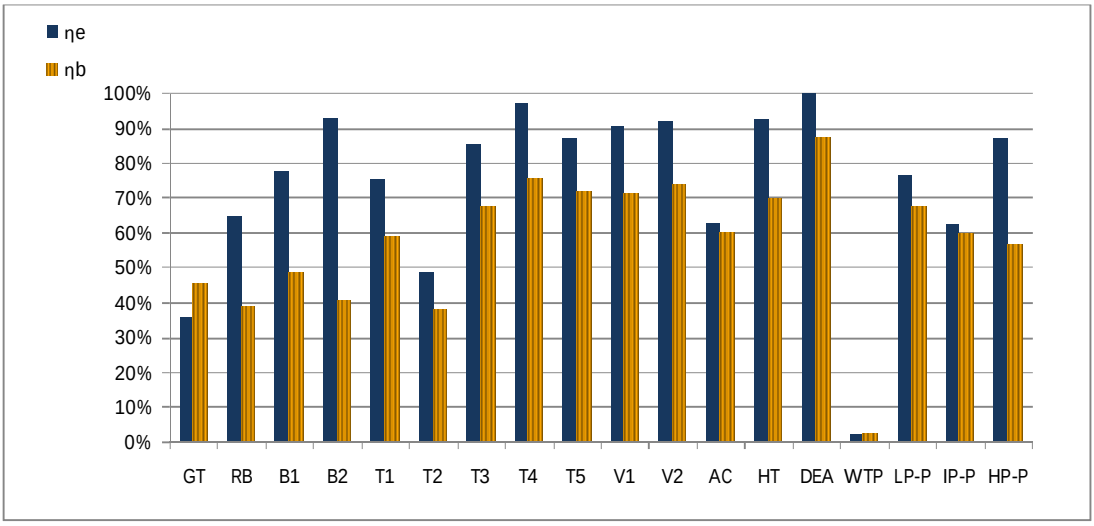

Fig. 10. Energy and exergy efficiency of utilities components

The main exergy destructions in utilities plant were presented in the components in which combustion occurs: boilers and gas turbines, these components are responsible for 85% of the all exergy destroyed, see Fig.11.

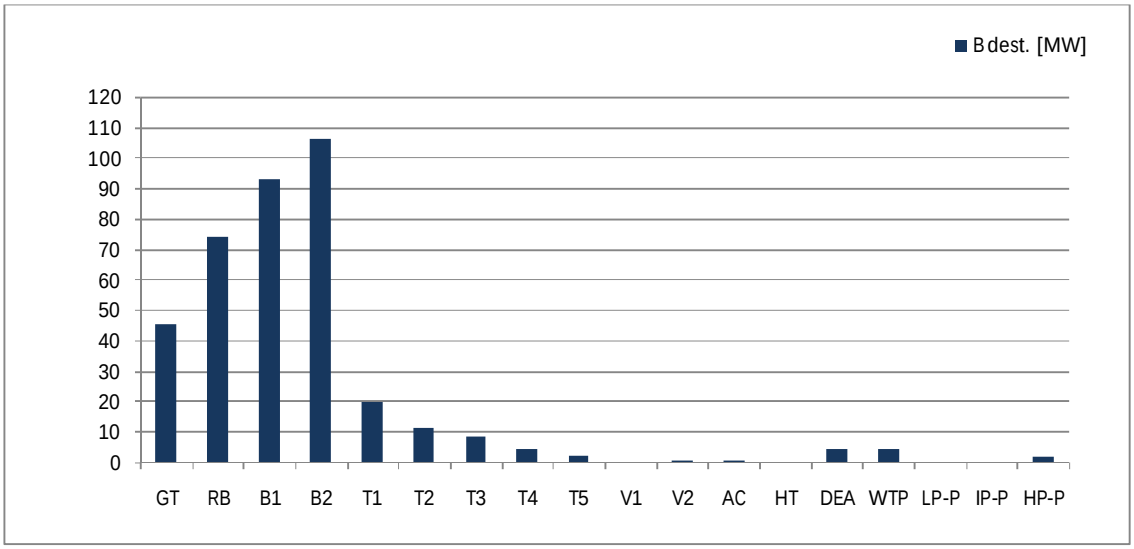

Fig. 11. Exergy destroyed in each utilities plant component

Taking into account all components of utilities plant, 249 MW of exergy are destroyed.

4.1.7. Exergy analysis summary

Table 2. presents a summary of the exergy analysis. Note that the total exergy destroyed is 749.8 MW. The exergy destroyed in SR and SWT treatment processes is allocated to the processes that make use of these units.

Table 2. Refinery exergy analysis summary

Unit	B_{in}[kW]	B_{out}[kW]	B_{dest} [kW]	% destroyed	η_b
CD	14,313,503	14,049,234	264,269	36%	98.18%
UT	355,931	107,065	248,866	33%	30.08%
DC	3,190,335	3,100,598	89,737	12%	98.00%
HDT	2,757,355	2,689,992	67,364	9%	92.88%
HG	142,457	104,686	37,770	5%	73.50%
FCC	3,418,041	3,384,802	33,239	4%	98.93%
TE	13,562,341	13,553,746	8,594	1%	99.94%
SR	36,754	28,346	8,408	1%	75.56%
SWT	15,668	14,058	1,610	0%	61.35%

4.1.8. Overall refinery efficiency

The overall exergy efficiency for the refinery is 94.4%. It is worth noting that more than 14 GW of exergy associated to crude oil, natural gas and water are processed and almost 800 MW of exergy are destroyed.

4.2. Improvements possibilities

Some possibilities to decrease exergy destruction are general, extensively studied and reported: Pinch Method for heat exchange network, pre-heating air systems and pre-heating water systems, both using waste heat, decrease the heat loss in the tanks between process, utilization of high efficiency utilities plants, the use of diagnosis and prognosis systems [27] and others. There are some improvement possibilities specific for refineries such as the development of better catalysts, the use of CO boilers as reported by [9,15] (already implemented in studied refinery) and the use of a turbo-expander to generate electricity during the CO gas pressure reduction before the CO boiler. This possibility is used in a great number of refineries and is reported in [28]. The use of the exergy of exhausting gases is very restricted, since for most of the furnaces and boilers the exhausting temperature is controlled to avoid acid condensation. However, the heat sent to cooling water circuit represents an actual improvement possibility since several streams are cooled prior entering transfer and storage area. From combined distillation unit 4.5 MW of exergy (~140ºC) are sent to cooling water circuit. The use of this exergy for power production using organic Rankine cycles (ORC) could improve the refinery efficiency by increasing the use of waste heat while decreases the cooling tower exergy and make-up water consumption.

4.3. Exergoeconomy results

In order to take into account the whole petroleum sector, the exergy spent during production and transportation were considered for evaluation.

4.3.1. Offshore production consideration

To take the primary separation into account, the work of Oliveira Jr. and Hombeeck [29] and Nakashima et al. [30] were considered. In [29] an exergy analysis of an offshore platform is performed while in [30] an exergoeconomy analysis of a petroleum artificial lift systems is conducted. Using a gas turbine efficiency of 30% and the extraction criterion, the related unit exergy cost of the crude oil is 1.006 (kJ/kJ) while 1.034 (kJ/kJ) is obtained for the natural gas. The higher value obtained for the natural gas is mainly due to post separation compression.

4.3.2. Petroleum and natural gas transportation

The unit exergy cost obtained for natural gas and petroleum from the offshore production facility includes their transportation up to an onshore base (~100km). In order to evaluate the transportation contribution from the onshore base to the refinery the following factors were used:

- 2.60 kJ/(kg.km) for natural gas. This value takes into consideration that the energy for compression comes from gas turbines with 30% of efficiency (LHV basis) and it is based on a real compression station data. The isentropic efficiency reported for gas compression is 87%.
- 0.18 kJ/(kg.km) for crude oil. This value takes into account that electricity is used to drive the pumps and it is obtained from local grid. This electricity is produced considering a local electricity matrix based on hydroelectricity with 80% of efficiency. A petroleum viscosity of 0.45 Pa.s (450 cP) was considered as well as a pumping efficiency of 50%.

By using the above mentioned considerations the basis for exergy unit cost calculations are the natural resources only: water in the reservoir and petroleum a natural gas in the well, both are the substances having unit exergy cost equals to one. Table 3 shows how the unit exergy cost varies with the distance between the onshore base and the refinery.

Table 3. Variation of unit exergy cost of NG and crude oil entering in the refinery

Distance (km)	**0**	**50**	**100**	**150**	**200**	**250**	**300**	**350**	**400**	**450**	**500**
NG (kJ/kJ)	1.0340	1.0366	1.0393	1.0419	1.0445	1.0471	1.0498	1.0524	1.0550	1.0576	1.0603
% accumulated		0.25%	0.51%	0.76%	1.02%	1.27%	1.52%	1.78%	2.03%	2.29%	2.54%
Crude oil (kJ/kJ)	1.0060	1.0062	1.0064	1.0066	1.0068	1.0070	1.0072	1.0074	1.0076	1.0078	1.0080
% accumulated		0.02%	0.04%	0.06%	0.08%	0.10%	0.12%	0.14%	0.16%	0.18%	0.20%

4.3.3. Overall results

The increment in the unit exergy costs for the products of refinery process units to a distance, between the onshore base and refinery, of 500 km is shown in Fig. 12. A very small sensibility is observed. The same variations are obtained for the exergy intensity.

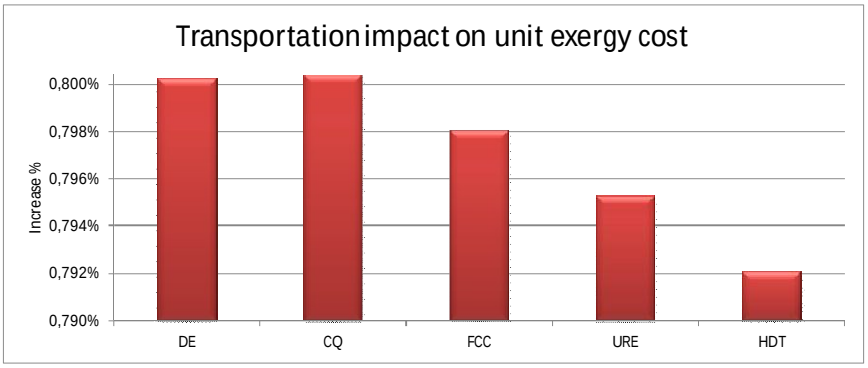

Fig. 12. Transportation impact on unit exergy cost in the products of the refining process for a 500 km variation

Since no relevant increment in unit exergy cost of products is observed due to transportation, even for long distances (500 km), the unit exergy costs for the crude oil and natural gas entering the refinery were considered the ones from offshore facility (0 km between onshore base and refinery). By solving the set of linear equation driven from exergy efficiencies provided in Table 1 and the exergoeconomy equations for each refinery process unit, (7), (8), (9), (10), (11) and (12), the unit exergy cost of all streams present in Fig.2 were calculated. Fig.13 shows the unit exergy cost of the utilities produced. It is worth noting that steam is produced by process units (_P) at a very low exergy cost, thus a medium cost is calculated (_M). Since the inverse of unit exergy cost is the exergy efficiency, the exergy efficiencies for electricity (EE), mechanical power (MechPw), high

pressure steam, medium pressure steam and low pressure steam generation are: 32%, 23%, 40%, 46% and 52%, respectively. These results show an inefficient mechanical power production and it is in accordance with the low efficiency obtained of some steam turbines, see Fig.10. These costs take into consideration all interaction present, thus they can be used as a quality indicator for utilities production.

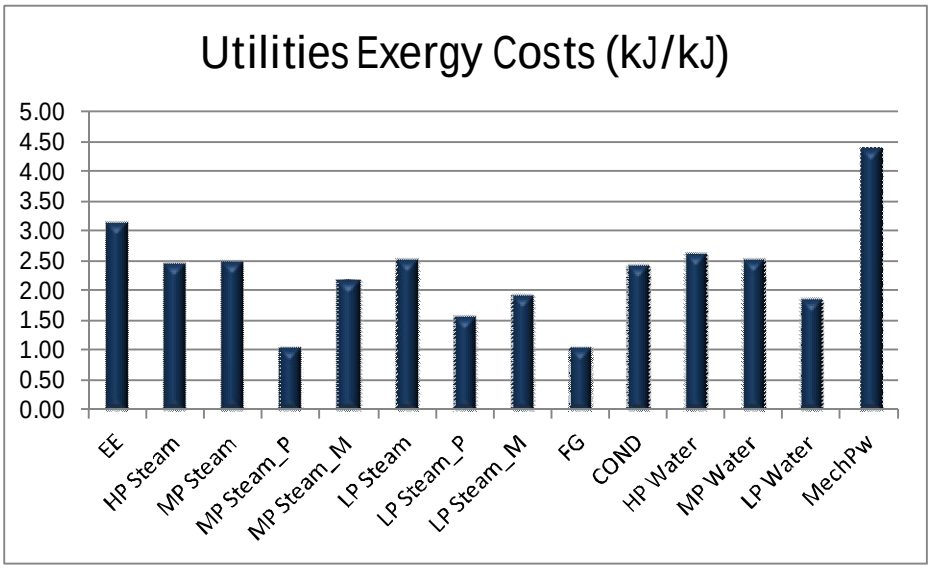

Fig. 13. Unit exergy cost of utilities

The unit exergy cost of the main refinery streams can be seen in Fig.14. It clearly shows the cost aggregation as a given substance is processed by an increasing number of processes. The streams leaving combined distillation (CD) have a unit exergy cost of 1.03 (kJ/kJ). The streams leaving the delayed coking (DC) unit were processed by CD and by DC since the feed of DC is the vacuum residue, thus a unit exergy cost of 1.07 is observed. For the streams leaving FCC process a unit exergy cost of 1.08 is obtained since the feed of this process is composed of products of CD and DC. The HDT products are the ones with highest unit exergy cost, 1.11 (kJ/kJ), due to hydrogen use and due the high unit exergy cost of its feed.

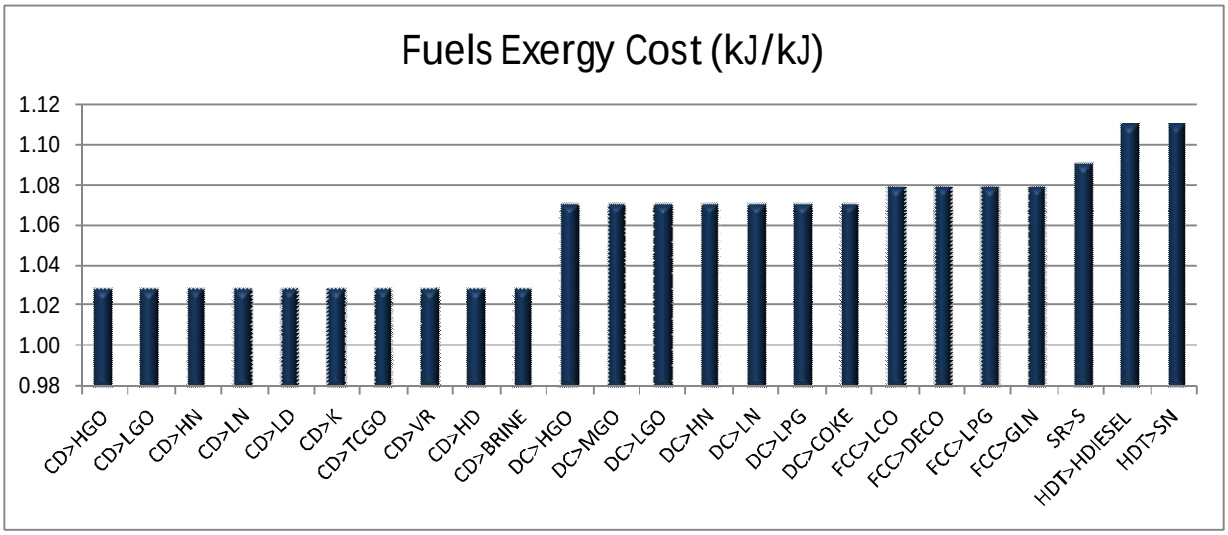

Fig. 14. Unit exergy cost of produced substances[5]

[5] In Figs 14-16 the mathematical symbol ">" are used to indicate the stream direction. E.g. CD>HGO means the heavy gasoil from combined distillation.

The exergy intensity of the streams, Fig.15, is calculated by multiplying the unit exergy cost (kJ/kJ) by the specific exergy (kJ/kg) of the stream. Therefore it provides an indicator that besides the cost aggregation due to processing also takes into account the exergy of the stream. As result the high exergy streams with long process chains are the most intensive in exergy: LPG produced by FCC and DC, naphtha produced by HDT, gasoline from FCC and hydrotreated diesel. As a consequence, the low exergy products have low exergy intensity: brine, elementary sulphur and coke.

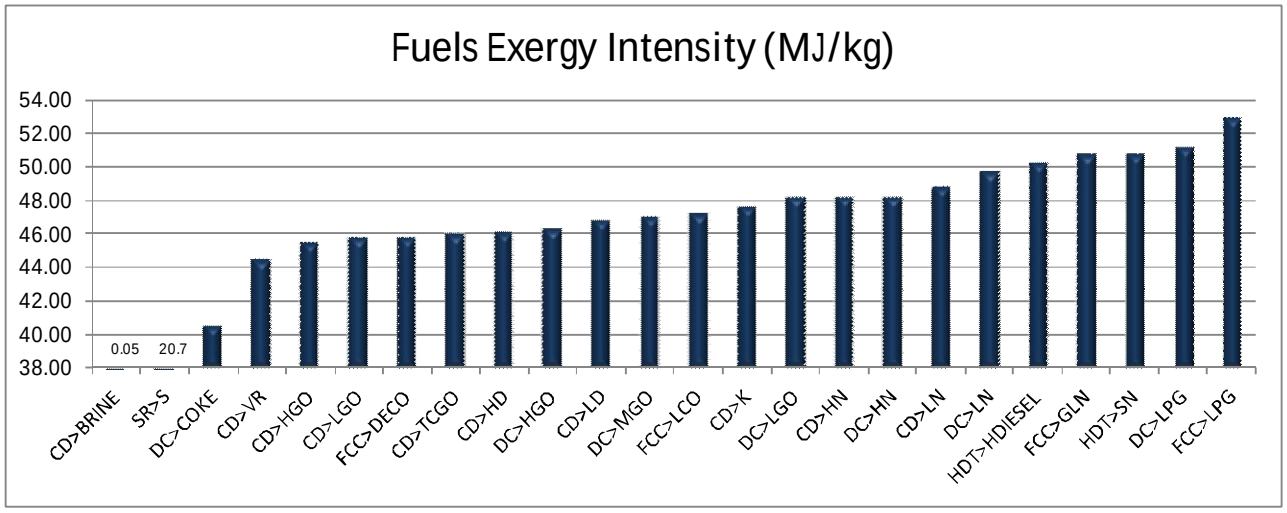

Fig. 15. Exergy intensity of the produced substances[5]

Figure 16 shows a comparison between unit exergy cost and exergy intensity. The unit exergy cost is function of process chain thus it is the same for the several products of a given process while exergy intensity is also function of the exergy accumulated in a given stream thus it varies from stream to stream. Table 4 shows the values informed in Figs 14, 15 and 16.

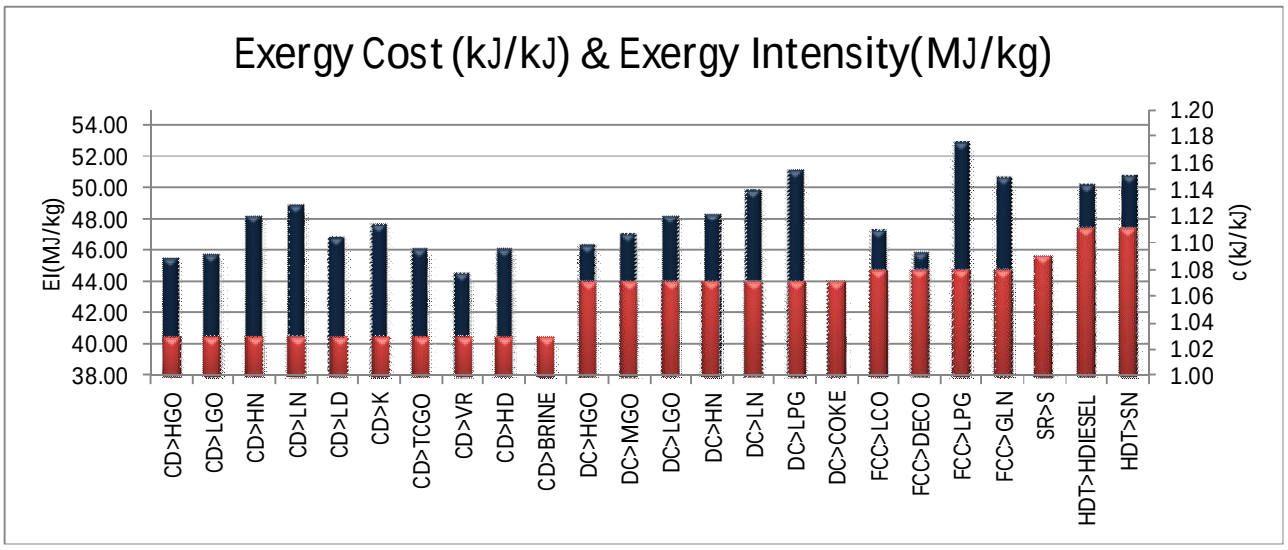

Fig. 16. Comparison between unit exergy cost and exergy intensity[5]

Table 4. Streams unit exergy cost(c) and exergy intensity(EI)

STREAM	c (kJ/kJ)	EI (MJ/kg)
CD>HGO	1.03	45.49
CD>LGO	1.03	45.76
CD>HN	1.03	48.20
CD>LN	1.03	48.83
CD>LD	1.03	46.82
CD>K	1.03	47.59
CD>TCGO	1.03	46.01
CD>VR	1.03	44.51
CD>HD	1.03	46.08
CD>BRINE	1.03	0.05
DC>HGO	1.07	46.32
DC>MGO	1.07	46.97
DC>LGO	1.07	48.18
DC>HN	1.07	48.24
DC>LN	1.07	49.78
DC>LPG	1.07	51.18
DC>COKE	1.07	40.46
FCC>LCO	1.08	47.18
FCC>DECO	1.08	45.81
FCC>LPG	1.08	52.89
FCC>GLN	1.08	50.71
SR>S	1.09	20.82
HDT>HDIESEL	1.11	50.19
HDT>WN	1.11	50.75

5. Conclusion

The exergy analysis was applied to a whole refinery. The processes responsible for the main exergy destruction rates are combined distillation, utilities plant (85% in gas turbines and boilers) followed by delayed coking. The overall exergy efficiency observed is 94.4%. This result demonstrates that only a small percentage of the exergy input (~14 GW) is destroyed (~800MW). Organic Rankine cycles to make use of the exergy sent to cooling tower hence reducing the exergy and make-up water consumption while increasing whole process efficiency is suggested as improvement. The exergoeconomy provided the necessary tool to calculated the exergy efficiency of utilities production in the highly integrated and multiproduct processes. By using the unit exergy cost provided by previous works for oil and natural gas from primary separation the exergy cost and exergy intensity of petroleum derived fuels were calculated. The oil and natural gas transportation to the refinery plays a minor role in comparison with refining and production exergy consumption. The exergy intensity of the petroleum derived fuels allows properly quantification of the exergy expenditures for production of petroleum derived goods and fuels. The exergy intensity observed for FCC gasoline and LPG, and for hydrotreated diesel are 50.71 (MJ/kg), 52.89 (MJ/kg) and 50.19 (MJ/kg), while the unit exergy costs are 1.08 (kJ/kJ), 1.08 (kJ/kJ) and 1.11(kJ/kJ), respectively. It is interesting to note that these values are significantly smaller than the value provided in [1] for a typical sugar cane ethanol, 3.4 (kJ/kJ) and 92.56 (MJ/kg).

Acknowledgments

The first and last authors of this paper would like to thank CNPq (grants 143302/2009-4 and 306505/2009-6) and Petrobras for the financial support.

Nomenclature

AC Air Compressor
B Boiler
c Unit exergy cost, (kJ/kJ)
CCR Carbon Conradson Residue
CD Combined Distillation
CO Carbon monoxide
CT Cooling Tower
DC Delayed Coking
DEA. Deaerator
DECO Decanted Oil
EE Electric Energy
EI Exergy Intensity, (MJ/kg)
FCC Fluidized Catalytic Cracking
FG Fuel Gas
GLN Gasoline
GO Gasoil
GT Gas Turbine
HD Heavy Diesel
HDT Hydrotreating
HG Hydrogen Generation
HGO Heavy Gasoil
HN Heavy Naphtha
HPW High Pressure Water
HRSG Heat Recovery Steam Generator
HT Heat transfer
IP Intermediate pressure
K Kerosene
LCO Light Cycling Oil
LD Light Diesel
LGO Light Gasoil
LHV Low Heating Value
LN Light Naphtha
LP Low Pressure
LPG Liquefied Petroleum Gas
LPW Low Pressure Water
MecPw Mechanical Power
MGO Medium Gasoil
MP Medium Pressure

MPW Medium Pressure Water
N Naphtha
NG Natural Gas
ORC Organic Rankine Cycle
P Pump
PI Plant Information
PSA Pressure Swing Adsorption
Q Heat
RB Recovery Boiler
RW Rectified Water
S Sulphur
SG Sour Gas
SR Sulphur Recovery
SW Sour Water
SWT Sour Water Treatment
T Steam Turbine
TBP True Boiling Point
TCFO Top Cycling Fuel Oil
TE Transport and Storage
V Valve
VR Vacuum Residue
WN Wild Naphtha
WTP Water Treatment Process

Greek symbols

η efficiency
φ Correction factor to transform LHV into chemical exergy

Subscripts and superscripts

b Exergy
Ci To cooling water
Cond. Condensed
CW From cooling water
e Energy
i General process
m General auxiliary unit
LP Low Pressure
MP Medium Pressure
RW Rectified Water
S Sulphur
SR Sulphur Recovery
SWT Sour Water Treatment
0 Environment

References

[1] Pellegrini L. F., Oliveira Jr, S. Combined production of sugar, ethanol and electricity: Thermoeconomic and environmental analysis and optimization. Energy 2011; 36: 3704-3715.

[2] Lazzaretto A., Tsatsaronis G., SPECO: A Systematic and General Methodology for Calculating Efficiencies and Costs in Thermal Systems. Energy 2006; 31: 1257-1289.

[3] Lozano M. A., Valero A., Theory of Exergetic Cost. Energy 1993; 18: 939-960.

[4] Erlach B., Serra L., Valero A., Structural Theory as a Standard for Thermoeconomics. Energy Conversion and Management 1999; 40: 1627-1649.

[5] Frangopoulos C., Thermo-Economic Functional Analysis and Optimization. Energy 1987; 12: 563-571

[6] Torres C., Valero A., Rangel V., Zaleta A., On the cost formation process of the residues. Energy 2008; 33: 144-152.

[7] Santos J., Nascimento M., Lora E., Reyes A. M., On the Negentropy Application in Thermoeconomics: a fictitious or an exergy component flow?. Int. J. of Thermodynamics 2009; 12: 163-176.

[8] Dinçer S., Erkan D., Available Energy Analysis of a Petroleum-Refinery Operation. Applied Energy 1986; 22 : 157-163.

[9] Rivero R., Application of the exergy concept in the petroleum refining and petrochemical industry. Energy conversion and Management, 2002; 43: 1199-1220.

[10] Rivero R., Urquiza J., Simulation, exergy analysis and application of diabatic distillation to thertiary amyl methyl ether production unit of a crude oil refinery. Energy 2004; 29: 467-489.

[11] Khoa T. D., Shuhaimi M., Hashim H., Panjeshahi M. H., Optimal design of distillation column using three dimensional exergy analysis curves. Energy 2010; 35: 5309-5319.

[12] Al-Muslim H., Dinçer I., Thermodynamic analysis of crude oil distillation systems. International Journal of Energy Research 2005; 29: 637-655.

[13] Frangopoulos C. A., Lygeros A. I., Markou C. T., Kaloritis P., Thermoeconomic Operation Optimization of the Hellenic Aspropyrgos Refinery Combined-Cycle Cogeneration System. Applied Thermal Engineering 1996; 16: 949-958.

[14] Cooper D., Do you value steam correctly? Hydrocarbon Processing 1989.

[15] Rivero R., Rendón C., Gallegos S., Exergy and Exergoeconomic analysis of a crude oil combined distillation unit. Energy 2004; 29: 1909-1927.

[16] Lima R. S., Schaeffer R., The energy efficiency of crude oil refining in Brazil: A Brazilian refinery plant case. Energy 2011, 1-12.

[17] Szklo A., Schaeffer R., Fuel specification, energy consumption and CO_2 in oil refineries. Energy 2007; 32 : 1075 -1092.

[18] Fahim M. A., Al-Sahhaf T. A., Elkilani A. S., Fundamentals of Petroleum Refining. Elsevier; 2010.

[19] Gary J. H., Handwerk G. E., Kaiser M. J., Petroleum refining - Technology and Economics. CRC Press; 2007.

[20] Szargut J., Morris D.R., Steward F.R., Exergy analysis of thermal, chemical and metallurgical processes. New York: Hemisphere Publ. Corp; 1988.

[21] KBC Advanced Technologies plc, Petro-SIM, V3. Hysys Base Portion Copyright.

[22] Riazi, M. R., Characterization and properties of petroleum fractions. ASTM manual series: MNL50, 2005.

[23] Rivero R., Rendón C., Monroy L., The exergy of crude oil mixtures and petroleum fractions: calculation and application. Int. J. Applied Thermodynamics 1999; 2: 115-123.

[24] Kotas, T. J., The exergy method of thermal plants analysis. London: Butterworths; 1985.

[25] Channniwala S. A., Parikh P. P. A., Unified correlation for estimating HHV of solid, liquid and gaseous fuels. Fuel 2002; 81: 1051-1063.

[26] Kein S. A., Engineering Equation Solver - EES. Professinal V8.876, 2011.

[27] Silva J. A. M., Venturini O. J., Lora E. E. S., Pinho A. F., Santos J. J. C. S., Thermodynamic information system for diagnosis and prognosis of power plant operation condition. Energy 2011: 36; 4072-4079.

[28] Fermoselli N. E. G., Predicting the impact of a FCC turbo expander on petroleum refineries. Cobem 2011. Proceedings of 21 Brazilian Congress of Mechanical Engineering, October 24-28, 2011, Natal, RN, Brazil.

[29] Oliveira Jr, S., Hombeeck M. V., Exergy analysis of petroleum separation processes in offshore platforms. Energy Conversion and Management 1997; 38: 1577-1584.

[30] Nakashima C. Y., Oliveira Jr. S., Caetano E. F. Subsea multiphase pumping system x gas lift: an exergo-economic comparison. Thermal Engineering 2004; 3: 1676-1790.

Exergy-based sustainability evaluation of a wind power generation system

J. Yang[a], B. Chen[a*], E. Sciubba[b]

[a] State Key Joint Laboratory of Environmental Simulation and Pollution Control, School of Environment, Beijing Normal University, Beijing 100875, China, email (J. Yang): yangjin_asang@163.com, email (B. Chen): chenb@bnu.edu.cn

[b] Department of Mechanical and Aerospace Engineering, University of Roma 1, La Sapienza, via Eudossiana 18, 00184, Roma, Italy, e-mail(E. Sciubba):enrico.sciubba@uniroma1.it

Abstract:

Huge greenhouse gas (GHG) emission from fossil fuel combustion and unsatisfied energy requirement have forced China to inquire into and change to environmental friendly alternatives that are renewable to sustain the increasing energy demand. Therefore, renewable energy in China has experienced a prosperous development in the last decade and will continue to be the focus and key issue of future energy development planning. However, some environmentalists have long argued that whether renewable energy sources such as wind are preferable to fossil fuels (oil, natural gas and coal), and which kind of renewable energy are more clean and sustainable. Quantitative evaluation to answer these questions thereby should be conducted. As extended exergy accounting (EEA) is a systematic exergo-economic method that adopts a single quantifier to account for materials, energy, labor and capital and to compute a presumed environmental impact based on remediation costs, it is a powerful tool for handling sustainability issues. Thus, aiming at evaluating the sustainability of renewable energy, we employ EEA to monitor the sustainability level of a wind power plant in China from the aspects of economic and environmental performance, and exergy efficiency. The results may provide some useful suggestions to support the environmentally sound renewable energy development.

Keywords:

Extended Exergy Evaluation, Wind Farm, Sustainability.

1. Introduction

Owing to its economic feasibility and great potential in reducing carbon emission, wind power, which is currently the environmentalists' favourite source of renewable energy, is thought to be the most likely renewable energy source to replace fossil fuels in the generation of electricity in the 21st century. However, controversies on if the wind power is more competitive compared with other renewable alternatives are still going on. For energy sources, it is difficult to measure and is often decided in a qualitative manner. Therefore, a quantitative approach aiming at making trade-offs among renewable energy sources is required.

Sustainability of energy sources is regarded an efficient way to determine which energy source is more appropriate. Clearly, judgements of sustainability include conversion efficiency, economic feasibility, and environmental loading that must be 'treated and recycled' by the environment. Ultimately, the comprehensive evaluation of sustainability for different energy sources could be factored into policy discussions of future renewable energy planning.

To make decisions towards sustainable energy generation and use, several methods and models have been developed, and classified into indicator-based analytic hierarchy process (AHP) method [1, 2], systematic energy analysis [3, 4], emergy analysis [5], and exergetic method [6, 7]. For AHP method, since there are no intrinsic principles for the selection of indicators, especially the identification of weight which is judged subjectively by experts, the derived indicators may be not

suitable to measure the long-term sustainability of energy systems. Although energy analysis (first law analysis) could overcome the subjectivity of AHP method, the non-additivity of different kinds of energy types which vary in quality poses great barriers for monitoring the energy flow of the energy system.

The concept of exergy was first proposed by Rant in 1956, and defined as the maximum amount of work which can be produced by a system or a flow of matter or energy as it comes to equilibrium with a reference environment [8]. This methodology has evolved since the early 1970's and has been extensively applied in empirical studies since late 1990's [9-17]. Compared with energy analysis, exergy is more appropriate in sustainability evaluation. Dincer (2002) has pointed out the importance of exergy from the following aspects: (1) It is a primary tool in best addressing the impact of energy resource utilization on the environment. (2) It is an effective method using the conservation of mass and conservation of energy principles together with the second law of thermodynamics for the design and analysis of energy systems. (3) It is a suitable technique for furthering the goal of more efficient energy-resource use, for it enables the locations, types, and true magnitudes of wastes and losses to be determined. (4) It is an efficient technique revealing whether or not and by how much it is possible to design more efficient energy systems by reducing the inefficiencies in existing systems. (5) It is a key component in obtaining sustainable development.

In the evolvement of exergy method, Szargut et al. [18] extended the conventional exergy analysis to cumulative exergy consumption analysis (CECA), which combines exergy analysis with life cycle analysis (LCA) together, and accounts the sum of the values of primary exergy consumed in all the links of the energy and technological network in connection with the fabrication of the considered product.

However, despite that exergy analysis could detailed trace the efficiency of each conversion process in a thermodynamics perspective, it is not regarded as the optimal approach in sustainable evaluation as it couldn’t reflect the economic property of a process. This inability of standard exergy analysis to evaluate sustainability and determine real design optima was perfected by extended exergy accounting (EEA), which was proposed by Sciubba [19]. The conceptual novelty of EEA is represented by the fact that it also includes externalities (capital, labour and environmental impact) measured in homogeneous units (Joules) by a theory of joint economic- and thermodynamic character, properly named ‘thermoeconomics’, This concept was further developed and illustrated by Sciubba [20-23], and Ptasinski et al. [24]. Now, some researchers began to employ extended exergy to evaluate the sustainability of renewable energy sources. Corrado et al. [25] analysed the performance of an innovative high-efficiency steam power plant by means of two ‘‘life cycle approach’’ methodologies, the life cycle assessment (LCA) and the ‘‘extended exergy analysis’’ (EEA). Talens Peiró et al. [26] assessed and compared the production of 1 ton of biodiesel from used cooking oil (UCOME) and rapeseed crops (RME). The cumulative exergetic method is used by Yang et al. [27] to identify the renewability of the total corn-ethanol production in China when capturing all natural nonrenewable resources consumed in the integrated process including agricultural crop production, corn transportation, industrial conversion and waste treatment. However, in the current stage, a comprehensive sustainable indicator system hasn’t been proposed.

In this paper, the extended exergy evaluation method is applied to a wind power generation system, and some extended exergy based sustainability indicators were proposed to comprehensively monitor its environmental, economic and sustainable performances. The rest of the paper is organized as follow: In section 2, the accounting framework as well sustainable indicators are proposed. Using the EEA method, a case study is performed in Section 3. The results and some discussions are then demonstrated in Section 4. Finally, some conclusions are drawn.

2. Methodology

2.1. Extended exergy accounting

Extended exergy, proposed by Sciubba, is an extension of traditional exergy analysis to highlight the primary production factors, including two of neo-classical economics, i.e., labour and capital, and the other three ones, i.e., the exergy, necessary materials and environmental remediation, thus bridging the gap concerning the 'production of value' between the majority of economists and energists [28]. Based on the concept of extended exergy, except for the primary exergy resource equivalent "embodied" in the materials and energy sources, the primary resource equivalent of the so-called "externalities": Labour-, Capital- and Environmental remediation costs is also included in the accounting framework. The calculation of extended exergy in demonstrated in (1).

$$EE = CExC + E_C + E_W + E_e, \tag{1}$$

where EE is the total extended exergy input of a specific system, $CExC$ is he cumulative exergy costs, E_C represents the exergy equivalent of the monetary flow, E_W represents the exergy equivalent of human labour, and E_e is specified as the environmental remediation costs.

2.2. Extended exergy indices

Extended exergy is observed to be a thermal-economic concept that adopts a single quantifier (exergy, expressed in Joules) to account for materials, energy, labour and capital and to compute a presumed environmental impact based on remediation costs. In consideration of its resource, economic, and environmental implications, a series of extended exergy-based indicators derived from this concept could thereby be proposed to reflect the conversion efficiency, resource consumption, environmental loading, economic benefits as well as sustainability. The calculations of these indicators are demonstrated in (2)-(5).

The conversion efficiency of ε_P can be computed as the ratio of the useful output to the sum of the inputs that concurred to produce it [19]:

$$\varepsilon_P = \frac{\sum EO_j}{\sum EI_i}, \tag{2}$$

where $\sum EO_j$ is the sum of useful outputs, $\sum EI_i$ is the total inputs of a specific process.

Renewability is defined as the ratio of renewable exergy inputs and cumulative non-renewable exergy inputs, indicating the percentage of the total energy driving a process that is derived from renewable sources. In the long run, only processes with high R% are sustainable.

$$R\% = E_R / CExC, \tag{3}$$

where E_R is the renewable exergy inputs and $CExC$ is the cumulative exergy input, which is the sum of renewable exergy inputs (E_R) and non-renewable exergy inputs (E_{NR}).

The economic yield ratio (EYR) is used to reflect the economic feasibility, and is defined as the ratio of the exergy output and the monetary costs, as demonstrated in Equation (4). The larger the amount of monetary costs in the process, the lower the economic yield ratio, vice versa.

$$EYR = E_C / Y, \tag{4}$$

where E_C is the exergy equivalent of the monetary flow, and Y is the exergy output of a process.

Environmental impact degree (EID) is expressed by the proportion of non-renewable exergy inputs and environmental remediation costs to the total exery input. It is used to quantify the environmental impacts exerted by human activities.

$$EID = (E_e + E_{NR}) / EE, \tag{5}$$

3. Case study

3.1. Study site

The wind farm concerned in this paper is constructed in Horqin Right Front Banner, which is located at 45°42'07"-47°01'36" north latitude and 119°31'51"-122°52'07" east longitude. The altitude there declines gradually from the northwest to the southeast. There is a northern continental climate where annual average temperatures of the south, central and north parts are 4.2 ℃, 2.1℃, -3.2℃, respectively. The annual precipitation is 1198.9 mm and the annual solar duration is 2800 hours. Horqin Right Front Banner is affluent in wind resources; the annual windy days on average about 23 days, with up to 47 days. Wind velocity varies yearly, representing a trend of heavier winds in the winter and spring while the winds abate in the autumn and summer. In addition, the wind velocity in the daytime is larger than at night.

The total installed capacity of the projected wind farm in Horqin Right Front Banner is 150MW and is expected to be completed in three phases. In this paper, the energy and economic feasibility analysis is conducted on the first phase. Based on the characteristic power curve and hourly wind data for the location of the wind farm, ultimately the optimal scheme the first phase is a goal of a gross electricity output of 183.5 GWh annually and the annual electricity to access grid is 111.7GWh, with the equivalent full load operating hours of 2257 h and capacity factor of 0.258. The construction of the wind farm will take 12 months while the operation period will be 20 years.

3.2. System boundary

The system boundary of the wind power generation system is demonstrated in Fig. 1. Exergy inputs include wind resource, non-renewable energy and material used in the electricity generation process, capital investment on equipment and construction, labour input and environmental remediation costs. Meanwhile, the main output of this wind farm is electricity.

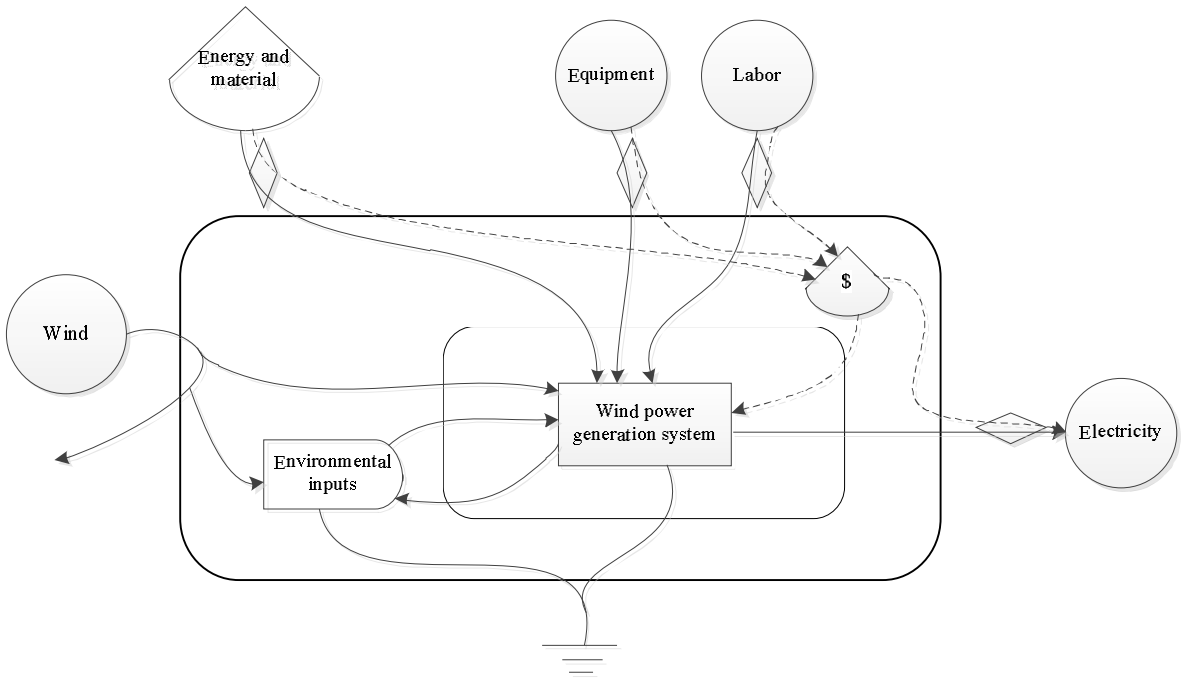

Fig. 1. Exergy flows of the wind power generation system

3.3. Data sources

For calculating the extended exergy of the concerned wind farm, we need disaggregated data of material and energy inputs, capital and labour and additional information about the remediation costs linked to its environmental impact. Material and energy inputs are quantified based on cumulative exergy content of each input, which was calculated by previous works. Economic data is

provided by China Xiehe Wind Power Investment Co., Ltd, including direct cost purchase of equipment cost and installation, instrumentation and control, building work, electrical equipment and materials and service facilities), indirect costs (construction and contingencies) plus maintenance. The environmental impact of the system is calculated based on the investments on waste gas emission, the waste water and solid waste treatment and vegetation restoration. The labour required in the construction and operation stages is also included.

4. Results and discussions

As illustrated in Table 1, the total extended exergy that flows into the wind power generation system is 8.40E+15 J, in which the proportions of renewable exergy input, non-renewable exergy from energy sources, capital input, labour input and environmental remediation input to the total extended exergy input are 83.30%, 0.07%, 15.20%, 1.32% and 0.11%, respectively (Figure 2). Obviously, renewable exergy input makes up the largest proportion, followed by capital input, indicating that although free wind resources are largely and efficiently used, the wind power generation is propelled by a vast of capital investment. The great investment on the wind power increases the cost and price of wind power. As a result, the higher price of wind power makes it less competitiveness compared with other power generation systems. Obviously, the non-renewable energy inputs and environmental remediation costs only constitute a small fraction, implying that the wind powered electricity generation system is a renewable and environmentally friendly energy utility mode.

Table 1. Exergy inputs of the wind power generation system

Items	Quantity	Unit	Exergy coefficients	Units	References	Exergy (J)
00Renewable energy inpputs						
Wind	7.00E+15	J	1	J/J	[18]	7.00E+15
Water	1.00E+04	t	0.05	MJ/kg	[12]	5.00E+11
Subtotal						**7.00E+15**
Non-renewable energy inputs						
Gasoline	1.21E+02	t	1.07	J/J	[29]	5.60E+12
Subtotal						**5.60E+12**
Capital inputs						
Equipment	3.18E+08	yuan	2.94	MJ/yuan	[28]	9.34E+14
Building works	6.10E+07	yuan	2.94	MJ/yuan	[28]	1.79E+14
Interest of loan	1.14E+07	yuan	2.94	MJ/yuan	[28]	3.37E+13
Others	4.50E+07	yuan	2.94	MJ/yuan	[28]	1.32E+14
Subtotal						**1.28 E+15**
Labor input						
Construction	9.39E+05	Hour	71.9	MJ/Hour	[28]	6.75E+13
Operation	6.01E+05	Hour	71.9	MJ/Hour	[28]	4.32E+13
Subtotal						**1.11E+14**
Environmental remediation costs						
NO_x	6.31E+03	kg	2963.3	kJ/kg	[30]	1.87E+10
SO_2	6.07E+03	kg	4892.3	kJ/kg	[30]	2.97E+10
CO	1.64E+02	kg	9825	kJ/kg	[30]	1.62E+09
CO_2	1.74E+03	t	0.45	PJ/Mt	[31]	7.84E+11
Waste treatment	6.15E+05	yuan	2.94	MJ/yuan	[28]	1.81E+12
Vegetation restoration	2.20E+06	yuan	2.94	MJ/yuan	[28]	6.47E+12
Subtotal						**9.11E+12**
Total input						**8.40E+15**

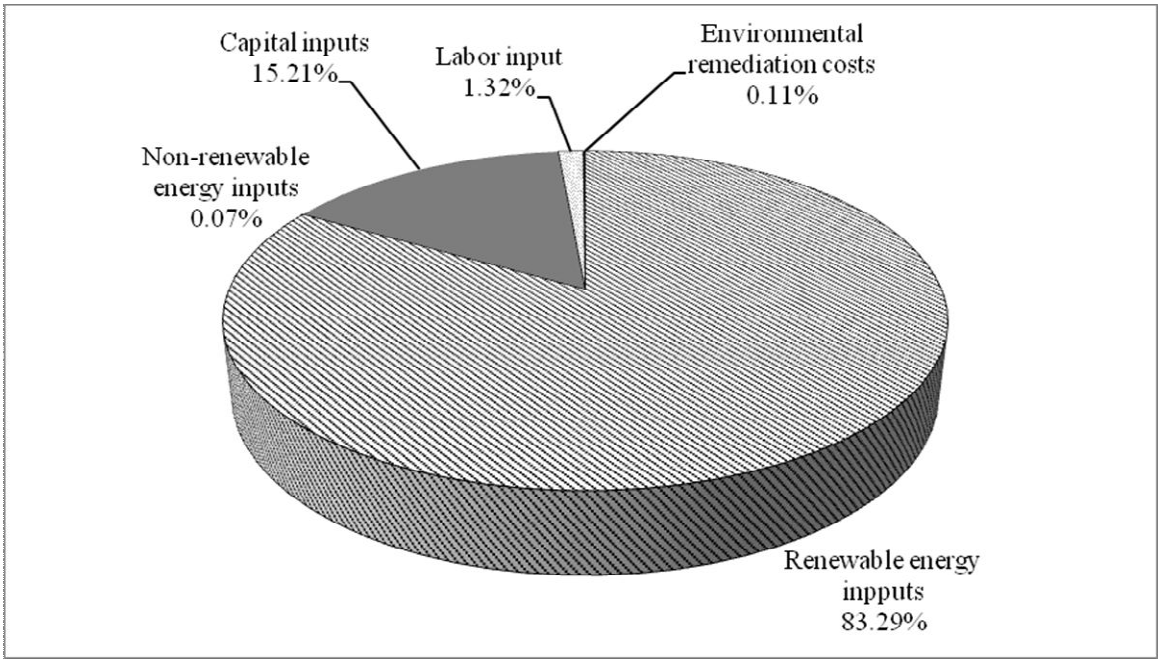

Fig. 2. The components of extended exergy inputs

The annual electricity output of the wind farm is 183.5 GWh, and the life span of this research is 20 years. As a result, the total electricity output is 3670 GWh. Based on the analysis above, and the extended exergy-based indicators are calculated and demonstrated in Table 2. Compared with the hydrogen-fed steam power plant [25], the renewability of wind power generation system is higher with the value of 0.99.

Table 2. The extended exergy-based indicators of the wind power generation system

Indicators	Conversion efficiency	Renewability	Economic yield ratio	Environmental impact degree
Value	2.29E+6 J/kWh	0.99	0.23	1.75E-03

5. Conclusions

Extended exergy is a powerful tool that adopts a single quantifier to account for materials, energy, labour and capital and to compute a presumed environmental impact based on remediation costs, and handle the sustainability issues. Thus, it is applied in this paper to evaluate the sustainability of wind powered electricity generation system. Also, some extended exergy-based indicators were proposed and used to reflect the resource, environmental and economic performances of the wind power system.

The wind power generation is propelled by a vast of capital investment. The great investment on the wind power increases the cost and price of wind power. As a result, a higher price of wind power makes it less competitiveness compared with other power generation system. Thus, a rational cost compensation mechanism that aims at cost reduction is expected to be established to make wind power competitive. A market oriented incentive mechanism among provinces could be established to mobilize the exploitation and utility positivity of provinces with affluent wind resources. CDM program and Build-Operate-Transfer (BOT) mode are also effective ways in raising capital for wind farm construction.

In addition, the non-renewable energy inputs and environmental remediation costs only constitute a small fraction, implying that the wind powered electricity generation system is a renewable and

environmentally friendly energy utility mode. Therefore, the development of wind power should be further accelerated in the 12th Five-Year plan period of China to cope with the energy security issue. Obviously, the extended exergy-based indicators provide a platform to compare the economic and environmental performance, conversion efficiency and sustainability of different renewable energy utility modes, and shed lights on the planning and policies of renewable energy development. However, the indicator system is still incomplete and need revisions in future works.

Acknowledgments

This study was supported by the Program for New Century Excellent Talents in University (NCET-09-0226), National High Technology Research and Development Program of China (No., 2009AA06A419), Key Program of National Natural Science Foundation (No., 50939001), and National Natural Science Foundation of China (Nos., 40701023, 40901269).

References

[1] Streimikiene D., Ciegis R., Grundey D., Energy Indicators for Sustainable Development in Baltic States. Renew Sust Energ Rev 2007;11(5): 877-93.

[2] Weidou N., Johansson TB., Energy for Sustainable Development in China. Energ Policy 2004;32(10): 1225-229.

[3] Tremeac B., Meunier F., Life cycle analysis of 4.5MW and 250W wind turbines. Renew Sust Energ Rev 2009;13: 2104-110.

[4] Kubiszewski I., Cleveland CJ., Endres PK., Meta-analysis of net energy return for wind power systems. Renew Energ 2010;35: 218-25.

[5] Brown MT., Ulgiati S., Emergy evaluations and environmental loading of electricity production systems. J Clean Prod 2002;10: 321-34.

[6] Wall G., Conditions and tools in the design of energy conversion and management systems of a sustainable society. Energ Convers Manage 2002; 43: 1235-248.

[7] Kaushik SC., Siva Reddy V., Tyagi SK., Energy and exergy analyses of thermal power plants: A review. Renew Sust Energ Rev 2011; 15: 1857-872.

[8] Wall G., Exergy: A useful concept within resource accounting. – Available at: http://www.exergy.se/ftp/ex77c.pdf [accessed 1.14.2011].

[9] Sciubba E., Beyond thermoeconomics? The concept of extended exergy accounting and its application to the analysis and design of thermal systems. Int J Exergy 2001;1 (2): 68-84.

[10] Rosen MA., Can exergy help us understand and address environmental concerns? Int J Exergy 2002;2 (4): 214-17.

[11] Chen B., Chen GQ., Yang ZF., Exergy-based resource accounting for China. Ecol Model 2006;196 (3-4): 313-28.

[12] Dincer I., Rosen MA., Exergy, Environment and Sustainable Development. in Exergy. Amsterdam. Elsevier. 2007. p. 36-59.

[13] Chen GQ., Chen B., Resource analysis of the Chinese society 1980–2002 based on exergy Part 1: Fossil fuels and energy minerals. Energ Policy 2007;35(4): 2038-50.

[14] Chen B., Chen GQ., Resource analysis of the Chinese society 1980–2002 based on exergy—Part 2: Renewable energy sources and forest. Energ Policy 2007;35 (4): 2051-64.

[15] Chen B., Chen GQ., Resource analysis of the Chinese society 1980–2002 based on exergy—Part 3: Agricultural products. Energ Policy 2007;35 (4): 2065-78.

[16] Chen B., Chen GQ., Resource analysis of the Chinese society 1980–2002 based on exergy—Part 4: Fishery and rangeland. Energ Policy 2007;35 (4): 2079-86.

[17] Chen GQ., Chen B., Resource analysis of the Chinese society 1980–2002 based on energy—Part 5: Resource structure and intensity. Energ Policy 2007;35(4): 2087-95.

[18] Szargut J., Morris D.R., Steward F.R., Exergy analysis of thermal, chemical and metallurgical processes. New York: Hemisphere Publ. Corp; 1988.

[19] Sciubba E., Beyond thermoeconomics? The concept of extended exergy accounting and its application to the analysis and design of thermal systems. Int J Exergy 2001;1 (2): 68-84.

[20] Sciubba E., Cost analysis of energy conversion systems via a novel resource based quantifier. Energy 2003;28 (5): 457-77.

[21] Sciubba E., From engineering economics to extended exergy accounting: a possible path from "monetary" to "resource-based" costing. J Ind Ecol 2004;8 (4): 19-22.

[22] Sciubba E., Exergoeconomics. In: Cleveland CJ, editor. Encyclopedia of Energy. Boston: U. Press. 2007. p.577-91.

[23] Sciubba E., A revised calculation of the econometric factors α- andβ for the Extended Exergy Accounting method. Ecol Model 2011;222: 1060-66.

[24] Ptasinski KJ., Koymans MN., Verspagen HHG., Performance of the Dutch Energy Sector based on energy, exergy and Extended Exergy Accounting. Energy 2006;31: 3135-144.

[25] Corrado A., Fiorini P., Sciubba E., Environmental assessment and extended exergy analysis of a "zero CO2 emission", high-efficiency steam power plant. Energy 2006;31: 3186–198.

[26] Talens Peiró L., Villalba Méndez G., Sciubba E., Gabarrell i Durany X., Extended exergy accounting applied to biodiesel production. Energy 2010;35 (7): 2861-869.

[27] Yang Q., Chen B., Ji X., He YF., Chen GQ., Exergetic evaluation of corn-ethanol production in China. Commun Nonlinear Sci 2009;14: 2450-461.

[28] Chen G Q, Chen B. Extended-exergy analysis of the Chinese society. Energy 2009;34: 1127-144.

[29] Kotas TJ., The exergy method of thermal plant analysis. London: Butterworths; 1985.

[30] Ji X., Chen GQ., Chen B., Jiang MM., Exergy-based assessment for waste gas emissions from Chinese transportation. Energ Policy 2009;37: 2231-240

[31] Szargut J., Exergy method: technical and ecological applications. Southampton: WIT Press; 2005.

Human body exergy metabolism

Carlos Eduardo Keutenedjian Mady[a], Silvio de Oliveira Junior[b]

*[ab] Polytechnic School of the University of São Paulo, Av. Prof. Mello Moraes, 2231, 05508-900, São Paulo, Brazil, cekm@usp.br[a] **(CA)**, soj@usp.br[b]*

Abstract:

The exergy analysis of the human body is a tool that can provide indicators of health and life quality. To perform the exergy balance it is necessary to calculate the metabolism in an exergy basis, or metabolic exergy, although there is not yet consensus in its calculation procedure. Hence, the aim of this work is to provide a general method to evaluate this physical quantity for human body based on indirect calorimetry data. Similarly to the chemical exergy definition for pure substances, the metabolic exergy may be defined as the maximum amount of work that the body can perform from the oxidation of the energy substrates, which are the carbohydrates, lipids and proteins. To calculate the metabolism in an exergy basis it is necessary to define the reference reactions and obtain their exergy variation. The reference reactions of the energy substrates are represented by the oxidation of the glucose, palmitic acid and a representative amino acid. The products of these reactions are carbon dioxide, liquid water and urea; being this last substance formed only in the reaction of the amino acid. From the Gibbs free energy of the oxidation of these substances it is possible to calculate the chemical exergy and their exergy variation. The indirect calorimetry permits the analysis of expired and inspired air (oxygen consumption and carbon dioxide production). Attaching these data to the stoichiometry of the reactions of oxidation it is possible to obtain the consumption rate of the energy substrates. Hence, from the exergy variation of the reactions and the rate consumption of the substrates, the metabolic exergy is determined. The method to calculate the metabolism in energy basis is well set; it is obtained from the consumption of nutrients and enthalpy variation of the reactions of oxidation. Results, for basal conditions and during physical activities, indicate that the exergy and energy metabolism have difference lower than 5% similar values only for basal conditions but the difference is not larger than 10%.

Keywords:

Human Body, Exergy Analysis, Metabolic Exergy.

1. Introduction

The application of the exergy analysis for the human body may be used to assess the quality of the energy conversion processes that takes place in its several systems, organs and even cells. Several authors applied the exergy analysis for the human body [1-8] and some of the methods were revised by [5]. To perform the exergy analysis it is necessary to calculate the metabolic exergy in human body, but there is still not a consensus in its calculation.

Initially, the Second Law of Thermodynamics was applied to living organisms as an attempt to confirm the principle of minimum entropy production or Prigogine and Wiame [9] principle. In this principle it is stated that all living organisms tend to sate of minimum entropy production. Therefore, for different types of species, ranging from fish to humans [8,10-15], the minimum entropy production was confirmed.

Batato et al. [1] were one of the first authors that applied the exergy analysis to the human body. In the analysis the energy and exergy metabolism were calculated from indirect calorimetry results, where it was selected representative reactions of oxidation of three types of substance (carbohydrates, lipids and proteins). A comparison between metabolisms in both basis indicated that the difference is not higher than 5%.

Prek [2,3], Prek and Butala [4] and Simone et al. [5] performed the exergy analysis for the human body to obtain relations of exergy destruction with thermal comfort and thermal sensation

conditions. In the analyses the metabolic exergy was considered as a heat source, therefore the metabolism in energy and exergy basis have one order of magnitude of difference.

Finally, [14,15] applied the concept of maximum amount of work to bichemical reaction defining the metabolic efficiency, and [7] performed the exergy analysis for the celluar metabolism of glucose and palmitic acid, but the metabolism was not calculated for the body.

Although there is a consensus in literature to calculate the metabolism in energy basis [16], there is not a consensus in its calculus in exergy basis. In this work it is proposed a method to calculate the metabolic exergy from indirect calorimetry results, based on [1,16]. Moreover, it will be held a discussion of the methods of literature to calculate this physical quantity to establish a procedure and an equation to calculate this physical quantity.

2. Model description

Figure 1 indicates a model with a schematic representation of the human body, where it is indicated the heat transfer rate and mass flow rates associated with radiation (Q_r), convection (Q_c), vaporization (H_e), respiration (H_{ex}-H_a), food intake, food wastes, water intake and urine. The term Q_M is the heat released to the body caused by the cellular metabolism (from the First Law of Thermodynamics $M = Q_M$). In this figure the human body is divided in two control volumes, CV1 and CV2. The first one represents the thermal system and respiratory system and the second the cellular metabolism.

According to Rahman [13] in a period of one day the mass input (food, liquids and inspired gases) is equivalent to the mass output (food wastes, urine, expired gases and vaporization). In shorter periods of time this may not be verified. In this article, for the sake of the simplicity, the variation of body mass due to food and water intake, wastes and accumulation are neglected. During the measurements: $m_{food\ intake}$, $m_{water\ intake}$, $m_{food\ wastes}$ and m_{urine} are considered as a constant rate with the following considerations:

- $m_{food\ intake} - m_{food\ wastes} = m_{carb}+m_{lip}+m_{ami}$;
- $m_{water\ intake} - m_{urine} = m_{w,ex} + m_e - m_{w,a} - m_{H2O} - m_{urea}$;
- $m_{inspired\ air} - m_{expired\ air} = m_{O2} - m_{CO2}$.

Where, $m_{w,ex}$ and $m_{w,a}$ are the mass of water in expired and inspired air; m_e is mass of water evaporated through skin; m_{carb}, m_{lip}, m_{ami} are the mass consumption rate of carbohydrates, lipids and proteins; m_{O2} is the mass consumption rate of oxygen; and m_{CO2}, m_{H2O} and m_{urea} are the mass production of carbon dioxide, water and urea.

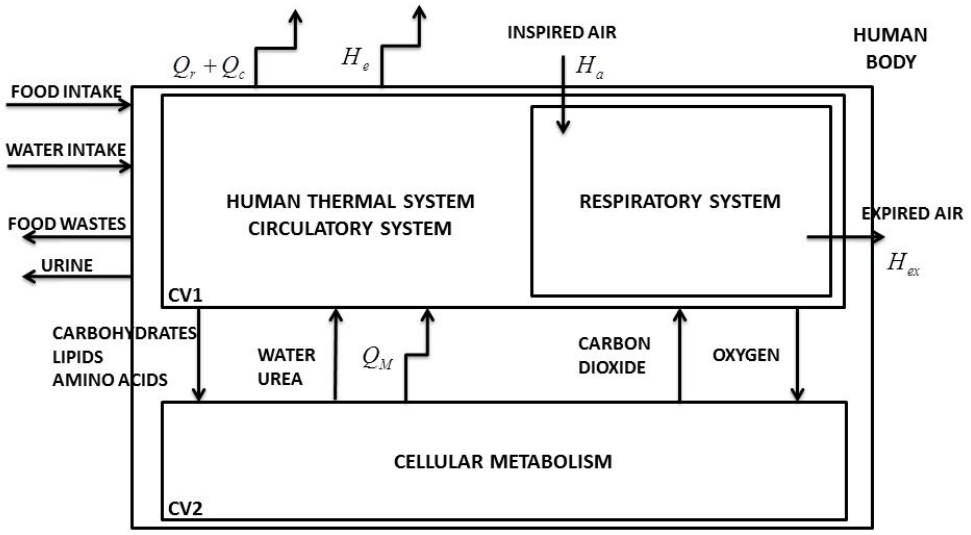

Figure 1. Schematic representation of the human body, with the intake of food, water and inspired air; and output of food, urine, expired air, vaporization trough skin and heat release due to radiation and convection

The Exergy Analysis is applied in the control volume shown in Fig. 1, with given environment and reference conditions such as temperature ($T_0 = T_a$), pressure ($P_0 = P_a$) and relative humidity ($\phi_0 = \phi_a$). Thus, (1) indicates a general equation of the exergy balance.

$$\frac{dB}{dt} = \sum B_{in} - \sum B_{out} + \sum_k Q_k \left(1 - \frac{T_0}{T_k}\right) - W - B_{dest}, \quad (1)$$

The exergy metabolism (B_M) for the whole body is part of the exergy variation of the body over time as indicated in (2). Where **B** is the body exergy and $d\mathbf{B}/dt|_{\Delta T}$ is the exergy variation of the body due to a variation in environmental conditions. This term is related to internal energy and entropy variation of the body over time. In (2) the variation of the volume of the body is neglected.

$$\frac{d\mathbf{B}}{dt} = -B_M + \left.\frac{d\mathbf{B}}{dt}\right|_{\Delta T}, \quad (2)$$

Equation (3) indicates the exergy balance applied to CV1. The exergy intake is B_{QM}, indicated by (4), where Q_M is the heat transferred to the body caused by the metabolism, T_0 is the environment/reference temperature and T_b the body temperature. The exergy rate and flow rates B_c, B_r, B_e and ΔB_{res} ($B_{ex} - B_a$) are the exergy associated with convection, radiation, vaporization and respiration, previously determined in [8].

$$B_{dest}^{CV1} = B_{Q_M} - \left(B_c + B_r + B_e + \Delta B_{res}\right) - \left.\frac{d\mathbf{B}}{dt}\right|_{\Delta T}^{CV1}, \quad (3)$$

$$B_{Q_M} = Q_M \left(1 - \frac{T_0}{T_b}\right), \quad (4)$$

The cellular metabolism is a representation of the human cells. In this control volume (CV2) the reactions of oxidation of the energy substrates, also called metabolism, take place. The destroyed exergy is indicated in CV2 by (5), where B_{reac} is the exergy content of the reactants (carbohydrates, lipids, amino acids and oxygen) and B_{prod} is the exergy content of the products (urea, liquid water and carbon dioxide).

$$B_{dest}^{CV2} = B_{reac} - B_{prod} - Q_M \left(1 - \frac{T_0}{T_b}\right) - \left.\frac{d\mathbf{B}}{dt}\right|_{\Delta T}^{CV2}, \quad (5)$$

The exergy metabolism is defined as (6)

$$B_M = B_{reac} - B_{prod}, \quad (6)$$

When the control volume is the whole body, the exergy balance for steady state conditions becomes a sum of (3) and (5). The result is indicated in (7).

$$B_{dest}^{body} = \left(B_M - \left.\frac{d\mathbf{B}}{dt}\right|_{\Delta T}\right) - \left(B_c + B_r + B_e + \Delta B_{res}\right), \quad (7)$$

Note that (3) is similar to the exergy analysis proposed by [2-4] (which takes into account only the thermal part of metabolism) and (7) is similar to the analysis proposed by [1]. The difference between these two approaches is that all the exergy destroyed in CV2 are neglected if (3) is used as the metabolic exergy.

2.1. Energy metabolism

As indicated by [16], the metabolism is defined as a set of chemical reactions that release energy from the oxidation of energy substrates and allow the vital processes in human body. Figure 1 indicates the cellular metabolism with the input of glucose, lipids, amino acids and oxygen; and the output of carbon dioxide, urea and water. Moreover, there is a heat rate released to the body caused by the metabolism (Q_M).

Diener [16] described a procedure to calculate the metabolism based on the indirect calorimetry technique. In order to calculate metabolic energy and exergy, it is assumed that the oxidation of carbohydrates, lipids and protein are represented by the reactions of oxidation of glucose ($C_6H_{12}O_6$), palmitic acid ($C_{16}H_{32}O_2$) and a representative amino acid with mean thermodynamic properties ($C_{4.98}H_{9.8}N_{1.4}O_{2.5}$).

The oxidations of these three organic compounds are indicated in (8) to (10). Note that the oxidation of glucose and palmitic acid results in the formation of carbon dioxide and liquid water, while the oxidation of amino acid results in the formation of carbon dioxide, liquid water and urea. In humans and most of mammals, the excretion of nitrogen content in the amino acids is mostly through urea.

$$C_6H_{12}O_6 + 6O_2 \rightarrow 6CO_2 + 6H_2O, \quad (8)$$

$$C_{16}H_{32}O_2 + 23O_2 \rightarrow 16CO_2 + 16H_2O, \quad (9)$$

$$C_{4.98}H_{9.8}N_{1.4}O_{2.5} + 5.13O_2 \rightarrow 4.28CO_2 + 3.5H_2O + 0,7CH_4N_2O, \quad (10)$$

It is important to define the respiratory quotient (*RQ*) that is the ratio of the carbon dioxide production and oxygen consumption (in molar basis). This value is 1 for (8), 0.7 for (9) and 0.83 for (10). In basal conditions *RQ* is approximately 0.83, during heavy aerobic activities it becomes close to 1 [17]. This quotient gives a clue whether the oxidation which prevails is only one type of substance (physical activities) or a combination (basal conditions).

From the stoichiometry of the reactions, it is possible to obtain the consumption of carbohydrates, lipids and proteins in unity of mass, as indicated by (11) to (13), based on [16]. In this equation, oxygen consumption ($m_{↓}(O_{↓}2)$) and carbon dioxide production ($m_{↓}(⟦CO⟧_{↓}2)$) are usually measured with the aid of a respirometer. The nitrogen excreted from the body ($m_{↓}N$) is measured from the urine analysis. In the literature, there is a convention adopted that each gram of nitrogen excreted in the urine represents the oxidation of 6.25g of amino acids [1,16].

$$m_{carb} = -2.14m_{O_2} + 2.24m_{CO_2} - 3.39m_N, \quad (11)$$

$$m_{lip} = 1.14m_{O_2} - 0.83m_{CO_2} - 1.50m_N, \quad (12)$$

$$m_{ami} = 6.25m_N, \quad (13)$$

The energy metabolism can be calculated as indicated in (14), where Δh is the enthalpy variation of the reactions indicated in (8) to (10). Note that this procedure is well established on literature and used to calculate the metabolism from indirect calorimetry results.

$$M = -\Delta H = -\left(m_{carb}\Delta h_{carb} + m_{lip}\Delta h_{lip} + m_{ami}\Delta h_{ami}\right), \quad (14)$$

It is important to mention that in literature exists a discussion that in basal conditions the oxidation of proteins may be neglected, because it represents only 2% of the total metabolism if the person is healthy [16].

2.2. Exergy metabolism

The chemical exergy of a compound (b_{ch}) may be calculated according to (15), where Δg_0 is the specific Gibbs free energy variation of the reference reaction (that has only substances present in the reference environment as co-reactants and products), and $b_{ch,i}$ is the chemical exergy of the products, or the co-reactants [17].

$$b_{ch} = -\Delta g_0 + \left[\sum_i x_i b_{ch,i}\right]_{\text{products}} - \left[\sum_i x_i b_{ch,i}\right]_{\text{co-reactants}}, \qquad (15)$$

To calculate the metabolic exergy it is necessary to define reference reactions that are indicated in (10) to (12). The exergy variation of the reactions of oxidation (ΔB) can be calculated as indicated in (16), where Δb is the specific exergy variation of each reaction. For the glucose and palmitic acid, the Δb terms are the chemical exergy of these substances, calculated from (15). For the amino acid, Δb is a linear combination of the chemical exergy of amino acid and urea. The consumption rate of the energy substrate is determined from (11) to (13).

$$\Delta B = m_{carb}\Delta b_{carb} + m_{lip}\Delta b_{lip} + m_{ami}\Delta b_{ami}, \qquad (16)$$

The definition of the metabolism in exergy basis is not as simple as in energy basis. Some authors [2-4] calculated the metabolic exergy as B_{QM}, similarly to (3). Herein the metabolic exergy will be considered as the exergy variation of the reactions of the oxidation (17).

$$B_M = -\Delta B, \qquad (17)$$

3. Experimental data and thermodynamic properties

3.1 Thermodynamic properties

To calculate the metabolism in energy and exergy basis, it is necessary to obtain thermodynamic properties of the energy substrates such as enthalpy variation (Δh) and Gibbs free energy variation (Δg) of the reactions of oxidation. The references which these data were obtained are Diener [16], Hayne [19] and Cortassa et al. [20]. Table 1 indicates the values of these thermodynamic properties for the complete oxidation of glucose and palmitic acid, and partial oxidation to the formation of liquid water, carbon dioxide and urea for the amino acids. The Δh of the reaction of oxidation of urea (CH_4N_2O) is obtained from Doran [21] (10527 kJ/kg) and the chemical exergy is obtained from Szargut et al. [17] (11483 kJ/kg).

Table 1. Enthalpy and Gibbs free energy variation of the complete oxidation of glucose, palmitic acid and a representative amino acid

	Δh (kJ/kg)			Δg (kJ/kg)		
	Glucose	Palmitic Ac.	Amino Ac.	Glucose	Palmitic Ac.	Amino Ac.
Diener [16]	-15648	-39581	-18075	-	-	-
Hayne [19]	-15600	-39200	-19000	-15946	-38212	-
Cortassa et al. [20]	-15594	-39020	-	-15956	-38281	-

Cortassa et al. [20] provides the value of enthalpy variation and Gibbs free energy variation of the complete oxidation for different amino acids. Table 2 indicates the value of these thermodynamic properties for the several amino acids and from these the calculated chemical exergy.

Nelson and Cox [22] provide the average occurrence of each amino acid in nature, indicated in Table 2 representing approximately 96% of the common amino acids found in proteins (exception

of methionine and cysteine). These percentages are used to calculate the mean molecular formula ($C_{4.98}H_{9.8}N_{1.4}O_{2.5}$) and mean thermodynamic properties.

Table 2. Thermodynamic properties of the oxidation of each amino acid until the formation of carbon dioxide, nitrogen and liquid water [17,20] and the average occurrence of each amino acid in nature [22]

Substance	Molecule	% Nature	Δh (kJ/kg)	Δg (kJ/kg)	b_{ch} (kJ/kg)*
Glycine	$C_2H_5NO_2$	7.2	-12987	-13480	14150
Alanine	$C_3H_7NO_2$	7.8	-19180	-18449	18991
Serine	$C_3H_7NO_3$	6.8	-13857	-14305	14783
Aspartic Acid	$C_4H_7NO_4$	5.3	-12090	-12677	13189
Asparagine	$C_4H_8N_2O_3$	4.3	-14667	-15144	15643
Threonine	$C_4H_9NO_3$	5.9	-17681	-17899	18446
Proline	$C_5H_9NO_2$	5.2	-23783	-	24856**
Glutamic Acid	$C_5H_9NO_4$	6.3	-15306	-15748	16312
Glutamine	$C_5H_{10}N_2O_3$	4.2	-17603	-18000	18553
Valine	$C_5H_{11}NO_2$	6.6	-24957	-24957	25623
Histidine	$C_6H_9N_3O_2$	2.3	-22103	-	22629**
Leucine	$C_6H_{13}NO_2$	9.1	-27389	-27214	27921
Isoleucine	$C_6H_{13}NO_2$	5.3	-27389	-27206	27914
Lysine	$C_6H_{14}N_2O_2$	5.9	-25233	-	26541**
Arginine	$C_6H_{14}N_4O_2$	5.1	-21517	-21759	22294
Phenylalanine	$C_9H_{11}NO_2$	3.9	-28200	-28164	29021
Tyrosine	$C_9H_{11}NO_3$	3.2	-24514	-24768	25560
Tryptophan	$C_{11}H_{12}N_2O_2$	1.4	-27608	-27691	28540
Average Value	$C_{4.98}H_{9.8}N_{1.4}O_{2.5}$		-21067	-	21890

*The chemical exergy of these amino acids were calculated for this article

** Chemical exergy calculated using group contribution method, from Szargut et al. [17]

3.2 Experimental data

3.2.1. Basal conditions

To calculate the metabolism in energy and exergy basis, for basal conditions the O_2 consumption, the CO_2 and H_2O production are considered, respectively: $1.79.10^{-4}$, $1.46.10^{-4}$ and $5.47.10^{-4}$ mol/s. The RQ is 0.82 (close to basal conditions defined in [17]). These data were obtained from Hardy and Du Bois [18], for basal conditions and were also used by Aoki [12]. Furthermore, it is possible to assume that in one day there is an excretion of 12 g of nitrogen in the urine [16] due to the oxidation of amino acids.

3.2.2 Physical activities

The experimental results for subjects under physical activities were obtained from Sports medicine group and FIFA medical center of excellence of institute of orthopedics and traumatology of the University of São Paulo Medical School. During the experimental procedure, the individuals are submitted to increasing levels of velocities, where it was measured the respiratory gas exchange (O_2 consumption and CO_2) production and the tympanic temperature (representative of the body temperature). Results of treadmill velocities, oxygen consumption rate and carbon dioxide production rate are indicated in Figure 2 for one runner.

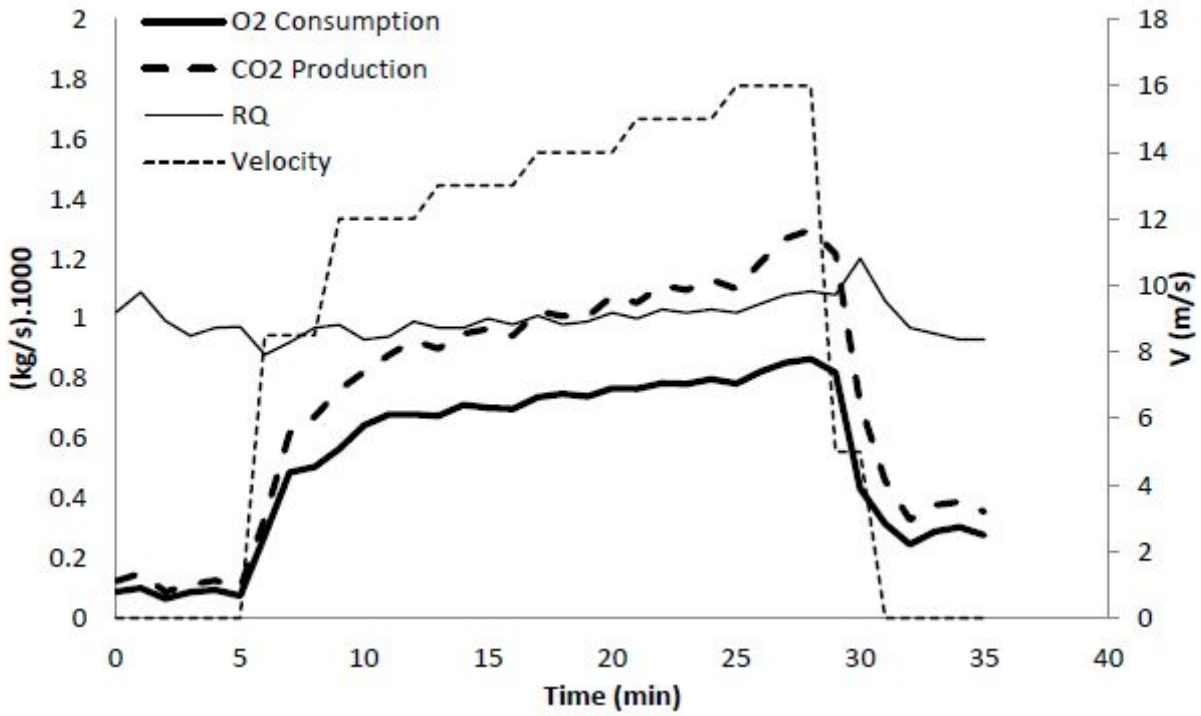

Figure 2. Oxygen consumption rate and carbon dioxide production rate as a function of time for different exercise levels for one subject

4. Results and Discussion

4.1 Thermal properties and metabolism equation

In the present analysis it is important to detach that, carbohydrates and lipids are represented by one substance (glucose and palmitic acid), but amino acids are represented by one amino acid with mean thermodynamic properties. Sorguven and Özilgen [23] obtained the chemical exergy for three types of fatty acids with 18, 20 and 22 carbons in its chain; the difference of the chemical exergy (in mass basis) was not larger than 1%. Table 2 indicates that the difference of the chemical exergy of the amino acids may achieve values as high as 50%. Each amino acid has a different type of chain, with different ramifications.

Table 3 indicates the Δh, Δg and Δb of the reactions partial oxidation (carbon dioxide, liquid water and urea) of several amino acids. The mean values are weighted by the occurrence in nature of each amino acid (Table 2). Furthermore, these results indicate a value of $\Delta b/\Delta h$ of 1.047.

Table 3. Enthalpy, Gibbs free energy and exergy variation of the reactions of partial oxidation (liquid water, carbon dioxide and urea) of the amino acids

Substance	Molecule	Δh (kJ/kg)	Δg (kJ/kg)	Δb (kJ/kg)
Glycine	$C_2H_5NO_2$	-8776	-8996	-9556
Alanine	$C_3H_7NO_2$	-15631	-14671	-15121
Serine	$C_3H_7NO_3$	-10850	-11102	-11502
Aspartic Acid	$C_4H_7NO_4$	-9716	-10148	-10599
Asparagine	$C_4H_8N_2O_3$	-9882	-10049	-10424
Threonine	$C_4H_9NO_3$	-15027	-15073	-15551
Proline	$C_5H_9NO_2$	-21037	-	-22110
Glutamic Acid	$C_5H_9NO_4$	-13158	-13461	-13969
Glutamine	$C_5H_{10}N_2O_3$	-13277	-13393	-13834
Valine	$C_5H_{11}NO_2$	-22258	-22083	-22678
Histidine	$C_6H_9N_3O_2$	-15991	-	-16517

Leucine	$C_6H_{13}NO_2$	-24979	-24647	-25291
Isoleucine	$C_6H_{13}NO_2$	-24979	-24639	-25284
Lysine	$C_6H_{14}N_2O_2$	-20907	-	-24378
Arginine	$C_6H_{14}N_4O_2$	-14257	-14028	-14375
Phenylalanine	$C_9H_{11}NO_2$	-26286	-26126	-26933
Tyrosine	$C_9H_{11}NO_3$	-22769	-22910	-23657
Tryptophan	$C_{11}H_{12}N_2O_2$	-24512	-24394	-25162
Average Value		-17830	-	-18359

In Table 1 the only value that Hayne [19] does not provide is the Gibbs free energy of the oxidation of amino acids. Applying the result of $\Delta h/\Delta b=1.04$, it is possible to obtain that Δb of the oxidation of amino acids is 19760 kJ/kg.

In Table 4, it is indicated the values of Δb of the reactions of oxidation as they occur in humans (glucose and palmitic acid the oxidation is complete, amino acids the oxidation is partial). From the values of Δh and Δb it is possible to formulate an equation of the metabolism in energy basis (which differ from [16] because of the oxygen consumption and carbon dioxide production are per unity of mass) and exergy basis.

Table 4. Exergy variation of the reactions of oxidation of glucose, palmitic acid and proteins.

	Δb (kJ/kg)		
Reference	Glucose	Palmitic Ac.	Amino Ac.
Hayne [19]	-16506	-39141	-19760
Cortassa et al [20]	-16516	-39223	-18359

Finally, (18) and (19) indicate the metabolism in energy basis using the data from Hayne [19]. Equations (20) and (21) indicate the metabolism in energy and exergy basis using the data from Cortassa [20].

$$M_{Hayne} = 11371m_{O_2} + 2366m_{CO_2} + 6891m_N \quad (18)$$

$$B_{M,Hayne} = 9363m_{O_2} + 4444m_{CO_2} + 8764m_N \quad (19)$$

$$M_{Cortassa} = 11179m_{O_2} + 2502m_{CO_2} - 1980m_N \quad (20)$$

$$B_{M,cortassa} = 9435m_{O_2} + 4399m_{CO_2} - 932.6m_N \quad (21)$$

4.1 Energy and exergy metabolism

4.1.1 Basal conditions

Results in Table 5 indicate the metabolism in energy and exergy basis, considering the oxidation of proteins (M and B_M) and disregarding the oxidation of proteins (M_p and B_{Mp}) for the data of Hardy and Du Bois [18]. For this condition, the authors obtained that the metabolism is 79.8W. In all cases the difference between this value and the ones calculated herein is not larger than 4%. Furthermore, the difference of the metabolism using the two different references of thermodynamic properties [19,20] did not differ 3%. The ratio of metabolism in energy and exergy basis (considering and disregarding the oxidation of proteins) does not exceed 1.03. Hence, as in Batato et al. [1], the approximation $B_M \approx M$ for basal conditions is valid.

Table 5. Metabolism in energy and exergy basis with the oxidation of amino acids (M and B_M) and without the oxidation of amino acids (M_p and B_{Mp})

	Hayne [19] (W)	Cortassa et al. [20] (W)
M	81.3	79.8
M_p	80.3	80.1
B_M	83.4	82.2
B_{Mp}	82.2	82.3

4.1.1 Physical activities

For the experimental results of Figure 2 the metabolism in energy and exergy basis was calculated, using the values of thermodynamic properties of Cortassa et al. [20] indicated in (20) and (21), due to the small difference between results in Table 5.

Figures 3 indicates *M*, B_M and B_{QM} for the experimental data indicated in Fig. 2. The difference of B_M and B_{QM} is one order of magnitude, indicating that when the metabolism is calculated as B_{QM} (taking into account only the thermal exergy), 95% of the exergy content of metabolism is disregarded.

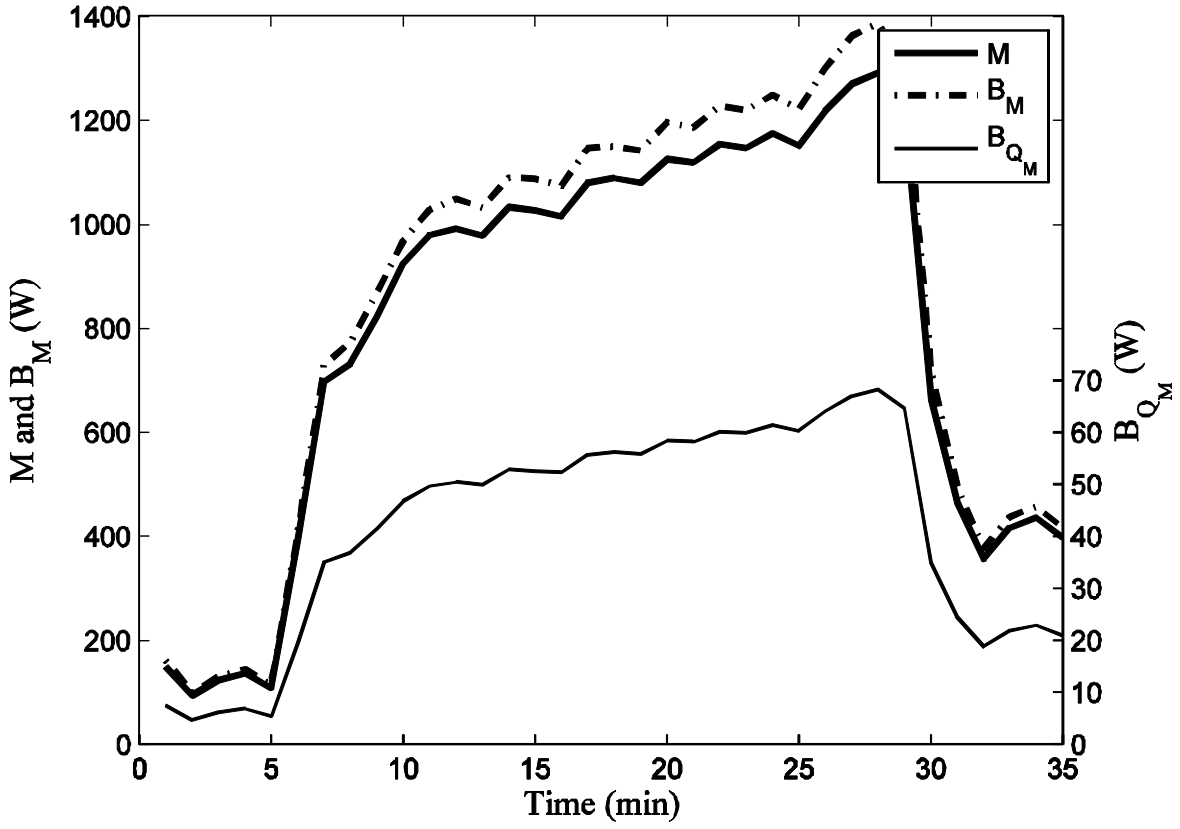

Figure 3. Result of M, B_M and B_{QM} as a function of time during the treadmill test. The first two properties are indicated in the left axis, the last on in the right side axis

In Fig. 4 it is demonstrated the ratio of the metabolism in energy and exergy basis as a function of time. In the first five minutes, the ratio B_M/M ranged from 1.04 to 1.08 (time when the subject controlled the respiration and was adapting to the respirometer). Between 5 and 30 minutes, the ratio remained between the same limits. Finally, on the final period of the test the ratio increased to values as close as 1.1. This result indicates that the approximation $B_M \approx M$ may not be always valid, although the ratio was not larger than 1.1.

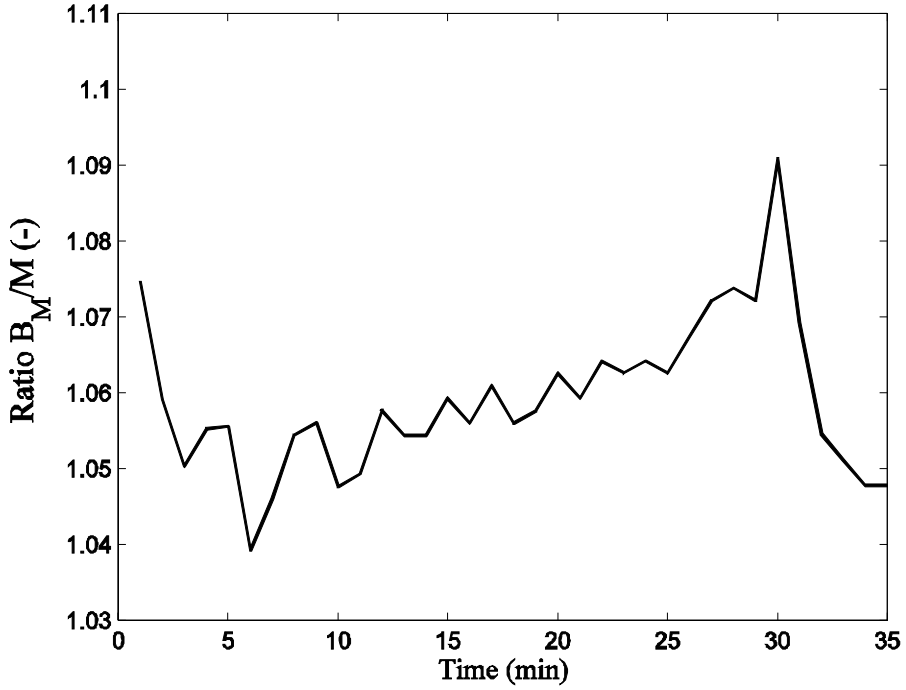

Figure 4. Ratio of the metabolism in energy and exergy basis during the treadmill test

Figure 5 indicates the ratio of the metabolism considering the oxidation of proteins (*M*) and disregarding the oxidation of this type of substance (M_p). The ratio was very close to 1 (5-30min), indicating that during the exercises the body uses more carbohydrates and lipids as energy source. In the beginning of the test the ratio was approximately 99.5%, indicating that the participation of proteins in the total metabolism is larger when the person is resting. Nevertheless, this figure indicates that for a healthy person under physical activities the oxidation of proteins can be disregarded.

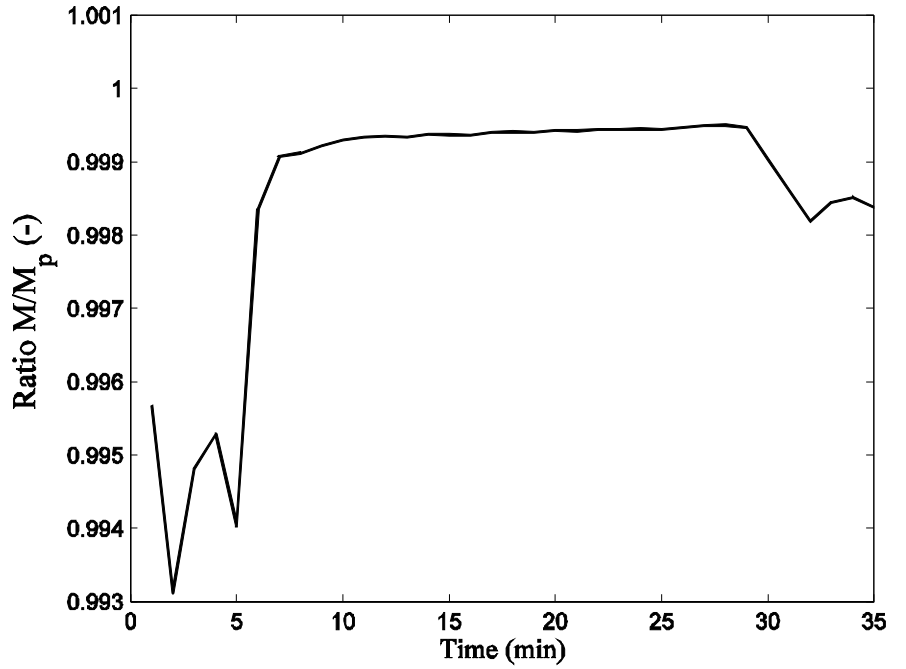

Figure 5. Ratio of the metabolism considering and disregarding the oxidation of proteins during the treadmill test

5. Conclusions

In this work analyses of the human metabolism in energy and exergy basis were performed and it was proposed a method and an equation to calculate the metabolic exergy. From the range of tests analyzed it was possible to conclude that:

- For basal conditions results of metabolism in energy and exergy basis did not differ more than 3%, for the different thermodynamic properties. For basal conditions, results obtained from Batato et al. [1] were verified;
- For the treadmill running tests, the results found in Batato et al [1] that the difference of metabolism in energy and exergy basis may not always verified. The ratio exceeds 1.05 in most of the test, but it was not larger than 1.10.
- Finally, the contribution of proteins did not exceed 3% of the total metabolism during physical activities and in basal conditions. The oxidation of proteins may be disregarded in a healthy person in basal conditions and under physical activities.

Acknowledgments

The authors acknowledge FAPESP (São Paulo Research Foundation) for his PhD grant 09/17578-0. The authors acknowledge the Sports medicine group and FIFA medical center of institute of orthopedics and traumatology of the University of São Paulo Medical School.

Nomenclature

b specific exergy, J/kg

B body exergy, J

B exergy flow rate, W

h specific enthalpy, J/kg

H enthalpy flow rate, W

M metabolism, W

m mass flow rate, kg/s

Q heat transfer rate, W

RQ respiratory quotient, -

T temperature, K

t time, min

V velocity, m/s

W work, W

Subscripts and superscripts

0 Reference

ami Amino acids

b Body

c Convective

carb Carbohydrates

dest Destruction

e Evaporative

ex Expired

in Inspired

lip Lipids

M Metabolic

p disregarding proteins

r Radiative

res Respiration

References

[1] Batato M., Borel L., Deriaz O., Jequier, E., Analyse exergétique théorique et expérimentale du corps humain. Entropie 1990;26(153-154):120-130.

[2] Prek M., Thermodynamic analysis of human heat and mass transfer and their impact on thermal comfort. International Journal of Heat and Mass Transfer 2005;48(3-4):731-739.

[3] Prek M., Thermodynamical analysis of human thermal comfort. Energy 2006;31(5):732-743.

[4] Prek M., Butala, V., Principles of exergy analysis of human heat and mass exchange with the indoor environment. International Journal of Heat and Mass Transfer 2010;48(25-26):731-739.

[5] Simone A., Kolarik J., Iwamatsu T., Asada H., Dovjak M., Schellen L., Shukuya M., Olesen B.W., A relation between calculated human body exergy consumption rate and subjectively assessed thermal sensation. Energy and Buildings 2011;43(1):1-9.

[6] Albuquerque Neto C, Pellegrini LF, Ferreira MS, Oliveira Jr S, Yanagihara JI. Exergy analysis of human respiration under physical activity. International Journal of Thermodynamics 2010;13(3):105-109.

[7] Lems, S., Thermodynamic explorations into sustainable energy conversion - Learning from living systems [dissertation]. Delft, Netherlands, Technische Universiteit Delft; 2009.

[8] Mady C.E.K., Ferreira M.S., Yanagihara J.I., Saldiva P.H.N., Oliveira Jr S., Modeling the exergy behavior of human body. In: Bojić M., Lior N., Petrović J., Stefanović, G. Stevanović, V., editors. ECOS 2011: Proceedings of the 24th International Conference on Efficiency, Cost, Optimization, Simulation, and Environmental Impact of Energy Systems; 2011 Jul 4-7; Novi Sad, Serbia. 245-257.

[9] Prigogine I., Wiame J., Biologie et Thermodynamique des phenomenes irreversibles. Experimentia 1946;2(11):451-453.

[10] Zotin A.I., Zotina R.S.. Thermodynamics aspects of developmental biology. Journal of Theoretical Biology 1967;17(1):57-75.

[11] Balmer R.T., Entropy and aging in biological systems. Chemical Engineering Communications 1984;17(1):171-181.

[12] Aoki I., Entropy principle for human development, growth and aging. Journal of Theoretical Biology 1991;150(2):215-223.

[13] Rahman M.A., A novel method for estimating entropy generation rate in human body. Thermal Science 2007;11(1):75-92.

[14] Silva C., Annamalai K., Entropy generation and human aging: lifespan entropy and effect of Physical Activity Level. Entropy 2008;10(2):100-123.

[15] Silva C., Annamalai K., Entropy generation and human aging: lifespan entropy and effect of diet composition and caloric restriction diets. Journal of Thermodynamics 2009;2009:1-10.

[16] Diener J.R.C., Indirect calorimetry (in Portuguese). AMB Rev. Assoc. Med. Bras. 1997;43(3):245–253.

[17] ASHRAE: American Society of Heating, Refrigerating and Air-Conditioning Engineers, Physiological principles and thermal comfort. In: Handbook of Fundamentals, Atlanta; 1993, p.1–29.

[18] Hardy J.D., Du Bois E.F., The technique of measuring radiation and convection. J Nutr 1938;15:461-475.

[19] Hayne D.T., Biological thermodynamics. Cambridge, UK: Cambridge University Press; 2008.

[20] Coratassa S., Aon M.A., Iglesias A.A., Lloyd D., An introduction to metabolic and cellular engineering. London: World Scientific Pub Co Inc; 2002.

[21] Doran M.D., Bioprocess engineering principles. . Cambridge, UK: Cambridge University Press; 1995.

[22] Nelson, D.L., Cox, M.M., Lehninger principles of biochemistry. New York, US: W.H. Freeman and company; 2000

[23] Sorguven E., Özilgen M., Thermodynamic assessment of algal biodiesel utilization. Renewable energy 2010;35(9):1956-1966.

Integrating an ORC into a natural gas expansion plant supplied with a co-generation unit

Sergio Usón[a], Wojciech J. Kostowski[b]

[a] Centre of Research for Energy Resources and Consumption – CIRCE, Universidad de Zaragoza, Spain, suson@unizar.es
[b] Silesian University of Technology, Gliwice, Poland, wojciech.kostowski@polsl.pl,

Abstract:
The paper presents a thermoeconomic analysis of a proposed novel system for natural gas expansion, based on the integration of gas expanders, ICE engine and an organic Rankine cycle (ORC). The objective of a natural gas expansion plant is to generate electric power while reducing the natural gas pressure. In contrast to the throttling process in pressure regulators, gas expanders allow one to utilize the physical exergy of the pressurized gas. However, the necessity of gas pre-heating bound to thy hydrate formation problem decrease the performance of existing expansion plants. Pre-heating systems based on co-generation modules with ICE-engines have better performance that boiler systems, however, as shown in authors' previous studies, they are burdened with a relatively high irreversibility bound to an excessive temperature difference between the engine exhaust gases and the pre-heated natural gas. The proposed system integrates an ORC between the exhaust gases and natural gas. Pre-heating of natural gas is carried out partially directly by the co-generation module, by means of the engine cooling cycle, and partially indirectly, by means of the engine exhaust gases supplying heat for the ORC, while the ORC condenser is coupled with the first stage of gas pre-heating. It has been demonstrated that the integration of ORC increases the system exergy efficiency to 0.526 compared to the reference case of 0.498. The performance ratio (electric output related to local fuel input) of the system reaches a favourable value of 0.77. The performed detailed thermoeconomic analysis points out the occurrences of irreversibilities and depicts the process of cost formation in particular devices.

Keywords:
Thermoeconomic analysis, Turboexpanders, ORC, Natural gas, Exergy, Hybrid energy systems

1. Introduction

Thanks to the accumulation of organic substances in the Earth's crust over millions of years, the nature provides us with fossil fuels enclosed in underground fields. Due to the gravity of rocks, the pressure of natural gas in underground reservoirs usually exceeds 100 bar [1] and may reach values as high as 700 bar [2]. However, this pressure may decrease during the extraction period; moreover, as the gas passes the well tubing, the flow control devices in the wellhead and the processing plant, the pressure may eventually decrease to the level of 10–40 bar [1]. Further transportation of the gas to large distances usually requires a higher degree of compression in order to reduce the volumetric flow rate, the resulting pipeline dimensions and the corresponding investment cost. Alternatively, the gas may be liquefied for overseas transportation. In the year 2011, 69.5% of gas traded worldwide was transported in pipelines and the remaining 30.5% was liquefied [3]. In the case of pipeline transportation, the typical pressure range varies between 35 and 100 bars depending on the design optimization result. As the gas reaches its destination (consumption) area, the pressure has to be adjusted to the level suitable for its utilization in gas burners. The latter is determined by the flame speed at a level of only 16–25 milibars above the atmospheric pressure. Hence, a multistage system of pressure reduction stations is required in order to deliver the natural gas to distribution networks and to the final consumers.

The vast majority of the pressure reduction stations (PRS, also called ‘pressure regulating stations’ or ‘city gate stations’) operate with a pressure regulator used to reduce the gas pressure. A pressure regulator is an automatically operated *throttling valve*, which has the primary purpose to adjust the flow to the current demand of consumers, and the secondary purpose to reduce the gas pressure and maintain it within the desired limits even in the case of unstable demand or supply conditions [4].

From the point of view of energy management, the use of pressure regulators is undesired, since the throttling process destroys the potential of energy generation available in the pressure reduction process. This fact can be detected and quantified by means of exergy analysis [5]. Exergy destruction in a pressure regulator corresponds to the maximum amount of mechanical work that could be generated between given inlet and outlet pressure levels and for the given flow rate. As stated by Szargut [6], accepting the exergy destruction can only be justified by economic reasons, otherwise it should be regarded as an ‘error in the art of engineering’. For this reason, and accounting for huge amounts of natural gas choked worldwide in throttling valves, the possibility of pressurized gas exergy utilization should be thoroughly investigated.

The available physical exergy contained in the pressurized gas may be converted into mechanical work by means of a piston, screw or, most frequently, a turbine expander (turboexpander). The generated work may be converted to electricity, or in particular industrial applications, may be utilized directly [7]. From the technical point of view, the expander technology is well-known and offered by many manufacturers.

The key issue related to the application of expanders is the temperature drop of natural gas. In the conventional throttling process, a moderate temperature drop is observed due to the real-gas Joule-Thompson effect, roughly estimated at 0.5K/bar. The temperature drop may provoke a separation of the solid phase (hydrates) from natural gas or cause external icing of pressure regulators and/or pressure safety valves. These phenomena pose a risk of blocking the devices, leading to excessive outlet pressure, which in turn can result in rare but severe accidents involving losses in human life [8]. Another risk factor is bound to the utilization of polyethylene pipes in distribution networks (downstream of the PRS). Mechanical properties of polyethylene are appropriate for a limited temperature range (lower temperatures decrease the material stress under which rapid crack propagation can occur [9]). In order to exclude any risk of system malfunction, the majority of PRSs are equipped with a gas-fired or electric preheating system. The objective of the preheating system is to maintain the temperature at the regulator outlet above the ‘permissible safe temperature’ [10]; detailed regulations may further specify the value of the limit (e.g. 5–8°C [11]).

If gas expansion is applied instead of throttling, the temperature drop becomes significant due to the conversion of internal energy of gas into mechanical work. It is therefore required to heat the gas upstream of the expander (pre-heating), or design the expander for low temperatures and heat the gas downstream of the expander (post-heating) in order to avoid the supply of cold gas to the downstream network. A review of possible technical solutions is presented in Table 1.

The use of IC engines entails an improvement of efficiency, however, the temperature difference between exhaust gases from the engine and the stream of gas to be heated indicates a potential for further improvement. In this paper, the integration of an ORC between both streams is analyzed by using exergy and thermoeconomic analyses.

The use of ORCs for producing electricity from low and medium temperature heat sources has been analyzed by several authors. In [19], ORC cycles are applied for increasing the power produced by micro-turbines, while in [20] a methodology for process integration of ORC is proposed. In [21] ORC is compared to Stirling and a new concept (the so called inverted Brayton cycle). In [22], the

use of ORC in a polygeneration plant producing power, heat, cold and water is investigated, and a comprehensive list of candidate working fluids is proposed.

Table 1. Natural gas expansion – methods applied for controlling the outlet temperature

Heat source	Advantages	Drawbacks
	A. Heating the gas prior to expansion (pre-heating)	
Electric	Low investment cost / space requirement	In most cases, negative net electricity production excludes this solution
Gas boilers [5], [12]	Robust design, moderate investment cost	Low performance ratio (power output/fuel consumption), no supporting mechanisms for selling the electricity;
Gas boilers (expander with low isentropic efficiency) [13]	Preheating cost increases only slightly compared to the throttling process; low investment cost.	Low performance ratio, low output power, the available exergy potential is used only partially;
CHP with IC engine [14],	High performance ratio, possible support for the generated electricity, high power output, proven successful applications;	Higher investment cost; exergy losses due to a high temperature difference between exhaust gases and natural gas;
Fuel cell [15]	High performance ratio,	Difficulties in accommodating fluctuating flow rates
Renewables (solar [16], geothermal)	Low operational cost, high feasibility, no local CO_2 emissions.	1. Availability 2. Known studies concern pre-heating for the throttling process. Achieving higher gas temperatures can be problematic.
Waste heat [17]	Low operational cost, high feasibility	Availability
	B. Heating the gas subsequent to expansion (post-heating)	
Ambient air / water	No preheating cost	Risk of destructing the expander by the solid/liquid phase
Refrigeration system [18]	Optimum use of the exergy potential, two products obtained, possible excellent feasibility indicators	Risk of desctructing the expander by the solid/liquid phase; requires integration with external processes; highest demand (summer) corresponds to lowest gas flux.

The use of ORC as a bottoming cycle for internal combustion engines (ICE) has been also investigated as a means for increasing electricity production and thus for improving efficiency. In [23], several types of working fluids (overhanging, nearly isentropic and bell shaped) are compared and Second Law analysis is performed. In [24], the use in automotive applications is analyzed while in [25] ORC and ICE are used in a biomass gasification plant.

In this paper, a hybrid energy generation system comprising turboexpanders, ICE and ORC is simulated and analyzed applying thermoeconomic analysis, and compared with a similar system without ORC. After presenting the fundamentals of thermoeconomic analysis, the thermodynamic and thermoeconomic models are presented. Finally, results of the analysis are shown and discussed.

2. Thermoeconomic analysis – methodology description

In this section, the fundamentals of exergy and thermoeconomic analysis are reviewed in relation to its application to the problem analyzed in this paper.

2.1. Exergy analysis

Exergy is the work potential of a thermodynamic medium with respect to the environment. The concept is particularly useful if pressurized gases are considered, since both the internal energy and enthalpy fail to represent the pressurized medium's ability to perform mechanical work. Methods

for calculating the exergy are given e.g. in [6]. Within this paper, the reference state of p_0=101325 Pa and T_0 = 288.15 K has been chosen for physical exergy calculations, and the chemical exergy of fuel has been assumed at the level of 1.04 LHV, after Szargut's results for high-methane gas [6].

Exergy does not satisfy the conservation law. Therefore, each process is characterized by an internal exergy loss, referred to as irreversibility I. For steady-state analyses, it may be written:

$$\sum_i \dot{m}_i b_i - \sum_e \dot{m}_e b_e + \sum_j \dot{Q}_j \frac{T_j - T_0}{T_j} - \dot{W} - I = 0, \tag{1}$$

where i denoted all entering flows, e denotes all exiting flows, j denotes all heat sources exchanging heat $\dot{Q}_j$ with the control volume, and $\dot{W}$ denotes work transferred across the control volume.

2.2. Thermoeconomic analysis

Thermoeconomic analysis is based on the 2nd law of thermodynamics (exergy) and economics (cost) and provides method for the analysis, diagnosis and optimization of complex energy systems [26]. In particular, the methodology applied in this paper is the thermoeconomic input-output analysis (formerly known as symbolic exergoeconomics) [27].

The thermoeconomic model of a system is represented by its productive structure, where physical flows are substituted by fuel, product and, eventually, waste flows. All system components are numbered starting from 1, and the number 0 corresponds to the environment. Eij is the part of the product of component i that becomes part of the fuel of component j. Accordingly, product and fuel of a component are calculated as:

$$P_i = \sum_{j=0}^{n} E_{ij}\,, \tag{2}$$

$$F_i = \sum_{j=0}^{n} E_{ji}\,, \tag{3}$$

A table containing the values of all elements Eij as well as their summations by columns and rows is called the fuel-product table. The unit exergy consumption is defined as the exergy that each component requires from the other components to obtain a unit of its product:

$$\kappa_{ij} = E_{ij} / P_j\,. \tag{4}$$

The sum of all unit exergy consumptions in a component is the inverse of its exergy efficiency:

$$\frac{1}{\eta_{b,j}} = \sum_{j=0}^{n} \kappa_{ij} = \frac{F_j}{P_j}\,. \tag{5}$$

Besides, it is possible to introduce waste flows: Rij is a waste flow produced by component i and charged to component j.

The unit exergy cost of a flow is the quotient between the cost of that flow (i.e. the amount of exergy resources needed for producing it) and its exergy:

$$k^*_{ij} = E^*_{ij} / E_{ij} \tag{6}$$

All product flows of a component are considered to have the same formation process and, accordingly, they have the same unit cost. Besides, the cost is formed by two parts, one due to productive flows and the other considering the contribution of waste flows. Thus, the following equation can be written:

$$k^*_{ij} = k^*_{P,i} = k^{*,e}_{P,i} + k^{*,r}_{P,i} \tag{7}$$

The previous costs can be calculated by applying the cost balance of all components. In particular, the term corresponding to productive flows can be obtained from the following equation:

$$\mathbf{k}_{\mathbf{P}}^{*,\mathbf{e}} = \left(\mathbf{U}_{\mathbf{D}} - \langle \mathbf{KP} \rangle\right)^{\mathrm{T}} \boldsymbol{\kappa}_{\mathbf{e}}. \tag{8}$$

where $\langle \mathbf{KP} \rangle$ is a (n × n) matrix whose elements are the values of the unit exergy consumption □ij and $\boldsymbol{\kappa}_{\mathbf{e}}^{\mathbf{T}} = \left(\kappa_{01,} \cdots, \kappa_{on}\right)$ is a (n × 1) vector whose elements contain the unit consumption of external resources. More details on thermoeconomic input-output analysis can be seen in [26].

3. Gas expansion system description

The gas expansion system analyzed within the present paper is partially based on the nominal data of the Arlesheim gas expansion plant in Switzerland [28]. In particular, the two-stage arrangement, the flux of gas and its parameters, including inlet and outlet pressures and temperatures are based on the plant data. However, the pre-heating system has been re-designed in order to include the ORC between the flux of exhaust gases and natural gas.

Table 2. Description of system devices

Device acronym	Description
D1. ICE	Internal Combustion Engine
D2. HRHE	Heat Recovery Heat Exchanger
D3. LHP	Low-temperature, High-pressure Pre-heater
D4. HHP	High-temperature, High-pressure Pre-heater
D5. GE1	Gas Expander 1st stage
D6. LMP	Low-temperature, Medium-pressure Pre-heater
D7. HMP	High-temperature, Medium-pressure Pre-heater
D8. GE2	Gas Expander 2nd stage
D9. PM	Power mixer (virtual device)
D10. EVAP	(ORC) EVAPorator
D11. ORCT	ORC Turbine
D12. REG	(ORC) heat REGeneration exchanger
D13. COND	(ORC) CONDenser
D14. ORCP	ORC Pump
D15. ST	Stack

The proposed system structure is presented in Fig. 1, and the system devices are listed in Table 2, also explaining the abbreviations used in the following description.

Natural gas (system points 1–9) is pre-heated in LHP and HHP and supplied to the expander GE1. Consecutively, at the medium pressure level is pre-heated in LMP and HMP and supplied to GE2. Low-pressure gas leaves the system, with the exception of a small share extracted as a fuel for the gas engine (ICE).

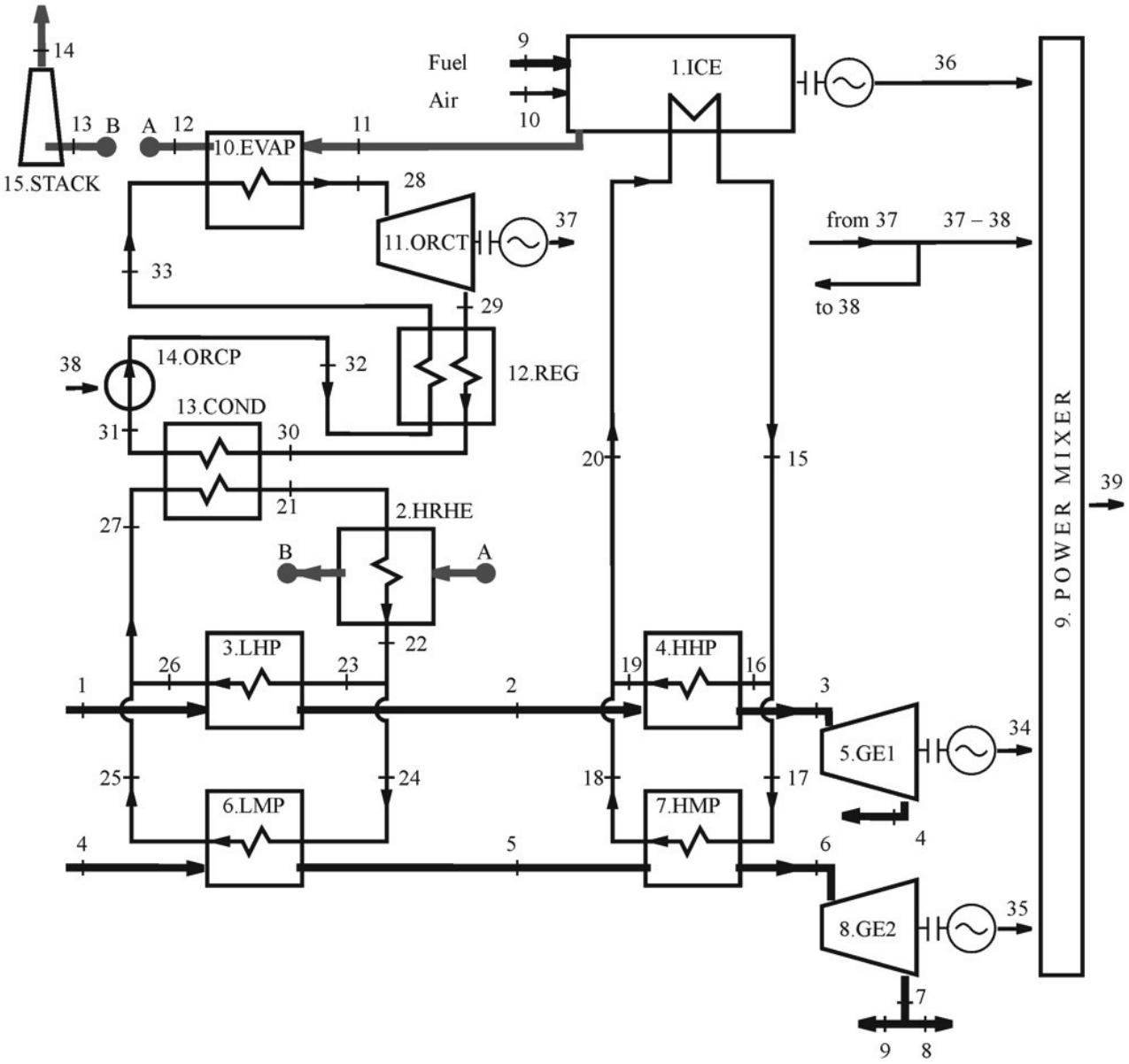

Fig. 1. Scheme of a natural gas expansion system integrated with an internal combustion engine and an Organic Rankine Cycle

As can be seen in Fig. 1, heat generated by the ICE is used in two independent subsystems. The high enthalpy of the engine exhaust gases is transferred the ORC evaporator (D10), and, at a lower temperature level, also to the heat recovery exchanger (D2). Instead of rejecting the ORC waste heat to the environment, it is utilized to supply the low-temperature water cycle (system points 21–27), which in turn serves as the low-temperature section of gas pre-heating (LHP and LMP).

The ICE jacket water is used to supply the high-temperature section of gas-preheating by means of the exchangers HHP and HMP.

The system has four electric outputs: the gas expanders (36 and 37), the ICE output 38, and the net ORC output, determined as the difference of the ORC turbine electric output (39) reduced by the power of the pump (40). The power mixer (D9) has been introduced as a virtual device in order to illustrate the hybrid origin of the total electricity production and to determine the cost of this electricity. The stack has been added because it will be needed as a dissipative device for the thermoeconomic model.

4. Thermodynamic model

A thermodynamic model of the analyzed system comprises a set of mass and energy equations as well as stoichometry calculations and formulation of the relevant efficiencies. The model has been built in Engineering Equation Solver v8.904. The set of equations describing the system comprises:

- mass balances for flow splits and junctions (steady state); for a given split/or junction it may be written:

$$\sum \dot{m}_{\text{in}} = \sum \dot{m}_{\text{out}} ; \tag{9}$$

- energy balances for system devices (heat losses to the ambient have been neglected); for a given heat exchanger or flow machine the balance is:

$$\sum (\dot{m}h)_{\text{in}} = \sum (\dot{m}h)_{\text{out}} + \dot{W} , \tag{10}$$

- formulation of ICE electric efficiency:

$$\eta_{el} = \frac{\dot{W}_{el,36}}{Q_{n,9} \cdot \text{LHV}} , \tag{11}$$

- stoichiometric equations for determination of exhaust gases composition (see e.g. [30]);
- formulation of electromechanical efficiency for the machinery, for *i*-th device:

$$\eta_{em,i} = \dot{W}_{el,i} / \dot{W}_i . \tag{12}$$

For heat exchangers and flow machines it is sufficient to analyze changes in the physical enthalpy. The reference state for physical enthalpy of all analyzed fluids has been chosen at 298.15 K and 101 325 Pa. Natural gas has been approximated by pure methane, for which the physical enthalpy has been calculated using real gas properties [29] implemented in the solver (EES). Enthalpy of ICE exhaust gas has been found for the ideal gas model with temperature-dependent specific heat.

All heat exchangers have been assumed isobaric.

Atmospheric air used for combustion has been assumed to have a temperature of 15°C, relative humidity 60% and CO_2 content of 380 ppm. Natural gas supplied to the ICE as a fuel is extracted at the outlet of GE2; the engine pressure regulator (i.e. throttling valve) has been assumed to be part of the engine.

Since the size of ICE is determined by a discrete sequence of available electric powers, the possibility of continuous variation of the power was modelled by choosing a specific engine and applying an engine load factor, defined as:

$$ELF = \dot{W}_{el,36} / \dot{W}_{el,36,\text{nom}} , \tag{13}$$

where $\dot{W}_{el,36}$ is the actual power of the engine in part-load operation and $\dot{W}_{el,36,\text{nom}}$ is the nominal power. Accordingly, it was also assumed that all flow rates bound to the ICE (fuel, air, exhaust gases, jacket water) are scaled linearly with the same ELF while the temperatures of fluxes remain unchanged. The exhaust gases temperature and oxygen concentration have been assumed according to catalogue data. The chosen engine was Caterpillar G3612 Genset DM5006, 50 Hz with the nominal data given in Table 3.

Within this work, three cases were analyzed in order to evaluate the impact of ORC application on system performance:

A. operation with ORC module;

B. operation without ORC module, this mode is simulated by setting the heat exchange in the evaporator and the ORC working fluid flow rate to 0; heat is transferred from exhaust gases to natural gas only by means of the HRHE. Moreover, the ELF is reduced in order to minimize the exhaust gases stack temperature;
C. operation without ORC module like in case B, however, the ELF is kept at the same level as in case A.

Table 3. Expansion plant data and assumptions

Parameter	Symbol	Value		
A. Generic parameters				
Natural gas inlet flux	Q_1	35000 m^3/h (at 0°C 101 325 Pa)		
NG inlet parameters	p_1 , T_1	67 bar abs, 10 °C		
NG parameters at GE1 inlet	p_3 , T_3	67 bar abs, 82 °C		
NG parameters at GE1 outlet	p_4 , T_4	17 bar abs, 10 °C		
NG parameters at GE2 inlet	p_6, T_6	17 bar abs, 72 °C		
NG parameters at GE2 outlet	p_7 , T_7	5.5 bar abs, 10 °C		
TE1/TE2 isentropic efficiency (calculated) [a)]	$\eta_{TE1/2}$	68.5%, 76.5%		
ICE Nominal electric power	$\dot{W}_{el,36,nom}$	2915 kW		
ICE electric efficiency	$\eta_{el,\,ICE}$	40.4%		
Exhaust gas temperature	T_{11}	405 °C		
Exhaust gas oxygen content (molar dry basis)	$[O_2]$	12.0%		
Heat rejection to jacket water (nominal)	$\dot{Q}_{JW,nom}$	1234 kW		
Jacket water temperature	T_{15} / T_{20}	95 / 70 °C		
Combustion air inlet temperature	T_{10}	15°C		
Pinch in LHP	$T_{26} - T_1$	10 K		
Pinch in LMP	$T_{25} - T_4$	10 K		
Temperature difference in LT water cycle	$T_{22} - T_{27}$	35 K		
Pinch in ORC condenser	$T_{31} - T_{21}$	5K		
B. Case-dependent parameters				
		Case 1	Case 2	Case 3
ORC fluid mass flow rate	$\dot{m}_{28}$	2.68 kg/s	**0 kg/s**	**0 kg/s**
ORC fluid max/min pressure	p_{28} / p_{29}	29.9 bar/ 0.44 bar	–	–
Electricity production, ICE	$\dot{W}_{el,36}$	2349 kW	1965 kW	**2349 kW**
Pinch in the evaporator (EVAP)	$T_{12} - T_{33}$	**10 K**	–	–
Pinch in the HRHE	$T_{13} - T_{21}$	**10 K**	20 K	115 K
Exhaust gases stack temperature	T_{13}	60.2°C	**56°C**	134.9°C

In part B of the table, input parameters are set in **bold**.
[a)] Values of efficiency are indirectly given by the values of turbine outlet temperature

Following assumptions have been done for the ORC subsystem:

- the working fluid is benzene;
- the regeneration ratio, defined as:

$$\varepsilon = \frac{h_{29} - h_{30}}{h_{29} - h_{32}} \tag{14}$$

has the value of ε = 0.7;

- the isentropic efficiency of the ORC expander and pump are 0.80 and 0.75, and the overall mechanic-to-electric conversion efficiency is 0.95 in both cases;
- the maximum temperature of the working fluid in the evaporator is 250°C;
- minimum allowable exhaust gas temperature has been fixed at 56 ºC (i. e. 10 degrees above the condensation temperature).

It should be noted that the maximum and minimum pressures of the ORC result from the assumed pinches for the evaporator and condenser. The main technical data and assumptions regarding the system are collected in Table 3. In part B of the table, case-specific parameters are described; in that part certain parameters are input values in one of the cases, and modelling results in the other.

Solving the mass and energy balance equations allows one to determine the values of flow rates and temperatures for all fluxes in the system as well as the energy fluxes exchanged between particular devices. Key results are presented in Table 5.

Exergy efficiency of the whole system can be calculated by considering total plant fuel and total plant product. If this information is taken from Table 9, it yields:

$$\eta_{b,\text{system}} = \frac{\dot{B}_{39}}{\dot{B}_9 + \dot{B}_{10} + \dot{B}_1 - \dot{B}_7}\,. \tag{15}$$

The CO_2 emission factor indicates the emission of carbon dioxide caused by the energy use. The factors can be calculated for primary, secondary or final energy carriers. Utilization of 1 kWh contained in natural gas (determined on the HHV basic) yields an emission of 0.1852 kg CO_2. The CO_2 equivalent of 1 kWh of electricity depends on the sources used and on the efficiency of generation, transmission and distribution. Data for Switzerland ([31], 2009) and Poland ([32], 2007) demonstrate the difference between hydropower and carbon-based generation, the emission factors for these countries are 0.0045 and 0.824 kg CO2/kWh respectively. The EU-27 averaged factor was 0.377 in 2010 [33].

Stoichiometric calculations performed as a background for the present study indicate the mole fraction of CO_2 equal 4.513% while the molar flux of exhaust gases equals 0.1605 kmol/s. This yields a CO_2 mass flow rate of $\dot{m}_{CO2}$ = 1148 kg/h. The system CO_2 emission factors can be obtained by referring this value to the total electric power generated in the system:

$$e_{CO2} = \frac{\dot{m}_{CO2}}{\dot{W}_{el,34} + \dot{W}_{el,35} + \dot{W}_{el,36} + \dot{W}_{el,37} - \dot{W}_{el,38}} \tag{16}$$

Values of the CO_2 emission factors depending on the considered case are presented in table 5.

5. Thermoeconomic model

The first step in the development of the thermoeconomic model is the identification of fuel, product and wastes for each component. This information appears in Table 4. The environment is the complement of the whole plant: receives the electricity produced and provides air, gas for the engine, and difference of exergy of gas before and after expansion. ICE consumes natural gas and air and produces electricity, exergy increment for cooling water, and exhaust gases. HRHE and EVAP use exergy of exhaust gases for increasing the exergy of water for heating gas and ORC, respectively. In gas pre-heaters (LHP, HHP, LMP and HMP), exergy of water decreases for increasing the exergy of gas. Expanders produce electricity from the exergy decrement of gas. The ORC turbine uses exergy drop for producing electricity while the ORC pump uses electricity for

increasing the pressure of the ORC fluid. In the ORC condenser, heat released by the condensing fluid is used for increasing the temperature of water, while in the regenerator, a reduction of temperature of superheated fluid is used for increasing the temperature of liquid fluid. The power mixer collects power of several devices in order to obtain the final product of the system. The stack is a dissipative device (the only one whose output is a waste); it should be noted that the cost of this waste is assigned to the ICE.

Table 4. Fuel-Product-Waste definition. Exergy fluxes are denoted by B *instead of* $\dot{B}$.

Device	Fuel	Product	Waste
ENVIRONMENT	B39	B9+B16+(B1-B7)	
D1. ICE	B9+B10	B36+(B16-B19)+(B17-B18)+B11	
D2. HRHE	B12-B13	B24+B23-B21	
D3. LHP	B23-B26	B2-B1	
D4. HHP	B16-B19	B3-B2	
D5. GE1	B3-B4	B34	
D6. LMP	B24-B25	B5-B4	
D7. HMP	B17-B18	B6-B5	
D8. GE2	B6-B7	B35	
D9. PM	B34+B35+B36+(B37-B38)	B39	
D10. EVAP	B11-B12	B28-B33	
D11. ORCT	B28-B29	B37	
D12. REG	B29-B30	B33-B32	
D13. COND	B30-B31	B21-B25-B26	
D14. ORCP	B38	B32-B31	
D15. ST	B13		B14

The next step is to create the generic fuel-product table (see annex). In most cases, terms of this table are straightforward from the explanations above, except in two situations: i) the product of condenser and HRHE is fuel for LHP and LMP, and ii) the product of evaporator, ORC pump and regenerator is fuel for the ORC turbine, regenerator and condenser. In these situations, distribution ratio has been introduced for defining the table.

6. Results

Based on the thermodynamic and thermoeconomic models discussed in sections 4 and 5, a set of results describing the plant as a system and its particular components has been obtained. All results are presented for three cases defined in section 4 (Case A – ORC, Case B – without ORC, decreased ICE power, Case C – without ORC, ICE power as in Case A).

Table 5 presents overall system results, showing the system output power, exergy efficiency, performance ratio and CO_2 emissions referred to the unit of produced electricity. The table illustrates the hybrid character of the energy generation system. The power generated in natural gas expanders (1790 kW in all cases) constitutes between 40 and 48% of the total system production, depending on the analyzed case. The ORC power (Case A) is only 7.7% of the total production. Therefore, it may be stated that the turboexpanders and the ICE are primary system devices, and the ORC is an auxiliary device, applied in order to improve the overall system performance.

If the operation of expanders were possible without gas pre-heating (i.e. with acceptance of low outlet temperatures), the local performance ratio would approach infinity (since energy would be

generated without on-site fuel input). On the other hand, a performance ratio for a stand-alone ICE corresponds to the engine electric efficiency (0.404 for the analyzed engine). The obtained values of the local performance ratio vary between 0.712 for Case C and roughly 0.77 for Cases A and B. Although the performance ratio should not be referred to as 'efficiency', its economic significance for the system operator exactly corresponds to that term, as it represents the ratio of the produced energy flux (intended for sales) to the fuel consumed on-site (determining the cost). From this point of view, the achieved values of the performance ratio should be evaluated as outstanding. Accordingly, also the system CO_2 emissions are very low even if compared to average emissions e.g. in Europe. Both advantages are due to the 'energy-invisible' part or the input potential, contained in the pressurized gas, and detected by means of exergy analysis.

Table 5. Results summary

Parameter	Unit	Value		
		Case A	Case B	Case C
ICE exhaust gas composition (molar, wet basis)	–	4.5% CO_2, 10.0% H_2O, 10.8% O_2, 74.7% N_2		
ORC Power	kW	343	0	0
Total power of NG expanders (GE1+GE2)	*kW*	*906 + 884 = 1790*		
Total system power	kW	4482	3810	4139
Performance ratio (local)	–	0.771	0.762	0.712
Exergy efficiency	–	0.526	0.496	0.485
Exergy cost of produced electricty	–	1.902	2.015	2.060
System CO_2 emissions	kg/kWh	0.256	0.259	0.277

[a)] – given quantity is a result of calculations, not an input parameter.

Table 6. Irreversibility

	Irreversibility (kW)		
Device	Case A	Case B	Case C
D1. ICE	2690.1	2313.9	2690.2
D2. HRHE	12.6	501.4	527.8
D3. LHP	18.6	15.7	18.6
D4. HHP	25.1	19.3	25.1
D5. GE1	516.3	516.3	516.3
D6. LMP	15.7	13.1	15.7
D7. HMP	20.6	15.5	20.6
D8. GE2	347.3	347.3	347.3
D9. PM	0	0	0
D10. EVAP	79.4	0	0
D11. ORCT	89.7	0	0
D12. REG	9.4	0	0
D13. COND	69.7	0	0
D14. ORCP	3.4	0	0
D15. ST	0	0	0

The system exergy efficiency varies between 0.485 for Case C and 0.526 for Case A. Assuming Case B as a reference, it can be seen that the application of ORC increases the system exergy efficiency by 2.8 percent points.

In order to understand better how this efficiency is formed, it is interesting to analyze separately the different components forming the installation. Irreversibility of all components appears in Table 6, for the three situations considered. The most interesting result is the strong reduction of irreversibility in the HRHE (around 500 kW); actually, the interest of using of an ORC is to reduce this irreversibility. Of course, this ORC, as a non-perfect device does not transform all this exergy in electricity but only 347 kW, however, exergy savings are clear. It can be argued that there are other components with higher irreversibility (mainly ICE and expanders). However, this is due because they process more exergy. It should be noted that irreversibility in expanders is the same in all columns, because they are the same components in the three cases. For the ICE, it can be noticed that irreversibility is lower in Case B because the power of the engine is also smaller. Irreversibility levels in gas preheaters (LHP, HHP, LMP and HMP) are by an order of magnitude lower since these devices process less exergy due to low temperature levels.

Table 6 shows the absolute magnitude of irreversibility. In order to eliminate the influence of the component size, a non-dimensional, qualitative parameter has to be used, such as the unit exergy consumption (inverse of the exergy efficiency), which can be seen in Table 7. This table shows clearly that the component with the lowest efficiency is the HRHE in the cases with no ORC. Accordingly, the analysis correctly points out that the matching between the high temperature of exhaust gases and the low temperature of preheated gas has to be improved. One possibility to do that is to introduce a heat engine that takes advantage of this temperature difference, and this is what is analyzed in the paper. Another component with high irreversibility is the ICE, which is bound to the current state of engine technology. It should be noted that most of the values of unit exergy consumption are the same for all cases, because the corresponding devices are either equal or a scaled version (ICE). Neither the power mixer nor the stack have internal irreversibility, accordingly, their unit exergy consumption is equal to one.

Both irreversibility and unit exergy consumption are local parameters characterizing the components individually. In order to have a clear picture, parameters taking into account the different role of the components in the whole system are needed. Unit exergy costs of the products of all components appear in Table 8. It can be seen how the cost increases as the chain of exergy transformation advances. For this reason, the highest values appear in LHP and LMP (they are affected by their own irreversibility, as well as by irreversibility of ICE, HRHE, and components of ORC when present). It can be seen how the use of ORC decreases substantially this value, because irreversibility in the chain decreases.

It may be surprising that, despite the high values commented above, the unit cost of the final product is quite low (around 2). This fact can be explained taking into account that the final electricity production is a result of two or three production chains: expanders, ICE and ORC (when present). As it is shown in Table 6, expanders are very efficient devices; accordingly the percentage of electricity produced by them should be maximized. This fact has to be balanced with the need of low temperature heat for increasing the gas temperature before expansion: if this heat is produced with an efficient system (Case A), efficiency of the whole system improves. However, if the CHP system is oversized (Case C), efficiency decreases. Accordingly, the choice of an optimum size of the ICE is a key point in the efficiency of the system.

Finally, the Fuel-Product table with the values of Case A can be seen in annex.

Table 7. Unit exergy consumption

	Unit exergy consumption (-)		
Device	Case A	Case B	Case C
D1. ICE	1.794	1.794	1.794
D2. HRHE	1.582	5.680	6.430
D3. LHP	1.556	1.378	1.556
D4. HHP	1.278	1.235	1.278
D5. GE1	1.570	1.570	1.570
D6. LMP	1.532	1.357	1.532
D7. HMP	1.394	1.342	1.394
D8. GE2	1.393	1.393	1.393
D9. PM	1	1	1
D10. EVAP	1.134	-	-
D11. ORCT	1.251	-	-
D12. REG	1.345	-	-
D13. COND	1.924	-	-
D14. ORCP	1.347	-	-
D15. ST	1	1	1

Table 8. Unit exergy cost of the products of devices.

	Unit exergy cost (-)		
Device	Case A	Case B	Case C
D1. ICE	1.875	1.873	1.922
D2. HRHE	2.966	10.641	12.360
D3. LHP	6.113	14.666	19.232
D4. HHP	2.396	2.314	2.457
D5. GE1	1.898	2.316	2.388
D6. LMP	6.019	14.43	18.936
D7. HMP	2.613	2.515	2.679
D8. GE2	1.656	2.029	2.091
D9. PM[a)]	**1.902**	**2.015**	**2.060**
D10. EVAP	2.127	-	-
D11. ORCT	2.736	-	-
D12. REG	2.940	-	-
D13. COND	4.206	-	-
D14. ORCP	3.686	-	-
D15. ST	1.875	1.873	1.922

a) Corresponds to the total plant product

7. Conclusions

The main conclusion of the performed analysis is that the objective of integrating the ORC into the system (to decrease exergy losses occurring due to irreversible heat transfer) was accomplished. As a result, efficiency of the system has improved around 3 points compared to the no-ORC case (B).

The fact that the global improvement is not very high compared to the local improvement in the section of heat recovery from exhaust gases can be commented by Jan Szargut's 16th rule of improving thermodynamic imperfection of processes [6]:

'Avoid the elongation of the chain of thermodynamic processes'.

In the analyzed case, the introduction of ORC allows one to generate supplementary electricity generation utilizing thus the thermal potential between the hot source (exhaust gases) and the sink (natural gas). However, introducing additional heat exchangers, including evaporators and condensers introduces new sources of exergy losses. Moreover, in order to integrate the ORC several pinch points have to be taken into account in a series of exchangers, and eventually the ICE engine has to be operated at higher load in order to provide sufficient heat as the ORC driving force. The thermoecomomic analysis performed provides rigorous results for assessing this fact.

The integration of the ORC into the gas expansion system does have a significant advantage: the system produces more electric energy with the performance ratio and CO_2 emission factor as high as in a case without ORC. For this reason the interest of the application of an ORC would depend strongly of economic reasons (mainly, the feed-in tariff) that should be analyzed by means of an economic feasibility study while designing a new expansion system for a particular application. Moreover, optimization of the ORC structure, parameters and the working fluid could contribute to the system performance and may be of interest for future research. Another interesting line of development would be the integration of the preheating system with renewable energy sources. Despite of the case-dependent results of this analysis, the study presented demonstrates the applicability of thermoeconomic analysis as a systemic method for pointing out the possibilities of energy savings.

Acknowledgements

This work has been developed within the RECENT project (REsearch Center for Energy and New Technologies), supported by EU within the 7th Framework Programme, Theme 4, Capacities and coordinated by Silesian University of Technology (SUT), Gliwice, Poland.

Nomenclature

b	specific exergy, kJ/kg
$\dot{B}$	exergy flux, kW
e_{CO2}	CO_2 emission factor, kg CO_2/kWh
E	exergy flow in a productive structure, kW
E^*	exergy cost of a flow in a productive structure, kW
F	fuel flux, kW
h	specific enthalpy, kJ/kg
I	irreversibility, kW
k^*	unit exergy cost, –
LHV	lower heating value, kJ/m^3 (at 0°C, 101325 Pa)
$\dot{m}$	mass flow rate, kg/s

n number of components of the plant, –

$\dot{n}$ molar flow rate, kmol/s

p pressure, Pa

P product flux, kW

Q_n normalized volumetric flow rate, m^3/h (at 0°C, 101325 Pa)

$\dot{Q}$ heat flux, kW

T temperature, K

$\dot{W}$ power, kW

$\mathbf{U_D}$ identity matrix ($n \times n$)

$\langle \mathbf{KP} \rangle$ matrix of unit exergy consumptions ($n \times n$)

Greek symbols

ε regeneration ratio

η_b exergetic efficiency

κ unit exergy consumption

$\boldsymbol{\kappa_e}$ vector of unit exergy consumption of external resources ($n \times 1$)

Subscripts and superscripts

0 exergy reference conditions

$_{el}$ electric

$_{em}$ electromechanical

$_{i,j}$ generic component in a productive structure

Abbreviations

abs absolute pressure

ICE Internal Combustion Engine

NG Natural gas

ORC Organic Rankine Cycle

References

[1] Guo B., Lyons W.C., Ghalambor A. Petroleum Production Engineering. Oxford: Elsevier Science & Technology Books; 2007.

[2] Yilin Wang, J. 2012, Well completion for effective deliquification of natural gas wells. Journal of Energy Resources Technology, Transactions of the ASME, vol. 134, no. 1.

[3] BP Statistical Review of World Energy 2011; available at http://www.bp.com [Accessed Jan 2012].

[4] Rami, E.G., Jean-Jacques, B., Bruno, D. & François, M. 2007, "Modelling of a pressure regulator", International Journal of Pressure Vessels and Piping, vol. 84, no. 4, pp. 234-243.

[5] Kostowski, W. 2010, "The possibility of energy generation within the conventional natural gas transport system", Strojarstvo, vol. 52, no. 4, pp. 429-440.

[6] Szargut J. Exergy Method: Technical and Ecological Applications, WIT Press, Southampton, 2005.

[7] Bisio G. Thermodynamic analysis of the use of pressure exergy of natural gas. Energy 1995;20(2):161-167.

[8] http://www.newpolandexpress.pl/polish_news_story-2656-home_explosions_cause_panic_.php [Accessed Jan 2012].

[9] Krishnaswamy, R.K., Lambom, M.J., Sukhadia, A.M., Register, D.F., Maeger, P.L. & Leevers, P.S. 2006, “Rapid crack propagation failures in HDPE pipes: Structure - Property investigations", Polymer Engineering and Science, vol. 46, no. 10, pp. 1358-1362.

[10] British Standard BS EN 12186:2000 Gas supply systems – Gas pressure regulating stations for transmission and distribution – Functional requirements.

[11] Polish Oil and Gas Company Standard ZN-G-4121:2004 Gas supply systems – Gas pressure regulating stations for transmission and distribution – Requirements (in Polish).

[12] Poživil J. Use of expansion turbines in natural gas pressure reduction stations. Acta Montan Slovaca 2004;9(3):258–60.

[13] Kostowski, W.; Przywara M., Łyczko J., Lipko D.: Application of expansion turbines for the purpose of electricity production in gas regulating and metering installations (in Polish), Proc. of the 3rd International Conference ‘Energy from Gas’, Institute of Power Engineering and Turbomachinery (IMiUE), Gliwice 2005.

[14] Kostowski, W., Usón, S., Piekarczyk, W.: Thermoeconomic assessment of a natural gas expansion system integrated with a co-generation unit. In: Proceedings of the 6th Conf on Sustainable Development of Energy, Water and Environment Systems, Dubrovnik, Croatia, Sep 25–29, 2011.

[15] Howard, C., Oosthuizen, P. & Peppley, B. 2011, "An investigation of the performance of a hybrid turboexpander-fuel cell system for power recovery at natural gas pressure reduction stations", Applied Thermal Engineering, vol. 31, no. 13, pp. 2165-70.

[16] Farzaneh-Gord M, Arabkoohsar A, Deymi Dasht-bayaz M., Farzaneh-Kord V., Feasibility of accompanying uncontrolled linear heater with solar system in natural gas pressure drop stations, Energy, Vol. 41, no. 1, 2012, pp 420-8.

[17] Jedynak, A.: Electricity production in gas pressure reduction systems (in Polish), Proc. of the 3rd International Conference ‘Energy from Gas’, Institute of Power Engineering and Turbomachinery (IMiUE), Gliwice 2005.

[18] Faddeev IP. Turbo expanders to utilize the pressure of natural gas delivered to Saint Petersburg and industrial centers. Chem and Petroleum Eng 1998; 34(11{12):704–11

[19] Costante Invernizzi, Paolo Iora, Paolo Silva, Bottoming micro-Rankine cycles for micro-gas turbines, Applied Thermal Engineering, Volume 27, Issue 1, January 2007, Pages 100-110.

[20] Nishith B. Desai, Santanu Bandyopadhyay, Process integration of organic Rankine cycle, Energy, Volume 34, Issue 10, October 2009, Pages 1674-1686..

[21] M. Bianchi, A. De Pascale, Bottoming cycles for electric energy generation: Parametric investigation of available and innovative solutions for the exploitation of low and medium temperature heat sources, Applied Energy, Volume 88, Issue 5, May 2011, Pages 1500-1509.

[22] D. Maraver, J. Uche, J. Royo. A. James Assessment of high temperature organic Rankine cycle engine for polygeneration with MED desalination: A preliminary approach. Energy Conversion and Management 2012; 56 :108-17.

[23] I. Vaja, A. Gambarotta, Internal Combustion Engine (ICE) bottoming with Organic Rankine Cycles (ORCs), Energy, Volume 35, Issue 2, February 2010, Pages 1084-1093.

[24] Tianyou Wang, Yajun Zhang, Zhijun Peng, Gequn Shu, A review of researches on thermal exhaust heat recovery with Rankine cycle, Renewable and Sustainable Energy Reviews, Volume 15, Issue 6, August 2011, Pages 2862-2871.

[25] J. Kalina, Integrated biomass gasification combined cycle distributed generation plant with reciprocating gas engine and ORC, Applied Thermal Engineering, Volume 31, Issues 14-15, October 2011, Pages 2829-2840.

[26] Valero A, Torres C. Thermoeconomic Analysis, EOLSS Publishers, Oxford UK, 2006. http://www.eolss.net (Accessed Jan 2012)

[27] Torres C. Symbolic thermoeconomic analysis of energy systems. EOLSS Publishers, Oxford, 2006. http://www.eolss.net (Accessed Jan 2012)

[28] Natural gas expansion plant Arlesheim (Erdgas-Entspannungsanlage Arlesheim, in German). Gasverbund Mittelland AG, Arlesheim, Switzerland. Information available at http://www.energiezukunftschweiz.ch/cms/liniee/fuehrungen/erdgasentspannunganlage/Doku.pdf [Accessed Jan 2012]

[29] Setzmann U., Wagner W. A New Equation of State and Tables of Thermodynamic Properties for Methane Covering the Range from the Melting Line to 625 K at Pressures up to 1000 MPa, J. Phys. Chem. Ref. Data 1991; 20(6):1061--1155.

[30] Çengel Y. A. and Boles M. A. Thermodynamics: An Engineering Approach, McGraw-Hill, New York, 2006.

[31] Switzerland. Energy efficiency report. ABB 2011. Available at: www05.abb.com/global/scot/scot316.nsf/veritydisplay/bc38d0b683dcd8b2c125788d004b15e3/$file/switzerland.pdf [Accessed May 2012]

[32] Energy generation and CO2 emission (in Polish), available at www.solis.pl/index.php/oferta/wytwarzanie_energii_elektrycznej_i_emisja_co2 [Accessed May 2012]

[33] European Environment Agency; data available at http://www.eea.europa.eu/data-and-maps/figures/trends-in-energy-ghg-emission [Accessed May 2012]

Table 9 (Annex). Generic FP table. Exergy fluxes are denoted by B instead of $\dot{B}$.

	F0	F1	F2	F3	F4	F5	F6	F7	F8	F9	F10	F11	F12	F13	F14	F15	PRODUCT
P0	0	B9+B10	0	0	0	B1-B4	0	0	B4-B7	0	0	0	0	0	0	0	B9+B10+B1-B7
P1	0	0	B12-B13	0	B16-B19	0	0	B17-B18	0	B36	B11-B12	0	0	0	0	B13	a
P2	0	0	0	(B22-B21)·b	0	0	(B22-B21)·c	0	0	0	0	0	0	0	0	0	B24+B23-B21
P3	0	0	0	0	0	B2-B1	0	0	0	0	0	0	0	0	0	0	B2-B1
P4	0	0	0	0	0	B3-B2	0	0	0	0	0	0	0	0	0	0	B3-B2
P5	0	0	0	0	0	0	0	0	0	B34	0	0	0	0	0	0	B34
P6	0	0	0	0	0	0	0	0	B5-B4	0	0	0	0	0	0	0	B5-B4
P7	0	0	0	0	0	0	0	0	B6-B5	0	0	0	0	0	0	0	B6-B5
P8	0	0	0	0	0	0	0	0	0	B35	0	0	0	0	0	0	B35
P9	B39	0	0	0	0	0	0	0	0	0	0	0	0	0	0	0	B39
P10	0	0	0	0	0	0	0	0	0	0	0	(B28-B33)·d	(B28-B33)·e	(B28-B33)·f	0	0	B28-B33
P11	0	0	0	0	0	0	0	0	0	B37-B38	0	0	0	0	B38	0	B37
P12	0	0	0	0	0	0	0	0	0	0	0	(B33-B32)·d	(B33-B32)·e	(B33-B32)·f	0	0	B33-B32
P13	0	0	0	(B21-B27)·b	0	0	(B21-B27)·c	0	0	0	0	0	0	0	0	0	B21-B25-B26
P14	0	0	0	0	0	0	0	0	0	0	0	(B32-B31)·d	(B32-B31)·e	(B32-B31)·f	0	0	B32-B31
P15	B14	0	0	0	0	0	0	0	0	0	0	0	0	0	0	0	B14
F	B39	B9+B10	B12-B13	B23-B26	B16-B19	B3-B4	B24-B25	B17-B18	B6-B7	g	B11-B12	B28-B29	B29-B30	B30-B31	B38	B13	
W	B14	0	0	0	0	0	0	0	0	0	0	0	0	0	0	0	

a = B11+B16+B17-B18-B19+B36 ; b = (B23-B26)/(B23+B24-B25-B26); c = (B24-B25)/(B23+B24-B25-B26); d = (B28-B29)/(B28-B31); e = (B29-B30)/(B28-B31); f = (B30-B31)/(B28-B31); g = B34+B35+B36+B37-B38.

Table 10. (Annex) FP table for the system with ORC (Case A). All values are given in kW exergy.

	F0	F1	F2	F3	F4	F5	F6	F7	F8	F9	F10	F11	F12	F13	F14	F15	PRODUCT
P0	0	6078.77	0	0	0	1298.52	0	0	1149.14	0	0	0	0	0	0	0	8526.44
P1	0	0	34.33	0	115.38	0	0	73.03	0	2348.83	670.53	0	0	0	0	146.55	3388.65
P2	0	0	0	11.62	0	0	10.09	0	0	0	0	0	0	0	0	0	21.71
P3	0	0	0	0	0	33.44	0	0	0	0	0	0	0	0	0	0	33.44
P4	0	0	0	0	0	90.28	0	0	0	0	0	0	0	0	0	0	90.28
P5	0	0	0	0	0	0	0	0	0	905.97	0	0	0	0	0	0	905.97
P6	0	0	0	0	0	0	0	0	29.48	0	0	0	0	0	0	0	29.48
P7	0	0	0	0	0	0	0	0	52.40	0	0	0	0	0	0	0	52.40
P8	0	0	0	0	0	0	0	0	0	883.76	0	0	0	0	0	0	883.76
P9	4485.15	0	0	0	0	0	0	0	0	0	0	0	0	0	0	0	4485.15
P10	0	0	0	0	0	0	0	0	0	0	0	419.97	34.45	136.68	0	0	591.10
P11	0	0	0	0	0	0	0	0	0	346.59	0	0	0	0	9.99	0	356.59
P12	0	0	0	0	0	0	0	0	0	0	0	19.34	1.59	6.29	0	0	27.22
P13	0	0	0	40.41	0	0	35.08	0	0	0	0	0	0	0	0	0	75.50
P14	0	0	0	0	0	0	0	0	0	0	0	6.93	0.569	2.26	0	0	9.76
P15	146.55	0	0	0	0	0	0	0	0	0	0	0	0	0	0	0	146.55
F	4485.15	6078.77	34.33	52.03	115.38	1422.25	45.17	73.03	1231.02	4485.15	670.53	446.24	36.60	145.24	9.99	146.55	
W	146.55	0	0	0	0	0	0	0	0	0	0	0	0	0	0	0	

One-dimensional Model of an Optimal Ejector and Parametric Study of Ejector Efficiency

Ronan K. McGovern[a], Kartik V. Bulusu[b], Mohammed A. Antar[c] and John H. Lienhard V[d]

[a] *Massachusetts Institute of Technology, Cambridge, MA, U.S.A., mcgov@mit.edu*
[b] *The George Washington University, Washington D.C., U.S.A., bulusu@gwmail.gwu.edu*
[c] *King Fahd University of Petroleum and Minerals, Dhahran, Saudi Arabia, antar@kfupm.edu.sa*
[d] *Massachusetts Institute of Technology, Cambridge, MA, U.S.A., lienhard@mit.edu*

Abstract:
Significant numerical and experimental analyses have been devoted to understanding the variety of flow regimes present in steady flow ejectors. Certain regimes are more conducive to achieving high performance (i.e. high entrainment ratios). In particular, the entrainment ratio is seen to be highest when the entrained fluid reaches a choked condition in the mixing region. In addition, the expansion regime of the motive nozzle (under-, perfectly- or over-expanded) appears to influence performance. In this paper, we propose a method to model an ejector of optimal geometry, designed for a favorable flow regime. Then, rather than focusing upon the maximization of efficiency, we seek operational conditions that maximise ejector efficiency, specifically the reversible entrainment ratio efficiency. Ejector efficiency is found to be highest at low compression ratios and at low driving pressure ratios. However, at lower compression ratios, the optimal area of the mixing chamber becomes large relative to the motive nozzle throat area.

Keywords:
Ejector Efficiency, Entrainment Ratio, One-Dimensional Model, Perfect Expansion.

1. Introduction

Ejectors are supersonic flow induction devices employed for the generation of a vacuum for compressing a fluid. Figure 1 shows a straight throat ejector. High pressure motive fluid enters a converging diverging nozzle and is accelerated to a supersonic Mach number. The pressure at section NE is below that of the entrained fluid at its inlet. Consequently, the entrained fluid is drawn into the ejector. The motive and entrained fluids mix between sections NE and U and the uniform mixture is diffused to reach the discharge pressure.

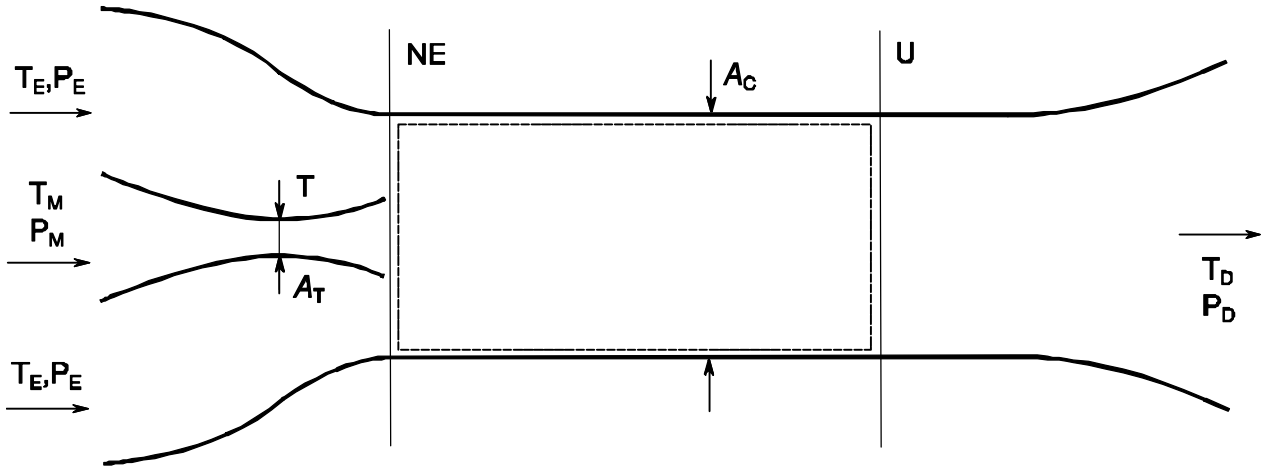

Fig. 1. Schematic diagram of a straight throat ejector

One common ejector application is the withdrawal of non-condensible gases from steam condensers. Other applications employ ejectors to compress a working fluid, such as vapor-compression refrigeration and vapor compression multi-pressure humidification-dehumidification desalination [3]. The operating conditions of an ejector in vacuum generation and compression applications differ significantly. When generating a vacuum, the compression ratio of the ejector, P_D/P_E, is very high whilst the ratio of the mass flow rate of entrained to motive fluid (known as the entrainment ratio) is very high. In compression applications, the compression ratio is low, whilst the entrainment ratio is high. The compression ratios also differ between compression applications. For example, Huang et al. [1] performed experiments on a refrigeration system using R141b. For an evaporator temperature of 8°C and a condenser temperature ranging from 28°C to 42.1°C, the compression ratio of the ejector varied from 2.2 to 3.6. Kamali et al. [2] optimised the design of a seven effect thermal vapour compression multi-effect distillation system with a condenser temperature of 45°C and a first effect temperature of 69°C, corresponding to a compression ratio of 3.1. Narayan et al. [3] optimised an ejector driven humidification dehumidification desalination system and found that the optimal compression ratio lies near 1.2.

For compression applications, the ejector efficiency is of significant importance as it dictates the energy input (or more correctly the exergy input) required to drive the ejector. One means of quantifying ejector performance, suggested by Elrod [4] and analysed in detail by McGovern et al. [5], is the reversible entrainment ratio efficiency, or η_{RER}. This efficiency compares the entrainment ratio of a real ejector to a reversible process with the same inlet fluid states and the same discharged pressure:

$$\eta_{RER} = \frac{ER}{RER} \qquad (1)$$

When designing an ejector, we could look for more than just a high value of entrainment ratio for fixed inlet conditions and a fixed discharge. Importantly, the entrainment ratio alone is not an indication of the quality of design or the performance of an ejector. We can ask what ejector geometry *and* what operating conditions are conducive to the highest ejector efficiency. This is the objective of the present work. In Section 2, we identify the flow regimes possible in steady flow ejectors that are most conducive to high efficiency. In Section 3, we discuss how an ejector of optimal geometry may be modelled using 1 dimensional theory. In Section 4, using fluid inlet conditions and ejector discharge pressure as parameters, we identify the operating conditions conducive to the highest values of efficiency. In summary, by focusing upon efficiency rather than solely the entrainment ratio we provide a new insight to optimising ejector design.

2. Regimes of Ejector Operation

One crucial consideration in the analysis and design of ejectors is the variety of flow regimes that are possible, depending on operating conditions and the ejector geometry. In order to design for maximum ejector efficiency one should be able to identify favorable flow regimes. To understand the flow regimes of an ejector we can describe the entrainment ratio in terms of the inlet fluid conditions, the discharged pressure, the motive fluid nozzle throat area and the mixing chamber area.

$$ER = f(P_M, T_M, P_E, T_E, P_D, A_T, A_C) \qquad (2)$$

First, we would like to explain the effect of the operating conditions upon an ejector of fixed geometry and second, the effect of the ejector geometry upon the entrainment ratio of an ejector with fixed operating conditions. This is done by considering experimental and numerical analyses present in literature.

2.1 Flow regimes within an ejector of fixed geometry

The explanation of flow regimes for a fixed ejector geometry is common in literature and revolves around the concept of critical back pressure, P_D*. A clear description of the critical pressure is provided by Bartosiewicz et al. and Huang et al. [6, 20] using experimental data and by Sriveerakul et al. [7] using a CFD analysis. The motive fluid throat area, the chamber area and the inlet motive and entrained fluid states at the inlet to the ejector are fixed. We may now describe three distinct regimes:

1. Reversed flow region – P_D is to the right of point A on the *x* axis of Fig. 2 and the discharged pressure is too high to allow entrainment. Flow through the converging diverging nozzle is overexpanded, resulting in compression shocks (see Bartosiewicz [6]). Motive fluid partially flows back through the entrained fluid inlet.
2. Unchoked entrainment – The discharged pressure drops to point A in Fig. 2, causing the compression shocks at the exit of the motive fluid nozzle to weaken, allowing the pressure at NE to drop and provoke entrainment.
3. Critical operation – The discharged pressure reaches P_D*, allowing a decrease in pressure upstream and causing the entrained flow to be accelerated to sonic speed within the mixing region.
4. Choked Flow – For values of P_D below P_D* the entrainment ratio remains constant. The motive fluid is choked at the motive fluid nozzle throat and the entrained flow remains choked in the mixing region.

The important message to take from these analyses is that the entrained mass flow rate is constant as the discharge pressure drops below critical. Since the entrained fluid pressure is held constant at the inlet this can only mean that the effective cross-sectional area at which choking occurs in the mixing region must be constant for fixed inlet conditions and ejector geometry, as concluded by Munday and Bagster [8].

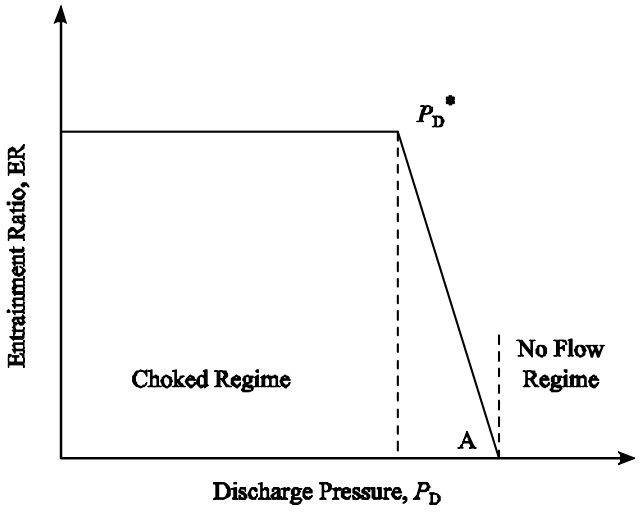

Fig. 2. Evolution of the entrainment ratio with discharge pressure

2.2 Flow regimes within an ejector with fixed operating conditions

Less common in literature is an intuitive explanation of the effect of ejector geometry upon the entrainment ratio. Nahdi et al. [9] and Lu et al. [10] draw important conclusions in this regard. By considering fixed inlet fluid states and a fixed discharged pressure we may identify three regimes which depend upon ejector geometry.

1. Overexpanded Flow – We consider operating conditions such that the motive and entrained fluids are choked at the motive nozzle throat and in the mixing chamber, respectively. The ratio

of chamber to motive nozzle throat area, φ, is small, such that the motive nozzle is overexpanded.

2. Perfectly Expanded Flow – The value of φ is reduced causing a higher value of ER. The pressure at cross section U in Fig. 1 drops, as does the pressure upstream of U. The compression shocks downstream of the motive fluid nozzle weaken until they cease to exist when the nozzle is perfectly expanded. The effective flow area of the entrained fluid increases (since φ increases) and the entrainment ratio increases. Nahdi et al. refer to φ at this point as the optimal area ratio for a given set of inlet conditions and discharged pressure. The entrainment ratio is maximum, the static pressures of the motive and entrained fluid are equal at section NE in Fig. 1 and the motive nozzle is perfectly expanded.
3. Underexpanded Flow – The value of φ is reduced below optimal, causing a decrease in entrainment. The underexpanded motive jet spreads at the exit of the motive nozzle, restricting the flow area of the entrained fluid. The flow structure takes the form of Fig. 3.

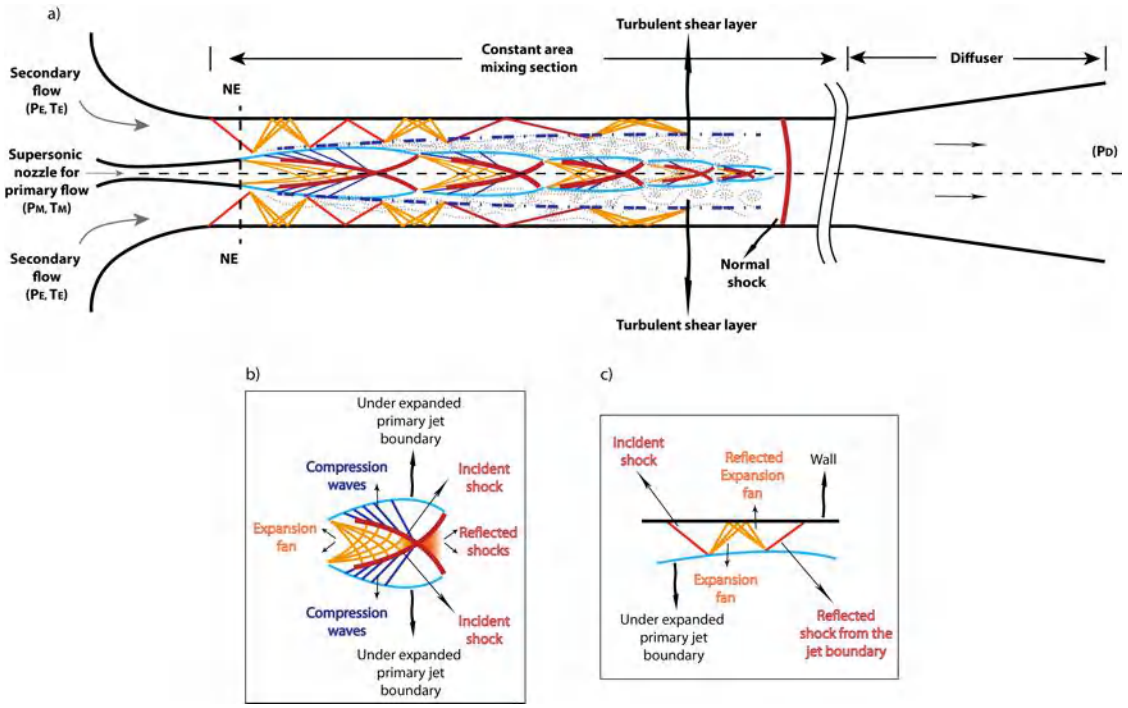

Fig. 3. Representation of the flow structure in an ejector with an underexpanded motive fluid nozzle and choked entrained flow

Using experimental results, Nahdi et al. [9] recognise that the entrainment ratio of an ejector is maximised when the primary nozzle is perfectly expanded and the entrained fluid reaches a choked condition. They identify, for a working fluid of R11, the area ratio which maximises the ER, as a function of ejector compression ratio, P_D/P_E, and driving pressure ratio, P_M/P_D.

3. One Dimensional Model of an Optimal Ejector

Using this knowledge we can build a one-dimensional ejector model that captures the performance of an optimal ejector. Coupled with the definition for efficiency (Section 1), this model can be used to identify the ejector operating conditions conducive to high efficiency (Section 4).

Nahdi et al. [9] identified the flow regime that maximised the ER for fixed conditions of operation. Since the reversible entrainment ratio is constant for fixed conditions of operation [4, 5], the flow regime that maximizes the ER must also maximize the reversible entrainment ratio efficiency. Consequently, the purpose of this section is to model an ejector operating in this optimal flow

regime. Using this knowledge we can build a one-dimensional ejector model that captures the performance of an optimal ejector. Coupled with the definition for efficiency (Section 1), this model can be used to identify the ejector operating conditions conducive to high efficiency (Section 4). To simplify the interpretation of results, an ideal gas ejector is modelled, with constant values of specific heats.

3.1 Nozzle Region

We begin by considering flow from the motive and entrained fluid inlets to the cross section NE in Fig. 1. The inlet fluid pressures and temperatures are fixed, P_M, P_E, T_M, T_E. According to Section 3, the motive fluid nozzle is perfectly expanded, meaning that the static pressures of the motive and entrained streams are equal at NE. In addition, the entrained flow is choked at section NE, *i.e.* the Mach number is unity, such that further decreases in the downstream pressure cannot induce a higher mass flow rate. Considering the motive and entrained flows both to be isentropic and adiabatic, we may solve for the entrained fluid pressure and temperature at the nozzle exit, and then for the motive fluid Mach number and the motive fluid temperature at NE.

$$\frac{T_E}{T_{NE,E}} = 1 + \frac{\gamma - 1}{2} \tag{3}$$

$$\frac{P_E}{P_{NE,E}} = \left(1 + \frac{\gamma - 1}{2}\right)^{\frac{\gamma}{\gamma - 1}} \tag{4}$$

$$\frac{P_M}{P_{NE,M}} = \left(1 + \frac{\gamma - 1}{2} M_{NE,M}{}^2\right)^{\frac{\gamma}{\gamma - 1}} \tag{5}$$

$$\frac{T_M}{T_{NE,M}} = 1 + \frac{\gamma - 1}{2} M_{NE,M}{}^2 \tag{6}$$

In order to fix the capacity of the ejector, we fix the motive fluid throat area, A_T. This allows the mass flow of the motive fluid to be calculated:

$$\dot{m}_M = \frac{\sqrt{\gamma} A_T P_M}{\sqrt{R T_M}} \left(1 + \frac{\gamma - 1}{2}\right)^{-\frac{\gamma + 1}{2(\gamma - 1)}} \tag{7}$$

At this point, the mass flow rate (and the flow area at NE) of the entrained fluid is yet to be determined. The modelling until this point is the same as Khoury et al. [11], although their work does not allude to the motive nozzle being perfectly expanded to justify the uniformity of pressure across NE. In the present analysis, the motive nozzle exit is located at the entrance to the mixing region (Fig. 1). In many experimental configurations, the nozzle exit is upstream of the constant area region. Zhu et al. [12] provide a detailed analysis of the influence of the axial position of the nozzle exit upon entrainment ratio.

3.2 Mixing Region

In the constant area mixing region, the mass, momentum, and energy conservation equations are applied between sections NE and U of Fig. 1. The fluid properties and velocity are taken to be uniform over the entrained flow area and motive flow area at NE and over the total flow area at U. Frictional forces on the fluid due to the no slip condition at the wall are assumed to be negligible.

$$\dot{m}_M + \dot{m}_E = \dot{m}_U \tag{8}$$

$$P_{NE}A_{NE} + \dot{m}_M V_{NE,M} + \dot{m}_E V_{NE,E} = P_U A_U + \dot{m}_U V_U \quad (9)$$

$$\dot{m}_M c_p T_{NE,M} + \dot{m}_E c_p T_{NE,E} = \dot{m}_U c_p T_U \quad (10)$$

In addition, there is a relationship between the mixing chamber area and the flow areas at the exit of the motive nozzle.

$$A_{NE} = A_{NE,M} + A_{NE,E} = A_U \quad (11)$$

A number of these assumptions merit further discussion. The mixing process within an ejector is characterised by highly irreversible oblique and sometimes normal shocks coupled with dissipative processes within the shear layer between the motive and entrained fluids. Entropy generation within this region is driven by pressure, velocity and temperature differences, in axial and radial directions. By employing a control volume approach, we are overlooking the details of the mixing process. Instead, by essentially varying the ratio of pressure, velocity and temperature, the motive and entrained fluids at NE and the pressure ratio between sections NE and U, we are essentially altering the scale of the disequilibria responsible for entropy generation. Examples of detailed experimental visualisations of internal flow structures are provided by Desevaux et al. [14] and Dvorak et al. [19], whilst numerical visualisations are provided by Desevaux et al. [13], Hemidi et al. [15], Bartosiewicz et al. [6] and Sriveerakul et al. [7].

By assuming properties and velocity to be uniform at section U in Fig. 1, we intend the ratio of the mixing chamber length to diameter to be sufficiently large for the motive fluid core and the entrained fluid annulus to have mixed very well. The consequence of incomplete mixing is inadequate pressure recovery and compression within the diffuser. The axial length of the mixing section is dependent on the rate of mixing between the two streams. The higher the rate of mixing the greater would be the transverse spread (or growth) of the turbulent shear layer leading to a shorter axial length of the mixing region. Li et al. [16] indicated that the optimum length varies greatly with the operation conditions. In numerical studies, one way to determine the appropriate mixing length is by employing a numerical die tracer, as suggested by Bartosiewicz et al. [6]. Sriveerakul et al. [7] also points out that as the mixing chamber is elongated, total pressure losses due to shear stress at the wall increase, implying that there is an optimal length of the mixing region.

3.3 Diffuser

Since the fluid velocity is considered to be uniform at cross section U in Fig. 1, the diffuser is modelled as isentropic.

$$\frac{T_D}{T_U} = 1 + \frac{\gamma - 1}{2} M_U{}^2 \quad (12)$$

$$\frac{P_D}{P_U} = \left(1 + \frac{\gamma - 1}{2} M_U{}^2\right)^{\frac{\gamma}{\gamma - 1}} \quad (13)$$

In practice, the performance of the diffuser depends largely upon the completeness of mixing in the constant area section. Diffuser efficiency was reported by Varga et al. [17] to be within the range 0.5 to 0.9 depending on both temperature and area ratio. For an ejector of fixed mixing chamber length, the diffuser efficiency is a function of the back pressure. As back pressure increases, normal or oblique shocks will be pushed back into the mixing section, resulting in a more uniform flow at cross section U and consequently improved diffuser performance. This is clearly illustrated by Sriveerakul et al. [7].

3.4 Solution of Equations

Given the following relations for mass flow rate, Mach number and the speed of sound in an ideal gas, the set of equations provided above are closed and may be solved.

$$\dot{m} = \rho A V \tag{14}$$

$$M = \frac{V}{c} \tag{15}$$

$$c = \sqrt{\gamma R T} \tag{16}$$

The equations are solved iteratively using the non-linear equation solver provided by Engineering Equation Solver [18] subject to the restriction that the Mach number obtained at cross section U must be subsonic. For compression applications, the conditions of the fluid obtained at the diffuser exit should be as close as possible to stagnation (zero velocity). Consequently, the flow must be subsonic at the diffuser exit, and preferably within the entire diffuser. For a set of operational conditions (inlet fluid states and discharge pressure), we may calculate the following key variables:

1. The ejector area ratio of A_C/A_T
2. The entrainment ratio, ER

4. Results

Given the model of an optimal ejector presented in Section 3, we now seek the conditions of operation that maximize ejector efficiency. We begin by considering the variation in ejector efficiency and area ratio with the compression ratio in Fig. 4. As the compression ratio decreases, the entrainment ratio of the optimal ejector increases at a faster rate than the reversible entrainment ratio, resulting in improved efficiency. Meanwhile, as the compression ratio drops, the optimal area ratio of the mixing chamber to the ejector throat increases to accommodate a greater flow rate of entrained fluid.

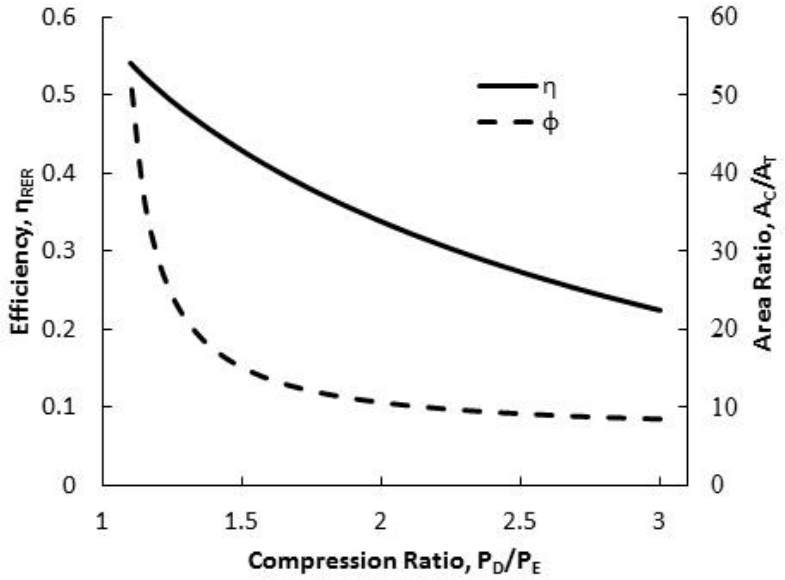

Fig. 4. Efficiency and area ratio for a driving pressure ratio of P_M/P_D=5 and an inlet temperature ratio of T_M/T_E=1

Figure 5 illustrates the effect of the driving pressure ratio upon ejector efficiency and area ratio. Ejector efficiency is less sensitive to the driving pressure ratio of the ejector than the compression

ratio. As the driving pressure ratio increases, the area ratio of the ejector also increases, resulting in an ejector that is larger in size.

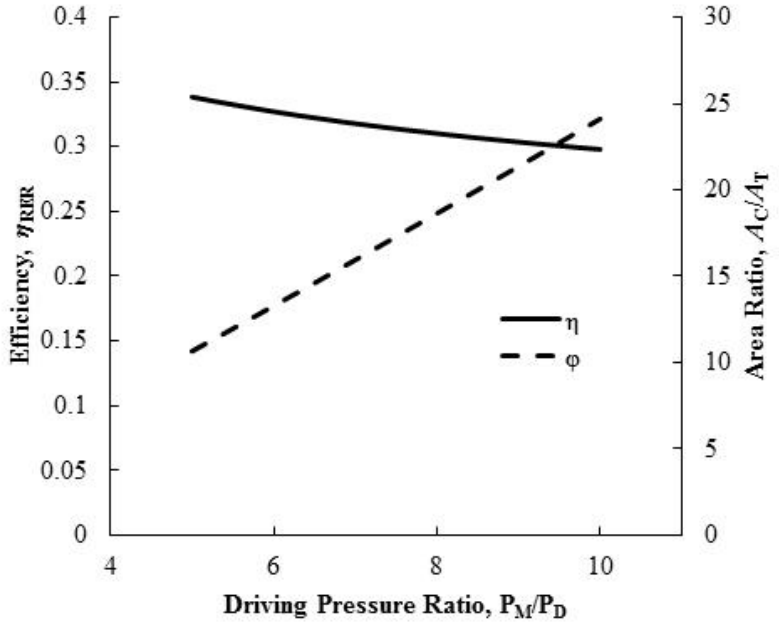

Fig. 5. Efficiency and area ratio for a compression ratio of $P_D/P_E=2$ and an inlet temperature ratio of $T_M/T_E=1$

Finally, we consider the effect of the inlet temperature ratio. In Fig. 5, the efficiency of the ejector reaches a maximum at an inlet temperature ratio just above unity. This is the point where the temperature difference between the motive and entrained streams at the nozzle exit are minimum. Also, the ejector area ratio is insensitive to the inlet temperature ratio.

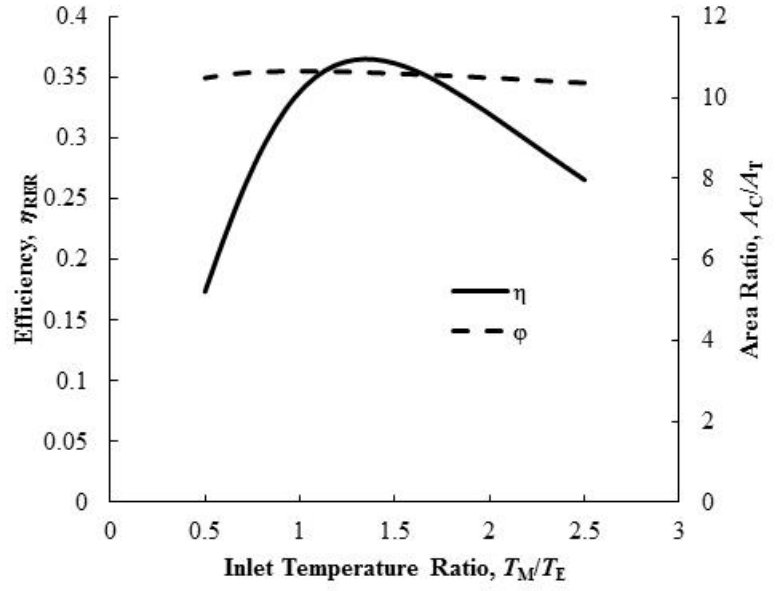

Fig. 6. Efficiency and area ratio for a driving pressure ratio of $P_M/P_D=5$ and an inlet temperature ratio of $T_D/T_E=2$

5. Conclusions

Using a simple model of an optimal ejector, a parametric study has been performed to identify operating conditions conducive to high ejector efficiency. This optimal ejector is designed such that

the motive fluid nozzle is perfectly expanded and the entrained fluid is choked at the entrance to the constant area mixing section. The following is concluded from the parametric study:

- The efficiency of an ideal gas ejector is highest when design for conditions of low compression ratio and low driving pressure ratio.
- At low compression ratios the area ratio of the mixing section to the motive nozzle throat increases, indicating that the required size of the ejector increases.
- As the driving pressure ratio increases, the required size of the ejector increases
- An optimal inlet temperature ratio of the inlet fluids appears to exist for fixed inlet and discharge pressures, although the ejector area ratio appears insensitive to the inlet temperature ratio

Acknowledgments

The first author would like to thank the US Department of State for conference funding through the Fulbright Science and Technology PhD program. The authors would like to thank the King Fahd University for Petroleum and Minerals for support for this research through the Center for Clean Water and Clean Energy at MIT and KFUPM.

Nomenclature

Letter Symbols

A area, m^2

c speed of sound, m/s

ER entrainment ratio, dimensionless

$\dot{m}$ mass flow rate, kg/s

M speed of sound, dimensionless

P pressure, Pa

R ideal gas constant, J/kg K

RER reversible entrainment ratio, dimensionless

T temperature, K

Greek symbols

η reversible entrainment ratio efficiency, dimensionless

γ ratio of specific heats, dimensionless

φ Ratio of mixing chamber area to motive nozzle throat area

Subscripts

C mixing chamber area

D discharge

E entrained fluid

M motive fluid

NE motive nozzle exit

T motive nozzle throat

U uniform flow cross section

Abbreviations

ER entrainment ratio

RER reversible entrainment ratio

References

[1] Huang B.J., Chang J.M., Wang C.P., Petrenko V.A., A 1-D analysis of ejector performance. International Journal of Refrigeration 1999;22:354–364.

[2] Kamali R.K., Abbassi A., Sadough Vanini S.A., Saffar Avval M., Thermodynamic design and parametric study of MED-TVC. Desalination 2008;222:596-604

[3] Narayan G.P. McGovern R.K., Zubair S.M., Lienhard V J.H., High-temperature-steam-driven, varied-pressure, humidification-dehumidification system coupled with reverse osmosis for energy-efficient seawater desalination. Energy 2012;27(1):482–493.

[4] Elrod H.G., The Theory of Ejectors. Journal of Applied Mechanics 1945;12:A170-A174

[5] McGovern R.K., Narayan G.P., Zubair S.M., Lienhard V J. H., Analysis of reversible ejectors and definition of an ejector efficiency. International Journal of Thermal Sciences 2012;54:153-166.

[6] Bartosiewicz Y., Aidoun Z., Desevaux P, Mercadier Y., Numerical and experimental investigations on supersonic ejectors, International Journal of Heat and Fluid Flow. 2005; 26:56–70.

[7] Sriveerakul K. , Aphornratana S., Chunnanond K., Performance predict tion o fsteam ejector using computational fluid dynamics: Part 2: Flow structure of a steam ejector influenced by operating pressure and geometries, International Journal of Thermal Sciences 2007;46:823–33.

[8] Munday J.T., Bagster D.F., A New Ejector Theory Applied to Steam Jet Refrigeration. Industrial & Engineering Chemistry Process Design and Development 1977;16(4):442-449.

[9] Nahdi E., Champoussin J.C., Hostache G., Cheron J. Optimal geometric parameters of a cooling ejector-compressor. Revue International du Froid 1993;16(1):67-72

[10] Lu T.C., Champoussin J.C., Nahdi E., Optimal performance and use of an ejector cycle refrigeration system. 17eme Congres International du Froid AARAC/IIR; 1987; Wien:969- 974.

[11] Khoury F., Heyman M., Resnick W., Performance Characteristics of Self-Entrainment Ejectors. ILEC Process Design and Development 1967;6(3):331-340.

[12] Zhu Y., Cai W., Wen C., Li Y., Simplified ejector model for control and optimization, Energy Conversion and Management.2008; 49:1424-32.

[13] Desevaux P., Marynowski T., Khan M., CFD prediction of supersonic ejector performance, International Journal of Turbo and Jet Engines. 2006; 23:173-81.

[14] Desevaux P., A method for visualizing the mixing zone between two co-axial flows in an ejector, Optics and Lasers in Engineering. 2001;35:317–23.

[15] Hemidi A., Henry F., Leclaire S., Seynhaeve J.M., Bartosiewicz Y., CFD Analysis of a Supersonic Air Ejector. Part I: Experimental Validation of Single-Phase and Two-Phase Operation. Applied Thermal Engineering 2008. Applied Thermal Engineering 2009;29(8-9):1523–1531.

[16] Li C., Li Y., Wang L., Configuration dependence and optimization of the entrainment performance for gas-gas and gas-liquid ejectors. ATE In press.

[17] Varga S., Oleviera A. C., Diaconu B., Numerical Assessment of Steam Ejector Efficiencies using CFD, Internatinal Journal of Refrigeration. 2009;32:1203-11.

[18] Klein S.A., Engineering Equation Solver, Academic Professional, Version 8, 2009; Madison, WI; www.fchart.com.

[19] Dvorak V., Safarik P., Supersonic Flow Structure in the Entrance Part of a Mixing Chamber of 2D Model Ejector, Journal of Thermal Science. 2003;12(4):344-349.

[20] Huang B. J., Jiang C. B.., Hu F. L., Ejector Performance Characteristics and Design Analysis of Jet Refrigeration System, Journal of Engineering for Gas Turbines and Power, Transactions of the ASME. 1985; 107(3):792-803.

Optimization and Design of Pin-Fin Heat Sinks Using Minimum Entropy Generation

J.L. Zúñiga-Cerroblanco[a], A. Hernández-Guerrero[a], C.A. Rubio-Jimenez[a], J.C. Rubio-Arana[a], S.Diaz-Mendez[b]

[a] *University of Guanajuato, Salamanca, Guanajuato, Mexico, abel@ugto.mx*
[b] *Department of Mechanical Engineering, Autonomous University of El Carmen, Mexico*

Abstract:

This work analyses the entropy generation production for different pin-fin heat sink configurations, optimizing the parameters that must be used in the manufacture of heat sinks. The pin-fin heat sinks are commonly used for cooling in the electronic devices, with the goal of improving the performance, as well as increasing the life span of electronic circuits. In addition to the design parameters, the type of geometrical arrangement is analyzed too (this is because both the in-line and the staggered arrangement could be employed). Once the optimal parameters are determined, the next step is to analyze the type of pin-fin cross-sectional geometry that can be used; for the present work the geometries analyzed are rectangular, circular, elliptical and a constructal theory-based arrangement. The entropy generation and Bejan number are reported for the different geometries, as well as the optimal parameters including fins diameter, the distance between the fins, the air velocity and the number of fins needed.

Keywords:

Entropy Generation, Bejan Number, Pin-Fin Heat Sink.

1. Introduction

Nowadays the electronic industry spends a great deal of capital in the development of faster, smaller and more efficient electronic devices; but this industry has put no interest in an extremely important area for the maintenance and the good operation of the electronic circuits: the thermal design area of the electronic industry. As power dissipation of components increases and component package size decreases, thermal engineers must innovate to ensure that the components will not overheat. Devices that are well cooled increase their period of life utility. Therefore, a heat sink must satisfy thermal design as well as mechanical requirements.

The main techniques for electronic circuits cooling are based on forced convection and using pin-fin heat sinks due to their low cost of manufacturing and easy installing. Different pin-fin heat sink configurations have been used as in-line and staggered arrangement, with different geometries [1]-[3],[23] for the pin-fin cross section: square, circular and elliptical. Aluminium is the material used commonly for its thermal properties, easy manufacturing and cost.

Nowadays the design engineer is faced with integrating coolant passages into an existing piece of equipment, where the space occupied by the coolant passage is at a premium and the available flow rates may be limited by the size of an existing or a retrofit fan or pump, therefore, the following question arises: is there an optimum pin-fin heat sink configuration that minimizes entropy generation and allows for the best performance? To answer that question different experimental and numerical analyses have been performed for the thermal and hydraulic behaviour of the pin-fin heat sinks [4]. Different pin-fins cases have been studied and the optimal parameters have been found. These optimal parameters present a better thermal and hydraulic performance.

2. Background

Several researches [4] have undertaken the characterization of pin-fin heat sinks, the behaviour of the flow within a heat sink is the same as that within a series of tubes of infinite length, except at the end of the walls. Idelchik et al. [21] present correlations for different geometries of tube banks, whereas Zhukauskas et al. [8] present experimental correlations for tubes in cross flow as a function of the Reynolds number, diameter of tubes and space between the tubes. Dugruoz et al. [4] show that the experimental correlations of tubes in cross flow can be used in pin-fin heat sinks analysis for high velocities (v>3 m/s) when the pin-fin geometry is square. On the other hand, Khan et al. [5] reported that the experimental correlations can be used for a wide range of velocities (v=1.5 to 5 m/s) when the pin-fin geometry is circular. In the present work a circular pin-fin geometry is employed for obtaining the optimal parameters for the arrangement.

Different studies [4] determine the optimal parameters for the design of a pin-fin heat sink, therefore the optimum number of fins that present the lower thermal resistance, thence finding the greater heat dissipation. However, the optimal configuration is determined by only taking into account the heat transfer performance, but the pressure drop should be also taken into account since it increases as a function of the number of fins.

In the last few years a parameter used for the optimization of thermo-fluidic systems is the entropy. The entropy generation rate has become a useful tool for evaluating the intrinsic irreversibilities associated with a given process or device [18]. The groundbreaking work by Bejan [20] introduced the concept of entropy generation analysis due to fluid flow and heat transfer as a powerful tool to evaluate the effectiveness of different configurations. Since the entropy generation destroys the work availability of a system, it makes good engineering sense to focus on the irreversibility due to heat transfer and fluid flow processes to understand the associated entropy generation mechanisms. References can be found where entropy generation is calculated and minimized in ducts with various cross-sectional shapes for laminar and turbulent flow configurations, with constant heat transfer rate per unit length, with constant heat flux, or with constant wall temperature, and in flows with temperature dependent viscosity [9]-[11].

Numerous studies have shown that in convective heat transfer arrangements the fluid friction and the heat transfer losses are coupled, and that attempts to reduce entropy generation associated with heat transfer will increase the entropy generation associated with fluid friction, and vice versa [12]. This coupling between fluid flow and heat transfer irreversibilities suggests that the geometry and operating conditions can be optimized to minimize the overall entropy generation. Khan et al. [13] employed the entropy generation minimization method as a unique measure to study the thermodynamic losses caused by heat transfer and pressure drop for a fluid in cross flow with tube banks. Analytical and empirical correlations for heat transfer coefficients and friction factors are used, where the characteristic length is used as the diameter of the tubes and reference velocity used in the Reynolds number, and the pressure drop is based on the minimum free area available for the fluid flow. A parametric study is also performed to show the effects of different design variables on the overall performance of tube banks.

On the other hand Culham et al. [14] worked in the specification and design of heat sinks for electronic applications, and presented a procedure that allows the simultaneous optimization of heat sink design parameters based on a minimization of the entropy generation associated with heat transfer and fluid friction. In addition, a novel approach for incorporating forced convection through the specification of a fan curve is integrated into the optimization procedure, providing a link between optimized design parameters and the system operating point.

An important parameter in the design of the pin-fin heat sink is the geometry of the fins. Important investigations in this area have been published like that of Behnia et al. [15]. In their work they compare the heat transfer dissipation capacity of several geometries of fins commonly used. Geometries were optimized to diminish the thermal resistance using moderate air speeds.

New geometries and adjustments are proposed to improve the performance of the pin-fin heat sinks, in this untiring search there is a configuration proposed by Bello et al. [16]; although they propose their configuration for a phenomenon of natural convection, in the present work it will be adapted for forced convection to observe the thermal and hydraulic behavior of such configuration. Bello found that in a space filled with cylinders used to dissipate heat by natural convection, the heat transfer dissipation capacity can be progressively increased by the use of cylinders of several sizes and the optimal place of each cylinder in the adjustment. These authors placed smaller cylinders at the entrance of the adjustment section (the regions of free flow occupied by still air and that is not being used for the heat transfer performance). The optimization of the flow and the development for structures with one and two sizes of cylinders is reported, which correspond to structures with one and two degrees of freedom. In Fig. 1 a) and b) the arrangement adjustments of the cylinders are observed, a) the original adjustment used commonly, and b) the proposed complex adjustment to be used in this work. The proposed arrangement is called honeycomb because it simulates the structure with which the bees construct their honeycomb. The optimal relation between the big and the small cylinders was found by Bello: $D_1/D_0=0.2$.

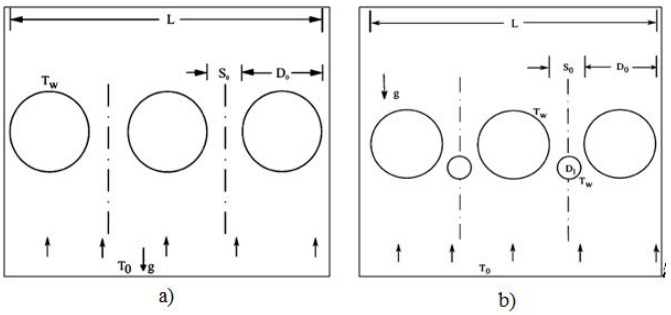

Fig. 1. Constructal arrangement.

3. Geometric parameters

The present work investigates the impact of the parameters modification on the entropy generation for a pin-fin heat sink. Fig. 2 shows the main parameters of the heat sink that need to be optimized: SL is the pitch longitudinal, ST is the pitch transversal, b is the distance between the fins and a is the magnitude of the fin side. Another parameter to optimize is the flow velocity.

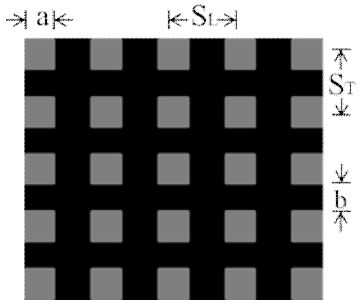

Fig. 2. Heat sink parameters.

The material used for the pin-fin heat sink manufacturing is aluminium, which has a thermal conductivity of 210 W/(m K). The base of the heat sink has the following dimensions: 6.35 cm of width, 6.35 cm of length and 0.635 cm of height. All fins have a height of 3.175 cm. The heat sink is placed in a channel of rectangular cross-section, air flow pass through this channel at ambient temperature; with this arrangement it is possible to simulate the electronics circuit cooling currently employed in the industry.

Once the optimal parameters of the design for the pin-fin heat sink are found, the different arrangements for the fins are studied; the arrangements studied in this work are shown in Fig. 3 a) and b), which are the in-line and staggered arrangement respectively.

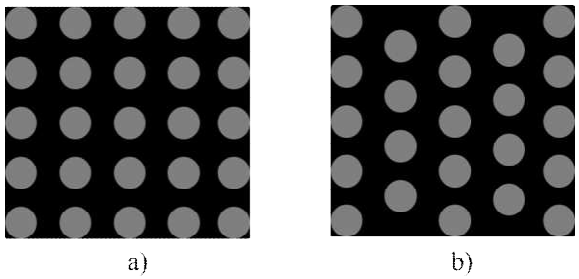

Fig. 3. a) In-line arrangement, b) staggered arrangement.

When the best arrangement for the minimum entropy generation is obtained considering specific geometrical configurations, the manufacturing processes, integration and costs have to be evaluated in order to obtain the best and most reliable heat sink geometrical configuration.

Fig. 4 shows the different fins geometries analyzed in this work: square, circular, elliptical and constructal arrangement; the dimensions of the fins are obtained using the same hydraulic diameter so they can be compared. In the incessant search to find new geometries and arrangements for a better performance of these heat sink new ideas are proposed, therefore the arrangement proposed by Bello [16] based on the constructal theory for the phenomenon of free convection is analyzed, this arrangement is adapted to forced convection, observing that improvements are observed with this configuration.

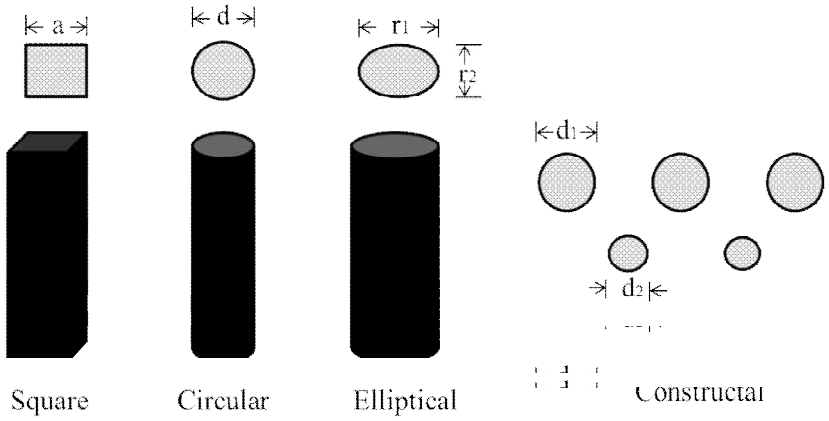

Fig. 4. Geometries analysed: square, circular, elliptical and constructal.

4. Entropy Analysis

Following Bejan´s discussions on the subject [12], and applying the mass conservation and energy laws with the entropy balance for a fluid that crosses through a heat sink, an expression for the entropy generation rate can be deduced.

$$\dot{S}_{gen} = \left(\frac{Q^2}{T_a T_b} \right) R_{hs} + \frac{\dot{m} \Delta P}{\rho T_a} \qquad (1)$$

This is the entropy generation due to heat transfer and pressure drop, therefore it is possible to use it as an objective function for the optimization of the design of the heat sink. The previous relations are based on the previous knowledge of the pressure drop correlations for tube bundles tubes

[6],[8],[13],[21],[22], which have very good results, as Dugruoz et al. [4] and Khan et al. [5] confirmed.

5. Results

This work finds the optimum variables that lead to the minimum entropy. The effects of certain parameters on the optimum design variables and the corresponding entropy generation rates are studied. Results are shown in Fig. 5; the curves show the entropy generation variation versus the fin diameter. It is observed that the entropy generation depends on the diameter, and the minimum entropy generation is obtained for a diameter between 3 and 3.7 mm. The air velocity and fins number used are 4 m/s and 8 fins.

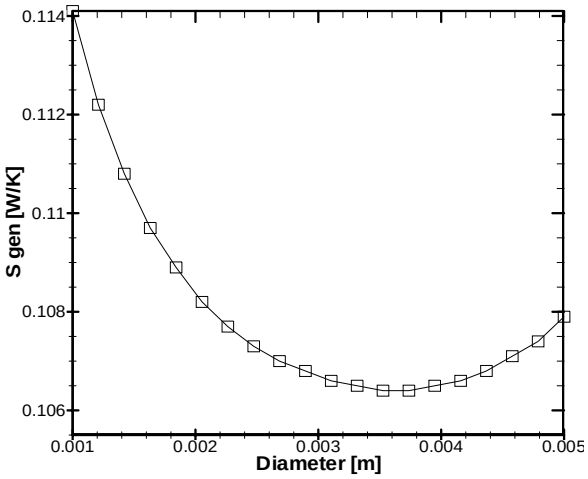

Fig. 5. Entropy generation versus fin diameter.

Another parameter of interest in the present work is the number of fins per row that generates the minimum entropy generation and therefore the optimal number of fins for the heat sinks design. Fig. 6 shows the entropy generations versus the number of fins; from this figure the optimal number of fins for a minimum entropy generation is 8 fins, thus the heat sink arrangement has a total of 64 fins. When the number of fins and the diameter optimal are found, the distance between the fins can be determined for the optimal performance of the heat sink.

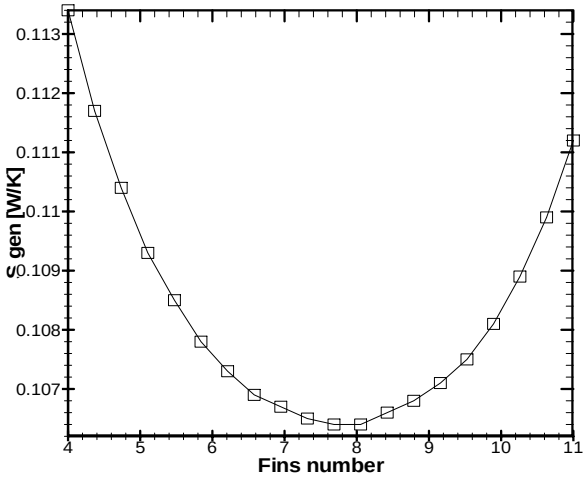

Fig. 6. Entropy generation versus number of fins.

The air velocity entering the heat sink is a factor affecting the pressure drop and the amount of heat removed by the heat sink. Therefore in Fig. 7 the entropy generation is plotted versus air velocity. Clearly, an air velocity of 2 m/s leads to obtaining the minimum entropy generation.

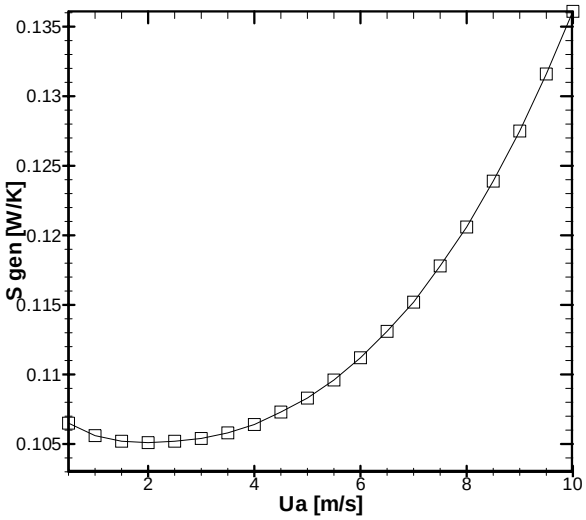

Fig. 7. Entropy generation versus air velocity.

Typically, a heat sink works with an air velocity of 4 m/s, and when the air velocity increases the thermal resistance decreases, although when greater velocities are used the pressure drop increases as well; therefore using the minimum entropy methodology an optimal flow velocity can be obtained. The graph in Fig. 8 shows the entropy generation for different number of fins and for air velocities of 2 and 4 m/s. Clearly a minimum for both velocities occurs: for the 4 m/s case the minimum entropy occurs for 8 fins, and for the 2 m/s case the minimum occurs for an arrangement of 10 fins.

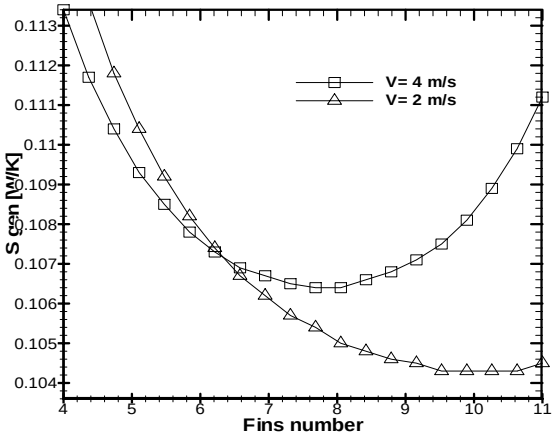

Fig. 8. Entropy generation versus number of fins for different air velocities.

The results for entropy generation variation versus diameter are observed in Fig. 9 for different inlet velocities; for each velocity a minimum occurs, and the smaller the velocity the lower the entropy generation. The minimum entropy generation is obtained when the air velocity is 1.5 m/s and a fin height of 6 mm is employed.

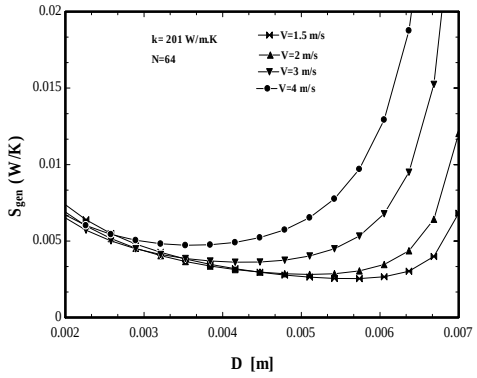

Fig. 9. Entropy generation for different diameters and air velocities.

A comparison of the in-line and staggered arrangement is shown in Fig. 10. Therefore the best arrangement for the heat sink is the in-line arrangement for the studied conditions, since it shows a minimum entropy generation.

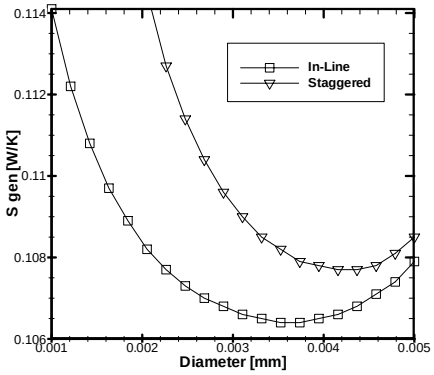

Fig. 10. Entropy generation versus fin diameter.

The optimal number of fins for both arrangements studied in this work is shown in Fig. 11. For a staggered and in-line arrangement the optimal number of fins for the arrangement is approximately 8 fins. These results depend on the air velocity (as shown in Fig. 9), then the air velocity must be taken into account in any analysis; for the results presented in Fig. 11, an air speed of 4 m/s was used.

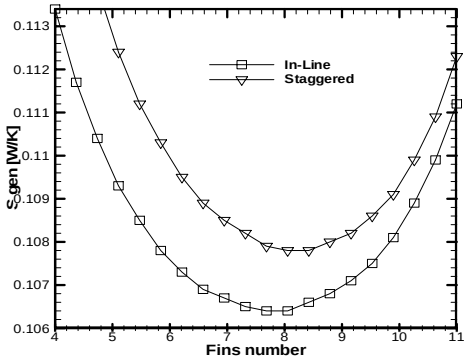

Fig. 11. Entropy generation versus number of fins.

In order to select a material to use in the manufacturing of the pin-fin heat sink, Fig. 12 allows to see that the aluminium (k=210 W/(m K)) is a good material for the heat sinks, because its entropy generation is not very different from that generated with materials of higher conductivity; on the

other hand, very interestingly, it is observed that the use of materials with low conductivity leads to an almost exponential increase in the entropy generation.

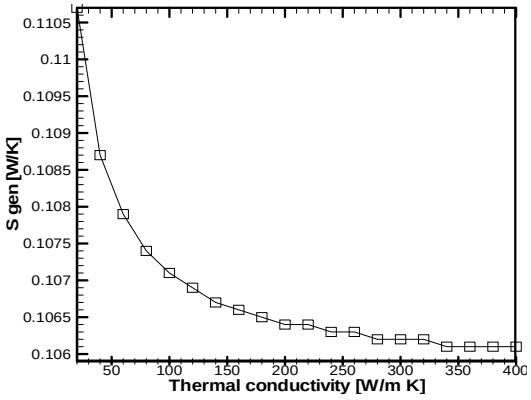

Fig. 12. Entropy generation variation versus thermal conductivity.

Considering the results shown in Figures 5 to 12, the behavior of the entropy generation by varying the operating and geometrical parameters can be observed. Thus, optimal geometrical configuration of heat sinks can be proposed.

When different fin geometries are analyzed, analytical and empirical correlations cannot be used, because the results will be the same for all geometries, and the best geometry cannot be found for the heat sink. Therefore, the general relation to determine the entropy generation should be written as:

$$\dot{S}_{gen} = q.\nabla\left(\frac{1}{T}\right) - \frac{1}{T}P^{v}\nabla\cdot v - \frac{1}{T}\overset{\circ}{P}^{v} : \overset{\circ}{V} \qquad (2)$$

where the first term is the entropy related to heat transfer, the second and third terms are due to mechanical dissipation.

A code was developed to solve Equation (2). The input variables for solving Equation (2) are the temperature and pressure drop contours; these are obtained previously with the aid of a commercial code.

In Fig. 13 it is possible to observe the entropy generation by volume unit for each fin geometry and for the constructal arrangement. The geometry that presents the lower entropy generation is the constructal arrangement proposed by Bello [16], although this arrangement is for a phenomenon in free convection but adapted in the present work to forced convection, offering very good results for the thermal and hydraulic performance.

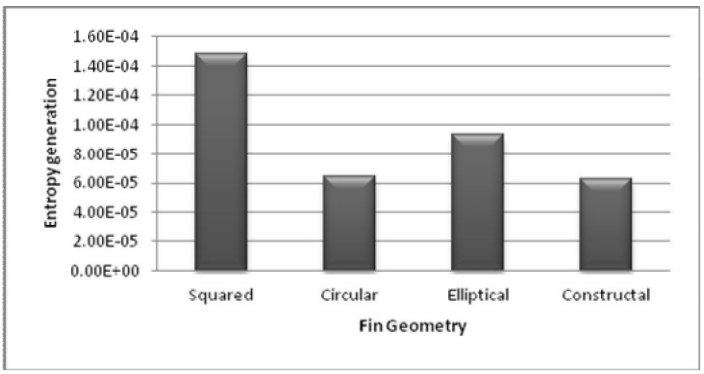

Fig. 13. Entropy generation for the fin geometries analyzed in the present work.

The Bejan number is calculated for each fin geometry and for the constructal arrangement; these results are reported in Fig. 14; the elliptical geometry has the largest Bejan number, indicating that the thermal affects are dominant in the phenomenon analyzed. The constructal arrangement has the smallest Bejan number since the entropy generated by pressure drop effects is considerable due to the large number of pin fins compared with other configurations. A larger hydrodynamic resistance is observed with this increase in the pin fin density.

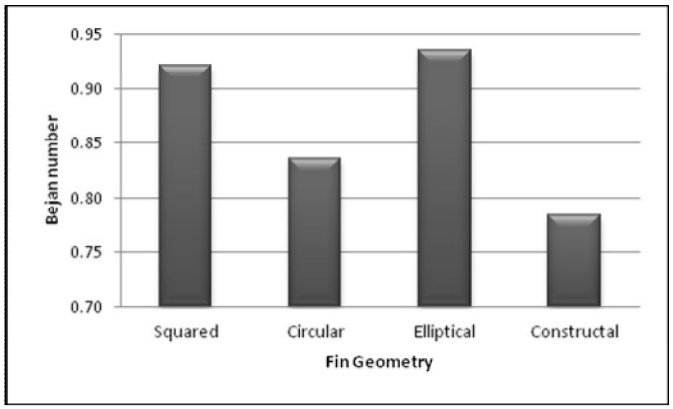

Fig. 14. Bejan number versus fins geometry.

6. Conclusions

In the present work an analysis of the entropy generation due to heat transfer and to pressure drop for a pin-fin heat sink arrangement is reported. Using empirical and analytical correlations the optimal diameter, optimal number of fins, the optimal arrangement and the optimal air velocity are found for the manufacturing a pin-fin heat sinks. The material to use for the heat sink manufacturing is analysed as well, this analysis indicated that aluminium is as good a material because it leads to low entropy generation and cost.

Analysing the results for different fin geometries it is concluded that that circular geometry is the best geometry for the performance of the heat sink, although surpassed slightly by the constructal arrangement, which has the minimum entropy generation of all geometries used in this investigation.

It is concluded, thus, that it is possible to obtain the optimal parameters with a new arrangement for pin-fin heat sinks; these results could be used to improve the cooling techniques for the current electronic devices, leading to optimal operating conditions and efficiency.

Nomenclature

a fin side, (m)
b distance between fins (m)
d diameter (m)
d_1 diameter major (m)
d_2 diameter minor (m)
H height of the finned section (m)
$\dot{m}$ mass flow (kg/s)
N fins number
P pressure (Pa)
Q heat flow rate from heater (W)
r_1 semi major axis length (m)
r_2 semi minor axis length (m)

R_{hs} thermal resistance (K/W)

S_L pitch longitudinal (m)

S_T pitch transversal (m)

$\dot{S}_{gen}$ entropy generation rate (W/K)

T_a ambient temperature (K)

T_b base temperature of the heat sink (K)

U_{int} inlet velocity (m/s)

v velocity (m/s)

Greek symbols

ΔP overall pressure drop in the finned section (Pa)

ρ density (kg/m^3)

μ viscosity (N s/m^2)

References

- **Journals**:

[1]Beauchemin M., Jinny Rhee J., 2006, "Investigation of Cylindrical Pin-Fin Heat Sink Thermal Performance at High Altitude." In Proceedings of ASME International Mechanical Engineering Congress and Exposition, Chicago, Illinois, USA.

[2]Issa J. S, and Ortega A., 2006, "Experimental Measurements of the Flow and Heat Transfer of a Square Jet Impinging on an Array of Square Pin Fins" Journal of Electronic Packaging, ASME.

[3]Dogruoz M.B., Ortega A and. Westphal R.V., 2006," A Model for Flow Bypass and Tip Leakage in Pin Fin Heat Sinks". Journal of Electronic Packaging. Vol. 128 / 53.

[4]M.B. Dogruoz, M. Urdaneta, A. Ortega, Experiments and Modeling of Heat Transfer of in-line Square Pin Fin Heat Links with Top by-Pass Floor, ASME Heat Transfer Div., Publ.-HTD 372(7), (2002), 195-206.

[5]Waqar A. Khan, J. Richard Culham, Optimization of Pin-Fin Heat Sinks Using Entropy Generation Minimization, IEEE, Transactions on Components and Packaging Technologies, vol. 28, No. 2, June 2005 247.

[6]R.W. Knight, J.S. Goodling, D.J. Hall, Optimal Thermal Design of Forced Convection Heat Sinks-Analytical, ASME J. Electron. Packaging 113 (1991) 313-321.

[7]Ledezma G., Morega A. M. and Bejan A. *"Optimal Spacing Between Pin-Fins With Impinging Flow"*, Journal of Heat Transfer, AUGUST 1996, Vol, 118 / 571, Copyright © 1996 by ASME**.**

[8]A. Zhukauskas, Heat Transfer from Tubes in Cross Flow, in: J.P. Harnett, T.F. Irvine Jr. (Eds.), Advances in Heat Transfer, 8, Academic Press, San Diego, 1972.

[9]E.B. Ratts, A.G. Raut, Entropy generation minimization of fully developed internal flow with constant heat flux, ASME J. Heat Transfer 126 (2004) 656–659.

[10] H.F. Oztop, Effective parameters on second law analysis for semicircular ductsin laminar flow and constant wall heat flux, Int. Commun. Heat Mass Transfer 32 (2005) 266–274.

[11] D.H. Richardson, D.P. Sekulic, A. Campo, Low Reynolds number flow inside straight micro channels with irregular cross-sections, Heat Mass Transfer 36 (2000) 187–193

[12] A. Bejan, General criterion for rating heat exchanger performance, Int. J. Heat Mass Transfer 21 (1978) 655–658.

[13] W. A. Khan, J. R. Culham and M. M. Yovanovich. Optimal Design of Tube Banks in Crossflow Using Entropy Generation Minimization Method. Journal of Thermophysics and Heat Transfer. Vol. 21, No. 2, April–June 2007.

[14] J. Richard Culham, and Yuri S. Muzychka. Optimization of Plate Fin Heat Sinks Using Entropy Generation Minimization. IEEE Transactions on Conponenets and Packaging Technologies, Vol. 24, No. 2, June 2001.

[15] Behnia M., Copeland D. and Soodphakdee D., 1998, "A Comparison of Heat Sink Geometries for Laminar Forced Convection: Numerical Simulation of Periodically Developed Flow." Thermal and Thermomechanical Phenomena in Electronic Systems, ITHERM apos; 98. The Sixth Intersociety Conference on Volume, Issue, P:310 315.

[16] T. Bello-Ochende, A. Bejan, *Constructal multi-scale cylinders with natural convection*, International Journal of Heat and Mass Transfer 48 (2005) 4300–4306.

[17] Bejan, A., "Entropy Generation Minimization", The Method of Thermodynamics Optimization of Finite-Size Systems and Finite-Time Processes.

- **Books and other monographs:**

[18] A. Bejan, Entropy Generation Minimization, CRC Press, Boca Raton, 1996.

[19] A. Bejan, Entropy Generation through Heat and Fluid Flow, Wiley, New York, 1982.

[20] A. Bejan, Heat Transfer, Wiley, New York, 1993.

[21] I.E. Idelchik, Flow Resistance: A. Design Guide for Engineers, Hemisphere, New York, 1989.

[22] Kakaç S., Shah R.K., Aung W., 1987, "Handbook of Single-Phase Convective Heta Transfer, John Wiley & Sons."

- **Conference Papers:**

[23] Zuñiga-Cerroblanco J. L., Hernandez-Guerrero A., Rubio-Arana J. C., Kowalski G., "Geometrical effects in optimal performance of energy dissipation of pin fin heat sinks", Proceedings of the 2009 ASME, International Mechanical Engineering Congress & Exposition, IMECE 2009, November 13-19, 2009, Lake Buena Vista, Florida, USA

Performance analysis of a district heating system

Andrej Ljubenko[a], Alojz Poredoš[b], Tatiana Morosuk[c], and George Tsatsaronis[d]

[a] *University of Ljubljana, Faculty of Mechanical Engineering, Ljubljana, Slovenia, Andrej.Ljubenko@fs.uni-lj.si, **CA***
[b] *University of Ljubljana, Faculty of Mechanical Engineering, Ljubljana, Slovenia, Alojz.Poredos@fs.uni-lj.si*
[c] *Technische Universität Berlin, Institute for Energy Engineering, Berlin, Germany, Morozyuk@iet.tu-berlin.de*
[d] *Technische Universität Berlin, Institute for Energy Engineering, Berlin, Germany, Tsatsaronis@iet.tu-berlin.de*

Abstract:

Lowering the exergy content of heat, required for heating purposes, can decrease the primary energy consumption. District heating systems are often an important link between facilities that generate heat with low exergy content and consumers. Exergetic efficiency of heat distribution is an important factor in heat supply to consumers and can serve as an optimization factor for a more sustainable distribution network operation.

This paper presents a methodology for an exergy-based distribution network analysis of a district heating system. Criterions for performance evaluations are defined. They can be used to evaluate heat supply to different points in the network, or individual system components. A case study is performed on an existing district heating system. Energetic and exergetic efficiencies of supply lines are analysed. Exergy destructions and exergy losses are studied. Exergy destruction rates present less than 1 % of exergy loss rates in their separate consideration. Distribution network operation is discovered as not optimal. An optimal ratio between exergy destruction and exergy losses at fictitious mass flow rate increment is searched. It is found to be in the interval 0.34 to 0.37.

Keywords:

District Heating System, Distribution Network, Energy, Exergy, Efficiency.

1. Introduction

Exergy of a stream at combustion temperatures of fuels is very close to its energy values. Exergy of a stream at temperatures of heated buildings or domestic hot water is typically in the magnitude of 10 % of its energy value. Direct usage of boilers to supply heat demands therefore results in large thermodynamic irreversibilities. These irreversibilities are in exergy analysis, in dependency of the selected boundaries, known as exergy destruction and exergy losses. With high values of exergy destruction and losses a potential to cause a change is therefore wasted in a great extent. This represents a waste of primary energy resources [1].

Several applications of an exergy analysis to space heating in buildings have been made in the literature. In ref. [2] it is stated that energy and exergy analyses must be conducted from the primary energy transformation until the building envelope including the envelope. It is shown that energy concept alone is not adequate in gaining a full understanding of all the important aspects of energy utilization processes. The building sector has a high potential for reducing the exergy content of energy demand and supply [3]. For this purpose the exergy concept is relevant for design of buildings, heating, ventilation and air-conditioning systems [4, 5]. The low exergy approach is the main object to constitute a sustainable built environment [6]. Low exergy (or LowEx) building systems are studied by many researches and are seen as a possibility for design of high performance buildings [3, 6, 7]. Future exergoeconomic analysis is recommended by some authors when using exergy analysis method for analysis of buildings [2, 8].

A prerequisite for low exergy building systems is low exergy content heat generation with low irreversibilities. This can be achieved by different means. In ref. [9] researchers studied different cases of heat pump systems and compared them to conventional condensation boiler heating system. Approach for energetic analyses, which they used, considers energy chain from primary energy source via building to the sink. The most efficient case in their analyses is a ground source heat pump system which has 25 % less primary energy and exergy demand compared to condensation boiler system. In ref. [10] geothermal resources are proposed to be classified as low, medium and high quality resources based on their exergy value. High quality resources can be used for direct generation of electricity. Lower quality resources are more appropriate for heating applications and their utilization results in lower irreversibilities. Solar radiation represents a high quality energy flow. Researchers in ref. [11] proposed a different boundary when analyzing solar energy systems from an exergy perspective, on a physical viewpoint. They stated that thermal energy output of a solar collector field at its corresponding temperature level or electricity output of a PV system should be regarded as primary energy sources. In this way inconsistencies from a physical point of view, when regarding direct (e.g. solar thermal, photovoltaic systems or windows in the building envelope) and indirect (e.g. heat pumps, wind turbines, etc.) use of solar radiation, are avoided. For efficiency determination of different direct-solar conversion systems they propose an additional parameter, namely the total required area to be installed. Accordingly an exergy output of a more efficient direct-solar system at a given area would be higher. This consideration adds solar energy to the heat generation systems with low irreversibility.

Cogeneration is a technique for generating multiple energy products simultaneously in a manner of utilizing high exergy flows for processes where they are needed and remaining low exergy flows where they can be used. Thus an important reduction in irreversibility is achieved in comparison with separate generation of these products. It is often related to generation of electricity and heat with low exergy content for heating and industrial purposes. In this field the implementation of exergy-based analyses for efficiency improvement has been made by researches in the highest extent. In recently published papers they are often in a form of thermoeconomic or exergoeconomic analyses, where costs of irreversibilities are also acquired [1, 12]. In ref. [13] a review is made on the exergoeconomic analysis and optimization of combined heat and power production.

Low exergy heat generation is often possible only at a scale which largely exceeds the local heat demands. In some cases the higher scale of heat generation facilities results in better energy and exergy efficiency. In these cases a district heating system can be used to connect consumers to the heat generation facility. There the distribution network of a district heating system becomes an important part in the heat supply chain. On the distribution network heat losses occur and pumping power is needed to transport the fluid, which carries the heat. Accordingly an exergy-based performance analysis of the distribution network in a district heating system is needed to discover the design and operating parameters that can decrease irreversibilities in supplying heat for thermal demands in buildings. Several authors have used exergy concept to analyze district heating systems. Many of them carried out an exergy analysis [14-18]. One study [19] proposed a model which can serve as a basis for differential tariff determination. There different price factors were calculated for heat supplied to different consumers based on the exergy losses of heat distribution. In ref. [20] authors presented strategies for improving the performance of waste-heat based district heating system. They concluded that an exergy analysis has a clear added value for characterizing and improving the performance of district heating systems. Some studies are also dealing with exergoeconomic analyses of district heating systems. In ref. [21] various studies conducted on geothermal district heating systems from the energetic, exergetic and exergoeconomic point of view are reviewed.

Distribution network of a district heating system is often spread out in a large area. Hot-water pipelines constricting it have a variety of diameters and isolative properties. The heat transported through an individual point in the network varies in a great extent. Distance from the heat generation facilities to the individual consumers is also dependent on the point in the distribution

network. Accordingly an energy or exergy efficiency of the whole distribution network in a district heating system is not informative of the efficiency of heat supply to individual consumer connected to the network. In order to improve the performance of a district heating system from an exergetic and economic point of view, several points in the network have to be considered. As a first step for future exergoeconomic analysis an approach for exergy analysis has to be defined which considers different points in the network and separates supply and return lines. We have not found such a model in the literature. Boundaries and definitions are in this paper in accordance with a widely used and accepted theory in exergoeconomics in [1, 22].

2. Methodology

2.1. Network description

Distribution network in a district heating system is described in this paper using graph theory. In graph theory a graph is a set of points and lines connecting some pairs of the points [23]. Points are called vertices and lines are called edges. Edges represent connections between points and can be attributed with individual properties. A connected graph which has no cycles is called a tree. Distribution network in a district heating system without internal loops can be represented by a directed tree. Fig. 1 shows a simple directed tree. In a distribution network this tree structure can be seen as follows. The first vertex in the network is *v1*. This is the first point which is subject of analyses. The parameters of the supply and return water here determine the thermal inputs into the distribution network. The edge *e1* is a pipeline connecting point *v2* to *v1*. From *v2* two edges (pipelines) are connecting vertices *v3* and *v4*. Vertices *v2* to *v4* can represent branching and/or consumers or just an arbitrary point in the network.

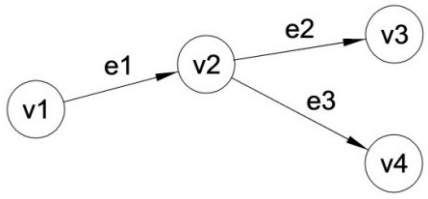

Fig. 1. Tree structure.

If two vertices are connected by an edge, they are called adjacent, otherwise they are called disjoint. To input graphs into computer adjacency matrix can be used. If vertex x_i is adjacent to vertex x_j, than (i,j) entry in the adjacency matrix is 1, else it is 0. Adjacency matrix for the directed graph in Fig. 1, denoted by M is:

$$M = \begin{pmatrix} 0 & 1 & 0 & 0 \\ 0 & 0 & 1 & 1 \\ 0 & 0 & 0 & 0 \\ 0 & 0 & 0 & 0 \end{pmatrix}. \qquad (1)$$

With the adjacency matrix connections between points in the distribution network of a district heating system are defined. To perform an energy and exergy analysis properties of edges and governing equations also need to be defined.

2.2. Energetic analysis

A *positive effect* (PE) of a district heating system is the heat supplied to the consumers. The *resource expended* (RE) to do it is the heat supplied to the distribution network and the energy required for the pumps. We can write an energy balance equation for the whole system:

$$\dot{E}_{RE} = \dot{E}_{PE} + \left(\dot{Q}_L - \dot{W}\right). \qquad (2)$$

The difference between heat losses and pumping power in Eq. (2) is the amount of heat which has to be supplied to the network in addition to the energy of the PE.

In analogy the PE and the RE can be defined for each individual pipeline (edge in Fig. 1). Resources expended can also be considered as resources needed to supply heat to an individual point in the network. E.g., heat which has to be supplied to the vertex *v1* and energy for the pumps to supply the product to *v3*. Accordingly, the definition of RE and PE depends on a chosen control volume. A flow is entering and exiting every pipe with different parameters, as seen in Fig. 2. Heat is being lost to the pipe surroundings with its temperature.

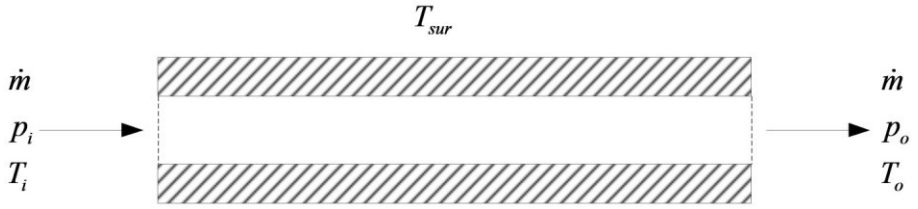

Fig. 2. Pipe (edge) in a distribution network.

To calculate the energetic efficiency the PE is divided by the RE:

$$\eta = \frac{E_{PE}}{E_{RE}}. \qquad (3)$$

2.2.1. Heat losses

When we have water flow inside a pipe and its temperature is higher than the one of the surroundings, heat losses cannot be avoided. To calculate heat losses Eq. (4) is used. There are many different methods how to determine the overall heat transfer coefficient of an insulated district heating pipeline and other network components. It can be calculated or experimentally acquired.

$$\dot{Q}_L = U \cdot A \cdot \Delta T_{lm} \qquad (4)$$

Log mean temperature difference in Eq. (4) is calculated as:

$$\Delta T_{lm} = \frac{(T_i - T_{sur}) - (T_o - T_{sur})}{\ln\left(\frac{T_i - T_{sur}}{T_o - T_{sur}}\right)}. \qquad (5)$$

2.2.2. Pumping power

Pumping power needed to supply the hot water to the consumers can be calculated using Eq. (6).

$$\dot{W}_{pump} = \frac{\dot{m} \cdot (p_i - p_o)}{\rho_w} \qquad (6)$$

Pressure drop (p_i - p_o) is dependent on the wall shear stress between the water and pipe surface. The overall pressure drop for the pipe system consists of the pressure loss due to viscous effects in the straight pipes termed the major loss and the pressure drop in various other components, termed the minor loss [24].

In a distribution network of a district heating system static pressure is maintained at a constant value. As mentioned before, pumping power is needed to cover the pressure losses. Pressure losses are a drop in static pressure over a length of pipe. Pumps are located at several locations in the network and increase the static pressure. However, the location of the pumps has little influence when analyzing the energy or exergy performance of a distribution network with given flow

parameters. Consequently we can, for a more generally applicable analysis, model the network as it would have a large number of pumps. So large, that their effect to the static pressure could be neglected. This way the whole network (or a part of the network which is physically separated) is considered to have the same static pressure on the length of the pipelines.

2.2.3. Water flow temperature

Heat losses cause a temperature change of the water on the length of the pipeline. It is a logarithmic function on the length of the pipeline [25]. For short pipelines, with low temperature change (<0.5 °C), it can be considered as linear. Temperature change is not dependent only on the amount of heat losses, because of the friction caused by the fluid flow. Energy needed to transport the water must also be accounted for. Especially in modern district heating systems with low supply and return temperatures and high pressure gradients in pipelines, as in [26]. Because of the temperature change the heat available to consumers is being decreased on the length of the pipeline. It is decreased by:

$$\dot{Q}_d = \dot{m} \cdot \left(h_i - h_o \right). \qquad (7)$$

We can also calculate it by knowing the heat losses and energy needed for the fluid flow:

$$\dot{Q}_d = \dot{Q}_L - \dot{W} . \qquad (8)$$

In a network as displayed in Fig. 1, the data used to analyze the system can include T_i at *v1* or a desired T_o at any other vertices. All of the unknown T_i and T_o for each of the edges can be calculated individually by using Eq. (8). The solution is acquired numerically.

2.3. Exergetic analysis

2.3.1. Reference state

In a reference state the system is in equilibrium with the environment. District heating system is a closed system. Consumers and heat generation facilities are physically separated from the distribution network. In an interaction with the environment only thermal energy is being transferred. Thus a restricted reference state exists, where temperature of the water is equal to the temperature of the environment. The pressure and chemical potential remain unchanged. The available exergy in a water flow in the distribution network is therefore defined by calculating the thermal part of the physical exergy [27]:

$$\dot{e}_j^T = \left[\left(\dot{h}_j - \dot{h}_{j,T_0} \right) - T_0 \left(\dot{s}_j - \dot{s}_{j,T_0} \right) \right]_{p=const} . \qquad (9)$$

2.3.2. Boundaries on supply and return lines

Exergy balance for a component as well as for the overall system can be written in form *exergy fuel/exergy product* [1]. Exergy of product is the desired result, expressed in exergy terms, achieved by the system (component). Exergy fuel are the exergetic resources expended to generate the exergy of the product.

Exergy fuel for a pipeline in Fig. 3 is defined as:

$$\dot{E}_F = \dot{E}_{\mathrm{sup,v1}} - \dot{E}_{\mathrm{ret,v1}} + \dot{W}_{\mathrm{sup}} + \dot{W}_{\mathrm{ret}} . \qquad (10)$$

Exergy of the product is:

$$\dot{E}_P = \dot{E}_{\mathrm{sup,v2}} - \dot{E}_{\mathrm{ret,v2}} . \qquad (11)$$

Selection of boundaries is an important topic to discuss for correct conduction of the exergy analysis. The choice of boundary determines whether the effect of heat transfer is charged as exergy destruction or an exergy loss. In Fig. 3 a supply line (edge) is defined as our control volume. Heat

losses of the supply pipeline are denoted as $Q_{L,sup}$ and heat losses of the return $Q_{L,ret}$. Two different boundaries are defined:

- Boundaries I include just the supply and return pipeline, and
- Boundary II is located outside the system where the temperature corresponds to the ambient temperature, taken here as the temperature of the exergy reference environment T_0.

With boundary II, heat transfer occurs at the temperature T_0, and thus there is no associated exergy transfer: $\dot{E}_Q = 0$. Accordingly, the value of the exergy loss is: $\dot{E}_L = 0$. The exergy destruction term accounts for exergy destruction owing to friction and the irreversibility of heat transfer to the environment:

$$\dot{E}_D = \dot{E}_F - \dot{E}_P . \qquad (12)$$

With Boundaries I the rate of exergy loss $\dot{E}_L$ equals the rate of exergy transfer associated with heat transfer, and is thus given by:

$$\dot{E}_Q = \int_{v1}^{v2} \left(1 - \frac{T_0}{T_w}\right) \cdot \dot{q}_L \cdot dl . \qquad (13)$$

With different boundary considerations the exergies of fuel and product remain the same. The relation between exergy destruction and exergy loss with different boundaries is described by the following term:

$$\dot{E}_D^{\text{Boundary II}} = \dot{E}_D^{\text{Boundary I}} + \dot{E}_L^{\text{Boundary I}} . \qquad (14)$$

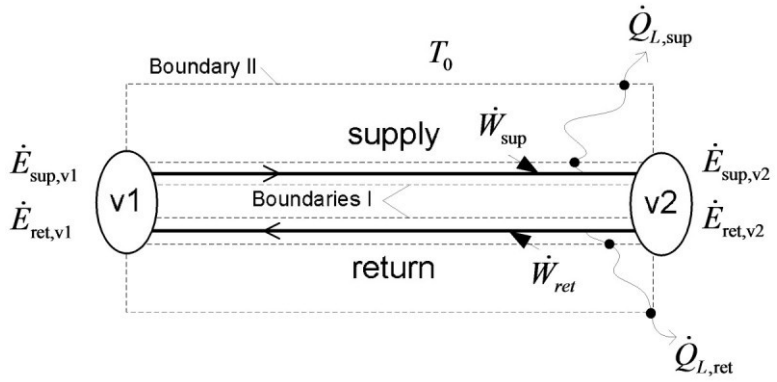

Fig. 3. Supply and return pipeline with heat transfer to the surroundings.

For a heat exchanger fuel is defined as the exergy difference between input and output of the hot stream [1]. The product is defined as the exergy difference between input and output of the cold stream.

With the definition of product and fuel in Eq. (10) and (11) the exergetic efficiency for the selected control volume can be calculated:

$$\varepsilon = \frac{\dot{E}_P}{\dot{E}_F} . \qquad (15)$$

Exergy destruction ratio is a ratio of the exergy destruction rate within a system (subsystem) to the exergy rate of the fuel for the overall system:

$$y_D = \frac{\dot{E}_D}{\dot{E}_F} . \qquad (16)$$

2.4. Consideration of return pipelines

Supply pipelines distribute water from one vertex to others in a tree structure. Direction of water flow in return pipelines is opposite. Let us consider that consumers at *v3* and *v4* in Fig. 1 are returning water with the same temperature. When the edges *e2* and *e3* are not identical, the temperature of booth return flows is not the same in *v2*. Mixing will take place. Similar occurs when the consumers are returning water with different temperatures. This affects the exergy fuel and exergy product through heat losses of the return pipeline and return water temperature in *v1*. Accordingly the return temperature of one consumer affects the efficiency of supplying heat to the other. In a district heating system there can be consumers with higher and lower return temperatures. Supplying heat to consumers with higher return temperatures reduces the distribution network efficiency and supplying heat to consumers with low return temperatures increases it. Accordingly it would be appropriate to separate the efficiencies of heat supply to different consumers as much as possible. We can achieve this by individually considering the return of each consumer. To do it first the return in *v4* (Fig. 1) defines the temperature in *v2* and *v1*. For the return in vertices *v3* and *v2* the calculations are then repeated. Mass flow rates on edges are in all calculations on the same value as in the supply pipelines. With this consideration we can calculate different efficiencies for consumers with different return temperatures. On the other hand the difference to actual conditions is small, because of much lower heat losses of return than supply pipeline. Therefore this consideration is used for the analyses in this paper.

3. Case study

3.1. District heating of Šaleška valley

In Slovenia 9 % of total heat demand in residential, services and other sectors is supplied by district heating. In Šaleška valley, which is positioned in the northern part of the country, Slovenia's second largest district heating system is in operation. The heat is produced by a coal-fired cogeneration plant and distributed through a branched distribution network. The electrical power of the cogeneration plant is 779 MW. The maximal heating power supplied to the distribution network is 192 MW. Cooling towers are used for the heat, which has to be transferred to the surroundings in the electricity production process and is not supplied to the distribution network. A part of the distribution network of the district heating system is analyzed in this paper. It covers approximately 25 % of the total distribution network. The analyzed part is presented as a tree structure in Fig. 4. The considered vertices and edges are marked there. To this part of the network heat is supplied through vertex *v1*. Following vertices were introduced where needed: change in diameter of the pipe, water mass flow rate, insulation properties of the pipeline or branching of the network.

Several physical parameters can be defined for edges because they represent pipelines. The ones needed for our analyses are: pipeline diameter, length, isolative properties (overall heat transfer coefficient), mass-flow rate of water and pressure in pipes. The temperature of the surroundings around each of the pipes has to be defined because heat is being transferred to it. Stationary conditions on a winter day were considered in our case study. The parameters used were acquired while determining energy efficiency of the distribution network [28]. They are summarized in Table 1. Pressure in supply pipelines is 16 bars and in return pipelines 15 bars. Temperature of the environment is 0.2 °C. Each edge in Fig. 4 represents supply and return pipeline. The same parameters from Table 1 are considered for booth. Internal pipe area was considered for heat transfer, when determining overall heat transfer coefficients.

Temperature of the supply water in vertex *v1* is defined as 126.5 °C. Temperature of the return for each of the vertices is 75 °C. An exergy analysis of heat exchangers is relatively simple on a level needed for distribution network. In addition the main goal of the case study in this paper is to present the tree structure exergy analysis with different boundaries and fuel – product selections. Consequently a part of the distribution network in Šaleška valley was selected which does not contain any heat exchangers.

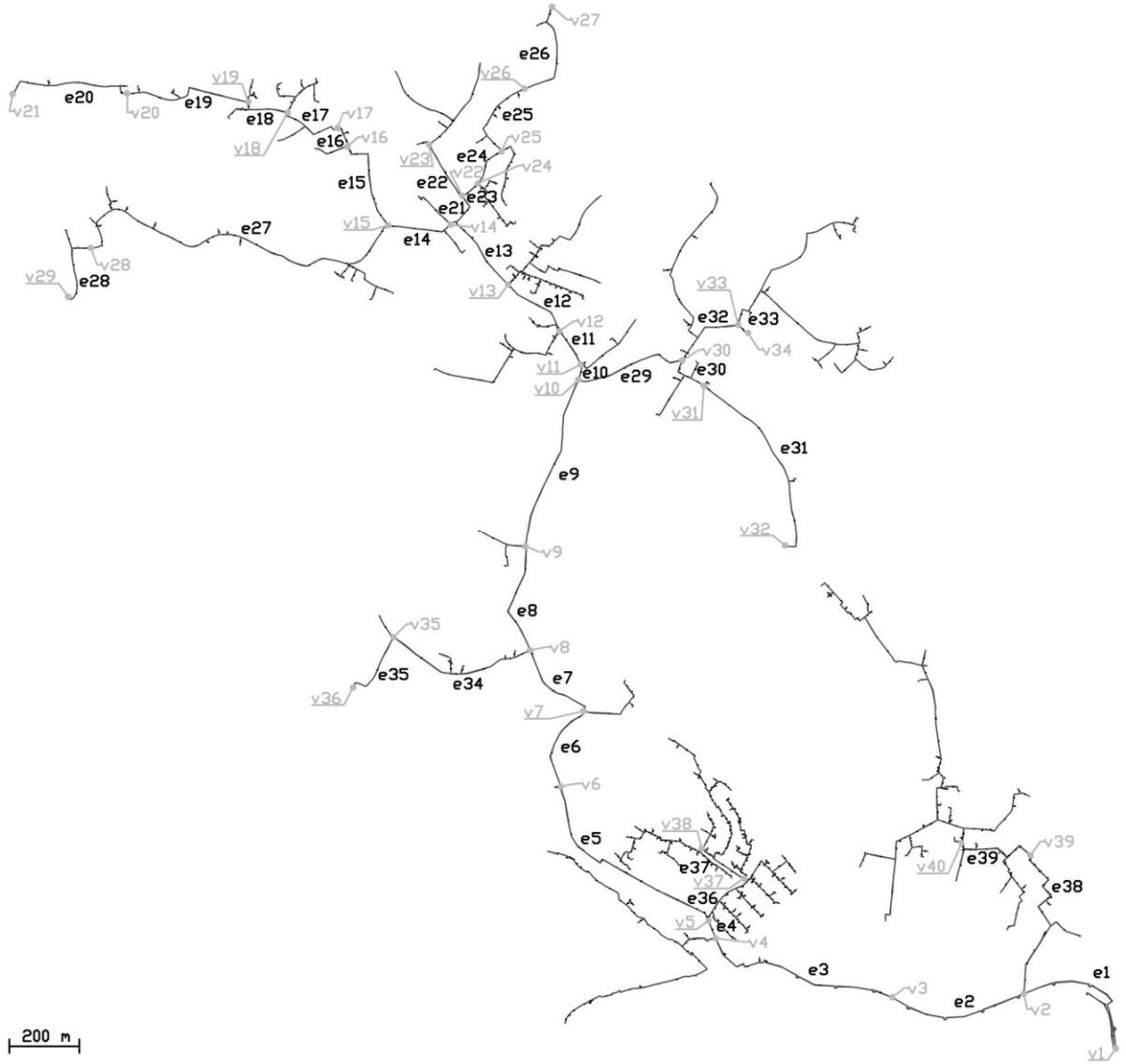

Fig. 4. Tree structure of considered distribution network in Šaleška valley.

Table 1. Physical parameters of edges in distribution network in Šaleška valley (stationary conditions on a winter day)

Edge	d, mm	l, m	U, W/m^2K	$\dot{m}$, kg/s	T_{sur}, °C	Edge	d, mm	l, m	U, W/m^2K	$\dot{m}$, kg/s	T_{sur}, °C	Edge	d, mm	l, m	U, W/m^2K	$\dot{m}$, kg/s	T_{sur}, °C
e1	350	455	0.64	39.3	0.2	e14	150	168	1.02	6.4	8.2	e27	65	1068	1.53	1.2	8.2
e2	350	445	0.64	39.3	0.2	e15	125	292	1.12	4.4	8.2	e28	40	220	1.94	0.5	8.2
e3	250	626	0.78	20.1	0.2	e16	125	72	1.12	4.4	8.2	e29	80	323	1.38	1.9	8.2
e4	250	55	0.78	17.7	0.2	e17	80	184	1.38	1.8	8.2	e30	60	120	1.59	1.0	8.2
e5	200	630	0.88	11.3	8.2	e18	76	134	1.42	1.6	8.2	e31	48	600	1.77	0.7	8.2
e6	200	259	0.88	11.3	8.2	e19	60	377	1.59	1.0	8.2	e32	76	211	1.42	1.6	8.2
e7	200	253	0.88	11.3	8.2	e20	42	368	1.89	0.5	8.2	e33	42	37	1.89	0.5	8.2
e8	200	321	0.88	11.3	8.2	e21	150	96	1.02	6.4	8.2	e34	60	438	1.59	1.0	8.2
e9	200	510	0.88	11.3	8.2	e22	114	181	1.17	3.7	8.2	e35	32	212	2.18	0.3	8.2
e10	150	46	1.02	6.4	8.2	e23	125	58	1.12	4.4	8.2	e36	250	191	0.78	17.7	8.2
e11	150	115	1.02	6.4	8.2	e24	65	122	1.53	1.2	8.2	e37	80	159	1.38	1.8	8.2
e12	150	216	1.02	6.4	8.2	e25	60	255	1.59	1.0	8.2	e38	100	515	1.24	2.8	8.2
e13	150	267	1.02	6.4	8.2	e26	42	309	1.89	0.5	8.2	e39	80	243	1.38	1.8	8.2

3.2. Results and discussion

In Table 2 results of the performance analysis on a part of the distribution network in Šaleška valley are presented. Representative vertices from Fig. 4 are selected. Table 2 is divided into two sections: Stationary conditions on a winter day and optimal mass flow. Fuel is defined for each vertex individually as exergy supplied to *v1* and pumping energy needed to transport hot water to this vertex. Product is the quantity of exergy at each vertex.

Analysis of the stationary conditions on a winter day is based on the data described in chapter 3.1. A temperature of water which reaches vertices varies in a significant extent. The biggest temperature change, among the analyzed vertices, occurs in heat supply to *v29*. The supply water there is 15.4 °C cooler than in *v1*. There are substantial variations in temperatures supplied to different points. PE and RE are calculated for heat supplied to individual points. E.g. to supply 1 kg/s of water from *v1* to *v2*, 217.9 kW of energy are needed. The heat available to consumers from 1 kg/s of water (product) in *v2* is 216.2 kW. Energetic efficiency of supplying heat to *v2* is thus 0.99. The vortex with the lowest energetic efficiency is *v29*. To supply 1 kg/s of water to it, 254.7 kW of energy are needed. The available heat is 151.8 kW and the energetic efficiency is 0.60. Exergy fuels and exergy products are calculated for individual point in the network. Exergetic efficiencies are also calculated. The benefits of exergy analyses can be seen in separation of exergy destruction and exergy losses in accordance with defined boundary I in chapter 2.2.2. Values of exergy destructions are very low, almost negligible, in comparison to exergy losses. This suggests that measures which would increase exergy destruction and decrease exergy losses could improve the exergy efficiency of heat supply. Exergy destruction in accordance with boundary II and exergy destruction ratio is also calculated (the results are in Table 2).

As discussed above the results of exergy analysis has shown that the operation of the network on the winter day may be far from optimal. The selection of optimal operating parameters for a distribution network is a complex process with possible regulations of supply and return temperatures with combination of water mass-flow rates. Parameter limitations are in the design of a distribution network, consumer equipment and heat generation facilities. Performance of heat generation facilities in dependence of output parameters also plays a key role. Thus optimal parameters are not general and differ in different district heating systems. Heat demands of consumers and the environment is changing during a year or a day. These also affect the optimal parameters. The aim of optimization in this paper is not to select optimal operating parameters, but to present a usage of exergetic analysis in an optimization process.

The ratio between exergy destruction and exergy losses in a distribution network can be increased by increasing the mass flow rate of the water and thus increasing the amount of heat distributed through the network. Optimal mass flow was searched for the distribution network in Fig. 4. Calculation is not based on any real possibilities for increased heat demands of consumers in the system. The purpose is to show the ratio between exergy destruction and exergy losses at the highest exergetic efficiency. Optimal mass flow was searched in series, first for heat supply from *v1* to *v2*, then from *v2* to *v3* and so on until *v40*. In this procedure mass-flow rate is iteratively increased until the exergetic efficiency is increasing. Because exergetic efficiency is a concave function, the maximum is discovered. Doing this all other parameters from chapter 3.1 are left unchanged. The highest calculated exergetic efficiencies for considered points are at the ratio of exergy destruction and exergy loss 0.34 to 0.37. To achieve it mass flow rates from Table 1 were increased on average for around 300 %. Maximal occurring velocities of water in pipes is 2 m/s. The optimal ratio ($\dot{E}_D/\dot{E}_L$) is higher for vertices with lower energetic and exergetic efficiencies. This results show the over dimensioned characteristics of the heat supply lines on the considered winter day and not the technical and physical options for improvement.

Table 2. Energy and exergy analyses results

Vertex	Stationary conditions on a winter day											Optimal mass flow		
	T_w, °C	$\dot{e}_{RE}$, kW/kg	$\dot{e}_{PE}$, kW/kg	η	$\dot{e}_F$, kW/kg	$\dot{e}_P$, kW/kg	ε	$\dot{e}_D^{\text{Boundary II}}$, kW/kg	$\dot{e}_D^{\text{Boundaries I}}$, kW/kg	$\dot{e}_L^{\text{Boundaries I}}$, kW/kg	$y_D^{\text{Boundary II}}$	η	ε	$\frac{\dot{e}_D^{\text{Boundaries I}}}{\dot{e}_L^{\text{Boundaries I}}}$
v2	126.3	217.9	216.2	0.99	58.3	58	0.99	0.33	0.00	0.33	0.01	1.00	1.00	0.34
v5	125.4	220.1	212.6	0.97	58.8	57	0.96	1.48	0.01	1.47	0.03	0.99	0.99	0.34
v8	123.9	223.8	206.1	0.92	59.6	55	0.92	3.52	0.02	3.50	0.06	0.98	0.97	0.34
v10	122.8	226.4	201.5	0.89	60.2	53	0.88	4.97	0.02	4.95	0.08	0.97	0.96	0.34
v14	121.5	229.6	195.9	0.85	60.9	52	0.85	6.69	0.03	6.66	0.11	0.96	0.95	0.35
v15	121.1	230.4	194.5	0.84	61.0	51	0.84	7.13	0.03	7.10	0.12	0.96	0.94	0.35
v21	111.2	254.5	152.2	0.60	65.9	39	0.58	19.8	0.07	19.73	0.30	0.89	0.85	0.36
v25	120.3	232.4	190.9	0.82	61.5	50	0.81	8.23	0.03	8.20	0.13	0.95	0.94	0.35
v27	114.4	246.7	165.8	0.67	64.4	43	0.66	15.8	0.05	15.74	0.25	0.91	0.88	0.36
v28	114.0	247.6	164.2	0.66	64.6	42	0.65	16.27	0.06	16.22	0.25	0.91	0.88	0.36
v29	111.1	254.7	151.8	0.60	66.0	38	0.58	19.9	0.07	19.83	0.30	0.89	0.85	0.37
v30	121.2	230.2	194.7	0.85	61.0	51	0.84	7.05	0.03	7.03	0.12	0.96	0.94	0.35
v32	114.0	247.7	164.2	0.66	64.6	42	0.65	16.29	0.06	16.23	0.25	0.91	0.88	0.36
v34	119.6	234.2	187.8	0.80	61.8	49	0.79	9.18	0.04	9.14	0.15	0.95	0.93	0.35
v35	120.4	232.1	191.5	0.83	61.4	50	0.82	8.04	0.03	8.01	0.13	0.95	0.94	0.35
v36	116.3	242.1	173.9	0.72	63.4	45	0.71	13.37	0.04	13.33	0.21	0.92	0.90	0.36
v37	125.2	220.5	211.8	0.96	58.9	57	0.96	1.72	0.01	1.72	0.03	0.99	0.98	0.34
v38	124.4	222.5	208.3	0.94	59.4	55	0.93	2.84	0.01	2.83	0.05	0.98	0.98	0.34
v39	124.3	222.6	207.9	0.93	59.4	55	0.93	2.94	0.01	2.93	0.05	0.98	0.98	0.34
v40	123.0	225.7	202.6	0.90	60.0	54	0.89	4.62	0.02	4.60	0.08	0.97	0.97	0.34

4. Conclusions

In this paper a methodology for an exergy-based analysis of a distribution network in a district heating system is presented. The main differences to other published papers on this subject are in the definition of energetic and exergetic efficiency for a single point in the distribution network and in exergy balance in the form fuel/product. Possibilities for efficiency improvements on different parts of the network can be discovered this way.

Separation of the exergy destruction and exergy losses points out guidelines for exergetic efficiency improvements. The choice of boundaries is important when doing the separation. Low exergy destruction in comparison to exergy losses suggests that with the increase of pumping power on behalf of decrease in heat losses will improve the exergetic efficiency of the distribution network.

Analysis of a part of the distribution network in Šaleška valley has shown large differences in energetic and exergetic efficiencies of heat supply to different points in the network. This part of the distribution network does not include heat exchangers.

Calculated exergy destruction rates on a considered winter day are less than 1 % of the exergy losses in the separate consideration. Accordingly we can conclude that the network is operating below its optimal capacity. The conditions that occur on this day present one of the highest annual heat demands by consumers in the district heating of Šaleška valley. Thus the distribution network, operating with this temperatures and mass-flow rates, is over dimensioned.

The increase of energy transported by individual pipelines, through the mass flow rate increase to optimal values, is searched. Maximal exergetic efficiencies determine the optimal mass flow rates. In separate consideration exergy destruction rates are in the interval 34 to 37 % of exergy loss rates at maximal exergetic efficiencies. They are higher for vertices with lower energetic and exergetic efficiencies.

Nomenclature

A surface, m^2

d internal diameter, m

$\dot{E}$ exergy rate, W

$\dot{e}$ specific exergy rate, W/kg

$\dot{E}$ energy rate, W

$\dot{e}$ specific energy rate, W/kg

$\dot{h}$ specific enthalpy rate, W/kg

h specific enthalpy, J/kg

l length, m

M adjacency matrix

$\dot{m}$ mass flow rate, kg/s

p pressure, bar

$\dot{Q}$ heat rate, W

$\dot{q}$ specific heat rate, W/m

$\dot{s}$ specific entropy rate, W/(kgK)

T temperature

U overall heat transfer coefficient, $W/(m^2K)$

$\dot{W}$ pumping power, W

y exergy destruction ratio

Greek symbols

ε exergetic efficiency

η energetic efficiency

ρ density, kg/m3

Subscripts and superscripts

0 thermodynamic environment (reference state)

D destruction

d decreased

F fuel

i in

L loss

o out

P product

PE positive effect

RE resource expended

ret return

sup supply

sur surroundings

w water

References

[1] Bejan A, Tsatsaronis G, Moran MJ. Thermal design and optimization: Wiley-Interscience, 1996.

[2] Yildiz A, Güngör A. Energy and exergy analyses of space heating in buildings. Applied Energy. 2009;86(10):1939-48.

[3] Hepbasli A. Low exergy (LowEx) heating and cooling systems for sustainable buildings and societies. Renewable and Sustainable Energy Reviews. 2012;16(1):73-104.

[4] Sakulpipatsin P, Itard LCM, van der Kooi HJ, Boelman EC, Luscuere PG. An exergy application for analysis of buildings and HVAC systems. Energy and Buildings. 2010;42(1):90-9.

[5] Balta MT, Dincer I, Hepbasli A. Performance and sustainability assessment of energy options for building HVAC applications. Energy and Buildings. 2010;42(8):1320-8.

[6] Tolga Balta M, Kalinci Y, Hepbasli A. Evaluating a low exergy heating system from the power plant through the heat pump to the building envelope. Energy and Buildings. 2008;40(10):1799-804.

[7] Meggers F, Ritter V, Goffin P, Baetschmann M, Leibundgut H. Low exergy building systems implementation. Energy. 2011.

[8] Yucer CT, Hepbasli A. Thermodynamic analysis of a building using exergy analysis method. Energy and Buildings. 2011;43(2):536-42.

[9] Lohani S, Schmidt D. Comparison of energy and exergy analysis of fossil plant, ground and air source heat pump building heating system. Renewable Energy. 2010;35(6):1275-82.

[10] Lee KC. Classification of geothermal resources by exergy. Geothermics. 2001;30(4):431-42.

[11] Torío H, Schmidt D. Framework for analysis of solar energy systems in the built environment from an exergy perspective. Renewable Energy. 2010;35(12):2689-97.

[12] Tsatsaronis G, Moran MJ. Exergy-aided cost minimization. Energy Conversion and Management. 1997;38(15):1535-42.

[13] Abusoglu A, Kanoglu M. Exergoeconomic analysis and optimization of combined heat and power production: A review. Renewable and Sustainable Energy Reviews. 2009;13(9):2295-308.
[14] Çomaklı K, Yüksel B, Çomaklı Ö. Evaluation of energy and exergy losses in district heating network. Applied thermal engineering. 2004;24(7):1009-17.
[15] Ozgener L, Hepbasli A, Dincer I. Energy and exergy analysis of geothermal district heating systems: an application. Building and environment. 2005;40(10):1309-22.
[16] Ozgener L, Hepbasli A, Dincer I. Exergy analysis of two geothermal district heating systems for building applications. Energy Conversion and Management. 2007;48(4):1185-92.
[17] Keçebaş A, Kayfeci M, Gedik E. Performance investigation of the Afyon geothermal district heating system for building applications: Exergy analysis. Applied thermal engineering. 2011;31(6-7):1229-37.
[18] Yüksel B, Aslan A, Akyol T. Investigation of seasonal variations in the energy and exergy performance of the Gonen geothermal district heating system. Applied thermal engineering. 2012;36(0):39-50.
[19] Poredoš A, Kitanovski A. Exergy loss as a basis for the price of thermal energy. Energy Conversion and Management. 2002;43(16):2163-73.
[20] Torío H, Schmidt D. Development of system concepts for improving the performance of a waste heat district heating network with exergy analysis. Energy and Buildings. 2010;42(10):1601-9.
[21] Hepbasli A. A review on energetic, exergetic and exergoeconomic aspects of geothermal district heating systems (GDHSs). Energy Conversion and Management. 2010;51(10):2041-61.
[22] George T. Definitions and nomenclature in exergy analysis and exergoeconomics. Energy. 2007;32(4):249-53.
[23] Voloshin VI. Introduction to Graph Theory: Nova Science Publishers, 2009.
[24] Munson BR, Young DF, Okiishi TH. Fundamentals of fluid mechanics: Wiley York, NY,, USA, 1998.
[25] Incropera FP, Bergman TL, Lavine AS, DeWitt DP. Fundamentals of heat and mass transfer: Wiley, 2011.
[26] Dalla Rosa A, Christensen JE. Low-energy district heating in energy-efficient building areas. Energy. 2011;36(12):6890-9.
[27] Morosuk T, Tsatsaronis G. Graphical models for splitting physical exergy. Shaping our future energy systems, S Kjelstrup, JE Hustad, T Gundersen, A Rosjorde and G Tsatsaronis, eds. 2005;1:377-84.
[28] Ljubenko A, Poredoš A. Energy efficiency of a district heating system and its possible improvements. 24th International Conference on Efficiency, Cost, Optimization, Simulation and Environmental Impact of Energy Systems. Novi Sad, Serbia2011. p. 2935-44.

Systems analysis of exergy losses in an integrated Oxy-Fuel Combustion power plant

Andrzej Ziębik[a], Paweł Gładysz[b]

[a] *Silesian University of Technology, Institute of Thermal Technology,*
Konarskiego 22, 44-100, Gliwice, Poland
e-mail: andrzej.ziebik@polsl.pl **CA**
[b] *Silesian University of Technology, Institute of Thermal Technology,*
Konarskiego 22, 44-100, Gliwice, Poland
e-mail: pawel.gladysz@polsl.pl

Abstract:

The paper presents a method of the systems analysis of exergy losses, as well as an example of application in the case of an integrated OFC power plant. The considered system consists of five interconnected modules, among which there also exist feedback relations. For the purpose of modelling an integrated OFC power plant "input-output analysis" was applied. Five main products (corresponding to the given modules) and also five by-products, as well as three supplies delivered entirely from outside are to be distinguished. The basis of the exergy system analysis of an integrated OFC plant is its completed energy balance. The algorithm of the systems analysis of exergy losses is also based on "input-output analysis". The way of expressing the exergy balance adapted to the convention of "input-output analysis" has been applied. The input exergy (exergy of substance, work, increase of exergy of the source of heat) supplied to given module is the sum of the respective items in the column of the input-output table corresponding to the given module. The output exergy is the exergy of the main product concerning the given module and the exergy of by-products. The difference between the input and the output exergy is the whole exergy loss (internal and external exergy losses) of the considered module. The systems analysis of exergy losses based on "input-output analysis" allows to asses the influence of decreasing the exergy losses in one module on changes of exergy losses in other modules of the integrated OFC plant. The paper presents the system analysis of exergy losses of an exemplary integrated OFC power plant operating using tonnage oxygen with a purity of 95%. Among the analysed five modules the highest relative exergy losses are to be observed in ASU (about 80%). The boiler island is charged with relative exergy losses exceeding 50%. The relative exergy losses in a CPU module amount to about 50%. The steam cycle is characterised by relative exergy losses below 20% and the cooling water system about 5%. The net exergy efficiency of electricity production amounts to 30% in comparison with the energy efficiency of about 34%.

Keywords:

Oxy-fuel combustion, systems analysis, exergy losses, mathematical modelling, input-output analysis.

1. Introduction

A power plant operating in compliance with the Oxy-Fuel Combustion (OFC) technology consists of such modules as boiler island, steam cycle, cooling water system, air separation unit (ASU) and CO_2 purification and compression unit (CPU). Between these modules there exist interbranch connections, some part of which are of feedback character. The interbranch connections become still more complex if process integration is being realised [1]. In an OFC power plant it is possible to integrate both on the thermal side (utilizing the heat from interstage cooling of air and CO_2 compressors) [2] and on the electrical side in the case of pressurized OFC power plant (expansion turbine of nitrogen).

Thus, an integrated OFC power plant is a large energy system, the design of which and also its exploitation ought to be optimized by means of system methods [3,4]. Also the analysis of exergy losses in an integrated OFC power plant requires a system approach [5]. Szargut and Sama state: "consider the influence of the proposed changes in energy management on the exergy losses in

other links of the system" [6]. This means that in a system consisting of many elements, not only the improvement of one of them should be considered, because the decrease of exergy losses in one element may involve in other elements of the system both positive and negative effects. This requirement can be satisfied if the exergy losses are assessed by means of system analysis.

System approach requires that all the balance equations resulting both from the I and II Law of Thermodynamics are considered jointly. In the analysis of large energy systems commonly Leontief's "input-output analysis" is applied.

The model of energy balance of an integrated OFC power plant is composed of linear equations of the "input-output" type, concerning main products (e.g. live steam, electricity, oxygen) and by-products (e.g. process steam, nitrogen), as well as energy carriers and materials from outside. The coefficients in "input-output" matrices result from the energy characteristics of the energy equipment determined in process models which are usually non-linear. The non-linear characteristics are then approximated by means of the segments of straight lines.

The linear mathematical model of the energy balance is the basis of the system model of exergy losses in an integrated OFC power plant. The input part of the exergy balance are vectors of the consumption of the exergy of the main and by-products, as well as the exergy of the supply from outside (mainly fuels and materials). The output part comprises the vectors of the exergy of main and by-production, as well as exergy losses which are the result of system analysis. The system of direct and indirect interconnections is expressed by the inverse matrix in relation to the "input-output" matrix of the energy balance of main products. From the viewpoint of energy analysis this inverse matrix is the matrix of indices of cumulative energy consumption. This inverse matrix applied in the model of the exergy balance permits to determine the system exergy losses. The suggested system model of exergy analysis will be applied in an integrated OFC power plant.

2. Why system analysis of exergy losses?

The utilization of the limited resources of non-renewable energy ought to comply with the principle of sustainable development. This means rational utilization and warranting ecological security, keeping in mind future generations. Rationalization of the use of energy consists, first of all, in the improvement of the thermodynamic imperfection of phenomena occurring in energy processes. This involves consequently an increased protection of the environment.

Thermodynamic imperfections involve a devaluation of energy (exergy losses). Although, in actual processes this cannot be avoided, they ought to be restricted as far as technically possible and economically justified. Exergy losses may be permitted only in the case when they are indispensable for the reduction of investment outlays. If exergy losses are economically not justified, we have to do with an error from the point of view of the Second Law of Thermodynamics [6]. The elimination of these errors favours the financial effects of the project ensuring most often savings both in exploitation and in the investment outlays. Every design which does not contain any Second Law errors may be considered to be an optimal design [6].

The observance of the twenty practical rules set up by Szargut an Sama [7], referring to previous publications by Sama, Quian and Gaggioli [6], leads to a reduction of the Second Law errors and to a rationalized utilization of energy. Two of these practical rules of thermodynamic imperfections stress the interdependence of thermal processes in the respective elements of energy systems. Any change occurring in one element of the system affects the operation of the other elements. The influence of the suggested energy changes on the losses of exergy should always be taken into account not only in the given considered process but also in the other elements of the system. It should also be kept in mind that by decreasing one exergy loss, no other parallelly occurring exergy loss should increase [7]. In other words, the reduction of the degree of thermodynamic imperfection of energy processes should be assessed by means of systems analysis.

System analysis was formally discovered again just before the Second World War by the biologist Ludwig von Bertalanffy [8]. The first attempt to define the system problem is contained in Aristotle's philosophy [9]. Before the Second World War (1936) also Leontief's "input-output analysis" was published, which belongs to the methods of system analysis [10]. This method was applied in the algorithm of systems analysis of exergy losses in an integrated OFC power plant. Wassily Leontief has written about "input-output analysis" [10], "In practical terms, the economic system to which it is applied may be as large as a nation or even the entire world economy, or even a single enterprise" (such a single enterprise is the integrated OFC power plant - the author's comment). "The advantage of the input-output analysis is that it permits the disentanglement and accurate measurement of the indirect effects" stressed the author of "Input-output economics" [10].

In energy systems many interconnections are feedbacks. The paper [11] provides such an example in a CHP plant with an extraction-condensing turbine. This can be presented more simply by choosing the connections between the boiler and the turbogenerator in the power plant (Fig.1).

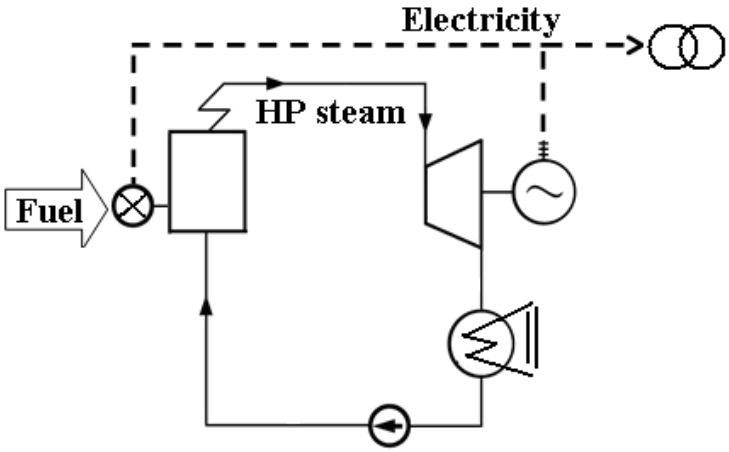

	HP steam	Electric energy
HP steam	0	1
Electric energy	1	1

Fig. 1. Diagram of the power plant cycle and binary input-output submatrix

If, for example, the production of electric energy is increased, the production of high-pressure steam grows. But this increased production of high-pressure steam leads to a further increase of electric energy production due to its consumption in the boiler (first of all in the coal pulverizer). And again, the demand for high-pressure steam will grow, causing a further increase of the demand for electric energy in the boiler house and so on, and so on due to the existence of the feedback relation between the turbogenerator and the boiler. Therefore, the system approach basing on input-output analysis is necessary. The method of exergy analysis based on a set of the balance equations of exergy of the respective modules of a complex system permits to determine the system exergy losses resulting from the interconnections of energy processes.

In mathematical models of energy systems their specific properties must be taken into account, not like as in Leontief's classical model [10]. In some energy branches the main production ought to be divided into the basic and peak parts. The basic part of heat production in CHP plants, for instance, is produced in the cogeneration part (heating steam from the outlet of the back-pressure turbine or from the bleed of the extraction-condensing turbine), whereas the peak part of heat production is produced in the hot water boiler [12]. Besides the main production there exists also a by-production which can supplement the main production or be a product not belonging to the set of main products [12]. The amount of by-production in the given energy branch depends on its main production.

3. Linear mathematical model of the energy balance of an integrated OFC power plant

A power plant operating in the oxy-fuel combustion technology consists of such modules as boiler island, steam cycle, cooling water system, air separation unit (ASU) and CO_2 processing unit (CPU) (Fig. 2). Between these modules there exist interbranch connections, which may be described by an "input-output matrix". The connections of the oxy-fuel combustion plant with the environment are described by input and output vectors.

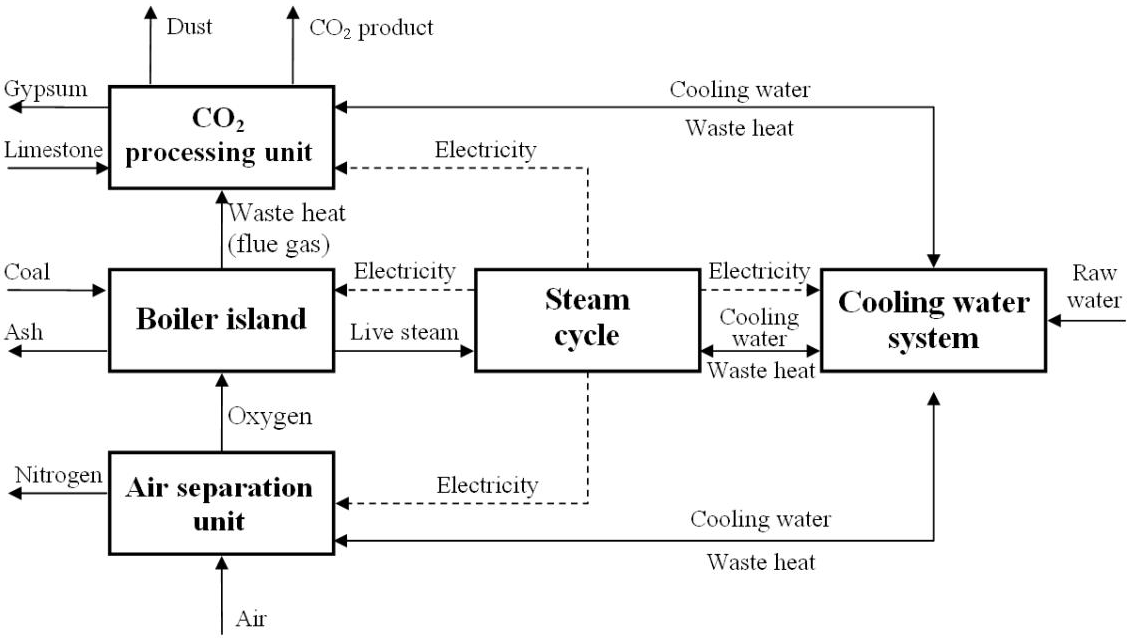

Fig. 2. Simplified block scheme of the Oxy-Fuel Combustion power plant.

The integrated OFC power unit is a system consisting of energy branches (technological modules) connected with each other by interbranch (intermodular) relations. Table 1 presents the system of interbranch connections concerning an oxy-fuel combustion power plant [1].The energy carriers have been divided into two groups:

I – energy carriers being the main products or by-products of the respective modules of the integrated oxy-fuel combustion power plants,

II – energy carriers supplied from outside (mainly fuels).

Table 1. Input-output table of an integrated OFC power unit

Group of energy carriers	Input part			Output part	
	Main production	By-production	Supply from outside	Interbranch flows	Final production
First group - I	$\underset{i}{\Lambda}: G_i$	0	0	$= \sum_{j=1}^{n} a_{ij}^{G} G_j$	$+ K_i$
	0	$\underset{l}{\Lambda}: \sum_{j=1}^{n} f_{lj} G_j$	0	$= \sum_{j=1}^{n} a_{lj}^{F} G_j$	$+ K_{Fl}$
Second group - II	0	0	$\underset{p}{\Lambda}: D_p$	$= \sum_{j=1}^{n} a_{pj}^{D} G_j$	0

where:

a_{ij}^{G} - coefficient of the direct consumption of energy carriers,

a_{lj}^{F} - coefficient of the consumption of by-products,

a_{pj}^{D} - coefficient of the of the direct consumption of external supplies of energy carriers,

f_{lj} - coefficient of by-production of energy carriers.

In matrix notation the equation from Table 1 can be presented as:

$$\mathbf{G} + \mathbf{A_G G} = \mathbf{K_G}, \quad (1)$$

$$\mathbf{F_G G} = \mathbf{A_F G} + \mathbf{K_F}, \quad (2)$$

$$\mathbf{D_D} = \mathbf{A_D G}. \quad (3)$$

Hence, from the set of balance equations concerning the main production of energy carriers we get [1]:

$$\mathbf{G} = \left(\mathbf{I} - \mathbf{A_G}\right)^{-1} \mathbf{K_G}, \quad (4)$$

where:

G - vector of the main production of energy carriers,

$\mathbf{A_G}$ - matrix of the coefficients of the direct consumption of energy carriers,

$\mathbf{K_G}$ - vector of the final production of main products,

$\mathbf{F_G}$ - matrix of the coefficients of by-production not supplementing the main production,

$\mathbf{A_F}$ - matrix of the coefficient of the consumption of by-production,

$\mathbf{K_F}$ - vector of the final production of by-products,

$\mathbf{D_D}$ - vector of external supplies of energy carriers,

$\mathbf{A_D}$ - matrix of the coefficients of the direct consumption of external supplies of energy carriers,

I - unit matrix.

Equations (1), (2) and (3) describe the mathematical simulation model of an integrated OFC power plant. The input data are in this case $\mathbf{A_G}$, $\mathbf{K_G}$, **F**, $\mathbf{A_F}$, $\mathbf{A_D}$, $\mathbf{D_D}$. The coefficients of the inverse matrix $\mathbf{(I - A_G)^{-1}}$ comprise direct and indirect connections existing in the integrated power plant. These coefficients may be called coefficients of cumulative energy consumption for the considered integrated power plant.

The main products corresponding to technological modules are live steam, electricity, cooling water, oxygen and the CO_2 product. Besides the mentioned main production, the following by-productions can be distinguished: heat from the interstage cooling system of ASU and CPU, nitrogen from ASU, bottom ash in the boiler island, dust and gypsum in CPU. This production depends strictly on the main production. External supplies are fuel (bituminous coal), raw water (supplied from the municipal system) and limestone for wet flue gas desulphurization.

The boiler was designed for pulverized coal as the main fuel. The parameters of live steam are: p = 28,4 MPa , t = 600 °C / 620 °C. The steam cycle is based on supercritical conditions, concerning the high- (HP), intermediate- (IP) and low-pressure (LP) part. The CO_2 processing unit (CPU) is based on the cryogenic distillation system. ASU is based on cryogenic distillation, producing 95% pure oxygen. The heat of compression from air and CO_2 compressors is directly transferred to the cooling-water system.

Table 2. Example of an input-output table (input part)

No	Energy carrier or material	Main product	By-production					External supply
			1	2	3	4	5	
1	Live steam [MJ]	G_1						
2	Electricity [MJ]	G_2						
3	Cooling water [Mg]	G_3						
4	Oxygen [Mg]	G_4						
5	CO_2 product [Mg]	G_5						
6	Waste heat [MJ]		$f_{61}G_1$	$f_{62}G_2$		$f_{64}G_4$	$f_{65}G_5$	
7	Nitrogen [Mg]					$f_{74}G_4$		
8	Bottom ash [Mg]		$f_{81}G_1$					
9	Dust [Mg]						$f_{95}G_5$	
10	Gypsum [Mg]						$f_{105}G_5$	
11	Bituminous coal [MJ]							D_{11}
12	Raw water [Mg]							D_{12}
13	Limestone [Mg]							D_{13}

Table 3. Example of an input-output table (output part)

No	Energy carrier or material	Interbranch flows					Final product
		1	2	3	4	5	
1	Live steam [MJ]		$a_{12}^{G}G_2$				
2	Electricity [MJ]	$a_{21}^{G}G_1$	$a_{22}^{G}G_2$	$a_{23}^{G}G_3$	$a_{24}^{G}G_4$	$a_{25}^{G}G_5$	K_2
3	Cooling water [Mg]		$a_{32}^{G}G_2$		$a_{34}^{G}G_4$	$a_{35}^{G}G_5$	
4	Oxygen [Mg]	$a_{41}^{G}G_1$				$a_{45}^{G}G_5$	
5	CO_2 product [Mg]						K_5
6	Waste heat [MJ]			$a_{63}^{F}G_3$		$a_{65}^{F}G_5$	
7	Nitrogen [Mg]						K_7
8	Bottom ash [Mg]						K_8
9	Dust [Mg]						K_9
10	Gypsum [Mg]						K_{10}
11	Bituminous coal [MJ]	$a_{111}^{D}G_1$					
12	Raw water [Mg]			$a_{123}^{D}G_3$			
13	Limestone [Mg]					$a_{135}^{D}G_5$	

In Tables 2 and 3 the input part and the output part have been presented concerning the “input-output table” of the considered integrated OFC power plant (Fig 1.). Three groups of energy carriers are to be distinguished. The fundamental part of the “input-output table” comprises energy carriers

or materials (e.g. CO_2 product) corresponding to the main products of basic technological modules of the integrated OFC power plant. As far as the first group of energy carriers and materials is concerned, the row 5 is characteristic for the CO_2 product, which is a typical output element with only one-sided connections with other energy carriers. That means that it is the consumer of energy carriers, but it is not consumed in other branches.

As we can see in Table 3, in the main production interbranch flows occur in the case of the first four energy carriers. From among these electricity is consumed in all the five modules (branches). For instance $a^{G}_{21}G_1$ denotes the consumption of electricity for the production of live steam and $a^{G}_{12}G_2$ the consumption of live steam for the production of electricity. Both these elements, situated on either side of the main diagonal, indicate a connection of feedback character. The main production is accompanied by six by-products, e.g. $f_{62}G_2$, $f_{64}G_4$ and $f_{65}G_5$ denote waste heat removed from the steam cycle, ASU and CPU, respectively. These streams are passed to the cooling water system - $a^{F}_{63}G_3$. Flue gases ($f_{61}G_1$) are also treated as waste heat, although they are passed to the CPU unit - $a^{F}_{65}G_5$. The analyzed system is fed by three external supplies, e.g. the supply of coal feeding the boiler - $a^{\mathrm{G}}_{11\,1}G_1$. The supply of raw water (after its conditioning) supplementing the water cooling system - $a^{\mathrm{D}}_{12\,3}G_3$. Limestone for wet flue gas desulphurization is delivered to CPU - $a^{D}_{13\,5}G_5$.

4. Calculation algorithms of system exergy losses

The calculation algorithms of system exergy losses are based on "input-output analysis". Figure 3 illustrates the diagram of the exergy balance concerning the module (energy branch) "*j*" formulated in compliance with Table 1 (Section 3).

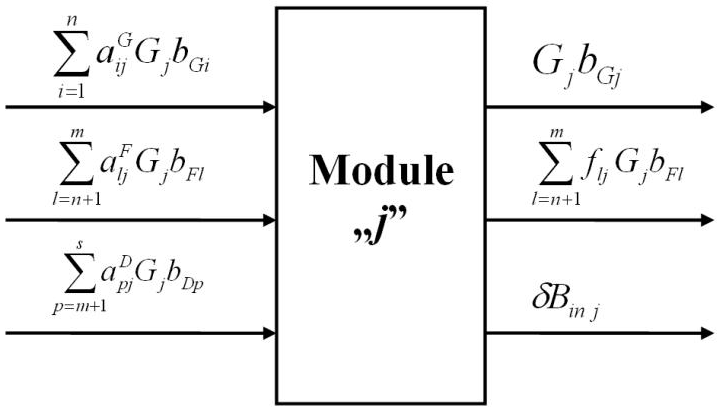

Fig. 3. Calculation diagram of exergy losses.

The set of exergy balances concerning all the modules takes the following form:

$$\bigwedge_{j=1}^{n} : \sum_{i=1}^{n} a^{G}_{ij} G_j b_{Gi} + \sum_{l=n+1}^{m} a^{F}_{lj} G_j b_{Fl} + \sum_{p=m+1}^{s} a^{D}_{pj} G_j b_{Dp} = G_j b_{Gj} + \sum_{l=n+1}^{m} f_{lj} G_j b_{Fl} + \delta B_{in\,j} \quad (5)$$

where:

b_{Gi}, b_{Gj} - specific exergy of the "*i*-th" or the "*j*-th" main product,

b_{Fl} - specific exergy of the "*l*-th" by-product,

b_{Dp} - specific exergy of the "*p*-th" external supply of energy carrier,

δB_j - exergy losses concerning the "*j*-th".

In matrix notation of the set of equations (5) looks as follows:

$$\left(\mathbf{A_G G^d}\right)^{\mathbf{T}}\mathbf{b_G} + \left(\mathbf{A_F G^d}\right)^{\mathbf{T}}\mathbf{b_F} + \left(\mathbf{A_D G^d}\right)^{\mathbf{T}}\mathbf{b_D} = \mathbf{G^d b_G} + \left(\mathbf{F G^d}\right)^{\mathbf{T}}\mathbf{b_F} + \boldsymbol{\delta}\mathbf{B} \qquad (6)$$

Hence:

$$\boldsymbol{\delta}\mathbf{B} = \left(\left(\mathbf{A_G G^d}\right)^{\mathbf{T}} - \mathbf{G^d}\right)\mathbf{b_G} + \left(\left(\mathbf{A_F G^d}\right)^{\mathbf{T}} - \left(\mathbf{F G^d}\right)^{\mathbf{T}}\right)\mathbf{b_F} + \left(\mathbf{A_D G^d}\right)^{\mathbf{T}}\mathbf{b_D} \qquad (7)$$

where:

$\mathbf{b_G}$ - column-vector of specific exergy of main products,

$\mathbf{b_F}$ - column-vector of specific exergy of by-products,

$\mathbf{b_D}$ - column-vector of specific exergy of external supplies of energy carriers.

The column vector **G** is calculated from (4) basing on the inverse input-output matrix. The indices **T** and **d** denote, respectively, the transposed matrix and the formation of the diagonal matrix from the column vector.

The notation of the balance equations of exergy, by means of which the exergy losses can be determined, are of a generalized character. The work and increase or decrease of the exergy of heat sources are not distinguished as separate terms in the balance equations. The symbols:

$a_{ij}^{G} G_j b_{Gi}$,

$a_{lj}^{F} G_j b_{Fl}$,

$a_{pj}^{D} G_j b_{Dp}$

denote the input exergy delivered to the module "*j*" (exergy of the substance, decrease of the exergy of the heat source, driving work).

Similarly, the symbols:

$G_j b_{Gj}$,

$f_{lj}\, G_j b_{Fl}$

are to be understood as output exergy (exergy of the main product and by-product, the increase of the exergy of heat sources or output work).

The chemical exergy of the homogenous substance "*i*" (with a known chemical formula) is determined basing on the tables of the normal chemical exergy [13] (corrections due to small differences between the normal and ambient temperature and the deviation of concentration in the actual environment from normal concentrations have been neglected):

$$B_{chi} = a_{ij}^{D} G_j b_{chn} \qquad (8)$$

where b_{chn} denotes the specific chemical exergy of homogenous "*i*-th" substance.

In the case of gases, for which the set of reference substances is the component of the atmospheric air (e.g. tonnage oxygen) the chemical exergy is calculated according to the equation:

$$B_{chi} = a_{ij} G_j (MR) T_a \sum_i z_k \ln \frac{z_k}{z_{ka}} \qquad (9)$$

where:

(MR) - universal gas constant,

T_a - ambient temperature,

z_k, z_{ka} - molar fraction of the "*k*-th" component in the considered mixture and in atmospheric air.

As far as solid fuels are concerned, the empirical formula is used [13]:

$$B_{chi} = a_{ij}^{D} G_j \left[\left(LHV + r_n w \right) \left(1.0437 + 0.1896 \frac{h}{c} + 0.0617 \frac{o}{c} + 0.0428 \frac{n}{c} \right) + \left(b_{chns} - LHV_s \right) s + w b_{chw} + p b_{chp} \right] \quad (10)$$

where:

LHV - lower heating value of solid fuel,

r_n - specific heat of evaporation,

w - mass fracture of moisture,

c, h, o, n, s, p - mass fractions of carbon, hydrogen, oxygen, nitrogen, sulphur and ash,

b_{chns}, LHV_s - specific exergy and lower heating value of sulphur,

b_{chp} - specific exergy of ash.

The presented calculation algorithms of system exergy losses can be used to analyze the influence of process changes in the respective modules of the integrated OFC power plant on the system exergy losses.

If the elements of the matrix $\mathbf{A_F}$, $\mathbf{F}$, $\mathbf{A_D}$ are changed, changes in the system exergy losses may be expressed as follows:

$$\Delta'(\delta \mathbf{B}) = \left(\left(\left(\mathbf{A_F G}^{\mathbf{d}} \right)^{\mathbf{T}} - \left(\mathbf{F G}^{\mathbf{d}} \right)^{\mathbf{T}} \right)'' - \left(\left(\mathbf{A_F G}^{\mathbf{d}} \right)^{\mathbf{T}} - \left(\mathbf{F G}^{\mathbf{d}} \right)^{\mathbf{T}} \right)' \right) \mathbf{b_F} + \left(\left(\mathbf{A_D G}^{\mathbf{d}} \right)^{\mathbf{''T}} - \left(\mathbf{A_D G}^{\mathbf{d}} \right)^{\mathbf{'T}} \right) \mathbf{b_D} \quad (11)$$

In such a case the inverse matrix $\mathbf{(I - A_G)^{-1}}$, whose elements express both direct and indirect interconnections, remains unchanged.

In the case of a process change affecting changes in the values of the elements of the matrix $\mathbf{A_G}$ a new inverse matrix must be determined and a new vector $\mathbf{G}$ must be calculated. Then the changes of system exergy losses are expressed by the equation:

$$\begin{aligned} \Delta''(\delta \mathbf{B}) = & \left(\left(\left(\mathbf{A_G G}^{\mathbf{d}} \right)^{\mathbf{T}} - \mathbf{G}^{\mathbf{d}} \right)'' - \left(\left(\mathbf{A_G G}^{\mathbf{d}} \right)^{\mathbf{T}} - \mathbf{G}^{\mathbf{d}} \right)' \right) \mathbf{b_G} + \\ & + \left(\left(\left(\mathbf{A_F G}^{\mathbf{d}} \right)^{\mathbf{T}} - \left(\mathbf{F G}^{\mathbf{d}} \right)^{\mathbf{T}} \right)'' - \left(\left(\mathbf{A_F G}^{\mathbf{d}} \right)^{\mathbf{T}} - \left(\mathbf{F G}^{\mathbf{d}} \right)^{\mathbf{T}} \right)' \right) \mathbf{b_F} + \left(\left(\mathbf{A_D G}^{\mathbf{d}} \right)^{\mathbf{''T}} - \left(\mathbf{A_D G}^{\mathbf{d}} \right)^{\mathbf{'T}} \right) \mathbf{b_D} \end{aligned} \quad (12)$$

The apostrophes $''$ and $'$ denote the state after and before the process changes, respectively.

5. Examples of applications of the system analysis of exergy losses

The mathematical model of the integrated OFC power plant described in (1), (2), (3) allows to strike an energy balance. The set of equations described by (5) permits to assess the exergy system losses. Basing on these equations and on the data base concerning the operation of an integrated OFC power plant with a purity of oxygen amounting to 95%, the exergy losses (internal and external ones) concerning the five modules have been investigated. The net exergy efficiency of the integrated OFC unit has been calculated and compared with the net energy efficiency.

The process analyses were carried out basing on the Thermoflex program, by means of which the respective modules of the integrated OFC unit have been modeled. These researches are run within the frame of the strategic project [14]. The results presented in this paper have been achieved in the course of the first tests of applying the Thermoflex program in process investigations. This paper presents possibilities of implementing the system approach in exergy analysis basing on an integrated OFC power plant.

Table 4 presents an example of "input-output" matrices $\mathbf{A_G}$ and $\mathbf{F_G}$ expressing respectively the coefficients of unit consumption of main product, as well as coefficients of the by-production of energy carriers and materials.

Table 4. "Input-output" matrices $\mathbf{A_G}$ *and* $\mathbf{F_G}$

$$\mathbf{A_G} = \begin{bmatrix} 0 & 1.9582 & 0 & 0 & 0 \\ 0.0226 & 0.0484 & 0.1124 & 603.59 & 519.34 \\ 0 & 0.0233 & 0 & 8.4313 & 30.285 \\ 0.0001 & 0 & 0 & 0 & 0.0083 \\ 0 & 0 & 0 & 0 & 0 \end{bmatrix}$$

$$\mathbf{F_G} = \begin{bmatrix} 0.000468 & 0.0233 & 0 & 8.7051 & 30.559 \\ 0 & 0 & 0 & 3.1482 & 0 \\ 9.21 \cdot 10^{-07} & 0 & 0 & 0 & 0 \\ 0 & 0 & 0 & 0 & 0.0369 \\ 0 & 0 & 0 & 0 & 0.0287 \end{bmatrix}$$

As has already been mentioned before line 5 of the matrix $\mathbf{A_G}$ contains merely 0 elements, which proves that the CO_2-product is an output element.

An exemplary exergy balance concerning ASU takes the following form:

$$a_{24}^{G} G_4 b_2 + a_{34}^{G} G_4 b_3 = G_4 b_4 + f_{64} G_4 b_6 + f_{74} G_4 b_7 + \delta B_{in} \qquad (13)$$

hence, the sum of internal and external exergy losses is:

$$\delta B_{in} + \delta B_{ex} = a_{24}^{G} G_4 b_2 - G_4 b_4 \qquad (14)$$

or the entire relative loss in relation to driving exergy:

$$\frac{\delta B_{in} + \delta B_{ex}}{B_{drive}} = 1 - \frac{b_4}{a_{24}^{G} b_2} \qquad (15)$$

where:

$a_{24}^{G} G_4 b_2$ - electric exergy (energy) - driving exergy,

$a_{34}^{G} G_4 b_3$ - exergy of cooling water,

$G_4 b_4$ - exergy of oxygen,

$f_{64} G_4 b_6$ - exergy of water heated in interstage cooling,

$f_{74} G_4 b_7$ - exergy of nitrogen,

δB_{in} - internal exergy loss,

δB_{ex} - external exergy loss,

B_{drive} - driving exergy.

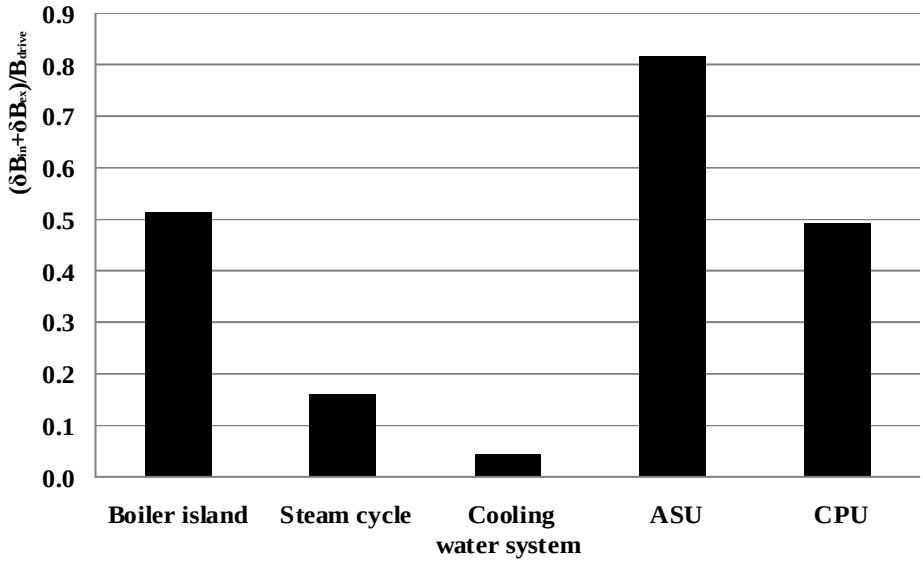

Fig. 4. Relative exergy losses in the energy subsystem

Figure 4 presents the relative exergy losses in the particular modules of the integrated OFC power plant. In each considered module the sum of internal and external exergy losses was determined basing on the results of the exergy balance prepared in compliance with the "input-output" model. Thus, both the direct and indirect interconnections between the respective modules constituting the integrated OFC power plant may be taken into account. Quantitatively these properties are expressed by the elements of the inverse matrix $\mathbf{(I - A_G)^{-1}}$ (Eq. 4). The sum of internal and external exergy losses corresponds generally to the driving exergy of the respective modules. An exception is the module "cooling water system", in which, due to the peculiarity of the cooling tower, the relative exergy losses are determined corresponding to the amount of heat given off by the cooling water [15]. The highest relative exergy losses are to be observed in ASU, where they reach almost 80%. This proves a large thermodynamic imperfection of ASU, particularly in the case when nitrogen is not utilized. The second highest relative exergy losses occur in the boiler island (above 50%), then in the CPU (about 50%) and steam cycle (below 20%). In the cooling water system the exergy losses corresponding to the heat are about 5%.

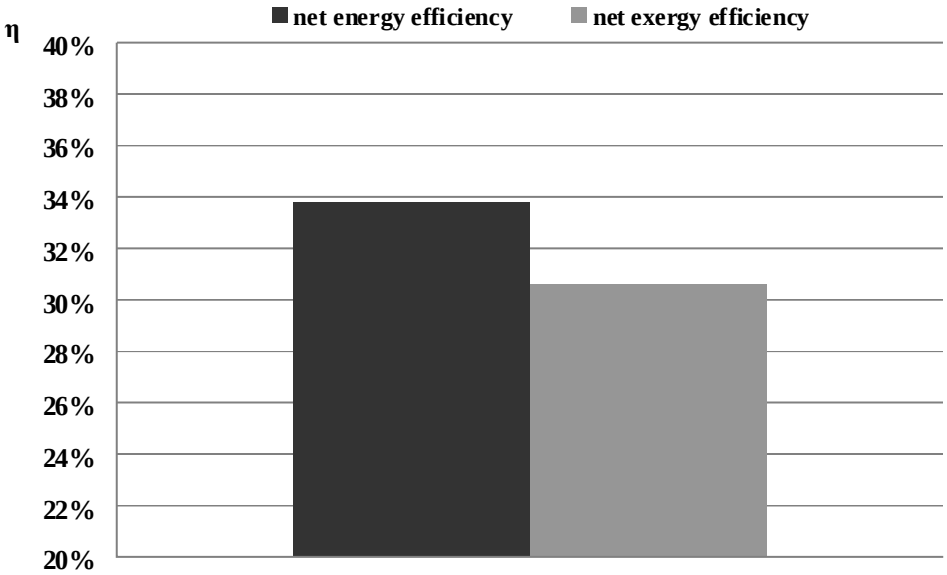

Fig. 5. The net energy and exergy efficiencies of an integrated OFC power plant

Figure 5 presents the energy and exergy efficiency of an integrated OFC power plant. The net exergy efficiency is defined as follows:

$$\eta_{B'} = \frac{K_2 b_2}{a^{D}_{11\,1} G_1 b_{11}}, \qquad (16)$$

where K_2 denotes the final production of electricity.

Paper [16] determines net exergy efficiency of an oxy-combustion system assuming also CO_2 to be a product, viz. 37.13%. For the seek of comparison also the net exergy efficiency of the analysed system was calculated taking into account CO_2 as a product. The obtained comparative result was 38.4%.

6. Conclusions

The rationalization of utilizing the energy is one of the main factors in the realisation of sustainable development. First of all, it depends on the improvement of the thermodynamic imperfections of phenomena occurring in energy processes. Thermodynamic imperfections involve exergy losses. Although in actual processes they are inevitable, they ought to be restricted as much as technically possible and economically justified.

In large-scale systems, e.g. in an integrated OFC power plant, it should be kept in mind that a decrease of exergy losses in one element of the system may involve exergy losses in other elements of the system due to existing interconnections, some part of which are of feedback character. Therefore the application of system approach is in such an analysis indispensable. A convenient tool is the “input-output analysis”.

For the considered integrated OFC power plant the investigation concerned relative exergy losses.

Systems analysis of exergy losses has proved that the highest relative exergy losses (related to driving exergy) occur in ASU, amounting to about 80%. The boiler island is charged with relative exergy losses of more than 50%. The relative exergy losses in a CPU module are about 50%. The steam cycle is also characterised by relative exergy losses below 20%, and the cooling water system by about 5%.

The net exergy efficiency of electricity production amounts to about 30% in comparison with the energy efficiency of about 34%.

Acknowledgments

The authors wish to express their gratitude to the National Centre for Research and Development for financing the researches dealt with in the paper within the frame of the strategy programme “Advanced Technologies for Energy Generation”, Research task 2 “Elaboration of oxy-fuel combustion technology concerning pulverized-coal and fluidized-bed boilers integrated with CO_2 capture” (PBS-4/RIE6/2010).

Nomenclature

Main symbols

A matrix of the coefficients of the consumption of energy carriers and materials

a_{ij} coefficient of consumption of energy carriers and materials

B exergy

b column-vector of specific exergy

b specific exergy

D vector of external supplies

D external supply

F matrix of the coefficients of the by-production

f_{ij} coefficient of by-production of energy carriers or materials

G column vector of the main production

G main product

I unit matrix

K column vector of the final production

K final product

p pressure, MPa

T temperature, K

Greek symbols

η efficiency

δ losses

Subscripts and superscripts

a ambient

D, *D* external supply

ex external

ch chemical

F, *F* by-product

G, *G* main product

in internal

Abbreviations

ASU Air Separation Unit

CPU CO_2 Processing Unit (CO_2 purification and compression unit)

OFC Oxy-Fuel Combustion

References

[1] Ziębik A., Gładysz P.: System Approach to the Energy Analysis of an Integrated Oxy-Fuel Combustion Power Plant. The 6th Dubrovnik Conference on Sustainable Development of Energy, Water and Environment Systems. 25-29 September 2011, Dubrovnik, Croatia

[2] Zheng L. (ed.): Oxy-fuel combustion for power generation and carbon dioxide (CO_2) capture. Woodhead Publishing Series in Energy: Number 17, 2011

[3] Simpson A.P., Simon A.J.: Second law comparison of oxy-fuel combustion and post-combustion carbon dioxide separation. Energy Conversion and Management 48 (2007):3034-3045

[4] Liszka M., Ziębik A.: Coal-fired oxy-fuel power unit – Process and system analysis. Energy 35 (2010):943-951

[5] Ziębik A.: Applications of second law analysis in industrial energy and technological system. Proc. of Second Law Analysis of Energy Systems: Towards the 21-st Century, Workshop School of Engineering, University of Roma 1 "La Sapienza", July 5-7, 1995:329-359

[6] Sama D. A.: A common sense 2nd law approach to heat exchanger network design. Proceedings ECOS '92, Zaragoza, 1992:329-338

[7] Szargut J., Sama D.A.: Practical rules of the reduction of Exergy losses caused by the thermodynamic imperfection of thermal processes. Proc. the Second Intern. Thermal Energy Congress, In: eds. E. Bilgren et al., Agadir, 1995:782-785

[8] Bertalanffy L.: General system theory (Polish translation). PWN, Warszawa, 1984

[9] Klir G. J. (ed.): General theory of systems (Polish translation). WNT, Warszawa, 1976

[10] Leontief W.: Input-Output Economics. Oxford University Press. New York, Oxford, 1986

[11] Ziębik A.: System analysis in thermal engineering. Archives of Thermodynamics. Vol. 177 (1996), 3-4:81-97

[12] Ziębik A.: Mathematical moddeling of energy management system in industrial plants. Ossolineum, Wrocław, 1990

[13] Szargut J.: Exergy method. Technical and ecological applications. WIT Press, 2005, Southampton

[14] Ziębik A., Liszka M. at al: Elaboration of oxy-fuel combustion technology concerning pulverised-coal and fluidized-bed boilers integrated with CO_2 capture. Strategy Project PBS-4/RIE6/2010

[15] Szargut J., Petela R.: Exergy (in Polish). WNT, Warszawa, 1965.

[16] Xiong J., Zhao H., Zheng C.: Exergy Analysis of a 600 MW_e Oxy-combustion Pulverized-Coal-Fired Power Plant. Energy & Fuels 2011, 25:3854-3864

What is the cost of losing irreversibly the mineral capital on Earth?

Alicia Valero [a] and Antonio Valero [a]

a CIRCE. Centro de Investigación de Recursos y Consumos Energéticos
Universidad de Zaragoza, Zaragoza, Spain, aliciavd@unizar.es

Abstract:

The exergy replacement cost is presented in this paper as a tool for assessing abiotic resource depletion. Each time we extract minerals from the mines, the deposits become depleted in quantity and grade. As a consequence, more energy is required for the extraction of the next ton of material.

The exergy and exergy replacement costs provide a measure for quantifying this degradation, which is systematically being ignored in conventional accounting systems. Hence, this approach allows performing an absolute Life Cycle Analysis, by including a new stage in the accounting: namely the grave to cradle stage. In this methodology, the "cradle" is the state of the mineral deposits at which they are currently found. The "grave" is assumed as being a hypothetical Earth with the absence of concentrated mineral resources and fossil fuels. This degraded planet named as "Thanatia" is the starting point for the assessment of abiotic resource depletion. The exergy measured from Thanatia gives a measure of the quality of the resource. It constitutes a universal, objective and useful tool for classifying resources according to their depletion states.

As the method provides values in energy units, the annual exergy decrease in the mineral endowment of the planet can now take into account the fossil fuel's exergy plus the nonfuel mineral bonus lost. The results obtained show that the useful energy that man saves thanks to the existence of mineral deposits accounts for about 32% of the whole energy stages. Furthermore, it is in the same order of magnitude as the yearly loss of coal, oil or natural gas.

Keywords:

Exergy, mineral capital, cost, LCA, Thanatia

1. Introduction

Conventional economics only accounts for the energy required in the extraction and refining processes of minerals. Nevertheless a fair accountability of resources should also take into account the use and the decrease of the non-fuel mineral capital endowment. The latter, and as opposed to fossil fuels, do not produce energy, but require huge amounts of energy for their extraction, beneficiation, refining and smelting processes. That energy is only lost when the obtained materials are dispersed. In such a case, more minerals need to be extracted from the Earth and this time with even more energy, as the ore grade decreases with extraction. Furthermore, the environmental and eventually the social impact will increase as well.

Hence, if no serious recycling measures are taken, the Earth will be gradually transformed by man into a depleted state with the absence of concentrated mineral resources. This is a consequence of the Second Law of Thermodynamics. In previous papers, we have described and modeled this end of the planet, which we have called "Thanatia" or the "Crepuscular Earth" [1, 2]. In a hopefully very distant future, there will be no concentrated mineral deposits from which to extract raw-materials. We will either need to obtain them from the bedrock, which is extremely costly, or we will have to recycle every single material used. If we want to avoid this situation, we have to include in the accountability an additional stage: the grave to cradle approach. The latter should

account for the gradual decrease of the concentrated mineral deposits, which will be unavailable for future generations.

It has been argued that the methods for assessing resource depletion in LCA must come from Thermodynamics and must take into account the Second Law of Thermodynamics [3]. We commonly admit that the Second Law plays a central role in the message of Ecological Sciences and Technology.

Energy and Life Cycle Analyses are techniques based on on material and energy flow analyses, which in turn are based on Thermodynamics. They do not need rigorous definitions of energy and still they are quite useful and far reaching. On the contrary, i.e., fixing in the Thermodynamic realm a concept well established in Energy and LC Analyses is a matter of precision. For many unrefined analyses we may use both the energy and embodied energy concepts as substitutes of exergy and exergy cost concepts respectively, but in fact, in no way they are synonyms. Both exergy and exergy cost require precise definitions. As is well known, LCA results are relative to the chosen system's boundary.

Nowadays, no absolute LCA values exist for a given good or service. Notwithstanding that, suppose we start our analysis from a hypothetical cradle in which all the commercial minerals and fossil fuels have been depleted, i.e., Thanatia. This crepuscular planet serves us both as a boundary limit and as a reference environment good enough for calculating the exergy and the exergy costs of any commodity at the industry gate. Theoretically speaking, this could be eventually the only way to get absolute LCA values, by converging LCA with Second Law Analysis using the crepuscular planet as a reference environment.

From now on, Thanatia may become the starting point for the assessment of abiotic resource depletion. The exergy measured from the Crepuscular Earth gives a measure of the quality of the resource and constitutes a universal, objective and useful tool for classifying resources according to their depletion states. Presented over time, exergy can give an indication of the speed at which degradation is occurring. However we must state that even considering a consequent baseline, exergy is still insufficient for realistically quantifying resource depletion and we should additionally resort to the exergy costs.

Hence, from the exergoecological point of view, we propose to introduce a new stage in the LCA's *cradle to grave* methodology, namely the *grave to cradle* approach, as depicted in Fig. 4. It is important to close the whole material's cycle, as stated by [4] in their book *Cradle to Cradle*.

2. Methodology

Chapman and Roberts [5] report that in the mining and concentrating stages the fuel is proportional to the quantity of ore processed. In the smelting and refining stages, the fuel is proportional to the quantity of metal produced. Hence, if we start mining from Thanatia, in principle only the fuel required in the mining and concentrating stages will be a_ected. Bearing in mind this fact, we will now develop the methodology required for assessing the exergy replacement costs of minerals. As explained in [6], the exergy of a mineral resource has at least 2 components (neglecting the cohesion exergy [7]): one associated to its chemical composition and one associated to its concentration.

Hence, the total exergy (b_t), representing the minimum exergy required for obtaining the resource from the reference to the initial conditions in the mineral deposit (steps R#0 → R#1) in Fig. 4, is calculated as the sum of the chemical b_{chi}[1] and concentration b_{ci} exergy components.

[1] The chemical exergy is calculated according to the well known formula proposed by Szargut [8].

$$b_{ti} = b_{chi} + b_{ci} \tag{1}$$

$$b_{ci} = -\bar{R}T^0\left[lnx_i + \frac{(1-x_i)}{x_i}ln(1-x_i)\right] \tag{2}$$

where R is the universal gas constant (8.314 kJ/kmole K), T^0 is the standard ambient temperature (298.15 K) and x is the mass concentration of the substance.

The calculation of the concentration exergy implies to know the ore grade which is the average mineral concentration in a mine x_m as well as the average concentration in the Earth's crust (in the Crepuscular Earth) x_c. The value of x in 2 is replaced by x_c or x_m to obtain their respective exergies, whilst the difference between them $\Delta b_c(x_c \rightarrow x_m)$ represents the minimum energy (exergy) required to form the mineral from the concentration in the Earth's crust to the concentration in the mineral deposits.

$$\Delta b_c(x_c \rightarrow x_m) = b_c(x = x_c) - b_c(x = x_m) \tag{3}$$

Hence, even if we use the term b_{ci} for simplification purposes, it is rather $\Delta b_c(x_c \rightarrow x_m)$ the correct notation.

On the other hand, the exergy replacement cost is defined as the total exergy required to mine and concentrate the mineral resources from the Crepuscular Earth, with the available technologies. Therefore, these are not absolute and universal values, as opposed to property exergy. The exergy costs are a function of the ore grades, extraction and separation technologies, which in turn vary with time, with the type of mineral analyzed, and with our ability to extract it, i.e. with its learning curve. The exergy costs b_t^* of the resource commonly have two contributions, its chemical cost ($k_{ch} \cdot b_{chi}$), accounting for the chemical production processes of the substance, and its concentration cost ($k_c \cdot b_{ci}$), accounting for the concentration processes.

$$b_{ti}^* = k_{ch} \cdot b_{chi} + k_c \cdot b_{ci} = b_{ch}^* + b_c^* \tag{4}$$

Variable k (dimensionless) represents the unit exergy cost of a mineral. It is defined as the relationship between the energy invested in the real obtaining process ($E_{Xm \rightarrow Xr}$) for mining and concentrating the mineral, and the minimum energy (exergy) required if the process from the ore x_m to the conditions before the smelting and refining processes take place $x_r\left(\Delta b_{Xm \rightarrow Xr}\right)$.

$$k = \frac{E(x_m \rightarrow x_r)}{\Delta b_{x_m \rightarrow x_r}} \tag{5}$$

The chemical exergy cost b_{ch}^* of the resource comes into play when the reference chosen does not contain the substance under consideration. Since the Crepuscular Earth contains in principle most of the minerals found in the crust, the chemical exergy will not appear. Therefore we will mainly focus on the concentration exergy replacement cost b_c^* and accordingly the unit concentration costs k_c.

Since the energy required for mining is a function of the ore grade of the mine and of the technology used, so is the unit exergy cost (Eq. 6). As [9] states, both variables have an opposite effect on the energy used. The lower the ore grade, the more energy is required for mining. On the contrary, technological development usually improves the efficiency of mining processes and hence, decreases the energy consumption. The latter will be discussed in more detail in the next section.

$$k = k(x, t) \tag{6}$$

The temporal function k is only definable for the past and for each particular mineral. It is therefore difficult to extrapolate it towards the future for the practical impossibility to predict changes in the scientific and technological knowledge that will eventually appear. The second problem with k is that it is not a continuous function. The technology applied can also vary with the concentration ranges of a particular deposit. And in turn, each mining technique (i.e. underground or open-pit mining), has a particular effect on the energy consumption due to different factors such as ore grade, grinding size, nature, depth and processing route. These factors have been analyzed for different commodities like copper and nickel [10], aluminium, iron and copper [11] and nickel laterites through the life cycle assessment methodology [12].

Bearing in mind these limitations and the kind of data available for mining (which is usually very scarce) we will assume that the same technology is applied for the range of concentration between the ore grade x_m in the mine and the pre-smelting and refining grade x_r , than between the dispersed state of the crepuscular crust x_c and x_m. For that purpose, we will analyze the average energy vs. ore grade trends for different minerals, calculate the corresponding unit exergy cost values, and extrapolate them to ore grades equal to those of the Crepuscular Earth.

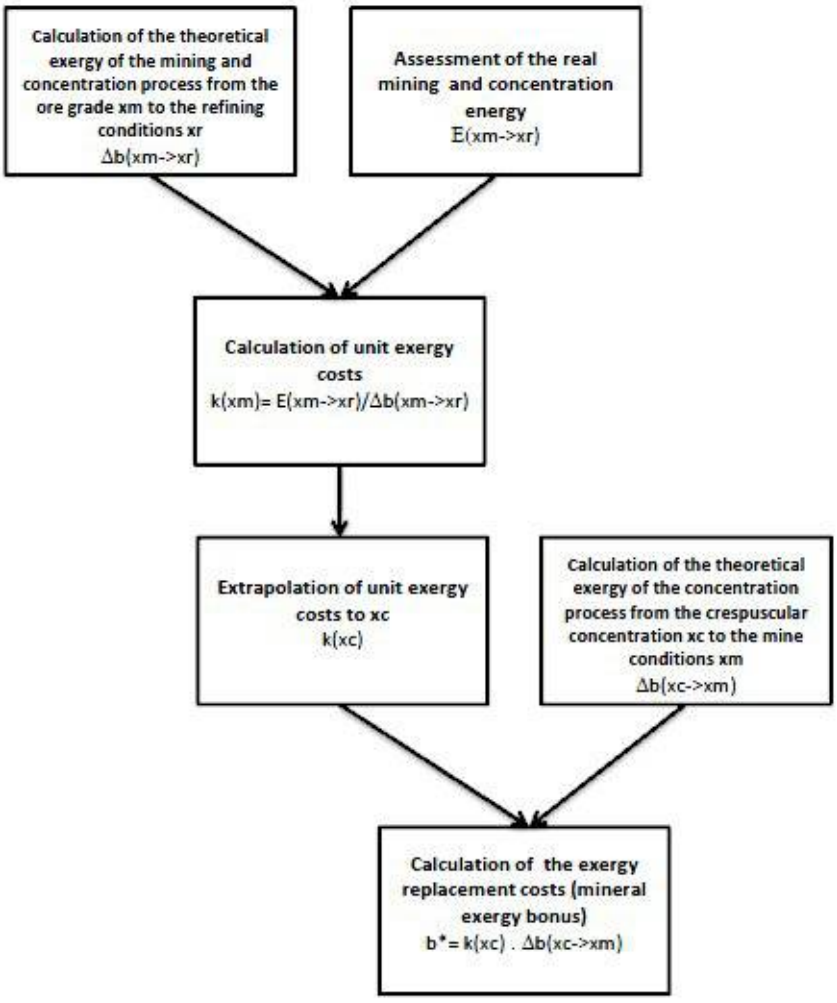

Figure 1. Calculation procedure for obtaining the mineral exergy bonus of a substance

Summarizing, the first step in obtaining the unit exergy cost for the commodities analyzed is to obtain their real energy consumptions in the mining and concentrating processes (going from x_m to x_r) as a function of the ore grade (x_m). This information can be obtained from data published in the literature. In a parallel way, the theoretical exergy of the same process is calculated as the difference in concentration exergy (Eq. 2) when $x = x_m$ and $x = x_r$. Finally, the unit exergy costs are calculated

with Eq. 5 as a function of the ore grade. The latter can be extrapolated to obtain the unit costs at the crepuscular grade x_c , which will eventually serve for calculating the exergy replacement costs of the mineral wealth on Earth with Eq. 4. The values used for the crepuscular grade are those x_c obtained in [13]. Average values for x_m have been obtained from the study of [14]. This procedure is depicted in Fig. 1.

Energy consumption values as a function of the ore grade are difficult to find. Very little studies compile these tendencies. Relevant works about this issue are those of [15, 16, 17] or [10]. Chapman and Roberts [5] proposed a general theoretical formula to describe the tendencies of the energy consumptions for metals mining. The latter estimates the energy consumption as a function of two components: 1) the energy used in mining and concentrating the ores, which is inversely proportional to the ore grade and 2) the energy used in smelting and refining.

Following [5], we could make the approximation that the energy required in the mining and concentration processes can be assumed as a constant divided by the ore grade. Note that the corresponding curve derived from this expression is similar to the curve derived from Fig. 2, i.e. as the ore grade tends to zero, the energy required to mining tends to infinity. With this very rough approximation, we could theoretically calculate the energy required in this step for each value of x_m. Obviously the results obtained through this approach are very questionable since the energy consumption as a function of the ore grade does not necessarily follow the path of x_m^{-1}, nor the technologies for all ranges of x_m must be the same. A more precise evaluation would require more research and compilation efforts of real data sets from companies in the mining industry like those performed by [15] or [10]. Empirical data of energy consumption as a function of the ore grade suggest relationships varying from $x_m^{-0.2}$ to $x_m^{-0.9}$. Hence, for the calculations, it is preferable to work with empirical data of energy vs. ore grade.

Unfortunately it is very uncommon to find data for most of the commodities and we need to resort to approximations.

3. The exergy bonus of the minerals on Earth

With the formulas described above and a comprehensive bibliographical search about mineral energy consumption, we can now make an initial assessment of the exergy bonus of the main produced minerals.

Only for five minerals gold, copper, nickel, cobalt and uranium, we could find empirical data of the energy for mining and concentration processes as a function of the ore grade $E(x_m)$ [15, 16, 18, 12]. For the rest of the commodities where no empirical data was found, it has been assumed that the general formula applying for the energy consumption as a function of the ore grade follows the exponential curve given by Eq. 7:

$$E(x_m) = A \cdot x_m^{0.5} \ [x_m, \text{metal concentration } \%] \tag{7}$$

Coefficient A is determined for each mineral since we know average ore grades x_m and the energy required for concentrating and extracting the mineral at that grade $E(x_m)$. The value of $E(x_m)$ for each commodity is obtained from different bibliographical sources [19, 20, 21, 22, 23, 24, 25, 26, 27, 28, 29, 30, 31, 32, 33, 34]It should be noted that xm values are expressed in Eq. 7 as mass percentage of the element under consideration.

The latter is a very rough approximation and it is derived observing the trends for other commodities where empirical values are available. As stated before, empirical data of energy consumption as a function of the ore grade suggest relationships varying from $x_m^{-0.2}$ to $x_m^{-0.9}$.

We have now all the ingredients required for assessing the exergy replacement costs of the minerals analyzed. This is done with the procedure shown in Fig. 1. Table 3 shows a summary of the replacement, mining & concentration and refining costs of the minerals considered. The exergy replacement costs of the considered deposit is expressed as "Bonus" in the table. The crustal, average mineral concentration of the deposits and average grade before the refining stage are represented by x_c , x_m and x_r , respectively. For those substances where no data was found concerning average refining grades, we have assumed a value of $x_r = 0.9$. The energy consumption trend as a function of the ore grade $E(x_m)$ requires that the ore grade is expressed in mass percentage of the metal considered if not otherwise specified. With Eq. 5, the unit exergy replacement costs $k(x_c)$ and $k(x_m)$ are obtained, assuming that the same energy trend applies for the whole concentration grade (from x_c to x_r). Finally, the mineral bonus is obtained with Eq. 4[2]. As stated before, the bonus represents the natural exergy of the deposit which is gradually being lost when the mine is exploited (replacement costs). To the latter, we have to add the conventional mining & concentration and refining costs presented in the table. From Table 3 we can extract some conclusions.

The empirical data found for minerals gold, copper, nickel, cobalt and uranium suggest that the energy required for mining follows an exponential growth with the ore grade. This observed fact which is in accordance with the Second Law of Thermodynamics, has allowed us to make a general approximation of the exponential energy trend with the ore grade for the rest of minerals where no empirical data was available.

As was explained previously, unit exergy costs are calculated as the ratio between the real energy required for mining and concentrating a substance and the minimum thermodynamic energy (exergy) required to achieve the same process. This means that they provide a measure for the irreversibility (or technological ignorance) of the process. The closer is the value of k to 1, the less irreversible is the process and hence, less energy is required. But k is also a function of the ore grade. The smaller the ore grade, the greater the unit exergy cost of the mineral.

For instance, gold has the highest $k(x = x_m)$ unit exergy cost values associated to the deposits of the metals analyzed in this work, attributable to its low concentration in mines and the consequent amount of energy needed to concentrate it. Besides, the actual ore grade in mines is close to that in Crepuscular Earth's crust. The opposite examples are silicon or lime which have a lower $k(x = x_m)$ value ascribed to their actual high ore grade in mines.

But the state of technology plays also an important role. This fact is highlighted with aluminium. Even if its ore grade is similar to that of chromium or manganese, the elevated value of $k(x = x_m)$ is an indicator of the significant irreversibility of the production process. The same thing happens with tantalum, which has a high unit exergy cost value compared to other minerals with similar ore grades such as tin or tungsten (wolfram). This can be attributed to the elevated energy intensity in the mining and concentration steps of tantalum.

A particular case is that of nickel and its ores. Historically, the metal was likely obtained from sulphide ores due to the major energy requirement of laterites in the refining process. Nevertheless, more Ni resources are in the form of laterites than of sulphides (around 60% for laterite ores vs. 40% for sulphide ores). But focusing only in the concentration energy, sulphide ores have larger concentration requirements than lateritic ores, as revealed by the larger unit exergy costs.

Of special interest is the value of $k(x = x_m)$. The latter multiplied by the minimum exergy required to concentrate the mineral from x_c to x_m represents the amount of energy required to mine and concentrate a substance from the bedrock (Crepuscular Earth) to the current conditions in the mineral deposits and provides a measure of the mineral exergy bonus on Earth. The value of the

[2] Here, only the concentration term is considered since Thanatia contains all considered minerals but at a lower concentration. This means that there would be no need to produce them chemically as they are already available with the same chemical structure.

crepuscular unit exergy cost of the different minerals is always greater than that of the current mineral deposits.

And the difference increases generally with the separation between the crepuscular grade and the average grade in the deposits. For instance, the crepuscular *k*-value of silicon, lime or titanium is in the same order of magnitude than the mine *k*-value, because their average ore grades are close to those of the Crepuscular Earth. The opposite happens with antimony, bismuth or tantalum, which have a very small crepuscular grade compared to current average ore grades, therefore its crepuscular *k*-value is considerably much larger compared to their unit exergy cost when the average ore grade in the mines are taken into account.

Considering all these facts, the exergy bonus provides hints about which are those minerals that would be difficult to replace after complete dispersion. Extracting and dispersing a mineral with a great exergy bonus implies losing irreversibly a natural capital that mankind could barely replace and if so, with huge amounts of energy. The minerals with the highest exergy replacement costs according to our calculations are gold, tantalum, mercury, silver, cobalt, cadmium or tungsten. This means that a good management of the latter metals becomes especially critical.

It should be stated that the values obtained are first assessments. Important assumptions have been made, such as assuming that the same technology is applied for the whole range of grades analyzed, including the crepuscular ore grade. One of the major limitations found is the lack of real data over time. So estimation of future trends of this issue without real and reliable information becomes subjective. Therefore, the results and data provided are an attempt to afford indicators based on physical facts rather than on subjective market policies for identifying challenges and opportunities in the mining sector and should not be taken as final and closed.

4. The decrease of the mineral capital endowment due to rawmaterial production

The method outlined in this study could be used to assess both the mineral capital endowment of the Earth's crust and its yearly depletion due to mining. However some additional remarks need to be done. The mining process does not imply an immediate loss of the mineral exergy bonus of the material itself. On the contrary, once extracted, it is elevated from R#1 to R#2 through further concentration and refining processes. The same happens when the material goes to landfills (R#2 to R#3). We only lose this bonus when materials cannot be recovered again, i.e. when a material goes from R#i to R#0. This is the case of metallic pigments in paintings, zinc in tyres, phosphorous in car surface treatments, lead in gasoline, phosphates in agriculture, metals as additives in steels, cadmium and other metal dispersion in waste incineration, many electroplating materials, mine tailings and hundreds of more examples. Also, all fossil fuels required to elevate the exergy of materials, from R#1 and R#3 to R#2, become degraded and slowly but irreversibly contribute to form Thanatia (R#0).

Taking these considerations into account, we can now assess the yearly depletion of the mineral capital endowment due mineral production. For that purpose, world primary production figures such as those reported by the Mineral Commodity Summaries 2008 [35] are required. Table 1 shows the total exergy costs of the studied production chains. According to our calculations, the exergy replacement costs (bonus) associated to the 2008 production of the studied minerals is equal to 5.3 Gtoe.

It is worth to note that conventional economics only accounts for the energy required in the extraction and refining processes. In the case of the materials studied, these account for around 9%

of the total world fossil fuel produced[3] in year 2008 (see Fig. 2). The latter value is in the range reported by the World Watch Institute (up to 7% of the total world energy consumption) and by the International Energy Agency (up to 10% also of the world energy consumption).

Nevertheless a fair accountability of resources should also take into account the use and the decrease of the non-fuel mineral capital endowment. This means that the true yearly balance of the exergy decrease in the mineral endowment of the planet should account for at least, the exergy of fossil fuels world production plus the loss of the mineral exergy bonus of the non-fuel minerals. As can be seen in Fig. 2, this accounts for 32% of the whole energy stages, if the cradle to grave stage is taken into account and is in the same order of magnitude as the yearly loss of coal, oil or natural gas.

Fig. 3 also shows in a schematic way the gross mineral exergy bonus of the extraction of the considered minerals for year 2008. But this bonus is not entirely lost. As explained above, only that part that is not recycled becomes in reality lost. The USGS reports recycling ratios for some important minerals in the US [35] (see Table 2).

We will assume the same recycling ratios for the whole world as in the US, which means that from the total mineral bonus extracted, only 72% is practically lost. Consequently, the exergy bonus lost due to mineral production in 2008, represents a decrease of the planetary mineral endowment of around 3.8 Gtoe. Adding the exergy of the fossil fuels used in the extraction and processing of the minerals, we obtain that the total exergy loss due to mineral production in 2008 was equal to 5.3 Gtoe. This represents around 41%, of the overall decrease respectively (taking into account fossil fuels and the mineral bonus lost). It should be stated that only 37 minerals have been considered. Hence, the previous reported value would increase, if all mineral commodities were to be included in the analysis.

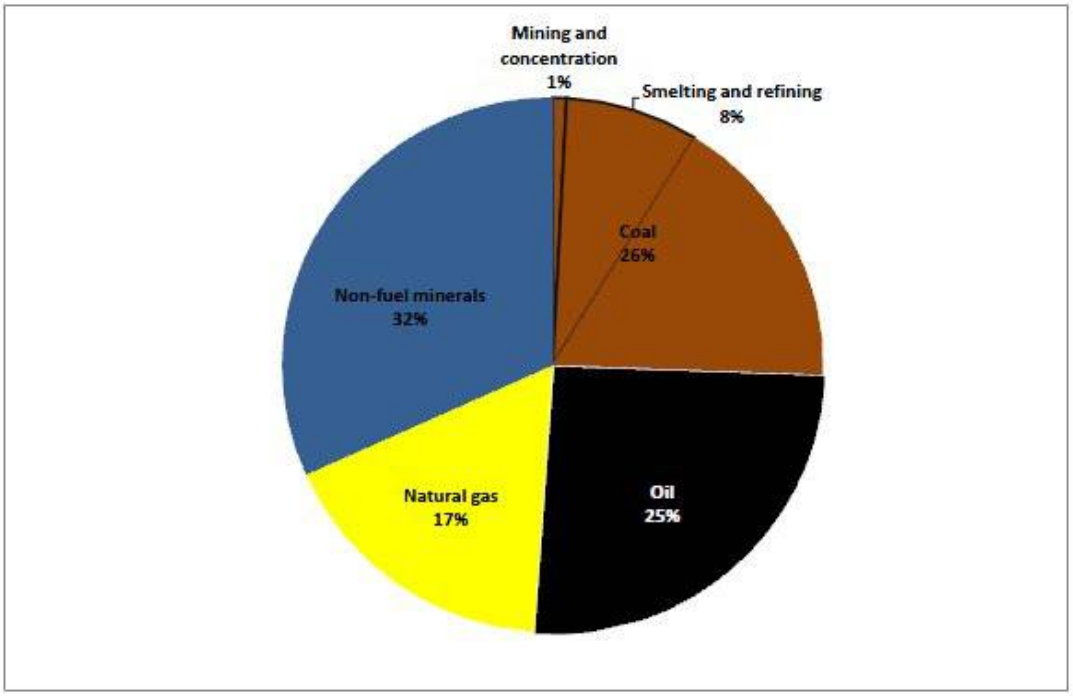

Figure 2. Distribution of the exergy costs associated to the 2008 world production of the main mineral commodities

[3] In Fig. 2, the energy associated to the mining and concentration, smelting and refining has been depicted as if it would come from coal. This is obviously a simplification, since that energy can come from other fossil fuels or even from renewable resources.

Table 1. Total exergy costs of 2008 world production. Values are expressed in Mtoe if not specified

Substance	2008 Production, t	Bonus	Mining & conc.	Smelting & refining
Aluminium	2.05E+08	3.06E+03	5.15E+01	1.16E+02
Antimony	1.97E+05	2.23E+00	6.57E-03	5.63E-02
Arsenic	5.27E+04	5.02E-01	1.13E-02	2.38E-02
Beryllium	1.38E+02	8.30E-04	2.37E-05	1.48E-03
Bismuth	7.70E+03	8.97E-02	6.60E-04	9.68E-03
Cadmium	1.96E+04	2.75E+00	1.23E-01	1.30E-01
Chromium	6.98E+06	7.54E-01	1.40E-02	6.03E+00
Cobalt	7.59E+04	1.96E+01	1.66E-02	2.33E-01
Copper	1.54E+07	4.05E+01	1.06E+01	7.86E+00
Fluorspar	6.04E+06	2.63E+01	2.09E-01	-
Gold	2.26E+03	3.14E+01	5.80E+00	-
Gypsum	1.59E+08	5.83E+01	7.65E-01	-
Iron	2.22E+09	9.38E+02	3.70E+01	1.04E+03
Lead	3.84E+06	3.35E+00	8.16E-02	3.00E-01
Limestone	1.23E+08	7.66E+00	1.06E+00	1.69E+01
Lithium	3.82E+05	4.96E+00	1.14E-01	3.82E+00
Manganese	1.33E+07	4.95E+00	5.13E-02	1.82E+01
Mercury	1.48E+03	9.97E-01	5.53E-03	8.88E-03
Molybdenum	1.84E+05	3.98E+00	5.96E-01	5.26E-02
Nickel - laterites	1.19E+06	4.76E+00	4.89E-02	1.17E+01
Nickel - sulfides	1.00E+06	1.82E+01	3.71E-01	2.39E+00
Phosphate rock	1.61E+08	1.35E+00	1.10E+00	1.77E+01
Potash	3.48E+07	1.01E+03	2.54E+00	-
Rhenium	5.65E+01	1.38E-01	2.10E-04	2.02E-05
Silicon	2.83E+06	4.92E-02	4.85E-02	5.12E+00
Silver	2.13E+04	3.74E+00	6.50E-01	1.44E-01
Sodium	N.A.	N.A.	N.A.	N.A.
Tantalum	1.17E+03	1.35E+01	8.59E-02	2.27E-04
Tin	2.99E+05	3.04E+00	1.08E-01	3.82E+01
Titanium-rutile	6.21E+05	1.30E-01	2.04E-01	3.61E+00
Titanium-ilmenite	6.79E+06	7.29E-01	1.17E+00	2.07E+01
Uranium	6.09E+04	1.31E+00	2.74E-01	0.00E+00
Vanadium	5.61E+04	1.41E+00	1.82E-01	5.09E-01
Wolfram	5.59E+04	9.89E+00	2.83E-01	1.92E-01
Zinc	1.16E+07	6.85E+00	4.13E-01	1.12E+01
Zirconium	1.28E+06	1.99E+01	2.25E+01	1.93E+01
TOTAL	**2.98E+09**	**5,307.97**	**137.87**	**1,335.97**

Table 2. US recycling rates of selected metals in 2008 [35]

Aluminium	48%	Iron	61%	Tin	34%
Chromium	34%	Lead	77%	Titanium	41%
Copper	32%	Nickel	43%	Zinc	30%

5. Conclusions

The extraction of materials from the Earth's crust implies a net reduction of the natural's exergy stock.

This is because we are unable to recycle all materials we mine. Consequently, the Earth approaches gradually to a degraded planet of minimum exergy, with the absence of fuel and non-fuel mineral deposits. And this is a consequence of the Second Law of Thermodynamics.

We have presented in this paper a methodology for measuring the mineral bonus that Nature grants us for providing the minerals concentrated in mines and not dispersed throughout the crust. The exergy replacement costs account for the actual exergy required to extract and concentrate the materials from the Crepuscular Earth to the conditions found in Nature, with current available technologies. Hence, the knowledge of mining practices of extraction and refining of minerals is a fundamental key for assessing them.

The obtained values give an idea of the great amount of exergy that man saves thanks to the existence of the concentrated mineral capital on Earth. The analyzed substances represent only a part of the globally used mineral resources, so the complete analysis including all minerals is even larger.

Furthermore, as the mines become depleted, the obtained number will continue to increase and presumably in an exponential way, coinciding with the exponential trend of extraction throughout history.

Our analysis enhances and puts numbers to the importance and necessity of material reuse and recycling.

The accuracy of the numbers to be obtained with this methodology relies strongly on the quality of the data used. The knowledge of metallurgical processes that imitate Nature in creating minerals is required. But most importantly, we need to know precisely geological facts on how our mineral wealth is being altered by man. Unfortunately, there is an enormous lack of information about our mineral capital.

The obtained values should serve as an assessment tool for decision-makers in the mineral industry. Because, how can we effectively manage our resources if we do not even know which is the cost of the mineral capital that we are irremediably destroying?

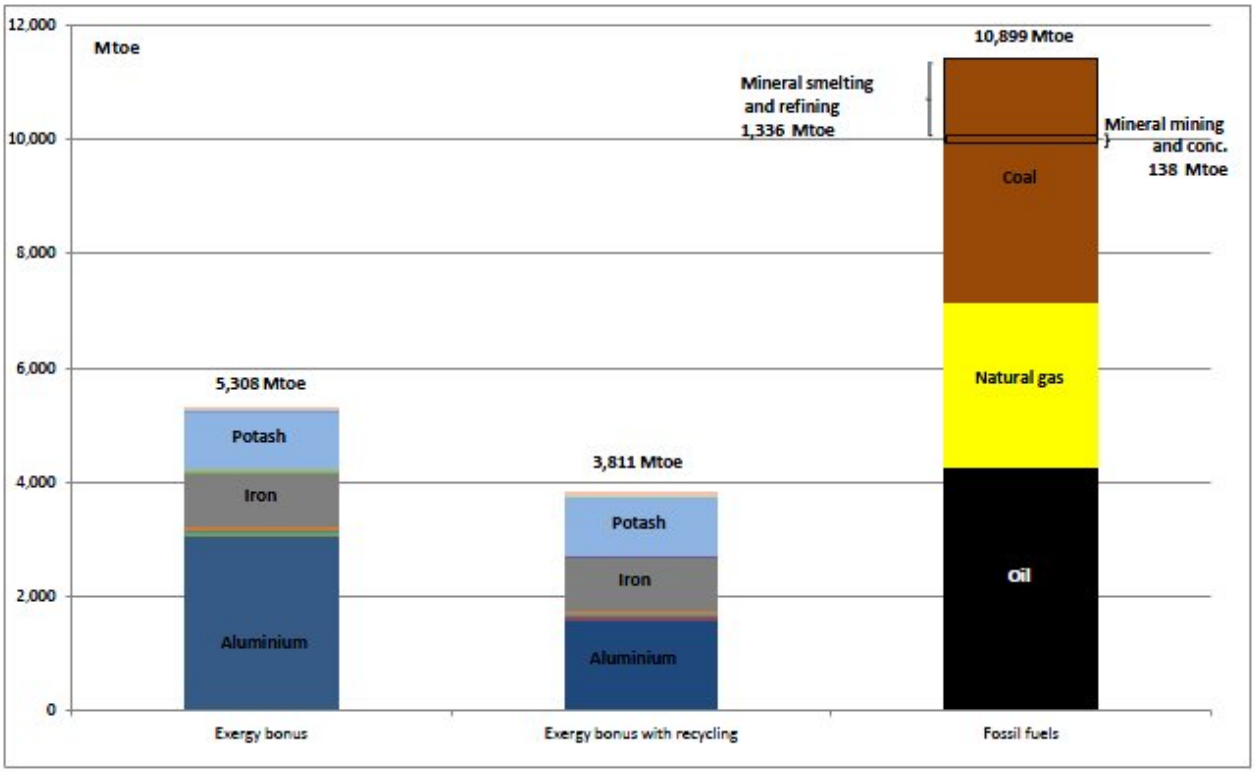

Figure 3. The decrease of the world mineral capital endowment due to raw-material production in 2008.

6. Acknowledgment

This paper has been financed by the IDERE II project from the Spanish Ministry of Industry and Science.

References

[1] Alicia Valero, Antonio Valero, and Javier B. Gómez. The crepuscular planet. a model for the exhausted continental crust. Energy, 36(1):694 – 707, 2011.

[2] A. Valero and Al. Valero. A prediction of the exergy loss of the world's mineral reserves in the 21st century. Energy, 36:1848–1854, 2011. Best paper award of the 5th Conference on Sustainable Development of Energy Water And Environment Systems held from 30 September to 3 October 2009 in Dubrovnik, Croatia.

[3] Stefan Gößling-Reisemann. Combining LCA with thermodynamics. Information Technologies in Environmental Engineering, 1:19–22, 2008.

[4] William McDonough and Michael Braungart. Cradle to Cradle. Remaking the way we make things. North Point Press, 2002.

[5] P.F. Chapman and F. Roberts. Metal Resources and Energy. Butterworths, 1983.

[6] Antonio Valero and Alicia Valero. Exergoecology: A thermodynamic approach for accounting the Earth's mineral capital. The case of bauxite-aluminium and limestone-lime chains. Energy, 35(1):229–238, 2010.

[7] Antonio Valero, Alicia Valero, and Cristobal Cortés. Exergy of Comminution and the Crepuscular Planet. In Proceedings of the 6th Dubrovnik Conference on Sustainable Development of Energy Water and Environmental Systems, Dubrovnik, Croatia, September, 25-29 2011.

[8] J. Szargut and D.R. Morris. Calculation of standard chemical exergy of some elements and their compounds based upon seawater as the datum level substance. Bulletin of the Polish Academy of Sciences. Techical Sciences., 33(5-6):293–305, 1985.

[9] M. Ruth. Thermodynamic constraints on optimal depletion of copper and aluminum in the United States: a dynamic model of substitution and technical change. Ecological Economics, 15:197–213, 1995.

[10] T. Norgate and S. Jahanshahi. Low grade ores. Smelt, leach or concentrate? Minerals Engineering, 23:65–73, 2010.

[11] T. Norgate and N. Haque. Energy and greenhouse gas impacts of mining and mineral processing operations. Journal of Cleaner Production, 266-274:18, 2010.

[12] T. Norgate and S. Jahanshahi. Assessing the energy and greenhouse gas footprints of nickel laterite processing. Minerals Engineering, November 2010.

[13] Alicia Valero and Antonio Valero. The crepuscular planet. A model for the exhausted continental crust. Energy, doi:10.1016/j.energy.2010.09.034, 2010.

[14] D. P. Cox and D. A. Singer, editors. Mineral Deposit Models, volume US Geological Survey Bulletin 1693. US Geological Survey, 1992. Online under: http://pubs.usgs.gov/bul/b1693/.

[15] G. M. Mudd. Global trends in gold mining: Towards quantifying environmental and resource sustainability? Resources Policy, 32(1-2):42–56, 2007.

[16] Gavin M. Mudd. Global trends and environmental issues in nickel mining: Sulfides versus laterites. Ore Geology Reviews, June 2010.

[17] Gavin Mudd. Radon releases from australian uranium mining and milling projects: assessing the unscear approach. Journal of Environmental Radioactivity, 99:288–315, 2008.

[18] G. Mudd and M. Diesendorf. Uranium Mining, Nuclear Power and Sustainability – Rhetoric versus Reality. In Sustainable mining conference, Kalgoorlie, WA, 17 - 19 August 2010 2010.

[19] E. Botero. Valoración exergética de recursos naturales, minerales, agua y combustibles fósiles. PhD thesis, Universidad de Zaragoza, 2000.

[20] IPPC. Integrated Pollution Prevention and Control (IPPC). Reference Document on Best Available Techniques for the Non-Ferrous Metals Industries. Technical report, Institute for Prospective Technological Studies. European Commision, 2009.

[21] Kennecott Utah Copper. Silver environmental profile. life cycle assessment. Technical report, Kennecott Utah Copper Corporation, 2006.

[22] J. C. Bravard, H. B. Flora, and C. Portal. Energy expeditures associated with the production and recycle of metals. Report ornl-nsf ep 24, Oak Ridge National Laboratory, Oak Ridge, Tenn., 1972.

[23] H. H. Kellogg. Sizing up the energy requirements for producing primary metals. Enginnering and Mining Journal, 178:61–65, April 1977.

[24] John Barkas. Patterns of energy consumption and greenhouse gas emission across primary base metals production. Joint Metal Study Group Energy and Climate Change Seminar, 2009.

[25] P.G. Kihlstedt. Energy and mineral exploitation techniques. Scandinavian journal of metallurgy, 4(4):145–149, 1975.

[26] Kenneth A. Walsh. Beryllium chemistry and processing. ASM International, USA, 2009.

[27] IPPC. Integrated Pollution Prevention and Control (IPPC); Draft Reference Document on Best Available Techniques for Management of Tailings and Waste-Rock in Mining Activities. Technical report, Institute for Prospective Technological Studies. European Commision, 2002. Retrieved at 01.03.2003 from http://www.jrc.es/pub/english.cgi/0/733169.

[28] IPPC. Integrated Pollution Prevention and Control (IPPC). Reference Document on Best Available Techniques on the production of Iron and Steel. Technical report, Institute for Prospective Technological Studies. European Commision, 2001.

[29] DOE. Mining Industry of the Future. Annual report. industrial technologies program., Office of Energy E_ciency and Renewable Energy and U.S. Department of Energy, 2005.

[30] Mischa Classen, Hans-Jörg Althaus, Silvio Blaser,Wolfram Scharnhorts, Matthias Tuchschmid, Jungbluthm Niels, and Faist Emmenegger Mireille. Life Cycle Inventories of Metals. Final report ecoinvent data v2.0. Technical report, Swiss Centre for Life Cycle Inventories, 2007.

[31] K. S. Yoshiki-Gravelsins, J. M. Toguri, and T. C. Choo. Metals Production, Energy, and the Environment, volume Part I: Energy Consumption. JOM, 1993.

[32] G. F. Hancock. Energy requirements for manufacture of some non-ferrous metals. Metals Technology, 11:290–299, 1984.

[33] G. Hagedorn and E. Hellriegel. Umweltrelevante masseneinträgen bei der herstellung verschiedener solarzellentypen. Endbericht-teil i: Konventionelle verfahren, Forschungsstelle für Energiewirtschaft (München), 1992.

[34] Batelle-Columbus-Laboratories. Energy use patterns in metallurgical and non-metallurgical mineral processing. U.S. Department of Commerce, Washington, 1975.

[35] USGS. Mineral commodity summaries. Technical report, US Geological Survey, 2010.

A new polygeneration system for methanol and power based on coke oven gas and coal gas

Hu LIN, Hongguang JIN*, Lin GAO, Rumou LIN

Institute of Engineering Thermophysics, Chinese Academy of Sciences, Beijing, China,
**Corresponding author E-mail: hgjin@mail.etp.ac.cn*

Abstract:

Polygeneration system for chemical and power co-production has been regarded as one of promising technologies to use fossil fuel more efficiently and cleanly. In this paper, a novel polygeneration system, with both coal-based syngas and coke oven gas inputs for methanol and power production, is proposed. New system demonstrates the superior performance to the single-product systems, whose energy saving ratio is as high as 15%, and exergy efficiency can reach about 65%. To clarify the characteristic of the new system, exergy balance sheet and Energy Utilization Diagrams (EUDs) are applied to reveal the essence of performance improvement. The results show the following reasons: Firstly, pressure swing absorption is used to remove the hydrogen from the coke oven gas, by which, the concentration of reformed methane is gone up, which reduces exergy destruction. Secondly, the thermal energy for partial methane reforming is supplied by syngas out of coal gasifier instead of fuel gas, which not only save chemical energy of fuel, but also recover the sensible thermal energy of the syngas. Finally, the mixed gas by coke-oven gas and coal syngas can make the composition more fit for chemical synthesis even without any energy consumption. This novel system has the capability of both effectively utilizing the coke-oven gas and developing coal based polygeneration system, which leads to a new direction for clean energy technology.

Keywords:

Coke oven gas, Syngas, Dual-gas complement, System integration, Performance character.

1. Introduction

Multi-energy complement and coproduction have been a main character and direction of energy system sustainable development. China is a country with abundant of coal but short of oil. Coal is the main energy resource in primary energy resource. The complement problem between coal and the second energy resource by-produced during coal utilization has been paid more attention. In traditional development, power system focuses on improvement of thermal energy utilization, and chemical production focuses on max product outputs. Both of the development directions could not break through the problems of higher energy consumption, chemical energy destruction and pollution [1-9]. Therefore, polygeneration system, integrating between chemical and power productions, has attracted more attention, and some science researches and demonstration projects have been carried out.

In China, coke production was about half of the total in the world, which by-produces about 36 billion cubic meters per year of coke oven gas (COG). But only 10 % of it has been utilized, and most of it was burned in the air, it is obvious that leads to good energy waste and air pollution [10-11]. So its effective utilization is necessary. Because hydrogen and methane are the main components of COG, and syngas from coal is rich in CO, syngas from coal or COG must be adjusted to fit for chemical production with large energy consumption, which is the critical point when system integration.

This paper is to integrate a new polygeneration system with syngas from coal and COG. The performance of the system is identified, and the characteristics of the new system are disclosed by exergy analysis with EUD method.

2. New polygeneration system based on COG and coal gas

2.1. A new approach for integrated utilization between COG and coal-based syngas

In this paper, we chose the coal, whose base analysis (weight, %) is as follows: 68.54%C, 3.97%H, 6.85%O, 0.74%N, 1.08%S, 9.98%Ash, and 8.84%W, and LHV was 26710 kJ/kg. The syngas produced by a Texaco gasifier was composed of 44.0%CO, 30.8%H_2, 10.5%CO_2, 12.7%H_2O, and 1.8%others, which comes from industrial data. In order to convert almost all syngas into methanol, H_2/CO ratio of fresh gas should be adjusted to the stoichiometric ratio. But the H_2/CO ratio in syngas is about 0.69, so the syngas is always been adjusted by shift reaction. Another way, coke-oven gas is rich in H_2 and CH_4 (about 8.8%CO, 57.3%H_2, 2.8%CO_2, 20.5%CH_4, and 10.8%others in volume). Traditionally, COG is reformed with steam firstly, by which, CH_4 is converted into CO and H_2, leading to much higher H_2/CO ratio in syngas. Furthermore, because of being rich in hydrogen, if CH_4 is reformed completely, much more energy is needed, which always supplies by COG or/and other fuel gases combustion.

Synergetic considering the characters of coal syngas and COG, the new energy utilization mode is concept as shown in Fig.1. COG is put into pressure swing absorb process (PSA) to separate H_2 firstly, and then put into the reformer. The thermal energy is not supplied by fuel combustion but the high temperature syngas out of the coal gasifier, whose temperature can be higher than 1200℃. Furthermore, CH_4 in COG don't need to be totally converted into CO and H_2. And the two flows of syngas out of reformer are mixed as fresh gas for methanol synthesis.

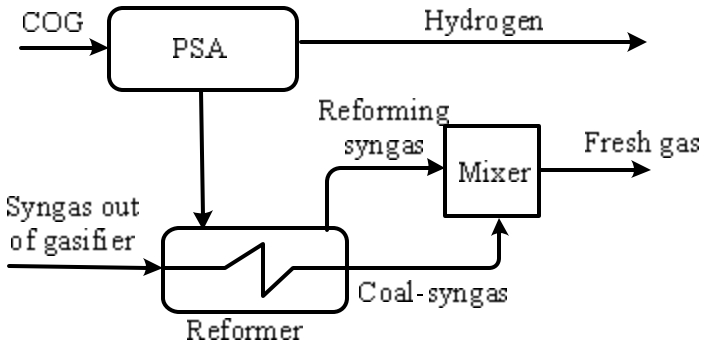

Fig. 1 Concept of complementation between coke oven gas and coal syngas

2.2. Description of the new polygeneration system

The flow sheet of the new system is shown in Fig 2. Through PSA process, 90 % hydrogen is separated, and the rich-methane gas is put into the reformer. The syngas out of gasifier is put into the reactor as the thermal energy donor. In the reformer, about 70% of methane is reacted, which is more different from that mentioned in reference [12]. After clean-up unit, the low temperature coal gas is mixed with the product gas of the reformer. Then the mixed gas is put into the methanol synthesis reactor. There are about 80 % un-reacted syngas is recycled to the reactor. And after recycled pressure energy, the excess un-reacted syngas and hydrogen out of PSA are put into combined cycle as fuel for power generation.

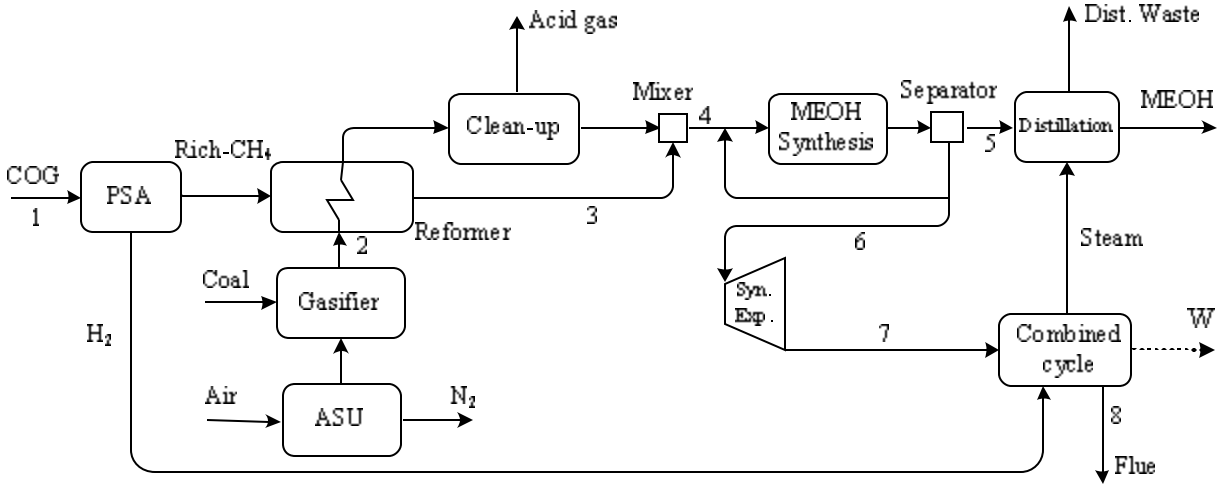

Fig. 2 Flow sheet of the new dual-gas polygeneration system (PG)

3. System simulation

3.1. Reference systems

The polygeneration system, based on COG and coal syngas input, is the complicated system with dual-energy inputs and dual-product outputs. When thermodynamic performance is analysed via contrast method, two or more conference systems must be chosen. In the paper, integrated coal gasification combined cycle (IGCC) system and methanol production system with COG input, which shown in Fig.3, are chosen as reference systems. In Fig.3, after being cleaned up and preheated at about 550 ℃, COG is reformed by steam to convert CH_4 into H_2 and CO. Then the reformed gas is sent to the methanol production subsystem. Some of purge gas in methanol synthesis unit is sent to reformer as fuel, and the rest is sent to a captive power plant. The energy consumption is about 40 GJ/t-CH_3OH.

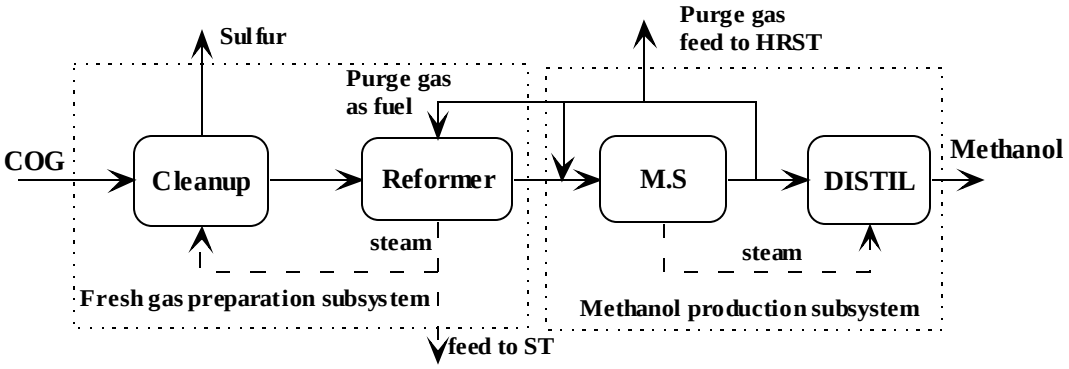

Fig. 3 Flow diagram of COG-based methanol production system

3.2. Simulation results

Mainly parameters of the processes come from industrial data. All the systems, including conference systems and the new system, are simulated by Aspen Plus. The thermodynamic properties of syngas and methanol were evaluated by the PR and RK equations respectively. The gas turbine was simulated basing on the technical level of 9FA class. The HRSG of the combined cycle works at two difference pressure levels. The turbine inlet temperature was 1260℃, and the pressure ratio in the gas turbine was 16. The isentropic efficiencies of the gas turbine, the high-

pressure steam turbine and the low-pressure steam turbine were 0.9, 0.88 and 0.86, respectively. With Aspen Plus simulation, the parameters of critical points (shown in Fig.2) are shown in Tab.1. Point 4 denotes the fresh gas for methanol synthesis, ratio of H2/CO is much closer to the stoichiometric ratio of methanol production.

Tab.1 Critical point parameters of the polygeneration system

Point	1	2	3	4	5	6	7	8
Flow	1.3	3.2	2.2	3.0	0.6	1.6	2.3	18.5
Pressure	1.0	68.0	23.0	78.0	75.0	75	18.5	1.0
Tem. ℃	25	1346	145	247	40	51	64	105
Mole component（%）								
CO	8.8	43.0	10.6	41.6	3.5	49.4	35.8	
H_2	57.3	30.5	41.3	48.0	0.2	30.6	47.0	
CH_4	20.5		3.8	2.2	0.7	4.2	3.2	
CO_2	2.8	11.7	7.4	3.7	6.5	7.9	7.3	6.0
H_2O		12.6	31.8		1.6			7.0
CH_4O					83.3	0.4	0.5	
N_2	6.6	0.9	3.0	3.0	0.4	6.0	4.4	73.7
O_2	1.6		1.0	0.6	0.1	1.1	0.8	13.3
H_2S		0.3						
C_2H_6	2.4							
C_2H_6O					2.7	0.3	0.9	

To evaluate the performance of the polygeneration system, the proposed system was compared with the reference single systems (including the COG-based methanol production system and IGCC system). The thermodynamic performance of the systems is shown in Tab.2. IGCC system and COG-based methanol production system have the same outputs as those of the polygeneration system, 300 MW power and 58.2 t/h methanol respectively. In the table, *Rc* denotes the ratio of methanol (in low heat value) to power output; *Ec* is the energy consumption for 1 ton methanol production; η_P and η_{th} symbol the thermal efficiencies of power generation and the total system. And we also chose primary energy saving ratio (*PES*) as a criterion to evaluate the thermodynamic performance of the new system. *PES* is defined as:

$$PES = \frac{W/\eta_P + Q_{ME}/\eta_{ME} - (Q_C + x \cdot Q_{COG})}{W/\eta_P + Q_{ME}/\eta_{ME}} \qquad (1)$$

Where W and Q_{ME} are the network output and methanol(LHV); η_P and η_{ME} are the efficiencies of power generation in IGCC system and methanol production system respectively; Q_C and Q_{COG} are the low heat value of coal gas and COG. Because the energy level of COG is higher than that of coal gas, we chose x as a coefficient to deal with this difference, as 1.1 in the paper [13].

The polygeneration system shows its better thermodynamic performance, whose primary energy saving ratio can reach about 15 %, thermal efficiency for power generation is about 10 percentage points higher than that of IGCC system, and energy consumption for methanol production is about 70 % of that in COG-based methanol production system.

To disclose the energy utilized advantage, exergy destructions of processes are shown in Tab. 3. The exergy efficiency of the proposal system is higher than 60%, which is much higher than those in the reference systems. The exergy destruction of reforming process is only about 1/15 of that in the COG based methanol production system.

Tab. 2 Main thermodynamic performance of the polygeneration system

	PG	Single-product system	
		IGCC	COG ME
Coal MW	710.6	683.4	
Coke-oven gas MW	405.8		606.2
Network output MW	300.0	300.0	
MEOH output t/h	58.2		58.2
Rc	1.1		
η_P %	58.8	43.9	
E_C GJ/t	26.8		37.5
η_{th} %	55.7	43.9	53.1
PES %	14.3		

Tab. 3 Exergy balance of the polygeneration system and single-product systems

System	PG		COG ME		IGCC	
Unit	MW	%	MW	%	MW	%
Exergy input						
Fuel exergy	1134.4	100.0	718.5	100.0	698.7	100.0
Coal	727.8	64.2			698.7	100.0
Coke oven gas	406.6	35.8	718.5	100.0		
Exergy destruction						
ASU	19.3	1.7	12.0	1.7	18.8	2.7
Gasification	104.4	9.2			106.2	15.2
PSA	5.7	0.5				
Coke-oven gas reform	7.9	0.7	103.8	14.4		
MEOH synthesis and distillation	43.6	3.8	47.2	6.5		
Power system and others	230.3	20.3	131.6	18.3	274.1	38.2
Product exergy output						
Network output	300.0	26.4			300.0	42.9
MEOH	423.2	37.3	423.2	58.9		
Destruction and outputs	1134.4	100.0	718.5	100.0	698.7	100.0

4. Discussion

4.1. EUD analysis of reforming process

From the results shown in tab.3, the new approach for integrated utilization between COG and coal syngas leads to less exergy destruction in reforming process. To disclose the reason of exergy destruction decrement, Energy Utilization Diagrams was used to analyze the process [14]. In Fig.4, ed means the energy donating side, and ea symbols the energy accepting side. A_{ea1} is the energy

degree of air heated process during fuel combustion, A_{ea2} and A_{ea3} are the energy degree of fuel and coke oven gas reheated processes respectively, A_{ea4} is the energy degree of reforming process. The area between energy donated side and accepted side is the exergy destruction of the total reforming process, including reheating and reacting processes. Fig.5 shows the exergy loss of the new reforming process. Compared Fig. 4 with Fig. 5, with system integration, the steam for reforming process in new system comes from power cycle, because of partial CH_4 reforming, the reforming temperature can be decreased, which means that the energy degree of steam much closer to that of the reforming process, and the energy denoted side is the syngas out of gasifier, then the fuel reheated process is cancel, which means that the processes 1 and 2 are deleted. Furthermore, partial reaction and different energy donated side make the exergy destruction decrease.

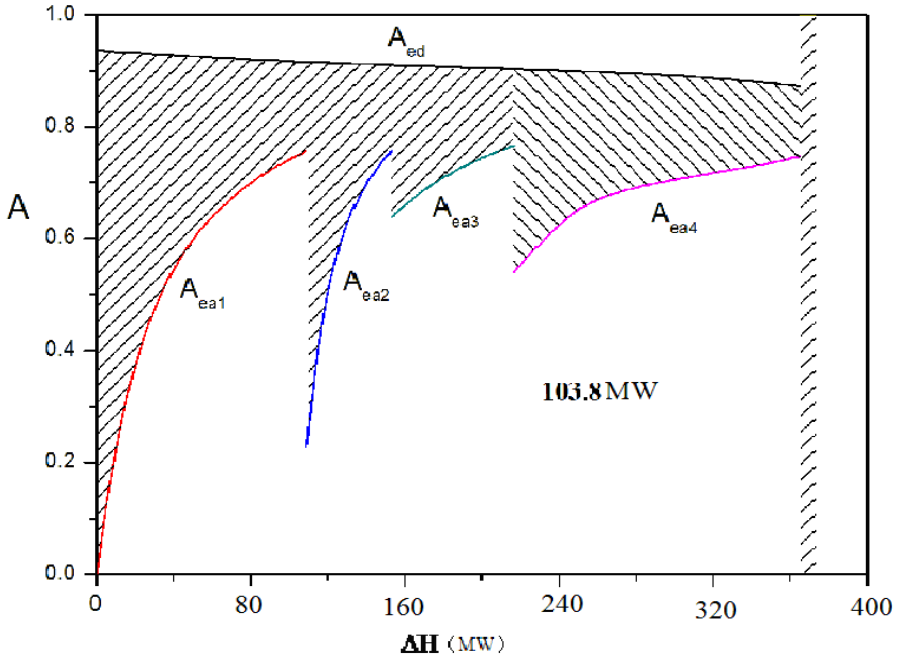

Fig.4 EUD of the conventional coke oven gas reforming

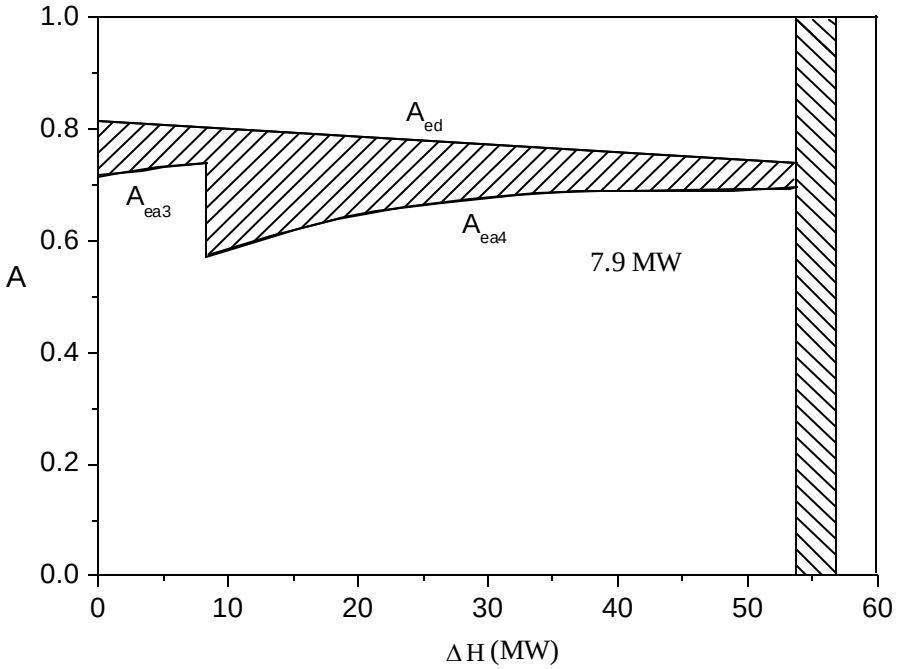

Fig. 5 EUD of coke oven gas reforming in dual-gas polygeneration system

4.2. Analysis of thermodynamic performance

From the flow sheet shown in Fig. 2, the methane partial reform configuration determines the complement between COG and coal gas from the aspect of energy integration, and the syngas out of separator partial recycled to the methanol reactor directly decides the energy into the power combined cycle, which determines the chemical energy integration between chemical process and power cycle. So the methane reformed ratio (R_f) of reformed methane to all methane and the ratio (*Ru*) of recycled gas to the syngas out of separator are the main critical variable to determine the whole system performance.

Fig.6 shows R_f how to impact on *PES*, the system thermodynamic performance. In the figure, *Ru* is defined as the ratio of recycled gas to the syngas out of separator. With certain *Ru* (as 2.2, un-reacted syngas about 80% recycled to methanol reactor) and mixed ratio of COG to coal gas, when R_f increasing, *PES* goes up quickly first, and has a highest value, about 15%. But with R_f continuously increasing, *PES* decreases. For every *PES* line with certain *Ru*, there is a R_f value corresponding to the best thermodynamic performance, with highest *PES*, which results from the effective components in fresh gas increased and H_2/CO much closer to stoichiometric ratio of methanol synthesis with R_f going up, but when R_f comes to a certain value, H_2/CO in fresh gas deviates the stoichiometric ratio, which results from more coal gas required for reforming. As about 70% methane reformed, because the concentration of methane is lower, much more reforming energy is needed, which means that the ratio of coal gas to coke oven gas is much higher. Therefore, with certain system configuration, there is an optimal reforming ratio (R_{fopt}) couple with recycled ratio and ratio of coal gas to coke oven gas resulting in the couple between chemical side and power generation side of the system, which leads to optimal thermodynamic performance.

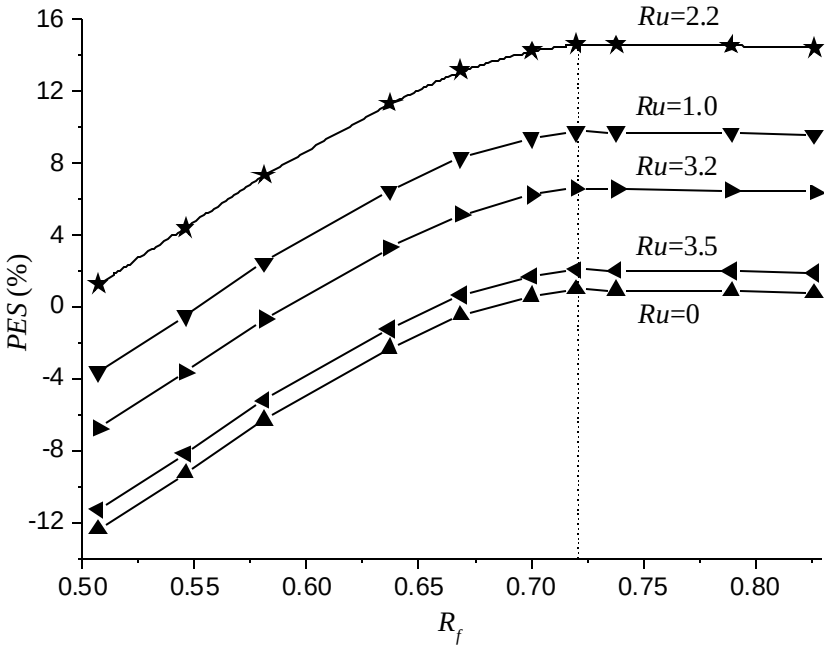

Fig. 6 Thermodynamic performance change with reforming ratio

Fig.7 shows *Ru* how to impact on *PES*, the system thermodynamic performance. With certain coke oven gas reforming ratio (70%) and H_2/CO (1.15) in refresh gas, *PES* goes up with *Ru* increasing first. This is because the effective components and chemical energy in fresh gas are utilized efficiently. But when *Ru* gone up to certain value, more recycled work is needed, and the synthesis ratio of methanol increases slowly, in the distillation unit, more energy consumption is needed too, so *PES* goes down. With every R_f, there is a *Ru* corresponding to the optimal *PES*, as optimal thermodynamic performance. Therefore, there is an optimal recycling ratio (Ru_{opt}). Appropriate

unreacted syngas recycle, methane reforming, and mixed ratio of coal gas to coke oven gas lead to couple of chemical side and power generation system, which results in optimal thermodynamic performance.

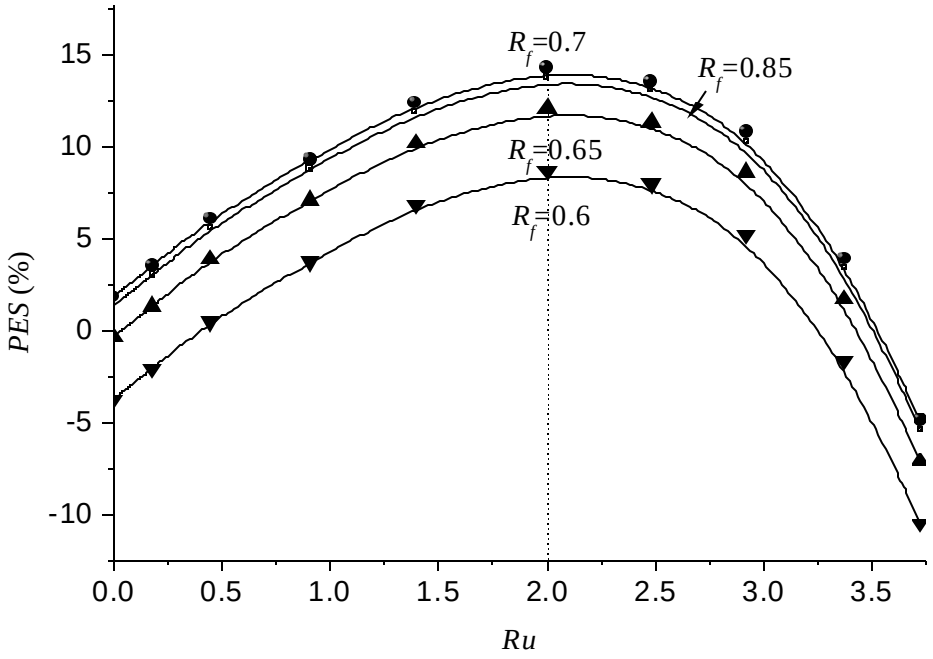

Fig.7 Thermodynamic performance change with syngas recycling ratio

5. Conclusions

Based on polygeneration definition and dual-fuel gas complement, a new polygeneration system for methanol and power has been proposed, which primary energy saving ratio can reach about 15%. And the thermodynamic performance has also been analyzed by EUD method, the conclusions can be drawn from the results as follow: 1) with coke oven gas and coal-based syngas integrating utilization, and methane partial reform, chemical exergy destruction of reforming process is reduced obviously; 2) with partial recycle configuration of methanol synthesis, chemical exergy destruction is decreased too; 3) the decrement of chemical exergy destruction in the chemical process make more energy into the power island and realizes couple between chemical process and power generation, which leads to improvement of the system thermodynamic performance. The polygeneration system shows the integrating cascade utilization between chemical energy and physical energy.

This novel system has the capability of both effectively utilizing the coke-oven gas and developing coal-based polygeneration system, which leads to a new direction for clean energy technology.

Acknowledgments

This study has been supported by China National High-Tech Research and Development Projects (2011AA050606).

References

[1] Nexant, Inc. Multi-client Study Prospectus: Polygeneration from Coal Integrated Power, Chemicals and Liquid Fuels. Nexant Report, New York, USA. September 2006

[2] WMPI PTY., LLC. Early Entrance Co-Production Plant. Report of U.S. Department of Energy National Energy Technology Laboratory, 2003.

[3] Jackson, R. G. Polygeneration System for Power and Methanol Based on Coal Gasification. Coal Conversion, 1989, Vol. 3: 60-64.
[4] Ni W., Li Z., Xue Y. Polygeneration Energy Systems Based on Coal Gasification, Energy and Environment. Engineering Science, 2000, 2 (8): 59-68.
[5] Chinese Academy of Science Energy Strategy Research Group. China Energy Sustainable Development Specific Research[M]. Beijing: Science Press, 2006
[6] JIN Hongguang, LIN Rumou. Energy Cascade Utilization and Gas Turbine Integrated Energy system [M]. Beijing：Science Press, 2008
[7] Yamashita, K.; Barreto, L.: Integrated Energy Systems for the 21st Century: Coal Gasification for Co-producing Hydrogen, Electricity and Liquid Fuels (Interim Report) [R]. IR-03-039, Laxenburg Austria: IIASA, 2003.
[8] Doug S., Albert T. Wabash River Integrated Methanol and Power Production from Clean Coal Technologies (IMPPCCT) [R]. Report of U.S. DOE and Gasification Engineering Corporation，2001.
[9] Xie K. Focus on Coal Chemical Engineering. Beijing: Chemical Industry Press, 2005:330-349.
[10] SUN Shi-en. Mechanism and Integration of Coke Oven Gas & Coal Gas Based Polygeneration Systems for Production of Coke, Chemicals & Power [D]. Beijing: Chinese Academy of Sciences, 2009
[11] LIN Hu. Study on Polygeneration System CCS Life Cycle Assessment and System Integration [D]. Beijing: Chinese Academy of Sciences, 2010
[12] GAO Jian, NI Wei-dou, LI Zheng. A Dual-fuel Methanol/Electricity Multi-generstion System with Methane Reforming for Sensible Heat Utilization [J]. Journal of Power Engineering, 2008 Vol.28(4):639-646
[13] LIN Ru-mou, SUN Shi-en, JIN Hong-guang, GAO Lin. Energy Saving Ratio of Polygeneration System and the Option for Reference Performance [J]. Proceedings of CSEE，2009，29（1：1-7)
[14] Gao, L., Jin, H., Liu, Z. Exergy Analysis of Coal-Based Polygeneration System for Power and Chemical Production [J]. Energy - The International Journal, 2004Vol. 29: 2359-2371.

ARGON-WATER CLOSED GAS CYCLE

Federico Fionelli * – Giovanni Molinari *

** Mechanical Engineer, Rome, Italy, f.fionelli@libero.it*

*** Prof. Ing., Dip. Meccanica e Aerospaziale, Università "La Sapienza" di Roma, g.molinari@dma.ing.uniroma1.it*

Abstract:

In the 40 forthcoming years, a substantial reduction of the electric energy production from oil and natural gas is expected; these sources are going to run out and therefore their price is going to increase markedly; the certain increase of the energy request will be met by a limited percentage increase of renewable energies, above all from coil and, despite the current situation, from the nuclear energy.

Due to technical-economic reasons, coal seems to be more recommended to meet the oscillations of the power request while the basic production is devolved upon the nuclear, in particular upon the fourth generation liquid metal reactors.

Super-hypercritical steam generators which are powered by coal have been reached a net output equal to 45%; leading companies research and development are oriented to the detection of high resistance metal alloys allowing to increase pressures and temperatures of operating fluid and therefore to increase the plant output from the current 45% to 50%; leading companies (i.e. Hitachi Power Europe GmbH) have been passed trials on pressurized parts in order to produce superheated steam at 350 bar and 700°C in coal fired boilers (Ref. http://www.hitachi-power.com/en/materials.html).

Against this background, the coal fired closed gas cycle, can become an important option for the electric power production thanks to its intrinsic advantages.

1. Introduction

The closed gas cycle works with fluid invariable both in nature and mass, excepting functional replenishments with an heat transfer to and from the cycle by heat exchangers. The disadvantage of the huge dimensions of these components is counterbalanced by some advantages; the most relevant ones are:

- The possibility of the gas choice
- The starting from initial thermodynamic condition independent on the environment, particularly for the pressure value
- Favourable effects deriving from employing a clean fluid.

It is important to consider also the favourable effects deriving from a clean fluid.

Regarding to the fossil fuel fired closed gas cycles, one of the main limits is represented by the low heat transfer capacity of the gas compared to the water in steam cycles; this results in a low *value of the cross loading of the combustion chambers*, which is expressed, as well known, by the ratio of input energy to the cross area of the chamber. For example, in the combustion chambers for air closed TG built in Germany in 1960-80, there were 1,2÷1,6 MW/m^2 against 6÷7 available in the steam power plants.

As a consequence the combustion chamber of Gelsenkirchen plant having volume of 500 m^3 was producing 17,25 MWe while a steam generator of the same dimensions can attain 75 MWe. (Ref.

MOLINARI, G., CASASANTA, P., *The Helium turbine in the energy conversion*, Sistema, Rome, 1980).

Actually, an efficiency enhancement is achievable either by increasing the cross sectional loading or by an enlargement of the combustion chamber. Using air as fluid these measures undergo some difficulties caused by its low heat transfer coefficient; in fact with a too high cross load, two different situations can occur: either the chamber temperature increases, and then the temperature of the exchange surfaces may become too high or increases the thermal content of the gas output, with an increase in energy losses and with imbalance of the entire downstream system. On the other hand with a lower cross load the chamber dimension get prohibitive for unit power nowadays requested for large plant.

2. The fluid choice

In order to overcome the difficulties encountered in the design and operation of the closed gas cycles, we focused our attention on gas-water mixtures. The injection of an appropriate amount of water in the gas downstream of the compressor allows to limit the temperature of the tube walls of the combustion chamber; the high heat transfer coefficient of boiling water vaporized in the tubes can significantly increase the thermal flow.

Moreover, the water in the mixtures leads to the increase the cycle work ratio.

To achieve this objective, in addition to the economic availability, the mixture should have the following two main properties:

- High density
- Specific heat at constant pressure lower than steam

The former allows to have comparable volumetric flow rates of the two fluids starting from an appropriate choice of the mass flow rate ratios in the tubes of the combustion chamber; the latter widens the gap between the P_T power of the turbine and compressor mechanical power P_C, which is expressed by the following (1) e (2):

$$P_C = M_G \times c_{pG} \times (T_{2r} - T_1) \qquad (1)$$

$$P_T = (M_G + M_W) \times c_{pGW} \times (T_1 - T_{2r}) \qquad (2)$$

where M_G and M_W are the gas and water mass flow rate, and c_{pGW} the specific heat at constant pressure of the steam-gas mixture.

The effect of the condition $c_{pG}<c_{pW}$ is higher in the reduction of the gas compression work compared to the lower contribution which gives to the expansion work of the mixture, with benefits to the useful work; substantially, the useful power $P = P_T - P_C$ increases because the turbine, in addition to working with a greater mass flow rate, develops an even higher mass work due also to the condition $c_{pGW}>c_{pG}$ (Ref. LOZZA, G., *Gas Turbines and Combined Cycles*, Esculapio, Bologna, 2006 – CAPETTI, A., *Thermal Engines*, UTET, Torino, 1964).

The gas which we think the best to meet the foreside requirements is the Argon, with a molecular mass of 40 and then a normal density of 1,786 kg/Nm^3 and Cp_A=0,52 kJ/(kg K) i.e. ¼ of that of the superheated steam at high temperature; the ratio Cp/Cv is equal to 1,667.

The ratio $\gamma=Cp_{AW}/Cv_{AW}$ of the mixture is calculated as weighted average on the mass flow rate of the two fluids. To this regard, it should be noted that since $\gamma_{AW} < \gamma_A$, for a given expansion ratio, the output mixture temperature from the turbine is higher than Argon. This is a thermodynamic disadvantage of the mixture, however mild compared to the above-mentioned benefits.

The properties Cp and γ of both components and consequently this of the mixture, particurarly their dependence on the pressure are very important not only for the nominal performances of the plant but also for their variation at partial load as specified speaking on the power plant regulation.

3. The proposed cycle

The proposed Argon-water closed cycle is characterized at full load by the following thermodynamic features;

- Maximum pressure: 343 bar
- Minimum pressure: 1 bar
- Maximum temperature: 700 °C
- Minimum temperature: 40 °C
- Inter-refrigerated three-stage compression
- Two reheaters

As an optimal Argon-Water mass ratio of the mixture, the value 2/3 was chosen (M_A/M_W=2/3). Actually, if the percentage of water of the mixture is higher, the total efficiency decreases owing to a lower inlet temperature in the boiler; if the percentage of water in the mixture is lower, the result is the same because the cycle work ratio becomes too low.

The choice was also supported by the fact that, with a view to implementing a plant of unit power which can be compared to that of the current coal-fired supercritical groups, the chosen mass flow rate of the two fluids are 320 and 480 kg/s, respectively (M_A = 320 e M_W = 480 kg/s) for a full load of 800 kg/s.

The proposed cycle is shown in figure 1.

3.1 Plant machinery

Referring to the Argon compression, the increase from 1 bar to 343 bar is obtained by three compressor each having the same compression ratio equal to 7. Enormous flow rate at the beginning leads to an axial compressor (1,7 Mm^3/h) leads to an axial compressor which is a feasible solution also for the second compressor (246000 m3/h). As regard the third compression we think it could be preferable a centrifugal machine because of the very low height of the axial blades (about 15 mm). The centrifugal compressor could be a two-stage machine each having 2,65 compression ratio. We assumed efficiencies 89 % and 84 % for axial and centrifugal machine respectively.

For the Argon Water mixture expansion we have a Curtis wheel for the high pressure turbine followed by a reaction medium and low pressure turbines. We assumed efficiencies 75 % for the Curtis turbine and 90 % for the reaction turbines.

The boiler feedwater pump is a variable centrifugal multistage machine electric motor driven with an efficiency of 70 %.

3.2 Plant heat exchangers

Main plant heat exchangers are the regenator, the two compressor intercooler including the argon cooling exchangers by service water, the mixer and the condenser. Figures 2-3-4-5 show the working conditions of the condensate regenerator, of the A e B exchangers, of the inter-refrigerator and of the mixer.

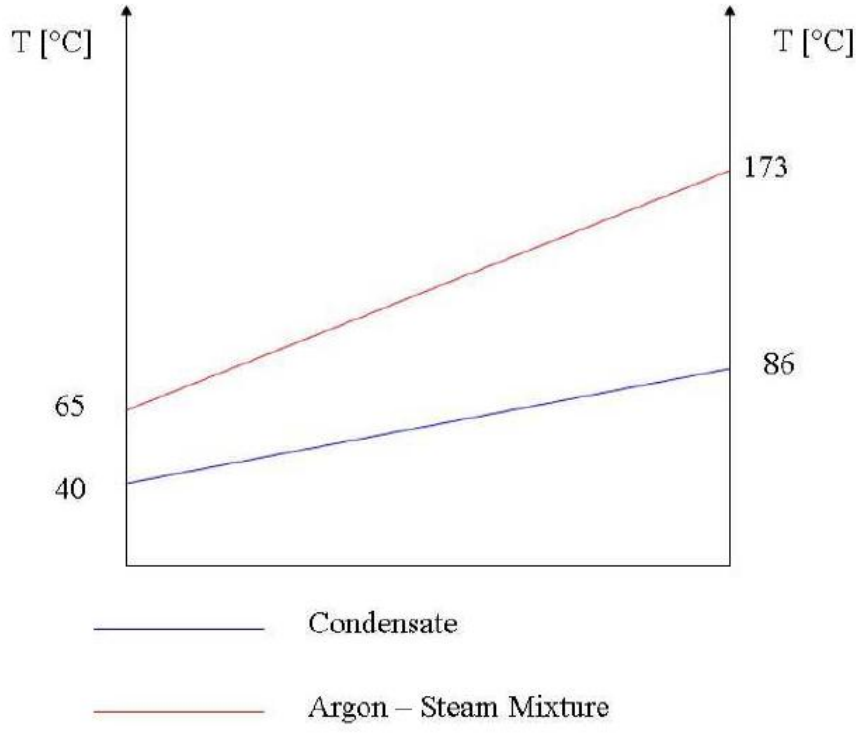

Fig. 2 – Condensate regenerator

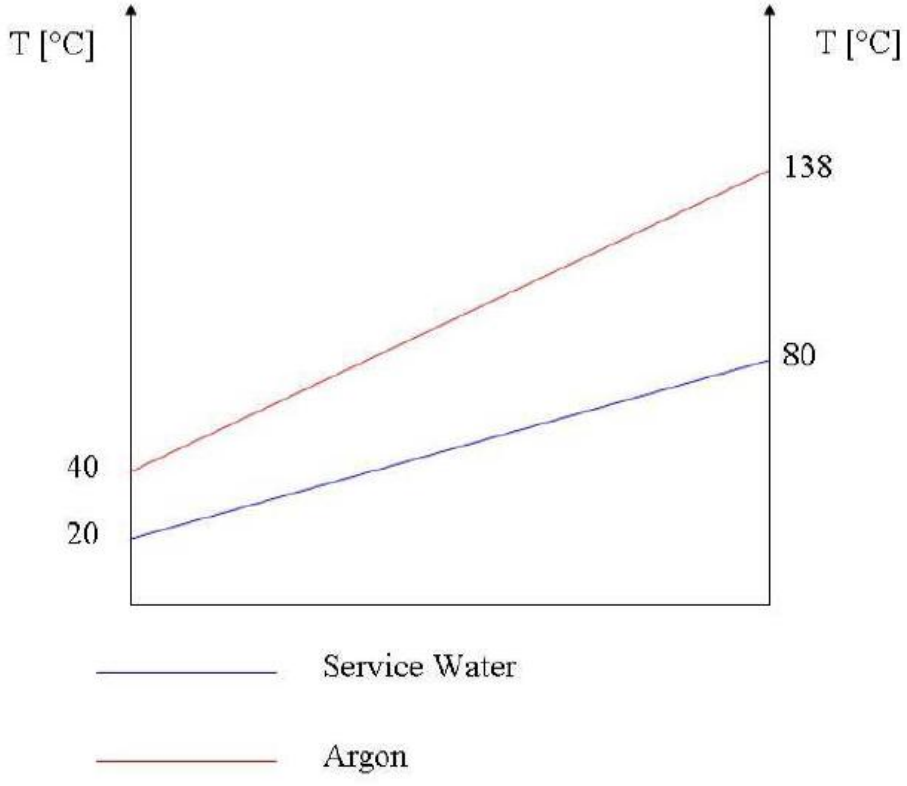

Fig. 3 – Intercooler 1 exchanger A

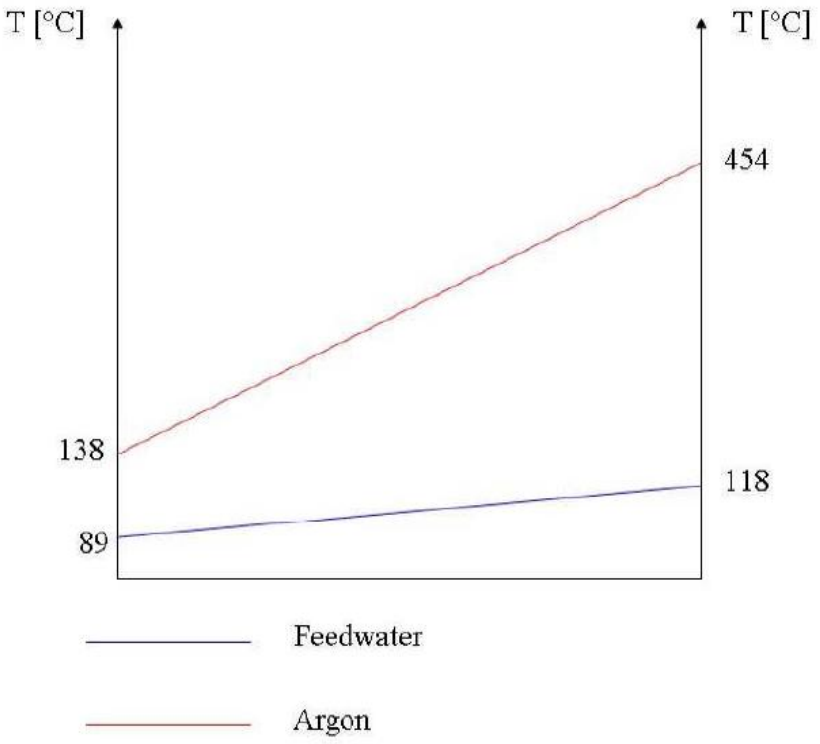

Fig. 4 – Intercooler 1 exchanger B

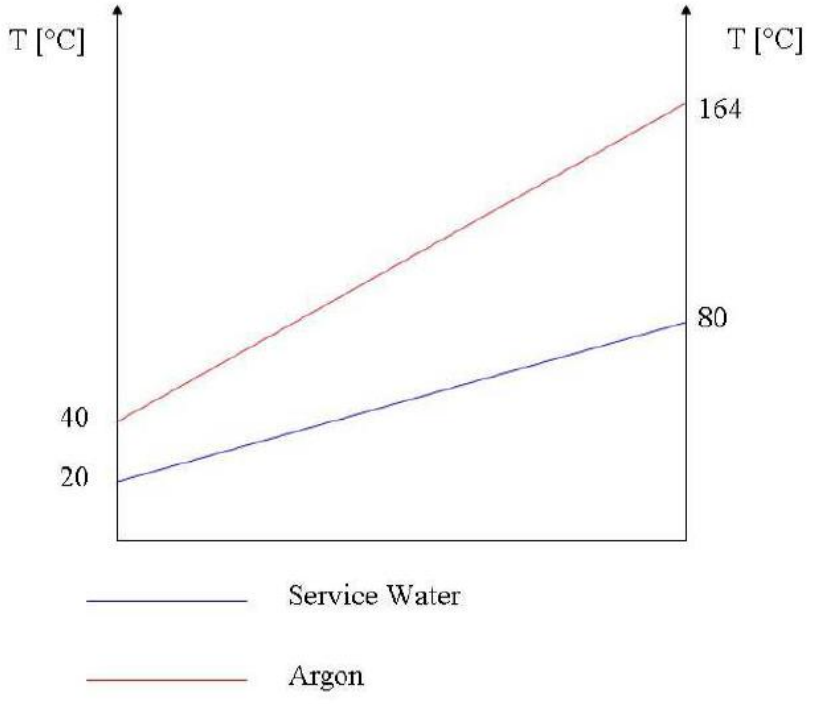

Fig. 5 – Intercooler 2 exchanger A

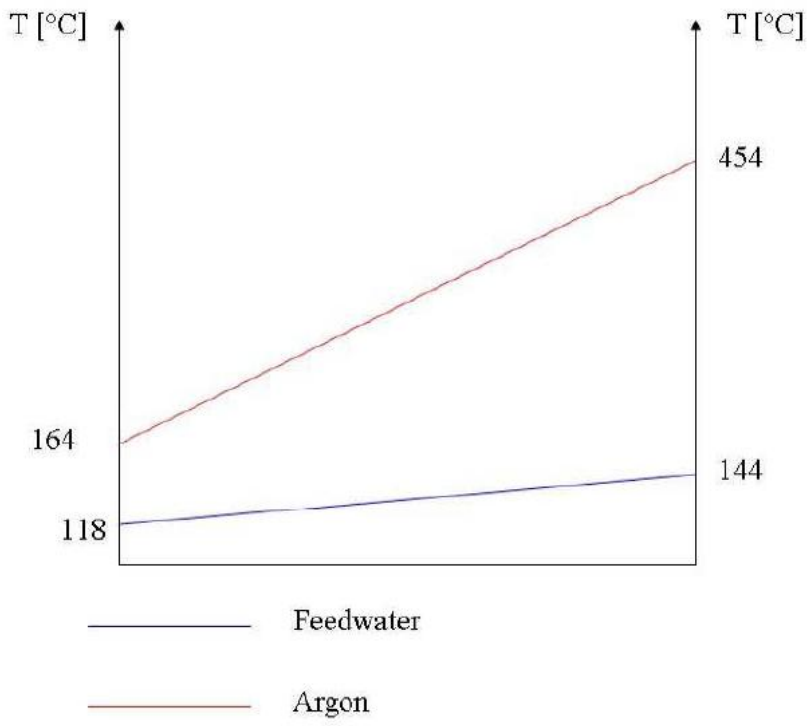

Fig. 6 – Intercooler 2 exchanger B

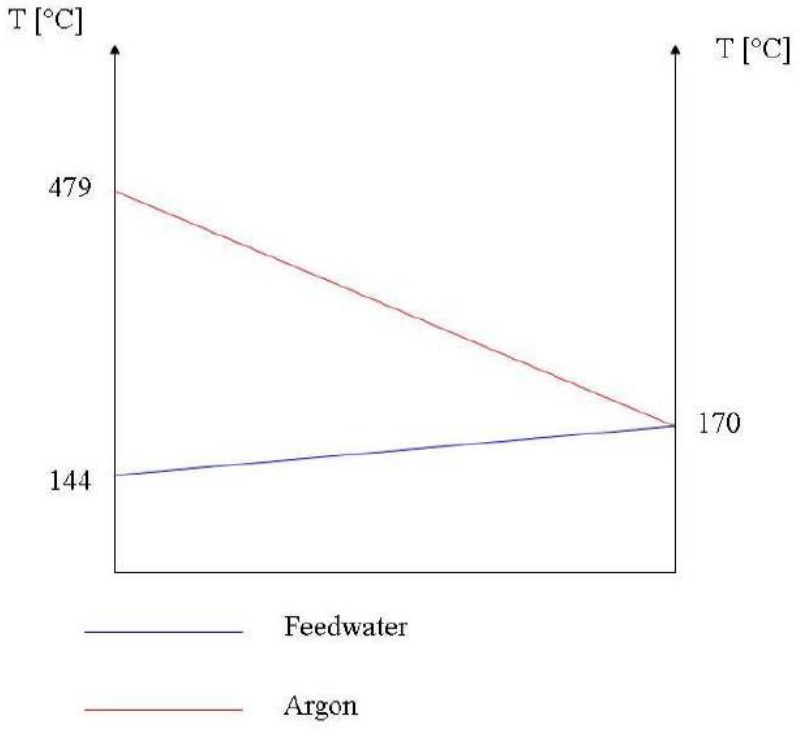

Fig. 7 – Mixer

Figure 8 shows schematically the thermodynamics of the mixture in T-S plan.

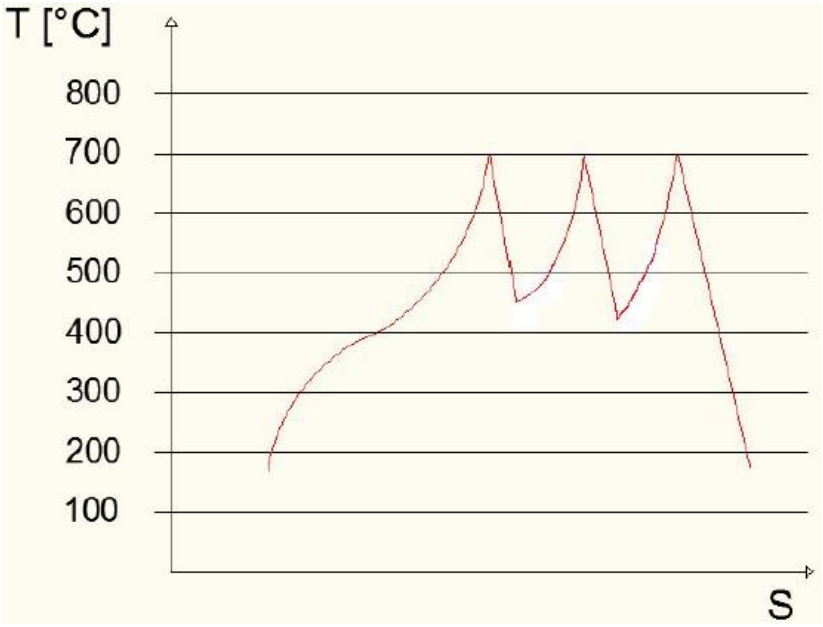

Fig. 8 – Thermodynamic of the mixture

3.3 The boiler

The combustion chamber is fuelled by coal (6000 Kcal/kg); the boiler it is composed by a combustion chamber which is cooled by wall screen with Argon water mixture coming from the mixer. After gas tempering fuel gases cross the RH2 then RH1-HT then SH-HT then RH1-LT then SH-LT. At this point we have a flue gas extraction for the gas tempering and finally the air-preheater.

The RH2 as the first heat exchanger because of the favourable low pressure considering the thermo-mechanical stress. Similar consideration have been taking in mind for the all other exchanger positioning.

Mixture inlet temperature even at partial load is about 170 °C; Argon water mixture exit from the combustion chamber at 400 °C. A schematic view of the boiler is showed in Fig. 9.

Because of the particular position and configuration of the various heat exchanger the mixture pressure drop is increasing from the RH2 to SH; it is a pressure drop distribution which is favourable for turbine power because leads to larger expansion ratio in the three turbines and then to plant efficiency enhancement.

4. Performances of the cycle

The proposed system efficiency is calculated as ratio between the alternator power output, reduced of the power consumed by the extraction and feeding pumps, and the thermal power of the fossil fuel.

The power output by the three turbines and the power input by the two compressors and the pumps are shown in table 1 together with the plant electrical power.

The contributions of the various machines to the above total values for both the expansion and compression are specified in table 2 and 3.

Table 1.

P HP Turbine [MW]	P MP Turbine [MW]	P LP Turbine [MW]
368,2	356,6	626,1
	P Tot Turbine [MW]	
	1351,0	
P LP Compr. [MW]	P MP Compr. [MW]	P HP Compr. [MW]
69,0	69,0	73,1
	P Tot Compr. [MW]	
	211,0	
	P Pumps [Mwe]	
	24,5	
	Plant Power [Mwe]	
	1081,2	

Table 2.

	T-HP	T-MP	T-LP
T1(°C)	700	700	700
β_t	3,5	3,5	20
c_{pAW} (kJ/kgK)	1,823	1,584	1,486
γ_{AW}	1,513	1,448	1,443
$T_{2,is}$ (°C)	363	387	115
T_2 (°C)	447	419	173

Table 3.

	C-LP	C-MP	C-HP
T1(°C)	40	40	40
β_t	7	7	7
c_{pAW} (kJ/kgK)	0,52		
γ_{AW}	1,667		
$T_{2,is}$ (°C)	408		
T_2 (°C)	454	454	479

The thermal power Q_{TOT} received in total by the fluid, calculated by the sum of thermal power in the plant exchangers (vaporizer, SH, RH1, RH2) amounts to Q_{TOT}=2232,8 MW.

The thermodynamic efficiency of the η_{TER} cycle is therefore given by the Eq. (3):

$$\eta_{Ter} = \frac{(P_{T-TOT} - P_{C-TOT}) \times \eta_o - P_P}{Q_{TOT}} \qquad (3)$$

where η_0 includes the mechanical and electrical efficiency of the group. Assuming η_0=97%, η_{TER}=48,4 % is obtained.

Finally, assuming an efficiency of the boiler η_{GV} = 93,5 % the plant efficiency results $\eta_{IMP} = \eta_{GV}$ = 45,3 %. We note that this efficiency has been obtained on the basis of the efficiencies assumed for the turbomachinery whose value could be slightly enhanced with benefit of plant efficiency aiming at achieve η = 50 %.

4.1 Performances and mixture composition

We examined the variations of the plant performances at full load as the dosage of the two components of the mixture changes. Figures 10-11-12-13 show in the order the cycle efficiency, the cycle work ratio, the electrical power of the plant and the boiler inlet temperature.

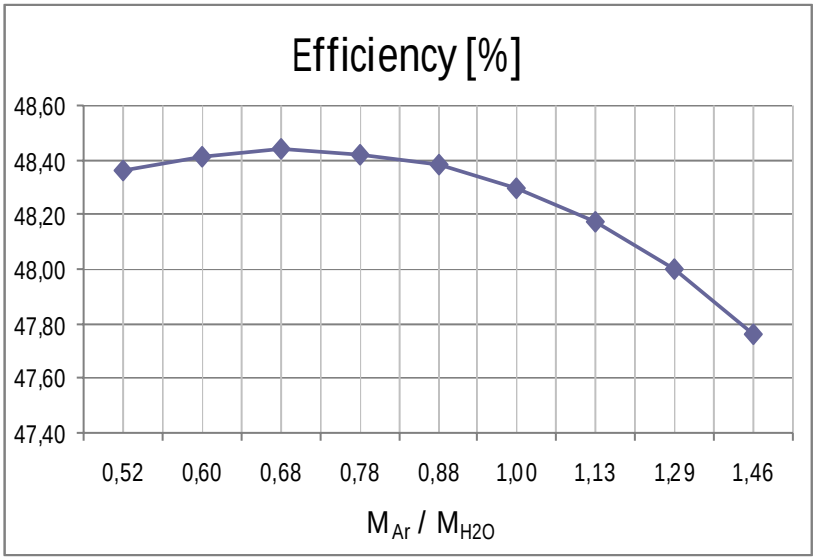

Fig. 10 – Plant efficiency VS mixture dosage change

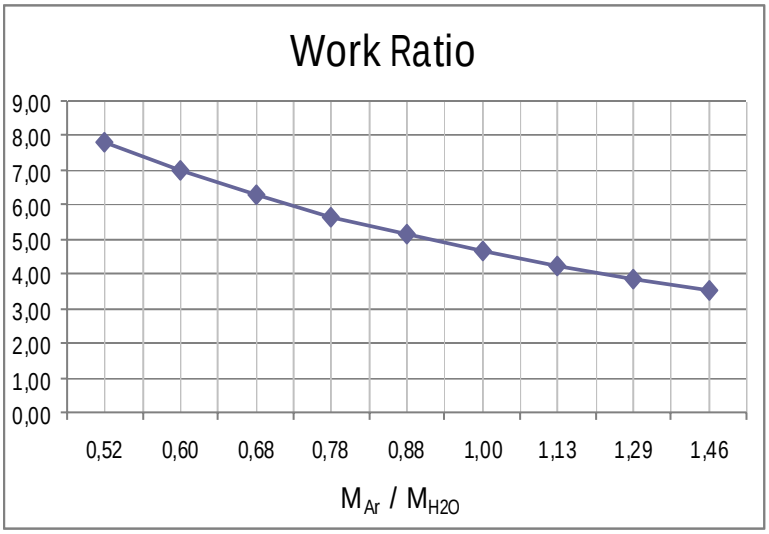

Fig. 11 – Work ratio VS mixture dosage change

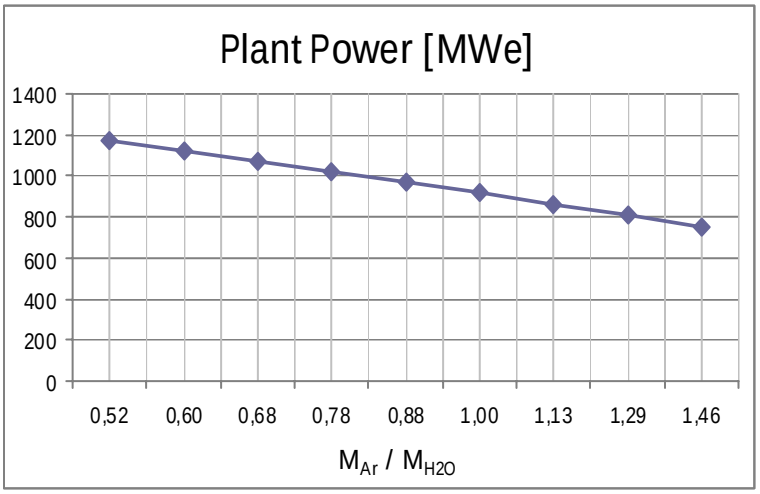

Fig.12 – Plant power VS mixture dosage change

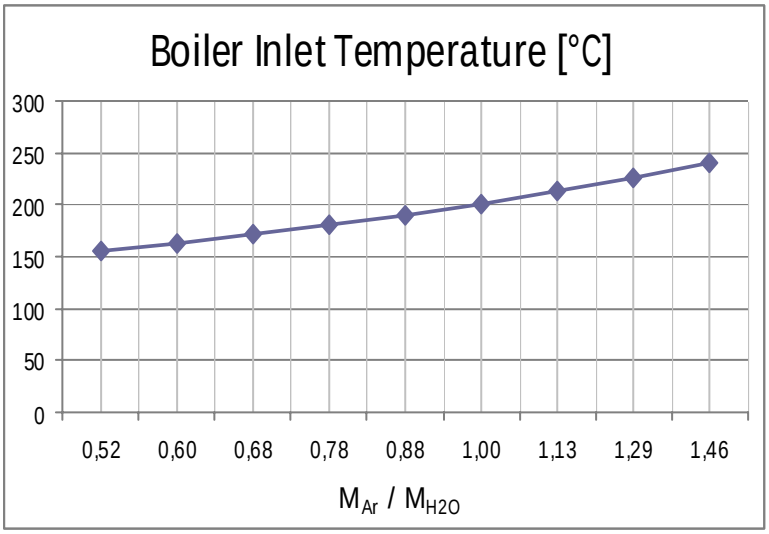

Fig. 13 –Boiler inlet temperature VS mixture dosage

5. Partial load performances

Finally, we examined the plant performances as the mixture nominal (2/3) mass flow rate changes. The results are gathered in figures 14-15-16-17-18 showing the cycle efficiency, the plant electrical power, the boiler inlet temperature, the heat specific at constant pressure and the outlet temperature of the turbines. As regards the efficiency we observed that its decreasing at lower loads is due to the diminution of the Cp and □ of the mixture flowing in the turbine.

In effect while Argon Cp is constant the steam one lowers, at constant temperature when the pressure decreases with the load.

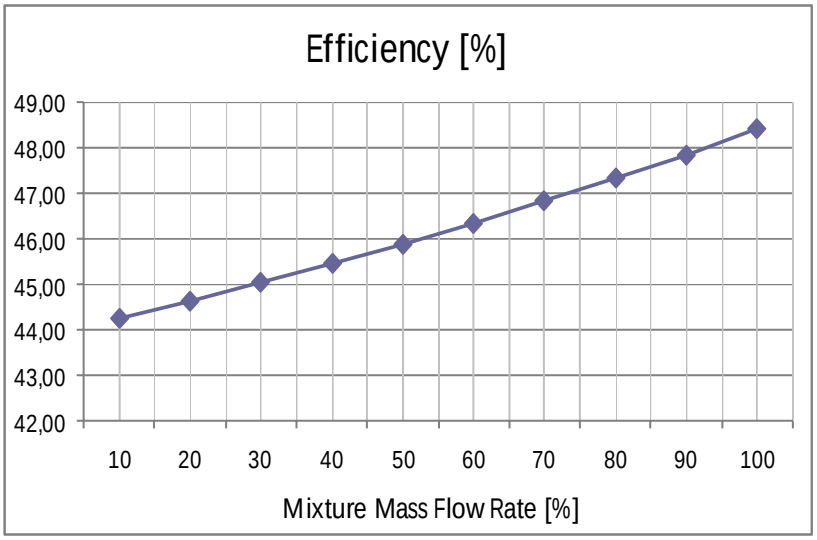

Fig. 14 – Plant efficiency VS mixture mass flow

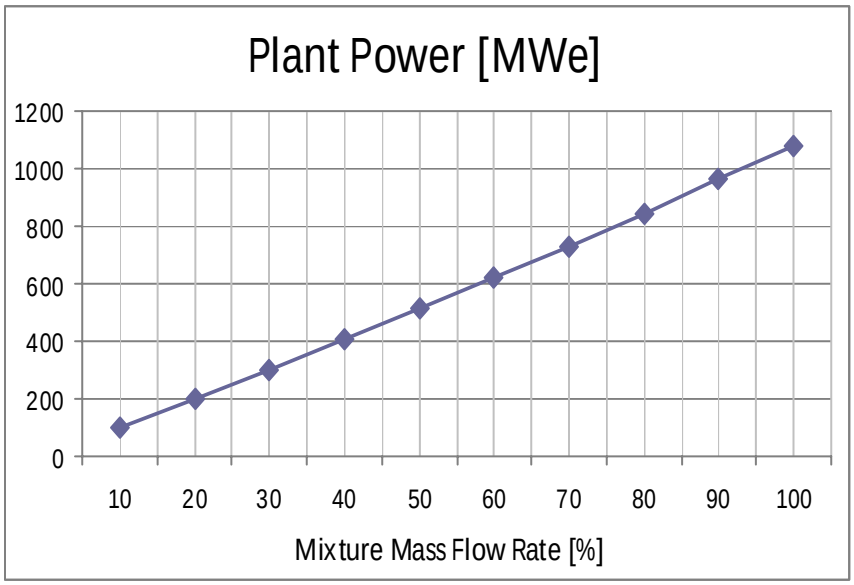

Fig. 15 – Plant power VS mixture mass flow

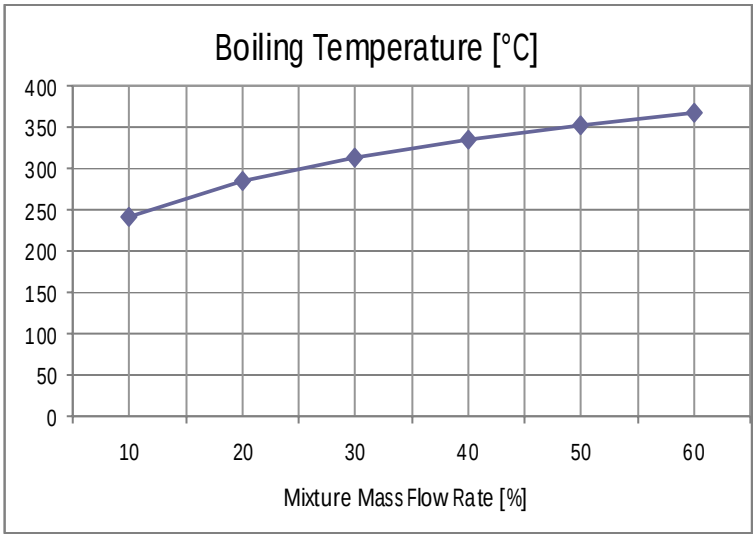

Fig. 16 – Boiler temperature VS the mixture mass flow rate

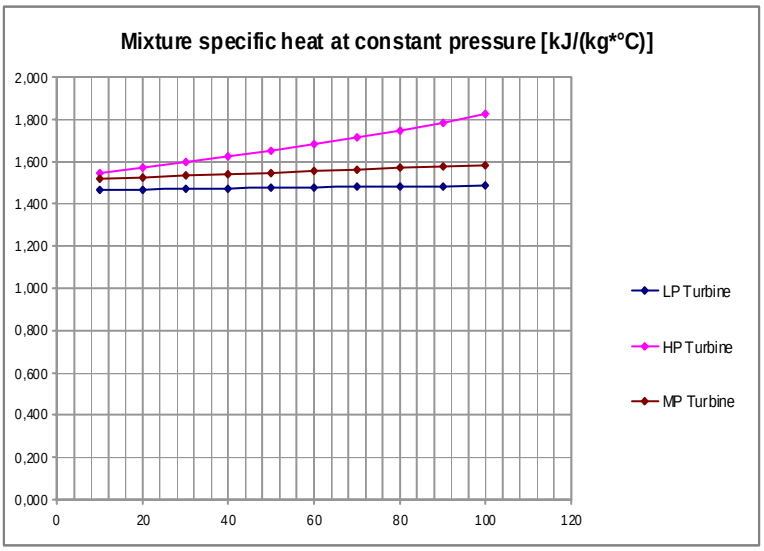

Fig. 17 – Mixture Cp VS the mixture mass flow rate

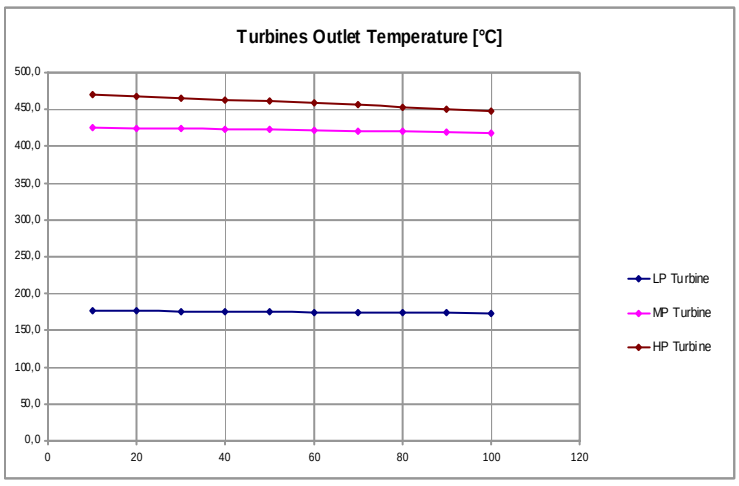

Fig. 18 – Turbines outlet temperature

6. Conclusions

The proposed thermodynamic cycle is presented as a suitable alternative for the generation of electrical power compared both to coal fired supercritical steam cycles that have to supply load variation, and the gas combined cycles if the fuel price gets prohibitive.

Concerning with the boiler design, it would be necessary to investigate experimentally the critical thermal flow of the argon-water mixture; particularly, for the design of the superheater and reheaters, the gas tempering has been considered in order to control the thermo-mechanical stress of the heat exchangers.

From our analysis the following features of the proposed plant can be focused;

- Cycle efficiency remains practically constant with load
- The maximum temperature of 700 °C in the turbine is permitted by available steel alloys and therefore do not require blade refrigeration; moreover turbines operate without moisture even at partial load.
- The absence of mass extraction in the turbine leads to simplification of the plant; concerning this we note that the utilization of mass extraction in the turbines could lead to an efficiency enhancement but with disadvantages of higher complexity power plant configuration and operation.
- Plant turbomachinery do not meet particular design problems being the Argon thermophysical properties similar to the air; on the other hand, the higher Cp/Cv ratio, under the same condition and compression ratio and axial velocity, Argon undergoes a minor flow area variation in comparison with air obtaining a better flow pattern.
- The results obtained in the analysis of the proposed plant lead to dimensions of the boiler comparable to the current supercritical steam power plant

References

[1] CAPETTI, A., Motori termici, UTET, Torino, 1964.

[2] MOLINARI, G., CASASANTA, P., I turbogruppi a elio nella conversione di energia, Sistema, Roma, 1980.

[3] MOLINARI, G., Turbogruppo a gas, Esa, Roma, 1997.

[4] LOZZA, G., Le turbine a gas ed i cicli combinati, Esculapio, Bologna, 2006

[5] “http://www.hitachi-power.com/en/materials.html”

[6] “http://www.energy.siemens.com/hq/en/power-generation/power-plants/steam-power-plants/benson.htm#content=Efficiency”

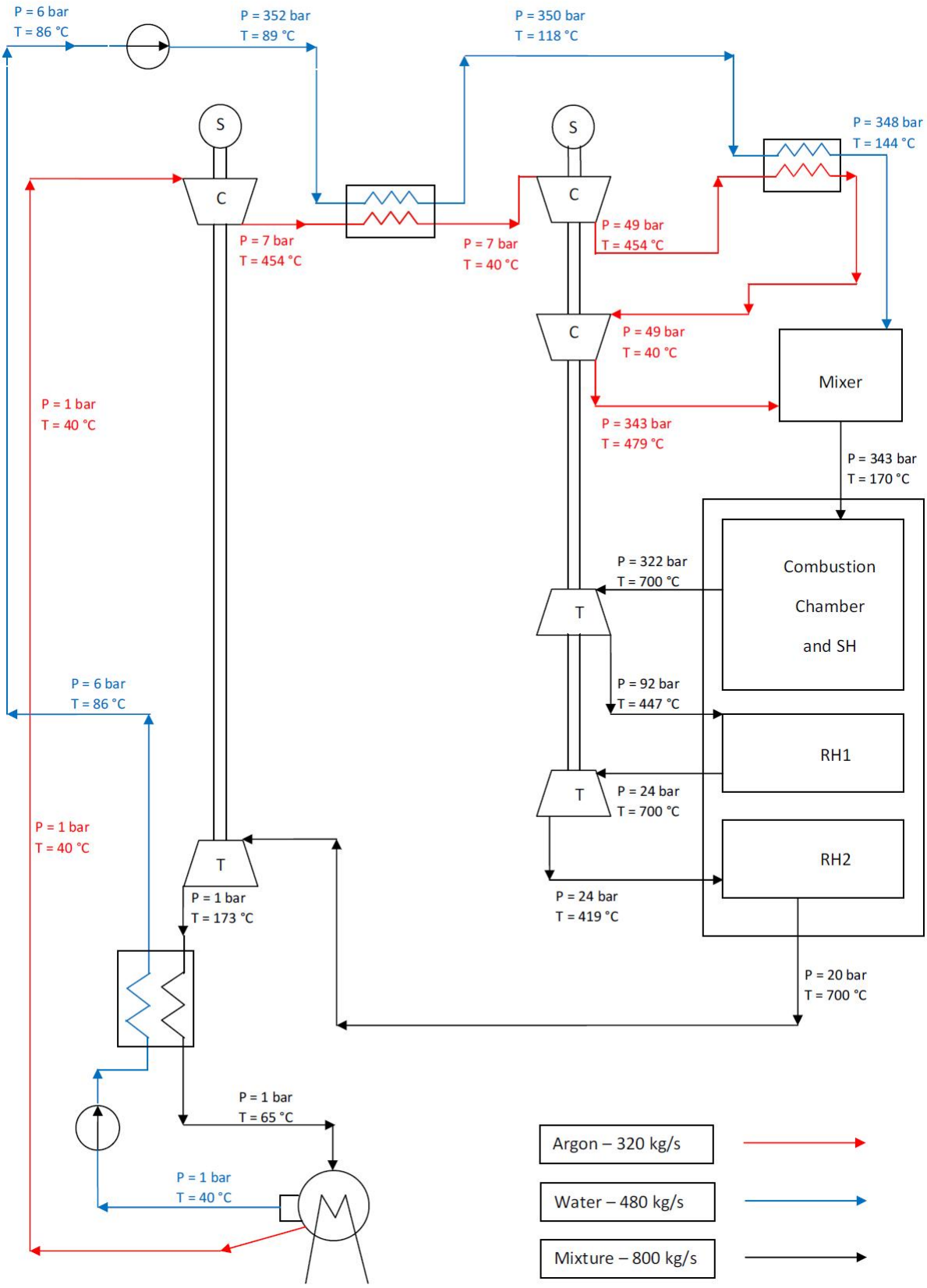

Fig. 1 – The proposed Argon Water cycle

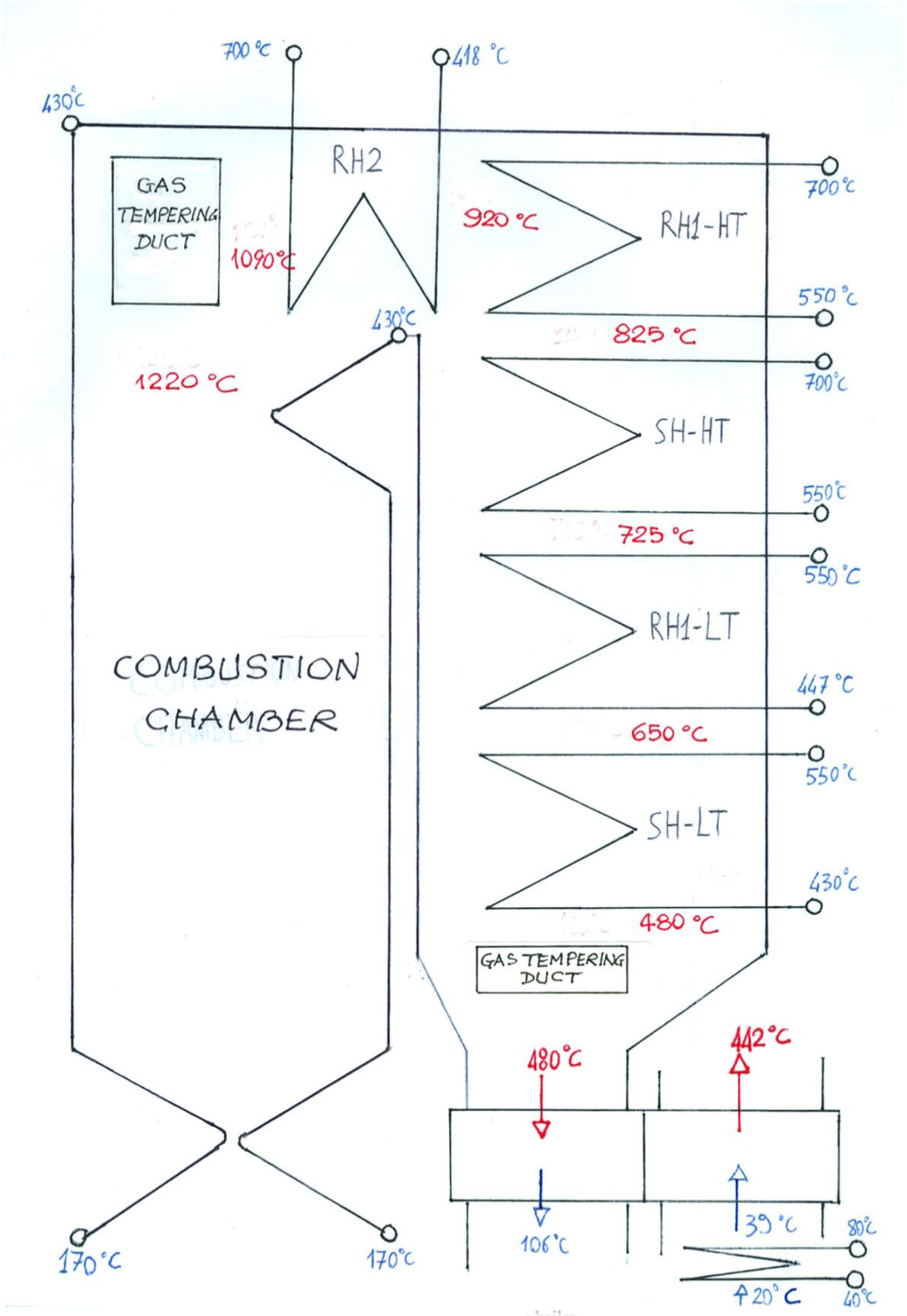

Fig. 9 – Schematic view of the boiler

Binary Alkane Mixtures as Fluids in Rankine Cycles

M. Aslam Siddiqi, Burak Atakan

Thermodynamics, IVG, Faculty of Engineering, University of Duisburg Essen,
Lotharstr. 1, 47048 Duisburg, Germany

aslam.siddiqi@uni-due.de(CA)
b.atakan@uni-due.de

Abstract:

Waste heat recovery from the exhaust gases of gas turbines, geothermal resources, and from industrial plants offers a great opportunity for energy conservation by productively using the waste energy. Organic Rankine cycles (ORC) have been used to convert low grade heat available as waste from exhaust gases from turbines and engines as well as from industrial plants. Different working fluids (generally pure substances) have been investigated and in part used for this purpose. This was also the theme of our previous work. Among others the efficiency of the process depends on the extent of losses from irreversible heat transfer from the source and to the sink. The losses depend on the levels of matching of *T*-$\dot{H}$ curves of heat source, working fluid and the heat sink. This can be achieved by matching the corresponding *T*-$\dot{H}$ curves. One way to tune the properties is to use a suitable mixture in place of pure substance. There are only a few studies which report the use of fluid mixtures as the working fluid for ORC. In the present communication we report the results of model calculations of binary mixtures of one short chain alkane with one long chain alkane (hexane + decane, hexane + dodecane) at different compositions. The upper pressure levels were selected up to 20 bar for safety reasons and the cooling temperatures were selected at levels suitable for co-generation. At a fixed condenser pressure the mixtures perform better than the pure components (20-50% higher efficiencies). At a fixed condenser temperature the efficiency varies with the condensation pressure and is higher at lower condenser pressures. The exergy losses occurring at various stages were also investigated. The results for the total heat recovery efficiency, second law efficiency and the surface area of the heat exchanger have been discussed.

Keywords:

ORC; Rankine cycle; Exergy loss; Thermal efficiency; *T*-H Diagrams

1. Introduction

The utilization of low, medium and high temperature heat has been studied extensively in the past [1-10]. The choice of working fluids is of key importance for the performance of an organic Rankine cycle (ORC). The number of working fluids which can be used in ORC systems is countless. The most important criteria for the selection of ORC working fluid are the high efficiency and low exergy loss which are basically governed by the thermodynamic properties. The efficiency of an ORC system depends on the entropy changes in the working fluid as well as in the environment during various stages. Thus it depends on the working fluid as well as on the working conditions (the temperature at which heat is available and the temperature at which it is rejected).

In our previous publications [11, 12] the results for some representative substances e.g. hydrocarbons, refrigerants, aromatics, were presented for the case of waste heat availability at 773.15 K, 623.15 K and 523.15 K. In contrast to most previous publications the combined generation of heat and power (CHP) using ORC is studied in our work, which is continued here, meaning that the heat rejection of the cycle shall be used for heating purposes. Such systems can be used as the energy supply for hospitals, small industries etc. Thus, to be useful for this purpose, a heating of the cooling water to 85°C was studied. The previous studies were limited to pure

substances. An important limitation of an ORC with a pure working fluid is the isothermal boiling, which often leads to a bad thermal matching between the working fluid and the heat source as well as between the working fluid and the cooling water stream due to pinch point limitations which again lead to large irreversibilities. A *T*-H -diagram helps to visualise [13] the complete process, as an example the heat transfer from hot air to two different fluids is depicted in Figure 1. In this case not only the ORC, but also the process lines for the hot exhaust gas and the cooling water are included and thus the whole process can be visualised. Any pinch point breach can be seen on it and the temperature differences along the heat transfer processes can easily be seen as a direct measure of thermodynamic irreversibilities. Fig.1 shows qualitatively the temperature variation in boiler in ORC with pure substance (full line) and a binary mixture (dashed line). Since the temperature difference between the heat source and the fluid mixture is throughout smaller than between the pure fluid and the heat source, the irreversibilities in the former case are smaller. This could lead to improved second law efficiencies. Also, similar losses from irreversible heat transfer to the sink will be observed.

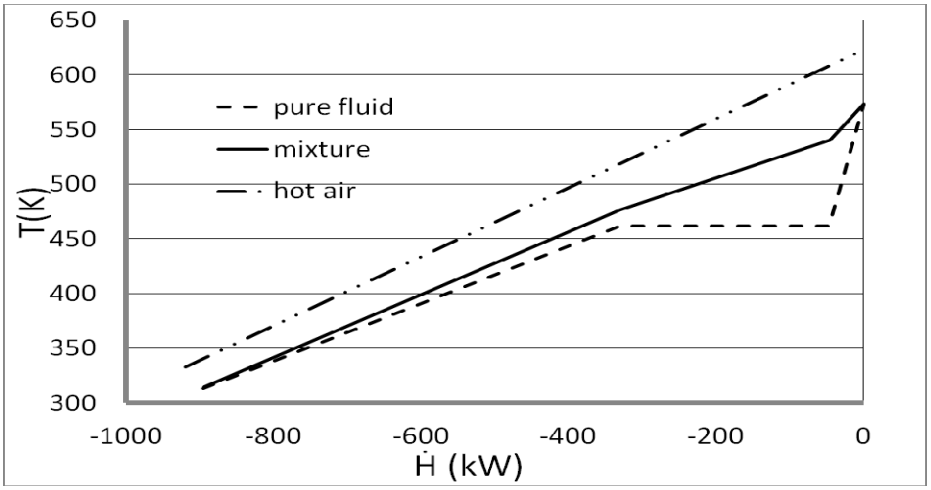

Fig. 1. Temperature variation in boiler for pure fluid and fluid mixture.

Some studies with binary and ternary mixtures of non-azeotropic working fluids featuring evaporation/condensation at different temperatures, i.e. non isothermal (variable) heat addition and rejection have been reported from time to time [7, 14-18]. However, the studies are limited and report the results obtained under quite different conditions. Due to the numerous parameters involved, a comparison of the performance of mixtures as working fluids to pure substances is difficult. In the present study it is attempted to systematize such a comparison. The results of model calculations of binary mixtures of one short chain alkane with one long chain alkane (hexane + decane, hexane + dodecane etc.) at different compositions are reported here. The model calculations have been performed keeping fixed as many parameters as possible and study the performance by varying only a limited number of parameters. Apart from the first law and the second law efficiencies, the required surface area for the heat exchanger and the condenser is roughly estimated for each process since this is an important factor regarding the investment costs. The cycles are studies for different evaporator pressures of up to 2000 kPa, which is a reasonable value for single stage turbines and also for safety reasons in small devices.

2. Method

ORC is a Rankine cycle in which the working fluid is not water but an organic fluid. The working fluids for Rankine cycle are classified in literature as dry with positive slope (dT/dS) or isentropic with infinitely large slope depending on the shape of temperature-entropy (T-S) diagram. A detailed description is found in [1]. Water (and Ammonia) with negative slope (dT/dS) have been termed as wet fluids. The model used for the calculations and the numbering of the different states is shown in Figure 2(a) for a ready reference.

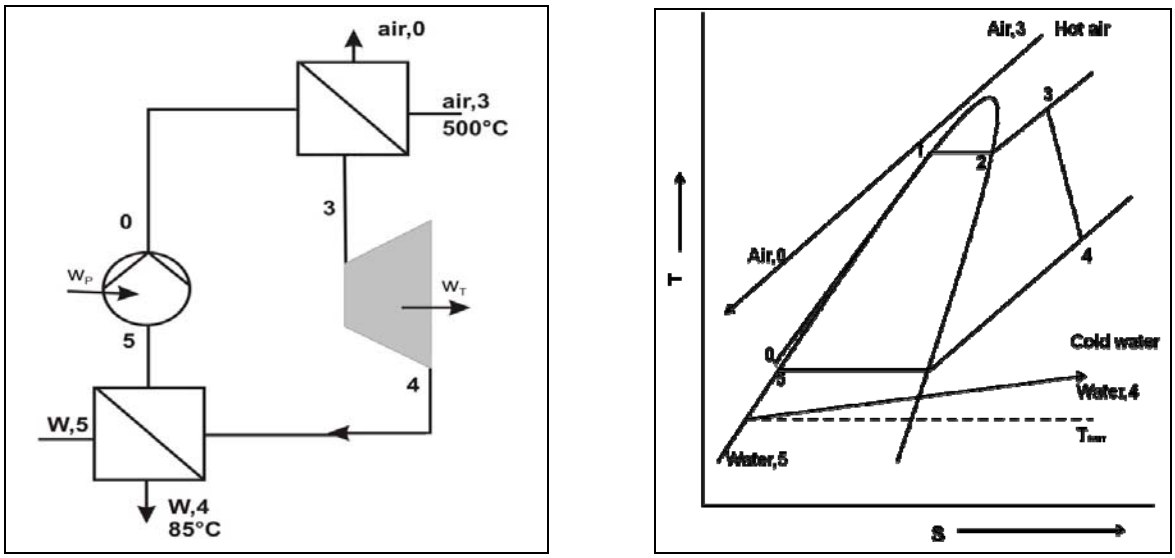

(a) *(b)*

Fig. 2. The ORC system used in this study (a) and the related schematic T-s diagram (b), the entropy scales will differ for the three different fluids.

The system consists of:

a) hot gas that enters the system boundary at $T_{air,3}$ transfers energy via heat exchanger to the working fluid (its temperature drops to $T_{air,0}$) and leaves the system boundary at $T_{air,surr}$.

b) working fluid that enters the system boundary at $T_{F,0}$ at a high specified pressure (state 0), is heated to $T_{F,3}$ by the heat energy delivered by the air, drives the turbine to produce electricity, passes through a condenser thereby delivering the rest heat energy to a cold water stream. It leaves the condenser at $T_{F,5}$. The working fluid is brought back to the initial state 0 through a pump. The difference between the temperatures $T_{F,5}$ and $T_{F,0}$ is very small (max. 0.7K). The power of the pump has been taken into account while calculating the net power of the ORC cycle or of the complete process.

c) cold water stream that enters the system boundary at $T_{W,5}$ is heated to a higher temperature $T_{W,4}$ for further use.

The temperature $T_{air,0}$ is at least 10 K higher than $T_{F,0}$ in all the cases.

The related qualitative T-s diagram is also drawn in Figure 2(b). An enthalpy stream of hot air, simulating an exhaust gas at a definite temperature, is available from an industrial process or an engine. Energy will be transferred as heat to the working fluid of a Rankine cycle. The Rankine

cycle produces electricity and rejects the heat at a lower temperature which can be used further for the heating of cold water (W). The equations used for the model process calculations are summarized below.

The working fluid which leaves the condenser as boiling liquid at a lower pressure (state 5, $p = p_{cond}$) is brought to a higher pressure ($p = p_{boiler}$, state 0) with the help of a feed pump.
The specific work of the feed pump is then

$$w_{50} = \frac{v(p_{boiler} - p_{cond})}{\eta_P} \tag{1}$$

where v is the specific volume of the saturated liquid in state 5. Thus

$$h_{F,0} = h_{F,5} + w_{50} \tag{2}$$

The subscript F refers to the fluid of the Rankine cycle and the numbers refer to different states.
The working fluid receives energy from the hot gas stream via a counter current heat exchanger and is vaporized in three stages:

a) Heating of the working fluid up to boiling (state 0 → state 1)
b) Complete vaporization of the working fluid (state 1 → state 2)
c) Superheating of the fluid (state 2 → state 3).

The energy balance across the heat exchanger gives:

$$\dot{m}_F \cdot (h_{F,3} - h_{F,0}) + \dot{m}_{air} \cdot (h_{air,0} - h_{air,3}) = 0 \tag{3}$$

The heat exchanger, which is assumed to be adiabatic towards the surrounding, may be thought to be made up of three parts and in each part one of the above operations takes place. So the first part, i.e. the heat transfer needed for raising the temperature of the working fluid to the boiling temperature can be written as:

$$\dot{Q}_{add,01} = k_{01} \cdot A_{01} \cdot \Delta T_{LMTD,01} = \dot{m}_F \cdot (h_{F,1} - h_{F,0}) \tag{4}$$

The logarithmic mean temperature difference ΔT_{LMTD} is defined as:

$$\Delta T_{LMTD,01} = \frac{\Delta T_0 - \Delta T_1}{\ln(\frac{\Delta T_0}{\Delta T_1})} \tag{5}$$

The pinch point for the heat exchanger (states: 0-3) restricts the maximum mass flow rate in the cycle, while the pinch point in the heat rejection from the cycle limits the maximum cooling water flow rate.

The temperature of air in state 1 is written as

$$T_{air,1} = T_{air,0} + \frac{\dot{m}_F \cdot (h_{F,1} - h_{F,0})}{\dot{m}_{air} \cdot c_{p,air}} \tag{6}$$

Similar equations hold for the second and the third part of the heat transfer.
The superheated vapour is then expanded in a turbine (state 3→state 4) to the pressure of the condenser, p_{cond}:

$$w_{34} = \eta_T \cdot (h_{F,4s} - h_{F,3}) \tag{7}$$

The isobaric condensation of the vapour to the state of boiling liquid (state 4 → state 5):
The heat will be transferred from the cycle to the cold water (Index: W) running in the condenser.

$$\dot{Q}_{rem} = -\dot{m}_F \cdot (h_{F,5} - h_{F,4}) = \dot{m}_W \cdot (h_{W,4} - h_{W,5}) \quad (8)$$

Various parameters (e.g. the thermal efficiency of the cycle $\eta_{th,ORC}$, the total efficiency $\eta_{th,total}$. the net power of the process P_{net}, the exergy loss of the hot stream and the $T - \dot{H}$ diagram for the process) are used to evaluate system performance.
The thermal efficiency of a Rankine cycle is defined as [9]

$$\eta_{th,ORC} = \frac{\left|w_{50} + w_{34}\right|}{q_{03}} = \frac{\left|w_{50} + w_{34}\right|}{(h_{F,3} - h_{F,0})} \quad (9)$$

The net power delivered by the system is

$$P_{net} = \left|\dot{m}_F \cdot (w_{50} + w_{34}) + \dot{m}_W \cdot w_{P,W}\right| \quad (10)$$

with

$$w_{P,W} = v_{W,5} \cdot \Delta p_{P,W} / \eta_{P,W} \quad (11)$$

The efficiency of the Rankine cycle given by equation (9) does not take into account any losses due to the release of the exhaust gases at temperatures which are higher than the one of the surroundings. However, the exhaust gas at the exit of the heat exchanger cannot be cooled down to the temperature of the surroundings due to the pinch point restriction and thus contributes to the exergy loss. A more realistic approach will be to consider this enthalpy loss and define the thermal efficiency of the complete process, viz. $\eta_{th,total}$

$$\eta_{th,total} = \frac{P_{net}}{\dot{m}_{air} \cdot c_{p,air} \cdot (T_{air,3} - T_{air,surr})} \quad (12)$$

In order to make the comparisons easier the mass flow rate of the air was chosen such that the term in the denominator gives 1000 kW. This means that the maximum possible heat transfer to the cycle would correspond to this value.

If the air is cooled up to $T_{air,surr}$ the exergy (loss+destruction) rate for the complete process can be calculated

$$\dot{I}_{Process} = \Delta\dot{E}_{Process} = \dot{E}_{air,3} - P_{net} - \Delta\dot{E}_{acc,water} = \Delta\dot{E}_{air,3,0} + \dot{E}_{loss,Exhaust} - P_{net} - \Delta\dot{E}_{acc,water} \quad (13)$$

with

$$\Delta\dot{E}_{air,3,0} = \dot{m}_{air} \cdot [(h_{air,3} - h_{air,0}) - T_{surr} \cdot (s_{air,3} - s_{air,0})] \quad (14)$$

$$\dot{E}_{loss,Exhaust} = \dot{m}_{air} \cdot [(h_{air,0} - h_{air,surr}) - T_{surr} \cdot (s_{air,0} - s_{air,surr})] \quad (15)$$

$$\Delta\dot{E}_{acc,water} = \dot{m}_W \cdot [(h_{W,4} - h_{W,5}) - T_{surr} \cdot (s_{W,4} - s_{W,5})] \quad (16)$$

This formula assumes that the air exhausted to the atmosphere will be equilibrated with the surrounding without further usage ($E_{loss,Exhaust}$). This is termed as exergy loss in the following, coming due to the unavoidable exhausting of the air at a higher temperature than ambient. Also some exergy is gained (accumulated) in the water stream which is used further for heating purposes

($\Delta E\square_{acc,water}$). The thermal efficiencies defined by equation (9) and equation (12) do not reflect the ability to energy from low grade waste heat into usable work. Therefore, the exergy efficiency (i.e. the second law efficiency), which can evaluate the performance of the waste heat recovery is needed. The second law efficiency for the process ψ_{total} is calculated as

$$\Psi_{total} = \frac{\Delta \dot{E}_{acc,water} + P_{net}}{\dot{E}_{air,3}} \tag{17}$$

Another way to analyse the exergy loss for the complete process is to sum up the exergy destruction rates in all parts and the other exergy loss rates ($\dot{I}$):

$$\dot{I}_{Process} = \Delta \dot{E}_{Process} = \dot{I}_{Boiler} + \dot{I}_{Turbine} + \dot{I}_{Condenser} + \dot{E}_{loss,Exhaust} + \dot{I}_{Pump} + \dot{I}_{P,W} \tag{18}$$

where $\dot{I}$,s denote the exergy destruction rate in boiler, turbine or condenser. These have been calculated from the difference of the exergy streams flowing into the device and out of the device:

$$\dot{I}_{Device} = \dot{E}_{In} - \dot{E}_{Out} \tag{19}$$

The exergy destruction rates in the two pumps are the power consumed by the pumps. These exergy losses/destruction rates with different working fluids will be discussed later in this paper.

Besides this, the surface area of the heat exchanger A and of the condenser $A_{Condenser}$ required for the complete heat transfer is also very important from the point of view of its cost. This may be estimated using equation (4) for the three parts of the heat exchanger as well as of the condenser using typical values for the overall heat transfer coefficient k.

Description of the model process: The properties of working fluids needed for the calculations were taken from [19]. The isentropic efficiencies of the turbine and the pump were taken as 0.85. The model process was described by the following parameters:

Surroundings: T_{surr} = 298.15 K, p_{surr} = 101.3 kPa

Gas Stream: Air, ideal gas [c_p = 1.004 kJ/(kg K)] entering at 773.15 K or 623.15 K. The mass flow rate was constant at 2.097 kg/s or 3.0647 kg/s resulting in a maximum possible heat flow rate of 1000 kW. The exit temperature of the gas stream from the heat exchanger was calculated according to a pinch point analysis for the studied maximum temperature and pressure of the cycle fluid, leading to gas exhaust temperature T_{surr}.

Heat Exchanger: The ideal heat exchanger with 100% effectiveness was considered to be adiabatic towards the surrounding and isobaric. The heat is transferred in three stages from hot gas to the working fluid. The overall heat transfer coefficients, gas to liquid: $k_{l,g}$ = 40 W/(m^2 K) [state 0 → state 1, heat transfer between liquid and gas; state 1 → state 2, heat transfer between evaporating liquid and gas (in 2-phase region)] and $k_{g,g}$ = 20 W/(m^2 K) [state 2 → state 3, heat transfer between two gases] were assumed. ΔT_{pinch}=10 K was taken as temperature difference at the pinch point for most of the cases. In a few cases ΔT_{pinch} was higher than 10 K. Thus, the temperature of the hot exhaust gas at the exit of the heat exchanger is throughout higher than the ambient temperature.

Condenser: The condenser was also treated as ideal with 100% effectiveness were considered to be adiabatic towards the surrounding and isobaric. As considered above for heat exchangers the

heat is transferred in three stages from superheated vapour to cold liquid water and different overall heat transfer coefficients were used [gas to liquid: $k_{l,g}$ = 40 W/(m^2 K), liquid as well as 2-phase region to liquid: $k_{l,l}$ = 1000 W/(m^2 K)] were assumed. The cooling water entered the condenser at $T_{W,5}$ = 298.15 K. The efficiency of the cold water pump $\eta_{P,W}$ was taken to be 0.7. The pressure increase due to the cold water pump was taken as 600 kPa. The mass flow rate was adjusted to ensure total heat transfer. The temperature of cold water at the exit $T_{W,4}$ was 358.15 K if not specified.

The boiler pressure was varied between 500 and 1500 kPa. The turbine entrance temperature $T_{F,3}$ was varied from the saturation temperature of the investigated fluid up to the maximum temperature calculated according to the pinch point analysis. At higher pressures the design of the turbine gets complex due to the flow velocities at the turbine exit more than one stage is needed.

3. Results and Discussions

Calculations were performed for n-hexane, n-decane, n-dodecane and the mixtures n-hexane(1) + n-decane(2), and n-hexane(1) + n-decane(2) having different concentrations (mass fraction of hexane = ξ_1). These were considered as the working fluid for the above mentioned ORC. The needed thermodynamic parameters, viz. the enthalpies and entropies for fluids and their mixtures in different states were adopted [19] or calculated using method [20] from software [19].

3.1. Calculations at constant condenser pressure

The first set of calculation was performed at a constant condenser pressure for all the working fluids. The condenser pressure (p_{cond}) was chosen as 37.389 kPa for n-hexane (1) + n-decane (2) mixtures. This is the saturation pressure for a mixture of 50% mass fraction of n-hexane (ξ_1= 0.5) at $T_{F,sat}$=323.15 K. For n-hexane (1) + n-dodecane (2) mixtures the condenser pressure was chosen as 40.864 kPa [the saturation pressure for a mixture with ξ_1=0.5 at $T_{F,sat}$=323.15 K]. The parameters defined by equations (9) – (19) and the required surface areas for the heat exchanger and the condenser were calculated. The pinch point temperature difference was kept 10 K. Some representative results for the various efficiencies obtained for n-hexane, n-decane and two of the representative mixtures without superheating for the case that the energy is available at the high temperature 773.15 K are summarized in Table 1 together with important process parameters. The values refer to a boiler pressure of 1500 kPa, hot air inlet temperature of 773.15 K and condenser pressure of 37.389 kPa. The high temperature of the cycle was dependent on the fluid and the boiler pressure and is also reported.

Table 1. Comparison of different parameters of ORC systems with hexane(1), decane(2) and their mixtures as working fluid.

	$\xi_1 = 0.0$	$\xi_1 = 0.5$	$\xi_1 = 0.9$	$\xi_1 = 1.0$
$T_{F,3}$ (K)	593.141	529.931	476.831	461.72
$\dot{m}_F$ (kg/s)	1.080	1.238	1.476	1.561
$\eta_{th,ORC}$	0.128	0.143	0.175	0.183
$\boldsymbol{\eta_{th,total}}$	**0.092**	**0.130**	**0.162**	**0.141**
$P_{Turbine}$ (kW)	97.3	135.5	169.0	177.3
P_{Pump} (kW)	2.9	3.2	3.9	4.2
P_{net} (kW)	92.2	129.6	161.9	141.3
$P_{P,W}$ (kW)	2.2	2.7	3.2	31.8
A (m^2)	364.5	384.7	332.0	319.4
$\Delta\dot{E}_{air,3,0}$ (kW)	358.9	397.8	399.4	399.7
$\dot{I}_{Boiler}$ (kW)	46.7	97.6	133.3	142.7
$\dot{I}_{Turbine}$ (kW)	9.6	15.4	22.2	24.5
$\dot{I}_{Condenser}$ (kW)	147.9	78.6	16.0	48.6
$\Delta\dot{E}_{acc,water}$ (kW)	57.4	70.6	58.8	6.6
$\dot{E}_{loss,Exhaust}$ (kW)	43.0	4.1	2.5	2.2
$\Delta\dot{E}_{Process}$ (kW)	252.4	201.7	181.2	254.0
$A_{Condenser}$ (m^2)	67.8	97.9	229.5	192.2
$T_{F,5}$ (K)	411.84	323.15	314.84	313.22
$\boldsymbol{\Psi_{total}}$	**0.372**	**0.498**	**0.549**	**0.368**

The increase of $\eta_{th,ORC}$, $\eta_{th,total}$ and Ψ_{total} with the increasing boiler pressure was reported when pure alkanes were used as working fluids in ORC [12]. The same trend is observed when their mixtures are used as working fluid. Also similar to pure organic substances the efficiency dropped with increasing temperature level and was highest without superheating. Similar observations have been reported in literature [21]. The decrease of efficiency with increasing turbine entrance temperature can be explained by the shape of the T-s diagram [compare Figure 2(b)]. An increased average temperature for the heat rejection is observed. This is not balanced by the increased average temperature of heat addition to the cycle. This is discussed in detail in [12].

It is observed from Table 1 that for under these conditions the thermal efficiency for the complete process, $\eta_{th,total}$ is lowest for decane (0.092 for ξ_1=0.0) and highest for a mixture (0.162 for ξ_1=0.9). The second law efficiency Ψ_{total} is also higher for mixtures (0.549 for ξ_1=0.9 and 0.498 for ξ_1=0.5) and low (0.368 or 0.372) when pure substances are used as working fluids. This means that when mixtures are used as working fluids the efficiency increases by 33% to 48.5% compared to pure n-decane or pure n-hexane, respectively. Obviously the exergy loss rate for the complete process is least for the case when the second law efficiency has a maximum.

A comparison of the exergy loss rates at various stages show that the exergy loss rates in exhaust is highest for decane as it leaves the system at a high temperature due to pinch point restrictions. The exergy destruction in the boiler is higher for n-hexane followed by mixtures (ξ_1=0.9), (ξ_1=0.5) and n-decane, while the losses in the condenser show the opposite tendency, leading to a minimum in the losses for the mixture with ξ_1=0.9. The losses in the turbine are comparatively low. The required surface areas for the heat exchanger do not differ much from each other. However, the required surface areas for condenser in case of n-hexane and the mixture (ξ_1=0.9) are higher than those required when n-decane and (ξ_1=0.5) mixtures are used.

The performance of an ORC system can be visualized by *T*-H□ diagrams [13]. For the description of the complete process not only the Rankine cycle, but also the process lines for the air and the cooling water are to be included. Any pinch point breach can be seen on it and the temperature differences along the heat transfer processes can easily be seen as a direct measure of thermodynamic irreversibilities. Figure 3 shows the *T*-H□ diagram for n-hexane, mixture (ξ_1=0.5) and n-decane under the conditions given in Table 1. The full line shows the step in which turbine produces power. It is noticed that the area bounded by the enthalpy lines is least for the system with n-decane as working fluid. This is also reflected in the values of the efficiency of the process which is lowest for n-decane. The best thermodynamic case would be when the lines along the heat transfer from and to the cycle would fall on each other, although the heat exchanger area would then increase towards infinity.

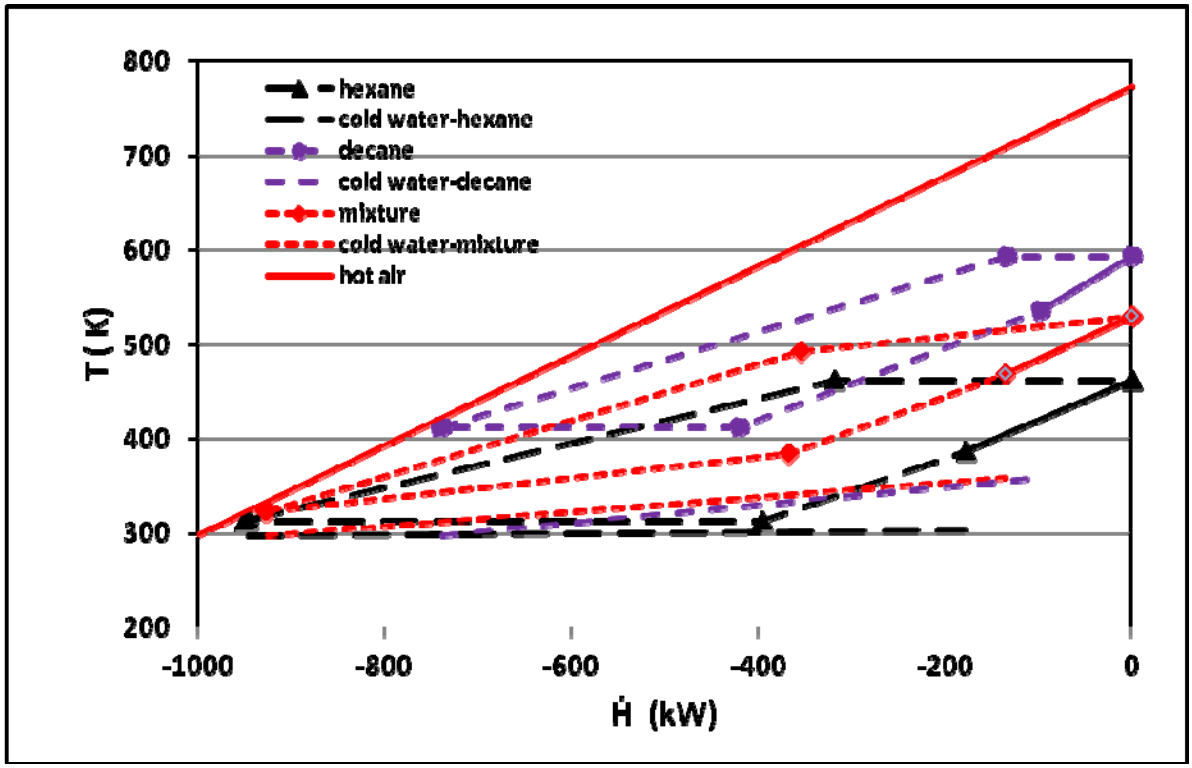

Fig. 3. T-H□ diagram n-hexane, n-decane and the mixture (ξ_1=0.5) at 1500 kPa without superheating (source temperature =773.15K).

Qualitatively the same trend in the values of exergy loss/destruction rates and the efficiencies was observed for the n-hexane (1) + n-dodecane (2) system. Here too, the highest second law efficiency is achieved (Ψ_{total}=0.561) for (ξ_1=0.9) mixture and lowest (Ψ_{total}=0.343) for n-dodecane as working fluid. A comparison of the results for the mixture of n-hexane + n-decane with the pure fluid n-octane showed that the mixtures always performed better than the equivalent pure fluid as working medium.

3.2. Calculations at constant condenser temperature

Calculations were performed for n-hexane, n-decane, n-dodecane and the mixtures n-hexane(1) + n-decane(2), and n-hexane(1) + n-decane(2) having different concentrations (mass fraction of hexane = ξ_1) as working fluid at a constant condensation temperature ($T_{F,5}$= 323.15 K). The saturation pressure for the liquid state varied from 0.88 kPa (n-decane) to 54.09 kPa (n-hexane). The parameters defined by equations (9) – (18) and the required surface areas for the heat exchanger and the condenser were calculated. Using the thermodynamic parameters from [19] the efficiencies and the required surface areas for the heat exchanger and the condenser were calculated. Some typical results are summarized in Table 2 together with important process parameters. The values refer to a boiler pressure of 1500 kPa and the hot air inlet temperature of 773.15 K.

The increase of $\eta_{th,ORC}$, $\eta_{th,total}$ and Ψ_{total} with the increasing boiler pressure was observed for n-hexane, n-decane and their mixtures. Also both the first law and second law efficiencies dropped with increasing temperature level and was highest without superheating. Hence the results without superheating for the case that the energy is available at the high temperature 773.15 K (range c) from above) are reported here.

Table 2. Comparison of different parameters of ORC systems with hexane(1), decane(2) and their mixtures as working fluid.

	ξ_1= 0.0	ξ_1 = 0.5	ξ_1 = 0.9	ξ_1 = 1.0
$T_{F,3}$ (K)	593.141	529.931	476.831	461.72
$\dot{m}_F$ (kg/s)	1.025	1.238	1.494	1.587
$\eta_{th,ORC}$	0.201	0.143	0.165	0.171
$\boldsymbol{\eta_{th,total}}$	**0.182**	**0.130**	**0.150**	**0.150**
$P_{Turbine}$ (kW)	188.9	135.5	156.8	162.3
P_{Pump} (kW)	2.6	3.2	4.0	4.3
P_{net} (kW)	182.4	129.6	149.7	150.2
$P_{P,W}$ (kW)	3.8	2.7	3.2	7.9
A (m^2)	465.9	384.7	324.7	311.3
$\Delta\dot{E}_{air,3,0}$ (kW)	397.8	397.8	397.8	397.8
$\dot{I}_{Boiler}$ (kW)	59.2	97.6	130.3	138.8
$\dot{I}_{Turbine}$ (kW)	20.2	15.4	20.4	22.0
$\dot{I}_{Condenser}$ (kW)	84.1	78.6	31.8	50.1
$\Delta\dot{E}_{acc,water}$ (kW)	45.6	70.6	58.4	24.5
$\dot{E}_{loss,Exhaust}$ (kW)	4.2	4.2	4.2	4.2
$\Delta\dot{E}_{Process}$ (kW)	173.9	201.7	193.8	227.2
$A_{Condenser}$ (m^2)	233.7	97.9.0	164.5	196.4
$p_{Condenser}$ *(kPa)*	0.88053	37.389	50.81	54.087
$\boldsymbol{\Psi_{total}}$	**0.567**	**0.498**	**0.518**	**0.435**

It is observed from Table 2 that under the conditions that the temperature of the condenser is held constant at 323.15 K the thermal efficiency for the complete process, $\eta_{th,total}$ is lowest for the mixture (ξ_1=0.5) and highest for n-decane. The second law efficiency Ψ_{total} is also highest for n-decane (0.567) followed by the mixtures (0.518 for ξ_1=0.9 and 0.498 for ξ_1=0.5). The second law efficiencies for different mixtures at constant condenser temperature (solid line) and constant condenser pressure (dashed line) are shown in Fig. 4. N-decane has the highest boiling temperature at a fixed boiler pressure while the condenser pressure is now very low for the fixed condenser temperature case, thus, the heat addition occurs at the highest average temperature and the heat rejected is same for all fluid compositions. The lowest second law efficiency is found with n-hexane as working fluid. The exergy loss for the process was lowest for n-decane followed by the different mixtures and by n-hexane. The exergy loss with the exhaust is very small in all the cases. The main difference in the exergy loss arises due to large exergy destruction in the boiler for n-hexane and for the mixtures.

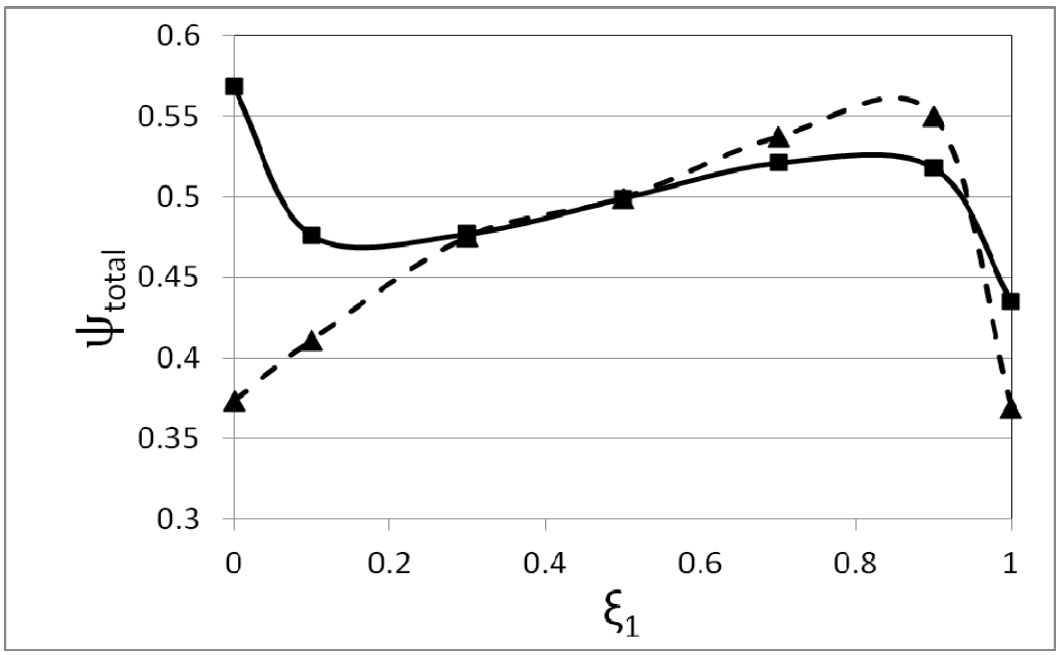

Fig. 4. Plot of ψ_{total} againstξ_1 for n-hexane + n-decane mixture at 1500 kPa without superheating (source temperature =773.15K); ———— $T_{condenser}$ = 323.15K, -------- $p_{condenser}$ = 37.389kPa.

3.3. Calculations for heat source at 623.15 K

An examination of $T - \dot{H}$ diagram given in Figure 3 shows a parallel course of the enthalpy curves for the heat source at 773.15 K and the working fluid. One observes also some free space above the heating line of the working fluid. The heating line for the heat source will have smaller slope and will be nearer to working fluid line for a heat source at a lower temperature, e.g. 623.15 K. In this case a good thermal match between the heat source line and the working fluid line (where a mixture is used) will be achieved and thus a better utilization of energy should be possible. Therefore, some exemplary calculations were performed with heat source at 623.15 K at constant condensation temperature of 323.15K. As expected higher second law efficiencies were obtained for mixtures as working fluid. The results are shown in Table 3. The values refer to a boiler pressure of 1500 kPa, hot air inlet temperature of 623.15 K.

Table 3. Comparison of different parameters of ORC systems with hexane(1), decane(2) and their mixtures as working fluid.

	$\xi_1 = 0.0$[(a)]	$\xi_1 = 0.5$	$\xi_1 = 0.9$	$\xi_1 = 1.0$
$T_{F,3}$ (K)	522.691	529.931	476.831	461.72
$\dot{m}_F$ (kg/s)	1.175	1.192	1.438	1.528
$\eta_{th,ORC}$	0.193	0.143	0.165	0.171
$\boldsymbol{\eta_{th,total}}$	**0.163**	**0.125**	**0.144**	**0.145**
$P_{Turbine}$ (kW)	171.7	130.5	151.0	156.3
P_{Pump} (kW)	1.0	3.1	3.9	4.1
P_{net} (kW)	163.4	124.7	144.1	144.6
$P_{P,W}$ (kW)	7.4	2.6	3.1	7.6
A (m^2)	1332.2	1127.5	644.3	581.4
$\Delta\dot{E}_{air,3,0}$ (kW)	317.8	317.7	317.6	317.6
$\dot{I}_{Boiler}$ (kW)	22.8	28.8	60.2	68.3
$\dot{I}_{Turbine}$ (kW)	20.2	14.8	19.6	21.2
$\dot{I}_{Condenser}$ (kW)	80.1	75.7	30.7	48.2
$\Delta\dot{E}_{acc,water}$ (kW)	23.1	68.0	56.2	23.6
$\dot{E}_{loss,Exhaust}$ (kW)	5.9	6.1	6.1	6.1
$\Delta\dot{E}_{Process}$ (kW)	137.3	131.0	123.4	155.6
$A_{Condenser}$ (m^2)	169.0	94.2	158.4	189.0
$p_{Condenser}$ *(kPa)*	0.88053	37.389	50.81	54.087
$\boldsymbol{\Psi_{total}}$	**0.576**	**0.595**	**0.619**	**0.519**

(a) For n-decane the calculations were performed only at 500 kPa boiler pressure due to pinch point restrictions. These are reported here.

As the same amount of power is to be transferred over a small temperature range the required mass flow rate of air is higher and so are the mass flow rates of the fluids. For heat transfer from the hot air to the working fluid it is necessary that the temperature of air is higher than the temperature of working fluid throughout the corresponding stages. Hence the temperature of air at state 1 ($T_{air,1}$) must be higher than the saturation temperature of fluid at the given turbine pressure ($T_{F,1}$). This is now the pinch point. $T_{air,1}$ had to follow the pinch point restrictions. It has to be increased. This is achieved by increasing $T_{air,0}$. The thermal efficiencies of the organic Rankine cycles $\eta_{th,ORC}$ do not change if the other conditions are kept the same [refer to equation (9)]. It is observed that both $\eta_{th,total}$ and Ψ_{total} with the heat source at 623.15 K is lower than that at 773.15 K. The highest total thermal efficiency is obtained with n-decane as working fluid. The second law efficiencies follow the order:

$\Psi_{total}(\xi_1 = 0.9) > \Psi_{total}(\xi_1 = 0.5) > \Psi_{total}$(n-decane) > Ψ_{total}(n-hexane).

Fig. 5 shows the T-H□ diagram for n-hexane, n-hexane + n-decane mixture ($\xi_1 = 0.9$) and n-decane at saturation vapour pressures at 1500 kPa boiler pressure and 323.15 K condenser temperature.

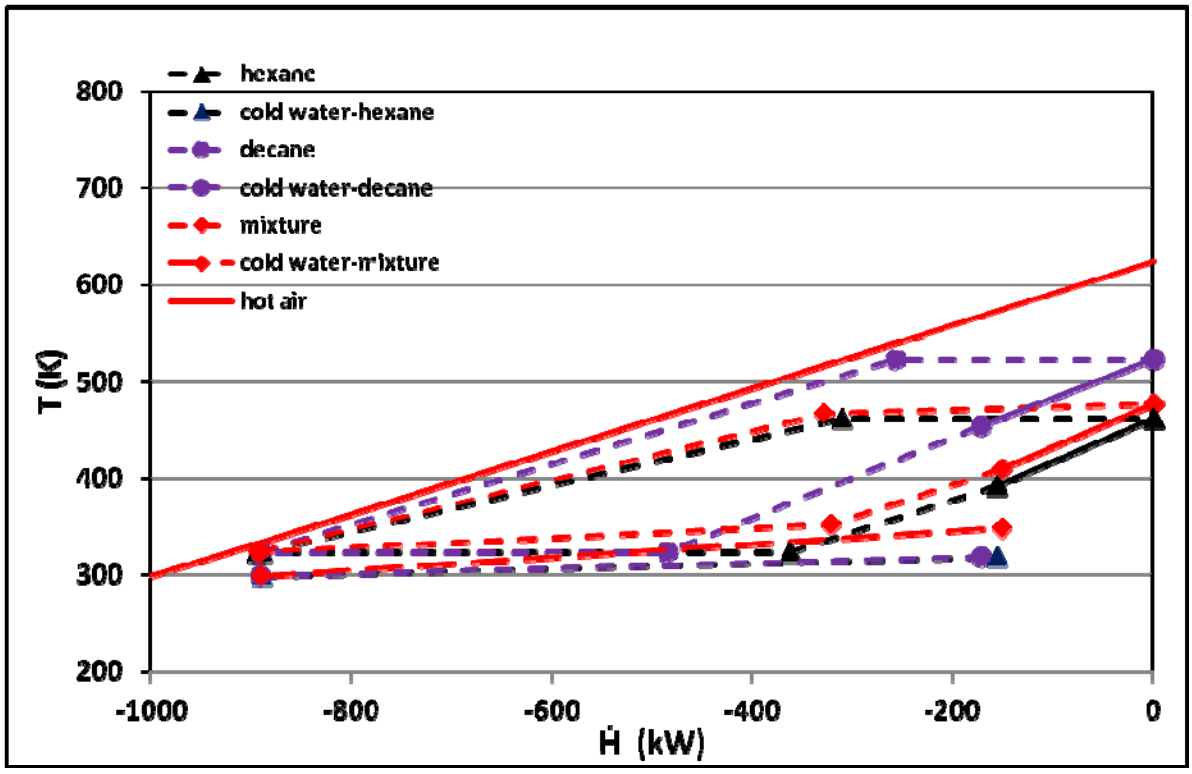

Fig. 5. T-H□ diagram n-hexane, n-decane and the mixture (ξ_1=0.9) at 1500 kPa without superheating (source temperature =623.15K).

Conclusions

Organic Rankine cycles working with pure fluids or their mixtures were investigated for their usage in combined heat and power generation systems, utilzing low grade heat available either at 773.15 K or at 623.15K from exhaust gases from turbines and engines as well as from industrial plants. Model calculations of binary mixtures of different compositions of one short chain alkane with one long chain alkane (hexane + decane, hexane + dodecane) were performed at a certain condenser pressure or temperature and different boiler pressures and temperatures. The usefulness of binary mixtures compared to pure fluids depends strongly on the parameters which are fixed. For pure fluids as well as for the mixtures higher first law ($\eta_{th,total}$) and second law efficiencies (Ψ_{total}) were obtained at higher boiler pressures. At a fixed boiler pressure the efficiencies decreased with increasing boiler temperatures due to the fact that the fluid left the turbine as superheated vapour. At a fixed condenser pressure the mixtures performed better than the pure fluids. The second law efficiency increased by 20-50%. The exergy destruction rate in the boiler is higher for small chain alkanes followed by the mixtures (ξ_1=0.9), (ξ_1=0.5) and the long chain alkanes. The exergy destruction rates in the turbine are comparatively low. The required surface areas for the heat exchanger do not differ much from each other. However, the required surface area in case of n-hexane and (ξ_1=0.9) mixture are higher than those required when n-decane and (ξ_1=0.5) mixtures are used. At a fixed condenser temperature which results in different pressure the first law efficiency with pure long chain alkane is much higher than that obtained with mixtures or short chain alkane. The second law efficiencies achieved with long chain alkane and mixtures do not differ much but the efficiency with pure short chain alkane n-hexane is lower. The required surface area for the heat exchanger and condenser was highest for long chain alkane. By using the heat source at 623.15 K and taking advantage of the non-isothermal boiling of fluid mixtures a better

thermal match between the working fluid and the heat source as well as between the working fluid and the cooling water stream could be obtained. A comparison of the results for the mixture of n-hexane + n-decane with the pure fluid n-octane showed that the mixtures always performed better than the equivalent pure fluid as working medium.

Nomenclature

A	area (surface area for heat exchanger), m^2
$\Delta\dot{E}_{air}$	total exergy loss rate air, kW
$\dot{E}_{air,3}$	exergy of air stream, kW
$\Delta\dot{E}_{air,3,0}$	exergy loss rate of air stream from state 3 to state 0, kW
$\dot{E}_{loss,Exhaust}$	exergy in exhaust, kW
$\Delta\dot{E}_{acc,water}$	exergy gain (accumulation) rate in water, kW
$c_{p,air}$	specific heat capacity of air, kJ/(kg K)
$\dot{H}$	enthalpy stream, kW
$h_{air,i}$	specific enthalpy of air in state i, kJ/kg
$h_{F,i}$	specific enthalpy of fluid in state i, kJ/kg
$\dot{I}_{Boiler}$	exergy destruction rate in boiler, kW
$\dot{I}_{Condenser}$	exergy destruction rate in condenser, kW
$\dot{I}_{Process}$	exergy (loss+destruction) rate for the process, kW
$\dot{I}_{Pump}$	exergy destruction rate in pump, kW
$\dot{I}_{P,W}$	exergy destruction rate in cold water pump, kW
$\dot{I}_{Turbine}$	exergy destruction rate in Turbine, kW
$k_{i,j}$	heat transfer coefficient $i \rightarrow j$, kJ/(m^2 K)
$\dot{m}_{air}$	mass flow rate of air, kg/s
$\dot{m}_F$	mass flow rate of fluid, kg/s
ORC	organic Rankine cycle
$P_{Turbine}$	turbine power, kW
P_{Pump}	*ORC* pump power, kW
P_{net}	the net power of the process, kW
$P_{P,W}$	power of cold water pump, kW
p_{boiler}	pressure in boiler, kPa
p_{cond}	pressure in condenser, kPa
$\dot{Q}_{add}$	rate of heat addition, kW
$\dot{Q}_{rem}$	rate of heat removal, kW
T	temperature, K
$T_{air,i}$	temperature o fair in state i, K
T-H□	temperature-enthalpy diagram
T-s	temperature-entropy diagram
$T_{F,i}$	temperature of fluid in state i, K
$T_{F,sat}$	saturation temperature of fluid at condenser pressure, K
$T_{W,i}$	temperature of cold water in state i, K
v	specific volume of saturated liquid, m^3/kg

$w_{5,0}$	specific work of ORC pump, kJ/kg
$w_{P,W}$	specific work of the pump for cold water, kJ/kg

Greek symbols

$\eta_{s,P}$	isentropic efficiency of pump
$\eta_{P,W}$	efficiency of cold water pump
$\eta_{th,ORC}$	thermal efficiency of ORC
$\eta_{th,total}$	total thermal efficiency of the process
$\Delta p_{P,W}$	pressure drop in cold water pump, kPa
$\Delta T_{LMTD,ij}$	logarithmic mean temperature difference between state *i* and *j*, K
ΔT_i	difference between the temperature of air and that of fluid in state *i*, K
ΔT_{pinch}	difference between the temperature of hot air and the fluid at pinch point, K
Ψ_{total}	second law efficiency
ξ_i	mass fraction of component *i* of a mixture

Subscripts and superscripts

air	*air*
cond	*condenser*
Device	*device such as boiler, condenser, pump*
F	*fluid*
i,j	*state points 0,1,2,3,4,5*
LMTD	*logarithmic mean temperature difference*
ORC	*organic Rankine cycle*
P,W	*cold water pump*
pinch	*pinch point*
s	*isentropic*
sat	*saturated*
surr	*surroundings*
th	*thermal*
W	*water, cold water*

References

[1] Saleh B., Koglbauer G., Wendland M., Fischer J., Working fluids for low-temperature organic Rankine cycles. Energy 2007; 32: 1210-21.

[2] Hung T.C., Waste heat recovery of organic Rankine cycle using dry fluids. Energy Conversion and Management 2001; 42: 539-53.

[3] Hung T.C., Shai T.Y., Wang S.K., A review of organic Rankine cycles (ORCs) for the recovery of low-grade waste heat. Energy 1997; 22: 661-67.

[4] Liu B-T., Chien K-H., Wang C-C., Effect of working fluids on organic Rankine cycle for waste heat recovery. Energy 2004; 29: 1207-1217.

[5] Lai N.A., Wendland M., Fischer J., Working fluids for high-temperature organic Rankine cycles. Energy 2011; 36: 199-211.

[6] Drescher U., Brüggemann D., Fluid selection for the Organic Rankine Cycle (ORC) in biomass power and heat plants. Applied Thermal Engineering 2007; 27: 223-28.

[7] Borsukiewicz-Gozdur A., Nowak W., Comparative analysis of natural and synthetic refrigerants in application to low temperature Clausius-Rankine cycle. Energy 2007; 32: 344-352.

[8] Larjola J., Electricity from industrial heat using high-speed organic Rankine cycle (ORC). Int. J Product Econom 1995; 41: 227-235.

[9] Mago P.J., Chamra L.M., Srinivasan K., Somayaji C., An examination of regenerative organic Rankine cycles using dry fluids. Applied Thermal Engineering 2008; 28:998-1007.

[10] Velez F., Segovia J.J., Martin M.C., Antolin G., Chejne F., Quijano A., Comparative study of working fluids for a Rankine cycle operating at low temperature. Fuel Processing Technology doi:10.1016/j.fuproc.2011.09.017.

[11] Siddiqi M.A., Atakan B., Investigation of the Criteria for Fluid Selection in Rankine Cycles for Waster Heat Recovery. Int. J. of Thermodynamics 2011; 14: 117-123.

[12] Siddiqi M.A., Atakan B., Alkanes as Fluids in Rankine Cycles in Comparison to Water. Benzene and Toluene.In: Bojic M., Lior N., Petrovic J., Stefanovic G., Stevanovic, V., editors. ECOS 2011: Proceedings of the 24th International Conference on Efficiency, Cost, Optimization, Simulation and Environmental Impact of Energy Systems; 2011 July 4-7; Novi Sad, Serbia. University of Nis, Serbia: 1544-1557. Also submitted to Energy.

[13] Bejan A. Tsatsaronis GJ. Moran M. Thermal design and optimization. New York Wiley; 1996.

[14] Angelino G. Di Paliano PC. Multicomponent working fluids for organic Rankine cycles (ORCs). Energy 1998; 23: 449-463.

[15] Chen H. Goswami DY. Rahman MM. Stefanakos EK. A supercritical Rankine cycle using zeotropic mixture working fluids for the conversion of low-grade heat into power. Energy 2011; 36: 549-555.

[16] Angelino G. Di Paliano PC. Organic Rankine cycles (ORCs) for energy recovery from molten carbonate fuel cells. AIAA2000-3052.

[17] Maizza V. Maizza A. Working fluids in non-steady flows for waste energy recovery systems. Applied Thermal Engineering 1996; 16: 579-590.

[18] Maizza V. Maizza A. Unconventional working fluids in organic Rankine-cycles for waste energy recovery systems. Applied Thermal Engineering 2001; 21: 381-390.

[19] Lemmon EW. Huber ML. Mclinden MO. NIST Standard Reference Database 23: Reference Fluid Thermodynamic and Transport Properties-REFPROP. Version 8.0, National Institute of Standards and Technology, Standard Reference Data Program, Gaithersburg; 2007.

[20] Lemmon EW. Jacobsen RT. A Generalized Model for the Thermodynamic Properties of Mixtures. Int. J. Thermophysics 1999; 20:825-835.

[21] Yamamoto T. Furuhata T. Arai N. Mori K. Design and testing of the Organic Rankine Cycle. Energy 2008; 26:239-51.

Excess Enthalpies of Second Generation Biofuels

Alejandro Moreau[a], José J. Segovia[a], M. Carmen Martín[a], Miguel A. Villamañán[a], César R. Chamorro[a], Rosa M. Villamañán[a]

[a] Research Group TERMOCAL; Escuela de Ingenierías Industriales, Universidad de Valladolid; Paseo del Cauce 59, 47011 Valladolid; Spain;alejandro.moreau@eii.uva.es; jose.segovia@eii.uva.es; mcarmen.martin@eii.uva.es; miguel.villamanan@eii.uva.es; cescha@eii.uva.es; rvillama@dce.uva.es.

Abstract:

The use of biofuels is increasing in the EU with the target of decrease the dependency of the petroleum and also to reduce CO_2 emissions and to support the agricultural community. A wide variety of biogenic products is added to fuels and the quality of these products becomes more important requiring an accurate knowledge of the thermodynamic properties of the new fuel blends. Between these properties the heats of mixing or the excess enthalpies are needed to calculate the energy balances.

The 1-pentanol is considered an alcohol of the second generation of biofuels, it has some advantages in comparison with ethanol such as a lower vapour pressure and higher heating values, quite similar to the gasoline.

In this work the experimental values of the excess enthalpies for the binary mixtures containing 1-pentanol and hydrocarbons as hexane, 1-hexene and 1,2,4-trimethyl benzene at 25°C and 40°C and atmospheric pressure are reported. A flow calorimeter developed in our laboratory was used for the measurements.

Keywords:

Biofuels, 1-pentanol, excess enthalpy, hexane, 1-hexene, 1,2,4-trimethyl benzene.

1. Introduction

The European Union is strongly dependent on fossil fuels for its transport needs so that the EU has adopted measures to encourage the production and use of sustainable biofuels because they can provide a very significant contribution in the short to medium term. Furthermore, biofuels can contribute to the EU's objectives of securing the EU fuel supply while improving the greenhouse gas balance and fostering the development of a competitive European (biofuels and other) industry.

To facilitate the wider use of biofuels in road transport, biofuels and blends need to become increasingly compatible with existing logistics as well as future ones but a good characterization of the thermodynamic properties is needed to obtain an in-depth understanding for example of the relationship between biofuels quality and engine performance.

In this context, 1-pentanol is a very important compound in the second generation of biogasolines due to the fact that it has high octane rating, up to 100 Research Octane Number (RON), better water tolerance and very high heat of combustion.

In this perspective and due to the fact that the new 'blends' of the second generation biofuels require reference materials with well-characterized reference values, our group decided to do a complete study of the mixtures 1-pentanol + hydrocarbons behaviour, as part of a research project. In this paper excess molar enthalpies measurements for the systems 1-pentanol with hydrocarbons as hexane, 1-hexene and 1,2,4-trimethyl benzene are reported. They have been measured at two different temperatures (298.15 to 313.15) K and at atmospheric pressure.

2. Experimental section

2.1. Materials

The compounds were purchased from Sigma-Aldrich and were of the highest purity available, chromatography quality reagents with a purity >0.99 (GC) for 1-pentanol, >0.99 (GC) for hexane, >0.97 (GC) for 1-hexene and >0.98 (GC) for 1,2,4-trimethyl benzene. Their purities were also checked by gas chromatography and all were found to be >0.997.

2.2. Apparatus and procedure

An automated quasi-isothermal flow calorimeter has been developed in our laboratory[1] for the accurate measurement of excess enthalpies at atmospheric pressure. It is based on the accurate measurement of the energy required to maintain the mixing vessel at a constant temperature. To achieve this condition, a Peltier cooler removes, at constant rate, energy from the flow cell and a control-heater compensates this energy and additionally the energy liberated (exothermic mixing) or absorbed (endothermic mixing) by the mixing process. Excess enthalpy is calculated by the determination of the net power exchanged.

A schematic view of the calorimeter is shown in Figure 1. Two precision isocratic pumps with dual floating pistons in series, (Agilent 1100 used in HPLC chromatography) delivers the pure compounds through the cell at a programmable constant flow rate. The fluids pass through a loop immersed in the bath (Hart Scientific, model 7041) to ensure that it reaches the bath temperature prior to entering the cell. The mixing point is at the bottom of the cell and it is made of two concentric tubes.

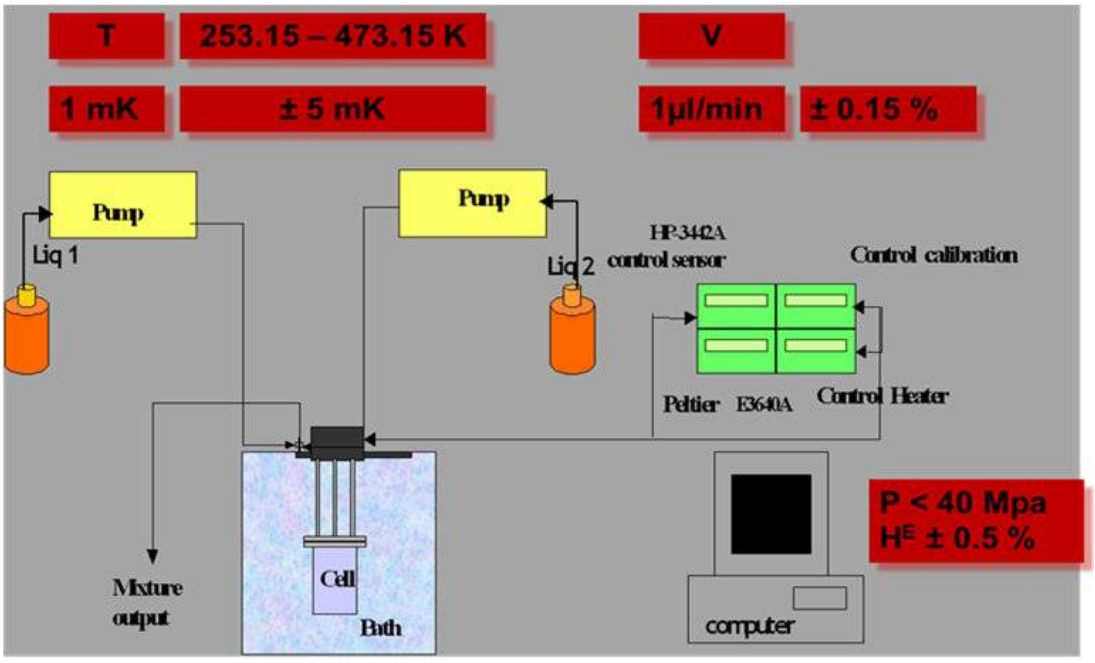

Figure 1. Schematic view of the calorimeter.

The cell is a stainless steel vessel containing a copper block where all the energy in the process is exchanged by conduction. The liquid flows through a stainless steel tube which is coiled around the copper block. The fluid inlet and outlet temperature has to be the same, and it is the bath temperature in which the cell is immersed.

At the top of the copper block is the Peltier cooler to remove at constant rate energy from the flow cell and the heater (100 Ω resistance used as a control heater). Refrigeration power is set and held constant through a DC power supply (Agilent E3640A) during the experiments and the control heater is connected to a function generator (Agilent 33220A) of arbitrary waveform, to change the power input into the cell.

The calorimeter is controlled using the value of an NTC thermistor connected to a multimeter (Agilent 3458 A) and located at the top of the flow cell, which is also used to measure the exit temperature. The cell is shown in Figure 2.

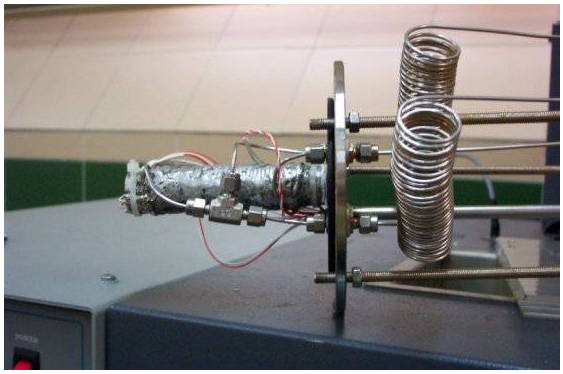

Figure 2. Photograph of the measuring cell.

A complete automation system supplies everything needed such as data acquisition, monitoring, and controlling to operate the calorimeter and take measurements from a single personal computer. The automation program has been done using Agilent-VEE language. The optimum total flow rate ranges from (0.5 to 1) ml/min which depends on the effect of mixing.

An electrical calibration of the calorimeter is carried out using the calibration resistance located on the bottom of the cell. It consists of the simulation of different energies in a calibration resistance by Joule effect at the same conditions as in the experimental measurements. The Peltier cooler, the control-heater and the calibration heater are each connected to their own DC power supplies. These devices are controlled using a computer with a GPIB connection and specific software developed in our laboratory.

The measuring procedure starts with a flow of one pure compound to set up the power input to maintain the gradient temperature (Q_{base}), it indicates the energy losses in the system. After that we program the different volumetric flows to measure the energy of the excess enthalpy at different compositions ($Q_{measured}$). Then you can calculate the net power (Q_{net}) with the difference between ($Q_{measured}$) and (Q_{base}). Finally the excess enthalpy is calculated using net power, electrical calibration and molar flow.

The properties measured directly and their corresponding uncertainties are: flow rate ± 0.15% (1-10 mL/min); temperature ± 10 mK; the heating and cooling systems have an stability better than 2.4 μW, and it results in an uncertainty of ± 0.0001 in the composition of the mixture and the extended uncertainty in the excess molar enthalpy is better than ± 1% for a cover factor of 2 which means a confidence level of 0.95.

3. Results

For the same three binary mixtures the excess enthalpies were measured at T= (298.15 and 313.15) K, these experimental data as a function of the composition and the calculated results are given in Figure 3. Density values and molecular weight of pure compounds, needed to compute mass flow from volumetric flow, it has been obtained from the literature. These data are given in Table 1.

Table 1. Density and molecular weight of pure compounds.

	Density at 293,15 K ($kg \cdot m^{-3}$)	Density at 303.15 K ($kg \cdot m^{-3}$)	Molecular Weight ($g \cdot mol^{-1}$)
1-Pentanol	815.10[a]	807.90[a]	88.149
Hexane	659.33[b]	650.18[b]	86.177
1-Hexene	673.00[c]	663.70[c]	84.159
1,2,4-Trimethyl benzene	873.66[d]	867.61[d]	120.19

[a] Reference 2. [b] Reference 3. [c] Reference 4. [d] Reference 5

The data have been correlated using Redlich-Kister equation:

$$H_m^E/\left(J \cdot mol^{-1}\right) = x \cdot (1-x) \cdot \sum_{i=1}^{n} A_i \cdot (2x-1)^{i-1} \Big/ \left[1 + C(2x-1)\right] \quad (1)$$

and the standard deviations $\sigma(H_m^E)$ were calculated by:

$$\sigma\left(H_m^E\right) = \left[\sum_{i=1}^{N} \left(H_{m,\exp}^E - H_{m,calc}^E\right)^2 / (N-n)\right]^{1/2} \quad (2)$$

where N is the number of experimental points and n is the number of coefficients A_i. The calculated parameters of the equation, standard deviations and absolute maximum deviation are summarized in Table 2.

Table 2. Parameters of Redlich-Kister equation, standard deviation of excess molar enthalpies σ and, absolute maximum deviation ($\left|\Delta H_{m,\max}^E\right|$) for the measured systems.

T (K)	A_1	A_2	A_3	A_4	A_5	C	σ	$\left\|\Delta H_{m,ma}^E\right.$
	($J \cdot mol^{-1}$)							
1-pentanol (1) + hexane (2)								
298.15	1916.5	-589.23	-973.47	-530.22	228.83	0.98	3.08	7.40
313.15	2620.0	-771.09	-1194.9	-320.28	516.14	0.93	2.55	4.25
1-pentanol (1) + 1-hexene (2)								
298.15	2133.6	-408.47	-1127.0	-174.68	154.42	0.96	1.74	3.10
313.15	2881.9	-745.68	-907.45	-520.79	180.92	0.93	3.95	8.70
1-pentanol (1) + 1,2,4-trimethyl benzene (2)								
298.15	3748.7	-1269.3	-988.91	-438.13	441.08	0.87	3.03	7.47
313.15	4734.3	-1767.6	-1502.14	-566.25	87.17	0.82	1.97	3.92

The experimental data as a function of the composition and the calculated results with Redlich-Kister equation are represented in Figure 3.

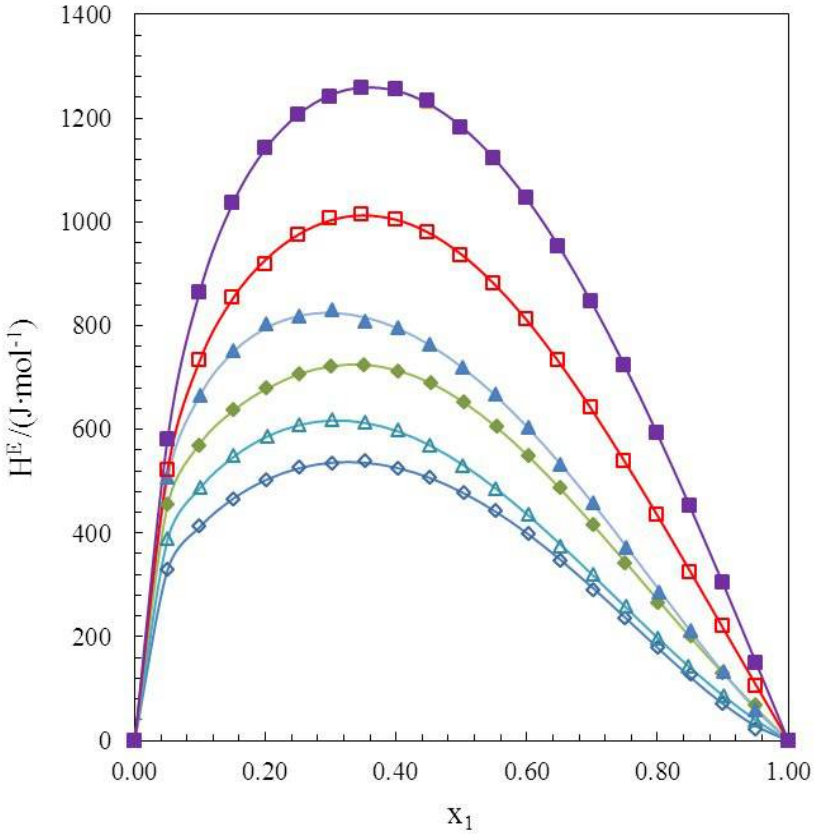

Figure 3. Experimental excess molar enthalpies as function of the composition for the binary systems 1-pentanol(1) + hexane(2) (◊) at 298.15 K and (♦) at 313.15 K; 1-pentanol(1) + 1-hexene(2) (△) at 298.15 K and (▲) at 313.15 K; and 1-pentanol(1) + 1,2,4-trimethyl benzene(2) (□) at 298.15 K and (■) at 313.15 K.

4. Discussion and Conclusions

We have chosen for this study a paraffin, an olefin and an aromatic hydrocarbon because these type of hydrocarbons are the most representative in the composition of any gasoline. We want to know the behavior of the blending with a second generation biofuel such as 1-pentanol. In this case we studied the excess enthalpies as function of the composition for the binary systems 1-pentanol with hexene, 1-hexene or 1,2,4-trimethyl benzene.

Concerning the effect of mixing, all systems have a strong endothermic behaviour which increases at higher temperatures, this behaviour is coherent with the results for the systems 1-pentanol with ciclohexane or toluene measured in our laboratory [6].

All the systems have a strong endothermic behaviour (positive excess enthalpy), the highest excess enthalpy is observed for the system 1-pentanol + 1,2,4-trimethyl benzene at 313.15 K. The maximum value is $H_m^E = 1257$ J·mol^{-1} for a mole fraction of 1-pentanol of 0.35 at T= 313.15 K and it decreases to $H_m^E = 1015$ J·mol^{-1} at the same composition at T= 298.15 K.

On the other hand, the binary mixture 1-pentanol + 1-hexene shows the maximum excess enthalpy at a mole fraction of 1-pentanol of 0.30 and the corresponding values are $H_m^E = 829$ J·mol^{-1} at 313.15 K and $H_m^E = 617$ J·mol^{-1} at 298.15 K.

Finally the binary mixture 1-pentanol + hexane presents the maximum excess enthalpy at a mole fraction of 1-pentanol of 0.35 and the corresponding values are $H_m^E = 724$ J·mol^{-1} at 313.15 K and $H_m^E = 538$ J·mol^{-1} at 298.15 K.

Acknowledgements

The authors are grateful for financial support from the Spanish Minister de Science and Innovation (MICINN) for Project ENE2009-14644-C02-01. Alejandro Moreau appreciate the support from European Social Fund (ESF) and from Consejería de Educación de la Junta de Castilla y León.

References

[1] Segovia J.J., Martín M.C., Vega-Maza D., Chamorro C.R., Villamañán M.A., Thermodynamics of biofuels: Excess enthalpies for binary mixtures involving ethyl 1,1-dimethylethyl ether and hydrocarbons at different temperatures using a new flow calorimeter. J. Chem. Thermodyn. 41 (2009) 759-763.

[2] TRC—Thermodynamic Tables of Hydrocarbons and Non Hydrocarbons, Densities, Thermodynamics Research Center, The Texas A&M University System, College Station, 1973.

[3] National Institute of Standards and Technology. NIST thermophysical properties of fluids - Available at: http://webbook.nist.gov/chemistry/fluid/.

[4] Riddick J.A., Bunger W.B., Sakano T.K., Organic Solvents, Physical Properties and Methods of Purification, Techniques of Chemistry, Vol.II; Wiley-Interscience: New York, 1986.

[5] Yang-Yi Y., Jian-Hong D., Hai-Ling Y., Xiu-Huan Z., Guan-Quan C., Zhong-Qi H., Densities, surface tensions, and derived surface thermodynamics properties of (trimethylbenzene + propyl acetate, or butyl acetate) from T = 298.15 K to 313.15 K. J. Chem. Thermodynamics 39 (2007) 438-448.

[6] Moreau A., Martín M.C., Chamorro C.R., Segovia J.J., Thermodynamic characterization of second generation biofuels: Vapour–liquid equilibria and excess enthalpies of the binary mixtures 1-pentanol and cyclohexane or toluene, Fluid Phase Equilib. (2012), doi:10.1016/j.fluid.2012.01.007.

Responsibility notice

The authors are the only responsible for the printed material included in this paper.

Local stability analysis of a Curzon-Ahlborn engine considering the Van der Waals equation state in the maximum ecological regime

Ricardo Páez-Hernández[a], Pedro Portillo-Díaz[b], Delfino Ladino-Luna[c] and Marco A Barranco-Jiménez[d]

[a,c]Área de Física de Procesos Irreversibles, [b]Dpto. Ciencias Básicas Universidad Autónoma Metropolitana Azcapotzalco, Distrito Federal, México, e-mail:[a]phrt@correo.azc.uam.mx, e-mail:[b]ppd@correo.azc.uam.mx, e-mail:[c]dll@correo.azc.uam.mx
[d]Escuela Superior de Cómputo del IPN, Distrito Federal, México, e-mail: mbarrancoj@ipn.mx,

Abstract:
In this work we analyze the stability of an endoreversible Curzon-Ahlborn-Novikov engine, using Van der Waals gas as a working substance and the corresponding efficiency for this engine working at temperatures within the maximum ecological regime. From the local stability analysis we find that a critical point of an almost linear system is stable and analytically expressed in eigenvalues. After an arbitrarily small perturbation, the system state exponentially decays to a critical point, with either of two characteristic relaxation times, which are a function of the thermal conductance (α), heat capacity (*C*) and $\tau=T_2/T_1$. The behavior of relaxation times and solution of the systems are qualitatively shown by sketching its phase portrait, which results susceptible to operating regimes, i.e. the eigenvectors in the maximum ecological regime have a clockwise rotation with respect to the eigenvectors in the regime of maximum power. Finally, we have to observe that after the approximation $\boldsymbol{\lambda_{VW}=1}$, we obtain $\boldsymbol{\eta_{VWE}=\frac{3}{4}\eta_C}$, where $\boldsymbol{\eta_{VWE}}$, is the van der Waals efficiency at maximum ecological regime and $\boldsymbol{\eta_C}$, is Carnot´s efficiency. Finally we discuss the local stability and steady state of the energetic properties of the endoreversible engine.
.

Keywords:
Endoreversible, Ecological Regime, Dynamics, Van der Waals equation, Stability, Steady State.

1. Introduction

One of the important topics in thermodynamics has been the formulation of the criteria for comparing the performance of real processes. For example, the Carnot engine provides an upper bound on the efficiency of all heat engines operating between two fixed-temperature thermal-reservoirs. Clausius, Kelvin and others carried out pertinent studies by identifying limits on works, heat input and efficiency of various heat engines. The use of reversible processes as standards of performance is no desirable because a reversible process must be carried out at an infinitesimally-slow pace, or requires an infinitely-large heat-exchanger surface-area. Since power produced by a heat engine is work divided by time, a finite time amount of work produced by the engine over an infinite time delivers no power. The need to produce a finite amount of power in a real heat-engine is one of the reasons why the performance criterion of an ideal, reversible heat-engine is seldom used. There is a strong need in industry to find new bounds in power and efficiency for comparing the performances of thermal-power cycles. In this direction a new branch of irreversible thermodynamics, called finite time thermodynamics (FTT) has been developed during the last pastyears [1-9]. This FTT originated from the pioneering Curzon-Ahlborn (CA) [10] as a non-equilibrium approach to systems undergoing irreversible processes; which are visualized as

networks of internally reversible (endoreversible [10]) subsystems exchanging energy in an irreversible fashion among themselves and with the environment. Perhaps the simplest and most extensively studied FTT system is the so-called Curzon-Ahlborn-Novikov (CAN) engine [5,6,8-10]. This engine consists on a Carnot engine which exchanges heat with thermal baths T_1 and T_2 ($T_1>T_2$) through thermal conductors governed by the linear Newton heat transfer law. The CAN engine has non-zero power output, a positive entropy production and a more realistic efficiency (in terms of T_1 and T_2) than of the Carnot engine.

It is important to mention that this theory has been heavily criticized, partially because of the mainframe thermodynamics community who does not consider this theory as an extension of irreversible thermodynamics. However, Salamon P.[11] and Andresen B.[12] have perfectly established the application of the FTT. In fact, Andresen B.[12] said that at least 597 papers have been written in the context of this branch of thermodynamics. The subject has also made its way into textbooks [13, 14].

Most of the studies of FTT have been concerned with their steady-state energetic properties, which are important from the designed point of view. On the other hand, only a few of these studies have dealt with the system's dynamic properties, such as the response to noisy perturbation or the stability of the system's steady-state.

More recently, Santillán et al. [15] studied the local stability of an endoreversible Curzon-Ahlborn-Novikov engine operating in a maximum-power-like regime. Huang [16] analyzed the local stability of an irreversible heat pump performing in the minimum input power state for a given heating load. Guzmán-Vargas et al. [17] have shown the effect of heat transfer laws and thermal conductivity on the local stability of an endoreversible heat engine. Páez-Hernández et al. [18] analyzed the stability of a non-endoreversible Curzon-Ahlborn engine, taking into account the engine´s implicit delays. Huang Y and Sun D [19] analyzed the stability of a non-endoreversible heat pump. Páez-Hernández et al. [20] analyzed the stability of an endoreversible CAN engine using a Van der Waals gas as working substance in the maximum power regime.

In 1991, Angulo-Brown [21] developed an ecological optimization criterion for FTT-thermal cycles. This criterion consists on the maximization of a function E that represents a good compromise between high power output and low entropy production. This function is given by $E = P - T_2\sigma$, where P is the power output of the cycle, σ the total entropy production (system plus surroundings) per cycle, and T_2 the temperature of the cold reservoir. When function E is maximized, the CA cycle has a configuration that produces around 80% of the maximum power and only about 30% of the entropy produced in the maximum power. Another important property of the maximum ecological regime is that the CA-engine's efficiency in this regime η_E, is given by $\eta_E \approx \frac{1}{2}(\eta_C + \eta_{CA})$, where η_C is the Carnot efficiency and η_{CA} is the CA efficiency.

The paper is organized as follows. In section 2, we describe the local stability analysis method applied to a two-dimensional system. In section 3, a brief description of an endoreversible engine is presented. In section 4, the local stability analysis of a CAN engine using a Van der Waals gas as working substance in the maximum power regime is presented. In section 5, we discuss our results in context of the thermodynamic. Finally, in section 6 we write some comments.

In this work we present a local stability analysis to an endoreversible CAN engine using a Van der Waals gas as working substance in the maximum ecological regime.

2. Linearization and stability analysis

In this section, we show a brief description of both the linearization technique for two-dimensional dynamical systems, and the fixed point local stability analysis [17]. Consider a dynamical system

$$\frac{dx}{dt} = f(x, y) \tag{1}$$

and

$\frac{dy}{dt} = g(x, y)$. (2)

Let $(\bar{x}, \bar{y})$ be a fixed point such as that $f(\bar{x}, \bar{y}) = 0$and $g(\bar{x}, \bar{y}) = 0$. Consider a small perturbation around this fixed point and write $x = \bar{x} + \delta x$and $y = \bar{y} + \delta y$, where δx and δy are small disturbances from the corresponding fixed point values. By substituting equations (1) and (2), expanding $f(\bar{x} + \delta x, \bar{y} + \delta y)$ and $g(\bar{x} + \delta x, \bar{y} + \delta y)$ in a Taylor series and using the fact that δx and δy are small to neglect quadratic terms, the following equations are obtained for the perturbations:

$$\begin{pmatrix} \frac{d\delta x}{dt} \\ \frac{d\delta y}{dt} \end{pmatrix} = \begin{pmatrix} f_x & f_y \\ g_x & g_y \end{pmatrix} \begin{pmatrix} \delta x \\ \delta y \end{pmatrix}, \quad (3)$$

where

$f_x = \partial f/\partial x|_{\bar{x},\bar{y}}$; $g_x = \partial g/\partial x|_{\bar{x},\bar{y}}$; $f_y = \partial f/\partial y|_{\bar{x},\bar{y}}$ and $g_y = \partial g/\partial y|_{\bar{x},\bar{y}}$.

Equation (3) is a linear system of differential equations. Thus, we assume that the general solution of the system is

$\delta\vec{r} = e^{\lambda t}\vec{u}$, (4)

with$\delta\vec{r} = (\delta x, \delta y)$ and$\vec{u} = (u_x, u_y)$. Substitution of the solution $\delta\vec{r}$ into equation (3) yields the following eigenvalue equation:

$A\delta\vec{r} = \lambda\delta\vec{r}$, (5)

where$A$ is the matrix given by the first term on the right-hand side equation (3). The eigenvalues of this equation are the roots of the characteristic equation.

$|A - \lambda I| = 0$ (6)

or

$(f_x - \lambda)(g_y - \lambda) - g_x f_y = 0$. (7)

If λ_1 and λ_2 are solutions of equation (7), the general solution of the system is

$\delta\vec{r} = c_1 e^{\lambda_1 t}\vec{u}_1 + c_2 e^{\lambda_2 t}\vec{u}_2$, (8)

wherec_1 and c_2 are arbitrary constants and $\vec{u}_1$ and $\vec{u}_2$ are the eigenvectors corresponding to λ_1 and λ_2, respectively. To determine $\vec{u}_1$ and $\vec{u}_2$ we use the equation (5) again for each eigenvalue. Information about the stability of the system can be obtained from the eigenvalues$\lambda_1$and λ_2. In general, λ_1 and λ_2 are complex numbers. If both λ_1 and $\lambda_2$have negative real parts, the fixed point is stable. Moreover, if both eigenvalues are real and negative, perturbations decay exponentially. In this case, it is possible to identify characteristic time scales for each eigendirections as

$t_1 = \frac{1}{|\lambda_1|}$ (9)

and

$t_2 = \frac{1}{|\lambda_2|}$. (10)

2.1 Van der Waals Model

To describe the behavior of real gases, Van der Waals proposed two corrections for the thermal equation of ideal gases $pV = RT$. The first idea was that one has to correct the "volume" of molecules, which cannot be treated as points. Roughly speaking, the molecules can be visualized as little hard spheres. Therefore there is a minimum volume *b* (for 1 mole) which cannot be passed even by applying very large pressures. The quantity *b* can be regarded as the volume of 1 mole of molecules in a closed-packed arrangement. An obvious and simple way to correct this behavior is to replace *V* by $V - b$, in the equation of ideal gases. The second correction is due to mutual attraction of the molecules. This attraction tends to decrease the volume or acts like an additive pressure. If

we consider a small surface layer of the gas, its attraction by the inner molecules should be proportional to the square of the density, i.e., proportional to .

3.The Curzon-Ahlborn-Novikov engine using a Van der Waals gas as working substance

Consider the endoreversible CAN heat engine Fig.1. This engine works between the heat reservoirs T_1 and T_2 (T_1 $_2$). The working temperatures at steady state are and (T_1 T_2). Heat flows from T_1 to and from y to T_2 through the thermal resistances are governed by the Newton's heat transfer law, with a thermal conductance denoted by α. Using the endoreversibility hypothesis, an engine working between the reservoir and acts like a Carnot engine, although it works in finite time cycles, i.e.

— (11)

and

— (12)

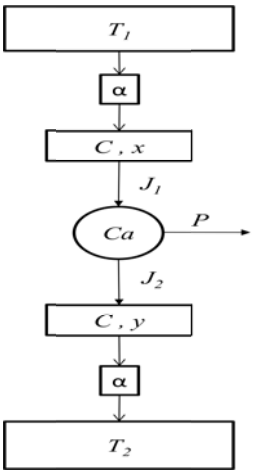

Fig.1 Schematic representation of a CAN engine consists of a Carnot engine (Ca) and the heat reservoirs T_1 and T_2. The heat exchange J_1 and J_2 takes place through both thermal conductors with the same conductance α.

$_1$ and $_2$ are the steady-state heat flows from to the engine, and from the engine to respectively. is the engine power output.

The CA engine works usually in steady state, so that the heat flux from a reservoir at temperature to is $_1$, and the heat flux from to the reservoir at temperature T_2 is $_2$,

(13)

and

. (14)

From equations (11) – (14), and from the definition of efficiency,

– (15)

it follows that

$$\bar{x} = \frac{T_1}{2}\left(1 + \frac{T_2/T_1}{1-\bar{\eta}}\right) \tag{16}$$

$$\bar{y} = \frac{T_1}{2}(1-\bar{\eta})\left(1 + \frac{T_2/T_1}{1-\bar{\eta}}\right). \tag{17}$$

The efficiency of a Curzon-Ahlborn-Novikov engine working at maximum ecological regime using a Van der Waals gas as working substance was found by Ladino-Luna [22]

$$\eta_{VWE} = 1 - \sqrt{\frac{1}{2}(\tau+\tau^2)}\left\{1 + \left[\frac{1}{4}(1+3\tau)\sqrt{\frac{2}{\tau+\tau^2}} - 1\right]\lambda_{VW} + \left[\frac{\frac{1}{16}(1+3\tau)}{\tau+\tau^2} - \frac{1}{2}\sqrt{\frac{2}{\tau+\tau^2}}\ln\sqrt{\frac{1}{2}(\tau+\tau^2)}\right]\left[1+3\tau - 4\sqrt{\frac{1}{2}(\tau+\tau^2)}\right]\lambda^2 vw\right\} + O(\lambda^3 vw), \tag{18}$$

where:

$$\lambda_{VW} = \frac{1}{\gamma-1}\left(\ln\frac{V_{max}-b}{V_{min}-b}\right)^{-1}, \tag{19}$$

where b is a constant which depends on the gas, γ is the ratio of the constant-pressure and constant-volume heat capacities $\gamma = C_p/C_V$, V_{max} and V_{min} are the subtended volumes, maximum and minimum respectively, by the gas in a cycle. Now if we consider that b is smaller than V_{max} and V_{min}, table 13.1 [23], then the ratio $(V_{max}-b)/(V_{min}-b)$ is approximately V_{max}/V_{min}, this ratio is called volumetric compression ratio r_C, for Diesel cycle the typical values are 12-15, table 10.1 [24], so we do the calculus using (19) obtaining $\lambda_{VW} = 1.006$, which shows that we can use for purposes of calculus $\lambda_{VW} = 1$, equation (19) give more values to λ_{VW}, but are all not have physically mean. If $\lambda_{VW} = 1$ we obtain the approximate expression,

$$\eta_{VWE} = \frac{3}{4}\eta_C. \tag{20}$$

In the above approximation, we observe a relation between Carnot's efficiency and Van der Waals's efficiency at maximum power, which is $\eta_{VWE} = 3\,\eta_C/4$. It is reasonable because η_{VW} is smaller than η_C, so the efficiency of a CA engine working in the maximum power regime using a Van der Waals gas working substance is given by (20), with $\tau = T_2/T_1$.

Now, substituting this efficiency (20), into equations (16) and (17) renders

$$\bar{x} = \frac{T_1}{2}\frac{(1+7\tau)}{(1+7\tau)} \tag{21}$$

and

$$\bar{y} = \frac{T_1}{8}(1+7\tau). \tag{22}$$

From (13), (15), (16) and (17) we can write the power output of the steady- state in terms of T_1 and $T_2(T_1 \text{and } \tau)$ and itbecomes

$$\bar{P} = \frac{3\alpha T_1}{8}\frac{(1-\tau)^2}{(1+3\tau)}. \tag{23}$$

Solving for $T_1$and T_2, from equations (21) and (22) gives

$$T_1 = -\frac{6\bar{x}\bar{y}}{\bar{x}-7\bar{y}} \tag{24}$$

and

$$T_2 = 2\left(\frac{-\bar{x}\bar{y}+4\bar{y}^2}{-\bar{x}+7\bar{y}}\right). \tag{25}$$

Finally substituting (24) and (25) in (23) we obtain the power output in steady-state $\bar{P}$ as function of $\bar{x}$and $\bar{y}$,

$$\bar{P} = -\frac{\alpha(\bar{x}-\bar{y})^2}{\bar{x}-7\bar{y}}. \tag{26}$$

4. Local stability of an endoreversible CAN engine

Following Santillán et al [15], a system of differential equations that provides information about how the stability engine is constructed. Santillán et al. developed a system of coupled differential equations to model the rate of change of intermediate temperature.

Assuming that the temperatures x and y correspond to macroscopic objects with heat capacity C, the differential equations for x and y are given by [15]

$$\frac{dx}{dt} = \frac{1}{C}[\alpha(T_1 - x) - J_1] \tag{27}$$

and

$$\frac{dy}{dt} = \frac{1}{C}[J_2 - \alpha(y - T_2)] \tag{28}$$

Both derivatives cancel when x, y,J_1 and J_2 take their steady state values. Under the endoreversibility assumption, the heat flux from x to the working fluid is J_1 and the heat flux from the Carnot engine to y is J_2, so J_1 and J_2 are given in terms of x and y, and the power output P as,

$$J_1 = \frac{x}{x-y}P \tag{29}$$

and

$$J_2 = \frac{y}{x-y}P. \tag{30}$$

It seems reasonable to assume that the power output produced by the CA engine is related to temperature x and y in the same way that the power output at steady state $\bar{P}$ depends of $\bar{x}$ and $\bar{y}$ in the maximum power regime (see equation (23)), i.e.,

$$P = -\frac{\alpha(x-y)^2}{x-7y}. \tag{31}$$

The substitution (29)- (31) in (27) and (28) leads to the following set of differential equations for temperatures x and y of a CA engine performing in maximum-power regime and using a Van der Waals gas as working substance.

$$\frac{dx}{dt} = \frac{\alpha[T_1(x-7y)+6xy]}{C(x-7y)} \tag{32}$$

and

$$\frac{dy}{dt} = \frac{\alpha[T_2(x-7y)-2y(x-4y)]}{C(x-7y)}. \tag{33}$$

To analyze the stability's system near to the steady state, we proceed by following the steps described in section 2. First we define

$$f(x,y) = \frac{\alpha[T_1(x-7y)+6xy]}{C(x-7y)} \tag{34}$$

$$g(x,y) = \frac{\alpha[T_2(x-7y)-2y(x-4y)]}{C(x-7y)}. \tag{35}$$

Now the matrix $A = \begin{pmatrix} f_x & f_y \\ g_x & g_y \end{pmatrix}$, where A is the matrix given by the first term on the right-hand side equation (3) where

$$f_x = \frac{\partial f}{\partial x}\Big|_{\bar{x},\bar{y}} = -\frac{14\alpha(1+3\tau)^2}{3C(1+7\tau)^2} \tag{36}$$

$$f_y = \frac{\partial f}{\partial y}\Big|_{\bar{x},\bar{y}} = \frac{32\alpha}{3C(1+7\tau)^2} \tag{37}$$

$$g_x = \frac{\partial g}{\partial x}\Big|_{\bar{x},\bar{y}} = \frac{2\alpha(1+3\tau)^2}{3C(1+7\tau)^2} \tag{38}$$

$$g_y = \frac{\partial g}{\partial y}\Big|_{\bar{x},\bar{y}} = -\frac{8\alpha(1+3\tau(2+7\tau))}{3C(1+7\tau)^2} \tag{39}$$

with $\tau = T_2/T_1$.

Due to the substitution (36)-(39) in equation (7), we found that both eigenvalues $\lambda_1$and λ_2, are given as

$$\lambda_1 = \frac{-\alpha}{3C}\frac{11+66\tau+147\tau^2+\sqrt{73+492\tau+774\tau^2-756\tau^3+441\tau^4}}{(1+7\tau^2)} \tag{40}$$

and

$$\lambda_2 = \frac{-\alpha}{3C}\frac{11+66\tau+147\tau^2-\sqrt{73+492\tau+774\tau^2-756\tau^3+441\tau^4}}{(1+7\tau^2)}, \quad (41)$$

since both are real and negative, it follows from equation (8) that any perturbation decays exponentially with time and thus that steady state is stable for every value of α, C and $\tau = T_2/T_1 > 0$.

5. Systems stability characteristics

The decay time depends on the absolute value of $\lambda_1$and λ_2. Indeed, we can define two relaxation times t_1 and t_2 as

$$t_1 = -\frac{1}{\lambda_1} = \frac{3C}{\alpha}\frac{3C(1+7\tau^2)}{11+66\tau+147\tau^2+\sqrt{73+492\tau+774\tau^2-756\tau^3+441\tau^4}} \quad (42)$$

and

$$t_2 = -\frac{1}{\lambda_2} = \frac{3C}{\alpha}\frac{3C(1+7\tau^2)}{11+66\tau+147\tau^2-\sqrt{73+492\tau+774\tau^2-756\tau^3+441\tau^4}}. \quad (43)$$

Note that both relaxation times are proportional to C/α. This means that in order to improve the system's stability, we can either increase α or decrease C. Both of the relaxation times depend on τ. The smaller $\lambda_1$and λ_2 are then t_1>t_2, where t_1, t_2 correspond to the slow and fast direction, respectively. Thus the steady state is stable because any perturbation would be decayed exponentially. The plot of t_1 and t_2 versus τ is shown in figure 2. We notice that in the limit $\tau \to 1$, both relaxation times tend to be closer to one another, indicating that the stability is preserved, but in the limit $\tau \to 0$ the stability is not preserved.

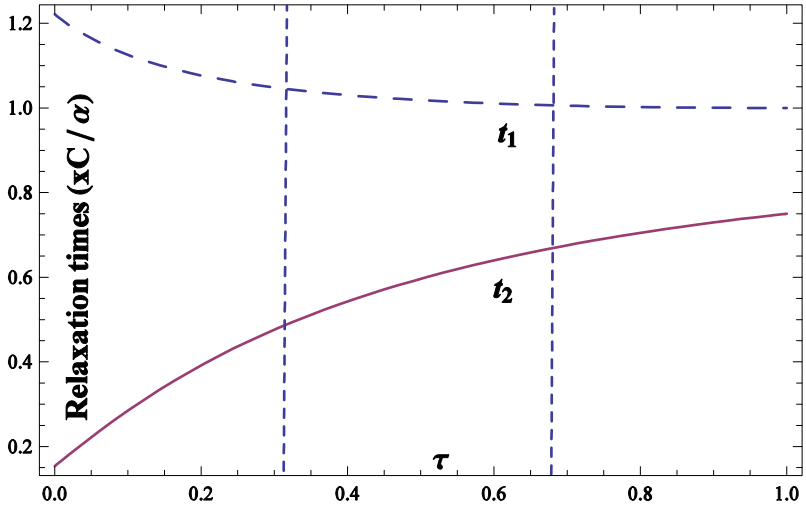

Fig. 2 Plots of the CAN engine relaxation times t_1 and t_2, after a small perturbation, versus τ.

Equations (20) and (23), respectively, determine the steady-state efficiency $(\bar{\eta})$ and power output$(\bar{P})$, as functions of $\tau = T_2/T_1$ and α, of an endoreversible Curzon-Ahlborn engine using a Van der Waals gas as working substance. It is easy to show that both $\bar{\eta}$ and $\bar{P}$ are decreasing functions of τ see Fig. 3 and Fig. 4, for every fixed values of α and C.

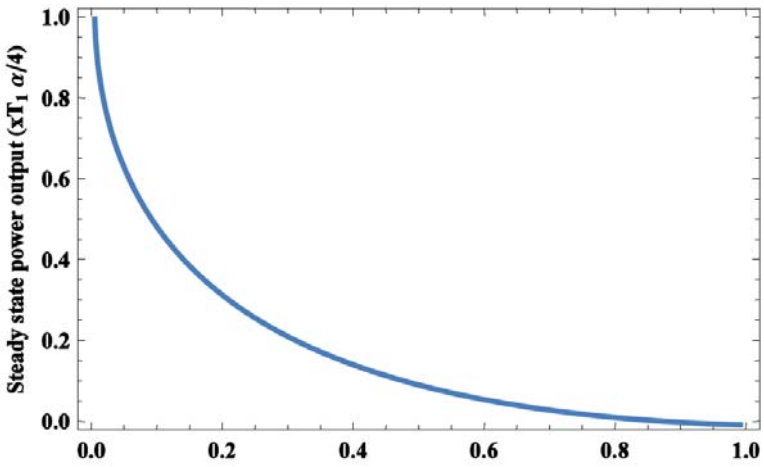

Fig. 3 Plot of the power output versus τ.

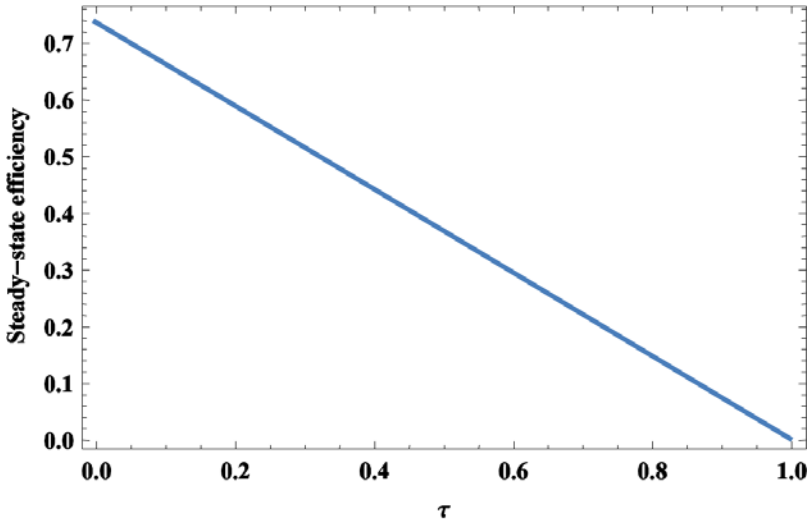

Fig. 4 Plot of the efficiency versus τ.

We conclude from the assertions in the previous paragraph that energetic properties of a Curzon-Ahlborn-Novikov engine using a Van der Waals gas as working substance, working in the maximum ecological regime worsen as τ decreases to zero and improve as τ increases to one. In Fig. 5 is shown the phase portrait for an endoreversible CAN engine working maximum power regime and maximum ecological regime and we can see that the trajectories approach the origin tangent to slow eigendirections which are susceptible to work regime.

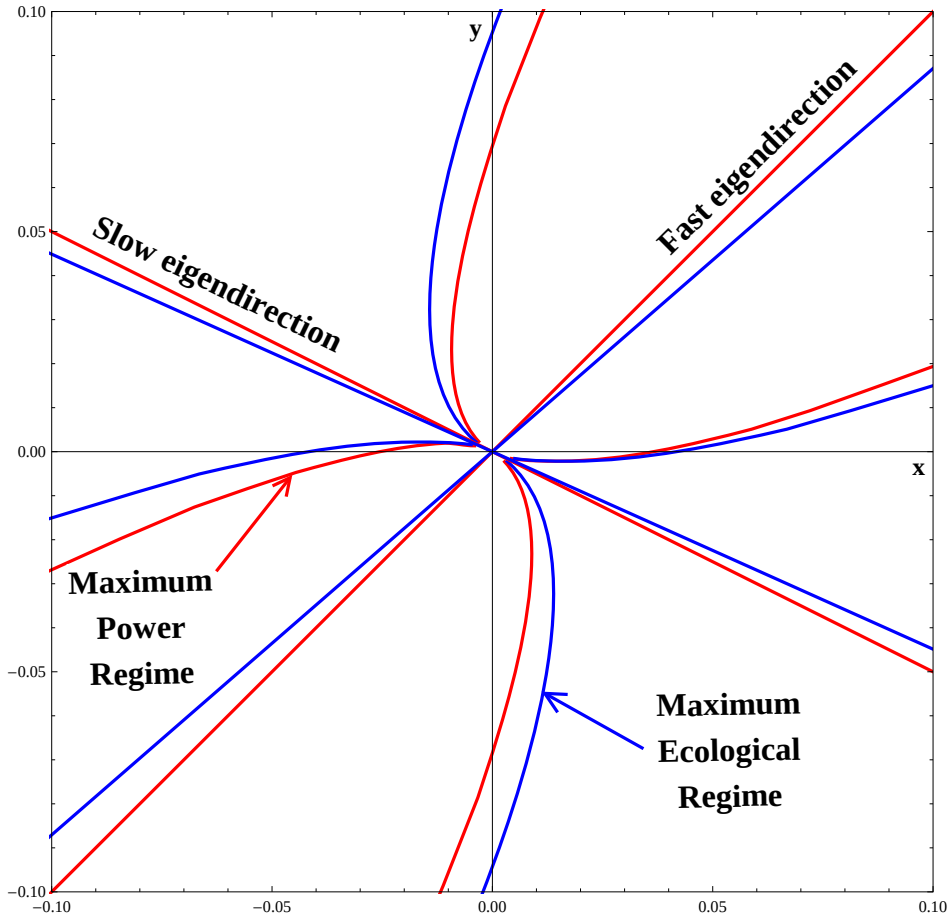

Fig. 5 Behavior of the portrait phase for an endoreversible CAN engine using a Van der Waals gas as working substance, working in the maximum ecological regime and the maximum power regime.

6. Comments

We obtain the same behavior at a CAN engine working at maximum power regime, see Santillán et al.[15]. In Fig. 2 the range where the engine has good thermodynamic and dynamic properties is shown similar to Santillán's results. From Figure 5 it is clear that all trajectories approach the origin tangentially to slow eigendirection, i.e. we can say that it is a stable point. In addition, it is shown that eigendirections are susceptible to both the heat transfer law and the work regime [17, 20], because the eigenvectors in the ecological regime have different angles with the maximum power regime. It is important to point out that we obtain an analytical expression to both eigenvalues, which depend of α, C and τ. Finally, we highlight the fact that the approach used $\lambda_{vW} = 1$, leads to the known relationship $\eta_{VWE} = \frac{3}{4}\eta_C$.

Acknowledgments

This work was partially supported by CONACYT (SNI).

References

[1] Rubin M.H., Optimal configuration of a class of irreversible heat engines I, Phys. Rev. A. 1979; **19**:1272-1276.

[2] Andresen B., Berry R.S., Ondrechen M.J., and Salamon P., Thermodynamics for processes in finite time; Acc. Chem. Res.1984; **17**:266.

[3] Sieniutycz S. and Salamon P., Advances in Thermodynamics, vol. 4: Finite Time Thermodynamics, Taylor & Francis, New York, 1990.

[4] De Vos A., Endoreversible Thermodynamics of Solar Energy Conversion, OxfordUniversity Press, Oxford, 1992.

[5] Bejan A., Entropy Generation Minimization: The new thermodynamics of finite-size devices and finite-time processes; J. Appl. Phys. 1996; **79**:1191-1219.

[6] Bejan A., Entropy Generation Minimization, CRC Press, Boca Raton, Florida, 1996.

[7] Berry R.S., Kazakov V.A.,Sieniutycz S., Szwast Z., and Tsirlin A.S.,Thermodynamics Optimization of Finite Time Processes, Wiley, Chichester, 1999.

[8] Chen L., Wu C. and Sun F., Finite Time Thermodynamic Optimization or Entropy Generation Minimization of Energy Systems, J. Non-Equilib. Thermodyn. 2005;**24**:327-359.

[9] Chen L. and Sun F., Advances in Finite Thermodynamics Analysis and OptimizationNova Science, New York, 2004.

[10] Curzon F.L. and Ahlborn B., Efficiency of a Carnot engine a maximum power output; Am. J. Phys.1975; **43:**22-24.

[11] Salamon P., Some Issues in Finite-Time thermodynamics, Auracher H., Feidth M., and Tsatsaronis G., editors. Proceedings of Seminaire Eurotherm No.59; Nancy France July 1998.

[12] Andresen B., Current Trend in Finite-Time Thermodynamics. Angew. Chem. Int. Ed. 2011: 2690-2705.

[13] Callen H.B., Thermodynamics an Introduction to Thermostatics, 2nd ed., Wiley, New York,1985.

[14] Radenco V.T., Generalized Thermodynamics, Editura Tehnica, Bucarest, 1994.

[15] Santillán M., Maya G. and Angulo-Brown F., Local stability analysis of an endoreversible Curzon-Ahlborn-Novikov engine working-power-like regime, J. Phys. D: Appl. Phys.2001;**34**: 2068-2072.

[16] Huang Y., A study on thermodynamic optimization of irreversible cycle and application to the absortion systems [in Chinese], Ph.D. thesis, Harbin Institute of Technology, PR China, 2003.

[17] Guzmán-Vargas L, Reyes-Ramírez I., and Sanchez N., The effect of heat transfer laws and thermal conductances on the local stability of an endoreversible heat engine; J. Phys. D: Appl. Phys.2005; **38**:1282-.

[18] Páez-Hernández R., Angulo-Brown F. and Santillán M., Dynamic Robustness and Thermodynamic Optimization in a non-endoreversible Curzon-Ahlborn engine; J. Non-Equilib. Thermodyn. 2006; **31**: 173-178.

[19] Huang Y. and Sun D., Local stability analysis of a non-endoreversible heat pump; J. Non-Equilib. Thermodyn. 2008; **33**: 61.

[20] Páez-Hernández R, Ladino-Luna D. and Portillo-Díaz P., Dynamic properties in an endoreversible Curzon-Ahlborn engine using a van der Waals gas as working substance. Physica A.2011;**390**: 3275-3282.

[21] Angulo-Brown F., An ecological optimization criterion for Finite-Time heat engines. J.Appl. Phys. 1991;**69**: 7465-7469.

[22] Ladino-Luna D. Ciclo de Curzon-Ahlborn para un gas de van der Waals,Rev.Mex.Fis. 2002;**48:** 575-578.

[23] Huang F.F., Engineering Thermodynamics: Fundamentals and Applications 2nd. ed. McMillan Publishing Company, New York, 1989.

[24] Heywood J. B., Internal Combustion Engine, McGraw-Hill Publishing Company 1988.

Some Remarks on the Carnot's Theorem

Julian Gonzalez-Ayala[a] and F. Angulo-Brown[b]

[a] *Escuela Superior de Fisica y Matematicas IPN, Mexico City, Mexico, noldor_21@yahoo.com.mx*
[b] *Escuela Superior de Fisica y Matematicas IPN, Mexico City, Mexico, angulo@esfm.ipn.mx.*

Abstract:

It is common in many thermodynamics textbooks to illustrate the Carnot's theorem through the usage of diverse equations of state for gases, paramagnets, and other simple thermodynamic systems. As it is well-known, the universality of the Carnot efficiency is easily demonstrated in a temperature-entropy diagram. In fact, any thermodynamic cycle depicted in a (w,z) diagram, being zdw the inexact differential of work, can be mapped into a (T,S) diagram. In this work we show that this property is consistent with a preserving area map with $Jacobian[(w,z),(T,S)]=-1$, and that any equation of state satisfying this Jacobian transformation fulfills the Carnot's theorem.

Keywords:

Second law of thermodynamics, Carnot's theorem, Legendre transformation, preserving areas transformation.

1. Carnot's Theorem

It is well known the limit imposed by the second law of thermodynamics about the maximum efficiency of any energy converter (thermodynamic cycle, heat engine, and so on) working between two extreme absolute temperatures T_1 and T_2, that is, the efficiency of the Carnot cycle, which is the following,

$$\eta = 1 - \frac{T_1}{T_2}, \qquad (1)$$

where $T_1 < T_2$ are the temperatures of the cold and the hot reservoirs at which the thermodynamical engine operates. This upper limit works for both, reversible and irreversible processes. There exist several possible demonstrations of this fact, but perhaps the most compact and easy way to do this is on the (T,S) plane, where S denotes the entropy. Such a demonstration can be easily found on any thermodynamics textbook. Although the Carnot's theorem is accompanied with (1), the original statement was that the efficiency was function solely of the temperature at which heat is respectively received and emitted and independent of the nature of the working substance. However it should be mentioned that it was Rankine who obtained the explicit form of equation (1) [1].

It is well known that any cycle on the (T,S) plane (the heat-plane) has a corresponding cycle on a (w,z) plane, where w and z are some conjugate variables in such a way that the inexact differential of work dW can be written as wdz (the work-plane).

Several examples are in the literature on the independency of (1) from any working substance and some of them are based on gases obeying the equation of state of the ideal gas, Van der Waals and other equations of state [2-7]. Some of the authors ask themselves about the validity of (1) for non ideal substances [6,7]. In fact [7] answers this question by introducing a general method to obtain the efficiency of the Carnot's cycle for an arbitrary equation of state. It is also common that in some textbooks (1) is found by using other simple thermodynamic systems as the working substance, for instance, a stretched elastic wire, a surface film [8] and ideal paramagnets [2-5].

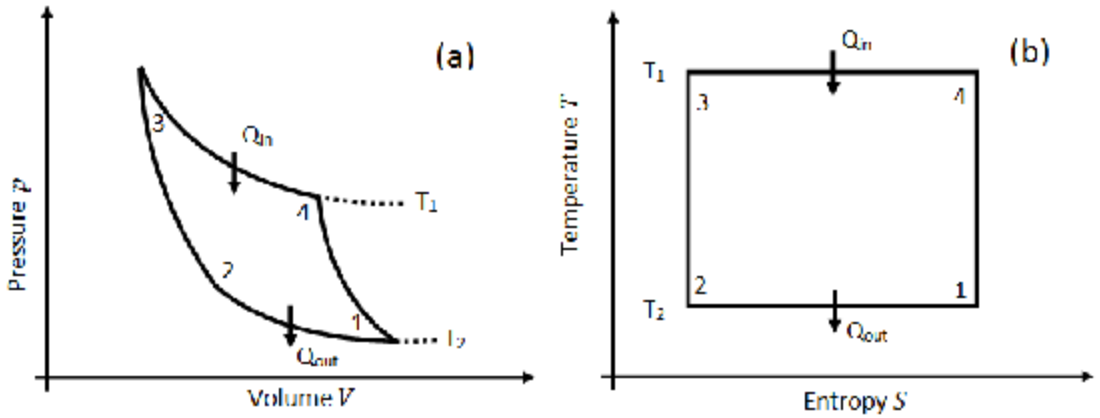

Fig. 1. Carnot cycles in the (p,V) diagram and in the (T,S) diagram, Q_{in} and Q_{out} are the income and output heat.

2. Consistency of equations of state with thermodynamics

Equations of state for several thermodynamic systems (as fluids, paramagnets, etc.) are built following empirical and semiempirical procedures, or methods based in first principles stemming from statistical mechanics, as is the case of the Virial equation for example. Despite this there are no much efforts on explaining if the many existing equations of state are compatible with first and second laws of thermodynamics (because it is not expected that these equations describe the behavior of gases near zero temperature, compatibility with third law can be relaxed).

About this subject Tykodi and Hummel [9] proposed a way to verify the thermodynamic validity of any gas state equation. The result obtained was that if any equation of state of the form $\mathrm{p} = \mathrm{p}(\mathrm{T},\mathrm{V})$ is expected to be in agreement with the first and the second laws of thermodynamics, where p is the pressure, T the temperature and V the volume, the equation of state should be expressible as,

$$[\mathrm{p} + \xi(\mathrm{T},\mathrm{V})]\phi(\mathrm{V}) = \mathrm{RT}, \qquad (2)$$

where $\phi(\mathrm{V})$ is a function of the volume, R the universal gas constant and $\xi(\mathrm{T},\mathrm{V})$ is a function of the temperature and the volume defined as follows,

$$\xi(\mathrm{T},\mathrm{V}) = -\mathrm{T}\int \mathrm{T}^{-2}\left(\frac{\partial \mathrm{U}}{\partial \mathrm{v}}\right)_{\mathrm{T}} \mathrm{dT}, \qquad (3)$$

integrated at constant V and U is the total internal energy. (2) and (3) stem from well-known simple thermodynamic identities. From the Gibbs' equation,

$$\mathrm{dU} = \mathrm{TdS} - \mathrm{pdV}, \qquad (4)$$

it immediately follows that,

$$\left(\frac{\partial \mathrm{U}}{\partial \mathrm{v}}\right)_{\mathrm{T}} = \mathrm{T}\left(\frac{\partial \mathrm{S}}{\partial \mathrm{v}}\right)_{\mathrm{T}} - \mathrm{p}, \qquad (5)$$

by using the Maxwell relation,

$$\left(\frac{\partial \mathrm{S}}{\partial \mathrm{v}}\right)_{\mathrm{T}} = \left(\frac{\partial \mathrm{p}}{\partial \mathrm{T}}\right)_{\mathrm{v}}, \qquad (6)$$

and replacing (6) into (5) one obtains,

$$\left(\frac{\partial U}{\partial V}\right)_T = T\left(\frac{\partial p}{\partial T}\right)_V - p, \qquad (7)$$

that can be written as,

$$\left(\frac{\partial U}{\partial V}\right)_T = T^2\left(\frac{\partial \frac{p}{T}}{\partial T}\right)_V. \qquad (8)$$

Integration of (8) at constant temperature gives (2) and (3). In addition, it is expected that in the limit of a very dilute gas, it behaves as an ideal gas, that is,

$$\lim_{V\to\infty} p = p_{\text{ideal gas}}, \qquad (9)$$

in other words,

$$\lim_{V\to\infty} \frac{V}{\phi(V)} = 1, \qquad (10)$$

and

$$\lim_{V\to\infty} V\xi(T,V) = 0. \qquad (11)$$

Substitution of (7) into (3) gives the following relation,

$$\xi(T,V) = -T\int T^{-2}\left(T\left(\frac{\partial p}{\partial T}\right)_V - p\right)dT. \qquad (12)$$

In this way, all we need is to know the equation of state to evaluate (12) and to obtain the function $\phi(V)$ to determine whether such equation of state is thermodynamically consistent or not. Some work has been made on equations of state like the ideal gas, Van der Waals, Dieterici and Redlich-Kwong[9].

In 1990 Agrawal and Menon [6] calculated the expression of the Carnot efficiency for the Van der Waals gas, pointing out that typically in textbooks [2-5] this treatment is only made with the ideal gas as a working substance. These authors emphasize the fact that for non ideal substances the calculation of (1) is not a trivial task, alluding that in general the heat capacities present a dependence on the volume. Later, in 2006 Tjiang and Sutanto [7] demonstrated that an arbitrary gas state equation fulfills (1). Recently, Penrose [10] has asserted that: “this law (the second law of thermodynamics) has a universality that goes beyond any particular system of dynamical rules that one might be concerned with… It applies also to hypothetical dynamical theories that we have no good reason to believe have relevance to the actual universe that we inhabit…”.

3. Carnot’s theorem for equations of state which do not fulfill the Tykodi-Hummel consistency criterion.

More can be said about the generality of (1). Since Carnot’s theorem is a thermodynamical principle, it is not expected that an equation in a non-agreement with the thermodynamics, that is a “non-thermodynamical” equation of state should fulfills this theorem. At first sight the statement that “any working substance reproduces the Carnot efficiency” should apply only to well behave thermodynamical equations of state seems reasonable, however, surprisingly (at least for the authors of this work) it is not the case, because even those equations not consistent with thermodynamics (see Appendix A) reproduce (1). The general method that we used in the calculation of the efficiency is an analogue to the one used in [7]. Some more about the mathematics of this method can be found in Appendix B.

In particular, the equation in a non-agreement with the first and the second laws of thermodynamics shown in Appendix A, reproduce (1). As much as we would like to prove this for every single equation of state one by one, we consider that it is more convenient do it with a general equation. The proposal is the following,

$$p = \sum_{j=-n}^{n} \sum_{i=-m}^{m} a_{ij} T^i v^j, \qquad (13)$$

p is the pressure, T^i and v^j are the temperature and the volume elevated to the i and j power respectively and a_{ij} are the constant coefficients of the series (equation (A1) is a particular case of equation (13)). This equation is general enough to cover any analytical function. For example, the virial equation which has the following form,

$$p = RT\left(\frac{1}{v} + \frac{B_2}{v^2} + \frac{B_3}{v^3} + \dots\right), \qquad (14)$$

where v is the molar volume and B_2, B_3, etc. are the second, the third, etc. virial coefficients and are functions of the temperature only. Since the virial coefficients B_j are related to the Mayer cluster integrals, which are integrals of an exponential function, then they are infinitely derivable on the variable T and then they are analytic functions and by the Taylor theorem they accept a power series representation. That means that one can write each B_j as follows,

$$B_j = \sum_{i=0}^{\infty} b_{ij} T^i, \qquad (15)$$

where each b_{ij} are the constant coefficients of the series. Then (14) is now written as,

$$p = RT\left(\frac{1}{v} + \frac{1}{v^2}\sum_{i=0}^{\infty} b_{i2} T^i + \frac{1}{v^3}\sum_{i=0}^{\infty} b_{i3} T^i + \dots\right), \qquad (16)$$

that can be rearranged as,

$$p = \frac{RT}{v} + RT \sum_{j=2}^{\infty} \sum_{i=0}^{\infty} \frac{b_{ij} T^i}{v^j}, \qquad (17)$$

by grouping one obtains the same kind of function as (13). For this equation, the total internal energy U is obtained according to (B7) and (B8) giving the following result,

$$U = \sum_{i=-m}^{m} (i-1) T^i \left(\sum_{\substack{j=-n \\ j \neq -1}}^{n} i a_{ij} \frac{v^{j+1}}{j+1} + a_{i,-1} \ln v \right) + \alpha T + F(T), \qquad (18)$$

where α is a constant and $F(T)$ is an arbitrary function of the temperature only (for the ideal gas $F(T) = 0$ and $\alpha = 3nR/2$). And from (B5) the entropy is,

$$S = \sum_{i=-m}^{m} \left(\sum_{\substack{j=-n \\ j \neq -1}}^{n} i a_{ij} \frac{T^{i-1} v^{j+1}}{j+1} + i T^{i-1} a_{i,-1} \ln v \right) + \alpha \ln T + \int \frac{F\prime(T)}{T} dT + S_0. \qquad (19)$$

Equation (B12) is,

$$\eta = 1 + \frac{T_2}{T_1} \frac{\sum_{i=-m}^{m} \left(\sum_{\substack{j=-n \\ j \neq -1}}^{n} i a_{ij} \frac{T_2^{i-1} v_1^{j+1}}{j+1} + i T_2^{i-1} a_{i,-1} \ln v_1 \right) - \sum_{i=-m}^{m} \left(\sum_{\substack{j=-n \\ j \neq -1}}^{n} i a_{ij} \frac{T_2^{i-1} v_2^{j+1}}{j+1} + i T_2^{i-1} a_{i,-1} \ln v_2 \right)}{\sum_{i=-m}^{m} \left(\sum_{\substack{j=-n \\ j \neq -1}}^{n} i a_{ij} \frac{T_1^{i-1} v_4^{j+1}}{j+1} + i T_1^{i-1} a_{i,-1} \ln v_4 \right) - \sum_{i=-m}^{m} \left(\sum_{\substack{j=-n \\ j \neq -1}}^{n} i a_{ij} \frac{T_1^{i-1} v_3^{j+1}}{j+1} + i T_1^{i-1} a_{i,-1} \ln v_3 \right)}. \qquad (20)$$

Subtracting (B13) from (B14) we have that,

$$\sum_{i=-m}^{m}\left(\sum_{\substack{j=-n\\ j\neq -1}}^{n} i a_{ij}\frac{{T_1}^{i-1}v_4^{j+1}}{j+1}+i{T_1}^{i-1}a_{i,-1}\ln v_4\right)-\sum_{i=-m}^{m}\left(\sum_{\substack{j=-n\\ j\neq -1}}^{n} i a_{ij}\frac{{T_1}^{i-1}v_3^{j+1}}{j+1}+i{T_1}^{i-1}a_{i,-1}\ln v_3\right)=$$

$$\sum_{i=-m}^{m}\left(\sum_{\substack{j=-n\\ j\neq -1}}^{n} i a_{ij}\frac{{T_2}^{i-1}v_1^{j+1}}{j+1}+i{T_2}^{i-1}a_{i,-1}\ln v_1\right)-\sum_{i=-m}^{m}\left(\sum_{\substack{j=-n\\ j\neq -1}}^{n} i a_{ij}\frac{{T_2}^{i-1}v_2^{j+1}}{j+1}+i{T_2}^{i-1}a_{i,-1}\ln v_2\right)$$

, (21)

then,

$$\frac{\sum_{i=-m}^{m}\left(\sum_{\substack{j=-n\\ j\neq -1}}^{n} i a_{ij}\frac{{T_2}^{i-1}v_1^{j+1}}{j+1}+i{T_2}^{i-1}a_{i,-1}\ln v_1\right)-\sum_{i=-m}^{m}\left(\sum_{\substack{j=-n\\ j\neq -1}}^{n} i a_{ij}\frac{{T_2}^{i-1}v_2^{j+1}}{j+1}+i{T_2}^{i-1}a_{i,-1}\ln v_2\right)}{\sum_{i=-m}^{m}\left(\sum_{\substack{j=-n\\ j\neq -1}}^{n} i a_{ij}\frac{{T_1}^{i-1}v_4^{j+1}}{j+1}+i{T_1}^{i-1}a_{i,-1}\ln v_4\right)-\sum_{i=-m}^{m}\left(\sum_{\substack{j=-n\\ j\neq -1}}^{n} i a_{ij}\frac{{T_1}^{i-1}v_3^{j+1}}{j+1}+i{T_1}^{i-1}a_{i,-1}\ln v_3\right)}=-1. \qquad (22)$$

Then by the substitution of (22) in (20) we arrive to the final form given by (1). Now we have the certainty that any equation generated from (13) will reproduce (1).

At this point we can propose some equations of state that are physically strange and to use them as the working substance in a Carnot cycle. As an example, let be

$$p=\frac{aV}{T}, \qquad (23)$$

a being a constant with the adequate units. From (13) we can see that the only non zero coefficient is the $a_{-1,1}$, then, from (18) its internal energy is,

$$U=-\frac{aV^2}{T}+\alpha T+F(T), \qquad (24)$$

Which in the usual monoatomic case ($\alpha=\frac{3}{2}nR$ and $F(T)=0$) becomes

$$U=-\frac{aV^2}{T}+\frac{3}{2}RT, \qquad (25)$$

by means of (19) its entropy is,

$$S=-\frac{aV^2}{2T^2}+\frac{3}{2}R\ln T+S_0. \qquad (26)$$

At first glance this is a non-physical equation of state, because when T grows p diminishes and when the gas expands the pressure increase. Expressions (25) and (26) in the limit of large volumes do not reproduce the ideal gas case. It is not logical that increasing the temperature of a gas produces a decrease of the energy. Also it has a problem with the entropy when $T\to 0$. In Fig. 2 it is shown the possible corresponding Carnot cycle for this equation of state.

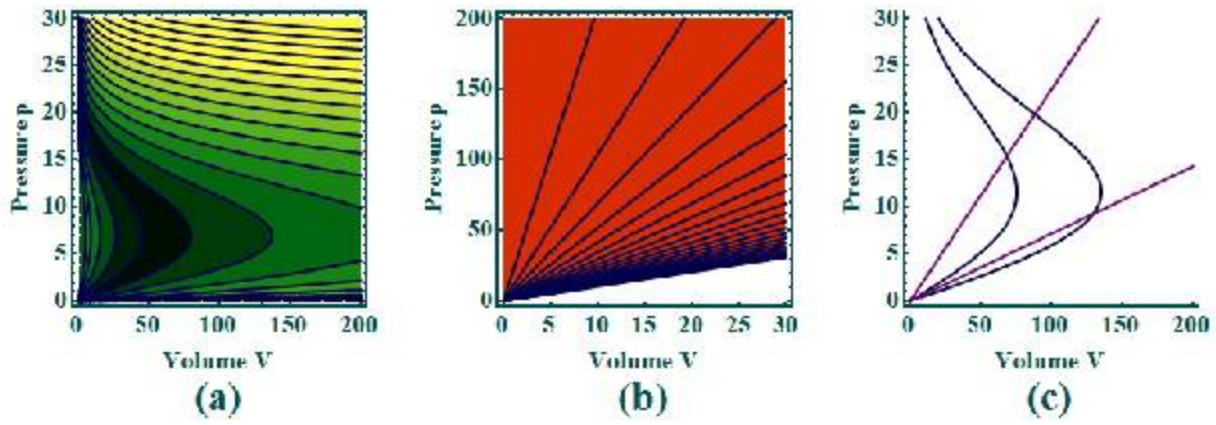

Fig. 2. (a) Adiabatic processes, (b) Isothermal processes and (c) a possible Carnot cycle for the equation of state $p = \frac{aV}{T}$.

Before moving to the next section we would like to mention that in the methods used in [7] and in Appendix A for finding the Carnot efficiency we use the well-known relation,

$$\left(\frac{\partial U}{\partial V}\right)_T = T\left(\frac{\partial p}{\partial T}\right)_V - p, \qquad (27)$$

that can only be obtained if the Maxwell relation [2-5]

$$\left(\frac{\partial S}{\partial V}\right)_T = \left(\frac{\partial p}{\partial T}\right)_V, \qquad (28)$$

is valid. It can be said that (1) is valid if (28) is also valid.

4. Legendre transformations and Jacobian identities

Maxwell relations, as it is well-known, come from Legendre transformations on the internal energy U. A highlight that has been left aside in textbooks is the connection between Maxwell relations and their little known and more compact form of Jacobian identities as it has been pointed by David Mermin and Vinay Ambegaokar in 2001[11], for example,

$$\frac{\partial(p,V)}{\partial(T,S)} = 1. \qquad (29)$$

From this identity it follows immediately the Maxwell relation, (a problem that can be found in [5])

$$\left(\frac{\partial S}{\partial V}\right)_T = \left(\frac{\partial p}{\partial T}\right)_V. \qquad (30)$$

Equation (30) is obtained from (29) by means of the Jacobian properties, that is, by using some called auxiliary variables (T,V),

$$\frac{\partial(p,V)}{\partial(T,S)} = \frac{\partial(p,V)}{\partial(T,V)}\,\frac{\partial(T,V)}{\partial(T,S)} = \left(\frac{\partial p}{\partial T}\right)_V\left(\frac{\partial V}{\partial S}\right)_T = 1. \qquad (31)$$

Now we will show a demonstration that we haven't found in textbooks. This demonstration shows in a simple manner that Legendre transformations would produce mappings that preserve areas (with a suitable choice of the range of the coordinate system). Some general comments about the Legendre transformations and its definition can be found in Appendix C.

4.1. Mappings that preserve areas

Let's take the function M defined in a subspace V of $\mathbb{R}^2$, then if $\vec{x}\epsilon V$ with $\vec{x} = (x,y)$, then

$$M(\vec{x}) = M(x,y). \qquad (32)$$

Its differential is

$$dM = m(x,y)dx + n(x,y)dy, \qquad (33)$$

where m and n are functions of x and y, but for simplicity we'll just denote them as m and n, then,

$$dM = mdx + ndy. \qquad (34)$$

Let's take the Legendre transformation K of M, which according to (C1) is,

$$K = -xm + M, \qquad (35)$$

we are changing the variable x for the variable m, that according to (C4), has the form

$$m = \left(\frac{\partial M}{\partial x}\right)_y. \qquad (36)$$

The differential of this new function is

$$dK = -xdm + ndy, \qquad (37)$$

And because dK is exact, then by the Schwarz theorem,

$$\left(\frac{\partial x}{\partial y}\right)_m = -\left(\frac{\partial n}{\partial m}\right)_y. \qquad (38)$$

Now let Ω be a mapping with $\Omega: (y,n) \mapsto (x,m)$ like the one illustrated in Fig. 3. It is easily shown that this mapping preserves areas (but changes orientations) given the fact that the Jacobian between this two coordinates systems is -1,

$$\frac{\partial(n,y)}{\partial(m,x)} = \frac{\partial(n,y)}{\partial(m,y)}\,\frac{\partial(m,y)}{\partial(m,x)} = \left(\frac{\partial n}{\partial m}\right)_y\left(\frac{\partial y}{\partial x}\right)_m = -\left(\frac{\partial x}{\partial y}\right)_m\left(\frac{\partial y}{\partial x}\right)_m = -1. \qquad (39)$$

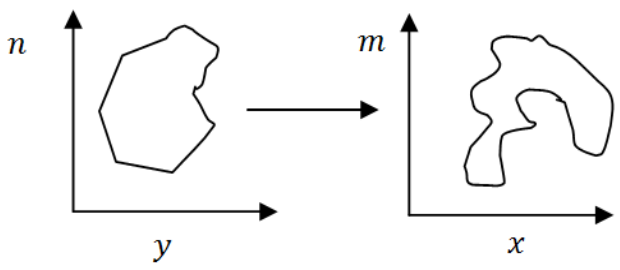

Fig. 3. Preserving areas maps between the (y,n) plane and the (x,m) plane.

What this means is that if the contour in the (y,n) plane is taken clockwise, then the corresponding contour in the (m,x) plane should be taken counterclockwise. Then the area in the (y,n) plane is the negative of the area in the (m,x) plane.

4.2. Application to thermodynamics

In particular the heat-plane, that is, the (T,S) plane and the work-plane (w,z) are of the same kind of those studied in the last subsection. All that is left to do is make the correct associations. Let's take the following substitution, in which the coordinate plane (x,y) is now (S,V),

$$(x,y) \to (S,V), \tag{40}$$

the function M is replaced by the total internal energy U,

$$\mathrm{M(x,y)} \to \mathrm{U(S,V)}, \tag{41}$$

following (C4) and (36),

$$\mathrm{m} = \left(\frac{\partial \mathrm{M}}{\partial \mathrm{x}}\right)_{\mathrm{y}} \to \mathrm{T} = \left(\frac{\partial \mathrm{U}}{\partial \mathrm{S}}\right)_{\mathrm{V}}, \tag{42}$$

$$\mathrm{n} = \left(\frac{\partial \mathrm{M}}{\partial \mathrm{y}}\right)_{\mathrm{x}} \to -\mathrm{p} = \left(\frac{\partial \mathrm{U}}{\partial \mathrm{V}}\right)_{\mathrm{S}}, \tag{43}$$

which are already familiar identities [2-5]. The Helmholtz potential F takes the place of K and it is given by,

$$\mathrm{F} = \mathrm{U} - \mathrm{TS}, \tag{44}$$

and because of (38)

$$\left(\frac{\partial \mathrm{S}}{\partial \mathrm{V}}\right)_{\mathrm{T}} = \left(\frac{\partial \mathrm{p}}{\partial \mathrm{T}}\right)_{\mathrm{V}}. \tag{45}$$

That is to say, from an application that maps a thermodynamical process from the $(-\mathrm{p},\mathrm{V})$ plane to the same process but in the (T,S) plane, it is possible to obtain the first law of thermodynamics for a cycle (see Fig. 4),

$$\mathrm{Q} = -\mathrm{W}, \tag{46}$$

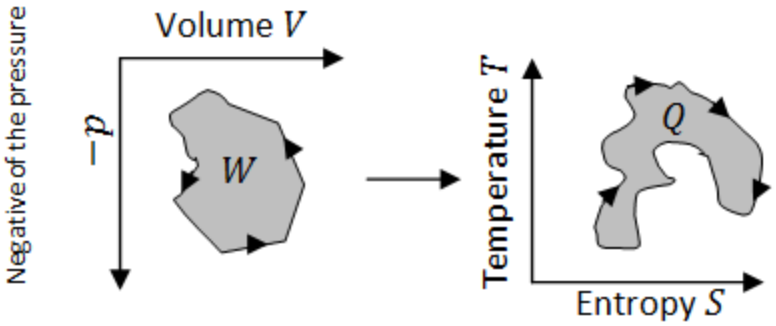

Fig. 4. Preserving areas maps between the $(-p,V)$ plane and the (T,S) plane.

Note in Fig. 4 the direction of the process. Usually we are more familiar with the (p,V) plane instead of the $(-\mathrm{p},\mathrm{V})$ plane. In Fig. 5 it is illustrated the trivial conversion from one another.

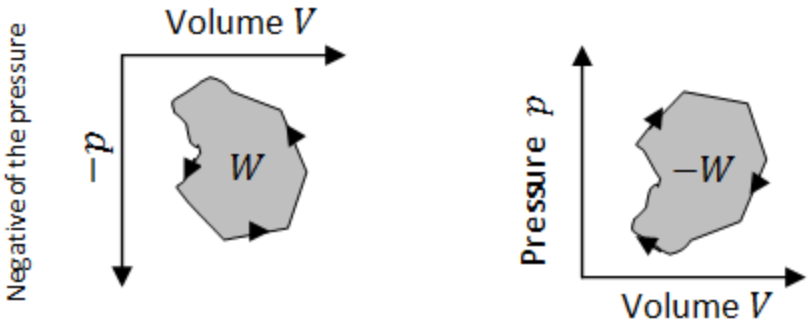

Fig. 5. Relation between the (p, V) plane and the $(-p, V)$ plane.

The generality of this result, which is purely mathematical in a certain manner is linked to the first law of thermodynamics. It is also connected directly to the second law of thermodynamics trough the Carnot's theorem and it seems to carry out a little bit more general property, since apparently extends Carnot's theorem beyond thermodynamics because there are not physics involved. Uncovering a possible contradiction in the sense that we have a thermodynamical principle that should be obeyed by non-thermodynamical or even non-physical entities. We believe that this geometrical property is a link between some aspects of the thermodynamics that have remained dissociated, but we intuitively believed that are connected.

5. Conclusions

In this work we have proposed a gas state equation in a general form (see equation (13)). This equation embraces any known gas state equation, remarkably those compatible with the virial expansion. All these equations fulfill the Tykodi-Hummel criterion of thermodynamic self-consistency. However, (13) also can generate a subset of equations of state, which present a phenomenological anomalous thermodynamic behavior, and on the other hand, they do not fulfill the Tykodi-Hummel criterion. In Sect. 3, we have shown that (13) satisfies the Carnot theorem, thus, the subset of anomalous gas state equations also fulfill with Carnot's theorem, nevertheless, they do not obey the Tykodi-Hummel criterion (see Appendix A). This result is in accordance with the Penrose's comment mentioned at the end of Sect. 2. In the present work we have also shown that this great universality of Carnot's theorem has to do with a geometrical property stemming from preserving areas maps between the work-plane and the heat-plane. As Mermin and Ambegaokar assert [11], this approach based in Jacobian transformations is apparently little known in the literature.

We believe that this geometrical property (preserving areas maps) has not been emphasized in most of standard thermodynamic textbooks. This approach can evidently enrich the conventional thermodynamic analysis.

Acknowledgments

The authors thank partial financial support from PIFI-IPN projects 20113510 and 20120427, and to CONACYT.

Appendix A

Let's take the following ansatz as a possible equation of state,

$$p(T,V) = \frac{aV}{T}. \qquad \text{(A1)}$$

From (12), one can obtain that

$$\xi(T,V) = -\frac{aV}{T} = -p, \qquad \text{(A2)}$$

and (2) yields to $0 = RT$, which is not possible. Then going on the other side, from (2)

$$\xi(T,V) = \frac{RT}{\phi(V)} - p, \qquad \text{(A3)}$$

if (5) is true then $\lim_{V\to\infty} \frac{V}{\phi(V)} = 1$, and applying (6),

$$\lim_{V\to\infty} V\xi(T,V) = RT - \lim_{V\to\infty} \frac{aV^2}{T} \neq 0, \quad \text{(A4)}$$

then this equation of state is not compatible with thermodynamics under the Tykodi-Hummel criterion.

Appendix B

The general method that we used in the calculation of the efficiency is the following:
Our aim is to obtain the efficiency, defined as,

$$\eta = \frac{W}{Q_{in}} = 1 + \frac{Q_{out}}{Q_{in}}, \qquad \text{(B1)}$$

where W is the total work, Q_{in} and Q_{out} are the input and output heats over the isothermal processes. Here we use the convention that Q_{out} is negative since the integration path is taken from $4 \to 1$ (see Fig. 1).
One way to find the heat is using the equality $\delta Q = TdS$ (because we have a reversible process), where δQ is the inexact differential of heat and dS the exact differential of entropy. As it is well known $\frac{1}{T}$ is the integrating factor of δQ. From (7)

$$dS = \frac{1}{T}dU + \frac{p}{T}dV, \qquad \text{(B2)}$$

because dU is exact, then,

$$dS = \frac{1}{T}\left[\left(\frac{\partial U}{\partial T}\right)_V dT + \left(\frac{\partial U}{\partial V}\right)_T dV\right] + \frac{p}{T}dV. \qquad \text{(B3)}$$

From (5) and (6) we have,

$$\left(\frac{\partial U}{\partial V}\right)_T = T\left(\frac{\partial p}{\partial T}\right)_V - p, \qquad \text{(B4)}$$

then,

$$dS = \frac{1}{T}\left(\frac{\partial U}{\partial T}\right)_V dT + \left(\frac{\partial p}{\partial V}\right)_T dV, \qquad \text{(B5)}$$

and,

$$dQ = \left(\frac{\partial U}{\partial T}\right)_V dT + T\left(\frac{\partial p}{\partial T}\right)_V dV. \qquad \text{(B6)}$$

From (B4),

$$\left(\frac{\partial^2 U}{\partial V \partial T}\right) = T\left(\frac{\partial^2 p}{\partial T^2}\right)_V, \qquad \text{(B7)}$$

an integration over the variables V and T yields to

$$U = \iint \left(\frac{\partial^2 U}{\partial V \partial T}\right) dV dT + \int f(T)\, dT + H(V), \quad \text{(B8)}$$

where $f(T)$ and $H(V)$ are functions to determine. At this point we can impose the condition that for a very dilute monoatomic gas it behaves as the ideal gas, that is,

$$\lim_{V\to\infty} U = \frac{3}{2} nRT, \qquad \text{(B9)}$$

where n is the molar number of the gas, then,

$$f(T) = \frac{3}{2} nR, \qquad \text{(B10)}$$

all this to calculate $\left(\frac{\partial U}{\partial T}\right)_V$ and to obtain from (B5) the entropy $S(T,V)$. Q_{in} and Q_{out} are over isothermal processes, then

$$\begin{aligned} Q_{in} &= T_1 \Delta S_{34} \\ Q_{out} &= T_2 \Delta S_{12}, \end{aligned} \qquad \text{(B11)}$$

and (B1) becomes,

$$\eta = 1 + \frac{T_2}{T_1}\frac{\Delta S_{12}}{\Delta S_{34}}, \qquad \text{(B12)}$$

where ΔS_{12} denotes $S(T_2,V_2) - S(T_2,V_1) > 0$, and $\Delta S_{34} = S(T_1,V_4) - S(T_1,V_3) < 0$ ($S(T,V)$ is a state function). Over the adiabatic processes we also have the following conditions,

$$S(T_1,V_3) = S(T_2,V_2), \qquad \text{(B13)}$$

$$S(T_1,V_4) = S(T_1,V_4), \qquad \text{(B14)}$$

the subtraction between (B13) and (B14) yields to

$$\Delta S_{34} = -\Delta S_{12}, \qquad \text{(B15)}$$

then (B12) is exactly (1), so in this way it is possible to arrive directly from the equation of state to the entropy and finally to the efficiency of Carnot.

As a manner of example, consider the following equation of state (which satisfies the Tykodi-Hummel criterion),

$$p(T,V) = \frac{aT}{V} + \frac{bT^2}{V^s}. \qquad \text{(B16)}$$

From (B4) we have that,

$$\left(\frac{\partial U}{\partial V}\right)_T = \frac{bT^2}{V^s}, \qquad \text{(B17)}$$

because of (B7),

$$\left(\frac{\partial^2 U}{\partial V \partial T}\right) = 2\frac{bT^2}{V^3}, \qquad \text{(B18)}$$

integration over the volume gives,

$$\left(\frac{\partial U}{\partial T}\right)_V = -\frac{bT}{V^2} + f(T), \qquad \text{(B19)}$$

and integration over the temperature results in,

$$U = -\frac{bT^2}{V^2} + \int \frac{3}{2} nRdT + H(V). \qquad \text{(B20)}$$

Then (B19) is,

$$\left(\frac{\partial U}{\partial T}\right)_V = -\frac{bT}{V^2} + \frac{3}{2} nR, \qquad \text{(B21)}$$

and from (B5), (B21) and (B16) one obtains,

$$dS = \left(-\frac{b}{V^2} + \frac{3}{2}\frac{nR}{T}\right) dT + \left(2\frac{bT}{V^3} + \frac{a}{V}\right) dV, \text{ (B22)}$$

then,

$$S = -\frac{bT}{V^2} + \frac{3nR}{2} \ln T + a \ln V. \qquad \text{(B23)}$$

Equation (B12) implies that

$$\eta = 1 + \frac{T_2}{T_1} \frac{a \ln \frac{V_4}{V_3} - bT_2\left(\frac{1}{V_4^2} - \frac{1}{V_1^2}\right)}{\left(a \ln \frac{V_2}{V_1} - bT_1\left(\frac{1}{V_2^2} - \frac{1}{V_1^2}\right)\right)}, \qquad \text{(B24)}$$

from (B13) and (B14),

$$a \ln \frac{V_4}{V_3} - bT_2\left(\frac{1}{V_4^2} - \frac{1}{V_1^2}\right) = -\left(a \ln \frac{V_2}{V_1} - bT_1\left(\frac{1}{V_2^2} - \frac{1}{V_1^2}\right)\right), \qquad \text{(B25)}$$

then,

$$\eta = 1 - \frac{T_2}{T_1}. \qquad (1)$$

Appendix C

The Legendre transformation maps functions in a vector space into functions in the tangent space [12]. Let's take a function $F(\vec{x})$ with $F: \mathbb{R}^n \to \mathbb{R}$. Its Legendre transformation named K to the variable $\vec{p} \in \mathbb{R}^n$ is given by,

$$K(\vec{x}, \vec{p}) = -\vec{x} \cdot \vec{p} + M(\vec{x}), \qquad \text{(C1)}$$

this function has the property that $\forall\, \vec{p}$, $K(\vec{x}, \vec{p})$ has a maximum with respect to $\vec{x}$ in a point $\vec{x}(\vec{p})$; which is defined by the extremal condition of $K(\vec{x}, \vec{p})$ respect to $\vec{x}$. In other words,

$$\vec{\nabla}_{\vec{x}} K(\vec{x},\vec{p}) = 0, \qquad \text{(C2)}$$

then,

$$\vec{p} = \vec{\nabla} M(\vec{x}). \qquad \text{(C3)}$$

If we now define the function $n(\vec{p}) = K(\vec{x}(\vec{p}),\vec{p})$, we have transformed the function $M(\vec{x})$ to a new function that has as a domain the tangent space to $M(\vec{x})$. The basis coordinates are the set,

$$p_i = \frac{\partial M}{\partial x_i}, \qquad \text{(C4)}$$

which is an already familiar result from the classical mechanics used to go by means of this Legendre transformation from the Lagrangian function to the Hamiltonian function.

References

[1] Truesdell C., The Tragicomical History of Thermodynamics 1822-1854. USA: Springer-Verlag; 1980.

[2] Greiner W., Neise L., Stöcker H., Thermodynamics and Statistical Mechanics. USA: Springer; 1995.

[3] Zemansky, M. W. and Dittman, R. H., Heat and thermodynamics. USA: Mc Graw-Hill; 1981.

[4] García-Colín L., Introducción a la Termodinámica Clásica. México: Ed. Trillas; 2005.

[5] Piña-Garza E., Termodinámica. México: Limusa; 1978.

[6] Agrawal D., Menon V.J., The Carnot cycle with the Van der Waals equation of state. Eur. J. Phys. 1990;11, 88-90.

[7] Tjiang P., Sutanto S., The efficiency of the Carnot cycle with arbitrary gas equation of state. Eur. J. Phys. 2006;27, 719-726.

[8] Hazlett-Crawford F., Heat, thermodynamics, and statistical physics. USA: Harcourt, Brace & World; 1963.

[9] Tykodi R.J., Hummel E., On the Equation of State for Gases. Am. J. Phys. 1972;41, 340-343.

[10] Penrose R., Cycles of Time, An Extraordinary New View of the Universe. New York: Alfred A. Knopf; 2011.

[11] Ambegaokar V., Mermin, D., Question #78. A question about the Maxwell relations in thermodynamics. Am. J. Phys. 2001;69 (4).

[12] Arnold, V.I., Mathematical Methods of Classical Mechanics. USA: Springer-Verlag; 1987.

The Dead State

Richard A. Gaggioli

Professor Emeritus, Marquette University
Milwaukee, WI 53201-1881 USA
Richard.Gaggioli@marquette.edu

Abstract:
The purpose of this paper is to provide guidance for the selection of the dead state for exergy analysis, guidance that is especially important in applications to energy-conversion and materials processing plant engineering, and to ecology. First, the general definition of the dead state is provided, based on the concept of 'the available energy of a body' as originally presented by Gibbs. Gibbs 'body' can be any overall system, no matter how complex, and a crucial point is that there is no need to include or have a 'reference environment.' On this groundwork, criteria underlying the selection of the appropriate dead state for a variety of practical engineering systems are referred to; while these cases are not exhaustive, they provide examples of the rationale for selection of an appropriate dead state for any case. Finally, the implications and relevance of the dead state on applications of exergy considerations to the issues of ecology and sustainability are discussed.

Keywords:
Dead State, Exergy, Reference Environment, Available Energy, Resource Assessment, Sustainability

1. Introduction

This paper has two principal parts: Fundamentals, and Practical Applications.

1.1 Fundamentals. Following Gibbs [1] the 'available energy of a body' is defined for any 'body' – i.e., for any overall system, no matter how *complex* the system's structure. The structure generally includes several subsystems or processes *and* how they interact. While a subsystem *may* be an 'environment', an environment is not necessary. Given the structure, the 'dead state' of the system follows directly from this general definition of available energy. Moreover, the dead state of the overall system dictates the dead state of each subsystem. The overall dead state and hence dead states of the subsystems can change with time.

In practice, the overall dead state and hence the subsystem dead states depend upon underlying *choices*. Above all, the practitioner must delineate the makeup of the overall system. That is, given the purpose of the analysis, choose the parts of the 'universe' to be included in the overall system (as subsystems). Moreover, it is essential to choose 'constraints' placed upon (i) spontaneous processes allowed within each subsystem, (ii) modes of interaction[1] between subsystems, (iii) modes whereby products are delivered from the overall system (to its 'market').

1.2 Applications. Exergy is an additive property. The exergy of a subsystem represents its contribution to the available energy of the overall system. Exergy is definable whether or not one of the subsystems is an 'environment.'

In many if not most engineering applications of 'exergy analysis' to a conversion plant – for efficiency analysis and/or costing – an important subsystem is a local environment with which it interacts.[i] The dead state of each plant subsystem and its contents depends upon the assumed constraints applied to it and to the environment. The choice of constraints can have a significant effect upon the conclusions drawn from the analysis.

Among the factors that are relevant to the choices of constraints (and hence to the outcome of an analysis) are:

[1] Interaction is synonymous with 'exchange of additive property.'

- The projected time-period for which the analysis will be relevant
- The scope of the environment
  - Its breadth
  - The accessibility of materials therein
  - The stability of the materials
  - Relevance of variations with time
- The scope of technology – i.e., the 'state of the art' for the projected time period
- The scope of science – i.e., its 'state of development' for the period

These choices (relevant to engineering applications) are all the more important when exergy and 'dead state' considerations are applied to ecology and sustainability.

1.3 Closure. The fundamentals will be presented and illustrated in the context of simple examples. Nevertheless, these examples will be used to draw (convincingly, it is hoped) broad, general principles relevant to complex practical applications.

2. Gibbs Available Energy

In 1873 Gibbs [1] defines the *available energy*, for two cases.

2.1 Case 1. The first, more general case, is for that of a 'body' – *any* closed system which, overall, may have parts (subsystems). At any instant t the system has values of energy, entropy and of volume. Using different symbols than Gibbs, here they are denoted by $E(t)$, $S(t)$, $V(t)$.[2] Its available energy at t, a characteristic of the system alone, is the maximum amount of energy deliverable with no *net* transfer of either entropy or volume to external systems. That is, during the hypothetical delivery, entropy and volume can be exchanged between its parts. External devices ('technology') may be employed to do so; but, in order to assure that no external object makes a net contribution to the energy delivered, the net change of every external device's energy must be zero.

Shown in Figure 1 is a very simple *example* of an overall system, in this case consisting of two identical subsystems, *1* and *2*. The subsystems are separated by an impermeable movable piston. Let us say that at an instant t each subsystem, by itself, is at equilibrium with a uniform temperature and pressure within. But, supposing $[p_1 - p_2] > 0$ and $[T_1 - T_2] > 0$, the *overall* system is not at equilibrium and has available energy. That is, energy could be delivered from the overall system by exchange of volume and/or entropy; the net amount of energy delivered would equal $\int p_1\, dV_1 + \int p_2\, dV_2 - \int T_1\, dS_{\tau 1} - \int T_2\, dS_{\tau 2} = \int [p_1 - p_2]\, dV_1 + \int [T_1 - T_2][dS_{\tau 2} - dS_\pi]$.[3] This net output of energy would be a maximum, equal to the available energy A, when the entropy production dS_π is zero throughout the delivery, and the overall system has reached an equilibrium state, with $[p_1 - p_2] = 0$ and $[T_1 - T_2] = 0$. The remaining energy content of the overall system would be the minimum value reachable from the initial state with its volume $V(t)$ and entropy $S(t)$.

[2] The existence of entropy (as well as energy and volume) is taken for granted here. See the Appendix for elaboration.

[3] Here, the equal sign depends upon volume and entropy balances for the case of no net transfers of volume or entropy to or from the overall system.

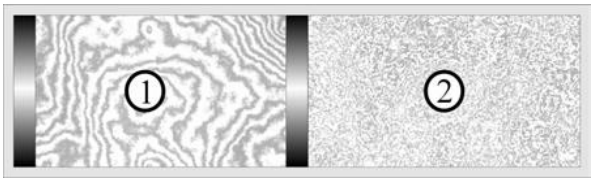

Figure 1

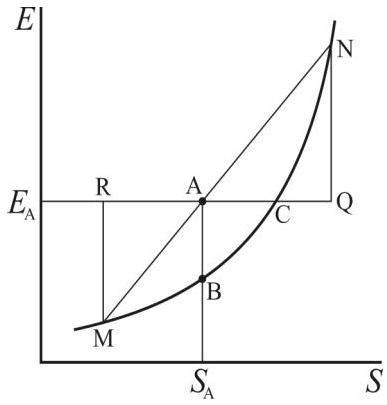

Figure 2

At *any* particular state of *any* overall system, with its particular entropy *S* and volume *V*, there is a minimum possible energy, E_{min}. That is, there is function $E_{min}(S, V)$. Thus, at any state of the system, the Gibbs available energy is given by $A \equiv E - E_{min}(S, V)$. When the energy of the body equals $E_{min}(S, V)$, the body is at an equilibrium state at (S, V), and there is no available energy. On Figure 2, from Gibbs [1], the curve through MBCN represents a hypothetical $E_{min}(S, V)$, at a fixed *V*. The location A represents an arbitrary nonequilibrium state of the system, and the distance AB is the available energy of that state. Figure 3 (from [2a]) shows a complete $E_{min}(S, V)$ surface and the points A and B. It is notable that Point A – with its unique values of *E*, *S* and *V* – does not represent a unique state of the overall system. For example, consider Figure 1 again. At any fixed (S, V) there are many conceivable states of the overall system with the same energy *E*.[4]

2.1.1 The Dead State. When the overall system is at Point B, it is at a 'dead state' – a state of zero available energy. Whenever the overall system is at any condition vertically above B, Point B is the corresponding dead state.

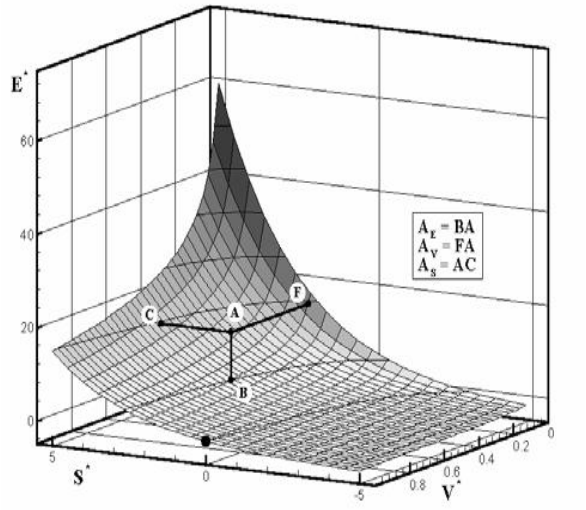

Figure 3.

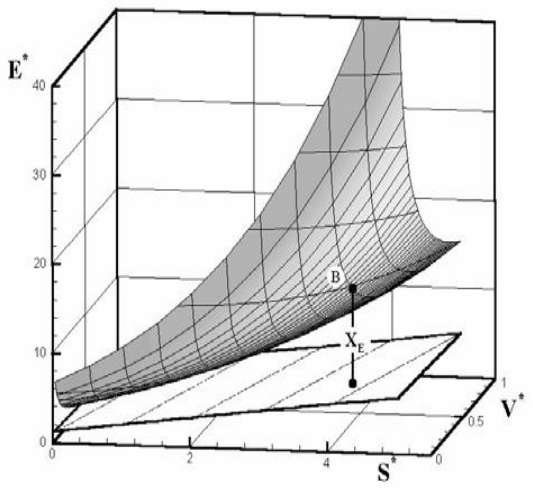

Figure 4.

Gibbs called $E_{min}(S, V)$ "the surface of dissipated energy". If an overall system, like that in Figure 1, were allowed to reach equilibrium without delivering energy (say by letting entropy flow

[4] States with the same *E* could differ as a result, simply, of disparities in pressure and temperature differences between the subsystems. Furthermore, many states with the same *E* will differ because of gradients within a subsystem, and so on.

through the piston and letting it oscillate, uncontrolled), entropy would be produced. The system would end up at Point C, another dead state.

2.1.2 Additional Measures of Potential Influence. The available energy represents the system's intrinsic potential to influence any other system. Gibbs defined other *equivalent* measures of disequilibrium and potential to influence. The distance AC on either figure (2 or 3) represents the system's 'capacity for entropy' – at least that amount of entropy could be extracted from any system (at $T > 0$), no matter how cold. AF on Figure 3 is Gibbs 'available vacuum.' At least this amount of volume increase could be imposed upon any system no matter how low its pressure.

These three characteristics (represented by AB, AC and AF) are measures of a system's disequilibrium and potential to influence *any* object; they are attributes of the system alone. Gibbs also described the potential influence upon specific objects. For example consider a large object at any temperature *T*, represented by the slope of the straight line MAN on Figure 2. The distance QA on the figure is the amount of entropy that could be extracted from the object; starting at A the system would end up at N. AR is the amount of entropy that could be imposed upon the object.

2.2 Case 2. This special case presented by Gibbs, is for a circumstance where one part of the *overall* system is a 'medium' – a large subsystem which has a constant temperature and a constant pressure. In Gibbs' terminology the overall system consists of a 'body' (*any* body) and the 'medium' (made up of the same components as the body). In both cases, **1** and **2**, his development is for circumstances where the *overall* system reaches equilibrium without *net* transports of entropy or volume between the *overall* system and its surroundings. In Case 2, net exchanges of entropy and volume between the body and the medium (two subsystems) are allowed. Figure 4 (from [2a])) shows two surfaces, the curved surface for the body alone, and a planar surface. The plane is tangent to the curved surface at the location where the body and the medium have the same temperature and pressure – namely the constant *T* and *p* of the medium. If the body is at *internal* equilibrium at B (of Figures 3 and 4), the vertical distance from B to the planar surface represents the available energy of the composite system of body and medium together. If the body is at A, the available energy from the composite equals that vertical distance plus AB. (As explained below, the available energy can be attributed to the body, and called the 'exergy' of the body. The exergy of the medium is zero.)

At the dead state of the overall system (body and medium) the body will be at the location where its *T* and *p* are equal to that of the medium – where the body's surface is tangent to that of the medium.

2.2.1 Gibbs Available Energy with Variable Composition. Subsequently, in 1875, Gibbs [3] presented – implicitly – the available energy of a body and medium for the case of open systems, where exchanges with a 'medium' include not only entropy and volume but also chemical *components*.[5]

3. Generalized Available Energy

In the foregoing review of Gibbs' 1873 development of available energy, leading to $A \equiv E - E_{min}(S, V)$, the entropy and volume were 'constrained'. That is, the hypothetical process that delivers available energy is carried out with limitations: no *net* transport of volume or entropy to or from the surroundings of the overall system. Such limitations will, herein, be called *constraints*. This word will be used not only for limitations upon *transports* but also for restrictions on *spontaneous changes* (such as changes of composition by chemical reactions within a subsystem).

[5] The word 'component' is to be understood as distinct from 'constituent'. Constituents are species actually present; components are species from which the constituents could be composed (e.g., see Hatsopoulos and Keenan [4].). In the case at hand, components are constituents of the 'medium' from which the constituents of the 'body' could be composed.

3.1 Constraints. To illustrate the concept of constraints, consider Figure 1 again. Suppose the piston to be fixed in place (or replaced by an immovable wall). This additional constraint upon the overall system could be represented by the symbol V_1 (for the volume of *1*). When V_1 is constrained, interchanges of volume between the two subsystems would be precluded, and full advantage of pressure difference between the two could not be taken. In general the available energy from the composite of *1* and *2* would be less. Because, the minimum energy reachable would in general be greater than that reachable if the constraint on V_1 were removed: $E_{min}(S, V, V_1) > E_{min}(S, V)$, and so $A(E, S, V, V_1) = E - E_{min}(S, V, V_1) < A(E, S, V) = E - E_{min}(S, V)$.[6]

This example illustrates that the existence of additional constraints changes the amount of available energy, and it changes the dead state. While additional constraints may *seem* to be 'strictly theoretical' and even questionable, later in this article it will be illustrated that it has important consequences in practice. There are relevant effects on delivery of available energy, on subsystem dead states, on calculated exergy values, and on costing.

Moreover, it is important to recognize that, in general, available energy is defined:

- For an overall system, consisting of specific relevant subsystems, and one subsystem *may be* a large 'medium',
- Subject to constraints, which may restrict
  - how subsystems can interact, and
  - spontaneous changes within a subsystem.
  - modes of interactions with external devices.

See [2b] for further elaboration on generalization of Gibbs available energy, including the relevance of constraints to equilibrium.

3.2 Exergy. Available energy is not an additive property, which is readily illustrated by considering Figure 1. Suppose that Subsystem 1, alone is at equilibrium; likewise for Subsystem 2. Then each, alone, has zero available energy. Whereas, when the two are not in equilibrium with each other, the composite of the two (the overall system) has available energy,. The author [5] has derived 'subsystem exergy' such that (i) exergy is additive, (ii) the sum of the subsystem exergies is equal to the available energy of the overall system, (iii) hence each subsystem's exergy can be viewed as its contribution to the overall available energy, and (iv) because it is additive, an 'exergy balance'can be written for any subsystem, so that 'exergy analysis' can be carried out.

Unlike the usual, 'textbook' derivations for exergy equations, which depend upon having a 'reference environment', the derivation in [5] is for any overall system. No reference environment (reservoir) is required. In the derivation, the dead state of the overall system becomes relevant, in lieu of a reference environment. The dead state of each subsystem is dictated by the dead state of the overall system. Incidentally, these dead states can change with time, when E_{min} increases because of dissipations.

For the case when subsystems are free to exchange entropy S, volume V, and chemical components N_i, the expression for exergy *content* of a subsystem is:

$$X = E + p_f V - T_f S - \Sigma \mu_{if} N_i$$

The subscript f denotes the pressure, temperature and component chemical potential at the dead state. The expressions for exergy *transports* follow directly from this expression for *content*.

When one of the subsystems is a 'medium', large and at equilibrium (or constrained equilibrium) – with pressure p_0, temperature T_0 and chemical potentials μ_{i0} – it has zero exergy. The medium dictates the dead state of all the subsystems. Then, in the foregoing expression for exergy, the f's

[6] In theory, the > and the < shown should be ≥ and ≤ because there are special, though rare circumstances when, upon taking advantage of temperature difference between *1* and *2*, upon reducing that difference to zero, the pressure difference would also happen to become zero. The $E_{min}(S, V, V_1)$ surface would be tangent to $E_{min}(S, V)$, Otherwise $E_{min}(S, V, V_1)$ will be above $E_{min}(S, V)$.

become the usual 0's. However, as argued later, there are many practical instances where it is erroneous (if not presumptuous) to assume an *equilibrium* environment (or a finite, non-equilibrium environment with a quasi-stable equilibrium 'dead state').

Understanding (a) the meaning of 'dead state' in general (including in the absence of an 'environment') and (b) the relevance of constraints upon the dead state is important. In practice, the choices made to determine the overall dead state are effected (even when one subsystem is an 'environment').

The derivation of exergy in [5] is a simplification of one presented earlier with Wepfer [6]. (In [6], by the way, there is an error in line 2 of Eq. (14); the subscripts shown as B should be A.)

4 Practical Examples

4.1 Relevance to Subsystem Dead States for Engineering Exergy Analysis and Costing Applied to Conversion Systems and Plants.

What is meant here by *Engineering* Exergy Analysis is this: analysis of an existing, operating plant (or system), or analysis of a plant that is being designed. The intent is that all of the subsystems consist of technologies that are currently available. (Comments relevant to R&D and resource assessment are presented later.)

Before a plant (or system) is analyzed it is important to ascertain (or make reasonable assumptions) regarding the dead state of the materials in every subsystem. That is, the p_f, T_f, and μ_{if} need to be determined for each subsystem. (When a material flows between two subsystems, it of course has the same dead state in both.)

Given a plant and its surroundings, (a) the first step in determining appropriate subsystem dead states is to *establish* the *relevant* "composite system" (overall system, consisting of subsystems). That is, what parts of the 'universe' have *significant effect* on performance of the plant or system.

- *Relevant*: considering the purpose of the analysis.
- *Significant effect*: having an effect that influences the outcome of the analysis within the desired significant figures.

In turn, (b) the practical, technological constraints on the interactions between subsystems need to be specified.

These principles – (a) and (b) – are illustrated with several cases, in [6]. That article includes a section on "The selection of reference datums [dead states] for subsystem [exergy]." Rather than duplicate that section, here only one of those cases will be presented, in order to illustrate the application of principles.

One case that illustrates the relevance of constraints is the situation where a 'working fluid' is confined, within some of the subsystems. An example is the H_2O confined in the 'cycle' of a power plant. Another is the refrigerant confined in a vapor-compression refrigeration system. In these circumstances the total volume of the working fluid is fixed, constrained. As long as a refrigeration system is intact (working, practically) the refrigerant cannot equilibrate its pressure (or composition) with that of the surrounding environment. Its equilibration would be constrained, so that only thermal equilibration could occur. The appropriate dead state for the refrigerant is that which it would reach upon system shut-down; typically that would be a state at environmental temperature and the refrigerant's saturation pressure at that temperature.

If one assumes that the dead state pressure should equal atmospheric pressure, erroneous subsystem efficiencies (and costs) will result. If the reader needs to be convinced that the correct dead state pressure should be the one recommended here, it is suggested that two exergy analyses be carried out. One with the recommended p_0 and one with p_0 equal to atmospheric. Then draw exergy flow diagrams for the two cases and compare – noting that all of the exergy enters as supply to the compressor, which then delivers exergy to the other subsystems. (By the way, if one argued

that atmospheric pressure is correct, then to be consistent the chemical exergy of the refrigerant should also be taken into account.)

Another, even more interesting, 'refrigerant example' would be for the case of a dual-purpose vapor compression system; one which delivered cooling to a load at temperature less than ambient and heating at a temperature higher than ambient (and with no interaction with the ambient). See Paulus and Gaggioli [7] for the rationale for proper specification of T_f and, hence, p_f.

Other circumstances discussed in [6], with different procedures for determining the dead states, include:

- Multiple, stable surrounding media
- Circumstances when variations in the environment, with time, are significant
- Metastable and Unstable Ambient Environments; e.g.
  - inherently unstable (such as weather changes; see [8,9])
  - unstable because of the impact of effluents from the plant

One point that can be made regarding the choice of an environment for analyzing a plant is this: *Alternative* choices may be appropriate, depending upon the purpose of the analysis. For example, suppose one analysis is being made for the purpose of improving efficiency or economy of a plant (which has state of the art equipment, and apparatus required in order to satisfy regulations and codes). Then an appropriate environment would be that immediately surrounding the plant. On the other hand, if a second analysis is to include assessment of environmental impact, then the selected environment (or subsystems) will need to include chemical components for neutralizing the emissions, to stable non-toxic conditions. Such components might exist only remotely from the plant. (If costing were part of the analysis, emissions could have negative unit exergy costs – so that the cost of bringing the neutralizing components would be charged to the plant.)

For further elaboration on selection of dead states, see [6] for details and examples.

4.2 Relevance to Analyses for R&D and for Resource and Sustainability Assessment.

This section will be devoted to the importance of the constraint concept, and to the significance of choosing a relevant dead state.

4.2.1 Significance of Constraints. Again, consider a simple *example*, referred to earlier. Suppose that the system in Figure 1 is at a condition like A in Figure 2, and consider a *real* process that is striving to deliver the available energy represented by AB. Invariably there would be entropy production, due to 'mechanical friction' and heat transfer through temperature differences. As a result the system would end up at a condition to the right of B on the curve toward C; the more the entropy production the closer to C (but never above C, which is the condition reached if the system is allowed, uncontrolled, to equilibrate internally, so no energy is delivered).

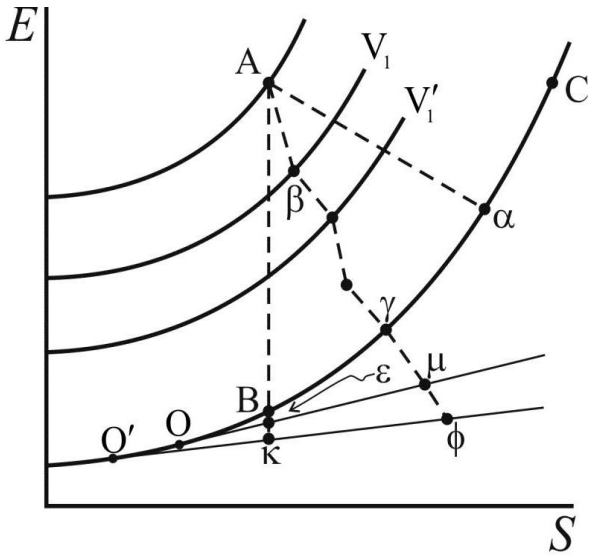

Figure 5

Let us suppose that, with more or less well-controlled, but real equilibration the final condition reached is at α, on Figure 5 (For convenience of the artwork the ordinate (for E) is not linear; α appears closer to C than if the ordinate were linear; i.e. the energy delivered (E_A - E_α) is significantly greater than the dissipation of available energy (E_α - E_B).). Moreover suppose that the entropy production is predominantly caused by mechanical, viscous friction. Consider the following alternative scheme, starting at A, for delivering available energy: If the piston were fixed in place (constraining V_1), and available energy were delivered with very little entropy production due to heat transfer, that delivery process would end up at a place like β, below and slightly to the right of A. Next, deliver more available energy by letting V_1 change by a modest amount (to V_1'), with some but less viscous friction (because of the controlling of V_1's change). By repeating, once more, this procedure of fixing and then changing V_1, the path to equilibrium could be like that from A to γ on Figure 5. More available energy, namely E_A - E_γ, would be delivered (less dissipated) than from the path A to α. (By increasing the number of steps the delivery could be increased all the more so.) This is a simplistic *example* of how adding constraints, and controlling them, can improve the delivery of available energy. The *general conclusion* to be drawn therefrom (which may appear obvious) is that improving the control of available energy transfer processes – by *adding*, **or** by **finding** *new* constraints – can improve the efficiency.

The objective of additional constraints is control; that is accomplished by reducing states that otherwise would proceed more spontaneously, toward successive constrained-equilibrium states.

Adding effective constraints will generally depend upon advances in technology. Finding *new* constraints will often depend on scientific advancement as well. New constraints 'produce' new constrained-equilibrium states.

It can be surmised that there exists unknown constraints that could even 'increase' the available energy. That is, by allowing states that (at the current status of science) are *believed* to be at equilibrium but are at metastable equilibrium – such that the metastability could be overcome by manipulation of 'newly discovered' constraints. Moreover, if the new constraints can be controlled well, the delivery of the additional available energy can be improved.

From the vantage point of one or two hundred years ago, that 'new' available energy could be what we call nuclear today.

4.2.2 Significance of the Dead State. Consider the object of Figure 1 again, but this time in conjunction with a medium like that depicted by the flat surface in Figure 4. And, for simplicity, assume that the curve through BC in Figures 2 and 5 is for the constant volume passing through the point of tangency in Figure 4. That point of tangency represents the dead state of the object, at the overall dead state of the composite of object and medium. Shown on Figure 5 is the line that is in

the plane and passes, through the point of tangency at 0. The slope of that line is the temperature at that overall dead state located at 0.

If the object is at A, the available energy of the composite (the overall system including the object and the medium) is equal to the distance E_A - E_ε on Figure 5. If the object is at B (with no available energy of its own), the available energy of the composite is E_B - E_ε

When delivering available energy, entropy production *within* the object, when starting at A, is represented by the horizontal distance between A and γ. Further entropy production, as a result of interactions with the medium, is the horizontal distance between γ and μ. The overall delivery when proceeding from A to μ is E_A - E_μ.

Finally, suppose there exists another medium at say a much lower temperature, represented by the tangent line through 0' on Figure 6. Now the overall available energy for the composite is [E_A - E_κ]; the delivery is represented by [E_A - E_ϕ]. Clearly, these are greater than [E_A - E_ε] and [E_A - E_μ], respectively. (Again, consider the nonlinearity of the E scale, and for example consider what the differences would be if the slope of the straight line through 0 were 273K and that through 0' were 27.3K or 2.73K.)[7]

4.2.3 Intermediate Conclusions. In general terms,

- Controlling with constraints that are available with current technology can improve the delivery of available energy (to desired products).
- Moreover, if additional constraints were found, it is conceivable that delivery can be improved.
  - An obvious, simple example is control of chemical composition. In the examples presented above, chemical composition of Subsystems **1** and **2** *could have* been changing,[8] and there would have been associated entropy production during delivery. Inasmuch as only entropy and volume exchanges were allowed between **1** and **2** (and with the mediums), then:
    - ♣ If the compositions of **1** and **2** (when the object was at B) differed, there could be additional available energy deliverable, *if* exchange of chemicals between them were allowed, and controlled, while bringing the two subsystems to chemical equilibrium.
    - ♣ Moreover, if **1** and **2** were each, alone, at chemical equilibrium but not at chemical equilibrium with an accessible medium, there would be additional available energy.
    - ♣ Additionally, if the left-hand piston in Figure 2 were controllable (in essence, making both V_1 and V_2 constraints that could be manipulated) spontaneous change of composition within **1** and **2** could be controlled, reducing (and in theory[9] eliminating) associated entropy production.
  - This simple example, chemical, is only an example. The *important* point is that it would be significant if new constraints can be found, to unlock heretofore unavailable energy. (Relatedly, there may exist available energy that is more or less 'hidden', within the context of today's science – like nuclear disequilibrium was hidden 200 years ago).
- If a medium is accessible with a lower temperature and/or with a lower pressure, and/or lower chemical potentials (or lower potentials associated with any new controlling constraint), the delivery can be increased.

5. Closure

Traditionally, the development of exergy has assumed the existence of a 'surrounding environment'. Necessarily then, in practice exergies are evaluated relative to a reference

[7] By the way, on Figure 5, the vertical lines ending on the straight lines correspond to exergies of the object. The mediums have no exergy.

[8] Earlier it was stated, for conceptual simplicity, that Subsystems **1** and **2** were identical. That assumption was unnecessary for the discussions that ensued, as long as **1** and **2** were constrained from exchanging chemicals.

[9] A theoretical scheme whereby chemical conversion of a fuel could be accomplished without entropy generation was proposed by Keenan ([10], p. 279). The method is also presented in [11], Article 3-19.

environment, which must be selected by the evaluator. Several alternative 'standard' reference environments have been proposed, and commonly the evaluator will choose one of them. In any case, the engineering 'dead state' is dictated by the selected reference environment. And it is commonly held that, in theory at least, the dead state should be the same for all of the contents of, and the flow streams between, the subsystems of the facility being analyzed.

These habitual practices have shortcomings. By and large the shortcomings can be circumvented by referring back to the more fundamental concept underlying exergy, namely available energy.

As shown above, *if* an overall system is *given*, then (at any moment) the overall dead state and the dead states of all subsystem and their materials is unique. No reference environment is necessary. If, as usual, one of the subsystems is a large surrounding medium, in a sense it is 'just one more subsystem'. Nevertheless, it may have a dominant (if not total) effect upon the dead state of the other subsystems. However, those subsystem dead states will not all be in *complete* equilibrium with the surrounding medium. Generally, subsystems will be in constrained equilibrium with the surroundings (For example, as referred to earlier, at its dead state the refrigerant in a vapor-compression system will be in thermal equilibrium with the system's surroundings, but not in pressure or chemical equilibrium.)[10]

The preceding paragraph began with ". . . *if* an overall system is *given* . . . the overall dead state . . . is unique." That statement is subject to several, related stipulations:

- The modes of interaction between subsystems must be specified.
- The constraints on subsystems must be specified.

That is, defining an overall system (making it 'given') requires not only identification of its parts, but also how they will be allowed to interact and what constraints are imposed upon the parts and the interactions.

5.1 Defining an Overall System

It is imperative that, whenever the results of an exergy analysis or exergy evaluation of resources is presented, it should be clear to the reader what the underlying "overall system" is – its make-up and the assumed interactions and constraints. In theory, this clarification should be made by the authors. If it has not been made explicitly, a careful reader will seek to determine what overall system has been *assumed*. If an answer cannot be found or assumed judiciously, the reader should question (if not be skeptical, or even dismiss) the conclusions that have been drawn.

5.2 Engineering Systems

In the case of exergy analyses of engineering systems, it is generally straightforward for the reader to ascertain the overall system, as long as a reference environment has been clearly stated. The reader will naturally assume that the subsystems shown on the flowsheet, are 'standard' – current technology. If some are not standard the authors hopefully will have made that known.

5.3 Resource and Ecologic Assessment

Many laudable applications of exergy to ecology and sustainability have been carried out. These studies refer to the future and often project into the future – making predictions (often dire) about the future – and then make recommendations. Care needs to be exercised when considering some

[10] Some might think that it doesn't matter what the dead state is, because when one calculates exergy differences between points in a cycle, the dead state values cancel. That thinking is flawed; it is important to know the correct, total values at every point. Otherwise significant mistakes can occur in evaluating subsystem efficiencies and especially unit costs [9].

of the conclusions drawn (especially when the conclusions and recommendations are presented ardently).

It seems that there generally are assumptions that go unrecognized or are taken for granted by both authors and readers. So the following kinds of questions arise:

- What is the overall system? Generally, it is evident that the overall system has been limited to the earth and its resources. Is that a reasonable limitation when predicting the future?
  - Are there resources outside our 'sphere' that will become accessible? Literal energy resources? Or subsystems that can be invoked?
    - In some remote places, the night sky is used as a source of exergy today. The background temperature of the universe is about 3K; could it be used as a 'medium'? Consider the two straight lines on Figure 5.
  - What's the point of 'all this'? Only that the reader of the assessments should realize that the *assumed* scope of the overall system has a very big effect on the results and conclusions.
- What is the overall system? (Same question!) For available energy and exergy to be meaningful, there must be a *complete* overall system; that is, besides the resources there must be means – theoretical and practical – for harvesting and converting them that are assumed.
  - What science and technologies have been assumed for the harvesting and converting? Presumably today's, with their 'control constraints'? If so, that dismisses prospective, relevant developments in science and technology.
    - Scientific advances can lead not only to new technologies but also to new resources (like fission and fusion have 'made' new resources – even if only theoretical so far, in the case of fusion).
    - A conjecture: Can means be found for controlling nuclear reactions, analogous say to fuel cells controlling chemical reactions, to eliminate 'heat generation' (entropy production) as the means for extracting the available energy? Why not?
- What *are* the 'controlling constraints'?
  - Is it implicit that the control variables are classical? Electrical, mechanical, chemical and perhaps nuclear? – such that the perceived resource conversion is subject to the laws of 'classical' science (e.g. today's chemical thermodynamics, with its assumed variables).
  - Again, the reader of assessments should realize that there is an implicit science and technology being assumed. Quite conceivably, future developments likely will introduce unforeseen variables, employable to control/constrain phenomena relevant to resource conversion.

5.4 Viewpoints

All 'energy resources' have usefulness because there exists an associated disequilibrium with our environment. It is typical of resources that the disequilibrium is constrained (thankfully) such that there is a metastable equilibrium. Their usefulness depends upon 'breaking' the metastable equilibrium via one constraint or another. The better the control of the ensuing equilibration, using constraints, the more efficient is the use of the resource.

Particularly regarding resources, history is filled with dreadful forecasts which have arisen in the face of challenging circumstances. Invariably, the forecasts have been made under the (inherently pessimistic) assumption that the then-current science and technology was definitive. However, humankind has not only overcome the challenges but in dealing with them has *advanced* – has discovered 'new' resources, unlocked them with new science and new technologies, improved the efficiency of usage, . . . and as a consequence has improved our subsistence.

One could say that the advances resulted, at least in part, as consequence of the challenges. So assessments of the type referred to above should be appreciated – as challenges.

Nevertheless, there is a great amount of disequilibrium, particularly metastable equilibrium in our *universe*. Our future technology is not earthbound. Moreover, it can be hoped (and from a historical perspective, *expected*) that – spurred on by challenges – future science and technology

will unlock not only remote resources but 'hidden' or currently 'unreachable' earthly resources as well. Some would say, "That's overly optimistic. Careless. We should 'play it safe!" The readers will have a variety of viewpoints (worth discussing!).[11]

In any case, let the readers of 'assessment' papers that refer to the future understand that there are implicit assumptions that are very important, and will prove to have been very important.

Acknowledgments

I would like to acknowledge and thank the following 'schools of thermo' that I have learned from: Obert, Hirschfelder-Curtiss-Bird, Hatsopoulos-Keenan-Gyftopoulos, Tribus-Evans-ElSayed. I have benefitted from many others of course, and I appreciate and thank all of you.

Appendix

The concept of entropy has been taken for granted in this presentation. The author [12] prefers to take the existence of entropy axiomatically, rather than derive it in manners such as the common $dS = dQ_{rev}/T$ or methods similar to the $dS = C\,d[E\text{-}\Omega]$ of [4], where Ω is the 'available work'. To the extent of the author's awareness, Obert [13] was the first to postulate the existence of entropy, and then Callen [14]; these authors defined entropy only for equilibrium states.

Using the likes of $dS = C\,d[E\text{-}\Omega]$, Hatsopoulos and Gyftopoulos [15] proved the existence of entropy for non-equilibrium states, too (or, see Gyftopoulos and Beretta [16]). If it is accepted that entropy exists for nonequilibrium states then there can be logical objection to postulating that it exists for these states as well as equilibrium states, as long as it can be proved that $dS = C\,d[E\text{-}\Omega]$ is then a result. Whether to 'begin' with $dS = C\,d[E\text{-}\Omega]$ or with the postulation of entropy's existence is then a matter of preference. The author contends that postulation is preferable, because then all of useful thermodynamic relations can be derived in a much more streamlined manner [12]. Many concepts that students struggle with and/or find 'superfluous' are eliminated. For examples, the concepts of reservoir or, even, reversibility are not needed. Unlike available work or adiabatic availability, available energy is deliverable by any mode – mechanical, with Force or Torque (momentum currents); electrical, with charge current; . . . ; thermal, with entropy current). By the way, available energy (and exergy) delivered with any one current is as good as that delivered with any other. With the postulation of entropy, maintaining strict logic doesn't require ponderous definitions of work and/or heat.[12] As a matter of experience, students find the concept of entropy and, in turn, all of thermodynamics easier to comprehend when entropy is postulated. Developing and then putting 'heat' – a transport not an additive property – ahead of entropy is in the author's opinion, putting the cart ahead of the horse, and very difficult to 'operate'.[13]

---

[11] There is an old saying, "Don't let a crisis go by without taking advantage of the opportunity." It should not be assumed that to 'play it safe' is without 'cost'.

[12] It is a matter of convenience and 'standard practice' that the assignment of units to energy is via mechanical work. Keenan and Shapiro [17] proposed a thermal method for stating the 1st Law and assigning units to energy. That possibility supports, implicitly, the rationality of postulating the existence of entropy.

[13] It should have been mentioned that, following Shannon and Jaynes, Tribus [18] postulates *an* entropy (call it η here) to be a certain probability-measure of uncertainty, namely $\eta = -\,k\Sigma[p_i \ln(p_i)]$ where p_i is the probability of the ith quantum state of the material. With that postulate certain 'general' and useful relationships of Statistical Thermostatics (the 'Boltzmann distribution' and the associated 'partition function') follow straightforwardly. To relate *that* entropy to the entropy of thermodynamics, a resulting equation for 'reversible' processes, $d\langle e\rangle = [1/\beta]d\eta - p\,dv$ is compared to $de = T\,ds - p\,dv$. Assuming that η and s are the same thing, and that the probable energy $\langle e\rangle$ is what e *is*, then it is rational to conclude that $\beta = 1/T$. The deduction is applicable only for equilibrium states.

REFERENCES

[1] Gibbs, J.W., 1873, "A Method of Geometrical Reperesenation of the Thermodynamic Properties of Substances by Means of Surfaces," in *The Scientific Papers of J.W. Gibbs,* vol. 1, Dover Publications, 1961.

[2] Gaggioli, R.A., Richardson, D.H., Bowman, A.J., Paulus, D.M. Jr., 1999, "Available Energy: a. Gibbs Revisited, b. Gibbs Extended", Proceedings of the Advanced Energy Systems Division, ASME, vol AES 39, pp. 285-296, 1999 (also published in Trans. ASME, J. of Energy Resource Technology)

[3] Gibbs, J.W., 1873, 1875, "On the Equilibrium of Heterogeneous Substances," in *The Scientific Papers of J.W. Gibbs,* vol. 1, Dover Publications, 1961.

[4] Hatsopoulos, G.N. and Keenan, J.H., 1965, *Principles of General Thermodynamics*, Wiley.

[5] Gaggioli, R.A., 1999, "Available Energy and Exergy", International Journal of Thermodynamics, Vol. 1, pp. 1-8.

[6] Wepfer, W.J. and Gaggioli, R.A., 1980, "Reference Datums for Available Energy [Exergy]", Ch. 5, pp. 78-92, *Thermodynamics: Second Law Analysis*, American Chemical Society, Symposium Series Vol. 122.

[7] Paulus, D.M. Jr. and Gaggioli, R.A., "The Dead State According to the Available Energy of Gibbs", AES-Vol. 40, ASME, New York, 2000

[8] Gaggioli, R.A., Wepfer, W.J. and Elkouh, A.F., 1978, "Available Energy Analysis for HVAC, I. Inefficiencies in a Dual-Duct System," *Energy Conservation and Building Heating and Air-conditioning Systems,* ASME Symposium Volume H00116, pp. 1-20.

[9] Wepfer, W.J, Obert, E.F. and Gaggioli, R.A., 1979, "Proper Evaluation of Available Energy for HVAC," *Trans. ASHRAE*. Vol. 85, pp. 1*ff*.

[10] Keenan, J.H., 1941, *Thermodynamics*, Wiley.

[11] Obert, E.F., 1973, *Internal Combustion Engines,* Harper and Row.

[12] Gaggioli, R., 2010, "Teaching Elementary Thermodynamics and Energy Conversion: Opinions," *Energy*, Vol. 35, pp. 1047–1056.

[13] Obert, E., 1949, *Elements of Thermodynamics and Heat Transfer*, McGraw-Hill.

[14] Callen, H., 1960, *Thermostatics and Thermodynamics*, Wiley

[15] Hatsopoulos, G. and Gyftopolous, E., 1976, "A Unified Quantum Theory of Mechanics and Thermodynamics," *Foundations of Physics*, Vol. 6, pp. 15-31, 127-141,439-455, 561-570.

[16] Gyftopolous, E.P, and Beretta, G.P., 1991, *Thermodynamics: Foundations and Applications*, Macmillan.

[17] Keenan, J. and Shapiro, A., 1947, "History and Exposition of the Laws of Thermodynamics," *Mechanical Engineering*, Vol. 69, pp. 915-921.

[18] Tribus, M., 1961, *Thermostatics and Thermodynamics*, Van Nostrand.

THE MAGNETOCALORIC ENERGY CONVERSION

Andrej Kitanovski[a], Jaka Tusek[b], Alojz Poredos[c]

University of Ljubljana, Faculty of Mechanical Engineering, Askerčeva 6, 1000 Ljubljana, Slovenia,
[a] andrej.kitanovski@fs.uni-lj.si, CA
[b] jaka.tusek@fs.uni-lj.si
[c] alojz.poredos@fs.uni-lj.si

Abstract:
The article presents a review on research and developments of the magnetocaloric energy conversion. This promising alternative technology has a large potential in domains of refrigeration and heat pumping. Moreover, it represents a potential alternative for the power generation by the application of low temperature energy sources. High energy efficiency and application of environmentally friendly refrigerants make this technology as a serious alternative to phase out vapour-compression. Substantially increased international research activities in the last two decades led to development of about 45 prototype devices. Despite strong research efforts are still required, the technology is ready to be developed for certain special market niches. This article shows some basic information on physics of the magnetocaloric energy conversion. It presents most important research activities and achievements. Temporary limits that researchers are facing at the moment are described in the article. Perspectives of the technology are presented and the guidelines for the future research and developments are given.

Keywords:
Magnetocaloric, Energy conversion, Energy efficiency, Magnetic refrigeration

1. Brief history of research and developments

The magnetocaloric energy conversion is a technology which applies the magnetocaloric effect (MCE). The technology applies solid refrigerants (magnetocaloric materials) which have global warming potential (GWP) and ozone depletion potential (ODP) equal to zero. The MCE of many of existing magnetocaloric materials represent a reversible process. Already the earliest prototypes have demonstrated exergy efficiency higher than that of existing compressor-based technologies. The magnetocaloric energy conversion has a potential of running machines with the very high exergy efficiency. A silent operation without vibrations makes this technology attractive for large number of applications. The magnetocaloric energy conversion regards the magnetic power generation, magnetic heat pumping, and the magnetic refrigeration.

The magnetocaloric effect (MCE) was first discovered by Warburg [1], who in 1881observed an increase of temperature when he had brought an iron sample into a magnetic field and a decrease when the sample was removed out of it. Soon after this discovery, approximately in 1890, Tesla [2] and Edison [3] independently and unsuccessfully tried to benefit from this effect by running heat engines for “power production”. In 1918 Weiss and Piccard [4] explained the magnetocaloric effect. Later Debye [5] and Giauque [6] proposed a method of magnetic refrigeration for low temperature physics in order to obtain sub-Kelvin temperatures. In 1933 Giauque and MacDougall [7]

successfully verified the method by experiment. Since the 1930's magnetic refrigeration is a standard technique in low temperature physics.

In the magnetic power generation, there were not much research and development activities performed until the 1950's, when a large interest of scientists was created by the idea of performing magnetic power generators by applying magnetocaloric suspensions as working fluids. Most of this pioneering work was performed by Resler and Rosensweig [8,9]. However, some single earlier publications than those may be found in [10-13]. There is no evidence that any of these early ideas were transformed to real working prototypes. Thirty years later most of the publications were related to studies of magnetocaloric power generators with solid working materials [14-16]. In the last few years activities on the magnetic power generation can be found in the following references [17-23].

In 1976 Brown [24, 25] designed the first magnetic refrigerator working at room temperature. After that a number of patents were announced, which describe such refrigerators. This may be noted to be the time of the first generation of magnetic refrigerators. With the discovery of the "giant magnetocaloric effect" [26], the development of magnetic refrigeration gained increased momentum. Since then, the number of papers published in international journals has grown exponentially. The number of patents in this area is also increasing The first "room temperature" magnetic refrigerator – containing permanent magnets – was designed and built in 2001 [27]. Then the start of the development of a new second generation family of magnetic refrigerators began.

Approximately forty five prototype magnetic refrigerators and heat pumps have been built in different parts of the world [28]. The research in magnetic refrigeration is nowadays focused on improvements on magnetocaloric materials, magnets and their materials, thermodynamics and fluid dynamics and an optimal design and building of devices. Large number of studies on the simulation and optimization of magnetocaloric regenerators have been performed [29], while other studies deal with the design and optimization of the permanent-magnet assemblies that are normally used in prototypes [30-35]. Large number of studies has been focused on the magnetocaloric materials [36-40], and few newer publications are related also to the economics of magnetic refrigeration [41-45].

2. Thermodynamics

The first law of thermodynamics for a closed thermodynamic-magnetocaloric system can be written as:

$$du = \delta q + \mu_0 H \, dM \tag{1}$$

where H represents the magnetic field intensity in the material and M represents the magnetization within the magnetocaloric material. For a reversible process it is permissible to rewrite the Eq.(1) into the following relation:

$$du = T \, ds + \mu_0 H \, dM \tag{2}$$

where s represents the total specific entropy of the magnetocaloric material. Its derivative for constant pressure and volume may be defined as:

$$ds(T,H) = \left(\frac{\partial s}{\partial T}\right)_H dT + \left(\frac{\partial s}{\partial H}\right)_T dH \,. \tag{3}$$

One of the most important thermodynamic potentials applied in engineering is enthalpy. It presents the potential to describe the behaviour of an open thermodynamic system with the work performed over its boundary.

$$h = u - \mu_0 H\, M\ , \tag{4}$$

The derivative of this potential is:

$$dh = du - \mu_0 H\ dM - \mu_0 M dH\ . \tag{5}$$

Inserting (3) it follows that:

$$dh(s,H) = \left(\frac{\partial h}{\partial s}\right)_H ds + \left(\frac{\partial h}{\partial H}\right)_s dH = T\, ds - \mu_0 M dH\ . \tag{6}$$

In the closed thermodynamic system, no magnetocaloric material is transferred in or out of the system boundaries. In an open magnetic thermodynamic system, the magnetocaloric material "flows" as the continuum in and out of the system boundaries The first law of thermodynamics for such systems states that the increase in the internal energy of the system equals the amount of energy added to the system by the "flow" (e.g., rotation) of the magnetocaloric material into the system's boundary and by heating, reduced by the amount of energy lost by the "flow" of the magnetocaloric material out of system's boundaries and reduced by the work done by the system. The specific technical work may be defined as:

$$dw_t = dq - dh = \mu_0\, M\, dH \tag{7}$$

The heat alternation in the magnetocaloric material in its specific form may be defined as:

$$dq = c_H(T,H)dT + c_T(T,H)\,dH\ . \tag{8}$$

where c_H denotes the specific heat capacity at a constant internal magnetic field H. The second specific heat c_T denotes the specific heat capacity at a constant temperature. The specific heat may also be expressed using Maxwell's relations:

$$c_H = \left(\frac{\partial q}{\partial T}\right)_H = T\left(\frac{\partial s}{\partial T}\right)_H\ . \tag{9}$$

and

$$c_T = \left(\frac{\partial q}{\partial H}\right)_T = T\left(\frac{\partial s}{\partial H}\right)_T = \mu_0 T\left(\frac{\partial M}{\partial T}\right)_H\ . \tag{10}$$

Magnetic refrigeration process can be based on different thermodynamic cycles, i.e. like Brayton, Ericsson, Carnot, etc. Those potential cycles are in general based on three processes, which will further be explained in detail.

The ***Isothermal (de)magnetization*** process occurs in the Carnot, Ericsson and Stirling magnetic cycles. Isothermal magnetization requires simultaneous magnetization and heat transfer within the magnetocaloric material in such a way that during the alternation of the volumetric magnetic flux the temperature does not change. Heat alternation in this particular case leads to:

$$dq = c_T(T,H)\,dH = T\left(\frac{\partial s}{\partial H}\right)_T dH = \mu_0\, T\left(\frac{\partial M}{\partial T}\right)_H dH\ . \tag{11}$$

The derivative of the specific enthalpy is then:

$$dh(s,H) = \mu_0 T\left(\frac{\partial M}{\partial T}\right)_H dH - \mu_0 M dH = \mu_0\left[T\left(\frac{\partial M}{\partial T}\right)_H - M\right]dH \tag{12}$$

The total specific entropy change is calculated by applying Eq. (3):

$$ds(T,H) = \left(\frac{\partial s}{\partial H}\right)_T dH\,. \tag{13}$$

Or by an integration between two magnetic fields:

$$\Delta s = s_2 - s_1 = \int_{H_1}^{H_2}\left(\frac{\partial s}{\partial H}\right)_T dH = \int_{H_1}^{H_2}\mu_0\left(\frac{\partial M}{\partial T}\right)_H dH = \int_{H_1}^{H_2}\frac{c_T}{T}dH\,, \tag{14}$$

where s_1 is the specific total entropy at the field H_1 and s_2 at H_2.

The ***isofield heating (cooling)*** processes of heating and cooling of the magnetocaloric material in a constant magnetic field correspond to the Brayton, Ericsson, and Stirling magnetic cycles. The heat transfer is mostly provided by the flow of the working fluid through the porous structure of the magnetocaloric material. Heat alternation in this particular case leads to the following expression:

$$dq = c_H\, dT = T\left(\frac{\partial s}{\partial T}\right)_H dT \tag{15}$$

Furthermore, the specific enthalpy derivative takes the following form:

$$dh = dq \tag{16}$$

Eq. (16) shows that the enthalpy difference may be defined for the isofield in a similar way as in conventional gas thermodynamics for the isobaric process where:

$$c_H = \left(\frac{\partial h}{\partial T}\right)_H \tag{17}$$

The ***Adiabatic (de)magnetization*** process occurs in the Brayton and Carnot cycles. In the ideal case the adiabatic magnetization can be considered as an isentropic process. Since the alternation of the heat equals zero, then Eq.(8) takes the following form:

$$c_H(T,H)dT = -c_T(T,H)\,dH = -\mu_0\left(\frac{\partial M}{\partial T}\right)_H\,. \tag{18}$$

The differential of the specific enthalpy equals:

$$dh = -\mu_0 M\, dH = -dw_t \tag{19}$$

Eq.(19) denotes that for isentropic magnetization or demagnetization, the derivative of the enthalpy is equal to the technical work. The same may be obtained in conventional thermodynamics for isentropic gas compression or expansion, where dw_t=-vdp. In an adiabatic process the total specific entropy does not alter (ds=0). It follows that:

$$\left(\frac{\partial s}{\partial T}\right)_H dT = -\left(\frac{\partial s}{\partial H}\right)_T dH\,. \tag{20}$$

Rearranging the Eq.(18), a further relation is obtained:

$$dT = -\frac{c_T}{c_H}dH\,. \tag{21}$$

It follows:

$$\frac{dT}{T} = -\frac{\mu_0}{c_H} \cdot \left(\frac{\partial M}{\partial T}\right)_H dH \ . \tag{22}$$

With a knowledge of the temperature as a function of the specific entropy for different isofields, it is more convenient to perform the following integration:

$$\Delta T = \int_{T_1}^{T_2} dT = T_2(s, H_2) - T_1(s, H_1), \tag{23}$$

where $T_2(s,H_2)$ is the temperature of the magnetocaloric material at the higher magnetic field H_2 and $T_1(s,H_1)$ at the lower magnetic field intensity, both evaluated at the same specific entropy.

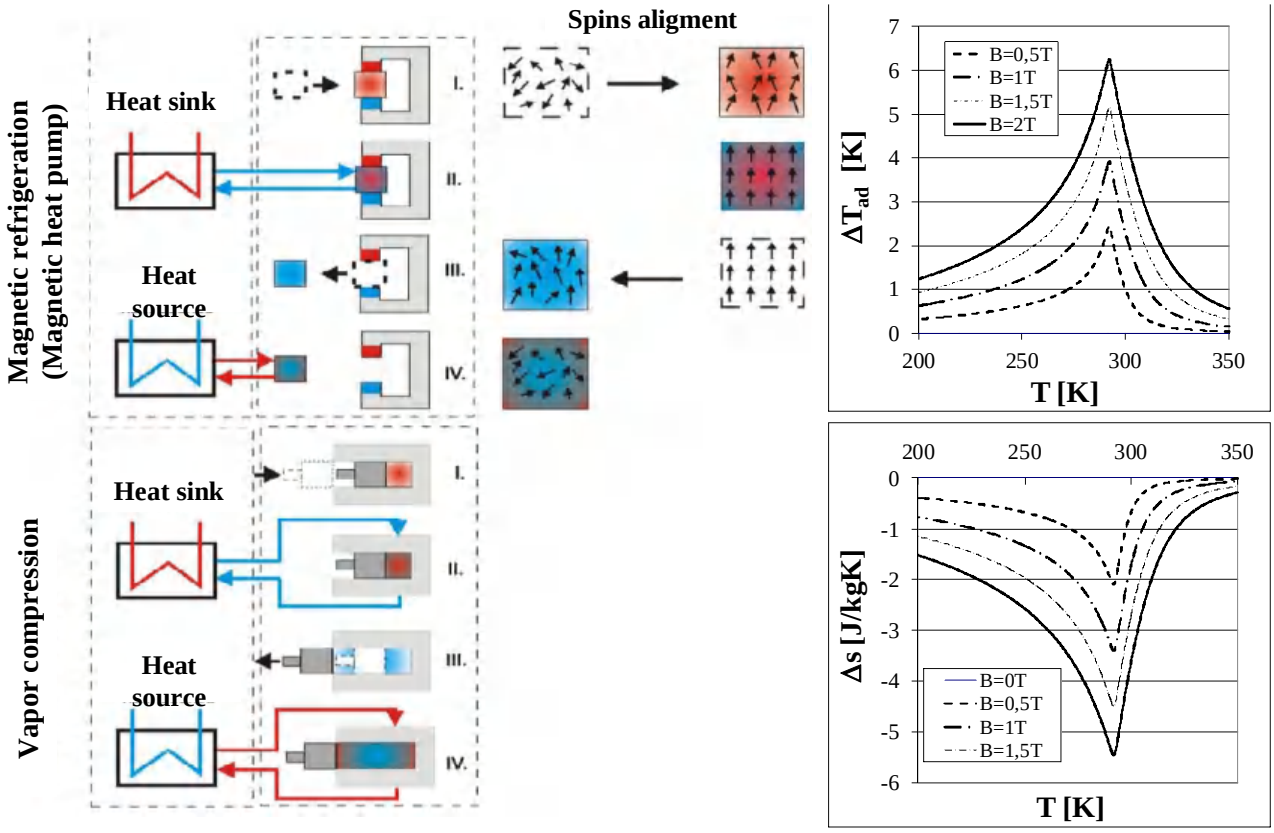

Figure 1: Left: The analogy with the vapour compression (I. magnetization vs compression, II:heat flow to heat sink vs condensation, III. Demagnetization vs expansion, IV. Heat flow from the heat source vs evaporation) , Right: Calculated adiabatic temperature change and isothermal entropy change for the reference magnetocaloric material Gadolinium

3. Magnetocaloric devices and their characteristics

The existing magnetocaloric materials in magnetic fields accessible by permanent magnets do not exhibit a sufficiently large magnetocaloric effect that would enable its direct application in a refrigeration device. This is especially true for systems based on rather small magnetic field changes; for instance, applications with permanent magnets. Therefore, most of magnetic refrigerators perform a regenerative process in order to increase the temperature span. The regenerator in magnetic refrigeration represents a device that serves for the heat transfer between different phases of a thermodynamic process and thus enables an increase of the temperature span. There are two basic types of regenerators, the passive and the active magnetic regenerator (AMR)

respectively. The passive regenerator may store and/or transfer heat during different processes of the thermodynamic cycle. It applies the working fluid for the heat transfer. In the domain of magnetic refrigeration, such regenerators are applied mostly in applications in low-temperature physics. At or near the room temperature, all the current prototypes of magnetic refrigerators are based on the AMR principle (Yu et.al [28]). A review of numerical models for the AMR was given by Nielsen et al. [29]. Following the early work of Brown [25], the concept of the active magnetic regenerator (AMR) refrigeration was introduced by Steyert [46] and developed by Barclay [47, 48]. After Barclay the research on the active magnetic regeneration led to several publications in the 1980s and 1990s (see, e.g., [14-15, 49-51]). Some examples of newer publications can be found in e.g. [29, 52, 53].

The active magnetic regeneration (AMR) is a process, when the magnetocaloric material itself acts as a regenerator, and as the source/sink of the heat induced by the magnetocaloric effect. In active regeneration (AMR) systems there is no overlapping of the "cycles", as is usually the case in a cascade system. As explained by Hall et al. [55] and Tishin and Spichkin [36], each particle of the AMR does not directly pump heat to the next-neighbour particle, but all particles accept or reject heat to the heat-transfer fluid at the same time and are coupled indirectly through the fluid. Because of the "counter current" fluid flow, particles and their internal (local) cycles interact with the neighbouring ones by the heat transfer of the fluid, thus performing the regenerative process. AMR therefore performs a unique thermodynamic process, where each infinitesimally small particle of the magnetocaloric material performs its own thermodynamic cycle. Almost all the existing analyses of the AMR are based on the Brayton-like thermodynamic cycle. However, there is a possibility to perform a number of different thermodynamic cycles in combination with the AMR process.

3.1. Types of magnetocaloric devices

The magnetic field sources, which can be applied in magnetocaloric devices, are: permanent magnets, superconducting magnets, electromagnets. Below are given certain most common features of magnetic refrigerators. Those, who have not been developed yet in practice, are underlined. Machines with moving parts are:

- rotary (rotation of magnetocaloric material or rotation of magnetic field source),
- linear (linear motion of magnetocaloric material or linear movement of the magnetic field source).

Without moving parts:
- magnetocaloric suspensions or, nanofluids,
- »on-off« magnetic field.

Rotary magnetic refrigerators
Rotary magnetic refrigerators present (at the moment) the most efficient way to perform magnetic refrigeration. Most of the prototypes apply rotation of the magnetocaloric material through the static magnetic field, performed by the permanent magnet assembly. Magnetocaloric material forms or it is embodied in the structure which has a form of a disc, torus or a cylinder. Rotary magnetic cooling devices can be realized in order to perform various thermodynamic cycles. Figure 2 shows a shematic example of the rotary type of magnetic refrigerator (heat pump), where the magnetocaloric material is contained in the ring, which rotates through static magnetic field (in the figure this is shown by grey region). The fluid flow in the case of the Figure 2 is such, that the magnetocaloric regenerator performs active magnetic regeneration. Since magnetocaloric materials have restricted

temperature range of their efficient operation, the regenerator must consist of different magnetocaloric materials, which are layered in a direction of a temperature gradient. If the operation of the magnetic refrigeration cycle is such that it operates between two constant magnetic fields (isofields, analogue to isobars in conventional refrigeration), and two isentropic processes (fast reversible adiabatic magnetization or demagnetization, e.g states 2-3 and 4-1 respectively), then such process is Brayton AMR process. By the simultaneous variation of the magnetic field intensity and the heat transfer it is possible to create also other types of magnetocaloric thermodynamic cycles. Such an example is shown in the Figure 5, where an Ericsson AMR magnetic refrigeration (heat pump) cycle is shown.

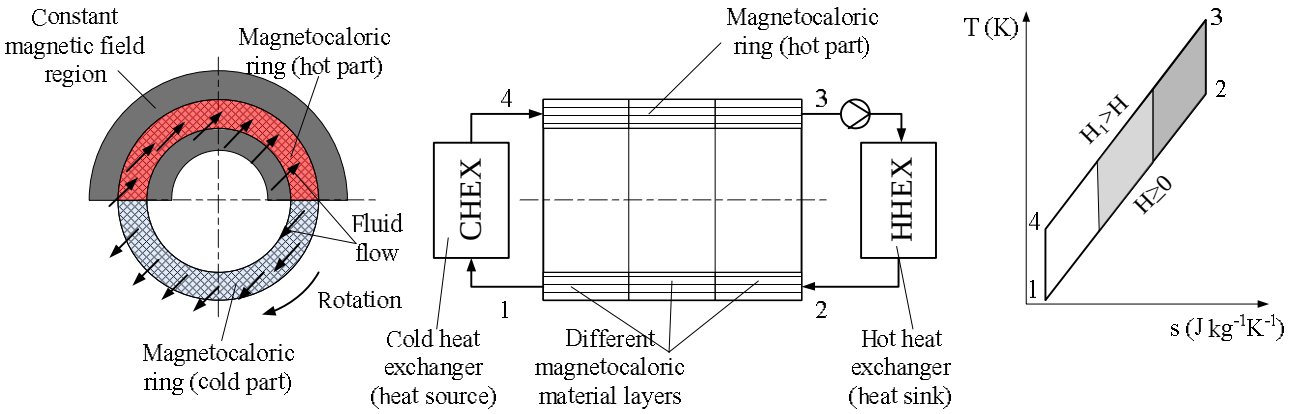

Figure 2: Left: An example of the "Brayton" type of magnetic refrigerator with the rotary motion of the magnetocaloric material Right: The T-s diagram of the Brayton AMR regenerative magnetic refrigeration cycle

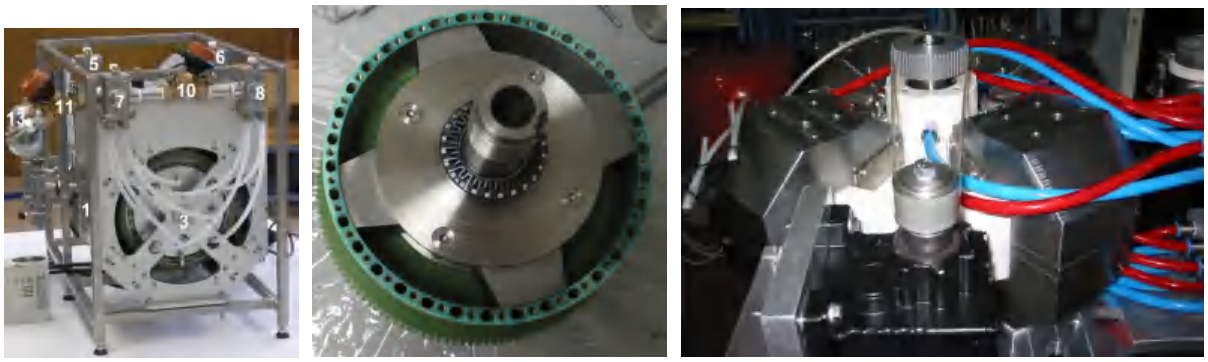

Figure 3: Left: The first rotary magnetic refrigerator built at the University of Ljubljana. In the middle, the coaxial ring is shown with 34 magnetocaloric regenerators[54]. Right: second rotary magnetic refrigerator built at the University of Ljubljana.

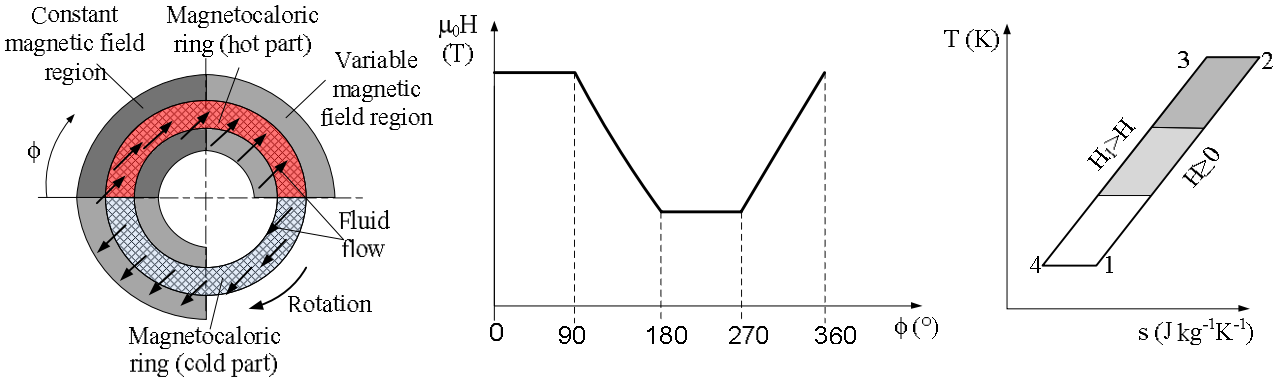

Figure 5: Left: An example of the "Ericsson" type of magnetic refrigerator with the rotary motion of the magnetocaloric material Right: The T-s diagram of the Ericsson AMR regenerative magnetic refrigeration cycle

Linear magnetic refrigerators

This kind of devices may be considered as experimental devices or demonstrators, rather than prototypes for potential market applications. The operation of such devices is based on the linear motion of magnet or magnetocaloric material through a magnetic field. All types of magnets have already been applied in such prototypes. Magnetocaloric material is usually in a form of a cylinder or a block. The last may be filled with the magnetocaloric material in a shape of rods, spheres, grains, plates, etc. The construction and design of such a device is simpler than for the rotary one. However, in order to perform a continuous operation, such have the rotary magnetic refrigerators, the device has to be consisted of two coupled devices, unless certain reservoirs are used. The frequency of the operation and related cooling power cannot be compared with the rotary device. Furthermore, the linear device has lower efficiency due to the acceleration and deceleration.

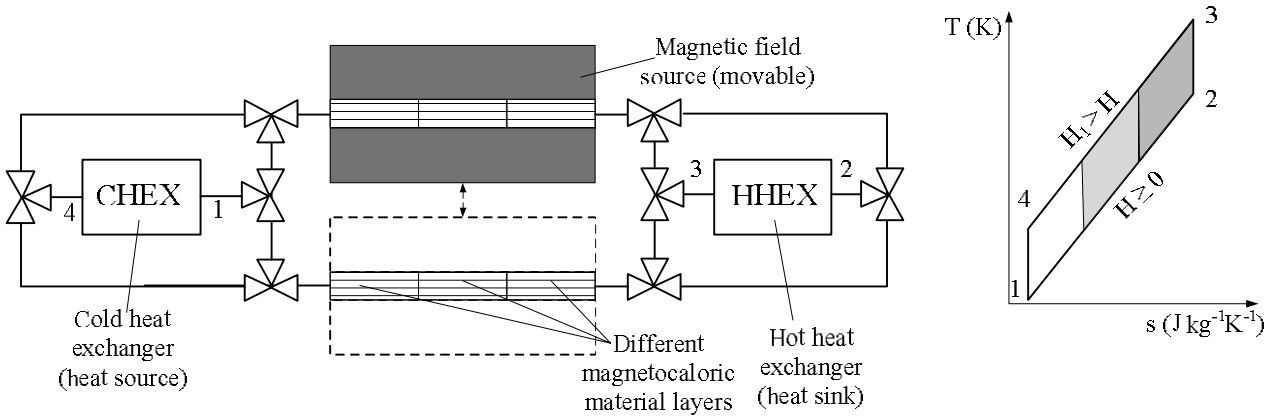

Figure 6: Left: An example of the "Brayton" type of magnetic refrigerator with linear motion of the magnetocaloric material or motion of the magnetic field source, Right: The T-s diagram of the Brayton AMR regenerative magnetic refrigeration cycle

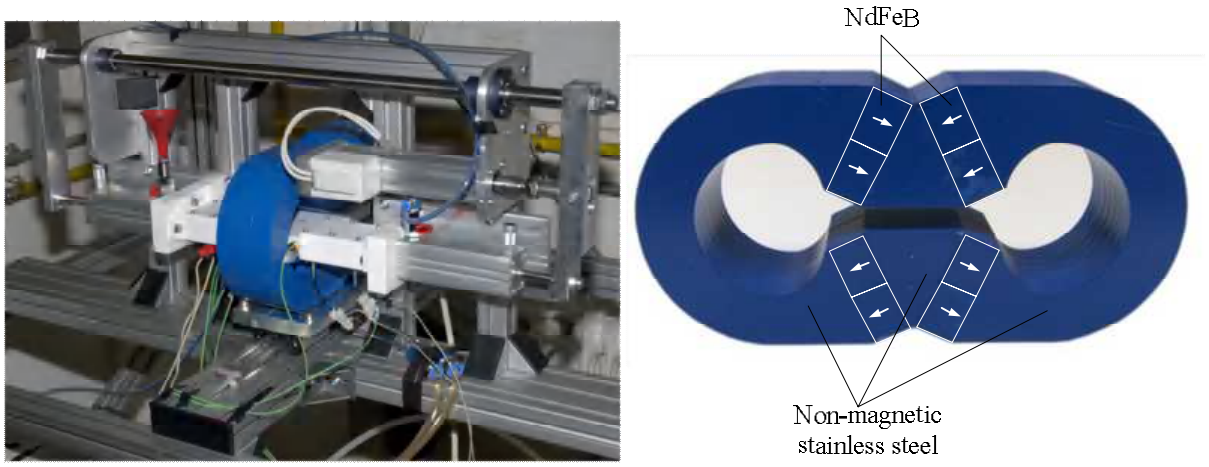

Figure 7: A photography of the linear magnetic refrigeration experimental device and the permanent magnet assembly developed at the University of Ljubljana

3.2. Magnetic field source and magnetocaloric materials

Magnetic field is a driving force of the magnetocaloric effect and consequently of the magnetic refrigerator. The magnetic field can be produced with electromagnets, superconducting magnets or permanent magnets. Electric magnets require additional power, and the electric resistance of conductors partly converts electricity into joule heating. Superconducting magnets are more interesting; however their price limits their use only to large scale applications. These are reasons why permanent magnets are applied in most of prototypes. Currently, the strongest permanent magnets are based on neodymium-iron-boron (Nd-Fe-B) due to the highest maximum energy product (BH_{max}), which is one of crucial parameters for the selection of a permanent magnet. In magnetic refrigeration (heat pumping) at room temperature, the magnetic fields applied in devices are in the range between 0.7 to 2.4 Tesla. The tendency is to reduce the magnetic field, since this is coupled with the third order with the mass of magnets, which are rather expensive.

A large number of different magnetocaloric materials can be applied in magnetocaloric energy conversion. From the periodic system, the rare earth metal gadolinium may be regarded to be the ideal substance of magnetic refrigeration, just as the ideal gas is for conventional refrigeration. However, the magnetocaloric effect of gadolinium is not so large as this is the case for some other magnetocaloric materials. Furthermore, each magnetocaloric material can operate in a limited temperature span. At present, most interesting materials are for example La(Fe,Si,H), La(Fe,Co,Si), or La(Fe,Co,Mn,Si), or Mn(Fe,Si,P). More information on magnetocaloric materials may be found in [36-40, 56, 57].

4. CONCLUSION

Magnetocaloric energy conversion did not reach yet market applications. The major obstacle of this green technology is the cost of device, which is strongly related to materials (mostly permanent magnet materials, partly magnetocaloric materials). Most of existing prototype devices operate with the low frequency of the operation (small number of thermodynamic cycles per unit of time, what leads to low power density). The reasons, not only for the low power density, but also for the low efficiency of existing prototype machines are related to low manufacturability of magnetocaloric

materials, high heat transfer irreversible losses, losses related to flow dividers, and losses related to fluid switching valves with internal leakage of the fluid. In certain cases high viscous losses are present, and some machines operate with high mechanical friction losses.

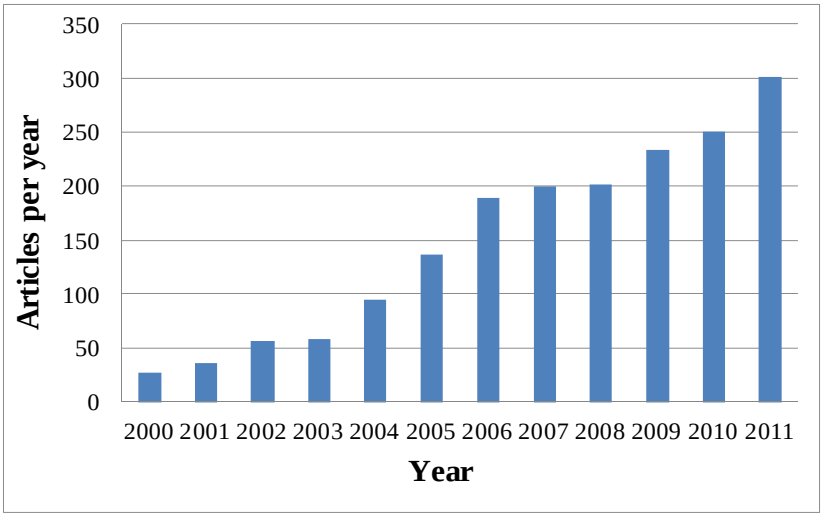

Figure 8: Yearly published papers (by keyword: "magnetocaloric" in ScienceDirect search engine)

Researchers are trying to solve each of the above issues by innovation of the new solutions. Improvements regard: optimization of magnet assemblies, application of new working liquids, better processing of magnetocaloric materials, new magnetocaloric materials, introduction of new thermodynamic cycles, introduction of new heat transfer mechanisms, new machine concepts, etc. And there still exists a large room for improvements, as it was proposed by Kitanovski and Egolf [58]. Such solutions may lead to an increase of the existing maximal frequency of the operation of 5 Hz up to an order higher, what will substantially influence the future of magnetocaloric devices and their market applications. Following the existing achievements, the magnetocaloric energy conversion, despite it was up to present mostly focused in the refrigeration domain, offers the possibility of market penetration in several different domains, especially for devices with rather smaller power of up to few kW.

5. Nomenclature

Standard

c	Specific heat capacity	$J\ m^{-3}\ K$
COP	Coefficient of performance	/
h	Specific enthalpy	$J\ m^{-3}$
H	Magnetic field intensity	$A\ m^{-1}$
M	Magnetization	$A\ m^{-1}$
Q	Heat	J
q	Specific heat	$J\ m^{-3}$
S	Entropy	$J\ K^{-1}$
S	Specific entropy	$J\ m^{-3}\ K^{-1}$
T	Temperature	K

Greek

ϕ	Azimuth angle	(°)
μ	Permeability of vacuum	$VsA^{-1}m^{-1}$

Subscripts

Ad	Adiabatic
H	Isofield
T	Isothermal
t	technical
0	vacuum

U	Internal energy	J
U	Specific internal energy	$J\ m^{-3}$
W	Work	J
W	Specific work	$J\ m^{-3}$

References

[1] Warburg E., Magnetische Untersuchungen über einige Wirkungen der Koerzitivkraft. Ann. Phys. 1881; 13:141 –164.

[2] Tesla N., Pyromagneto-electric generator, US patent 428,057, 1890.

[3] Edison T.A., Pyromagnetic generator, US patent 476,983, 1892.

[4] Weiss P., Piccard A., Sur un nouveau phénomene magnétocalorique, Compt. Rend. Ac. Sc. 1918; 166:352

[5]Debye P., Einige Bemerkungen zur Magnetisierung bei tiefer Temperatur, Ann Phys.1926; 81: 1154 –1160.

[6]Giauque, W.F., A proposed method of producing temperatures considerably below 1° absolute. J. Amer. Chem. Soc. 1927; 49:1864 –1870.

[7] Giauque, W.F., MacDougall, D.P., Attainment of temperatures below 1° absolute by demagnetization of Gd2(SO4)3·8H2O, Phys. Rev. Lett. 1933, 43(9):768.

[8] Resler E. L. Jr, Rosensweig R. E., Magnetocaloric power, AIAA Journal 1964; 8(2):1418-1422.

[9] Resler E. L. Jr, Rosensweig R. E., Regenerative thermomagnetic power, J. of Eng. Pow.1967; 89, 399 406.

[10] Van der Voort E., Ideal magnetocaloric conversion, Appl. Sci. Res. 1969; 20: 98-114.

[11] Chilowsky C., Thermomagnetic generator and refrigerator, US 2.619.603, 1952.

[12]Technical Assets, Improvements in and relating to thermomagnetic generators and refrigerators, GB 674.284, 1952.

[13] Elliott J.F., Thermomagnetic generator, J. Appl. Physics 1959; 11(30): 1774-1777.

[14] Kirol L. D., Mills J. I., Thermomagnetic generator, Proc. Intersoc. Energy Conversion Eng. Conf. 1984; 3:1361-1368.

[15] Kirol L. D., Mills J. I., Numerical analysis of thermomagnetic generators, J. Appl. Phys.1984; 56 (3): 824-828

[16] Salomon D., Thermomagnetic mechanical heat engines, J. Appl. Phys.1989; 65(9):3687-3693.

[17] Palmy C., A thermo-magnetic wheel, Europhysics News 2007; 38(3): 32-34.

[18] Palmy C., Egolf P.W., Levitation and acceleration of a thermo-magnetic wheel, Proc. of the 2nd int.conf. mag. ref. of the International Institute of Refrigeration 2007: 299-307

[19] Diebold M., Kitanovski A., Vuarnoz D., Egolf P.W., Force, torque and energy of machines with porous magnetisable wheels, 2nd Workshop on Magnetostr. Mat. and Mag. Ref.2007: 15-16

[20] Egolf P.W., Kitanovski A., Diebold M., Gonin C., Vuarnoz D., Magnetic power conversion with full or porous wheel heat exchangers. J. magn. magn. mater.2009; 321(7): 758-762

[21] Kitanovski A., Diebold M., Vuarnoz D., Gonin C., Egolf P.W., Applications of magnetic "Power Production" and its assessment, A feasibility study - final report, SFOE 2008.

[22] Gama S., Tesla Type Thermomagnetic motor powered by water heated using solar Energy, 4th Int. IIR Conf. on Mag. Refr. .PR China, Inner Mongolia, 2010

[23] Brück E., Dung N.H., Ou Z.Q., Caron L., Zhang L., Buschow K.H.J., de Wijs G.A., de Groot R.A., Magnetocaloric Materials – not only for cooling applications, Presentation at Delft days on Magnetocalorics, Delft University (NL), 2011

[24] Brown G.V., Magnetic heat pumping, US Patent 4.069.028, 1978 (filed in Nov. 1976).

[25] Brown G.V., Magnetic heat pumping near room temperature, J.Appl.Phys 1976;47:3673 – 3680.

[26] Pecharsky V.K., Gschneidner K.A., Giant Magnetocaloric Effect in Gd5(Si2Ge2), Phys. Rev. Lett.1997; 78(23): 4494–4497.

[27] Zimm C.B., Sternberg A., Jastrab A.G., Boeder A.M., Lawton L.M., Chell J.J., Rotating bed magnetic refrigeration apparatus, US Patent 6.526.759.4, 2003

[28] Yu B., Liu M., Egolf P. W., Kitanovski A.., A review of magnetic refrigerator and heat pump prototypes built before the year 2010. Int. j. refrig.2010; 1029-1060

[29] Nielsen K.K., Tusek J., Engelbrecht K., Schopfer S., Kitanovski A., Bahl C.R.H., Smith A., Pryds,N., Poredos A., 2011, Review on numerical modeling of active magnetic regenerators for room temperature applications, Int. J. Refr.2011; 34(3):603-616.

[30] Bjørk R., Bahl C.R.H., Smith A., Pryds N., Review and comparison of magnet designs for magnetic refrigeration, Int. J. Refr.2010; 33(3): 437-448.

[31] Roudaut J., Yonnet J.P., Kedous-Lebouc A, Müller Ch, Comparison of Magnetic Field Sources for Magnetic Refrigeration at Room Temperature, Proc. 4th IIR Int. Conf. Mag. Ref. Room Temp. 2010, Baotou, China: 497-506.

[32] Tušek J. Zupan S. Šarlah A., Prebil I., Poredoš A., Development of a rotary magnetic refrigerator, Int. J. Refr.2010, 33(2): 294-300.

[33] Zimm C., Boeder A., Chell J., Sternberg A., Fujita A., Fujieda S., Fukamichi K., Design and performance of a permanent-magnet rotary refrigerator, Int. J. Refr.2006; 29(8):1302-1306.

[34] Okamura T., Yamada K, Hirano N, Nagaya S, Performance of a room-temperature rotary magnetic refrigerator, Int. J. Refr. 2006; 29(8):1327-1331.

[35] Rowe A, Configuration and performance analysis of magnetic refrigerators, Int. J. Refr.2011; 34(1):168-177

[36] Tishin A.M., Spichkin Y.I., The Magnetocaloric Effect and its Applications, Series in Condensed Matter Physics, Institute of Physics Publishing 2003, Bristol and Philadelphia.

[37] Pecharsky, V.K., Gschneidner, K.A., Advanced magnetocaloric materials: What does the future hold?, Int. J. Refr.2006; 29: 1239-1249.

[38] Brück E, Tegus O., Cam Thanh D.T., Trung N. T., Buschow K.H.J., A review on Mn based materials for magnetic refrigeration: Structure and properties, Int. J. Refr.2008; 31(5):763-770.

[39] Gutfleisch O., Willard M. A., Brück E., Chen C. H., Sankar S. G. and Liu J. P., Magnetic Materials and Devices for the 21st Century, Advanced Materials 2010; 23(7): 821-842.

[40] Bjørk R., Bahl C.R.H., Katter M, Magnetocaloric properties of LaFe13−x−y CoxSiy and commercial grade Gd, J. Mag. Mag. Mater 2010; 322(24):3882-3888.

[41] Egolf P.W., Gendre F., Kitanovski A., Sari O., Machbarkeitsstudie für magnetische Wärmepumpen: Anwendungen in der Schweiz Final report of project no. 100873/151017, Swiss Federal Office of Energy 2006: 1-69.

[42] Russek S.L., Zimm C.B., Potential for cost effective magnetocaloric air conditioning systems, Int. J. Refr. 2006; 29(8):1366-1373.

[43] Kitanovski A., Egolf P.W., Gonin C., Central magnetic cooling and refrigeration machines (chiller) and their assessment, Final report of a feasibility study, Swiss Federal Office of Energy 2010, Contract/Project no. 102873/153691.

[44] Rowe A, Configuration and performance analysis of magnetic refrigerators, Int. J. Refr.2011; 34(1):, 168-177.

[45] Kitanovski, A., Egolf, P.W., Poredos, A.,Rotary magnetic chillers with permanent magnets, , Submitted to Int. J. Refr. 2012.

[46] Steyert W.A., Stirling-cycle rotating magnetic refrigerators and heat engines for use near room temperature, J.Appl.Phys 1978, 49; 1216-1226.

[47] Barclay J.A., Steyert W.A.,, Active magnetic regenerator, U.S. Patent 1982, No. 4.332.135

[48] Barclay J.A., Wheel-type magnetic refrigerator, U.S. Patent 1983, No. 4.408.463

[49] DeGregoria A., Modeling the active magnetic regenerator, Adv.Cryog.Eng. 1991; 37: 867-873.

[50] Matsumoto K., Hashimoto T., Thermodynamic analysis of magnetically active regenerator from 30 to 70 K with a Brayton-like cycle, Cryogenics 1990; 30: 840-845.

[51] Smailli A., Chahine R.,Thermodynamic investigations of optimum active magnetic regenerators, Cryogenics 1998; 38: 247-252.

[52] Tušek J., Kitanovski A., Prebil I., Poredoš A., Dynamic operation of an active magnetic regenerator (AMR), Int. J. Refr 2011; 34(6): 1507-1517

[53] Sarlah A., Kitanovski A., Poredos A., Egolf P.W., Sari O., Gendre F., Besson C., Static and rotating active magnetic regenerators with porous heat exchangers for magnetic cooling Int. J. Refr. 2006; 29(8): 1332-1339

[54] Tušek J., Zupan S., Šarlah A., Prebil I., Poredoš A., Development of a rotary magnetic refrigerator, Int. J. Refr. 2010, 33 (2): 294-300.

[55] Hall J.L., Reid C.E., Spearing I.G., J.A. Barclay, Thermodynamic consideration for the design of active magnetic regenerative refrigerators, Adv. Cryog. Eng. 1996; 41: 1653-1659

[56] Gschneidner K.A. Jr, Pecharsky V.K., Tsokol A.O., Recent Developments in Magnetocaloric Materials, Institue of Physics Publishing, Rep. Prog. Phys. 2005; 68: 1479-1539.

[57] Katter M., Zellmann V., Barcza A, Solid Hydrogenation (SH) Process for Massive La(Fe,Co,Mn,Si)13Hx parts, Delft days Magnetocalorics 2011

[58] Kitanovski A., Egolf P.W., Innovative ideas for future research on magnetocaloric technologies. Int. J. Refr. 2010; 33(3): 449-464.

ECOS 2012

The 25th International Conference on Efficiency, Cost, Optimization and Simulation of Energy Conversion Systems and Processes

(Perugia, June 26th-June 29th, 2012)

edited by
Umberto Desideri, Giampaolo Manfrida,
Enrico Sciubba

firenze university press
2012

ECOS 2012 : the 25th International Conference on Efficiency, Cost, Optimization and Simulation of Energy Conversion Systems and Processes (Perugia, June 26th-June 29th, 2012) / edited by Umberto Desideri, Giampaolo Manfrida, Enrico Sciubba. – Firenze : Firenze University Press, 2012.
(Proceedings e report ; 90)

http://digital.casalini.it/9788866553229

ISBN 978-88-6655-322-9 (online)

Progetto grafico di copertina Alberto Pizarro, Pagina Maestra snc
Immagine di copertina: © Kts | Dreamstime.com

Peer Review Process
All publications are submitted to an external refereeing process under the responsibility of the FUP Editorial Board and the Scientific Committees of the individual series. The works published in the FUP catalogue are evaluated and approved by the Editorial Board of the publishing house. For a more detailed description of the refereeing process we refer to the official documents published on the website and in the online catalogue of the FUP (http://www.fupress.com).

Firenze University Press Editorial Board
G. Nigro (Co-ordinator), M.T. Bartoli, M. Boddi, F. Cambi, R. Casalbuoni, C. Ciappei, R. Del Punta, A. Dolfi, V. Fargion, S. Ferrone, M. Garzaniti, P. Guarnieri, G. Mari, M. Marini, M. Verga, A. Zorzi.

© 2012 Firenze University Press
Università degli Studi di Firenze
Firenze University Press
Borgo Albizi, 28, 50122 Firenze, Italy
http://www.fupress.com/
Printed in Italy

ECOS 2012

The 25th International Conference on

Efficiency, Cost, Optimization and Simulation
of Energy Conversion Systems and Processes

Perugia, June 26th-June 29th, 2012

Book of Proceedings - Volume III

Edited by:
Umberto Desideri, Università degli Studi di Perugia
Giampaolo Manfrida, Università degli Studi di Firenze
Enrico Sciubba, Università degli Studi di Roma "Sapienza"

ECOS 2012 - THE 25TH INTERNATIONAL CONFERENCE ON
EFFICIENCY, COST, OPTIMIZATION, SIMULATION AND ENVIRONMENTAL IMPACT OF ENERGY SYSTEMS
JUNE 26-29, 2012, PERUGIA, ITALY
EDITED BY UMBERTO DESIDERI, GIAMPAOLO MANFRIDA, ENRICO SCIUBBA
FIRENZE UNIVERSITY PRESS, 2012, ISBN ONLINE : 978-88-6655-322-9

Advisory Committee (Track Organizers)

Building, Urban and Complex Energy Systems
V. Ismet Ugursal
Dalhousie University, Nova Scotia, Canada

Combustion, Chemical Reactors, Carbon Capture and Sequestration
Giuseppe Girardi
ENEA-Casaccia, Italy

Energy Systems: Environmental and Sustainability Issues
Christos A. Frangopoulos
National Technical University of Athens, Greece

Exergy Analysis and Second Law Analysis
Silvio de Oliveira Junior
Polytechnical University of Sao Paulo, Sao Paulo, Brazil

Fluid Dynamics and Power Plant Components
Sotirios Karellas
National Technical University of Athens, Athens, Greece

Fuel Cells
Umberto Desideri
University of Perugia, Perugia, Italy

Heat and Mass Transfer
Francesco Asdrubali, **Cinzia Buratti**
University of Perugia, Perugia, Italy

Industrial Ecology
Stefan Goessling-Reisemann
University of Bremen, Germany

Poster Session
Enrico Sciubba
University Roma 1 “Sapienza”, Italy

Process Integration and Heat Exchanger Networks
Francois Marechal
EPFL, Lausanne, *Switzerland*

Renewable Energy Conversion Systems
David Chiaramonti
University of Firenze, Firenze, Italy

Simulation of Energy Conversion Systems
Marcin Liszka
Polytechnica Slaska, Gliwice, Poland

System Operation, Control, Diagnosis and Prognosis
Vittorio Verda
Politecnico di Torino, Italy

Thermodynamics
A. Özer Arnas
United States Military Academy at West Point, U.S.A.

Thermo-Economic Analysis and Optimisation
Andrea Lazzaretto
University of Padova, Padova, Italy

Water Desalination and Use of Water Resources
Corrado Sommariva
ILF Consulting M.E., U.K

Scientific Committee

Riccardo Basosi, University of Siena, Italy
Gino Bella, University of Roma Tor Vergata, Italy
Asfaw Beyene, San Diego State University, United States
Ryszard Bialecki, Silesian Institute of Tecnology, Poland
Gianni Bidini, University of Perugia, Italy
Ana M. Blanco-Marigorta, University of Las Palmas de Gran Canaria, Spain
Olav Bolland, University of Science and Technology (NTNU), Norway
Renè Cornelissen, Cornelissen Consulting, The Netherlands
Franco Cotana, University of Perugia, Italy
Alexandru Dobrovicescu, Polytechnical University of Bucharest, Romania
Gheorghe Dumitrascu, Technical University of Iasi, Romania
Brian Elmegaard, Technical University of Denmark , Denmark
Daniel Favrat, EPFL, Switzerland
Michel Feidt, ENSEM - LEMTA University Henri Poincaré, France
Daniele Fiaschi, University of Florence, Italy
Marco Frey, Scuola Superiore S. Anna, Italy
Richard A Gaggioli, Marquette University, USA
Carlo N. Grimaldi, University of Perugia, Italy
Simon Harvey, Chalmers University of Technology, Sweden
Hasan Heperkan, Yildiz Technical University, Turkey
Abel Abel Hernandez-Guerrero, University of Guanajuato, Mexico
Jiri Jaromir Klemeš, University of Pannonia, Hungary
Zornitza V. Kirova-Yordanova, University "Prof. Assen Zlatarov", Bulgaria
Noam Lior, University of Pennsylvania, United States
Francesco Martelli, University of Florence, Italy
Aristide Massardo, University of Genova, Italy
Jim McGovern, Dublin Institute of Technology, Ireland
Alberto Mirandola, University of Padova, Italy
Michael J. Moran, The Ohio State University, United States
Tatiana Morosuk, Technical University of Berlin, Germany
Pericles Pilidis, University of Cranfield, United Kingdom
Constantine D. Rakopoulos, National Technical University of Athens, Greece
Predrag Raskovic, University of Nis, Serbia and Montenegro
Mauro Reini, University of Trieste, Italy
Gianfranco Rizzo, University of Salerno, Italy
Marc A. Rosen, University of Ontario, Canada
Luis M. Serra, University of Zaragoza, Spain
Gordana Stefanovic, University of Nis, Serbia and Montenegro
Andrea Toffolo, Luleå University of Technology, Sweden
Wojciech Stanek, Silesian University of Technology, Poland
George Tsatsaronis, Technical University Berlin, Germany
Antonio Valero, University of Zaragoza, Spain
Michael R. von Spakovsky, Virginia Tech, USA
Stefano Ubertini, Parthenope University of Naples, Italy
Sergio Ulgiati, Parthenope University of Naples, Italy
Sergio Usón, Universidad de Zaragoza, Spain
Roman Weber, Clausthal University of Technology, Germany
Ryohei Yokoyama, Osaka Prefecture University, Japan
Na Zhang, Institute of Engineering Thermophysics, Chinese Academy of Sciences, China

The 25th ECOS Conference 1987-2012: leaving a mark

The introduction to the ECOS series of Conferences states that "ECOS is a series of international conferences that focus on all aspects of Thermal Sciences, with particular emphasis on Thermodynamics and its applications in energy conversion systems and processes". Well, ECOS is much more than that, and its history proves it!

The idea of starting a series of such conferences was put forth at an informal meeting of the Advanced Energy Systems Division of the American Society of Mechanical Engineers (ASME) at the November 1985 Winter Annual Meeting (WAM), in Miami Beach, Florida, then chaired by Richard Gaggioli. The resolution was to organize an annual Symposium on the Analysis and Design of Thermal Systems at each ASME WAM, and to try to involve a larger number of scientists and engineers worldwide by organizing conferences outside of the United States. Besides Rich other participants were Ozer Arnas, Adrian Bejan, Yehia El-Sayed, Robert Evans, Francis Huang, Mike Moran, Gordon Reistad, Enrico Sciubba and George Tsatsaronis.

Ever since 1985, a Symposium of 8-16 sessions has been organized by the Systems Analysis Technical Committee every year, at the ASME Winter Annual Meeting (now ASME-IMECE). The first overseas conference took place in Rome, twenty-five years ago (in July 1987), with the support of the U.S. National Science Foundation and of the Italian National Research Council. In that occasion, Christos Frangopoulos, Yalcin Gogus, Elias Gyftopoulos, Dominick Sama, Sergio Stecco, Antonio Valero, and many others, already active at the ASME meetings, joined the core-group.

The name ECOS was used for the first time in Zaragoza, in 1992: it is an acronym for **Efficiency, Cost, Optimization and Simulation** (of energy conversion systems and processes), keywords that best describe the contents of the presentations and discussions taking place in these conferences. Some years ago, Christos Frangopoulos inserted in the official website the note that "ècos" ('οικος) means "home" in Greek and it ought to be attributed the very same meaning as the prefix "Eco-" in environmental sciences.
The last 25 years have witnessed an almost incredible growth of the ECOS community: more and more Colleagues are actively participating in our meetings, several international Journals routinely publish selected papers from our Proceedings, fruitful interdisciplinary and international cooperation projects have blossomed from our meetings. Meetings that have spanned three continents (Africa and Australia ought to be our next targets, perhaps!) and influenced in a way or another much of modern Engineering Thermodynamics.
After 25 years, if we do not want to become embalmed in our own success and lose momentum, it is mandatory to aim our efforts in two directions: first, encourage the participation of younger academicians to our meetings, and second, stimulate creative and useful discussions in our sessions. Looking at this years' registration roster (250 papers of which 50 authored or co-authored by junior Authors), the first objective seems to have been attained, and thus we have just to continue in that direction; the second one involves allowing space to "voices that sing out of the choir", fostering new methods and approaches, and establishing or reinforcing connections to other scientific communities. It is important that our technical sessions represent a place of active confrontation, rather than academic "lecturing".
In this spirit, we welcome you in Perugia, and wish you a scientifically stimulating, touristically interesting, and culinarily rewarding experience. In line with our 25 years old scientific excellency and friendship!

Umberto Desideri, Giampaolo Manfrida, Enrico Sciubba

CONTENT MANAGEMENT

The index lists all the papers contained all the eight volumes of the Proceedings of the ECOS 2012 International Conference.
Page numbers are listed only for papers within the Volume you are looking at. The ID code allows to trace back the identification number assigned to the paper within the Conference submission, review and track organization processes.

CONTENT

VOLUME III

THERMO-ECONOMIC ANALYSIS AND OPTIMIZATION

» A comparison of optimal operation of residential energy systems using clustered demand patterns based on Kullback-Leibler divergence (ID 142) ……..... *Pag. 1*
Akira Yoshida, Yoshiharu Amano, Noboru Murata, Koichi Ito, Takumi Hashizume

» A Model for Simulation and Optimal Design of a Solar Heating System with Seasonal Storage (ID 51) ……..... *Pag. 17*
Gianfranco Rizzo

» A thermodynamic and economic comparative analysis of combined gas-steam and gas turbine air bottoming cycle (ID 232) ……..... *Pag. 34*
Tadeusz Chmielniak, Daniel Czaja, Sebastian Lepszy

» Application of an alternative thermoeconomic approach to a two-stage vapor compression refrigeration cycle with intercooling (ID 135) ……..... *Pag. 54*
Atilio Barbosa Lourenço, José Joaquim Conceição Soares Santos, João Luiz Marcon Donatelli

» Comparative performance of advanced power cycles for low temperature heat sources (ID 109) ……..... *Pag. 67*
Guillaume Becquin, Sebastian Freund

» Comparison of nuclear steam power plant and conventional steam power plant through energy level and thermoeconomic analysis (ID 251) ……..... *Pag. 84*
S. Khamis Abadi, Mohammad Hasan Khoshgoftar Manesh, M. Baghestani, H. Ghalami, Majid Amidpour

» Economic and exergoeconomic analysis of micro GT and ORC cogeneration systems (ID 87) ……..... *Pag. 98*
Audrius Bagdanavicius, Robert Sansom, Nick Jenkins, Goran Strbac

» Exergoeconomic comparison of wet and dry cooling technologies for the Rankine cycle of a solar thermal power plant (ID 300) ……..... *Pag. 109*
Philipp Habl, Ana M. Blanco-Marigorta, Berit Erlach

» Influence of renewable generators on the thermo-economic multi-level optimization of a poly-generation smart grid (101) ……..... *Pag. 123*
Massimo Rivarolo, Andrea Greco, Francesca Travi, Aristide F. Massardo

» Local stability analysis of a thermoeconomic model of an irreversible heat engine working at different criteria of performance (ID 289) ……..... *Pag. 138*
Marco A. Barranco-Jiménez, Norma Sánchez-Salas, Israel Reyes-Ramírez, Lev Guzmán-Vargas

» Multicriteria optimization of a distributed trigeneration system in an industrial area (ID 154) ……..... *Pag. 152*
Dario Buoro, Melchiorre Casisi, Alberto de Nardi, Piero Pinamonti, Mauro Reini

» On the effect of eco-indicator selection on the conclusions obtained from an exergoenvironmental analysis (ID 275) ……..... *Pag. 168*
Tatiana Morosuk, George Tsatsaronis, Christopher Koroneos

FIRENZE UNIVERSITY PRESS, 2012, ISBN ONLINE : 978-88-6655-322-9

» Optimisation of supply temperature and mass flow rate for a district heating network (ID 104) ……..... *Pag. 181*
Marouf Pirouti, Audrius Bagdanavicius, Jianzhong Wu, Janaka Ekanayake

» Optimization of energy supply systems in consideration of hierarchical relationship between design and operation (ID 389) ……..... *Pag. 193*
Ryohei Yokoyama, Shuhei Ose

» The fuel impact formula revisited (ID 279) ……..... *Pag. 194*
Cesar Torres, Antonio Valero

» The introduction of exergy analysis to the thermo-economic modelling and optimisation of a marine combined cycle system (ID 61) ……..... *Pag. 221*
George G. Dimopoulos, Chariklia A. Georgopoulou, Nikolaos M.P. Kakalis

» The relationship between costs and environmental impacts in power plants: an exergy-based study (ID 272) ……..... *Pag.237*
Fontina Petrakopoulou, Yolanda Lara, Tatiana Morosuk, Alicia Boyano, George Tsatsaronis

» Thermo-ecological evaluation of biomass integrated gasification gas turbine based cogeneration technology (ID 441) ……..... *Pag. 250*
Wojciech Stanek, Lucyna Czarnowska, Jacek Kalina

» Thermo-ecological optimization of a heat exchanger through empirical modeling (ID 501) ……..... *Pag. 265*
Ireneusz Szczygieł, Wojciech Stanek, Lucyna Czarnowska, Marek Rojczyk

» Thermoeconomic analysis and optimization in a combined cycle power plant including a heat transformer for energy saving (ID 399) ……..... *Pag. 285*
Elizabeth Cortés Rodríguez, José Luis Castilla Carrillo, Claudia A. Ruiz Mercado, Wilfrido Rivera Gómez-Franco

» Thermoeconomic analysis and optimization of a hybrid solar-electric heating in a fluidized bed dryer (ID 400) ……..... *Pag. 297*
Elizabeth Cortés Rodríguez, Felipe de Jesús Ojeda Cámara, Isaac Pilatowsky Figueroa

» Thermoeconomic approach for the analysis of low temperature district heating systems (ID 208) ……..... *Pag. 311*
Vittorio Verda, Albana Kona

» Thermo-economic assessment of a micro CHP systems fuelled by geothermal and solar energy (ID 166) ……..... *Pag. 321*
Duccio Tempesti, Daniele Fiaschi, Filippo Gabuzzini

» Thermo-economic evaluation and optimization of the thermo-chemical conversion of biomass into methanol (ID 194) ……..... *Pag. 333*
Emanuela Peduzzi, Laurence Tock, Guillaume Boissonnet, François Marechal

» Thermoeconomic fuel impact approach for assessing resources savings in industrial symbiosis: application to Kalundborg Eco-industrial Park (ID 256) ……..... *Pag. 346*
Sergio Usón, Antonio Valero, Alicia Valero, Jorge Costa

» Thermoeconomics of a ground-based CAES plant for peak-load energy production system (ID 32) ……..... *Pag. 357*
Simon Kemble, Giampaolo Manfrida, Adriano Milazzo, Francesco Buffa

CONTENTS OF ALL THE VOLUMES

VOLUME I

I . 1 – SIMULATION OF ENERGY CONVERSION SYSTEMS

» A novel hybrid-fuel compressed air energy storage system for China's situation (ID 531)
Wenyi Liu, Yongping Yang, Weide Zhang, Gang Xu,and Ying Wu

» A review of Stirling engine technologies applied to micro-cogeneration systems (ID 338)
Ana C. Ferreira, Manuel L. Nunes, Luís B. Martins, Senhorinha F. Teixeira

» An organic Rankine cycle off-design model for the search of the optimal control strategy (ID 295)
Andrea Toffolo, Andrea Lazzaretto, Giovanni Manente, Marco Paci

» Automated superstructure generation and optimization of distributed energy supply systems (ID 518)
Philip Voll, Carsten Klaffke, Maike Hennen, André Bardow

» Characterisation and classification of solid recovered fuels (SRF) and model development of a novel thermal utilization concept through air- gasification (ID 506)
Panagiotis Vounatsos, Konstantinos Atsonios, Mihalis Agraniotis, Kyriakos D. Panopoulos, George Koufodimos,Panagiotis Grammelis, Emmanuel Kakaras

» Design and modelling of a novel compact power cycle for low temperature heat sources (ID 177)
Jorrit Wronski, Morten Juel Skovrup, Brian Elmegaard, Harald Nes Rislå, Fredrik Haglind

» Dynamic simulation of combined cycles operating in transient conditions: an innovative approach to determine the steam drums life consumption (ID 439)
Stefano Bracco

» Effect of auxiliary electrical power consumptions on organic Rankine cycle system with low-temperature waste heat source (ID 235)
Samer Maalouf, Elias Boulawz Ksayer, Denis Clodic

» Energetic and exergetic analysis of waste heat recovery systems in the cement industry (ID 228)
Sotirios Karellas, Aris Dimitrios Leontaritis, Georgios Panousis, Evangelos Bellos, Emmanuel Kakaras

» Energy and exergy analysis of repowering options for Greek lignite-fired power plants (ID 230)
Sotirios Karellas, Aggelos Doukelis, Grammatiki Zanni, Emmanuel Kakaras

» Energy saving by a simple solar collector with reflective panels and boiler (ID 366)
Anna Stoppato, Renzo Tosato

» Exergetic analysis of biomass fired double-stage Organic Rankine Cycle (ORC) (ID 37)
Markus Preißinger, Florian Heberle, Dieter Brüggemann

» Experimental tests and modelization of a domestic-scale organic Rankine cycle (ID 156)
Roberto Bracco, Stefano Clemente, Diego Micheli, Mauro Reini

» Model of a small steam engine for renewable domestic CHP system (ID 31)
Giampaolo Manfrida, Giovanni Ferrara, Alessandro Pescioni

» Model of vacuum glass heat pipe solar collectors (ID 312)
Daniele Fiaschi, Giampaolo Manfrida

» Modelling and exergy analysis of a plasma furnace for aluminum melting process (ID 254)
Luis Enrique Acevedo, Sergio Usón, Javier Uche, Patxi Rodríguez

» Modelling and experimental validation of a solar cooling installation (ID 296)
Guillaume Anies, Pascal Stouffs, Jean Castaing-Lasvignottes

» The influence of operating parameters and occupancy rate of thermoelectric modules on the electricity generation (ID 314)
Camille Favarel, Jean-Pierre Bédécarrats, Tarik Kousksou, Daniel Champier

» Thermodynamic and heat transfer analysis of rice straw co-firing in a Brazilian pulverised coal boiler (ID 236)
Raphael Miyake, Alvaro Restrepo, Fábio Kleveston Edson Bazzo, Marcelo Bzuneck

» Thermophotovoltaic generation: A state of the art review (ID 88)
Matteo Bosi, Claudio Ferrari, Francesco Melino, Michele Pinelli, Pier Ruggero Spina, Mauro Venturini

I . 2 – HEAT AND MASS TRANSFER

» A DNS method for particle motion to establish boundary conditions in coal gasifiers (ID 49)
Efstathios E Michaelides, Zhigang Feng

» Effective thermal conductivity with convection and radiation in packed bed (ID 60)
Yusuke Asakuma

» Experimental and CFD study of a single phase cone-shaped helical coiled heat exchanger: an empirical correlation (ID 375)
Daniel Flórez-Orrego, Walter Arias, Diego López, Héctor Velásquez

» Thermofluiddynamic model for control analysis of latent heat thermal storage system (ID 207)
Adriano Sciacovelli, Vittorio Verda, Flavio Gagliardi

» Towards the development of an efficient immersed particle heat exchanger: particle transfer from low to high pressure (ID 202)
Luciano A. Catalano, Riccardo Amirante, Stefano Copertino, Paolo Tamburrano, Fabio De Bellis

I . 3 – INDUSTRIAL ECOLOGY

» Anthropogenic heat and exergy balance of the atmosphere (ID 122)
Asfaw Beyene, David MacPhee, Ron Zevenhoven

» Determination of environmental remediation cost of municipal waste in terms of extended exergy (ID 63)
Candeniz Seckin, Ahmet R. Bayulken

» Development of product category rules for the application of life cycle assessment to carbon capture and storage (537)
Carlo Strazza, Adriana Del Borghi, Michela Gallo

» Electricity production from renewable and non-renewable energy sources: a comparison of environmental, economic and social sustainability indicators with exergy losses throughout the supply chain (ID 247)
Lydia Stougie, Hedzer van der Kooi, Rob Stikkelman

» Exergy analysis of the industrial symbiosis model in Kalundborg (ID 218)
Alicia Valero Delgado, Sergio Usón, Jorge Costa

» Global gold mining: is technological learning overcoming the declining in ore grades? (ID 277)
Adriana Domínguez, Alicia Valero

» Personal transportation energy consumption (ID305)
Matteo Muratori, Emmanuele Serra, Vincenzo Marano, Michael Moran

» Resource use evaluation of Turkish transportation sector via the extended exergy accounting method (ID 43)
Candeniz Seckin, Enrico Sciubba, Ahmet R. Bayulken

» The impact of higher energy prices on socio-economic inequalities of German social groups (ID 80)
Holger Schlör, Wolfgang Fischer, Jürgen-Friedrich Hake

VOLUME II

II . 1 – EXERGY ANALYSIS AND 2ND LAW ANALYSIS

» A comparative analysis of cryogenic recuperative heat exchangers based on exergy destruction (ID 129)
Adina Teodora Gheorghian, Alexandru Dobrovicescu, Lavinia Grosu, Bogdan Popescu, Claudia Ionita

» A critical exploration of the usefulness of rational efficiency as a performance parameter for heat exchangers (ID 307)
Jim McGovern, Georgiana Tirca-Dragomirescu, Michel Feidt, Alexandru Dobrovicescu

» A new procedure for the design of LNG processes by combining exergy and pinch analyses (ID 238)
Danahe Marmolejo-Correa, Truls Gundersen

» Advances in the distribution of environmental cost of water bodies through the exergy concept in the Ebro river (ID 258)
Javier Uche Marcuello, Amaya Martínez Gracia, Beatriz Carrasquer Álvarez, Antonio Valero Capilla

» Application of the entropy generation minimization method to a solar heat exchanger: a pseudo-optimization design process based on the analysis of the local entropy generation maps (ID 357)
Giorgio Giangaspero, Enrico Sciubba

» Comparative analysis of ammonia and carbon dioxide two-stage cycles for simultaneous cooling and heating (ID 84)
Alexandru Dobrovicescu, Ciprian Filipoiu, Emilia Cerna Mladin, Valentin Apostol, Liviu Drughean

» Comparison between traditional methodologies and advanced exergy analyses for evaluating efficiency and externalities of energy systems (ID 515)
Gabriele Cassetti, Emanuela Colombo

» Comparison of entropy generation figures using entropy maps and entropy transport equation for an air cooled gas turbine blade (ID 468)
Omer Emre Orhan, Oguz Uzol

» Conventional and advanced exergetic evaluation of a supercritical coal-fired power plant (ID 377)
Ligang Wang, Yongping Yang, Tatiana Morosuk, George Tsatsaronis

» Energy and exergy analyses of the charging process in encapsulted ice thermal energy storage (ID 164)
David MacPhee, Ibrahim Dincer, Asfaw Beyene

» Energy integration and cogeneration in nitrogen fertilizers industry: thermodynamic estimation of the efficiency, potentials, limitations and environmental impact. Part 1: energy integration in ammonia production plants (ID 303)
Zornitza Vassileva Kirova-Yordanova

» Evaluation of the oil and gas processing at a real production day on a North Sea oil platform using exergy analysis (ID 260)
Mari Voldsund, Wei He, Audun Røsjorde, Ivar Ståle Ertesvåg, Signe Kjelstrup

» Exergetic and economic analysis of Kalina cycle for low temperature geothermal sources in Brazil (ID 345)
Carlos Eymel Campos Rodriguez, José Carlos Escobar Palacios, Cesar Adolfo Rodríguez Sotomonte, Marcio Leme, Osvaldo José Venturini, Electo Eduardo Silva Lora, Vladimir Melián Cobasa, Daniel Marques dos Santos, Fábio R. Lofrano Dotto, Vernei Gialluca

» Exergy analysis and comparison of CO2 heat pumps (ID 242)
Argyro Papadaki, Athina Stegou - Sagia

» Exergy analysis of a CO2 Recovery plant for a brewery (ID 72)
Daniel Rønne Nielsen, Brian Elmegaard, C. Bang-Møller

» Exergy analysis of the silicon production process (ID 118)
Marit Takla, Leiv Kolbeinsen, Halvard Tveit, Signe Kjelstrup

» Exergy based indicators for cardiopulmonary exercise test evaluation (ID 159)
Carlos Eduardo Keutenedjian Mady, Cyro Albuquerque Neto, Tiago Lazzaretti Fernandes, Arnaldo Jose Hernandez, Paulo Hilário Nascimento Saldiva, Jurandir Itizo Yanagihara, Silvio de Oliveira Junior

» Exergy disaggregation as an alternative for system disaggregation in thermoeconomics (ID 483)
José Joaquim Conceição Soares Santos, Atilio Lourenço, Julio Mendes da Silva, João Donatelli, José Escobar Palacio

» Exergy intensity of petroleum derived fuels (ID 117)
Julio Augusto Mendes da Silva, Maurício Sugiyama, Claudio Rucker, Silvio de Oliveira Junior

» Exergy-based sustainability evaluation of a wind power generation system (ID 542)
Jin Yang, B. Chen, Enrico Sciubba

» Human body exergy metabolism (ID 160)
Carlos Eduardo Keutenedjian Mady, Silvio de Oliveira Junior

» Integrating an ORC into a natural gas expansion plant supplied with a co-generation unit (ID 273)
Sergio Usón, Wojciech Juliusz Kostowski

» One-dimensional model of an optimal ejector and parametric study of ejector efficiency (ID 323)
Ronan Killian McGovern, Kartik Bulusu, Mohammed Antar, John H. Lienhard

» Optimization and design of pin-fin heat sinks based on minimum entropy generation (ID 6)
Jose-Luis Zuniga-Cerroblanco, Abel Hernandez-Guerrero, Carlos A. Rubio-Jimenez, Cuauhtemoc Rubio-Arana, Sosimo E. Diaz-Mendez

» Performance analysis of a district heating system (ID 271)
Andrej Ljubenko, Alojz Poredoš, Tatiana Morosuk, George Tsatsaronis

» System analysis of exergy losses in an integrated oxy-fuel combustion power plant (ID 64)
Andrzej Ziębik, Paweł Gładysz

» What is the cost of losing irreversibly the mineral capital on Earth? (ID 220)
Alicia Valero Delgado, Antonio Valero

II . 2 – THERMODYNAMICS

» A new polygeneration system for methanol and power based on coke oven gas and coal gas (ID 252)
Hu Lin, Hongguang Jin, Lin Gao, Rumou Li

» Argon-Water closed gas cycle (ID 67)
Federico Fionelli, Giovanni Molinari

» Binary alkane mixtures as fluids in Rankine cycles (ID 246)
M. Aslam Siddiqi, Burak Atakan

» Excess enthalpies of second generation biofuels (ID 308)
Alejandro Moreau, José Juan Segovia, M. Carmen Martín, Miguel Ángel Villamañán, César R. Chamorro, Rosa M. Villamañán

» Local stability analysis of a Curzon-Ahlborn engine considering the Van der Waals equation state in the maximum ecological regime (ID 281)
Ricardo Richard Páez-Hernández, Pedro Portillo-Díaz, Delfino Ladino-Luna, Marco Antonio Barranco-Jiménez

» Some remarks on the Carnot's theorem (ID 325)
Julian Gonzalez Ayala, Fernando Angulo-Brown

» The Dead State (ID 340)
Richard A. Gaggioli

» The magnetocaloric energy conversion (ID 97)
Andrej Kitanovski, Jaka Tusek, Alojz Poredos

VOLUME IV

IV . 1 – FLUID DYNAMICS AND POWER PLANT COMPONENTS

» A control oriented simulation model of a multistage axial compressor (ID 444)
Lorenzo Damiani, Giampaolo Crosa, Angela Trucco

» A flexible and simple device for in-cylinder flow measurements: experimental and numerical validation (ID 181)
Andrea Dai Zotti, Massimo Masi, Marco Antonello

» CFD Simulation of Entropy Generation in Pipeline for Steam Transport in Real Industrial Plant (ID 543)
Goran Vučković, Gradimir Ilić, Mića Vukić, Milan Banić, Gordana Stefanović

» Feasibility Study of Turbo expander Installation in City Gate Station (ID 168)
Navid Zehtabiyan Rezaie, Majid Saffar-Avval

» GTL and RME combustion analysis in a transparent CI engine by means of IR digital imaging (ID 460)
Ezio Mancaruso, Luigi Sequino, Bianca Maria Vaglieco

» Some aspects concerning fluid flow and turbulence modeling in 4-valve engines (ID 116)
Zoran Stevan Jovanovic, Zoran Masonicic, Miroljub Tomic

IV . 2 – SYSTEM OPERATION CONTROL DIAGNOSIS AND PROGNOSIS

» Adapting the operation regimes of trigeneration systems to renewable energy systems integration (ID 188)
Liviu Ruieneanu, Mihai Paul Mircea

» Advanced electromagnetic sensors for sustainable monitoring of industrial processes (ID 145)
Uroš Puc, Andreja Abina, Anton Jeglič, Pavel Cevc, Aleksander Zidanšek

» Assessment of stresses and residual life of plant components in view of life-time extension of power plants (ID 453)
Anna Stoppato, Alberto Benato and Alberto Mirandola

» Control strategy for minimizing the electric power consumption of hybrid ground source heat pump system (ID 244)
Zoi Sagia, Constantinos Rakopoulos

» Exergetic evaluation of heat pump booster configurations in a low temperature district heating network (ID 148)
Torben Ommen, Brian Elmegaard

» Exergoeconomic diagnosis: a thermo-characterization method by using irreversibility analysis (ID 523)
Abraham Olivares-Arriaga, Alejandro Zaleta-Aguilar, Rangel-Hernández V. H, Juan Manuel Belman-Flores

» Optimal structural design of residential cogeneration systems considering their operational restrictions (ID 224)
Tetsuya Wakui, Ryohei Yokoyama

» Performance estimation and optimal operation of a CO2 heat pump water heating system (ID 344)
Ryohei Yokoyama, Ryosuke Kato, Tetsuya Wakui, Kazuhisa Takemura

» Performances of a common-rail Diesel engine fuelled with rapeseed and waste cooking oils (ID 213)
Alessandro Corsini, Valerio Giovannoni, Stefano Nardecchia, Franco Rispoli, Fabrizio Sciulli, Paolo Venturini

» Reduced energy cost through the furnace pressure control in power plants (ID 367)
Vojislav Filipović, Novak Nedić, Saša Prodanović

» Short-term scheduling model for a wind-hydro-thermal electricity system (ID 464)
Sérgio Pereira, Paula Ferreira, A. Ismael Freitas Vaz

VOLUME V

V . 1 – RENEWABLE ENERGY CONVERSION SYSTEMS

» A co-powered concentrated solar power Rankine cycle concept for small size combined heat and power (ID 276)
Alessandro Corsini, Domenico Borello, Franco Rispoli, Eileen Tortora

» A novel non-tracking solar collector for high temperature application (ID 466)
Wattana Ratismith, Anusorn Inthongkhum

» Absorption heat transformers (AHT) as a way to enhance low enthalpy geothermal resources (ID 311)
Daniele Fiaschi, Duccio Tempesti, Giampaolo Manfrida, Daniele Di Rosa

» Alternative feedstock for the biodiesel and energy production: the OVEST project (ID 98)
Matteo Prussi, David Chiaramonti, Lucia Recchia, Francesco Martelli, Fabio Guidotti

» Assessing repowering and update scenarios for wind energy converters (ID 158)
Till Zimmermann

» Biogas from mechanical pulping industry – potential improvement for increased biomass vehicle fuels (ID 54)
Mimmi Magnusson, Per Alvfors

» Biogas or electricity as vehicle fuels derived from food waste - the case of Stockholm (ID 27)
Martina Wikström, Per Alvfors

» Compressibility factor as evaluation parameter of expansion processes in organic Rankine cycles (ID 292)
Giovanni Manente, Andrea Lazzaretto

» Design of solar heating system for methane generation (ID 445)
Lucía Mónica Gutiérrez, P. Quinto Diez, L. R. Tovar Gálvez

» Economic feasibility of PV systems in hotels in Mexico (ID 346)
Augusto Sanchez, Sergio Quezada

» Effect of a back surface roughness on annual performance of an air-cooled PV module (ID 193)
Riccardo Secchi, Duccio Tempesti, Jacek Smolka

» Energy and exergy analysis of the first hybrid solar-gas power plant in Algeria (ID 176)
Fouad Khaldi

» Energy recovery from MSW treatment by gasification and melting technology (ID 393)
Fabrizio Strobino, Alessandro Pini Prato, Diego Ventura, Marco Damonte

» Ethanol production by enzymatic hydrolysis process from sugarcane biomass - the integration with the conventional process (ID 189)
Reynaldo Palacios-Bereche, Adriano Ensinas, Marcelo Modesto, Silvia Azucena Nebra

» Evaluation of gas in an industrial anaerobic digester by means of biochemical methane potential of organic municipal solid waste components (ID 57)
Isabella Pecorini, Tommaso Olivieri, Donata Bacchi, Alessandro Paradisi, Lidia Lombardi, Andrea Corti, Ennio Carnevale

» Exergy analysis and genetic algorithms for the optimization of flat-plate solar collectors (ID 423)
Soteris A. Kalogirou

» Experimental study of tar and particles content of the produced gas in a double stage downdraft gasifier (ID 487)
Ana Lisbeth Galindo Noguera, Sandra Yamile Giraldo, Rene Lesme-Jaén, Vladimir Melian Cobas, Rubenildo Viera Andrade, Electo Silva Lora

» Feasibility study to realize an anaerobic digester fed with vegetables matrices in central Italy (ID 425)
Umberto Desideri, Francesco Zepparelli, Livia Arcioni, Ornella Calderini, Francesco Panara, Matteo Todini

» Investigations on the use of biogas for small scale decentralized CHP applications with a focus on stability and emissions (ID 140)
Steven MacLean, Eren Tali, Anne Giese, Jörg Leicher

» Kinetic energy recovery system for sailing yachts (ID 427)
Giuseppe Leo Guizzi, Michele Manno

» Mirrors in the sky: status and some supporting materials experiments (ID 184)
Noam Lior

» Numerical parametric study for different cold storage designs and strategies of a solar driven thermoacoustic cooler system (ID 284)
Maxime Perier-Muzet, Pascal Stouffs, Jean-Pierre Bedecarrats, Jean Castaing-Lasvignottes

» Parabolic trough photovoltaic/thermal collectors. Part I: design and simulation model (ID 102)
Francesco Calise, Laura Vanoli

» Parabolic trough photovoltaic/thermal collectors. Part II: dynamic simulation of a solar trigeneration system (ID 488)
Francesco Calise, Laura Vanoli

» Performance analysis of downdraft gasifier - reciprocating engine biomass fired small-scale cogeneration system (ID 368)
Jacek Kalina

» Proposing offshore photovoltaic (PV) technology to the energy mix of the Maltese islands (ID 262)
Kim Trapani, Dean Lee Millar

» Research of integrated biomass gasification system with a piston engine (ID 414)
Janusz Kotowicz, Aleksander Sobolewski, Tomasz Iluk
» Start up of a pre-industrial scale solid state anaerobic digestion cell for the co-treatment of animal and agricultural residues (ID 34)
Francesco Di Maria, Giovanni Gigliotti, Alessio Sordi, Caterina Micale, Luisa Massaccesi

» The role of biomass in the renewable energy system (ID 390)
Ruben Laleman, Ludovico Balduccio, Johan Albrecht

» Vegetable oils of soybean, sunflower and tung as alternative fuels for compression ignition engines (ID 500)
Ricardo Morel Hartmann, Nury Nieto Garzón, Eduardo Morel Hartmann, Amir Antonio Martins Oliveira Jr, Edson Bazzo, Bruno Okuda, Joselia Piluski
» Wind energy conversion performance and atmosphere stability (ID 283)
Francesco Castellani, Emanuele Piccioni, Lorenzo Biondi, Marcello Marconi

V. 2 – FUEL CELLS

» Comparison study on different SOFC hybrid systems with zero-CO2 emission (ID 196)
Liqiang Duan, Kexin Huang, Xiaoyuan Zhang and Yongping Yang

» Exergy analysis and optimisation of a steam methane pre-reforming system (ID 62)
George G. Dimopoulos, Iason C. Stefanatos, Nikolaos M.P. Kakalis

» Modelling of a CHP SOFC power system fed with biogas from anaerobic digestion of municipal wastes integrated with a solar collector and storage units (ID 491)
Domenico Borello, Sara Evangelisti, Eileen Tortora

VOLUME VI

VI . 1 – CARBON CAPTURE AND SEQUESTRATION

» A novel coal-based polygeneration system cogenerating power, natural gas and liquid fuel with CO2 capture (ID 96)
Sheng Li, Hongguang Jin, Lin Gao

» Analysis and optimization of CO2 capture in a China's existing coal-fired power plant (ID 532)
Gang Xu, Yongping Yang, Shoucheng Li, Wenyi Liu and Ying Wu

» Analysys of four-end high temperature membrane air separator in a supercritical power plant with oxy-type pulverized fuel boiler (ID 442)
Janusz Kotowicz, Sebastian Stanisław Michalski

» Analysis of potential improvements to the lignite-fired oxy-fuel power unit (ID 413)
Marcin Liszka, Jakub Tuka, Grzegorz Nowak, Grzegorz Szapajko
» Biogas Upgrading: Global Warming Potential of Conventional and Innovative Technologies (ID 240)
Katherine Starr, Xavier Gabarrell Durany, Gara Villalba Mendez, Laura Talens Peiro, Lidia Lombardi

» Capture of carbon dioxide using gas hydrate technology (ID 103)
Beatrice Castellani, Mirko Filipponi, Sara Rinaldi, Federico Rossi

» Carbon dioxide mineralisation and integration with flue gas desulphurisation applied to a modern coal-fired power plant (ID 179)
Ron Zevenhoven, Johan Fagerlund, Thomas Björklöf, Magdalena Mäkelä, Olav Eklund

» Carbon dioxide storage by mineralisation applied to a lime kiln (ID 226)
Inês Sofia Soares Romão, Matias Eriksson, Experience Nduagu, Johan Fagerlund, Licínio Manuel Gando-Ferreira, Ron Zevenhoven

» Comparison of IGCC and CFB cogeneration plants equipped with CO2 removal (ID 380)
Marcin Liszka, Tomasz Malik, Michał Budnik, Andrzej Ziębik

» Concept of a "capture ready" combined heat and power plant (ID 231)
Piotr Henryk Lukowicz, Lukasz Bartela

» Cryogenic method for H2 and CH4 recovery from a rich CO2 stream in pre-combustion CCS schemes (ID 508)
Konstantinos Atsonios, Kyriakos D. Panopoulos, Angelos Doukelis, Antonis Koumanakos, Emmanuel Kakaras

» Design and optimization of ITM oxy-combustion power plant (ID 495)
Surekha Gunasekaran, Nicholas David Mancini, Alexander Mitsos

» Implementation of a CCS technology: the ZECOMIX experimental platform (ID 222)
Antonio Calabrò, Stefano Cassani, Leandro Pagliari, Stefano Stendardo

» Influence of regeneration condition on cyclic CO2 capture using pre-treated dispersed CaO as high temperature sorbent (ID 221)
Stefano Stendardo, Antonio Calabrò

» Investigation of an innovative process for biogas up-grading – pilot plant preliminary results (ID 56)
Lidia Lombardi, Renato Baciocchi, Ennio Antonio Carnevale, Andrea Corti, Giulia Costa, Tommaso Olivieri, Alessandro Paradisi, Daniela Zingaretti

» Method of increasing the efficiency of a supercritical lignite-fired oxy-type fluidized bed boiler and high-temperature three - end membrane for air separation (ID 438)
Janusz Kotowicz, Adrian Balicki

» Monitoring of carbon dioxide uptake in accelerated carbonation processes applied to air pollution control residues (ID 539)
Felice Alfieri, Peter J Gunning, Michela Gallo, Adriana Del Borghi, Colin D Hills

» Process efficiency and optimization of precipitated calcium carbonate (PCC) production from steel converter slag (ID 114)
Hannu-Petteri Mattila, Inga Grigaliūnaitė, Arshe Said, Sami Filppula, Carl-Johan Fogelholm, Ron Zevenhoven

» Production of Mg(OH)2 for CO2 Emissions Removal Applications: Parametric and Process Evaluation (ID 245)
Experience Ikechukwu Nduagu, Inês Romão, Ron Zevenhoven

» Thermodynamic analysis of a supercritical power plant with oxy type pulverized fuel boiler, carbon dioxide capture system (CC) and four-end high temperature membrane air seprator (ID 411)
Janusz Kotowicz, Sebastian Stanisław Michalski

VI . 2 – PROCESS INTEGRATION AND HEAT EXCHANGER NETWORKS

» A multi-objective optimization technique for co- processing in the cement production (ID 42)
Maria Luiza Grillo Renó, Rogério José da Silva, Mirian de Lourdes Noronha Motta Melo, José Joaquim Conceição Soares Santos

» Comparison of options for debottlenecking the recovery boiler at kraft pulp mills – Economic performance and CO2 emissions (ID 449)
Johanna Jönsson, Karin Pettersson, Simon Harvey, Thore Berntsson

» Demonstrating an integral approach for industrial energy saving (ID 541)
René Cornelissen, Geert van Rens, Jos Sentjens, Henk Akse, Ton Backx, Arjan van der Weiden, Jo Vandenbroucke

» Maximising the use of renewables with variable availability (ID 494)
Andreja Nemet, Jiri Jaromír Klemeš, Petar Sabev Varbanov, Zdravko Kravanja

» Methodology for the improvement of large district heating networks (ID 46)
Anna Volkova, Vladislav Mashatin, Aleksander Hlebnikov, Andres Siirde

» Optimal mine site energy supply (ID 306)
Monica Carvalho, Dean Lee Millar

» Simulation of synthesis gas production from steam oxygen gasification of Colombian bituminous coal using Aspen Plus® (ID 395)
John Jairo Ortiz, Juan Camilo González, Jorge Enrique Preciado, Rocío Sierra, Gerardo Gordillo

VOLUME VII

VII . 1 – BUILDING, URBAN AND COMPLEX ENERGY SYSTEMS

» A linear programming model for the optimal assessment of sustainable energy action plans (ID 398)
Gianfranco Rizzo, Giancarlo Savino

» A natural gas fuelled 10 kW electric power unit based on a Diesel automotive internal combustion engine and suitable for cogeneration (ID 477)
Pietro Capaldi

» Adjustment of envelopes characteristics to climatic conditions for saving heating and cooling energy in buildings (ID 430)
Christos Tzivanidis, Kimon Antonopoulos, Foteini Gioti

» An exergy based method for the optimal integration of a building and its heating plant. Part 1: comparison of domestic heating systems based on renewable sources (ID 81)
Marta Cianfrini, Enrico Sciubba, Claudia Toro

» Analysis of different typologies of natural insulation materials with economic and performances evaluation of the same buildings (ID 28)
Umberto Desideri, Daniela Leonardi, Livia Arcioni

» Complex networks approach to the Italian photovoltaic energy distribution system (ID 470)
Luca Valori, Giovanni Luca Giannuzzi, Tiziano Squartini, Diego Garlaschelli, Riccardo Basosi

» Design of a multi-purpose building "to zero energy consumption" according to European Directive 2010/31/CE: Architectural and plant solutions (ID 29)
Umberto Desideri, Livia Arcioni, Daniela Leonardi, Luca Cesaretti ,Perla Perugini, Elena Agabitini, Nicola Evangelisti

» Effect of initial systems on the renewal planning of energy supply systems for a hospital (ID 107)
Shu Yoshida, Koichi Ito, Yoshiharu Amano, Shintaro Ishikawa, Takahiro Sushi, Takumi Hashizume

» Effects of insulation and phase change materials (PCM) combinations on the energy consumption for buildings indoor thermal comfort (ID 387)
Christos Tzivanidis, Kimon Antonopoulos, Eleutherios Kravvaritis

» Energetic evaluation of a smart controlled greenhouse for tomato cultivation (ID 150)
Nickey Van den Bulck, Mathias Coomans, Lieve Wittemans, Kris Goen, Jochen Hanssens, Kathy Steppe, Herman Marien, Johan Desmedt

» Energy networks in sustainable cities: temperature and energy consumption monitoring in urban area (ID 190)
Luca Giaccone, Alessandra Guerrisi, Paolo Lazzeroni and Michele Tartaglia

» Extended exergy analysis of the economy of Nova Scotia, Canada (ID 215)
David C Bligh, V.Ismet Ugursal

» Feasibility study and design of a low-energy residential unit in Sagarmatha Park (Nepal) for envirnomental impact reduction of high altitude buildings (ID 223)
Umberto Desideri, Stefania Proietti, Paolo Sdringola, Elisa Vuillermoz

» Fire and smoke spread in low-income housing in Mexico (ID 379)
Raul R. Flores-Rodriguez, Abel Hernandez-Guerrero, Cuauhtemoc Rubio-Arana, Consuelo A. Caldera-Briseño

» Optimal lighting control strategies in supermarkets for energy efficiency applications via digital dimmable technology (ID 136)
Salvador Acha, Nilay Shah, Jon Ashford, David Penfold

» Optimising the arrangement of finance towards large scale refurbishment of housing stock using mathematical programming and optimisationg (ID 127)
Mark Gerard Jennings, Nilay Shah, David Fisk

» Optimization of thermal insulation to save energy in buildings (ID 174)
Milorad Bojić, Marko Miletić, Vesna Marjanović, Danijela Nikolić, Jasmina Skerlić

» Residential solar-based seasonal thermal storage system in cold climate: building envelope and thermal storage (ID 342)
Alexandre Hugo and Radu Zmeureanu

» Simultaneous production of domestic hot water and space cooling with a heat pump in a Swedish Passive House (ID 55)
Johannes Persson, Mats Westermark

» SOFC micro-CHP integration in residential buildings (ID 201)
Umberto Desideri, Giovanni Cinti, Gabriele Discepoli, Elena Sisani, Daniele Penchini

» The effect of shading of building integrated photovoltaics on roof surface temperature and heat transfer in buildings (ID 83)
Eftychios Vardoulakis, Dimitrios Karamanis

» The influence of glazing systems on energy performance and thermal comfort in non-residential buildings (ID 206)
Cinzia Buratti, Elisa Moretti, Elisa Belloni

» Thermal analysis of a greenhouse heated by solar energy and seasonal thermal energy storage in soil (ID 405)
Yong Li, Jin Xu, Ru-Zhu Wang

» Thermodynamic analysis of a combined cooling, heating and power system under part load condition (ID 476)
Qiang Chen, Jianjiao Zheng, Wei Han, Jun Sui, Hong-guang Jin

VII . 2 – COMBUSTION, CHEMICAL REACTORS

» Baffle as a cost-effective design improvement for volatile combustion rate increase in biomass boilers of simple construction (ID 233)
Borivoj Stepanov, Ivan Pešenjanski, Biljana Miljković

» Characterization of CH4-H2-air mixtures in the high-pressure DHARMA reactor (ID 287)
Vincenzo Moccia, Jacopo D'Alessio

» Development of a concept for efficiency improvement and decreased NOx production for natural gas-fired glass melting furnaces by switching to a propane exhaust gas fired process (ID 146)
Jörn Benthin, Anne Giese

» **Experimental analysis of inhibition phenomenon management for Solid Anaerobic Digestion Batch process (ID 348)**
Francesco Di Maria, Giovanni Gigliotti, Alessio Sordi, Caterina Micale, Claudia Zadra, Luisa Massaccesi

» **Experimental investigations of the combustion process of n-butanol/diesel blend in an optical high swirl CI engine (ID 85)**
Simona Silvia Merola, G. Valentino, C. Tornatore, L. Marchitto , F. E. Corcione

» **Flameless oxidation as a means to reduce NOx emissions in glass melting furnaces (ID 141)**
Jörg Leicher, Anne Giese

» **Mechanism of damage by high temperature of the tubes, exposed to the atmosphere characteristic of a furnace of pyrolysis of ethane for ethylene production in the petrochemical industry (ID 65)**
Jaqueline Saavedra Rueda, Francisco Javier Perez Trujillo, Lourdes Isabel Meriño Stand, Harbey Alexi Escobar, Luis Eduardo Navas, Juan Carlos Amezquita

» **Steam reforming of methane over Pt/Rh based wire mesh catalyst in single channel reformer for small scale syngas production (ID 317)**
Haftor Orn Sigurdsson, Søren Knudsen Kær

VOLUME VIII

VIII . 1 – ENERGY SYSTEMS : ENVIRONMENTAL AND SUSTAINABILITY ISSUES

» **A multi-criteria decision analysis tool to support electricity planning (ID 467)**
Fernando Ribeiro, Paula Ferreira, Madalena Araújo

» **Comparison of sophisticated life cycle impact assessment methods for assessing environmental impacts in a LCA study of electricity production (ID 259)**
Jens Buchgeister

» **Defossilisation assessment of biodiesel life cycle production using the ExROI indicator (ID 304)**
Emilio Font de Mora, César Torres, Antonio Valero, David Zambrana

» **Design strategy of geothermal plants for water dominant medium-low temperature reservoirs based on sustainability issues (ID 99)**
Alessandro Franco, Maurizio Vaccaro

» **Energetic and environmental benefits from waste management: experimental analysis of the sustainable landfill (ID 33)**
Francesco Di Maria, Alessandro Canovai, Federico Valentini, Alessio Sordi, Caterina Micale

» **Environmental assessment of energy recovery technologies for the treatment and disposal of municipal solid waste using life cycle assessment (LCA): a case study of Brazil (ID 512)**
Marcio Montagnana Vicente Leme, Mateus Henrique Rocha, Electo Eduardo Silva Lora,Osvaldo José Venturini, Bruno Marciano Lopes, Claudio Homero Ferreira

» **How will renewable power generation be affected by climate change? – The case of a metropolitan region in Northwest Germany (ID 503)**
Jakob Wachsmuth, Andrew Blohm, Stefan Gößling-Reisemann, Tobias Eickemeier, Rebecca Gasper, Matthias Ruth, Sönke Stührmann

» **Impact of nuclear power plant on Thailand power development plan (ID 474)**
Raksanai Nidhiritdhikrai, Bundhit Eua-arporn

» **Improving sustainability of maritime transport through utilization of liquefied natural gas (LNG) for propulsion (ID 496)**
Fabio Burel, Rodolfo Taccani, Nicola Zuliani

» Life cycle assessment of thin film non conventional photovoltaics: the case of dye sensitized solar cells (ID 471)
Maria Laura Parisi, Adalgisa Sinicropi, Riccardo Basosi

» Low CO2 emission hybrid solar CC power system (ID 175)
Yuanyuan Li, Na Zhang, Ruixian Cai

» Low exergy solutions as a contribution to climate adapted and resilient power supply (ID 489)
Stefan Goessling-Reisemann, Thomas Bloethe

» On the use of MPT to derive optimal RES electricity generation mixes (ID 459)
Paula Ferreira, Jorge Cunha

» Stability and limit cycles in an exergy-based model of population dynamics (ID 128)
Enrico Sciubba, Federico Zullo

» The influence of primary measures for reducing NOx emissions on energy steam boiler efficiency (ID 125)
Goran Stupar, Dragan Tucaković, Titoslav Živanović, Miloš Banjac, Srđan Belošević,Vladimir Beljanski, Ivan Tomanović, Nenad Crnomarković, Miroslav Sijerčić

» The Lethe city car of the University of Roma 1: final proposed configuration (ID 45)
Roberto Capata, Enrico Sciubba

VIII . 2 - POSTER SESSION

» A variational optimization of a finite-time thermal cycle with a Stefan-Boltzmann heat transfer law (ID 333)
Juan C.Chimal-Eguia, Norma Sanchez-Salas

» Modeling and simulation of a boiler unit for steam power plants (ID 545)
Luca Moliterno, Claudia Toro

» Numerical Modelling of straw combustion in a moving bed combustor (ID 412)
Biljana Miljkoviü, Ivan Pešenjanski, Borivoj Stepanov, Vladimir Milosavljeviü, Vladimir Rajs

» Physicochemical evaluation of the properties of the coke formed at radiation area of light hydrocarbons pyrolysis furnace in petrochemical industry (ID 10)
Jaqueline Saavedra Rueda , Angélica María Carreño Parra, María del Rosario Pérez Trejos, Dionisio Laverde Cataño, Diego Bonilla Duarte, Jorge Leonardo Rodríguez Jiménez, Laura María Díaz Burgos

» Rotor TG cooled (ID 121)
Chiara Durastante, Paolo Petroni, Michela Spagnoli, Vincenzo Rizzica, Jörg Helge Wirfs

» Study of the phase change in binary alloy (ID 534)
Aroussia Jaouahdou, Mohamed J. Safi, Herve Muhr

» Technip initiatives in renewable energies and sustainable technologies (ID 527)
Pierfrancesco Palazzo, Corrado Pigna

ECOS 2012

VOLUME III

A comparison of optimal operation of residential energy systems using clustered demand patterns based on Kullback-Leibler divergence

Akira Yoshida[a], Yoshiharu Amano[a], Noboru Murata[b], Koichi Ito[a] and Takumi Hashizume[a]

[a] Research Institute for Science and Engineering, Waseda University, 17 Kikui-cho, Shinjuku-ku, Tokyo, 162-0044, Japan, yoshida@power.mech.waseda.ac.jp
[b] School of Science and Engineering, Waseda University, 1-4-3 Okubo, Shinjuku-ku, Tokyo, Japan

Abstract:
Residential energy demand varies widely in terms of time-series behaviors, amounts consumed between families, and even within one family. Residential energy demand profiles have a high degree of uncertainty in their essentials because the demand profile is entirely based on the occupant-driven load. When evaluating residential energy systems like co-generation systems, hot water and electricity demand profiles are critical. In this paper, in order to clarify rational energy system selection guidelines and rational operation strategies, authors aim to extract basic demand time-series patterns from two kinds of measured demand (electricity and domestic hot water), measured over 26307 days of data in Japan. Authors also aim to reveal the relationship between primary energy consumption and demand patterns. Demand time-series data are categorized by means of a kind of "unsupervised" learning, which is a hierarchical clustering method using a statistical pseudo-distance. The statistical pseudo-distance is calculated from the generalized Kullback-Leibler divergence with the Gaussian mixture distribution fitted to the demand time-series data. The classified demand patterns are built using a hierarchical clustering and then a comparison is performed between the optimal operation of the two systems (a polymer electrolyte membrane fuel cell co-generation system, and a CO_2 heat pump system) and the operation of a reference system (a conventional combination of a condensing gas boiler and electricity purchased from the grid) using the demand profiles appropriately built.
Our results show that basic demand patterns are extracted by the proposed method. The demand patterns, the amount of daily demand and heat-to-power ratio of demand affect the primary energy reduction ratio of the polymer electrolyte membrane fuel cell co-generation system.

Keywords:
Co-generation, Demand Pattern, Gaussian Mixture Model, Hierarchical Clustering, KL-divergence, Optimal Operation.

1. Introduction

A variety of water heaters are commercially available in Japan. Condensing gas boilers and heat pump water heaters, which are operated with CO_2 as a working fluid, and co-generation systems (CGS), which have polymer electrolyte fuel cells, are available. Residential energy consumption has been increasing slowly but surely in Japan. Residential energy consumption accounted for 81.3% of all residential energy consumption by domestic hot water (DHW) and electricity (excluding heating, ventilation and air conditioning (HVAC)) demand [1]. There is a need for introducing high-efficiency equipment. Residential energy demand varies widely in terms of time-series behaviors, amounts consumed between families, and even within one family. Residential energy demand profiles have a high degree of uncertainty in their essentials because of the occupant-driven load. When evaluating residential energy systems, demand profiles are critical. In order to reduce the primary energy consumption when introducing an energy supply system, we need rational energy system selection guidelines and rational operation strategies that consider a variety of demand profiles. Therefore, it is important to clarify the matches between the characteristics of energy systems and the characteristics of demand profiles.

Hashimoto et al. [2] carried out a comparative evaluation on both a CO_2 heat-pump system (HP-S) and two kinds of polymer electrolyte membrane fuel cell co-generation system (PEFC-CGS). At that time, because there was no commercial PEFC-CGS, they estimated the model parameters with assumptions based on some ideal physics model.

In our previous study [3], the daily optimal operations of the PEFC-CGS and the HP-S were analyzed using measured operated system data and measured demand. It showed that primary energy consumption is reduced when an energy system is introduced with characteristics matching the characteristics of the demand profiles. Thus, one of the selection criteria of introducing an energy system is the amount of daily demand. The primary energy consumption of the PEFC-CGS shows large differences in spite of the similarity in the amount of daily demand and the similarity of the heat-to-power ratio of non-HVAC electricity and DHW demand. We guess that other factors affect the primary energy consumption of each system. Here we hypothesize that demand patterns have an effect on the primary energy consumption. We make an analysis of the demand patterns.

In this paper, in order to clarify the rational energy system selection guidelines and the rational operation strategies, our main purposes are

1. To extract basic demand time-series patterns from the measured operated system data and two kinds of demand (non-HVAC electricity and DHW), measured over 26307 days, and

2. To reveal the relationship between demand patterns and the primary energy consumption of each system.

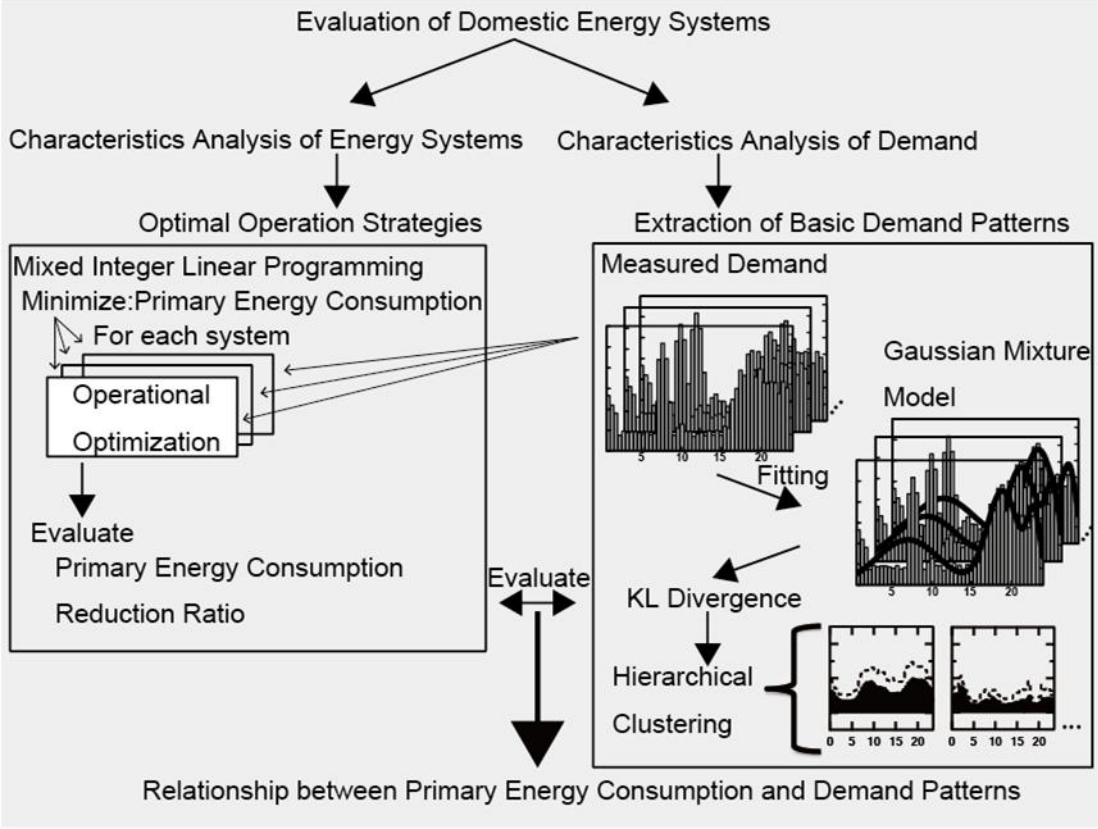

Fig. 1. Analysis framework.

Figure 1 shows the analysis framework of this paper. It does not use demographic data but uses only demand time-series data for the extraction of demand patterns. Demand time-series data are categorized by means of a kind of "unsupervised" learning, which is a hierarchical clustering method using a statistical pseudo-distance. The statistical pseudo-distance is calculated from the generalized Kullback-Leibler (KL) divergence [4] with the Gaussian mixture distribution (GMD) fitted to the demand time-series data. The method was proposed by Shen et al. [5]. The classified

clusters are evaluated by the optimal operation of each energy system. The main consideration is the relationship between the clustered demand time-series data and the primary energy consumption of each energy system, one PEFC-CGS, and one HP-S. Each system is compared to a reference system (C-S): a conventional combination of a condensing gas boiler and electricity purchased from the grid.

2. Hot water and non-HVAC electricity demand

Figure 2 shows demand maps measured in 40 households in detached houses and 32 households in residential buildings. Data were gathered for a total of 26307 days, measured with a sampling interval of 30 minutes. As shown in Fig. 2 (a), the annual non-HVAC electricity demand is 15.49 GJ/year (about 11.79 kWh/day), and the annual DHW demand is 13.05 GJ/year (about 9.93 kWh/day) on average for the 72 households. As shown in Fig. 2 (b), the modal value of daily non-HVAC demand,E, is around 8 kWh/day, and the modal value of daily DHW demand,Q,is around 4 kWh/day. Daily demand varies widely because DHW demand accrues to over 60 kWh/day, which is 15 times more than the modal value. Since the operational strategy might be implemented in co-generation systems on daily, time-series data should be analyzed on daily time scale.

As shown in Fig. 2 (b), measured demand data are separated from the daily heat-to-power ratio,R, and DHW demand,Q, by red lines. The 26307 days are divided into 6 sets of groups, defined by each zone of heat-to-power ratio,R, for descriptive purposes as shown in Table 1. Measured demand data are separated based on information obtained from our earlier study [3]. This showed that the targeted PEFC-CGS increases primary energy consumption compared with the simple condensing gas boiler and grid electricity system in the zone under 6 kWh/day of DHW demand, Q. We do a clustering analysis for each group.

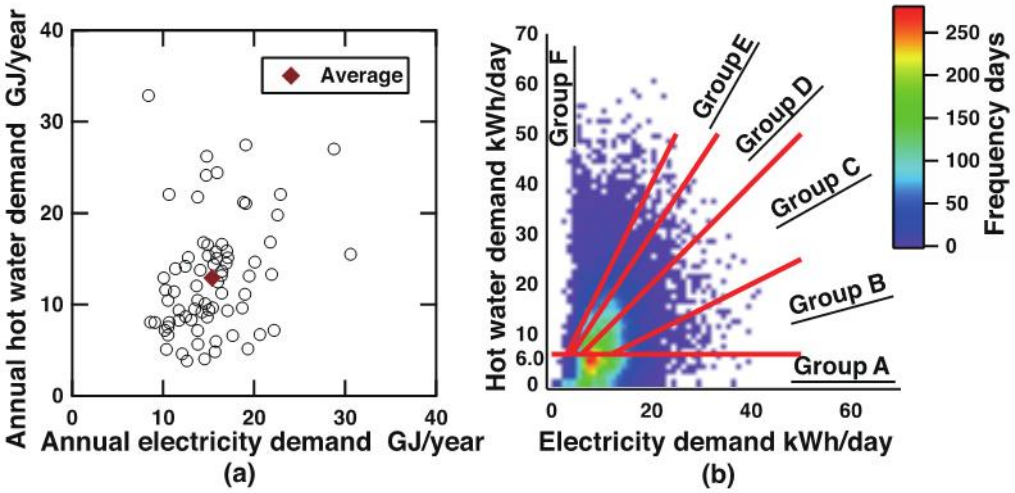

Fig. 2. Measured demand: a) yearly, b) daily.

Table 1. Demand groups.

Group name	Number of Elements, days	DHW demand Q, kWh/day	Heat-to-power ratio R
A	9807	$Q < 6.0$	---
B	971	$6.0 \leq Q$	$R < 0.5$
C	6958	$6.0 \leq Q$	$0.5 \leq R < 1.0$
D	4920	$6.0 \leq Q$	$1.0 \leq R < 1.5$
E	1926	$6.0 \leq Q$	$1.5 \leq R < 2.0$
F	1725	$6.0 \leq Q$	$2.0 \leq R$

3. Clustering Model

Demand time-series data are categorized by a hierarchical clustering method using a statistical pseudo-distance. A statistical pseudo-distance is the distance between two points in a pseudo-metric, which defined by identity of indiscernibles, symmetry and triangle inequality. The statistical pseudo-distance is calculated from the generalized KL divergence with the GMD fitted to the demand time-series data. Actually, this process fits the GMD to some peaks of daily non-HVAC electricity and daily DHW demands. The GMD is represented by three parameters: the mean, the covariance, and the coefficient in the linear combination. 48-dimensional vectors, which are 48 terms accumulated every 30 minutes through a day, are translated to vectors with up to 12 dimensions. The demand time-series data are categorized by the hierarchical clustering method using the distance, which is calculated with information per day represented by vectors with up to 12 dimensions. The KL divergence, which represents the dissimilarity measure between two distributions, is often used for cluster analyses. The Bregman divergence [6] is a pseudo-distance for measuring the discrepancy between two functions. The generalized KL divergence is extended by the framework of the Bregman divergence, and can handle distributions and others. In this paper, the generalized KL divergence between two biased distributions, which represents the dissimilarity measure of the histogram of daily demand time-series data, is used as the pseudo-distance of the clustering. Please refer [5] for details.

3.1. Gaussian Mixture Model

For a d-dimensional vector $\mathbf{x} = (x_1, \dots, x_d)^{\mathrm{T}}$ of continuous variables, the Gaussian distribution (GD) is defined by

$$\mathcal{N}(\mathbf{x}|\boldsymbol{\mu}, \boldsymbol{\Sigma}) = \frac{1}{(2\pi)^{\frac{d}{2}}} \frac{1}{|\boldsymbol{\Sigma}|^{\frac{1}{2}}} \exp\{-\frac{1}{2}(\mathbf{x} - \boldsymbol{\mu})^{\mathrm{T}} \boldsymbol{\Sigma}^{-1} (\mathbf{x} - \boldsymbol{\mu})\}, \quad (1)$$

where $\boldsymbol{\mu}$ is a d-dimensional mean vector, and $\boldsymbol{\Sigma}$ is a $d \times d$ covariance matrix. A superposition of K Gaussian densities of the form

$$p(\mathbf{x}|\boldsymbol{\theta}) = \sum_{k=1}^{K} \pi_k \mathcal{N}(\mathbf{x}|\boldsymbol{\mu}_k, \boldsymbol{\Sigma}_k), \quad (2)$$

is called a mixture of Gaussians. The parameters π are called mixing coefficients. If we integrate both sides of (2) with respect to $\mathbf{x}$, and note that both $p(\mathbf{x})$ and the individual Gaussian components are normalized, we obtain

$$\sum_{k=1}^{K} \pi_k = 1. \quad (3)$$

The form of the GMD is governed by the parameters $\boldsymbol{\pi} \equiv \{\pi_1, \dots, \pi_K\}, \boldsymbol{\mu} \equiv \{\boldsymbol{\mu}_1, \dots, \boldsymbol{\mu}_K\}, \boldsymbol{\Sigma} \equiv \{\boldsymbol{\Sigma}_1, \dots, \boldsymbol{\Sigma}_K\}$. Here, the unknown parameters $\boldsymbol{\theta}$ are defined by

$$\boldsymbol{\theta} = \{\pi_k, \boldsymbol{\mu}_k, \boldsymbol{\Sigma}_k\}_{k=1}^{K}. \quad (4)$$

We determine values for the unknown parameters $\boldsymbol{\theta}$ in the GMD by maximizing the likelihood function. Here, the maximum likelihood solution for the parameters no longer has a closed-form analytical solution. We use the expectation-maximization (EM) algorithm [7], which is a method of approximating inference, to estimate the parameters of the Gaussian mixture model. Mclust function [8] with mclust packages in R language, which is an open source programming language and software environment for statistical computing, is utilized. The numbers of the Gaussian mixture elements are chosen by the Bayesian information criterion (BIC) from one to four. In other words, the GMD fits the demand patterns, which might have up to four peaks in a day, at morning, noon, evening and midnight. In this process, 48-dimensional daily demand vectors are represented by a maximum of $3 \times 4 = 12$-dimensional vectors of the GMD, because the GMD is represented by the three parameters, namely the mean, the covariance, and the coefficient in the linear combination.

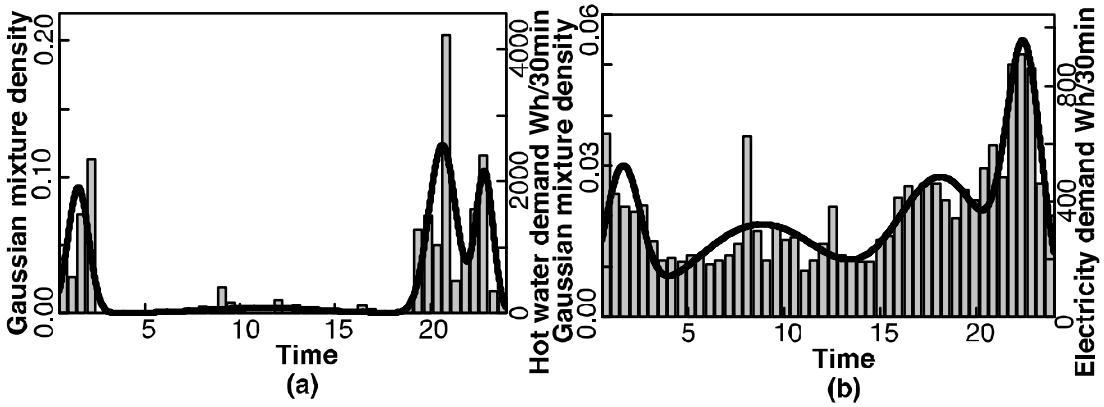

Fig. 3. A sample of fitting the Gaussian mixture model: a) Hot water demand, b) Electricity demand.

Figure 3 shows a sample of fitting the Gaussian mixture model for demand time-series data. As shown in Fig. 3 (a), the bar charts represent the hot water demand of a sample day, and the solid curves represents the Gaussian mixture density. It shows the four peaks, which mean the four GDs. Similarly, as shown in Fig. 3 (b), the non-HVAC electricity demand of this sample day has four peaks.

3.2. Kullback-Leibler Divergence

Statistical pseudo-distances between all days are represented by the KL divergence, which is known as the "relative entropy". The KL divergence between two probability density functions, $f(x)$ and $g(x)$, is given by

$$\mathcal{D}_{\mathrm{KL}}(f,g) = \int f(x) \ln \frac{f(x)}{g(x)} dx. \tag{5}$$

The KL divergence between d-dimensional GDs $\tilde{f}(x)$ and $\tilde{g}(x)$ is given by

$$\mathcal{D}_{\mathrm{g}}(\tilde{f},\tilde{g}) = \frac{1}{2}\left[\log\frac{|\Sigma_{\tilde{g}}|}{|\Sigma_{\tilde{f}}|} + \mathrm{Tr}\left[\Sigma_{\tilde{g}}^{-1}\Sigma_{\tilde{f}}\right] - d + \left(\mu_{\tilde{f}} - \mu_{\tilde{g}}\right)^{\mathrm{T}}\Sigma_{\tilde{g}}^{-1}(\mu_{\tilde{f}} - \mu_{\tilde{g}})\right]. \tag{6}$$

The KL divergence between two mixture of Gaussian $p(\mathbf{x}|\boldsymbol{\theta})$ and $q(\mathbf{x}|\boldsymbol{\theta}')$ is approximated by

$$\mathcal{D}_{\mathrm{gm}}(p,q) = \Sigma_{a=1}^{K_a}\pi_a \log\frac{\Sigma_{a'=1}^{K_a}\pi_{a'}\exp\left(-\mathcal{D}_{\mathrm{g}}(p_a,p_{a'})\right)}{\Sigma_{b=1}^{K_b}\pi_b\exp\left(-\mathcal{D}_{\mathrm{g}}(p_a,q_b)\right)}, \tag{7}$$

where Gaussian, $p_a(\mathbf{x})$, is the a^{th} component of the GMD $p(\mathbf{x}|\boldsymbol{\theta})$. Specifically, in this context, $\mathbf{x}$ represents the measured demand of a day, $p(\mathbf{x}|\boldsymbol{\theta})$ represents the characteristics of one day of the waveform regarding demand time-series data as a histogram, and $p_a(\mathbf{x})$ represents the characteristics of a peak fitted to the GD. $q(\mathbf{x})$ represents the characteristic of the wave form of the other day. Until this point, we have considered the KL divergence as the difference between the shapes of the histogram of daily demand time-series data. In this paper, it is important to consider both the amount of daily total demand and time-series behaviors, because the balance of electricity and heat demand is critical for CGS performance. Here, we consider a biased GMD, $\tilde{p}(\mathbf{x})$ for one day and $\tilde{q}(\mathbf{x})$ for the other day, which are multiplied by daily total non-HVAC electricity demand, E_p, E_q kWh/day. The KL divergence of non-HVAC electricity demand is explained in the following context:

$$\tilde{p}(\mathbf{x}) = \frac{E_p}{1000}p(\mathbf{x}),$$

$$\tilde{q}(\mathbf{x}) = \frac{E_q}{1000}q(\mathbf{x}). \tag{8}$$

For calculating the KL divergence from the biased GMD, (8), the generalized KL divergence, $\mathcal{D}_{\mathrm{gen}}$, which is extended by the framework of the Bregman divergence, is given by

$$\mathcal{D}_{\mathrm{gen}}(\tilde{p},\tilde{q}) = \int_x \left(\tilde{p}(\mathbf{x}) \log \frac{\tilde{p}(\mathbf{x})}{\tilde{q}(\mathbf{x})} - \tilde{p}(\mathbf{x}) + \tilde{q}(\mathbf{x})\right) dx,$$

$$= \frac{E_p}{1000}\mathcal{D}_{\mathrm{gm}}(p,q) + \frac{E_p}{1000}\log\frac{E_p}{E_q} - \frac{E_p}{1000} + \frac{E_q}{1000}. \quad (9)$$

The KL divergence is not a symmetrical quantity, that is to say $\mathcal{D}_{\mathrm{gen}}(\tilde{p},\tilde{q}) \neq \mathcal{D}_{\mathrm{gen}}(\tilde{q},\tilde{p})$. In order to use the KL divergence for a distance measure in cluster analysis, we adopt the symmetrized KL divergence, $\mathcal{D}^{\mathrm{ELE}}_{\mathrm{symm}}$, given by

$$\mathcal{D}^{\mathrm{ELE}}_{\mathrm{symm}}(\tilde{p},\tilde{q}) = \frac{\mathcal{D}_{\mathrm{gen}}(\tilde{p},\tilde{q})+\mathcal{D}_{\mathrm{gen}}(\tilde{q},\tilde{p})}{2}. \quad (10)$$

A distance matrix $\boldsymbol{\mathcal{D}}^{\mathrm{ELE}}_{\mathrm{symm}}$ for the clustering is composed the symmetrized KL divergences. The symmetrized KL divergence for DHW demand $\mathcal{D}^{\mathrm{HW}}_{\mathrm{symm}}$, and a distance matrix $\boldsymbol{\mathcal{D}}^{\mathrm{HW}}_{\mathrm{symm}}$ are also calculated in the same manner.

3.3. Hierarchical Clustering

The hierarchical clustering analysis uses a distance matrix, $\boldsymbol{\mathcal{D}}$, with the KL divergence of both non-HVAC electricity and DHW demands as the distance measure between clusters by Ward's method [9]. Because both distance matrices $\boldsymbol{\mathcal{D}}^{\mathrm{ELE}}_{\mathrm{symm}}$ and $\boldsymbol{\mathcal{D}}^{\mathrm{HW}}_{\mathrm{symm}}$ are calculated independently until this point, they are normalized by dividing by the median of each $\boldsymbol{\mathcal{D}}^{\mathrm{ELE}}_{\mathrm{symm}}$ and $\boldsymbol{\mathcal{D}}^{\mathrm{HW}}_{\mathrm{symm}}$ in order to compute the sum of the two distance matrices. The distance matrix, $\boldsymbol{\mathcal{D}}$, which sums the two kinds of symmetrized KL divergence, is given by:

$$\boldsymbol{\mathcal{D}} = \frac{\boldsymbol{\mathcal{D}}^{\mathrm{ELE}}_{\mathrm{symm}}}{\mathrm{Median}(\boldsymbol{\mathcal{D}}^{\mathrm{ELE}}_{\mathrm{symm}})} + \frac{\boldsymbol{\mathcal{D}}^{\mathrm{HW}}_{\mathrm{symm}}}{\mathrm{Median}(\boldsymbol{\mathcal{D}}^{\mathrm{HW}}_{\mathrm{symm}})}, \quad (11)$$

where "Median" represents the median of the matrix. Demand is classified into 16 clusters for each group by the hierarchical clustering method. The reason for 16 clusters is because we assume DHW demand patterns vary widely while non-HVAC electricity demand patterns do not vary widely. In other words, 2^4=16 clusters represent the combination of the four existing or non existing DHW demand peaks, which are morning, noon, evening and midnight.

4. Optimization Model

The clusters, which are classified in the previous section, are evaluated relative to the optimal operation of each energy system. The main consideration is the relationship between the clustered demand time-series data and the primary energy consumption of each energy system, the PEFC-CGS and the HP-S. Each system is compared to the reference system: a conventional combination of a condensing gas boiler and electricity purchased from the grid. A optimal operational planning method for cogeneration systems with thermal storage was proposed by Yokoyama et al. [10]. Schematic diagrams with the specifications [3] of the PEFC-CGS, the HP-S and the C-S are shown below. The parameters in the model are taken up from catalog values. If measured values are available, model parameters are identified from them. This problem is formulated as a Mixed Integer Linear Programming (MILP) problem. The models were coded by the algebraic modeling language AMPL version 12.1 [11] as MILP, and were solved by the general optimization solver CPLEX version 12.1 [12].

4.1. Objective Function

The objective function to be minimized is the daily primary energy consumption calculated from summation of purchased electricity and gas consumption multiplied by each primary energy

conversion factor. In particular, the primary energy consumption of purchased gas is converted by higher heating value of 45 MJ/m^3 [13]. The primary energy conversion factors of electricity mean all of the conversion efficiency of input fuel between thermal power plants and end users. In other words, they mean transmission loss, the efficiency of thermal power plant and so on. The primary energy conversion factor of purchased electricity in the daytime is 9.97 MJ/kWh [14], and the primary energy conversion factor of purchased electricity in the nighttime is 9.28 MJ/kWh [14]. The objective function P, which is the daily operating cost at the viewpoint of the primary energy consumption, is given by

$$\text{Minimize } P = \Sigma_{t=1}^{T} f(x_t)\delta t, \quad (12)$$

where $t = 1, \dots, T$ represents the time index. T is the number of time periods. The sampling period, δt, is 30 minutes. One day is discretized to $T = 48$ terms. We stack optimal solutions and operations for each day to evaluate the characteristics of the energy systems.

4.2. Constraints

A T-dimensional vector $\mathbf{x} \equiv (x_1, \dots, x_T)$ of continuous variables represents the energy flow, a T-dimensional vector $\mathbf{z} \equiv (z_1, \dots, z_T)$ of binary variables represents the start-stop status of each device in each term. The linear equality, h, corresponds to the energy balance of the system. The inequality, g, corresponds to a special case for mitigating the strict energy balance. This inequality means loss of heat due to transport, and is introduced in order to relax the computational load.

$$\text{Subject to } h(x_{t-1}, x_t, z_{t-1}, z_t) = 0,$$

$$g(x_t, z_t) > 0,$$

$$z_t \in \{0,1\}. \quad (13)$$

4.3. CO_2 Heat Pump System (HP-S)

As shown in Fig. 4, the HP-S consists of two main parts: the heat pump (HP) unit, which is operated with CO_2as the heat-transfer medium, and the thermal storage tank (HW tank), which has a capacity of 370 liters. The rated hot-water output of the HP unit is 4.5 kW. The Coefficient of Performance (COP) of the HP unit is assumed to be a function of the hot water outlet temperature and ambient temperature [15]. Hot water is stored by the HP-S in the thermal storage tank at nighttime, using the cheaper electricity available then. The thermal storage tank has to match the heat quantities at the beginning and end of the day.

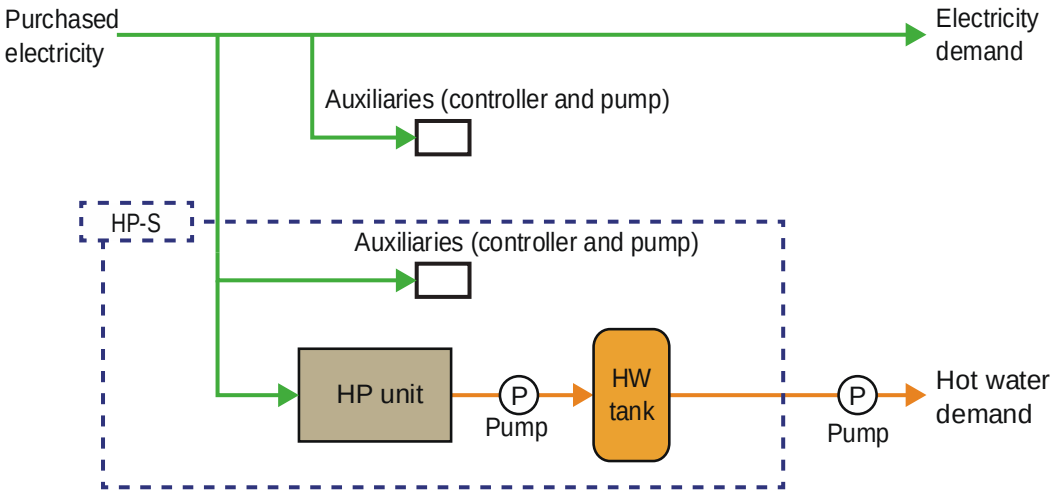

Fig. 4. HP-S.

4.4. Polymer Electrolyte Membrane Fuel Cell Co-Generation System (PEFC-CGS)

As shown in Fig. 5, the PEFC-CGS consists of four main parts: the polymer electrolyte membrane fuel cell (PEFC) unit, the thermal storage tank, which has a capacity of 200 liters, the auxiliary boiler, which has an 83% conversion efficiency (lower heating value of the fuel: LHV), and the electric heater (H), which has a 95% conversion efficiency to hot water. Electricity demand is supplied from the grid and the PEFC unit. Because reverse flow of electricity from a CGS to the grid is not allowed in Japan, surplus electricity produced by the CGS is supplied to the electric heater to prevent reverse flow to the grid. The rated hot water output of the PEFC unit is 1.0 kW (100% load), which is smaller than the output of the HP unit. The DHW demand is supplied from the auxiliary boiler, in case of supply shortages of the PEFC unit and the thermal storage tank. The relationship between the output of the PEFC unit and gas consumption identified piecewise-linear function based on measured data, as shown in Fig. 6. Table 2 shows the partial load efficiency of the PEFC unit. The rated electricity output is 700 W. At rated load, the overall efficiency is 50.0+35.0=85.0%, the heat-to-power ratio of the rated output is 50.0/35.0=1.43. The minimum electricity output is 0.25 kW (35.7% load), and the heat-to-power ratio of the output is 30.0/30.0=1.0. When starting up, the PEFC-CGS has the following three requirements: 60 minutes, 0.5 kWh of electricity consumption, and 0.04 Nm^3 of gas consumption.

Table 2. Partial load performance of PEFC unit.

Load factor %	35.7	71.4	100
Electricity power output kW	0.25	0.50	0.70
Electricity power efficiency (LHV) %	30.0	34.0	35.0
Thermal efficiency (LHV) %	30.0	45.0	50.0

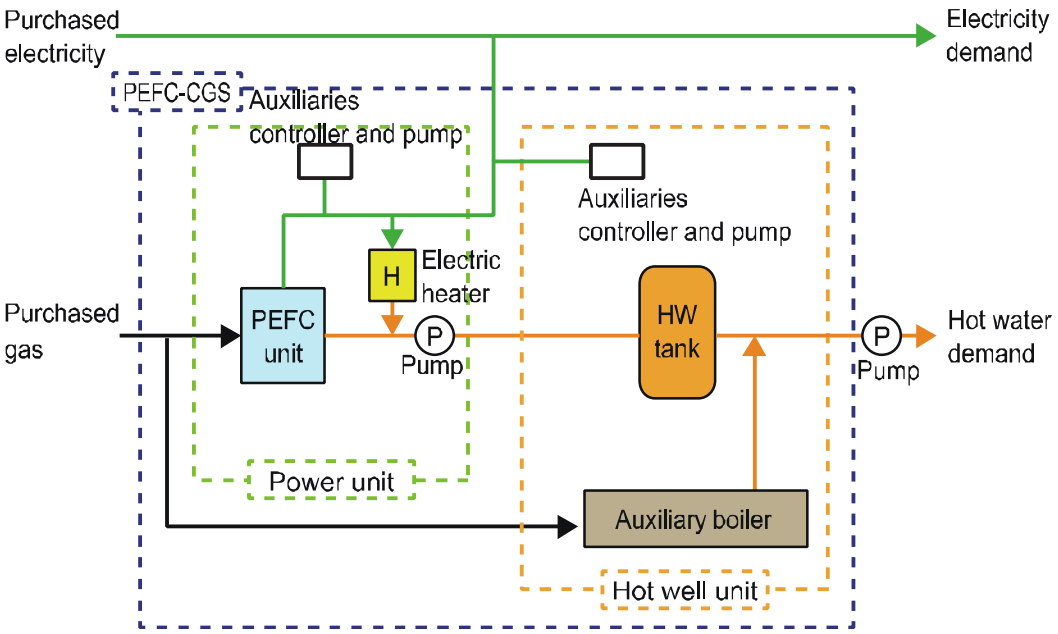

Fig. 5. PEFC-CGS.

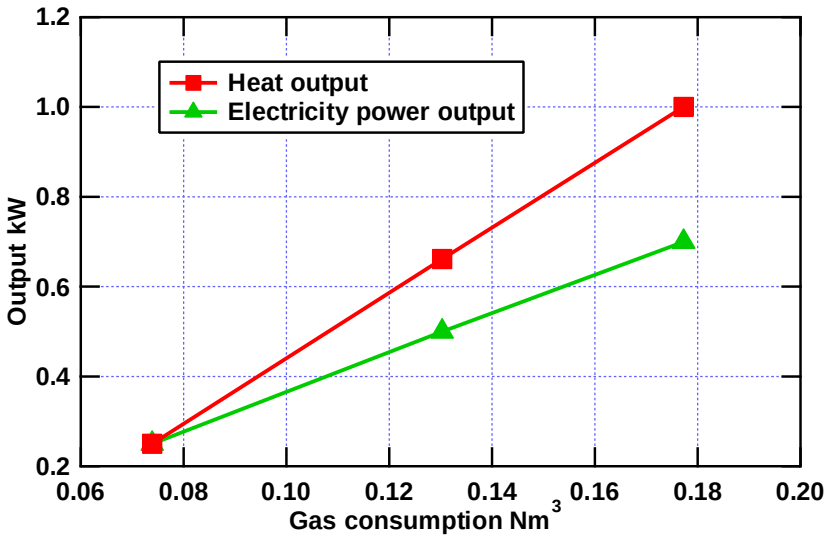

Fig. 6. Partial load characteristics of PEFC unit.

4.5. Conventional System (C-S)

Figure 7 shows the reference system: a condensing gas boiler, which has a 92% conversion efficiency (LHV), with electricity from the grid. It has no thermal storage tank. DHW demand is supplied from the boiler just in time. Electricity demand is supplied from the grid only.

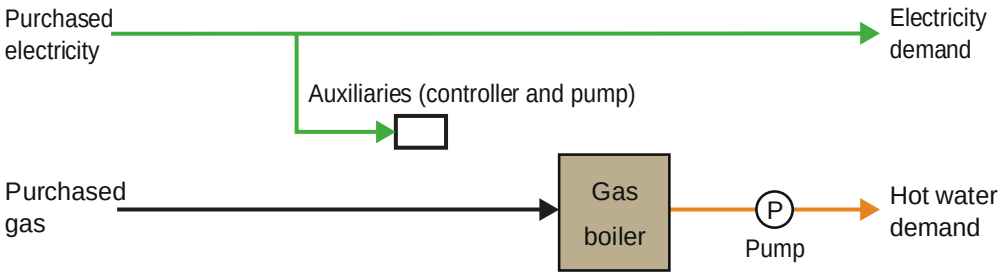

Fig. 7. C-S.

5. Numerical Results

5.1. Optimal Operation

In order to compare the PEFC-CGS and the HP-S, we introduce an index, $\varphi_{\mathrm{X}}^{\mathrm{ene}}$, representing the primary energy reduction ratio.

$$\varphi_{\mathrm{X}}^{\mathrm{ene}} = \frac{P_{\mathrm{cs}} - P_{\mathrm{X}}}{P_{\mathrm{cs}}} \times 100, \qquad (14)$$

where subscript X represents the primary energy consumption of each system, and subscript cs represents the primary energy consumption of the C-S. This index, $\varphi_{\mathrm{X}}^{\mathrm{ene}}$, which is called the primary energy reduction ratio, represents the difference between the two optimal solutions, the primary energy consumption of each system. Figure 8 shows the distribution of the daily primary energy reduction ratio. The peak of the distribution for the PEFC-CGS, which is the blue line, is shifted to the negative side relative to the peak of the distribution of the HP-S, which is the red line. As shown in Fig. 8, for the average of all 26307 days, the primary energy reduction ratio of the HP-S is 9.88%, which is shown by the red dotted line. The primary energy reduction ratio of the PEFC-CGS is 5.64%, which is shown by the blue dotted line. One of the dominant factors, the negative primary energy reduction ratio, is the hot water supplied by the auxiliary boiler on the PEFC-CGS. This is because the efficiency of the auxiliary boiler of the PEFC-CGS is inferior to that of the condensing gas boiler of the C-S. There are two possible cases: the PEFC-CGS operation is ineffective because

of lower DHW demand, or higher DHW demand is supplied from the auxiliary gas boiler in addition to the PEFC unit. In these cases, the characteristics of the PEFC-CGS don't match the demand, because of lower DHW demand for the operations of the PEFC-CGS over an entire day.

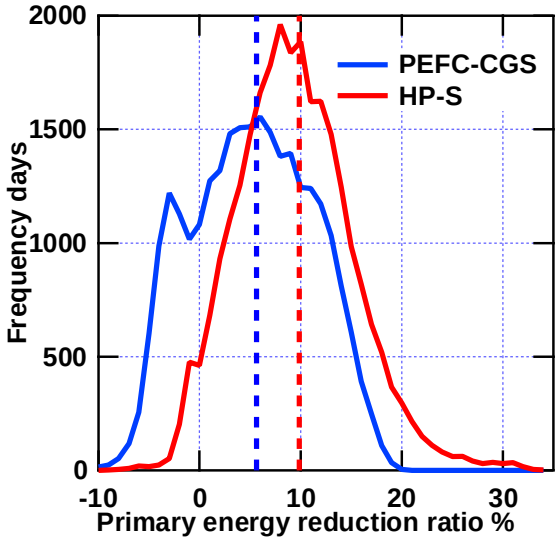

Fig. 8. Distribution of primary energy reduction ratio in optimal operation.

5.2. Extraction of Demand Patterns

Six sets of groups of demand were defined in terms of heat-to-power ratio. Because of space limitations, the following section shows the numerical results of Group-D, which matches the characteristics of the PEFC-CGS output. Figures 9 to 10 show the demand patterns clustered into 16 groups from Group-D. The bar charts, which are shown in Figs. 9 and 10, represent the average demand of each term in each cluster. The dotted lines shown in Figs. 9 and 10 represent the demand ± standard deviation on average of each term.

It is confirmed that the basic demand patterns are extracted by the hierarchical clustering with the generalized KL divergence. As shown in the second row and the 1st, 4th, 5th, and 7th columns in Table 3, four basic demand patterns, which have about 10% of the elements in each cluster, are recognized. As shown in Figs. 9 (a), (d), (e), and (g), clusters show the peak of DHW demand at evening. Others, Cluster 12 shows the two peaks of DHW demand: at morning and evening, as shown in Fig. 10 (l). Cluster 9 shows the three peaks of DHW demand: at morning, evening, and midnight, as shown in Fig. 10 (i).

On average in Group-D, the primary energy reduction ratio of the PEFC-CGS is 11.07%, and that of the HP-S is 13.01%. From the viewpoint of the primary energy reduction ratio of the PEFC-CGS, there is 11.07-5.64=5.43% difference between the average in the 4920 days of Group-D and the average of all 26307 days. Therefore, it is confirmed that the heat-to-power ratio defined by the relationship between non-HVAC electricity and DHW demand has an influence on the primary energy reduction ratio of the PEFC-CGS.

It is confirmed that the distributions of the primary energy reduction ratio differ for each cluster, as shown in Figs. 9 and 10. It means the amount of daily demand and demand patterns have an effect on the primary energy reduction ratio of each system. As shown in the sixth-to-last and third-to-last rows and the 1st, 2nd, 3rd, 9th, 11th, 12th, 13th, and 16th columns in Tables 3 and 4, the primary energy reduction ratio of the PEFC-CGS is better than that of the HP-S at Clusters1, 2, 3, 9, 11, 12, 13, and 16, on average in each cluster. As shown in the second row and those same columns in Tables 3 and 4, these clusters have 10.28+4.04+4.49+2.93+5.63+4.65+6.04+2.46=40.52% of the elements of Group-D.

As shown in Figs. 9 and 10, DHW demand and the standard deviations vary widely by hour on average for each term in each cluster. On the other hand, as shown in Figs. 9 and 10, there is a certain amount of non-HVAC electricity demand throughout the day. As shown in the hot water demand row and the electricity demand row in Tables 3 and 4, DHW demand standard deviations are larger than that of non-HVAC electricity, on average in each cluster.

As shown in the third-to-last row and the 7^{th} column in Table 3, 6.05% of Cluster 7, which has the minimum daily non-HVAC electricity and DHW demand, is at the worst primary energy reduction ratio of the PEFC-CGS on average in each cluster for Group-D. As shown in the last row and the 16^{th} column in Table 4, 15.15% of Cluster 16, which has the maximum daily non-HVAC electricity and DHW demand, is at the best primary energy reduction ratio of the PEFC-CGS on average in each cluster for Group-D.

Thus, in overall, because of a high degree of uncertainty of demand, it is difficult to exercise better performance of the PEFC-CGS than that of the HP-S.

6. Conclusion

Demand time-series data are categorized by means of a hierarchical clustering method using a statistical pseudo-distance. The statistical pseudo-distance is calculated using the generalized KL divergence with the GMD fitted to the demand time-series data of non-HVAC electricity and DHW demand from 26307 days of data, measured in Japan. The demand patterns are useful means to compare the performance of conventional and non-conventional systems. We formulated an analytical framework of the characteristics of the energy systems, and of the characteristics of the demand profiles. The following main results were obtained.

1. Basic demand patterns are extracted by the proposed method.
2. Factors which are at least associated with the primary energy reduction ratio of the PEFC-CGS, are heat-to-power ratio, demand patterns, and the amount of daily demand.
3. The average primary energy reduction ratio of the PEFC-CGS is better than that of the HP-S at Clusters1, 2, 3, 9, 11, 12, 13, and 16.
4. These clusters contain 40.52% of the elements of Group-D.
5. The primary energy reduction ratio of the PEFC-CGS varied from 6.05% to 15.15% on average for each cluster of Group-D.

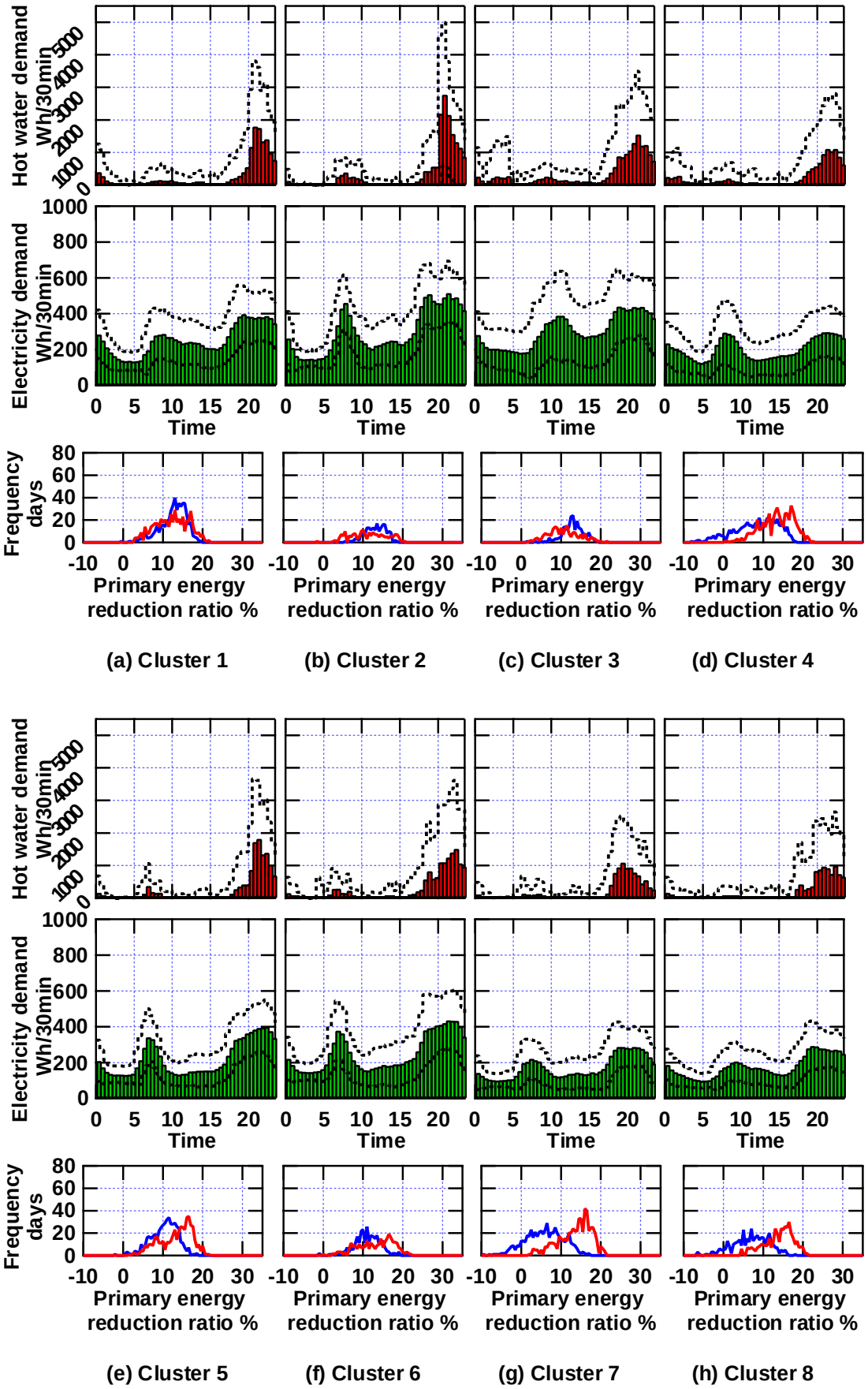

Fig. 9. Clusters in Group-D (1/2).

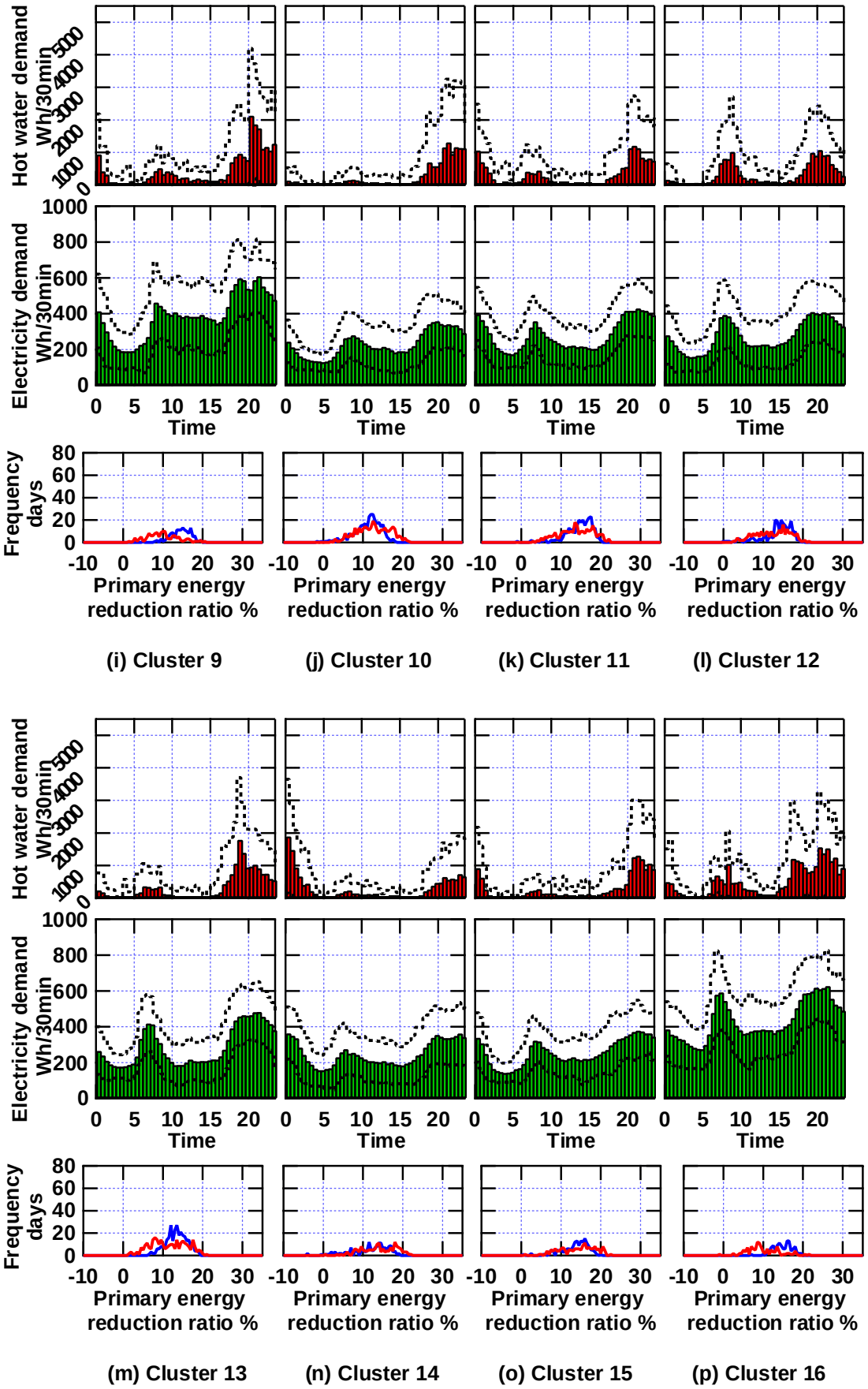

Fig. 10. Clusters in Group-D (2/2).

Table 3. Clustering data of Group-D (1/2).

Group-D			Cluster							
Total elements		4920	1	2	3	4	5	6	7	8
Number of elements		days	506	199	221	532	491	296	566	392
		%	10.28	4.04	4.49	10.81	9.98	6.02	11.50	7.97
Hot water demand	Mean	Wh/30min	307.64	371.36	365.04	254.54	269.04	305.82	207.81	216.61
	Median	Wh/30min	0.00	0.00	0.00	0.00	0.00	0.00	0.00	0.00
	Maximum	Wh/30min	11408.58	8649.48	11542.30	10354.05	10242.69	10458.39	9688.55	10262.62
	Minimum	Wh/30min	0.00	0.00	0.00	0.00	0.00	0.00	0.00	0.00
	Standard deviation		887.42	967.17	987.21	799.92	823.45	952.94	701.63	764.48
Electricity demand	Mean	Wh/30min	258.28	304.46	307.80	207.96	226.84	255.88	176.05	182.39
	Median	Wh/30min	231.46	265.35	264.51	170.44	179.47	203.58	142.14	154.57
	Maximum	Wh/30min	1651.77	1329.62	1909.49	1253.07	1188.22	1326.76	1347.63	1036.94
	Minimum	Wh/30min	28.98	38.78	22.67	11.09	28.11	33.34	7.62	15.28
	Standard deviation		147.01	178.61	192.89	134.92	141.08	162.45	112.70	108.97
Primary energy reduction ratio of the HP-S	Mean	%	12.49	11.66	10.90	13.71	13.50	13.46	13.82	14.14
	Maximum	%	21.55	20.53	21.81	22.52	21.63	22.00	21.39	21.45
	Minimum	%	3.09	-1.33	2.35	0.50	1.99	0.46	2.14	4.64
Primary energy reduction ratio of the PEFC-CGS	Mean	%	12.86	13.37	13.15	8.46	10.59	11.28	6.05	7.16
	Maximum	%	19.55	18.52	19.45	18.21	18.76	19.46	17.32	18.17
	Minimum	%	-0.43	5.67	1.62	-7.92	-1.78	-0.76	-9.43	-6.43

Table 4. Clustering data of Group-D (2/2).

Group-D			Cluster							
Total elements		4920	9	10	11	12	13	14	15	16
Number of elements		days	144	318	277	229	297	163	168	121
		%	2.93	6.46	5.63	4.65	6.04	3.31	3.41	2.46
Hot water demand	Mean	Wh/30min	484.62	274.72	349.65	334.48	350.71	313.06	312.74	552.09
	Median	Wh/30min	50.00	0.00	0.00	0.00	0.00	0.00	0.00	137.94
	Maximum	Wh/30min	10841.97	10046.06	9302.10	11358.01	9333.45	9282.30	9819.48	9711.63
	Minimum	Wh/30min	0.00	0.00	0.00	0.00	0.00	0.00	0.00	0.00
	Standard deviation		1020.72	933.00	822.97	818.57	833.86	781.56	849.59	952.34
Electricity demand	Mean	Wh/30min	391.88	234.04	285.96	280.69	294.44	252.33	261.09	439.16
	Median	Wh/30min	361.68	200.75	259.31	251.81	251.20	224.63	237.76	415.29
	Maximum	Wh/30min	1643.08	1310.84	1493.83	2148.11	1429.03	1297.27	1469.93	1799.64
	Minimum	Wh/30min	8.85	20.58	35.68	28.51	26.16	28.84	35.33	61.22
	Standard deviation		215.91	137.40	151.16	165.90	168.51	150.18	136.88	197.55
Primary energy reduction ratio of the HP-S	Mean	%	10.15	12.81	13.93	12.55	11.64	14.22	14.43	10.14
	Maximum	%	20.52	21.73	22.38	21.87	21.48	22.26	22.58	21.54
	Minimum	%	1.72	2.44	3.41	2.58	1.57	0.57	1.04	-0.95
Primary energy reduction ratio of the PEFC-CGS	Mean	%	14.66	11.34	14.81	13.77	13.68	11.84	13.84	15.15
	Maximum	%	19.87	18.09	20.34	20.28	19.41	19.16	20.08	19.91
	Minimum	%	5.01	-1.14	-0.62	0.38	6.68	-3.96	0.58	7.18

Acknowledgement

The authors acknowledge Mr. H.Shen and Associate Professor H.Hino of Murata Laboratory of Waseda University for technical suggestions about implementation using the R language. Part of this work is supported by a Strategic Research Foundation Grant-aided Project for Private Universities grant from MEXT(2010). The authors would like to acknowledge the support of the "Distributed Autonomous Urban Energy Systems for Mitigating Environmental Impact" project of

Osaka University. This research was conducted under Optimal Planning of Energy Supply Systems for Various Buildings, 09P05 at RISE, Waseda University.

Nomenclature

d number of dimensions
$\mathcal{D}$ distance measure
$\boldsymbol{\mathcal{D}}$ distance matrix
E non-HVAC electricity demand, kWh/day
f, g a probability density function
$\tilde{f}, \tilde{g}$ Gaussian probability density function
k discretized index
K number of discrete value
P primary energy consumption, MJ/day
$p, \tilde{p}, q, \tilde{q}$ Gaussian mixture distribution
Q DHW demand, kWh/day
R heat-to-power ratio
t discretized time index
T number of time index
$\mathbf{x}$ vector of continuous variables
$\mathbf{z}$ vector of binary variables

Greek symbols

δt sampling period, hour
$\boldsymbol{\theta}$ unknown parameters
$\boldsymbol{\mu}$ mean vector
π mixing coefficient
$\boldsymbol{\Sigma}$ covariance matrix
φ primary energy reduction ratio, %

Subscripts and superscripts

a,b component index of the Gaussian mixture distribution
CS conventional system
ELE non-HVAC electricity demand
ene primary energy consumption
$\tilde{f}, \tilde{g}, p, q$ a probability density function
g Gaussiandistribution
gen generalized
gm Gaussian mixture distribution
HW hot water demand
KL KL divergence
symm symmetrized
X each system

References

[1] Jyukankyo Resarch Institute Inc., (Ed.), 2009. Household energy handbook, 2009th ed.

[2] Hashimoto, K., Takahashi, T., Yoshiha, T., Saikawa, M., Hamamatsu, T., 2001. Evaluation of energy saving and environment potential about new domestic energy systems. – Comparison of hot water supplying and air-conditioning electric heat pumps, and of PEFC co-generation, with consideration to daily and yearly estimated demand curve. –. Central Research Institute of Electric Power Industry, No. W00021.

[3] Yoshida, A., Inagaki, K., Amano, Y., Ito, K., Hashizume, T., 2011. Comparative Evaluation of Residential Energy Systems to Reduce CO_2 Emissions, in: Proceedings of WEC 2011. pp. 2-9.

[4] Hershey, R.J., Olsen, A.P., 2007. Approximating The Kullback Leibler Divergence Between Gaussian Mixture Models, in: Proceedings of the International Conference on Acoustics, Speech, and Signal Processing 2007. pp. 317-320.

[5] Shen, H., Hino, H., Murata, N., Wakao, S., 2011. Extraction of Basic Patterns of Household Energy Consumption, in: Proceedings of the International Conference on Machine Learning and Applications 2011. pp. 275-280.

[6] Banerjee, A., Merugu, S., Dhillon, I.S., Ghosh, J., 2005. Clustering with Bregman Divergences. Journal of Machine Learning Research 6, 1705-1749.

[7] Dempster, A.P., Laird, N.M., Rubin, D.B., 1977. Maximum likelihood from incomplete data via the EM algorithm. Journal of the Royal Statistical Society 39, 1-38.

[8] Fraley, C., Raftery, A.E., 2010. MCLUST Version 3 for R : Normal Mixture Modeling and Model-Based Clustering, Office.

[9] Ward, H.J., 1963. Hierarchical Grouping to Optimize An Objective Function. Journal of the American Statistical Association 58, 236-244.

[10] Yokoyama, R., Ito, K., 1993. Optimal Operational Planning Method for Cogeneration Systems with Thermal Storage. Journal of the Japan Society of Mechanical Engineers 59, 1817-1823.

[11] Fourer, R., Gay, M.D., Kernighan, W.B., 2003. AMPL: A Modeling Language for Mathematical Programming, Second Edition, 2nd ed. Curt Hinrichs.

[12] IBM ILOG CPLEX Optimizer [WWW Document], n.d. . URL http://www-01.ibm.com/software/integration/optimization/cplex-optimizer/

[13] OSAKA GAS Co. [WWW Document], n.d. . URL http://www.osakagas.co.jp/kankyo/gas/03.html

[14] Law Concerning the Rational Use of Energy in Japan [WWW Document], 2010. . Ministry of Economy, Trade and Industry. URL http://law.e-gov.go.jp/htmldata/S54/S54F03801000074.html

[15] Yokoyama, R., Wakui, T., Kamakuri, J., Takemura, K., 2008. Performance Analysis of a CO_2 Heat Pump Water Heating System Under a Daily Change in a Standardized Demand, in: Proceedings of ECOS 2008. pp. 391-399.

A Model for Simulation and Optimal Design of a Solar Heating System with Seasonal Storage

Gianfranco Rizzo[a]

[a] *Department of Industrial Engineering, University of Salerno,Fisciano (SA), Italy, grizzo@unisa.it*

Abstract:

A thermo-economic model for the simulation and optimization of a Central Solar Heating Plant with Seasonal Storage (CSHPSS) is presented. The model, written in Matlab, is used to investigate the effects of different design variables on thermal performance and cost. Daily and seasonal variations of solar irradiation at different latitudes are considered, and an original approximate model for thermal stratification is included. The simulation model has been also integrated with a non-linear constrained optimization procedure, in order to determine the optimal choice of design variables for different locations and operating conditions.

Keywords:

Solar Thermal Plant, Seasonal Storage, Model, Optimization

1. Introduction

The perspective depletion of fossil fuels and the concerns about climate changes due to carbon dioxide emission in the atmosphere are strongly stimulating the recourse to renewable energy sources and to energy savings [1]. European Community [2] and governments are committed to achieve significant improvements in terms of renewable share of final energy (Fig. 1).

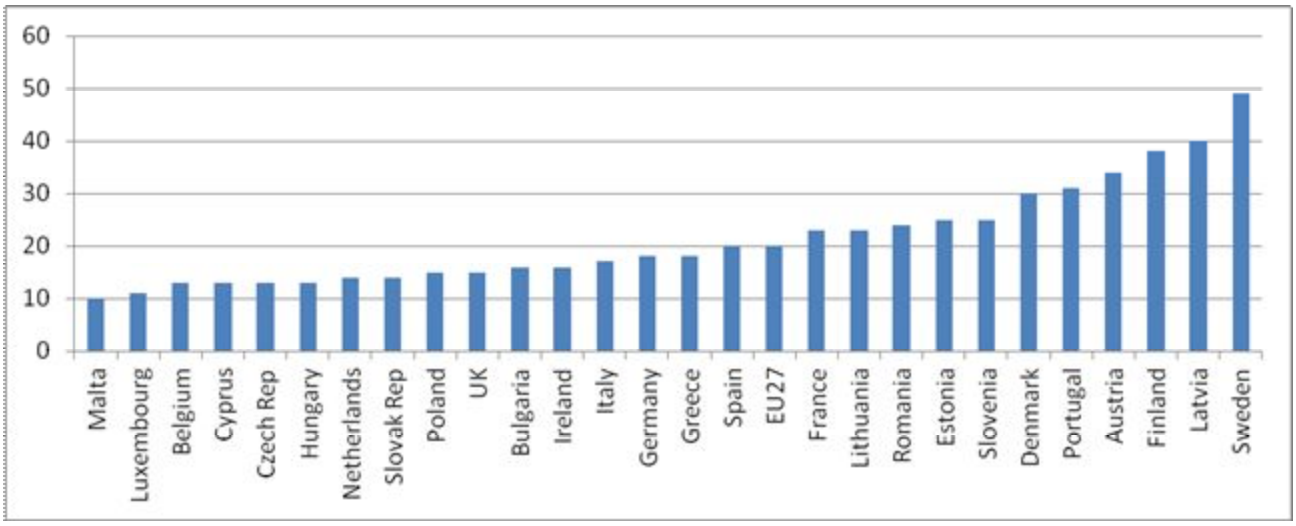

Fig. 1. EU Renewable Shares, Targets for 2020

Thermal uses represent a relevant fraction of the energy consumption. Solar thermal power is largely used in many countries, particularly in China, to cover this energy demand (*Fig. 2*). At the end of 2010, a thermal installed power of 185 GW for solar collectors for hot water/space heating was already in existence, and other 30 GW were installed during 2010 [1]. Solar plants can provide part of the thermal power needed for space heating, but they have an intrinsic drawback, since most of the solar power would be available during summer, whereas the demand for thermal power is at its minimum level. In this case, most of the thermal power produced during summer would be wasted.

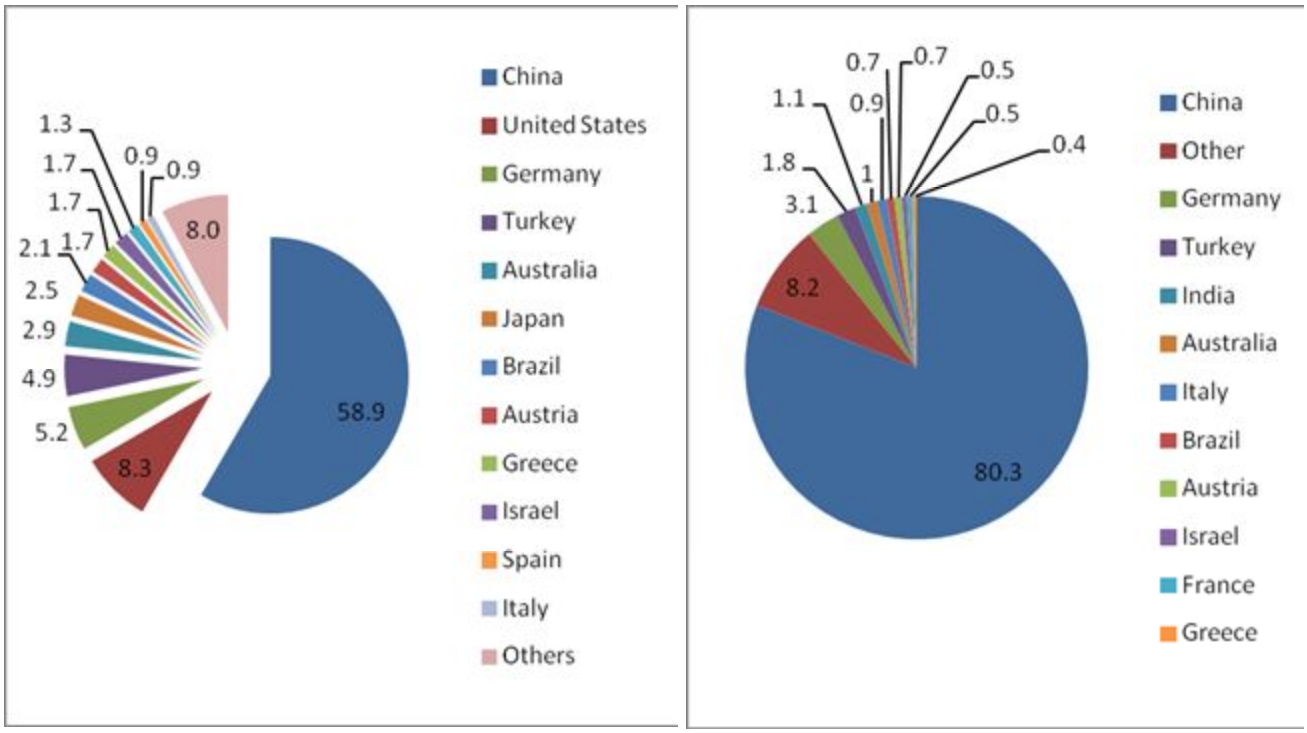

Fig. 2. *Solar heating, Top Countries, 2009: Percent Existing (left) [3] and Added Capacity (right) [1]*

The usage of solar-cooling may partly overcome this problem, since the exceeding thermal power could be used for refrigeration and air-conditioning through absorption cooling plants. This solution, anyway, is limited by the relatively high cost and low efficiency of such plants. Moreover, there are many cases in which air-conditioning is not needed: significant examples are represented by schools, normally closed during summer. In these cases, a possible solution is resorting to Central Solar Heating Plant with Seasonal Storage (CSHPSS).

In next chapter, a review of the systems for seasonal heat storage is presented, and the modeling approaches are discussed. Then, a model for simulation and optimization of a thermal solar plant with a seasonal water storage is presented, and some results are discussed.

2. Seasonal Heat Storage Systems

In the last decades, several pilot projects on CSHPSS plants have been developed, mainly in Central and Northern Europe. Attention was particularly given to the costs involved in heat storage, since economic feasibility is the most critical factor for this technology.

2.1. Literature review

A technical assessment of the different technologies for solar thermal energy storage is presented in [4]. Both sensible heat and latent heat storage technologies can be adopted. Storage systems are usually classified as “Water storage”, “Earth storage”, “Ground diffusive storage” and “Aquifer storage” (Fig. 3) [5] [6] [7].

Water Storage use tanks constructed from concrete, steel or fiberglass. The thank is located underground to benefit from the insulating and structural properties of the surrounding ground, and to minimize the above-ground space requirements. Insulation is applied to any above-ground surface of the tank [6][8].

Earth Storage (or Pit) Systems are essentially large artificially-dug holes usually filled with water and gravel. They are one of the most popular type of seasonal storage systems, due to low cost and

ease of construction. The gravel provides structural support but reduces the effective storage capacity compared to water alone. An insulated floating cover completes the storage unit.

In Ground Diffusive Storage (or Borehole Systems), heat is stored directly in the ground. Heat exchangers are installed in boreholes drilled in ground that is suitable for heat storage [9]. These bores can be between 30-100 m in depth and 100-150 mm in diameter. The heat exchangers are U-shaped tubes, providing an inlet and outlet for the heat transfer fluid, which is usually water. Insulation is installed at the ground level to minimize heat losses from this top surface. Studies have also been carried out on use of ground source heat pumps [10].

In Aquifer Storage Systems, a naturally-occurring water-saturated media (usually sand) is used as the storage medium. Because the natural occurrence of such bodies in the right location is uncommon, the system is not as diffused as the previous three types.

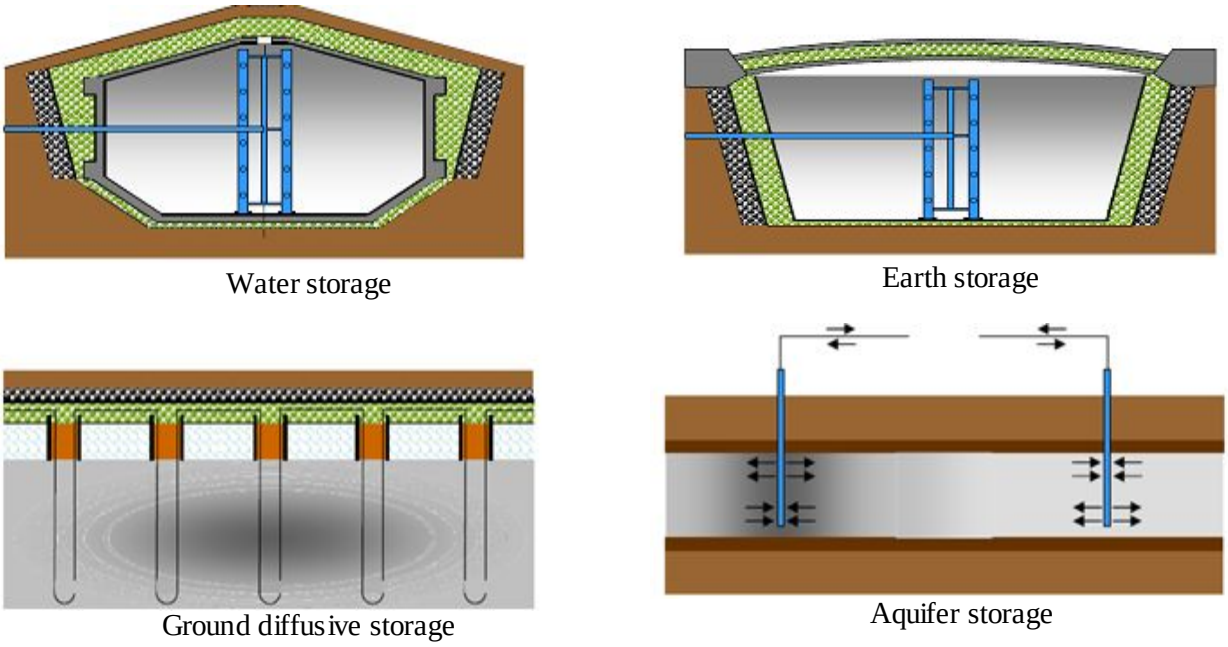

Fig. 3. Schemes of different type of storage systems [14]

For space heating applications, usually low temperature (less than 100°C) sensible heat storage is generally used. Water is the most suitable thermal storage liquid in such temperature range, due to its high thermal capacity, large availability and low cost. Rocks can also be used as a storage medium.

Since the '90s, several pilot and demonstration CSHPSS plants have been built in Germany, within a governmental R&D program. The monitoring of such plants has proved to be well matched with the simulation performed during the design phase. Moreover, no major problems during their construction and operation occurred. In 2003, the cost for solar heating with such systems were, at maximum, twice as high as the conventional heat cost [5]. An accurate study on construction techniques and costs of water seasonal storage, based on three pilot projects in Germany, has been published in 1977 [11]. The cost sharing between the component was studied, and different solutions analyzed and discussed. A unit cost of about 90 €/m^3, including cost for insulation, were estimated for large volume storage (10.000 m^3), while the long term goal was set to about 50 €/m^3. Studies on the techniques to prevent oxygen penetration in the storage were performed, since the storage would be used in direct connection with district heating network. Use of steam cushion and of nitrogen atmosphere was discussed [11].

The thermal performance and economic feasibility of two types of central solar heating systems with seasonal storage in Turkey have been investigated by Ucar and Inalli [12] [13]. The effects of different ground types were studied with a finite element analysis. Pay-back time ranging from 19

to 34 years has been found. A study on a CSHPSS under construction in Cheju Island (Korea) is also available [8]. The plant has been simulated using TRNSYS to predict thermal performances and economic outcomes for two different types of solar collectors (flat plate and vacuum tube). Return of investment ranging from 18 to 30 years resulted by these studies.

2.2. Modelling approaches

In most papers, a simulation approach has been followed, also with a parametric analysis of the main design variables: particularly, storage volume and solar panels area. In some cases, thermal stratification has been considered, also with FEM analysis. In most cases, the simulation has been performed with TRNSYS simulation model [15].

Although TRNSYS includes an optional optimization tool (TRNOPT) that would allow to minimize a cost function [15], there are no studies in literature on CSHPSS performed via optimization analysis. A study on the optimization of a near-zero energy solar home via Genetic Algorithms has been presented [16], but seasonal storage was not investigated. In order to limit the computational time required by the optimization analysis, a simplified (one-zone) modeling approach was used. In case of a seasonal storage, a multi-year simulation is needed in order to reach steady operation. Therefore, there is a need for simplified models realizing a good compromise between precision and computational time, in order to allow their use in an optimization tool. A simplified model of a thermal solar plant with seasonal storage, also considering thermal stratification, is presented in next chapter.

3. Model of Thermal Solar Plant with Seasonal Storage

A simplified analytical model of solar irradiation has been adopted, able to describe seasonal and daily variations of irradiance, and the effects of latitude, also considering real sky conditions.

Two different types of solar collectors have been considered, flat pate and vacuum tube. Their efficiency curves are shown in Fig. 4.

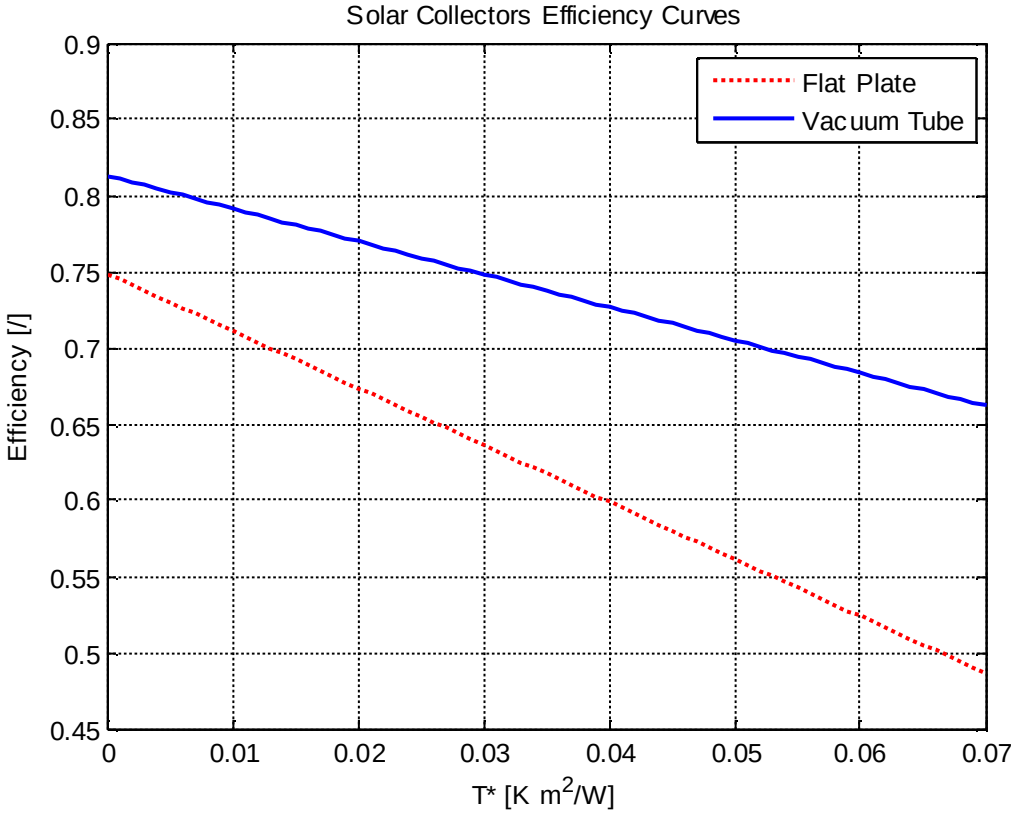

Fig. 4. Solar collector efficiency curves.

A parabolic efficiency curve has been implemented in the model:

$$\eta = \eta_0 + U_1 T^* + U_2 T^{*2} \quad (1)$$

where:

$$T^* = \frac{t_m - t_{amb}}{Irr} \quad (2)$$

The parameters for the two collectors are presented in Table 1. It can be observed that the quadratic terms are zero (Flat Plate) or almost negligible (Vacuum Tube).

Table 1. Parameters for collector efficiency models

Collector type	η_0	U_1	U_2
Flat Plate	0.7486	-3.7465	0
Vacuum Tube	0.8131	-2.16	-0.001

In order to precisely estimate solar collector performance, an analytical model for the time varying value of ambient temperature has been developed, considering sinusoidal variations between daily minimum and maximum temperatures. Daily minimum and maximum temperatures are estimated by linear interpolation from monthly average values, available on-line for many locations [17]. The equations of the solar collector simplified performance model are reported in the Appendix.

Thermal losses are estimated by the following equation:

$$P_{loss} = \frac{\lambda}{L} A_{st} (t_{mean} - t_g) \quad (1)$$

as a function of insulation thickness L, thermal conductivity λ, storage area A_{st}, mean storage temperature t_{mean} and ground temperature t_g. This latter is computed as the yearly average value of ambient temperatures, for each location [17].

3.1. Stratification effects

Thermal stratification occurring in water storage plays an important role in the thermal plant management. Stratification has been studied both in experimental way and numerically [18][19]. Usually, rather complex models are used to describe thermal stratification [15]. Although these models are adequate to perform detailed design analysis of the water storage system, they are not suitable to be integrated in optimization studies, sometimes requiring hundreds or thousands of iterations. Therefore, a different approach is pursued in this paper, consisting in the development of a simple model based on the synthesis of physical data describing the most relevant aspects of thermal stratification (grey-box approach). The model has been developed starting from a detailed study on thermal stratification in water thermal storage of different aspect ratio in static mode, published by Khalifa et al. [18]. The results have confirmed that thermal stratification is maximized at higher aspect ratio (i.e. AR=2), while it is less pronounced at lower aspect ratio (AR=0.5). AR is in this case defined as ratio between height and diameter.

The results obtained with AR=1 are shown in Fig. 5. Temperature values in four subsequent times (a, b, c, d) are shown. For each time frame, the difference ΔT between maximum temperature t_{top} and minimum temperature t_{bottom}, and the mean temperature t_{mean} (computed as the mean value between t_{top} and t_{bottom}) have been computed and plotted in Fig. 6. It can be observed that the relationship between these variables is remarkably linear.

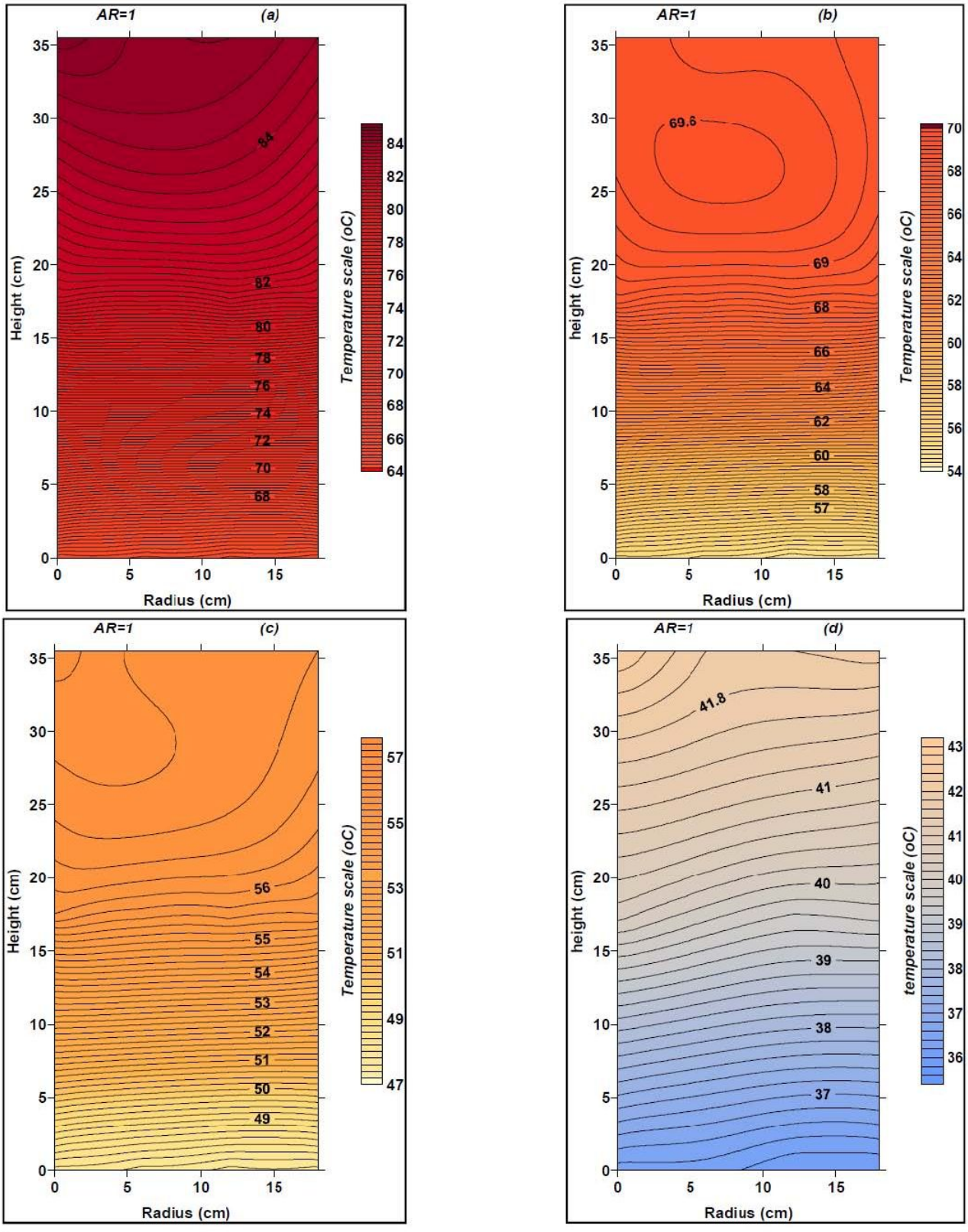

Fig. 5 – Thermal stratification in static conditions in a water storage (Aspect Ratio=1). From [18].

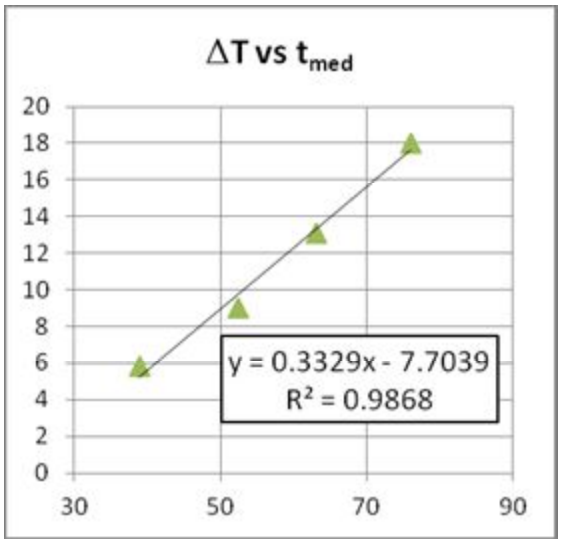

Fig. 6 – Difference between top and bottom temperature vs mean temperature in a water storage [18].

The linear model has been then integrated by further relations, in order to take into account that thermal stratification tends to zero when water mean temperature approaches external temperature t_{min}, or in case it approaches maximum allowed water temperature t_{max}. The model, synthesized in the following equations (2)-(5), is represented in Fig. 7.

$$t_{top} = t_{mean} + \Delta t/2 \tag{2}$$

$$t_{bottom} = t_{mean} - \frac{\Delta t}{2} \tag{3}$$

$$\Delta t = \min\left[(k_1 + k_2 t_{mean});\ 2(t_{max} - t_{mean});\ 2(t_{mean} - t_{min})\right] \tag{4}$$

$$\Delta t \geq 0 \tag{5}$$

The parameters of the linear model k_1 and k_2 in (4) have been identified by linear regression techniques: their values are respectively -7.7039 and 0.3329.

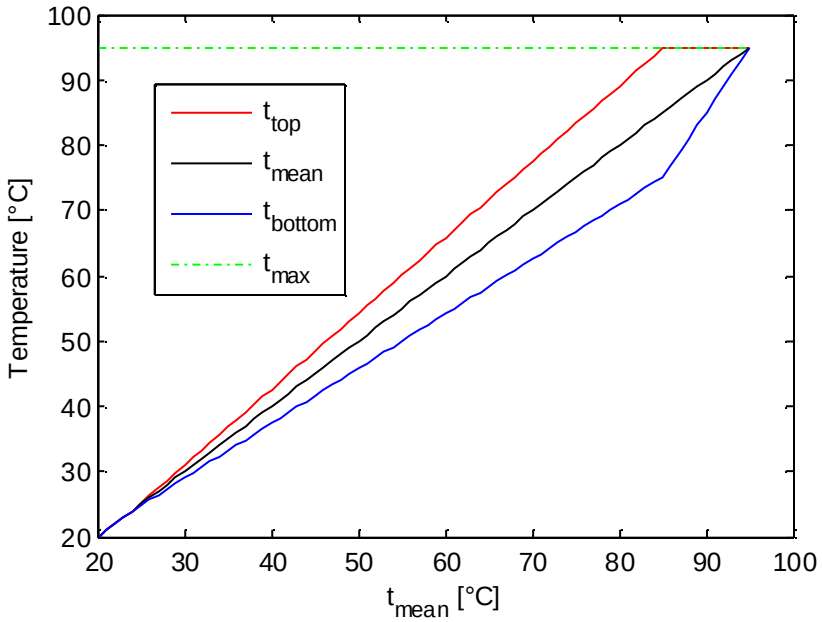

Fig. 7. Thermal stratification model

The model has been validated over the measured data available for a water reservoir of a CSHPSS in Germany [21]. The mean temperature has been computed as the mean of top and bottom measured temperature (red and blue lines). Then, the estimated top and bottom temperatures (red and blue dotted lines) have been computed by means of the model (2)-(5). It can be observed that the matching between measured and computed data is quite satisfactory, suggesting that most of thermal stratification occurring in a typical water reservoir for CSHPSS can be explained considering static effects. Some significant deviations occur in first starting phase, where transient effects may be more relevant. Although this conclusion cannot be generalized, it comes out that the model can be used to make an approximate estimate of thermal stratification in water if a more detailed model is unavailable or cannot be used due to excessive computational time (i.e. for optimization studies).

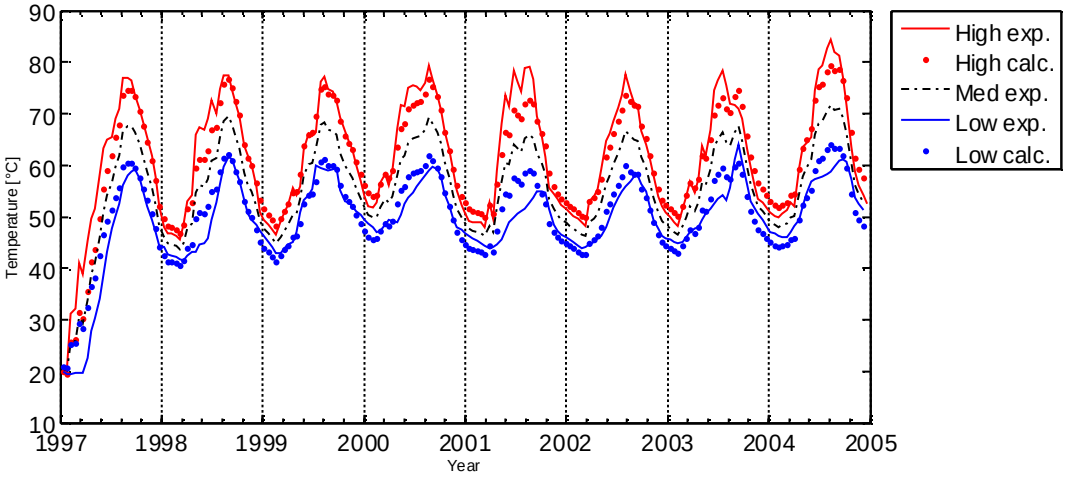

Fig. 8 – Comparison of measured and estimated high and low temperatures in a water storage.

The model is integrated starting from given initial conditions for a number of years, until convergence is reached, in terms of difference between initial and final value of the water storage temperature. The thermal and economic performance is then evaluated with reference to the last year. A variable step 4th order Runge-Kutta method, implemented in the "ode45" routine of Matlab [22], has been used. Preliminary numerical studies were performed in order to set proper values of maximum allowable integration step and of termination criteria, in order to find the best compromise between numerical precision and stability, and computational time. This aspect is particularly relevant, since the model has to be integrated within an optimization procedure, where hundreds of iterations may occur. Computational time is about 50 [s] for a year simulation (CPU Intel® Core™ i3, 4 GB RAM, 3.07 GHz).

4. Simulation results

A parametric analysis has been performed, by varying storage volume V and solar panel area A in a large range of values (A=25÷1000 m^2, V=25÷1000 m^3). The values assumed for the other variables are reported in Table 2. Insulation unit cost is referred to the volume of insulating material. Total insulation cost is then computed considering insulation thickness and area. When reservoir volume increases, the incidence of insulation cost decreases, since the ratio between insulating area and reservoir volume decreases.

Table 2. Data for simulation analysis

Component	Value	Unit Costs	
Solar panel type	Flat plate	Insulation	48 [€/m^3]
Solar panel tilt	40 [deg]	Solar panels	300 [€/m^2]
Insulation thickness	0,25 [m]	Natural gas	0,076 [€/kWh]
Thermal conductivity	0,04 [W/(mK)]	Storage (except insulation)	80 [€/m^3]

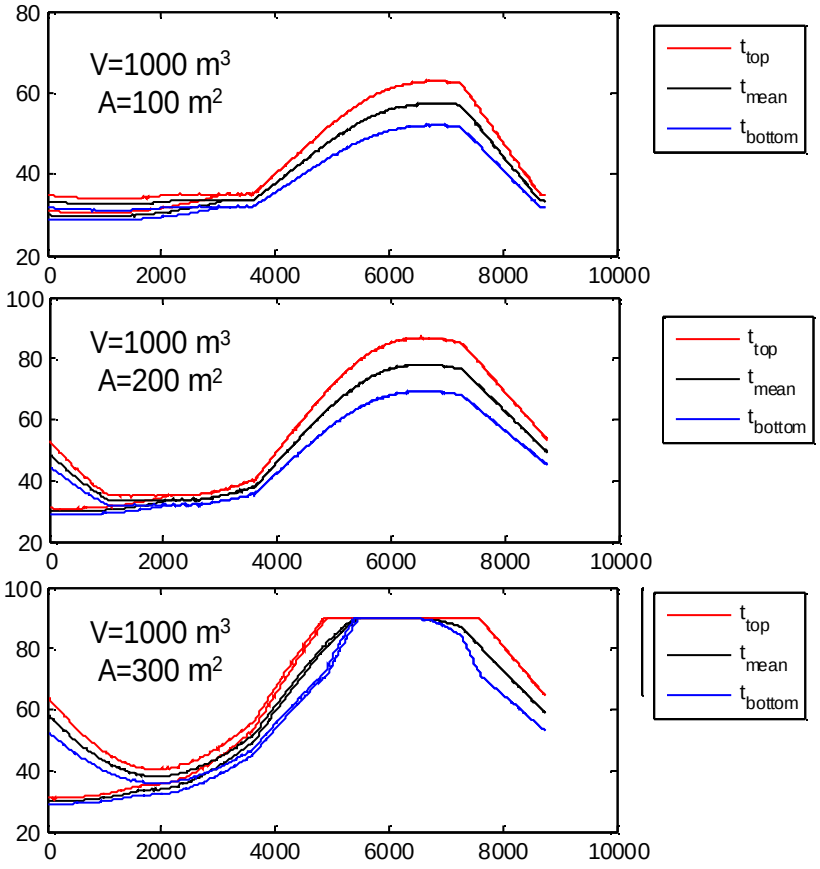

Fig. 9. Simulation analysis. Reservoir temperature [°C] vs time [hours]. Solar surface=100-300 m^2. Reservoir volume=1000 m^3. Collector type: Flat plate. Location: Naples.

Thermal power utilized by the user was assumed to be 100 kW, distributed from 8 AM to 1 PM for six days in a week. The plant is supposed to be off from June 1st to October 31st. A total thermal load of 91,5 MWh/year resulted. More articulated load schedules, also taking into account external temperature effects, can be adopted with minor changes. It is assumed that low temperature space heaters are used. Input and output water temperatures can be varied, to account for different heating systems. In the following computations, the values of 35°C and 30°C were assumed for water flow in and out, respectively.

The graphs presented in Fig. 9 show the storage temperature versus time (in hours) for three different cases, characterized by the same storage volume (1000 m^3) and decreasing solar panel area (300-200-100 m^2). The black, red and blue lines represent respectively the mean, top and bottom water temperature, estimated by the stratification model. Temperature trajectories of both starting year and steady solution are represented in the graphs.

The following figures report the solar fraction (defined as the fraction of the thermal energy demand covered by solar energy) versus storage volume and panel area for all the computed cases. The contour plots of payback (Fig. 10), mean solar collector efficiency (Fig. 11) and storage thermal losses (Fig. 12) are also shown. The solutions at the left of the purple line are characterized by heat dissipation during summer, indicating that storage volume is undersized with regard to solar panel area. This case occurs for the lower graph of Fig. 9 (300 m^2) in fact, during summer part of solar heat must be dissipated, to avoid that the storage temperature exceeds the maximum allowed temperature (90°C). It can be observed that temperature stratification is not present during such phase, since it is assumed that heat from solar panel is added until all the storage is at its maximum allowable temperature, to maximize heat storage. Solar fraction is 100%, in this case (Fig. 10). In the second case (A=200 m^2) maximum temperature reaches about 80°C and no dissipation occurs, while a solar fraction of about 92% is reached. In the third case (A=100 m^2) the storage is oversized and therefore underutilized: maximum temperature is about 60°C, and solar fraction stops at about 59%. The best payback is reached in the second case (A=200 m^2) (Fig. 10), while the third case (A=100 m^2) is characterized by higher average solar collector efficiency (Fig. 11) and lower storage losses (Fig. 12), due to lower storage temperatures.

The study of the results (Fig. 10, Fig. 11, Fig. 12) shows that the effect of solar collectors area over solar fraction is non-linear: an increase in solar area from 100 m^2 to 200 m^2 produces a significant improvement in solar fraction (from 43% to 68% about, at the minimum storage volume), while passing from 300 m^2 to 400 m^2 results in a much lower improvement (from 78% to 85% about). Also the effect of storage volume is non-linear: the slope of the constant solar area curves is positive and almost constant until the saturation conditions (purple lines) are reached, tending to assume an asymptotic behavior afterwards. The observed effects of storage volume and panel area over solar fraction and the pay-back time values, ranging from 15 years up, are consistent with other studies available in literature [9] [12] [13].

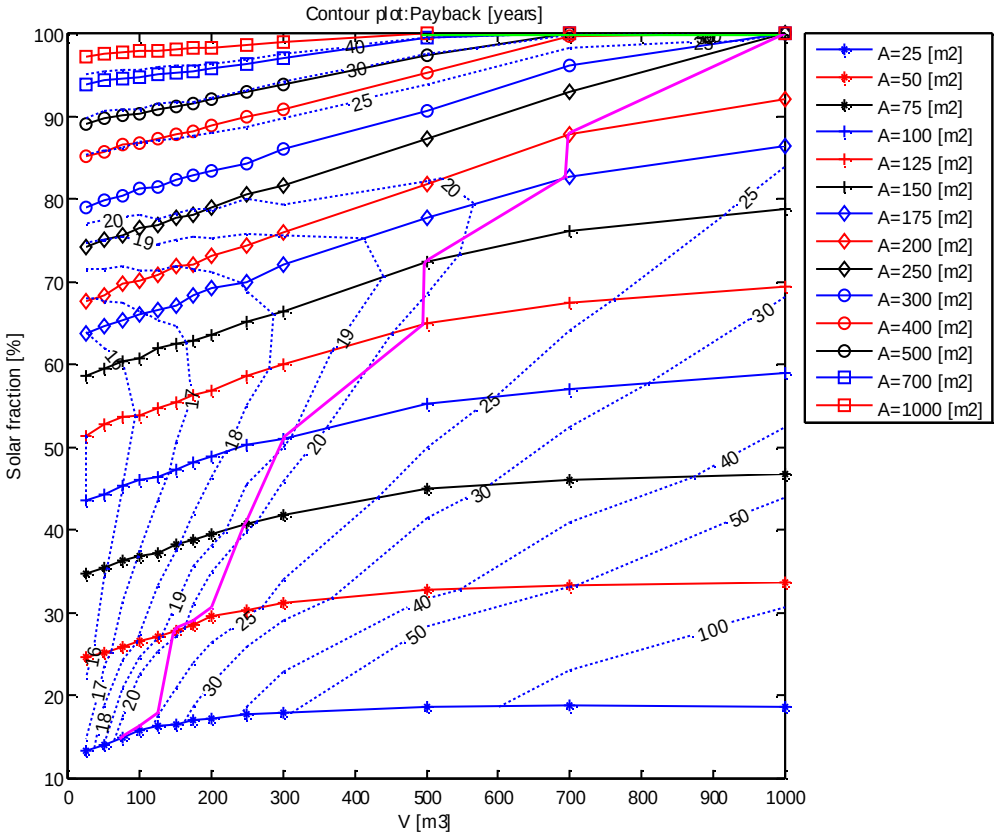

Fig. 10. Solar fraction vs reservoir volume, for different solar panel area. Dotted lines: pay-back time [years]. Collector type: Flat plate. Location: Naples.

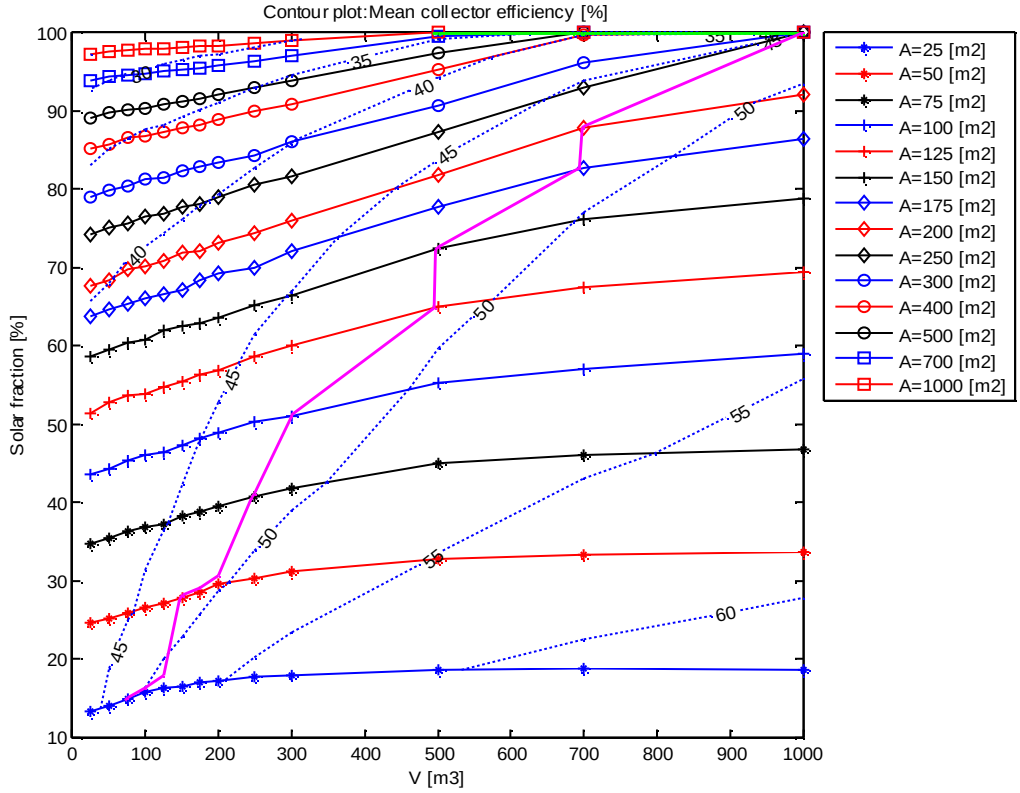

Fig. 11. Solar fraction vs reservoir volume, for different solar panel area. Dotted lines: solar collector efficiency [%]. Collector type: Flat plate. Location: Naples.

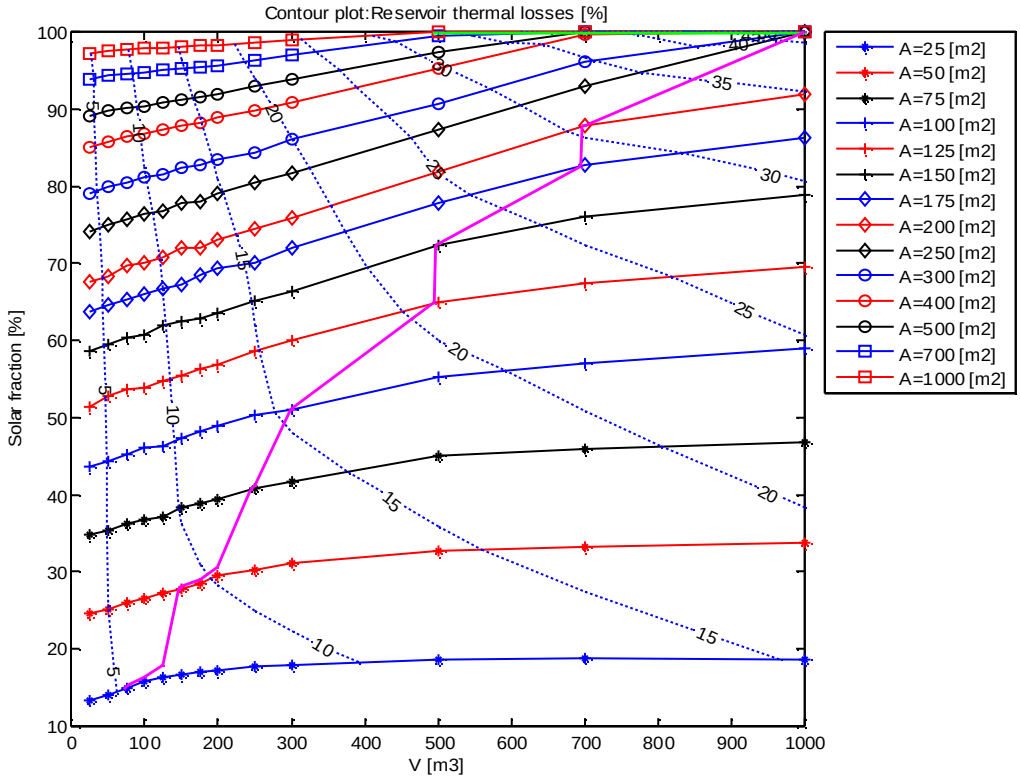

Fig. 12. Solar fraction vs reservoir volume, for different solar panel area. Dotted lines: reservoir thermal losses [%]. Collector type: Flat plate. Location: Naples.

5. Optimization approach

Non-linear effects occur for most of the variables affecting plant performance. In this case, the best set of design variables cannot be determined solely by analyzing each variable independently of other variables, since they are interdependent. Therefore, the adoption of a non-linear optimization approach is suitable [24]. The plant model has been then integrated within a nonlinear constrained optimization algorithm, in order to determine the optimal combination of design and operating variables corresponding to the best values of the performance indices. The mathematical problem is formulated in the following way:

$$min_x f(x) \tag{6}$$

$$G(x) \leq \mathbf{0} \tag{7}$$

$$E(x) = \mathbf{0} \tag{8}$$

$$LB \leq x \leq UB \tag{9}$$

The objective function (6) is represented by the simple pay-back time, defined as the ratio between the plant cost and the yearly savings. The equality constraint (8) may express the condition that the solar fraction must be equal to a given value (i.e. 100%), while inequality constraints (7) may express the condition that no dissipation occurs, and therefore storage temperature is always below the maximum allowed value.

All the design variables are assumed to be positive, i.e. LB=0 in (9). A classical 2nd order Quasi-Newton approach is used [24], as implemented in the routine "fmincon" of the optimization toolbox of Matlab [22].

Preliminary tests have been performed, to verify the functionality of the procedure. The graphs in Fig. 13 show the values of design variables (storage volume and panel area) and of the objective function (pay-back time) versus the iterations, for two different cases (Flat Plate and Vacuum Tube). For this computation, lower values for storage cost (40 €/m^3) and for insulation cost (40 €/m^3) were assumed with respect to the values reported in Table 2.

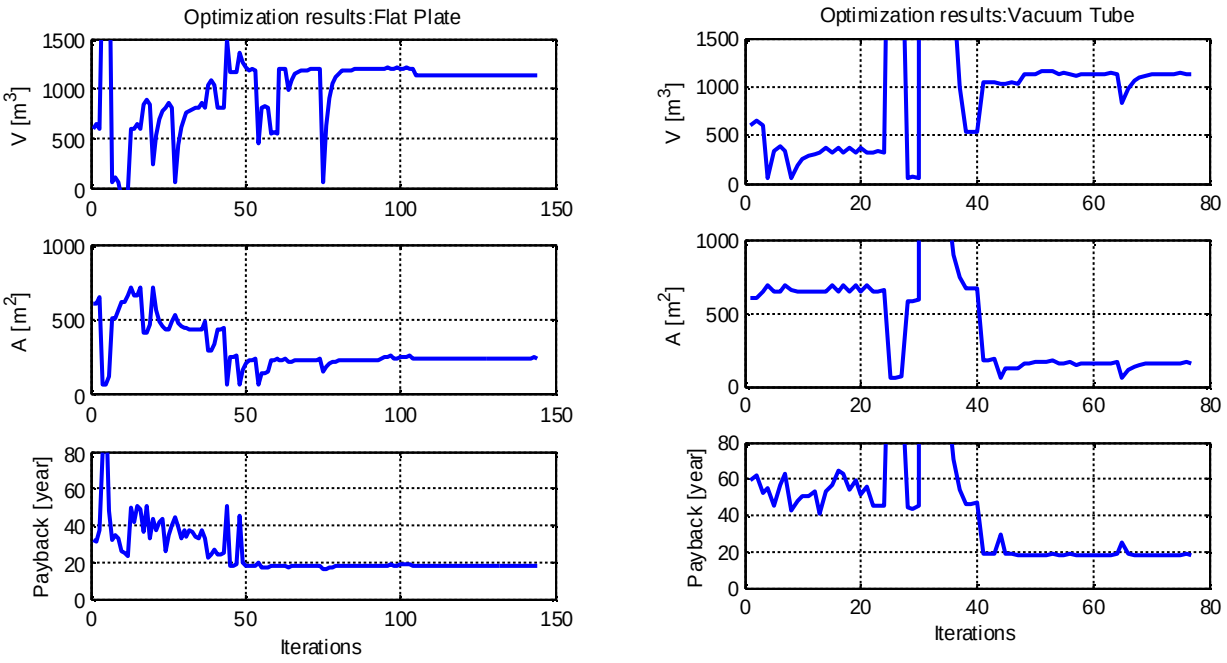

Fig. 13. Optimization results: design variables and objective function vs iterations.

It can be observed that, starting from arbitrary initial values (A=600 m^2, V=600 m^3), optimal solutions are found in both cases in approximately 60 iterations. Very similar optimum pay-back time were obtained (about 17,9 years). The optimal storage volume V is also quite similar in the two cases (about 1130 m^3). In case of vacuum tube, however, lower surface is suggested for solar panels, as expected (Table 3).

Computational time for each test is less than two hours, and therefore compatible with the use of model for design purposes.

Table 3. Optimization results: optimal values of design variables and objective function.

Solar collector type	V [m3]	A [m2]	Pay-back time [year]
Flat plate	1125	239	17,8
Vacuum tube	1136	161	17,9

Conclusions

Thermal solar plants with seasonal water storage have been considered as an environmentally valuable, but expensive, solution to cover thermal energy demand in buildings. In recent years their economic feasibility is improving, due to the parallel increase of fuel cost and decrease of solar collectors cost. A thermo-economic model of a thermal solar plant with seasonal water storage has been presented. The model includes also a simple sub-model for the estimation of thermal stratification in water storage, successfully validated by literature data. The results of a parametric analysis on the effects of storage volume and panel area over solar fraction, pay-back time, average collector efficiency and thermal losses have been presented and compared with other studies available in literature, and non-linear effects have been evidenced.

The model has been integrated within a non-linear constrained optimization procedure. Preliminary tests have demonstrated that the results are sound and that computational time is compatible with practical uses of this tool for design purposes.

In future research, the model will be used to make a systematic study of the effects of design variables, as tilt angle, insulation thickness, panel type, as well as of operating and control variables. The effects of plant location over optimal design variables will be also investigated by means of the optimization procedure.

Acknowledgments

The contributions given to the present analysis by Claudia Poto and Vito Della Corte during their Master Thesis in Mechanical Engineering at the University of Salerno are gratefully acknowledged.

Appendix

The following equations describe the solar power absorbed by a solar collector with tilt angle β and azimuth ψ, in a location of latitude φ. The model predicts the direct solar irradiance with sunny sky *Irr*. The reduction factor f_{SUN} is introduced in (17) to predict irradiance under real sky conditions. This factor has been identified for different locations (Fig. 14) [25], starting from average real monthly solar data [23].

$$\delta = 0.4093\ sin\left(2\pi\frac{284+d}{365}\right) \quad (10)$$

$$\omega = 2\pi\,{}^{(12-h)}/_{24} \quad (11)$$

$$z = acos(\sin(\delta)\cdot\sin(\varphi) + \cos(\delta)\cdot\cos(\varphi)\cdot\cos(\omega)) \quad (12)$$

$$AM = min\left[{}^{1}/_{sin\left(\frac{\pi}{2}-z\right)}, 38\right] \quad (13)$$

(14)

$$Irr = 1.1\cdot I_0\cdot 0.7^{AM^{0.678}} \quad (15)$$

$$\psi_{SUN} = acos\left(\left(\sin(\delta)\cdot\cos(\varphi) - \cos(\omega)\cdot\cos(\delta)\cdot\sin(\varphi)\right)\Big/\cos\left(\frac{\pi}{2}-z\right)\right)$$

$$\theta = acos\left(\cos\left(\frac{\pi}{2}-z\right)\cdot\cos(\Psi-\Psi_{SUN})\cdot\sin(\beta)\right) \quad (16)$$

$$P_{SUN} = Irr\cdot f_{SUN}\cdot\cos(\theta) \quad (17)$$

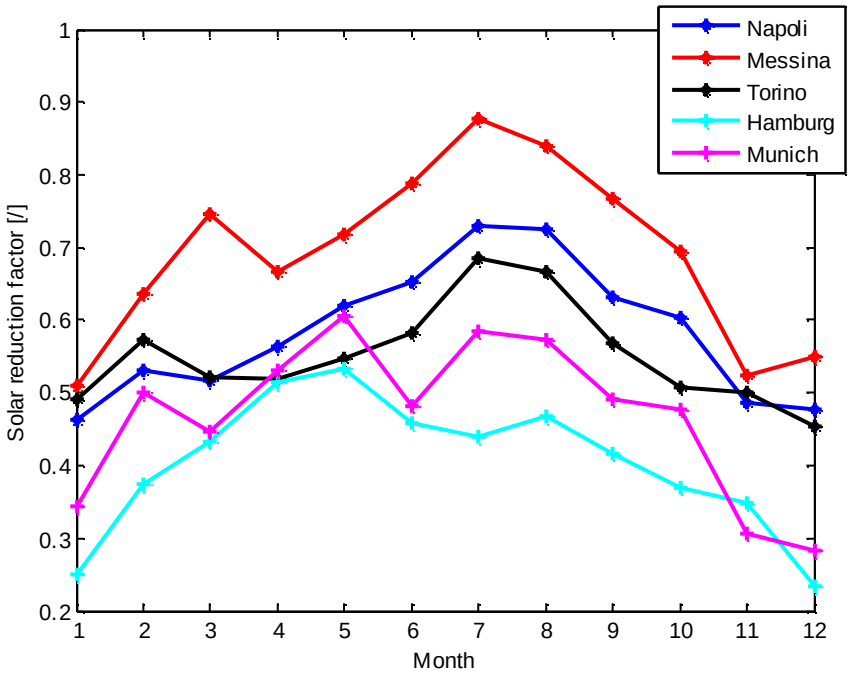

Fig. 14. Solar reduction factor for different locations

Nomenclature

A	Solar collector area [m^2]
AM	Air Mass [/]
A_{st}	Water storage area [m^2]
d	Day index (1-365) [/]
E	Equality constraint
f	Objective function
f_{SUN}	Solar radiation reduction factor [/]
G	Inequality constraint
h	Hour (1-24) [/]
I_0	Solar constant=1366 [W/m^2]
Irr	Irradiance [W/m^2]
k_1, k_2	Parameters in the stratification model
L	Insulation thickness [m]
LB	Lower bound
P_{loss}	Reservoir thermal losses [W]
P_{SUN}	Solar power [W/m^2]
T^*	Variable in collector efficiency model
t_{amb}	Ambient temperature [°C]
t_{bottom}	Bottom temperature in the water reservoir [°C]
t_g	Ground temperature [°C]
t_m	Solar collector mean temperature [°C]
t_{max}	Maximum allowed temperature in the water reservoir [°C]
t_{mean}	Mean temperature in the water reservoir [°C]
t_{top}	Top temperature in the water reservoir [°C]
U_1, U_2	Parameters of the collector efficiency model
UP	Upper bound
V	Reservoir volume [m^3]
x	Decision variables
z	Zenith angle [rad]

Greek Symbols

η	Solar collector efficiency [/]
η_0	Parameter in the collector efficiency model
Δt	Difference between top and bottom temperature in the water reservoir
β	Tilt angle [rad]
δ	Declination [rad]
θ	Incidence angle [rad]
λ	Thermal conductivity [W/mK]
φ	Latitude [rad]
Ψ	Azimuth [rad]

ω Hour angle [rad]

References

[1] Renewables 2010 Global Status Report, available at <http://www.ren21.net>

[2] European Commission, Reenewable Energy, Target for 2020, available at <http://ec.europa.eu/energy/renewables/targets_en.htm>

[3] W.Weiss, F.Mauthner, Solar Heat Worldwide, Markets and Contribution to the Energy Supply 2009, IEA Solar Heating & Cooling Programme, May 2011

[4] Fath, Hassan E.S., Technical assessment of thermal energy storage technologies, Renewable Energy (1998) Vol.14, 1-4, pp.35

[5] T. Schmidt, D. Mangold, H. Muller-Steinhagen, Central solar heating plants with seasonal storage in Germany, Solar Energy 76 (2004) 165-174.

[6] R.Fuller, L.Aye, Seasonal storage for solar systems in Australia?, in "Is Solar our only Nuclear option?", ANZSES Solar 07.

[7] Lottner, V., Schulz, M.E. and Hahne, E. (2000). Solar-assisted district heating plants: status of the German Programme Solarthermie-2000. Solar Energy, 69, 6, 449-459.

[8] Mo Chung, Jun-Un Park and Hyung-Kee Yoon, Simulation of a central solar heating system with seasonal storage in Korea, Solar Energy Vol. 64, Nos 4–6, pp. 163–178, 1998.

[9] K.Lim, S.Lee, C.Lee, An experimental study on the thermal performance of ground heat exchanger, Experimental Thermal and Fluid Science 31 (2007) 985–990.

[10] B.Sannera, C.Karytsasb, D.Mendrinosb, L.Rybachc, Current status of ground source heat pumps and underground thermal energy storage in Europe, Geothermics 32 (2003) 579–588.

[11] R.Kubler, N.Fisch, E.Hahne, High temperature water pit storage projects for the seasonal storage of solar energy, Solar Energy Vol. 61 No.2 pp.97-105, 1997.

[12] Ucar A., Inalli M., Thermal and economical analysis of a central solar heating system with underground seasonal storage in Turkey, Renewable Energy 30 (2005) 1005–1019.

[13] Ucar A., Inalli M., Thermal and economic comparisons of solar heating systems with seasonal storage used in building heating, Renewable Energy 33 (2008) 2532– 2539.

[14] Vito Della Corte, Studio delle caratteristiche e dei parametri funzionali dei sistemi ad accumulo stagionale di energia termica solare, Thesis in Mechanical Engineering, University of Salerno, 2010 (in Italian).

[15] TRNSYS, available at <http://www.trnsys.com/>

[16] R.Charron and A.Athienitis, The Use of Genetic Algorithms for a Net-Zero Energy Solar Home Design Optimisation Tool, PLEA2006 - The 23rd Conference on Passive and Low Energy Architecture, Geneva, Switzerland, 6-8 September 2006.

[17] Database of weather data, available at <http://www.weatherbase.com>

[18] A.N.Khalifa, A.T.Mustafa, F.A.Khammas, Experimental study of temperature stratification in a thermal storage tank in the static mode for different aspect ratios, ARPN Journal of Engineering and Applied Sciences, Vol.6, NO.2, February 2011, ISSN 1819-6608.

[19] C.Cruickshank and S.Harrison, Analysis of a Modular Thermal Storage for Solar Heating Systems, Canadian Solar Buildings Conference, Montreal, August 20-24, 2004.

[20] H.Kerskes, Seasonal Thermal Storage, Institute for Thermodynamics and Thermal Engineering, Universitat Stuttgart.

[21] Thomas Schimidt, Janet Nuβbicker, Monitoring results from German central solar heating plants with seasonal storage, Solar World Congress, Orlando Florida USA (2005).

[22] Matlab technical documentation, available at <http://www.mathworks.it/help/techdoc/index.html>

[23] Database of solar data, available at < http://www.nrel.gov/rredc/ >

[24] Gill, P.E., W. Murray, and M.H. Wright, Practical Optimization, Academic Press, London, 1981.

[25] Claudia Poto, Sviluppo di modelli per lo studio di impianti solari con accumulo stagionale, Thesis in Mechanical Engineering, University of Salerno, 2010 (in Italian).

[26] Department of Defense, USA, Active Solar Preheat Systems, Unified Facilities Criteria, available at <http://buildingcriteria2.tpub.com/ufc_3_440_01/index.htm>

A thermodynamic and economic comparative analysis of combined gas-steam and gas turbine air bottoming cycle

Tadeusz Chmielniak[a], Daniel Czaja[b], Sebastian Lepszy[c]

[a] Institute of Power Engineering and Turbomachinery, Silesian University of Technology, Gliwice, Poland, tadeusz.chmielniak@polsl.pl
[b] Institute of Power Engineering and Turbomachinery, Silesian University of Technology, Gliwice, Poland, daniel.czaja@polsl.pl ***CA***
[c] Institute of Power Engineering and Turbomachinery, Silesian University of Technology, Gliwice, Poland, sebastian.lepszy@polsl.pl

Abstract:

An increase in the efficiency of energy systems can be achieved by the development of combined cycles. Examples of high efficiency cycles are combined cycle power plants (CCPP) and gas turbine air bottoming cycles (GT-ABC), which are a combination of a gas turbine and air turbine cycle coupled by means of a heat exchanger referred to as the Air Heat Exchanger (AHX). The main feature of the GT-ABC is a low water consumption. For this reason, it can be used in gas transport and storage systems.
In this paper the GT-ABC and the combined gas-steam cycle designed for the same class of application are compared. An example of the considered technological structures is presented. The calculations include thermodynamic characteristics and a preliminary economic analysis determining the capital expenditure for each installation. In particular, the GT-ABC (either a simple system or a version with an intercooled compressor) and the combined gas-steam cycle with a single-pressure Heat Recovery Steam Generator (HRSG) are compared. Due to a limited access to cooling water at a potential place of application, the combined gas-steam cycle with an air fan cooling tower and an air-cooled condenser are used.

Keywords:

Air turbine, ABC (Air Bottoming Cycle), GT (Gas Turbine), HRSG (Heat Recovery Steam Generator), efficiency, combined gas-steam cycle, heat exchanger, AHX (Air Heat Exchanger), cogeneration, economic analysis, thermodynamic analysis.

1. Introduction

Gas turbines are one of the basic technologies used to produce electricity and power working machinery. The popularity of the technology results from its advantages, the most important of which are: the fast start-up, high efficiency, low pollutant emissions, the short time needed for the installation to be constructed and a reasonable size. Gas turbines are becoming increasingly important in new power installations [1-8]. They find application in hierarchical power systems, e.g.

- gas-steam systems,
- combined multi-fuel systems,
- pressure fluidised bed boiler systems,
- partial and complete gasification systems,
- gas-air systems [9-12].

So far, cycles with steam or an organic medium have been the ones employed in combined systems with gas turbines [13-16]. The main factor that decided about the popularity of these systems was their high power efficiency.

Another option is to couple the gas turbine with an air turbine (GT-ABC) by means of an air heat exchanger (AHX). The construction of this type of systems may turn out to be energy-effective due to the advancement in flow machinery construction, especially in the field of improvement to blade profiles and sealing. Other features that make gas-air systems interesting are the following:

- an increase in the efficiency of power installations with gas turbines,
- the potential to meet the peak demand for power,
- mobility,
- no demand for water,
- no toxic substances,
- a harmless working medium,
- lower investment costs compared to gas-steam systems,
- fuel diversification for a given coal-fired power plant.

The GT-ABC systems can find application in the food industry (industrial bakeries, powdered milk factories and as a source of hot air in glass melting furnaces), in cogenerative systems with air as the working medium or in high-temperature furnaces where the pre-heated air comes from the ABC. Gas-air systems can also be used as a potential improvement to the efficiency of simple power units with gas turbines operating at locations without access to large amounts of water. It seems that these systems could be applied in other technologies, such as power engineering of renewable sources, energy recovery from gases, especially where water availability is limited. The potential applications of gas-air systems in coal-fired plants as a source of heat feeding the carbon dioxide capture installations, as well as in heat engineering are also considered [11,13]. The mechanical power obtained from the turbine can be used either to support the gas turbine system or to generate electricity. Due to the short start-up time of the air turbine, the ability to meet the peak demand for power may also be significant.

Air turbine systems are simple in terms of operation. This results from the fact that there is no combustion process and there are no toxic mediums or mediums causing erosion or needing to be topped up.

2. Systems under analysis

It is assumed that the source of heat for gas-air and gas-steam systems is the turbine ABB GT10, whose basic data are listed in Table 1 [17-19].

Table 1. Basic data of ABB GT10 gas turbine

Model	ABB GT10
Power N_{GT}, MW	23.92
Turbine inlet temperature t_4, °C	1220
Net efficiency η_{GT}, %	34.22
Pressure ratio β_{GT}, -	14.02
Heatrate q_{GT}, kJ/kWh	11080

The following composition of flue gases at the outlet from the gas turbine expander is assumed for the modelling:

- N_2 75.76%
- O_2 13.56%
- CO_2 3.28%
- H_2O 7.40%

2.1. Gas-air systems

The simplest model of an air turbine with a gas turbine system is shown in Fig. 1. The system is composed of a simple gas turbine, an air turbine and a compressor.

The crucial element is the structure of the air heat exchanger (AHX) [20-26], which has a decisive impact on the efficiency of the entire system. A rationally designed system must take account of the differences in the medium temperature which determine its size, as well as the pressure drops which determine the efficiency of both the air and the gas turbine. A high efficiency of the system is obtained for small temperature differences in the heat exchanger. Therefore the heat exchanger will have a large size. Shell-and-tube heat exchangers or plate heat exchangers can be applied. Preliminary calculations show that lower pressure drops are obtained for plate structures. Also, the area of a plate heat exchanger is significantly smaller.

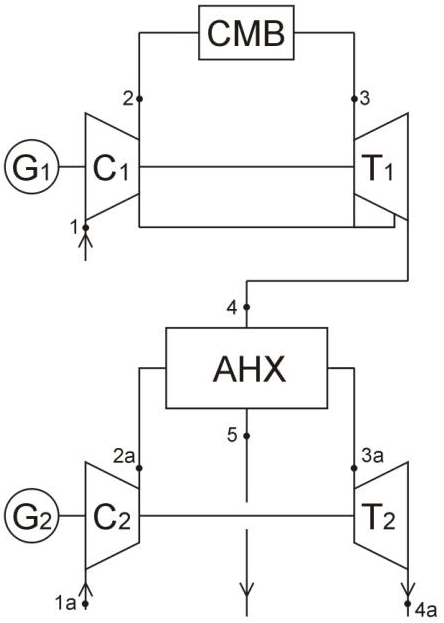

Fig. 1. Schematic diagram of a simple gas-air system

The air turbine system is composed of compressor C_1, an air heat exchanger (AHX) and expander T_1. The main advantage of this type of system is its simplicity; the downside, however, is the fact that the air temperature at the compressor outlet is high, which causes that a relatively small amount of heat is exchanged in the AHX. Due to the low values of the upper heat source temperature, this system achieves high efficiency values only if the internal efficiency of the compressor and the turbine is also high.

In order to improve the efficiency of air turbine installations, it is necessary to employ more complex system configurations. An example of a complex system of the air turbine is the installation shown in Fig. 2. In this system two compressors and an intercooler are used. The outlet air from compressor C_3 has a lower temperature compared to the simple system, which allows a

more intense cooling of the gas turbine flue gases and a reduction in the driving operation of the compressors. In the calculations of this system it is assumed that the air in the intercooler is cooled to the temperature of 40°C.

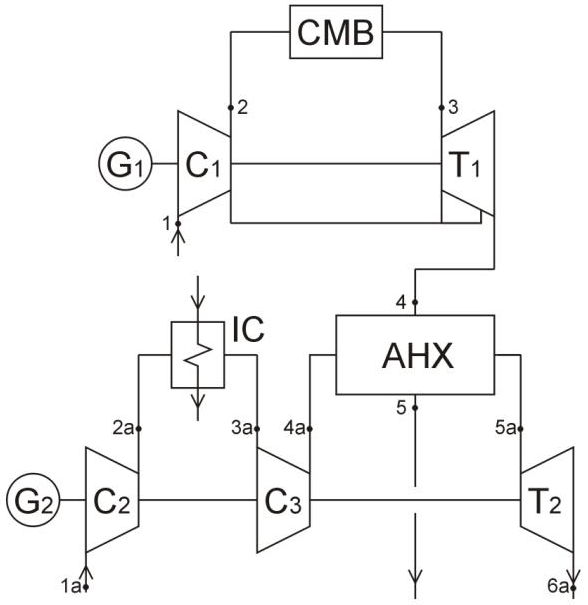

Fig. 2. Complex gas-air system with an air intercooler

2.2. Gas-steam system

In order to compare gas-air and gas-steam systems, the same gas turbine (ABB-GT10) is used in it. The flowchart of the gas-steam system under consideration is presented in Fig. 3. In the analysed system the heat recovery steam generator (HRSG) is a single-pressure boiler composed of three different heat exchange surfaces: the economiser (ECO), the evaporator (EVAP) and the steam superheater (SH). The deaerator (DEA) is fed with steam from the steam turbine (ST) bleed. The task of the heat exchanger (HX) after the condensate pump (CP) is to stabilise the boiler feed water temperature at a constant level, which is a standard solution in gas-steam power plants. The system electricity generation efficiency reaches 48.4%. A downside of a system with a single-pressure heat recovery boiler is the large exhaust loss (approx. 180°C).

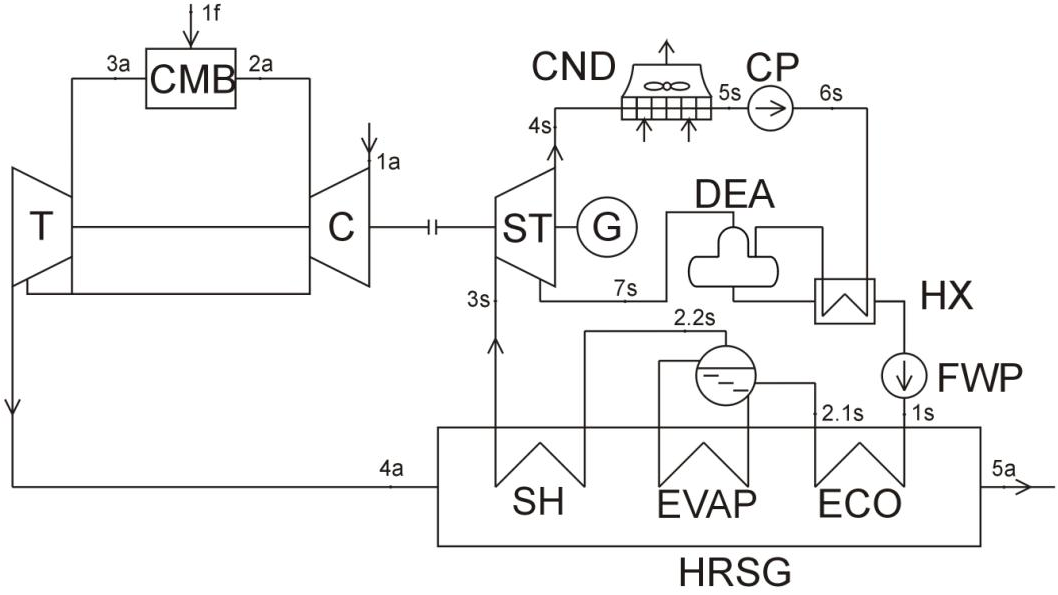

Fig. 3. The flowchart of the gas-steam system with single pressure HRSG

A subcooling temperature at the level of t_{sc} = 10°C is assumed in the economiser. The pinch point in the evaporator is t_{pp} = 6°C, and the live steam temperature is t_{ls} = 535°C.

In order to minimise the demand for water, and thereby ensure a better comparison of the gas-steam cycle to gas-air systems, an air-cooled condenser with an air fan cooling tower (CND) is used. The air-cooled condenser is composed of bays; in each bay several fans can be placed. Each bay is fed with steam from a common collector. Due to the fact that the condensate is also carried away to the common collector, the whole can be treated as a group of coolers. The facility is available in two variants:

- condensation,
- cooling.

In the former case, the air sucked in from the environment is used to cool the steam to saturation temperature. In the latter, the sucked-in air is used to cool water to a set temperature value (enthalpy). Fig. 4 schematically presents the two modes of the air condenser operation [18,27].

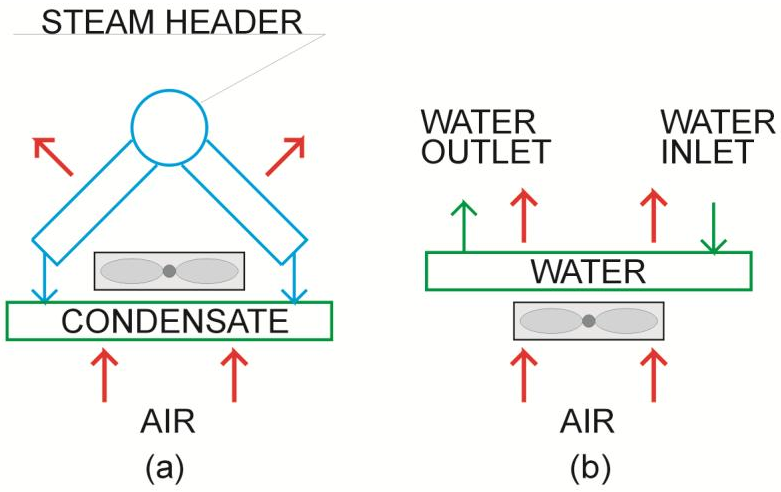

Fig. 4. Two variants of air cooled condenser operation (a. – condensation, b. – cooling)

3. Calculation results

In the case of the standalone operation of a gas turbine, the important parameter is electricity generation efficiency defined by the formula:

$$\eta_{elGT} = \frac{N_{elGT}}{\dot{m}_f \cdot LHV}, \qquad (1)$$

The target of a gas-air system analysis should be the maximisation of the ratio of the amount of generated electricity to the chemical energy of the fuel. In this case, the power efficiency of the system can be defined as follows:

$$\eta_{elGT-ABC} = \frac{N_{elGT} + N_{elAT}}{\dot{m}_f \cdot LHV} \qquad (2)$$

The system efficiency can be evaluated using the following definition of power efficiency:

$$\eta_{eAT} = \frac{N_{mAT}}{\dot{Q}_4} \qquad (3)$$

where: $\dot{Q}_4$ – the heat of cooling flue gases to the reference temperature.

In order to simplify the analyses, it is assumed in the calculations presented in this paper that Q_4 corresponds to the cooling of flue gases to temperature t_5 = 15°C, while the water vapour contained in flue gases is not condensed.

The cycle efficiency is defined by following dependence:

$$\eta_{cAT} = \frac{N_{mAT}}{\dot{I}_4 - \dot{I}_5} \qquad (4)$$

where:

$\dot{I}_4$ and $\dot{I}_5$ are values of enthalpy corresponding to point 4 and 5 (Fig.1 and Fig.2).

The electricity generation efficiency of the gas-steam power plant is defined as follows:

$$\eta_{elCCPP} = \frac{N_{elGT} + N_{elST}}{\dot{m}_f \cdot LHV} \qquad (5)$$

The air system is optimized in terms of efficiency. The pressure ratio and the air mass flow are chosen as decision variables. The other values are selected according to the parameters of the machines and equipment operating in gas turbine systems. For set parameters of the heat exchanger, pressure value p_{2a} is varied within the range of 0.15-0.6 MPa. The procedure is repeated for different mass flow values of the air sucked in by compressor C_2.

It is important to chose an appropriate pressure value at the outlet of the compressor's first stage. The optimum pressure value which minimizes the power consumption to drive the compressor can be determined by minimizing the following objective function:

$$\frac{1}{\eta_i}\left[T_{1a}\left(\varsigma_1 - 1\right) + T_{3a}\left(\varsigma_3 - 1\right)\right] \rightarrow \min \qquad (6)$$

where: $\varsigma_1 = \frac{T_{2ai}}{T_{1a}}, \varsigma_3 = \frac{T_{4ai}}{T_{3a}}$

3.1. Air Heat Exchanger calculations

Parameters which have a significant impact on the efficiency of the entire system are overall heat transfer coefficient value and pressure drop in the air heat exchanger (AHX). The higher the pressure drop in AHX, the lower efficiency η_{eAT}. On the other hand, a bigger pressure drop makes it possible to obtain high heat transfer coefficients, which leads to a reduction in the heat exchange area and, consequently – to a smaller size of the device. In order do to determine the heat transfer coefficient many physical properties of air and flue gas were take into account:

$$\alpha = f\left(\eta, \lambda, c_p, \rho, \nu, \Delta t, a...\right) \qquad (7)$$

The calculation algorithm is based on the LMTD method. [22-24]. To determine the heat surface area the Nusselt number should be found. The plate heat exchanger was taken into account. The Nusselt number for this type of heat exchangers can be defined by the formula:

$$Nu = 0.022 \cdot \sqrt{\xi_0} \cdot \beta \cdot \beta_t \cdot \mathrm{Re}^{0.825} \cdot \mathrm{Pr}^{0.54} \qquad (8)$$

where:

β – turbulence damping ratio,

β_t – forced turbulence ratio,

ξ_0 – flow resistance ratio.

In order to obtain reduced surface of heat exchange with relatively high values of the heat transfer coefficient, higher velocities of the working mediums are required. This, however, results in a bigger flow resistance and a higher pressure drop. Finally the low velocity values (especially on the air side) were chosen. The loss in the AHX also depends on the equivalent diameter of the duct and

on the heat radiation losses. In calculation the radiation losses were assumed at a level equal $\dot{Q}_{amb} = 1\%$. The velocity of flue gases and equivalent diameter of ducts (flue gas side) has been also assumed. Assumption of flue gas velocity equal 15m/s resulted in a very low air speeds, but also very low pressure drop value (especially in the air side).

The overall heat transfer coefficient was between 23-30 W/(m2K). The example results of the analysis performed for the plate heat exchanger are given in Table 2. In the case of simple system an air inlet temperature was at a level of about t_{ain} = 170°C with the isentropic efficiency of compressor equal η_{iC2} = 85% (in the case of complex system t_{ain} = 105°C and η_{iC2} = 85% respectively).

Determining of the pressure drop value is done by calculating the sum of hydraulic resistance (local resistance) as well as longitudinal resistance.

It is assumed that the wall which separates mediums in AHX are made of P235GH, 16Mo3 and 14CrMo4-5 steel, and its heat conductivity depends on temperature [22].

Table 2. Example of AHX calculation results

	Simple system	Complex system
Heat transfer surface, m^2	approx. 58700	approx. 58200
Pressure drop (flue gas side), %	approx. 1.65	approx.1.65
Pressure drop (air side), %	approx. 0.3	approx 0.3
Overall heat transfer coefficient, W/(m^2K)	approx 25	approx 25
Equivalent diameter of flue gas duct, m	0.04	0.04
Effectiveness, %	95	95

The heat transfer surface area is strongly dependent on overall heat transfer coefficient and assumed equivalent diameter. Determination of AHX geometry is broad issue of thermoeconomic optimization. A trade-off between the system energy efficiency and the size of the AHX will be required (minimization of investment expenditures and maximizing the energy efficiency). It should be mentioned that also plate fin heat exchanger will be considered as an element which coupled topping and bottoming cycle.

3.2. Gas Turbine Air Bottoming Cycle - Results and discussion

Most often, the optimum parameters of the air turbine cycle with respect to the power efficiency of cycle η_{eAT} and the efficiency of cycle η_{cAT} are different, which is shown in the example chart in Fig. 5, which presents the dependence of the air turbine system efficiency as a function of the compressor outlet pressure. Pressure drop in AXH is ΔP_a = ΔP_{fg} = 1%, isentropic efficiency of compressor and air turbine is η_{iC2} = η_{iT} = *0.9*, t_{cpt} = 10°C. Flue gas temperature which is a function of pressure ratio is equal t_4 = 500℃.

Nomenclature used:

ΔP_a – relative pressure drop (air side),

ΔP_{fg} – relative pressure drop (flue gas side),

t_{cpt} – cold pinch temperature,

η_{iCi} – compressors internal efficiency,

η_{iT} – turbine internal efficiency.

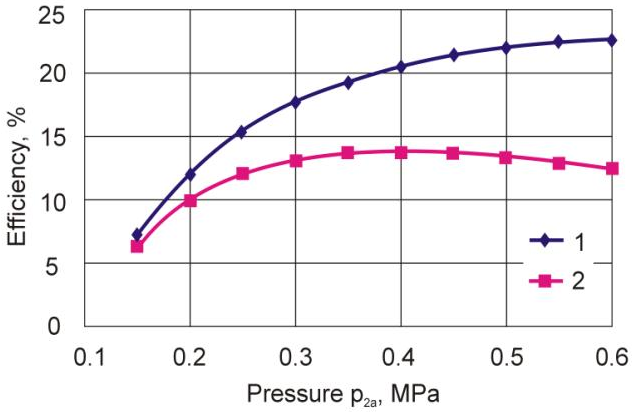

Fig. 5. Dependence of efficiency as a function of compressor outlet pressure (1 – efficiency of cycle η_{cAT}; 2 – power efficiency of cycle η_{eAT}

It's should be noted that every point of each characteristic in Fig 5-8 represents other engine. That's why the analysis was conducted with constant isentropic efficiency.

Energy efficiency as a function of compressor outlet pressure for simple cycle with ABB GT10 is presented in Fig 6. Isentropic efficiency of compressor and air turbine is $\eta_{iC2} = \eta_{iT} = 0.85$ and $t_{cpt} = 10°C$.

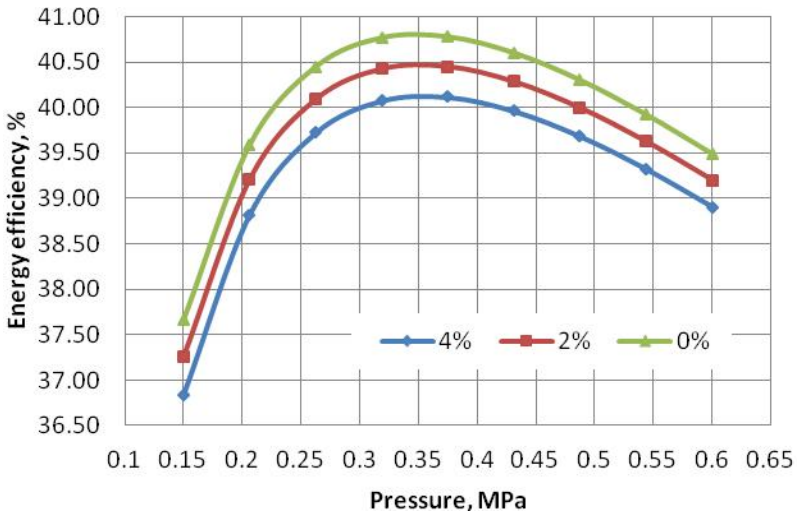

Fig. 6. Dependence of efficiency as a function of compressor outlet pressure for simple cycle with ABB GT10 (results for different value of pressure drop in AHX)

The factor which most affects the installation efficiency is the temperature of flue gases. A drop in the flue gas temperature results in a considerable decrease in efficiency, with other optimum values, such as the compressor outlet pressure, changed at the same time. In ABB GT10 the turbine outlet temperature is relatively high ($t_4 = 540°C$).

Table 3 presents the results of the power efficiency of a simple gas-air system depending on the efficiency of the gas turbine system for a given temperature difference between the flue gas outlet and the air inlet in the AHX (three values of isentropic efficiency of the turbomachinery in the air system are distinguished). The pressure drop on part of both flue gases and air is 4%.

The impact of the pressure drop in the AHX on the efficiency of the simple gas-air system was also analysed. The difference in temperatures between the air inlet and the flue gas outlet is 10K. The results are listed in Table 4.

Table 3. Power efficiency of a simple gas-air system for different values of the difference in the flue gas and air temperature in the AHX (t_{fg}=540 °C, $\Delta P_a = \Delta P_{fg}$ = 4%)

ΔT, K	η_{eGT}, %	$\eta_{iC2}=\eta_{iT}$, %		
		82.50%	85.00%	87.50%
10	30	35.03	36.27	37.60
	35	39.67	40.82	42.06
	40	44.31	45.37	46.51
20	30	34.77	35.97	37.29
	35	39.43	40.54	41.77
	40	44.09	45.12	46.25
30	30	34.52	35.69	36.98
	35	39.19	40.28	41.48
	40	43.87	44.88	45.98

Table 4. Power efficiency of a simple gas-air system for different values of the pressure drop in the AHX (t_{fg}=540 °C)

ΔP, %	$\eta_{GT,}$ %	$\eta_{iC2}=\eta_{iT}$, %		
		82.50%	85.00%	87.50%
3	30	35.22	36.45	37.78
	35	39.84	40.99	42.23
	40	44.47	45.53	46.67
5	30	34.85	36.09	37.41
	35	39.39	40.65	41.88
	40	44.16	45.22	46.35
7	30	34.48	35.72	37.03
	35	39.16	40.31	41.53
	40	43.84	44.90	46.03

In order to improve the efficiency of air turbine installations, it is necessary to employ more complex system configurations. In the system two compressors and an air intercooler are used. The outlet air from compressor C_3 has a lower temperature compared to the simple system, which allows a bigger cooling of the gas turbine flue gases and a reduction in the driving operation of the compressors. In the calculations of this system it is assumed that the air in the intercooler is cooled to the temperature of 40˚C.

Energy efficiency as a function of compressor C_3 outlet pressure for complex cycle with ABB GT10 is presented in Fig 7. Isentropic efficiency of compressor and air turbine is

$\eta_{iC2} = \eta_{iT} = 0.85$ and, $t_{cpt} = 10°C$. Compressor C_2 outlet pressure value was assumed according to dependence 6.

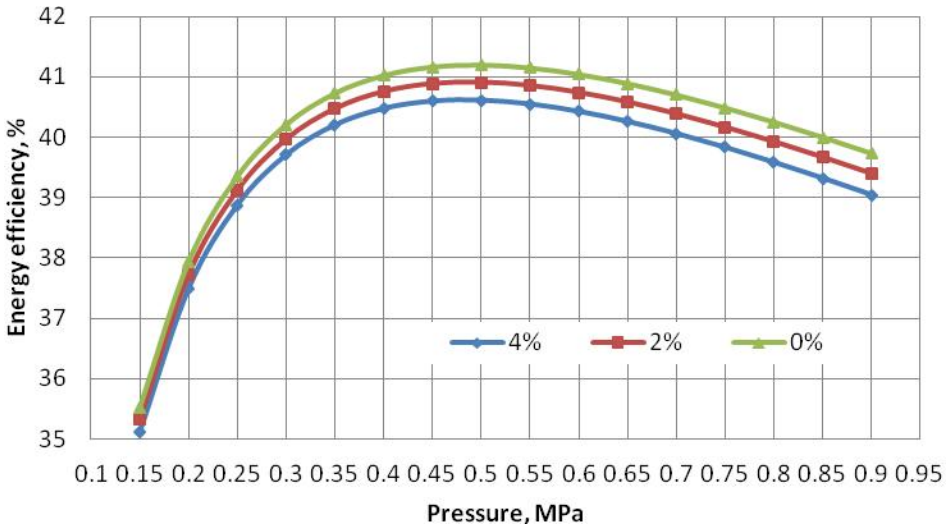

Fig. 7. Dependence of efficiency as a function of compressor C_3 outlet pressure for complex cycle with ABB GT10 (results for different value of pressure drop in AHX)

The impact of the isentropic efficiency of the compressors and of the turbine on the power efficiency was also analysed (Fig. 8). A decrease in the internal efficiency values results in a reduction in the power efficiency and in a drop in the optimum values of compressor C_3 outlet pressure. Pressure drop in AHX is $\Delta P_a = \Delta P_{fg} = 1\%$, isentropic efficiency of compressors and air turbine is $\eta_{iC2} = \eta_{iC3} = \eta_{iT}$, $t_4 = 550°C$, $t_{cpt} = 10°C$.

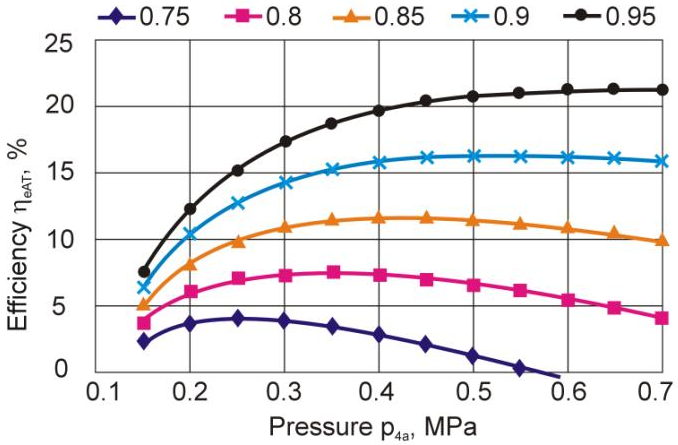

Fig. 8. Dependence of efficiency η_{eAT} as a function of the compressor outlet pressure for different values of the isentropic efficiency of the compressors and the turbine ($\eta_{iC2} = \eta_{iC3} = \eta_{iT}$)

Table 5 presents the results of the power efficiency of a complex gas-air system depending on the efficiency of the gas turbine system for a given temperature difference between the flue gas outlet and the air inlet in the AHX (three values of isentropic efficiency of the turbomachinery in the air system are distinguished). The pressure drop on part of both flue gases and air is 4%.

The impact of the pressure drop in the AHX on the efficiency of the complex gas-air system was also analysed. The difference in temperatures between the air inlet and the flue gas outlet is 10K. The results are listed in Table 6.

The gas-steam cycle was analysed with regard to the determination of the highest value of electricity generation efficiency for a given pressure of generated steam. The analysis was conducted parametrically for various pressure values in the air condenser (Fig. 9). In the gas-steam cycle the steam turbine featured internal efficiency at the level of η_{iST} = 90%.

Table 5. Power efficiency of a complex gas-air system for different values of the difference in the flue gas and air temperature in the AHX (t_{fg}=540°C)

ΔT, K	η_{eGT}, %	$\eta_{iC2}=\eta_{iC3}=\eta_{iT}$, %		
		82.50%	85.00%	87.50%
10	30	36.01	37.51	39.07
	35	40.57	41.97	43.42
	40	45.15	46.44	47.77
20	30	35.68	37.15	38.68
	35	40.27	41.64	43.06
	40	44.87	46.13	47.44
30	30	35.36	36.80	38.30
	35	39.97	41.31	42.71
	40	44.59	45.83	47.11

Table 6. Power efficiency of a complex gas-air system for different values of the pressure drop in the AHX (t_{fg}=540°C)

ΔP, %	$\eta_{GT,}$ %	$\eta_{iC2}=\eta_{iC3}=\eta_{iT}$, %		
		82.50%	85.00%	87.50%
3	30	36.16	37.67	39.23
	35	40.72	42.12	43.57
	40	45.28	46.57	47.91
5	30	35.84	37.35	38.91
	35	40.43	41.82	43.27
	40	45.01	46.30	47.64
7	30	35.52	37.02	38.58
	35	40.12	41.52	42.87
	40	44.73	46.02	47.36

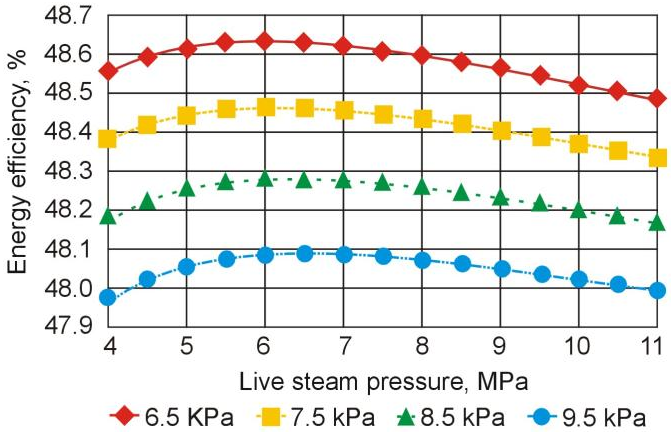

Fig.9. Electricity generation efficiency depending on steam pressure for different pressure values in the air cooled condenser

Even if the condenser pressure is p_{5s}=10 kPa, by selecting an appropriate steam pressure value, it is possible to achieve the system electricity generation efficiency at the level exceeding η_{eCCPP} = 48%. Considering the above, the gas-steam cycle turns out to be thermodynamically better than the gas-air cycle (both simple and complex with interstage cooling).

4. Economic analysis

The execution of an investment involves incurring certain investment expenditures. The determination of the size of the outlays is based on the information obtained from design departments. This information is often supplemented with feasibility studies, concerning for example:

- the costs related to the installation and start-up of the machinery and equipment,
- the costs related to the purchase and preparation of the site intended for the investment,
- the costs related to the construction works, etc.

The design of a consolidated statement of costs for a power engineering investment consists of:

- Studies, documentation and site preparation:
  - research works and related project documentation,
  - site acquisition and preparation.
- Basic and auxiliary facilities:
  - basic production facilities,
  - auxiliary and service facilities,
  - energy management facilities,
  - transport and communication management facilities,
  - external networks and structures related to them.
- Temporary structures together with the construction site equipment:
  - infrastructure for the contractor's needs,
  - temporary structures for the investor's needs.
- Investment-related services, training, start-up:
  - maintenance of investment staff,
  - preparation of the operational staff,
  - start-up costs.

- Reserve for incidental works and expenses.

This paper is focused on the estimation of the purchase costs of the basic machinery and equipment operating in the gas-air and the gas-steam installations. Two variants are distinguished in the case of the former installation:

- a simple system,
- a complex system.

4.1. Gas turbine purchase cost

The same gas turbine is used in each of the installation type mentioned above. The cost of generation of 1kWh was taken from [28] and adjusted with appropriate economic indicators for year 2011 [29].

The cost of the gas turbine can be determined from the dependence [30,31]:

$$C_{GT} = 10764 \cdot N_{elTG}^{0.7} \qquad (9)$$

The costs resulting from investment outlays on the purchase of machines and equipment are often related to their technical and thermodynamic parameters. For example, the compressor price can be defined by the following dependence [30]:

$$C_C = \alpha_1 \frac{39.5 \cdot m_{1a}}{0.9 - \eta_{ik}} \cdot \beta_k \cdot \ln \beta_k \qquad (10)$$

And the cost of the expander for the gas turbine installation by [30]:

$$C_T = \alpha_1 \frac{266.3 \cdot m_{3a}}{0.92 - \eta_{iT}} \cdot \ln \beta_T \cdot [1 + \exp(0.036 \cdot T_{3a} - 54.4 \cdot \alpha_2)] \qquad (11)$$

where [30]:

α_i – constants,

m_{1a} – amount of air fed into the compressor, kg/s

β_k – compressor pressure ratio, -

β_t – turbine pressure ratio, -

m_{3a} – amount of flue gases at the turbine inlet, kg/s

T_{3a} – turbine flue gas inlet temperature, K

η_i – internal efficiency, -

The purchase cost of the entire gas turbine system is about:

C_{GT} = \$12,500,000

4.2. Gas-air (GT-ABC) system purchase cost

In the case of the gas-air system, in addition to the gas turbine installation, it is necessary to determine the purchase cost of the air heat exchanger AHX , whose price is estimated in the same way as in the case of the heat recovery steam generator of the steam system, i.e. using the information obtained from industry [32]. The materials taken into account here are steels: P235GH, 16Mo3 or 13CrMo4-5 (EN 10216). Chromium steel would only be used at places where the working temperature exceeds the maximum permissible temperature for steel 16Mo3. The cost of purchase of the compressor and the expander was determined in the same way as for individual machines in the gas turbine system. In the case of the gas-air system with an intercooling installation it is necessary to include additionally the purchase cost of the heat exchanger (the interstage cooler), for which material P235GH (EN 10216) is used.

The cost of turbomachinery for simple system depending on the assumed isentropic efficiency is listed in Table 7.

Table 7. Purchase cost of individual air installation turbomachines (simple system)

Machine type	Price, USD (at given isentropic efficiency)		
	82.5%	85.0%	87.5%
Compressor	260,000	390,000	790,000
Expander	380,000	500,000	800,000

Undoubtedly, the biggest cost is the purchase of the AHX. Preliminary studies show that plate heat exchangers are more effective in minimising the pressure drops in the working media and the heat exchange area. Assuming a counterflow heat exchanger, three steel grades can be used in it at the same time: P235GH, 16Mo3 and 13CrMo4-5 (the following proportion is assumed: 43% of steel P235GH, 36% of steel 16Mo3 and 21% of steel 13CrMo4-5). Dividing costs in this way, the cost of purchase of the heat exchange area only will be about \$1,850,000[1]. For simple system the purchase cost is bigger (approx. \$2,300,000[2]). The shell and tube construction is not longer taken into account because of both bigger heat transfer area and bigger pressure drop of flue gases and air.

In the case of the gas-air system with an interstage cooler, the heat exchanger (the cooler) between the two groups of compressor stages has to be additionally included in the costs. Steel P235GH is assumed for the cooler. The interstage cooler is an air-to-air exchanger. For the assumed heat exchange effectiveness of $\varepsilon = 0.74$, and keeping the temperature at the inlet into the second compressor at the level of $t_{3a} = 40$°C, the cost of purchase for this machine would be about \$110,000.

The purchase cost of complex system turbomachinery is shown in Table 8. The presented prices are calculated for the maximum pressure ratio values. Due to the fact that the pressure value before the AHX in the system with an interooler cooler is higher than in the simple gas-air system, the expander price rose.

Table 8. Expander purchase cost for a complex gas-air system

Machine type	Price, USD (at given isentropic efficiency)		
	82.5%	85.0%	87.5%
Compressor	490,000	740,000	1,300,000
Ekspander	400,000	550,000	850,000

The price of the generators for the respective gas-air systems is [30,31]:

- a simple system – \$1,650,000, (net power output – approx. 29.2 MW; η_g=0.985),
- a complex system – \$1,600,000, (net power output – approx. 28.5 MW; η_g=0.985).

According to [33] the purchase cost of other components like ducts, dampers, stack, instrumentation, etc. was estimated on approx \$1,200,000 - \$1,300,000.

[1] Heat transfer surface area is equal approx. 66500m^2.

[2] Heat transfer surface area is equal approx. 83000m^2.

4.3. Gas-steam (CCPP) system purchase cost

In the case of the steam system, the heat recovery steam generator purchase cost plays an important role. The cost of the facility is estimated based on the information obtained from industry concerning the price of steel of which the individual parts of the heat exchange surfaces are made, on the area of individual heat exchangers, as well as on the coil thickness [32]. The materials used for the individual components of HRSG are shown in Table 9.

Table 9. Materials used to estimate the purchase cost of main HRSG's heat transfer surfaces

HRSG component	Material according to EN 10216	Material according to DIN
Economizer	P235GH	St 35.8 I/III
Evapurator	16Mo3	15 Mo 3
Superheater	13CrMo4-5	13 CrMo 44

The steam turbine purchase cost is of significant importance [30,31]:

$$C_{ST} = 1.36 \cdot \left(3197280 A_{ST}^{0.261} + 823.7 N_{elST}^{1.543}\right) \quad (12)$$

Cost of generators [30,31]:

$$C_G = 1.36 \cdot 3082 \cdot \left(\frac{N_{elGT}}{\eta_{gGT}} + \frac{N_{elST}}{\eta_{gST}} \right)^{0.58} \quad (13)$$

Cost of the condenser: [30,31]:

$$C_{CON} = 1.36 \cdot 275.4 \cdot A_{CON}^{1.01} \quad (14)$$

where:

A_{st} – exhaust annulus area, m^2

η_g – generator efficiency, %

The costs related to the gas-steam installation including the cost of the heat recovery steam generator, the steam turbine, the generator and the condenser are listed in Table 10. It should be noted that the turbine price was estimated for internal efficiency η_{iST} = 90%.

Table 10. Cost of purchase of the steam installation major machines and equipment

GT komponent	Price, USD
HRSG	4,000,000
Steam turbine	6,760,000
Generator*	1,800,000
Condenser	1,990,000

* net power output – approx. 34.2 MW

In the case of CCPP with single pressure HRSG the purchase cost of the entire system including other facilities is according to [34] approx. $31,600,000 (includes the price of gas turbine).

4.4. Comparison of the costs of purchase of individual installations

The costs of the three installations under analysis are listed in Table 11. In the case of the gas-air system, the isentropic efficiencies of turbomachines in the air part are assumed at the level of

$\eta_{iC} = \eta_{iE} = 87.5\%$. It should be noted that the presented costs do not include the purchase cost of the gas turbine.

Table 11. Cost of purchase of major machines and equipment of individual installations

	Simple gas-air system	Complex gas-air system	Gas-steam system
Purchase cost, thousand USD	approx. 6,740	approx. 6,960	approx. 14,550

Based on the electric power which can be obtained from the systems under analysis, it is possible to determine unit investment expenditures for individual installations. The results are presented in Table 12. In order to estimate unit investment expenditures, the power capacities of both the cycles under consideration and of the gas turbine system are totalled.

Table 12. Unit investment expenditures of the power systems under consideration

	Simple gas-air system	Complex gas-air system	Gas-steam system
Unit investment expenditure, USD/kW	approx. 660	approx. 690	approx. 930

Conclusions

Gas-air systems involve smaller investment expenditures than gas-steam cycles. However, they feature a lower efficiency. Both system types include expensive heat exchangers which recover heat energy from flue gases. In either case, the gas turbine is the most expensive component. Obtaining information on the nature of the system operation is an essential element in economic calculations. Is the task of the system to satisfy peak demand for electricity generation, or is the system intended for continuous operation. Is it to power working machines, such as the gas compressor in gas pumping stations etc., or is it to provide the power feed for the electric generator. The detailed data concerning investment expenditures are obtained only after the project has been completed. Studies are the basis for making investment decisions. The price of a gas-air system is predominantly determined by the amount of steel needed to make the AHX. The purchase price of turbomachinery depends mainly on isentropic efficiency. However, the costs related to the compressor and the air expander are not high due to moderate values of the working medium pressure. In the case of the gas-steam system, the principal cost-generating facilities are the heat recovery steam generator and the steam turbine. The total of these components is in fact equal to the price of the gas turbine. Like in the case of the gas-air system, the cost is determined by the amount of the material used for individual areas of heat exchange in the boiler and by the internal efficiency of the turbine. It should also be borne in mind that the gas-steam system is composed of more machinery and equipment, which undoubtedly affects the purchase price of individual installations. As for the heat exchangers, in both installations their price can be lowered at the expense of their effectiveness. Consequently, the purchase costs will be lower but so will be lower the electricity generation efficiency.

The current-generation combined cycles are usually gas-steam cycles. However, the heat contained in the flue gases after the gas turbine can be used differently. If another Brayton cycle with air as the working medium is added after the gas turbine, a combined gas-air system is created whose main advantage is a simple structure of the cycle. The point is that there are no facilities such as the condenser and there is no need to top up the water in the cycle. In the light of the thermodynamic analysis, gas-steam systems appear to be more efficient than gas-air ones. The most efficient

installation of a simple system composed of the ABB GT10 gas turbine and an air part reached 46.51% (Table 2) . Using an additional facility such as an intercooler, the efficiency of electricity generation was raised to 47.3% (Table 4). The simple gas-steam system reached a 48.4% efficiency, despite a high exhaust loss. The information on the nature of the future installation operation will be one of the main assumptions for a broad economic analysis. Considering the fact that they are less complex technologically, gas-air systems definitely have an advantage. It should be expected that the assembly of a gas-air system will take less time and, consequently, that the costs related to the commissioning of the new installation will be lower. If a system is placed where there is no access to water (gas pumping stations, for example), gas-air systems have a considerable advantage.

In this paper gas-steam and gas-air cycles are discussed and compared to each other thermodynamically and economically. The efficiency of individual systems and the purchase cost of major machines and equipment are determined.

Acknowledgments

„The results presented in this paper were obtained from research work co-financed by the National Centre of Research and Development in the framework of Contract SP/E/1/67484/10 – „Strategic Research Programme – Advanced Technologies for obtaining energy: Development of a technology for highly efficient zero-emission coal-fired Power units integrated with CO_2 capture".

Nomenclature

a - Thermal diffusivity, m^2/s
A - Exhaust annulus area, m^2
ABC - Air Bottoming Cycle
AHX - Air Heat Exchanger
AT - Air Turbine
C - cost, USD or compressor
CCPP - Combined Cycle Power Plant
CMB - combustion chamber
CND - condenser
c_p - specific heat, J/(kg K)
CP - condensate pump
DEA - deareator
ECO - Economizer
EVAP - Evapurator
FWP - feed water pump
G - Generator
GT - gas turbine
HRSG - Heat Recovery Steam Generator
HX - heat exchanger
IC - intercooler
LHV - low heat value
$\dot{m}$ - mass flow rate, kg/s
N - power, MW
Nu - Nusselt number, -

p,P - pressure, MPa
Pr - Prandtl number, -
R - gas constant, J/(kg K)
Re - Reynolds number, -
SH - superheater
ST - steam turbine
T, t - temperature, K, °C
$\dot{Q}$ - heat, W

Greek symbols

α - heat transfer coefficient, W/(m^{2}K)
β - pressure ratio
Δ - difference, -
ε - effectiveness, %
η - efficiency, %, dynamic viscosity, Pa·s
λ - thermal conductivity, W/mK
ρ - density, kg/m^3
υ - kinematic viscosity, m^2/s
ξ - relative pressure drop
ζ - temperature ratio, -

Subscripts and superscripts

a - Air
amb - Ambient
ABC - Air Bottoming Cycle
AT - Air turbine
c - Cycle
cpt - Cold pinch temperature
C - Compressor
e - Energetic
el - Electric
f - fuel
fg - Flue gas
G - Generator
GT - Gas turbine
i - Internal, isentropic
in - In
ls - Live steam
m - Mechanical
out - Out
pp - Pinch point
sc - Subcooling
ST - Steam turbine

t - temperature, K, °C

T - Turbine

References

[1] Chmielniak T., Lepszy S. Technical and economical analysis of gas-turbine systems with external combustion of the biomass. Archives of thermodynamics Vol. 28 (2007) No. 3, 67-80.

[2] Chmielniak T., Lepszy S. External combustion of biomass parallely coupled with the gas turbine unit. Międzynarodowe Sympozjum SYMKOM'05 Compressor and turbine flow systems – theory and application areas, Łódź, 21-23 wrzesień 2005r. Institute of Turbomachinery, Technical University of Łódź.

[3] Lepszy S., Chmielniak T. Energy and exergy analyses of micro gas turbine system with external combustion of the biomass. Proceedings of 15th European Biomass Conference "From Research To Market Deployment", Berlin, 7-11 may 2007, ETA-Renewable Energies.

[4] Chmielniak T., Rusin A., Czwiertnia K. Turbiny gazowe. Maszyny przepływowe tom 25. Zakład Narodowy im. Ossolińskich Wydawnictwo Polskiej Akademii Nauk. Wrocław 2001.

[5] Miller A. Maszyny i urządzenia cieplne i energetyczne. Wydawnictwo Szkolne i Pedagogiczne, Warszawa 1989.

[6] Miller A., Lewandowski J. Układy gazowo-parowe na paliwo stałe. WNT Warszawa 1993.

[7] Chmielniak T. Technologie energetyczne. Wydawnictwo Politechniki Śląskiej, Gliwice 2004.

[8] Skorek J., Kalina J. Gazowe układy ko generacyjne. WNT, Warszawa 2005.

[9] Najjar Y. S. H., Zaamout M. S. Performance Analysis of Gas Turbine Air-Bottoming Combined System. Energy Conversion And Management Vol. 37, No. 4, pp 399-403, 1996.

[10] Korobitsyn M. Industrial applications of the air bottoming cycle. Energy Conversion and Menagement 43 (2002) 1311-1322.

[11] Chmielniak T., Czaja D., Lepszy S. Wykorzystanie układów gazowo-powietrznych w ciepłownictwie. Rynek Ciepła 2011, Wydawnictwo Kaprint Lublin 2011.

[12] Chmielniak T., Lepszy S., Czaja D. Analysis of gas turbine air-bottoming-cycle and heat exchanger modelling. Proceedings of ECOS 2011, Novi Sad, Serbia 2011.

[13] Chmielniak T., Lepszy S., Czaja D. The use of air-bottoming cycle as a heat source for the carbon dioxide capture installation of a coal-fired power unit. Konferencja „Problemy Badawcze Energetyki Cieplnej", Warszawa 13 – 16.12.2011, Archieves of Thermodynamic Vol. 41(2011), No. 3, 4.

[14] Kotowicz J. Analiza efektywności elektrowni gazowo-parowych; układ z trójciśnieniowym kotłem i przegrzewem międzystopniowym. Archiwum Energetyki, tom XXXI, nr 1-2, 29-49.

[15] Kotowicz J. Dobór optymalnych parametrów w części parowej układu gazowo-parowego. IX Konferencja Kotłowa 2002. Prace IMiUE Politechniki Śląskiej.

[16] Kotowicz J., Chmielniak T. Badanie wpływu struktury elektrowni gazowo-parowych na charakterystyki sprawności. IV Międzynarodowa Konferencja Naukowo-Techniczna Expo-Ship 2006. Zeszyty Naukowe Nr 10(82) Akademii Morskiej w Szczecinie.

[17] Steinbach C., Goudeaux D., Troger C., Moore R. Operation experience with Alstom Power's GT10 gas turbine and ultra low NO_x combustion control.

[18] Gate Cycle™ Getting Started & Installation Guide – opis programu Gate Cycle.

[19] Modern Power Systems (July 2011).

[20] Smith E. Thermal design of heat exchangers. John Wiley & Sons Ltd, Baffins Lane, Chichester 1997.

[21] Hewitt G. Heat Exchanger design handbook. York, Begell House 2002.

[22] Kostowski E. Przepływ ciepła. Wydawnictwo Politechniki Śląskiej, Gliwice 2000.

[23] Hobler T. Ruch ciepła i wymienniki. WNT Warszawa 1986.

[24] Pudlik W. Wymiana i wymienniki ciepła. Wydawnictwo Politechniki Gdańskiej, Gdańsk 1988.

[25] Edwards J. Design and rating sheel and tube heat exchangers. P&I Design Ltd, UK.

[26] Shankar R. Heat transfer to or from a fluid flowing through a tube.

[27] Larinoff M., Reichhelm M. and R. Design and specification of air-cooled steam condensers – Hudson Products Corporation; Houston, Texas; Reprint from Chemical Engineering, 1978.

[28] Parson Brickerhoff New Zeland Ltd. Cost estimates for thermal peaking plant – final report (June 2008).

[29] Marshall & Swift Equipment Cost Index. Chemical Engineering. Oct. 2011 Vol. 118 Issue 10, p80-80.

[30] Kotowicz J. Elektownie gazowo-parowe. Wydawnictwo KAPRINT. Lublin 2008.

[31] Attala L., Facchini B., Ferrara G. Thermoeconomic optimization method as design tool in gas-steam combined plant realization. Energy Conversion and Managment 42 (2001) 2163-2172.

[32] Own information obtained from industry 2011 (Information related to the cost factors).

[33] Bolland O., Forde M., Hande B. Air Bottoming Cycle: Use of Gas Turbine Waste Heat for Power Generaton. Journal of Engineering for Gas Turbines and Power, 1996 – Volume 118, Issue2, 359.

[34] Gas Turbine World Handbook 2009.

Application of an Alternative Thermoeconomic Approach to a Two-Stage Vapor Compression Refrigeration Cycle with Intercooling

Atilio B. Lourenço[a], José Joaquim C. S. Santos[b], João Luiz M. Donatelli[c]

Federal University of Espírito Santo, Vitória-ES, Brazil.
*[a] atiliobl@gmail.com (**CA**), [b] jjcssantos@yahoo.com.br, [c] donatelliufes@gmail.com*

Abstract:

In any energy system, in the same manner that there are productive components, there also exist dissipative components. Although there has been an advance in the development of thermoeconomic criteria for dissipative components allocation, this problem is still open. The introduction of the negentropy in thermoeconomics represented a great advance, since this magnitude allows quantifying the condenser product. However, negentropy itself does not allow defining the product of valves. To overcome such a limitation, in this paper an alternative thermoeconomic approach is applied to a two-stage vapor compression refrigeration cycle with intercooling. The approach is based on disaggregation of the physical exergy into three terms, namely internal energy ($U–U_0$), flow work ($pV–p_0V_0$) and the here called entropic term ($T_0S–T_0S_0$). The so-called UFS Model allows the valves isolation in the productive structure. The goal is to obtain the exergetic unit cost of each internal flow, considering an ideal cycle and an actual cycle, as application examples. Such an alternative approach yields consistent results, because exergetic unit costs of internal flows are greater than or equal to one and product-fuel ratio of each productive unit are less than or equal to one, depending on the situation, i.e., when considering the actual cycle or the ideal cycle, respectively. Besides the allocation of the external power of the plant, analyses on irreversibilities of each cycle unit are carried out by the exergy balance and by the difference between the defined fuels (resources) and products, according to the systematic of this alternative approach. Thus, it is shown that the UFS Model can be used in order to quantify irreversibilities as well as the conventional exergy analysis. Results show that the product-fuel ratio of each component of the proposed structure varies from zero (for totally irreversible processes) to one (for totally reversible processes).

Keywords:

Exergy Disaggregation, Refrigeration Cycle, Thermoeconomics, Valves Isolation.

1. Introduction

Thermoeconomics can be considered a new science which, by connecting Thermodynamics and Economics, provides tools to solve problems in complex energy systems that can hardly or not be solved using conventional energy analysis techniques based on First Law of Thermodynamics (mass and energy balance), as for instance a rational price assessment to the products of a plant based on physical criteria [1].

In any energy system, in the same manner that there are productive components, there also exist dissipative components. An energy system has a defined productive structure, but also dissipative ones and both structures are not independent. Although there has been an advance in the development of criteria for the cost allocation of residues, this problem is still open [2].

One of the thermoeconomic methodologies challenges is to define the productive structure of thermal systems that allows allocating rationally the cost of dissipative components to final products. The way in which we define the productive structure is a key point of the thermoeconomic modeling [3]. Different thermoeconomic methodologies can provide different cost values when they define different productive structures. Cost validation is a key issue in thermoeconomics which has not been properly solved yet. However, one considers that cost

validation can be designed using the physical behavior of the plant together with Thermodynamics, because irreversibility is the physical magnitude generating the cost [4].

According to [5], depending on the type of analysis, different levels of accuracy of the results are required. Sometimes, under a thermoeconomic analysis point of view, it is necessary to consider a component as a group of subsystem (made up of a group of subsystem) or a mass or an energy flow rate consisting of several components, for example thermal, mechanical or chemical exergy, as proposed by [6], or even to include fictitious flow stream (negentropy) without a physical existence in the flow sheet of the plant, as proposed by [7].

The negentropy flow was applied in thermoeconomics joined up with exergy flow [7]. Negentropy was defined as the negative variation of entropy multiplied by the temperature of the environment. This application represented a great advance in the discipline, since it allowed one to quantify the condenser product, which was not possible before because the condenser is a dissipative component, whose product cannot be expressed in terms of exergy. The concept of negentropy was also used in order to define the productive structure of a gas turbine cogeneration system [3,8].

However, when negentropy is applied as a fictitious flow (joined up with exergy flow), it is not possible to obtain an efficiency based on the Second Law of Thermodynamics (product-resource ratio), since the product of dissipative units might be higher than its resource, yielding unit costs lesser than one for some flows [9]. This happens because exergy loss is considered as fuel and negentropy (in this work also called syntropy) as product. To overcome this problem, the H&S Model was developed [9] to allocate wastes of dissipative component (the condenser) in the thermoeconomic analysis of energy systems. The basis of this method is the breakup of exergy into enthalpy and negentropy. Enthalpy flows replace exergy flows and negentropy flows are used as a component of exergy. Therefore, the productive structure is defined using enthalpy and negentropy flows.

The disaggregation of exergy in thermal and mechanical components does not allow defining the product of the condenser. On the other hand, this goal is achieved when negentropy is used both as a fictitious flow [7] and as an exergy component flow [9]. But none of them allows defining the product of valves (for instance, in a refrigeration cycle). Thus, this paper presents an alternative thermoeconomic approach, which is so-called UFS Model, based on disaggregation of physical exergy into internal energy ($U-U_0$), flow work ($pV-p_0V_0$) and the here called syntropy ($T_0S-T_0S_0$). This disaggregation of the physical exergy allows the isolation of valves in the productive structure, so defining their resources and products, without generating any problems [10].

2. Physical Model

A two-stage vapor compression refrigeration cycle with intercooling is used, in this paper, to illustrate the application of the UFS Model. The intercooling of the working fluid is achieved by using both a flash tank and a mixing tank. By using this cycle, this paper shows the capacity of the UFS Model to treat an important point in discussion related to the thermoeconomic methodologies: the dissipative components, as condensers and valves. Figure 1 represents the physical structure of the refrigeration cycle, which is defined as having eight units: the high-pressure compressor (cmp.h), the low-pressure compressor (cmp.l), the high-pressure expansion valve (vlv.h), the low-pressure expansion valve (vlv.l), the evaporator (evp), the condenser (cnd), the flash tank (flt) and the mixing tank (mxt).

Assumptions made for the modeling are:

- Equipments are analyzed as control volumes at steady state and are adiabatic;
- The exergy provided by the evaporator to the cold region is modeled as an exergy flow associated with the heat transfer;
- There is no pressure drop for flow through heat exchangers;

- Kinetic and potential energy effects are negligible.

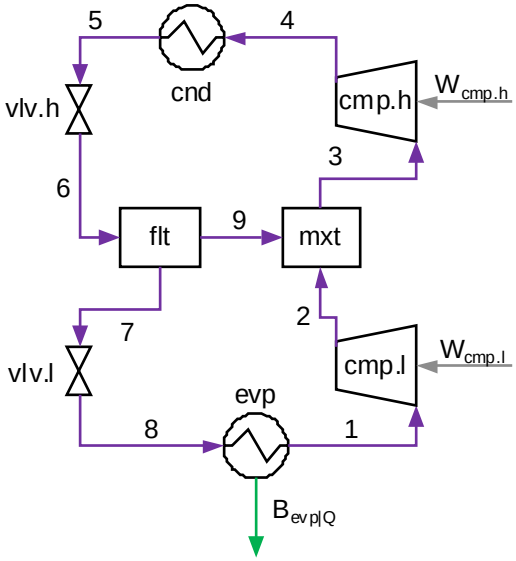

Fig. 1. Physical Structure of the Refrigeration Cycle.

3. Exergy and Thermoeconomic Modelling

In order to carry out a thermoeconomic analysis, the UFS Model defines the productive purpose of the subsystems (resources and products), as well as the distribution of the external resources and internal products throughout the system. The productive structure could be represented by means of a functional diagram. In this section, basic concepts of the cost formation are shown. After that, the UFS Model is applied to generate the productive structure of the studied refrigeration cycle. Finally, the exergy balances are done for each equipment of such a cycle.

3.1. Productive Structure and Costs Formation

The productive structure represents the cost formation process of the cycle. The external resources consumed by the cycle are the mechanical power demanded by the high-pressure compressor ($W_{cmp.h}$) and the low-pressure compressor ($W_{cmp.l}$). The functional product is the exergy, which is associated to the heat transfer, provided by the evaporator ($B_{evp|Q}$). Rectangles are real units that represent the actual equipment of the cycle. Rhombus and circles are fictitious units called junctions and bifurcations, respectively. Each productive unit has inlet and outlet arrows that represent its resources and products, respectively. Each productive flow is defined based on physical flows.

The mathematical model for the mechanical power allocation is obtained by formulating the cost balance equation in each productive unit, or subsystem, of the productive structure, as shown in (1), where k is the exergetic unit cost of productive flows (unknown variable) and Y represents the generic productive flow, which can be internal or external. The exergetic unit cost of the mechanical power is equal to one.

$$\sum (k \cdot Y) = 0 . \qquad (1)$$

Efficiency is defined as the ratio of the desired result for an event to the input required to accomplish such an event. Therefore, when one defines the fuel and the product during the thermoeconomic modeling, one takes into account that the Second Law efficiency ranges from zero, for a totally irreversible process, to 100 percent, for a totally reversible process [11]. Thus, the exergetic unit cost is the inverse of an efficiency, which is defined as the ratio between the products of a productive unit and the external fuels of the plant.

Since the number of flows is always greater than the number of productive units, some auxiliary equations attribute the same exergetic unit cost to all of productive flows leaving the same bifurcation. The solution of the set of cost balance equations allows the attainment of the exergetic unit cost of each internal flow and final product.

3.2. The UFS Model

The physical exergy (B_i) of a refrigerant stream is written as shown in (2), where h_0 and s_0 are the specific enthalpy and the specific entropy, both at the dead state, respectively. Dead state is at T_0, the reference temperature, and at p_0, the reference pressure.

$$B_i = m_i \cdot [(h_i - h_0) - T_0 \cdot (s_i - s_0)]. \quad (2)$$

To generate the productive structure, the so-called UFS Model considers that the physical exergy must be disaggregated into three components, which are the internal energy (U_i), the flow work (F_i) and the syntropy (S_i). The productive structure is shown in Fig. 2.

The products and the fuels of each subsystem, in terms of internal energy, flow work and chemical exergy component, are defined based on the quantity of these magnitudes added to and removed from the working fluid, respectively. On the other hand, the entropic component flows are the products of the subsystems that decrease the working fluid entropy, and subsystems that increase the working fluid entropy are entropic components consumers.

The physical flows are calculated as shown in (3-5), where u_0 and v_0 are the specific internal energy and the specific volume, both at the dead state, respectively. One must remind that the enthalpy is defined as the sum between the internal energy and the flow work.

$$U_i = m_i \cdot (u_i - u_0), \quad (3)$$

$$F_i = m_i \cdot (p_i v_i - p_0 v_0), \quad (4)$$

$$S_i = m_i \cdot T_0 \cdot (s_i - s_0). \quad (5)$$

Chemical exergy is not considered because there is no changing in the composition of the fluid throughout the processes of the cycle.

The disaggregation of the enthalpy is done because when one evaluates an adiabatic valve at steady state, the enthalpy variation between its upstream and downstream flows is equal to zero, but the increasing of its flow work is equal to the decreasing of its internal energy. In light of this, it is now possible to define a product for a valve.

Internal flows of the productive structure are calculated using (6-11).

$$U_{i:j} = m_i \cdot (u_i - u_j), \quad (6)$$

$$F_{i:j} = m_i \cdot (p_i v_i - p_j v_j), \quad (7)$$

$$S_{i:j} = m_i \cdot T_0 \cdot (s_i - s_j), \quad (8)$$

$$U_{i:j'} = m_j \cdot (u_i - u_j), \quad (9)$$

$$F_{i:j'} = m_j \cdot (p_i v_i - p_j v_j), \quad (10)$$

$$S_{i:j'} = m_j \cdot T_0 \cdot \left(s_i - s_j\right). \tag{11}$$

The set of cost balance equations is given by (12-22).

$$k_{cmp.l} \cdot \left(U_{2:1} + F_{2:1}\right) - k_S \cdot S_{2:1} = W_{cmp.l}, \tag{12}$$

$$k_{cmp.h} \cdot \left(U_{4:3} + F_{4:3}\right) - k_S \cdot S_{4:3} = W_{cmp.h}, \tag{13}$$

$$k_{vlv.l} \cdot F_{8:7} - \left(k_U \cdot U_{7:8} + k_S \cdot S_{8:7}\right) = 0, \tag{14}$$

$$k_{vlv.h} \cdot F_{6:5} - \left(k_U \cdot U_{5:6} + k_S \cdot S_{6:5}\right) = 0, \tag{15}$$

$$k_{cnd} \cdot S_{4:5} - \left(k_U \cdot U_{4:5} + k_F \cdot F_{4:5}\right) = 0, \tag{16}$$

$$k_{evp} \cdot \left(B_{evp|Q} + U_{1:8} + F_{1:8}\right) - k_S \cdot S_{1:8} = 0, \tag{17}$$

$$k_{flt} \cdot \left(U_{9:6} + F_{9:6} + S_{6:7'}\right) - \left(k_U \cdot U_{6:7'} + k_F \cdot F_{6:7'} + k_S \cdot S_{9:6}\right) = 0, \tag{18}$$

$$k_{mxt} \cdot \left(U_{3:9'} + F_{3:9'} + S_{2:3}\right) - \left(k_U \cdot U_{2:3} + k_F \cdot F_{2:3} + k_S \cdot S_{3:9'}\right) = 0, \tag{19}$$

$$\begin{aligned} &k_U \cdot \left(U_{7:8} + U_{5:6} + U_{4:5} + U_{6:7'} + U_{2:3}\right) \\ &- \left(k_{cmp.l} \cdot U_{2:1} + k_{cmp.h} \cdot U_{4:3} + k_{evp} \cdot U_{1:8} + k_{flt} \cdot U_{9:6} + k_{mxt} \cdot U_{3:9'}\right) = 0 \end{aligned}, \tag{20}$$

$$\begin{aligned} &k_F \cdot \left(F_{4:5} + F_{6:7'} + F_{2:3}\right) \\ &- \left(k_{cmp.l} \cdot F_{2:1} + k_{cmp.h} \cdot F_{4:3} + k_{vlv.l} \cdot F_{8:7} + k_{vlv.h} \cdot F_{6:5} + k_{evp} \cdot F_{1:8} + k_{flt} \cdot F_{9:6} + k_{mxt} \cdot F_{3:9'}\right) = 0 \end{aligned}, \tag{21}$$

$$\begin{aligned} &k_S \cdot \left(S_{2:1} + S_{4:3} + S_{8:7} + S_{6:5} + S_{1:8} + S_{9:6} + S_{3:9'}\right) \\ &- \left(k_{cnd} \cdot S_{4:5} + k_{flt} \cdot S_{6:7'} + k_{mxt} \cdot S_{2:3}\right) = 0 \end{aligned}. \tag{22}$$

In Fig. 2, orange lines represent $U_{i:j}$ and $U_{i:j'}$, blue lines represent $F_{i:j}$ and $F_{i:j'}$, red lines represent $S_{i:j}$ and $S_{i:j'}$, gray lines represent mechanical power, black lines represent the resource and the product of productive units and the green line represents the product of the refrigeration cycle.

One should note that Fig. 2, i.e., the productive structure of the refrigeration cycle, is the graphical representation of (12-22).

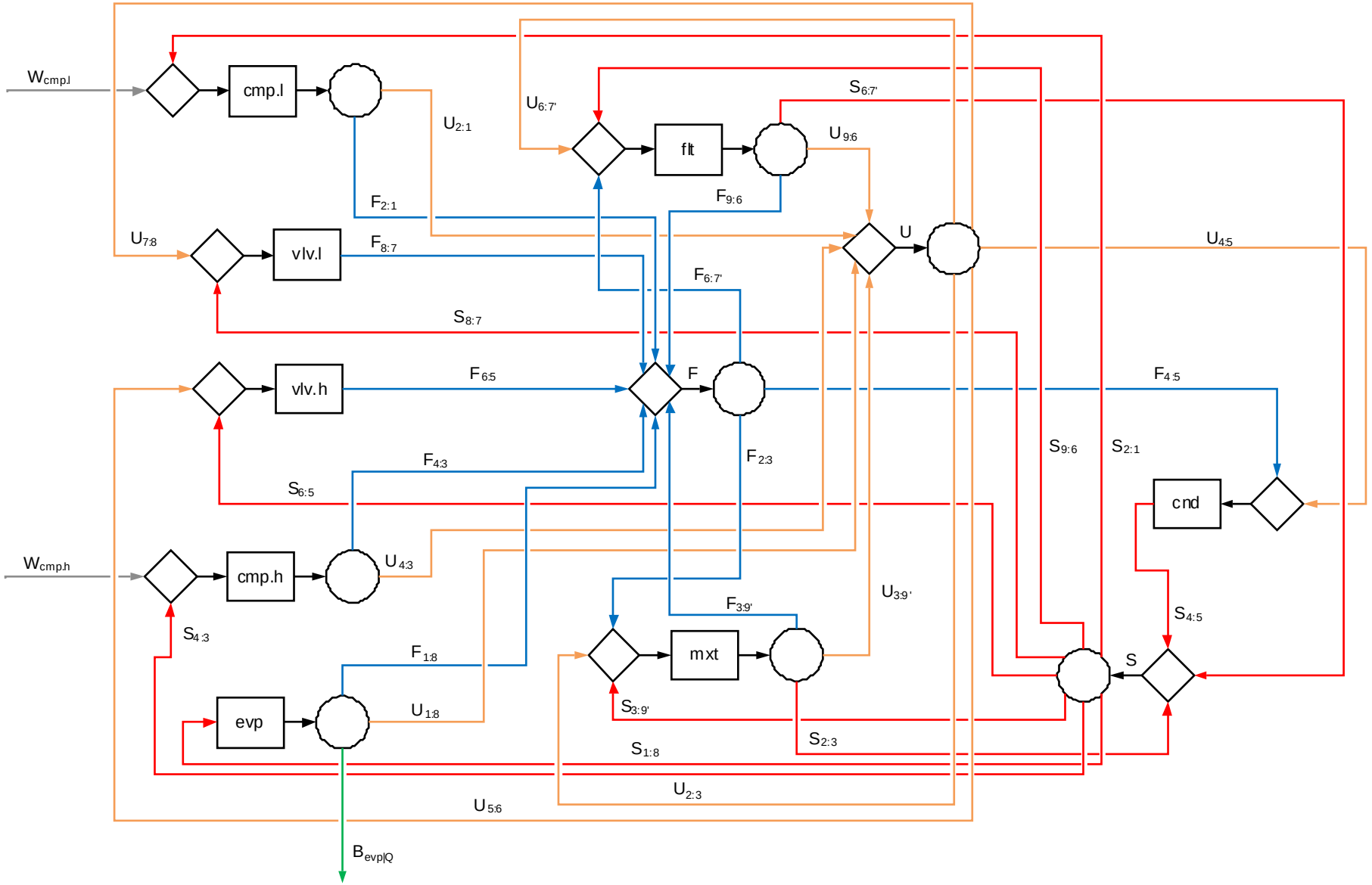

Fig. 2. Productive Structure of the Refrigeration Cycle

Equations (23-33) are generated by taking the difference between resources and products for all units, both real and fictitious ones, of the productive structure.

$$(R-P)_{cmp.l} = (W_{cmp.l} + S_{2:1}) - (U_{2:1} + F_{2:1}), \tag{23}$$

$$(R-P)_{cmp.h} = (W_{cmp.h} + S_{4:3}) - (U_{4:3} + F_{4:3}), \tag{24}$$

$$(R-P)_{vlv.l} = (U_{7:8} + S_{8:7}) - F_{8:7}, \tag{25}$$

$$(R-P)_{vlv.h} = (U_{5:6} + S_{6:5}) - F_{6:5}, \tag{26}$$

$$(R-P)_{cnd} = (U_{4:5} + F_{4:5}) - S_{4:5}, \tag{27}$$

$$(R-P)_{evp} = S_{1:8} - (B_{evp|Q} + U_{1:8} + F_{1:8}), \tag{28}$$

$$(R-P)_{flt} = (U_{6:7'} + F_{6:7'} + S_{9:6}) - (U_{9:6} + F_{9:6} + S_{6:7'}), \tag{29}$$

$$(R-P)_{mxt} = (U_{2:3} + F_{2:3} + S_{3:9'}) - (U_{3:9'} + F_{3:9'} + S_{2:3}), \tag{30}$$

$$(R-P)_{U} = (U_{2:1} + U_{4:3} + U_{1:8} + U_{9:6} + U_{3:9'}) - (U_{7:8} + U_{5:6} + U_{4:5} + U_{6:7'} + U_{2:3}), \tag{31}$$

$$(R-P)_{F} = (F_{2:1} + F_{4:3} + F_{8:7} + F_{6:5} + F_{1:8} + F_{9:6} + F_{3:9'}) - (F_{4:5} + F_{6:7'} + F_{2:3}), \tag{32}$$

$$(R-P)_{S} = (S_{4:5} + S_{6:7'} + S_{2:3}) - (S_{2:1} + S_{4:3} + S_{8:7} + S_{6:5} + S_{1:8} + S_{9:6} + S_{3:9'}). \tag{33}$$

3.3. Exergy Balances

The exergy balance is done for each control volume in the physical structure. The sum between the exergy destruction (B_D) and the exergy loss (B_L) is evaluated for each equipment that lies in such a structure. Applying the exergy balance for control volumes at steady state, (34), it generates (35-42).

$$\left(1 - \frac{T_0}{T}\right) Q - W - B_D = \sum_{out|m} B_{out|m} - \sum_{in|m} B_{in|m}, \tag{34}$$

$$B_{D.cmp.l} = W_{cmp.l} + B_1 - B_2, \tag{35}$$

$$B_{D.cmp.h} = W_{cmp.h} + B_3 - B_4, \tag{36}$$

$$B_{D.vlv.l} = B_7 - B_8, \tag{37}$$

$$B_{D.vlv.h} = B_5 - B_6, \tag{38}$$

$$B_{D.cnd} + B_{L.cnd} = B_4 - B_5, \tag{39}$$

$$B_{D.evp} = B_8 - B_1 - B_{evp|Q}, \tag{40}$$

$$B_{D.flt} = B_6 - B_7 - B_9, \tag{41}$$

$$B_{D.mxt} = B_9 + B_2 - B_3. \tag{42}$$

On the condenser, it is considered that the exergy loss is equal to the net exergy associated to the cooling water flow, i.e., the difference between the exit and inlet water flows exergies. Nevertheless, for purposes of this paper, it is not necessary to know the value of that exergy loss, because such a loss is internalized in the productive structure.

3.4. Applying Examples

In order to exemplify the applying of the UFS Model, such an approach is going to be used to evaluate a defined actual cycle and a defined non-actual cycle, according to the data given in the next paragraph. This is done to check the consistency of the proposed thermoeconomic approach.

Considering the actual cycle, let the isentropic efficiencies of both high-pressure compressor ($\eta_{C.high}$) and low-pressure compressor ($\eta_{C.low}$) be equal to 0.90, the temperature difference between the cold region that receives the exergy provided by the evaporator (ΔT_{evp}) and the state 8 be equal to 5 K and the temperature difference between the state 5 of the physical structure and the environment (ΔT_{cnd}) be equal to 5 K. Considering the non-actual cycle, the compression processes are isentropic ($\eta_{C.high} = \eta_{C.low} = 1$) and there are no temperature differences ($\Delta T_{cnd} = \Delta T_{evp} = 0$ K).

Streams parameters of the refrigeration cycle for both the actual and non-actual situations are presented in Table 1. Streams 2, 3 and 4 have different thermodynamic properties in each situation (subscripts *a* and *n-a*, respectively). Values are based on [12]. The refrigerant is R-134a. Thermodynamic properties, in this case specific internal energy, specific volume and specific entropy, of the fluid are evaluated from the database of the software Engineering Equation Solver (EES).

Considering the actual cycle, the reference temperature is equal to 314.44 K. Considering the non-actual cycle, the reference temperature is equal to 319.44 K. The exergy provided by the evaporator is calculated by multiplying the exergetic temperature factor, considering the evaporation temperature, and the value of the heat transfer associated to such equipment.

Table 1. Streams Parameters and Thermodynamic Properties of R-134a

Physical Flow		*m* [kg/s]	*p* [kPa]	*T* [K]	*u* [kJ/kg]	*v* [m³/kg]	*s* [kJ/kg-K]
i	Description						
1	Vapor ($x = 1$)	2.091	84.43	243.15	213.11	0.22580	0.9558
2_a	Vapor	2.091	400.00	294.76	245.49	0.05464	0.9678
2_{n-a}	Vapor	2.091	400.00	290.15	242.38	0.05363	0.9558
3_a	Vapor	2.907	400.00	291.17	242.56	0.05369	0.9565
3_{n-a}	Vapor	2.907	400.00	288.44	240.32	0.05296	0.9478
4_a	Vapor	2.907	1,200.00	334.08	268.47	0.01851	0.9645
4_{n-a}	Vapor	2.907	1,200.00	329.13	263.61	0.01794	0.9478
5	Liquid ($x = 0$)	2.907	1,200.00	319.44	116.70	0.00089	0.4244
6	Mixture ($x = 0.2809$)	2.907	400.00	282.06	111.79	0.01495	0.4385
7	Liquid ($x = 0$)	2.091	400.00	282.06	63.62	0.00079	0.2476
8	Mixture ($x = 0.2336$)	2.091	84.43	243.15	59.44	0.05331	0.2639
9	Vapor ($x = 1$)	0.817	400.00	282.06	235.07	0.05120	0.9269

4. Results and Discussion

Table 2 shows the exergy balance sheet for the given numerical data. Percentages are based on total exergy, which is defined by the sum between the mechanical power inlets. Such a value is also equal to the sum between the exergy provided by the refrigeration cycle and the exergy destructions and losses of all equipments.

Table 2. Exergy Balance Sheet

Description		Actual Cycle		Non-Actual Cycle	
		Value [kW]	Percentage	Value [kW]	Percentage
Total Exergy		151.01	100%	134.88	100%
Power in:	HP Compressor	77.47	51.30%	68.69	50.93%
	LP Compressor	73.54	48.70%	66.19	49.07%
Product Exergy:	Evaporator	93.96	62.22%	110.35	81.82%
Exergy Destructions and Losses:	LP Compressor	7.90	5.23%	0.00	0.00%
	HP Compressor	7.32	4.85%	0.00	0.00%
	LP Valve	10.74	7.11%	10.91	8.09%
	HP Valve	12.84	8.50%	13.05	9.67%
	Condenser	8.95	5.93%	0.51	0.38%
	Evaporator	9.14	6.05%	0.00	0.00%
	Flash Tank	0.00	0.00%	0.00	0.00%
	Mixing Tank	0.17	0.11%	0.08	0.06%

The exergetic efficiency of the refrigeration cycle, (43), is equal to the ratio between the product exergy of the cycle and its mechanical power inputs. As seen in Table 2, such a value is equal to 62.22% for the actual cycle and equal to 81.82% for the non-actual cycle.

$$\varepsilon = \frac{B_{evp|Q}}{W_{cmp.h} + W_{cmp.l}}. \tag{43}$$

Table 3 shows productive flows, its values and its respective exergetic unit costs for the given numerical data. One should note that there is no exergetic unit cost value less than one.

Taking the inverse of the exergetic unit cost of the product exergy, (44), one obtains the same value of the exergetic efficiency of the refrigeration cycle, i.e., 62.22% for the actual cycle and 81.82% for the non-actual cycle.

$$\varepsilon = \frac{1}{k_{evp}}. \tag{44}$$

Table 4 shows the values of the difference between resources and products of both real and fictitious units of the productive structure for the given numerical data.

For the real productive units, the differences between resources and products (Table 4) are equal to the sums of both exergy destruction and loss of the same units of the physical structure (Table 2). Actually, one can do some algebra from (23-30) and (6-11) and obtain (35-42). For the fictitious productive units, the differences between resources and products (Table 4 and 31-33) are equal to zero. Therefore, exergetic costs are fairly distributed among the productive structure.

Considering the non-actual cycle and its values from Table 4, the difference of the condenser is not equal to zero because the desuperheating and the difference of the mixing tank is not equal to zero because its inlet streams are at different thermodynamic states.

Table 3. Exergetic Unit Costs

Productive Flow	Value [kW]		Exergetic Unit Cost [kW/kW]	
	Actual Cycle	Non-Actual Cycle	Actual Cycle	Non-Actual Cycle
$U_{1:8}$	321.25	321.25	1.607	1.222
$U_{2:1}$	67.71	61.19	1.169	1.000
$U_{2:3}$	6.13	4.30	1.486	1.170
$U_{3:9'}$	6.11	4.29	1.579	1.231
$U_{4:3}$	75.33	67.70	1.149	1.000
$U_{4:5}$	441.25	427.12	1.486	1.170
$U_{5:6}$	14.27	14.27	1.486	1.170
$U_{6:7'}$	100.70	100.70	1.486	1.170
$U_{7:8}$	8.75	8.75	1.486	1.170
$U_{9:6}$	100.70	100.70	1.559	1.219
$F_{1:8}$	30.45	30.45	1.607	1.222
$F_{2:1}$	5.83	4.99	1.169	1.000
$F_{2:3}$	0.79	0.56	2.015	1.594
$F_{3:9'}$	0.81	0.57	1.579	1.231
$F_{4:3}$	2.14	0.99	1.149	1.000
$F_{4:5}$	61.46	59.46	2.015	1.594
$F_{6:5}$	14.27	14.27	2.903	2.287
$F_{6:7'}$	11.84	11.84	2.015	1.594
$F_{8:7}$	8.75	8.75	3.419	2.694
$F_{9:6}$	11.84	11.84	1.559	1.219
$S_{1:8}$	454.80	462.03	1.575	1.222
$S_{2:1}$	7.90	-----	1.575	-----
$S_{2:3}$	7.43	5.36	1.579	1.231
$S_{3:9'}$	7.60	5.44	1.575	1.222
$S_{4:3}$	7.32	-----	1.575	-----
$S_{4:5}$	493.75	486.07	1.579	1.223
$S_{6:5}$	12.84	13.05	1.575	1.222
$S_{6:7'}$	125.45	127.45	1.559	1.219
$S_{8:7}$	10.74	10.91	1.575	1.222
$S_{9:6}$	125.45	127.45	1.575	1.222
$B_{evp\|Q}$	93.96	110.35	1.607	1.222
$W_{cmp.l}$	73.54	66.19	1.000	1.000
$W_{cmp.h}$	77.47	68.69	1.000	1.000

Table 4. Differences between Resources and Products of Productive Units

Productive Unit	Difference Value [kW]	
	Actual Cycle	Ideal Cycle
LP Compressor (cmp.l)	7.90	0.00
HP Compressor (cmp.h)	7.32	0.00
LP Valve (vlv.l)	10.74	10.91
HP Valve (vlv.h)	12.84	13.05
Condenser (cnd)	8.95	0.51
Evaporator (evp)	9.14	0.00
Flash Tank (flt)	0.00	0.00
Mixing Tank (mxt)	0.17	0.08
Internal Energy (U)	0.00	0.00
Flow Work (F)	0.00	0.00
Syntropy (S)	0.00	0.00

Taking the ratios between products and resources of the productive units, such ratios are defined based on the Second Law of Thermodynamics, the set (45-55) is generated.

$$\eta_{cmp.l} = \frac{U_{2:1} + F_{2:1}}{W_{cmp.l} + S_{2:1}}, \tag{45}$$

$$\eta_{cmp.h} = \frac{U_{4:3} + F_{4:3}}{W_{cmp.h} + S_{4:3}}, \tag{46}$$

$$\eta_{vlv.l} = \frac{F_{8:7}}{U_{7:8} + S_{8:7}}, \tag{47}$$

$$\eta_{vlv.h} = \frac{F_{6:5}}{U_{5:6} + S_{6:5}}, \tag{48}$$

$$\eta_{cnd} = \frac{S_{4:5}}{U_{4:5} + F_{4:5}}, \tag{49}$$

$$\eta_{evp} = \frac{B_{evp|Q} + U_{1:8} + F_{1:8}}{S_{1:8}}, \tag{50}$$

$$\eta_{flt} = \frac{U_{9:6} + F_{9:6} + S_{6:7'}}{U_{6:7'} + F_{6:7'} + S_{9:6}}, \tag{51}$$

$$\eta_{mxt} = \frac{U_{3:9'} + F_{3:9'} + S_{2:3}}{U_{2:3} + F_{2:3} + S_{3:9'}}, \tag{52}$$

$$\eta_{U} = \frac{U_{7:8} + U_{5:6} + U_{4:5} + U_{6:7'} + U_{2:3}}{U_{2:1} + U_{4:3} + U_{1:8} + U_{9:6} + U_{3:9'}}, \tag{53}$$

$$\eta_{F} = \frac{F_{4:5} + F_{6:7'} + F_{2:3}}{F_{2:1} + F_{4:3} + F_{8:7} + F_{6:5} + F_{1:8} + F_{9:6} + F_{3:9'}}, \tag{54}$$

$$\eta_{S} = \frac{S_{2:1} + S_{4:3} + S_{8:7} + S_{6:5} + S_{1:8} + S_{9:6} + S_{3:9'}}{S_{4:5} + S_{6:7'} + S_{2:3}}. \tag{55}$$

Table 5 shows the values of the product-resource ratios of the productive units for the given numerical data. One should note that there is no product-resource ratio value greater than 100%.

Table 5. Product-Resource Ratios of Productive Units

Productive Unit	Ratio Value	
	Actual Cycle	Non-Actual Cycle
LP Compressor (cmp.l)	90.30%	100.00%
HP Compressor (cmp.h)	91.37%	100.00%
LP Valve (vlv.l)	44.90%	44.51%
HP Valve (vlv.h)	52.64%	52.24%
Condenser (cnd)	98.22%	99.90%
Evaporator (evp)	97.99%	100.00%
Flash Tank (flt)	100.00%	100.00%
Mixing Tank (mxt)	98.86%	99.19%
Internal Energy (U)	100.00%	100.00%
Flow Work (F)	100.00%	100.00%
Syntropy (S)	100.00%	100.00%

The UFS Model was proposed in order to define a product for valves and, in general, for units or processes that are modelled as isenthalpic, because the H&S Model is not able to do it. Nevertheless, the UFS Model keeps all features of the H&S Model, i.e., one can say that the UFS Model is an extension of the H&S Model and the application of the former only could be justified, e.g., whether there is a valve in the structure, because of the increasing of the modeling complexity.

5. Closing Remarks

In this paper, an exergy and a thermoeconomic analyses were carried out to a two-stage vapor compression refrigeration cycle with intercooling. The thermoeconomic approach used was the UFS Model, which is based on the disaggregation of physical exergy into internal energy (U_i), flow work (F_i) and syntropy (S_i).

Results of both exergy and thermoeconomic evaluations were compared. It was seen that the sum between the exergy destructions and losses of each physical structure equipment were equal to the difference between the fuels and the products of each real equipment of the productive structure. Besides that, the exergetic efficiency of the refrigeration cycle evaluated by the product-fuel ratio was equal to the one evaluated by the inverse of exergetic unit cost value of the productive unit associated to the product of the cycle. Thus, one can conclude that this thermoeconomic modeling can be used as well as the exergy balance in order to quantify both internal and external irreversibilities of each equipment that lies in the cycle. One can conclude as well that the exergetic costs were fairly allocated throughout the cycle. It was seen as well that exergetic unit costs of internal flows and products are greater than or equal to one and product-resource ratio of each productive unit are less than or equal to one, depending on the situation, i.e., when considering the actual cycle or the non-actual cycle, respectively. Thus, one can say that the UFS Model is in accordance with the Second Law of Thermodynamics. Results also show that the product-resource ratio of each component of the productive structure varies from zero (for totally irreversible processes) to one (for totally reversible processes), whether one considers the trend of such ratios.

Acknowledgments

Authors of this paper would like to thank the Brazilian National Agency for Petroleum, Natural Gas and Biofuels (ANP) for the financial support.

References

[1] Erlach B., Serra L., Valero A., Structural Theory as Standard for Thermoeconomics. Energy Conversion and Management 1999;40:1649-1627.

[2] Torres C., Valero A., Rangel V., Zaleta A., On the Cost Formation Process of the Residues. Energy 2008;33:152-144.

[3] Lozano M.A., Valero A., Thermoeconomic Analysis of a Gas Turbine Cogeneration System. In: Richter H.J. et al., editors. ASME-WAM Book No. H00874 AES-Vol. 30; 1993 Nov 28-Dec 3; New Orleans, USA. 320-312.

[4] Valero A., Serra L., Uche J., Fundamentals of Exergy Cost Accounting and Thermoeconomics. Part I: Theory. Journal of Energy Resources Technology 2006;128:8-1.

[5] Torres C., Serra L., Valero A., Lozano M.A., The Productive Structure and Thermoeconomic Theories of System Optimization. In: Duncan A.B. et al., editors. ASME-IMECE Book No. G01022 AES-Vol. 36; 1996 Nov 17-22; Atlanta, USA. 436-429.

[6] Tsatsaronis G., A Review of Exergoeconomic Methodologies. In: Moran M.J., Sciubba E., editors. Proceedings of the Fourth International Symposium on Second Law Analysis of Thermal Systems; 1987 May 25-29; Rome, Italy. 87-81.

[7] Frangopoulos C.A., Thermo-Economic Functional Analysis and Optimization. Energy 1987; 12(7):571-563.

[8] von Spakovsky M.R., Application of Engineering Functional Analysis to the Analysis and Optimization of the CGAM Problem. Energy 1994;19(3):364-343.

[9] Santos J., Nascimento N., Lora E., Reyes A.M., On the Negentropy Application in Thermoeconomics: A Fictitious or an Exergy Component Flow?, International Journal of Thermodynamics 2009;12(4):176-163.

[10] Lourenço A.B., Santos J.J., Donatelli J.L., Thermoeconomic Modeling of a Simple Heat Pump Cycle: An Alternative Approach for Valve Isolation. In: Mitrović D., Laković M., editors. SimTerm 2011: Proceedings of the Fifteenth Symposium on Thermal Science and Engineering of Serbia; 2011 Oct 18-21; Sokobanja, Serbia. 453-446.

[11] Çengel Y.A., Boles M.A., Thermodynamics: An Engineering Approach. New York: McGraw-Hill; 2006.

[12] Moran M.J., Shapiro H.N., Boettner D.D., Bailey M.B., Fundamentals of Engineering Thermodynamics. New Jersey: John Wiley & Sons. 2011. 624-605.

Comparative Performance of Advanced Power Cycles for Low-Temperature Heat Sources

Guillaume Becquin[a], Sebastian Freund[b]

[a,b] GE Global Research, Freisinger Landstrasse 50, 85748 Garching b. Muenchen, Germany
[a] guillaume.becquin@ge.com, CA
[b] sebastian.freund@ge.com

Abstract:

In this study the performance benefit of numerous advanced power cycles including supercritical, dual-pressure and several cycles using an ammonia/water mixture is assessed against a baseline of a state-of-the-art single pressure organic Rankine cycle with heat source temperatures ranging from 80°C to 200°C. Different sets of boundary conditions (heat exchanger minimum approach temperature and pressure loss) are investigated in order to evaluate their influence on each of the cycles. Both the relative power output of these cycles and the relative increase in the size of the heat exchangers are reported in order to allow estimating their economic benefits. Each of the investigated cycles is optimized to maximize the net power output over the whole range of heat source temperatures. Several heat exchanger designs are laid out for the boilers and condensers of selected cycles in order to assess their relative size from one cycle to another, taking into account the properties of the different working fluids and the operating conditions. The pressure loss and the overall heat transfer coefficient for the different working fluids are showing no significant benefit for ammonia/water mixtures or hydrocarbons over refrigerants that would justify applying lower temperature differences and losses as design boundary conditions for cycle comparison. To meet given approach and pinch temperatures, however, different cycles require very different sizes of heat exchangers and the total amount of required UA (heat transfer coefficient (U) multiplied by the transfer area (A)) is shown. The study shows that advanced cycles can significantly increase the power output over the range of temperatures considered. With similar temperature boundary conditions, the power output can be increased by up to 35% compared to the baseline at the lowest heat source temperatures, but little benefit was found at the higher end of the temperature range. Ammonia/water mixture cycles, dual-pressure organic Rankine cycles and supercritical cycles can each offer a significant increase in power production for different heat source temperatures, generally at the cost of an increased system complexity and heat exchanger size.

Keywords:

Low-temperature cycles, advanced organic Rankine cycles, ORC comparison, ORC heat exchanger.

1. Introduction

The industrial sector energy consumption in the U.S. accounted in 2002 for roughly 22 quadrillions Btu/year (or 6.5 PWh/year), 25% to 55% of this energy being lost to the surroundings in the form of heat [1]. The IEA Blue Map Hi-REN scenario [2] aiming to reduce CO_2 emissions by 50% in 2050 predicts an installed geothermal power capacity of 200 GWe by that date. While the potential for industrial waste heat recovery and geothermal power is great, a large fraction of these resources is dominated by low grade heat sources. The organic Rankine cycle (ORC) is a proven technology which allows generating electricity from low-temperature heat sources in a far more efficient way than conventional steam cycles. However, for heat source temperatures below 200°C, the performance of ORCs is hampered by the large fraction of exergy being destroyed during the heat exchange process, mainly due to the constant temperature boiling phase of the working fluid. This evaporation phase compromises the thermal efficiency of the system to maintain good heat source utilization in order to maximize the power generation. Advanced solutions exist in order to minimize this exergy destruction at low heat source temperature and increase the overall system

efficiency. These solutions enhance the match between the heat source and the working fluid heating curves by working in the supercritical regime (removing the evaporation phase), increasing the number of evaporating pressure levels or using a fluid mixture as working fluid (thereby taking advantage of a temperature glide during the evaporation). The enhanced performance results from the better match between the heat source and the working fluid but comes at the cost of a (desired) lower overall temperature difference over the heat exchangers, leading to a higher cost for this equipment. This study aims at evaluating the relative power generation advantage and the penalty in required heat exchanger area of advanced low-temperature power cycles. Seven cycles, including a supercritical cycle, a dual-pressure organic Rankine cycle and several ammonia/water mixture cycles ("Kalina" cycles) are optimized for net power output on heat source temperatures ranging from 80°C to 200°C and compared to a single-pressure ORC baseline. These cycles are investigated using two sets of boundary conditions, mainly affecting the heat exchangers. The impact of these boundary conditions on the cycle performance and the relative size increase of the heat exchangers will be evaluated to assess the potential economic benefits of each cycle. As absolute power scales with the mass flow of the heat source for an optimized cycle and the cycles are calculated for comparison to one another with the same heat source, only relative power, normalized by a baseline cycle, is used throughout this paper. Finally, heat exchangers designs will be laid out for a selection of heat source temperatures and cycles in order to assess the impact of the different working fluids and operating conditions on the predicted cost of the heat exchangers, and to quantify possible advantages for some fluid/cycle combinations which might motivate the use of a different set of boundary conditions to make a fair comparison with the ORC baseline.

2. Investigated Cycles

Several cycles offering a better match between the heat source and working fluid heating curve have been investigated. Their relative net power output and relative heat exchanger size are compared to a state of the art subcritical, single-pressure organic Rankine cycle, referred to as "subcritical ORC" in the following.

2.1 - Subcritical Organic Rankine cycle

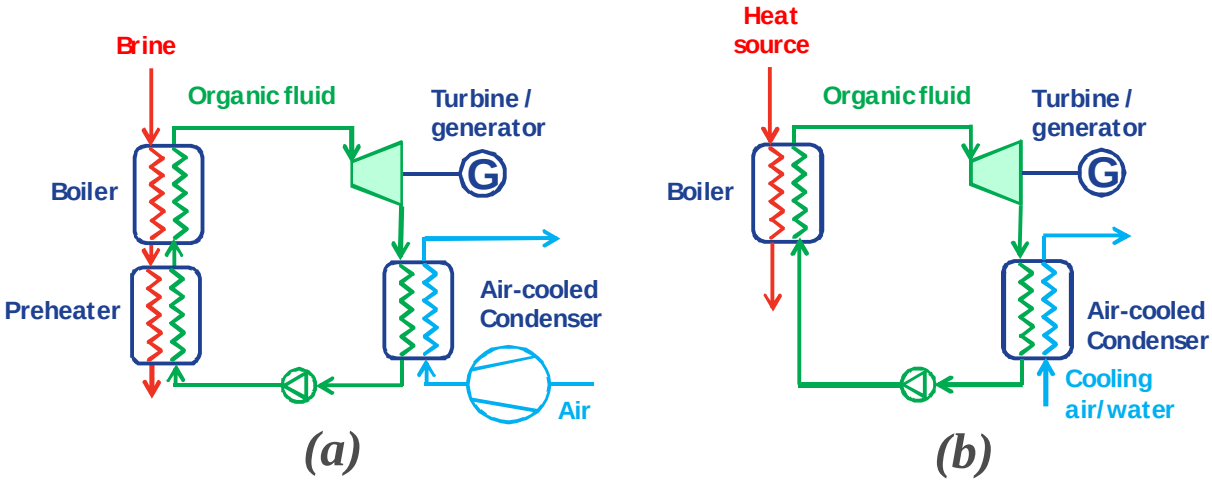

Fig. 1. a) Subcritical, single-pressure ORC, b) Supercritical ORC

Subcritical ORCs are a proven technology based on the steam Rankine cycle. Water is replaced by a working fluid more suitable for low-temperature heat sources such as hydrocarbons or refrigerants. The layout of the subcritical ORC cycle is given in Fig. 1-a. The lower boiling temperature of these fluids, combined with their "dry fluid" properties allows increasing the efficiency of these cycles while reducing the need for superheating even at low temperatures. However, subcritical ORCs

suffer from the constant temperature boiling phase for low heat source temperature. The pinch point occurring at the beginning of the working fluid evaporation indeed limits the extent to which the heat source can be cooled, affecting the system's second law efficiency. Considering the low heat source temperatures investigated, a recuperator is usually not beneficial from a net power output point of view [3] (the minimum heat source temperature is set to 40°C, which is low enough for it not to become a limiting factor for the net power output optimization). These systems can be either water- or air-cooled, however in this study all the cycles investigated will be assumed to be air-cooled.

2.2 - Supercritical Organic Rankine Cycle

One way to reduce the exergy destruction caused by the imperfect heat transfer is to simply remove the constant temperature evaporation by working in the supercritical regime. The layout is similar to the subcritical ORCs given in Figure 1-b.

2.3 - Dual-Pressure, Subcritical ORC

Dual-pressure cycles introduce an additional pressure level, leading to an evaporation occurring at two different temperatures. The power cycle is split into a high-pressure and a low-pressure loop. The high temperature part of the heat source is used to evaporate the high-pressure loop. Where a single-pressure ORC would keep the same mass flow to preheat the high-pressure loop, the dual-pressure cycle splits the heat source around the beginning of the high-pressure loop evaporation. The minimum amount required for the high-pressure loop preheating is sent to the high-pressure preheater, while the rest of the flow is used to evaporate a low-pressure loop, as seen in Figure 2. The layout given in Figure 2, describing the cycle used in this study, is just one solution for the implementation of a dual-pressure ORC among others.

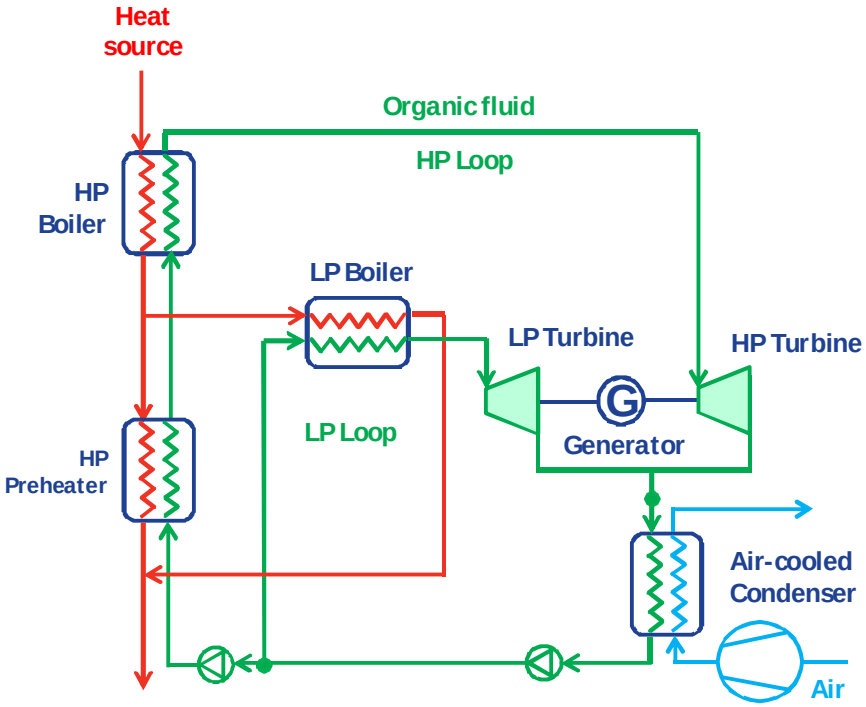

Fig. 2. Subcritical, dual-pressure organic Rankine cycle (dual-pressure ORC)

The dual-pressure cycle allows working with high pressure while still offering high heat source utilization. This concept can be generalized with more pressure levels, approaching the theoretical Lorenz cycle with an infinite number of pressure levels. In this study, however, the analysis is limited to the assessment of cycles with two pressure levels. It should be noted that on top of the

overall increase in system complexity, working with two pressure levels may require to use two turbines, potentially leading to a further increase of the system cost.

2.4 - Ammonia/Water Mixture (Kalina) Cycles

Power cycles designed with fluid mixtures benefit from a temperature glide both during the evaporation and the condensation process, as those will occur at non-constant temperature and reduce the losses associated with imperfect heat transfer between the heat source or the heat sink and the working fluid. Examples of these cycles are the ammonia/water mixture cycles, commonly referred to as Kalina cycles [4]. This study investigates several configurations with variable complexity using an ammonia/water mixture as a working fluid. These configurations can be classified into first and second generation's cycles (the second generation cycles are more complex than the first generation). Each of this generation is declined into a low and a high temperature version. In total, five ammonia/water cycle (AW) configurations are investigated: three first generation (AWa, AWb, AWc), and two second generation cycles (AWd, AWe). Configuration (AWa), shown in Figure 3, is the low-temperature version of the first generation ammonia/water mixture cycle, commonly referred to as KCS34 Kalina cycle [3].

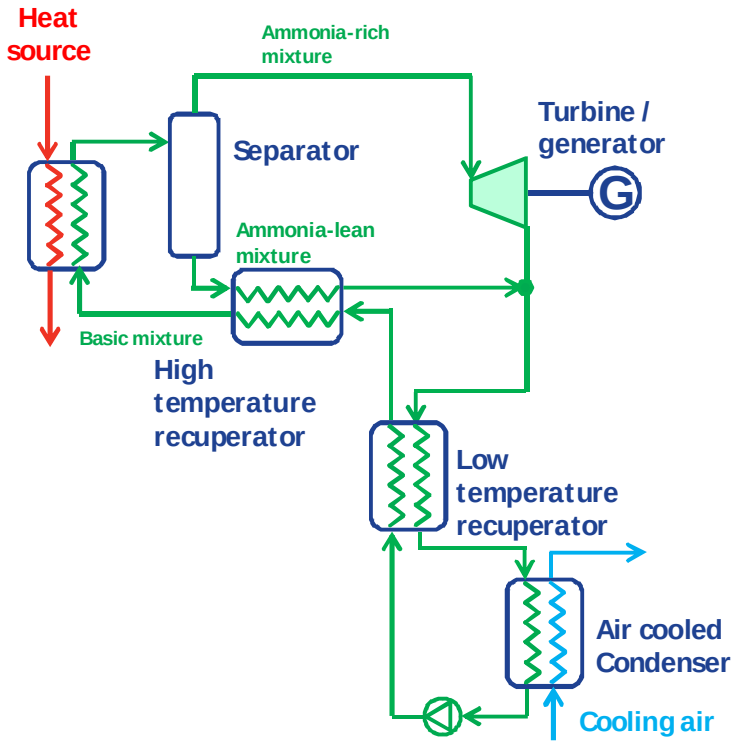

Fig. 3. Ammonia/water mixture cycle (AWa)

In this cycle a basic ammonia/water mixture is partially evaporated using the heat source and internal recuperation. The stream is then separated, where the ammonia-rich vapour is sent to the turbine and the ammonia-lean liquid is used for recuperation before being absorbed at the turbine exhaust. This recuperated cycle maximizes the efficiency cooling the source down to low temperatures thanks to the temperature glide during the evaporation. The effects of the operating pressure and the ammonia concentration on the performance of the cycle have already been investigated in previous research work [5]. This cycle is now proven and operating in several geothermal (e.g. in the Húsavik power plant [4]) and industrial heat sources.

It is possible that the pinch point at the beginning of the evaporation occurs during the recuperation step. In such cases it is possible to further increase the heat source utilization and therefore the power output of the system by slightly modifying the (AWa) layout with the introduction of a heat source heat exchanger in parallel to the low-temperature recuperator. This configuration (AWb),

shown in Figure 4 allows a better management of the heat source utilization at a moderate cost of complexity.

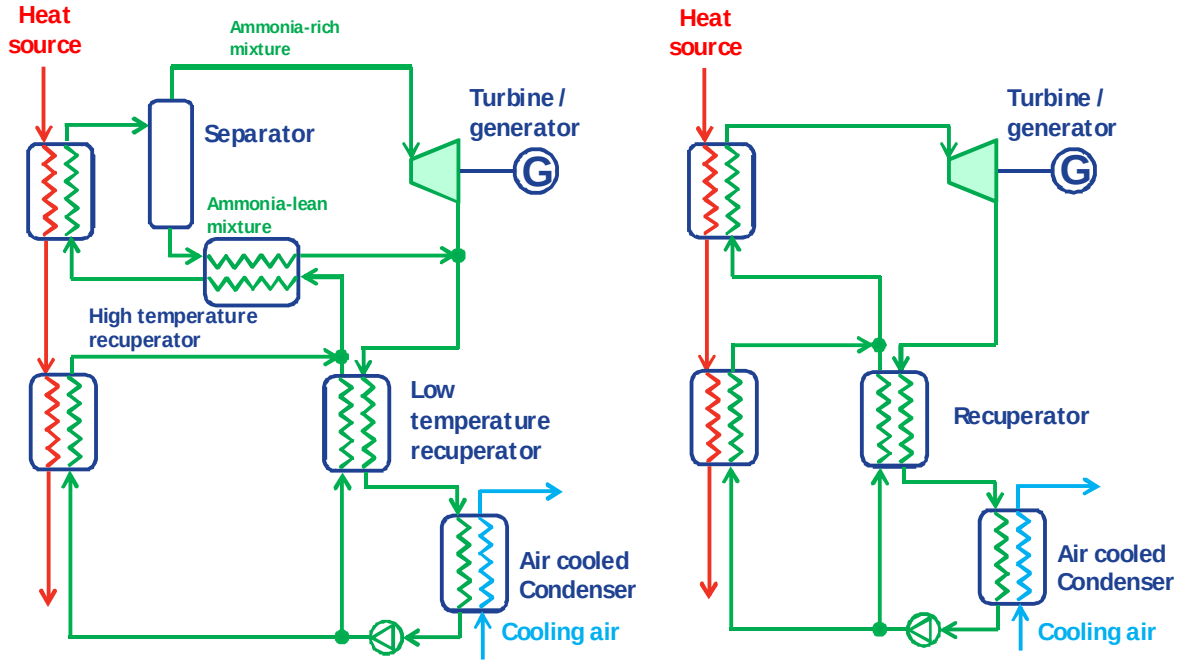

Fig. 4 and Fig. 5. Ammonia/water mixture cycle (AWb), left and (AWc), right.

For high-temperature heat sources, the optimum design fully evaporates the ammonia/water mixture at the heat exchanger outlet. In these cases, a separator is not required anymore, and the first generation ammonia/water mixture cycles degenerates into configuration (AWc), shown in Figure 5. This cycle, often referred to as KCS11 [7], is a simplified version of the previous cycle. The main difference here is that a constant concentration of ammonia is used on the whole cycle as opposed to the two previous cycles where three different ammonia concentrations occur in the cycle. More complex configurations designed for higher temperature heat source using two condensers exist [8, 9, 10], but are not investigated in this study. The main advantage of variable concentration cycles is their off-design capability; it is indeed possible to change the ammonia concentrations in order to optimize for different ambient temperatures [6].

The next two cycles investigated belong to the second generation of ammonia/water mixture cycles, developed by Kalex LLC [6]. The low-temperature version of these cycles, configuration (AWd), is shown in Figure 6-a. The main feature of these second generation cycles (often referred to as SG2 cycles [6]) is an internal recirculation loop which allows decreasing the condenser load. This has a positive impact on the condenser parasitic load since it decreases the working fluid flow rate through the condenser while maintaining a higher flow rate through the turbine. The liquid resulting from the first separation process is flashed to an intermediate pressure, and undergoes a second separation. The vapour stream is then sent back to the heat exchangers without being condensed, thereby reducing the condensation heat load. In order to pump this vapour stream back to the cycle's top pressure, it is absorbed by a liquid stream resulting from the third separator placed downstream of the turbine.

If the heat source temperature is high enough, the optimum design for the (AWd) cycle leads to full evaporation of the ammonia/water mixture after the second heat source heat exchanger. In that case, the cycle can be simplified and degenerates into the (AWe) cycle shown in Figure 6-b.

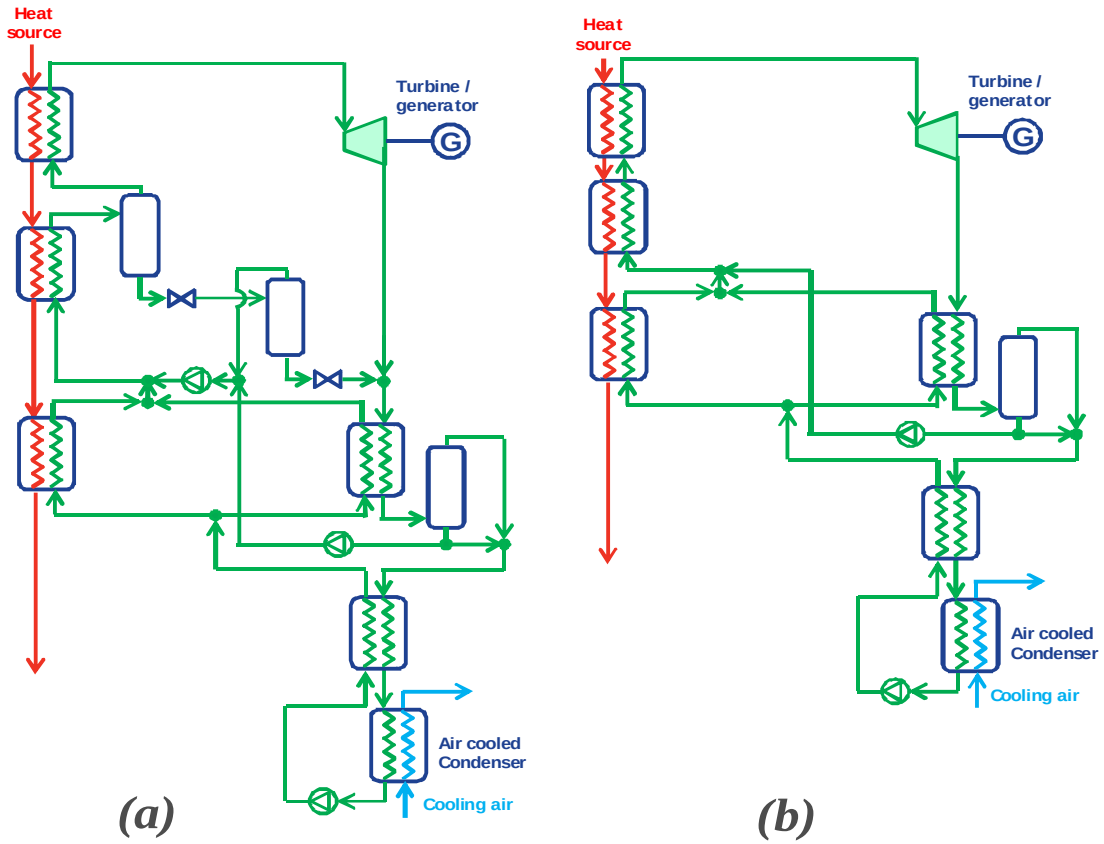

Fig. 6. Ammonia/water mixture cycle: a) (AWd), b) (AWe)

3. Boundary Conditions

The previously described cycles are optimized for net power output on a set of eight heat source temperatures ranging from 80°C to 200°C with steps of 100°C, 110°C, 120°C, 130°C, 150°C and 175°C. Two sets of boundary conditions have been used for this study in order to evaluate the sensitivity of the investigated cycles relative to the heat exchangers design. “Conservative” and “aggressive” boundary conditions are defined, with different allowable minimum approach and pressure loss for the heat exchangers. The rest of the boundary conditions (i.e. isentropic and electrical efficiencies, ambient temperature, allowable air temperature rise over the air-cooled condenser, minimum heat source temperature) remain essentially unchanged. Table 1 shows the conservative boundary conditions in use for the heat exchangers and heat sink.

The set of boundary conditions described in Table 1 is slightly modified when simulating ammonia/water mixture cycles. Given the lower mass and volume flow rate at the expander outlet in ammonia/water cycles, the expected pressure loss in the condenser and the recuperator can be expected to be lower with similarly sized equipment when compared to organic Rankine cycles. For this reason, the pressure loss for the condenser and the recuperators in cycles running with ammonia/water mixture as a working fluid has been decreased to 1% of the absolute inlet pressure, while the other boundary conditions remain unchanged.

Table 1. Conservative boundary conditions

Heat exchangers		**Heat sink**	
Minimum approach (heat source heat exchanger)	10 K	Ambient temperature	15°C
Minimum approach (recuperators)	5 K	Minimum air temperature rise over condenser	10°C
Minimum approach (condenser)	10 K	Cooling medium	air
Pressure loss (heat source heat exchanger)	7% of absolute inlet pressure	Condenser fan power	1% of condensing duty
Pressure loss (recuperators)	3% of absolute inlet pressure		
Pressure loss (condenser)	5% of absolute inlet pressure		
Minimum heat source temperature	40 °C		

The aggressive boundary conditions are derived from a paper published by Dr. Kalina, describing the second generation Kalina cycles [7]. The boundary conditions for the heat exchangers calculated from the state points of an SG-2a cycle given in this paper are given in Table 2. It can be seen that the minimum approach and the pressure losses on the heat exchangers are much lower than for the previous "conservative" set of boundary conditions. The rest of the boundary conditions and the ambient temperature remain unchanged.

Table 2. Aggressive boundary conditions

Heat exchangers	
Minimum approach (heat source heat exchanger)	2.8 K
Minimum approach (recuperators)	2.8 K
Minimum approach (condenser)	5 K
Pressure loss (heat source heat exchanger)	2 psia / 0.14 bar
Pressure loss (recuperators)	2 psia / 0.14 bar
Pressure loss (condenser)	2 psia / 0.14 bar
Minimum heat source temperature	40°C

The list of the optimization variables for each of the cycles investigated is given in table 3. The rest of the cycle parameters are imposed by fixed conditions (e.g. degree of superheating) or their optimum value can be calculated directly without optimization (e.g. condensing pressure).

Table 3. Optimization variables for each cycle

Cycle	**Optimization variables**
Subcritical, single pressure ORC	Top cycle pressure
Supercritical ORC	Top cycle pressure
	Top cycle temperature
Dual-pressure ORC	Top cycle pressure
	Intermediate cycle pressure
(AWa), (AWb), (AWc)	Top cycle pressure
	Ammonia concentration
(AWd), (AWe)	Top cycle pressure
	Ammonia concentration
	Recirculation loop flow rate

The cycles are modeled using the commercial chemical process modeling tool Aspen HYSYS. For organic Rankine cycles, a set of common refrigerants and hydrocarbons are investigated (including, but not limited to R125, R134a, R245fa, R152a, isobutane, n-butane, propane, isopentane, n-pentane), and the fluid properties are calculated using the Zudkevitch-Joffee [11] equation of state available in HYSYS. For ammonia/water mixture cycles, the SRK [12] equation of state is used in order to calculate the fluid properties.

4. Cycle Performance Comparison

The previously introduced cycles are optimized for net power output for each of the eight heat source temperatures, for both sets of boundary conditions.

4.1. Conservative Boundary Conditions

Figure 7 shows the relative net power output of the investigated cycles against the single-pressure, subcritical ORC using the conservative set of boundary conditions. The working fluid used for the reference subcritical ORC is given at the bottom of the graph. As a general trend, the advanced cycles tend to offer larger power output benefits for lower heat source temperatures: the power output increase can reach up to 35% with an 80°C heat source, while benefits up to only 10% can be expected for a 200°C heat source. This can be explained by the strong increase in performance of the subcritical ORC as we leave the very low heat source temperature range.

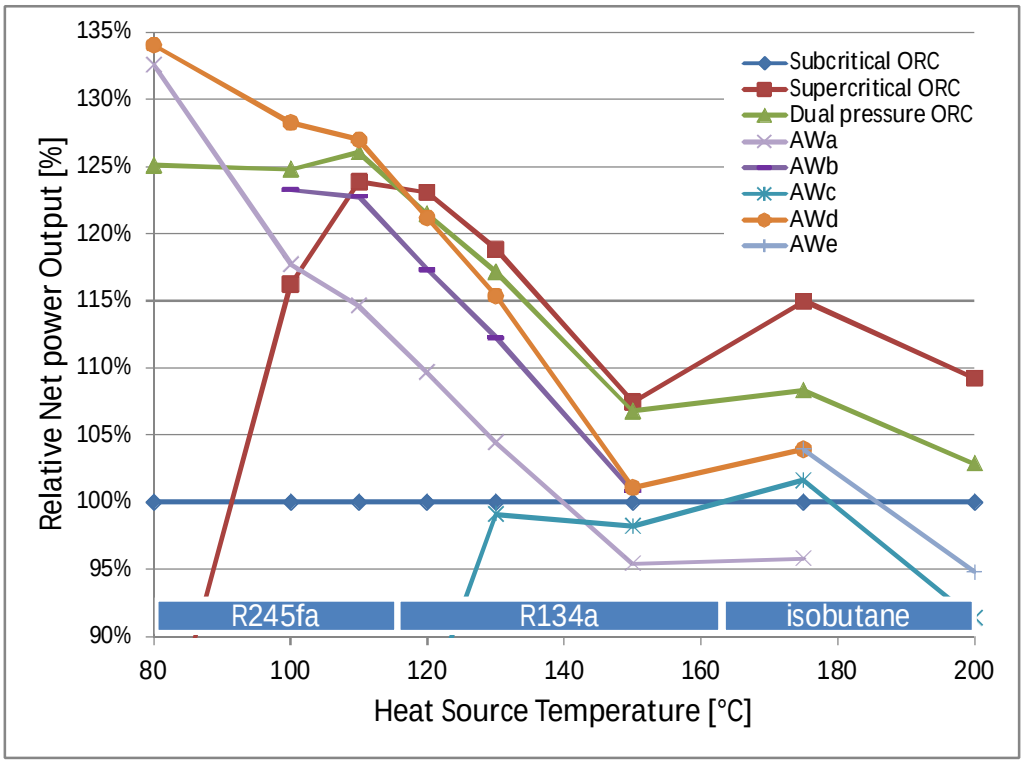

Fig. 7. Relative performance comparison, conservative boundary conditions

When looking closer into the power output of the different cycles, it is apparent that ammonia/water cycles perform significantly better than the ORC baseline for heat source temperatures below about 150°C. Among these cycles, the second generation cycles offer greater benefits than the first generation cycles over the same temperature range. The modified version of KCS34, the AWb cycle, significantly increases the performance of the first generation cycles to bring them close to the second generation configuration. For heat source temperatures below 110°C, the second

generation ammonia/water cycles offer the highest performance. It should be noted that with the same set of conservative boundary conditions, the ammonia/water mixture cycles investigated cannot compete with the organic Rankine cycles for temperatures above 175°C. Dual-pressure cycles are the only advanced solution to offer a power output increase over the whole range of heat source temperature considered, even though this advantage decreases with the heat source temperature. Above 120°C, supercritical cycles become the most efficient cycles. It is worth noting that for very low heat source temperature, the choice of working fluids that can operate supercritical is very limited, which partly explains the strong decrease in performance for this temperature range. If an ideal fluid could be tailored for any temperature with an adjusted critical point, one could expect that the power output benefit would be maintained even for very low heat source temperatures.

Considering the net power output by itself may not be enough for a comprehensive cycle assessment. The advanced cycles aim at improving the match between the cooling curve of the heat source and the heating curve of the working fluid to reduce the second-law losses during the heat transfer. The direct consequence in a cycle where the input and approach temperature boundary conditions are fixed is a reduction of the average temperature difference across the heat exchangers. A reduced mean temperature difference typically will result in a larger heat exchanger area to transfer the same amount of heat, hence an increase in size and cost. In order to capture this effect, the total UA value of the heat exchangers in the cycle is recorded for each of the optimized cycles (the UA of a heat exchanger is the overall heat transfer coefficient multiplied by the heat transfer area and equals the quotient of the heat duty divided by the mean temperature difference. The mean temperature difference takes into account the non-linear temperature-heat load profile in the heat exchangers for the supercritical and ammonia/water based cycles). The total UA value (summed over the heat source heat exchangers, recuperators and condenser) required per unit of power produced is calculated to represent the size of the heat exchangers relative to the power output increase of the advanced cycles. This value is shown in Figure 8 for each cycle and heat source temperature.

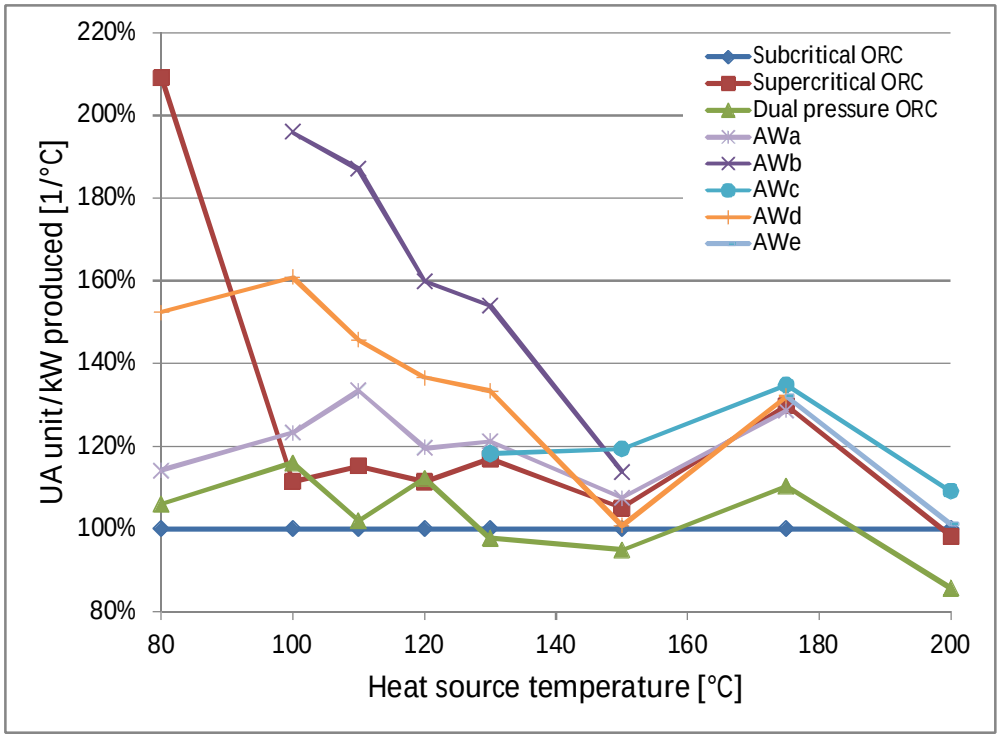

Fig. 8. Relative total heat exchanger UA per unit of power produced, conservative boundary conditions

Figure 8 shows that even if the AWb configuration helped to bring the performance of the first generation of ammonia/water mixtures closer to the second generation, it requires far more heat exchanger area under the same boundary conditions. The second generation cycles indeed achieve a higher power output increase while being relatively less demanding from a heat exchanger size point of view. This can be explained by the use of more separators and mixers in the second generation configurations which achieve internal recuperation via direct mixing, therefore saving on heat exchanger UA.
The required total UA per unit of power produced is remarkably constant for the first generation AWa and AWc configurations and for the supercritical cycle. This value oscillates between 115% and 135% for the range of heat source temperatures where these cycles offer a performance advantage. For the dual-pressure cycle the required UA per unit of power produced is barely higher than for the subcritical, single-pressure ORC, or even lower for temperatures around 150°C. This means that the dual-pressure cycle will offer a strong power output increase, while the relative size of the heat exchanger is expected to stay almost the same. The dual-pressure and ammonia/water based cycles however have an additional cost associated with the increase in cycle complexity, additional components (mixers, separators) and controls, and with the possible need for two expanders instead of one for the dual-pressure cycle.

4.2. Aggressive Boundary Conditions

The same exercise as above is repeated with the second set of boundary conditions; the results are shown in Figure 9. The general trend is the same: under comparable boundary conditions, the performance advantage offered by the advanced cycles decreases with increasing heat source temperature, with a maximum benefit of about 35% at a heat source temperature of 80°C, down to about 5% at 200°C.

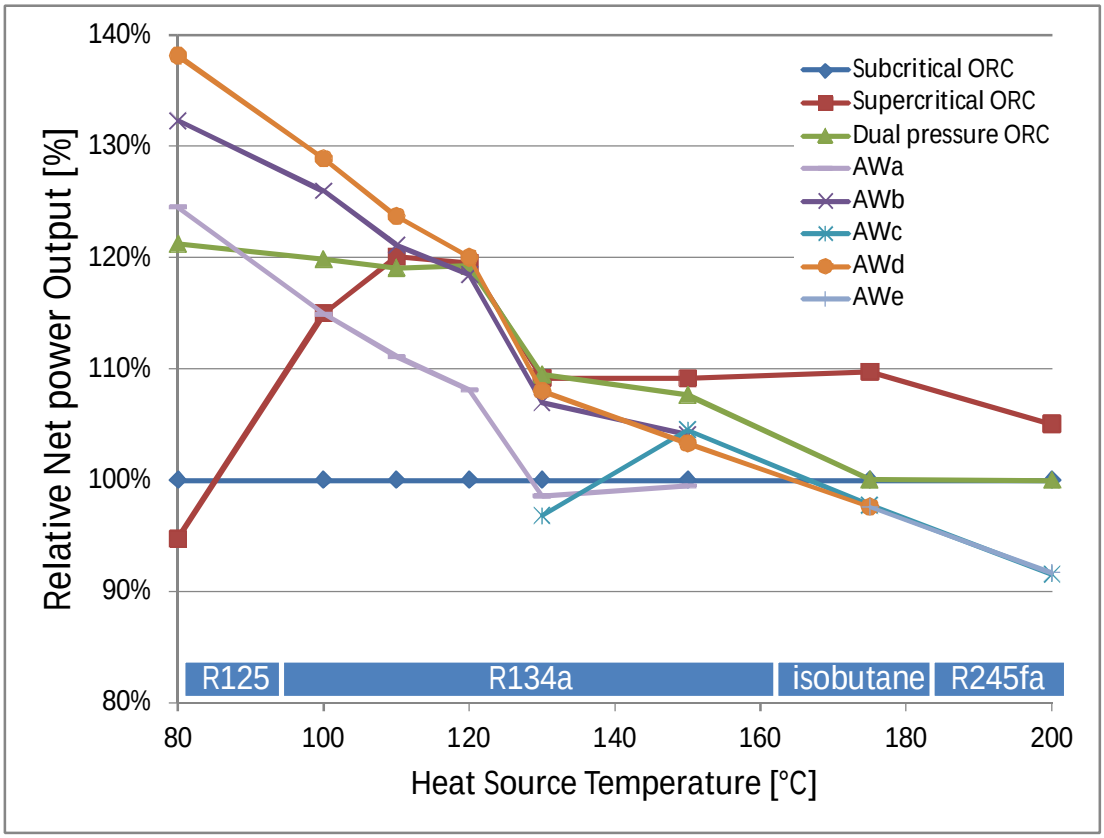

Fig. 9. Relative performance comparison, aggressive boundary conditions

Similar to the previous conservative boundary conditions case, the ammonia/water cycles perform significantly better than the organic Rankine cycles for heat source temperatures of 150°C and

below. For heat source temperatures below 120°C, the second generation ammonia/water cycle is the best cycle from a pure performance point of view. In the region where they offer benefits over the baseline, the second generation ammonia/water cycles perform significantly better than the first generation at base configuration (AWa). The modified version, AWb, brings the performance of the first generation closer to the second generation configurations, especially for heat source temperatures of 120°C and above.

The dual-pressure cycle offers a strong performance increase for heat source temperatures between 80°C and 150°C, with a gain of roughly 10% to 20% in net power in that range. The power increase offered by dual-pressure cycles increases as the heat source temperature gets lower, but reaches a plateau of 20% net power increase for heat source temperatures of 120°C and below. The supercritical cycle offers the best performance increase for heat source temperatures of 130°C and above. It can be noted again that for very low heat source temperatures the benefit of the supercritical cycle decreases dramatically, and even drops below the subcritical ORC performance for an 80°C heat source temperature. This is because the choice of working fluids with a critical temperature low enough to be used in these cycles is limited as the heat source temperature goes below 100°C.

The relative increase in size of the heat exchangers for each cycle is calculated for the whole temperature range. This increase is measured by considering the amount of heat exchanger UA required in order to generate a unit of power. Figure 10 shows how this value evolves for each cycle and heat source temperature relatively to the subcritical, single pressure ORC baseline.

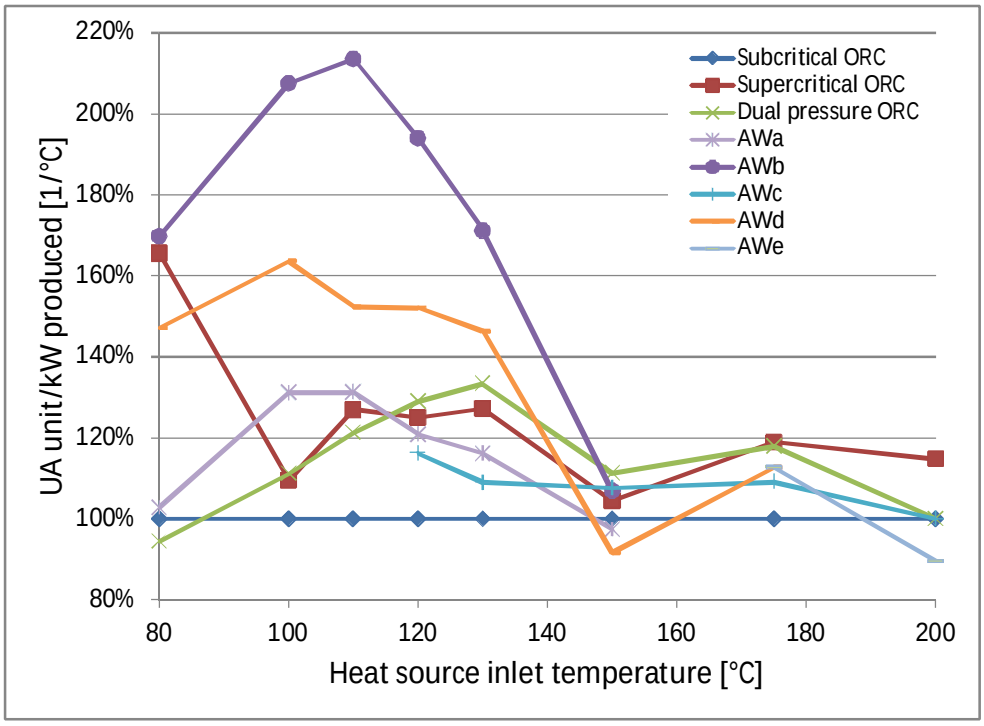

Fig. 10. Relative total heat exchanger UA per unit of power produced, aggressive boundary conditions

The trend for the total UA required per unit of power produced is very similar to the trends identified for the conservative boundary conditions case. Even though the AWb configuration brings the performance of the first generation ammonia/water cycles closer to their second generation counterpart, they are likely to require far more heat exchanger area relatively to the power they produce, and might not represent an economical solution. The second generation cycles offer equal or superior performance at a relatively lower required heat exchanger area per unit of power produced. It is interesting to note that for a 150°C heat source, the required heat exchanger UA per unit of power produced for the AWd configuration is lower than for the subcritical ORC

baseline. This means that this cycle not only produces more power than the baseline on a 150°C heat source, but it is also likely to have smaller heat exchangers relatively to the power produced by the cycle. The AWa configuration and the dual-pressure cycle are for the same reasons particularly interesting for the lowest heat source temperatures considered, where they offer strong performance benefits at only a moderate increase in the relative UA of the heat exchangers. It has been shown that the supercritical cycle offers the highest performance benefits for heat source temperatures of 130°C and above. In this same range of heat source temperatures, its relative required UA per unit of power produced remains between 5% and 20% higher than the subcritical ORC baseline.

4.3. Mixed Boundary Conditions

While the previous results help to assess the attractiveness of one cycle to another with the same set of boundary conditions being applied to all cycles, they do not give any indication on the best choice for boundary conditions or specifications for the heat exchangers. The following figures 11 and 12 show the net power output increase and the impact on the required total heat exchanger UA per unit of power produced for both sets of boundary conditions relative to the subcritical ORC baseline with conservative boundary conditions.

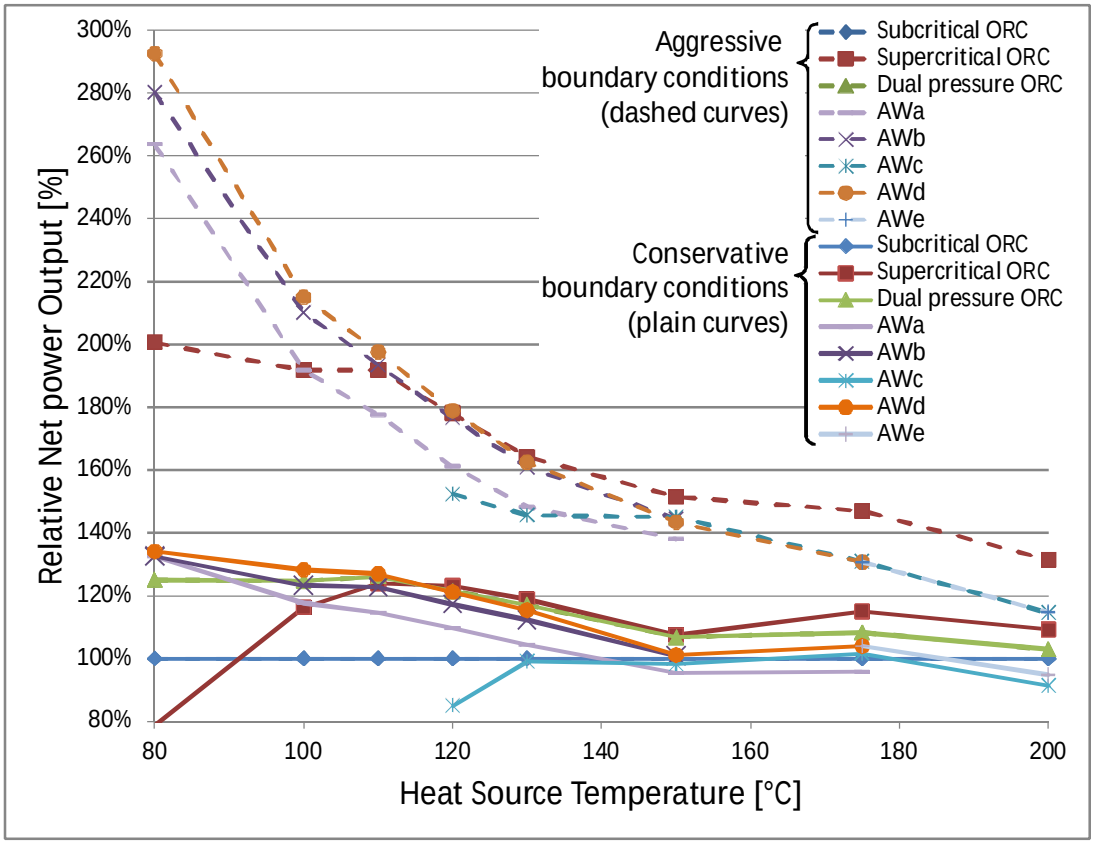

Fig. 11. Mixed boundary condition cycle performance comparison

A first observation is that within the same set of boundary conditions, the difference between the different cycles seems to decrease, especially for the relative net power output. The important conclusion is that the change from one set of boundary conditions to another has at least as much impact as the change from one cycle to another assuming the same set of boundary conditions. Another observation is that the advantage of using an aggressive set of boundary conditions is the highest for the lowest heat source temperature range. At the same time, the relative required total heat exchanger UA per unit of power produced tends to get much higher with the aggressive set of boundary conditions than with the conservative set at higher heat source temperatures. This is an indication that the aggressive set of boundary conditions may provide high power production

benefits at a moderate increase of the relative size of the heat exchangers for the lowest heat source temperature range. This is particularly interesting when working with very expensive heat sources such as geothermal brines. On the other hand, the conservative set of boundary conditions seems most appropriate when working with higher heat source temperatures, as the power output benefits relative to the baseline tends to decrease when switching to more aggressive set of boundary conditions while the relative size of the heat exchangers increases dramatically. The previous observations are made considering only the heat exchanger UA required to meet certain design temperatures and pressure losses given in the boundary condition sets. The required UA is a good indication of the variations of the heat exchanger size when working with the same fluid under similar operating conditions and heat exchanger geometries. However, variations of the overall heat transfer coefficient U can be expected between the subcritical ORC, supercritical ORC and the ammonia/water cycles owing to different fluid properties and flow conditions even between geometrically similar heat exchangers. These variations influence the required area and ultimately the size and cost of the heat exchangers. For instance, an increase of the U value of one cycle would decrease the area for the required UA; despite a higher UA requirement, one cycle with higher U may not require a larger area than another. The UA required for a certain cycle is therefore not fully sufficient to fairly compare different cycles in order to estimate relative equipment cost. In order to assess the impact of the fluid and the flow conditions on the heat exchanger size and cost for a given UA resulting from the boundary conditions set in this study, detailed heat exchanger designs are laid out for a selection of cycles and common heat source temperatures.

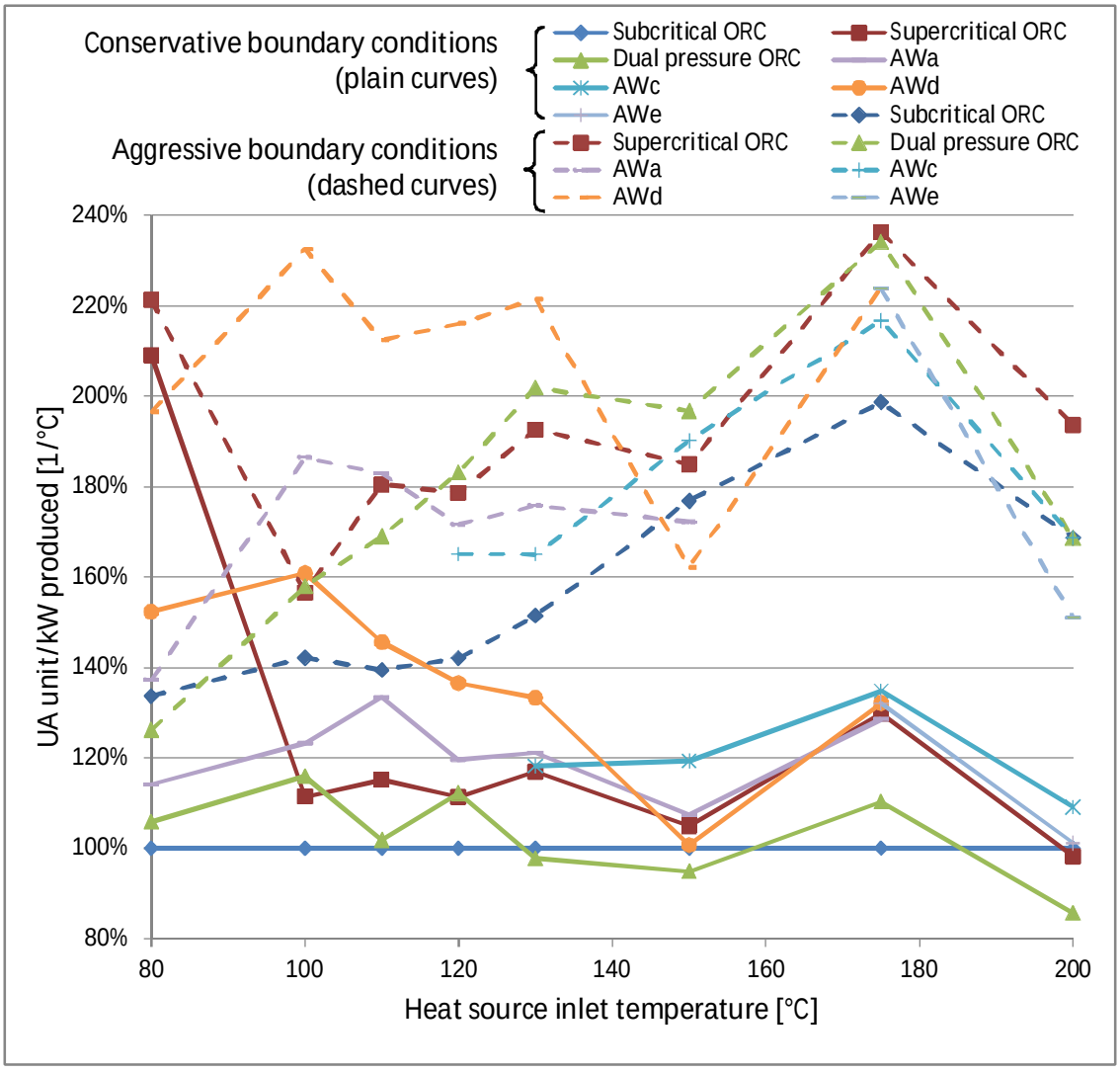

Fig. 12. Mixed boundary conditions, relative total heat exchanger UA per unit of power produced comparison

5. Detailed Heat Exchanger Design Comparison

Different cycles under given fluid temperature and pressure boundary conditions and a fixed heat source mass flow and inlet temperature require not only different heat flows but also different approach and pinch point temperatures because of the different heating (boiling or condensing) curves, resulting in different overall heat transfer and surface area (UA) requirements for each heat exchanger. To answer questions about how the UA requirement for different cycles affects the size and cost of the heat exchangers, shell-and-tube (S&T), plate and fin-tube boilers (PHE) and fin-tube (F-T) condensers have been designed using Aspen Exchanger Design and Rating software (Aspen v7.2). The cycles selected for this investigation are the subcritical ORC with isobutane and with a refrigerant, the supercritical ORC and the recuperated simple KCS34 Kalina cycle (AWa) with a heat source temperature of 120°C and "conservative" boundary conditions. The heat exchangers are designed with consistent features and design guidelines across the range of cycles to ensure these are comparable one to another and the area and cost implications due to fluid and cycle specifics are expressed clearly.

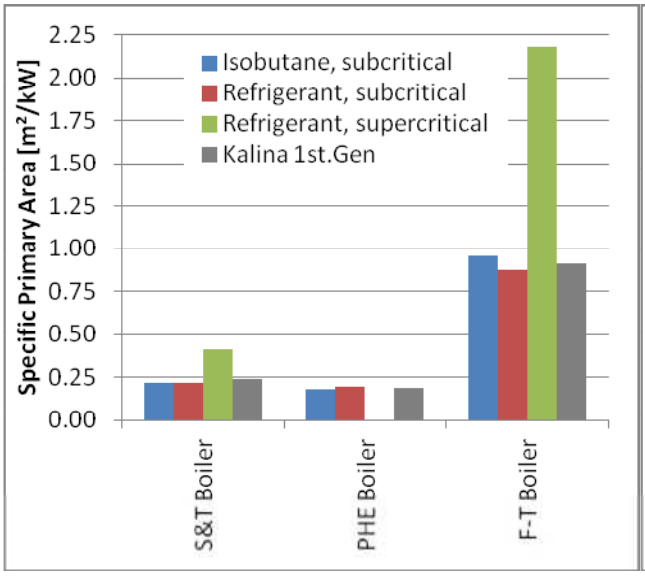

Fig. 13. Boiler surface area

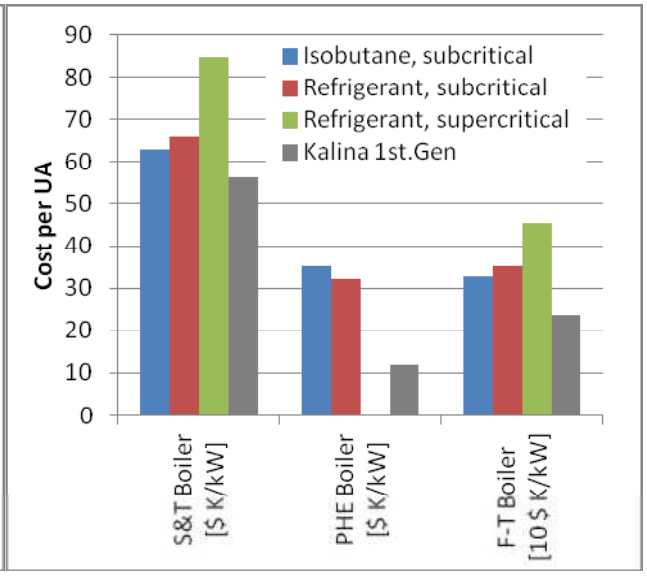

Fig. 14. Cost per unit UA of the boilers

For the three types of boilers the required surface areas for the different cycles are shown in Figure 13. "Specific" here refers to normalization by the cycle net power output. For the ammonia/water cycles with a boiling two-phase ammonia-water mixture, the average fluid-side heat transfer coefficients in a heat exchanger can be more than twice as high as hydrocarbons or refrigerants, particularly when allowing for higher pressure losses on the grounds of smaller volume mass flow rate in the feed pump. However, when the heat transfer coefficients on the other side of the boiler or condenser, single-phase water or air, enter the equation, the overall heat transfer coefficient (U) that determines the heat exchanger's area and cost, does not increase dramatically over that seen for hydrocarbons or refrigerants, by about 10% for shell-and-tube and fin-tube heat exchangers, hence the modest decrease in required area. Still, the relatively low mass flow and a mostly lower pressure of the ammonia/water cycles compared to ORCs allow designing a shell-and-tube or fin-tube boiler somewhat more compact and inexpensive, with the cost per unit tube surface area about 10% lower than for an ORC in the cases studied. Together with the higher U for the ammonia/water heat exchangers, the cost per unit UA of shell-and-tube and fin-tube boiler can be more than 10% lower for the ammonia/water cycle than for refrigerants and hydrocarbons; this cost is shown in Figure 14.

The boilers designed in this study showed that for a shell-and-tube heat exchanger the pressure losses on both sides are significantly below the limits set in the boundary conditions, size and cost are driven primarily by the desired UA. For plate heat exchangers, however, for cycles with

relatively large volume flow, such as for an ammonia water mixture or an evaporating refrigerant, the exchanger size and cost is primarily driven by acceptable pressure loss rather than by the desired UA alone, hence a larger UA than required came out of the design and the cost per unit UA (Figure 14) is very low. Thus, for a plate heat exchanger in ammonia/water cycles further opportunity for reduced surface area due to increased U compared to ORCs exist if pressure losses are allowed to rise as pointed out in the following considerations on design boundary conditions based on pumping power. A plate heat exchanger is not a likely choice for a supercritical ORC because of the high pressure. For a fin-tube boiler, the design, size and cost is mostly driven by the air-side pressure loss limit and associated limited velocity and heat transfer coefficient; achieving high values for U and reaching small approach temperatures to meet more "aggressive" boundary conditions is very difficult and costly.

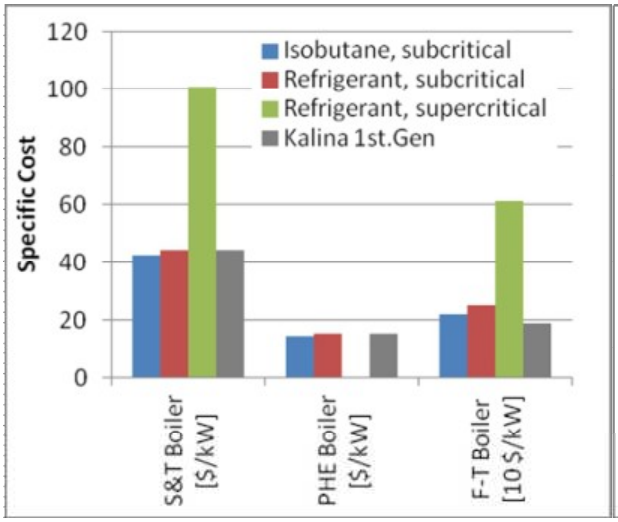

Fig. 15. Specific cost of boiler

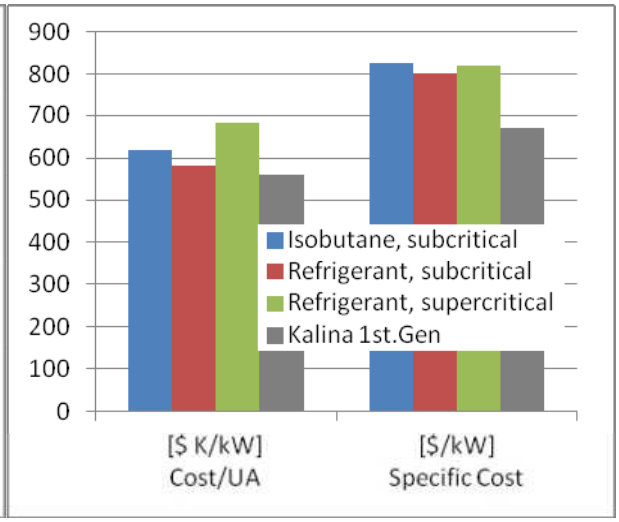

Fig. 16. Condenser cost specific to UA and to cycle net power

Generally speaking, a boiler with a liquid heat source does not present a significant cost challenge under either set of boundary conditions considered here, whereas a fin-tube boiler for a gaseous heat source does come at a significant cost, about five times that of a shell-and-tube boiler for "conservative" conditions. The specific cost relative to the net power output of the boilers is shown in Figure 15. Attempting to meet more "aggressive" design boundary conditions by decreasing the desired approach temperatures may lead to size and cost increases beyond what is economical.

Customarily the boundary conditions for heat exchanger design are given as minimum approach temperatures, pinch-points and relative pressure losses, such as in the sets of boundary conditions used in this paper. An alternative to setting the desired temperatures is to design for matching a desired UA that is deemed economical, as the UA is more closely related to the cost than minimum temperature differences as this investigation has shown. An alternative way to set the fluid-side pressure loss limit in the boiler to a fixed fraction of absolute pressure is instead setting a required pumping power to overcome the losses as a fraction of the cycle's net power. This way cycles with low mass flow, such as hydrocarbons or ammonia-water mixture, allow for higher absolute pressure losses in the boiler (smaller or longer pipes), which may further reduce the boiler size and the approach temperatures depending on the design and the heat source-side pressure loss limit relative to ORCs, specifically for a pressure loss limited plate heat exchanger.

An air-cooled condenser is arguably the largest and most costly heat exchanger in a Rankine cycle. To save cost at the cold end, a water-cooled condenser (shell-and-tube or plate heat exchanger) and a source of cooling water, such as a river or a cooling tower could be applied. In this study, only an air-cooled fin-tube condenser with forced convection electric fans is considered. To trade the cost of fan power requirements against the area of the condenser, the design fan power has been kept at or

below about 1% of the heat duty. For the boiler and the condenser the performance impact in terms of relative change in power output versus relative change in required UA are basically similar (roughly 1% net power for 4% UA, depending on the design point, resulting ultimately from Carnot's efficiency for low source temperature). However, the cost impact of an air-cooled condenser on a cycle is almost an order of magnitude larger than that of a shell-and-tube or plate boiler. The specific cost of the air-cooled condenser is shown in Figure 16, along with the cost per unit UA in $-K/kW.

The ammonia/water cycles have a rather small required UA as they are usually recuperated and less heat is discharged in the condenser although the temperature differences are also smaller than for ORCs because of the temperature glide when condensing a mixture, overall resulting in a lower specific cost, shown in Figure 16. Despite the higher heat transfer coefficients on the inside compared to refrigerants and hydrocarbons, the cost per unit UA is only insignificantly lower for ammonia/water cycles condensers, shown also in Figure 16. The supercritical ORC with its high mass flow rate has a somewhat higher cost per UA to meet pressure loss limits but the specific cost is not higher than for other ORCs. The fluid-to-air condenser heat transfer is mainly limited by the air-side, as the inside heat transfer coefficients are about two times higher than on the outside relative to the bare tube area. Since the outside heat transfer resistance is independent of the fluid conditions and similar air velocities result from the fan power limits, the differences between the cycles are rather small.

When designing the condensers to meet either the "conservative" or the "aggressive" boundary conditions, it emerges that the differences in required area and estimated cost are rather small, but the fan power requirement increases to allow a higher mass flow of air and the arrangement of fin tubes and headers can be different to meet the fluid pressure loss limitations. Only for supercritical ORC and the ammonia/water cycles, the required UA to meet the "aggressive" boundary conditions increased by about 20%.

6. Conclusions

The performance of advanced power systems, including dual-pressure ORCs, supercritical cycles and ammonia/water cycles for low temperature heat sources have been evaluated relatively to an organic Rankine cycle baseline. These cycles have been compared using two different sets of boundary conditions in order to evaluate their sensitivity to the heat exchanger design. Under the same set of boundary conditions, ammonia/water mixture cycles outperform all other cycles for heat source temperatures below 120°C. For this same range of heat source temperatures, the second generation cycles offer better performance than the first generation of ammonia/water cycles. These performance benefits are achieved at the price of a larger required total heat exchanger UA for these cycles compared to the subcritical ORC baseline. For heat source temperatures between 120°C and 150°C, the dual pressure cycle offers a solid performance benefit over the subcritical ORC, at a moderate increase of the relative size of the heat exchangers. For heat source temperatures above 150°C, the supercritical cycle is the best advanced cycle solution. However, the general performance benefit of advanced cycles over subcritical organic Rankine cycles tends to decrease as the heat source temperature increases, resulting from an increase of the baseline performance as the heat source temperature approaches 200°C.

Ammonia/water mixture based cycles need somewhat less primary area for the boilers per unit UA because of a higher U, but at the same time require higher UA to meet the same approach temperatures compared to ORCs. The result is that any effect on specific area or cost reduction is small and more "aggressive" temperature design boundary conditions than in an ORC are not justified. Supercritical ORCs entail higher costs for the boiler than other cycles because of high UA requirements and higher mass flow. Thermally efficient cycles that reject relatively less heat for the same input have an advantage of a smaller condenser requirement. The specific cost for air-cooled condensers is about one order of magnitude higher than that of shell-and-tube or plate boilers and

several times that of fin-tube boilers. Although having a similar impact on the efficiency of low-temperature cycles, an economic condenser will require more generous approach temperatures than a shell-and-tube or plate boiler to optimize the cycle. Generally, meeting more “aggressive” boundary conditions than the “conservative” set seems practicable for air-cooled condensers and boilers, specifically for plate boilers, while larger approach temperatures are to be expected in fin-tube boilers for gaseous heat sources. Reasonable boundary conditions for design need to account for the type of heat exchanger and the media on both sides and cost considerations; an apple-to-apple comparison of cycles should include comparable heat exchanger areas or costs.

In any case, there is no single best technology for low temperature waste heat recovery. The optimum design will indeed vary strongly from one application to another and the author’s company supports specific studies to offer the appropriate solution fitting each customer’s needs.

References

[1] International Energy Agency, IETS. Industrial Excess Heat Recovery Technologies & Applications, 2010.

[2] Beerepoot, Milou. Interim Results IEA Technology Roadmap: Geothermal Heat and Power. 2010.

[3] Dai et al., Parametric optimization and comparative study of ORC for low grade waste heat recovery, Energy Conversion and Management, 2009

[4] Páll Vladimarsson, Exorka, The Kalina power plant in Husavik - why Kalina and what has been learned. Strasbourg: Electricity generation from Enhanced Geothermal Systems, 2006.

[5] Ogriseck S., Integration of Kalina cycle in a combined heat and power plant, a case study, Applied Thermal Engineering, 2009

[6] Kalex LLC. Kalex Kalina Cycle Power Systems for Geothermal Applications. 2010.

[7] Kalina, Alexander I, New Binary Geothermal Power System. Sochi, Russia: International Geothermal Workshop, Geothermal Energy Society, 2003.

[8] Kalina A.I., Combined cycle system with novel bottoming cycle, Journal of Eng. For Gas Turbines and Power, 1984

[9] Wall et al., Exergy Study of the Kalina Cycle, AES Vol. 10-3, pp. 73-77 ASME 1989

[10] Nag and Gupta, Exergy Analysis of the Kalina Cycle, Applied Thermal Engineering, 1998

[11] Joffee, Joseph, David Zudkevitch. Prediction of Liquid Phase Enthalpies with the Redlich-Kwong Equation of State. Ind. Eng. Chem. Fundamen. 1970, Bd. 9.

[12] Soave, Giorgio. Equilibrium constants from a Modified Redlich-Kwong equation of state. Chemical Engineering Science. 1972, Bd. 27.

Comparison of Nuclear Steam Power Plant and Conventional Steam Power Plant through Energy Level and Thermoeconomic Analysis

S.Khamis Abadi[a], M.H.Khoshgoftar Manesh[b], M.Baghestani[b], H.Ghalami[a] , M.Amidpour[b]

a. Department of Energy Engineering, Science and Research Branch, Islamic Azad University, Tehran, Iran.
b. Energy Integration Laboratory, Mechanical Faculty, K.N. Toosi University of Technology, Tehran, Iran. amidpour@kntu.ac.ir;mh.khoshgoftar@gmail.com

Abstract:
Exergetic and thermoeconomic analyses were performed for a 315 MW conventional steam and 1076 MW VVER nuclear power plants. In these analyses, mass and energy conservation laws were applied to each component of the system. Quantitative balances of the exergy and exergetic cost for each component, and for the whole system was carefully considered. The exergoeconomic model, which represented the productive structure of the system considered, was used to visualize the cost formation process and the productive interaction between components. The computer program developed in this study can determine the production costs of each component of steam and combined cycle power plant such as electricity production in steam turbines or gas turbine. The code can be also be used to study plant characteristics, namely, thermodynamic performance and sensitivity to changes in process and/or component design variables.

Keywords:
Exergy, Exergoeconomic, Steam power plant, Nuclear power plant.

1. Introduction

Energy systems involve a large number and various types of interactions with the world outside their physical boundaries. The designer must, therefore, face many issues, which deal primarily with the energetic and economic aspects of the system. Thermodynamic laws govern energy conversion processes, costs are involved in obtaining the final products (expenses for the purchase of equipment and input energy resources, operation and maintenance costs), and the effects of undesired fluxes to the ambient must be evaluated in order to answer environmental concerns.
Second law analysis has been widely used in the last several decades by many researchers. Exergy analysis usually predicts the thermodynamic performance of an energy system and the efficiency of the system components by accurately quantifying the entropy-generation of the components [1]. Furthermore, exergoeconomic analysis estimates the unit cost of products such as electricity, steam and quantifies monetary loss due to irreversibility. Also, this analysis provides a tool for the optimum design and operation of complex thermal systems [1], [2], [3]. At present, such analysis is in great demand because proper estimation of the production costs is essential for companies to operate profitably. In addition, it is vital to display the system information graphically for one to visualize the performance of system in different cases by applying improved combined pinch and exergy analysis. In contrast, the power of exergy analysis is that it can identify the major causes of thermodynamic imperfection of thermal and chemical processes and thus promising modifications can be determined [4]. By combining the strengths of pinch and exergy methods, the

proposed method can represent a whole system, including individual units on one diagram, which helps to screen the promising modifications quickly for improving a base case design [5].
In this study, exergetic, thermoeconomic and combined pinch and exergy analyses have been performed for 1076MW nuclear steam cycle and 315MW gas fired steam power plants. In these analyses, mass and energy conservation laws were applied to each component. Quantitative balance of the exergies and exergy costs for each component and for the whole system was carefully considered. The exergy-balance equation developed by Oh et al. [6] and the corresponding exergy cost-balance equations developed by Kimet al. [7] were used in these analyses.
In this regard, computer program has been developed for energy, exergy, exergoeconomic and exergy analysis of both of cases in different load conditions. Furthermore, it can also use to study plant characteristics, namely, thermodynamic performance and sensitivity to changes in process and/or component design variables.
In this paper, the authors evaluate and compare gas fired steam and nuclear power plants in view of exergy and thermoeconomic analysis at different load conditions. The main objective of this study is to provide insights into the performance of system components in particular by applying methods.

2. Process Description

In this paper, two cases have been considered at different load conditions. The first case is 315 MW gas fired steam power plant such as RAMIN power plant that is located in southwest of Iran in Ahvaz city. The scheme of 315 MW power plant and its steam turbines have been shown in Figure 1. The type of fuel is natural gas that its Low Heating Value (LHV) is 48748 kJ/kg and the net plant efficiency based on LHV is about 38.5.
The second case is 1076 MW nuclear steam power plant such as BUSHEHR power plant that is located in south of Iran in BUSHEHR city. Figure 2 represents the flow diagram of this plant. The net plant electricity efficiency in BOSHEHR power plant is 34.98.

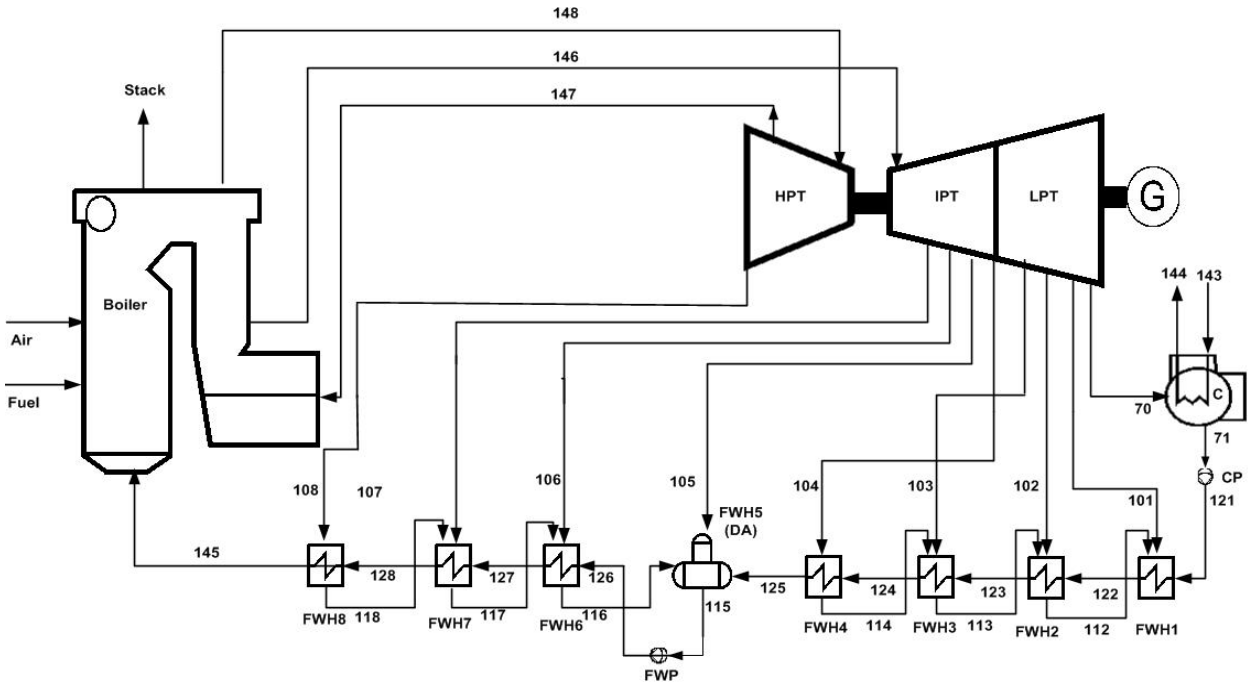

Fig 1. The scheme of a 315 MW Steam Power Plant

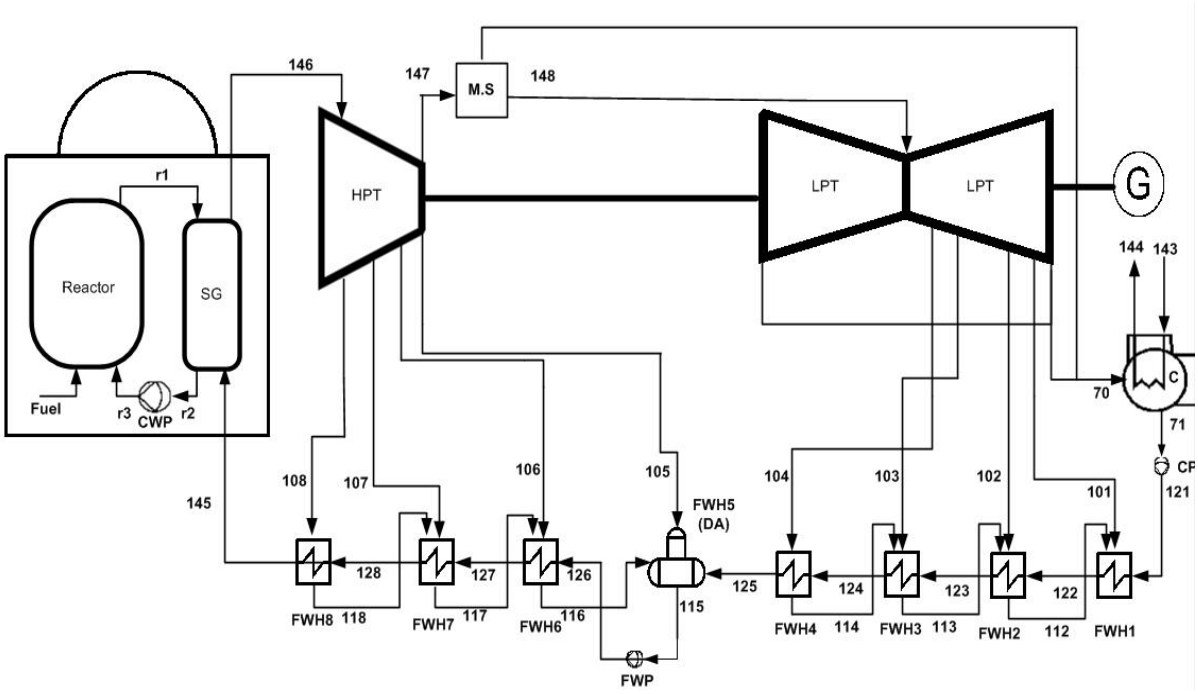

Fig 2. The scheme of 1076 MW Steam Power Plant

3. Exergoeconomic Analysis

3.1.Exergy Analysis

Exergy is the maximum theoretical useful work attainable from an energy carrier under the conditions imposed by an environment at given pressure p_0 and temperature T_0, and with given amounts of chemical elements [8]. The purpose of an exergy analysis is generally to identify the location, the source, and the magnitude of true thermodynamic inefficiencies in thermal systems. Disregarding kinetic and potential energy changes the specific flow exergy of a fluid at any cycle state is given by:

$$e = h - h_o - T_o(s - s_o) \quad (1)$$

The reversible work as a fluid goes from an inlet state to an exit state is given by the exergy change between these two states. That is:

$$e_2 - e_1 = h_2 - h_1 - T_o(s_2 - s_1) \quad (2)$$

Where the subscripts 1 and 2 represent the inlet and the exit state for a flowing fluid. Now, we present the exergy destruction and exergy efficiency relations for various cycle components in plant [9].

3.2. Cost equation for plant component

All costs due to owning and operating a plant depend on the type of financing, the required capital, the expected life of a component, and so on. The annualized (levelized) cost method of Moran [was used to estimate the capital cost of system components in this study. The amortization cost for a particular plant component may be written as:

$$PW = C_i - \$_u PWF(i, n) \quad (3)$$

$$\dot{C}\left(\frac{\$}{year}\right) - PW \times CFR(i,n) \quad (4)$$

The present worth of the component is converted to annualized cost by using the capital recovery factor CRF(*i*,*n*), i.e [2]. Dividing the levelized cost by 8000 annual operating hours, we obtain the following capital cost for the *k*th component of the plant.

$$Z_k - \frac{\Phi_k \dot{C}_k}{3600 \times 8000} \quad (5)$$

The maintenance cost is taken into consideration through the factor $\Phi_k = 1.06$ for each plant component whose expected life is assumed to be 15 years [2].

3.3. Exergoeconomic Modelling

The results from an exergy analysis constitute a unique base for exergoeconomics, an exergy-aided cost reduction method. A general exergy-balance equation, applicable to any component of a thermal system may be formulated by utilizing the first and second law of thermodynamics [1], [2], [11], [12].

The cost balance expresses that the cost rate associated with the product of the system (C_P), the cost rates equals the total rate of expenditure made to generate the product, namely the fuel cost rate (C_F), the cost rates associated with capital investment (Z^{CI}), operating and maintenance (Z^{OM}) [13].

In a conventional economic analysis, a cost balance is usually formulated for the overall system (subscript tot) operating at steady state [14]:

$$C_{P,tot} = C_{F,tot} + C_L Z_{tot} \quad (6)$$

Accordingly, for a component receiving a heat transfer and generating power, we would write [2]:

$$\sum \dot{E}_{e,k} + \dot{E}_{w,k} = \dot{E}_{q,k}$$

(7)

To solve for the unknown variables, it is necessary to develop a system of equations applying Eq. (6) to each component, and it some cases we need to apply some additional equations, to fit the number of unknown variables with the number of equations [15],[16],[17].

To derive the cost balance equation for each component, we assigned a unit cost to the principal product for each component. Depending on the type of fuel consumed in the production process different unit cost of product should be assigned [18], [19], [20],[21].

3.4. Energy Level Analysis

Pinch analysis has become a general methodology for targeting and design of thermal and chemical processes and associated utilities [4]. The composite curves (CC) and the grand composite curves (GCC) are two basic tools in pinch analysis, and they are constructed using temperature versus enthalpy axes. The energy targets set by the CC and GCC are mainly in terms of heat loads. To deal with systems involving heat and power, the concepts of both the composite curves and the grand composite curves have been extended. As a result, the exergy composite curves (ECC) and the exergy grand composite curves (EGCC) were proposed which are based on Carnot factor (η) versus enthalpy [4].

The composite curves (T-H diagram) for a heat transfer system can be converted into the exergy composite curves and the grand composite curves. The shaded areas indicate the exergy loss associated with the heat transfer process. By combining pinch analysis and exergy analysis in such a

manner, it is possible to predict the shaft work requirement or generation for both power systems and refrigeration systems with certain accuracy [4]. It must be noted that this combined pinch and exergy analysis was developed mainly for the purpose of shaft work targeting. When dealing with process modifications, it has severe limitations. Particularly, only processes related to heat transfer can be represented on the ηc-H diagram but not the processes associated with pressure and composition changes, since the diagram is constructed based on temperatures [4]:

$$\eta = 1 - \frac{T_0}{T} \tag{8}$$

To overcome limitation of ηc-H diagram, a generic diagram has been introduced which is the so called Ώ-H by Feng in 1996 [4], where Ω indicates the energy level and H states the amount of energy. Both energy and exergy balances for a whole system can therefore be represented simultaneously on this diagram. Using this diagram, the major advantages of both pinch and exergy analysis are combined since the diagram enables one to view the performance of a system and set targets for improvement.

The Energy Level Representation (ELR) based on pinch and exergy analysis draw on the earlier strategies of the thermodynamic approach to process integration, namely the concept of composite curves and the methodology of combined pinch and exergy analysis.

The graphical representation of process units involving energy in terms of heat and power has been made possible with the introduction of a variable referred to as energy level (Ώ) defined [23]:

$$\Omega = \frac{Exergy}{Energy} \tag{9}$$

Thus, for work

$$\Omega = 1 \tag{10}$$

and for heat

$$\Omega = 1 - \frac{T_0}{T} \tag{11}$$

and for a steady-state-flow system

$$\Omega = \frac{\Delta E}{\Delta H} \tag{12}$$

4. Computer Program

A computer program for exergy, exergoeconomic, exergy destruction and exergy destruction level analyses of the 1076-MW nuclear and 315-MW steam gas fired power plants have been developed. The program uses the following input data:

(a) Standard pressure (P_0) and temperature (T_0);

(b) Fuel compositions and costs

(c) Air composition and relative humidity of air;

(d) Different load conditions;

(d) Gross shaft power of gas turbine, steam turbine;

(e) Shaft work consumption in compressor and pumps;

(f) Mass flow rate (kg/s), pressure (MPa) and temperature (°C) for fluid streams at the inlet and outlet of each component;

(g) Initial investment of capital cost, interest rate, salvage value factor;

Using these input data; one can calculate the number of moles of combustion products, adiabatic flame temperature and enthalpy (MW) and entropy (MW/K) for fluid streams at various states. Using the values of these properties, we calculated the net flow rate of various exergies and entropies, the exergy efficiencies of the components and the lost exergy occurred in each component. The heat transfer rate from a component was calculated to satisfy the exergy balance for the component. Once exergy balances for the components, junctions and the plant boundary were established, the unit cost of various exergies and products were calculated by solving the cost balance equations simultaneously. Also, this program can generate Energy Level representations that can be used for combined pinch and exergy analysis.

5. Results and discussion

In this paper, computer program have been developed for thermodynamic simulation and analysis of 315-MW gas fired steam and 1076-MW nuclear power plants in different load conditions. The enthalpy and entropy of non-interacting gas species were calculated by using appropriated polynomials fitted to the thermophysical data in the JANAF Tables [22]. Also the values of physical properties such as enthalpy and entropy for water and steam were evaluated by using equations suggested by the International Association for the Properties of Water and Steam IAPWS-IF97) [23]. Exergy and exergoeconomic rates of each streams in both thermal power plants calculated by computer program have been provided in this study. Also, exergy and exergeconomic analysis have been performed for each component to calculation of exergy and exergy cost destruction with and without considering capital investment at various load conditions in steam gas fired and VVER nuclear steam power plants as shown in Table 1 and Table 2.

Table 1. Exergy flow and cost flow rates of exergy destruction with and without considering capital investment for each streams in a 315 MW steam power plant at various load condition.

Load	**100**			**75**			**50**			**25**		
Parameter	E_D	C_{D0}	C_D	E_D	C_{D0}	C_D	E_D	C_{D0}	C_D	E_D	C_{D0}	C_D
Equip Unit	MW	$/hr	$/hr	MW	$/hr	$/hr	MW	$/hr	$/hr	MW	$/hr	$/hr
FWH1	1.74	19.40	20.02	0.59	6.98	7.19	0.60	6.94	7.37	0.12	1.46	1.67
FWH2	0.76	8.46	7.94	0.39	4.58	3.69	0.28	3.26	1.73	0.14	1.83	2.09
FWH3	0.89	9.96	10.28	0.86	10.17	10.48	0.33	3.85	4.09	0.17	2.10	2.40
FWH4	0.79	8.80	9.08	0.42	4.96	5.11	0.36	4.18	4.44	0.21	2.60	2.97
FWH5	0.99	12.55	13.33	0.61	8.08	8.70	0.05	0.63	0.71	0.23	3.68	4.57
FWH6	0.69	7.65	7.90	0.75	8.97	9.24	0.35	4.09	4.34	0.21	2.60	2.97
FWH7	1.24	13.75	14.20	0.36	4.30	4.43	0.52	5.94	6.31	0.21	2.60	2.96
FWH8	0.73	7.92	8.65	0.80	9.27	9.87	0.56	6.25	7.38	0.13	1.65	2.00
CR	16.2	181.37	187.22	5.48	65.10	67.07	1.69	19.52	20.75	0.72	9.13	10.43
STLP	12.2	86.88	87.29	10.60	80.44	80.88	7.19	53.05	55.96	5.61	46.87	51.55
STIP	8.70	96.44	99.49	0.23	1.04	2.79	0.91	10.45	11.10	0.12	1.51	1.73
STHP	17.3	86.73	91.55	16.93	105.38	113.49	11.02	67.56	74.67	16.13	155.98	184.34
Boiler	425	4595.6	4748.8	337.2	3884.4	4005.8	229.3	2558.9	2724.0	141.0	1776.8	1979.9
BFPT	2.60	27.57	28.98	1.37	15.77	12.54	0.68	7.77	8.64	1.52	18.92	21.68
CP	1.22	18.96	25.19	1.04	16.92	24.87	0.24	2.91	3.51	0.43	4.85	6.73
BFP	2.54	35.72	37.55	2.21	31.07	24.70	1.60	20.69	22.99	1.72	29.73	34.07
TED	494.3	5217.77	5397.46	379.83	4257.46	4390.85	255.69	2776.03	2958.04	168.69	2062.36	2312.2

Table 2. Exergy flow and cost flow rates of exergy destruction with and without considering capital investment for each streams in a 1076 MW nuclear power plant at various load conditions.

Load	**100**			**75**			**50**			**25**		
Parameter	E_D	C_{D0}	C_D	E_D	C_{D0}	C_D	E_D	C_{D0}	C_D	E_D	C_{D0}	C_D
Equipment/Unit	MW	$/hr	$/hr	MW	$/hr	$/hr	MW	$/hr	$/hr	MW	$/hr	$/hr
HPT	94.70	409.12	1340.31	84.76	396.67	1238.48	85.81	556.03	1654.85	80.00	921.70	2909.61
LPTIPT	98.82	426.89	1494.13	69.53	325.40	1076.33	48.72	315.72	1017.33	28.36	326.79	1113.14
Condenser	99.54	765.58	1505.03	51.54	241.19	797.78	11.34	80.85	236.71	10.20	38.18	400.47
FWH1	1.73	7.46	26.12	1.435	6.72	22.21	1.45	9.42	30.36	0.42	4.84	16.49
FWH2	5.38	23.24	81.32	3.23	15.10	49.95	1.96	12.70	40.93	0.45	5.18	17.65
FWH3	4.77	20.63	72.19	2.97	13.91	46.01	1.51	9.80	31.58	1.15	13.30	45.31
FWH4	3.74	16.18	56.62	2.41	11.29	37.33	1.534	9.94	32.03	0.66	7.60	25.91
FWH5(DA)	4.03	43.53	161.72	2.37	13.81	61.29	2.49	14.69	58.30	0.88	17.67	78.51
FWH6	3.14	13.58	46.41	2.35	11.01	35.58	0.35	2.28	7.09	0.05	0.57	1.89
FWH7	3.57	15.44	52.74	3.45	16.15	52.19	0.19	1.21	3.78	0.17	1.93	6.34
FWH8	2.95	12.73	43.51	0.26	1.21	3.91	4.76	30.87	96.03	0.48	5.51	18.08
SG	170.16	245.24	980.36	129.12	511.34	976.36	50.76	219.37	548.39	10.02	108.23	213.13
Reactor	1621	5253	15342	1216	4815	13695	811	4961	13214	364.83	3940	10278
Moisture Separator	6.38	27.75	94.18	1.47	6.87	22.16	0.951	6.14	19.07	0.61	7.08	23.17
Condenser Pump	0.98	17.03	68.47	1.87	13.46	78.72	7.41	56.04	314.90	2.75	78.11	424.19
Coolant Pump	2.15	37.20	149.57	1.61	11.63	68.00	1.07	8.14	45.72	0.54	15.30	83.12
SG Feed Water Pump	5.56	96.15	386.60	6.95	50.03	292.69	5.99	45.32	254.65	6.97	198.37	1077.28

These results represented that boiler in gas fired steam and reactor in nuclear power plant have most exergy and exergy cost destruction due to nature of combustion and fission; however boiler in steam plant shares about 86 % TED, 88 % TCD0 and 87% TCD and reactor in nuclear plant shares about 76% TED, 71% TCD0 and 70% TCD. In next steps, condenser and steam turbines for gas fired steam and steam generator, condenser and steam turbine for nuclear case have most exergy and exergy cost destruction. As results shown, TCD0 and TCD reduce when load condition decreases and vice versa because the fuel consumption decreases when load condition reduces and vice versa, so TCD0 and TCD have direct relation with load conditions.

In this study, exergy and energy efficiency comparison of both power plants at different load conditions have been considered as represented in Fig.3. The energy and exergy efficiency based on first and second laws of thermodynamics for RAMIN steam power is more than BUSHEHR nuclear plant in different load conditions; however, we can divide two sections for analysis of energy and exergy comparison of both power plants. In section 1, that refer to 25-75 % load, both efficiency in both plants approach together when load condition increase to 75% (efficiency will be about 35% for BUSHEHR and 38% for RAMIN). Section 2 begins from 75% and be finished in full load condition that in this domain with increasing load condition form 75%, both efficiency in both plants almost be fixed.

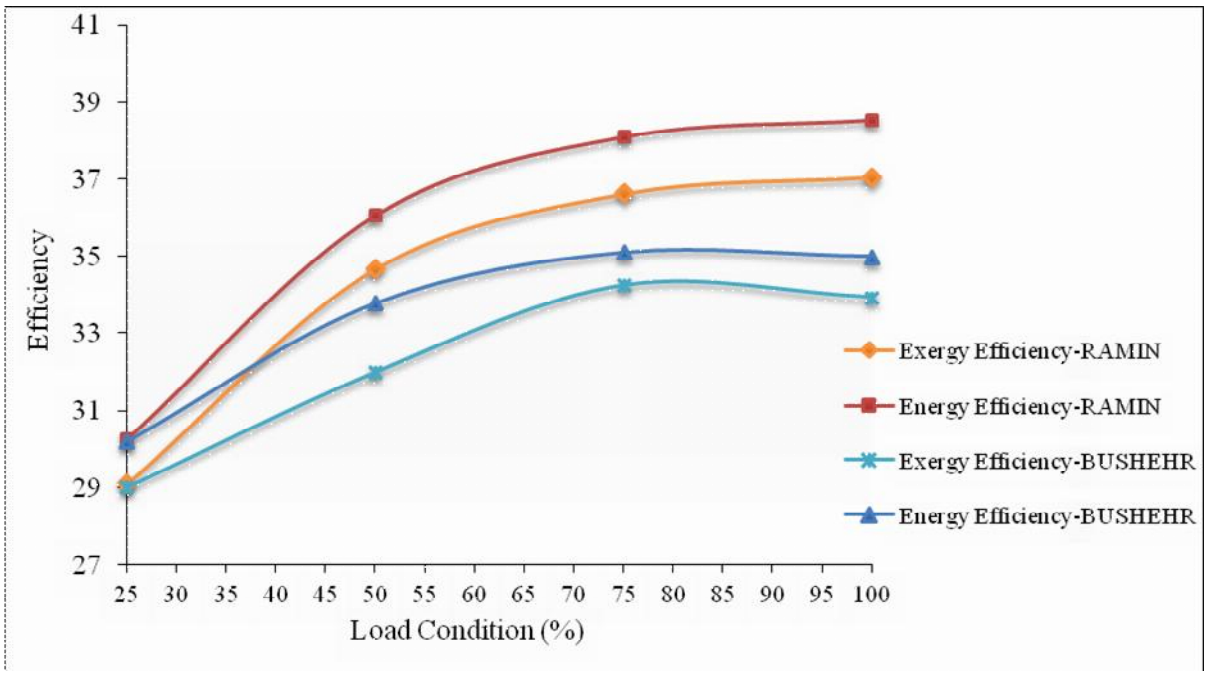

Fig. 3. Exergy and energy efficiency comparison of BUSHEHR and RAMIN power plants at different load.

The details comparison of main parameters such as TED (total exergy destruction), EF (rate of exergy related to fuel) and Wnet (net power generation) in RAMIN and BUSHEHR plants have been illustrated in Fig. 4.

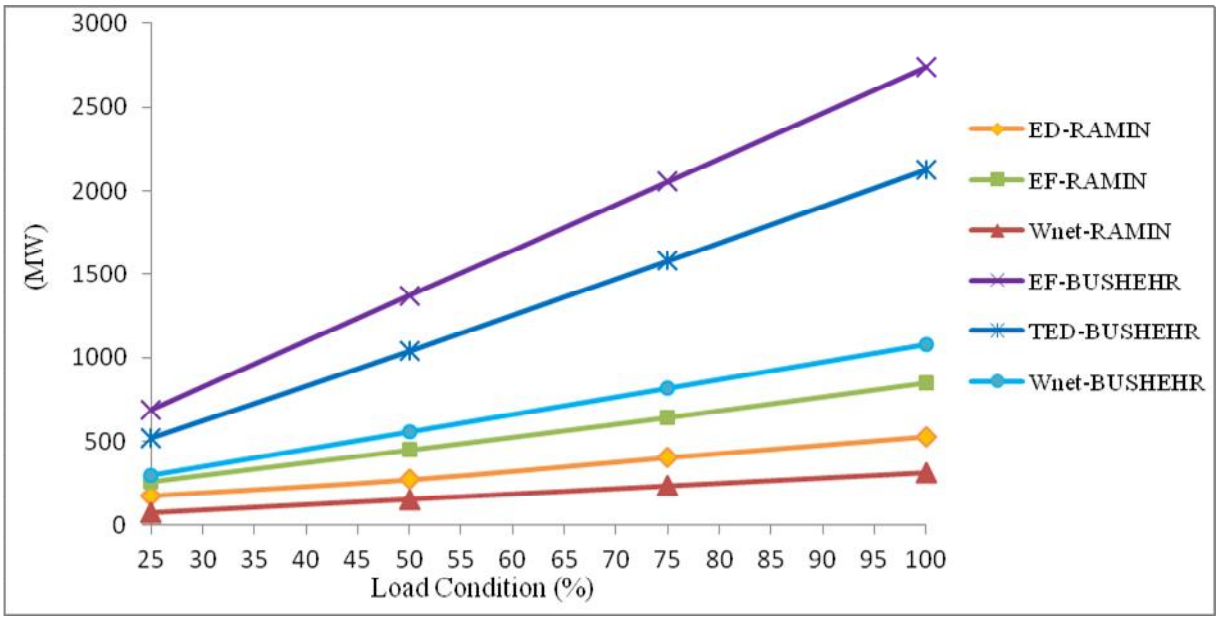

Fig. 4. EF, TED and net power comparison of BUSHEHR and RAMIN power plants at different loads.

As shown in Fig. 4, rate of exergy related to fuel in BUSHEHR is more than in RAMIN but with increasing load condition the difference between them is increased subsequently. In addition, net power generation in BUSHEHR is more than RAMIN in different loads; however load difference between net power in both plants is increased. Also, total exergy destruction (TED) in both plants is increased and difference between TED of BUSHEHR and RAMIN is increased.

The comparison of cost per unit exergy of product for turbine systems of both plants at different load conditions with and without considering capital cost have been demonstrated in Fig. 5 and Fig. 6 consecutively. As shown in these figures, c_{P0} of HP steam turbine in BUSHEHR in full load is more than other turbines significantly; however between 25-60% loads, c_{P0} and c_P of BUSHEHR HP steam turbine are decreased, between 60-100% loads these parameters are increased. After c_{P0} and c_P of BUSHEHR HP steam turbine, high pressure steam turbine (STHP) in RAMIN has most c_{P0} and c_P than other turbines. Also, in domain 25-50% loads c_{P0} and c_P are decreased quickly, between 50-75% loads they are fixed and both parameters between 50-100% load are decreased slowly. RAMIN low pressure steam turbine (STLP) locates in next level and it behavior similar to STHP but sloop between 25-50% is gentler than STHP. RAMIN intermediate pressure steam turbine (STIP) locates in next level Also, between 25-50% these parameters are decreased, between 50-100% are almost fixed and between 75-100% are increased with very gentle sloop. Finally, BUSHEHR low pressure steam turbine (STLP) has lowest c_{P0} and c_P.

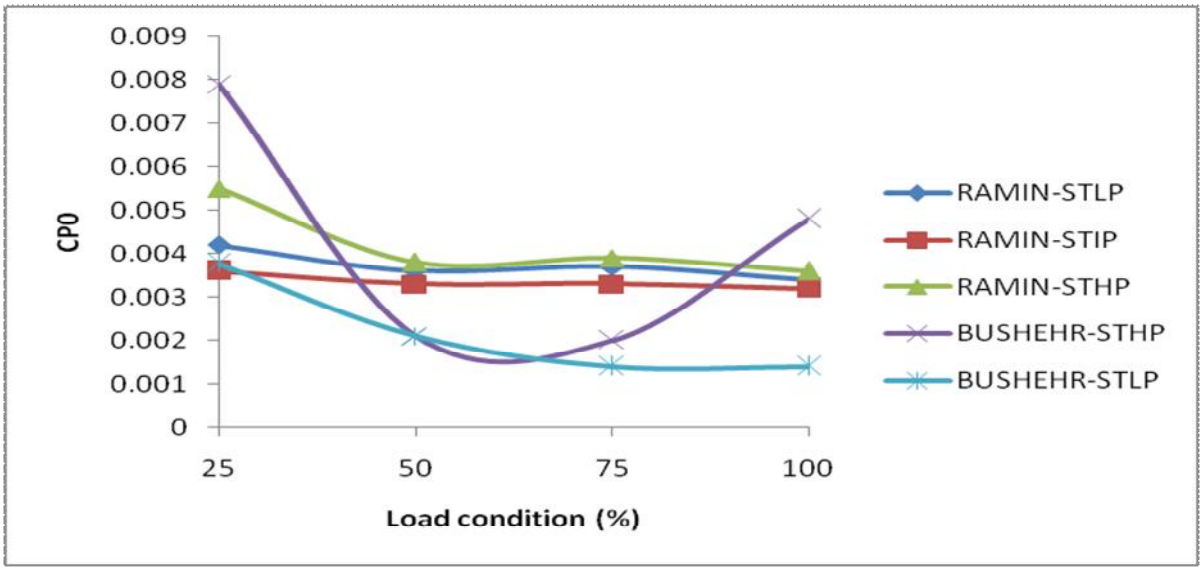

Fig. 5. C_{p0} comparison of BUSHEHR and RAMIN power plants at different loads.

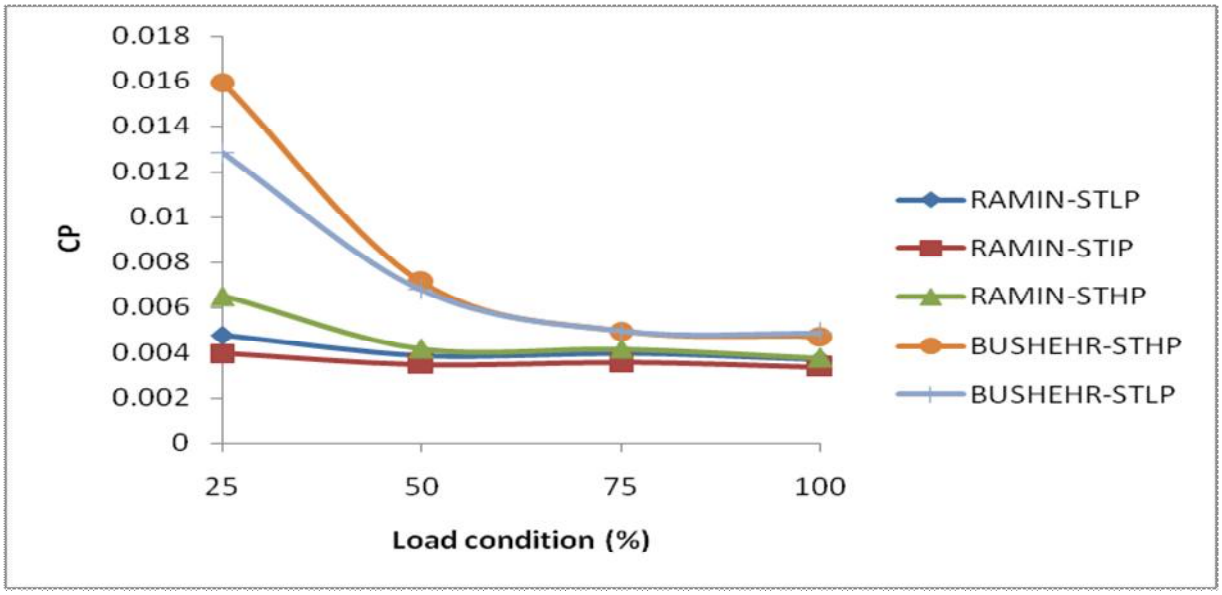

Fig. 6. C_p comparison of BUSHEHR and RAMIN power plants at different loads.

Comparison of cost per hour of exergy destruction of both plants at different load conditions with and without considering capital cost has been demonstrated in Fig.7. As shown in these figure, cost exergy destruction (CD and CD_0) in BUSHEHR is more than cost exergy destruction in RAMIN. Both parameters are increased when load condition increase to full load. However but RAMIN sloop is gentler than BUSHEHR. Also, the energy level representation of BUSHEHR and RAMIN power plants at full load condition have been shown in Fig 8 and Fig 9 consequently. The interaction between different components in each power plant have been demonstrated.

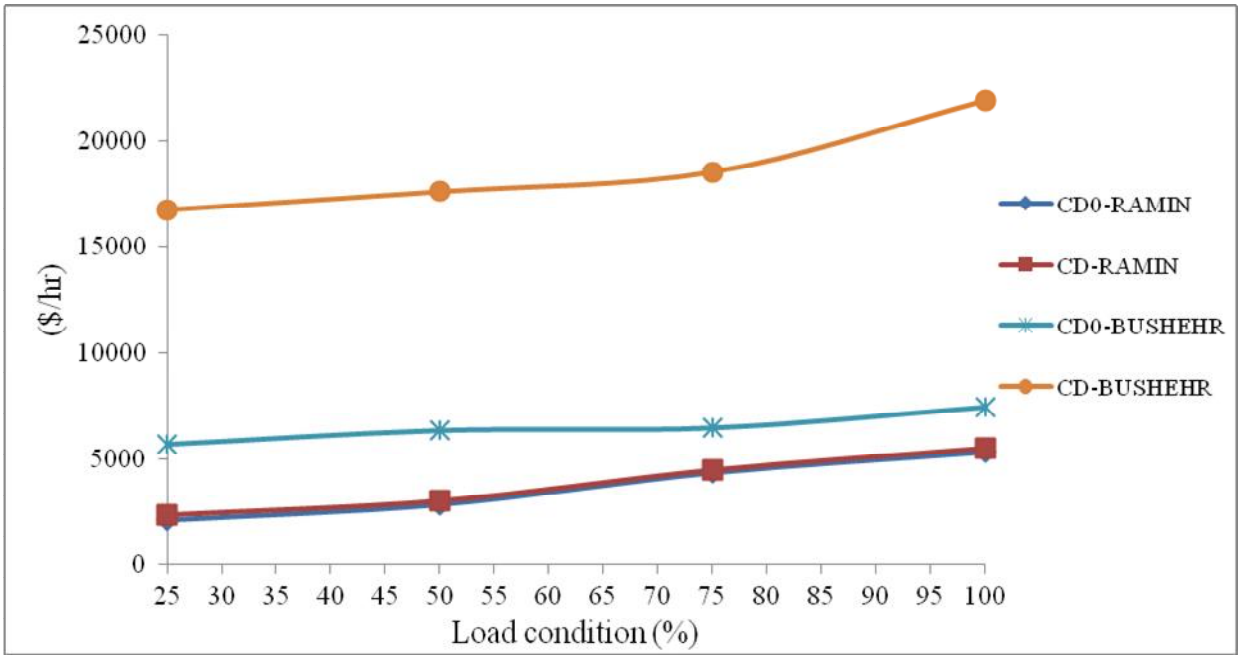

Fig. 7. CD, CD_0 and net power comparison of BUSHEHR and RAMIN power plants at different loads.

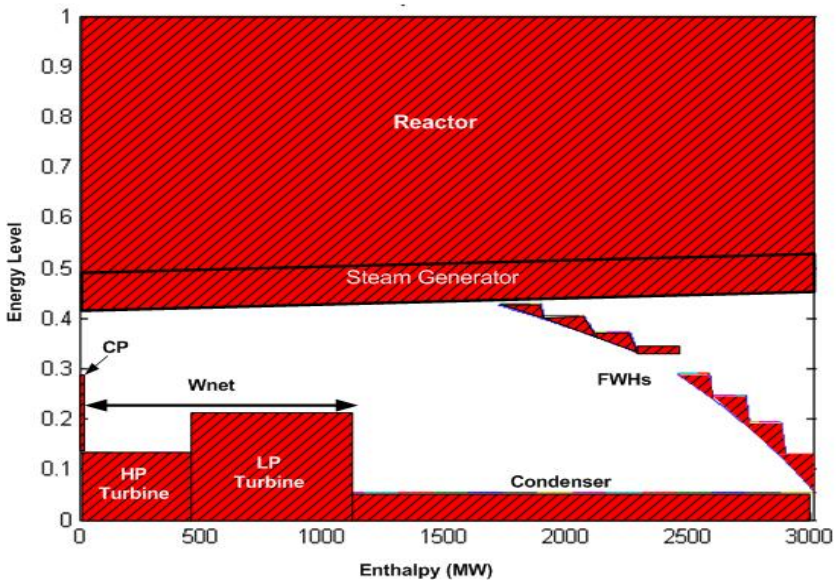

Fig. 8. Energy Level Representation of BUSHEHR power plant

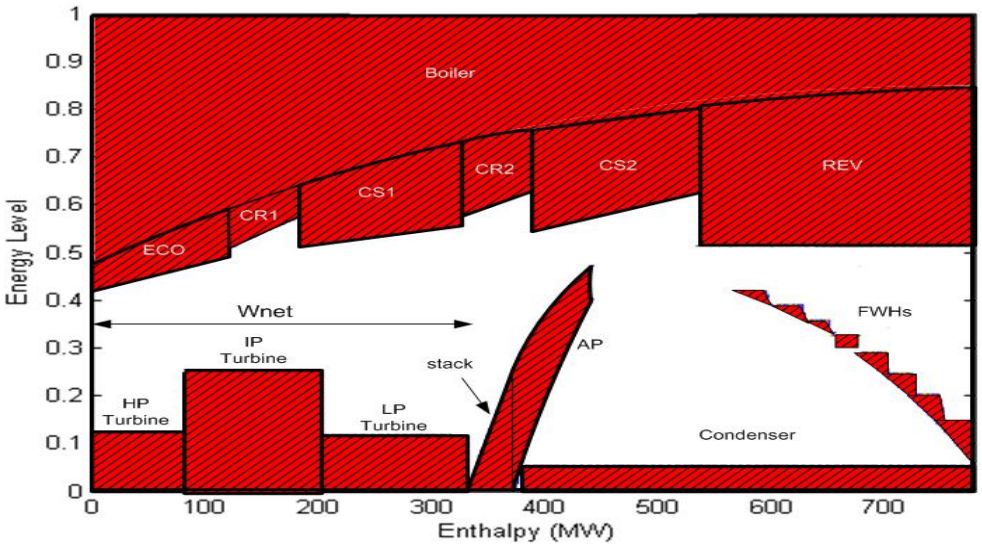

Fig. 9 Energy Level Representation of RAMIN power plant

6. Conclusions

In this paper, exergy and exergoeconomic methods have been applied for analysis and comparison of a 315-MW steam gas fired and a 1076-MW nuclear steam cycle power plants in different load conditions.

An exergy-costing method has been applied to both cases to estimate the unit costs of electricity produced from steam turbines. The computer program that was developed which shows that the exergy and the thermoeconomic analysis presented here can be applied to any energy system systematically and elegantly. If correct information on the initial investments, salvage values and maintenance costs for each component can be supplied, the unit cost of products can be evaluated.

Although the overall picture of a system can be shown and major directions for improving the system performance can be identified from the above two levels of analysis, the maximum potential or the limit of improvement for individual units and processes are still uncertain, since the exergy loss analysis so far is based on the concept of total exergy loss. In some cases, the suggestions for promising modifications based on the total exergy loss may be misleading, since they do not consider the minimum exergy loss which is required to operate a process.

The combined pinch and exergy analysis or Energy Level Representation shows the maximum potential for improvement or limitations. There are three significant advantages of knowing the practical maximum potential and limit for improvement. First, the performance of a process and equipment can be evaluated based on the maximum potential which is achievable in current technical and economical conditions. The practical maximum potential for improvement defined as such distinguishes itself from the theoretical maximum potential, which cannot be realized either technically or economically. Therefore, the practical maximum potential indicates what can be done and what cannot be done in current conditions. Secondly, by knowing the practical maximum potential for improvement, a designer sets the target for improvement by making modifications. Different modifications can then be compared in terms of how much benefit can be achieved and what is the capital cost involved. Thirdly, any processes or units with very small potential for improvement can be immediately ruled out from consideration.

Nomenclature

c	cost per unit exergy ($/MW)
cp	molar specific heat capacity (J/kmol.K)
C	cost flow rate ($/hr)
CP	heat capacity (J)
CRF	capital recovery factor
e	exergy rate per mass (MW/kg)
E	specific exergy (MW)
h	specific enthalpy (kJ/kg)
i	interest rate
m	mass flow rate (kg/s)
N	Molar mass flow rate of saline water
PWF	Present forth factor
PW	Present worth
p	pressure (bar)
R	universal gas constant ($bar.m^3K^{-1}$)
s	specific entropy (MW/K)
T	temperature (°C)
T_0	ambient temperature (°C)
W	shaft work, electricity (MW)
Z	capital cost rate of unit ($/hr)
TED	Total exergy destruction
TCD	Total exergy cost of destruction
STHP	steam turbine high pressure
STIP	Steam turbine Intermediate pressure
STLP	Steam turbine low pressure
GT	gas turbine
ST	steam turbine

Greek symbols

ρ	density (kg/m^3)

Superscript

CI	capital investment
OM	en operating and maintenance cost
ph	Physical
ch	Chemical

Subscript

P	Product
f	Fuel
tot	Total
D	Destruction

L	Loss
k	kth component
0	without considering capital investment
Q	Heat transfer
i	Inlet
o	Outlet
st	Steam
W	shaft work

References

[1]Sanjay Y, Singh O, Prasad BN. Energy and exergy analysis of steam cooled reheat gas–steam combined cycle. *Applied Thermal Engineering* 2007; 27: 2779–2790.

[2]Chao Z, Yan W. Exergy cost analysis of a coal fired power plant based on structural theory of thermoeconomics. *Energy Conversion and Management* 2006; 47:817–843.

[3]Modesto M, Nebra SA. Analysis of a repowering proposal to the power generation system of a steel mill plant through the exergetic cost method, *Energy* 2006; 31: 3261–3277.

[4]Feng X, Zhu XX. Combining pinch and exergy analysis for process modifications. *Applied Thermal Engineering* 1997*;* 17: 250-260.

[5]Kotas TJ. The exergy method of thermal plant analysis. New York:Krieger; 1995.

[6] S. Oh, H. Pang, S. Kim, H. Kwak, 1996, Exergy analysis for a gas–turbine cogeneration system, Journal of Engineering for Gas Turbines and Power 118 : 782–791.

[7] S. Kim, S. Oh, Y. Kwon, H. Kwak, 1998, Exergoeconomic analysis of thermal systems, Energy 23: 393–406.

[8]Uhlenbruck S, Lucas K. Exergoeconomically-aided evolution strategy applied to a combined cycle power plant. *International Journal of Thermal Science* 2004; 43: 289–296.

[9]Bejan A, Tsatsaronis G, Moran M. Thermal design and optimization. New York: Wiley; 1996.

[10] Dobrowolski R, Witkowski A, Leithner R, Simulation and optimization of power plant cycles, in: G. satsaronis, M. Moran F. Cziesla T. Bruckner (Eds.), ECOS 2002, Proceedings of the 15th International Conference on Efficiency, Costs, Optimization, Simulation and Environmental Impact of Energy Systems, Berlin, Germany, 2002, pp. 766–772.

[11]Emmerich M, Gr¨otzner M, Gross B, Sch¨utz M. Mixed-integer evolution strategy for chemical plant optimization with simulators, in: I. Parmee (Ed.), Evolutionary Design and Manufacture, Springer Verlag, Berlin, 2000, pp. 55–67.

[12]Emmerich M, Schutz M. Design of graph-based evolutionary algorithms: A case study for chemical process networks. *Evolutionary. Computation* 2001; 9 (3): 329–354.

[13]Durmayaz A, Yavuz Y. Exergy analysis of a pressurized water reactor nuclear power plant. *Applied Energy 2001;* 69: 39-57.

[14]Nafey AS, Fath HES, Mabrouk AA. Exergy and thermoeconomic evaluation of MSF process using a new visual package. *Desalination 2006;* 201: 224-240.

[15]Dobrowolski R, Witkowski A, Leithner R. Simulation and optimization of power plant cycles. ECOS 2002, Proceedings of the 15th International Conference on Efficiency, Costs, Optimization, Simulation and Environmental Impact of Energy Systems, Berlin, Germany, 2002, pp. 766–772.

[16]Emmerich M, Gr¨otzner M, Gross B, Schutz B. Mixed-integer evolution strategy for chemical plant optimization with simulators. Evolutionary Design and Manufacture, Springer Verlag, Berlin, 2000, pp. 55–67.

[17] Emmerich M, Grotzner M, Schutz M. Design of graph-based evolutionary algorithms: A case study for chemical process networks. Evolutionary Computation 2001; 9 (3): 329–354.
[18]Moreno RM. Exergoeconomic analysis of a nuclear power plant, PhD THESIS, University of Arizona, UMI number : 9806823 (1997).
[19]Sato N. Chemical energy and exergy:An introduction to chemical thermodynamics for engineers. Sapporo: Japan: Elsevier Science & Technology Books; 2004.
[20]Arons JS, Kooi H, Sankaranarayanan K. Efficiency and Sustainability in the Energy and Chemical Industries. New York: Marcel Dekker: 2004.
[21]Tsatsaronis G. Thermoeconomic analysis and optimization of energy system. *Progress in Energy and Combustion Science* 1993; 19:, pp. 227-257,
[22]Joint Army-Navy–Air Force Thermochemical Tables. NSRDS-N3537, Washington, DC: National Bureau of Standard Publications; 1985.
[23]M.H.Khoshgoftar Manesh, M. Amidpour, New Graphical Methodology for Energy Integration in Nuclear Steam Power Plant ,*Proceeding of 16th International Conference On Nuclear Engineering*, May 2008, Orlando, Florida.

Economic and exergoeconomic analysis of micro GT and ORC cogeneration systems

Audrius Bagdanavicius[a], Robert Sansom[b], Nick Jenkins[c], Goran Strbac[d]

[a] Cardiff University, Cardiff School of Engineering, Cardiff, UK, bagdanaviciusa@cardiff.ac.uk (CA)
[b] Imperial College, London, UK, r.sansom10@imperial.ac.uk
[c] Cardiff University, Cardiff School of Engineering, Cardiff, UK ,jenkinsn6@cardiff.ac.uk
[d] Imperial College, London, UK, g.strbac@imperial.ac.uk

Abstract:

Exergoeconomic analysis is a powerful tool which can be used to analyse energy generation systems. However, due to its complexity it is rarely used, especially for smaller systems. These systems are usually assessed using traditional energy and economic analysis. The aim of this study is to compare the differences between the two approaches, i.e. economic and exergoeconomic. For that purpose a commercial micro gas turbine (GT) cogeneration system and a cogeneration system consisting of a gas turbine and micro organic Rankine cycle (GT-ORC) have been investigated. Results show that exergy costs of products calculated using exergoeconomic analysis depend on ambient reference temperature and these costs reduce when the temperature decreases. Heat energy costs, calculated using the exergy factor from exergy costs, increase slightly when the reference temperature decreases. It is also noted that exergoeconomic cost analysis may provide an attribution of costs which gives a better guide to the relative value of electricity and heat than economic cost analysis.

Keywords:

CHP; cogeneration; economic analysis; exergy analysis; exergoeconomic analysis; gas turbine; ORC

1. Introduction

Traditionally energy efficiency and economic analyses are used when energy conversion systems have to be assessed, particularly for investment purposes. Sometimes energy analysis is not sufficient, especially when different types of cogeneration systems are compared. Therefore, economic evaluation plays an important role in deciding which cogeneration system should be chosen. However, economic analysis cannot be relied upon when attributing costs to electricity and heat as it may not reflect their quality or value and alternative methods such as thermoeconomic analysis need to be used.

Thermoeconomic analysis combines economic and thermodynamic analysis by applying the concept of cost [1]. First attempts to combine exergy and costs were undertaken in early 1930's [2]. Later many more thermoeconomic methods were developed. During the last decade several attempts to generalise all thermoeconomic methods were made. It led to the evolution of two thermoeconomic methods. One of them, Structural Theory of Thermoeconomics, is a standard mathematical formulation for all methodologies [3]. Another, Specific Exergy Costing (SPECO) is a methodology for defining and calculating exergy efficiencies and exergy related costs in thermal systems [4].

The SPECO method provides an unambiguous and systematic procedure for exergy cost calculations. This method has been used to study community energy supply systems [5] and micro cogeneration plants [6]. In this paper the investigation of micro cogeneration systems is extended. As in the previous papers the SPECO method has been used but the micro gas turbine cogeneration system (GT) has been modified by connecting an organic Rankine cycle turbine (GT-ORC). Then exergoeconomic analysis has been performed and the effect of ambient reference temperature on

the product costs has been investigated. Finally an economic assessment of both systems has been conducted from a cost and investment perspective.

2. System description

The GT and GT-ORC systems were modelled using the Cycle-Tempo modelling tool [7] with an ambient reference temperature of 288K (T_0) and a pressure of 101.3kPa (P_0) used for exergy calculations.

2.1. Micro GT cogeneration system

A micro gas turbine cogeneration system available on the market was chosen (Fig. 1). Air for combustion is compressed in the compressor (1) and passes through the recuperator (4). The temperature of the air is increased in the recuperator (4) and the hot air supplied to the combustion chamber (2), where air and gas mixture is burned. The gas expands in the gas turbine (3) and is supplied to the heat exchanger (5), passing by the recuperator (4), where it is cooled. In the heat exchanger (5), high temperature exhaust gas cools and heats water in the heating system (6). Pump (7) is used to circulate water in the heating system (6). Finally the cooled exhaust gas is delivered to the flue stack (8). Electrical energy generated in the gas turbine and heat energy generated in the heating system (6) are shown using arrows (13) and (15). Simulation data are presented in table 1.

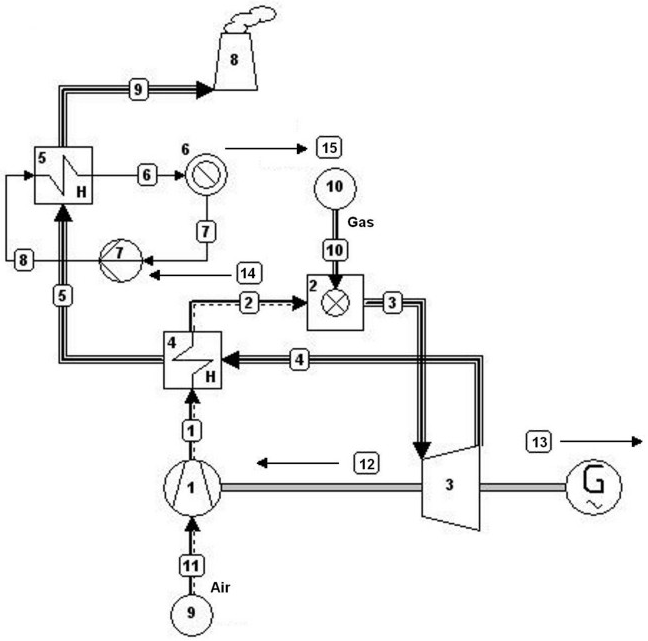

Fig. 1. Micro GT cogeneration system model [6]

2.2. Micro GT-ORC cogeneration system

This consists of the micro GT-ORC system described in 2.1 and a commercially available ORC turbine [8] (Fig. 2).

The main difference with this cogeneration system is that in the heat exchanger (5) high temperature exhaust gas is used to heat water to +140°C under elevated pressure conditions. Pump (7) is used to circulate water between heat exchangers (5) and (8). In the heat exchanger (8) water heats the refrigerant pentafluoropropane (R245fa), which is used as working fluid in the ORC system. Cooled water is then supplied back to the heat exchanger (5). High pressure and temperature R245fa vapour is delivered to the turbine (9), where it expands. Exhaust vapour from

turbine (9) is condensed in the heat exchanger (10). Then the liquid is pumped to the heat exchanger (8) and the cycle repeats. Water in the heating system is heated from 50°C to 70°C in the heat exchanger (10) and is supplied to the heating system (15) using the circulation pump (14).

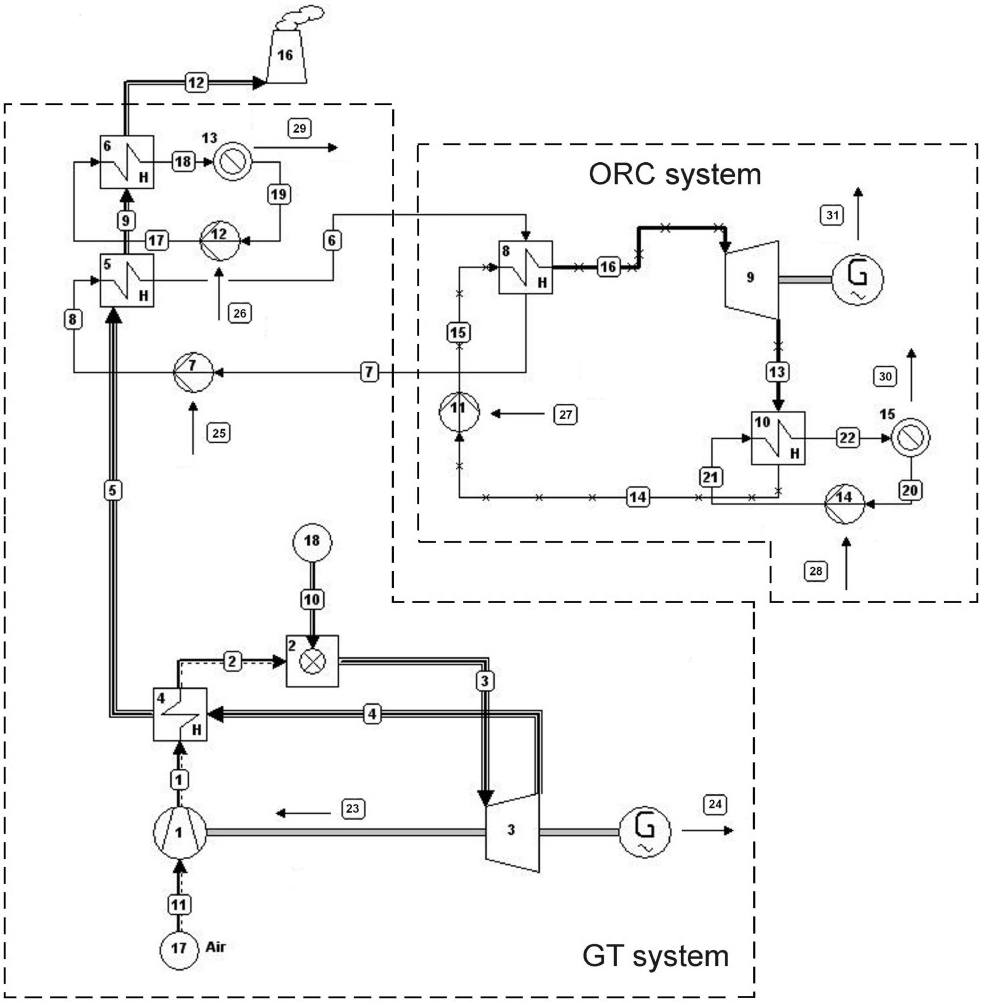

Fig. 2. Micro GT-ORC cogeneration system model

Table 1. Micro GT and micro GT-ORC simulation data

Parameter	Micro GT	Micro GT-ORC
Fuel energy (HHV), kW	369.7	369.7
Electrical output, kW	102.1	112.1
Thermal output, kW	157.6	148.0
Exhaust gas temperature after GT recuperator, °C	270	270
Gas temperature in chimney, °C	70	70
Supply/return heating system temperature , °C	70°/50°	70°/50°
Supply/return water temperature for ORC cycle, °C	-	140°/115°
Maximum refrigerant vapour temperature, °C	-	120°

In the GT-ORC system, electricity is generated in gas turbine (3) and ORC turbine (9) (electrical energy streams (24) and (31)), and heat is generated in heating systems (13) and (15) (heat energy streams (29) and (30)). Simulation data are presented in table 1.

3. Energy and exergy efficiency analysis

Energy and exergy efficiencies of the micro GT and micro GT-ORC systems including auxiliary pumps are shown in Table 2. Efficiencies are calculated using the higher heating value (HHV) of fuel.

Table 2.Energy and exergy efficiency of the micro GT and micro GT-ORC (HHV based)

Parameter	Micro GT	Micro GT-ORC
Electric energy efficiency[1], %	27.5	29.9
Heat energy efficiency, %	42.6	40.0
Total energy efficiency, %	**70.1**	**69.9**
Electric exergy efficiency[1], %	29.3	31.8
Heat exergy efficiency, %	6.2	5.8
Total exergy efficiency, %	**35.5**	**37.6**

Notes: 1 - Including auxiliary power consumption

The total energy efficiency of the GT-ORC system is slightly lower than that of the GT system. However, more electrical energy is generated in the GT-ORC system. The reduction of heat exergy efficiency in the GT-ORC system by 0.4% is accompanied by a 2.5% increase in electrical exergy efficiency. Consequently, the total exergy efficiency of the GT-ORC system is higher than that of the GT system.

4. Exergoeconomic analysis

In order to perform exergoeconomic and economic analysis, capital costs were required. The total cost of the micro GT system was provided by the manufacture and component costs were then estimated based on the cost functions provided by Galanti and Massardo [9] supplemented by manufactures' quotes. The total cost of the micro GT system is €130.2 k.

The costs of components: heat exchangers, ORC turbine and pumps for the GT-ORC system, were obtained from the manufactures' pricelists. The total cost of the micro GT-ORC system is €156.7 k.

The following assumptions were made for both cogeneration systems:

- 10 % return on investment,
- 15 years investment repayment period,
- 7000 hours annual operating hours,
- operation and maintenance costs are not included,
- 2.31 c/kWh fuel price (HHV) based on natural gas for industrial consumers in UK in 2011 (taken from EU Energy Portal (www.energy.eu)).

4.1. Exergoeconomic calculations

The Specific Exergy Costing (SPECO) method [4] was used in this study. At first, identification of the exergy streams was carried out using Cycle-Tempo software. Total exergy was used in this study because the use of separate forms of exergy, such as: thermal, mechanical or chemical, only marginally improves calculation accuracy [4]. The next step, definition of *products* and *fuels*, was carried out using the methodology described by Tsatsaronis [10, 11]. Finally the last step, construction of cost equations, was carried out by constructing cost equations for each component in the model and by formulating auxiliary cost equations. More detailed description of application of SPECO method can be found in [5, 6].

Using the exergoeconomic approach cost rates of exergy destruction, capital cost rates and exergoeconomic factors of the micro GT and micro GT-ORC systems were calculated. The exergeoeconomic factor was calculated using equation [11]:

$$f_k = \frac{\dot{Z}_k}{(\dot{Z}_k + \dot{C}_{D,k})} \quad (1)$$

Here f_k – exergoeconomic factor of k-th component (%), $\dot{Z}_k$ – capital cost rate (€/h), $\dot{C}_{D,k}$ – cost rate of exergy destruction based on fuel (€/h). The exergoeconomic factor shows the contribution of non-exergy related cost (investment cost) to the total cost increase. A low value indicates that a higher cost of the component would be acceptable if the exergy destruction were reduced. A high value of f_k indicates the cost of the component should be reduced, even if the exergy efficiency of the component decreases.

Results of calculation of the GT system are presented in Fig. 3. It is seen that the cost rate of exergy destruction in the combustor is the highest. The exergoeconomic factor of the combustor is low, which suggests further investment in this component may be justifiable if higher exergy efficiency were achieved.

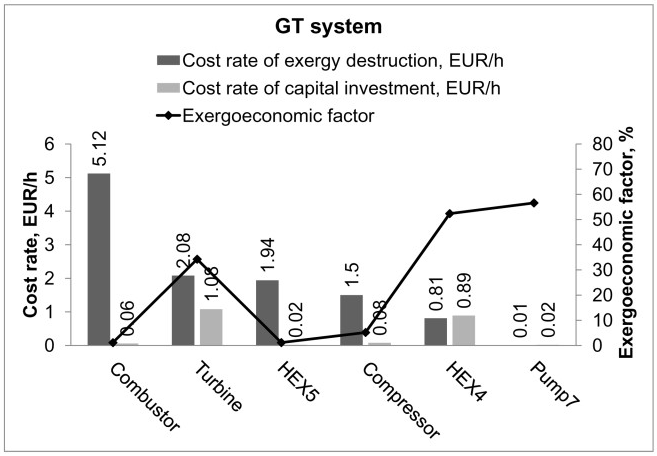

Fig. 3.Cost rate and exergoeconomic factors of micro GT system components

The cost rate of exergy destruction of turbine, heat exchanger (5) (HEX5) and compressor are similar. The exergoeconomic factor of turbine is around 34 %. This suggests that a less efficient gas turbine produced at lower cost can be chosen, if its exergy efficiency were not significantly reduced.

The cost rate of exergy destruction (0.81 €/kWh) of the recuperator (4) (HEX4) is low compared with other system components. However its capital cost rate (0.89 €/kWh) is significantly higher than that of other components. The exergoeconomic factor of the recuperator (4) is about 52%, which indicates that its capital cost should be reduced even if the exergy efficiency decreased.

Results of calculation of the GT-ORC system are presented in Fig. 4. It is seen that the cost rate of exergy destruction in the combustor and turbine are the highest, as in the GT system.

A similar cost rate of exergy destruction of the recuperator (4) (HEX4) is observed in both the GT (Fig. 3) and GT-ORC systems (Fig. 4). However the cost rate of exergy destruction of the heat exchanger (5) (HEX5) is significantly lower in the GT-ORC system (Fig. 4) compared with the GT system (Fig. 3).

A single heat exchanger is used to reduce the temperature of the flue gas in the GT system (heat exchanger (5), Fig. 1) whereas two heat exchangers (5) and (6) are used in the GT-ORC system (Fig. 2). The cost rate of exergy destruction of the heat exchanger (5) in the GT system (1.94 €/h, Fig. 3) is higher than the sum of two cost rates of exergy destruction of the heat exchangers (5) and

(6) (1.03 €/h, Fig. 4) in the GT-ORC system. It shows that gradual reduction of the exhaust gas temperature is more beneficial than sudden reduction of temperature using one heat exchanger.

There are more components, such as: heat exchangers (6), (8) and (10), turbine (9) and pump (11) and (14) (Fig. 2), which contribute to the increase of the total cost rate of exergy destruction in the GT-ORC system compared with the GT system. The contribution of pumps (7) and (12) (Fig. 2) to the cost of exergy destruction formation is negligibly small. However, the total cost rate of exergy destruction of the GT system (11.46 €/h) is higher than that of the GT-ORC system (11.30 €/h). The decrease exergy destruction cost is obtained because the additional ORC system is used. However, the use of additional system increases the total cost rate, which is the sum of cost rates of exergy destruction and capital costs. The total cost rate is 13.61 €/h in the GT system and 13.93 €/h in the GT-ORC system.

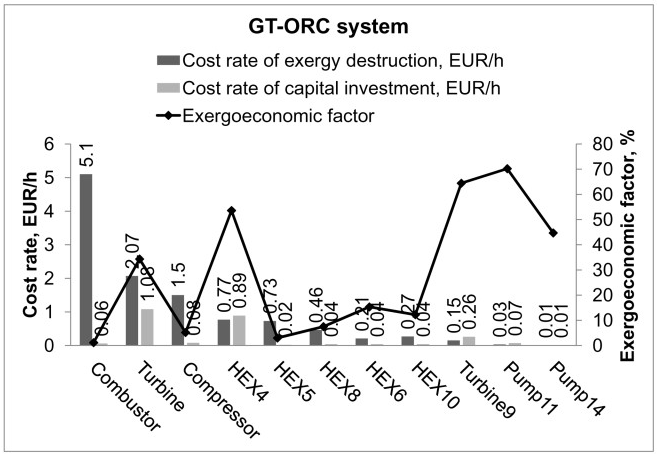

Fig. 4. Cost rate and exergoeconomic factors of micro GT-ORC system components

One of the main objectives of exergoeconomic analysis is to evaluate the production costs of products in an energy conversion system [2]. The exergy costs of electricity and heat generated in the micro GT and micro GT-ORC systems are shown in Figure 5. It is seen that electricity exergy costs of the GT system is lower than the average cost of the GT-ORC system. However, the heat exergy cost of the GT is higher than the average heat exergy cost of the GT-ORC system. The exergy cost of electricity generated in the ORC turbine of GT-ORC system is significantly higher than the exergy cost of electricity generate in the gas turbine. The reason for that is low electrical efficiency of the ORC.

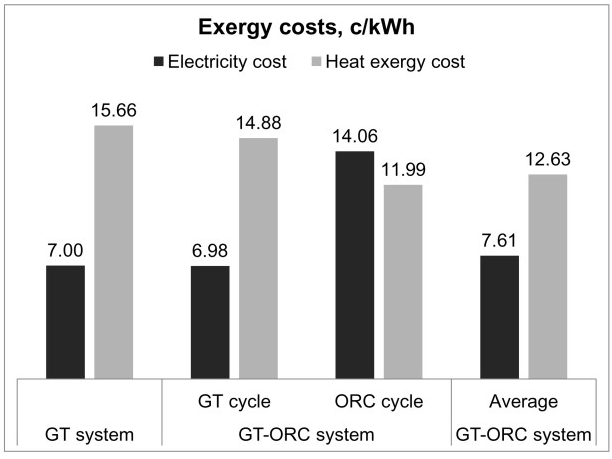

Fig. 5. Exergy costs

4.2. Calculation of energy cost based on exergoeconomic analysis

Exergoeconomic analysis is a powerful tool which allows an understanding of the cost formation process and the calculation of the costs of each product. However, exergy is not a commodity. Therefore, exergy cost calculated using exergoeconomic analysis, has little practical value. In order to use the exergoeconomic method for practical calculations exergy costs must be converted to energy costs.

When conducting exergy and exergoeconomic analysis the reference ambient temperature T_0 must be carefully selected as any variation affects the exergy efficiency of the system. In this study exergy and exergoeconomic analysis were conducted using an ambient reference temperature +15°C. Other ambient reference temperatures of +9°C and +4°C were explored to understand how exergy costs are affected for the GT system only.

In order to calculate the heat energy costs from heat exergy costs the exergy factor τ is used determined from:

$$\tau = {}^{E}\Big/_{Q} = 1 - \frac{\frac{T_0 \ln T_S}{T_R}}{T_S - T_R} \qquad (2)$$

Here E is heat exergy; Q is heat energy, T_0 (K) is ambient reference temperature, T_S (K) is heating system supply water temperature and T_R (K) is heating system return water temperature. Calculated energy and exergy costs at different reference temperature for micro GT system are shown in Fig.6.

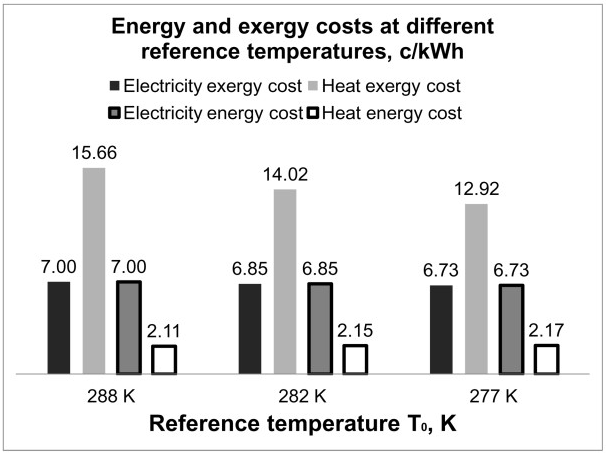

Fig. 6. Energy and exergy costs of products in micro GT system at different reference temperatures

It is seen that exergy costs of electricity and heat reduces when the lower ambient reference temperature is used with a larger reduction in heat cost than electricity. This is because there is an increased quantity of exergy when the lower reference temperature is used. Electricity energy cost is equal to its exergy cost whereas heat energy cost increases with temperature due to the augmentation of exergy factor. In general the change of reference temperature has little effect on electricity and heat energy costs.

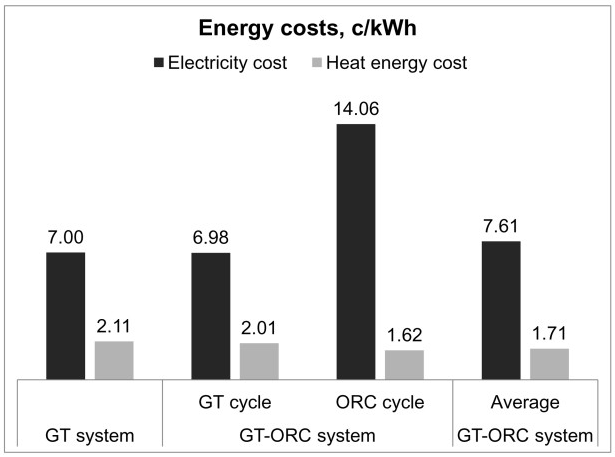

Fig. 7. Energy costs

The energy costs, calculated using exergoeconomic analysis at ambient reference temperature +15°C for the GT and GT-ORC systems are presented in Fig. 7. These costs ensure that all fuel and capital costs are recovered. As expected, electricity energy costs are the same as exergy costs but it can be seen that the heat energy costs, calculated using exergoeconomic analysis, are significantly lower than heat exergy costs.

5. Economic analysis

Exergy analysis can identify elements of the system where the exergy destruction is the greatest and exergoeconomics enables the costing of that destruction to be performed. From this the scope for improvements can be identified. However, this costing may bear little relationship to traditional economic analysis which will ultimately form the basis of any investment case. The economic analysis of both co-generation systems is presented here and then compared with those from the exergoeconomic analysis.

The following assumptions have been made:

1. The main objective of the investment is for electricity production with heat as a by-product. Hence heat production is marginal to electricity production. So only the capital and variable costs which can be solely attributed to heat are allocated to heat.
2. The asset capital costs which can be attributed to heat production are:
   a. GT system - heat exchanger 5 and pump 7 with a total cost of €2200.
   b. GT-ORC system – heat exchangers 6 and 10, pumps 12 and 14 with a total cost of €5500.
3. Overheads, operating and maintenance costs have not been included.

Otherwise all other assumptions are the same as those for the exergoeconomic analysis.

5.1. Cost analysis

This comprises the fixed and variable costs. Fixed costs are the capital costs associated with the investment. In practice there will be other fixed costs such as overheads but for the purpose of this analysis they have not been included. The capital repayment is based on 10% return on investment with a 15 year repayment period and 7000 hours/years of operation. Cost attribution of heat is determined from those costs that can be directly attributed to heat only with the remainder to electricity.

Table 4. Costs of micro GT and GT-ORC cogeneration systems based on economic analysis

	Micro GT	Micro GT-ORC
Total capital cost, €	130200	156700
Heat asset costs, €	2200	5500
Fixed electricity cost, c/kWh	2.35	2.53
Fixed heat cost, c/kWh	0.03	0.07
Total fuel cost, €/a	59780	59780
Variable electricity cost, c/kWh	8.36	7.62
Variable heat cost, c/kWh	0	0
Total electricity cost, c/kWh	**10.72**	**10.15**
Total heat cost, c/kWh	**0.03**	**0.07**

Variable costs are the fuel costs associated with plant operation. In practice there will be other running costs such as plant maintenance but for the purpose of this analysis they have not been included. Fuel is converted to produce both electricity and heat and so the methodology for attributing fuel needs to be considered. For both of these cogeneration systems heat production has no impact on fuel input or electricity output and as a consequence the variable cost of heat production is zero. Thus the fuel cost must be fully attributed to electricity production. The fixed, variable and total costs for heat and electricity are shown in Table 4.

5.2. Investment analysis

The results of the cost analysis do not permit a decision to be made in terms of choice of cogeneration system or whether or not to proceed with either investment. This is because the costing of the electricity and heat products may not reflect their market value. For example, the heat cost shown in table 4 is less than 0.1 c/kWh, which places a very low value on heat.

For an investment to be justified the economic analysis needs to include an assessment of the market value of the products in order to determine the potential sales revenue. For the purposes of this analysis the electricity price 10.9 c/kWh has been obtained from the EU Energy Portal for industrial customers. Heat prices are not published and so an estimate has been made from the production cost of heat using a gas boiler based on an efficiency of 80% and using the same gas price as used for the cogeneration systems to give 2.89 c/kWh. Table 5 shows the results of the investment analysis.

Table 5.Investment analysis of micro GT and GT-ORC cogeneration systems

	Micro GT	Micro GT-ORC
Total revenue, €k pa	**110**	**115**
Capital repayment, €k pa	17	21
Fuel cost, €k pa	61	60
Total cost, €k pa	**77***	**81**
Gross margin (Total revenue – Total costs), €k pa	**33**	**35***
Project Net Present Value (NPV), €k	**250**	**266**

* Rounding applied.

The investment analysis shows that both projects have a positive NPV and has also identified that the GT-ORC generation system has a higher NPV and on this criterion only should be preferred.

5.3. Comparison of exergoeconomics with economic analysis

Both exergoeconomic and economic energy costing analysis ensure all cogeneration costs (i.e. capital and fuel) are fully recovered in their attribution to the electricity and heat produced. However, it is can be seen from table 6 that the cost attribution is very different.

Table 6.Electricity and heat costs from exergoeconomic and economic analysis of micro GT and GT-ORC cogeneration systems.

	Micro GT	Micro GT-ORC
Exergoeconomic cost		
Electricity, c/kWh	7.00	7.61
Heat, c/kWh	2.11	2.17
Economic cost		
Electricity, c/kWh	10.72	10.15
Heat, c/kWh	0.03	0.07
Market price (based on prices for UK industry)		
Electricity, c/kWh	10.9	10.9
Heat, c/kWh (estimated)	2.89	2.89

In a commercial environment an investment decision is more likely to be dependent on the market value of the product streams but it is important to note that these may bear no relationship to the costs derived from either methodology. This in itself can be problematic as energy prices have been very volatile [12] and substantial changes in market prices could continue to be seen over the economic life of the cogeneration system.
It is worthwhile noting that the exergoeconomic cost of electricity relative to heat is comparable to that of market price of electricity to heat and thus seems to provide a better estimate of heat value than that from economic cost analysis.

6. Conclusion

Exergoeconomic and economic analysis of micro GT and GT-ORC systems was conducted and the effect of ambient reference temperature on the exergy costs of products was investigated. The results of this study show:

- Exergoeconomic analysis can assist in identifying improvements in performance and capital costs.
- Exergy costs fall with a reduction in reference temperature.
- Exergoeconomic analysis can be used to ensure all cogeneration costs are fully recovered through their attribution to electricity and heat.
- The change of reference temperature has little effect on electricity and heat energy costs when calculated using exergoeconomic analysis and exergy factor.
- Exergoeconomic cost analysis may provide an attribution of costs which gives a better guide to the relative value of electricity and heat than economic cost analysis.
- Economic cost analysis is fundamental to any investment case but it is not affected by the quality or value of the product streams. Hence it must be supplemented by the market value of the energy products in order to enable an investment decision to be made.

Acknowledgments

This research formed part of the programme of the UK Energy Research Centre and was supported by the UK Research Councils under Natural Environment Research Council award (NE/G007748/1) (Phase II) and by the Higher Education Funding Council for Wales (HEFCW).

References

[1] Serra L, Valero A, Torres C, Uche J. Thermoeconomic analysis: Fundamentals. In: Husain A, editor. Integrated power and desalination plants: Eolss Publishers Co Ltd; 2003.

[2] Tsatsaronis G. Thermoeconomic Analysis and Optimization of Energy Systems. Progress in Energy and Combustion Science. 1993;19:227-57.

[3] Erlach B, Serra L, Valero A. Structural theory as standard for thermoeconomics. Energy Conversion and Management. 1999;40:1627-49.

[4] Lazzaretto A, Tsatsaronis G. SPECO: A systematic and general methodology for calculating efficiencies and costs in thermal systems. Energy. 2006;31:1257-89.

[5] Bagdanavicius A, Jenkins N, Hammond GP. Assessment of community energy supply systems using energy, exergy and exergoeconomic analysis. Proceedings of ECOS 2011, Novi Sad, Serbia, July 4-7, 2011. 2011:3117-30.

[6] Bagdanavicius A, Jenkins N. Exergoeconomic evaluation of small scale CHP systems Proceedings of the 8th International Conference "Environmental Engineering", Vilnius, Lithuania, May 19-20, 2011. 2011:727-34.

[7] Cycle-Tempo Release 5. Delft University of Technology; 1980-2007.

[8] http://www.infinityturbine.com/ORC/ORC_Waste_Heat_Turbine.html.

[9] Galanti L, Massardo AF. Thermoeconomic Analysis of Micro Gas Turbine Design in the Range 25-500 kW_e. Proceedings of ASME Turbo Expo 2010: Power for Land, Sea and Air. June 14-18, 2010, Glasgow, UK2010.

[10] Tsatsaronis G. Combination of Exergetic and Economic Analysis in Energy-Conversion Processes. Energy Economics and Management in Industry. Algarve, Portugal, April 2-5: Proceedings of the European Congress, Pergamon Press, Oxford, England; 1984. p. 151-7.

[11] Bejan A, Tsatsaronis G, Moran M. Thermal Design and Optimization. New York: A Wiley-Interscience Publication, 1996.

[12] DECC. Quarterly energy prices December 2011. http://www.decc.gov.uk/assets/decc/11/stats/publications/qep/3906-qep-dec11.pdf. London, 2011.

Exergoeconomic comparison of wet and dry cooling technologies for the Rankine cycle of a solar thermal power plant

Philipp Habl[a], Ana M. Blanco-Marigorta[b] and Berit Erlach[c]

[a] *Technische Universität Berlin, Berlin, Germany, philipphabl@gmail.com*
[b] *Universidad de Las Palmas de Gran Canaria, Las Palmas de G.C., Spain, ablanco@dip.ulpgc.es*
[c] *Technische Universität Berlin, Berlin, Germany, berit.erlach@tu-berlin.de*

Abstract:

This work describes and analyses the Rankine cycle of the 50 MW parabolic trough power plant Andasol 1 in the Spanish region of Andalusia, a prime example of the use of solar energy for electricity generation. By means of an exergoeconomic analysis, all components of the thermal plant are considered individually. Thermodynamic inefficiencies within the system are located, quantified and economically evaluated.
Generally, various wet and dry cooling methods come into consideration for the re-cooling of the steam. Andasol 1 uses the more effective wet cooling method, because in the vicinity sufficient water reserves are available. In this work, the water-cooled system is replaced by an air-cooled condenser and the two variants are compared under exergoeconomics aspects. Also the impact of a construction of Andasol 1 in a hotter and drier climate than the northern Sahara is simulated.
The analysis shows that within the air-cooled condenser much more exergy is destroyed than within the wet cooling system. Thereby the achievable condenser pressure is one of the critical process parameters. The electricity production cost in the zone around the Andalucian Granada are 15.27 ct/kWh when using wet cooling and 16.08 ct/kWh in case of dry cooling. In the Sahara, these costs increase to 15.52 ct/kWh for wet cooling and 17.52 ct/kWh for dry cooling technology.

Keywords:

Exergy analysis, Exergoeconomic analysis, Thermal power plant, Rankine cycle, Cooling tower, Air cooled condenser.

1. Introduction

For the last few years, the energy industry finds itself in a noticeable change. Sustainable, safe and resource-saving energy will play a key role in the coming years to keep nature and environment safeguarded for future generations and to strengthen and expand the current prosperity. This requires that the renewable energy conversion methods have to be optimized and distributed and further practical experiences have to be collected.

This paper describes and analyses the parabolic trough power plant Andasol 1, a prime example of the use of solar energy for electricity generation. In a steam cycle (Rankine cycle) heat is converted into mechanical energy. This is done in a steam turbine which is coupled to a generator to produce electricity. Once the steam has passed through the turbine, it is condensed by heat transfer to the ambient. Generally, various wet and dry cooling methods come into consideration for the re-cooling of the steam. For wet cooling a cooling water cycle including cooling tower, cooling pump and water-cooled condenser is the most common method. For dry cooling an air-cooled condenser is the most used variant.

In this paper the Rankine cycle of the power plant is simulated and analyzed by using the exergoeconomic method. Furthermore, the water-cooled system which is used in the real Andasol 1 plant (Configuration 1) is replaced by an air-cooled condenser (Configuration 2) and the two variants are compared under exergoeconomics aspects. Also the impact of a construction of Andasol 1 in a hotter and drier climate as the northern Sahara is simulated.

In an exergoeconomic analysis, all components of the thermal plant are considered individually. Thermodynamic inefficiencies within the system can be located, quantified and economically evaluated. Thus, the process variants presented in this work can be compared to each other objectively and suggestions for improvements to reduce electricity generation costs can be made.

One exergy analysis of Andasol 1 power plant with wet and dry cooling at two different condenser pressures has already been made in a previous paper Blanco-Marigorta et al. [1]. This analysis is optimized and economic and exergoeconomic analysis are added.

Related to solar-thermal power plants, Singh et al [2] presented a second law analysis based on an exergy concept for a solar thermal power system. Singh et al evaluated the respective losses as well as exergetic efficiency for typical solar thermal power systems under given operating conditions. They found that the main energy loss takes place in the condenser. Their exergy analysis shows that the collector–receiver assembly is the part where the losses are maximal. Gupta and Kaushik [3] carried out the energy and exergy analysis for the different components of a proposed conceptual direct steam generation solar-thermal power plant. In Kaushik et al [4], a 35 MW solar thermal power plant was analyzed with the aid of exergoeconomics.

2. Description of the plant

The parabolic trough power plant Andasol 1 has a net power capacity of 50 MWe. The power cycle is a conventional reheat design with 5 closed and 1 open extraction feedwater heaters. A schematic of the Rankine Cycle of the plant is shown in Fig. 1. The streams S50 and S52 come from the solar part and the streams S51 and S55 go back to the solar part.

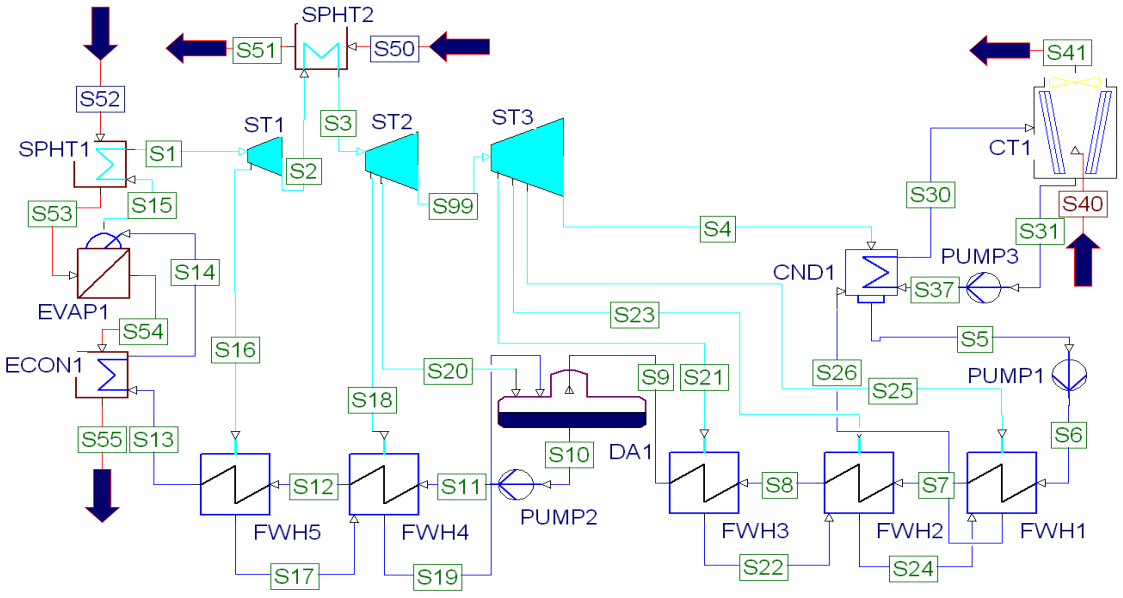

Fig. 1. GateCycle flow diagram 50 MWe Rankine cycle with wet heat rejection.

GateCycle [5] software has been used in this work for simulation purposes. Real operation parameters have been introduced in the simulation.

Thermo oil VP1 is used as heat transfer fluid: it is heated up in the solar collectors and cooled down while producing steam in the steam generator. A part of this heat transfer fluid is also used to heat up the molten salt-storage tanks. The hours at which the plant runs with the stored heat in the heat tanks is considered in the total annual time of system operation at full load. The steam generation system consists of two parallel heat exchanger trains (preheater (ECON1)/ evaporator (EVAP1)/ superheater (SPHT1)) and two reheaters (SPHT2), again connected in parallel. The produced superheated steam enters the high-pressure turbine with a pressure of 100 bar, a mass flow of 60.34

kg/s and a temperature of 373 °C. A conventional Rankine cycle begins.

After expanding in the high-pressure turbine, the steam is reheated and enters the low-pressure turbine with a pressure of 16.5 bar and a temperature of 373 °C. To preheat feedwater in one of the five feedwater heaters, one extraction is taken from the high-pressure turbine. After expanding in the low-pressure turbine, the steam reaches the condenser at a pressure of 0.063 bar. In the low-pressure turbine, five steam extractions take place. One goes to the deaerator, the other four preheat the feedwater in the remaining four feedwater heaters. In the condenser the steam is cooled down by means of wet cooling technology. The feedwater pump leads the deaerated water through two more consecutive feedwater heaters and to the heat recovery steam generator, where the cycle closes. Thermodynamic parameters of the most important streams can be seen in Table 1.

In contrast to other solar thermal trough projects, the electricity production of Andasol 1 can be adjusted to the demand thanks to a molten salt thermal storage system. A part of the thermal energy received by the solar field during the day is stored in one of two liquid salt-tanks. A full storage tank, which holds 1 010 MWh of heat, can generate power at full load for 7.5 hours [6].

Table 1. Thermodynamic parameters of the most important streams

Stream	$\dot{m}$, kg/s	p, bar	T, °C	$\dot{E}^{PH}$, kW	$\dot{E}^{CH}$, kW	$\dot{E}^{TOT}$, kW
1	60.08	100.0	373.0	72 158	150	72 308
2	53.87	18.5	208.5	47 053	135	47 187
3	53.87	16.5	373.4	57 789	135	57 923
4 (Conf. 1)	40.98	0.063	37.1	3 495	102	3 598
4 (Conf. 2)	41.18	0.075	40.1	4 404	103	4 507
5 (Conf. 1)	48.47	0.063	37.1	43	121	165
5 (Conf. 2)	48.47	0.073	39.7	66	121	188
13	60.08	103.0	235.0	13 945	150	14 096
26	7.48	0.370	42.2	14	19	33
30 (Conf. 1)	2 814	1.9	36.3	2663	7 035	9 698
31 (Conf. 1)	2 814	0.948	28.7	237	7 035	7 272
37 (Conf. 1)	2 814	1.9	28.7	500	7 036	7 535
40 (Conf. 1)	1 645	0.948	28.1	72 304	12 691	84 995
41 (Conf. 1)	1 677	0.946	3.4	72 685	18 874	91 559
40 (Conf. 2)	10 740	0.948	301.2	471 955	82 839	554 794
41 (Conf. 2)	10 740	0.948	309.7	474 166	82 839	557 004
50	68.5	15.8	393.1	19 256	0*	19 256
51	68.5	13.5	225.0	6 050	0*	6 050
52	533.4	15.8	393.1	149 968	0*	149 968
55	533.4	11.8	301.0	86 687	0*	86 687

*neglected

The wet cooling system of the solar trough power plant Andasol 1 consists of five induced draft cooling tower cells, three cooling pumps and a surface condenser (Conf. 1). To cool down the steam of the Rankine cycle and for other water-consuming equipment, 870 000 m^3 of water of the nearby Sierra Nevada mountains are required a year. In water scarce regions, a hypothetic alternative is dry cooling technology by means of air cooled condensers (ACC) (Fig. 2). In the process with air cooled condenser no further cooling tower and no cooling water pump is needed (Conf. 2). However, heat transfer by forced air convention is less effective than evaporative heat transfer; therefore, larger heat exchanger areas and greater fan power are required to achieve the same heat rejection.

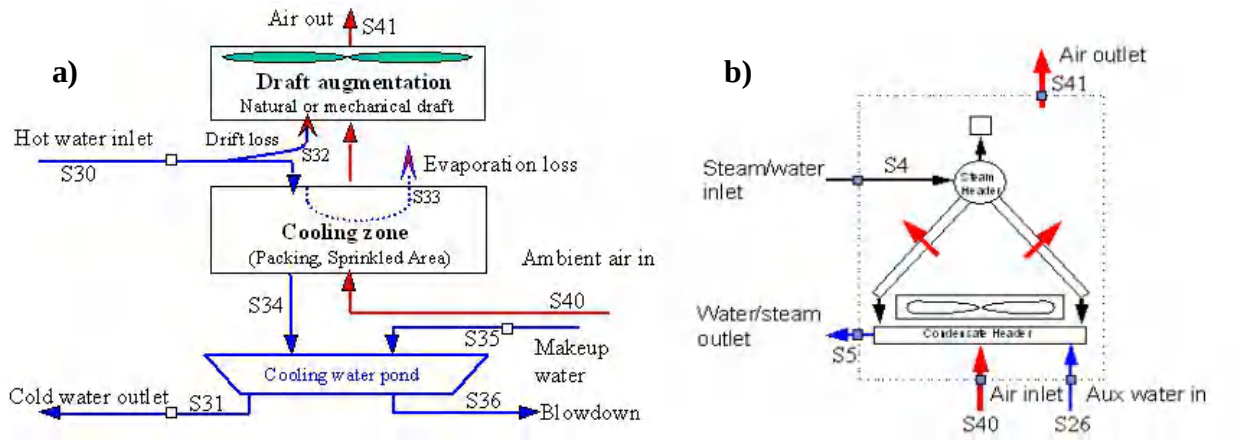

Fig. 2. a) Cooling Tower or b) Air cooled condenser, connected to the Rankine Cycle of Andasol 1.

3. Thermodynamic evaluation

3.1. Basic assumptions for the thermodynamic analysis

A representative steady flow process at design conditions is analyzed. Start-up, shutdown and part load procedures and processes are not subject of this work. A constant solar radiation (900 W/m^2) which allows running the plant at design conditions is assumed [7].

In the Rankine cycle only the components shown in figure 1 and 2 are taken into consideration. All other components such as valves and auxiliary systems are neglected. The same applies to the solar part. It is treated as one component including the solar field, the expansion and overflow tank, the main HTF-pumps, the HTF anti-freeze system, the HTF piping system, the salt tanks, the heat exchangers between oil and salt and the salt circulation pumps. It is assumed that in the pipes connecting the main components no losses take place.

The cooling tower cells are designed in GateCycle as close as possible to the ones used in the real power plant. Main plant operation data [8] were fed to the software as input variables. The theoretical cooling alternative of an air cooled condenser is designed with an ACC calculator [9].

The net work output is the net electricity fed into the grid. The plant's consumption due to solar field tracking, auxiliary components, HTF- and liquid salt-pump are estimated to 4 250 kW [10].

3.2. Energy assessment

The pressure and the temperature of the steam both entering and leaving the turbine define, in large part, the efficiency of the Rankine Cycle. The steam conditions at the turbine outlet are defined by the temperature at which the steam is condensed and the latent heat of vaporization can be transferred to the environment. The lower the ambient temperature, the lower the feasible operation pressure of the condenser (p_{CND}) and the higher the energetic efficiency of the cycle. For wet cooling technologies, the lowest ambient temperature available is the wet bulb temperature since an evaporation process is used to provide the cooling water source for the condenser. Taken into account the ambient conditions of the region where Andasol 1 is located, p_{CND} was set to 0.063 bar.

Dry cooling technologies reject heat to the environment at the dry bulb temperature. Therefore, first of all, an optimal condenser pressure has to be found. Fig. 3 shows the condenser pressure as a function of the net work output of the process using either a wet cooling or a dry cooling technology in the Rankine Cycle of Andasol 1 at design conditions. The ambient temperature in Granada is assumed to be 28.05 °C and the relative air humidity is assumed to be 60 %.

For this purpose, in calculations, air mass flow streaming through ACC and water flow streaming through the wet condenser have been adjusted. In both cases all other parameters such as steam

mass flow or ambient conditions are kept constant. It is assumed that the design condenser pressure of 0.063 bar used in the real power plant is the lowest reachable condenser pressure for this plant.

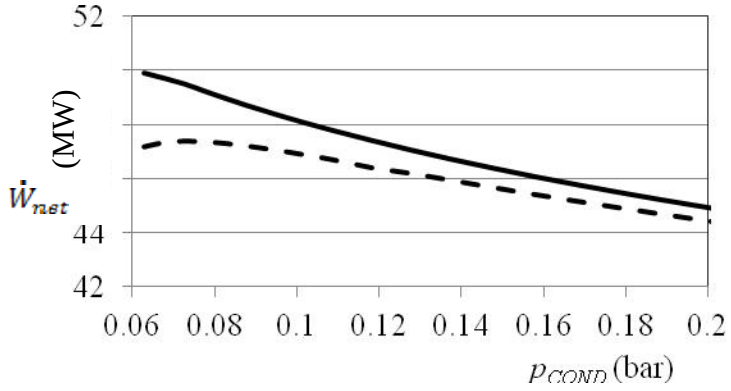

Fig. 3. Net power versus condenser pressure using (——) wet cooling or (- - -) dry cooling in the Rankine cycle of Andasol 1.

Rankine cycle with ACC shows a maximum net power value of 47.37 MW corresponding to an optimum pressure value of 0.073 bar (at lower pressures, additional fan power outweighs additional electricity production by the steam turbine). This output is 2.54 MW lower compared to the possible maximum in configuration with wet cooling. From this pressure operation value on, the higher the condenser pressure, the more both curves converge and the lower gets the efficiency of the cycle.

According to GEA's ACC calculator [9], 15 fan modules divided in 3 A-frames are required for this optimum configuration. ACC's plot area is 2 100 m^2 and inlet height is 18 m; the diameter of each fan is 9.75 m.

To reach a worse condenser pressure, dry cooling system consumes over three times more electricity (2 660 kW) in confront to the wet cooling system (810 kW). This shows that from an energetic point of view a wet cooling system would be much more efficient and using a dry cooling system could only be justified with a lack of a water source close to the plant.

The dry ambient temperature, the wet ambient temperature and the relative humidity of the ambient change within a year. Therefore, also condenser pressure may change to avoid a too high power consumption of the fans in the cooling tower cells as well as in the ACC.

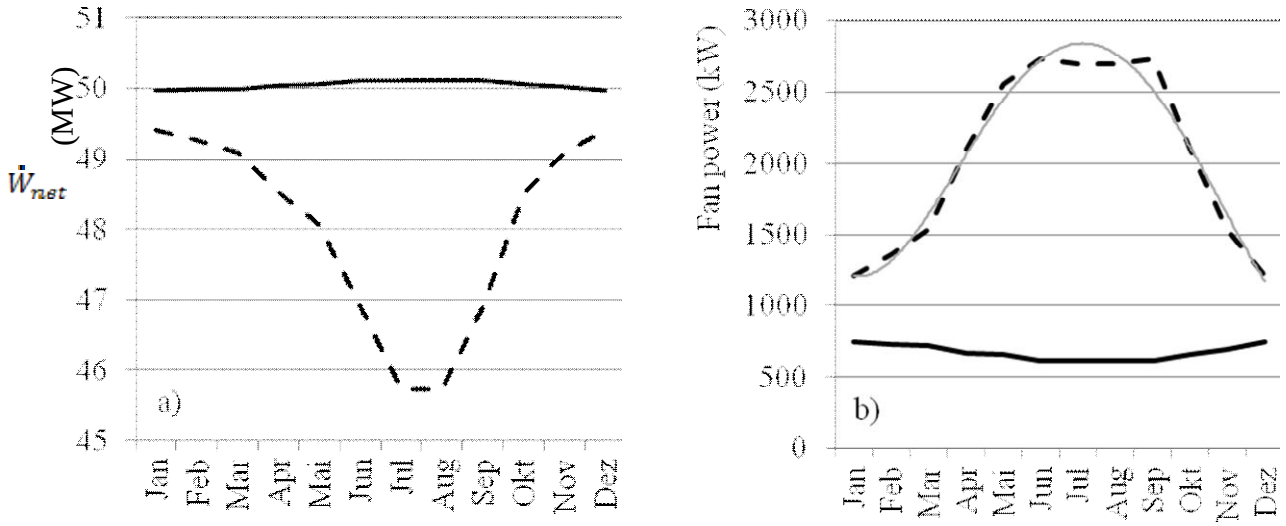

Fig.4. (a) Net power output or (b) fan power output during a year using (———) wet cooling or (- - - -) dry cooling in the Rankine cycle of Andasol 1 in Granada.

The diagram in Fig. 4 (a) shows the net electrical power output of both configurations in a year. Fig. 4 (b) shows the consumption of the fans in the same period; a polynomial trend line of the development of ACC's fan-consumption is added.

Fig. 4 shows that the ambient temperature during the year has a high impact on the effectiveness of ACC fans and electric power output. On the contrary, net electric output of configuration with wet cooling technology does not change significantly over the year. For dry cooling technology, condenser pressure has to be increased in summer to avoid a high consumption of ACC-fans.

At outside temperatures over about 20 ºC the difference in net power output between the two configurations gets higher than 1 MW. In the simulated extreme case of the Sahara (45 °C, 20 % relative air humidity) there is even a difference of 5.6 MW of net power output between the two configurations.

4. Exergoeconomic Analysis

An exergoeconomic analysis, also called thermoeconomic analysis, is a combination of exergy and economic analysis. Therefore, a complete exergoeconomic investigation consists of an exergy analysis, an economic analysis and a thermoeconomic analysis [11]. The questions how much thermodynamic inefficiencies in the process cost and which variables have to be changed in order to obtain a cost-effective system are answered. [12].

4.1. Exergy Analysis

An exergy analysis is the first step for the exergoeconomic analysis. With an exergy analysis it is possible to get to know the thermodynamic inefficiencies in a thermal system. The location, the size and the sources of the inefficiencies can be discovered. The exergy of each stream, the exergy losses, the exergy destruction and the exergetic efficiency can be identified.

The exergy of the flow streams was calculated according to the definitions given in [11]. In this work, the conditions of thermodynamic environment are set to T_0 =298.15 K and p_0 =1.013 bar [15]. This implicates that thermodynamic environment and ambient conditions are not equal. Kinetic and potential exergy are neglected and chemical exergy is calculated with Ahrendts [13].

Thermodynamic properties of Water are calculated from IAPWS 97 [14] Air is presumed to be a mixture of N_2, O_2 and H_2O (60 % relative air humidity) treated as ideal gases and neglecting all other substances. Enthalpy and entropy of air is taken from [15]. Thermo oil VP1 is a mixture of 73.5 % biphenyl oxide and 26.5 % diphenyl [16]. The physical exergy of this fluid has already been calculated [1]; the chemical exergy of the HTF has been neglected because it does not play a role.

Table 2 shows the values of exergy rates associated with fuel and product, exergy destruction, $\dot{E}_{D,k}$, exergetic efficiencies, ε_k,as well as the exergy destruction ratio, $y_{D,k}$,for the Rankine Cycle of the system. Solar part is excluded.

It is not possible to define exergy rates associated with fuel and product for the dissipative components CT1, CND1 and ACC1. To be able to define an exergetic product and an exergetic fuel of the two cooling systems and to make them more comparable, both cooling variants are packed together in a system with the low pressure steam turbine ST2&3 [17, 18]. Exergy rates associated with fuel and product as well as exergy destruction for a system with LP turbine and wet cooling system are defined as follows:

$$\dot{E}_{F,ST2\&3+WCS} = \dot{E}_3 + \dot{E}_{26} - \dot{E}_5 - \dot{E}_{18} - \dot{E}_{20} - \dot{E}_{21} - \dot{E}_{23} - \dot{E}_{25} \quad (1)$$

$$\dot{E}_{P,ST2\&3+WCS} = \dot{W}_{ST2\&3} + \dot{W}_{PUMP3} - \dot{W}_{FAN,CT} \quad (2)$$

$$\dot{E}_{L,ST2\&3+WCS} = \dot{E}_{32} + \dot{E}_{33} + \dot{E}_{36} + \dot{E}_{41} - \dot{E}_{35} - \dot{E}_{40} \quad (3)$$

For a system with LP turbine and dry cooling system, instead:

$$\dot{E}_{F,ST2\&3+DCS} = \dot{E}_3 + \dot{E}_{26} - \dot{E}_5 - \dot{E}_{18} - \dot{E}_{20} - \dot{E}_{21} - \dot{E}_{23} - \dot{E}_{25} \quad (4)$$

$$\dot{E}_{P,ST2\&3+DCS} = \dot{W}_{ST2\&3} - \dot{W}_{FAN,ACC} \quad (5)$$

$$\dot{E}_{L,ST2\&3+DCS} = \dot{E}_{41} - \dot{E}_{40} \quad (6)$$

Table 2. Exergetic variables of the main plant components of the Rankine cycle $\dot{E}_{P,k}$

Component	$\dot{E}_{P,k}$, kW	$\dot{E}_{F,k}$, kW	$\dot{E}_{D,k}$, kW	ε_k	$y_{D,k}$
Low-pressure turbine ST2&3	39 803	45 409	5 606	0.877	0.073
Steam generator EVAP1	39 111	42 323	3 212	0.924	0.042
Reheater SPHT2	10 736	13 206	2 470	0.813	0.032
High-pressure turbine ST1	16 725	19 008	2 283	0.880	0.030
Economizer ECO1	10 369	11 696	1 327	0.887	0.017
Superheaters SPHT1	8 732	9 262	530	0.943	0.007
Feedwater heaters 5 FWH5	4 716	5 133	417	0.919	0.005
Feedwater heater 1 FWH1 (Conf. 1)	551	873	323	0.631	0.003
Feedwater heaters 4 FWH4	2 484	2 787	303	0.891	0.004
Feedwater heater 1 FWH1(Conf. 2)	527	810	281	0.653	0.004
Feedwater heater 2 FWH2	1 009	1 274	266	0.791	0.003
Feedwater heater 3 FWH3	1 410	1 668	258	0.845	0.003
Deaerator DA1	1 832	2 059	227	0.890	0.003
Feedwater pump PUMP2	687	791	104	0.868	0.001
Condensate pump PUMP1 (Conf. 2)	40	56	15	0.725	0.0002
Condensate pump PUMP1 (Conf. 1)	41	56	14	0.741	0.0002
ST2&3-CND1-CT1-PUMP3 (Conf. 1)	38 993	48 876	7 472	0.798	0.098
ST2&3-ACC1 (Conf. 2)	36 446	48 928	10 271	0.745	0.134
Total Rankine cycle (Conf. 1)	54 871	76 487	19 205	0.717	0.251
Total Rankine cycle (Conf. 2)	52 324	76 487	21 952	0.684	0.287

The exergetic efficiency of the system which includes low pressure steam turbine and wet cooling system $\varepsilon_{ST2\&3+WCS}$ is 79.8 % while with dry cooling $\varepsilon_{ST2\&3+DCS}$ is 74.5 %. This difference and the fact that $\dot{E}_{D,ACC1}$ (4 806 kW) is more than twice as high as $\dot{E}_{D,CND1}$, $\dot{E}_{D,CT1}$ and $\dot{E}_{D,PUMP3}$ together (1 865 kW), shows among others that from an exergetic point of view, the air cooled condenser is much more ineffective than the water-cooled system.

The exergy destruction ratio $y^*_{D,CT1+CND1+PUMP3}$, which is the quotient of the exergy destruction in CND1, CT1 as well as PUMP3 and the total exergy destruction in configuration 1 is 9.7 %. In configuration 2, $y^*_{D,ACC1}$ is 21.9 %.

It should be noted that the biggest exergy destruction in the whole process of the parabolic trough power plant takes place in the solar part. If the exergy destruction within the solar part (387 021 kW) is included in the calculation of total exergy destruction, $y^*_{D,SP}$ is 95.3 % in configuration 1 and 94.6 % in configuration 2. Therefore exergy destruction of the Rankine cycle is only about 5 % in both configurations. The exergetic efficiency of the solar part is around 16.5 % in both configurations. Thereby it is assumed that the only exergetic product of the solar part is to heat the streams 2, 13, 14 and 15.

4.2. Economic Analysis

The aim of an economic analysis as a part of a thermoeconomic analysis is to relate entire costing on the total annual time of system operation at full load. Levelized carrying charges,CC_l, and operating and maintenance costs, OMC_l, can be assigned to components according to the relative fraction of the k th component associated to the purchased-equipment costs. In this paper is used the total revenue requirement method, TRR [17].

Therefore the cost rates linked with capital investment $\dot{Z}_k^{CI}$ as well as the cost rate coupled with operating and maintenance cost $\dot{Z}_k^{OMC}$ each related to the k th component have been calculated. The sum of these terms is defined as $\dot{Z}_k$:

$$\dot{Z}_k = \dot{Z}_k^{CI} + \dot{Z}_k^{OMC} \tag{7}$$

Parameters for the economic calculation are given in Table 3. Depreciation is linear. Income taxes and costs of licensing, research and development are neglected. Overnight construction is assumed. Calculations will be made in constant 2011 € (without inflation).

Table 3. Basic conditions for economic calculations

Parameter	Value
Average annual inflation rate, r_i	0 %/a
Average annual nominal discount rate, $i_{eff,n}$	7 %/a
Nominal average annual escalation rate for fuel, $r_{n,FC}$	4 %/a
Nominal average annual escalation rate for other costs, $r_{n,}$	3 %/a
Average annual real discount rate, $i_{eff,r}$	3.92 %/a
Real average annual escalation rate for fuel, $r_{r,FC}$	0.98 %/a
Real average annual escalation rate for other costs, $r_{r,}$	1.96 %/a
Full load hours	3600 h/a
Economic life time	40 years

The costs of the generator which converts mechanical into electrical energy are neglected. In contrast to conventional power plants, fuel costs of solar radiation are equal to zero. For part load situations, an auxiliary fossil fuel is necessary. In case of Andasol 1, liquefied natural gas or liquefied petroleum gas is used [8]. But because at base load there is not used a co-firing gas stream, fuel costs have to be treated in a special manner. In this analysis they are apportioned to the components, a similar procedure as for the operating and maintenance costs.

The total capital investment of both configurations is the same (314.2 million €), because the package consisting of cooling tower, cooling pump and wet condenser (configuration 1) and ACC (configuration 2) are assumed to cost the same.

In this plant the levelized main product unit costs are equal to the electricity generation costs. In case of configuration 1 with the ambient conditions of Granada, $MPUC_{l,Conf1}$ are 15.27 ct/kWh of generated electricity. With the same ambient conditions, levelized main product unit costs in configuration 2 are 16.08 ct/kWh. This shows that using an air cooled condenser is 0.81 ct/kWh more expensive than using wet cooling tower cells.

$MPUC_{l,Conf1,Sahara}$ which are the levelized main product unit costs in configuration 1 when the power plant is built in the Sahara, are 15.52 ct/kWh. This is still more economic than configuration 2 in Granada. When air cooling is used in the northern Sahara, the electricity generation costs $MPUC_{l,Conf2,Sahara}$ are 17.52 ct/kWh. From the economic analysis follows that water cooled systems are much more economic than air cooled systems.

4.3. Exergoeconomic analysis

For the exergoeconomic analysis, cost flows are assigned to exergy flows [17]. This method is called "Exergy Costing". Combining the results of the exergetic and the economic analyses, the cost rates of all exergy streams within the process were calculated according to the definitions given in [11]. To calculate the costs of exiting streams auxiliary relations based on the P-rule and the F-rule [17] are used.

Following variables are used in a exergoeconomic analysis for improving the cost effectiveness of the k-th component:

The average costs per exergy unit of fuel:

$$c_{F,k} = \frac{\dot{C}_{F,k}}{\dot{E}_{F,k}} \tag{8}$$

The average costs per exergy unit of product:

$$c_{P,k} = \frac{\dot{C}_{P,k}}{\dot{E}_{P,k}} \tag{9}$$

By the use of the average costs per exergy unit of fuel the current costs of exergy destruction can be calculated:

$$\dot{C}_{D,k} = c_{F,k}\dot{E}_{D,k} \tag{10}$$

It is assumed that the average costs per supplied exergy unit of product and the exergetic product stay constant even if the exergy destruction of the component changes [17].

The relative cost difference between the average costs per exergy unit of product $c_{P,k}$ and the average costs per exergy unit of fuel $c_{F,k}$ can be determined as follows:

$$r_k = \frac{c_{P,k} - c_{F,k}}{c_{F,k}} \tag{11}$$

Exergy destruction and investment costs have the biggest impact on r_k value. By exergoeconomic factor the values of these two main variables are compared:

$$f_k = \frac{\dot{Z}_k}{\dot{Z}_k + \dot{C}_{D,k}} \tag{12}$$

To interpret the system exergoeconomically, the exergoeconomic key figures of both configurations have to be determined. Primarily the exergoeconomic interpretation gives information about whether the investment costs in single components should be increased or reduced. Increasing the investment costs would also increase the exergetic efficiency and vice versa.

The values of the exergoeconomic key figures average costs per exergy unit of product and fuel, sums of investment cost rates of the components plus cost streams of exergy destruction, relative cost differences as well as exergoeconomic factors of both configurations are shown in Table 4.

In accordance with exergoeconomic analysis, the most significant component in the Rankine cycle in both configurations is the low pressure steam turbine, which has at the same time the highest values of exergy destruction and the highest investment costs. Although in the evaporator takes place the second highest exergy destruction, the high-pressure turbine has the second highest exergoeconomic significance in the process due to its high investment cost. However, the f_k - factors of the turbines are within the acceptable range. Nevertheless a reduction of exergy destruction and an increase of exergetic efficiencies are recommended.

Table 4. Exergoeconomic data of main components of the Rankine cycle $\dot{Z}_k + \dot{C}_{D,k}$

Component	$c_{F,k}$, €/MWh	$c_{P,k}$, €/MWh	$\dot{Z}_k + \dot{C}_{D,k}$, €/h	r_k	f_k
Low-pressure turbine ST2&3	103.4	136.9	1333.0	0.324	0.565
High-pressure turbine ST1	101.1	139.9	649.3	0.384	0.645
Evaporator EVAP1	84.5	94.7	397.1	0.120	0.316
Reheater SPHT2	84.5	113.7	313.4	0.345	0.338
Economizer ECO1	84.5	96.5	124.4	0.142	0.098
Superheaters SPHT1	84.5	97.3	111.8	0.151	0.599
Feedwater pump PUMP2	137.8	216.0	53.7	0.568	0.732
Feedwater heaters 5 FWH5	101.1	381.0	46.5	0.098	0.094
Deaerator DA1	89.2	109.3	37,0	0.225	0.453
Feedwater heater 1 FWH1(Conf. 1)	103.4	170.4	36.9	0.648	0.095
Feedwater heaters 4 FWH4	102.8	116.9	35.1	0.137	0.112
Feedwater heater 1 FWH1(Conf. 2)	103.4	165.0	32.6	0.596	0.108
Feedwater heater 2 FWH2	103.4	133.9	30.8	0.295	0.109
Feedwater heater 3 FWH3	103.4	124.6	29.9	0.205	0.109
Condensate pump PUMP1(Conf. 2)	137.9	389.6	10.1	1.826	0.792
Condensate pump PUMP1(Conf. 1)	137.8	110.9	10.0	1.765	0.802
ST2&3, CND1, CT1, PUMP3	103.4	136.9	1720.0	0.324	0.551
ST2&3 and ACC1	103.4	137.0	2009.0	0.326	0.472
Total (Conf. 1)	84.6	137.8	3382.0	0.623	0.520
Total (Conf. 2)	84.5	137.9	3614.0	0.631	0.486

Low-pressure turbine, high-pressure turbine, evaporator, reheater and economizer have in descending order the highest $\dot{Z}_k + \dot{C}_{D,k}$ - values. With these components is a need of action within the framework of an exergoeconomic optimization.

The SPHT1 is the only component with a f_k - factor outside of the desired range. The high f_k - factor (59.9 %) of the SPHT1 recommends a reduction of the investment costs of the component that can be accomplished by accepting the increase of the exergy destruction within the component.

FWH1 should be redesigned for both configurations, not least due to its low exergetic efficiencies of 63.1 % (configuration 1) and 65.3 % (configuration 2) respectively. The simplifying assumption in this work that FWH1 can be designed with the same size in both configurations is not recommended and has to be reconsidered.

The system with ST2&3, CND1, CT1 and PUMP3 has a much lower $\dot{Z}_k + \dot{C}_{D,k}$ - value (1 720 €/h) in comparison to the system with ST2&3 and ACC1 (2 009 €/h), thus a larger f_k - factor (55.1 % in comparison to 47.2 %). This shows that the exergy destruction in the system with ST2&3 and ACC1 is much higher.

In the solar part $c_{F,SP}$ is very low, because the sun as a fuel is free of charge. This implicates that costs of exergy destruction are therefore very low as well. The fact that about 95 % of the exergy destruction in both configurations takes place in the solar part is not expressed by r_{SP} and f_{SP} (63.6 % and 0.92). However, the investment costs are still very high, because of the rare usage of this solar technology. Research and development work in order to reduce the investment costs are therefore necessary. As proposed in [19], investment costs can be reduced as well by improving the efficiency of the turbine and reducing the efficiency of the solar part.

5. Conclusions

Two configurations with different cooling systems for the Rankine cycle of Andasol 1 power plant are simulated. Configuration 1 includes a wet cooling system (cooling tower cells, wet condenser and cooling pump) and is used in the real Andasol 1 plant. In configuration 2, the wet cooling system is replaced by an air cooled condenser.

When using an air cooled condenser in Granada (28.05 °C, 60 % relative air humidity), the optimal condenser pressure increases to 0.073 bar in comparison to 0.063 bar with a wet cooling technology. For the dry cooling system 2 660 kW have to be used on electrical energy. For the wet cooling system have to be spent only 810 kW. These facts result in a net power output of 47.34 MW for configuration 2 and 49.91 MW in configuration 1.

In case of the construction of an Andasol-type plant in the northern Sahara (45 °C, 20 % relative air humidity), the optimal condenser pressure increases drastically and only 43.50 MW net power output can be obtained. With wet cooling technology it is still possible to provide 49.10 MW net power output in the Sahara.

The main unit product costs of configuration 1 with a wet cooling system in Granada are 15.27 ct/kWh and 16.08 ct/kWh for configuration 2 with a dry cooling system. In the Sahara they increase to 15.52 ct/kWh in configuration 1 and 17.52 ct/kWh in configuration 2.

The difference in electricity generation costs of both configurations (0.81 ct/kWh in Granada and 2 ct/kWh in the Sahara) compared to the costs, which make water supply possible, are crucial to be able to judge which cooling system to take.

The values of exergoeconomic factors are all in the frame of the values determined in conventional power plant technology, except the one of the SPHT1.

The $\dot{Z}_k + \dot{C}_{D,k}$ - value of the system with ST2&3 and AC1 is much higher than the one of the system with ST2&3, CND1, CT1 and PUMP3 (2 009 €/h in comparison to 1 720 €/h).

This implies that the exergy destruction in the system with ST2&3 and AC1 is much higher, for the reason that the investment costs of both systems are the same.

The trade-off between investment cost and fuel cost which is found in fossil-fuel fired plants does not exist to the same extend in solar plants, because the main fuel, solar energy, is for free. Therefore, the meaningfulness and the validity of empirical exergoeconmical factors from conventional power plant which are used to judge solar power plant technology are questionable. Nevertheless it is evident that increasing the effectiveness of the turbine and decreasing the investment costs of the solar part are most important potentials to theoretically improve the cost effectiveness of both configurations.

Nomenclature

c	cost per unit of exergy, €/MWh
$\dot{C}$	cost rate associated with exergy, €/h
e	specific exergy, kJ/kg
$\dot{E}$	exergy flow rate, kW
f	exergoeconomic factor, %
h	specific enthalpy, kJ/kg
$\dot{m}$	massflow rate, kg/s
p	pressure, bar
$\dot{Q}$	heat rate
r	relative cost difference

s specific entropy, kJ/kg

$\dot{S}$ entropy flow rate, kW

S stream

T temperature, K

$\dot{W}$ power

y exergy destruction ratio, %

$\dot{Z}$ cost rate associated with capital investment, €/h

Greek letters

ε exergetic efficiency, %

τ total annual time of system operation at full load, h

Subscripts

D destruction

F fuel

gen generated

j *j*th stream

k *k*th component

P product

q associated with transfer of heat

L loss

l levelized

tot total

w associated with transfer of work

0 thermodynamic environment (reference state)

Superscripts

CH chemical

KN kinetic

PH physical

PT potential

Abbreviations

ACC air cooled condenser

CND condenser

CC carrying charges

CI capital investment

Conf configuration

CT cooling tower

DA deaerator

DCS dry cooling system

ECON economizer

EVAP evaporator

FC fuel costs

FWH feedwater heater

HTF heat transfer fluid

LP low pressure

MPUC main product unit cost

PEC purchased-equipment cost

OMC operating and maintenance costs

SPHT superheater

ST steam turbine

SP solar part

TRR total revenue requirement

WCS wet cooling system

References

[1] Blanco-Marigorta A.M., Sánchez Henríquez M.V., Peña-Quintana J.A., Exergetic comparison of two different cooling technologies for the power cycle of a thermal power plant. Energy 2011;36:1966-72.

[2] Singh N, Kaushik SC, Misra RD., Exergetic analysis of a solar thermal power system. Renewable Energy 2000;19:135-43.

[3] Gupta MK, Kaushik SC., Exergy analysis and investigation for various feed water heaters of direct steam generation solarethermal power plant. Renewable Energy 2010;35:1228-35.

[4] Kaushik SC, Abhyankar YP, Bose S, Mohan S., Exergoeconomic evaluation of a solar thermal power plant. International Journal of Sustainable Energy 2001;21:293-314.

[5] GateCycle^{TM} version 5.61.0.r. The General Electric Company; 2005.

[6] The parabolic trough power plants Andasol 1 to 3, Solar Millenium AG, Project report, Available at: <http://www.solarmillennium.de> [accesed 20.5.2008].

[7] Herrmann U, Geyer M., Kistner R., The AndaSol Project, Workshop on Thermal Storage for Trough Power Systems, Feb 20-21, 2002.

[8] Proyecto de Ejecución AndaSol-1. Technical Description of Andasol 1 Proyect 7: 2006.

[9] ACC calculator. GEA Aircooled Systems (Pty) Ltd. Feb. 2007. Available at:< http://www.gea-energytechnology.com> [accessed 15.6.2011]

[10] Kern H., Head of Proposal Department Flagsol GmbH. Personal communication, 2011.

[11] Tsatsaronis G., Cziesla F., Thermoeconomics, In: Encyclopedia of Physical Science and Technology. Volume 16, 2002. p. 659-80.

[12] Tsatsaronis G., Application of Thermoeconomics to the Design and Synthesis of Energy Plants, in *Exergy, Energy System Analysis, and Optimization*, [Ed. Christos A. Frangopoulos] in *Encyclopedia of Life Support Systems (EOLSS)*, Developed under the Auspices of the UNESCO, Eolss Publishers, Oxford ,UK, [http://www.eolss.net], 2007.

[13] Ahrends J., Die Exergie chemisch reaktionsfähiger Systeme, VDI-Forschungsheft 579, VDI-Verlag, Düsseldorf, 1977.

[14] Wagner W., Cooper J.R., Dittmann A., Kijima J., Kretzschmar H.-J., Kruse A., Mares R., Oguchi K., Sato H., Stöcker I., Sifner O., Takishi Y., Tanishita I., Trübenbach J., Willkommen Th., The IAPWS Industrial Formulation 1997 for the Thermodynamic Properties of Water and Steam. J. Eng.Gas Turbine Power 2000;122:150-120.

[15] Knacke O., Kubaschewski O., Hesselmann, Thermochemical Properties of Inorganic Substances, Springer, Berlin, 1991.

[16] Therminol VP-1, Fragol Schmierstoff GmbH, Available at:www.fragol.de [accessed 20.4.2011].

[17] Bejan A., Tsatsaronis G., Moran M., Thermal design and optimization. New York: Wiley; 1996.

[18] Mendes da Silva J., Santos J., Oliveira Jr S., The Condenser Product and Residues Allocation in Thermoeconomics. ECOS 2010: Proceedings of the 23th International Conference on Efficiency, Cost, Optimization, Simulation, and Environmental Impact of Energy Systems; 2010 Jun 14-175; Lausanne, Switzerland Book 1: 381-388.

[19] Waninger H., Exergoökonomische Bewertung eines Parabolrinnenkraftwerks, Fachgebiet für Energietechnik und Umweltschutz Institut für Energietechnik Fakultät III, Technische Universität Berlin, 2007.

Influence of renewable generators on the thermo-economic multi-level optimization of a poly-generation smart grid

M. Rivarolo, A.Greco, F.Travi, A.F. Massardo

DIME – Thermo-chemical Power Group (TPG), University of Genoa, Italy

Abstract:

In this paper, the impact of not controllable renewable energy generators (wind turbines or solar photovoltaic panels) on the thermo-economic optimum performance of poly-generation smart grids is investigated using an original time dependent hierarchical approach.

The grid used for the analysis is the one installed at the University of Genoa for research activities. It is based on different prime movers: (i) 100 kWe micro gas turbine, (ii) 20 kWe internal combustion engine powered by gases to produce both electrical and thermal (hot water) energy and (iii) a 100 kWth adsorption chiller to produce cooling (cold water) energy. The grid includes thermal storage tanks to manage the thermal demand load during the year and appropriate systems to model any kind of thermal and electrical load profiles. The system is also equipped with two renewable non-controllable generators: a small size wind turbine and photovoltaic solar panels.

The system optimization (size and management) including the renewable generators has been carried out using a time-dependent thermo-economic hierarchical approach developed by the authors, considering the time-dependent electrical, thermal and cooling load demands during the year as constraints, in order to minimize both grid capital and variable costs.

The results are presented and discussed in depth and show the strong interaction between fossil and renewable resources, and the importance of an appropriate storage system to optimize the RES impact taking into account the multiproduct character of the grid under investigation.

Keywords:

Poly-generative smart grid, renewable sources, thermo-economic time-dependent optimization, optimal size.

1. Introduction

The development of poly-generation smart grids represents an interesting solution to satisfy electricity and heat demand and emission reduction[1][2]: poly-generation smart grids generate electricity and heating and cooling thermal power close to end users, solving the main disadvantages of the centralized generation approach, due to energy transmission [3]. In fact, the distributed generation approach has several benefits over the others, such as (i) reduction of transmission and distribution costs: about the 30% of the costs related to electricity supply relates to these costs. Local connections do not generate high capital costs and energy losses for long distances to be wired with overhead facilities; (ii) decrease of energy dissipation: piping and conversion devices dissipate almost 6% of produced energy,[4] increasing costs and emissions; in a smart grid these kinds of losses are avoided; (iii) increase of energy efficiency: the simultaneous supply of electrical and thermal demand allows to reduce energy waste, improving system global efficiency; since thermal energy is less easily transported than electricity, distributed generation approach (production close to users) is essential; (iv) integration of renewable generators: traditional prime movers could be easily integrated at local site with renewable generators decreasing emissions.

Therefore, the main goal is to analyze and optimize a poly-generation smart grid, analyzing the effect of renewable generators and correlation with the storage tank for hot thermal energy. To understand the importance of renewable generators in influencing the whole system, it is worth

remembering that an optimal poly-generation smart grid must assure the end users' demands (multi product systems) simultaneously (heating, cooling and electrical demand).

Increasing the size of renewable generators involves several advantages such as low environmental impact and fossil fuel consumption reduction; on the other hand, renewable generation is intrinsically random over time, thus their "***unpredictable behaviour***" could affect the operating conditions of prime movers over time. Since prime movers are co-generative, changes to operating conditions influence simultaneously electrical and thermal production. Thus, by varying the optimal size of renewable electrical generators, thermal storage size and behaviour could be influenced too. Therefore, the most important point of the analysis is represented by the integration between the prime mover constraints (continuous operation, high performance, etc.) and the uncontrolled renewable production (whose performance are random according to wind and solar irradiation condition).

2. Prime movers and device test rig

The poly-generation smart grid analyzed here is based on the one installed in the laboratory of the University of Genoa. The facilities installed are based on different kinds of technology with the aim to produce both electrical and thermal energy [5] and designed using different tools developed at TPG lab.[6-9]

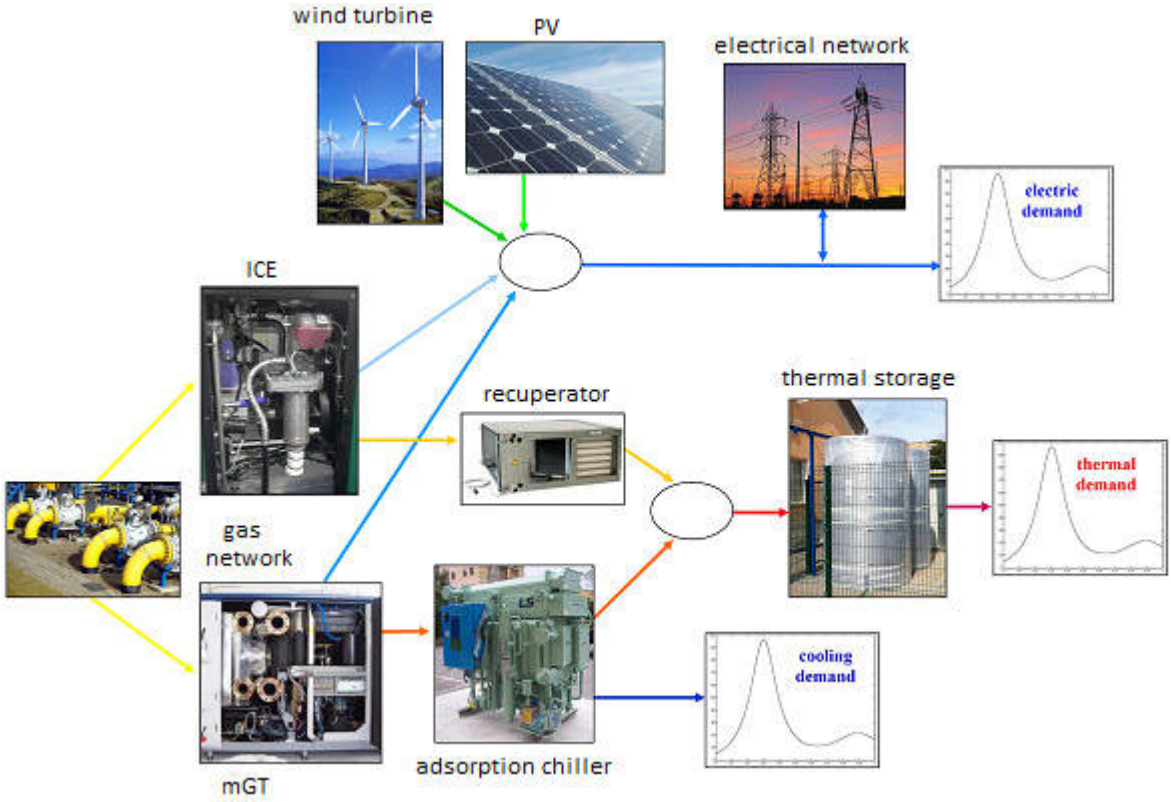

Fig.1: University of Genoa poly-generation grid laboratory.

Referring to Fig.1 the poly-generative smart grid main components are [10]:

- **<u>100 kWe Recuperated Micro Gas Turbine:</u>** It is the largest prime mover installed and produces the highest amount of both thermal and electrical energy; the machine is a Turbec T100 PHS Series [11]**Errore. L'origine riferimento non è stata trovata.**. This commercial unit

consists of a power generation module (100 kW of electrical power at nominal conditions), a cogeneration heat exchanger located downstream of the recuperator outlet (hot side).

- **20 kWe Internal Combustion Engine:** the internal combustion engine installed is a FIAT TANDEM-T20-A, powered by natural gas; this commercial unit generates 20 kW of electrical power at nominal conditions; a cogenerative heat exchanger (named recuperator) is placed downstream of the ICE outlet. It produces 47.5 kW of thermal power at nominal conditions.
- **100 kWc Adsorption Chiller:** in order to generate cooling thermal power, mGT T100 has been connected to an adsorption chiller LWM-W300 produced by LS. It is powered directly by the mGT heat, assuring 100kW cooling power generation.
- **Renewable generators:** the grid also includes renewable generators; photovoltaic solar panels, model eco line 72/180-185 W produced by Luxor; wind energy produced by wind turbines of MAGLEV series.
- **Storage tank:** the grid analyzed is equipped with several storage tanks (i.e., for hot and cold water of the whole grid, and for each main engines). However in this analysis only the storage tank (Pufferspeicher series. [5]) for thermal energy is considered.

The grid is also integrated with a 450 kW SOFC Hybrid System Emulator developed by the authors in collaboration with Rolls-Royce FCS [12-15] for cogeneration applications, but it is not considered in the analysis carried out this paper.

3. EPoMP multilevel thermo-economic optimization approach

To optimize a poly-generative smart grid optimal size and management including RES, a time-dependent thermo-economic analysis is mandatory. The approach used here represents the further development of the one for co-generative power plants [16][17]. The model has been developed by the authors and a modular program named EPoMP (*Economic Poly-generation Modular Program*) has been created [18].

Fig. 2 shows the model structure which is based on a hierarchical optimization structure. There are two different optimization levels: the low and the high level respectively. At the low level, lay-out and plant size are fixed (therefore capital costs are fixed) and the code finds the best operational strategy, in order to minimize the function that represents the hourly (or less time period) variable cost.

$$C_{\mathrm{var}} = F_i \cdot \sum_{i=1}^{N} c_{fuel,i} + c_{el} \cdot E_{acq} + c_{virt} \cdot \left(F_{virt} + E_{virt} + Q^{*}_{virt} \right) \tag{1}$$

Variable costs are made up of the following terms: (i) a term related to fuel consumption costs, (ii) a term related to electrical energy costs, and (iii) a term that represents "virtual costs".

The electrical energy costs term represents the product of the electrical energy purchased from external grid and the electricity specific cost: when the electricity produced by the plant is not sufficient to satisfy the electrical load (which is one of the problem constraints), electricity is purchased from the external grid. About the term "*virtual flows*", added to the cost function, it is important to underline that it is not a real cost, but rather represents exchanges between system and environment (electrical grid, fuel grid, storage system, etc.) necessary only to meet during the calculation the optimization procedure constraints. Since the virtual cost is considered very high, to find the optimum conditions without any virtual energy request (constraint violation such as the gas flow rate or available electricity from the grid), the code is forced to find a plant configuration which minimizes virtual flows [16] (i.e. zero virtual costs).

The main inputs of the model are: (i) electricity, heating, cooling, etc. load curves versus time; (ii) economic scenario where the grid operates, including trade prices (fuel cost, energy cost, plant lifetime etc.); (iii) component capital costs vs. size; (iv) operating and maintenance costs vs. time;

(v) prime movers off design performance curves; (vi) technology constraints for grid devices (i.e. starting time, flexibility, etc.).

Constraints of the problem are the balance equation between supply and demand of the components. For example, in the energy balance, the energy produced by the prime movers (ICE, gas turbines, etc.) in the system, the energy sold to the user and the energy consumed by system components (i.e. electrolytic cells, etc.) are included:

$$E_{req} = \sum_{i=1}^{N} E_{i,prod} + E_{acq} + E_{virt} - \sum_{i=1}^{N} E_{i,cons} \tag{2}$$

The same concept is the basis of the thermal energy balance:

$$Q_{req} = \sum_{i=1}^{N} Q_{prod} + Q_{virt} \tag{3}$$

At the high level, the plant component optimal size, minimizing total annual cost, is evaluated as the sum of variable costs C_{var} calculated at low level analysis and capital plant costs C_{cap}.

$$C_{tot} = C_{\text{var}} + C_{cap} \tag{4}$$

The plant total capital cost is the sum of the total capital cost of any plant component.

$$C_{cap} = \sum_{i=1}^{N} C_{cap,i} \tag{5}$$

Therefore, the approach optimizes simultaneously the plant and the component sizes, together with plant operation management [16][17].

EPoMP, using two different optimization routines (one for each level of the model at every iterative cycle), calculates the total annual cost changing the value of the component nominal size: in this step virtual flows are very important to find the optimal component size, in order to determine the global minimum value of the objective function. At low levels, only variable costs are optimized, reducing to zero the penalty costs associated with the virtual flows that would represent not satisfied constraints. At the high optimization levels, the model also takes into account fixed costs, finding the optimal size for plant components. At every optimization level, different constraints must be satisfied; if these conditions are not verified, strong penalties are applied and objective functions are raised because of costs C_{virt} associated with virtual flows [18].

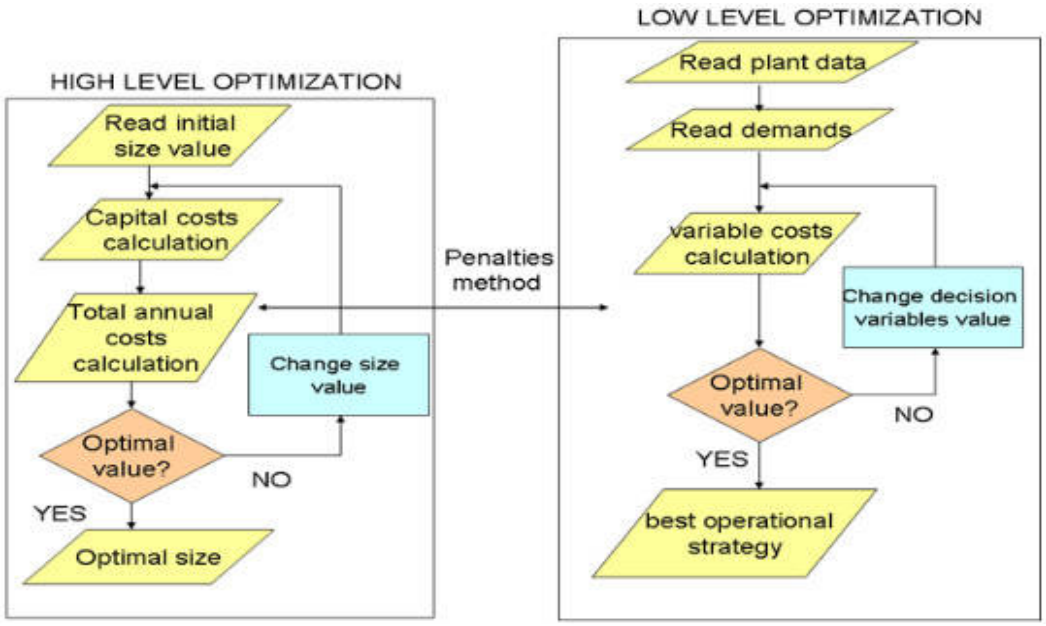

Fig. 2: EPoMP code hierarchical structure

To build in an easy way complex plant configurations, a modular visual approach has been developed by the authors (37 different modules are available at the moment), as already presented

in [19]. For each component, four subroutines are developed to calculate (i) design and off design performance; (ii) capital costs; (iii) variable costs, and (iv) operating and maintenance costs. The calculation is then carried out by dividing the operational time (usually a year) into a sufficient number of representative periods, one hour or less depending by the particular application.

Due to their high importance in the poly-generative smart grid under analysis in this paper, a short description of renewable generators and thermal storage models is presented.

- **Renewable generator module:** the innovative aspect of this module is its ability to simulate the functional behaviour and the energy production of any kind of renewable generator, including random aspects, such as wind turbines, hydraulic plants, solar panels, etc. Thanks to its generic nature, it is possible to simulate several plant configurations. The module needs, as inputs: (i) solar radiation and wind curves [20] in order to take properly into account the random character of these energy resources; (ii) nominal size of the installed renewable generator; (iii) number of the modules installed in the plant; (iv) kind of the installed renewable generators. Energy production is computed as the product of renewable generator installed power and the availability curves, varying in each period, as reported in Eq. (6):

$$P_{prod,i} = P_{inst} \cdot \alpha_i \tag{6}$$

  α_i is strictly related to renewable sources availability curves, thus it can assume all the values between 0 and 1. As far as the economical analysis is concerned, for any kind of renewable generator, specific cost functions are implemented, in order to calculate both fixed and variable costs.

  It is worth noting the innovative feature of this module; in a standard prime mover (ICE, mGT, etc.) powered by fuel, working conditions are optimized at hierarchical low level taking into account off-design curves, implemented in the model, and satisfying load demands (constraints of the problem) in each period; on the contrary, renewable generators behaviour cannot be regulated by the users, since energy production amounts depend only on random renewable sources (water, solar, wind) availability curves.

- **Thermal storage module**: the optimization of this component is realized by the introduction of appropriate virtual flows and virtual costs. The calculation is carried out over a selected period of time, in order to predict the weighted average performance of the plants working under variable loads. The new system of virtual costs has been introduced in order to optimize storage management, associating virtual costs with the filling and emptying operations [21]**Errore. L'origine riferimento non è stata trovata.** taking carefully into account that any kind of storage system moves the model toward a strong non linearity. These virtual terms are implemented in order to take into account the management effect of the storage on the whole system. Virtual costs give priority to the nominal working conditions of prime movers in order to assure a high efficiency of the plant and they have been set in order to promote filling operation, in order to consistently guarantee a sufficient tank level. Model equations are not reported here: further details can be found in [19][21].

3.1 Thermo-economic simulation

To achieve thermo-economic optimization, EPoMP needs a large number of input, most of them related to the economic scenario where the plant is installed. The main plant data considered here are as follow:

Electrical and thermal load curves: The simulation was carried out on an entire year time period, considering average monthly values for electrical, thermal and cooling demand values. Load curves versus time represent the problem constraints to avoid penalties; they are shown in Fig. 3 and represent typical university campus energy demands, as reported in [20].

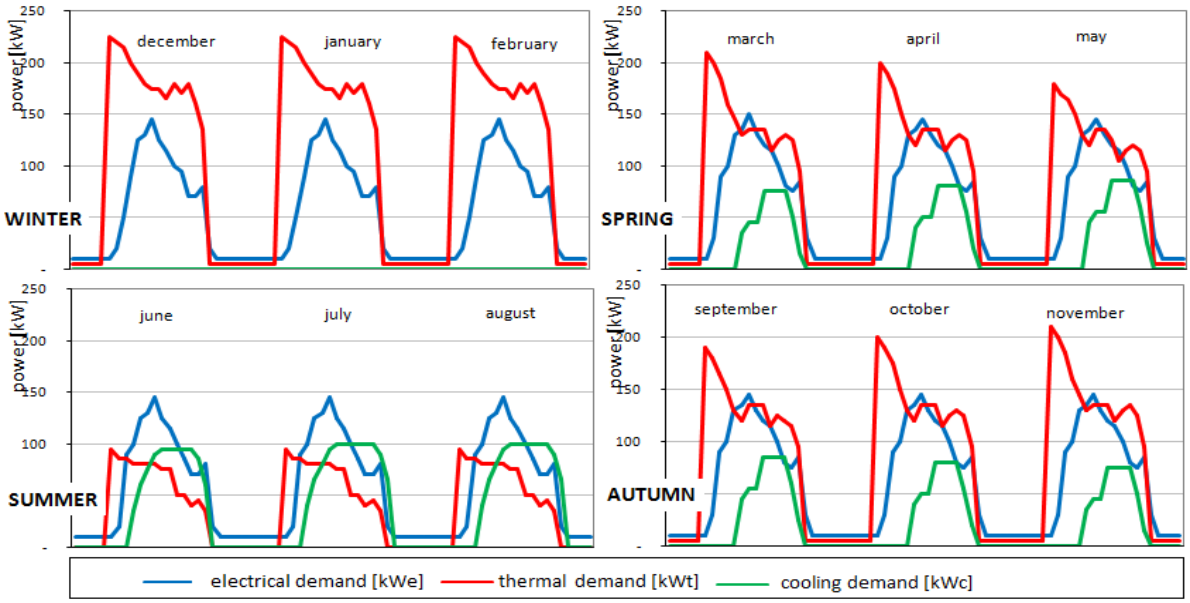

Fig. 3: Energy load demands

Energy cost: electricity cost has been assumed to be equal to 0.20 €/kWh; for both hot and cold thermal energy a sale rate of 0.10 €/kWh has been assumed [20].

Capital costs of each installed device have been assumed based on laboratory plant data [5][11][5]. In particular, for renewable generators a value of 2,500 €/kW peak for photovoltaic panels and of 2,000 €/kW for wind generator have been considered.

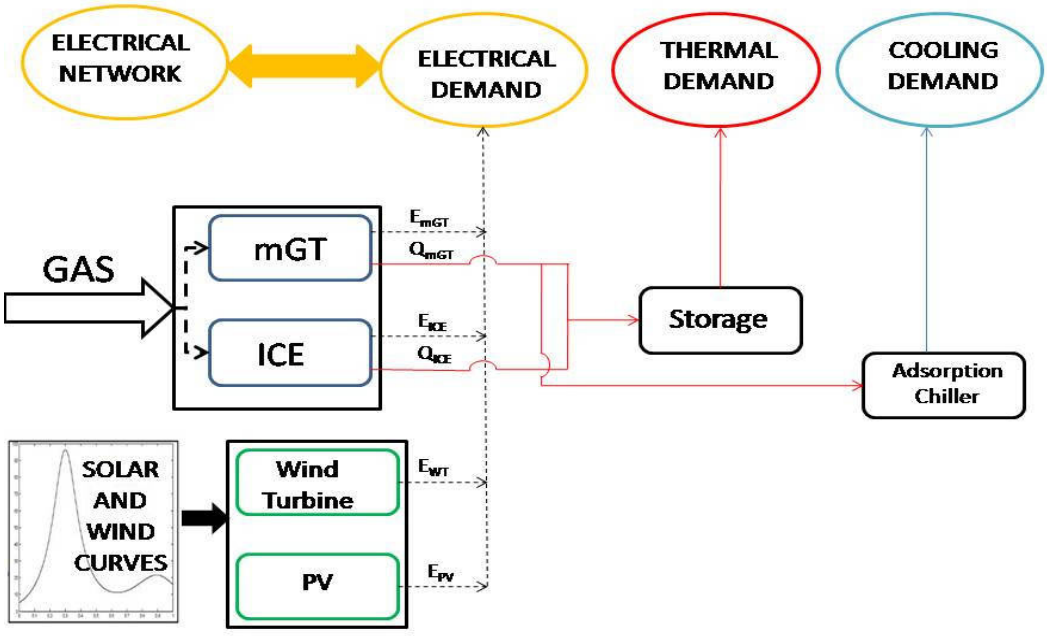

Fig. 4: Scheme of the virtual and real energy flows of the polygenerative grid installed at University of Genoa laboratory.

Fig. 4 shows the constraints of the problem, in particular: *(i)* cooling demand, satisfied by adsorption chiller, which is fuelled by mGT heat; *(ii)* thermal demand, satisfied by a storage tank, whose level depends on operation of the prime movers (Q_{mGT} and Q_{ICE}); *(iii)* electrical demand,

satisfied by the prime movers (E_{mGT} and E_{ICE}) and renewable generators (E_{SP} and E_{WT}). As shown in Fig. 4, electrical demand may also be satisfied by taking electricity from the external electrical network (i.e. when a peak demand is higher than maximum installed plant production capacity). In this case, a limit to the electricity from the external grid is considered for contract cost reasons, and therefore a virtual cost may be applied also for this connection.

The plant analysis was performed on an entire year time period (8760 hourly periods) considering the percentage load of the prime movers (mGT, ICE, adsorption chiller) as decision variables at model low level; renewable generators (solar panels and wind turbines) and thermal storage size have been assumed as decision variables at high level optimization. The analysis was performed at high levels considering storage volume and renewable generators size as decision variables. Renewable generators have been considered in the range between 1 and 25 kW for both photovoltaic panels and wind turbines.

4. Results

Through the use of the EPoMP code, an optimum value of 17 kW for photovoltaic panels peak power, 3 kW for wind turbine size, and 34 m^3 for the storage tank volume has been obtained.

To carry out a detailed analysis of the results for the different aspects of the grid along the year, they have been properly organized in "***power or size vs. time plots***" showing the entire year behaviour.

In Fig. 5, the mGT, the internal combustion engine, the renewable generators productions and the electricity taken from the grid are shown; the electrical load demand is represented by a black line. Specifically, mGT production satisfies the base load, ICE supplies electricity during peak periods and at night hours as well, when the demand is lower and mGT would work at strong off design conditions, where efficiency is particularly low and emissions high. In some periods, electrical demand could be higher than maximum prime movers production, thus the system has to buy electricity from the external network to satisfy the load demand, previously shown in Fig. 4. The electrical demand trend is nearly the same throughout the entire year, no significant differences between the seasons are evident. It is worth noting that the optimization minimizes the number of mGT start-up and shut-down, which affects the operating life of the engine (similarly for ICE): the cost related to these operations is considered in the fuel consumption term, included in Eq. (1).

As far as renewable generators are concerned, their behaviour is shown in Fig. 6. It is worth remembering that their production follows not only night/day variation, but it also depends on the season of the year and is substantially "random", therefore it is unpredictable and not controllable. It is also necessary to highlight the great difference between photovoltaic panels (17 kW) and wind turbine (3 kW) optimal size. Although both of them are uncontrollable generators, photovoltaic panels follow the night/day insulation (i.e. easily predictable) behaviour: this feature allows a less complex matching for PV panels with mGT and ICE, compared to wind turbine. In particular, since wind turbine works even during night periods, a further size increase would result in the shut-down of the ICE during night periods, a thermal power reduction and greater difficulty in satisfying thermal load demand in classical morning peak periods. In this case, a larger storage would be necessary and plant capital costs would increase. For this main reason, the optimal size of wind turbines is lower than the size of photovoltaic panels.

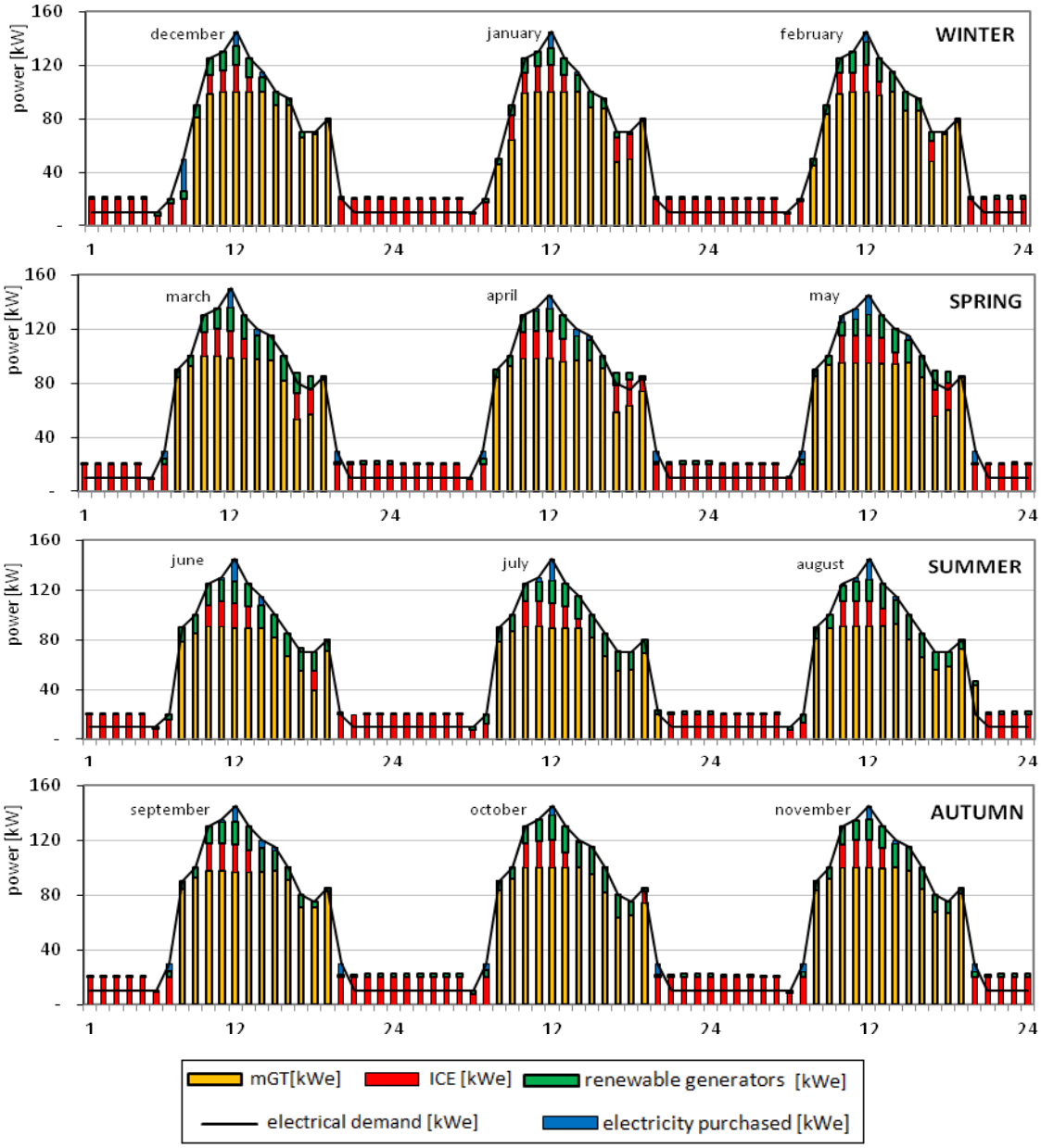

Fig. 5: Electrical power vs. time plots

In Fig. 7 the mGT and the ICE thermal productions are shown; storage tank supply is also shown; thermal demand is represented by black line. During the winter season thermal power production (cogeneration effect) exceeds the demand at midday, when a peak of electrical demand is present, and in the late afternoon. Since the prime movers are co-generative, surplus heat produced is used to fill the storage tank. Likewise, during night hours, since ICE works to cover electrical demand, its thermal power production, which exceeds the demand, is sent to the storage. As Fig. 7 shows, the storage tank operates to cover thermal load in the early morning, when thermal demand presents a peak and the prime movers are not sufficient to satisfy the thermal demand, and in the afternoon, when electrical demand gets lower and co-generative prime movers are off (in the case of MCI) or work at strong part load (mGT).

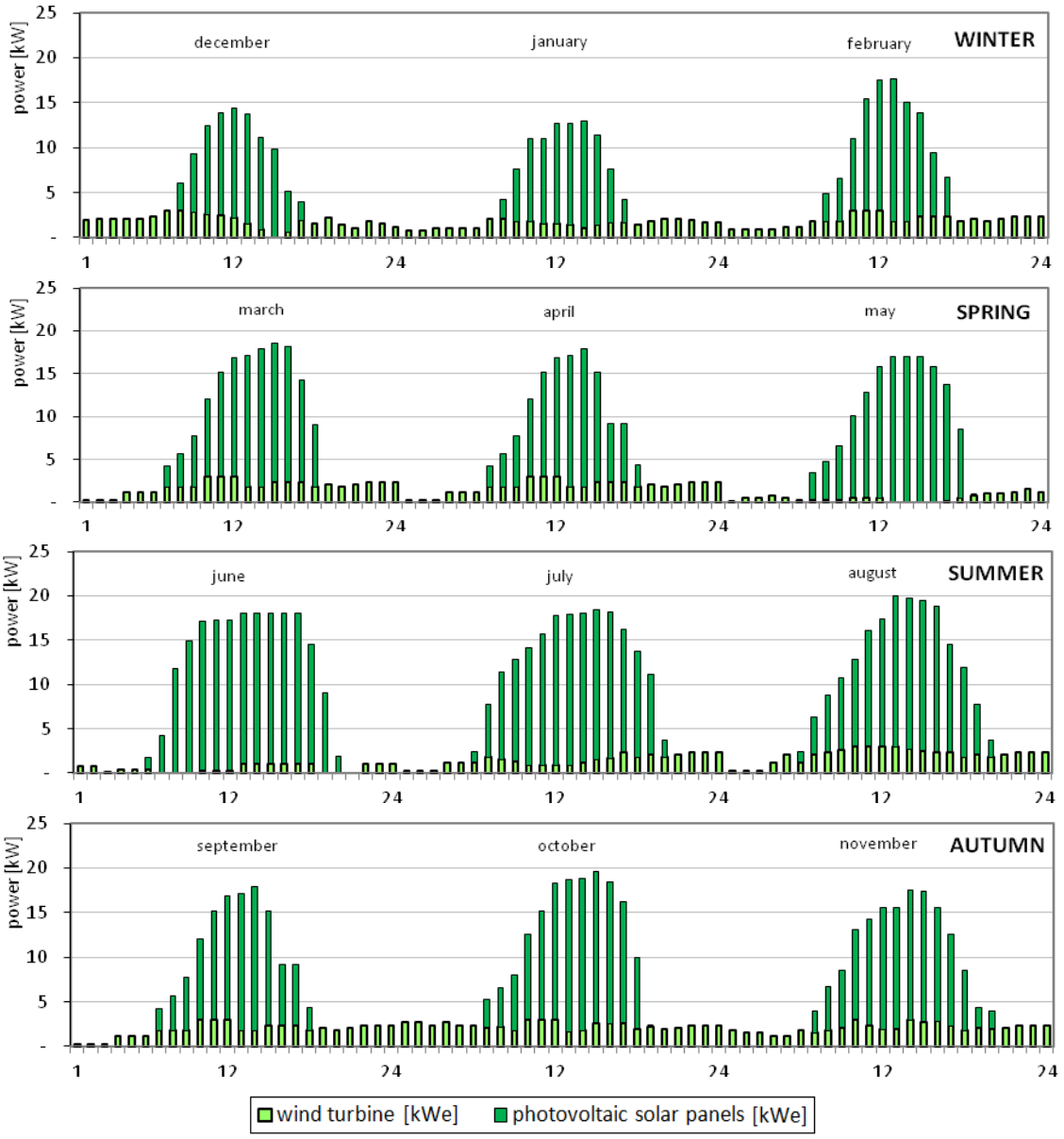

Fig.6: Renewable generators behaviour vs. time (note: since the wind model is fully random, electricity generated by wind turbines is not repetitive for different days or months of the year, while PV generation is mainly related to day and night solar insulation with possible cloud effects considered in the model).

In the other seasons, in particular in summer, thermal demand gets low: as consequence, a higher surplus thermal power amount is present, a fact that could bring strong economical penalties due to storage tank overfilling. Since hot and cooling thermal demands are complementary (see Fig. 3), a significant part of the thermal power surplus generated by mGT is used by adsorption chiller (see Fig. 4) in the summer, supplying the cooling demand and avoiding thermal storage overfilling. Thermal power used by chiller is represented in dashed lined yellow columns in Fig. 7.

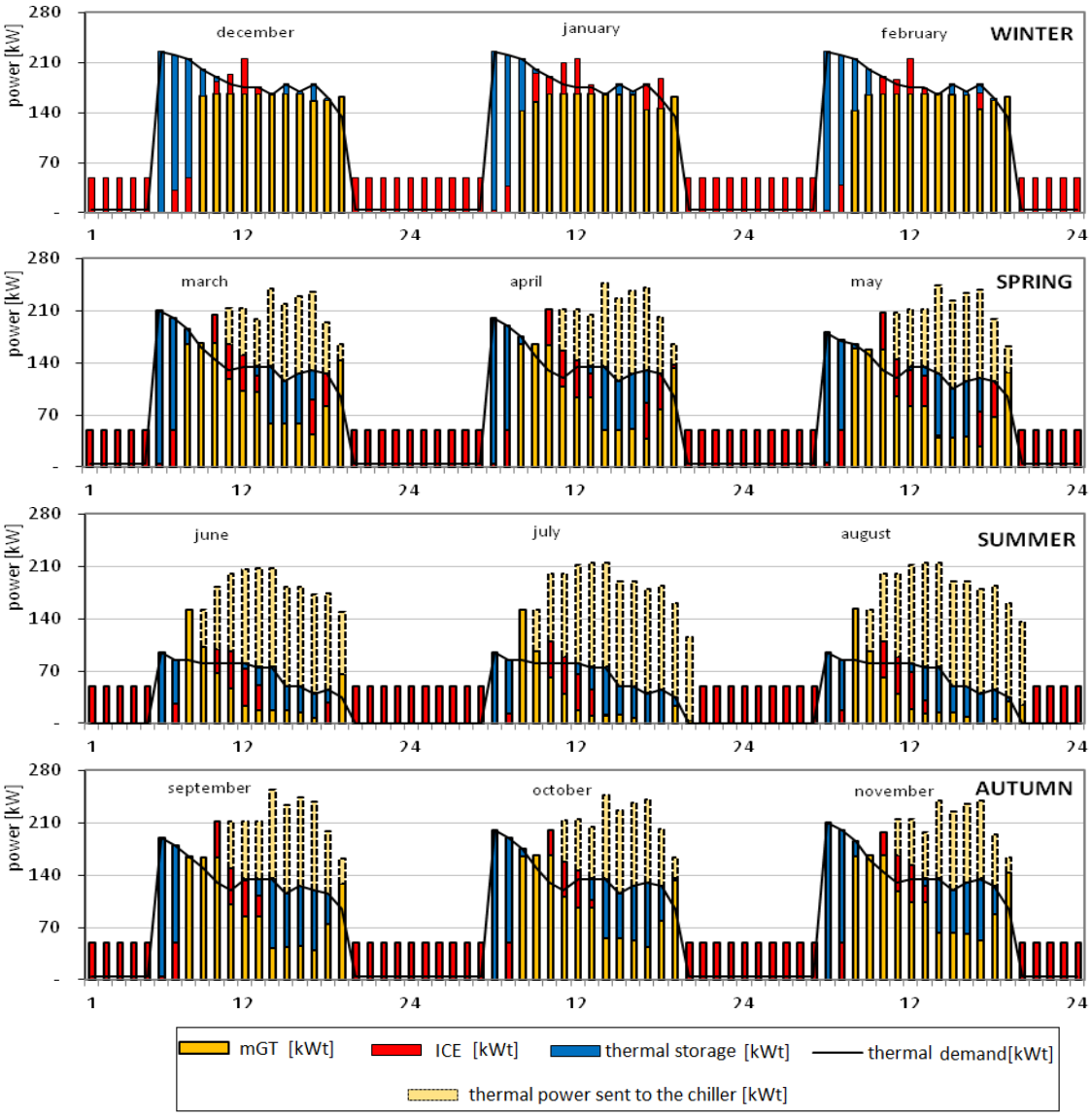

Fig.7: Thermal power vs. time plots

Cooling thermal demand is supplied by the adsorption chiller which is powered directly by mGT. In the case under investigation, cooling power demand is zero and the adsorption chiller does not work during the winter. It is worth noting (see Fig. 3) that cooling power load demand is practically complementary to thermal load demand; it is the highest in summer (when thermal load demand is the lowest) and zeros out in winter (when thermal load is the highest). Thus, the surplus thermal power produced by mGT in summer time, that would not be necessary in the storage tank, finds an application in the adsorption chiller, allowing cooling power production without any additional fuel cost and obtaining revenue from the cooling water.

Storage tank behaviour during the year is shown in Fig. 8 where storage tank level vs. time for each season is reported. The poly-generation plant with renewable generators (continuous line) results are compared to the only fossil configuration (dashed line), investigated in a previous work [20], considering the same load curves shown in Fig. 8.

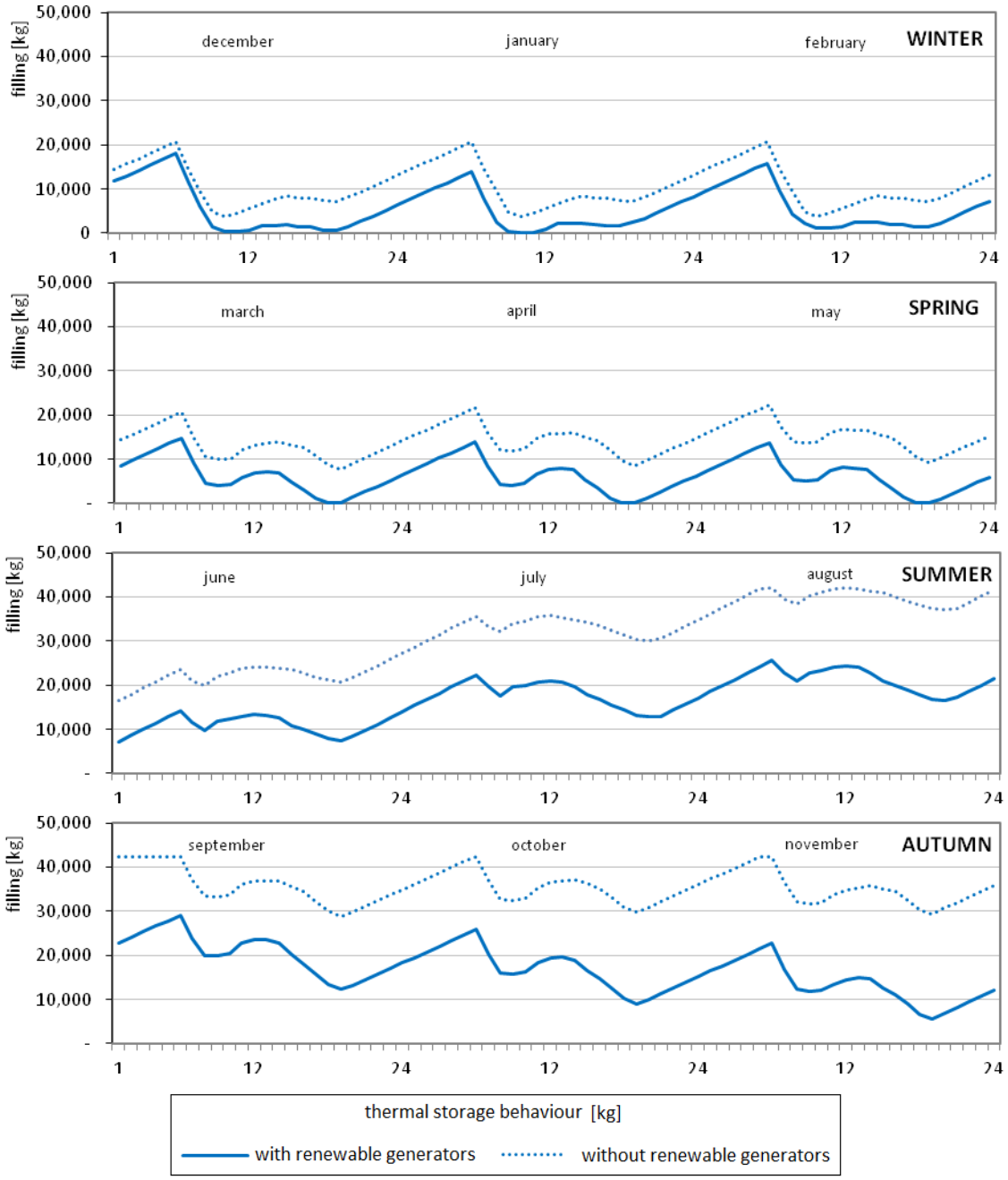

Fig.8: Storage tank level vs. time plots

Without renewable generators, electrical energy is produced by traditional prime movers only (mGT and MCI). Due to their co-generative nature, all the heat produced is sent to storage tank, without any dissipation. Thus, as Fig. 8 shows, tank level gets higher and the minimum volume to avoid overfilling penalties is 45 m^3. Since renewable generators produce only electrical energy, their integration in the poly-generation system implies lower co-generative device utilization, thus a lower thermal storage maximum filling. As Fig. 8 shows, storage tank optimal dimension is reduced to 30 m^3, allowing a significant decrease in terms of volume and capital costs.

Analyzing the whole grid operating period, it is worth noting that starting level and final level are the same. This result proves how prime movers operation, renewable generators size and energy load demands are perfectly balanced. Storage tank levels get higher in summer, when the demand for heat is low, while it gets empty in winter, when the demand for heat is higher.

Fig. 9 compares economic results for the poly-generative system plant lay-out, considering two different configurations: (a) without any renewable production (configuration A); (b) including 17 kW photovoltaic panels and 3 kW wind turbine installation (configuration B). For both configurations, annual cash flows are reported, including revenues and costs: revenues (on the left) are represented by electrical, hot and cooling thermal energy selling, costs are composed of the depreciation rate, gas consumption and electricity purchased from external network.

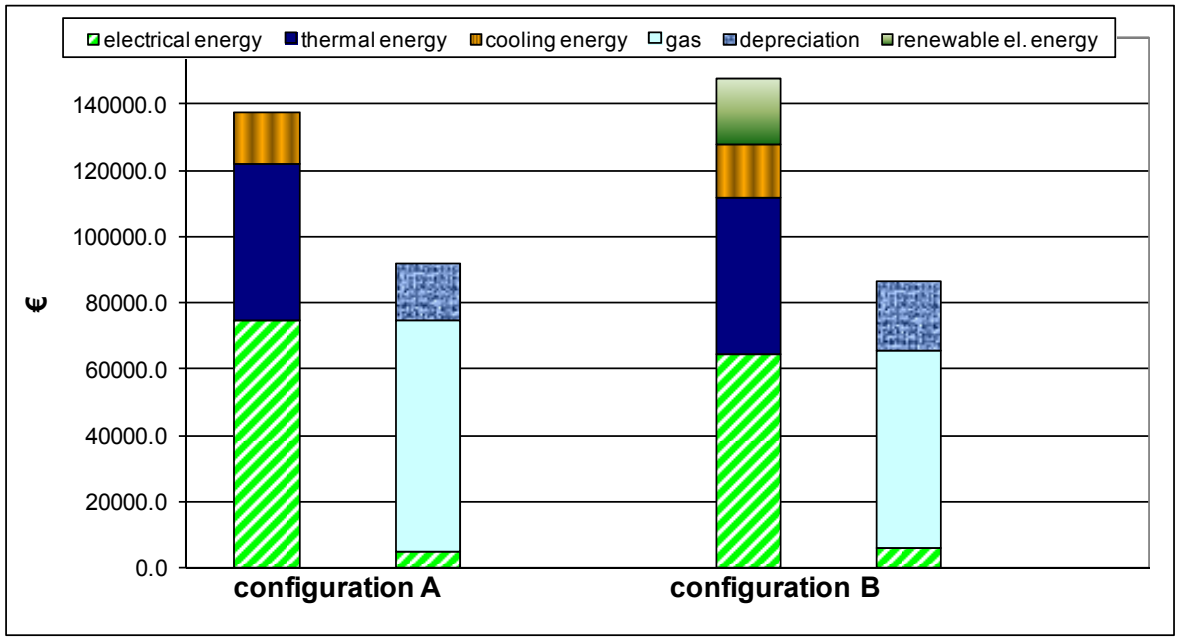

Fig. 9: Poly-generation grid annual cash flows (revenues and costs): configuration A includes only fossil systems; configuration B also includes RES.

It is worth noting that installation of renewable generators (configuration B) implies increasing revenues; moreover, it has primary effects on the whole thermo-economic annual results:

a) ***Electrical energy increase***, since new configuration includes 17kW$_e$ solar panels and 3kW$_e$, installed power increase from 120 kW to 140 kW, thus during peak hours electricity purchased from the external grid is reduced;

b) ***Fuel consumption decrease,*** since prime movers average utilization is reduced

c) ***Depreciation rate increase,*** since capital costs are higher

To sum up, total annual costs are nearly constant, since effects (b) and (c) balance each other; on the other hand, revenues get higher since electrical energy increases, thus introducing the renewable generators is significant from a thermo-economic point of view. Moreover, annual fuel consumption is reduced by 13.5 tons: since specific methane emissions are 2.75 kg CO_2 / kg CH_4, about 37 tons/year of CO_2 can be avoided thanks to renewable generators production.

5. Conclusions

In this paper, the influence of renewable non-controllable sources (wind turbines or solar photovoltaic panels) on the thermo-economic performance of a poly-generation smart grid, similar to the one installed in the laboratory of the University of Genoa [5], has been investigated.

The analysis was carried out using a hierarchical thermo-economic approach for poly-generative system optimization, developed by the authors [18][19]. The code, named EPoMP, found the optimal size for both renewable generators and hot storage system.

The results allow the following main conclusions to be carried out:

- Two different renewable non-controllable generators were considered, specifically photovoltaic panels and wind turbines. Although both of them are random generators, photovoltaic panels follow at least the alternation night/day, a feature which allows a better matching with prime movers compared to wind turbine (i.e. the random grade is higher for wind energy). For this reason, the optimum result is a size of 17 kW for PV panels and only 3 kW for wind turbine.
- Since renewable generators considered here produce only electrical energy, optimal size has been optimized by also taking into account that the poly-generative system must satisfy thermal and cooling demands throughout the year too. Since they are non controllable, higher renewable sizes (i.e. 20 kW solar panels, 5 kW wind turbine) would not verify the problems constraints and costs (capital and variable) increase largely.
- Renewable generator utilization influences the storage system optimal size too; since co-generative prime movers working time and load (they operate largely at part load) is reduced due to RES generators, thermal energy production is lower and storage optimal volume decreases (in this case from 45 to 30 m^3) allowing a reduction in storage tank capital costs too.
- The optimized system integrated with non-controllable renewable generators was compared from a thermo-economic point of view with the same poly-generative plant without RES installed; the main result is that optimizing solar panels, wind turbine sizes and system management allows annual revenues increasing to be obtained, while annual costs are nearly constant (capital costs increase, but variable costs reduce).

It is worth noting that the model developed here can be applied to any poly-generative plant including any kind of renewable generator. Moreover, the presented results have a generalized value, since the method takes into account the type and size of the prime movers, the energy load profiles, the plant location, and the economic scenario.

Using the laboratory poly-generation grid at University of Genoa with a very flexible approach not only for generation aspects, but also for load profile generation, the EPOMP model will be validated and different options will be investigated such as low geothermal heat, solar panel, hydrogen generation and utilization with the intention to define case by case the best option for multi product distributed generation grids.

6. Nomenclature

Abbreviations:

ICE	Internal Combustion Engine
PV	Photo Voltaic
mGT	Micro Gas Turbine
RES	Renewable Energy Sources

Symbols:

C	Cost [€]
E	Electricity flow [kWh]
P	Power [kW]
α	RES availability coefficient
c	Specific cost [€/kWh]
F	Fuel consumption [kg]
Q	Heat flow [kWh]

Subscripts:

acq	acquired

cons	consumed
i	i-th step
prod	produced
var	variable
cap	capital
el	electrical
inst	installed
req	required
virt	virtual

Acknowledgements

This work has been partially supported through the EU-FP7 European Project E-HUB, grant agreement n° 260165.

The authors wish to thank the colleagues at TPG working on the grid design and installation Mario Ferrari, Matteo Pascenti, Alberto Nicola Traverso, Loredana Magistri, Alberto Traverso and Francesco Caratozzolo for their help in the design and modelling of the different parts of the grid including the hybrid System Emulator.

References

[1] Sheikhi A., Ranjbar A.M., Oraee M., Moshari A., "Optimal Operation and Size for an Energy Hub with CCHP", Energy and Power Engineering, 2011, 3, 641-649.

[2] US EPA, "Inventory of US Greenhouse Gas Emissions and Sinks: 1990–2001". EPA 430-R-03-004. US Environmental Protection Agency, Washington, DC, 2003.

[3] McDonald, J., "Adaptive Intelligent Power Systems: Active Distribution Networks", *Energy Policy*, 2008, 36, 4346–4351.

[4] Mendez, V.H., Rivier, J., De La Fuente, J.I, Gomez,T., Arceluz, J., Marin, J., 2002, "Impact of Distribute Generation on Distribution Network", Universidad Pontificia Comillas, Madrid.

[5] Ferrari M.L., Pascenti M., Traverso A., Rivarolo M., "Smart polygeneration grid: a new experimental facility", ASME Turbo Expo 2012, June 11-15, Copenhagen, Denmark.

[6] Agazzani A., Massardo A.F., "A tool for thermoeconomic analysis and optimization of gas, steam, and combined plants", ASME Journal of Engineering for Gas Turbines and Power, 1997, 120, 557-565, doi 10.1115/1.2818183.

[7] Borchiellini R., Massardo A.F., Santarelli, M., 2000, "Analytical procedure for carbon tax evaluation", Energy Conversion and Management, Vol. 41, pp. 1509-1531, doi10.1016/S0196-8904(99)00184-3

[8] Massardo A.F., Magistri L., "Internal reforming solid oxide fuel cell gas turbine combined cycles (IRSOFC-GT) - Part II: Exergy and thermoeconomic analyses", ASME Journal of Engineering for Gas Turbines and Power, 2003, 125, 67-74, doi 10.1115/1.1492837

[9] Santin M., Traverso A., Magistri L., Massardo A.F., 2010, "Thermoeconomic analysis of SOFC-GT hybrid systems fed by liquid fuels", Energy, Vol. 35, pp. 1077-1083, doi 10.1016/j.energy.2009.06.012

[10] Ferrari M.L., Pascenti M., Traverso A., Massardo A.F., 2012, "An Experimental Facility for Tests on Distributed Generation Systems", International Conference on Applied Energy 2012, Suzhou, China.

[11] Turbec T100 Series 3, “Installation Handbook” , 2002.

[12] Ferrari M.L., Pascenti M., Magistri L, Massardo A.F. “Hybrid System Test Rig: Start-up and Shutdown Physical Emulation”, Journal of Fuel Cell Science and Technology 2010, 7: 021005_1-7.

[13] Ferrari M.L., Pascenti M., Magistri L., Massardo A.F. “MGT/HTFC Hybrid System Emulator Test Rig: Experimental Investigation on the Anodic Recirculation System”, Journal of Fuel Cell Science and Technology, 2010, 8, 021012,1-9.

[14] Ferrari M.L. “Solid Oxide Fuel Cell Hybrid System: Control Strategy for Stand-Alone Configurations”, Journal of Power Sources 2011, Elsevier, 196, 5, 2682-2690.

[15] Magistri, L., Costamagna, P., Massardo, A.F., Rodgers, C., McDonald, C.F., “A hybrid system based on a personal turbine (5 kW) and a solid oxide fuel cell stack: A flexible and high efficiency energy concept for the distributed power market”, ASME Journal of Engineering for Gas Turbines and Power, 124, 2002, pp.850-857.

[16] Massardo A.F., “Cogeneration”, John Wiley Encyclopedia of Electronic and Electrical Engineering, New York, J.Webster Ed., March 2001.

[17] Gamou S., Yokohama R., Ito K., “Optimal unit sizing of cogeneration systems in consideration of uncertain energy demands as continuous random variables”, Energy Conversion and Management 2002, 43, 1349-1361.

[18] Torti C., “Development of Time Depending Calculation Tools for Plant Optimization”, 2009, Doctoral Thesis, University of Genoa.

[19] Rivarolo M., Bogarin J., Magistri L., Massardo A.F., 2011, “Time-dependent optimization of a large size hydrogen generation plant using “spilled” water at Itaipu 14 GW hydraulic plant”, International Journal of Hydrogen Energy, doi:10.1016/j.ijhydene.2011.09.015.

[20] Travi F., Greco A., “Design and thermoeconomic optimisation of poly-generation smart grid including thermal storage” (in Italian), University of Genoa, Faculty of Engineering, 2011.

[21] Nicolini M., “Thermal energy storage systems optimization for forest biomass and natural gas-fired cogeneration plants” (in Italian), University of Genoa, Faculty of Engineering, 2010.

Local stability analysis of a thermo-economic model of an irreversible heat engine working at different criteria of performance

M. A. Barranco-Jiménez[a], N. Sánchez-Salas[b] , I. Reyes-Ramírez[c] and L. Guzmán-Vargas[c]

[a] *Escuela Superior de Cómputo del IPN, México DF, México, mbarrancoj@ipn.mx,*
[b] *Escuela Superior de Física y Matemáticas del IPN, México DF, México, norma@esfm.ipn.mx,*
[c] *Unidad Profesional Interdisciplinaria en Ingeniería y Tecnologías Avanzadas del IPN, México DF, México, lguzmanv@ipn.mx, ireyesr@ipn.mx*

Abstract:
In recent works [1, 2], we reported a local stability analysis of a thermo-economic model of an irreversible heat engine working at maximum power conditions. In those works, we calculated the relaxation times in terms of τ, f and R (a parameter which comes from the Clausius inequality and measures the degree of the internal irreversibilities). Besides $\tau = T_2/T_1$, with $T_1 > T_2$, being the temperatures of the external heat reservoirs and the parameter f is the fractional fuel cost, which is associated to several energy resources considering energy sources where de investment is the preponderant cost ($f = 0$), until energy sources where the fuel is the predominant cost ($f = 1$). In those works, we showed that, after a small perturbation the system decays exponentially to the steady state determined by two different relaxation times. In this work, we extend the local stability analysis considering other regimes of performance: The Maximum Efficient Power and the Ecological Function regime. We show that the relaxation time under maximum ecological function conditions is lesser than the relaxation times under both maximum power and maximum efficient power, that is, under maximum ecological conditions we have better stability conditions than for the other two regimes. Besides, we observe that the stability of the system improves as τ increases whereas the steady-state energetic properties of the engine declines for all cases of energy sources.

Keywords:
Thermo-economics, Local stability, Irreversible heat engine.

1. Introduction

Since the work of Curzon–Ahlbom(CA) [3], most of the studies on Finite-Time Thermodynamics (FTT) have focused on steady-state energetic properties [3-8], which are important from the point of view of design. However, all thermal engine works in many cycles per unit time and they are never identical, that is, there exists intrinsic cyclic variability (CV) in any sequence of cycles. For example, in internal combustion engines, the CV is produced for incomplete combustion of fuel and other causes [9]. It is crucial to know how much each cycle allows external perturbations, while still preserving the steady-state regime that lets it carry out its function well. In order to have a well-designed system, it is important to analyse the effect of noisy perturbations on the stability of the system's steady state. This study may allow us to guarantee proper dynamical behaviour of a system like stability and small relaxation times, or to warn about possible failure in the performance of a thermal engine. In 2001, Santillán et al. [10] studied the local stability analysis of an endo-reversible Curzon-Ahlborn heat engine operating under maximum power conditions. Later, Guzmán-Vargas et al. [11] investigated the effect of the heat transfer laws and the thermal conductances on the local stability of an endo-reversible heat engine. Recently, Páez-Hernández et al. [12], analyzed the local stability of a non-endo-reverible Curzon-Ahlborn cycle taking into

account the engine's implicit time delays when operating at maximum power regime. However, the local stability analysis described in these works have not considered the effect of economicalaspects. Within the context of Finite-Time Thermodynamics, the effect of the economical aspects was early introduced by De Vos [13] for the study of the thermo-economic performance of a model of power plant of the Novikov type [14,15]. Later, Sahin and Kodal [16] studied the thermo-economics of an endo-reversible heat engine in terms of the maximization of a profit function defined as the quotient of the power output and the annual investment and the full consumption costs. This thermo-economic performance analysis [17], consists in to maximize a benefit function in terms of the power output and the cost involved in the performance of the power plant. Recently, Barranco-Jiménez et al. [1,2] reported a local stability analysis of a thermo-economic model of an irreversible heat engine working under maximum power conditions. In those studies they used two different heat transfer laws, the Newton heat transfer law [1] and the Dulong-Petit heat transfer law [2]. In this work, we extend the local stability analysis considering other regimes of performance: The Maximum Efficient Power [18,19,20]and the Ecological Function regime [21-22]. We show that the relaxation time under maximum ecological function conditions is lesser than the relaxation times under both maximum power and maximum efficient power, that is, under maximum ecological conditions we have better stability conditions than for the other two regimes. The paper is organized as follows: In section 2, we present the thermo-economic analysis of the irreversible heat engine with different criteria of performance. In section 3, we describe the local stability analysis method applied to a two-dimensional system. In section 4, the local stability analysis of the irreversible heat engine is presented. Finally, en section 5, we present our conclusions.

2.Thermo-economic analysis of the steady-state irreversible heat engine under different criteria

In Fig. 1 a schematic diagram of the irreversible heat engine (Curzon-Ahlbornmodel) is shown. This engine consists in a Carnot-like thermal engine that works in irreversible cycles and exchanges heat with external thermal reservoirs at temperatures T_1 and T_2 ($T_1 > T_2$). In the steady state, the temperatures of the Carnot-like cycle isothermal branches are $\bar{x}$ and $\bar{y}$, here overbars are used to indicate the corresponding steady-state value. The steady-state heat flows from the hot to the cold thermal reservoirs are denoted as $\bar{J}_1$ and $\bar{J}_2$, respectively (Fig.1).

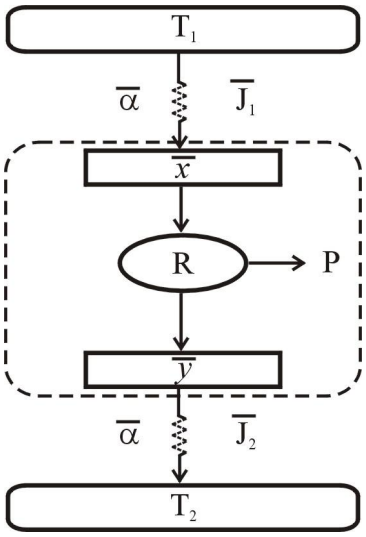

Fig. 1.Schematic representation of an irreversible heat engine. R is a measure of the departure of the endo-reversible regime

Applying the Clausius theorem and using the fact that the inner Carnot-like engine works in irreversible cycles, we get the following inequality,

$$\frac{\overline{J}_1}{\overline{x}} - \frac{\overline{J}_2}{\overline{y}} < 0, \tag{1}$$

this expression can be transformed into an equality by introducing a parameter R leading to,

$$\frac{\overline{J}_1}{\overline{x}} = R\frac{\overline{J}_2}{\overline{y}}, \tag{2}$$

The parameter R, which in principle is within the interval $0 \le R \le 1$ (R = 1 for the endo-reversible limit), can be seen as a measure of the departure from the endo-reversible regime [23-25]. If we assume that the heat flows from T_1 to $\overline{x}$ and from $\overline{y}$ to T_2 are of the Newton type, then

$$\overline{J}_1 = \alpha\left(T_1 - \overline{x}\right), \tag{3}$$

$$\overline{J}_2 = \alpha\left(\overline{y} - T_2\right), \tag{4}$$

where α is the thermal conductance. For simplicity of the calculations, we have assumed that the heat exchanges take place in conductors with the same thermal conductance α ; that is, the materials of both conductors are the same. The effect of the thermal conductances on the local stability of an endo-reversible heat engine was investigated by Guzmán-Vargas et al [11], in fact the power is a strong function of the conductances ratio [26]. The system's steady-state power output and the efficiency can be defined as,

$$\overline{P} = \overline{J}_1 - \overline{J}_2, \tag{5}$$

and

$$\overline{\eta} = \frac{\overline{P}}{\overline{J}_1} = 1 - \frac{\overline{J}_2}{\overline{J}_1} = 1 - \frac{1}{R}\frac{\overline{y}}{\overline{x}}. \tag{6}$$

By combining Eqs. (2), (3), (4) and (6), we can write $\overline{x}$ and $\overline{y}$ in terms of T_1, T_2, R and $\overline{\eta}$ as,

$$\overline{x} = \frac{T_1}{1+R}\left(1 + \frac{\tau}{1-\overline{\eta}}\right) \tag{7}$$

$$\overline{y} = \frac{R}{1+R}T_1\left(1 + \frac{\tau}{1-\overline{\eta}}\right)\left(1-\overline{\eta}\right) \tag{8}$$

where $\tau = T_2/T_1$. The De Vos thermo-ecomical analysis considers a profit function $\overline{F}$, which is maximized [13]. This profit function is given by the quotient of the power output ($\overline{P}$) and the total cost involved in the performance of the power plant ($\overline{C}_{tot}$), that is,

$$\overline{F} = \frac{\overline{P}}{\overline{C}_{tot}}. \tag{9}$$

In his early study, De Vos assumed that the running cost of the plant consists in two parts: a capital cost which is proportional to the investment and, therefore, to the size of the plant and, a fuel cost that is proportional to the fuel consumption and, therefore, to the heat input rate $\overline{J}_1$. Assuming that $\overline{J}_{\max}$ is an appropriate measure for the size of the plant, the running cost of the plant exploitation is defined as [13],

$$\overline{C}_{tot} = a\overline{J}_{\max} + b\overline{J}_1 = a\alpha T_1\left[(1-\tau)+\beta\left(1-\frac{\overline{x}}{T_1}\right)\right], \tag{10}$$

where the proportionality constants a and b have units of $\$/Joule$, $\beta = b/a$ and $\overline{J}_{\max} = \alpha(T_1 - T_2)$ is the maximum heat that can be extracted from the heat reservoir without supplying work (see Fig. 1). By using Eqs. (3), (6), (7), (9) and (10), the profit function can be written as,

$$a\overline{F}_{MP} = \frac{\overline{\eta}\left[\frac{1}{1+R}\left(R-\frac{\tau}{1-\overline{\eta}}\right)\right]}{(1-\tau)+\frac{\beta}{1+R}\left(R-\frac{\tau}{1-\overline{\eta}}\right)}. \tag{11}$$

If we calculate the derivative of $a\overline{F}$ with respect to $\overline{\eta}$, and we solving for the efficiency $\left(d\left(a\overline{F}_{MP}\right)/d\overline{\eta}\big|_{\overline{\eta}=\overline{\eta}^*} = 0\right)$we get [27],

$$\overline{\eta}^*(\beta,\tau,R) = 1-\sqrt{\frac{\tau}{R}}\,\frac{R(1-\tau)-\tau\beta}{(1-\tau)R\sqrt{1+\frac{\beta(R-\tau)}{(1-\tau)R}}-\sqrt{R\tau}\,\beta}. \tag{12}$$

We can observe in Eq. (12) that for $R=1$ the result obtained previously by De Vos [13] is recovered. Besides, when $\beta = 0$, we obtain $\overline{\eta}_{opt} = 1-\sqrt{\tau/R}$, which was previously obtained by Wu and Kiang [28], and by Arias-Hernández et al. [25]. Instead of expressing the result in terms of the parameter β, a number that is difficult to obtain in the literature [13], we can also express the efficiency in terms of the fractional fuel cost,which is defined as [13],

$$f = \frac{b\overline{J}_1}{a\overline{J}_{\max}+b\overline{J}_1} = \frac{\overline{J}_1\beta}{\overline{J}_{\max}+\beta\overline{J}_1}. \tag{13}$$

The fractional fuel costs (f) for various technologies were reported by De Vos for different energy sources; that is, for example; renewable energy $f = 0$, for Uranium $f = 0.25$, for Coal $f = 0.35$ and for natural gas $f = 0.5$ [13]. By using Eqs. (3), (7) and (13), we can write theparameter β in terms of the fractional fuel cost as follows [13],

$$\beta = \frac{f}{1-f}\,\frac{(1+R)(1-\tau)}{\left(R-\frac{\tau}{1-\overline{\eta}}\right)}. \tag{14}$$

Therefore, the efficiency that maximizes the profit function is given by [27],

$$\bar{\eta}_{MP}(f,\tau,R)=1-\frac{f}{2R}\tau-\frac{\sqrt{4(1-f)\tau R+f^2\tau^2}}{2R}, \tag{15}$$

and the power output is given by

$$\bar{P}=\alpha T_1\frac{\left[(f-2)\tau-\sqrt{4(1-f)\tau R+f^2\tau^2}\right]\left[f\tau-2R+\sqrt{4(1-f)\tau R+f^2\tau^2}\right]}{2(1+R)\left[-f\tau-\sqrt{4(1-f)\tau R+f^2\tau^2}\right]}. \tag{16}$$

Eqs. (15) and (16), represent the steady-state efficiency($\bar{\eta}$) and power output ($\bar{P}$)respectively. They are function of τ, f and R for a nonendo-reversibleNovikov-Curzon-Alhborn heatengine working at the maximum-power regime. It is straightforward to show that both $\bar{\eta}$ and $\bar{P}/\alpha T_1$ are decreasing functions of τ for every fixed value of R [1].Analogously to Eq. (9), for our thermo-economic optimization approach, we define two objective functions in terms of the so-called Efficient Power [18, 19,20] and the so-called Ecological Function [21, 22], both divided by the fractional fuel cost.The Maximum Efficient Power performance [18,19] for heat engines was studied for Yilmaz [18] and previously defined for Stucki [20] as the product of power output (P) by the efficiency (η) in the context of the first order irreversible thermodynamics (FOIT) in 1980.The ecological optimization criterion for the FTT-thermal cycles was proposed by Angulo-Brown [21]. This criterion considers the maximization of a function E which represents a compromise between high power output (P) and low entropy production Σ. The E function is given by $E=P-T_2\Sigma,$ where P is the power output of the cycle, Σ the total entropy production per cycle and T_2 is the temperature of the cold reservoir. One of the most important characteristics of a CA engine operating under maximum E conditions is that it produces around 80% of the maximum power and only 30% of the entropy produced in the maximum power regime [21, 22]. Another interesting property of the maximum-E regime is that the CA-engine's efficiency in this regime, is given by $\eta_E\approx(\eta_C+\eta_{CA})/2$, where η_C is the Carnot efficiency and η_{CA} the Curzon-Ahlborn efficiency [9].

For our thermo-economical approach, these objective functions are given by $\bar{F}_{EP}=\frac{\eta\bar{P}}{\bar{C}_{tot}}$ and $\bar{F}_E=\frac{\bar{P}-T_2\Sigma}{\bar{C}_{tot}}$ respectively. In the same way that Eq. (11) the profit function can be written as,

$$a\bar{F}_{EP}=\frac{(\bar{\eta})^2\left[\frac{1}{1+R}\left(R-\frac{\tau}{1-\bar{\eta}}\right)\right]}{(1-\tau)+\frac{\beta}{1+R}\left(R-\frac{\tau}{1-\bar{\eta}}\right)}. \tag{17}$$

and

$$a\bar{F}_E = \frac{\left(2\bar{\eta}+\tau-1\right)\left[\frac{1}{1+R}\left(R-\frac{\tau}{1-\bar{\eta}}\right)\right]}{(1-\tau)+\frac{\beta}{1+R}\left(R-\frac{\tau}{1-\bar{\eta}}\right)}. \tag{18}$$

In Eq. (18) we have applied the second law of thermodynamics to calculate the total entropy production given by $\Sigma = \frac{\bar{J}_2}{T_2} - \frac{\bar{J}_1}{T_1}$ (see Fig. 1). Analogously to Eq. (11), If we calculate the derivatives of $a\bar{F}_{EP}$ and $a\bar{F}_E$ with respect to $\bar{\eta}$, and we solve for the efficiency $\left(\left.\frac{d\left(a\bar{F}_{EP}\right)}{d\bar{\eta}}\right|_{\bar{\eta}=\bar{\eta}^*} = 0 \quad and \quad \left.\frac{d\left(a\bar{F}_E\right)}{d\bar{\eta}}\right|_{\bar{\eta}=\bar{\eta}^*} = 0\right)$ and using Eq. (14) we get,

$$\bar{\eta}_{EP}(f,\tau,R) = 1-\frac{(1+f)}{4R}\tau - \sqrt{\frac{(1-f)\tau}{2R}+\frac{(1+f)^2\tau^2}{16R^2}}. \tag{19}$$

$$\bar{\eta}_E(f,\tau,R) = 1-\frac{f}{2R}\tau - \sqrt{\frac{(1-f)(1+\tau)\tau}{2R}+\frac{f^2\tau^2}{4R^2}}. \tag{20}$$

Eqs. (19) and (20), represent the steady-state efficiencies working both under maximum- efficient power ($\bar{\eta}_{EP}$) and under maximum ecological function conditions ($\bar{\eta}_E$), respectively. In analogous way to Eq. (12) or Eq. (15), for the endo-reversible case $(R=1)$, from Eqs. (19) and (20), when $f=0, \quad (\beta=0)$, we obtain $\bar{\eta}=1-\tau/4-\sqrt{\tau(8+\tau)}/4$ and $\bar{\eta}=1-\sqrt{\tau(\tau+1)/2}$, respectively, which were previously obtained byGuzmán-Vargas et al. and Yilmaz [11, 18], and by Angulo-Brown [21], for the case of a Curzon-Ahlborn heat engine, working at maximum efficient power and maximum ecological function conditions respectively.

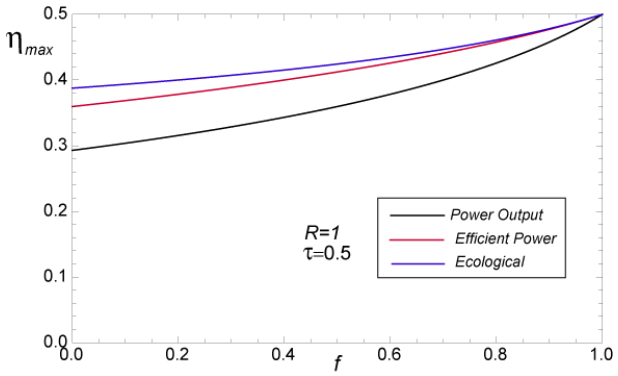

Figure 2. The steady-state efficiencies working under maximum power output ($\bar{\eta}_P$), maximum-efficient power ($\bar{\eta}_{EP}$) and maximum ecological function conditions ($\bar{\eta}_E$).

We can see in Fig. 2, how the optimal efficiencies smoothly increase from the maximum efficiency point, $f=0$, corresponding to energy sources where the investment is the preponderant costup to the Carnot value for $f=1$, that is, for energy sourceswhere the fuel is the predominant cost [13].

3. Linearization and stability analysis

In this section, we present a brief description of the linear stability analysis of a two-dimensional system[29]. Consider the dynamical system,

$$\frac{dx}{dt} = h(x, y)\,, \tag{17}$$

$$\frac{dy}{dt} = g(x, y)\,, \tag{18}$$

where h an g are functions of x and y. Let $(\bar{x}, \bar{y})$ be a fixed point such that $h\ (\bar{x}, \bar{y}) = 0$ and $g(\bar{x}, \bar{y}) = 0$. Consider a small perturbation around this fixed point and write $x = \bar{x} + \delta x$ and $y = \bar{y} + \delta y$, where $\delta x$and δy are small disturbances from the corresponding fixed point values. By substituting into equations (17) and (18), expanding $h\ (\bar{x} + \delta x\,, \bar{y} + \delta y)$ and $g(\bar{x} + \delta x\,, \bar{y} + \delta y)$ in a Taylor series, and using the fact that δx and δy are small to neglectquadratic terms, the following equations are obtained for theperturbations:

$$\begin{pmatrix} \dfrac{d\delta x}{dt} \\ \dfrac{d\delta y}{dt} \end{pmatrix} = \begin{pmatrix} h_x & h_y \\ g_x & g_y \end{pmatrix} \begin{pmatrix} \delta x \\ \delta y \end{pmatrix}, \tag{19}$$

where $h_x = \left.\dfrac{\partial h}{\partial x}\right|_{\bar{x},\bar{y}}$, $h_y = \left.\dfrac{\partial h}{\partial y}\right|_{\bar{x},\bar{y}}$, $g_x = \left.\dfrac{\partial g}{\partial x}\right|_{\bar{x},\bar{y}}$ and $g_y = \left.\dfrac{\partial g}{\partial y}\right|_{\bar{x},\bar{y}}$. Equation (19) is a linear system of differentialequations. Thus, we assume that the general solution of the system is of the form,

$$\delta \bar{r} = e^{\lambda t} \bar{u}\,, \tag{20}$$

with $\delta \vec{r} = (\delta x, \delta y)$ and $\vec{u} = (u_x, u_y)$. Substitution of the solution $\delta \vec{r}$ into equation (19) yields the following eigenvalueequation:

$$A\delta \bar{r} = \lambda \delta \bar{u}\,, \tag{21}$$

where A is the matrix given by the first term on the right-handside of equation (19). The eigenvalues of this equation are the roots of the characteristic equation,

$$|A - \lambda I| = (h_x - \lambda)(g_y - \lambda) - g_x h_y = 0\,. \tag{22}$$

If λ_1 and λ_2 are solutions of equation (22), the general solution of the system is

$$\delta \bar{r} = c_1 e^{\lambda_1 t} \bar{u}_1 + c_2 e^{\lambda_2 t} \bar{u}_2\,, \tag{23}$$

where c_1 and c_2 are arbitrary constants and $\vec{u}_1$ and $\vec{u}_2$ are the eigenvectors corresponding to λ_1 and λ_2, respectively. To determine $\vec{u}_1$ and $\vec{u}_2$ we use equation (21) again for eacheigenvalue.

Information about the stability of the system can be obtained from the eigenvalues λ_1 and λ_2.In general, λ_1 and λ_2 are complex numbers. If both λ_1 and λ_2 have negative real parts, the fixed point is stable. Moreover, if both eigenvalues are real and negative, the perturbations decay exponentially. In this last case, it is possible to identify relaxation times for each eigendirection as

$$t_1 = \frac{1}{|\lambda_1|}, \tag{24}$$

$$t_2 = \frac{1}{|\lambda_2|}, \tag{25}$$

4. Local stability analysis

Following Santillán et al [10], due to the reservoirs x and y are not real heat reservoirs but macroscopic objects (the working substance at the isothermal branches of the cycle) with heat capacity C. Their temperatures change according to the following differential equations:

$$\frac{dx}{dt} = \frac{1}{C}\left[\alpha\left(T_1 - x\right) - J_1\right], \tag{26}$$

$$\frac{dy}{dt} = \frac{1}{C}\left[J_2 - \alpha\left(y - T_2\right)\right], \tag{27}$$

where J_1 and J_2 are the heat flows from x to the working substance and from the Carnot engine to y, respectively. According to the non-endoreversibility hypothesis [23,24], J_1 and J_2 are given by

$$J_1 = \frac{Rx}{Rx - y} P \tag{28}$$

and,

$$J_2 = \frac{y}{Rx - y} P, \tag{29}$$

On the other hand, we can use Eqs. (6) and (15) to construct the expression which relates the internal variables x and y, to the external temperatures T_1 and T_2, in this case under maximum power conditions we get,

$$\tau = \frac{\bar{y}^2}{\bar{x}^2(1-f)R + \bar{x}\bar{y}f}, \tag{30}$$

In a similar way to Eq. (30), by using Eqs. (7) and (15), we can obtain an expression for T_1, given by,

$$T_1 = \frac{2(f-1)(1+R)\bar{x}}{2(f-1) + \dfrac{f\bar{y}^2}{\bar{x}(1-f) + R\bar{x}^2 + f\bar{x}\bar{y}} + \dfrac{2(1-f)R\bar{x}\bar{y} + f\bar{y}^2}{\bar{x}(1-f)R\bar{x} + f\bar{y}}}, \tag{31}$$

and the corresponding steady-state values of $\bar{x}$ and $\bar{y}$ as functions of T_1 and T_2 at maximum-profit function (in this case defined by Eq. (11)) are obtained by substituting Eq. (15) into Eqs. (7) and (8), respectively

$$\bar{x} = \frac{T_1}{1+R}\left(1 + \frac{2R\tau}{f\tau + \sqrt{4(1-f)\tau R + f^2\tau^2}}\right), \tag{32}$$

$$\bar{y} = \frac{RT_1}{2(1+R)}\left[(f+2R)\tau + \sqrt{4(1-f)\tau R + f^2\tau^2}\right] \tag{33}$$

We can observe from Eqs. (30) - (33) that for the case $f = 0$ and $R = 1$, the results previously obtained by Santillán et al. [10] and Guzmán-Vargas et al. [11] are recovered. Finally, by substituting Eqs. (30) and (31) into Eq. (16), the steady-state power output can be expressed by,

$$\bar{P}(\bar{x}, \bar{y}, f, R) = \alpha \frac{\left[\bar{x}\Lambda + \dfrac{(f-2)\bar{x}\bar{y}^2}{(1-f)R\bar{x} + f\bar{x}\bar{y}}\right]\left[\Lambda - 2R + \dfrac{f\bar{y}^2}{(1-f)R\bar{x} + f\bar{x}\bar{y}}\right]}{2\left[\Lambda + \dfrac{(f+2R)\bar{y}}{(1-f)R\bar{x} + f\bar{x}\bar{y}}\right]}, \tag{34}$$

where $\Lambda = \sqrt{\dfrac{\bar{y}^2\left[2(1-f)R\bar{x} + f\bar{y}\right]^2}{\bar{x}^2\left[(f-1)R\bar{x} - f\bar{y}\right]^2}}$. Using the assumption [10] that out of the steady state but not too far away, the power output of a Curzon-Ahlborn heat engine depends on x and y in the same way that it depends on $\bar{x}$ and $\bar{y}$ at the steady-state $\left(\bar{P}(\bar{x}, \bar{y}, f, R) \to P(x, y, f, R)\right)$, that is, this assumption is applicable only in the vicinity of the steady state, we can write the dynamical equations for x and y as follows:

$$\frac{dx}{dt} = \frac{1}{C}\left[\alpha(T_1 - x) - \frac{Rx}{Rx - y}P(x, y, f, R)\right], \tag{36}$$

$$\frac{dy}{dt} = \frac{1}{C}\left[\frac{y}{Rx - y}P(x, y, f, R) - \alpha(y - T_2)\right]. \tag{37}$$

To analyze the system stability near the steady state, we proceed following the steps described in the previous section, where

$$h(x, y, f, R) = \frac{1}{C}\left[\alpha(T_1 - x) - \frac{Rx}{Rx - y}P(x, y, f, R)\right], \tag{38}$$

$$g(x, y, f, R) = \frac{1}{C}\left[\frac{y}{Rx - y} P(x, y, f, R) - \alpha\left(y - T_2\right)\right], \tag{39}$$

After solving the correspondingeigenvalue equation, we findthat both eigenvalues (λ_1 and λ_2) are function of α , C , τ , f and R . The final expression and the algebraic details are not shown because they are quite lengthy and can be easily reproduced with the help of a symbolic algebra package. Moreover, our calculations show that both eigenvalues are real and negative. Thus, the steady state is stable because any perturbation would be decay exponentially. For the case $f = 0$, expressions for the eigenvalues previously obtained by Santillán et al. [10] and Guzmán-Vargas et al. [11] are recovered. In Figs. 3, 4 and 5, the relaxation times are plotted against τ for different values of fractional fuel cost *f*, for a fixed value of R ($R = 1$), that is, the endo-reversible case. We observe that t_1 (Eq. 24) is a decreasing function of τ . This relaxation time decreases as the fuel cost increases, indicating a faster decay as $f \to 1$.

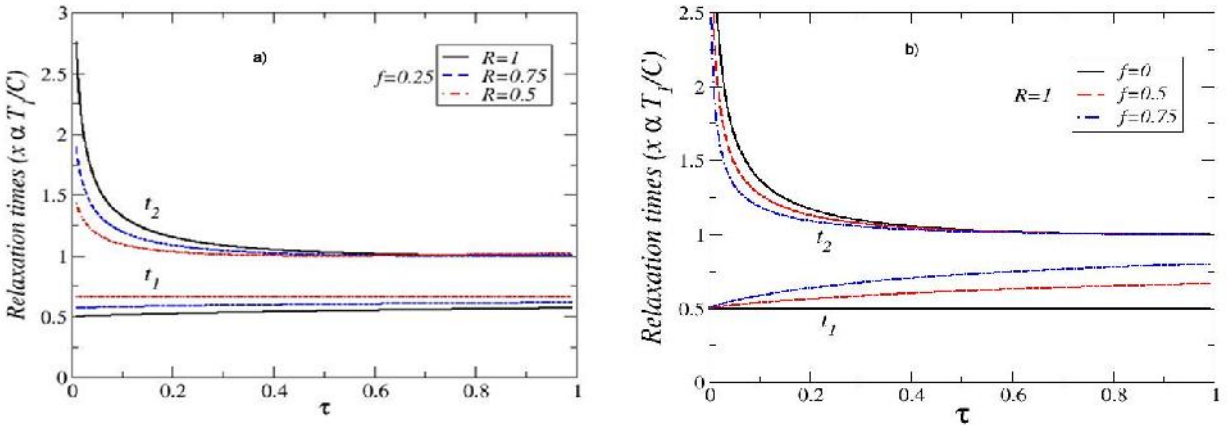

Figure 3. Plot of relaxation times under maximum power conditions $(t_1$ *and* $t_2)$ *versus* τ *for a) several values of the endorreversibility parameter and a value of the fractional fuel cost and b) for several values of the fractional fuel cost* f *in the endoreversible case (R = 1).*

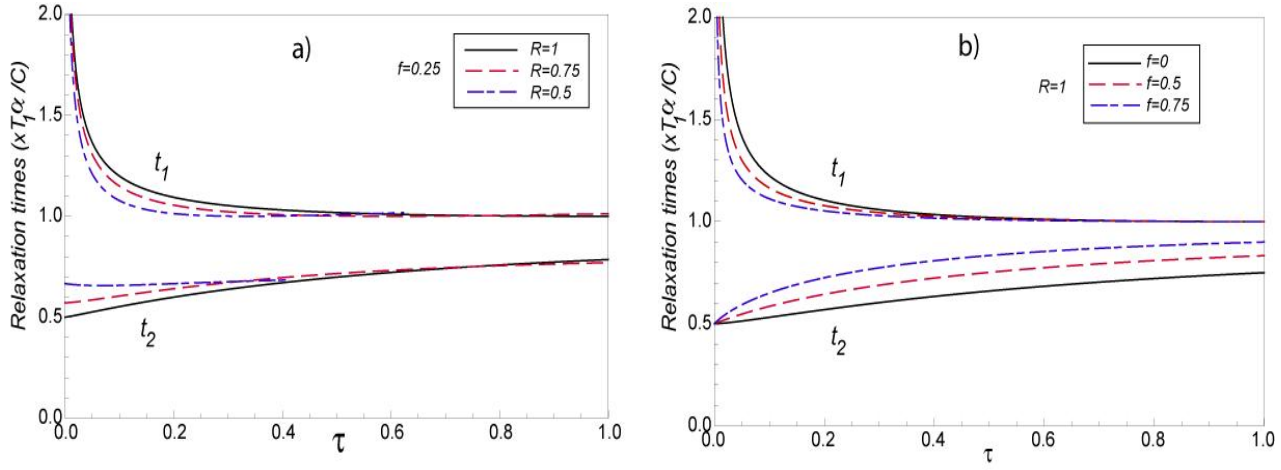

Figure 4. Plot of relaxation times under maximum efficient power $(t_1$ *and* $t_2)$ *versus* τ *for a) several values of the endo-reversibility parameter and a value of the fractional fuel cost and b) for several values of the fractional fuel cost* f *in the endo-reversible case (R = 1).*

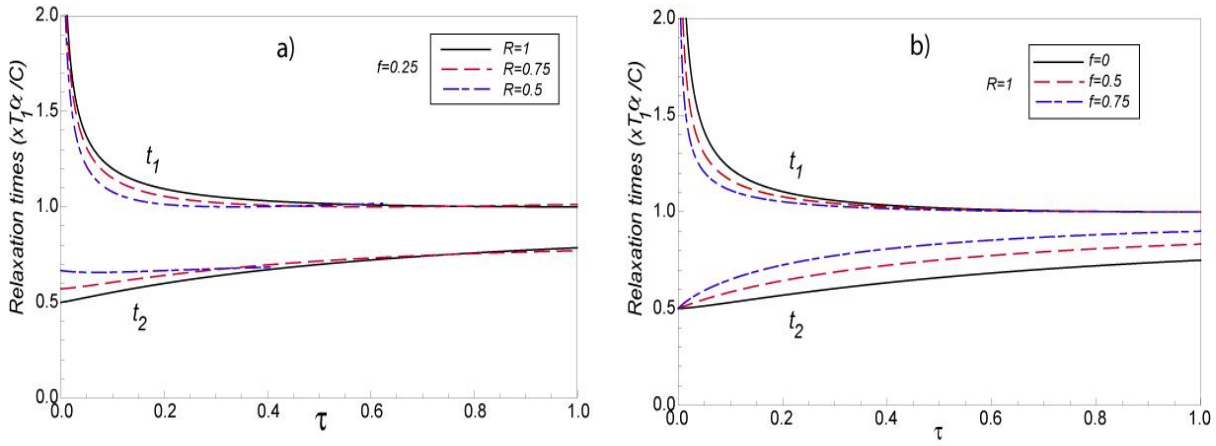

Figure 5. Plot of relaxation times under maximum ecological function conditions $(t_1$ *and* $t_2)$ *versus* τ *for a) several values of the endo-reversibility parameter and a value of the fractional fuel cost and b) for several values of the fractional fuel cost* f *in the endo-reversible case (R = 1).*

For t_2 (see Eq. 25), we observe that this relaxation time remains almost constant for $f = 0$. As the fractional fuel cost f increases, t_2 slowly increases too. We notice that in the limit $f \to 1$, both relaxation times tend to be closer each other, but there is a stronger inequality $t_2 < t_1$ in the interval $0 < \tau < 1$. In fig. 4 we also show the relaxation times as a function of τ, for several values of the parameter R, and for a fixed value of the fractional fuel cost *f*. We can see in Figs. 3 4 and 5, that t_1 is a decreasing function of τ and decreases as the parameter R decreases. We also observe that t_2 remains almost constant when the irreversibility parameter changes. From the findings of Figs. 3, 4 and 5, we can conclude that the system is stable for $\tau > 0$. We notice that as the fractional fuel cost f increases, t_1 decreases whereas t_2 increases, for a given value of R. In contrast, for a given value of f, as the irreversibility parameter R decreases, t_1 decreases whereas t_2 increases. We also remark that the power output and the efficiency depend on τ for the cases analyzed here, and both energetic quantities are decreasing functions of this parameter, that is, the system's stability moves in the opposite direction to that of the steady – state as P, η and τ varies.

Additionally, in Fig. 6, for the cases of maximum power output, maximum efficient power and maximum ecological function conditions, we show the relaxation times *versus* fuel fractional costfor several values of τ. We can see, in this case, how the fast (slow) relaxation time slightly increases (decreases) as f changes from 0 to 1.

Conclusions

In this work, we present a local stability analysis of a thermo-economic model of an irreversible heat engine working at different regimes of performance: The Maximum Efficient Power and the Ecological Function regimeand by considering a linear heat transfer law (the Newton law case). We show that the relaxation times are function of α, C, τ, f and R; that is, they depend on the materials that separate the working fluid form the reservoirs (through α); on the working fluid (through C); on the reservoirs temperatures (through τ); on fractional fuel costs (through f, which is associate to various energy sources from renewable energy until natural gas, see Table 1. reported by De Vos [13]) and on the internal irreversibilities (through R).

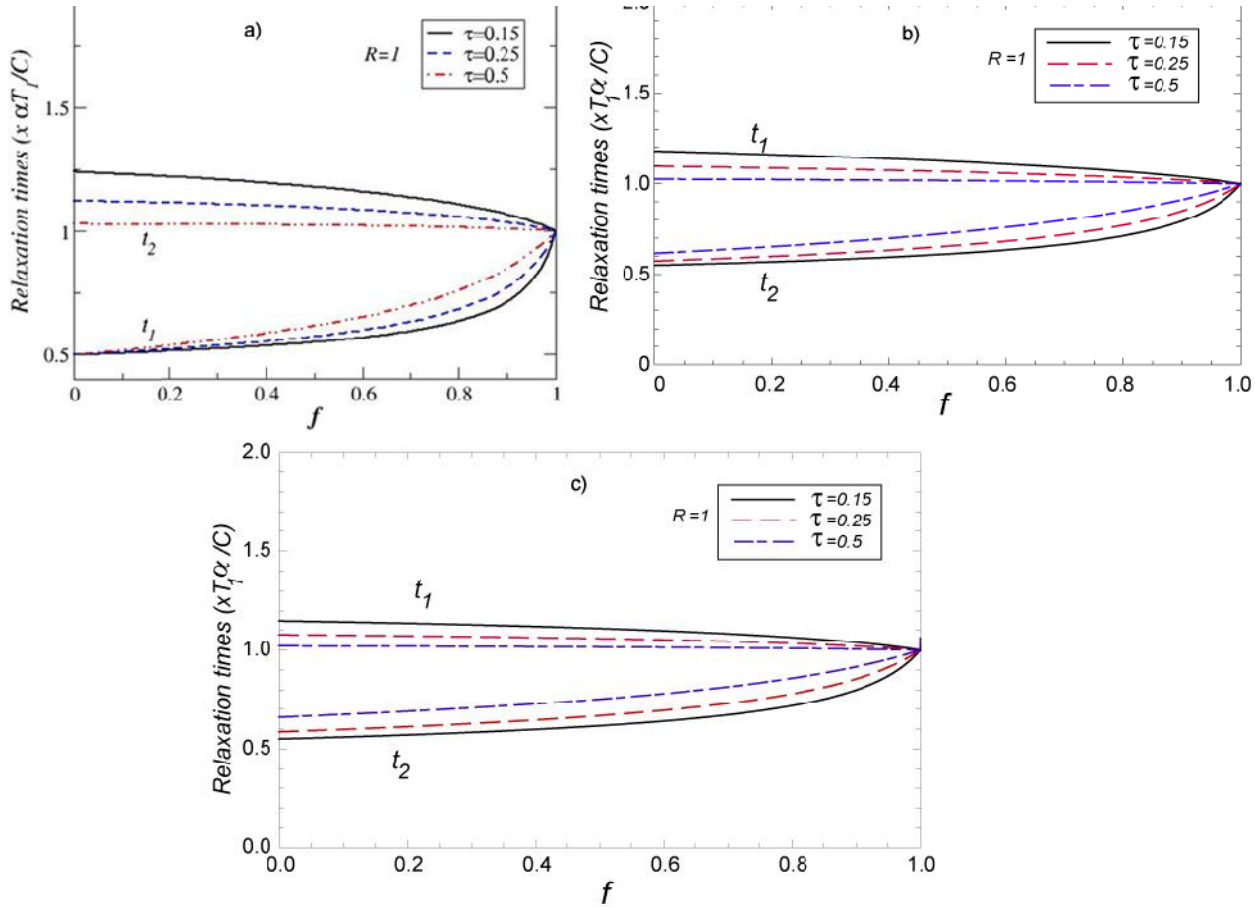

Figure 6. Relaxation times $(t_1$ *and* $t_2)$ *in the endo-reversible case (R = 1) versus* f *for several values of* τ *for a) Maximum Power output, b) Maximum Efficient Power conditions and c) Maximum Ecological Function.*

After a small perturbation the system decays exponentially to the steady state determined by two different relaxation times. We show that the relaxation time under maximum ecological function conditions is lesser than the relaxation times under both maximum power and maximum efficient power, that is, under maximum ecological conditions we have better stability conditions than for the other two regimes. Besides, we observe that the stability of the system improve as τ increases whereas the steady-state energetic properties of the engine declines for all cases of energy sources. Our cycle's model is an FTT version of a Carnot-type engine, but considering in addition the fractional fuel costs. In this sense, it has the same general idealized characteristics of any other model stemming from FTT. However such as it has been showed by Fisher and Hoffmann [6] and Curto-Riso et al. [30], this kind of models are useful to describe yet very elaborated dynamical models of heat engines of the Otto-type for example.

Acknowledgments

This work was supported in part by CONACYT, COFAA and EDI-IPN-México. The authors thank to Professor F. Angulo-Brown for all fruitful discussions.

Nomenclature

$\overline{F}$	Profit function (W/$)
$\overline{P}$	Steady-state power output ($)
$\overline{J_i}$	Steady-state heat flows ($i = 1,2$)
$\overline{C}_{tot}$	Total costs ($)

f Fractional fuel cost
R Parameter of the internal irreversibilities

C Heat capacity

Greek symbols

$\bar{\eta}$ Steady-state efficiency
β Economical parameter
τ Temperature ratio
α Thermal conductance
λ_i Relaxation times ($i = 1,2$)

References

[1] Barranco-Jiménez M. A., Páez-Hernández R. T., Reyes-Ramírez I., Guzmán-Vargas L., Local Stability Analysis of a Thermo-Economic Model of aChambadal-Novikov-Curzon-Ahlborn Heat Engine. Entropy 2011; 13:1584-94.

[2] Barranco-Jiménez M. A. et al. Local Stability Analys of thermoeconomic model of a Curzon-Ahlborn heat engine with a Dulong-Petit heat transfer law, Proceedings of ECOS2011, (2011), July 4-7, 410-418.

[3] Curzon F. and Ahlbom B.Efficiency of a Carnot engine at maximumpower output. Am. J. Phys. 1975;43:22-24.

[4] Chen L. and Sun F. Advances in Finite Time Thermodynamics: Analysis and Optimization, Nova Science Pub Inc, 2004.

[5] De Vos A, "Endoreversible Thermodynamics of Solar Energy Conversion", Oxford University Press. 1992.

[6] Fisher M. and Hoffmann K. H. Can a quantitative simulation of an Otto enginebe accurately rendered by a simple Novikov model with heat leak? J. Non-Equil. Thermodyn. 2004;29:9-28.

[7] Velasco S, Roco J. M. M. Medina A. White J. A. and Calvo-Hernández A. Optimization of heat engines including the saving of natural resources and thereduction of thermal pollution. J. Phys. D. 2000;33**:**355-359.

[8] Sieniutycs S. and Salamon P. (ed). Finite Time Thermodynamics and Themoeconomics (London: Taylor and Francis) 1990.

[9] Sen A. K. and Zheng J. and Huang Z. Dynamics of cycle-to-cycle variations in a natural gas direct-injection spark-ignition engine. Appl. Energy. 2011;8:2324-2334., Curto-Risso P. L. and Medina A. and Calvo-Hernández A. and Guzmán-Vargas L. and Angulo-Brown F. "On cycle-to-cycle heat release variations in a simulated spark ignition engine. Appl. Energy. 2010;88:1557-1567.

[10] Santillán M. and Maya-Aranda G. and Angulo-Brown. Local stability analysis of an endoreversible Curzon–Ahlborn–Novikov engine working in a maximum-power like regime. J. Phys. D. 2001;34:2068-.

[11] Guzmán-Vargas L. and I. Réyes-Ramírez and Sánchez-Salas N. The effect of heat transfer laws and thermal conductances on the local stability of an endoreversible heat engine. J. Phys. D. 2005;38:1282-1291.

[12] Páez-Hernández R. T. and Angulo-Brown F. and Santillán M. Dynamic Robustness and ThermodynamicOptimization in a Non-EndoreversibleCurzon–Ahlborn EngineJ. Non-Equilib. Thermodyn. 2006;36:173-178.

[13] A. De Vos. Endoreversiblethermoeconomics. Energy. Convers. Magnagement. 1995;36:(1)1-5.

[14] I. I. Novikov, the efficiency of atomic power stations (a review). AtomimayaEnergiya, **3**(1957); 409: in English translation; I. Nuclear Energy, **7** (1958) 125.

[15] P. Chambadal. Les Centrales Nucleaires. Paris: Armand Colin, 1957:4158.

[16] B. Sahin and A. Kodal, Energy. Convers. Manage. “Performance analysis of an endo-reversible heat engine based on a new thermo-economic optimization criterion. 2001; 42:1085-1093.
[17] Wu, C., Chen, L., Chen, J., eds., Recent Advances in Finite-Time Thermodynamics, Nova Science, New York, 1999.
[18] Yilmaz T; A new performance criterion for heat engine: efficient power. J. Energy Inst. 2006; 79(1):38-41.
[19] Arias-Hernández L. A; BarrancoJiménez M. A; Angulo-Brown F; Comparative analysis of two ecological types modes of performance for a simple energy converters. J. Energy Inst. 2009; 82(4):223-227.
[20] J. W. Stucki: Eur. J. Biochem., The optimal efficiency and the economic degrees of coupling of oxidative phosphorylation, 1980, 109, 269–283.
[21] Angulo-Brown F; An ecological optimization criterion for finite-time heat engines. J. Appl. Phys. 1991; 69:7465-7469.
[22] Arias-Hernández L. A; Angulo-Brown F; A general property on endoreversible thermal engines. J. Appl. Phys. 1997; 81:2973-2979.
[23] J. Chen. The maximum power output and maximum efficiency of an irreversible Carnot heat engine.*J. Phys. D: Appl. Phys.* 1994;*27*:1144–1149.
[24] Ozcaynak, S.; Goktan, S.; Yavuz, H. Finite-time thermodynamics analysis of a radiative heat enginewith internal irreversibility. *J. Phys. D: Appl. Phys.* 1994;*27*:1139–1143.
[25] L. A. Arias-Hernández, G. Ares de Parga and F. Angulo-Brown, On Some Nonendoreversible Engine Models with Nonlinear Heat Transfer Laws. Open Sys. & Information Dyn. 2003; 10:351-375.
[26] G.Grazzini, Work from Irreversible HeatEngines. Energy, 1991; Vol.16, n.4, 747-755.
[27] Barranco-Jiménez M. A. Finite-time thermodynamics optimization of a non endoreversible heat engine. Rev. Mex. Fis. (2009) 55 (3), 211-220.
[28] C. Wu and R.L. Kiang, “Finite-time thermodynamic analysis of a Carnot engine with internal irreversibility”. Energy, **1** (12) (1992) 1173-1178.
[29] S. H. Strogatz, Nonlinear Dynamics and Chaos with Applications to Physics, Biology, Chemistry and Engineering, Addison-Wesley Publishing Company, 1994.
[30] P. L. Curto-Risso, A. Medina and A. Calvo-Henández, “Theoretical and Simulated models for an irreversible Otto cycle”, J. Appl. Phys. 2008, 104, doi: 10.1063/1.2986214.

MULTICRITERIA OPTIMIZATION OF A DISTRIBUTED ENERGY SUPPLY SYSTEM FOR AN INDUSTRIAL AREA

D. Buoro[a], M. Casisi[b], A. De Nardi[c], P. Pinamonti[d], M. Reini[e]

[a] Dept. of Electrical, Management and Mechanical Engineering, University of Udine, Italy, dario.buoro@uniud.it
[b] Dept. of Electrical, Management and Mechanical Engineering, University of Udine, Italy, melchiorre.casisi@uniud.it
[c] Dept. of Engineering and Architecture, University of Trieste, Italy, ing.alberto.denardi@gmail.com
[d] Dept. of Electrical, Management and Mechanical Engineering, University of Udine, Italy, piero.pinamonti@uniud.it
[e] Dept. of Engineering and Architecture, University of Trieste, Italy, reini@units.it

Abstract:

In the paper a multi-objective optimization model for distributed energy supply systems optimization is presented. The superstructure of the system comprehends a distri1ct heating network that connects the users to each other, small scale CHP systems (e.g. micro gas turbines or internal combustion engine), conventional integration boilers, large centralized solar plant and a seasonal thermal storage. The optimization has to determine the optimal structure of the system, the size and the load of each component inside the optimal solution, as well as the optimal operation strategy. The multi-objective optimization is based on a Mixed Integer Linear Programming model (MILP) and it takes into account as objective function a linear combination of the total annual cost (for owning, maintaining and operating the whole system) and the CO_2 emissions amount, associated to the system operation. The model allows to obtain different optimal solutions by varying the relative weight of the economic and the environmental objectives. In this way the Pareto Front is identified and the possible improvements in both economic and environmental terms can be highlighted. The model has been applied as an example to a specific case study made of nine industrial facilities and it has been optimized for different superstructure configurations and for two different values of the electricity greenhouse emissions factor. The obtained results shows that the solar plant, coupled with the seasonal thermal storage, allows reaching both environmental and economic goals. If the centralized solar plant is not considered in the superstructure, CO_2 emissions related to electricity affect the optimal structure of the energy supply system.

Keywords:

Multicriteria optimization, District heating, Mixed Integer Linear Programming, Solar thermal plant, CHP

1 Introduction

Distributed energy systems have already been recognized as an efficient and reliable alternative to the traditional energy supply [1]. It must be said also that nowadays a purely economic analysis is not anymore sufficient due to growing environmental concerns like global warming and depletion of fossil fuel reserves. Therefore, the operation problems become more challenging when the environmental burdens should be minimized at the same time when costs, too, are to be minimized [2]. The reason is because the minimization of costs and pollutant emissions are normally contradictory objectives, as it is often expensive to utilize environmentally friendly technologies.

The multi-objective optimization can help to solve this problem combining the supply energy cost together with the environmental impact. These goals have to be both minimized. Multi-objective optimization tackles the issue of conflicting objective functions, finding a set of solutions by varying the impact of the single objective functions in the global optimum. For such solutions, called Pareto optimal solutions or non-dominated solutions, no improvement is possible without sacrificing the other objective functions [3]. Reviews on multi-criteria analysis and examples of multi-objective optimizations of distributed energy supply systems can be found in [4-9].

The paper proposes an optimization model that helps to determine the optimal configuration and operation of a distributed energy supply system. The developed model has been applied as an example to the energy supply system serving nine industrial facilities. They may be connected to each other through a district heating network of fixed size and layout. Heating and electric demands are known in advance and they can be satisfied by small-scale CHP systems (ICE or μTG), properly located at or near the end-users. Conventional integration boilers can also be installed inside the factories or in the centralized plant and each user is free to purchase and sell electricity from/to the national grid.

The paper also introduces the integration between conventional power sources and renewable energies, designing a solar district heating plant coupled with a long term thermal energy storage. This alternative is increasing in importance, as it is a valid solution to overcome the mismatch problem between the availability of the solar source and the energy user demands, especially for domestic applications[10-12]. As all users can be connected together through the DHN, the heat produced by the solar thermal plant and by the production units may be exchanged to one another or sent to the thermal storage.

The model used to solve the optimization problem is based on a Mixed Integer Linear Programming (MILP). In previous works of the authors, MILP models were developed to optimize the design and operation of distributed CHP systems in a tertiary sector scenario, considering different technologies and taking into account the effects of various economic support policies [13-16]. A similar model was applied to an industrial area considering also the thermal inertia of the network in [17].

The two objective functions of the model to be minimized consider the total operating CO_2 emissions and the total annual cost for owning, maintaining and operating the whole distributed system. The optimization is subject to the constraints that express component operation characteristics, energy balances of nodes and district heating network behavior. The optimization specifies the size, the kind and the location of cogeneration equipment and integration boilers, the size of the solar thermal plant and of the heat storage, as well as the optimal operation of each component included in the optimal solution.

In the specific application, the Pareto frontiers associated to four different system configurations and for two different values of the electricity carbon intensity, were evaluated. The results of the optimizations were used to identify the best trade-off solutions.

2 Optimization model

The proposed model aims at providing decision support to planners for selecting the configuration system and the operating levels of various generation units throughout the planning period.

Recently a lot of research has been carried out to optimize the design and operation of distributed energy supply systems [3, 18-20] integrated also with the district heating network [21-23]. The mathematical problem of optimizing the operation of an energy system composed of CHP units, solar thermal modules and DHN has to be generally regarded as a variational calculus problem, because the optimization variables expressing partial load operation of each CHP engine are time dependent. However, a realistic description of the system may be represented by an MILP formulation by properly discretizing the load curves (in each time interval the thermal and the electrical demands are assumed to be constant) and approximating performance maps with a set of linear functions [24, 25]. The thermal losses along pipelines have been approximated as a fixed fraction of the thermal energy transferred in each time interval. All other relations that describe the system (energy balances, load limits, cost of energy vectors) are intrinsically linear and they do not need to be approximated. A detailed description of the model and the approximation introduced with the linearization of the performance curves can be seen in [26].

The optimization of an energy supply system begins with the definition of the superstructure. The superstructure must include all components that can be potentially part of the optimal solution, so

that generally it depends on the specific application case. After the optimization process, the superstructure will be reduced to the optimal configuration.

Figure 1 shows the system superstructure. The distributed energy supply system has to supply the thermal and electrical energy required by a set of users. The electric energy can be produced by the CHP systems installed in each production unit or purchased from the electric grid. The thermal energy can be produced by the CHP systems, by conventional boilers or by a large centralized solar plant. All users can be connected to each other and to the solar field by a district heating network. Additionally, the superstructure includes also a hot water storage. Many large scale solar district heating systems have been built already in central and northern Europe, mainly in Sweden, Denmark, The Netherlands, Germany and Austria [27]. They consist of ground mounted collector fields integrated into a DHN for supplying heat to residential and industrial areas. The sizes of those plants allow lower specific investments compared to small applications. When the system is coupled with a heat water storage it is possible to reach solar fractions of approximately 50% [28].

In the superstructure, a typical user *k* can be equipped with a cogeneration unit and a boiler. The central production unit includes a boiler and a solar field. The district heating network connects the users to one another and to the heat storage. The model is completely general and it can be applied to different applications with a similar superstructure, by changing the values that describe the components only. An MILP model has been used for properly describing the choice of centralized/decentralized components inside the system superstructure by means of binary variables, as well as the on/off operation of chosen components in the optimal operation strategy.

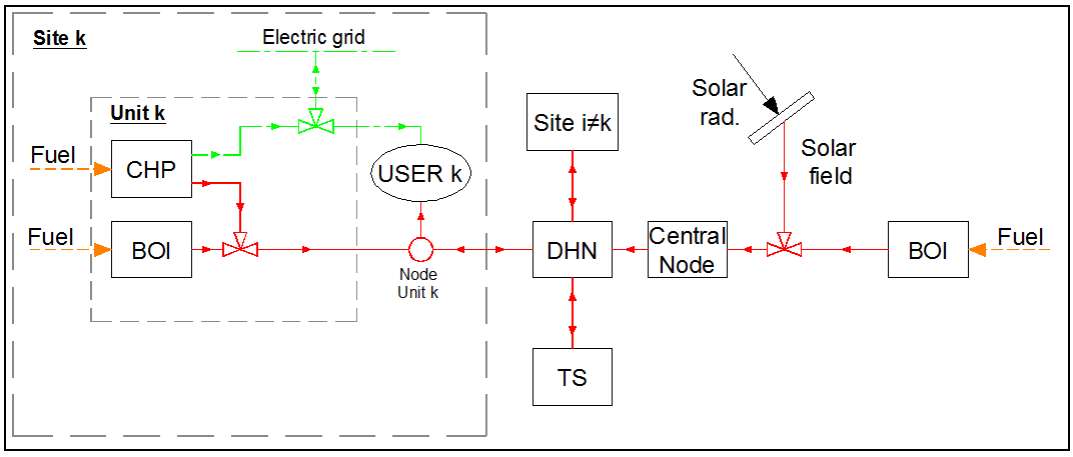

Figure 1: Superstructure of the energy supply system described by the optimization model.

2.1 Decision variables

The degrees of freedom that characterize the model are the decision variables, both binary and continuous. The optimization procedure finds the set of decision variables that allows the minimization of the objective function. The identified decision variables are:

- Existence and size of each component;
- Operation status and load level of each component in each time interval;
- Electricity to be exchanged with the electricity network;
- Thermal flows inside the district heating network;
- Size of the thermal energy storage;
- Level of the thermal energy stored in the storage.

Binary variables represent existence and operation status of components, while all other variables are continuous. The decision variables can be set in advance to describe cases when only a subset of the components included in the superstructure can be adopted. For example in the conventional

solution the district heating network has to be excluded by setting to zero the decision variable related to its existence.

2.2 Objective functions

The MILP model considers two different objective functions, which quantify the total annual cost and the environmental impact, both to be minimized. The environmental impact objective function attempts to capture the increasing awareness of environmental pollution resulting from energy generation.

The objectives have been kept separated inside the model. It allows to find and to rank the best integrated solutions from the superstructure, which are both economical convenient and less polluting. The solutions returned by the optimization are used to identify the Pareto Front. The Pareto Front solutions cannot be made less polluting without being more costly, or cheaper without emitting more.

2.2.1 Economic objective function

The economic objective function C_{tot} considers the energy supply system in terms of the total annual cost for owning, operating and maintaining the whole system. The objective function is linear with respect to all decision variables and consists of:

$$C_{tot} = C_{inv} + C_{ope} \tag{1}$$

The sum of the investment costs of all components (*Inv*) multiplied by the related capital recovery factor *rf* gives the annual investment cost C_{inv}. Capital recovery factor takes into account the interest rate *i* and the life span *n* of each components *j* contained in the superstructure.

$$C_{inv} = \sum_{j} rf(j) \cdot Inv(j) \tag{2}$$

$$rf(j) = \frac{i \cdot (1+i)^{n(j)}}{(1+i)^{n(j)} - 1} \tag{3}$$

The whole year has been subdivided in a set of discrete time intervals *t*. The annual operating and maintaining cost C_{ope} associated to the energy supply system is expressed by:

$$C_{ope} = \sum_{t} \left(c_{gas} \cdot F_g(t) + c_{ep} \cdot E_p(t) - c_{es} \cdot E_s(t)\right) + \sum_{j,t} C_{man}(j,t) \tag{4}$$

The maintenance cost $C_{man}(j,t)$ of the j^{th} component in the t^{th} time interval is assumed to be proportional to the energy produced.

2.2.2 Environmental objective function

The environmental impact objective function *CE* totalizes the CO_2 emissions of the electricity taken from the grid and of the consumed fuel, subtracted by the avoided CO_2 emissions related to the sold electricity:

$$CE = CE_G + CE_{Ep} - CE_{Es} \tag{5}$$

The CO_2 emissions from consumed fuels are calculated by multiplying the total amount of fuel consumption with the carbon intensity of the fuel:

$$CE_G = \sum_{t} F_g(t) \cdot CI_G \tag{6}$$

The CO_2 emissions due to the usage of electricity from the grid are calculated by multiplying the total amount of purchased power by the carbon intensity of grid electricity CI_E:

$$CE_{Ep} = \sum_t E_p(t) \cdot CI_E \quad (7)$$

While the avoided CO_2 emissions related to the sold electricity are obtained by multiplying the total amount of the sold electricity by the carbon intensity of grid electricity:

$$CE_{Es} = \sum_t E_s(t) \cdot CI_E \quad (8)$$

The carbon intensity CI_E is the amount of CO_2 emissions per unit of electricity generated within the specific utility grid. It can be measured in kg/kWh and depends on the electricity mix of the electricity network.

2.3 Model Constraints

In the MILP optimization model, three main different categories of constraints can be identified:

- Components constraints: relate output and input energy of each component;
- Energy balances: ensure that the amount of input energy is equal to the output, for each time interval and for each node;
- Network constraints: describe thermal losses and the maximum thermal energy transfer from units to users.

2.3.1 Component constraints

This kind of constraints have been introduced for each component. Equality constraints represent the relation between fuels, products and sub-products, while inequality constraints describe the load and size ranges. The thermal production of the solar thermal plant is related to the size of the plant. The energy production per surface unit has been supposed to be known in advance, for each time interval. This means that position and tilt angle are fixed in advance. A long term thermal storage is considered a component too, and the equality constraints relate the thermal level of the storage to the input/output flow, taking into account the thermal losses. The stored energy depends on the temperature of the medium multiplied by the volume contained in the storage, so that volume and temperature cannot be both decision variables because each relation inside the model has to be linear. The volume has been chosen as a decision variable, while the temperature is considered constant. This choice corresponds to the hypothesis of a perfect stratification of the fluid inside the heat storage, so that if the storage is not completely empty, the residual energy is stored at the same temperature required by the DHN.

2.3.2 Energy balances

These constraints are equality constraints and represent the thermal and electric energy balances, in each time interval. Taking the thermal balance as an example, for each production unit the heat produced by the cogeneration unit and by the boiler has to be equal to the heat consumed by the local user and sent to other users through the DHN.

2.3.3 Network constraints

These constraints describe the DHN and limit the thermal flows in each pipeline based on its size. Moreover they represent the thermal energy balance of the network taking into account the thermal losses along each pipeline.

2.4 Multicriteria optimization method

Steps towards the design of sustainable energy systems must include tools for simultaneously considering the broad range of criteria linked to the thermodynamic, economic and environmental performance assessment of a system. The increasing needs for more efficient systems, that are attractive both from the economical and environmental point of view, request the development of

new criteria and determine new design rules. In fact, up until recently, the main criterion to choose the best plant was the economic one. Introducing a new decision criterion that considers the impact of the system in the environment, it is obvious that the design of such a system is associated with conflicting objectives [4,5], as it is often expensive to utilize environmentally friendly technologies.

Cogeneration systems are usually studied from an economic, energetic or environmental point of view, but not optimized. In the case of multiple objectives, there does not necessarily exist a solution that is the best with respect to all targets because of differentiation between objectives. A solution may be the best in one objective but worse in another. For this reason the same problem has a lot of optimal solutions that can be intended as a compromise between the objectives. For such solutions, forming the Pareto frontier, there is not any other solution that reduces one objective without increasing another. The Pareto frontier represents a set of alternatives among them the decision maker can choose the best solution suited to its needs.

There are a lot of methods for solving multi-objective optimization problems, such as compromise programming, global criterion method, and goal programming [29]. In this study, the compromise programming method has been employed to solve this problem through the implementation in the commercial optimization software X-press® [30].

In order to apply compromise programming, the optimization model has been modified including only one objective function. In this method the aim is to minimize the distance of the criterion values from their utopia point. Considering this, the objective function of the problem is formulated as follows:

$$F_{obj} = \alpha \cdot C_{tot} + \beta \cdot CE \tag{9}$$

Where C_{tot} and CE are the economic and environmental objective function, respectively.

The optimization of this problem for different values of α and β gives the Pareto optimal solutions and the Pareto frontier can be obtained. For each combination of α and β only one optimal solution exists and it is a weighted combination of economic and environmental benefits.

In order to reduce the number of iterations (infinite combinations of α and β), a different formulation of the problem can be expressed as:

$$\mathbf{Min}\ F_{obj} = \varepsilon \cdot C_{tot} + (1-\varepsilon) \cdot CE \tag{10}$$

For $\forall \varepsilon = \varepsilon_1 1, \varepsilon_1 2, \ldots \mid 0 \le \varepsilon \le 1$

ε represents the slope of the Pareto front tangent. For $\varepsilon = 1$ the solution that minimizes C_{tot} can be obtained, while the solution that minimizes CE can be obtained for $\varepsilon = 0.$ Intermediate values of ε give other intermediate solutions appertaining to the Pareto front.

Usually, the single objective functions that constitute the overall objective function of the multicriteria optimization problem assume values that can have different orders of magnitude. In this situation the resulting optimization would be led by the objective function with the greatest order of magnitude, because the objective function with the lowest one would not affect the value of the objective function F_{obj}. In order to avoid this a scale coefficient has to be multiplied by the objective functions C_{tot} and CE so that they have the same order of magnitude.

3 The case study

The nine users considered in the study belong to different economic sectors, like plastic, food, furniture, engineering and tertiary. Despite the heterogeneity of the goods produced, their energy consumptions show quite regular trends along the year. The electrical and heating demands have been evaluated by means of energy audits. Figure 2a represents a plan view of the whole industrial area. The blue line represents the layout of the main DHN that is 5 km long and provides the heat required by the users. The locations of the nine users are marked by red spots, while the yellow spot indicates the space available for positioning the central unit, the solar field and the heat storage.

Figure 2b shows the annual electric and heating load duration curves of the nine users. Electric load is higher than zero all year round. This is because a certain amount of electricity is always required, even when factories are closed. Heating load is higher than zero for about 7,000 hours, higher than 2 MW for almost 6,000 hours and higher than 4 MW for almost 3,000 hours.

Figure 3a shows the aggregated electric and heating demand of the nine users in a typical winter and summer week. The profile is quite predictable, with peaks during intensive working hours, low consumption during nights and a very low demand in the weekend, when the most of the factories are closed. The two trends are very similar; the difference is a higher consumption in summer because of the electricity required to power the air conditioning systems of the factories.

Figure 3b shows the aggregated heating demand of the nine users in a typical winter and summer week. It can be noted that heating load is slightly higher during coldest months, when space heating is operating. The Saturday heat consumption is very small, while in Sunday neither process heat nor space heating is required.

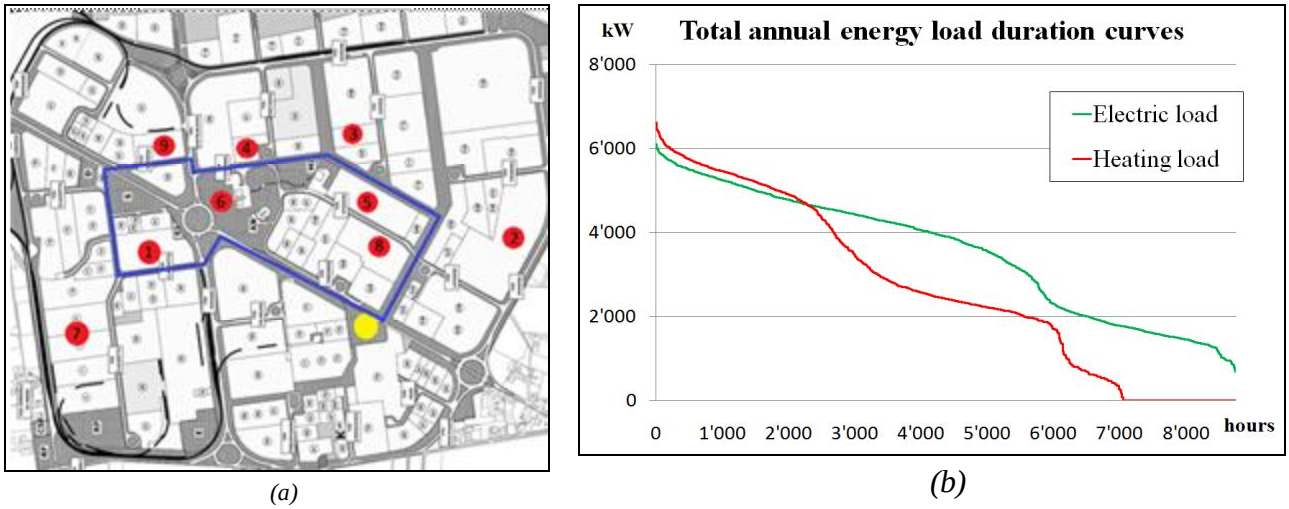

(a) *(b)*

Figure 2a: Plan view of the industrial disctrict. Figure 2b: Total annual energy load duration curves.

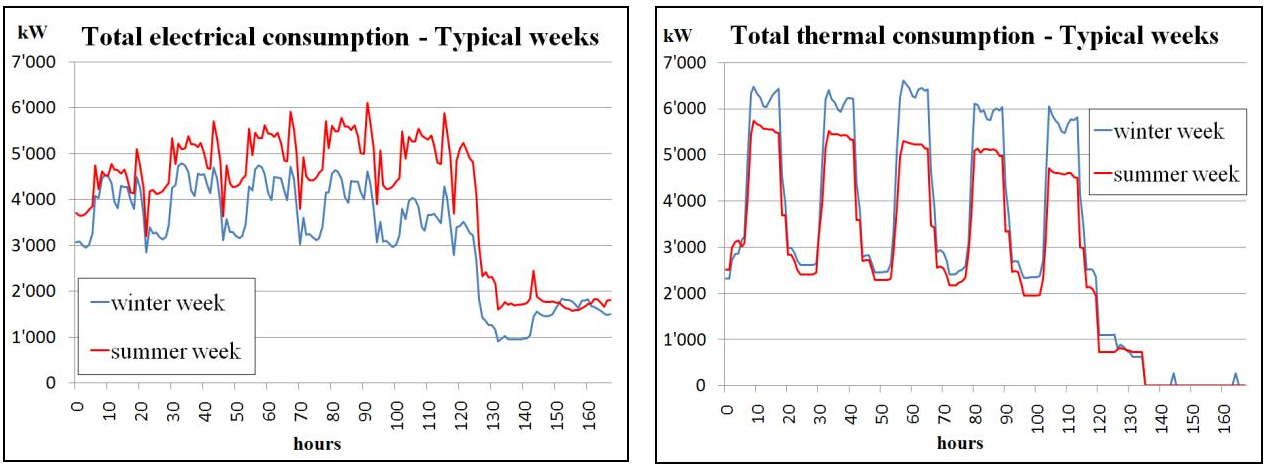

(a) *(b)*

Figure 3: Total electric and thermal demand profile in a typical winter and summer week.

Table 1: Users' energy consumptions.

USER	ELECTRIC		HEATING	
	Peak power [kW_{el}]	Year demand [MWh]	Peak power [kW_{th}]	Year demand [MWh]
1	945	4,381	518	394
2	1,181	5,152	-	-
3	801	1,607	686	1,008
4	652	1,710	996	1,700
5	742	3,039	516	790
6	14	62	136	115
7	690	2,699	2,976	4,426
8	2,540	7,352	3,720	14,946
9	1,283	4,837	81	58
Total	6,112	30,838	6,619	23,436

Table 1 shows the peak power and the yearly energy consumption of each user for both electric and heating demands. Total peak power is the actual maximum hourly energy demand of the all users and it is clearly lower than the sum of the single user peaks because they do not appear simultaneously.

In order to reduce the variables number and the model complexity, the whole year is represented by twelve typical weeks (1 week per month), each composed of seven days of 24 hours, for a total of 2,016 time intervals. This kind of discretization allows keeping a realistic picture of the actual annual behaviour of the whole system and also allows the solar district heating plant and the thermal storage producing their effects on the optimal operation.

Table 2 was produced considering the energy requirements and the energy load profiles of each user. For each component it shows: the life span, the possible location and the minimum and maximum sizes and costs [31]. Machine prices are considered linear with the size. It can be observed that units 3 through 9 have the same structure: a CHP system (ICE or µGT) and a boiler, both of variable sizes. Moreover, in unit 1 only a 500 kW GT can be installed, while unit 2 includes only a ICE of variable size.

Table 2: Components costs and sizes

COMPONENT	SIZE [kW]	COST [k€]	UNIT	LIFE SPAN [year]
ICE	300-4,000	350-3,000	2, 7, 8	10
GT	500	500	1	10
µGT	30-300	70-160	3, 4, 5, 6, 9	10
BOILER	100-2,500	8-50	3, 4, 5, 6, 7, 8, 9, Central	10

Table 3 shows the energy prices and the solar plant costs used in the application, with reference to a current Italian market scenario. A life span of 20 years is considered for the solar thermal panel and 40 years for both the DHN and the seasonal storage. The unitary heat storage cost generally depends on its kind and size and can vary between 120 and 180 €/m^3[11, 32, 33]. An intermediate cost of 150 €/m^3 has been assumed in this case study in order to maintain the problem linear. An interest rate equal to 6% has been adopted for the calculation of all capital recovery factors.

Table 3. Energy and solar thermal plant prices

	PRICE
Electricity purchased	0.15 €/kWh
Electricity sold	0.12 €/kWh
Natural Gas	0.05 €/kWh
District Heating Network	4,500 k€
Heat storage	150 €/m^3
Solar thermal panel	200 €/m^2

In this application case the CO_2 emissions are associated with the carbon intensity of both natural gas and electricity because they are the only input fuels at the system boundary. While the natural gas has similar carbon intensity all around the world, the electricity carbon intensity strictly depends on the electricity mix of the network at which the system is connected. The optimizations has been conducted for a value 0.202 kg/kWh related to the emissions of burning natural gas [34, 35]. The greenhouse emissions of the electricity have been assumed equal to 0,504 and 0,356 kg/kWh. The first value is representative of the average electricity greenhouse emissions of the world in the years 2007-2009 and it is similar to the greenhouse emissions of the USA in 2009. The second value refers to the average CO_2 emissions in Europe in the years 2007-2009 and it is similar to the emissions of Italy in 2009 [36].

4 Results and discussion

The model defined for the specific case study has been optimized considering different superstructures and different values of the electricity carbon intensity. The optimization MILP model includes 160,000 decision variables and 240,000 constraints and can be solved in about two hours with a processor Intel Core Due T9400 @2,52 GHz, 4GB RAM, with the stopping criteria based on the GAP, that is the percentage difference between the current value of the objective function and the current value of the objective function of the relaxed problem. The GAP assumed in the calculation is equal to 0.05%.

In the specific, the Pareto frontiers have been obtained for the following four superstructures and for two different values of the electricity carbon intensity:

- Isolated Solution (IS): the users are not connected with the DHN, therefore heat has to be produced locally while the electricity can also be bought from the grid;
- Distributed Cogeneration Solution (DCS): the users can be connected to each other through the district heating network;
- Distributed Cogeneration Solution integrated with the Thermal Storage (DCS + TS): a thermal storage is added to the suprestructure of the Distributed Cogeneration Solution;
- Distributed Renewable Solution (DRS): the superstructure includes also a large solar thermal plant.

Figure 4a and 4b report the Pareto frontiers obtained by varying the weight of the two objective functions and for two different values of the electricity carbon intensity. The purely environmental and purely economic optima can been obtained by setting to 0 and 1 respectively the value of $\mathcal{E}$ in eq.10. Therefore, these optima correspond to the two extremities of each points series.

Comparing Figure 4a with Figure 4b a sensible reduction of the annual CO_2 emissions can be noted when the electricity carbon intensity is lowered. As the variation of the carbon intensity operate only in the environmental objective function, the purely economic optima in the two figures are the same, for each superstructure.

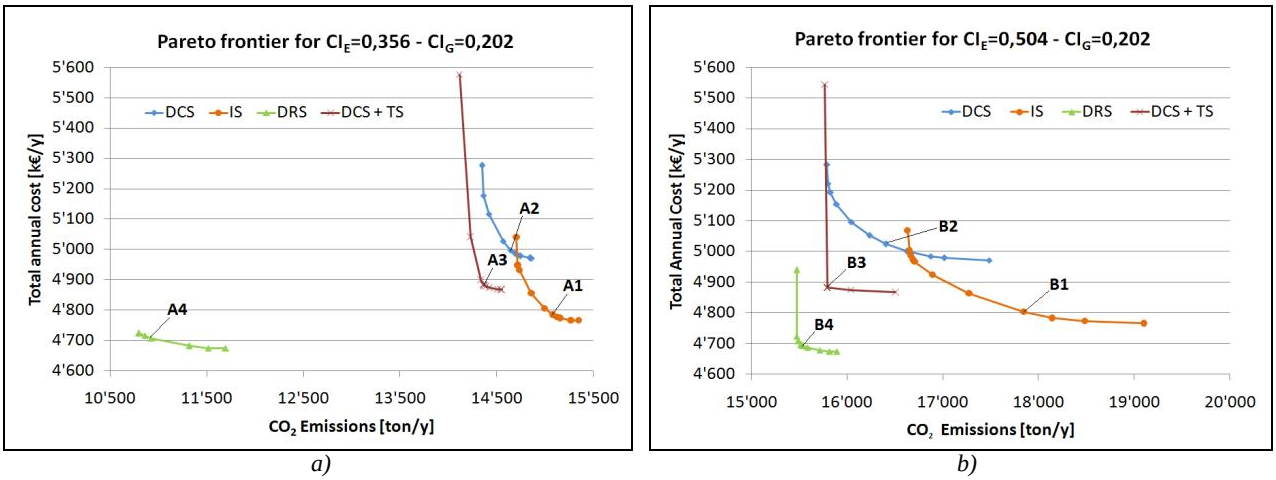

a) *b)*

Figure 4: Pareto Frontier for different plant configurations

If the solar plant (DRS) is not taken into account, the best economic performance can be achieved with the Isolated Solution (IS), while including the DHN in the system (DCS), total annual costs increase allowing an improvement of the environmental benefits. The Pareto frontiers obtained optimizing the solution including also the thermal storage (DCS + TS) dominate the DCS Pareto frontiers, therefore the adoption of a thermal storage together with the District Heating Network allows achieving better results in term of both economic and environmental benefits.

Figure 5 shows the values of the main energy parameters for each optimization performed. Each diagram refers to a specific Pareto frontiers, obtained by varying the coefficient Ɛ from 0 to 1.

The IS optimal results shows that the thermal energy produced by the CHP increases moving from the economic optimum (Ɛ=1) towards the environmental optimum (Ɛ=0), while the thermal energy produced by boilers decreases. When the district heating network is included in the superstructure (DCS), the thermal energy produced by CHP is greater, while the one produced by boilers is lower. This effect is more evident approaching the purely environmental optima, up to reach a complete absence of boilers. This trend is still more pronounced if the thermal storage is included in the superstructure (DCS + TS). In fact the thermal energy produced by CHP is greater than the other cases and quite constant, while the contributions of the boilers are negligible for a wide range of $\mathcal{E}$ values.

Generally, by comparing the optimal solutions obtained for the electricity carbon intensity equal to 0.356 (figures on the left) with the ones obtained for a value of 0.504 (figures on the right), it can be pointed out that the former are characterized by a higher usage of boilers and a lower usage of cogeneration units in the environmental optima. This trend is due to the fact that the electric production by means of cogeneration units is more environmental convenient when CI_E is higher. An additional set of optimizations performed for a lower value of electricity greenhouse emissions (CI_E=0.25) showed that such a low value of emissions brings to the adoption of boilers instead of cogeneration units in the environmental optima, according to the results presented by Carvalho et al. [3]. This can be easily understood thinking at an extreme situation where the electric energy available from the grid were produced without CO_2 emissions, for example from nuclear or solar sources. In this case the usage of natural gas cogeneration units would certainly imply an increase of global CO_2 emissions.

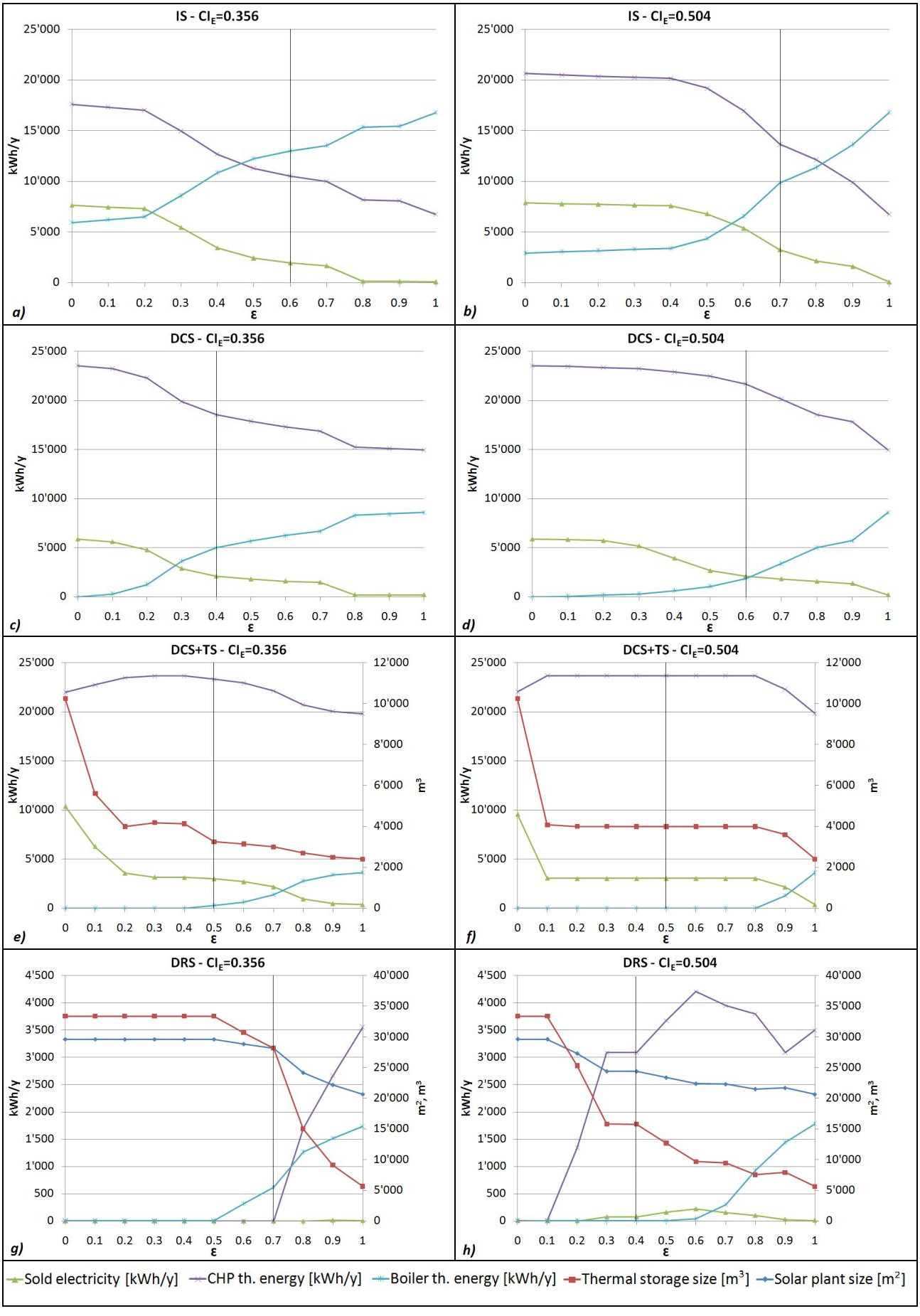

Figure 5: Results of electricity, thermal energies, plant and thermal storage size varying the weight of the objective functions

Table 4: Optimal solutions resulting from the analysis of the Pareto Front

	IS		DCS		DCS + TS		DRS	
	CI_E=0.356	CI_E=0.504	CI_E=0.356	CI_E=0.504	CI_E=0.356	CI_E=0.504	CI_E=0.356	CI_E=0.504
Points in Figure 5:	A1	B1	A2	B2	A3	B3	A4	B4
Cogeneration units power [kWel]	1,703	2,318	3,139	4,090	3,083	3,160	0	779
Cogeneration units number	2	3	4	7	4	4	0	2
Boilers power [kWth]	7,872	4,973	3,241	2,065	677	0	2,322	1,462
Boilers number	8	8	1	1	1	0	1	1
DH network	No	No	Yes	Yes	Yes	Yes	Yes	Yes
Solar field [m2]	-	-	-	-	-	-	28,153	24,407
Thermal Storage [m3]	-	-	-	-	3,242	3,994	28,147	15,786
CHP fuel cost [k€/y]	1,100	1,438	1,938	2,284	2,438	2,477	0	323
Boiler fuel cost [k€/y]	613	465	235	87	14	0	29	0
Bought electricity cost [k€/y]	2,787	2,621	1,935	1,637	1,522	1,486	3,701	3,374
Sold electricity income [k€/y]	154	260	167	169	238	241	0	6
Maintenance cost [k€/y]	223	279	375	427	465	472	1	62
Amortization charge [k€/y]	208	262	680	759	680	688	977	944
Total investment cost [k€/y]	1,460	1,837	6,907	7,457	6,976	7,050	11,528	10,766
Total annual cost Ctot [k€/y]	4,777	4,804	4,997	5,024	4,880	4,882	4,707	4,697
CS annual cost [k€/y]	4,864							
PBP	5	6	13	12	11	11	10	10
CO2 emission of the CS [ton/y]	15,757	20,435	15,757	20,435	15,757	20,435	15,757	20,435
Saved CO2 em. wrt CS [ton/y]	630	2,591	1,110	4,032	1,382	4,643	4,833	4,920

Better results can be achieved in terms of both economic and environmental benefits if the solar plant is included in the superstructure (DRS, Figure 4) and the total convenience of these integrated systems is more pronounced for low values of CI_E. This is because the recourse to renewable energy sources is more effective with respect to the usage of natural gas cogeneration, if the cogenerated electric energy implies a lower CO_2 emission reduction. Focusing on the main energy parameters obtained varying the $\mathcal{E}$ coefficient (Figure 5) the DRS trends are significantly different from the others. In particular, approaching the environmental optima the usage of CHP decreases, thanks to the important contribution of the solar plant. For $\mathcal{E}$=0 boilers and cogeneration units are not included in the optimal configurations and all thermal energy required by the users is produced by the solar plant. These results can be attained also thanks to the adoption of a large seasonal thermal storage. In the economic optima, the thermal energy produced by the solar plant covers about 60% of the thermal demand.

An analysis of Pareto front (Figure 4) and the related energy parameters (Figure 5) can lead to the identification of the most attractive economic/environmental compromise solutions for each plant configuration, that are indicated in Figure 4 with A1÷A4, B1÷B4. The relating main data concerning the configurations, the economic and the environmental performance are reported in Table 4.

Figure 6 summarizes the optimal operation results of the identified trade-off points, in terms of electric energy and thermal energy amounts (Figure 6a and b, respectively). Generally, a little amount of electricity is sold to the grid if the solar plant is not considered. When it is included in the configuration the CHP are less convenient and consequently no electricity is sold to the grid.

Focusing on Figure 6b it can be noted that for solutions 3 and 4, the thermal energy produced is greater than the thermal energy required by the users because of the thermal losses through the storage wall.

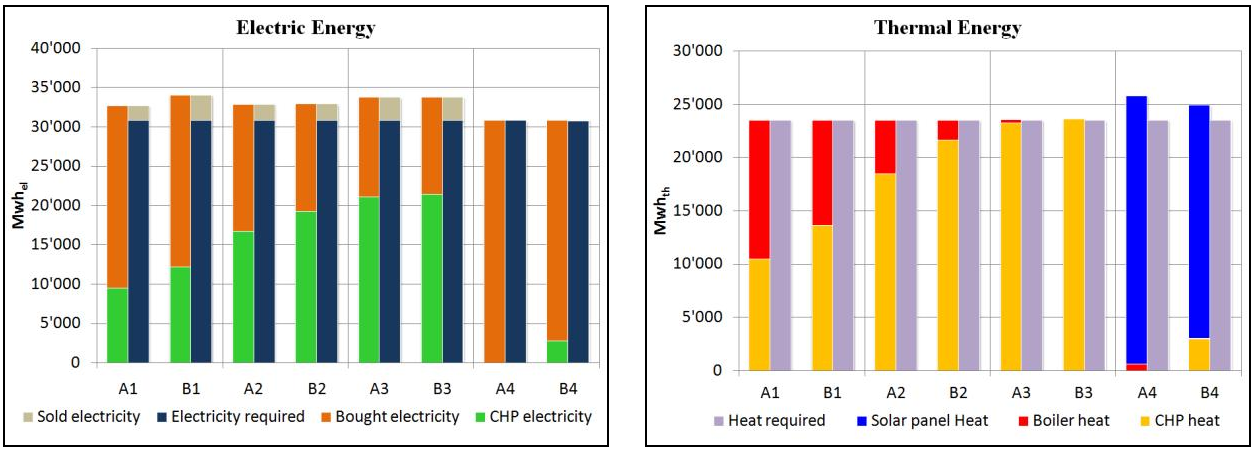

(a) *(b)*

Figure 6: Optimal operation results at the various trade-off points

5 Conclusions

In this paper, a MILP multi-objective model has been developed for identifying the operational synthesis and operation of a distributed energy system, in order to meet the energy demands of a set of users while considering both economic and environmental objectives. The two objective functions of the model to be minimized consider the total annual cost for owning, maintaining and operating the whole distributed system and the total operating CO_2 emissions. The solution allows identifying the location, size and optimal operation of boilers and CHP, as well as the optimal size of the solar plant and of the seasonal thermal storage.

The model has been applied as an example to a specific case study made of nine industrial facilities. It has been optimized for four different configurations, beginning with a distributed cogeneration systems made up of CHP and boilers only, up to the more integrated configuration which includes the district heating network, the thermal storage and the solar field.

Without considering the solar field, the best economic performances can be achieved with the optimal mix of boilers and cogeneration units, without adopting neither the district heating network nor the thermal storage. The adoption of these components made the total annual cost increase, but allows a reduction of the operating CO_2 emissions. It is worth noting that the adoption of a thermal storage together with the District Heating Network allows achieving better results in term of both economic and environmental benefits, with respect to the district heating network alone. In the considered hypotheses, the optimal integrated solution which includes the solar field, turns out to be the most convenient and the most environmentally friendly, at the same time.

A comparison between optimal solutions obtained for two different values of the electricity greenhouse emission factor shows that lower value of this coefficient brings to a lower usage of cogeneration units and a higher usage of boilers. In addition, the lower the electricity carbon intensity is, the lower the environmental benefit of natural gas cogeneration is, so that the recourse to renewable energy sources (e.g. solar fields) becomes the most effective strategy for the emission reduction. The cogeneration could be still attractive if renewable sources had used as primary energy.

Nomenclature

BOI	Boiler
CE	Total Annual CO2 Emission, ton/y
CE_G	Annual Natural Gas CO_2 Emissions, ton/y
CE_{Ep}	Purchased Electricity CO_2 Emissions, ton/y
c_{ep}	Purchase Price of Electricity, €/kWh
CE_{Es}	Sale Electricity CO_2 Emissions, ton/y
c_{es}	Sale Price of electricity, €/kWh
c_{gas}	Purchase Price of Natural Gas, €/kWh
CHP	Combined Heat and Power
CI_E	Electricity Carbon Intensity, t/kWh

CI_G	Natural Gas Carbon Intensity, t/kWh	i	Interest Rate
C_{inv}	Annual Investment Cost, €/y	*ICE*	Internal Combustion Engine
C_{man}	Maintenance Cost, €	*Inv*	Investment Cost, €
C_{ope}	Annual Operating Cost , €/y	*MILP*	Mixed Integer Linear Programming
CS	Conventional Solution	n	Life Span
C_{tot}	Total Annual Cost, €/y	*rf*	Capital recovery factot, y-1
DCS	Distributed Cogeneration Solution	*STOR*	Thermal Storage
DHN	District Heating Network	t	Time Interval, h
DRS	Distributed Renewable Energy Solution	j	Component
E_p	Purchased Electricity, kWh		
E_s	Sold electricity, kWh	α, β	Coefficients
F_g	Natural Gas Consumption, kWh	$\mathcal{E}$	Slope of Pareto Front
F_{obj}	Objective Function	μGT	Micro Gas Turbine
GT	Gas Turbine		

References

[1] Alanne K., Saari A., Distributed energy generation and sustainable development. Renewable and Sustainable Energy Reviews, 2006; 10(6):539–58.

[2] Ren H., Zhou W., Nakagami K., Gao W., Wu Q., Multi-objective optimization for the operation of distributed energy systems considering economic and environmental aspects. Applied Energy 2010; 87(12):3642–51.

[3] Carvalho M., Lozano M.A., Serra L., Multicriteria synthesis of trigeneration systems considering economic and environmental aspects, Applied Energy 2012; 91(1):245-54.

[4] Pohekar SD., Ramachandran M., Application of multi-criteria decision making to sustainable energy planning – a review. Renewable and Sustainable Energy Reviews 2004; 8:365–81.

[5] Wang JJ., Jing YY., Zhang CF., Zhao JH., Review on multi-criteria decision analysis aid in sustainable energy decision making. Renewable and Sustainable Energy Reviews 2009; 13: 2263–78.

[6] Alarcón A., Ault G., Galloway S., Multi-objective planning of distributed energy resources a review of the state-of-the-art. Renewable and Sustainable Energy Reviews. 2010; 14: 1353–66.

[7] Lazzaretto A., Toffolo A., Energy, economy and environment as objectives in multi-criterion optimization of thermal systems design. Energy 2004; 29(2004):1139–57.

[8] Tsay MT., Applying the multi-objective approach for operation strategy of cogeneration systems under environmental constraints. International Journal of Electrical Power & Energy Systems, 2003; 25:219–26.

[9] Kavvadias KC., Maroulis ZB., Multi-objective optimization of a trigeneration plant. Energy Policy, 2010; 38:945–54.

[10] Faninger G., Combined solar-biomass district heating in Austria. Solar Energy, 2000; 69(6): 425–35.

[11] Schmidt T., Mangold D., Muller-Steinhagen H. Central solar heating plants with seasonal storage in Germany. Solar Energy, 2004; 76(1-3): 165–74.

[12] Chung M., Park J., and Yoon H., Simulation of a central solar heating system with seasonal storage in Korea". Solar Energy, 1998; 64(4-6): 163–78.

[13] Buoro D., Casisi M., Pinamonti P., Reini M.,. Optimal lay-out and operation of district heating and cooling distributed trigeneration systems. (GT2010-23416). Proceedings of AMSE TurboExpo 2010, June 14-18; Glasgow, UK.

[14] Casisi M., Castelli L., Pinamonti P., Reini M., Effect of different economic support policies on the optimal definition and operation of a CHP and RES distributed generation system. (GT2008-50353). Proceedings of ASME TurboExpo 2008, June 9-13; Berlin, Germany.

[15] Casisi M., Pinamonti P., Reini M.,. Optimal lay-out and operation of CHP distributed energy systems. Energy, 2009; 34(12): 2175–83.

[16] Casisi M., Reini M.,. Energy production through distributed urban cogeneration systems: preliminary definition of lay-out, units size and operation. Proceedings of ASME/ATI 2006, May 14-17; Milan, Italy.

[17] Buoro D., Covassin C., De Nardi A., Pinamonti P., Reini M.,. Optimization of a distributed trigeneration system with heating micro-grids for an industrial area. Proceedings of 2nd European Conference on Polygeneration 2011, March 30-April 1. Tarragona, Spain.

[18] Chicco G., Mancarella P.,. "Matrix modelling of smallscale trigeneration systems and application to operational optimization". Energy 2009; 34(3): 261–73.

[19] Kayo G., Ryozo O.,. Application multiobjective genetic algorithm for optimal design method of distributed energy system. Proceedings of 11th International IBPSA Conference 2009, July 27-30. Glasgow, Scotland.

[20] Lozano M., Carvalho M., Serra L.,. Operational strategies and marginal costs in a symple trigeneration systems". Energy, 2009; 34(11): 2001–08.

[21] Weber C., Shah N., Optimisation based design of a district energy system for an eco-town in the united kingdom. Energy, 2011; 36: 1292–08.

[22] Tveit T., Savola T., Gebremedhin A., Fogelholm C., Multi-period MINLP model for optimising operation and structural changes to chp plants in district heating networks with long-term thermal storage". Energy Conversion and Management, 2009; 50:. 639–47.

[23] Molyneaux A., Leyland G., Favrat D., Environomic multi-objective optimisation of a district heating network considering centralized and decentralized heat pumps. Energy, 2010; 35: 751-58.

[24] Gerogiorgis DI., Pistikopoulos EN., Modeling and optimization of polygeneration energy systems", Catalysis Today, 2007; 127: 347-59.

[25] Yokoyama R., Ito K., Operational strategy of a cogeneration system under a complex utility rate structure. Journal of energy resources technology, 1996; 118(4): 256–62.

[26] Buoro D., Casisi M., Pinamonti P., Reini M., Optimization of distributed trigeneration system integrated with district heating and cooling micro-grids. Distributed generation and alternative energy journal, 2011; 26(2): 7–33.

[27] Dolenback JO., European large scale solar heating network. In Institutionen for Installationsteknik, Chalmers Tekniska Hogskola, Goteborg, Sweden.

[28] Bauer D., Marx R., Nussbicker-Lux J., Ochs F., Hedemann W., Muller-Steinhagen,. German central solar heating plants with seasonal heat storage. Solar Energy2010, 84, pp. 612–23.

[29] Collette Y, Siarry P., Multiobjective optimization. Springer, 2004, Berlin.

[30] Fico Xpress Optimization Suite, 2011. X-press Mosel – Reference Manual - Release 3.2, March. http://www.fico.com/.

[31] Chinese D., Optimal size and layout planning for district heating and cooling networks with distributed generation options. Int. Journal of Energy Sector Management, 2008, 2(3):385-419.

[32] Pauschinger T., Solar district heating with seasonal thermal energy storage in germany. Solar District Heating guidelines 2011, p. Fact Sheet 30.5.

[33] Verda V., Colella F., Primary energy savings through thermal storage in district heating networks. Energy, 2011;, 36: 4278–86.

[34] Eurostat, 2009, "Environment, transport and energy indicators", ISSN-1725-4566; Eurostat Pocketbooks, http://epp.eurostat.ec.europa.eu/

[35] IPCC, 2006, “Revised 1996 IPCC Guidelines for National Greenhouse Gas Inventories – Reference manual”, Bruxelles, International Energy Agency.

[36] IPCC, 2011, “Guidelines for National Greenhouse Gas Inventories – CO_2 emissions from fuel combustion”, Bruxelles, International Energy Agency.

On the Effect of Eco-indicator Selection on the Conclusions Obtained from an Exergoenvironmental Analysis

Tatiana Morosuk[a], George Tsatsaronis[b] and Christopher Koroneos[c]

[a] *Technische Universität Berlin, Germany, morozyuk@iet.tu-berlin.de*
[b] *Technische Universität Berlin, Germany, tsatsaronis@iet.tu-berlin.de*
[c] *Aristotle University of Thessaloniki, Greece, koroneos@aix.meng.auth.gr*

Abstract:
An exergoenvironmental analysis is conducted at the component level of a system and identifies (a) the relative importance of each component with respect to environmental impact, and (b) options for reducing the environmental impact associated with the overall system. In an exergoenvironmental analysis, a one-dimensional characterization indicator is obtained using a Life Cycle Assessment (LCA). An index (a single number) describes the overall environmental impact associated with system components and exergy carriers. It should be emphasized that the evaluation of environmental impacts will always be subjective to some degree and associated with some uncertainties. Exergoenvironmental analysis identifies the magnitude, location and causes of thermodynamic inefficiencies and environmental impacts. The information supplied by such exergy-based methods is very useful in understanding the operation of energy conversion systems and in developing strategies for improving them.

The paper presents the exergoenvironmental analysis applied to a gas-turbine cogeneration system (the CGAM problem that is used here as an example), and discusses the effect of the Eco-indicator used in an exergoenvironmental analysis on the conclusions obtained from the analysis. Five indicators are used here to conduct the LCA: Eco-indicator 95, Eco-indicator 99, Cumulative Exergy Consumption, a method developed at the Center Environmental Studies of the University of Leiden (The Netherlands), and ECO-factor 2006.

Keywords:
Exergy analysis, LCA, Eco-indicator, Exergoenvironmental Analysis.

1. Introduction

The detailed evaluation of an energy conversion system from the ecological point of view is a relative new area in engineering. The thermodynamic evaluation is part of the ecological evaluation: By increasing the thermodynamic efficiency, the fuel consumption is decreased and this affects positively the improvement of the energy system from the ecological and thermodynamic points of view. In general, the relationship between thermodynamic variables and ecological variables is complex and, and if we want to successfully reduce thermodynamic inefficiencies and environmental impacts, we must understand their formation process, i.e. we need a deep understanding of

- the real thermodynamic inefficiencies and the processes that cause them,
- the environmental impact associated with equipment and thermodynamic inefficiencies as well as the connection between these two sources of environmental impact,
- the interconnections among efficiency and component-related environmental impact associated with the selection of specific system components, and
- possible measures that would improve the efficiency and would reduce the environmental impact of the system being studied.

A thermodynamic analysis should be conducted in terms of exergy. The exergy destruction caused by the irreversibilities within the system being considered is the most important thermodynamic inefficiency and is identifiable with the aid of an exergetic analysis.

There are many publications where the exergetic analysis and the ecological (environmental) analysis are applied to energy-conversion and chemical systems. The most interesting conclusions can be obtained if the exergetic analysis and the environmental assessment are discussed simultaneously. Different approaches have been developed to combine these analyses, for example, cumulative exergy consumption [1], exergoecological analysis [2], extended exergy accounting [3], environomic analysis [4]. A recently developed exergoenvironmental analysis has been introduced in [5] and already applied to different energy-conversion systems [5-10].

An exergoenvironmental analysis consists of an exergetic analysis, a Life Cycle Assessment (LCA) of the environmental impact and an exergoenvironmental evaluation [5].

Life cycle assessment is a method used to evaluate the inputs and outputs of systems and to organize and convert those inputs and outputs into environmental impacts relative to resource use, human health and ecological areas [12]. The quantification of inputs and outputs of a system is called Life Cycle Inventory (LCI). At this stage, all emissions are reported on a volume or mass basis. Life Cycle Impact Assessment (LCIA) converts these flows into simpler indicators. The Eco-indicator of a material or process is a number that indicates the environmental impact of a material or process, based on data from a life cycle assessment. The higher the indicator, the greater the environmental impact.

During the last 15 years many LCIA methods have developed, for example, Eco-indicator 95 [13], Eco-indicator 99 [14], EDIP 97 [15], EDIP 2003 [16], EPS 2000d [17], Impact (2002)+ [18], JEPIX [19], LIME [20], CML [21], ECO-Factors 2006 [22], etc.

However, only few of them are applicable to an energy conversion system (because of the availability of data that can be used for this purpose), but almost all these methods have already been applied to estimate environmental impacts of land, processes in agriculture, transport, buildings, etc. In the previous publications related to an exergoenvironmental analysis only the Eco-indicator 99 has been used, for example in [5-8]. In recently published papers also the Eco-indicator 95 and the Cumulative Exergy Consumption method are used for the exergoenvironmental evaluation of a simple refrigeration machine [9] and an open-cycle gas-turbine system [11].

Since different approaches (from environmental impact point of view) are used to develop LCIA methods, it is interesting to analyze the effect of selection of the indicator to the results and conclusions obtained from the exergoenvironmental analysis.

2. Exergoenvironmental analysis

The *exergoenvironmental costing principle* which is used in an exergoenvironmental analysis, states that exergy is the only rational basis for assigning environmental impact to energy streams and to the thermodynamic inefficiencies within a system [5].

An exergoenvironmental analysis is conducted at the component level of a system and identifies (a) the relative importance of each component with respect to environmental impact, and (b) options for reducing the environmental impact associated with the overall system. In an exergoenvironmental analysis, a one-dimensional characterization indicator is obtained using an LCA. An index (a single number) describes the overall environmental impact associated with system components and exergy carriers.

It should be emphasized that the evaluation of environmental impacts will always be subjective and associated with uncertainties. However, the information extracted from an exergoenvironmental analysis is very useful.

2.1. Exergetic analysis

Using the exergy rates associated with fuel and product, $\dot{E}_F$ and $\dot{E}_P$ [24], respectively, the exergetic balances for the *k*th component and for the overall system are, respectively

$$\dot{E}_{F,k} = \dot{E}_{P,k} + \dot{E}_{D,k} \qquad \text{and} \qquad \dot{E}_{F,tot} = \dot{E}_{P,tot} + \sum_n \dot{E}_{D,k} + \dot{E}_{L,tot} \tag{1}$$

The exergetic efficiencies for the *k*th component and for the overall system are, respectively

$$\varepsilon_k = \frac{\dot{E}_{P,k}}{\dot{E}_{F,k}} \qquad \text{and} \qquad \varepsilon_{tot} = \frac{\dot{E}_{P,tot}}{\dot{E}_{F,tot}} \tag{2}$$

The exergy destruction ratios for the *k*th component and for the overall system are, respectively

$$y_k = \frac{\dot{E}_{D,k}}{\dot{E}_{F,tot}} \qquad \text{and} \qquad y_k = \frac{\dot{E}_{D,tot}}{\dot{E}_{F,tot}} \tag{3}$$

2.2. Life Cycle Assessment (LCA)

In this paper the following five indicators (given with the corresponding units) are used for the analysis:

- Eco-indicator 95 (ECO-95) [13], with mPts (milipoints of the ECO-indicator 95);
- Eco-indicator 99 (ECO-99) [14], with mPts (milipoints of the ECO-indicator 99 that is different than milipoints of the ECO-indicator 95);
- Cumulative Exergy Consumption (CExC) [1], with kJ of cumulative exergy;
- Method of the Centre for Environmental Studies (CML) of the University of Leiden, The Netherlands, also known as "The Dutch Guide" [21], with ELU (environmental load units), and
- The Ecological Scarcity Method, ECO-Factors 2006 (ECO-F2006) or BUWAL methodology [22], with EP (Endpoints).

2.3. Exergoenvironmental evaluation

The exergoenvironmental model of an energy conversion system consists of balances and auxiliary equations associated with environmental impact [5].

The *environmental impact balances* are written for the *k*th system component in the following form

$$\dot{B}_{P,k} = \dot{B}_{F,k} + \left(\dot{Y}_k + \dot{B}_k^{PF}\right) \qquad \text{or} \qquad b_{P,k}\dot{E}_{P,k} = b_{F,k}\dot{E}_{F,k} + \left(\dot{Y}_k + \dot{B}_k^{PF}\right) \tag{4}$$

Here $\dot{B}_{P,k}$ and $\dot{B}_{F,k}$ are the environmental impact rates associated with the product and fuel respectively, and $b_{P,k}$ and $b_{F,k}$ are the corresponding environmental impacts per unit of exergy for product and fuel.

The component-related environmental impact $\dot{Y}_k$, which considers the entire life cycle of the *k*th component, consists of the following contributions:

$$\dot{Y}_k = \dot{Y}_k^{CO} + \dot{Y}_k^{OM} + \dot{Y}_k^{DI} \tag{5}$$

Here $\dot{Y}_k^{CO}$ is the environmental impact that is associated with construction, including manufacturing, transport and installation, $\dot{Y}_k^{OM}$ is associated with operation and maintenance, including production of pollutants during operation, and $\dot{Y}_k^{DI}$ refers to the environmental impact associated with disposal.

To account for *pollutant formation* within the kth component, a new variable was recently introduced $\dot{B}_k^{PF}$ [9]. This term $\dot{B}_k^{PF}$ is zero if no pollutants are formed within a process, i.e. for processes without a chemical reaction (compression, expansion, heat transfer, etc.). For components, where chemical reactions occur (combustion, for example), the value of $\dot{B}_k^{PF}$ is calculated from

$$\dot{B}_k^{PF} = \sum_i b_i^{PF} \left(\dot{m}_{i,out} - \dot{m}_{i,in} \right) \tag{6}$$

where only pollutant streams which finally will be emitted to the environment are taken into account: CO, CO_2, CH_4, N_2O, NO_x and SO_x [5].

The following variables may be used for evaluating and improving the kth component and the overall system [5]:

- Environmental impact rate associated with the exergy destruction within the kth component

$$\dot{B}_{D,k} = b_{F,k} \dot{E}_{D,k} \tag{7}$$

Total environmental impact associated with a component $\left(\dot{Y}_k + \dot{B}_k^{PF} + \dot{B}_{D,k} \right)$.

- Relative environmental impact difference

$$r_{b,k} = \frac{b_{P,k} - b_{F,k}}{b_{F,k}} = \frac{1 - \varepsilon_k}{\varepsilon_k} + \frac{\dot{Y}_k + \dot{B}_k^{PF}}{\dot{B}_{D,k}} \tag{8}$$

- Exergoenvironmental factor

$$f_{b,k} = \frac{\dot{Y}_k^{CO} + \dot{B}_k^{PF}}{\dot{Y}_k^{CO} + \dot{B}_k^{PF} + \dot{B}_{D,k}} = \frac{\dot{Y}_k^{CO} + \dot{B}_k^{PF}}{\dot{Y}_k^{CO} + \dot{B}_k^{PF} + b_{F,k} \cdot \dot{E}_{D,k}} \tag{9}$$

3. Example

Figure 1 shows a cogeneration system based on an open-cycle gas-turbine power system. This cogeneration system is known as CGAM problem – an academic example used to demonstrate the different exergy-based methods for optimization [23] as well as the application of exergetic and exergoeconomic analyses [24]. An exergoenvironmental analysis for this system was already presented in [5,6]. Here only main data from References [6,23,24] are repeated, in order to understand the new results. The cogeneration system generates net power $\dot{W}_{net} =$ 30 MW and saturated steam (stream 9) with $\dot{m}_{water} = 14$ kg/s at a pressure of 20 bar.

Table 1 contains the main results of the simulation. Table 2 (first column) and Table 3 show the definition and the values of the exergy of fuel and exergy of product for the kth component of the cogeneration system and results obtained from the exergetic analysis.

The equations used for the kth component in the exergoenvironmental analysis are given in the second column of Table 2. The value of the environmental impact associated with the fuel (methane) b_{10} depends on the approach used for LCA. There are two approaches to estimate the value of b_{10}.

- Approach 1: The value of b_{10} associated only with the fuel itself without pollutant formation. The values of b_{10} for the different eco-indicators are given in Table 4. The value of $\dot{B}_k^{PF}$ should be estimated separately using Eq. (6). For the system being analyzed, only CO_2 and NO_x are taken into account, i.e. $\dot{B}_{CC}^{PF} = b_{CO_2}^{PF}\left(\dot{m}_{CO_2,out} - \dot{m}_{CO_2,in}\right) + b_{NO_x}^{PF}\left(\dot{m}_{NO_x,out} - \dot{m}_{NO_x,in}\right)$, with $\dot{m}_{CO_2,in}$=0.019 kg/s, $\dot{m}_{CO_2,out}$=0.322 kg/s, and $\dot{m}_{NO_x,out}$=0.001 kg/s. The values of $b_{CO_2}^{PF}$ and $b_{NO_x}^{PF}$ for the different eco-indicators are also given in Table 4 as well as the values of $\dot{B}_{CC}^{PF}$.
- Approach 2: The value of b_{10} associated with the fuel includes the pollutant formation, for example, according to the average data for a combustion process. This data is available for few eco-indicators (Table 4). For this approach the value of $\dot{B}_k^{PF}$ is equal to 0. Note that the variable $\dot{B}_k^{PF}$ cannot be estimated and used in conjunction with the method of cumulative exergy consumption, because in CExC the effect of pollutants cannot be appropriately considered since exergy is the only measure of environmental impact.

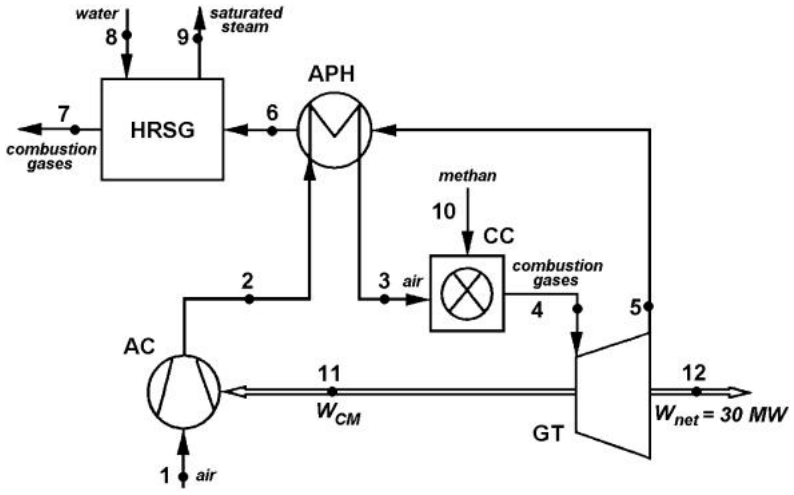

Fig. 1. A gas-turbine-based cogeneration system (CGAM problem)

Table 1. Thermodynamic data for the cogeneration system shown in Figure 1

Stream	Material of stream	$\dot{m}$ [kg/s]	T [K]	p [bar]	e [MJ/kg]
1	Air	91.28	298.1	1.01	0
2	Air	91.28	603.7	10.13	0.302
3	Air	91.28	850.0	9.62	0.459
4	CG	92.92	1520.0	9.14	1.092
5	CG	92.92	1006.2	1.10	0.417
6	CG	92.92	779.8	1.07	0.234
7	CG	92.92	426.9	1.01	0.030
8	Water	14.00	298.1	20	0.04
9	Water	14.00	485.6	20	0.915
10	CH4	1.64	298.1	12	51.825
11	Power to AC*)	-	-	-	
12	Net power**)	-	-	-	

*) $\dot{W}_{AC}$ =29.662 MW, **) $\dot{W}_{net}$ =30 MW

Table 2. Equations used for the exergetic and exergoenvironmental analysis

Component	Exergetic analysis	Exergoenvironmental analysis
AC	$\dot{E}_{F,AC} = \dot{W}_{AC}$	$b_w \dot{W}_{AC} + \dot{Y}_{AC} = b_2 \dot{E}_2 - b_1 \dot{E}_1$
	$\dot{E}_{P,AC} = \dot{E}_2 - \dot{E}_1$	with $b_1 = 0$
APH	$\dot{E}_{F,APH} = \dot{E}_5 - \dot{E}_6$	$\left(b_5 \dot{E}_5 - b_6 \dot{E}_6\right) + \dot{Y}_{APH} = b_3 \dot{E}_3 - b_2 \dot{E}_2$
	$\dot{E}_{p,APH} = \dot{E}_3 - \dot{E}_2$	with $b_5 = b_6$ (F rule [5])
CC	$\dot{E}_{F,CC} = \dot{E}_{10}$	$b_{10} \dot{E}_{10} + \left(\dot{Y}_{CC} + \dot{B}_{CC}^{PF}\right) = b_4 \dot{E}_4 - b_3 \dot{E}_3$
	$\dot{E}_{P,CC} = \dot{E}_4 - \dot{E}_3$	b_{10} = known (Table 4)
GT	$\dot{E}_{F,GT} = \dot{E}_4 - \dot{E}_5$	$\left(b_4 \dot{E}_4 - b_5 \dot{E}_5\right) + \dot{Y}_{GT} = b_w \dot{W}_{GT}$
	$\dot{E}_{P,GT} = \dot{W}_{GT}$	with $b_4 = b_5$ (F rule)
HRSG	$\dot{E}_{F,HRSG} = \dot{E}_6 - \dot{E}_7$	$\left(b_6 \dot{E}_6 - b_7 \dot{E}_7\right) + \dot{Y}_{HRSG} = b_9 \dot{E}_9 - b_8 \dot{E}_8$
	$\dot{E}_{P,HRSG} = \dot{E}_9 - \dot{E}_8$	with $b_6 = b_7$ (F rule)
		and $b_8 = 0$ (arbitrary assumption)

Table 3. Exergetic analysis the cogeneration system shown in Figure 1

Component	$\dot{E}_{F,k}^{real}$ [MW]	$\dot{E}_{P,k}^{real}$ [MW]	$\dot{E}_{D,k}^{real}$ [MW]	ε_k [%]	y_k [%]
AC	29.66	27.54	2.12	92.84	2.50
APH	16.93	14.40	2.53	84.55	3.09
CC	85.00	59.52	25.48	80.37	29.98
GT	62.67	59.66	3.01	95.20	3.54
HRSG	18.98	12.75	6.23	67.17	7.33
Overall system	**85.000**	**42.750**	**39.370**	**50.3**	**46.3**

Table 4. Environmental impact of the fuel and pollutants

Substance	ECO-95	ECO-99	ECO-99	CExC	CML	ECO-F2006	ECO-F2006
Methane as fuel, b_{10}	0.063*) mPts/MJ	3.5 mPts/MJ	5.38*) mPts/MJ	0.00104 kJ/MJ	0.02671 ELU/MJ	0.97 EP/MJ	3.3*) EP/MJ
CO_2 as pollutant, $b_{CO_2}^{PF}$	–	5.454 mPts/kg	–	–	0.0636 ELU/kg	310 EP/kg	–
NO_x as pollutant, $b_{NO_x}^{PF}$	–	2749.36 mPts/kg	–	–	0.395 ELU/kg	92000 EP/kg	–
$\dot{B}_{CC}^{PF}$ based on Eq. (6)	–	4.402 mPts/s	–	–	0.01967 ELU/s	185.93 EP/s	–

*) average statistical data for a low NO_x combustion process

Approach 1 is more accurate, whereas Approach 2 can be used if the b_i^{PF} data necessary for Approach 1 are not available.

$\dot{Y}_k$ is a term in the exergoenvironmental balance (Eqs. (4) and (5)). In the previous applications of the exergoenvironmental analysis [5-11], the value of $\dot{Y}_k$ was set equal to $\dot{Y}_k^{CO}$ that is the biggest contributor to $\dot{Y}_k$. In Ref. [6] the values of $\dot{Y}_k$ for the system being analyzed have already been discussed. In all publications related to an exergoenvironmental analysis [5-11] the authors conclude that the value of $\dot{Y}_k$ is very small compared with the value of the environmental impact associated with the exergy destruction ($\dot{B}_{D,k}$) and can be neglected in the analysis without effect to the results. In this paper we considered the value of $\dot{Y}_k$ only in conjunction with ECO-99.

Table 5 presents the results obtained from the exergoenvironmental analysis using five eco-indicators and three approaches for considering the values of $\dot{B}_k^{PF}$ and $\dot{Y}_k$.

The environmental impact associated with the total product of the cogeneration system (electricity and heat) can be calculated from the environmental impact balance applied to the overall system as

$$b_{P,tot}\dot{E}_{P,tot} = b_{F,tot}\dot{E}_{F,tot} + \left(\dot{Y}_{tot} + \dot{B}_{tot}^{PF}\right) - \dot{B}_{L,tot} \tag{10}$$

When the environmental impact associated with the exergy losses of the overall system ($\dot{B}_{L,tot} = \dot{B}_7$) is charged to the product, we obtain

$$b^*_{P,tot} = \frac{b_{P,tot}\dot{E}_{P,tot} + \dot{B}_{L,tot}}{\dot{E}_{P,tot}} \tag{11}$$

In order to estimate the environmental impacts associated with electricity and steam, the value of $\dot{B}_{L,tot}$ should be split using the terms $\dot{W}_{net}$ and $\left(\dot{E}_9 - \dot{E}_8\right)$ as weighting factors:

$$b^*_w = \frac{b_w\dot{W}_{net} + \dot{B}_{L,tot}\dfrac{\dot{W}_{net}}{\left(\dot{E}_9 - \dot{E}_8\right) + \dot{W}_{net}}}{\dot{W}_{net}} = b_w + \frac{\dot{B}_{L,tot}}{\left(\dot{E}_9 - \dot{E}_8\right) + \dot{W}_{net}} \tag{12}$$

The following data are obtained:

- Using ECO-95, we obtained $b^*_w =$ 0.39 mPts/kWh while the average value for Europe measured in ECO-95 points is 0.75 mPts/kWh [13],
- Using ECO-99, we obtained three values $b^*_w =$ 2.54 mPts/kWh if $\dot{B}_k^{PF}$=0 (for the case with the pollutant formation included in the value of b_{10}), $b^*_w =$ 1.702 mPts/kWh (with separate consideration of the formation of pollutants) and $b^*_w =$ 1.703 mPts/kWh (with separate consideration of the formation of pollutants and consideration of the values $\dot{Y}_k$). The average value for electricity in Europe according to ECO-99 is 27 mPts/kWh [14].
- For CExC we obtain $b^*_w =$ 1.795 kJ/kJ while the average environmental impact associated with electricity generation according to Ref. [25] is equal to 12.857 kJ/kJ. Note that in Ref. [25] a coal power plant is discussed. Apparently, coal power plants have a much higher relative environmental impact than gas-turbine power systems.

Table 5. Exergoenvironmental analysis of the cogeneration system shown in Figure 1

Compo-nent	$\dot{Y}_k$	$\dot{B}_{D,k}$	$\dot{B}_k^{PF}$	$\dot{Y}_k + \dot{B}_{D,k} + \dot{B}_k^{PF}$	$b_{F,k}$	$b_{P,k}$	$r_{b,k}$	$f_{b,k}$
				ECO- 95				
	(mPts/h)	(mPts/h)	(mPts/h)	(mPts/h)	(mPts/MJ)	(mPts/MJ)	(%)	(%)
AC	–	780	–	780	0.1022	0.1132	10.73	0
APH	–	950	–	950	0.1003	0.1187	18.26	0
CC	–	5779	–	5779	0.0630	0.0900	42.81	0
GT	–	1087	–	1087	0.1003	0.1022	1.86	0
HRSG	–	2250	–	2250	0.1003	0.1494	48.88	0
Overall system	**–**	**8952**	**–**	**8952**	**0.0630**	**0.1228**	**94.92**	**0**
				ECO – 99 ($\dot{B}_k^{PF}=0,\ \dot{Y}_k=0$)				
	(mPts/h)	(mPts/h)	(mPts/h)	(mPts/h)	(mPts/MJ)	(mPts/MJ)	(%)	(%)
AC	–	65625	–	65625	8.599	9.521	10.73	0
APH	–	79923	–	79923	8.441	9.983	18.26	0
CC	–	486158	–	486158	5.300	7.569	42.81	0
GT	–	91471	–	91471	8.441	8.599	1.86	0
HRSG	–	189324	–	189324	8.441	12.570	48.88	0
Overall system	**–**	**753088**	**–**	**753088**	**5.300**	**10.330**	**94.91**	**0**
				ECO – 99 ($\dot{B}_k^{PF}\neq 0,\ \dot{Y}_k=0$)				
	(mPts/h)	(mPts/h)	(mPts/h)	(mPts/h)	(mPts/MJ)	(mPts/MJ)	(%)	(%)
AC	–	43978	–	43978	5.762	6.381	10.73	–
APH	–	53561	–	53561	5.657	6.690	18.26	–
CC	–	321048	15847	336895	3.500	5.072	44.92	4.70
GT	–	61299	–	61299	5.657	5.762	1.86	–
HRSG	–	126876	–	126876	5.657	8.422	48.88	–
Overall system	**–**	**497322**	**15847**	**513169**	**3.500**	**6.922**	**97.77**	**3.09**

Table 5 (continuation)

ECO – 99 ($\dot{B}_k^{PF} \neq 0,\ \dot{Y}_k \neq 0$)

	(mPts/h)	(mPts/h)	(mPts/h)	(mPts/h)	(mPts/MJ)	(mPts/MJ)	(%)	(%)
AC	126	43989	–	44115	5.764	6.382	10.73	0.03
APH	145	53571	–	53716	5.658	6.694	18.31	0.27
CC	20	321048	15847	336915	3.500	5.072	44.92	4.71
GT	58	61311	–	61369	5.658	5.764	1.87	0.09
HRSG	119	126900	–	127019	5.658	8.426	48.92	0.09
Overall system	**468**	**497322**	**15847**	**513637**	**3.500**	**6.925**	**97.86**	**3.18**

Cumulative exergy consumption (CExC)

	(kJ/h)	(kJ/h)	(kJ/h)	(kJ/h)	(kJ/MJ)	(kJ/MJ)	(%)	(%)
AC	–	12.88	–	12.88	0.00169	0.00187	10.73	0
APH	–	15.68	–	15.68	0.00166	0.00196	18.26	0
CC	–	95.40	–	95.40	0.00104	0.00148	42.81	0
GT	–	17.95	–	17.95	0.00166	0.00169	1.86	0
HRSG	–	37.15	–	37.15	0.00166	0.00247	48.88	0
Overall system	**–**	**147.8**	**–**	**147.8**	**0.00104**	**0.00203**	**95.19**	**0**

C M L

	(ELU/h)	(ELU/h)	(ELU/h)	(ELU/h)	(ELU/MJ)	(ELU/MJ)	(%)	(%)
AC	–	334	–	334	0.0437	0.0484	10.73	0
APH	–	406	–	406	0.0429	0.0507	18.26	0
CC	–	2450	71	2521	0.0267	0.0385	44.05	2.81
GT	–	465	–	465	0.0429	0.0437	1.86	0
HRSG	–	962	–	962	0.0429	0.0639	48.88	0
Overall system	**–**	**3795**	**71**	**3866**	**0.0267**	**0.0525**	**96.63**	**1.84**

ECO - F2006

	(EP/h)	(EP/h)	(EP/h)	(EP/h)	(EP/MJ)	(EP/MJ)	(%)	(%)
AC	–	40861	–	40861	5.354	5.928	10.73	0
APH	–	49764	–	49764	5.256	6.216	18.26	0
CC	–	302702	–	302702	3.300	4.713	42.81	0
GT	–	56954	–	56954	5.256	5.354	1.86	0
HRSG	–	117881	–	117881	5.256	7.825	48.88	0
Overall system	**–**	**468904**		**468904**	**3.300**	**6.432**	**94.91**	**0**

Table 5 (continuation)

				ECO - F2006				
	(EP/h)	(EP/h)	(EP/h)	(EP/h)	(EP/MJ)	(EP/MJ)	(%)	(%)
AC	–	39097	–	39097	5.123	5.672	10.73	0
APH	–	47616	–	47616	5.029	5.948	18.26	0
CC	–	88976	669348	758324	0.970	4.509	364.90	88.27
GT	–	54496	–	54496	5.029	5.123	1.86	0
HRSG	–	112793	–	112793	5.029	7.487	48.88	0
Overall system	**–**	**137829**	**669348**	**807177**	**0.970**	**6.154**	**534.43**	**82.92**

- Using the CML method, the environmental impact associated with the electricity generation is $b^*_w = 0.0129$ ELU/kWh, and
- Using the ECO-factor 2006 $b^*_w = 1.582$ EP/kWh (for the case with the pollutant formation included in the value of b_{10}) and $b^*_w =$ 1.514 EP/kWh (with separate consideration of the formation of pollutants).

Note that for the CML and the ECO-factor 2006 average data for the environmental impact associated with electricity generation are not reported; therefore, we cannot compare the obtained results with the data mentioned in References [21] and Ref.[22].

If $\dot{Y}_k$ and $\dot{B}_k^{PF}$ are not considered (ECO-95, ECO-99, CExC and ECO-F2006), then the following conclusions can be obtained: Independently of the used method for the LCA, the absolute results of the exergoenvironmental analysis are different, but the relative values remain the same (for example, values $r_{b,k}$ and $r_{b,tot}$). Therefore, the conclusions (recommendations for improving the system) are independent of the method used for the LCA. The variable $f_{b,k}$ cannot be meaningfully used in this approach.

If $\dot{Y}_k$ is considered (ECO-99), this value does not significantly affect the results, and the conclusions from the analysis are the same as without considering the value $\dot{Y}_k$.

If the value of $\dot{B}_k^{PF}$ is considered as a separate term in Eq. (4), then different methods used for the LCA lead to different results: For example, (a) using ECO-99, $\dot{B}_{CC}^{PF} < \dot{B}_{D,CC}$ and $r_{b,tot}$=98%, (b) using CML, $\dot{B}_{CC}^{PF} << \dot{B}_{D,CC}$ and $r_{b,tot}$=97%, whereas (c) using ECO-F2006 $\dot{B}_{CC}^{PF} >> \dot{B}_{D,CC}$ and $r_{b,tot}$=534 %.

Conclusions

An exergoenvironmental analysis demonstrates the formation of environmental impacts associated with energy conversion systems at the component level.

This paper deals with the effect of the selected eco-indicator on the results and the conclusions obtained from the exergoenvironmental analysis. Five eco-indicators (ECO-95, ECO-99, CExC, CML and ECO-F2006) with two approaches for estimating the pollutants formation process were used for the environmental evaluation of a gas-turbine system (the so-called CGAM problem).

The total environmental impact associated with a component of the overall system consists in three terms: component-related environmental impact, environmental impact associated with the pollutant formation (only for the combustion chamber) and environmental impact associated with exergy destructions (e.g., Ref.[5]). The value of the environmental impact of pollutant formation can be calculated only if the used eco-indicator provides the necessary data. Calculating the value of the component-related environmental impact is a difficult task because many data related to the material consumption for manufacturing the equipment must be estimated. For the exergo-environmental analysis, however, this value can in the majority of the energy conversion systems be neglected (independently of the selected eco-indicator). The value of environmental impact associated with exergy destruction and, where appropriate, the value of pollutant formation should be considered in the analysis. Finally we can conclude that in many cases an exergy conversion system can be improved from the environmental point of view simply by improving its thermodynamic efficiency because the lower the exergy destruction within a component, the lower the environmental impact associated with it. Note that the environmental impact associated with pollutant formation is calculated only for the "pollutant producing" components.

Nomenclature

b	environmental impact per unit of exergy, Pts/J, kJ/J, ELU/J, EP/J or per unit of mass, Pts/kg, kJ/kg, ELU/kg, EP/kg
$\dot{B}$	environmental impact rate associated with exergy, Pts/s, kJ/s, ELU/s, EP/s
e	specific exergy, J/kg
$\dot{E}$	exergy rate, W
j	j th stream
f_b	exergoenvironmental factor, %
k	k th component
$\dot{m}$	mass flow rate, kg/s
p	pressure, bar
r_b	relative environmental impact difference, %
T	temperature, °C
$\dot{W}$	power, W
y	exergy destruction ratio, %
$\dot{Y}$	environmental impact, Pts/s, kJ/s, ELU/s, EP/s

Greek symbols

Δ	difference
ε	exergetic efficiency, %

Superscripts

$\bullet$	time rate
BF	pollutants formation

Subscripts

D	exergy destruction
F	exergy of fuel
j	j th stream

k k th component

P exergy of product

Abbreviations

AC air compressor

APH air preheater

CC combustion chamber

HRSG heat-recovery steam generator

GT gas turbine

References

[1] Szargut J., Minimization of the consumption of natural resources. Bulletin of the Polish Academy of Sciences: Tech Sci, 1978, 26(6):41–6.

[2] Valero A., Thermoeconomics as a conceptual basis for energy − ecological analysis. In: Ulgiati S., editor. Proceedings of the international workshop on advances in energy studies, Portovenere, Siena, Italy, 1998:415–44.

[3] Sciubba E., Extended exergy accounting: towards an exergetic theory of value. In: Proceedings of the ECOS '99, Tokyo, Japan, 1999:85–94.

[4] Frangopoulos C.A., Caralis Y.C. A method for taking into account environmental impact in the economic evaluation of energy systems, Energy Conversion Management, 1997, 38 (15-17): 1751-1763.

[5] Meyer L., Tsatsaronis G., Buchgeister J., Schebek L., Exergoenvironmental analysis for evaluation of the environmental impact of energy conversion systems, Energy Int. J., 2009, 34:75-89.

[6] Tsatsaronis G., Morosuk T., A general exergy-based method for combining a cost analysis with an environmental impact analysis. Part I, Proceedings of the ASME International Mechanical Engineering Congress and Exposition, Boston, Massachusetts, USA, 2008: IMECE2008-67218.

[7] Tsatsaronis G., Morosuk T., A general exergy-based method for combining a cost analysis with an environmental impact analysis. Part II, Proceedings of the ASME International Mechanical Engineering Congress and Exposition, Boston, Massachusetts, USA, 2008: IMECE2008-67219.

[8] Tsatsaronis G., Morosuk T., Advances in exergy-based methods for improving energy conversion systems. In: Optimization using exergy-based methods and computational fluid dynamics, Tsatsaronis G., Boyano A., editors, Clausthal-Zellerfeld: Papierflieger Verlag, 2009:1-10.

[9] Boyano A., Blanco-Marigorta A.M., Morosuk T., Tsatsaronis G., Exergoenvironmental analysis of a steam methane reforming process for hydrogen production, Energy Int. J., 2011, 36: 2202-14.

[10] Morosuk T., Tsatsaronis G., Koroneos C., Reduction of Environmental Impact Using Exergy-Based Methods. Accepted for publication in the Proceedings of the ECOS-2011 Conference, Novi Sad, Serbia, 4-7 July 2011, CD-ROM.

[11] Morosuk T., Tsatsaronis G., Koroneos C., The effect of eco-indicator on the results of exergoenvironmental analysis. Accepted for publication in the Proceedings of the 2nd International Exergy, Life Cycle Assessment, and Sustainability Workshop & Symposium (ELCAS2), Nisyros, Greece, 19 - 21 June, 2011, CD-ROM.

[12] International Organization for Standardization (ISO). Environmental management — life cycle assessment. European Standard ENISO14040 and 14044, Geneva, Switzerland, 2006.

[13] http://www.pre.nl/eco-indicator95/

[14] http://www.pre.nl/eco-indicator99/
[15] http://ipt.dtu.dk/~mic/EDIP97
[16] http://ipt.dtu.dk/~mic/EDIP2003
[17] http://eps.esa.chalmers.se/
[18] http://www.epfl.ch/impact
[19] www.jepix.org
[20] http://www.jemai.or.jp/lcaforum/index.cfm
[21] http://media.leidenuniv.nl/legacy/new-dutch-lca-guide
[22] http://www.e2mc.com/BUWAL297%20english.pdf
[23] Valero A., et al., CGAM Problem: Definition and Conventional Solution, Energy – The International Journal, 1994, 19:279-86.
[24] Bejan A., Tsatsaronis G., Moran M., Thermal Design and Optimization, J. Wiley, New York, 1996.
[25] Szargut J., Local and System Exergy Losses in Cogeneration Processes, Int. J. Thermodynamics, 2007, 10 (4): 135-42.

Optimisation of supply temperature and mass flow rate for a district heating network

Marouf Pirouti[a], Audrius Bagdanavicius[b], Jianzhong Wu[c], Janaka Ekanayake[d]

Institute of Energy, Cardiff University, Cardiff, UK
[a]Piroutim@cardiff.ac.uk, [b]BagdanaviciusA@cardiff.ac.uk, [c]WuJ5@cardiff.ac.uk,
[d]EkanayakeJ@cardiff.ac.uk

Abstract:
Heat losses and pump electrical energy consumption are inevitable during the operation of a district heating (DH) network. Therefore, the appropriate design and operating strategy of a DH network is required in order to reduce the heat losses and pump energy consumption. This study is aimed at optimising the supply water temperature and mass flow rate in a DH network, according to the heating load variations. For this purpose, two different design cases of a DH pipe network were considered. An optimisation model was developed using FICO™ Xpress optimisation tool. Hydraulic and thermal calculations of the model were validated with the commercial software PSS SINCAL. The DH networks were optimised with respect to the annual energy (heat losses and pump energy consumption), and associated costs. The optimum supply temperature and mass (volume) flow rate were obtained for each case. Consequently, optimum heat losses and pump power were calculated.

Keywords:
District heating network, Modelling, Design, Optimisation, Supply temperature

1. Introduction

District heating (DH) systems provide multiple buildings or dwellings with heat and domestic hot water (DHW) from a central energy centre. Heat is transferred from the central energy centre through a network of insulated pipes, carrying the hot water to each building.

DH systems, particularly for densely populated urban environments, have proved to be sustainable and efficient systems compared with individual boilers [1]. However operational costs, related to the pump's power and heat losses in DH pipe networks, present the major drawback of DH compared to the individual heating system. The operational costs can be reduced by energy efficient design as well as a better energy management during the operation. Therefore the reduction of heat energy losses and pump energy consumption is one of the most important tasks, which reduces costs and improves the efficiency of a DH system.

Modelling and operation of a DH network is addressed in a number of studies .Short-term optimal operation of a DH system to find the most economic way of fulfilling consumer's heat requirement, is presented in ref [2-6]. An optimisation model, considering the dynamic of the network, which incorporates the consumers, the district heating network and the production plant was developed to minimise operational costs [2-3]. An equivalent model of DH network with regards to on-line optimisation of the operational costs of the complete system was developed [4]. An optimisation model, taking into account the dynamic character of the DH network, was formulated to minimise operating costs and maximise the profit of the system [5]. Reference [6] specifically addresses the modelling and optimal operation of Micro-grid system.

Determination of pipe sizes is a first task in a DH pipe network. Pipe diameters are usually chosen based on maximum flow and pressure loss. Target pressure loss (TPL) is a common design parameter of DH pipe networks. DH networks are designed using pressure losses of 50-200 Pa/m [7]. Many DH networks in Denmark and other EU countries have been designed based on pressure loss of 100 Pa/m [8]. However, in newer studies much higher pressure loss is used. In a study of Li

et al. [9] for the determination of pipe size, the pressure loss of 500 Pa/m was used for main pipes. In the mean time, pressure loss of 1500 Pa/m was used as the dimension criteria for the street pipes [9]. A much higher pressure loss of 2000 Pa/m was used for low energy DH systems in energy efficient building area [10-11].

In this study two different design cases of a DH pipe network were prepared using SINCAL. Optimal annual operation of each DH design case was carried out, using FICO^{TM} Xpress. The objective of the optimisation was to determine the optimum annual supply temperature and flow rate. Consequently, using obtained temperature and flow rate, optimum heat losses and pump energy consumption were calculated. The obtained results were compared and analysed.

2. District heating model

District energy model based upon a real project redevelopment in South Wales, UK, was applied [12]. A simplified diagram of the DH pipe connection is shown in Fig.1. Consumers were geographically split into a set of clusters. Consumers have different occupancy type and building size within a cluster.

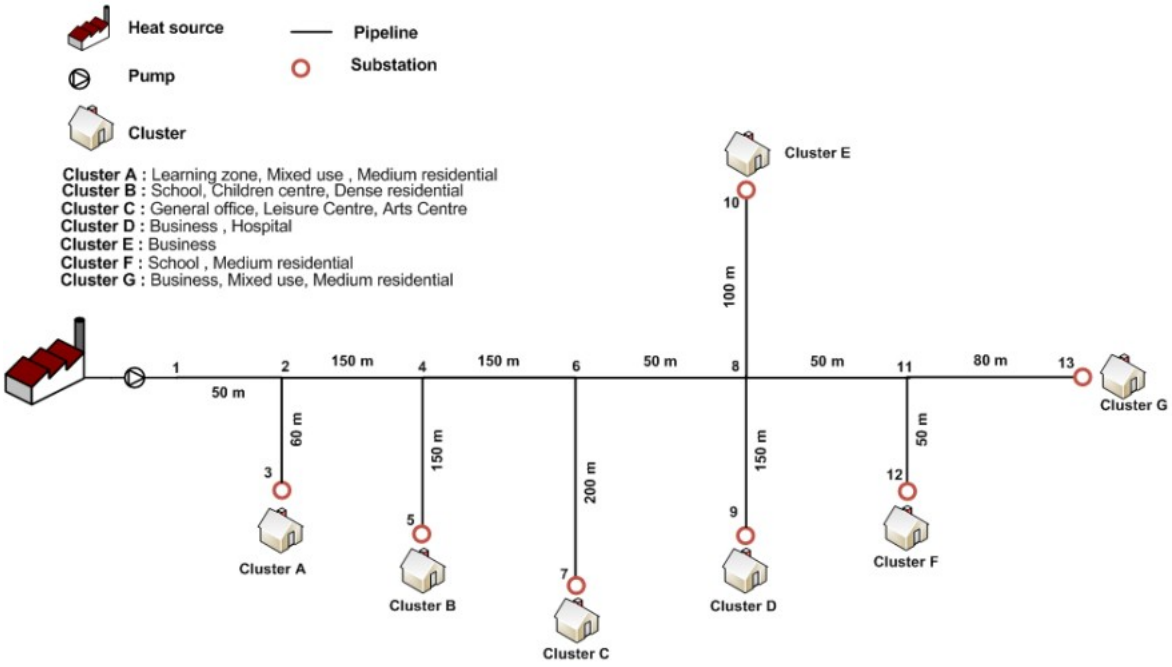

Fig.1. Simplified diagram of DH case study

Each cluster was connected to the DH network using heating substation. Maximum energy demand for space heating (SH) and domestic hot water (DHW) was calculated based on estimated area for each building [13-14].

Mean daily DHW requirement calculated for each building was assumed to be constant over the whole year. Energy demand for SH varied proportionally to the outdoor temperature. Daily SH demand was calculated using the concept of heating degree days (HDD) [15-17]. The base temperature of 15.5 °C was assumed and the minimum outdoor temperature was considered to be -3 °C in this study. The total heating demand of SH was calculated for each day over the year. The heating load was divided into two main seasons. The winter season lasts for 182 days and includes energy demand for SH and DHW. For the rest of the year (summer season) only energy demand for DHW was taken into account. The total heat demand (right) and annual load duration curve (left) are shown in Fig.2.

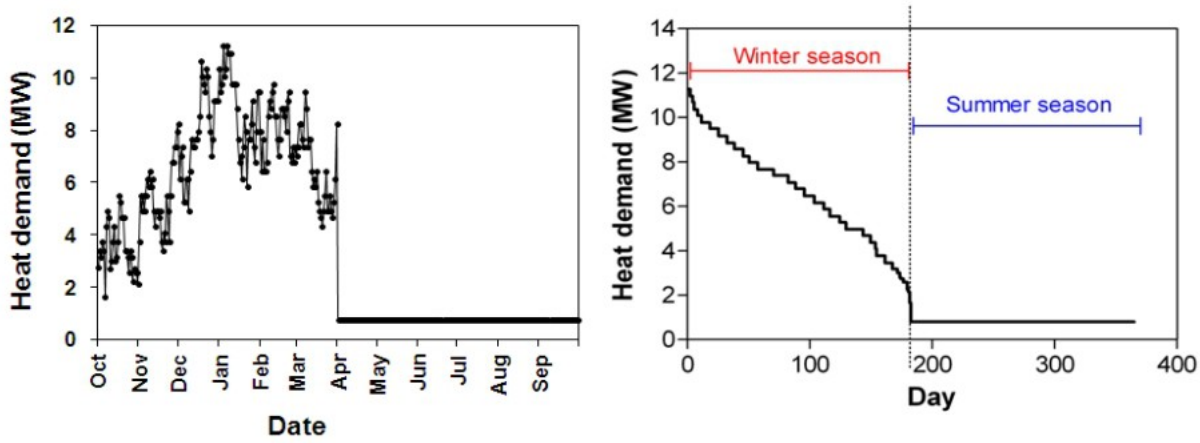

Fig.2.Total annual heat demand

2.1. Design cases

In this study, two approaches were used. First, system was designed based on low pressure loss (Case 1: TPL of 100 Pa/m). Then, the design was reiterated for much higher pressure loss (Case 2: TPL of 1200 Pa/m). The pipe diameters and heating system design parameters for both design cases are given in Table 1, and Table 2.

The difference between TPL and actual pressure loss is due to the selection of standard pipe sizes available in the market [18]. Standard sizes of pre-insulated steel pipes were selected. Pipes diameters, calculated in PSS SINCAL, were different compared with the standard size. The pipe with the diameter which was closest to the calculated pipe diameter was selected. By reiterating the calculation with actual pipes diameter the actual pressure loss in the system was obtained.

Table 1. DH design

Pipe No.	Length (m)	From node	To node	Pipe diameter (mm)	
				Case 1	Case 2
1	50	1	2	250	150
2	60	2	3	125	80
3	150	2	4	250	125
4	150	4	5	125	80
5	150	4	6	200	125
6	200	6	7	125	80
7	50	6	8	150	125
8	150	8	9	125	80
9	100	8	10	100	65
10	50	8	11	125	80
11	50	11	12	80	50
12	80	11	13	100	65

Table 2. Heating system design parameters

Case	$T_{s,\max} / T_{r,\max}$ (°C)	$\dot{V}_{\max}$ (m^3/s)	$p_{loss,\max}$ (Pa/m)	$\Delta p_{p,\max}$ (kPa)	$P_{p,\max}$ (kW)	$v_{\max}$ (m/s)
Case 1	120/70	0.062	99	158	12	1.7
Case 2	120/70	0.062	1276	1454	112	4.2

2.2. Optimisation model

The optimisation model determines the optimum system flow rate and system supply temperature at each time step over a year, at a steady state condition.
The suitable method to describe a DH pipe network is to use the concept of graph theory [19]. A graph is commonly defined as a combination of

- A set of nodes
- A set of branches, and
- And incident relation

Each branch within the graph is connected to a pair of nodes, the node where the branch starts and the node where it ends. A DH network can be treated as a network graph. The branches represent pipes and nodes symbolise the points where pipes are connected. In the study the DH network graph consists of 13 nodes and 12 pipes (Fig.1.)
The connectivity matrix was created to explain the DH network with k_n nodes and m_f flow stream (branches). The program stores the network graph in a matrix data structure such as *(A)* which is a $k_n \times m_f$ matrix, containing the incidence elements ($a_{k,j}$).

$a_{k,j}$=-1 If pipe j starts at node k,
$a_{k,j}$=1 If pipe j ends at node k,
$a_{k,j}$=1 If source j ends at node k,
$a_{k,j}$=-1 If load j starts at node k,
$a_{k,j}$=0 Otherwise

The connectivity matrix has one column for each flow stream, and one row for each node. The connectivity matrix (A) was used to calculate flow in supply pipes. The flow rates in the return pipes are calculated in the same manner as in supply pipes. For the calculation of flow in the return pipes, the connectivity matrix was simply multiplied by -1. In this study, since supply and return pipes are assumed to be identical, it was found that flow and pressure loss in the supply and return pipes were nearly the same.
The energy flow and flow rate in each branch, temperature (supply and return), and pressure at each node were calculated using equations found in the thermal engineering textbooks [20- 21].
The total heat supplied (SH and DHW) to the network was calculated using the following equation.

$$Q_{SH,DHW} = c\dot{m}(T_s - T_r) \quad (1)$$

Heat supply at each branch was obtained using Kirchhoff rule at nodes.

$$\sum_{j=1}^{m} Q_{jk} = 0 \tag{2}$$

A linear approximation of the exponential decay of temperature was used to calculate temperature at the outlet of the pipes [6].

$$T_{out,j} = \begin{cases} (T_{in,j} - T_g)(1 - \dfrac{U_j l_j}{c\dot{m}_j}) + T_g & \dfrac{U_j l_j}{c\dot{m}_j} \le 1 \\ T_g & \dfrac{U_j l_j}{c\dot{m}_j} \ge 1 \end{cases} \tag{3}$$

At nodes with more than one braches or supply sources, the nodes temperature was calculated as the mixed of incoming streams temperatures to the node [19-20]. For example, if pipe 1 receives hot water from pipe 2 and 3, then temperature at node l is:

$$T_k = \frac{\sum_{j=1}^{m} \dot{m}_j T_{out,j}}{\sum_{j=1}^{m} \dot{m}_j} = \frac{\dot{m}_2 T_{out,2} + \dot{m}_3 T_{out,3}}{\dot{m}_2 + \dot{m}_3} = T_1 \tag{4}$$

Heat loss in each pipe section was obtained by the equation:

$$Q_{loss,j} = c\dot{m}_j (T_{in,j} - T_{out,j}) \qquad for \quad j = 1,2,3.....m \tag{5}$$

The total heat loss in the DH pipe network is the sum of the heat loss in each pipe section of supply and return pipes.

According to the law of conservation of mass, flow in each pipe was calculated using the Kirchhoff law.

$$\sum_{j=1}^{m} \dot{m}_{jk} = 0 \tag{6}$$

The pump head of variable speed pump was obtained using the equation [22]:

$$\Delta p_p = \left(\frac{\dot{m}}{\dot{m}_{\max}} \right)^2 . \Delta p_{p,\max} \tag{7}$$

Pump power (in kW) was calculated by the following equation:

$$P_p = \frac{\Delta p_p \dot{m}}{1000 \rho \eta_p} \tag{8}$$

2.3. Validation

Model validation, guarantees the credibility of the results. Hence, the heating calculations of the model were validated with the commercial software PSS SINCAL.

For this purpose, for both cases the heat losses and pump power over the whole year calculated in Xpress model were validated with the commercial software PSS SINCAL. Model validation is shown in Fig.3. In terms of credibility of the result, it is seen that Xpress model provides

approximately the same result as PSS SINCAL model. Therefore Xpress model was used for further analysis of the DH network.

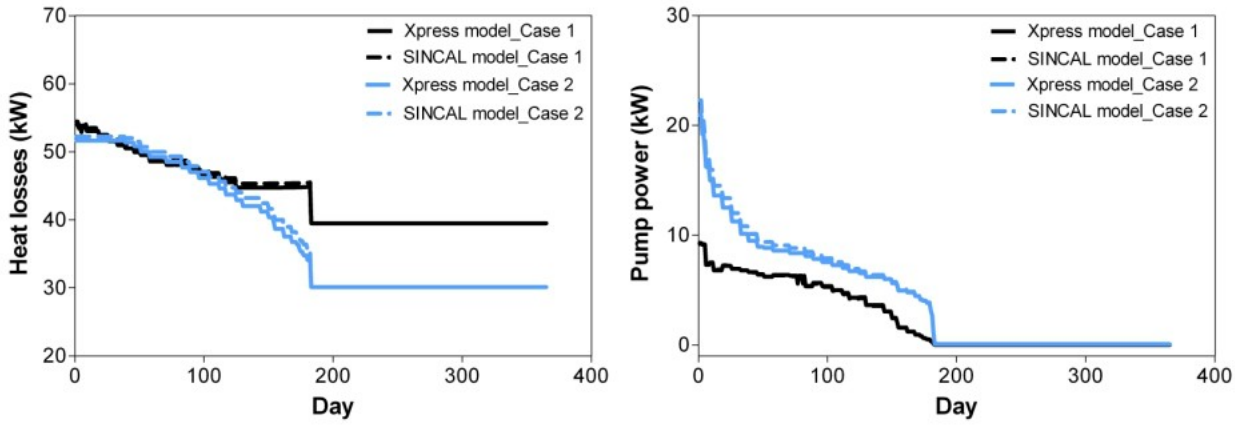

Fig.3. Model validation

2.4. Objective function

The optimisation model determines the optimum system flow rate and system supply temperature when total annual energy consumption and losses of the main pipe network is minimal. Detailed modelling of the secondary network was not considered.

In a DH network, total energy consumption and losses include pump electrical energy requirement and heat energy losses to the ground. Therefore, total operational costs consist of pumping cost and heat losses cost. The objective function was:

$$Min \quad \sum_{t=1}^{n} \left\{ 24 \times \left(P_{p,t} + Q_{loss,t} \right) \right\} \tag{9}$$

$$Min \quad \sum_{t=1}^{n} \left\{ 24 \times \left(P_{p,t} \times CE_t + Q_{loss,t} \times CH_t \right) \right\} \tag{10}$$

Subject to:

- System supply temperature, flow and pressure loss constraints

Two objective functions were considered. The equation (9) considers the minimisation of energy losses and pump energy consumption, regardless of the energy price. Exergy losses were not calculated in this study. In equation (10) minimisation of operational costs is addressed. The only difference between equation (9) and equation (10) is the inclusion of energy price.

Supply and return temperature of the pipes was within the permissible range:

$$T_{s,\min} \le T_s \le T_{s,\max} \tag{11}$$

$$T_{r,\min} \le T_r \le T_{r,\max} \tag{12}$$

Maximum supply temperature of 120 ℃ during winter season was considered. For the entire summer regime, supply temperature was fixed at 70 ℃ in both cases, as there was only demand for DHW. For both cases, the return temperature was assumed to be constant in the consumer's substations. For the entire winter season, return temperature was assumed to be 40 ℃ in all substations. In the summer season, the return temperature of 30 ℃ was taken into account.

The system flow rate (total flow in the source side) was required to be within minimum and maximum limits.

$$\dot{m}_{\min} \le \dot{m} \le \dot{m}_{\max} \tag{13}$$

The maximum differential pressure of pump was equal or higher than the maximum pressure drop in the network.

$$\Delta p_p \le \Delta p_{p,\max} \tag{14}$$

The optimisation model was formulated as a nonlinear objective function with nonlinear constraints, using FICO™ Xpress optimisation. Xpress optimisation allows modelling and solving of large and complex optimisation problems. For the study, successive (sequential) linear programming (Xpress-SLP) was used. Xpress-SLP is a solver for nonlinear optimisation problems. It uses successive linear approximation which has been developed from techniques used in the process industries and it can solve large problems with many thousands of variables [23, 24].

3. Results

3.1. Minimisation of energy consumption

The results of the optimisation based on minimisation of energy losses and consumption are shown in Fig.4. The energy demand for heating decreases over the year (according to the outdoor temperature). Therefore, the temperature and the flow rate decrease. As a result, heat losses and pump power reduce in both cases. However, the temperature and flow rate profiles of different cases are very different.

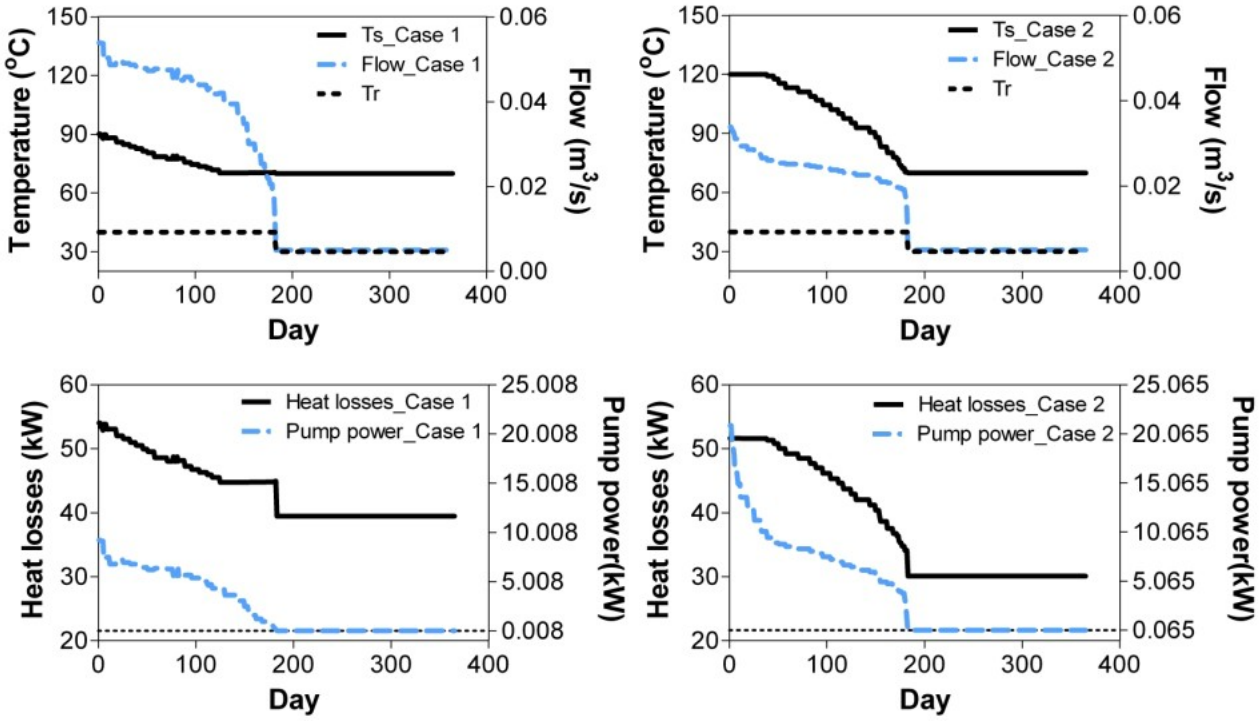

Fig.4. Optimal DH network parameters, based on minimising energy

The difference is rooted in the design of the DH pipe network. For the case 1, since pipes with larger diameters were selected, pressure loss and pump energy consumption is less compared with the case 2. Heat losses are higher for larger diameter pipes. Therefore, in case 1, larger flow rate and lower supply temperature were obtained compared with the case 2. Due to lower supply temperature, heat losses decrease in case 1 while due to lower flow rate in case 2, the pump energy consumption is reduced.
In case 1, higher heat losses and lower pump power compared with the case 2 is observed, due to the different design conditions. It is clear that in terms of energy losses and consumption, heat losses in both cases are more important than pump energy requirement. In both cases during summer season, as a result of reduction in flow rate pump energy consumption is very low (Case 1: 8 W, Case 2: 65 W), since demand for DHW is less than demand for SH (about 7 % of the total peak demand). However, because supply temperature is still relatively high, heat losses are substantial in both cases.

3.2. Minimisation of costs

For the optimisation based on minimisation of costs, electricity and heat price were assumed to be constant over the year. An average price per kWh was considered for this purpose. The price of 0.095 (£/kWh) was taken into account for electricity [25, 26], while heat price was assumed to be 0.07 (£/kWh) over the whole year [27]. The results of the optimisation are shown in Fig.5.

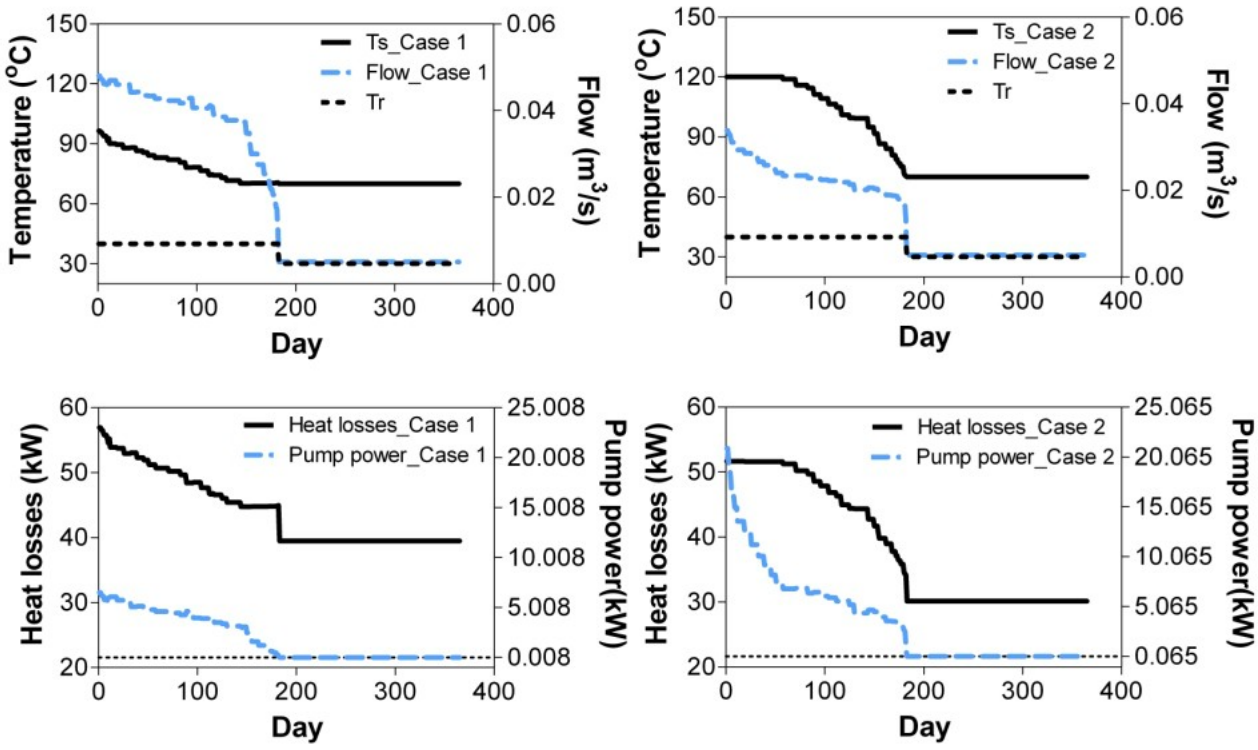

Fig.5. Optimal DH network parameters, based on minimising costs

It is seen that as the energy demand changes over the year and supply temperature and flow rate change accordingly. As energy demand decreases heat losses and pump power requirement decrease, due to the reduction in supply temperature and flow rate. However, for different DH pipe networks, different results were obtained. As it was explained earlier, this is the consequence of the selection of pipe with different diameters and different size of pumps.

3.3. Comparison

Optimisation results for both approaches, based on minimisation of energy and costs, are shown in Fig.6.

A slight difference is seen when system is optimised based on minimisation of energy and costs. For the optimisation based on minimising costs a slightly higher temperature and smaller flow rate are observed in both cases. This is due to the price of heat energy losses and pump electricity consumption. Since the price of electricity which is consumed by pump is higher than the heat price, the optimiser increases supply temperature and reduces flow rate to avoid excessive pumping costs. Hence, the amount of optimal supply temperature, flow rate, heat losses and pump power can vary with regards to the energy price. When electricity price is higher than the heat price, it is better to reduce flow rate and increase supply temperature to avoid higher pumping cost. In the mean time, when heat price is more than the electricity price, it may be beneficial to reduce supply temperature and increase flow rate to avoid higher heat losses cost. It is worth mentioning, that results of the both optimisation approaches (minimisation of energy and costs) show similar trends of the change in supply temperature and flow rate. As the heat demand changes according to outdoor temperature, system supply temperature and flow rate change to balance the production and demand.

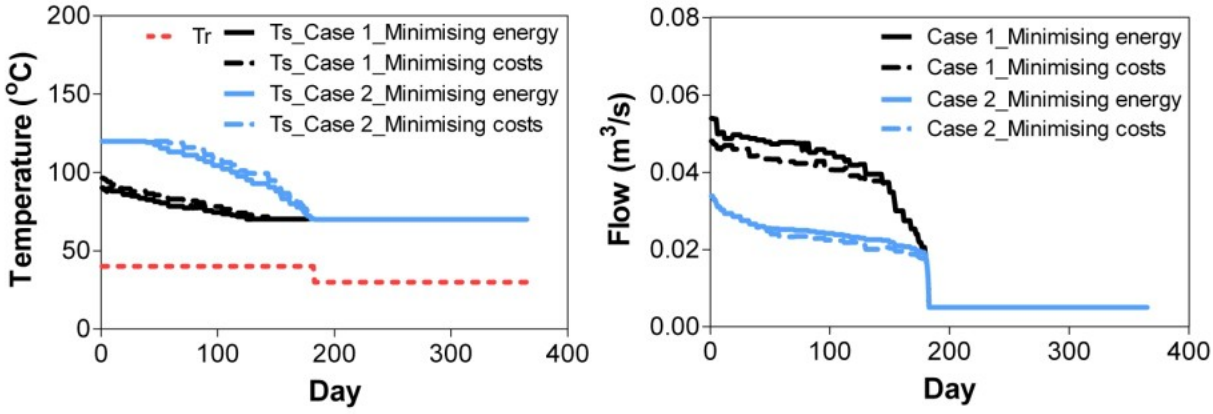

Fig.6. Optimal supply temperate and flow based on minimisation of energy and costs

4. Conclusion

In this study, an optimisation model was developed to optimise supply temperature and flow rate for a DH network. Optimal heating system parameters, temperature and flow rate, were found and validated. Due to the uncertainty in the price of heat and electricity, two objective functions were taken into account, one based on minimisation of energy losses and energy consumption, and another based on minimisation of operational costs. In addition, two different DH networks were designed and then optimised.

It was shown that for the DH pipe networks, optimisation results were different, due to the selection of pipes and pumps with different sizes. For a DH pipe network designed based on low pressure loss (100 Pa/m), pump energy consumption was not substantial and high heat losses were due to the selection of pipes with larger diameters. Therefore, in order to reduce heat losses, supply temperature had to be reduced and flow rate had to be increased. When the DH pipe network was designed using high pressure loss (1276 Pa/m), pipes with smaller diameters were selected. Hence, reduction of pump energy consumption was achieved by increasing supply temperature and reducing flow rate.

Heat losses were higher than pump energy consumption in both cases as well as for both optimisation approaches. It was observed, that the design case based on high pressure drop performed better since lower heat losses were obtained.
Finally, it was found that price of energy (electricity and heat) have impact on optimum supply temperature and flow rate and consequently heat losses and pump energy consumption.

Acknowledgments

The research comprises part of the Supergen-Highly Distributed Energy Future (HiDEF) work streams via EPSRC funding. The authors wish to thank Supergen-HiDEF consortium for their continued financial and technical support. The authors also thank Marc Rees for access to the case study data.

Nomenclature

CE	electricity price, £/(kWh)
CH	heat price , £/(kWh)
c	specific heat capacity, kJ/(kg K)
l	pipe length, m
$\dot{m}$	mass flow rate, kg/s
p	pressure , Pa
Δp	differential pressure, Pa
P	pump power , kW
Q	thermal power , kW
T	temperature , °C
$\dot{V}$	volume flow rate , m^3/s
v	velocity, m/s
U	heat transition coefficient, W/(m K)

Greek symbols

η	efficiency
ρ	water density , kg/m^3

Subscripts and superscripts

g	Ground
in	Inlet
j	Index for pipe
k	Index for node
max	Maximum
min	Minimum
out	Outlet
p	Pump
r	Return
s	Supply
t	Index for time step

References

[1] Ljubenko A., Poredoš A., Energy efficiency of a district heating system and its possible improvements. Proceedings of the 24th International Conference on Efficiency, Cost, Optimization, Simulation, and Environmental Impact of Energy Systems, 2011, July 4-7, Novi Sad, Serbia, pp.2935-2944.

[2] Benonysson A., Bøhm B., Ravn H.F., Operational optimization in a district heating system. Energy. Conversion and Management, 1995, Vol.36, No.5, pp.297-314.

[3] Bøhm B., et al., Simple model for operational optimization.IEA District Heating and Cooling, 2002, Annex VI: Report 2002:S1.

[4] Pálsson H., et al., Equivalent models of district heating systems for on-line minimization of operational costs of the complete district heating system. Department of Energy Engineering Technical University of Denmark and RISØ National Laboratory Systems Analysis Department, ISBN 87-7475-221-9, 179p.

[5] Wigbel M., Bøhm B., Sipilae K., Dynamic heat storage optimisation and demand side management.IEA R&D Programme on District Heating and Cooling, Annex VII, 2005:8DHC-05-.06.

[6] Awad B., Operation of energy micro grids [PhD Dissertation]. Cardiff, UK, Cardiff University: 2010.

[7] Yildirim N., Toksoy, M., Gokcen, G., Piping network design of geothermal district heating systems: Case study for a university campus. Energy, 35 (2010), pp.3256-3262.

[8] Phetteplace G., Optimal design of piping system s for district heating. U.S. Army Corps of Engineers. Cold Regions Research & Engineering Laboratory: 1995.

[9] Li H., Dalla rosa A., Svendsen S., Design of low temperature district heating network with supply water recirculation. The 12th International Symposium on District Heating and Cooling, 2010, September 5-7, Tallinn, Estonia, pp.73-80.

[10] Dalla rosa A., Christensen J. E., Low energy district heating in energy efficient building areas. Energy, 36 (2011), pp.6890-6899.

[11] Zinko H., et al., District heating distribution in areas with low heat demand density. International Energy Agency, IEA implementing agreement on district heating and cooling including the integration of CHP: 2008.

[12] Rees M., et al., A total energy approach to integrated community infrastructure design. IEEE Power and Energy Society General Meeting, 2011, July 24-29 , USA, pp.1-8

[13] Barry H., et al., Energy efficiency in buildings. CIBSE Guide F, Second edition, 2004, The Chartered Institution of Building Services Engineers, London.

[14] Beegs C., Energy management supply and conservation. Second edition, Butterworth-Heinemann, Oxford, UK: 2009.

[15] Heating degree days (HDD)-Available at :<http://www.degreedays.net/> [accessed 15.07.2011].

[16] BizEE Software Ltd, Business Energy Efficiency Software- Available at: < http://www.bizeesoftware.com/> [accessed 15.07.2011].

[17] Day T., et al., Degree-days theory: and application. CIBSE, 2006, The Chartered Institution of Building Services Engineers, London.

[18] LOGSTOR, Pre insulated pipe catalogue-Available at :< http://www.logstor.com> [accessed 15.07.2011].

[19] Hassine B.H., Eicker U., Simulation and optimization of the district heating network in Scharnhauser Park. 2nd European Conference on Polygeneration, 2011, Tarragona, Spain, pp.1-12.

[20] PSS® SINCAL 6.5 Heating, 2009. Heating calculations in flow networks. SIEMENS AG.

[21] Moran M.J., Shapiro H.N., Munson B.R., DeWitt D.P., Introduction to thermal systems engineering: Thermodynamic, Fluid Mechanic, and Heat Transfer. John Wiley & Sons, Inc: 2003.

[22] Snok C., et al., Optimization of district heating systems by maximizing building heating system temperature difference. Programme of Research, Development and Demonstration on District Heating and Cooling, 1999, International Energy Agency IEA District Heating and Cooling, pp.89-90.

[23] Fico Xpress optimization suite, getting start with Xpress-Available at: <http://www.fico.com/en/Products/DMTools/xpress-overview/Pages/Xpress-Documentation.aspx>[accessed 15.07.2011].

[24] Fico Xpress optimization suite, Xpress Mosel, user guide- Available at: <http://www.fico.com/en/Products/DMTools/xpress-overview/Pages/Xpress-Documentation.aspx>[accessed 15.07.2011].

[25] Weber C. Shah N. Optimisation based design of a district energy system for an eco-town in the United Kingdom. Energy, 36(2011), pp.1292-1308.

[26] Europe Energy's portal-Available at :< (http://www.energy.eu/#Industrial-Elec)> [accessed 15.07.2011].

[27] Pöyry Energy Consulting. The potential and costs of district heating networks, A report to the Department of Energy and Climate Change, Oxford, UK.

Optimization of Energy Supply Systems in Consideration of Hierarchical Relationship Between Design and Operation

Ryohei Yokoyama[a] and Shuhei Ose[b]

a Department of Mechanical Engineering, Osaka Prefecture University
*Sakai, Osaka, Japan, yokoyama@me.osakafu-u.ac.jp, **CA***
b Department of Mechanical Engineering, Osaka Prefecture University
Sakai, Osaka, Japan, ose@ese.me.osakafu-u.ac.jp

Abstract:

To attain the highest performance of energy supply systems, it is necessary to rationally determine types, capacities, and numbers of equipment in consideration of their operational strategies corresponding to seasonal and hourly variations in energy demands. Combinatorial optimization methods based on the mixed-integer linear programming (MILP) have been proposed to solve this design problem, and integer variables are used to express the selection, number, and on/off status of operation of equipment. However, the number of these variables increases with the numbers of equipment and periods for variations in energy demands, and affects the computation efficiency significantly. In this paper, a MILP method utilizing the hierarchical relationship between design and operation variables is proposed to solve the optimal design problem of energy supply systems efficiently: At the upper level, the values of design variables are optimized by the conventional branch and bound method; At the lower level, the values of operation variables are optimized independently at each period by the conventional branch and bound method; Both the levels are connected with each other to exchange data for optimization calculations. The proposed method is applied to a numerical study on the optimal design of a gas engine cogenetation system for electric power and hot water supply, and its validity and effectiveness are clarified.

Keywords:

Energy supply systems, Design, Operation, Optimization, Mixed-integer linear programming, Branch and bound method, Hierarchical approach.

1. Introduction

In designing energy supply systems, it is important to rationally determine their structures by selecting energy producing and conversion equipment from many alternatives so that they match energy demand requirements. It is also important to rationally determine capacities and numbers of selected equipment in consideration of their operational strategies such as on/off status of operation and load allocation corresponding to seasonal and hourly variations in energy demands.

Recently, distributed energy supply systems have been widespread and diversified, and many types of equipment have been installed into them, which means that many alternatives for system design and operation have arisen. Thus, it has become more and more difficult for designers to design the systems properly in consideration of their operational strategies only with their experiences. In addition, not only reliability in energy supply but also economics, energy saving, and environmental impact have become more and more important criteria for system design and operation, with which designers have been burdened more heavily. For the purpose of assisting designers in system design and operation, therefore, it is necessary to develop a tool for providing rational design and operation solutions flexibly and automatically.

One of the ways to rationally determine the aforementioned design and operation items of energy supply systems is to use combinatorial optimization methods, which are based on the mathematical programming such as the mixed-integer linear programming (MILP) [1–6] and the mixed-integer nonlinear programming [7], as well as the meta heuristics such as the simulated annealing [8] and

the genetic algorithm [9]. For example, in the method based on the MILP, the selection, numbers, and on/off status of operation of equipment are expressed by integer variables, and the capacities and load allocation of equipment by continuous ones. However, the optimal design problem has often been treated in consideration of single-period operation [1], or multi-period one for a small number of periods [2], to avoid excessive difficulty of the problem. This is because the number of integer variables increases with those of equipment and periods, and it becomes difficult to obtain the optimal solution in a practical computation time using the conventional solution algorithm for the MILP which combines the branch and bound method with the simplex one.

Some efforts have been made to treat the optimal design problem in consideration of multi-period operation for a larger number of periods [3–5]. Nevertheless, equipment capacities have still been treated as continuous variables, and correspondingly performance characteristics and capital costs of equipment have been assumed to be continuous functions with respect to their capacities. This is because if equipment capacities are treated discretely, the number of integer variables increases drastically, and the problem becomes too difficult to solve. As a result, the treatment of equipment capacities as continuous variables causes discrepancies between existing and optimized values of capacities, and expresses the dependence of performance characteristics and capital costs on capacities with worse approximations. On the other hand, an optimal design method has been proposed in consideration of discreteness of equipment capacities [6]. In this method, a formulation for keeping the number of integer variables as small as possible has been presented to solve the optimal design problem easily. However, the aforementioned difficulty in the MILP method still exists essentially. Even commercial MILP solvers which are recently available may not derive the optimal solutions in practical computation times.

In this paper, a MILP method utilizing the hierarchical relationship between design and operation variables is proposed to efficiently solve the optimal design problem of energy supply systems in consideration of discreteness of equipment capacities: At the upper level, the values of the design variables are optimized by the conventional branch and bound method; At the lower level, the values of the operation variables are optimized independently at each period by the conventional branch and bound method; Both the levels are connected with each other to exchange data for optimization calculations. Since this MILP method utilizing the hierarchical relationship cannot be incorporated into commercial MILP solvers currently, it is incorporated into an open solver at the initial stage. Finally, a numerical study on the optimal design of a gas engine cogeneration system for electric power and hot water supply is conducted using the proposed method, and its validity and effectiveness are investigated.

2. Formulation of optimal design problem

2.1. Summary of optimal design problem

To consider seasonal and hourly variations in energy demands, a typical year is divided into multiple periods, and energy demands are estimated for each period. As shown in Fig. 1, a super structure for an energy supply system is created to match energy demand requirements. The super structure is composed of all the units of equipment considered as candidates for selection, and a real structure is created by selecting some units of equipment from the candidates. Furthermore, some units of equipment are operated to satisfy energy demands for each period. The selection, capacities, and numbers of equipment are considered as design variables, and the on/off status of operation and load allocation of equipment as operation ones. The hierarchical relationship between the design and operation variables is shown in Fig. 2. The selection and capacities are expressed by binary variables, the numbers and on/off status of operation by integer ones, and the load allocation by continuous ones.

As fundamental constraints, performance characteristics of equipment and energy balance relationships are considered. If necessary, other constraints such as relationships between maximum

contract demands and consumptions of purchased energy, and operational restrictions are considered.

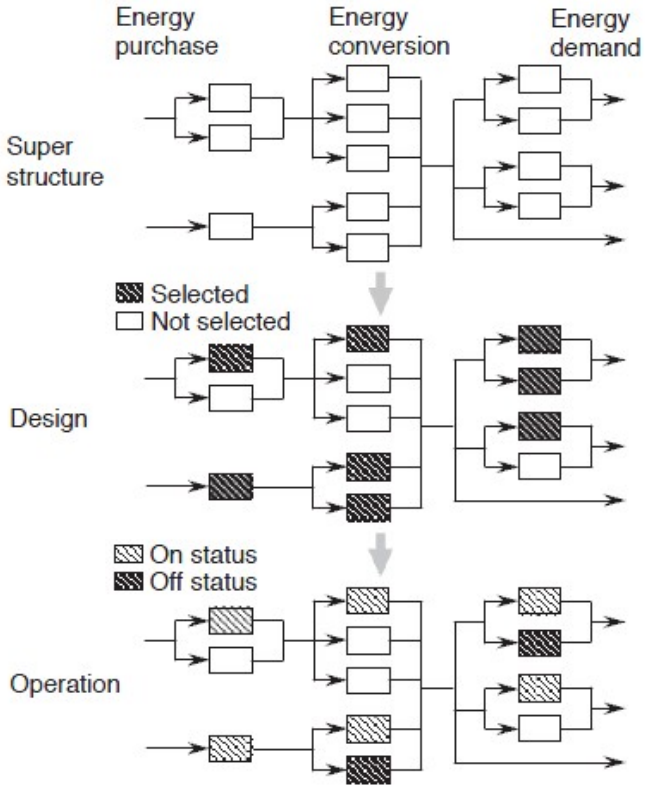

Fig. 1. Concept of super structure.

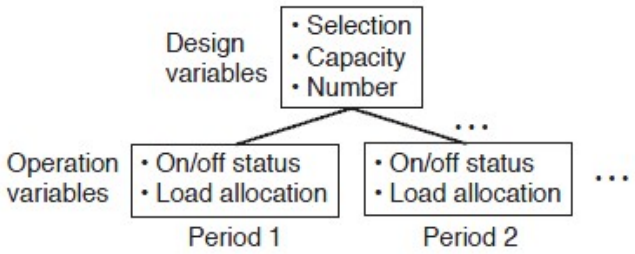

Fig. 2. Hierarchical relationship between design and operation variables

As the objective function to be minimized, the annual total cost is adopted typically, and is evaluated as the sum of annual capital cost of equipment and annual operational cost of purchased energy.

These constraints and objective function are expressed as functions with respect to the design and operation variables.

In the following, an optimal design problem is formulated for the energy supply system with a simple super structure shown in Fig. 3. The formulation can easily be extended to energy supply systems with complex super structures.

2.2. Selection, capacities, and numbers of equipment

The energy supply system is composed of I blocks, each of which corresponds to a type of equipment. The capacity of the ith type of equipment is selected from its J_i candidates. In addition, the number of the ith type and the jth capacity of equipment is determined within its maximum N_{ij}.

The selection and number of the *i*th type and the *j*th capacity of equipment are designated by the

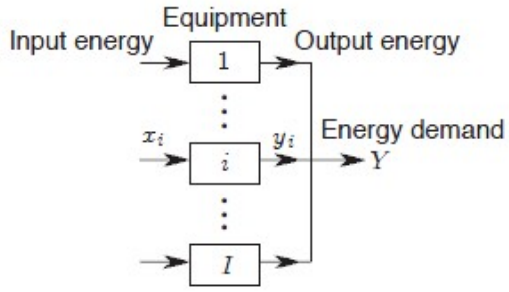

Fig. 3. Energy supply system with simple super structure

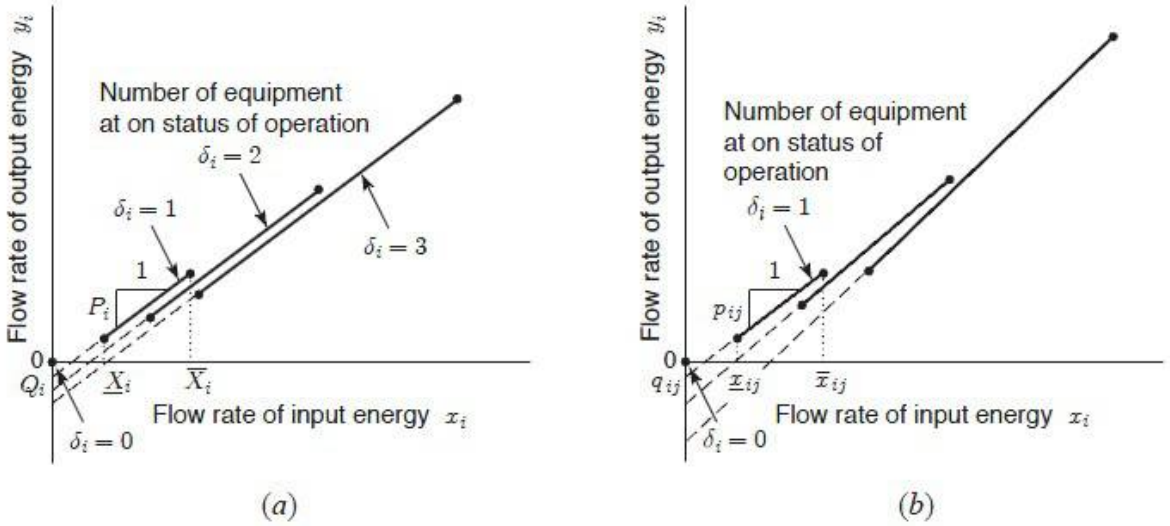

Fig. 4. Modeling of performance characteristics of equipment: a) dependence on number of equipment at on status of operation, b) dependence on capacity of equipment.

binary variable γ_{ij} and the integer variable η_{ij}, respectively. By these definitions, the following equations are obtained:

$$\left.\begin{aligned} &\eta_{ij}/N_{ij} \le \gamma_{ij} \le \eta_{ij} \quad (j = 1, 2, \cdots, J_i) \\ &\sum_{j=1}^{J_i} \gamma_{ij} \le 1 \\ &\gamma_{ij} \in \{0, 1\} \quad (j = 1, 2, \cdots, J_i) \\ &\eta_{ij} \in \{0, 1, \cdots, N_{ij}\} \quad (j = 1, 2, \cdots, J_i) \end{aligned}\right\} (i = 1, 2, \cdots, I) \qquad (1)$$

Here, it is assumed that multiple units with the same capacity can be selected for a type of equipment. To select multiple units with different capacities for a type of equipment, multiple blocks for the type of equipment should be included in the system.

2.3. Performance characteristics of equipment

A relationship between the flow rates of input and output energy is shown in Fig. 4 as performance characteristics of a piece of the *i*th type of equipment. Here, the discontinuity of the relationship due

to the number of equipment at the on status of operation is expressed by an integer variable, and the relationship for all of equipment is approximated by a linear equation as follows:

$$\left.\begin{aligned} & y_i(k) = P_i x_i(k) + Q_i \delta_i(k) \\ & \underline{X}_i \delta_i(k) \le x_i(k) \le \overline{X}_i \delta_i(k) \\ & \delta_i(k) \in \{0, 1, \cdots, \max_{1 \le j \le J_i} N_{ij}\} \end{aligned}\right\} (i = 1, 2, \cdots, I;\ k = 1, 2, \cdots, K) \qquad (2)$$

where δ_i is the integer variable for the number of equipment at the on status of operation. Here, it is assumed that δ_i units of equipment are operated at the same load level, and the sums of the flow rates of input and output energy are expressed by the continuous variables x_i and y_i, respectively. This assumption is validated if the simple performance characteristics expressed by Eq. (2) are used. P_i, Q_i, $\underline{X}_i$, $\overline{X}_i$ and are the performance characteristic values, i.e., P_i and Q_i are the slope and intercept, respectively, of the linear relationship between the flow rates of input and output energy for a piece of equipment at the on status of operation, and $\underline{X}_i$ and $\overline{X}_i$ are the lower and upper limits, respectively, for the flow rate of input energy for a piece of equipment at the on status of operation. The argument k is the index for periods, and K is the number of periods. The first equation in Eq. (2) expresses the flow rate of output energy as a function with respect to that of input energy when a part of equipment are at the on status of operation, and makes the flow rate of output energy zero when all of equipment are at the off status of operation. The second equation in Eq. (2) makes the flow rate of input energy within its lower and upper limits when a part of equipment are at the on status of operation, and zero when all of equipment are at the off status of operation. The third equation in Eq. (2) means that the number of equipment at the on status of operation may not be larger than that selected. Since δ_i is common to all the capacities, $\max_{1 \le j \le J_i} N_{ij}$ is used as its maximum in this equation.

The values of P_i, Q_i, $\underline{X}_i$, and $\overline{X}_i$ depend on the selected capacity, and are expressed as follows:

$$\left.\begin{aligned} P_i &= \sum_{j=1}^{J_i} p_{ij}\gamma_{ij} \\ Q_i &= \sum_{j=1}^{J_i} q_{ij}\gamma_{ij} \\ \underline{X}_i &= \sum_{j=1}^{J_i} \underline{x}_{ij}\gamma_{ij} \\ \overline{X}_i &= \sum_{j=1}^{J_i} \overline{x}_{ij}\gamma_{ij} \end{aligned}\right\} (i = 1, 2, \cdots, I) \qquad (3)$$

where p_{ij}, q_{ij}, $\underline{x}_{ij}$, and $\overline{x}_{ij}$ are the performance characteristic values of the ith type and the jth capacity of equipment, i.e., p_{ij} and q_{ij} are the slope and intercept, respectively, of the linear relationship between the flow rates of input and output energy, and $\underline{x}_{ij}$ and $\overline{x}_{ij}$ are the lower and upper limits, respectively, for the flow rate of input energy. In addition, the number of equipment at the on status of operation is smaller than or equal to that selected, and the following equation is obtained:

$$\delta_i(k) \le \sum_{j=1}^{J_i} \eta_{ij} \quad (i = 1, 2, \cdots, I;\ k = 1, 2, \cdots, K) \qquad (4)$$

Therefore, Eqs. (2) to (4) result in

$$\left.\begin{aligned} & y_i(k) = \sum_{j=1}^{J_i} p_{ij}\gamma_{ij}x_i(k) + \sum_{j=1}^{J_i} q_{ij}\gamma_{ij}\delta_i(k) \\ & \sum_{j=1}^{J_i} \underline{x}_{ij}\gamma_{ij}\delta_i(k) \le x_i(k) \le \sum_{j=1}^{J_i} \overline{x}_{ij}\gamma_{ij}\delta_i(k) \\ & \delta_i(k) \le \sum_{j=1}^{J_i} \eta_{ij} \\ & \delta_i(k) \in \{0, 1, \cdots, \max_{1 \le j \le J_i} N_{ij}\} \end{aligned}\right\} (i = 1, 2, \cdots, I;\ k = 1, 2, \cdots, K) \qquad (5)$$

Since δ_i is common to all the capacities, this formulation keeps the number of integer variables as small as possible, which makes the computation time as short as possible.

2.4. Capital costs of equipment

The capital cost of each unit of equipment depends on its capacity and performance characteristics. The capital cost of the *i*th type of equipment C_i is calculated as follows:

$$C_i = \sum_{j=1}^{J_i} c_{ij}\eta_{ij} \quad (i = 1, 2, \cdots, I) \qquad (6)$$

where c_{ij} is the capital cost of the *i*th type and the *j*th capacity of equipment.

2.5. Objective function and energy balance relationship

As mentioned previously, the annual total cost is adopted as the objective function z to be minimized, and is expressed by

$$\begin{aligned} z &= \sum_{i=1}^{I} \left(RC_i + \varphi_i \sum_{k=1}^{K} T(k)x_i(k) \right) \\ &= \sum_{i=1}^{I} \left(R \sum_{j=1}^{J_i} c_{ij}\eta_{ij} + \varphi_i \sum_{k=1}^{K} T(k)x_i(k) \right) \end{aligned} \qquad (7)$$

where R is the capital recovery factor, φ_i is the unit cost for energy charge of the input energy consumed by the *i*th type of equipment, and T is the duration per year of each period.

As the energy balance relationship, the following equation is considered:

$$\sum_{i=1}^{I} y_i(k) = Y(k) \quad (k = 1, 2, \cdots, K) \qquad (8)$$

where Y is the energy demand for each period.

3. Solution of optimal design problem

3.1. Linearization of nonlinear terms

The aforementioned formulation leads to the following optimal design problem:

Find γ_{ij}, η_{ij}, $\delta_i(k)$, $x_i(k)$, and $y_i(k)$
$(i = 1, 2, \cdots, I;\ j = 1, 2, \cdots, J_i;\ k = 1, 2, \cdots, K)$
which minimize z of Eq. (7)
subject to Eqs. (1), (5) and (8).

To reformulate this optimal design problem as a MILP one, the nonlinear terms due to the products of γ_{ij} and x_{ij}, γ_{ij} and and in Eq. (5) are replaced by the continuous variables ξ_{ij} and ζ_{ij}, respectively, as follows:

$$\xi_{ij}(k) = \gamma_{ij} x_i(k) \quad (i = 1, 2, \cdots, I;\ j = 1, 2, \cdots, J_i;\ k = 1, 2, \cdots, K) \tag{9}$$

$$\zeta_{ij}(k) = \gamma_{ij} \delta_i(k) \quad (i = 1, 2, \cdots, I;\ j = 1, 2, \cdots, J_i;\ k = 1, 2, \cdots, K) \tag{10}$$

As a result, Eq. (5) is reduced to

$$\left.\begin{aligned} & y_i(k) = \sum_{j=1}^{J_i} p_{ij} \xi_{ij}(k) + \sum_{j=1}^{J_i} q_{ij} \zeta_{ij}(k) \\ & \sum_{j=1}^{J_i} \underline{x}_{ij} \zeta_{ij}(k) \le x_i(k) \le \sum_{j=1}^{J_i} \bar{x}_{ij} \zeta_{ij}(k) \\ & \delta_i(k) \le \sum_{j=1}^{J_i} \eta_{ij} \\ & \delta_i(k) \in \{0, 1, \cdots, \max_{1 \le j \le J_i} N_{ij}\} \end{aligned}\right\} (i = 1, 2, \cdots, I;\ k = 1, 2, \cdots, K) \tag{11}$$

In addition, the following constraints are employed:

$$\left.\begin{aligned} & \underline{x}_i(k) \gamma_{ij} \le \xi_{ij}(k) \le \tilde{x}_i(k) \gamma_{ij} \\ & x_i(k) - \tilde{x}_i(k)(1 - \gamma_{ij}) \le \xi_{ij}(k) \le x_i(k) \end{aligned}\right\} \\ (i = 1, 2, \cdots, I;\ j = 1, 2, \cdots, J_i;\ k = 1, 2, \cdots, K) \tag{12}$$

$$\left.\begin{aligned} & \underline{\delta}_i(k) \gamma_{ij} \le \zeta_{ij}(k) \le \tilde{\delta}_i(k) \gamma_{ij} \\ & \delta_i(k) - \tilde{\delta}_i(k)(1 - \gamma_{ij}) \le \zeta_{ij}(k) \le \delta_i(k) \end{aligned}\right\} \\ (i = 1, 2, \cdots, I;\ j = 1, 2, \cdots, J_i;\ k = 1, 2, \cdots, K) \tag{13}$$

where ($\underset{\sim}{}$) and ($\tilde{}$) are lower and upper bounds, respectively, and these values can be set as follows:

$$\left.\begin{aligned} & \underline{x}_i(k) = 0 \\ & \tilde{x}_i(k) = \max_{1 \le j \le J_i} N_{ij} \bar{x}_{ij} \end{aligned}\right\} (i = 1, 2, \cdots, I;\ k = 1, 2, \cdots, K) \tag{14}$$

$$\left.\begin{aligned} & \underline{\delta}_i(k) = 0 \\ & \tilde{\delta}_i(k) = \max_{1 \le j \le J_i} N_{ij} \end{aligned}\right\} (i = 1, 2, \cdots, I;\ k = 1, 2, \cdots, K) \tag{15}$$

The validity of the constraints of Eqs. (12) and (13) are shown as follows: Eq. (12) means that if $\gamma_{ij} = 0$, then $\xi_{ij}(k) = 0$, and that else if $\gamma_{ij} = 1$, then $\xi_{ij}(k) = x_i(k)$, which makes Eq. (9) valid indirectly; Similarly, Eq. (13) means that if $\gamma_{ij} = 0$, then $\zeta_{ij} = 0$, and that else if $\gamma_{ij} = 1$, then $\zeta_{ij} = \delta_i(k)$, which makes Eq. (10) valid indirectly.

This procedure can linearize the nonlinear terms without any approximations and transform the optimal design problem into a MILP one as follows:

Find γ_{ij}, η_{ij}, $\delta_i(k)$, $x_i(k)$, $y_i(k)$, $\xi_{ij}(k)$, and $\zeta_{ij}(k)$
$(i = 1, 2, \cdots, I;\ j = 1, 2, \cdots, J_i;\ k = 1, 2, \cdots, K)$
which minimize z of Eq. (7)
subject to Eqs. (1), (8), and (11) to (13).

3.2. Solution in consideration of hierarchical relationship

Some commercial MILP solvers which are recently available can solve large scale problems in practical computation times [10]. The reformulated MILP problem may be solved by such solvers. However, the MILP problem under consideration has the feature that it becomes extremely large scale with increases in the numbers of equipment and periods, *I*, *J*, and *K*. In such cases, even commercial MILP solvers may not derive the optimal solutions in practical computation times. In this paper, a special solution method is developed in consideration of the hierarchical relationship between the design and operation variables. However, this special solution method cannot be incorporated into commercial MILP solvers currently, because they are not open for revision. Therefore, the special solution method is incorporated into a MILP solver published in reference [11], because it is open for revision.

The original optimal design problem has the hierarchical relationship between the design and operation variables as shown in Fig. 2. The reformulated MILP problem also has a similar relationship.

Namely, the design variables at the upper level are the binary and integer variables, γ_{ij} and η_{ij} , respectively, while the operation variables at the lower level are the integer variable $\delta_i(k)$ as well as the continuous variables $x_i(k)$, $y_i(k)$, $\xi_{ij}(k)$, and $\zeta_{ij}(k)$ at each period *k*. The values of these design

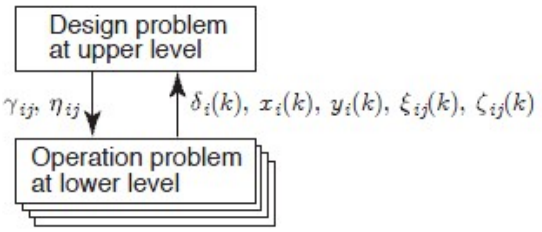

Fig. 5. Solution process in consideration of hierarchical relationship between design and operation variables.

and operation variables at all the periods should be optimized simultaneously. However, if the values of the design variables are assumed tentatively at the upper level, the values of the operation variables can be optimized independently at each period at the lower level. This feature leads to the following hierarchical solution process as shown in Fig. 5.

In place of the reformulated MILP problem, the design and operation problems at the upper and lower levels, respectively, are defined as follows:

Design problem

Find	γ_{ij}, η_{ij}, $\delta_i(k)$, $x_i(k)$, $y_i(k)$, $\xi_{ij}(k)$, and $\zeta_{ij}(k)$ $(i = 1, 2, \cdots, I;\ j = 1, 2, \cdots, J_i;\ k = 1, 2, \cdots, K)$
which minimize	z of Eq. (7)
subject to	Eqs. (1), (8), and (11) to (13)
by relaxing	$\delta_i(k)$ as a continuous variable.

Operation problem $(k = 1, 2, \cdots, K)$

Find	$\delta_i(k)$, $x_i(k)$, $y_i(k)$, $\xi_{ij}(k)$, and $\zeta_{ij}(k)$ $(i = 1, 2, \cdots, I;\ j = 1, 2, \cdots, J_i)$
which minimize	$\sum_{i=1}^{I} \varphi_i T(k) x_i(k)$ as a part of Eq. (7)
subject to	Eqs. (8) and (11) to (13)
by giving	γ_{ij} and η_{ij} which satisfy Eq. (1).

The design problem at the upper level is defined by relaxing $\delta_i(k)$ as a continuous variable in the reformulated MILP problem, while the operation problem at the lower level is defined at each period by adopting $\sum_{i=1}^{I} \varphi_i T(k) x_i(k)$ as the objective function and giving the values of γ_{ij} and η_{ij} .

The optimal values of the design variables, γ_{ij} and η_{ij} are searched by the branching and bounding operations used in the conventional branch and bound method. In the proposed method, however, when the branching operation is conducted for all the design variables and their values are assumed tentatively, the operation problem at the lower level is solved independently at each period by the conventional branch and bound method, and its result is returned to the design problem at the upper level as follows: If an operation problem at a period is infeasible, or the deficit in energy supply arises, the tentative values of the design variables cannot become the optimal solution, and therefore the bounding operation is conducted; If the operation problems at all the periods are feasible, the values of the operation variables, $\delta_i(k)$, $x_i(k)$, $y_i(k)$, $\xi_{ij}(k)$, and $\zeta_{ij}(k)$, and are determined, and a part of the objective function $\sum_{i=1}^{I} \sum_{k=1}^{K} \varphi_i T(k) x_i(k)$ is evaluated correspondingly; Then, the value of the objective function z is evaluated using the tentative value of η_{ij} ; If z is larger than that for the tentative optimal solution obtained previously, the bounding operation is conducted; Else if z is smaller than that for the tentative optimal solution, this solution is a new candidate for the optimal solution, and the tentative optimal solution is replaced with it.

The number of all the variables in the design problem is the same as that in the reformulated MILP problem. However, the number of the binary and integer variables in the design problem is much smaller than that in the reformulated MILP problem. Therefore, the design problem needs a smaller memory size as well as a shorter computation time for conducting the branching and bounding operations. In addition, the number of the variables of the operation problem at each period is quite small, and the operation problem can be solved easily. As a result, the proposed method has better features in memory size and computation time as compared with the direct solution of the reformulated MILP problem.

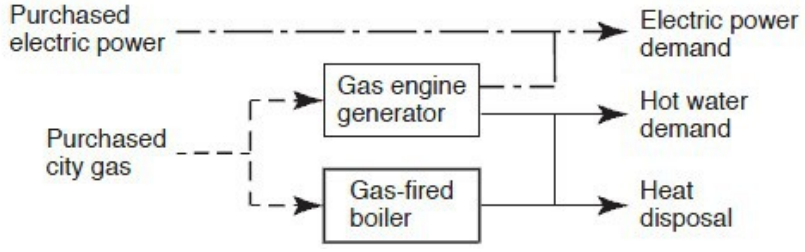

Fig. 6. Super structure for gas engine cogeneration susyem

The aforementioned proposed method is incorporated into the open solver in the following way: Two sets of general programs by the conventional branch and bound method are prepared for both the design and operation problems; Specific programs for creating matrices for simplex tableaus are also prepared for both the design and operation problems. These specific programs are generated automatically from the equations for the objective function and constraints in consideration of the structure of an energy supply system and the number of periods. All the programs are connected with one another to exchange data for conducting the branching and bounding operations in the design and operation problems.

Table 1. Capacities of equipment for selection

Equipment	Capacity	Item	Value
Gas engine generator	1	Maximum power output Maximum hot water output	25.0 kW 138.2 MJ/h
	2	Maximum power output Maximum hot water output	35.0 kW 189.6 MJ/h
Gas-fired boiler	1	Maximum hot water output	356.4 MJ/h
	2	Maximum hot water output	712.9 MJ/h

4. Numerical study on optimal design of cogeneration system

4.1. Conditions

The proposed method is applied to a numerical study on the optimal design of a gas engine cogenetation system for electric power and hot water supply. Figure 6 shows the super structure for the system, which has two gas engine generators with a same capacity and two gas-fired boilers with a same capacity. Table 1 shows the capacities of the gas engine generators and gas-fired boilers to be selected. In addition to the equipment, the maximum contract demands of electric power and city gas purchased from outside utility companies are also determined. However, the proposed method can treat only binary and integer variables in the design problem at the upper level. Thus, the maximum contract demands of electric power and city gas are treated using integer variables, and are selected among discrete values by 10.0 kW and 1.0 Nm^3/h, respectively. Table 2 shows the capital costs of equipment as well as the unit costs for demand and energy charges of utilities. The capital recovery factor is set at 0.7782 by assuming the interest rate and life of equipment as 0.02 and 15 y respectively.

Table 2. Capital costs of equipment and unit costs for demand and energy charges of utilities

Equipment/Utility	Item	Value
Gas engine generator	Capital cost	225.0 $x10^3$ yen/kW
Gas-fired boiler	Capital cost	2.5 $x10^3$ yen/kW
Electric power	Unit cost for demand charge Unit cost for energy charge	1685 yen/(kW·month) 12.08 yen/kWh
City gas	Unit cost for demand charge Unit cost for energy charge	630 yen/(Nm3/h·month) 60 yen/Nm3

A hotel with the total floor area of 3000 m^2 is selected as the building which is supplied with electric power and hot water by the cogeneration system. To take account of seasonal and hourly variations in energy demands, a typical year is divided into three representative days in summer, midseason, and winter whose numbers of days per year are set as 122, 122, and 121 d/y, respectively, and each day is further divided into 3, 6, and 12 sampling time intervals with 8, 4, and 2 h, respectively. Thus, the year is divided into 9, 18, and 36 periods correspondingly. Figure 7 shows the hourly changes in energy demands in each season for the case with 12 sampling time intervals per day.

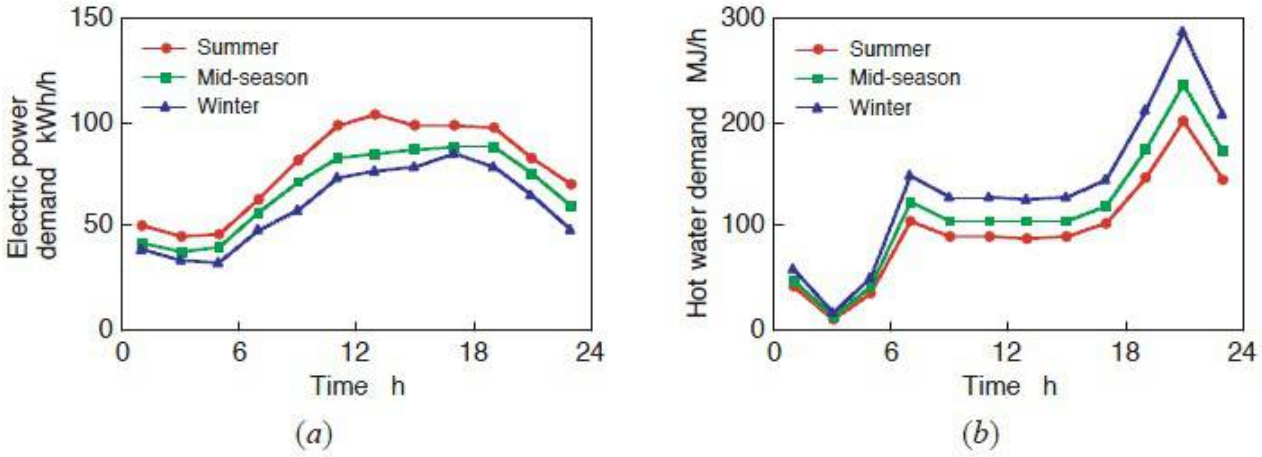

Fig. 7. Energy demands in three seasons at hotel: a) electric power, b) hot water.

Table 3. Results by optimization calculations

Number of periods	Conventional method		Proposed method		Capacity and number of gas engine generator kW	Capacity and number of gas-fired boiler MJ/h	Electric Power contract demand kW	City gas contract demand Nm^3/h
	Solution and Objective $\times 10^6$ yen/y	Computation time	Solution and Objective $\times 10^6$ yen/y	Computation time				
9 (3×3)	Optimal 10.45	3072 s	Optimal 10.45	2 s	25.0×2	—	50	13
18 (6×3)	Feasible 10.54	3600 s*	Optimal 10.44	6 s	25.0×1	356.4×1	80	10
36 (12×3)	Feasible 10.90	3600 s*	Optimal 10.49	192 s	25.0×1	356.4×1	80	13

* Attains limit for computation time.

4.2. Results and discussion

Table 3 shows the results obtained by the optimization calculations on a MacBook Air with Mac OS X 10.6.7. The optimal design problem is solved by both the conventional and proposed methods. Both the design and operation variables are simultaneously optimized by the conventional method. This calculation is conducted using the same program as that used for the design problem by the proposed method. The results obtained by both the methods are compared with each other in terms of solutions and computation times. In addition, the values of the design variables obtained by the proposed method are also shown.

In the case with the number of periods of 9, both the methods derive the optimal solution. However, the conventional method needs a much longer computation time. In the cases with the number of periods of 18 and 36, the proposed method derives the optimal solutions in practical computation times. However, the conventional method does not derive the optimal solutions but only feasible ones within the limit for the computation time. In the case with the number of periods of 9, the

optimal solution adopts two smaller gas engine generators. In the cases with the number of periods of 18 and 36, the optimal solutions adopt one smaller gas engine generator and one smaller gas-fired boiler. These are because in the former case the electric power and hot water demands are averaged and resultantly balanced, which is advantageous to cogeneration, and in the latter cases the electric power and hot water demands are not balanced in some periods.

As an example, Fig. 8 shows the allocation in electric power and hot water supply in summer in the case with the number of periods of 36. The gas engine generator is stopped, is operated at a part load status, or is operated at the rated load status, depending on the electric power and hot water demands. The heat flow rate of hot water generated by the gas engine generator is larger than the hot water demand during 10:00 to 18:00, and its excess is disposed of. This is because the purchased electric power attains its contract demand. In addition, the heat flow rate of hot water generated by the gas-fired boiler is larger than the hot water demand during 2:00 to 6:00, and its excess is disposed of. This is because the lower limit for the hot water output of the gas-fired boiler is larger than the hot water demand.

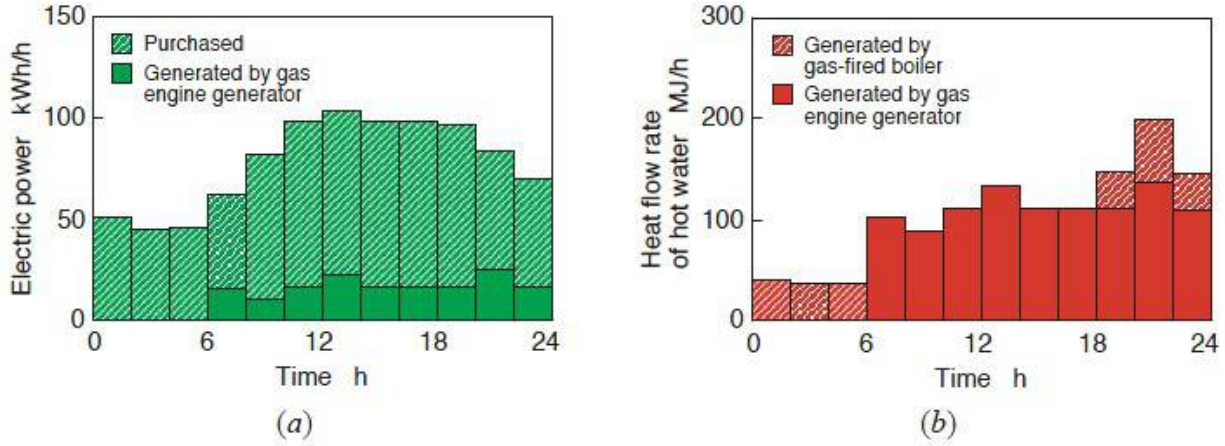

Fig. 8. Allocation in energy supply in summer: a) electric power, b) hot water

5. Conclusions

A MILP method utilizing the hierarchical relationship between design and operation variables has been proposed to efficiently solve the optimal design problem of energy supply systems in consideration of discreteness of equipment capacities: At the upper level, the values of the design variables are optimized by the conventional branch and bound method; At the lower level, the values of the operation variables are optimized independently at each period by the conventional branch and bound method; Both the levels are connected with each other to exchange data for optimization calculations. This MILP method utilizing the hierarchical relationship has been incorporated into an open solver at the initial stage. Finally, the proposed method has been applied to a numerical study on the optimal design of a gas engine cogenetation system for electric power and hot water supply. The optimal design problem has been solved with a change in the number of periods by both the conventional and proposed methods. The results obtained by both the methods have been compared with each other in terms of solutions and computation times. Through the study, it has turned out that the proposed method is much superior to the conventional one in terms of computation time. In addition, some features concerning the optimal design and operation of the cogeneration system have been clarifired.

As a subsequent subject, the proposed method should be incorporated into commercial solvers so that much larger scale optimal design problems can be solved in practical computation times.

Nomenclature

C, c : capital cost of equipment
I : number of types of equipment
J : number of capacities of equipment
K : number of periods
k : index for periods
N : maximum number of selected equipment
P, p : slope of linear relationship between flow rates of input and output energy of equipment
Q, q : intercept of linear relationship between flow rates of input and output energy of equipment
R : capital recovery factor
T : duration per year of period
$\underline{X}$, $\underline{x}$: lower limit for flow rate of input energy of equipment
$\overline{X}$, $\overline{x}$: upper limit for flow rate of input energy of equipment
x : flow rate of input energy
Y : energy demand
y : flow rate of output energy
z : annual total cost
γ : selection of equipment
δ : number of equipment at on status of operation
ζ : product of γ and δ
η : number of selected equipment
ξ : product of γ and x
φ : unit cost for energy charge of input energy
($\underset{\sim}{}$): lower bound
($\tilde{}$): upper bound

Subscripts

i : index for types of equipment
j : index for capacities of equipment

References

[1] Papoulias SA, Grossmann IE. A structural optimization approach in process synthesis—I: utility ystems. Computers and Chemical Engineering 1983; 7 (6): 695–706.

[2] Horii S, Ito K, Pak PS, Suzuki Y. Optimal planning of gas turbine co-generation plants based n mixed-integer linear programming. International Journal of Energy Research 1987; 11 (4):507–518.

[3] Iyer RR, Grossmann IE. Synthesis and operational planning of utility systems for multiperiod operation. Computers and Chemical Engineering 1998; 22 (7–8): 979–993.

[4] Yokoyama R, Hasegawa Y, Ito K. Structural optimization of energy supply systems by a decomposition method for mixed-integer linear programming. Transactions of the JSME, ser. C 2000; 66 (652): 4016–4023 (in Japanese).

[5] Yokoyama R, Hasegawa Y, Ito K. A MILP decomposition approach to large scale optimization in structural design of energy supply systems. Energy Conversion and Management 2002; 43 (6): 771–790.

[6] Yokoyama R, Ito K. Optimal design of gas turbine cogeneration plants in consideration of discreteness of equipment capacities, Transactions of the ASME, Journal of Engineering for Gas Turbines and Power 2006; 128 (2): 336–343.

[7] Adjiman CS, Schweiger CA, Floudas CA. Mixed-integer nonlinear optimization in process synthesis. In: Du D-Z, Pardalos PM, editors. Handbook of combinatorial optimization, vol. 1, Dordrecht: Kluwer Academic Publishers; 1998, p. 1–76.

[8] Painton LA, Diwekar UM. Synthesizing optimal design configurations for a Brayton cycle power plant. Computers and Chemical Engineering 1994; 18 (5): 369–381.

[9] Fujita K, Akagi S, Hirokawa N, Yoshida K. Optimal planning method of energy plant configurations based on a genetic algorithm. Transactions of the JSME, ser. C 1998; 64 (617): 354–361 (in Japanese).

[10] Rosenthal RE, GAMS—a user's guide. Washington: GAMS Development Corporation; 2008.

[11] Kuester JL, Mize JH. Optimization techniques with FORTRAN. NewYork: McGraw-Hill;

[12] 1972.

The Fuel Impact Formula Revisited

César Torres[a] and Antonio Valero [b]

[a] Research Centre for Energy Resources and Consumption – CIRCE, Universidad de Zaragoza, Mariano Esquillor, 15, 50018, Zaragoza (Spain), cesar.torres@endesa.es
[b] Research Centre for Energy Resources and Consumption – CIRCE, Universidad de Zaragoza, Mariano Esquillor, 15, 50018, Zaragoza (Spain), valero@unizar.es

Abstract:

Energy systems comprise complex networks structures, where the irreversibility of a process depends on those of other processes. Thermoeconomics provides tools to identify and to quantify the additional consumption of resources caused by an irreversibility increase of some component affecting the other components. The fuel impact formula is the mathematical expression of the non-equivalence of energy losses in energy systems, i.e. the same irreversibility change on several system components has a different effect on the corresponding change on the total irreversibility of the system. This formula is used for diagnosis of malfunctions in energy plants and also for evaluating the potential energy saving that could be obtained by the efficiency improving in one or more processes. For this last purpose simulations or approximation formulae are used, but error estimation has not yet been studied.

The aim of this paper is to review the fundamentals of the principle of non-equivalence of the exergy losses and its connection with the thermoeconomic isolation principle, which allows to analyse the potential savings of each individual process instead on the overall system. A revised *exact* expression of the global exergy savings due to the improvement of the efficiency of a component and a new indicator of the thermoeconomic isolation of process within the global system are obtained. These results provide a better understanding of the effects of local savings and the productive structure in the total energy saving of any energy system.

Keywords:

Irreversibility, Fuel Impact Formula, Thermoeconomic isolation, Energy Savings

1. Introduction

According to the exergy cost theory [1], the fuel impact is the effect on total resources consumption, which can be achieved if the efficiency of a process, or equivalently its unit consumption, is improved. It will be assessed by multiplying its local exergy saving $\Delta I_i = P_i \Delta k_i$, by the unit exergy cost of the fuel consumed by this process, and defined as:

$$\mathrm{A}_{T,i} \equiv k^*_{F,i} P_i \Delta k_i \tag{1}$$

The fuel impact formula (1) states that the location of an irreversibility do not coincide with the location of the causes that provoke these losses. When a system's process degrades, we will need more local resources to obtain the same required production. These resources are product of some upstream process that will readapt its production, and subsequently increasing its irreversibility. Moreover, the increase of the unit exergy consumption of a process causes the increase of its unit production cost and consequently the increase of the unit production costs of all process downstream. The unit exergy cost of fuel, say $k^*_{F,i}$, is the measure of this propagation. The fuel impact formula expresses the non-equivalence of irreversibilities in different components of a system.

Consider the case of a sequential system, like the one shown in the figure 1. In this example, which corresponds to a simplified steam cycle, the variation of irreversibility of 1 MW on each process

has different fuel impacts, 2.96 MW in case the generator, 2.70 MW in case of the turbine and only 1MW in case of de boiler. However, a relative variation of its unit exergy consumption, for example $\%\Delta k = 1\%$, has the same fuel impact 0.92 MW for all components.

It is because the local irreversibility change on a process does not have the same equivalence in relative efficiency change, 1 MW in the turbine is a relative change of 3%, meanwhile in the boiler is only 1%.

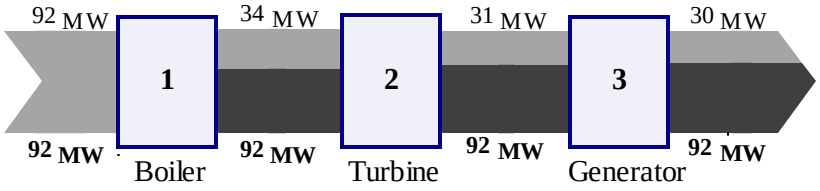

Figure 1. Exergy cost diagram of a simplified steam cycle

The fuel impact of an irreversibility variation does not depend only for the unit exergy cost of fuel, but also the amount of resources consumed by the process. In fact equation (1) could be rearranged as:

$$\mathrm{A}_{T,i} = F_i^* \%\Delta k_i \tag{2}$$

in which F_i^* is the cost of the resources consumed, and $\%\Delta k_i = \Delta k_i / k_i$.

We could see, in case of a sequential system, eq. (2) measures the real fuel impact $\Delta F_{T,i}$, due to a variation in the *i*-th process efficiency, if the efficiency of the remaining components doesn't change.

For more complex systems, this expression has been proved [2] that it is a reasonable approximation for small variations. But, several theoretical questions arise here: could we find an estimation of the relative error between $\mathrm{A}_{T,i}$ and $\Delta F_{T,i}$, which explain the discrepancies? Is there an exact expression for fuel impact formula?

The fuel impact formula is the basis of Thermoeconomic Diagnosis. It was proposed by Valero et al. [3], and developed by several authors [4-8]. The formula permits to compute the fuel impact generated by each process, as a function of its unit exergy consumption changes.

2. The fuel impact formula revisited

In this section we will obtain an exact expression for external resources variation due to the efficiency variation of an individual process, with the condition that the unit exergy consumption ratios of the rest of processes do not change.

Using Thermoeconomic Input-Output (see Appendix A), Torres et al. [9] introduce an exact formula, for the fuel impact generated by process, at constant production, when the unit exergy consumption of the processes $\Delta\kappa_{ij}$ change:

$$\Delta F_T = \sum_{i=1}^{n} \left(\Delta\kappa_{0i} + \sum_{j=1}^{n} k_{P,i}^*(\bar{x}) \Delta\kappa_{ji} \right) P_i(x_0) \tag{3}$$

To compute the fuel impact it is required to know two states of the system, a reference state, say x_0, and a current state $\bar{x}$, and compute the unit production cost at the current state. Equation (3) will be our starting point to answer the question posed above.

Let´s consider now a relative change $\%\Delta k_i$ on the unit consumption of the *i*-th process, under the condition the unit exergy consumption of the rest of components do not change, i.e. $\Delta\kappa_{jl}=0$ for $l\neq i$, Hence, only the *i*-th column, say $\mathbf{k}_i$, of the matrix $\langle\mathbf{KP}\rangle$ is change and $\Delta\kappa_{ji}=\kappa_{ji}\%\Delta k_i$.

Under these conditions (3) is rewritten as:

$$\Delta F_{T,i}=\left(\kappa_{0i}+\sum_{j=1}^{n}\bar{k}^{*}_{P,j}\kappa_{ji}\right)P_i\%\Delta k_i \tag{4}$$

and:

$$\Delta F_{T,i}-\mathrm{A}_{T,i}=\left(\sum_{j=1}^{n}\Delta k^{*}_{P,j}\kappa_{ji}\right)P_i\%\Delta k_i \tag{5}$$

Therefore, to solve the problem we should compute $\Delta k^{*}_{P,j}$, for a relative change $\%\Delta k_i$.

According to equations of Thermoeconomic Input-Output (see appendix A), the unit production cost satisfy:

$${}^{\mathrm{T}}\mathbf{k}^{*}_{P}={}^{\mathrm{T}}\mathbf{k}_{e}\left|\mathbf{P}\right\rangle \tag{6}$$

Let's $\bar{\mathbf{k}}^{*}_{P}$ to be the unit production cost in the new state $\bar{x}$, when the efficiency or technical coefficients of one or several processes change, therefore:

$${}^{\mathrm{T}}\bar{\mathbf{k}}^{*}_{P}=\left({}^{\mathrm{T}}\mathbf{k}_{e}+\Delta{}^{\mathrm{T}}\mathbf{k}_{e}\right)\left|\bar{\mathbf{P}}\right\rangle \tag{7}$$

in which, the production matrix $\left|\bar{\mathbf{P}}\right\rangle$ in the new state is:

$$\left|\bar{\mathbf{P}}\right\rangle=\left|\mathbf{P}\right\rangle\left(\mathbf{U}-\Delta\left\langle\mathbf{KP}\right\rangle\left|\mathbf{P}\right\rangle\right)^{-1} \tag{8}$$

Under our problem conditions:

$$\Delta{}^{\mathrm{T}}\mathbf{k}_{e}=\%\Delta k_i\kappa_{0i}\,\mathbf{p}_i$$
$$\Delta\left\langle\mathbf{KP}\right\rangle\left|\mathbf{P}\right\rangle=\%\Delta k_i\mathbf{k}_i\otimes\mathbf{p}_i$$

where $\mathbf{p}_i$ denote the *i*-th row of matrix $\left|\mathbf{P}\right\rangle$.

Therefore, applying the Sherman-Morrison formula (see Appendix C), we get:

$$\left(\mathbf{U}-\Delta\left\langle\mathbf{KP}\right\rangle\left|\mathbf{P}\right\rangle\right)^{-1}=\mathbf{U}+\frac{\%\Delta k_i}{1-\tau_i\%\Delta k_i}\mathbf{k}_i\otimes\mathbf{p}_i \tag{9}$$

Note that the quotient of the right side equation is a scalar, and τ_i is also a scalar defined as:

$$\tau_i\equiv\mathbf{p}_i\cdot\mathbf{k}_i=\sum_j p_{ij}k_{ji}=p_{ii}-1 \tag{10}$$

Substitution of (9) into (7) yields:

$${}^{\mathrm{T}}\bar{\mathbf{k}}^{*}_{P}-{}^{\mathrm{T}}\mathbf{k}^{*}_{P}=\Delta{}^{\mathrm{T}}\mathbf{k}^{*}_{P}=\frac{\%\Delta k_i}{1-\tau_i\%\Delta k_i}k^{*}_{F,i}\,k_i\,\mathbf{p}_i \tag{11}$$

and, substitution of (11) into (5), follows:

$$\Delta F_{T,i}-\mathrm{A}_{T,i}=F^{*}_{i}\frac{\tau_i\%\Delta k_i}{1-\tau_i\%\Delta k_i}\%\Delta k_i \tag{12}$$

Therefore, we get an exact expression of the fuel impact formula, as a function of the relative variation of the efficiency:

$$\Delta F_{T,i} = F_i^* \frac{\%\Delta k_i}{1-\tau_i \%\Delta k_i} \tag{13}$$

where the relative error is given by:

$$\text{ò} = \frac{\left|\Delta F_{T,i} - \mathrm{A}_{T,i}\right|}{\left|\Delta F_{T,i}\right|} = \frac{\tau_i \%\Delta k_i}{1-\tau_i \%\Delta k_i} \approx \tau_i \%\Delta k_i \tag{14}$$

It means than the relative error between the original fuel impact formula and the new expression is linear, and it depends on the value of τ_i, and as consequence also depends on p_{ii}.

If the graph which represents the productive structure of the system is acyclic (see Appendix B), it means that without recirculation, the diagonal elements of the Leontief inverse matrix are $p_{ii} = 1$, and consequently $\tau_i = 0$. In these conditions, as we stated in the introduction section, the original fuel impact formula gives the correct value. Hence, the parameter τ_i measures the recirculation degree of a process and we will call it, *recirculation factor*. If a process has no feedback flows then its recirculation factor is zero. The elements of matrix $|\mathbf{P}\rangle$ represents the total requirements of product of process *i* to obtain a unit of the product of the process *j*. In particular, if $p_{ii} > 1$, it means that there is a feedback in process *i*. The larger the feedback of a process, the larger the recirculation factor is.

To simplify previous equations, we will denote $\%\Delta\bar{k}_i = \%\Delta k_i / (1-\tau_i \%\Delta k_i)$, which measure the feedback effect on the relative change of the unit exergy consumption of a process. Observe that, if $\tau_i = 0$ then $\%\Delta\bar{k}_i = \%\Delta k_i$.

Therefore the fuel impact formula (2) could be expressed as:

$$\bar{\mathrm{A}}_{T,i} = \Delta F_{T,i} = F_i^* \%\Delta\bar{k}_i \tag{15}$$

As a conclusion, if a process has no feedback the fuel impact formula coincides with the real external resources change due to a relative change of the efficiency of such process. If the system has cycles the formula maintains the same structure and only is modified by a correction factor $1/(1-\tau_i \%\Delta k_i)$, which depends on the recirculation factor and the amplitude of the change.

Table 1. Fuel Impact and related parameters caused by a deviation $\%\Delta k_i = 1\%$ in each process of the combined cycle power plant case study. Appendix D

Nr	Process	A_T	ΔF_T	ò	τ	$\%\Delta\bar{k}$	$\%\Delta F_T$
1	Combustor	2198,8	2198,8	0,000%	0,000	1,000%	1,000%
2	Compressor	1960,886	1978,531	0,892%	0,892	1,009%	0,900%
3	Gas Turbine	3219,867	3248,840	0,892%	0,892	1,009%	1,478%
4	HRSG	939,819	939,819	0,000%	0,000	1,000%	0,427%
5	Steam Turbine	943,692	943,709	0,002%	0,002	1,000%	0,429%
6	Pump	3,87306	3,87313	0,002%	0,002	1,000%	0,002%
7	Generator	2202,673	2202,712	0,002%	0,002	1,000%	1,002%

Table 1, shows the fuel impact and associated parameters for a relative change of the unit exergy cost $\%\Delta k_i = 1\%$, in each process of the combined cycle power plant, described in the Appendix D.

Note that, the relative error "ò" is directly related with the recirculation factor τ. If we observe the corresponding fuel-product diagram of the plant, see figure 2, the combustor and the HRSG has no feedback, thus, their recirculation factors are zero. The steam cycle has a small recirculation for the feedwater pump, whose fuel is provided by the generator, and its recirculation factor is very small,

and then $A_{T,5}$ provides a good value for the fuel impact of steam turbine. Compressor and gas turbine have a strong feedback loop, therefore its recirculation factor is high, and then the relative error is near to 1%. In general, for each process of this plant, as it has been put forward in the introduction, the fuel impact A_T is a reasonable approximation to the real value. But now we know how good the approximation is and why. It depends of the productive structure of the system, and in particular of their feedbacks.

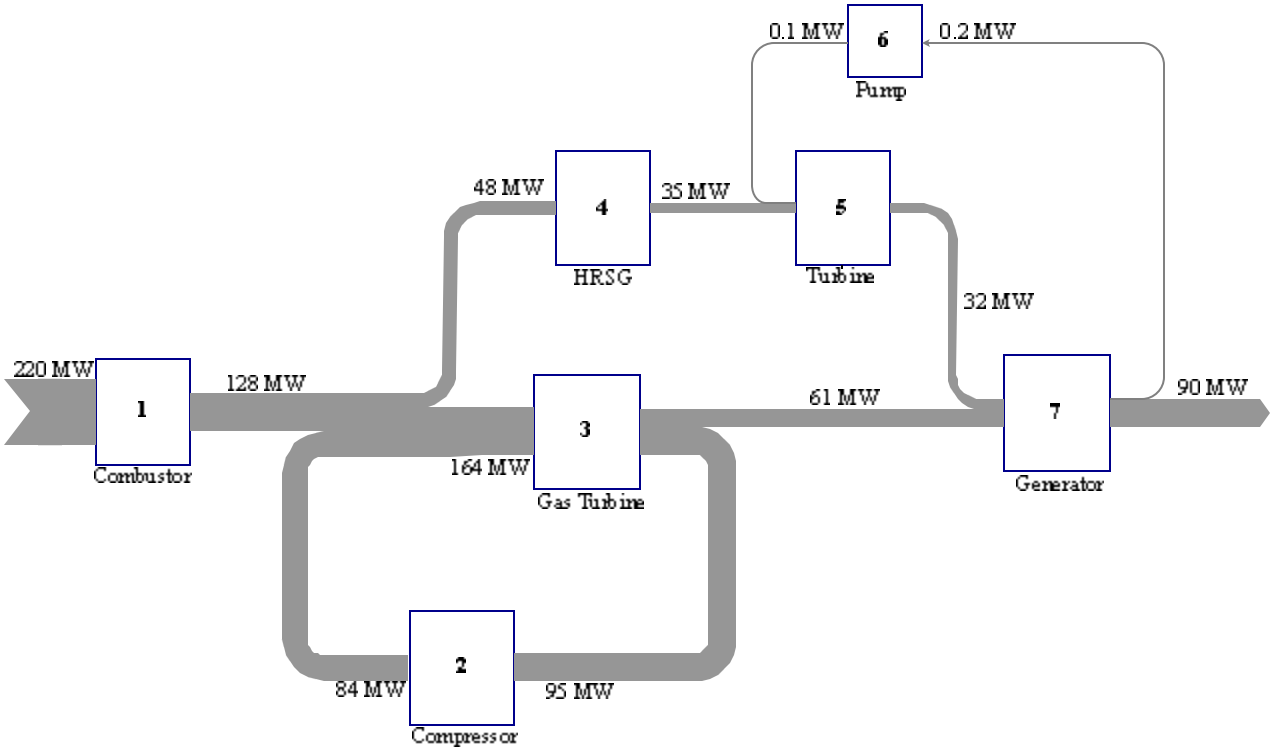

Figure 3. Fuel-Product Diagram of the Combined Cycle Power Plant

Obviously, we can use the revised fuel impact formula (13), we do not need additional calculation to compute the corrected value, the recirculation factor is obtained from the production matrix, required to calculate the unit production cost.

In last column it is shown the relative change of the total fuel due to a process efficiency change. This parameter, called total fuel elasticity factor, shows the importance of a process on the overall system, and the sensitivity of the system efficiency besides an efficiency change in a local process.

3. Production cost stability matrix

As application of the fuel impact formula, we developed in the previous section, we will determine the effect of process efficiency on the variation of the production cost, that could be expressed by means of its elasticity matrix of the type: $\%\Delta\mathbf{k}_P^* = \left[\boldsymbol{\varepsilon}_A^k\right]\%\Delta\mathbf{k}$.

From (11) the unit production cost variation of process *j* is related with the efficiency variation of process *i*, as:

$$\Delta k_{P,j}^* = k_{P,i}^* p_{ij} \%\Delta\bar{k}_i \tag{16}$$

Therefore, if a process has no recycling its unit production cost variation is $\%\Delta k_{P,i}^* = \%\Delta k_i$, it means that a variation of 1% in its unit consumption represents 1% in the unit production cost variation. But if the process has feedbacks the effect of a positive variation (malfunction) on the unit production cost variation is bigger: $\%\Delta k_{P,i}^* = p_{ii}\%\Delta\bar{k}_i > \%\Delta k_i$, because $p_{ii} > 1$.

Let denote $\left|\mathbf{P}^*\right\rangle \equiv \left[p_{ij}^*\right]$ the matrix of cost normalized total requirement values defined as $p_{ij}^* \equiv k_{P,i}^* p_{ij} / k_{P,j}^*$, therefore the elasticity matrix is $\left[\boldsymbol{\varepsilon}_A^k\right] = {}^{\mathrm{T}}\left|\mathbf{P}^*\right\rangle$ and:

$$\%\Delta k_{P,j}^* = p_{ij}^* \%\Delta \bar{k}_i \tag{17}$$

In systems without flow recirculation, the elasticity matrix is lower triangular, therefore an efficiency change only affects to downstream process, and every element is lower or equal to one.

In real plants, the measures used to calculate the efficiency of a process have a certain measurement error, and usually average values with error deviation are used. This elasticity matrix could be used to analyse the sensitivity of cost against efficiency measurement uncertainty.

In our example, the elasticity matrix of the combined cycle is:

$$\left[\varepsilon_A^k\right] = \begin{bmatrix} 1 & 0 & 0 & 0 & 0 & 0 & 0 \\ 1 & \mathbf{1.909} & \mathbf{1.909} & 0 & 0 & 0 & 0 \\ 1 & 0.9 & \mathbf{1.909} & 0 & 0 & 0 & 0 \\ 1 & 0.9 & 0.9 & 1 & 0 & 0 & 0 \\ 1 & 0.9 & 0.902 & 1 & \mathbf{1.002} & \mathbf{0.004} & \mathbf{0.004} \\ 1 & 0.9 & 1.478 & 0.427 & 0.429 & \mathbf{1.002} & \mathbf{1.002} \\ 1 & 0.9 & 1.478 & 0.427 & 0.429 & 0.002 & \mathbf{1.002} \end{bmatrix}$$

In bold characters, the values corresponding to processes with recirculating flows are shown. In the case of the gas turbine cycle (rows 2 and 3), the values are high and the process is very sensitive to changes on its efficiency, meanwhile in the Rankine cycle these values are not significant. For example an increase of 1% in the unit consumption of the gas turbine, increases 1.9% the unit cost of the compressor, meanwhile in the rest of processes an increase of 1% in the unit consumption increase the unit cost of the affected process less or equal than 1%, and recirculation in the Rankine cycle affects less than 0.005%. The last row, which corresponds to the electric generator, it shows the effect of the variation in the efficiency of each process to the production cost of the electricity, and indicates the weight of each process on the system. A malfunction in the gas turbine, column #3, has more effect that the rest of processes, meanwhile the feeder pump, column #6, has no effect.

4. Thermoeconomic Isolation

According to Evans and Frangopoulus [10,11] a process of an energy system is thermoeconomically isolated (TI), from the rest of the system if the product of the process and the unit cost of the products used as fuel in the process are constant and have known quantities. As a consequence, if a process is thermoeconomically isolated from the rest of system, then may optimized "by itself", i.e. without considering the variation made in the rest of the system processes, and the optimum solution thus obtained for the process coincides with the optimum solution for the system as a whole.

In this section we will show that the recycling factor could be used as an indicator of the thermoeconomic isolation degree of a process, and give some criteria to improve the local optimization methodology.

The first premise for thermoeconomic isolation is equivalent to say that the fuel unit cost of a process remains constant when its efficiency is modified.

The unit cost of fuel variation could be written as:

$$\Delta k_{F,i}^* = \frac{1}{k_i} \sum_{j=1}^{n} \Delta k_{P,j}^* \kappa_{ji} \tag{18}$$

and applying (16) we obtain:

$$\Delta k^*_{F,i} = \tau_i \, k^*_{F,i} \% \Delta k_i \tag{19}$$

Therefore, if the recirculation factor of a process is zero, its unit cost of fuel is constant and the first condition for TI is satisfied. If a process has no feedback, the production matrix $|\mathbf{P}\rangle$ is upper triangular, therefore, from (16) only the processes downstream modify their unit production cost.

The second premise for thermoeconomic isolation says that if the efficiency of the process varies the production remains constant, or an efficiency change in a process only modified the production of the processes upstream it.

The production variation is $\Delta\mathbf{P} = \Delta|\mathbf{P}\rangle\boldsymbol{\omega}_s$, and applying (8), we obtain:

$$\Delta|\mathbf{P}\rangle = \frac{\%\Delta k_i}{1-\tau_i \%\Delta k}|\mathbf{P}\rangle\mathbf{k}_i \otimes \mathbf{p}_i \tag{20}$$

therefore the production change is given as:

$$\Delta\mathbf{P} = P_i \%\Delta\bar{k}_i \boldsymbol{\tau}_i \tag{21}$$

where $\boldsymbol{\tau}_i$ is the i-th column of matrix of matrix $|\mathbf{P}\rangle\langle\mathbf{KP}\rangle = |\mathbf{P}\rangle - \mathbf{U}$. Hence the production change in a process due to a change in its unit consumption is:

$$\Delta P_i = \tau_i P_i \%\Delta\bar{k}_i \tag{22}$$

Equation (22) shows that the production of a process remains constant when its efficiency changes, if and only if the recirculation ratio of the process is zero. This means that the process has no recirculations or feedbacks. For the rest of processes their production changes deal $\Delta P_j = p_{ji} P_i \%\Delta\bar{k}_i$, thus if the recirculation factor of the *i*-th process is zero, then the production of every process downstream does not change.

Hence, from both results we can state that a process is thermoeconomically isolated if and only if the recirculation ratio of the process is zero. Furthermore, to fulfil this condition in a real case, a completely disjoint set of mutually independent free variables affect unit consumption for each process, is required. It means that all interdependences between processes must be banished from the thermodynamic model.

Finally as a corollary of this result, we will prove that if a process is TI, then the local fuel impact is equal to the total fuel impact $\Delta F_{T,i} = \Delta F_i^*$. In fact, the local fuel impact of a process is given by:

$$\Delta F_i^* = \Delta P_i^* = \Delta k^*_{P,i} P_i + \bar{k}^*_{P,i} \Delta P_i \tag{23}$$

If the process is TI then $\Delta P_i = 0$, applying (16) we have: $\Delta F_i^* = p_{ii} F_i^* \%\Delta\bar{k}_i$, and applying that $\tau_i = 0$, then $p_{ii} = 1$ and $\%\Delta\bar{k}_i = \%\Delta k_i$, so this results in:

$$\Delta F_{T,i} = \Delta F_i^* = F_i^* \%\Delta k_i \tag{24}$$

Thermoeconomic Isolation is an ideal condition which cannot be achieved in most of real systems, but the closer to zero of the recirculation factor is the closer to TI conditions will be, and the less iteration loops will be needed in the local optimization procedure [12].

In our study case combustor and HRSG satisfy the TI conditions. The processes of the steam cycles have recirculation factors close to zero and could be consider thermoeconomically isolated. Here, the gas turbine and compressor do not satisfy TI conditions.

Systems as Rankine cycles are near the TI conditions and this method works well. However, other systems based on gas turbine cycles have strong feedbacks and then high recirculation factors, in these cases TI is not satisfied and the convergence of local optimization procedures will not be good.

By means of graph theory algorithms [13], we can determine which processes are strongly connected and determine its recirculation factor. To apply local optimization procedures these processes should be aggregated. In case of the example of the paper, the gas turbine system should be considered as a component in order to apply local optimization.

5. Conclusions

The fuel impact formula is the mathematical representation of the principle of non-equivalence of the irreversibilities [14], therefore it needs a rigorous formalization. In this paper it has been shown that the fuel impact formula is a linear approximation to the fuel impact due to the increase of the local irreversibility of an individual process of a system. Moreover, a revised formula for the real fuel impact has been obtained, which coincides with the original exergy cost theory formula (1), when the system is sequential. For a non-sequential branched system including feedbacks, this expression becomes more complex, but essentially maintains the same idea. There exists a relationship between local irreversibility and the additional consumption of resources. Feedbacks or recyclings amplify the effect of malfunctions or local savings, thus we must pay more attention on processes where recycling plays an important role.

The importance of the fuel impact formula is paramount, because it justifies the practical reason for internal cost accounting. Or in other words, it answers the question of how many additional expenses we must pay because of presence of malfunctions in a process [15]. If the local investment ΔZ_i is related with the irreversibility that could be achieved, by means of the saving-investment formula, then a potential local investment is feasible if $\Delta Z_i < \mathrm{A}_{\mp,i}$.

The paper also introduces a new parameter, the *recirculation factor*, which measures the degree of thermoeconomic isolation of a process and could be used to improve the Local-Global Optimization methodologies.

The main drawback to use the Fuel Impact Formula to analyse the feasibility of local improvements, lies in the interdependence between the processes efficiencies, which are not taken into consideration in the formula, which is based on the hypothesis that local changes do not affect the local behaviour of the rest of processes.

From the thermodynamic model of a system, the unit consumption of a process depends of a set of free variables. But, in general, several processes could have common free variables. Insofar as the number of parameters of the thermodynamic model is greater than the number of parameters of the thermoeconomic model, i.e. unit consumptions, the former will be more sensitive to the calculation of marginal costs of the type (∂Resources/∂Parameter), than the information of the fuel impact formula.

However, as it is shown in reference [16], when the system structure is complex, the change of characteristic parameters of a process have mainly local not global effects on the rest of processes, and structural effects predominate over local effects. As far as the processes are independent, i.e. $\partial \kappa_{jl} / \partial \kappa_i \approx 0$, the accuracy of the fuel input formula is improved, and gives a good picture of the plant behaviour.

Appendix

This appendix shows a brief review of some mathematical questions required to understand the paper development, and a description of the plant used as study case.

A. Thermoeconomic Input-Output Analysis

Thermoeconomic input-output [17] is an extension of the Input-Output analysis [18], based on the second law of thermodynamics and the concept of productive purpose [19]. An energy system is formed by, say *n* processes. Let P_i denote the exergy of the *i*-th process production, which is used in part to meet the intermediate requirement as input resources of other processes and in part to meet the final demand of the system. If E_{ij} denotes the exergy of process *i* uses as resource for process *j*, and E_{i0} denotes the final demand produced in process *i*, we have the following condition:

$$P_i = E_{i0} + E_{i1} + \cdots + E_{in} \quad i = 1,...,n \tag{25}$$

On the other hand, the input resources of each process *i*, say F_i, are in part coming from external resources and in part from the production of other processes. If E_{0i} the exergy of the external resources used in process *i*, we have the condition:

$$F_i = E_{0i} + E_{1i} + \cdots + E_{ni} \quad i = 1,...,n \tag{26}$$

Furthermore, Second Law states $F_i - P_i = I_i \geq 0$, where I_i denotes the irreversibility of the process *i* and $k_i = F_i / P_i \geq 1$ represents the unit exergy consumption of process *i*. Now let κ_{ij} denote the quantity (exergy) of the process *i* production, which is used to obtain one unit of product in process *j*, then we have $E_{ij} = \kappa_{ij} P_j$, these ratios are calling *technical coefficients*, and satisfy:

$$k_i = \kappa_{0i} + \kappa_{1i} + \cdots + \kappa_{ni} \tag{27}$$

Therefore eq.(25) could be written in terms of technical coefficients as follows:

$$P_i = E_{i0} + \kappa_{i1} P_1 + \cdots + \kappa_{in} P_n \quad i = 1,...,n \tag{28}$$

Let F_i^* and P_i^* denote respectively the *exergy cost* of resources and product of a process, i.e. the amount of external resources, measured in terms of exergy, required to produce a unit of exergy, Then, the cost balance established:

$$P_i^* = F_i^* = E_{i0} + k_{P.1}^* E_{1i} + \cdots + k_{P.n}^* E_{ni} \quad i = 1,...,n \tag{29}$$

where $k_{P,i}^*$ denotes the cost per production unit of process *i*, applying the definition of technical coefficient to eq. (29) ,we obtain a system of *n* simultaneous equations, which let to determine the unit production cost of each process given the values of technical coefficients:

$$k_{P,i}^* = \kappa_{i0} + k_{P,1}^* \kappa_{1i} + \cdots + k_{P,n}^* \kappa_{ni} \quad i = 1,...,n \tag{30}$$

In matrix notation, eq. (28) may be compactly expressed as:

$$\mathbf{P} = \boldsymbol{\omega}_s + \langle \mathbf{KP} \rangle \mathbf{P} \tag{31}$$

in which $\langle \mathbf{KP} \rangle \equiv \left[\kappa_{ij} \right]$ is the $(n \times n)$ matrix of technical coefficients, $\mathbf{P} \equiv [P_i]$ is the $(n \times 1)$ column vector of process production, and $\boldsymbol{\omega}_s \equiv \left[E_{i0} \right]$ is the $(n \times 1)$ column vector of final demand. The matrix $\langle \mathbf{KP} \rangle$ is, in the input-output methodology, the matrix of *direct requirement* because it shows the quantity of product *i* required directly in the production of one unit of process *j*.

To solve this system for the production vector **P**, known the final demand vector $\boldsymbol{\omega}_s$, we have:

$$\mathbf{P} - \langle \mathbf{KP} \rangle \mathbf{P} = \left(\mathbf{U} - \langle \mathbf{KP} \rangle \right) \mathbf{P} = \boldsymbol{\omega}_s \tag{32}$$

If the demand vector is positive, the matrix $\mathbf{U} - \langle \mathbf{KP} \rangle$ is non-singular, then the desired production vector is evaluated as a function of the final demand and the technical coefficients:

$$\mathbf{P} = \left(\mathbf{U} - \langle \mathbf{KP} \rangle \right)^{-1} \boldsymbol{\omega}_s \tag{33}$$

In a similar way, (30) may be compactly expressed as:

$$\mathbf{k}_P^* = \boldsymbol{\kappa}_0 + {}^T\langle \mathbf{KP} \rangle \mathbf{k}_P^* \tag{34}$$

where $\mathbf{k}_\mathbf{P}^* \equiv \left[k_{P,i}^* \right]$ is the $(n \times 1)$ column vector of unit production costs and $\boldsymbol{\kappa}_0 \equiv \left[\kappa_{0i} \right]$ is the $(n \times 1)$ column vector of external resources direct requirements. Therefore the unit production exergy cost vector could be obtained as a function of the technical coefficients:

$$\mathbf{k}_P^* = {}^T\left(\mathbf{U} - \langle \mathbf{KP} \rangle \right)^{-1} \boldsymbol{\kappa}_0 \tag{35}$$

The total production requirement of process i in the production of a unit of process j, both direct plus indirect, is revealed by, say p_{ij}, the element i, j-th of the Leontief inverse matrix $|\mathbf{P}\rangle \equiv \left(\mathbf{U} - \langle \mathbf{KP} \rangle \right)^{-1}$, which verifies $\langle \mathbf{KP} \rangle |\mathbf{P}\rangle = |\mathbf{P}\rangle - \mathbf{U}$.

The total exergy of the external resources could be written as:

$$F_T = {}^T\mathbf{k}_e \mathbf{P} = {}^T\mathbf{k}_P^* \boldsymbol{\omega}_s \tag{36}$$

B. Directed Graphs

The productive structure of an energy system could be represented by a weight directed graph, where the $(n \times n)$ matrix $\mathbf{E} \equiv \left[E_{ij} \right]$ is its adjacency matrix. Here we review some interesting results related with directed graphs [20], applied on this paper.

A *directed graph* or digraph is a pair G=(V,E) of a set V, whose elements are called nodes, and a set E of ordered pairs of nodes call edges. (loops are not allowed in simply digraph). A *weighted digraph* or *network* is a digraph with weights assigned for its edges. The adjacency matrix of a digraph is a matrix with rows and columns corresponding to the digraph nodes, where a non-diagonal entry a_{ij} is the weight of arcs from node i to node j, and the diagonal entry $a_{ii} = 0$ if loops are not allowed.

A *path* in a graph is a sequence of nodes such that from each of its nodes there is an edge to the next vertex in the sequence. A cycle is a path such that the start vertex and end vertex are the same. The vertices of a directed cycle are said to be strongly connected. A digraph with no cycles is called directed acyclic graph (DAG). The *strongly connected components* of a directed graph are their maximal strongly connected subgraphs. If each strongly connected component is contracted to a single vertex, the resulting graph is a DAG.

A *topological ordering* of a directed graph is a linear ordering of its nodes such that, for every edge (u,v), u comes before v in the ordering. A topological ordering is possible if and only if the graph has is a DAG, and any DAG has at least one topological ordering, For this topological ordering the adjacency matrix of the DAG is strictly upper triangular, it means all the entries below the main diagonal are zero: $a_{ij} = 0 \; \forall i \geq j$.

If the graph which represents an energy system is acyclic then its adjacency matrix **E**, is strictly upper triangular, and consequently $\langle \mathbf{KP} \rangle$ is also strictly upper triangular. Therefore, the Leontief inverse matrix $|\mathbf{P}\rangle$ is upper triangular and its main diagonal is the unity vector.

C. The Sherman-Morrison Formula

Given a non-singular matrix **A** and its inverse $\mathbf{L} \equiv \mathbf{A}^{-1}$, assume that several elements of **A** are changed, i.e. $\bar{a}_{ij} = a_{ij} + \Delta a_{ij}$, producing $\bar{\mathbf{A}} = \mathbf{A} + \Delta\mathbf{A}$, therefore the new inverse matrix $\bar{\mathbf{A}}^{-1}$ can be found by adjusting the known matrix $\mathbf{A}^{-1}$, by means of:

$$\bar{\mathbf{L}} \equiv \bar{\mathbf{A}}^{-1} = \mathbf{L} - \frac{\mathbf{L}\Delta\mathbf{A}\mathbf{L}}{\mathbf{U} + \Delta\mathbf{A}\mathbf{L}} = \frac{\mathbf{L}}{\mathbf{U} + \Delta\mathbf{A}\mathbf{L}} \tag{37}$$

If the change is on the form $\Delta\mathbf{A} = \mathbf{v} \otimes \mathbf{w}$, for some vectors **v** and **w**, where the outer product $\mathbf{v} \otimes \mathbf{w}$ is defined as $\Delta a_{ij} = v_i w_j$, then previous equation is simplified as:

$$\bar{\mathbf{L}} = \mathbf{L} - \frac{(\mathbf{Lv}) \otimes ({}^{\mathrm{T}}\mathbf{wL})}{1+\lambda} \tag{38}$$

where $\lambda \equiv {}^{\mathrm{T}}\mathbf{wLv}$ is a scalar. This equation is called [21] Sherman-Morrison formula.

If **v** is a unit vector $\mathbf{u}_i = (0,\ldots,1,\ldots 0)$ then $\mathbf{v} \otimes \mathbf{w}$ adds the elements of **w** to the *i*-th row of **A**, meanwhile if **w** is the unit vector $\mathbf{u}_i$ then $\mathbf{v} \otimes \mathbf{w}$ adds the elements of **v** to the *i*-th column of **A**. This formula let to compute easily the inverse of a matrix when only the elements of a row or column are modified.

D. Thermoeconomic model of a combined cycle

This appendix describes the model of a simple combined cycle power plant used a case study though this paper. Figure 3, shows its physical structure and the exergy of their flows.

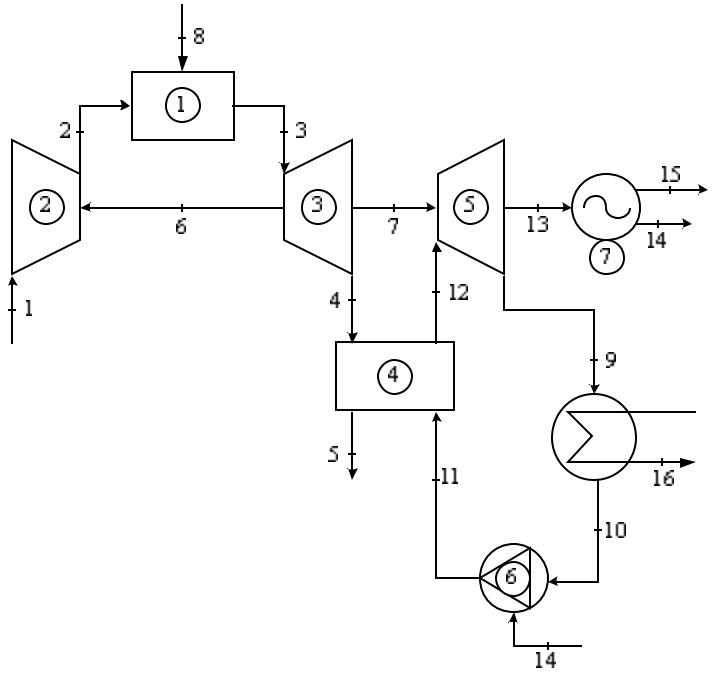

Flow	Exergy (kW)
1	0.00
2	88091.00
3	224086.00
4	60266.00
5	12450.00
6	95289.00
7	61180.00
8	219880.00
9	3723.00
10	65.00
11	193.00
12	38817.00
13	31767.00
14	158.53
15	90000.00
16	3633.00

Figure 3. Physical diagram of study case, a combined cycle power plant.

Its basic operational parameters are:

- The system is fueled by natural gas, with a LHV=45000 kJ/kg
- Net electric power of 90 MW, of which about 60 MW come from gas turbine and 30 MW come from steam turbine.
- Life steam conditions: 40 bar and 420ºC
- Gas turbine inlet temperature: 870ºC
- Gas turbine outlet temperature: 450ºC
- Compression rate: 9

The Fuel-Product definition and the thermoeconomic properties of the plant are shown in Table 2, and have been obtained using TAESS [22]. The gases leaving the HRSG and the waste heat of condenser are considered as external exergy losses.

Table 2. Thermoeconomic properties of the combined cycle power plant

Nr	Process	Fuel	Product	F (kW)	P(kW)	k	k_F^*	k_P^*
1	Combustor	E_8	E_3–E_2	219880	128439.3	1.7119	1.0000	1.7119
2	Compressor	E_6	E_2–E_1	95289	83196.7	1.1453	2.0578	2.3569
3	Gas Turbine	E_3–E_4	E_7+E_6	163820	156469.0	1.0470	1.9655	2.0578
4	HRSG	E_4–E_5	E_{12}–E_{11}	47816	34978.1	1.3670	1.9655	2.6869
5	Steam Turbine	E_{12}–E_9	E_{13}	35094	31767.0	1.1047	2.6890	2.9707
6	Pump	E_{14}	E_{11}– E_{10}	158.53	115.9	1.3676	2.4431	3.3412
7	Generator	E_7+E_{13}	E_{14}+E_{15}	92947	90158.5	1.0309	2.3698	2.4431

Nomenclature

n Number of processes
E Exergy of a flow (kW)
F Fuel exergy of a process (kW)
P Product exergy of a process (kW)
I Irreversibility of a process
Z Equipment investment (€/year)
k Unit exergy consumption (kW/kW)
k_P^* Unit cost of product (kW/kW)
k_F^* Unit cost of fuel (kW/kW)
F_T Total Fuel of the system (kW)
$A_{\mp}$ Fuel Impact (kW)

Greek symbols

Δ increment
κ technical coefficients
τ recirculation factor
ω System output

Subscripts and superscripts

* Exergy Cost
T Transpose Matrix

Matrix and vectors

$\langle \mathbf{KP} \rangle$ Matrix of technical or direct requirement coefficients $(n \times n)$
$|\mathbf{P}\rangle$ Production or total requirement coefficients matrix $(n \times n)$
$|\mathbf{P}^*\rangle$ Cost normalized production matrix $(n \times n)$

References

[1] Lozano M.A, Valero A., Theory of exergy cost. Energy 1993;18(9):939-960.

[2] Lozano M.A. and Valero A., Application of the Exergetic Costs Theory to a Steam Boiler in a Thermal Generation Station. In: Moran M.J., Stecco S., and Reistad G.M. Eds. ASME AES 1987; 3(2): 41-52.

[3] Valero A., Torres C. and Lozano M.A. On causality in organized energy systems. Part III: Theory of perturbations. In proceedings of Flowers90: A Future for Energy; 1990; Florence, Italy. 401-410.

[4] Lozano M.A., Bartolome J., Valero A., Reini M., Thermoeconomic diagnosis of energy systems. In proceedings of Flowers94, Florence World Energy Research Symposium; 1994; Florence, Italy. 149-156.

[5] Reini M., Lazzaretto A. and Macor A., Average Structural and Marginal Costs as Result of a Unified Formulation of the Thermoeconomic Problem. In Proceedings of Second Law Analysis of Energy System: Towards the 21st Century; 1995 July 5-7; Rome, Italy.

[6] Valero A., Correas L., Zaleta A., Lazzaretto A., Verda V., Reini M. and Rangel V., On the Thermoeconomic Approach to the Diagnosis of Energy Systems Malfunctions. Part 2: Malfunction Definitions and Assessment. Energy 2004; 29 (12-15); 1889-1907.

[7] Lazaretto A., Toffolo A., A Critical Review of the Thermoeconomic Diagnosis Methodologies for the Location of Causes of Malfunctions in Energy Systems. ASME Journal of Energy Resour. Technolo. 2006; 128 (4): 335-343

[8] Verda V., Accuracy Level in Thermoeconomic Diagnosis of Energy Systems. Energy 2006; 31: 3248-3260

[9] Torres C., Valero A., Serra L., Royo J., Structural Theory and Thermoeconomic Diagnosis. Part I: On Malfunction and Dysfunction Analysis. Energy Convers Manage 2002;43:1503-18.

[10] Evans R.B., Thermoeconomic isolation and Essergy analysis. Energy 1980; 5(8):804-821.

[11] Frangopoulos C.A, Thermoeconomic Functional Analysis and optimization. Energy 1987;12(7): 563–571.

[12] Uche J., Serra L. and Valero A, Fundamentals of Exergy Cost Accounting and Thermoeconomics. Part II: Applications. J. Energy Resour. Technolo. 2006; 128(1):9-16.

[13] Tarjan R.E., Deep first Search and linear graphs algorithms. SIAM J. Computing 1972;1(2):146-60.

[14] Kotas T.J., The exergy method of thermal plant analysis. London, UK: Butterworths; 1985.

[15] Verda V., Torres C.; Valero A., Application of Thermoeconomic Analysis to the Evaluation of Potential Improvements for Energy Resources Saving in Process Plants. In Proceedings of the ASME International Mechanical Engineering Congress and Exposition 2008 : Energy Systems: Analysis, Thermodynamics and Sustainability; 8: 501-506.

[16] Torres C., Valero A. and Cortes C., Application of Symbolic Exergoeconomics to Thermal System Simulation. In: Wepfer W.J., Moran J., Eds. ASME AES 1989, 9: 75-84.

[17] Torres C., Symbolic Thermoeconomic Analysis of Energy Systems. In: Frangopoulos C, editor. Energy System Analysis and Optimization Vol. 2. Oxford, UK. EOLSS Publisher. 2009. p. 61-82.

[18] Miller R.E, Blair P.D.; Input-Output Analysis. Foundations and Extensions 2º edition. Cambrige, UK: Cambridge University Press; 2009.

[19] Valero A., Exergy accounting: capabilities and drawbacks. Energy 2006; 31(1):164-180.

[20] Bang-Jensen J., Gutin G., Diagraphs: Theory, Algorithms and Applications, 2nd edition. London, UK: Springer-Verlag; 2008.

[21] Golub, G.H., Van Loan C.F. Matrix Computation 3rd edition. Baltimore, USA. Johns Hopkins University Press; 1996

[22] Perez E., Torres C., TAESS. Thermoeconomic Analysis of Energy Systems Software, CIRCE Research Centre for Energy Resources and Consumption.
Available at: <http://www.exergoecology.com> [accessed 12.5.2012]

The introduction of exergy analysis to the thermo-economic modelling and optimisation of a marine combined cycle system

George G. Dimopoulos[a], Chariklia A. Georgopoulou[b] and Nikolaos M.P. Kakalis[c]

[a] *Det Norske Veritas, Research & Innovation, Piraeus, Greece, George.Dimopoulos@dnv.com*
[b] *Det Norske Veritas, Research & Innovation, Piraeus, Greece, Chara.Georgopoulou@dnv.com*
[c] *Det Norske Veritas, Research & Innovation, Piraeus, Greece, Nikolaos.Kakalis@dnv.com* ***CA***

Abstract:

Combined cycle systems are promising solutions for the efficient, cost-effective and environmentally friendly power generation and propulsion onboard ocean-going ships. However, their complexity is significantly increased by machinery space and weight limitations, multiple safety and operational constraints and inherently higher capital costs. To address concurrently these issues, a thermo-economic approach is required that is able to take into account the design, operation and control of the marine energy system throughout its mission profile in an integrated manner. In addition to that, the use of exergy analysis could further strengthen such a thermo-economic approach by associating the exergetic losses of each component to the overall system irreversibility and, thus, revealing and quantifying the internal sources of thermodynamic losses.
In this paper, we present an exergy analysis approach in thermo-economic modelling and optimisation of an advanced marine combined cycle system for an ocean-going container vessel. A thermo-economic model based on energy (first-law) analysis, that is used for model-based design and operation optimisation, is coupled with exergy analysis with the objective to: a) gain better insight of the complex energy conversion process through the identification and ranking of the components which contribute most to the overall system exergy destruction at each operating mode, and, b) to enhance the optimisation of the system by retrofitting/re-designing selected high irreversibility components.
The introduction of exergy analysis to the thermo-economic modelling of the combined cycle system resulted in better insight and understanding of its energy conversion processes, and of the sources of exergy losses. The contribution of components to the total system irreversibility was found to vary with the mode of operation of the vessel. The components that were identified to contribute most to the total irreversibility and that were able to be further re-designed and/or retrofitted, were allowed for further model-based design and operation optimisation. The optimisation results yielded an improved and more cost-effective combined cycle design. The presented approach of integrating exergy analysis in thermo-economic modelling and optimisation is generic and can be applied to various marine energy systems aiding significantly system designers and operators.

Keywords:
Marine energy systems, Thermo-economics, Exergy analysis, Optimisation.

1. Introduction

Combined cycle systems are promising integrated solutions for increasing the overall efficiency, reducing fuel costs and emissions of marine powerplants. However, there are certain challenges to handle including higher capital costs, space and weight requirements, operational and safety constraints and complexity. Advanced thermo-economic modelling, simulation and optimisation approaches have the ability to shed light on such issues.

Exergy analysis is a well-established method for the assessment, improvement and optimization of energy systems [1-4]. Exergy-based approaches have been widely applied on a range of energy systems applications spanning from optimisation [5-11], system assessment and improvement [12-20], monitoring and diagnostics [21-24] to multidisciplinary optimisation of complex aero-

thermodynamic processes [25, 26]. The level of complexity of these exergy-based approaches ranges from simple exergy analysis to more advanced approaches that incorporate categorisation of exergy losses and monetary costs.

This work builds upon the thermo-economic modelling and optimisation of an advanced marine combined cycle system for an ocean-going containership that was presented in [27]. Herein we extend the study with exergy analysis so as to gain better insight of the energy conversion process by identifying and ranking the components of the system with respect to their contribution to the overall exergy destruction. Subsequently, the optimisation problem has been solved again, this time retrofitting/re-designing selected high irreversibility components.

The following sections present the marine combined system description, the exergy analysis and its results and the second round of the thermo-economic design and operation optimisation of the system. Finally, the results and the benefits of this approach are discussed with respect to the potential added value to marine energy systems designers and operators.

2. Marine combined cycle system modelling and optimisation

2.1. System description

We consider a marine combined cycle system for a containership. The generic system model flowsheet and its mission profile are shown in Fig. 1, while the main application characteristics are given in Table 1. The detailed description of this system and its modelling can be found in [27]. The system consists of a marine Diesel engine for propulsion with its exhaust gases driving a power turbine and a dual pressure heat recovery module. The steam produced is expanded through a steam turbine. The steam and power turbines are in a single shaft arrangement with an electricity generator. The produced electric power is supplied to the ship's grid to cover the demand. In addition, an electric motor is coupled to the main engine shaft-line, able to supply the propulsion shaft with excess power from the combined cycle. In cases where the ship's electricity demand is not covered by the combined cycle system, the Diesel gen-sets supply the rest of the electricity.

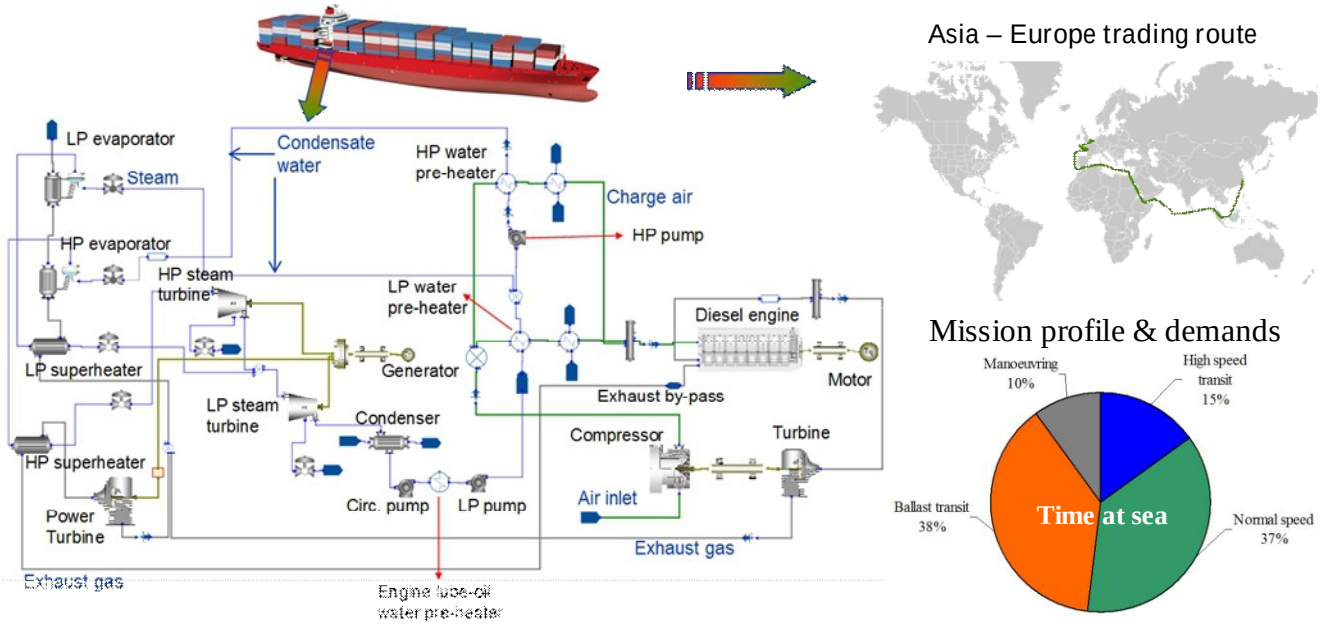

Fig. 1. The marine combined cycle system flowsheet and mission profile characteristics.

There are two key features of the combined cycle system of Fig. 1: the turbocharger exhaust gas by-pass and the integration of water pre-heating with charge air cooling. A part of the cylinders exhaust by-passes the turbocharger to feed the high pressure superheater and the power turbine. The by-pass stream is then mixed with the bulk flow after the turbocharger to feed the rest of the heat recovery

module. This concept offers advanced heat recovery potential at the expense of reduced charge air pressure which has a negative impact on the engine's efficiency. This trade-off is subject to the overall optimisation of the system. The water condensate is preheated in three-stages: a) in the engine's lubricating oil cooler, b) in a stage of one of the charge air-coolers of the main engine, and c) the high pressure condensate is further preheated in a similar charge air-cooler stages. This integration of pre-heating with the engine cooling system can offer significant efficiency improvements in the steam cycle.

A generic model of the marine combined cycle system has been computer implemented to our in house developed modelling framework DNV COSSMOS. COSSMOS is an acronym for Complex Ship Systems MOdelling and Simulation. We have developed a modular library of reconfigurable generic component models suitable for design, performance and transient operation analyses, and optimisation of ship machinery systems in a hierarchical process modelling environment. Our methodology is based on the mathematical modelling of the steady-state and dynamic thermofluid behaviour of marine machinery components resulting in systems of non-linear Partial Differential and Algebraic Equations (PDAE), subject to initial and boundary conditions. The DNV COSSMOS modelling framework is described in detail in [27-29].

Table 1. Principal application characteristics.

Ship		**Main engine**		**Diesel generators**	
Ship Type	Containership	Engine Type	2S-Diesel	Generator-sets type	4S-Diesel
Capacity	4500 TEU	Number of cylinders	8	Number	4
Length overall	260.05 m	Number of TCs	3	Nominal power	1700 kW
Breadth	32.25 m	Bore / Stroke	0.9m / 2.3m	Nominal speed	720 rpm
Depth	19.30 m	Nominal power	36540 kW	Fuel consumption	191 gr/kWh
Draft	12.60 m	Nominal speed	104 rpm		
Service speed	24.5 kn	Exhaust gas flow	92.5 kg/s		
Year of built / Class	2004 / DNV	Exh. gas temperature	275^{o}C		
		Fuel consumption	186 gr/kWh		

2.2. Optimisation problem formulation

In [27] a thermo-economic design and time-varying operation optimisation problem was formulated based on an energy (first-law) analysis model. The time-varying operational profile and power demand for a typical trading route of the vessel (Fig. 1) were also incorporated in the thermo-economic model.

The optimisation objective was the maximisation of the Net Present Value (NPV) of the investment on the combined cycle system compared to the traditional / baseline system configuration of the propulsion and electric power production, consisting of a propulsion marine Diesel engine and independent auxiliary Diesel generator sets:

$$\max_{\mathbf{x}}(NPV) = -\phi \cdot \sum_{Y} C_Y + \sum_{i=1}^{N_{years}} \left(\frac{\sum_{t=1}^{N_T} \left[\left(C_{op,base,t} - C_{op,t} \right) \cdot \Delta\tau_t - c_{TEU} \cdot \Delta(TEU) \right]}{(1+ir)^i} \right) \quad (1)$$

where Y={SUP_{HP}, SUP_{LP}, $EVAP_{HP}$, $EVAP_{LP}$, ST, PT, CND, HP pump, LP pump, HP piping, LP piping, Exhaust path piping, GEN, SM}. The cost of components, appearing both in the heat

recovery and in the baseline system (main engine, gen-sets, etc.), is not included in the capital cost formulation since the NPV was calculated on a comparative basis.

The set $\mathbf{X}$ of independent decision variables was divided in three subsets: $\mathbf{X_1}$ with heat exchanger geometry variables, $\mathbf{X_2}$ nominal performance variables and $\mathbf{X_3}$ time-varying operation variables:

$$\mathbf{X} = [\mathbf{X}_1, \mathbf{X}_2, \mathbf{X}_3]^T \tag{2}$$

$$\begin{aligned} \mathbf{X}_1 &= \begin{bmatrix} \left(D_i, L, l_p, l_b, h_f, N_{tubes,row}, N_{tubes,col}\right)_{Y=(HP\,\mathrm{sup},HPevap,LP\,\mathrm{sup},LPevap)}, \\ D_{i,CND}, L_{CND}, N_{tubes,CND} \end{bmatrix} \\ \mathbf{X_2} &= \left[p_{HP}, p_{LP}, \pi_{PT,n}, \eta_{is,PT,n}, p_{CND}\right] \\ \mathbf{X_3} &= \left[\dot{m}_{f,ME}, x_{bp}\right]_{t=1,\ldots,N_T} \end{aligned} \tag{3}$$

This optimisation problem formulation captured successfully the main techno-economic drivers and technical challenges relevant to the introduction of the marine combined cycle when compared to a baseline/ not integrated system; namely:

- The additional capital of combined cycle components (by the use of component cost functions).
- The potential gain in operational expenses in fuel and lubricating oil consumptions by covering electric needs with the combined cycle additional output and utilising less the Diesel gen-sets.
- The potential loss of profit from the reduction of containers onboard due to the larger engine room size to host the combined cycle system.
- The influence of the time-varying operational strategy.

Finally, the optimisation problem was subject to numerous design, space, demand, operability and safety equality and inequality constraints, the most important of which are:

- Coverage of all of the onboard propulsion and electric energy needs;
- Operation of the turbocharger within safe surge margin limits (exhaust gas by-pass results to operation closer to the surge limit);
- Overall exhaust gas pressure drop (heat recovery sections) under an allowable limit to ensure safe operation of the main engine;
- Exhaust gas velocity within allowable limits in all operating modes;
- Outlet exhaust gas temperature higher than a minimum to avoid sulphuric acid condensation and subsequent corrosion;
- Dimensions of heat exchange components bounded by engine room space constraints.

This formulation resulted in a mixed integer non-linear problem (MINLP) consisting of 44 independent optimisation variables, 8 equality constraints and 35 inequality constraints. It is also noted that the combined cycle process model flowsheet, depicted in Fig. 1, consists of 9,674 equations.

2.3. Thermo-economic optimal solution

The results of the first-law thermo-economic optimisation of [27] are presented in Tables 2 and 3. The combined cycle system has an NPV of about 3.6 million USD, over 25 years lifetime, with a market interest rate of 10% and base fuel price 600 USD/ton. This corresponds to approximately 8 years discounted pay-back period. The overall system energy efficiency is 51.31% which represents an 11% increase compared to the baseline system efficiency of 46.19% [27]. The system delivers 5.9 MW additional electric power at nominal load. In all operating modes the use of the Diesel gen-sets is minimised, resulting in additional fuel and maintenance cost savings. In high loads (>85%) the combined cycle system supports the propulsion power plant, through the shaft motor, delivering

approximately 3% of the demand. Finally, for main engine loads below 50%, the exhaust by-pass is closed and the power turbine as well as the HP superheater is shut-down.

3. Introduction of exergy analysis

In this paper the exergy analysis is introduced to the thermo-economic model of the marine combined cycle system of [27]. For every node of the system process streams the specific physical, chemical exergy and exergy rate are evaluated from the relevant physical properties and process variables. Based on these figures the exergetic efficiency and irreversibility of the major system components are derived. For clarity, the numbering of stream nodes and short names of system components are depicted in Fig. 2 and the listing of system components is given in Table 4.

In the system flowsheet of Fig. 2 three types of process streams appear: air flowing into the Diesel engine, exhaust gas supplied to the heat recovery sections and water both in vapour and liquid phases. In addition, there are also mechanical connections in all rotating components for the torque (i.e. mechanical power) production. It is noted that the exergy rate of mechanical and electrical connection nodes is equal to the respective mechanical or electric power. The specific physical and chemical exergy at any node of a process stream are:

$$\varepsilon_{ph} = h - h_0 - T_0 \cdot (s - s_0) \tag{4}$$

$$\varepsilon_{ch} = \left[\sum_{i=1}^{N_{sp}} x_i \cdot \varepsilon_{ch,0} + RT_0 \cdot \sum_{i=1}^{N_{sp}} x_i \cdot \ln(x_i) \right] / MW \quad \forall i = 1,..., N_{sp} \tag{5}$$

The specific chemical exergy is calculated under the assumption of perfect gas mixtures [2]. The reference state is set at a pressure of p_0 = 1.013 bar and temperature T_0 = 298.15 K.

For liquid hydrocarbons of the form $C_xH_yO_zN_wS_v$ the following empirical relation is valid [3]:

$$\varepsilon_{ch,f} = \left[1.0401 + 0.1728 \frac{y}{x} + 0.0432 \frac{z}{x} + 0.2169 \frac{v}{x} \cdot \left(1 - 2.0628 \frac{y}{x} \right) \right] \cdot H_u \tag{6}$$

The total exergy rate at each node of the process flowsheet is calculated:

$$\dot{E} = \dot{m} \cdot (\varepsilon_{ph} + \varepsilon_{ch}) \tag{7}$$

Table 2. Thermo-economic optimal combined cycle system design [27].

Component Geometry	HP sup.	HP evap.	LP sup.	LP evap.	CND	Nominal Characteristics	Value
D_i (m)	0.049	0.0168	0.0173	0.018	0.030	p_{HP} (bar)	10.210
L (m)	6.000	3.867	3.000	4.014	5.000	p_{LP} (bar)	2.388
l_p (m)	0.098	0.200	0.200	0.200	-	$\dot{W}_{ST,n}$ (kW)	2670
l_b (m)	6.000	1.229	3.000	1.108	-	p_{CND} (bar)	0.050
h_f (m)	0.003	0.000	0.000	0.0003	-	$\pi_{PT,n}$	3.533
$N_{tubes,row}$	12	28	25	28	1000	$\dot{m}_{PT,n}$	18.590
$N_{tubes,col}$	2	28	13	27	-	$\eta_{is,PT,n}$	0.8596
$C_{capital}^* = 2.631 \cdot 10^6 USD$			$A_{HRB} = 36.533 m^2$			$\dot{W}_{PT,n}$ (kW)	3318
$Profit^* = 682 \cdot 10^3 USD/year$			$H_{HRB} = 14.826 m$			$\dot{m}_{st,HP,n}$ (kg/s)	2.631
Payback period = 8.16 years			$\eta_{tot}^* = 0.5131$			$\dot{m}_{st,LP,n}$ (kg/s)	2.338
$NPV^* = 3.561 \cdot 10^6 USD$							

Table 3. Thermo-economic optimal combined cycle operation [27].

Operating Mode	Optimal operating characteristics									
	$\dot{m}_{f,ME}$ (kg/s)	x_{bp} (-)	SM (%)	$f_{L,ME}$ (-)	$\dot{W}_{ME}$ (kW)	$\dot{W}_{SM}$ (kW)	$\dot{W}_{PT}$ (kW)	$\dot{W}_{ST}$ (kW)	$\dot{W}_{DG}$ (kW)	η_{tot} (-)
High speed tr.	1.5795	0.1788	9.11	0.8276	30241	908	2121	1888	0	0.5401
Normal speed	1.2521	0.1634	12.69	0.6500	23751	0	1264	1594	231	0.5295
Ballast transit	0.9032	0	35.14	0.4500	16443	0	0	1330	213	0.4905
Manoeuvring	0.7926	0	45.23	0.3500	12789	0	0	1553	1592	0.4509

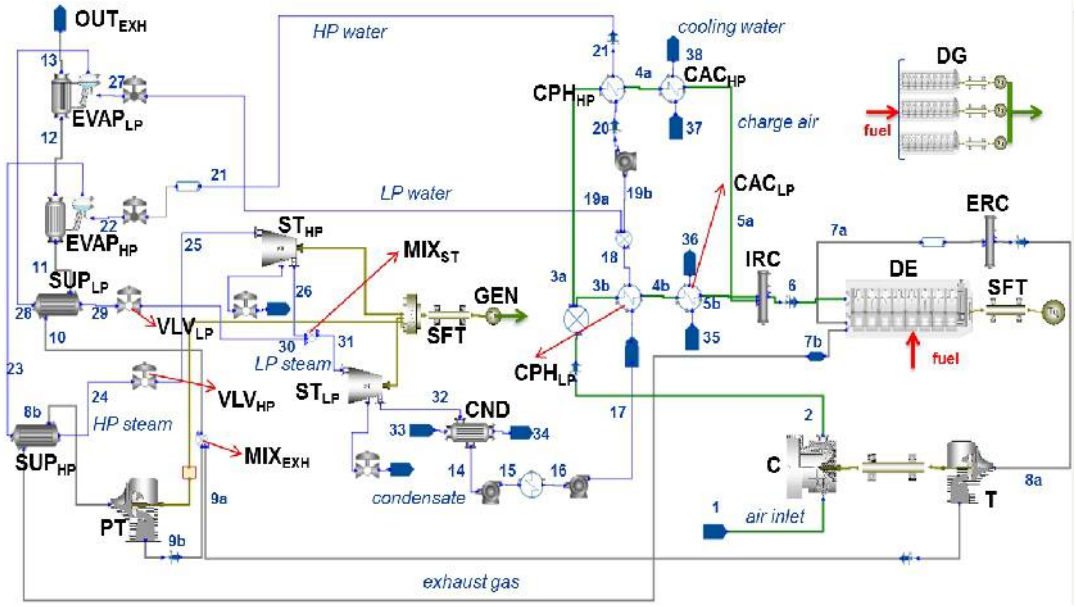

Fig. 2. Combined cycle system flowsheet with listing of components and numbering of stream nodes used in the exergy analysis.

Table 4. Combined cycle system components listing.

Component	Short-name	Component	Short-name	Component	Short-name
Diesel engine	DE	Power turbine	PT	HP steam turbine	ST_{HP}
TC compressor	C	Exhaust gas mixer	MIX_{EXH}	LP steam turbine	ST_{LP}
TC turbine	T	HP superheater	SUP_{HP}	HP/LP steam mixer	MIX_{ST}
Diesel generators	DG	LP superheater	SUP_{LP}	Vacuum condenser	CND
Charge air cooler HP	CAC_{HP}	HP evaporator	$EVAP_{HP}$	Exhaust gas outlet	OUT_{EXH}
Charge air cooler LP	CAC_{LP}	LP evaporator	$EVAP_{LP}$	Generator/ shaft motor	GEN
Water pre-heater HP	CPH_{HP}	HP steam valve	VLV_{HP}	Shaft lines	SFT
Water pre-heater HP	CPH_{LP}	LP steam valve	VLV_{LP}		

The total exergy rate of the fuel input to the system is:

$$\dot{E}_{f,tot} = \dot{E}_{f,DE} + \dot{E}_{f,DG} = \left(\dot{m}_{f,DE} + \dot{m}_{f,DG}\right) \cdot \varepsilon_{ch,f} \tag{8}$$

For the heat exchange components the definitions for the exergetic efficiency and irreversibility rate depend on their purpose, i.e. heating or cooling [1]. For heating components, i.e CPH_{HP}, CPH_{LP}, SUP_{HP}, SUP_{LP}, $EVAP_{HP}$ and $EVAP_{LP}$, the exergetic efficiency and the irreversibility rate are:

$$\zeta = \frac{\dot{E}_{Cold,out} - \dot{E}_{Cold,in}}{\dot{E}_{Hot,in} - \dot{E}_{Hot,out}} \tag{9}$$

$$\dot{I} = \left(\dot{E}_{Hot,in} - \dot{E}_{Hot,out}\right) - \left(\dot{E}_{Cold,out} - \dot{E}_{Cold,in}\right) \tag{10}$$

with the indexes “Hot” and “Cold” denoting the heating and heated streams, respectively, while indexes “in” and “out” denoting the inlet and outlet from the component.

In a similar fashion, for the cooling components, i.e. CAC_{HP}, CAC_{LP} and CND:

$$\zeta = \frac{\dot{E}_{Cold,in} - \dot{E}_{Cold,out}}{\dot{E}_{Hot,out} - \dot{E}_{Hot,in}} \tag{11}$$

$$\dot{I} = \left(\dot{E}_{Hot,out} - \dot{E}_{Hot,in}\right) - \left(\dot{E}_{Cold,in} - \dot{E}_{Cold,out}\right) \tag{12}$$

with the indexes “Hot” and “Cold” denoting the cooling and cooled streams, respectively.

For the expansion components in the system, i.e. T, PT, ST_{HP} and ST_{LP} the exergetic efficiency and the irreversibility rate are [1]:

$$\zeta = \frac{\dot{W}}{\dot{E}_{in} - \dot{E}_{out}} \tag{13}$$

$$\dot{I} = \left(\dot{E}_{in} - \dot{E}_{out}\right) - \dot{W} \tag{14}$$

with $\dot{W}$ the expansion work produced per unit of time.

For the turbocharger compressor:

$$\zeta = \frac{\dot{E}_{out} - \dot{E}_{in}}{\dot{W}} \tag{15}$$

$$\dot{I} = \dot{W} - \left(\dot{E}_{in} - \dot{E}_{out}\right) \tag{16}$$

The two junctions MIX_{EXH} and MIX_{ST} that serve the mixing of exhaust gas prior to the SUP_{LP} and of HP with LP steam prior to ST_{LP}, respectively, have:

$$\zeta = \frac{\dot{E}_{out}}{\dot{E}_{in,1} + \dot{E}_{in,2} + \ldots} \tag{17}$$

$$\dot{I} = \left(\dot{E}_{in,1} + \dot{E}_{in,2} + \ldots\right) - \dot{E}_{out} \tag{18}$$

The HP/LP steam valves (VLV_{HP} and VLV_{LP}) have:

$$\zeta = \frac{\dot{E}_{out}}{\dot{E}_{in}} \tag{19}$$

$$\dot{I} = \dot{E}_{in} - \dot{E}_{out} \tag{20}$$

The exergetic efficiency and the irreversibility rate of mechanical and electrical components, i.e. SFT and GEN, are equal to the mechanical efficiency and losses, respectively. The form of the respective calculation equations is that of Eqs. (19) and (20).

In the exhaust gas outlet, OUT_{EXH}, the stream is dumped to the environment. Therefore, the exergetic efficiency is considered to be equal to zero. Similarly, the irreversibility rate is equal to the exergy of the outlet stream (Fig. 2):

$$\dot{I}_{EXH_{OUT}} = \dot{E}_{13} \tag{21}$$

For the combustion block of the main engine (DE) an exergy balance is formulated (Fig. 2) and the irreversibility rate and exergetic efficiency are derived:

$$\dot{E}_{f,DE} + \dot{E}_6 = \dot{W}_{DE} + \dot{E}_{7a} + \dot{E}_{7b} + \dot{I}_{DE} \tag{22}$$

$$\zeta_{DE} = \frac{\dot{W}_{DE}}{\dot{E}_{f,DE} + \dot{E}_6} \tag{23}$$

Finally, for the Diesel generators a simpler ("black-box") exergy balance is employed yielding:

$$\dot{I}_{DG} = \dot{E}_{f,DG} - \dot{W}_{DG} \tag{24}$$

$$\zeta_{DG} = \frac{\dot{W}_{DG}}{\dot{E}_{f,DG}} \tag{25}$$

The irreversibility ratio (δ) of each component is defined:

$$\delta = \frac{\dot{I}_i}{\dot{E}_{f,tot}}, \text{ for each component } i \tag{26}$$

4. Exergy analysis results

We performed exergy analysis to the optimal marine combined cycle design of [27], which is briefly presented in Tables 2 and 3. The analysis covered the entire mission profile of the system. In Table 5 the component exergetic efficiencies, irreversibility rates, irreversibility ratios and component contributions to total system irreversibility are given. The results give a clear insight of the energy conversion processes within the system. The exergy losses are obtained on a component basis for each operating mode of the system. Therefore, the components that contribute the most to the overall exergy losses of the system are readily identified for the various operating modes. The analysis of the results on a component level reveals:

- The combustion block of the main propulsion engine (DE) is the biggest contributor to the overall exergy losses with an irreversibility of 49 to 50% of the chemical exergy of the fuel input for all modes of operation.
- The Diesel gen-sets (DG) have low exergetic efficiency causing high exergy losses. Their contribution to the overall irreversibility depends on their utilisation which is high at low loads.
- Excluding the combustion engines (i.e. DE and DG), the rest of the system components have a total irreversibility of 8.8 to 10.5% of the chemical exergy of the fuel input for all modes of operation. This represents a contribution to the overall exergy losses of 13 to 18% increasing with load demand.

- The main engine charge air cooler stages CAC_{HP} and CAC_{LP} have very low exergetic efficiency in all operating modes. This is due to the heat rejection, i.e. exergy destruction, to the sea water cooling circuit. This allows for further low temperature heat recovery in these units as a subsequent improvement to the system. A first step towards that direction is the integrated condensate pre-heaters CPH_{HP} and CPH_{LP}, already installed. The exergy losses in CAC_{HP} and CAC_{LP} correspond to 0.7 to 3.7% of the total system irreversibility, having a greater impact on high loads (i.e High speed transit and Normal speed modes). Thus, exergy analysis offers a formal justification for the introduction of the integrated condensate pre-heaters CPH_{HP} and CPH_{LP} as a means to minimise the exergy destruction in the charge air cooling module.
- The condenser has also low exergetic efficiency since heat is again rejected to sea cooling water. However the condenser's contribution to the overall system irreversibility is relatively low.
- The steam valves VLV_{HP} and VLV_{LP} have a minimal contribution to the overall system irreversibility, since the amount of throttling is kept at a minimum, as their purpose is the HP/LP pressure regulation prior to admission to the steam turbine.
- The mixing process at the two junctions MIX_{EXH} and MIX_{ST} has a very low (even negligible) contribution to the overall exergy losses, despite the fact that mixing is a usual source of high irreversibility in most cases. This is mainly due that in both junctions the inlet streams have very similar pressure and temperature and the same composition.
- The exhaust gas outlet to the environment causes the loss of roughly 3 to 4% of the chemical exergy of the fuel input. The contribution of OUT_{EXH} to the total system irreversibility varies from 4% to 6%. This source of losses cannot easily be alleviated due to minimum exhaust temperature constraints. However, the use of low sulphur fuels or SO_X scrubbers will result into lower minimum permissible exhaust temperatures and, therefore, the exergy losses will be lower.
- The LP section of the steam turbine contributes 1.2 to 1.6% to the total system irreversibility, with the higher rates at low loads. On the other hand, the HP section has a relatively low contribution to the total exergy losses. The ST_{LP} high contribution is primarily due to its lower isentropic efficiency (compared to the HP section). In addition, at low loads the exhaust gas by-pass is closed and the PT and SUP_{HP} are switched-off. Therefore, the LP steam is then becoming more crucial to the combined cycle power production.
- At low loads (i.e. Ballast transit and Manoeuvring modes), when the exhaust gas by-pass is closed and the PT and SUP_{HP} are switched-off, the contribution of the HP evaporator in the overall system irreversibility is increased up to 1.6%. Therefore, its importance for efficient low load operation is high.
- The main engine turbocharger (C and T) is responsible for the loss of roughly 2% of the exergy of the fuel input. This amounts to a contribution to the overall irreversibility of 2.7 to 3.9%, depending on the operating mode. Therefore, the turbocharger is an important sub-system with a high potential for improvement through re-designing and matching with the main engine.

On a system level, the exergetic efficiency at each operating mode ranges from 34 to 40%, being minimum at low loads. It is noted that the system energy efficiencies (Table 3) range from 45 to 54%. Hence, there is a significant difference between the energetic and exergetic approach in the system analysis. As shown in Table 5, the combined cycle system efficiencies are significantly higher to those of the baseline system (i.e. independent power production), yielding an improvement from 18 to 25%, increasing at low loads. This strongly supports the marine combined cycle system concept as a means to save primary energy onboard. Further to the results of Table 5, the system overall exergetic efficiency, considering the entire mission profile is: ζ_{tot} = 37.83%, whereas the overall exergetic efficiency of the baseline system is 32.39%. It is noted that the comparison between combined cycle and baseline system using first-law energy efficiencies (paragraph 2.3), yielded an improvement of 11%.

Table 5. Combined cycle system exergetic efficiencies and irreversibilities.

Mode:	Nominal point				1. High speed transit				2. Normal Speed				3. Ballast transit				4. Manoeuvring			
Components	ζ [%]	$\dot{I}$ [kW]	δ [%]	δ/δ_{tot} [%]	ζ [%]	$\dot{I}$ [kW]	δ [%]	δ/δ_{tot} [%]	ζ [%]	$\dot{I}$ [kW]	δ [%]	δ/δ_{tot} [%]	ζ [%]	$\dot{I}$ [kW]	δ [%]	δ/δ_{tot} [%]	ζ [%]	$\dot{I}$ [kW]	δ [%]	δ/δ_{tot} [%]
DE	32.53	52338	48.998	81.63	33.58	42387	49.168	82.38	33.57	34180	49.865	82.46	32.70	26010	52.227	82.42	29.88	24061	50.118	75.90
C	88.61	1794	1.680	2.80	88.51	1360	1.578	2.64	87.57	967	1.410	2.33	85.47	600	1.205	1.90	83.82	368	0.766	1.16
T	95.67	713	0.668	1.11	95.24	591	0.686	1.15	94.08	489	0.714	1.18	86.68	635	1.275	2.01	82.00	499	1.039	1.57
CAC_{HP}	11.65	1874	1.754	2.92	10.38	1329	1.542	2.58	8.72	773	1.128	1.87	7.07	330	0.663	1.05	5.78	152	0.317	0.48
CAC_{LP}	11.30	814	0.762	1.27	10.11	579	0.672	1.13	8.55	340	0.495	0.82	6.99	150	0.301	0.47	5.75	72	0.150	0.23
CPH_{HP}	78.60	61	0.057	0.10	79.42	31	0.036	0.06	79.64	17	0.025	0.04	76.88	7	0.015	0.02	71.49	4	0.008	0.01
CPH_{LP}	53.86	132	0.124	0.21	57.07	74	0.086	0.14	61.86	36	0.052	0.09	70.82	10	0.019	0.03	76.69	3	0.006	0.01
PT	87.57	473	0.442	0.74	87.19	317	0.367	0.62	85.94	206	0.300	0.50	0.00	0	0.000	0.00	0.00	0	0.000	0.00
MIX_{EXH}	99.99	0	0.000	0.00	100.0	0	0.000	0.00	100.00	0	0.000	0.00	0.00	0	0.000	0.00	0.00	0	0.000	0.00
SUP_{HP}	64.03	91	0.085	0.14	67.75	51	0.059	0.10	69.18	34	0.050	0.08	0.00	0	0.000	0.00	0.00	0	0.000	0.00
SUP_{LP}	55.84	33	0.031	0.05	59.55	23	0.027	0.05	62.04	20	0.029	0.05	97.12	18	0.037	0.06	60.61	26	0.054	0.08
$EVAP_{HP}$	84.07	351	0.329	0.55	86.10	218	0.253	0.42	85.04	215	0.314	0.52	81.89	262	0.525	0.83	74.78	515	1.073	1.63
$EVAP_{LP}$	76.11	407	0.381	0.64	77.02	328	0.381	0.64	77.11	276	0.402	0.66	76.62	234	0.469	0.74	74.82	228	0.474	0.72
VLV_{HP}	99.14	20	0.019	0.03	99.14	14	0.016	0.03	99.13	12	0.018	0.03	99.06	12	0.024	0.04	99.06	15	0.031	0.05
VLV_{LP}	97.05	43	0.040	0.07	97.06	36	0.042	0.07	97.09	30	0.043	0.07	97.12	24	0.048	0.08	97.17	21	0.044	0.07
ST_{HP}	85.53	110	0.103	0.17	81.98	95	0.110	0.18	79.65	91	0.132	0.22	74.33	93	0.187	0.30	77.63	103	0.215	0.32
ST_{LP}	73.31	723	0.677	1.13	70.90	606	0.703	1.18	68.98	549	0.800	1.32	66.75	501	1.005	1.59	67.70	526	1.095	1.66
MIX_{ST}	99.93	2	0.002	0.00	99.96	1	0.001	0.00	99.91	2	0.003	0.00	99.32	11	0.023	0.04	99.04	17	0.036	0.06
CND	23.38	215	0.201	0.34	27.51	157	0.182	0.31	29.70	130	0.190	0.31	31.61	109	0.218	0.34	30.70	119	0.247	0.37
GEN	90.00	285	0.267	0.44	90.00	97	0.113	0.19	0.00	0	0.000	0.00	0.00	0	0.000	0.00	0.00	0	0.000	0.00
SFT	99.00	60	0.056	0.09	99.00	41	0.047	0.08	99.00	28	0.041	0.07	99.00	13	0.026	0.04	99.00	15	0.030	0.05
OUT_{EXH}	0.00	3573	3.345	5.57	0.00	3119	3.617	6.06	0.00	2559	3.734	6.17	0.00	2013	4.041	6.38	0.00	1563	3.255	4.93
DG	0.00	0	0.000	0.00	0.00	0	0.000	0.00	32.96	497	0.725	1.20	32.96	527	1.058	1.67	32.96	3397	7.076	10.72
System	**39.98**	**64114**	**60.023**	**100**	**40.31**	**51455**	**59.686**	**100**	**39.53**	**41450**	**60.472**	**100**	**36.63**	**31558**	**63.366**	**100**	**33.96**	**31703**	**66.036**	**100**
Baseline	34.11				34.19				33.18				31.48				27.15			

The exergetic efficiency of the combined cycle is improved by 17%, compared to the baseline system. Therefore, exergy analysis provides an improved quantitative argument in favour of the combined cycle system.

A final step to utilise and exploit further the exergy analysis results of Table 5, is the ranking of the system components based on their contribution to the overall system irreversibility (δ/δ_{tot}) weighted over the operating hours of each mode of the system's mission.

$$\left(\frac{\delta_i}{\delta_{tot}}\right)_w = \frac{\sum_{t=1}^{N_T}\left[\left(\frac{\delta_i}{\delta_{tot}}\right)_t \cdot \Delta\tau_t\right]}{\sum_{t=1}^{N_T}\Delta\tau_t} \quad , \quad \forall \text{ component i} \tag{27}$$

The weighted component contributions to the overall system irreversibility are given in Table 6. Via this ranking the individual components that should be carefully considered when designing and operating marine combined cycle systems are identified. The combustion engines, the exhaust losses, the turbocharging system, the charge air coolers (HP and LP) and the steam evaporators (HP and LP) are among the largest 10 contributors to the exergy losses of the system.

5. System re-design and optimisation

Based on the ranking results of Table 6, further system re-design and optimisation is considered, focusing on the components with the higher contribution to the overall system irreversibility. The improvement of the combustion engines (ranking positions 1 and 3) requires detailed modelling of engine design and combustion, which is a very broad field, yet outside the scope of this system-oriented study. The exhaust losses (rank 2) are already incorporated in the thermo-economic modelling and optimisation through appropriate minimum exhaust gas temperature constraints [27]. In addition, the HP and LP evaporators are also incorporated in the optimisation problem formulation, with their design characteristics being independent decision variables. Similarly the heat integration of the charge air coolers (ranking positions 6 and 10) with the condensate water pre-heaters is already implemented in the marine combine cycle system. Finally, only the turbocharger compressor and turbine (ranking positions 4 and 5) was selected for re-design and optimisation in order to improve further the combined cycle system.

Table 6. Ranking of combined cycle system components based on their irreversibility contributions.

Component	Rank	$\left(\frac{\delta_i}{\delta_{tot}}\right)_w$ [%]	Component	Rank	$\left(\frac{\delta_i}{\delta_{tot}}\right)_w$ [%]	Component	Rank	$\left(\frac{\delta_i}{\delta_{tot}}\right)_w$ [%]
DE	1	81.776	$EVAP_{LP}$	9	0.695	SUP_{LP}	17	0.055
OUT_{EXH}	2	6.110	CAC_{LP}	10	0.675	SUP_{HP}	18	0.045
DG	3	2.150	CND	11	0.330	CPH_{HP}	19	0.035
C	4	2.098	PT	12	0.276	VLV_{HP}	20	0.034
T	5	1.531	ST_{HP}	13	0.253	GEN	21	0.028
CAC_{HP}	6	1.523	VLV_{LP}	14	0.072	MIX_{ST}	22	0.021
ST_{LP}	7	1.435	CPH_{LP}	15	0.066	MIX_{EXH}	23	0.000
$EVAP_{HP}$	8	0.733	SFT	16	0.057			

In the initial study [27], the turbocharger design and matching with the main engine in the combined cycle system are the same as in the baseline system. However, for marine combined cycle systems with exhaust gas by-pass it is strongly recommended in the technical literature [30-32] that the turbocharger selection and matching processes are revised. The exergy analysis results (Section

4) highlight and justify in a formal way this technical guideline to re-match the turbocharger for exhaust-gas by-pass operation.

In order to introduce the turbocharger re-design to a new thermo-economic optimisation formulation, the compressor and turbine maps [27] are expressed in non-dimensional form as functions of their nominal point. Then, a set of scaling factors are introduced on the nominal compressor and turbine flow rate and pressure ratio. By changing these scaling factors new compressor and turbine nominal points are created and, in turn, new component performance maps are generated. These scaling factors are introduced as new independent decision variables to the thermo-economic optimisation problem formulation. It is noted that the isentropic efficiency maps have not been scaled, under the assumption that the current and the re-designed (by scaling) turbocharger have the same efficiency. In addition, it is assumed that no additional capital cost is introduced by the turbocharger re-design.

Let $x_{C,m}$, $x_{C,p}$, $x_{T,m}$ and $x_{T,p}$ be the aforementioned scaling factors. In the optimisation problem formulation of Eqs. (1) – (3), the nominal performance independent variables $\mathbf{X_2}$ of Eq. (3) are now given by:

$$\mathbf{X}_{2,new} = \left\lfloor p_{HP}, p_{LP}, \pi_{PT,n}, \eta_{is,PT,n}, p_{CND}, x_{C,m}, x_{C,p}, x_{T,m}, x_{T,p} \right\rfloor \tag{28}$$

The optimisation problem is solved again subject to the same constraints as in Section 2.2. The new optimisation results are briefly presented in Table 7. It is noted that the geometry of the heat exchange components is not given in Table 7, since there were only minor differences to the previous results of Table 2. The new optimal solution yields a significant improvement of the cost-effectiveness of the system. The new NPV* = 4.8 million USD represents more than 30% improvement than the optimal results without turbocharger re-design. This halves the payback period of the investment, to 4 years. The overall energy efficiency is now 51.73%, improved by 0.8% from the previous configuration, while the overall exergy efficiency is 38.34%, improved by 1.3%. Once again the exergetic efficiency is able to capture effectively the improvement to the performance of the system. The results indicate that the fuel consumption (hence the efficiency) is the main and very strong driver to the economic performance of such systems. An exergy efficiency relative improvement of 1.3% leads to cost savings of 20%.

Table 7. Design and operation optimisation results with turbocharger re-design.

Nominal Characteristics	*Value*	Nominal Characteristics	*Value*	Operating characteristics		
p_{HP} (bar)	10.050	$\dot{W}_{PT,n}$ (kW)	3325	*Operating* Mode	$\dot{m}_{f,ME}$ (kg/s)	x_{bp} (-)
p_{LP} (bar)	2.410	$\dot{m}_{st,HP,n}$ (kg/s)	2.645	High speed transit	1.5624	0.1776
$\dot{W}_{ST,n}$ (kW)	2701	$\dot{m}_{st,LP,n}$ (kg/s)	2.334	Normal speed	1.2387	0.1617
p_{CND} (bar)	0.050	$x_{C,m}$ (-)	0.9900	Ballast transit	0.8931	0
$\pi_{PT,n}$	3.560	$x_{C,p}$ (-)	0.9968	Manoeuvring	0.7826	0
$\dot{m}_{PT,n}$ (kg/s)	18.526	$x_{T,m}$ (-)	0.9900			
$\eta_{is,PT,n}$	0.8586	$x_{T,p}$ (-)	1.0000			
System characteristics						
$C_{capital}^{*} = 2.638 \cdot 10^{6} USD$				$NPV^{*} = 4.787 \cdot 10^{6} USD$		
$\mathrm{Pr}ofit^{*} = 818 \cdot 10^{3} USD/year$				$\eta_{tot}^{*} = 0.5173$		
Payback period = 4.09 years				$\zeta_{tot}^{*} = 0.3834$		

The results also indicate that the system efficiency is very sensitive to the turbocharger performance. The new maps, scaled at a maximum of 1% relative to the original ones, are able to yield the aforementioned improvements in both efficiency and cost-effectiveness of the system.

6. Conclusions

In this work, exergy analysis was introduced to the thermo-economic modelling and optimisation of a marine combined cycle system. With the aid of exergy analysis, a better insight of the system was gained and the internal sources of exergy losses were identified. The analysis provided a formal and quantifiable basis of ranking the importance of the system components with respect to their contributions to the overall irreversibility of the system. The most important components proved to be the combustion engine(s), turbocharging modules, charge air coolers, steam evaporators and steam turbines, with their contribution varying with the mode of operation of the vessel.

As a result of the exergy analysis, the re-design of the main engine turbochargers was formally justified. Therefore, a new thermo-economic design and operation optimisation problem incorporating the turbocharger re-design was solved. This resulted into a significantly improved system design and operation. By re-design of the turbocharger, a 30% improvement on the optimum NPV of the investment is attained with a payback period of 4 years. The overall exergetic efficiency of the system is also improved by 1.3%, reaching 38.3%. These results confirm the key importance of the turbocharging module as it was assessed and quantified through the exergy analysis.

The insights from the exergy analysis provide the system designers and operators with a clear picture of the internal energy conversion process and the potential focus areas for overall system improvements. In addition, the importance of the individual components is quantified in terms of their irreversibility. The results of the exergy analysis provide an improved quantitative argument in favour of the marine combined cycle system as a viable and cost-effective concept to save primary energy onboard vessels.

Nomenclature

A Area, m^2

C Cost, USD

c Specific cost, USD / (kW or kWh or kg)

D_i Internal diameter, m

$\dot{E}$ Exergy rate, kW

f_L Load factor

h Specific enthalpy, kJ/kg

h_f Tube fin height, m

H Height, m

H_u Lower heating value, kJ/kg

$\dot{I}$ Irreversibility rate, kW

ir Market interest rate

L Length, m

l_p Tube pitch, m

l_b Buffle spacing, m

$\dot{m}$ Mass flow rate, kg/s

MW Molecular weight, kg/kmol

N_{sp} Number of species in a mixture

N_T Number of time intervals

N_{years} Economic life of the investment, years

p Pressure, bar

R_g Gas constant, kJ/(kmolK)

s Specific entropy, kJ/(kgK)

SM Surge margin

T Temperature, K

$\dot{W}$ Power, kW

x Molar composition

$\mathbf{X}$ Set of independent optimisation variables

x_{bp} Exhaust gas by-pass ratio

Greek Symbols

δ Irreversibility to chemical exergy of the fuel ratio

$\Delta\tau$ Time interval duration, hours

ε Specific exergy, (kJ/kg)

η Energy efficiency

ζ Exergy efficiency

π Pressure ratio

ϕ Capital cost scaling factor

Subscripts

0	reference
a	Air
AUX	Auxiliaries
base	Baseline system
C	Compressor
CAC	Charge air cooler
ch	Chemical
CND	Condenser
DE	Diesel engine
DG	Diesel generator
el	electric
exh	Exhaust (gas)
f	Fuel
GEN	Generator
HP	High pressure
HRB	Heat recovery boiler
in	Inlet
is	Isentropic
LP	Low pressure
ME	Main engine
n	Nominal
op	Operation
out	Outlet
ph	Physical
PT	Power turbine
SM	Shaft motor
ST	Steam turbine
st	Steam
T	Turbine

Superscripts

*	Optimum

References

[1] A. Bejan, G. Tsatsaronis and M. J. Moran, 1996, *Thermal design and optimization*, John Wiley, New York ; Chichester.

[2] T. J. Kotas, 1995, *The Exergy Method of Thermal Plant Analysis*, Krieger Publishing Co., Malabar, Florida.

[3] J. Szargut, D. R. Morris and F. R. Steward, 1988, *Exergy Analysis of Thermal, Chemical and Metallurgical Processes*, Hemisphere Publishing, New York

[4] C. A. Frangopoulos, 2003, Methods of Energy Systems Optimization, (available at: http://www.itc.polsl.pl/centrum.).

[5] C. A. Frangopoulos, 1991, Intelligent Functional Approach: A method for analysis and optimal synthesis-design-operation of complex systems, *Energy*, Vol. 1, No. 4, pp. 267-274.

[6] C. A. Frangopoulos, 1994, Application of the thermoeconomic functional approach to the CGAM problem, *Energy*, Vol. 19, No. 3, pp. 323.

[7] G. Tsatsaronis and J. Pisa, 1994, Exergoeconomic evaluation and optimization of energy systems--application to the CGAM problem, *Energy : technologies, resources, reserves, demands, impact, conservation, management, policy*, Vol. 19, No. 3, pp. 287.

[8] A. Valero, M. A. Lozano, L. Serra and C. Torres, 1994, Application of the exergetic cost theory to the CGAM problem, *Energy : technologies, resources, reserves, demands, impact, conservation, management, policy*, Vol. 19, No. 3, pp. 365.

[9] M. R. Von Spakovsky, 1994, Application of engineering functional analysis to the analysis and optimization of the CGAM problem, *Energy : technologies, resources, reserves, demands, impact, conservation, management, policy*, Vol. 19, No. 3, pp. 343.

[10] G. Tsatsaronis and M. J. Moran, 1997, Exergy-aided cost minimization, *Energy conversion and management*, Vol. 38, No. 15/17, pp. 1535-1542.

[11] M. Jüdes and G. Tsatsaronis, 2009, Improving Mathematical Optimization Techniques with the Aid of Exergy-Based Variables, *International Journal of Thermodynamics*, Vol. 12, No. 2, pp. 75-82.

[12] M. A. Lozano and A. Valero, 1993, Theory of the exergetic cost, *Energy*, Vol. 18, No. 9, pp. 939-960.

[13] B. Erlach, L. Serra and A. Valero, 1999, Structural theory as standard for thermoeconomics, *Energy conversion and management*, Vol. 40, No. 15-16, pp. 1627.

[14] E. Sciubba, 2001, Beyond thermoeconomics? The concept of Extended Exergy Accounting and its application to the analysis and design of thermal systems, *Exergy, An International Journal*, Vol. 1, No. 2, pp. 68-84.
[15] E. Cardona and A. Piacentino, 2006, A new approach to exergoeconomic analysis and design of variable demand energy systems, *Energy*, Vol. 31, No. 4, pp. 490-515.
[16] F. Cziesla, G. Tsatsaronis and Z. Gao, 2006, Avoidable thermodynamic inefficiencies and costs in an externally fired combined cycle power plant, *Energy*, Vol. 31, No. 10-11, pp. 1472-1489.
[17] A. Lazzaretto and G. Tsatsaronis, 2006, SPECO: A systematic and general methodology for calculating efficiencies and costs in thermal systems, *Energy*, Vol. 31, No. 8-9, pp. 1257-1289.
[18] N. Lior and N. Zhang, 2007, Energy, exergy, and Second Law performance criteria, *Energy*, Vol. 32, No. 4, pp. 281-296.
[19] G. Tsatsaronis, K. Kapanke and A. María Blanco Marigorta, 2008, Exergoeconomic estimates for a novel zero-emission process generating hydrogen and electric power, *Energy*, Vol. 33, No. 2, pp. 321-330.
[20] A. Boyano, A. M. Blanco-Marigorta, T. Morosuk and G. Tsatsaronis, 2010, Advanced exergetic analysis of a steam methane reforming system for hydrogen production, *Proceedings of The 23rd International Conference on Efficiency, Cost, Optimization, Simulation and Environmental Impact of Energy Systems (ECOS)*, Lausanne
[21] A. Stoppato and A. Lazzaretto, 1996, The Exergetic Analysis for Energy System Diagnosis, *Proceedings of AES: Thermodynamics and the Design, Analysis and Improvement of Energy Systems*.
[22] C. Torres, A. Valero, L. Serra and J. Royo, 2002, Structural theory and thermoeconomic diagnosis: Part I. On malfunction and dysfunction analysis, *Energy conversion and management*, Vol. 43, No. 9-12, pp. 1503-1518.
[23] A. Toffolo and A. Lazareto, 2004, On the Thermoeconomic Approach to the Diagnosis of Energy System Malfunctions Indicators to Diagnose Malfunctions: Application of a New Indicator for the Location of Causes, *International Journal of Thermodynamics*, Vol. 7, No. 2, pp. 41-49.
[24] A. Valero, L. Correas, A. Lazareto, V. Rangel, M. Reini, R. Taccani, A. Toffolo, V. Verda and A. Zaleta, 2004, Thermoeconomic philosophy applied to operating analysis and diagnosis of energy utilty systems, *International Journal of Thermodynamics*, Vol. 7, No. 2, pp. 33-39.
[25] D. F. Rancruel and M. R. v. Spakovsky, 2003, Decomposition with Thermoeconomic Isolation Applied to the Optimal Synthesis/Design of an Advanced Tactical Aircraft System, *International Journal of Thermodynamics*, Vol. 6, No. 3, pp. 93-105.
[26] K. Alabi, F. Ladeinde, M. R. v. Spakovsky, D. Moorhouse and J. Camberos, 2006, The Use of the 2 nd Law as a Potential Design Tool for Aircraft Air Frame Subsystems, *International Journal of Thermodynamics*, Vol. 9, No. 4, pp. 1-14.
[27] G. G. Dimopoulos, C. A. Georgopoulou and N. M. P. Kakalis, 2011, Modelling and optimisation of an integrated marine combined cycle system, *Proceedings of 24th International Conference on Energy, Cost, Optimization, Simulation and Environmental Impact of Energy Systems (ECOS)*, Novi-Sad, Serbia.
[28] G. G. Dimopoulos and N. M. P. Kakalis, 2010, An integrated modelling framework for the design, operation and control of marine energy systems, *Proceedings of 26th CIMAC World Congress*, Bergen, Norway.
[29] N. M. P. Kakalis and G. Dimopoulos, 2012, Managing the complexity of marine energy systems, Position Paper 11/2012, Det Norske Veritas, Research & Innovation, (available at: www.dnv.com).
[30] MAN, 2010, SFOC Optimisation Methods For MAN B&W Two-stroke IMO Tier II Engines, MAN Diesel SE, (available at: www.mandiesel.com).

[31] MAN, 2011, Thermo Efficiency System (TES) for Reduction of Fuel Consumption and CO2 Emission, MAN Diesel SE, (available at: www.mandiesel.com).
[32] MHI, 2011, Mitsubishi Energy Recovery System for Container Vessels, Mitsubishi Heavy Industries (MHI), (available at: http://www.mhi.co.jp/en/products/detail/mers.html).

The Relationship Between Costs and Environmental Impacts in Power Plants: An Exergy-Based Study

Fontina Petrakopoulou[a], Yolanda Lara[b], Tatiana Morosuk[c], Alicia Boyano[d], George Tsatsaronis[e]

[a] *IMDEA Energy Institute, Madrid, Spain, fontina.petrakopoulou@imdea.org*
[b] *Research Centre for Energy Resources and Consumption, Zaragoza, Spain, ylara@unizar.es*
[c] *Technische Universität Berlin, Germany, morozyuk@iet.tu-berlin.de* ***(CA)***
[d] *Institute for Prospective Technological Studies, Sevilla, Spain, alicia.boyano@ec.europa.eu*
[e] *Technische Universität Berlin, Germany, tsatsaronis@iet.tu-berlin.de*

Abstract:

Exergy-based methods (exergetic, exergoeconomic and exergoenvironmental analyses) are powerful tools for developing, evaluating and improving energy-conversion systems. In an exergoeconomic analysis, thermodynamic inefficiencies – represented by exergy destruction – are used together with investment cost to calculate the "cost-optimal" alternative for the overall plant. Analogously, in an exergoenvironmental analysis, the aim is to reduce the total environmental impact. Normally, exergoeconomic and exergoenvironmental analyses are conducted independently of each other. Thus, until now, the improvement of a plant has been considered in terms of reduction of either costs or environmental impact. To simultaneously decrease the investment costs and the component-related (manufacturing or construction-related) environmental impacts, their relationship with exergy destruction must be studied in parallel. This paper examines the relationship between exergoeconomic and exergoenvironmental data under various plant operating conditions. A combined-cycle power plant is analyzed and options for a simultaneous improvement from the economic and environmental viewpoints are discussed.

Keywords:

Exergy analysis, Exergoeconomic Analysis, Exergoenvironmental Analysis.

1. Introduction

Thermodynamic, economic, and environmental-impact analyses are three tools used for the evaluation and improvement (optimization) of an energy conversion system. These analyses reveal

(a) The real thermodynamic inefficiencies and the processes that cause them,
(b) The costs associated with equipment and thermodynamic inefficiencies as well as the connection between these two important factors,
(c) The environmental impact associated with equipment and thermodynamic inefficiencies as well as the connection between these two sources of environmental impact, and
(d) Possible measures that would improve the efficiency and the cost effectiveness and would reduce the environmental impact of the system being studied.

An exergoeconomic analysis [1-4] consists of an exergetic analysis, an economic analysis, and an exergoeconomic evaluation. An exergoenvironmental analysis [4,5] consists of an exergetic analysis, a life cycle assessment (LCA) of the environmental impact and an exergoenvironmental evaluation conducted in analogy with the exergoeconomic one.

In the exergoeconomic and exergoenvironmental analyses (which are already known as powerful tools for analyzing, evaluating and improving energy-conversion systems) the economic analysis and the LCA (therefore the exergoeconomic and the exergoenvironmental analysis) are conducted independently of each other. Obviously, then the conclusions from these analyses are also obtained independently.

In this paper we try to obtain consistent conclusions on how to improve an energy conversion system by reducing simultaneously cost and environmental impact. Note that we do not want to assign cost values to environmental impacts (or vice versa) because of the arbitrariness associated with this procedure. As before, the main assumption is that data obtained from an LCA and from a cost analysis are independent from each other.

2. Exergy-based Analyses

2.1 Exergetic analysis

Using the exergy rates associated with fuel and product [1-3], $\dot{E}_{F,k}$ and $\dot{E}_{P,k}$, respectively, the exergetic balance for the *k*-th component is

$$\dot{E}_{F,k} = \dot{E}_{P,k} + \dot{E}_{D,k} \tag{1}$$

The total exergy destruction within the *k*-th component ($\dot{E}_{D,k}$) can be determined through an exergy balance.

The exergetic efficiency for the *k*-th component is

$$\varepsilon_k = \frac{\dot{E}_{P,k}}{\dot{E}_{F,k}} = 1 - \frac{\dot{E}_{D,k}}{\dot{E}_{F,k}} . \tag{2}$$

Additional variables used in the exergetic analysis can be found in many publications, for example, [2-4].

2.2 Exergoeconomic analysis

The exergoeconomic analysis is an exergy-based method that identifies and calculates the location, magnitude, causes and costs of thermodynamic inefficiencies in an energy conversion system. An exergoeconomic analysis is conducted at the component level of a system and reveals (a) the relative cost importance of each component, and (b) options for improving the overall cost effectiveness.

The exergoeconomic model of an energy conversion system [2-4] consists of:

(a) *Cost balances* written for each system component

$$\dot{C}_{P,k} = \dot{C}_{F,k} + \dot{Z}_k , \tag{3a}$$

or

$$c_{P,k}\dot{E}_{P,k} = c_{F,k}\dot{E}_{F,k} + \dot{Z}_k \tag{3b}$$

Here $\dot{C}_{P,k}$ and $\dot{C}_{F,k}$ are the cost rates associated with fuel and product, whereas $c_{P,k}$ and $c_{F,k}$ are the corresponding costs per unit of exergy. Finally $\dot{Z}_k$ is the sum of cost rates associated with capital investment (*CI*) and operating & maintenance (*O&M*) expenditures for the *k*-th component

$$\dot{Z}_k = \dot{Z}_k^{CI} + \dot{Z}_k^{OM} \tag{4}$$

To simplify the discussion, we assumed in the present paper, that the contribution of $\dot{Z}_k^{OM}$ remains constant when the design is changed, and, therefore, the changes in the value of $\dot{Z}_k$ are associated only with changes in the capital investment cost $\dot{Z}_k^{CI}$.

(b) *Auxiliary costing equations* based on the P-rule and the F-rule as, they have been finalized in [3].

The following exergoeconomic variables may be used for improving the overall effectiveness of the *k*-th component in an iterative optimization:

- Cost rate associated with the exergy destruction within the *k*-th component

$$\dot{C}_{D,k} = c_{F,k}\dot{E}_{D,k} \tag{5}$$

- Total costs associated with the component, which are the sum ($\dot{Z}_k^{CI} + \dot{C}_{D,k}$)

- Relative cost difference

$$r_k = \frac{c_{P,k} - c_{F,k}}{c_{F,k}} = \frac{1-\varepsilon_k}{\varepsilon_k} + \frac{\dot{Z}_k}{\dot{C}_{D,k}} \tag{6}$$

- Exergoeconomic factor

$$f_k = \frac{\dot{Z}_k^{CI}}{\dot{Z}_k^{CI} + \dot{C}_{D,k}} = \frac{\dot{Z}_k^{CI}}{\dot{Z}_k^{CI} + c_{F,k} \cdot \dot{E}_{D,k}} \tag{7}$$

2.3 Exergoenvironmental analysis

An exergoenvironmental analysis is an exergy-based method that identifies and calculates the location, magnitude, causes and environmental impact of thermodynamic inefficiencies in an energy conversion system [4,5]. An exergoenvironmental analysis is also conducted at the component level of a system and identifies (a) the relative importance of each component with respect to environmental impact, and (b) options for reducing the environmental impact associated with the overall system. In an exergoenvironmental analysis a one-dimensional characterization indicator is obtained using a Life Cycle Assessment (LCA). This indicator is used in a similar way as the cost is used in exergoeconomics. An index (a single number) describes the overall environmental impact associated with system components and exergy carriers. The Eco-indicator 99 [6] is an example of such an index and is used here. It should be emphasized that the evaluation of environmental impacts will always be subjective and associated with uncertainties. However, the information extracted from the exergoenvironmental analysis is very useful, and future work should also focus on reducing the arbitrariness associated with the LCA and the index used in the analysis.

The exergoenvironmental model of an energy conversion system consists of:

(a) The *environmental impact balances* written for each system component

$$\dot{B}_{P,k} = \dot{B}_{F,k} + \left(\dot{Y}_k + \dot{B}_k^{PF}\right), \tag{8a}$$

or

$$b_{P,k}\dot{E}_{P,k} = b_{F,k}\dot{E}_{F,k} + \left(\dot{Y}_k + \dot{B}_k^{PF}\right). \tag{8b}$$

Here $\dot{Y}_k$ is associated with the component-related (manufacturing, operation and retirement) environmental impact [5]; $\dot{B}_{P,k}$ and $\dot{B}_{F,k}$ are the environmental impact rates associated with product and fuel respectively, and $b_{P,k}$ and $b_{F,k}$ are the corresponding environmental impacts per unit of exergy for product and fuel [5]. To separately account for *pollutant formation* within the k th component during system operation, a new variable was introduced $\dot{B}_k^{PF}$ [7]. This term $\dot{B}_k^{PF}$ is zero if no pollutants are formed within a process, i.e. for processes without a chemical reaction (compression, expansion, heat transfer, etc.). For components, where chemical reactions occur (for example, combustion), the rule on how to calculate the value of $\dot{B}_k^{PF}$ is described in detail in [7].

(b) *Auxiliary environmental impact equations* based on the P-rule and the F-rule, which are applied in analogy to exergoeconomics [4,5].

The following exergoenvironmental variables may be used for reducing the environmental impact associated with the *k*-th component:

- Environmental impact rate associated with the exergy destruction within the *k*-th component

$$\dot{B}_{D,k} = b_{F,k}\dot{E}_{D,k} \tag{11}$$

- Relative environmental impact difference

$$r_{b,k} = \frac{b_{P,k} - b_{F,k}}{b_{F,k}} = \frac{1-\varepsilon_k}{\varepsilon_k} + \frac{\dot{Y}_k}{\dot{B}_{D,k}} \tag{12}$$

- Exergoenvironmental factor

$$f_{b,k} = \frac{\dot{Y}_k^{CO}}{\dot{Y}_k^{CO} + \dot{B}_{D,k}} = \frac{\dot{Y}_k^{CO}}{\dot{Y}_k^{CO} + b_{F,k}\cdot\dot{E}_{D,k}} \tag{13}$$

2.4 3D Analysis

Figure 1 shows some possible relationships among exergy destruction, capital investment cost and construction-of-component-related environmental impact [8]. The effect of component size is taken into consideration in this figure by relating $\dot{E}_{D,k}$, $\dot{Z}_k^{CI}$ and $\dot{Y}_k^{CO}$ to the product exergy rate associated with the same component at the given operation conditions ($\dot{E}_{P,k}$).

In Fig.1 single curves are shown for simplicity. In reality each curve should be replaced by a rather wide area representing the fact that for each value of relative exergy destruction ($\dot{E}_{D,k}/\dot{E}_{P,k}$), both the $\dot{Z}_k^{CI}/\dot{E}_{P,k}$, and the $\dot{Y}_k^{CO}/\dot{E}_{P,k}$ values can vary within a rather wide range.

The values of $\dot{Y}_k^{CO}/\dot{E}_{P,k}$ shown in the lower left part of each plot (quarter II) in Fig.1 could have different shapes since some design changes might correspond to entirely different materials and/or

manufacturing methods being used for the construction of component *k*, and, thus, to various curves for the environmental impact. Until now the character of this curve has not been studied, therefore the four curves (a-d) shown here in quarters II are just some examples of possible options. The resulting functions given in the upper right part of each plot (quarter III) are of particular importance for the simultaneous reduction of investment cost and environmental impact.

In this paper, and for the first time, we study the relationship among three variables: $\dot{E}_{D,k} / \dot{E}_{P,k}$, $\dot{Z}_k^{CI} / \dot{E}_{P,k}$, and $\dot{Y}_k^{CO} / \dot{E}_{P,k}$ using a particular example (a combined-cycle power plant).

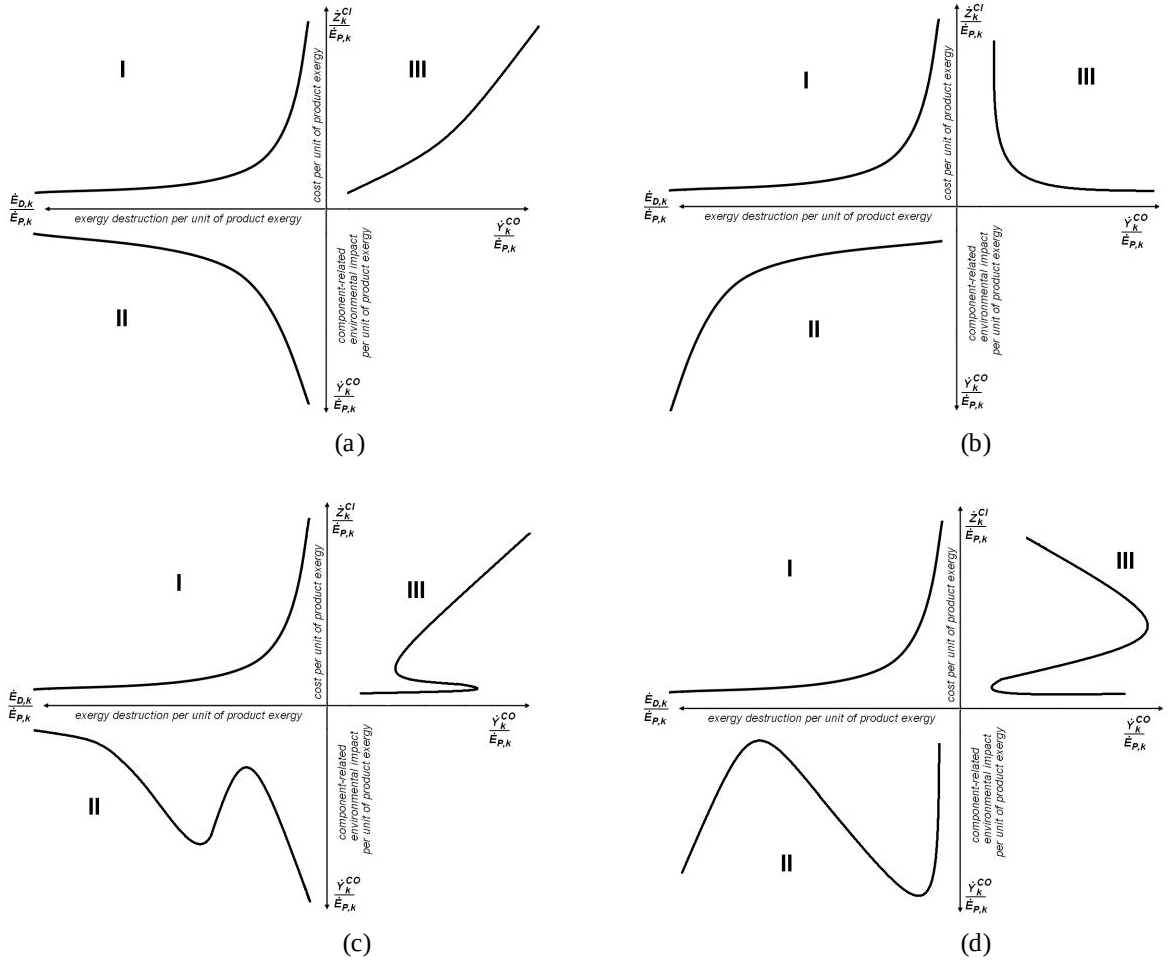

Figure 1: Expected relationships among capital investment, construction-of-component-related environmental impact and exergy destruction for the k th component of an energy conversion system

3. Study Case

The power plant studied in this paper is a three-pressure-level combined-cycle plant with one reheat stage. The plant has one product – electricity – and works with natural gas that was assumed here to be pure methane. The configuration of the process is shown in Figure 2. The thermodynamic variables for selected streams of the plant are shown in Table 2. The total exergy, $\dot{E}_{tot,j}$, includes both the chemical and physical exergy of each material stream *j*.

High-temperature flue gas with a mass flow rate of 628 kg/s exits the plant's *gas turbine* (GT) and is led to the *heat recovery steam generator* (HRSG), where it provides thermal energy to produce steam at three different pressure levels, 124, 22, and 4.1 bar. The combustion products enter the HRSG with a pressure of 1.058 bar at 580°C and are exhausted to the atmosphere at 95°C. The

high-pressure steam at 560°C is expanded to 23 bar in the *high-pressure steam turbine* (HPST) and returns to the HRSG, where it is reheated to 560°C. The reheated steam is sent to the *intermediate-pressure steam turbine* (IPST), where it is expanded to 4.1 bar. This low-pressure steam is mixed with low-pressure superheated steam and it is then led to the *low-pressure steam turbine* (LPST), where it is expanded to 0.05 bar. The steam is condensed in the condenser, preheated, led to the deaerator of the plant and further conveyed to the feedwater pumps to continue the cycle.
Results from the exergetic, exergoeconomic and exergoenvironmental analyses of this combined-cycle power plant have been reported in several publications (for example, [9]), where the performance of the complex combined cycle power plant including different systems for CO_2 capture has been discussed. Some data obtained from the exergetic, exergoeconomic and exergoenvironmental analyses for selected components of the power plant (Figure 2) are presented in Table 2. For the base case, the cost of electricity is equal to 7.39 €/kWh, whereas the environmental impact associated with electricity production is equal to 14.69 mPts/kWh.
From the economic point of view, we need to find a way to reduce the total cost associated with the component, i.e. the sum ($\dot{Z}_k + \dot{C}_{D,k}$); from the environmental viewpoint we want to reduce the total environmental impact associated with the component, i.e. the sum ($\dot{Y}_k + \dot{B}_{D,k}$). The main final goal for the improvements is to decrease the cost of the final product, electricity. Afterwards, the effect of the economics-based modifications on the environmental impact of the final product should also be investigated. Taking into account these modifications, an exergoenvironmental analysis has been carried out to obtain the total environmental impact of the produced electricity.

Table 2: Calculated thermodynamic variables for selected material streams [9].

Stream, j	$\dot{m}_j$ [kg/s]	T_j [°C]	p_j [bar]	$\dot{E}_{tot,j}$ [MW]
1	614.50	15.0	1.01	0.96
2	614.50	392.9	17.00	232.25
3	14.00	15.0	50.00	729.62
4	14.00	15.0	17.00	727.37
5	628.50	1264.0	16.49	741.01
6	628.50	580.6	1.06	189.87
7	268.50	580.6	1.06	81.11
8	268.50	447.6	1.05	54.64
9	360.00	580.6	1.06	108.75
10	360.00	449.3	1.05	73.68
11	628.50	448.6	1.05	128.33
12	628.50	341.2	1.04	84.69
13	628.50	257.9	1.04	55.77
14	628.50	257.3	1.04	55.59
15	628.50	237.6	1.04	49.49
16	628.50	234.1	1.04	48.43
17	628.50	229.3	1.04	47.01
18	628.50	156.4	1.03	27.98
19	628.50	95.3	1.03	16.49
20	94.58	32.9	3.73	0.47
21	94.58	135.6	3.62	8.18
22	95.41	140.0	3.62	8.79
23	72.43	140.0	3.62	6.67
24	7.22	140.0	3.62	0.67
25	7.22	140.5	25.13	0.68
26	7.22	216.6	24.38	1.56
27	7.22	222.6	24.38	7.23
28	7.22	237.9	23.16	7.35
29	94.58	32.9	0.05	0.44
30	72.43	305.1	23.16	79.53
31	72.43	560.6	22.00	103.42
32	72.43	317.2	4.10	66.03
33	22.15	214.1	4.10	18.01
34	22.15	146.4	4.32	16.96
35	0.83	146.4	4.32	0.63
36	22.97	140.0	3.62	2.12
37	22.97	140.0	4.32	2.12
38	22.97	146.4	4.32	17.60
39	65.21	140.0	3.62	6.01
40	65.21	141.8	134.56	6.96
41	65.21	325.2	130.53	31.88
42	65.21	331.2	130.53	71.79
43	65.21	560.6	124.00	103.51
44	65.21	313.2	23.16	72.22
45	94.58	293.0	4.10	83.86
46	94.58	32.9	0.05	12.87

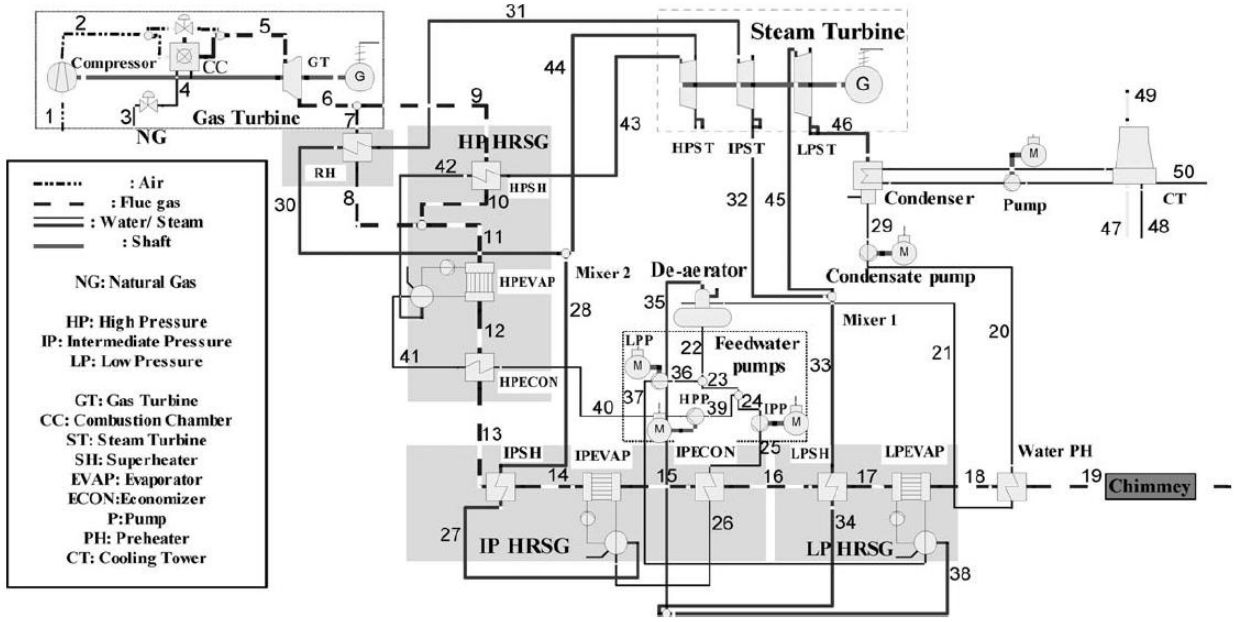

Figure 2: Schematic of a three-pressure-level combined cycle power plant

Table 3: Some data obtained from the exergetic, exergoeconomic and exergoenvironmental analyses for the selected components of the power plant shown in Figure 2.

Component	Exergetic analysis	Exergoeconomic analysis			Exergoenvironmental analysis		
	$\dot{E}_{D,k}$ [MW]	$\dot{Z}_k$ [€/h]	$\dot{C}_{D,k}$ [€/h]	$\dot{Z}_k + \dot{C}_{D,k}$ [€/h]	$\dot{Y}_k$ [Pts/h]	$\dot{B}_{D,k}$ [Pts/h]	$\dot{Y}_k + \dot{B}_{D,k}$ [Pts/h]
CC	220.87	202.12	926.46	8202.79	0.381	2862	2862
GT	20.47	31.33	1482.34	2610.20	1.126	396	397
Compressor	11.38	18.97	1297.05	1979.83	0.236	228	228
PHSH	3.35	5.12	149.46	333.92	1.237	65	66
HPEVAP	3.73	5.70	183.60	388.93	0.139	72	72
LPST	9.64	20.40	696.33	1430.61	0.493	232	232

4. Sensitivity Analysis

The improvement suggestions can be divided into two groups:

- Design changes that lead to an increase in the exergetic efficiency of the components (to a decrease in the exergy destruction), i.e., to a decrease in the values of $\dot{C}_{D,k}$ and $\dot{B}_{D,k}$, or

- Design changes that lead to a decrease in the values of $\dot{Z}_k$ and $\dot{Y}_k$ by decreasing the exergetic efficiency and increasing the exergy destruction.

The following assumptions for the sensitivity analysis were used.

4.1 Combustion Chamber

From the viewpoint of all three analyses, the combustion chamber can be improved by increasing its exergetic efficiency. In order to achieve this goal, the following effects have been studied:

- Effect of excess air (Figure 3a). For the sensitivity analysis, we assumed λ=2.1; 2.05 (Base Case), 1.95 and 1.9, and

- Effect of the fuel inlet temperature (Figure 3b). For the sensitivity analysis, we assumed for T_4 the values 15ºC (Base Case), 50ºC, 100ºC and 150ºC.

4.2 Gas Turbine

For the sensitivity analysis, we assumed that the isentropic efficiency of the gas turbine remains constant and an improvement of this component is possible only through modification of the operation conditions, for example, through a change in the temperature of the combustion gases entering the gas turbine. For the sensitivity analysis (Figure 4) we assumed for T_5 the values 1264ºC (Base Case), 1300ºC, 1324 ºC and 1350ºC.

4.3 Compressor

The two effects were considered for the improvement of the compressor:

- Effect of the isentropic efficiency (Figure 5a). For the sensitivity analysis, we assumed η_{CM}= 0.91, 0.915 (Base Case), 0.92 and 0.925.

- Effect of the pressure ratio (Figure 5b). For the sensitivity analysis we assumed p_2/p_1= 16/1.013, 17/1.013 (Base Case), 18/1.013 and 19/1.013.

4.4 High-pressure superheater

The modifications can be conducted by changing the temperature difference between hot inlet and cold outlet streams (Figure 6). For the sensitivity analysis we assumed ($T_9 - T_{43}$)= 15K, 20K (Base Case), 25K and 30K.

4.5 High-pressure evaporator

The modifications can be done by changing the pinch temperature. For the sensitivity analysis (Figure 7) we assumed ΔT_{pinch}=9K, 10K (Base Case), 15K and 20K.

4.6 Low-pressure steam turbine

The following two options were considered for the improvement of the low-pressure steam turbine:

- Effect of the isentropic efficiency (Figure 8a). For the sensitivity analysis we assumed η_{CM}= 0.85, 0.88 (Base Case), 0.90, 0.91 and 0.915.

- Effect of the pressure at the outlet from the turbine (Figure 8b). For the sensitivity analysis we assumed p_2/p_1= 125 bar, 130.5 bar (Base Case), 135 bar and 140 bar.

4.7 Overall system

The effects of the improvement of the selected components to the overall cost and the environmental impact of the electricity are shown in Figures 9 and 10. For this analysis we selected only variables that have a positive effect to the reduction of the cost and the environmental impact of electricity.

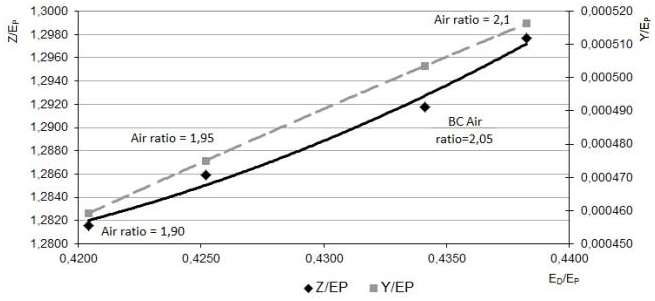

(a)

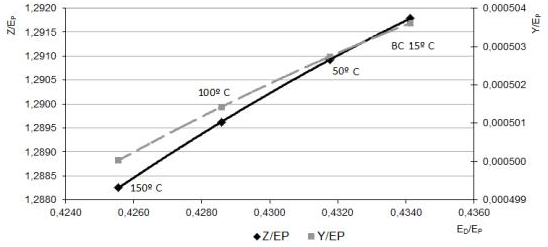

(b)

Figure 3: Combustion Chamber:(a) Effect of the excess air, and (b) effect of the inlet temperature of the fuel

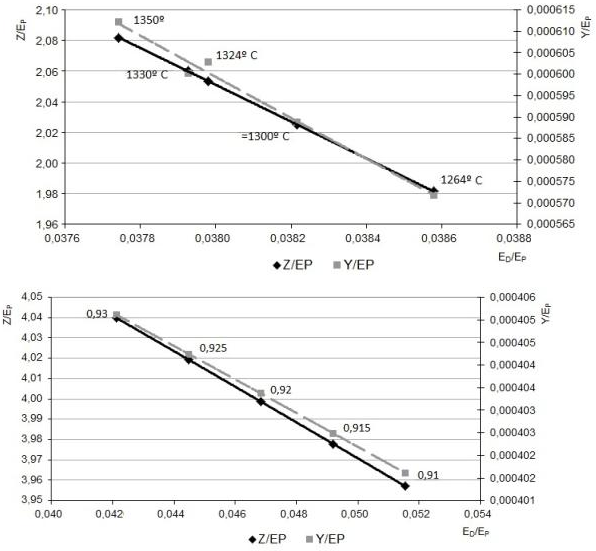

(a)

Figure 4: Gas turbine

(Effect of the temperature at the inlet)

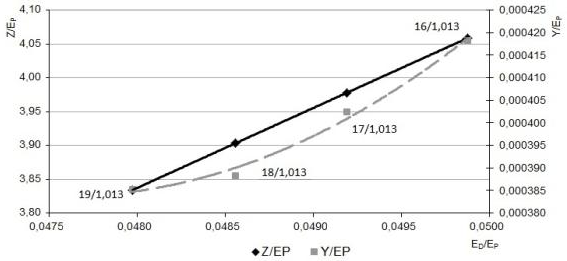

(b)

Figure 5: Compressor: (a) Effect of the isentropic efficiency, and (b) effect of the pressure ratio.

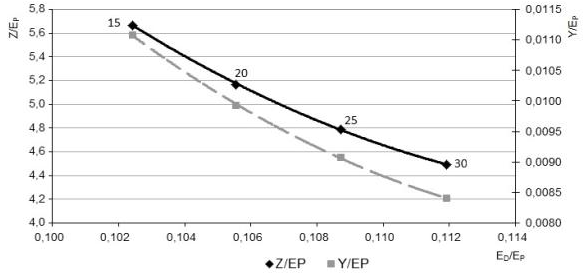

Figure 6: High-pressure superheater (Effect of the minimum temperature difference between hot stream inlet and cold stream outlet).

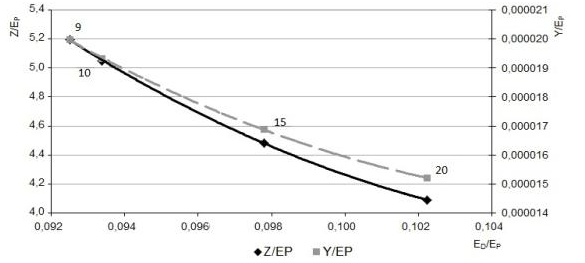

Figure 7. High-pressure evaporator (effect of the pinch temperature difference).

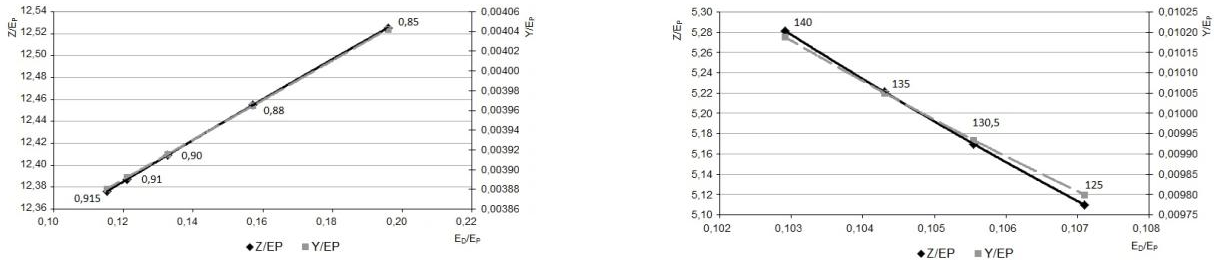

(a) (b)

Figure 8: Low-pressure steam turbine: (a) Effect of the isentropic efficiency, and (b) effect of the pressure at the outlet from the turbine.

5. Results and Discussion

The results of the sensitivity analysis (Figures 3 through 8) for the selected components of the analyzed combined-cycle power plant show, that for the assumptions made, the results obtained from the exergoeconomic and the exergoenvironmental analyses are qualitatively the same. We have two types of curves:

- Rising curves - for the combustion chamber (Figures 3a and 3b), compressor (Figure 5b), and low-pressure steam turbine (Figure 8a), and
- Falling curves – for the gas turbine (Figure 4), compressor (Figure 5a), High-pressure superheater (Figure 6), high-pressure evaporator (Figure 7), and low-pressure steam turbine (Figure 8b).

With respect to the character of the resulting curves among the three variables: $\dot{E}_{D,k}/\dot{E}_{P,k}$, $\dot{Z}_k^{CI}/\dot{E}_{P,k}$, and $\dot{Y}_k^{CO}/\dot{E}_{P,k}$ (Figure 1), the case of a rising curve corresponds to Type I (Figure 1a) and the case of a falling curve corresponds to Type II (Figure 1b).

If during the variation of a given process variable we obtain a Type I curve, then optimization is not required, because the lower the value of $\dot{E}_{D,k}/\dot{E}_{P,k}$ (i.e., of the thermodynamic inefficiencies), the lower the values of $\dot{Z}_k^{CI}/\dot{E}_{P,k}$ and/or $\dot{Y}_k^{CO}/\dot{E}_{P,k}$ (i.e., of the investment costs and/or of the component-related environmental impact. It is apparent that in this case we would select the most efficient option that happens to exhibit also the lowest investment cost and/or the lowest environmental impact. Thus, for example, for the combustion chamber and according to the assumptions made in this paper, we would select the lowest possible amount of excess air and the highest possible preheating temperature of the fuel (see Figures 3a and 3b). Along the same line for the compressor we would select the highest possible pressure ratio, and for the low-pressure steam turbine we would select the highest possible isentropic efficiency.

If during the variation of a given process variable we obtain a Type II curve, then optimization is necessary, because the higher the value of $\dot{E}_{D,k}/\dot{E}_{P,k}$ the lower the values of $\dot{Z}_k^{CI}/\dot{E}_{P,k}$ and/or $\dot{Y}_k^{CO}/\dot{E}_{P,k}$. Thus, an optimal value needs to be determined, for example, for the temperature of the

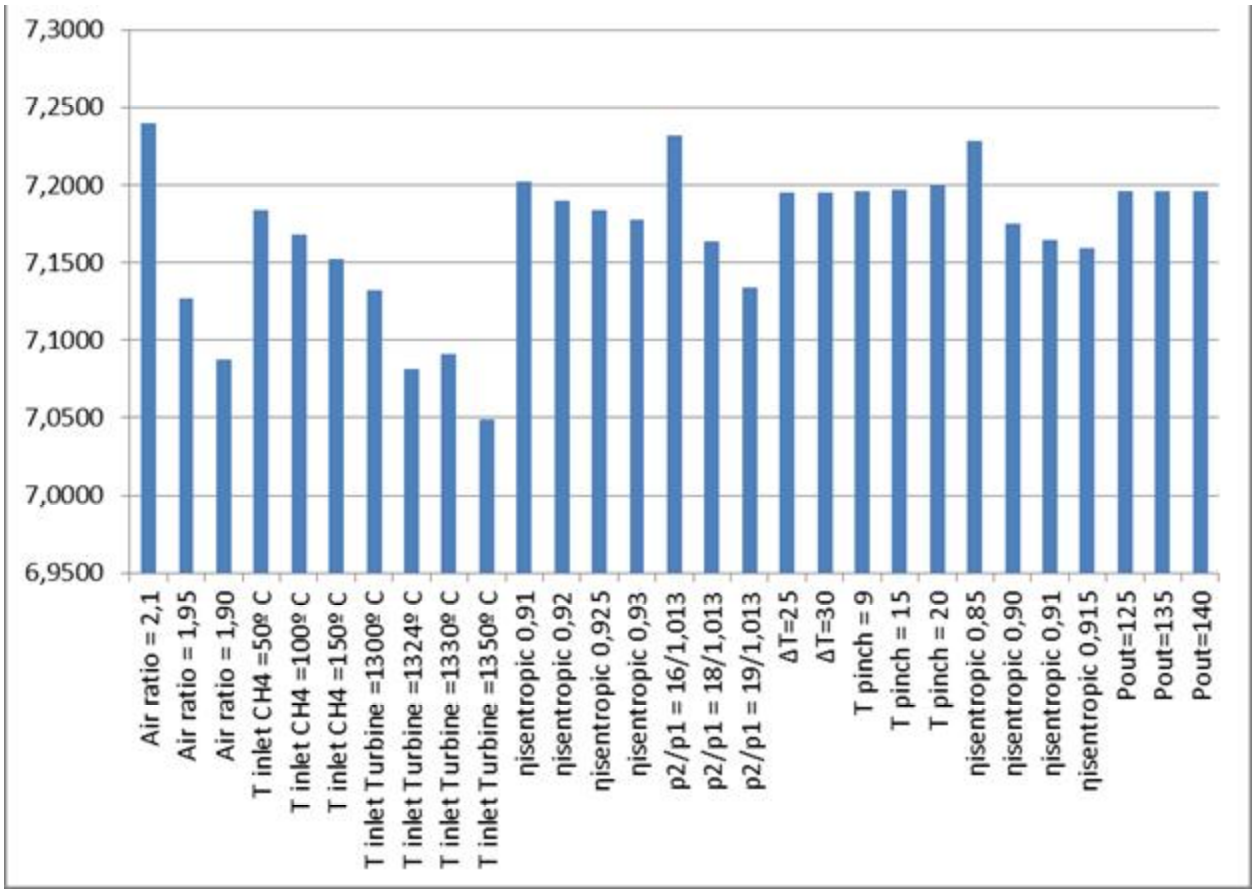

Figure 9: Specific cost of the generated electricity, $c_{P,tot}$ [€/kWh]. The effects of improving selected components on the overall cost (Base Case 7.39 €/kWh).

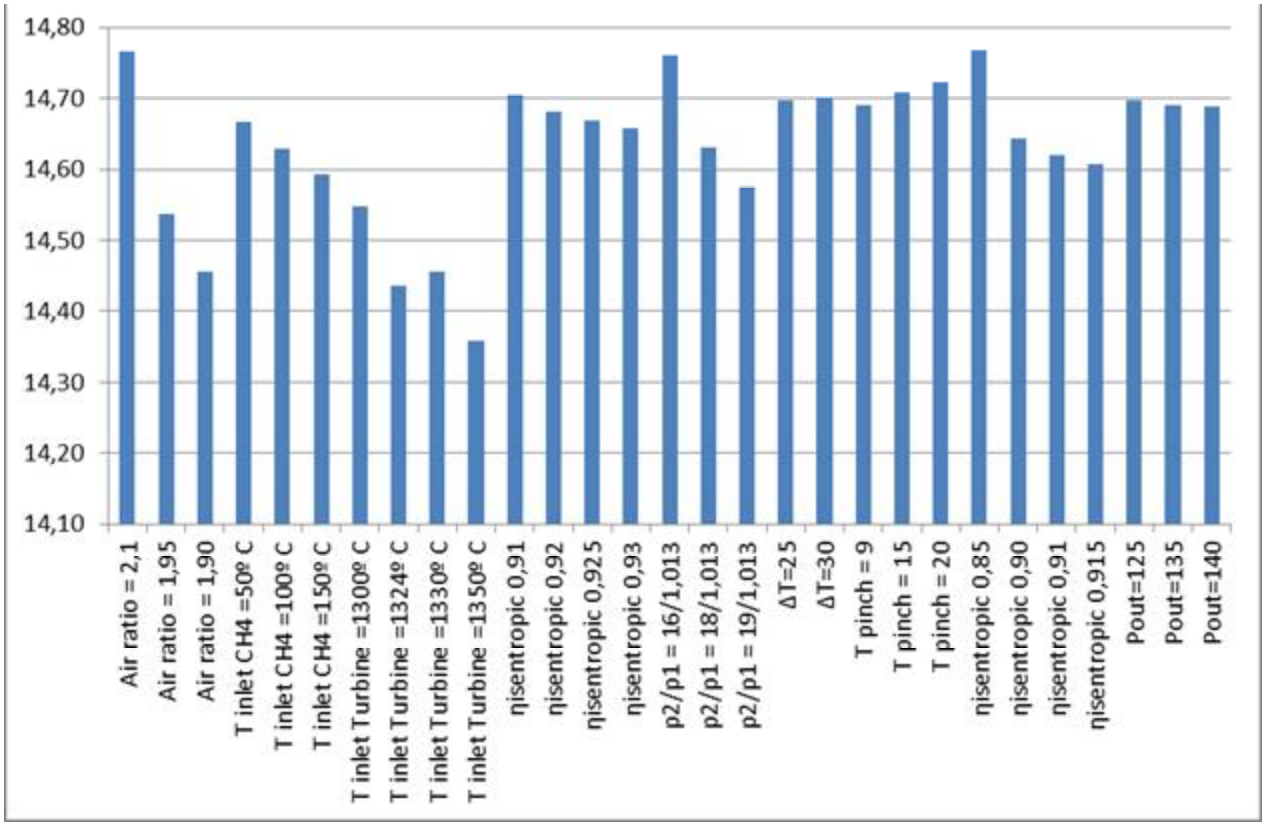

Figure 10: Specific environmental impact of the generated electricity, $b_{P,tot}$ [mPts/kWh]. The effects of improving selected components on the overall environmental impact (Base Case 14.69 mPts/kWh).

combustion gases at the inlet of the gas turbine, for the isentropic efficiency of the compressor, for the minimum temperature difference between hot inlet and cold outlet streams in the high-pressure superheater, the pinch temperature difference for the high-pressure evaporator, and for the inlet pressure in the low-pressure steam turbine.

Figures 9 and 10 show how the considered options for improving the components of the combined-cycle power plant affect the cost and the environmental impact of the generated electricity. Significant improvements are achieved when improving the performance of the combustion chamber and the turbomachinery.

6. Conclusions

A complex energy conversion system (a three-pressure-level combined cycle power plant) was used in this paper to study the interdependencies among costs, environmental impacts and thermodynamic inefficiencies. Exergoeconomic and exergoenvironmental analyses and considerations have been applied. The data obtained from these analyses under various plant operating conditions have been considered simultaneously.

The results demonstrate that, for the three-pressure-level combined cycle power plant, improvements in efficiency result - in most cases - in the decreases of both costs and environmental impact. However, the trends of the functions $\dot{Z}_k / \dot{E}_{P,k}$ and $\dot{B}_{D,k} / \dot{E}_{P,k}$ are not always similar. The analysis presented here suggests ways for improving a three-pressure-level combined cycle power plant simultaneously from the thermodynamic, economic and ecological viewpoints. Future work should focus on more detailed analysis such as the examination of the relationship between the three functions: $\dot{E}_{D,k} / \dot{E}_{P,k}$, $\left(\dot{Z}_k + \dot{C}_{D,k}\right) / \dot{E}_{P,k}$ (i.e., consideration of the total cost associated with the component) and $\left(\dot{Y}_k + \dot{B}_{D,k}\right) / \dot{E}_{P,k}$ (i.e. consideration of the total environmental impact associated with the component).

Nomenclature

B environmental impact associated with an exergy stream, Points
b environmental impact per unit of exergy, Points/J
C cost associated with an exergy stream, €
c cost per unit of exergy, €/J
E exergy, J
e specific exergy, J/kg
f exergoeconomic factor
f_b exergoenvironmental factor
k k th component
m mass, kg
p pressure, bar
r relative cost difference
r_b relative environmental impact difference
T temperature [K]
Y construction-of-component-related environmental impact, Points

Z cost associated with investment expenditures, €

Greek symbols

ε exergetic efficiency

η isentropic efficiency

λ stoichiometric amount of air

Subscripts

D refers to exergy destruction

F fuel

P product

tot refers to the total system

References

[1] Tsatsaronis G., Combination of Exergetic and Economic Analysis in Energy-Conversion Processes. In: Energy Economics and Management in Industry, Proceedings of the European Congress, Algarve, Portugal, April 2-5, 1984, England, Oxford: Pergamon Press, Vol. 1: 151-157.

[2] Bejan A., Tsatsaronis G., Moran M. Thermal Design and Optimization, Wiley, New York, 1996.

[3] Lazzaretto A., Tsatsaronis G. SPECO: A systematic and general methodology for calculating efficiencies and costs in thermal systems, Energy Int. J., 31, 2006: 1257-1289.

[4] Tsatsaronis G. Recent developments in exergy analysis and exergoeconomics', *Int. J. Exergy*, Vol. 5 (5/6), 2006:489–499.

[5] Meyer L., Tsatsaronis G., Buchgeister J., Schebek L. Exergoenvironmental Analysis for Evaluation of the Environmental Impact of Energy Conversion Systems**,** Energy Int. J., Vol. 34, 2009: 75-89.

[6] Goedkoop M., Spriensma R. The Eco-indicator 99: A damage oriented method for Life Cycle Impact Assessment. Methodology Report. Amersfoort, Netherlands, 2000, (http:\\www.pre.nl).

[7] Boyano A., Blanco-Marigorta A.M., Morosuk T., Tsatsaronis G. Exergoenvironmental analysis of a steam methane reforming process for hydrogen production. Energy Int. J., 2011, Vol.36 (4): 2202-2214.

[8] Tsatsaronis G., Morosuk T. A general exergy-based method for combining a cost analysis with an environmental impact analysis. Proceedings of the ASME International Mechanical Engineering Congress and Exposition, Boston, Massachusetts, USA, 2008, files IMECE2008-67218 and IMECE2008-67219.

[9] Petrakopoulou F., Boyano A., Cabrera M., Tsatsaronis G. Exergoeconomic and exergoenvironmental analyses of a combined cycle power plant with chemical looping technology. International Journal of Greenhouse Gas Control 5 (2011): 475-482.

Thermo-Ecological Evaluation of Biomass Integrated Gasification Gas Turbine Based Cogeneration Technology

Wojciech Stanek [a], Lucyna Czarnowska and Jacek Kalina

Institute of Thermal Technology, Silesian University of Technology, Gliwice, Poland
[a]e-mail: wojciech.stanek@polsl.pl

Abstract:

Biomass integrated gasification combined cycle cogeneration is nowadays considered as one of the most attractive technology for CO_2 emission reduction and non-renewable fuel savings. Different criterions such as primary energy savings or emission reduction are usually taken into account in order to evaluate potential energy and environmental benefits resulting from the technology. On the other hand investment decision is in most cases based on financial profitability of a project. Nowadays the biomass energy conversion plants, especially the integrated gasification ones, cannot compete effectively with fossil fuel fired technologies without an effective financial support. Therefore in many countries, in order to satisfy political priorities, there have been established supportive mechanisms that are based on different forms of financial subsidies. The subsidies are usually allocated between projects according to the amount of electricity generated, therefore promoting rather power generation than its efficiency or the influence on the depletion of non-renewable resources. In the face of growing scarcity of non-renewable natural resources, it seems to be reasonable that additional criterion is applied to evaluate biomass conversion technologies. The Thermo-Ecological Cost (TEC), which expresses the cumulative consumption of non-renewable exergy, seems to be an appropriate indicator in this matter. Moreover, to express the total effect of considered energy conversion systems the TEC should be supplemented with the data resulting from Life Cycle Analysis (LCA). In this paper the proposed methodology has been applied to the analysis of a gas turbine based cogeneration plant integrated with gasification of biomass. There are investigated different gasification technologies and configurations of CHP plant. There are taken into account atmospheric fluidized bed gasification (AFB), pressurized fluidized bed gasification (PFB) and allothermal gasification using pure steam as gasification agent (FICFB) as well as simple and combined power cycles based on a recuperated gas turbine. The performance of the plant has been investigated using the combined model developed using Engineering Equation Solver and GateCycle software. The results reveal that simple cycle with gas turbine and waste heat recovery water boiler offers better effects than combined cycle configuration. The best performance has been reported for pressurized gasification technology.

Keywords:

Cogeneration, Heat and Power Plant, Biomass Gasification, Exergy, Life Cycle Analysis, Thermo-Ecological Cost.

1. Introduction

Depletion of natural non-renewable resources is accelerated by continuously increasing energy consumption. From the economic point of view the increase of consumption is a base for further development [1] of societies. On the other hand, it provides an ecological threat to the existence of future generations. Environmental risks associated with the growth of consumption can be divided into two groups: depletion of non-renewable natural resources and discharge of harmful waste products into the environment. Damages caused by the waste products can also be expressed through the impact on the depletion of non-renewable natural resources as the losses should be compensated or prevented. In order to reduce the consumption of non-renewable natural resources, the use of renewable ones should increase. The replacement of non-renewable fuels by biomass is an option. However, the effects of biomass utilisation in the energy sector should be evaluated using system analysis, not pure direct effects appearing at the boundary of a conversion plant. Moreover,

it is highly recommended to take into account beside the classical economic criterion the one based on physical laws in non-renewable management. The global effects of natural resources management can be investigated applying the methods of cumulative calculus and Life Cycle Assessment (LCA) [2,3]. The calculation of the cumulative coefficients was initiated by Chapman, who introduced the concept of energy cost [4-6]. The theory of the energy cost of useful products was developed by Boustead and Hancock [7]. Szargut introduced the important concept of cumulative exergy consumption (CExC) [8,9], and then basid on CExC the Thermo-Ecological Cost (TEC), which extends the applications of exergy analysis onto the field of environmental considerations. The TEC expresses the cumulative consumption of non-renewable exergy of natural resources [10,11]. The Szargut's method in comparison with other methods of ecological assessment can bring all environmental impacts to one measure which is the exergy. The minimization of the TEC [13,14] ensures a mitigation of the depletion of non-renewable resources. Such optimisation can be a base of ecological economy that is in line with the concept of sustainable development.

The original Szargut's TEC analysis concerns only the operational phase of a production plant. In order to evaluate a global (or total) impact of a considered production process the method should be supplemented with tools offered by the LCA. Nowadays the problem of emissions becomes a very important one. Therefore Szargut proposed adaptation of the TEC algorithm for the calculation of the cumulative emissions. In the case of green house gasses (GHG) he proposed a new term that is the Thermo-Climatic Cost (TCC) [14,15]. The combination of the TEC, LCA and TCC methods can be a comprehensive tool for sustainable management of non-renewable resources. In this paper there is proposed the algorithm of thermo-ecological evaluation based on TEC, TCC and LCA principles for environmental evaluation of biomass to energy conversion technology.

2. Exergetic cost of natural resources

Szargut [15] defined the TEC as the cumulative consumption of non-renewable exergy connected with the fabrication of a particular product, including also an additional consumption, that results from the necessity of compensation of environmental losses caused by rejection of harmful substances into the environment. The index of operational TEC can be determined by solving a set of balance equations. The equations are formulated using the scheme presented in Fig. 1.

The physical cost of any product expressed by the TEC is mainly the consumption of chemical exergy b_s extracted directly from the nature as fuels, mineral ores, nuclear ores or fresh water. However this consumption appears only in the production processes directly connected with an extraction of a substance from the natal deposits, e.g. in coal mine. Not all branches of economy are directly connected to the nature. However, due to interconnections in the production systems, the TEC is generated also by consumption of domestic semi-finished products a_{ij} exchanged between branches of the system. Additionally, if within the national system there are some imported and exported goods a part of TEC can result from an interregional exchange. For example, in Polish conditions 70% of natural gas is imported from outside the balance boundary of domestic economy. In this case the total TEC of a *j*-th product results from consumption of a *r-th* imported good in a *j*-th branch a_{rj}. In some branches a by-production can appear. By-products replace main products in other branches and for this reason the value of TEC of a considered main product is reduced. In the balance presented in Fig. 1 by-products are taken into account by the coefficient of by-production f_{ij}. TEC of useful by-product should be determined using the principles of avoided exergetic cost method. The balance of TEC of a *j*-th production branch includes also an additional consumption of resources ψ_{j0} connected with rejection of wastes into the environment. This additional consumption is connected with the consumption at an abatement installation ψ'_{j0}. as well as it results from the necessity of compensation of losses in the environment. By the definition the exergetic TEC takes into account only the consumption of non-renewable resources.

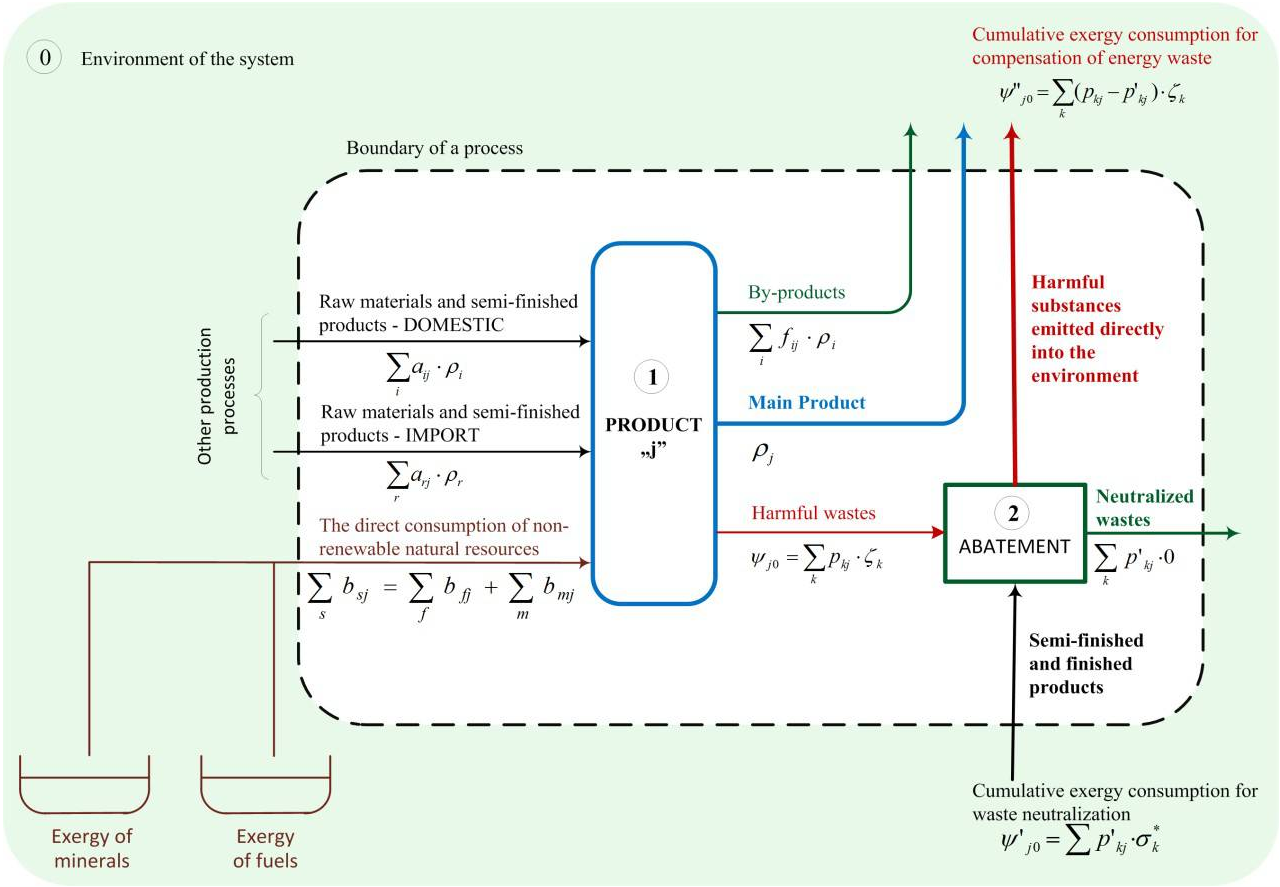

Fig. 1. Idea of TEC balance equation

Therefore if a process driven by a renewable energy is being examined the direct consumption of chemical exergy should not be taken into account in the balances of TEC. This is because the consumption of renewable exergy, e.g. biomass, doesn't make any deleterious impact on depletion of deposits of limited natural resources. However, it does not mean the TEC of biomass should be equal to zero. The TEC of biomass is positive and it results from cumulation of some external expenses of non-renewable natural resources appearing in the total life cycle of a conversion technology. For this reason, the original TEC algorithm should be supplemented with LCA tools and new comparative indices of technology performance should be derived. According to the balance scheme given in Fig. 1 the equations for calculation of the operational TEC take the form [10,11,15]:

$$\rho_j+\sum_i\left(f_{ij}-a_{ij}\right)\rho_i-\sum_r a_{rj}\rho_r=\sum_s b_{sj}+\psi_{j0} \tag{1}$$

The last part of the Eq.(1) includes the additional expenses of cumulative exergy of non-renewable resources arising from the formation of waste products within the *j*-th production process. These additional expenses $\psi_{j0}=\psi'_{j0}+\psi''_{j0}$ are divided between abatement of wastes and losses in environment:

$$\psi'_{j0}=\sum_k p'_{kj}\cdot\sigma_k \tag{2}$$

An abatement of a negative impact of *k*-th waste substance requires the consumption of additional quantities of cumulative exergy of non-renewable resources and can be expressed as follows:

$$\psi''_{j0}=\sum_k(p''_{kj}-p'_{kj})\cdot\zeta_k \tag{3}$$

The concept of evaluation of exergetic abatement cost has been exhaustively described by Valero and Botero in [29] and this method has been adopted within the TEC algorithms. A residual amount of harmful k-th substance $(p''_{kj} - p'_{kj})$ that is not removed in an abatement installation is transferred into the environment and causes damages. The additional thermo-ecological cost arising from the environmental losses results from necessity of either compensation or repair. Determination of the exergetic cost of compensation ζ_k is one of the most difficult task within the analysis of TEC [30]. Szargut [20] proposed the simplified method based on the knowledge of external impacts of the process using so called monetary indices of harmfulness:

$$\zeta_k = \frac{Bw_k}{PKB + \sum_k P_k w_k} \tag{4}$$

Practical application of this method is shown by Stanek and Czarnowska in [16,17]. The results of ζ_k obtained using external costs w_k for main harmful gaseous substances are presented in Table 1.

Table 1. External cost and TEC of major air pollution

No.	Indicator	Units	Harmful substance		
			SO_2	NO_X	PM
1.	Monetary external cost, w_k	€$_{2008}$/kg	12.81	9.41	7.00
2.	Thermo-Ecological Cost, ζ_k	MJ$_{ex}$/kg	97.82	71.88	53.42

The exergetic abatement cost σ_k can be determined on the basis of mass and energy balances for abatement technology. In the case of CO_2 removal by MEA the obtained value of abatement cost [19] is σ_{CO2}=4.4 MJ/kg.

3. Thermo-Climatic Cost

The methodology for determination of depletion of non-renewable resources (Eq. 1) can be also used for investigation of cumulative emissions. It seems to be an appropriate approach in the case of GHG emissions, because these gases are supposed to be responsible for global warming effect. Therefore the TCC has been defined as the cumulative emission of the GHG. In order to modify the TEC balance for the analysis of GHG cumulative emissions, first of all the specific consumption of exergy b_s should be replaced by the total direct emission $e_{GHG,j}$ of GHG from a considered process. In the energy conversion processes the direct emission consists mainly of:

- anthropogenic CO_2 emission from combustion processes e_{CO2},
- methane emission in the processes of fossil fuels delivery and processing e_{CH4}.

The direct anthropogenic CO_2 emission is closely dependent on the energy efficiency of the transformation of chemical energy of fuels. Direct emission of carbon dioxide can be evaluated assuming complete combustion of fuels. Basing on the law of conservation the specific emission of CO_2 related to the chemical energy of a fuel can be calculated using simple stoichiometric formula:

$$e_{CO2} = \frac{M_{CO2}}{M_C} \cdot \frac{c}{LHV} = 3.667 \cdot \frac{c}{LHV}, \frac{\text{kg CO}_2}{\text{MJ}} \tag{5}$$

The calculated direct emission of CO_2 associated with combustion of primary fuels is shown in Table 2. It is important to emphasis the fact that wrong conclusions can be drawn if the impact of different fuels on global warming is analysed using the direct emission indicators. Such approach shows that combustion of coal gives almost two times higher emission than combustion of natural gas. This results from the fact that the additional external emissions are not taken into account. To

have a complete picture of the influence of a given technology on the GHG emission, the emission in all links of the process of energy conversion should be considered. A solution to this problem is to apply cumulative emission calculus [14,18] and LCA [13,19,20]. The approach allows for the inclusion of greenhouse gases in the entire cycle of investment and operation of a considered production system e.g. power plant.

The external emissions result from consumption a_{ij} of i-th semi-finished product in considered j-th branch or from by-production f_{ij} of i-th product per unit of main j-th product. The direct emission is a sum of specific emission of k-th GHG in j-th branch e_{jk} multiplied by its global warming potential $(GWP)_k$. Moreover, if the balance is formulated in global scale the part concerning imported goods a_{ij} is not necessary. The formula of the TCC takes the form:

$$e_j^* = \sum_i \left(a_{ij} - f_{ij}\right) e_i^* + \sum_k (GWP)_k e_{jk} \qquad (6)$$

Coefficients a_{ij} and f_{ij} in Eq. 6 have the same meanings and take the same values like in the case of Eq. 1.

The GHG cumulative emission e_j^* connected with coal and natural gas has been investigated by Stanek and Białecki [21]. Selected results concerning fuels consumed in Poland are given in Table 2 (rows 2,3 for coal and rows 5-10 for imported natural gas).

Table 2. Direct and cumulative GHG emissions burdening combustion of coal and natural gas

No.	Variant	Emission, t CO_{2e}/TJ
1	Coal – direct emission	92
2	Coal – cumulative emission	96
3	Coal – cumulative emission withleakage of methane from coal mine	108
4	Natural gas – direct emission	56
5	Gas variant 1: 21 GWP + 0,11 % natural gas leakage form mine to consumer	72
6	Gas variant 2: 21 GWP + 3,25 % natural gas leakage form mine to consumer	85
7	Gas variant 3: 30 GWP + 0,11 % natural gas leakage form mine to consumer	72
8	Gas variant 4: 30 GWP = 1,5 % natural gas leakage form mine to consumer	80
9	Gas variant 5: 30 GWP + 3,5 % natural gas leakage form mine to consumer	91
10	Gas variant 6: 30 GWP + 4,2 % natural gas leakage form mine to consumer	97

If the utilisation of biomass is considered it is important to take into account the savings in the TCC. First of all the direct emission of CO_2 from biomass combustion is not taken into account because it is closed in the biomass cultivation life cycle. The only emission burdening the biomass utilisation is the external emission resulting from delivery and processing of biomass and production of fertilizers for cultivation purposes. The savings caused by replacement of fossil fuels by biomass result from the avoided cumulative emissions related to the chemical energy of replaced fuels, according to the results data given in Table 2. Two possibilities can be taken into account – replacement of coal or replacement of natural gas.

4. Life cycle exergetic cost

The Thermo Ecological Cost Life Cycle Assessment (LC-TEC) should cover the following phases:

1. *Construction Phase,* that encompasses project, extraction of raw materials, semi-finished products fabrications, transport expenditures in the construction phase. All these expenses influence the final thermo-ecological cost burdening the final useful product. This phase has a significant contribution in case the processes is based on renewable sources of energy. For instance, in case of wind power plant the thermo-ecological cost results mainly from expenses in construction phase.

2. *Operational phase,* that is defined as a period between the end of construction phase and the beginning of decommissioning phase. In processes utilising non-renewable resources, this phase is predominant in the cumulative consumption of natural resources, mainly chemical exergy of fossil fuels.

3. Decommissioning phase of plant concerns the period at the end of plant's life. In this phase, the thermo-ecological cost results from expenditures connected with retirement as for instance for re-cultivation of terrain and disposal of remains.

General form of the equation for determination of LC-TEC has been formulated by Szargut and [15]. The methodology has been used so far for Thermo-Ecological optimisation of solar collector. Results of the optimisation have been presented by Szargut and Stanek in [12,13]. The LC-TEC expresses an annual thermo-ecological cost of investigated useful product with inclusion of the whole life of this product. The formula takes the following form:

$$\Theta_{LCA} = \tau_n \left(\sum_j \dot{G}_j \rho_j + \sum_k \dot{P}_k \zeta_k - \sum_u \dot{G}_u \rho_i s_{iu} \right) + \frac{1}{\tau} \left(\sum_m G_m \rho_m (1 - u_m) + \sum_r G_r \rho_r \right) \tag{7}$$

5. Thermo-ecological indicators of environmental benefits

The indices of operational TEC: ρ_i, ρ_j, ρ_m, ρ_r, that appear in Eq. 7, are determined by means of TEC

balance (Eq. 1). Equation (7) can be applied to optimize construction and operational parameters of different resources intensive systems and can be a supplementary criterion in ecological economy. After the specific emission e_k in Eq. 7 had been introduced instead of the TEC the formula for calculation of cumulative emission was obtained. The methodology of TEC, TCC and LC-TEC, briefly explained in previous sections, has been applied for the evaluation of the influence of utilisation of biomass in CHP plant on the depletion of non-renewable resources. Also the emissions on the entire life cycle have been considered.

In order to evaluate the ecological advantages of biomass utilisation for energy production three additional indicators are being proposed. The indicators are based on the results of analysis of TEC, TCC or LC-TEC These are as follows:

- Index of natural resources savings (NRS):

$$NRS = \frac{\Delta m_F \cdot (\rho_F + \sum_k p_{k,F} \cdot \zeta_k + p_{CO2} \cdot \sigma_{CO2})}{m_{bio} \cdot (\rho_{bio,LCA} + \sum_k p_{k,bio} \cdot \zeta_k)} \tag{8}$$

This NRS index expresses the ratio of decrease of consumption of exergy of non-renewable resources, that results from the replacement of Δm_F of fossil fuel by biomass in the amount of m_{bio}. This index can be interpreted as the cumulative efficiency of non-renewable exergy savings thanks to application of biomass.

- Index of greenhouse gasses cumulative emission reduction Δ(GHG):

$$\Delta(GHG) = \frac{\Delta m_F \cdot e^*_{GHG}}{m_{bio} \cdot (e^*_{GHG} - e_{CO2})} \tag{9}$$

The Δ(GHG) is expressed as the ratio of cumulative reduction of GHG emissions resulting from decrease of consumption of fossil fuel Δm_F to increase of external emission of GHG $(e^*_{GHG} - e_{CO2})$ burdening the unit of biomass m_{bio}. The external emissions of GHG results e.g. from transport or cultivation of biomass whereas it does not take into account the direct emissions of CO_2.

- Index of natural resources savings resulting from decrease of GHG emissions $\Delta(\text{NRS})_{\text{GHG}}$:

$$NRS_{GHG} = \frac{\Delta m_F \cdot e^*_{GHG} \cdot \sigma_{CO2}}{m_{bio} \cdot \rho_{bio,LCA}} \tag{10}$$

The reduction of GHG emissions expressed by the Δ(GHG) leads not only to the decrease of GHG emission expressed in mass units but also as a final result to the savings of natural resources. The avoided e^*_{GHG} emissions of CO_{2e} lead to the savings of exergy of non-renewable natural resources for CO_2 removal. For this reason it leads finally to the reduction of consumption of non-renewable resources in the amount $e^*_{GHG} \cdot \sigma_{CO2}$ per unit of a fossil fuel saved. The natural resources that we have to pay for this savings is equal to the cumulative exergy consumption that has to be spend to produce unit of biomass for energetic purposes.

6. LC-TEC analysis of gasification and gas turbine based cogeneration technology for biomass utilisation

The methodology given in the previous sections has been applied to the analysis of biomass powered cogeneration plant. All stages of constructing, producing and dismantling of the plant have been considered. Additionally, the strongly connected branches have been introduced within LC-TEC procedure. The boundary of the investigated system includes biomass farming and harvesting, fertilizers production and all connections by transport. These connected processes with indication of supply of energy carriers, non-energetic materials and unavoidable emissions of harmful substances are presented in Fig. 2.

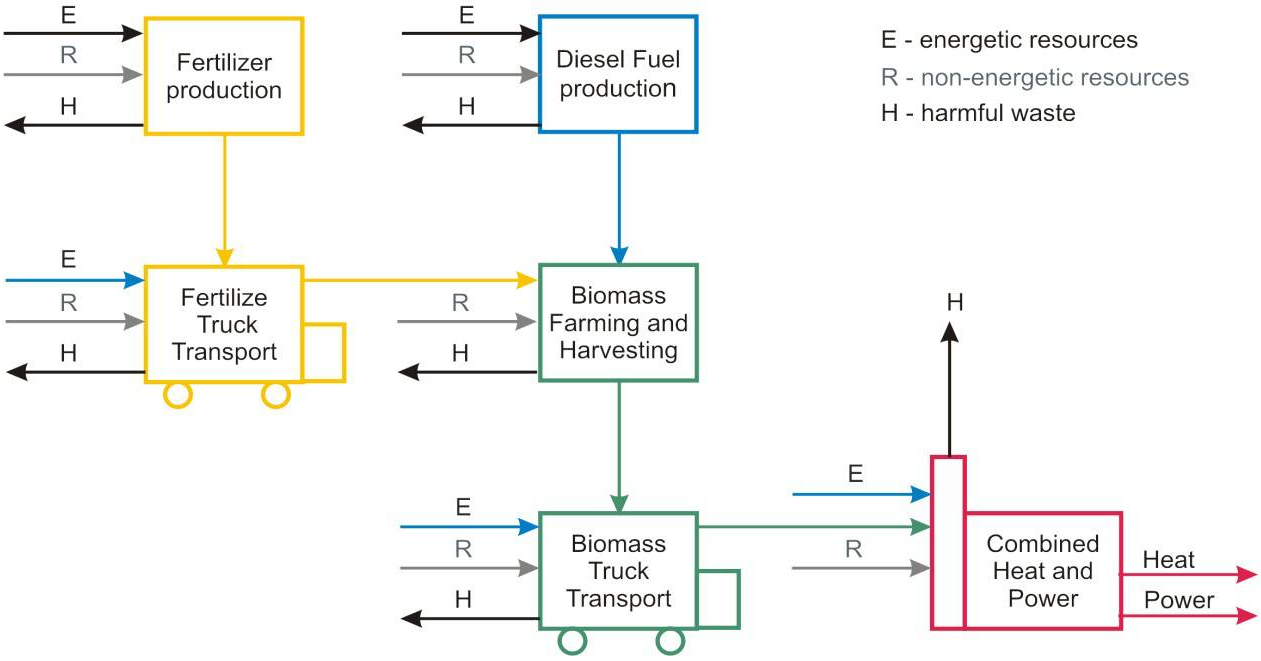

Fig. 2. LC-TEC system boundary of CHP fed with biomass

Different configurations of a cogeneration plant fed with biomass are taken into account. There are also taken into account different biomass gasification technologies. The total number of seven alternative designs of the system, that are numbered A.1 to A.3.1 (Table 3), are examined.

The example system presented in Fig. 3 is made up of fluidized bed gasifier, Mercury 50 Recuperated Gas Turbine and either a bottoming steam cycle or heat recovery water boiler. Detailed energy analysis of different configurations of the plant has been presented in [22, 23].

Within the first alternative design (named A.1) an autothermal Atmospheric Fluidized Bed (AFB) gasification technology and combined gas and steam turbine cycle are taken into account. The disadvantages of this technology are considerable gas cleaning requirements and high consumption of power for compression of large amount of the low calorific value GT fuel gas. The parameters of steam within the bottoming steam turbine cycle are relatively low due to the low temperature of GT exhaust gas. The scheme of the plant within the configuration A.1 is presented in Fig. 3.

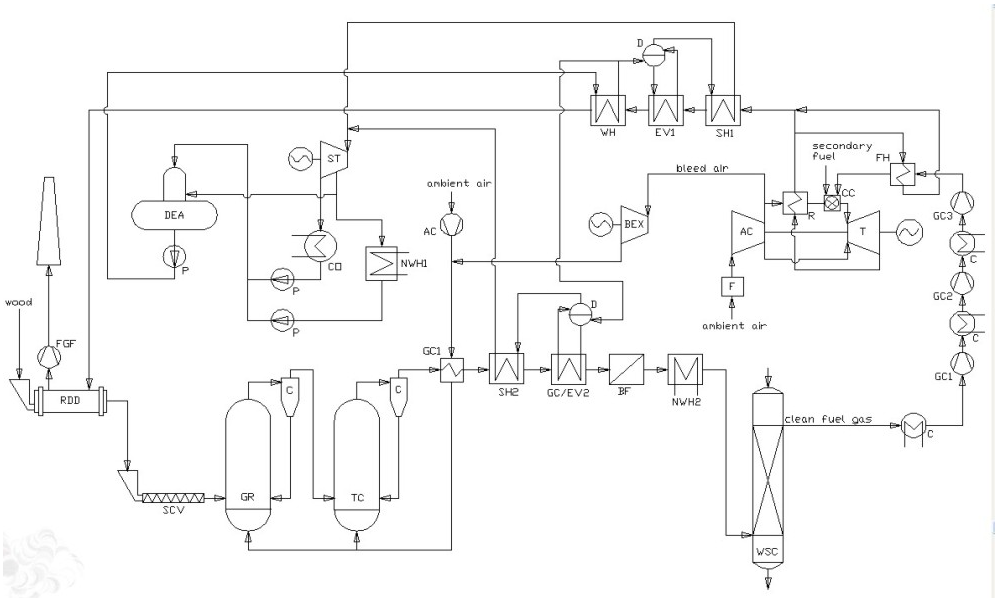

Fig. 3. Scheme of IBGCHP plant with atmospheric fluidised bed gasifier, gas turbine and bottoming steam cycle (design no. A.1)[22,23]

Within the alternative configuration A.1.1 there is a supplementary firing applied. It leads to an increased electric and heating power of the plant. On the other hand however there is an increased demand for wet biomass and considerable heat consumption for drying purposes.

In another alternative design A.1.2 a simple GT cycle is coupled to a heat recovery water boiler. Within this configuration there is no bottoming steam cycle, what results in a lower investment cost.

Configurations number A.2 and A.2.1 are designed basing on pressurized fluidized bed gasification technology (PFB). There is no demand for producer gas compression as well as gas cleaning requirements are significantly reduced. In the configuration A.2 a combined cycle is taken into account while in A.2.1 a simple cycle with boiler is assumed.

In the alternative designs No. A.3 and A.3.1 there is applied the allothermal gasification technology using pure steam as gasification agent (FICF). This technology leads to much higher calorific value of the GT fuel gas. Therefore the flow of fuel gas is smaller and the power consumption for compression is reduced. Using the integrated gasification and combustion double circulating fluidized bed reactor technology helps to solve gasification waste substances related problems.

The highest level of net efficiency of electricity generation (in full cogeneration mode) is reached in alternative design A.2 (combined cycle integrated PFB gasification technology). On the other hand GT simple cycle in the alternative design A.2.1 offers the highest value of biomass energy utilization factor. These two design alternatives also lead to high values of non-renewable energy

replacement index (ERI) and specific global CO_2 emission reduction within the regional energy system (calculated per GJ of biomass energy consumed). The simple cycle configuration with waste heat recovery water boiler offers slightly better energy and emission savings.

The weakest performance of the plant is represented by the alternative design A.1.1 (AFB gasification technology integrated with combined cycle plant with supplementary firing). All indices that are taken into account have the lowest value in this case. Although the configuration A.1.1 leads to the highest electric power of the system the performance is poor due to high demand for wet biomass, significant drying requirements and relatively high fraction of electricity generated at the low efficient steam cycle.

An interesting conclusion is that the FICFB gasification technology offers the energy and environmental effects better than the AFB technology but slightly worse than PFB technology. The FICFB technology offers relatively high calorific value of the product gas. On the other hand the high demand for gas recirculation into the combustion zone of the reactor results in the net value of cold gas efficiency at the level of other gasification technologies.

Table 3. Main results of annual mass and energy balance [22]

Alternative configuration	**A.1**	**A.1.1**	**A.1.2**	**A.2**	**A.2.1**	**A.3**	**A.3.1**
Gasification technology	**AFB**	**AFB**	**AFB**	**PFB**	**PFB**	**FICFB**	**FICFB**
Plant own electricity consumption, MWh	9 142	10 594	9 064	3 442	3 321	5 703	5 585
Nett electricity to grid, MWh	38 783	49 507	34 965	43 215	36 963	39 782	33 994
Network heat, GJ	127 352	247 608	178 752	125 393	178 951	130	175 562
Network heat from cogeneration, GJ	110 436	247 608	100 190	125 393	126 330	77 654	97 835
Electricity from cogeneration, MWh	23 380	34 934	44 029	27 925	40 284	16 500	38 105
Wet biomass consumed m_{bio}, tons	44 278	71 300	44 278	41 898	41 898	41 936	41 936
Biomass energy consumed, GJ	498 635	802 937	498 635	471 833	471 833	472	472 257
Saved coal Δm_F, tons	6 896	13 409	9 680	6 790	9 691	7 053	9 507
CO_2 emission reduced $\Delta m_F e_{CO2}$,	52 092	76 334	54 360	56 136	56 308	53 390	53 056
Non-renewable energy saved within the regional energy system (loco generation plants), GJ	543 134	797 030	567 641	585 071	587 861	556 655	554 040

Investigation of LC-TECand evaluation of indices defined by the authors (Eqs. 8 – 10) requires the initial calculations of TEC of fertilizers, TEC of biomass cultivation and TEC of biomass transport. The TEC of nitrogen fertilizer is calculated using data from Polish big fertilizers factory [24]. Ammonia takes part of the reactions for forming the N-fertilizer. The ammonia production process of producing very energy consuming and for this reason the TEC of N-fertilizer is high. According to [25,26] the TEC of phosphorus fertilizer, potassium fertilizer and lime is established for further calculations. Table 4 presents the LC-TECof fertilizers production using the balance of TEC expressed by Eq. 1.

Table 4. Unit TEC of fertilizers production and CO_2 direct emissions

Useful product	**TEC**	**CO_2 direct emissions**
	MJ $_{ex}$/kg $_{fertilizer}$	kg $_{emission}$/kg $_{fertilizer}$
Nitrogen fertilizer	49.15	2.6410
Phosphorus fertilizer	15.11	0.6735
Potassium fertilizer	10.39	0.4656
Lime production	1.32	0.0079

According to [27] the demand of fertilizers for biomass production is presented in Table 5.

Table 5. Fertilizer requirements for production of different biomass

Fertilizer	Units	Bundles, short-rotation wood	Miscanthus bales	Wheat straw, bales
N-fertilizer	$kg_{fertilizer}/kg_{DB}$	0.0052	0.0040	0.0022
P2O5-fertilizer	$kg_{fertilizer}/kg_{DB}$	0.0040	0.0031	0.0011
K2O-fertilizer	$kg_{fertilizer}/kg_{DB}$	0.0064	0.0051	0.0009
Lime	$kg_{fertilizer}/kg_{DB}$	0.0065	0.0036	0.0044

The indices of fertilizes specific consumption included in Table 5 and the TEC of fertilizers (Table 4) are the basic information required for LC-TECof biomass calculation. Additionally according to Fig. 3 the TEC resulting from transport has to be taken into account. The authors assumed that biomass is transported by Lorries. The TEC of lorry production is presented in Table 6. The values are calculated using Life Cycle Inventory [28] and TEC of useful products [19].

Table 6. Unit TEC and CO_2 direct emission burdening car transport

Parameter	Units	Lorry	Lorry	Lorry
Input data				
Load capacity	Mg	16	28	40
Useful truck life	years	15	15	15
Annual mileage	km	50 000	50 000	50 000
CO_2 direct emissions	kg	633	633	633
Results of TEC calculations				
TEC	MJ_{ex}/km	0.603	0.863	1.165
TEC	$MJ_{ex}/(km \cdot Mg)$	0.038	0.054	0.073

The TEC of biomass cultivation is presented in Table 7. It was calculated taking into account fertilizer production (Table 4), fertilizer transportation (Table 6) and usage of this fertilizer for growing three different crops (Table 5).

Table 7. TEC and CO_2 emission of biomass cultivation

Units	Bundles, short rotation wood	Miscanthus bales	Wheat straw, bales
MJ_{ex}/kg_{DB}	0.3965	0.3949	0.3932
kg_{CO2}/Mg_{DB}	20.04	15.52	6.99

For the process of biomass cultivation the TEC is on very similar level for different types of biomass (Table. 7). The TEC index for example non-renewable fuel as coal can be on the level 27.0 MJ/kg and results mainly from chemical exergy of coal (about 90%). One can easily see that the (TEC) burdening the cultivation of bio-fuels is significantly lower than TEC resulting from chemical exergy of non-renewable fuels. TEC of biomass besides cultivation is influenced by the needs for transport. First of all the transportation needs can be higher than in the case of fossil fuels because of relatively low energy density of biomass (esp. wet biomass). Moreover, TEC of biomass can be dependent on the distance of transportation. Table 8 presents the results of biomass resulting from transport taking into account the distances between 25 and 100 km.

Table 8 TEC of biomass transportation as a function of distance

Distance	TEC	CO_2 emissions
km	MJ_{ex}/kg_{DB}	kg_{CO2}/Mg_{DB}
25	0.031	1.838
50	0.063	3.676
75	0.094	5.514
100	0.125	7.353

Similarly as in the case of the TEC resulting from cultivation also the part burdening the transport of biomass (Table 8) is significantly lower than TEC index burdening non-renewable fuels. Even if we consider the transportation distance of about 100 km the TEC on the level of 0.125 MJ/kg_{DB} is significantly lower than for instance chemical exergy of coal which can be about 24 MJ/kg.
TEC burdening the construction of the system has to be also introduced into the modified LC-TECalgorithm proposed in this work. Table 9 includes the investment part of LC-TECof different power plants. This investment part is divided between construction and dismantling. The second one can decrease the total LC-TEC if the factor of recovery of *m*-th material appearing in Eq. 8 $u_m > 0$.

Table 9. TEC of power plants

Parameter	Units	Hard Coal	Hard Coal	Natural Gas/Sng	Lignite	Hard Coal/ Wood Co-Firing
Power	MW	400	800	950	950	400
TEC construction	MJ_{ex}/MJ_{el}	0.65	0.58	0.29	0.88	0.87
TEC dismantling	MJ_{ex}/MJ_{el}	0.0020	0.0018	0.0015	0.0075	0.0043

Basing on the results enclosed in table 9 it can be concluded that for two systems taken into account as a power technologies prepared for energetic conversion of biomass, the net TEC index resulting from construction decreased by TEC of recycled materials is as follows:
- synthetic natural gas power plant TEC = 0.288 MJ_{ex}/MJ_{el},
- hard coal / wood cofiring power plant TEC = 0.866 MJ_{ex}/MJ_{el}.

Also in this case the TEC is relatively low, but not negligible. For example the TEC burdening generation of electricity in Polish conditions is on the level of about 3.6 MJ/MJ. The constructional net TEC mentioned above represents about 8% in the case of natural gas power, 14% in the case of hard coal power plant and 17% in the case of lignite power plant. Analysing the obtained results (Table 7 – 9) one can also conclude that the investment part can be the most important in (LC-TEC) of biomass. Nevertheless, the total (LC-TEC) is significantly lower in the case of biomass than that of non-renewable fed energy system. Such presumptions are confirmed by obtained results that are presented in Table 10.

Table 10. Greenhouse gas avoidance and natural resources avoidance in comparison to coal

Gasification system	A.1	A.1.1	A.1.2	A.2	A.2.1	A.3	A.3.1
NRS	6.0	8.7	10.1	7.5	10.7	7.8	10.5
$\Delta(GHG)$	22.39	27.04	31.43	23.30	33.26	24.18	32.60
NRS_{GHG}	4.93	5.96	6.92	5.13	7.32	5.33	7.18

It should indicate that the proposed indices of decreasing the GHG emissions (Eq. 9) and of natural resources savings (Eq. 8 and 10) should confirm high profitability of biomass utilisation from the

point of view of greenhouse effects as well as from the point of view of non-renewable resources savings.

7. Summary and conclusions

The methodology of thermo-ecological evaluation of biomass utilization in energy production sector has been presented in the paper. The performance indices of an energy conversion technology have been introduced taking into account reduction of the GHG emissions as well as the savings of non-renewable natural resources.

The comparison of the proposed cogeneration plant technologies in the aspect of LC-TEC revealed that the best environmental performance is obtained for the alternative design no. A.2.1. (Table 10). The previous study [22], where the economic effectiveness of an investment project was examined, showed that the best values of Net Present Value (NPV) and Internal Rate of Return (IRR) were obtained in the case of the variant A.1.2. However, the difference in profitability between A.1.2. and A.2.1 was not significant. The general conclusion from present and previous works is that in the case of the gas turbine based biomass-to-energy conversion technology in relatively small-scale of the plant the simple cycle is more effective than the combined one. On the other hand in Europe the combined cycle configurations have been tested so far in ARBRE and Värnamo projects [22].

The presented results confirm the high ecological profitability of biomass conversions. In the case of savings of natural non-renewable resources the TEC of biomass plant is 6.0 to 10.7 times lower than that in a plant fed with non-renewable chemical energy. It leads to the obvious conclusion that the share of biomass power plants and CHP plants should be maximised within the area of economic profitability. In other words the results of optimisation are only economically constrained. In the Polish conditions the economic profitability of renewable power plants strongly depends on subsidies (green certificates). But in the practice this system does not take into account that different renewable systems have different influence on depletion or savings in non-renewable resources, as has been widely demonstrated by the authors. The results presented in table 10 of this paper clearly show such influence. Moreover the overestimated prices of certificates can lead to the competition in agriculture between production of food and production of “food for fuels”. For this reason the proposed LC-TEC algorithm can be also used for division of green subsidies between renewable power plants basing on objective criterions as is the NRS – non-renewable resources savings. The same algorithm can be used for other renewable power systems eg. wind turbines or photo-voltaic. One of the most important issues in the application of biomass energy is GHG emission. The index $\Delta(GHG)$ is between 4.9 and 7.3. It is scientifically confirmed that the problem is global but the technology selection based on single economic criterion of profitability maximisation limits this problem often to local scale. Frankly speaking the biomass is transported for thousand kilometres and these external emission are not taken into account in the system of subsidies because the external expenditures that have been discussed in this paper are intentionally neglected.

Nomenclature

a_{ij} coefficient of the consumption of the i-th product per unit of the j-th major product, e.g in kg/kg or kg/MJ,

a_{rj} coefficient of the consumption of the r-th imported product per unit of the j-th major product, e.g in kg/kg or kg/MJ,

B exergy extracted per year from the domestic non-renewable natural resources,

b_{sj} exergy of the s-th non-renewable natural resource immediately consumed in the process under consideration per unit of the j-th product, MJ/kg,

c mass fraction of carbon element in the fuel in kg/kg or in kg/kmol;

e^*_{GHG} index of cumulative GHG emissions,

e^*_i coefficient of cumulative emission of greenhouse gasses burdening *i*-th useful product,

e^*_j cumulative emission of greenhouse gasses in *j*-th production branch,

e_{CO2} index of CO_2 direct emission.

e_{jk} coefficient of direct emission of *k*-th greenhouse gas in *j*-th production branch.

f_{ij} coefficient of the consumption and by production of the *i*-th product per unit of the *j*-th major product, e.g in kg/kg or kg/MJ,

GDP Gross Domestic Product,

G_m consumption of mth material or energy carrier used for construction of installation,

$\dot{G}_j$ nominal flow rate of the *j*th major product,

$\dot{G}_u$ nominal flow rate of the useful uth by-product,

GWP_k coefficient of global warming potential of k-th gas (1 for CO2 and depending on source 21 – 30 for methane),

LHV lower heating value of the fuel in MJ/kg,

M_{CO2}, M_C molar mass of CO_2 and of element C, kg/kmol.

p'_{kj} amount of *k*-th waste product abated from waste products.

P_k annual amount of *k*-th waste product,

$\dot{P}_k$ nominal flow rate of the kth deleterious waste product rejected to the environment,

$p_{k,bio}$, $p_{k,F}$ amount of waste k-th substance rejected to the environment burdening the combustion of conventional (F) and renewable (bio) fuel,

p_{kj} total amount of *k*-th waste product generated in *j*-th production branch.

s_{iu} replacement ratio in units of the ith replaced product per unit of the uth by-product,

u_m expected recovery factor of the mth material,

w_k monetary factor of harmfulness of *k*-th substances.

Δm_F decrease of non-renewable fuel consumption,

ζ_k the total expenditure of non-renewable resources exergy for compensation loses in environment caused by rejection of *k*-th contaminant,

$\rho_{bio,LCA}$ LC-TEC of biomass,

ρ_f TEC of avoided consumption of non-renewable fuel,

ρ_i, ρ_j, ρ_r specific thermo-ecological cost of the *i*-th, *j*-th domestic product and the *r*-th imported good, e.g. in MJ/kg,

ρ_m thermoecological cost of *m*th material or energy carrier used for construction of installation,

σ_k cumulative exergy consumption of non-renewable resources due to the removing of *k*-th aggressive product from wastes in abatement installation (abatement TEC),

τ nominal life time of installation,

τ_n annual operation time with nominal capacity.

ψ_{j0} requirement for natural resources exergy to compensate or to avoid the environmental losses resulting from operation of *j*-th production process, MJ/kg of *k*-th waste product.

Acknowledgments

This work was carried out within the frame of research project no. N N513 004036, titled: Analysis and optimization of distributed energy conversion plants integrated with gasification of biomass. The project is financed by the Polish Ministry of Science.

The paper has been also supported by the RECENT project (REsearch Center for Energy and New Technologies) supported by 7th Framework Programme, Theme 4, Capacities.

References

[1] Macmillan P., Human Development Report 2009, Overcoming barriers: Human mobility and development. Publish for the United Nations Development Programme, 1 UN Plaza, New York, NY 10017, USA

[2] International Standard ISO/FDIS 14040.

[3] Kowalski Z., Kulczycka J., Góralczyk M. Ekologiczna ocean cyklu życia procesów wytwórczych (LCA)PWN, Warszawa 2007 (Environmentallife cycle assessmentof manufacturing processes)

[4] Chapman P.F., Energy costs: a review of methods. Energy Policy. June 1974 pp. 91 – 103.

[5] Chapman P.F., Leach G., Slesser M., The energy cost of fuels. Energy Policy. September 1974 pp. 231 – 243.

[6] Chapman P.F., The energy cost of materials. Energy Policy. March 1975 pp. 47 – 57.

[7] Boustead I., Hancock G.F., Handbook of industrial energy analysis, Ellis Horwood Publisher, 1979.

[8] Szargut J., Analiza egzergochłonności skumulowanej. Archiwum Energetyki nr 3, 1987.

[9] Szargut J., Analysis of cumulative exergy consumption. Energy Research, 1987, No 4, pp. 541 – 547.

[10] Szargut J., Application of exergy for the determination of ecological costs, Bull. Pol. Acad. Sci., Techn., No 7 - 8, 1986

[11] Szargut J., Depletion of unrestorable natural exergy resources. Bulletin of the Polish Academy of Sciences, Vol. 45, No. 2, 1997.

[12] Szargut J., Stanek W. Comparison of economic and thermo-ecologic optimization of thermal processes. Report from research project 8T10B05518, Gliwice 2005 (in Polish).

[13] Szargut J., Stanek W.: Thermo-ecological optimization of a solar collector. Energy 32 (2007) 584–590.

[14] Szargut J., Stanek W., Thermo-climatic cost of the domestic consumption products. Energy Vol. 35 Issue 2, Feb. 2010, pp. 1196-1199.

[15] Szargut J., Exergy Method: Technical and Ecological Applications.WITpress, 2005, Southampton, Boston.

[16] Stanek W., Czarnowska L., Environmental externalities and their effect on the cost of consumer products Poceding of SWEDES Dubrovnik 2011

[17] Stanek W., Czarnowska L., Environmental externalities and its influence on the thermo-ecological costPoceding of SWEDES Dubrovnik 2011

[18] Stanek W.: Cumulative emissions of harmful substances burdening the fabrication of metallurgical products.Proc. Conf. Gospodarka Cieplna i Eksploatacja Pieców Przemysłowych. Poraj k. Częstochowy 2000 (in Polish).

[19] Stanek W.: Method of evaluation of ecological effects in thermal processes with the application of exergy analysis. Silesian University of Technology Press, 2009 (in Polish).

[20] Szargut J. Exergy method, technical and ecological applications. Southampton, Boston: WIT Press, 2005.

[21] Stanek W.,Białecki R.,Can natural gas warm the climate more than coal? Proc. Conf. CareTech 2011, Gliwice, Poland 2011.

[22] Kalina J. Kalina J.: Comparative Analysis of Alternative Configurations of the Mercury 50 Recuperated Gas-Turbine-Based Biomass Integrated Gasification Combined Heat and Power (BIGCHP) Plant. Energy Fuels, Article ASAP. DOI: 10.1021/ef201624h

[23] Kalina J. Comparative analysis of alternative configurations of mercurytm 50 recuperated gas turbine based BIGCHP plant CaReTECH 2011

[24] Hunt S., Stanek W.; Analiza systemowa Zakładu Azotowego Puławy S.A. pod względem kosztu termoekologicznego; Gliwice 2006

[25] Daugherty E., Stripple H.; Biomass Energy Systems Efficiency: Analyzed through a Life Cycle Assessment; Lund University; Gothenburg; Sweden 2001

[26] Borjesson P.I.I.; Energy analysis of biomass production and transportation; Pergamon; Lund; Sweden 1996

[27] Jungbluth N., Busser S., Frischknecht R., Tuchschmid M., Life Cycle Assessment of biomass-to-liquid fuels Berne, 2008

[28] Spielmann M., Bauer C., Dones R., Transport Service, Ecoinventreport 14, Swiss Centre for Life Cycle Inventory, Villigen and Unster 2007

[29] Valero A., Botero E.: An assessment of the Earth's clean fossil exergy capital based on Exergy Abatement Cost. Proc. Conf. ECOS'02 - Efficiency, Cost, Optimization, Simulation of Energy Systems, Berlin 2002.

[30] Szargut J.: Exergy and ecology. Proc. of the Conference Second Law Analysis of Energy Systems; towards the 21-th Century. Roma 1995.

Thermo-ecological optimization of a heat exchanger through empirical modelling

Szczygiel Ireneusz, Stanek Wojciech, Czarnowska Lucyna*, Rojczyk Marek

Silesian University of Technology
Institute of Thermal Technology
Konarskiego 22, 44-100 Gliwice, POLAND
**e-mail: lucyna.czarnowska@polsl.pl*
tel. (+48 32) 237 24 40; fax. (+48 32) 237 28 72

Abstract:
The thermodynamic optimization of thermal devices requires information about the influence of operational and structural parameters on its behaviour. The interrelations among parameters can be estimated by different tools such as computational fluid dynamics (CFD) or experimental statistics of the device. Although precise and comprehensive results can be obtained by CFD, the time required for the computations is relatively long. This disadvantage often cannot be tolerated in the case of optimization or online control. In contrast to CFD, neural network and regression methods are characterized by short computational times, but these techniques do not take into account the physical phenomena underlying the investigated process. For this reason, the results of some CFD physical models can be transferred to empirical models. CFD models are used in such a case as a numerical experiment that generates a grid of operational states of the device under consideration. In this study, a CFD model of a heat exchanger (HEX) is built using the commercial package Fluent/Ansys. Based on a set of pseudo-measurements generated with an exact CFD model, an empirical HEX model is developed by applying regression and neural networks. In this case, the heat exchanger is treated as a black-box that connects parameters such as the tube diameter, number and length, the thermal power of the heat exchanger, the pressure drop and the Reynolds number. The results obtained by training and verifying the applied models are discussed. Furthermore, the authors demonstrate the usage of the developed empirical HEX model for the minimisation of thermo-ecological cost (TEC). The TEC expresses the cumulative exergy consumption of non-renewable resources. The example presented in this paper concerns the optimisation of the operational parameters of a heat exchanger. Calculations concerning the minimisation of the TEC are based on the objective function formulated by Szargut. This function adheres to the rules of life cycle analysis (LCA) because it includes the investment expenditures (measured by the cumulative exergy consumption of non-renewable natural resources), the device operation and the final effects of decommissioning the installation.

Keywords:
Heat exchanger, CFD, Optimization, Neural Networks, Thermo-Ecological Cost

1. Introduction

Each technological process requires different devices and activities. In many cases, the proper selection of devices requires the application of an optimization procedure, which determines what type of device will assure optimal operational results. After the device is chosen, its parameters can also be optimized. Of course, the result of optimization is strongly dependent on the optimization criterion. For the criterion formulation, various approaches can be used, such as those based on economic or thermodynamic considerations. As a thermodynamic criterion, the minimisation of entropy generation is often used [1,2]. This method is useful, but its application is very limited because it is a process, not a system, approach. One possible solution is to use the thermo-ecological cost (TEC) as the desired criterion [3]. Such approaches make use of exergy as a thermodynamic measure of the quality of resources [4-

10]. Szargut [11] defined TEC as the cumulative consumption of non-renewable exergy associated with producing a particular useful product. In general, a TEC analysis can be applied for the solution of the following problems [7,11]:

- the examination of the influence of the operational parameters of energy and technological systems on the depletion of non-renewable natural resources,
- the selection of technology that ensures the minimal consumption of non-renewable natural resources,
- the optimisation of construction and operational parameters to ensure the minimum depletion of natural resources,
- the evaluation of harmful impacts from waste products, i.e., exergetic externalities,
- the investigation of the influence of interregional exchange on the depletion of domestic natural resources,
- the evaluation of the ecological harmfulness of particular useful goods over their entire lifetime (thermo-ecological life cycle analysis),
- the determination of pro-ecological taxes.

The results of calculations for thermo-ecological costs have been presented, for example, in [3,12,13,14]. In [7,13], Szargut proposed an extension of the analysis of operational TEC to other phases of production systems. For this purpose, an objective function was formulated to fulfil the rules of life cycle analysis (LCA) because such an approach includes both the investment expenditures (measured by the cumulative exergy consumption of non-renewable natural resources) and the final effects of decommissioning the installation. Moreover, the proposed TEC minimisation goes a step beyond the classic LCA by introducing a common measure for different ecological impacts. The application of the proposed LC-TEC objective function for the optimization of a solar collector is presented in [13]. However, this optimisation is based on a simplified mathematical model of the collector and it should be noted that the description of the optimized device plays an important role in the optimisation procedure. This description, which can be called the device characterisation, should simulate the operation of the device, namely, it should be able to generate the values of the output parameters (temperature, pressure of the working fluids, heat loads, etc.) based on the device input parameters.

Different types of characterisation can be provided. Currently, the most popular type employs experimental characteristics based on the measurements of real devices. Such an attempt has its drawbacks: it is expensive during the creation phase (a number of devices should be thoroughly investigated) and this method cannot be used for new constructions. Another method involves approximate characteristics based on measurements and approximate theoretical relationships. This solution is cheaper, but its accuracy is, in many cases, unacceptable. Currently, due to the rapid development of computer technology and advances in numerical modelling, another solution can be considered. In the place of device characteristics, a numerical model can be inserted. The numerical model simulates the characteristics of a device; it returns the output parameters based on the values of input parameters, supplemented with boundary and initial conditions. The most precise and sophisticated approach is computational fluid dynamics (CFD), in which thermal devices are efficiently modelled [15]. Although precise and comprehensive results can be obtained by CFD, the time required for these computations is relatively long; moreover, advanced computer equipment is required. These disadvantages are often unacceptable for optimization or online control. The alternative of using models directly based on statistical data does not take into account the physical phenomena occurring in the device under investigation. In contrast to CFD, neural networks are characterized by a short

computational time and high precision. For this reason, some CFD results can be transferred to empirical models. CFD models can be used in a numerical experiment, generating a grid of operational states of the considered devices. Based on this set of pseudo-measurements, an empirical model can be identified. In this paper, a heat exchanger is presented as an example of a thermal device. In this case, the heat exchanger (HEX) is treated as a black-box that connects parameters such as the tube diameter, number and length, the thermal power of the heat exchanger, the pressure drop and the Reynolds number. The neural network and regression methods are assessed for selected heat exchanger parameters. Additionally, the results obtained by training and verifying the applied models are discussed. Finally, the possibility of applying the developed models for optimization purposes is described.

2. Minimisation of thermo-ecological cost

The index of operational TEC can be determined by solving the TEC balance, as presented in Fig. 1. The equation for the balance of operational takes the following form [11,14]:

$$\rho_j + \sum_i (f_{ij} - a_{ij})\rho_i - \sum_r a_{rj}\rho_r = \sum_s b_{sj} + \psi_{j0} \tag{1}$$

This set should comprise all branches of domestic economy. However, it would be difficult to solve such a problem. For this reason, practical calculations only consider strongly connected production [7,12]. To express the total natural resource expenditures, the TEC method should include the total life of the installation [4]. A thermo-ecological life cycle assessment (LC-TEC) consists of three main parts:

1. ***The construction phase*** encompasses the project, the extraction of raw materials, semi-finished product fabrication and transport expenditures in the construction phase. All of these expenses influence the TEC burdening the final useful consumptive product. This phase can have a significant contribution to the TEC in the case of processes based on renewable energy. For instance, the TEC of a wind power plant results mainly from expenses in the construction phase.

2. ***The operation phase*** is defined as the period of time between the end of the construction phase and the beginning of the decommissioning phase. In processes utilising non-renewable resources, this phase is the predominant consumer of natural resources, mainly energy carriers.

3. ***The decommissioning phase*** concerns the period at the end of installation. The TEC in this phase results from expenditures for developing the remnants of the system and for terrain reclamation.

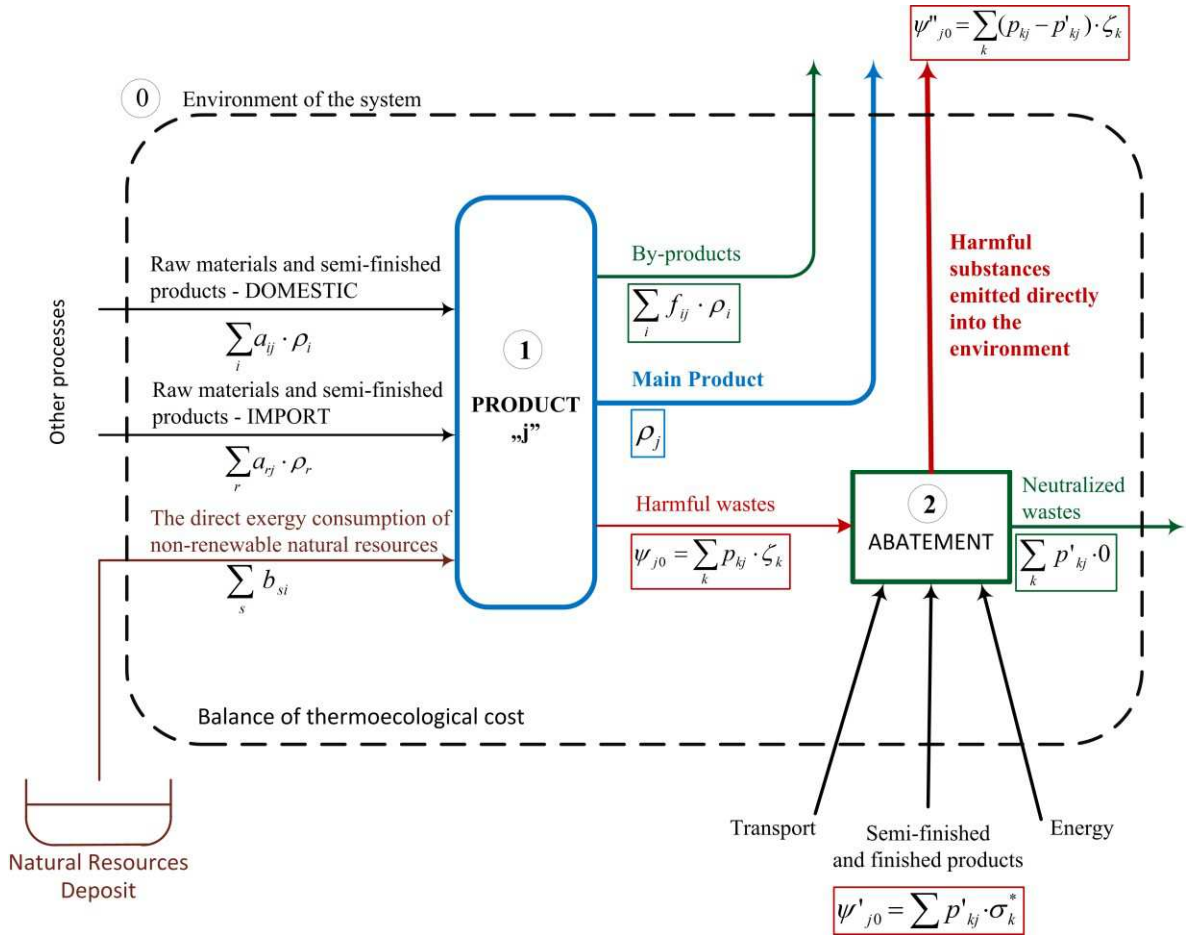

Fig. 1. TEC balance.

The general form of the objective function, based on the LC-TEC concept of TEC minimisation, taking into account the lifetime of the product, was formulated by Szargut [7,8] and applied for a sample investigation in the work of Szargut and Stanek [13]. This function has the following form:

$$TEC = \tau_n \left(\sum_j \dot{G}_j + \sum_k \dot{P}_k \zeta_k - \sum_u \dot{G}_u s_{iu} \right) + \frac{1}{\tau} \left(\sum_m G_m \rho_m (1 - u_m) + \sum_r G_r \right) \quad (2)$$

The presented formula expresses the yearly TEC of a given product, with a consideration of its complete lifetime. Equation (2) can also be used for the optimisation of construction and operational parameters of different resource-intensive systems. In this case, the function should be minimised: TEC → min.

The objective function (2) can also be used for economic LCA optimization. In such cases, the indices ρ and ζ should be expressed as monetary costs. TEC optimisation based on Equation (2) requires a mathematical model of the process or device.

3. Numerical simulation of a heat exchanger using CFD

A numerical model of a device can be developed from the physical laws appropriate for the considered device. In thermal technology, the numerical description of devices is quite often based on conservation equations. One can enumerate the mass balance, the energy conservation equation and the momentum equation. These equations cover the phenomena found in the solid parts of a device (e.g., heat transfer through the solid wall) as well as in the working media (fluid flow in engines, turbines, etc.). The branch of fluid mechanics that utilizes numerical methods to solve such problems is called computational fluid dynamics (CFD) and can be successfully employed to create numerical models of thermal devices. With CFD, in many cases, empirical equations for modelling thermal devices are being used [15] .

The procedure of CFD model creation can be divided into several steps:

- geometry creation,
- meshing,
- computation,
- result processing.

The first three steps can be called pre-processing, while the fourth step can be called post-processing. The first step, geometry creation, is usually accomplished by using specialized commercial software, e.g., CATIA or Design Modeler. Depending of the complexity of the considered device, this step can be very time-consuming [16].

The second step divides the created geometry into finite volumes, for which partial equations are solved. Meshing (discretization) is usually performed automatically by sophisticated software, but the results should be carefully checked to avoid computational errors resulting from an improper mesh. The time required for meshing also depends on the complexity of the object and the computational power of the machine used. Within the computation step, the discretized governing equations are solved, returning discrete values of the desired parameters. The time required for this step is strongly dependent on the number of finite volumes under study (which is a function of the complexity of the geometry) and the power of the machine. The computational time can be significantly shortened by using parallel computations in computational clusters or multi-core processors.

For each device, each step of the procedure must be completed. If the aim is to optimize the device's working parameters, step one need only is performed once at the beginning of the optimization process. However, the shape often needs to be changed during device optimisation. This requires a reconstruction of the geometry, which results in some difficulties in process automation. Fortunately, contemporary software makes it possible to automatically redefine the geometry. This feature allows CFD models to be used in optimization procedures, as will be described later in this paper.

As mentioned above, the computational time is strongly dependent on the complexity of the object and the computational power of the machine used. In more complex cases, this time can be counted in days or even in weeks. This significantly decreases the appeal of employing CDF in optimization loops. This disadvantage can be circumvented by applying another modelling method (a neural network). In the place of the CFD model, a neural algorithm can be used, which significantly decreases the computational time. Neural algorithms are quick and

straightforward. The cloud of data with which the neural algorithm operates can be generated by the CFD model for an entire series of types of the optimized device. Of course, the CFD generation of the input data is still time-consuming, but it can be performed outside the optimization loop and can be used in the optimization of different devices from the same series of types. During this generation, the need for geometry reconstruction may also arise.

The geometry reconstruction can be automated by utilizing the new features of commercial CFD software. In this paper, the commercial software Ansys was used. The new version of the Ansys CFD package is called Workbench [15]. This software allows one to design the CFD process, including loops and process flow control. Both the computational parameters and the geometry can be altered. This is performed through a so-called parameterization of the geometry. During the CFD process, the geometrical parameters can be modified, which, in fact, results in a redefinition of the entire geometry. Then, the model is remeshed and the computations can be repeated many times. The tool used by the authors is semi-automatic, which is one of the main advantages of using this application. At the beginning of the process, all of the parameters, such as those mentioned above, e.g., the geometrical and physical parameters, must be set by the user. After that, all of the computations, which may take up to one month or more, can be performed without the user. In this paper, as an example, the data generation for a tube and shell heat exchanger is presented. In this section, a sample algorithm of data generation, demonstrating the need for a neural algorithm, is presented. A heat exchanger is a device that is used, among other purposes, for exchanging heat between two media: one hot and one cold. Here, a tube and shell heat exchanger working with two streams of water was chosen as a model. Such devices consist of several pipes surrounded by a steel shell. One medium flows within the pipes, while the second flows within the shell outside the pipes. The pipes are fixed by one or two perforated bottoms, depending on the exchanger construction. The heat flows through the heat transfer area, which, in this case, is constituted by the pipes. Due to variations in material consumption, this area significantly influences the cost of the apparatus. A schematic of the analysed heat exchanger is shown in Fig. 2.

The amount of heat exchanged strongly depends on the size of this area and on the medium temperature difference, as governed by the Peclet equation [18]:

$$\dot{Q} = kA\,\Delta t_m \tag{3}$$

To evaluate the heat load, one should know the values of the heat transfer area A and the heat transfer coefficient k. Both quantities are based, among others, on the geometry of the exchanger. The size of the inner tubes directly influences the heat transfer area and the flow inside and outside the tubes, which is strongly related to the overall heat transfer coefficient. Thus, for each geometrical configuration, the velocity, pressure and temperature fields should be computed. This step can be performed with any CFD solver; in the sample case, the Ansys Fluent solver was employed [19].

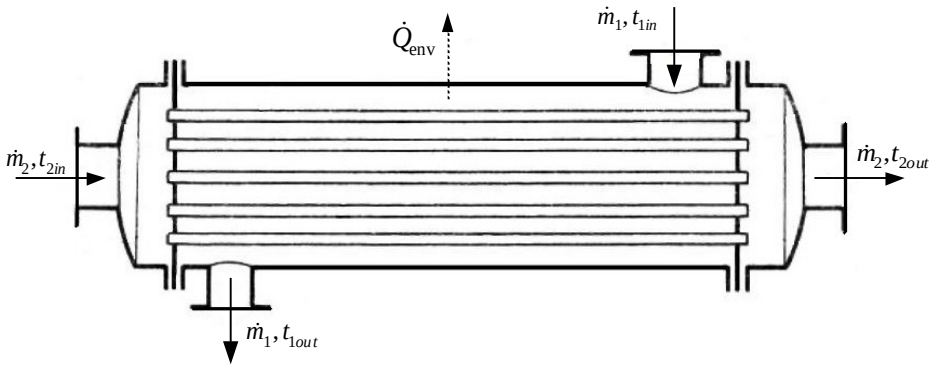

Fig. 2 Diagram of the heat exchanger under investigation.

In the computations, the following parameters were assumed to be constant:

- number of tubes,
- outer diameter of tubes,
- hot fluid inlet temperature and mass flow rate,
- cold fluid inlet temperature and mass flow rate.

During data generation, the thickness and length of the tubes were changed. As a result, different heat loads, outlet temperatures and material consumption values were computed.

As the geometry was modified, the flow in the pipes was altered, which influenced the heat transfer coefficient of the pipes and, consequently, the overall heat transfer coefficient. This also changed the heat transfer area, which directly influenced the heat load of the exchanger.

A flow diagram of the data generation process is shown in Fig. 3. In each step, due to the variable geometrical parameters, the whole geometry was rebuilt and, as a consequence, was remeshed in each step. This was performed in a fully automatic way, without user interaction. An example of the geometry mesh is shown in Fig. 4.

In each step, after the geometry and mesh generation, the velocity, pressure and temperature fields of both fluids were computed using the commercial code Fluent. The resulting data were stored for later use with the neural algorithm. In Fig. 4, a sample mesh for one of the cases is shown.

The computational time depends on the power of the machine performing the computations. The analysed case (number of finite volumes ~1 million) required approximately 8 hours on an 8-processor machine and approximately 13 hours on a 4-processor machine. However, due to the full automation of the computations, no interventions by the user were required. This relatively long computational time is not acceptable for optimisation procedures. For this reason, the results of CFD modelling were used for empirical modelling of the HEX.

4. Empirical model of a HEX

In general, the empirical models, both the regression and neural models, belong to the group of black-box models. Such models are purely statistical models without any knowledge about the physical phenomenon proceeding in the investigated system [13, 20-22]. The concept of a black-box model is presented in Fig. 6.

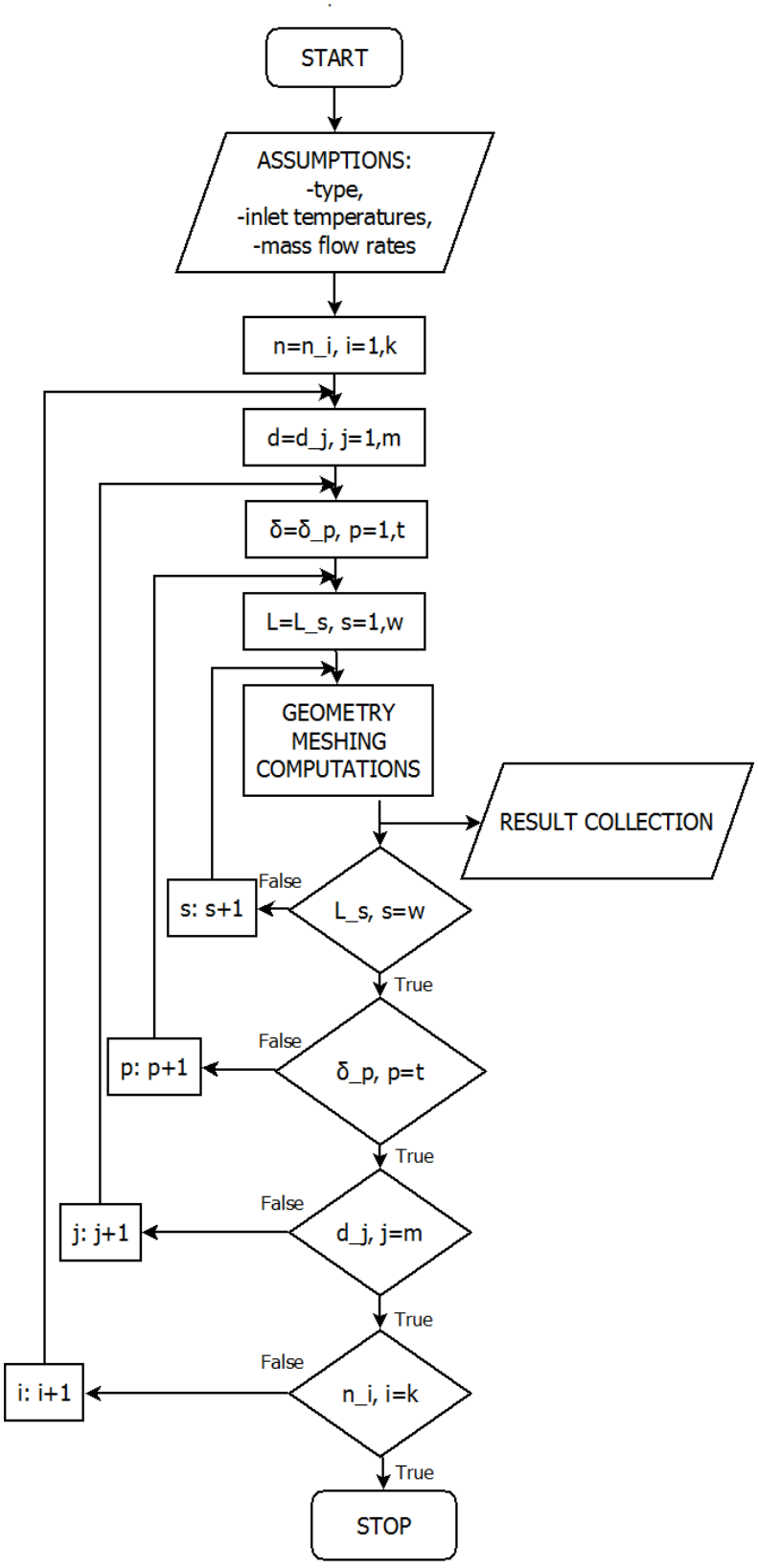

Fig. 3 Flow diagram of the data generation process.(n – number of the tubes, d - external diameter of the tubes, δ - wall thickness of the tubes, l - length of the tubes, i, j, p, s, k, m, t, w - variables).

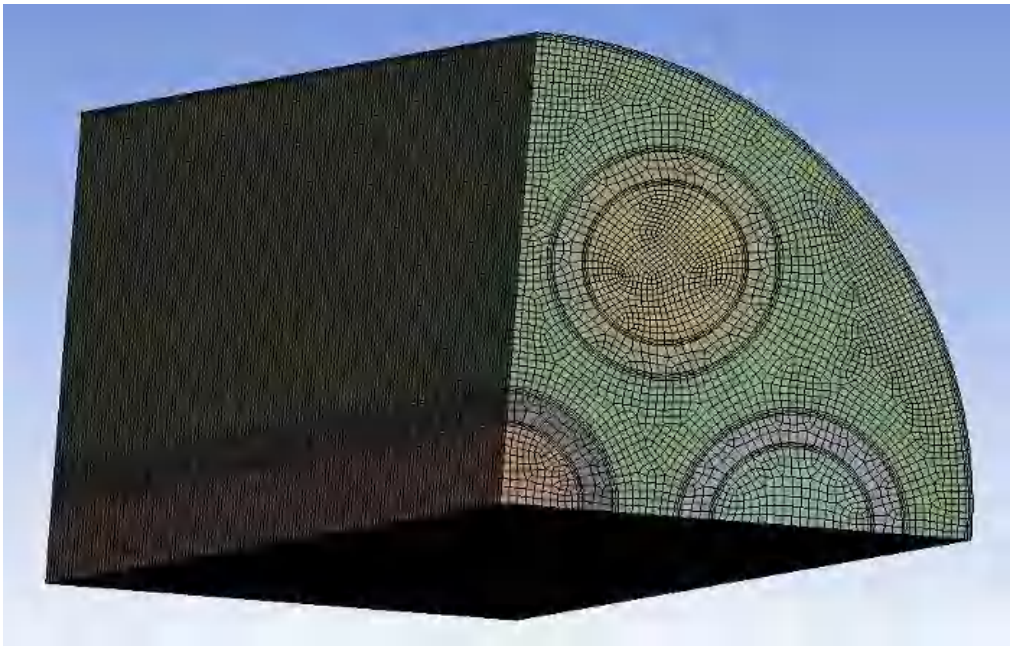

Fig. 4 A mesh example.

Figure 5 presents the heat load of the series of types of heat exchangers analysed as a function of the internal diameter of the pipes and the length of the exchanger.

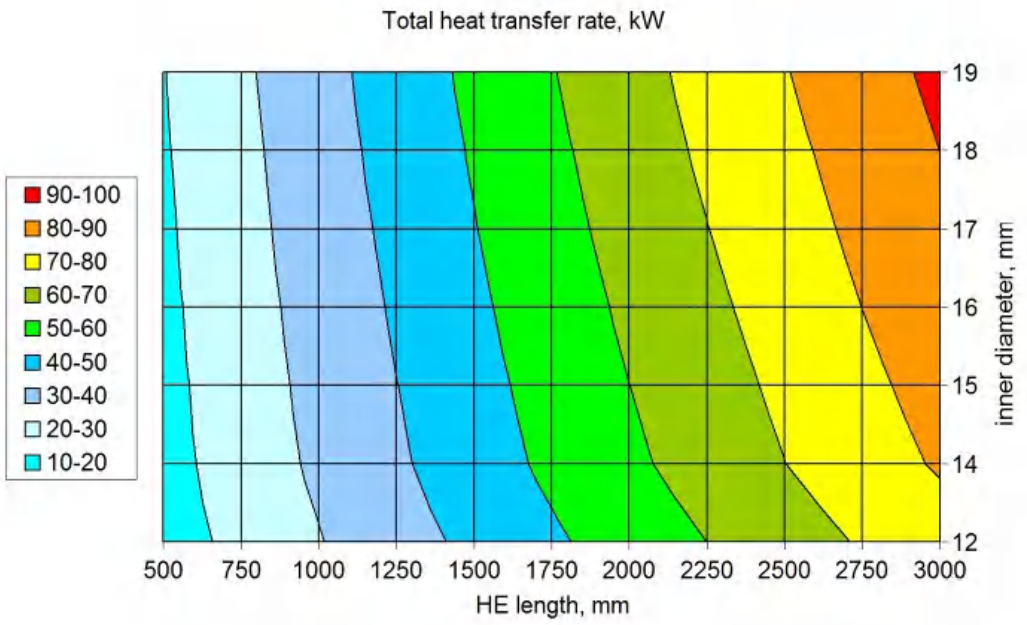

Fig. 5 Heat load of the series of types of heat exchanger analysed as a function of the internal diameter of the pipes and the length of the exchanger.

In the case of a HEX, the thermal power of the HEX, the inner and outer diameters of the inner tubes and the inner temperature of both fluids are generally independent variables.

The identification of a black-box model comprises two main steps:

- calibration of the model,
- verification of the model.

It is important that the verification of the model be based on a statistical dataset other than that used for calibration. The verification step is the base for determining the possibility of usage of the model. Empirical models of the black-box type are characterised by the following features:

- short calculation time – for this reason, they can be used online and for optimisation purposes,
- lack of physics knowledge,
- strong influence of the quality of data used for calibration on the quality of the model,
- calibration is simple, with commonly accessible commercial computer codes.

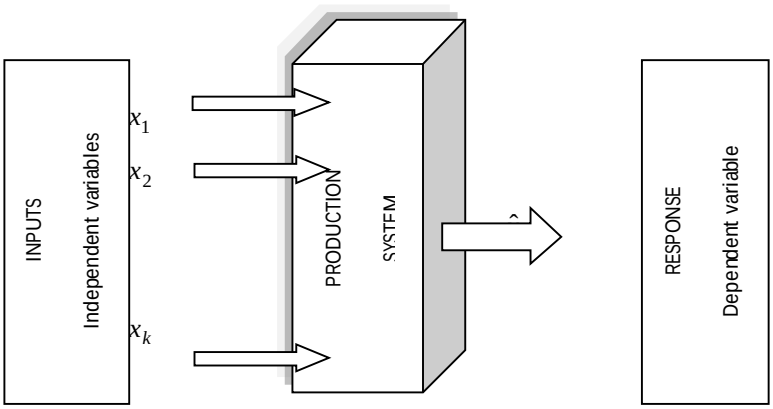

Fig. 6 Black-box emission model.

Although the authors developed an exact physical model, its usage for TEC analysis was inconvenient due to a relatively long computational time. For this reason, the development of faster models is necessary. This aim can be obtained through empirical modelling. The authors compared two methods – regression and neural networks – to choose the more efficient model for describing the influence of operational and constructional parameters on the pressure drop of fluids in a heat exchanger. Better results were achieved in the case of neural network models. It should be noted that the models describing the pressure drop of agents in heat exchangers are very important for the objective function and the results of optimisation. The product that is most particularly burdened by cumulative exergy consumption is electricity. Pressure drops in a HEX directly influence the demand for electricity for pumping purposes. For this reason, an efficient model for the pressure drop is crucial to optimisation.

4.1 Regression

The choice of the model structure is the aim of structural identification [22]. Most often, a linear structure is applied in relation to the estimated parameters. The most general type of linear model, the multi-input single output (MISO) approach, can be described by the following equation:

$$y_i = m_0 + m_1 x_{i1} + \ldots\ldots + m_k x_{ik} + \varepsilon_i \tag{3}$$

Estimators for the coefficients of the linear regression model can be determined by means of the following formula:

$$\mathbf{m} = (\mathbf{X}^T \mathbf{X})^{-1} \mathbf{X}^T \mathbf{y} \tag{4}$$

Each evaluation of the model's parameters introduces errors. To determine the relation between y and $\hat{y}$, the coefficient of multiple determinations R^2 is applied [22]:

$$R^2 = \frac{R_R}{R_T} = \frac{\mathbf{m}\mathbf{X}^{\mathbf{T}}\mathbf{y} - \frac{\left(\sum_{i=1}^{n} y_i\right)^2}{n}}{\mathbf{y}^{\mathbf{T}}\mathbf{y} - - \frac{\left(\sum_{i=1}^{n} y_i\right)^2}{n}} \tag{5}$$

The coefficient of multiple determinations R^2 is applied as a measure of the quality of the model with respect to the data variability. The model's accuracy is higher if the value of the coefficient of determination is closer to 1. However, as more independent variables are added, the R^2 coefficient increases, even though the dependence can be smaller.

4.2 Neural network

Several signals x_k of the model are supplied to the neural inputs. These signals come either from the inputs of the neural network or from the outputs of other neurons. Each signal reaching the neuron is multiplied by its weight w_k and then, all of the signals are summed up. The sum of the input signals φ multiplied by their weights represents the argument of the neuron activation function. The output (answer) of a neuron is the result of the neuron activation function $y=f(\varphi)$. Figure 7 presents the scheme of a single artificial neuron.

The possibilities of applying a single neuron as a model are considerably limited due to its constrained computation capacity. To obtain advanced computation possibilities and a higher calculation accuracy, the single neurons are interconnected into a net [20,22]. The calculation of the neural network is called the learning process.

The Lavenberg Marquardt algorithm has been investigated as a training method [23].

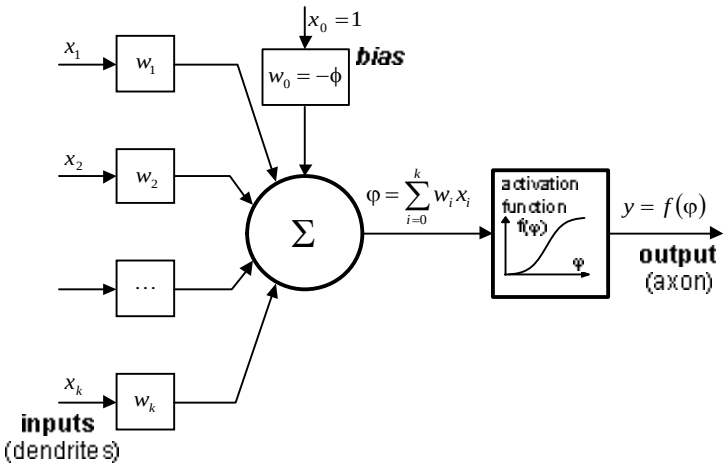

Fig. 7 Model of an artificial neuron.

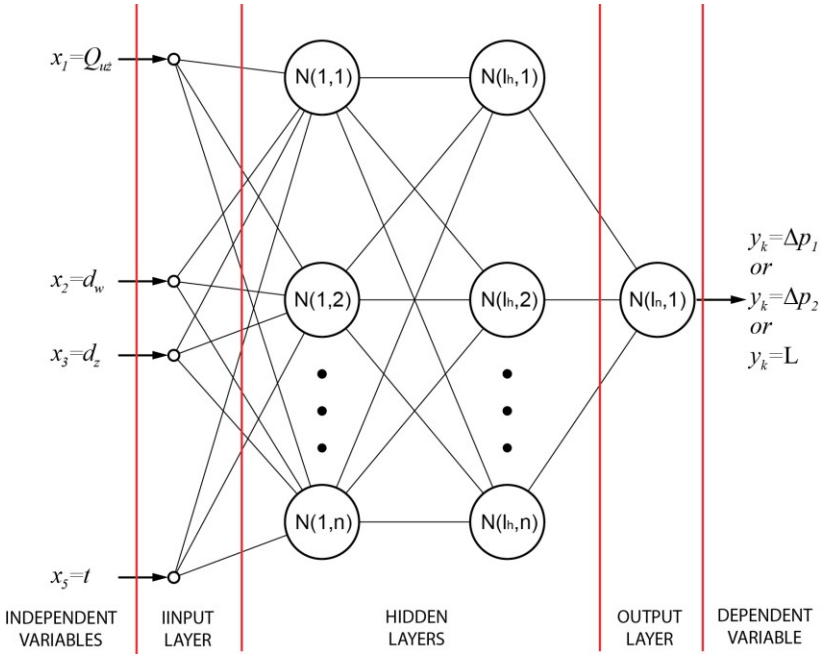

Fig. 8 Structure describing a change in pressure in the inner and outer tubes.

Neural simulations were carried out ten times for j=5,10,..,50 neurons for each layer with k=1,2,3 layers. The best R^2 coefficient for the hot stream was obtained for the case of one layer with 15 neurons; however, for the cool stream, the best value was obtained in the case of two layers with 15 neurons each. In the case of length, the best correlation was obtained for one layer with 15 neurons.

Regression was conducted twice for the hot and cool streams and the length. Firstly, regression was carried out for all CFD data, as shown in Fig. 9 – 11, designated as full regression; secondly, regression was conducted for the data used in training the neural network. In both cases, the correlation coefficient was high.

The correlation coefficients for the regressions and neural networks are presented in Table 1 and the adjustment is shown in Fig. 9 – 11.

In sum, the results of the pressure drops in the hot and cool streams for the neural network and regression methods are similar to those found by the CFD model.

Table 1 Correlation coefficients for the neural network and regression methods

	δp_1	δp_2	Length
Layer	2	1	2
Neurons in layer	15	15	15
Correlation coefficient			
Neural network	0.9136	0.9812	0.8568
Regression	0.9993	0.9314	0.9727
Full regression	0.8630	0.8681	0.7898

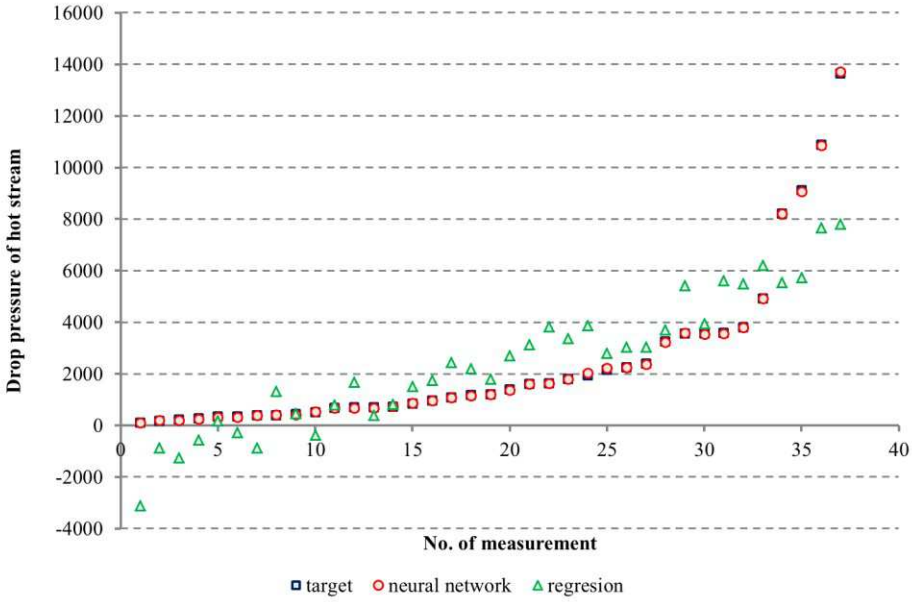

Fig. 9 Adjustment of neural network and regression to CFD simulation results for the hot stream.

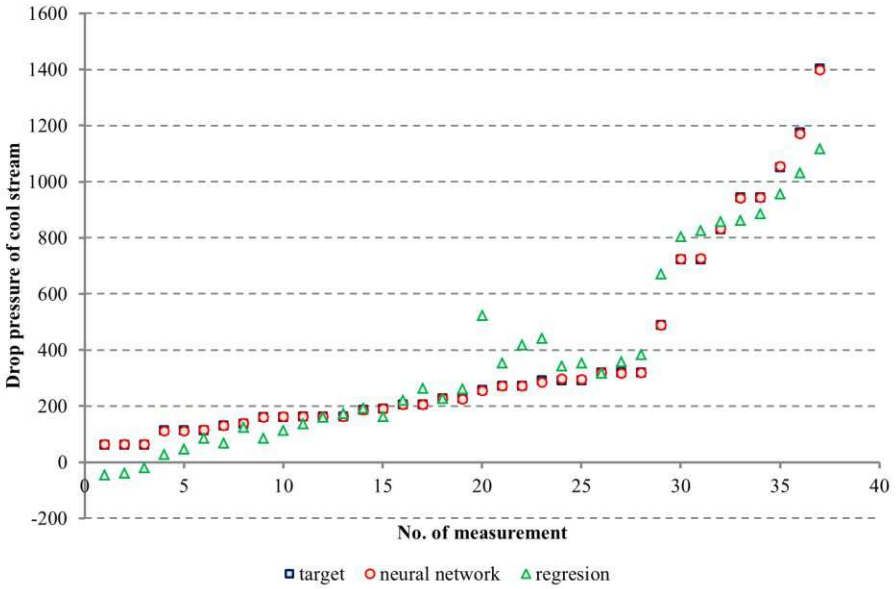

Fig. 10 Adjustment of neural network and regression to CFD simulation results for the cool stream.

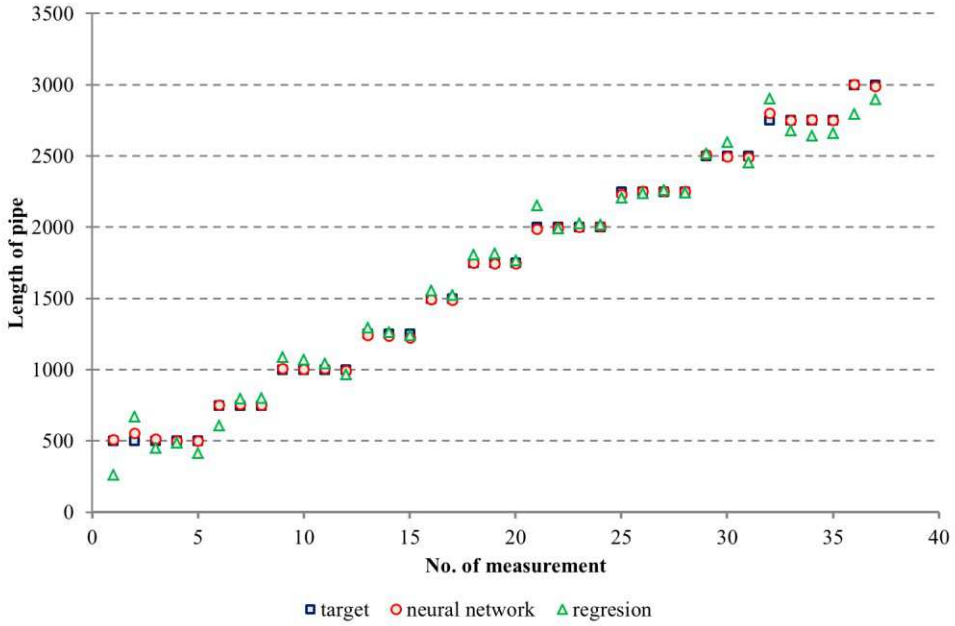

Fig. 11 Adjustment of neural network and regression to CFD simulation results for length.

5. TEC optimisation of heat exchangers

The yearly TEC of the heat exchanger operation can be expressed as follows [7,20,24]:

$$(TEC) = \frac{\rho_{el}}{\eta_p} \int_0^{\tau_p} \left(\dot{V}_1 \cdot \delta p_1 + \dot{V}_2 \cdot \delta p_2 \right) d\tau + \frac{\rho_s \cdot (1 - u_s)}{\tau_z} \cdot \left(G_p + G_s^{'} \right) + E_{el} \cdot \rho_{el} \rightarrow \min \tag{6}$$

The amount of steel needed for the pipe in the heat exchanger is determined from the following equation [13]:

$$G_p = \left(\frac{\pi}{4} (D + 2t)^2 - \frac{\pi D^2}{4} \right) L \gamma_s \tag{7}$$

It can be assumed [13] that the diameter of the heat exchanger jacket is proportional to the diameter of the tubes and the square root of the number of tubes:

$$G_s' = \sigma D \sqrt{n} (1 + \kappa L) \tag{8}$$

The electricity consumption for the construction of the heat exchanger should be a function of influential variables, as follows [13]:

$$E_{el} = \mu D n + \nu D \sqrt{n} \tag{9}$$

The following data have been assumed:

- TEC index of electricity [13] ρ_{el}, as shown in Fig. 12
- TEC index of steel products ρ_s = 35.7 MJ/MJ
- Empirical coefficients in Eqs. (7) – (9):

σ =700 kg/m; κ =0.151 /m; μ=0.08 kJ/m; ν =0.3 kJ/m

The example of a tailed structure of the TEC of electricity calculated by the algorithm presented in Fig. 1 is illustrated in Fig. 12. The highest value arises for the exergy of the resources bar, corresponding to the exploitation cost of the selected system.

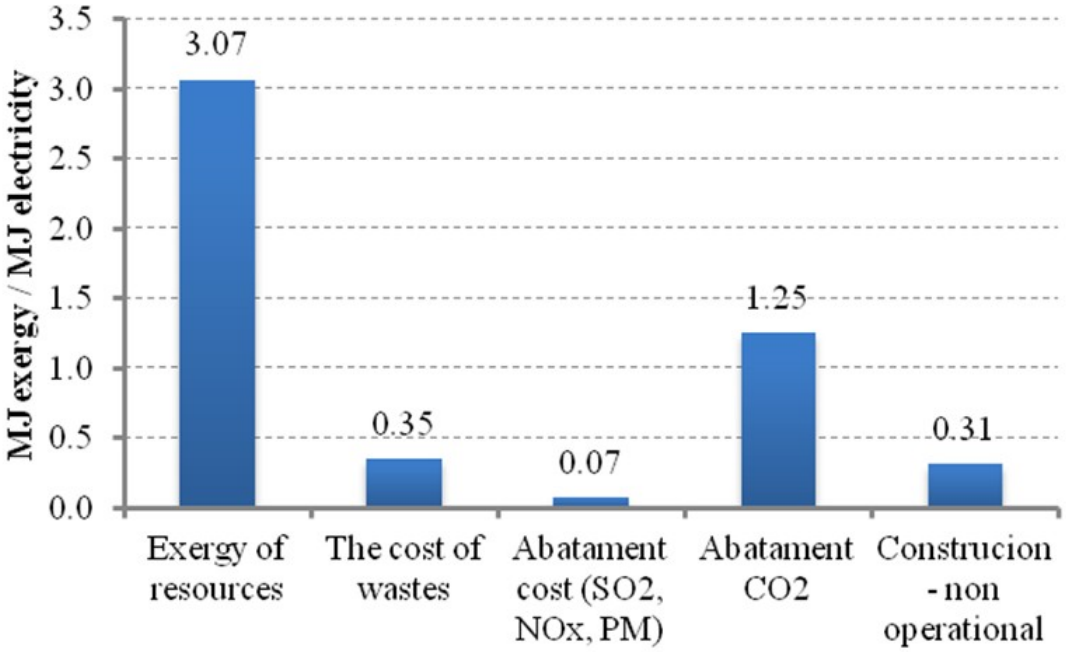

Fig. 12 Structure of the TEC of electricity.

Equation (6) contains two main components:

1. the investment component, including the TEC of the materials used for the construction of the exchanger and
2. the operational components expressing the electricity consumption of the pump.

The investment component takes into account the lifetime τ_Z of the installation and the possibility of reusing the steel after the completion of the installation lifecycle. The operational components take into account the yearly operation time τ_P of the pump. The entire optimisation procedure is shown in Fig. 13. In the present work, to shorten the calculation time of the optimisation procedure, the CFD model is replaced by the empirical model.

The applied method of TEC analysis is directly connected with the assumption that the boundary is not local, but system-wide. However, the authors consider the heat exchanger boundary to be much broader. For example, there is a power requirement for pumping agents that exchange heat. It is assumed that the pumps are driven by an electric motor. For this reason, the boundary is extended for the process of electricity generation, which is included in the TEC of electricity. This index is introduced as ρ_{el} in the objective function (6/10). Similarly, some materials are used for the construction of the exchanger. In this case, we use steel. The cost of steel is introduced in the index of ρ_s, the TEC of steel. The introduction of this cost is equivalent to the assumption of a balance boundary comprising the processes of steel production.

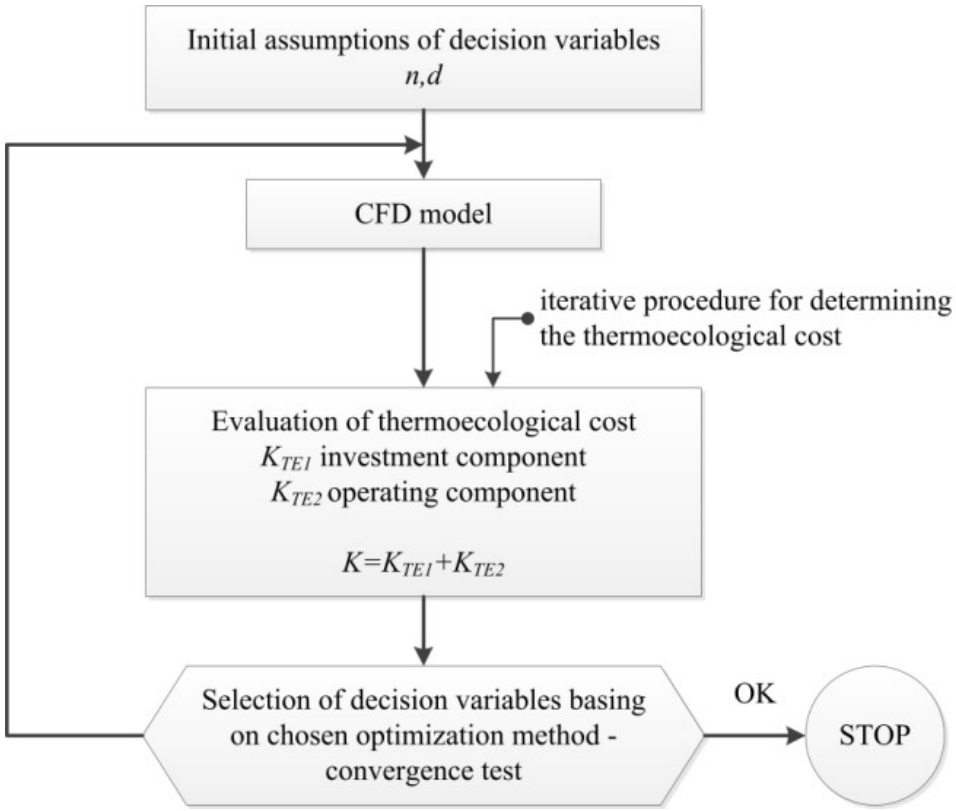

Fig. 13. Schematic of the optimisation procedure.

Sample results for the minimisation of the heat exchanger TEC are shown in Fig. 14.

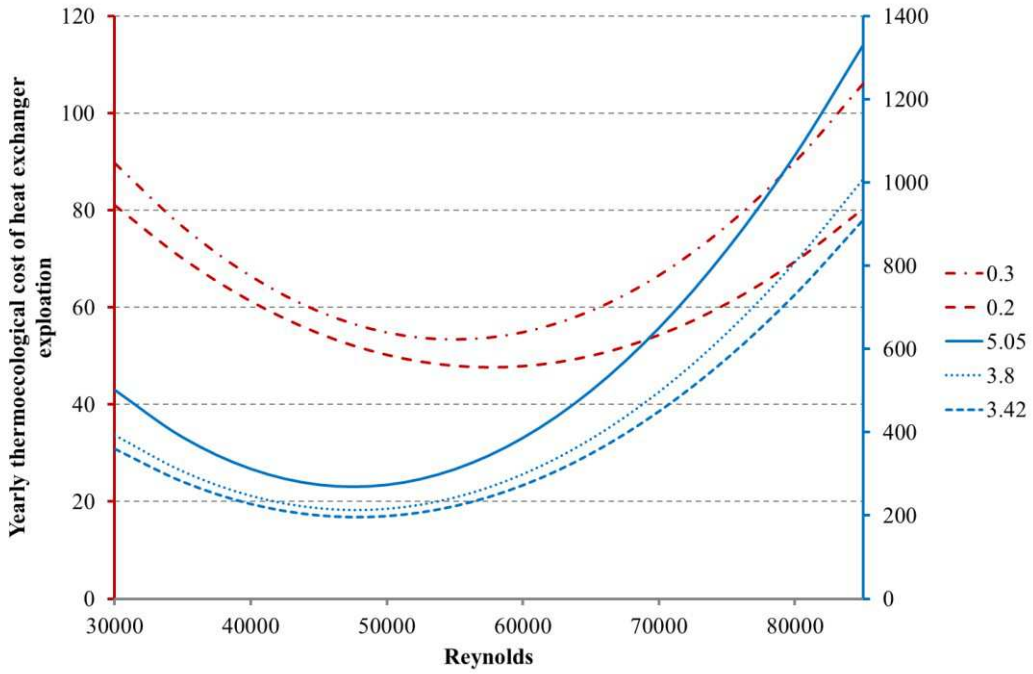

Fig. 14. Yearly TEC of heat exchanger exploitation as a function of the Reynolds number.

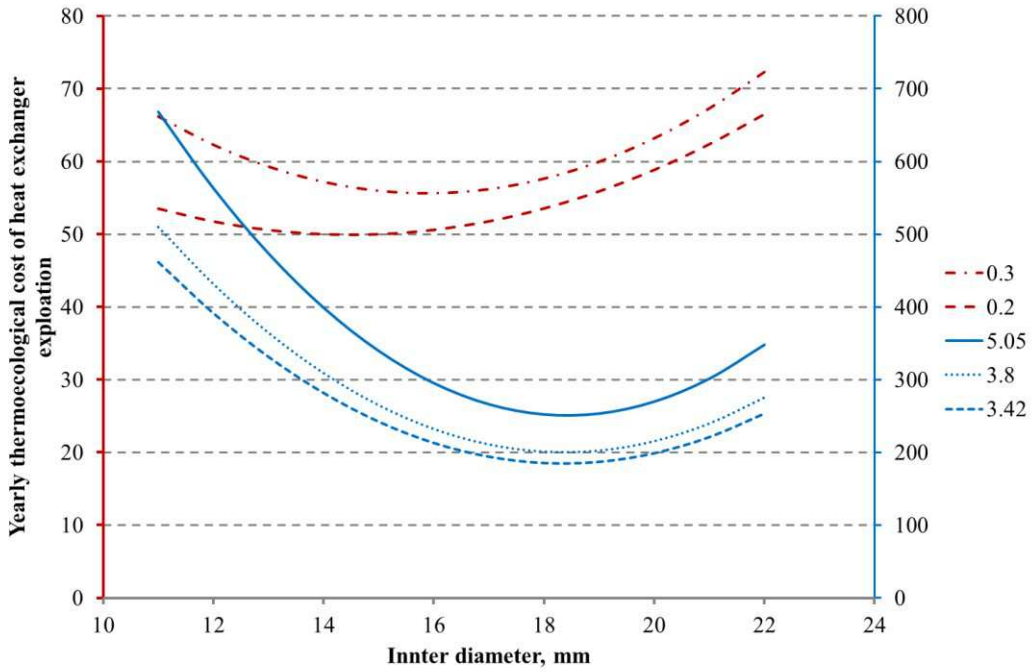

Fig. 15. Yearly TEC of heat exchanger exploitation as a function of the inner diameter.

Figures 14 and 15 illustrate the results of the optimisation function, Eq. 6, in conjunction with the TEC of electricity presented in Fig. 12. The calculation results plotted in red in Fig. 14 correspond to rather low levels of electricity TEC (ρ_{el} in Eq. 6) in the range of 0.2 – 0.3 MJ/MJ. Such values would be obtained for the production of electricity from renewable sources and result only from the construction of a power plant (compare with Fig. 8). However, in the domestic energy market, non-renewable power plants fired with solid fuels have the dominant share. These plants are characterised by a TEC on the level of 3.4 – 3.8. The highest TEC (approximately 5 MJ/MJ) for electricity would appear in the case of CCS technologies. It can be observed that the results of minimisation are strongly dependent on the TEC index. In the case of a lower TEC, the minimum corresponds to higher *Re* numbers and the curves are rather flat, while the obtained values of the optimal TEC result mainly from the TEC of materials used for heat exchanger construction. In the case of higher values of electricity TEC, the operation expenditures dominate and the minimum TEC values shift toward lower *Re* numbers. For all cases of higher electricity TEC, the heat exchanger minimum corresponds to an Re number of approximately 50000.

6. Summary and conclusion

The results of preliminary attempts to utilise CFD models in thermo-ecological optimization procedures are quite encouraging. The replacement of the experimental characteristics of devices with numerical models decreases the costs of determining such characteristics and extends the possible application of this method to new devices. The main problem lies in the computational time, which significantly increases the time of optimization. The rapid development in computer technology gives hope for machines that will be, in the not so distant future, able to solve such complicated problems in a reasonable amount of time. Currently, this problem can be overcome by the use of neural networks, which operate on a data cloud generated by a multi-variant numerical model.

Neural network modelling is rapid and, for trained, validated and tested networks with high correlation coefficients for the given range of parameters, is an easy and fast way to obtain the desired results. This article shows the adjustment of points with neural network models and multi-regression to the results of CFD modelling. In this case, for pressure drops and tube lengths, a high correlation coefficient was obtained between the input and output parameters. Both the regression and neural network methods are very useful in determining the correlation between variables and the results can be obtained very quickly.

In this paper, a CFD algorithm to generate data for a neural algorithm is presented. Due to the new features of the commercial package Ansys Workbench, geometry modifications can be provided automatically, which significantly shortens the time required for data generation.

Sample computations of a heat exchanger were carried out. The sample results and a discussion concerning the computational time are given. The presented algorithm can be used on any device for which one can construct a CFD model.

7. Nomenclature

A heat transfer area,
a_{ij} coefficient of the consumption of the *i*-th product per unit of the *j*-th major product
a_{rj} coefficient of the consumption of the *r*-th imported product per unit of the *j*-th major product
b_{sj} exergy of the *s*-th non-renewable natural resource immediately consumed in the process under consideration per unit of the *j*-th product
d inner dimension
D inner diameter of tubes
E_{el} electricity consumption during exchanger construction
f_{ij} coefficient of by-production of the *i*-th product per unit of the *j*-th major product
G_j nominal flow rate of the *j*-th major product
G_u nominal flow rate of the useful *u*-th by-product
G_m consumption of the *m*-th material or energy carrier used for the construction of installation
G_p, G'_s mass of steel tubes and exchanger jacket
k overall heat transfer coefficient
L length of the tube
$m_0, m_1, m_2, \ldots, m_k$ regression coefficients, determined during the calibration of the model
n number of tubes
$n-p$ degrees of freedom
δp difference between inlet and outlet total pressure
p_{kj} amount of the *k*-th aggressive component of waste products emitted to the environment per unit of the *j*-th product
P_k nominal flow rate of the *k*-th deleterious waste product emitted to the environment
$\dot{Q}$ heat load of the apparatus
Re Reynolds number
R_R regression sum of squares
R_T regression total sum of squares
s_{iu} replacement ratio in units of the *i*-th replaced product per unit of the *u*-th by-product
t thickness of pipe wall
Δt_m logarithmic temperature difference in the exchanger

u_m expected recovery factor of the *m*-th material
y_i actual observation from measurements
$\dot{V}$ volumetric flow rate
z_{lj} amount of the *l*-th aggressive component of waste products entering the cleaning installation

Greek symbols

γ_s density of steel
ε error, uncorrelated random variable
σ,κ coefficients resulting from construction of the exchanger
σ_l cumulative exergy consumption of non-renewable resources due to the removal of the *k*-th aggressive product from wastes
ζ_k cumulative exergy consumption of non-renewable resources due to the emission of one unit of the *k*-th waste product
η_p electric efficiency of the pump and electric engine
ψ_{j0} requirement for natural resource exergy to compensate or to avoid environmental losses resulting from operation of the *j*-th production process
μν proportionality coefficients (as determined by the producer of the exchanger, for example)
ρ_{el} unit thermo-ecological cost of electricity
ρ_s thermo-ecological cost of steel
ρ_i,ρ_j thermo-ecological cost of the *i*-th product
ρ_m thermo-ecological cost of the *m*-th material or energy carrier used for the construction of installation
ρ_r specific thermo-ecological cost of the *r*-th imported good
τ lifetime of installation
τ_n annual operation time with nominal capacity
τ_z nominal lifetime of installation
$)_1$ hot medium
$)_2$ cold medium

Acknowledgments

This paper was prepared with the support of the following projects:

- RECENT project (REsearch Center for Energy and New Technologies) supported by the 7th Framework Programme, Theme 4, Capacities;
- Research Project N N512 455540, financed by the science budget resources.

References

[1] Bejan A. Entropy generation minimization: The new thermodynamic of finite-size devices and finite-time processes. Journ. Applied Physics Reviews, 1996;79 February.
[2] Bejan A., Entropy Generation through Heat and Fluid Flow, John Wiley & Sons, New York, 1982

[3] Szargut J., Stanek W. Comparison of economic and thermo-ecologic optimization of thermal processes. Report from research project 8T10B05518, Gliwice 2005 (in Polish).
[4] Cornellisen RL, Marquart EN, Hirs GG. The value of exergetic life cycle assessment besides LCA. In: M. Ishida, G. Tsatsaronis, MJ. Moran, H. Kataoka (eds), Proc. ECOS'99, Tokyo 1999, p. 282-203.
[5] Finneveden G., Ostlund P.: Exergies of natural resources in life-cycle assessment and other applications, Energy, Vol. 22, No. 9, 1997.
[6] Sciubba, E. Beyond thermoeconomics? The concept of Extended Exergy Accounting and its application to the analysis and design of thermal systems. Exergy Int. J., Vol.1., 2001.
[7] Szargut J. Minimization of the depletion of non-renewable resources by means of the optimization of design parameters. Energy 2004;29(12-15):2161-2169.
[8] Valero A., Botero E. An exergetic assessment of natural mineral capital (1): Reference environment, a thermodynamic model for degradated Earth, Proc. Conf. ECOS 2002, Berlin.
[9] Valero A., Botero E., An assessment of the Earth's clean fossil exergy capital based on Exergy Abatement Cost. Proc. Conf. ECOS'2002, Berlin
[10] Wall, G., Gong M. On exergy and sustainable development, Exergy Int. J., Vol.1., 2001.
[11] Szargut J. Exergy method, technical and ecological applications. Southampton, Boston: WIT Press, 2005.
[12] Stanek W. Iterative evaluating method of the ecological cost of imported goods. Proc. of ECOS'01, Istanbul 2001, 575-80.
[13] Szargut J., Stanek W.: Thermo-ecological optimization of a solar collector. Energy 32 (2007) 584–590.
[14] Szargut J., Ziębik A., Stanek W.: Depletion of the Unrestorable Natural Exergy Resources as a Measure of the Ecological Cost, Energy, Conversion and Management 42, 2002.
[15] Joel H. Ferziger and Milovan Peric.Computational Methods for Fluid Dynamics, Springer-Verlag, Berlin, Heidelberg 2002
[16] Szczygieł I.: Temperature-Velocity Coupling of the Convective Heat Transfer-Sensitivity Analysis; Numerical Heat Transfer, An International Journal, Part B, 48: pp. 165-190, 2005
[17] ANSYS Workbench Help © 2010 SAS IP, Inc.
[18] Cengel Y.A., Heat Transfer, McGraw Hill, New York, 2003.
[19] Szczygieł I., Stanek W., Rojczyk M.: Thermo-ecological optimisation of the heat exchanger based on CFD modelling, Proceedings of ECOS 2010, Lausanne, Switzerland
[20] Tadeusiewicz R. Neural networks. Academic Press RM, Warszawa, 1993. In Polish
[21] Deutsch R. Theory of estimation. Warszawa: PWN 1969 (In Polish.)
[22] Draper NR, Smith H. Applied regression analysis. Warszawa: PWN 1973. (In Polish).
[23] Documentation of MathWorks http://www.mathworks.com/help/
[24] Szczygieł I., Stanek W., Rojczyk M., Czarnowska L.: "CFD aided thermo-ecological optimization of selected thermal device.", Thermodynamics in Science and Technology. Part 2. 1-st International Congress on Thermodynamics, 4-7 September 2011, Poznań

THERMOECONOMIC ANALYSIS AND OPTIMIZATION IN A COMBINED CYCLE POWER PLANT INCLUDING A HEAT TRANSFORMER FOR ENERGY SAVING

Elizabeth Cortés Rodríguez[a], José Luis Castilla Carrillo[a], Claudia A. Ruiz Mercado[a]
Wilfrido Rivera Gómez-Franco[b]

aFacultad de Ingeniera Química. Universidad Autónoma de Yucatán, México.
bCentro de Investigación en Energía, Universidad Nacional Autónoma de México.

Abstract:

Nowadays, the use of renewable energy is not capable of replacing the fossil energy, so, new technologies such as the combined cycle power, have been developed using the minimum fuel to obtain the maximum performance.

In this research, through the exergy analysis and thermoeconomics techniques a predictive analysis was developed according two possible scenarios: the sulfur content increase in the fuel composition and the implementation of an innovative heat recycling technology such as the heat transformers.

Exergy analysis was applied to each of equipment in an existing combined power cycle plant of 531 MW of power capacity, the individual and global efficiency were obtained, as well as, the effects of different concentrations of sulfur in natural gas composition before and during combustion were analyzed, and also the implementation of a heat transformer was proposed in order to reduce waste heat discharged to the atmosphere.

As a result of the study, the use of a heat transformer was suggested in the gas turbines, where the biggest exergy loss was located with the purpose to reduce the consumed fuel in an order of 4.5% with important economic savings. Also a predictive model of the corrosion in thermoeconomics terms was obtained, allowing determining the irreversibility cost due to corroded pipes and the presence of sulfur in the fuel composition, which will increase due to the location of new fossil fuel reserves in inaccessible sites will be expected, so that fossil fuels with higher impurities will be obtained.

Predictive models, related to exergy consumed and the implementation of new technologies are useful to estimate in a quick and easy way the main variables in a process.

Keywords:

Combined Cycle Power Plant, Heat Transformer, Corrosion, Thermoeconomic, Predictive Energy Saving.

1. Introduction

In general, electric power generation consists in the transformation of some kind of energy like chemical, mechanical or thermal, into electrical energy. Combined Cycle Power Plant (CCPP) stands out among the technologies developed for electric generation, because of the high energy efficiency obtained through the co-existence of two thermodynamic cycles in one system, using steam and combustion gases as working fluids and natural gas (NG) as fuel for power generation.

During the last decades, joined to the technology development, different strategies for the energetic optimization have emerged as response to the increase in the energy demand. Being the exergy analysis, one of the energy integration methods more useful because, the energy quality and the maximum work obtained have been utilized in the design and selection of the best equipments such as gas turbines [1], to establish the best operation parameters in a feasible way [2] considering the technical limits [3] and optimization of process and equipment with good results [4], moreover, the

combination of exergy analysis with economy has allowed the development of disciplines like thermoeconomic, which, is one of the most used at industrial level [5] due to the correlation exergy-cost, allows to realize a complete analysis according the available technology [6], to predict the operational performance [7] in thermal devices, and other applications more, with the purpose to suggest modifications in the current operational parameters and the implementation of new equipment existent [8] or in recent development [9].

In this research, a predictive analysis was developed, considering the operational performance range, construction material, fuel characteristics and energy use as main factors to be considered through the application of exergy analysis and thermoeconomic optimization in an existing CCPP, which produces 531 MW of electricity. Exergy efficiency was obtained and analyzed for each equipment and the global system; likewise the best operation conditions for a double heat absorption heat transformer implementation were determined, economic savings in order of 14,810,240.00 USD/year were obtained with the respective reductions in the NG and energy utilized. A thermoeconomic predictive model was developed to estimate the corrosion inside the Heat Recovery Steam Generators (HRSG), at different concentrations of sulfhydric acid (H_2S) in NG, because of the future expectatives about this pollutant, which estimate NG content will be increased because the lack of fossil resources and high costs of extraction and refinement. Therefore, it is important to analyze the effects of increasing H_2S concentration to suggest preventive actions against the acid corrosion since it constitutes a serious and expensive maintenance problem

2. System description

2.1 A combined cycle power plant

The study system is a 2x1 CCPP, because two combustion turbines and one steam turbine conform the generation system of 531 MW. The main equipments considered in the combined cycle power flowsheet are shown in Fig.1. The two combustion turbines were designed to operate with NG as fuel and are capable to produce together a combined total of 336 MW. Steam is generated in two Heat Recovery Steam Generators (HRSGs) by heat exchange between the combustion gases (CG) and water. The HRSG is a heat recovery unit with natural circulation, which contains 6 superheaters, 3 evaporators, 3 drums, 4 economizers and 2 reheaters. The components are included within an outer isolated cover, designed to receive hot exhaust gas from the combustion turbine at 550°C and are released to the environment from the chimneys at 90°C. The internal components of the HRSG are arranged to obtain a CGs horizontal flow through vertical pipes. This equipment operates with three different pressure levels: low pressure (LP) 393 kPa, intermediate pressure (IP) 2000 kPa, and high pressure (HP) 9545 kPa. Each pressure level has the same sections: economizer or pre heater, evaporator and superheater. The economizer heats water at temperature near the saturation, which varies according to the vapor pressure in the corresponding evaporators. In evaporators, saturated steam is generated. The superheaters raise the temperature of vapor above the saturation temperature.

The feed water for the LP level is provided by the condenser at 40°C to the LP drum, passing or bypassing the LP economizer. The LP drum supplies water to IP and HP levels where fed water is evaporated and superheated at 294 °C and 526 °C respectively and receives the steam from the LP section. All the steam produced in both HRSGs is fed to the Steam Turbine (ST) with capacity of 195 MW. The steam leaves the turbine in a saturated state and then passes through the condenser at 10 kPa where all the steam is condensed and it is send to the HRSGs to restart the cycle. Note: The data above indicated are average measured values from an existing CCPP.

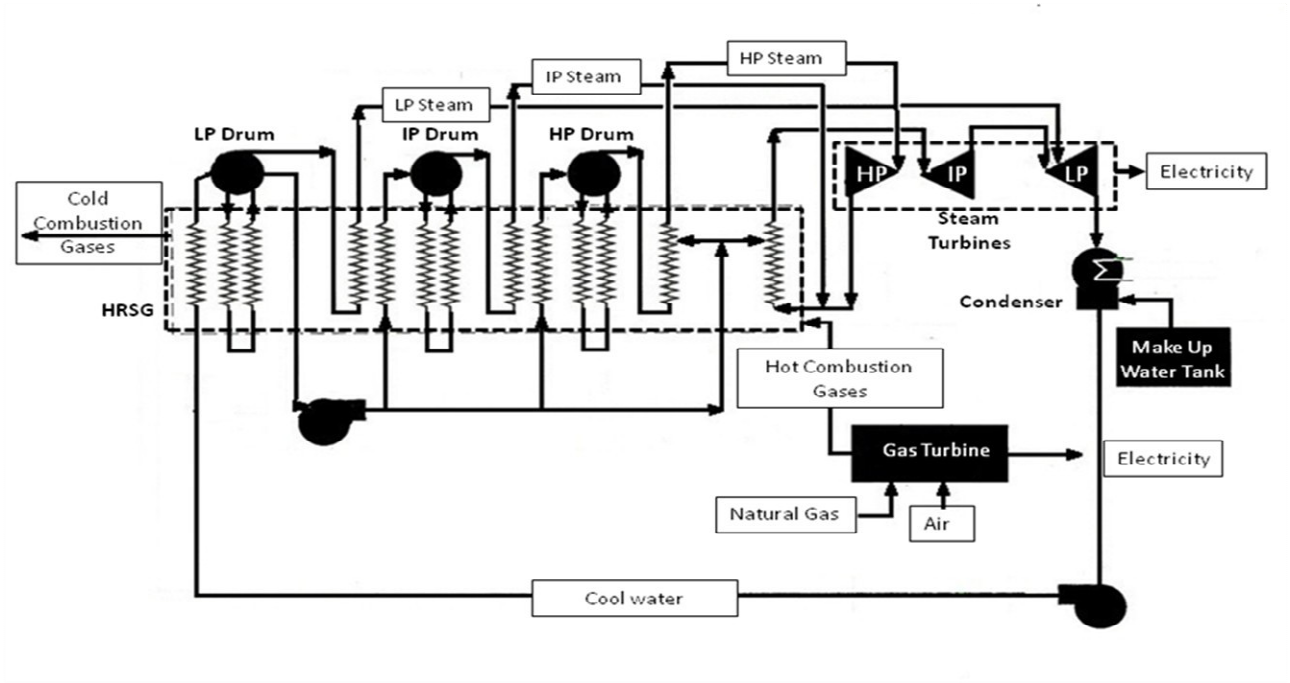

Fig.1. Combined Cycle Power Plant flowsheet.

2.2 Corrosion

In general, fossil fuels cannot be considered as free of sulfur with the exception of the wood. Small amounts of sulfur have been found in commercial NG components, or in significant amounts in liquid fuels such as diesel or fuel oil [10].

The corrosion is a latent problem in HRSGs, it can be developed inside the pipes where, the protective magnetite layer could be dissolved by the ammonia concentration in water and the operation temperatures. Outside the pipes, corrosion could take place by acid depositions on the metal surfaces, caused by the impurites content and temperature of CG, specifically concentrations of NOx and SO_2, due to the proximity of dewpoint of NOx, SO_2 and water in shut down and star up. Corrosion by SO_3 is possible in plants in operation, where more serious consequences occur when the gas temperature is below the dew point within the process. Corrosion is an inevitable consequence provided the hot sulfuric acid is deposited on a metal surface. SO_3 formation occurs when the sulfur content in any fuel is burned and oxidized to SO2 (1). If oxygen is presented, a fraction of SO_2 is oxidized to form SO_3 (2). In most cases, SO_3 forms a small but significant fraction of oxidized sulfur. If water vapor is present and the gas temperature is below the acid dew point this can react with SO_3 to produce H_2SO_4 in spray form (3), and a film formed will also be deposited onto any exposed surface to a temperature below the dew point inside the HRSGs [11].

$$H_2S + O_2 \rightarrow SO_2 + H_2 \quad (1)$$

$$2SO_2 + O_2 \rightarrow 2SO_3 \quad (2)$$

$$SO_3 + H_2O \leftrightarrow H_2SO_4 \quad (3)$$

Sulfuric acid is condensed at temperatures near 100 °C. In general, it is preferable to maintain the process temperature above the dew point, however, during the star up and shut down is inevitably a temperature decrease below the dew point of sulfuric acid or water and condensation will occur, so that, corrosion of sulfuric acid may not always be avoided [12], due to CCPP operators need to decide between low flue gas temperatures that may cause H_2SO_4 deposition, with consequent corrosion, and high flue gas temperatures, which may avoid corrosion but increase heat losses and reduce efficiency [13,14].

Corrosion by formation of SO_2 and H_2SO_4 has been documented [15], but there has not considered the corrosion from the point of view of H_2S content in the NG and the operational times, being

these, important factors due to the efficiency and replace equipment are affected by the exposition time, material composition and temperature [16,17]. In literature, there was not developed a thermoeconomic analysis like the developed in this research, considering corrosion rates and natural gas composition in a CCPP, like this analysis so important due to allows estimating and determining the energy losses and costs in a more realistic form.

2.3 Heat Transformers

There is a growing interest in using heat transformers systems in industrial and domestic sectors. A heat transformer uses low grade calorific energy such as waste heat from industries, solar, geothermal to obtain energy with a greater potential for industrial applications. Single-stage heat transformers can be used to retrieve industrial waste heat at intermediate temperatures when 50 °C gross lift temperature or less are required in an industrial process. However, when higher gross lift temperatures are required, advanced absorption heat transformers, such as two-stage heat transformers and double absorption heat transformer must be considered [18].

This equipment has been analyzed in changing operating and design parameters as measure to increase efficiency [19], in the industrial sector, at pilot scale has been used in the waste heat recovery [20], in the production of environmentally clean steam [21], also the simulation and analysis of its implementation in industrial processes such as pulp and paper effluent in the area [22] has been done, and its optimization in the process area, or integration with other devices distillation processes [23] has been considered.

2.3.1 Double absorption heat transformers

A double absorption heat transformer consists of a generator, a condenser, an evaporator, an absorber, an absorber/evaporator and an economizer Fig.2. A heat source is supplied to separate the working fluid in the generator at an intermediate temperature; the working fluid is evaporated and condensed at a low temperature. Then, the condensed working fluid is split into two streams, one is pumped to the evaporator where is vaporized at intermediate temperature and pressure. The other stream is pumped at a higher pressure to be evaporated in the absorber/evaporator. The vaporized working fluid is absorbed at an elevated temperature in the absorber, by a rich salt solution coming from the generator. The salt solution at intermediate concentration is split into two streams; one goes to the generator to preheat the rich solution in the heat exchanger, the other stream is fed to the absorber / evaporator, where the vaporized working fluid coming from the evaporator and delivers an amount of heat. Finally, the salt solution at a low concentration leaves the absorber/evaporator and is pumped to the generator to restart the cycle [24].

3. Exergy and thermoeconomic analysis

3.1 Methodology

A new methodology developed recently by the authors [9] allows to simulate and optimize the energy and economic sources considering the integration of several the methods above mentioned with pinch technology to obtain the best scenario in an industrial process. This was used in this predictive analysis as follows:

1. Establishing the dead state, temperature and pressure of reference, surroundings and volume control.

2. The balances of mass and energy in the system and the conceptual flowsheet was obtained, to establish the real energy and mass flow.

3. The global system was divided in subsystems, according to the exergy flow, complexity and the different involved processes.

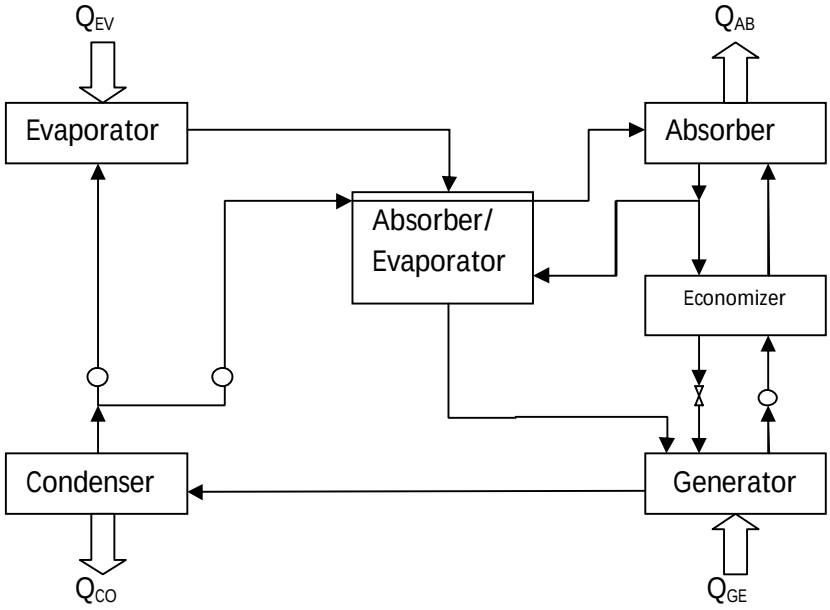

Fig.2. Schematic diagram of a double absorption heat transformer.

4. The initial conditions of the global system and the selected subsystems were determined through the exergy analysis, such as exergy flow, efficiency, and the irreversibility.

5. The sensibility analysis was developed to determine the possible causes of irreversibility in the main components, subsystems and the integrated system.

6. Several mathematical models of the considered subsystems in efficiency and fuel terms and the relationship among the global efficiency were obtained, which allowed to establish the relationship between the main variable of the global system and each subsystem.

7. The models obtained made possible to propose improvements such as the modification of the operating conditions and the implementation of new equipment.

8. New exergy analyses were carried out again for each improvement choosing the ones with lower irreversibility to establish the operation conditions modifications.

9. The Pinch technology was useful to determine the location of the new equipment.

10. Once the previous steps were finished, and thermoeconomic analysis were carried out by means of optimization techniques developing and solving the objective function which was the optimum operation conditions of the existing equipment and the design of new equipment increasing the global efficiency at lowest cost.

4. Mathematical Models

According to the outlined methodology, atmospheric air with the conditions of temperature, pressure, and relative humidity of T0 = 303.15 K, P0 = 101.3 KPa and Hr = 90% respectively was chosen as dead state. The global system was made up for: two gas turbines, one steam turbine, two HRSGs and one condenser. It was a simple system, so it was divided in the four main subsystems, and the surroundings were chosen as from each subsystem to the part of the near atmosphere to the same ones. In a global form, the equations and concepts used in the exergy and exergoeconomic analysis are described as follows:

The exergy, also well-known as availability it is a measure of the useful work that can be obtained of the system in a state given in a specific atmosphere. The exergy balance for an open system that experiences physical and chemical processes can be written in the following way (4):

$$I = \sum (mE)_{in} - \sum (mE)_{out} + \sum W_{in} - \sum W_{out} + \sum \left(Q\left(1 - \frac{To}{T}\right)\right)_{in} - \sum \left(Q\left(1 - \frac{To}{T}\right)\right)_{out} \quad (4)$$

Where I is the irreversibility, the first two terms in the right side to the equation are referred to the mass flow entering and leaving the system. The following terms are related to the input and output of work (Win, Wout) and heat transfer (Qin, Qout) respectively, at a specified temperature (T). Therefore, energy balances were obtained applying the (4) to the main components considered in the studio system, the equations obtained are as follows(5-8).

Gas Turbines:

$$I = \quad (E_{NG} + E_{Air}) - E_{CGin} - W_{GTE} \quad (5)$$

Heat Recovery Steam Generators:

$$I = (E_{CGin} + E_{CW} + E_{CRH}) - (E_{LPS.} + E_{IPS} + E_{HPS} + E_{HRH}) - Q_{loss} \quad (6)$$

Steam Turbine:

$$I = \left(E_{LPS} + E_{IPS} + E_{HPS} + E_{HRH}^{'}\right) - \left(E_{SST} + E_{Condensate} + E_{CRH}\right) - W_{STE} \quad (7)$$

Condenser:

$$I = E_{SST} - Q_{cond} \quad (8)$$

Where: E_{NG} and E_{CG} is the Exergy content in NG and GC and E_{LPS}, E_{IPS} , E_{HPS} are referred to the Exergy streams at Low, Intermediate, and High Pressure respectively; E_{CRH}, E_{HRH} are the Exergy of Cold Reheat and Hot Reheat Steams Exergy respectively; Ccondensate and E_{SST} is the Condensate and Saturated Steam Exergy; Q_{Loss} , Q_{Cond} is the exergy associated with the heat transfer from the HRSG and the Condenser; W_{GTE} , W_{STE} are the Exergy associated with the work transfer produced from the Gas and Steam Turbines, all in [kW] units.

The exergetic efficiency (η) is obtained through the following equation (9):

$$\eta = \frac{-\left(1 - \frac{To}{Ti}\right) \times Q_i}{-\left(1 - \frac{To}{Ti}\right) \times Q_i - LW} \quad (9)$$

Where: T_0 and T_i is the initial and final Temperature from the heat transfer [kW] and Q_i and LW is the heat transfer and lost work respectively [kW].

Thermoeconomics provides to the system designer or operator, information crucial to the design and operation of a cost effective system. The cost balance for a system is as follows (10):

$$\sum_e \dot{C}_{e,k} + \dot{C}_{w,k} = \dot{C}_{q,k} + \sum_e \dot{C}_{i,k} + \dot{Z}_k \quad (10)$$

where: Ce,kand Ci,k are the average costs per unit of exergy in dollars per gigajoule ($/GJ), Cw,k and Cq,k are the costs associated with a work and heat transfer respectively and Zk is the cost rate associated with capital investment or operating and maintenance.

From Eq. (10) and using the auxiliary equation cost for each one of the equipment, it was possible to determine the global system cost and the exergoeconomic optimization for the main components and the whole plant (11-14).

Gas Turbines:

$$C_{CGin} + C_{GTE} = C_{NG} \tag{11}$$

Heat Recovery Steam Generators:

$$C_{LPS} + C_{IPS(W3)} + C_{HPS} + C_{HRH} + C_{CGout} + C_{Loss} = C_{CGin} + C_{CRH} + C_{CW} \tag{12}$$

Steam Turbine:

$$C_{SST} + C_{Condensate} + C_{STE} = C_{HPS} + C_{IPS} + C_{LPS} + C_{HRH} \tag{13}$$

Condenser:

$$C_{RW} + C_{CW} = C_{Condensate} + C_{SST} + C_{RW} \tag{14}$$

Where: C_{NG}, C_{CG}, C_{LPS}, C_{IPS}, C_{HPS} are the NG, CG and Low, Intermediate and High Pressure Steams costs respectively; being C_{CRH}, C_{HRH} $C_{Condensate}$ and C_{SST} the costs referred to Cold Reheat and Hot Reheat Steams and Condensate and Saturated Steam costs; C_{Loss} are the costs associated with the heat transfer from the HRSG and C_{GTE}, C_{STE} are the costs associated with the work transfer produced from the Gas and Steam Turbines, all in [$/kW] units. Being the water, the electric energy and the NG costs, known values.

5. Results and discussions

The current irreversibility distribution into the study system was determined by the Exergy analysis, with a 0 % H_2S composition in the NG (Fig.3), being the greatest irreversibility (65 %) located in the gas turbine due to the inherent irreversibility in the combustion chamber, however, despite the value obtained of irreversibility, none changes were suggested in the combustion process due to the efficiency is an acceptable value in these power systems. Therefore, the whole system was analyzed and as a result of a sensibility analysis, two situations were considered: the increase of sulfur content in NG and the implementation of a new thermal device according the developed model by Rivera [18].

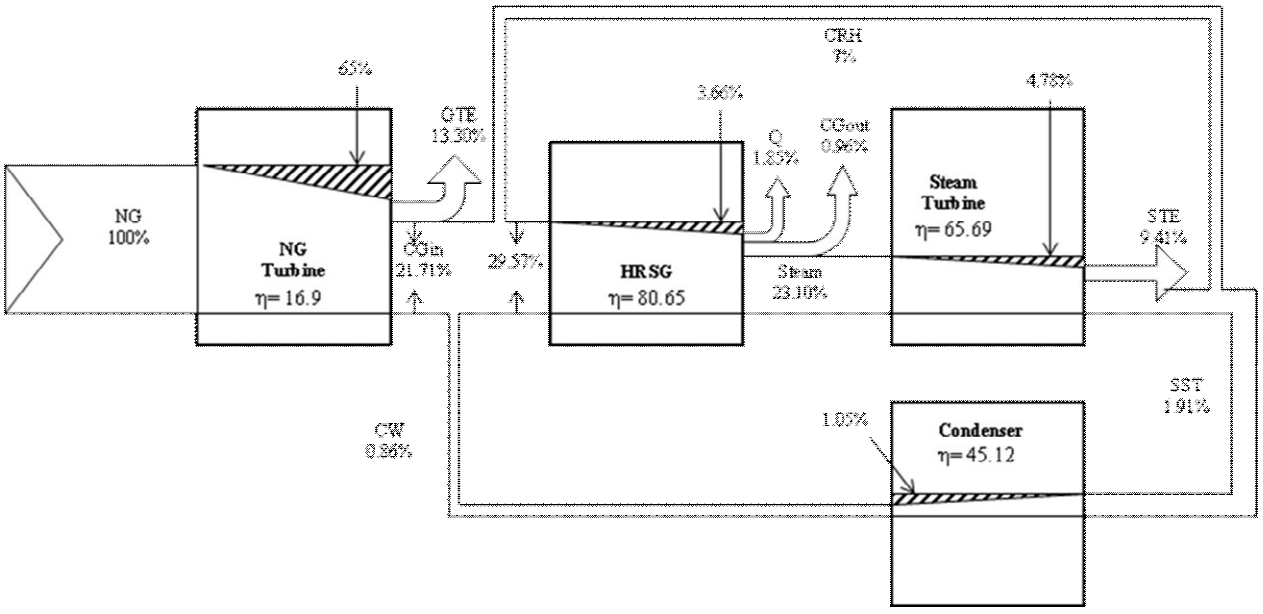

Fig.3. Grassman diagram of the combined cycle power plant without a heat transformer.

The corrosion model development was initiated through the determination of the acid dewpoint temperatures according the H_2S content as well as the H_2SO_4 deposition percentage expected according the operation conditions into the equipment analyzed.

The H_2S content in NG was related with the H_2SO_4 dew point temperature, an exponential function was obtained (15) with a R^2 of 0.9996. Being 72.61°C the temperature initial value at 0% H_2S (This is the current situacion in the existing CCPP analyzed) (Fig 4). .

$$T_R = 72.61\, y_{H2S}^{0.0637} \quad (15)$$

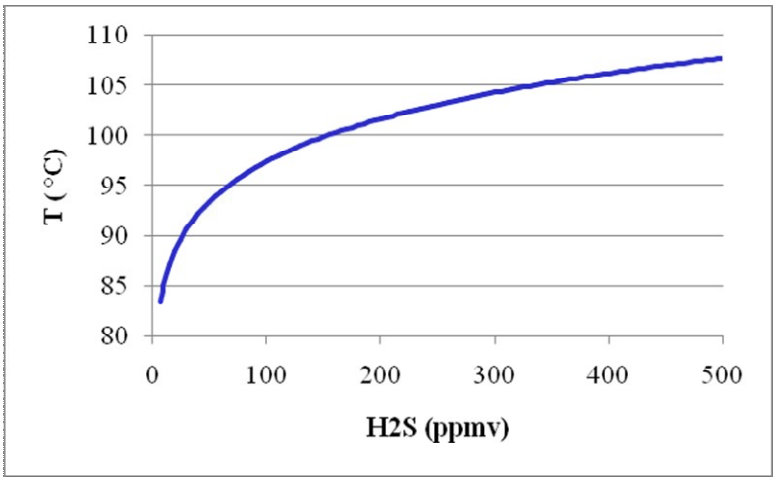

Fig. 4. Dewpoint temperature of H_2SO_4 from the content of H_2S in the NG.

Through the temperature profile obtained, inside the HRSG was the corrosion prone zone, specifically the economizer located in LP zone (Fig. 5) and starting from a H2S concentration of 25 ppm in NG, corrosion will occur in operational times with 65% in volume of H_2SO_4 in solution.

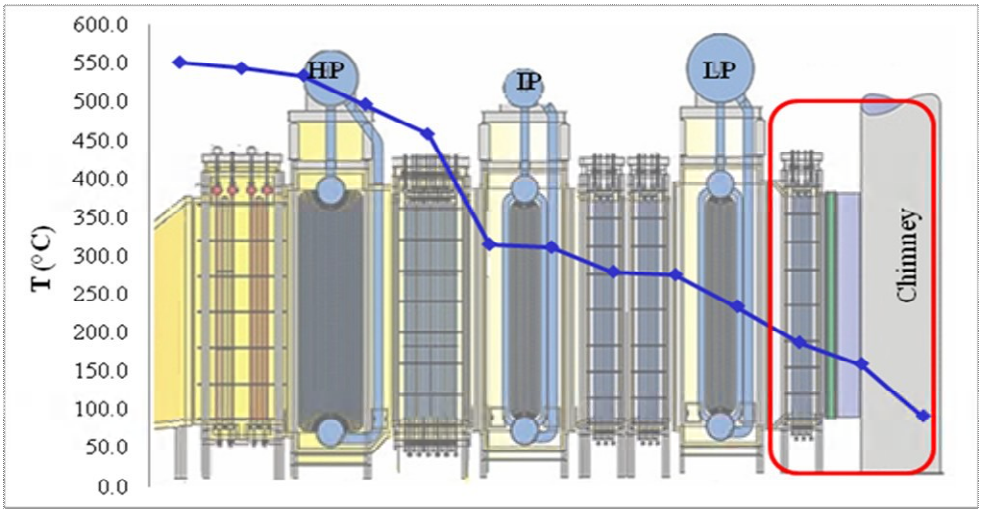

Fig. 5. Temperature profile of CG through the HRSG.

According to the equations proposed by Kiang, Okkes and Land [25,26,27] a model was obtained, considering the total number of tubes to be corroded (NT) being the two most important variables: water fed temperature in ° C to the HRSG (T_{CW}) and the concentration of H2S in percentage in GN (y_{H2S}), the best fit (16) was obtained using linear regression with a 0.999968 R^2. The model obtained allows determining the amount of corroded pipes, which will increase while the concentration is increasing and the temperature is decreasing (Fig 6). It is worth to note that the pipes of the HRSG are circular finned pipes, with an area of 46.5 m^2 and height of 18 m, the nominal diameter and thickness are 0.044 m and 0.002 m respectively, the construction material is SA178A.

$$NT = 987.75 + 884.60(y_{H2S}) - 1.08(T_{CW}) + 0.13(y_{H2S})(T_{CW}) \quad (16)$$

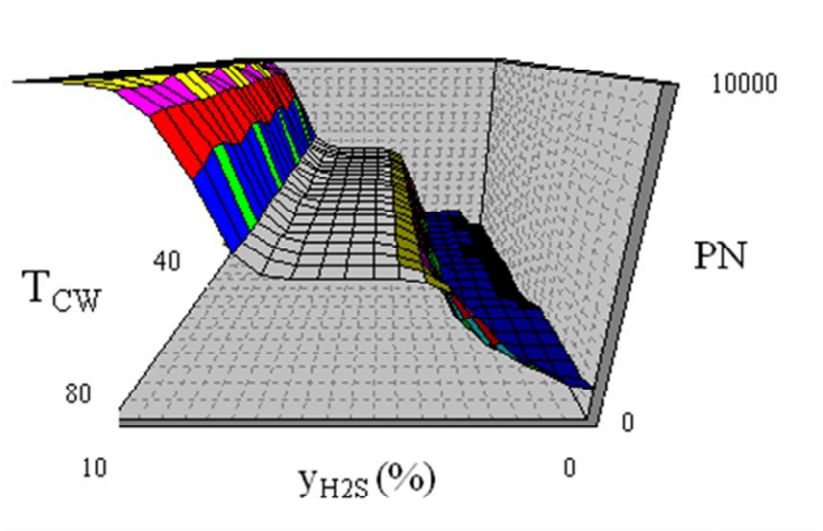

Fig.6. Response surface for corrosion in the HRSG.

By Thermoeconomic analysis, was possible to quantify the economic losses associated to the energy required to form the corrosion in situ (deposition stage) and the corrosion attack (H_2SO_4 formation). The models above developed allowed to establish a model, which predicts the irreversibility cost of the system in MUSD/year (C_I) considering two of the most important variables: the number of pipes to be entirely corroded (NP) and the H_2S composition in percentage in the NG (y_{H2S}), the behavior obtained shows two stages, the first one is related to the formation and deposition of condensed sulfuric acid, it refers to incipient corrosion in which the irreversibility and number of affected pipes remains constant, occurring corrosion in situ, in the second stage exists an linear increasing behavior of the irreversibility and the number of affected pipes Fig. 7. The model (17) was obtained from a linear regression with an R-Squared of 0.999 in the software NCSS 2007 ©, it is worth to note that according the H_2S current concentration in NG, there is not corrosion inside the HRSGs and the model obtained will allow to estimate the costs related to the pipes replacement according the sulfur in NG in operational times.

$$C_I = 92.70 + 19.39(y_{H2S}) - 2.18x10^{-2}(PN) + 5.40(y_{H2S})(PN) \quad (17)$$

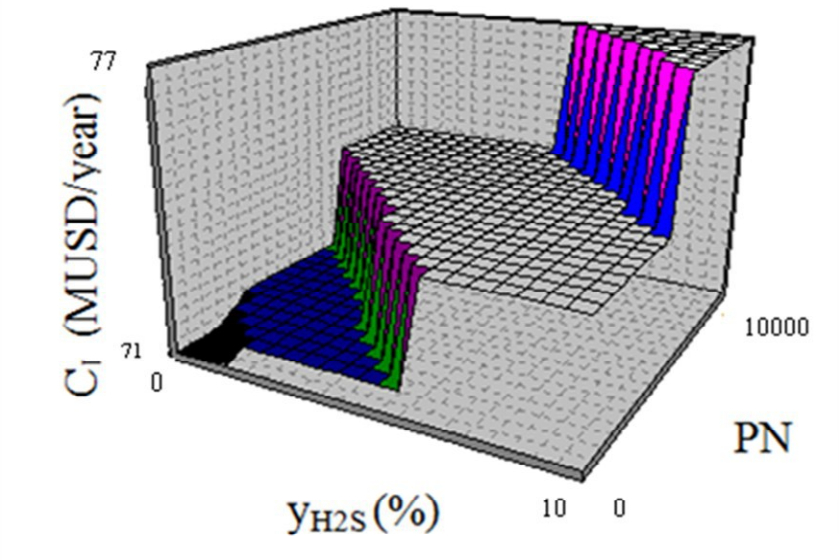

Fig.7. Thermoeconomic analysis of corrosion in the HRSG.

By using of pinch technology, the chimney exit, was selected as the best site for the implementation of a double absorption Heat Transformer (HT), to improve the plant efficiency, where the HT will use the residual energy of the CG at the chimneys exit (90 °C), preheating 91.5% of the total water fed by the condenser from 40 °C to 120 °C, being the CG output at 40°C. The Exergy analysis was developed and the Grassman diagrams with the HT implementation (Fig 8), the electric production from the ST was increased in 0.25% while the CG exergy at the exit was decreased in 0.47 %, when the HT was implemented. The whole system efficiency was slightly increased in 0.5 % in the H_2S scenarios considered with the HT. With the thermoeconomic analysis, it was possible to quantify the economic losses by CG thrown to the environment, which were reduced by the implementation of the HT being this the main advantage due to a 4.5% reduction in fossil fuel consumption, leading economic savings in order of 14,810,240.00 USD/year.

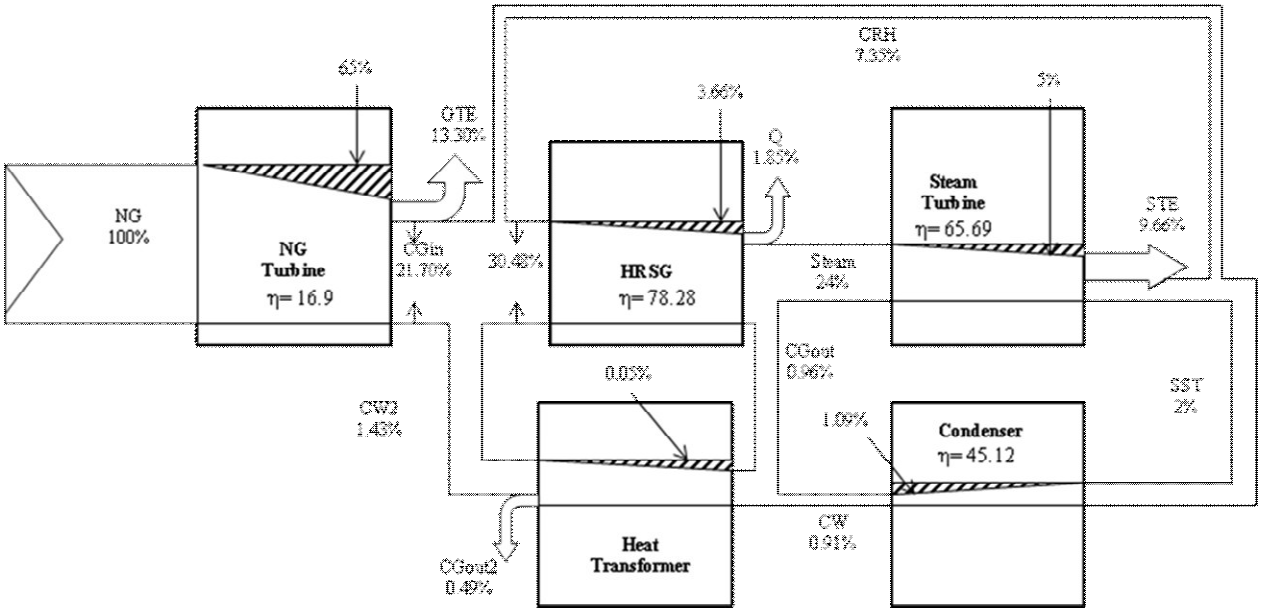

Fig.8. Grassman diagram of the combined cycle power plant with a heat transformer.

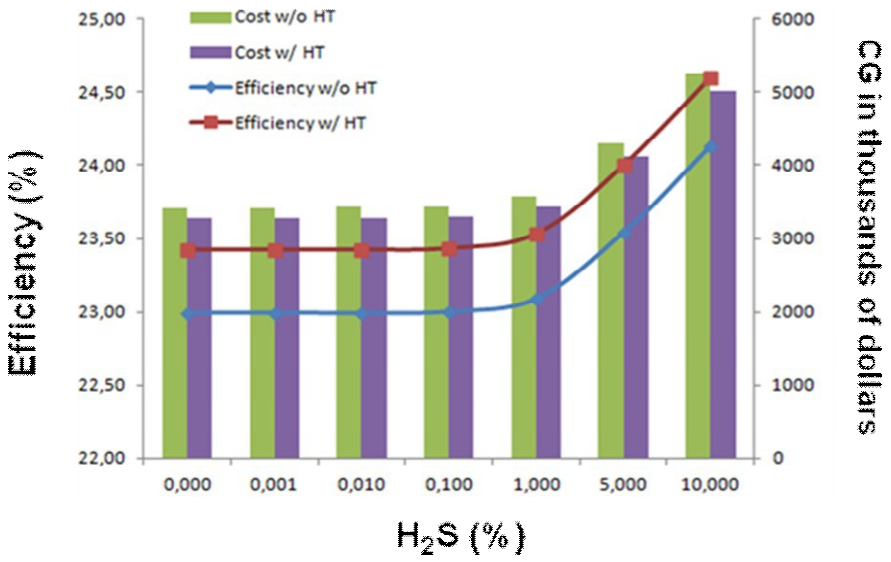

Fig.9. Exergetic efficiency and Cost of the CG with (w/HT) and without (w/o HT) the Heat Transformer.

6. Conclusions and recommendations

A predictive mathematical model was developed capable to predict the irreversibility costs in an existent CCPP, based on the quality of the NG and the corrosive effects inside the HRSGs, being the thermoeconomics a useful technique for real process with good results.

With the implementation of the HT savings about of $14,810,240.00 dollar/year savings will be expected, allowing suggest the use and implementation of this new thermal devices in industrial processes, since they improve the efficiency and decrease costs and irreversibility.

The study of complex systems demands a good methodology as the used in this research, is necessary to consider the use of different energy integration techniques to obtain the best operating conditions and to determine the major irreversibility within a system, considering several scenarios.

References

[1] J. Luz-Silveira, A. Beyene, E. Leal, J. Santana and D. Okada, Thermoeconomic analysis of a cogeneration system of a university campus. Applied thermal engineering 2002; 22: 1471-1483.
[2] A. Franco and C. Casarosa, Thermoeconomic evaluation of the feasibility of highly efficient combined cycle power plants. Elsevier Energy 2004; 29: 1963-1982.
[3] S. Sieniutycz, M. Kubiak, Dynamical energylimits in traditional and work-driven operations I. Heat-mechanical systems. Elsevier 2002; 45(14): 2995-30102.
[4] J.L. Silveira and C.E. Tuna, Thermoeconomic analysis method for optimization of combined heat and power systems—part II. *Progress in Energy and Combustion Science 2004; 30(6): 673-678.*
[5] El-Sayed, Y.M. The Thermoeconomics of Energy Conversions. Hungary, Elsevier 2003.
[6] N. Ferdelji, A. Galovic and Z. Guzovic, Exergyanalisis of a co-generation plant. Thermal science 2008; 12(4): 75-88.
[7] Sözen A., Arcaklioğlu E., Erisen A. and Akcayol M.A.,. Performance prediction of a vapour-comprenssion heat-pump. Applied Energy 2004.
[8] A. Cihan, O. Hacihafizoglu and K. Kahveci, Energy-exergy analysis and modernization suggestions for a combined-cycle power plant. International Journal Of Energy Research 2006; 30:115-126.
[9] E. Cortés, W. Rivera, Exegetic and exergoeconomic optimization of a cogeneration pulp and paper mill plant including the use of a heat transformer. Energy 2010; 35:1289-1299.
[10] B. Buecker, Corrision control in HRSGs. Power Engeniering 2011.
[11] R. Leferink, and W. Huijbregts, Nitrate stress corrosion cracking in Waste Heat recovery boilers. Anti-Corrosion Methods and Materials 2002; 49(2): 118-126.
[12] D.Stuart, Acid dewpoint temperature measurement and its use in estimating sulfur trioxide concentration,Analysis Division Symposium 2010; 3:12.
[13] S. Harris, Efficiency *vs*corrosion: sulphuric acid dewpoint monitors find the right balance, Modern Power Systems 2007.
[14] R. Tamayo, I. Lucio and P. Rodríguez, Corrosión en generadores de vapor en la refinería hermanos Díaz. TecnologiaQuimica 2003; 23(2).
[15] H. Tallermo, I. Klevtsov and A. Dedov, Corrosion of air preheater tubes of oil shale CFB boiler. Part II.Oil Shale, 2009; 26(1):13–18.

[16] P. Viklund, R. Pettersson, A. Hjo¨rnhede, P. Henderson and P. Sjo¨vall, Effect of sulphur containing additive on initial corrosion of superheater tubes in waste fired boiler.Corrosion Engineering, Science and Technology 2009; 44(3): 234-240.
[17] M. Mobin, A. U. Malik and M. Al-Hajri, Investigations on the Failure of Economizer Tubes in a High-Pressure Boiler. J Fail. Anal.andPreven. 2008; 8:69–74.
[18] R. Best,W. Rivera, M. J. Cardoso, R. J. Romero and F. A. Holland, Modelling of single-stage and advanced absortion heat transformers operating with the water/carrol mixture. Applied Thermal Engineering 1997; 17(11):1111-1112.
[19] Qin X., Chen L. and Sun F., (2007). Performance of real absorption heat-transformer with a generalized heat transfer law. Applied Thermal Engineering.
[20] Mostofizadeh Ch., and Kulick C., Use of a new type of heat transformer in process industry; Applied Thermal Engineering 1997.
[21] Rivera W., Best R., Baker J.N., Fletcher W.H., Heard C.L. and Holland F.A., Mobile Pilot-Plant for the Production of Enviromentally Clean Steam; AppliedThermal Engineering 1996.
[22] Gidner A., Jernqvist Å. and Aly G., An energy efficient evaporation process fortreating bleach plant effluents; Applied Thermal Engineering 1995.
[23] Tufano V., Heat recovery in distillation by means of absorption heat pumps andheat transformers; Applied Thermal Engineering1996.
[24] W. Rivera, J. Cerezo, R. Rivero, J. Cervantes and R. Best, Single stage and double absortion heat transformers used to recover energy in a distillation column of butane and pentane. International Journal of Energy Research 2003; 27(14):1279-1292.
[25] Yen HsiungKiang, Predicting dewpoints of gases. *Chemical Engineering* 1981; 88 (3): 127
[26] Okkes A. G., Get acid dewpoint of flue gas. Hydrocarbon Processing 1987; 7: 53-55.
[27] Land E., The theory of acid deposition and its application to the dewpoint meter. Journal of the Institute of Fuel 1977; June.

THERMOECONOMIC ANALYSIS AND OPTIMIZATION OF A HYBRID SOLAR-ELECTRIC HEATING IN A FLUIDIZED BED DRYER

Elizabeth Cortés Rodríguez[a], Felipe de Jesús Ojeda Cámara[a], Isaac Pilatowsky Figueroa[b]

[a]Facultad de Ingeniería Química. Universidad Autónoma de Yucatán, México.
[b]Centro de Investigación en Energía. Universidad Nacional Autónoma de México.

Abstract:

In the last decades, the technological development based in alternative energy sources has been increased. Hybrid systems are still an emerging technological option and it is expected this technology will continue to evolve in the future, so that it will have wider applicability and lower costs, therefore, the application of techniques such as exergy analysis and thermoeconomic are useful to determine the basic energy cost and the possible competitiveness of these systems.

In this research, a pilot prototype of a hybrid solar – electric system for air heating using a low temperature collector was developed as part of a redesign in the habanero chili drying, where a pre treatment by a solar dryer and a fluidized bed dryer were combined. Habanero chili is an important seasonal food product, so drying is so important for the Mexican producers. Exergy analysis was carried out to identify the operation conditions for the whole system and the potential savings, which can be made, such as, the air temperature and velocity (333 K and 6 m/s), while the product quality was preserved.

As a demo for the ECOS 2012 template, text has been uploaded from the Universal Declaration of Human Rights. Detailed info on paper preparation can be found from Section 2 on.

Whereas recognition of the inherent dignity and of the equal and inalienable rights of all members of the human family is the foundation of freedom, justice and peace in the world,

The results showed that the rates of heat and moisture transfer are related to the velocity and temperature of the drying air utilized. A reduction in the average drying time of 50% and in the energy usage of 77% in the fluidized bed dryer were obtained, with an exergy saving of 2.6 KW that represents 0.52 kg of natural gas per kg of fresh habanero chili with the final moisture required of 5%. A thermoeconomic model was developed for the whole system to determine the optimum operation conditions; also, it predicts the savings in energy cost terms at industrial level. An innovative sustainable and efficient process was developed in drying, one of the most demanding and wasteful of energy in the industrial sector.

Keywords:

Hybrid system, Solar Drying, Thermoeconomics, Optimization, Habanero chili

1. Introduction

1.1 Hybrid power systems

In the present times, a considerable interest has emerged in combined or ‘hybrid’ energy systems.

The term of hybrid energy systems refers to applications, where, different types of energy converters are involved for the same requirement.

These systems are usually isolated applications and at least one renewable energy source is included. The hybrid energy systems are used as an alternative operation form of conventional systems, which typically use energy from fossil fuels. The general definition refers to "Hybrid energy systems are a combination of two or more energy sources working in an integrated manner". Nowadays, there are several reasons to use hybrid systems. The main goal is the reduction in fossil fuel usage; also, there is an increase in the energy efficiency.

However, these systems are more expensive in installation and operation aspects, compared to common devices that use petroleum products like gasoline, coal or natural gas as fuels, when in the design stage, the cost of energy of a hybrid system is not considered, which, it is determined primarily by two factors: the cost of the system and the amount of useful energy that is produced. Other factors that are also important include the value of the energy, the cost of conventional energy, lifetime of the system, maintenance costs, and financial costs.

The cost of a hybrid energy system is first of all affected by the cost of the individual components that make up the system. Installation of the components and integrating them into a functioning unit will also contribute to the total cost. The cost of the useful energy will depend on the type of application and the nature of the resources available [1].

Therefore, when the equipment and energy available have a low or zero cost, an important economic advantage is been obtained by the hybrid systems over the conventional energy systems.

Solar energy stands out from other renewable energy, being more available, accessible and free, and it is considered such as one of the greatest technological potential areas. Conversion technologies from solar energy are focused into two main branches: solar-thermal and solar electric. The solar-electric technology is performed by photovoltaic cells to obtain electric power by using materials such as silicon and germanium. The solar-thermal technology is performed with solar collectors, which are devices designed to capture solar radiation, transform it into thermal energy to raise the temperature of a fluid for later use. Solar collectors are divided into two groups: without and with energy concentration, the first ones allow obtaining temperatures in the order of 100 ° C, while with the last ones, temperatures above of 100ºC are reached using methods of optical concentration. The materials used in the collectors have lower cost than solar cells and their applications are diverse, so, the solar-power tends to have more costly components, this in relation to copper used in solar-thermal technology also has solar thermal applications varied, so it has become a future field of study, within the most common applications, where solar collectors are used, are: the heating of water for domestic use, thermal conditioning of swimming pools, drying of leave tea and power generation.

In many practical applications, the drying process consumes a high amount of energy, due to high latent heat of water, and low energy efficiency of industrial dryers. Has been reported that industrial dryers consume on average 12% of the total energy used in manufacturing processes [2].In the drying industry the main energy sources to operate the dryers are fossil fuels, industrial oil, natural gas, electric Power, waste materials (biomass) and solar energy [3]. So, drying process is one of the most demanding and wasteful of energy in the industrial sector being an opportunity area to redesign through a hybrid system, due to the low temperature requirements.

In this research, a low temperature solar collector (flat plate) and a open sky dryer were chosen between the technologies available due to its low cost and the maximum daily solar radiation of 560 W/m^2 existing in Yucatan, Mexico, the first one was coupled with an electric system for air heating in a pilot fluidized bed dryer and due to the habanero chili is a hygroscopic material there are practical restrictions to be fluidizable (up 90% humidity) was necessary to include a solar drying pretreatment (open sky dryer) to dry habanero chili into the fluidized bed dryer. Being the useful energy determine by the exergy analysis and the best conditions of temperature, air velocity and exergetic efficiency was obtained by the thermoeconomic optimization according the primary energy cost to heat air. Therefore, a reduction in fossil fuel consumption was obtained through the redesign of a drying system with important economic savings.

1.2 Solar drying

A true sustainable development requires the efficient usage of energy and resources, so that, solar drying is a sustainable process. [4]

Solar drying is used in fruits and vegetables because good results are obtained, also it is efficient, providing a longer product life and preserving properties and vitamins.

Solar dryers can be classified into three groups, which are defined based on the power source to operate, such as

1. Solar dryers using environmental natural energy only.

2. Semi-artificial solar dryers with a fan and a motor that maintains continuous airflow on drying area.

3. Artificial Solar-assisted drying, they use electricity as backup energy power.

1.3 Fluidized bed dryer

Fluidized bed dryer is an emerging technology also is one of the most used in the industry because of it allows drying a wide variety of products like granular materials, cereals, polymers, chemical compounds, pharmaceutical compounds, fertilizers, crystalline products and minerals. Fluidized bed dryer can operate in batch and continuous form compared with other drying techniques, also it has great advantages, such as: high transfer of energy and matter between gas and solid particles is obtained, good and rapid mixing of solids, a control in the temperature within the bed is possible, the dry sample is handled in an easy way to dry and the construction is simple. [5]

1.4 Habanero Chili

Mexico has the highest genetic diversity of Capsicum and ranks second after China in terms of world production. Among the biological properties of the chilies, highlight the antioxidant activity, anticancer properties, antimicrobial properties, anti-inflammatory and analgesic property of the hot varieties, because of the capsaicin presence. [6]

The habanero chili (Capsicum chinense Jacq) is a crop of great economic importance for Mexican producers in the state of Yucatán (Fig.1). The major crop is located in the north of the state and contributes over 90% of the volume of state production, which is for local marketing and some is used in industry as raw material for hot sauce preparation. Local consumers prefer the orange fresh chili [7]. The condiments production is the main application of dehydrated habanero chili, as well as the extraction of capsaicin, which is the substance that gives the itch to chili, and may also have other uses, including the making of tear gas, insects or rodents repellents. Traditionally dehydration of habanero chili is done in ovens wood, built by the same producers. These furnaces are characterized by being built in a rudimentary form and consequently have many energy losses. The drying process can take several hours, requiring a constant supply of wood, causing the unwanted emissions of pollutants to the environment. [8] Industrial drying of habanero chili takes place in trays, the disadvantage of this equipment is the high maintenance and operation costs and the average drying time is 12 hours, this process is wasteful of energy to get a moisture content of 5% wet basis. That is the main reason to use a new technology to energy saving like a hybrid energy system. Using the solar energy to pre-treatment the habanero chili and the fluidized bed drying can take place using a system solar electric for air heating, the optimum energy use in the global process was obtained, according the environmental and climatic conditions existing in Yucatan, Mexico, where a monthly average number of solar hours per day, is between 6 and 8.5 hours, an average ambient temperature per day is over 30 ° C from March to October, with a critical period in the months of April, May and June with average maximum temperature of 37 ° C and maximum 40 ° C. extreme and there is an availability of solar radiation per hour in the summer period in May and June, with a maximum daily solar radiation of 560 W/m2 integrated [9].

Fig 1. Fresh habanero chili (Capsicum chinense Jacq) native of the Yucatan Peninsula.

2. Exergy Analysis and Thermoeconomic

A sustainable energy system is more efficient, safer and friendlier to the environment compared to a system that operates with conventional energy for local use, being the exergy analysis widely used for design, simulation and performance of these energy systems. [10]

The exergy analysis is applied to several system for studying the efficiency of photovoltaic cells and heaters, to increase efficiency [11]of the drying of porous materials, different studies have been developed to analyzed the energy and exergy flow and it was found that many variables need to be measured such as the ambient humidity, moisture and texture of the product and air heating temperature [12], particularly in the food area the energy applied to the drying process, is a greater amount than the needed to dry the product, so that, dryers use a great quantity of energy making the process inefficient.

The exergy flow in the drying process of food has been analyzed, concluding that the main variables are the total drying time, the amount of initial moisture of the product concerned as well as operation temperature of the drying air because of they are the most representative variables of the process [13-14].

In the solar area, several energy and exergy analysis have been conducted,[15] in an open solar dryer using mint leaves, exergy efficiencies were high, since the amount of useful energy was greater than in conventional drying, being the solar dryer temperatures used from 35℃ to 60 ° C, the best results were obtained with temperature of 60 ° C, and the drying time was 8 hours to dehydrate mint leaves from 84.7% to 10% of wet basis moisture, [16] another research establishing that the characteristics of the solar collector, such as the length of collector, its surface as well as, the operating conditions, are the main variables in the heat transfer process and exergy efficiencies were found due to the low value of usefulness of energy sun, because only a little part of it is captured [17]. Also the coupling of a solar collector to drying system has been analyzed and it increased the exergetic efficiency values of the process [18].

In general, an efficient drying process has been obtained through the use of low-temperature solar collectors, being the temperatures close to 60 ° C, with a better yield in energy use and a good quality dry product. [19]

From the economic point of view a solar pretreatment in a drying process offers many economical savings, also reduces the residence time in the final dryer, obtaining a process more efficient and sustainable. Energy utilization in this treatment type, increase the energetic and exergetic efficiency of drying process, this potential decreases with increasing temperature and drying time.[15-18]

Several analyses have been realized to the habanero chili to determine its content features like pungency, capsaicin, water content, antioxidant and nourishing properties. [7-8], also 50℃-70℃ has been established as the range of temperature operation for drying process, to avoid thermal degradation of product assuring final product quality. The drying kinetics of the habanero chili normally is realized in times greater than 20 hours in rotary dryers [20]. The process, reflects a high

operating cost because it is a continuous process where the amount to be treated is in function of the capacity of the dryer.

3. Methodology

The methodology used for thermoeconomic optimization of the hybrid solar-electric heating system in this research has been implemented previously. (Fig.2) [21]

1. Temperature, pressure and relative humidity of the surroundings were established as the reference dead state, which are To= 308.15 K, P = 1 bar, RH = 70% respectively. The fluidized bed dryer was selected as the control volume.

2. Mass and energy balances were developed for the control volume, to determine the exergy flow, efficiency and irreversibility.

3. A sensibility analysis was carried out in order to determine the possible causes of the irreversibility.

4. The global system was divided in two subsystems, mass and energy balances were obtained for two subsystems, which are as follow:

Subsystem 1: Open Sky Solar Dryer.

Subsystem 2: Fluidized Bed Dryer.

5. New exergy analyses were carried out again for each subsystem, to establish the modifications in the operating conditions. Once the previous steps were finished, a thermoeconomic analysis was carried out by means of optimization techniques solving the objective function.

As a result of this, the optimum operation conditions of the old and new equipment were determined, reducing the costs and increasing the global efficiency.

3.1. Mathematical Model

3.1.1 Initial system and hybrid system

For overall system, the exergy balance for an open system can be written as (1).

$$I = \sum (mE)_{in} - \sum (mE)_{out} + \sum W_{in} - \sum W_{out} + \sum \left(Q\left(1 - \frac{To}{T}\right)\right)_{in} - \sum \left(Q\left(1 - \frac{To}{T}\right)\right)_{out} \quad (1)$$

Where I is the irreversibility, the first two term in the right side to the equation are related with the mass flow entering $(mE)_{in}$ and leaving $(mE)_{out}$ the system. The following two terms are related to the work (Win, Wout) and the two last ones with the heat transfer to the system and from the system respectively (Q). Therefore making exergy balances in the main components of the system the following equations are obtained.

Applying the general equation to the drying column, considering that the main heat transfer is due to heat of evaporation between the solid and the drying air, and also, the heat transfer to the surroundings and the kinetic and potential energy are neglected, being the mass flow of dry air and the mass of dry material within the control volume, constants with respect to time, the following form (2) was obtained:

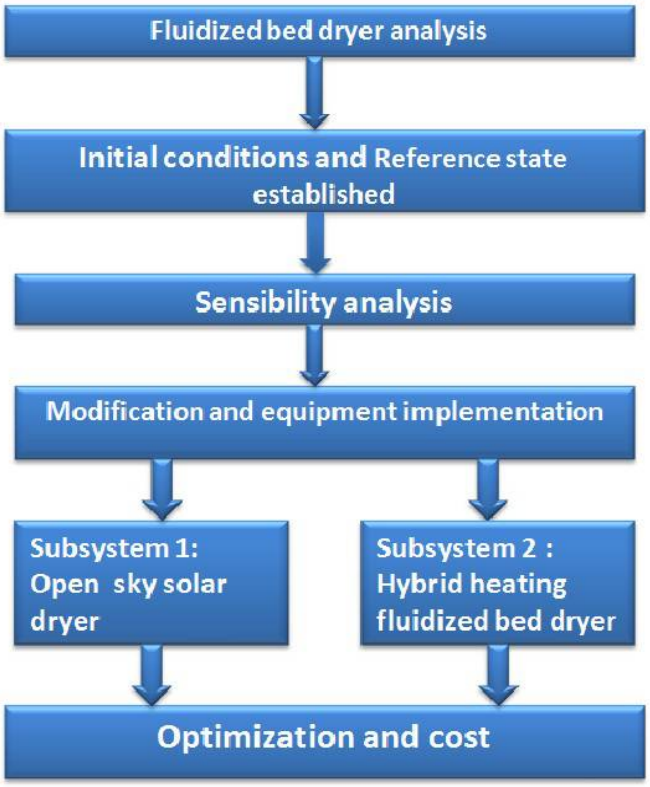

Fig. 2. - Methodology used for the exergetic optimization in the habanero chili drying process.

$$\frac{W_d(Ex_{m_1}-Ex_{m_2})}{\Delta t} = m_a(h_1-h_2)+\left(1-\frac{T_o}{T_m}\right)Q_{evap}-\left(1-\frac{T_o}{T_b}\right)Q_{loss}-T_o m_a(s_1-s_2)-T_o S_{gen} \quad (2)$$

Or the above equation could be expressed as follows (3):

$$\Delta Ex_{m1-2} = \Delta Ex_{air\,1-2}+Ex_{evap}-Ex_{loss}-Ex_D \quad (3)$$

Where is ΔEx_{m1-2} the exergy loss in the column of fluidized bed dryer, $\Delta Ex_{air\,1-2}$is the difference in exergy of the air at the inlet and outlet of the column, Ex_{evap} the exergy of evaporation of water in the system, Ex_{loss} the exergy loss in the environment and the Ex_D the exergy destroyed in the drying phenomenon is the irreversibility.

Being the generated energy obtained from an entropy balance for the same volume of control (4):

$$\frac{W_d(s_{m_1}-s_{m_2})}{\Delta t} = \frac{Q_{evap}}{T_m}+m_a(s_1-s_2)-\frac{Q_{loss}}{T_b}+S_{gen} \quad (4)$$

Where $\frac{W_d(s_{m_1}-s_{m_2})}{\Delta t}$is the change in entropy of the habanero chili during the drying time, Q_{evap} is the heat required to evaporate the excess moisture in the habanero chili, T_m is the temperature at which is conducting evaporation, $m_a(s_1-s_2)$ is the entropy change of the drying air from the entry and exit of the column respectively, Q_{loss} is the heat that is lost to the surroundings, T_b the temperature when heat loss occurs and S_{gen} is the entropy generated in the control volume.

The exergy efficiency (ψ) is the main parameter for yield measure is obtained from the exergy balance, and it is the ratio between the required evaporation exergy (Ex_{evap}) and the drying air exergy of the next to the column ($Ex_{air\,1}$) is expressed as (5):

$$\psi = \frac{Ex_{evap}}{\Delta Ex_{air\,1-2}} \quad (5)$$

For the hybrid system, the above equations were used to determine the exergetic efficiency of the drying column, considering pre-treatment of the solid in the open sky solar dryer, with the new conditions of the system. P = 1 bar, To = 308.15 K, T = 333.15 K and RH = 70%.

3.2 Thermoeconomics

Thermoeconomics provides the system designer or operator, crucial information to the design and operation of a cost effective system [20]. The cost balance for a system is as follows (6):

$$\sum_e \dot{C}_{e,k} + \dot{C}_{w,k} = \dot{C}_{q,k} + \sum_e \dot{C}_{i,k} + \dot{Z}_k \quad (6)$$

where: Ce,k and Ci,k are the average costs per unit of Exergy in US dollars per KWh ($USD/KWh), Cw,k and Cq,k are the costs associated with a work and heat transfer respectively and Zk is the cost rate associated with capital investment or operating and maintenance.

The thermoeconomic equation of studio system is as follows (7):

$$C_{i\text{-}a} + C_{w,e} + C_{f\text{-}ch} = C_{d\text{-}ch} + C_{o\text{-}a} + C_{irrev} \quad (7)$$

Where Ci-a andC o-a is the cost of inlet air and ouput air into the system respectively, C w,e is the cost associated with electric energy , C f-ch and C d-ch is the cost of fresh and dry chili and Cirrev is the irreversibility cost of system. Being the cost of Air, electric energy and fresh chilli known values.

4. Results

4.1 Initial system

The volume control and initial system was a pilot fluidized bed dryer operated with electric power. The system was characterized by the mass, energy and exergy balance. High power consumption and low energy and exergy efficiency were detected, due to the relationship among the transport phenomenon along the fluidized bed dryer column: momentum in the base to form the bed, heat and mass in the rest of the column to dry the wet solid (Fig 3).

These phenomenon were analyzed to identify the main low efficiency causes, such as:

1) The initial high moisture content of the solid at the dryer inlet (around 90%), affected the bed formation and the fluidization process by the solid wet loss due to the tendency to stick it on the column walls, also the velocity utilized was a greater value than the fluidization minimum velocity (11m/s instead of 2.4 m/s).

2) The operating temperature was T= 70°C, causing thermal degradation in the final product, also, there was a significant heat loss due to the lack of insulation along the column.

3) The mass transfer related to the postcritic period of moisture loss was not reached, because of the high velocity and temperature used even during long operation times, being the time an important factor during the post critic period.

Therefore, according the above analysis developed, velocity, temperature and time are the main variables associated to the transport phenomena developed in the fluidized bed dryer, they are related with the energy efficiency. The initial system had higher energetic efficiency with moisture content higher than 5% (Fig. 4) at 70°C during 7.5 hrs, being this process inefficient in energetic and economical aspects therefore (efficiency 4%), the scaling process was not possible to realize under this conditions, so the initial system was analyzed through the exergy analysis and thermoeconomic optimization to determine the useful energy and the real cost of the final product in base of the air heating system.

Through a technical-economic analysis, the use of solar technology of low cost such as a flat plane collector and an open sky dryer to redesign the initial system were chosen. The first one was

coupled to the electric air heating existent into the fluidized bed dryer (Fig 3) and the open solar dryer was the pretreatment for habanero chili before the fluidized bed dryer, avoiding the stick effect.

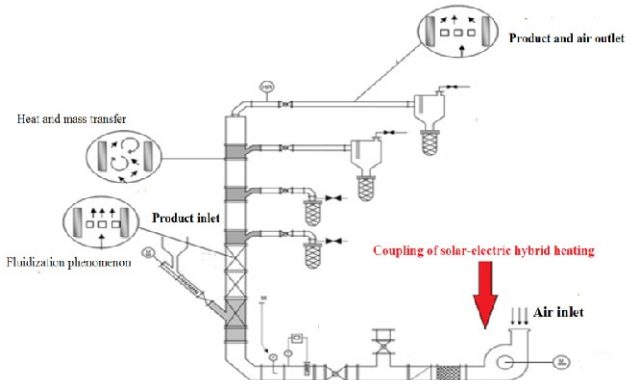

Fig.3. Initial Fluidized bed dryer.

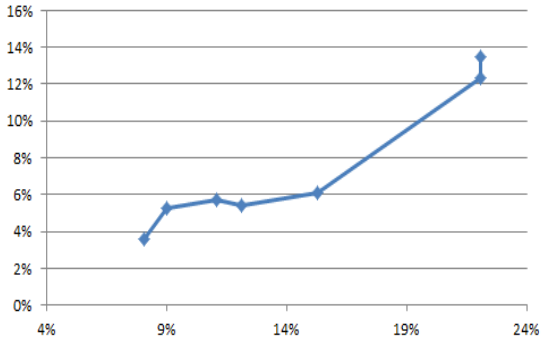

Fig.4. Energy efficiency of the initial operation conditions into the fluidized bed

4.2 Hybrid System Description

The system was conforming by 2 subsystems: an open sky solar dryer and a flat plane collector coupled a pilot fluidized bed dryer (Fig. 5)

Subsystem 1: Open sky solar dryer. The moisture content of the fresh chili was reduced from 90% to 30% in 6.8 hrs, this process required the major quantity of energy 70% (Table 1) in the drying process due to the biggest water lost takes place. (Fig.5a). this subsystem avoided the stick effect and reduced the time and electric energy used in the fluidized bed dryer.

Subsystem 2:.A flat plane solar collector coupled to a fluidized bed dryer (Fig. 5b): In this system the solid got into the fluidized bed dryer which has an electric blower, the leaving air from the blower exchanged heat with the hot water from the storage vessel from the flat plane collector, to obtain the required temperature (T=60°C) then, the drying process was completed and the final product had the moisture required of 5% in 3.5 hrs requiring 30% (Table 1) of the drying energy.

The initial drying process was developed at 70°C with thermal degradation of the product and great heat losses. The energy analysis indicated the energy efficiency was almost the same value at 50 and 60 °C (4.80 and 4.87% respectively) and considering the efficiency of the solar flat plane collector (80%) according to maximum daily solar radiation of 560 W/m^2 integrated existing in Yucatan, the optimum air temperature was established at 60°C. Therefore, improvements in the energy efficiency (11%) and in the drying time (3.5 hrs) into the fluidized bed dryer were obtained (Table 1).

Fig 5a. Open sky solar dryer

Fig.5b. Fluidized bed dryer

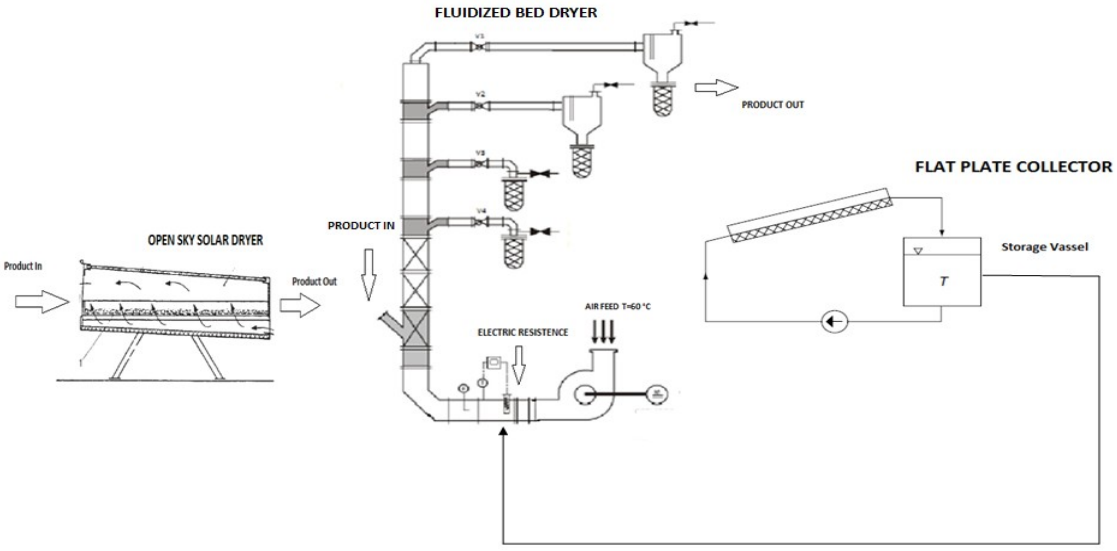

Fig.5. Hybrid drying process.

Table 1: Heat streams involved in drying process.

Process	Qinlet**(kJ)**	Qevap **(KJ)**	**Qloss (KJ)**	**Time(h)**	**η** Efficiency	Energy input **(%)**
Open Sky Solar Dryer	21,092.70	2137.173	18,955.53	6.8	10.13%	70
Solar - Electric Fluidized Bed Dryer	9,187.89	100.9553	9,086.93	3.5	11%	30
ALL PROCESS	30,280.59	2238.1283	28,042.46	10.3	7%	100

4.3 Exergy Analysis

The initial and hybrid systems were analyzed through exergy analysis, to determine the useful energy (exergy) into the process, the real efficiency and the cost of the hybrid system. The results obtained of the energy analysis indicated that there was an increase in the process efficiency from 4 to 7%, also in the drying time (10.3 hrs.), but the heat loss is 92% (Q_{loss}) of the heat total, according the exergy analysis, the hybrid system reduced the input exergy around of 35%, (2.6 kW) that represents 0.52 kg of natural gas per kg of fresh habanero chili with the final moisture required of 5%.

The irreversibility in the hybrid system was reduced from 16% (3.47kW Fig 6a) to 2% (0.31 kW Fig 6b) respectively. Therefore, despite the fact the hybrid system increased the useful energy and reduced the irreversibility, the drying time was increased from 7.5 to 10.3 hrs (Fig 7), despite the fact of the drying time into the fluidized bed dryer was reduced 50%, the cost of the hybrid system need to be determined by the thermoeconomic analysis to establish the economic feasibility of the hybrid system.

(a) Initial system *(b) Final system*

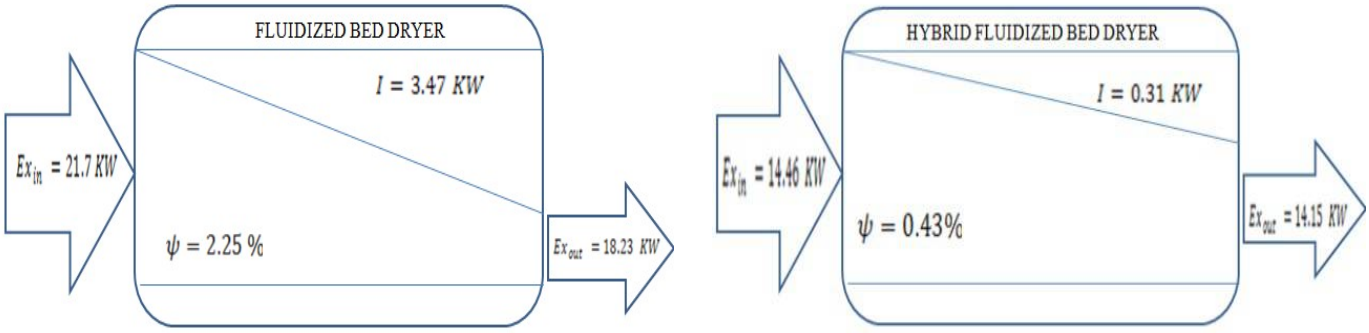

Fig. 6.Grassman Diagrams for the initial (a) and hybrid system(b).

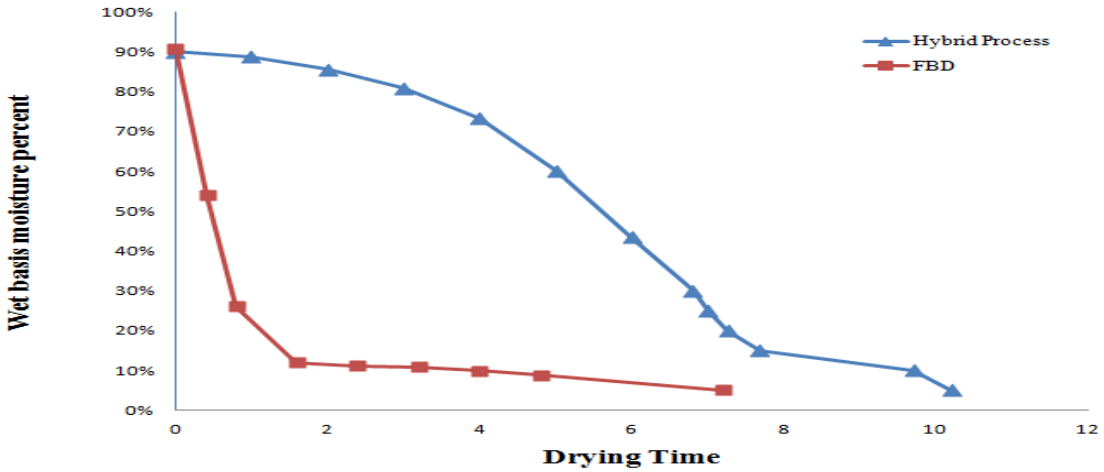

Fig.7.Drying kinetics of habanero chili before and after the process redesign Hybrid Process (FBD).

4.4Thermoeconomic model

The real cost of the hybrid system developed was determined by the thermoeconomic model considering the main variables involved in the process: temperature, exergy cost of the air drying, time and exergetic efficiency.

The exergetic efficiency depends on the air cost and the temperature, through a canonical analysis considering the drying temperature from 50 to 70°C, maximum costs were obtained at the highest temperature (70°C) and lowest exergetic efficiency in the hybrid drying process. (Fig.8). The exergy efficiency and cost obtained between 50 and 60°C (black zone in Fig 8) are very close values, then the drying temperature of 60°C was selected to realize the drying into the fluidized bed dryer .

Thermoeconomic analysis was developed to determine the energy cost of the hybrid system, considering the environmental temperature air and the drying time into the fluidized bed dryer, due to in this equipment there was an electric consumption. The results obtained indicated that the drying time used in the fluidized bed dryer process (3.5 hours) had the biggest exergetic efficiency of 0.5% with a drying cost of 0.33 $ USD / KWh of heating (Fig. 9).

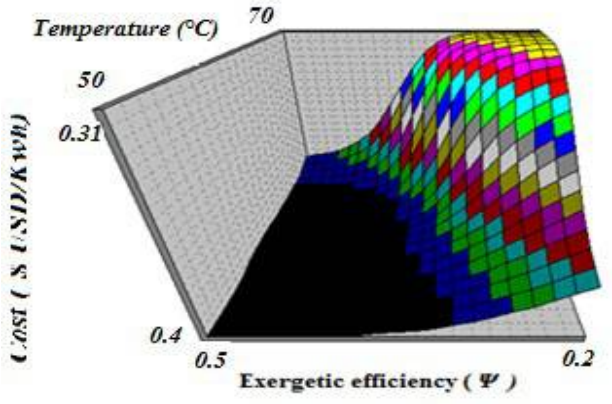

Fig.8. Canonical analysis of the hybrid system.

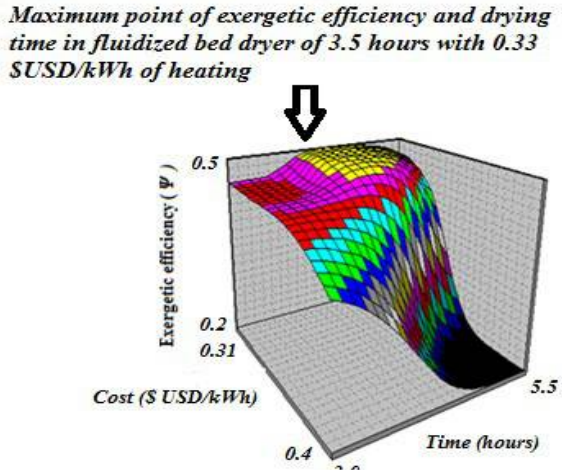

Fig.9.Thermoeconomic results of the drying process developed.

The air drying cost (C_{air}) in the fluidized bed dryer, was obtained by the thermoeconomic model in function of temperature air feed and the exergetic efficiency of the system with the software NCSS2000 © with a lineal behavior with a $R^2 = 0.9999$.

$$C_{Air} = 6.567 - 1.0628x10^{-2}(T) + 3.907\ (Efi) \quad (8)$$

Where $\mathbf{C_{Air}}$ is the air drying cost into the hybrid process in $ USD/KWh, ***T*** is the drying air temperature at °C and ***Efi*** is the global efficiency of the drying process.

The thermoeconomic model obtained was useful to establish the real cost of heating of the hybrid system to establish the dried habanero chili cost obtained by this process, being the cost reduced in 50% respect the commercial technology (Table 2).

Therefore, the hybrid system is a feasible and economic option for redesign the habanero chili drying at industrial scale.

Table 2.Comparison of different drying process.

Cost per kg of dried chili ($ USD)	Drying time (hours)	Energy source	Type of process	Final moisture of dried chili (%)
15.4	12	Gas natural	Comercial	8
40.4	7.5	Electric Power	Fluidized bed dryer	5
7.7	10.3	Solar Electric	Hybrid process	5

5. Conclusions

The redesign process, distributes the total of the energy usage, being 70% of the energy used in the pretreatment of open sky solar dryer while 30% was used in the fluidized bed dryer. Being obtained an exergy saving of 2.6 KW that represents 0.52 kg of natural gas per kg of fresh habanero chili.

Habanero chili drying by a solar electric hybrid system is a real alternative to dehydrate this product, being comparable with other industrial dryers such as forced convection heat dryer and tray industrial dryer, improving the overall drying time, obtaining an efficient energy use and cost saving operation.

The Hybrid system developed is a feasible and economic option for redesign the habanero chilli drying at industrial scale. A new technology has been developed

The energy cost and the advantages of new technologies like hybrid sistems only can be determined by the exergy analysis and thermoeconomic optimization in a real and feasible way.

Acknowledgements

Special thanks to Secretaría de Educación Pública (SEP) through the Programa para el mejoramiento del profesorado (PROMEP) for funding this project with reference numbers UADY-CA-30.

Nomenclature

Efi	Overall efficiency of the drying process in function of the drying air cost.
Ex_{evap}	Exergy due to evaporation of water in the solid, kW
Ex_{loss}	Exergy loss to the environment, kW
Ex_D	Exergy destroyed in the drying phenomenon, kW
h_1 , h_2	Enthalpy of the air inlet and outlet air of fluidized bed dryer, kJ/kg
I	Rate of Irreversibility, kW
m_a	Air stream fed to the fluidized bed dryer, kg/s
Q	Heat involved in the process, kJ
Q_{evap}	Heat required to evaporate the excess moisture in the habanero chili , kJ/s.
S_{gen}	Entropy generated into the column, kJ/K
S_1, S_2	Entropy of the air inlet and outlet air of fluidized bed dryer, kJ/(kg K)
Tm.To,Tb	Drying temperature , Reference state temperature ,Evaporation temperature, K
T	The temperature of drying ire presented in the thermoeconomic model, °C
W_{in}, W_{out}	Work done inside and outside the system , kg/s
Greek symbols	
Ψ	Exergetic efficiency of the drying process
η	Energetic efficiency of the drying process
ΔEx_{m1-2}	Rate of exergy loss in the fluidized bed dryer
ΔEx_{air1-2}	Exergy difference between the air outlet and inlet to fluidized bed dryer
Subscripts and superscripts	
$C_{e,k}$, $C_{i,k}$	The average costs per unit of Exergy , $USD/(kWh)
$C_{w,k}$	Cost associated with work in the system for thermoeconomic equation , $ USD
$C_{q,k}$	Cost associated with work in the system for thermoeconomic equation, $USD
C_{i-a} C_{o-a}	The cost of inlet and output air for the drying system ,$USD
$C_{w,e}$	The cost associated with electric energy in system, $USD
C_{f-ch}	The cost of fresh chili, $USD.
C_{d-ch}	The cost of dry chili in the process at the end of the process, $USD

C_{irrev}	The cost of system irreversibility, $USD / (kWh)
$(mE)_{in}$	Mass flow input system, kg/s
$(mE)_{out}$	Mass flow output system,kg/s
$\frac{W_d(s_{m1}-s_{m2})}{\Delta t}$	Entropy of the habanero chili during the drying time, kJ/K
Z_k	The cost for operating and maintenance of the fluidized bed dryer,$USD

References

[1] Cutler J. Cleveland, Encyclopedia of energy. Boston, USA: Elsevier; 2004

[2] Ibrahim Dincer, Marc A. Rosen, Energy, environment and sustainable development. Ontario, Canada: Elsevier; 2007.

[3] A. S. Mujumdar, Handbook of industrial drying USA: CRC Press (2007).

[4] Ibrahim Dincer, Marc A. Rosen, , Energy, environment and sustainable development. Ontario, Canada: Elsevier; 2007.

[5] M. Özbey , M.S Söylemez., Effect of swirling flow on fluidized bed drying of wheat grains , *Energy Conversion and Management* 2005, (46) 1495–1512.

[6] Rubio-Pino J.L , Iloki-Assanga , S.B , et all , (2010), Caracterización química, nutrimental y evaluación de la actividad biológica in vitro de chiles habaneros (Capsicum Chinense), chiltepín (Capsicum anuum var.Glabriusculum) , morrón verde y rojo (Capsicum annum L).VII Congreso del Noreste y III Nacional de Ciencias Alimentarias y Biotecnología

[7] José Jorge Gerardo Trujillo-Aguirre, Omar Gutiérrez-Alonzo y Capullo del Rocío Pérez Llanes. (2003). Características Morfológicas de flor y fruto de nuevo genotipos de chile habanero (Capsicum Chinense Jacq.) colectados en Yucatán México. Breeding and Genetic Resources

[8] R. Hernández, Martínez, D. Quinto, D. Cuevas, O. Acosta, J. Aguilar (2010) .Secado de chile habanero con energía solar. Revista Iberoamericana de Tecnología Postcosecha, (10)120-127.

[9] Weather Station of Facultad de Ingeniería, Universidad Autónoma de Yucatán [consulted 20.10.11].

[10] S. Nayak, and G. N. Tiwari, Energy and exergy analysis of photovoltaic thermal integrated with a solar greenhouse, *Energy and Buildings* 2008; 40(11):2015-2021.

[11] A. Hepbasli , key review on exergetic analysis and assessment of renewable energy resources for sustainable future, *Renewable & Sustainable Energy Reviews* 2008*;* 12(3):593-661.

[12] R. Prommas, P. Rattanadecho, and D. Cholaseuk, Energy and exergy analyses in drying process of porous media using hot air, *International Communications in Heat and Mass Transfer* 2010*;* 37(4):372-378.

[13] O.Corzo , N.Bracho , A.Vazquez , A.Pereira , Energy and Exergy analyses of a thin layer drying of coroba slices, *Journal Of Food Engineering* 2007; 86(2): 151-161.

[14] E. Kavar Akpinar, A. Midilli, and Y. Bicer, Energy and exergy of potato drying process via cyclone type dryer, *Energy Conversion and Management* 2005*;* 46(15-16):2530-2552.

[15] E.Kavar Akpinar, Drying of mint leaves in a solar dryer and under open sun: Modelling performance analyses, *Energy Conversion and Management* 2010*; 51*(1):2407-2418

[16] S.Farahat, F.Sarhaddi, H.Ajam,Exergetic optimization of flat plate solar collectors ,*Renewable Energy* 2009,32(1):1169-1174

[17] Jorge Facao and Armando C.Olivera, Analysis of a plate heat pipe solar collector, *International Conference on Sustainable Energy Technologies 2004*.

[18] S. Sami, N. Etesami, and A. Rahimi, Energy and exergy analysis of an indirect solar cabinet dryer based on mathematical modeling results, *Energy* 2011*;* 36(5):2847-2855.

[19] B. K. Bala, M. A. Morshed and M. F. Rahman, Solar drying of mushroom using solar tunnel dryer, *International Solar Food Processing Conference 2009*.

[20] S.Kaleemullah, R.Kailappan, Drying Kinetics of Red Chilies in a Rotary Dryer, *Biosystems Engineering* 2005; 92(1):15-23.

[21] E.Cortés, W.Rivera, Exergetic and exergoeconomic optimization of a cogeneration pulp and paper mill plant including the use of a heat transformer, *Energy*. Elsevier 2009; 35(3): 1289-1299.

Thermoeconomic approach for the analysis of low temperature district heating systems

Verda Vittorio[a] and Albana Kona[b]

[a] *Politecnico di Torino, Torino, Italy, vittorio.verda@polito.it*
[b] *Politecnico di Torino, Torino, Italy, albana.kona@polito.it*

Abstract:

In this paper a thermoeconomic analysis of district heating systems is performed. The analysis aims at comparing possible options to supply heat to the users, using low temperature networks. Thermoeconomic analysis consists a powerful tool to perform such analysis as it allows one to evaluate the possible options in terms of primary energy cost or economic costs. In the first case, the use of exergy as the quantity that is transported along the network makes it possible to properly consider the various qualities of energy that are used to supply heat to the network and to distribute it to the users. In the case of economic cost, the various cost contributions are considered: investment cost, cost of heat supplied to the network, pumping cost. A different cost can be calculated for the various users depending on their position and characteristics of the heating devices. This is a useful information in order to compare possible options for supply them heat.

Keywords:

District heating, low temperature heating, thermoeconomic analysis

1. Introduction

District heating is a rational and reliable way to supply heat to multiple users from a unique or few centralized thermal plants. Heat is mainly produced with systems as combined heat and power plants, biomass boilers and industrial processes heat recovery systems, integrated with high efficiency boilers to cover peak loads. One of the most interesting contributions of district heating networks to future energy systems is the opportunity to integrate heat productions from renewables [1].

The use of renewables in district heating may involve reduction of the operating temperatures. This idea is behind the concept of “low temperature district heating”. Low temperature district heating is typically characterized by supply temperatures between 75°C and 50 °C (even if lower temperatures may be considered) and return temperatures between 40 °C and 20 °C [2,3]. This allows the direct use of renewable energy sources as solar [4] and geothermal [5] or in combination with large-scale heat storages [6]. In addition, there is big potential for utilization of waste heat from cogeneration plants, waste-to-energy plants, heat pumps and industrial processes [7,8]. Low temperature networks allow one to increase the amount of heat recovery from exhausts and also to recover heat from low temperature processes.

The main issue on this kind of systems is referred to investment and operating costs. As any other system it needs to be more convenient than the alternatives. In addition, its energy sustainability should be carefully analyzed in order to ensure that the total primary energy required to supply heat to the users is smaller than possible alternatives.

To build district heating networks several years are usually necessary, with large expenses and discomfort to the community. For this reason, the system must be designed in its final structure, with few possibilities of making changes. In particular it is necessary to determine the possible users to be connected, the topology and the pipe diameter of each branch. Such a problem can be solved as a synthesis problem, i.e. an optimization where the system structure is not defined a priori

[9]. In this way it is possible to define the optimal network that minimize (or maximize) an objective function, such as the minimum cost of heat or the maximum benefit.

This paper deals with the problem of district heating network (DHN) synthesis, i.e the search for the optimal configuration of the network, which consists in the identification of users that should be connected to the network and those to which heat should be supplied through alternative systems. In particular, a low temperature district heating network fed with solar energy is considered. The analysis is conducted considering a supply temperature between 55 °C and 40 °C, while the return temperature is assumed 25 °C or 20 °C. Groundwater heat pumps run with solar photovoltaic are considered as the possible alternative, in order to obtain 100% renewable configurations.

A thermoeconomic approach [10] is applied to a small network by considering both monetary and energy cost as the objective functions in the optimization.

2. Thermoeconomic analysis

The optimal synthesis of energy systems is here approached by starting with a superstructure, which is a DHN involving all of the possible zones and thus all the users. The use of a superstructure is the most common approach to synthesis problems (see for example [11]). Once the superstructure is built, the synthesis problem can be solved as an optimization problem, provided that particular values of the variables associated with the components or with the internal flows correspond to the condition of absence of that component or flow. In the case of DHN when the optimal mass flow rate in a pipe is zero means that the pipe must be eliminated from the structure.

The procedure starts with the evaluation of the objective function in the initial configuration, corresponding to all the users connected with the network. The network is then reduced, through successive elimination of the users characterized by high costs and the corresponding pipes connecting these users with the rest of the network. The selection of the user to be disconnected to the network is operated using a probabilistic approach. The probability of a user to be disconnected increases with increasing unit cost of heat supplied to that user. As this procedure is not deterministic, it should be repeated several times in order to increase the possibility to find the true optimal configuration. The procedure is stopped when all the users are disconnected.

The details of the selected procedure are shown by considering the average primary energy consumption of heat provided to the users as the objective function to be minimized. This quantity is calculated as the exergetic unit cost of heat. The first step consists then in calculating the productive function:

$$\bar{c} = \frac{C_{tot}}{Q_u} = \frac{C_{net} + c_F \cdot Q_F + c_p \cdot L_p + c_a \cdot Q_a}{Q_u} \qquad (1)$$

The cost of network C_{net} is the amount of primary energy required to produce and install the insulated pipes. Components as heat exchangers, pumps, valves have been neglected in the analysis. Primary energy associated with excavation, installation and paving restoration has been also considered. C_{net} is an annual cost. Year is the best unit time to be used for thermoeconomic analysis of such system due to the production variation depending on the average external temperature and during the day. Cost functions used in this analysis are discussed in the annex.

The energy unit cost of heat has been calculated considering heat production from solar collectors only. The following expression for collector efficiency has been considered [12]:

$$\eta = \eta_0 - a_1 \frac{\Delta T}{I_t} - a_2 \frac{\Delta T^2}{I_t} \qquad (2)$$

ΔT is the difference between the average temperature of the fluid inside the collectors and the air temperature and I_t is the total radiation. Ambient temperature and solar radiation of Turin have been considered (see Table 1).

Table 1. Solar radiation and temperature for Turin

	Jan	Feb	Mar	Apr	May	Jun	Jul	Aug	Sep	Oct	Nov	Dec
I_t (MJ/month/m^2)	155	218.4	378.2	340	607.6	645	728.5	573.5	405	288.3	165	145.7
T (°C)	1.7	5.3	8.5	15.7	19.1	20.5	21.3	24	20.3	13.2	7.7	4.1

In the case of the available collectors: η_0 =0.718, a_1=0.974 W/m^{2}K, a_2 =0.004 W/m^{2}K^2. Excess heat produced when the heating demand is small is considered to be stored in a seasonal storage system. Efficiency is considered to be linearly dependent on the difference between the internal temperature and ground temperature. Efficiency is assumed 0.9 when the internal temperature is 90 °C and ground temperature is 13 °C [13].

Heat request by the users Q_u and heat supplied by the thermal plant Q_F differ because of heat losses Q_L. Heat losses have been calculated by considering each branch.

$$Q_L = \pi \cdot D \cdot L \cdot k \cdot \left(\overline{T} - T_g\right) \cdot t \qquad (3)$$

where k is the overall heat transfer coefficient and $\overline{T}$ is the average temperature between outgoing an return network, T_g is the ground temperature an t is time period (a year).

Last term on numerator of equation (1) accounts for the primary energy association with electricity required for pumping, being c_P the exergetic unit cost of electricity and L_p is the annual electricity consumption, calculated as:

$$L_p = \frac{1}{\eta_p} \int_{year} G \cdot v \cdot \Delta p \cdot dt \qquad (4)$$

where η_p is the average pump efficiency, G is the water mass flow rate, v is the water specific volume (constant) and Δp the total pressure losses due to pipe friction and localized resistances.

The last term on the right hand side of equation (1) is the cost of heat supplied to the users fed with alternative systems. This is obtained as the product of the exergetic unit cost of the heat produced with these systems (c_a) times the annual heat supplied to the users not connected with the district heating (Q_a). In the initial network configuration this term is zero.

Terms in equation (1) depend on the thermal load supplied by the network and on its extension. The possible area to be heated by the thermal plant must be chosen. This area can be divided into zones, each including one or more buildings. The number of zones should be selected as trade-off between result accuracy (large number of zones) and time required for design and calculation (small number of zones). For each zone, the total volume of buildings is determined. The thermal barycentre can be easily located in the area by considering the position of buildings and their respective volume (the geometric barycentre can be used as well, especially when the building structure is sufficiently regular). At this point, the network connecting the thermal plant with TBs can be traced.

The annual heat load of each single zone Q_z is calculated by considering, for the whole heating season, the daily difference between the internal temperature (20 °C) and the external temperature, the average thermal transmittance of buildings (through walls, windows, floor, etc.), the number of daily heating hours (hh). The thermal transmittance of building can be multiplied for a shape factor defined as the ratio of external surface and building volume; this quantity, here indicated as r, expresses the volumetric heat losses per unit temperature difference. This value has been measured for several buildings; an average value of 0.9 W/(m^{3}K) can be assumed. The annual heat load for a zone, in kWh, is then calculated as

$$Q_z = \frac{r \cdot DTD \cdot hh \cdot V_z}{1000} \qquad (5)$$

where V_z is the total volume of buildings in the zone and DTD is the summation of daily difference between internal and external temperature, calculated for the whole heating season (degree day). The number of daily heating hours is considered to be the same as for buildings with individual

heating system, which is established by law, depending on DTD. In the specific case analyzed in this paper, this quantity is about 2730 °C, being the heating season from the middle of October to the middle of April, while the number of heating hours is 12 per day.

The total heat load is calculated as summation of the contributions of all zones. The network operates for longer time than specified, mainly due to four causes: 1) non contemporary request by the users, 2) presence of particular users, like hospitals, that requires heat for more than 14 hours per day and for an extended period, 3) domestic water demand, 4) presence of users that requires heat in summer for air conditioning through absorption chillers. For all these reason, the total load calculated through equation (5) has been considered as spread on 18 hours per day in the seasonal heating, moreover the thermal flow outside this period has been assumed non null, but calculated on the basis of the thermal losses.

The cost of the network is calculated by considering each single branch and depends on its diameter. Internal diameter of pipes is calculated by first determining the mass flow rate in each branch. The mass flow rate is imposed by the thermal requirement of each user downstream that branch:

$$\Phi = G \cdot (h_o - h_r) \qquad (6)$$

where Φ is the thermal flow provided to the users (the maximum load is considered in design), G the water mass flow rate, h_0 and h_r the enthalpies of fluid feeding and returning from the users. The diameter is determined by imposing the maximum velocity v_{max} allowed in the pipes. This value is mainly defined on the basis of economic criterion, since friction losses and thus pumping cost depend on the square of velocity. On the other hand, a too low velocity would determine a large pipe diameter, thus high investment costs. In this analysis a value of 1.5 m/s is considered. The water mass flow rate G is expressed as:

$$G = \rho \frac{\pi D_{int}^{\ 2}}{4} v_{max} \qquad (7)$$

A thermoeconomic analysis is then implemented for the designed network, where all the possible users are connected. In particular, a useful approach that can be adopted for this purpose is that proposed by Valero and co-workers in the eighties [14, 15]. One of its main characteristics is the matrix based approach, in particular the use of incidence matrix for expressing the equation of cost conservation. The only auxiliary equation to be applied is the assignment of the same unit cost to the flow exiting each bifurcation [16].

The unit cost of a flow *c* can then be calculated, by dividing the costs for the corresponding exergy flow:

$$c = \frac{B}{\Psi} \cdot 3600 \qquad (8)$$

Where B is the exergetic cost of a general flow and Ψ its exergy.

At this point, the unit cost for each user, can be calculated. This cost is not the same for all of them because of the different exergy destruction (mainly due to friction) and the pipe cost associated to the different paths joining the thermal plant with the users.

The network is then optimized using a probabilistic approach similar to simulated annealing [17]. The probability of users to be disconnected to the district heating network is assumed to be dependent on their unit cost. In the optimization procedure, users are progressively disconnected from the network. Each iteration the user to be disconnected is randomly selected from an ensemble where the number of samples for each user is proportional to its probability. The users disconnected with the network are considered to be heated through the alternative system, which is, in this case a solar photovoltaic driven groundwater heat pump. The average COP of the heat pump is assumed equal to 4 in the case of unperturbed groundwater temperature. In the case of multiple installations, possible interferences between heat pumps are considered, as discussed in [18]. A simplified

expression for the effects of the distance *d* between an upstream installation on a downstream installation is assumed:

$$COP = COP_0 \cdot (0.9 + 0.0108 \cdot \ln(d)) \quad (9)$$

Since a probabilistic approach has been considered, the complete optimization procedure has been repeated several times in order to increase the probability to find the true optimum.

The entire procedure is similar in the case of economic costs, the only difference is that unit costs are expressed in monetary units. Costs of insulated pipes have been considered as in [10], while the cost of solar collectors and storage system have been taken from [13]. No incentives have been considered for solar energy.

In the cases where minimum primary energy and minimum economic cost are competing, the optimization has been performed by imposing a variable constraint on the maximum acceptable cost of heat (i.e. the economic objective function), so that the problem can be treated as single objective optimization. Once an optimal point is found, the optimization is repeated by modifying the maximum acceptable cost of heat.

3. Application

Figure 1 shows a schematic of the district heating network that has been considered as the case study. It is a network located in a small town in the north west part of Italy. The maximum thermal request is about 7 MW [19]. Heat to this network is supplied by an internal combustion engine (about 3 MW) and gas boilers. This case study is considered since it is a reasonable size of network that can be fed with renewable energy and because there is availability of groundwater to feed groundwater heat pumps, that can be considered as potential alternatives to the district heating network.

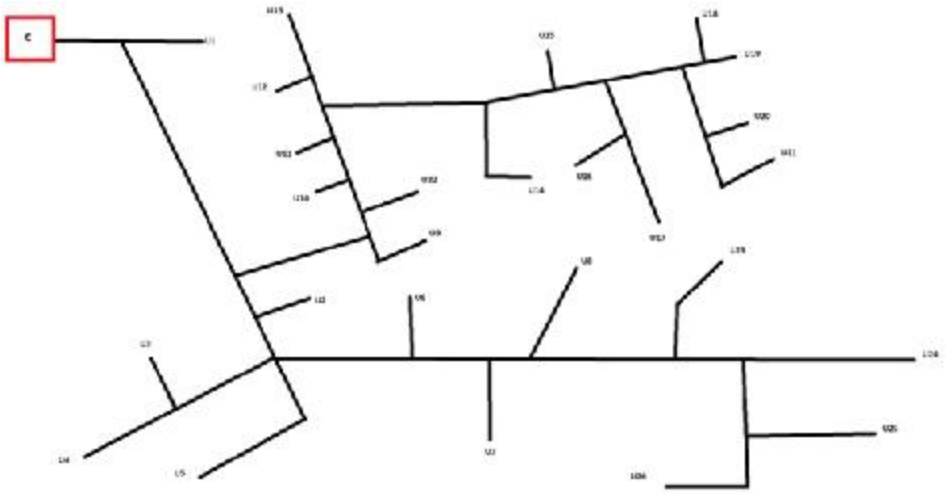

Fig. 1. Schematic of the District Heating Network.

The network shown in the figure corresponds to all the users connected to the district heating system. This superstructure is progressively simplified in order to discover the optimal configuration. The analysis is conducted by considering various combinations of the supply temperature and return temperature, which are here assumed as parameters in the analysis instead of design variables. Therefore, several optimal curves are obtained for each couple of these parameters. These results are shown in figure 2 for the following cases: 40-20 °C, 45-20 °C, 50-20 °C, 55-20 °C and 55-25 °C.

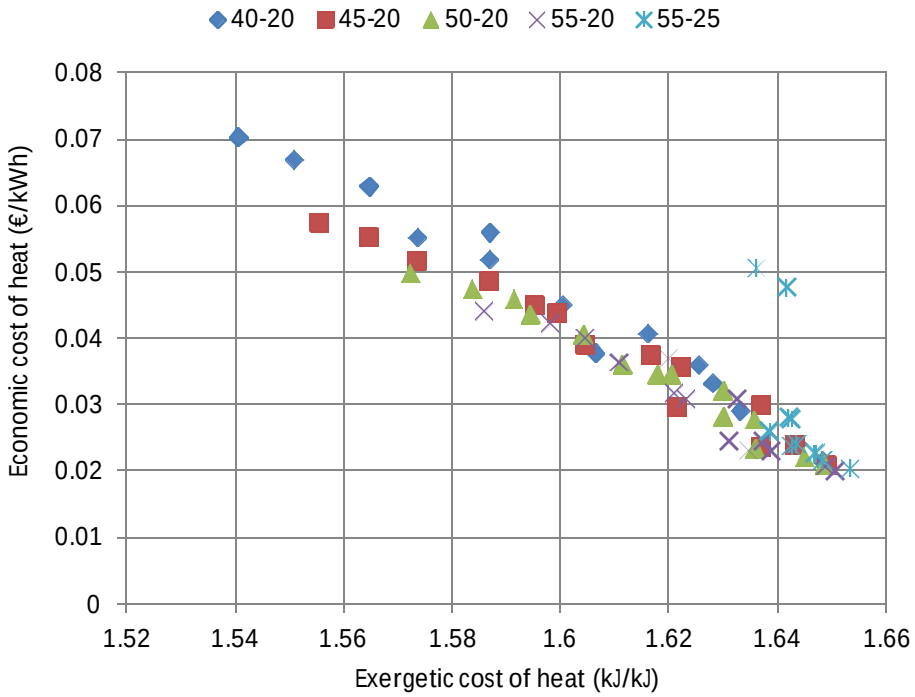

Fig. 2. Optimization results.

Results show that the two objective functions are competing for the values of the supply and return temperatures here considered. The lowest exergetic unit cost of heat is obtained in the case of smallest supply and return temperature. This also corresponds to the highest economic cost. This configuration corresponds to 54% of the users connected to the district heating network. This percentage refers to the annual heat demand with respect to the total heat demand of the users in the urban area. Increasing the supply temperature, the number of users connected to the district heating network in this condition (i.e. minimum exergetic cost of heat) increases. It becomes 67% in the case of supply temperature of 45 °C, 80% in the case of supply temperature of 50 °C and 93% in the case of supply temperature of 55 °C. The reason of such behaviour can be analyzed by considering the diagram in figure 3.

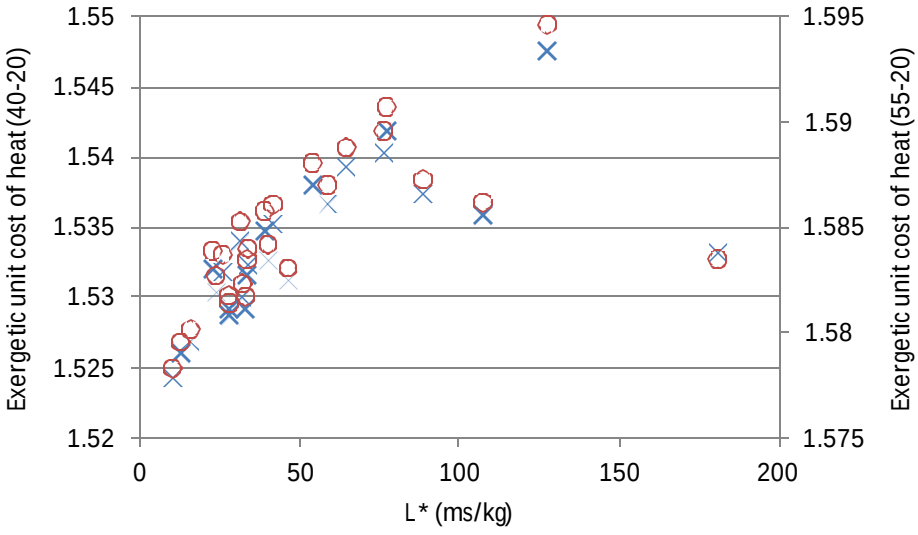

Fig. 3. Effect of weighted distance from the thermal plant to the unit cost of heat in (kWh/kWh).

Figure 3 shows the exergetic cost of heat associated to the users when they are all connected to the network. In the figure this is represented as the function of L*, which is the ratio between the distance of the user from the thermal plant and the mass flow rate required by the user. The graph shows that when the users are far from the plant, the efficient use of primary energy decreases. The only exception is represented by very small users (i.e. small mass flow rate required to satisfy the thermal request) located quite close to the thermal plant.

When the supply temperature is increased from 40 °C (crosses) to 55 °C (circles), the behaviour remains the same, but the exergetic costs increases of about 3%. This is due to the increase in the term due to heat production, which is basically associated to the efficiency of solar collectors, which decreases (of about 4.5%) because of the larger operating temperature.

Starting from the points in figure 2 corresponding with all users connected with the network (for each series, these are the points on the left part of the diagram), it is possible to reduce the economic unit cost of heat by disconnecting some users from the network (those characterized with larger economic unit cost of heat) and supplying them heat with groundwater heat pumps.

This can be observed by analyzing the exergetic and economic unit costs of heat as the users are disconnected to the network. This is analyzed in figure 4 in the case of supply temperature of 55 °C and return temperature of 20 °C.

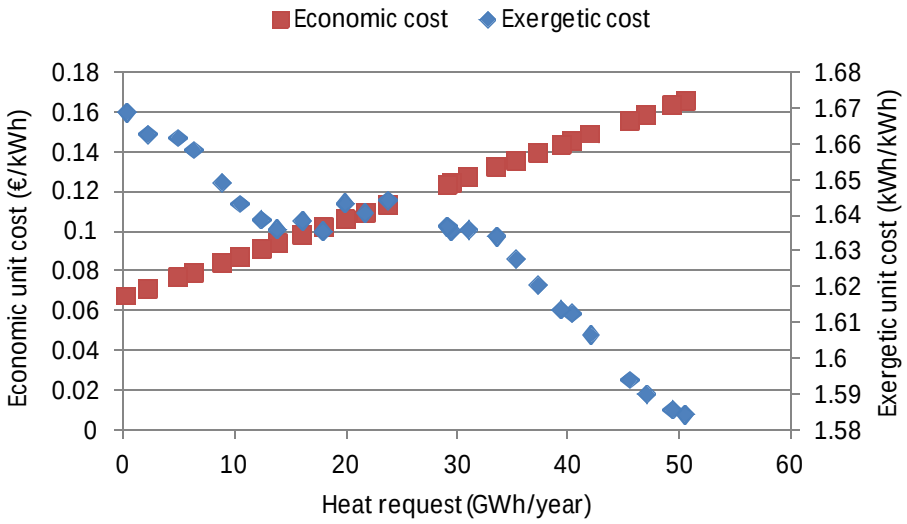

Fig. 4. Trends of exergetic and economic unit costs during a iterative network simplification.

The reasons why the exergetic unit cost tends to increase as the users are disconnected is that solar district heating is more efficient than the alternative. In addition, there are interactions between the various heat pump installations that affect their efficiency, as discussed above. In contrast, the economic cost tends to decrease. The minimum economic cost is obtained with few users still connected with the district heating system (about 6-10% of the annual heat, depending on the combination of temperatures). This is due to the interferences between heat pumps, that cause a reduction in the COP of downstream installation and thus an increase in the primary energy consumption.

Also, it is interesting to compare the unit costs corresponding to a fixed amount of heat supplied to users connected with the district heating network, for the various supply temperatures and fixed return temperature (20 °C). The amount of heat supplied through district heating network is considered to be 55% of the total annual request. Figure 5 shows that an increase in the supply

temperature causes an increase in the exergetic unit cost but a decrease in the economic unit cost. The latter is due to the reduction of the investment costs associated with heat storage and pipe network. Nevertheless the economic advantage obtained increasing the supply temperature tends to decrease with increasing temperature, in fact the distance between points at fixed increase in the supply temperature tends to reduce.

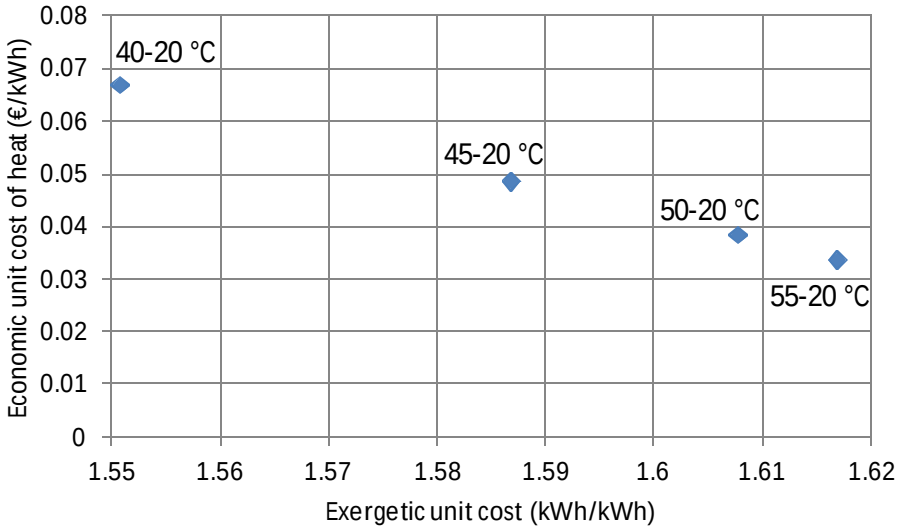

Fig. 5. Unit costs for fixed users connected to the network as the function of supply temperature.

In the case of higher return temperature (e.g. 25 °C), the Pareto front presents sudden increase in the economic unit cost of heat with decreasing exergetic cost. It should be also mentioned that in the case of high temperatures (65-40 °C, 70-35 °C, 75-30 °C...) no Pareto front takes place and the optimal system is obtained with most users heated through groundwater heat pumps.

4. Conclusions

In this paper the energy and economic optimization of a district heating network is conducted using a thermoeconomic based probabilistic procedure. The procedure is applied to a small low temperature district heating network. Groundwater heat pumps are considered as the possible alternative systems to supply heat to the users not connected to the district heating network.

A multi-objective optimization is performed for various combinations of the supply and return temperatures. The analysis shows that supply and return temperatures play a crucial role in the optimal configuration. In particular a reduction of both temperatures allows one to achieve smaller cost of heat in terms of required primary energy, but causes an increase in the economic costs. An increase in the return temperature causes an increase in both costs, which conducts to non competing objective functions.

The most important terms that affect to optimal configuration are the efficiency of solar collectors and the possible thermal interferences between heat pump, and, from the economic viewpoint only, the investment cost due to the seasonal thermal storage and the pipe network.

Appendix: cost calculation

Purchase cost for pre-insulated pipes has been calculated through the following equation [20]:

$$C_{pipe} = (a_0 + a_1 \cdot D + a_2 \cdot D^2) \cdot 1.25 \cdot 2 \cdot L$$

where D is the internal diameter and L the length of the pipe, 1.25 is a corrective factor used to include the cost of special components also determined through available data and 2 accounts for the double pipe. The values of polynomial coefficients have been updated with respect to those available in [20]: a_0=11.7 €/m, a_1=133.7 €/m^2, 1575 €/m^3.

Installation costs include the excavation (5.2 €/m^3) and pavement restoring (10.3 €/m^2).

Concerning heat generation, the following specific equipment costs are considered: solar collectors 250 €/m^2, photovoltaic panels 2500 €/kW, heat pumps 500 €/kW [21], seasonal storage tank 80 €/m^3 [13]. Linear cost functions have been considered for these components.

References

[1] H. Lund, B. Moller, B.V. Mathiesen, A. Dyrelund (2010).The role of district heating in future renewable energy systems. Energy 35: 1381–1390

[2] http://www.iea-dhc.org/index.php (accessed on 10/02/2012)

[3] A. Dalla Rosa, J.E. Christensen (2011).Low-energy district heating in energy-efficient building areas. Energy 36: 6890-6899

[4] V. Lottner, M.E. Schulz, E. Hahne (2000). Solar-Assisted District Heating Plants: Status of the Germal Program SOLARTHERMIE-2000. Solar Energy 69: 449–459

[5] P.A. Østergaard, H. Lund (2011).A renewable energy system in Frederikshavn using low-temperature geothermal energy for district heating. Applied Energy 88: 479–487

[6] D. Lindenberger, T. Bruckner, H.M. Groscurth , R. Kummel (2000). Optimization of solar district heating systems: seasonal storage, heat pumps, and cogeneration. Energy 25: 591–608

[7] P.K.Olsen, H. Lambertsen, R. Hummelshøj, B. Bøhm, C.H. Christiansen, S. Svendsen, C.T. Larsen, J. Worm (2008). A New Low-Temperature District Heating System for Low-Energy Buildings. The 11th International Symposium on District Heating and Cooling, August 31-September 2, Reykjavik, Iceland

[8] S. Svendsen, M. Brand (2010). Performance of Low Temperature District Heating Systems for Low Energy Houses Final conference Annex 49 “Low Exergy Systems for High Performance Building and Communities”.

[9] C.A. Frangopoulos, M.R. von Spakovsky, E. Sciubba. (2002). A Brief Review of Methods for the Design and Synthesis Optimization of Energy Systems. The International Journal of Applied Thermodynamics. Vol.5, No. 4. pp 151-160.

[10] V. Verda, C. Ciano (2005). Procedures for the Search of the Optimal Configuration of District Heating Networks. Int. J. of Thermodynamics, 8: 143-153.

[11] C.A. Frangopoulos, G.G. Dimopoulos (2004). Effect of reliability Considerations on the Optimal Synthesis, Design and Operation of a Cogeneration System. Energy, 29, pp. 309-329.

[12] http://www.kloben.it/ (accessed on 10/02/2012)

[13] M.A. Lozano, A. Anastasia, L.M. Serra, V. Verda (2010). Thermoeconomic Cost Analysis of Central Solar Heating Plants combined with Seasonal Storage. Proceedings of the ASME International Mechanical Engineering Congress & Exposition IMECE 2010. November 12-18, 2010, Vancouver, British Columbia, Canada

[14] M.A. Lozano, A. Valero (1993). Theory of the Exergetic Cost. Energy, Vol.18 No.9, pp.939-960.

[15] A. Valero , M. A. Lozano, M. Muñoz (1986). A general Theory of exergy saving I, II, III. AES Vol. 2-3. ASME Book H0341C, pp. 1,9,17.

[16] V. Verda, R. Borchiellini, M. Calì (2001). A thermoeconomic approach for the analysis of district heating systems. The International Journal of Applied Thermodynamics. Vol.4, No. 4. pp 183-190.

[17] N. Metropolis, A. Rosenbluth, A. Teller, T. Teller (1953). Equation of State Calculations by Fast Computing Machines. Journal of Chemical Physics, Vol. 21, No. 6, pp. 1087-1092.

[18] V. Verda, G. Baccino, A. Sciacovelli, S. Lo Russo (2012). Impact of District Heating and Groundwater Heat Pump Systems on the Primary Energy Needs in Urban Areas. Applied Thermal Engineering. 10.1016/j.applthermaleng.2012.01.047

[19] L. Carta Fornon (2011). Economic and Energetic Analysis of a District Heating Network. Master Thesis. Politecnico di Torino. (In Italian)

[20] Verda V., Ciano C. (2005). Procedures for the Search of the Optimal Configuration of District Heating Networks. The International Journal of Thermodynamics. Vol. 8. No. 3. pp.143-154

[21] Lazzarin R., Noro M. (2006). Local or district heating by natural gas: Which is better from energetic, environmental and economic point of views? Applied Thermal Engineering 26: 244–250.

Thermo-economic assessment of a micro CHP system fuelled by geothermal and solar energy

Duccio Tempesti [a], ***Daniele Fiaschi*** [b], ***Filippo Gabuzzini*** [c]

[a,b,c] *Università degli Studi di Firenze, Dipartimento di Energetica "Sergio Stecco"*
C/o Centro Didattico Morgagni Viale Morgagni 40/44 - 50134 Firenze Italy
[a] *CA: duccio.tempesti@unifi.it*
[b] *daniele.fiaschi@unifi.it*
[c] *filippodrummer@msn.com*

Abstract:

A micro combined heat and power (CHP) plant operating through an Organic Rankine Cycle (ORC) using renewable energy is analyzed. The reference system is designed to produce 50 kWe. The heat sources of the system are geothermal energy at low temperature (80-100°C) and solar energy. The system uses a solar field composed only by evacuated solar collectors, and work is produced by a single turbine. Different working fluids (e.g. R134a, R236fa, R245fa) are considered in the analysis. The aim of this paper is to assess the cost of the proposed CHP plant and to determine the most convenient working fluid through a thermo-economic analysis. The system is sized in base of the weather data of a city in the centre of Italy in three different months (January, March, July), and the main characteristics of the system (i.e. heat exchanger surface, solar collector area) are presented. The results of the thermo-economic analysis show that R245fa allows the lowest price of electricity production and the lowest overall cost of the CHP plant.

Keywords:

Organic Rankine Cycle, Combined Heat and Power, geothermal energy, solar energy, thermo-economic analysis.

1. Introduction

Organic Rankine Power Cycles are well proven and reliable technology for energy conversion, particularly for exploiting low-temperature heat source. The use of an organic vapour in place of water steam is very interesting for small and medium size power plants (50 to 5000 kW), with applications varying from heat recovery at gas turbine discharge [1-3] or internal combustion engines [4], to energy conversion from biomass [5-6], solar [7-9] and geothermal resources [10-12] (these last two cases with no significant market alternative, considering the low level of temperature of the resource). Today, Organic Rankine Cycles are increasing in popularity with several manufacturers of equipment available on the market [13-17].

In scientific literature concerning ORC system fuelled by low-temperature geothermal resources, much research has been dedicated to the selection of the optimal working fluid. The few works on the geothermal hybrid systems [6,18-20] investigated only the exploitation of geothermal resource at medium temperature [6,18,20] for electricity production (with power plant size ranging from 1 MWel to 550 Mwel). Only [19] considered a power plant for electricity production fuelled by geothermal at low-temperature and another renewable energy resource, i.e. biomass. In a previous paper [21], the authors presented an innovative CHP ORC system powered by low-temperature geothermal resource (i.e. 90°C) and solar energy captured by solar collectors. In this paper, the authors will investigate the innovative CHP ORC system through a thermo-economic analysis. The system proposed has a small size (i.e. 50 kWel) because it designed for small CHP applications.

2. CHP ORC power plant description

The reference case here considered has been previously presented in [21]. Figure 1 represents the layout of the power plant. The liquid organic fluid coming from the condenser is first pre-heated in a heat exchanger (Geothermal Heater) by a geothermal flow rate at low temperature (90 °C). Then, solar energy collected by an Evacuated Tube Collectors (ETC) field is used to heat the organic fluid up to the maximum temperature, set at 147°C (420 K). This temperature reflects the interest of using solar collectors without concentrators or with a limited concentration ratio, which have a low cost for installed unit surface. After producing mechanical work in the turbine, the organic fluid is still in superheated condition (high temperature and enthalpy values). This heat can be recovered in building space heating and domestic hot water production (CHP unit). From CHP point of view, the de-super-heater DSH, that provides heat at higher temperature, but with limited heat capacity, should be separated from the condenser, which instead provides heat at low and constant temperature, but with infinite heat capacity. The DSH cools the organic fluid at turbine outlet from superheated conditions down to saturated vapour conditions at variable temperature. Then, before being circulated to the Geothermal Heater by the pump to start the cycle again (point 1, Fig. 1), the saturated organic vapour that leaves the DSH is condensed at constant temperature.

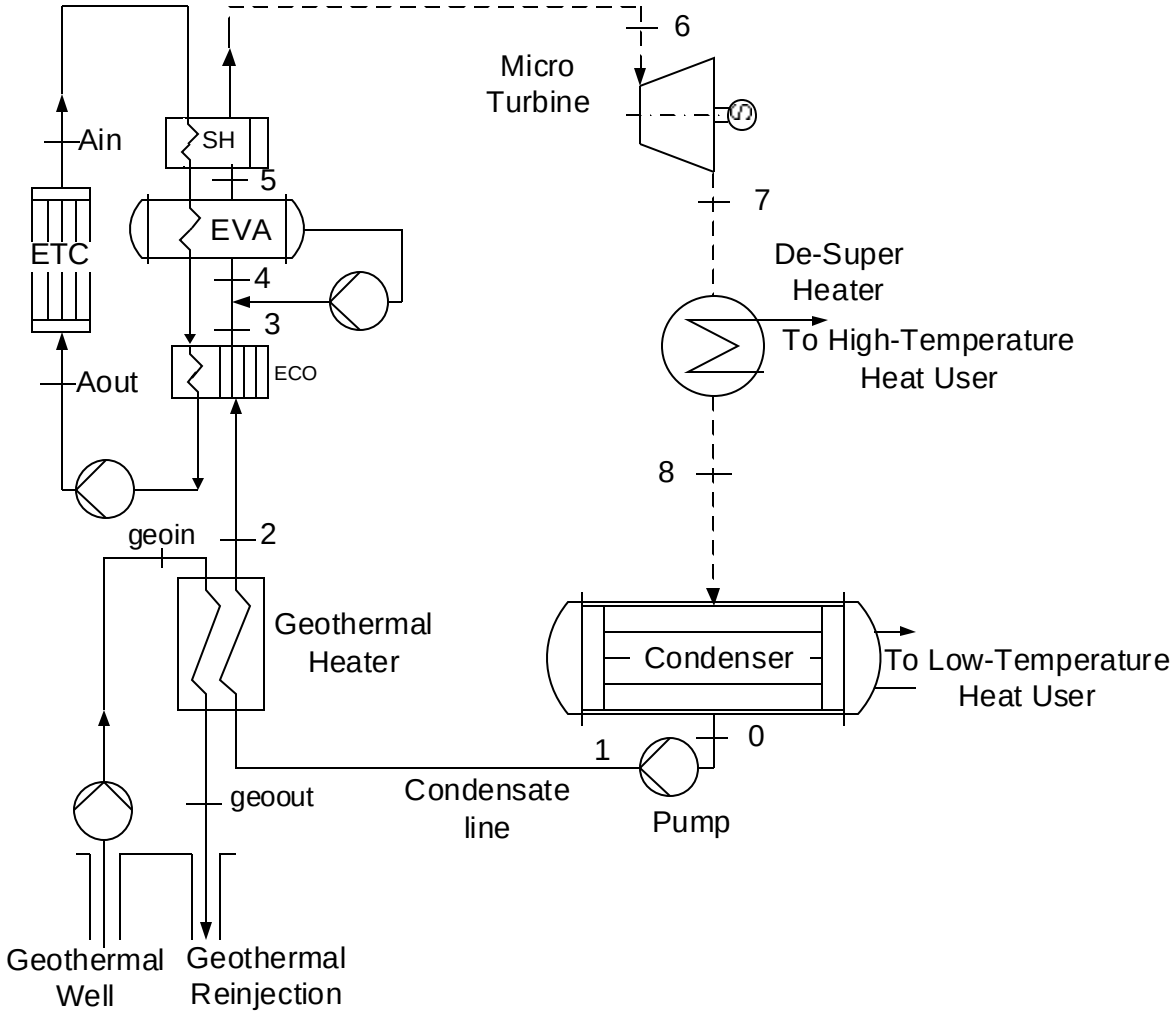

Figure 1 – Low temperature geothermal and solar CHP-ORC layout

The system was modelled through Engineering Equation Solver (EES® [22]), using data acquired from a long term local data source [23] for Florence, Italy. The CHP plant was designed in three different months: January, March and July. These months are selected to cover three different cases

for air temperature and global radiation. In January, the global radiation is the lowest of the year, and this leads to the highest area of solar collectors; on the contrary, in July the yearly highest global radiation implies the lowest area of solar collectors. The design in March, indeed, is an intermediate situation between January and July. The design conditions in terms of air temperature and global radiation were taken at 13:00 of a reconstructed standard day for each of the three months (Table 1). Three different engineered refrigerants suitable for low-temperature energy conversion were selected: R134a, R236fa, R245fa [6,14]. The critical temperatures and pressures of these analyzed fluids are reported in Table 2. The different shape of the cycle in the T-s diagram is shown in Figure 2, referring only to fluids R134a (left) and R245fa (right). Table 3 reports the parameters assumed for the calculations. The collector efficiency is modeled by the following quadratic approximation [24]:

$$\eta_{coll} = c_0 - \left[\left(c_1 + c_2 \cdot \left(T_{avcoll} - T_{amb} \right) \right) \cdot \left(\frac{T_{avcoll} - T_{amb}}{G_{tot}} \right) \right] \quad (1)$$

Where T_{avcoll} is the average temperature of the collector thermal fluid and T_{amb} is the air temperature. The operating data for the evacuated solar collector reported in Table 3 are taken from [24] for an ESTEC VR12 CPC®. The temperature of the collector thermal fluid at collector outlet is set 10 °C above the maximum temperature of the superheated organic vapour (point [6]). Heat exchanger surfaces are calculated through the NTU-effectiveness method [25], and each overall heat transfer coefficient U is assumed to be the same for all the fluids for each different heat exchanger (Table 3). This assumption is justified by the fact that the overall heat transfer coefficient of the heat exchangers is mainly affected by the thermal conductivity of the water, which is at least four times higher than the thermal conductivity of the organic fluid. For all the three fluids, the temperature difference of the water in all the heat exchangers is quite the same. In addition, the variation of the thermal conductivity among the three organic fluids is very low, so this means that the U of each heat exchanger is independent from the organic fluid. In order to contain the surface of the geothermal heat exchanger, the temperature difference T_{geoout}-T_1 is set at high value (15 °C).

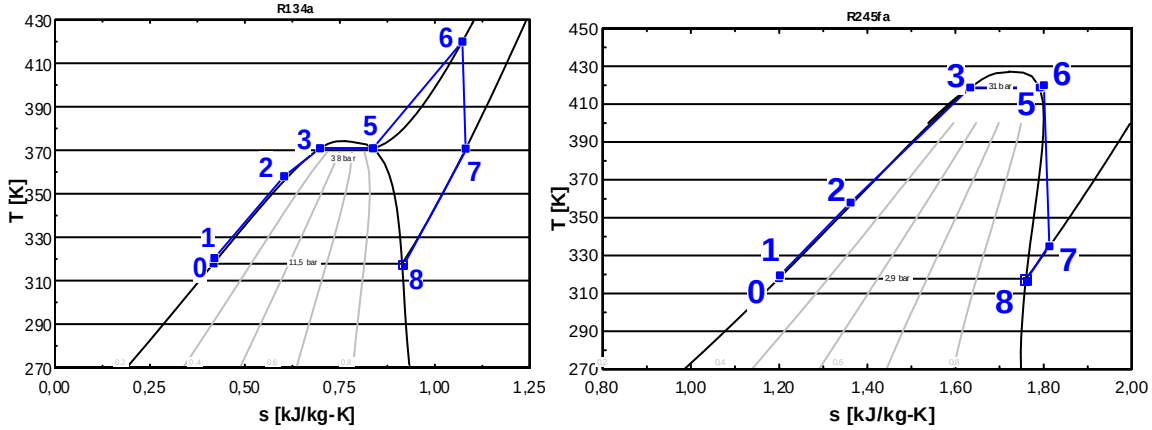

Figure 2 – ORC thermodynamic cycle for R134a (left) and R245fa (right)

Table 1: Ambient design conditions for each month [20]

Month	**January**	**March**	**July**
Global Irradiation on the 30° tilted surface G_{tot} [W/m^2]	690	931	1011
Ambient temperature T_{amb} [°C]	6	11	26

Table 2: Fluids critical temperature and pressure

Fluid	R134a	R236fa	R245fa
Critical pressure [bar]	40.6	32	36.5
Critical temperature T_0 [°C]	101	125	154

Table 3: ORC system parameters

CYCLE		SOLAR	
Turbine Power output W_t [kW]	50	Tilt angle [°]	30
Condenser temperature T_0 [°C]	45	Optical efficiency c_0	82.5
Maximum cycle temperature T_6 [°C]	147	Coefficient c_1 [W/(m^2°C)]	0.91
Pump/Turbine isentropic efficiency	0.8	Coefficient c_2 [W/(m^2°C ^{2})]	$0.6*10^{-3}$
ECO - U [kW/(m^2°C)]	0.25	T_{ain}-T_6 [°C]	10
EVA - U [kW/(m^2°C)]	0.20	Pinch point temperature difference [°C]	5
SH - U [kW/(m^2°C)]	0.125		
GEOTHERMAL		**CONDENSER**	
Geothermal temperature (T_{geoin}) [°C]	90	Refrigerant inlet temperature [°C]	37
Temperature difference T_{geoin}-T_2 [°C]	5	Temperature difference pinch point [°C]	5
Temperature difference T_{geoout}-T_1 [°C]	15	DSH U [kW/(m^2 °C)]	0.125
GEO HX U [kW/(m^2°C)]	0.30		

The main parameters of the CHP plant calculated for the value of p[1] (upper cycle pressure) that maximizes the cycle efficiency are reported in Table 4.

Table 4: Main parameters of the CHP plant

Fluid	R134a	R236fa	R245fa
Upper cycle pressure p[1] [bar]	38	29.3	31
Condenser pressure p[0] [bar]	11.6	5	2.92
Geothermal reinjection temperature [°C]	335	336	335
T[6]-T[5] [°C]	49	26	1.3
Temperature at DSH inlet T[8] [°C]	98	93	62
Water temperature at DSH outlet [°C]	93	87	57
Organic fluid flow rate [kg/s]	1.77	1.84	1.33
Geothermal flow rate [kg/s]	0.95	0.87	0.60
Water flow rate at DSH [kg/s]	0.45	0.43	0.32
Water flow rate at Condenser [kg/s]	22.3	19.72	18.93
Geothermal power input Q_{geo} [kW]	111	98.5	72.4
Solar power input Q_{solar} [kW]	316	273.5	235
DSH heat recovered [kW]	102	82.5	23
Condenser heat recovered [kW]	280	247	237.5

3 CHP ORC thermo-economic analysis

The exergy analysis of the power plant was performed following the reference literature [26-28]. Since it is not a reactive system, the following classical definition of exergy was used:

$$ex = h - h_0 - T_0 \cdot (s - s_0) \qquad (2)$$

where h_0 and s_0 are the specific enthalpy and the specific entropy of the element at the reference state, which was fixed at a pressure of 1 atm and a temperature given in Table 1 for each month.

The exergy inputs to the system come from (I) geothermal and (II) sun. The exergy from the sun is given by:

$$Ex_{sun} = G_{tot} \cdot A_{coll} \cdot \left[1 - \frac{T_{amb}}{T_{sun}}\right] \qquad (3)$$

where T_{sun} is taken as 75% of the equivalent black-body sun temperature, in agreement with [9, 29].

The thermo-economic analysis was developed applying the following thermo-economic balance for each component of the system:

$$C_e + C_{Qe} + C_{We} = C_i + C_{Qi} + C_{Wi} + Z_{comp} \qquad (4)$$

Where on the left side there are the costs per second (€/s) related to all the mass (C_e), heat ($C_{Q;e}$) and work ($C_{W;e}$) fluxes that enter the component, on the right side there are the costs per second related to all the mass (C_i), heat ($C_{Q;i}$) and work ($C_{W;i}$) fluxes that exit the component and also the cost per second of the component (Z_{comp}). C_e, C_Q and C_W are calculated as follow:

$$\dot{C} = c \cdot \dot{E} \qquad (5)$$

$$\dot{C}_Q = c_Q \cdot \dot{Q} \qquad (6)$$

$$\dot{C}_W = c_W \cdot \dot{W} \qquad (7)$$

Where c, c_Q and c_W are the exergy specific cost respectively for mass flow rate, heat $\dot{Q}$ and work $\dot{W}$, while $\dot{E}$ is defined as the product of the mass flow rate and the exergy:

$$\dot{E} = \dot{m} \cdot ex \qquad (8)$$

The cost per second of the component $\dot{Z}_{comp}$ includes the cost of the component and costs for operation and maintenance (O&M). In the calculation, it was assumed that the system works for 15 years for 6000 hours per year. The following Table 5 reports the thermo-economic balance according to (4-8) for each component of the system. Differently from all the other points of the system, the exergy of the geothermal mass flow rate m_{geo} at the depth of 700 m - which is involved in the calculation of E_{well} through (8) - takes into account also the potential exergy - $m_{geo}gz$, where g is the gravitational constant, z is the depth of the well and the sign minus indicates that level of zero potential exergy is set at the CHP plant level (i.e. sea level).

Table 5: Thermo-economic balance for each system component.

COMPONENT	THERMO-ECONOMIC BALANCE
Geothermal wells	$E_{well} \cdot c_{well} = Z_{well}$
ORC Pump	$E_0 \cdot c_0 + \frac{W_p}{\eta_p} \cdot c_p + Z_p = E_1 \cdot c_1$
Geothermal pump	$E_{well} \cdot c_{well} = E_{geoin} \cdot c_{geoin} + W_{p;geo} \cdot c_p + Z_{p;geo}$
Geothermal heater	$E_{geoin} \cdot c_{geoin} + E_1 \cdot c_1 + Z_{geohx} = E_{geoout} \cdot c_{geoout} + E_2 \cdot c_2$
Solar Collectors ETC	$E_{ain} \cdot c_{ain} = E_{aout} \cdot c_{aout} + Z_{coll} + Ex_{sun} \cdot c_{Qsol}$
ECO+EVA+SH	$E_{ain} \cdot c_{ain} + E_2 \cdot c_2 + Z_{solarhx} = E_{aout} \cdot c_{aout} + E_6 \cdot c_6$
Turbine	$Z_t \cdot + E_6 \cdot c_6 = W_t \cdot c_t + E_7 \cdot c_7$
Desuperheater	$Z_{dsh} \cdot + E_7 \cdot c_7 = E_Q \cdot c_Q + E_8 \cdot c_8$
Condenser	$E_8 \cdot c_8 + Z_{cond} = E_0 \cdot c_0 + E_{Q;cond} \cdot c_{Q;cond}$

Using the equations of Table 5 it is possible to calculate c_t, which is the cost of the energy produced by turbine, and c_Q and $c_{Q;cond}$ which are respectively the cost of the heat released at the DSH and at the condenser. In order to solve the system of equations of Table 5 some auxiliary equations are needed. First of all, the following equations are added:

$$c_6 = c_7 = c_8 = c_0 \quad (9)$$

$$c_{geoout} = c_{geoin} = c_{pumpgeoin} \quad (10)$$

$$c_{aout} = c_{ain} \quad (11)$$

Then, the cost of the sun energy c_{Qsol} is supposed to be zero, since it can be taken for free. However, the cost of the solar collectors Z_{coll} is considered in the calculation. The power to run the ORC and geothermal pumps is supposed to be given by the electrical grid. Then, the cost of the electricity c_p was taken from the Italian market database for 2011 [30] for each month studied. The c_p values were fixed at: 76,1 €/MWh for January, 63,87 €/MWh for March, 87,26 €/MWh for July.

4. Results

The heat exchanger surfaces for each fluid are reported in Table 6: they are not influenced by the variation of the design month, since the operating temperature and pressure are fixed. Instead, the effective area of the solar collectors is affected by the design month, and it decreases as the solar radiation G_{tot} increases (i.e. from January to July).

Table 6: Heat exchanger surface in each month studied (January, March, July).

Fluid	R134a	R236fa	R245fa
Geothermal Heater surface [m^2]	79	53	31
ECO surface [m^2]	35	31	14
EVA surface [m^2]	37	32	58
SH surface [m^2]	40	34	4
DSH surface [m^2]	224	100	37
Condenser surface [m^2]	146	129	124

Table 7: Solar Collectors effective area [m^2] for each fluid in each month (January, March, July).

Fluid	R134a	R236fa	R245fa
January ETC area [m^2]	555	482	413
March ETC area [m^2]	411	356	305
July ETC area[m^2]	378	328	281

The cost of the geothermal and ORC pumps were taken from commercial catalogue [33,34]. The two geothermal wells were assumed to be deep 700 m with a cost of 50 € per meter of perforation. Hence, Z_{well} is the cost of the two wells, and it computes the cost for making the geothermal resource available to the use in the CHP plant. The geothermal pump, instead, consumes power in order to bring the geothermal resource from the 700 m of depth up to the CHP system.

For the cost of the ETC, we overlooked the high price (598 €/m^2) reported in [24]. The price was set at 187 €/m^2 which is an average value of the price reported in [35-37]. The O&M cost was fixed at 5% of the component cost for the heat exchangers and the pumps, and at 3% for the solar collectors. Table 8 contains all the costs of the plant components that are not influenced by the design month, while Table 9 reports the costs of the solar collectors for each fluid for the three design months. Table 10 summarizes the overall cost of the power plant for each fluids in each design month.

Table 8: ORC component cost [k€] for each fluid (constant for every month).

Fluid	R134a	R236fa	R245fa
Geothermal Heater cost [€]	13.170	8.830	5.100
ECO+EVA+SH cost [€]	24.640	20.810	16.645
DSH cost [€]	98.560	21.900	5.475
Condenser cost [€]	87.600	76.650	65.700
Geothermal pump [€]	21.470	21.470	21.470
Geothermal wells [€]	70.000	70.000	70.000
ORC pump [€]	4.000	4.000	4.000
Turbine [€]	50.000	50.000	50.000

Table 9: Solar Collectors cost [k€] for each fluid in each month (January, March, July).

Fluid	R134a	R236fa	R245fa
January cost [€]	107.230	93.000	79.740
March cost [€]	79.320	68.780	58.980
July cost [€]	73.050	63.350	54.300

Table 10: ORC plant overall cost [k€]for each fluid in each design month (January, March, July).

Month	January	March	July
R245fa [€]	318.200	297.450	292.780
R236fa [€]	366.670	342.450	337.020
R134a [€]	476.660	448.760	442.510

The overall cost of the ORC plant with R134a is approximately 50% higher than the cost with R245fa, which has the lowest cost in each design month. This result is due to the higher heat exchangers surfaces needed by R134a in comparison to R245fa (see Table 6). The ORC plant overall cost diminishes when design month passes from January to July, and this result is due to the lower ETC surface (Table 7) that decreases the overall costs for solar collectors (Table 9).

Table 11 reports the cost in €/MWh of the work produced by the turbine c_t for each fluid in each design month. R245fa is still the fluid with the lowest cost for MWh produced, while R134a presents the highest cost. These results are in agreement with the results showed in Table 10 for the overall cost of the ORC plant. Besides, the lowest value of c_t is obtained in March for each fluid. This result is justified by the fact that at March there is the proper balance between ambient temperature and global solar radiation increase. High value of solar radiation allows to strongly decrease the ETC cost (Table 9), which diminishes of almost 30 k€ from January to March, but less than 8 k€ from March to July. At the same time, an ambient temperature of 11°C allows to control the exergy losses of the solar collectors and of the plant (Figure 3).

Table 11: specific cost of the work produced by the turbine [€/MWh] for each fluid in each design month (January, March, July).

Month	**January**	**March**	**July**
R245fa [€/MWh]	39	37	46
R236fa [€/MWh]	43	41	52
R134a [€/MWh]	41	39	49

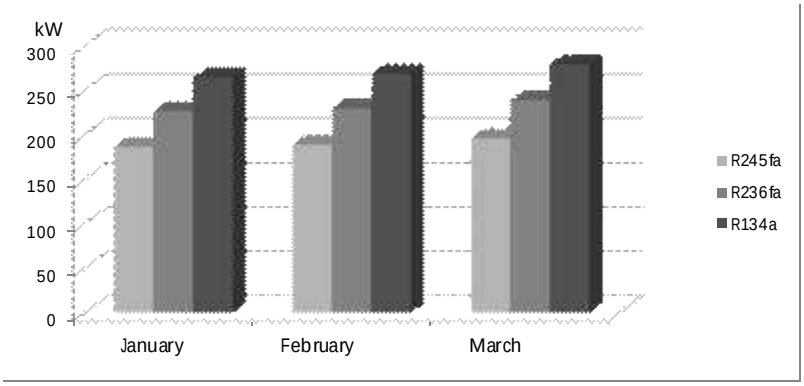

Figure 3: Solar Collectors exergy losses for each fluid in each month (January, March, July).

Table 12 reports the cost in €/MWh of the heat released at the DSH, c_Q, for each fluid in each design month. R245fa has the lowest cost for MWh of heat produced, while R134a presents the highest cost. This result is given by the fact that for R245fa the DSH surface (Table 6), and consequently its cost (Table 8), is much lower in comparison to R134a. Instead, the values of c_Q, for R245fa e R236fa are similar because the slight higher cost of DSH for R236fa is almost compensated by the largest amount of heat recovered. Instead, at the condenser (Table 13), the highest specific cost is obtained with R245fa, because the quantity of heat recovered at the condenser with R245fa is lower than the heat recovered with R134a, while the costs are similar (Tables 4 and 8). Table 14 summarizes the specific cost of all the fluxes for each fluid in each design month involved in the thermo-economic analysis.

Table 12: specific cost of the heat released at the DSH [€/MWh] for each fluid in each design month (January, March, July).

Month	**January**	**March**	**July**
R245fa [€/MWh]	49	51	81
R236fa [€/MWh]	54	55	81
R134a [€/MWh]	99	106	154

Table 13: specific cost of the heat released at the condenser [€/MWh] for each fluid in each design month (January, March, July).

Month	**January**	**March**	**July**
R245fa [€/MWh]	49	51	78
R236fa [€/MWh]	45	46	60
R134a [€/MWh]	43	43	56

Table 14: specific cost c_i [€/MWh] of all the fluxes involved in Table 3 for each fluid in each design month (January, March, July).

Fluid	R134a			R236fa			R245fa		
Month	January	March	July	January	March	July	January	March	July
c_1 [€/MWh]	34	31	40	79	63	65	66.6	67.6	56
c_2 [€/MWh]	38	36	47	60	57	71	63	68.4	79
$c_6 = c_7 = c_8 = c_0$ [€/MWh]	27	26	34.5	29	27	37	25.6	24	31
$c_{ain} = c_{aout}$ [€/MWh]	13	10	10.6	12	10	10	11	8.6	9
c_p [€/MWh]	76.1	67.8	87.3	76.1	67.8	87.3	76.1	67.8	87.3
$c_{geoin} = c_{geoout}$ [€/MWh]	36	40	67	38	42	71	50	56	92
c_{well}[€/MWh]	22	26	46	24	28	50	34	41	72

5. Conclusions

In this work, a thermo-economic analysis of a new micro CHP ORC system fuelled by two renewable energy resources (solar and low-temperature geothermal) was presented. The system was sized in base of the weather data of a city in the centre of Italy in three different months (January, March, July). The thermo-economic performance of three different working fluids (e.g. R134a, R236fa, R245fa) were compared. The results showed that the plant operating with R245fa is the less expensive, due to the fact that requires the lower surface of heat exchangers and the lower solar collector area. R245fa is also the most convenient working fluid in terms of cost of power produced by the system. In terms of heat recovered from the CHP system, the cost of the heat recoverd at high temperature is less expansive for R245fa, while R134a present the lowest cost of the heat recovered at low temperature. Finally, the results also showed that the lowest cost of the CHP system for all the fluid is obtained in March, when there is the proper balance between the ambient temperature and the global solar radiation.

Acknowledgements

This research has been funded by Regione Toscana, project "BT-GEO H&P: - Sistemi di Generazione Distribuita di Energia Elettrica e Termica da Fonti Geotermiche", using European Social Fund (FSE) resources.

Nomenclature

A_{coll}: Solar collector area [m^2]
C: Cost [€/s]
c: Exergy specific cost of the material streams [€/kJ]
c_Q: Exergy specific cost for the transfer of heat [€/kJ]

c_W:	Exergy specific cost for the transfer of power [€/kJ]
E:	Exergy [kJ/s]
ex:	Specific Exergy [kJ/kg]
Ex_{sun}:	Exergy from the sun [kW]
G_{tot}:	Global radiation on the tilted surface
h	Enthalpy [kJ/kg]
m:	Mass flow rate [kg/s]
p:	Pressure [bar]
Q:	Heat rate [kW]
Q_{solar}:	Solar radiation incident to collector [kW]
s:	Entropy [kJ/kgK]
T:	Temperature [K]
T_{avcoll}	Average temperature of the collector thermal fluid [K]
T_{sun}:	Temperature of the sun [K]
U	Global Heat exchange coefficient [kW/m^2-K]
x:	Quality
W:	Work [kW]
W_t:	Power output of the cycle[kW]
Z:	Component cost [€]
[1]...[n]:	Thermodynamic point of the cycle
η_{coll} :	Collector efficiency
η:	Isentropic efficiency

Suffixes

ain:	Collectors outlet
amb:	Ambient
aout:	Collectors inlet
coll:	Collector
cond:	Condenser
e:	Component exit
geoin:	Geothermal inlet to the system
geoout:	Geothermal reinjection into the well
geo:	Geothermal
i:	Component inlet
p:	Pump
solarhx:	Solar Heat exchanger, i.e. ECO+EVA+SH
t:	Turbine
well:	Geothermal well

Acronyms

CEPCI:	Chemical Engineering's Plant Cost Index
CHP	Combined Heat and Power
COND	Condenser

DSH	De-Super-heater
ECO	Economizer
ETC	Evacuated Solar Collectors
EVA	Evaporator
GEO HX	Geothermal Heater
O&M:	Operation and Maintenance
SH	Super-heater

REFERENCES

[1] Invernizzi C., Iora P., Silva P., Bottoming micro-Rankine cycles for micro-gas turbines. Applied Thermal Engineering 2007;27:100–110.

[2] Chacartegui R., Sánchez D., Muñoz J.M., Sánchez T., Alternative ORC bottoming cycles for combined cycle power plants. Applied Energy 2009;86:2162–2170.

[3] Al-Sulaiman F.A., Dincer I., Hamdullahpur F., Exergy analysis of an integrated solid oxide fuel cell and organic Rankine cycle for cooling, heating and power production. Journal of Power Sources 2010;195: 2346–2354.

[4] Vaja I., Gambarotta A., Internal Combustion Engine (ICE) bottoming with Organic Rankine Cycles (ORCs). Energy 2010;35: 1084–1093.

[5] Dong L, Liu H, Riffat S. Development of small-scale and micro-scale biomass-fuelled CHP systems – a literature review. Applied Thermal Engineering 2009;29**:**2119–2126.

[6] Drescher U, Bruggemann D. Fluid selection for the Organic Rankine Cycle (ORC) in biomass power and heat plants. Applied Thermal Engineering 2007;27:223–228.

[7] Schuster A., Karellas S., Kakaras E., Spliethoff H., Energetic and economic investigation of Organic Rankine Cycle applications, Applied Thermal Engineering 2009;29:1809–1817.

[8] Zhai H., Dai Y.J., Wu J.Y., Wang R.Z., Energy and exergy analyses on a novel hybrid solar heating, cooling and power generation system for remote areas. Applied Energy 2009;86:1395–1404.

[9] Fiaschi D., Lifshitz A., Manfrida G., Fuel-Assisted Solar Thermal Power Plant with supercritical ORC cycle. ECOS 2010: Proceedings of the 23rd International Conference on Efficiency, Cost, Optimization, Simulation, and Environmental Impact of Energy Systems; 2010 June 14-17; Lausanne, Switzerland.

[10] Heberle F., Brüggemann D., Exergy based fluid selection for a geothermal Organic Rankine Cycle for combined heat and power generation, Applied Thermal Engineering 2006;30:1326-1332.

[11] Lentz A., Almanza R., Solar–geothermal hybrid system, Applied Thermal Engineering 2006;26: 1537–1544.

[12] Di Pippo R., Geothermal Power Plants: Principles, Applications and Case Studies. London, UK: Elsevier Advanced Technology; 2006.

[13] Pratt and Whitney Corp., Model 280 kW PureCycle® Power System, http://www.pw.utc.com/media_center/assets/model_280_purecycle_power_system.pdf.

[14] ElectraTherm's Heat to Power Generation Systems available at http://www.electratherm.com/products.html last access 10 February 2012.

[15] Turboden Combined Heat And Power Orc Units For The Pellet Industries, 2008, (available at: http://www.turboden.eu/en/public/press/Turboden_ORC_for_pellets_english.pdf).

[16] Obernberger I., Hammerschmid A., Biomass fired CHP plant based on an ORC cycle – Project ORC-STIA-Admont. Final Report, Bios-energy systems; 2001 (available at: http://www.bios-bioenergy.at/uploads/media/Report-ORCAdmont-Thermie-2001-03-26.pdf).

[17] GE Energy Announces Industrial Waste-Heat Recovery Innovation for Onsite Power Plants, http://www.genewscenter.com/content/detail.aspx?releaseid=7229&newsareaid=2, 6 July, 2009 (last access 4 January 2012).

[18] Bruhn M., Hybrid geothermal–fossil electricity generation from low enthalpy geothermal resources: geothermal feed water preheating in conventional power plants. Energy 2002;27:329–346.

[19] Borsukiewicz-Gozdur A., Dual-fluid-hybrid power plant co-powered by low-temperature geothermal water. Geothermics 39;2010:170-176.

[20] Astolfi M., Xodo L., Romano M.C. , Macchi E., Technical and economical analysis of a solar–geothermal hybrid plant based on an Organic Rankine Cycle. Geothermics 2011;40:58-68.

[21] Tempesti D., Manfrida G., Fiaschi D. Thermodynamic analysis of two micro CHP systems operating with geothermal and solar energy. Applied Energy, 2012, available at: doi:10.1016/j.apenergy.2012.02.012

[22] EES Engineering Equation Solver, available at http://www.fchart.com/.

[23] Agency for environmental protection of Tuscany, Meteorological Measured Data Internal Report, 1991-2004. Florence, 2005.

[24] European Commission Directorate General Energy and Transport, Poship Final Report: The Potential of Solar Heat for Industrial Processes. 2001, Project No. NNE5-1999-0308.

[25] Nellis GF, Klein SA. Heat Transfer. Cambridge (UK): Cambridge University Press; 2009.

[26] Bejan A. Entropy generation through heat and fluid flow. John Wiley & Sons inc; 1982.

[27] Kotas TJ. The Exergy Method of Thermal Plant Analysis, London; Boston: Butterworths; 1985.

[28] Bejan A., Tsatsaronis G., Moran M.J., Thermal design and optimization New York: John Wiley & Sons, 1996.

[29] Bejan A., Kearney D.W., Kreith F., Second law analysis and synthesis of solar collector systems, ASME J. Solar Energy Engineering. 1981;103: 23–28.

[30] Gestione Mercati Energetici spa www.mercatoelettrico.org/It

[31] Peters M., Timmerhaus K.D, West R.E., Plant design and economics for chemical engineers, London: McGraw-Hill, 2003.

[32] CEPCI, chemical engineering's plant cost, available at www.che.com/pci.

[33] Wilo pump catalogue, available at: http://www.wilo.it.

[34] Danfoss Italia catalogue, available at: www.danfoss.com/Italy.

[35] Hang Y., Ming Q., Fu Z., Economical and environmental assessment of an optimized solar cooling system for a medium-sized benchmark office building in Los Angeles, California. Renewable Energy 2011;36:648-658.

[36] Al-Alili A., Islam M.D., Kubo I., Hwang Y., Radermacheret R., Modeling of a solar powered absorption cycle for Abu Dhabi. Applied Energy, 2012;93:160-167

[37] Mokhtar M. Tauha Ali M., Bräuniger S., Afshari A., Sgouridis S., Armstrong P., Chiesa M., Systematic comprehensive techno-economic assessment of solar cooling technologies using location-specific climate data. Applied Energy 2000;87:3766-3778.

Thermo-Economic Evaluation and Optimization of the Thermo-Chemical Conversion of Biomass into Methanol

Emanuela Peduzzi[a], Laurence Tock[b], Guillaume Boissonnet[c] and François Marechal[d]

[a] CEA, Grenoble, France, emanuela.peduzzi@cea.fr
[b] EPFL LENI, Lausanne, Switzerland, laurence.tock@epfl.ch,
[c] CEA, Grenoble, France, guillaume.boissonnet@cea.fr
[d]EPFL LENI, Lausanne, Switzerland, francois.marechal@epfl.ch,

Abstract:

In a carbon and resources constrained world, thermo-chemical conversion of lignocellulosic biomass into fuels and chemicals is regarded as a promising alternative to fossil resources derived products. Methanol is one potential product which can be used for the synthesis of various chemicals or as a fuel in fuel cells and internal combustion engines. This study focuses on the evaluation and optimization of the thermodynamic, economic and environmental performance of methanol production from biomass by applying process integration and optimization techniques. Results show the importance of the energy integration and in particular of the cogeneration of electricity for the improvement of the overall efficiency. The energy efficiencies of the evaluated scenarios reach up to 45% and chemical efficiencies up to 51%.

Keywords:

Biomass, Energy Integration, Methanol, Multi-Objective Optimization, Process Design.

1. Introduction

Methanol was produced since the early 1800s through the distillation of wood to make 'wood alcohol'. This method was replaced in the 1920s by large scale processes producing methanol from hydrogen and carbon oxides mixture obtained from the incomplete combustion and reforming of fossil fuels. Today, Methanol is produced mainly by reforming of natural gas, naphtha or refinery light gas [1]. Other ways to produce methanol, which are currently being investigated, include direct methane oxidation without the intermediate step of syngas production and reductive hydrogenative recycling of CO_2, requiring hydrogen, but providing a way to use CO_2.

The price of methanol is about 16 $€_{2011}$/GJ[1] [2], while as a reference, the OPEC basket price of crude oil is 107.46 US$/bbl, or approximately 14.7 $€_{2011}$/GJ. The recent peaks in methanol prices at the end of 2007 and 2008 are mainly due to plants shutting down for scheduled maintenance but also to the increasing demand in the growing economies. High natural gas prices, especially in North America, have also driven the prices up but the subsequent slowdown of the world economy helped lowering the prices [3].

Methanol is mainly used as a feedstock for the synthesis of other products. Being a fuel with an octane number of 100, it can be blended with gasoline as an oxygenated additive or used directly in internal combustion engines with only minor modifications [3]. Furthermore, methanol can be used to produce electricity in direct methanol fuel cells (DMFC) or DME which can be used as a substitute to diesel fuel as well as household gas for cooking and heating, and gasoline (Methanol to Gasoline Synthesis) [4].

Previous studies have analyzed the technical and economic feasibility of the thermo-chemical conversion of biomass into methanol, exploring different scenarios. A comparison of the biomass

[1] Values calculated considering 20.094 MJ/kg as the low heating value of methanol. Energy values are always expressed in terms of the LHV unless otherwise stated

derived methanol production costs is carried out by Spath and Dayton [5] who reported values varying from 10 - 19.6 $\$_{1989}/GJ_{HHV}$ (28-54 $€_{2011}/GJ$)[1] for the study of Wyman et al. [6] to 9 - 12 $\$/GJ_{HHV}$ (18-23 $€_{2011}/GJ$)[2] for the study of Hamelinck et al. [7]. Hamelinck et al. investigated promising conversion concepts and compared different types of gasifiers and gas cleaning steps obtaining overall HHV (High Heating Value) energy efficiency of 55%. More recently the models developed by Van Rens et al. [8] and Huisman et al. [9] addressed two scenarios: a present day design relying on proven technologies (though not on commercial scale for biomass applications) and a near future design studied within the CHRISGAS project [10] in particular for syngas cleaning and conditioning. Their results show, for the present day design relying on an oxygen/steam blown circulating fluidized bed gasifier, an energy efficiencies of 47.8% and a chemical efficiency of 50% (without considering the heat available for district heating). These evaluations focus on case-studies operating at fixed conditions, for which only limited process integration has been taken into consideration. Comparing the results of the various studies on a common basis is a very difficult task, because of the different technologies considered, the different assumptions made and the degree of process integration. The objective of the present work is to systematically investigate the thermo-chemical conversion of lignocellulosic biomass into methanol applying multi-objective optimization techniques and including a detailed heat integration model to evaluate the potential for heat recovery and valorization.

2. Methodology

The present work is based on a model superstructure that was previously developed to analyze and compare the thermo-chemical conversion of lignocellulosic biomass into syngas and liquid fuels (FT, MeOH, DME) [12,13]. The analysis is completed here by applying the thermo-economic process optimization methodology described by Gassner et al. [13], focusing on the gasification technology. An EF (Entrained Flow) gasifier and a FICFB (Fast Internally Circulating Fluidized Bed) gasifer are compared, as represented in Figure 1. The superstructure is built of single process-units thermo-economic models that can be assembled to systematically study different process configurations. The thermo-chemical models are developed using commercial flowsheet calculation software *Belsim-Vali* [14] providing the chemical transformation and the heat requirements of the process units. These models are coupled with the economic and the energy integration models. The energy integration model computes the minimum energy requirements of the process using the mass balance between the unit operations and the heat cascade as constraints. If the combustion of the waste streams is not sufficient to provide the heat requirement above the pinch, selected process streams may be used as fuels. Available excess heat can be recovered in a Rankine cycle producing electricity. The energy integration model is detailed in [13], [15]. The economic model evaluating the profitability of the plant is based on equipment sizing and costing taking into account the operating conditions. The superstructure approach allows a flexible and systematic analysis of different process configurations. Sets of optimal design solutions are generated by the simultaneous optimization of the process in terms of thermodynamic performance and economic performance as a function of the decision variables.

3. Process Description

The overall process of thermo-chemical conversion of biomass into liquid fuels consists of: feed preparation, gasification, gas cleaning and treatment, and fuel synthesis and purification. Figure 1 represents the unit operations of the process, as well as the energy integration options. It is focused

[2] Consumer Price Index (CPI) for prices actualization. [33]

on two scenarios shown in the superstructure; the first, employing a FICFB gasifier and the second, an EF gasifier. These scenarios are referred to as FICFB and EF scenario.

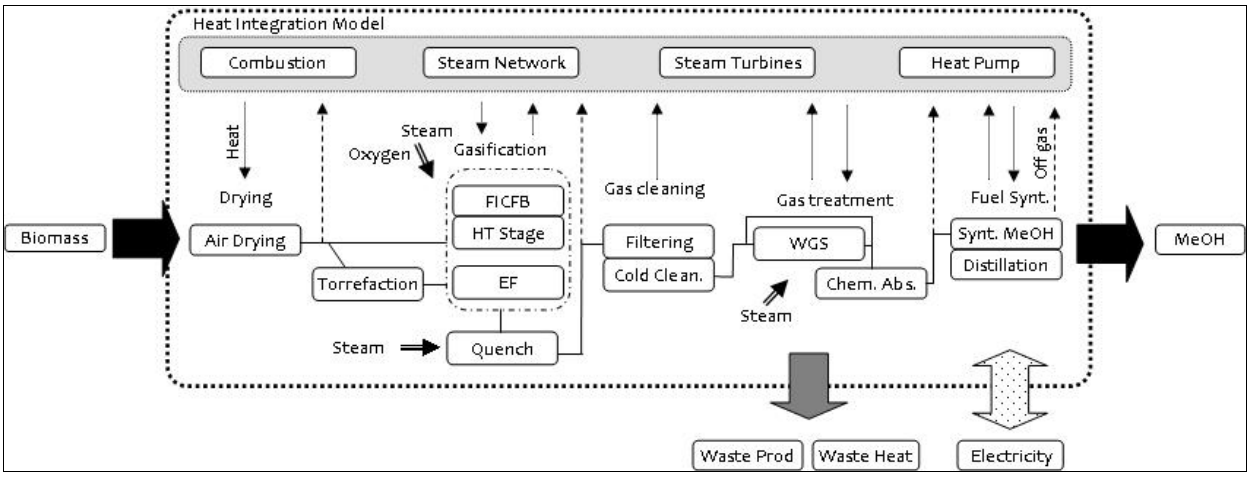

Figure 1 Simplified process superstructure for MeOH production, including the energy integration options (full arrow: heat exchange, double arrow: steam and oxygen, broken arrow: possible streams that could be used as additional fuels).

3.1. Thermo-Economic Models

The thermo-economic models used in this study are based on the work of Tock et al. [16]. The models used for biomass pre-treatment, gasification and gas cleaning are identical to those previously developed by Gassner et al. [12,18].

3.1.1. Thermo-Chemical Conversion Models

The biomass supplied to the process (50% humidity) is dried in an *air drying* unit which is optimized in respect to the residual humidity $\Phi_{d,wood}$ and the inlet air temperature T_d. The dried biomass is then directly grinded for FICFB gasification or torrefied ($T_{T,out}$ = 260°C) in order to be pulverized as required by the EF gasification. The model of the torrefaction unit is based on simple conversion ratios [17].

The FICFB gasifier consists of an indirectly heated circulating fluidized bed where the heat required for gasification is provided by circulating the bed material between two physically separated combustion and gasification chambers. The model of the FICFB gasifier is described in detail by Gassner et al. [18]. In the combustion chamber ungasified char and fuels are oxidized with air to heat up the bed material which is transferred via a cyclone to a gasification chamber where steam reacts with the biomass feed to produce the syngas. The advantage of this gasification technology is that it produces an essentially nitrogen-free product gas without requiring air separation for the oxygen supply. The main disadvantages arise from the methane and tar content of the synthesised gas and from the high investments costs due to the complicated construction. A directly heated high temperature stage (HT stage) is introduced to reduce the methane and hydrocarbon content in the product gas through autothermal steam methane reforming. The heat for the endothermic reforming is thus satisfied by partial oxidation with pure oxygen.

In the EF gasifier, the pulverized feed is entrained with the reacting gases, solid particles and gases move at approximately the same velocity. Consequently, smaller particles are required making the torrefaction step necessary. In this case, gasification is carried out using both oxygen and steam, and heat is provided directly by the oxidation of the feed. Advantages of this technology are the high capacity per unit volume (especially for the pressurized reactors) and the simpler geometry [19] (relatively to a fluidized bed). Because of the high temperature (1350°C), the product gas is almost

tar-free and a leach resistant molten slag is produced [20]. Disadvantages include the high oxygen consumption and a higher conversion of the energy of the feed into sensible heat [21].

The main operating conditions of the FICFB gasifier and the EF gasifier are summarized in Table 1. For both gasification scenarios the product gas is quenched with steam to a temperature of 800°C. In the *gas cleaning* step the product gas is cooled to 150°C before entering the filter and the scrubber where it is cooled to atmospheric temperature. The *water gas shift (WGS) reactor* and the *acid gas removal* (AGR) step are used to bring the synthesis gas to the specifications required for the synthesis of methanol, that is to a stoichiometric ratio s ($s=(H_2-CO_2)/(CO+CO_2)$) of 2. The exothermic WGS reaction produces extra H_2 (and CO_2) at the expense of CO by the addition of steam. It has been shown that, for kinetic reasons and in order to control by-products, a value slightly greater than two is preferred [5]. The CO_2 concentration is typically adjusted to 4-8% for optimal activity and selectivity [5,22]. Furthermore, an excess of steam is required to allow an almost complete conversion of CO and to push the reaction away from solid carbon formation. The molar steam to carbon ratio is usually between 2-6, depending on the feedstock and reactor conditions [5]. In the model a steam to carbon (mainly CO) ratio of 2.5 was used. The absence of solid carbon at reactor conditions and at thermodynamic equilibrium is verified using the software Gemini [23], which calculates the equilibrium composition by minimization of the Gibbs energy of the system. The absence of solid carbon is verified at equilibrium but this does not guarantee that any carbon soot is produced. In order to maintain the steam to CO ratio and obtain the required gas compositions only part of the stream needs to be shifted. The WGS unit is modeled as a single intermediate temperature reactor optimized with regard to the water gas shift reaction temperature T_{WGS} and the inlet temperature ($T_{in,WGS}=T_{WGS} - \Delta T_{WGS}$). The AGR step is modeled taking into consideration the values for the energy integration and economic analysis for chemical absorption as described by Tock [24]. *Methanol synthesis* is modeled by a multistage reactor with four beds in series [12, 23, 24] and it is optimized in respect to the synthesis gas inlet temperature $T_{m,in}$ and the reactors temperature and pressure (T_m, P_m). A fraction of the off-gases ($R_m = 0.95$) is recycled into the synthesis reactors, to increase methanol conversion. In order to increase the purity of the produced methanol a final *purification* step is required. Two distillation columns allow achieving a methanol purity of over 99% (Tock [24]). *Oxygen* is required for the EF gasifier and for the directly heated high temperature stage of the FICFB gasifier. Oxygen for gasification is conventionally produced by pressure swing adsorption or cryogenic distillation. An ASU (Air Separation Unit) is not included in the current model superstructure but it will be integrated in future studies. The energetic and economic costs of the oxygen supply have been considered. From an economic standpoint oxygen is considered as a utility, purchased at the price indicated by Kirschner [19]. The energetic cost of oxygen is taken into account considering an electricity consumption of 1080 kJ/kg_{O2} for off-site oxygen production. Oxygen is delivered at standard ambient temperature and pressure. The decision variables relative to the integration of the steam network, for the heat integration model, include two steam production pressures (p_{sp1}, p_{sp2}) and one steam consumption temperature (T_{sc2}).

The reference scenario considered for the thermo-chemical conversion of biomass into methanol is a 20 MW_{th} sized plant. The main fixed operating conditions and the decision variables are summarized in Table 1.

3.1.2. Economic Evaluation

The economic performance is evaluated by the total production cost including investment and operating costs. The capital cost estimates provide a basis for the overall comparison by assessing the trends implied by the decision variables, rather than an accurate estimate of the project. The cost estimation approach follows the one adopted by Gassner et al. [11] and Tock et al. [12] relying on data available in the literature.

Table 1 Main operating conditions and decision variables with their variation range

Section	Description	Variable	Value/Range	Unit
Dryer	air dryer inlet T	T_d	[180 240]	°C
	Wood Φ at outlet	$F_{d,wood}$	[10 35]	%
Torrefaction	Torrefaction T	$T_{T,out}$	260	°C
Gasfier (FICFB)	Steam to biomass ratio	$R_{s/b}$	0.5	-
	Gasification P	p_g	1.15	bar
	Gasification T	Tg	847	°C
	HT stage outlet T	T_{HT}	1350	°C
	Steam preheating T	T_{steam}	400	°C
Gasfier (EF)	Steam to biomass ratio	$R_{s/b}$	0.6	-
	Gasification P	p_g	30.15	bar
	Gasification T	T_g	1350	°C
Water Gas Shift	difference between unit inlet and reactor T	ΔT_{WGS}	[0.1 50]	°C
	WGS react T	T_{WGS}	[250 320]	°C
	steam to CO for WGS	$R_{s/co}$	2.5	-
Methanol Synthesis	S = $(H_2-CO_2)/(CO+H_2)$	S	2.05	-
	methanol synthesis inlet T	$T_{m,in}$	[227 387]	°C
	MeOH process P	p_m	[75 90]	bar
	MeOH synthesys T	T_m	[252 267]	°C
	Recycled fraction	R_m	0.95	mol
Steam Network	Steam production P	p_{sp1}	[40 120]	bar
	Steam production P additional level	p_{sp2}	[40 120]	bar
	T of additional steam consumption level	T_{sc2}	[50 250]	°C
	Steam superheating T	T_{SH}	[350 550]	°C

The currency exchange rates used are the yearly average exchange rates for 2010 [26] and all costs have been updated to year 2010 by using the Marshall and Swift Index. The investment costs are calculated on the basis of the methodology outlined in [26,27]. The major process equipments are roughly sized and their purchase cost is calculated and adjusted to account for specific process pressures and materials using correlations from literature. The *total investment cost* is then calculated using multiplication factors to take into account indirect expenses like labour, transportation, fees, contingencies and auxiliary facilities. The *operating costs* [€/GJ_{MeOH}] take into account the cost of labour, maintenance (5% of the total investment), raw materials (biomass, oxygen) and utilities (electricity). The *production cost* [€/GJ_{MeOH}] is the sum of the operating cost and the *depreciation cost*, the latter being the total investment cost divided by the present worth of annuity (1) (depending on the investment rate *ir* and the economic lifetime *t*) and the yearly production of methanol.

$$\textit{present worth of annuity} = \frac{(1+ir)^t - 1}{ir \cdot (1+ir)^t} \qquad (1)$$

The main assumptions for the economic evaluation are summarized in Table 2.

Table 2. Economic evaluation assumptions

Marshall and Swift Index (2010)	1473
US$ equivalency	1.3 US$/€
Expected lifetime *(t)*	15 y
Interest rate *(ir)*	6%
Plant availability	90%
Operators [a]	4 p./shift [12]
Operator's salary	66000 €/y
Biomass price [b] (Φ= 50%)	6 €/GJ_{BM} (21 €/MWh_{BM})
Electricity price [b]	43 €/GJ_e (155€/MWh_e)
Oxygen price ($1 – 10^5$ m^3/h)[19]	0.03- 0.7 €/kg

[a] For a plant size of 20 MW_{th} biomass input. For other production scales, an exponent of 0.7 with respect to plant capacity is used.

[b] The prices of electricity and biomass are representative of the European market. The high price of electricity accounts for the production/consumption of "green" electricity.

3.2. Process Performance Indicators

To assess the process performance, thermodynamic, economic and environmental indicators can be defined. The considered indicators are:

- Energy efficiency:

$$\eta_{en} = \frac{LHV_{MeOH} \cdot \dot{m}_{MeOH} + \dot{E}^{-}}{LHV_{Biomass} \cdot \dot{m}_{biomass} + \dot{E}^{+}} \quad (2)$$

- Chemical Efficiency:

$$\eta_{chem} = \frac{LHV_{MeOH} \cdot \dot{m}_{MeOH}}{LHV_{Biomass} \cdot \dot{m}_{biomass}} \quad (3)$$

- Equivalent efficiency:

$$\eta_{en_{eq}} = \frac{LHV_{MeOH} \cdot \dot{m}_{MeOH} + \frac{1}{\eta_{CC}} \cdot \left(\Delta \dot{E}^{-}\right)}{LHV_{Biomass} \cdot \dot{m}_{biomass}} \quad (4)$$

Where the superscripts – and + refer respectively to produced (output) and consumed (input) services. The equivalent energy conversion efficiency aims at correctly assessing the value of the produced or consumed by-products. In equation (4), contrary to definition (2), the consumed amount of power at the denominator is omitted and represented by the net overall output of electricity (ΔE^{-}) at the numerator [17]. The electrical power required is substituted by the equivalent amount of SNG (synthetic natural gas) which would be used for its generation in a CC (combined cycle).

The economic indicators are the total investment and the production cost previously described. The only environmental indicator taken into consideration is the *yearly avoided CO_2 emissions* [ktonCO_2/year] obtained by the substitution of conventionally produced methanol with the biomass derived methanol. The account of the CO_2 emissions assumes that the combustion of the biomass and derived methanol is carbon neutral, while it takes into account the emissions due to the harvesting and transport of biomass and the consumption of electricity which is dependent on the electricity mix. The CO_2 emissions relative to the use of fossil derived methanol take into account its production and combustion. The data used for environmental evaluation refers to the Swiss context and are taken from [29].

4. Optimization

The multi-objective optimization was carried out selecting as the objective functions, the minimization of the capital investment cost and the maximization of the equivalent efficiency (4). The generated pareto fronts for the two conversion scenarios employing the EF and the FICFB gasifiers are represented in Figure 2, in terms of specific investment cost (€/kW$_{BM}$) and equivalent efficiency:

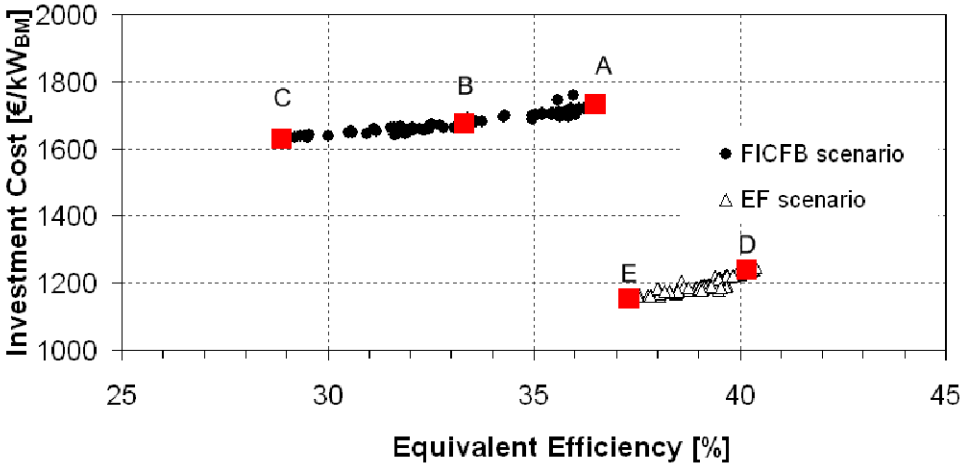

Figure 2 Optimization results for the FICFB and the EF scenarios

The designs A, B, and C are shown as representative of a high efficiency - investment cost, intermediate efficiency – investment and low efficiency – investment cost optimal designs for the FICFB scenario. The designs D and E are representative of a high efficiency – investment cost and low efficiency – investment cost optimal designs for the EF scenario. The performances of these designs are summarized in Table 3, and the composite curves of designs A, B, and C are represented in Figure 4.

Table 3 Summary of results for different design solutions

	Design	Capacity [MW$_{th,BM}$]	η_{en_eq} [%]	η_{en} [%]	η_{chem} [%]	Steam Cycle Power [kW/MW$_{BM}$]	Elec Net Cons* [kW/MW$_{BM}$]	Inv. Costs [€/kW$_{BM}$]	Op. Costs [€/GJ]	Prod. Costs [€/GJ]
FICFB	**A**	20	36.50	42.55	44.71	70.3	70.3 (15.6)	1736	29.6	44.6
	B	20	33.31	44.78	49.18	37.2	98.4	1677	30.9	44.0
	C	20	28.88	44.62	50.64	7.5	134.9	1632	32.9	45.4
EF	**D**	20	40.15	44.28	45.84	84.8	35.3 (38.5)	1241	24.1	34.6
	E	20	37.30	43.12	45.25	68.7	49.2	1155	25.4	35.3

* The share of power required for oxygen production is reported in parenthesis. Design D results in a net exporter of electricity, if the electricity required for oxygen production is not accounted for. The electricity consumption due to oxygen production is similar across the FICFB and the EF scenarios. The oxygen requirement for a capacity of 20MWth is of 0.28 kg/s and 0.47 kg/s for the FICFB and the EF scenarios respectively.

4.1. Analysis of the optimization results

The comparison of the composite curves of designs A and D are represented in Figure 3. Design A, with a FICFB, presents a pinch at the gasification temperature, while in design D the pinch

disappears because for the EF gasifier the heat is directly provided by the partial oxidation of the feed.

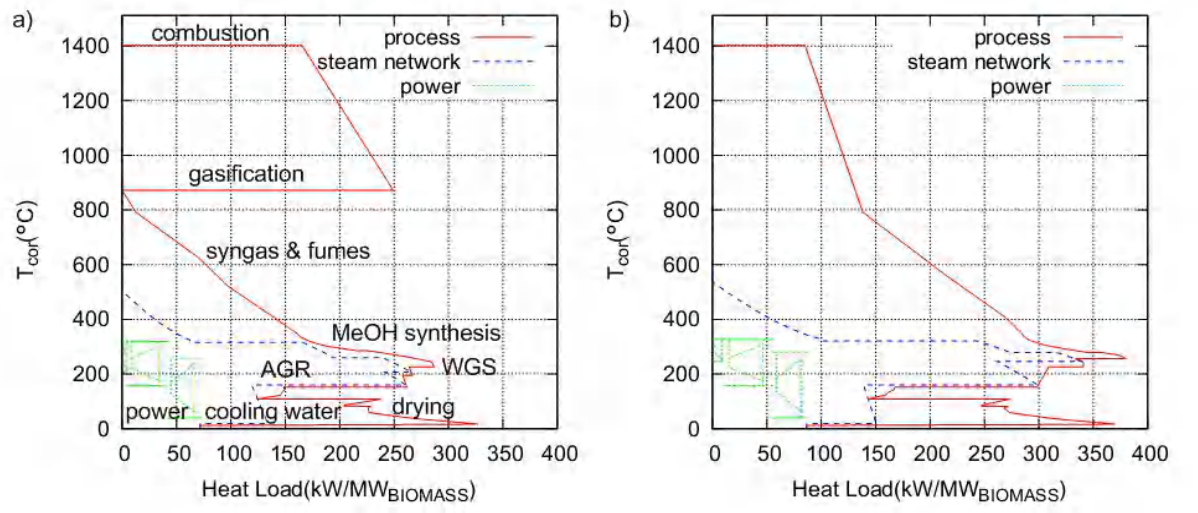

Figure 3 Comparison of the composite curves of (a) design A, with a FICFB gasifer, and (b) design D with an EF gasifier.

The analysis of the optimization results of both scenarios suggests that the co-generation of electricity has a determining importance in the positioning of the designs on the pareto front for both gasifier options. Designs with the lowest efficiency are the ones with smaller units for heat recovery and electricity generation, which are also the cheapest ones. Moving from the lowest efficiency designs to the highest ones, the amount of electricity produced increases, the process remaining a net importer of electricity all along the pareto front. This can be visualized by the composite curves of the three designs A, B, and C represented in Figure 4.

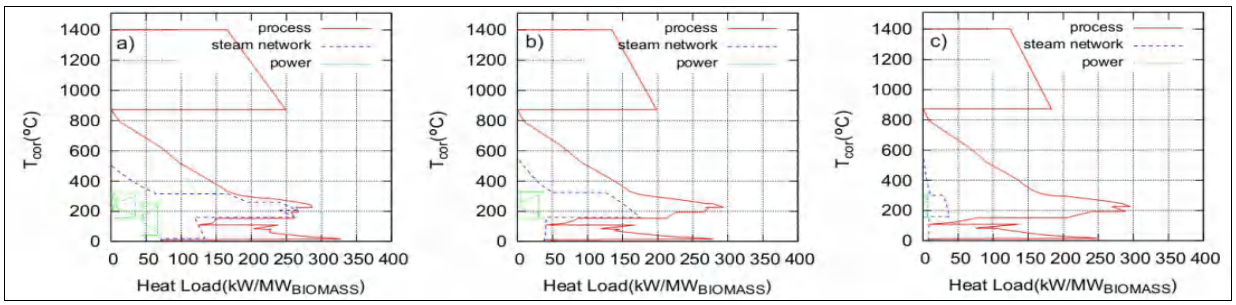

Figure 4 Composite curves of designs A (a) B (b) and C (c) belonging to the FICFB scenario

The role of the energy integration is also shown in Figure 5 where electric power and total electricity required by the process are represented as a function of the equivalent efficiency (4) for the FICFB and the EF scenario. The secondary axis indicates the chemical (2) and energy (3) efficiencies. These results show the importance of the heat integration and the cogeneration of electricity in improving the overall efficiency of the process. For both design solutions the highest equivalent efficiency processes are the ones displaying a higher fraction of the required electricity produced via a Rankine cycle. The overall equivalent energy efficiency results are higher for the EF designs than for the FICFB. This is in part due to the integration of the combined cycle which is able to provide a larger fraction of the electricity requirement. The EF gasifier, in fact, makes available a higher fraction of the feed as high temperature heat which may be converted into electricity. As explained before, an inconvenient of the FICFB gasifier is the presence of methane and tars in the produced gas. In this study tar removal and methane reforming is carried out by a HT stage following the FICFB gasifier. The temperature of the HT stage depends on technological constraints and the nature of the biomass resource. Its value greatly affects the performance of the

process, as higher temperatures impose larger oxygen consumption (and therefore energy requirements). For design A, for example, the equivalent efficiency η_{en_eq} could be raised by 1.7% point to 38.2 % (η_{en} = 44.2%, η_{chem} = 46.5 %) if the HT stage temperature was reduced by 100°C to 1250°C. In a subsequent optimization study the influence of the temperature can be studied in more detail. Other technological options for the reduction of tars and the reforming of methane have been investigated in other studies, such as catalytic cracking and mechanism methods (i.e. scrubbers). A review of tar reduction and control technologies for biomass gasification is presented by Han et al. [30].

The energy efficiencies are similar for both scenarios and range between 42 and 45%. The chemical efficiencies range between 45 and 51%, corresponding to mass yields between 42 and 48%. These values are in the same range of the efficiencies reported in the literature but the comparison results difficult because of the different process options and operating conditions. The efficiency of the FICFB is slightly lower than what is reported by Hamelinck et al. [7] for a fluidized bed, this difference is mainly due to the presence of the HT stage in the present study.

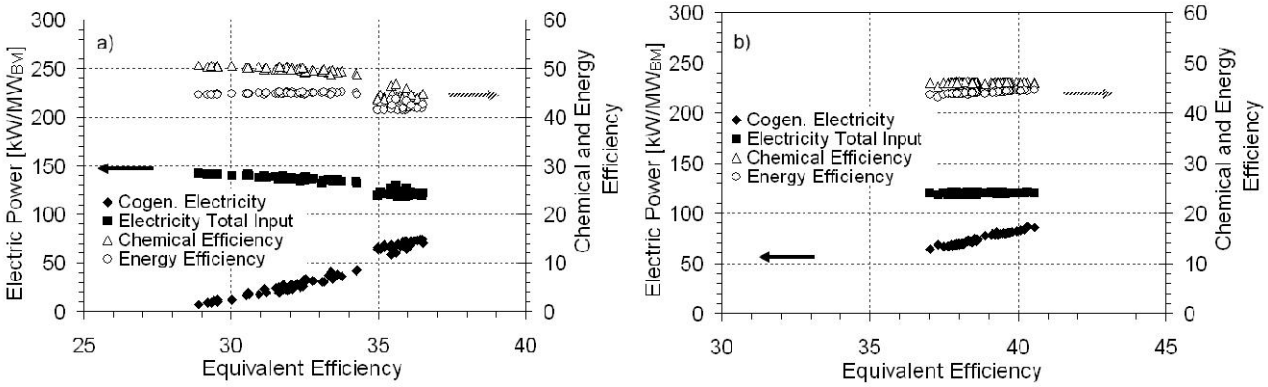

Figure 5 Effect of heat integration on the optimal conceptual designs for the FICFB scenario (a) and the EF scenario (b). The cogeneration power, total electricity requirement, the chemical and energy efficiency are represented as a function of the equivalent efficiencies. The x-axes do not have the same scale.

The investment cost build-up for the high efficiency designs of the FICFB scenario and the EF scenario are shown in Figure 6.

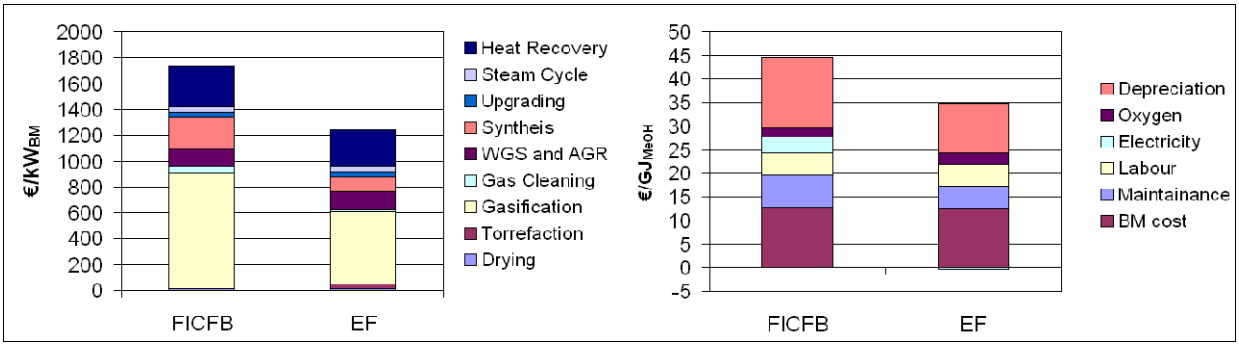

Figure 6 Investment production cost build-up for the FICFB (design A) and the EF (design D) scenarios.

The cost of the gasifier represents a large fraction of the total investment cost. The higher cost for the FICFB is in large part due to the cost of the gasifier itself. The lower estimated cost of the EF gasifier is due to its simpler design and the possibility of building larger units. Furthermore for the FICFB scenario, two gasification units are required, while only one gasifier is required in the EF scenario. The production costs results are also lower for the EF gasifier mainly because of the impact of the lower investment costs. The oxygen required by the processes appears in the

production costs as it is purchased [19]. This is why design D results a slight net exporter of electricity. Nevertheless, for a more reliable comparison of the cost of the two technologies more information would be needed.

5. Sensitivity Analysis

The base price considered for biomass is 6 €/GJ and for electricity, 43 €/GJ (Table 2). For comparison, the price of electricity for industry in France is about 20 €/GJ [31], but in Italy and Switzerland about 40 €/GJ [30,31]. Furthermore, if the product is to be considered renewable, the imported electricity should also be provided by a renewable resource, which may result in a higher electricity price. The sensitivity analysis was carried out considering a price range for electricity between 20 and 50 €/GJ and for biomass between 3 and 12 €/GJ. The sensitivity of the production and operating costs of the electricity and biomass prices for the three previously described designs, belonging to the FICFB scenario is represented in Figure 7. The strong impact of the biomass cost highlights the importance of the chemical efficiency to obtain favourable methanol production costs.

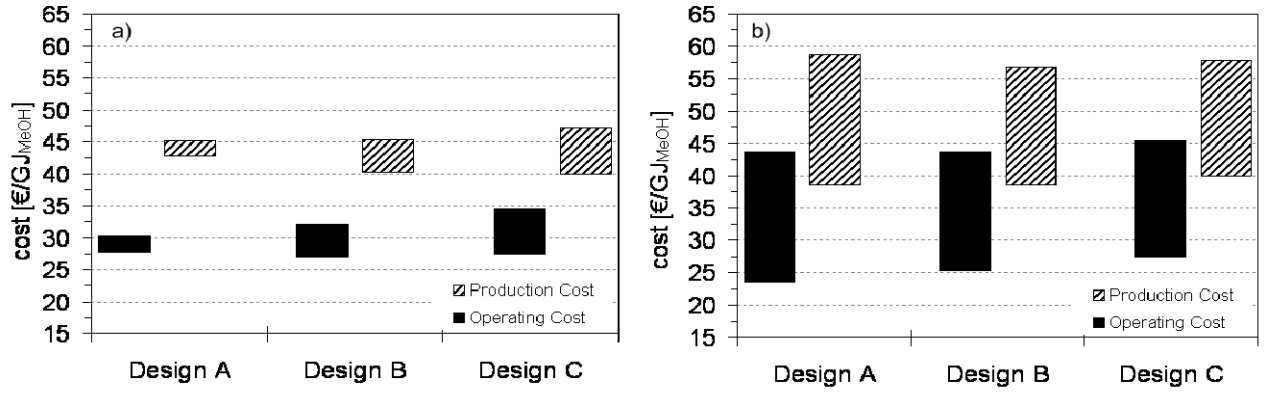

Figure 7 Sensitivity analysis for the FICFB scenario a) base price for biomass is 6 €/GJ, electricity price range 20-50 €/GJ. b) base price for electricity is 43 €/GJ, biomass price range 3-12€/GJ.

The reference scenario considered for this study is a 20 MW_{th} sized plant. Figure 8 shows the variation of operating and production costs and the environmental impact in terms of yearly CO_2 avoided emissions as a function of the plant size, for designs A and C.

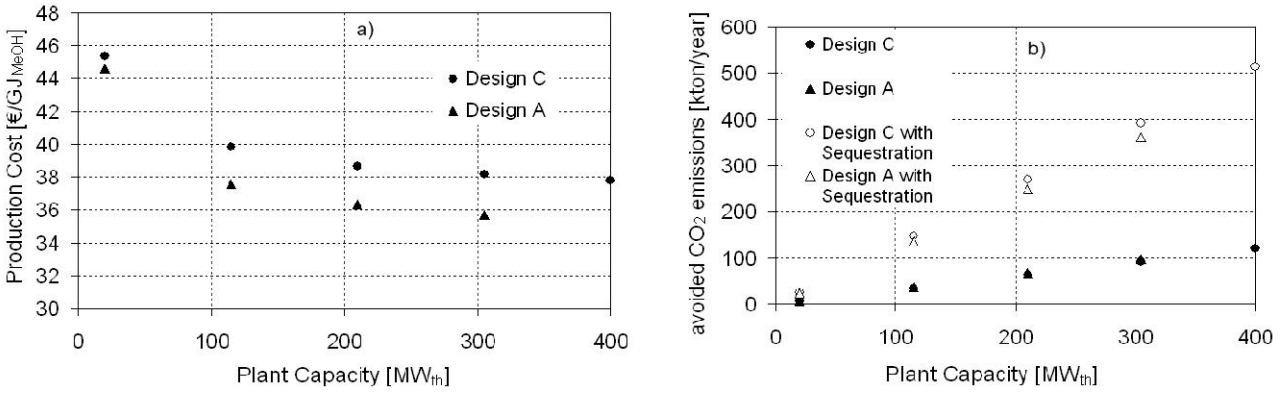

Figure 8 a) Production cost and b) avoided CO_2 emissions sensitivity analysis on the plant capacity.

As expected, the economies of scale have non-linear impact on the production costs which decrease by about 15% from a plant capacity of 20 MW_{th} of biomass input to about 200 MW_{th}. The

production cost reduction between 200 MW_{th} and 400 MW_{th} is only about 2%. The avoided CO_2 emissions increase linearly with the plant capacity as they are proportional to the produced methanol. The distance at which biomass is sustainably available also affects the evaluation of the production cost and the CO_2 emissions in terms of the optimal plant capacity, but it hasn't been the focus of this study.

6. Conclusions

The thermo-economic optimization of biomass thermo-chemical conversion into methanol was carried out considering as alternative scenarios, a FICFB gasifier and an EF gasifier. The performances of the optimized conceptual designs were evaluated consistently in terms of efficiency, costs and environmental performance. Results show the importance of the energy integration and in particular of the Rankine/cogeneration cycle for the improvement of the overall efficiency of the process. The EF scenario displays higher equivalent efficiencies in comparison to the FICFB scenario because the integration of a steam cycle allows for a larger production of electricity, satisfying part of the energy requirement of the plant. On the other hand, the overall energy efficiencies are similar for the two scenarios and result of about 43-45%. The chemical efficiencies range between 45-51%. From an economic standpoint, the production costs, ranging from 35 to 45 €/GJ remain well above the current price for natural gas derived methanol but the evaluation of the avoided CO_2 emissions highlights the potential of this biomass conversion route in a carbon constrained world.

Acknowledgments

Thanks are due to Geert Haarlemmer for helpful discussions.

Nomenclature

Abbreviations

AGR Acid Gas Removal
BM Biomass
DME Dimethyl ether
EF Entrained Flow
FT Fischer- Tropsch
FICFB Fast Internally Circulating Fluidized Bed
HHV Higher Heating Value, MJ/kg
LHV Lower Heating Value, MJ/kg
MeOH Methanol
WGS Water Gas Shift

Roman Letters

P Pressure, bar
T Temperature, °C
$\dot{E}$ Mechanical/electrical power, kW
$\dot{m}$ Mass flowrate, kg/s

Greek symbols

Φ Humidity, %

η_{en} Energy Efficiency, %

η_{chem} Chemical Efficiency, %

η_{en_eq} Equivalent Efficiency, %

References

[1] E. Fiedler, G. Grossmann, D. B. Kersebohm, G. Weiss, and C. Witte, "Methanol," *Ullmann's Encyclopedia of Industrial Chemistry*, Jun. 2000.

[2] "Methanex," 2012. [Online]. Available: www.methanex.com/products/methanolprice.html. [Accessed: 01-Jan-2012].

[3] G. A. Olah, A. Goeppert, and G. K. S. Prakash, *Beyond Oil and Gas: The Methanol Economy*. Wiley-VCH, 2009, p. 334.

[4] M. Iglesias Gonzalez, B. Kraushaar-Czarnetzki, and G. Schaub, "Process comparison of biomass-to-liquid (BtL) routes Fischer–Tropsch synthesis and methanol to gasoline," *Biomass Conversion and Biorefinery*, vol. 1, no. 4, pp. 229-243, Oct. 2011.

[5] P. L. Spath and D. C. Dayton, "Preliminary Screening - Technical and Economic Assessment of Synthesis Gas to Fuels and Chemicals With Emphasis on the Potential for Biomass-Derived Syngas," Dec. 2003.

[6] C. E. Wyman, N. D. Hinman, R. L. Bain, and D. J. Stevens, "Chapter 21 -Ethanol and Methanol from Cellulosic Materials," in *Renewable energy: sources for fuels and electricity*, Island Press, Washington, D.C.,, 1993.

[7] C. N. Hamelinck and A. P. . Faaij, "Future prospects for production of methanol and hydrogen from biomass," *Journal of Power Sources*, vol. 111, no. 1, pp. 1-22, Sep. 2002.

[8] G. L. M. a. Van Rens, G. H. Huisman, H. De Lathouder, and R. L. Cornelissen, "Performance and exergy analysis of biomass-to-fuel plants producing methanol, dimethylether or hydrogen," *Biomass and Bioenergy*, pp. 1-10, Jun. 2011.

[9] G. H. Huisman, G. L. M. A. Van Rens, H. De Lathouder, and R. L. Cornelissen, "Cost estimation of biomass-to-fuel plants producing methanol, dimethylether or hydrogen," *Biomass and Bioenergy*, May 2011.

[10] S. Bengtsson, "The CHRISGAS project," *Biomass and Bioenergy*, vol. 35, p. S2-S7, 2011.

[11] M. Gassner and F. Maréchal, "Thermo-economic process model for thermochemical production of Synthetic Natural Gas (SNG) from lignocellulosic biomass," *Biomass and Bioenergy*, vol. 33, no. 11, pp. 1587-1604, 2009.

[12] L. Tock, M. Gassner, and F. Maréchal, "Thermochemical production of liquid fuels from biomass: Thermo-economic modeling, process design and process integration analysis," *Biomass and Bioenergy*, vol. 34, no. 12, pp. 1838-1854, Aug. 2010.

[13] M. Gassner and F. Marechal, "Methodology for the optimal thermo-economic, multi-objective design of thermochemical fuel production from biomass," *Computers & Chemical Engineering*, vol. 33, no. 3, pp. 769-781, 2009.

[14] Belsim S.A., "Belsim Vali." [Online]. Available: www.belsim.com. [Accessed: 01-Jan-2012].

[15] F. Maréchal and B. Kalitventzeff, "Process integration: Selection of the optimal utility system," *Computers & Chemical Engineering*, vol. 22, no. 98, p. S149--S156, 1998.

[16] L. Tock, M. Gassner, and F. Maréchal, "Thermo-economic Evaluation of the Thermochemical Production of Liquid Fuels from Biomass," *23rd International Conference on Efficiency, Cost, Optimization, Simulation and Environmental Impact of Energy Systems*, vol. 2, p. 35, 2010.

[17] M. Gassner, *Process design methodology for thermochemical production of fuels from biomass. Appliaction to the production of synthetic natural gas from lignocellulosic resources*. École Polytechnique Fédérale de Lausanne, Switzerland, 2010.

[18] M. Gassner and F. Maréchal, "Thermodynamic comparison of the FICFB and Viking gasification concepts," *Energy*, vol. 34, no. 10, pp. 1744-1753, 2009.

[19] M. J. Kirschner, "Oxygen," in *Ullmann's Encyclopedia of Industrial Chemistry*, Weinheim, Germany: Wiley-VCH Verlag GmbH & Co. KGaA, 2000.

[20] E. Henrich and F. Weirich, "Pressurized Entrained Flow Gasifiers for Biomass," *Environmental Engineering Science*, vol. 21, no. 1, pp. 53-64, Jul. 2004.

[21] R. Reimert, F. Marschner, H.-J. Renner, W. Boll, E. Supp, M. Brejc, W. Liebner, and G. Schaub, "Gas Production, 2. Processes," *Ullmann's Encyclopedia of Industrial Chemistry*, 2011.

[22] I. Wender, "Reactions of synthesis gas," *Fuel Processing Technology*, vol. 48, no. 3, pp. 189-297, 1996.

[23] B. Cheynet, *Computer Software in Chemical and Extractive Metallurgy*. Pergamon Press, 1989.

[24] L. Tock, *Evaluation Thermo-économique des productions de carburants liquides à base de biomasse*. École Polytechnique Fédérale de Lausanne, Switzerland, 2009.

[25] F. Maréchal, G. Heyen, and B. Kalitventzeff, "Energy savings in methanol synthesis: Use of heat integration techniques and simulation tools," *Computers & Chemical Engineering*, vol. 21, no. 97, p. S511-S516, 1997.

[26] Internal Revenue Service, "Yearly Average Currency Exchange Rates," 2012. [Online]. Available: http://www.irs.gov. [Accessed: 03-Jan-2012].

[27] R. Turton, B. Richard C., W. Wallace B., and S. (Author) Joseph A., *Analysis, Synthesis, and Design of Chemical Processes*. Prentice Hall; 2 edition, 2002, p. 987.

[28] G. D. Ulrich and T. V. Palligarnai, *Chemical Engineering Process Design and Economics, a Practical Guide [Hardcover]*. Process Publishing; 2nd edition, 2004, p. 706.

[29] "Ecoinvent." [Online]. Available: www.ecoinvent.ch. [Accessed: 01-Jan-2012].

[30] J. Han and H. Kim, "The reduction and control technology of tar during biomass gasification/pyrolysis: An overview," *Renewable and Sustainable Energy Reviews*, vol. 12, no. 2, pp. 397-416, Feb. 2008.

[31] "Europe's Energy Portal," 2012. [Online]. Available: www.energy.eu. [Accessed: 01-Jan-2012].

[32] "Commission fédérale de l'électricité," 2010. [Online]. Available: www.news.admin.ch. [Accessed: 01-Jan-2011].

[33] "U.S. Department Of Labor - Bureau of Labor Statistics." [Online]. Available: ftp://ftp.bls.gov/pub/special.requests/cpi/cpiai.txt. [Accessed: 01-Jan-2012].

Thermoeconomic Fuel Impact Approach for Assessing Resources Savings in Industrial Symbiosis: Application to Kalundborg Eco-industrial Park

Sergio Usón[a], Antonio Valero[b], Alicia Valero[c] and Jorge Costa[d]

[a] *CIRCE-Universidad de Zaragoza, Zaragoza, Spain, suson@unizar.es CA*
[b] *CIRCE-Universidad de Zaragoza, Zaragoza, Spain, valero@unizar.es*
[c] *CIRCE-Universidad de Zaragoza, Zaragoza, Spain, aliciavd@unizar.es*
[d] *CIRCE-Universidad de Zaragoza, Zaragoza, Spain, jorge_frg@hotmail.com*

Abstract:

Thermoeconomics is a powerful analysis tool for Industrial Symbiosis because: i) it provides a systemic approach and ii) the use of exergy allows the characterization of both energy and matter flows by using a common basis. Furthermore, techniques developed within Thermoeconomics for the analysis, synthesis, optimization and diagnosis of energy systems may be adapted for its application to Industrial Symbiosis.
A general methodology for relating the savings of resources of a given eco-park with improvements in local efficiencies of components, introduction of integrations and variations of park production is presented. The approach is based on the fuel impact approach developed in Thermoeconomics for the diagnosis of the operation of energy systems, but introduces significant improvements: i) the introduction of integrations requires the modelling of discrete changes in the productive structure of the system and ii) the purpose of the comparison is to analyze effects of improvements instead of reduction of efficiency.
The formulation is applied to the example of symbiosis in Kalundborg, where the present situation is compared to a reference state without symbiosis. Exchange flows considered include waste heat, steam, ash, waste gas and gypsum, which are shared among a power plant, a refinery, a district heating system, a plaster board industry, a cement plant, a fish farm and others. Application of the methodology points out how the integration of by-products causes local savings that, in turn, produce savings at eco-park level.

Keywords:

Industrial Symbiosis, Thermoeconomics, Kalundborg, Fuel Impact Formula

1. Introduction

The aim of Industrial Symbiosis is the transformation of conventional linear productive chain into material cycles by using wastes from industries as raw materials for others [1-3]. Accordingly, it is a core part of Industrial Ecology, which is a multidisciplinary area looking for achieving a more rational and balanced industrial organization, trying to imitate the structure and operation of natural ecosystems [1,4]. The ideas of Industrial Symbiosis are implemented in eco-industrial parks, which are defined as "a community of businesses that cooperate with each other and with the local community to efficiently share resources (information, materials, water, energy, infrastructure and natural habitat), leading to economic gains, gains in environmental quality, and equitable enhancement of human resources for the Business and local community" [5].

Several analysis tools are used in Industrial Symbiosis. The most widely used is Input-Output analysis [6,7]. This powerful methodology has a drawback: it uses different measurement units for the different flows. This disadvantage is overcome by using monetary costs, introducing subjectivity. The use of exergy can be seen as solution for this problem, because it allows one to

express all flows in the same physical units. Exergy has been used in several applications related to Industrial Ecology such as quantification of resource depletion [8] or life cycle assessment [9-11].

A first step towards the application of Thermoeconomics [12,13] to Industrial Symbiosis was the application of exergy to input-output analysis [14], while the actual application was developed in [15]. This research was continued in [16] where a methodology for cost analysis formation in eco-industrial parks was proposed.

Besides, one of the most interesting applications of Thermoeconomics developed during the last years is the diagnosis of energy systems [17-19]. This area of research aims at the detection of malfunctioning components in energy systems and the quantification of the additional fuel consumption caused by each one of them. In this paper, a methodology for quantifying resources savings in Industrial Symbiosis based on the fuel impact-approach developed for diagnosis is developed and applied. The goal of the approach is to compare two situations: with and without integration. Due to integration, the amount of resources consumed by the whole system is reduced. The method is able to quantify which part of these savings corresponds to: i) improvements in components (either by improving their efficiency or by using by-products), ii) reduction of the generation of wastes and iii) variation of the production of useful streams. As an example of application, a simplified version of the Kalundborg eco-industrial park is used.

2. Methodology

In this section, the methodology proposed is presented. In the first part, the main concepts of thermoeconomic analysis are reviewed while in the second, the method itself is described.

2.1. Review of thermoeconomic input-output analysis

Thermoeconomic input-output, also known as symbolic exergoeconomics, provides a general framework for thermoeconomic analysis based on matrix notation which can be easily implemented in computers [20]. In order to apply the approach, the physical structure of the system, where all physical flows appear, has to be substituted by the productive structure, where fuel and product flows are depicted. All components of this productive structure are numbered starting from 1, and the number 0 corresponds to the environment. E_{ij} is the part of the product of component i that becomes part of the fuel of component j. A generic component i with its fuel and product is represented in Fig. 1.

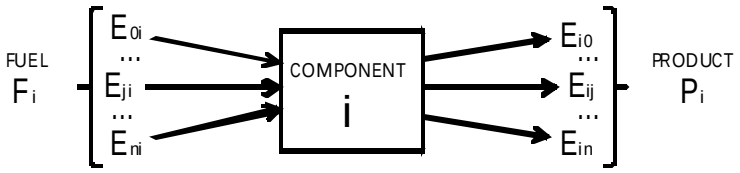

Fig. 1. Fuel and product of a generic component i.

Accordingly, product (P_i) and fuel (F_i) of a given component i are:

$$P_i = \sum_{j=0}^{n} E_{ij} \qquad (1)$$

$$F_i = \sum_{j=0}^{n} E_{ji} \qquad (2)$$

A table containing the values of all elements E_{ij} as well as their summations by columns and rows is called fuel-product table.

The unit exergy consumption (κ_{ij}) is defined as the number of units of exergy that each component requires from the other components to obtain a unit of its product:

$$\kappa_{ij} = \frac{E_{ij}}{P_j} \tag{3}$$

The sum of all unit exergy consumptions (k_j) in a component is the inverse of the exergy efficiency of that component (η_j):

$$k_j = \sum_{i=0}^{n} \kappa_{ij} = \frac{F_j}{P_j} = \frac{1}{\eta_j} \tag{4}$$

Exergy cost of a flow E_{ij} is the amount of exergy resources entering the system needed to produce that flow; it is represented as E^*_{ij} and has units of exergy. The unit exergy cost (k*) is the quotient between the exergy cost and the exergy of the flow, accordingly, it is non-dimensional:

$$k^*_{ij} = \frac{E^*_{ij}}{E_{ij}} \tag{5}$$

All flows of the product of a component are considered to have the same formation process and, accordingly, they have the same unit cost. This assumption constitutes a limitation of the method that can be overcome by a suitable definition of the productive structure. Thus, the following equation can be written:

$$k^*_{ij} = k^*_{P,i} \tag{6}$$

By applying the cost balance of all components, it can be demonstrated that the unit cost of the flows can be obtained by using the following equation:

$$\mathbf{k}^*_{\mathrm{P}} = (\mathrm{U_D} - \langle \mathrm{KP} \rangle^{\mathrm{t}})^{-1} \boldsymbol{\kappa}_{\mathrm{e}} \tag{7}$$

where ${}^{t}\kappa_e \equiv (\kappa_{01},\ldots,\kappa_{0n})$ is a (n x 1) vector whose elements contain the unit consumption of external resources and $\langle \mathbf{KP} \rangle$ is a (n x n) matrix whose elements are the unit exergy consumptions κ_{ij}. More details on thermoeconomic analysis can be seen in [20,21].

2.2. Application of thermoeconomic analysis to the quantification of resources savings

One possibility for quantifying resources savings is to apply an increment formulation of the exergy balance of the plant. Reduction of the resources consumed by the plant (PS) is, thus due to three effects: reduction of irreversibility in components ($-\Delta I_i$), reduction of plant production of useful products ($-\Delta P_s$), and reduction of amount of waste ($-\Delta P_r$):

$$PS = \sum_{i=1}^{n} (-\Delta I_i) - \Delta P_s - \Delta P_r \tag{8}$$

The problem of the previous formula appears because when savings occurs in a component, irreversibility usually varies also in other components in order to keep the plant production. For example, if there is a substitution of a turbine of a power plant that leads to higher efficiency, this turbine will need less steam in order to keep the power produced and, accordingly, irreversibility of the boiler will also decrease. For this reason, more detailed analysis is needed.

When the unit exergy consumption of a component decreases ($-\Delta\kappa_{ji}$), the irreversibility in this component also decreases leading to local savings (LS) in that component.

$$LS_{ji} = -\Delta\kappa_{ji} P_i(x_0) \tag{9}$$

where $P_i(x_0)$ is the product of component i in the reference situation (before the improvement). The total local savings in that component are:

$$LS_i = -\Delta k_i P_i(x_0) = \sum_{j=0}^{n} LS_{ji} \quad (10)$$

This reduction of irreversibility is interesting because it is associated to the behavior of the component (it is proportional to the variation of its unit exergy consumption). However, it is not the variation in resources consumed by the plant. This correspondence is made through the unit exergy cost of fuel of the component. Accordingly, *plant savings* (PSk) are defined as the additional amount of fuel entering the plant (or park) caused by *local savings*, and it is calculated as:

$$PSk_{ji} = k^*_{P,j}(x) LS_{ji} \quad (11)$$

$$PSk_i = \sum_{j=0}^{n} PSk_{ji} \quad (12)$$

where $k^*_{p,j}(x)$ is the unit cost of the product of j in the operation situation (after improvements). If the amount of product leaving the plant is reduced (ΔP_s), it causes also plant savings (PSp) that can be calculated as:

$$PSp_i = -k^*_{P,i}(x) \cdot \Delta P_{s,i} \quad (13)$$

Besides, the reduction of the amount of waste leaving the plant (ΔP_r) also causes plant savings (PSr) that can be calculated as:

$$PSr_i = -k^*_{P,i}(x) \cdot \Delta P_{r,i} \quad (14)$$

Finally, the total amount of plant savings fuel impact is a summation of plants savings due to variation in the components (PSk), plant savings due to reduction in plant production of useful products (PSp), and reduction of plant generation of wastes (PSr):

$$PS = \sum_{i=1}^{n} PSk_i + \sum_{i=1}^{n} PSp_i + \sum_{i=1}^{n} PSr_i \quad (15)$$

3. Example of application

3.1. Description and exergy of flows

In order to demonstrate the applicability of the methodology proposed, an example based on Kalundborg eco-industrial park will be used. Since the application to the whole system is out of the scope of the present work and would be difficult because the lack of data, a simplified example has been defined considering the more representative flows of this eco-park. The working case is defined around the thermal power plant of Asnaes, which represents the core of the park, and includes the following symbiotic exchanges:

- Waste gas from the refinery is used in the boiler of the power plant, substituting part of the coal consumed in that plant.
- Process steam is bleed from the steam cycle of the power plant.
- Steam for district heating is bleed from steam cycle.
- Hot sea water at low temperature from power plant condenser is used in fish farm.
- Ash and slag from the power plant boiler are used as substitute for clinker in cement manufacturing.
- Gypsum produced in the desulfurization process of the power plant is used in a plasterboard industry.

In order to assess the effect that industrial symbiosis has on resources savings, the working case described is divided into two situations: with and without integration. The first case considers the

situation corresponding to industrial symbiosis with the six integrations considered before. The second case simulates a fictitious situation where no integration is present, in a way that symbiotic matter and energy flows are substituted by others produced by conventional processes. In other words: waste gas is flared thus causing an additional coal consumption in the boiler, integrations of steam and hot water are substituted by natural gas-fired boilers, ash and slag are replaced by clinker produced in a kiln and gypsum is imported from Spain by sea. Figure 2 represents a physical diagram corresponding to a superstructure able to represent both cases.

Exergy of all flows present in Fig. 2 are listed in Table 1, for both situations. Asterisks are used to indicate flows dissipated in the non-integrated case. Exergy values have been calculated using a data from [20-22], and details of calculations can be found in the first part of this paper[1].

3.2. Productive structure

The starting point for thermoeconomic analysis is the definition of the productive structure, which is represented in Fig. 3. This structure is the graphical representation of the Fuel, Product and Waste flows of the system considered. For this reason, the structure contains the Fuel-Product-Residue definition of each component. It should be noted that these flows of the productive structure are, in general, different from the actual flows of the physical structure; for instance, the product of the boiler going to steam turbine is the flow of live steam minus the flow of condensate water; accordingly, it is represented as a single flow in the productive structure.

The most interesting aspect of the productive structure defined is that components representing the considered integration do not operate in the same way in both cases considered. In other words, in the integrated situation they act as junctions directly connected to the power plant without consuming external resources, while in the example without integration they act as processes isolated from the power plant consuming external resources.

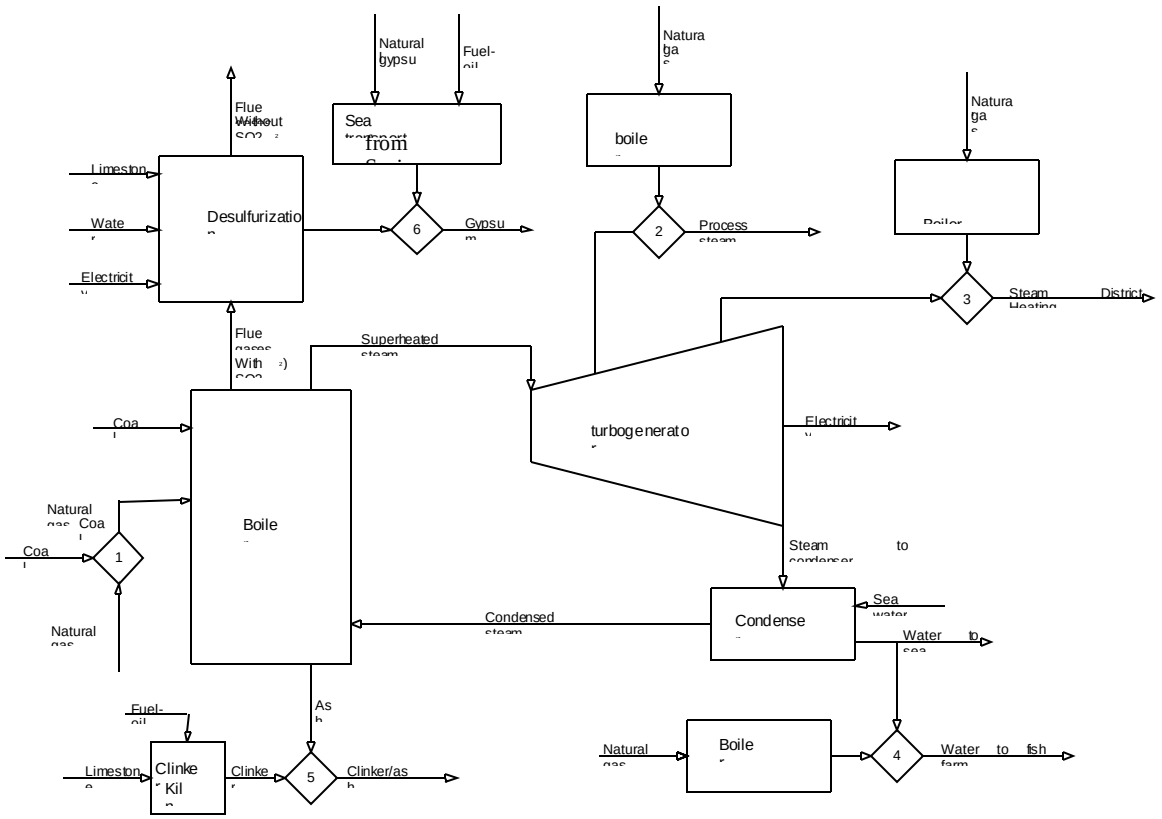

Fig. 2. Physical structure.

[1] Alicia Valero, Sergio Usón and Jorge Costa. Exergy Analysis of the Industrial Symbiosis Model in Kalundborg. Accepted for presentation in ECOS 2012.

Table 1. Yearly exergy of flows in the working example.

	B_{year} [GWh/year]	
Flow	*Integration*	*No integration*
Coal	16.376	10.591
Waste gas*	841.7	841.7
Electricity power plant	3.968	3.968
Ash and slag*	21.79	22.24
Sulphur dioxide	25.98	26.51
Limestone for desulfurization	1.933	1.973
Water desulfurization	4.51	4.604
Gypsum from desulfurization*	2.036	2.078
Electricity for desulfurization	24.8	24.8
Process steam	193.4	193.4
District heating steam	63.8	63.8
Hot water for fish farm	14	14
Steam for turbines	4.487	4.487
Natural gas process	-	495.8
Natural gas district heating	-	307.7
Natural gas fish farm	-	254.4
Limestone clinker	-	16.26
Fuel-oil clinker	-	213.4
Clinker	-	59.51
Natural gypsum	-	2.036
Fuel-oil gypsum transport	-	9.703

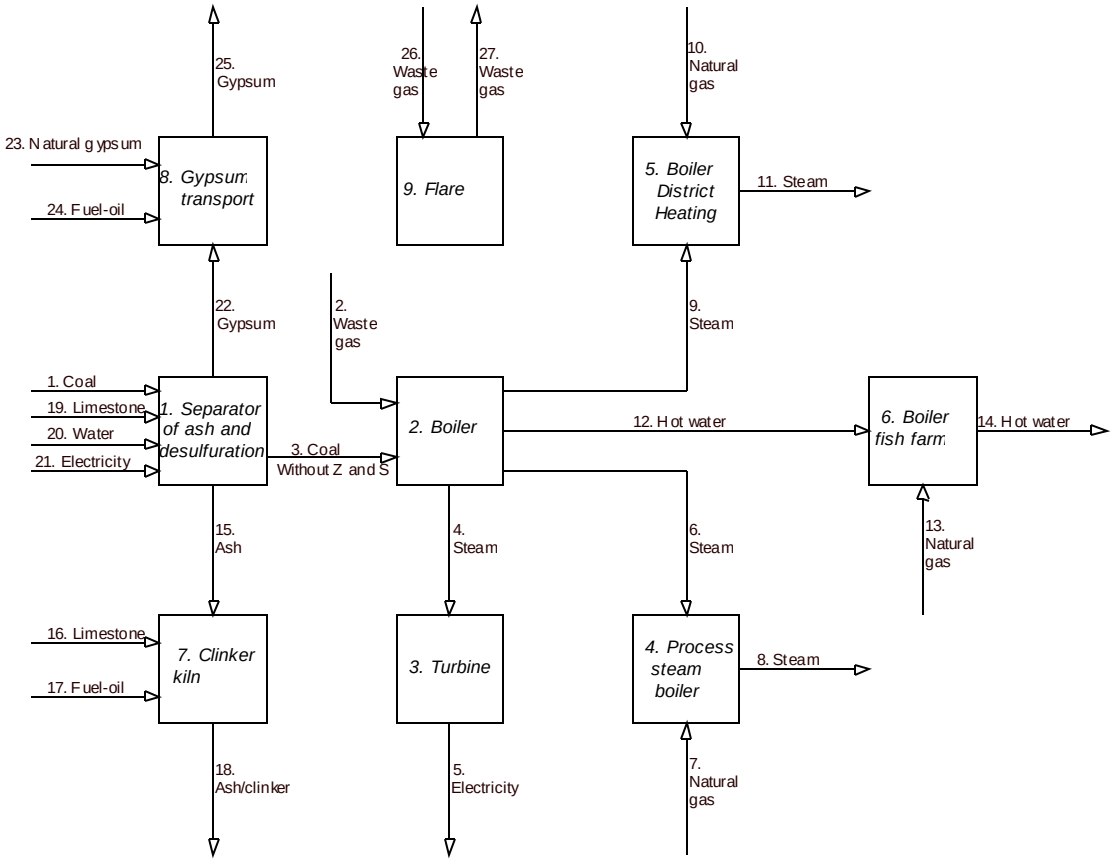

Fig. 3. Productive structure

This type of structure able to properly representing both situations is a key innovative point of the work presented. It should be noted that the cost of waste flow leaving the flare is assigned to the boiler of the power plant. Once the productive structure has been defined, it is possible to calculate unit exergy costs for all flows and to apply the resources savings decomposition with the methodology presented above.

3.3. Unit exergy costs

As it was presented previously, the unit exergy cost is the amount of resources, measured in exergy, needed to obtain a unit of product of each component. Table 2 contains unit exergy costs of the products of each component for both situations.

Table 2. Unit exergy costs of the products of the components

	Unit exergy cost [-]	
Component	*Integration*	*No integration*
1. Separator + desulfurization	1.0054	1.0076
2. Boiler	2.3591	2.5550
3. Turbine	2.6676	2.8891
4. Process steam boiler	2.3591	2.5636
5. District heating boiler	2.3591	4.8229
6. Fish farm boiler	2.3591	18.1714
7. Clinker kiln	1.0054	3.8592
8. Gypsum transport	1.0054	5.7657
9. Flare	1.0000	1.0000

Table 2 shows how the unit exergy cost of integrated components is decreased, except the flare. These reductions appear because integrations, which act as junctions in the integrated case, are substituted by alternative processes consuming resources and having irreversibility. These reductions are analyzed in detail below.

- Separator + desulfurization. The variation is negligible and appears because in the case without integration flows of ash and gypsum entail irreversibilities due to the component. Accordingly, it was expected that the cost would remain almost constant, considering that processes of separation of ash and desulfurization keep their exergy efficiency constant.
- Boiler and steam turbine. The turbine keeps its exergy efficiency while the boiler has a small variation because irreversibility changes since, in the case without integration, water that was sent to the fish farm must be dissipated in the condenser. However, a small variation in the costs of the products of both components appears because of the assignation of a part of the cost of the flare. Accordingly, it should be highlighted that, in the non integrated case, the cost of the waste increases slightly the unit cost of the product of the boiler and, accordingly, the unit cost of electricity generated.
- Process steam boiler. The ancillary boiler is less efficient in exergy terms than the boiler of the power plant. However, in the example without integration they have similar unit cost. This fact is due because of the variation of unit cost of the boiler due to the dissipation of waste gas.
- District heating boiler. It can be seen how the unit cost of the district heating boiler is more than twice in the case without integration. This is due because of the low exergy efficiency of using natural gas for producing low temperature thermal energy for district heating.
- Fish farm boiler. This unit cost is the highest one, because the exergy efficiency of producing thermal energy at low temperature by using natural gas is very low.
- Clinker kiln and gypsum transport. It should be noted the high difference of unit cost of clinker kiln and gypsum transport, which are multiplied times 4 and 6, respectively. This is also due to

the consumption of external resources for producing or transporting these flows. Besides, it should be noted that the cost of ash and gypsum in the integrated example is roughly one, which means that every real process considered in the case without integration would entail an increment of the unit cost of these products.

3.4. Resources saved decomposition by using fuel impact approach

The analysis of unit exergy cost is very useful for assigning a cost to the product by using physical criteria. However, this parameter does not provide information about the resources savings caused by the integration of flows. Accordingly, to know these savings, resources impact approach has to be applied.

The total amount of resources savings is calculated at the difference between the consumption of resources in the non integrated case minus the consumption in the integrated situation. In this example, these savings are equal to 1514 GWh/year. However, the determination of resources savings is not enough, because it is needed to identify the causes that have generated it and to share this total amount into partial savings originated by each cause. A first idea to perform this decomposition may be to consider the variation of irreversibility, products and waste, as it can be seen in Table 3.

Table 3. Impact on savings based on irreversibility

Component	$-\Delta I$ [GWh/year]	$-\Delta P_s$ [GWh/year]	$-\Delta P_r$ [GWh/year]	
1. Separator + desulfurization	25	0	0	
2. Boiler	-357	0	0	
3. Turbine	0	0	0	
4. Process steam boiler	302	0	0	
5. District heating boiler	244	0	0	
6. Fish farm boiler	240	0	0	
7. Clinker kiln	170	38	0	
8. Gypsum transport	10	0	0	
9. Flare	0	0	842	
TOTAL	635	38	842	1514

It should be noted that, for the decomposition of resources savings according to irreversibility, only exergy analysis is needed. However, this approach is not suitable for pointing out where savings are caused. For example, the boiler of the power plant can be considered. This component causes additional resources consumption (negative savings) because it has increased its production (and, thus, its irreversibility) but not because it has decreased its efficiency. In other words, it needs more fuel not because it works worse, but because its production is higher.

Accordingly, a more detailed methodology that considers the variation of efficiency of components, as well as changes in fuel used, is needed. This decomposition is shown in Table 4 and uses the concept of local savings and plant savings presented before.

Table 4 shows the decomposition of plant savings according to the methodology proposed. The total value is obviously the same as in Table 3, but the method is able to point out where savings are caused. The main contributions are due to the following components:

- Ancillary boilers. They show in terms of plant savings that the autonomous production of thermal energy is less efficient than the use of steam from the power plant. In other words, this shows the advantages of combined heat and power (CHP). Besides, it can be seen how the lower the temperature of thermal energy generated, the higher the impact on plant savings.
- Clinker kiln. This component has an impact on local savings caused mainly because of the substitution of clinker by another flow with lower exergy (ash), what originates a variation in its

product. Besides, there is also an impact caused by the consumption of external resources needed for producing clinker.

- Flare. This component has the highest impact, which appears because of the use in the system of a flow of high exergy (waste gas) that previously was wasted (flared).

Table 4. Impact on savings based on local savings and plant savings

Component	*LS [GWh/year]*	*PSk [GWh/year]*	*PSp [GWh/year]*	*PSr [GWh/year]*	*PS [GWh/year]*
1. Separator + desulfurization	24	24	0	0	24
2. Boiler	9	16	0	0	16
3. Turbine	0	0	0	0	0
4. Process steam boiler	302	38	0	0	38
5. District heating boiler	244	157	0	0	157
6. Fish farm boiler	240	221	0	0	221
7. Clinker kiln	62	62	146	0	208
8. Gypsum transport	10	10	0	0	10
9. Flare	0	0	0	842	842
TOTAL		527	146	842	1514

Finally, it should be commented an interesting fact related to ancillary boilers: plant savings are smaller than local savings. This may be surprising because plants savings are calculated by multiplying local savings times the unit exergy cost of fuels, which is always higher than 1. This fact can be explained taking into account that plant savings of each component are calculated as a summation of several terms, and local savings in these boilers is produced by a positive term (less resources from the environment are consumed) and a negative term (more steam from the power plant is needed).

4. Conclusion

The analysis of integrations characterizing industrial symbiosis need the use of methodologies that should be systemic and also able to deal with the diverse nature of the flows involved. Thermoeconomic analysis accomplishes these premises because it uses a well structured matrix formulation and uses exergy as indicator for measuring.

In this paper, a methodology has been proposed for analyzing the savings in resources obtained in these integrations. The method compares the system with integration and an equivalent system without this integration. The comparison is performed by using an impact approach developed from the formulation used for diagnosis, and a suitable definition of the productive structure able to deal with both situations.

The methodology is applied to a simplified version of Kalundborg eco-industrial park. Although not all integrations present in the park are considered, the example is representative enough because it includes flows of energy (steam and hot water at several temperatures, as well as waste gas) and materials (ash and gypsum). Cost assessment shows how integration causes reduction of cost of different products (e. g. Unit exergy cost of steam for district heating decreases from 4.82 to 2.36, or unit exergy cost of gypsum is reduced from 5.77 to 1.01). Besides, the methodology is able to share total plant savings (1514 GWh/year) into different causes (e.g. 157 GWh/year for the integration of district heating, 62 GWh/year for the use of ash in the clinker or 842 GWh/year for the use of waste gas from the refinery).

Since the method is focused on energy and material resources savings during operation, capital, operation and maintenance costs are not considered. The extension of the methodology to consider also these important issues is an interesting research line.

Acknowledgments

Authors would like to acknowledge ARAID and IberCaja for its support within the project "Thermoeconomics and Industrial Ecology. Application to Teruel coalfield", Young researchers program, 2010.

Nomenclature

E exergy flow in a productive structure, kW
E^* exergy cost of a flow in a productive structure, kW
F fuel flux, kW
I irreversibility, kW or GWh/year
k^* unit exergy cost, –
LS plant savings, kW or GWh/year
P product flux, kW
PS plant savings, kW or GWh/year
$\mathbf{U_D}$ identity matrix ($n \times n$)
$\langle \mathbf{KP} \rangle$ matrix of unit exergy consumptions ($n \times n$)
$\boldsymbol{x}$ operation situation
$\boldsymbol{x_0}$ reference situation

Greek symbols

η exergy efficiency
κ unit exergy consumption
$\boldsymbol{\kappa_e}$ vector of unit exergy consumption of external resources ($n \times 1$)

Subscripts and superscripts

P product
r waste plant output
s productive plant output
$_{em}$ electromechanical
$_{ph}$ physical

References

[1] Graedel T, Allenby B. Industrial Ecology. Englewood Cliffs, NJ, USA: Prentice Hall; 1995.
[2] Chertow M. Industrial symbiosis: Literature and taxonomy. Annu. Rev. Energy Environment 2000;25:313-37
[3] Chertow M. Uncovering industrial symbiosis. Journal of Industrial Ecology 2007;11:11-30.
[4] Frosch R, Gallopoulos N. Strategies for Manufacturing. Scientific American 1989; 261:144-52

[5] USPCSD (US President's Council on Sustainable Development). Eco-Industrial Park Workshop Proceedings, Cape Charles, Virginia, 1996, 17th-18th October.

[6] Miller R, Blair P. Input-Output Analysis. Foundations and Extensions, 2nd Ed. Cambridge, UK: Cambridge University Press; 2009.

[7] Suh S., Ed. Handbook of Input-Output Economics in Industrial Ecology; NY, USA: Springer Science; 2009.

[8] Connelly L, Coshland C. Exergy and industrial ecology. Part 2: A non-dimensional analysis of means to reduce resource depletion. Exergy International Journal2001;1:134-55.

[9] Finnveden G, Ostland P. Exergies of natural resources in life cycle assessment and other applications. Energy 1997; 22: 923-31.

[10] Cornelissen R, Hirs G. The value of the exergetic life cycle assessment besides the LCA. Energy Conversion and Management 2002; 43: 1417-24.

[11] Dewulf J, Langenhove HV. Assessment of the sustainability of technology by means of a thermodynamically based Life Cycle Analysis. ESPR. Environ. Sci. Pollut. Res. Int 2002; 9: 267-73.

[12] Tribus M, Evans RB. A contribution to the theory of thermoeconomics. 1962 Technical report, Report no. 62-63; Department of Engineering UCLA: Los Angeles, CA, USA.

[13] Valero A, Lozano M, Muñoz M. A general theory of exergy saving. Part I: On the exergetic cost. In: Computer Aided Engineering and Energy systems, Vol. 3: Second Law Analysis and Modeling; Gaggioli R. Ed.; New York, USA: ASME; 1986.

[14] Hau J, Bakshi B. Expanding exergy analysis to account for ecosystem products and services. Environment Science and Technology 2004;38:3768-77.

[15] Valero A, Usón S, Torres C, Valero A. Application of Thermoeconomics to Industrial Ecology. Entropy 2010;12:591-612.

[16] Usón S, Valero A, Agudelo A. Thermoeconomics and industrial symbiosis. Effect of by-product integration in cost assessment. In: Proceedings of ECOS 2011, Novi Sad, Serbia. 2011 4th-7th July.

[17] Valero A, Correas L, Zaleta A, Lazzaretto A, Verda V, Reini M, Rangel VH. On the thermoeconomic approach to the diagnosis of energy system malfunctions. Part 1: the TADEUS problem. Energy 2004; 29:1875-87.

[18] Valero A, Correas L, Zaleta A, Lazzaretto A, Verda V, Reini M, Rangel VH. On the thermoeconomic approach to the diagnosis of energy system malfunctions. Part 2: Malfunction definitions and assessment. Energy 2004; 29:1889-907.

[19] Valero A, Torres C. Application of thermoeconomics to operation diagnosis of energy plants. Oxford, UK: EOLSS Publishers; 2006. www.eolss.net.

[20] Torres C. 2006. Symbolic thermoeconomic analysis of energy systems. Oxford, UK: EOLSS Publishers; 2006. www.eolss.net.

[21] Valero A, Torres C. 2006. Thermoeconomic analysis. Oxford, UK: EOLSS Publishers; 2006. www.eolss.net.

[22] Jacobsen NB. Industrial Symbiosis in Kalundborg, Denmark. A quantitative assessment of economic and environmental aspects. Journal of Industrial Ecology 2006;10(1-2):239-55.

[23] Lowe EA. Eco-industrial park handbook for Asian developing countries. A report to Asian Development Bank. Environment Department. Oakland, CA: Indigo Development; 2001.

[24] Kalundborg symbiosis. – Available at: <http://www.symbiosis.dk> [accessed 10.2.2012]

Thermoeconomics of a ground-based CAES plant for peak-load energy production system

S. Kemble[a], G. Manfrida[b], A. Milazzo[c], F. Buffa[d]

[a]GE O&G Nuovo Pignone SrL, Firenze, Italy, Simon.Kemble@ge.com

[b]Università degli Studi di Firenze, Dipartimento di Energetica "Sergio Stecco", Firenze, Italy, Giampaolo.Manfrida@unifi.it

[c]Università degli Studi di Firenze, Dipartimento di Energetica "Sergio Stecco", Firenze, Italy, Adriano.Milazzo@unifi.it

[d]GE O&G Nuovo Pignone SrL , Firenze, Italy, Francesco.Buffa@ge.com

Abstract:

Compressed Air Energy Storage is recognized as a promising technology for applying energy storage to grids which are more and more challenged by the increasing contribution of renewable such as solar or wind energy.

The paper proposes a medium-size ground-based CAES system, based on pressurized vessels and on a multiple-stage arrangement of compression and expansion machinery; the system includes recovery of heat from the intercoolers, and its storage as sensible heat in two separate (hot/cold) water reservoirs, and regenerative reheat of the expansions.

The CAES plant parameters were adapted to the requirements of existing equipment (compressors, expanders and heat exchangers). A complete exergy analysis of the plant was performed. For all components, cost data were sought on the market or from reference bibliographic sources. The results allow to calculate the final cost of the electricity unit (kWh) which is made available under peak-load (production) mode, and to identify the contribution within the plant of capital costs and component inefficiencies.

Keywords:

CAES, exergy, thermoeconomics

1. Field of application of CAES

Compressed Air Energy Storage (CAES) and Pumped Hydro Energy Storage (PHES), air and water being the most inexpensive fluids, are likely to be the most reliable and technologically sound options for massive energy storage [1, 2].

PHES systems require two reservoirs at different elevation and a pump/turbine for storing/recovering energy in form of water head. Their high energy efficiency (60-78% - [1]) has gained them a widespread application, but development of new PHES is often constrained by localization difficulties. In many situations where cost-effective and environmentally acceptable sites for PHES are unavailable, alternative technologies may be useful.

CAES systems replace water basins with underground storage volumes (caverns in salt or rock formations, porous rocks, depleted natural gas fields) which are used as reservoirs for pressurized air (60-70 bar). Normally, for a given capacity, a CAES uses less land surface than a PHES and doesn't require an elevated reservoir. Natural storage volumes may be scarce or too distant from the energy grid, but artificial storage volumes can be developed in form of high-pressure vessels or underground pipes.

Artificial storage is obviously more expensive than a natural one. It has been shown [3] that an increase in the storage pressure (>100 bar) decreases the material cost of the vessels, although it makes the compression/expansion train more complex.

It is likely that artificial storage CAES would be preferable on a small scale (1-10 MW), whenever the convenience of a given site overcomes the lack of a natural reservoir. Incidentally, an artificial storage is easier to control in terms of air contaminants at turbine inlet.

Existing CAES plants are all gas fuelled, compressed air being heated in a combustion chamber ahead of the turbine during the expansion phase. Hence, these systems combine energy storage within a power plant. The first 290 MW plant built at Huntdorf (Germany) in 1978 is very simple [4]: no attempt was made to recover any thermal energy at turbine exhaust or at compressor exit, before storage in the cavern. The main purpose of this earlier plant was to transfer energy produced by nuclear or coal plants from low to peak demand hours.

A second plant, Mcintosh – Alabama [5], has a recuperator between the hot turbine exhaust and the cold air stream coming from the cavern, in order to reduce the fuel consumption. Many refined schemes have been proposed [6, 7], with notable energy efficiency improvements or using alternative fuels [8].

A significant breakthrough is the so-called "Adiabatic CAES" (ACAES) [9, 10] that has been prompted by the increasing market share of renewable, intermittent energy sources. This configuration gets rid of the combustion chamber and takes full advantage of the thermal recovery from the hot, compressed air to raise the air temperature before expansion. If compression is performed in a common radial or axial machine, i.e. it is practically adiabatic, the recoverable thermal energy at compressor exit is of the same order of magnitude of compression work. Being compression and expansion performed in different phases, a Thermal Energy Storage (TES) is necessary. Expected benefits of this configuration are:

- improved energy efficiency,
- avoidance of a connection to the natural gas grid or any other fuel distribution,
- elimination of pollutant emissions
- lower turbine operating temperature.

The second point may be useful if the CAES is thought as an addendum to a wind farm or any other discontinuous, remote energy source. According to the economic analysis presented in [9], ACAES may be useful as:

- centralized plants – size around 300 MW – in countries with high spread between base and peak energy price;
- decentralized plants – size around 150 MW –near large windfarms in order to increase full load operation, peak price sales and increase utilization of the power lines;
- remote island solutions – size around 30 MW – integrated with wind power, aimed at increase of full load operation of wind turbines and savings of grid connection costs or fuel consumption.

When designing the heat recovery, storage and reclaim system, the simplest option is to introduce one or more heat exchangers on the compression and on the expansion train. Heat storage medium can be liquid or solid or phase change material. In principle, the optimum thermodynamic design should pursue a quasi-isothermal compression/expansion. In the limit of isothermal transformations, the work consumed per unit mass of compressed air would be minimum and the same amount would be returned during expansion, i.e. energy recovery would be complete. In this case, the TES would be ambient air itself and hence would have infinite thermal capacity at no cost. The energy recovery efficiency is hence expected to increase with the number of stages (compressor plus cooler or heater plus turbine) as demonstrated in [11].

In practice, when the compression/expansion is divided in a large number of stages in order to approximate an isothermal behaviour, concentrated losses in the connections between stages and heat exchangers become predominant. A compromise, accounting for system complexity and cost, must be pursued. In any case, increasing the number of stages reduces the maximum temperature of

the TES during compression and hence simplifies its design. For example, if the TES temperature is kept below 100°C, the storage medium can be liquid water at moderate pressure.

All components of a CAES plants are commercially available: compressors, heat exchangers, large volume vessels for high pressure (in case of artificial storage), radial expanders, insulated water reservoirs. Variable Inlet Guide Vanes (IGVs) may be used to adapt the compressors/expanders at the variable storage pressure. Variable configurations of the compression/expansion train have been shown in [3, 11] to extend the operating range. Reciprocating compressors may be integrated in the train for the last stages, when the storage pressure approaches its maximum.

Some caution must be used when comparing ACAES energy efficiency with gas fuelled CAES. For example the ACAES efficiency (energy output divided by input) should not be matched against the "round trip efficiency" of a non-adiabatic CAES [12], where a significant part of the energy is produced from a primary source at the time of peak demand, i.e. is not affected by a storage penalty.

1.1 - Mode of operation

The proposed CAES system (Figure 1) (from an original idea by "ENEL Ingegneria e Innovazione"), is designed as a typical backup unit for wind energy plants. It is based on a seven-stage intercooled compression train. The inlet air (25 °C, 1 bar, dry air) passes through the compression train (an air-based version of that described in [13]), driven by an electric motor (MD), and is stored in pressurized vessels with an overall volume of 6340 m^3. The compressed air storage reservoir (CAR) is built as a system of interconnected vessels; it is pre-pressurized at 77 bar, so that the compressor train starts operating at this pressure, and finishes its operating cycle when the discharge pressure reaches 125 bar. The compressors operated most of the time in off-design conditions (variable IGV setting helps maintaining a good efficiency at off-design). The intercoolers (IC) are water-cooled: the heat from the intercoolers is recovered and stored in a hot water reservoir (TES). Following the description of the air path, the plant is completed by a six-stage expansion train (TE), geared to the electric generator (EG). The expansion is reheated after each stage, recovering heat stored in the hot water tank in a water/air heat recovery heat exchanger (RH). The cold water flow at the RH discharge is recovered in the cold water reservoir (CWR), from which it is re-used in a closed loop for the next operating cycle. Before re-use, water is cooled down to the temperature of the environment by an external cooler.

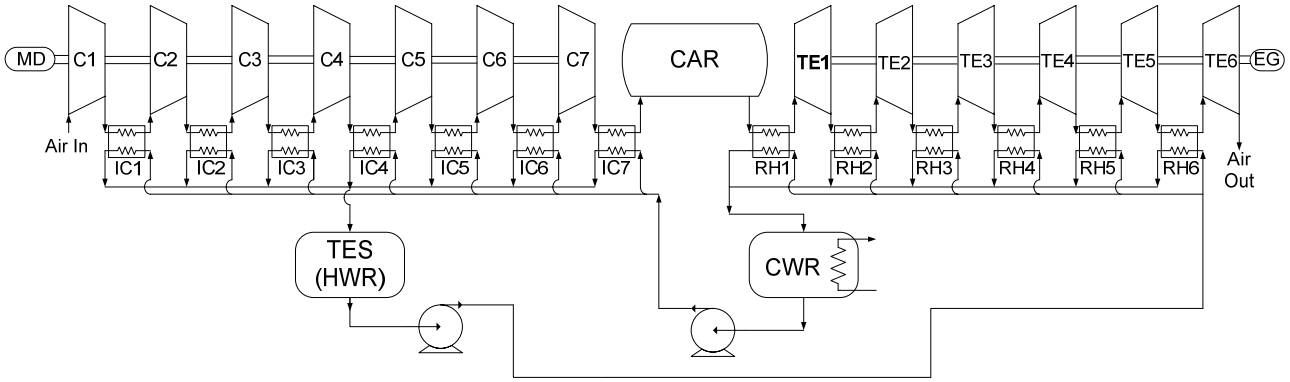

Fig. 1. Schematic of CAES plant

2. CAES plant components

2.1 – Compressor train

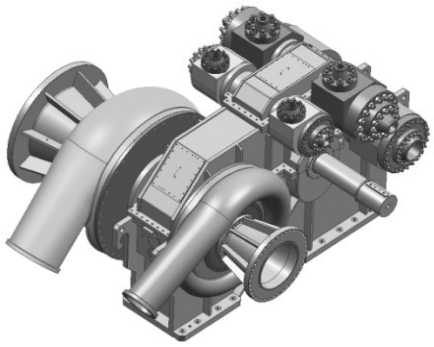

Fig. 2. SRL Compressor

The reference case is built around a typical multi-stage centrifugal compressor train using a GE O&G Nuovo Pignone SRL compressor (Figure 2), as it allows the modular selection of the required number of impellers optimizing the speed using different gear ratios between the High Speed Shafts and main shaft. This design allows also relatively simple inter-stage extraction, as is needed in the present case for intercooling (IC in Figure 1). The first three stages of the compressor train are equipped with variable-IGV control, which can adjust the IGV setting angle from + 15° to -60°. It should be remarked that the compressor train is operated at constant mass flow (12,2 kg/s) and variable discharge pressure (fixed volume of the CAR): accordingly, the characteristic curve can be adjusted along the pressure range, as is shown in Figure 3.

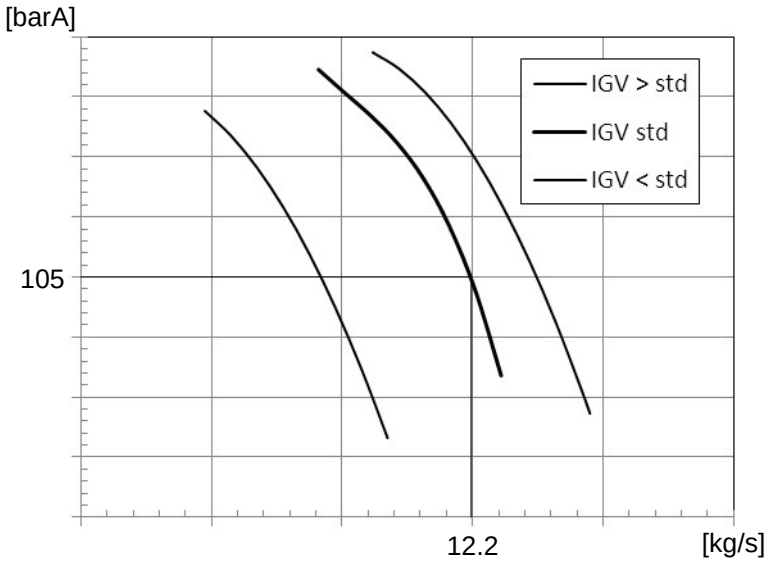

Fig. 3. SRL Compression Train pressure-flow rate characteristic curve with variable IGV setting

The variable-IGV operating mode allows also to maintain a good efficiency under off-design operating conditions; Figure 3 shows the efficiency achievable (obtained with the optimal IGV setting) under the main reference operating conditions, over the full pressure range considered in the CAES application.

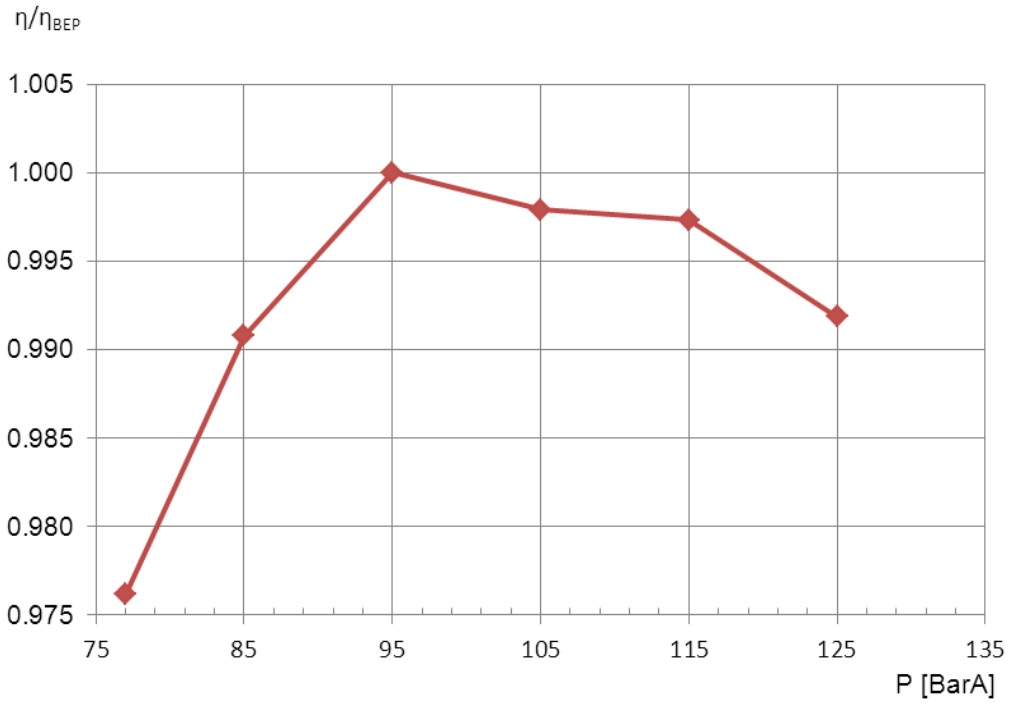

Fig. 4. Compression Train calculated polytropic efficiency along the charging cycle (Varying IGV)

The GE internal tool CCS was used to select each impeller of the SRL compressor. CCS is based on an internal database of different types of centrifugal impellers which have already been designed for other applications and whose performance has been checked against test data. The tool has a number of inputs: P_{in}, T_{in}, m_{in}, RPM, D_i for each stage; moreover, the inter-stage pressure drops, the casing size and rating, the size of flanges and volutes. The discharge pressure p_{out} is a code output, as well as the IGV pre-rotation angle and the BEP efficiency at design conditions.

The nominal design condition was assumed at a discharge pressure of 105 bar. The calculation of the operating point conditions was then repeated for off design, setting 5 discrete operating points: 125, 115, 95, 85 and 77 bar, and calculating the optimal IGV setting and the off-design efficiency. The power absorbed by the compression train ranges from 7,5 MW for p_{out} = 75 bar to 8,1 MW p_{out} = 125 bar. The SRL motor drive is an asynchronous electric motor having the following target data: W = 9600 kW; Nominal rotational speed = 1500 rpm; Nominal voltage V = 13.8 kV.

2.2 – Turbo-expander train

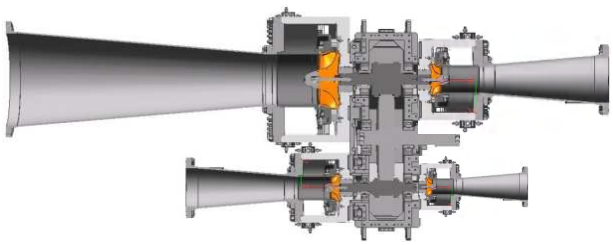

Fig. 5. Integrally-Geared Turbo-Expander

The turbo-expander is again of the integrally-geared type: an example is shown in Figure 5. In the present case, 6 stages were considered, geared on three shafts (rotating respectively at 26000, 14000

and 7300 rpm). Each stage is preceded by a Reheat Heat Exchanger (RH in Figure 1). Here again, each stage is equipped with variable-setting IGVs.

The turbo-expander mass flow rate was adjusted to maintain as far as possible a constant power output with variable inlet pressure: this operating condition results from the electric market day-ahead arbitrage pricing which is required by the Italian grid operator. In the present case, three reference conditions were assumed for calculating the design and off-design performance, which are summarized in Table 1:

Table 1 Turbo-expander train reference operating conditions

	HP	IP	LP
P_{CAR}, bar	125	98	75
m, kg/s	24,5	26,6	27,4
W, MW	8,60	8,62	8,34

The EG is an asynchronous electric generator having the following target data: W = 10500 kVA; Nominal rotational speed = 1500 rpm; Nominal voltage V = 13.8 kV;

2.3 – Heat Exchangers (IC, RH)

The heat exchangers were designed by an external provider after specifications by GE O&G Nuovo Pignone; a shell and tube arrangement was required; shell/tube arrangement between air and water were switched with variable pressure: in fact, air passes through shells (and water through the pipes) when the air pressure is low (first stages), while in the last stages air passes inside the pipes (and water through the shell side) in order to minimize heat exchanger capital costs. The shell side is provided with baffles which ensure a correct cross-flow arrangement. The water inlet/outlet conditions were specified as 20°C/90°C for the IC; and 89°C/80°C for the RH heat exchangers. Due attention was paid in not exceeding the boiling water temperature balancing the amount of water mass flow. Referring for example to coolers, the water mass flow rates were adjusted for each cooler under each operating condition in order to have a delivery temperature of 90°C, with a heat exchanger pinch temperature difference of 15 °C. The calculation was done by traditional HE sizing rules, assuming a constant overall heat transfer coefficient and surface. So, considering heat exchangers duty, it is possible, knowing the air inlet and outlet temperature, to calculate the water flow rates (data reported in Table 2).

Table 2 Main data for CAES plant heat exchangers

Unit	External Diameter [mm]	L [mm]	m_w [kg/s]	Q [kW]
Intercooler 1	900	4000	4.8	1414
Intercooler 2	900	5000	5	1500
Intercooler 3	900	4500	5.9	1800
Intercooler 4	650	6000	3.2	1000
Intercooler 5	600	6500	3.4	1000
Intercooler 6	580	7000	3.3	1000
Aftercooler	500	7500	3.5	1100
Heater 1	700	6000	12	2700
Heater 2	800	6000	9.5	1600
Heater 3	950	5000	9.3	1500
Heater 4	950	5000	9.3	1600
Heater 5	1000	5000	8.7	1500
Heater 6	1000	5000	8.9	1500

2.4 – Reservoirs (CAR, CWR, TES)

Air storage vessels (CAR) were selected considering an above ground storage ACAES plant, using 2115 TENARIS pressure vessels with a unit capacity of 3 m^3. The admissible work pressure for this vessel is 140 bar, tested following the 97/23/EC-PED standard. Each cylinder features 622mm external diameter and 12m length.

In the Thermal Energy Storage (TES), hot water reservoir works at ambient pressure, therefore water cannot exceed the boiling temperature. An average temperature of the hot tank of 89 °C was estimated , with an overall volume of water equal to 810 m^3, including 50 m^3 used as fixed quantity to make sure that the tank never empties.

The Cold Water Reservoir (CWR) has the same size; it starts its operation (storage mode) at 20 °C; at the end of the production mode, it is full of warm water at 47°C, which has been delivered from the TES passing through the HR network. The cooling load needed for reducing the CWR temperature from 47 to 20°C is provided by an external heat exchanger.

3. Exergy and Thermoeconomic Analysis

3.1 – Exergy analysis

Exergy Analysis was set in the classical reference form [14, 15]. Exergy is evaluated as an extensive property, so it can be transferred into or out of a control volume where steams of matter enter and exit. For each component, generally:

$$\frac{dE_{CV}}{dt} = \sum_j \left(1 - \frac{T_0}{T_j}\right)\dot{Q}_j - \left[\dot{W}_{cv} - p_0 \frac{dV_{CV}}{dt}\right] + \sum_i \dot{m}_i e_i - \sum_e \dot{m}_e e_e - \dot{E}_D - \dot{E}_L \quad (1)$$

The term $\dot{m}_i e_i$ accounts for the time rate of exergy transfer at the inlet *i*. Similarly, $\dot{m}_e e_e$ accounts for the time rate of exergy transfer at the outlet *e*.

The analyses considered in this work involves a slow evolution of steady-state operating conditions (as the pressure in the CAR is varied); for the analysis of most components, it is sufficient to consider the steady-state form of the exergy rate balance. At steady state, $\frac{dE_{CV}}{dt}$ = 0 and $\frac{dV_{CV}}{dt}$ = 0, so equation (1) reduces to

$$0 = \sum_j \left(1 - \frac{T_0}{T_j}\right)\dot{Q}_j - \dot{W}_{cv} + \sum_i \dot{m}_i e_i - \sum_e \dot{m}_e e_e - \dot{E}_D - \dot{E}_L \quad (2)$$

This equation states that the rate at which exergy is transferred into the control volume exceeds the rate at which exergy is transferred out. The difference is the rate at which exergy is destroyed within the control volume due to irreversibilities. In compact form Eq. 2 reads:

$$0 = \sum_j \dot{E}_{q,j} - \dot{W}_{cv} + \sum_i \dot{E}_i - \sum_e \dot{E}_e - \dot{E}_D - \dot{E}_L \quad (3)$$

e_i and e_e can be calculated from enthalpy and entropy referring to unit mass of the fluid:

$$e_i - (h_i - h_0) - T_0(s_i - s_0) \quad (4)$$

In this study, the compressors were assumed to be working without any heat transfer to the external environment (Adiabatic conditions). Both Heat Exergy and the Exergy Loss terms disappear, leading to:

$$\dot{E}_{D,C} = -\dot{W}_C + \dot{E}_i - \dot{E}_e \quad (5)$$

The compression power is easily found

$$\dot{W}_c = \dot{m}\,(h_i - h_e) \tag{6}$$

The compressor work is negative, as the sign convention defines as negative an energy flow entering the system.

Heat exchangers are treated as steady-state adiabatic, no-work components; under these assumptions, $\dot{E}_D$ can be calculated from:

$$\dot{E}_{D,HE} = \dot{E}_{i,air} + \dot{E}_{i,w} - \dot{E}_{e,air} - \dot{E}_{e,w} \tag{7}$$

Exergy destruction within the piping (air and water sides) were evaluated calculating the friction losses by traditional correlations. The piping was considered adiabatic; the total pressure loss is converted into an entropy generation, and the exergy destruction is calculated consequently [14]:

$$E_D = T_0 \dot{S}_{gen} \tag{8}$$

A closed-system balance was used to evaluate the total exergy E_{CAR} stored in the compressed air reservoir (vessels). Only physical exergy was considered, neglecting kinetic and potential contributions; air vessels were assumed, at the end of the charge, at a temperature of 25 °C (same as environment).

The specific physical exergy is

$$e^{PH} = (u - u_0) + p_0(v - v_0) - T_0(s - s_0) \tag{9}$$

In the case of an ideal gas with constant specific heat ratio, the specific physical exergy can be expressed as:

$$\frac{e^{PH}}{c_p T_0} = \frac{T}{T_0} - 1 - \ln\frac{T}{T_0} + \frac{k-1}{k}\left[\ln\frac{p}{p_0} + \frac{T}{T_0}\left(\frac{p_0}{p} - 1\right)\right] \tag{10}$$

From the assumptions made, air temperature is constant at ambient value, hence:

$$e^{PH} = RT_0\left[\ln\frac{p}{p_0} + \left(\frac{p_0}{p} - 1\right)\right] \tag{11}$$

Note that in this case, the assumption of constant *k* is no longer necessary.

E_{CAR} over one operating cycle can be calculated by the difference between exergy stored at 125 bar and 77 bar, simply as:

$$E_{CAR} = E_{125}^{PH} - E_{77}^{PH} \tag{12}$$

The exergy loss corresponding to heat release to the environment to cool the water in the CWR at the end of the cycle can be estimated using the difference between two exergy levels, calculated by a closed system balance:

$$E_{CWR,W} = (U_W - U_0) - T_0(S_W - S_0) \tag{13}$$

$$E_{CWR,C} = (U_C - U_0) - T_0(S_C - S_0) \tag{14}$$

Where $E_{CWR,W}$ and $E_{CWR,C}$ are respectively the exergies of the CWR at the final temperature of 47 °C and at the starting value of 20 °C. Then the exergy loss can be estimated as:

3.2 – Thermoeconomic analysis

Thermoeconomics [14] is the branch of engineering that combines exergy analysis and economic principles to provide the system designer or operator with information not available through conventional energy analysis and economic evaluations, but crucial to the design and operation of a cost-effective system involving transformation of energy.

At the base of a thermoeconomic analysis there is an economic analysis in order to detect and define each cost relative to the system. The system was modelled considering a sequence of steady states; all relevant entering and exiting material streams, as well as both heat and work interactions with the surroundings were included. Associated with these transfers of matter and energy are exergy transfers into and out of the system, and exergy destructions caused by the irreversibilities within the system. Since exergy measures the true thermodynamic value of such effects, and costs should only be assigned to commodities of value, it is meaningful to use exergy as a basis for assigning costs in thermal systems.

The cost balance applied to the *k*-th system component can be generally written as:

$$\sum_{e}(c_e\dot{E}_e)_k + c_{w,k}\dot{W}_k - c_{q,k}\dot{E}_{q,k} + \sum_{i}(c_i\dot{E}_i)_k + \dot{Z}_k \tag{16}$$

In the specific case of compressors, for each stage:

$$c_{e,k}\dot{E}_{e,k} = c_{i,k}\dot{E}_{i,k} + c_w\dot{W} + \dot{Z}_k \tag{17}$$

No auxiliary relation is needed for compressor stages [14]. In the first compressor stage $c_{i,1}$ was considered equal to zero (ambient air); in the other stages, $c_{i,k}$ is equal to the cost stream exiting the preceding cooler. c_w was considered equal to 38 €/MWh, corresponding to use of off-peak electricity.

Each heat exchanger was evaluated referring to the component model shown in Figure 6, using the following relations:

$$c_2\dot{E}_2 + c_4\dot{E}_4 = c_1\dot{E}_1 + c_3\dot{E}_3 + \dot{Z}_k \tag{18}$$

Considering that the coolers work as a heat exchanger with double purpose (cooling + heat recovery), the thermo-economic assumption $c_2 = c_4$ was applied (equal cost of the two exit streams, which are both products of the component); additionally, the cost of cold water was assumed to be negligible $c_3 = 0$ (the pumping cost is marginal, and anyway a calculation of the friction losses in the water loop was not performed, so that even pumping power was not calculated at this level of the analysis, which focuses on thermal and compressor/expander performance).

For heaters, the only purpose is that of heating air. c_1 in this case is equal to the cost of the water stored in the hot tank (TES). As for any heat exchanger whose purpose is heating a cold stream [14], the auxiliary relation is $c_2 = c_1$. For the first RH, c_3 is equal to the cost of air coming from the CAR; for all the others, it is given by the cost of the exit flow from each expansion stage.

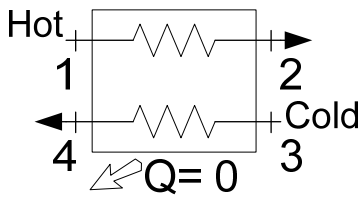

Fig.6 Schematic of heat exchanger

The expander thermo-economic balance is similar to that of the compressor, considering now the work stream as an outlet:

$$c_{e,k}\dot{E}_{e,k} + c_{w,k}W_k = c_{i,k}\dot{E}_{i,k} + \dot{Z}_k \tag{19}$$

The auxiliary relation in this case is [14]: $c_{e,k} = c_{i,k}$.

For the storage (CAR) reservoir (a component in which the capital cost is expected to be very high), the thermo-economic relation is applied over the complete lifetime considering the overall scheduled operating time in charge/discharge modes, and it reads:

$$\sum_e c_{e,CAR}\dot{E}_{e,CAR}t_{e,disch} = \sum_i c_{i,CAR}\dot{E}_{i,CAR}t_{i,ch} + Z_{CAR} \tag{20}$$

The operating time in the different states of charge/discharge is considered in Equation 20, and the values calculated (based on the CAR size and on the operating lines of compressors and expanders) are presented in the following section.

4. Results - Exergy Analysis

4.1 Charge and discharge time

The application of the compressor characteristic curve to the ACAES plant gives the charge curve in Figure 7, which was calculated with reference to the CAR considered as a closed system, integrating the mass flow with a time step Δt for each intermediate condition.

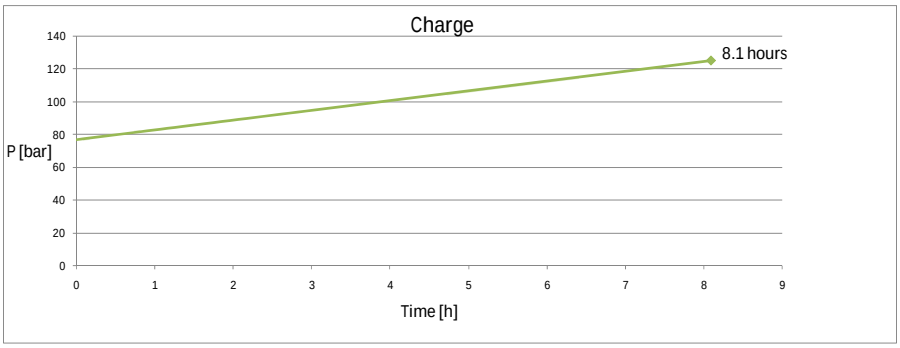

Fig.7 Charge pressure history

The CAR pressure time history is approximately a linear function of time. The result shows a theoretical time of 8.1 hours to fill completely the air storage vessels with a volume of 6340 m^3.

During the discharge process, the expander unit was simulated according to its characteristic curve with variable IGV setting. As the CAR pressure varies in a limited range (125-75 bar), the discharge function results approximately linear. The complete discharge time is 3.77 hrs.

4.2 – Results - Exergy analysis

The exergy balance was divided into CAES plant sections: compressors, intercoolers, expanders, re-heaters. As an example, for the case p_{CAR} = 125 bar, the overall exergy destruction in compressors amounts to 1,3MW (for an absorbed power of 7,5 MW). The distribution of exergy destruction over the 7 stages is shown in Figure 8.

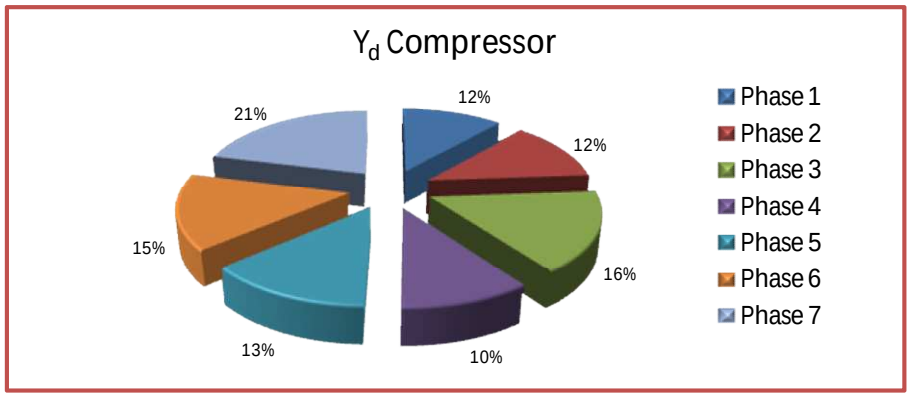

Fig.8 Relative distribution of Compressors exergy destruction (p_{CAR} = 125 bar)

The overall IC exergy destruction amounts to 517 kW, and its distribution is shown in Figure 9.

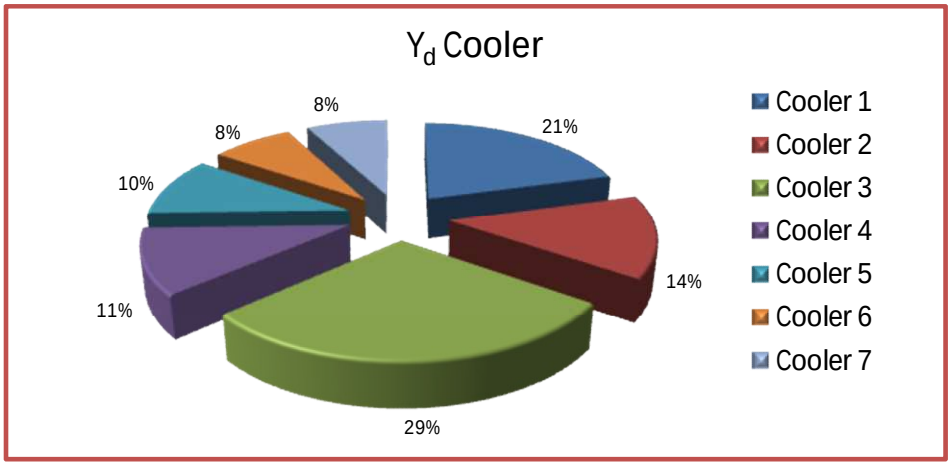

Fig.9 Relative distribution of IC exergy destruction (p_{CAR} = 125 bar)

The overall RH exergy destruction amounts to 625 kW, and its distribution is shown in Figure 10.

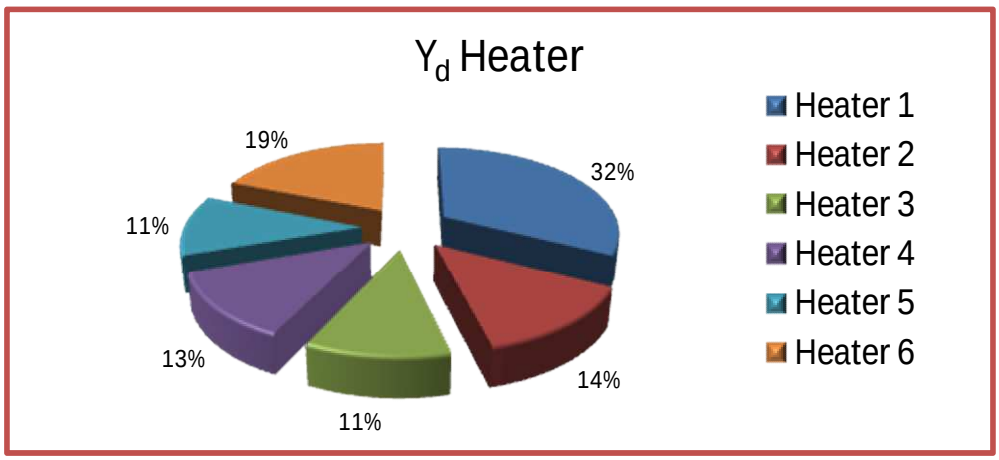

Fig.10 Relative distribution of RH exergy destruction (p_{CAR} = 125 bar)

The piping exergy destruction was very low (18 kW for all the IC connection pipes.

The overall expander exergy destruction amounts to 1654 kW, and its distribution among the different stages is shown in Figure 11.

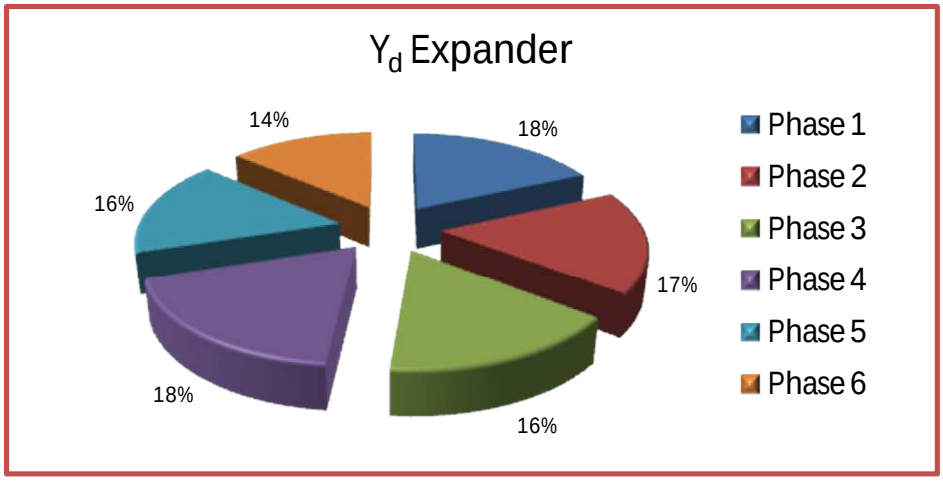

Fig.11 Relative distribution of expander exergy destruction (p_{CAR} = 125 bar)

In practice, the operating conditions are continuously varying in time, as the delivery pressure in the CAR is increased from 75 to 125 bar. As an example, the trend of exergy destruction in time for the compressor train is shown in Figure 12. $\dot{E}_D$ was calculated for every compressor stage in each off-design condition considered (the minimum exergy destruction is achieved very close to the nominal design conditions). Interpolating the values with a polynomial function allows to define an approximate trend line, which was integrated in time to give the overall expected value over one charge cycle, E_D = 10.1 MWh.

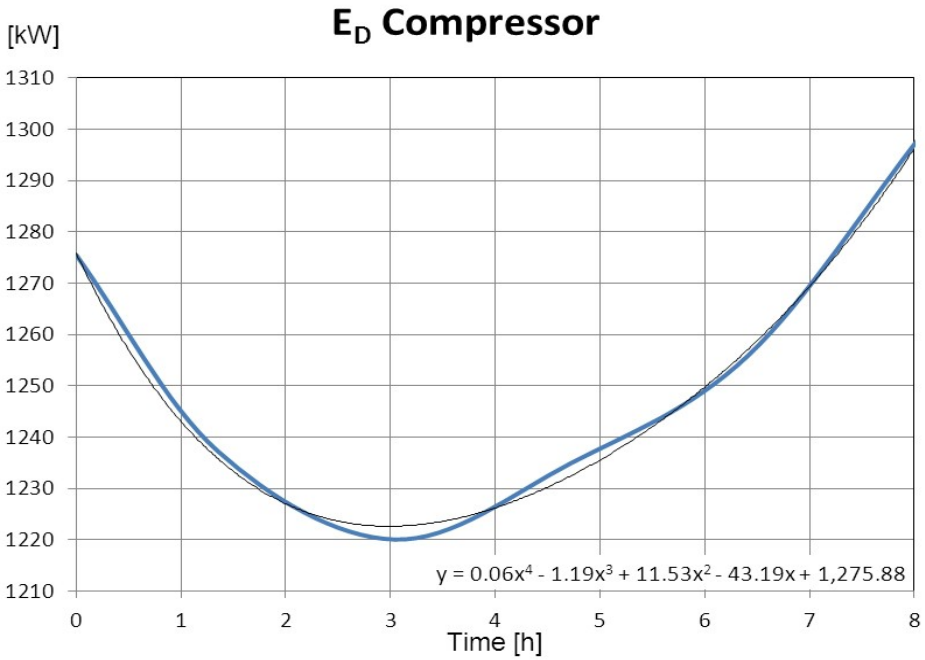

Fig.12 Time history of calculated compressor exergy destruction

A Sankey diagram showing the exergy destruction during the charge and discharge phases is shown in Figure 13.

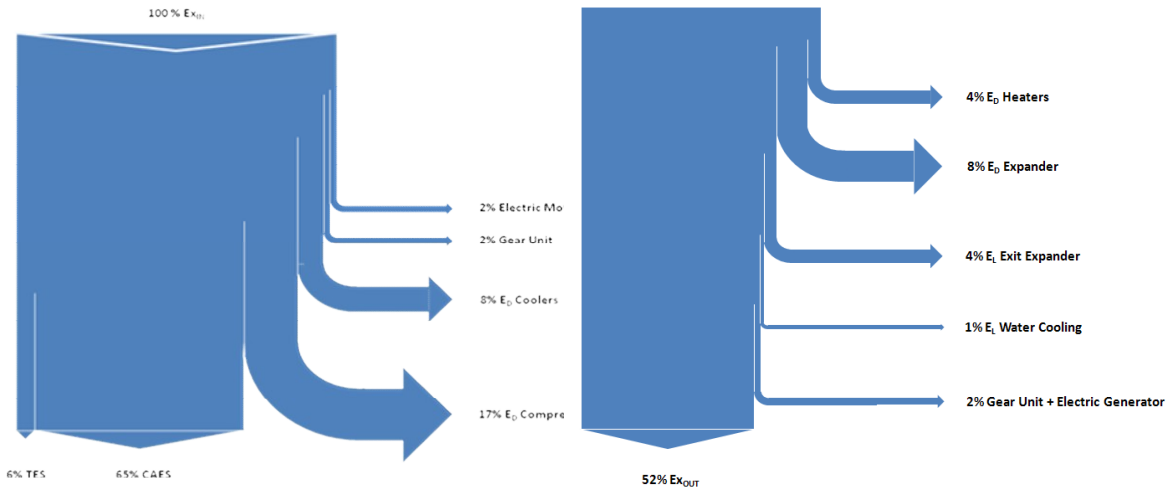

(a) *(b)*

Fig.13 Exergy flow Sankey diagram; (a) Charging (b) Discharging

5. Results – Thermoeconomic analysis - Conclusions

Detailed results about exergy analysis have been shown in Section 4, consequently the conclusions here reported represent only a synthesis of this case study. The cumulated exergy efficiency of the process (calculated through a time-resolved integration of the sequence of system operating conditions, along a complete charging/discharging cycle) is about 52%. Referring to the maximum pressure (125 bar), the power production distribution among the 6 expander stages is shown in Figure 14, and the cost of electricity produced by each stage, according to the thermo-economic analysis of the plant, is summarized in Figure 15.

The power-averaged cost of the electricity produced is calculated at 70 €/MWh, which corresponds to a marginal cost of (70 – 38) = 32 €/MWh of the equivalent stored electrical energy; in practice, a 84% increase with respect to the base-load cost of electricity assumed (38 €/MWh). This is considered as a promising result for proposing ground-built ACAES systems as storage devices for the near future.

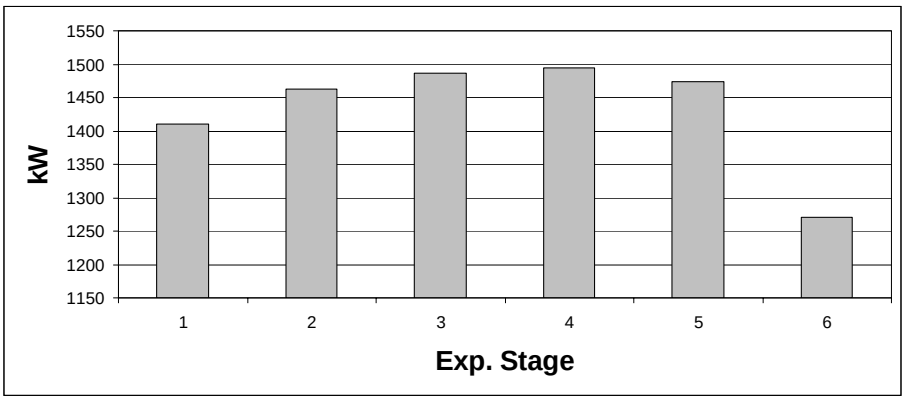

Fig.14 Power produced by each expander stage (p_{CAR} = 125 bar)

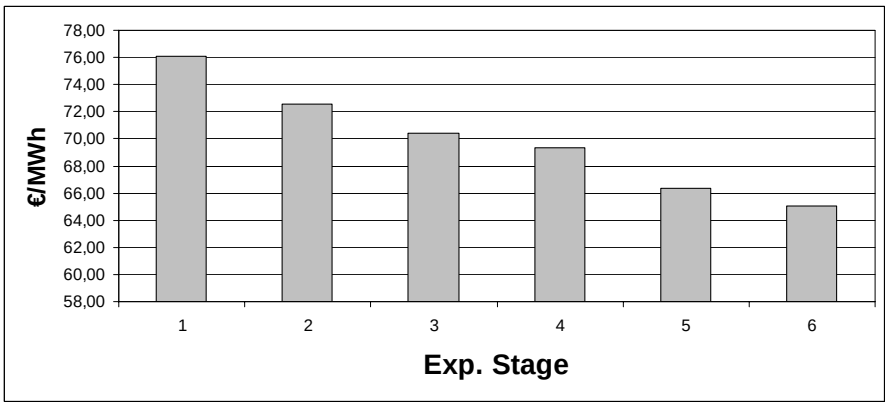

Fig.15 Electricity production cost for each expander stage (p_{CAR} = 125 bar)

The distribution of the marginal cost buildup among the main plant components, in terms of cost of exergy destruction and capital+O&M costs, is shown in Figure 16.

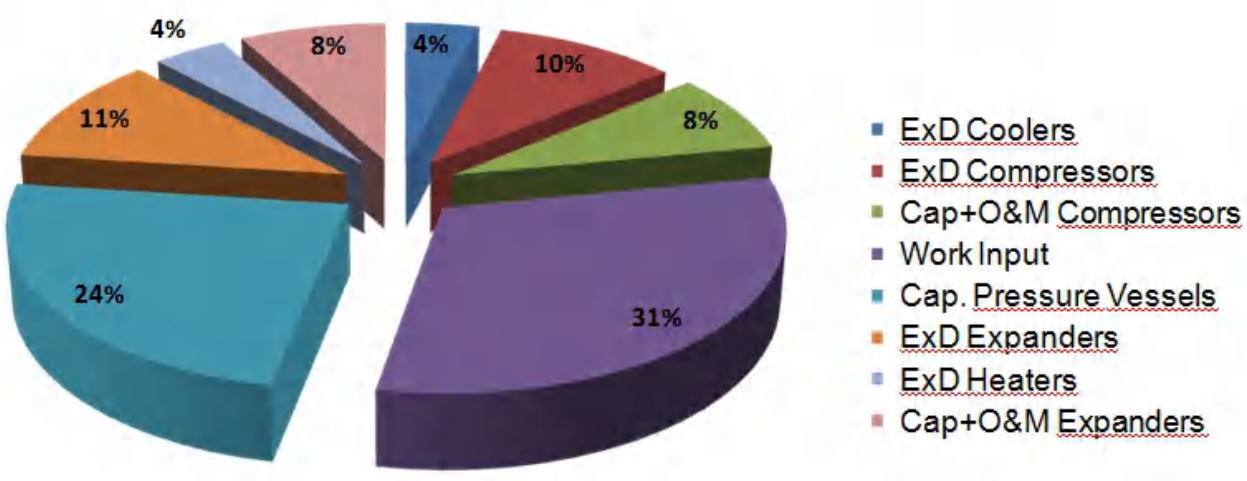

Fig.16 Relative distribution of the marginal costs among ACAES plant components.

Exergy destruction and Capital + O&M costs (p_{CAR} = 125 bar)

It can be noticed that the work input amounts to 31% of the expenses; exergy destruction during plant operation (storage and production modes) respresents 29% of the marginal cost; about 40 % can be accounted to capital expenses, with the largest share due to the pressure vessels (24%).

Acknowledgments

The Authors are grateful to GE O&G Nuovo Pignone SrL and to ENEL Ingegneria e Innovazione for having allowed publication of the present work, which was object of the placement/master thesis project work of one of the Authors (Simon Kemble) in the frame of an established University/Industry cooperation program.

Nomenclature

c	Cost of unit exergy, €/J
c_p	Constant-pressure specific heat, J/(kg K)
e	Exergy, J/kg
E	Overall system Exergy, J
h	Enthalpy, J/kg
$\dot{m}$	Mass flow rate, kg/s
P	Pressure, bar
Q	Heat Rate, W
R	Gas Constant, J/(kgK)
s	Entropy, J/(kg K)
S	System Entropy, J/K
t	Time, s
T	Temperature, °C
u	Internal energy, J/kg
U	System Internal Energy, J
V	Volume, m^3
W	Power, W
Z	capital cost, €

Acronyms

ACAES	Adiabatic CAES
BEP	Best Efficiency point
C	Compressor
CAES	Compressed Air Energy Storage
CAR	Compressed Air Reservoir
CWR	Cold Water Reservoir
EG	Electric Generator
HE	Heat Exchanger
TES	Thermal Energy Storage
IC	Intercooler (heat exchanger)
IGV	Inlet Guide Vanes
LPR	Low Pressure Reservoir
MD	Motor Drive (electric)
PHES	Pumped Hydro Energy Storage
RH	Reheater (heat exchanger)

Subscripts and superscripts

0	Reference state
air	Air
C	Compressor
ch	Charge
CV	Control Volume (delimiting component)
D	Destroyed

disch	Discharge
e	Component Exit (thermodynamic conditions)
gen	Entropy generation
i	Impeller
i	Component Inlet (thermodynamic conditions)
in	Inlet (stage)
k	k-th element
L	Lost
out	Outlet (stage)
w	water

References

[1] Bradshaw D.T., "Pumped hydroelectric storage (PHS) and compressed air energy storage CAES)",presented at the IEEE PES Meeting Energy Storage, Seattle, WA, 2000

[2] Schoenung S.M., "Characteristics and technologies for long- vs. short-term energy storage", Sandia Rep. SAND2001-0765, 2001.

[3] Grazzini G., Milazzo A., "Exergy analysis of a CAES with thermal energy storage", 5th European Thermal-Science Conf., Eindhoven, The Netherlands, May 18–22, 2008.

[4] Crotogino F., Mohmeyer K. U., Scharf R., "Huntorf CAES: More than 20 years of successful operation", SMRI Spring Meeting 2001, Orlando, FL, April 2001, pp. 351 – 357

[5] D. R. Mack, "Something new in power technology", IEEE Potentials, 12, 2, pp. 40–42, Apr. 1993.

[6] Nakhamkin M., Chiruvolu M., Daniel M. "Available compressed air energy storage (CAES) plant concepts". [Online]. Available: http://espcinc.com/library/PowerGen_2007_paper.pdf.

[7] Wolf D., "Methods for Design and Application of Adiabatic Compressed Air Energy Storage Based on Dynamic Modelling". Oberhausen, Germany: Verlag Karl Maria Laufen, 2011

[8] Denholm P., "Improving the technical, environmental and social performance of wind energy systems using biomass-based energy storage", Renewable Energy, 31, 2006, pp. 1355–1370

[9] Bullough C., Gatzen C., Jakiel C., Koller M., Nowi A., Zunft S., "Advanced adiabatic compressed air energy storage for the integration of wind energy", Proceedings of the European Wind Energy Conference, EWEC 2004, London UK, November 2004.

[10] Zunft S., Jakiel C., Koller M., Bullough C., „Adiabatic compressed air energy storage for the grid integration of wind power", 6th Int. Workshop on Large-Scale Integration of Wind Power and Transmission Networks for Offshore Wind-Farms, Delft, The Netherlands, Oct. 2006.

[11] Grazzini G., Milazzo A., "A Thermodynamic Analysis of Multistage Adiabatic CAES", Proceedings of the IEEE, Special Issue "Addressing the intermittency challenge: Massive energy storage in a sustainable future", 99, 12, pp. 1-12 (2011)

[12] Greenblatt J.B., Succar S., Denkenberger D.C., Williams R.H., Socolow R.H., "Baseload wind energy: modelling the competition between gas turbines and compressed air energy storage for supplemental generation", Energy Policy, 35 (2007) 1474–1492

[13] Botero, C., Finkenrath, M., Belloni, C., Bertolo, S., D'Ercole, M., Gori, E., Tacconelli, R., "Thermoeconomic Evaluation of CO2 Compression Strategies For Post-Combustion CO2 Capture Applications", ASME Paper GT2009-60217, Orlando, FL, USA.

[14] Bejan, A., Tsatsaronis, G., Moran, M., 1996, Thermal Design and Optimization, Wiley Interscience, New York.

[15] Kotas, T.J., 1985, The Exergy Method of Thermal Plant Analysis, Butterworths.

ECOS 2012

The 25th International Conference on Efficiency, Cost, Optimization and Simulation of Energy Conversion Systems and Processes

(Perugia, June 26th-June 29th, 2012)

edited by
Umberto Desideri, Giampaolo Manfrida,
Enrico Sciubba

firenze university press
2012

ECOS 2012 : the 25th International Conference on Efficiency, Cost, Optimization and Simulation of Energy Conversion Systems and Processes (Perugia, June 26th-June 29th, 2012) / edited by Umberto Desideri, Giampaolo Manfrida, Enrico Sciubba. – Firenze : Firenze University Press, 2012.
(Proceedings e report ; 90)

http://digital.casalini.it/9788866553229

ISBN 978-88-6655-322-9 (online)

Progetto grafico di copertina Alberto Pizarro, Pagina Maestra snc
Immagine di copertina: © Kts | Dreamstime.com

Peer Review Process
All publications are submitted to an external refereeing process under the responsibility of the FUP Editorial Board and the Scientific Committees of the individual series. The works published in the FUP catalogue are evaluated and approved by the Editorial Board of the publishing house. For a more detailed description of the refereeing process we refer to the official documents published on the website and in the online catalogue of the FUP (http://www.fupress.com).

Firenze University Press Editorial Board
G. Nigro (Co-ordinator), M.T. Bartoli, M. Boddi, F. Cambi, R. Casalbuoni, C. Ciappei, R. Del Punta, A. Dolfi, V. Fargion, S. Ferrone, M. Garzaniti, P. Guarnieri, G. Mari, M. Marini, M. Verga, A. Zorzi.

© 2012 Firenze University Press
Università degli Studi di Firenze
Firenze University Press
Borgo Albizi, 28, 50122 Firenze, Italy
http://www.fupress.com/
Printed in Italy

ECOS 2012

The 25th International Conference on

Efficiency, Cost, Optimization and Simulation
of Energy Conversion Systems and Processes

Perugia, June 26th-June 29th, 2012

Book of Proceedings - Volume IV

Edited by:
Umberto Desideri, Università degli Studi di Perugia
Giampaolo Manfrida, Università degli Studi di Firenze
Enrico Sciubba, Università degli Studi di Roma "Sapienza"

ECOS 2012 - THE 25TH INTERNATIONAL CONFERENCE ON
EFFICIENCY, COST, OPTIMIZATION, SIMULATION AND ENVIRONMENTAL IMPACT OF ENERGY SYSTEMS
JUNE 26-29, 2012, PERUGIA, ITALY
EDITED BY UMBERTO DESIDERI, GIAMPAOLO MANFRIDA, ENRICO SCIUBBA
FIRENZE UNIVERSITY PRESS, 2012, ISBN ONLINE : 978-88-6655-322-9

Advisory Committee (Track Organizers)

Building, Urban and Complex Energy Systems
V. Ismet Ugursal
Dalhousie University, Nova Scotia, Canada

Combustion, Chemical Reactors, Carbon Capture and Sequestration
Giuseppe Girardi
ENEA-Casaccia, Italy

Energy Systems: Environmental and Sustainability Issues
Christos A. Frangopoulos
National Technical University of Athens, Greece

Exergy Analysis and Second Law Analysis
Silvio de Oliveira Junior
Polytechnical University of Sao Paulo, Sao Paulo, Brazil

Fluid Dynamics and Power Plant Components
Sotirios Karellas
National Technical University of Athens, Athens, Greece

Fuel Cells
Umberto Desideri
University of Perugia, Perugia, Italy

Heat and Mass Transfer
Francesco Asdrubali, **Cinzia Buratti**
University of Perugia, Perugia, Italy

Industrial Ecology
Stefan Goessling-Reisemann
University of Bremen, Germany

Poster Session
Enrico Sciubba
University Roma 1 “Sapienza”, Italy

Process Integration and Heat Exchanger Networks
Francois Marechal
EPFL, Lausanne, *Switzerland*

Renewable Energy Conversion Systems
David Chiaramonti
University of Firenze, Firenze, Italy

Simulation of Energy Conversion Systems
Marcin Liszka
Polytechnica Slaska, Gliwice, Poland

System Operation, Control, Diagnosis and Prognosis
Vittorio Verda
Politecnico di Torino, Italy

Thermodynamics
A. Özer Arnas
United States Military Academy at West Point, U.S.A.

Thermo-Economic Analysis and Optimisation
Andrea Lazzaretto
University of Padova, Padova, Italy

Water Desalination and Use of Water Resources
Corrado Sommariva
ILF Consulting M.E., U.K

Scientific Committee

Riccardo Basosi, University of Siena, Italy
Gino Bella, University of Roma Tor Vergata, Italy
Asfaw Beyene, San Diego State University, United States
Ryszard Bialecki, Silesian Institute of Tecnology, Poland
Gianni Bidini, University of Perugia, Italy
Ana M. Blanco-Marigorta, University of Las Palmas de Gran Canaria, Spain
Olav Bolland, University of Science and Technology (NTNU), Norway
Renè Cornelissen, Cornelissen Consulting, The Netherlands
Franco Cotana, University of Perugia, Italy
Alexandru Dobrovicescu, Polytechnical University of Bucharest, Romania
Gheorghe Dumitrascu, Technical University of Iasi, Romania
Brian Elmegaard, Technical University of Denmark , Denmark
Daniel Favrat, EPFL, Switzerland
Michel Feidt, ENSEM - LEMTA University Henri Poincaré, France
Daniele Fiaschi, University of Florence, Italy
Marco Frey, Scuola Superiore S. Anna, Italy
Richard A Gaggioli, Marquette University, USA
Carlo N. Grimaldi, University of Perugia, Italy
Simon Harvey, Chalmers University of Technology, Sweden
Hasan Heperkan, Yildiz Technical University, Turkey
Abel Abel Hernandez-Guerrero, University of Guanajuato, Mexico
Jiri Jaromir Klemeš, University of Pannonia, Hungary
Zornitza V. Kirova-Yordanova, University "Prof. Assen Zlatarov", Bulgaria
Noam Lior, University of Pennsylvania, United States
Francesco Martelli, University of Florence, Italy
Aristide Massardo, University of Genova, Italy
Jim McGovern, Dublin Institute of Technology, Ireland
Alberto Mirandola, University of Padova, Italy
Michael J. Moran, The Ohio State University, United States
Tatiana Morosuk, Technical University of Berlin, Germany
Pericles Pilidis, University of Cranfield, United Kingdom
Constantine D. Rakopoulos, National Technical University of Athens, Greece
Predrag Raskovic, University of Nis, Serbia and Montenegro
Mauro Reini, University of Trieste, Italy
Gianfranco Rizzo, University of Salerno, Italy
Marc A. Rosen, University of Ontario, Canada
Luis M. Serra, University of Zaragoza, Spain
Gordana Stefanovic, University of Nis, Serbia and Montenegro
Andrea Toffolo, Luleå University of Technology, Sweden
Wojciech Stanek, Silesian University of Technology, Poland
George Tsatsaronis, Technical University Berlin, Germany
Antonio Valero, University of Zaragoza, Spain
Michael R. von Spakovsky, Virginia Tech, USA
Stefano Ubertini, Parthenope University of Naples, Italy
Sergio Ulgiati, Parthenope University of Naples, Italy
Sergio Usón, Universidad de Zaragoza, Spain
Roman Weber, Clausthal University of Technology, Germany
Ryohei Yokoyama, Osaka Prefecture University, Japan
Na Zhang, Institute of Engineering Thermophysics, Chinese Academy of Sciences, China

The 25th ECOS Conference 1987-2012: leaving a mark

The introduction to the ECOS series of Conferences states that "ECOS is a series of international conferences that focus on all aspects of Thermal Sciences, with particular emphasis on Thermodynamics and its applications in energy conversion systems and processes". Well, ECOS is much more than that, and its history proves it!

The idea of starting a series of such conferences was put forth at an informal meeting of the Advanced Energy Systems Division of the American Society of Mechanical Engineers (ASME) at the November 1985 Winter Annual Meeting (WAM), in Miami Beach, Florida, then chaired by Richard Gaggioli. The resolution was to organize an annual Symposium on the Analysis and Design of Thermal Systems at each ASME WAM, and to try to involve a larger number of scientists and engineers worldwide by organizing conferences outside of the United States. Besides Rich other participants were Ozer Arnas, Adrian Bejan, Yehia El-Sayed, Robert Evans, Francis Huang, Mike Moran, Gordon Reistad, Enrico Sciubba and George Tsatsaronis.

Ever since 1985, a Symposium of 8-16 sessions has been organized by the Systems Analysis Technical Committee every year, at the ASME Winter Annual Meeting (now ASME-IMECE). The first overseas conference took place in Rome, twenty-five years ago (in July 1987), with the support of the U.S. National Science Foundation and of the Italian National Research Council. In that occasion, Christos Frangopoulos, Yalcin Gogus, Elias Gyftopoulos, Dominick Sama, Sergio Stecco, Antonio Valero, and many others, already active at the ASME meetings, joined the core-group.

The name ECOS was used for the first time in Zaragoza, in 1992: it is an acronym for **Efficiency, Cost, Optimization and Simulation** (of energy conversion systems and processes), keywords that best describe the contents of the presentations and discussions taking place in these conferences. Some years ago, Christos Frangopoulos inserted in the official website the note that "ècos" ('οικος) means "home" in Greek and it ought to be attributed the very same meaning as the prefix "Eco-" in environmental sciences.
The last 25 years have witnessed an almost incredible growth of the ECOS community: more and more Colleagues are actively participating in our meetings, several international Journals routinely publish selected papers from our Proceedings, fruitful interdisciplinary and international cooperation projects have blossomed from our meetings. Meetings that have spanned three continents (Africa and Australia ought to be our next targets, perhaps!) and influenced in a way or another much of modern Engineering Thermodynamics.
After 25 years, if we do not want to become embalmed in our own success and lose momentum, it is mandatory to aim our efforts in two directions: first, encourage the participation of younger academicians to our meetings, and second, stimulate creative and useful discussions in our sessions. Looking at this years' registration roster (250 papers of which 50 authored or co-authored by junior Authors), the first objective seems to have been attained, and thus we have just to continue in that direction; the second one involves allowing space to "voices that sing out of the choir", fostering new methods and approaches, and establishing or reinforcing connections to other scientific communities. It is important that our technical sessions represent a place of active confrontation, rather than academic "lecturing".
In this spirit, we welcome you in Perugia, and wish you a scientifically stimulating, touristically interesting, and culinarily rewarding experience. In line with our 25 years old scientific excellency and friendship!

Umberto Desideri, Giampaolo Manfrida, Enrico Sciubba

CONTENT MANAGEMENT

The index lists all the papers contained all the eight volumes of the Proceedings of the ECOS 2012 International Conference.
Page numbers are listed only for papers within the Volume you are looking at. The ID code allows to trace back the identification number assigned to the paper within the Conference submission, review and track organization processes.

CONTENT

VOLUME IV

IV. 1 FLUID DYNAMICS AND POWER PLANT COMPONENTS

» A control oriented simulation model of a multistage axial compressor (ID 444) ……..... *Pag. 1*
Lorenzo Damiani, Giampaolo Crosa, Angela Trucco

» A flexible and simple device for in-cylinder flow measurements: experimental and numerical validation (ID 181) ……..... *Pag. 15*
Andrea Dai Zotti, Massimo Masi, Marco Antonello

» CFD Simulation of Entropy Generation in Pipeline for Steam Transport in Real Industrial Plant (ID 543) ……..... *Pag. 36*
Goran Vučković, Gradimir Ilić, Mića Vukić, Milan Banić, Gordana Stefanović

» Feasibility Study of Turbo expander Installation in City Gate Station (ID 168) ……..... *Pag. 47*
Navid Zehtabiyan Rezaie, Majid Saffar-Avval

» GTL and RME combustion analysis in a transparent CI engine by means of IR digital imaging (ID 460) ……..... *Pag. 56*
Ezio Mancaruso, Luigi Sequino, Bianca Maria Vaglieco

» Some aspects concerning fluid flow and turbulence modeling in 4-valve engines (ID 116) ……..... *Pag. 66*
Zoran Stevan Jovanovic, Zoran Masonicic, Miroljub Tomic

IV. 2 SYSTEM OPERATION CONTROL DIAGNOSIS AND PROGNOSIS

» Adapting the operation regimes of trigeneration systems to renewable energy systems integration (ID 188) ……..... *Pag. 82*
Liviu Ruieneanu, Mihai Paul Mircea

» Advanced electromagnetic sensors for sustainable monitoring of industrial processes (ID 145) ……..... *Pag. 92*
Uroš Puc, Andreja Abina, Anton Jeglič, Pavel Cevc, Aleksander Zidanšek

» Assessment of stresses and residual life of plant components in view of life-time extension of power plants (ID 453) ……..... *Pag. 104*
Anna Stoppato, Alberto Benato and Alberto Mirandola

» Control strategy for minimizing the electric power consumption of hybrid ground source heat pump system (ID 244) ……..... *Pag. 114*
Zoi Sagia, Constantinos Rakopoulos

» Exergetic evaluation of heat pump booster configurations in a low temperature district heating network (ID 148) ……..... *Pag. 126*
Torben Ommen, Brian Elmegaard

» Exergoeconomic diagnosis: a thermo-characterization method by using irreversibility analysis (ID 523) ……..... *Pag. 140*
Abraham Olivares-Arriaga, Alejandro Zaleta-Aguilar, Rangel-Hernández V. H, Juan Manuel Belman-Flores

» Optimal structural design of residential cogeneration systems considering their operational restrictions (ID 224) ……..... *Pag. 156*
Tetsuya Wakui, Ryohei Yokoyama

FIRENZE UNIVERSITY PRESS, 2012, ISBN ONLINE : 978-88-6655-322-9

» **Performance estimation and optimal operation of a CO2 heat pump water heating system (ID 344)** ……..... *Pag. 173*
Ryohei Yokoyama, Ryosuke Kato, Tetsuya Wakui, Kazuhisa Takemura

» **Performances of a common-rail Diesel engine fuelled with rapeseed and waste cooking oils (ID 213)** ……..... *Pag. 188*
Alessandro Corsini, Valerio Giovannoni, Stefano Nardecchia, Franco Rispoli, Fabrizio Sciulli, Paolo Venturini

» **Reduced energy cost through the furnace pressure control in power plants (ID 367)** ……..... *Pag. 203*
Vojislav Filipović, Novak Nedić, Saša Prodanović

» **Short-term scheduling model for a wind-hydro-thermal electricity system (ID 464)** ……..... *Pag. 212*
Sérgio Pereira, Paula Ferreira, A. Ismael Freitas Vaz

CONTENTS OF ALL THE VOLUMES

VOLUME I

I . 1 – SIMULATION OF ENERGY CONVERSION SYSTEMS

» **A novel hybrid-fuel compressed air energy storage system for China's situation (ID 531)**
Wenyi Liu, Yongping Yang, Weide Zhang, Gang Xu,and Ying Wu

» **A review of Stirling engine technologies applied to micro-cogeneration systems (ID 338)**
Ana C Ferreira, Manuel L Nunes, Luís B Martins, Senhorinha F Teixeira

» **An organic Rankine cycle off-design model for the search of the optimal control strategy (ID 295)**
Andrea Toffolo, Andrea Lazzaretto, Giovanni Manente, Marco Paci

» **Automated superstructure generation and optimization of distributed energy supply systems (ID 518)**
Philip Voll, Carsten Klaffke, Maike Hennen, André Bardow

» **Characterisation and classification of solid recovered fuels (SRF) and model development of a novel thermal utilization concept through air- gasification (ID 506)**
Panagiotis Vounatsos, Konstantinos Atsonios, Mihalis Agraniotis, Kyriakos D. Panopoulos, George Koufodimos,Panagiotis Grammelis, Emmanuel Kakaras

» **Design and modelling of a novel compact power cycle for low temperature heat sources (ID 177)**
Jorrit Wronski, Morten Juel Skovrup, Brian Elmegaard, Harald Nes Rislå, Fredrik Haglind

» **Dynamic simulation of combined cycles operating in transient conditions: an innovative approach to determine the steam drums life consumption (ID 439)**
Stefano Bracco

» **Effect of auxiliary electrical power consumptions on organic Rankine cycle system with low-temperature waste heat source (ID 235)**
Samer Maalouf, Elias Boulawz Ksayer, Denis Clodic

» **Energetic and exergetic analysis of waste heat recovery systems in the cement industry (ID 228)**
Sotirios Karellas, Aris Dimitrios Leontaritis, Georgios Panousis, Evangelos Bellos, Emmanuel Kakaras

» Energy and exergy analysis of repowering options for Greek lignite-fired power plants (ID 230)
Sotirios Karellas, Aggelos Doukelis, Grammatiki Zanni, Emmanuel Kakaras

» Energy saving by a simple solar collector with reflective panels and boiler (ID 366)
Anna Stoppato, Renzo Tosato

» Exergetic analysis of biomass fired double-stage Organic Rankine Cycle (ORC) (ID 37)
Markus Preißinger, Florian Heberle, Dieter Brüggemann

» Experimental tests and modelization of a domestic-scale organic Rankine cycle (ID 156)
Roberto Bracco, Stefano Clemente, Diego Micheli, Mauro Reini

» Model of a small steam engine for renewable domestic CHP system (ID 31)
Giampaolo Manfrida, Giovanni Ferrara, Alessandro Pescioni

» Model of vacuum glass heat pipe solar collectors (ID 312)
Daniele Fiaschi, Giampaolo Manfrida

» Modelling and exergy analysis of a plasma furnace for aluminum melting process (ID 254)
Luis Enrique Acevedo, Sergio Usón, Javier Uche, Patxi Rodríguez

» Modelling and experimental validation of a solar cooling installation (ID 296)
Guillaume Anies, Pascal Stouffs, Jean Castaing-Lasvignottes

» The influence of operating parameters and occupancy rate of thermoelectric modules on the electricity generation (ID 314)
Camille Favarel, Jean-Pierre Bédécarrats, Tarik Kousksou, Daniel Champier

» Thermodynamic and heat transfer analysis of rice straw co-firing in a Brazilian pulverised coal boiler (ID 236)
Raphael Miyake, Alvaro Restrepo, Fábio Kleveston Edson Bazzo, Marcelo Bzuneck

» Thermophotovoltaic generation: A state of the art review (ID 88)
Matteo Bosi, Claudio Ferrari, Francesco Melino, Michele Pinelli, Pier Ruggero Spina, Mauro Venturini

I . 2 – HEAT AND MASS TRANSFER

» A DNS method for particle motion to establish boundary conditions in coal gasifiers (ID 49)
Efstathios E Michaelides, Zhigang Feng

» Effective thermal conductivity with convection and radiation in packed bed (ID 60)
Yusuke Asakuma

» Experimental and CFD study of a single phase cone-shaped helical coiled heat exchanger: an empirical correlation (ID 375)
Daniel Flórez-Orrego, Walter Arias, Diego López, Héctor Velásquez

» Thermofluiddynamic model for control analysis of latent heat thermal storage system (ID 207)
Adriano Sciacovelli, Vittorio Verda, Flavio Gagliardi

» Towards the development of an efficient immersed particle heat exchanger: particle transfer from low to high pressure (ID 202)
Luciano A. Catalano, Riccardo Amirante, Stefano Copertino, Paolo Tamburrano, Fabio De Bellis

I . 3 – INDUSTRIAL ECOLOGY

» Anthropogenic heat and exergy balance of the atmosphere (ID 122)
Asfaw Beyene, David MacPhee, Ron Zevenhoven

» Determination of environmental remediation cost of municipal waste in terms of extended exergy (ID 63)
Candeniz Seckin, Ahmet R. Bayulken

» Development of product category rules for the application of life cycle assessment to carbon capture and storage (537)
Carlo Strazza, Adriana Del Borghi, Michela Gallo

» Electricity production from renewable and non-renewable energy sources: a comparison of environmental, economic and social sustainability indicators with exergy losses throughout the supply chain (ID 247)
Lydia Stougie, Hedzer van der Kooi, Rob Stikkelman

» Exergy analysis of the industrial symbiosis model in Kalundborg (ID 218)
Alicia Valero Delgado, Sergio Usón, Jorge Costa

» Global gold mining: is technological learning overcoming the declining in ore grades? (ID 277)
Adriana Domínguez, Alicia Valero

» Personal transportation energy consumption (ID305)
Matteo Muratori, Emmanuele Serra, Vincenzo Marano, Michael Moran

» Resource use evaluation of Turkish transportation sector via the extended exergy accounting method (ID 43)
Candeniz Seckin, Enrico Sciubba, Ahmet R. Bayulken

» The impact of higher energy prices on socio-economic inequalities of German social groups (ID 80)
Holger Schlör, Wolfgang Fischer, Jürgen-Friedrich Hake

VOLUME II

II . 1 – EXERGY ANALYSIS AND 2ND LAW ANALYSIS

» A comparative analysis of cryogenic recuperative heat exchangers based on exergy destruction (ID 129)
Adina Teodora Gheorghian, Alexandru Dobrovicescu, Lavinia Grosu, Bogdan Popescu, Claudia Ionita

» A critical exploration of the usefulness of rational efficiency as a performance parameter for heat exchangers (ID 307)
Jim McGovern, Georgiana Tirca-Dragomirescu, Michel Feidt, Alexandru Dobrovicescu

» A new procedure for the design of LNG processes by combining exergy and pinch analyses (ID 238)
Danahe Marmolejo-Correa, Truls Gundersen

» Advances in the distribution of environmental cost of water bodies through the exergy concept in the Ebro river (ID 258)
Javier Uche Marcuello, Amaya Martínez Gracia, Beatriz Carrasquer Álvarez, Antonio Valero Capilla

» Application of the entropy generation minimization method to a solar heat exchanger: a pseudo-optimization design process based on the analysis of the local entropy generation maps (ID 357)
Giorgio Giangaspero, Enrico Sciubba

» Comparative analysis of ammonia and carbon dioxide two-stage cycles for simultaneous cooling and heating (ID 84)
Alexandru Dobrovicescu, Ciprian Filipoiu, Emilia Cerna Mladin, Valentin Apostol, Liviu Drughean

» Comparison between traditional methodologies and advanced exergy analyses for evaluating efficiency and externalities of energy systems (ID 515)
Gabriele Cassetti, Emanuela Colombo

» Comparison of entropy generation figures using entropy maps and entropy transport equation for an air cooled gas turbine blade (ID 468)
Omer Emre Orhan, Oguz Uzol

» Conventional and advanced exergetic evaluation of a supercritical coal-fired power plant (ID 377)
Ligang Wang, Yongping Yang, Tatiana Morosuk, George Tsatsaronis

» Energy and exergy analyses of the charging process in encapsulted ice thermal energy storage (ID 164)
David MacPhee, Ibrahim Dincer, Asfaw Beyene

» Energy integration and cogeneration in nitrogen fertilizers industry: thermodynamic estimation of the efficiency, potentials, limitations and environmental impact. Part 1: energy integration in ammonia production plants (ID 303)
Zornitza Vassileva Kirova-Yordanova

» Evaluation of the oil and gas processing at a real production day on a North Sea oil platform using exergy analysis (ID 260)
Mari Voldsund, Wei He, Audun Røsjorde, Ivar Ståle Ertesvåg, Signe Kjelstrup

» Exergetic and economic analysis of Kalina cycle for low temperature geothermal sources in Brazil (ID 345)
Carlos Eymel Campos Rodriguez, José Carlos Escobar Palacios, Cesar Adolfo Rodríguez Sotomonte, Marcio Leme, Osvaldo José Venturini, Electo Eduardo Silva Lora, Vladimir Melián Cobasa, Daniel Marques dos Santos, Fábio R. Lofrano Dotto, Vernei Gialluca

» Exergy analysis and comparison of CO2 heat pumps (ID 242)
Argyro Papadaki, Athina Stegou - Sagia

» Exergy analysis of a CO2 Recovery plant for a brewery (ID 72)
Daniel Rønne Nielsen, Brian Elmegaard, C. Bang-Møller

» Exergy analysis of the silicon production process (ID 118)
Marit Takla, Leiv Kolbeinsen, Halvard Tveit, Signe Kjelstrup

» Exergy based indicators for cardiopulmonary exercise test evaluation (ID 159)
Carlos Eduardo Keutenedjian Mady, Cyro Albuquerque Neto, Tiago Lazzaretti Fernandes, Arnaldo Jose Hernandez, Paulo Hilário Nascimento Saldiva, Jurandir Itizo Yanagihara, Silvio de Oliveira Junior

» Exergy disaggregation as an alternative for system disaggregation in thermoeconomics (ID 483)
José Joaquim Conceição Soares Santos, Atilio Lourenço, Julio Mendes da Silva, João Donatelli, José Escobar Palacio

» Exergy intensity of petroleum derived fuels (ID 117)
Julio Augusto Mendes da Silva, Maurício Sugiyama, Claudio Rucker, Silvio de Oliveira Junior

» Exergy-based sustainability evaluation of a wind power generation system (ID 542)
Jin Yang, B. Chen, Enrico Sciubba

» Human body exergy metabolism (ID 160)
Carlos Eduardo Keutenedjian Mady, Silvio de Oliveira Junior

» Integrating an ORC into a natural gas expansion plant supplied with a co-generation unit (ID 273)
Sergio Usón, Wojciech Juliusz Kostowski

» One-dimensional model of an optimal ejector and parametric study of ejector efficiency (ID 323)
Ronan Killian McGovern, Kartik Bulusu, Mohammed Antar, John H. Lienhard

» Optimization and design of pin-fin heat sinks based on minimum entropy generation (ID 6)
Jose-Luis Zuniga-Cerroblanco, Abel Hernandez-Guerrero, Carlos A. Rubio-Jimenez, Cuauhtemoc Rubio-Arana, Sosimo E. Diaz-Mendez

» Performance analysis of a district heating system (ID 271)
Andrej Ljubenko, Alojz Poredoš, Tatiana Morosuk, George Tsatsaronis

» System analysis of exergy losses in an integrated oxy-fuel combustion power plant (ID 64)
Andrzej Ziębik, Paweł Gładysz

» What is the cost of losing irreversibly the mineral capital on Earth? (ID 220)
Alicia Valero Delgado, Antonio Valero

II . 2 – THERMODYNAMICS

» A new polygeneration system for methanol and power based on coke oven gas and coal gas (ID 252)
Hu Lin, Hongguang Jin, Lin Gao, Rumou Li

» Argon-Water closed gas cycle (ID 67)
Federico Fionelli, Giovanni Molinari

» Binary alkane mixtures as fluids in Rankine cycles (ID 246)
M. Aslam Siddiqi, Burak Atakan

» Excess enthalpies of second generation biofuels (ID 308)
Alejandro Moreau, José Juan Segovia, M. Carmen Martín, Miguel Ángel Villamañán, César R. Chamorro, Rosa M. Villamañán

» Local stability analysis of a Curzon-Ahlborn engine considering the Van der Waals equation state in the maximum ecological regime (ID 281)
Ricardo Richard Páez-Hernández, Pedro Portillo-Díaz, Delfino Ladino-Luna, Marco Antonio Barranco-Jiménez

» Some remarks on the Carnot's theorem (ID 325)
Julian Gonzalez Ayala, Fernando Angulo-Brown

» The Dead State (ID 340)
Richard A. Gaggioli

» The magnetocaloric energy conversion (ID 97)
Andrej Kitanovski, Jaka Tusek, Alojz Poredos

VOLUME III

THERMO-ECONOMIC ANALYSIS AND OPTIMIZATION

» A comparison of optimal operation of residential energy systems using clustered demand patterns based on Kullback-Leibler divergence (ID 142)
Akira Yoshida, Yoshiharu Amano, Noboru Murata, Koichi Ito, Takumi Hashizume

» A Model for Simulation and Optimal Design of a Solar Heating System with Seasonal Storage (ID 51)
Gianfranco Rizzo

» A thermodynamic and economic comparative analysis of combined gas-steam and gas turbine air bottoming cycle (ID 232)
Tadeusz Chmielniak, Daniel Czaja, Sebastian Lepszy

» Application of an alternative thermoeconomic approach to a two-stage vapor compression refrigeration cycle with intercooling (ID 135)
Atilio Barbosa Lourenço, José Joaquim Conceição Soares Santos, João Luiz Marcon Donatelli

» Comparative performance of advanced power cycles for low temperature heat sources (ID 109)
Guillaume Becquin, Sebastian Freund

» Comparison of nuclear steam power plant and conventional steam power plant through energy level and thermoeconomic analysis (ID 251)
S. Khamis Abadi, Mohammad Hasan Khoshgoftar Manesh, M. Baghestani, H. Ghalami, Majid Amidpour

» Economic and exergoeconomic analysis of micro GT and ORC cogeneration systems (ID 87)
Audrius Bagdanavicius, Robert Sansom, Nick Jenkins, Goran Strbac

» Exergoeconomic comparison of wet and dry cooling technologies for the Rankine cycle of a solar thermal power plant (ID 300)
Philipp Habl, Ana M. Blanco-Marigorta, Berit Erlach

» Influence of renewable generators on the thermo-economic multi-level optimization of a poly-generation smart grid (101)
Massimo Rivarolo, Andrea Greco, Francesca Travi, Aristide F. Massardo

» Local stability analysis of a thermoeconomic model of an irreversible heat engine working at different criteria of performance (ID 289)
Marco A. Barranco-Jiménez, Norma Sánchez-Salas, Israel Reyes-Ramírez, Lev Guzmán-Vargas

» Multicriteria optimization of a distributed trigeneration system in an industrial area (ID 154)
Dario Buoro, Melchiorre Casisi, Alberto de Nardi, Piero Pinamonti, Mauro Reini

» On the effect of eco-indicator selection on the conclusions obtained from an exergoenvironmental analysis (ID 275)
Tatiana Morosuk, George Tsatsaronis, Christopher Koroneos

» Optimisation of supply temperature and mass flow rate for a district heating network (ID 104)
Marouf Pirouti, Audrius Bagdanavicius, Jianzhong Wu, Janaka Ekanayake

» Optimization of energy supply systems in consideration of hierarchical relationship between design and operation (ID 389)
Ryohei Yokoyama, Shuhei Ose

» The fuel impact formula revisited (ID 279)
Cesar Torres, Antonio Valero

» The introduction of exergy analysis to the thermo-economic modelling and optimisation of a marine combined cycle system (ID 61)
George G. Dimopoulos, Chariklia A. Georgopoulou, Nikolaos M.P. Kakalis

» The relationship between costs and environmental impacts in power plants: an exergy-based study (ID 272)
Fontina Petrakopoulou, Yolanda Lara, Tatiana Morosuk, Alicia Boyano, George Tsatsaronis

» Thermo-ecological evaluation of biomass integrated gasification gas turbine based cogeneration technology (ID 441)
Wojciech Stanek, Lucyna Czarnowska, Jacek Kalina

» Thermo-ecological optimization of a heat exchanger through empirical modeling (ID 501)
Ireneusz Szczygieł, Wojciech Stanek, Lucyna Czarnowska, Marek Rojczyk

» Thermoeconomic analysis and optimization in a combined cycle power plant including a heat transformer for energy saving (ID 399)
Elizabeth Cortés Rodríguez, José Luis Castilla Carrillo, Claudia A. Ruiz Mercado, Wilfrido Rivera Gómez-Franco

» Thermoeconomic analysis and optimization of a hybrid solar-electric heating in a fluidized bed dryer (ID 400)
Elizabeth Cortés Rodríguez, Felipe de Jesús Ojeda Cámara, Isaac Pilatowsky Figueroa

» Thermoeconomic approach for the analysis of low temperature district heating systems (ID 208)
Vittorio Verda, Albana Kona

» Thermo-economic assessment of a micro CHP systems fuelled by geothermal and solar energy (ID 166)
Duccio Tempesti, Daniele Fiaschi, Filippo Gabuzzini

» **Thermo-economic evaluation and optimization of the thermo-chemical conversion of biomass into methanol (ID 194)**
Emanuela Peduzzi, Laurence Tock, Guillaume Boissonnet, François Marechal

» **Thermoeconomic fuel impact approach for assessing resources savings in industrial symbiosis: application to Kalundborg Eco-industrial Park (ID 256)**
Sergio Usón, Antonio Valero, Alicia Valero, Jorge Costa

» **Thermoeconomics of a ground-based CAES plant for peak-load energy production system (ID 32)**
Simon Kemble, Giampaolo Manfrida, Adriano Milazzo, Francesco Buffa

VOLUME V

V . 1 – RENEWABLE ENERGY CONVERSION SYSTEMS

» **A co-powered concentrated solar power Rankine cycle concept for small size combined heat and power (ID 276)**
Alessandro Corsini, Domenico Borello, Franco Rispoli, Eileen Tortora

» **A novel non-tracking solar collector for high temperature application (ID 466)**
Wattana Ratismith, Anusorn Inthongkhum

» **Absorption heat transformers (AHT) as a way to enhance low enthalpy geothermal resources (ID 311)**
Daniele Fiaschi, Duccio Tempesti, Giampaolo Manfrida, Daniele Di Rosa

» **Alternative feedstock for the biodiesel and energy production: the OVEST project (ID 98)**
Matteo Prussi, David Chiaramonti, Lucia Recchia, Francesco Martelli, Fabio Guidotti

» **Assessing repowering and update scenarios for wind energy converters (ID 158)**
Till Zimmermann

» **Biogas from mechanical pulping industry – potential improvement for increased biomass vehicle fuels (ID 54)**
Mimmi Magnusson, Per Alvfors

» **Biogas or electricity as vehicle fuels derived from food waste - the case of Stockholm (ID 27)**
Martina Wikström, Per Alvfors

» **Compressibility factor as evaluation parameter of expansion processes in organic Rankine cycles (ID 292)**
Giovanni Manente, Andrea Lazzaretto

» **Design of solar heating system for methane generation (ID 445)**
Lucía Mónica Gutiérrez, P. Quinto Diez, L. R. Tovar Gálvez

» **Economic feasibility of PV systems in hotels in Mexico (ID 346)**
Augusto Sanchez, Sergio Quezada

» **Effect of a back surface roughness on annual performance of an air-cooled PV module (ID 193)**
Riccardo Secchi, Duccio Tempesti, Jacek Smolka

» **Energy and exergy analysis of the first hybrid solar-gas power plant in Algeria (ID 176)**
Fouad Khaldi

» **Energy recovery from MSW treatment by gasification and melting technology (ID 393)**
Fabrizio Strobino, Alessandro Pini Prato, Diego Ventura, Marco Damonte

» **Ethanol production by enzymatic hydrolysis process from sugarcane biomass - the integration with the conventional process (ID 189)**
Reynaldo Palacios-Bereche, Adriano Ensinas, Marcelo Modesto, Silvia Azucena Nebra

» Evaluation of gas in an industrial anaerobic digester by means of biochemical methane potential of organic municipal solid waste components (ID 57)
Isabella Pecorini, Tommaso Olivieri, Donata Bacchi, Alessandro Paradisi, Lidia Lombardi, Andrea Corti, Ennio Carnevale

» Exergy analysis and genetic algorithms for the optimization of flat-plate solar collectors (ID 423)
Soteris A. Kalogirou

» Experimental study of tar and particles content of the produced gas in a double stage downdraft gasifier (ID 487)
Ana Lisbeth Galindo Noguera, Sandra Yamile Giraldo, Rene Lesme-Jaén, Vladimir Melian Cobas, Rubenildo Viera Andrade, Electo Silva Lora

» Feasibility study to realize an anaerobic digester fed with vegetables matrices in central Italy (ID 425)
Umberto Desideri, Francesco Zepparelli, Livia Arcioni, Ornella Calderini, Francesco Panara, Matteo Todini

» Investigations on the use of biogas for small scale decentralized CHP applications with a focus on stability and emissions (ID 140)
Steven MacLean, Eren Tali, Anne Giese, Jörg Leicher

» Kinetic energy recovery system for sailing yachts (ID 427)
Giuseppe Leo Guizzi, Michele Manno

» Mirrors in the sky: status and some supporting materials experiments (ID 184)
Noam Lior

» Numerical parametric study for different cold storage designs and strategies of a solar driven thermoacoustic cooler system (ID 284)
Maxime Perier-Muzet, Pascal Stouffs, Jean-Pierre Bedecarrats, Jean Castaing-Lasvignottes

» Parabolic trough photovoltaic/thermal collectors. Part I: design and simulation model (ID 102)
Francesco Calise, Laura Vanoli

» Parabolic trough photovoltaic/thermal collectors. Part II: dynamic simulation of a solar trigeneration system (ID 488)
Francesco Calise, Laura Vanoli

» Performance analysis of downdraft gasifier - reciprocating engine biomass fired small-scale cogeneration system (ID 368)
Jacek Kalina

» Proposing offshore photovoltaic (PV) technology to the energy mix of the Maltese islands (ID 262)
Kim Trapani, Dean Lee Millar

» Research of integrated biomass gasification system with a piston engine (ID 414)
Janusz Kotowicz, Aleksander Sobolewski, Tomasz Iluk

» Start up of a pre-industrial scale solid state anaerobic digestion cell for the co-treatment of animal and agricultural residues (ID 34)
Francesco Di Maria, Giovanni Gigliotti, Alessio Sordi, Caterina Micale, Luisa Massaccesi

» The role of biomass in the renewable energy system (ID 390)
Ruben Laleman, Ludovico Balduccio, Johan Albrecht

» Vegetable oils of soybean, sunflower and tung as alternative fuels for compression ignition engines (ID 500)
Ricardo Morel Hartmann, Nury Nieto Garzón, Eduardo Morel Hartmann, Amir Antonio Martins Oliveira Jr, Edson Bazzo, Bruno Okuda, Joselia Piluski

» Wind energy conversion performance and atmosphere stability (ID 283)
Francesco Castellani, Emanuele Piccioni, Lorenzo Biondi, Marcello Marconi

V. 2 – FUEL CELLS

» Comparison study on different SOFC hybrid systems with zero-CO2 emission (ID 196)
Liqiang Duan, Kexin Huang, Xiaoyuan Zhang and Yongping Yang

» Exergy analysis and optimisation of a steam methane pre-reforming system (ID 62)
George G. Dimopoulos, Iason C. Stefanatos, Nikolaos M.P. Kakalis

» Modelling of a CHP SOFC power system fed with biogas from anaerobic digestion of municipal wastes integrated with a solar collector and storage units (ID 491)
Domenico Borello, Sara Evangelisti, Eileen Tortora

VOLUME VI

VI . 1 – CARBON CAPTURE AND SEQUESTRATION

» A novel coal-based polygeneration system cogenerating power, natural gas and liquid fuel with CO2 capture (ID 96)
Sheng Li, Hongguang Jin, Lin Gao

» Analysis and optimization of CO2 capture in a China's existing coal-fired power plant (ID 532)
Gang Xu, Yongping Yang, Shoucheng Li, Wenyi Liu and Ying Wu

» Analysys of four-end high temperature membrane air separator in a supercritical power plant with oxy-type pulverized fuel boiler (ID 442)
Janusz Kotowicz, Sebastian Stanisław Michalski

» Analysis of potential improvements to the lignite-fired oxy-fuel power unit (ID 413)
Marcin Liszka, Jakub Tuka, Grzegorz Nowak, Grzegorz Szapajko

» Biogas Upgrading: Global Warming Potential of Conventional and Innovative Technologies (ID 240)
Katherine Starr, Xavier Gabarrell Durany, Gara Villalba Mendez, Laura Talens Peiro, Lidia Lombardi

» Capture of carbon dioxide using gas hydrate technology (ID 103)
Beatrice Castellani, Mirko Filipponi, Sara Rinaldi, Federico Rossi

» Carbon dioxide mineralisation and integration with flue gas desulphurisation applied to a modern coal-fired power plant (ID 179)
Ron Zevenhoven, Johan Fagerlund, Thomas Björklöf, Magdalena Mäkelä, Olav Eklund

» Carbon dioxide storage by mineralisation applied to a lime kiln (ID 226)
Inês Sofia Soares Romão, Matias Eriksson, Experience Nduagu, Johan Fagerlund, Licínio Manuel Gando-Ferreira, Ron Zevenhoven

» Comparison of IGCC and CFB cogeneration plants equipped with CO2 removal (ID 380)
Marcin Liszka, Tomasz Malik, Michał Budnik, Andrzej Ziębik

» Concept of a "capture ready" combined heat and power plant (ID 231)
Piotr Henryk Lukowicz, Lukasz Bartela

» Cryogenic method for H2 and CH4 recovery from a rich CO2 stream in pre-combustion CCS schemes (ID 508)
Konstantinos Atsonios, Kyriakos D. Panopoulos, Angelos Doukelis, Antonis Koumanakos, Emmanuel Kakaras

» Design and optimization of ITM oxy-combustion power plant (ID 495)
Surekha Gunasekaran, Nicholas David Mancini, Alexander Mitsos

» Implementation of a CCS technology: the ZECOMIX experimental platform (ID 222)
Antonio Calabrò, Stefano Cassani, Leandro Pagliari, Stefano Stendardo

» Influence of regeneration condition on cyclic CO2 capture using pre-treated dispersed CaO as high temperature sorbent (ID 221)
Stefano Stendardo, Antonio Calabrò

» Investigation of an innovative process for biogas up-grading – pilot plant preliminary results (ID 56)
Lidia Lombardi, Renato Baciocchi, Ennio Antonio Carnevale, Andrea Corti, Giulia Costa, Tommaso Olivieri, Alessandro Paradisi, Daniela Zingaretti

» Method of increasing the efficiency of a supercritical lignite-fired oxy-type fluidized bed boiler and high-temperature three - end membrane for air separation (ID 438)
Janusz Kotowicz, Adrian Balicki

» Monitoring of carbon dioxide uptake in accelerated carbonation processes applied to air pollution control residues (ID 539)
Felice Alfieri, Peter J Gunning, Michela Gallo, Adriana Del Borghi, Colin D Hills

» Process efficiency and optimization of precipitated calcium carbonate (PCC) production from steel converter slag (ID 114)
Hannu-Petteri Mattila, Inga Grigaliūnaitė, Arshe Said, Sami Filppula, Carl-Johan Fogelholm, Ron Zevenhoven

» Production of Mg(OH)2 for CO2 Emissions Removal Applications: Parametric and Process Evaluation (ID 245)
Experience Ikechukwu Nduagu, Inês Romão, Ron Zevenhoven

» Thermodynamic analysis of a supercritical power plant with oxy type pulverized fuel boiler, carbon dioxide capture system (CC) and four-end high temperature membrane air seprator (ID 411)
Janusz Kotowicz, Sebastian Stanisław Michalski

VI . 2 – PROCESS INTEGRATION AND HEAT EXCHANGER NETWORKS

» A multi-objective optimization technique for co- processing in the cement production (ID 42)
Maria Luiza Grillo Renó, Rogério José da Silva, Mirian de Lourdes Noronha Motta Melo, José Joaquim Conceição Soares Santos

» Comparison of options for debottlenecking the recovery boiler at kraft pulp mills – Economic performance and CO2 emissions (ID 449)
Johanna Jönsson, Karin Pettersson, Simon Harvey, Thore Berntsson

» Demonstrating an integral approach for industrial energy saving (ID 541)
René Cornelissen, Geert van Rens, Jos Sentjens, Henk Akse, Ton Backx, Arjan van der Weiden, Jo Vandenbroucke

» Maximising the use of renewables with variable availability (ID 494)
Andreja Nemet, Jiri Jaromír Klemeš, Petar Sabev Varbanov, Zdravko Kravanja

» Methodology for the improvement of large district heating networks (ID 46)
Anna Volkova, Vladislav Mashatin, Aleksander Hlebnikov, Andres Siirde

» Optimal mine site energy supply (ID 306)
Monica Carvalho, Dean Lee Millar

» Simulation of synthesis gas production from steam oxygen gasification of Colombian bituminous coal using Aspen Plus® (ID 395)
John Jairo Ortiz, Juan Camilo González, Jorge Enrique Preciado, Rocío Sierra, Gerardo Gordillo

VOLUME VII

VII . 1 - BUILDING, URBAN AND COMPLEX ENERGY SYSTEMS

» A linear programming model for the optimal assessment of sustainable energy action plans (ID 398)
Gianfranco Rizzo, Giancarlo Savino

» A natural gas fuelled 10 kW electric power unit based on a Diesel automotive internal combustion engine and suitable for cogeneration (ID 477)
Pietro Capaldi

» Adjustment of envelopes characteristics to climatic conditions for saving heating and cooling energy in buildings (ID 430)
Christos Tzivanidis, Kimon Antonopoulos, Foteini Gioti

» An exergy based method for the optimal integration of a building and its heating plant. Part 1: comparison of domestic heating systems based on renewable sources (ID 81)
Marta Cianfrini, Enrico Sciubba, Claudia Toro

» Analysis of different typologies of natural insulation materials with economic and performances evaluation of the same buildings (ID 28)
Umberto Desideri, Daniela Leonardi, Livia Arcioni

» Complex networks approach to the Italian photovoltaic energy distribution system (ID 470)
Luca Valori, Giovanni Luca Giannuzzi, Tiziano Squartini, Diego Garlaschelli, Riccardo Basosi

» Design of a multi-purpose building "to zero energy consumption" according to European Directive 2010/31/CE: Architectural and plant solutions (ID 29)
Umberto Desideri, Livia Arcioni, Daniela Leonardi, Luca Cesaretti ,Perla Perugini, Elena Agabitini, Nicola Evangelisti

» Effect of initial systems on the renewal planning of energy supply systems for a hospital (ID 107)
Shu Yoshida, Koichi Ito, Yoshiharu Amano, Shintaro Ishikawa, Takahiro Sushi, Takumi Hashizume

» Effects of insulation and phase change materials (PCM) combinations on the energy consumption for buildings indoor thermal comfort (ID 387)
Christos Tzivanidis, Kimon Antonopoulos, Eleutherios Kravvaritis

» Energetic evaluation of a smart controlled greenhouse for tomato cultivation (ID 150)
Nickey Van den Bulck, Mathias Coomans, Lieve Wittemans, Kris Goen, Jochen Hanssens, Kathy Steppe, Herman Marien, Johan Desmedt

» Energy networks in sustainable cities: temperature and energy consumption monitoring in urban area (ID 190)
Luca Giaccone, Alessandra Guerrisi, Paolo Lazzeroni and Michele Tartaglia

» Extended exergy analysis of the economy of Nova Scotia, Canada (ID 215)
David C Bligh, V.Ismet Ugursal

» Feasibility study and design of a low-energy residential unit in Sagarmatha Park (Nepal) for envirnomental impact reduction of high altitude buildings (ID 223)
Umberto Desideri, Stefania Proietti, Paolo Sdringola, Elisa Vuillermoz

» Fire and smoke spread in low-income housing in Mexico (ID 379)
Raul R. Flores-Rodriguez, Abel Hernandez-Guerrero, Cuauhtemoc Rubio-Arana, Consuelo A. Caldera-Briseño

» Optimal lighting control strategies in supermarkets for energy efficiency applications via digital dimmable technology (ID 136)
Salvador Acha, Nilay Shah, Jon Ashford, David Penfold

» Optimising the arrangement of finance towards large scale refurbishment of housing stock using mathematical programming and optimisationg (ID 127)
Mark Gerard Jennings, Nilay Shah, David Fisk

» Optimization of thermal insulation to save energy in buildings (ID 174)
Milorad Bojić, Marko Miletić, Vesna Marjanović, Danijela Nikolić, Jasmina Skerlić

» Residential solar-based seasonal thermal storage system in cold climate: building envelope and thermal storage (ID 342)
Alexandre Hugo and Radu Zmeureanu

» Simultaneous production of domestic hot water and space cooling with a heat pump in a Swedish Passive House (ID 55)
Johannes Persson, Mats Westermark

» SOFC micro-CHP integration in residential buildings (ID 201)
Umberto Desideri, Giovanni Cinti, Gabriele Discepoli, Elena Sisani, Daniele Penchini

» The effect of shading of building integrated photovoltaics on roof surface temperature and heat transfer in buildings (ID 83)
Eftychios Vardoulakis, Dimitrios Karamanis

» The influence of glazing systems on energy performance and thermal comfort in non-residential buildings (ID 206)
Cinzia Buratti, Elisa Moretti, Elisa Belloni

» Thermal analysis of a greenhouse heated by solar energy and seasonal thermal energy storage in soil (ID 405)
Yong Li, Jin Xu, Ru-Zhu Wang

» Thermodynamic analysis of a combined cooling, heating and power system under part load condition (ID 476)
Qiang Chen, Jianjiao Zheng, Wei Han, Jun Sui, Hong-guang Jin

VII . 2 – COMBUSTION, CHEMICAL REACTORS

» Baffle as a cost-effective design improvement for volatile combustion rate increase in biomass boilers of simple construction (ID 233)
Borivoj Stepanov, Ivan Pešenjanski, Biljana Miljković

» Characterization of CH4-H2-air mixtures in the high-pressure DHARMA reactor (ID 287)
Vincenzo Moccia, Jacopo D'Alessio

» Development of a concept for efficiency improvement and decreased NOx production for natural gas-fired glass melting furnaces by switching to a propane exhaust gas fired process (ID 146)
Jörn Benthin, Anne Giese

» Experimental analysis of inhibition phenomenon management for Solid Anaerobic Digestion Batch process (ID 348)
Francesco Di Maria, Giovanni Gigliotti, Alessio Sordi, Caterina Micale, Claudia Zadra, Luisa Massaccesi

» Experimental investigations of the combustion process of n-butanol/diesel blend in an optical high swirl CI engine (ID 85)
Simona Silvia Merola, G. Valentino, C. Tornatore, L. Marchitto , F. E. Corcione

» Flameless oxidation as a means to reduce NOx emissions in glass melting furnaces (ID 141)
Jörg Leicher, Anne Giese

» Mechanism of damage by high temperature of the tubes, exposed to the atmosphere characteristic of a furnace of pyrolysis of ethane for ethylene production in the petrochemical industry (ID 65)
Jaqueline Saavedra Rueda, Francisco Javier Perez Trujillo, Lourdes Isabel Meriño Stand, Harbey Alexi Escobar, Luis Eduardo Navas, Juan Carlos Amezquita

» Steam reforming of methane over Pt/Rh based wire mesh catalyst in single channel reformer for small scale syngas production (ID 317)
Haftor Orn Sigurdsson, Søren Knudsen Kær

VOLUME VIII

VIII . 1 - ENERGY SYSTEMS : ENVIRONMENTAL AND SUSTAINABILITY ISSUES

» A multi-criteria decision analysis tool to support electricity planning (ID 467)
Fernando Ribeiro, Paula Ferreira, Madalena Araújo

» Comparison of sophisticated life cycle impact assessment methods for assessing environmental impacts in a LCA study of electricity production (ID 259)
Jens Buchgeister

» Defossilisation assessment of biodiesel life cycle production using the ExROI indicator (ID 304)
Emilio Font de Mora, César Torres, Antonio Valero, David Zambrana

» Design strategy of geothermal plants for water dominant medium-low temperature reservoirs based on sustainability issues (ID 99)
Alessandro Franco, Maurizio Vaccaro

» Energetic and environmental benefits from waste management: experimental analysis of the sustainable landfill (ID 33)
Francesco Di Maria, Alessandro Canovai, Federico Valentini, Alessio Sordi, Caterina Micale

» Environmental assessment of energy recovery technologies for the treatment and disposal of municipal solid waste using life cycle assessment (LCA): a case study of Brazil (ID 512)
Marcio Montagnana Vicente Leme, Mateus Henrique Rocha, Electo Eduardo Silva Lora,Osvaldo José Venturini, Bruno Marciano Lopes, Claudio Homero Ferreira

» How will renewable power generation be affected by climate change? – The case of a metropolitan region in Northwest Germany (ID 503)
Jakob Wachsmuth, Andrew Blohm, Stefan Gößling-Reisemann, Tobias Eickemeier, Rebecca Gasper, Matthias Ruth, Sönke Stührmann

» Impact of nuclear power plant on Thailand power development plan (ID 474)
Raksanai Nidhiritdhikrai, Bundhit Eua-arporn

» Improving sustainability of maritime transport through utilization of liquefied natural gas (LNG) for propulsion (ID 496)
Fabio Burel, Rodolfo Taccani, Nicola Zuliani

» Life cycle assessment of thin film non conventional photovoltaics: the case of dye sensitized solar cells (ID 471)
Maria Laura Parisi, Adalgisa Sinicropi, Riccardo Basosi

» Low CO2 emission hybrid solar CC power system (ID 175)
Yuanyuan Li, Na Zhang, Ruixian Cai

» Low exergy solutions as a contribution to climate adapted and resilient power supply (ID 489)
Stefan Goessling-Reisemann, Thomas Bloethe

» On the use of MPT to derive optimal RES electricity generation mixes (ID 459)
Paula Ferreira, Jorge Cunha

» Stability and limit cycles in an exergy-based model of population dynamics (ID 128)
Enrico Sciubba, Federico Zullo

» The influence of primary measures for reducing NOx emissions on energy steam boiler efficiency (ID 125)
Goran Stupar, Dragan Tucaković, Titoslav Živanović, Miloš Banjac, Srđan Belošević,Vladimir Beljanski, Ivan Tomanović, Nenad Crnomarković, Miroslav Sijerčić

» The Lethe city car of the University of Roma 1: final proposed configuration (ID 45)
Roberto Capata, Enrico Sciubba

VIII . 2 - POSTER SESSION

» A variational optimization of a finite-time thermal cycle with a Stefan-Boltzmann heat transfer law (ID 333)
Juan C.Chimal-Eguia, Norma Sanchez-Salas

» Modeling and simulation of a boiler unit for steam power plants (ID 545)
Luca Moliterno, Claudia Toro

» Numerical Modelling of straw combustion in a moving bed combustor (ID 412)
Biljana Miljkoviü, Ivan Pešenjanski, Borivoj Stepanov, Vladimir Milosavljeviü, Vladimir Rajs

» Physicochemical evaluation of the properties of the coke formed at radiation area of light hydrocarbons pyrolysis furnace in petrochemical industry (ID 10)
Jaqueline Saavedra Rueda , Angélica María Carreño Parra, María del Rosario Pérez Trejos, Dionisio Laverde Cataño, Diego Bonilla Duarte, Jorge Leonardo Rodríguez Jiménez, Laura María Díaz Burgos

» Rotor TG cooled (ID 121)
Chiara Durastante, Paolo Petroni, Michela Spagnoli, Vincenzo Rizzica, Jörg Helge Wirfs

» Study of the phase change in binary alloy (ID 534)
Aroussia Jaouahdou, Mohamed J. Safi, Herve Muhr

» Technip initiatives in renewable energies and sustainable technologies (ID 527)
Pierfrancesco Palazzo, Corrado Pigna

ECOS 2012

VOLUME IV

A Control Oriented Simulation Model of a Multistage Axial Compressor

Lorenzo Damiani [a], Giampaolo Crosa and Angela Trucco

[a] *University of Genoa, Lorenzo.Damiani@unige.it*

Abstract:

As known, the diagnostic and control – oriented dynamic turbomachinery simulation tools have to be simple and fast running, to achieve the short calculation times compatible with the real – time operation to which they are finalized.

This paper describes a mathematical model, implemented in the Matlab-Simulink environment, able to reproduce the design and off-design performances of multi stage compressors. The simulator was built to be integrated into an industrial gas turbine dynamic simulator, with the purpose to describe the behaviour of the whole plant as the operational conditions are changed, for a better prevision of the turbine cooling flows thanks to the model ability of inter – stage pressure and temperature prediction. The model was identified with an industrial axial compressor in commerce, part of the AE94.3A gas turbine, using both the results of a more complex numerical programme and the compressor characteristic maps (efficiency and pressure ratio in function of reduced mass flow rate and IGV angle).

The tests effected on the simulator demonstrate a satisfactory behaviour in reproducing the design and off-design performances.

Keywords:

Compressor, modelling, control, gas turbine.

1. Introduction

A dynamic physical simulator of a heavy-duty combined cycle, designed to tune up the control system, to predict the maintenance intervals, or also for diagnostic use or staff training [1, 2, 3], consists of a coordinate set of separated simulation modules each describing, by simple mathematical relations, one plant component. The different modules, once connected, have the task to reproduce the plant design and off-design performance with precision and rapidity.

Turbomachinery mathematical models are in general built on the ground of their characteristic maps: pressure ratio and efficiency versus reduced mass flow rate, reduced rotational speed and IGV angle. In a multistage machinery simulation context, a step forward could be a quasi-one-dimensional fluid-dynamic approach [4]. Nevertheless, this method is not reliable for an axial flow multistage compressor, owing to the validity limits of loss correlations and flow angle predictions at partial load conditions.

In this paper, a multi stage axial compressor was considered and, as an alternative approach to obtain information on pressures and temperatures between the stages, a stage by stage method was tested and its potentialities investigated. Said technique becomes a suitable and very indicated simulation instrument in case sufficiently powerful calculation tools are available: these allow the rapid solution of the equations involved in the problem, making the simulation model able to a real-time monitoring of an operating plant.

One more advantage of a stage by stage technique is the possibility of interposing, between the stage blocks, well fitted inter-stage volumes. Applying to each of them the continuity and energy equations in their time-varying form, the whole compressor can be simulated, appreciating its dynamic behaviour [5].

The simulation model presented in this work was particularized on a 15-stage axial compressor produced by Ansaldo Energia, equipped with variable inlet guide vanes (IGV) and outlet guide vane diffusion duct (OGV). The compressor is part of the heavy-duty AE94.3A gas turbine representing, with its 285 MW nominal power and 39.6% efficiency, the peak model of Ansaldo commercial offer.

In the simulator described in this paper, non dimensional stage performance parameters were used to characterize stages operating in subsonic regime; instead, since the 1st and the 2nd stage of the machine in exam work in transonic conditions, the first stages set upstream of the first air bleeding and the IGV cascade were grouped into a single block, whose performance are reproduced by means of an overall characteristic map.

The single stage characteristic curves were determined by the use of a compressor model having as inputs the mass flow rate and two reference arrays containing total pressure and temperature data at the outlet of each stage. These values were derived with the aid of a more complex through-flow model. By means of a correction loop, the compressor model forces each stage to attain the reference pressure and temperature values, so deriving the non-dimensional parameters for each given working point. If input data include a sufficient number of operating conditions, the dimensionless characteristic maps are obtained by interpolation of the points on the related charts.

The simulator was finally validated, with satisfactory agreement, comparing its output data with those of the through-flow model, for different compressor working conditions.

2. The compressor simulator

The complete compressor simulator, of which the overall scheme is provided in Figure 1, is composed by two main sub-systems:

- The first sub-system includes the IGV row and the first five stages, which were grouped into a single simulation block containing overall working maps: its role is to provide the correct inlet total pressure and temperature to the 6th stage as well as the compressor inlet mass-flow rate actual value. This settlement is suitable to avoid characteristic maps calculation problems connected to the transonic operation of the first stages, as they do not work in quasi-incompressible flow regime. This sub-system is named “IGV + Stages 1-5” in Figure 2. Downstream of this block, the first air bleeding is drawn out.
- The second sub-system groups the 6th to 15th stages, which were implemented by a classical Stage-Stacking approach, explained in detail in Appendix A; OGV was simulated as a divergent duct, by means of the continuity and energy equations.

In the AE94.3A gas turbine, the air needed for turbine blade cooling is provided by several “bleeds”, delivering air from the compressor stages to the turbine cooling devices. In Figure 2 is shown the compressor bleedings scheme, characterised by some external cooling air ducts and some others passing through the shaft.

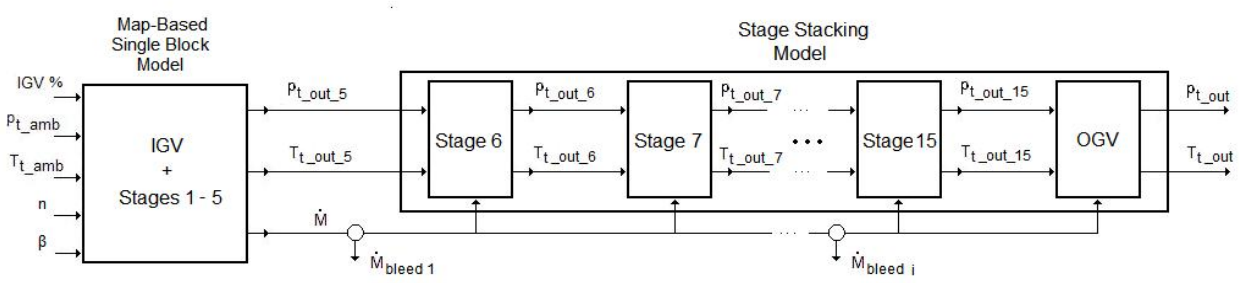

Figure 1: Simulation model overall scheme.

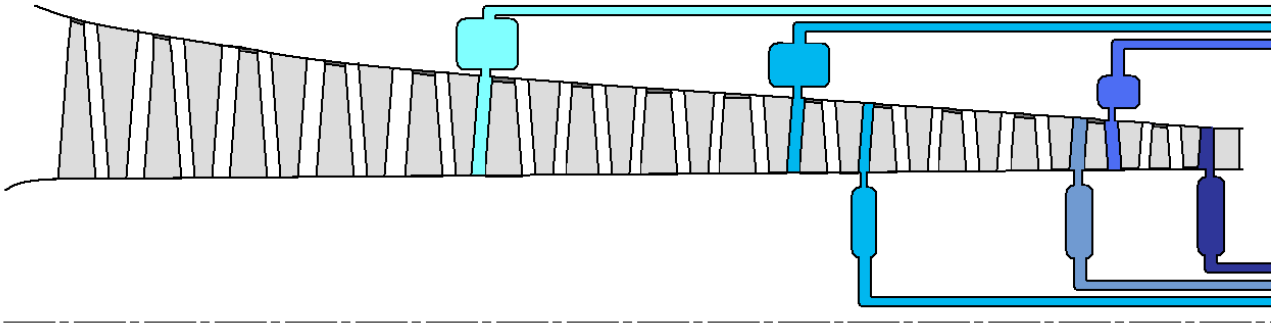

Figure 2: Scheme of the air cooling system.

In order to obtain a simple but correct model of the cooling bleeds, these last were simulated subtracting from the total evolving flow-rate a fixed percentage on the basis of the design point value; this simplification is believed to be a good approximation of the real machine operating conditions.

3. Stage characteristic maps

3.1. Stage characteristics of the AE94.3a compressor

The stage-by-stage simulation of an axial compressor requires information about the blade cascades geometry. In the examined compressor, the non-transonic cascades are characterised by geometrical similarity among the different stages, translating into an equality of the related non-dimensional characteristic curves [6]; the stage model (Appendix A) needs no geometrical compressor data other than air flow passage area, a parameter necessary to determine air axial velocity, and mean stage diameter [7].

The stage model utilised in the present approach strongly depends on the stage characteristic maps. It is thus of primary importance for the good operation of the model the acquisition of reliable $\Psi_i = \Psi_i(\Phi_i)$ and $\eta_i = \eta_i(\Phi_i)$ stage non-dimensional characteristic curves [8], being:

- Φ_i the ith stage flow-rate coefficient:

$$\Phi_i = \frac{c_{a_i}}{u_i} \tag{1}$$

It is related to volumetric flow rate, as it indicates the stage outlet axial velocity c_{a_i}, turned into a non-dimensional quantity dividing by rotor speed u_i calculated at the mean blade radius.

- Ψ_i the ith stage pressure rise coefficient:

$$\Psi_i = \frac{\Delta H_{s_i}}{u_i^2} = \frac{c_p T_{t_i-1} \cdot \left(\beta_i^{\frac{k-1}{k}} - 1 \right)}{u_i^2} \tag{2}$$

It is related to the ideal energy increase experimented by the fluid in its passage through the stage: the formula includes, in fact, the term ΔH_{s_i}, stage isentropic total enthalpy rise, divided by rotor speed to the square.

- η_i the ith stage efficiency:

$$\eta_i = \frac{\Delta H_{s_i}}{\Delta H_{r_i}} \tag{3}$$

where ΔH_{r_i} is the real enthalpy increase, including losses.

The thermodynamic quantities appearing in the mentioned equations are referred to the stage outlet [9, 10].

The construction of such curves was realised basing on inter-stage total temperature and pressure reference data series, calculated by means of a through-flow approach employed by Ansaldo Energia. The inter-stage data were calculated for four compressor working conditions (the Design Point and three Off-Design conditions) as shown in Figures 3a and 3b, where the pressures and temperatures are divided by "reference" pressure and temperature values p_{t_ref} and T_{t_ref}.

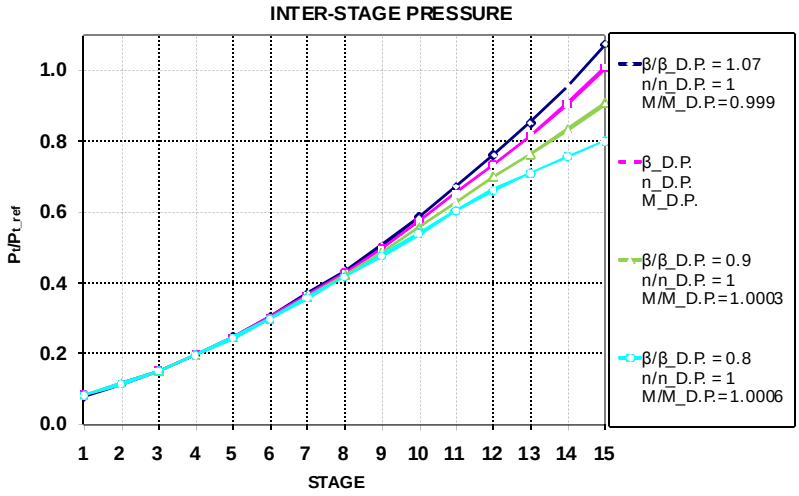

Figure 3a: Reference inter-stage total pressure through-flow data.

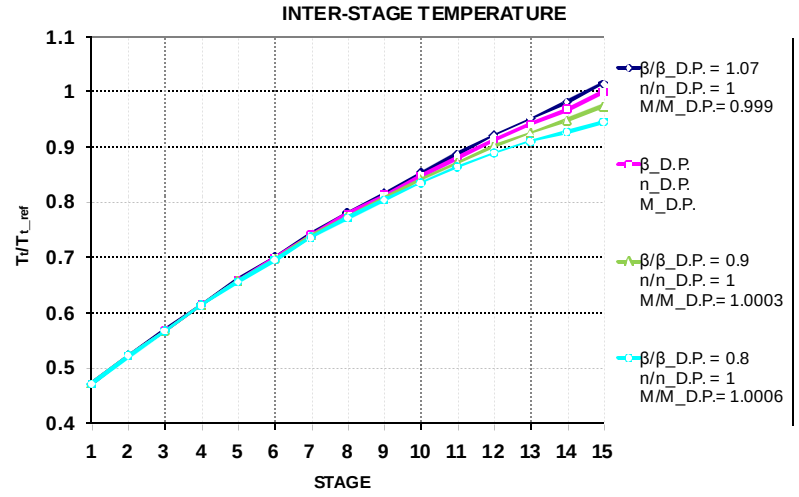

Figure 3b: Reference inter-stage total temperature through-flow data.

In order to generate the stage maps $\Psi_i = \Psi_i(\Phi_i)$ and $\eta_i = \eta_i(\Phi_i)$, an auxiliary stage by stage model was created, able to provide as output the three non-dimensional parameters Φ_i, Ψ_i and η_i for all the stages, having as input the mass flow rate and the two arrays containing the reference data of figures 3a and 3b.

This auxiliary model is composed by a sequence of 15 blocks each representing one compressor stage; each stage is forced, thanks to a time-marching control loop, to obtain as output the reference total pressure and temperature data. The correct values of Φ_i, Ψ_i and η_i, needed for each stage

characteristic maps construction have then been determined. Figure 4 provides a graphical explanation of the control loop operation.

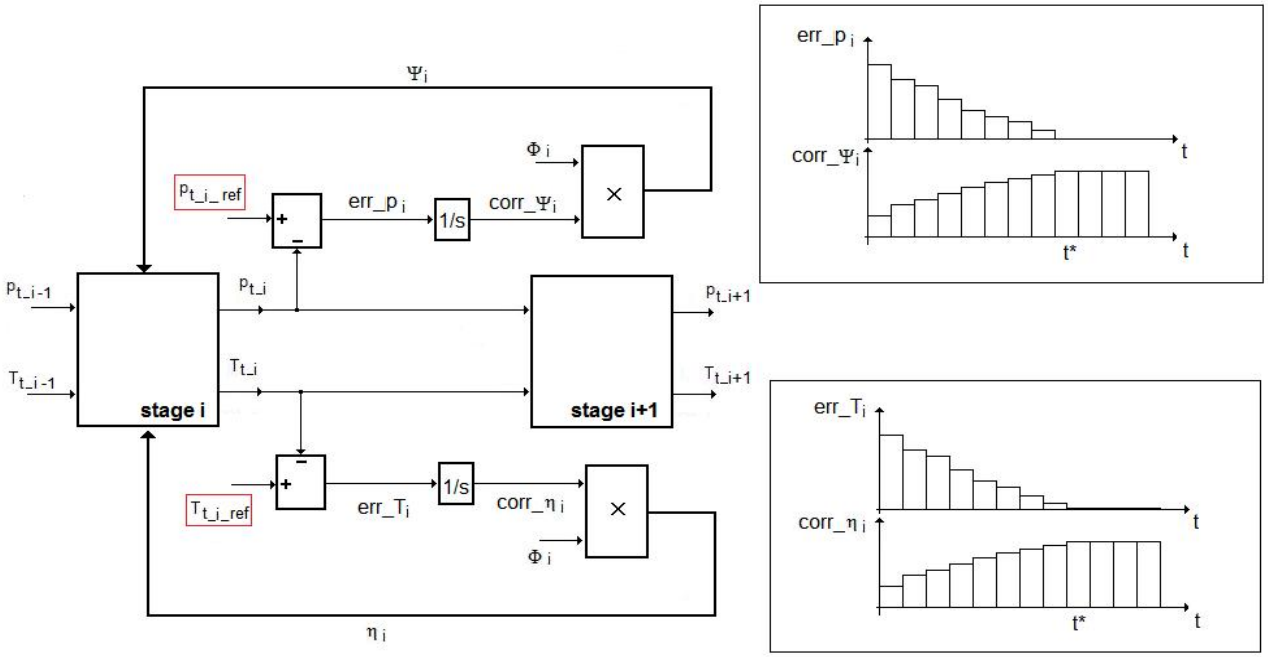

Figure 4: Correction loop in the auxiliary stage by stage model.

Referring to Figure 4, the i[th] stage output total pressure and temperature values (p_{t_i} and T_{t_i}) are continuously compared with the reference values ($p_{t_i_ref}$ and $T_{t_i_ref}$), and the errors (err_p_i and err_T_i) are integrated in time in the 1/s block, to supply adjustment coefficients ($corr_\Psi_i$ and $corr_\eta_i$) by which Φ_i is multiplied, providing stage Ψ_i and η_i correct values. Once reached the steady state condition (time step t^* in the figure), i[th] stage total pressure and temperature are equal to the reference ones, to which correspond the correct stage pressure rise and efficiency coefficients.

The auxiliary stage by stage model was utilised to determine the values of Φ_i, Ψ_i and η_i for each of the stages 6 to 15 in the four compressor working conditions provided by Ansaldo, obtaining four points on the (Φ_i, Ψ_i) map and other four on the (Φ_i, η_i) map.

3.2. Normalised characteristic maps

According to several authors [11, 12, 13, 14, 15] and basing on the Similitude Theory, stage by stage models based on the Stage-Stacking technique are capable of operating with two characteristic curves in common for all the stages, one for the pressure rise coefficient and one for efficiency, called “normalised characteristics”, instead of working with a couple of curves for each stage.

These two curves were determined, for each stage, dividing the values of non-dimensional parameters Φ_i, Ψ_i and η_i, obtained from the auxiliary stage by stage model in the four aforementioned operating conditions, by the non-dimensional parameters at the Design Point ($\Phi_{i_D.P.}$, $\Psi_{i_D.P.}$ and $\eta_{i_D.P.}$). The non-dimensional and normalised parameters so obtained, for the stages 6 to 15, were positioned on two charts $(\Phi_i/\Phi_{i_D.P.}, \Psi_i/\Psi_{i_D.P.})$ and $(\Phi_i/\Phi_{i_D.P.}, \eta_i/\eta_{i_D.P.})$, from which results evident the settlement of the related points approximately on two curves, as shown in Figures 5a and 5b.

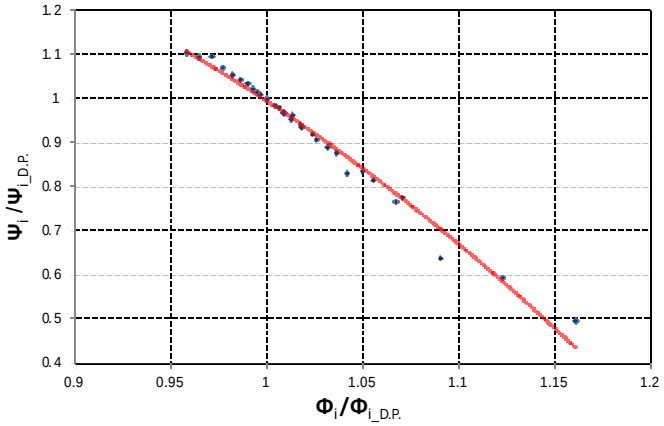

Figure 5a: Normalised pressure rise coefficient characteristic curve.

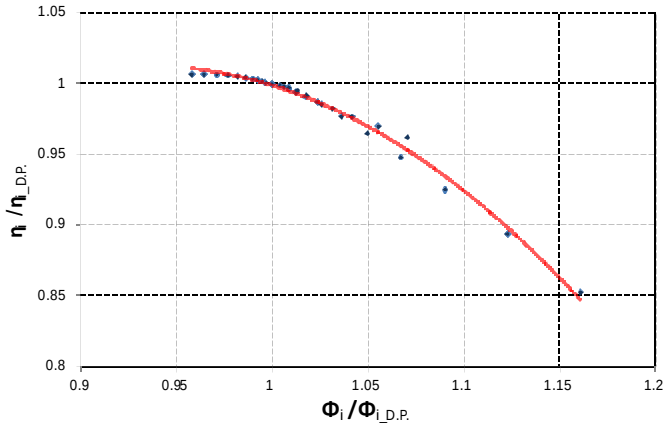

Figure 5b: Normalised efficiency characteristic curve.

The points so obtained were joined together by minimum error parabolas (red curves in Figures 5a and 5b), whose mathematical functions $\Psi/\Psi_{D.P.} = F(\Phi/\Phi_{D.P.})$ and $\eta/\eta_{D.P.} = G(\Phi/\Phi_{D.P.})$ were included in the 6th to 15th stage blocks.

Therefore, according to the calculation procedure described in Appendix A, the normalised stage characteristic maps were used to calculate the performance of each compressor stage starting from the 6th one, known the ith stage Design Point values ($\Phi_{i_D.P.}$, $\Psi_{i_D.P.}$ and $\eta_{i_D.P.}$), by the scheme of Figure 6.

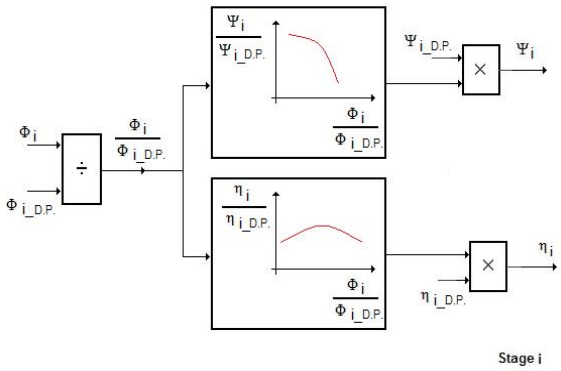

Figure 6: Determination of ith stage Ψ_i and η_i values from the normalised characteristic maps.

4. Mapping of the first five stages and IGV

Since a stage simulation method based on Φ_i, Ψ_i and η_i non-dimensional parameters is not suitable for representing stages with transonic flow (the first one and the second one, in the presented case) [16], the IGV and the stages 1 to 5 were simulated by means of a classical single block provided of its proper characteristic maps. Since the first cooling mass flow bleeding is positioned downstream of the 5th stage, this solution does not influence the capability of the complete simulator to reproduce correctly the compressor operation.

In this phase, the activity was turned to the determination of:

- efficiency maps, with the structure $\eta = \eta(IGV, \beta, n_{red})$;
- reduced mass flow maps, with the structure $\dot{M}_{red} = \dot{M}_{red}(IGV, \beta, n_{red})$;

where for n_{red} is intended the reduced shaft rotational speed ($n\ (T_{t1})^{-0.5}$) and for $\dot{M}_{red}$ the reduced mass flow rate ($\dot{M}\ (T_{t1})^{0.5}\ (p_{t1})^{-1}$)

The maps were generated following the scheme represented in Figure 7, taking as reference the output pressure and temperature values provided by a single block model of the whole compressor, described in detail in [17]. The stage by stage model output values (p_{t_out} and T_{t_out} in Figure 7), were forced to reproduce the single block model output values ($p_{t_out_ref}$ and $T_{t_out_ref}$) by varying the 6th stage inlet total pressure and temperature ($p_{t_out_5}$ and $T_{t_out_5}$) coming from the block named "Maps Generator". This last block, together with the same inputs of the whole compressor model, has as further input the output pressure and temperature errors (*Err_p* and *Err_T* in Figure 7), which are minimized by a control loop similar to that described in section 3 for stage maps (Φ_i, Ψ_i) and (Φ_i, η_i) generation. As a result, this calculation scheme provides the 5th stage correct values of total pressure and temperature, useful for determining the "IGV + Stages 1 to 5" block characteristic maps.

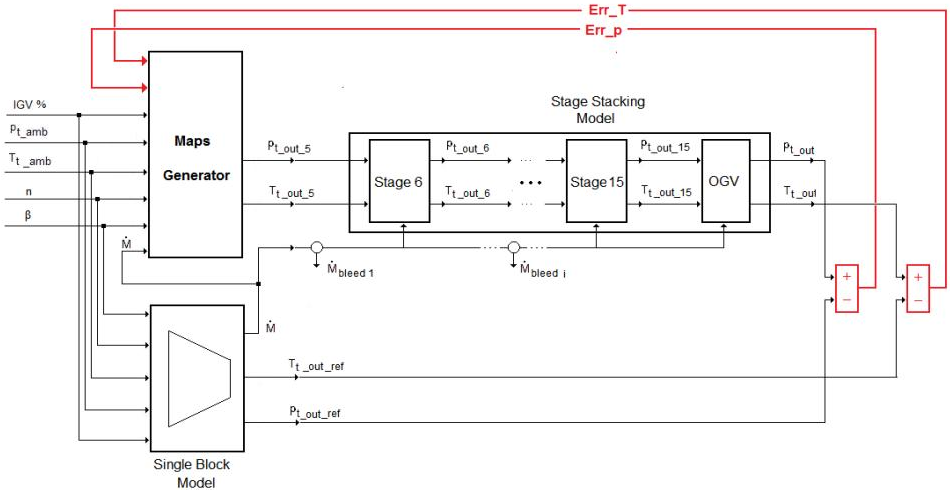

Figure 7: Matching between stage by stage model and single block reference model, for the creation of stages 1-5 maps.

A Matlab script was used in order to control the Simulink model and automate the maps build-up procedure of the "IGV + Stages 1-5" block, by changing, for various rotational speeds, the pressure ratio and the IGV opening. Reduced mass-flow rates and 6th stage inlet total pressure and temperature values were automatically saved and used to build the series of reduced mass-flow and efficiency maps necessary to model the compressor first five stages characteristics.

The maps so derived were introduced into the block comprising stages 1 to 5, making it able to reproduce the behaviour of the first five stages and to provide the mass flow rate to the stage by stage block downstream.

5. Results

The simulation model described in the previous paragraphs was tested against the reference data provided by Ansaldo Energia, resulting from the through-flow calculations.

The results here presented are related to the following simulation conditions tested:

- four 100% IGV opening operating conditions; these last are the same utilised for the characteristic maps generation;
- two off-design conditions providing two IGV opening values of respectively 95% and 85%.

Table 1 indicates the mass-flow rate errors between reference data and simulations output, in terms of percentage of the reference mass-flow rate, at the different conditions tested.

Table 1: Relative mass-flow rate errors between calculated values and reference values.

	$\beta / \beta_{D.P.} = 1.07$ IGV = 100%	$\beta / \beta_{D.P.} = 1.0$ IGV = 100%	$\beta / \beta_{D.P.} = 0.9$ IGV = 100%	$\beta / \beta_{D.P.} = 0.8$ IGV = 100%	$\beta / \beta_{D.P.} = 0.95$ IGV=95%	$\beta / \beta_{D.P.} = 0.85$ IGV=85%
$\dot{M} / \dot{M}_{D.P.}$	0.999	1	1.000	1.001	0.944	0.859
$\frac{\lvert \dot{M}_{calc} - \dot{M}_{ref} \rvert}{\dot{M}_{ref.}}$ [%]	1.33	1.34	1.33	1.35	1.75	0.49

As noticeable, the errors show a peak of 1.75% at the 95% IGV opening condition. For the other working points, the error does not exceed 1.35%.

In the following diagrams (Figures 8-13) the results of the complete compressor simulator are presented, in terms of inter-stage total pressure rise and inter-stage total temperature rise, from the 6th stage on. The output values obtained through the presented Matlab-Simulink model was compared with the results obtained from the reference through-flow calculations effected by Ansaldo Energia.

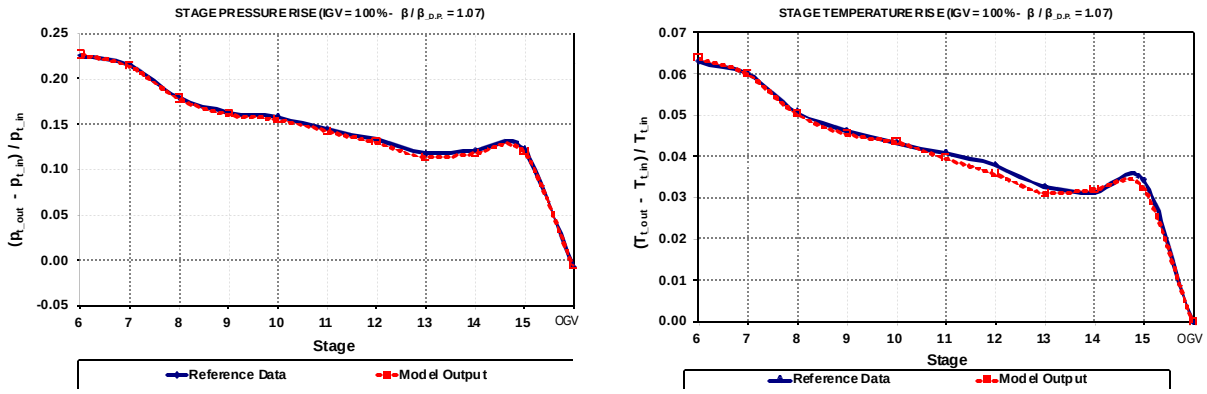

Figure 8: Inter-stage total pressure rise (left) and total temperature rise (right); comparison between model output and reference data (IGV = 100%, $\beta/\beta_{D.P.}$=1.07).

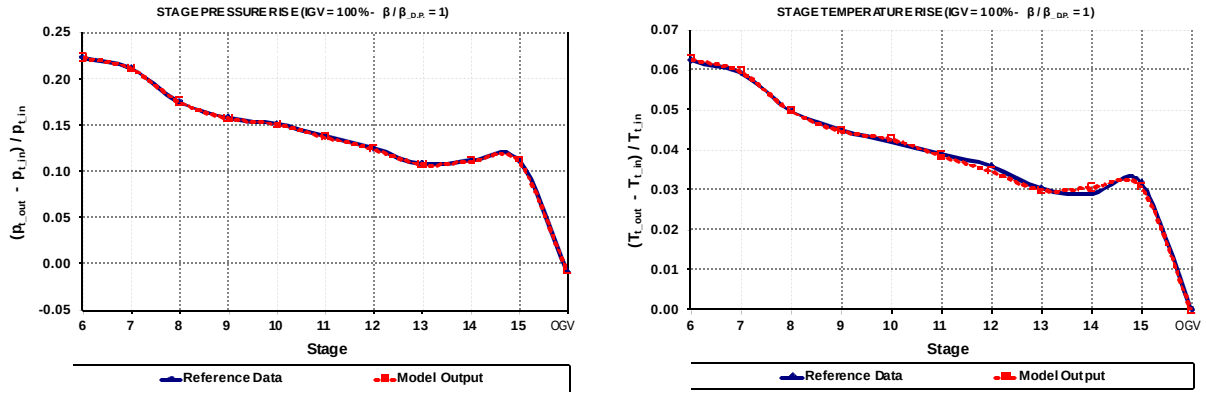

Figure 9: Inter-stage total pressure rise (left) and total temperature rise (right); comparison between model output and reference data (IGV = 100%, $\beta/\beta_{D.P.}=1$).

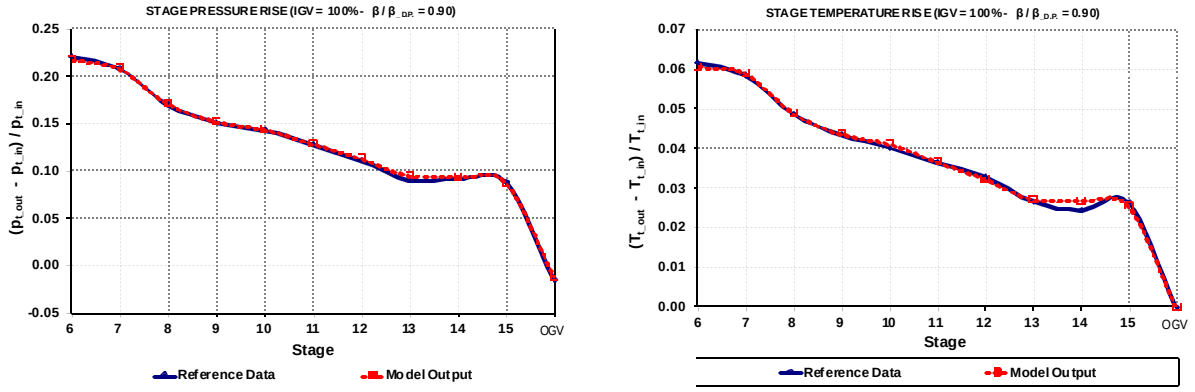

Figure 10: Inter-stage total pressure rise (left) and total temperature rise (right); comparison between model output and reference data (IGV = 100%, $\beta/\beta_{D.P.}=0.9$).

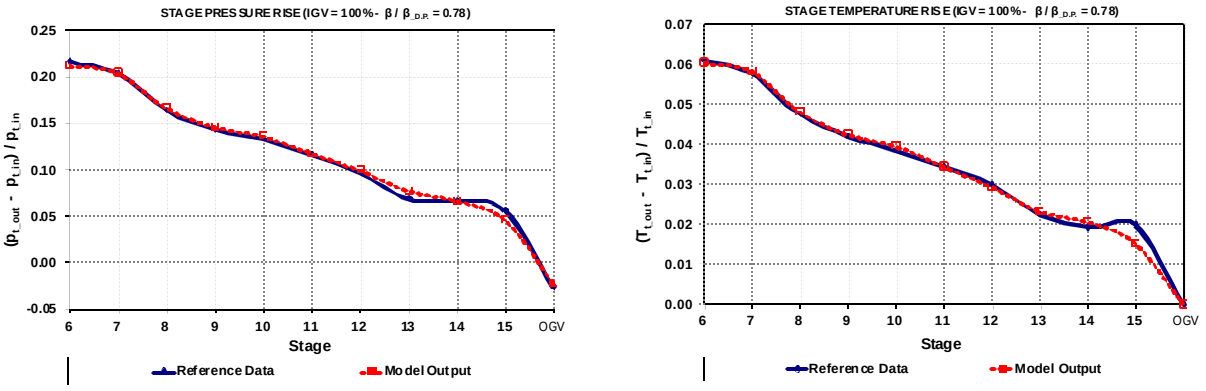

Figure 11: Inter-stage total pressure rise (left) and total temperature rise (right); comparison between model output and reference data (IGV = 100%, $\beta/\beta_{D.P.}=0.78$).

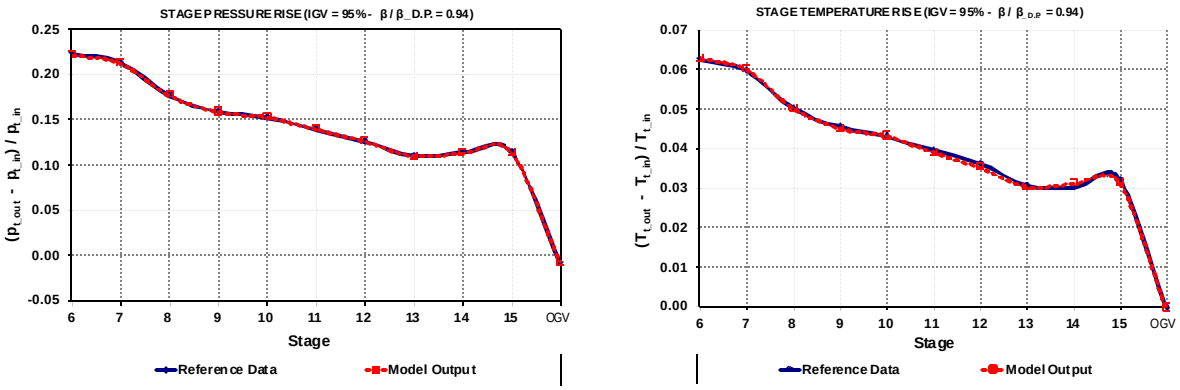

Figure 12: Inter-stage total pressure rise (left) and total temperature rise (right); comparison between model output and reference data (IGV = 95%, $\beta/\beta_{D.P.}$=0.94).

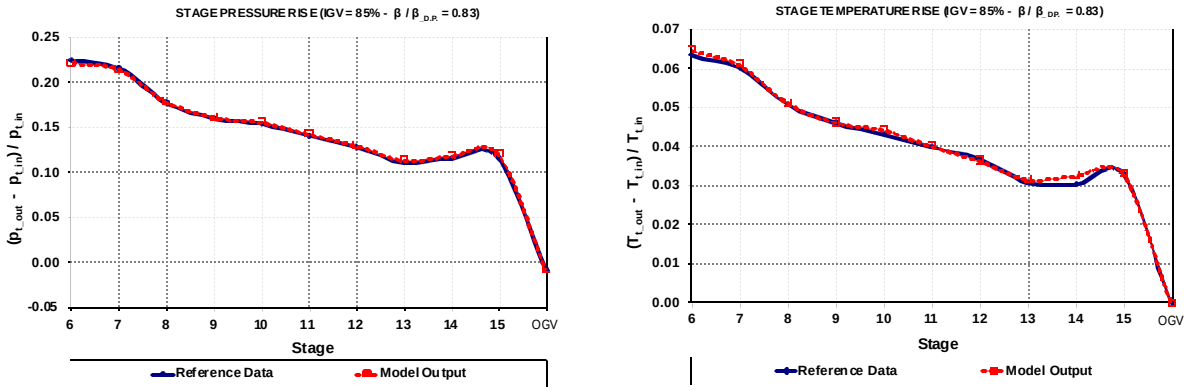

Figure 13: Inter-stage total pressure rise (left) and total temperature rise (right); comparison between model output and reference data (IGV = 85%, $\beta/\beta_{D.P.}$=0.83).

Model outputs show a well acceptable agreement with the reference inter-stage total pressure and temperature rise data.

6. Conclusions

A one-dimensional stage by stage model, integrated with a classical map-based single block model, was developed to predict the design and off-design performance of a multistage axial flow compressor.

Being the first stages affected by transonic flow, not reproducible by the simple similitude theory based on Φ_i, Ψ_i and η_i non-dimensional parameters not variable in function of Mach number, stages 1 to 5 were simulated by a map-based block. The remaining ten stages were simulated by the ordinary Stage Stacking method.

The individual stage non-dimensional characteristics ($\Psi_i=f_i(\Phi_i)$ and $\eta_i=g_i(\Phi_i)$) were estimated by means of an auxiliary stage by stage model, basing on inter-stage total pressure and temperature reference data calculated by a through-flow simulator. Moreover, according to Similitude Theory, the single stage characteristic maps were normalised by the Design Point values ($\Phi_{i,D.P.}$, $\Psi_{i,D.P.}$ and $\eta_{i,D.P.}$), obtaining two general stage maps valid for the whole machine.

As shown in the presented results, the model is able to reproduce with good precision the machine performance for a wide range of working conditions.

The new stage by stage compressor model has been developed to replace the old single-block map-based one into the dynamic simulator of the Ansaldo AE94.3A gas turbine, enhancing its prediction capability; in particular, thanks to the model stage by stage structure, a better reproduction of the blade cooling system performances is possible, since the total pressure and total temperature values of the cooling air bleedings are correctly calculated.

The next step to be done is the incorporation in the compressor model of the inter-stage volumes provided of continuity and energy equations in the time-varying form, making the simulator able to reproduce the machinery dynamic behaviour.

Appendix A

The mathematical model utilised for the stage by stage simulator is based on the known Stage-Stacking technique, and has been developed in the Matlab-Simulink environment; its construction was effected following three steps:

1. introduction of the physical equations that rule the stacking of stages and OGV duct in the simulation programme;
2. evaluation, for different machine working conditions, of the set of non-dimensional parameters Φ_i, Ψ_i and η_i for each stage i [11] [16];
3. on the basis of the data collected in step 2), construction of the stage non-dimensional characteristic curves $\Psi_i = \Psi_i(\Phi_i)$ and $\eta_i = \eta_i(\Phi_i)$ [18].

The non-dimensional parameters Φ_i, Ψ_i and η_i utilised are defined in equations (1), (2) and (3).

The parameters needed to apply the Stage-Stacking procedure are: total temperature and pressure at the compressor inlet station, shaft rotational speed, geometrical stage data (inlet flow passage areas Ω_i and mean stage diameter), relative air humidity, mass flow rate and 10 stage characteristic curves $\Psi_i = \Psi_i(\Phi_i)$ and $\eta_i = \eta_i(\Phi_i)$, (i = 6,…,15) [8 ,13]. The evolving fluid was considered as a perfect gas.

Mass flow rate $\dot{M}$ evolving in the compressor is calculated in the single block model (stages 1 to 5 + IGV, described in Paragraph 5), working with its typical performance maps [17]; the calculated flow rate value deviates from the reference data of no more than 1,75%, as indicated in Table 1, in the totality of the working conditions investigated.

Figure 14 shows the structure of one stage block; the sequence of steps by which the input signals are elaborated to calculate the output values [12] is described in the following.

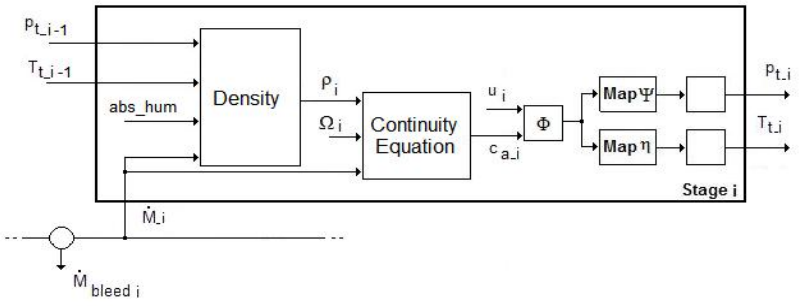

Figure 14: Scheme of one stage.

1. The "Density" block calculates the flow inlet static density from the inlet total pressure and temperature and the absolute air humidity exploiting, in sequence, the general formulas:

$$p = \frac{p_t}{\left(1+\frac{k-1}{2}M^2\right)^{\frac{k}{k-1}}} \tag{4}$$

$$T = \frac{T_t}{\left(1+\frac{k-1}{2}M^2\right)} \tag{5}$$

$$\rho = \frac{p}{RT} \tag{6}$$

2. In the "Continuity Equation" block, known flow passage area and mass flow rate, it is possible to obtain axial velocity c_{a_i} and derive the flow-rate coefficient Φ_i, dividing c_{a_i} by the mid-span rotor velocity, u_i. This operation takes place into the block indicated with the label "Φ".
3. Pressure coefficient Ψ_i is calculated in the block "Map Ψ ", containing the $\Psi_i = \Psi_i(\Phi_i)$ characteristic curve for the i^{th} stage.
4. Pressure coefficient definition permits to find the stage pressure ratio, through Equation 7:

$$\beta_i = \frac{p_{t_i}}{p_{t_i-1}} = \left(\frac{\Psi_i u_i^2}{c_p T_{t_i-1}} + 1\right)^{\frac{k}{k-1}} \tag{7}$$

From this relation, it is immediate to find stage outlet total pressure, p_{t_i}.

5. Stage efficiency η_i is calculated in the block "Map η", containing $\eta_i = \eta_i(\Phi_i)$ stage characteristic curve.
6. Once known the efficiency, it is possible to obtain the outlet total temperature by means of Equation 8:

$$T_{t_i} = T_{t_i-1} + \left(\frac{\Psi_i u_i^2}{\eta_i c_p}\right) \tag{8}$$

7. Stage outlet total pressure and temperature represent the inlet values for the following stage: in this way, proceeding stage by stage, it is possible to calculate the compressor outlet conditions.

Acknowledgements

The Authors wish to thanks Franco Rocca, Raffaele Traverso and Daniela Marino of Ansaldo Energia for the reference data of the AE94.3A gas turbine, and for the permission of their publishing in this paper.

Nomenclature

c_a	axial flow velocity, m s^{-1}
F, G	generic function
H	enthalpy, J kg^{-1}
c_p	specific heat capacity at constant pressure, J kg^{-1} K^{-1}
IGV	inlet guide vanes
k	specific heat ratio, -
$\dot{M}$	mass-flow rate, kg s^{-1}
Ma	Mach number,-

n shaft rotational speed, rev s^{-1}

p pressure, Pa

R individual gas constant, J kg^{-1} K^{-1}

T temperature, K

u rotor speed at the mean diameter, m s^{-1}

Greek symbols

β pressure ratio, -

η efficiency, -

Φ mass-flow coefficient, -

Ψ pressure rise coefficient, -

Ω flow passage area, m^2

Subscripts

D.P. design point

i related to the i^{th} stage

red reduced

ref reference

r real

s isentropic

t total (stagnation)

References

[1] Aretakis N., Roumeliotis L., Mathioudakis K., "Performance Model Zooming for in-depth Component Fault Diagnosis", 2011, *ASME J. of Engineering for Gas Turbines and Power* **133** (3).

[2] Morini M., Pinelli M., Spina P.R., Venturini M., "Influence of blade deterioration on compressor and turbine performance", 2010, *ASME J. of Engineering for Gas Turbines and Power*, **132** (3).

[3] Reza Hosseini S.H., Khaledi H., Soltani M.R., "New Model Based Gas Turbine Fault Diagnostics Using 1D Engine Model and Nonlinear Identification Algorithms" 2009, *Proceedings of the ASME Turbo Expo*, **1**, pp. 575-585.

[4] White N.M., Tourlidakis A., Elder R.L., "Axial compressor performance modelling with a quasi-one-dimensional approach", 2002, *Proc Instn Mech Engrs, Part A: Journal of Power and Energy*, **216** (2), pp. 181-193.

[5] Schulte H., Schmidt K.J., Weckend A., Staudacher S., "Multi Stage Compressor Model for Transient Performance Simulations", 2008, *Proceedings of the ASME Turbo Expo*, **1**, pp. 185-195.

[6] Saravanamuttoo H.I.H., "Component performance requirements", 1992, Nato, Agard-LS-183, pp. 1-4.

[7] Horlock J. H., "A Rapid Method for Calculating the "Off-Design" Performance of Compressors and Turbines", 1958, *The Aeronautical Quarterly*, pp. 346-360.

[8] Tsalavoutas A., Stamatis A., Mathioudakis K., "Derivation of Compressor Stage Characteristics for Accurate Overall Performance Map Prediction", 1994, *Proceedings of the International Gas Turbine and Aeroengine Congress in Exposition*, Hague (Netherlands), 13-16 June.

[9] Robbins H., Dugan J.F., "Prediction of Off-Design Performance of Multistage Compressors", 1965, *Aerodynamic Design of Axial-Flow Compressors*, NASA SP-36, pp. 302-304.

[10] Benser W.A., "Compressor Operation with One or More Blade Rows Stalled", 1965, *Aerodynamic Design of Axial-Flow Compressors*, NASA SP-36, pp. 341-364.

[11] Howell A.R. and Bonham R.P., "Overall and stage characteristics of axial flow compressors", 1950, *Institutions of Mechanical Engineering*, **163**, pp. 235-248.

[12] Mellor G.L., Root T., "Generalized Multistage Axial Compressor Characteristics", 1961, *Transactions of the ASME*, Series D.

[13] Song T.W., Kim T.S., Kim J.H., Ro S.T., "Performance Prediction of Axial Flow Compressors Using Stage Characteristics and Simultaneous Calculation of Interstage Parameters", 2001, *Proc Instn Mech Engrs, Part A: Journal of Power and Energy*, **215**, pp 89-98.

[14] Aker, G. F., and Saravanamuttoo, H. I. H., 1989, "Predicting Gas Turbine Performance Degradation Due to Compressor Fouling Using Computer Simulation Techniques," *ASME J. of Engineering for Gas Turbines and Power*, **111** , pp. 343-350.

[15] Muir, D. E., Saravanamuttoo, H. I. H., and Marshall, D. J., 1989, "Health Monitoring of Variable Geometry Gas Turbines for the Canadian Navy," *ASME J. of Engineering for Gas Turbines and Power*, **111**, pp. 244-250.

[16] Ma W., Liu Y., Su M., Yu N., "Multi-stage axial flow compressors characteristics estimation based on system identification", 2007, *Energy Conversion and Management*, **149** (2), pp. 143-150.

[17] Crosa G., Pittaluga F., Trucco A., Beltrami F., Torelli A., Traverso F., "Heavy Duty Gas Turbine Plant Aerothermodynamic Simulation Using Simulink", 1998, *ASME J. of Engineering for Gas Turbines and Power*, **120** pp.550-556.

[18] A.R. Howell and W.J. Calvert, "A New Stage Stacking Technique for Axial-Flow Compressor Performance Prediction" , 1978, *Journal of Engineering for Power, Transactions of the ASME*, **100**, pp. 698-703.

A flexible and simple device for in-cylinder flow measurements: experimental and numerical validation

Andrea Dai Zotti[a], Massimo Masi[b], Marco Antonello[c]

[a] *Ebara Pumps Europe S.p.A., R&D Dept., Brendola-Vicenza, Italy, Andrea_DaiZotti@ebaraeurope.com*
[b] *University of Padova, Dept. of Management and Engineering, Vicenza, Italy, massimo.masi@unipd.it*
[c] *University of Padova, Padova, Italy, marco.antonello@unipd.it*

Abstract:

Deep knowledge of intake process aerodynamics is fundamental to development and optimisation of modern internal combustion engines. In particular, the intake port flow strongly affects both volumetric efficiency, i.e. power output, and in-cylinder charge motion which influences combustion behaviour and pollutants formation.
The paper presents an experimental and numerical study of intake airflow through ports and cylinder in a four-valves pent-roof motorbike high-speed engine.
A very simple mechanical device specifically designed for quick and low-cost measures of swirl and tumble motions in steady-state discharge flow coefficient test rigs was developed and checked on two twin-cylinder stock production heads featuring intake ports design typical of modern motorbike high speed SI engines. Simultaneous measures of discharge flow and tumble coefficients proved the limited error due to device insertion.
A detailed CFD model of cylinder, intake ports, and manifolds within the engine head was build and experimentally validated by discharge-flow coefficient measurements performed at different valve lift. The sensitivity to grid refinement and the performance of a realizable k-ε and a modified k-ω turbulence models is investigated.
The numerical model is used to evaluate the reliability of tumble measurements. The correlation between experimental data and the whole CFD velocity field within cylinder volume is very good proving that the device appears well-suited for rapid and reliable analysis of aerodynamic bulk performance of engine heads.

Keywords:

Tumble measure, Tumble and discharge flow coefficients, in-cylinder flow CFD calculation, grid and turbulence model for intake ports computations.

1 Introduction

Design of intake ports for high speed engines equipping stock production motorbikes results from an aerodynamic trade-off between two counteracting requirements: high volumetric efficiency and intense motion of fresh charge trapped within cylinders. It is well-known (see e.g. [1-6]) that processes like air-fuel mixing, start and development of combustion, cylinder wall heat transfer and pollutant formation are greatly influenced by squish, swirl and tumble motions. These two latter can be experimentally studied by means of both mechanical and optical instrumentation. Many types of paddle wheel or honeycomb flow straightener used to sense angular velocity or momentum, respectively, belong to the first category of instrumentation. Angular speed of the wheel ω or torque T exerted by the vortex flow on the impulse-meter within an appropriately located equivalent of the cylinder, are measured during traditional steady-state tests at discharge flow test rigs. Thus, meaningful similarity parameters such as swirl or tumble coefficients and numbers are defined as in [7, 8]. The main difference in the experimental measurements of swirl and tumble motions is the location of the sensor. In fact, the quite simple location of the swirl-meter directly within the equivalent of the cylinder is usually substituted by the more complex apparatus constituted by a cylindrical reversed T-junction, required to symmetrically split the tumbling flow towards the two openings each one provided of an impulse-meter or a paddle wheel.

On the other hand, the up-to-date optical and electronic instrumentation allows very detailed measurements of the local vector field within the cylinder both under steady-state ([5, 8-10]) and unsteady test rig operations (see e.g. [5, 11-14]). Other parameters of swirl and tumble are more properly suited to this type of instrumentation [2-4, 14, 16].

Many researchers studied the correlations between traditional test rig data of discharge flow and the newer optical measurement systems. Omori et al. [6] investigated the airflow vector field featured by various intake runner layouts in the region upstream and around the valve, and within the cylinder. Tumble index calculated from LDV data, collected for engine heads featuring different runner design (traditional, straight, straight with shielded valves), was compared to tumble coefficient, derived by traditional measurements performed on discharge-flow test rig for the same engine heads. In this work an excellent correlation between experimental tumble parameters is assessed. Kim et al. [18], focusing on the correlation between tumble parameters calculated from data obtained by PIV, PTV, and traditional impulse-meter, corroborated the experimental findings of Omori et al. [6]. Algieri et al. [19] verified good reliability of swirl measurements obtained by impulse sensor extrapolated from optical systems data. In [8, 10] Kang and Reitz studied swirl intensity within a medium-bore compression ignition engine. Once again, they proved the good agreement between optical instrumentation and torque sensor data.

The flow field of port-valve-cylinder systems is widely studied from many years also through CFD techniques, which give very detailed predictions that can be useful to better explain experimental evidences, and to aid the designer work. Pioneering CFD researches on engines modelled the flow field close to and downstream of intake valves. In 1985 Gosman [20] obtained qualitative good agreement between calculated and measured flow fields and, in a succeeding work [21], proved that the discharge-flow coefficient for a simplified valve port can be numerically predicted with acceptable accuracy. Brandstaatter et al. [12] focused their effort on in-cylinder flow performing 3D CFD simulation of cylinder volume starting from results of 1D gas-dynamic code and velocity measure at the curtain valve section. They succeeded on capturing the vortex flow in the recirculating zone between valve and cylinder liner wall, and the swirl motion structure on various cylinder heights. However, they highlight limitations related to standard k-ε turbulence model. Among other works Dent and Chen [22] accurately predicted valve lifts for which flow separation from valve lip and from valve seat occur. Steady-state calculations capable to correctly estimate the discharge-flow coefficient and satisfactorily correlate numerical and experimental swirl indices were performed by Befrui [23], Godrie and Zellat [16]. In 2000 Kang and Reitz [8] compared their experiments with previous CFD computations performed with KIVA 3V code in [24], and showed the calculations under-estimation in both swirl and tumble charge motion. In the same period Hong and Tarng [9], using KIVA 3 and optical LDV measurements, find appreciable correlation between rather basic calculations and experimental data for tumble ratios. However, both their local and overall in-cylinder flow calculations with standard k-ε turbulence model, notably over-predict tumble intensity. Ramajo and Nigro [25] after the validation of their numerical model by comparison of discharge-flow coefficient, tumble, and swirl indices with corresponding parameter value measured during steady-state flow tests, performed time-dependent calculations for the whole engine cycle. They proved that tumble moment versus valve lift shows the same features during steady and unsteady operation.

The paper presents an experimental and numerical study of intake airflow through ports and cylinder in a four-valves pent-roof motorbike high-speed engine. The main aim of the work is to verify the reliability of a very simple mechanical device specifically designed for quick and low-cost measurements of swirl and tumble motions in steady-state discharge-flow coefficient test rigs. A “spherical” paddle wheel, which has to be located in the cylinder downstream the head under analysis and does not require special T-junction ducts to sense tumble motion, was used to experimentally test two twin-cylinder stock production heads featuring different intake port design, which are typical of modern motorbike high speed engines. The more traditional head, featuring low tumble intensity, is then selected to check the designed device in the less favourable condition.

Since CFD results are used to better understand swirl and tumble data, numerical predictions require an experimental validation by different measured flow parameters. For this purpose, since the test rig is a traditional steady-state flow bench, the choice of discharge-flow coefficient is straightforward.
Concerning numerical simulations, the selection of an appropriate RANS turbulence model is an important issue. Indeed, in-cylinder flows are mainly characterised by jet interactions with walls, recirculation regions, vortex flow, and three-dimensional effects. Reynolds-stress transport models (RSTM) are able to describe all the above-mentioned features but they suffer from a great computational cost [26], and from a strongly simplified near-wall modelling [27]. For these reasons, in the simulation of industrial complex flows, the class of nonlinear eddy viscosity models (NLEVM), based on k and ε transport equations, and the class of k-ω models are most frequently employed. Concerning in-cylinder flows, numerical studies confirmed that Wilcox k-ω model and NLEVMs are suitable to reproduce the flow field inside the combustion chamber and the quantification of the overall angular momentum with respect to the cylinder axis (see e.g. [34, 35]). For all the reasons the present numerical study has been carried out with the realizable model of Shih et al. [36], which is one of the most successful NLEVM, and with the modified k-ω model of Wilcox [31].
Finally the validated CFD model is used to evaluate the reliability of the tumble measurements looking at the correlation between numerical and experimental tumble indices.

2 Experimental facility

The test rig used for present experiments is a traditional discharge-flow test rig, derived from an A-type industrial fan test rig built according to the UNI 10531 Italian Standard [37], which is equivalent to the ISO 5801 Standard. The main scheme of the original test rig is described in details by Martegani et al. [38]. The original facility has been modified in a previous work [39] by substituting the auxiliary fan with a variable speed fan that generates a negative relative constant pressure inside the plenum chamber faced to the engine head to be analysed. The mass flow across valve port is derived from conventional measurements: dry and wet-bulb ambient temperature and the temperature inside the plenum chamber are measured using mercury thermometers; barometric pressure is measured using a mercury barometer, whereas a water manometer is used to measure the pressure in the plenum chamber. Finally, a differential water manometer measures differential pressure of orifice plate, which is needed for flow rate determination. The accuracy estimated by the Kline-McClintock criterion is about 1% for all the presented discharge coefficient measurements.

2.1 Swirl and tumble meter

Classically adopted mechanical devices to measure in-cylinder motion are usually paddle wheels or honeycomb flow straightener impulse-meters. They provide in-cylinder flow parameters such as the following swirl or tumble coefficient and number (see e.g.[7, 8]):

$$C = \frac{\omega D}{v_{is}} \qquad N = \frac{8T}{\dot{m} D v_{is}} \qquad (1)$$

Where v_{is} is the isentropic velocity due to the actual pressure drop across the inlet ports, $\dot{m}$ is the actual mass-flow rate, and D is the cylinder bore.

The well-established set-up for these devices usually is not conceived to allow an easy switch from swirl to tumble analysis layout. The device used to measure charge motion intensities within the cylinder has been designed to cope with the following requirements:

- suitability for both swirl and tumble tests to simplify the test rig instrumentation required for basic measurements;
- low flow field modification to allow simultaneous analysis of charge motion and discharge-flow performance, if desired;
- easy manufacturing to allow in-house building without sophisticated machining and remarkable cost of sensors;
- quickness and simplicity of use with usual steady-state discharge flow test rigs to assure rapid and repeatable measurements with minimum risk of human error.

Figure 1 shows exploded views of the main parts arranged within the core of the mechanical assembly for charge motion measurement.

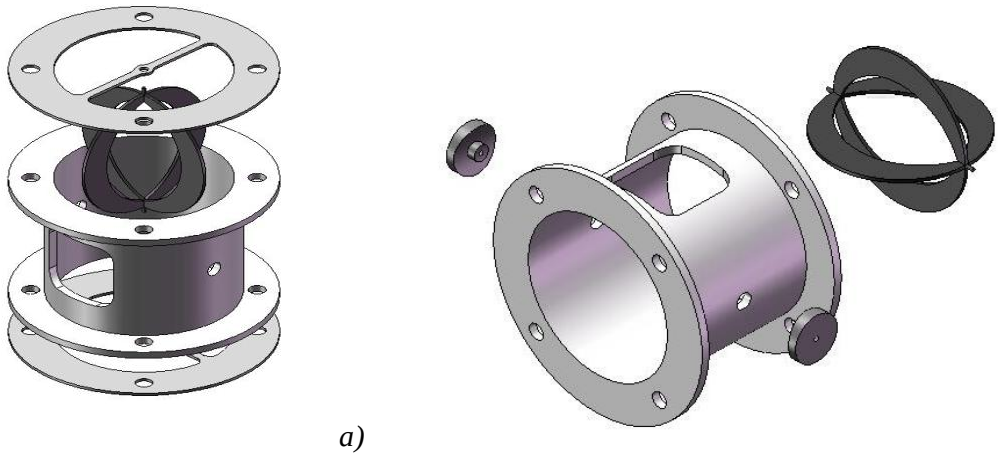

a) *b)*

Fig. 1. Exploded views of the mechanical assembly including the charge motion transducer: a) swirl measurement layout, b) tumble measurement layout.

To deal with first item the charge motion transducer has spherical shape so that it can be inserted within a cylinder of actual engine bore, which is flanked downstream the assembly of runners, valves, and combustion chamber under analysis (i.e. the proper engine head section). Depending on the layout, the transducer can spin around an axis overlaid or perpendicular to cylinder axis (see figure 1).

Since impulse sensors act like walls counteracting flow motion and greatly affect discharge flow coefficient measurement, paddle wheel is mandatory to try fulfilment of second requirement. Moreover, the circular plates arranged in the wheel has been machined to be lens shaped in order to reduce flow blockage, device inertia, and mechanical friction due to weight action on wheel pivotal bearings.

The third item can be fulfilled using cheap metallic duct sections for the equivalent of the cylinder (alloy if the overall assembly weight is a problem, or plexiglass if money saving is not so strict) and light sheets as prime matter to be lens shaped machined, which is actually the sole process requiring some carefulness. Being the paddle wheel steel made, a simple and inexpensive proximity sensor, which counts blade passing, can be used.

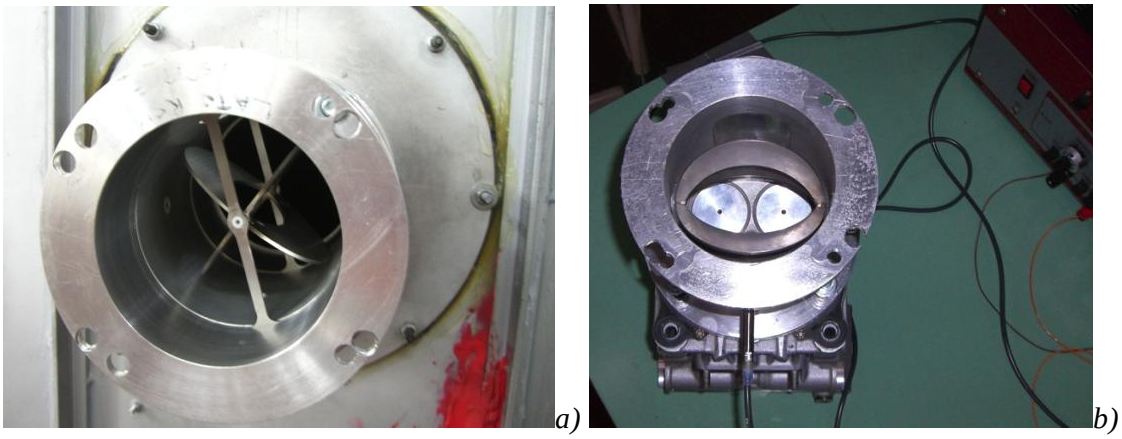

Fig. 2. Complete assembly of charge motion mechanical meter: a) swirl measurement layout mounted on test chamber of the used discharge-flow coefficient rig, b) tumble measurement layout mounted on one of the two actual engine heads analysed.

Finally, the last needing can be well satisfied. In fact Figure 2a) shows that effort to set-up the discharge-flow test rig is very slightly affected by the simple insertion at openings of the main cylindrical duct section of two annular slices, required to pivot the paddle wheel for swirl measurements. Similarly, the easy repositioning of the two low friction plug bearings for tumble measurements, which are well visible in Figure 1b), ends in the assembly illustrated in Figure 2b).

The specific equipment used for present measurements includes an electric power unit, which can be both voltage and current regulated, and the "virtual oscilloscope" library tool provided with Labview®, which easily counts the blade passing close to the proximity sensor. The main features of this proximity sensor are reported in Table 1. Since the paddle wheel counts 4 blades, the resolution of present instrumentation is a quarter of the last paddle wheel revolution occurred during the measurement time interval. As a consequence, the higher the charge motion intensity and the time interval the higher the overall accuracy. Following this reasoning the accuracy error is negligible.

The main cylinder section features a transparent window in the paddle wheel location zone, which is clearly visible in both Figure 1 and Figure 2. This window provides the immediate feeling on effectiveness and proper assembly of instrumentation.

Table 1. Main features of proximity sensor equipping charge motion meter assembly

Manufacturer	OMRON
Model	EA-S08LS01-WP-B1
Sensing distance	1.5 mm (iron-magnetic materials)
Maximum frequency	2000 Hz
Voltage input	10-32 V (DC)
Current output (max)	200 mA (32 VDC)
Output type	PNP with signal occurring for distance ≤ sensing distance

2.2 Ports, valves and combustion chamber assemblies

The main characteristics of the two twin-cylinder stock production heads used to check the instrumentation presented in the previous section, are reported in Table 2. These heads feature different intake ports design typical of modern motorbike high speed engines. Both of them are swirl-free, as usual for high speed SI engines. Nevertheless Aprilia's head shows the classical layout for high volumetric efficiency featuring curved intake runners and reduced angle between intake and exhaust. On the other hand, Ducati's head favours rapid combustion thanks to in-cylinder tumble induced by straight intake runners.

Table 2 Main features of production engine heads under analysis.

Manufacturer	Aprilia S.p.A.	Ducati S.p.A.
Motorbike model	RSV 1000	999
Engine architecture	Twin-cylinder V 60° liquid cooled	Twin-cylinder V 90° liquid cooled
Distribution	4 valve DOHC	4 valve DOHC
Combustion camber layout	pent-roof	pent-roof
Stroke/Bore	67.5 mm / 97 mm	63.5 mm / 100 mm
Compression ratio	11.8	11.4
Intake valve diameter d_v	37.95 mm	40 mm
Valve seat diameter d_s	33.6 mm	36.95 mm
Valve lift (measured)	11.78 mm	11.78 mm
Sketch of intake runners, intake ports, valves and combustion chamber assembly		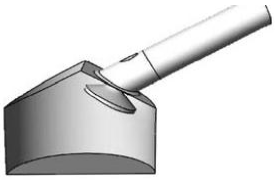

3 Tumble meter validation

Imposing no-lift to one of the two intake valves to artificially induce in-cylinder swirling flow, a preliminary check on capability of the assembly to measure swirl motion has been performed, through discharge-flow coefficient tests. However, the device validation is focused on tumble motion measurements, being this charge motion the most critical to be characterised with an unique tumble coefficient. In fact, it is well-known that tumble vortex can present different shape, eccentricity, and vertical position of its axis depending to valve lift [13] also in steady-state tests. Moreover the effectiveness of such a device to give reliable data about in-cylinder tumble motion need to be verified just because of the original layout, which does not include nor actual piston crown nor any other piston dummy always provided in steady-flow rigs tumble meters. Actually, it is a matter of fact that in a real engine the presence of the piston surface plays a relevant role in the onset of tumble vortex. On the other hand, just due to the presence of the piston surface, every pent-roof four-valve head in actual engines features a certain degree of tumble motion. Following the results of [6] what is hypothesised as the base for the design of present device is that not the piston surface, but the intake ports design and their interaction with cylinder liner are the more relevant items in the establishing of different tumble intensity level.

Thus, the validation procedure develops as follows:

1) comparison between tumble coefficient measured for the two heads in order to verify the sensitivity to different head design;
2) comparison of these coefficients with published data typical of engine heads featuring similar layout;
3) comparison between discharge-flow coefficient measurements performed with and without paddle wheel, in order to quantify the blockage effect of the rotating device and, consequently, the experimental error related to simultaneous discharge-flow and tumble coefficient measurements.

3.1 Tumble coefficients

The intensity of charge motion is measured at different valves lift for both the engine head under analysis. Starting from zero-lift condition, which is needed to verify the negative pressure-proof of the test chamber and zero-offset condition of the whole instrumentation, the lift is increased by 0.5 mm steps until 1.5 mm lift. Higher lift values are tested by 1 mm steps until 11.25 mm for both the heads. Five non-sequential measurement repetitions are made for each valve lift conditions featuring paddle wheel rotation (i.e. appreciable tumble), in order to reduce random accuracy error.

The arithmetic mean value of tumble coefficient defined according to (1a) is assumed as experimental tumble data. Figure 3 shows the tumble coefficient values against valves lift for both the heads under analysis. Error bars refers to a confidence of 99.5% for experimental data according to Student distribution. It appears that present instrumentation is capable to sense the difference in tumble intensity existing between two runner-valve-combustion chamber assemblies featuring different conceptual design. In fact, the behaviour of tumble coefficient against lift is in line with the figures provided by Omori et al. [6] discussed in the next section. As a general comment Aprilia head, not specifically conceived to originate high tumble, shows a quite regular increase in tumble intensity which, however, reaches values for high valve lift well above the corresponding ones featured by Ducati. This latter, designed for a more pronounced tumble motion, shows lower intensities than Aprilia until the proper onset of tumble vortex.

Other tests, not presented here, were performed for different pressure ratio values across intake valve measurements. However, they revealed to be less sensitive to Reynolds and Mach numbers than discharge flow coefficient measurements. Thus, this tumble coefficient measurement defines a cinematic property of in-cylinder flow field, which is to be considered as a similarity parameter, at least in the limits stated for discharge flow coefficients.

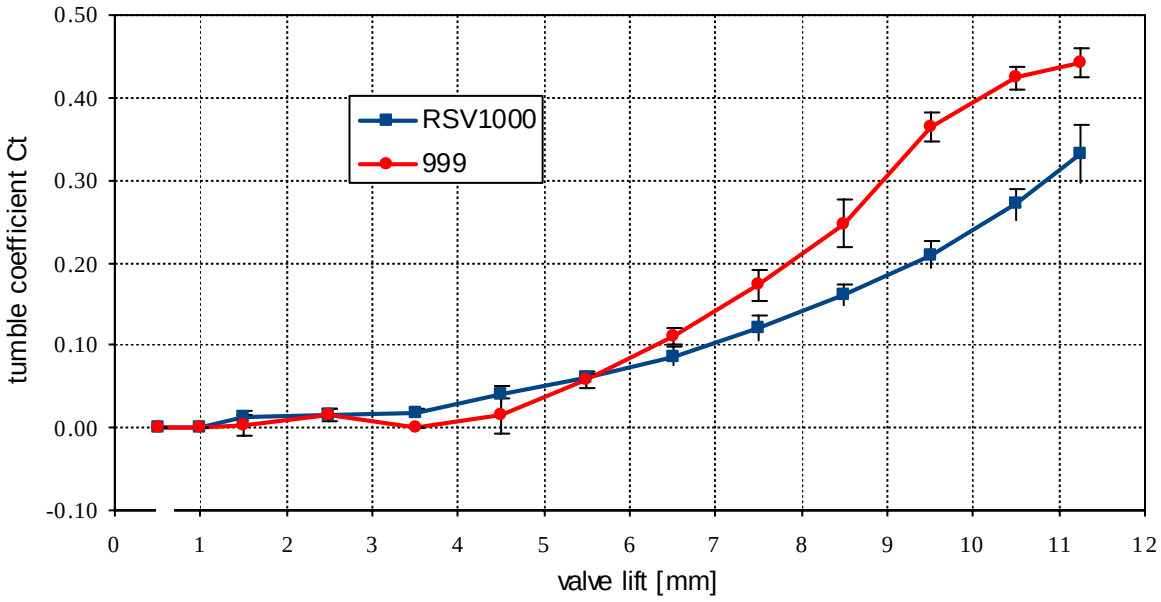

Fig. 3. Tumble coefficient against valve lift for Aprilia RSV1000 (blue) and Ducati 999 (red) heads.

3.2 Comparison with other published data

In order to check if present device may be used to acquire something more than the hierarchic rank of tumble flow onset capability, due to different intake port design, a comparison with some published data [6, 43, 44] measured by tumble meter devices of consolidated use is presented. Although the head designs are not radically different to the present ones, a complete comparison with previously referenced data is almost impossible, because of the uncertainty both on detailed features of engine heads and on values used by some of those authors to provide non-dimensional data. Thus, Figure 4 compares to present measurements the referenced data some of which were scaled by an arbitrary factor reported in figure legend. First considering the classical reference (1991) of Omori et al. [6] which offers measurements collected from a series of intake ports of different conceptual design, it appears that the quite low-tumble design of Aprilia head shows tumble coefficient figure in line with the low-tumble head design F of the cited reference [6], since the higher tumble design of Ducati head shows figure more similar to the head design E of the same reference [6]. The comparison appears to be satisfactory enough only for medium-to-high valve lifts. More recent (2000) measurements of tumble coefficient on a pent-roof four-valve car engine

head were presented by Yun and Lee [15]. They used the classical honeycomb wheels at the end of a T-junction duct. Green curve of Fig.4 refers to these data without any rescaling. Slope of the curve is in the middle of the present measurements and the agreement appears acceptable also for low valve lift values. Finally, a very recent work (2011) of Moore et al. [17] is considered. These authors show, among other interesting data, the tumble index map measured at the flow bench in a SI direct injection turbocharged engine head where many combinations of intake valves lift are tested. To make possible a comparison with the tumble index used by those the rescale by the arbitrary factor 3 is performed to originate orange curve in Fig.4. This data trend, except for the very low valve lift values, is in very good agreement with present measurements on Ducati 999 head. Note that Moore and co-authors stated that the port design of the engine head used in their work was conceived for high tumble intensity making possible to argue an head design more similar to the Ducati one than the Aprilia one.

At least within the limits of this incomplete comparison, present device appears to be capable to capture the main tumble features of the bulk in-cylinder flow in the medium-to-high valve lift ranges, which are the most relevant in the onset of tumble intensity level at the compression top dead centre in actual engines, as assessed by LDV measurements on the single-cylinder optical engine arrangement performed by [6]. However, it is worth noting that present measurements lack of the abrupt rise of the tumble torque typical of very high tumble intensity head designs. This could be due to the design of the heads used for present work. On the other hand the possibility that the absence of a piston crown dummy in present device affects especially low lift valve measurements has to be accounted for.

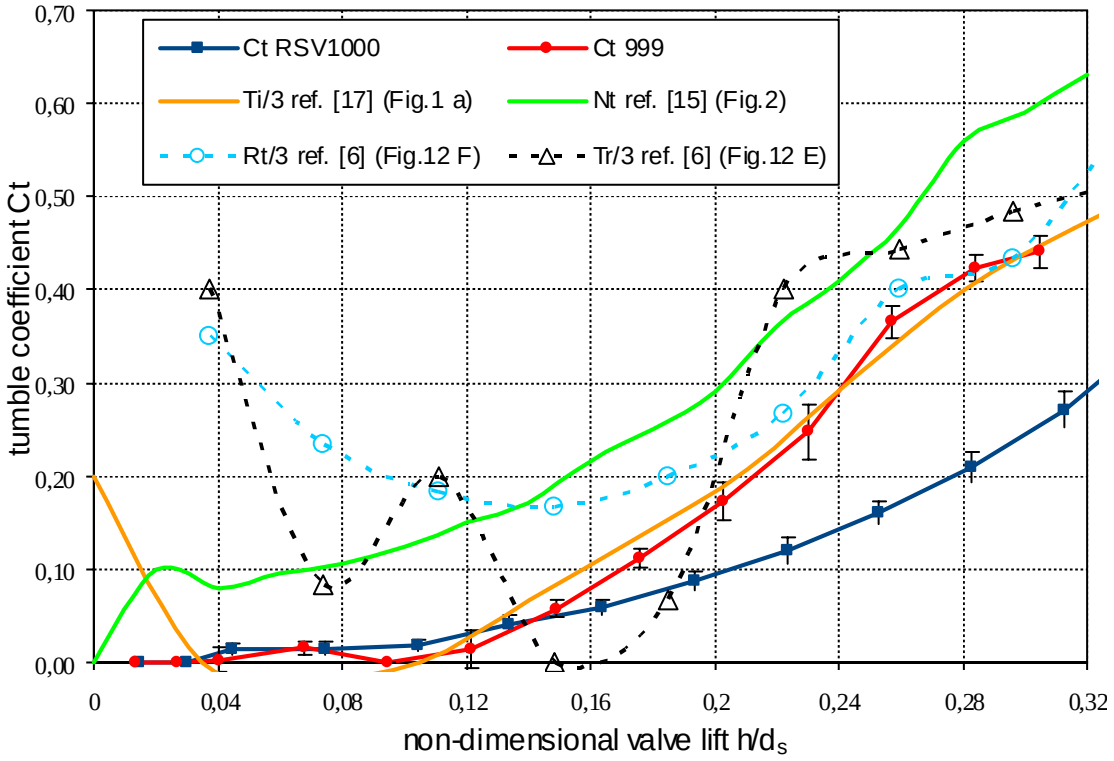

Fig.4. Tumble coefficient against non-dimensional valve lift for Aprilia RSV1000 (blue), Ducati 999 (red), ref. [6] (cyan and black) ref. [15] (green) and ref [17] (orange) heads.

3.3 Discharge-flow coefficients

Overall aerodynamic performance of the engine heads are measured through the well-known discharge-flow coefficient

$$C = \frac{\dot{m}_r}{\dot{m}_i} \qquad 3),$$

where $\dot{m}_r$ and $\dot{m}_i$ are actual and ideal constant-entropy one-dimensional steady-state mass flow rate across the conventional throttle section of the port, which is calculated for the actual valves pressure drop.

As stated in section 2 the overall mass flow accuracy estimated for maximum lift is about 1%.

In order to quickly evaluate aerodynamic performance at high and low valve lift values, the following well-known reference sections are assumed, respectively:

- valves head area, which is lift independent and gives the non-dimensional coefficient C_d;
- curtain area, which is lift dependent and gives non-dimensional coefficient C_f [7].

Figure 5 shows the steady-state direct discharge-flow coefficients measured for Aprilia and Ducati heads, for lift values ranging from 0 mm to 7 mm with 0.5 mm lift step, and with 1 mm lift step until maximum valve opening is reached.

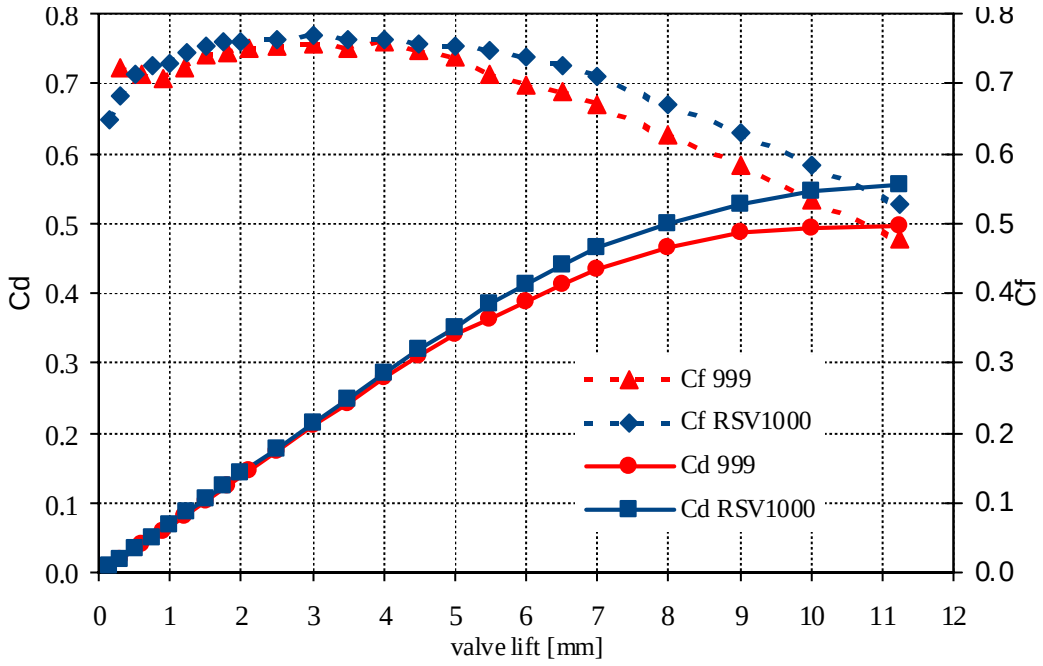

Fig. 5. Discharge-flow coefficients against valve lift for Aprilia RSV1000 (C_d continuous blue; C_f dotted blue) and Ducati 999 (C_d continuous red; C_f dotted red) heads.

Finally, to quantify the effect of flow blockage and aerodynamic obstruction due to the simultaneous measure of discharge-flow and tumble coefficients, Figure 6 compares the solid lines referring to the discharge-flow coefficients C_d already shown in Figure 5 with the same coefficients measured during the tumble flow tests discussed in the previous section.

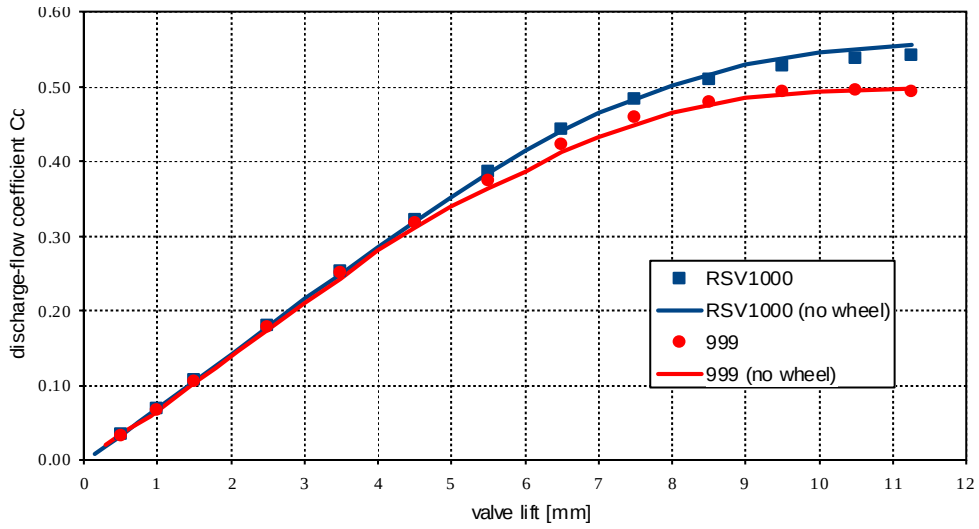

Fig. 6. Discharge-flow coefficients C_d against valve lift for Aprilia RSV1000 (blue) and Ducati 999 (red) heads, measured with and without paddle wheel.

Maximum error on discharge-flow measurements due to aerodynamic interference of paddle wheel results 2.3% for Aprilia head and 0.7% for Ducati head at maximum valve lift (11.25 mm). This evidence demonstrates the limited sensitivity of steady-state in-cylinder flow field to present instrumentation. Moreover, the instrumentation appears to reduce its interference on in-cylinder flow field as more as higher the charge motion intensity is, revealing to be well-suited for quick in-cylinder charge motion analysis, especially in engine heads designed to maximise the charge motion itself. Indeed, it is quite secure the occurrence of a small blockage effect on the valve flow originated by the paddle wheel insertion, which penalises the higher discharge flow coefficient of Aprilia at higher lift values. Less clear is the improvement of discharge flow coefficient featured by test performed on Ducati head when the paddle wheel is inserted. A possible explanation of this occurrence is that the paddle wheel strengthens the rigid body motion character of bulk flow. This reduces near-wall recirculation close to the intake runner exit on the opposite side of the exhaust. Thus, viscous losses and vortices blockage are smoothed. However, detailed information about actual flow motion within the cylinder enclosing paddle wheel must be acquired to support this reasoning.

4 Numerical analysis

The limited influence of paddle wheel on in-cylinder flow field assessed by experiments suggests comparing the measured tumble intensity with the detailed charge motion description achievable from a validated CFD model of the fluid domain enclosing the intake manifold, valves and cylinder system. This comparison appears particularly useful to reduce the uncertainty related to the reliability of tumble measurements. This is not a style exercise for all those researchers and applied engineers who can not dispose of very sophisticated and expensive optical instrumentation. Indeed, numerical results can be used like optical measurements to evaluate the correlation existing between motion intensity of overall charge, measured by mechanical instrumentation, and velocity fields. Moreover, CFD data give whole cylinder volume velocity field and, thanks to in-cylinder integration, allow proper comparison with mechanical charge motion measurements. This comparison can be more effective than that between mechanical and optical measurements collected within a very limited number of plane sections.

The more traditional head design, i.e. Aprilia RSV1000, is selected for the numerical analysis. The selection of a low tumble intensity configuration is aimed at checking the designed mechanical device in the less favourable condition.

4.1 Computational domain

The physical domain, which was meshed to be numerically analysed, has been obtained by use of a reverse engineering technique. The manifolds, valves and combustion chamber geometry have been acquired by applying a laser scanning technique to a rubber 'core' obtained by filling the empty space within the ports and cylinder volumes (see left side of Figure 7). Surface data have then been handled with the Rapidform® 3D Scanning Software, before CAD surfaces reconstruction and addition of inlet and outlet plenums have been made as showed in right side of Figure 6. The detail of the whole reverse engineering work is reported in [40]. Summarising, the whole geometrical domain used for CFD analysis encloses an hemisphere used as inlet plenum (similarly to [41]), the bell-mouth duct before the intake runners, the air volume surrounding intake valves and pent-roof combustion chamber, the cylinder before experimental test rig plenum, and its CFD equivalent modelled by another hemisphere. The domain is almost symmetrical and this could advantage numerical calculation. However, the entire domain is discretised to account for un-symmetries due to casting and for the spark plug region within the dome of the combustion chamber, the axis of which intersects but does not lie in the mean cylinder plane.

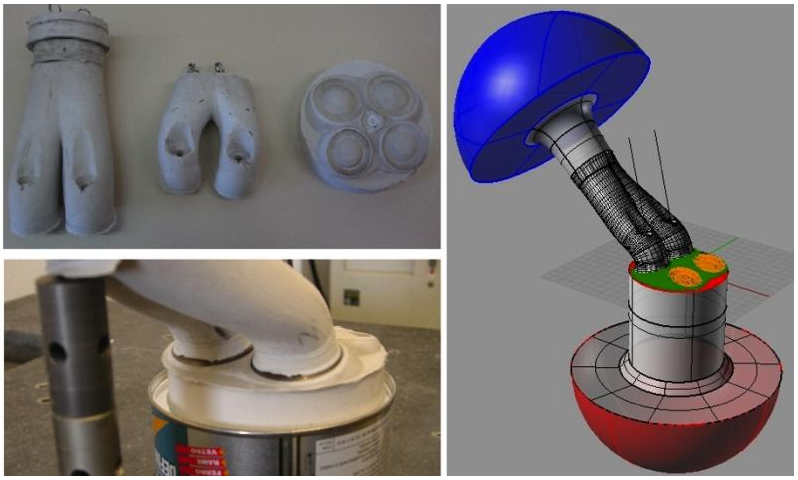

Fig. 7. Reverse engineering of Aprilia RSV1000 cylinder geometry: "rubber" cores of combustion chamber and manifolds (upper left); intake system assembly to be 3D scanned (lower left); reconstructed CAD surface of the whole intake system CFD domain (right).

4.2 CFD model

The steady-state RANS equations for turbulent incompressible and isothermal airflow are solved by commercial finite volume code Star CCM+® version 6.0.009 of CD-Adapco. These flow hypotheses are justified by the low pressure ratios involved in the experimental tests which, however, are not considered to be inadequate for intake valves within the limits of steady-state flow bench data.

As mentioned in section 1, the complexity of in-cylinder flows requires a careful selection of the turbulence model to be used. From a theoretical point of view, Reynolds-stress transport models (RSTM) are able to describe all complex flow effects. However, they suffer from two main drawbacks: the computational effort is much larger than that of two equation models [26]; strongly simplified near-wall models must be introduced to systematically integrate transport equations in complex geometries [27]. As a result, in many cases where near-wall effects are relevant RSTM give similar or even worst predictions compared to those of two equation models [26, 28, 29]. For these reasons, in the simulation of industrial complex flows, the class of nonlinear eddy viscosity models (NLEVM), based on k and ε transport equations, and the class of k-ω models are most frequently employed. The first group, which also embodied the explicit algebraic Reynolds stress

models (EARSM), has the advantage of retaining to some degree the Reynolds stress anisotropy effects associated with a full differential closure [30]; while the second group, nevertheless the simpler representation of the stress tensor, gives rather good prediction for many flows with strong adverse pressure gradient and recirculations, and three-dimensional jets [26, 28, 29, 31] as well. This is due to the fact that these models describe quite well both the near-wall effects and the mechanisms of production and dissipation of the turbulent quantities. Wallin and Johansson [32] developed an EARSM based on k and ω equations that, however, has no met with much success in the simulation of engineering flows. One of the reasons is the too large value of turbulence dissipation predicted in some situations, which prevent to improve the results of the simpler k-ω model [33]. According to the above considerations, some numerical studies of in-cylinder flows confirmed that Wilcox k-ω model and NLEVMs improve the reproduction of the flow field inside the combustion chamber and the quantification of the overall angular momentum with respect to the cylinder axis (see e.g. [34, 35]). Thus, following these works, the present numerical study has been carried out with the realizable model of Shih et al. [36], which is one of the most successful NLEVM, and with the modified k-ω model of Wilcox [31].

The polyhedral grid capability is preferred to the more classical hexahedral trimmed grid approach to speed up mesh generation process, to minimise grid clustering in regions far from valves, to obtain high cell regularity also in proximity of surfaces of complex shape, to keep low advection term spreading and, finally, to take advantage of polyhedral cells to more accurately capture vortex flows. Near wall prism sub-layer is generated for all the solid surfaces. Dimension and number of layers as well as clustering and number of core cells are discussed in the following. Figure 8 shows the computational domain and particulars of the grid selected for 7 mm valve lift, after the grid sensitivity analysis.

A pressure drop of 1500 Pa (derived by experimental data) is imposed between the two hemispherical openings of the simulation domain, shown in left side of Figure 8. The inflow turbulence intensity and length scale are 1.5% and 40 mm, respectively. The solid walls are modelled with the adiabatic no-slip condition, and a surface roughness ranging from 0.1 mm to 0.25 mm is imposed from upstream valve seats to valve guides zone. In fact, the intake valve manifold surface of the engine head is cast without finish, and the measured wall roughness for the previously mentioned zones is reported in Tab. 3.

Numerical simulations are carried out using the realizable eddy viscosity model of Shih et al [36] and the k-ω model of Wilcox [31]. In the first model modifications of both the eddy viscosity expression and the transport equation for the dissipation rate are introduced. The eddy viscosity formulation ensures realizability through an expression that is nonlinear in mean strain rate components. The transport equation for ε is based on the dynamic equation for fluctuating vorticity. In the modified model of Wilcox the dissipation terms of both k and ω equations are modified to improve the predictions for free shear flows, giving boundary layer results equal to the original model. These models are selected, among most used two-equation models, because they give good descriptions of jet flows, expansions and recirculations [26, 28, 29, 31, 35], and the computational effort is moderately greater than that of the standard k-ε model.

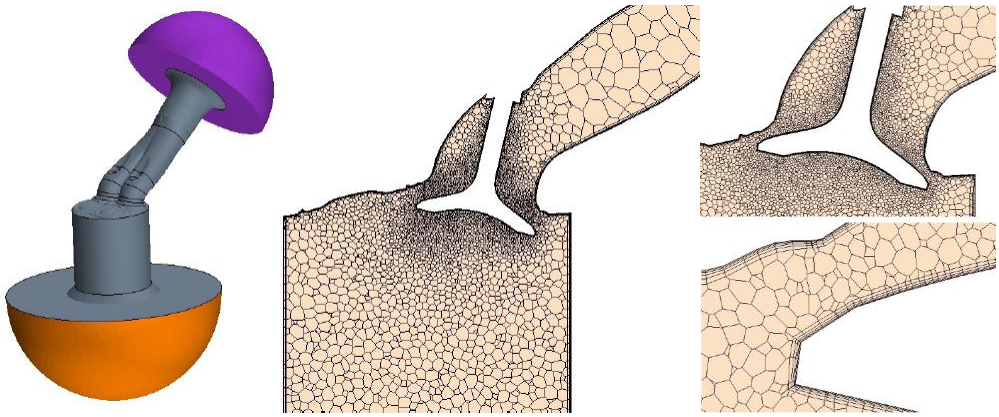

Fig. 8. CFD model for steady-state flow analysis of Aprilia RSV1000 intake valves and cylinder: computational domain (left); volume mesh section lying on valve axis and parallel to cylinder mean plane (centre); valve zone grid (upper right); near-wall sub-layer near the curtain area (lower right)half-valve half-manifold plane of the main domain region used to model.

Wolfstein two-layer approach [42] is coupled with the realizable k-ε for near-wall calculation being wall-y^+ values always lower than 30 (see following section).

Second order upwind scheme is adopted to solve the steady-state RANS equations by means of a segregated SIMPLE-like algorithm. Calculations are considered to be converged when normalised residuals of conservation equations are below 1.5 E^{-5} and the mass flow rate is constant.

Table 3 Intake manifold surface roughness data.

Region	Upstream valve seats [mm]	Valves guide [mm]
Cut off length L_c	2.50	2.50
$R_a = 1/L_c \int_{L_c} \lvert y \rvert (x) dx$	11.8 E^{-3}	32.4 E^{-3}
$R_q = \sqrt{1/L_c \int_{L_c} y^2(x) dx}$	15.4 E^{-3}	48.6 E^{-3}
$R_y = y_{p,\max} - y_{v,\max}$	94 E^{-3}	231 E^{-3}

4.2.1 Grid and turbulence models sensitivity analysis

Independence of results from grid refinement has been verified before the execution of CFD analysis. The numerical validation of the grid has been performed focusing on discharge-flow coefficient value calculated for valve lift equal to 7 mm. This typical mean lift value for present configuration is representative both of mean topology layout and important flow separations at cylinder inlet. The realizable two-layer k-ε turbulence model was used for this validation. It is worth noting that the implementation of this model within Star CCM+ code operates a switch to standard log law at walls if the near-wall refinement is not suitable for two-layer calculations. Thus, starting from a very coarse grid counting around 80000 cells, which is almost the minimum cells number required to follow all the relevant geometrical features of present domain, the mesh has been progressively refined according to the following criterion: cells number and clustering in the inlet and outlet plenum, in the bell-mouth entry, and in cylinder bottom have been almost unchanged in all the tested grids. Thus, the successive refinements have involved the region roughly centred in the curtain zone of valves. Taking advantage of polyhedral foam the cell clustering is gradually increased and the same cell dimension in the peripheral zones is smoothly reached, for each grid. Figure 8 (centre and right) shows sections of the final volume mesh and clearly illustrates what just explained, evidencing high shape regularity and smooth clustering change of the core cells.

The refinement strategy is to firstly halve cell side dimension from two successive grids in order to theoretically allow the refined grid to capture the first larger flow structure unaccountable by

previously less refined grid. This rigorous approach to grid sensitivity analysis requires a multiplying factor of 8 for cell number between two successive grids, and takes quickly to huge need of computational effort. However, Figure 9 shows the discharge flow computed for the base 80000 cell grid and for the about 640000 cell refined grid both solved using the realizable k-ε model, and compared to experimental data for 7 mm intake valve lift. The comparison shows the dependency of calculated parameter to grid refinement and underlines the decreasing over-estimation of calculated mass flow rate across intake valves. In absence of detailed measurement of flow field it can be argued that an excess of turbulent viscosity predicted by CFD limits the extent of flow separation across valve passage favouring an unreal better use of geometrical throat section. Thus, being the successive rigorous step of grid refinement beyond the scope of present numerical model, and according to many numerical researches (see e.g. [35]) that considered 640000 cells almost entirely placed around the two intake valves to be close to the minimum cell number required to grid independent discharge flow coefficient calculation, the last refinement has been limited to around 800000 cells. The result confirms the over-climbing of grid independency limit and assesses the over-estimation of discharge-flow coefficient provided by present RANS model to be around 10% for mean valve lifts. Calculations performed on other less-fine grids have indicated in about 500000 the definitive value of polyhedral cells number limit for mesh independent discharge-flow coefficient computation, and have evidenced that an un-properly refined grid which does not reach cell independence limit and counts a significant cells number may give results also more unreliable than coarser grids.

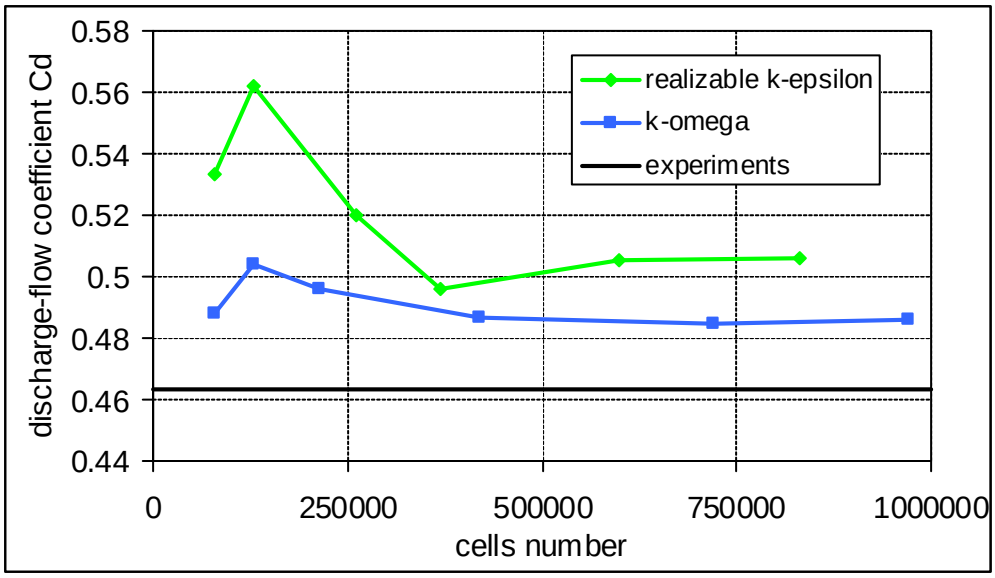

Fig. 9. Steady-state discharge-flow coefficient calculated by numerical models against their cells number: realizable k-ε (green); linear k-ω (blue); experimental value (black).

Another grid sensitivity analysis has been performed solving RANS equations coupled to the modified k-ω of Wilcox. Blue curve in Figure 9 shows the results of this analysis. Main results are:

- the grid independence limit for discharge-flow coefficient calculation remains almost unchanged;
- Wilcox k-ω model, despite its simpler eddy-viscosity representation performs better than the realizable k-e in terms of
  - prediction accuracy;
  - grid refinement sensitivity;
  - reliability of coarse grid calculations.

4.2.2 Tumble momentum validation

Results of the previous sensitivity analysis applied to the calculation of in-cylinder tumble flow angular momentum are shown in Figure 10. In this case it must be underlined that the numerical calculation of the tumble coefficient by means of flow field quantities is questionable; on the contrary, the overall tumble angular momentum within cylinder volume is undoubtedly determined by:

$$M_t = \int \mathbf{r} \times (\rho w \mathbf{u}) dV = \int \rho w [u(z - z_c) - w(x - x_c)] dV \qquad 4)$$

Where u and w are the velocity components along x and z directions, respectively, both perpendicular to paddle wheel axis, which lies on a pole of (x_c, z_c) coordinates within cylinder volume V.

Once again Wilcox k-ω reveals less sensitivity to grid refinement and provides tumble lower intensity value than realizable k-ε. It is worth noting that the predictions of tumble angular momentum provided by the two turbulence models can differ from each other much more than the predictions of discharge-flow coefficient. In fact, the difference between tumble intensities obtained by mesh independent calculations over-climb 15%, becoming very remarkable for less finer grids (also greater than 50%!). Moreover, the cell number limit for grid independent calculations is higher than that for discharge-flow coefficient calculation.

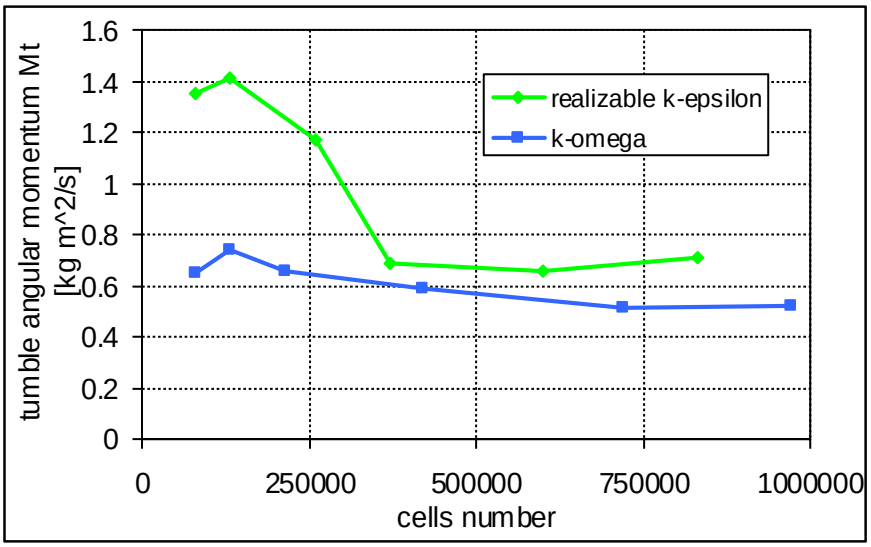

Fig. 10. Steady-state tumble motion angular momentum calculated by numerical models against their cells number: realizable k-ε (red); linear k-ω (blue).

In particular, the analysis highlight that more computational cells are needed in the upper part of cylinder volume to obtain tumble angular momentum no more dependent to grid refinement. The k-ω turbulence model requires less than about 700000 cells to achieve the condition of independence from grid, whereas the realizable k-ε needs for more than 800000 cells.

5 Results

Sensitivity analysis of previous sections has suggested meshing the fluid domain with 650000 polyhedral cells, featuring a 4-5 near-wall prism layers for all the computation performed at various intake valve lift values.

Figure 11 shows discharge-flow coefficient C_f comparison between experimental data and numerical steady-state calculations, performed using the two previously discussed turbulence models. All the two models well describe the experimental trend and over-predict the measured data, especially for the mean lift range. However, according to [35], Wilcox k-ω performs better

than realizable k-ε in the whole lift domain. Moreover, the k-ω model predicts the maximum C_f experimental lift value (3 mm), whereas the realizable k-ε model locates maximum C_f at a higher lift value. The better behaviour of the k-ω model is probably due to the fact that the dissipation terms of both k and ω equations are specifically modelled to give good predictions of free shear flows (see e.g. [26, 28, 29, 31, 35]).

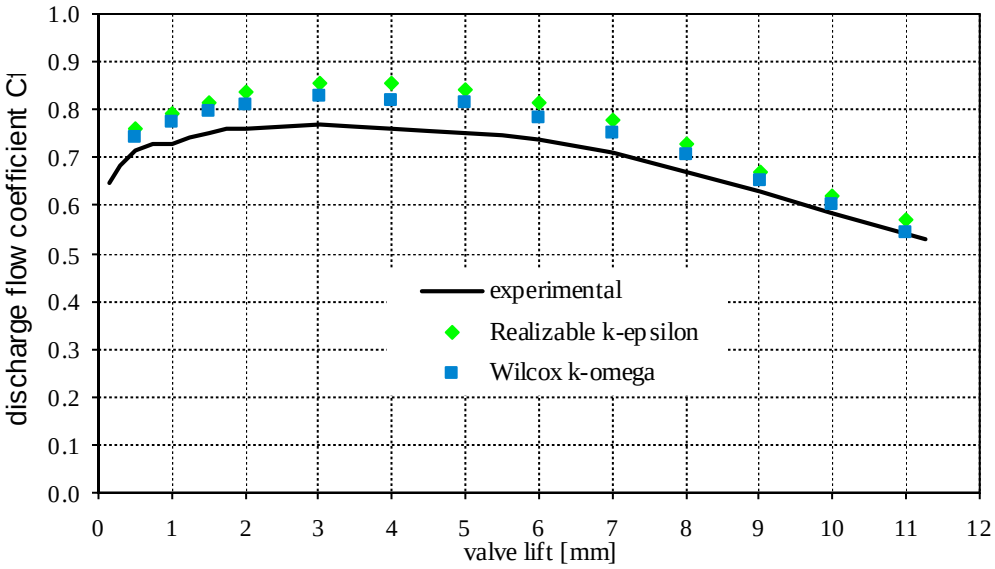

Fig. 11. Steady-state discharge-flow coefficient C_f against valve lift comparison: calculated realizable k-ε (green); calculated linear k-ω (blue); experiments (black).

As well-known [7], the descending trend of discharge-flow coefficient C_f in the medium valve lift range mainly depends on the increasing extent of flow separation from both valve lip and seat, which reduce the curtain area effectiveness. The velocity magnitude contour-plot in figure 12 proves that this occurrence is qualitatively well captured by computations.

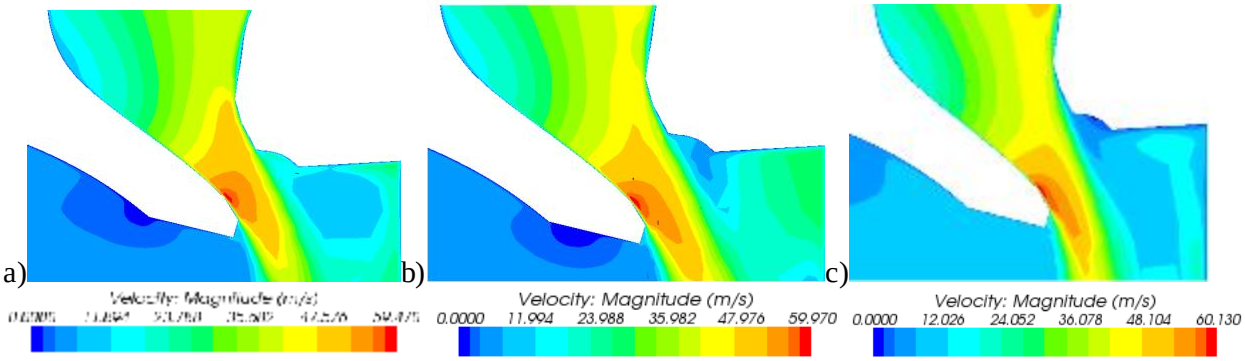

Fig. 12. Intake valve velocity magnitude contour-plots on the plane lying in valve axes at different valve lift: a) 4 mm; b) 5 mm; c) 6 mm.

Figure 13 shows the relative difference between numerical and experimental data against lift value for the two turbulence model calculations. Once again, the two curves feature the same trend, being the maximum departure from experimental data evident in the low-to-medium valve lift range for both the two turbulence model calculations. In fact, it is well-known that the medium valve lift range is strongly affected by complex turbulent effects, which are not enough precisely quantified by two equation turbulence models currently available.

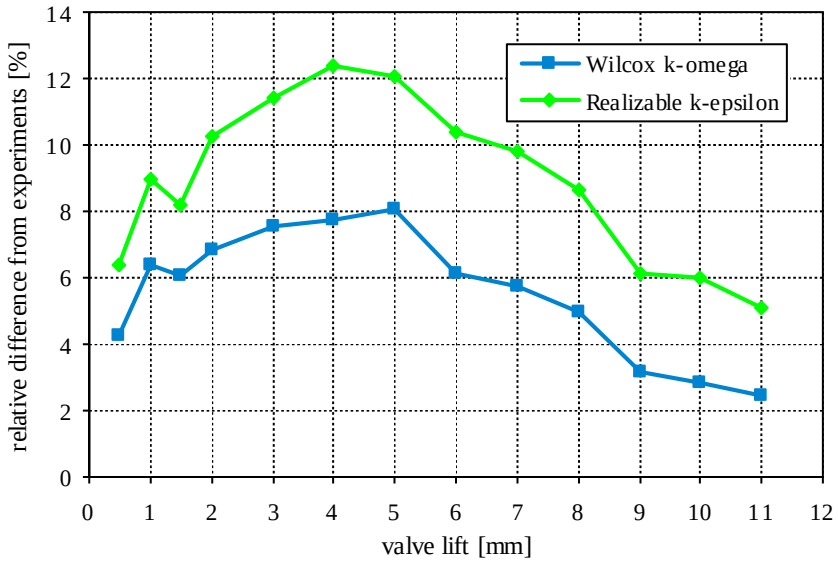

Fig. 13. Steady-state discharge-flow coefficient C_f experimental/numerical relative difference against valve lift: realizable k-ε (green); linear k-ω (blue).

Nevertheless, the value of the difference between numerical and experimental data is comparable with other research findings. Recently, Ramajo and Nigro [25] studied an engine head quite similar to present case and, however, their calculations, performed on tetrahedral grids, under-predicted experiments. Both under and over-prediction of calculation were reported by Befrui [23] as results of less recent calculations performed on almost entirely hexahedral grids. This author showed results regarding many engine heads, which, however, featured, swirl motion layouts. In 2009, Fontana and Galloni [41], modelled the entire engine cycle on an unstructured hexahedral grid, less refined than present one. Their preliminary steady-state calculation results on the reverse discharge-flow coefficient of exhaust valve showed numerical over-prediction at low-to-medium lifts values. Less clear was the direct intake findings, which were declared to be affected also by some difference between actual and modelled geometry. Finally, Algieri et al. [35], using tetrahedral and wedge grid counting about 800000 cells, compared experiments with the prediction of four different turbulence models (comprising present Shih k-ε and Wilcox k-ω models). Numerical results of the flow within the cylinder and valve zone proved that the discharge-coefficient is over-estimated at the specific medium-high valve lift value investigated. Indeed, at measured flow rate value, they calculated a pressure drop across valve assembly that was 0.09% and 2.5% lower than experimental value for k-ω and realizable k-ε models, respectively. Moreover, they find predictions of charge motion intensity, which was very close to experiments for k-ω calculations and very under-estimated for realizable k-ε calculations.

Looking at in-cylinder flow field, Figure 14 shows velocity vectors in the cylinder symmetry plane and in the parallel plane lying on intake valve axis calculated at 11 mm valve lift, which is the intake valves lift experimentally featuring nearly maximum tumble coefficient (see Figure 3). According to previous reasoning about turbulence models accuracy, the presented results were obtained by the modified k-ω model of Wilcox. It is worth noting the different vector field behaviour in the two plane analysed. The symmetry plane evidence a clear tumbling structure almost centred in the location of paddle wheel pivoting axis. On the other hand, the valve plane features the well-known counter-rotating vortices due to interaction between incoming jet and cylinder wall [7] typical of traditional valve port designs. This difference entails the requirement of more than two measure planes for the detailed 2-D optical studies of in-cylinder motion, in order to properly quantify tumbling region extension and tumble flow intensity, especially for low-to-medium tumble manifold design.

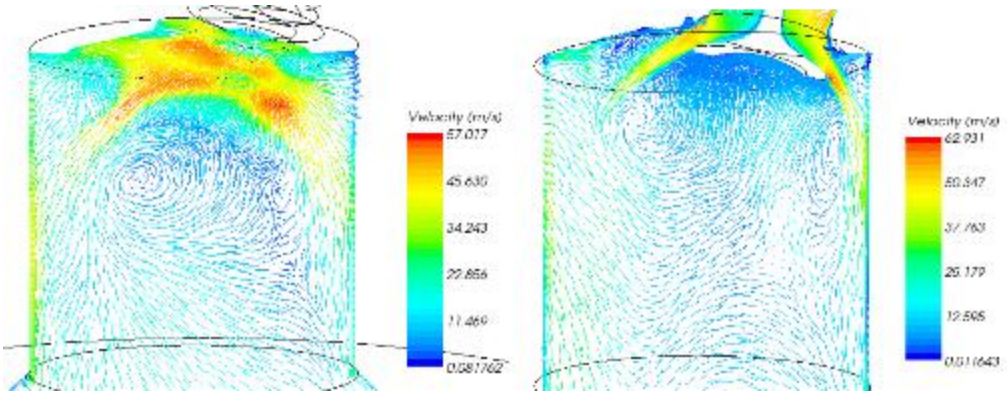

Fig. 14. Steady-state in-cylinder velocity field: mean cylinder plane (left); valve axis plane (right).

Figure 15a shows the comparison between the calculated and the measured tumble motion intensity. Being not proper a direct comparison of measured tumble coefficient and calculated moment of momentum within in-cylinder volume, the figure refers to correlation existing between these quantities, as suggested by many authors (see e.g. [16, 23]). Each one of the markers represents a specific lift value data and the solid line is the linear regression curve. Obviously, if measured and calculated data are identical the markers will fall in a rectilinear line passing through the axes origin with a slope of 45 deg. Kim et al. [18] stated that comparison between relative values is more significant than that between absolute values. In fact, experimental data referring to different tumble parameters, even if perfectly correlated, fall in a rectilinear line featuring slope that depends on the chosen tumble parameter. Moreover, they clarified that, comparing measurements of the same tumble parameter derived by different rig type, the correlation curve usually does not pass through the origin of axes. In particular, they observed that tumble ratios, measured by steady rig equipped with mechanical charge motion instrumentation, were dependent on the T-type adaptor design and changed with its body and branches length. It is worth noting the very good correlation degree (0.995) existing between the integration on the whole in-cylinder volume of the moment of momentum and the experimental data collected by present instrumentation. Moreover, quite surprisingly, present measurements show a correlation curve with calculations that passes close to the origin of both axes, assessing the capability of the proposed instrumentation to well capture the overall features of tumble motion within the cylinder assembly of Aprilia RSV1000.

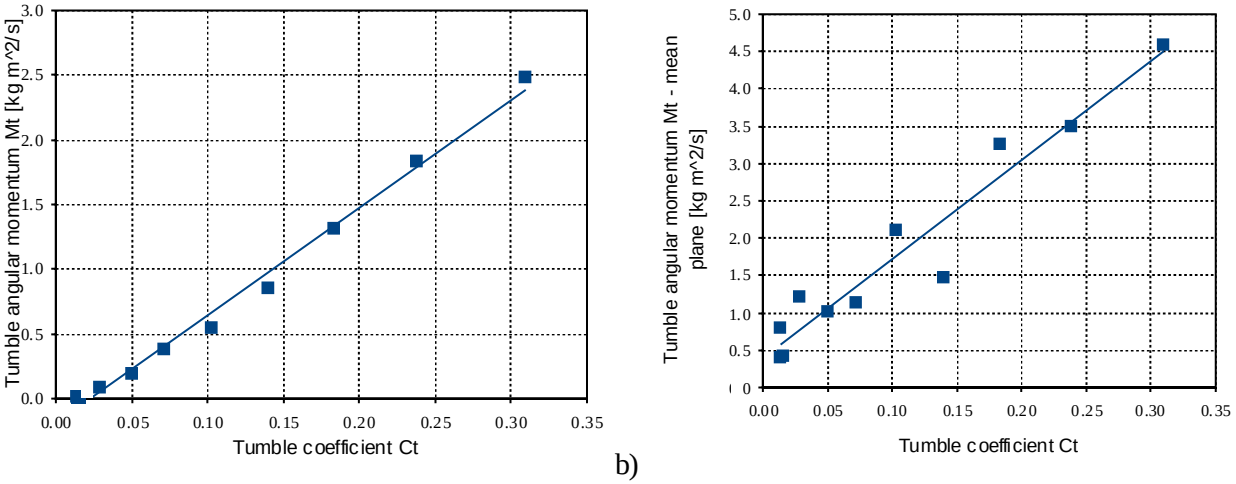

Fig. 15. Correlation between calculated moment of momentum (ordinate) and measured tumble coefficient (abscissa): a) in the whole cylinder; b) in cylinder symmetry plane.

Figure 15b shows the correlation curve between measurements and the integration of tumble moment of momentum limited to the cylinder symmetry plane. The correlation index is still acceptable (0.967) assessing the capability of cylinder mean plane to be quite representative of the whole tumble motion. However, the spreading of the markers corroborates the need of data for more planes, in order to satisfactory capture charge motion features.

6 Conclusions

A mechanical instrumentation featuring a spherical lens-shaped paddle wheel is designed to quickly measure overall intensity of both swirl and tumble in-cylinder charge motion by mean of traditional steady-state discharge-flow test rigs. The sensitivity to tumble motions due to different design of runner-valves-cylinder is experimentally checked on two different engine head of production high-speed motorbike engines. The limited fluid-dynamic blockage of the device affecting discharge-flow coefficient measurements is proven as well. Finally, a comparison with the result of a detailed CFD model is presented to verify the reliability of tumble intensity measurements within a low-medium tumble cylinder assembly. The CFD model, featuring polyhedral grids, is validated both numerically and experimentally. Grid sensitivity study demonstrates the need of 650000 cells with a 4-to-5 near-wall prism-layer within intake runners, ports and whole cylinder to reach discharge-flow coefficient results independent to grid size. As other researchers stated before, the modified Wilcox k-ω turbulence model predictions are confirmed to be closer to experiments than realizable k-ε results. Moreover, k-ω exhibits the property to be less sensitive to grid refinements and to give acceptable results also for very coarse grid computations.

The comparison between CFD results and tumble measurements assesses a very good correlation if the overall in-cylinder flow is considered. This stated the capability of present instrumentation to well capture the relevant features of tumble motion, despite its inherent simplicity and structure of tumble, which change between planes perpendicular to vortex axis as evidenced by CFD results.

Acknowledgments

Authors acknowledge Roberto Meneghello for the fundamental contribution to the results of reverse-engineering activity and Fabio Zanotto for the CAD modelling work.

References

[1] Fujimoto M., Iwai K.; Kataoka M., Tabata M., Effect of combustion chamber shape on tumble flow, squish-generated flow and burn rate. JSAE Review 2002; 23(3): 291-96.

[2] Huang RF., Lin KH., Yeh C-N, Lan J., In-cylinder tumble flows and performance of a motorcycle engine with circular and elliptic intake ports. Exp Fluids 2009; 46: 165-79.

[3] Huang RF., Yang HS., Yeh C-N, In-cylinder flows of a motored four-stroke engine with flat-crown and slightly concave-crown pistons. Experimental Thermal and Fluid Science 2008; 32: 1156-67.

[4] Huang RF., Huang CW., Chang SB., Yang HS., Lin TW., Hsu WY., Topological flow evolution in cylinder of a motored engine during intake and compression strokes. Journal of Fluids and Structures 2005; 20: 105-27.

[5] Lee K., Bae C., Kang K., The effects of tumble and swirl flows on flame propagation in a for-valve S.I. Engine. Applied Thermal Engineering 2007; 27: 2122-30.

[6] Omori S., Iwachido K., Motomochi M., Hirako O., Effect of Intake Port Flow Pattern on the In-Cylinder Tumbling Air Flow in Multi-Valve SI Engines. In: Proceedings of the International Congress & Exposition; 1991 February; Detroit, MI, USA. SAE Technical Paper 910477.

[7] Heywood JB., Internal Combustion Engine Fundamentals. Singapore: McGraw-Hill Inc.; 1988.

[8] Kang KY., Reitz RD., Intake Flow Structure and Swirl Generation in a Four-Valve Heavy-Duty Diesel Engine. ASME J. Eng. for Gas Turbines Power 2000; 122(4): 570-79.

[9] Hong CW., Tarng SD., In-Cylinder Tumble Flow Field Measurements and Predictions. ASME J. Eng. for Gas Turbines Power 2001; 123(1): 139-45.

[10] Kang KY., Reitz RD., The effect of intake valve alignment on swirl generation in a DI diesel engine. Experimental Thermal and Fluid Science 1999; 20(2): 94–103.

[11] Arcoumanis C., Hu Z., Vafidis C., Whitelaw JH., Tumbling Motion: A Mechanism for Turbulence Enhancement in Spark-Ignition Engines. In: Proceedings of International Congress & Exposition; 1990 February; Detroit, MI, USA. SAE Technical Paper 900060.

[12] Brandstätter, W., Johns RJR, Wigley G., The Effect of Inlet Port Geometry on In-Cylinder Flow Structure. 1985; SAE Technical Paper 850499.

[13] Kang KY., Baek JH., LDV Measurement and Analysis of Tumble Formation and Decay in a Four-Valve Engine. Experimental Thermal and Fluid Science 1995; 11: 181-189.

[14] Murali Krishna B., Mallikarajuna JM., Comparative study of in-cylinder tumble flows in an internal combustion engine using different piston shapes-an insight using particle image velocimetry. Exp. Fluids 2010; 48: 863-74.

[15] Yun J. E., Lee J. J., A study on Combine effects between swirl and tumble flow on intake port system in cylinder head. In : Proceedings of FISITA World Automotive Congress; 2000 June, Seoul, Korea. F2000A094.

[16] Godrie P., Zellat M., Simulation of Flow Field Generated by Intake Port-Valve-Cylinder Configurations-Comparison with Measurements and Applications. In: Proceedings of International Congress & Exposition; 1994 February; Detroit, MI, USA. SAE Technical Paper 940521.

[17] Moore W., Foster W., Lai M.-C., Xie X.-B., Zheng Y., Matsumoto A., Charge motion benefits of valve deactivation to reduce fuel consumption and emission in a GDI, VVA Engine. In: SAE 2011 World Congress & Exhibition, 2011 April, Detroit, MI, USA. SAE Technical Paper 2011-01-1221.

[18] Kim M., Lee S., Kim W., Tumble Flow Measurements Using Three Different Methods and its Effects on Fuel Economy and Emissions. In: Proceedings of Powertrain & Fluid Systems Conference and Exhibition; 2006 October; Toronto, ON, CANAD. SAE Technical Paper 2006-01-3345.

[19] Algieri A., Bova S., De Bartolo C., Influence of valve lift and throttle angle on intake flow in a high performance four-stroke motorcycle engine. ASME J. Eng. for Gas Turbines Power 2006; 128(4): 934-42.

[20] Gosman AD., Multidimensional Modelling of Cold Flows and Turbulence in Reciprocating Engines. 1985; SAE Technical Paper 850344.

[21] Gosman AD. Ahmed AMY., Measurement and Multidimensional Prediction of Flow in a Axisymmetric Port/Valve Assembly. 1987; SAE Technical Paper 870592.

[22] Dent, JC., Chen A., An Investigation of Steady Flow Through a Curved Inlet Port. In: Proceedings of International Congress & Exposition; 1994 February; Detroit, MI, USA. SAE Technical Paper 940522.

[23] Berfrui B. A., CFD Simulation and Comparison with Measurement of Steady Flow in Intake Ports and Combustion Chambers. In: COMODIA 94: Proceedings of the 3rd International Symposium on Diagnostics and Modeling of Combustion in Internal Combustion Engines; 1994 July 11-14; Yokohama, Japan. 535-40.

[24] Fuchs TR., Rutland CJ., Intake Flow Effects on Combustion and Emissions in a Diesel Engine. In: Proceedings of the International Congress & Exposition; 1998 February; Detroit, MI, USA. SAE Technical Paper 980508.

[25] Ramajo DE., Nigro NM., In-Cylinder Flow Computational Fluid Dynamics Analysis of a Four-Valve Spark Ignition Engine: Comparison Between Steady and Dynamic Tests. ASME J. Eng. for Gas Turbines Power 2010; 132(5): 052804-1-10.

[26] El-Behery SM., Hamed MH., A comparative study of turbulence models performance for separating flow in a planar asymmetric diffuser. Computers & Fluids 2011; 44: 248–57.

[27] So RM., Lai YG., Hwang BC., Second-order near-wall turbulence closure: A review. AIAA J. 1991; 29: 1819-35.

[28] Jia R., Sundén B., Miron P., Léger B., A Numerical and experimental investigation of the slot film-cooling jet with Various Angles. J. Turbomach. 2005; 127: 635-45.

[29] Paul SS., Ormiston SJ., Tachie MF., Experimental and numerical investigation of turbulent cross-flow in a staggered tube bundle. Int. J. Heat and Fluid Flow 2008: 29: 387–414.

[30] Speziale CG, So RMC., Turbulence modeling and simulation. In: Johnson RW, editor. The Handbook of fluid dynamics. Boca Ratom, FL: CRC Press. 1998. p. 14.1-14.111.

[31] Wilcox DC., Turbulence modeling for CFD. La Canada, CA: DCW Industries; 1998.

[32] Wallin S., Johansson AV., An explicit algebraic Reynolds stress model for incompressible and compressible turbulent flows. Journal of Fluid Mechanics 2000; 403: 89–132.

[33] Gullman-Strand J., Törnblom O., Lindgren B., Amberg G., Johansson AV., Numerical and experimental study of separated flow in a plane asymmetric diffuser. Int. J. Heat and Fluid Flow 2004; 25: 451–60.

[34] Bianchi GM., Fontanesi S., On the applications of low-Reynolds cubic k-ε turbulence models in 3D simulations of ICE intake Flows. In: Proceedings of the International Congress & Exposition; 2003 February; Detroit, MI, USA. SAE Technical Paper 2003-01-0003.

[35] Algieri A., Bova S., De Bartolo C., Nigro A., Numerical and Experimental Analysis of the Intake Flow in a High Performance Four-Stroke Motorcycle Engine: Influence of the Two-Equation Turbulence Models. ASME J. Eng. for Gas Turbines Power 2007; 129: 1095-105.

[36] Shih T-H., Liou WW., Shabbir A., Yang Z., Zhu J., A New k-ε eddy viscosity model for high Reynolds number turbulent flows-Model development and validation. Comput. Fluids 1995; 24: 227–38.

[37] UNI 10531, (In Italian) Ventilatori industriali - Metodi di prova e condizioni di accettazione (Industrial fans – Test methods and conditions for the acceptance), Milano, Italy; 1995.

[38] Martegani AD., .Lazzaretto A, Taffurelli A., A User's Guide to the UNI 10531 Standard on Performance Testing of Industrial Fans; 2003, 4 Dec. Document ISO/TC117 No: 306 Annex 3.

[39] Masi M., Toffolo A., Antonello M., Experimental analysis of a motorbike high speed racing engine. Applied Energy 2010; 87: 1641-50.

[40] Zanotto F., Studio sperimentale e numerico dei condotti valvola di scarico di un motore 4 tempi con il supporto di tecniche di ingegneria inversa (in Italian) [MSc thesis]. Padova, Italy: University of Padova; 2011.

[41] Fontana G., Galloni E., Variable valve timing for fuel economy improvement in a small spark ignition engine. Applied Energy 2008; 86: 96-105.

[42] Wolfstein M., The velocity and temperature distribution in one-dimensional flow with turbulence augmentation and pressure gradient. Int. J. Heat Mass Transfer 1969; 12:301-318.

CFD Simulation of Entropy Generation in Pipeline for Steam Transport in Real Industrial Plant

Goran Vučković[a], Gradimir Ilić[b], Mića Vukić[c] Milan Banić[d] and Gordana Stefanović[e]

[a] *University of Niš, Faculty of Mechanical Engineering, Niš, Serbia, vucko@masfak.ni.ac.rs, CA*
[b] *University of Niš, Faculty of Mechanical Engineering, Niš, Serbia, gradei@masfak.ni.ac.rs*
[c] *University of Niš, Faculty of Mechanical Engineering, Niš, Serbia, micav@masfak.ni.ac.rs*
[d] *University of Niš, Faculty of Mechanical Engineering, Niš, Serbia, banic@masfak.ni.ac.rs*
[e] *University of Niš, Faculty of Mechanical Engineering, Niš, Serbia, goca@masfak.ni.ac.rs*

Abstract:

The success of methods to increase the energy efficiency, to a large extent depends on the efficiency of individual elements, devices and apparatus, which are in the system. Energy efficiency operation of each of the elements of the system can be achieved with good design, which requires knowledge of the processes that take place in the device. The pipelines are an integral part of every industrial plant.
The objective of this paper is to illustrate the CFD simulation of entropy generation in one part of pipeline for steam transport in complex industrial plant, like a way of reducing irreversibility production in pipelines. The irreversibility of any fluid flow in pipelines is due to two factors, the transfer of heat across the stream to stream temperature difference (heat transfer irreversibility) and the frictional pressure drop that accompanies the circulation of fluid through the apparatus (fluid friction irreversibility).
In this paper the pipeline for steam transport in rubber industry is analysed. The superheated steam at the pressure 10 bar is a fluid that transfers the energy from the steam boiler to the apparatus in the factory. For a defined geometry of pipeline, the model was created, and as results are represented the fields of local entropy generation due to heat transfer and fluid friction, and the total entropy generation in the pipeline.
The minimum values of the local entropy generation rate in the steam flow meter (2.801×10^{-7} W/m^{3}K and 6.274×10^{-7} W/m^{3}K) are obtained in the core of fluid at the straight part of pipeline with constant cross-section. The maximum values (1.705 W/m^{3}K and 14.360 W/m^{3}K) are occurs near the wall. In the case of pipe curve at 90º turns the local entropy generation rate has a minimum values (3.223×10^{-10} W/m^{3}K and 4.730×10^{-10} W/m^{3}K) in the core of stream in the inlet of curve, and maximum values (1.733 W/m^{3}K and 14.580 W/m^{3}K) near the wall due to heat transfer and friction between the fluid and the wall. On the entropy generation has a dominant influence of irreversibility due to friction in comparison to the irreversibility caused by heat transfer.

Keywords:

CFD, entropy generation, energy efficiency, pipeline.

1. Introduction and Background

Heat transfer, as a way of thinking and formulation problems, is considerably older than thermodynamics. The foundation of knowledge of entropy production goes back to Clausius and Kelvin's studies on the irreversible aspects of the Second law of thermodynamics. Since then the theories based on these foundations have rapidly developed [1]. Entropy generation is associated with thermodynamic irreversibility, which is common in all types of heat transfer processes. Different sources are responsible for generation of entropy like heat transfer across finite temperature gradient, characteristic of convective heat transfer, viscous effect etc. Entropy generation through heat and fluid flow is designed to bridge the gap between three cornerstone subjects: heat transfer, thermodynamics and fluid mechanics. From historical point of view entropy generation through heat and fluid flow became a part of engineering thermodynamics in the last decade of previous century [2].

Flow through pipelines and heating situations find wide applications in industry. Bejan [2] focused on the different reasons behind entropy generation in applied thermal engineering. Generation of entropy destroys available work of a system. Therefore, it makes good engineering sense to focus on irreversibility of heat transfer and fluid flow processes and try to understand the function of

entropy generation mechanism. Bejan [3] presented a study of four basic convective heat transfer phenomena from the unique point of view of entropy generation, and illustrated, in a very modest way, the place thermodynamics duly occupies in heat transfer. Mahmud and Fraser [1] analyzed Second law characteristics of heat transfer and fluid flow due to forced convection of steady-laminar flow of incompressible fluid inside channel with circular cross-section and channel made of two parallel plates. Different problems are discussed with their entropy generation profiles and heat transfer irreversibility characteristics. Guo, et all [4] presented the viscous dissipation effect on the entropy generation for laminar flow region in curved square microchannles is numerically investigated. Aniline and ethylene glycol are selected as the working fluids. Sahin and Mansour [5] investigated a numerical solution to the entropy generation in laminar viscous fluid flow through a circular pipeline, with uniform heat flux at wall boundary condition. Zaharnah and Yilbas [6] the influence of fluid viscosity on the entropy generation rate is investigated in the pipeline flow at different wall temperatures. The temperature and flow fields are computed numerically using the control volume method. It is found that fluid viscosity influences considerably temperature distribution in the fluid close to the pipeline wall. Yapici et all [7] presented in study the investigation of the local entropy generation in compressible flow through a suddenly expanding pipe. Air is used as fluid. To determine the effects of the mass flux, the ambient heat transfer coefficient and the inlet temperature on the entropy generation rate, the compressible flow is examined for various cases of these parameters. The flow and temperature fields are computed numerically with the help of the computational fluid dynamics (CFD) code. In addition to this CFD code, a computer program has been developed to calculate numerically the entropy generation and other thermodynamic parameters by using the results of the calculations performed for the flow and temperature fields. Ko [8] three-dimensional laminar forced convective flow and entropy generation in a 180-deg curved rectangular duct with longitudinal ribs equipped on the heated wall have been investigated by numerical methods. The effects of rib size under different flow conditions with various Dean number and external flux are particularly highlighted. Ko and Ting [9] numerically analyzed entropy generation for laminar forced convection in curved rectangular ducts and air as the working fluid under constant heat flux condition; and found that there exists an optimal Dean number for each aspect ratio, and the optimal Dean number increases as the dimensionless heat flux increases.

2. Methodology

2.1 Local Rate of Entropy Generation in Convective Heat Transfer

The purpose is to study the volumetric entropy generation rate distribution throughout the fluid in the pipeline. This requires solution of velocity and temperature fields in the fluid. The governing equations and the boundary conditions for this steady problem with constant thermophysical properties are as follows:

Continuity ($\nabla \cdot \rho \vec{w} = 0$):

$$\frac{\partial}{\partial x}(\rho w_x) + \frac{\partial}{\partial y}(\rho w_y) + \frac{\partial}{\partial z}(\rho w_z) = 0 \tag{1}$$

Momentum ($\rho(\vec{w} \cdot \nabla w) = -\nabla p + \mu \nabla^2 \vec{w}$):

$$\rho\left(w_x \frac{\partial w_x}{\partial x} + w_y \frac{\partial w_x}{\partial y} + w_z \frac{\partial w_x}{\partial z}\right) = -\frac{\partial p}{\partial x} + \mu\left(\frac{\partial^2 w_x}{\partial x^2} + \frac{\partial^2 w_x}{\partial y^2} + \frac{\partial^2 w_x}{\partial z^2}\right) \tag{2a}$$

$$\rho\left(w_x \frac{\partial w_y}{\partial x} + w_y \frac{\partial w_y}{\partial y} + w_z \frac{\partial w_y}{\partial z}\right) = -\frac{\partial p}{\partial y} + \mu\left(\frac{\partial^2 w_y}{\partial x^2} + \frac{\partial^2 w_y}{\partial y^2} + \frac{\partial^2 w_y}{\partial z^2}\right) \tag{2b}$$

$$\rho\left(w_x\frac{\partial w_z}{\partial x}+w_y\frac{\partial w_z}{\partial y}+w_z\frac{\partial w_z}{\partial z}\right)=-\frac{\partial p}{\partial z}+\mu\left(\frac{\partial^2 w_z}{\partial x^2}+\frac{\partial^2 w_z}{\partial y^2}+\frac{\partial^2 w_z}{\partial z^2}\right) \tag{2c}$$

Energy ($\rho c_p\left(\vec{w}\cdot\nabla T\right)=\lambda\nabla^2 T+\mu\Phi$):

$$\rho c_p\left(w_x\frac{\partial T}{\partial x}+w_y\frac{\partial T}{\partial y}+w_z\frac{\partial T}{\partial z}\right)=\lambda\left(\frac{\partial^2 T}{\partial x^2}+\frac{\partial^2 T}{\partial y^2}+\frac{\partial^2 T}{\partial z^2}\right)+\mu\Phi \tag{3}$$

In the fluid flow, irreversibility arises due to the heat transfer and the viscous effects of the fluid. The entropy generation rate can be expressed as the sum of contributions due to thermal and viscous effects, and thus it depends functionally on the local values of temperature and velocity in the domain of interest. In these systems, when both temperature and velocity fields are known, the local or volumetric entropy generation rate at each point can be calculated as follows equation, in tensor notation [10]:

$$\dot{S}'''_{gen}=\frac{\lambda}{T^2}\left(\nabla T\right)^2+\frac{\mu}{T}\Phi\ , \tag{4}$$

or in development form:

$$\dot{S}'''_{gen}=\frac{\lambda}{T^2}\left[\left(\frac{\partial T}{\partial x}\right)^2+\left(\frac{\partial T}{\partial y}\right)^2+\left(\frac{\partial T}{\partial z}\right)^2\right]+\frac{\mu}{T}\Phi \tag{5}$$

In equitation (3) and (5) Φ is the viscous dissipation function, which is [11]:

$$\Phi=\left\{2\left[\left(\frac{\partial w_x}{\partial x}\right)^2+\left(\frac{\partial w_y}{\partial y}\right)^2+\left(\frac{\partial w_z}{\partial z}\right)^2\right]+\left(\frac{\partial w_y}{\partial x}+\frac{\partial w_x}{\partial y}\right)^2+\left(\frac{\partial w_z}{\partial y}+\frac{\partial w_y}{\partial z}\right)^2+\left(\frac{\partial w_x}{\partial z}+\frac{\partial w_z}{\partial x}\right)^2\right. \tag{6}$$

$$\left.-\frac{2}{3}\left(\frac{\partial w_x}{\partial x}+\frac{\partial w_y}{\partial y}+\frac{\partial w_z}{\partial z}\right)^2\right\}.$$

The first and second term on the right side in equitation (4) and (5) represent, respectively, the local entropy generation rate due to heat transfer and fluid friction.

In accordance with the foregoing, equation (5) can be symbolically represent in the form:

$$\dot{S}'''_{gen}=\left(\dot{S}'''_{gen}\right)_{HT}+\left(\dot{S}'''_{gen}\right)_{FF}\ , \tag{7}$$

The total entropy generation rate over the volume can be calculated as follows [7]:

$$\dot{S}_{gen}=\oint_V \dot{S}'''_{gen}dxdydz\ . \tag{8}$$

Based on the known values of entropy generation can be by applying the theorem of lost available work, or Gouy-Stodola theorem, determine the amount of exergy destruction. The destruction of exergy is proportional to the value of the generated entropy, where the coefficient of proportionality is the reference temperature [12]:

$$\dot{E}_D=T_0\dot{S}_{gen} \tag{9}$$

Owing to exergy destruction, but and exergy loss, the exergy rate at the outlet is less than the exergy rate at the inlet. These exergy quantities are related by the exergy rate balance, which at steady state can be expressed as [13]:

$$\dot{E}_i = \dot{E}_e + \dot{E}_D + \dot{E}_L \tag{10}$$

The rate of exergy loss equals the rate of exergy transfer associated with heat transfer, and is thus given by [10]:

$$\dot{E}_L = \dot{E}_q = \int_i^e \left(1 - \frac{T_0}{T_b}\right) \dot{q}' dL \tag{11}$$

where is:

$$\dot{q}' = k_l \left(t_{f,l} - t_0\right) \tag{12}$$

To obtain the information which irreversibility dominated for entropy generation, due to heat transfer or fluid friction, Bejan was define dimensionless parameter - Irreversibility distribution ratio. The irreversibility distribution ratio is equal to the ratio of entropy generation due to fluid friction to heat transfer [2]:

$$\phi = \frac{\left(\dot{S}'''_{gen}\right)_{FF}}{\left(\dot{S}'''_{gen}\right)_{HT}} . \tag{13}$$

Heat transfer irreversibility dominates over fluid friction irreversibility for $0 < \phi < 1$ and fluid friction dominates when $\phi > 1$. For $\phi = 1$, both the heat transfer and fluid friction have the same contribution for generating entropy In the case $\phi \gg 1$ or $\phi \to \infty$ entropy generation is occurs only due to friction.

As an alternative irreversibility distribution ratio, defined Bejan number [1] which describes the contribution of heat transfer entropy on overall entropy generation, is defined as [8]:

$$\mathrm{Be} = \frac{\left(\dot{S}'''_{gen}\right)_{HT}}{\dot{S}'''_{gen}}, \tag{14}$$

Bejan number ranges from 0 to 1. Accordingly, $\mathrm{Be} = 1$ is the limit at which the heat transfer irreversibility dominates, $\mathrm{Be} = 0$ is the opposite limit at which the irreversibility is dominated by fluid friction effects, and $\mathrm{Be} = 0.5$ is the case in which the heat transfer and fluid friction entropy generation rates are equal. [1, 7].

Using equations (7) and (13) can be established a relationship between Bejan's number and irreversibility distribution ratio [1]:

$$\mathrm{Be} = \frac{1}{1+\phi}. \tag{15}$$

2.2 Computational Procedure

The general theory of fluid motion is too difficult to enable the user to attack arbitrary geometric configurations. It is possible to apply merely numerical techniques to arbitrary geometries. Computational fluid dynamics turns out the methods are applicable to a number of systems of equations which fall under the category of conservation laws. Therefore, a suitable numerical method and/or computational fluid dynamics code is frequently used to solve the governing equations in this field. The CFD code is the program by which fluid flow can be predicted through arbitrary geometries, giving such information as flow speed, pressures, residence times, flow patterns, etc. The main advantage of this approach is in its potential for reducing the extent and number of experiments required to describe such types of flow.

2.2.1 Calculation Tools

The ANSYS CFX 13 program was chosen as the CFD computer code to calculate entropy generation in a steam pipeline. The software was chosen due the ease with which the analysis model can be created, and because the software allows input of new equations necessary for calculation of entropy generation rate. Furthermore, ANSYS CFX computer code enables the definition of wall heat transfer coefficient as a user function, which parameters are solved during the solving of fluid flow equations. The ANSYS CFX computer code uses a finite-volume procedure to solve the Navier-Stokes equations of fluid flow in primitive variables such as velocity (w_x, w_y, w_z) and pressure. Noted computer code includes various turbulence models [14] among which k-ε model was selected in entropy generation rate calculation. k-ε model calculates turbulent viscosity (μ_t) as a function of turbulent kinetic energy (k) and turbulence dissipation rate (ε). Fluid flow equations include the viscous term in order to calculate entropy generation rate due to fluid friction.

The thermo-physical properties of steam were adopted according to the International Association for the Properties of Water and Steam (IAPWS) equation of state, incorporated into ANSYS CFX computer code. In ANSYS CFX, the analytical equation of state is used to transfer properties into tabular form. These IAPWS tables are defined in terms of pressure and temperature, which are then inverted to evaluate states in terms of other property combinations, such as pressure/enthalpy or entropy/enthalpy [14].

As ANSYS CFX calculates automatically derivates of temperature and velocity components, the expressions necessary to calculate volumetric entropy generation were inserted into solver by the CFX Command Language (CCL).

The finite element mesh was created from pipeline geometrical model by patch confirming method. Boundary layer was inflated with 20 layers with total thickness of 3 mm. The finite element mesh has 3508655 nodes which form 2662769 tetrahedrons and 5972280 wedge elements. All mesh quality parameters (Orthogonality angle, Expansion factor and Aspect ratio) are in permissible range for a double precision solver.

2.2.2 Simulation Values

Steam pipeline boundary conditions were defined based on actual measurement of mass flow rate, temperature and pressure at inlet and outlet. The simulation parameters are given in Table 1.

Table 1. Overview of simulation parameters

Parameters	Value/setting
Analysis type	steady state
Steam properties	IAPWS IF97
Thermodynamic state	gas
Temperature of the surrounding, ^oC	10
Reference pressure, atm	0
Heat transfer model	total energy
Inlet flow regime	subsonic
Inlet volumetric flow rate, m^3/h	150/400
Inlet steam temperature, ^oC	181.4/182.6
Inlet turbulence	medium intensity and eddy viscosity ratio
Outlet flow regime	subsonic
Outlet static pressure, bar	9.85/9.25
Wall mass and momentum	no slip wall
Wall roughness, mm	0.2
Wall heat transfer coefficient, W/m^2K	calculated during solve[1]
Turbulence numerics	high resolution
Advection scheme	high resolution
Execution control	double precision
Convergence criteria - Residual Target	RMS $\leq 10^{-5}$

[1]The wall heat transfer coefficient was calculated during the solve procedure based on equation:

$$k = \frac{1}{\frac{1}{\alpha_{ex}} + \frac{d_{is}}{2\lambda_{is}} \ln \frac{d_{is}}{d_{ew}} + \frac{d_{is}}{2\lambda_{pw}} \ln \frac{d_{ew}}{d_{iw}} + \frac{d_{is}}{d_{iw}} \frac{1}{\alpha_{in}}} \tag{16}$$

3. Background of Industrial Plant and Pipeline Geometry

The energy system in a representative industrial plant, Fig. 1, consists of four parts: Energy supply sector (EN), Factory 1 (F1), Factory 2 (F2) and Engineering department (IN).

Energy supply sector is a part of the factory complex where chemical and thermal treatment of water is being carried out, and superheated steam for their own use and supply of all other consumers is produced.

The boiler produces superheated steam at the pressure of 10 bars, which is then distributed to factories 1 and 2, and partly reduced at lower pressures in accordance with the needs of consumers. Factory 1 is the largest consumer of energy in the whole complex and is supplied with energy using the superheated steam at the pressure of 10 bars. The focus point in this paper is a pipeline in which distributed superheated steam at 10 bars from Energy supply sector to Factory 1.

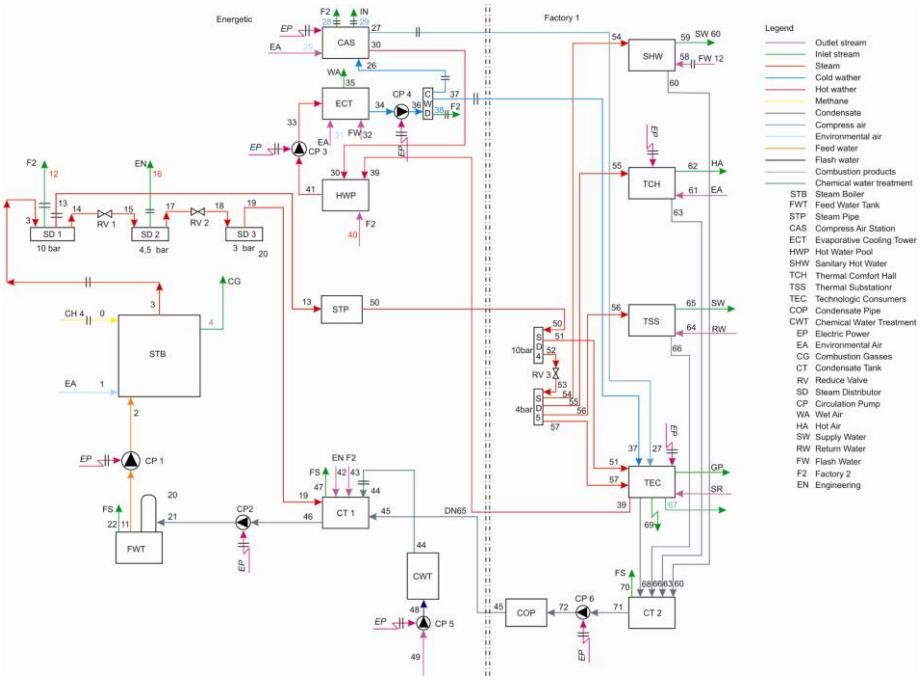

Fig. 1. Flow diagram of the representative industrial plant

The present steam pipeline, Fig. 2, is made of steel with a nominal diameter of DN 150 with total length of 148.7 m. In one part of the pipeline cross-section is reduced for the steam flow meter. Pipeline contains more curves at angle of 90^{o} and two elements for compensate expansion due to temperature change.

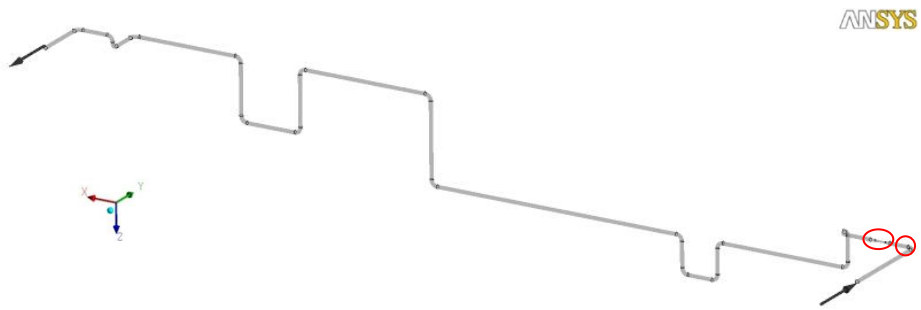

Fig. 2. Real steam pipeline

The pipeline is to reduce heat losses to the environment covered with insulation material thickness of 80 mm. Due to that pipeline mainly located in open space, insulation material is protected by aluminium tin. From the inside area pipeline is not an ideal smooth, but has a certain roughness, which is characterized with roughness height 0.2 mm.

4. Results and Discussion

4.1 Analysis Results for the whole Steam Pipeline

The results of numerical calculations for the whole pipeline are given in Table 2. From the collected results, it can be concluded that with increasing volumetric flow rate of 2.67 times, respectively with 150 m^3/h to 400 m^3/h, the total entropy generated due to irreversibility in the pipeline increases more than 10 times, and in the same amount increases exergy destruction. The dominant effect of entropy generation is due by fluid friction. On the other hand, at higher volumetric flow rates decreases the value of entropy generation due to the irreversibility caused by convective heat transfer, but to a much lesser extent than the increase of entropy generation by friction of fluids. The dominance of irreversibility due to fluid friction is expressed through the values of irreversibility distribution ratio, which in both cases is greater than 1 (3.200 and 120.464). For the higher volumetric flow rate (Case 2), irreversibility distribution ratio has a far higher value, 120.464. Also, both the values for the dimensionless criterion, Bejan's number, are close to zero (0.238 and 0.00824), indicating little impact of irreversibility due to convective heat transfer in the steam flow of 150 m^3/h, and almost insignificant impact of irreversibility due to convective heat transfer in the steam flow of 400 m^3/h.

Table 2. Overview of results for whole steam pipeline

Parameters	Units	Case 1	Case 2
	m^3/h	150.00	400.00
p_i (measured)	bar	10.000	9.420
p_i (simulation)	bar	9.883	9.277
p_e (measured)	bar	9.850	9.250
p_e (simulation)	bar	9.850	9.250
T_i (measured)	K	454.540	455.740
T_e (simulation)	K	451.823	454.555
T_o	K	283.140	283.140
T_0	K	298.150	298.150
	W/K	0.0003755	0.003792
	W/K	8.942e-5	3.122e-5
	W/K	0.0002861	0.003761
ϕ	-	3.200	120.464
Be	-	0.238	0.00824
k	W/m^2K	0.307597	0.308593
t_z	K	452.90	455.01
	W	-1,309.68	-1,332.24
	W	0.112	1.121

4.2 Analysis Numerical Results for Local Entropy Generation and Bejan Number for Characteristics Parts of Steam Pipeline

In general, the local entropy generation rate is maximal, as expected, near the wall due to heat transfer and friction between the fluid and the wall. The temperature of the fluid will decrease gradually towards the pipe wall and outlet, and the temperature gradients in the radial and axial directions will occur, which in turn will increase the local entropy generation rate.

Furthermore, the local entropy generation rate is maximal at the flow meter (Fig. 3) and in pipeline curves (Fig. 5). In this paper we analyzed first curve at the pipeline and fluid flow meter (Fig. 2).

As known, in a pipe flow, the cross-section contraction in flow meter accelerates fluid, and the sudden expansion in the pipe produces the high velocity gradients which also increase the local entropy generation rate. It is obvious from Fig. 3 that local entropy generation rate increases with the increase in fluid mass flow rate i.e. fluid velocity. The minimum values of the local entropy generation rate in the both cases (2.801×10^{-7} W/m^{3}K and 6.274×10^{-7} W/m^{3}K) are obtained in the core of fluid at the straight part of pipeline with constant cross-section. The maximum values (1.705 W/m^{3}K and 14.360 W/m^{3}K) are occurs near the wall.

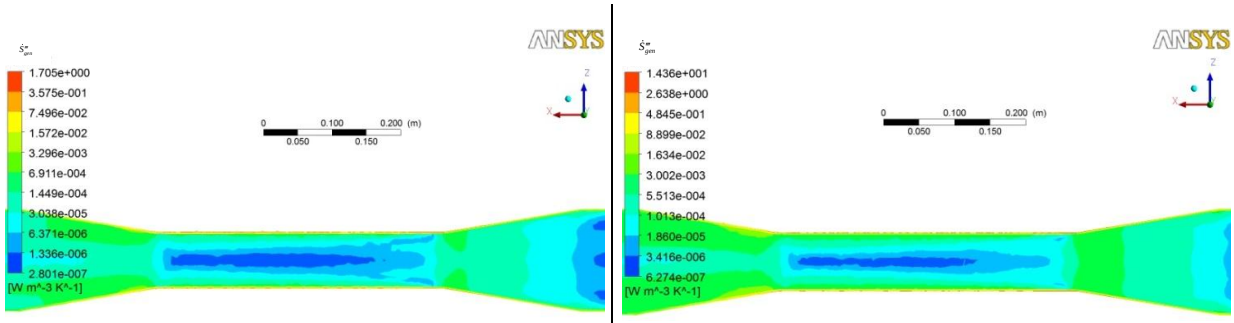

a) volumetric flow rate 150 m^3/h *b) volumetric flow rate 400 m^3/h*

Fig. 3. Local entropy generation rate at flow meter (logarithmic)

Fig. 4 shows the distribution of Bejan number in steam flow meter. As Bejan number values are smaller than 0.8 for the lower mass flow rate, and smaller than 0.2 for higher mass flow rate.

In the first case in very small area (only part of red zone, $0.5 < Be \leq 0.7882$) irreversibility from convective heat transfer is dominate for local entropy generation. In the point where is Be=0.5 irreversibility from convective heat transfer and fluid friction are equal for local entropy generation. In the other part of flow meter values of Bejan number is very close to zero, it is clear that irreversibility from heat transfer has less influence on resultant local entropy generation rate then irreversibility from fluid friction.

In the second case, all values of Bejan number are smaller than 0.5 and for these reason, in whole part of flow meter irreversibility from fluid friction is dominate for entropy generation.

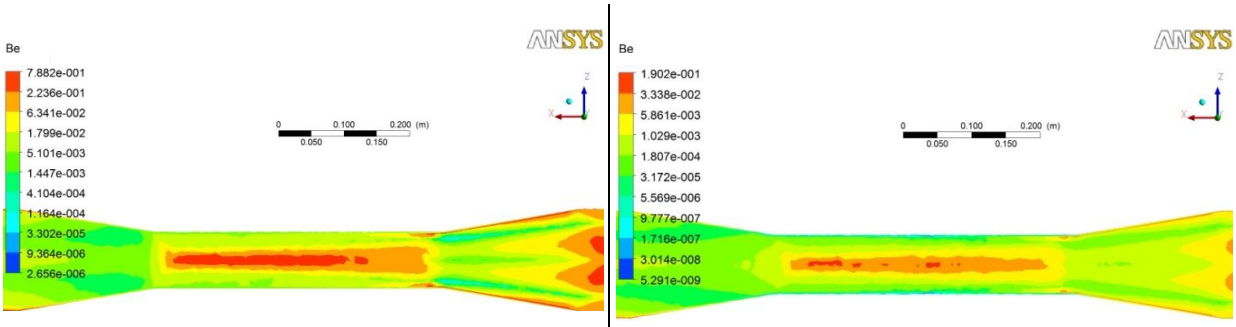

a) volumetric flow rate 150 m^3/h *b) volumetric flow rate 400 m^3/h*

Fig. 4. Bejan number at flow meter (logarithmic)

The velocity change in curves and the consequent change in velocity gradients also increases the local entropy generation rate (Fig. 5). Again, the local entropy generation rate increases with the increase in fluid mass flow rate. The local entropy generation rate in the both cases has a minimum values (3.223×10^{-10} W/m^{3}K and 4.730×10^{-10} W/m^{3}K) in the core of stream in the inlet of curve, and maximum values (1.733 W/m^{3}K and 14.580 W/m^{3}K) near the wall due to heat transfer and friction between the fluid and the wall.

Fig. 6 shows the distribution of Bejan number in pipeline curve.

As maximal Bejan number values are relatively high (0.9984) for the lower mass flow rate is clear that irreversibility from heat transfer has dominant influence on resultant local entropy generation. But this value and values higher than 0.5 valid only in very small area having in mind that the red

zone includes values for Bejan number from 0.1990 to 0.9984. In the point where is Be=0.5 irreversibility from convective heat transfer and fluid friction are equal for local entropy generation. In the other part of pipe curves values of Bejan number is very close to zero, it is clear that irreversibility from heat transfer has less influence on resultant local entropy generation rate then irreversibility from fluid friction.

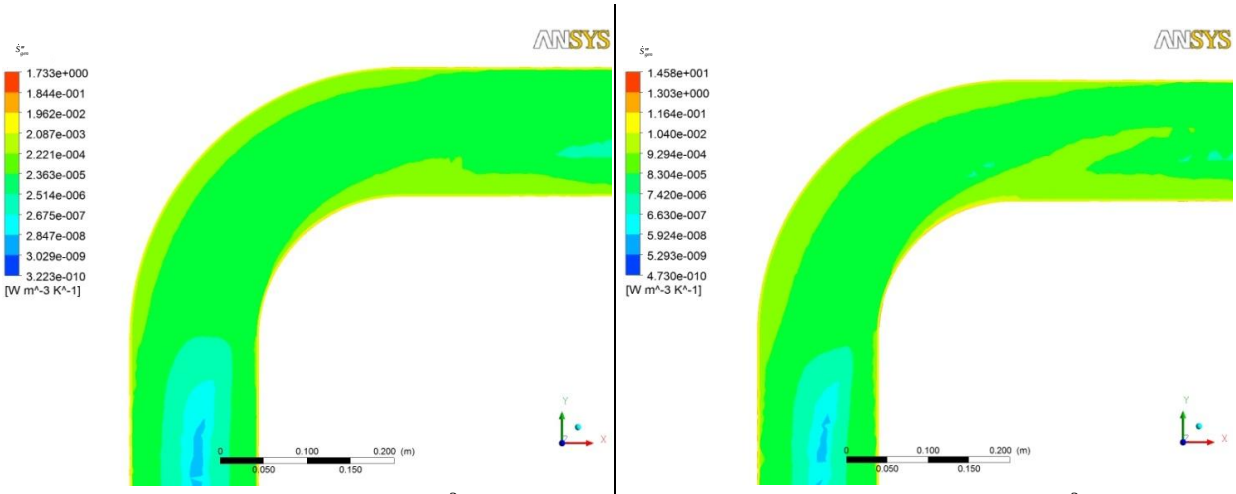

a) volumetric flow rate 150 m^3/h *b) volumetric flow rate 400 m^3/h*

Fig. 5. Local entropy generation rate at pipeline curve (logarithmic)

In the second case, all values of Bejan number are smaller than 0.5 and for these reason, in whole part of pipe curve irreversibility from fluid friction is dominate for entropy generation. Furthermore, no matter what heat transfer losses are greater for higher volumetric flow rate, influence of irreversibility from heat transfer on entropy generation is decreases with increase fluid flow.

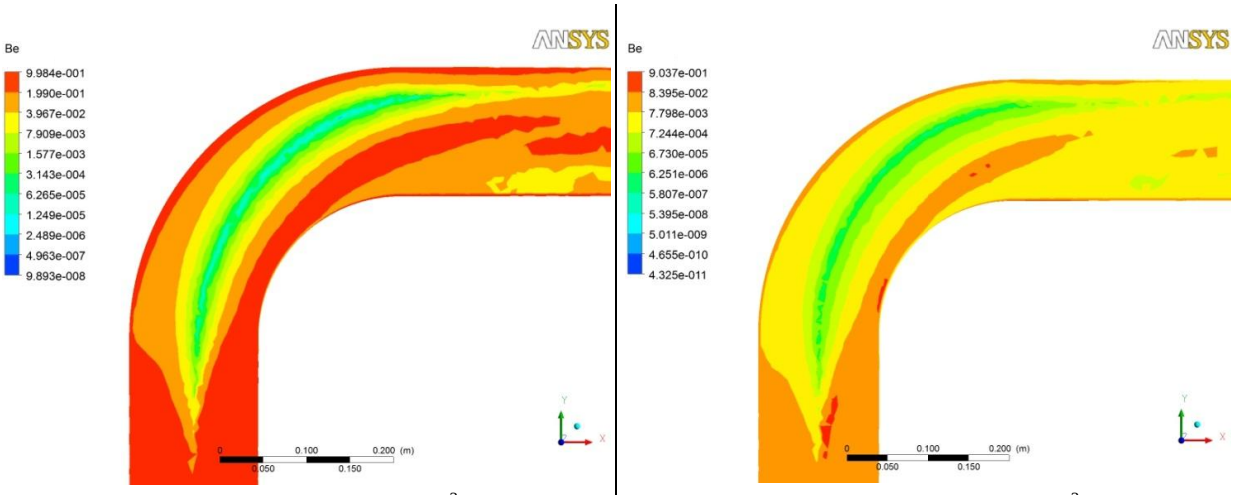

a) volumetric flow rate 150 m^3/h *b) volumetric flow rate 400 m^3/h*

Fig. 6. Bejan number at pipeline curve (logarithmic)

5. Conclusions

The paper presents a numerical simulation of entropy generation in the real pipeline superheated steam. The results of numerical simulation show good agreement with measured data in regard to temperature. The inability to predict pressure drop is a consequence of relatively coarse mesh in the core of the pipeline. Due to relatively coarse mesh the CFX solver cannot accurately calculate fluid friction losses and thus irreversibility from fluid friction. Noted trade-off in coarse mesh in central fluid region was introduced to decrease the computational resources necessary to perform calculations i.e. decrease of time necessary to perform calculations to a reasonable frame. Regardless of the above simplifications, examples of steam flow meter and pipe curve, it is shown

that the irreversibility of friction far more influence on the generation of entropy than irreversibility from heat transfer, and therefore on the loss of available work or exergy destruction. Having in mind previous, the general conclusion is that in order to increase the energy efficiency of the system should significantly decrease the friction between the pipe wall and fluid.

Nomenclature

Be - Bejan number

$\dot{E}$ - exergy flow rate, W

d - diameter, m

k - heat transfer coefficient, W/(m^2·K)

p - pressure, bar

q' - heat transfer rate per unit of length, W/m

$\dot{Q}$ - heat transfer rate, W

$\dot{S}_{gen}$ - entropy generation rate, W/K

$\dot{S}'''_{gen}$ - local entropy generation rate, W/(m^3·K)

t - temperature, ^{o}C

T - temperature, K

$\dot{V}$ - volumetric flow rare, m^3/h

w - velocity, m/s

Greek symbols

α - convective heat transfer coefficient, W/(m^2·K)

ϕ - irreversibility distribution ratio

Φ - viscous dissipation function, s^{-2}

λ - thermal conductivity, W/(m·K)

Greek symbols (continue)

μ - viscosity, kg/(s·m)

ρ - density, kg/m^3

Subscripts

b - boundary

D - destruction

e - outlet

ew - external wall

ex - external

FF - fluid friction

HT - heat transfer

i - inlet

in - internal

is - isolation

iw - internal wall

L - loss

o - environment

pw - pipe wall

q - heat transfer

0 - reference state

References

[1] Mahmud S., Fraser A.R.: The Second Low Analysis in Fundamental Convective Heat Transfer Problems, Thermal Science 2003; 42: 177-86.

[2] Bejan A: Entropy Generation through Heat and Fluid Flow, John Wiley&Sons; 1982.

[3] Bejan A.: A Study of Entropy Generation in Fundamental Convective Heat Transfer, Journal of Heat Transfer 1979; 101: 718-25.

[4] Guo J., Xu M., Cai J., Huai X.: Viscousn Dissipation Effect on Entropy Generation in Curved Square Microchannels, Energy 2011; 33: 5416-23.

[5] Sahin Z.A., Mansour B.R.: Entropy Generation in Laminar Fluid Flow through a Circular Pipe, Entropy 2003; 5: 404-16.

[6] Zaharnah A.T., Yilbas S.B.: Thermal Analysis in Pipe Flow: Influence of Variable Viscosity on Entropy Generation, Entropy 2004; 6: 344-63.

[7] Yapici H., Kayatas N., Kahraman N., Baştürk G.: Numerical Study on Local Entropy Generation in Compressible Flow through a Suddenly Expanding Pipe, Entropy 2005; 7: 38-67

[8] Ko H.T.: Numerical Investigation on Laminar Forced Convection and Entropy Generation in a Curved Rectangular Duct with Longitudinal Ribs Mounted on Heated Wall Ducts, Thermal Science 2006; 45: 390-404.

[9] Ko H.T., Ting K.: Entropy Generation and Optimal Analysis for Laminar Forced Convection in Curved Rectangular Ducts: A Numerical Study, Thermal Sciences 2006; 45(2): 138-50.

[10] Bejan A., Tsatsaronis G., Moran M.: Thermal Design and Optimization, New York: John Wiley&Sons; 1996.

[11] Bird B., Steward W., Lightfoot E.: Transport Phenomena, John Wiley&Sons; 2002.

[12] Szargut J., Morris D.R, Steward F.R.: Exergy Analysis of Thermal, Chemical, and Metallurgical Processes, New York: Hemisphere Publishing Corporation; 1988.

[13] Edited by Frangopoulos C.: Exergy, Energy System Analysis and Optimization - Exergy and Thermodynamic Analysis, Vol. 1, EOLSS Publishers Co. Ltd; 2009.

[14] ANSYS CFX 13.0, Theory manual.

Feasibility Study of Turbo expander Installation in City Gate Station

Navid Zehtabiyan Rezaie[a], Majid Saffar-Avval[b]

[a] Amirkabir University of Technology, Tehran, Iran, n.zehtabiyan@gmail.com
[b] Amirkabir University of Technology, Tehran, Iran, mavval@aut.ac.ir,CA

Abstract:
Natural gas pressure has to be increased in natural gas distribution network; meanwhile, before entering the low-pressure lines, this high pressure must be reduced. Pressure let-down in city gate stations is traditionally performed as natural gas passes through a throttle valve, although this method is simple, a considerable irreversibility is imposed to the system. A turbo expander can be used as an alternative way for reducing the gas pressure. The generated mechanical power may be used to produce electricity or drive a compressor.
As natural gas flow rate varies during the year, the turbo expander almost operates in off-design conditions. The generated power is evaluated for each day of the year. The study has been applied for Takestan, Iran city gate station with nominal flow rate of 20000 cubic meters per hour. The recovered annual electrical energy is about 1104737 kWh and the project is economic for interest rate up to 18%.

Keywords:
City gate stations, Natural gas, Pressure reduction, Turbo expander.

1. Introduction

Nominal gas pressure in distribution pipelines is about 5-7 MPa, there are several stations for reduction of natural gas pressure, the first step in gas pressure let-down is performed in the city gate station. The process includes the natural gas expansion in a throttle valve, which decreases the pressure and temperature of the gas. Natural gas pre-heating is necessary to avoid condensation and a fraction of pipe gas is burned for this purpose. Replacing the throttle valve with a turbine is an approach to decrease the entropy generation in city gate stations as well as in natural gas distribution system. Replacement of throttle valve with turbo expander does not mean that the throttle valve is eliminated. The turbo expander is installed in parallel with the former system, to avoid any interruptions in gas distribution as a result of turbo expander failure.

As stated in [1], turbo expanders were first installed in 1980s in San Diego, Memphis, Stockbridge and Hamilton New Jersey. Joining the turbo expander and fuel cell was first done in 2008 in Toronto Canada. Combination of turbo expanders installed in London natural gas distribution system with bio-fuel burning generator was started in 2009 and was expected to produce 20 MW.

Mirandola and Minca [2] showed that for an inlet pressure of 1.13-5.1 MPa and an outlet pressure of 0.15-0.6 MPa, with design flows varying from 5000 to 30000 Nm3/h, a power recovery of about 300-1400 kW is expected.

Mirandola and Macor [3] analysed the real data from a prototype built in Ravenna Italy in 1987.

Pozivil [4] simulated a natural gas station in Czech Republic. This analysis showed that the temperature drop in the turbo expander will be greater than throttle valve and is about 1.5-2 ˚C per kPa depending on gas composition. The outlet temperature was maintained at 3 ˚C where the inlet and outlet pressures varied from 4.5 to 6.3 MPa and 1.4-2.3 MPa respectively. The flow rate was 60000 Nm^3/h and was assumed to be fixed.

The study [5] was made for Shahrekord, Iran city gate station having nominal flow rate of 120000 Nm^3/h. Average values for flow rates were used for each month, where the monthly flow rates varied from 5 to 40 million cubic meters. The inlet pressure varied from 4.9 to 5.5 MPa, where the outlet pressure was assumed to be 1.8 MPa and fixed. Inlet and outlet temperatures were assumed to

be fixed. It was shown that the flow rate of pre-heater is 0.32% of total flow and power recovery was about 0.15-1.18 GWh per month.

Rahman [6] studied a number of natural gas wells and pressure reduction stations. It was shown that the power recovery at wellhead is in the range of 150-500 kW and it is about 200 kW to 5 MW in pressure reduction stations.

2. Mathematical modelling of turbo expander

Turbo expander is designed to adjust the nominal flow rate of the city gate station as the flow rate varies during the year and it is often less than the nominal flow rate. Inlet pressure and temperature are usually constant. Outlet pressure of the city gate station is an important factor and it shouldn't be less than 1.7 MPa. If the turbo expander results an outlet pressure less than 1.7 MPa, the aim of the city gate station is missed. Since flow rate variation will cause the outlet pressure variation, an outlet pressure more than 1.7 MPa is selected. Outlet temperature is controlled through generated power and outlet pressure. The main point is that this temperature should always be greater that the dew point of natural at outlet pressure. The composition of natural gas has to be considered as well.

Table 1. Selected natural gas composition for calculations

Constituent	Mole fraction, x_i	Molecular weight, M_i	Mass fraction, y_i
Methane	0.8900	16.0400	0.8044
Ethane	0.0410	30.0700	0.0695
Propane	0.0120	44.1000	0.0298
Nitrogen	0.0500	28.0100	0.0789
Carbon dioxide	0.0070	44.0100	0.0174

2.1. Design of turbo expander

According to [7] the important parameters in turbo expander design are

$$N_s = \frac{0.076N\sqrt{Q}}{(\Delta h)^{3/4}}, \qquad (1)$$

$$D_s = \frac{2.36D_2(\Delta h)^{1/4}}{\sqrt{Q}}. \qquad (2)$$

Where

N shaft speed, rpm

Q volumetric flow, m^3/s

Δh ideal enthalpy differential, kJ/kg

D_2 blade tip diameter, m

Radial turbo expanders are more sufficient for natural gas application. According to [7] the efficiency of radial turbo expanders as a function of specific speed, N_s is illustrated in Fig. 1. It is evident that the turbine efficiency is not solely a function of specific speed, but using the diagram offers a primary approach in feasibility studies with many unknown factors. Exact values must be calculated in detailed designs afterwards.

One needs to find shaft rotational speed to calculate specific shaft speed. Reference [7] specifies the rotational speed to be a function of estimated shaft power with an efficiency of 0.8 for the turbo expander in Fig. 2. Same reference also presents a diagram that helps to estimate the turbo expander blade tip speed and consequently blade diameter in Fig. 3.

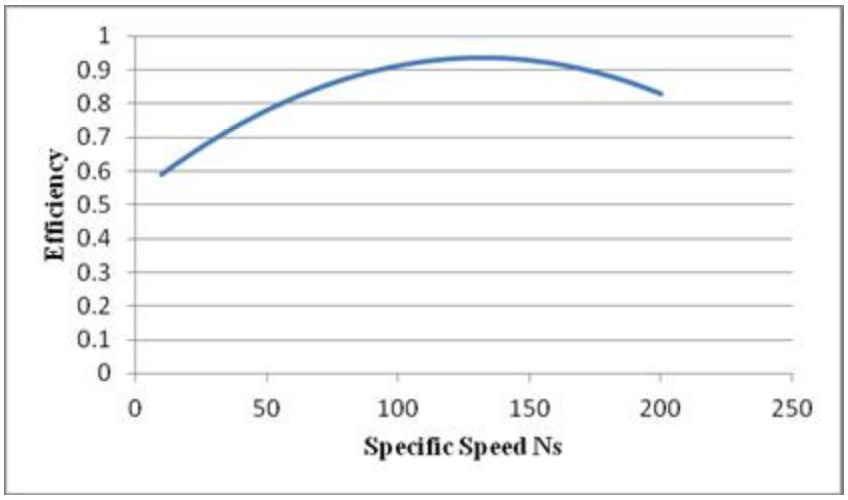

Fig. 1. Radial turbo expanders efficiency as a function of specific speed N_s .

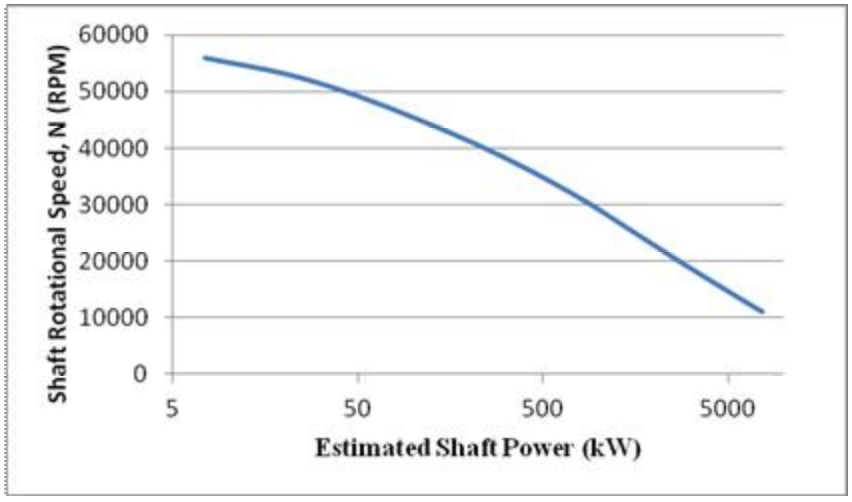

Fig. 2. Shaft rotational speed as a function of estimated shaft power.

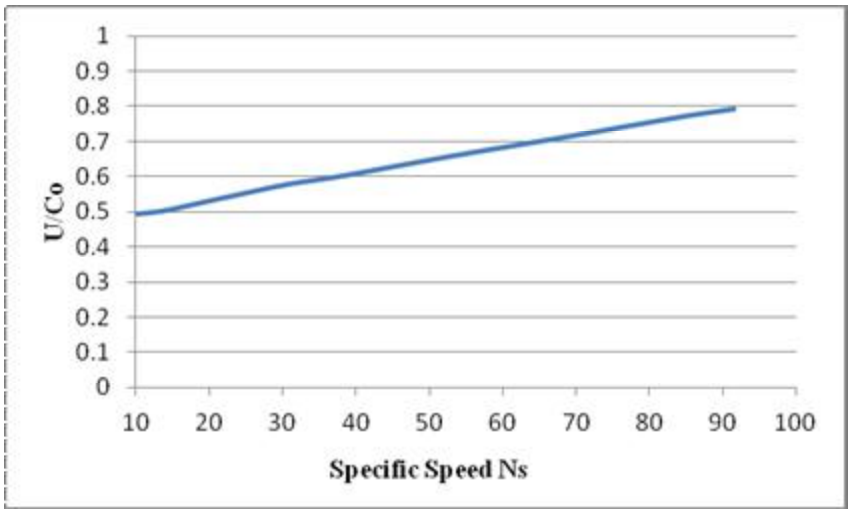

Fig. 3. Blade tip speed to spouting velocity as a function of specific speed.

Spouting velocity is defined in [7] as

$$C_0 = 44.57\sqrt{\Delta h}. \qquad (3)$$

Where

Δh ideal enthalpy differential, kJ/kg

Flow rate variation over the year is an important issue. It may result an outlet pressure not equal to the design outlet pressure. Choosing a reliable safety factor for the outlet pressure, leads to the design outlet pressure equal to 2.75 MPa, while a throttle valve is placed after the turbo expander to give a pressure equal to 1.7 MPa leaving the city gate station. Fig. 4 shows the new station schematically.

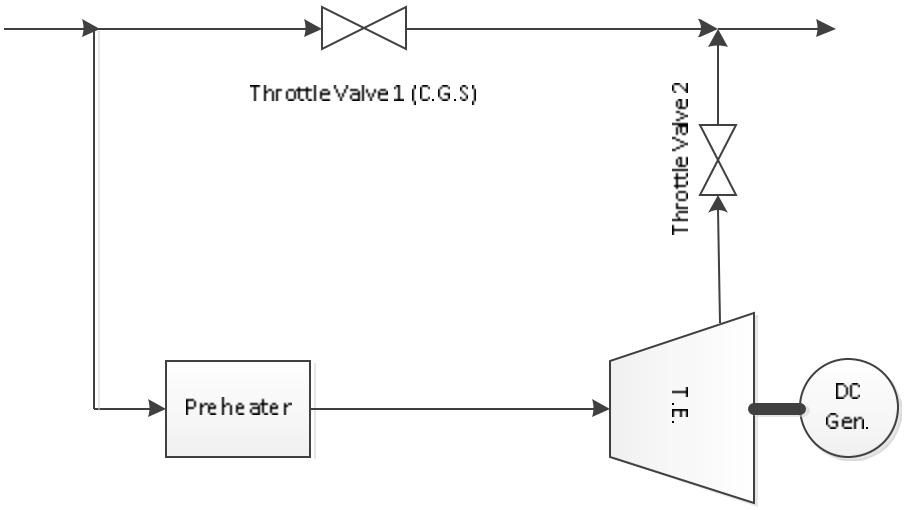

Fig. 4. Schematic form of city gate station with turbo expander.

According to [8] the dew point of natural gas can be predicted by

$$T_{dp} = \frac{5}{9}(36.76P^{0.285} - 32). \qquad (4)$$

Where

P pressure, MPa

For an outlet pressure of 2.75 MPa, the dew point is 10˚C, where a throttle valve is installed after the turbo expander. The dew point temperature of natural gas after the throttle valve is 6.11˚C. Taking advantage of other studies about throttle valve analysis, leads to Ardali and Heybatian [5] who claim that natural gas temperature, drops 18˚C passing through the throttle valve, so the outlet temperature of the turbo expander is expected to be 24.11˚C instead of 10˚C.

Inlet pressure is assumed constant and equal to 5.5 MPa. By making a comparison of [5] with this study, it is found that there will be 44.78˚C temperature drop in the turbo expander so the inlet temperature must be 68.88˚C to ensure the outlet temperature. Ardali and Heybatian [5] also state that the flow rate of pre-heater is 0.32% of the total flow. This study showed that the flow rate of the pre-heater will be 0.2268% of the total flow which is reasonable comparing to [5].

2.2. Off-Design analysis

Fig. 5 shows the daily variation of flow rate during the year. This variation will affect the performance of the turbine and must be accounted. It has to be mentioned, natural gas is treated as an ideal solution and a real gas. It is essential to use an equation of state in order to study the process under off-design conditions. In some equations of state such as Redlich-Kwong, despite their complexity of calculations the results are not too far away from the results obtained by ideal gas assumption.

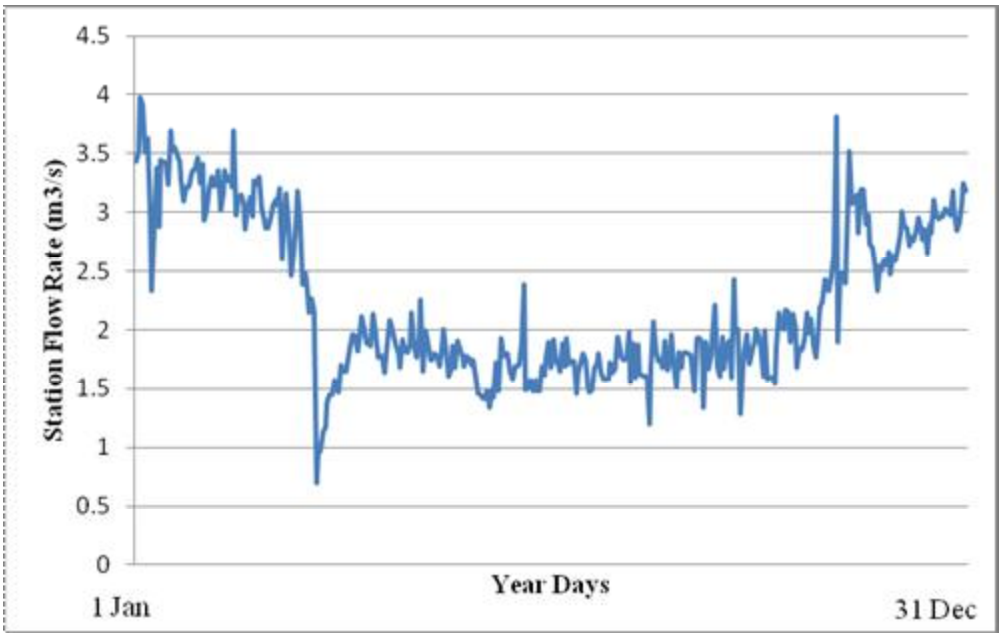

Fig. 5. Variation of gas flow rate during the year.

Because of the flow rate variation, the efficiency of the turbo expander is usually different from the design value. Prediction of efficiency changes is made by using the results of [7]. Fig. 6 shows the ratio of efficiency of the turbo expander to design efficiency as a function of ratio of flow rate to design flow rate.

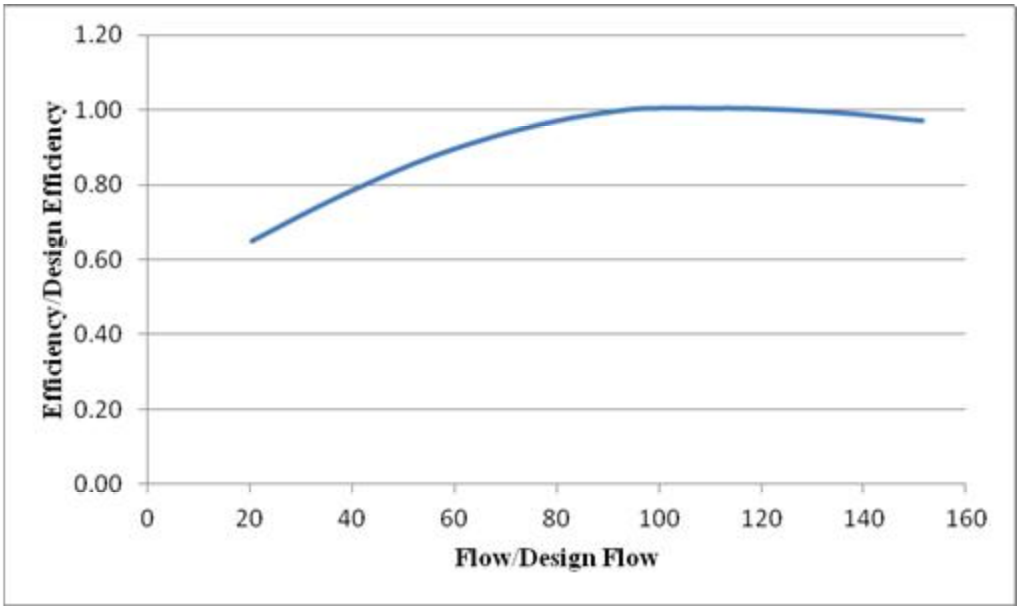

Fig. 6. Efficiency of turbo expander in varying flow rate presented by Atlas Copco.

As mentioned above, outlet pressure differs from the design value as the flow rate is different from design flow. According to [9] the ratio of off-design outlet pressure to design outlet pressure can be calculated by relation

$$\frac{P_{out}}{P_{outDesign}} = \frac{\left(1-\frac{U^2}{\eta.c_p.T_{in}}\right)^{\frac{\gamma-1}{\gamma}}}{\left(1-\frac{U_{Design}^2}{\eta_{Design}.c_p.T_{in}}\right)^{\frac{\gamma-1}{\gamma}}} \quad . \qquad (5)$$

Where

U	tip velocity in off-design conditions, m/s
U_{design}	tip velocity in design conditions, m/s
η	efficiency in off-design conditions
η_{design}	efficiency in design conditions
c_p	specific heat, kJ/(kg K)
T_{in}	inlet temperature, K
γ	c_p/c_v

The whole design and off-design process can be seen in Fig. 7.

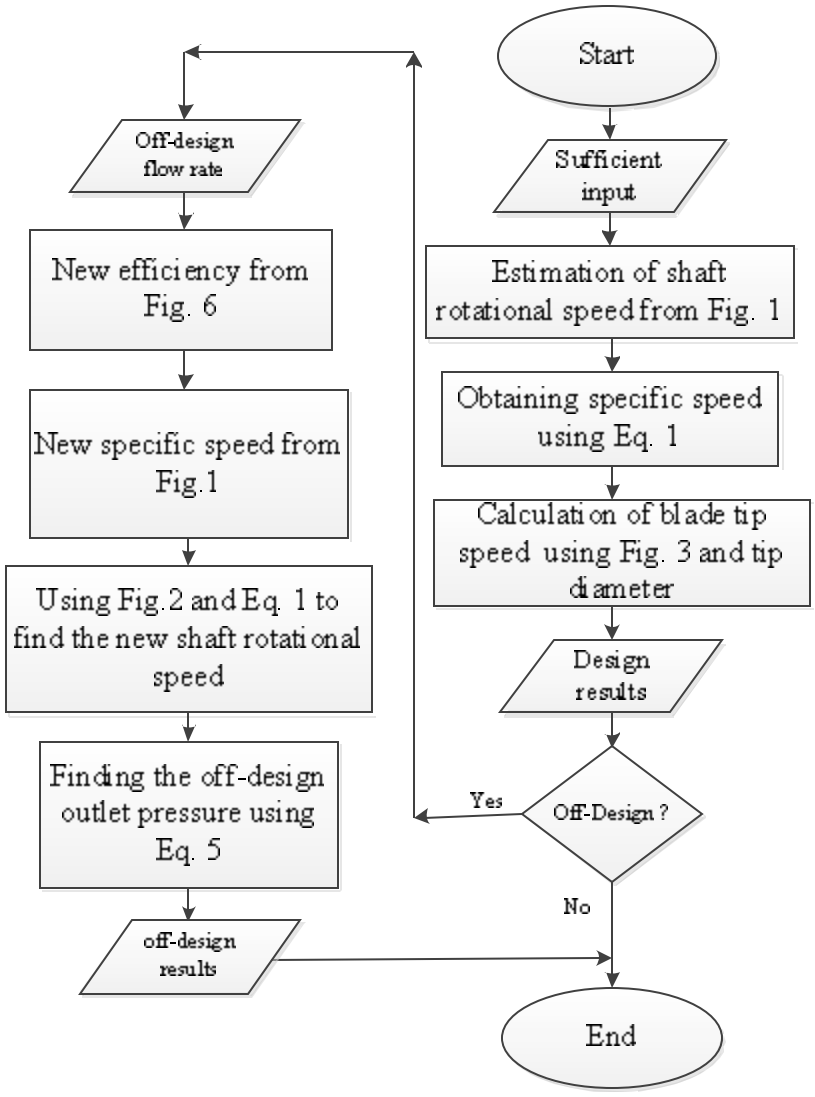

Fig. 7. Design and off-design process.

3. Results and economic analysis

Fig. 8 represents the daily generated power during the year. The energy produced in a year is calculated 1104737 kWh by integration. It is assumed that the generator is DC and invertor produces AC electric to sell. The income due to electric power selling is 46.230 thousand dollars. The capital cost including turbo expander price and installation costs is about 184.56 thousand dollars. Annual costs comprising pre-heater gas burning cost and operation and maintenance costs are estimated 6.8 and 1.8 thousand dollars respectively. Fig. 9 represents the pre-heater gas consumption which equals to 157238 cubic meters of natural gas in the year. Assuming a lifetime of 15 years for the project the IRR[1] equals to 18% according to [10].

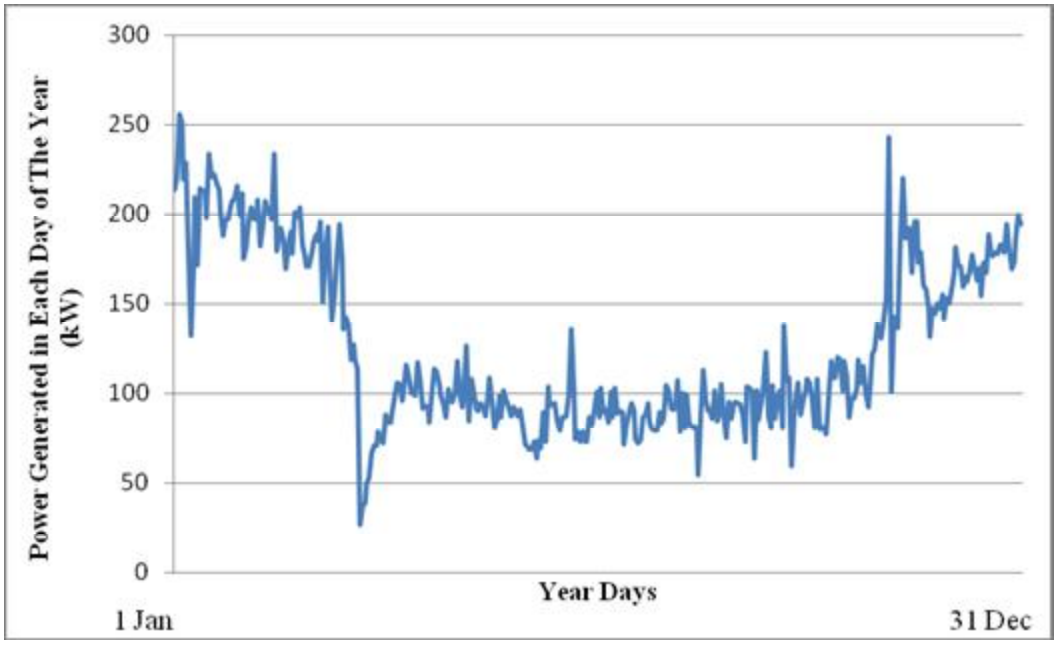

Fig. 8. Generated power in each day of year.

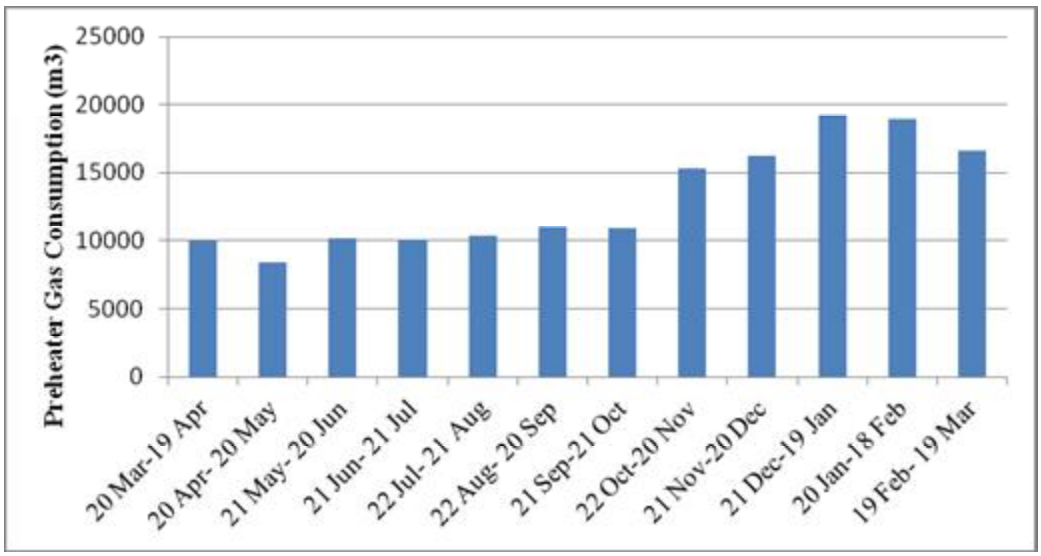

Fig. 9. Monthly pre-heater gas consumption.

[1] Internal rate of return

4. Conclusion

This feasibility study with some simplifying assumptions reveals interesting results about Takestan C.G.S. The variation of flow rate of this station causes a considerable variation in power production. Although the power output is acceptable in Iran winter, with increase in flow rate, the outlet temperature of the turbo expander is much higher than expected, because of the safety factors selected. The pre-heater consumes 157238 cubic meters of natural gas and 1104737 kWh of electrical energy is recovered in the year. The internal rate of return of the project is 18%. The average efficiency of turbo expander is 67.79 % which is less that the design value because of the variation in flow rates. These variations in flow rate are not considered in other studies but the effect is not negligible particularly for economic investigations.

Nomenclature

C_o spouting velocity, m/s
c_p specific heat, kJ/(kg K)
D_2 blade tip diameter, m
D_s specific diameter
Δh ideal enthalpy differential, kJ/kg
N shaft speed, rpm
N_s specific speed
P pressure, MPa
Q volumetric flow, m^3/s
T temperature, °C
U tip velocity, m/s
w specific work, kJ/kg

Greek symbols

η efficiency

Subscripts and superscripts

dp Dew point

References

[1] Rheuban J., Turbo Expanders: Harnessing the Hidden Potential of Our Natural Gas Distribution System. Article. 2009. Available at: <http://jacobrheuban.com/2009/03/09> [accessed 29.4.2011].

[2] Mirandola A., Minca L., Energy Recovery by Expansion of High Pressure Natural Gas. In: Proceedings of the 21st Intersociety Energy Conversion Engineering Conference; 1986 Aug; San Diego, California.

[3] Mirandola A., Macor A., Experimental Analysis of an Energy Recovery Plant by Expansion of Natural Gas. In: Proceedings of the 23rd Intersociety Energy Conversion Engineering Conference; 1988 Aug; Denver, Colorado.

[4] Požívil J., Use of Expansion Turbines in Natural Gas Pressure Reduction Stations. Acta Montanistica Slovaca 2004.

[5] Ardali E.K., Heybatian E., Energy regeneration in natural gas pressure reduction stations by use of turbo expanders; evaluation of available potential in Iran . In: Proceedings of the 24th world gas conference; 2009 Oct; Buenos Aires , Argentina.

[6] Rahman M.M., Power Generation from Pressure Reduction in the Natural Gas Supply chain in Bangladesh. Journal of Mechanical Engineering 2010.

[7] Bloch H., Soares C., Turbo expander and process application.Butterworth-Heine; 2001.

[8] Fattah K.A.A,Evaluation of empirical correlation for natural gas hydrate prediction. Oil and gas businesses. 2004.

[9] Montazerin N., Turbomachines (In Persian). Amirkabir University Publications. 1999. p.88-98.

[10] Kreith F., Engineering economics and project management. In: Kreith F, Goswami Y, editors. The Mechanical Engineering Handbook Series. CRC press. 2004. p. 2121-2180.

[11] Data sheet from Takestan city gate station.

GTL and RME Combustion Analysis in a Transparent CI Engine by means of IR Digital Imaging

Ezio Mancaruso, Luigi Sequino, Bianca Maria Vaglieco

Istituto Motori - CNR, Naples, Italy, e.mancaruso@im.cnr.it

Abstract:

In the present paper, infrared (IR) measurements were performed in order to study the behaviour of biofuels combustion in a transparent Euro 5 diesel engine operating in premixed mode. Commercial diesel fuel (REF) Gas To Liquid (GTL) and Rapeseed Methyl Ester (RME) biofuels have been used. An elongated single cylinder transparent engine equipped with the multi-cylinder head of commercial passenger car and common rail (CR) injection system was used. A sapphire window was set in the bottom of the combustion chamber, and a sapphire ring was placed in the upper part of the cylinder. Measurements were carried out through both accesses by means of high-speed infrared digital imaging system. IR camera was able to detect the emitted light in the wavelength range 1.5-5 μm. In a previous paper UV and visible cameras were used, infrared imaging allowed acquiring larger amount of information than those experiments. In particular the IR camera was used for the characterization of injection and combustion process. Analysing the IR images, it was possible to identify clearly the seven jets of vaporized fuel that react with air in the bowl. During the late combustion phase, the IR image showed a good capability to follow the hot burned gas both in the bowl and above the piston. The IR camera has shown high sensibility permitting to follow carefully the soot oxidation process within the cylinder. The GTL shows an advance of about 2°CA in the evolution of combustion process with respect to the RME. On the contrary a longer chemical activity has been detected for the latter biofuel. Finally, the IR camera was revealed very useful tool to characterize the combustion process for long time allowing high quality of the results. Images of the reactions that happen in the combustion chamber and above the piston head were clearly acquired even if the optical windows were obscured by the soot produced from the previous combustion cycles.

Keywords:

Biofuels, In-cylinder combustion analysis, Infrared digital imaging.

1. Introduction

Nowadays, one of the possible solutions to make cleaner and more efficient the internal combustion engine (ICE) seems to be the use of biofuels. The fast reduction of fossil fuel resources and their contribution to environmental pollution from ICE, and the increasing request for efficient and eco-friendly energy management have led to an increase in interest among researchers on study combustion characteristics of alternative fuels. Their blends in a certain percentage can be used without modification of engine structure. In particular, great attention is paid to the 1st and 2nd generation of biodiesel. The former is obtained from vegetable resources; it is commonly referred to as FAME (Fatty-Acid Methyl Esters). Its performance is quite similar to those of diesel, in particular, its main characteristic is the higher content of O_2 with respect to conventional fuels. On the other hand, moral-social debates are in place because its derivation from edible oil and interferences with the human food chain [1]. The 2nd generation of biodiesel, is produced by the Fischer-Tropsch synthesis process, able to produce liquid fuels from the so-called syngas. It is usually indicated as xTL, where 'x' denotes the specific source feedstock and TL (to Liquid) the conversion to liquid state. The input feedstock can be either renewable Biomass (hence BTL) or fossil fuels, as natural Gas (GTL) or Coal (CTL). Furthermore, the chemical origin of the xTL fuels provides them better combustion characteristic as attitude to autoignition and stability in the

chemical composition than FAME, which is essentially driven by the synthesis process itself and not by the baseline feedstock [2, 3].

Moreover, in the last decades, the development of high performance devices and their application in the research fields has provided new techniques suitable for the monitoring of natural phenomena. In the motorist area, the growing attention on these methods is motivated by the need to achieve a more precise description of the processes occurring in the combustion chamber, in order to implement new optimized control methods assuring more efficient and clean combustion systems. Optical diagnostic strongly benefits from technological innovation; the microscopic and macroscopic analysis of the in-cylinder processes gives the possibility to collect significant information. In particular, the opportunity to inspect the phenomena in the infrared (IR) range makes it possible to investigate an area, outside the visible spectrum, where a lot of reactions take place. Each body with a temperature higher than 0 K emits energy, as an electromagnetic radiation, in the whole spectral range from the ultraviolet (UV) up to the infrared (IR). The visible range goes from 380 to 750 nm, so human eyes can't detect energy emitted at higher or lower wavelength. Infrared cameras can detect radiation with a wavelength longer than 750 nm, the infrared range goes from 750 nm to 1000 μm and it is divided in Near Infrared (0.78 - 3 μm), Mid Infrared (3 - 50 μm) and Far Infrared (50 - 1000 μm) [4]. The use of infrared cameras in a diesel engine with the aim to gather information about its functioning has many benefits; the main challenge in this field is the definition of the most representative flame signals and to derive the meaningful information required to diagnose the state of a flame. Fuel vapour is not easily observed in the visible wavelength range but is well resolved in the infrared region [5]. In the IR range it is also possible to capture the radiation emitted by species of low-temperature reactions prior to running into rapid heat-releasing reactions [6]. Parker et al. monitored soot formation in the near-infrared for a diesel spray, observing that 9.4 μm was an appropriate wavelength for quantitative measurements of soot mass in the spray [7]. Moreover, filtering images from combustion chamber in the IR range allows eliminating the effects due to other substances; it is so possible to study better the stability of combustion [8]. Finally, more information of the energy released are obtained and for a longer time period. However, it is important to consider some limitations and shortfalls of current infrared technologies. In fact, for phenomenon as rapid as combustion process, only little image resolution is available for the high acquisition frequency needed. Moreover, some hot gases, such as oxygen and nitrogen, are mostly transparent in the infrared wavelengths due to their low emissivity. So the temperature measurements will consider the radiation transmitted through these gases rather than the direct radiation emitted by flames, causing difficulties in determination of temperatures [5-8].

This paper deals with the analysis of combustion process in a transparent Euro5 diesel engine operating in premixed mode. The investigation of the phenomena occurring in the combustion chamber is made through IR digital imaging. A single cylinder engine equipped with the head of a Euro5 production engine has been used. A multi injection strategy, consisting of a pilot and a main injection, has been performed with last generation high pressure Common Rail (CR) injection system. IR images have been acquired from two different views: one from the bottom of the cylinder and the other from the side; image luminosity has been computed by using image processing techniques. The aim is to explore the reactions that are not detectable using a visible detector. In particular, the engine, running at 1500 rpm, has been fed with three different fuels: commercial diesel fuel (REF), Gas To Liquid (GTL) and Rapeseed Methyl Ester (RME) biofuels, in order to investigate how fuel properties influence combustion reaction.

2. Experimental apparatus and engine operating condition

A single-cylinder (SC) optical engine equipped with the combustion system architecture and injection system of a four-cylinder, 16 valves, 1.9 liter, Euro5 engine has been used. Details and specifications of the engine and the injection system are reported in Table 1. The elongated single cylinder transparent engine had the stroke and bore of 92 mm and 85 mm, respectively, and the

compression ratio is 16.5:1. The engine was equipped with a Common Rail (CR) injection system managed by a fully opened electronic control unit (ECU). Bosch second-generation CR system injects fuel through a CRI2.2 injector, minisac type, with 7-hole nozzle, hole diameter 0.141 mm.

Table 1. Engine and injection system specifications

Engine type	4-stroke diesel single cylinder
Bore	85 mm
Stroke	92 mm
Swept volume	522 cm^3
Combustion bowl	19.7 cm^3
Vol. compression ratio	16.5:1
Injection system	Common Rail
Injector type	Solenoid driven
Numbers of holes	7
Cone angle of fuel jet axis	148°
Hole diameter	0.141 mm
Rated flow at 100 bar	440cm/30s

An external air compressor was used to supply pressurized intake air in order to obtain the same in-cylinder conditions of the real multi-cylinder engine. The intake air, before reaching the intake manifold, was filtered, dehumidified, and preheated. Moreover, a variable swirl actuator (VSA) system was employed in order to manage the air swirl motion in the intake manifold.

Finally, the presence of a pressure valves in the exhaust pipe permitted the recirculation of the right amount of burned gases through the cooled Exhaust Gas Recirculation system (EGR). A Hall-effect sensor was applied to the injector current line in order to detect the drive injector signal. Moreover, the in-cylinder pressure, in motored and fired conditions, was monitored by a piezoelectric pressure transducer set in the glow plug seat of the engine head. The in-cylinder pressure and the drive injector current were digitalized and recorded at 0.2°Crank Angle (°CA) increments and ensemble-averaged over 150 consecutive combustion cycles.

Commercial diesel engine (REF), first generation biofuel Rapeseed Methyl Ester (RME) and second generation biofuel Gas To Liquid (GTL) have been used. RME is a biofuel from vegetable sources obtained from seeds of rape. In Table 2 their properties have been briefly summarized.

Table 2. Fuel properties

	Density @ 15°C [kg/m3]	Viscosity @ 40°C [mm2/s]	Cetane number	Lower heating value [MJ/kg]
REF	840	3.14	51.8	43.11
GTL	777	2.56	73.9	43.53
RME	883	3.26	52.3	37.35

The engine operating condition analyzed is representative of the new European driving cycle (NEDC). It corresponded to engine speed of 1500 rpm, and low load of 2 bar of break mean effective pressure (BMEP), with exhaust gas recirculation (EGR) of 57%. The high EGR level allows realizing a strong premixed combustion. Both injection and engine parameters for all tested fuels have been reported in Table 3. The injection strategy consisted of two injections per cycle, pilot and main, performed with injection pressure of 615 bar. It can be noted that the Energizing Time (ET) of the main injection is longer for RME fuel. It in fact has a Lower Heating Value smaller than other fuels tested.

Table 3. Injection strategies

Fuel	Rpm	SOI Pilot [°CA]	ET Pilot [µs]	SOI Main [°CA]	ET Main [µs]	Prail [bar]	EGR [%]	VSA [%]
REF	1500	-16	290	-6	545	615	46	66
GTL	1500	-16	290	-6	545	615	46	66
RME	1500	-16	290	-6	587	615	46	66

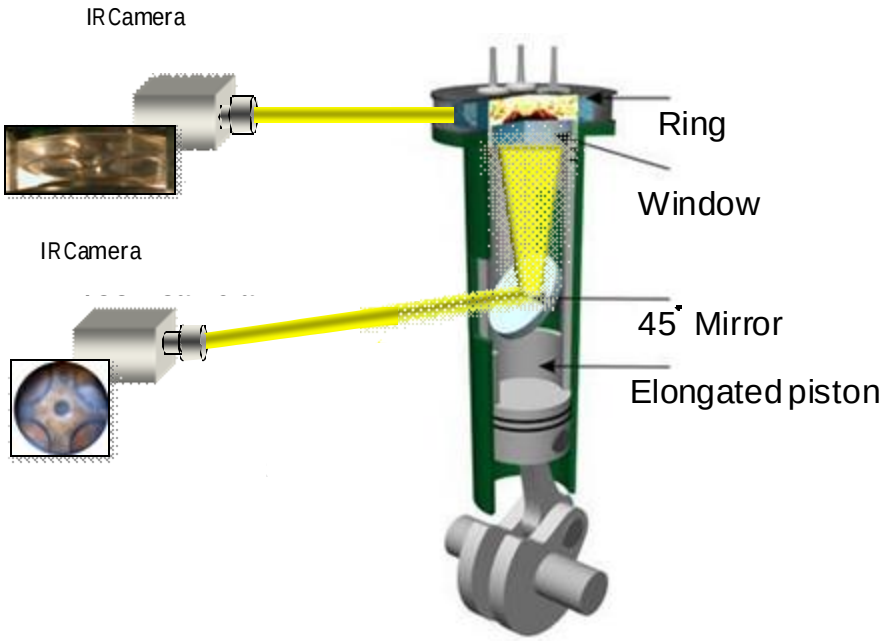

Fig. 1. Optical setup

Figure 1 shows the engine lay-out and optical apparatus. The optical engine utilizes a conventionally extended piston with a piston crown sapphire window. In order to provide a full view of the combustion bowl a flat window was fitted in the piston head and a fixed 45° visible-IR mirror was set inside the extended piston. Moreover, a sapphire ring was placed on the top of the cylinder; it provided a view of the in-cylinder volume above the piston head even if it is influenced by the piston movement. IR imaging was performed using a fast camera (320×256 pixels) able to detect light in the range 1.5-5 µm. The IR camera had a sensor made of Indium Antimonide (InSb). It was equipped with a 70 mm objective, F/1:2.3. The resolution of camera was 2 pixels per mm at 2.25 kHz and 9 pixels per mm at 650 Hz. IR images were acquired at 4°CA step in the same engine cycle. The high sensitivity IR camera did not require a light source for the spray imaging. Images from both cameras were acquired with an exposure time of 111 µs, corresponding to 1° ca at 1500 rpm. The synchronization of the camera with the engine was made by a delay unit connected to the engine shaft encoder.

3. Results and discussion

The engine operating condition reported in table 3 for several pure fuels were widely investigated in previous paper by means of digital imaging in the visible and UV wavelength range [9]. The two injections performed (pilot and main) were well discernible on the drive injector current signals. Moreover, the in-cylinder pressure gave macroscopic information on the combustion evolution of the alternative fuels with respect to the REF. In particular, the start of combustion (SOC) was identified analyzing the rate of heat release trace and it corresponded to the point where the energy released begins to exceed the energy lost due to the fuel evaporating process. The rate of heat release (ROHR) was computed from the ensemble-averaged pressure data using the typical first law and the perfect gas analysis [10]. At the start of main combustion, a fast rate due to the exothermic

reactions of combustion was observed. Two well resolvable peaks were discernible on the ROHR curve for REF fuel. SOC of Pilot and main injections occurred at 8° BTDC and 1° BTDC, respectively [9]. Moreover, a comparison between all tested fuels was made with respect to the curve of in-cylinder pressure, the ROHR and the current signals. It was noted that the in-cylinder combustion peak pressure was around 50 bar for all the fuels; in particular, GTL reached the highest value (51 bar) and in advance with respect to the REF and RME. This is due to its high Cetane Number that allows faster chemical reactions in the combustion chamber. On the contrary the lower peak of pressure was detected for RME (49.5 bar). The pilot injection ignited at 8° BTDC for all fuels, after this phase, the curves of heat release raised. In particular, it was found that GTL shows the same start of pilot combustion of REF but it had the highest peak rate of heat release peak due to the pilot combustion. While the RME fuel showed later SOC and the lowest pilot combustion peak. These features influenced the ignition delay time of the subsequent main injection and its combustion evolution. Regarding the main combustion, the GTL fuel had the fastest ROHR behaviour; on the contrary, the RME fuel had the lowest and retarded peak this is ascribed to its smaller heating value. Also its combustion duration is longer, because the injected fuel mass is bigger.

In this paper, in order to focus the analysis on the behaviour of biofuels in the IR range, a set of images of combustion from the bottom view, has been reported in Fig. 4. They are for GTL and RME at several crank angle degrees after top dead centre (°ATDC). In the images, the white areas denote maximum energy, as indicated in the colour bar. It can be noted that the IR camera detects clearly the seven jets of vaporized fuel before the starting of main injection. The flames due to the pilot injection were recorded at 4° BTDC. However, as reported in the previous paper [11], the IR images show better the seven burning jet than a visible CCD camera. The latter detected only some bright spots near the nozzle tip. Moreover, in the IR images it seems that the vaporized jets are not strongly affected by the in-cylinder air motion. It is so possible to identify the non homogeneous distribution of reactants in the bowl, a fundamental factor that influences the evolution of the process. At TDC, the seven atomized jets of main injection are burning and the energy released by the flames is detected by the IR camera. At 8° ca ATDC, the combustion flame moved towards the bowl wall and consumed the fuel along the jet direction. At 20° ca ATDC, the IR emission is still intense, while the visible light is very weak [11]. Another peculiarity is that IR camera can follow the reactions that take place during the late combustion. In particular, in the IR wavelength residual flame and hot burned gas distributed in the bowl and above the piston head emitted energy and impressed the IR detector. The combustion activity was recorded up to 60° ca ATDC. This can help to better understand the motion of the hot gas and air into the cylinder and their evolution during the soot reduction. The energy released by the hot burned gases was detected up to 40° and 60° ca ATDC for RME and GTL, respectively where the heat release is already finished [10].

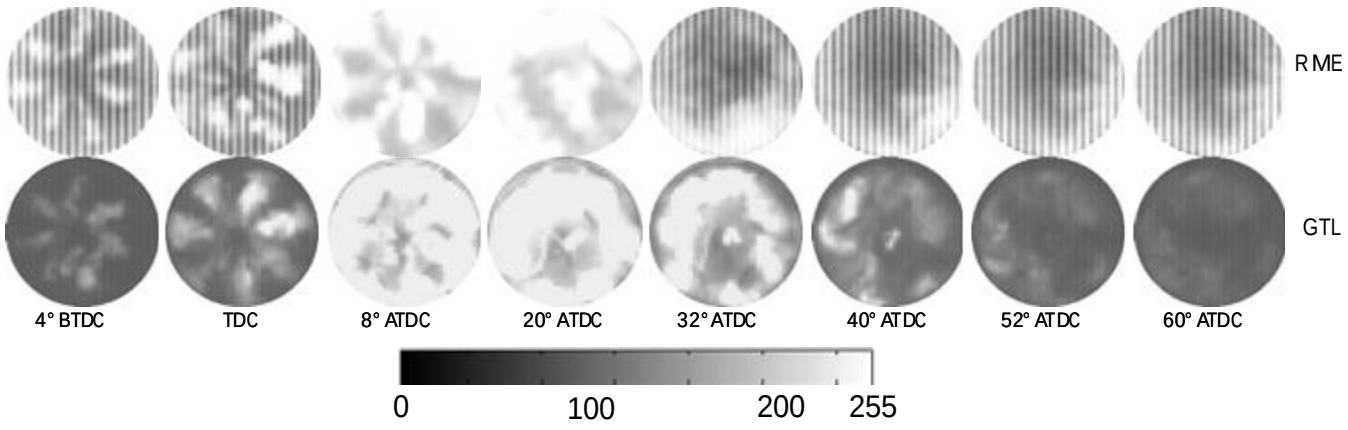

Fig. 4. Combustion images from the bottom for RME and GTL fuels.

Moreover, it is interesting to analyze the results detected through the sapphire ring from the lateral view. The images reported in Figure 5 show the combustion reactions taking place outside the bowl, on the top of the piston surface. As the expansion stroke goes on, the piston goes down and a higher percentage of the ring window can be investigated. It must be remembered that it is not possible to have images across the TDC because the piston blocks the visibility. In Fig. 5, images of combustion from the side have been reported for REF, GTL and RME. Images refer to the late combustion from 18° ca ATDC. A cloud of hot burned gases lies above the piston head, it can be explained considering that the oxygen stored in the crevice, when the piston was at TDC, now is mixing with the hot gas and continues to oxidize the unburned species [12] in the cylinder volume during the expansion stroke.

Making a comparison between the three fuels, it can be noted that an intense cloud of burned gases on the top of the piston is present for all. In particular, at 18°ATDC the images are not able to put in evidence relevant differences between the fuels. After, the gases exiting from the bowl, they are clearly discernible in the images at 30°ATDC, until they fill the entire available volume as the piston goes down (42°ATDC).

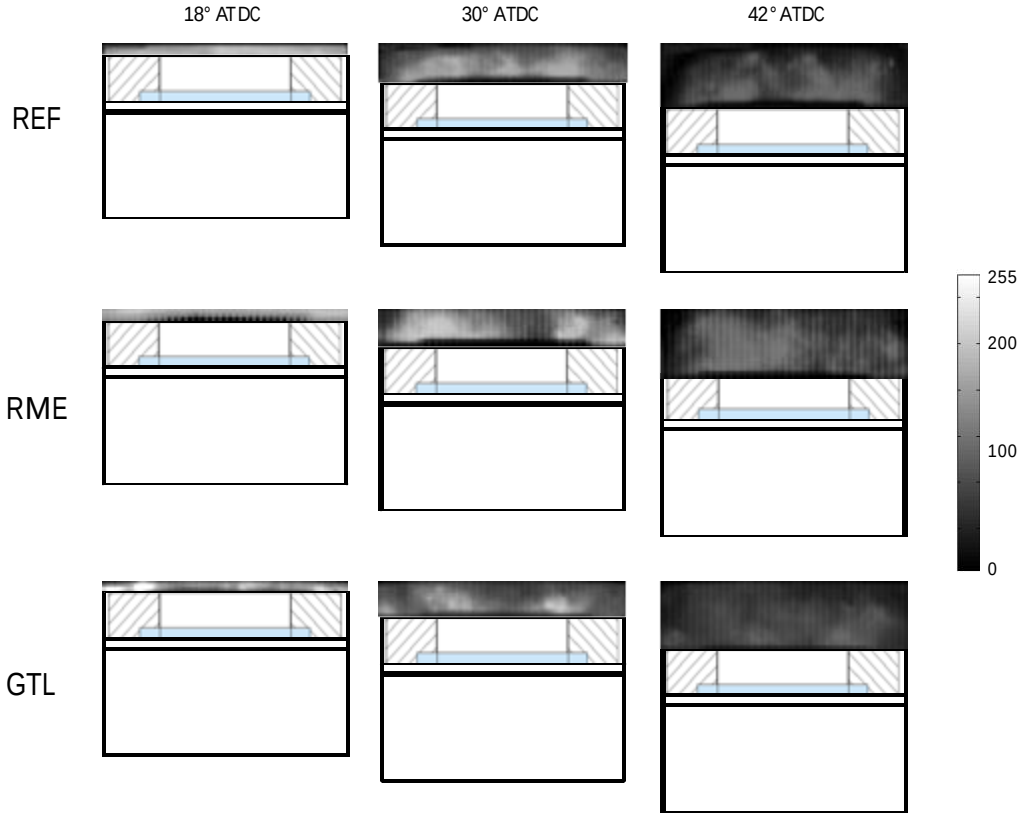

Fig. 5. Combustion images from the side for REF, GTL and RME fuels.

In order to evaluate the variation of IR intensity during the evolution of the combustion process, images have been post-processed, in particular, the integral luminosity of the images at each crank angle has been calculated. The methodology applied for the computation has been faithfully described in [11]. In Fig. 6, the IR luminosities detected through the piston window (bottom view) have been reported for all the investigated fuels. It is the integrated value of the pixel intensity reported in figure 4 for each crank angle. In order to make a comparison with the physical and chemical processes that happens in the engine during the combustion we must to take in mind that the IR images were recorded with 4° ca step. For this reason, it is not possible to detect exactly the start of combustion of the several fuels. However the IR evolution can characterize the energy released during the first phase of combustion. From the analysis of the intensities emitted through the bottom window, it can be noted that the IR luminous emissions start to increase from 12° ca

BTDC for GTL, before the SOC of pilot injection detected from ROHR curve. It is the earliest detected IR signal. However, we must consider that the next frame analysed with this procedure was at 8° ca BTDC, when the SOC of pilot was detected. Probably, the IR camera is also able to catch the energy during the evaporation and mixing formation phases. Moreover, this is due to the cold combustion that occurs before the luminous combustion, it releases a small quantity of energy that doesn't influence the ROHR computation. Then, the intensities increase slowly up to TDC. After this crank angle the main combustion occurs into the bowl and produces strong light emission in a broad wavelength range. The peak of the curves is at about 9° ca ATDC, it occurs 5°CA after the peak of the ROHR curve. This happens because, only after the energy release has reached its maximum rate, that is the peak of ROHR curve, in the cylinder can be detected the maximum energy. In fact, the IR camera acquires the energy emitted in the cylinder during a certain period, the exposure time, as integral of the instantaneous values. At 9°ATDC, the highest contribution to the total release of energy has already been given. Finally, it can be noted that during the late combustion, after 60°ATDC, the IR emission hasn't reached the zero value yet, sign that chemical reactions are still in place. In the IR range it has been possible to investigate the combustion for a total duration longer than 90° ca ATDC.

Form the analysis of two biofuels tested some interesting consideration can be made. For GTL, first IR emission anticipates the REF, due to the high value of its Cetane Number. Moreover, it keeps higher values for the entire rising phase, until it reaches a peak value quite similar to that of REF. Finally, the reduction of the IR emission is similar to the values of REF. Finally, the analysis of the RME behavior showed a delay in the activation of this fuel with respect to others. In fact, even if it reaches its peak of IR emission almost at the same crank angle of REF, its intensity is very low with respect to other fuels. This may be due to a delay in the chemical reaction of fuel in the bowl, because of a slower mix with the air due to its higher density and low cetane number. On the other hand, the first generation biofuel has shown a delay also in the reduction of the IR emission. Its values are higher than REF and GTL up to 30° ca ATDC. This means that the chemical activity is still in progress during the late combustion phase. This is also due to the longer main injection time.

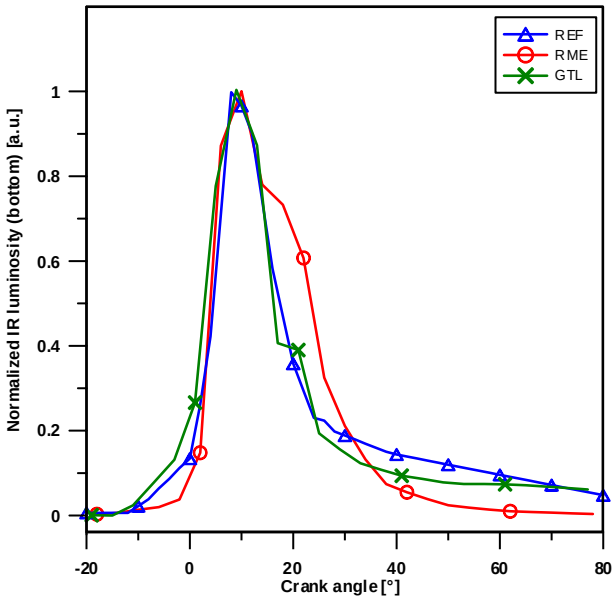

Fig. 6. Normalized IR integrated luminosity measured from the bottom view for REF, RME, and GTL fuels.

In Figure 7, the normalized integrated IR luminosity from the side view has been reported for all investigated fuels. Images represent the luminous emissions above the piston head during the expansion strokes. In the first phase (before 40°ATDC), it is due to the flames that burns outside the

bowl. In fact, the air stored in the crevice, when the piston was at TDC, now moves toward the center of the cylinder, when the piston goes down, mixes with the remaining vaporised hydrocarbons and ignites [12]. In the second phase (after 40°ATDC), images regards the hot gases that moves on the head of the piston while it goes down.

From the computation of the IR emission it can be noted, as explained above, that no data are available across the TDC due to the presence of the piston that covers the area of interest. Moreover, at about 10°ATDC it is possible to see the first luminous emission above the piston head. Despite of the first instants of the expansion stroke, where the view available is very thin and the detection of the emission is highly subjected by errors, the REF, GTL and RME have the same emission intensity at 20°ATDC. After this crank angle, the behavior is very different; it rises with various slopes, REF is the one that shows first high intensity, followed by RME and GTL. This configuration is evident also after the peak value, when the emission drops. For this reason, the position of the maximum values are at 30°, 40°, and 55° ca ATDC for REF, RME, and GTL, respectively. Moreover, the REF peak unless some uncertainty remains constant up to 50° ca ATDC. These behaviors can be explained considering also the curves of IR emission from the bottom. For example, REF emission decreases and shows a knee at 30°ATDC, corresponding to the peak from the side view, this means that the combustion is moving toward the volume which has become available on the top of piston. Moreover, the fuel has not burned completely yet, so it needs about 20°CA for the combustion. Similarly, RME and GTL reach their maximum intensities from the side, when the emission from the bottom view extinguishes. In particular, it is retarded with respect to REF and burns in the bowl volume for a longer period.

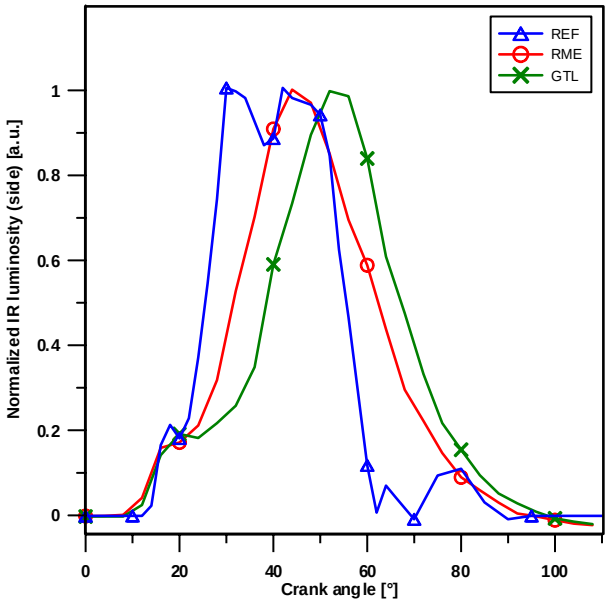

Fig. 7. Normalized IR integrated luminosity from the side view for REF, RME, and GTL fuels.

4. Summary and conclusions

In the present paper IR digital imaging has been carried out to study the combustion process of alternative diesel fuels. Two biofuels, GTL and RME, have been tested, and compared with commercial diesel, REF. They fuelled a transparent single cylinder diesel engine equipped with the latest generation Euro 5 engine head. Images have been recorded via two optical accesses: one in the head of the piston and another along the cylinder line. The integrated values of energy released in the IR wavelength range have been calculated as function of the crank angle and analysed. Infrared imaging has allowed acquiring a large amount of information. It allows distinguishing

chemical and/or physical activity of the injection and combustion process in advance or with more detail with respect to typical visible images.

GTL emission starts before the energy released by the other fuels this is ascribed to the high value of its Cetane number. This means that the GTL has less time to premix it with the air in the bowl and thus realize more soot during the combustion. This is also in good agreement with the results of high PM emission and in-cylinder OH rates detected in previous papers. Moreover, the energy released on the top of the piston is the slowest than the other fuels, while it decreases quickly as the REF fuel. This is in good agreement with the fastest rate both for the formation and the oxidation of the soot. Probably, the GTL completes its combustion in the bowl and the unburned fuel and burned hot gases moves out the bowl slowly producing retarded IR energy detection. The GTL combustion behaviour entirely offset the benefit of fuel lack of aromatics.

RME showed the most retarded start of combustion due to its LHV. Very low energy during the pilot combustion with respect to the other fuels has been detected. Moreover, the longest time for the autoignition, due to its lower Cetane Number, and the high oxygen content improved the RME mixing process providing a low soot combustion process. RME had the largest IR emission due to the highest energizing time of the main injection. Chemical activity is in progress up to 30° ATDC. Finally, the analysis of reactions occurring outside the piston bowl, shown RME flames have a propensity to migrate toward the volume which has become available on the top of the piston during the expansion stroke slower than REF and faster than GTL.

The introduction of infrared technologies in the study of combustion engine functioning has revealed a good way to investigate the influence of alternative fuel in the combustion process especially when the visible imaging is not able to catch useful information. In particular, during the late combustion phase, the IR image showed a good capability to follow the hot burned gases both in the bowl and above the piston. Finally, the IR digital imaging of combustion process has revealed a tool with high potential

Acknowledgments

The authors thank Mr. Carlo Rossi and Mr. Bruno Sgammato for their precious help.

Nomenclature

ATDC After Top Dead Centre
BTDC Before Top Dead Centre
ca Crank Angle
CCD Charge Coupled Device
CR Common Rail
DI Direct Injection
ECU Electronic Control Unit
EGR Exhaust Gas Recirculation
ET Energizing Timing
IR Infrared
ROHR Rate Of Heat Release
SOC Start Of Combustion
SOI Start Of Injection
TDC Top Dead Centre
UV Ultraviolet
VIS Visible
VSA Variable Swirl Actuator

References

[1] Assessment of barriers to the trade of biofuels between the European Union and Latin America Prepared for BioTop project BioTop Deliverable 5.3 Project Nr 1412 Date April 2010 <http://www.btgworld.com/uploads/documents/Biofuel%20Trade%20Barriers%20BTG%20April%202010.pdf>

[2] McCormick, R. L., Alleman T. L., Fischer-Tropsch Diesel Fuels – Properties and Exhaust Emissions: A Literature Review. SAE Paper, 2003, 2003-01-0763.

[3] Peterson, C. L., Vegetable oil as a diesel fuel: Status and research priorities. Transactions of the ASAE 1986, 29(5), 1413-1422.

[4] Manca, D., Rovaglio, M., Infrared thermographic image processing for the operation and control of heterogeneous combustion chambers. Combustion and Flame, 2002 130, pp. 277-297.

[5] Founti, M., Kolaitis, D., Zannis, G., Kastner, O., Trimis, D., Experimental determination of fuel evaporation rates using IR-Thermography. QIRT 2002, 2002, Collegium Ragusinum, Dubrovnik, Croatia, September 24-27.

[6] Jansons, M., Lin, S., Fang, T., Rhee, K. T., Visualization of Preflame and Combustion Reactions in Engine Cylinders. SAE Paper, 2000, 2000-01-1800.

[7] Parker, T. E., Morency, J. R., Foutter, R. R., Rawlins, W. T., Infrared Measurements of Soot Formation in Diesel Sprays. Combustion and Flame, 1996, 107(3), 271–290.

[8] Chimenti, M., Di Natali, C., Mariotti, G., Paganini, E., Pieri, G., Salvetti, O., An IR image processing approach for characterising combustion instability. Infrared Physics & Technology, 2004, 46, 41–47.

[9] Mancaruso, E., Vaglieco, B. M., Premixed combustion of GTL and RME fuels in a single cylinder research engine. Applied Energy, 2012, 91, 385–394.

[10] Heywood, J. B., Internal Combustion Engine Fundamentals. McGraw-Hill, NewYork, 1988.

[11] Mancaruso, E., Sequino, L., Vaglieco, B. M., IR Imaging of Premixed Combustion in a Transparent Euro5 Diesel Engine. SAE Paper, 2011, 2011-24-0043.

[12] Benajesa, J., Novella, R., García, A., Arthozoula, S., The role of in-cylinder gas density and oxygen concentration on late spray mixing and soot oxidation processes. Energy, 2011, 36(3), 1599-1611.

Some aspects concerning fluid flow and turbulence modeling in 4-valve engines

Zoran Jovanovic[a], ZoranMasonicic [b], Miroljub Tomic[c]

[a]*Institute "Vinca", Head of Dept. for IC Engines, Univ. of Belgrade, zoranj@vin.bg.ac.rs*
[b]*Institute "Vinca", Dept. for IC Engines, Univ. of Belgrade, masonicicz@vin.bg.ac.rs*
[c] *Faculty of Mech. Engineering, Head of Dept. for IC Engines, Univ. of Belgrade, mtomic@mas.bg.ac.rs*

Abstract

In this paper some results concerning the structure and evolution of fluid flow pattern during induction and compression in 4-valve engines with tilted valves were presented. Results were obtained by dint of multidimensional modeling of non-reactive flows in arbitrary geometry with moving boundaries. During induction fluid flow pattern was characterized with organized tumble motion followed by small but clearly legible deterioration in the vicinity of BDC. During compression the fluid flow pattern is entirely three-dimensional and fully controlled by vortex motion located in the central part of the chamber. In order to annihilate negative effects of tumble deterioration and to enhance swirling motion one of the intake valves was deactivated. Some positive and negative effects of such attempt were elucidated. The effect of turbulence model variation was tackled as well. Namely, some results obtained with eddy-viscosity model i.e. standard k-ε model were compared with results obtained with k-ξ-f model of turbulence in domain of 4-valve engine in-cylinder flow. Some interesting results emerged rendering impetus for further quest in the near future. In the case of combustion all differences ensuing from turbulence model variation, encountered in the case of non-reactive flow were annihilated entirely. Namely the interplay between fluid flow pattern and flame propagation is invariant as regards both turbulence models applied.

Keywords:

Computational Fluid Dynamics (CFD), Automotive Flows, Turbulence Modelling

1. Introduction

It is known for a long time that various types of organized flows in combustion chamber of IC engines are of predominant importance for combustion particularly with regards to flame front shape and its propagation. Some results related to the isolated or synergic effect of squish and swirl on flame propagation in various combustion chamber layouts are already analysed and published [1, 2] but results concerning the isolated or combined effect of the third type of organized flow i.e. tumble are relatively less presented and sometimes ambiguous [3, 4]. For instance some authors [5] studied the development of swirl and tumble in five different intake valve configurations and found that when both inlet valves are opened no defined tumble flow structure was created rendering quick vortices dissipation before BDC. In spite of the fact that tumble flow is inherent to multi-valve engines some authors have demonstrated that some two-valve engines exhibit characteristics similar to tumble flow [6, 7]. In addition, the fairly similar fluid flow patterns in the vicinity of BDC in various combustion chamber geometries yield entirely different fluid flow patterns, spatial distribution of kinetic energy of turbulence and integral length scales of turbulence in the vicinity of TDC [8]. In such occasions the significance of organized tumble flow is fairly relative. Some theoretical and experimental results show that tumble is of prime importance for specific power and fuel economy increase in modern engines with multi-valve systems. The beneficial effects of tumble on CO, CH and NOx were also demonstrated. From the theory of turbulence is known that vortex filament subjected to compression reduces its length and promotes rotation around its axis yielding the movement on the larger scale ("spin-up" effect). It can be presumed that tumble

pursues the same rule i.e. the destruction of formed and expressive tumble during compression stroke generates the higher turbulence intensity and larger integral length scale of turbulence in the vicinity of TDC contributing to the flame kernel formation period reduction and faster flame propagation thereafter. The aforementioned logic imposes the conclusion that the most beneficial fluid flow pattern in the vicinity of BDC is well shaped high intensity tumble. Some additional objectives in this paper were qualitative and quantitative characterization of fluid flow pattern during induction and compression in a particular 4-valve engine, the analysis of the valve/port assembly from the point of compliance with presumed ideal fluid flow pattern, the effect of port deactivation and the clout of turbulence model variation on fluid flow and turbulence parameters.

2. Model and computational method

The analysis of this type is inherent to multidimensional numerical modelling of non-reactive fluid flow and therefore it is quite logical to apply such a technique particularly due to fact that it is the only technique that encompasses the valve/port geometry layout in an explicit manner. In lieu of the fact that, in its essence, multidimensional models require initial and boundary conditions only their applications is fairly complicated and imply some assumptions and simplifications [9]. The full 3D conservation integral form of unsteady equations governing turbulent motion of non-reactive mixture of ideal gas is solved on fine computational grid with moving boundaries (piston and valves) in physical domain (66.000-682.000 cells) by dint of two different codes. The first one is KIVA 3V release 2 code running on UNIX Ultra SUN II computer [10, 11, 12, 13]. This code is used in the first part of this paper in order to scrutinize clouts of intake port geometry variations on in-cylinder fluid flow. The second code used is well known AVL FIRE 2009.1 code [14] used to investigate the effect of turbulence model variations on fluid flow and flame propagation. In both cases the numerical solution method is based on a fully conservative finite volume approach (CGR method). All dependent variables such as momentum, pressure, density, turbulence kinetic energy, dissipation rate, and passive scalar are evaluated at the cell centre. A second-order midpoint rule is used for integral approximation and a second order linear approximation for any value at the cell-face. A diffusion term is incorporated into the surface integral source after employment of the special interpolation practice. The convection is solved by a variety of differencing schemes (upwind or donor cell, interpolated donor cell, quasi second order differencing, central differencing, MINMOD and SMART). The rate of change is differenced by using implicit schemes i.e. Euler implicit scheme and three time level implicit scheme of second order accuracy. The overall solution procedure is iterative and is based on the Semi-Implicit Method for Pressure-Linked Equations algorithm (SIMPLE). For the solution of a linear system of equations, a conjugate gradient type of solver (CGS) is used. Two different models of turbulence were used. The first one is nearly forty years old k-ε model based on Boussinesq's assumption which is certainly the most widely used model for engineering computations. On the contrary to some other models, such as Reynolds-stress closure model [15], its implementation is numerically robust due to simplicity of the model and at the same provides an acceptable level of accuracy for particular applications. The second one is relatively recent k-ξ-f model of turbulence i.e. eddy-viscosity model based on Durbin's elliptic relaxation concept [16, 17]. This model solves a transport equation for the velocity scale ratio ξ instead of imaginary turbulent normal stress component. In addition, the pertinent hybrid boundary conditions were applied. The combustion model implemented is well known Eddy Breakup model. This model implies the assumption that reactants are in the same eddies and are clearly separated from eddies that contain hot combustion products. Due to the fact that chemical reactions have time scale very short in comparison to the characteristics of turbulent transport processes it can be assumed that the rate of combustion is determined by the rate of intermixing on a molecular scale of the eddies reactants and those containing hot products. The major feature of this model is the fact that it does not call for predictions of fluctuations of reacting species.

3. Results and discussion

The analysis of fluid flow pattern during induction and compression was based on a fairly complicated geometry layout presented in figs.1.and2. Obviously, combustion chamber is constrained with dual intake and exhaust valves. In spite of the fact that it is not of crucial importance the inclination of intake and exhaust port is 20^0 and 22^0 respectively. The basic block data sheet consists of bore/stroke ratio = 9.2/8.5 cm, inlet valve head diameter = 3.65 cm, exhaust valve diameter = 3.25 cm, squish gap = 0.115 cm, engine speed RPM = 2500 min^{-1} and mixture quality λ=1. It should be stated that maximum valve lift is Li=0.962 cm while the other geometrical data (relative location, valve shape etc.) could be seen in fig.1 and 2. In the case with simultaneous valve opening the commencement of intake valves opening was set at 15^0 BTDC and their closure at 195^0 ATDC.

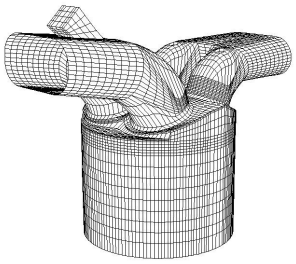

Fig.1: Perspective view of the combustion chamber geometry layout with 4-valves (upper view)

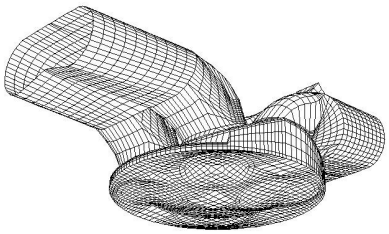

Fig.2: Perspective view of the combustion chamber geometry layout with 4-valves (bottom view)

The results presented in figures 3-27 are obtained with KIVA 3V release 2 code and k-ε model of turbulence, while the rest are obtained with the AVL FIRE 2009.1 code and two different turbulence models (k-ε and k-ξ-f). The evolution of fluid flow pattern and turbulence was pursued in five cut-planes (in x-z plane, y=2.1 cm, passing through one intake and one exhaust valve, in symmetry x-z plane, y=0, in y-z plane, x=-2.1 cm, passing through both intake valves, in y-z plane, x=2.1 cm, passing through both exhaust valves and in x-y plane at z=8.6 cm). The evolution of fluid flow pattern, represented as vectors, in vertical x-z plane (y=2.1 cm or y=-2.1cm for simultaneous valve opening) is shown in fig. 3, 4 and 5. As can be seen in fig.3 high velocity intake jet flows over the valve, strikes upon the piston crown, curls and commences to form an elliptically-shaped vortex around y-axis in counter-clockwise direction, provided that it is stipulated as such, on the left side of the valve. A small tumble-like vortex motion is created by the intake jet in clockwise direction to the right of the valve (fig.3).

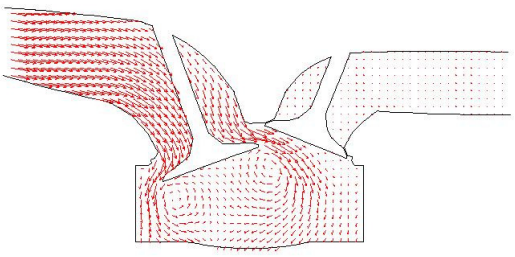

Fig.3: Fluid flow pattern in x-z plane, y=2.1cm, at 60^0 ATDC, k-ε

At 60^0 ATDC these two vortices are of the same intensity (fig.3) indicating the zone of coinciding flow followed by separation region just beneath the intake valve face. These two vortices are part of thoroidalring vortex that can be verified in fig. 6.

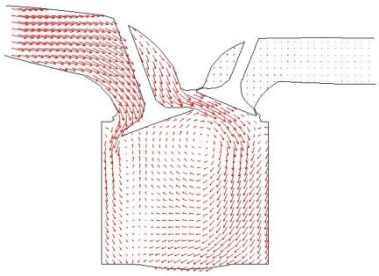

Fig.4: Fluid flow pattern in x-z plane, y=2.1 cm, at 120^0 ATDC, k-ε

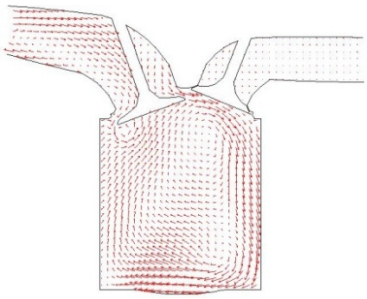

Fig.5: Fluid flow pattern in x-z plane, y=2.1 cm, at 170^0 ATDC, k-ε

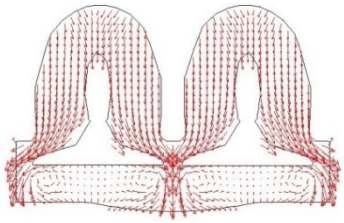

Fig.6: Fluid flow pattern in y-z plane, x=-2.1cm, at 30^0 ATDC, k-ε

Namely, the centre of rotation is equally distributed around the perimeter beneath the valve face. The increase of tumble motion intensity at maximum valve lift and further movement of piston downward exerts the attenuation of the vortex flow on the left side of intake valve. Obviously, the vortex flow is squeezed out and its shape becomes elongated (along z-axis). It's interesting to note that the centre of rotation of tumble motion is in the same position. The formed tumble flow around y-axis reduces the activity of that vortex to the zone in the vicinity of cylinder wall particularly from the moment when valve movement changes its direction (fig.4). In the vicinity of BDC the direction of vortex flow is changed due to tumble motion and its role reduced entirely to the close proximity of intake valve face (fig.5). In addition, the centre of rotation of tumble motion is slowly displaced to the right side of cylinder wall Such a movement is followed by new vortex formation in the corner located adjacent to the bottom right side indicating the subtle deterioration of general tumble motion. Non-uniform distribution of tumble intensity along y-axis and two symmetric vortices in x-y plane in the vicinity of cylinder wall are responsible for the deterioration of tumble flow near BDC. Namely, as can be seen in fig.7 the tumble intensity in vertical plane for y=0 is more expressive than tumble intensity for y=± 2.1 cm. No deterioration of tumble motion in vertical plane for y=0 is encountered. In addition, larger velocities are encountered in the central part of the chamber ensuing partly from jet penetration from the flanks. This activity is enhanced by vortices in

x-y plane which prevent the tumble motion in vertical plane (y=± 2.1) to reach the cylinder wall. The net result is the deflection of fluid flow in y-z plane (x=2.1 cm) along z-axis and formation of symmetric vortices adjacent to piston crown (fig.8).

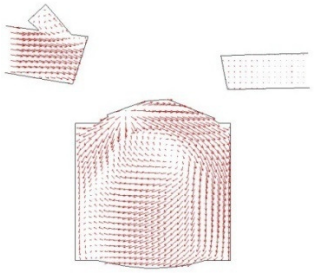

Fig.7: Fluid flow pattern in x-z plane, y=0 cm, at 150^0 ATDC, k-ε

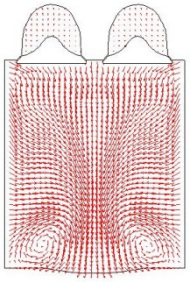

Fig.8: Fluid flow pattern in y-z plane, x=2.1 cm, at 175^0 ATDC, k-ε

The formation of tumble motion is observed as well through evolution of fluid flow pattern in x-y plane, as shown in fig. 9 and 10.

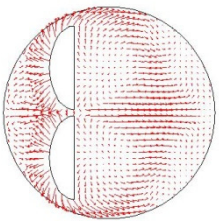

Fig.9: Fluid flow pattern in x-y plane, z=8.6 cm, at 60^0 ATDC, k-ε

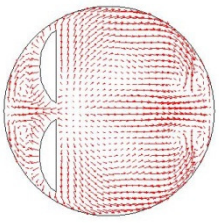

Fig.10: Fluid flow pattern in x-y plane, z=8.6 cm, at 175^0 ATDC, k-ε

A symmetric flow structure is created about the plane of symmetry of the cylinder head, y=0, even though no conditions of symmetry were applied to the flow. It should be noted that variable visible segments of valves are due to valve movement. As can be seen in fig. 9 the synergic action of the flows over the two intake valves generates a jet travelling across the cylinder away from intake valves, formed approximately in the midway from the cylinder centre to the right wall. Two counter-rotating vortices are observed on the very left side of the cylinder. Regions of low velocity magnitude are identifiable on the very right of the cylinder indicating large velocity component in z-direction. Annihilating effect of the combination of the flow is evident in the upper part of the

symmetry plane (fig.7). As can be seen in fig.10 two counter rotating vortices are clearly legible on the very right side of the cylinder as well. The entire region is engulfed with counter rotating vortex motion in the vicinity of BDC. Namely the curling of the flow is obvious in the central part as well indicating the ingress of the fluid flow from the flank followed by deterioration of tumble motion. During compression, the quick decay of vortex motion in the zone beneath intake valves and in the vicinity of piston crown is encountered. Further movement of piston upwards yields the restitution of organized vortex motion with its centre of rotation around x=0. The fairly expressive w-component of the velocity in the zone of intake valves is observed rendering 1D fluid flow thereafter. In x-z plane, z=8.61 cm, on the very beginning of compression the intensive flank flows

exerts detention of strong coinciding flow along x-axis, y=0, and changes its direction to intake valves.

Fig.11: Fluid flow pattern in x-y plane, z=8.6 cm, at 270^0 ATDC, k-ε

Fig.12: Fluid flow pattern in x-y plane, z=8.6 cm, at 345^0 ATDC, k-ε

High intensity coinciding flow in x-y plane is fairly similar to the fluid flow pattern in x-y plane during induction but in opposite direction (fig. 11 and 12)

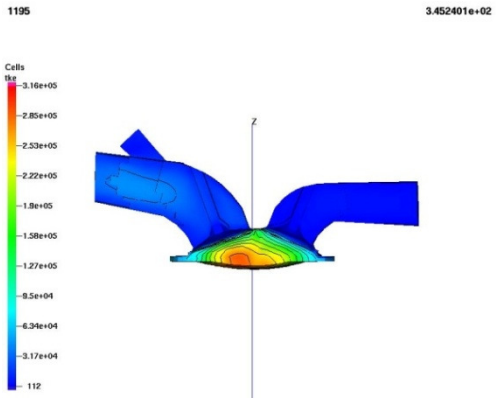

Fig.13 Spatial distr. of kinetic energy of turbulence in x-z plane, y=-2.1 cm, at 345^0 ATDC, k-ε

Non-uniformity of fluid flow pattern along y-axis is followed by non-uniform spatial distribution of kinetic energy of turbulence along y-axis. Namely, in x-z plane, y=-2.1 cm, the zone with relatively high kinetic energy of turbulence is spread out through the entire region (fig.13) while in symmetry plane, y=0, the zone with high kinetic energy of turbulence is, due to strong coinciding flow (u-component dominant flow) squeezed to the zone between cylinder wall and intake valves (fig.14).

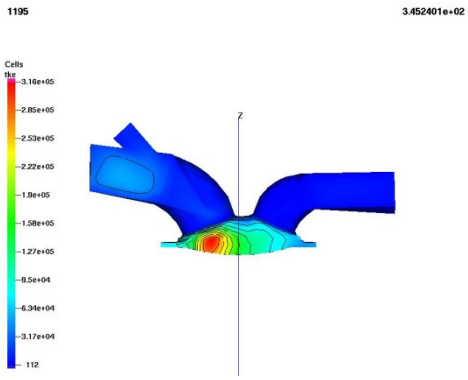

Fig.14: Spatial distribution of kinetic energy of turbulence in x-z plane, y=0, at 345^0 ATDC

Such a non-uniformity along y-axis yields characteristic and fairly inconvenient "bean-like" shape of spatial distribution of kinetic energy of turbulence in x-y plane, as can be seen in fig.15.

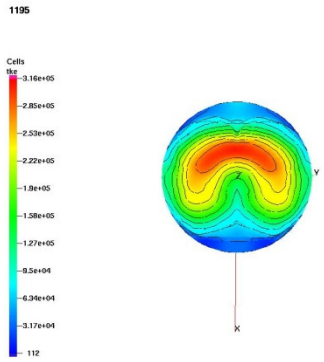

Fig.15: Spatial distribution of kinetic energy of turbulence in x-y plane, z=8.6 cm, at 345^0 ATDC

In order to prevent strong coinciding flow along x-axis yielding inconvenient spatial distribution of kinetic energy of turbulence in the vicinity of TDC port deactivation was included in analysis as well. The rationale for such a step is the presumption of fairly convenient mutual interaction between tumble and swirl, not observed in the case with simultaneous valve openings that could contribute to the better spatial distribution of kinetic energy of turbulence in the vicinity of TDC.

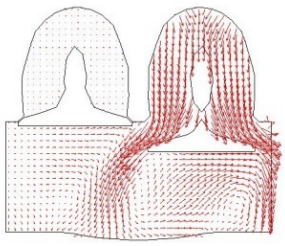

Fig.16: Fluid flow pattern in y-z plane, x=-2.1 cm, at 60^0 ATDC, port deactivation, k-ε

As can be seen in fig.16 port deactivation means that one of the intake valves is kept closed and as a consequence the fluid flow pattern is entirely asymmetric. The evolution of the fluid flow in the cut-plane passing through one active and one exhaust valve is shown in fig.17 and 18.

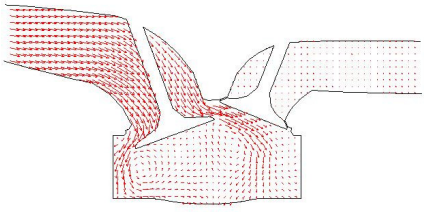

Fig.17: Fluid flow pattern in x-z plane, y=2.1 cm, at 60^0 ATDC, port deactivation, k-ε

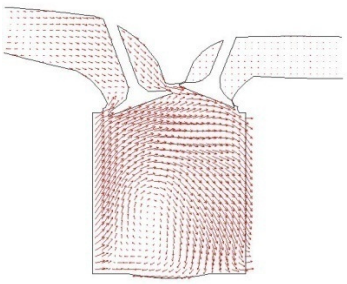

Fig.18: Fluid flow pattern in x-z plane, y=2.1 cm, at 170^0 ATDC, port deactivation, k-ε

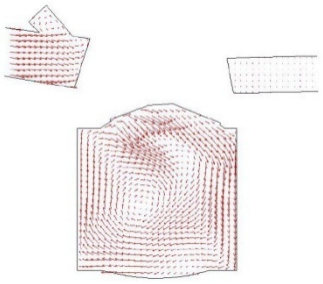

Fig.19: Fluid flow pattern in x-z plane, y=0, at 120^0 ATDC, port deactivation, k-ε

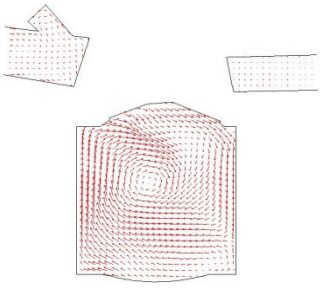

Fig.20: Fluid flow pattern in x-z plane, y=0, at 170^0 ATDC, port deactivation, k-ε

At the very beginning of induction the fluid flow pattern is fairly similar to the previous case (fig.17). Namely, two counter rotating vortices around y-axis are observed as well. On the contrary to the case with both intake valves opened there is no constraint imposed by fluid flow through another intake valve and therefore no squeezing out of vortex motion in the intake valve zone is encountered. The majority of the fluid flow is directed astray and promotes vortex motions around y-axis in a set of parallel x-z planes (fig. 18 and 19). The flank flows from the zone with active intake valve promotes the formation of two concentric vortex flows around y-axis in symmetry plane, y=0 (fig.19). The intensity of the inner vortex prevails and its axis of rotation gradually moves to the central part of the chamber (fig.20) and persists there up to the end of compression stroke (fig.21).

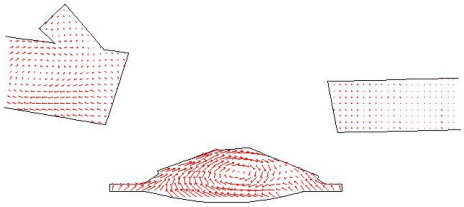

Fig.21: Fluid flow pattern in x-z plane, y=0, at 345^0 ATDC, port deactivation, k-ε

The evolution of the fluid flow pattern in x-z cut plane passing through inactive intake valve is shown in fig.22 and 23.

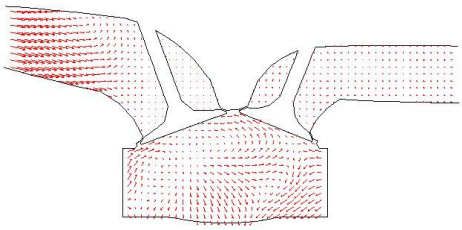

Fig.22: Fluid flow pattern in x-z plane, y=-2.1 cm, at 60^0 ATDC, port deactivation, k-ε

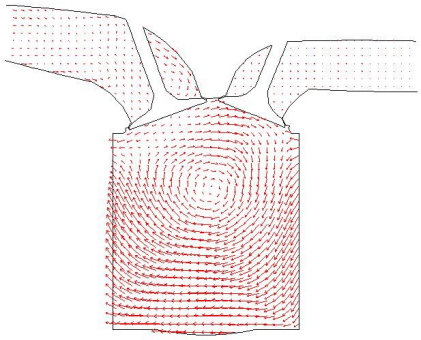

Fig.23: Fluid flow pattern in x-z plane, y=-2.1 cm, at 170^0 ATDC, port deactivation, k-ε

Large soothing zones in fig.22 indicate strong v-component velocities. In the vicinity of BDC formed vortex motion around y-axis, similar to that in symmetry plane, y=0, is observed as well (fig.23).

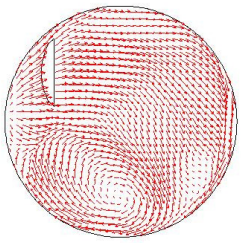

Fig.24: Fluid flow pattern in x-y plane, z=8.6 cm, at 170^0 ATDC, port deactivation, k-ε

It's interesting to note that the entire zone of inactive intake valve is engulfed with large-scale vortex motion. In addition to the vortex motion around y-axis, strong vortex motion around z-axis, in the vicinity of BDC, is encountered as well (fig.24) being transformed, due to its increased intensity, into formed swirling flow in the vicinity of TDC thereafter (fig.25).

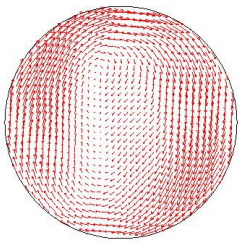

Fig.25: Fluid flow pattern in x-y plane, z=8.6 cm, at 345^0 ATDC, port deactivation k-ε

The spatial distribution of kinetic energy of turbulence replicates entirely the fluid flow pattern and is shown in fig.26 and 27.

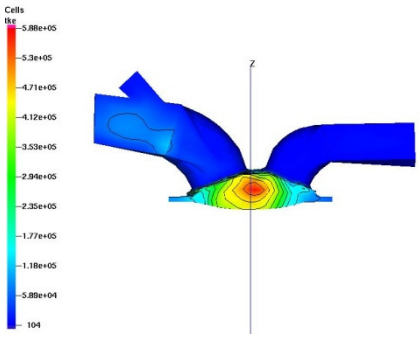

Fig.26: Spatial distribution of kinetic energy of turbulence in x-z plane, y=0, at 345^0 ATDC, port deactivation, k-ε

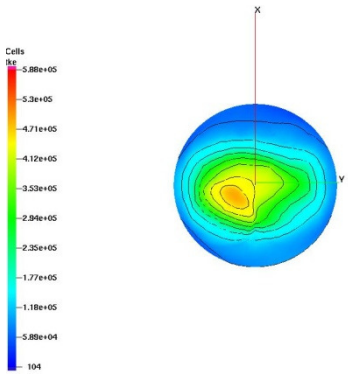

Fig.27: Spatial distribution of kinetic energy of turbulence in x-y plane, z=8.6 cm, at 345^0 ATDC, port deactivation, k-ε

As can be seen in fig.26 and 27 the spatial distribution of kinetic energy of turbulence is more convenient than in the case with simultaneous intake valve opening. Namely, regularly shaped zone of high kinetic energy of turbulence is located in the central part of the chamber and occupies the entire region along z-axis between piston crown and cylinder head. The effects of turbulence model variation on the evolution of fluid flow pattern and spatial distribution of kinetic energy of turbulence in 4.-valve engine were presented in figs.28-39 below. Namely, figs. 28, 31, 34 and 37 are related to standard k-ε model of turbulence while figs. 29, 32, 35 and 38 are related to k-ξ-f model of turbulence. Due to symmetry in x-y plane results for both model of turbulence were presented in the same figure (figs. 30, 33, 36 and 39). In order to alleviate comparisons of fluid flow patterns particularly in the case of subtle differences colours were employed as well.

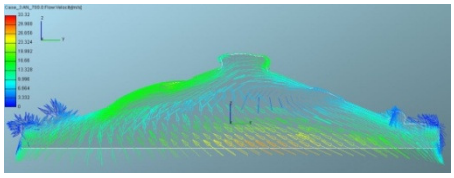

Fig.28: Fluid flow pattern in x-z plane, y=const.at 340 deg. ATDC, k-ε

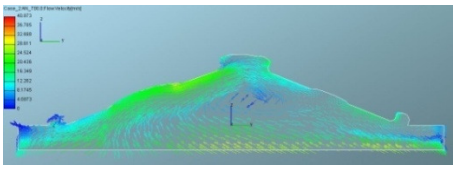

Fig.29: Fluid flow pattern in x-z plane, y=const.at 340 deg. ATDC, k-ξ-f

During induction and large portion of compression stroke (up to 270 deg. ATDC) no legible differences as regards the evolution of fluid flow pattern and spatial distribution of kinetic energy of

turbulence were observed and therefore not presented due to economy of the paper. The significant differences are commencing in the vicinity of TDC. Namely, the fluid flow pattern and less intensive colours in figs. 29, 32, 30 (right) and 33(right) than in figs. 28, 31, 30(left) and 33(left) indicate less expressive vortex flow and generally smaller velocities in the case of k-ξ-f model of turbulence yielding somehow the detention of vortex displacement to the exhaust valve zone thereafter. Larger velocities in the case of k-ε model of turbulence are encountered in x-y plane as well (figs. 30 and 33, left).

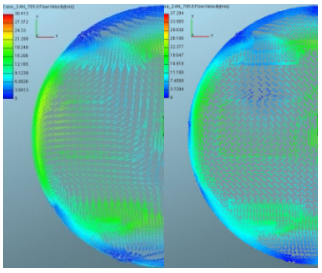

Fig.30: Fluid flow pattern in x-y plane, z=const.at 345 deg. ATDC, k-ε (left) and k-ξ-f(right)

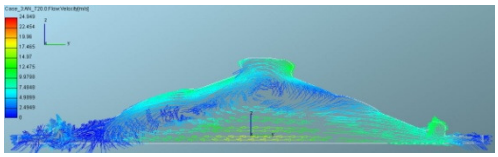

Fig.31: Fluid flow pattern in x-z plane, y=const.at 360 deg. ATDC, k-ε

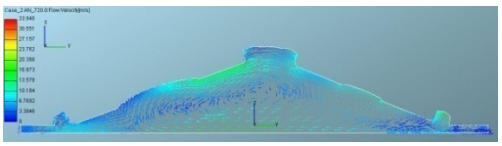

Fig.32: Fluid flow pattern in x-z plane, y=const. at 360 deg. ATDC, k-ξ-f

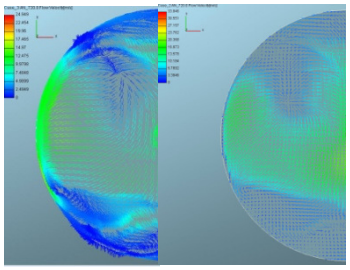

Fig.33: Fluid flow pattern in x-y plane, z=const.at 360 deg. ATDC, k-ε (left) and k-ξ-f(right)

Differences in fluid flow patterns are pursued in a straightforward fashion by certain differences in turbulence intensity and spatial distribution of kinetic energy of turbulence in all planes. It can be seen that in the case of k-ε model of turbulence the maximum kinetic energy of turbulence is located in the central part of the chamber (figs. 34 and 37) while in the case of k-ξ-f model of turbulence the maximum kinetic energy of turbulence is shifted to the intake valve zone (figs. 35 and 38). In addition, in the case of k-ε, high values of kinetic energy of turbulence prevail and engulf nearly the entire chamber (figs. 36 and 39, left) while in the case of k-ξ-f these zones are obviously smaller and akin to characteristic bean-like form (figs. 36 and particularly 39, right). Such behaviour could largely affect all other in-cylinder processes that incur such as mixing, combustion and etc. In general k-ε model of turbulence generates higher values of kinetic energy of turbulence over the broader part of the chamber. Namely, k-ε over predicts its value.

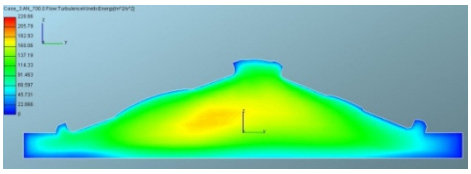

Fig.34: Spatial distribution of kinetic energy of turbulence in x-z plane, y=const. at 340 deg. ATDC, k-ε

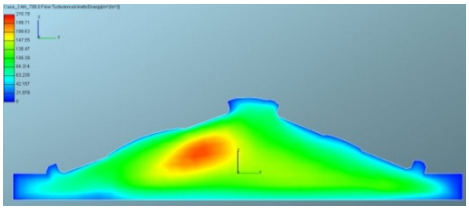

Fig.35: Spatial distribution of kinetic energy of turbulence in x-z plane, y=const. at 340 deg. ATDC, k-ξ-f

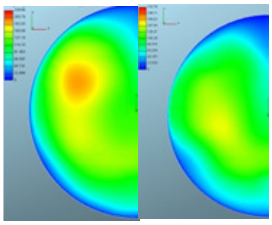

Fig.36: Spatial distribution of kinetic energy of turbulence in x-y plane, z=const. at 340 deg. ATDC, k-ε (left) and k-ξ-f(right)

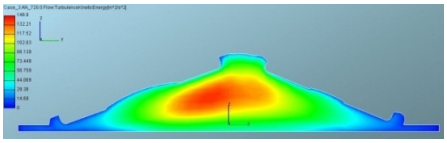

Fig.37: Spatial distribution of kinetic energy of turbulence in x-z plane, y=const. at 360 deg. ATDC, k-ε

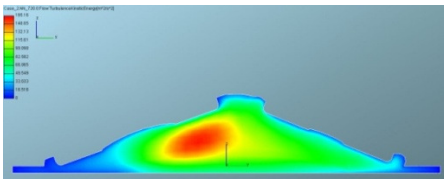

Fig.38: Spatial distribution of kinetic energy of turbulence in x-z plane, y=const. at 360 deg. ATDC, k-ξ-f

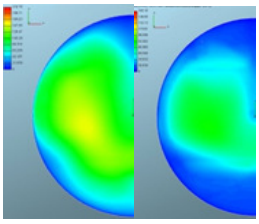

Fig.39: Spatial distribution of kinetic energy of turbulence in x-y plane, z=const. at 360 deg. ATDC, k-ε (left) and k-ξ-f(right)

The fairly interesting results were obtained in the case of combustion that was tackled as well. Namely, combustion was modelled in an eclectic, worldwide theoretically and experimentally

validated way [9]. In the case of combustion all the subtleties as regards fluid flow pattern and spatial distribution of kinetic energy of turbulence due to turbulence model alteration, observed in figs. 28-39, were annihilated entirely. The fluid flow pattern and flame propagation (represented as iso-contours of temperatures) in various cut planes, for two different models of turbulence (k-ε and k-ξ-f) were presented in figs. 40-47, below.

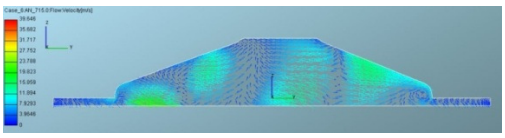

Fig.40: Fluid flow pattern in x-z plane, y=const. (0.0) at 355 deg. ATDC, k-ε

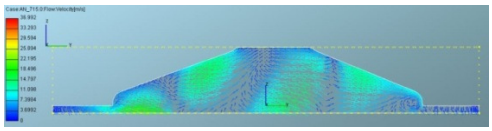

Fig.41: Fluid flow pattern in x-z plane, y=const. (0.0) at 355 deg. ATDC, k-ξ-f

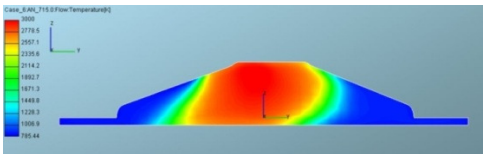

Fig.42: Spatial distribution of temperature in x-z plane, y=const. (0.0) at 355 deg. ATDC, k-ε

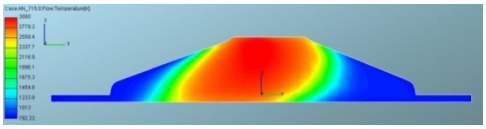

Fig.43: Spatial distribution of temperature kinetic in x-z plane, y=const. (0.0) at 355 deg. ATDC, k-ξ-f

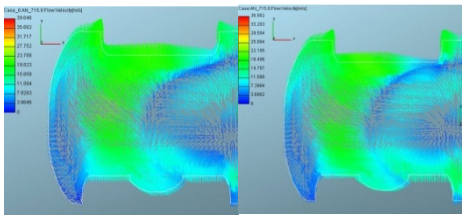

Fig.44: Fluid flow pattern in x-y plane, z=const. (mid-height of the wedge chamber) at 355 deg. ATDC, k-ε (left) and k-ξ-f (right)

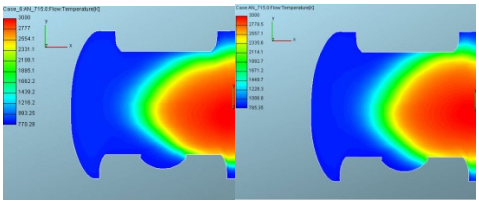

Fig.45: Spatial distribution of temperature in x-y plane, z=const. (mid-height of the wedge chamber) at 355 deg. ATDC, k-ε (left) and k-ξ-f (right)

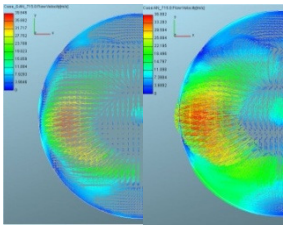

Fig.46: Fluid flow pattern in x-y plane, z=const. (squish zone) at 355 deg. ATDC, k-ε (left) and k-ξ-f (right)

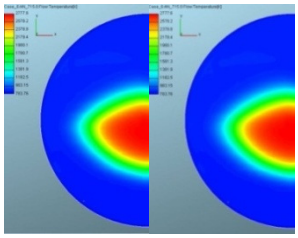

Fig.47: Spatial distribution of temperature in x-y plane, z=const. (squish zone) at 355 deg. ATDC, k-ε (left) and k-ξ-f (right)

It can be seen, in figs. 40, 41, 44 and 46 that, in the case of combustion, no clear difference in fluid flow pattern is observed. Namely, the well-known "flame dominated fluid flow pattern" is encountered characterized with higher velocities in front of the flame front and relaminarization behind the flame front (figs. 40, 41, 44 and 46). This is legible in all cut planes considered. In comparison with corresponding fluid flow pattern in no combustion case (figs. 31, 32 and 33) clear differences are indicated. The main reason for the relaminarization of the fluid flow behind the flame front lies in the fact that flame propagation through un-burnt mixture, entire of itself, accelerates the hot gas in front of the flame front. In the case of shear the production of turbulence increases with the effect of flame acceleration thereafter. In the compressed zone in front of the flame front the divergence of the mean velocity is negative yielding the generation of turbulence as well. In addition the sign and the magnitude of the density gradient within the flame affect the diffusion of turbulence. Referring to the energy conservation equation one can find the maximum enthalpy in the zone of minimal density, i.e. behind the flame front so these higher temperatures cause the intensive increase of viscosity with the consequential increase of Re_t-number, the increase of viscous dissipation of turbulence and shifting of the velocity fluctuations to the low frequency part of spectrum. In the heat release zone the dilatation of turbulence reduces the turbulent kinetic energy yielding fairly legible soothing or attenuation (relaminarization) of the fluid flow. It can be seen, in figs. 42, 43, 45 and 47, that in a particular combustion chamber geometry layout, flame propagation as regards its velocity and its flame front shape is entirely invariant vis-à-vis alteration of k-εmodel of turbulence to k-ξ-f model of turbulence.

4. Conclusions

The fluid flow pattern during induction and compression in the particular combustion chamber geometry of 4-valve engine is extremely complex and entirely three-dimensional. In the case with two valves opened tumble motion during induction is clearly legible and followed by gradual deterioration in the vicinity of BDC due to non-uniform distribution along y-axis. During compression strong vortex flow around y-axis and fairly expressive coinciding flow along x-axis in reverse direction is encountered contributing to the inconvenient spatial distribution of kinetic energy of turbulence in the vicinity of TDC. Some benefits concerning generation of swirling flow and better spatial distribution of kinetic energy of turbulence in the vicinity of TDC were gained with port deactivation. The modelling of turbulence strongly affects the evolution of fluid flow pattern and spatial distribution of kinetic energy of turbulence in 4-valve engines. In general k-ε model of turbulence generates higher values of kinetic energy of turbulence over the broader part of

the chamber than corresponding k-ξ-f model of turbulence. In the case of combustion all differences ensuing from turbulence model variation, encountered in the case of non-reactive fluid flow were annihilated entirely. This is verified elsewhere [18] particularly when Reynolds stress closure is excluded. This occurs in the case of so called "flame dominated fluid flow", where the situation before combustion has slight effect on the flame propagation ahead. This is only one of three possible cases of macro flows that can be encountered in IC engines. In the case of other two types of macro flows i.e. "squish dominated" and "coincident" flows respectively, the situation before combustion has a major effect on flame propagation [2]. Namely, in the case of squish dominated flow the radial component is responsible for flame propagation while in the case of coincident flow there is a balance between squish (macro flows) and turbulence intensity generated by the flame.

5. References

[1] J. Danneman, K. Pielhop, M. Klaas, W. Schroeder(2010) „Cycle resolved multi planar flow measurements in a four valve combustion engine", Exp.Fluids, Research article, DOI 10.1007/s00348-010-0963-4

[2] Z. Jovanovic, S. Petrovic "The mutual interaction between squish and swirl in IC Engines", (1997) Mobility and Vehicle Mechanics 23, 3, 72-86

[3] K. Lee, C. Bae, K. Kang "The effects of tumble and swirl flows on flame propagation in a four-valve S.I.engine", Applied Thermal Engineering 27 (2007) 2122-2130

[4] G.J.Micklow, W. D. Gong "Intake and in cylinder flow field modeling of a four valve diesel engine" Proc.IMechE(2007) vol. 221, Journal of Automobile Engineering, 1425-1440

[5] B. Khaligi "Intake generated swirl and tumble motion in a 4.-valve engine with various intake configurations" SAE Paper 900059

[6] Z.Jovanovic, S. Petrovic, M. Tomic "The effect of combustion chamber geometry layout on combustion and emission" (2008) Thermal Science vol.12, No.1, pp. 7-24

[7] Z. Jovanovic, Z.Masonicic, M. Tomic „The vice-verse movement of the reverse tumble centre of rotation in a particular combustion chamber", MTM Machines Technologies Materials, Year II, issue 6-7, (2008) ISSN 1313-0226l, pp. 17-20

[8] Z. Masonicic, Z. Jovanovic "The effect of combustion chamber geometry layout variations onto fluid flow pattern", International Automotive Conference with Exhibition, SCIENCE AND MOTOR VEHICLES, NMV0774, Belgrade, 2007, ISBN 978-86-80941-31-8

[9] Z.Jovanovic "The role of tensor calculus in numerical modeling of combustion in IC engines" Computer Simulation in Fluid Flow, Heat and Mass Transfer and Combustion in Reciprocating Engines, Hemisphere Publishers (1989) 457-542, ISBN 0-89116-392-1

[10] A. A. Amsden, KIVAII: Acomp. prog. for reactive flows with sprays,LA-11560-MS,1989

[11] A. A. Amsden, KIVA3V, Rel.2 Improvements to KIVA3V, LA-UR-99-915, 1999

[12] A. A. Amsden, SALE3D: A simplified ALE computer program for calculating 3D fluid flows, NUREG-CR-2185, 1982, 11560-MS, 1989

[13] D. J. Torres, M. F. Trujillo, KIVA-4: An unstructured ALE code for compressible gas flow with sprays, Journal of Computational Physics, 219 (2006), pp.943-975

[14] CFD Solver, AVL FIRE 2009.1

[15] C.G. Speciale, S. Sarkar, T. B. Gatski „Modelling the pressure strain correlation of turbulence – an invariant dynamical system approach", pp.1-51, ICASE Report No. 90-5, 1990

[16] K.Hanjalic, M.Popovac, M.Hadjiabdic „A robust near-wall elliptic relaxation eddy viscosity turbulence model for CFD", International Journal of Heat and Fluid Flow, 25(2004) 1047-1051

[17] P.A.Durbin „Near wall turbulence closure modeling without damping functions",Theor.Comput. Fluid Dynamics (1991) 3 1-13

[18] B. Basara, Z. Jovanović: "The current capabilities of turbulence modeling in Automotive Flows“ YUMV 010021, pp. 93-96, Beograd , 2001

Adapting the operation regimes of trigeneration systems to the renewable energy systems integration

Liviu Ruieneanu[a] and Mihai Paul Mircea[b]

[a] *University of Craiova, Craiova, Romania, lruieneanu@elth.ucv.ro*
[b] *University of Craiova, Craiova, Romania, imircea@elth.ucv.ro*

Abstract:

The purpose of the paper is to evaluate the potential for parallel operation of conventional CHP/trigeneration plants and wind turbines. This approach allows the identification of the best possible operation scenarios for the conventional plants in order to contribute to a fast integration of the wind turbines into the energy production mix.

The mathematical model presented in the paper allows the determination of a safe operation domain where the power variations of the wind turbines are fully compensated by the conventional plant for different operation regimes. The results also reveal the necessity of a differentiated CO_2 emissions tax calculated at system level and not at the level of the conventional power plants. This is important because sometimes increased CO_2 emissions of the conventional power plants might lead to an overall decrease of the CO_2 emissions at system level (for example when conventional plants are operating at partial loads in order to allow an increased electricity production of the wind turbines).

Keywords:

Trigeneration, District heating/cooling.

1. Introduction

In Romania the installed power of the wind turbines was at the end of 2011 around 500 MW. By the end of 2012 the installed power will increase rapidly due to new subsidies for renewable sources. Even if Romania has a high number of hydro power plants (covering 30% of the total demand), the stability of the national grid is often ensured by conventional power plants with steam turbines. The main reason for that resides in the high price of the electrical energy sold by these plants. By maintaining the stability of the system these power plants receive a higher price for the electrical energy, remaining competitive.

However reserving this role for conventional power plants is somehow complicated because these plants were designed for base loads. The problem becomes acute when power plants on coal are operating in parallel with wind turbines due to the coal power plants high inertia. In this paper we are trying to evaluate the cogeneration and trigeneration potential to increase the flexibility in power supply of these plants.

2. Indicators used for the analysis

In order to analyse the implications of an important role for the renewable sources on the energy market we have considered a complex system consisting of a trigeneration plant and a wind farm. The purpose of the mathematical model is the calculation of the electrical energy that might be produced by the wind turbines within this complex system without an exchange of energy outside the system borders. In other words the power supply of the trigeneration plant has to be flexible enough to compensate the power variations of the wind turbines.

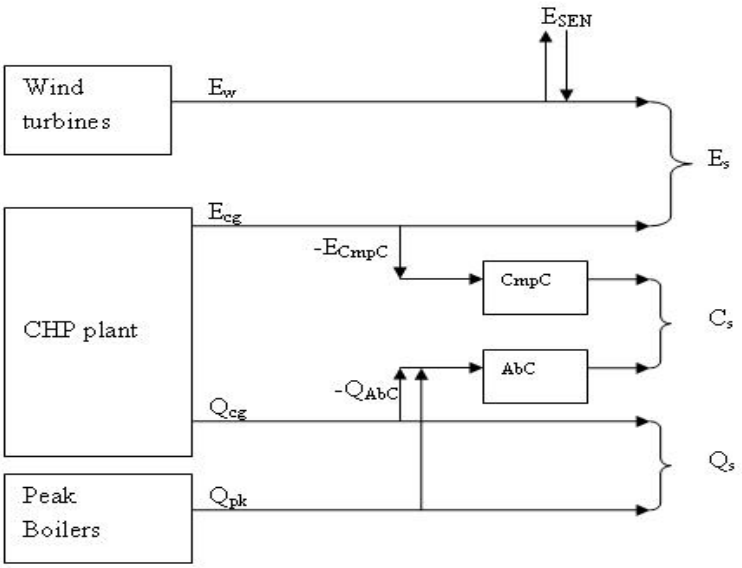

Fig. 1. The scheme of the analysed system

In order to evaluate the best solution for the trigeneration plant we have considered both absorption and compressor chillers. For the purpose of the analysis, both types of chillers have to be able to supply the entire cooling demand of the consumers.

In order to analyse the influence of the wind turbines operation over the trigeneration we have used the trigeneration plants efficiency relation proposed in [8], particularized for the scheme presented in figure 1:

$$\eta_{tr} = \frac{E_{cg} - E_{CmpC} + Q_{cg} + Q_{pk} - Q_{AbC} + C_{CmpC} + C_{AbC}}{Q_{epcg} + Q_{epb}} \qquad (1)$$

When there is no cooling demand, the trigeneration efficiency becomes the total efficiency of the CHP plant [13]. In fact by grouping different terms this becomes obvious:

$$\eta_{tr} = \eta_{tcg} + \frac{Q_{AbC}(COP_{AbC} - 1)}{Q_{epcg} + Q_{epb}} + \frac{E_{CmpC}(COP_{CmpC} - 1)}{Q_{epcg} + Q_{epb}} \qquad (2)$$

In a similar way it might also be defined an equivalent efficiency for the entire system depicted in figure 1 (trigeneration plant plus wind farm) as follows:

$$\eta_{tr} = \frac{Es + Qs + Cs}{Q_{epcg} + Q_{epb}} = \eta_{tr} + \frac{Ew}{Q_{epcg} + Q_{epb}} \qquad (3)$$

In order to highlight the integration of the wind turbines all the calculation were made in relation with the quota of the electricity produced by the wind turbines:

$$f_w = \frac{E_w}{E_s} \qquad (4)$$

In this paper we wanted to study the effect of the wind turbines operation over the trigeneration plant, so we have always calculated the trigeneration plant efficiency as function of the electrical energy quota of the wind turbines (f_w). The environmental impact of the system was quantified by the calculation of system's specific CO_2 emissions for all the analysed cases.

3. Operation in condensing regime (the plant produces only electricity)

Even if it was designed as a combined heat and power plant, today the analysed plant operates in condensing regime producing only electrical energy. The power plant consist of two groups each one having an installed power of 315 MW. The power plant uses coal as fuel.

In the past, the plant provided heat to a series of greenhouses situated in its vicinity. Due to the past operation as a combined heat and power plant there are 5 peak boilers still operational.

In order to operate again as a CHP plant, a supplementary investment (table 1) is necessary in order to construct a heat network that connects the plant with the district heating system of one neighbourhood of our city.

Table 1. The investment structure

Investment	*Investment, mil. €*
Investment for the construction of new heat network	12.42
Rehabilitation of the thermal substations that are operating now in the district heating system of the neighbourhood	3

The purpose of our analysis is to determine the electrical energy that might be produced by the wind turbines in an insular operation with one of the power plant's groups. The power plant operation in condensing regime imposes certain limitations for the analysed system, the electricity demand of the system dictating the operation of the wind turbines.

In figure 2 we have calculated the main indicators for the operation of the analysed system, assuming the power demand of the consumers is equal to the installed power of the conventional plant.

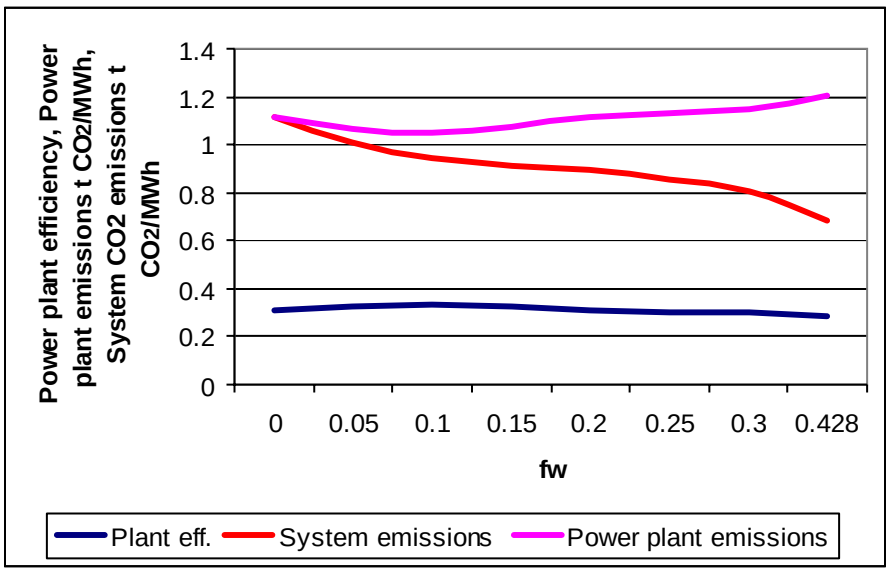

Fig. 2. Present day operation (the plant produces only electricity)

The graph shows that the maximum power quota of the wind turbines (f_w=0.42) is conditioned by the minimum operational power of the conventional power plant's group (180 MW). The quota of the wind turbines power will decrease with the overall power demand of the system.

The graph shows that the integration of the wind turbines is decreasing the system's CO_2 emissions. So, even if partial load operation of the conventional plant decreases it's efficiency and that leads to an increase of the power plant's CO_2 emissions; the overall emissions for the entire system are decreasing (obvious if we compare the orange and the pink line).

This effect imposes the introduction of a differentiated CO_2 tax so that the conventional plants that are operating at partial loads for the integration of the wind turbines will not to be further affected by an increase of the CO_2 emissions tax.

The operation in domain of the system was dictated by the minimum operation limit in condensing regime of the conventional plant (table 2).

Table 2. Operation domains for the condensing operation regime

Domain	*MW*
System operation domain	180-450
Safe operation domain	180 - 315

4. Operation in cogeneration regime

The link between the generated power and the heat output for the steam extraction turbines, might be used to increase the flexibility of the power supply of the conventional power plants. The condition is the use of oversized peak boilers that might provide the entire heat demand of the consumers (not only the peak load). This practice is common to many combined heat and plants designs so that these plants could provide heat to the consumers when a malfunction occurs.

By increasing the quota of the heat produced by the peak boilers or by using exclusively it's peak boilers, the plant increases it's power by shifting from cogeneration to separate production of electricity and heat.

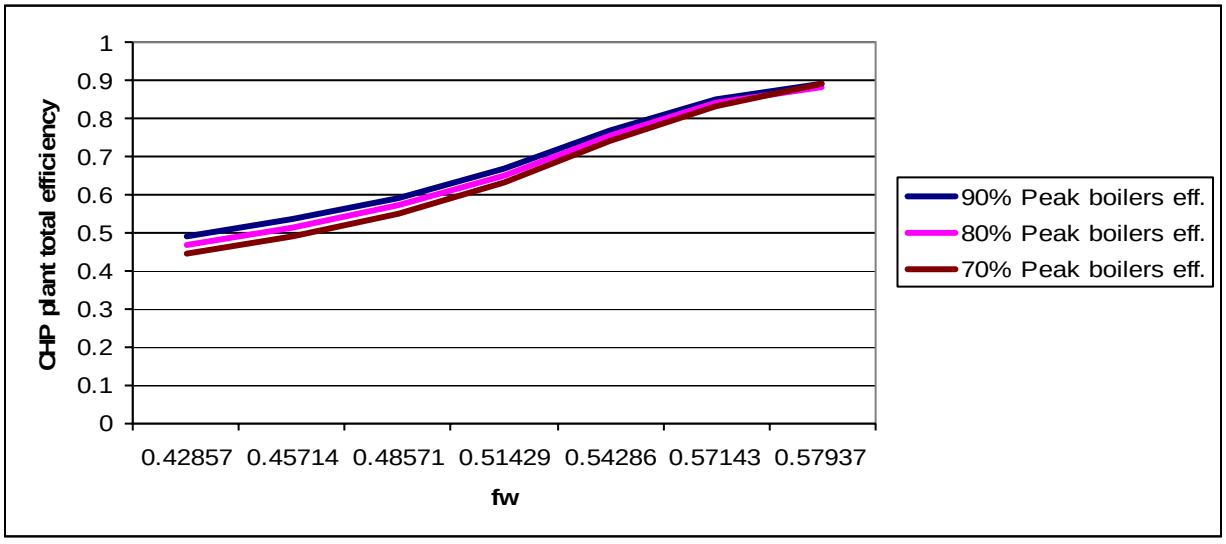

Fig. 3. CHP plant efficiency variation for different peak boilers efficiency (when compensating a wind farm power drop)

Figure 3 depicts the behaviour of the system for a 100% heat demand (319.6 MW). By shifting from cogeneration to separate production the power of the conventional plant decreases with the increase of the power injected by the wind turbines. The use of peak boilers operating with high efficiencies improves the global efficiency of the system (figure 3).

In figure 4, for a 100% heat demand the power of the wind turbines might get close to 58 % of the total power injected by the system. The method is very effective because the cogeneration plant might compensate any decrease of the wind turbines power in the safe operation domain. The downside of the method is the decrease of the global efficiency with the shift to separate production.

The lower operation point of the system drops to a power of 132.5 MW (table 3) from 180 MW in condensing regime (table 2). Therefore by supplying heat in cogeneration the conventional power plant has a better power supply flexibility, thus increasing the reserve of the system for parallel operation with the wind farm.

Table 3. Operation domains for 100% heat demand

Domain	*MW*
System operation domain	132.5-500
Safe operation domain	132.5 - 315

If the total electricity demand of the consumers decreases, than the power injected by the wind turbines has to decrease since the conventional plant produces the technological minimum power (132.5 MW).

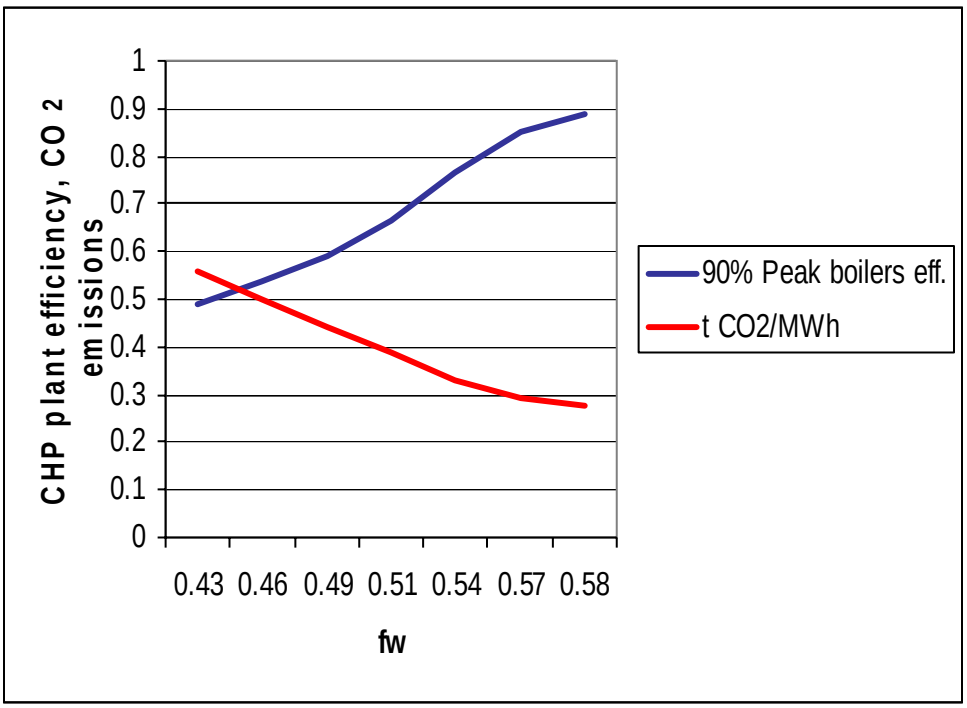

Fig. 4. Compensating a wind farm power drop in cogeneration operation regime at 100% heat demand

The decrease of the heat demand limits the CHP plant ability to compensate sudden drops of wind turbines power and leads to an increase of the CO_2 emissions of the system.

Figure 5 depicts the system's behaviour at 50 % heat demand.

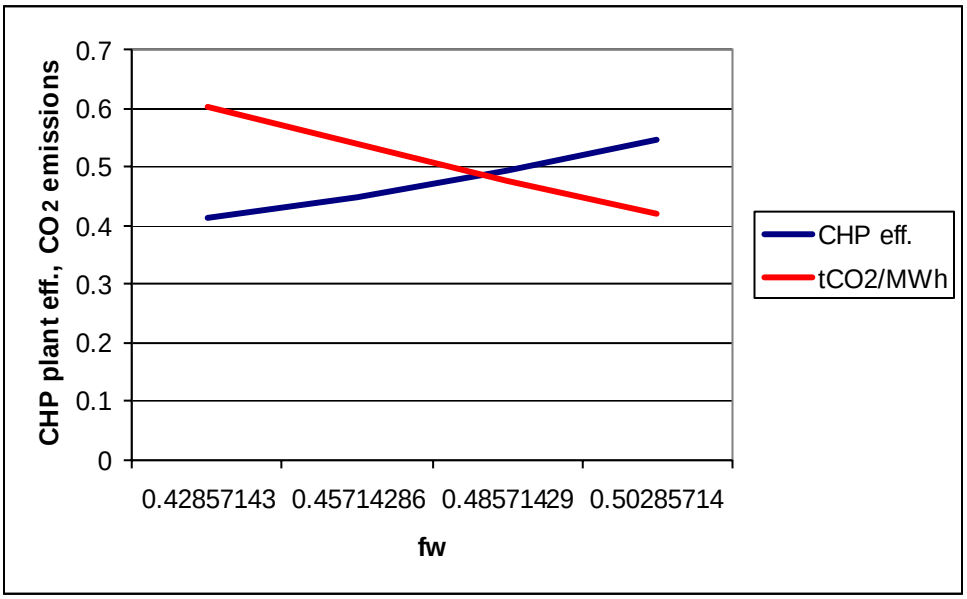

Fig. 5. Compensating a wind farm power drop in cogeneration operation regime at 50% heat demand

Figure 5 shows that even in the worst case, when the efficiency of the CHP plant drops to nearly 40 % (separate production of electricity and heat) because the plant has to compensate power drop of the wind turbines, the CO_2 emissions are considerably low. In both cases the decrease of the electricity demand leads to a decrease of the wind turbines power (because the CHP plant is at the minimum value). The safe operation domain of the system decreases with heat demand (table 4).

Table 4. Operation domains for 50 % heat demand

Domain	*MW*
System operation domain	156-473
Safe operation domain	156 - 315

5. Trigeneration operation regime with absorption chillers

In order to operate as a trigeneration plant the company has to invest an even larger sum (table 5), however the absorption chillers are increasing the flexibility of the conventional plant's power supply during the summer.

Table 5. Investment structure

Chillers type	*Capacity, MW*	*COP*	*Specific investment,€/kW*
Single effect absorption chillers	224	0.7	160
Compressor chillers	224	5	145

As in the case of the cogeneration regime the existence of oversized peak boilers allows an increase of the installed power of wind turbines operating in parallel with the cogeneration plant. In this case the conventional plant is increasing the trigeneration plant power supply by producing the necessary heat for the absorption chillers partially or totally with peak boilers.

Figure 6 depicts the wind turbines power supply quota that might be reached by the use of absorption chillers.

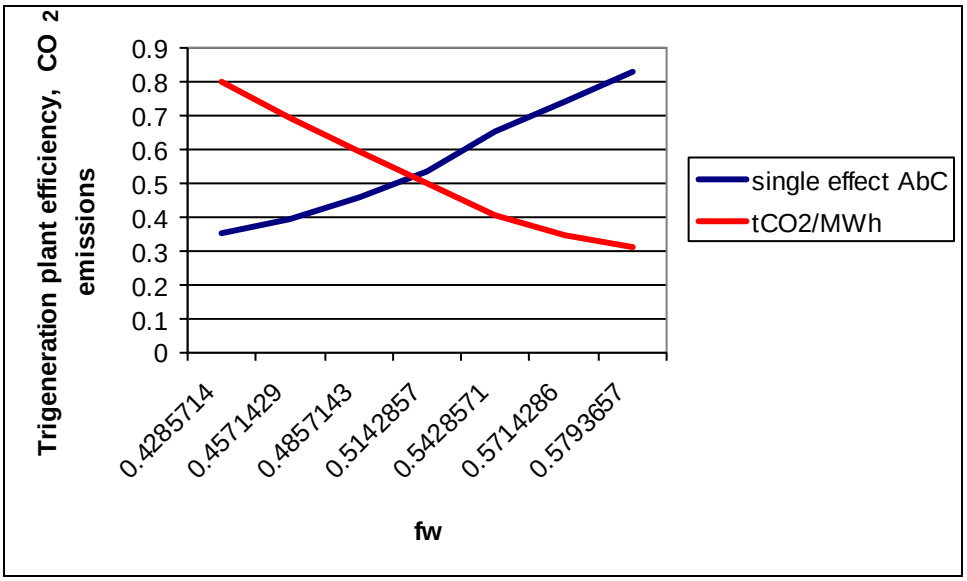

Fig. 6. Compensating a wind farm power drop in trigeneration operation regime for 100% cooling demand and a small heat demand during the summer

The calculations presented in figure 6 show that in trigeneration regime, the plant operates with a relatively high efficiency that leads to small CO_2 emissions. When the power injected by the wind turbines decreases, the efficiency of the trigeneration plant drops resulting an increase of the CO_2 emissions.

Table 6. Operation domains for trigeneration regime at 100% cooling demand

Domain	*MW*
System operation domain	133-497
Safe operation domain	133 - 315

The decrease of the cooling demand limits the trigeneration plant ability to compensate large variations of the wind turbines supply.

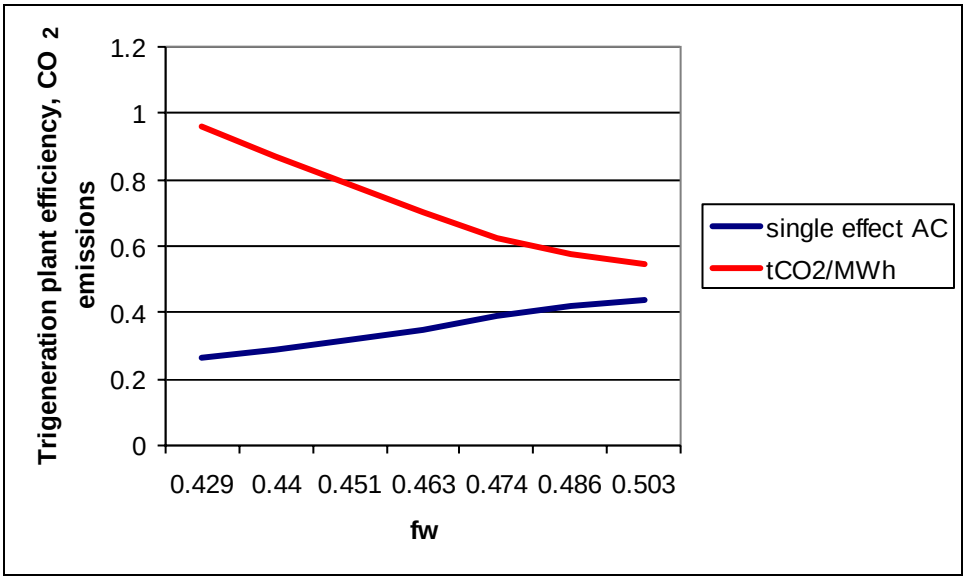

Fig. 7. Compensating a wind farm power drop in trigeneration operation regime for a 50 % cooling demand

The safe operation domain for the 50% cooling demand is presented in table 7. The results are very close to the cogeneration operation during the winter period, trigeneration operation allowing in this case an increased electrical energy production for the wind farm during the summer.

Table 7. Operation domains for trigeneration regime at 50% cooling demand

Domain	*MW*
System operation domain	157-473
Safe operation domain	157 - 315

5. Trigeneration operation regime with compressor chillers

The use of compressor chillers for the construction of the trigeneration plant allows the increase of the wind turbine power quota.

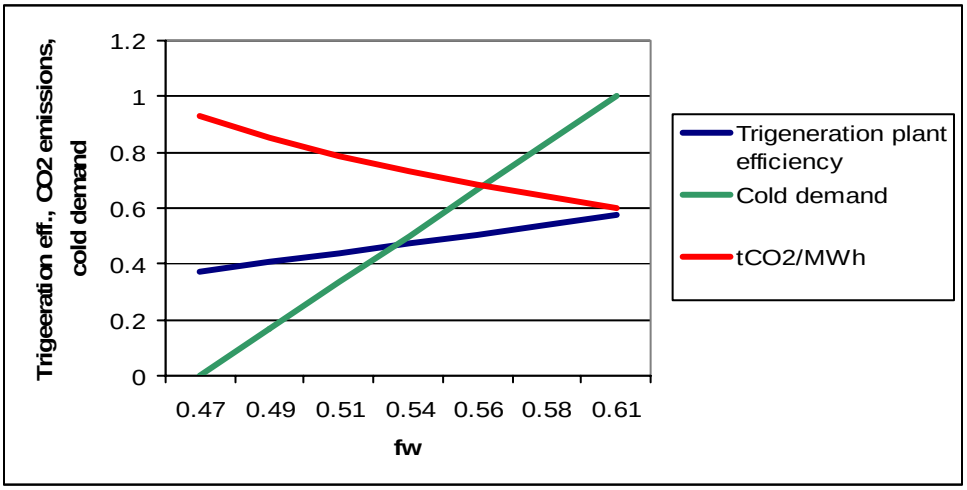

Fig. 8. Compensating a wind farm power drop in cogeneration trigeneration operation regime with compressor chillers

The use of compressor chillers lowers even further the minimum power of the trigeneration plant and that allows a further increase of the power injected by the wind turbines (figure 8). However there is also the downside of a direct link between the cooling demand of the consumers and the power that might be injected at one time by the wind turbines.

Another downside is the necessity of both compressor and absorption chillers (when the power of the wind farm drops, the plant must use the absorption chillers operating with the heat produced by peak boilers). This also means that if the power of the wind turbines decreases (with the wind speed) the system has to buy some electrical energy from the grid ($E_{SEN} \neq 0$). Even so the parallel operation with the trigeneration plant has some advantages because it decreases the electrical energy "imported" from the grid.

5. Conclusions

The decentralisation of the electrical energy market tends to increase the pressure over the operating companies complicating the stability of the grids. Hydro power plants that might help the integration of the renewable sources, are in many cases operating with bilateral contracts with important (industrial) consumers, so the role of maintaining the grid stability is designated to conventional power plants (due to a higher price of the electrical energy).

Parallel operation of wind turbines and conventional plants within a system is possible and reduces the negative effects over the energy system of one country. However a successful operation necessitates an understanding of the conventional plant operational limits.

From the results presented in this paper it was possible to determine a safe system operation domain for each operation regime of the trigeneration plant. In other words cogeneration and trigeneration might increase the flexibility of the power supply of existing conventional plants and therefore these technologies could facilitate the integration of the renewable energy sources in the energy production mix.

The success of the trigeneration plant in compensating the power variations of the wind turbines is directly related with the heat and /or cooling demand. The operation with absorption chillers ensures an increase of the safe power operation domain for the trigeneration-wind turbines system.

This is possible if there is a shift of the heat delivered to the consumers or used by the absorption chillers from the combined heat and power plant to the peak boilers. The main advantage is in this case the increased power availability for the conventional plant.

The compressor chillers allow an even further decrease of the power produced by the trigeneration plant so the installed power of the wind turbines might be even higher in this case. The problem with the compressor chillers is that the cooling demand dictates the power that might be produced by the wind turbines tacking into consideration the availability of the electrical energy from the national grid (E_{SEN}).

The paper shows also the necessity of a differentiated CO_2 tax that takes into account that by partial load operation some conventional power plants allow an overall decrease of the CO_2 emissions for the entire system, compensating the discontinuous operation of the wind turbines. A linear CO_2 tax would only increase, in this case, an already high price of the energy.

Nomenclature

E_w	Electrical energy produced by the wind turbines
E_{cg}	Electrical energy produced by the CHP plant
E_{CmpC}	Electrical energy consumed by the absorption chillers

E_s	Electrical energy produced by system
Q_{cg}	Heat produced by the CHP plant
Q_{pk}	Heat produced by the peak boilers
Q_{AbC}	Heat used by the absorption chillers
Q_s	Heat produced by the system
C_s	Cooling demand
COP_{AbC}	Coefficient of performance for the absorption chillers
COP_{CmpC}	Coefficient of performance for the compressor chillers.
η_{cg}	Total efficiency of the cogeneration plant [5]

References

Journals:

[1] Athanasovici V. and Dumitrescu I. S., - Global total efficiency of district heating systems, Energetica Review, december 2005.

Books and other monographs:

[2] Liviu Ruieneanu General Method for the Analysis of Cogeneration Systems. LAP Lambert Academic Publishing AG & Co KG., ISBN : 978-3-8443-2300-9, Germany, 2011

[3] Chic Wu, Thermodynamic cycles, Marcel Decker Inc., New York, 2003.

[4] Meyer-Krahmer F, Kuntze U and Walz R, Innovation and Sustainable Development. Lessons for Innovation Policies, Lessons for Innovation Policies. Physica, Heidelberg, 1998

[5] Flin D. Cogeneration – User's Guide The Institution of Engineering and Technology, 2010

[6] Logan E, Roy R. Handbook of turbomachinery Marcel Decker Inc., New York, 2003.

Conference Papers:

[7] Ruieneanu, L., Mircea I., Technical-economical evaluation of CHP plants, WESC 2006, Torino, Italy 2006

[8] Minciuc, E., Bitir-Istrate I. Patrascu R., Constantin C., Athanasovici V. Energetic analysis of cogeneration, WEC Regional Energy Forum – FOREN 2004, Neptun, 13-17 June 2004

[9] V. Athanasovici, I. S. Dumitrescu A unitary method for the definition of technical indices specific to medium and small scale cogeneration solutions, Energetica, Romania, April 1998.

[10] Ruieneanu, L., Goşea, I. Considerations regarding the competitiveness of the CHP plants, pg. 503-505, SIELMEN, Chisinau, Moldavia 2005.

[11] Ruieneanu L., Mircea I , The unit costs method. A method for a CHP plant cots allocation on both types of energy CNE 2004, Neptun Romania. 2004

[12] Monica Carvalho, Luis M. Serra*, Miguel A. Lozano Geographic evaluation of trigeneration systems in the tertiary sector. Effect of climatic and electricity supply conditions. SDEWES 2009, Dubrovmik, Croatia.

Web references:

[13] EUROPA- the official web site of the European Union. Official Journal of the European Communities. Directive of the European parliament *2004/8/EC*.

[14] Greenhouse Gas Emissions from the U.S. Transportation Sector 1990-2003.EPA 420 R06 003 March 2006 www.epa.gov

Advanced electromagnetic sensors for sustainable monitoring of industrial processes

Uroš Puc[a], Andreja Abina[b], Anton Jeglič[c], Pavel Cevc[d] and Aleksander Zidanšek[e]

[a] *Jožef Stefan International Postgraduate School, Ljubljana, Slovenia, uros.puc@mps.si, (CA)*
[b] *Jožef Stefan International Postgraduate School, Ljubljana, Slovenia, andreja.abina@mps.si*
[c] *Faculty of Electical Engineering, University of Ljubljana, Ljubljana, Slovenia, anton.jeglic@fe.uni-lj.si*
[d] *Jožef Stefan Institute, Ljubljana, Slovenia, pavel.cevc@ijs.si*
[e] *Jožef Stefan International Postgraduate School, Ljubljana, Slovenia, aleksander.zidansek@mps.si*

Abstract:

Utilization of non-destructive and non-invasive methods for real-time monitoring of industrial processes is one of the challenging and desired tasks in industrial ecology. The aim of this work was to verify advanced electromagnetic (EM) sensors for material properties characterizing within industrial systems. To achieve this goal, we chose two EM sensors, an electromagnetic induction (EMI) sensor and ground penetrating radar (GPR). The operation of GPR is based on observation of EM waves reflections at the interface boundaries where the dielectric permittivity changes. We found out that the operation of the EMI sensor is in principle the same as that for GPR. In EMI method, the primary magnetic field produced by transmitter coil is changed in such a way that a higher density of magnetic flux lines occur due to the presence of metallic objects. Additionally, eddy currents occur which originate by metallic objects and have an important effect on the induction of the receiver coil field. In both methods, the changes due to material interactions with EM waves or magnetic fields are detected. The EMI method is used to characterize if the material within the industrial process is metallic or not. In case of non-metallic material, the object is sent into the next level, where GPR is applied to determine the dielectric properties of the material. The proposed method is capable to monitor material flow through industrial system. In such a manner, an imperfect material or any other impurity could be detected and eliminated from the process. Furthermore, the eliminated material can be either reused in the same process or recycled in order to reduce disposal cost and energy consumption. Through modification and adaptation of GPR and EMI sensor, the applications of these technologies are expanding, and the advantages could also be used beneficially in the energy sector.

Keywords:

Electromagnetic Induction Sensor, Ground Penetrating Radar, Industrial Ecology, Material Properties, Monitoring.

1. Introduction

Nowadays, different techniques are used for non-destructive and non-invasive sensing. The utilization of such methods in industry provides the opportunity of real-time monitoring of industrial processes in a sustainable way [1-5]. Some sensing techniques are depicted in Fig. 1, which shows that the technology costs go up with the increased sensors availability and complexity. This paper is focused on two of those techniques - ground penetrating radar (GPR) and electromagnetic induction (EMI) sensor. Their applications have been growing rapidly and there was a great progress in the development of theory, technique and technology over the past few decades. The diversity of GPR and EMI applications includes a variety of areas [6-13], but in this work the focus will be on industrial applications such as concrete inspection in construction industry, subsurface infrastructure detection in transportation industry and water utility industry, food inspection and applications of these technologies in the energy sector.

The aim of this work was to verify advanced electromagnetic (EM) sensors for material properties characterisation within feasible industrial systems. First, the basic principles of operation and physical background of GPR and EMI senor will be presented. Furthermore, the experimental setup will be explained to understand how these two sensors could be included into industrial processes. Experimental results will also be shown and discussed. We will demonstrate and evaluate how the

proposed methods are capable to monitor material flow through industrial system in such a manner that an imperfect material or any other impurity could be detected and eliminated from the process.

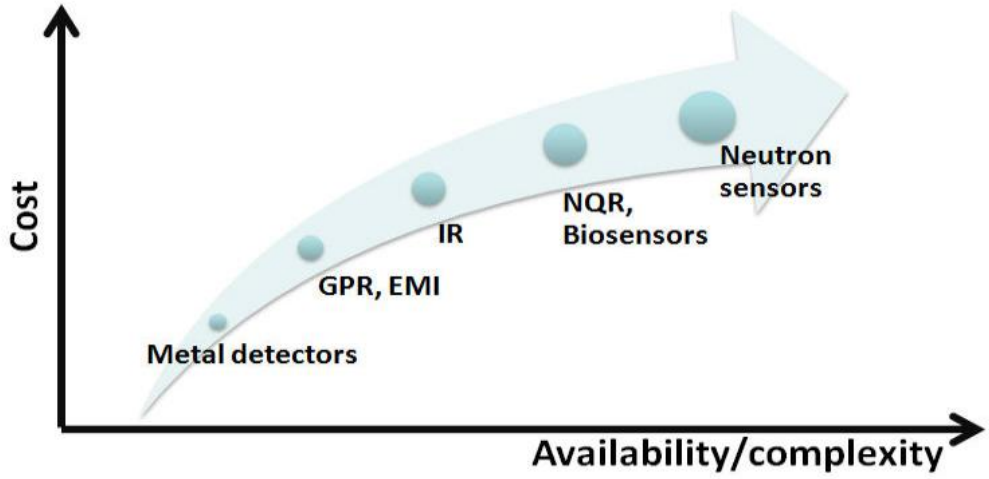

Fig. 1. Electromagnetic and similar sensing techniques used for monitoring and material properties characterizing.

2. Principles of EM sensors operation

Electromagnetic waves comprise both electric and magnetic fields that oscillate at right angles to each other in the direction of propagation [14]. Furthermore, the EM waves are classified by frequency or by wavelength into radio wave, microwave, terahertz radiation, infrared wave, the visible region, ultraviolet, X-rays and gamma rays. Currently, various sensors exist in the range of all possible frequencies of EM spectrum [3-5]. The behaviour of EM waves as well as its interaction with matter depends on the selected working frequency. In this work the focus is on radio waves and microwaves which are used by GPR and EMI sensors. The operation of GPR is based on observation of EM waves' reflections at the interface boundaries where the dielectric permittivity changes [15]. The operation of the EMI sensor is similar as that for GPR because both methods detect changes due to material interactions with EM waves or magnetic fields.

2.1. Physical foundation of GPR

The GPR sensor uses electromagnetic wave energy to obtain information about the subsurface structures. Basically, this method operates by transmitting a very short EM pulse into the medium using an antenna at selected frequency. In practice, any GPR system contains a signal generator, a control unit, transmitting and receiving antenna. By using such a system configuration, the GPR measurements could be divided into two categories, reflection and transillumination, as shown in Fig. 2. The most useful is a reflection mode configuration in which a single transmitter and a single receiver are used. Typical GPR survey is conducted by moving a transmitter and receiver antenna, separated by a fixed distance, along a survey line [7]. For other more specialized applications multiple source and receiver configurations are recommended [16]. However, basic characteristics of the GPR investigation are related with a very high precision of the data, continuous surveying, highest survey resolution, entirely non-destructive and very fast collecting of data [17].

The principle of GPR is based on electromagnetic wave propagation. Maxwell's equations are used to mathematically describe the physics of electromagnetic fields, while constitutive relationships provide a macroscopic description of how electrons, atoms, molecules, and ions respond to the application of EM field. These two sets of equations are used for describing the GPR signals. The propagation of the radar signals within the medium depends on the electromagnetic properties of the material, mainly the dielectric permittivity and electrical conductivity [18-19]. If there is a difference in dielectric permittivity between adjacent layers or objects in the medium the reflection

of incident EM radiation occurs. Synchronization between the transmitter and the receiver systems allows the determination of the time taken for the electromagnetic pulse to be reflected back. The travel time of the electromagnetic wave, which travels from the transmitter to the object in the medium and back to the receiver is known as two way travel time *TWTT*. The greater the contrast between media is the greater will be the amount of reflected energy. The proportion of reflected energy is given by the reflection coefficient *R*, which is determined by the contrast in radio wave velocities *v* or dielectric permittivities ε of adjacent media. The amplitude of reflection coefficient *R* is given by one of these two equations [7]:

$$R = \frac{(v_1 - v_2)}{(v_1 + v_2)} \tag{1}$$

$$R = \frac{\sqrt{\varepsilon_2} - \sqrt{\varepsilon_1})}{\sqrt{\varepsilon_2} + \sqrt{\varepsilon_1}} \tag{2}$$

However, the electromagnetic wave-matter interactions are usually expressed by the complex formulation of the dielectric permittivity:

$$\tilde{\varepsilon} = \varepsilon' - j\varepsilon'' = \varepsilon_0 \varepsilon'_r - j\varepsilon_0 \varepsilon''_r \tag{3}$$

where ε_0 is the dielectric permittivity of a vacuum, ε' and ε'' are the real and imaginary parts of the complex dielectric permittivity, and ε'_r and ε''_r are the real and imaginary parts of the relative complex dielectric permittivity. The real part carries the information about the electromagnetic energy, whereas the imaginary part is a measure of the energy loss in the material due to time varying field [20]. Radar signal velocity v_m in low-loss medium like ambient air is related to the real part of a dielectric permittivity:

$$v_m = \frac{c}{\sqrt{\varepsilon'}} \tag{4}$$

Although the velocity of radar waves can be expressed by:

$$v_m = \frac{2d}{TWTT} \tag{5}$$

where *d* is the distance between the GPR antenna and reflected point and *TWTT* is the two-way travel time of the GPR signal.

The electrical response in medium is affected by various variables, such as selected frequency, material porosity, water content, aggregation state, component geometry, electrochemical interactions, temperature and density. Over the frequency range of 10 MHz – 1000 MHz, the real part of the dielectric constant does not appear strongly frequency dependent. When operating in this frequency range and if the medium is a good dielectric, the dependence of radar velocity on electrical conductivity is negligible. In such medium, the velocity of electromagnetic waves is related only to the real part of the dielectric constant [19].

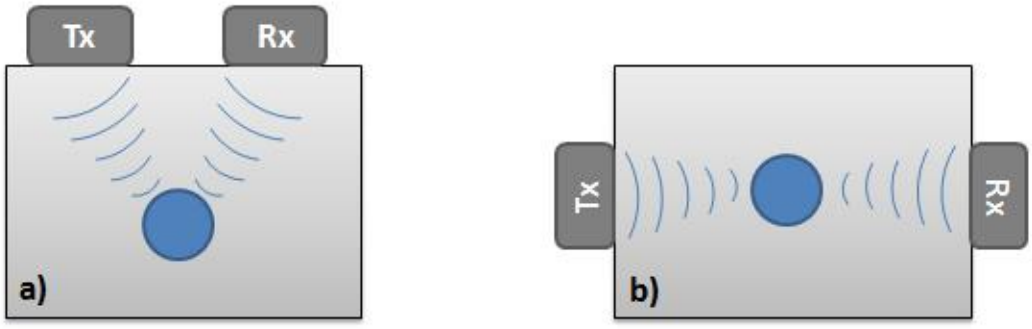

Fig. 2. GPR measurements in reflection (a) and transillumination (b) geometry.

2.2. Physical foundation of EMI sensor

Electromagnetic-induction is typically operated as an active sensor. EMI sensors are widely used to locate buried landmines [12-13, 21-23] by detecting the metal content in such objects. This sensor usually consists of a pair of concentric, circular coils, one of which is used to transmit electromagnetic waveform. The transmitted field induces a secondary current in any buried or hidden conducting object. A receiving coil senses the secondary field returned from the buried objects [21]. This is the foundation of the well known EMI method whereas the physics of EMI operation is completely described by Maxwell's four equations [24]. Additionally, eddy currents occur which originate by metallic objects and have an important effect on the induction of the receiver coil field. These eddy currents are particularly expressed in case of conductor materials such as aluminium and not as much in case of ferro-magnetic materials such as iron. Unlike EMI sensors that can only detect mines with metal content, GPR is capable of detecting very low metal and plastic mines. In fact, the EMI principle is the basis of common metal detectors even those for treasure hunting on the beach, especially because they are not expensive and complex to produce.

A partly or wholly metal object has a distinct combination of electrical conductivity, magnetic permeability, and geometrical shape and size. When this object is exposed to a low-frequency electromagnetic field, it produces a secondary magnetic field. When using EMI spectroscopy a distinct unique spectral signature could be obtained. This method could be used to identify different metal objects. EMI spectroscopy explores the frequency dependence of the EMI response in a broad frequency band in order to detect and characterize the object's geometry and material composition [24].

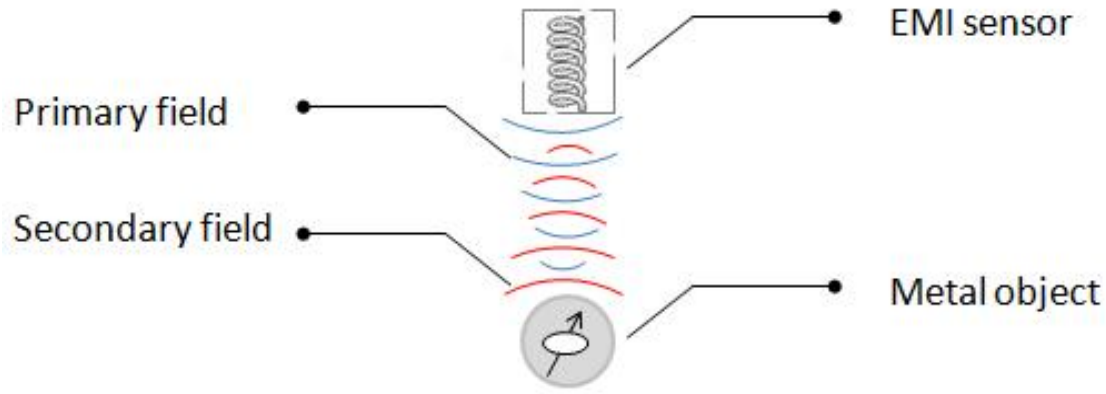

Fig. 3. Principle of operation for EMI sensor.

3. Experimental setup

Utilization of non-destructive and non-invasive methods for real-time monitoring of industrial processes is one of the challenging and desired tasks in industrial ecology. The realization of this task is possible with advanced EM sensors such as EMI sensor and GPR. In our experimental setup the EMI method is used within Level 1 to characterize if the material within the industrial process is metallic or not. Moreover, the proposed method is also capable to estimate the shape and orientation of detected metallic objects. In case of non-metallic material, the object is sent into the next level, where GPR is applied to determine the dielectric properties of the material by estimation of the reflection coefficient. Furthermore, the thickness of the sample could be estimated because the conveyor belt in this setup contains metal part which serves as a reference plate. However, the proposed method shown in Fig. 4 is capable to monitor material flow through industrial system. In such a manner an imperfect material or any other impurity could be detected and eliminated from the process.

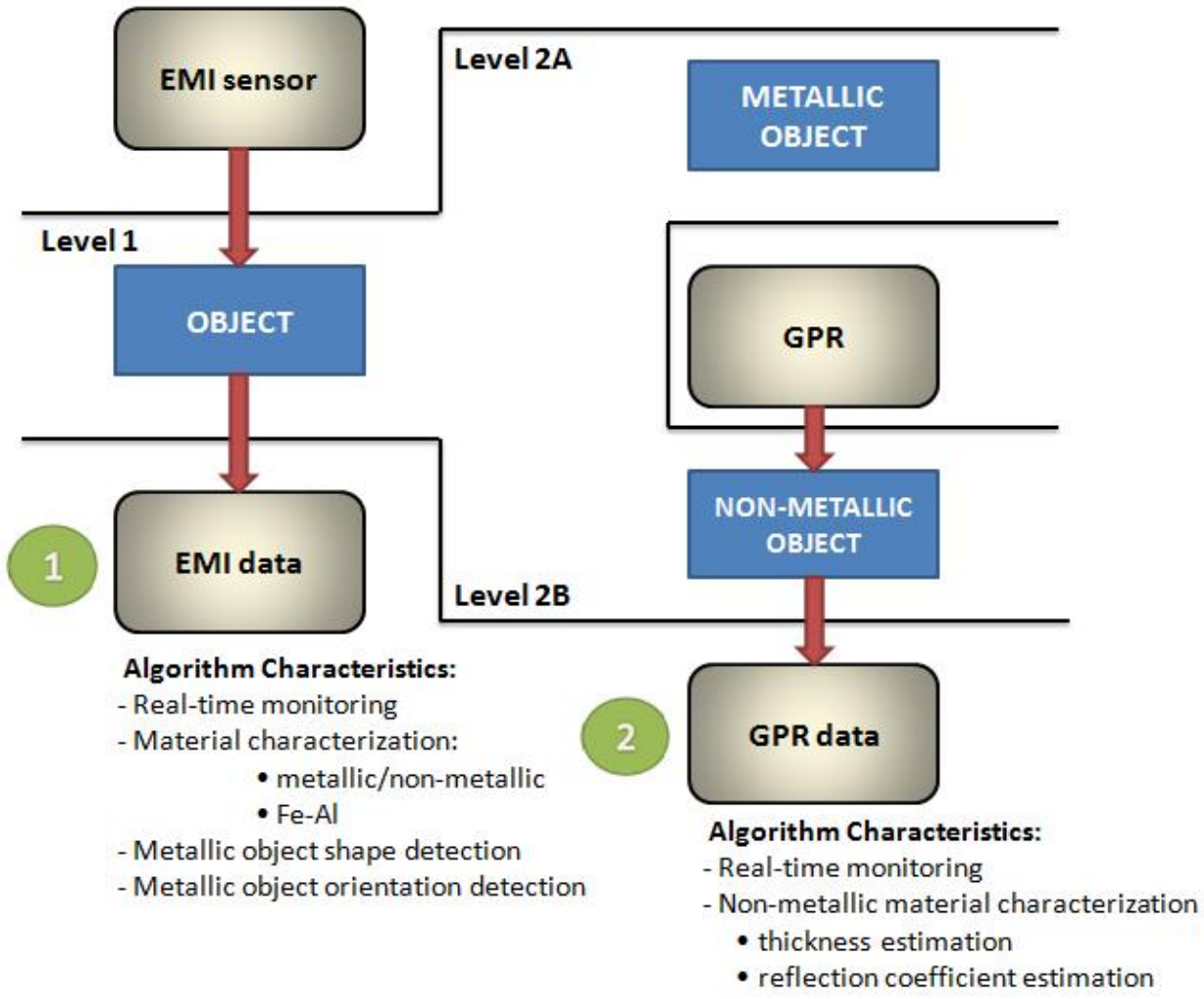

Fig. 4. Method of real-time monitoring of industrial processes with EMI sensor and GPR.

3.1. Monitoring by GPR

The research work was conducted using a commercial georadar system manufactured by Mala Geoscience Inc. The GPR system was equipped with a 1.6 GHz antenna. The software for data acquisition run in the GPR processing unit, from where the raw data were transferred to the computer used for further calculations. The proposed method for reflection coefficient calculation is based on analyzing the raw GPR signals. Each 1-D GPR target response provides some unique information; therefore the signal needs to be acquired in an appropriate way. As a reference signal we used the reflection from the large metal plate which was placed behind the plastic sample holder as shown in Fig. 5. The sample holder filled with dry sand was located on the same place in each measurement with the constant distance from the antenna which was in the range of few centimetres.

The reflected sample signal contains both reflections from the top and the bottom of the sample, thus the reflection coefficient of the material inside the sample holder could be estimated. This is the reason why we extracted the early-time response from the GPR signal and excluded the late-time response, which is always distorted by other uncontrollable environmental factors. Later on, the reference signal through the ambient air is subtracted from the measured signal of the dry sand. The subtraction between reference signal and sample signal at two different distances between antenna and metal plate is shown in Fig. 9.

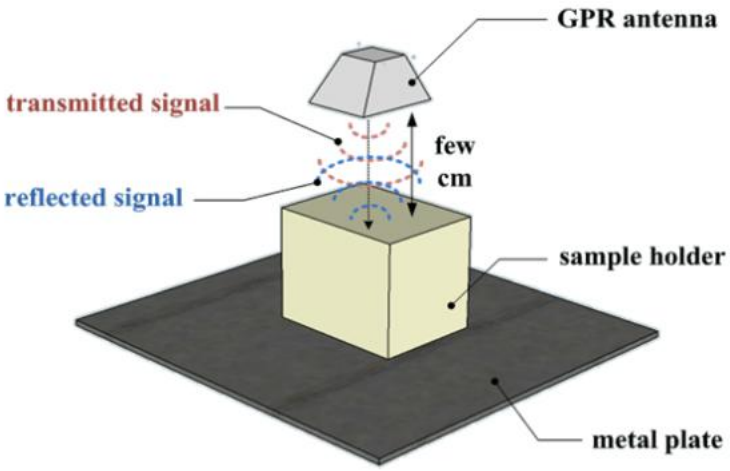

Fig. 5. The measurement setup for GPR data acquisition with a reference metal plate and sample holder.

3.2. Monitoring by EMI

The scenario for EMI monitoring comprised EMI sensor composed of four probes mounted on a wooden pole (Fig. 6). Moreover, the home-made EMI sensor was moving on a quadratic holder made from wood to reduce destructive interferences from other objects. For the investigation purposes, samples with simple circular and rectangular cross sections were selected. For carrying out laboratory experiments we consider dynamic sensor system and static samples which were located on the wooden plate with the constant distance from the sensor which was in the range of few centimetres. The investigated area was limited with dimensions of 45 cm by 85 cm. However, the inverse case is also possible where EMI probes are fixed on a pole, e.g. above the production line and as such serve as an in-line monitoring tool. In such a manner, EMI can be applied in real-time monitoring of material flow through industrial systems.

Special software was prepared to acquire signals from all four probes simultaneously. The raw signals in a matrix form were imported in Matlab programming environment. In order to obtain a more realistic circular or rectangular cross section of the detected objects the 2-D interpolation between the matrix elements was applied. Furthermore, the obtained plots were smoothed using MatLab's built-in cubic interpolation function. The final results were visualized as an intensity plot.

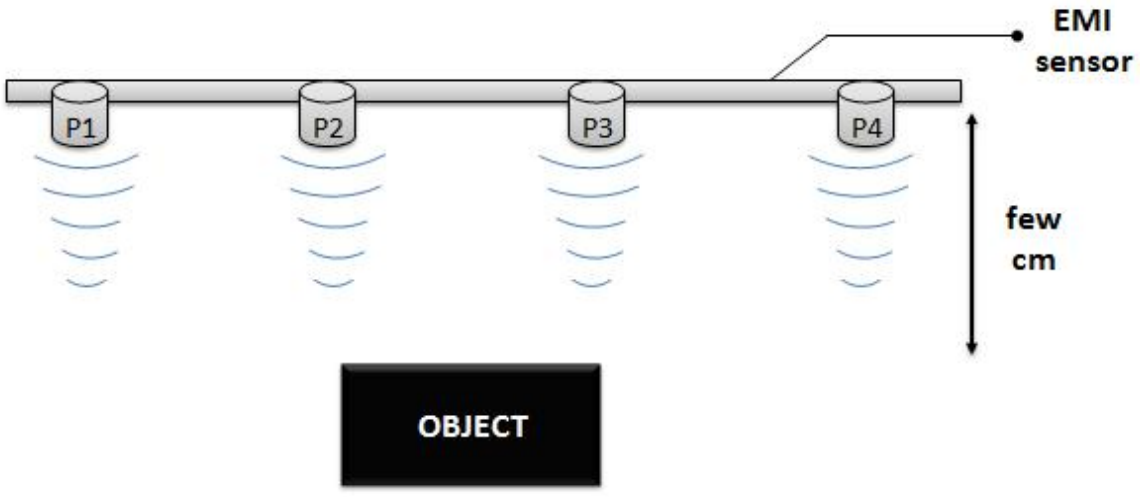

Fig. 6. The measurement setup for data acquisition with the EMI sensor composed of four individual probes.

4. Results and discussion

The proposed method for reflection coefficient calculation is based on analyzing the raw GPR signals. As a reference signal we used the reflection from the large metal plate which was placed behind the sample holder. The sample located in front of the metal plate modifies the signal shape and its amplitude. Hence, from the signals fingerprint one can notice that the sign of the polarization is changed where the sample is present. In Fig. 7 the sign of the polarization is changed at 51st sample whereas in Fig. 8 this change is shifted for 7 samples to the right corresponding to the longer distance between the GPR antenna and reference plate.

For accurate reflection coefficient calculation some initial optimization parameters had to be determined, such as sampling rate and time window in ns. Size of the time window was set to 10.781626 ns. The total number of samples was 176. These two parameters are used for signal velocity calculation. With the subtraction function between the reference signal and sample signal it is possible to determine the top and the bottom of the sample. In Fig. 9 the bottom of the sample can be clearly identified as a maximum positive peak whereas the end of the ground signal is defined as a point where the difference between the signals starts to rise. The distance between these two points is actually the distance between a GPR antenna and reference plate. For instance, at distance of 12 cm this difference counts 19 samples, at distance of 18 cm it counts 26 samples. Within this distance both media ambient air and dry sand are included. Thus, it is important to recognize the point representing the top of the sample which is in our case the second positive peak at 41st and 48th samples. By knowing all these locations in plot and distance from antenna to metal plate, one can calculate the signal velocity through the air and the sample by equation:

$$v_m = \frac{2d}{TWTT} = \frac{c}{\sqrt{\varepsilon'}} \tag{6}$$

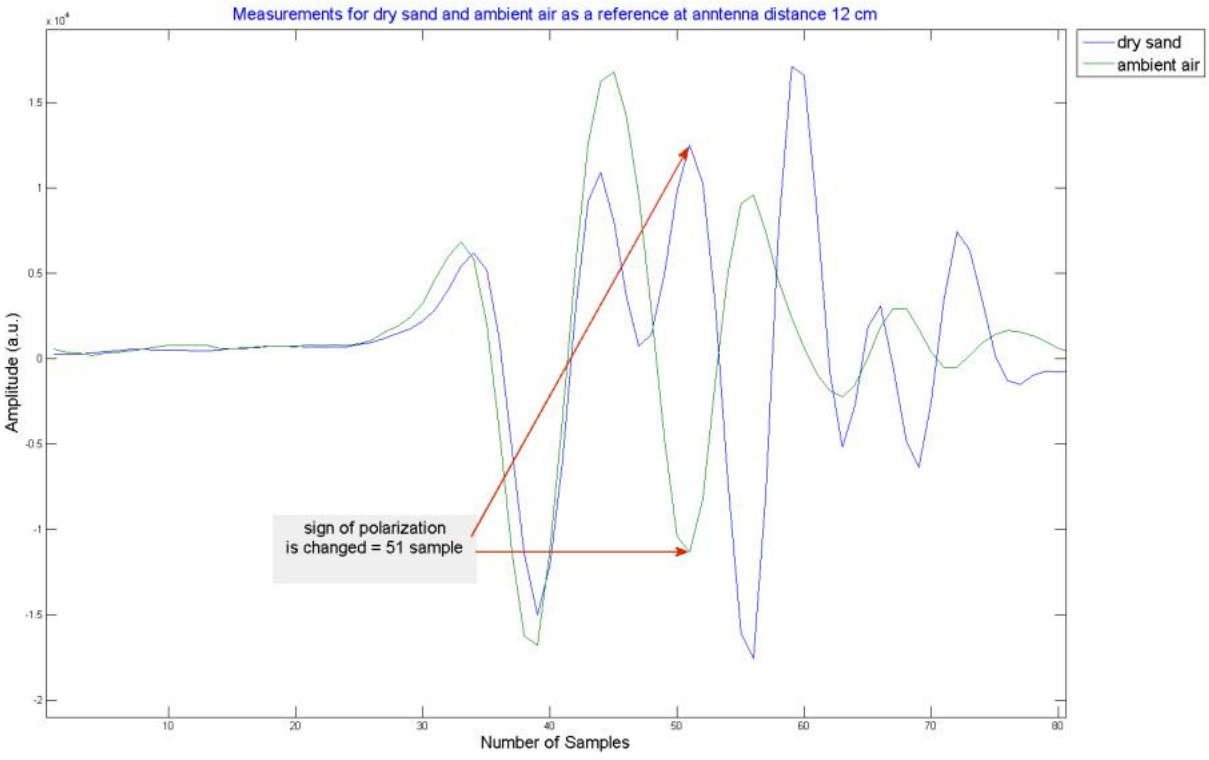

Fig. 7. The comparison between acquired signals with and without a sample of dry sand at a distance of 12 cm between antenna and reference plate.

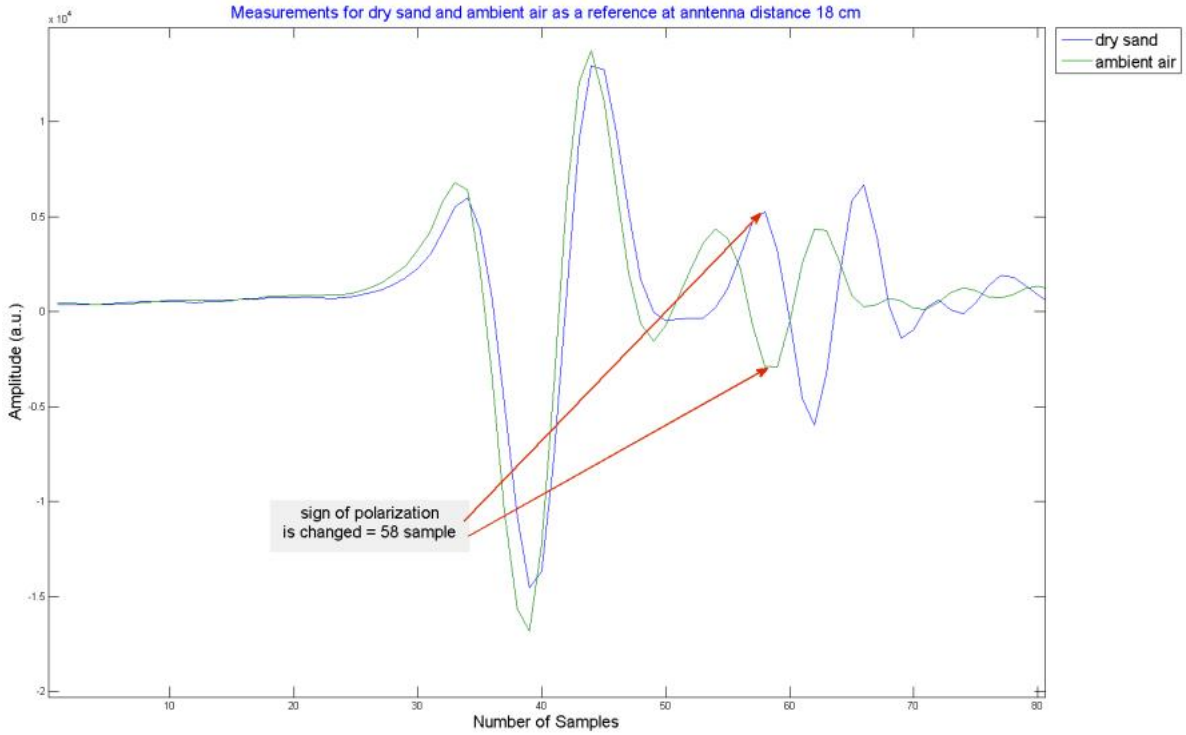

Fig. 8. The comparison between acquired signals with and without a sample of dry sand at a distance of 18 cm between antenna and reference plate.

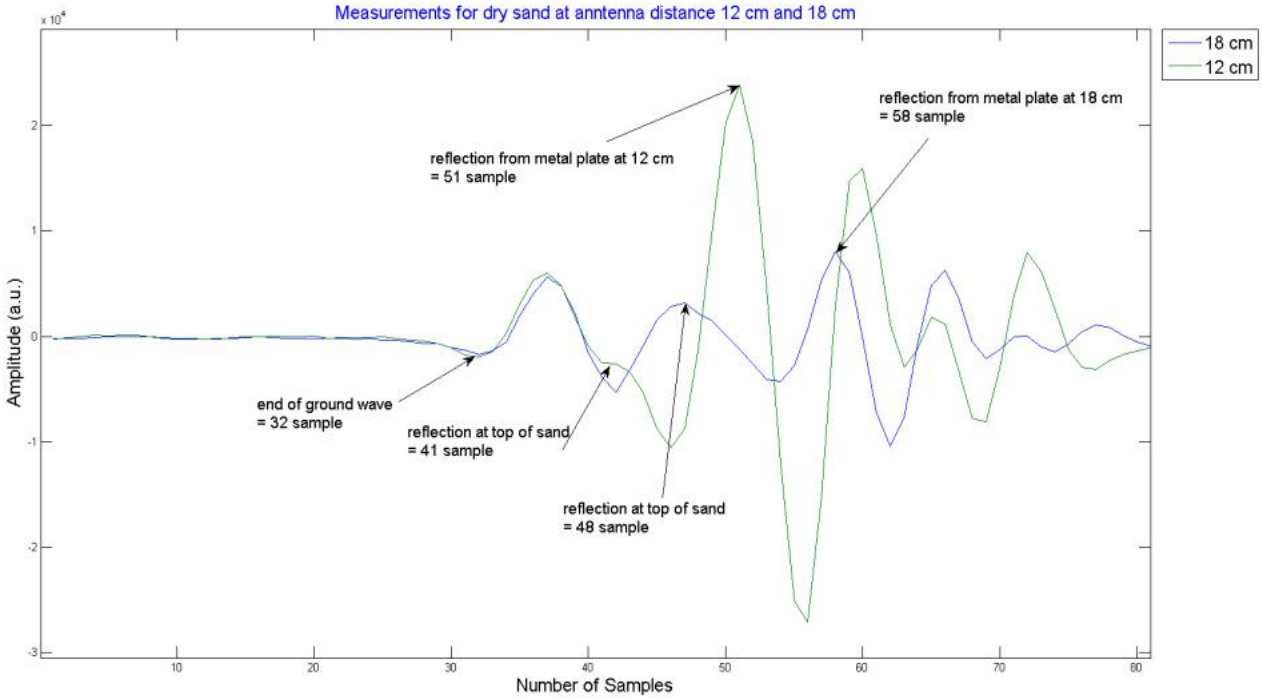

Fig. 9. The comparison between signals at a distance of 12 cm and 18 cm after s subtracting the waveforms captured with and without object.

The calculated values for velocities in dry sand are given in Table 1. As a sample for GPR monitoring we used dry sand with relative dielectric permittivity between 4 and 7 [25]. Theoretical

value of the reflection coefficient *R* given by equation (2) and is in the range between 0.333 and 0.451. Practically estimated reflection coefficient *R* given by equation (1) has a value of 0.428 for a distance of 12 cm and 18 cm between antenna and reference plate. The estimated and calculated values of reflection coefficients are given in Table 1. Additionally, range detection could be also performed by GPR technique. Thus, the distance from a GPR antenna to the object could be estimated. If the distance from the antenna to the reference plate is constant, one can determine the thickness of the sample as well. This concept could be adapted to in-line and real-time monitoring of material samples within various industrial processes which is a key for ensuring final quality of products as well as eliminating waste from the industrial process. If the production lines contain an embedded metallic layer it serves as a reference, similar to the metal plate used in our experiment. The wider area where material samples are placed can be sensed by an array of GPR antennas. Hence, the reflection coefficient calculated with the above described method can be acquired from various sites of the sample simultaneously. In case of any impurity or imperfection within the homogenous material, the value of reflection coefficient at this site will differentiate from the rest of the sample. For instance, this technology could be used for in-line monitoring of cracks and voids inside concrete slabs as well as for detection of impurities within the food samples (e.g. flour) or any other solid samples with a significant difference in the reflection coefficient between the impurity and the surrounding homogenous material.

Table 1. Signal velocities for ambient air and dry sand calculated from acquired signals

Medium	Distance (cm)	Signal velocity (cm/ns)	Estimated reflection coefficient	Calculated reflection coefficient (ε = 4-7)
dry sand	12	13.059	0.428	0.333-0.451
	18	13.059	0.428	0.333-0.451

The EMI method is used to characterize if the material within the industrial process is metallic or not. Apart from this, we also found out that different metallic objects give various EMI responses. Fig. 10 shows four different EMI responses from four probes acquired synchronously. The probes are equidistantly positioned on a wooden pole. In this case, we investigated two rectangular objects with different dimensions. Probe 1 and probe 2 were located on the outside of the pole, therefore only the larger object was detected with all four probes. The smaller object was visible only for probe 2 and probe 3.

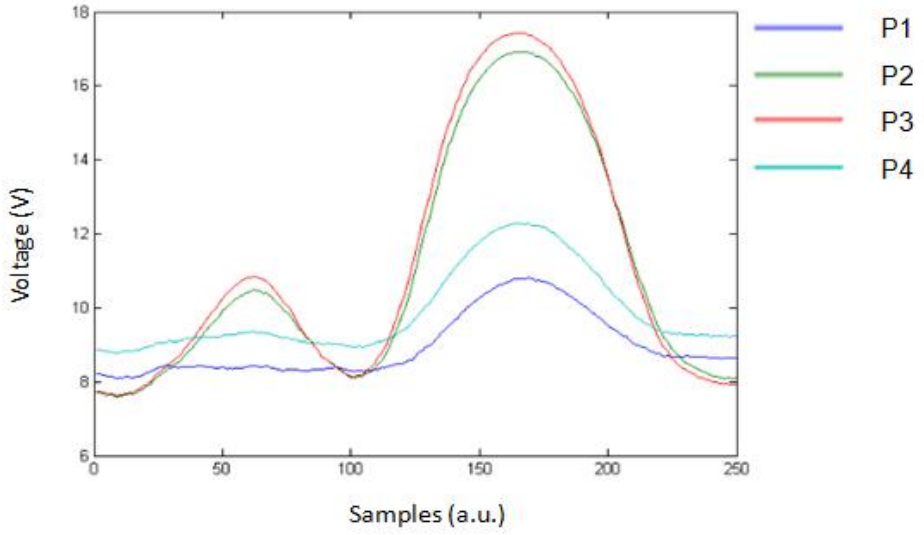

Fig.10. Four different EMI responses from four probes of EMI sensor acquired synchronously.

The raw EMI responses were recorded in a matrix form. With basic imaging method based on cubic interpolation 2-D images were obtained. From these images one can notice that not only the shape

(Fig. 12a) and orientation (Fig. 11) of the objects could be detected but also some information regarding metal material characterization could be defined. In Fig. 12b there is a major difference in EMI responses between aluminium and iron objects due to the eddy currents which originate by metallic objects and they are particularly expressed in case of conductor materials such as aluminium and not as much in case of ferromagnetic materials such as iron.

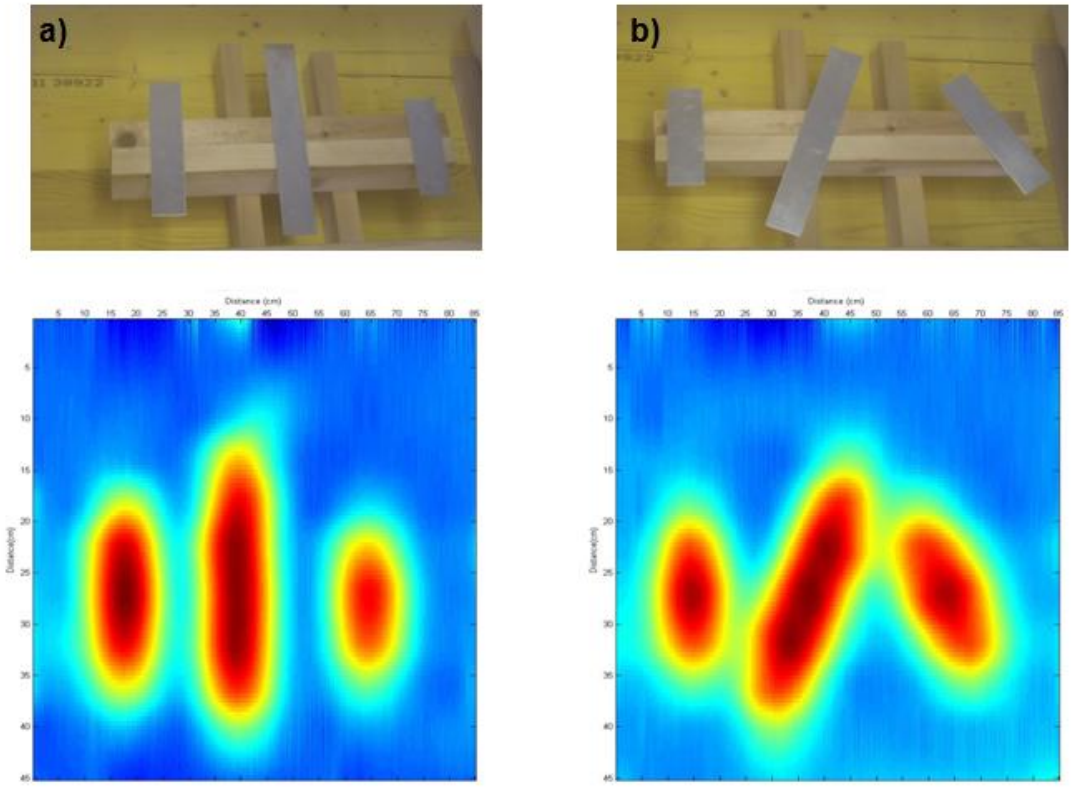

Fig.11. 2-D EMI images of different objects orientation, parallel (a) and inclined (b.

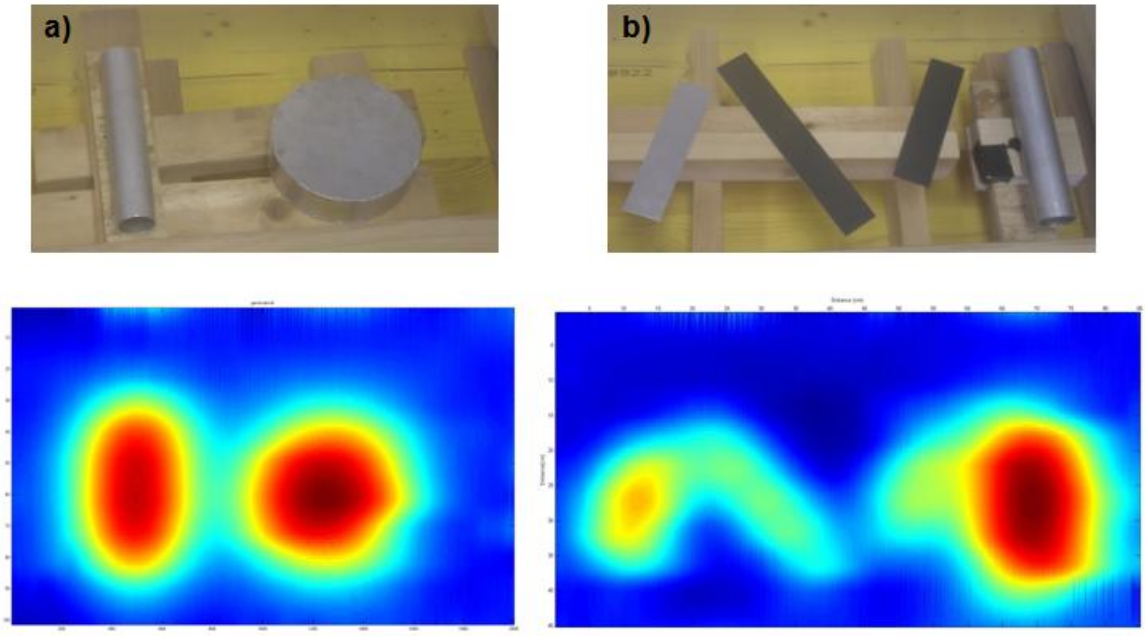

Fig.12. 2-D EMI images of different object shapes (a) and various material composition (b)

Through modification and adaptation of GPR and EMI sensor, the applications of these technologies are expanding, and the advantages could also be used beneficially in the energy sector. For instance, GPR offers great possibilities to identify suitable locations for geothermal energy generation considering the exploration of geological and hydrological sites. GPR can also be used as a tool for defining geological properties of soil based on dielectric properties determination. Thus, if the suitable soil properties are found the commercial use of the geothermal energy is possible. Another potential use of GPR and EMI sensor is in the field of energy efficiency, where these technologies can be used as additional sensors to monitor energy efficiency in buildings. As we demonstrated in this paper, these sensors allow characterizing the material properties and as such evaluating the state of maintenance of the building coatings. For this reason, the insulation materials can be investigated with respect to thickness measurements of walls and floors, void and cracks detection as well as moisture detection. Currently, we are developing adaptive EMI sensor and GPR which would be used in water environments (lake, river, sea). In such a way these technologies will be able to detect and map oil or gas pipelines at sea bottom. In case if reservoirs of energy sources in water environments are rather close to the sea bottom surface, the method is however also capable to seeing potential new sources of oil or gas.

5. Conclusions

In-line process monitoring often requires several sensing techniques in order to get relevant information. The methods proposed in this work EMI and GPR sensors are non destructive methods which could increase the efficiency of industrial processes through in-line and real-time monitoring of materials with the possibilities to detect defects and impurities as well as to provide information about the object's size, shape and orientation. Furthermore, the material eliminated from the process can be either reused in the same process or recycled in order to reduce disposal cost and energy consumption. With some modification and adaptation of GPR and EMI sensors, the applications of these technologies are expanding, and the advantages could also be used beneficially in the energy sector.

Acknowledgments

The authors would like to thank J. Polanc and V. Eržen for the support at GPR and EMI system development; Slovenian Research Agency grants no, P2—0348 and J2—4266 and EC 7th Framework Project Uncoss for financial support.

References

[1] Matikas T.E., Paipetis A., Kostopoulos V., Real-time Monitoring Of Damage Evolution In Aerospace Materials Using Nonlinear Acoustics. In: AIP Conference Proceedings. 2008;1022(1):549-552.

[2] Cano A.J., Plaza-Gonzalez P.J., Penaranda-Foix F., Catala-Civera J.M., Non-invasive Microwave Sensors for the Monitoring of the state of Liquids Used in the Polyurethane Industry. In: Proceedings of the 2007 International Conference on Sensor Technologies and Applications; 2007.

[3] Lasri T., Glay D., Achraït L., Mamouni A., Leroy Y., Microwave Methods and Systems for Nondestructive Control. Subsurface Sensing Technologies and Applications. 2000;1(1):141-60.

[4] Nielsen S.A., Bardenshtein A.L., Thommesen A.M., Stenum B., Non-Contact Ultrasound for Industrial Process Monitoring of Moving Objects. In: AIP Conference Proceedings. 2004;700(1):1499-506.

[5] Yao-Chun S., Taday P.F., Development and Application of Terahertz Pulsed Imaging for Nondestructive Inspection of Pharmaceutical Tablet., IEEE Journal of Selected Topics in Quantum Electronics. 2008;14(2):407-15.

[6] Chen C., Zhang J., A Review on GPR Applications in Moisture Content Determination and Pavement Condition Assessment. In: Proceedings of ACE, 2009.

[7] Knight R., Ground penetrating radar for environmental applications. Annu Rev Earth Planet Sci. 2001;29:229-55.

[8] Hubbard S., Jinsong C., Williams K., Rubin Y., Peterson J., Environmental and agricultural applications of GPR. Advanced Ground Penetrating Radar. In: Proceedings of the 3rd International Workshop on IWAGPR; 2005 May 2-3, 2005.

[9] Olhoeft G.R., Applications and frustrations in using ground penetrating radar. Aerospace and Electronic Systems Magazine, IEEE. 2002;17(2):12-20.

[10] Olhoeft G.R., Applications and limitations of ground penetrating radar. SEG Technical Program Expanded Abstracts. 1984;3(1):147-8.

[11] Lai W.L., Kind T., Wiggenhauser H., Using ground penetrating radar and time-frequency analysis to characterize construction materials. NDT & E International. 2011;44(1):111-20.

[12] Druyts P., Craeye C., Acheroy M., Volume of Influence for Magnetic Soils and Electromagnetic Induction Sensors. IEEE Transactions on Geoscience and Remote Sensing. 2010;48(10):3686-97.

[13] Sezgin M., Kaplan G., Birim M., Bahadirlar Y., Buried metalic object identification by EMI sensor. 2007: SPIE.

[14] Manoj G., Eugene W.W.L., Introduction to Microwaves. Microwaves and Metals. Singapore: John Wiley & Sons; 2007.

[15] Ghasemi F.S.A., Abrishamian M.S., A novel method for FDTD numerical GPR imaging of arbitrary shapes based on Fourier transform. NDT & E International. 2007;40(2):140-6.

[16] Jol H.M., Ground penetrating radar: Theory and applications. First ed: Elsevier Science; 2009.

[17] Cukavac M., Klemcic G., Lazovic C., Reconstruction Of Buried Objects by Implementation of Ground-penetrating radar technique: Example on Roman Tomb in Brestovik (Serbia). In: Proceedings of the International Conference on Geoarchaeology & Archaeomineralogy; 2008: 333-338.

[18] Annan A.P., Electromagnetic Principles of Ground Penetrating Radar. In: Jol H.M., editor. Ground Penetrating Radar Theory and Applications. 1st ed. Oxford: Elsevier; 2009. p. 3-40.

[19] Gloaguen E., Chouteau M., Marcotte D., Chapuis R., Estimation of hydraulic conductivity of an unconfined aquifer using cokriging of GPR and hydrostratigraphic data. Journal of Applied Geophysics. 2001;47(2):135-52.

[20] Stuerga D., Microwave–Material Interactions and Dielectric Properties, Key Ingredients for Mastery of Chemical Microwave Processes. In: Loupy A, editor. Microwaves in Organic Synthesis. 2nd ed.; 2006. p. 1-61.

[21] Collins L., Gao P., Makowsky L., Moulton J., Reidy D., Weaver D., Improving detection of low-metallic content landmines using EMI data. In: Proceedings of the Geoscience and Remote Sensing Symposium, 2000.

[22] Ho K.C., Collins L.M., Huettel L.G., Gader P.D., Discrimination mode processing for EMI and GPR sensors for hand-held land mine detection. IEEE Transactions on Geoscience and Remote Sensing. 2004;42(1):249-63.

[23] Xuejun L., Carin L., Application of the theory of optimal experiments to adaptive electromagnetic-induction sensing of buried targets. IEEE Transactions on Pattern Analysis and Machine Intelligence. 2004;26(8):961-72.

[24] Won I.J., Keiswetter D.A., Bell T.H., Electromagnetic induction spectroscopy for clearing landmines. IEEE Transactions on Geoscience and Remote Sensing. 2001;39(4):703-9.

[25] Rudge A.W., The Handbook of antenna design. London: Peter Peregrinus Ltd.; 1983.

Assessment of stresses and residual life of plant components in view of life-time extension of power plants

Anna Stoppato[a](CA), Alberto Benato[b] and Alberto Mirandola[c]

[a] D.I.I. University of Padova, Padova, Italy, anna.stoppato@unipd.it
[b] D.I.I. University of Padova, Padova, Italy, alberto.benato@unipd.it
[c] D.I.I. University of Padova, Padova, Italy, alberto.mirandola@unipd.it

Abstract:
The deregulated energy market requires strong, irregular and discontinuous operation in order to meet the user demand and produce energy mainly during peak hours, when the electricity price is higher. The increasing number of plants powered by non-predictable renewable sources and of cogenerative units has amplified this need. For this reason, over the last decade new more flexible strategies in thermal power plants and systems management have been applied, which ensure greater income in the short term, but likely cause a lifetime reduction of the most critical components, due to thermo-mechanical fatigue, creep and corrosion.
A procedure aimed at evaluating this extra cost related to a flexible operation, and at assisting the management decision about power plants' operation and maintenance scheduling has been implemented by the Authors.
The procedure, on the basis of the historical data, predicts the residual life of the most critical components, considering the effects of creep, thermo-mechanical fatigue, welds, corrosion and oxidation, as a function of the past and the forecasted operation strategy. The core of this procedure is the simulation tool, able to evaluate the variation of the most important thermodynamic parameters versus load during the transitory periods and then to estimate the creep and fatigue stresses on plant devices.
In this paper the model for the analysis of a combined power plant will be presented. It permits to simulate the load variation of the plant also during start-up and shut-down. The velocity of these variations is taken into consideration too. Then, the stresses of the most critical components are calculated and the related damage evaluated. Finally, the residual lifetime can be estimated and the consequences on the long term profit of the plant assessed.

Keywords:
Deregulated market, Combined plants, Super-heater, Creep-fatigue model, Sustainability.

1. Introduction

The gradual liberalization of the gas and electricity markets in Europe [1-2] has caused growing competition among different electricity producers and this makes more and more important optimizing management strategies and plant control in order to reduce production costs. This optimization must also take into account the severe environmental laws which restrict the operating margins of power plants [3].

The operating economy is therefore essential for all the electric operators since it is the requisite for the survival in the energy market, but the variability of fuel costs [4], the new and more efficient technology systems [5], the connection to the grid of many plants powered by renewable sources, often small in size and not able to plan their production [6-7], the daily variability of electricity demand and price [8] pose complex problems to the plant operator which has to develop operational models aimed at improving the system management in terms of efficiency, flexibility and reliability.

All these aspects result in new strategies for plant and systems management: strongly irregular and discontinuous operation of power plants is required in order to meet the user demand, satisfy the CO_2 emission limits and maximize profits by producing as much as possible during peak hours, when the electricity price is higher, while stopping the plant or greatly reducing the load during off-peak hours. Consequently, many plants have to work in the so-called "two shift run" [9-11], operating for 12-15 hours/day, and usually stopping for the whole weekend. Essential characteristics for the correct functioning of the power system is the ability to satisfy the load changes required by the electricity demand (especially the demand for short term, that has a higher profit) and operating at minimum load during off-peak periods. Therefore, each unit should have design features that make it capable to work either at high loads or at a technical minimum and make night and weekend shutdowns with short time restart. Gas turbines and combined plants, that are powered by expensive high-quality fuel, which are more flexible than other thermal power plants, are especially asked to make frequent and rapid load variations, but also steam power plants are often operated at variable load with several stops [10,12].

Going from a basic to a flexible usage involves the need of verifying the suitability of plants to develop a different role for which they were designed and studying types of plant management to reduce problems related to flexibility.

This type operation guarantees greater profits in the short term, but can cause a reduction in the lifetime of the most critical components, due to thermo-mechanical fatigue loadings. Since the correct target of good management is to obtain the best average performance during the whole life of the system, the decision makers need suitable tools that are able to give information about the long-term consequences of the operation choices. The boilers, in particular the parts at higher temperature, gas and steam turbines are subjected to higher thermo-mechanical cycles due to an increase of heating velocity and to the number of these transitional periods. Each cycle damages the components and the accumulated damages end up causing frequent breakdowns and unplanned maintenance. Moreover, the methods used to start and stop the plant influence its reliability and its life expectancy.

The Authors in the past have investigated [13] the relationship between a plant's operation and its components' residual life. A model to assess damage from creep and thermo-mechanical fatigue has been proposed and its application was presented to find the cumulative mechanical damage of the most critical components of thermoelectric power plants. The effects of corrosion and erosion on the residual life are considered too and included in the model of damage. The presence of weak points in the devices, such as welding in the pipes of boilers, where the problems are accentuated, is considered too.

This model has been introduced into a procedure for power plant on-line monitoring, control, production and maintenance scheduling already presented [14-15]. It can be used to evaluate the effect of the current management strategy in terms of reduction of residual life. To take into account the high uncertainty of the electricity market, the procedure has been improved with the possibility of modifying the production strategy during operation.

In this paper, the focus is on the combined gas-steam power plants which currently gives the 57.5% of the electric energy produced in Italy (69.4% of that from thermal plants) and for this reason, are now the most interesting in regard to operating flexibility problems. Moreover, the spinning and cold reserve service is a prerogative of these plants. This will permit greater profits, but asks for:

- Reducing characteristic time of start-up and transitional load.
- Extending the field of possible operating conditions by increasing the peak power or reducing the technical minimum load.
- Higher recurrence of transient conditions already provided.

2. Combined cycle

Gas cycles are flexible while steam ones are “slow”, so during transitional operation of a combined plant the Heat Recovery Steam Generator (HRSG), where the coupling of two cycles actually occurs, must work as a thermal flywheel and for this reason it is subjected to high thermo-mechanical fatigue.

ASME (section-Power Boiler Code) [16], British Standard (BS1113) [17], EN 12952[18] and TRD301 [19] are guidelines for HRSG design taking into account these problems.

The most stressed element is the high temperature super-heater (SH), which is subject to high temperatures and pressures; so during transitional operation the thermo-mechanical fatigue is added to creep phenomenon. Some typical examples of how cycling creates or enhances damaging the mechanism are given below:

- Creep damage by definition is caused by a prolonged exposure to high temperature and stress. Creep may be the only process which is not caused or enhanced by cycling. However if the creep is coupled with fatigue due to cycling, the damage will be much higher than that occurring if the same fatigue or creep is working alone.
- Fatigue damage is the most prevalent action affecting the boiler life and is a direct consequence of cycling. For example, for rapid starting, the SH is exposed to high temperature on the outside of tubes and headers whereas inside may still be cool, while at shut down cool gasses are sent on hot surfaces. Similarly, the condensed steam in the tubes after shut down impinges on hot surfaces if condensate remains in the tubes. The high pressure components are more vulnerable to top fatigue effects due to higher thickness.
- Thermal shock: condensate in the super-heater would result in thermal shock to the inner surface of the tubes hand headers.
- Oxidation: is caused by the exposure of the metal to high temperature in comparison to design specifications. Oxidation and corrosion can happen inside and outside due to gas or steam. The reaction with water results in corrosion this is due to cycling or because of water treatment failure.
- Differential expansion: uneven heating of tubes due to flow and temperature bad distribution causes adjacent tubes to expand differently. This problem can also present itself when devices made of difference materials or having different thickness are connected; for example between headers and tubes.

Operation in a two-shift regime has two main effects on steam turbines:

- Thermal fatigue and creep/thermal fatigue associated with thick walled component, including start and stop valves and HP and IP turbines inlet belts.
- Mechanical fatigue as a result of load and speed variations. It arises from two sources: a) during the run up, the passages of critical speed where vibration levels increase; b) the very high centrifugal stress on the route area of blades, which is more important in LP stages.

Other problems are related to the overheating of turbines as a result of windage, to differential expansion of rotors and casings, to erosion as a result of oxide impact of blades.

2.1. The model

Mechanical parameters in the devices, that are stress and strain deriving from creep and thermo-mechanical fatigue, are used to calculate the cumulative mechanical damage to each single component. They depend on the thermodynamic variable trends which define the energy conversion process, both during constant and transient operation.

A model of a simple one level combine cycle has been built by means Dymola software [20] and CombiPlant Library [21] in order to estimate the thermodynamic variable trends during different operation modes. Since at the present the main focus is on the HRSG the gas cycle has been modeled as a hot gas source.

The design power of the plant is 40 MW of which 13 MW from steam section. The load variation is simulated using a control on the gas sub-section. The layout of the model is reported in Fig. 1. It also includes all the control systems, whose role is very important during load variations. Drum vent, admission valves and pump speed control are implemented. They are in charge of maintaining the correct water level in the drum. Steam temperature control is needed to avoid that the steam temperature from the HRSG is too high. The geometry of all the devices (number, length and diameter of pipes in the heat exchangers and their configuration, turbine and pump dimensions, connection pipes dimensions), their materials and turbine and pump maps have been introduced into the parameters windows of Dymola Software.

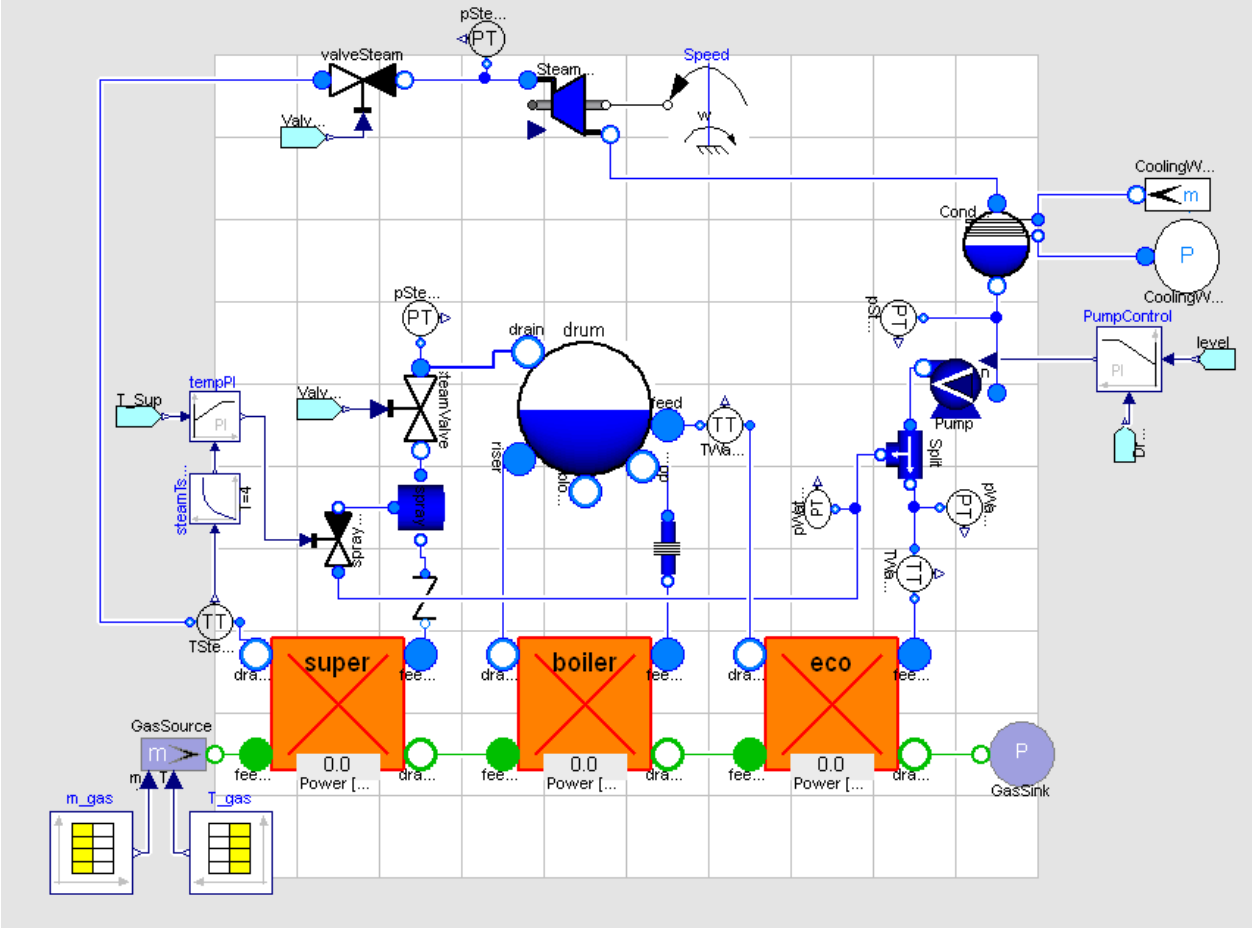

Fig. 1. Model of the Combined Plant.

2.2. Model results

The response of the steam section is analyzed using the Model reported in Fig. 1. To evaluate the influence of the load variation velocity on devices lifetime, Authors studied load variations from design point to the technical minimum (40% of design electric power). The simulations differ for the duration of rise and fall times on the gas side (from 20 to 40 minutes) and for the duration of the operation at minimum load between two successive transient periods (from 15 to 120 minutes).

Fig. 2 shows the gas and steam mass flow rate and the mechanical power by the steam turbine for a transient period of 20 min. As we can see, steam plant time constant is about twice than that of gas while the two trends are very similar.

In Fig. 3 the water level in the drum is shown during the fastest load variation. It is evident that both raise and fall do not present control problems.

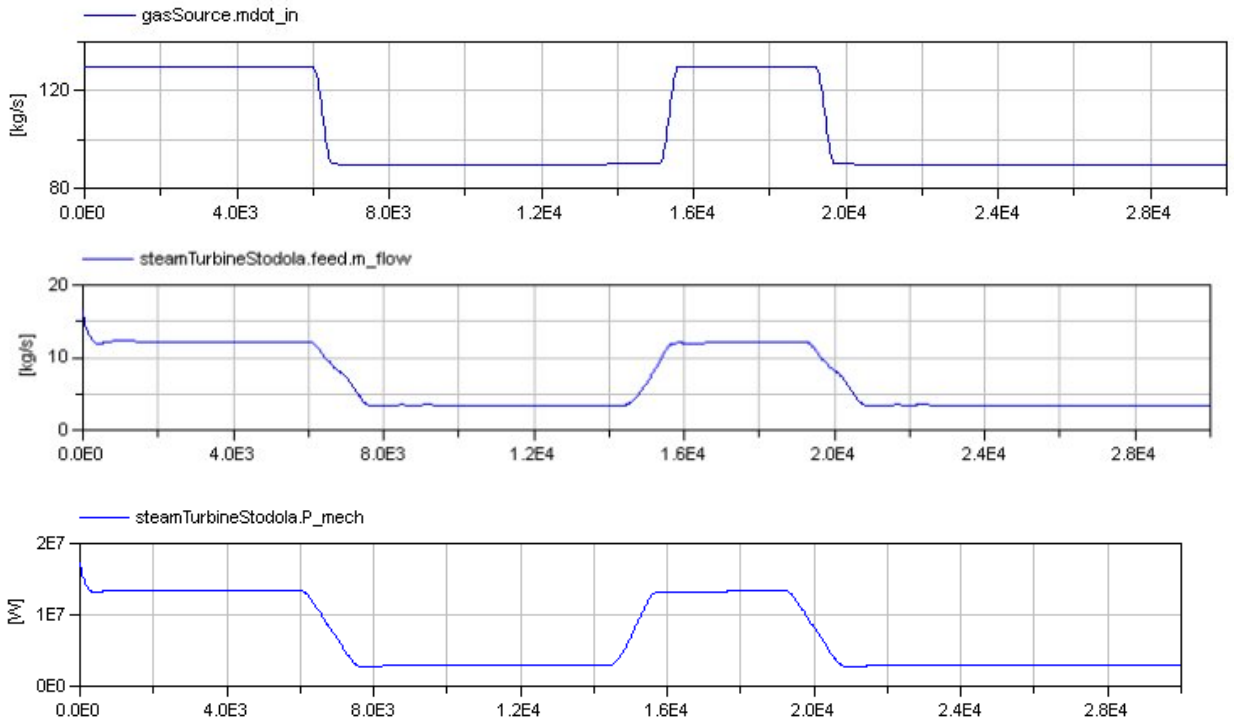

Fig. 2. Trend of gas and steam mass flow rate and of steam turbine mechanical power (W) vs. time (s) for a load variation from design to minimum load in about 20 min.

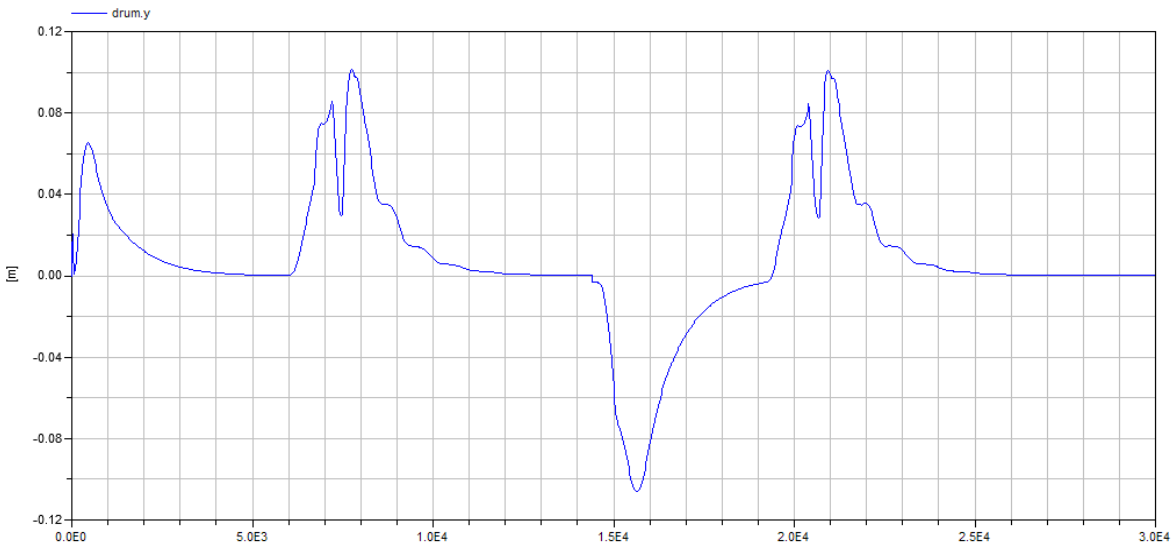

Fig. 3. Water level in the drum (m) and drum air vent signal vs. time (s).

During transient operation, plant components are subject to variations of pressure and temperature that cause thermal stress and thermo-mechanical fatigue. The super-heater is one of the most critical components. For this component, Fig. 4 shows the medium diameter wall temperature trends vs. time in different positions along the flow path for the most severe (i.e. rapid) raise and fall conditions. As we can see, there is a large temperature variation along the longitudinal development of each tube (more than 120°C from the wall near gas inlet and that near gas outlet at design point). This difference is about 70°C lower at minimum load, while reaches higher values during raise time. Note also that the maximum wall temperature is about 20°C higher during transitory that its design value; at minimum load this temperature is about 220°C lower.

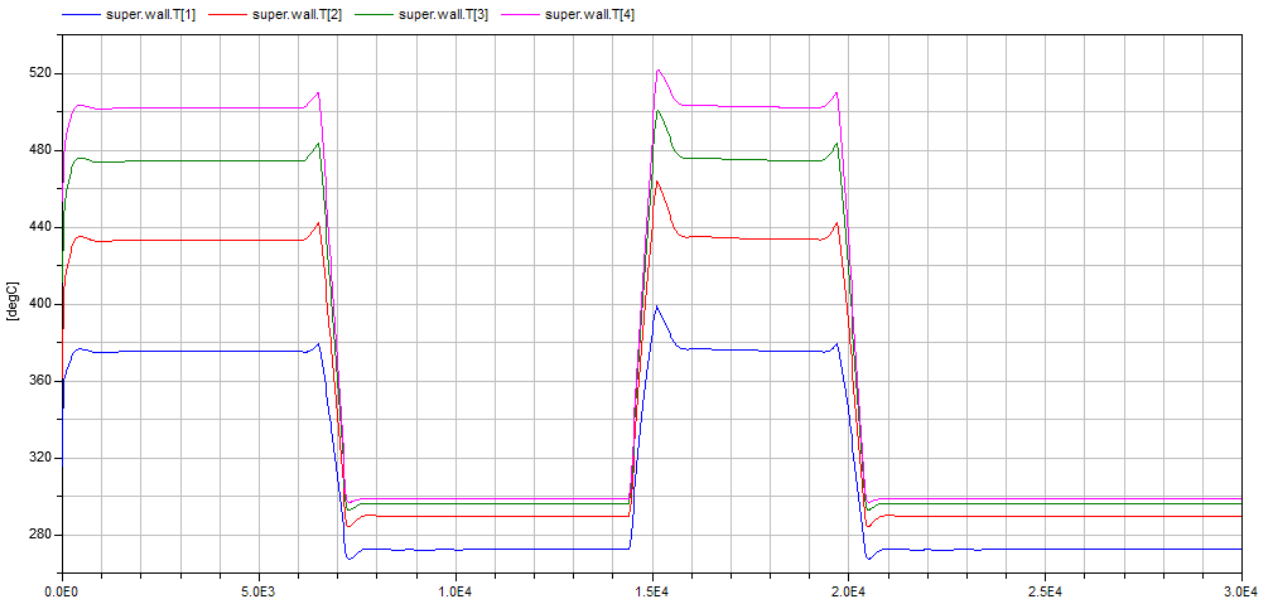

Fig. 4. Medium diameter wall temperature (°C) trends in super heater vs. time in different positions along the longitudinal development form gas inlet [4] to gas outlet [1].

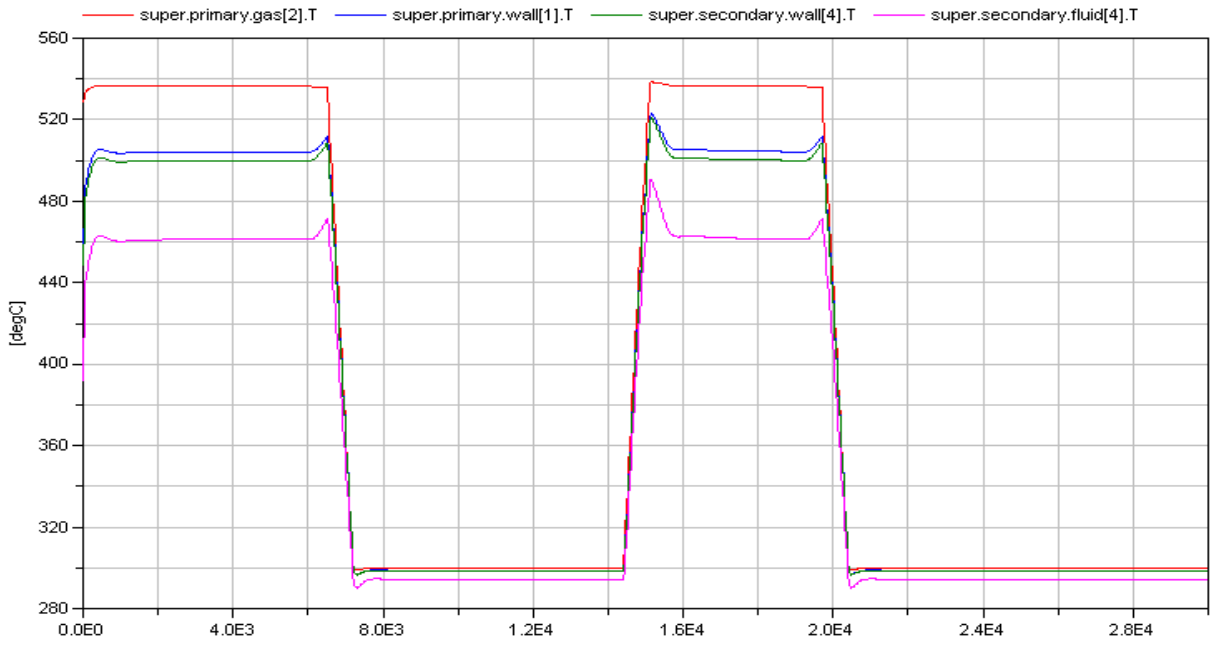

Fig. 5. Gas, steam and wall inner and outer diameter temperature (°C) trends in the hottest point of the superheater (i.e. at gas inlet).

In addition, due to the heat transfer from hot gas to colder steam, there is a temperature difference between inner and outer diameters of pipe walls. Fig. 5 shows the temperature trends for the hottest point: there are about 4.3°C along the pipe thickness (2.5 mm) at design point, but this value vary with load up to about 0°C at minimum load. This variation causes a thermo-mechanical fatigue stress, too.

For the same load variation, the steam pressure varies from 64.1 bar to about 15.1 bar.

2.2. Life time reduction calculation

The super heater is made of AISI SA335P91 (P91) with a high mechanical strength up to 650 – 700°C. This material is commonly used for the super-heaters of high performance three level combined cycles, but it could be used also for simpler plants. Pipes have an inner radius of 10 mm and a thickness of 2.5 mm.

As said, all the pressure and temperature variations during transient period generate thermo-mechanical fatigue stress in addition to creep. Using the model described in [15], the strain range in the most sollecited point of super-heater wall, which is the inner diameter in the hottest position, has been evaluated during each cycle as a function of steam pressure and temperature variations. Then, by means of the experimental Manson-Coffin curve of P91, reported in Fig.6 [16], the cycles number to complete failure has been calculated for each simulation.

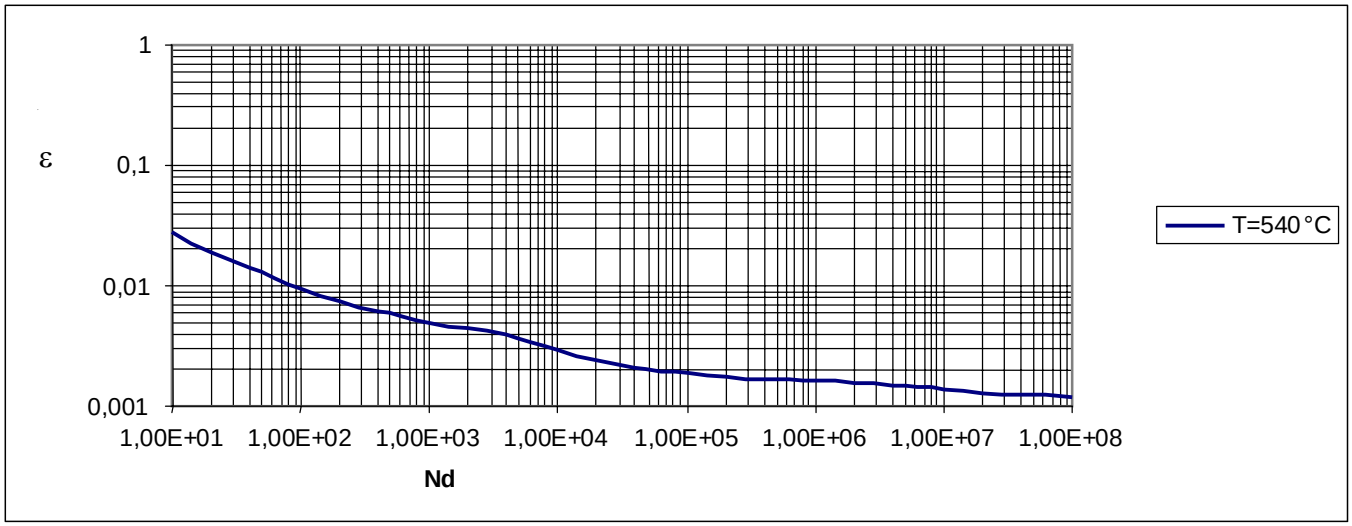

Fig. 6. Manson-Coffin curve for P91 at 540°C [16].

For the load variation from the design point to the technical minimum in 20 minutes analysed in the previous section, the strain range is 0.003566. It corresponds to about 1400 cycles before failure. For a load variation with double time constants (about 40 min from design to minimum load) the strain range is 0.003566 and the life is about 1750 cycles. This difference is mainly related to the lowest temperature peak in the most stressed point, as shown in Fig.7.

In both these cases, the duration of operation at the minimum load before the following raise up has been simulated 120 min long, while the operation at design load is 60 minutes long. If this duration is reduced up to 30 minutes, the effects on life time is not significant, but if it is reduced to 15 minutes the strain range becomes 0.0035736 corresponding to 1200 cycles before rupture, always with a transient duration of 20 minutes. This reduction is due to an increase in the peak temperature, caused by the not complete achievement of stationary conditions on steam side between load fall and raise.

Considering a management strategy aimed at the maximum production only when electricity prices are higher, where the plant operates at design load from 9 am to 6 pm, and at the minimum technical from 6 pm to 9 am, these results correspond to a life time of about 4 years if the hypothesis of load variation within 20 minutes, of 5 years if the variation is within 40 minutes.

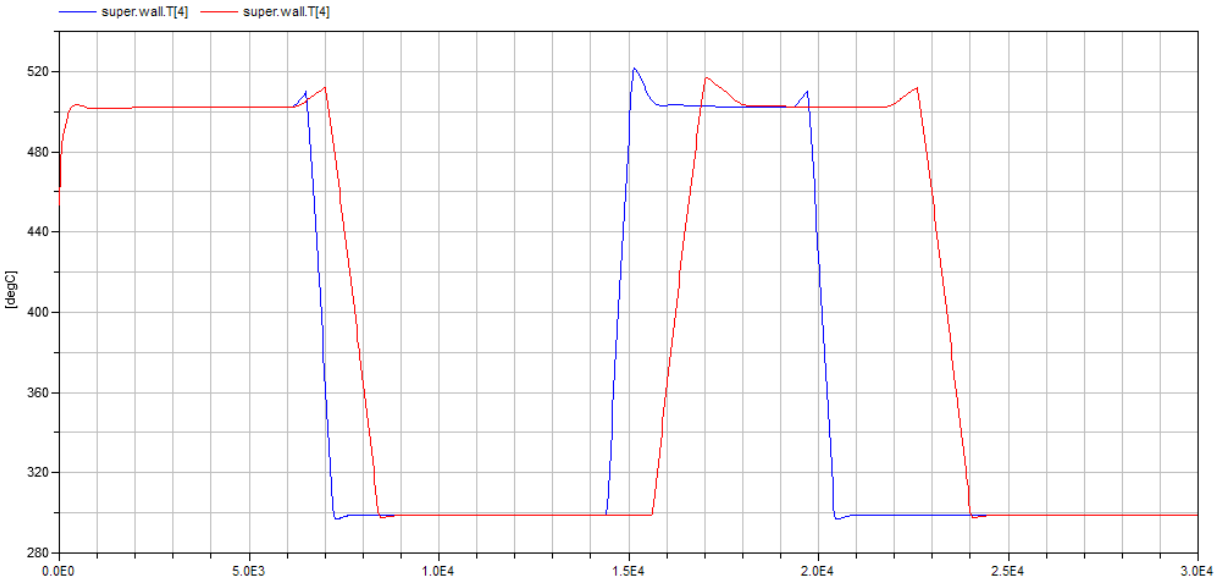

Fig. 7. Wall external diameter temperature (°C) trends in the hottest point of the superheater for two different velocities of load variations.

3. Steam plant turbine

A model was also built of a steam turbine for thermal power plant having seven extractions. The turbines are very critical in steam plants, since they often have been not designed for a cyclic operation and so have small axial and radial clearances between rotors and casings and thick walls, while the bypass of the turbine during start-up is not present. The model was tested using data derived from tests at stationary load from an existing plant sized 320 MW. Subsequently, authors used this model to implement the transition from nominal power to zero power; situation that normaly occurs during an operation to stop the plant or the occurence of a break. Fig. 6 shows the scheme of the turbine model. In Fig. 7 the measured power generated by the HP section during a shut down for a out of load problem is presented. Fig. 8 reports the simulated mass flow rate and turbine inlet pressure trends for the same event. There is a good correspondence between measured during a transient period and simulated values for temperature and pressure of drains.

Also in this case, these results can be used to evaluate the stress and strain on turbine blades and casing and consequently the lifetime reduction due to a sudden shut down.

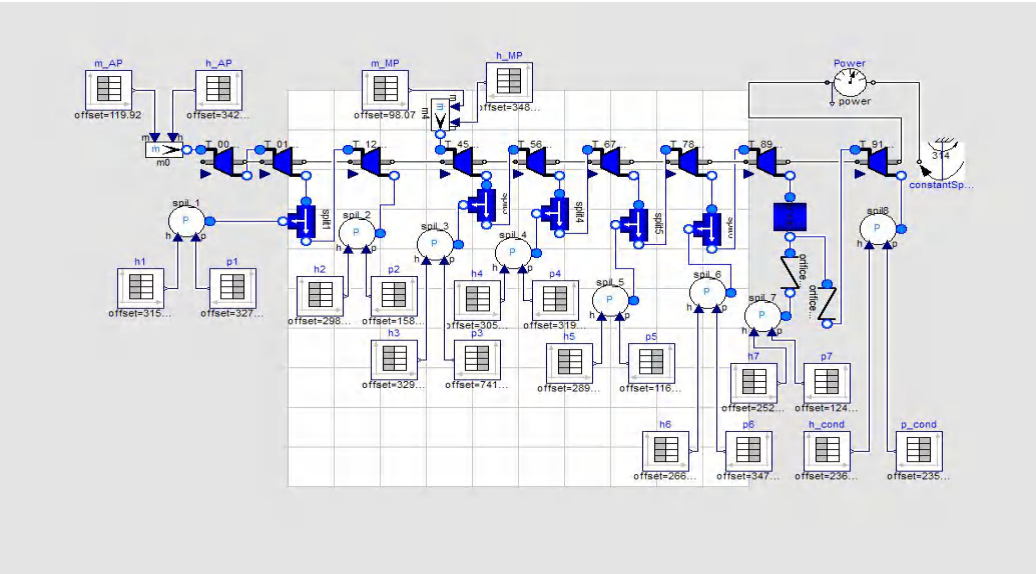

Fig. 8. Scheme of a 320 MW turbine model.

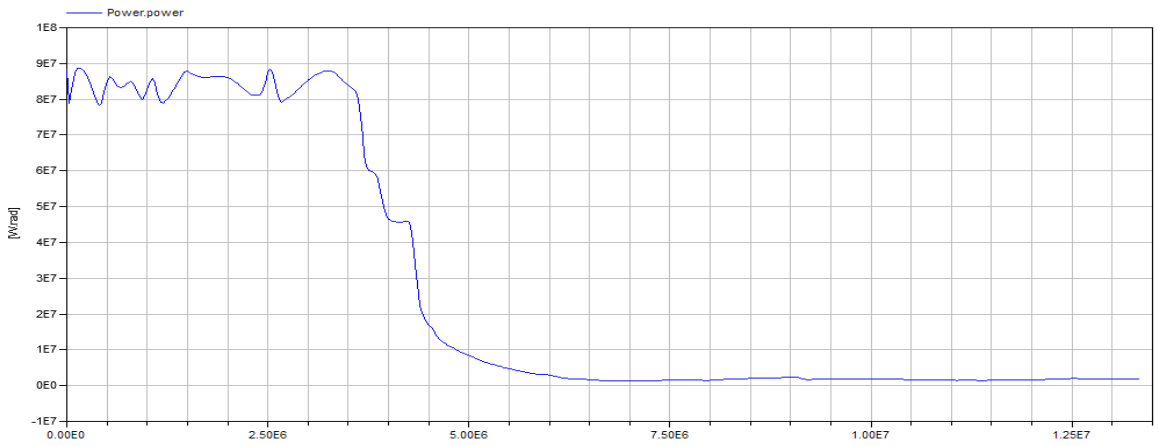

Fig. 9. Trend of power (MW) generated by the HP turbine section vs. time (s).

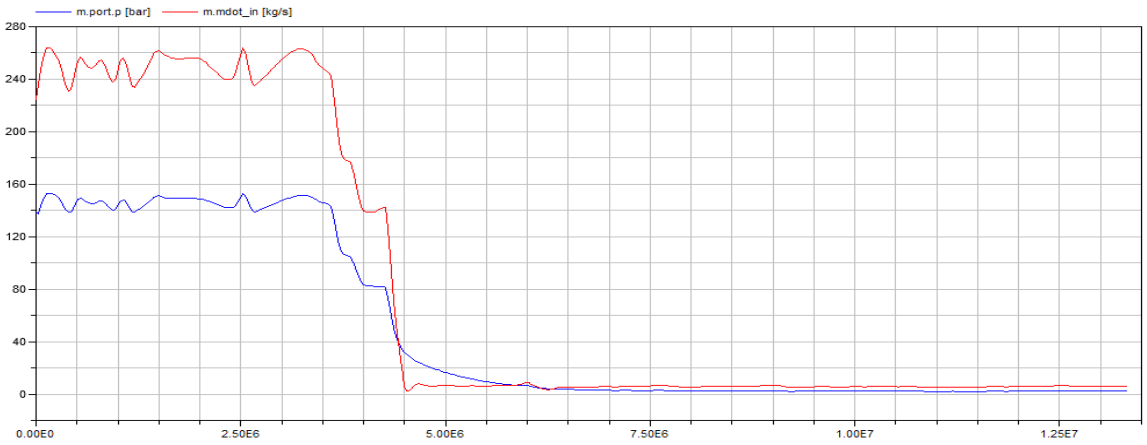

Fig. 10. Trend of mass flow rate (kg/s) and inlet pressure (bar) for the HP turbine vs. time (s).

4. Conclusions

Some models for the simulation of plants operation during load variations have been presented. They can be used to calculated thermodynamic variable trends which influence creep and thermo-mechanical fatigue damage in plant devices. So, the lifetime of devices can be forecasted as a function of operation management. The models permit to simulate management strategies different: for number of annual hot or cold start-ups, velocity of load variations, for hours of operation at design and off-design load. The results give a comparison among strategies in terms of devices lifetime, which can be translated in economic terms.

References

[1] Directive 2003/54/EC of the European Parliament and of the Council of 26 June 2003 concerning common rules for the internal market in electricity and repealing Directive 96/92/EC

[2] Directive 2009/72/EC of the European Parliament and of the Council of 13 July 2009 concerning common rules for the internal market in electricity and repealing Directive 2003/54/EC]

[3] Italian National Emission Plan, D.lgs. April 4, 2006, n. 216 and its modifications (in Italian).

[4] DOE/EIA International Energy Outlook 2011- Available at: <www.eia.gov> [accessed 2.2.2012].

[5] Roques F.A., Technology choices for new entrants in liberalized markets: The value of operating flexibility and contractual arrangements. Utilities Policy 2008; 16(4): 245-253.

[6] Tsao C.C., Campbell J.E., Chen Y., When renewable portfolio standards meet cap-and-trade regulations in the electricity sector: Market interactions, profits implications, and policy redundancy. Energy Policy 2011; 39 (7): 3966-3974.

[7] Milstein I., Tishler A., Intermittently renewable energy, optimal capacity mix and prices in a deregulated electricity market. Energy Policy 2011; 39 (7): 3922-3927.

[8] GME Statistics Monitoring-Electricity Market- summary data - Available at: http://www.mercatoelettrico.org/en/Statistiche/ME/DatiSintesi.aspx [accessed 2.2.2012].

[9] Concari S, Fedeli G., Cyclic Operation Experience at ENEL with Conventional Thermal Power Plant, Proceedings of the International seminar "Cyclic Operation of Power Plant- Technical, Operation and Cost Issues. London, 25-27 June 2001.

[10] Dukashe MP, Nieuwoudt T, Begg J., Operational Experience of two shifting Large Coal Fired Unit, Proceedings of the International seminar Cyclic Operation of Power Plant-Technical, Operation and Cost Issues, London, 25-27 June 2001.

[11] Chow J, Ho K, Du X, Lee HS, Pearson M. Experience from extensive two-shift operation of 680 MW coal/gas fired Units at Castle Peak, Hong Kong, Proceedings of the International seminar Cyclic Operation of Power Plant- Technical, Operation and Cost Issues, London, 25-27 June 2001.

[12] Lefton SA, Besuner P, Grimsrud P, Kunts T. Experience in Cycling Cost Analysis of Thermal Power Plants in North America and Europe, Proceedings of the International seminar Cyclic Operation of Power Plant- Technical, Operation and Cost Issues, London, 25-27 June 2001

[13] Carraretto C, Lo Casto E, Meneghetti G, Polo F, Stoppato A., Comparison Among Thermo-Mechanical Fatigue Criteria in The Context of Long-Term Power Plants Optimisation, Proceedings of ECOS 2007, Padova – Italy, June 25-28 2007: 1637-44.

[14] Mirandola A, Lo Casto E, Stoppato A., A procedure for the evaluation of residual life of steam Power plant devices. Proc. of the 22nd International Conference on Efficiency, Cost, Optimisation, Simulation and Environmental Impact of Energy Systems ECOS 2009, Iguaçu (Brazil).

[15] Lo Casto E, Mirandola A, Stoppato A., Evaluation of the effects of the operation strategy of a steam power plant on the residual life of its devices. Energy, The International Journal, 2010; 35: 1024-32

[16] ASME Code. Boiler and pressure vessel code. Section II, III, New York, USA, 2001.

[17] British Energy. R5, Assessment procedure for the high temperature response of structures. Issue 3, Gloucester, UK, 2003.

[18] UNI EN 12952-5:2011 Water-tube boilers standards

[19] TRD 301 Annex1 – Calculation for cyclic loading due to pulsating internal pressure or combined changes of internal pressure and temperature

[20] Elmqvist H, Brück D, Otter M. Dymola User's Manual, Dynasim AB, Research Park Ideon, Lund, Sweden, 1996.

[21] CombiPlant Library, Modelon AB in:ww.modelica.org/libraries/CombiPlant.

Control Strategy for minimizing the electric power consumption of Hybrid Ground Source Heat Pump System

Zoi Sagia[a], Constantinos Rakopoulos[b]

National Technical University of Athens, School of Mechanical Engineering, Department of Thermal Engineering, Laboratory of Thermal Processes, 9 Heroon Polytechniou St., Zografou Campus, 15780 Athens, Greece
[a]zoisagia@mail.ntua.gr, CA
[b]cdrakops@central.ntua.gr

Abstract:

Hybrid Ground Source Heat Pump Systems (HGSHPSs) which include cooling towers are widely used so as to improve Ground Source Heat Pump Systems (GSHPSs) efficiency in cooling dominated applications. A Greek office building with total cooled area 1000 m^2 is examined. The whole system is modelled using TRNSYS 17. System's operation is optimized using TRNOPT 17 so as to meet the maximum cooling load during the net cooling period, when no heating loads occur, by minimizing Ground Heat Exchangers (GHEs) depth. Three control strategies, based on continuous observation of critical temperatures, are applied to the optimized system. Each strategy attempts to achieve a further optimization of HGSHPS's operation by minimizing the electric power consumption. In the first one, the cooling tower is turned on when the difference between the fluid temperature exiting heat pumps and ambient air wet bulb temperature exceeds 10 ^oC. In the second one, the cooling tower is on when the fluid temperature exiting GHEs is greater than 28 ^oC. In the third one, the cooling tower starts to operate when the fluid temperature exiting heat pumps is greater than 32 ^oC. Each of these control points is normalized by the fluid temperature exiting the hot side of Heat Exchanger which comes in between the ground loop and the Closed Circuit Cooling Tower loop. The new set points define three new control strategies which are examined so as to achieve a further improvement to HGSHPS's operation.

Keywords:

Hybrid Ground Source Heat Pump System, Ground Heat Exchanger, Closed Circuit Cooling Tower, heat pump, Control Strategy.

1. Introduction

The use of Hybrid Ground Source Heat Pump Systems (HGSHPSs) has become very popular, nowadays. This happens due to the fact that HGSHPSs achieve a better energy saving performance than conventional Ground Source Heat Pump Systems (GSHPSs) thanks to supplemental heat rejection or extraction subsystems.

In the current work a HGSHPS which is coupled with a Heat Exchanger loop and a Closed Circuit Cooling Tower loop is examined. The studied HGSHPS is applied to a Greek office building with total cooled area 1000 m^2 and accounts for a cooling dominated climate. Different control strategies are applied to cooling tower's operation so as to minimize the whole system's electric power consumption during the net cooling period or in other words the period when only cooling loads occur.

Various studies have been done so as to propose control methods which lead to a more efficient operation of cooling towers in HGSHPSs. Kavanaugh (1998) [1], revises the HGSHPS sizing which has been proposed in ASHRAE (1995) [2] and suggests a balancing method so as to make up for the heat pump lessening performance due to the ground temperature increase in the borehole field. He concludes that the use of HGSHPSs is more energy and money saving in warm and hot climates than in moderate ones. Yavutzurk and Spitler (2000) [3] perform a comparative study of different

operating and control strategies of a HGSHPS using an hourly short time step simulation. This system includes a mechanical draft, open circuit cooling tower which is coupled with the ground loop by a plate heat exchanger. The best strategy is the one which activates the cooling tower fan when the temperature difference between the fluid exiting the heat pump and the ambient air wet bulb temperature is greater than a set point, which could be increased, and it is depended on system's operating characteristics and climate. However, the control strategy with the least operating hours per year is not necessarily the most cost effective one. Xu (2007) [4] proposes three control strategies. The first one determines set point at which the cooling tower starts its operation according to the temperature difference across the heat pump. The second one is a forecast/historical control strategy which depends on the ability to estimate the possible loads and energy savings of the heat pumps. The third one is based on linear functions of entering and exiting fluid temperatures of the heat pump with the average loop temperature deviation. All of them have satisfactory energy saving percentage to the studied HGSHPSs without the need of separate optimization of each system. Hackel et al (2009) [5] develop design guidelines for hybrid cooling and heating dominated systems. The cooling dominated HGSHPS includes a closed circuit cooling tower which is coupled with the heat pump system without the presence of heat exchanger. The optimal control set point for this tower is when the fluid temperature entering it is greater than the ambient wet bulb temperature plus a temperature difference which is chosen according the ASHRAE 1% design wet bulb temperature for the building's climate in July.

2. HGSHPS Modelling

2.1. Building Modelling

In the present article, a mainly glass office building with total cooled area 1000 m^2 is the case study. It bears insulating, Ar, 4/16/4 glazing with thermal transmittance $u = 1.4\,W/m^2K$ and solar heat gain coefficient $g = 0.589$.

The climatic data referred to Athens city and have been derived from Meteonorm 6.1 [6] in the form of Typical Meteorological Year TMY 3.

The cooled area of the building is modelled as one thermal zone in which the set point cooling temperature is 26 ^oC with 45% air humidity according to new, Greek legislation on buildings [7], applied on January 2011.

The whole system is modelled using TRNSYS 17 [8]. However, two different .tpf files have been built so as to perform the simulation by decreasing the demanded computational time. The first one determines the building loads and the second one simulates the HGSHPS's operation. The cooling load output of the first file is used to create an Excel file which is read by the second .tpf file. The distribution cooling system to the building is not examined.

Fig.1 shows the annual building load profile. It is very obvious that the annual cooling loads are much higher than the heating ones and this leads to a cooling dominated system. The annual cooling demand is 105.79 kWh/m^2 and the total cooling demand for the period of interest in this work, which is the net cooling period when only cooling loads exist in the building, is 74 kWh/m^2 (70% of the annual load). This period is running through June to September and it is defined in Fig.1 between the dashed lines. The peak cooling load is 70.3 kW.

2.2. HGSHPS Modelling

As it has been mentioned in Section 2.1 the HGSHPS is modelled in a separate .tpf file which includes useful TESS components [9]. Fig. 2 depicts a schematic diagram of simulation. The system is divided into three main loops which are depicted in different colours: the Ground Heat Exchangers' (GHEs') loop coupled with the heat pumps in blue, the Heat Exchanger loop which comes in between the GHEs' loop and the Closed Circuit Cooling Tower loop in green and the Closed Circuit Cooling Tower loop in cyan blue.

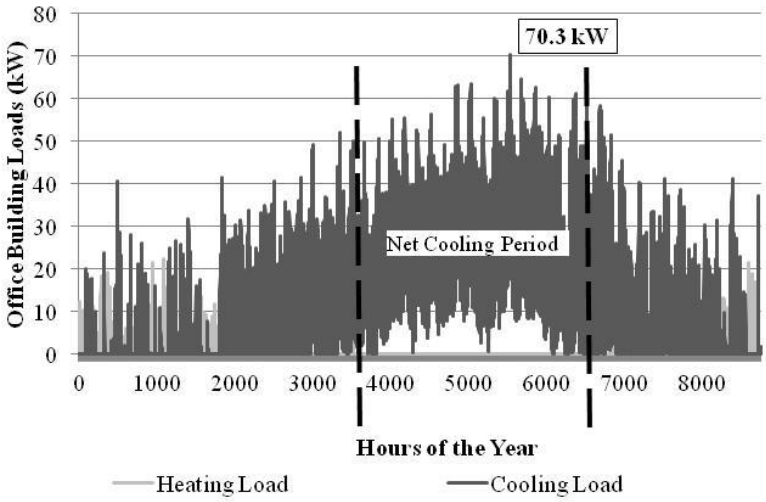

Fig. 1. Annual building load profile.

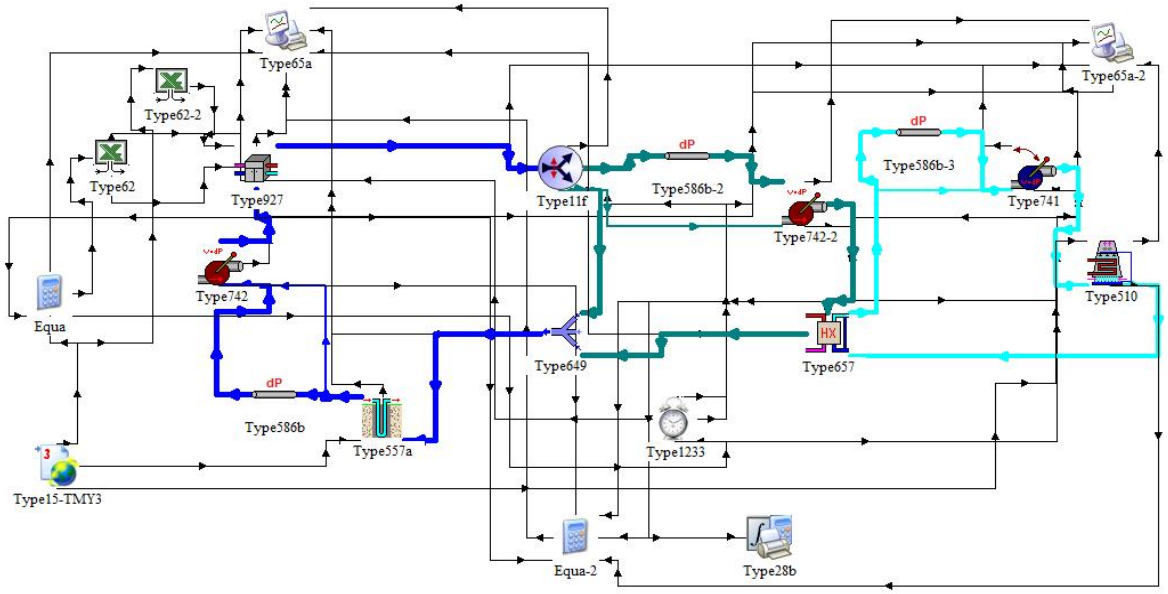

Fig. 2. HGSHPS TRNSYS 17 Modelling.

The main parts of HGSHPS are: the GHEs (Type 557a), the Heat Pumps (Type 927), the Heat Exchanger (Type 657), the Closed Circuit Cooling Tower (Type 510) and the circulating pumps.

The system is designed so as to cover the maximum cooling load during the net cooling period. Heat pumps and cooling tower cooling capacity are inputs which have been empirically selected so as to cover cooling demand with a safety coefficient of approximately 20%. It is optimized using TRNOPT 17 [10]. A parametric analysis is performed considering as parameters: the hot-side outlet temperature set point of the Heat Exchanger, the Closed Circuit Cooling Tower working fluid flow rate and the desired outlet fluid temperature from the Closed Circuit Cooling Tower so as to minimize borehole depth. The parametric algorithm is performed, allowing parametric runs where one parameter at a time is varied and all others are fixed at their initial values. The parameters are assumed discrete and have a lower and upper limit.

Table 1 summarizes main parameters of the optimum HGSHPS at which the control strategies will be applied.

2.2.1. GHEs

In the current work 15 boreholes are used to exploit ground's cooling capacity. Type 557a models a set of equal vertical U-tube heat exchangers which thermally interact with the ground. Each one is placed in a separate borehole, filled with grout.

The boreholes are placed uniformly within a cylindrical storage volume of ground. There is convective heat transfer between the circulating fluid and the pipes, and conductive heat transfer between the ground and the pipes. The depth below the surface of the top of GHEs determines the depth below the surface of the horizontal header pipe which is in conjunction with the GHEs. According to Hellström (1989) [9, 11], the temperature in the ground is determined by superposition of three terms: the global temperature, the local solution, and the steady-flux solution. The global and local problems are solved with the use of an explicit finite difference method. The steady flux solution is obtained analytically.

As the undisturbed ground temperature is relatively high 17 ^{o}C, the circulating fluid through GHEs is water.

Table 1. Main parameters of the optimum HGSHPS at which the control strategies will be applied

Parameter	*Value*
Borehole number	15
Borehole depth	130 m
Borehole separation	4.5 m
Borehole radius	0.055 m
Reference borehole flow rate	1032 kg/h
U-tube inside diameter	0.0218 m
U-tube outside diameter	0.0267 m
Header depth	1 m
Storage volume	34164 m^3
Ground thermal conductivity	2.42 W/m K
Ground volumetric heat capacity	2343 kJ/m^3 K
Undisturbed ground temperature	17 ^{o}C
Grout thermal conductivity	1.5 W/m K
Pipe thermal conductivity	0.4 W/m K
Source/Load fluid heat capacity	4.19 kJ/ kg K
Source/Load Fluid density	1000 kg/m^3
Load flow rate	15480 kg/h
Rated cooling capacity per heat pump	43kW
Rated cooling power per heat pump	8.98 kW
Rated source/load flow rate per heat pump	4.3 l/s
Overall circulating pumps efficiency	0.6
Circulating pumps motor efficiency	0.9
Effectiveness of heat exchanger	0.65
Cooling tower design inlet fluid temperature	35 ^{o}C
Cooling tower design outlet fluid temperature	29.44 ^{o}C
Cooling tower design fluid flow rate	7494 kg/h
Cooling tower design ambient air temperature	35 ^{o}C
Cooling tower design wet bulb temperature	25.56 ^{o}C
Cooling tower design air flow rate	14334 kg/h
Cooling tower's air pressure at design conditions	1 atm
Cooling tower's rated fan power	2.24 kW
Number of simulation years	15

2.2.2. Heat Pumps

Two equal single-stage water-to-water heat pumps are modelled through Type 927 [9]. In most time they work at partial load whereas bigger load coverage takes place at very hot summer days from the 5th year until the 15th so as to compromise for ground's cooling depletion. Heat pumps are dimensioned at 60% of the peak cooling load in an attempt to avoid repeatedly interruptions of their operation due to fluctuations of demand.

Input data files have been built for the normalized capacity and power draw, based on the entering load and source temperatures and the normalized source and load flow rates. These data have been derived from Water Furnace heat pumps catalog [12].

In addition two Excel data files are built. The first one provides Type 927 the inlet load temperature which is calculated by:

$$T_{load,out} = T_{load,in} + \frac{\dot{Q}_{cooling}}{\dot{m}_{load} c_{p,load}} \Rightarrow T_{load,in} = T_{load,out} - \frac{\dot{Q}_{cooling}}{\dot{m}_{load} c_{p,load}}, \qquad (1)$$

where $T_{load,out} = 12^{o}C$, $c_{p,load} = 4.19 kJ/kgK$ and $\dot{m}_{load} = \dot{m}_{source}$ for the current simulation.

Total cooling capacity $\dot{Q}_{cooling}$ is defined by:

$$\dot{Q}_{rejected} = \dot{Q}_{cooling} + \dot{P}_{cooling}, \qquad (2)$$

where $\dot{Q}_{rejected}$ is the heat rejected and $\dot{P}_{cooling}$ is the heat pump power.

$T_{source,out}$ is given by:

$$T_{source,out} = T_{source,in} + \frac{\dot{Q}_{rejected}}{\dot{m}_{source} c_{p,source}}. \qquad (3)$$

The second one defines the control signal which indicates when the unit should be on or off in cooling mode. Assuming that the building is occupied 12 hours every day except Sundays, from 9 a.m. to 9 p.m., the control signal function for a whole week would be as it is plotted in Fig. 3, where 1 is on-signal and 0 is off-signal. It is useful to highlight that this signal is the operating signal of the whole HGSHPS and it has also been taking into consideration for the building load calculation.

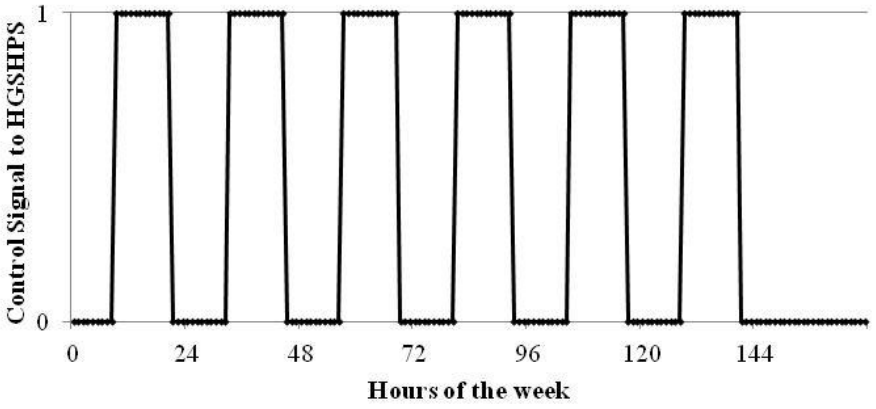

Fig. 3. Weekly Control Signal to HGSHPS.

2.2.3. Heat Exchanger

Heat Exchanger is modelled by Type 657 [9]. This type models a constant effectiveness heat exchanger which is able to automatically by-pass cold-side fluid around the heat exchanger in order to maintain the hot-side outlet temperature below a set point.

2.2.4. Closed Circuit Cooling Tower

Type 510 [9] models a Closed Circuit Cooling Tower or in other words an indirect cooling tower or evaporator, based on Zweifel et al [13] algorithm. This device is used to cool a liquid stream by evaporating water just outside of coils which contain the working fluid. The working fluid is completely isolated from air and water. In the current work the closed circuit cooling tower is operating at low speed (the fraction of rated fan speed does not exceeds 0.60) which leads to an oversized tower selection. Cooling tower's catalog data are derived from Baltimore Aircoil Company [14].

2.2.5. Circulating pumps

In this study there are three circulating pumps, each one per loop. In reality each pump represents a series of pumps which should be placed in an actual installation. The amount of water flowing through each pump equates to the amount of water that should flow through the series of pumps of each loop.

Type 742 [9] models a pump which sets its fluid outlet mass flow rate equal to a desired inlet mass flow rate. It can model a constant or a variable speed pump by passing the inlet mass flow rate through to its output but, does not take any control signal. The pump's power draw is calculated from the pressure drop, overall pump efficiency, motor efficiency, fluid flow rate and fluid characteristics. Pump's starting and stopping characteristics are not modelled.

Type 586b [9] calculates the input pressure drop for circulating pumps' calculations. As this case study is not referred to an actual installation but, to a possibly existing one the estimation of piping length is difficult. Based on [5] methodology for piping length estimation, the piping network of GHEs' loop is assumed to be 856.5 m, of Heat Exchanger loop 20 m and of Closed Circuit Cooling Tower loop 20 m.

Type 741 [9] models a variable speed pump that is able to produce any mass flow rate between zero and its rated flow rate. The pump's power draw is calculated similarly to Type 742. The reason for which this type is chosen for modelling the circulating pump of Closed Circuit Cooling Tower loop instead of Type742 is its ability to modify the outlet flow rate based on its rated flow rate parameter and the current value of its control signal input.

3. Control Strategies

Control strategies utilized in the present work define when the Closed Circuit Cooling Tower should be turned on or off. Three different control strategies are examined so as to minimize HGSHPS's electric power consumption. Type 1233 is utilized so as to send the appropriate control signal to fluid diverter (Type 11f) and to circulating pump Type 741. The system's electric power consumption is the sum of five terms: heat pump power, power of each circulating pump (three values of power for the current simulation, each one per loop) and cooling tower fan power.

Apart from the control strategies two other control functions are used to ensure the temperature and flow rate control in the studied HGSHPS. The first one is the hot-side outlet temperature set point of the Heat Exchanger which is:

$$T_{HEX,set} = 38^{o}C. \qquad (4)$$

The second one is the desired outlet fluid temperature which the Closed Circuit Cooling Tower tries to maintain and is:

$$T_{CT,set} = 28^{o}C. \qquad (5)$$

3.1. Control Strategy 1

Control Strategy 1 suggests that the cooling tower should operate when the temperature difference between the fluid temperature exiting heat pumps and ambient air wet bulb temperature exceeds a given set point:

$$\Delta T_1 = T_{source,out} - T_{wetbulb} > 10^{o}C \ . \qquad (6)$$

In an attempt to define the climatic area for which the HGSHPS is designed, Athens monthly average climatic data are presented in Table 2.

Table 2. Average Climatic data [6]

Month	*Ambient Air Temperature*, °C	*Mean irradiance of global radiation horizontal*, W/m^2	*Mean irradiance of diffuse radiation horizontal*, W/m^2	*Wet Bulb Temperature*, °C
JUN	25.6	297	105	17.5
JUL	28.4	299	98	19.4
AUG	28.0	271	90	19.3
SEP	23.5	216	80	17.1

3.2. Control Strategy 2

Control Strategy 2 activates the cooling tower when the fluid temperature exiting GHEs is greater than a certain value:

$$T_{GHE,out} > 28^{o}C \ . \qquad (7)$$

3.3. Control Strategy 3

Control Strategy 3 sets cooling tower on when the fluid temperature exiting heat pumps is greater than a given value:

$$T_{source,out} > 32^{o}C \ . \qquad (8)$$

3.4. New Control Strategies

Each of the control set points discussed above is normalized by the fluid temperature exiting the hot side of heat exchanger, $T_{HEX,hot,out}$. New set points are calculated which define three new control strategies. Equations (6) to (8) are transformed into:

$$\frac{\Delta T_1}{T_{HEX,hot,out}} = \frac{T_{source,out} - T_{wetbulb}}{T_{HEX,hot,out}} > 0.3 \qquad (9)$$

$$\frac{T_{GHE,out}}{T_{HEX,hot,out}} > 1.3 \qquad (10)$$

$$\frac{T_{source,out}}{T_{HEX,hot,out}} > 1.3 \qquad (11)$$

and define three new control strategies 1, 2, 3 respectively.

4. Results

Moving to the results section, the average monthly electric power consumption for Control Strategies 1, 2, 3 is presented in Figs 4, 5, 6 respectively. For the optimum borehole depth of 130 m, different desired outlet fluid temperature $T_{CT,set}$ and cooling tower set point flow rates $\dot{m}_{CT,set}$ are examined. In all Control Strategies the first scenario, the black one, that is $T_{CT,set} = 28^{o}C$ and $\dot{m}_{CT,set} = 3000kg/h$ accounts for the smallest overall electric power consumption. However, in August the second scenario, the dark grey one, that is $T_{CT,set} = 29^{o}C$ and $\dot{m}_{CT,set} = 3000kg/h$ leads to the smallest electric power consumption for Control Strategies 1 and 3.

Control Strategies 1 and 3 have similar results, with Control Strategy 1 to account for the smallest electric power consumption in all scenarios. To validate this remark, it should be mentioned that previous works [3, 15] which have examined the same scenario among others, into different HGSHPSs have reached to the same conclusion. This conclusion becomes more obvious in Fig. 7

where the total electric power consumption for one-year net cooling period is plotted. The x-axis coordinate 'OPTIMUM of Strategy' is referred to scenario that is borehole depth=130 m, $T_{CT,set} = 28^{o}C$ and $\dot{m}_{CT,set} = 3000kg/h$ and 'OPTIMUM of New Strategy' is referred to the same scenario at which the New Control Strategies are applied. It is worth saying that New Control Strategy1 accounts by far for the least electric power consumption which is approximately 28895 kW. All New Control Strategies lead to better results that is to say less demand for electric power in comparison with the optimum of each strategy. The optimum of New strategies 2 and 3 is 29127 kW and 29130 kW respectively. These values are very close but still smaller than the optimum of Control Strategy 1 which is 29137 kW. It should be noted that the range of examined values for the electric power consumption is small and that is an expected remark as they referred to a previous optimized system.

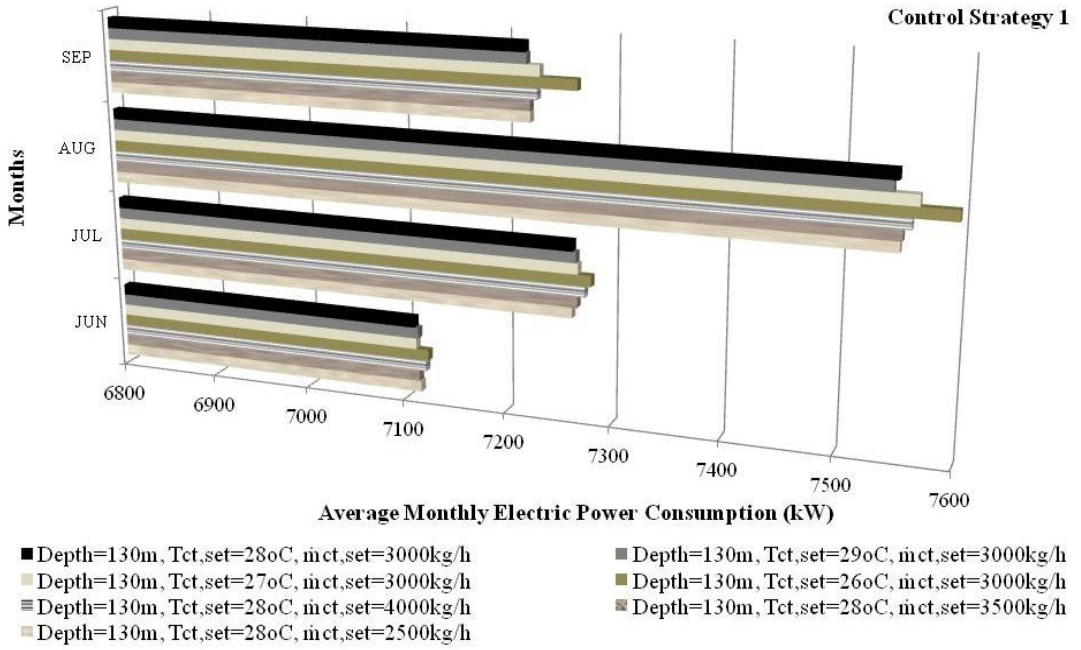

Fig. 4. Average monthly electric power consumption for Control Strategy 1.

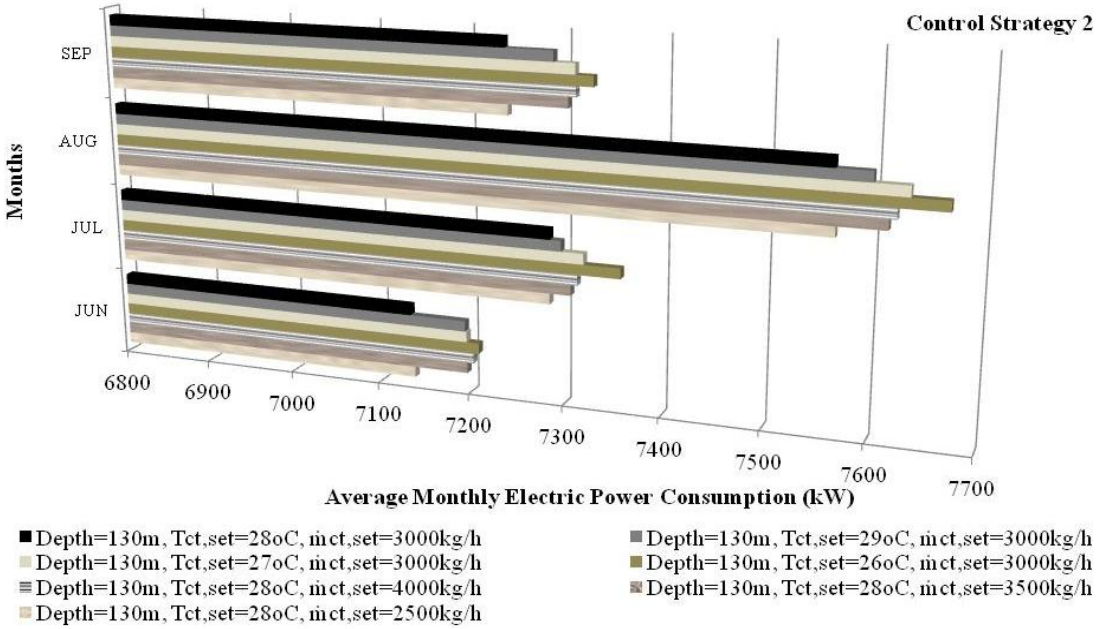

Fig. 5. Average monthly electric power consumption for Control Strategy 2.

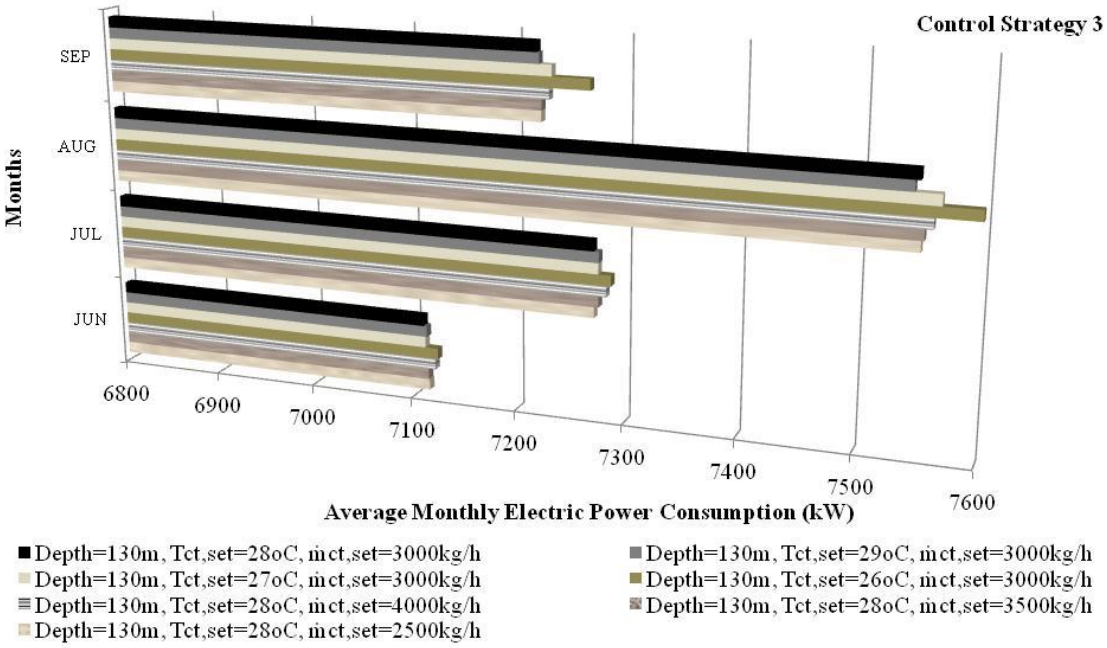

Fig. 6. Average monthly electric power consumption for Control Strategy 3.

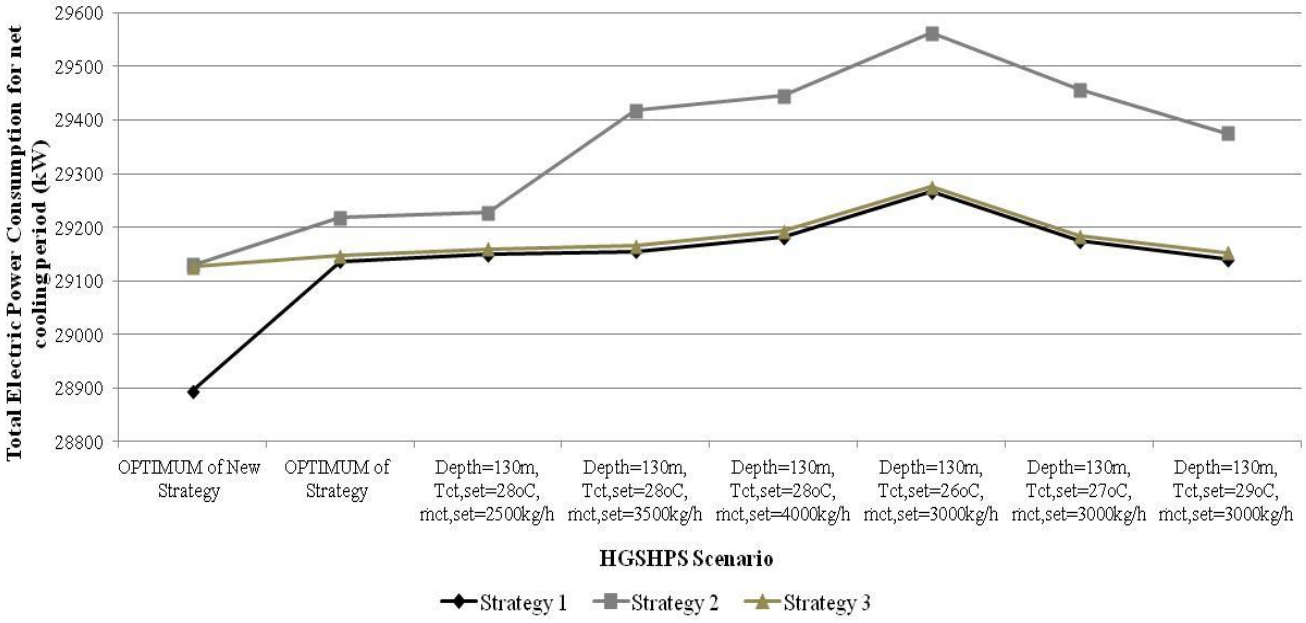

Fig. 7. Total electric power consumption for net cooling period.

However, as certain critical parameters such as heat pumps' and cooling tower cooling capacity have not been considered in the optimization procedure as variables, the optimization may be considered as restricted under the studied conditions. Despite the fact of the above mentioned assumptions, the results indicate the optimum control policy for the cooling tower operation in the HGSHPS and can provide useful guidance to future attempts for solving this complex sizing problem.

Fig. 8 shows the distribution of total electric power consumption in the 'optimum' HGSHPS which is regulated by New Control Strategy 1 and Control Strategy 1 for the net cooling period. In both pie-diagrams of Fig. 8 the biggest power consumption derives from the heat pumps and then with declining order from the circulating pump of GHEs' loop, cooling tower fan, circulating pump of

Closed Circuit Cooling Tower loop and circulating pump of Heat Exchanger loop. The relatively small increase in heat pumps' and fan power consumption in comparison with the relevant decrease in total circulating pumps' power is indicative of the improvement to fluid circulation.

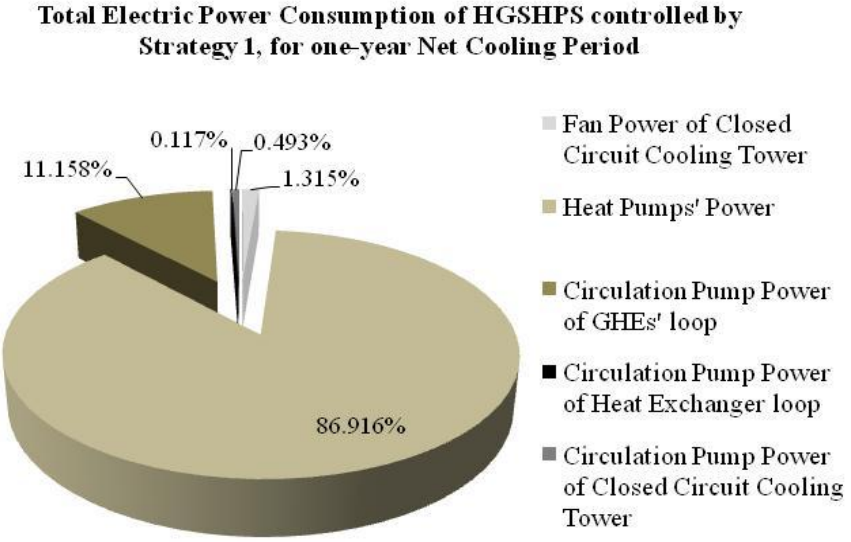

(a)

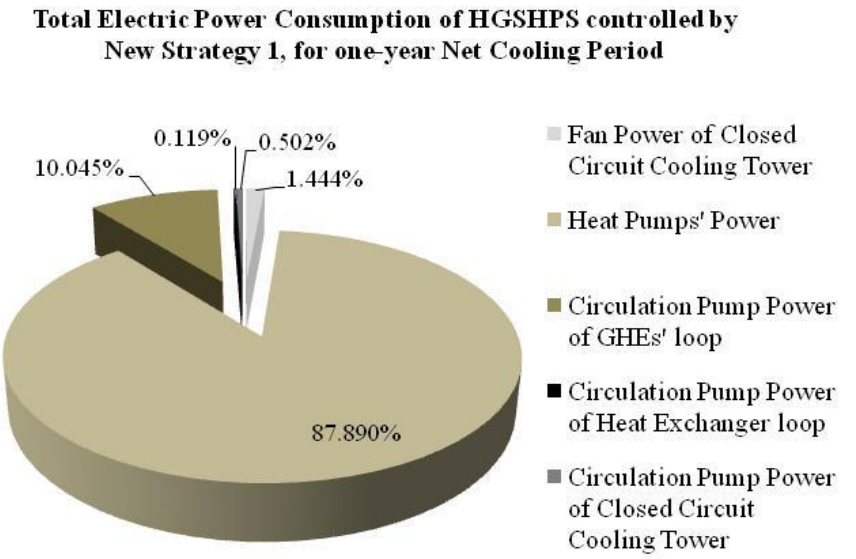

(b)

Fig. 8. Distribution of total electric power consumption of HGSHPS for one-year net cooling period controlled by: a) Strategy 1, b) New Strategy 1.

Fig. 9 is plotted in an attempt to visualize the conditions at which the optimum HGSHPS of our study operates. System's parameters are borehole depth=130 m, $T_{CT,set} = 28^{o}C$ and $\dot{m}_{CT,set} = 3000kg/h$, as it has been mentioned above, and Closed Circuit Cooling Tower operation is regulated by New Control Strategy 1. Distribution of inlet and outlet temperatures of load and source side of heat pumps, of GHEs, of Heat Exchanger and Closed Circuit Cooling Tower is presented for a very hot, cooling week in August. Inlet GHEs temperature is smaller than outlet source heat pumps temperature but still significant high in comparison with Heat Exchanger outlet temperature due to by-pass flow. The temperature difference between the fluid entering and exiting GHEs is 2 ^{o}C greater than the temperature difference between the load and source side of heat pumps. The temperature difference between the fluid entering and exiting Closed Circuit Cooling

Tower is on average 6.5 °C, while the outlet hot-side temperature of Heat Exchanger during the last working days do not succeed to maintain below the set point of 38 °C.

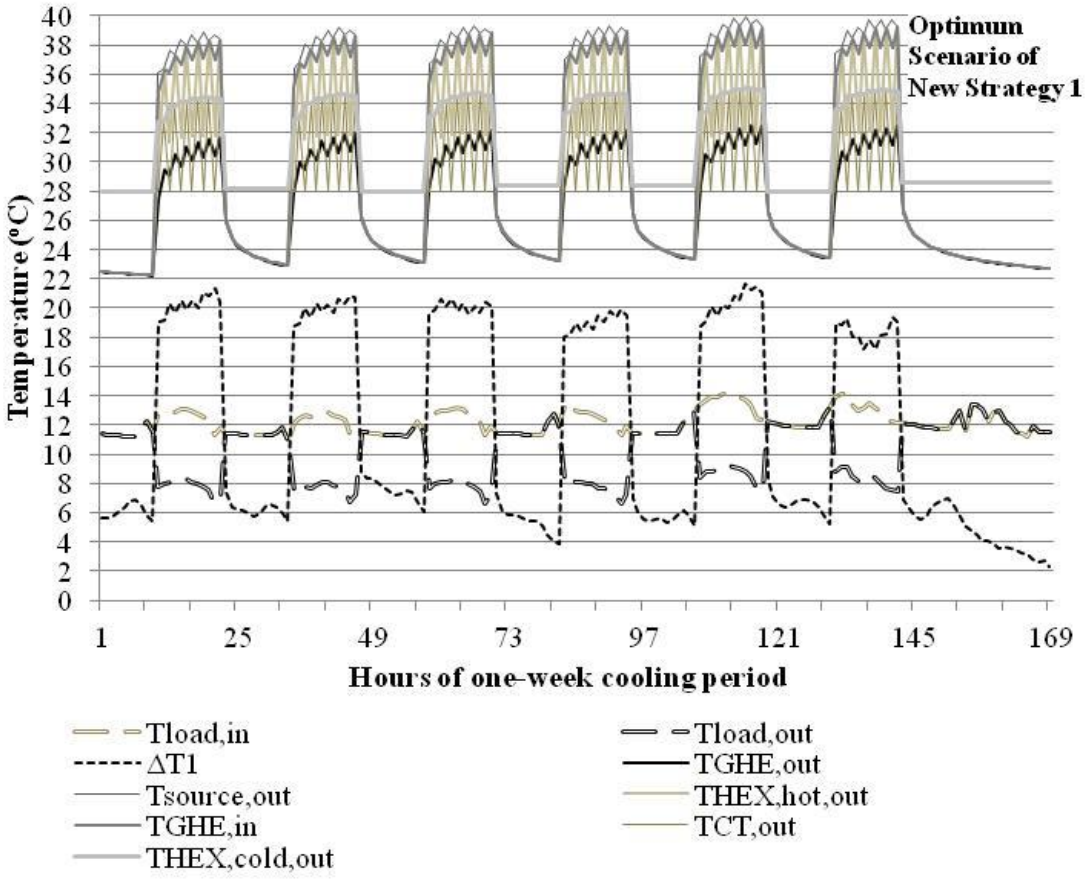

Fig. 9. Temperature distribution in HGSHPS controlled by New Strategy 1 for one-week cooling period in August.

5. Conclusion

To conclude, in the current work different control policies for HGSHPS optimization during the net cooling period have been applied to a Greek office building. The optimization is focused on the minimization of electric power consumption assuming certain values for the building load, the heat pumps' and cooling tower maximum cooling capacity. Therefore, it might not be considered as a full system optimization but it still could be considered as a determining improvement in system's operation.

By minimizing the electric power consumption, a significant reduction to HGSHPS operating cost should be achieved. However, it is difficult to claim that this is the most economically beneficial scenario, not only because the heating period is not examined but, also because the investment and maintain cost have not been considered in unit selection.

New control strategy1 is the best of the examined so as to regulate Closed Circuit Cooling Tower's operation in the HGSHPS. All new control strategies achieve a better regulation to system operation which leads to an extra reduction in the electric power consumption. These remarks can be used as guidance to future HGSHPS designers.

Nomenclature

c_p	specific heat capacity, kJ/(kg K)
g	solar heat gain coefficient
$\dot{m}$	mass flow rate, kg/h

$\dot{P}_{cooling}$ heat pump power, kW

$\dot{Q}_{cooling}$ heat pump cooling capacity, kW

$\dot{Q}_{rejected}$ heat rejected by heat pump, kW

T temperature, °C

u thermal transmittance, W/(m^2 K)

Subscripts and superscripts

CT Cooling Tower

GHE Ground Heat Exchanger

HEX Heat Exchanger

in/out Inlet/ Outlet

load/source Heat Pump load-side/source-side

set Set point

wetbulb Wet bulb

References

[1] Kavanaugh S.P., A design method for hybrid ground-source heat pumps. ASHRAE Transactions 1998;104(2):691-698.

[2] ASHRAE, Commercial/institutional ground-source heat pumps engineering manual. Atlanta: American Society of Heating, Refrigerating and Air-Conditioning Engineers Inc; 1995.

[3] Yavurtzuk C., Spitler J.D., Comparative study to investigate operating and control strategies for Hybrid Ground Source Heat Pump Systems using a short time-step simulation model. ASHRAE Transactions 2000;106(2):192-209.

[4] Xu X., Simulation and optimal control of hybrid ground source heat pump systems [doctor of philosophy]. Oklahoma, United States of America: Oklahoma State University; 2007.

[5] Hackel S.P. et al., Development of Design Guidelines for Hybrid Ground-Coupled Heat Pump Systems. ASHRAE TRP-1384; 2009.

[6] Meteonorm Software 2010; v.6.1.

[7] Technical Chamber of Greece, Comprehensive national standards parameters for calculating the energy performance of buildings and issuing of energy performance certificate. Technical Instruction 20701-1/2010; 2010. Building PECA Minister Decision 17178/2010. Official Gazette 1387/B/9-2-2010.

[8] TRNSYS Software 2010; v.17.

[9] TESS Library 2010.

[10] TRNOPT 17;2010.

[11] Hellström G., Duct ground heat storage model. Lund, Sweden: University of Lund, Department of Mathematical Physics; 1989. Manual for Computer Code.

[12] Water Furnace website – Available at:<http://waterfurnace.com> [accessed 12.12.2011].

[13] Zweifel G., Dorer V., Koschenz M., Weber A., Building Energy and System Simulation Programs: Model Development, Coupling and Integration. IBPSA 1995: Proceedings of International Building Performance Simulation Association Conference; 1995.

[14] Baltimore Aircoil Company website – Available at:<http://www.baltimoreaircoil.eu/ > [accessed 12.12.2011].

[15] Thermal Energy Systems Specialists (TESS), Hybrid Geothermal Heat Pumps at Fort Polk, Louisiana; 2005. Final Report to Oak Ridge National Laboratory.

Exergetic evaluation of heat pump booster configurations in a low temperature district heating network

Torben Ommen [a], Brian Elmegaard [b]

[a] *Technical University of Denmark, Kgs. Lyngby, Denmark, tsom@mek.dtu.dk* ***CA***
[b] *Technical University of Denmark, Kgs. Lyngby, Denmark, be@mek.dtu.dk*

Abstract:

In order to minimise losses in a district heating network, one approach is to lower the temperature difference between working media and soil. Considering only direct heat exchange, the minimum forward temperature level is determined by the demand side, as energy services are required at a certain temperature. As domestic hot water is required at a temperature range where legionella is no longer a threat, forward temperatures in a traditional low temperature district heating network cannot be lowered beyond approximately 55 ^{o}C. One solution is to boost the temperature of the forward tap water stream with a heat pump, as the remaining heat demands are often not required at temperature levels as high as the tap water. The scope of this work is to evaluate the power consumption and second law efficiency of booster heat pumps for tap water production in a low temperature district heating network. The heat pump and storage arrangement is evaluated based on a tapping sequence from the Danish standards (DS439). Based an initial investigation of possible designs, three configurations have been chosen for the evaluation. Of the three heat pumps, two are implemented on the primary side to boost the network stream, and one is intended to increase the temperature of the tap water directly. Results show that one of the three configurations are superior to the two remaining, when considering temperature levels of forward stream between 35 ^{o}C and 47 ^{o}C. The overall results remain the same regardless of heat exchanger sizes and the isentropic efficiency of the compressor used in the heat pump. The superior configuration shows exergetic efficiencies higher than 0.5 when forward temperatures is around 45 ^{o}C.

Keywords:

Domestic hot water, Exergy analysis, Heat pumps, Low temperature district heating.

1. Introduction

Using district heating in urban areas is a measure to increase overall energy efficiency and reduce consumption of fossil fuels. These systems are implemented in many northern cities and even rural areas where incineration plants provide surplus waste heat. As the market value of heat is increasing (due to numerous reasons - mainly due to increase in fuel prices), so is the interest in lowering the losses affiliated with transportation of heat. One simple measure is to reduce the temperature of the network, as this reduces the driving potential of the heat loss in the distribution system.

Novel parts of existing Danish district heating networks tend to be built with a forward temperature of around 60-55 ^{o}C [1] as this is the lowest temperature for which direct conversion into domestic hot water is possible. Domestic hot water (hot tap water) and space heating are the common heat demands in residential areas, of which the domestic hot water constitute approximately one third of the combined consumption [2]. Lowering the forward temperatures of the district heating network could potentially be beneficial, if only a small amount of electricity is required to increase the temperature of the tap water, while the temperature is high enough to provide space heating without using additional means. In this way heat losses of the combined district heating stream can be minimized while using only a small amount of electricity to boost the temperature of a minor part. Many of the new networks are coupled to the existing district heating networks. In case of the build of a completely new network and production unit (combined heat and power plant or district

heating boiler) several effects may be experienced from changing the temperatures levels of both forward and return in the network [3]. Changed production or efficiencies of these production units are not considered in this paper, as the entire production facility and district heating network must be changed for these effects to become realized.

Several heat pump solutions have been considered in the on-going research affiliated with this paper. Below the most promising candidates are evaluated based on electricity consumption, district heating network considerations and exergetic efficiency.

2. Concept considerations for low temperature DH systems.

2.1. Main obstacles

In trying to reach a lower supply temperature in the district heating system - beyond 55 ^{o}C, new steps must be taken to utilise the heat, as several constraints appear in this temperature range. In residential areas, the load for the district heating system consists mainly of two parts; space heating and hot tap water.

For space heating, the temperature difference between indoor heaters and the room temperature is minimised when using the lowered temperature in the system. Assuming a constant heat demand, the low temperature difference requires larger surfaces for heat transfer. In these situations floor heating is often utilised. Still quite some temperature difference is needed, as building materials are often inferior to slim iron constructions in terms of heat transfer. A minimum of 15 K higher floor heating inlet temperatures, compared to the required room temperature is considered a requirement in this evaluation [4]. In addition to this heat transfer consideration, the flow rates and pressure losses in both the district heating network and the house installations must be considered before choosing the appropriate temperature levels.

Considering the tap water requirements, the main issues are related to the bacterium “Legionella”. To prevent problems with bacteria two simple measures can be taken. Either the hot tap water must exceed a predefined temperature limit where the bacteria can no longer exist when stored, or the tap water is not to be stored after being heated. Either way, some constraints are encountered.

Additionally the Danish building standard must be met, where hot tap water is assumed at two temperature levels – 45 ^{o}C and 40 ^{o}C, respectively, differentiated by their use in kitchens or bathrooms. Even with small pinch temperature differences in the heat exchanger network, it is unlikely that forward temperatures in district heating can be reduced below 50 ^{o}C without considering heat pumps or other efforts to increase the temperature of tap water. In order to evaluate an overall conversion efficiency of systems with very low forward temperature (below 50 ^{o}C), small heat pump installations for individual houses are considered.

2.2. Different implementation schemes

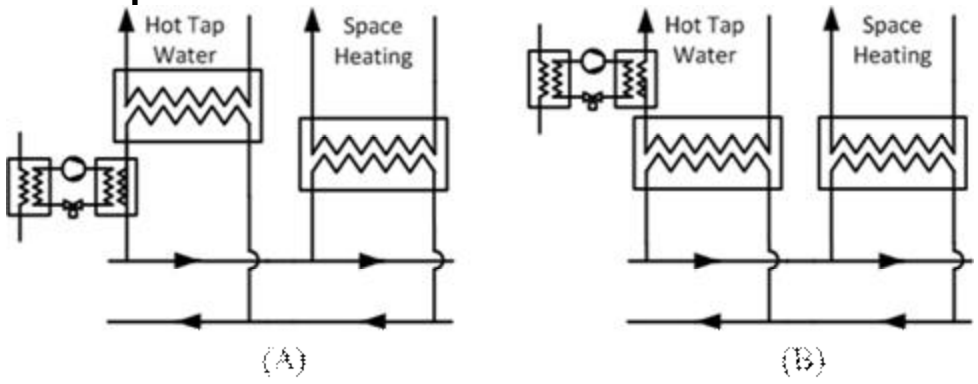

Fig. 1. Two different implementation schemes: (A) Heat pump on primary side of the tap water heat exchanger. (B) Heat pump on secondary side of the tap water heat exchanger.

In individual house installations for low temperature networks, heat pumps can be implemented in two different operating schemes, either to boost the temperature level of the district heating water prior to heat exchange with the tap water (named “primary”), or to boost the tap water temperature after the district heat network heat exchanger (“secondary”).

Within these two schemes, many individual concepts are plausible. Several different conceptual ideas have been tested and evaluated, based on “back of the envelope” calculations. The three most promising concepts are presented in this paper. This focus is to evaluate the most promising candidates in terms of energy efficiency. The evaluated systems consist principally of the tap water heat exchanger, heat pump and the storage system. The evaluation is considering both first and second laws of thermodynamic.

The results presented are intended for further analysis, as the impact of reducing supply temperature will influence the entire district heating system, among others; space heating requirements, pressure losses, cost of implementation and dimensioning of the piping system. Tap-water corresponds to between one half and one third of the combined heat consumption in the house.

2.3. Assumptions

The calculations are based on the assumptions presented in Table 1. Assumptions are made based on estimates of state of the art technology for a small decentralized heat pump producing hot tap water by use of low temperature district heating network.

Table 1 - Assumptions for low temperature district heating network heat pump

Variable	Assumption
Pinch temperature in Tap-water HEX (Q_{MAX}=32 kW)	8 [K]
Initially assumed forward temperature of DH network	40 [°C]
Initially assumed return temperature of DH network	22 [°C]
Refrigerant	R134a
Isentropic efficiency of compressor	0.5 [/]
HEX pinch temperature difference in both Condenser and Evaporator	2.5 [K]
Hot tap water	45 [°C]
Tap water in	10 [°C]
Minimum temperature if water stored on secondary side	58 [°C]

In the conducted calculations heat exchange between district heating water and tap water is assumed to have a constant pinch temperature of 8 K, as high flow rates occur in the tap water system. The assumed pinch temperature corresponds to the highest flow of tap water, but is assumed constant across the entire range of tap water flows. In practice the temperature difference would decrease at lower flow.

As the temperature difference between the forward and return stream of the district heating network is reduced (by a factor of minimum 2) [2] while assuming no change in the demand profile, significantly higher flow rates are required in the district heating network. Furthermore the high flow rates in the system will require high heat exchanger area and intermittent operation of the heat pump. To reduce these issues, storage of hot water is introduced in each scenario. The storage is regarded as a means to lower heat exchanger sizes and service life of components and will as such require an economic optimisation, which is not part of this paper.

In order to dimension the different heat pumps and storage tank sizes, the heat demand profile from DS439 is used [5]. As the recovery time for the system (storage empty -> storage full) is not expected to exceed 3 hours, only the time interval between 6.00 AM and 7.05 AM (morning showers and cooking) is considered in these calculations, as the time until next tap is almost 2 hours according to the standard. Only for the tapping sequence from 6.00 AM to 7.05 AM the full capacity of the heat storage will be needed. The preceding hours are assumed without any tapping,

thus the storage can be full before the tapping sequence. In the calculations presented below, the interaction between heat pump and storage tank is dimensioned to allow a “refilling” (leaving a heated volume of water corresponding to the desired) in two hours.

Regarding heat storage and heat pump on either primary or secondary side, some assumptions are introduced:

- With heat pump and storage on primary side of the network, only the tapping temperature dictates the temperature of the storage in the calculations.
- Employing the Heat pump on the secondary side of the system, the tap water is stored at high temperatures. Concern must be regarded towards legionella, so the heat pump system must be able to prevent and even remove the bacteria. Taking into account some of the heat losses that may emerge in a real system, the heat pump must deliver the tap water at minimum 58 °C.

The profile presented in figure 2 corresponds to the tapping and refilling profile considered. The concept considered in the figure corresponds to configuration A, but identical profiles are experienced in the two remaining configurations. The tapping sequence is assumed to correspond to a tapping temperature of 45 °C during the entire profile (this is a small offset from standard – where some are 40 °C).

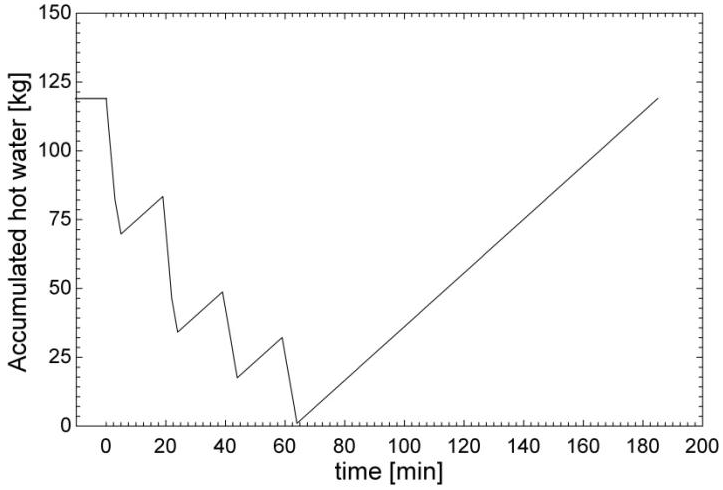

Fig. 2. Tapping and refilling sequence considered.

It is assumed that the heat pump is in operation from the initial tapping sequence and until the heated water volume is restored. The heat pump is working continuously during the tapping procedure in order to reduce the required amount of stored hot water. The tapping and refilling sequence is presented in Fig. 2. Thus proper dimensioning of the heat pump capacity can reduce the required volume of storage. Heat loss from the hot storage of water is neglected, as an almost equivalent amount of stored hot water is required in all the configurations at equally comparable temperature levels.

3. Method

Numerical models have been implemented in Engineering Equation Solver (EES) [6], corresponding to each individual heat pump implementation scheme. Operation assumptions are listed either in Table 1 or in the section considering each individual heat pump solution. The calculation of the state of all streams is primarily based on energy and mass balances. Pressure losses in heat exchange and pipes are neglected throughout the paper.

Heat exchange is modelled according to Nellis and Klein [7] using pinch temperatures in heat exchangers both with and without phase change. The used formulation of pinch point results in

lowered condensation pressure as the pinch point is not assumed at either end of the considered heat exchanger, but at the location of minimum temperature difference.

Calculation of the exergetic efficiency is based on the formulation of physical exergy presented in Bejan et al [8]. There are no changes in chemical composition of the working media or district heating media, leaving only changes in the physical exergy of each separate stream:

$$\dot{E}_i^{PH} = \dot{m}_i((h_i - h_0) - T_0(s_i - s_0)), \qquad (1)$$

Massflow $\dot{m}_i$, enthalpy h_i and entropy s_i is based on the above mentioned EES calculations for each concept. The dead state is based on $t_0 = 10\ ^{o}\text{C}$ and $p_0 = 1\,\text{bar}$, from where h_0 and s_0 can be calculated for the working media. The dead state is related to the cold tap water at ambient pressure.

Exergetic efficiency is modelled according to the formulation in Bejan et al. [8]. As exergetic efficiency is calculated as a relative term, the location of the dead state does not matter for the final results presented [9].

4. Individual concepts and initial calculations

4.1. A (primary side)

The heat pump is modelled according to the simplified PI-diagram presented in Figure 3. The forward stream supplies DH water for both the evaporator and the condenser. The two streams are mixed in the return flow, combining the residue heat from the evaporator and tap water HEX. During tapping, heated water is removed from the hot layer in the stratified tank, heat is transferred in the tap water heat exchanger and returned to the cold bottom layer in the tank. This is done to avoid high mass flows of district heating water in the heat pump condenser and in the district heating network. During recharging heated water is filled in the tank, displacing the bottom cold layer, which is returned to the District heating network.

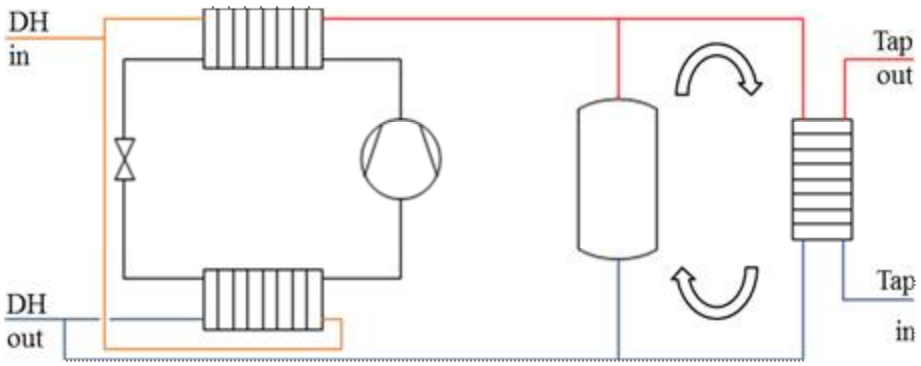

Fig. 3. Simplified diagram of A, with arrows to indicate the short circuit during tapping

Table 2. Initial calculations of variant A based on information from table 1.

Variant	$\dot{V}_{DH}$ [m^3/h]	Condenser [kW]	P [kW]	Heat pump COP [/]	Water Volume [m^3]	Exergetic eff. [/]
A	0.107	0.89	0.157	5.62	0.118	0.44

The results shown in Table 2 indicate that condenser capacity of approximately 0.9 kW is required in order to boost the temperature of the district heating water. The temperature levels in both the condenser and the evaporator allow the heat pump to operate with a COP of approx. 5.6. The combination of the tapping profile and the temperature of the boosted storage dictate the required amount of water in the storage.

4.2. B (primary side)

Source heat for the heat pump system can also be supplied from other sources than the forward district heating line. Heat can be extracted from space heating return flow, or even from the system return line. High temperatures in the heat supply for the evaporator is of cause an advantage in order to minimize the temperature lift between condenser and evaporator. The advantage of this system is a reduction in the district heating network forward flow compared to the variant A. This is achieved by increasing the temperature difference between DH forward and return beside the assumptions in Table 1.

To allow evaluation of introducing additional "waste" heat before the evaporator, two different calculations is performed in this variant.

- 'B1 is only using the return stream from either the tap water heat exchanger or the storage tank.
- 'B2' is an additional amount of return flow (most likely from the space heating circuit) with temperature 22 ^{o}C and mass flow corresponding to the assumption that the district heating requirement of a house can be divided into 2/3 space heating and 1/3 tap water [2]. The additional flow is subject to some uncertainties, as it is not always likely that the space heating flow is available when the tap water is required. On the other hand, utilising the space heating return flow would enable a lower return temperature than the one otherwise considered, which is dictated by the space heating heat transfer.

Figure 4 presents the simple flow diagram. The concept is quite similar to A, except for the addition of surplus waste heat prior to the evaporator.

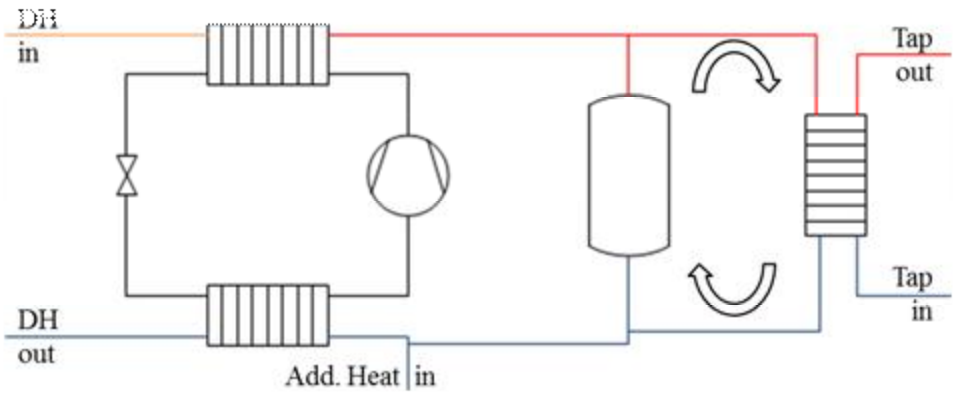

Fig. 4. Simple diagram of variant B (primary), with arrows to indicate the "short circuit" during tapping

Table 3. Initial calculations of variant B based on information from table 1.

Variant	$\dot{V}_{DH}$ [m^3/h]	Condenser [kW]	P [kW]	Heat pump COP [/]	Water Volume [m^3]	Exergetic eff. [/]
'B1'	0.059	0.89	0.252	3.52	0.118	0.38
'B2'	0.059	0.89	0.207	4.27	0.118	0.42

Table 3 shows the initial calculations of both variant B1 and B2. The condenser load is in both cases equal to the one presented in table 2, as the hot DH water stream for the condenser is identical to the one in variant A. Due to the changed temperature levels of the evaporator in both B1 and B2 the heat pump COP is changed, which calls for a higher electricity consumption. Considering available surplus heat (according to 'B2'), the system efficiency improves, as this reduces the temperature lift between heat pump sink and source. As the system changes only influence the evaporator, the new system provides similar effects with a variation in forward temperature. In

cases with no additional heat requirements in the house, the heat pump unit will operate on only the return stream from the tap water heat exchanger.

As the two systems have similarities in operation, only the 'B1' system is considered for further analysis, as this system composes the simple solution, where both streams from Figure 1 are not available in the same location due to practical constraints.

4.3. C (secondary side)

The last variant proposes the most efficient solution for boosting the tap water with the heat pump (secondary side implementation). The configuration of this system allows preheating to be utilized in an efficient way, where the high flow rates of the tap water does not influence the temperature lift. The forward stream of the district heating network is supplied both to the evaporator of the heat pump and the heat exchanger for preheating of tap water. In modelling the system the preheater was considered both as a tap water heat exchanger (pinch temperature in tap-water HEX = 8 K) or as a separate type (pinch temperature in HEX = 2.5 K = Condenser pinch temperature). As only a limited constant stream of tap water is heated, the heat exchanger (named 'preheater') was assumed to resemble the condenser based on the load profile. The pinch temperature defines the thermal load of the heat pump, and as such the losses in this heat exchanger must be minimised for efficient water heating.

The simple diagram of B2 is presented below in Figure 5. The arrow represents the continuous heating of tap water, which is independent of the tapping stream. The high flow from the Tapping procedure will only affect the amount of hot water in the stratified tank.

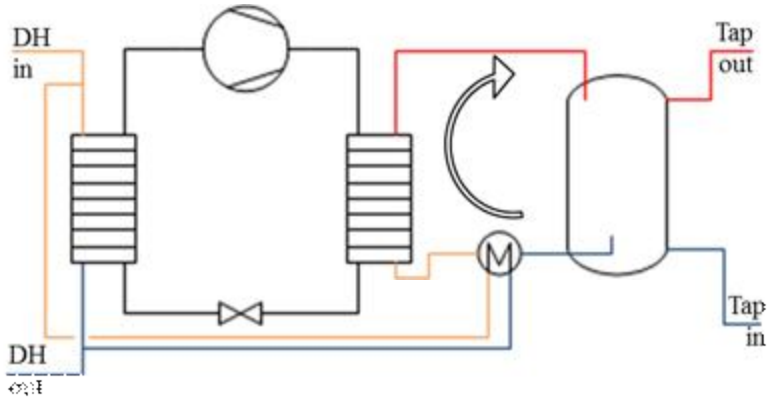

Fig. 5. Simple diagram of C, the arrow represents the continuous heating of tap water through the heat pump.

Table 4. Initial calculations of variant C based on information from table 1.

Variant	$\dot{V}_{DH}$ [m^3/h]	Condenser [kW]	P [kW]	Heat pump COP [/]	Water Volume [L]	Exergetic eff. [/]
C	0.105	1.02	0.193	5.26	0.086	0.40

Table 4 reveals a slightly increased heat pump condenser load is in variant C compared to the primary configurations. The increased load is due to the heat exchanger losses introduced in the secondary solution, where the district heating water is directly used (without temperature loss) in variant A and B. The configuration has a slightly lower requirement of DH flow than configuration A, and a lower storage volume than the both A and B.

As the heated water in the tank is hotter than the desired tapping temperature, cold tap water is mixed with the hot tap water during tapping, as is common practise when using district heating water today.

4.4. Evaluation

Based on table 2 to 4, a simple evaluation of electricity consumption and exergetic efficiency is possible. However, a variation of some of the parameters from table 1 may reveal changes in performance of the different booster configurations.

Heat exchanger sizes is a major interest, as the assumptions in Table 1 may not prove the economic optimum in later calculations. Other economic evaluations may include improvement in isentropic efficiency of the heat pump compressor, which may become possible through the use of different compression technologies and/or development of a compressor specifically designed for the temperature levels of the booster heat pump.

Heat exchange pinch temperature difference: In the evaluation of different heat exchangers, an increase in pressure losses from a decrease in pinch temperature difference is neglected. Such pressure losses would only affect the heat pump performance, as the pressure difference between forward and return DH stream is controlled at the district heating central, and as such not included in this paper.

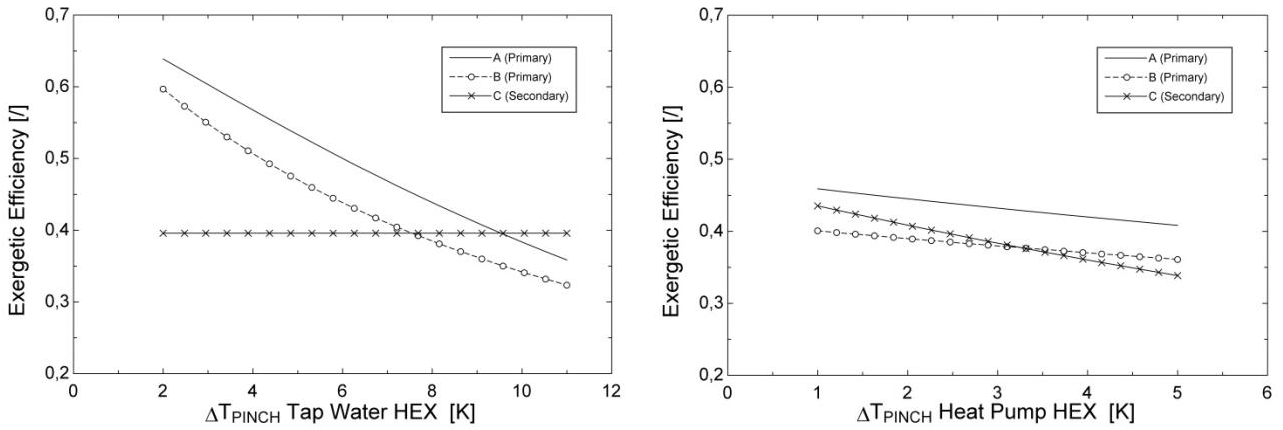

(A) (B)

Fig. 6. (A) The impact of tap water HEX pinch temperature on the 3 proposed configurations. (B) Impact of pinch temperature difference in evaporator and condenser on the 3 proposed configurations.

From Figure 6 (A) it is clear that the tap water HEX performance will influence the efficiency of Variant A and B, indicating that with poor heat exchange in these system, optimal performance will shift from variant A to variant C (as described in section 4.3, the heat exchanger in configuration C is not regarded as a tap water heat exchanger due to the constant flow rate of the HEX) . The steeper gradient of variant C in Figure 6 (B) is due to a higher number of HEX controlled by this pinch temperature difference (same explanation as in Fig. 6 (A))

Isentropic efficiency of heat pump compressor: The evaluation presented in Figure 7 cover a broader band of isentropic efficiency than what is reasonable to expect. A compressor for high temperature heat pumps in the condenser capacity range expected and at a reasonable cost is unlikely to have a higher efficiency than 0.65 [/] [9].

The evaluation presents the COP (coefficient of performance) for the heat pump pack and exergetic efficiency for the combined system with variable isentropic efficiency of the compressor. It is noticeable from Figure 7 (B), that an increase of isentropic efficiency above 0.65 [/] changes the relation between variant B and C. Configuration A has the highest performance of the three in both fig. 7 (A) and (B).

The difference between the first and the second law evaluation of performance is the influence of the condenser load on the electricity consumption. The increased load for the heat pump in configuration C is mainly due to the pinch temperature differences discussed above.

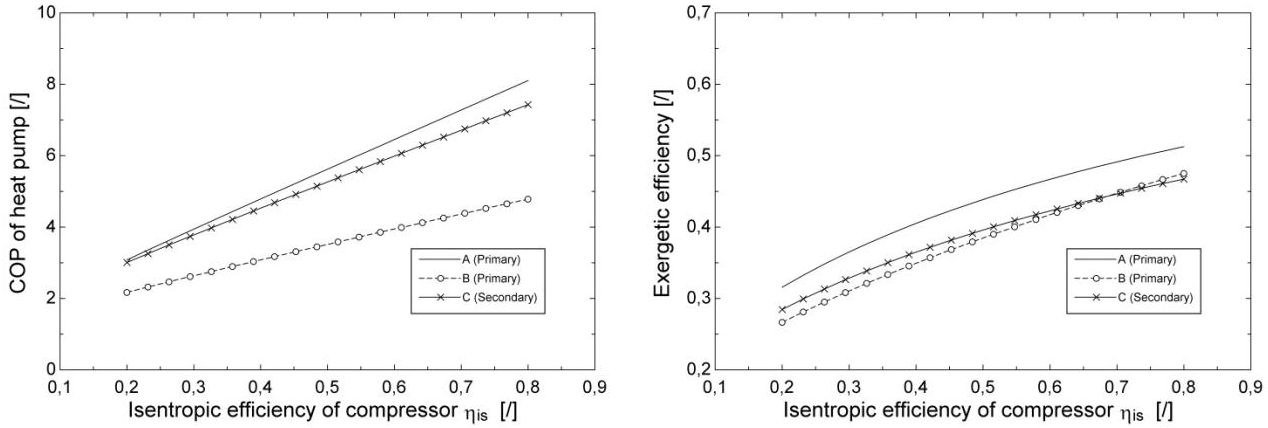

(A) (B)

Fig.7. (A) COP of heat pump with variable isentropic efficiency for each of the 3 proposed configurations. (B) Exergetic efficiency of individual configurations with variable isentropic efficiency.

5. Results

5.1. Variation of forward temperature of the DH network

The forward temperature of the DH has a high impact on the system performance, as the temperature is directly linked to the heat pump capacity and temperature lift in all the different configurations. Figure 8 shows the variation of the described configurations in terms of both volume flow of district heating water and electricity consumption, with variation in forward temperatures of the district heating network. Electricity consumption is presented as a function of the product – this is to represent how much power (and the remaining heat load) is required in order for the system to produce one [kWh] of hot tap water at 45 ^{o}C according to the assumptions explained above and the Danish building standard.

Heat is calculated on the basis of enthalpy difference between forward and return temperatures (in the case of Figure 8 the return temperature can be found in Table 1). The full heat content between forward and the lowered return temperature can be found by subtracting the curve of variant B from Figure 8 (B) from the product (energy balance calculation where the product is 1).

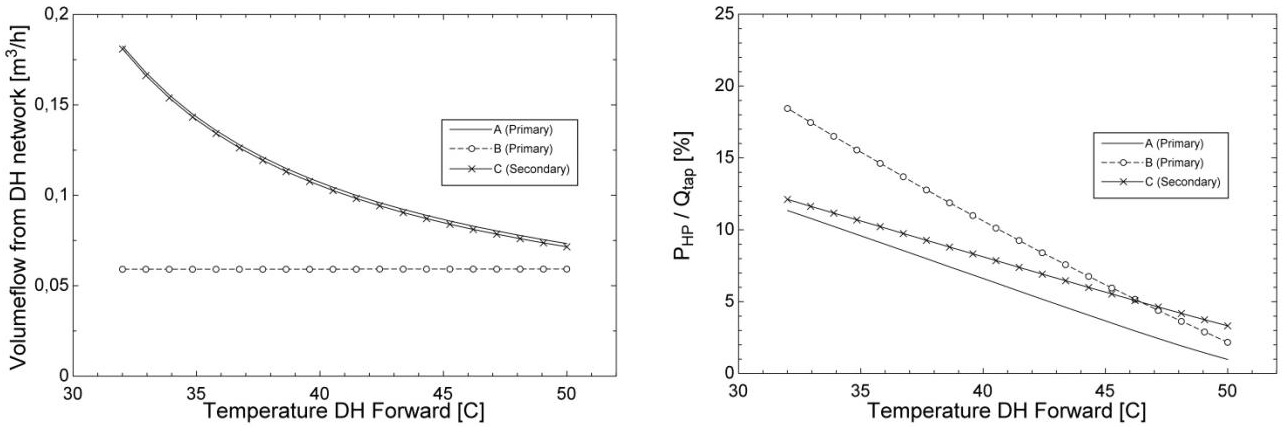

(A) (B)

Fig. 8. (A) Required volume flow of hot DH stream with variable forward DH temperature. (B) Relation between electricity consumption and product with variable forward DH temperature.

When the DH forward temperature approaches the temperature required for tap water heating (53 ^{o}C for primary side when considering a pinch temperature of 8 K, 58 ^{o}C for secondary side

according to the assumptions of Table 1), the consumption of electricity is reduced significantly; while almost the full energy flow is required from the district heating network. This is due to the significantly reduced thermal load in each of the heat pump configurations. As discussed above, configuration C has a slightly higher condenser load as in variant A, thus increasing the electricity consumption for the heat pump correspondingly at all temperature levels.

5.2. Variation of return temperature of the DH network

Changes in return temperatures are highly important, as not only the electricity consumption of the heat pump booster configuration is affected, but also the temperature difference between the forward and return of the district heating network. Thus the optimal heat pump must perform with high efficiency in a range of high temperature differences between forward and return temperatures.

Assuming tap water at 10 ^{o}C, and a finite heat exchanger (8 K), 18 ^{o}C is the lowest reachable temperature for the return water in the district heat system by direct heat exchange. Lower temperatures can only be achieved by using the heat pump evaporator to cool the stream further, which in this study only is considered in variant B.

With an increase in return temperature of the district heating network, power consumption is reduced as the evaporation temperature of the heat pump refrigerant can be increased. An evaluation of the heat pump characteristics with a change in return temperature is considered in Figure 9 (constant forward temperature corresponding to Table 1). From the curvature of variant A and C in Figure 9 (B) it is clear that an optimum exists if the district heating water from Figure 9 (A) has a change in value.

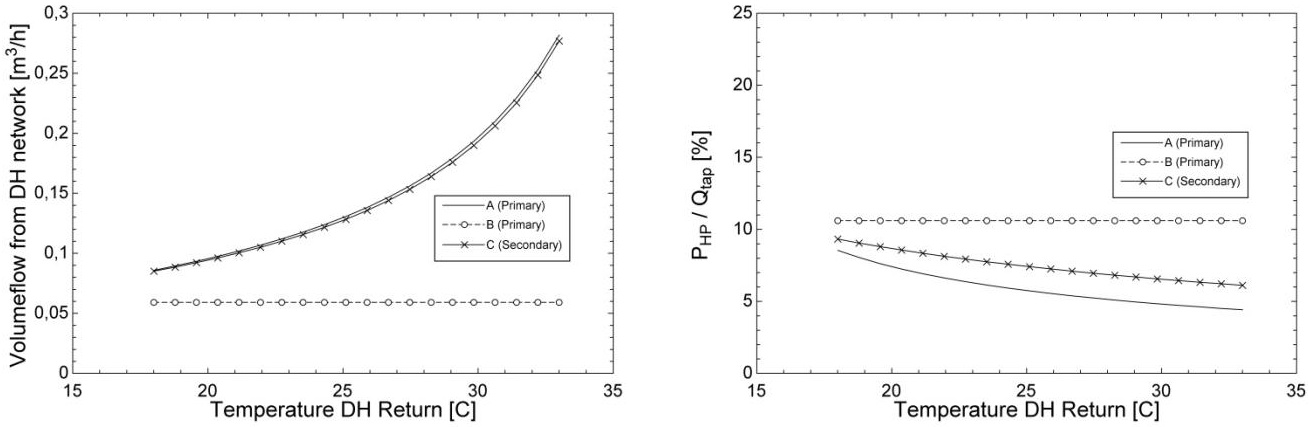

(A) (B)

Fig. 9. (A) Required volume flow of hot DH stream with variable forward DH temperature. (B) Relation between electricity consumption and product with variable return DH temperature

The differences between configurations A and C are quite hard to spot in Figure 9. In principle it does not make sense to display variant B, as the return temperature of the DH network is not controlled. The visible changes in Figure 9 (A) correspond to the previously addressed wish to show the differences in flow of DH water required to fulfil the tapping process.

5.3. Comparison of results using exergy

Exergy is used as another way to evaluate the performance of the different concepts. In this evaluation the different temperature levels of the district heating network is evaluated. Exergy is furthermore a good evaluation parameter when more than one fuel stream combine into only one product, as optimum between the different fuel streams is easily spotted.

The lower electricity consumption of configuration A is rewarded in the calculation of exergetic efficiency throughout the entire range of forward and return temperatures considered in the paper. Considering the initial calculations, and the sensitivity study of heat exchanger performance and

isentropic efficiency, the distribution between the performances of the individual configurations is distinct.

Figure 10 shows the exergetic efficiency of the three different variants, considering both the forward and the return temperatures. From Figure 10 (B) it seems that the second law efficiency is not improved with a return temperature above 25 ^{o}C in either of the cases, because the trade-off between reductions in electricity consumption is no longer compensating the increased exergy content of the heat consumption. The influence of pressure losses on exergy destruction is not considered in the systems and would lower efficiency further at the higher temperature due to higher flow rates. Increasing the forward temperature seems to be beneficial to the point where heat pump is no longer needed in the system. This is further discussed in section 6.

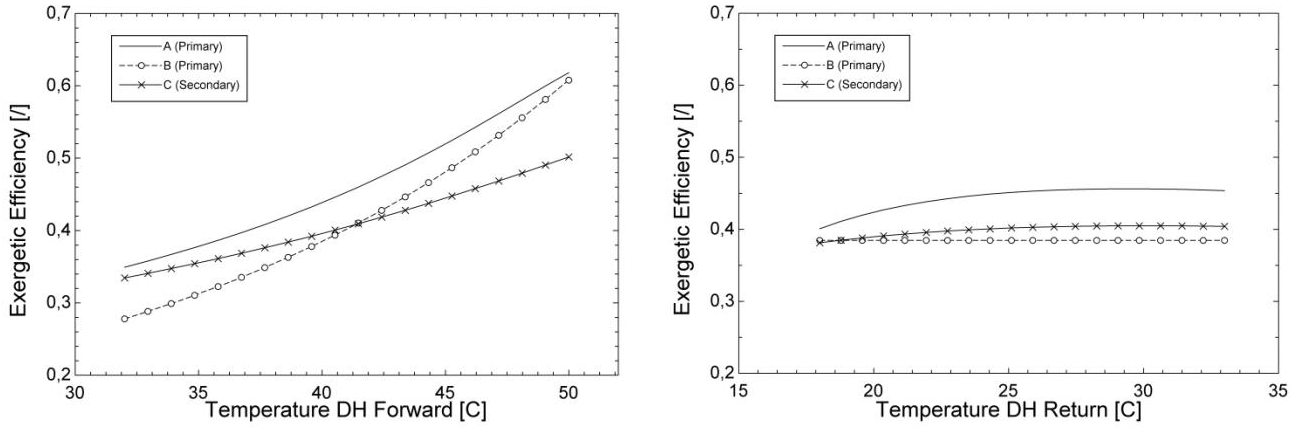

Fig. 10. (A) Exergetic efficiency of individual configurations with variable DH forward temperature. (B) Exergetic efficiency of individual configurations with variable DH return temperature.

Variant B performs well with a low temperature return stream, or very high forward temperatures. Allowing this configuration additional heat from the space heating as proposed in section 4.2 might improve the performance of the configuration considerably, but in the temperature regime proposed in the above calculations, the configuration is not advantageous in any part of the temperature span considered.

5.4. Constant temperature difference between forward and return

As it is not easy to find the optimal forward temperature from the above calculations, an additional calculation has been performed with a constant temperature difference (18 K) between forward and return of the district heating network. This is to rule out the coinciding effects of very high temperature lifts in the heat pump in one end and high thermal heat pump load in the other end of the studied temperature range.

In figure 11, most of the range is clearly covered by the configuration A. Only at very high temperature levels configuration B is advantageous. The secondary system C is inferior in the entire range.

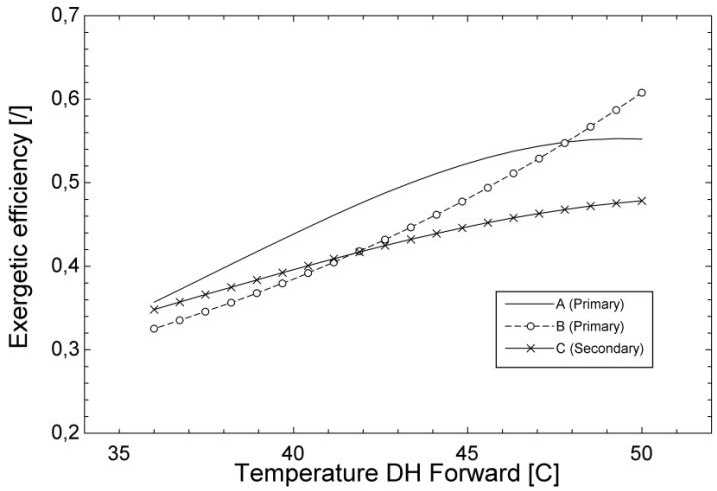

Fig. 11. Exergetic efficiency of the individual configurations with constant temperature difference between forward and return line of the district heating network.

6. Discussion

Several system configurations have been considered in the initial work of the project based on forward and return temperatures corresponding to table 1. Of the investigated systems, the three configurations presented in this paper have provided the best performance. It is not unlikely that other energy efficient solutions can exist. The three variants have been chosen based on the criteria considered in the overall project, not only to satisfy energy efficiency, but also to comply with e.g., state of the art technology and DH network considerations.

Considering both Fig. 8 and Fig. 10 (A), the optimal operation temperature of the district heating forward is not easily determined. The method used in fig. 11 show, that with a reasonable temperature difference throughout the range (18 K), the thermal load is the important factor to observe, as the COP is (almost) constant. Determination of optimal forward temperature of a low temperature district heating network will therefore not depend on the heat pump booster unit, but rather on external factors such as heat loses in the distribution network, sustainable sources and optimum production criteria for the combined heat and power plant.

This effect is also shown in In Fig. 10 (B), as the exergetic efficiency levels out without consideration to the improvement in COP from increasing the evaporator temperature.

From the same figure it is clear, that with a constant forward temperature (40 ^{o}C), the return temperature has an optimum (25 ^{o}C – 30 ^{o}C), which presumably would not be beneficial for the remaining network.

Consulting Figure 10 (A) it is clear that the exergetic efficiency decreases with consumption of electricity in the heat pump configurations. When approaching the temperatures where direct heat exchange is possible, the exergetic efficiency increases, as heat losses are not considered in the network.

If the heat pump booster unit is used in a system where it is coupled with a traditional district heating network, changes in the heat and power prices can be neglected. The reason for this is that the new system does not significantly change the operating conditions of the combined heat and power plant or the capacity of the transmission line in the district heating network. In this case only the heat losses in the novel DH system, and the increased end user capacity of the DH system from using lower temperatures can be compared with the additional electricity consumption.

7. Conclusion

Three heat pump schemes were singled out for evaluation in a low temperature district heating network in order to increase tap water temperature to meet the Danish standard. Out of the three

heat pumps, two are used to boost the network temperature prior to heat exchange with the tap water, while the third is used to boost the temperature of the heated tap water. Variant A was found to be the most efficient configuration in the temperature range considered. In the expected temperature range the heat pump has an exergetic efficiency between 0.4 [/] and 0.6 [/]. Variant B proved that power consumption might not become significantly increased, if the heat pump is used to actively lover the temperature of the return flow as source heat. This would allow for lower flow rates to meet the tap water requirements.

Acknowledgments

This work was supported by the Danish Energy Technology Development and Demonstration Programme (EUDP).

Nomenclature

$\dot{E}$ Time rate of exergy, kW

h Enthalpy, kJ/kg

$\dot{m}$ Mass flow rate, kg/s

p Pressure, kPa

P Electricity, kW

Q Heat, kW

s Entropy, kJ/(kg*K)

t Temperature, C

$\dot{V}$ Volume flow rate, m^3/h

subscripts

0 Dead state

i Index (component)

DH District heating network

References

[1] Thorsen J E, Christiansen C H, Brand M, Olesen P K, Larsen C T. Experiences on Low-Temperature District Heating in Lystrup – Denmark. Procedings of International Conference on District Energy 2011, Slovenia.

[2] Bøhm B, Danig P O. Monitoring the energy consumption in a district heated apartment building in Copenhagen, with specific interest in the thermodynamic performance. Energy and Buildings 2004; 36; 229 – 236

[3] Elmegaard B, Houbak N. Simulation of the Avedøreværket Unit 1 Cogeneration Plant with DNA. Proceedings of The 16th International Conference on Efficiency, Cost, Optimization, Simulation, and Environmental Impact of Energy Systems 2003; 1659-1666

[4] Asada H, Boelman EC. Exergy analysis of a low temperature radiant heating system. Building Services Engineering Research & Technology 2004; 25 (3); 197-209

[5] Danish Standards. Code of Practise for domestic water supply installations (DS 439). 2009; Fourth edition.

[6] Engineering Equation Solver (EES). 2011 F-Chart Software, LLC. http://www.fchart.com/ees/ [accessed 20.01.2012]

[7] Nellis G., Klein S A. Heat Transfer. Cambridge university press, NY. 2008. ISBN 978-0-521-88107-4.

[8] Bejan A, Tsatsaronis G, Moran M. Thermal Design and Optimization. Wiley, NY. 1996 ISBN 978-0-471-58467-4

[9] Rosen M A, Dincer I. Effect of varying dead state properties on energy and exergy analyses of thermal systems. Int J Therm Sci 2004; 43: 121–133

Exergoeconomic Diagnosis: a Thermocharacterization Method by Irreversibility Analysis

Olivares-Arriaga A.[a], Zaleta-Aguilar A[b], Rangel-Hernández V. H.[c] and Belmán-Flores J. M.[d]

[a] University of Guanajuato, Salamanca, Gto., México, abraoliaga@hotmail.com ,
[b] azaleta@ugto.mx ,[c] vrangel@ugto.mx, [d] jmbelman@ugto.mx

Abstract:

The paper at hand proposes an exergoeconomic diagnosis based upon the irreversibility characterization of the components by setting up the Rerefence Operating State (ROS) of the thermal power plant. The diagnosis introduces a new parameter, B, which represents the total irreversibilites attained to a subsystem or component at either design or off-design conditions (either partial or full loads). The elementary characterization of the reference state permits to detect changes on irreversibilities due to intrinsic or induced malfunctions. Reliability of the method is proven by its application to an actual Combined Power Plant. Data is obtained by means of software and hardware installed in the power plant. This has pemitted to obtaining a real-time exergoecomic diagnosis. Results from the study have been useful to detect the deviations in the thermal regime in terms of the irreversibilities of the components.

Keywords:

Irreversibility, Exergo-characterization, Diagnosis.

1. Introduction

The main idea of a thermoeconomic diagnosis is to pinpoint malfunctions into the components of a system as well as to quantify the additional consumption of resources because of them. The need to improve thermal processes have led to researchers to propose different methodologies for thermoeconomic diagnosis. Valero et. al. proposed the Exergy Cost Theory, which consisted in indentifying the causes and assessing their impact on additional consumption (i.e. Fuel Impact). However, the method required to be applied at constant power output. A first formulation to determine the causes of irreversibilities was proposed by Valero and Lozano et. al.[1] $\Delta F_T \cong k^*_{P_i} \Delta I_j$, this formulation relates the exergetic costs of each component, changes of irreversibilities to find the change in resources. An alternative formula was presented by Lozano and Valero [2] $\Delta F_T \cong k^*_{P_j} P \Delta \kappa_j$, however, this formulation does not consider changes in the local products of each component. Reini, Lazzaretto, and Macor [3] developed a new formulation to calculate the impact to Fuel.

$$\Delta F_T \cong \sum_{i=1}^{n} \left(\sum_{j=0}^{n} k^*_{P_i}(x_0) \Delta \kappa_{ji} \right) P_i(x_0) + \sum_{i=1}^{n} k^*_{P_i}(x_0) \Delta P_{s_i} \qquad (1)$$

This equation allows finding the contribution of each component to the final variation of resources. One of the main problems of exergoeconmic formulation is that it takes to get all the exergy of both reference state and test state of all the components and perform complex matrix formulations. The philosophy of these methods is to compare the actual operating conditions with the reference operating conditions, maintaining the product (power) of the plant and environmental conditions constant.

The main disadvantage of these methods is that it requires complex calculations so it is necessary to have expensive software and hardware.

Zaleta [4], proposes to make the diagnosis through of a thermodynamic simulation based on the first and second laws of thermodynamics. The methodology is able to analyze the changes produced by malfunctions in two global indicators of the thermodynamic cycle: the total power produced and the thermal regime (inverse of efficiency). This is based on a comparison between two operating conditions, a condition is the test operation (COP) which reflects the current operating conditions, and the other is the reference operating condition (COR) which can be taken in thermal balance or acceptance testing, it also uses energy and exergy analysis for the evaluation of the thermal regime and the total power generated; which are the most appropriate indicators to indicate the operation of a power plant. This diagnostic method has been used in actual power plants, where several malfunctions and external variations are common during operation and are detected in real time.

The series of papers, Tadeus, presented by Valero compiled the evolution of different kinds of diagnostic methods. The complexity of the mathematical formulations and solution arrays, the high degree of instrumentation in the overall process (which is affected when there is no energy balances), the low accuracy of the results and the lack of understanding and comprension of the results by plant operators.

The thermo-characterization theory proposed by Zaleta (2009) aims to diagnose each component in isolation on the impact of anomalies and using formulas to determine the overall effect on the process. The methodology of this theory was validated with the Method of Reconciliation and the results yielded a percentage relative error less than 5%. However, this new thermo-characterization theory considers not simultaneously enthalpy and entropy changes; therefore, two analysis most performed to find the change in the thermal regime first with respect to variation of the parameter ω and other with respect to the parameter σ.

In this paper we set out again the premises of the theory of thermo-characterization but based on exergy analysis. This new approach considers variations of the parameters ω and σ in a new single parameter β.

2. Diagnosis theory based on exergy thermo-characterization

Premise 1: Distribution of an energy system and local processes. All advanced energy system can be subdivided into *n* isolated subsystems, delimited by a control volume with strategically defined boundaries according to the instrumentation, process sections, etc. Figure 1, Shows the disaggregation of an open Brayton cycle.

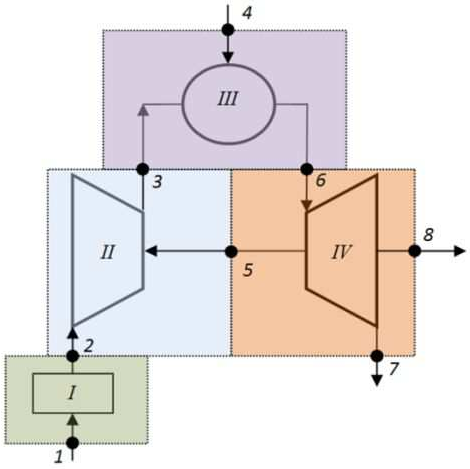

Fig. 1. Gas turbine cycle with subsystems (n=4 components) and (p=8) estrategy points.

Each control volume comply the mass and energy balances. Changes in thermodynamic conditions of input and output of the mass flow rates in each component *i*, during a process (heating, cooling, work, reaction, etc.), can be characterized by the parameters (***ωi, σi, βi, FR***) applied according to the control volume and the properties of defined mass flux, shown in the figure 2. Therefore, (4) describes the changes in the parameter β_j and (5) defines the mass flow ratio.

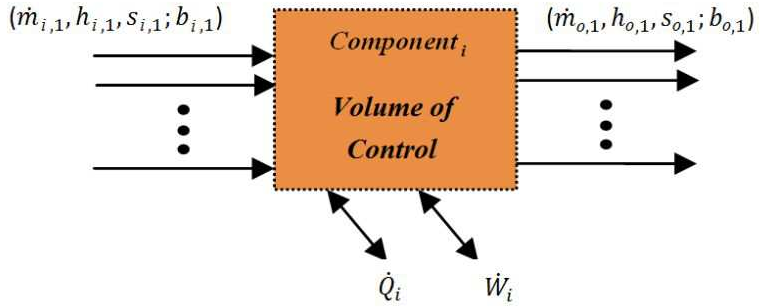

Fig. 2. Volume of control of i-th component.

The parameter ω_i is calculated from the enthalpy difference between the input minus output enthalpies.

$$\omega_i \left[\frac{kJ}{kg}\right] = h_e - h_s = \sum_{i=1}^{n} \dot{x}_i h_{e,i} - \sum_{j=1}^{m} \dot{y}_j h_{s,j} \qquad (2)$$

where:

$$h = h_{estatica} + \frac{c^2}{2} + gz + \mu x$$

$$\dot{x}_i = \frac{\dot{m}_{e,i}}{\sum \dot{m}_e}\ ; \qquad \dot{y}_j = \frac{\dot{m}_{s,j}}{\sum \dot{m}_s}$$

The difference of entropy is determinate with the next equation:

$$\sigma_i \left[\frac{kJ}{kg \cdot K}\right] = s_e - s_s = \sum_{i=1}^{n} \dot{x}_i s_{e,i} - \sum_{i=1}^{m} \dot{y}_j s_{s,j} \qquad (3)$$

The parameter β_i refers to the difference between the flows of inlet and outlet exergy, this is calculated from the parameters ω_i, σ_i and the chemical exergy.

$$\beta_i \left[\frac{kJ}{kg}\right] = \omega_i - T_0 \sigma_i + \sum_{i=1}^{n} \dot{x}_i e_s^Q - \sum_{i=1}^{m} \dot{y}_j e_e^Q =$$

$$= \sum_{i=1}^{n} \dot{x}_i h_{e,i} - \sum_{i=1}^{m} \dot{y}_j h_{s,j} - T_0 \left[\sum_{i=1}^{n} \dot{x}_i s_{e,i} - \sum_{i=1}^{m} \dot{y}_j s_{s,j}\right] + \sum_{i=1}^{n} \dot{x}_i e_s^Q - \sum_{i=1}^{m} \dot{y}_j e_e^Q \qquad (4)$$

The relationship between the actual mass or volume flow regarding to the design indicates the load which is operating the thermal cycle.

$$FR = \frac{\dot{m}_{test}}{\dot{m}_{ref}} \sqrt{\frac{p/v\big|_{ref}}{p/v\big|_{test}}} \qquad (5)$$

Premise 2: State of reference to different loads and modes of operation. An energy system is designed to operate at different loads depending on energy demand. The adjustment of the load control systems have been used in the admission of the working fluid, regulation of *IGV* (Inlet Guide Vane) for gas turbine or control valves for steam turbines. Load change (*FR*) produces changes in power, is well known that the power generated is directly proportional to the mass flow used to produce, in addition the properties change; however, these can be calculated for each load

from the parameters β. If malfunctions are not considered in the exergy balance of the components, these parameters calculated allow us to establish the reference state of i-th component, i.e. we will know the trajectory in two-dimensional space (β, P) of the component. The reference state is calculated from the heat balances provided by the manufacturer and / or performance testing and thermodynamic simulator.

Figure 3a shows the reference trajectory to be followed by the component in space β, P). β values can be characterized (using polynomial regression) as a function of P.

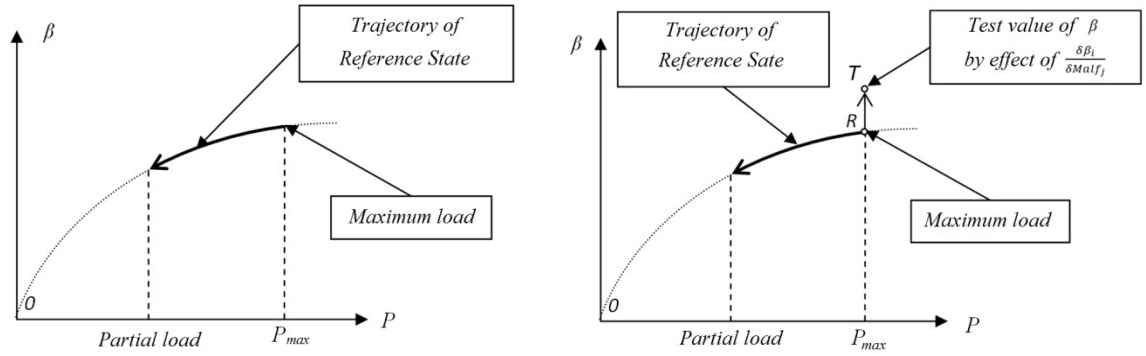

(a) *(b)*

Fig. 3. a) Trajectory of reference State, b)Effect of the j-th malfunction on the i-th β parameter.

Premise 3: Effect of malfunctions or anomalies. Figure 3b shows the effect of a malfunction. The point *"R"* is the reference point that component should be presented for current load if there not were any anomalies. The vectors in the plane (β, P) are the deviations in the parameters β due to the malfunction. The malfunctions can be selected by the criterion of the designers, operators, or by free variables of a thermodynamic simulation of the plant as proposed Zaleta [4]. These variables can be classified into three categories of m variables:

a) Environmental (P_0, T_0, *HR*, *HHV*, etc.)
b) Control and set Point (*IGV*, *T*, $\dot{m}$, etc.)
c) Internal Indicators (η_{iso}, *UA*, etc.)

If there would be more than a malfunction, these would always be in the same plane and their overall effect will be equal to the vector sum of each of the malfunctions. To find the β parameter variations in function of each of the possible malfunctions applies the concept of the derivation of these parameters in relation to each malfunction. Mathematically:

$$\frac{\delta\beta_i}{\delta Malf} = \frac{\delta\omega_i}{\delta Malf} - T_0 \frac{\delta\sigma_i}{\delta Malf} \quad (6)$$

We may establish a matrix of malfunctions which represents the variation of the parameter β for each component with respect to each possible malfunctions. To find each term within the matrix is necessary to use a simulator that allows us to independently vary each of the malfunctions and to find the effect of these variations in the parameter β. It should be noted that the matrix of malfunctions correspond to a single power (P), however, we can obtain these matrices to principal workloads: *VWO* (Valve wide open), 100%, 75%, 50% and 25%.

$$Malf_{\beta[n\times m]}\Big|_{FR} = \begin{bmatrix} \frac{\delta\beta_1}{\delta Malf_1} & \cdots & \frac{\delta\beta_n}{\delta Malf_1} \\ \vdots & \ddots & \vdots \\ \frac{\delta\beta_1}{\delta Malf_m} & \cdots & \frac{\delta\beta_n}{\delta Malf_m} \end{bmatrix} \quad (7)$$

As mentioned in the previous paragraph we can determine the variation of β with respect to each malfunction and to different loads, then it can be said that the variation of β is a function of the malfunctions and workload.

$$\frac{\delta\beta_i}{\delta Malf_j} = f\left(P, Malf_j\right) \tag{8}$$

Premise 4: Test performance. There are rules or procedures for conducting performance tests to energy systems such as performance tests codes (*PTC*) of the ASME. For testing is necessary to install strategically local instrumentation points (*p*) to find the basic thermodynamic properties (such as *p, T,* $\dot{m}$ *, Q,* etc..). The main objective of performance testing is to obtain the current values of:

I. P

II. $Malf_{j,test}$ y $Malf_{j,ref} = Malf\left(P\big|_{cte}\right)$

III. $\Delta Malf_j = Malf_{j,test} - Malf_{j,ref}$

IV. $\beta_{i,test}$

V. $\beta_{i,ref} = \beta\left(P\right)$

VI. $\Delta\beta_i = \beta_{i,test} - \beta_{i,ref}$

VII. $\eta_{ref} = \eta\left(P\right)$ y $RT_{ref} = RT\left(P\right)$

VIII. $\Delta\eta = \eta_{test} - \eta_{ref}$ y $\Delta RT = RT_{test} - RT_{ref}$

Premise 5: Reconciliation of local malfunctions. Deviations found in each thermo-characterización parameter $\Delta\beta_i$ by specific test performance can be disaggregated as the effect of malfunctions $\Delta Malf_j$, this is the total effect of each of the malfunctions. Equation (9) shows this variation:

$$\Delta\beta_i = \Delta\beta_{i,1} + \cdots + \Delta\beta_{i,m} = \sum_{j=1}^{m} \int_{Malf_{j,ref}}^{Malf_{j,act}} \left.\frac{\delta\beta_i}{\delta Malf_j}\right|_{FR} dMalf_j \tag{9}$$

For *n* components, the reconciliation of malfunctions is represented as the sum of all deviations of the parameter:

$$\Delta\beta_{[n\times1]} = \int Malf_{\beta[n\times m]} \times dMalf_{[m\times1]} \tag{10}$$

Premise 6: Global Impact. Global parameters of a plant are function on the characteristics of the equipment and the β parameters of each component. Using a simulator of the plant, the efficiency (η) or thermal regime *RT* (inverse of the efficiency) are a function of the parameters β and of the workload *P*, (11), (12).

$$\eta = f\left(\beta_1, \ldots, \beta_j, \ldots \beta_m, P\right) \tag{11}$$

$$RT = f\left(\beta_1, \ldots, \beta_j, \ldots \beta_m, P\right) \tag{12}$$

Any variation in the parameters β will indicate that there is a malfunction that can be characterized by the impact on global parameters η and RT in a vector of dimensions $m\times1$, (13) y (14):

$$\frac{\partial\eta}{\partial\beta_i} = \left[\left.\frac{\partial\eta}{\partial\beta_1}\right|_P, \ldots, \left.\frac{\partial\eta}{\partial\beta_j}\right|_P, \ldots, \left.\frac{\partial\eta}{\partial\beta_m}\right|_P\right] \tag{13}$$

$$\frac{\partial RT}{\partial\beta_i} = \left[\left.\frac{\partial RT}{\partial\beta_1}\right|_P, \ldots, \left.\frac{\partial RT}{\partial\beta_j}\right|_P, \ldots, \left.\frac{\partial RT}{\partial\beta_m}\right|_P\right] \tag{14}$$

From the information of the performance test we find deviations in the global indicators; however, we do not know which malfunctions are presented and their impact in these parameters. To determine the effect of each malfunction in these global parameters, we can apply the method of reconciliation [6]. However, as we only have the variations of the parameters β as effect of malfunctions a modification must be made to the method of reconciliation (chain rule for total derivation) that is:

$$\Delta\eta = \sum_{i=1}^{n}\sum_{j=1}^{m}\int_{Malf_{j,ref}}^{Malf_{j,test}} \frac{\partial\eta_T}{\partial\beta_i}\frac{\partial\beta_i}{\partial Malf_j}\bigg|_P dMalf_j \quad (15)$$

$$\Delta RT = \sum_{i=1}^{n}\sum_{j=1}^{m}\int_{Malf_{j,ref}}^{Malf_{j,test}} \frac{\partial RT_T}{\partial\beta_i}\frac{\partial\beta_i}{\partial Malf_j}\bigg|_P dMalf_j \quad (16)$$

The above equations represent the change in the global parameters of the plant as function to local variations of the parameters β of each component. These variations of the parameters β are in turn the effect of the plant malfunctions presented in.

3. Implementation of the exergo-characterization to a 420 MW combined cycle

The culmination of each new theory is to find the energy assessment of this application in real cases. This paper will talk about the use of make use of the exergo-characterization to find deviations from the thermal regime of a combined cycle operation. As a first step in the application describes the main features of the combined cycle components are described to be analyzed and then follow the application of the methodology or assumptions presented in the previous paragraph. Only the exergy balances for the components is shown , but to create the reference state and test state was performed in the program EES (Engineering Equation Solver®) which considers mass balances, energy and exergy.

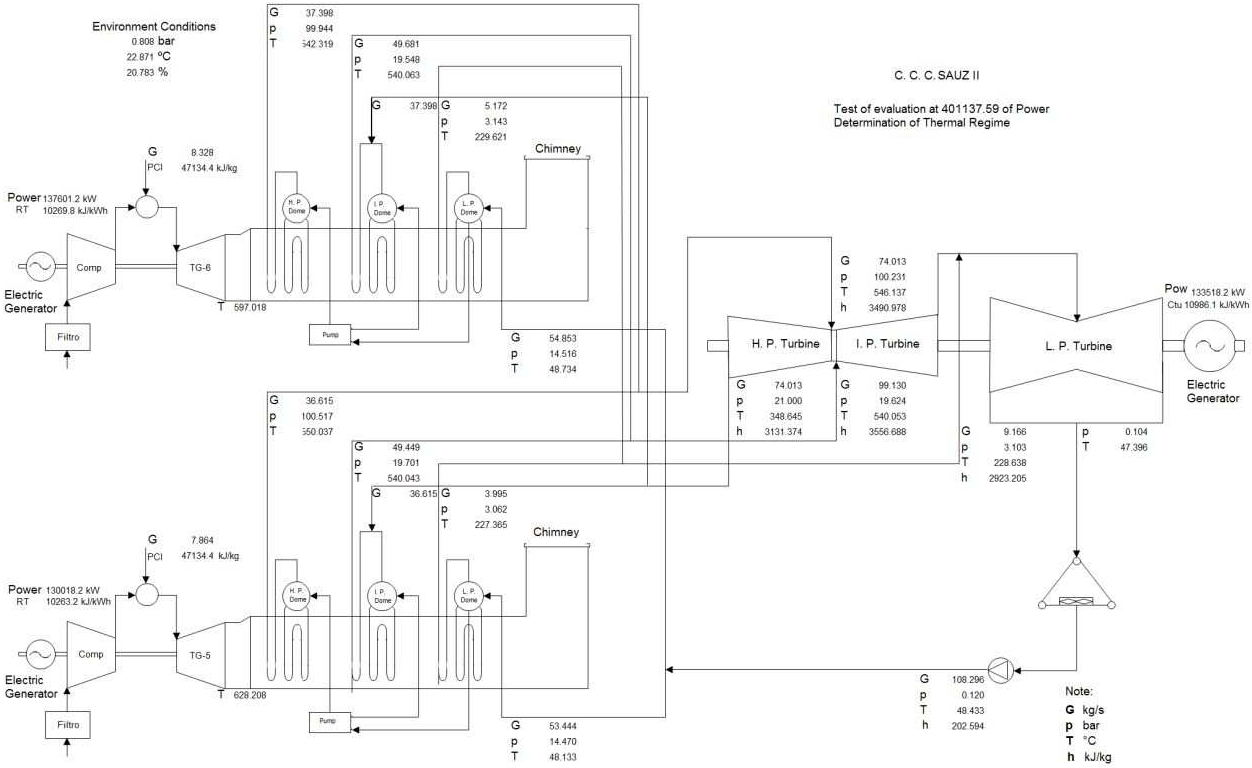

Fig. 6. Scheme of the real combined cycle.

3.1. Description of the combined cycle

The case of study of this work is referred to a combined cycle (Figure 6) consisting of a gas turbine of 128.98 MW Westinghouse with an efficiency of 34.8%, a Siemens gas turbine of 131.59 MW with an efficiency of 34.74% and a steam turbine ABB-Alstom with a capacity of 127.67 MW and an efficiency of 33.03%, data from a performance test conducted in January 2004 by staff of the Laboratory test Equipment and Materials (*LAPEM*).

Figure 6 shows the entire outline of the combined cycle that serves as a guide for the identification of the main equipment and flows in which the plant is discretized. Each has a tag number that identifies itself. Given the level of detail, the whole scheme is divided, in order of appearance in gas turbines, heat recovery, steam turbine and the air condenser.

Flows definition. In Table 1 all flows are systematically identified (exchange of mass and energy) of the combined cycle. It helps in the interpretation of the cycle scheme. The numbering of the flows and their interaction with each of the equipment in the plant, we propose a logic numeration according to the start of the cycle, i.e. cycle gas, putting a zero in this cycle for their distinction and avoid some confusion with vapor cycle, and so on until the end of it in the air cooled condenser.

3.2. Implementation of the premises of the exergo-characterization

Premise 1. Disaggregation of energy system and its local processes. In this case of study, the combined cycle was divided into 17 major components (n = 17) each delimited by its volume control. In the scheme of the combined cycle, likewise settled 32 points of interaction between the different volumes of control (p = 32). For each control volume are established mass and energy balances. Table 1 shows the values of the design parameters (FR = 1) of all the 32 points defined in the cycle. Table 2 shows the major components that form the thermodynamic cycle.

Premise 2. Reference state at different loads and modes of operation. As mentioned thermodynamic cycles are designed to work at different loads in the case of gas turbines, this is achieved decreasing the inlet compressor area by operating the *IGV's*. By reducing the inlet area decreases the mass flow and hence the power of the gas cycle. Using a thermodynamic simulator performed in software and data based on the design of components and design heat balances and / or acceptance testing is possible to vary the value of the *IGV* to find the variation of the parameters ω, σ and β as a function of the load P without abnormalities (reference state). Figure 4 shows the variation of the parameter β as a function of the load P, it should be noted that this parameter relates the enthalpy and entropy changes into one. For each component reference graphs must be calculated considering that the load P of each component will vary depending on the percentage of power.

Premise 3. Effects of malfunctions or anomalies. In order to understand the perturbation and effect of different anomalies or malfunctions on the reference state of each n component is necessary two steps:

I. Definition of malfunctions or anomalies.
II. Analysis of the perturbation by effects of each of the anomalies in each of the components.

Definition of malfunctions or system failures. The definition of m free variables of the system is necessary. Each variable corresponds to each possible malfunctions that may occur in the system. These variables should be chosen based on experience of the analyzer; Table 3 shows the variables and the corresponding description of malfunctions for the combined cycle.

Analysis of the perturbation of malfunctions on the reference state of the n sub-systems. Once identified malfunctions or anomalies in the whole system, the next step is to calculate the variation of the parameter β with respect to each of the malfunctions to the different load levels.

Table 1. Description of conditions in the combined cycle

TAG	Description	*T* [ºC]	*p* [bar]	*h* [kJ/kg]	*s* [kJ/kg K]	· [kg/s]	b [kJ/kg]	W [MW]
	Gas Turbine (Units 5 & 6)							
00	Environment Conditions	20	0.8077	20.20	0.07136		0	
01_5	Air Compressor suction	20	0.79	20.20	0.07136	285.49	0	
02_5	compressor discharge	381.1	9.29	392.33	0.8956	285.49	130.51	
03_5	Fuel Flow Combustion Chamber			47134.4		7.864	0	
04_5	Combustion gases at the inlet to turbine	1238	9.11	1620.12	1.459	293.35	1193.11	
05_5	Discharge of the combustion gases in the gas turbine	656.96	0.83	809.24	1.552	293.5	355.07	
06_5	Chimney flue gas	125.3	0.8077	144.70	0.5079	293.5	-3.47	
WC_5	Power consumed by the compressor							106.24
WG_5	Power developed by the turbine							237.87
01_6	Air Compressor suction	20	0.80	20.20	0.07135	331.3	0.00001	
02_6	compressor discharge	399.34	10.45	411.84	0.9250	331.3	141.40	
03_6	Fuel Flow Combustion Chamber			47134.4		8.328		
04_6	Combustion gases at the inlet to turbine	1191	10.24	1534	1.358	339.62	1137.0	
05_6	Discharge of the combustion gases in the gas turbine	612.38	0.83	742.33	1.470	339.62	312.02	
06_6	Chimney flue gas	120.0	0.8077	138.56	0.4924	339.62	-5.07	
WC_6	Power consumed by the compressor							129.75
WG_6	Power developed by the turbine							269.01
	Heat Recovery Steam Generator (HRSG 1 & 2) – Steam Turbine							
1	Principal steam	548	115	3481.66	6.6736	79.35	1528.23	
2	Hot Reheat steam	548	20.02	3574.52	7.5667	97.96	1359.25	
3	Cold Reheat Steam	327.91	22.82	3081.27	6.8079	77.63	1088.47	
4	Outlet Steam from Intermediate Pressure Steam Turbine	301.46	3.51	3071.30	7.6342	99.36	836.24	
45	Inlet Steam to Low Pressure Steam Turbine	294.55	3.48	3057.25	7.6143	108.24	828.04	
5	Outlet Low Pressure Steam from HRSG	217.20	3.5	2898.7	8.8602	8.86	759.05	
6	Exhaust Steam outlet from LPST	41.51	0.08	2427.68	7.7553	108.44	157.14	
61	Suction water of principal pump	137.8	3.40	579.9	1.717	97.32	86.81	
60M	Discharge Intermediate Pressure water of principal pump	137.9	22.30	581.6	1.718	77.59	88.73	
60A	Discharge High Pressure water of principal pump	138.4	115	589.5	1.721	19.732	98.09	
71	Suction water of condensate pump	41.51	0.08	173.84	0.5925	108.44	3.07	
70	Discharge water of condensate pump	41.62	15.45	175.66	0.5934	108.44	4.64	
	Electric Generator							
WNETA	Power net							404.96
WBC	Power to condensate pump							0.1977
WBA	Power to principal pump							5.3211
WAUX	Power to auxiliary equipment							6.320

Table 2. Principal components in the thermodynamic cycle

	Equipment	Integration in the cycle
I	Filters	Gas Cycle 5
II	Compressor	Gas Cycle 5
III	Combustor	Gas Cycle 5
IV	Drive turbine	Gas Cycle 5
V	HRSG	Gas Cycle 5 – Steam cycle
VI	Principal pump	Gas Cycle 5 – Steam cycle
VII	Filters	Gas Cycle 6
VIII	Compressor	Gas Cycle 6
IX	Combustor	Gas Cycle 6
X	Drive turbine	Gas Cycle 6
XI	HRSG	Gas Cycle 6 – Steam cycle
XII	Principal pump	Gas Cycle 6 – Steam cycle
XIII	High Pressure Turbine	Steam cycle
XIV	Intermediate Pressure Turbine	Steam cycle
XV	Low Pressure Turbine	Steam cycle
XVI	Condensate pump	Steam cycle
XVII	Air cooled condenser	Steam cycle

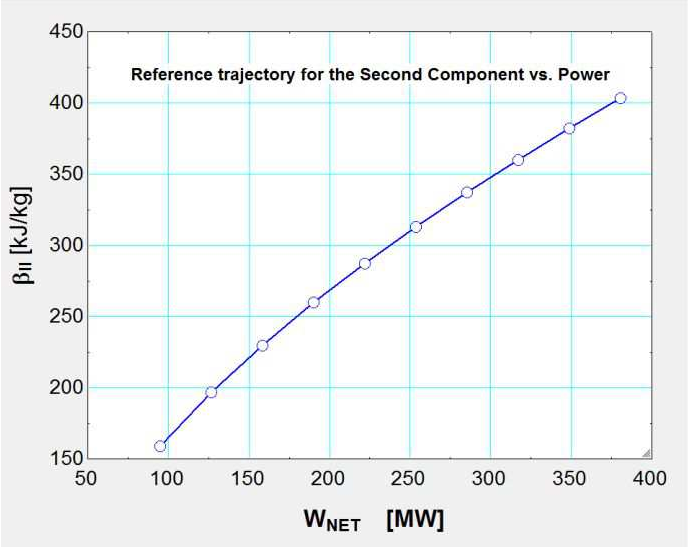

Fig. 4. Effect of the j-th malfunction on i-th parameter.

The variance of each parameter β depends on each of malfunctions; in the present case we have 20.

$$\Delta\beta_1 = \frac{\delta\beta_1}{\delta Malf_1} dMalf_1 + \frac{\delta\beta_1}{\delta Malf_2} dMalf_2 + \cdots + \frac{\delta\beta_1}{\delta Malf_{20}} dMalf_{20} \quad (17)$$

for each component we find in similar form the parameter β variation as a function of all malfunctions.

Premise 4. Performance test of a generating plant can be performed using the procedures provided by the test codes (PTC' s). To determine the reference state of the combined cycle was a performed

simulator which reproduces the design conditions that each flow has in the cycle and efficiencies of the main components.

Table 3. Definition of malfunctions with their reference and test values

Malfunction	Variable	Description	Test value	Reference value	Difference
$Malf_1$	$DPF_1[\%]$	Drop Pressure in Filters – Gas Turbine 5	3.02	2	1.02
$Malf_2$	$\eta_{comp,1}[\%]$	Efficiency of compressor – Gas Turbine 5	79.3	80.74	-1.44
$Malf_3$	$\eta_{exp,1}[\%]$	Efficiency of turbine – Gas Turbine 5	85.733	87.67	-1.937
$Malf_4$	$DPC_1[\%]$	Drop Pressure in combustor – Gas Turbine 5	3.5	2	0.015
$Malf_5$	$TIT_1[°C]$	Temperature Inlet to Turbine – Gas Turbine 5	1185	1200	-15
$Malf_6$	$DP_{HRSG,1}$ $[mmH_2O]$	Drop Pressure in HRSG side Gases – Gas Turbine 5	330	230	100
$Malf_7$	$DPF_2[\%]$	Drop Pressure in Filters – Gas Turbine 6	2.5	1.5	1
$Malf_8$	$\eta_{comp,2}[\%]$	Efficiency of compressor – Gas Turbine 6	80.36	81.58	-1.22
$Malf_9$	$\eta_{exp,2}[\%]$	Efficiency of turbine – Gas Turbine 6	86.425	87.05	-0.625
$Malf_{10}$	$DPC_2[\%]$	Drop Pressure in combustor – Gas Turbine 6	5.2	2	3.2
$Malf_{11}$	$TIT_2[°C]$	Temperature Inlet to Turbine – Gas Turbine 6	1205	1200	5
$Malf_{12}$	$DP_{HRSG,2}$ $[mmH_2O]$	Drop Pressure in HRSG side Gases – Gas Turbine 6	506.61	230	170.61
$Malf_{13}$	$\eta_{THP}[\%]$	Efficiency of High Pressure Turbine	81.87	83.58	-1.71
$Malf_{14}$	$\eta_{TIP}[\%]$	Efficiency of Intermediate Pressure Turbine	91.52	92.95	-1.43
$Malf_{15}$	$\eta_{TLP}[\%]$	Efficiency of Low Pressure Turbine	92.96	93.39	-0.43
$Malf_{16}$	P_{vacuum} $[bara]$	Vacuum Pressure in condenser	0.086	0.08	0.006
$Malf_{17}$	$P_1[bara]$	Pressure of Principal Steam to HPST	115.5	115	0.5
$Malf_{18}$	$T_1[°C]$	Temperature of Principal Steam to HPST	549.4	548	1.4
$Malf_{19}$	$T_2[°C]$	Temperature of Reheat Steam to IPST	550.3	548	2.3
$Malf_{20}$	$T_5[°C]$	Temperature of Steam to Low Pressure Steam Turbine	219.3	217.2	2.1
	$W_{net}[MW]$	Power Net	372.5	380.75	-8.25

One of the requirements to know the actual or test operation of the plant is to know the implementation details of the important points of the cycle. The combined cycle plant has a distributed control system and an OPC (OLE for process control) that communicates with the control to extract data from the instrumentation. The data obtained from the operation malfunctions of the plant are summarized in Table 3.

Premise 5. The deviations found for each specific test performance in exergo-parameter characterization $\Delta\beta_i$ can be disaggregated as the effect of the 20 malfunctions $\Delta Malf_j$, this is the total effect of each of the malfunctions in the first component.

$$\Delta\beta_1\big|_{P=372,5MW} = \Delta\beta_{1,1} + \Delta\beta_{1,2} + \cdots + \Delta\beta_{1,20} \quad (18)$$

similarly we found the deviations of each parameter β. Table 4 shows the effects that each malfunctions produces in the parameters β_i corresponding to each principal component in the combined cycle. This table shows that there are malfunctions that affect the operation of equipment even if this is present on equipment; these malfunctions are known as induced malfunctions. It is also noticed that there are components which are not affected by all malfunctions

Table 4. Matrix of partial derivatives $\frac{\partial \beta_i}{\partial Malf_j}$ *for* $i = 1 \ldots 17$ *and* $j = 1 \ldots 20$

	$Malf_1$	$Malf_2$	$Malf_3$	$Malf_4$	$Malf_5$	$Malf_6$	$Malf_7$	$Malf_8$	$Malf_9$	$Malf_{10}$	$Malf_{11}$	$Malf_{12}$	$Malf_{13}$	$Malf_{14}$	$Malf_{15}$	$Malf_{16}$	$Malf_{17}$	$Malf_{18}$	$Malf_{19}$	$Malf_{20}$
β_1	0,87	0	0	0	0	0	0	0	0	0	0	0	0	0	0	0	0	0	0	0
β_2	-1,5	-5,7	-2,08	-5376	-1,54	28,9	-1,6	-1,6	0.79	-5250	1,115	1,1E9	-0,2452	-0,2704	-0,189	-0,4437	0,022	0,028	0,064	0
β_3	-1,506	-5,759	-2,084	-5376	-1,548	2,8e5	-1,65	-1,64	-0,798	-5250	0,52	616,4	-0,115	-0,127	-0,091	-0,21	0,01	0,013	0,030	0,00092
β_4	-0,665	-3,92	-0,99	-694,1	-5,053	1,6e5	-0,78	-0,777	-0,379	-2324	-1,185	-1,5e6	0,256	0,2847	0,2027	0,4887	-0,023	-0,029	-0,068	0,00019
β_5	-0,714	1,52	-8,5	1261	-6,4	3,3	1,752	1,754	0,8571	5029	0,16	282,8	-0,016	-0,046	-0,029	-0,33	-0,031	-0,037	-0,072	0,0026
β_6	0,086	-0,276	1,97	-210	-2,001	-1,57	-0,251	-0,259	-0,14	-714,2	-6e-5	6,15	-0,0014	-0,0013	-0,0004	-0,002	72,44	-0,0011	-0,0022	0,00029
β_7	-1,4e-4	-0,0025	-0,012	-2291	0,0016	1508	-0,0011	-0,0029	-0,0046	-9086	0	0	0	0	0	0	0	0	0	0
β_8	-0,518	0	0	0	0	0	1,352	0	0	0	0,74	1,13e6	-0,25	-0,27	-0,19	-0,45	0,022	0,028	0,065	0
β_9	-1,53	-1,6	-2,12	-1407	-2,75	2,9	-1,67	-5,38	-0,81	-16,5	1,776	627,5	-0,115	-0,125	-0,089	-0,21	0,01	0,013	0,0306	0
β_{10}	-0,15	-0,74	-0,98	-622,2	-1,26	15,2	-1,269	-3,47	-0,377	-2431	2,415	11,8e6	0,24	0,27	0,19	0,47	-0,022	-0,028	-0,066	0
β_{11}	1,515	1,83	2,147	1409	3,27	-3,84	-0,488	1,254	-2773	4062	-28,98	-5,7E6	-0,021	-0,05	-0,027	-0,31	-0,028	-0,032	-0,075	0,00052
β_{12}	-0,22	-0,083	-0,357	-87,34	0,0243	62,4	0,064	-0,384	0,651	13,5	0	6,147	-0,0014	-0,0013	-0,00039	-0,0018	72,44	-0,0011	-0,0022	0,00029
β_{13}	-1,5e-4	-0,0025	-0,012	-2291	0,0016	1508	-0,0011	-0,0029	-0,0046	-9086	-0,016	3,39e6	-4,9	-0,19	-0,14	-0,70	0,90	1,03	0,014	0,024
β_{14}	-0,2894	-1,011	-4,767	-879,1	0,6631	845490	-0,4052	-1,164	-1842	-3548	0,0014	42,3	-0,021	-4712	-0,0024	-0,017	0,0016	-0,0009	1533	-0,041
β_{15}	-0,0061	-0,024	-0,12	-24,15	0,024	14,9	-0,0094	-0,031	-0,044	-102	0,0014	42,3	-0,021	-4712	-0,002	-0,017	0,0016	-9,4e-4	1533	-0,04
β_{16}	0,17	0,60	2,845	514,6	-0,3998	-55,06	0,2472	0,6935	1096	2050	0	-66,01	0	0	0	0	0	0	0	0
β_{17}	-0,014	-0,050	-0,24	-44,81	0,035	44,06	-0,025	-0,0593	-0,094	-177,1	0,0068	-2,2e6	0,37	4046	-0,162	-9398	-0,0359	-0,031	1439	0,183

3.3. Calculations for the deviation of the thermal regime of the combined cycle

Premise 6: Efficiency relationship by Second Law is:

$$\psi = \frac{\sum \dot{B}_o}{\sum \dot{B}_i} \tag{19}$$

or in terms of the thermal regime by Second Law is calculated as follows:

$$RT\big|_{2nd.Law} = 1 + \frac{\sum \dot{I} + \dot{L}}{\sum \dot{B}_o} \tag{20}$$

For calculating the deviations of each of the malfunctions to the thermal regime, it must be used the program of reference made in ESS to find optimum values that aims to show the thermodynamic cycle, ie the values that would have thermodynamic properties of the streams or efficiencies of the components if there were any malfunction. In addition, a test of the equipment is regarded with to evaluate the current condition of the plant. Once the evaluation of equipment is done a regulatory of regulatory procedures as well as the isentropic efficiency models and characteristic curves of the equipment can be considered.

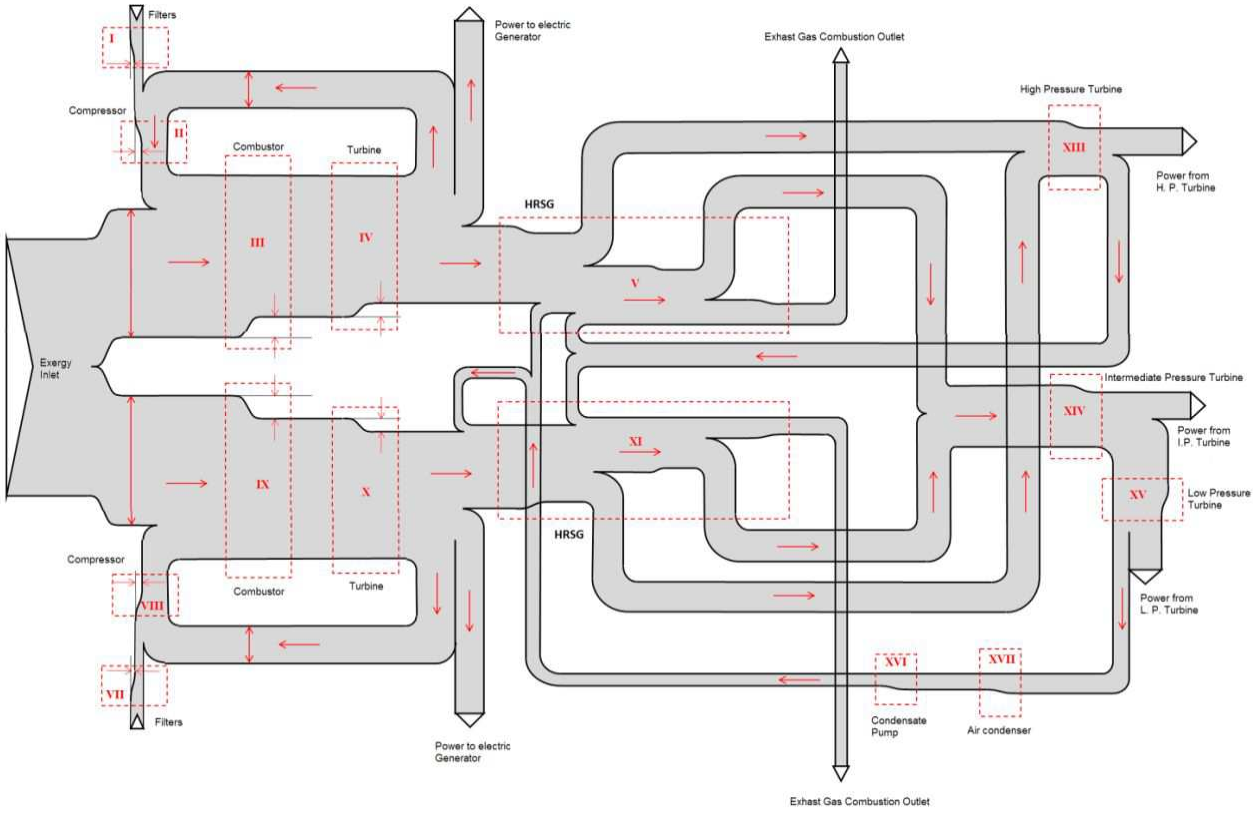

Fig. 7. Grassman diagram of the combined cycle.

Figure 7 shows the Grassman diagram of the combined cycle, we see that the input exergy (exergy of fuel) had divided the two combustion chambers of the two gas turbines. The output of the hot gases from both gas turbine are introduced into the heat recovery (HRSG's) to produce steam for the Rankine cycle, eventually the gases are expelled to the atmosphere which represents the total loss of the combined cycle. Shown in this diagram the irreversibilities present in each cycle of the equipment. The air condenser uses electrical energy to move the fan for condensing the steam, however, this exergy comes from the same turbine after passing through the electric generator so

that there is no flow of exergy that is sent to the atmosphere for this reason exergy losses should only be the exergy that is lost in the flow gas of HRSG's. As example,

I. Compressor 1

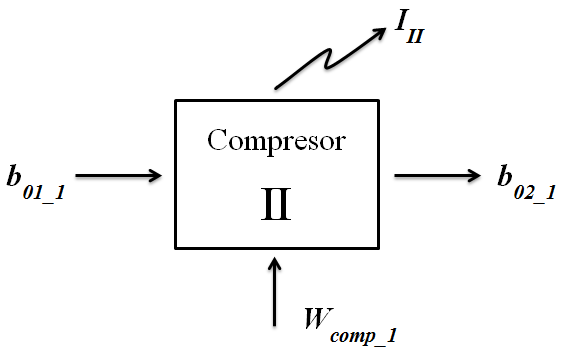

Fig. 5. Exergy balance for compressor 1.

Figure 5 shows the exergy balance for compressor and the equations used to find the irreversibility. We found all exergy balances for each component in the cycle.

$$\dot{I}_{T,II} = \dot{m}_{01,1}\left(b_{01,1} - b_{02,1}\right) + W_{comp_1} + x_{II}\dot{L}$$

$$\dot{I}_{T,II} = \dot{m}_{01,1}\beta_{II} + W_{comp_1} + x_{II}\dot{L} \qquad (21)$$

where:

$x_{II} = I_{II} / \sum I$ is the entropy loss generated in the compressor

L is the exergy loss in the flow gas to the output HRSG's

Finally, we found mathematical models of irreversibility on each component in function of the power and each malfunction. Below the equation for the steam turbine is only shown high pressure to illustrate their use in calculating the deviation of the thermal regime by Second Law.

$$I_{XIII,\eta_{comp1}} = 2468.05 + 7.933P - 8.221\eta_{comp1} - 0.00633P^2 + 4.4776\times10^{-02}\eta_{comp1}^2 - 0.0047P\eta_{comp1} \qquad (22)$$

The change in thermal regime must be equal to the change of the irreversibilities as defined by Second Law, that is:

$$dRT_{2nd,Law}\Big|_{P=cte} = \frac{1}{P}\sum_{k=1}\sum_{i=1}\frac{\partial I_{T,k}}{\partial Malf_i}dMalf_i \qquad (23)$$

There is already a relationship between each irreversibility with respect to power and each malfunction, all the contributions can be calculated of each malfunction affecting each thermal cycling equipment, namely the variation of each irreversibility with respect to malfunctions. From the above definition it also follows that the sum of the changes in the total irreversibilities is the change thermal regime cycle. Equation (23) shows each contribution to the thermal regime based on the irreversibility of all components.

$$dRT_{2nd,Law}\Big|_{P=372,5} = \underbrace{1.79266}_{\Delta I_I} + \underbrace{5.11770}_{\Delta I_{II}} + \underbrace{1.44992}_{\Delta I_{III}} + \underbrace{7.15927}_{\Delta I_{IV}} + \underbrace{1.58317}_{\Delta I_V} + \underbrace{0.00464}_{\Delta I_{VI}} + \underbrace{1.95410}_{\Delta I_{VII}} + \underbrace{5.37127}_{\Delta I_{VIII}} +$$
$$+ \underbrace{7.21231}_{\Delta I_{IX}} + \underbrace{4.17898}_{\Delta I_X} + \underbrace{5.23907}_{\Delta I_{XI}} + \underbrace{0.00203}_{\Delta I_{XII}} + \underbrace{0.97790}_{\Delta I_{XIII}} + \underbrace{1.23373}_{\Delta I_{XIV}} + \underbrace{1.42685}_{\Delta I_{XV}} + \underbrace{0.00515}_{\Delta I_{XVI}} + \underbrace{5.57756}_{\Delta I_{XVII}} \qquad (24)$$

giving as total variation:

$$dRT_{2nd,Law}\Big|_{P=372,5} = 50.286 \quad (25)$$

It is seen from equation (24) that the thermal regime is affected by intrinsic causes, i.e. which can be attributed to poor operation of the same components as well as induced malfunctions in a component where they are not presented but is affected by the change in properties at the entrance or exit in the component.

3. Conclusions

The exergo-characterization includes in a single exergetic parameter β the effect of malfunctions in the equipment that makes up a generation cycle. Also has been able to include the overall effect of each malfunction in the efficiency of the cycle or regime thermal as function of the irreversibility generated in the components of power cycles. As it has precision of a simulator, due the characterization performed in based on one, there are a good approximation of the effects produced by malfunctions regardless of the nature of them as it makes reference a simulator modeling with balances of First and Second Law. We show the exergo-characterization methodology applied on simple Gas turbine cycle developed in a practical way to understand your application.

The methodology is applied to an advanced generation cycle. The application allowed knowing the deviation of the thermal regime by Second Law (inverse of the Second Law efficiency) as a function of the variation of irreversibility in each of the components of the combined cycle in consequence of the occurrence of malfunctions, seeing Table 4 and (24). However, it is necessary to have a cycle simulator to characterize in terms of exergy flow behavior of the cycle. Once you have completed this step only requires mathematical models generated for exergy parameters for diagnosis. For this reason, we can say that there is an improvement over the method of reconciliation that requires a simulator for the reconciliation of malfunctions every time you want to do the exergy assessment.

Another improvement is that it has in terms of exergy evaluation of each component by itself or the entire cycle, the first as function of the parameters β_i and the second depending on the irreversibilities of each component.

Nomenclature

b	Exergy, kJ/kg
B	Exergy, kJ
DPC	Drop pressure combustor
DPF	Drop pressure filters
e	Exergy, kJ/kg
F	Fuel consumption, kW
FR	Mass flow ratio
h	Enthalpy, kJ/kg
I	Irreversibility, kW
k	Exergetic cost
L	Loss Exergy, kW
$\dot{m}$	Mass rate, kg/s
$Malf$	Malfuction
RT	Thermal regime
T	Temperature, °C

TIT Turbine inlet temperature, °C

x Reference values, mass fraction of inlet flow

y *M*ass fraction of outlet flow

W Power, MW

Greek symbols

β Exergy difference

Δ Difference

η Efficiency

κ Exergetic consumption

v *V*olume, m^3/kg

σ Entropy difference

ψ exergy efficiency

ω Enthalpy difference

Subscripts and superscripts

0 Reference state

comp Compressor

i Inlet, i-th component

iso *I*sentropic

j j-th component

o *O*utlet

p Pressure , bar

P Product

Q Chemistry

ref *R*eference load

T Total

test Actual load

References

[1] Antonio Valero, M A Lozano, J A Alconchel, M Muñoz, and Cesar Torres. Guadeamo: A system for energetic /exergetic optimization of coal power plants. ASME AES Vol 2-1, Computer-Aided Engineering of Energy Systems, Optimization, ed R.A. Gaggioli, ASME Book No. H0341 A, pp 43-49. New York, 1, 1986.

[2] Antonio Valero and M A Lozano. Application of the exergetic costs theory to a steam boiler in thermal generating station. AES Vol. 3-2 Analysis and Design of Advanced Energy Systems: Applications, eds. M. J. Moran, S.S. Steco, and G.M. Reistad, ASME Bokk No. G0377 B, pp 41-51. New York, 1987.

[3] M Reini, A Lazzareto, and A Macor. Average structural and marginal costs as result of a unified formulation of the thermoeconomic problem. Proceedings of Second Law Analysis of Energy System: Towards the 21st Century, Rome, 1995.

[4] Alejandro Zaleta, Armando Gallegos, and Victor Rangel. A reconciliation method based on a module simulator an approach to the diagnosis of energy system malfunctions. Int. J. Thermodynamics, Vol 7, No. 2. Pp 51-60, June 2004, ISSN 1301-9724, 2004.

[5] Vittorio Verda, Luis Serra, and Antonio Valero. Effects of the regulation system on the thermoeconomic diagnosis of a power plant part II: Application to a gas turbine- based

cogeneration plant. First International Conference on Applied Thermodynamics, ECOS 2001, July 4-6, 2001 ISTANBUL, 2001.

[6] A Toffolo and A Lazzaretto. On the thermodynamic approach to the diagnosis of energy system malfunctions indicators to diagnose malfunctions: Application of a new indicator for the location of causes. Int J. Thermodynamics, Vol. 7. No. 2, pp 41-49, June 2004, 2004.

[7] ASME PTC 6s 1988 (R 1995): Procedures for Routine Performance Tests of Steam Turbines. 1995.

[8] Alejandro Zaleta, Rosa Adriana Dominguez Vega, Abraham Olivares Arriaga, and Victor Hugo Rangel Hernandez. Thermoeconomic diagnosis theory based on thermocharacterization. Int. J. Thermodynamics, Vol 13, No. 4. Pp 143-152, 2010, ISSN 1301- 9724, 2010.

[9] D H Cooke. Modeling of off-design multistage turbine pressures by stodola´s ellipse. Energy Incorporated Pepser User´s Group Meeting Richmond, Virginia November 2-3, 1983.

[10] K C Cotton. Evaluating and Improving Steam Turbine Performance. ISBN 0-9639955-0-2, USA, 1998.

[11] T J Kotas. The exergy method of thermal plant analysis. Krieger Publishing, New York, 1995.

[12] A. Zaleta, H. Jimenez, J. Chavez, J. Pacheco, A. Campos, and A. Gallegos. Three statements for a reliable on-line thermoeconomic monitoring and diagnosis.dynamic reference state , acceptable performance tests, and the equalized reconciliation method. Proceedings of ECOS 2005, Trondheim, Norway June 20-25,2005, 2005.

[13] L. Correas. On the thermoeconomic approach to the diagnosis of energy system malfunctions suitability to real-time monitoring. Int.J.Thermodynamics,Vol.7,No.2,pp.85-84, June-2004, 2004.

[14] A. Zaleta, J. Royo, and A. Valero. Thermodynamics model of the loss factor applied to steam turbines. Int.J.Thermodynamics,Vol.4,No.3,pp.127-133,September-2001, 2001.

[15] J. Royo, A. Zaleta, and A. Valero. Analysis and evaluation of malfunctions in thermomechanical systems. AES.Vol.37,pp.103-108.ASME Book HO1126.1997, 1997.

Optimal Structural Design of Residential Cogeneration Systems Considering Their Operational Restrictions

Tetsuya Wakui[a] and Ryohei Yokoyama[b]

[a] Department of Mechanical Engineering, Osaka Prefecture University
1-1 Gakuen-cho, Naka-ku, Sakai, Osaka 599-8531, Japan
*wakui@ese.me.osakafu-u.ac.jp, **CA***

[b] Department of Mechanical Engineering, Osaka Prefecture University
1-1 Gakuen-cho, Naka-ku, Sakai, Osaka 599-8531, Japan
yokoyama@ese.me.osakafu-u.ac.jp

Abstract:

An optimal structural design method of residential cogeneration systems considering various kinds of operational restrictions of system components is developed from the energy-saving viewpoint. The optimal structure of a residential cogeneration system, which consists of a cogeneration unit and its peripheral devices, is determined in considertation of multi-period operation, based on their operational restrictions, so that annual primary energy consumption may be minimized. The selection, operational restriction, and operation status of system components are expressed by binary variables, and input and output rates of energy flow, and stored energies of system components are expressed by continuous variables. As principal operational restrictions of cogeneration units without reverse power flow to commercial electric power systems, a constant power output operation, daily start–stop operation, and continuous operation are focused on. By formulating the relationship between the binary variables expressing the selection and those expressing operation status for system components, their selection and multi-period operation are simultaneously optimized. The formulated optimal structural design problem results in a mixed-integer linear programming problem. Moreover, the proposed method is applied to the structural design of a residential cogeneration system consisting of a cogeneration unit, whose candidates are a gas engine employing a constant power output operation, polymer electryte fuel cell empoying a daily start–stop operation, and solid oxide fuel cell employing a continuous operation, with a storage tank and gas-fired boiler, and peripheral devices, whose candidates are an electric water heater and air-cooled heat exchanger, for simulated energy demands. The results reveal that the selection of the cogeneration unit is influenced more by the generation and heat recovery efficiencies and the operational restrictions of the cogeneration units than by the consistency in the heat-to-power ratios of the cogeneration unit and energy demand.

Keywords:

Cogeneration, Optimization, Structural design, Operational planning, Energy savings, Residential use.

1. Introduction

Cogeneration applications to archive energy savings and cost reduction have been extended to ordinary residences due to the development of small-scale, high-performance energy-conversion machines, including gas engines, fuel cells, and Stirling engines. In Japan, a 1-kWe gas engine-based cogeneration unit (GE-CGS) [1] and 1-kWe class polymer electrolyte fuel cell-based cogeneration units (PEFC-CGSs) [2, 3] have been available for residential use. Recently, a 0.7-kWe solid oxide fuel cell-based cogeneration unit (SOFC-CGS) has been released [4]. These residential cogeneration units have differing heat-to-power supply ratios and operational restrictions. The GE-CGS has the highest heat-to-power supply ratio of the three types of residential cogeneration units; however, it must be operated under the constant power output in order to maintain a generation efficiency. PEFC-CGSs have higher generation efficiencies than the GE-CGS, and adopt a daily start–stop operation, in which they are started and stopped a maximum of once a day. This is because their performances are degraded by thermal cycling from operating temperature to a low temperature and back [5], and because input energy is required for start-up. The SOFC-CGS has the highest generation efficiency of the three types of residential cogeneration units; however, it must

be operated continuously because its high operating temperature requires a long warm-up time and high level of input energy. Moreover, in Japan, surplus electric power from residential cogeneration units cannot be transmitted to commercial electric power systems. Thus, they must be operated in response to variations in the electric power demand of individual residences; however, the PEFC-CGS and SOFC-CGS may have minimum electric power output because their generation efficiencies decline under partial-load conditions. Furthermore, residential cogeneration units require storage tanks to intermittently supply hot water. Hence, peripheral devices may be required, including an electric water heater to consume surplus electric power, an air-cooled heat exchanger to waste surplus hot water, and a gas-fired boiler to compensate for the shortage in the hot water supply. Combining plural peripheral devices with residential cogeneration units in accordance with various operational restrictions increases the flexibility of the optimal system structure; thus, a rational design of the residential cogeneration units and their peripheral devices for various energy demands is strictly required to archive energy savings and cost reduction.

The benefits obtained by utilizing the three types of residential cogeneration units were previously analyzed. Paepe et al. [6] investigated the energy-saving effect of 4.7-kWe and 5.5-kWe GE-CGSs and a 4-kWe PEFC-CGS operated in a detached house and terraced family house in Belgium, through a whole-year simulation. Cockroft et al. [7] reported that a GE-CGS and SOFC-CGS meeting the maximum heat demand of typical residences in the United Kingdom needed to operate at a total utilization efficiency of more than 80% to achieve energy savings. Hawkes et al. [8] reported a cost-effective operation strategy for a 2-kWe GE-CGS and 2-kWe SOFC-CGS. Staffell et al. [9] developed a suitable operation strategy and cost target for a 1-kWe PEFC-CGS and 1-kWe SOFC-CGS in the United Kingdom, employing a Monte Carlo analysis. Dorer et al. [10] assessed the performance of a 4.7-kWe GE-CGS, 4.5-kWe PEFC-CGS, and 1-kWe SOFC-CGS under different power plant configurations in electric power systems, using a dynamic simulation model. In these previous studies, the residential cogeneration units could be operated flexibly to obtain the reported benefits because surplus electric power generated by them could be transmitted to commercial electric power systems. Some previous studies considered the constant power output operation of the GE-CGSs [6, 7] and continuous operation of the SOFC-CGSs [8, 10]; however, the daily start–stop operation of the PEFC-CGSs was not considered. Moreover, they did not attempt to optimize the system structure, comprising the cogeneration unit and its peripheral devices, for various energy demands. Yokoyama et al. [11] developed the optimal structure design method for large-scale energy supply systems, in which the selection and discrete capacity of system components were determined in consideration of their operations, using a mixed-integer linear programming approach. However, in this method, the input–output relationship of system components was formulated by single linear equations, and only their on-off status was considered as the operational restrictions.

Against such a background, an optimal structural design method of residential cogeneration systems considering various kinds of operational restrictions of system components is developed from the energy-saving viewpoint. The optimal structure of a residential cogeneration system, which consists of a cogeneration unit and its peripheral devices, is determined in consideration of multi-period operation, based on their operational restrictions, so that annual primary energy consumption may be minimized; this means that the selection and multi-period operation of system components are simultaneously optimized. As principal operational restrictions of cogeneration units without reverse power flow to commercial electric power systems, a constant power output operation, daily start–stop operation, and continuous operation are focused on. Moreover, the variations in the generation and heat recovery efficiencies of cogeneration units under partial-load conditions were formulated using multiple linear equations. The proposed method is applied to the structural design of a residential cogeneration system consisting of a cogeneration unit, whose candidates are a GE-CGS employing the constant power output operation, PEFC-CGS employing the daily start–stop operation, and SOFC-CGS employing the continuous operation, with a storage tank and gas-fired boiler, and peripheral devices, whose candidates are an electric water heater and air-cooled heat exchanger, for simulated energy demands.

2. Optimal structural design of residential cogeneration systems

2.1. Summary of optimal structural design problem

To consider seasonal and hourly changes in residential energy demands, a typical year is divided into M representative days; the index for the representative days is designated by m. Each representative day is divided into K sampling times, with a period of Δt (i.e., $\Delta t = 24/K$), and the index for the sampling times is designated by k. First, a superstructure for a residential cogeneration system is created; this consists of all the system components considered as candidates for selection and previously selected. Then, a real structure is created by selecting the system components from among the candidates [11]. The selected system components are operated in accordance with their operational restrictions and energy demands for each period. As a result, the selection and multi-period operation of the system components are simultaneously optimized so that annual primary energy consumption may be minimized. The operation of a residential cogeneration system with a storage tank cannot be determined independently at each sampling time; thus, a daily cyclic operation is considered, assuming that the energy demands change cyclically with a period of 24 h on each representative day; this means that the operation pattern of the selected system components is derived on each representative day.

2.2. Decision variables

In this optimal structural design problem, the decision variables are classified into two types: design variables and operation variables. The selection of the system components is expressed by binary variables, classified as the design variables; the design variables do not depend on representative days and sampling times. For the operation variables, continuous variables are used to express the input and output rates of energy flow, and the stored energies of the system components at the kth sampling time on the mth representative day; and the operation status of the system components at the kth sampling time on the mth representative day is expressed by binary variables.

2.3. Constraints

The constraints consist of the selection and performance characteristic in accordance with operational restriction of each system component, and energy balance relationships.

2.3.1. Selection of system components

The selection of the system components is formulated using the design variables. As an example, a superstructure for the cogeneration unit, which has I candidates for the selection, is shown in Fig. 1. For any candidate, the input is the natural gas because fuel cell-based cogeneration units are driven by hydrogen reformed from natural gas in built-in fuel reformers; and the outputs are the electric

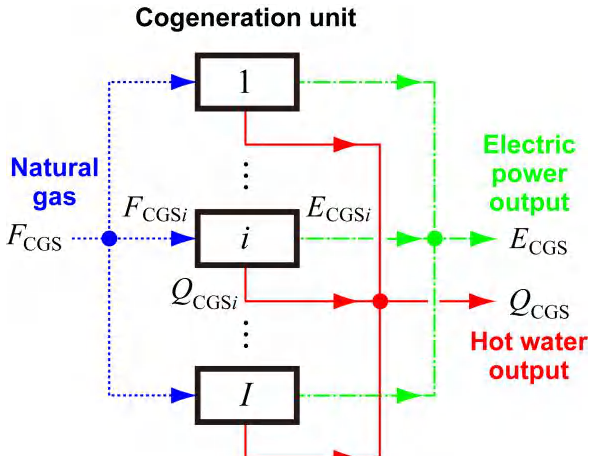

Fig. 1. Superstructure for selection of cogeneration unit.

power and hot water. Generally, one cogeneration unit is installed per single-family residence; thus, the constraint for the selection is formulated as follows:

$$\left.\begin{aligned} &\sum_{i=1}^{I} \gamma_{\mathrm{CGS}i} \le 1 \\ &\gamma_{\mathrm{CGS}i} \in \{0,1\} \quad (i = 1, 2, \cdots, I) \end{aligned}\right\} \tag{1}$$

where $\gamma_{\mathrm{CGS}i}$ denotes the binary variable (design variable) expressing the selection of the *i*th candidate for the cogeneration unit. Equation (1) indicates the possibility that any cogeneration unit is not selected as the optimal system structure. This constraint can be applied to other system components, which are selected from multiple candidates.

2.3.2. Performance characteristic of system components considering their operational restrictions

The performance characteristic of candidates for the system components in accordance with their operational restrictions is formulated at each sampling time on each representative day.

(a) Cogeneration units

Some cogeneration units can be operated under partial-load conditions; however, the generation and heat recovery efficiencies depend on their load factors. Thus, the input–output relationship of the cogeneration units may have nonlinear characteristics, and it is modeled using multiple linear equations, as shown in Fig. 2. The input–output relationship of the cogeneration units between their minimum and rated outputs is divided into *N* parts; the index for the divided parts is designated by *n*. The input–output relationship in the *n*th part of the *i*th candidate at the *k*th sampling time on the *m*th representative day is formulated as follows:

$$\left.\begin{aligned} &E^n_{\mathrm{CGS}i}(k,m) = p^n_{\mathrm{CGS}i} F^n_{\mathrm{CGS}i}(k,m) + q^n_{\mathrm{CGS}i} \delta^n_{\mathrm{CGS}i}(k,m) \\ &Q^n_{\mathrm{CGS}i}(k,m) = r^n_{\mathrm{CGS}i} F^n_{\mathrm{CGS}i}(k,m) + s^n_{\mathrm{CGS}i} \delta^n_{\mathrm{CGS}i}(k,m) \\ &\underline{F}^n_{\mathrm{CGS}i} \delta^n_{\mathrm{CGS}i}(k,m) \le F^n_{\mathrm{CGS}i}(k,m) \le \bar{F}^n_{\mathrm{CGS}i} \delta^n_{\mathrm{CGS}i}(k,m) \\ &\delta^n_{\mathrm{CGS}i}(k,m) \in \{0,1\} \end{aligned}\right\} \tag{2}$$
$$(n = 1, 2, \cdots, N; i = 1, 2, \cdots, I; k = 1, 2, \cdots, K; m = 1, 2, \cdots, M)$$

where $E^n_{\mathrm{CGS}i}$, $Q^n_{\mathrm{CGS}i}$, and $F^n_{\mathrm{CGS}i}$ denote the electric power output minus the power consumption of auxiliary machines including a water pump, heat flow rate of the hot water output, and natural gas consumption, respectively; $\underline{F}^n_{\mathrm{CGS}i}$ and $\bar{F}^n_{\mathrm{CGS}i}$ denote the lower and upper limits of natural gas consumption, respectively; $\delta^n_{\mathrm{CGS}i}$ denotes the binary variable expressing whether the current output is included in the *n*th part; and the coefficients $p^n_{\mathrm{CGS}i}$, $q^n_{\mathrm{CGS}i}$, $r^n_{\mathrm{CGS}i}$, and $s^n_{\mathrm{CGS}i}$ express the performance characteristic in the linear equations.

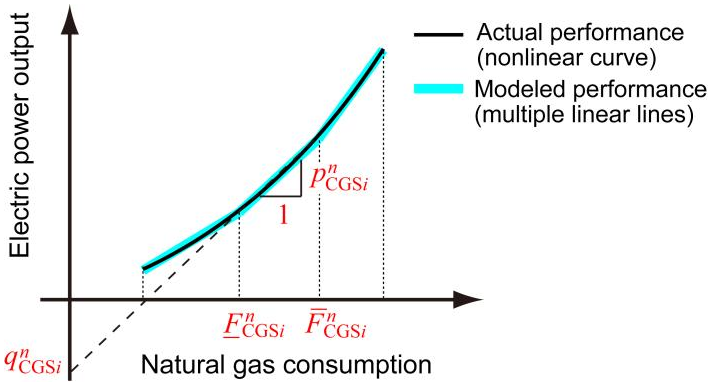

Fig. 2. Modeling of performance characteristic of cogeneration unit.

The following constraint is also considered to express the minimum power output operation.

$$\underline{F}^{1}_{\mathrm{CGS}i} = \bar{F}^{1}_{\mathrm{CGS}i} \qquad (i = 1, 2, \cdots, I) \tag{3}$$

The actual electric power output, $E_{\mathrm{CGS}i}$, heat flow rate of hot water output, $Q_{\mathrm{CGS}i}$, and natural gas consumption, $F_{\mathrm{CGS}i}$, of the *i*th candidate at the *k*th sampling time on the *m*th representative day are expressed by the following equation:

$$\left.\begin{aligned} E_{\mathrm{CGS}i}(k,m) &= \sum_{n=1}^{N} E^{n}_{\mathrm{CGS}i}(k,m) \\ Q_{\mathrm{CGS}i}(k,m) &= \sum_{n=1}^{N} Q^{n}_{\mathrm{CGS}i}(k,m) \\ F_{\mathrm{CGS}i}(k,m) &= \sum_{n=1}^{N} F^{n}_{\mathrm{CGS}i}(k,m) \\ \delta_{\mathrm{CGS}i}(k,m) &= \sum_{n=1}^{N} \delta^{n}_{\mathrm{CGS}i}(k,m) \\ \delta_{\mathrm{CGS}i}(k,m) &\in \{0,1\} \end{aligned}\right\} \quad (i = 1, 2, \cdots, I; k = 1, 2, \cdots, K; m = 1, 2, \cdots, M) \tag{4}$$

where $\delta_{\mathrm{CGS}i}$ denotes the binary variable expressing the on–off status of the *i*th candidate.

The constraints expressing the operational restrictions are also formulated. The model focuses on constant power output operation, daily start–stop operation, and continuous operation, which form principal operational restrictions of various types of cogeneration units. For the cogeneration unit employing the constant power output operation, the constraint, $N = 1$, is added. For the cogeneration unit employing the daily start–stop operation, the following constraint is considered.

$$\left.\begin{aligned} &\left.\begin{aligned} &\delta_{\mathrm{CGS}i}(k,m) - \delta_{\mathrm{CGS}i}(k-1,m) = \delta^{\mathrm{STA}}_{\mathrm{CGS}i}(k,m) - \delta^{\mathrm{STO}}_{\mathrm{CGS}i}(k,m) \\ &\delta^{\mathrm{STA}}_{\mathrm{CGS}i}(k,m) + \delta^{\mathrm{STO}}_{\mathrm{CGS}i}(k,m) \le 1 \\ &\delta^{\mathrm{STA}}_{\mathrm{CGS}i}(k,m) \in \{0,1\} \\ &\delta^{\mathrm{STO}}_{\mathrm{CGS}i}(k,m) \in \{0,1\} \end{aligned}\right\} \\ &\qquad (i = 1, 2, \cdots, I; k = 1, 2, \cdots, K; m = 1, 2, \cdots, M) \\ &\sum_{k=1}^{K} \left\{\delta^{\mathrm{STA}}_{\mathrm{CGS}i}(k,m) + \delta^{\mathrm{STO}}_{\mathrm{CGS}i}(k,m)\right\} \le 2 \quad (i = 1, 2, \cdots, I; m = 1, 2, \cdots, M) \end{aligned}\right\} \tag{5}$$

where $\delta^{\mathrm{STA}}_{\mathrm{CGS}i}$ and $\delta^{\mathrm{STO}}_{\mathrm{CGS}i}$ denote the binary valuables expressing the state migration from stopping to operation and that from operation to stopping, respectively. If the cogeneration unit is started at the *k*th sampling time, $\delta_{\mathrm{CGS}i}(k,m) = 1$ and $\delta_{\mathrm{CGS}i}(k-1,m) = 0$; thus, $\delta^{\mathrm{STA}}_{\mathrm{CGS}i}(k,m) = 1$ and $\delta^{\mathrm{STO}}_{\mathrm{CGS}i}(k,m) = 0$. On the other hand, if the cogeneration unit is stopped at the *k*th sampling time, $\delta_{\mathrm{CGS}i}(k,m) = 0$ and $\delta_{\mathrm{CGS}i}(k-1,m) = 1$; thus, $\delta^{\mathrm{STA}}_{\mathrm{CGS}i}(k,m) = 0$ and $\delta^{\mathrm{STO}}_{\mathrm{CGS}i}(k,m) = 1$. In addition, assuming the daily cyclic operation, the on–off status in the initial state is considered to be equal to that in the terminal state on each representative day.

Furthermore, the constraint to create an association between the design variable and the operation variables is considered; it is classified, depending on the operational constraints, as follows:

$$\left.\begin{aligned} &\delta_{\mathrm{CGS}i}(k,m) \le \gamma_{\mathrm{CGS}i} \quad \text{(without continuous operation)} \\ &\delta_{\mathrm{CGS}i}(k,m) = \gamma_{\mathrm{CGS}i} \quad \text{(with continuous operation)} \end{aligned}\right\} \\ (i = 1, 2, \cdots, I; k = 1, 2, \cdots, K; m = 1, 2, \cdots, M) \tag{6}$$

The electric power output, E_{CGS}, heat flow rate of hot water output, Q_{CGS}, and natural gas consumption, F_{CGS}, of the selected cogeneration unit at the *k*th sampling time on the *m*th representative day are expressed by the following equation:

$$\left.\begin{aligned} E_{\mathrm{CGS}}(k,m) &= \sum_{i=1}^{I} E_{\mathrm{CGS}i}(k,m) \\ Q_{\mathrm{CGS}}(k,m) &= \sum_{i=1}^{I} Q_{\mathrm{CGS}i}(k,m) \\ F_{\mathrm{CGS}}(k,m) &= \sum_{i=1}^{I} F_{\mathrm{CGS}i}(k,m) \end{aligned}\right\} \qquad (k=1,2,\cdots,K;\ m=1,2,\cdots,M) \tag{7}$$

(b) Other system components

The performance characteristics of other system components are also formulated by linear equations using the design variables and the operation variables.

The storage tank is selected along with the cogeneration unit, and its capacity depends on the selected cogeneration unit. The heat balance relationship, including heat loss, is considered by the balance equation between two consecutive sampling times. Moreover, in order to express the full storage, the stored heat is divided into two parts, and the binary variable, $\delta^{n}_{\mathrm{STi}}\ (n=1,2)$, is introduced to express in which part the current heat is included. The performance characteristic of the *i*th candidate of the storage tank at the *k*th sampling time on the *m*th representative day is formulated as follows:

$$\left.\begin{aligned} &\frac{S_{\mathrm{STi}}(k,m)-S_{\mathrm{STi}}(k-1,m)}{\Delta t} = Q^{\mathrm{in}}_{\mathrm{STi}}(k,m) - Q^{\mathrm{out}}_{\mathrm{STi}}(k,m) - \Lambda_{\mathrm{L}} S_{\mathrm{STi}}(k-1,m) \\ &\qquad (i=1,2,\cdots,I;\ k=1,2,\cdots,K;\ m=1,2,\cdots,M) \\ &\left.\begin{aligned} &\underline{S}^{n}_{\mathrm{STi}}\delta^{n}_{\mathrm{STi}}(k,m) \le S_{\mathrm{STi}}(k,m) \le \bar{S}^{n}_{\mathrm{STi}}\delta^{n}_{\mathrm{STi}}(k,m) \\ &\delta^{n}_{\mathrm{STi}}(k,m) \in \{0,1\} \end{aligned}\right\} \\ &\qquad (n=1,2;\ i=1,2,\cdots,I;\ k=1,2,\cdots,K;\ m=1,2,\cdots,M) \\ &\sum_{n=1}^{2} \delta^{n}_{\mathrm{STi}}(k,m) = \gamma_{\mathrm{CGS}i} \qquad (i=1,2,\cdots,I;\ k=1,2,\cdots,K;\ m=1,2,\cdots,M) \end{aligned}\right\} \tag{8}$$

where S_{STi} denotes the heat stored in the storage tank; $Q^{\mathrm{in}}_{\mathrm{STi}}$ and $Q^{\mathrm{out}}_{\mathrm{STi}}$ denote the heat flow rates of hot water stored into and supplied from the storage tank, respectively; Λ_{L} denotes the heat loss rate of the storage tank; and $\underline{S}^{n}_{\mathrm{STi}}$ and $\bar{S}^{n}_{\mathrm{STi}}$ denote the lower and upper limits of the stored heat in the *n*th part, respectively. In order to express the full storage, the following constraint is also considered.

$$\underline{S}^{2}_{\mathrm{STi}} = \bar{S}^{2}_{\mathrm{STi}} \qquad (i=1,2,\cdots,I) \tag{9}$$

Furthermore, based on the assumption of the daily cyclic operation, the heat stored in the initial state is considered to be equal to that stored in the terminal state on each representative day.

Peripheral devices, consisting of L types, are operated only when they are selected and their operating conditions are satisfied; the index for the peripheral devices is designated by *l*. The performance characteristic of the *l*th peripheral device at the *k*th sampling time on the *m*th representative day is formulated as

$$\left.\begin{aligned} &Y_{\mathrm{PD}l}(k,m) = a_{\mathrm{PD}l}X_{\mathrm{PD}l}(k,m) + b_{\mathrm{PD}l}\delta_{\mathrm{PD}l}(k,m) \\ &\underline{X}_{\mathrm{PD}l}\delta_{\mathrm{PD}l}(k,m)\gamma_{\mathrm{PD}l} \le X_{\mathrm{PD}l}(k,m) \le \bar{X}_{\mathrm{PD}l}\delta_{\mathrm{PD}l}(k,m)\gamma_{\mathrm{PD}l} \end{aligned}\right\} \\ (l=1,2,\cdots,L;\ k=1,2,\cdots,K;\ m=1,2,\cdots,M) \tag{10}$$

where $X_{\mathrm{PD}l}$ and $Y_{\mathrm{PD}l}$ denote the input and output rates of energy flow, respectively; the coefficient $a_{\mathrm{PD}l}$ and $b_{\mathrm{PD}l}$ express the performance characteristic in the linear equation; $\underline{X}_{\mathrm{PD}l}$ and $\bar{X}_{\mathrm{PD}l}$ denote the lower and upper limits of the energy flow rate of input; $\gamma_{\mathrm{PD}l}$ denotes the binary variable (design variable) expressing the selection; and $\delta_{\mathrm{PD}l}$ denotes the binary variable (operation variable)

expressing the on–off status that is associated with its operating condition. The input–output relationship of the peripheral devices can also be formulated using multiple linear equations as in the case of the cogeneration units.

2.3.3. Energy balance relationships

The energy balances are considered at the connecting points between the system components and the boundaries of the residential cogeneration system, meaning the supply points to the energy demands.

2.4. Objective function

Many evaluation criteria, including the energy savings, CO_2 emission reduction, and cost reduction, are required to quantify the benefits of using a cogeneration system [10]. First, a cost reduction should be discussed on the basis of the total cost consisting of initial costs and operational costs of selected system components; the operational costs can be calculated from purchased electric power and natural gas consumption of selected system components. Currently, a cost reduction by utilizing a PEFC-CGS or SOFC-CGS is not expected because their initial costs are rather expensive as compared with the reduction in the operational cost by utilizing them. Second, CO_2 emission reduction can also be calculated form purchased electric power and natural gas consumption of selected system components; however, the CO_2 emission factor of electric power purchased from an electric power company must be estimated appropriately. In Japan, the following two estimation methods have been discussed for several years. One estimation method is based on the average CO_2 emission of only thermal power plants in the commercial electric power system; this means that thermal power plants are considered as a power regulator for load variations in the commercial electric power system. The other estimation method is based on the average CO_2 emission of all power plants in the commercial electric power system. Although this discussion remains inconclusive, the Act on the Rational Use of Energy of Japan officially states that the conversion factor for primary energy of purchased electric power shall be calculated on the basis of the average consumption of only thermal power plants [12]. Thus, this study on the optimal structural design of residential cogeneration systems focuses on the energy savings; that is, the objective function to be minimized is the annual primary energy consumption, which is calculated from purchased electric power and natural gas consumption of the cogeneration unit and peripheral devices on each representative day. The objective function, J_{CGS}, is expressed by the following linear equation:

$$J_{\mathrm{CGS}} = \sum_{m=1}^{M} R(m) \left\{ \phi_{\mathrm{E}} \sum_{k=1}^{K} E_{\mathrm{p}}(k,m)\,\Delta t + \phi_{\mathrm{G}} \sum_{k=1}^{K} \left[F_{\mathrm{CGS}}(k,m) + \sum_{i=1}^{I} F_{\mathrm{CGS}i}^{\mathrm{S}} \delta_{\mathrm{CGS}i}^{\mathrm{STA}}(k,m) + \sum_{l=1}^{L} F_{\mathrm{PD}l}(k,m) \right] \right\} + \kappa \left(\sum_{i=1}^{I} \gamma_{\mathrm{CGS}i} + \sum_{l=1}^{L} \gamma_{\mathrm{PD}l} \right) \tag{11}$$

where R denotes the number of the representative days in a typical year; E_{p} denotes the purchased electric power; $F_{\mathrm{CGS}i}^{S}$ denotes the natural gas to start up the cogeneration unit employing the daily start–stop operation; $F_{\mathrm{PD}l}$ denotes the natural gas consumption of the lth peripheral device; and ϕ_{E} and ϕ_{G} denote the conversion factors for the primary energy of purchased electric power and natural gas, respectively. To avoid installing the cogeneration unit and peripheral devices when they are not operated on any representative day, a negligible energy for their selection, κ, is added in the objective function.

2.5. Solution method

The formulated problem has the nonlinear term, which is the product of $\delta_{\mathrm{PD}l}(k,m)$ and $\gamma_{\mathrm{PD}l}$ in Eq. (10). To reformulate this problem as a mixed-integer linear programming problem, this nonlinear term is replaced by the continuous variable $\xi_{\mathrm{PD}l}(k,m)$ as follows:

$$\xi_{\mathrm{PD}l}(k,m) = \delta_{\mathrm{PD}l}(k,m)\gamma_{\mathrm{PD}l} \qquad (l = 1,2,\cdots,L; k = 1,2,\cdots,K; m = 1,2,\cdots,M) \tag{12}$$

Moreover, the following constraint for $\xi_{\mathrm{PD}l}(k,m)$ is employed:

$$\left.\begin{aligned} &\underline{\delta}_{\mathrm{PD}l}\gamma_{\mathrm{PD}l} \le \xi_{\mathrm{PD}l}(k,m) \le \bar{\delta}_{\mathrm{PD}l}\gamma_{\mathrm{PD}l} \\ &\delta_{\mathrm{PD}l}(k,m) + \bar{\delta}_{\mathrm{PD}l}(\gamma_{\mathrm{PD}l} - 1) \le \xi_{\mathrm{PD}l}(k,m) \le \delta_{\mathrm{PD}l}(k,m) \end{aligned}\right\} \quad (l = 1,2,\cdots,L; k = 1,2,\cdots,K; m = 1,2,\cdots,M) \tag{13}$$

where $\underline{\delta}_{\mathrm{PD}l}$ and $\bar{\delta}_{\mathrm{PD}l}$ denote lower and upper limits of $\delta_{\mathrm{PD}l}(k,m)$, respectively and they are set as 0 and 1, respectively. In Eq. (13), if $\gamma_{\mathrm{PD}l} = 0$, $\xi_{\mathrm{PD}l}(k,m) = 0$, or else if $\gamma_{\mathrm{PD}l} = 1$, $\xi_{\mathrm{PD}l}(k,m) = \delta_{\mathrm{PD}l}(k,m)$. This means that Eq. (13) meets Eq. (12) indirectly. Thus, this procedure can linearize Eq. (12) without any approximation and transform the optimal structural design problem into a mixed-integer linear programming problem. The reformulated problem can be solved using the CPLEX optimization solver, which combines the branch and bound method with the simplex one, in the GAMS (General Algebraic Modeling System) language [13].

3. Case study

As a case study, the proposed method is applied to the structural design of an residential cogeneration system without reverse power flow to a commercial electric power system.

3.1. Superstructure of residential cogeneration system

The superstructure of a residential cogeneration system investigated as a case study is shown in Fig. 3. The solid, dash-dotted, and dotted lines in the figure denote the flows of hot water, electric power, and natural gas, respectively.

The electric power demand is met by operating the cogeneration unit and purchasing electric power from an electric power company; thus, there is no reverse power flow from the cogeneration unit to the commercial electric power system. This restriction is considered in the energy balance relationship. The hot water output of the cogeneration unit is stored in the storage tank. The hot water demand is met by supplying from the storage tank and gas-fired boiler. For the winter days, the two methods of heating are separately employed: heating by electric air conditioners and that by

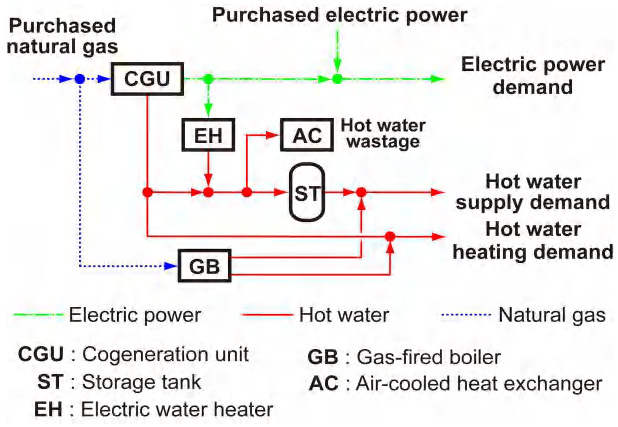

Fig. 3. Superstructure of residential cogeneration system.

hot water. When employing the winter heating by hot water, the required hot water is supplied from the gas-fired boiler and cogeneration unit.

Candidates for the cogeneration unit comprise a GE-CGS employing the constant power output operation, PEFC-CGS employing the daily start–stop operation, and SOFC-CGS employing the continuous operation; i.e., $I = 3$. Only the GE-CGS can directly supply hot water to meet the heating demand. The storage tank is selected along with the cogeneration unit. As peripheral devices, an electric water heater (EH) to utilize surplus electric power from the cogeneration unit, an air-cooled heat exchanger (AC) to waste surplus heat of hot water output of the cogeneration unit, and gas-fired boiler are considered; i.e., $L = 3$. The EH is operated only when the surplus electric power is generated under the minimum power output operation of the cogeneration unit, and the AC is operated only when the heat stored in the storage tank reaches its capacity. Thus, the binary variables, $\delta^{1}_{\mathrm{CGS}i}$ and $\delta^{2}_{\mathrm{ST}i}$, are employed to express the on–off status of the EH and AC, respectively. The gas-fired boiler is pre-selected as a system component by setting the binary variable to select the gas-fired boiler to 1; in Eq. (11), the negligible energy for the selection of the gas-fired boiler is omitted. Thus, this study determines the appropriate selection of the cogeneration unit with the storage tank, EH, and AC. If any cogeneration unit is not selected based on Eq. (1), the electric power demand is met only by purchasing electric power, and the hot water supply and heating demands are met by supplying only from the gas-fired boiler.

3.2. Input data

3.2.1. Performance characteristic values of system components

The performance characteristic values of the system components are listed in Table 1. These values are estimated on the basis of [1] for the GE-CGS, [3] for the PEFC-CGS, and [4] for the SOFC-CGS. The rated electric power outputs, which minus the power consumption of the auxiliary machines, of the GE-CGS, PEFC-CGS, and SOFC-CGS are 0.95 kW, 0.75 kW, and 0.7 kW, respectively. The minimum electric power outputs of the PEFC-CGS and SOFC-CGS are 0.25 kW and 0.15 kW, respectively.

Table 1. Performance characteristic values of system components

System component	Item	Value	
Gas engine-based cogeneration unit (GE-CGS)	Rated electric power output	0.950	kW
	Rated hot water output	2.50	kW
	Rated natural gas consumption	0.337	m^3/h
Polymer electrolyte fuel cell-based cogeneration unit (PEFC-CGS)	Rated electric power output	0.750	kW
	Rated hot water output	0.940	kW
	Rated natural gas consumption	0.167	m^3/h
	Natural gas consumption for start-up	0.0800	m^3/h
Solid oxide fuel cell-based cogeneration unit (SOFC-CGS)	Rated electric power output	0.700	kW
	Rated hot water output	0.620	kW
	Rated natural gas consumption	0.138	m^3/h
Storage tank	Capacity (GE-CGS)	5.25	kWh
	Capacity (PEFC-CGS)	9.33	kWh
	Capacity (SOFC-CGS)	5.78	kWh
	Heat loss rate	1.50	%/h
Latent heat recovery type gas-fired boiler	Hot water supply efficiency (HHV)	90.0	%
	Hot water heating efficiency (HHV)	84.0	%
Electric water heater (EH)	Maximum electric power input	0.950	kW
	Heating efficiency	90.0	%
Air-cooled heat exchanger (AC)	Maximum heat discharge rate	1.00	kW

Figure 4 shows the generation and heat recovery efficiencies of the three types of cogeneration units as a function of the electric power output, calculated using the higher heating value (HHV) of natural gas. The input–output relationship between the minimum and rated outputs of the PEFC-CGS and SOFC-CGS is divided into three (N = 3) and five (N = 5) parts, respectively.

The performance characteristic of the cogeneration units is summarized as follows: the GE-CGS has the highest heat-to-power supply ratio at the rated electric power output; the PEFC-CGS has high generation efficiency under partial-load conditions; and the SOFC-CGS has the smallest minimum and rated electric power outputs and the highest generation efficiency at the rated electric power output. Generally, fuel cells under high-temperature operation, e.g., the SOFC-CGS, may have restrictions for the load-following characteristic [5]. However, as described later, the sampling period of the residential energy demand is 1 h, in which the electric power output of the SOFC-CGS can be widely changed, and the demonstration by Suzuki et al. [14] reported that the electric power output of a prototype SOFC-CGS can follow the variations in the electric power demand of a residence in Japan. Thus, the load-following characteristic of the SOFC-CGS is not considered in this study. The capacity of the storage tank varies according to the selected cogeneration unit. For the gas-fired boiler, a latent heat recovery type, which is more efficient than a conventional type, is employed in any selection of the cogeneration unit; its supply capacity is assumed to be sufficient to meet the hot water demand described later.

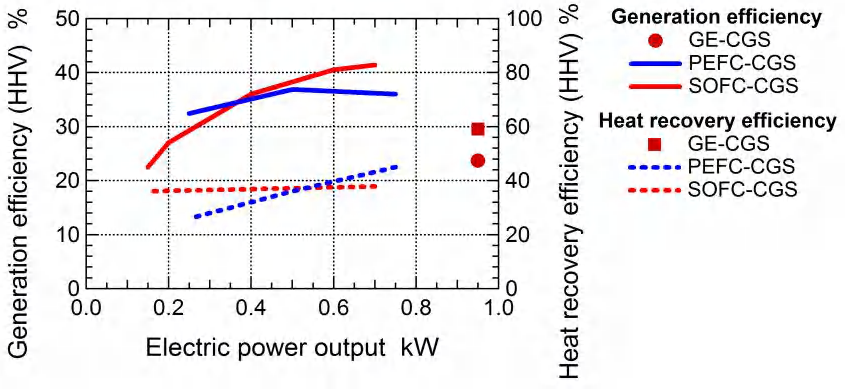

Fig. 4. Generation and heat recovery efficiencies of three types of cogeneration units.

3.2.2. Residential energy demands

This study focuses on the simulated energy demands of a typical single-family house in Japan, as defined by the Institute for Building Environment and Energy Conservation in Japan [15]. From these energy demands, the energy demands on five representative days are newly specified for the analysis; i.e., M = 5: a summer day, summer day with peak demand, mid-season day, winter day, and winter day with peak demand. The energy demands on each representative day are estimated at 24 sampling times; i.e., K = 24 and Δt = 1 h. The time evolution of the specified energy demands is shown in Fig. 5; the electric power demand varies with the winter heating methods, while the hot water supply demand is the same for the both winter heating methods.

In order to analyze the optimal structure of the residential cogeneration system, the energy demands at each sampling time is varied from the specified demands, shown in Fig. 5, in proportion to the annual energy demands as follows:

$$\left.\begin{aligned} E_{\mathrm{D}}(k,m) &= r_{\mathrm{E}} E_{\mathrm{D}}^{\mathrm{Ori}}(k,m) \\ Q_{\mathrm{D}}(k,m) &= r_{\mathrm{Q}} Q_{\mathrm{D}}^{\mathrm{Ori}}(k,m) \\ Q_{\mathrm{H}}(k,m) &= r_{\mathrm{Q}} Q_{\mathrm{H}}^{\mathrm{Ori}}(k,m) \end{aligned}\right\} \qquad (k = 1,2,\cdots,K; m = 1,2,\cdots,M) \qquad (12)$$

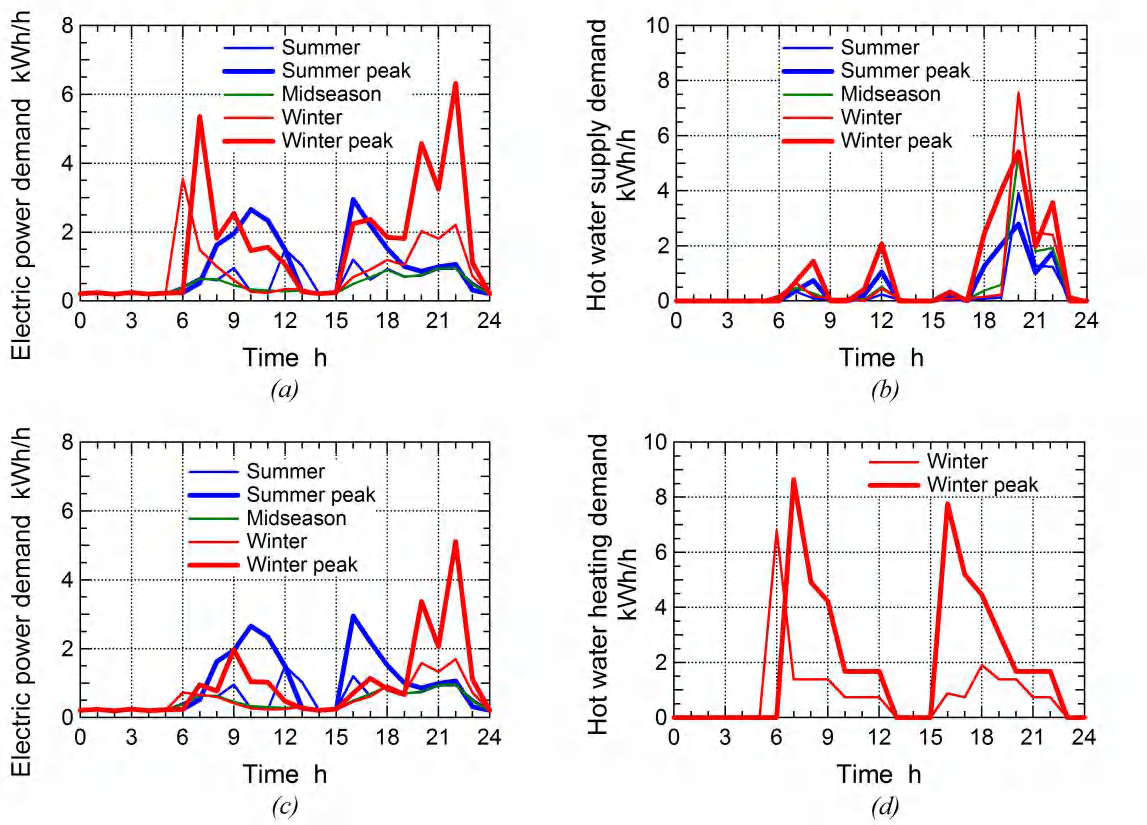

Fig. 5. Time evolution of specified energy demands: a) electric power demand (winter heating by electric air conditioners), b) hot water supply demand, c) electric power demand (winter heating by hot water), d) hot water heating demand.

where E_{D}, Q_{D}, and Q_{H} denote the electric power demand, hot water supply demand, and hot water heating demand, respectively, varied for the analysis; r_{E} and r_{Q} denote the ratio of the varied demand to the specified demand for electric power and heat, respectively; and $E_{\mathrm{D}}^{\mathrm{Ori}}$, $Q_{\mathrm{D}}^{\mathrm{Ori}}$, and $Q_{\mathrm{H}}^{\mathrm{Ori}}$ denote the electric power demand, hot water supply demand, and hot water heating demand, respectively, which are originally specified. For the residence employing the winter heating by electric air conditioners, r_{E} is varied discretely in the range of 0.29 to 1.25 and r_{Q}, in the range of 0.30 to 2.0. For the residence employing the winter heating by hot water, r_{E} is varied discretely in the range of 0.33 to 1.55 and r_{Q}, in the range of 0.33 to 1.65.

3.2.3. Conversion factors for primary energy

The conversion factors for the primary energy of purchased electric power and natural gas are listed in Table 2. For the purchased electric power, an average thermal power conversion factor is introduced [16]; this has two values, depending on the time of day, because the thermal power plant configuration in the electric power system varies. For natural gas, the values of the conversion factor is reported as the statistics by Japanese gas companies [17]; it is determined using the HHV.

Table 2. Conversion factors for primary energy.

Energy source	Value	
Purchased electric power (8:00 to 22:00)	9.97	MJ/kWh
Purchased electric power (22:00 to 8:00)	9.28	MJ/kWh
Natural gas	45.0	MJ/m^3

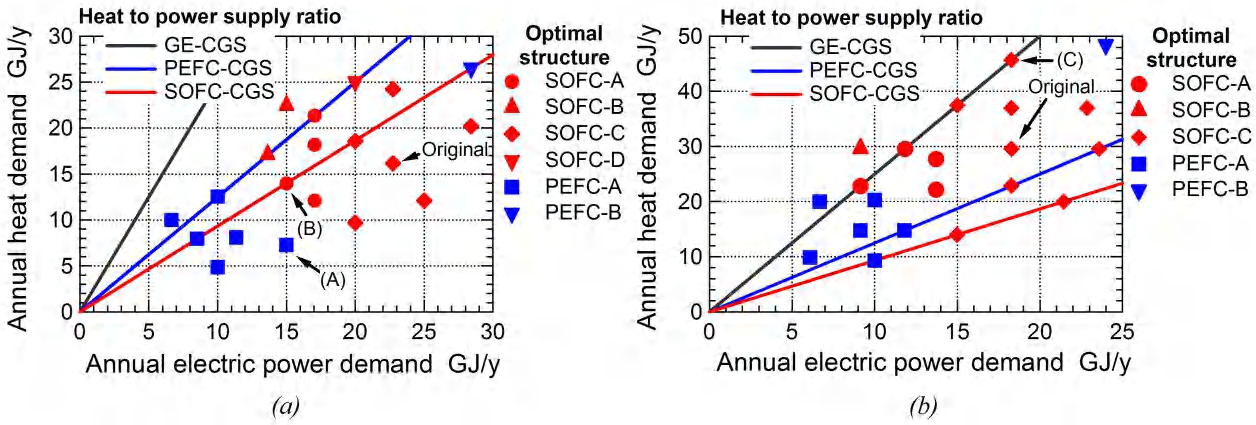

Fig. 6. Result of optimal structures of residential cogeneration system: a) winter heating by electric air conditioners, b) winter heating by hot water

Table 3. Detail of optimal structures of residential cogeneration system.

	Selected (S) / not selected (NS)				
Optimal structure	GE-CGS	PEFC-CGS	SOFC-CGS	EH	AC
SOFC-A	NS	NS	S	S	S
SOFC-B	NS	NS	S	S	NS
SOFC-C	NS	NS	S	NS	S
SOFC-D	NS	NS	S	NS	NS
PEFC-A	NS	S	NS	S	NS
PEFC-B	NS	S	NS	NS	NS

3.3. Results and discussion

3.3.1. Optimal structure analysis

The optimal structures of the residential cogeneration system for various energy demands are plotted in Fig. 6, showing the relationship between the annual electric power demand and the annual heat demand, which is the sum of the annual hot water supply demand and annual hot water heating demand; and the heat-to-power supply ratio of the three types of cogeneration units at the rated electric power output. The detail of the optimal structures of the residential cogeneration system, which have six types, are listed in Table 3.

Although Eq. (1) indicates the possibility that any cogeneration unit is not selected, the SOFC-CGS or the PEFC-CGS is selected for any case of the energy demands. The distribution of the optimal structures in the relationship between the annual electric power and heat demands is almost the same for both the winter heating methods. In case of high electric power demands, the SOFC-CGS, which has the smallest rated electric power output but the highest generation efficiency at the rated electric power output, is selected; in case of low electric power demands, the PEFC-CGS, which has high generation efficiency under partial-load conditions and can cease the operation during periods of low electric power demand, is selected. In case of high electric power and heat demands, the PEFC-CGS, whose heat-to-power supply ratio is higher than that of the SOFC-CGS, is selected.

Moreover, it should be noted that for the same electric power demand, the SOFC-CGS with a low heat-to-power supply ratio is selected in case of a large heat demand, indicated by (B) in Fig. 6-(a), while the PEFC-CGS with a high heat-to-power supply ratio is selected in case of a small heat

demand, indicated by (A) in Fig. 6-(a). To analyze this distinction, for demand (A) where r_E = 0.66 and r_Q = 0.45, the optimal operation patterns of the PEFC-CGS, which is identified as the optimal cogeneration unit, and the SOFC-CGS, is identified as the sub-optimal cogeneration unit, on the representative summer day are shown in Figs. 7 and 8, respectively. The result for the SOFC-CGS is derived by setting the binary variable to select the SOFC-CGS to 1 in Eq. (1). The operation time of the PEFC-CGS is limited so that the generated hot water meets the daily heat demand; although the result is not shown, it was confirmed that all the heat demand is supplied from the storage tank. On the other hand, the SOFC-CGS operates continuously in response to the variation in the electric power demand and wastes the surplus heat of hot water output. Due to a high level of wastage of surplus hot water, the energy-saving effect of the SOFC-CGS is lower than that of the PEFC-CGS. For demand (B) where r_E = 0.66 and r_Q = 0.87, the operation time of the PEFC-CGS is increased with the heat demand, while the wastage of surplus hot water generated by the SOFC-CGS is decreased. Since the latter provides a greater contribution to energy savings, the SOFC-CGS is selected as the optimal cogeneration unit. Furthermore, the GE-CGS is not selected in this analysis although the heat-to-power demand ratio of some of energy demands is close to the heat-to-power supply ratio of the GE-CGS. In order to analyze this result, for demand (c) where r_E = 1.0 and r_Q = 1.54, indicated in Fig. 6-(b), the energy supply patterns in using the GE-CGS on the representative winter day are shown in Fig. 9; the heat-to-power ratios of the GE-CGS and the energy demand are the same. The electric power supply from the GE-CGS can be decreased as compared with the rated electric power output, by consuming the surplus electric power at the EH.

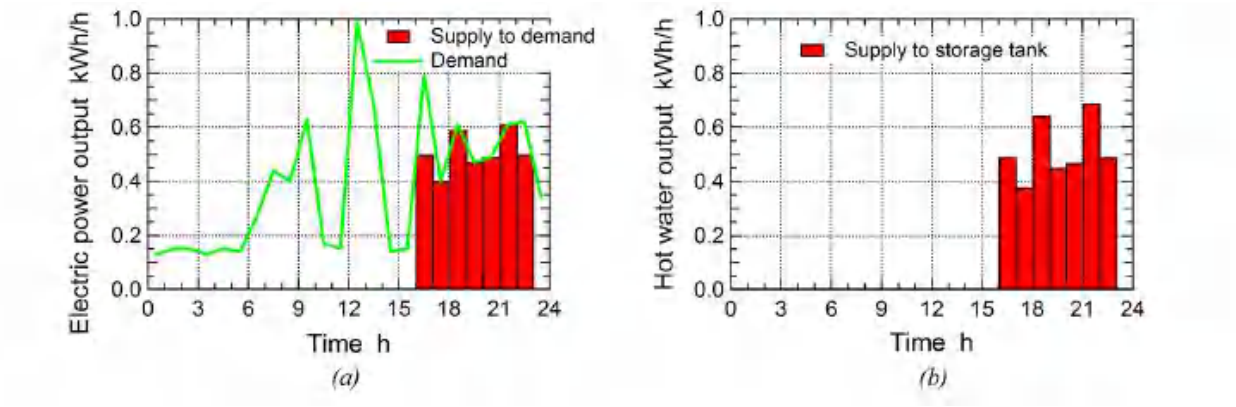

Fig. 7 Optimal operation pattern of PEFC-CGS on representative day of summer (r_E = 0.66, r_Q = 0.45): a) electric power output of PEFC-CGS, b) hot water output of PEFC-CGS.

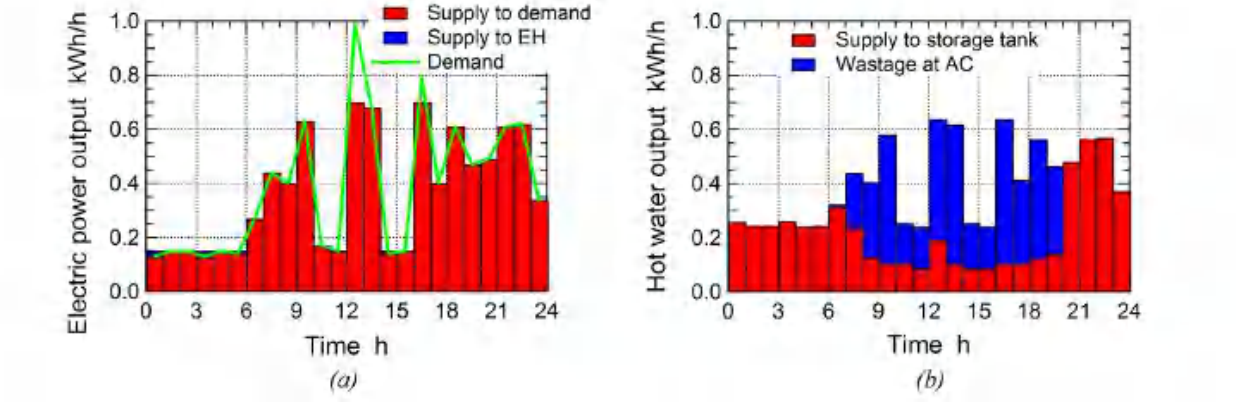

Fig. 8 Optimal operation pattern of SOFC-CGS on representative day of summer (r_E = 0.66, r_Q = 0.45): a) electric power output of SOFC-CGS, b) hot water output of SOFC-CGS.

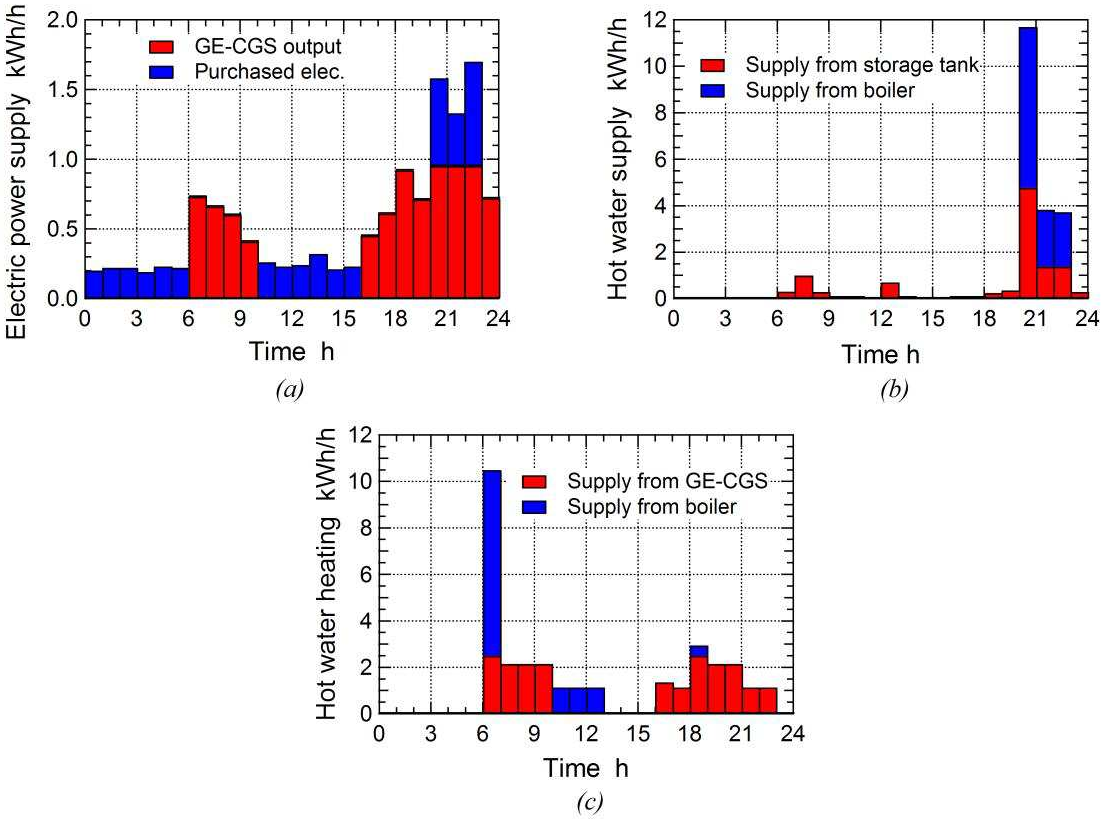

Fig. 9 Energy supply pattern in using GE-CGS on representative day of winter (r_E = 1.0, r_Q = 1.54): a) electric power supply, b) hot water supply, c) hot water heating.

However, the operation time of the GE-CGS is limited, and the shortage in the hot water supply from the storage tank and the hot water heating from the GE-CGS is compensated for by the gas-fired boiler. This is because the GE-CGS cannot be operated until the generated hot water meets the daily heat demand, due to a low energy-utilizing efficiency of the partial-load operation using the EH. These results reveal that the selection of the optimal cogeneration unit is influenced more by the generation and heat recovery efficiencies and the operational restrictions of the cogeneration units than by the consistency in the heat-to-power ratios of the cogeneration unit and energy demand.

The selection of the peripheral devices, which are the EH and AC, varies with the selected cogeneration unit and energy demands. The AC is selected only with the SOFC-CGS employing the continuous operation; this means that the PEFC-CGS with a high heat-to-power supply ratio needs to effectively utilize the generated hot water to archive energy savings. However, the AC is not required for the large heat demands (SOFC-B and SOFC-D). Although the EH is selected along with both the PEFC-CGS and SOFC-CGS, it is not required for the large electric power demands because the minimum electric power demands exceed the minimum electric power output of the PEFC-CGS and SOFC-CGS (SOFC-C, SOFC-D, and PEFC-B).

3.3.2. Energy-saving effect

The energy-saving effect of the residential cogeneration systems with the optimal and sub-optimal structures is analyzed. The reduction rate of the annual primary energy consumption by utilizing the residential cogeneration system, α, is defined as

$$\alpha = \frac{J_{CO} - J_{CGS}}{J_{CO}} \times 100 \quad (13)$$

where J_{CO} denotes the annual primary energy consumption of a conventional energy supply system, in which the electric power demand is met only by purchasing electric power, and the heat demand is met only by supplying from a conventional gas-fired boiler. Based on the HHV of natural gas, the hot water supply and heating efficiencies of the conventional gas-fired boiler are 80% and 75%, respectively. Table 4 shows the reduction rate of the annual primary energy consumption for the energy demands originally specified (r_E = 1.0 and r_Q = 1.0), indicated in Fig. 6, along with the selected structure of the residential cogeneration system. The results are also shown for the sub-optimal cogeneration units, and the energy supply system without the cogeneration units; the results are derived by setting the binary variable to select the target cogeneration unit to 1, and by setting all the binary variables to select the cogeneration units to 0 in Eq. (1), respectively.

For both the winter heating methods, there is a slight difference in the reduction rate of the annual primary energy consumption between the SOFC-CGS, which is selected as the optimal cogeneration unit, and the PEFC-CGS. Although the GE-CGS also greatly reduces the annual primary energy consumption as compared with the energy supply system without the cogeneration

Table 4. Energy-saving effect and system structure of residential cogeneration system.

Winter heating	Cogeneration unit	Reduction rate of annual primary energy consumption %	Selected (S) / not selected (NS)	
			EH	AC
Electric air conditioners	SOFC-CGS (Optimal)	19.7	NS	S
	PEFC-CGS	18.6	S	NS
	GE-CGS	10.8	S	NS
	NS	2.75	NS	NS
Hot water	SOFC-CGS (Optimal)	20.0	NS	S
	PEFC-CGS	18.6	S	NS
	GE-CGS	13.7	S	NS
	NS	4.75	NS	NS

units, especially in case of the winter heating by hot water, the reduction rate of the annual primary energy consumption of the GE-CGS is smaller than those of the SOFC-CGS and PEFC-CGS for both the winter heating methods. If the GE-CGS or PEFC-CGS is selected, the EH is selected, but the AC is not required because their heat-to-power supply ratios are high.

4. Conclusions

An optimal structural design method of residential cogeneration systems that considers various kinds of operational restrictions of system components was developed from the energy-saving viewpoint. The optimal structure of an residential cogeneration system, consisting of a cogeneration unit and its peripheral devices, was determined in consideration of multi-period operation, based on their operational restrictions, so that annual primary energy consumption may be minimized. As principal operational restrictions of cogeneration units without reverse power flow to commercial electric power systems, a constant power output operation, daily start–stop operation, and continuous operation were focused on. Moreover, the variation in the generation and heat recovery efficiencies of cogeneration units under partial-load conditions was formulated using multiple linear

equations. By formulating the relationship between the binary variables expressing the selection from their candidates and those expressing their operation status, the selection and multi-period operation of system components were simultaneously optimized. The formulated optimal structural design problem resulted in a mixed-integer linear programming problem.

The proposed method was applied to the structural design of an residential cogeneration system, consisting of a cogeneration unit, whose candidates are a GE-CGS employing the constant power output operation, PEFC-CGS employing the daily start–stop operation, and SOFC-CGS employing the continuous operation, with a storage tank and gas-fired boiler and peripheral devices, whose candidates are an electric water heater and air-cooled heat exchanger, for simulated energy demands. The results revealed that the selection of the optimal cogeneration unit is influenced more by the generation and heat recovery efficiencies and the operational restrictions of the cogeneration units than by the consistency in the heat-to-power ratios of the cogeneration unit and energy demand, which is generally regarded as important for the design of cogeneration systems. This is because the cogeneration units without reverse power flow must be operated in the response to variations in the electric power demand. In addition, it was revealed that the selection of the peripheral devices varies with the selected cogeneration unit and energy demands.

In a further study, the optimal structure of a residential cogeneration system and its energy-saving effect under various energy demands will be analyzed in more detail. Furthermore, the structural design will be optimized from the cost-reduction viewpoint in order to analyze the optimal sizing of the system components.

References

[1] Honda Motor Co., Ltd. Honda to Begin Sales through Gas Utilities of All-New Ultra-Efficient Household Gas Engine Cogeneration Unit Featuring World's Most Compact Design – Available at: <http://world.honda.com/news/2011/p110523Gas-Engine-Cogeneration/index.html> [accessed 3.4.2012]

[2] Tokyo Gas Co.. Commercial Unit of Residential Fuel Cell Cogeneration Systems Launch into the Market – Available at:<http://www.tokyo-gas.co.jp/Press_e/20041206-2e.pdf> [accessed 3.4.2012].

[3] Panasonic Co.. Tokyo Gas and Panasonic to Launch New Improved "Ene-Farm" Home Fuel Cell with World-Highest Power Generation Efficiency at More Affordable Price – Available at: <http://panasonic.co.jp/corp/news/official.data/data.dir/en110209-2/en110209-2.html> [accessed 3.4.2012]

[4] Institute of Energy Economics. Japan Energy Brief. 2011; 12: 10-11 – Available at: <http://eneken.ieej.or.jp/en/jeb/1103.pdf> [accessed 3.4.2012]

[5] Hawkes A.D., Brett D.J.L., Brandon N.P., Fuel cell micro-CHP techno-economics: part 2 – model application to consider the economic and environmental impact of stack degradation. International Journal of Hydrogen Energy 2009; 34(23): 9558-69.

[6] Paepe M.D., D'Herdt P., Mertens D., Micro-CHP systems for residential applications. Energy Conversion and Management 2006; 47(18-19): 3435-46.

[7] Cockroft J., Kelly N., A comparative assessment of future heat and power sources for the UK domestic sector. Energy Conversion and Management 2006; 47(15-16): 2349-60.

[8] Hawkes A.D., Leach M.A., Cost-effective operating strategy for residential micro-combined heat and power. Energy 2007; 32(5): 711-23.

[9] Staffell I., Green R., Kendall K., Cost targets for domestic fuel cell CHP. Journal of Power Sources 2008; 181(2): 339-49.

[10] Dorer V., Weber A., Energy and CO_2 emissions performance assessment of residential micro-cogeneration systems with whole-building simulation programs. Energy Conversion and Management 2009; 50(3): 648-57.

[11] Yokoyama, R., Ito, K., Optimal Design of Gas Turbine Cogeneration Plants in Consideration of Discreteness of Equipment Capabilities. Journal of Engineering for Gas Turbines and Power 2006; 128(2): 336-43.

[12] Act on the Rational Use of Energy– Available at:
< http://www.asiaeec-col.eccj.or.jp/law/revised/rue_2.pdf> [accessed 3.4.11]

[13] Rosenthal RE. GAMS - a user's guide. Washington, DC, USA: GAMS Development Corp.; 2008.

[14] Suzuki M., Iwata S., Higaki K., Inoue S., Shigehisa T., Miyachi I., Nakabayashi H., Shimazu K., Development and field test results of residential SOFC CHP system. ECS Transaction 2009; 25 (2); 143-47.

[15] Institute for Building Environment and Energy Conservation. Calculation method of primary energy consumption in standards of judgment for residential construction clients – Available at: <http://ees.ibec.or.jp/documents/img/kaisetsu200903_all_ver2.pdf> [accessed 3.4.2012] (in Japanese)

[16] Ministry of Economy, Trade and Industry/Ministry of Land, Infrastructure and Transport. Standards of Judgment for Construction Clients and Owners of Specified Buildings on the Rational Use of Energy for Buildings – Available at: <http://www.asiaeec-col.eccj.or.jp/law/ken1_e.html> [accessed 3.4.2012]

[17] Energy Statistics, Tokyo Gas Co., Ltd. – Available at:
<http://www.stat.go.jp/english/index/official/210.htm> [accessed 3.4.2012]

Performance Estimation and Optimal Operation of a CO2 Heat Pump Water Heating System

Ryohei Yokoyama [a], Ryosuke Kato[b], Tetsuya Wakui [c], and Kazuhisa Takemurad [d]

a Department of Mechanical Engineering, Osaka Prefecture University
*Sakai, Osaka, Japan, yokoyama@me.osakafu-u.ac.jp, **CA***
b Department of Mechanical Engineering, Osaka Prefecture University
Sakai, Osaka, Japan, katou@ese.me.osakafu-u.ac.jp
c Department of Mechanical Engineering, Osaka Prefecture University
Sakai, Osaka, Japan, wakui@me.osakafu-u.ac.jp
d Research and Development Center, Kansai Electric Power Co., Inc.
Amagasaki, Hyogo, Japan, takemura.kazuhisa@a5.kepco.co.jp

Abstract:

The daily performance of a CO2 heat pump water heating system with a hot water storage tank is affected by the history of daily hot water demand and heat pump operating conditions. To attain the maximum system performance, it is important to estimate the daily changes in the system performance values accurately in relation to those in hot water demand and heat pump operating conditions, and determine the operating conditions optimally based on the estimation. In this paper, neural network models are used for this estimation, and the values of model parameters are identified by a global optimization method. In addition, the outlet water temperature for during operation and the inlet water temperature for shutdown are determined to maximize the system efficiency subject to a lower limit for the volume of unused hot water. The validity and effectiveness of this approach are ascertained by a numerical study using a simulated hot water demand.

Keywords:
Heat pump, Water heater, Thermal storage, Natural refrigerant, Carbon dioxide, System performance, Estimation, Optimization.

1. Introduction

Hot water demand occupies about one-third of the energy consumption in the residential sector in Japan, and energy saving in hot water supply has been an important issue. Under this situation, water heating systems each of which is composed of a heat pump using CO_2 as a natural refrigerant and a hot water storage tank have been developed and commercialized widely [1, 2]. The performance of CO_2 heat pumps has been enhanced dramatically through the technological development of their components such as compressors and gas coolers. On the other hand, importance has also been given to the performance of water heating systems in case they are operated under a daily change in hot water demand.

As for the CO_2 heat pump only, its performance, or coefficient of performance (COP) is affected by the air temperature as well as the inlet and outlet water temperatures. Many theoretical and experimental studies have been conducted for the performance analysis on CO_2 heat pumps [3–15]. As for the water heating system composed of the CO_2 heat pump and storage tank, on the other hand, the ambient conditions such as air and feed water temperatures, the hot water demand, and the operating conditions such as startup and shutdown, and outlet water temperature during operation of the CO_2 heat pump affect the inlet water temperature and resultantly the COP through the temperature distribution in the storage tank. In addition to the COP, the storage and system efficiencies, and the volumes of stored and unused hot water are considered as system performance values, and these are also affected by the aforementioned various conditions through the temperature distribution in the storage tank. As a result, the system performance is affected by the

operational history on past several days, and changes complexly with days. Therefore, in order to attain the maximum system performance, it is necessary to estimate the daily changes in system performance values accurately in relation to those in the ambient conditions, hot water demand, and operating conditions, and determine the operating conditions optimally based on them.

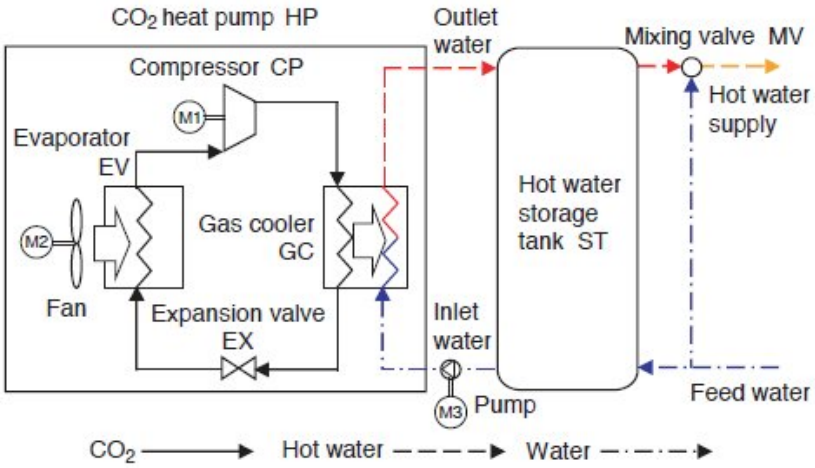

Fig. 1. Configuration of CO2 heat pump water heating system

Some studies have been conducted for the performance analysis on water heating systems [16–18]. However, few studies have been conducted in consideration of daily changes in the aforementioned conditions. In order to investigate the daily changes in system performance values, laboratory and field tests have been tried under simulated and practical hot water demands, respectively. However, hot water demands depend on residential houses, and it takes extremely long time to conduct the tests. Thus, it is not necessarily easy to investigate the system performance systematically and obtain useful results only by limited tests. On the other hand, numerical simulations have been conducted in place of the tests [19, 20]. The daily changes in system performance values have recently been investigated under a daily change in hot water demand by a numerical simulation [21, 22]. However, it is difficult to estimate the daily changes in system performance values under various operating conditions by numerical simulations from the viewpoints of computation complexity and time, and thus it is also difficult to determine the operating conditions optimally by numerical simulations. Therefore, it is necessary to establish easier methods of estimating the daily changes in system performance values accurately, and determining the operating conditions optimally.

In this paper, a method of estimating the daily changes in system performance values by neural network models is proposed for a CO_2 heat pump water heating system. In addition, the values of model parameters are identified by a global optimization method. Moreover, the operating conditions are determined optimally based on the system performance values obtained by the estimation.

This approach is applied to estimating the daily changes in system performance values and determining the operating conditions optimally under a simulated monthly hot water demand, and its validity and effectiveness is investigated through the comparison between estimated and simulated system performance values.

2. CO2 heat pump water heating system

Fig. 1 shows the configuration of the CO2 heat pump water heating system investigated in this paper. This system is composed of a CO2 heat pump and a hot water storage tank. The CO_2 heat pump is composed of a compressor, a gas cooler, an expansion valve, and an evaporator. The

system is equipped with a fan, a pump, and motors M1 to M3 as auxiliary machinery. Here, inlet and outlet water is defined as water at the inlet and outlet of the gas cooler, respectively. In the heating mode, the system heats water using the refrigeration cycle of the CO2 heat pump and stores hot water in the storage tank. In the tapping mode, hot water stored in the storage tank is retrieved and supplied to a tapping site.

3. Performance estimation and optimal operation

3.1. Basic assumptions

Existing systems are operated under complex conditions. In this paper, however, the performance estimation and optimal operation are considered under simple conditions by setting the following basic assumptions:

- The heating and tapping modes do not arise simultaneously and switch alternately. Namely, the heat pump is operated during the period from 0:00 to 6:00, and the hot water demand arises during the period from 6:00 to 24:00.
- The outlet water temperature during operation and the inlet water temperature for shutdown are considered as fundamental operating conditions of the heat pump. The heat pump is shut down with the shutdown condition that the inlet water temperature attains an appropriate value satisfied, and is started up at an appropriate time so that it is shut down before 6:00.
- Since the system performance is determined certainly by physical characteristics, it may be estimated accurately. However, since the hot water demand affecting the system performance is essentially uncertain, it cannot by predicted accurately by any methods. At the first phase of this research, it is assumed that the hot water demand is certainly given, and it is used to estimate the system performance.
- The system performance depends on ambient conditions such as air and feed water temperatures. However, the system performance during a short period hardly depends on the ambient conditions. Therefore, it is assumed that the ambient conditions are constant.

3.2. Evaluation of system performance values and hot water demand

A procedure is presented to estimate the system performance values accurately and determine the operating conditions optimally.

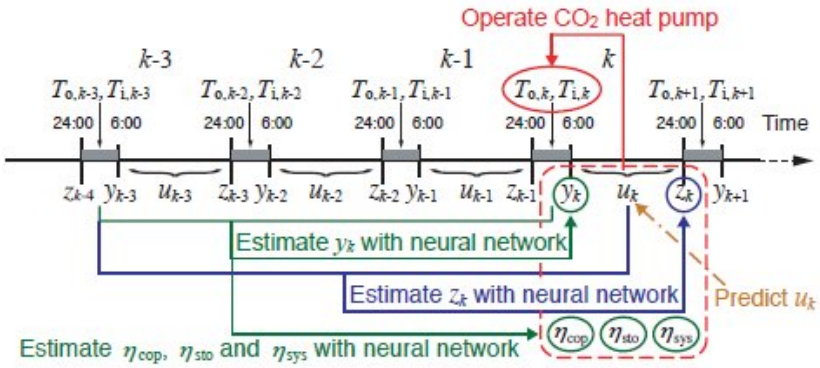

Fig. 2. Procedure for performance estimation and optimal operation.

Figure 2 shows the procedure in which the operational history on the past three days is used as an example. The outlet water temperature during operation and the inlet water temperature for shutdown of the heat pump are designated by T_0 and T_i, respectively. The volumes of hot water

stored at 6:00 and unused at 24:00 are designated by y and z, respectively. The total hot water demand during the period from 6:00 to 24:00 is designated by u. The subscript like k denotes a value on the kth day. In addition, the COP, storage efficiency, and system efficiency are designated by η_{COP} , η_{STO}, and η_{SYS} , respectively.

First, at 0:00 on the kth day, the volume of hot water stored at 6:00 on the kth day is y_k estimated using the outlet water temperature during operation, the inlet water temperature for shutdown, the volumes of stored and unused hot water, and the total hot water demand on the (k-3)th to (k-1)th days as well as the candidates for the outlet water temperature during operation and the inlet water temperature for shutdown on the kth day. Next, the volume of hot water unused at 24:00 on the kth day z_k is also estimated using the estimated value for the volume of stored hot water and the predicted value for the total hot water demand u_k on the kth day in addition to the aforementioned values. Finally, the COP η_{COP} , storage efficiency η_{STO}, and system efficiency η_{SYS} on the kth day are also estimated similarly as the volume of stored hot water y_k. This is based on the following reasons: The COP depends on the inlet water temperature, and the inlet water temperature depends significantly on the temperature distribution in the storage tank at 24:00; The storage efficiency depends on the temperature distribution in the storage tank throughout the day, and is roughly expressed by the temperature distributions in the storage tank at 6:00 and 24:00; The system efficiency is equal to the product of the COP and storage efficiency, and is also roughly expressed by the temperature distributions in the storage tank at 6:00 and 24:00.

The optimal operating conditions are determined as follows: The aforementioned system performance values are estimated under all the possible combinations of the candidates for the outlet water temperature during operation and the inlet water temperature for shutdown of the heat pump as operating conditions; Based on the estimated system performance values, the optimal combination of the candidates for the operating conditions is selected so that an objective function is optimized subject to constraints. For example, the objective function to be maximized is the system efficiency so that the system performance can be enhanced as much as possible, and the constraint to be satisfied is that the volume of unused hot water is larger than a certain value so that the shortage in hot water supply can be avoided.

3.4. Application of neural network models

As shown in Fig. 3, three-layered neural network models are used to estimate the system performance values.

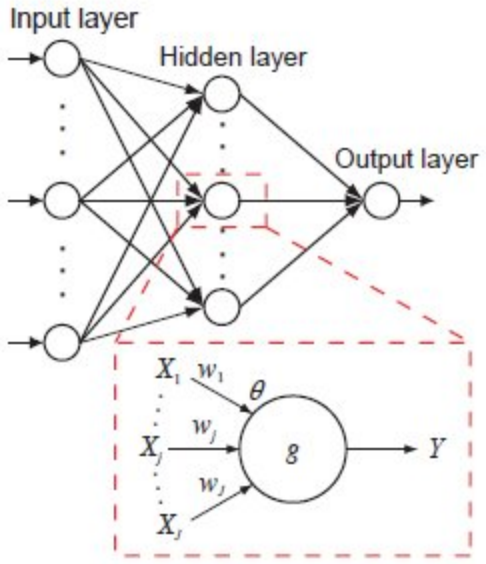

Fig. 3. Three-layered neural network model

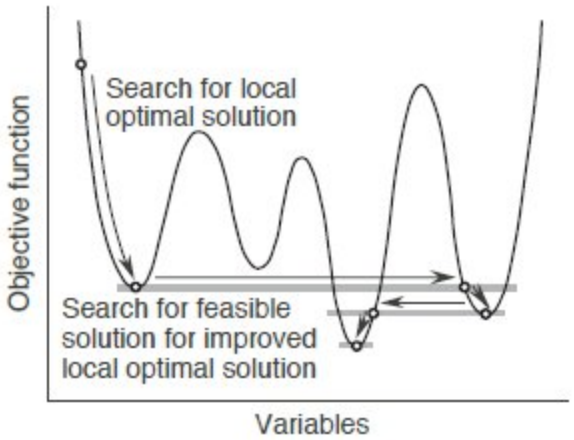

Fig. 4. Concept of modal trimming method

As aforementioned, each system performance value is estimated independently by the corresponding model. For long-term operation of existing systems, it is necessary to measure necessary data continuously and identify model parameter values repeatedly, and estimate system performance values correspondingly. Here, the estimation only for short-term operation is considered.

In the input layer, the operating conditions, the volumes of stored and unused hot water, and the total hot water demand on the past days as well as the operating conditions on the current day are adopted commonly as the inputs to the model to estimate all the system performance values. The estimated volume of stored hot water and the predicted total hot water demand on the current day are adopted additionally to estimate the volume of unused hot water. In the other layers, each neuron has multiple inputs and single output, and converts the weighted sum of the J inputs X_j minus the threshold θ to the output Y by the following response function:

$$Y = g\left(\sum_{j=1}^{J} w_j X_j - \theta \right) \quad (1)$$

Where ω_j is the weight for each input. The sigmoid function is usually used as the response function $g(x)$. In this paper, however, the hyperbolic tangent function $g(x) = \tanh x$ is used to obtain positive and negative values from the output. Here, the value from the output ranges only from -1.0 to 1.0 by normalizing the values to the inputs and from the output in advance.

3.5. Identification of model parameter values

To estimate the system performance values by the neural network models, it is necessary to identify the values of model parameters, weights and thresholds in Eq. (1). The squared error between the estimated value and the corresponding measured value is evaluated for each pattern, and its summation for all the patterns is minimized as the objective function to identify the values of model parameters. In the back propagation method, the error function for each pattern is minimized sequentially. Here, to secure the local optimality of solutions and make the convergence faster, the total error function for all the patterns is minimized simultaneously.

The search for local optimal solutions can be conducted by gradient methods for unconstrained nonlinear programming problems such as steepest descent, conjugate gradient, and quasi-Newton methods. However, these methods have the significant drawback that they can derive only local optimal solutions. In this paper, the modal trimming method proposed for nonlinear programming problems is adopted as a global optimization one [23]. This method has been applied to a neural network model for energy demand prediction, and its validity and effectiveness have been ascertained [24].

The concept of the modal trimming method is shown in Fig. 4. This method is composed of the following two procedures: A local optimal solution is searched to obtain a tentative global quasi-optimal one; A feasible solution with the value of the objective function equal to or smaller than that for the tentative global quasi-optimal one is searched to obtain an initial point for finding a better local optimal one. These procedures are repeated until a feasible solution with the value of the objective function equal to or smaller than that for the tentative global quasi-optimal one cannot be found, and the tentative global quasi-optimal one is adopted as the global quasi-optimal one. A local optimal solution is searched by a conventional gradient method. On the other hand, a feasible solution is searched by an extended Newton-Raphson method based on the Moore-Penrose generalized inverse of the Jacobi matrix of the objective function. The method can have a high possibility of deriving global optimal solutions, if it has the capability of global search for feasible ones.

The renewal of the values of the variables based on the extended Newton-Raphson method has the following features: In the region with a feasible solution, the renewal can have the convergence to it; In the region with no feasible solution, the renewal can create a chaotic behavior and has the

capability of global search; In the region with no feasible solution, the renewal can also create a cyclically vibrating behavior and has the possibility of trap into a local optimal solution. To prevent the trap, a decelerating parameter is changed randomly in the range from 0.0 to 1.0 at each renewal.

4. Numerical study on performance estimation

First, the parameter values of the neural network models are identified based on the system performance values obtained by numerical simulation, and their validity is investigated by comparing the estimated and simulated system performance values.

4.1. Numerical simulation

It is necessary to use some system performance values to identify the values of model parameters. In applying the method of performance estimation to existing systems, measured data on system performance values must be used. In this paper, values obtained by numerical simulation are used in place of measured values. Here, only a summary on the numerical simulation is described as follows:

A simplified static model is adopted for the CO_2 heat pump [21]: Although the heat pump includes several components, they are not taken into account explicitly, and it is expressed by one model. The mass flow rates and temperatures of water at the inlet and outlet, COP, heat output, power consumption, and air temperature are adopted as basic variables whose values are to be determined.

The mass and energy balance relationships as well as the energy input and output relationship are adopted as basic equations to be satisfied. The remaining equations to be considered are approximate functions of the power consumption and COP, and they are expressed in relation to the air and inlet/outlet water temperatures.

A detailed dynamic model is adopted for the storage tank [19, 21]. To consider the one-dimensional vertical temperature distribution in the storage tank, it is vertically divided into many control volumes with the same volume, in each of which the water temperature is assumed to be constant. It is also assumed that the heat transfer occurs by water flow and heat conduction as well as heat loss from the tank surface. The mass flow rates and temperatures of water for each control volume are adopted as basic variables whose values are to be determined. The mass and energy balance relationships for each control volume are adopted as basic equations to be satisfied.

A static model is adopted for the mixing valve. The mass flow rates and temperatures of water at the inlets and outlet are considered as basic variables, and the mass and energy balance relationships are considered as basic equations.

At the connection points among the heat pump, storage tank, and mixing valve, connection conditions are taken into account to equalize the values of the corresponding variables. The outlet water temperature is given as a control condition. The feed water temperature as well as the mass flow rate and temperature of hot water to the tapping site are given as boundary conditions. The air temperature is given as an ambient condition.

As for the concrete formulation of the simulation model, refer to reference [21]. The validity of the simulation model has been verified through an experiment and a three-dimensional thermo-fluid numerical simulation. As for this verification, also refer to reference [21].

The aforementioned modeling for the performance analysis by numerical simulation is conducted by a building block approach. The equations for the heat pump and mixing valve are static, while those for the storage tank are dynamic. Therefore, the modeling results in a set of nonlinear differential algebraic equations. It is solved by a hierarchical combination of the Runge-Kutta and Newton-Raphson methods.

Table 1. Specifications of CO_2 heat pump water heating system

Equipment	Specification	Value
CO2 heat pump	Rated heat output	4.50 kW
Hot water storage tank	Volume	370 L
	Height	1.45 m
	Diameter	0.57 m
	Overall heat transfer coefficient	0.80 W/(m2·°C)

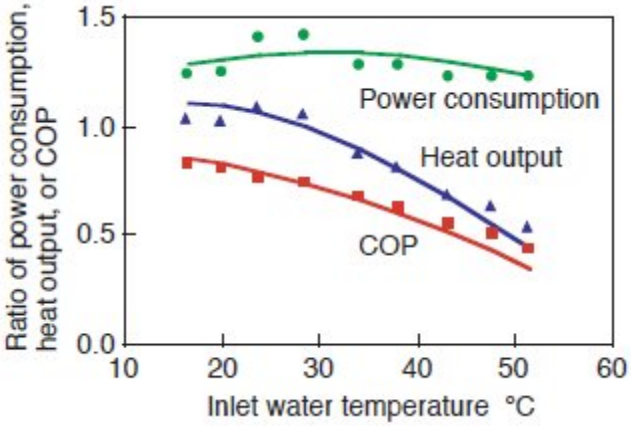

Fig. 5. Performance characteristics of CO_2 heat pump

4.2. Conditions for numerical simulation

A numerical simulation is conducted to obtain the daily changes in system performance values under a daily change in a simulated hot water demand. The following are the conditions used in the numerical simulation:

Table 1 shows the specifications of the CO2 heat pump water heating system. The values of model parameters included in the equations are estimated based on measured data for an existing system.

The rated heat output of the heat pump is set at 4.5 kW. As an example, Fig. 5 shows measured values and approximate functions for the power consumption, COP, and their resultant heat output of the heat pump in relation to the inlet water temperature for the air and outlet water temperatures of 16 and 85 °C, respectively. Here, each value is relative to its rated one for the air and inlet/outlet water temperatures of 16, 17, and 65 °C, respectively. This is because the existing system used here was developed initially by a manufacturer, and the values of COP of existing systems have

been enhanced significantly afterwards.

The volume of the storage tank is set at 370 L. The number of control volumes for the storage tank is set at 200, and the sampling time interval for the Runge-Kutta method is set at 10 and 180 s for the cases with and without water flow, respectively.

The mid-season is selected, and the corresponding air and feed water temperatures are set at 16 and 17 °C, respectively, which are prescribed by the Japanese Industrial Standards [25].

The numerical simulation is conducted for 6 representative days and a month, or consecutive 30 days composed of the 6 representative days [26]. On each representative day, an hourly change in a simulated hot water demand is prescribed. Figure 6 shows the total hot water demands on the 6 representative days. The 1st and 2nd representative days correspond to holidays with smaller and larger hot water demands, respectively, on which residents are out of the house. The 3rd and 4^{th} representative days correspond to weekdays with smaller and larger hot water demands, respectively. The 5th and 6th representative days correspond to holidays with smaller and larger hot water demands, respectively, on which residents are in the house. As an example, Fig. 7 shows the hourly change in the hot water demand on the 4th representative day. Here, the height and thickness of each vertical line means the flow rate and duration, respectively. The temperature of hot water supplied to the tapping site is set at 42 °C. Figure 8 shows the daily change in the total hot water demand on the 30 consecutive days.

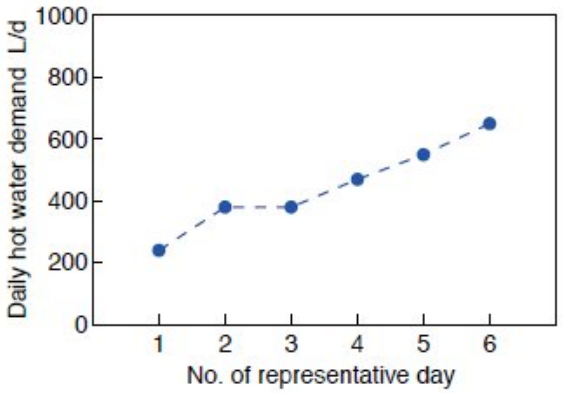

Fig. 6. Total hot water demands on 6 representative days

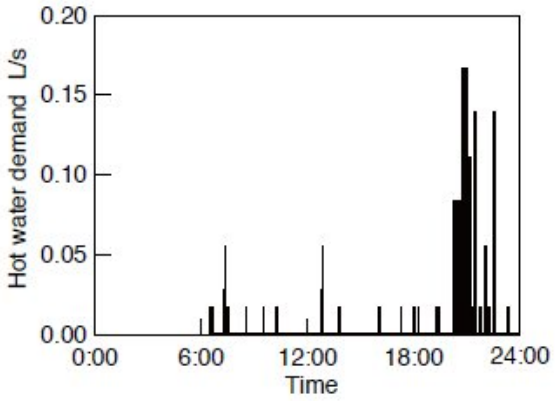

Fig. 7. Hourly change in hot water demand on 4th representative day

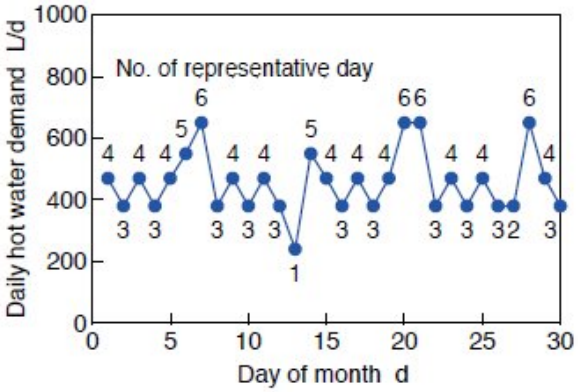

Fig. 8. Daily change in total hot water demand on consecutive 30 days

Table 2. Operating conditions for identification and verification of neural network models

Case	Purpose	Hot water demand	Outlet water temperature	Inlet water temperatuer for heat pump shutdown
1 ~ 54	Identification	Each of 6 representative days	Constant (each of 65, 75, and 85 °C)	Constant (each of 30, 40, and 50 °C)
55 ~ 63		Pattern of consecutive 30 days	Constant (each of 65, 75, and 85 °C)	Constant (each of 30, 40, and 50 °C)
64 ~ 66		Pattern of consecutive 30 days	Variable (comb. of 65, 75, and 85 °C)	Constant (each of 30, 40, and 50 °C)
67 ~ 69		Pattern of consecutive 30 days	Constant (each of 65, 75, and 85 °C)	Variable (comb. of 30, 40, and 50 °C)
70, 71		Pattern of consecutive 30 days	Variable (comb. of 65, 75, and 85 °C)	Variable (comb. of 30, 40, and 50 °C)
72	Verification	Pattern of consecutive 30 days	Variable (comb. of 65, 75, and 85 °C)	Variable (comb. of 30, 40, and 50 °C)

The heat pump is started up at 0:00 and 1:00, when the total hot water demand on the previous day is larger than or equal to and smaller than 500 L/d, respectively. The outlet water temperature during operation is selected among 65, 75, and 85 °C, and the inlet water temperature for shutdown is selected among 30, 40, and 50 °C. The daily operating conditions are set by combining these values.

72 cases are investigated by the numerical simulation. Table 2 shows the conditions on the outlet water temperature during operation and the inlet water temperature for shutdown in cases 1 to 72. Cases 1 to 71 are used to identify model parameter values, while case 72 is used to verify the validity of model parameter values. In cases 1 to 54, the numerical simulation is conducted for the periodically steady state on each representative day under each combination of the constant outlet and inlet water temperatures. In cases 55 to 63, the numerical simulation is conducted on the consecutive days under each combination of the constant outlet and inlet water temperatures. In cases 64 to 66, the numerical simulation is conducted on the consecutive days under variable outlet water temperature and each constant inlet water temperature. In cases 67 to 69, the numerical simulation is conducted on the consecutive days under each constant outlet water temperature and

variable inlet water temperature. In cases 70 to 72, the numerical simulation is conducted on the consecutive days under variable outlet and inlet water temperatures.

In cases 1 to 54, the initial temperature in the storage tank at 0:00 on the 1st day is set at 17 °C. In cases 55 to 72, the initial temperature distribution in the storage tank at 0:00 on the 1st day is set as follows: Since the 1st day corresponds to the 4th representative day as shown in Fig. 8, the temperature distribution in the storage tank at 0:00 obtained for the periodically steady state on the 4^{th} representative day is adopted as the initial temperature distribution in the storage tank at 0:00 on the 1st day.

4.3. Conditions for performance estimation

The numbers of neurons for the neural network models used for the performance estimation are set as follows: The data on the past two days are used; The numbers of neurons in the input and output layers are 12 and 1, respectively, for the models to estimate the COP, storage and system efficiencies, and volume of stored hot water; The numbers of neurons in the input and output layers are 14 and 1, respectively, for the model to estimate the volume of unused hot water; The number of neurons in the hidden layer is 3 commonly for all the models.

4.4. Results and discussion

Figure 9 shows the operating conditions and the system performance values in case 70. Figure (a) shows the operating conditions given in advance, and Figs. (b) and (c) show the system efficiency, and the volumes of stored and unused hot water, respectively, estimated by the neural network models under the given operating conditions. These figures also show the corresponding values obtained by the numerical simulation. The system efficiency is shown as the ratio of the system efficiency to its value on the 1st day. The estimated system performance values coincide well with the simulated ones. This result shows that the values of model parameters are identified properly by the global optimization method, and that the system performance values are estimated with high accuracy.

Figure 10 shows the operating conditions and the system performance values in case 72. Figures (a) to (c) show the same items as aforementioned. Although these simulated system performance values are not used to identify the values of model parameters, the estimated system performance values coincide well with the simulated ones. This result shows that the system performance values are estimated with high accuracy by the same neural network models even under different daily changes in the operating conditions.

5. Numerical study on optimal operation

Next, the operating conditions are determined optimally based on the estimation by the neural network models whose parameter values are identified previously.

5.1. Conditions for optimal operation

It is important to enhance the system efficiency and prevent the shortage in hot water supply. In this paper, therefore, the system efficiency is maximized subject to a lower limit for the volume of hot water unused at 24:00. The outlet water temperature during operation and the inlet water temperature for shutdown are adopted as the variables, and their values are determined so as to attain the objective and satisfy the constraint. Here, the lower and upper limits for the outlet water temperature during operation are set at 65.0 and 85.0 °C, respectively, and those for the inlet water temperature for shutdown are set at 30.0 and 50.0 °C, respectively.

On each day, each system performance value is estimated for all the combinations for the outlet and inlet water temperatures. For simplicity, the outlet water temperature is selected among its discrete values set by 1 °C from 65.0 to 85.0 °C, and the inlet water temperature is selected among its discrete values set by 1 °C from 30.0 to 50.0 °C. Here, the outlet water temperature is constrained so that the stratification in the storage tank is kept. Based on this estimation, the combination of the outlet and inlet water temperatures is selected so that the estimated system efficiency has its maximum and the estimated volume of unused hot water is larger than its lower limit.

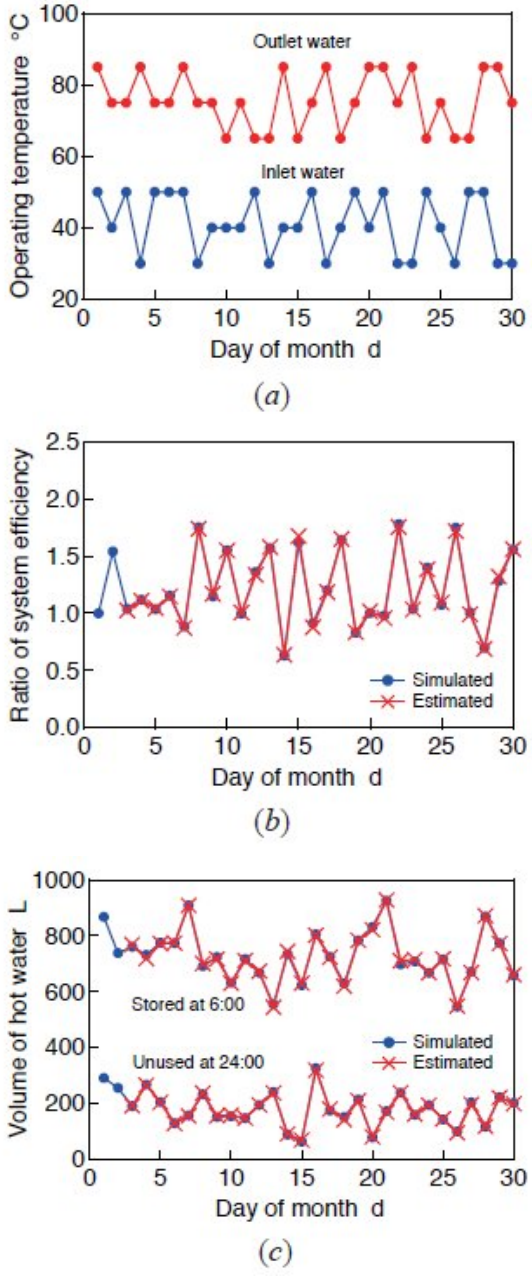

Fig. 9. Daily changes in operating conditions and system performance values in case 70: a) operating conditions, b) ratio of system efficiency, c) volumes of stored and unused hot water

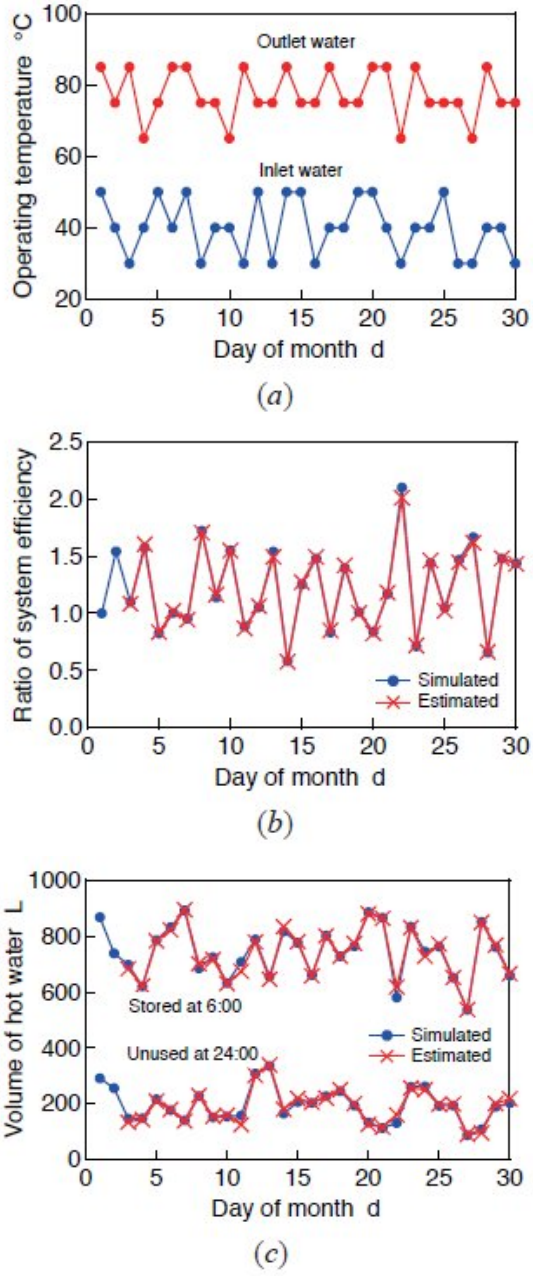

Fig. 10. Daily changes in operating conditions and system performance values in case 72: a) operating conditions, b) ratio of system efficiency, c) volumes of stored and unused hot water

In case there is no combination by which the estimated volume of unused hot water is larger than its lower limit, the combination by which the estimated volume of unused hot water is the closest to its lower limit is selected.

In the numerical study, the lower limit for the volume of unused hot water is changed by 50 L from 50 to 250 L in cases 73 to 77, respectively, and its influence on the system performance is investigated.

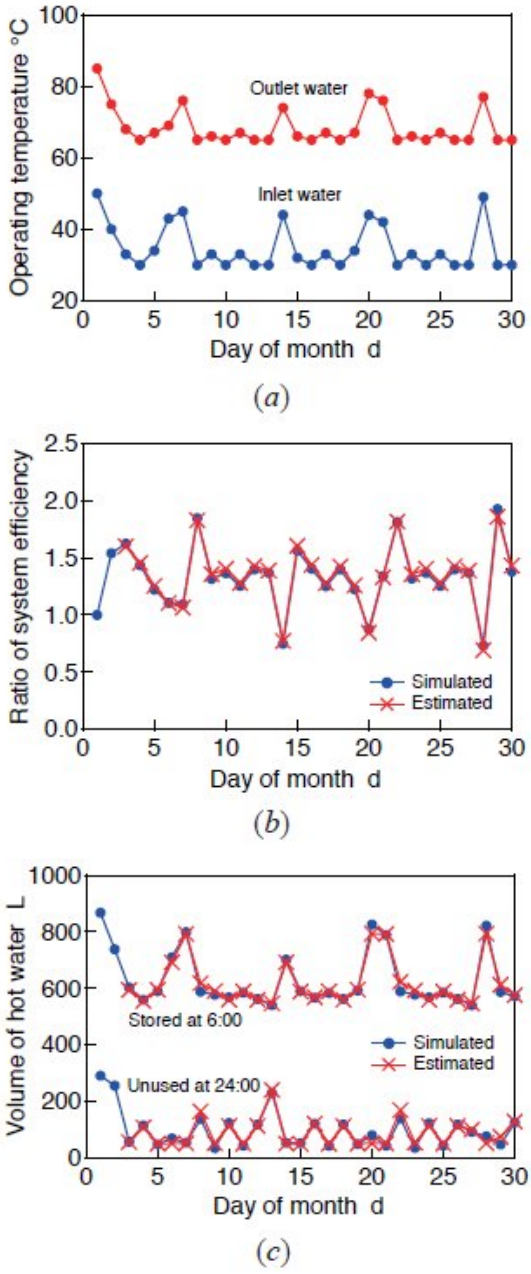

Fig. 11. Daily changes in operating conditions and system performance values in case 73: a) operating conditions, b) ratio of system efficiency, c) volumes of stored and unused hot water.

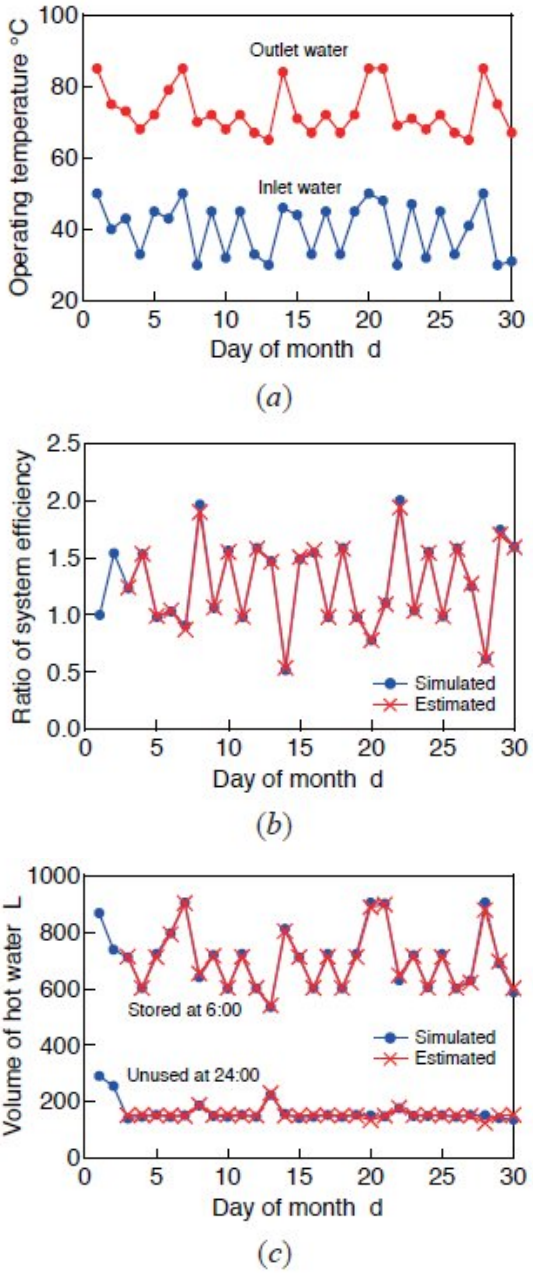

Fig. 12. Daily changes in operating conditions and system performance values in case 75: a) operating conditions, b) ratio of system efficiency, c) volumes of stored and unused hot water.

5.2. Results and discussion

Figures 11 to 13 show the operating conditions and the system performance values in cases 73, 75, and 77, respectively. Figure (a) shows the operating conditions determined optimally, and Figs. (b) and (c) show the system efficiency, and the volumes of stored and unused hot water, respectively, estimated by the neural network models under the optimal operating conditions. These figures also show the corresponding values obtained by the numerical simulation. Although these operating

conditions and the corresponding system performance values are not used to identify the values of model parameters, the estimated system performance values coincide well with the simulated ones. This result shows that the system performance values are estimated with high accuracy by the same neural network models even under daily changes in the optimal operating conditions.

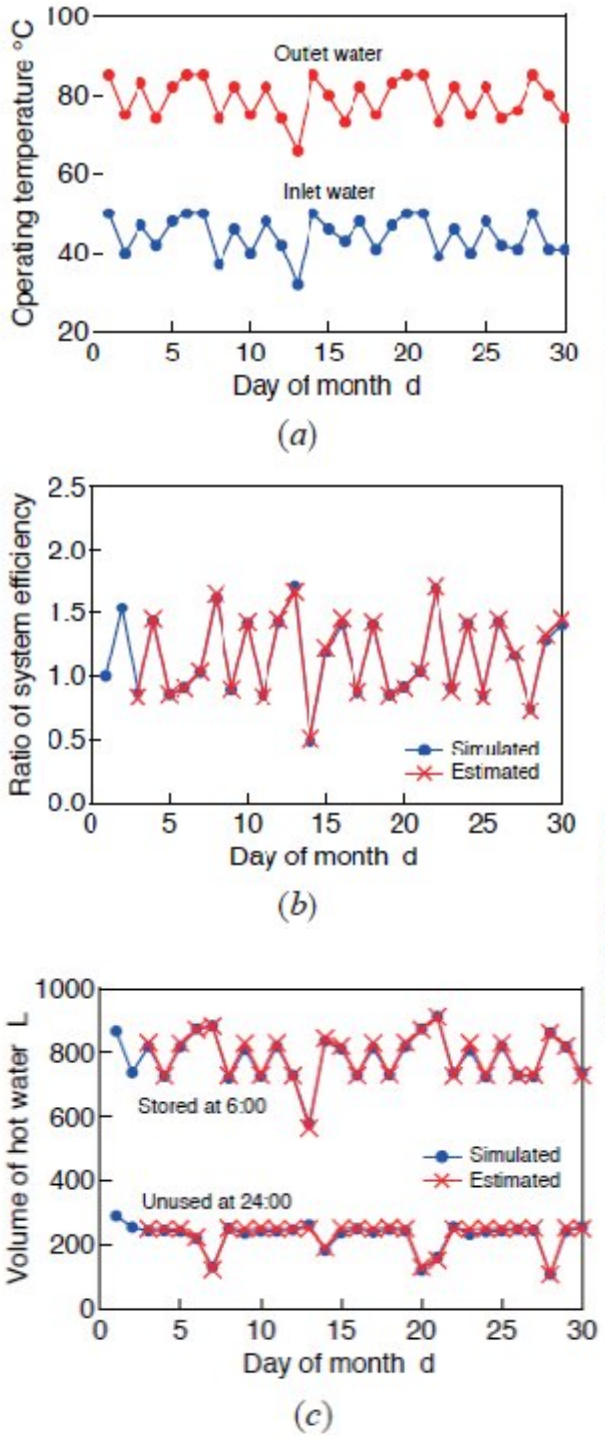

Fig. 13. Daily changes in operating conditions and system performance values in case 77: a) operating conditions, b) ratio of system efficiency, c) volumes of stored and unused hot water

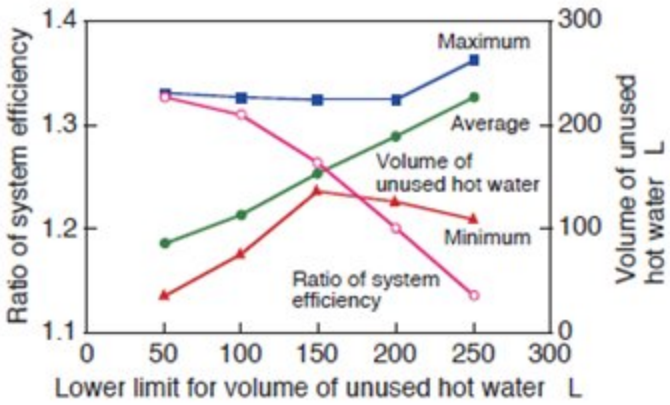

Fig. 14. Relationship between monthly system performance values

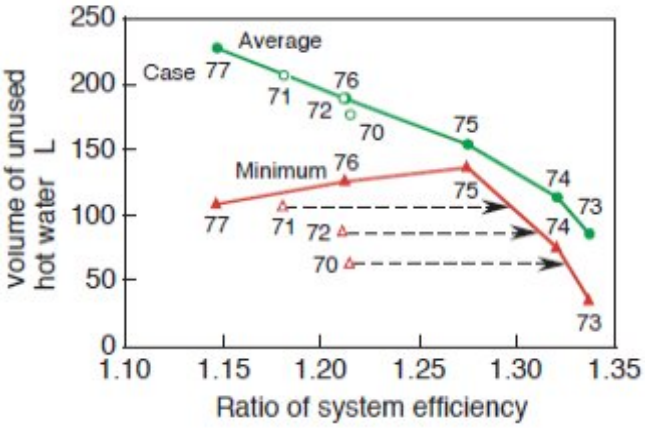

Fig. 15. Comparison between monthly system performance values under optimal and non-optimal operating conditions

In case 75, as shown in Fig. 12, although the volume of unused hot water changes around 150 L, it becomes larger than 150 L on a few days. This is because both the operating conditions attain their lower limits, or the outlet water temperature attains the temperature at the top of the storage tank on those days. As a result, the daily change in the volume of unused hot water is small. In case 73, as shown in Fig. 11, the volume of unused hot water changes above 50 L on many days. This is also because both the operating conditions attain their lower limits, or the outlet water temperature attains the temperature at the top of the storage tank on those days. As a result, the daily change I the volume of unused hot water is large. On the other hand, in case 77, as shown in Fig. 13, the volume of unused hot water changes below 250 L on several days. This is because the operating conditions attain their upper limits on those days. As a result, the daily change in the volume of unused hot water is slightly large.

Figure 14 shows the relationship between the lower limit for the volume of unused hot water and the monthly values of the ratio of system efficiency and the volume of unused hot water. The average value is adopted for the ratio of system efficiency, and the average, maximum, and minimum values are adopted for the volume of unused hot water. The average values of the ratio of system efficiency and the volume of unused hot water have a trade-off relationship. However, the average value of the ratio of system efficiency and the maximum or minimum value of the volume of unused hot water do not have a trade-off relationship. This is because, as shown in Figs. 11 and 13, in case the lower limit for the volume of unused hot water is small or large, the daily change in the volume of unused hot water becomes large, and the difference between the maximum and minimum values of the volume of unused hot water also becomes large.

Figure 15 shows the comparison of the monthly values of the ratio of system efficiency and the volume of unused hot water in cases 70 to 77. The average value is adopted for the ratio of system efficiency, and the average and minimum values are adopted for the volume of unused hot water.

As aforementioned, the average values of the ratio of system efficiency and the volume of unused hot water under the optimal operating conditions in cases 73 to 77 have a trade-off relationship. In addition, those under the non-optimal operating conditions in cases 70 to 72 are very close to the trade-off relationship. Thus, the optimal operation is not effective from the viewpoint of the average system performance values. On the other hand, the average value of the ratio of system efficiency and the minimum value of the volume of unused hot water under the optimal operating conditions in cases 73 to 77 have a trade-off relationship partly in cases 75 to 77. In addition, those under the non-optimal operating conditions in cases 70 to 72 are far from the trade-off relationship.

As for the volume of unused hot water, the minimum value is more important than the average one to prevent the shortage in hot water supply. Thus, as shown by arrows, it is possible to enhance the average value of the system efficiency with the minimum value of the volume of unused hot water kept constant. The increases in the average value of the system efficiency are expected to be about 9.0, 9.9, and 8.2 % in cases 70 to 72, respectively.

6. Conclusions

In this paper, a method of estimating the daily changes in system performance values by neural network models is proposed for a CO2 heat pump water heating system. In addition, the values of model parameters are identified by a global optimization method. Moreover, the operating conditions are determined optimally based on the system performance values obtained by the estimation.

This approach is applied to estimating the daily changes in system performance values and determining the operating conditions optimally under a simulated monthly hot water demand, and its validity and effectiveness is investigated through the comparison between estimated and simulated system performance values. The following main results are obtained:

- It is possible by this approach to estimate all the system performance values, or COP, storage and system efficiencies, and volumes of stored and unused hot water with high accuracy not only under the operating conditions used for identifying model parameter values but also under different operating conditions including the optimal ones.
- It is important to enhance the system performance and prevent the shortage in hot water supply. It is possible by this approach to determine the operating conditions optimally so as to maximize the system efficiency subject to a lower limit for the volume of unused hot water for the purpose.
- It is possible by this approach to enhance the average value of the system efficiency with the minimum value of the volume of unused hot water kept constant by changing the non-optimal operating conditions to the optimal ones. The increase in the average value of the system efficiency is expected to be 8 to 10 % under the conditions investigated in the numerical study.

Acknowledgment

A part of this work was supported by the JSPS Grant-in-Aid for Scientific Research (C) No. 22560838.

References

[1] Saikawa M. CO_2 heat pump water heater. Energy and Resources 2004; 25 (2): 101–105 (in Japanese).

[2] Hashimoto K. Technology and market development of CO_2 heat pump water heaters (ECO CUTE) in Japan. IEA Heat Pump Centre Newsletter 2006; 24 (3): 12–16.

[3] Hwang Y, Radermacher R. Theoretical evaluation of carbon dioxide refrigeration cycle. International Journal of Heating, Ventilating, Air-Conditioning and Refrigerating Research 1998; 4 (3): 1–20.

[4] Nekså P, Rekstad H, Zakeri R, Schiefloe PA. CO_2-heat pump water heater: characteristics, system design and experimental results. International Journal of Refrigeration 1998; 21 (3): 172–179.

[5] Saikawa M, Hashimoto K, Hasegawa H, Iwatsubo T. Study on efficiency and control method of CO_2 heat pump, report no. W98004. Central Research Institute of Electric Power Industry, 1999 (in Japanese).

[6] Saikawa M, Hashimoto K. Evaluation on efficiency of CO_2 heat pump cycle for hot water supply-evaluation on theoretical efficiency and characteristics. Transactions of the JSRAE 2001; 18 (3): 217–223 (in Japanese).

[7] Nekså P. CO_2 heat pump systems. International Journal of Refrigeration 2002; 25 (4): 421–427.

[8] White SD, Yarrall MG, Cleland DJ, Hedley RA. Modelling the performance of a transcritical CO_2 heat pump for high temperature heating. International Journal of Refrigeration 2002; 25 (4): 479–486.

[9] Skaugen G, Nekså P, Pettersen J. Simulation of trans-critical CO_2 vapour compression systems. Proceedings of the 5th IIR-Gustav Lorentzen Conference on Natural Working Fluids, Guangzhou, 2002; 82–89.

[10] Richter MR, Song SM, Yin JM, Kim MH, Bullard CW, Hrnjak PS. Experimental results of transcritical CO_2 heat pump for residential application. Energy 2003; 28 (10): 1005–1019.

[11] Yokoyama R, Shimizu T, Takemura K, Ito K. Performance analysis of a hot water supply system with a CO_2 heat pump by numerical simulation (1st report, modeling and analysis of heat pump). JSME International Journal, ser. B 2006; 49 (2): 541–548.

[12] Laipvadit P, Tiansuwan J, Kiatsiriroat T, Aye L. Theoretical performance analysis of heat pump water heaters using carbon dioxide as refrigerant. International Journal of Energy Research 2008; 32 (4): 356–366.

[13] Yan JL, Ma YT, Li MX, Hua J. Modeling and simulating the transcritical CO_2 heat pump system. Energy 2010; 35 (12): 4812–4818.

[14] Sarkar J, Bhattacharyya S, Ram Gopal M. Performance of a transcritical CO_2 heat pump for Simultaneous water cooling and heating. ASHRAE Transactions 2010; 116 (1): 534–541.

[15] Yamaguchi S, Kato D, Saito K, Kawai S. Development and validation of static simulation model for CO_2 heat pump. International Journal of Heat and Mass Transfer 2011; 54 (9–10): 1896–1906.

[16] Cecchinato L, Corradi M, Fornasieri E, Zamboni L. Carbon dioxide as refrigerant for tap water heat pumps: a comparison with the traditional solution. International Journal of Refrigeration 2005; 28 (8): 1250–1258.

[17] Stene J. Residential CO_2 heat pump system for combined space heating and hot water heating. International Journal of Refrigeration 2005; 28 (8): 1259–1265.

[18] Minetto S. Theoretical and experimental analysis of a CO_2 heat pump for domestic hot water. International Journal of Refrigeration 2011; 34 (4): 742–751.

[19] Yokoyama R, Shimizu T, Ito K, Takemura K. Influence of ambient temperatures on performance of a CO_2 heat pump water heating system. Energy 2007; 32 (4): 388–398.

[20] Yokoyama R, Okagaki S, Wakui T, Takemura K. Influence of operation temperatures on performance of a CO_2 heat pump water heating system. Journal of Environment and Engineering 2008; 3 (1): 61–73.

[21] Yokoyama R, Wakui T, Kamakari J, Takemura K. Performance analysis of a CO_2 heat pump water heating system under a daily change in a standardized demand. Energy 2010; 35 (2): 718–728.

[22] Yokoyama R, Kohno Y, Wakui T, Takemura K. Performance analysis of a CO_2 heat pump water heating system under a daily change in a simulated demand. Transactions of the JSRAE 2010; 27 (4): 355–364.

[23] Yokoyama R, Ito K. Capability of global search and improvement in modal trimming method for global optimization. JSME International Journal, ser. C 2005; 48 (4): 730–737.

[24] Yokoyama R, Wakui T, Satake R. Prediction of energy demands using neural network with model identification by global optimization, Energy Conversion and Management 2009; 50 (2): 319–327.

[25] Japanese Industrial Standards Committee. Residential heat pump water heaters, standard no. JIS C 9220: 2011. Japanese Standards Association, 2011 (in Japanese).

[26] Ukaji M, Sawachi T, Akimoto T, Hori Y, Kuwasawa Y, Mae M, Hosoi A. Study on low energy and resource saving technologies for autonomous housing (part 6, basic schedule for the verification of energy consumption in daily human activities). Procedings of the SHASE Annual Conference, Nagoya, 2004; 209–212 (in Japanese).

Performance of a common-rail Diesel engine fuelled with rapeseed and waste cooking oils

A. Corsini[a], V. Giovannoni[b], S. Nardecchia[c], F. Rispoli[d], F. Sciulli[e] and P. Venturini[f]

[a] *Dipartimento di Ingegneria Meccanica e Aerospaziale, Sapienza Università di Roma, Rome, Italy, corsini@dima.uniroma1.it*
[b] *AzzeroCO2 s.r.l., Rome, Italy, val.g85@gmail.com*
[c] *Dipartimento di Ingegneria Meccanica e Aerospaziale, Sapienza Università di Roma, Rome, Italy, stefano.nardecchia@alice.it*
[d] *Dipartimento di Ingegneria Meccanica e Aerospaziale, Sapienza Università di Roma, Rome, Italy, rispoli@uniroma1.it*
[e] *Dipartimento di Ingegneria Meccanica e Aerospaziale, Sapienza Università di Roma, Rome, Italy, fabrizio.sciulli@gmail.com*
[f] *Dipartimento di Ingegneria Meccanica e Aerospaziale, Sapienza Università di Roma, Rome, Italy, venturini@dima.uniroma1.it, CA.*

Abstract:

The EU energy strategy for 2020 forces scientists and industries to develop new generation of bio-fuels and increase the use of the ones available nowadays. Straight vegetable oils (SVO) and waste cooking oils (WCO) could represent an interesting alternative fuel for Diesel engines, representing a good solution in some niches sectors (i.e., public transportation, hybrid or marine propulsion, etc.).
As a matter of fact the use of SVO as fuel do not requires large production plants as in the case of biodiesel, thus it can be used in a large number of countries without requiring new costs. On the other hand SVO has some shortcomings due to the different characteristics comparing with the gasoil fuel. Main differences are related to its smaller heating value, a different density, and a larger viscosity, and this may provoke some problems to the injection system and power loss in a Diesel engine.
Aim of this work is to analyse the behaviour of a Diesel engine in automotive configuration when fuelled with SVO and WCO, to study the feasibility of use them in small public transport hybrid vehicles. To this aim a series of bench tests are performed; results are here presented. Tests are performed using a turbocharged, four stroke, four cylinders, water cooled, common-rail multijet Diesel engine operating on Diesel fuel, rapeseed oil (RO) and waste cooking oil (WCO) are presented. The influence of fuel used on engine power, specific consumption, efficiency, and exhaust opacity, are compared with those obtained fuelling with Diesel fuel.

Keywords:

Straight vegetable oil; waste cooking oil; common-rail Diesel engine; bio-fuels.

1. Background

The limited reserves of fossil fuels, the continuously increasing oil cost, and the environment pollution due to the combustion of fossil fuels are forcing the countries to revise their energy policies and put more and more attention to renewable energy sources. EU recently approved a new Directive aiming at changing its energy strategy. The Directive 2009/28/EC [1] fixes three main challenging objectives for 2020: to reduce the greenhouse gas (GHG) emissions by 20%; to reduce the final energy consumption by 20% (improving energy efficiency); to provide 20% of European energy consumption using renewable. A particular attention is also put to the use of fuels in transport. Indeed, the same Directive stats that by 2020 at least 10% of the whole fuels used in transport must be renewable. This new approach to energy forces scientists and industries to develop new generation of bio-fuels and efficiently increase the use of the ones already available. For Diesel engines the most suitable solution nowadays is the use of bio-diesel (BD), the bio-fuel derived by vegetable oils. It can be used alone or in blend with Diesel fuel (DF) and it is widely studied and tested ([2]-[6]). Although BD is a suitable substitution of DF, in the last years the interest in the use of SVO as fuel

has been increasing. This is due to the fact that BD requires large production plants, thus accordingly big economical efforts, and also consumes energy. Besides, the possibility of using vegetable oil directly as a fuel would widen the available alternative to DF, and would allow a lot of countries to use this alternative thus reducing their dependence on fossil fuels. At the moment the availability of vegetable oil, as well as of land to dedicate to oilseed crops, do not allow to look at the SVO as a global alternative to DF. However it can be used in blend with gasoil or also alone in some niche applications, such as public transport, hybrid and marine propulsion, electricity generation units, etc.. The situation may change with the use of oil from algae which seems to be very promising ([7]-[10]).

Despite there are several advantages in using the SVO as a fuel, it also may provoke some economical and technical problems. Focusing the attention to the latter aspect, there are two main issues related to the use of SVO as fuel: the first one is its environmental implication (i.e., pollution and energy consumption during SVO production, transport, etc.), and the second is how a Diesel engine behaves when fuelled with SVO (i.e., power loss, efficiency, etc.).

Environmental implication can be analysed using the Life Cycle Assessment (LCA) approach. In this kind of analysis all the factors influencing the life of a product are considered and evaluated to study the actual environmental impact of the product itself for a particular application. Here the Italian situation is considered, but the analysis might be applied to every other country and application. Today in Italy several small electricity generation units (<1 MWel) operate using RO (or SVO in general), but due to the scarcity of RO on the Italian market, plant managers turn more often to Eastern Europe countries (i.e., Romania, Hungary, Poland, etc.) for vegetable oil supply. This has an environmental cost that may overcome the advantages due to the use of a bio-fuel. In a previous study [11] some of the authors evaluated the LCA of such a situation. It came out that, due to the fact that oilseed crops productivity in those countries (i.e., Romania) is not very high, part of the advantage of using RO as a fuel is loss during production and transport. Nevertheless, the GHG saving (with reference to the use of DF) is still large, about 54% [11]. On the contrary, in the case of WCO collected through a short chain (maximum 70 km far from the power plant) the GHG emissions are extremely low. This is due to two main reasons: first, WCO is a waste product thus no emissions should be accounted for its production; second, the short chain reduces the emissions due to fuel transport. These aspects make the WCO an extremely interesting fuel from the GHG emissions point of view. Fig. 1 shows the GHG emissions caused by the use of RO and WCO as fuel in comparison with two conventional power production approaches, that is production using DF or electricity bought from the national grid. It is evident the advantage of using WCO or RO instead of the conventional solutions.

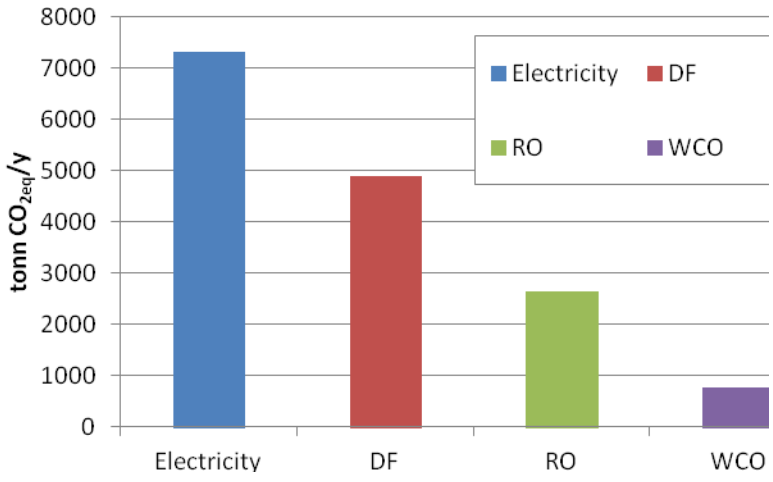

Fig. 1. GHGs emissions for four different Italian scenarios.

Once the environmental advantages given by the use of these bio-fuels are clear, then a more technical aspect has to be studied, that is the behaviour of an engine operating with SVO.

Aim of this work is to analyse the behaviour of a Diesel engine configured for automotive (public transport) applications, fuelled with RO and WCO. This will be the focus of the sections 2-4. Concluding remarks will close the paper.

2. Fuel characteristics

Even though Rudolf Diesel developed what would become the Diesel engine using peanuts oil as a fuel, oil products took over, and the engines were developed and optimized for them. This results in a wide diffusion of internal combustion engines (because of the past large availability of oil) but a very narrow adaptability to other fuels. The use of SVO or WCO in a Diesel engine may provoke problems due to different fuel characteristics. Average physical characteristics of several vegetable oils are listed in Table 1 [12],[13]. These are only indicative characteristics since they may vary quite widely according to the ground properties, the kind of crops, the productions process, etc..

Generally speaking, SVO has lower calorific value with reference to DF (about 10-15% less), and an higher density. This reduces the difference in energy content when considering a fixed volume of fuel. Indeed, the volumetric heating value of SVO results only 5-6% less than that of DF. At room temperature SVO viscosity is about 10-30 times larger than that of DF, thus resulting in possible problems to the feeding and injection systems, and to the combustion chamber [12]-[17]. The cetane number of the reported SVO varies between 32 and 45 as opposed to 45-55 of DF. Since the cetane number is a measure of the flammability of a fuel it may result in combustion problems when the engine is cold. Flash point measures the temperature at which the vapours given off by a substance. SVO has a higher flash point as compared to DF, and this increases the safety of the former in the storage or in the transport phase.

Table 1. Average characteristics of some vegetable oils and DF ([12],[13]).

Oil	Net heating value (MJ/kg)	Density (kg/m^3)	Kinematic viscosity (mm^2/s)	Cetane number	Flash point (°C)
Diesel fuel	39.5-43.8	830-860	3.0-7.5	50	76-93
Palm	36.9	915-918	95.0-106.0	38-42	267-280
Rapeseed	37.4-39.7	911-915	77.0	32-38	246-320
Sunflower	37.1-37.7	916-925	55.0-61.0	35-37	274-316
Soybean	37.3-39.6	914-920	58.0-63.0	36-38	254-330
Jatropha	38.8	915	55.0	45	240

Table 2. Reference characteristics of RO, WCO and DF.

Oil	Net heating value (MJ/kg)	Density at 20°C (kg/m^3)	Kinematic Viscosity at 20°C (Pa·s)
DF	43.3 [18]	868.88	6.33E-03
RO	37.6 [18]	960.85	51.54E-03
WCO	36.9 [14]	963.44	91.59E-03

In the present study RO and WCO will be used as fuel. Their characteristics are reported in Table 2 together with DF ones.

Density and viscosity may remarkably vary with temperature, hence it is important to know their variation in order to exactly compute the engine performance and to avoid problem with the pump-

ing system. To this aim preliminary measurements are performed as reported in the following sections.

2.1. Density as a function of temperature

Density is measured using a small volume tank (about 1.5 l), a digital scale having 1.0E-4 kg accuracy, and a thermocouple connected to a digital multimeter to visualise the fuel temperature. Using a couple of RTDs, electronically controlled by a Gefran 1000 unit, fuel is heated up to the desired temperature then poured into the tank. The volume of oil within the tank is kept constant thanks to a an overflow hole made on the tank surface. Therefore a constant volume is scaled in all the tests. Knowing the volume and its weight, the density is readily computed. The scale system is reported in Fig. 2.

Fig. 3 shows density measurements for the three analysed fuels as a function of temperature. Starting from the measured data (symbols in figure) an interpolation function for each fuels is computed (lines in figure). Thanks to this function it is possible to evaluate the fuel density even at temperature out of the measurement field. As shown in figure, DF has the smallest density in the whole temperature range, whilst RO ad WCO show a similar density up to about 65 °C then they diverge, with the RO being more sensitive to the temperature. As can be seen, interpolation curves are almost linear.

Fuel density ratios are reported in Fig. 4. RO/DF ratio is almost constant with the temperature (oscillating around 10%), whilst the WCO/DF ratio increases (from 10% up to 15% at 150 °C) , as well as the WCO/RO density ratio showing the maximum (about 5%) at 150 °C. These variations may affect the specific consumption, and in turn the engine efficiency.

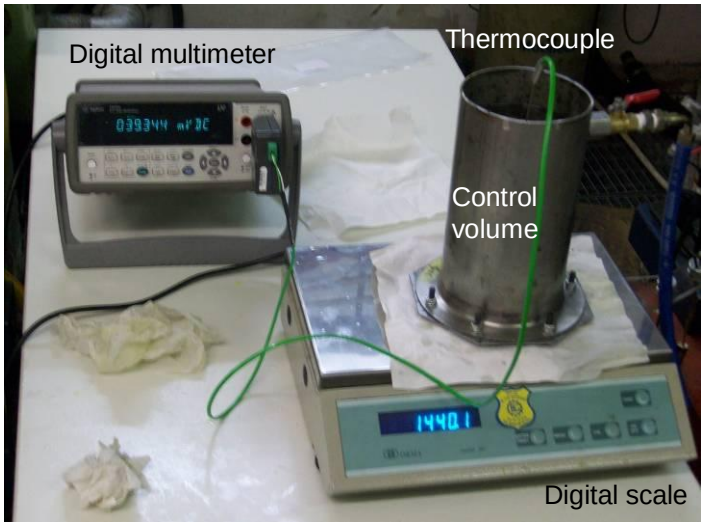

Fig. 2. Scale system for evaluation of density.

2.2. Viscosity as a function of temperature

A Bohlin Visco 88BV viscometer is used to measure dynamic viscosity of the considered fuels at different temperatures. A thermostatic bath, using distilled water as thermostatic liquid, provides a constant and adjustable temperature up to 100 °C. The thermostatic liquid flows through the viscometer and heat up the fuel. A temperature sensor (PT100) measures the actual fuel temperature. The viscometer and thermostatic bath are shown in Fig. 5.

Fig. 6 shows results of the viscosity tests for the three fuels as a function of temperature. As shown, DF viscosity is not really sensitive to temperature. Looking at Fig. 7 it is clear the difference between the three fuels: at 20 °C RO viscosity is about eight times larger than that of DF, and the WCO one is even larger (about fifteen times). As reported above, such high values of viscosity may

provoke problems to the fuel filters, the feeding system, the injectors, as well as combustion problems due to weak spray of fuel.

The viscosity of any fuel can be computed following the Mac-Coull's equation [19]:

$$\log\left[\log\left(\nu + A\right)\right] = B\log T + C$$

where: ν is the kinematic viscosity (in cSt); A = 0.6-0.8 is a model constant; B and C are constants experimentally determined; T is the temperature in K. In the present work the Mac-Coull's equation is used as interpolating function of the experimental data (constants are reported in Table 4). Interpolation curves are reported in Fig. 6 with temperature ranging from 15 to 150 °C. From Fig. 6 and Fig. 7 it can be seen that above 90 °C RO and WCO viscosities are very close to that of DF, being less than the double of it. Thus in the engine tests, temperature of the vegetable oils is maintained at not less than 90 °C.

Table 3. Values of the constants of the Mac-Coull equation for the present study.

Oil	A	B	C
DF	0.8	-3.068	7.478
RO	0.8	-3.759	9.510
WCO	0.8	-3.856	9.808

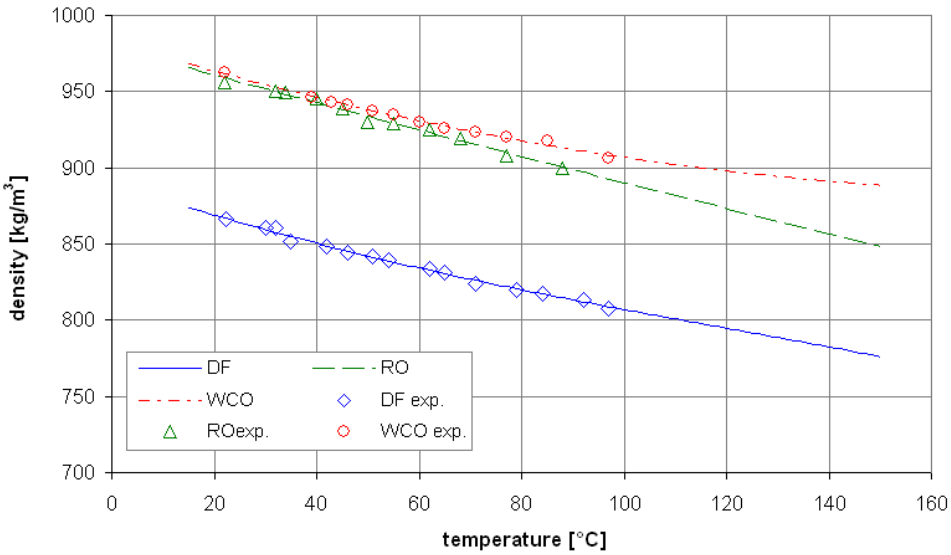

Fig. 3. Experimental end interpolated data for fuel density at different temperatures.

3. Experimental setup

The use of SVO as a fuel in automotive applications is growing and there are several small companies producing kits to switch from DF to SVO. Some of them propose their products also for common-rail engine, but so far very few studies involving real automotive common-rail engines have been performed. Recently Labeckas and Slavinskas [16] reported on the experiments performed on a direct-injection off-road Diesel engine fuelled with RO, but it was a low speed, naturally aspired, not common-rail engine. Fontaras et al. [15] used a Renault Laguna 1.9 dCi passenger car for their tests, but it was fuelled with a RO-DF blend (10% of RO). So the real effect of using SVO on these kind of applications is still not fully known. In the following sections the experimental setup and test results on a Diesel engine fuelled with RO and WCO are presented and discussed.

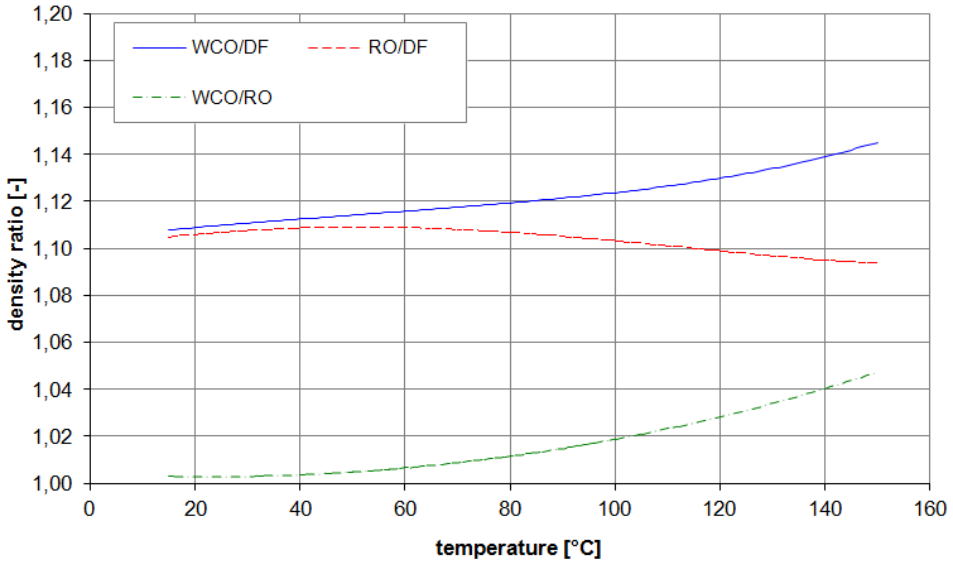

Fig. 4. Density ratios between the analysed fuels.

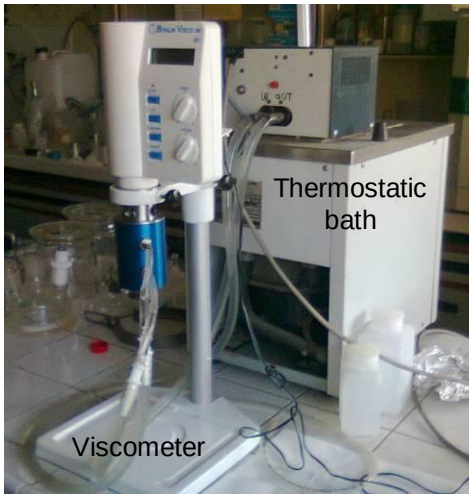

Fig. 5. Viscometer and thermostatic bath.

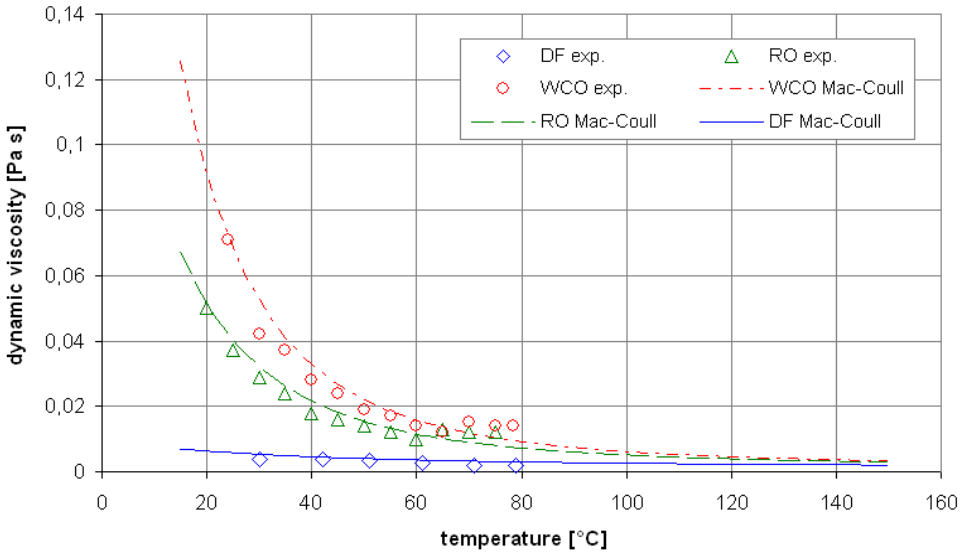

Fig. 6. Experimental end interpolated data for fuel dynamic viscosity at different temperatures.

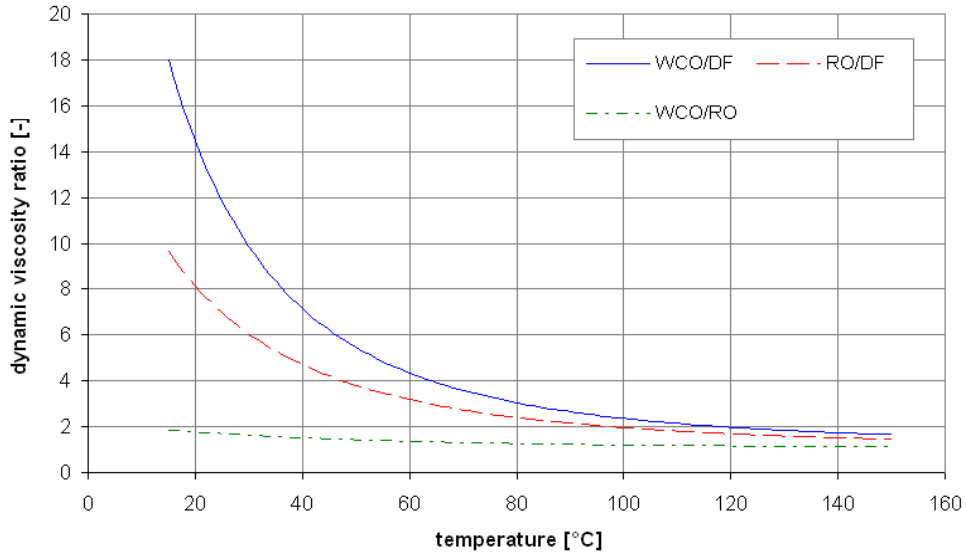

Fig. 7. Viscosity ratios between the analysed fuels.

3.1. Engine and experimental setup

Since the objective of this work is to study the feasibility of using SVO in small (conventional or hybrid) vehicles for public transport, the engine chosen is one commonly installed in mini-buses or van. It is a FIAT 1.9 JTD, a 4 strokes, common-rail, multijet, turbocharged Diesel engine (Fig. 8). Main characteristics of the engine is reported in Table 4. The engine is taken from a real vans and installed to the bench test at the laboratory of the Engineering Faculty of Sapienza Università di Roma. Few changes, only involving the supports, the throttle control, the gear box, the flywheel, the exhaust pipe and the fuel tank, have been done to adapt the engine to the test bench. A new support structure was built according to the bench test geometry; the throttle control was modified in order to maintain a given position; the gear box and the flywheel were removed since they are not needed for the present tests; the exhaust pipe was shortened to fit the bench test room. The fuel tank has been replaced by a specially designed bi-fuel system. In particular a new small tank was built to house the original fuel pump and a thermocouple for the measurement of the actual temperature of pumped fuel. This tank is connected to a switching valve which allows to feed the engine alternatively with DF or vegetable oil. The fuels are stored in two separate tanks, each equipped with a fuel filter at the exit. For DF a paper micro-fiber filter commonly used in cars is installed, whilst in order to avoid problems due to the high viscosity of the vegetable oils, the second tank is equipped with a plastic filter commonly used in trucks and tractors. Temperature within the vegetable oil tank is controlled by an electronic unit Gefran 1000, which in turn activates/deactivates four RTDs immersed in the fuel. Fig. 9 shows the whole bi-fuel system.

The bench test is equipped with a Schenck hydraulic brake, and a Bosch unit (BEA 350) to analyse the exhaust gas opacity and the main pollutant compounds. Moreover, two thermocouples within the fuel pump tank and the engine oil pan, measure the temperature of the fuel fed and engine lubrication oil respectively.

The engine crankshaft is connected to the brake through a cardan joint. The engine rotating speed is computed by the engine sensor and also by the brake system.

A sketch of the whole measurement system is shown in Fig. 10.

3.2. Tests description

Tests aimed at evaluating the torque and power, as well as the specific fuel consumption, at different rpm, the exhaust opacity and the main pollutant compounds (i.e., HC, CO, NO_x).

3.2.1. Torque and power

For all the tests performed with vegetable oil, the start and stop phases (about 10 minute each) are performed fuelling with DF. At the start, as the lube oil reaches about 100 °C, the tank housing the feed pump is almost completely emptied using the fuel draining valve (Fig. 10), and then the feeding system is switched to vegetable oil. After few minute the residual DF in the tank is completely used by the engine, thus the test can start.

The maximum throttle extent is divided into six parts. Torque and power are measured at each of the six possible positions, and at several engine rpm (namely 4200, 3700, 3200, 2700, 2200, 1700, 1500, and 1250 rpm).

Fig. 8. The FIAT 1.9 JTD Multijet engine used for the tests campaign.

Table 4. Main characteristics of the engine used for the tests.

Type	1.9 MultiJet
Charge	Turbocharge (with intercooler)
Fuel	Diesel fuel
Displacement	1910 cc
Power	89.5 kW (120 hp)
Maximum torque	200 Nm

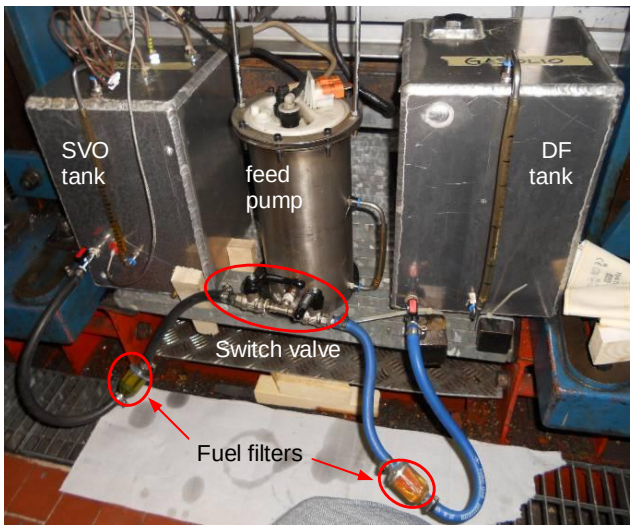

Fig. 9. Bi-fuel system.

3.2.1. Specific fuel consumption

The specific fuel consumption is computed measuring the time the engine takes to use 250 ml of fuel, under a given load. Tests are performed at 1/6 of maximum throttle extent, and at 2000, 2800 and 3600 rpm. Knowing the specific fuel consumption it is possible to evaluate the engine performance, computed as the inverse of the non-dimensional specific fuel consumption.

3.2.1. Exhaust opacity and pollutant compounds

Opacity tests are performed following the Bosh unit (BEA 350) user's manual. After a warm up phase, a series of throttle strokes is recorded by the unit and an average value is computed. At each stroke the throttle should go from minimum to maximum in no more than 4 s; after a rest of 5-45 s, a new stroke can be given. Three throttle strokes should be given at least to have a sufficient accuracy of results; in the present work more than six throttle strokes are given for each test.

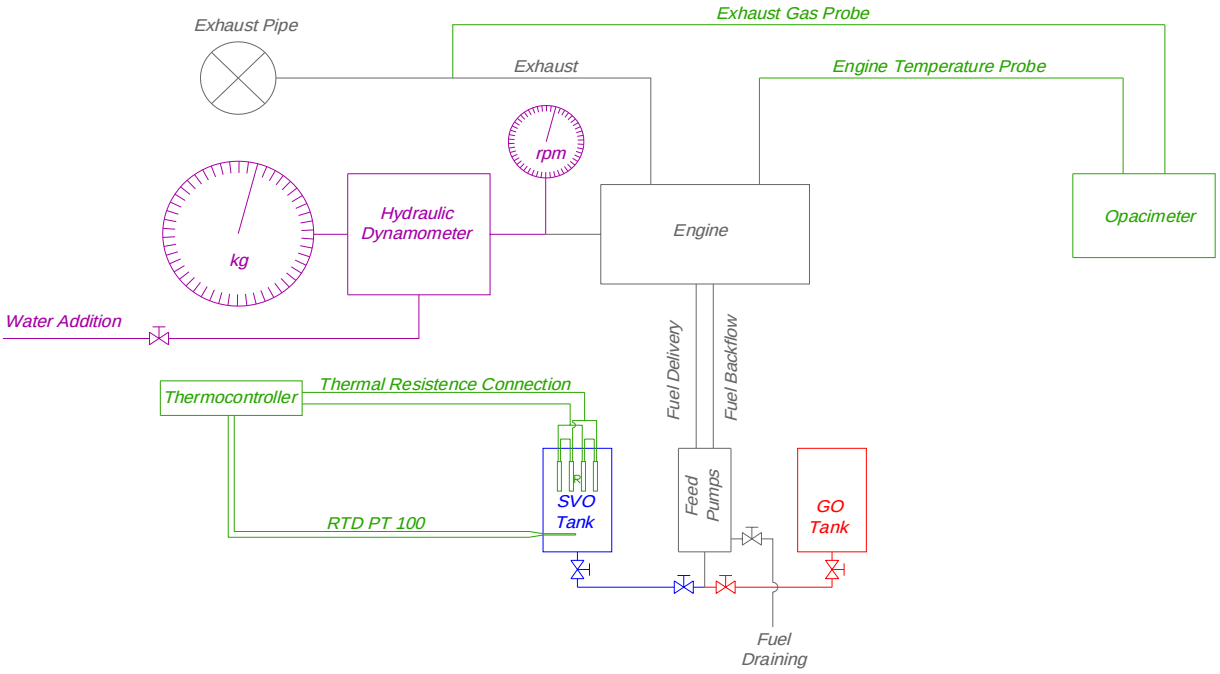

Fig. 10. Sketch of the measurement system.

The same Bosh unit is used to measure the main pollutant compounds. In particular HC, CO, CO_2, and NO_x, are measured. Even in this case tests are performed at 1/6 of maximum throttle extent, and at 2000, 2800 and 3600 rpm; each measure is repeated several times and then an average value is computed.

4. Results

4.1. Power curves

Fig. 11 shows power curves at each of the six throttle positions, and for the three different fuels tested. From the tests it is clear that the power loss due to fuelling with vegetable oils is not always present and constant. At low throttle (i.e., 1/6) the power loss is evident (about 18% with RO and 26% with WCO, at 2200 rpm). This effect is surely, but not only, due to the lower net heating value of SVO. Moreover the effect of viscosity on spray has to be considered. A high viscosity results in a worst spray, thus in a less efficient combustion, especially at low rpm. This may be also correlated to the injection time. As a matter of fact, at low rpm a small amount of fuel is needed, and thus a short injection time. In this situations the transient phases (i.e., the injector opening and closing),

during which spray is not optimal, represent a relevant fraction of the whole injection time, thus combustion efficiency may be smaller than in the reference case.

Power losses decrease as throttle increases, especially in the range around 2200-3200 rpm. Outside this range and with a throttle up to 3/6 power loss fuelling with RO and WCO is still remarkable. Curves with throttle at 4/6 show an inverse trend: there is a small range between 2200 and 3100 rpm where power loss fuelling with WCO is still clear, whilst fuelling with RO gives almost the same power as with the DF. Outside this range DF provides the smallest power, being the difference larger at higher rpm. At 5/6 and 6/6 throttle, power curves are not really consistent: at 5/6 WCO provides the highest power at any rpm, while RO stays below the DF curve up to about 3200 rpm then overcome it. On the contrary, at 6/6 throttle, power provided by vegetable oils returns to be smaller than that of DF, apart from two picks (at about 2000 rpm for RO, and 3300 rpm for WCO). This oscillating trends can be ascribed to the electronic unit control. It can check several parameters, such as the number of fuel jets, the fuel temperature, the exhaust temperature an composition, etc., and on the basis of their values the electronic unit tries to best fit the engine map recorded in it. Working with different fuels may then provoke an unpredictable behaviour of the electronic unit, hence engine operates irregularly.

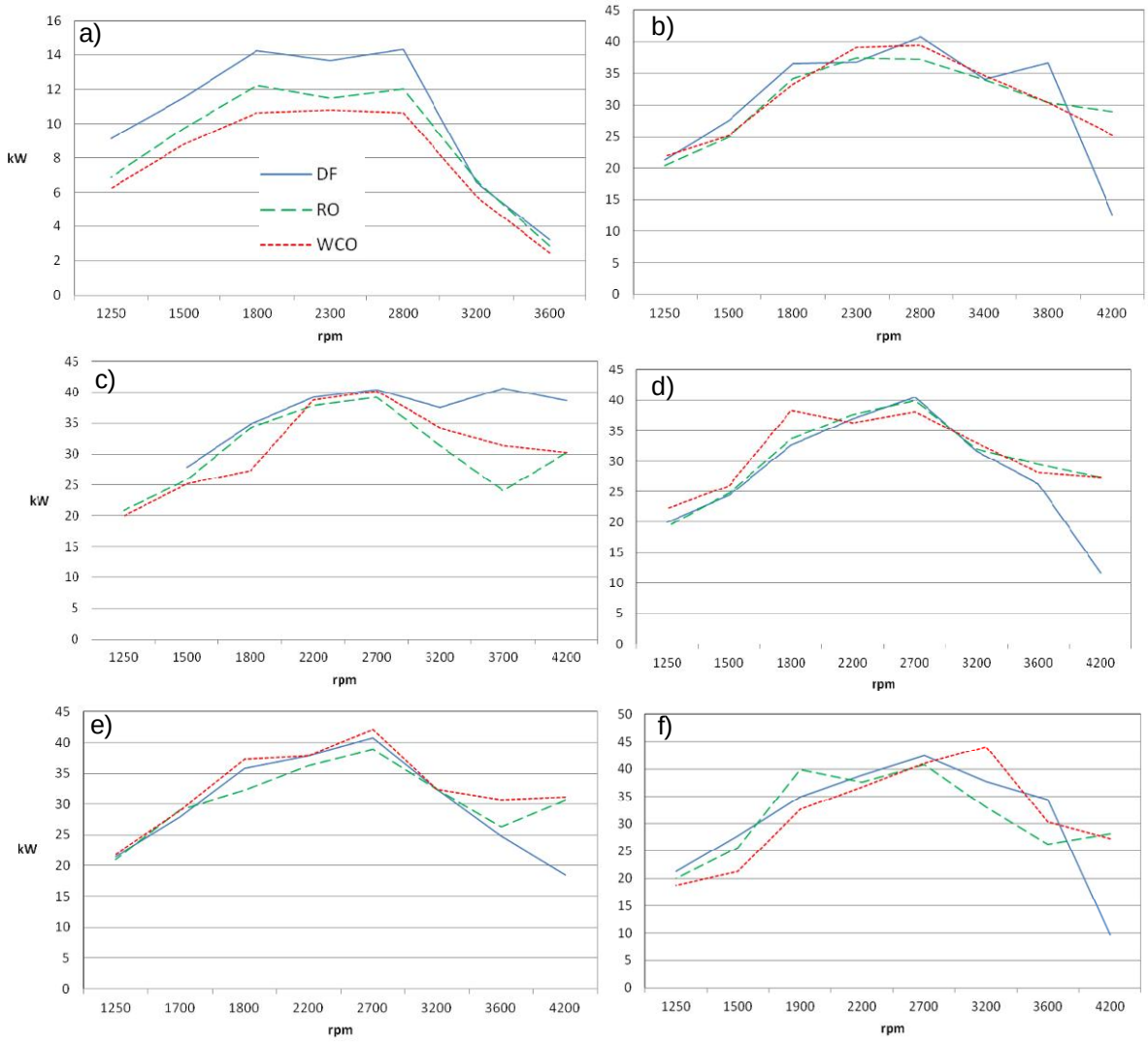

Fig. 11. Power curves at different throttle positions for DF, RO and WCO: a) 1/6 throttle; b) 2/6 throttle; c) 3/6 throttle; d) 4/6 throttle; e) 5/6 throttle; f) full throttle.

4.2. Specific fuel consumption and engine efficiency

Fig. 12 shows the specific fuel consumption for DF, RO and WCO. In the range 2000-2800 rpm DF shows a specific consumption about 30% less than the two vegetable oils, which in that range show almost the same consumption. Above 2800 rpm fuel consumption increases as well as the difference between DF and vegetable oils. Comparing the consumption at 3600 rpm it can be seen that the use of RO results in about 250% larger consumption with reference to DF case, whilst with WCO the difference approaches 300%. This larger specific consumption is the sum of three main effects: the lower net heating value and higher density of vegetable oils as compared to DF, and the electronic unit which, as written before, tries to match the map and the actual behaviour of the engine.

Multiplying the specific fuel consumption by the net heating value of the fuels (Table 2) and inverting the quantity, the engine efficiency is computed. Fig. 13 shows about the engine efficiency evaluated on the basis of the specific fuel consumption tests. RO and WCO show the same efficiency. The difference with respect to the DF fuelling increases according to the rpm, starting from about 25% at 2000 rpm and approaching 50% at 3600 rpm.

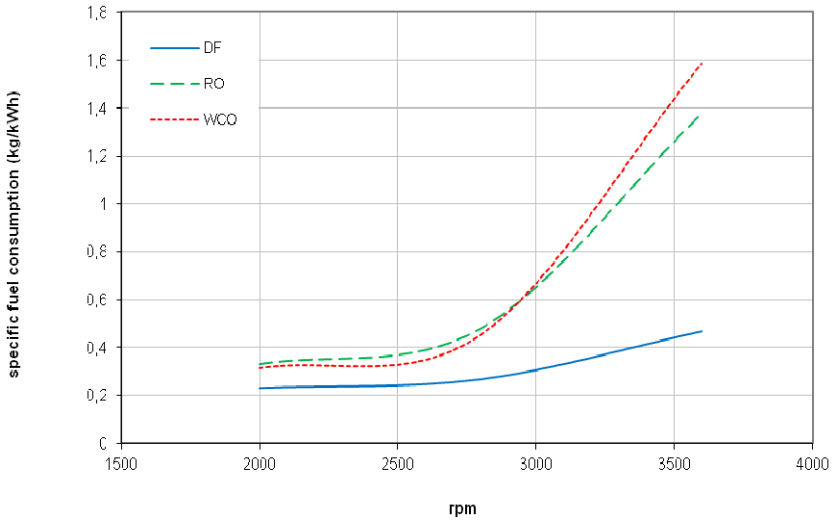

Fig. 12. Specific fuel consumption curves.

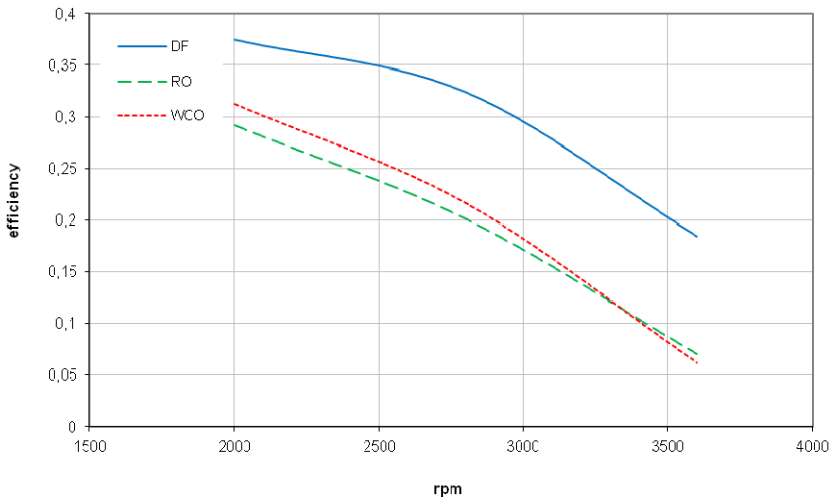

Fig. 13. Engine efficiency.

4.3. Exhaust opacity

The opacity of exhaust from DF is larger than those of WCO and RO (Fig. 14). This may be explained considering the operative condition of the engine. Opacity of exhaust measures somehow particulate (soot) emissions produced during combustion. Soot is mainly formed in case of lack of oxygen and large presence of carbon. Comparing the formula of the DF and RO for instance (DF: $C_{16}H_{34}$, RO: $C_{57}H_{105}O_6$, [18]) it is clear that vegetable oils have a larger content of carbon; nevertheless they contain oxygen contrary to DF which does not contain it at all. Moreover the stoichiometric air ratio is smaller for DF than for vegetable oils. Since the electronic unit regulates the air quantity ratio as if it is working with DF, when fuelling with vegetable oils it results in a higher air/fuel ratio, as confirmed by the lambda ratio measured by the Bosh unit (Fig. 15). This coupled with the larger content of oxygen, probably avoids the conditions for soot production when vegetable oils are used, even if their combustion is less efficient.

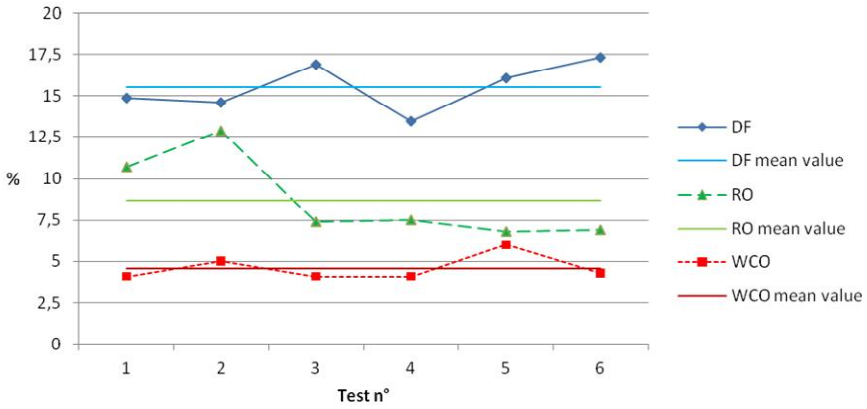

Fig. 14. Exhaust opacity.

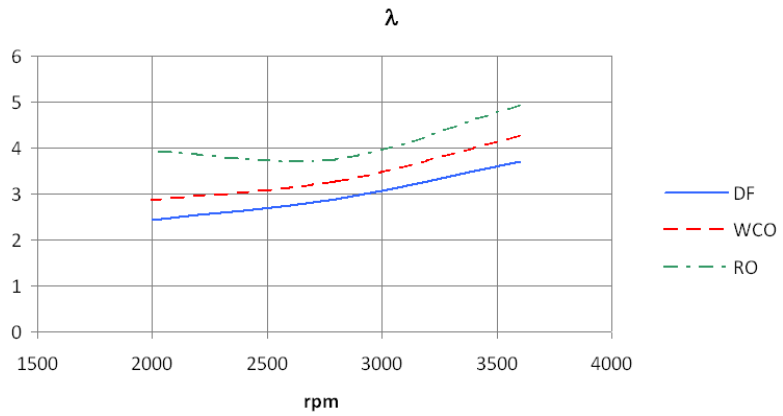

Fig. 15. Lambda ratio.

4.4 Pollutant emissions

Figs. 16-18 show the main pollutant compounds measured in the exhaust stream. CO emission is not shown because in all the tests it is null.

Fig. 16 shows the HC concentration expressed as ppm. The three tested fuels show different behaviours. In particular RO has the highest value of HC emission while WCO has the lowest one, both showing an almost linear behaviour with rpm (but different trend). The high HC emission level reached with RO can be related to its chemical composition. Indeed, vegetable oils have long C-chains which are broken during pre-combustion reactions. In WCO these long chains have been partially broken by the cooking process, thus it burns more easily and faster than RO. NO_x emissions are shown in Fig. 17. RO and WCO produce lower NO_x then DF. As reported in literature (i.e., [13]), this can be ascribed to the low heating value of RO and WCO. This reduces the peak

temperature within the cylinders and thus the thermal-NO_x which give the main contribution to NO_x emission in an internal combustion engine.

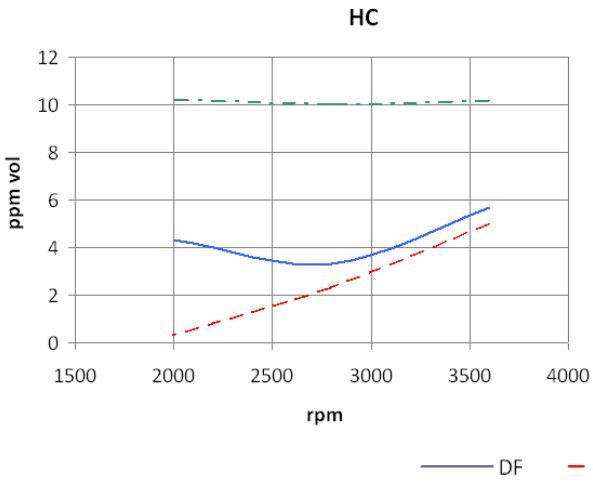

Fig. 16. HC emission.

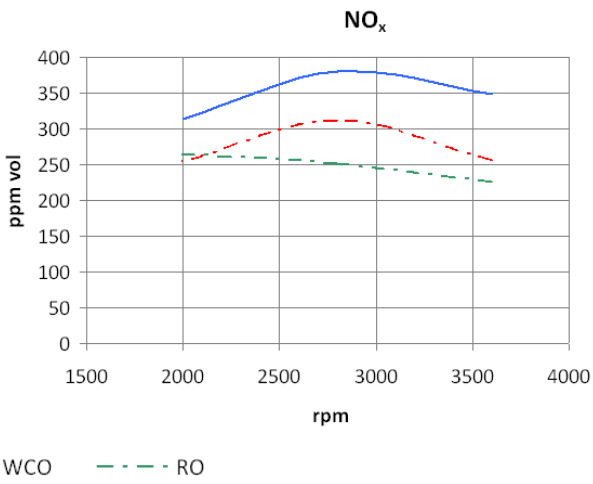

Fig. 17. NO_x emission.

CO_2 emitted by bio-fuels does not add to the greenhouse gas because it represents more or less the same quantity absorbed by plants during their growth. CO_2 emissions for the three fuels used are shown in Fig. 18. In this case CO_2 emission from DF is larger for each load in compare to those of RO and WCO, decreasing as rpm increases. As can be seen form the figure, at low rpm RO emission is larger than that of WCO, inverting the trend as rpm increases.

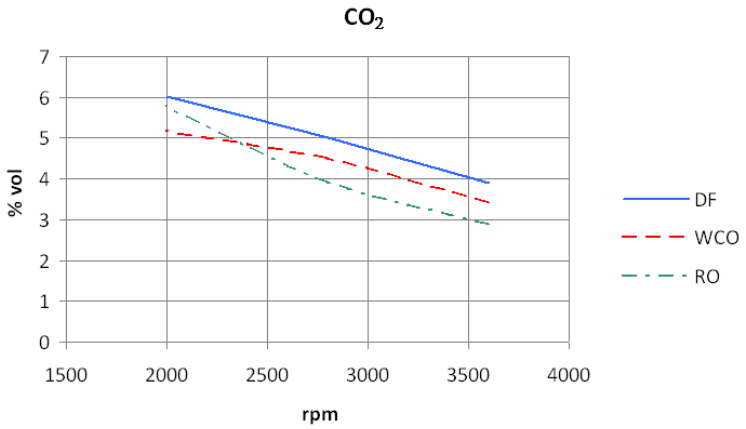

Fig. 18. CO_2 emission.

5. Conclusions

Bench tests on a FIAT 1.9 JTD, a 4 strokes, common-rail, multijet, turbocharged Diesel engine, fuelled with RO, WCO and DF are performed. The engine is in real automotive configuration, equipped with its original electronic unit. Beside bench tests, some preliminary tests are performed to determine the fuel density and viscosity as a function of temperature. Bench tests demonstrate that power loss due to the use of RO and WCO is relevant mainly at low loads (ranging from 18 to 26 %). At higher loads the power loss decreases and in some cases, vegetable oils provide a higher power as compared to DF. This behaviour may be due to several effects, i.e., the different density and viscosity of vegetable oils, the electronic unit, and the injection time which varies according to load.

The use of RO and WCO results also in a different specific fuel consumption. This is clearly due to the lower net calorific value of vegetable oils, which is just partly reduced by their higher density.

This reflects on the engine efficiency which is smaller than that of DF, showing a difference which varies for 25% at low load, up to 50% at higher load.

A positive result is obtained as for the exhaust opacity, since vegetable oils produce smaller values as compared to DF. This could be explained considering the chemical composition of vegetable oils. Soot forms mainly when a rich carbon fuel is used and in lack of oxygen. Since the oxygen is a main component of the vegetable oils, probably this avoid the conditions to let the soot form. Pollutant emissions are comparable to or less than those of DF, apart from HC emission from RO which reaches the highest level. This effect is probably related to the long C-chain compounds forming the RO.

Despite the engine used for this work may operates with vegetable oils, the electronic unit and fuel characteristics play an important role in engine performance. Fuel characteristics (i.e., viscosity) may be controlled by pre-heating the fuel as demonstrated by the preliminary tests performed. Electronic unit has to be tuned to work with vegetable oils, and this would be the next step of this research project.

Acknowledgments

We thank the CURSA (*University Consortium for Socio-economic and Environmental Research*) Italy, especially Eng. S. Binotti and Eng. M. Napoleoni, for their interest and help in this project. We also thank Dr. L. Monteleone for the assistance given during tests; S. Nardecchia for its work and help in assembling and preparing the engine; and I. Campolo for the work done during tests.

References

[1] Directive 2009/28/EC of the European Parliament and of the Council of 23 April 2009 on the promotion of the use of energy from renewable sources and amending and subsequently repealing Directives 2001/77/EC and 2003/30/EC. Available at: eur-lex.europa.eu.

[2] Canacki M., Combustion characteristics of a turbocharged DI compression ignition engine fueled with petroleum diesel fuels and biodiesel. Bioresource Technology 2007;98(6):1167-1175.

[3] Kalligeros S., Zannikos F., Stournas S., Lois E., Anastopoulos G., Teas Ch, Sakellaropoulos F., An investigation of using biodiesel/marine diesel blends on the performance of a stationary diesel engine. Biomass and Bioenergy 2003;24(2):141-149.

[4] Wang G.W., Lyons D.W., Clark N.N., Gautam M., Norton P.M., Emissions from nine heavy trucks fuelled by diesel and biodiesel blend without engine modification. Environmental Science & Technology 2000;34(6):933-939.

[5] Lapuerta M., Armas O., Rodriguèz-Fernàndez J., Effect of biodiesel fuels on diesel engine emissions. Progress in Energy and Combustion and Science 2008;34(2):198:223.

[6] Ramadhas A.S., Muraleedharan C., Jayaraj S., Performance and emission evaluation of a diesel engine fuelled with methyl esters of rubber seed oil. Renewable Energy 2005;30(12):1789-1800.

[7] Vijayaraghavan K., Hemanathan K., Biodiesel production from freshwater algae. Energy & Fuels 2009;23:5448-5453.

[8] Demirbas A., Fatih Demirbas M., Importance of algae oil as a source of biodiesel. Energy Conversion and Management 2011;52:163-170.

[9] Scott S.A., Davey M.P., Dennis J.S., Horst I., Howe C.J., Lea-Smith D., Smith A.G., Biodiesel from algae: challenges and prospects. Current Option in Biotechnology 2010;21:277-286.

[10] Demirbras A., Biodiesel from algae, biofixation of carbon dioxide by microalgae: a solution to pollution problems. Applied Energy 2011;88:3541-3547.

[11] Scarascia Mugnozza G., Binotti S., Napoleoni M., Rispoli F., Sciulli F., Venturini P., Babbini S., Straight vegetable oil as a fuel in an internal combustion engines for power and heat production. 4th Energy Conference – Palestine, 26-27 January, Ramallah, Palestine.

[12] Misra R.D., Murthy M.S., Straight vegetable oil usage in a compression ignition engine – A review. Renewable and Sustainable Energy Reviews 2010;14:3005-3013.

[13] Sidibé S.S., Blin J., Vaitilingom G., Azoumah Y., Use of crude filtered vegetable oil as a fuel in Diesel engines state of the art: literature review. Renewable and Sustainable Energy Reviews 2010;14:2748-2759.

[14] Pugazhvadivu M., Jeyachandran K., Investigation on the performance and exhaust emissions of a Diesel engine using preheated waste frying oil as fuel. Renewable Energy 2005;30:2189-2202.

[15] Fontaras G., Kousoulidou M., Karavalakis G., Bakeas E., Samaras Z., Impact of straight vegetable oil-diesel blends application on vehicle regulated and non-regulated emissions over legislated and real world driving cycles. Biomass and Bioenergy 2011;35:3188-3198.

[16] Labeckas G., Slavinskas S., Performance of direct-injection off-road diesel engine on rapeseed oil. Renewable Energy 2006;31:849-863.

[17] Hossain A.K., Davies P.A., Plant oils as fuels for compression ignition engines: A technical review and life-cycle analysis. Renewable Energy 2010;35:1-13.

[18] Altin R., Cetinkaya S., Husein S.Y., The potential of using vegetable oil fuels as fuel for diesel engine. Energy Conversion and Menagement 2001;42:529-538.

[19] Briant J., Denis J., Parc G., Propièteè rhèologiques des lubrifiants. Paris, France: Editions Technip et Institut Francais du Petrole; 1985.

Reduced Energy Cost through the Furnace Pressure Control in Power Plants

Vojislav Ž. Filipović[a], Novak N. Nedić[b] and Saša Lj. Prodanović[c]

[a] *University of Kragujevac, Faculty of Mechanical Engineering Kraljevo, Kraljevo, Serbia, v.filipovic@open.telekom.rs ,*
[b] *University of Kragujevac, Faculty of Mechanical Engineering Kraljevo, Kraljevo, Serbia, nedic.n@mfkv.kg.ac.rs ,*
[c] *University of East Sarajevo, Faculty of Mechanical Engineering, East Sarajevo, Bosnia and Herzegovina, elsing123@yahoo.com,* ***CA***

Abstract:

Maintaining pressure in the boiler's furnace is one of the key requirements for proper combustion in steam boilers in thermal power plants. This paper proposes a control strategy that eliminates flap in the channel for the output gases. This is achieved by applying the frequency regulator for asynchronous motor speed control. Reference value for the frequency regulator is obtained through the PI controller. Special attention is given to tuning of PI controller. Well-tuned PI controller with the use of frequency regulator provides significant energy savings, because asynchronous motor for ventilator of steam boiler in thermal power plants has a large power. Modification of relay feedback experiment has supported λ-tuning of controller whose two types (faster and robust) were tuned. This modification consists in:

a) Replacement of relay characteristic with saturation curve,

b) Fourth-order process identification with first-order process plus dead time.

The methodology is illustrated by simulations.

Keywords:

Energy saving, Combustion, Frequency regulator, PI controller, λ-tuning.

1. Introduction

Steam boiler, as well as the other components of power plant, performs energy transformation. Therefore, energy dissipation, during combustion process, is present here. This paper considers and suggests possibilities for energy saving by changing in strategy of furnace pressure control as part of boiler. That means replacing of damping control with strategy which is based on frequency regulators (variable-speed drives). Namely, furnace output gases are controlled by ventilators (fans) instead by flap (valve) in output channel. The aim of this paper is to build new control loop for furnace pressure using frequency regulators for asynchronous motor speed control, which drives ventilator.

In this control system, PI (proportional – integral) controller generates reference values for frequency regulator [1]. In order to explore an adequate tuning of PI controller, the method for process identification using relay feedback test was carried out using simulation. Saturation relay will be applied instead ideal relay because of its well known advantages [1]. Unlike previous research, fourth-order process was identified as true first-order process plus relative small dead time [2]. Afterward, method of λ-tuning gives parameters of PI controller, which is adequate for first-order process. Because of the possibility of different conditions during operation of the system, two types of PI controller (faster and robust) will be tuned [1]. Their quality will be explored after simulation of entire control loop for furnace pressure and analysing of process response. Essentially, this survey tends to exploit simulation as a tool for considering improvements of existing control system. Accordingly, researches in this paper are focused on reducing the energy consumption that is neces-

sary for the operation of thermal power plant, which directly means increasing the amount of electricity for delivery to customers [3].

2. Model of system

Good combustion in furnace of steam boiler enables better parameters of steam and better utilization of coal and in that way greater efficiency and lower costs. It is being obtained by maintenance of the furnace pressure on reference value which is required for well combustion. Furnace pressure control is necessary for controlling of quantities of O_2 and CO during combustion process [4]. Mentioned pressure depends on air circulation through the furnace. There are four ventilators, one couple for input of air and the other for output of gases. Because of larger flow on outlet, furnace is under vacuum. It is shared in two parts: upper and lower. In following exposures two approaches of furnace pressure control will be presented.

2.1. Damping model for furnace pressure control

This model is very widespread in thermal power plants. It is based on valve (flap) for furnace output gases. Therefore, asynchronous motors for ventilators always work with full power during exploitation. That causes energy dissipation on valves, as its main drawback, because output flow of gases is being controlled only by flap rotating. Namely, valves perform a damping here. Knowledge of the constituent components of the control system and connection between them and than their behaviour equations have enabled the formation of a general block diagram of the said control system. Of course, as so often in the modelling, to simplify a constructed mathematical model assumptions have been introduced [5]. General block diagram for this strategy is shown in Fig. 1.

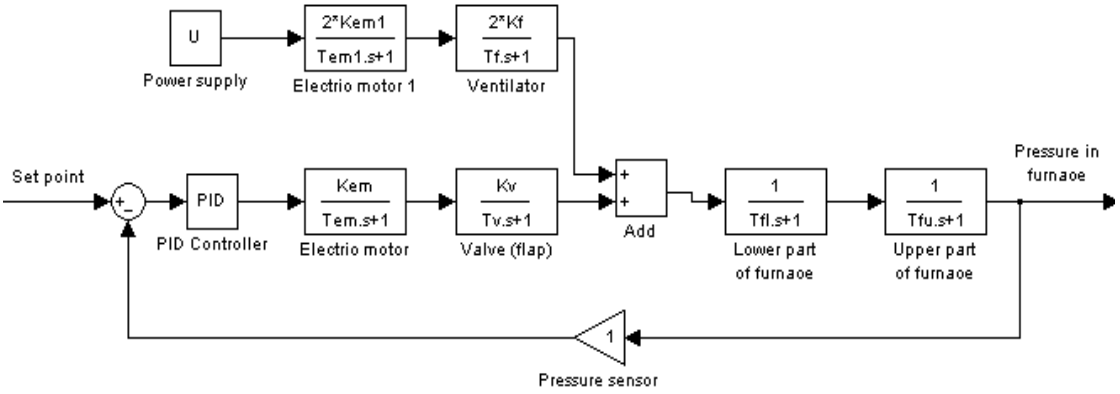

Fig. 1. General block diagram for damping control strategy [5]

2.2. Suggested model with frequency regulators

High power of asynchronous motors for ventilators leads to significant possibilities for energy saving by reducing their consumption. That might be enabled using frequency regulators for speed control of asynchronous motor. For example, in the thermal power plant Gacko (Bosnia and Herzegovina) both electric motors for ventilators in output channel of furnace have the same power P = 3,2 MW [6]. Configuration for application of this energy saving strategy is shown in Fig. 2, where dynamics of frequency regulators and pressure sensor haven't been considered because of small values of their gains and time constants. Hence those transfer functions have been assumed as 1.

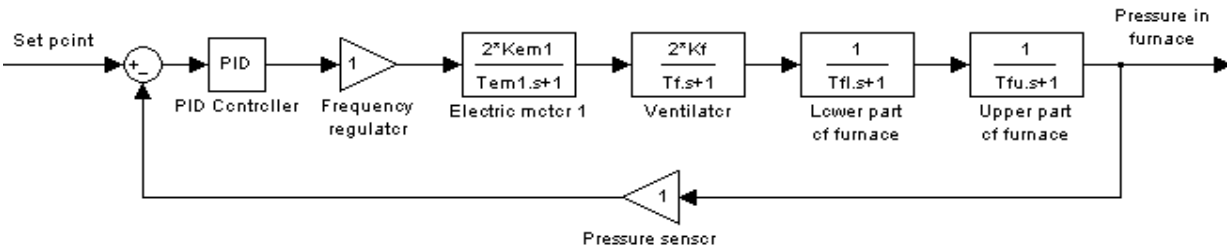

Fig. 2. General block diagram for strategy which is based on frequency regulators

In the both of strategies, gain and time constant of each component (i.e. transfer function) can be determined according physical laws or experimentally by recording their input and output signal.

The meanings of indexes of those components (blocks) have been given in nomenclature.

PI controller forms reference value for frequency regulator which is necessary for appropriate motor speed obtaining. Motor speed is being controlled by changing of power frequency. In order to keep constant torque, supply voltage should be controllable by frequency. In this way, frequency regulators provide power supply, which load (in our case ventilators) requires, and that is the key for energy saving [7]. Namely, torque for fan (ventilator) is:

$$M_f(t) = k_1 \omega^2(t) \quad (1)$$

power that should be obtained from the motor is:

$$P_f(t) = k_2 \omega^3(t) \quad (2)$$

where:

- $\omega(t)$ – angular speed,
- k_1 and k_2 – constants.

Now, reduction average speed of motor by 10% (which is usually feasible) leads to decrease in energy consumption by 27%, because it is calculated: $1 - (0,9)^3 \approx 1 - 0,73 = 0,27$.

This approach involves omission of valves, electric motors for its drive, and other components such as gearboxes and valve position sensors and thus increases savings.

In order to present general values of savings, here are calculated and shown in Table 1 possible savings in mentioned thermal power plant Gacko, i.e. in its electric motors for ventilators. In this calculation was taken into account that that thermal power plant operates up to 7000 hours per year, because of its regular maintenance and unexpected failures.

Table 1. Energy saving of electric motor with reduction of its average speed by 10%

	Daily		Annual	
	Consumption MWh	Energy saving MWh	Consumption MWh	Energy saving MWh
Electric motor for ventilator P=3,2x2=6,4 MW	153,6	41,5	44800	12096

Therefore, annual saving in the amount of 12,096 GWh is very significant and enables greater delivery of electricity to consumers.

In addition to energy saving frequency regulators allows: optimization of the process, "softer" functioning of driving and operating machines because of their smaller number of starts and stops, lower maintenance costs, longer equipment life and improved operating environment (for example, less fan noise). This theoretic approach, through these two control strategy, has been served as guideline for order assessment of process transfer function, which will be explained in next chapter.

3. Process identification

The knowledge transfer function of the process opens the opportunities of its analysis but also tuning of PI controller by various methods. It can be found on two ways: by modelling based on physical rules and using methodologies of identification.

Relay feedback test, which is often used for autotuning of PI controllers, here has been utilized for process identification [2]. In real conditions, this procedure involves introducing relay (as nonlinearity) into system in order to cause steady oscillations in its response and then obtain necessary information of the process. That method will be simulated in Matlab software.

For that purpose transfer function of process will be assumed. According general block diagram of system for furnace pressure control in Fig. 2, (where are four first-order components) this process can be taken as fourth-order process. Following exposure contains simulated and suggested methodology for process identification which is presented on example. Namely, in the absence of a real process model, transfer function is taken arbitrarily, as shown in Figs 4. and 7. In this case it is not disadvantage, but proof that the identification procedure which is carried out can be applied to any process.

Relay feedback test is based on saturation relay because of its advantages over ideal relay in estimating of ultimate gain and ultimate period.

In order to carry out process identification, i.e. obtain transfer function; following parameters should be determined [1]:

- K – steady state gain,
- L – dead time,
- T – time constant.

Then, this transfer function of first-order process is:

$$G(s)=\frac{K}{Ts+1}e^{-Ls} \qquad (3)$$

where: $K=\Delta y/\Delta u$ as it shown in Fig. 3.

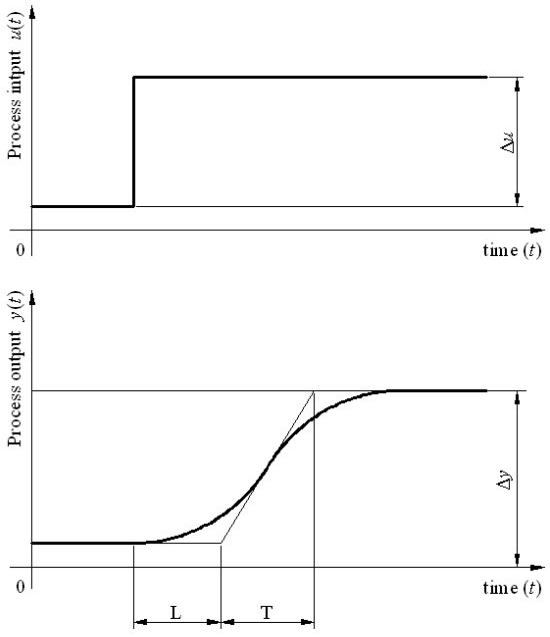

Fig. 3. Process input and output

Order of transfer function is obtained depending on category of system (based on integrated absolute error from frequency response), which is determined by *L/T* ratio and assumed order of the process. According partially demonstration in [2], in this example process will be presented with first-order process plus relative small dead time, as it shown in (3). In the following chapter its validation will be proved.

Now, mentioned parameters are given by [2] and follows:

first iteration to compute time constant, hence

$$T_1 = \frac{tg(\pi - L\omega_u)}{\omega_u} \tag{4}$$

afterwards, the second iteration follows

$$T = \frac{T_u / 2}{\ln\left(2e^{L/T_1} - 1\right)} \tag{5}$$

and

$$K = \frac{a}{h\left(1 - e^{-L/T_1}\right)} \tag{6}$$

As previously stated, general procedure for identification will be presented on arbitrarily chosen process in folowing three steps:

First step

Performing relay feedback test using ideal relay to determine slope of saturation relay (*k*).

Fig. 4. shows configuration for carry out relay feedback test in Matlab software.

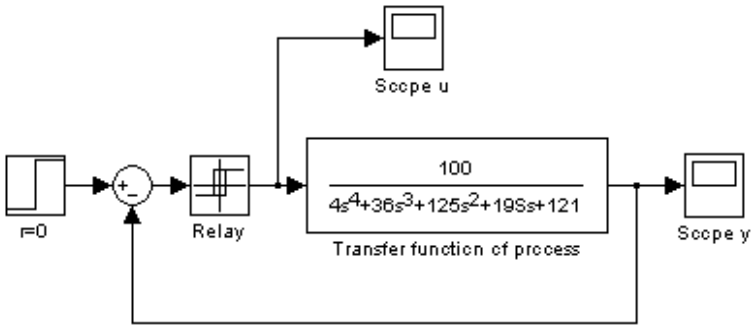

Fig. 4. Configuration for ideal relay feedback test [8]

At the beginning, height of ideal relay characteristic h = 0,03 bar has been set as Fig. 5 shows. Because $h = 0{,}1 \cdot SP$, where *SP* is set point of furnace pressure (in thermal power plant Gacko *SP* = 0,3 bar) [6]. This simulation gives relay output and relay feedback response, which is shown in Fig. 5 and 6, respectively.

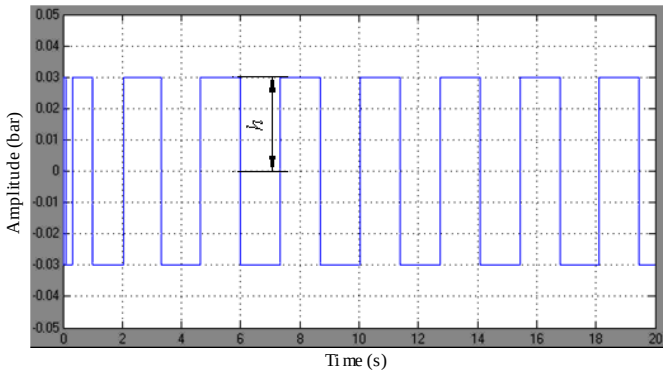

Fig. 5. Ideal relay output

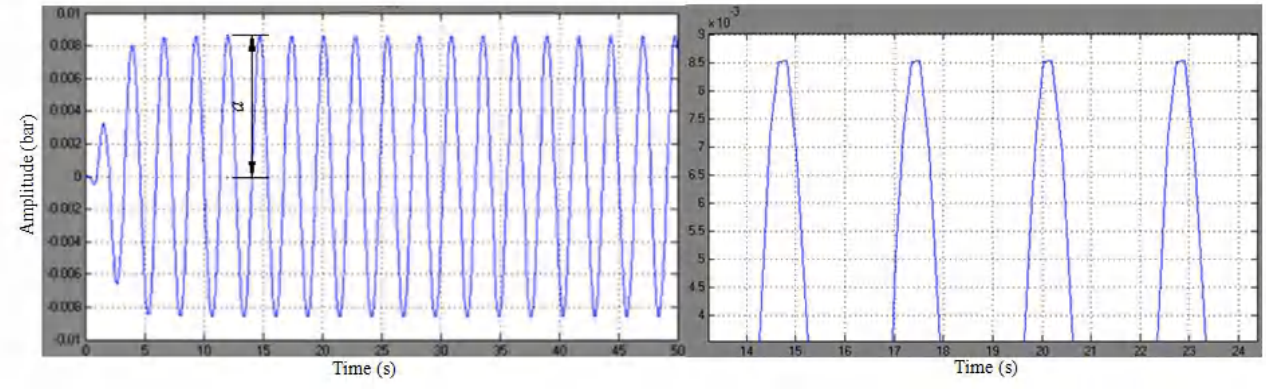

(a) *(b)*

Fig. 6. Ideal relay feedback response: a) whole view, b) zoomed segment

Using diagrams in Fig. 6 amplitude of response has been determined: a = 0,0085 bar.
Now, ultimate gain is [1]:

$$K_u = 4h/\pi a = 4{,}5 \qquad (7)$$

where $K_u = k_{\min}$,

the slope of saturation relay is given by

$$k = 1{,}4 \cdot k_{\min} = 6{,}3 \qquad (8)$$

Second step

Carry out relay feedback test using saturation relay as it is presented in Fig. 7., and result is diagram shown in Fig. 8.

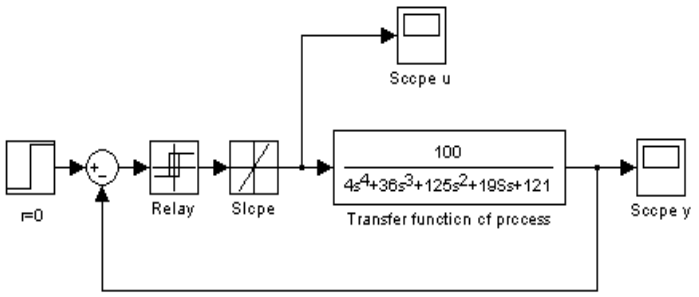

Fig. 7. Configuration for saturation relay feedback test

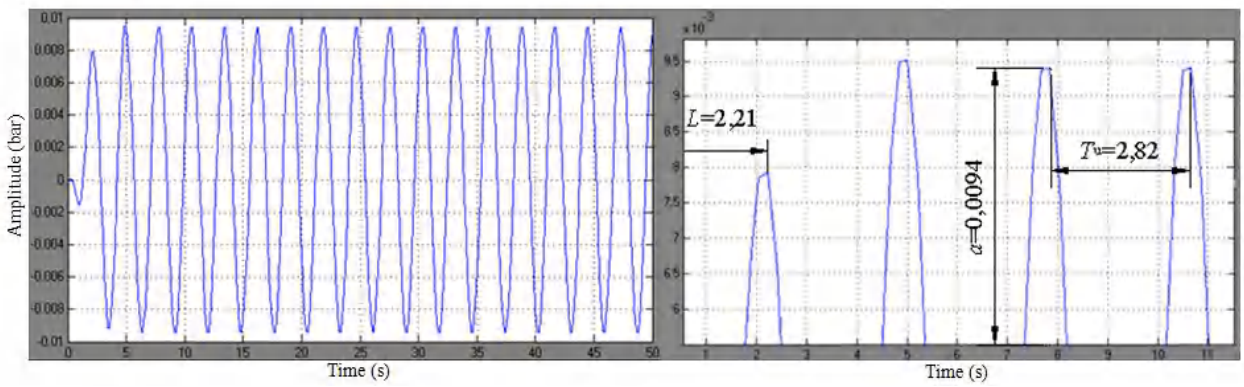

(a) *(b)*

Fig. 8. Saturation relay feedback response: a) whole view, b) zoomed segment

Amplitude of response a = 0,0094 bar, dead time L = 2,21 s and ultimate period T_u = 2,82 s have been determined from diagrams in Fig. 8. Than ultimate frequency can be calculated:

$$\omega_u = 2\pi / T_u = 0{,}71\pi \qquad (9)$$

Third step

Calculate necessary parameters to complete desired transfer function.

Afterward, using (4), (5) and (6) required parameters are obtained: T_1 = 2 s, T = 0,87 s and K = 0,47.

Using (3) gives transfer function of process

$$G(s) = \frac{0{,}47}{0{,}87s + 1} e^{-2{,}21s}$$

It is very important to say that this process is described as true first-order process plus *relative small* dead time, because relay feedback response doesn't develop stationary oscillation in the first cycle (Fig. 8), unlike the previous practice whereby this process should be described by high-order process without dead time, because ratio L/T = 2,54 [2].

4. Tuning of PI controller

Since the process has been identified as first-order process, the best type of controller is PI.

λ-tuning method (Dalin) will be used for obtaining appropriate parameters of controller. This method is special case of method of pole design [1]. It is based on two assumptions:

1. integral time constant T_i is equal to time constant of the process T,
2. it is assumed that system's feedback contains one real pole s = –1 / λ where λ is desired time constant of that system.

Approximation of exponential article in (3) with two article of Taylor progression gives

$$G(s) = \frac{K(1 - Ls)}{Ts + 1} \qquad (10)$$

Using first assumption transfer function of PI controller is

$$G_c(s) = K_c\left(1 + \frac{1}{Ts}\right) \qquad (11)$$

Than characteristic equation of system derived with (10) and (11) is

$$1 + G(s)G_c(s) = 0 \qquad (12)$$

Based on mentioned assumptions and (10), (11) and (12) parameters of PI controller are obtained as follows

$$K_c = \frac{1}{K}\frac{T}{L + \lambda} \qquad (13)$$

$$T_\text{i} = T \qquad (14)$$

According this method, heuristic rules are being used for determining of λ:

- $\lambda = T$ for faster controller,
- $\lambda = 3T$ for robust controller.

Afterward, parameters of PI controller for considered process are calculated:

- K_c = 0,6 and T_i = 0,69 for faster controller,

- K_c = 0,38 and T_i = 0,44 for robust controller.

How tuned controllers operate within the system was tested by simulating the entire control system. Configuration in Fig. 9 performs mentioned simulation and required responses are given in Fig. 10.

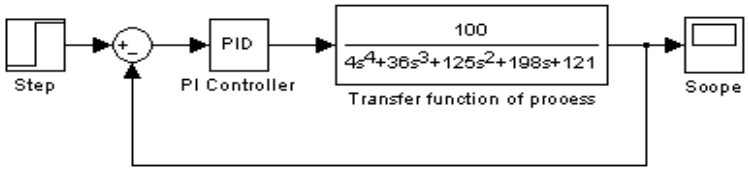

Fig. 9. Configuration for simulation of entire control system

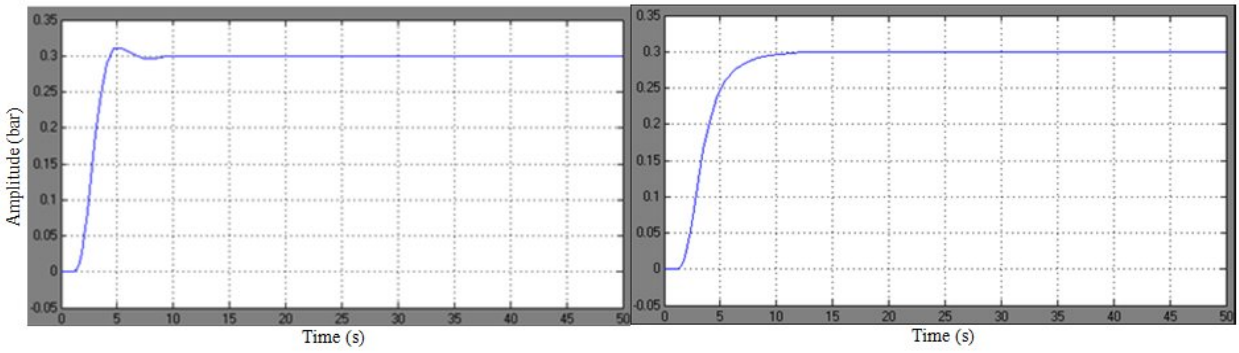

(a) *(b)*

Fig. 10. Response of control system: a) with faster PI controller, b) with robust PI controller

These two responses directly reflect the names of controllers which causes them. Namely, response in Fig. 10.*a)* has shorter rise time and dead time as well as less than 10% overshoot, while other response is without overshoot and has monotonous rise what are the characteristics of its robustness. Responses have appropriate shape, i.e. both kind of PI controller are good, but their application depends on the operating conditions in which the system supposed to work.

Finally, presented responses justify applied identification process (i.e. assumed first-order process) and λ-tuning method for PI controller.

5. Conclusions

Control strategy which is based on frequency regulators ensures energy saving in two ways. First, through the total speed control of asynchronous motor and second, because enabling appropriate functioning conditions. That has been proved on furnace pressure control in thermal power plant, where was suggested replacing damping control method for output gases flow with strategy which involves variable speed drives for ventilator's speed control.

The main contribution of this paper is proposing of procedure for process identification and λ-tuning of PI controller. In this research emphasis was placed on the use of exact method of tuning that is based on the estimated characteristics of the process. That procedure enables such control loops which can provides good behaviour of process and in that way make possible energy saving strategy. One of possibilities how to use simulations as tool for overcoming lack of laboratory equipment and real systems were proposed.

Nomenclature

a amplitude,

G(s) transfer function,

h height of ideal relay characteristic,
K steady state gain,
k slope of saturation relay,
L dead time, s
P power, W
s complex variable,
T time constant, h
t time, s
U voltage, V

Greek symbols

Δ change of signal,
λ desired time constant, s
ω angular speed, s^{-1}

Subscripts and superscripts

c controller,
em electric motor,
f fan (ventilator),
fl lower part of furnace,
fu upper part of furnace,
i integral,
u input and ultimate,
v valve,
y output.

References

[1] Filipović VŽ, Nedić NN. PID Controllers. Kraljevo: University of Kragujevac, Faculty of Mechanical Engineering; 2008. (in Serbian).

[2] Yu, CC. Autotuning of PID controllers. Taipei, Taiwan: National Taiwan University, Springer; 2006.

[3] Prodanović S. Analysis and improvement of control system of condensate level in condenser of turbine in thermal power plant Gacko (master thesis). Kraljevo, Serbia: University of Kragujevac; 2009. (in Serbian).

[4] Buljubašić I. Modelling of processes in steam boilers as a part of performance monitoring. TTEM Journal 2006;1(2):34 – 39.

[5] Komatsu T. Instrumentation for boiler plant. Fuji Denki Review;9(6):164 – 168.

[6] Technical documentation of the control system of condensate level in condenser of turbine and of the entire thermal power plant Gacko.

[7] Filipović V, Nedić N, Pršić D, Dubonjić LJ. Energy saving with variable speed drives. Proceedings of the VI International Triennial Conference, Heavy Machinery – HM 2008: Kraljevo, Mataruška banja, pp. A1 – A6.

[8] Prodanović SLJ, Nedić NN, Filipović VŽ. Improved Auto-tuning PID Controller of Level in Condenser of Turbine in Thermal Power Plant Using Saturation-relay Feedback. Proceedings of the X Triennial International SAUM Conference on Systems, Automatic Control and Measurement, Niš, Serbia, 2010.

Short-term scheduling model for a wind-hydro-thermal electricity system

Sergio Pereira [a], Paula Ferreira [a] A. Ismael F. Vaz [a]
[a]Department of Production and Systems, University of Minho, Guimarães, Portugal

Abstract:

This study addresses the problem of the self-scheduling of an electricity system mainly based on hydro, fossil fuel thermal and wind power plants. A binary mixed integer non-linear optimization model is described and applied to short-term electricity planning of a system close to the expected Portuguese one on the year 2020. The model is written in a GAMS code and a global optimization solver is used to obtain the numerical results. The objective function encompasses the minimization of total system production costs through a centralized unit commitment. Different constraints, essentially related to operating parameters that characterize the power plants available for dispatch, are included in the model. The obtained results show the importance of the renewable energy sources seasonality on the thermal power plants operating conditions and on the total cost of the system.

Keywords:
Electricity planning, Electricity system analysis, Unit Commitment problem.

1. Introduction

The emergence of new technologies such as wind power, characterized by production of variable output, not subject to dispatch and benefiting from feed–in tariffs, creates new challenges to the electricity power management. On the contrary, the large thermal and hydropower groups need to compete in the market for dispatch. Also, adding more variability and unpredictability to a power system, due to wind power curve characteristics, will frequently originate that thermal units will experience increased number of startups and shutdowns, and periods of operation at low load levels (see [1]).

It is well known that the principal aim of power planning, whether it is applied to long term planning horizon or to short term horizon, is to minimize the operational costs of the system while that a certain forecasted demand is fulfilled. In order to accomplish this aim, optimization models for both short-term electrical power generation scheduling and strategic power planning are seen as useful and powerful tools to be used by decision makers.

Short-term electricity power generation scheduling, also known as unit commitment (UC) problem, is essential for the planning and operation of power systems. The basic goal of the UC problem is to properly schedule the on/off states of all the units in the system. Furthermore, the UC problem should consider the predicted load demand and spinning reserve requirement, minimizing the total cost of production [2].

Uyar, A. et al. in [3] described the short-term electrical power generation scheduling as an optimization problem, in which optimal startup and shutdown schedules, for a group of power generators, need to be determined over a given time horizon and considering operational constraints. The model objective remains as the minimization of the power generation costs meeting the hourly forecasted power demands. The short-term electricity power generation scheduling is well documented in the literature, with special concerns about the wind power penetration on the traditional thermal units systems, and on the market prices (see, for example, [4] and [1]).

Despite the economic interests considered in these models, environmental concerns are also increasingly relevant. The Catalão, J. et al. study [5] focused on a multi-objective formulation, where two objective functions were considered, namely the total fuel cost and total CO2 emissions.

Chao–Lung and Chiang [6] also presented a multi-objective formulation for the economic emission dispatch of a hydrothermal power systems. Again, two objective functions were considered, one for the total cost and the other for the total emissions. The results included the optimal total cost and the optimal gas emission solutions. Compromise solutions were presented in a form of a Pareto-optimal front, representing the trade-off between the total cost and environmental objectives.

The major goal of the present work is to propose an optimization model for the short-term electricity power generation scheduling problem. The objective function encompasses the minimization of total system production and maintenance costs through a centralized unit commitment problem. The model considers different constraints essentially related to operating parameters that characterize the power plants available for dispatch. A mixed hydro-thermal-wind power system, with characteristics close to the Portuguese case, that presents by itself a set of typical technical and geographical characteristics, is addressed.

This paper is organized as follows. Section 2. describes the proposed optimization model. In Section 3. and Section 4. a realistic case study, close to the Portuguese system, is modeled and the results are analyzed. Conclusions are stated in Section 5..

2. Model formulation

2.1. Objective function

The proposed model considers only one objective function, which aggregates all the assumed costs of the electricity system. These costs includes the variable operation and management (O&M) costs, fuel and pumping costs, *CO2* emissions costs, and startup and shutdown costs for each group. The objective function is measured in € and is defined by:

$$\sum_{t\in T}\sum_{j\in J}\left[C_{t,j}+Su_{t,j}+Sd_{t,j}\right]+\sum_{t\in T}\left[CVOM_{h_d}\times phd_t\right]+\sum_{t\in T}\left[CVOM_{h_r}\times phr_t\right]+$$
$$\sum_{t\in T}\left[(Cp_p\times ppump_t)+(CVOM_p\times ppump_t)\right]+\sum_{t\in T}\left[(pwind_t\times CVOM_e)\right] \quad (1)$$

where T is a set of the time period (in hours) considered in the model, J is a set of all groups of thermal power plants included in the system, $C_{t,j}$ is the total cost of thermal power groups (€), $S\,u_{t,j}$ is the startup cost of thermal power groups (€), $CVOM_{hd}$ is the O&M cost of hydropower plants with reservoir (€/MWh), phd_t is the power output of hydro power plant with reservoir in hour t (MWh), $CVOM_{hr}$ is the O&M cost of run–of–river power plants (€/MWh), phr_t is the power output of run–of–river power plant in hour t (MWh), Cp_p is the cost of pumping (€/MWh), $ppump_t$ is the power output of pumping power plant in hour t (MWh), $CVOM_p$ is the O&M cost of pumping power plant (€/MWh), $pwind_t$ is the power output of wind power plant in hour t (MWh) and $CVOM_e$ is the O&M cost of wind power plants (€/MWh). Additionally, the costs of thermal power groups, i.e., the fuel cost of each group, the O&M cost, the emissions allowance cost, and the startup and shutdown costs, are defined as follows.

$$C_{t,j}=\left[F_j+CVOM_j+(CO_{2_j}\times EC)\right]pt_j \quad (2)$$

$$Sd_{t,j}=CSd_j\times(v_{t-1,j}\times(1-v_{t,j})) \quad (3)$$

$$Su_{t,j} = ColdS_j\left(v_{t,j} \times (1 - v_{t-1,j})\right) \times \prod_{n=1 \to N_j} 1 - v_{t-n,j} \tag{4}$$

$$Su_{t,j} = HotS_j\left(v_{t,j} \times (1 - v_{t-1,j})\right) \times \left(1 - \prod_{n=1 \to N_j} 1 - v_{t-n,j}\right) \tag{5}$$

where F_j is the fuel cost of group j (€/MWh), $CVOM_j$ is the O&M cost of thermal power group j (€/MWh), EC is the $CO2$ emission allowance cost (€/ton), $CO2_j$ is the $CO2$ emission factor of type j power group (ton/MWh), CSd_j is the shutdown cost of thermal power group j, $v_{t,j}$ is a binary variable w.r.t. the thermal power group j on hour t, $ColdS_j$ is the cold startup cost of power group j (€), N_j is the shutdown time necessary for a cold startup (in hours) and $HotS_j$ is the hot startup cost of power group j (€).

2.2. Constraints

The set of adopted constraints for the unit commitment problem includes constraints derived from physical processes, demand requirements, capacity limitations and legal/policy impositions. These constraints, presented as mathematical equations, define values of the decision variables that are feasible [7].

2.2.1. Demand constraint

To ensure the reliability of the system, the total power plants electricity production should meet the total system demand in each hour of the planning period. Thus, the total demand power has be equal to the total power output from power plants plus the total power output from the special regime producers, minus pumping consumption. The mathematical formulation of this constraint is

$$\sum_{j \in J} pt_{t,j} + phd_{t,h_d} + phr_{t,h_r} + pwind_{t,e} - ppump_{p,j} + Psrp_t = D_t \quad \forall t \in T \tag{6}$$

where D_t is the demand in hour t of the planning period (MWh) and $Psrp_t$ is the special regime producers power output in hour t of the planning period (MWh), excluding the large hydropower and wind power plants, and including co-generation in each t hour of respective planning period (MWh).

2.2.2. Thermal power capacity and ramp constraints

Power capacity constraints ensures that all power groups included in the model will not produce more than the respective group capacity, for each hour of the planning period. A minimum power output of 35% of both coal and gas thermal power groups is considered, due to technical characteristics. Furthermore, startup and shutdown ramp constraints are also included, to ensure a more reliable system representation. The constraints of the mathematical formulations are presented in the following equations.

$$\overline{p_{t,j}} \leq \overline{P_j}\left[v_{t,j} - (v_{t,j} \times (1 - v_{t+1,j}))\right] + (v_{t,j} \times (1 - v_{t+1,j})) \times Sdr_j \tag{7}$$

$$\overline{p_{t,j}} \leq pt_{t-1,j} + Ru_j \times v_{t-1,j} + Sur_j \times (v_{t,j} \times (1 - v_{t-1,j})) \tag{8}$$

$$\overline{p_{t,j}} \geq 0 \tag{9}$$

$$\overline{p_{t,j}} \geq pt_{t,j} \tag{10}$$

$$\underline{P_j} \times v_{t,j} \leq pt_{t,j} \tag{11}$$

$$pt_{t-1,j} - pt_{t,j} \leq Rd_j \times v_{t,j} + Sdr_j \times (v_{t-1,j} \times (1 - v_{t,j})) \tag{12}$$

$$pt_{t,j} \geq 0 \tag{13}$$

where $\overline{p_{j,t}}$ is the group j maximum power generation in time t (MWh), P_j is the thermal group j maximum capacity (MW), Sdr_j is the group j shutdown ramp limit (MWh), Ru_j is the group j ramp upper limit (MWh), $Surj$ is the group j startup ramp limit (MWh), P_j is the thermal power group j minimum capacity (MW) and Rd_j is the group j ramp lower limit (MWh) [8].

2.2.3. Thermal power groups minimum up and down time

Minimum up and down time constraints enforce the feasibility of the system in terms of proper technical operation of units. Once a shutdown is verified the group must remain off for a certain period of time (minimum down time). The same occurs when a startup happens, the group must remain working for a certain time period (minimum up time). Equations (14) and (15) ensure the minimum up and down time constraints for thermal power plants, respectively.

$$\sum_{i \in i \leq UT_j} v_{t+i,j} \geq UT_j \times (v_{t,j} \times (1 - v_{t-1,j})) \tag{14}$$

$$\sum_{i \in i \leq DT_j} 1 - v_{t+i,j} \geq DT_j \times (1 - v_{t,j}) \times (v_{t-1,j}) \tag{15}$$

where UT_j is the thermal group j minimum up time and DT_j is the thermal group j minimum down time.

2.2.4. Large hydropower constraints

For the large hydropower plants with reservoir, constraints regarding the expected storage and production capacity are considered in the model. The following equations allow to relate the reservoir level on hour t to the previous (hour t - 1) reservoir level, inflows and hydropower output. Two sets of constraints are considered, since an initial reserve is considered.

$$reserve_t = Inflows_t + \left(\eta_p \times ppump_t\right) - phd_t + Ir \qquad t = 0 \tag{16}$$

$$reserve_t = Inflows_t + \left(\eta_p \times ppump_t\right) - phd_t + reserve_{t-1} \qquad \forall t \in T \setminus \{0\} \tag{17}$$

where $reserve_t$ is the reservoir level on hour t of the planning period, $In\ flows_t$ is the hydro inflow on hour t of the planning period, Ir is the initial reserve and η_p is the efficiency of the pumping units.

Additional upper and lower bounds must be used to define maximum and minimum allowed reservoir levels, respectively. An upper bound on the power output of the group is also considered. These bounds are described in the following equations.

$$reserve_t \leq reserve_{max} \tag{18}$$

$$reserve_t \geq reserve_{min} \tag{19}$$

$$phd_{h_d,t} \leq \overline{P_{h_d}} \tag{20}$$

where $reserve_{max}$ and $reserve_{min}$ are the maximum and minimum reservoir level allowed, respectively, and $\overline{P_{hd}}$ is the maximum power capacity of hydropower units with reservoir.

Run–of–river power plants are characterized by a reduced water storage capacity. As such, the next set of constraints make the run–of–river power plants production equal to the installed power, taking into consideration the availability of these units.

$$phr_t = \phi_{h_r,t} \times \overline{P_{h_r}} \tag{21}$$

where $\Phi h_{r,t}$ is the run–of–river units availability in hour t, which is strongly dependent on the seasonality.

2.2.5. Pumping constraints

Two reservoirs must be taken into account for a proper mathematical formulation of hydropower plants with pumping capacity. The upper level reservoir storages water from inflows and from the pumping itself, while the lower level reservoir storages water already used for electricity generation. Water may be pumped from the lower level storage to the upper level storage, in order to take advantage of the over electricity production of the system. Again, two set of constraints are described in order to consider the initial pumping reserve.

$$Preserve_t = phd_t - \left(\eta_p \times ppump_t\right) + PIr \qquad t = 0 \tag{22}$$

$$Preserve_t = phd_t - \left(\eta_p \times ppump_t\right) + Preserve_{t-1} \qquad \forall t \in T \setminus \{0\} \tag{23}$$

where $Preserve_t$ is the pumping storage hydropower plant reserve in hour t and PIr is the lower level reservoir initial reserve.

Upper and lower bound constraints are considered on the pumping reservoirs and on the power production of the pumping units. These bounds are represented in the following constraints.

$$Preserve_t \leq Preserve_{max} \tag{24}$$

$$Preserve_t \geq Preserve_{min} \tag{25}$$

$$ppump_{t,p} \leq \overline{P_p} \tag{26}$$

where $Preserve_{max}$ and $Preserve_{min}$ are the maximum and minimum capacity of lower level reservoir, respectively, and $\overline{Pp}$ is the pumping groups maximum capacity.

2.2.6. Wind power constraints

It is assumed that wind power is not subject to dispatch and has priority access to the grid. As such, the proposed constraint ensures that the wind power generation capacity is equal to the total installed power, taking into account the wind availability. Wind constraint is described by

$$pwind_{t,e} = \phi_{t,e} \times \overline{P_e} \tag{27}$$

where $\overline{Pe}$ is the wind power units maximum capacity (MW) and $\Phi_{t,e}$ is the wind availability in hour t.

2.2.7. Security constraints

Power units outages, although not being frequent, must be considered and prevented. While there are several reasons for power units outage, the power units breakdown and stoppages for maintenance are the main ones. Furthermore, the system should take into consideration a possible suddenly increase on power consumption. Equation (28) represent this security constraint.

$$\sum_{j \in J} \left(\overline{P_j} - pt_{t,j}\right) + \sum_{h_d \in H_d} \left(\overline{P_{h_d}} - phd_{t,h_d}\right) + \sum_{h_r \in H_r} \left(\overline{P_{h_r}} - phr_{t,h_r}\right) \geq D_t \times \alpha \tag{28}$$

where α is the parameter that will ensure the reliability of the system, usually taken as 10%.

3. Case Study

The previous section presents a typical unit commitment problem, designed with the final aim of being used in the analysis of a mixed hydro-wind-thermal power system, with characteristics close to the Portuguese one.

The Portuguese electricity system comprises essentially large thermal and hydro power plants. Recently, the investment in new technologies, mainly wind power, is increasing due to environmental and social concerns along with the need to reduce the external energy dependence. According to [9] in 2011, Portugal occupied the tenth world position in wind power capacity with 3960 MW installed, from which, 260 MW were installed during the first half of 2011. In the end of 2010, and according to [10], wind power represented 21% of the Portuguese national system installed power.

The Portuguese system comprise two different regimes. The ordinary regime production (ORP) encompasses thermal and large hydropower plants and the special regime production (SRP) encompasses renewable energy sources and cogeneration (except large hydropower plants). Wind power still represents the major renewable energy source of the SRP with a share of 50%. In what concerns the ORP, in 2011, a reduction of 27% of the total hydropower production was observed totaling 10808 GWh, with an hydraulic productivity index (HPI)[1] of 0.92, in compare with a production of 14869 GWh in 2010 with an HPI of 1.31. On the contrary, thermal power groups production experience an increase of 12%, totaling in 2011 19435 GWh against the 17299 GWH in 2010. This variability is quite informative of the changes on production that variable output units can bring to the system. Weather conditions and the seasonality will influence the power output in each year, and consequently, will have an impact on the electricity system operation, mainly on the thermal power units. Figure 1 and 2 show the variability of the hydro and wind production for January and August[2]. As may be observed, the production for both hydro and wind power plants is

[1] Ratio between the hydropower production during a time period and the hydropower production that would be expected for the same period under average hydro conditions.

[2] Availability used as an approximation of the variability of the resource measured as power output divided by the

much higher during the winter week (in January) than during the summer week (in August), due to the availability of the underlying resources. In fact in 2011, during the winter, RES production represented approximately 66% of the total electricity demand, but during summer the share was only 24%. This demonstrates the need to analyze the short term scheduling of electricity systems with a large share of variable output RES.

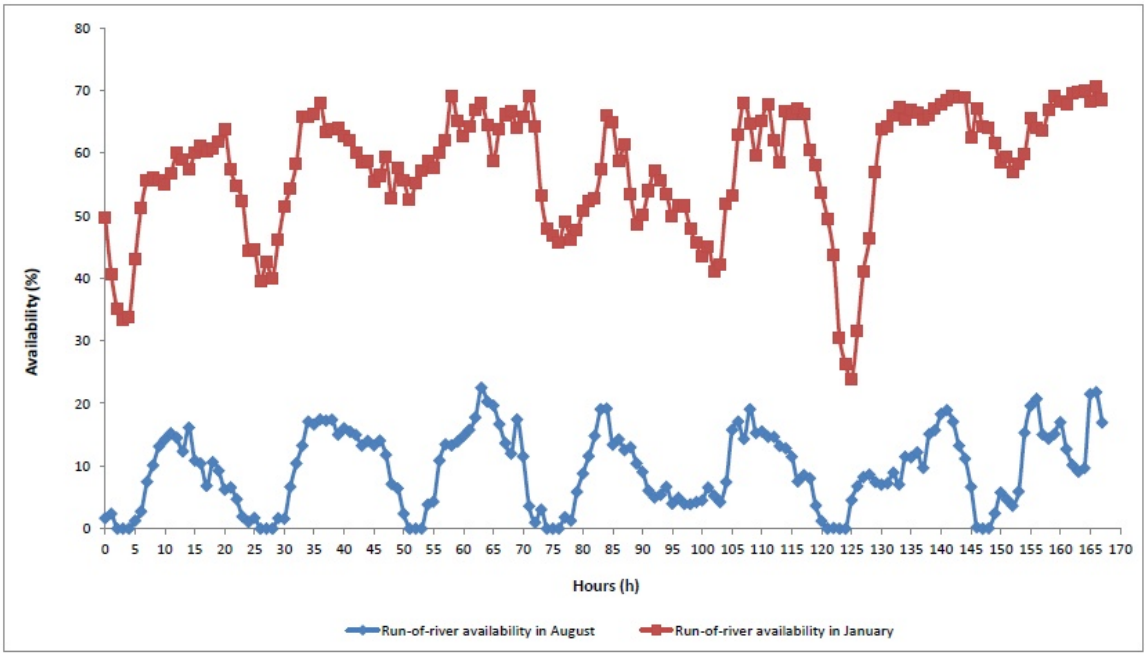

Figure 1: Weekly production of run–of–river power units in January and August 2011. [Own elaboration from REN data]

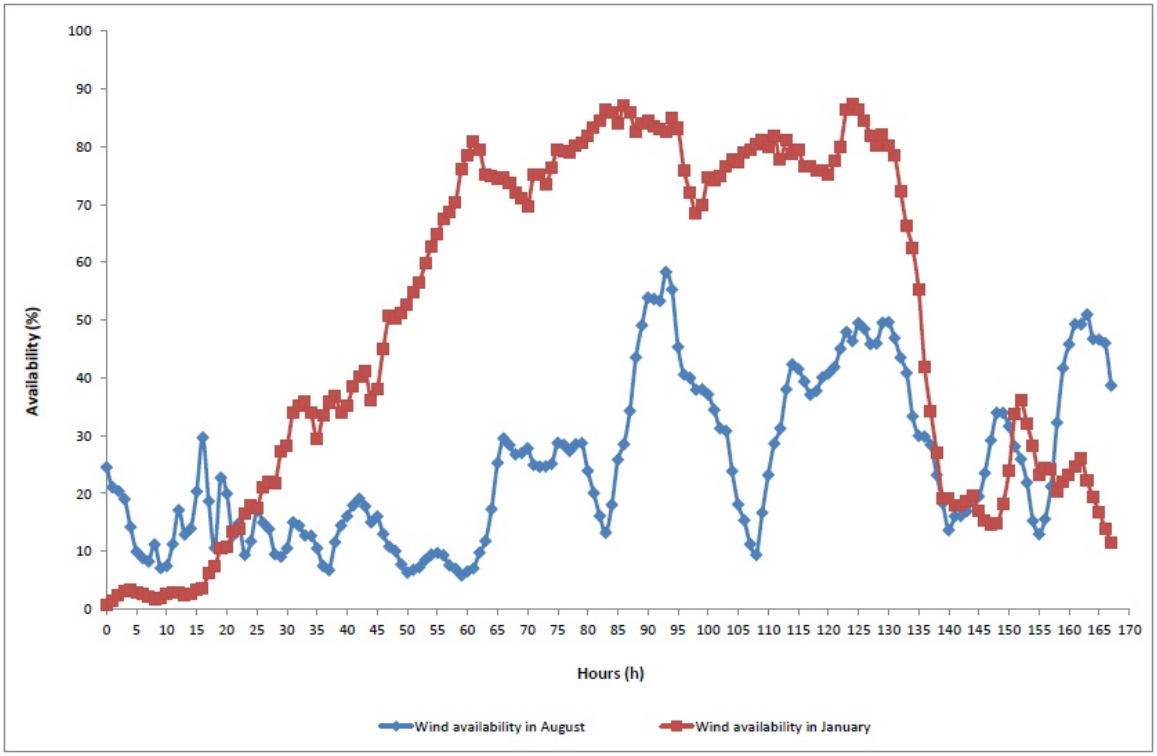

Figure 2: Weekly production of wind power units in January and August 2011. [Own elaboration from REN data]

maximum capacity.

In the next section, numerical results corresponding to a week horizon planning are presented. A short term electricity power generation scheduling is considered for the year 2020 forecasted Portuguese system (see reference [11]).

4. Numerical results

The forecasted Portuguese system over a week horizon planning for 2020 is considered in order to validate the proposed model. Considering a set of 168 hourly load blocks allow to obtain a more accurate analysis of results. In agreement with the year 2020 forecasted Portuguese system, a mix of 32 thermal power groups comprising gas, coal and fueloil technologies were considered in the model.

The previously described model, represented in equations (1) to (28), originates a single objective mix integer nonlinear optimization problem (MINLP) with 11089 continuing variables, 5208 binary variables and 26016 nonlinear inequality constraints, written in the GAMS [12] modeling language. The AlphaECP [13] solver was selected to obtain the numerical results reported herein, since it proved to be the most efficient solver available. The numerical results were obtained in a Microsoft Windows operating system using a Intel core i5 processor with 4GB of memory.

For simplicity, it was considered January as representative of the winter season and the August as representative of the summer season. Table 1 shows the optimal objective function values for January and August.

Table 1: Optimal objective function values

	Cost (M€)	
	January	August
Optimal cost	13.5	27.8

Results presented in Table 1 show that for January, the minimum cost of total power generation is lower than for August. This can easily be explained by comparing both figures A.1 and A.2 presented in Appendix A.. During the winter season, the variability of thermal power groups production is higher and the average thermal power production was 1273 MW. Also during winter, a reduction of the system variable cost is achieved, strongly dependent of the fossil fuel consumption. Nevertheless, an increase in the number of shutdowns and startups of the thermal power plants (with a direct impact on the ramping) is observed. In opposition, during summer, thermal power production remains rather steady with an average production of 3021 MW. Furthermore, no startups or shutdowns occurred, due to the low wind and hydropower production. The increase on the optimal cost is in part justified by the increase in the thermal power production during August, when compared with January. The higher summer cost is also explained by the need to fulfill the minimum up and downtime constraint of thermal power groups, in order to meet the load demand and compensate the lower wind and hydropower production. Despite the higher number of startups and shutdowns of thermal power plants in the winter season, this solution becomes less expensive due to the high availability of wind and hydropower. Thermal units are only used to compensate the lack of the RES reserves and for higher demand hours. This explains a higher wind and hydropower production with no fuel costs associated and consequently leading to a lower production cost of the entire power system.

5. Conclusions

This paper analysis the short-term electricity power generation scheduling in a mixed hydro-thermal wind power system based on data close to the ones characterizing the Portuguese electricity system.

A MINLP was proposed aiming to support the short term strategic decision, taking into account the

cost objective.

The results indicate that the seasonality associated with the renewable power sources affects the behaviour of the system, and consequently its total cost. Although the electricity demand during winter increases, the higher availability of wind and hydropower production ensure that thermal power groups will remain working at a lower rate than during summer. This leads to a reduction of the variable cost of the system, strongly driven by the fuel costs. The higher number of startups and shutdowns occurred in the winter season do not necessarily reflect an increase in the system costs. The startups and shutdowns costs are in fact less relevant then the fuel cost of thermal power groups, representing 54% of the total cost of the system during winter and 0% during summer.

The importance of designing short range planning models is crucial to study problems like the self-scheduling of a thermal electricity producer in day-ahead electricity markets. Future work will address the need to combine long term energy expansion strategies with short-term electrical power generation scheduling, for an hourly time step during one year horizon planning, evaluating the impact that the hydro-wind power combination strategies may have on the efficiency of thermal power plants. The model is expected to be expanded in order to increase the analysis period and to include the possibility of cross-border trading.

Acknowledgments

This work was financed by: the QREN – Operational Programme for Competitiveness Factors, the European Union – European Regional Development Fund and National Funds and Portuguese Foundation for Science and Technology, under Project FCOMP-01-0124-FEDER-011377 and Project Pest-OE/EME/UI0252/2011.

Appendix A

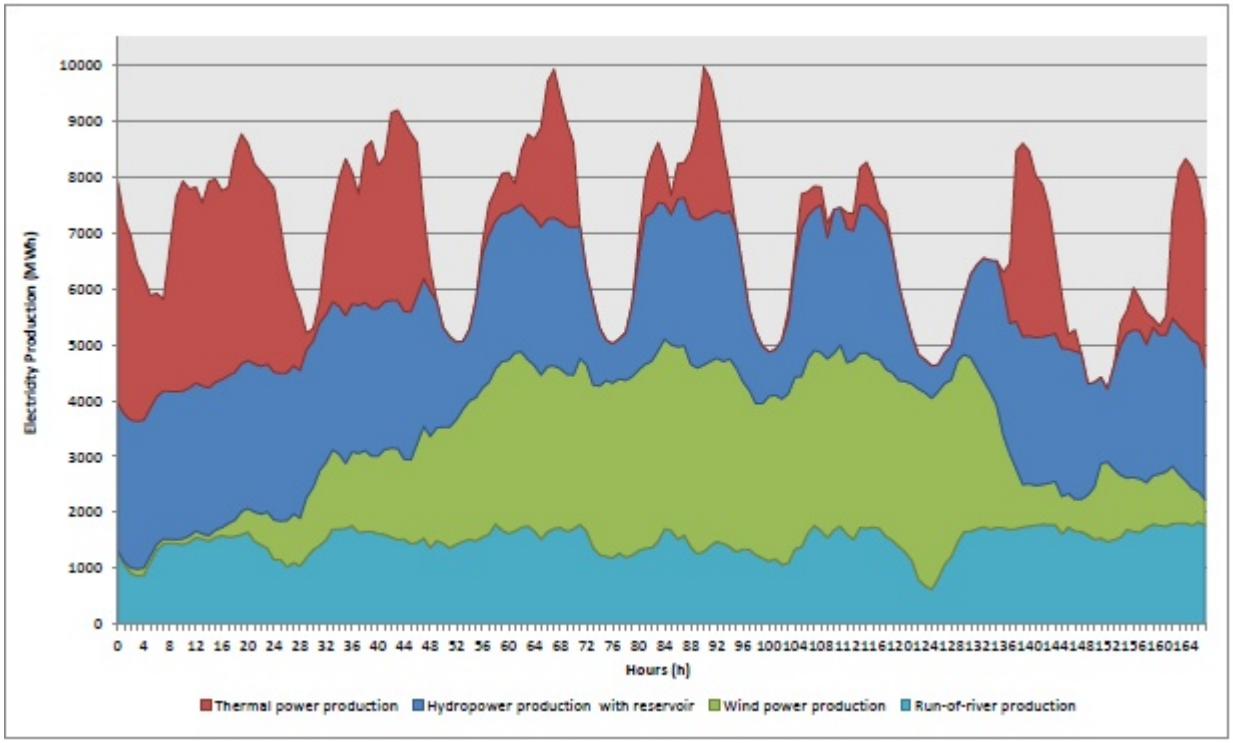

Figure A.1: Power units production for January (week planning).

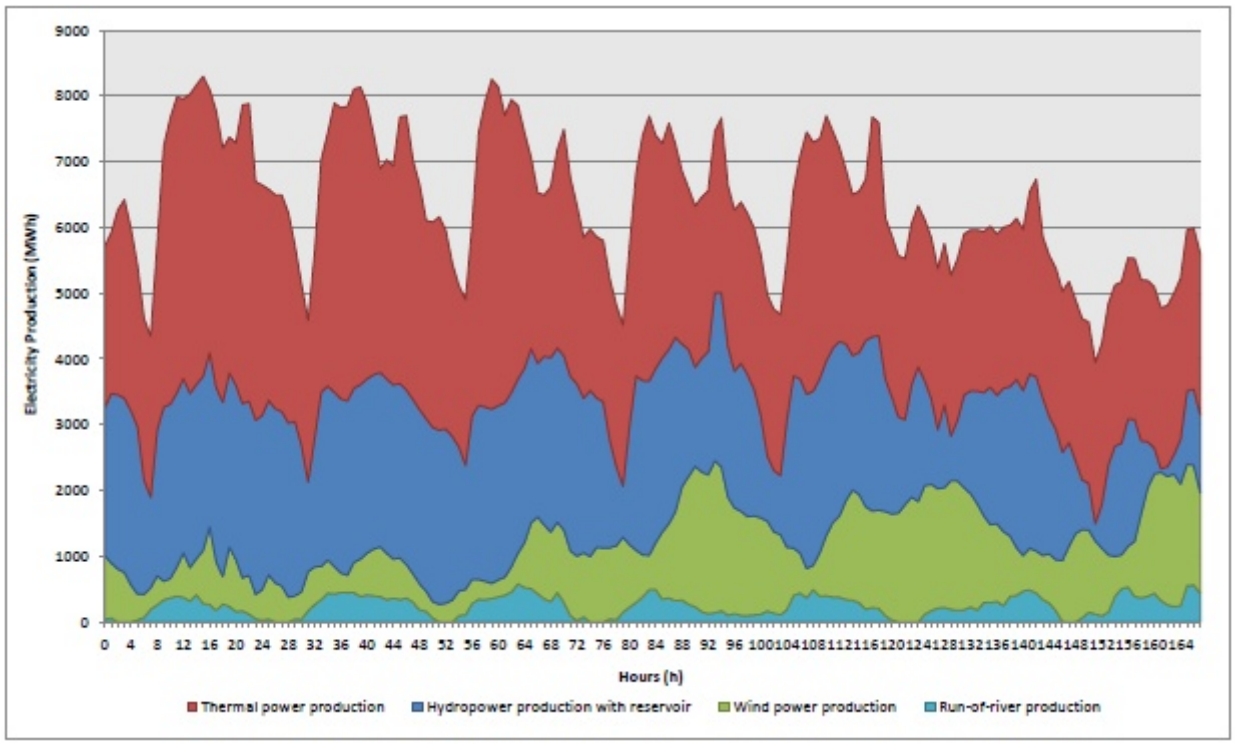

Figure A.2: Power units production for August (week planning).

References

[1] N. Troy, E. Denny, and M. O'Malley. Base-load cycling on a system with significant wind penetration. Power Systems, IEEE Transactions on, 25(2):1088 –1097, may 2010.

[2] T. Senjyu, K. Shimabukuro, K. Uezato, and T. Funabashi. A fast technique for unit commitment problem by extended priority list. Power Systems, IEEE Transactions on, 18(2):882 – 888, may 2003.

[3] A. Şima Uyar, T. Belgin, and Ali Keleş. A novel differential evolution application to short-term electrical power generation scheduling. International Journal of Electrical Power &; Energy Systems, 33(6):1236 – 1242, 2011.

[4] Thure Traber and Claudia Kemfert. Gone with the wind? electricity market prices and incentives to invest in thermal power plants under increasing wind energy supply. Energy Economics, 33(2):249 – 256, 2011.

[5] J. P. S. Catalão, S. J. P. S. Mariano, V. M. F. Mendes, and L. A. F. M. Ferreira. Short-term scheduling of thermal units: emission constraints and trade-o_ curves. European Transactions on Electrical Power, 18(1):1–14, 2008.

[6] Chao-Lung and Chiang. Optimal economic emission dispatch of hydrothermal power systems. International Journal of Electrical Power &; Energy Systems, 29(6):462 – 469, 2007.

[7] F. Hobbs. Optimization methods for electric utility resource planning. European Journal of Operational Research, 83:1–20, 1995.

[8] J. Arroyo and A. Conejo. Modelling of start-up and shut-down power trajectories of thermal units. IEEE Transactions on power systems, 19:1562–1568, 2004.

[9] WWEA. Half-year report 2011, 2011. The World Wind Energy Association.

[10] REN. A energia eólica em portugal, 2010. Redes Energ´eticas Nacionais, in Portuguese.

[11] S. Pereira, P. Ferreira, and A.I.F. Vaz. Electricity planning in a mixed hydro-thermal-wind power system. submitted, 2011.

[12] GAMS. General Algebraic Modeling System. GAMS Corporation, 2011. http://www.gams.com.

[13] Westerlund T. and Pörn R. Solving pseudo-convex mixed integer optimization problems by cutting plane techniques. Optimization and Engineering, 3:253–280, 2002.

ECOS 2012

The 25th International Conference on Efficiency, Cost, Optimization and Simulation of Energy Conversion Systems and Processes

(Perugia, June 26th-June 29th, 2012)

edited by
Umberto Desideri, Giampaolo Manfrida,
Enrico Sciubba

firenze university press
2012

ECOS 2012 : the 25th International Conference on Efficiency, Cost, Optimization and Simulation of Energy Conversion Systems and Processes (Perugia, June 26th-June 29th, 2012) / edited by Umberto Desideri, Giampaolo Manfrida, Enrico Sciubba. – Firenze : Firenze University Press, 2012.
(Proceedings e report ; 90)

http://digital.casalini.it/9788866553229

ISBN 978-88-6655-322-9 (online)

Progetto grafico di copertina Alberto Pizarro, Pagina Maestra snc
Immagine di copertina: © Kts | Dreamstime.com

Peer Review Process
All publications are submitted to an external refereeing process under the responsibility of the FUP Editorial Board and the Scientific Committees of the individual series. The works published in the FUP catalogue are evaluated and approved by the Editorial Board of the publishing house. For a more detailed description of the refereeing process we refer to the official documents published on the website and in the online catalogue of the FUP (http://www.fupress.com).

Firenze University Press Editorial Board
G. Nigro (Co-ordinator), M.T. Bartoli, M. Boddi, F. Cambi, R. Casalbuoni, C. Ciappei, R. Del Punta, A. Dolfi, V. Fargion, S. Ferrone, M. Garzaniti, P. Guarnieri, G. Mari, M. Marini, M. Verga, A. Zorzi.

© 2012 Firenze University Press
Università degli Studi di Firenze
Firenze University Press
Borgo Albizi, 28, 50122 Firenze, Italy
http://www.fupress.com/
Printed in Italy

ECOS 2012

The 25th International Conference on

Efficiency, Cost, Optimization and Simulation
of Energy Conversion Systems and Processes

Perugia, June 26th-June 29th, 2012

Book of Proceedings - Volume V

Edited by:
Umberto Desideri, Università degli Studi di Perugia
Giampaolo Manfrida, Università degli Studi di Firenze
Enrico Sciubba, Università degli Studi di Roma "Sapienza"

ECOS 2012 - THE 25TH INTERNATIONAL CONFERENCE ON
EFFICIENCY, COST, OPTIMIZATION, SIMULATION AND ENVIRONMENTAL IMPACT OF ENERGY SYSTEMS
JUNE 26-29, 2012, PERUGIA, ITALY
EDITED BY UMBERTO DESIDERI, GIAMPAOLO MANFRIDA, ENRICO SCIUBBA
FIRENZE UNIVERSITY PRESS, 2012, ISBN ONLINE : 978-88-6655-322-9

Advisory Committee (Track Organizers)

Building, Urban and Complex Energy Systems
V. Ismet Ugursal
Dalhousie University, Nova Scotia, Canada

Combustion, Chemical Reactors, Carbon Capture and Sequestration
Giuseppe Girardi
ENEA-Casaccia, Italy

Energy Systems: Environmental and Sustainability Issues
Christos A. Frangopoulos
National Technical University of Athens, Greece

Exergy Analysis and Second Law Analysis
Silvio de Oliveira Junior
Polytechnical University of Sao Paulo, Sao Paulo, Brazil

Fluid Dynamics and Power Plant Components
Sotirios Karellas
National Technical University of Athens, Athens, Greece

Fuel Cells
Umberto Desideri
University of Perugia, Perugia, Italy

Heat and Mass Transfer
Francesco Asdrubali, **Cinzia Buratti**
University of Perugia, Perugia, Italy

Industrial Ecology
Stefan Goessling-Reisemann
University of Bremen, Germany

Poster Session
Enrico Sciubba
University Roma 1 “Sapienza”, Italy

Process Integration and Heat Exchanger Networks
Francois Marechal
EPFL, Lausanne, *Switzerland*

Renewable Energy Conversion Systems
David Chiaramonti
University of Firenze, Firenze, Italy

Simulation of Energy Conversion Systems
Marcin Liszka
Polytechnica Slaska, Gliwice, Poland

System Operation, Control, Diagnosis and Prognosis
Vittorio Verda
Politecnico di Torino, Italy

Thermodynamics
A. Özer Arnas
United States Military Academy at West Point, U.S.A.

Thermo-Economic Analysis and Optimisation
Andrea Lazzaretto
University of Padova, Padova, Italy

Water Desalination and Use of Water Resources
Corrado Sommariva
ILF Consulting M.E., U.K

Scientific Committee

Riccardo Basosi, University of Siena, Italy
Gino Bella, University of Roma Tor Vergata, Italy
Asfaw Beyene, San Diego State University, United States
Ryszard Bialecki, Silesian Institute of Tecnology, Poland
Gianni Bidini, University of Perugia, Italy
Ana M. Blanco-Marigorta, University of Las Palmas de Gran Canaria, Spain
Olav Bolland, University of Science and Technology (NTNU), Norway
Renè Cornelissen, Cornelissen Consulting, The Netherlands
Franco Cotana, University of Perugia, Italy
Alexandru Dobrovicescu, Polytechnical University of Bucharest, Romania
Gheorghe Dumitrascu, Technical University of Iasi, Romania
Brian Elmegaard, Technical University of Denmark , Denmark
Daniel Favrat, EPFL, Switzerland
Michel Feidt, ENSEM - LEMTA University Henri Poincaré, France
Daniele Fiaschi, University of Florence, Italy
Marco Frey, Scuola Superiore S. Anna, Italy
Richard A Gaggioli, Marquette University, USA
Carlo N. Grimaldi, University of Perugia, Italy
Simon Harvey, Chalmers University of Technology, Sweden
Hasan Heperkan, Yildiz Technical University, Turkey
Abel Abel Hernandez-Guerrero, University of Guanajuato, Mexico
Jiri Jaromir Klemeš, University of Pannonia, Hungary
Zornitza V. Kirova-Yordanova, University "Prof. Assen Zlatarov", Bulgaria
Noam Lior, University of Pennsylvania, United States
Francesco Martelli, University of Florence, Italy
Aristide Massardo, University of Genova, Italy
Jim McGovern, Dublin Institute of Technology, Ireland
Alberto Mirandola, University of Padova, Italy
Michael J. Moran, The Ohio State University, United States
Tatiana Morosuk, Technical University of Berlin, Germany
Pericles Pilidis, University of Cranfield, United Kingdom
Constantine D. Rakopoulos, National Technical University of Athens, Greece
Predrag Raskovic, University of Nis, Serbia and Montenegro
Mauro Reini, University of Trieste, Italy
Gianfranco Rizzo, University of Salerno, Italy
Marc A. Rosen, University of Ontario, Canada
Luis M. Serra, University of Zaragoza, Spain
Gordana Stefanovic, University of Nis, Serbia and Montenegro
Andrea Toffolo, Luleå University of Technology, Sweden
Wojciech Stanek, Silesian University of Technology, Poland
George Tsatsaronis, Technical University Berlin, Germany
Antonio Valero, University of Zaragoza, Spain
Michael R. von Spakovsky, Virginia Tech, USA
Stefano Ubertini, Parthenope University of Naples, Italy
Sergio Ulgiati, Parthenope University of Naples, Italy
Sergio Usón, Universidad de Zaragoza, Spain
Roman Weber, Clausthal University of Technology, Germany
Ryohei Yokoyama, Osaka Prefecture University, Japan
Na Zhang, Institute of Engineering Thermophysics, Chinese Academy of Sciences, China

The 25th ECOS Conference 1987-2012: leaving a mark

The introduction to the ECOS series of Conferences states that "ECOS is a series of international conferences that focus on all aspects of Thermal Sciences, with particular emphasis on Thermodynamics and its applications in energy conversion systems and processes". Well, ECOS is much more than that, and its history proves it!

The idea of starting a series of such conferences was put forth at an informal meeting of the Advanced Energy Systems Division of the American Society of Mechanical Engineers (ASME) at the November 1985 Winter Annual Meeting (WAM), in Miami Beach, Florida, then chaired by Richard Gaggioli. The resolution was to organize an annual Symposium on the Analysis and Design of Thermal Systems at each ASME WAM, and to try to involve a larger number of scientists and engineers worldwide by organizing conferences outside of the United States. Besides Rich other participants were Ozer Arnas, Adrian Bejan, Yehia El-Sayed, Robert Evans, Francis Huang, Mike Moran, Gordon Reistad, Enrico Sciubba and George Tsatsaronis.

Ever since 1985, a Symposium of 8-16 sessions has been organized by the Systems Analysis Technical Committee every year, at the ASME Winter Annual Meeting (now ASME-IMECE). The first overseas conference took place in Rome, twenty-five years ago (in July 1987), with the support of the U.S. National Science Foundation and of the Italian National Research Council. In that occasion, Christos Frangopoulos, Yalcin Gogus, Elias Gyftopoulos, Dominick Sama, Sergio Stecco, Antonio Valero, and many others, already active at the ASME meetings, joined the core-group.

The name ECOS was used for the first time in Zaragoza, in 1992: it is an acronym for **Efficiency, Cost, Optimization and Simulation** (of energy conversion systems and processes), keywords that best describe the contents of the presentations and discussions taking place in these conferences. Some years ago, Christos Frangopoulos inserted in the official website the note that "ècos" ('οικος) means "home" in Greek and it ought to be attributed the very same meaning as the prefix "Eco-" in environmental sciences.
The last 25 years have witnessed an almost incredible growth of the ECOS community: more and more Colleagues are actively participating in our meetings, several international Journals routinely publish selected papers from our Proceedings, fruitful interdisciplinary and international cooperation projects have blossomed from our meetings. Meetings that have spanned three continents (Africa and Australia ought to be our next targets, perhaps!) and influenced in a way or another much of modern Engineering Thermodynamics.
After 25 years, if we do not want to become embalmed in our own success and lose momentum, it is mandatory to aim our efforts in two directions: first, encourage the participation of younger academicians to our meetings, and second, stimulate creative and useful discussions in our sessions. Looking at this years' registration roster (250 papers of which 50 authored or co-authored by junior Authors), the first objective seems to have been attained, and thus we have just to continue in that direction; the second one involves allowing space to "voices that sing out of the choir", fostering new methods and approaches, and establishing or reinforcing connections to other scientific communities. It is important that our technical sessions represent a place of active confrontation, rather than academic "lecturing".
In this spirit, we welcome you in Perugia, and wish you a scientifically stimulating, touristically interesting, and culinarily rewarding experience. In line with our 25 years old scientific excellency and friendship!

Umberto Desideri, Giampaolo Manfrida, Enrico Sciubba

CONTENT MANAGEMENT

The index lists all the papers contained all the eight volumes of the Proceedings of the ECOS 2012 International Conference.
Page numbers are listed only for papers within the Volume you are looking at. The ID code allows to trace back the identification number assigned to the paper within the Conference submission, review and track organization processes.

CONTENT

VOLUME V

V. 1 RENEWABLE ENERGY CONVERSION SYSTEMS

» A co-powered concentrated solar power Rankine cycle concept for small size combined heat and power (ID 276) ……..... *Pag. 1*
Alessandro Corsini, Domenico Borello, Franco Rispoli, Eileen Tortora

» A novel non-tracking solar collector for high temperature application (ID 466) ……..... *Pag. 17*
Wattana Ratismith, Anusorn Inthongkhum

» Absorption heat transformers (AHT) as a way to enhance low enthalpy geothermal resources (ID 311) ……..... *Pag. 26*
Daniele Fiaschi, Duccio Tempesti, Giampaolo Manfrida, Daniele Di Rosa

» Alternative feedstock for the biodiesel and energy production: the OVEST project (ID 98) ……..... *Pag. 38*
Matteo Prussi, David Chiaramonti, Lucia Recchia, Francesco Martelli, Fabio Guidotti

» Assessing repowering and update scenarios for wind energy converters (ID 158) ……..... *Pag. 47*
Till Zimmermann

» Biogas from mechanical pulping industry – potential improvement for increased biomass vehicle fuels (ID 54) ……..... *Pag. 56*
Mimmi Magnusson, Per Alvfors

» Biogas or electricity as vehicle fuels derived from food waste - the case of Stockholm (ID 27) ……..... *Pag. 68*
Martina Wikström, Per Alvfors

» Compressibility factor as evaluation parameter of expansion processes in organic Rankine cycles (ID 292) ……..... *Pag. 78*
Giovanni Manente, Andrea Lazzaretto

» Design of solar heating system for methane generation (ID 445) ……..... *Pag. 94*
Lucía Mónica Gutiérrez, P. Quinto Diez, L. R. Tovar Gálvez

» Economic feasibility of PV systems in hotels in Mexico (ID 346) ……..... *Pag. 106*
Augusto Sanchez, Sergio Quezada

» Effect of a back surface roughness on annual performance of an air-cooled PV module (ID 193) ……..... *Pag. 114*
Riccardo Secchi, Duccio Tempesti, Jacek Smolka

» Energy and exergy analysis of the first hybrid solar-gas power plant in Algeria (ID 176) ……..... *Pag. 130*
Fouad Khaldi

» Energy recovery from MSW treatment by gasification and melting technology (ID 393) ……..... *Pag. 144*
Fabrizio Strobino, Alessandro Pini Prato, Diego Ventura, Marco Damonte

» Ethanol production by enzymatic hydrolysis process from sugarcane biomass - the integration with the conventional process (ID 189) ……..... *Pag. 159*
Reynaldo Palacios-Bereche, Adriano Ensinas, Marcelo Modesto, Silvia Azucena Nebra

» **Evaluation of gas in an industrial anaerobic digester by means of biochemical methane potential of organic municipal solid waste components (ID 57)** ……..... *Pag. 173*
Isabella Pecorini, Tommaso Olivieri, Donata Bacchi, Alessandro Paradisi, Lidia Lombardi, Andrea Corti, Ennio Carnevale

» **Exergy analysis and genetic algorithms for the optimization of flat-plate solar collectors (ID 423)** ……..... *Pag. 185*
Soteris A. Kalogirou

» **Experimental study of tar and particles content of the produced gas in a double stage downdraft gasifier (ID 487)** ……..... *Pag. 197*
Ana Lisbeth Galindo Noguera, Sandra Yamile Giraldo, Rene Lesme-Jaén, Vladimir Melian Cobas, Rubenildo Viera Andrade, Electo Silva Lora

» **Feasibility study to realize an anaerobic digester fed with vegetables matrices in central Italy (ID 425)** ……..... *Pag. 209*
Umberto Desideri, Francesco Zepparelli, Livia Arcioni, Ornella Calderini, Francesco Panara, Matteo Todini

» **Investigations on the use of biogas for small scale decentralized CHP applications with a focus on stability and emissions (ID 140)** ……..... *Pag. 218*
Steven MacLean, Eren Tali, Anne Giese, Jörg Leicher

» **Kinetic energy recovery system for sailing yachts (ID 427)** ……..... *Pag. 229*
Giuseppe Leo Guizzi, Michele Manno

» **Mirrors in the sky: status and some supporting materials experiments (ID 184)** ……..... *Pag. 253*
Noam Lior

» **Numerical parametric study for different cold storage designs and strategies of a solar driven thermoacoustic cooler system (ID 284)** ……..... *Pag. 274*
Maxime Perier-Muzet, Pascal Stouffs, Jean-Pierre Bedecarrats, Jean Castaing-Lasvignottes

» **Parabolic trough photovoltaic/thermal collectors. Part I: design and simulation model (ID 102)** ……..... *Pag. 290*
Francesco Calise, Laura Vanoli

» **Parabolic trough photovoltaic/thermal collectors. Part II: dynamic simulation of a solar trigeneration system (ID 488)** ……..... *Pag. 309*
Francesco Calise, Laura Vanoli

» **Performance analysis of downdraft gasifier - reciprocating engine biomass fired small-scale cogeneration system (ID 368)** ……..... *Pag. 331*
Jacek Kalina

» **Proposing offshore photovoltaic (PV) technology to the energy mix of the Maltese islands (ID 262)** ……..... *Pag. 350*
Kim Trapani, Dean Lee Millar

» **Research of integrated biomass gasification system with a piston engine (ID 414)** ……..... *Pag. 363*
Janusz Kotowicz, Aleksander Sobolewski, Tomasz Iluk

» **Start up of a pre-industrial scale solid state anaerobic digestion cell for the co-treatment of animal and agricultural residues (ID 34)** ……..... *Pag. 373*
Francesco Di Maria, Giovanni Gigliotti, Alessio Sordi, Caterina Micale, Luisa Massaccesi

» **The role of biomass in the renewable energy system (ID 390)** ……..... *Pag. 381*
Ruben Laleman, Ludovico Balduccio, Johan Albrecht

» Vegetable oils of soybean, sunflower and tung as alternative fuels for compression ignition engines (ID 500) ……..... *Pag. 409*
Ricardo Morel Hartmann, Nury Nieto Garzón, Eduardo Morel Hartmann, Amir Antonio Martins Oliveira Jr, Edson Bazzo, Bruno Okuda, Joselia Piluski

» Wind energy conversion performance and atmosphere stability (ID 283) ……..... *Pag. 427*
Francesco Castellani, Emanuele Piccioni, Lorenzo Biondi, Marcello Marconi

V. 2 FUEL CELLS

» Comparison study on different SOFC hybrid systems with zero-CO2 emission (ID 196) ……..... *Pag. 440*
Liqiang Duan, Kexin Huang, Xiaoyuan Zhang and Yongping Yang

» Exergy analysis and optimisation of a steam methane pre-reforming system (ID 62) ……..... *Pag. 456*
George G. Dimopoulos, Iason C. Stefanatos, Nikolaos M.P. Kakalis

» Modelling of a CHP SOFC power system fed with biogas from anaerobic digestion of municipal wastes integrated with a solar collector and storage units (ID 491) ……..... *Pag. 472*
Domenico Borello, Sara Evangelisti, Eileen Tortora

CONTENTS OF ALL THE VOLUMES

VOLUME I

I . 1 – SIMULATION OF ENERGY CONVERSION SYSTEMS

» A novel hybrid-fuel compressed air energy storage system for China's situation (ID 531)
Wenyi Liu, Yongping Yang, Weide Zhang, Gang Xu,and Ying Wu

» A review of Stirling engine technologies applied to micro-cogeneration systems (ID 338)
Ana C Ferreira, Manuel L Nunes, Luís B Martins, Senhorinha F Teixeira

» An organic Rankine cycle off-design model for the search of the optimal control strategy (ID 295)
Andrea Toffolo, Andrea Lazzaretto, Giovanni Manente, Marco Paci

» Automated superstructure generation and optimization of distributed energy supply systems (ID 518)
Philip Voll, Carsten Klaffke, Maike Hennen, André Bardow

» Characterisation and classification of solid recovered fuels (SRF) and model development of a novel thermal utilization concept through air- gasification (ID 506)
Panagiotis Vounatsos, Konstantinos Atsonios, Mihalis Agraniotis, Kyriakos D. Panopoulos, George Koufodimos,Panagiotis Grammelis, Emmanuel Kakaras

» Design and modelling of a novel compact power cycle for low temperature heat sources (ID 177)
Jorrit Wronski, Morten Juel Skovrup, Brian Elmegaard, Harald Nes Rislå, Fredrik Haglind

» Dynamic simulation of combined cycles operating in transient conditions: an innovative approach to determine the steam drums life consumption (ID 439)
Stefano Bracco

» Effect of auxiliary electrical power consumptions on organic Rankine cycle system with low-temperature waste heat source (ID 235)
Samer Maalouf, Elias Boulawz Ksayer, Denis Clodic

» Energetic and exergetic analysis of waste heat recovery systems in the cement industry (ID 228)
Sotirios Karellas, Aris Dimitrios Leontaritis, Georgios Panousis, Evangelos Bellos, Emmanuel Kakaras

» Energy and exergy analysis of repowering options for Greek lignite-fired power plants (ID 230)
Sotirios Karellas, Aggelos Doukelis, Grammatiki Zanni, Emmanuel Kakaras

» Energy saving by a simple solar collector with reflective panels and boiler (ID 366)
Anna Stoppato, Renzo Tosato

» Exergetic analysis of biomass fired double-stage Organic Rankine Cycle (ORC) (ID 37)
Markus Preißinger, Florian Heberle, Dieter Brüggemann

» Experimental tests and modelization of a domestic-scale organic Rankine cycle (ID 156)
Roberto Bracco, Stefano Clemente, Diego Micheli, Mauro Reini

» Model of a small steam engine for renewable domestic CHP system (ID 31)
Giampaolo Manfrida, Giovanni Ferrara, Alessandro Pescioni

» Model of vacuum glass heat pipe solar collectors (ID 312)
Daniele Fiaschi, Giampaolo Manfrida

» Modelling and exergy analysis of a plasma furnace for aluminum melting process (ID 254)
Luis Enrique Acevedo, Sergio Usón, Javier Uche, Patxi Rodríguez

» Modelling and experimental validation of a solar cooling installation (ID 296)
Guillaume Anies, Pascal Stouffs, Jean Castaing-Lasvignottes

» The influence of operating parameters and occupancy rate of thermoelectric modules on the electricity generation (ID 314)
Camille Favarel, Jean-Pierre Bédécarrats, Tarik Kousksou, Daniel Champier

» Thermodynamic and heat transfer analysis of rice straw co-firing in a Brazilian pulverised coal boiler (ID 236)
Raphael Miyake, Alvaro Restrepo, Fábio Kleveston Edson Bazzo, Marcelo Bzuneck

» Thermophotovoltaic generation: A state of the art review (ID 88)
Matteo Bosi, Claudio Ferrari, Francesco Melino, Michele Pinelli, Pier Ruggero Spina, Mauro Venturini

I . 2 – HEAT AND MASS TRANSFER

» A DNS method for particle motion to establish boundary conditions in coal gasifiers (ID 49)
Efstathios E Michaelides, Zhigang Feng

» Effective thermal conductivity with convection and radiation in packed bed (ID 60)
Yusuke Asakuma

» Experimental and CFD study of a single phase cone-shaped helical coiled heat exchanger: an empirical correlation (ID 375)
Daniel Flórez-Orrego, Walter Arias, Diego López, Héctor Velásquez

» Thermofluiddynamic model for control analysis of latent heat thermal storage system (ID 207)
Adriano Sciacovelli, Vittorio Verda, Flavio Gagliardi

» Towards the development of an efficient immersed particle heat exchanger: particle transfer from low to high pressure (ID 202)
Luciano A. Catalano, Riccardo Amirante, Stefano Copertino, Paolo Tamburrano, Fabio De Bellis

I . 3 – INDUSTRIAL ECOLOGY

» Anthropogenic heat and exergy balance of the atmosphere (ID 122)
Asfaw Beyene, David MacPhee, Ron Zevenhoven

» Determination of environmental remediation cost of municipal waste in terms of extended exergy (ID 63)
Candeniz Seckin, Ahmet R. Bayulken

» Development of product category rules for the application of life cycle assessment to carbon capture and storage (537)
Carlo Strazza, Adriana Del Borghi, Michela Gallo

» Electricity production from renewable and non-renewable energy sources: a comparison of environmental, economic and social sustainability indicators with exergy losses throughout the supply chain (ID 247)
Lydia Stougie, Hedzer van der Kooi, Rob Stikkelman
» Exergy analysis of the industrial symbiosis model in Kalundborg (ID 218)
Alicia Valero Delgado, Sergio Usón, Jorge Costa

» Global gold mining: is technological learning overcoming the declining in ore grades? (ID 277)
Adriana Domínguez, Alicia Valero

» Personal transportation energy consumption (ID305)
Matteo Muratori, Emmanuele Serra, Vincenzo Marano, Michael Moran

» Resource use evaluation of Turkish transportation sector via the extended exergy accounting method (ID 43)
Candeniz Seckin, Enrico Sciubba, Ahmet R. Bayulken

» The impact of higher energy prices on socio-economic inequalities of German social groups (ID 80)
Holger Schlör, Wolfgang Fischer, Jürgen-Friedrich Hake

VOLUME II

II . 1 – EXERGY ANALYSIS AND 2ND LAW ANALYSIS

» A comparative analysis of cryogenic recuperative heat exchangers based on exergy destruction (ID 129)
Adina Teodora Gheorghian, Alexandru Dobrovicescu, Lavinia Grosu, Bogdan Popescu, Claudia Ionita

» A critical exploration of the usefulness of rational efficiency as a performance parameter for heat exchangers (ID 307)
Jim McGovern, Georgiana Tirca-Dragomirescu, Michel Feidt, Alexandru Dobrovicescu

» A new procedure for the design of LNG processes by combining exergy and pinch analyses (ID 238)
Danahe Marmolejo-Correa, Truls Gundersen

» Advances in the distribution of environmental cost of water bodies through the exergy concept in the Ebro river (ID 258)
Javier Uche Marcuello, Amaya Martínez Gracia, Beatriz Carrasquer Álvarez, Antonio Valero Capilla

» Application of the entropy generation minimization method to a solar heat exchanger: a pseudo-optimization design process based on the analysis of the local entropy generation maps (ID 357)
Giorgio Giangaspero, Enrico Sciubba

» Comparative analysis of ammonia and carbon dioxide two-stage cycles for simultaneous cooling and heating (ID 84)
Alexandru Dobrovicescu, Ciprian Filipoiu, Emilia Cerna Mladin, Valentin Apostol, Liviu Drughean

» Comparison between traditional methodologies and advanced exergy analyses for evaluating efficiency and externalities of energy systems (ID 515)
Gabriele Cassetti, Emanuela Colombo

» Comparison of entropy generation figures using entropy maps and entropy transport equation for an air cooled gas turbine blade (ID 468)
Omer Emre Orhan, Oguz Uzol

» Conventional and advanced exergetic evaluation of a supercritical coal-fired power plant (ID 377)
Ligang Wang, Yongping Yang, Tatiana Morosuk, George Tsatsaronis

» Energy and exergy analyses of the charging process in encapsulted ice thermal energy storage (ID 164)
David MacPhee, Ibrahim Dincer, Asfaw Beyene

» Energy integration and cogeneration in nitrogen fertilizers industry: thermodynamic estimation of the efficiency, potentials, limitations and environmental impact. Part 1: energy integration in ammonia production plants (ID 303)
Zornitza Vassileva Kirova-Yordanova

» Evaluation of the oil and gas processing at a real production day on a North Sea oil platform using exergy analysis (ID 260)
Mari Voldsund, Wei He, Audun Røsjorde, Ivar Ståle Ertesvåg, Signe Kjelstrup

» Exergetic and economic analysis of Kalina cycle for low temperature geothermal sources in Brazil (ID 345)
Carlos Eymel Campos Rodriguez, José Carlos Escobar Palacios, Cesar Adolfo Rodríguez Sotomonte, Marcio Leme, Osvaldo José Venturini, Electo Eduardo Silva Lora, Vladimir Melián Cobasa, Daniel Marques dos Santos, Fábio R. Lofrano Dotto, Vernei Gialluca

» Exergy analysis and comparison of CO2 heat pumps (ID 242)
Argyro Papadaki, Athina Stegou - Sagia

» Exergy analysis of a CO2 Recovery plant for a brewery (ID 72)
Daniel Rønne Nielsen, Brian Elmegaard, C. Bang-Møller

» Exergy analysis of the silicon production process (ID 118)
Marit Takla, Leiv Kolbeinsen, Halvard Tveit, Signe Kjelstrup

» Exergy based indicators for cardiopulmonary exercise test evaluation (ID 159)
Carlos Eduardo Keutenedjian Mady, Cyro Albuquerque Neto, Tiago Lazzaretti Fernandes, Arnaldo Jose Hernandez, Paulo Hilário Nascimento Saldiva, Jurandir Itizo Yanagihara, Silvio de Oliveira Junior

» Exergy disaggregation as an alternative for system disaggregation in thermoeconomics (ID 483)
José Joaquim Conceição Soares Santos, Atilio Lourenço, Julio Mendes da Silva, João Donatelli, José Escobar Palacio

» Exergy intensity of petroleum derived fuels (ID 117)
Julio Augusto Mendes da Silva, Maurício Sugiyama, Claudio Rucker, Silvio de Oliveira Junior

» Exergy-based sustainability evaluation of a wind power generation system (ID 542)
Jin Yang, B. Chen, Enrico Sciubba

» Human body exergy metabolism (ID 160)
Carlos Eduardo Keutenedjian Mady, Silvio de Oliveira Junior

» Integrating an ORC into a natural gas expansion plant supplied with a co-generation unit (ID 273)
Sergio Usón, Wojciech Juliusz Kostowski

» One-dimensional model of an optimal ejector and parametric study of ejector efficiency (ID 323)
Ronan Killian McGovern, Kartik Bulusu, Mohammed Antar, John H. Lienhard

» Optimization and design of pin-fin heat sinks based on minimum entropy generation (ID 6)
Jose-Luis Zuniga-Cerroblanco, Abel Hernandez-Guerrero, Carlos A. Rubio-Jimenez, Cuauhtemoc Rubio-Arana, Sosimo E. Diaz-Mendez

» Performance analysis of a district heating system (ID 271)
Andrej Ljubenko, Alojz Poredoš, Tatiana Morosuk, George Tsatsaronis

» System analysis of exergy losses in an integrated oxy-fuel combustion power plant (ID 64)
Andrzej Ziębik, Paweł Gładysz

» What is the cost of losing irreversibly the mineral capital on Earth? (ID 220)
Alicia Valero Delgado, Antonio Valero

II . 2 – THERMODYNAMICS

» A new polygeneration system for methanol and power based on coke oven gas and coal gas (ID 252)
Hu Lin, Hongguang Jin, Lin Gao, Rumou Li

» Argon-Water closed gas cycle (ID 67)
Federico Fionelli, Giovanni Molinari

» Binary alkane mixtures as fluids in Rankine cycles (ID 246)
M. Aslam Siddiqi, Burak Atakan

» Excess enthalpies of second generation biofuels (ID 308)
Alejandro Moreau, José Juan Segovia, M. Carmen Martín, Miguel Ángel Villamañán, César R. Chamorro, Rosa M. Villamañán

» Local stability analysis of a Curzon-Ahlborn engine considering the Van der Waals equation state in the maximum ecological regime (ID 281)
Ricardo Richard Páez-Hernández, Pedro Portillo-Díaz, Delfino Ladino-Luna, Marco Antonio Barranco-Jiménez

» Some remarks on the Carnot's theorem (ID 325)
Julian Gonzalez Ayala, Fernando Angulo-Brown

» The Dead State (ID 340)
Richard A. Gaggioli

» The magnetocaloric energy conversion (ID 97)
Andrej Kitanovski, Jaka Tusek, Alojz Poredos

VOLUME III

THERMO-ECONOMIC ANALYSIS AND OPTIMIZATION

» A comparison of optimal operation of residential energy systems using clustered demand patterns based on Kullback-Leibler divergence (ID 142)
Akira Yoshida, Yoshiharu Amano, Noboru Murata, Koichi Ito, Takumi Hashizume

» A Model for Simulation and Optimal Design of a Solar Heating System with Seasonal Storage (ID 51)
Gianfranco Rizzo

» A thermodynamic and economic comparative analysis of combined gas-steam and gas turbine air bottoming cycle (ID 232)
Tadeusz Chmielniak, Daniel Czaja, Sebastian Lepszy

» Application of an alternative thermoeconomic approach to a two-stage vapor compression refrigeration cycle with intercooling (ID 135)
Atilio Barbosa Lourenço, José Joaquim Conceição Soares Santos, João Luiz Marcon Donatelli

» Comparative performance of advanced power cycles for low temperature heat sources (ID 109)
Guillaume Becquin, Sebastian Freund

» Comparison of nuclear steam power plant and conventional steam power plant through energy level and thermoeconomic analysis (ID 251)
S. Khamis Abadi, Mohammad Hasan Khoshgoftar Manesh, M. Baghestani, H. Ghalami, Majid Amidpour

» Economic and exergoeconomic analysis of micro GT and ORC cogeneration systems (ID 87)
Audrius Bagdanavicius, Robert Sansom, Nick Jenkins, Goran Strbac

» Exergoeconomic comparison of wet and dry cooling technologies for the Rankine cycle of a solar thermal power plant (ID 300)
Philipp Habl, Ana M. Blanco-Marigorta, Berit Erlach

» Influence of renewable generators on the thermo-economic multi-level optimization of a poly-generation smart grid (101)
Massimo Rivarolo, Andrea Greco, Francesca Travi, Aristide F. Massardo

» Local stability analysis of a thermoeconomic model of an irreversible heat engine working at different criteria of performance (ID 289)
Marco A. Barranco-Jiménez, Norma Sánchez-Salas, Israel Reyes-Ramírez, Lev Guzmán-Vargas

» Multicriteria optimization of a distributed trigeneration system in an industrial area (ID 154)
Dario Buoro, Melchiorre Casisi, Alberto de Nardi, Piero Pinamonti, Mauro Reini

» On the effect of eco-indicator selection on the conclusions obtained from an exergoenvironmental analysis (ID 275)
Tatiana Morosuk, George Tsatsaronis, Christopher Koroneos

» Optimisation of supply temperature and mass flow rate for a district heating network (ID 104)
Marouf Pirouti, Audrius Bagdanavicius, Jianzhong Wu, Janaka Ekanayake

» Optimization of energy supply systems in consideration of hierarchical relationship between design and operation (ID 389)
Ryohei Yokoyama, Shuhei Ose

» The fuel impact formula revisited (ID 279)
Cesar Torres, Antonio Valero

» The introduction of exergy analysis to the thermo-economic modelling and optimisation of a marine combined cycle system (ID 61)
George G. Dimopoulos, Chariklia A. Georgopoulou, Nikolaos M.P. Kakalis

» The relationship between costs and environmental impacts in power plants: an exergy-based study (ID 272)
Fontina Petrakopoulou, Yolanda Lara, Tatiana Morosuk, Alicia Boyano, George Tsatsaronis

» Thermo-ecological evaluation of biomass integrated gasification gas turbine based cogeneration technology (ID 441)
Wojciech Stanek, Lucyna Czarnowska, Jacek Kalina

» Thermo-ecological optimization of a heat exchanger through empirical modeling (ID 501)
Ireneusz Szczygieł, Wojciech Stanek, Lucyna Czarnowska, Marek Rojczyk

» Thermoeconomic analysis and optimization in a combined cycle power plant including a heat transformer for energy saving (ID 399)
Elizabeth Cortés Rodríguez, José Luis Castilla Carrillo, Claudia A. Ruiz Mercado, Wilfrido Rivera Gómez-Franco

» Thermoeconomic analysis and optimization of a hybrid solar-electric heating in a fluidized bed dryer (ID 400)
Elizabeth Cortés Rodríguez, Felipe de Jesús Ojeda Cámara, Isaac Pilatowsky Figueroa

» Thermoeconomic approach for the analysis of low temperature district heating systems (ID 208)
Vittorio Verda, Albana Kona

» Thermo-economic assessment of a micro CHP systems fuelled by geothermal and solar energy (ID 166)
Duccio Tempesti, Daniele Fiaschi, Filippo Gabuzzini

» Thermo-economic evaluation and optimization of the thermo-chemical conversion of biomass into methanol (ID 194)
Emanuela Peduzzi, Laurence Tock, Guillaume Boissonnet, François Marechal

» Thermoeconomic fuel impact approach for assessing resources savings in industrial symbiosis: application to Kalundborg Eco-industrial Park (ID 256)
Sergio Usón, Antonio Valero, Alicia Valero, Jorge Costa

» Thermoeconomics of a ground-based CAES plant for peak-load energy production system (ID 32)
Simon Kemble, Giampaolo Manfrida, Adriano Milazzo, Francesco Buffa

VOLUME IV

IV . 1 – FLUID DYNAMICS AND POWER PLANT COMPONENTS

» A control oriented simulation model of a multistage axial compressor (ID 444)
Lorenzo Damiani, Giampaolo Crosa, Angela Trucco

» A flexible and simple device for in-cylinder flow measurements: experimental and numerical validation (ID 181)
Andrea Dai Zotti, Massimo Masi, Marco Antonello

» CFD Simulation of Entropy Generation in Pipeline for Steam Transport in Real Industrial Plant (ID 543)
Goran Vučković, Gradimir Ilić, Mića Vukić, Milan Banić, Gordana Stefanović

» Feasibility Study of Turbo expander Installation in City Gate Station (ID 168)
Navid Zehtabiyan Rezaie, Majid Saffar-Avval

» GTL and RME combustion analysis in a transparent CI engine by means of IR digital imaging (ID 460)
Ezio Mancaruso, Luigi Sequino, Bianca Maria Vaglieco

» Some aspects concerning fluid flow and turbulence modeling in 4-valve engines (ID 116)
Zoran Stevan Jovanovic, Zoran Masonicic, Miroljub Tomic

IV . 2 – SYSTEM OPERATION CONTROL DIAGNOSIS AND PROGNOSIS

» Adapting the operation regimes of trigeneration systems to renewable energy systems integration (ID 188)
Liviu Ruieneanu, Mihai Paul Mircea

» Advanced electromagnetic sensors for sustainable monitoring of industrial processes (ID 145)
Uroš Puc, Andreja Abina, Anton Jeglič, Pavel Cevc, Aleksander Zidanšek

» Assessment of stresses and residual life of plant components in view of life-time extension of power plants (ID 453)
Anna Stoppato, Alberto Benato and Alberto Mirandola

» Control strategy for minimizing the electric power consumption of hybrid ground source heat pump system (ID 244)
Zoi Sagia, Constantinos Rakopoulos

» Exergetic evaluation of heat pump booster configurations in a low temperature district heating network (ID 148)
Torben Ommen, Brian Elmegaard

» Exergoeconomic diagnosis: a thermo-characterization method by using irreversibility analysis (ID 523)
Abraham Olivares-Arriaga, Alejandro Zaleta-Aguilar, Rangel-Hernández V. H, Juan Manuel Belman-Flores

» Optimal structural design of residential cogeneration systems considering their operational restrictions (ID 224)
Tetsuya Wakui, Ryohei Yokoyama

» Performance estimation and optimal operation of a CO2 heat pump water heating system (ID 344)
Ryohei Yokoyama, Ryosuke Kato, Tetsuya Wakui, Kazuhisa Takemura

» Performances of a common-rail Diesel engine fuelled with rapeseed and waste cooking oils (ID 213)
Alessandro Corsini, Valerio Giovannoni, Stefano Nardecchia, Franco Rispoli, Fabrizio Sciulli, Paolo Venturini

» Reduced energy cost through the furnace pressure control in power plants (ID 367)
Vojislav Filipović, Novak Nedić, Saša Prodanović

» Short-term scheduling model for a wind-hydro-thermal electricity system (ID 464)
Sérgio Pereira, Paula Ferreira, A. Ismael Freitas Vaz

VOLUME VI

VI . 1 - CARBON CAPTURE AND SEQUESTRATION

» A novel coal-based polygeneration system cogenerating power, natural gas and liquid fuel with CO2 capture (ID 96)
Sheng Li, Hongguang Jin, Lin Gao

» Analysis and optimization of CO2 capture in a China's existing coal-fired power plant (ID 532)
Gang Xu, Yongping Yang, Shoucheng Li, Wenyi Liu and Ying Wu

» Analysys of four-end high temperature membrane air separator in a supercritical power plant with oxy-type pulverized fuel boiler (ID 442)
Janusz Kotowicz, Sebastian Stanisław Michalski

» Analysis of potential improvements to the lignite-fired oxy-fuel power unit (ID 413)
Marcin Liszka, Jakub Tuka, Grzegorz Nowak, Grzegorz Szapajko

» Biogas Upgrading: Global Warming Potential of Conventional and Innovative Technologies (ID 240)
Katherine Starr, Xavier Gabarrell Durany, Gara Villalba Mendez, Laura Talens Peiro, Lidia Lombardi

» Capture of carbon dioxide using gas hydrate technology (ID 103)
Beatrice Castellani, Mirko Filipponi, Sara Rinaldi, Federico Rossi

» Carbon dioxide mineralisation and integration with flue gas desulphurisation applied to a modern coal-fired power plant (ID 179)
Ron Zevenhoven, Johan Fagerlund, Thomas Björklöf, Magdalena Mäkelä, Olav Eklund

» Carbon dioxide storage by mineralisation applied to a lime kiln (ID 226)
Inês Sofia Soares Romão, Matias Eriksson, Experience Nduagu, Johan Fagerlund, Licínio Manuel Gando-Ferreira, Ron Zevenhoven

» Comparison of IGCC and CFB cogeneration plants equipped with CO2 removal (ID 380)
Marcin Liszka, Tomasz Malik, Michał Budnik, Andrzej Ziębik

» Concept of a "capture ready" combined heat and power plant (ID 231)
Piotr Henryk Lukowicz, Lukasz Bartela

» Cryogenic method for H2 and CH4 recovery from a rich CO2 stream in pre-combustion CCS schemes (ID 508)
Konstantinos Atsonios, Kyriakos D. Panopoulos, Angelos Doukelis, Antonis Koumanakos, Emmanuel Kakaras

» Design and optimization of ITM oxy-combustion power plant (ID 495)
Surekha Gunasekaran, Nicholas David Mancini, Alexander Mitsos

» Implementation of a CCS technology: the ZECOMIX experimental platform (ID 222)
Antonio Calabrò, Stefano Cassani, Leandro Pagliari, Stefano Stendardo

» Influence of regeneration condition on cyclic CO2 capture using pre-treated dispersed CaO as high temperature sorbent (ID 221)
Stefano Stendardo, Antonio Calabrò

» Investigation of an innovative process for biogas up-grading – pilot plant preliminary results (ID 56)
Lidia Lombardi, Renato Baciocchi, Ennio Antonio Carnevale, Andrea Corti, Giulia Costa, Tommaso Olivieri, Alessandro Paradisi, Daniela Zingaretti

» Method of increasing the efficiency of a supercritical lignite-fired oxy-type fluidized bed boiler and high-temperature three - end membrane for air separation (ID 438)
Janusz Kotowicz, Adrian Balicki

» Monitoring of carbon dioxide uptake in accelerated carbonation processes applied to air pollution control residues (ID 539)
Felice Alfieri, Peter J Gunning, Michela Gallo, Adriana Del Borghi, Colin D Hills

» Process efficiency and optimization of precipitated calcium carbonate (PCC) production from steel converter slag (ID 114)
Hannu-Petteri Mattila, Inga Grigaliūnaitė, Arshe Said, Sami Filppula, Carl-Johan Fogelholm, Ron Zevenhoven

» Production of Mg(OH)2 for CO2 Emissions Removal Applications: Parametric and Process Evaluation (ID 245)
Experience Ikechukwu Nduagu, Inês Romão, Ron Zevenhoven

» Thermodynamic analysis of a supercritical power plant with oxy type pulverized fuel boiler, carbon dioxide capture system (CC) and four-end high temperature membrane air seprator (ID 411)
Janusz Kotowicz, Sebastian Stanisław Michalski

VI . 2 – PROCESS INTEGRATION AND HEAT EXCHANGER NETWORKS

» A multi-objective optimization technique for co- processing in the cement production (ID 42)
Maria Luiza Grillo Renó, Rogério José da Silva, Mirian de Lourdes Noronha Motta Melo, José Joaquim Conceição Soares Santos

» Comparison of options for debottlenecking the recovery boiler at kraft pulp mills – Economic performance and CO2 emissions (ID 449)
Johanna Jönsson, Karin Pettersson, Simon Harvey, Thore Berntsson

» Demonstrating an integral approach for industrial energy saving (ID 541)
René Cornelissen, Geert van Rens, Jos Sentjens, Henk Akse, Ton Backx, Arjan van der Weiden, Jo Vandenbroucke

» Maximising the use of renewables with variable availability (ID 494)
Andreja Nemet, Jiri Jaromír Klemeš, Petar Sabev Varbanov, Zdravko Kravanja

» Methodology for the improvement of large district heating networks (ID 46)
Anna Volkova, Vladislav Mashatin, Aleksander Hlebnikov, Andres Siirde

» Optimal mine site energy supply (ID 306)
Monica Carvalho, Dean Lee Millar

» Simulation of synthesis gas production from steam oxygen gasification of Colombian bituminous coal using Aspen Plus® (ID 395)
John Jairo Ortiz, Juan Camilo González, Jorge Enrique Preciado, Rocío Sierra, Gerardo Gordillo

VOLUME VII

VII . 1 - BUILDING, URBAN AND COMPLEX ENERGY SYSTEMS

» A linear programming model for the optimal assessment of sustainable energy action plans (ID 398)
Gianfranco Rizzo, Giancarlo Savino

» A natural gas fuelled 10 kW electric power unit based on a Diesel automotive internal combustion engine and suitable for cogeneration (ID 477)
Pietro Capaldi

» Adjustment of envelopes characteristics to climatic conditions for saving heating and cooling energy in buildings (ID 430)
Christos Tzivanidis, Kimon Antonopoulos, Foteini Gioti

» An exergy based method for the optimal integration of a building and its heating plant. Part 1: comparison of domestic heating systems based on renewable sources (ID 81)
Marta Cianfrini, Enrico Sciubba, Claudia Toro

» Analysis of different typologies of natural insulation materials with economic and performances evaluation of the same buildings (ID 28)
Umberto Desideri, Daniela Leonardi, Livia Arcioni

» Complex networks approach to the Italian photovoltaic energy distribution system (ID 470)
Luca Valori, Giovanni Luca Giannuzzi, Tiziano Squartini, Diego Garlaschelli, Riccardo Basosi

» Design of a multi-purpose building "to zero energy consumption" according to European Directive 2010/31/CE: Architectural and plant solutions (ID 29)
Umberto Desideri, Livia Arcioni, Daniela Leonardi, Luca Cesaretti ,Perla Perugini, Elena Agabitini, Nicola Evangelisti

» Effect of initial systems on the renewal planning of energy supply systems for a hospital (ID 107)
Shu Yoshida, Koichi Ito, Yoshiharu Amano, Shintaro Ishikawa, Takahiro Sushi, Takumi Hashizume

» Effects of insulation and phase change materials (PCM) combinations on the energy consumption for buildings indoor thermal comfort (ID 387)
Christos Tzivanidis, Kimon Antonopoulos, Eleutherios Kravvaritis

» Energetic evaluation of a smart controlled greenhouse for tomato cultivation (ID 150)
Nickey Van den Bulck, Mathias Coomans, Lieve Wittemans, Kris Goen, Jochen Hanssens, Kathy Steppe, Herman Marien, Johan Desmedt

» Energy networks in sustainable cities: temperature and energy consumption monitoring in urban area (ID 190)
Luca Giaccone, Alessandra Guerrisi, Paolo Lazzeroni and Michele Tartaglia

» Extended exergy analysis of the economy of Nova Scotia, Canada (ID 215)
David C Bligh, V.Ismet Ugursal

» Feasibility study and design of a low-energy residential unit in Sagarmatha Park (Nepal) for envirnomental impact reduction of high altitude buildings (ID 223)
Umberto Desideri, Stefania Proietti, Paolo Sdringola, Elisa Vuillermoz

» Fire and smoke spread in low-income housing in Mexico (ID 379)
Raul R. Flores-Rodriguez, Abel Hernandez-Guerrero, Cuauhtemoc Rubio-Arana, Consuelo A. Caldera-Briseño

» Optimal lighting control strategies in supermarkets for energy efficiency applications via digital dimmable technology (ID 136)
Salvador Acha, Nilay Shah, Jon Ashford, David Penfold

» Optimising the arrangement of finance towards large scale refurbishment of housing stock using mathematical programming and optimisationg (ID 127)
Mark Gerard Jennings, Nilay Shah, David Fisk

» Optimization of thermal insulation to save energy in buildings (ID 174)
Milorad Bojić, Marko Miletić, Vesna Marjanović, Danijela Nikolić, Jasmina Skerlić

» Residential solar-based seasonal thermal storage system in cold climate: building envelope and thermal storage (ID 342)
Alexandre Hugo and Radu Zmeureanu

» Simultaneous production of domestic hot water and space cooling with a heat pump in a Swedish Passive House (ID 55)
Johannes Persson, Mats Westermark

» SOFC micro-CHP integration in residential buildings (ID 201)
Umberto Desideri, Giovanni Cinti, Gabriele Discepoli, Elena Sisani, Daniele Penchini

» The effect of shading of building integrated photovoltaics on roof surface temperature and heat transfer in buildings (ID 83)
Eftychios Vardoulakis, Dimitrios Karamanis

» The influence of glazing systems on energy performance and thermal comfort in non-residential buildings (ID 206)
Cinzia Buratti, Elisa Moretti, Elisa Belloni

» Thermal analysis of a greenhouse heated by solar energy and seasonal thermal energy storage in soil (ID 405)
Yong Li, Jin Xu, Ru-Zhu Wang

» Thermodynamic analysis of a combined cooling, heating and power system under part load condition (ID 476)
Qiang Chen, Jianjiao Zheng, Wei Han, Jun Sui, Hong-guang Jin

VII . 2 – COMBUSTION, CHEMICAL REACTORS

» Baffle as a cost-effective design improvement for volatile combustion rate increase in biomass boilers of simple construction (ID 233)
Borivoj Stepanov, Ivan Pešenjanski, Biljana Miljković

» Characterization of CH4-H2-air mixtures in the high-pressure DHARMA reactor (ID 287)
Vincenzo Moccia, Jacopo D'Alessio

» Development of a concept for efficiency improvement and decreased NOx production for natural gas-fired glass melting furnaces by switching to a propane exhaust gas fired process (ID 146)
Jörn Benthin, Anne Giese

» Experimental analysis of inhibition phenomenon management for Solid Anaerobic Digestion Batch process (ID 348)
Francesco Di Maria, Giovanni Gigliotti, Alessio Sordi, Caterina Micale, Claudia Zadra, Luisa Massaccesi

» Experimental investigations of the combustion process of n-butanol/diesel blend in an optical high swirl CI engine (ID 85)
Simona Silvia Merola, G. Valentino, C. Tornatore, L. Marchitto , F. E. Corcione

» Flameless oxidation as a means to reduce NOx emissions in glass melting furnaces (ID 141)
Jörg Leicher, Anne Giese

» Mechanism of damage by high temperature of the tubes, exposed to the atmosphere characteristic of a furnace of pyrolysis of ethane for ethylene production in the petrochemical industry (ID 65)
Jaqueline Saavedra Rueda, Francisco Javier Perez Trujillo, Lourdes Isabel Meriño Stand, Harbey Alexi Escobar, Luis Eduardo Navas, Juan Carlos Amezquita

» Steam reforming of methane over Pt/Rh based wire mesh catalyst in single channel reformer for small scale syngas production (ID 317)
Haftor Orn Sigurdsson, Søren Knudsen Kær

VOLUME VIII

VIII . 1 – ENERGY SYSTEMS : ENVIRONMENTAL AND SUSTAINABILITY ISSUES

» A multi-criteria decision analysis tool to support electricity planning (ID 467)
Fernando Ribeiro, Paula Ferreira, Madalena Araújo

» Comparison of sophisticated life cycle impact assessment methods for assessing environmental impacts in a LCA study of electricity production (ID 259)
Jens Buchgeister

» Defossilisation assessment of biodiesel life cycle production using the ExROI indicator (ID 304)
Emilio Font de Mora, César Torres, Antonio Valero, David Zambrana

» Design strategy of geothermal plants for water dominant medium-low temperature reservoirs based on sustainability issues (ID 99)
Alessandro Franco, Maurizio Vaccaro

» Energetic and environmental benefits from waste management: experimental analysis of the sustainable landfill (ID 33)
Francesco Di Maria, Alessandro Canovai, Federico Valentini, Alessio Sordi, Caterina Micale

» Environmental assessment of energy recovery technologies for the treatment and disposal of municipal solid waste using life cycle assessment (LCA): a case study of Brazil (ID 512)
Marcio Montagnana Vicente Leme, Mateus Henrique Rocha, Electo Eduardo Silva Lora,Osvaldo José Venturini, Bruno Marciano Lopes, Claudio Homero Ferreira

» How will renewable power generation be affected by climate change? – The case of a metropolitan region in Northwest Germany (ID 503)
Jakob Wachsmuth, Andrew Blohm, Stefan Gößling-Reisemann, Tobias Eickemeier, Rebecca Gasper, Matthias Ruth, Sönke Stührmann

» Impact of nuclear power plant on Thailand power development plan (ID 474)
Raksanai Nidhiritdhikrai, Bundhit Eua-arporn

» Improving sustainability of maritime transport through utilization of liquefied natural gas (LNG) for propulsion (ID 496)
Fabio Burel, Rodolfo Taccani, Nicola Zuliani

» Life cycle assessment of thin film non conventional photovoltaics: the case of dye sensitized solar cells (ID 471)
Maria Laura Parisi, Adalgisa Sinicropi, Riccardo Basosi

» Low CO2 emission hybrid solar CC power system (ID 175)
Yuanyuan Li, Na Zhang, Ruixian Cai

» Low exergy solutions as a contribution to climate adapted and resilient power supply (ID 489)
Stefan Goessling-Reisemann, Thomas Bloethe

» On the use of MPT to derive optimal RES electricity generation mixes (ID 459)
Paula Ferreira, Jorge Cunha

» Stability and limit cycles in an exergy-based model of population dynamics (ID 128)
Enrico Sciubba, Federico Zullo

» The influence of primary measures for reducing NOx emissions on energy steam boiler efficiency (ID 125)
Goran Stupar, Dragan Tucaković, Titoslav Živanović, Miloš Banjac, Srđan Belošević,Vladimir Beljanski, Ivan Tomanović, Nenad Crnomarković, Miroslav Sijerčić

» The Lethe city car of the University of Roma 1: final proposed configuration (ID 45)
Roberto Capata, Enrico Sciubba

VIII . 2 - POSTER SESSION

» A variational optimization of a finite-time thermal cycle with a Stefan-Boltzmann heat transfer law (ID 333)
Juan C.Chimal-Eguia, Norma Sanchez-Salas

» Modeling and simulation of a boiler unit for steam power plants (ID 545)
Luca Moliterno, Claudia Toro

» Numerical Modelling of straw combustion in a moving bed combustor (ID 412)
Biljana Miljkoviü, Ivan Pešenjanski, Borivoj Stepanov, Vladimir Milosavljeviü, Vladimir Rajs

» Physicochemical evaluation of the properties of the coke formed at radiation area of light hydrocarbons pyrolysis furnace in petrochemical industry (ID 10)
Jaqueline Saavedra Rueda , Angélica María Carreño Parra, María del Rosario Pérez Trejos, Dionisio Laverde Cataño, Diego Bonilla Duarte, Jorge Leonardo Rodríguez Jiménez, Laura María Díaz Burgos

» Rotor TG cooled (ID 121)
Chiara Durastante, Paolo Petroni, Michela Spagnoli, Vincenzo Rizzica, Jörg Helge Wirfs

» Study of the phase change in binary alloy (ID 534)
Aroussia Jaouahdou, Mohamed J. Safi, Herve Muhr

» Technip initiatives in renewable energies and sustainable technologies (ID 527)
Pierfrancesco Palazzo, Corrado Pigna

ECOS 2012

VOLUME V

A co-powered Concentrated Solar Power Rankine cycle concept for small size Combined Heat and Power

Alessandro Corsini[a], Domenico Borello[b], Franco Rispoli[c] and Eileen Tortora[d]

[a]Facoltà di Ingegneria, Sapienza Università di Roma, Latina, Italy, alessandro.corsini@uniroma1.it
[b]Dipartimento di Meccanica e Aeronautica, Sapienza Università di Roma, Roma, Italy, domenico.borello@uniroma1.it
[c]Dipartimento di Meccanica e Aeronautica, Sapienza Università di Roma, Roma, Italy, franco.rispoli@uniroma1.it
[d]Dipartimento di Meccanica e Aeronautica, Sapienza Università di Roma, Roma, Italy, eileen.tortora@uniroma1.it (CA)

Abstract:

The present work investigates the matching of an advanced small scale combined heat and power Rankine cycle plant to end-user thermal and electric load. The power plant consists of a concentrated solar power field co-powered by a biomass furnace to produce steam in a Rankine cycle, with a Combined Heat and Power configuration. A hotel was selected as the end user. The power plant design and its operation were modelled and investigated by adopting transient simulations with a hourly distribution. The study of the load matching of the proposed renewable power technology and the final user has been carried out by comparing two different load tracking scenarios, i.e. the thermal and the electric demands. As a result, the power output follows fairly well the given load curves, supplying, on a selected winter day, about 50 GJ/d of thermal energy and the 6 GJ/d of electric energy, with reduced energy dumps when matching the load. Furthermore, for the same winter day, the system allows the reduction of about 4·103 kgCO_2 of greenhouse gas emissions.

Keywords:

Co-powered Concentrated Solar Power, Rankine Cycle, Transient Simulation, Load Matching.

1. Introduction

In recent years the use of Combined Heat and Power (CHP) was commonly considered to supply energy to end users in the service or residential sectors. The basic argument in favour of CHP is the possibility to obtain electric and thermal energy in situ, improving the power generation efficiency and reducing the losses usually related to the energy distribution [1, 2]. Notably among the existing CHP technologies, only some exceptions are based on the exploitation of different fuels from natural gas, i.e. small-scale power plants based on biomass derived fuel exploitation, like wood or biogas [3, 4].

In most applications the main factor which determines the economic viability of CHP schemes is the high utilisation of heat and electric energy, which are produced simultaneously. Most of the literature indicates that a CHP plant needs to be fully utilised providing heat and power for a minimum duty of 4,500 h per annum to gain its breakeven point [5].

When designing renewable energy based CHP technologies, in a distributed generation concept, one of the key factors is the capability of tracking the time-dependent end-user load. Renewable Energy Sources (RES), intermittent by nature, produce inconsistently and somewhat unpredictably power outputs uncorrelated with the end user power demands, typically variable according to predictable

daily load profiles. As a consequence of this mismatch the available RES energy may not meet the energy demand, resulting in deficit and surplus energy situations.

Several solutions have been proposed to attenuate the RES-user matching inconsistency. The conventional remedial strategy is to plug the supply gap providing alternative capacity, known as spinning reserve [6]. Among the solutions devoted to RES electric grid integration, it is worth mentioning the use of high capacity energy storage to save the produced energy surplus and postponing the energy surplus delivery [7,8], or combining renewable energy sources with complementary intermittencies [9].

In this respect, the present study investigates a CHP scheme combining a parabolic trough field for concentrated solar power (CSP), a thermal energy storage and a biomass furnace as complementary source. It is worth noting that the biomass source is a *sui generis* RES, in fact its storage simplicity permits to customize the power production management, exactly like the fossil fuel sources.

Concerning the parabolic trough field, that device was selected for its high worldwide development among the CSP systems [10]. Nonetheless, an important aspect of these plants is the size, which, is usually large. In fact solar trough plants are characterised by multi-MW sizes, which range up to about 50 MW_{el} for parabolic trough systems. Also the biomass power plants are usually rated in the range 5–100 MW. Even so, while CSP plants size is still growing [11, 12], in the biomass field there are several applications on small-scale biomass power plants [13, 14].

The aim to exploit CSP technology and limit the plant footprint led to the design of a small scale plant, recently presented in [15, 16], composed by a 2,580 m^2 parabolic trough field, a thermal energy storage system (TES) and a 1,163 kW biomass furnace to face the solar source fluctuations. A heat transfer fluid (HTF), i.e. diathermic oil, is heated by the parabolic through field and biomass furnace and subsequently it is sent to a heat recovery steam generator where it produces low enthalpy saturated steam that is sent to a 130 kW reciprocating steam engine for the electric energy production. Moreover, the Rankine cycle (RC) economizer is fed by the exhaust gases derived from the biomass combustion. A heat recovery for thermal energy production is obtained, using hot water as heat carrier, in a back-pressure scheme at 134 °C and 300 kPa.

The investigations on the proposed RES-based small-scale CHP Rankine cycle plant, when matched to a typical hotelier end-user were carried out by transient model simulations. The selection of a hotel as end-user was made for its high heat/electricity consumption ratio. The system matching behaviour is analyzed for both thermal and electric load tracking with the aim to demonstrate its capability to meet the end-users energy request on a 24 hour period in a winter day as more challenging for the solar field performance.

The transient model and the simulations were performed in the TRNSYS environment [17] supported by the in-house made types of the biomass furnace and reciprocating steam engine and the STEC component model library [18]. The software TRNSYS was selected as it is a well-known instrument to model complex energy systems, as demonstrated by several studies appeared in the open literature which mostly deal on RES applications in a few fields like small-islands stand alone power systems [8, 19], or, more related to the present paper, on CSP field simulations [20], TES behaviour in solar trough plants [21] and matching to a hotel end-user [16].

2. Co-powered solar-biomass plant and model description

2.1. Component and system description

The proposed CHP concept, Figure 1, concerns of a solar-biomass Rankine cycle system. The basic equipment of the power block consists of 1,200 kW solar trough field, 360 kW thermal energy storage (TES) and 1,163 kW biomass furnace to feed the heat transfer fluid (HTF) loop and the related RC. Although biofuel can be easily stored and is promptly available, the TES allows avoiding the dump of surplus CSP energy occurring during the mismatch with respect to the load.

It is worth noting that the biomass furnace is constantly on duty at a minimum power that is the 35% of its maximum power (i.e. 407 kW_{th}), in order to ease its complementary source role avoiding

power output deficits and/or furnace start-up problems related to the Direct Normal Insulation (DNI) sudden variations.

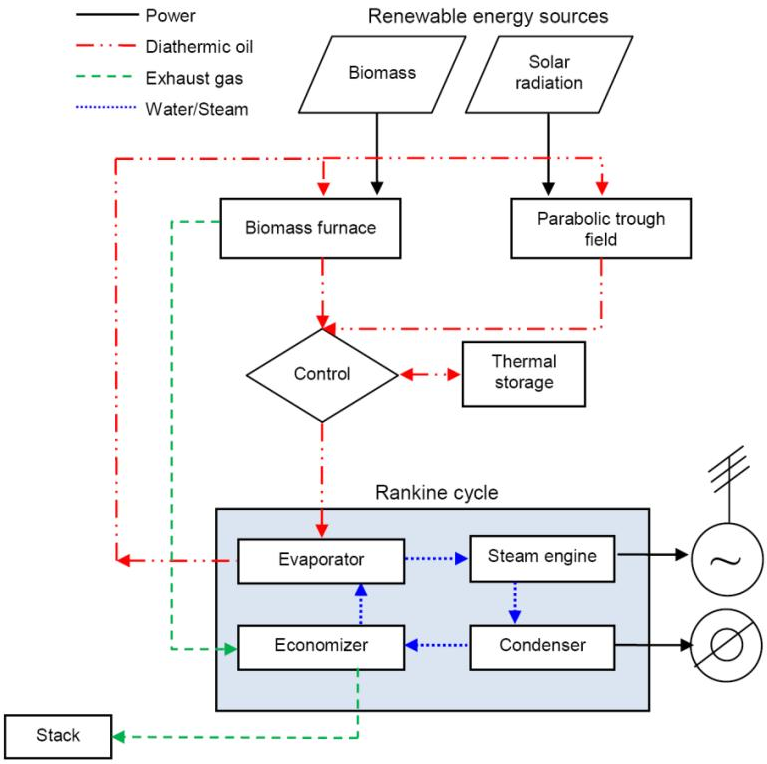

Figure 1.Power plant diagram.

Table 1. Main components description and nominal size.

Component description		Size
Solar parabolic trough field (2,580 m^2)	kW_{th}	1,200
TES	kW_{th}	360
Biomass furnace	kW_{th}	1,163
Reciprocating steam engine	kW_{el}	130
Condenser	kW_{th}	1,240
Diathermic oil circuit		
Maximum/minimum temperature	°C	300/240
Maximum/minimum specific heat	kJ/kg K	2.36/ 2.19
Operating pressure	kPa	800
Water/Steam circuit		
Maximum/minimum pressure	kPa	2,800/300
Maximum/minimum temperature	°C	230/134
Water/steam mass flow rate	kg/s	0.51
Electric power	kW	130
Thermal power	kW	1,100

The HTF circuit supplies the thermal energy to the RC for the production of saturated steam to be expanded in a 130 kW reciprocating steam engine fitted with an electric generator. According to a bottomer CHP configuration, the expanded steam is condensed producing a thermal power output

available at a constant temperature of 80 °C, i.e. the temperature demand of typical district heating networks. Figure 2 illustrates the temperature-entropy diagram of the Rankine cycle and the thermodynamic parameters in the reference points.The main components and system thermodynamic parameters, subdivided in diathermic oil and water/steam circuit, are described in Table 1. Additional details concerning the power system components are given in [15].

The temperature-heat diagram is shown in Figure 3. The exhaust gas, diathermic oil and water-steam temperatures with the Rankine cycle exchanged heat rate are shown. In particular, two lines are plotted for the exhaust gas respectively showing the temperature evolution at CSP design operation with the biomass furnace working at 35% duty rate (Gas-35%), and at 100% of the biomass heat contribution (Gas-100%). In between these two limiting lines the solar contribution to the Rankine cycle spans from maximum (Gas-35%) to zero (Gas-100%). Notably, the pinch point temperature difference for the evaporator is set to 10 °C.

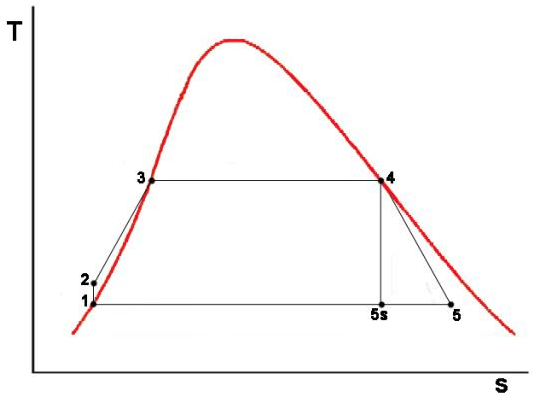

	1	2	3	4	5
T [K]	406,73	407,15	503,29	503,29	406,73
P [bar]	3,00	28,00	28,00	28,00	3
ρ [kg/m^3]	931,78	932,75	827,10	13,99	1,83
u [kJ/kg]	561,27	562,06	987,39	2604,02	2345,94
h [kJ/kg]	561,60	565,06	990,78	2804,11	2509,69
s [kJ/kg K]	1,67	1,67	2,61	6,21	6,46
quality	0,0	0,0	0,0	1,0	0,9

Figure 2. Temperature-Entropy diagram of power cycle.

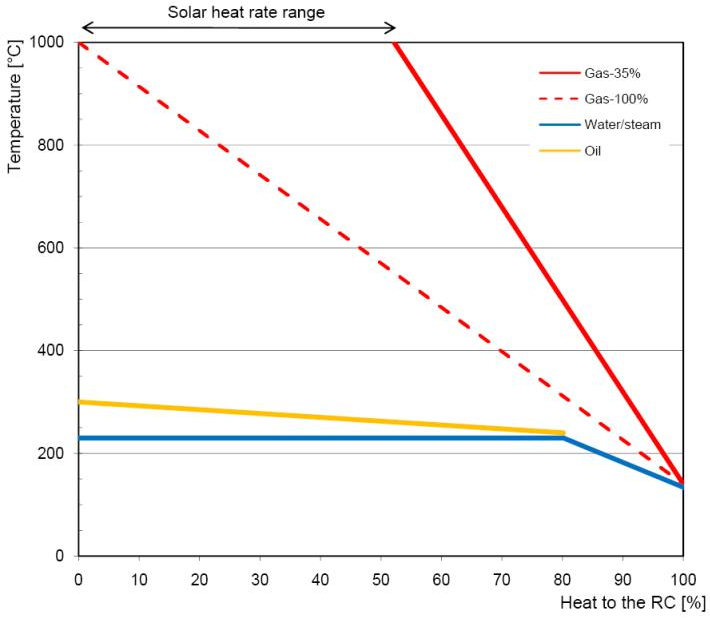

Figure 3. Temperature-Heat diagram.

2.2. Transient model description

In order to evaluate the time-dependent behaviour and the performance of the proposed system a transient model was developed in the TRNSYS framework [17] integrated with the STEC library [18]. The RC transient model also includes in-house made types for the biomass furnace and for the reciprocating steam engine [15]. The model subsets and their linkages are described by the flow

diagram in Figure 4. The present solar-biomass CHP plant is broadly based on a configuration recently investigated and assessed [15].

The base-line model has been implemented by a control logic targeted to the tracking of different loads, namely heat or power demands. The development of the load tracking strategy has been based on the definition of algebraic correlations between the HTF flow rate, directly related to the RES power input, and the system thermal power output (P_{th}) or the system electric output (P_{el}), respectively. The HTF flow rate was selected as the reference parameter because it governs the actual power outputs according to the instantaneous renewable energy availability. A sensitivity analysis, was carried out on the power system configuration by varying $\dot{m}_F$ and recording P_{el} and P_{th} values. Figure 5shows the values obtained with the sensitivity analysis (grey lines) and the corresponding trend lines (black lines) and equations. The HTF control equations, accordingly derived, read as

$$\dot{m}_F = 2 \cdot 10^{-6} \cdot P_{th}^{3}.289 \ ,$$

$$\dot{m}_F = 3.6 \cdot 10^{-2} \cdot P_{el}^{2}.713 \ .$$

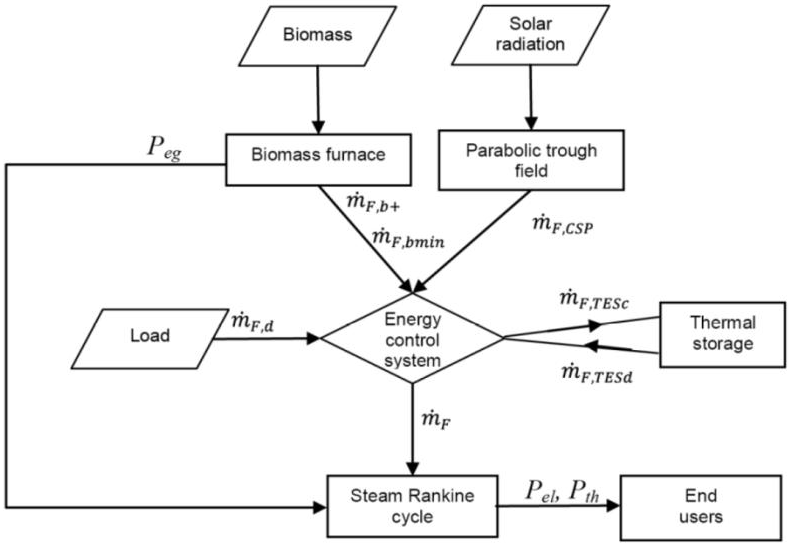

Figure4. Energy conversion system flow diagram.

The control logic was implemented, Figure 4, in order to match the requested HTF flow rate target ($\dot{m}_{F,d}$) at each time-step with the actual power demand according to the adopted load tracking law. Hence, the HTF flow rate target tracks the load evolution following a two-level control strategy, respectively driving the solar section and the whole system. In particular, the solar section control verifies the state of charge of the TES, giving priority to the storage charging in case of emptiness ($\dot{m}_{F,TESc}$). The flow rate not needed to charge the TES can be can be directly supplied to the Rankine cycle. The second control acquires the load data ($\dot{m}_{F,d}$) and compares the HTF flow rate target with the actual HTF flow rate achievable from the available solar field and the minimum biomass furnace rate ($\dot{m}_{F,bmin}$) at each time step, giving rise to three possible situations:

1. direct CSP contribution surplus, the exceeding HTF flow rate will be dumped;
2. direct CSP contribution deficit, the missing heat flux will be first requested to the TES (flow rate $\dot{m}_{F,TESd}$); and
3. in case of insufficient flux from the solar section and minimum biomass contributions, an additional heat flux is requested to the biomass furnace (flow rate $\dot{m}_{F,b+}$).

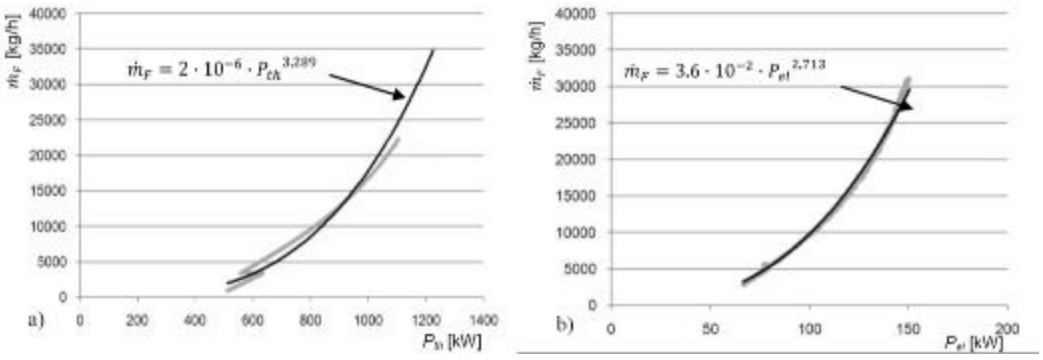

Figure5. Thermal a) and electric b) output control equations.

3. End user description

3.1. End-user load profile

The behaviour of the proposed RES-based small-scale CHP Rankine cycle plant is investigated in the matching of load curve of a typical hotelier end-user during a 24 hour time period. The hotel was chosen, among tertiary sector end-users, for its high annual heat/electricity consumption ratio. The end-user characteristics are summarized, in Table 2. The energy data gives a heat/electric consumption ratio higher than five, Table 2 [22], which is typical of European hotelier end-user figure, in contrast to the standard North-American hotel energy profile [23]. Furthermore, in order to take into account the cooling load also, it is worthy referring to the equivalent thermal load (obtained by the addition of the actual thermal load and the thermal load resulting if fulfilling the cooling load with a absorption chiller) with a 0,7 COP. In this case the heat/electric rises to a value of 7.44. The cooling load takes place only in the months from June to September, with a constant distribution of about 600 GJ/month.

Table 2. End users characteristics [22].

	Hotel
Volume [m^3]	43,000
Number of sleeping accommodations	350
Heat load [GJ/y]	8,640
Electric load [GJ/y]	1,656
Cooling load [GJ/y]	2,580
Equivalent thermal load	12˙326
Heat/electric consumption ratio [GJ_{th}/GJ_{el}]	5.23
Equivalent heat/electric consumption ratio [GJ_{th}/GJ_{el}]	7.44

Figure 6 shows the monthly distribution of the electric and equivalent thermal load for the selected end-user; the average daily energy demand (dot sign) is represented in relationship with the daily average power demand (x sign) and the power demand excursion (bar). It is evident that the electric energy request has an almost constant behaviour with average daily energy demand always below 200 GJ/day. Whereas the thermal monthly profile has a seasonal connotation which entails a thermal load range from 250 GJ on the summer period to 1,370 GJ on the winter one. It is worth noting that generally the average power demand is positioned on the lower part of the power demand excursion bars, indicating that the energy demand is composed by frequent low power demand values and rare high power values. This behaviour is highlighted in the summer equivalent

thermal load curves (from June to September) of both the end users, when high peaks of cooling energy are requested during the day.

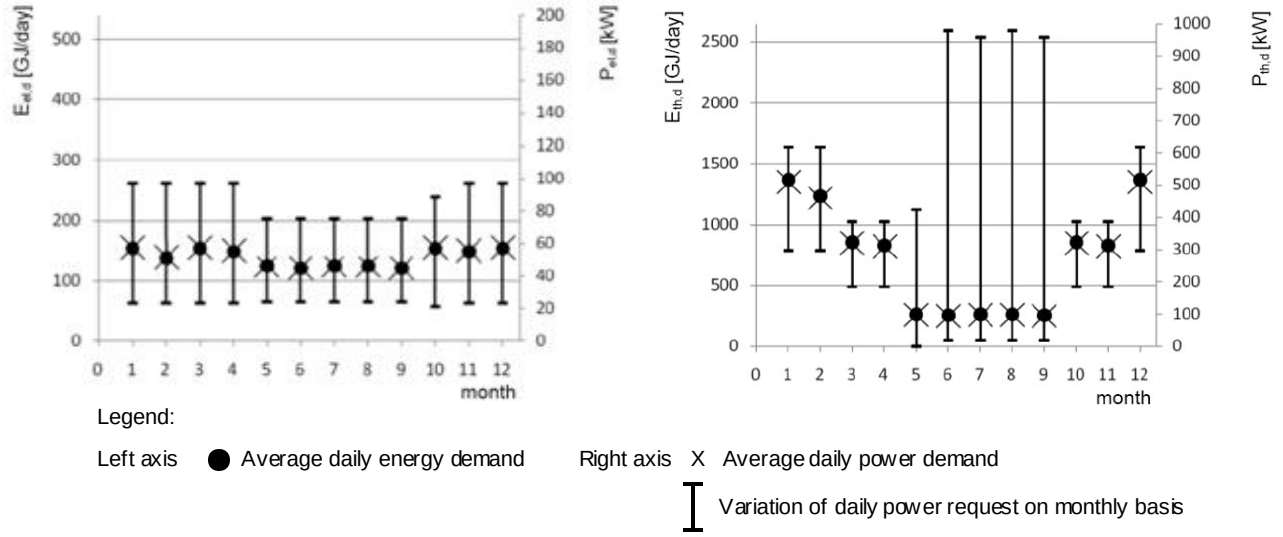

Figure 6. Hotel monthly electric and thermal load yearly behaviour.

3.2. RES data input

The RES input data are available on a hourly distribution over a year period. The direct normal insulation data [24], are referred to Rome's latitude, i.e. 41°54'39"24 N, as indicative of a central Italian location DNI data show a maximum value in the month of July, with 733.68 MJ/m^2 and a minimum value of 253.04 MJ/m^2 in December, with an annual cumulative irradiation of 5,760 MJ/m^2. The DNI hourly distribution data on the selected winter day are provided in Table 3.

Table 3. Direct normal insulation data for the selected winter day [24].

Hour	DNI [W/m^2]	Hour	DNI [W/m^2]
1	0	13	938.06
2	0	14	918.06
3	0	15	848.06
4	0	16	560.83
5	0	17	18.33
6	0	18	0
7	0	19	0
8	18.33	20	0
9	560.83	21	0
10	848.06	22	0
11	918.06	23	0
12	938.06	24	0

As far as the biomass is concerned, the thermo-chemical characteristics are typical of short rotation forestry derived woody pellet, with a lower heating value of about 17 MJ/kg and high carbon and oxygen ratios.

4. Solar-biomass power plant performance

The analysis of solar-biomass plant is based on the comparison of transient and overall performance under two power modulation scenarios. Namely, i. the tracking of the end-user thermal load in the hypothesis of electric energy surplus sale to the grid, and ii. the tracking of the end-user electric load with a dump of the thermal energy surplus.

In the following, the overall CHP plant performances are first discussed on a yearly and monthly basis and then the time-dependent results on a winter day are shown and discussed. In particular, the study focuses on a typical winter day in order to discuss the behaviour of the system in operating conditions which are not favourable to the solar sub-system. The thermal and electric load curves are shown in Figure 7. The thermal load ranges from 300 to 640 kW, with a sharp min-max modulation. On the other hand, the electric load, always below 100 kW, achieves its peak level in the morning and then it decreases during the day being nearly constant in the afternoon and evening times.

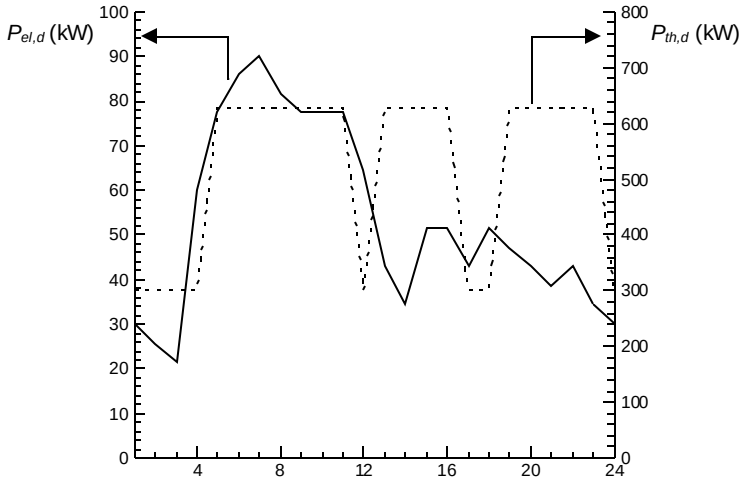

Figure 7. End user electric and thermal load for a typical winter day [22].

4.1. Overall performance

In order to compare the performance of the solar-biomass CHP system under the two proposed load-tracking logics, a number of indicators have been considered (Table 4). In particular the indices concern the RES system performance, the output performance and the RC efficiency. The surplus and deficit index for the output performance were calculated by adding the surplus or deficit thermal and electric energy production which occurred hour per hour with respect to the corresponding load energy request. The overall performances have been computed over a year period.

The integration over the duty time showed that the parabolic trough field collect s 4,277.53 GJ/y of solar energy. Furthermore, as the energy input need varies in the two scenarios in reason of the different loads, the effective solar energy supply, which is a balance between the available solar energy and the TES charge discharge rates, differs in the two cases with an amount of about 4,172 GJ/y in the electric tracking scenario and 4,093 GJ/y in the thermal tracking one. The biomass energy supply varies for the same reason, leading to an effective solar supply fraction, calculated as the percentage of the effective solar energy with respect to the sum of the effective solar energy and the biomass furnace energy, of 18.71% in the electric tracking case and 19.20% in the thermal tracking one. It is worth noting that the selected sizing of the solar collector field is made in accordance to the Italian existing feed in tariff minimum size of 2,500 m^2 for the concentrated solar power.

Looking at the RC system performance Table 4, the value of 1.2 for the primary energy ratio demonstrates that the presented solar-biomass Rankine cycle systems can effectively allow the saving of conventional primary energy sources in each presented scenario. Looking at the electric output, globally the system produces more electric energy than the need with a peak production/request ratio of 124% for the electric tracking.

Table 4. Overall performance data.

		Electric Tracking	Thermal Tracking
RES system	Solar energy [GJ/y]	4,277.53	4,277.53
	Effective solar energy supply [GJ/y]	4,172.09	4,092.72
	Biomass energy [GJ/y]	18,132.39	17,221.31
	Solar fraction	18.71	19.20
	Biomass consumption [ton/y]	990.84	941.06
	Global effective energy input E_g [GJ/y]	22,304.48	21,314.03
Electric output	Plant electric energy output E_{el} [GJ/y]	**2,064.37**	2,017.10
	$E_{el,d}$ [GJ/y]	**1,664.68**	1,664.46
	$E_{el}/E_{el,d}$[%]	**124.01**	121.19
	Surplus [%]	**19.80**	25.80
	Deficit [%]	**0.44**	8.32
Thermal output	Plant thermal energy supply E_{th}[GJ/y]	17,291.93	**16,895.49**
	$E_{th,d}$[GJ/y]	11,656.13	**11,653.99**
	$E_{th}/E_{th,d}$[%]	148.35	**144.98**
	Surplus [%]	40.09	**33.27**
	Deficit [%]	7.49	**2.26**
RC system	Net electric efficiency = E_{el}/E_g [%]	9.26	9.46
	Net thermal efficiency = E_{th}/E_g [%]	77.53	79.27
	Electric index = E_{el}/E_{th} [-]	11.94	11.94
	Primary energy ratio = $(E_{el}/\eta_{el}+E_{th}/\eta_{th})/E_g$ [-][1]	1.21	1.24

4.2. Hourly power system performance

The global data in a RES based plant are not indicative of the effective load covering. As a matter of fact, analyzing the hourly behaviour of the systems, there are both surplus and deficit situations. It is worth noting that the hotel electric tracking scenario offers a completely absence of thermal supply deficits, but shows a 132% of thermal energy surplus. Considering that the electric source is easier to manage than the thermal one, as it can be sold or bought from the grid, the most suitable configuration appears to be the thermal tracking one.

Figure 8 shows the surplus (values higher than zero) and deficits (values lower than zero) behaviour of the electric and thermal power supply for both the electric and thermal tracking scenario. The graphs, presented on a monthly basis, are based on hourly data, and show, on the left axis, the minimum and maximum difference registered in the month between the load and the supplied power. On the right axis the cumulative surplus and deficit energy is shown for each month. The electric output of the electric tracking configuration, Figure 8 a), shows the smaller values variation. Nevertheless, as this good result corresponds to the electric behaviour on the electric tracking

[1] For the primary energy ratio evaluation, the values for the reference electric and thermal efficiencies are $\eta_{el} = 0.38$ and $\eta_{th} = 0.8$.

configuration, the thermal behaviour is worst, with a high rate of surplus distributed all over the reference year and a deficit peak during the summer period, as the electric energy request is not sufficiently high to let the system to produce the requested thermal energy too. The deficit and surplus events have a quadruple explanation. The first one is that half of the results are load-independent, e.g. when discussing the electric tracking configuration, the thermal output does not follow any production law, but is dependent from the electric production trend, without any correlation to the thermal load. Secondly, in most of the occasions the gaps with the requested load are entailed to the used correlation among load energy and hot thermal fluid flowrate, which do not perfectly fit the sensitivity analysis data, conducing to gaps between the desired output and the obtained one. Nevertheless, those gaps are not particularly remarkable. The third reason, instead, explains the high surplus peaks that occur, by observing that sometimes there are contemporarily an elevated available solar supply and full thermal energy storage. In those cases the system, which has to deliver the collected heat, sends all the hot flowrate directly to the Rankine cycle. The last reason is that the biomass furnace is always on duty, even if on a minimum rate, supplying energy also in extremely low energy request.

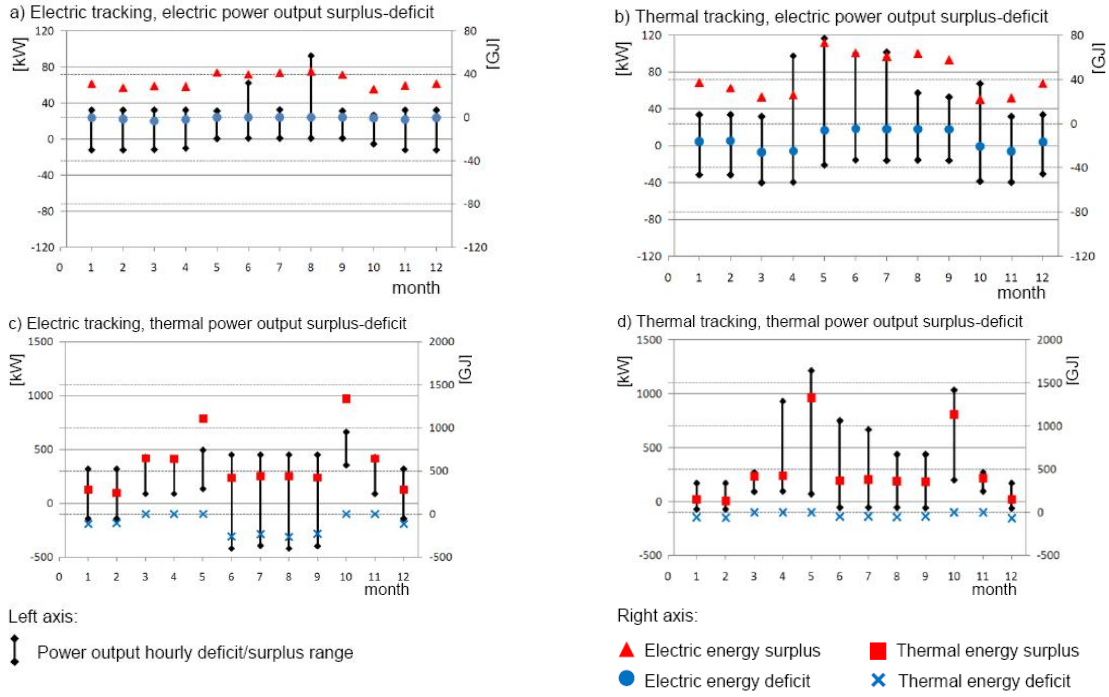

Figure 8. Hotel electric and thermal power surplus/deficit behaviour during a one year period under electric and thermal load tracking conditions.

4.3. Matching through the load tracking

The thermal and electric load tracking are analysed by comparing hourly distribution of the different power components. Figure 9 shows the thermal power inputs to the RC, respectively from the solar field (P_{CSP}) and the biomass furnace (P_b), the TES contribution during the charge/discharge cycles ($P_{TES,c}$, $P_{TES,d}$), and the thermal power recovered from the exhaust gas (P_{eg}).

As evident, the CSP power is available only between 9 a.m. and 4 p.m., with two peaks, respectively ante- and post-meridian, of about 400 kW. It is worth noting that the P_{CSP} reduction at 12 a.m. is caused by the reflection losses due to multiple reflections occurring for high solar incidence angles [25].

In the thermal load tracking (Figure 9.a) the P_{CSP} is not sufficient to meet the thermal load ($P_{th,d}$) which rapidly rises to its peak value about 600 kW. For this reason the control system driven by the thermal demand, activates the TES system to store fractions of the solar energy ($P_{TES,c}$) available in

the peak hours and to buffer it ($P_{TES,d}$) in the day time when the sun DNI falls below 3,000 kJ/h m^2. The passage to the electric load tracking logic (Figure 9.b) appears to influence remarkably the RES power inputs/outputs and the TES charge/discharge cycle. In particular, the TES charge cycle is no more driven by solar radiation a.m. and p.m. peaks and it is shifted in the afternoon hours when the overall electric power request reduces. This circumstance causes the shifting of the TES discharge cycle to the evening time and unbalances the power input from the biomass furnace which is mainly concentrated in the early morning hours. This finding confirms that the TES and the biomass furnace have complementary behaviours by implementing an effective reserve to the solar source.

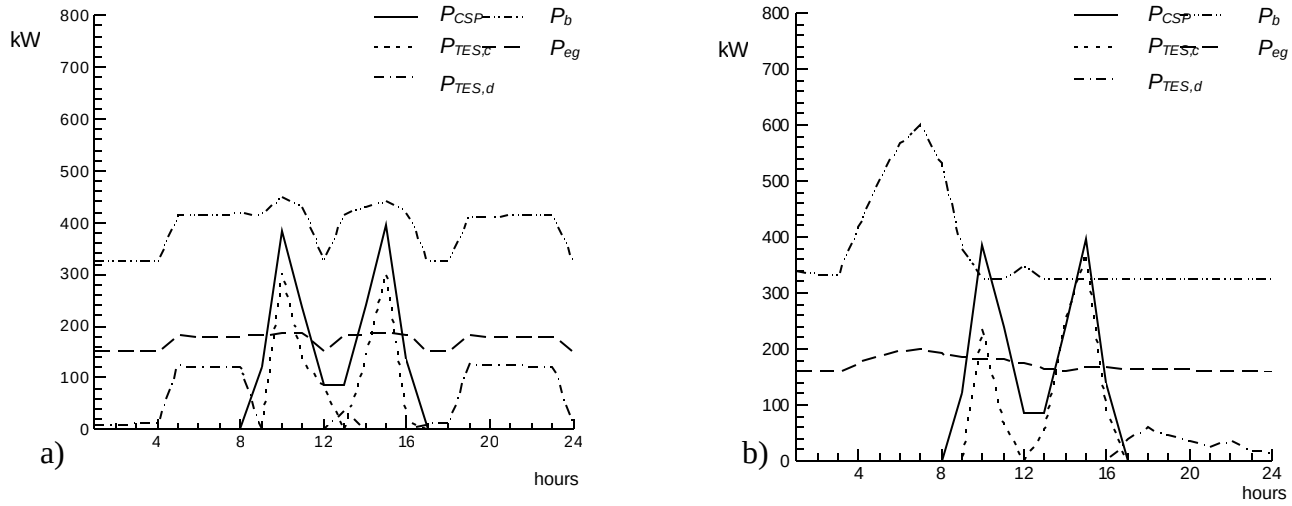

Figure 9. RES power contribution with the a) thermaland b) electric load tracking matching.

The matching of the power plant with the end-user demand, as driven respectively by the thermal and electric profile, is described in Figure 10 and Figure 11, by plotting the thermal power output (P_{th}) against the thermal power request ($P_{th,d}$) (Figure 10.a and Figure 11.a), and the electric power output (P_{el}) against the electric demand ($P_{el,d}$) (Figure 10.b and Figure 11.b).

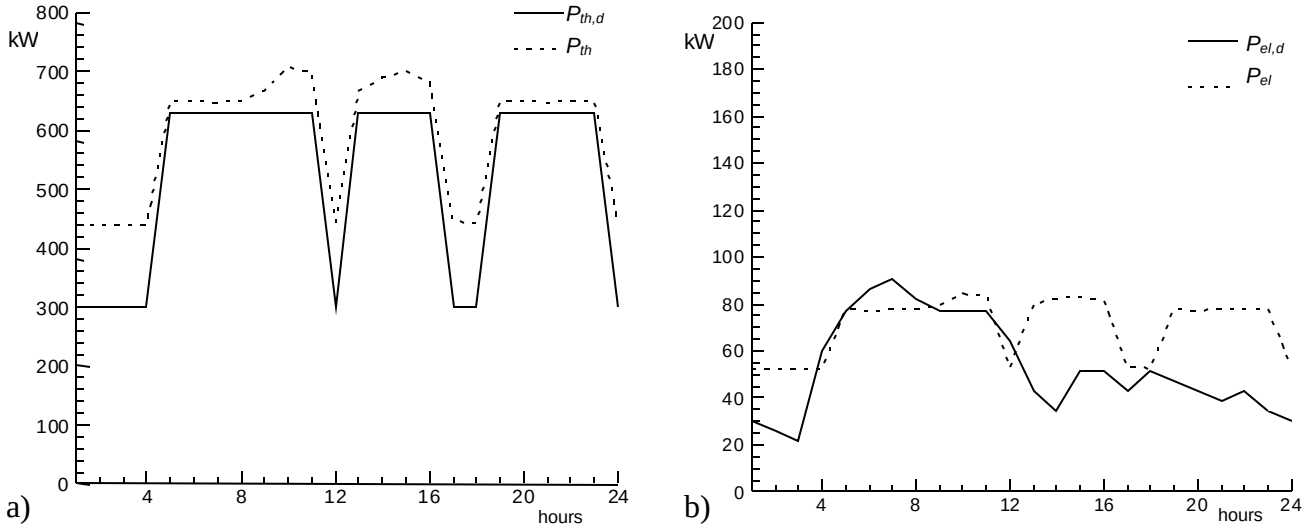

Figure 10. Thermal a) and electric b) behaviour with the thermal load tracking matching.

In the thermal load tracking case, Figure 10.a, the thermal load ($P_{th,d}$) is completely satisfied by the solar-biomass plant output (P_{th}). The exceeding heat production during the periods of minimum request is consequent to the control regime of the biomass furnace which is kept at a constant minimum level. When looking at the electric matching, Figure 10.b, it is remarkable that the power plant electric output (P_{el}) mimics the shape of the leading load component. As a result, the correct

sizing of the solar-biomass CHP system provides a fair matching in the period of peak electric request, while the load tracking logic drives the system to an over-production of electricity during the remaining duty time.

Looking at the electric load tracking case, as a matter of fact, the thermodynamic characteristics of the solar-biomass CHP system determine the significant overproduction of the thermal power output when the overall control is given to the electricity production. Figure 11.a shows the electric peak request in the early morning which, giving rise to the intervention of the biomass, in absence of any direct or stored solar contribution, results in a large surplus of heat availability. Moving to the electric matching, Figure 11.b, it is shown that the delivered electric power (P_{el}) follows fairly the load ($P_{el,d}$) between 4 a.m. and 12 p.m. while keeping it nearly constant in the remaining hours.

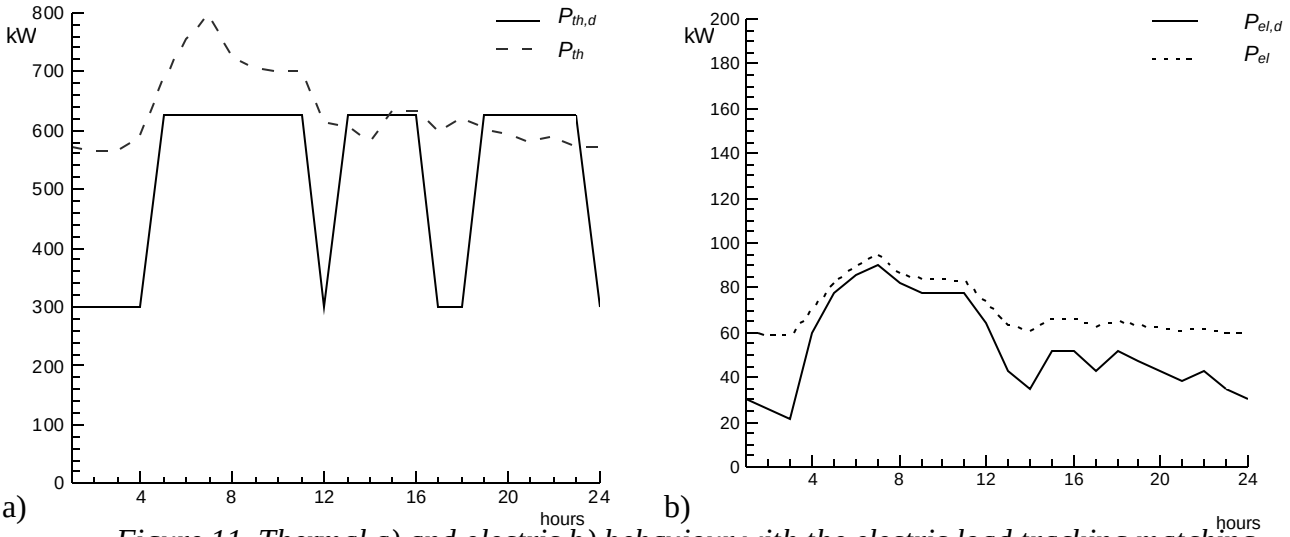

Figure 11. Thermal a) and electric b) behaviour with the electric load tracking matching.

5. Environomic issues

here the environmental and economic aspects will be analyzed. An effect of the application of this system are the entailed Greenhouse Gases (GHG) emission savings related to the solar fraction, estimated by means of emission factors related to the Italian thermoelectric power stations at reference year 2003 [22]. The emissions savings are evaluated considering the entire electric energy supply, in the hypothesis of grid transfer of the surplus, and the fraction of thermal energy supplied to the end users, in the hypothesis of dump of the thermal energy surplus

The result is a higher emission saving in the thermal tracking scenario, which avoids the emissions of 661 ton/y of carbon dioxide.

Table 5. Global emission savings for a typical winter day from solar fraction.

	Electric tracking	Thermal tracking
CO_2 [ton/y]	555.29	661.00
SO_x[ton/y]	0.58	0.69
NO_x[ton/y]	0.35	0.41
TSP [ton/y]	0.02	0.03

Another essential environmental aspect is the land use of the plant. Considering the net land use, Table 6, the plant needs about 13,000 m^2, nevertheless, taking into account security distances and the need of space for the power conversion block the needed surface amounts to 31,000 m^2. Even if

the solar field accounts for the 51.56% of the global footprintit is meaningful to reflect on the higher specific power of the parabolic trough field, i.e. 0.46 kW_p/m^2, when compared to the most commercial photovoltaic power plants (0.17 kW_p/m^2) referring only to the devices surface area.

Concerning the plant costs, Table 7 indicates that the parabolic trough field with the thermal energy storage are the most expensive devices of the proposed system. In particular, the capital cost of a solar trough field with thermal storage has been evaluated in 4,820 $/kW for the reference year 2006 [10]. It is worth noting that these data refer to large CSP technologies and must be considered only as a rough estimate of the present CSP device. Referring to the other technologies, the capital costs have been obtained by private communications with producers. In the utilities heading, it entails costs for electric panels, electric and hydraulic connections, civil works &c.

It is obvious that such high costs are constraining to the development of the proposed system when thinking to the standard fossil fuel based power technologies. Nevertheless, in a fossil fuel free power generation perspective, given from the exhaustion of fossil energy sources and from the need to pull down the fossil sources related emissions, the current high costs become a side issue in behalf of the sustainable development of the energy sector.

Table 6. Plant land use.

	Net land use [m^2]
Solar field	6,780
TES	570
Biomass furnace, filter and stack	700
Biomass storage	3,000
Buildings (Rankine cycle elements, desalting units, offices)	2,100
Total	**13,150**

Table 7. Plant estimated capital costs.

Technology	Cost [€]
CSP field with TES	7,870,000
Biomass furnace	130,000
Economizer	15,000
Evaporator	45,000
Steam engine	220,000
Condenser	15,000
Utilities	300,000
Total	**8,595,000**

6. Conclusions

A model of a combined solar-biomass CHP plant devoted to feed an hotelier end-user was presented. The well-established TRNSYS software was adopted for transient simulation.

An analysis of thermal and electrical power production on a yearly basis demonstrated the feasibility of the present configuration in satisfying the energy requirements of the hotel using a fully renewable and sustainable approach.

Furthermore the model was matched with a thermal and an electric winter day load in transient simulations. The results for the two different load tracking scenarios were compared in terms of delivered power, matched load, RC system efficiencies and global GHG emission savings.

When looking at the output performance, the results show a most suitable behaviour for the thermal load tracking scenario, as it delivers both electric and thermal energy with less gap from the end-user requested energy.

The Primary Energy Ratio values, in both electric and thermal tracking cases, indicate the capability of the system to save energy in comparison of two separated plant for the single electric and thermal energy production. Nevertheless, as the high plant capital costs, i.e. 7.2 k$/kW, are mostly related to the solar section, the improvements must be oriented to the exploitation of low-tech solar field entailing the passage from parabolic troughs to Compound Parabolic Concentrators (CPC) and the adoption of Direct Steam Generators (DSG) systems with supercritical steam Rankine cycles.

Nomenclature

CHP	Combined Heat and Power
CSP	Concentrated Solar Power
DNI	Direct Normal Irradiation
E_{el}	Electric energy output
E_g	Global energy input from biomass and solar radiation
E_{th}	Thermal energy output
HTF	Heat Transfer Fluid
$\dot{m}_F$	HTF flow rate
$\dot{m}_{F,CSP}$	Solar field HTF delivered flow rate
$\dot{m}_{F,bmin}$	Minimum biomass furnace HTF delivered flow rate
$\dot{m}_{F,b+}$	Additional biomass furnace HTF delivered flow rate
$\dot{m}_{F,d}$	HTF demanded flow rate
$\dot{m}_{F,s}$	Solar direct and TES delivered flow rate
$\dot{m}_{F,TESc}$	TES HTF charge flow rate
$\dot{m}_{F,TESd}$	TES HTF discharge flow rate
P_b	Biomass derived power
$P_{b,min}$	Biomass furnace power at minimum duty
P_{CSP}	CSP derived thermal power
P_{eg}	Exhaust gas power
P_{el}	Electric power output
$P_{el,d}$	Electric load power
P	Storage charge power
$P_{TES,d}$	Storage discharge power
P_{th}	Thermal power output
$P_{th,d}$	Thermal load power
RC	Rankine Cycle
RES	Renewable Energy Source
TES	Thermal Energy Storage
η_{el}	Reference electric efficiency
η_{th}	Reference thermal efficiency

References

[1] Maidment, G.G., Zhao, X., Riffat, S.B. and Prosser G., "Application of combined heat-and-power and absorption cooling in supermarkets", Applied Energy 63 (1999) 169-190.

[2] Maidment, G.G. and Tozer, R.M., "Combined cooling heat and power in supermarkets", Applied Thermal Engineering 22 (2002) 653-665.

[3] Corsini, V. Naso, G. Mattei, P. Venturini. "Biomass co-firing: analysis of the main technical problems in coal power plants". 15th European Biomass Conference, 7-11 May, Berlin, Germany.

[4] Corsini, V. Naso, G. Mattei, P. Venturini. "Biomass co-firing: estimation of fuel requirements and land needed to feed some Italian coal power plants". 15th European Biomass Conference, 7-11 May, Berlin, Germany.

[5] Eastop T.D. and Croft D.R., "Energy efficiency for engineers and technologists" (1st ed.), Longman Scientific and Technical, Halow, Essex, 1990, p. 335.

[6] Fröhlke, K. and Haidn, O.J., "Spinning reserve system based on H_2/O_2 combustion". Energy Conversion, S0196-8904(96)00128-8.

[7] Kélouwani, S., Agbossou, K. and Chahine R., "Model for energy conversion in renewable energy system with hydrogen storage". Journal of Power Sources 140 (2005) 392-399.

[8] Corsini, A., Rispoli, F., Gamberale, M., and Tortora, E., 2009, "Assessment of H2- and H2O-based renewable energy-buffering systems in minor islands", Renewable Energy 34 (2009) 279–288.

[9] Sinden, G. Environmental Change Institute University of Oxford, "The practicalities of developing renewable energy stand-by capacity and intermittency". Submission to The Science and Technology Select Committee of the House of Lords, 2004.

[10] Sargent & Lundy LLC Consulting Group Chicago, Illinois, "Assessment of Parabolic Trough and Power Tower Solar Technology Cost and Performance Forecasts", NREL/SR-550-34440, October 2003.

[11] Jun Li, "Scaling up concentrating solar thermal technology in China", Renewable and Sustainable Energy Reviews 13 (2009) 2051-2060.

[12] Al-Soud, M.S. and Hyayshat E.S., "A 50 MW concentrating solar power plant for Jordan", Journal of Cleaner production 17 (2008) 625-635.

[13] Dong, L., Liu, H. and Riffat, S., "Development of small-scale and micro-scale biomass fuelled CHP systems. A literature review", Applied Thermal Engineering 29(2009) 2119-2126.

[14] Badami, M. and Mura, M., "Preliminary design and controlling strategy of small-scale wood waste Rankine Cycle (RC) with a reciprocating steam engine (SE)", Energy 34 (2009) 1315-1324.

[15] Borello, D., Corsini, A., Rispoli, F. and Tortora E., "A combined solar-biomass Rankine cycle concept for small-size cogeneration", Proceedings of ECOS 2009 Conference.

[16] Borello, D., Corsini, A., Rispoli, F. and Tortora E., "Load matching for a combined solar-biomass Rankine cycle plant" Proceedings of ASME-ATI-UIT 2010 Conference.

[17] Klein, S.A., Beckam, W.A., Mitchell, J.W., Braun, J.E., Evan,s B.L., Kummert J.P., et al., 2000, "TRNSYS – a transient system simulation program. Version 15.1", Madison: Solar Energy Laboratory, University of Wisconsin; 2000.

[18] Schwarzbözl, P., Eiden, U., Pitz-Paal, R., Jones, S., 2002, "A TRNSYS model library for solar thermal electric components (STEC). A reference manual." Release 2.2.

[19] Corsini, A., Gamberale, M., and Rispoli F., 2006, "Assessment of renewable energy solutions in an Italian small island energy system using a transient simulation model", ASME Journal of Solar Energy Engineering 2006;128:237–44.

[20] Jones, S.A., Pitz-Paal, R., Schwarzboezl, P., Blair, N. and Cable R., 2001, "TRNSYS modeling of the SEGS VI parabolic trough solar electric generating system", Proceedings of Solar Forum 2001: Solar Energy: The Power to Choose, April 21-25, 2001, Washington, DC.

[21] Kolb, G.J. and Hassani, V., 2006, Performance of thermocline energy storage proposed for the 1 MW Saguaro solar trough plant, ISEC2006-99005.

[22] Macchi, E., Campanari, S., Silva, P., "La micro-cogenerazione a gas naturale", Polipress - Politecnico di Milano, 2005.

[23] National Action Plan for Energy Efficiency Sector Collaborative on Energy Efficiency, Hotel Energy Use Profile, EPA Summer Workshop Report, 2007.

[24] SEL, 25 July 2003, Generated Hourly Weather Data. Solar Energy Laboratory, University of Wisconsin-Madison. 12 November 2008 <http://sel.me.wisc.edu/trnsys/weather/generate.htm>.

[25] Ronnelid, M., Perers, B., Karlsson, B., "On the factorization of incidence angle modifiers for CPC collectors", S0038-092X(97)00016-9, Solar Energy, 1997.

A Novel Non-Tracking Solar Collector for High Temperature Application

Wattana Ratismith and Anusorn Inthongkhum

Energy Research Institute, Chulalongkorn University,10330, Bangkok, Thailand,
wattana@eri.chula.ac.th and anusornaun@hotmail.com

Abstract:
A parabolic trough solar collector is improved the efficiency by a novel design of compound parabolic trough solar collector where the aim is three-fold. Firstly, one aim is to achieve day-long collection efficiency without the need for mechanical tracking of the sun. Secondly, the collector must be designed to operate efficiently under diffuse solar irradiation as experienced for example in rainforest climate. Thirdly, one seeks to achieve as a high an output temperature as possible. Newly developed system consists of multiple compound parabolic troughs facing the sun at different angles. The salient feature of this design is that the system can collect the sunlight energy at every angle without any moving parts at the same time can receive the diffused light, the maximum efficiency of the collector is 32% and has an ability to achieve high output temperature, the maximum temperature at header of evacuated tube is 235 degrees Celsius, and is therefore suitable for high temperature application such as industrial uses or cooling application.

Keywords:
solar energy, compound parabolic trough, non-tracking solar collector.

1. Introduction

A parabolic trough is a type of solar thermal energy collector which is generally used in solar power plants. The solar collector is constructed as a long parabolic trough with a tube running its length at the focal point. Sunlight is reflected by the trough and concentrated on the tube filled with synthetic oil, which heats to 300-400 degrees Celsius [1-5]. The trough is usually aligned on a north-south axis, and rotated to track the sun as it moves across the sky each day. Therefore it seems unavoidable that there needs to be a tracking system that follows the position of the sun.

The disadvantage of the parabolic trough solar collector is that concentrating systems require sun tracking to maintain sunlight focus at the collector. The tracking system increases the cost, complexity and the maintenance cost due to the moving parts. This type of solar collector is not preferred in a small residential house. Another problem is an inability to provide power in diffused light conditions, which is due to the fact that the power output from concentrating systems drops in cloudy conditions. As Thailand has a tropical rainforest climate, which causes the ratio of diffused solar radiation to global solar radiation to be rather high (in the range of 31% to 58%) [8], one faces a serious problem in utilizing such a solar collector to collect solar energy, especially in rainforest climate.

A parabolic trough solar collector is improved the efficiency by a novel design of compound parabolic trough solar collector which does not contain a solar tracking system and has an ability to collect diffused sunlight by using compound parabolic troughs facing the sun at different angles [6-7]. The non-tracking parabolic trough solar collectors were presented in ref. [8-20]. The advantage of this design is that there are no moving parts in the system, which leads to reductions in the cost and maintenance. This collector yields higher temperatures than flat plate solar collector and could be used in the residential house, the maximum temperature at header of evacuated tube is 235 degrees Celsius, and is therefore suitable for high temperature application such as industrial uses or cooling application.

2. The Model

In order to design and develop the non-tracking solar collector, the mathematical model of reflection of compound trough is calculated. Let the shape of a parabolic trough be described by the curve $y = f(x)$ on the x-y plane in Fig. 1. The law of reflection states that the angle of incidence θ is equal to the angle of reflection relative to the tangent of the curve $y = f(x)$ at any point (x,y). The slope of this tangent line at point (x,y) is denote by $m_t = df(x)/dx$, the slope of the incident ray by m_0 and the slope of the reflected ray by m_1.

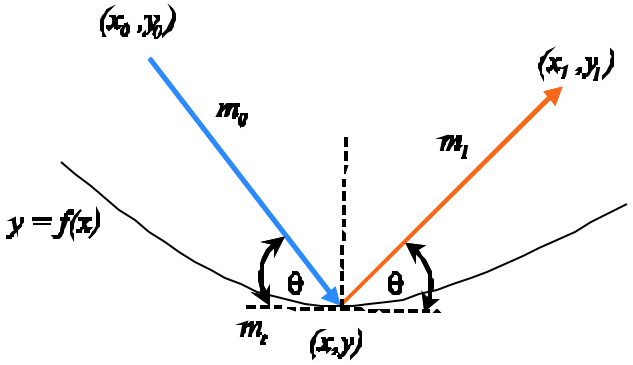

Fig. 1. The reflection of a light ray by a curve $y = f(x)$. θ is represented an angle of incidence and an angle of reflection. m_t, m_0 and m_1 are slope of a tangent line, an incident ray and a reflected ray respectively.

From trigonometry [5], the relationship between the angle θ between two lines and their relative slopes m_t, m_0 and m_1 is given as

$$\tan\theta = \frac{m_t - m_0}{1 + m_t m_0} = \frac{m_1 - m_t}{1 + m_t m_1}, \tag{1}$$

which yields a slope of the first reflected ray m_1 as

$$m_1 = \frac{m_0 - m_t\left(2 + m_t m_0\right)}{m_t^2 - 2m_t m_0 - 1}. \tag{2}$$

Similarly, the i^{th} reflected rays can be calculated by using the relation

$$\frac{m_t - m_{i-1}}{1 + m_t m_{i-1}} = \frac{m_i - m_t}{1 + m_t m_i}, \tag{3}$$

where i are integers. From Eq. 1 and Eq. 2, the reflection of a parabolic trough can be simulated as shown in Fig. 2.

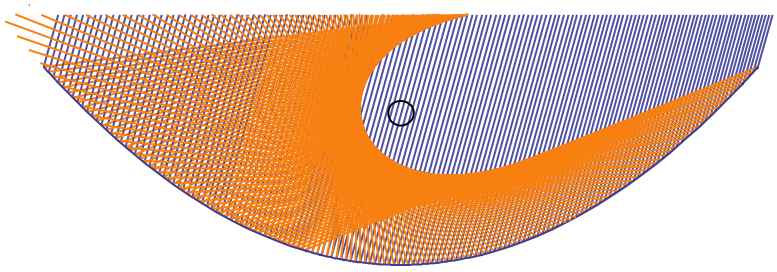

Fig. 2. The reflection of parabolic trough solar collector at incident angle of 75 degrees where blue and orange lines are incident and 1^{st} reflected rays respectively. The circle is the position of the focus point.

For the incident angle of 75 degrees, the conventional parabolic trough in Fig. 2 cannot receive the reflected rays. Therefore it needs solar tracking system to maintain sunlight at the focus point. The parabolic trough solar collector is designed to have an ability to achieve day-long collection efficiency without the need for mechanical tracking of the sun by using 3 compound parabolic troughs facing the sun at different angles. Using Eq.(1-3), the reflection of non-tracking solar collector at various time are shown in Fig. 3.

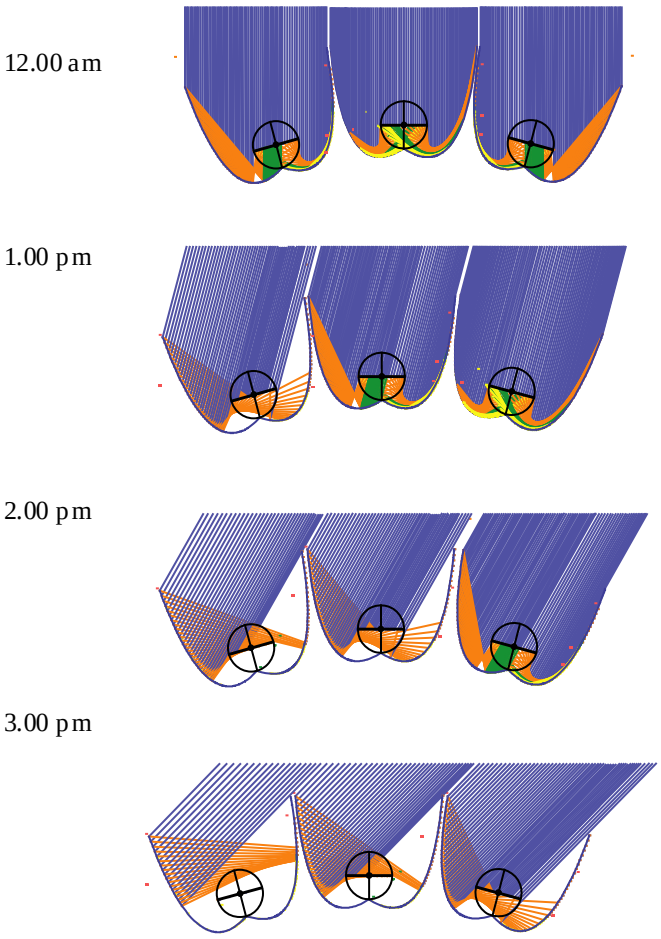

Fig. 3. The reflection of three-compound parabolic trough solar collector where blue, orange, green and yellow lines are incident, 1st reflected, 2nd reflected and 3rd reflected rays respectively. The circle in each trough is the position of evacuated tube.

The 3-compound parabolic trough shows that it has an ability to receive the sunlight at various time. For 12.00 a.m., the solar collector can collect all reflected rays, the reflected rays in the middle trough are concentrated at the lowest position of the tube and for both side of the middle trough, the reflected rays are concentrated on the higher position inside the tube. When the time changes, the reflected rays move up and down inside a tube. For this principle, this collector can collect the sunlight in any time. However there are some ray losses when the time changes especially after 3.00 p.m. which could be ignored because of very low solar power.

The collector is designed to have an ability to collect diffused light. In Fig. 4, compound parabolic trough can receive the incident rays in the period of 80 degrees. This implies that this collector has a probability to collect incident rays from sunlight in both direct and diffused light in the period of 80 degrees at the same time while a conventional parabolic trough can collect the incident rays which are nearly perpendicular to the trough. Although a parabolic trough could provide a high concentration, the parabolic trough could not work effectively under diffused light conditions. The experimental results have shown that the efficiency of the new design of solar collector is higher than parabolic trough under diffuse solar irradiation as shown in Fig.10 and Fig. 11.

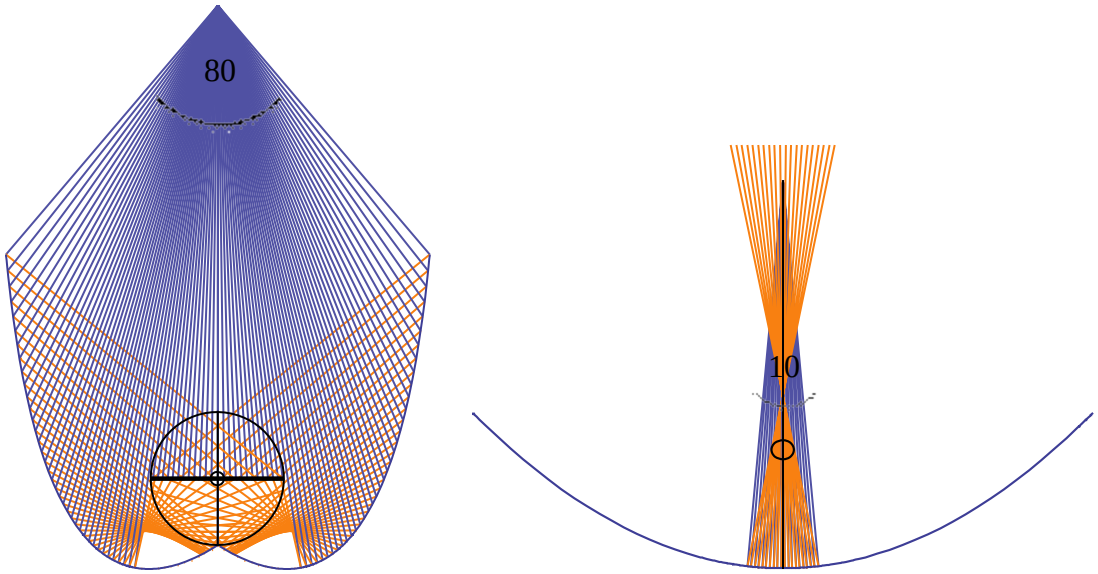

Fig. 4. The reflection of light rays at various angles of the incident rays. This design has an ability to collect incident rays in the period of 80 degrees while the conventional parabolic trough can receive the incident rays in the period of 10 degrees.

In this paper, SUNDA vacuum tubes (SEIDO1) are used to receive the concentrated light from the trough. This tube is composed of flat plate absorber as shown in Fig. 5.

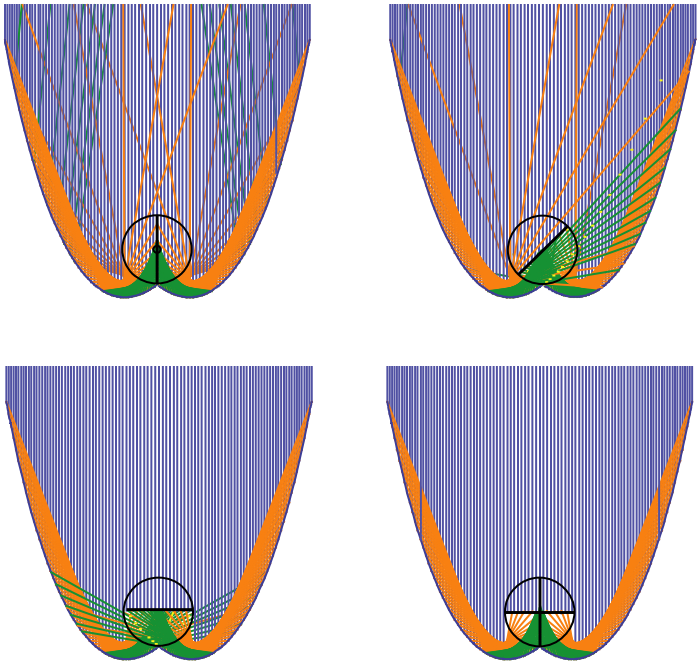

Fig. 5. The method to place an evacuated tube with flat plate absorber in compound parabolic trough.

From Fig. 5, the flat plate absorber which is placed horizontally can receive reflected rays better than the flat plate absorber which is placed vertically and cross shape absorber can collect all rays but there are no cross shape absorber product at the moment. For this reason, flat plate absorber is considered to place horizontally in each trough.

3. Experiment

The solar collector in Fig. 3 has been invented consisting of three compound parabolic troughs made of stainless sheets, oriented at different angles. The solar collector has an overall width of 1 m and a length of 1.9 m, and the evacuated tubes (SUNDA vacuum tube, (SEIDO1)) are placed along its axis. These evacuated tubes are connected to a manifold header pipe and connected with the pump to feed the oil. The flow rate is set at 5 lpm. The collectors are fixed on Earth and aligned along the north-south direction as shown in fig (6-7).

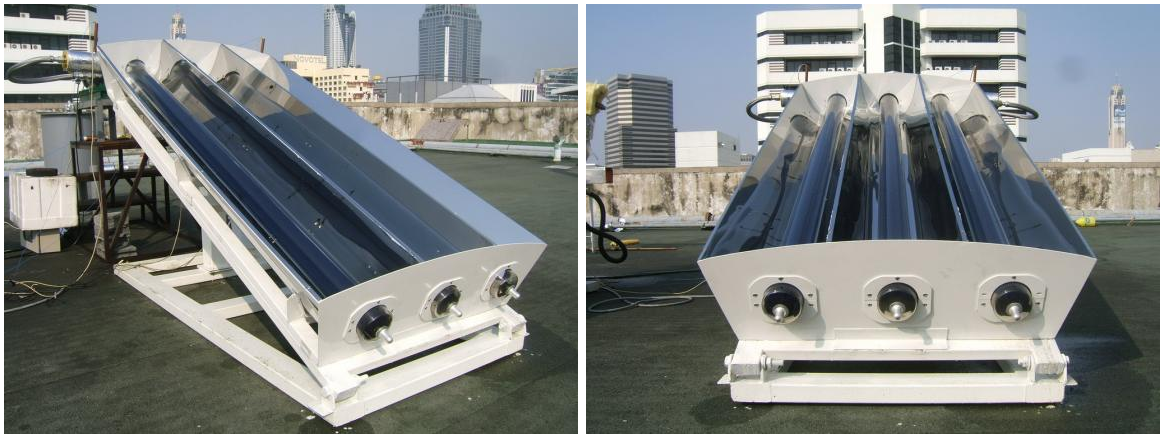

Fig. 6. The novel non-tracking solar collector has an overall width of 1 m and a length of 1.9 m.

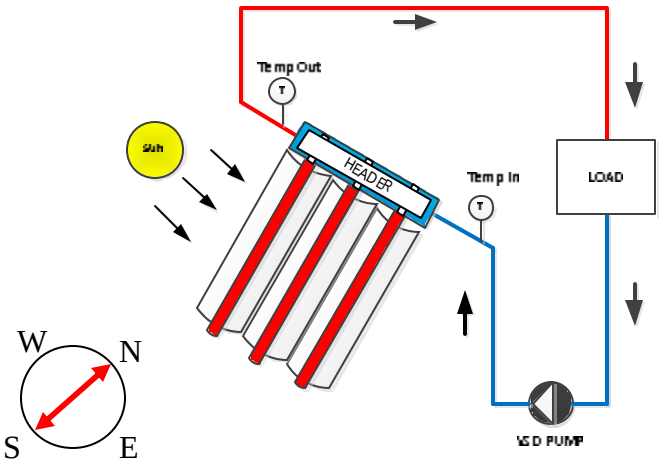

Fig. 7. Diagram of test arrangement.

The experiment was performed in Bangkok, Thailand. The data was taken during the period of 9.00 a.m. to 4.00 p.m. on the 10th, 11th, 12th ,13th and 14th January 2012, The sky was not very clear which lead the solar power is not smooth in any time. The diagram of test arrangement is shown in fig. 7.

When the evacuated tubes absorb the sunlight from troughs, the heat from the tubes is transferred to hot oil which flows in the system. The energy of the system can be calculated by [21]

$$Q_C(t) = \dot{m}C(T_{out} - T_{in})_l \tag{4}$$

where *t* represents time, $\dot{m}$ and *C* are flow rate and the specific heat of the thermal oil respectively. The efficiency of the system in any time is

$$\eta(t) = \frac{Q_C}{Q_{in}}, \tag{5}$$

where Q_{in} is the solar power. The evacuated tube is placed in the trough and measured the temperature at the header. The maximum temperature at heat pipe is 235 degrees Celsius as shown in Fig. 8 and the maximum temperature of hot oil is 180 degrees Celsius for 0.5 litres of oil as shown in Fig. 9.

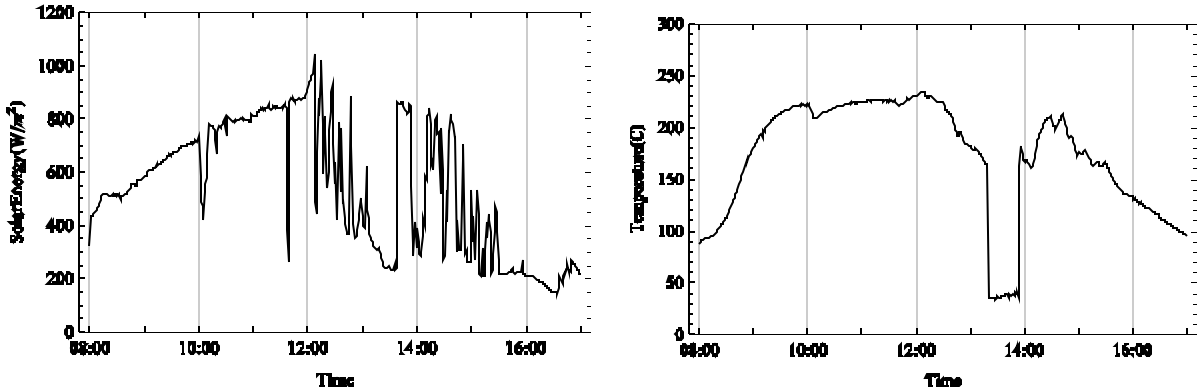

Fig. 8. The maximum temperature at the header of evacuated tube plotted against time from 8.00 a.m. to 5.00 p.m. on the 12th December 2011.

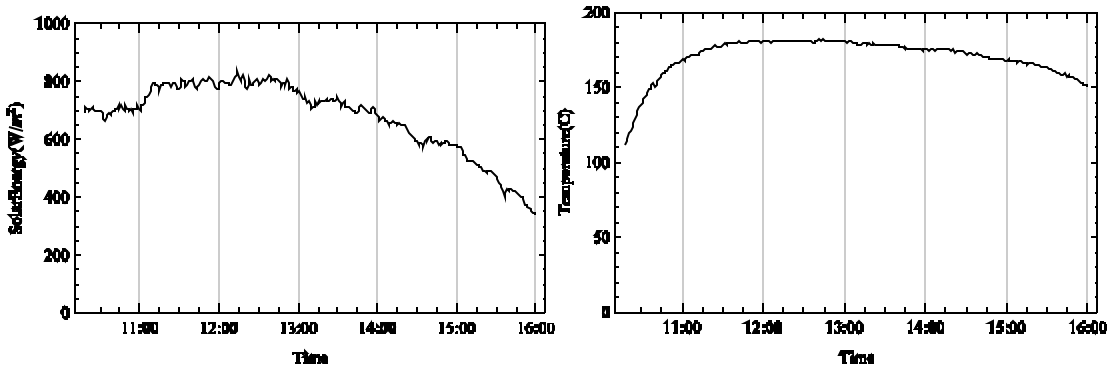

Fig. 9. The hot oil temperature plotted against time from 9.00 a.m. to 4.00 p.m. on the 14th November 2011. The maximum temperature is 180 degrees Celsius for 0.5 litres of oil.

From the experiment, the solar power on the 11th ,12th ,13th and 14th of January 2012 in Bangkok had been collected and its average is shown in Fig. 10. The results show that the efficiency of the new-design solar collector at any time is fairly constant, which is similar to the parabolic trough with solar tracking system, while the efficiency of a conventional parabolic trough at any time distributes like a Gaussian curve having its maximum at around 11.30 a.m. as shown in Fig.11. The three-compound parabolic trough solar collector yields higher temperature than flat plate or evacuated tube solar collector. The average efficiency of solar collector is 25-32% .

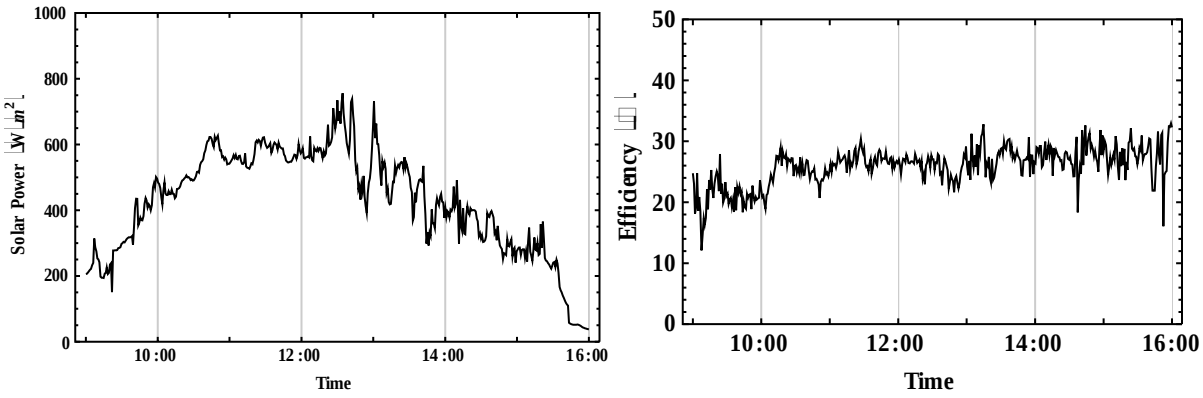

Fig. 10. The average solar power and efficiency of 3-compound parabolic trough plotted against times in the period of 9.00 a.m. to 4.00 p.m. on the 10th , 11th ,12th ,13th and 14th January 2012 in Bangkok.

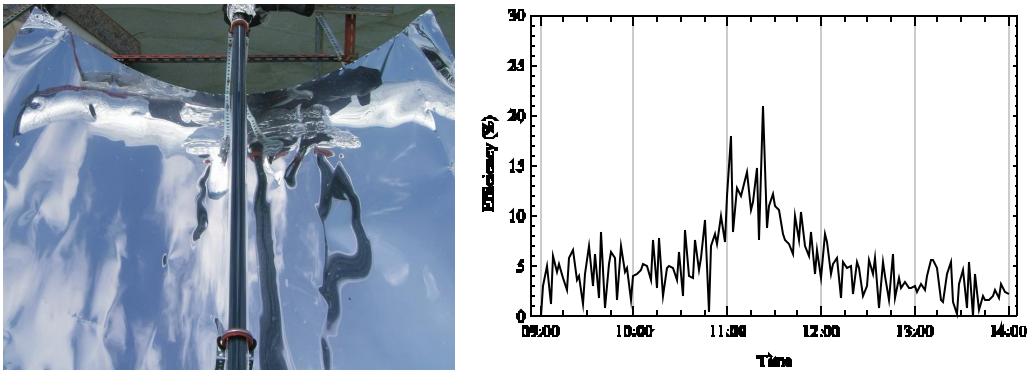

Fig. 11. The parabolic trough in Fig. 4 has been invented. The average efficiency of parabolic trough plotted against time from 9.00 a.m. to 2.00 p.m. on the 4th, 6th and 8th January 2010[9]

4.Conclusions

The new-design of solar collector has an ability to collect the sunlight at every angle, similar to the parabolic trough with a solar tracking system. This solar collector has an ability to receive the diffused light, and this make it suitable for using in all kinds of climate. There are no moving parts in the system, which results in the reductions in the cost of the system, the cost of maintenance and complexity. This collector needs only 3 evacuated tubes while SUNDA collector (SEIDO1) needs 8 tubes at the same area. This collector yields higher temperatures than flat plate or evacuated tube solar collector. The maximum temperature at heat pipe is 235 C and oil temperature is 180 C. It is, therefore, suitable for high temperature application such as industrial uses or cooling application.

5.Acknowledgements

The authors would like to thank the National Research University Project of CHE, the Ratchaphiseksomphot Endoment Fund (Project No. EN1180I), 2-V research program of National Research Council of Thailand (NRCT) and Energy Research Institute of Chulalongkorn University for the financial supports. We also would like to thank Mr. Narong Amornpitakpunt, AMP METALWORKS [Thailand] Co.,Ltd for his help for inventing the 1st and 2nd prototype of solar collector.

References

[1] Kearney, D., 1989. Solar Electric Generating Stations (SEGS). IEEE Power Engineering Review (IEEE) 9, 4-8.

[2] Mills D., 2004. Advances in Solar Thermal Electricity Technology. Solar Energy 76, 19-31.

[3] Hodge B. K., 2010. Alternative Energy Systems and Application. John Wiley & Sons, Inc.

[4] Frank Kreith, D. Yogi Goswami, 2007. Handbook of Energy efficiency and Renewable Energy, CRC Press.

[5] Milton Matos Rolim, Naum Fraidenraich and Chigueru Tiba, 2009. Analytic Modeling of Solar Power Plant with Parabolic Linear Collectors. Solar Energy 83, 126-133.

[6] Wattana Ratismith, Parabolic Troughs Solar Collector with no Need of Solar Tracking System, December, 9 2009 patent no.: 0901005526 (patent pending)

[7] Wattana Ratismith, Compound Parabolic Troughs Solar Collector with no Need of Solar Tracking System, July, 21 2011 patent no.: 1101001216 (patent pending)

[8] Wattana Ratismith, Novel Parabolic Troughs without Solar Tracking System, Proc. Renewable Energy 2010, Pacifico Yokohama, Japan, (2010)

[9] Wattana Ratismith and Urith Archakositt, Parabolic Troughs without Solar Tracking System, Third International Conference on Applied Energy, Perugia, Italy (2011)

[10] Standard Mathematical Table, 25th Ed., CRC Press, Inc., 1978.

[11] Zambolin E., Del Col D., 2010. Experimental analysis of thermal performance of flat plate and evacuated tube solar collectors in stationary standard and daily conditions, Solar Energy 84, 1382-1396.

[12] Grass C., Schoelkopf W., Staudacher L., Hacker Z., 2004. Comparison of the optics of non-tracking and novel types of tracking solar thermal collectors for process heat applications up to 300 C. Solar Energy 76, 207-215.

[13] Winston R., and Hinterberger H., 1975. Principles of Cylindrical Concentrators for Solar Energy. Solar Energy 17, 255-258.

[14] Winston R., 1974. Principles of Solar Concentrators of a Novel Design, Solar Energy 16, 89-95.

[15] Blanco J., Malato S. et al, 1999. Compound Parabolic Concentrator Technology Develop to Commercial Solar Detoxification Applications. Solar Energy 67, 4-6.

[16] Rabl A., O'Gallagher J. and Winston R., 1980. Design and Test of Non-Evacuated solar Collectors with Compound Parabolic Concentrators. Solar Energy 24, 335-351.

[17] Rabl A., Bendt P., and Gaul H. W., 1982. Optimization of Parabolic Trough Solar Collectors. Solar Energy 29, 407-417.

[18] Pei Gang, Li Guiqiang, Zhou Xi, Ji Jie, Su Yuehong, 2012. Experimental study and exergetic analysis of a CPC-type solar, Solar Energy 86, 1280–1286.

[19] M. Souliotis, P. Quinlan, M. Smyth, Y. Tripanagnostopoulos, A. Zacharopoulos, M. Ramirez, P. Yianoulis. 2011. Heat retaining integrated collector storage solar water heater with asymmetric CPC reflector, Solar Energy 85, 2474–2487.

[20] O. Helal, B. Chaouachi, S. Gabsi, 2011, Design and thermal performance of an ICS solar water heater based on three parabolic sections, Solar Energy 85, 2421–2432.

[21] Duffie J. A. and Beckmen W. A, 1991. Solar Engineering of Thermal Process, New York, Wiley.

Absorption Heat Transformers (AHT) as a way to enhance low enthalpy geothermal resources

Daniele Fiaschi[a, CA], Duccio Tempesti[b] , Giampaolo Manfrida[c] , Daniele Di Rosa[d]

[a,b,c,d] Università degli Studi di Firenze, Dipartimento di Energetica "Sergio Stecco"
C/o Centro Didattico Morgagni Viale Morgagni 40/44 - 50134 Firenze Italy
a daniele.fiaschi@unifi.it
b duccio.tempesti@unifi.it
c manfrida@unifi.it
d daniele.dirosa@stud.unifi.it

Abstract:

Exploiting low enthalpy geothermal resources (hot water at 45 to 90 °C) is increasing its attractiveness, due to their higher widespread compared to high enthalpy ones. Anyway, at these temperature levels, their application is almost solely related to district heating, due to the marginal efficiency achievable when eventually converted to electricity by a power plant. The possibility of applying an Absorption Heat Transformer (AHT) to enhance low enthalpy geothermal resources available in the range from 45 to 90 °C and produce electricity with an acceptable efficiency was investigated. A thermodynamic model of an AHT working with a Lithium Bromide (LiBr) solution was developed. It showed the possibility of enhancing low temperature heat, ranging from 45 to 90 °C, to the higher value heat at 130 – 140 °C with a COP variable within 40 to 50%. The enhanced heat can be used as the hot source of an Organic Rankine Cycle (ORC), which exploits the geothermal heat (available at 80 ÷ 90 °C) in summer time. Generally the geothermal resource supplies district heating in winter, but when heat demand resets, it becomes attractive to convert a fraction to electricity instead of leaving it waste. Even if the primary heat lost in the AHT (having COP in the 40 to 45% range) is less than compensated by the increase in the ORC efficiency, leading to a lower system efficiency, the adoption of an AHT is worth up to about 80 – 100 °C, because geothermal heat source temperatures below 100°C are not suitable for the current ORC technology When the temperature of the heat source is higher than 100 °C, the direct use of the geothermal resource into the ORC bypassing AHT is more performing and convenient.

Keywords:

Absorption Heat Transformer (AHT), Organic Rankine Cycle (ORC), Low Enthalpy Geothermal.

1. Heat transformers and their potential for upgrading geothermal resources

Absorption heat transformers (AHT) are devices which transform a large heat resource, which is available at temperature too low for correct thermal matching within an industrial process, in a smaller amount of heat available at a higher temperature level. They differ from traditional heat pumps, in that they use no (or a very limited amount of) electrical power or work. Basically, AHTs work on the principle of an absorption inverse cycle: however the net effect is that of transferring an amount of heat (smaller than the originally available) at a higher temperature level. This allows recovering this heat into industrial processes.

Examples of heat transformers can be found in the petroleum refinery industry [1] and have been proposed as a useful add-on to industrial waste heat recovery [2-4] and for applications related to renewable energies [5-7]. Being based on absorption inverse cycles, AHTs are not very suitable for small-scale, individual applications. However, they can prove to be very attractive when there is the opportunity to deal with relatively large heat rates (>200 kW) available at low temperatures. In these applications, they can be more competitive in comparison to large, distributed renewable

energy harvesting technologies (such as low-temperature, non-concentrating solar collectors; or parabolic troughs with low concentration ratio). The commercial attractiveness of AHTs lies in the possibility of building a relatively compact unit, which can effectively upgrade a large quantity of heat without needing – for example - a large solar field. In this sense, they can be an effective alternative to hybrid geothermal-solar power plants [7], which are currently being proposed as a promising technology.

With reference to geothermal applications, heat transformers can find applications for two purposes:

a) In geothermal heating networks, AHTs can be employed to convert a large amount of heat at low temperature (50-90 °C) into a smaller amount at higher levels (80-130°C). This is interesting as the district heating network is usually not used for a long period (e.g., March to October, depending on the local climate). It can instead be used to distribute heat at higher temperature, to be used locally with absorption cooling units during summer. Preliminary studies demonstrate that the rate of return of the overall system (Heat transformer/district heating network/local secondary heat exchangers/absorption cooling units) is promising [8].
b) When large amounts of heat are available from the geothermal resource at medium-low temperatures (80-100 °C), the current technology and thermodynamic limits (Carnot efficiency) do not allow to propose binary (ORC) energy conversion systems. However, as small ORC units operating at levels between 120°C and 150°C with engineered fluids are coming to the market [9,10], it makes sense to try to upgrade the resource using an AHT.

In both cases (a) and (b), the original geothermal resource would be unavailable for commercial exploitation (heat and/or electricity): then, it should be considered as wasted.

2. Thermodynamic layout and model of AHT

Basically, an AHT system operates with a reverse cycle of the AHP. Then, the AHT consists of an absorber (AB), an evaporator (EVA), a generator (GE), a condenser (CO) and an internal liquid–liquid solution heat exchanger (EX), as shown in Fig. 1, together with the related thermodynamic behaviour of steam into the T – s diagram. The working fluid considered in this article is water-Lithium bromide solution (water – LiBr) where water acts as a refrigerant in the cycle, and LiBr as an absorbent. A geothermal energy resource at low temperature (45 – 90 °C) feeds the Generator, where water is vaporized and then separated from the liquid solution rich in LiBr. The steam from generator (GE) flows into the condenser (CO), where is condensed, releasing heat to the ambient (i.e. to cooling water). The saturated water is pumped to higher-pressure level to the evaporator (EVA), where it is totally evaporated by heat still given by the low temperature geothermal resource. It must be noticed that the EVA and the GE work at the same temperature (Fig. 1). The steam evaporated then flows into the absorber (A), where the useful heat is recovered at higher temperature. Hence, the main capability of the AHT is to raise the temperature of the solution above the temperature of the geothermal resource. AHT thermal efficiency is improved using a counter flow heat exchanger between the dilute and the concentrated solutions. Fig. 1 shows the temperature and pressure levels of the AHT cycle. The Generator and the Condenser work at lower pressure, which is the saturation pressure of the condenser, while the Evaporator and the Absorber operate at higher pressure, which is the saturation pressure of the evaporator. Moreover, the Evaporator and the Generator work at same temperature, while the Condenser works at the lower cycle temperature and the Absorber works at the higher cycle temperature. Thus, there are three temperature levels in the AHT system: the generator (T_{GE}=T_{EVA}), the absorber (T_{AB}) and the condenser (T_{CO}) temperatures.

Several analyses and optimization studies of AHT can be found in the technical literature [1-6; 11-13]. In the present study, the work of Horuz and Kurt [3] is taken as a fundamental reference, and a complete thermodynamic model was written in a simulation environment which includes the link to common absorption fluid mixtures [14]. According to the existing literature [2-3;12-13] the main assumptions made are the following:

- The system is analyzed assuming steady state and thermodynamic equilibrium conditions.
- Pressure drops and heat losses (or gains) are neglected.
- The mechanical work consumed by the pumps is neglected.
- The evaporator and generator temperatures are the same.
- The refrigerant at the condenser and evaporator outlets are all saturated.

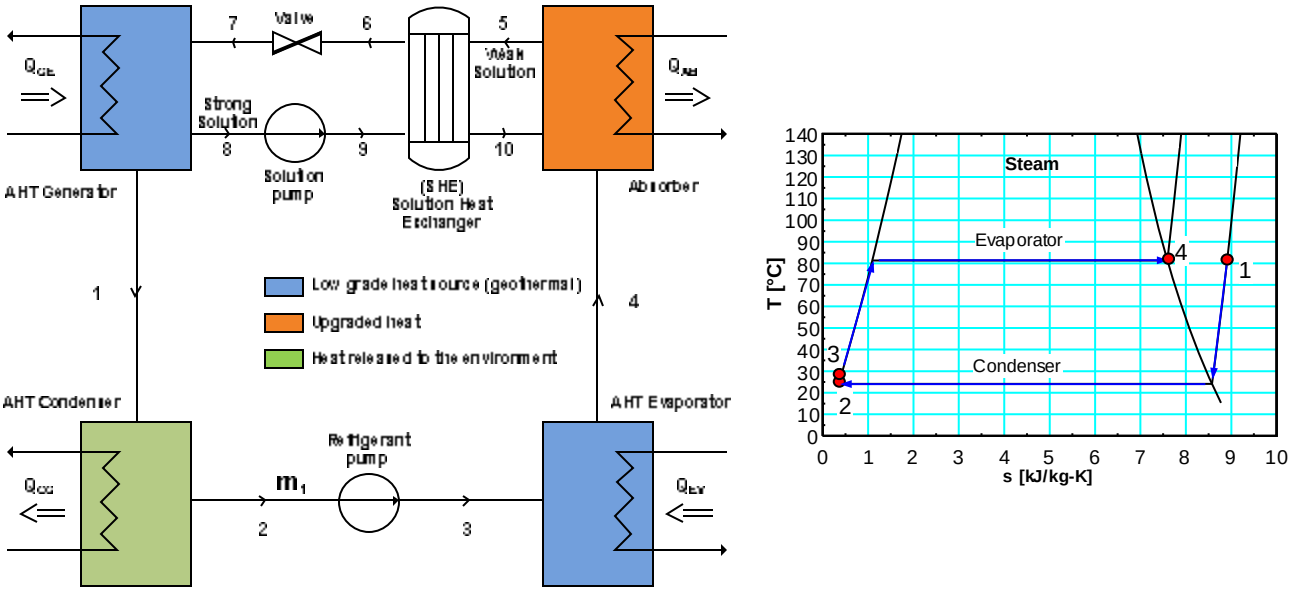

Figure 1a-1b: Absorber Heat Transformer layout (1a, left) and thermodynamic behavior of steam at evaporator and condenser on T – s diagram (1b, right).

It must be noticed that, as shown in [3], evaporator temperature higher than generator temperature leads to a very slight increase of COP, especially for temperatures higher than 80°C.

Furthermore, the temperature difference between the strong solution at the Absorber inlet (T_{10}) and the weak solution at the absorber outlet T_5 is fixed at 10 °C, as in [3]. Finally, the refrigerant mass flow rate (m_1) is fixed at 0,1139 kg/s, as in [3].

The thermodynamic analysis was carried out calculating the energy and the mass balance for each AHT component. For the mass balance, the balance at the Generator must be highlighted:

$$m_7 = m_1 + m_8 \quad (1)$$

$$m_7 \cdot x_7 = m_8 \cdot x_8 \quad (2)$$

Where x_7 and x_8 are the lithium bromide concentration in the weak and strong solution respectively. An important design parameter is the flow ratio (f), which is defined as the ratio between the strong

solution mass flow rate (m_8) and the refrigerant mass flow rate (m_1). Hence, considering (1) and (2), the flow ratio can be defined as:

$$f = \frac{x_7}{x_8 - x_7} \quad (3)$$

The performance of the AHT is measured by the COP, which is the ratio between the heat delivered from the absorber and the heat supplied to the evaporator and generator [14]:

$$COP_{AHT} = \frac{Q_{AB}}{Q_{EV} - Q_{GE}} \quad (4)$$

Table 1 shows the thermodynamic conditions of the AHT cycle points (as referred on figure 1a), in case of T_{AB}=130°C, T_{GE}=T_{EVA}= 80°C, T_{CO}=25°C, while Table 2 reports the heat exchanged at the absorber, evaporator, condenser, generator, the weak and strong solution concentration and the COP in various cases.

Table 1. AHT thermodynamic states if T_{AB}=130°C, T_{GE}=T_{EVA}= 80°C, T_{CO}=25°C.

	T [C]	m [kg/s]	P [bar]	T [C]	h [kJ/kg]	s [kJ/kg-K]
1	100	0.1139	0.03169	80	2650	8.875
2	0	0.1139	0.03169	25	104.8	0.367
3	-100	0.1139	0.4737	25	104.8	0.3669
4	1	0.1139	0.4737	80	2643	7.611
5	0.5926	1.171	0.4737	130	291.5	0.7226
6	0.5926	1.171	0.4737	98	226.9	0.5564
7	0.5926	1.171	0.03169	98	226.9	0.5564
8	0.6565	1.057	0.03169	80	227.6	0.4204
9	0.6565	1.057	0.4737	80	227.6	0.4204
10	0.6565	1.057	0.4737	120	299.2	0.6126

Table 2. AHT results for various cases.

	Unit	Case 1	Case 2	Case 3
TAB (Absorber Temperature)	°C	65	115	155
TCO (Condenser Temperature)	°C	25	25	25
TGE (Generator Temperature)	°C	45	70	90
TEV (Evaporator Temperature)	°C	45	70	90
T10 (Solution Heat Exchanger Outlet Temp.)	°C	55	105	145
f (Flow Ratio)		30.25	17.77	11.5
COP_{AHT}		0.4108	0.4667	0.4855
COP_{Carnot}		0.5314	0.5656	0.5895
QAB (Absorber Heat Transfer)	kW	196.9	251.8	275.6
QEV (Evaporator Heat Transfer)	kW	282.2	287.2	291
QCO (Evaporator Heat Transfer)	kW	282.4	287.7	292
QGE (Evaporator Heat Transfer)	kW	197.1	252.3	276.7
QSOL EXCH (Solution Heat Exch. Heat Transfer)	kW	77.84	136.3	120
Xw (Weak Solution Concentration)		0.4642	0.5779	0.6457
Xs (Strong Solution Concentration)		0.4795	0.6104	0.7018

3. AHT sensitivity analysis

The main performance parameters of the AHT, COP and Q_{AB}, depend on the three temperatures at heat sources and releases: T_{CO}, T_{GE} and T_{AB}. The results of the sensitivity analysis to these parameters are presented in Figs 2-5. As shown in Fig. 2, when T_{GE} and T_{AB} are fixed, the COP and the heat released at the absorber decrease as the condenser temperature increase. This result is justified by the fact that as the condenser temperature increases, the minimum AHT pressure also increases (as it works under saturated conditions), leading to a lower LiBr concentration in the strong solution (x_8), and finally to a lower enthalpy value at the absorber inlet (h_{10}).

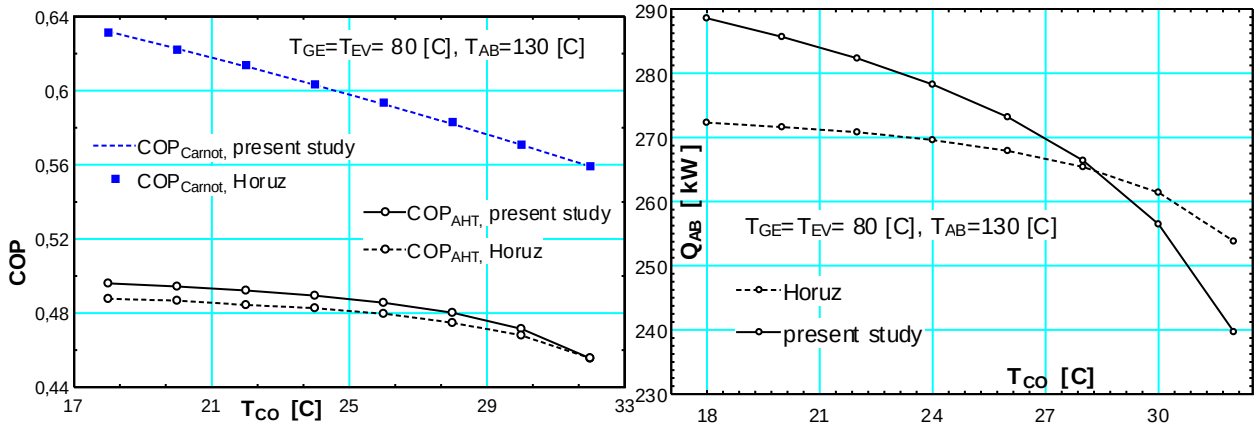

Figure 2: COP(left) and Absorber heat (right) vs the variation of the condenser temperature.

In Fig. 2 the values for COP and Q_{AB} obtained with the presented model are compared with the values given in [3]. COP values show a good agreement, with an average relative error of 1%, while for Q_{AB} the average relative error is slightly higher (3,5%). It is due to the strong influence that small error on the Li-Br concentration in the strong solution value has on Q_{AB}. However, taking into account that our model is developed with a software having probably different (and unknown to the reader) thermodynamic libraries of Li-Br than the one used in [3], the average error may be considered acceptable.

On the other hand, Fig. 3 shows that if the evaporator - and thus the generator – temperature raises, also the COP and the absorber output heat increases. In fact, in this case the maximum pressure increases and the LiBr concentration in the weak solution decreases, leading to a lower enthalpy value at the absorber outlet (point 5, Fig. 1) and then to a higher absorption heat and COP.

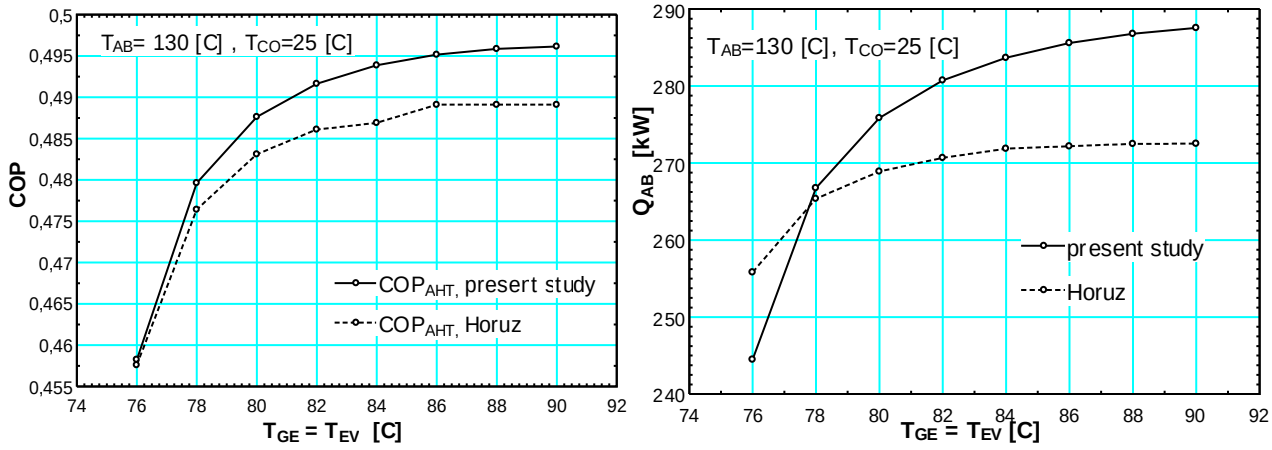

Figure 3: COP(left) and Absorber heat (right) vs the variation of the generator temperature.

Also in this case our results are compared with [3]: COP values are approximately in agreement, confirming an average error of 1%, while Q_{AB} values show, once again, higher discrepancies , with an average error of approximately 3,5%.

Finally, Figs 4 and 5 show, respectively, the variation of the COP and Q_{AB} with the absorber temperature at different generator (i.e. evaporator) temperatures. The increase of the absorber temperature leads, obviously, to decrease of COP and Absorber released heat. In fact, a higher T_{AB} implies a higher enthalpy value of the weak solution at absorber outlet (point 5) which means a lower heat released at the absorber. At each fixed value of T_{GE}, an absorber temperature which optimizes COP and Q_{AB} is found.

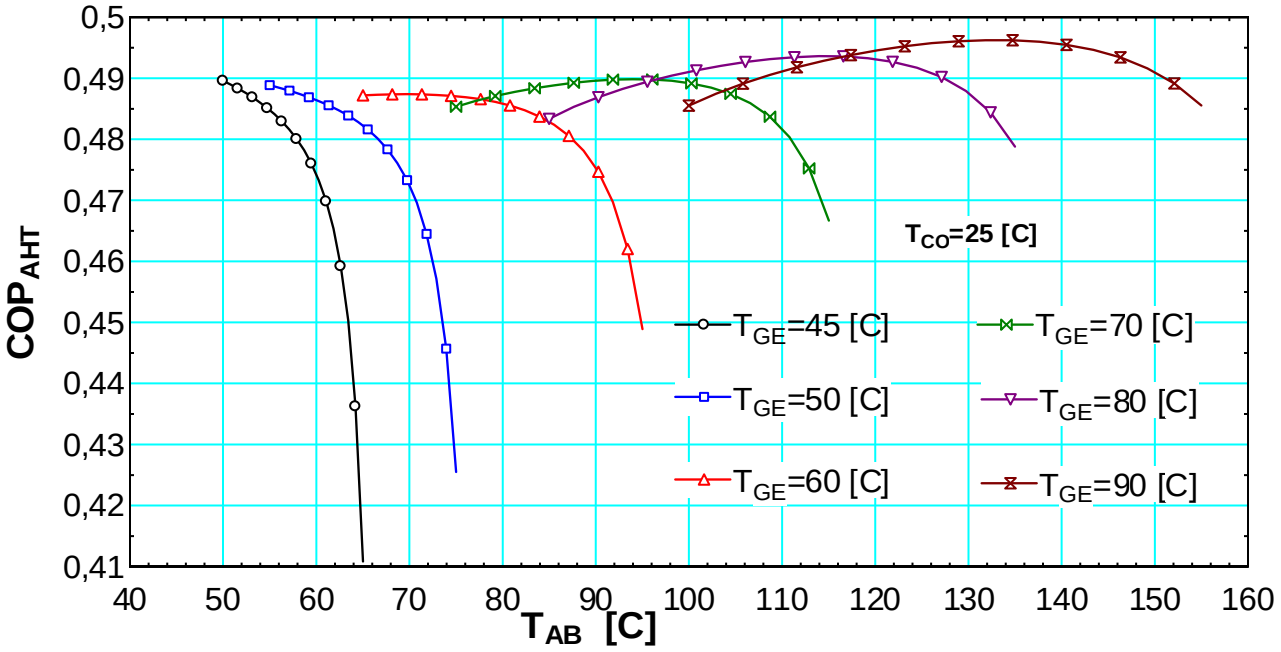

Figure 4: COP vs absorber temperature at different generator (evaporator) temperatures.

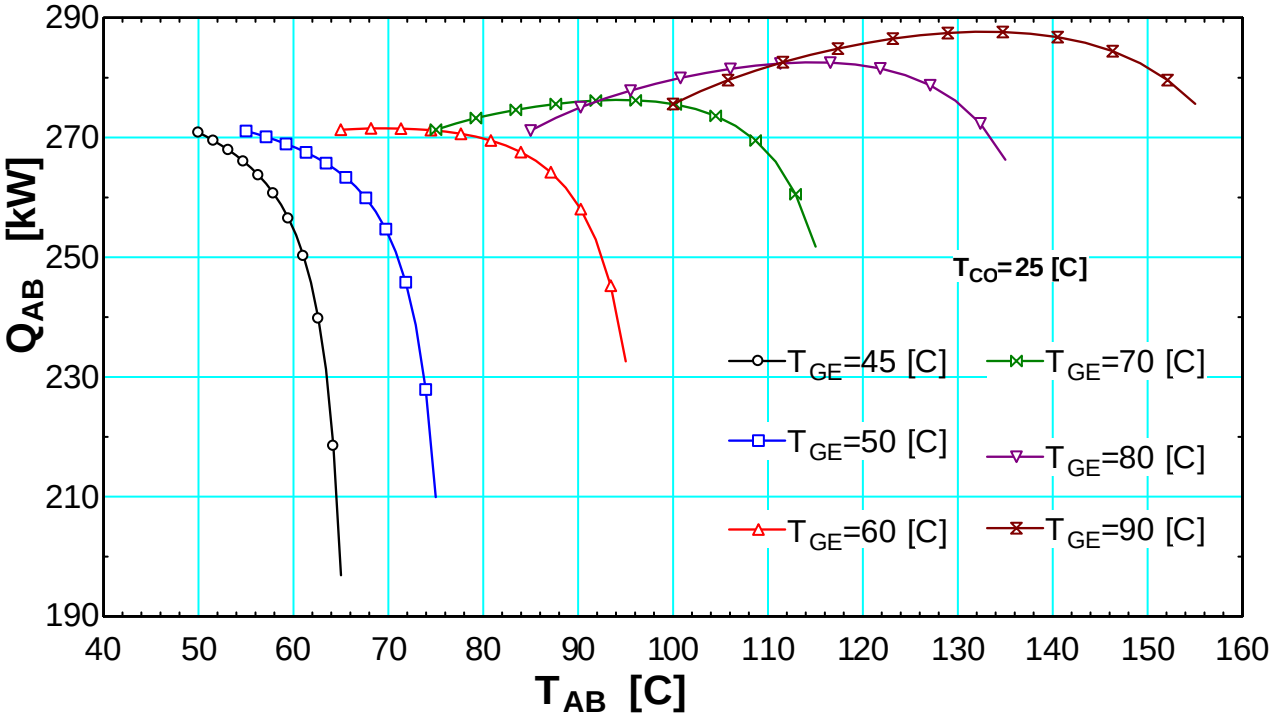

Figure 5: Absorber heat vs absorber temperature at different generator (evaporator) temperatures.

The results shown in Figs 4 and 5 are in a good agreement with those presented in [13]. It can also be observed that the optimized values of COP and Q_{AB} can be kept almost constant at relatively high values, provided that the decrease of the heat source temperature is followed by an adequate reduction of the temperature at the absorber.

4. ORC system

The Organic Rankine Cycle (ORC) is a market proven technology [15-18]. In this work we considered a standard ORC (Fig. 6), where a secondary, low boiling-point working fluid (i.e. R245fa) is vaporised (points 16-18), then it expands in a turbine, and it is subsequently condensed in the condenser before being returned to the economiser and the evaporator by the cycle pump. An internal heat exchanger (IHE) is added to recover the heat from the turbine outlet stream, in order to improve the cycle efficiency. Thermodynamically, the power plant works with a pure Rankine cycle, without superheater.

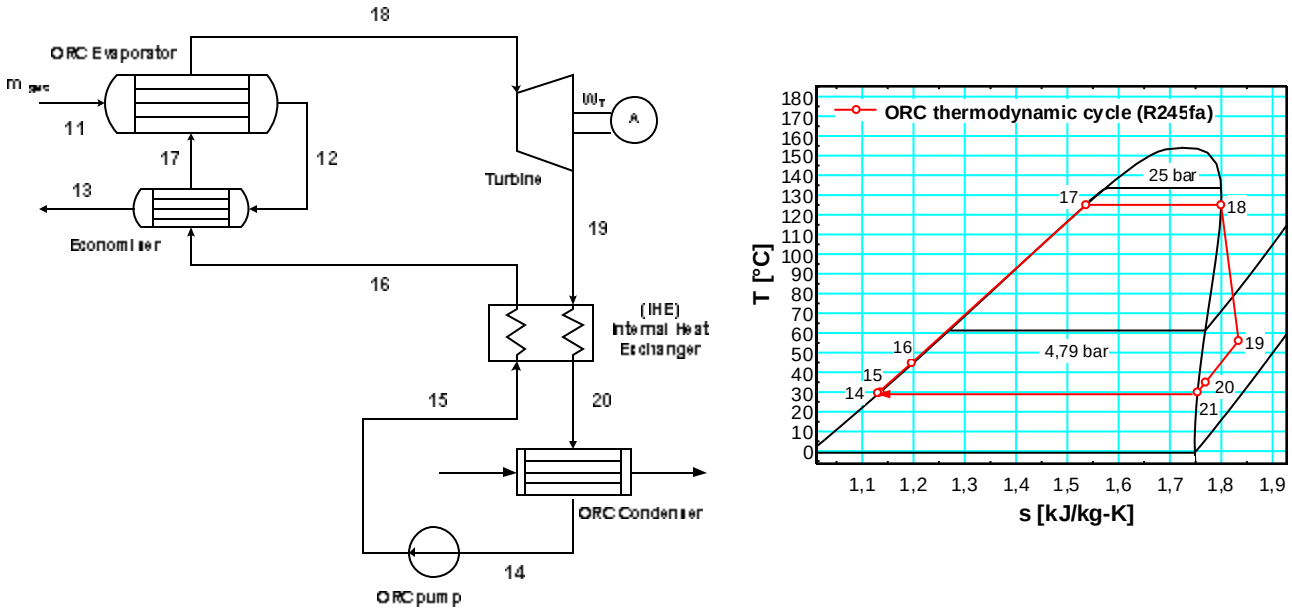

Figure 6: layout of the proposed Organic Rankine Cycle (ORC, left) and the related thermodynamic cycle (right)

The following assumptions for the ORC model are done:

- The ORC operates in a steady-state condition.
- The pressure drops throughout the heat exchangers and pipelines are neglected.
- The turbine isentropic efficiency is fixed at 0.76.
- The mechanical work consumed by the pump is neglected.
- The organic fluid exits the vaporizer under saturated conditions (x=1).
- The temperature at the condenser of the ORC is fixed at 25 °C.

The main purpose of this work is to compare the efficiency of two systems for the exploitation of a low enthalpy geothermal resource (45 to 90 °C): in the first system (called Geo-ORC), the geothermal resource is used to directly vaporize the organic fluid in the ORC vaporizer and economizer (Fig. 6). In the second system (called ORC-AHT), the ORC vaporizer is fed by the heat

released at the absorber of the AHT previously described. In the Geo-ORC system, for a given temperature of the geothermal resource (T_{source}, i.e. T_{11}), the temperature of the organic fluid at point 18 is calculated by (5), where the Approach temperature difference ($\Delta T_{app;ORC}$) is fixed by technical constraints at the heat exchanger at 10°C:

$$T_{18} = T_{source} - \Delta T_{app;ORC} \quad (5)$$

Furthermore, since the geothermal flow rate is given as an input data, the temperature difference at the pinch point ($\Delta T_{pp;ORC}$) is fixed at 5 °C by the following equation:

$$T_{17} = T_{geo;pp} - \Delta T_{pp;ORC} \quad (6)$$

The energy balance at the vaporizer and at the economizer are then given by the following equations, where (7) provides the organic fluid flow rate (m_{ORC}), while (8) calculates the reinjection temperature of the geothermal resource ($T_{geo;out}$):

$$m_{geo} \cdot c_{p;geo} \cdot (T_{source} - T_{geo;pp}) = m_{orc} \cdot (h_{18} - h_{17}) \quad (7)$$

$$m_{geo} \cdot c_{p;geo} \cdot (T_{geo;pp} - T_{geo;out}) = m_{orc} \cdot (h_{17} - h_{16}) \quad (8)$$

In the second system, i.e. the ORC-AHT, the geothermal resource is used in the evaporator and generator, which work at the same temperature. Since Q_{GE} (or Q_{EV}) is fixed to the operating value obtained by the AHT pure model, m_{geo} and T_{GE} (or T_{EV}) are given by the following equations:

$$Q_{GE} = m_{geo} \cdot c_{p;geo} \cdot (T_{source} - T_{geo;out;GE}) \quad (9)$$

$$T_{GE} = T_{source} - \Delta T_{app;GE} \quad (10)$$

The geothermal resource temperature at the outlet of the generator (or evaporator) is calculated by:

$$T_{geo;out;GE} = T_{GE} + \Delta T_{out;GE} \quad (11)$$

From (9) it can be stated that, as the geothermal resource temperature increases, T_{GE}, and then Q_{GE}, rises, leading to an augmentation of m_{geo}. The geothermal mass flow rate calculated by (9) is used as input in the GEO-ORC system, i.e. in (7) and (8). Approach temperature difference at the generator ($\Delta T_{app;GE}$) is fixed at 10°C, while the temperature difference at the geothermal resource outlet from generator ($\Delta T_{out;GE}$) is fixed at 5°C. Finally, in the ORC-AHT system, the heat Q_{AB} is coupled with the vaporizer and economizer. A heat carrier fluid is used between the two systems. However, as the temperature of the heat source and the evaporation temperature of the organic fluid are constant and respectively equal to T_{AB} and T_{18}, the temperature difference ($\Delta T_{app;ORC}$) between T_{AB} and T_{18} is fixed by technical constraints at the heat exchanger at 10°C. Hence, the energy balance at the vaporizer and economizer is calculated by the equation (12), where the temperature at point 18 is fixed using (13):

$$m_{orc} \cdot (h_{18} - h_{16}) = Q_{AB} \quad (12)$$

$$T_{18} = T_{AB} - \Delta T_{app;ORC} \quad (13)$$

5. Model results of the ORC-AHT combined system

In Table 3, the thermodynamic parameters (pressure, temperature, mass flow rate) of the ORC cycle in both AHT-ORC and GEO-ORC configurations for different temperatures of the heat source are shown. As previously explained, the geothermal flow rate and power input are the same for ORC-AHT and GEO-ORC at each source temperature. As the temperature of the resource is raised through the AHT, the maximum ORC Temperature (i.e. the turbine inlet temperature) is higher for ORC-AHT in every case, leading to higher ORC efficiency. The system efficiency is given by the ORC efficiency for GEO-ORC, while for ORC-AHT it is the COP of the AHT times ORC efficiency. Since the COP of the AHT is always very low, i.e. never higher than 0.5 for the simple AHT configuration here considered, the ORC-AHT system efficiency is lower than the GEO-ORC one. It must be noticed that, as both systems operate between the same temperature (i.e. source and condenser temperature), the Carnot efficiency and the Carnot turbine power output are the same for both systems. Since the geothermal power input and flow rate are the same for ORC-AHT and GEO-ORC at the same heat source temperature, the lower system efficiency leads to a lower turbine power output in case of ORC-AHT in comparison to GEO-ORC. In Table 3, columns for source temperature of 60°C and 80 °C are shown in grey, because the current ORC technology does not allow to exploit such low temperature resource. The minimum temperature at the evaporator of the ORC, at current level technology, is about 120°C, even though in a relatively short term it seems reasonable to expect evaporator temperature of about 100°C. Hence, the AHT-ORC system here proposed can convert this geothermal resource into electricity at such low temperature, which, otherwise, would be wasted.

Table 3. Geo-ORC and ORC-AHT results for various T_{SOURCE}.

		ORC-AHT				**GEO-ORC**			
Heat Source Temperature [C]	**80**	**90**	**100**	**110**	**120**	**60**	**80**	**100**	**120**
Absorber temperature [C]	115	135	155	160	160	-	-	-	-
Geothermal flow rate [kg/s]	25.74	26.48	26.95	27.61	26.32	23.6	25.74	26.95	26.32
Geothermal power input [kW]	539	556.1	568	583.6	558	493	539	568	558
Maximum ORC temperature [C]	105	125	145	150	150	50	70	90	110
Maximum pressure [bar]	14.16	21.27	30.84	33.81	33.81	3.432	6.097	10.09	15.74
Condenser pressure [bar]	1.478	1.478	1.478	1.478	1.478	1.478	1.478	1.478	1.478
Temperature at turbine outlet [C]	48.7	52.7	51.2	47.4	47.4	32.2	38.3	44.5	49.9
Geothermal fluid outlet temperature [C]	75	85	95	105	115	55	75	95	115
Organic fluid flow rate [kg/s]	1.11	1.147	1.17	1.229	1.11	2.39	2.51	2.56	2.45
ORC efficiency [%]	**14**	**16**	**17.2**	**17.2**	**17.2**	**5.5**	**9.1**	**12.1**	**14.5**
ORC Carnot efficiency [%]	23.2	27	30.4	31.2	31.2	10.5	15.6	20	24.2
System efficiency [%]	**6.5**	**7.7**	**8.4**	**8.5**	**8**	**5.5**	**9.1**	**12.1**	**14.5**
System Carnot efficiency [%]	15.6	17.9	20.1	22.2	24.2	10.5	15.6	20	24.2
COP AHT [-]	0.467	0.479	0.486	0.50	0.469	-	-	-	-
COP Carnot AHT [-]	0.672	0.664	0.662	0.712	0.775	-	-	-	-
Turbine power output [kW]	**35**	**42.5**	**47**	**49.6**	**45**	**27**	**49**	**68**	**81**
Turbine Carnot Power output [kW]	84	99.54	114	129.5	135	52	84	114	135
Absorber heat transfer [kW]	252	266.3	276	289.4	262	-	-	-	-
Internal heat recovered [kW]	25	30.3	29	26.2	24	16	32	47	58
ORC Condenser heat [kW]	217	223.7	228	239.8	217	466	490	499	477
AHT Condenser heat [kW]	288	289.9	292	294.2	296	-	-	-	-
Specific power output [kW/kg_{ORC}]	31.6	**90**	40.6	**110**	40.4	11.4	19.5	26.8	33.1

This analysis suggests that, with the proposed ORC, the adoption of AHT to upgrade the geothermal heat is worth for low temperature of geothermal resource, up to 85 – 100 °C.

6. Conclusions

The possibility of using an AHT system with a LiBr – water solution to upgrade the low temperature heat available from geothermal resources has been discussed. The upgraded heat is used to feed an ORC working with R245fa in a pure Rankine recuperative power cycle.
Both systems are modeled by calculation codes developed with the same calculation tool, which includes the thermodynamic libraries of LiBr solution and ORC working fluid. The results showed that the COP of the AHT and the amount of upgraded heat (Q_{AB}, for a fixed value of m_1) are strongly dependent on the three main design temperatures, i.e. T_{CO} (close to the environmental value), T_{GE} and T_{EV} (close to the available geothermal source), and T_{AB} (the value of upgraded heat). Specifically, for temperatures of low grade heat variable between 45 and 90 °C and the corresponding upgraded heat variable into the 55 – 155 °C range, the achieved COP varies between 38 and 50%. The condenser (i.e. environmental) temperature has a slight influence on AHT performance: with fixed upgraded heat from 80 °C (T_{GE}=T_{EV}) to 130 °C (T_{AB}), the COP is reduced from about 48% to about 45% for an increase of condenser temperature from 15 to 32 °C. The results agree with those found on literature [3].
The enhanced heat released by the absorber of the AHT can be used into the boiler of an ORC, which has the possibility to use the geothermal heat source, which otherwise would be unexploited, and thus wasted. However, the convenience of AHT – ORC combined system over the simple GEO – ORC is strongly related to the temperature of the geothermal heat source. Generally, coupling AHT – ORC is convenient until the geothermal resource temperature is below 120°C, which is the lowest temperature suitable for current ORC technology.

Nomenclature

COP	Coefficient of Performance
ΔT	Temperature difference [°C]
LiBr	Lithium Bromide
m:	Mass flow rate [kg/s]
p:	Pressure [bar]
Q:	Heat rate [kW]
T:	Temperature [K]
x:	Lithium bromide mass fraction in the solution
W:	Power [kW]
[1]...[n]:	Thermodynamic point of the cycle
Suffixes	
app;GE	Approach difference to GE
app;ORC	Approach difference to ORC
source:	Geothermal inlet to the system
geo;pp:	Geothermal at the pinch point
geo;out:	Geothermal reinjection into the well
geo:	Geothermal
out;GE	Geothermal outlet from GE

p:	Pump
pp;ORC	Pinch point ORC
sp	Specific
t:	Turbine

Acronyms

AB	AHT Absorber
AHT	Absorption Heat Transformer
CO	AHT Condenser
EVA	AHT Evaporator
EX	AHT Liquid to liquid heat exchanger
GE	AHT Generator
GEO-ORC	ORC directly fed by the Geothermal resource
ORC	Organic Rankine Cycle
ORC-AHT	ORC coupled with AHT
IHE	Internal Heat Exchanger

References

[1] Tufano, V., Heat recovery in distillation by means of absorption heat pumps and heat transformers, Applied Thermal Engineering 1997; II(2): 171-178.

[2] Zhao, Z., Ma, Y., Chen, J, Thermodynamic performance of a new type of double absorption heat transformer, Applied Thermal Engineering 2003;23: 2407–2414

[3] Horuz,I., Kurt, B., Absorption heat transformers and an industrial application, Renewable Energy 2010;35: 2175-2181

[4] Xuehu Ma, Jiabin Chen, Songping L., et alii, Application of absorption heat transformer to recover waste heat from a synthetic rubber plant, Applied Thermal Engineering 2003;23: 797–806

[5] Rivera, W., Romero, R.J, Thermodynamic design data for absorption heat transformers: Part 7: Operating on an aqueous ternary hydroxide, Applied Thermal Engineering, 1998;18(3-4): 147-156

[6] Best, Rivera, W. Thermodynamic design data for absorption heat transformers: Part 6: Operating on water-carrol, Heat Recovery Systems and CHP, 1994;14(4): 427-436

[7] Lentz, A., Almantza, R., Solar–geothermal hybrid system, Applied Thermal Engineering 2006;26: 1537–1544

[8] Fangtian Sun, Lin Fu, Shigang Zhang, Jian Sun, New waste heat district heating system with combined heat and power based on absorption heat exchange cycle in China, Applied Thermal Engineering 37 (2012) 136 – 144

[9] Pratt and Whitney Corp., Model 280 kW PureCycle® Power System, http://www.pw.utc.com/media_center/assets/model_280_purecycle_power_system.pdf

[10] ElectraTherm's Heat to Power Generation Systems available at http://www.electratherm.com/products.html last access 10 February 2012

[11] Yin J, Ming-Shan Z, Li-Zhong H. Performance analysis of an absorption heat transformer with different working fluid combinations. Applied Energy 2000;67(3):281-92.

[12] Sozen A, Yucesu HS. Performance improvement of absorption heat transformer. Renewable Energy 2007;32:267-84.

[13] Scott M., Jernqvist A., Olsson J., Aly G. Experimental and theoretical study of an open multi-compartment absorption heat transformer for different steam temperatures. Part I: hydrodynamic and heat transfer characteristics. Applied Thermal Engineering 1999;19: 279-298.

[14] EES Engineering Equation Solver, http://www.fchart.com/.

[15] Di Pippo R. Geothermal Power Plants: Principles, Applications and Case Studies. London, UK: *Elsevier Advanced Technology*; 2006.

[16] Turboden Combined Heat And Power Orc Units For The Pellet Industries, 2008, (see also http://www.genewscenter.com/content/detail.aspx?releaseid=7229&newsareaid=2http://www.turboden.eu/en/public/press/Turboden_ORC_for_pellets_english.pdf)

[17] Obernberger I, Hammerschmid A, Biomass fired CHP plant based on an ORC cycle – Project ORC-STIA-Admont. Final Report, Bios-energy systems; 2001 (see also http://www.bios-bioenergy.at/uploads/media/Report-ORCAdmont-Thermie-2001-03-26.pdf)

[18] GE Energy Announces Industrial Waste-Heat Recovery Innovation for Onsite Power Plants, http://www.genewscenter.com/content/detail.aspx?releaseid=7229&newsareaid=2, 6 July, 2009 (last access 4 January 2012).

Alternative feedstock for the biodiesel and energy production: the OVEST project

Matteo Prussi[2], David Chiaramonti[1], Lucia Recchia[3], Francesco Martelli[2], Fabio Guidotti[4]

[1]RE-CORD c/o Dept.of Energetics "S.Stecco", University of Florence (Italy);
[2]CREAR, c/o Dept.of Energetics "S.Stecco", University of Florence (Italy);
[3]CREAR - DEISTAF, University of Florence (Italy);
[4]Silo S.p.A.

Abstract:

A large share of the vegetable oil market is today shifting from food to energy sector. This trend led to discussions about the chance of a confliction between these two chains and its possible social and environmental consequences. Moreover the increasing interest in pure vegetable oils for energy and biodiesel production promotes market volatilities and, in recent years, high and peak prices. The economics of the biodiesel production is suffering the actual market situation.
In this framework, the present work presents the results of the OVEST project, which is supported by the Tuscany region. Aim of the project is the investigation of the possibility to use waste oil streams of the food industry to obtain an alternative feedstock for bioliquids and biofuels production. In the current food market, a number of waste streams are available from the food industry: oleins and fatty acids, sludge oils and WCO (Waste Cooking Oils) represent several examples of these waste streams from edible oil production. Most of these feedstock oil streams are composed by distilled fractions obtained during vegetable oil refining, i.e. free fatty acids, di- and mono-glyceride, etc. In the OVEST project, vegetable oil is obtained from waste materials by the re-esterification process, in order to obtain a new feedstock for biodiesel production and for power generation.
A market analysis has been carried out in OVEST, to estimate the economic viability and the potential of each waste streams. PFAD (Palm Fatty Acid Distillate), fatty acids from vegetable oils and WCO are very interesting feedstock to obtain "re-esterified" oils. The new vegetable oils obtained in OVEST show promising chemical-physical characteristics for biodiesel production, such as the fatty acid composition and the contamination from solids and inorganics.
Test on a modified Micro Gas Turbine (30 kWel) have been carried out. Performances and pollutant missions have been monitored. The results of the experimentation confirmed the viability of these materials for the energy production.
From the environmental point of view, the use of these feedstock allows to meet the requirements of the European Directive EC/28/2009 (RED), that introduces minimum targets in terms of GHGs saving for bioliquids and biofuels. According to the EC Directive, LCA must be carried out considering equal to zero the wastes and residual products GHG emissions before processing.
The present work showed that most of the input materials to the esterification plant may be classified as wastes or residues, and that assuring an accurate traceability for each treatment and transport phase is a really complex issue. However the GHG savings indicated in the RED for bioliquids from wastes, was confirmed by the work here carried out.
Therefore OVEST project demonstrates the viability of the use of re-esterified oils (reconstructed oils) for biodiesel production.

Keywords:

Vegetable Oil, organic waste, conversion technology.

1. INTRODUCTION

The European biofuels market is rapidly growing in recent years and it can be defined by three main actors: biodiesel (78.5% on energy base), bioethanol (17.5%) and pure vegetable oil (4.0%). Biogas is rapidly growing in EU market; the application to the transport sector is often proposed but still represent a minor component.

Biodiesel is the most important biofuel in European region, both for consumption and for production, representing about 78% of the total biofuels market in the transport sector. The EU27 production, in 2008, was 6,860 million liters, for a total consumption of 9,465 million liters [USDA, 2008]. Germany, France and Italy are the leaders of this market and together accounted for 80% of the EU biodiesel production.

The recent issued Renewable Energy Directive (RED [EU Parliament, 2009]) confirms the 10% target, set by the EC, for energy from renewable sources in transport. This 10% is a minimum target to be achieved by all Member States for the share of biofuels in transport petrol and diesel consumption by 2020. Even if the EU directive poses a rigid framework for the fuel sustainability, focusing on the GHGs reduction potential, the main reasons to set such ambitious target deals with the EU fuels supply security.

From this point of view, it is necessary to underline that demand is not growing only in Europe. China set a target of biodiesel penetration for 2020 and New Zealand, Australia, Japan, among the others, have mandates for biofuels blends [New Zealand Parliament, 2008]. Biofuels worldwide consumption accounted for 24.4 Mtoe in 2006, compared to only 10.3 in 2000. Despite this considerable increase, they still represent only 1.5% of the total road-transport fuel demand in 2006 [IEA, 2008] and rooms are today present for an increase in the demand.

As regards the feedstock, in contrast with the United States, where about 50% of biodiesel is produced from soybean oil, rapeseed oil and sunflower oils represent the major source of biodiesel for the European industry (4.7 Mton [Pelkmans, 2009]).

The issue of the cost is today one of the critical issue for the biodiesel producers. During the entire 2007 and part of 2008 the price of the food oils rose up, constituting an example of the price instability of this kind of market. Causes have been identified in the rapid growth of the Asian market, in the temporary decrease in the yield of several crops, due to unfavorable climatic conditions, in the increasing demand for biofuels and in the speculation on food and fuel commodities, the crude oil price to 147 US$/barrel [US EIA, 2009]. Nevertheless price instabilities still continue to appear cyclically and they can be still considered the major risk factor for transport fuel market.

The total world vegetable oil production has increased in the last decades: the main growth has been recorded for palm oil (+8% annually), followed by palm kernel oil (+7.6% annually) and soybean oil (+5.7% annually) [Pelkmans, 2009]. Palm oil and soybean oil represent more than half of the market, being 30% and 28% respectively. Rapeseed oil is also important, especially for Europe [Lieberz, 2009].

The vegetable oil consumption is divided between food industry and other industrial applications, among which, the biodiesel industry is rapidly rising in importance. Nonetheless more than 80% of the vegetable oil produced worldwide is destined to the food market.

The sector of vegetable oil trade is today dramatically changing. In the framework of the international scenario, European Union vegetable oil market is strongly affected by biodiesel sector. Despite palm oil is often perceived as the major actor in the biofuel market, the production of biodiesel from this feedstock is very limited due to the poor winter stability of the product. An increasing use of palm oil is observed as bioliquid for co-generative systems (high displacement reciprocating engine for power generation with heat recovery), or in substitution of rapeseed oil for food industry.

Despite the intensive productions, European Union (EU-27) is a net importer of oil. The total import of oil for food and industrial uses is estimated equal to 34% of the total domestic consumption [USDA, 2009].

The OVEST project aims to investigate alternative feedstock for biodiesel and direct energy production starting from food industry by-products and wastes. The main goal of the project are related to the techno-economic demonstration of the viability of the use of this low quality feedstock to produce energy in stationary systems. Moreover the lower costs of this materials

(figure 1), compared to the standard oils, are interesting as a potential answer for the biodiesel sector.

2. THE OVEST PROJECT

Many waste materials are today available from different markets. The possibility to consider these waste streams as potential feedstock for energy production, it is very interesting topic. Feedstock from waste materials are profitable in the actual context as an open discussion is on-going about the land use and the competition between the food and the energy chains for bioenergy sector.

Supported by the Tuscany Region, the OVEST project focuses its attention on several possible feedstock rich in fatty-acids content for oil production. There are several by-products of the processing of edible vegetable oils; there are mainly fatty-acids and oleins, Waste Cooking Oils (WCO) and sludge oils (the residues of tanks washings). The esterification process allows to obtain tri-glycerides from these materials, creating a product useful for both energy of biodiesel industries.

3. NON-STANDARD FEEDSTOCK

Oleins and Fatty-Acids are by-products of the same food chain: the de-acidification of the edible vegetable oils. This process is carried out to obtain a low acid-content edible oil, usually lower than 1%. Oleins and Fatty-acids are the results of different techniques. Oleins are obtained by treating a soapy paste, resulting from the chemical de-acidification of the oil, with sulfuric acid. This kind of chemical de-acidification produces a material with over the 50% of FFA (Free Fatty-Acids) content [Dumont M-J et al. 2007]. Fatty-acids are secondary products of distillation (physical de-acidification) of vegetable oils: their FFA content is very high (over 80%) [Hartman L. 1978], with also a normally lower content of impurities and contaminant than oleins.

While the previous described feedstock may present a relatively little fluctuation of their FFA content, different is the case of WCO and sludge oils. The properties of WCO are highly influenced by the kind of heating treatment they undertook. In the case of the sladge oils, their property are linked with the characteristics of the tanks they came from.

WCO can be a high quality feedstock if well pre-treated and in particular filtered for the removal the solid impurities [Balat M. 2010].

The most interesting qualities of this kind of feedstock is related to their cost. This is generally lower than the Pure Vegetable Oil. The price of this class of materials is subjected to volatility like the price of the oil, nevertheless this it has been noticed that these fluctuations are smaller, which make these substances interesting even in critical market situations.

Figure 1- Recent oil market price trend (CPO: crude palm oil; PFAD: palm fatty acids distilled).

In this framework, the sludge oils have to be considered for being very available and cheap, compared to the other by-products. Nevertheless their utilization may be not easy in the actual technologies, as their quality is poor. They can be used by a proper dilution with other purer materials.

Particular is the case of WCOs; they represent a good-quality feedstock to start with, their cost is similar to PFAD and they are available in large quantities even on regional scale. WCO has a high potential which needs to be supported by a well-coordinated collection mechanism. An interesting example is the experience carried out in Tuscany (Italy). In this Region, in the past years, the collection of WCO was limited to the restaurants. Today it has been powered and WCO are also available from a domestic collection system. The availability of this material has increased strongly and it is still developing, so it may become possible the implementation of a highly positive environmental short-chain embracing the attention to social and environmental sustainability proposed by the European RED Directive (Renewable Energy Directive EC/28/2009).

The actual market price is guiding the use of these non-standard feedstock. WCO is widely used as feedstock for biodiesel production, even because the European directives allow to associate at this material a double positive effect on the GHGs reduction. Sludge oils are more interested for the use in engines for the direct power generation, as their quality is lower compared to the other materials but also their costs.

4. RE-ESTERIFICATION PROCESS

The esterification process allows to obtain a new vegetable oil from FFA and glycerol. This process is well known in the biofuels area to be also a pre-treatment stage for the biodiesel production.

Controlling the stoichiometric ratio between Free Fatty Acids and glycerol it is possible to re-built an oil which is not edible (because of the reaction may alter the chemical residues from the previous processing) [Bhosle B. M. 2004] that can be directed to the energy chain without conflicting with the food sector. The feedstock required is largely available on international markets (for example Palm Fatty Acid Distilled) and on regional scales.

The technology described in the present work is a non-catalyzed reaction, which will take place in two separate reactors. In the first stage the glycerol and the FFA are introduced in the reactor and then heated up at 200-250 °C for two hours. The glycerol evaporates with the water produced by the reaction itself, so it is necessary to discharge water outside while force the glycerol to condensate back in the reactor, so to be re-circulated.

Depending on the kind of feedstock used, the esterification process needs some upstream treatments on the feedstock, in order to obtain a high quality oil. To reduce the impurities and contaminant: for example, on the WCOs, a severe filtration is required; de-phosphoration and dehumidification are advised in any case.

The esterified oil could not immediately suitable for power generation or as feedstock for biodiesel production. It is often necessary to provide further processes, like post-filtrations and deodorization.

5. POWER GENERATION FOR RE-ESTERIFIED OILS

Stationary power generation is an interesting market for the feedstock described. Standard technology for energy conversion are the reciprocating engines, based on diesel cycle and the gas turbine. The chemical and physical characteristics of the re-esterification process are different from fossil diesel oil and rather far from the common technical specifications for engines. Major

differences are the kinematic viscosity and the Lower Heating Value, but also as regards contaminant levels and composition, fuel cold properties, ignition behavior, etc.

A standard for the use of vegetable oils in engines is the DIN 51605 (table 1). It has been defined for the use of rapeseed oil in transports engine. It is a reference to qualify the characteristics of the vegetable oil for the power generation.

Table 1 – DIN51605 technical specification of the use of vegetable oil in engines.

Parameter	Method	Specification E DIN 51 605	Unit
Density (15 °C)	DIN EN ISO 12185	900 - 930	kg/m3
Flash point	DIN EN ISO 2719	min. 220	°C
Kin. viscosity (40 °C)	DIN EN ISO 3104	max. 36,0	mm2/s
Calorific value, lower	DIN 51 900-2	min. 36000	kJ/kg
Cetane number (DCN)	IP 498	min. 39	-
Carbon residue	DIN EN ISO 10370	max. 0,40	% (m/m)
Iodine value	DIN EN 14111	95 - 125	g Iodine/100g
Sulfur content	DIN EN ISO 20884	max. 10	mg/kg
Total contamination	DIN EN 12662	max. 24	mg/kg
Acid value	DIN EN 14104	max. 2,0	mg KOH/g
Oxidation stability 110 °C	DIN EN 14112	min. 6,0	h
Phosphorous content	DIN EN 14107	max. 12	mg/kg
Earth alkali content (Ca + Mg)	DIN EN 14538	max. 20	mg/kg
Ash content	DIN EN ISO 6245	max. 0,01	% (m/m)
Water content	DIN EN ISO 12937	max. 750	mg/kg
Free fatty acid content	AOCS Ca 5d-01 (03)	-	% (m/m)

As previously stated, the sludge oils are an interesting class of materials for power generation. The oil obtained by the sludge has presented the highest chemico-physical characteristics variation, especially in terms of impurities and contaminants, because of the wide variation of the original material. In general the quality of this oil is far from the technical specification defined in the standard. In table 2 is reported the concentration of several important elements in the vegetable oil. The high value shown confirm the difficulty to directly use these oils for engine application.

Their use is interesting when diluted to highest quality feedstock in order to reduce the cost of the final product.

Table 2 - Metal content in oil from sludge .

	Sulfur	Sodium and potassium	Vanadium
Limits	[ppm]	[ppm]	[ppm]
max	18,40	114	-
Min	0,26	86	<1
Mean	7,99	104	-
	Calcium and magnesium	Calcium	Copper
	[ppm]	[ppm]	[ppm]
Max	83,10	31,00	1
Min	44,50	18,00	0,1
Mean	58,18	24,53	-

For what concerns the other considered feedstock, the best results has been noticed for the fatty acids and WCOs.

Table 3 - Examples of analysis resulted on samples of esterified oil from WCO

Sample	A	B	C
Impurities (ppm)	3	1.5	1.5
Humidity (% d.b.)	5.44	3.03	4.82
Acidity (mg KOH/g)	2.98	2.62	2.69

In OVEST project the re-esterified oil has been tested in a 30 kW Micro Gas Turbine. This machine has been modified to be fed by this oils. In particular the fuel line has been adapted to the characteristics of the oil in input. The functioning resulted very stable and the performances substantially unmodified. After 250h of stable functioning many parts of the engine have been examined. In particular analysis have been carried out on the deposits of the injectors. The concentration of phosphorous in the oil appeared to be the most critical parameter as it was the main constituent of the deposits.

The analysis of the pollutant concentration in the exhaust gases from the turbine confirmed the good quality of the combustion. The concentration of NOx resulted to be higher when turbine works with re-esterified vegetable oil compared with regular Diesel but CO concentration appeared to be significantly lower. In figure 2 is shown a direct comparison with Diesel on the pollutants emissions.

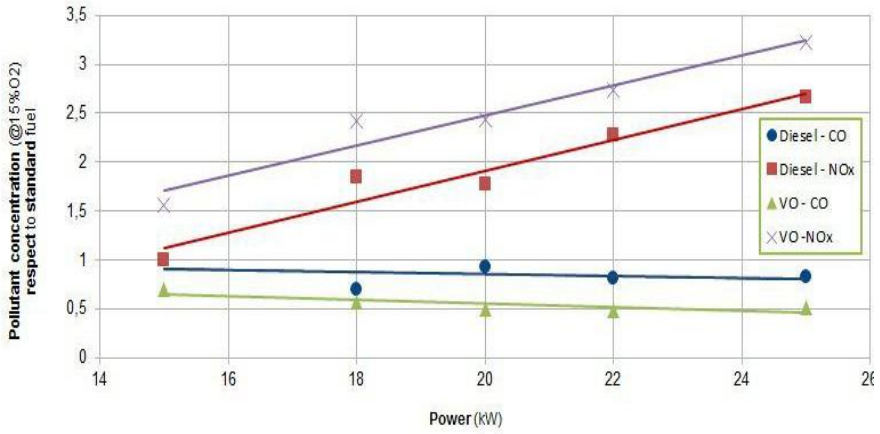

Figure 2: MGT C30 pollutant emission measured for pure vegetable oil feeding.

6. LIFE CYCLE ASSESSMENT

The economical potential benefits in the use of these non–standard products is not the only positive effect. In the present work the LCA has been carried out starting with the definition and classification of the feedstock. The classification as waste or by-product is a crucial point to assess the environmental balance: according to the European RED Directive (EC/28/2009) definitions, the emission of CO2 associated to the original chain are not taken into account if the product in exam is a waste. This is an crucial starting point to meet the 35% minimum target of GHGs saving.

In order to verify the achieving of the RED target the CO_{2eq} calculation basing on the methodology proposed by the directive has been implemented. Moreover, considering that the energetic consumptions and therefore the fossil energy requirements are significant along the re-esterification process also the CER parameter has been evaluated.

Besides the work provide to identify the production chain and the geographical origins of the feedstock (especially when classified as 'by-product') and to define clearly the stages of production and eventually the LCA methodology. The phases modeled (see, figure 3) in the LCA carried out can be summarized in the following steps:

- Transportation to the esterification reactor;
- Re-esterification phase;
- Use of oil for energy production.

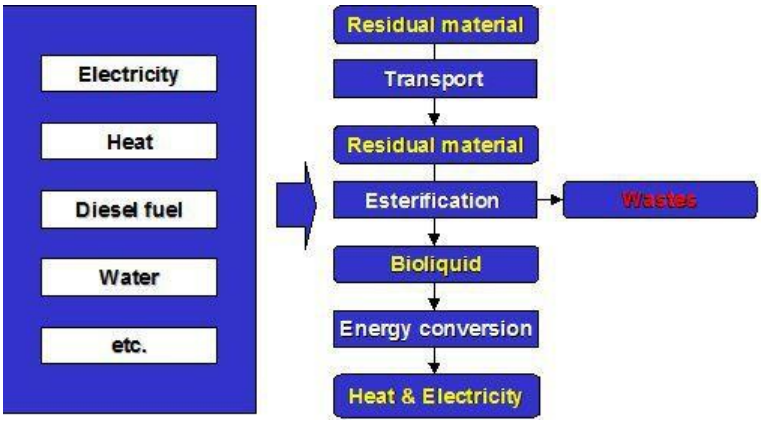

Figure 3 - Scheme for the definition of the new oil in LCA analysis.

The LCA has been carried out through a spreadsheet built using the Biograce project assumptions: particularly the Biograce emission factors have been considered (see table 4).

Table 4 - Emission factors used in the LCA (Source: Biograce).

GHG	g/g		
CO_2	1		
CH_4	23		
N_2O	296		
Transport	MJ/tkm	gCO_2/tkm	MJ/tkm
Road transport (liquid materials)	1.01	88.34	1.1693
Ship transport	0.12	10.85	0.1437
Train transport	0.21	26.81	0.5660
Re-esterification	gCO_2/MJ	MJ/MJ	
Diesel	87.64	1.16	
Natural gas	67.58	1.13	
Grid electricity - MV	127.65	2.70	
Grid electricity - LV	129.19	2.73	

The transport phase has been evaluated considering the geographical provenience of the current feedstock treated in the Silo SpA, hypothesizing the means of transport and estimating the average distance.

For the re-esterification process the energetic consumptions have been measured in the plant of the Silo SpA (see table 5): the values measured do not highlight a difference due to the feedstocks characteristics.

Finally, for the energy production a 250 kWel engine with 41% of electrical efficiency and 85% of thermal efficiency has been considered.

As shown in table 6, the potential GHGs saving is near 90%. The important results allows to meet the requirements of the directive EC/28/2009 on sustainability.

Moreover, the results obtained highlight that the transport phase have higher GHG emissions than these expected by the RED because of the far distances to be covered for delivering the feedstocks to the re-esterification plant. On the other hand the emissions are comparable to these indicated in the directive for the biodiesel production from waste materials.

Table 5 - Energy consumption for the production phase

Power consumption	47.81	kWh/t
Methane consumption	48.72	kg/t

Than has been calculated the equivalent CO_2 and the CER parameters, which consider the fossil energy consumptions for the process.

Table 6 - Results of LCA

Phase	gCO2/MJ_oil
Trasport	2.54
Esterificaztion	4.53
Total	7.08
Saving for cogenation	92%

CER analysis

Process	MJ/MJ_oil
Trasport	0.0364
Esterification	0.0783
Total	0.11

As shown in table 5, the potential GHGs saving is near 90%. The important results allows to meet the requirements of the directive EC/28/2009 on sustainability.

7. CONCLUSIONS

Biodiesel industry and power generation applications are today suffers for the market price and the price volatility of the traditional feedstock. Alternative feedstock are available from food industry, mainly from edible oils processing. By-products are oleins and the acid oils. Sludge oils and Waste Cooking Oils (WCO) are also interesting materials, rich in free fatty acids, that can be converted into re-esterified oils.

A new non-edible oil has been obtained thanks to the esterification process, adding glycerol to the inlet materials. The characteristics of the re-esterified oil are variable, mainly based on the characteristic of the feedstock. The oil could need further treatments but are mostly compatible with the use in engines and for the biodiesel industry. The lower quality for engine feeding is an aspect that can be improved, especially for very low cost feedstock, such as the sludge oils.

Test has been carried out in a 30 kW micro gas turbine. Good performances have been observed for re-esterified feeding.

From technical and economical point of views the best results were given by Palm Fatty Acid Distilled for the biofuel production. A good potential is for the Waste Cooking Oils, available also at regional level.

For power production in engine the cost is a key factor and sludge oils are very interesting even if the poor quality is today limiting their use.

The LCA resulted very interesting for the oils obtained from this process: the potential GHGs saving resulted higher than 90% compared to the traditional fossil fuels, so the target (35%) set by EU Directive can be reached.

ACKNOWLEDGMENT

The authors wish to acknowledge the Tuscany Region, for the support, project coordinator SILO SpA and the project partner Il Trebbiolo.

The authors would also to acknowledge Eng. Lisa Bigozzi for her precious support.

BIBLIOGRAPHY

[1] Balat M, "Potential alternatives to edible oils for biodiesel production – A review of current work", Energy Conversion and Management vol. 52, Elsevier Journal, Ottobre 2010.

[2] Bhosle B. M, Subramanian R, "New approaches in deacidification of edible oils—a review", Journal of food engineering vol. 69, Elsevier Journal, November 2004

[3] Dumont M-J, Narine S, "soapstock and deodorizer distillates from North American vegetable oils: Review on their characterization, exrtation and utilization", Food Reserch International n° 40, Elsevier Journal, June 2007.

[4] EU Parliament. "DIRECTIVE OF 2008/28/EC OF THE EUROPEAN PARLIAMENT AND OF THE COUNCIL", 2009.

[5] Hartman L, "Deacidification of edible oils by short path distillation", Rivista- Italiana-delle-Sostanze-Grasse Vol. 55, 1978.

[6] IEA, "World Energy Outlook", 2008.

[7] Lieberz S.,"EU27 Oilseeds annual", Global agricultural information network, NLE49039, 2009.

[8] New Zealand Parliament, "Biofuel bill", www.parliament.nz, 2008.

[9] Pelkmans, F., Walter, F., Rosillo-Calle, C. (2009) 'A global overview on vegetable oils, with reference to biodiesel', IEA Task 40, report.

[10] USDA. "United states department of agriculture foreign agricultural service". www.fas.usda.gov, 2008.

[11] US Energy Information Administration, "Policy research working pape", tonto.eia.doe.gov, 2009.

[12] USDA, "EU27 biofuels annual", Global agricultural information network, NL9014, 2009.

Assessing repowering and update scenarios for wind energy converters

Till Zimmermann[a]

[a] *University of Bremen, Faculty of Production Engineering & artec | Research Center for Sustainability Studies, Bremen, Germany, tillz@uni-bremen.de*

Abstract:

Wind energy converters are a major technology for the generation of power with even increasing relevance in the future. The shares of wind energy in the grid mixes of many countries are growing steadily. This growth is not only due to new converters on new sites but also due to repowering of sites already in use as well as updating of old wind energy converters. There is a huge potential for repowering and updating but since wind energy is supposed to reduce anthropogenic impacts on the environment, it is important to consider environmental aspects, for repowering as well as for updating. The methodological approach described in this paper allows identifying the environmentally preferable option from a variety of product scenarios using the specific energy demand as an exemplary indicator, while other indicators can be included, too. The method facilitates life cycle data regarding the converters energy balance or –depending on the desired indicators- other figures from the converters life cycle inventory. The described assessment can also be performed considering case (and site) specific factors. However, it has to be noted that data demand and availability might occur as a burden.

Keywords:

Wind energy converters, Wind turbines, Energy demand, Repowering, Updating, Sustainability.

1. Introduction

Wind energy is a technology of increasing importance – the installed capacity and the total number of installed wind energy converters (WEC) are steadily growing, in Europe as well as globally [1,2]. As a consequence thereof, repowering and updating of old converters have an increasing relevance within the wind energy sector. While various LCA studies have been performed for new WEC, environmental assessments of specific repowering scenarios or of updated second-hand WEC are rarely found. Still, the question about the environmental benefits from updating or repowering old WEC should not be discounted for. Also, the question whether updating or repowering is the environmentally favorable option for a particular old WEC might be of increasing relevance in the future. To address these aspects a method for comparing different product scenarios has been developed based on a previous work that focused exclusively on assessing repowering scenarios [3]. This method uses the specific energy demand as an exemplary indicator; including other indicators is possible, too. To demonstrate the method two exemplary assessments are performed illustrating use and possible outcomes of an assessment.

2. Background: today's situation of wind power generation, expected developments and the roles of repowering and updating

Wind energy is a major technology within the grid mix of the future since it is supposed to provide the world with "clean" and almost carbon neutral energy, reducing anthropogenic greenhouse gas emissions and other environmental impacts.

Germany as the leading European country in terms of installed wind power capacities has an installed capacity of more than 27,000 Megawatts [4] contributing already a significant share to the German grid mix. This share is constantly growing in Germany as well as in other European countries. The European Wind Energy Association, for example, has the announced target of 190 GW onshore and 40 GW offshore installed in 2020 and 250 GW onshore and 150 GW offshore in 2030 respectively [1]. This is accompanied by individual goals in different European countries. The German government for example has the goal to increase the share of renewable energies in power supply to 35% in 2020 [5]. A steady growth can also be observed globally [2]. Here, the installed capacity grew within the past years already by 22.9% (mid-2010 to mid-2011) and 23.6% (mid-2009 to mid-2010) respectively [2]. This growth is not only due to newly installed wind energy converters but it is also caused by repowering or updating of already existing converters and the installation of second hand converters, respectively. Repowering means the replacement of older WEC by new state-of-the-art WEC, hereby improving the utilization of existing sites and reducing the total number of installed converters. Since in most countries the most suitable sites for onshore wind energy are already in use, this is the main motivation for repowering. Also potential land use conflicts are hereby reduced. Updating of WEC includes refurbishing of an existing WEC, replacement of obsolete parts and possibly a slight increase of its rated power.

Germany, for example, has a potential for repowering of about 25,000 MW, which equals approximately the rated power of WEC already installed in 2010 [6,7]. The worldwide development of wind energy indicates that also in many regions outside of Germany repowering is going to be an issue as well as updating of WEC.

As –besides economic interests- the reasons for using wind energy are to a large extent environmental aspects, it is important also for repowering and updating, that they results in an overall improved environmental performance. Choosing the (ecologically and environmentally) preferable option from a variety of available repowering and updating scenarios as well as finding the (ecologically and environmentally) right moment in time for the respective measures is a challenging task. The methodological approach, described in the next section addresses this task.

3. Methodological approach

To assess the respective product scenarios we used a method comparing the specific energy yield of the different product scenarios to each other. Here, a product scenario is regarded as the combination of an old WEC that reaches the end of its life span and a repowering WEC or an updated version of the old WEC. If, for example, a 0.6 MW WEC reaches the end of its life span and there are two repowering options (A and B) available with updating/ refurbishing being another option (C), this results in three different product scenarios. Additionally, the repowering options might become available at different points in time, resulting in different repowering points:

a) 0.6 MW WEC + repowering WEC A at point A
b) 0.6 MW WEC + repowering WEC B at point B
c) 0.6 MW WEC + updated/refurbished 0.6 MW WEC at point C

For the identified (generic) product scenarios the specific energy demand is compared in the next step. This can be done calculative as well as graphically, which will be demonstrated in the next section. If required, the method can be used for additional impact categories like the carbon footprint (as demonstrated in [3]) or aggregated measures of several impact categories depending on the availability of the required data. Using several different impact categories might lead, of course, to inconclusive results (or at least to results that might need intensive discussion), since there will not always be an option that minimizes all assessed impact categories. Focusing on one impact category on the other hand will provide more conclusive results but discounts other relevant aspects. Still, this relevance always depends on the goal of the study that also might give indications on which impact categories should be assessed with priority.

However, to demonstrate the methodological approach within an exemplary assessment, the specific energy demand has been selected, since it can be regarded as one of the most discussed impact categories for WEC besides the global warming potential and –upcoming- the abiotic depletion potential. It indicates the required energy input (consumed energy) per energy fed into the grid (energy output) and can be calculated according to the following formula (cf. [3]); a description of the variables is given in Table 1:

$$e_x(t) = \frac{CED_{old}(t_r) + CED_x(t_x)}{E_{net,old}(t_r) + E_{net,x}(t_x)}$$

Table 1. Overview of variables

Scenario	*year of installation*
t_r	repowering/updating point (EoL point of old WEC)
$CED_{old}(t_r)$	Cumulative energy demand (CED) of the old WEC up to the repowering point t_r
$E_{net,old}(t_r)$	net energy production of old WEC up to repowering point t_r
X	index of potential repowering WEC, or of the potential repowering scenario, respectively
t_x	expected life span of repowering WEC X
$CED_x(t_x)$	CED of repowering WEC X subject to its life span
$E_{net,x}(t_x)$	net energy production of repowering WEC X (full lifecycle)
$e_x(t)$	specific energy yield in repowering scenario X at point t

As it can be seen in the formula e_x is a time dependent variable. The specific energy demand decreases over time with (usually) different gradients for the assessed scenarios which can lead to different results depending on the analyzed time frame.

The data demand within the described methodology varies depending on the desired quality of the results. To assess the specific energy demand as sole impact category, the minimum data demand includes the net energy production for the respective converters as well as their cumulated energy demand and data regarding boundary conditions like installation points or repowering points respectively. Depending on the goal of the study, this data needs to be case specific meaning that it needs to be based on the specific production, transport, site and end-of-life conditions, or it can be generic allowing the use of aggregated or average data from other studies. If life cycle inventories for the converters in question are available, it will provide the necessary data. If for example the specific carbon footprint (i.e. the CO_{2e}-emissions per kWh) is to be included as an indicator, the global warming potential (GWP) needs to be calculated based on the inventory data. The specific carbon footprint (cf_x) is then calculated according to the following formula, analogously to the specific energy demand with GWP_{old} being the GWP of the old WEC subject to the repowering/ updating point t_r and GWP_x being the GWP of the product option X subject to its life span:

$$cf_x(t) = \frac{GWP_{old}(t_r) + GWP_x(t_x)}{E_{net,old}(t_r) + E_{net,x}(t_x)}$$

Other impact categories or result indicators like the abiotic depletion potential which is of growing relevance can be included accordingly.

4. Exemplary assessments

Within this section, the previously described method is applied to two examples. In the first example different repowering scenarios are compared to each other, while two different update scenarios are assessed in the second example.

The underlying data represents generic converters of different rated powers, i.e. it is based on other studies (see [3,8]) and does not consider any site specific factors that would need to be considered in a case or site specific assessments of specific converter types. In some cases, site specific factors may have a critical influence on the results. Therefore, the following examples basically demonstrate how the described method can be used in order to compare different product scenarios to each other, rather than providing decisive conclusions or recommendations on how the life cycle of particular WEC should be designed.

Generally, the maximum life span of WEC is considered to be 20 years. This needs to be taken into consideration when analyzing the results of the assessment.

4.1. Repowering scenarios

For the exemplary assessment of repowering scenarios a 0.6 MW WEC installed in 1998 has been selected as base scenario. For this converter three possible repowering scenarios have been assessed: repowering in 2007 with a 1.8 MW converter, repowering in 2009 with a 2.0 MW converter and repowering in 2014 with a 3.0 MW converter. An overview of these scenarios is given in Table 2. Besides their increased rated power, the repowering WEC also have a higher number of annual full load hours, due to their increased hub height, which is based on an expert judgment from an industry partner (see [3]). Also, the 1.8 MW WEC has a rather high CED compared to the 2.0 MW and especially the 3.0 MW WEC. As a first indication on the energetic performance, the ratio of rated power to CED or the energetic payback time (*[annual net energy production / CED] * 12*) could be calculated prior to the graphical or calculative assessment of the different product scenarios. For a comparison of repowering scenario with identical repowering points this figure even is sufficient to identify the preferable choice.

Table 2. Overview of assessed repowering scenarios

Scenario	*year of installation*	*rated power [MW]*	*annual full load hours*	*CED [kWh]*
base scenario: WEC_{old}	1998	0.6	2,500	1,880,000
scenario 1	2007	1.8	2,800	3,600,000
scenario 2	2009	2.0	3,100	3,053,000
scenario 3	2014	3.0	3,100	3,100,000

Based on the method described in section 3 and the above data the comparison of the different scenarios is carried out. The results of this comparison are shown in Fig. 1.

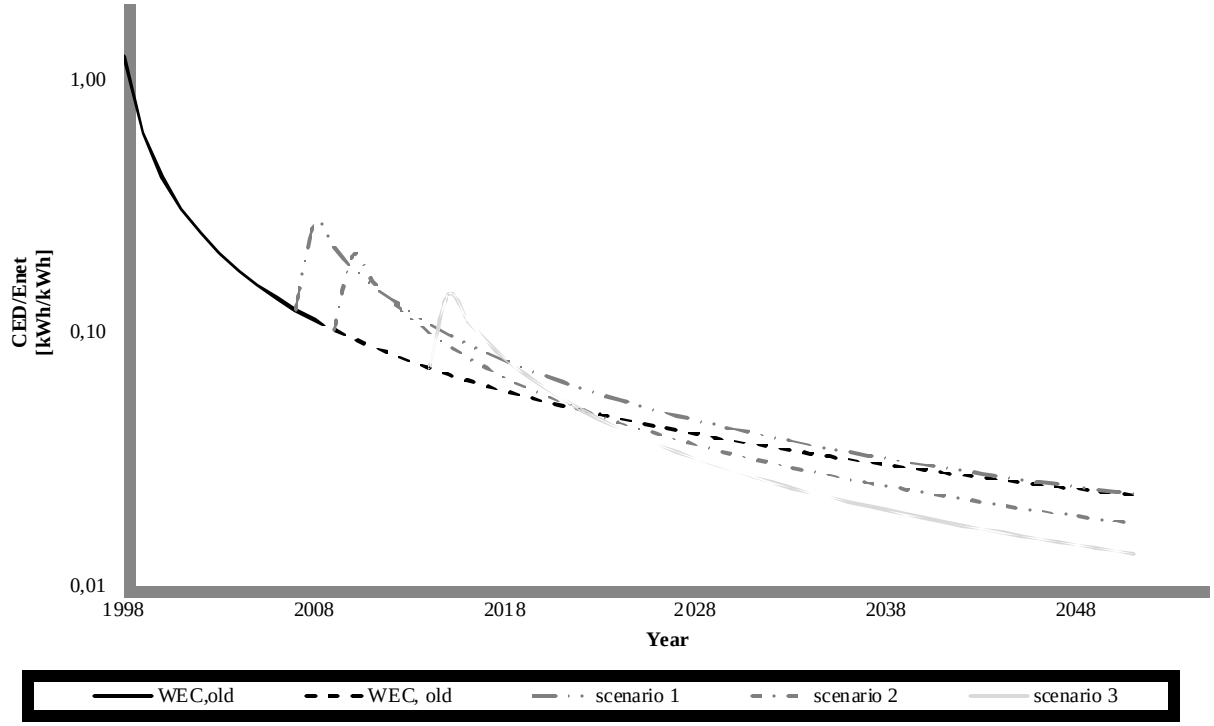

Fig. 1. Assessing the specific energy demand of different repowering scenarios.

In the figure, additionally to the different repowering scenarios, a reference scenario representing no repowering is shown by the dashed black graph. This reference scenario functions basically as an orientation; no repowering is not a real option due to the limited life span of WEC but may still function as a benchmark (however, updating/refurbishing could be an option, which is assessed in the following section).

In the diagram, the x-axis marks the installation of the original WEC which is associated with a high energy consumption (including production, transport and other factors influencing the CED) while energy production starts right after the installation. The resulting graph showing the specific energy demand falls with proceeding time as the produced net energy grows. The installation points of the different repowering scenarios are also associated with energy consumption appearing as peaks within the figure, falling with proceeding time, too.

It can be observed, that the repowering scenario 1 does not fall below the reference scenario within the assessed time scope, while scenarios 2 and 3 show a better performance. Scenario 2 falls below the reference line in 2023, which is 14 years after its installation. Scenario 3 shows an even better performance, falling below the reference line already in 2022, i.e. eight years after its installation. So, the graphical assessment (and the calculative assessment, too) shows scenario 3 as the favorable option of the assessed product scenarios; i.e., here, repowering of the 0.6 MW WEC in 2014 with the 3 MW WEC is the best option in terms of the specific energy demand.

4.2. Update scenarios

For the exemplary assessment of different update scenarios a 2 MW WEC has been chosen as the converter reaching its end-of-life. For this converter three different product scenarios are assessed:

1. Updating of the 2 MW WEC, increasing its rated power to 2.3 MW; installation at a different site,
2. Updating of the 2 MW WEC, increasing its rated power to 2.3 MW; installation at the same site,

3. Repowering with a 3 MW WEC; installation at a different site.

For scenario 1 it has been assumed that rotor blades and tower cannot be reused and need to be replaced. Rotor blades have a life span of maximum 20 years and usually after 12-15 years refurbishing is not economically feasible anymore. Concrete towers are usually not suited for reuse, either. So, it has been assumed that rotor blades and tower need to be re-produced, resulting in an energy demand equal to the original primary production of these components. The same applies to access roads, crane hard-standing and foundation. For the electrics it has been assumed that 90% can be reused while 10% need replacement (cf. [9]). For the nacelle including the generator it has been assumed that refurbishing and updating require an energy demand of 10% of the original CED of these components. This can be considered as a rather conservative assumption based on [9] with regard to the fact that around 80% of the production CED comes from material production, with 20% resulting from additional processing and transport (cf. [9]).

For scenario 2 with utilization of the same site it has been assumed that the existing infrastructure (access roads, crane hard-standing, foundation) and the tower – however requiring refurbishing equal to 5% of the original CED – can be used again; given that a life span of about 60 years can be regarded as realistic for concrete towers (cf. [9]). For the other main components – rotor blades, generator, nacelle and electricity – the same assumptions as for scenario 1 apply.

For both update scenarios 2,300 annual full hours have been assumed.

An overview of these parameters is shown in Table 3.

Table 3. Update scenarios

Component	*Scenario 1*	*Scenario 2*
rotor blades	new	new
tower	new	reuse, 5% of original CED
generator	reuse, 10% of original CED	reuse, 10% of original CED
nacelle	reuse, 10% of original CED	reuse, 10% of original CED
electric components	reuse, 10% of original CED	reuse, 10% of original CED
infrastructure	new	reuse
full load hours	2,300	2,300

The third scenario has been chosen as a benchmark for the update scenarios. It is identical with the 3 MW WEC that has been assessed in the previous section except for its earlier date of installation.

Within each product scenario, end-of-life credits are given 100% to the second product system. This way, a consistent approach for each product system is assured and the comparability of the results is increased. End-of-life credits are given according to the base end-of-life scenario described in [9] using system expansion.

Using these assumptions and boundary conditions the graphical assessment of the update scenarios has been carried out according to the described method, too, leading to the picture shown in Fig. 2.

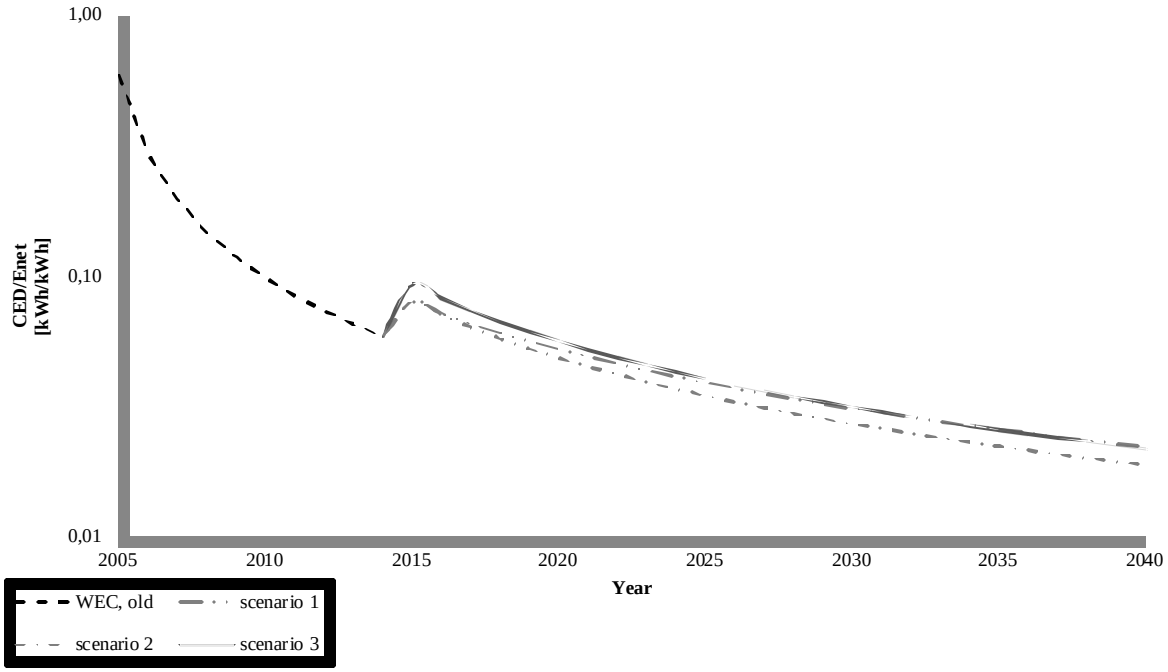

Fig. 2. Assessing the specific energy demand of different update scenarios.

In the diagram, the dashed black line shows the original WEC. It is continued by the alternative scenarios for updating and repowering, respectively. Contrary to the assessment in section 4.1 this assessment is not focused on (or limited to) one particular site but assessed different possible life cycle or product options resulting from the original WEC reaching its end-of-life.

As it can be seen in the figure, scenario 2 not requiring infrastructure shows the best performance of the assessed scenarios. The assessment of scenarios 1 and 3 leads to rather similar results; here considering site specific factors could give a better understanding of the environmental burdens.

This shows that, if the utilization of an existing infrastructure is possible, updating appears to be a preferable option with regard to optimizing the energy yield, even more attractive than repowering assuming that a new infrastructure is required, here. For the use of updated WEC as second-hand WEC at a different site, the difference to new WEC is not that significant.

5. Conclusions and discussions

Repowering and updating of WEC are trends of increasing importance. It has been demonstrated how both can be assessed under environmental aspects, using the specific energy demand as an exemplary indicator. Within the exemplary assessment it has been shown how different repowering or update scenarios can be compared in terms of their specific energy demand, a method that can be adapted to other impact categories, too. In this exemplary assessment generic data has been used, basically demonstrating how to use the described method and allowing only general conclusion on the benefits of different repowering and update strategies.

Regarding repowering, the method allows assessing different repowering options at one particular site in terms of their specific energy demand. Given a selection of available repowering scenarios preferable options can be identified, also indicating the optimal point in time for repowering (cf. [3]). General recommendations on repowering strategies cannot be deduced, here, except that significant differences between the different repowering scenarios are possible and need to be assessed, if the favorable option in terms of energy balance or other indicators shall be identified.

Based on the exemplary assessment of update scenarios, it can be said that the use of updated converters as second-hand WEC is definitely associated with environmental benefits but since components like tower and rotor blades that usually do not have second-hand potential are responsible for a significant share of the CED, the advantages compared to state-of-the-art WEC are reduced- at least regarding the assessed indicator. If however re-using tower and infrastructure is possible as well, updating shows a supreme performance also compared to state-of-the-art repowering WEC. Still, if the favorable option needs to be identified in a specific situation a case specific assessment needs to be performed. In general, however, it has to be said, that second-hand WEC and new WEC serve different markets and do not compete against each other. Also, re-use can be generally recommended; this also applies to wind energy converters. Giving WEC a second life makes sense in terms of energy balance as well as other environmental impact categories and economically (since selling and reuse is more profitable than disposal). Especially from a resource point of view re-use of WEC can be generally recommended. Even though recycling of WEC is relatively unproblematic – with the rotor blades being an exception – re-use still is the most resource saving option.

While an assessment using the described method can provide valuable information and help to better understand the environmental implications of different product scenarios, it requires a significant amount of data. To assess the specific energy demand, for example, knowledge of several figures is required: rated power, time of availability, number of annual full load hours and cumulated energy demand. While the first three are usually known, the latter requires some effort to be identified, especially when site specific aspects shall be included in the assessment. Here, conducting a life cycle wide assessment of the energy balance for all identified product scenarios might be necessary, or – if other indicators shall be included – a full life cycle assessment (LCA). These assessments require some effort and might not always be feasible due to data availability. The development and use of customized LCA tools (cf. [8]) can be of help, here, and significantly reduce the effort related with such assessments (a onetime extensive data collection is still required, though). Performing LCAs and additional case studies using the described methodology would allow creating a data basis that could be used for future assessment. This data basis might also allow drawing more specific conclusions on the environmental benefits and chances of repowering and updating of WEC.

References

[1] European Wind Energy Association, Statistics and Targets. Factsheet, 2011. Available at <http://www.ewea.org/fileadmin/swf/factsheet/1_statisticsandtargets.pdf>. [accessed 13.12.2011].

[2] World Wind Energy Association, Half year report 2011, Bonn, 2011.

[3] Zimmermann T., Gößling-Reisemann S., Optimal repowering of wind energy converters: Energy demand and CO2 intensity as indicators. Life Cycle Management Conference 2011, 2011 Aug 28-31; Berlin, Germany.

[4] European Wind Energy Association, Wind in power: 2010 European statistics, 2011. Available at <http://ewea.org/fileadmin/ewea_documents/documents/statistics/-EWEA_Annual_Statistics_2010.pdf> [accessed 13.12.2011].

[5] Bundesregierung, Erneuerbare Energien ausbauen, 2011. Available at <http://www.bundesregierung.de/Content/DE/Artikel/2011/06/2011-06-06-eeg-novelle.html> [accessed 13.12.2011].

[6] Bundesverband WindEnergie e.V., Zukunftsmarkt Repowering, 2010. Available at <http://www.wind-energie.de/de/themen/repowering/> [accessed 22.10.2011].

[7] Windenergie Agentur, Repowering von Windenergieanlagen in der Metropolregion Bremen-Oldenburg: Handlungsempfehlungen zur Steigerung der Akzeptanz von Repowering, Bremerhaven, Germany, 2010.

[8] Zimmermann T., Fully parameterized LCA tool for wind energy converters. Life Cycle Management Conference 2011, 2011 Aug 28-31; Berlin, Germany. Available at <www.lcm2011.org/papers.html?file=tl_files/pdf/poster/day2/Zimmermann-Fully_parameterized_LCA_tool_for_wind_energy_converters-567_b.pdf>, [accessed 23.12.2011].

[9] Zimmermann T., Entwicklung eines Life Cycle Assessment Tools für Windenergieanlagen. Thesis, Bremen, Germany, 2011.

Biogas from mechanical pulping industry – potential improvement for increased biomass vehicle fuels

Mimmi Magnusson[a] and Per Alvfors[a]

[a] *Division of Energy Processes, School of Chemical Science and Engineering, KTH – Royal Institute of Technology, Stockholm, Sweden, mimmim@kth.se (CA), alvfors@kth.se.*

Abstract:

Biogas is a vehicle fuel of the first generation of biofuels with great potential for reducing the climate impact from the transport sector. Today biogas is mainly produced by digestion in Sweden and the total amounts to 1.4 TWh_{LHV}/year (2010) of which about 0.6 TWh_{LHV} is upgraded and used in the transport sector. Using industrial wastewater, e.g. from a pulp and paper mill, as substrate for production of biogas, the amount of renewable fuel to the transport sector could be increased. In the pulping industry, substantial amounts of organic matter are generated; this is commonly treated aerobically to reduce the chemical oxygen demand (COD) in the effluent streams before discharge to a recipient. Treating these effluent streams mainly anaerobically instead could contribute to the transport sector's energy supply. The aim of this study is to investigate the potential for using effluent streams from the Swedish mechanical pulp and paper industry to produce biogas. A typical Swedish mechanical pulp mill is considered for anaerobic treatment of the wastewaters. This type of pulp mill presently uses conventional methods for wastewater treatment to reduce COD, but converting most of this to anaerobic treatment would increase the amount of biogas produced. When considering this conversion in a larger context, supposing that anaerobic treatment would be applied to all Swedish mechanical pulp mills, which stand for about 30% of the total Swedish pulp production, it is shown that the production could amount to as much as 0.5 TWh_{LHV}/year of biogas. This represents about one third of the biogas produced in Sweden today. The main conclusion of this study is that if anaerobic treatment of effluent streams from the pulping industry were introduced, the biogas production in Sweden could be significantly increased, thus moving one step further in reducing the transport sector's climate impact.

Keywords:

Anaerobic digestion, Biofuel, Biogas, Mechanical Pulping, Vehicle Fuel, Wastewater Treatment.

1. Introduction

The transport sector is seen as one of the most problematic areas when it comes to reduction of climate impact, due to its heavy dependence on fossil fuels. Biogas is a vehicle fuel of the first generation of biofuels, meaning that it is presently available on a commercial scale and has a well-developed infrastructure for distribution and filling, in some areas via a gas grid. In total, the biogas production in Sweden amounts to 1.4 TWh_{LHV}/year (2010) of which about 0.6 TWh_{LHV}/year is upgraded and used in the transport sector [1]. The production of biogas is commonly performed by anaerobic digestion, a technology that has been seen as one of the oldest to stabilise waste and sludge [2]. The production today is mainly based on sludge digestion and takes place in sewage treatment plants, but co-digestion plants, for instance with food wastes or agricultural wastes as substrates also exist, and there is further anaerobic treatment as a method for wastewater treatment in other types of industries.

The pulp and paper industry has been one of the most important base industries in Sweden for a long time, and still holds a strong position domestically as well as internationally. The annual production of pulp in Sweden is 12 million tonnes of the world total which is 178 million tonnes [3]. Pulp and paper production requires large amounts of water for the process and the effluent waters are rich in dissolved organic matter, measured as chemical oxygen demand (COD). Great

progress has been made to reduce the water use at the mills by closure of the water circuits and also to improve the wastewater treatment of the effluents. Since the late 1970s the environmental impact from pulp and paper industries has decreased substantially, for instance the emissions of COD in Sweden has decreased from 1.6 to 0.2 million tonnes of COD per year, while the pulp production has increased by about 4 million tonnes per year [3]. In Sweden the most common way to treat wastewaters from the pulp and paper industry has been by aerobic methods, which are rather electricity demanding: anaerobic wastewater treatment has so far not reached a break-through.

1.1 Aim

The aim of this study is to investigate the potential for using effluent streams from the Swedish pulp and paper industry to produce biogas. A case study is made on a typical Swedish mechanical pulp mill, the Rottneros mill, where a combination of anaerobic and aerobic treatment is considered an alternative to conventional aerobic methods for wastewater treatment. In the case study, design calculations are performed based on present effluent data from the mill. Based on the results from the case study on the Rottneros mill a potential biogas production for all Swedish mechanical pulp mills (producing groundwood, thermomechanical and/or chemi-thermomechanical pulp) is estimated as a possible way of increasing the share of renewable fuels in the transport sector.

2. Background

Biogas is a vehicle fuel that is well suited for both light and heavy vehicles. It is commercially available and can be distributed either in a gas grid, or to filling stations by trucks. The most common way of production is by anaerobic digestion, one of the oldest processes for treating organic wastes [4, 5]. Although used to a great extent in sewage treatments plants (for sludge digestion), the anaerobic methods for wastewater treatment have not reached a break-through in the pulp and paper industry in Sweden, where other wastewater treatment methods are more common. In the following sections, a short introduction to anaerobic digestion and to the pulp and paper industry is given.

2.1. Anaerobic digestion

Digestion of organic material to produce biogas is a process used on a commercial scale. All types of organic material may be subject to digestion; amongst the most commonly used substrates are food waste, sewage sludge, manure and agricultural waste. It is one of the standard methods used in wastewater treatment (WWT) technology, to reduce effluent treatment sludge from municipal plants and various industries. The conditions for the digestion process are dependent on the type of substrate used; the main difference between anaerobic treatment of wastewaters and digestion of organic wastes concerns the reactor design and the retention times. The main stages are, however, more or less the same, namely: collection of the substrate, pre-treatment, digestion, and, depending on end-use, upgrading. The digestion itself is a complex series of reactions where the substrate is degraded in four stages: hydrolysis (rate-limiting step); acidogenesis; acetogenesis and methanogenesis, where the methane (CH_4) is formed [6, 7]. In this series of reactions different groups of microorganisms work together in converting the substrates and intermediate products to final products. Together with methane the main product from the digestion is carbon dioxide (CO_2). The ratio between these varies depending on the substrate and process used, but the methane content is typically in the region of 45-85% [6]. The by-products are, aside from possible traces of other gases (e.g hydrogen sulphide and ammonia), water and the digestion residue (a solid fraction). To be used as a vehicle fuel the raw gas has to be upgraded to a quality with high methane content (97 +/- 2% according to Swedish standard, SS 15 54 38, European standards vary between 85% and 97% [8, 9, 10]) and thus most of the CO_2, and water have to be removed. Traces of other gases, such as sulphur-containing gases, have to be removed to not cause disturbances in the engine. The CO_2 may be vented to the atmosphere, used in other industries, used for carbon capture and storage

(CCS) or, as described in a study by Mohseni et al [11], be used to produce additional methane by reacting with hydrogen.

There are several parameters influencing the digestion and the rate of the different stages; among these are, e.g. temperature, number of fermentation steps, pH, retention time, alkalinity and moisture content of the substrate. These parameters are specific for each process and may be adjusted to enhance the biogas production. The temperature for digestion, however, is often seen as one of the most sensitive process parameters. There are three temperature intervals where the digestion is performed optimally: psychrophilic/cryophilic (0–20 °C), mesophilic (30–42 °C) and thermophilic (45–60 °C): industrial digestion is most commonly performed with the two higher intervals [6, 7]. Generally, a higher temperature gives a faster reaction rate, which is an advantage since smaller reactor volumes are needed. However, the thermophilic digestion is more sensitive when it comes to temperature and concentration variations and needs more process control, whereas the mesophilic digestion is a more stable process [6]. Whether mesophilic or thermophilic, the process requires heating to keep the reactor at the appropriate temperature.

The upgrading of the raw biogas, needed if the gas is to be used as vehicle fuel, is usually performed adjacent to the digestion, mainly only at large facilities since upgrading is rather costly. Common techniques for upgrading include water scrubbing, pressure swing adsorption (PSA) and chemical absorption. After upgrading the biogas may be compressed or condensed to liquid biogas (LBG) before being distributed to a gas grid, if available, or by trucks to filling stations [8].

2.2. Pulp and paper

The forestry industry is one of the largest industries in Sweden, and accounts for 10-12% of the employment, export, sales and added value in the Swedish industry. On an international level, the Swedish forestry industry also holds a strong position, being the third largest in Europe and second largest combined exporter of pulp, paper and sawn wood products in the world. The Swedish pulping industry produces a little less than 12 million tonnes of pulp each year, of which 3.7 million tonnes are for the pulp market and the remaining portion is processed to paper. The largest share of the pulp in Sweden is produced by chemical processes (mainly sulphate/kraft pulp), whereas the mechanical pulps (groundwood, thermomechanical and/or chemi-thermomechanical pulp) account for about 30%. On a global level, however, mechanical pulps only account for about 21% [3].

The purpose of the pulping process is to separate the cellulose fibres in the wood from each other in order to use them as raw material i.e. in papermaking; this can be achieved either mechanically or chemically. In mechanical pulping the cellulose fibres in the wood are physically torn from each other by grinding. In the groundwood pulping (GWP) process the logs are pressed against a rotating grinder stone while water is added; if the system is also pressurised the process is called pressure groundwood pulping (PGWP). In the refiner mechanical pulping (RMP) processes wood chips are ground between refiner discs; two variants of this process are thermomechanical (TMP) and chemi-thermomechnical pulping (CTMP), where the pressurised grinding is preceded by heat or chemical treatment, respectively. Other variations of the above-mentioned processes also exist. Mechanical pulping has a very high fibre yield where 90-97% of the raw material is found in the end product, compared to chemical pulping where about half of the wood is transformed to pulp and the rest (i.e. lignin) is used for energy conversion. However, pure mechanical pulping is very energy demanding: the higher the process temperature the higher the energy demand. Most of the electric energy input is transformed to heat, which is removed from the wood by cooling water. This energy can be recovered either for pulp and paper drying or as hot process water [12].

The emissions from mechanical pulping include emissions to air, water and solid wastes. The water emissions depend on the process used and increases if bleaching is applied, but they are mainly comprised of organic compounds with a chemical oxygen demand (COD) that can cause oxygen deficiency, acute or chronic toxicity, mutagenicity or eutrophication in the recipient water [4, 12]. The predominant methods for reducing COD from pulp and paper wastewaters are presently aerobic effluent treatment methods, such as the activated sludge process and biofilm treatment; another type

of treatment method is chemical precipitation [12]. Most WWT facilities at pulp and paper mills today are external treatment plants handling effluent streams before discharge to the recipient. Aerobically based WWT methods are generally rather energy demanding and also produce large amounts of sludge. The solid wastes from the process include wood and bark residues, fibre rejects (primary sludge) and biological sludge from the WWT [12]. Solids that are dry enough are usually incinerated in the bark boiler or at external combustion plants, but the main fraction of solid wastes – primary sludge and biological sludge – has to be dewatered, and possibly also dried, before further treatment, for instance incineration, which is of course energy demanding [12, 13].

3. Anaerobic treatment of effluent streams in mechanical pulping

Anaerobic treatment of wastewater to reduce COD has so far not been implemented to any large extent in Swedish pulp and paper mills, however it is more common in European mills. A few of the reasons for that are that the effluent volumes from the pulp and paper are very large (and thus have been seen as difficult to handle anaerobically) and that the anaerobic system is very sensitive to disturbances, which might be a problems since the wastewaters may contain large amounts of sulphur or other substances that are toxic [12, 14]. However, TMP as well as GWP effluents are well suited for anaerobic treatment. The carbohydrate content in the effluent is rather high (higher in groundwood pulping than in TMP), as is the anaerobic degradability, while the methanogenic toxicity is low. For CTMP the anaerobic degradability is not quite as high as for TMP and GWP, mainly because of the high contents of lignin and wood extractives in the effluent [4], but the potential for anaerobic digestion is still rather good. In a study by Sivard and Ericsson [15], different process alternatives for effluent treatment of process flows from the pulping industry (mechanical as well as chemical) have been suggested. The treatment alternatives included combinations of anaerobic treatment, flocculation and membrane filtration and the aim was to accomplish more energy- and resource-efficient wastewater treatment with low discharges and more recirculation of process waters. The results from that study were promising: not only could the process water be returned to the process to a greater extent, the anaerobic treatment also gave a substantial biogas production. According to [12], the power demand for removal of 1 tonne of COD by anaerobic treatment is about half of the power needed when using aerobic methods.

In following sections the case study and the potential for Sweden are presented. The present situation for the WWT at the studied mills is described in Section 3.1, as well as the suggested treatment with anaerobic digestion together with the relevant data for the calculations. As for the Swedish potential, an overview of the mechanical pulp mills is given in Section 3.2, together with the data and the assumptions made for the basis of calculations for the potential for biogas production.

3.1. Case study – The Rottneros mill

As stated previously this study uses a Swedish pulp mill to exemplify how anaerobic digestion could be implemented for appropriate effluent streams, to produce biogas. The case study is based on design calculations from a master thesis [16] performed at KTH – the Royal Institute of Technology in cooperation with ÅF and Rottneros. The subject for the case study, is the Rottneros mill, one of the two production sites in Sweden own by the Rottneros Group. The Rottneros mill has two separate production lines where two grades of pulp are produced: GWP and CTMP. Their yearly production capacity is about 170 000 tonnes of pulp; in 2010 the production amounted to 138 500 tonnes, of which 53% was groundwood pulp. [17].

Currently the Rottneros mill uses an aerobic wastewater treatment: a combination of activated sludge treatment and chemical precipitation, which is a traditional and rather power-demanding treatment (a simplified process diagram may be seen in Fig. 1). Simply described, the process waters from the pulping process and the wood yard are taken to the primary clarifier, where solids (primary sludge) are separated. The clarified water is then pumped to the activated sludge treatment,

including aeration basin and secondary clarifier. Nutrients (phosphorus and nitrogen) are added at the activated sludge stage. Part of the sludge from the secondary clarifier is returned to the aeration basin. There is no withdrawal of excess sludge from the secondary treatment stage. Water and the remaining sludge are led to tertiary treatment comprising chemical addition (of polyaluminum chloride) and flotation. The pH of the effluent water from the flotation is measured and adjusted before discharge to the recipient, lake Fryken. The sludge from the flotation is dewatered and the reject water is returned to the secondary clarifier, whereas the biologic and chemical sludge, together with the primary sludge, is taken care of by an external company. The total degree of COD reduction in the present wastewater treatment is 83% [16].

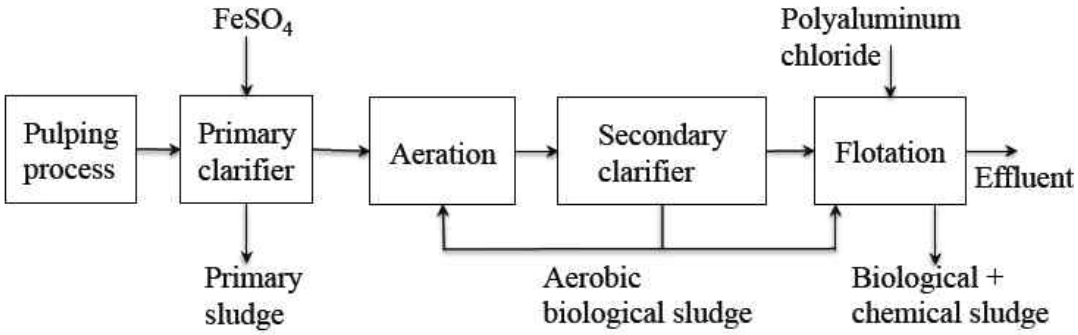

Fig. 1. Simplified process diagram over the present WWT for Rottneros.

In the suggested WWT for the Rotteros mill, anaerobic treatment in an upflow anaerobic sludge blanket (UASB) reactor is combined with aerobic treatment, see Fig. 2 for a simplified process diagram. Before entering the anaerobic reactor the flow is treated by chemical precipitation with $FeSO_4$ in the primary clarifier to reduce the amount of organic matter that is difficult to degrade and to make the wastewater less toxic to the micro-organisms present in the anaerobic process. The COD reduction in this primary precipitation stage is approximately 15%. The water from the primary clarifier is pH-adjusted with acid, and then taken to the UASB reactor. The degree of COD reduction in this stage is 70%. The produced biogas, with methane content of 70%, is separated and compressed. After the anaerobic treatment some further biological degradation is performed in the present aerobic treatment at Rottneros. An aerobic polishing is needed to avoid odours from the effluent. The flotation stage is used for final removal of suspended solids and if needed some chemicals may also be used for further reduction of COD [16]. The total degree of COD reduction for the entire WWT (including the primary clarifier, aeration and secondary clarifier) is 84%. The data for the present and for the suggested anaerobic treatment for Rottneros are presented in section 4.1.

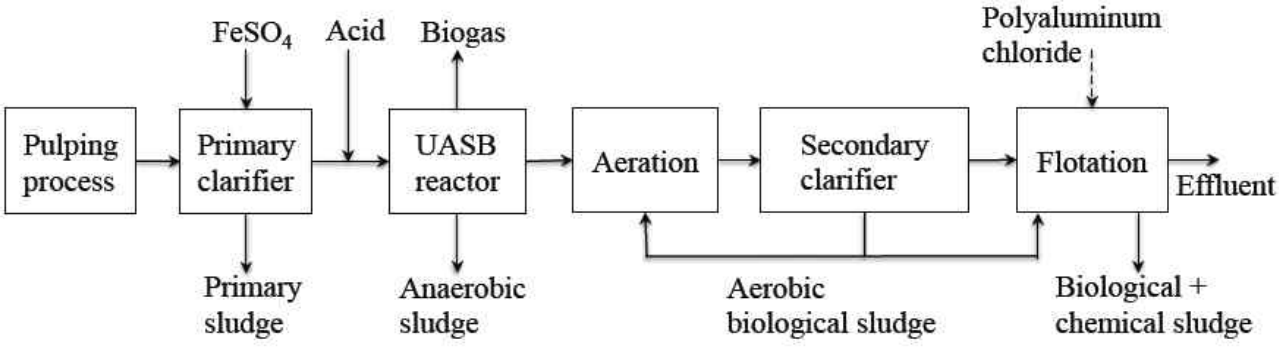

Fig. 2. Simplified process diagram over the suggested WWT for Rottneros.

3.2. Potential for Sweden – basis for calculations

There are presently 12 mills in Sweden producing GWP, TMP and/or CTMP. Their total pulp production amounts to 3.6 million tonnes of pulp per year (2010) and, as mentioned, this stands for 30% of the total Swedish pulp production. The situation at these mills is of course variable; most of them are integrated pulp and paper mills while three are market pulp mills. The pulp grades produced also vary, where four mills produce only one grade (CTMP: two mills, TMP: one mill, GWP: one mill) whereas the rest produce two or more grades. These mills include two mills producing sulphate pulp and CTMP and two mills producing recycled fibre pulps as one of their grades. [18] This means that the situation concerning the effluent WWT is different at these mills. All mills, except two, use the activated sludge process, in some cases in combination with other biological treatment stages and/or chemical precipitation. Because of their different conditions, these mills have varying potential for using anaerobic digestion with biogas production as part of their wastewater treatment system. However, as stated in the aim of this study, this potential is roughly estimated based on the results of the case study. The pulp production and the present emissions of organic compounds for the Swedish mechanical pulp mills are presented in Table 1.

Table 1. Total production of mechanical pulps and emissions of COD (based on [18]).

Groundwood pulp, t/year	400 000
TMP, t/year	2 400 000
CTMP, t/year	740 000
Total pulp production, t/year	**3 600 000**
COD emissions in effluent, t/year	26 000

In this study two scenarios concerning the potential for biogas production are presented: one moderate and one optimistic. Three parameters are varied in the assumptions for the calculations for these two scenarios; these parameters and other relevant data are summarised in Table 2, below. The first one concerns the degree of COD reduction at the current wastewater treatments at the mills, which is needed to be able to calculate the amount of COD from the process: the digestible potential. As mentioned, the WWT methods are different at the Swedish mills and thus have different degrees of COD reduction. According to [12], typical values for COD removal at biological treatment plants are in the range of 80% to 90% of the COD. In this study, two levels of reduction are assumed, the same for all mills: 85% in the moderate scenario and 90% in the optimistic scenario. Secondly it is assumed that not all the effluent streams from the process are suitable for anaerobic digestion, therefore it is assumed that 90% of the COD is possible to treat anaerobically in the moderate scenario and in the optimistic scenario the corresponding figure is 95% [19]. The third parameter varied is the anaerobic degradability of COD in the digestion, which depends on the material treated and the process conditions, such as the loading rate, for the anaerobic system. According to [4] the anaerobic degradability is in the range of 60-87% for TMP and somewhat lower for CTMP. In the case study, the anaerobic degradability was 70%, which is reasonable for a mill with GWP and CTMP. The mechanical pulps produced in Sweden consist of a large share of TMP though, and therefore the anaerobic degradability could be assumed to be somewhat higher in average. In this study the degradability is assumed at two different levels, 75% and 85% for the moderate and optimistic scenarios, respectively. The methane content in the produced biogas is assumed to be 70% in both scenarios (common contents are in the range of 65-75% according to [12]).

Table 2. Parameters used in calculations of the potential for biogas production from mechanical pulp mills.

	Moderate scenario	Optimistic scenario
Total pulp production, t/year	3 600 000[a]	3 600 000[a]
COD emissions in effluent, t/year	26 000[a]	26 000[a]
Total degree of COD reduction in present WWT, %	85	90
Amount COD possible to treat anaerobically, %	90	95
Anaerobic degradability in digester, % of COD	75	85
Specific gas production, Nm^3/kg COD removed	0.35[b]	0.35[b]
Methane content of produced gas, %	70	70
Energy content of produced biogas, kWh_{LHV}/Nm^3 biogas	6.98[c]	6.98[c]

[a] From [18].
[b] In [15, 20 and 21] specific gas productions in the range of 0.18 to 0.54 Nm^3/kg COD removed are reported.
[c] The energy content of biogas varies with the methane content. The energy content for pure methane is 9.97 kWh_{LHV}/Nm^3 [8].

4. Results

In this section, the results from the design calculations are given, both for the case study on the Rottneros mill and for the potential in the moderate and optimistic scenarios, respectively, if implemented in all Swedish mechanical pulp mills.

4.1. Case study results

The present WWT and the suggested process for the anaerobic wastewater treatment for Rottneros were described in section 3.1. Given that the pulp production and the amount of COD in the streams from the process are the same as in the present situation, the biogas production could be calculated from the COD reduction in digester. This would yield in a biogas production of 27 GWh_{LHV}/year. As shown in Table 3, further advantages are noted: both the total sludge from the treatment and the electricity demand is lower in the anaerobic treatment compared to the present, aerobic, treatment. The COD in the effluent discharge to the recipient is also somewhat lower for the anaerobic case than for the present WWT.

Table 3. Data for the present situation and the suggested anaerobic digestion at the Rottneros mill[a].

	Present situation	With anaerobic digestion
Pulp production, t/year	140 000	140 000
COD emissions in effluent, t/year	3 100	3 000
Total degree of COD reduction in WWT, %	83	84
Anaerobic degradability in digester, % of COD	-	70
Total sludge, t DS/year	15 000	9 000
Electricity demand, GWh_{LHV}/year	11	4.4
Biogas production, Nm^3/year	-	3 800 000
Biogas production, GWh_{LHV}/year	-	27

[a] All data from [16]

The Rottneros mill today has a sufficient and adequate WWT that is well suited for its production. If it, however, aims to expand the production at the mill, an anaerobic digestion treatment combined with the existing one is a promising alternative.

4.2. Assessment of the Swedish potential

When considering the entire Swedish mechanical pulping industry and the possible conversion to anaerobic wastewater treatment, this study uses two scenarios to estimate the potential biogas production. In the moderate scenario lower values were assumed considering degree of reduction in the present WWT, amount of COD possible to treat anaerobically and anaerobic degradability in the anaerobic reactor, than in the optimistic scenario.

To find the potential for producing biogas from the Swedish mechanical pulp mills, the amount of digestible material in the process water was calculated from the present emissions of COD in the effluents from the mills, using the assumed degree of COD reduction in the present WWT (see Table 2). From this material, the amount of COD degraded in the anaerobic reactor and, further, the amount of biogas produced from this was calculated using the parameters given in Table 2. The biogas production from Swedish mechanical pulp mills was calculated to 285 GWh_{LHV}/year for the moderate scenario, and 511 GWh_{LHV}/year for the optimistic scenario.

Table 4. Summary for biogas production from mechanical pulp mills in Sweden

	Moderate scenario	Optimistic scenario
COD from process, t/year	173 000	259 000
Amount COD degraded in reactor, t/year	117 000	209 000
Biogas production, Nm^3/year	40 800 000	73 300 000
Biogas production, GWh_{LHV}/year	285	511

As was stated in section 3.2, the WWT used presently is mill specific, and thus the two scenarios reflect the range of reduction degrees that actually exists. Concerning the amount of material suitable for digestion, the situation will vary between mills, depending on the grades of pulp produced, whether bleaching is applied or not and other types of process-specific reasons. This means that some streams may be toxic to the anaerobic bacteria and thus must be treated separately before taken to the anaerobic stage, if possible to treat anaerobically at all. The third variable that differs between the two scenarios is the degree of COD reduction in the anaerobic reactor and here it is assumed that the anaerobic system may be processed at better conditions in the optimistic scenario, thus giving a higher production rate.

5. Discussion

This study has first investigated the change to anaerobic wastewater treatment in a case study mill by design calculations, partly as a way of decreasing the energy demand in the WWT system, partly as a way of producing biogas. Secondly, the potential for biogas production from all Swedish mechanical pulp mills was estimated, assuming that anaerobic treatment was introduced at these sites. This estimation was made for two different scenarios, a moderate and an optimistic. The difference between these scenarios can be found in the assumptions regarding the degree of COD reduction in the present WWT, amount of COD possible to treat anaerobically and the degree of COD reduction in the anaerobic reactor. The figures for the moderate scenario reflect the fact that there might be disturbances in the production during the year, that full load is not always possible and is overall a more "careful" estimation. The optimistic scenario assumes that production is more stable and without disturbances; that a larger share of the streams is possible (or made possible) to treat anaerobically and that the process improvements that may increase the biogas production are implemented. These factors would give the possibility for the higher biogas production shown in the optimistic scenario, however it should not be seen as easily achievable.

The focus of this study is biogas used as vehicle fuel in the transport sector. To be used for this purpose the raw biogas has to be upgraded to vehicle standard. An upgrading facility might not be an alternative for a smaller mill because of the rather large investment this would require. If not being upgraded on-site, a possibility would be to transport the biogas to an external upgrading

facility, even though the raw biogas requires large volumes. The biogas could of course also be used for other purposes, for instance internally in the pulp mill, replacing fossil and/or biomass-based fuels needed for the production. In [16], the biogas was assumed to replace either oil or biomass internally in the mill and, as expected, it was shown that it was more economic to replace the oil. Biogas could also be used for heating, power or combined heat and power, especially use for heating purposes is common for biogas produced in Sweden today. In 2010, about the same amount of biogas was used for heating as for upgrading in the Swedish energy system (0.6 TWh_{LHV}) [1].

The size of the anaerobic facility, producing 27 GWh_{LHV}/year, is comparable to other digestion facilities. The average production for industrial digestion plants and co-digestion plants in Sweden is 19-23 GWh_{LHV}/year. The average size for a wastewater treatment plant in Sweden is lower, about 5 GWh_{LHV}/year, but the number of plants as well as range of their production is large, for instance three of the wastewater treatment plants in the Stockholm area produce around 50 GWh_{LHV}/year respectively [1,22, 23]. It would thus be reasonable to believe that investing in anaerobic wastewater treatment could be economic for the mill. Considering the production, as well as COD emissions in effluent, of the Rottneros mill in comparison to other Swedish mechanical pulp mills, it may be seen that the mill is within the range of an average sized mill [18] and thus possible anaerobic wastewater treatment facilities at several of the mechanical pulp mills in Sweden should also be in the same size.

The process for anaerobic treatment assumed to be used in this study is, as in most industrial digestion facilities in Sweden, of the mesophilic type. However, as has been discussed, the higher the temperature used, the faster the reaction rate and therefore it is possible to digest at thermophilic conditions, which even may be preferable at TMP or CTMP mills because of the high temperature (close to the thermophilic working interval) of the effluent streams from the process [14]. This was also investigated in [15], where digestion in the thermophilic interval was assumed to be more energetically favourable, compared to mesophilic digestion, since most process streams from the pulp mill have rather high temperatures and cooling of the process streams would thus be avoided.

The WWT processes investigated in [15] have similarities to the one used in this study, however these processes also use different set-ups of membrane filtration in combination with the anaerobic digestion, as mentioned. Another difference between the processes in [15] and the one here is that the sludge from the aerobic treatment following the anaerobic reactor is returned to this reactor to be treated together with the rest of the effluent material. This is an efficient way of reducing the sludge from the WWT and thus also the need for further sludge treatment. Depending on the amount of sludge a separate sludge digestion stage might be needed.

The Swedish mechanical pulp mills all have their mill specific conditions and thus the biogas potential estimated in this study should be considered carefully. To implement a change in the wastewater treatment such as suggested in this study a thorough evaluation of the mill, and the specific process used there, would be necessary. Depending on the process type, i.e. whether bleaching is applied and, if so, which type of bleaching, only few of the effluent streams might be suitable for anaerobic treatment. However, for a mill that currently has a satisfactory WWT but is looking to increase their production, investing in an anaerobic treatment could be a promising option for coping with the increased effluents.

This study only investigated pulp mills producing mechanical pulps. It is also possible to treat some effluent streams from chemical pulp mills, thus investigating the potential for these mills is also relevant. The production of chemical pulp in Sweden is about three times as large as the production of mechanical pulps. Moreover, these types of mills give higher amounts of COD per tonne produced pulp. However, the situation at the chemical mills is more complex than at mechanical mills, for instance, the streams from the chemical mills are even more varying and may also contain other types of chemicals that might disturb the anaerobic process. A potential assessment for biogas production from the whole pulp and paper industry in Sweden will be made in a coming study.

6. Conclusions

Using effluent streams from the mechanical pulping industry in anaerobic digestion to produce biogas could increase the share of biofuels to the transport sector. The main conclusions of this study are summarised below:

- Using anaerobic wastewater treatment combined with aerobic "polishing" stage as an alternative to conventional aerobic wastewater treatment methods at mechanical pulp mills gives a satisfactory wastewater treatment as well as a substantial contribution of biogas.
- When using anaerobic digestion both electricity consumption and sludge production at the mill are decreased, giving additional environmental advantages.
- The production size of an anaerobic wastewater treatment facility at a typical Swedish mechanical pulp mill is about the same as other industrial digestion plants and anaerobic wastewater treatment plants and such an investment should therefore have the potential of being be economic for a mill.
- If implemented in the whole Swedish mechanical pulping industry the biogas produced could amount to 0.3 TWh_{LHV} (moderate scenario) or as much as 0.5 TWh_{LHV} (optimistic scenario) annually.
- With a biogas production from the mechanical pulping industry according to the optimistic scenario (0.5 TWh_{LHV}/year), the total Swedish biogas production would increase by one third compared to today's production.

Acknowledgments

This work has been carried out under the auspices of The Energy Systems Programme, which is primarily financed by the Swedish Energy Agency. The authors would like to thank Mats Westermark (prof. at the division of Energy Processes) for valuable comments, Åsa Sivard, Tomas Ericsson (ÅF) and Nippe Hylander (ÅF and Adj. prof. at the division of Energy Processes) for contributing with the basis for the potential estimation and for valuable comments throughout the work and Yi Liu, author of the master thesis on which the case study in this paper is based.

Nomenclature

CCS Carbon capture and storage
CH_4 Methane
CO_2 Carbon dioxide
COD Chemical oxygen demand
CTMP Chemi-thermomechanical pulp
DS Dried substance
GWh Gigawatt hour
GWP Groundwood pulp
kWh Kilowatt hour
LBG Liquid biogas
LHV Lower heating value
Nm^3 Normal cubic meter
PGWP Pressurises groundwood pulp
PSA Pressure swing adsorption
t Tonne
TMP Thermomechanical pulp
TWh Terawatt hour

UASB Upflow anaerobic sludge blanket
WWT Wastewater treatment

References

[1] Swedish Energy Agency, Production and use of biogas 2010 (Produktion och användning av biogas 2010) [in Swedish]. Eskilstuna, Sweden: Swedish Energy Agency; 2011 Nov. Report No: ES 2011:07.

[2] van Lier, J.B., Tilche, A., Ahring, B.K., Macarie, R., Moletta, M., Dohanyos, L.W., Hulshoff Pol, L.W., Lens, P., Verstraete, W., New perspectives in anaerobic digestion. Water Science and Technology 2001;43(1):1-18.

[3] Swedish Forestry Industry Federation. The Swedish Forest Industries 2010. Facts and figures. Available at <http://www.skogsindustrierna.se/web/Utgivningsar_2011.aspx> [accessed 2011-10-03]

[4] Rintala, J.A., Puhakka, J.A., Anaerobic treatment in pulp and paper-mill waste management: a review. Bioresource Technology 1993;47:1-18.

[5] Yadvika, Santosh, S., Sreekrishnan, T.R., Kohli, S., Rana, V., Enhancement of biogas production from solid substrates using different techniques – a review. Bioresource Technology 2004;95:1-10.

[6] Appels, L., Baeyens, J., Degrève, J., Dewil, R., Principles and potential of the anaerobic digestion of waste-activated sludge. Progress in Energy and Combustion Science 2008;34:755-781.

[7] Weiland, P., Biogas production: current state and perspectives. Applied Microbiology and Biotechnology 2010;85:849-860.

[8] Swedish Gas Centre. Biogas folder 2011 – Basic data on biogas (Biogas – Basdata om biogas 2011) [in Swedish]. Available at <http://www.sgc.se/uk/display.asp?ID=1352&Typ=Rapport&Menu=Rapporter> [accessed 2011-09-29].

[9] Svensson, M., Evaluation of Swedish biogas standard – Basis for a future revision (Utvärdering av svensk biogassatandard – Underlag för en framtida revision) [in Swedish]. Malmö, Sweden: Swedish Gas Centre; 2011 April. Report No: SGC 229.

[10] Danish Gas Technology Center. Adding gas from biomass to the gas grid. Final report of Altener, Contract No: XVII/4.1030/Z/99-412. Available at <http://www.dgc.eu/publi2.htm> [accessed 2012-04-02].

[11] Mohseni, F., Magnusson, M., Görling, M., Alvfors, P., Biogas from renewable electricity – Increasing a climate neutral fuel supply. Applied Energy 2012;90:11-16.

[12] EUROPA – The official website of the European Union. European Commission, Joint Research Center, Institute for Prospective Technological studies, Integrated Pollution Prevention and Control. Draft reference document on best available techniques in the pulp and paper industry, Draft April 2010. Available at: <http://eippcb.jrc.es/reference/> [accessed 2011-12-20]

[13] Stoica, A., Sandberg, M., Holby, O., Energy use and recovery strategies within wastewater treatment and sludge handling at pulp and paper mills. Bioresource Technology 2009;100: 3497-3505.

[14] Salkinoja-Salonen, M., Apajalahti, J:, Silakoski, L:, Hakulinen, R., Anaerobic fluidised bed for the purification of effluents from chemical and mechanical pulping. Biotechnology Advances 1984;2:357-375.

[15] Sivard, Å., Ericsson, T., Process integration of wastewater treatment technique – decrease of the energy and resource use in the forestry industry (Processintegration av vattenreningsteknik

– minskning av energi- och resursanvändningen i skogsindustrin) [in Swedish]. Stockholm, Sweden: ÅF-Industry AB; 2011 Jan. Report for Swedish Energy Agency Project No 32218-1.
[16] Liu, Y., Combination of the membrane method, aerobic and anaerobic wastewater treatment for mechanical pulping (Kombination av membranmetoden, aerob och anaerob vattenrening vid mekanisk massaproduktion) [master thesis – in Swedish], Stockholm, Sweden: Royal Institute of Technology (KTH); 2011.
[17] Rottneros. Annual report 2010. Available at: <http://www.rottneros.com/en/ir/annual-reports> [accessed 2011-12-13].
[18] Swedish Forestry Industry Federation. The environmental database for the Swedish Forestry Industry Federation – Compiled data from all mills in the same table, year 2010. Available at: <http://miljodatabas.skogsindustrierna.org/si/main/main.aspx?l1=home> [accessed 2012-01-09].
[19] Sivard, Å. Process Consultant, Water and Effluent treatment, ÅF. Private Communication.
[20] Habets, L.H.A, de Vegt, A.L, Anaerobic treatment of bleached TMP and CTMP effluent in the BIOPAQ UASB system. Water Science and Technology 1991;24(3/4);331-345.
[21] Elliott, A., Mahmood, T., Pretreatment technologies for advancing anaerobic digestion of pulp and paper biotreatment residues. Water research 2007;41;4273-4286.
[22] Käppala Wastewater Treatment Plant. Käppala Association and the Käppala Wastewater Treatment Plant, information brochure. Available at: http://www.kappala.se/default.asp?show=1&varuid=&lid=1&ulid=82 [accessed 2012-02-07].
[23] Stockholm Vatten. Key figures 2001-2010 (Nyckeltal 2001-2010) [in Swedish]. Available at: http://www.stockholmvatten.se/sv/Om-oss/Broschyrer-rapporter-och-filmer/Rapporter/Om-Stockholm-Vatten/ [accessed 2012-02-08].

Biogas or Electricity as Vehicle Fuels Derived from Food Waste - the Case of Stockholm

***Martina Wikström*[a], *Per Alvfors*[b]**

a KTH Royal Institute of Technology, Department of Chemical Engineering and Technology, Division of Energy Processes, Stockholm, Sweden, marbjor@kth.se
b KTH Royal Institute of Technology, Department of Chemical Engineering and Technology, Division of Energy Processes, Stockholm, Sweden, alvfors@kth.se

Abstract:
The demand for renewable energy is increasing in Stockholm as well as the rest of the world. Imperative factors, such as the need to reduce anthropogenic green house gas emissions and security of supply, force this development. The European Commission distinguishes the organic compound in municipal solid waste as food waste. Food waste may be digested, form biogas and after upgrading, the biogas may be used as fuel in automotive applications.

This study is based on the food waste potential estimations performed by the Stockholm County Administration Board in the County of Stockholm, both in 2009 and in 2030. The County Administration Board aim for this food waste to be converted to the vehicle fuel biogas since this would improve the share of renewable transport fuels and, simultaneously, decrease the green house gas emissions coupled with the degradation of organic material. In 2009, Stockholm generated 122 000 tonnes of food waste which could have been converted to 130 GWh biogas. This amount of biogas corresponds to approximately 15 million litres of petrol. In 2030, the County Administration Board estimates the food waste has increased to 152 000 tonnes, which converted would correspond to 170 GWh biogas. This study will expand the analysis and will consider the option where the biogas from the food waste is use to generate electricity to fuel electric vehicles in Stockholm. In 2009, no large-scale introduction of electric vehicles in Stockholm had begun but it is vital for decision-makers to assess this option for 2030 in order to obtain a resource and energy efficient Stockholm.

When considering electricity as vehicle fuel, converting the energy carrier will include additional steps such as electricity generation, distribution, charging of the vehicle as well as the electric powertrain. The overall energy efficiency, from biogas to electric propulsion, is in the order of 40 %. Even though when adding process steps, which imply losses, the more energy efficient energy carrier is electricity. Converting the biogas from the food waste to electricity adds approximately another 10 % of driving distance. Assuming an annual driving distance of 15 000 kilometres, in 2030 this would imply either 27 450 biogas or 27 200 electric passenger cars in the county of Stockholm. The most resource and energy efficient usage of the biogas from food waste would be to convert it to electricity for electric vehicles.

Keywords:
Automotive applications, Biogas, Electricity, Food waste, Stockholm

1. Introduction

Today, the global transport sector is heavily dependent on fossil fuels and fossil-originated fuels accounts for 98 % worldwide [1] and 92 % in Sweden [2]. The demand for renewable energy carriers is increasing in Stockholm as well as the rest of the world. A transition towards a renewable-fuelled road transport system is desirable for a number of imperative factors, such as the need to reduce anthropogenic green house gas emissions and security of supply. One measure to increase the share of renewable fuels in a region, is to benefit from its generated organic waste, which may be digested, form biogas and when purified, be used as fuel in automotive applications.

The European Commission distinguishes the organic compound in municipal solid waste as food waste [3].

To investigate the biogas potential derived from food waste in the region, the Stockholm County Administration Board carried out a regional inventory of available food waste in the Stockholm County and the results was published in February 2011. The final estimations from this report constitute the foundations for the calculations carried out in this paper. The analysis in this paper is expanded to also consider utilisation of produced biogas as fuel for renewable electricity generation aimed for automotive applications and tank-to-wheel (TTW) analysis including the actual vehicles, in order to assess the overall energy efficiency of the two vehicle fuels.

2. Objectives and methodology

To assess the potential of biogas production from food waste, the Stockholm County Administration Board initiated a study in 2010 to evaluate the amount of petrol that could be replaced by more resource efficiently utilising food waste as an energy carrier. The final report, [4], considers the option of biogas production utilizing available food waste as raw material and estimates the production potential in its administrated territory. The biogas is considered a substitute for fossil fuels in the transport sector. The usage of biogas may be differentiated, and in the context of increasing the share of renewable fuels in the road transport system, the biogas could also function as fuel in order to generate renewable electricity for an electrified vehicle fleet.

This paper will consider biogas both as a transportation fuel and also as a renewable resource for producing electricity to fuel an electrified transport system. This paper will assess each conversion system's overall energy efficiency and will exemplify this by the means of absolute driving distance produced by each fuel and the corresponding number of units by each vehicle technology. The aim with this paper is to determine the most energy efficient way of utilising the biogas that The Stockholm County Administration Board has acknowledged as possible to produce from the County's food waste potential.

1.1 Input data

Input data for this paper will consist of both direct results from the report [4] and additional estimations and calculations applied onto these reported results. To distinguish the two separate sources of input data, it has been characterized into two categories:

- *Direct data* – reported results from the report [4]
- *Generated data* – further work carried out and applied upon the direct data

1.1.1 Direct data

Estimating the available amount of food waste in the Stockholm County, four sources were considered:

- Households
- Restaurants
- Large-scale catering establishments
- Grocery stores

From the theoretical total amount of available food waste, 60 % is considered possible to convert to biogas [5]. The relationship between the available and the food waste with biogas potential is illustrated in *Figure 1*.

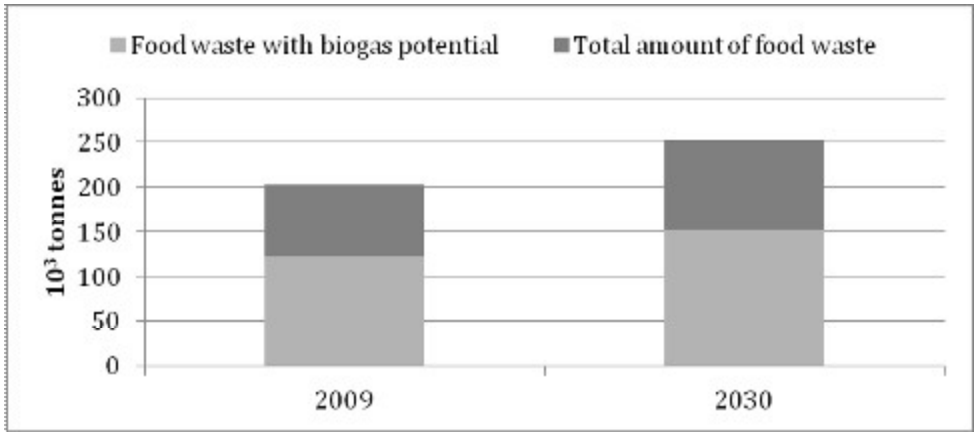

Figure 1. Estimated amount of food waste available in the Stockholm County and the corresponding share with biogas potential accounted as thousand tonnes.

The report [4] does not include any considerations regarding the biogas production process. All process steps are therefore assumed to been accounted for as well as the produced biogas is assumed to maintain Swedish automotive quality standard, SS 15 54 38.

The report [4] expresses its main result as litres of petrol possible to substitute with the food waste originated biogas. The fossil fuel substitution potential concluded in the report [4] is complied in *Table 1*. To reach these conclusions, assumptions such as energy content and conversion efficiency has been made but is not included in the report. Relevant thermodynamic assumptions fundamental for this paper will be presented in section 1.1.2.

Table 1. Fossil fuel substitution potential corresponding the available food waste

	2009	**2030**
Food waste [tonnes]	122 000	152 000
Petrol substituted [litre]	15 000 000	19 000 000

1.1.2 Generated data

According to the EU Directive 2009/30/EC, also referred to as the EU Fuel Quality Directive, the petrol sold in Sweden constitutes of 5 % ethanol [6]. The E5 petrol has the lower heating value (LHV) of 8,94 kWh/l [7]. The production capacity of biogas is calculated from the reported amount of petrol substituted. The produced amount of biogas corresponding to the substituted petrol, see *Table 1*, is found in *Table 2*:

Table 2. Potential biogas production (LHV) originated from food waste in Stockholm County

	2009	**2030**
Biogas [GWh]	134,1	169,9

To illustrate the production of biogas from food waste, *Figure 2* is a simplified schematic illustration of the conversion system.

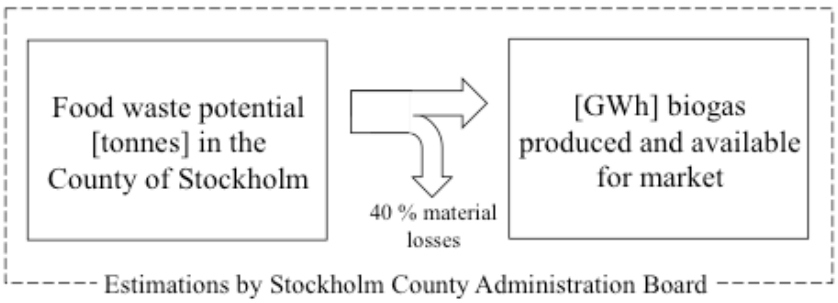

Figure 2. System description adopted from the report [4]

1.2 Description of the expanded system

The expanded system include, in addition to the biogas production in *Figure 2*, the two considered options of utilising the renewable resource food waste as vehicle fuel. The produced amount of biogas (*Table 2*) is the shared input parameter as energy content. Produced biogas is assumed to maintain automotive quality. This assumption implies the initial system would include upgrading steps not necessary prior combustion of biogas. The implications of this assumption are discussed in section 4 Discussion. The available amount of produced biogas may be utilised as vehicle fuel in two ways:

- Directly as transportation fuel – to a biogas vehicle.
- As a renewable fuel for electricity production - to an electric vehicle.

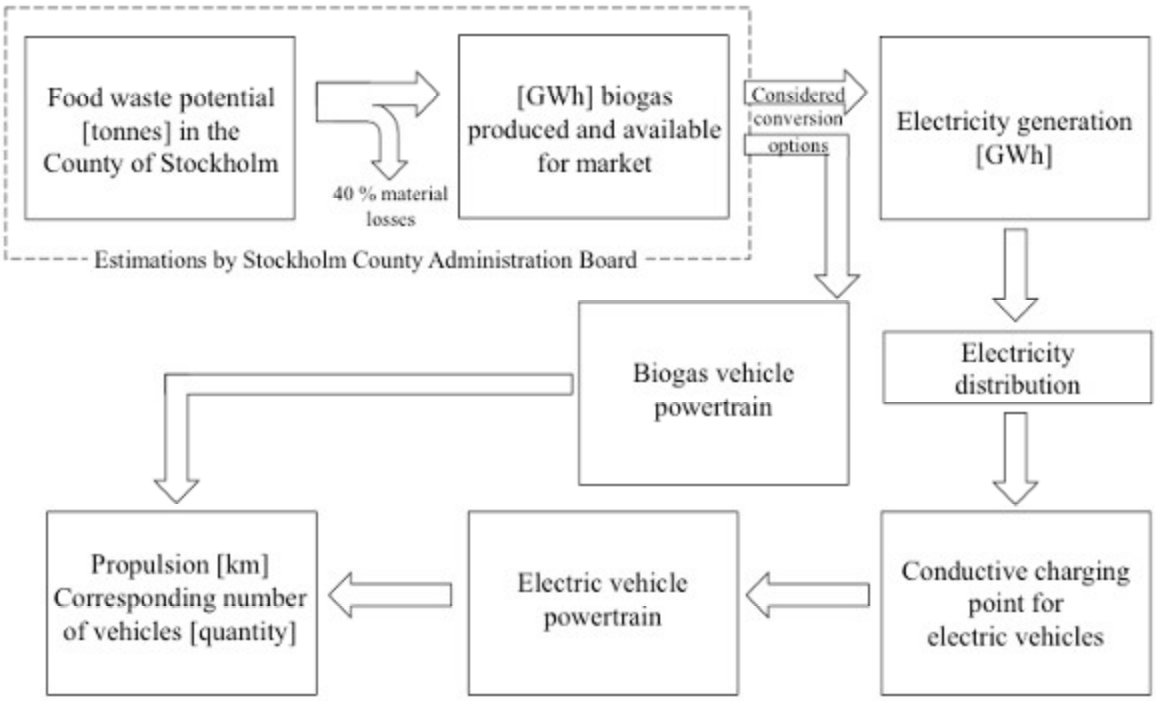

Figure 3. System description of two possible vehicle fuel options utilising biogas as a renewable resource

3. Analysis of conversion routes

This paper will assess the absolute driving distance inflicted by the available biogas when considering two vehicle technologies, either a biogas or an electric vehicle. As *Figure 3* show, there

are different parameters that determine each route's energy efficiency, which influence the absolute driving distance of the vehicle.

To ensure an accurate comparison, a model vehicle is designed using the shared classification system of the European Commission and Euro NCAP [8] and the vehicle size is assumed to correspond to a C-segment medium car/ small family car, for example Ford Focus or Opel Astra.

To obtain an additional measure of the total energy efficiency for each transportation fuel, an annual driving distance for such model vehicle is determined. This paper will assume an annual driving distance of 15 000 kilometres, which is the statistic distances a Swedish C-segment vehicle owner drive every year [9]. The total number of each vehicle, respectively, function as an additional comparison of the overall energy efficiency of the systems.

1.3 Biogas as road transportation fuel

Since the produced biogas is assumed to maintain automotive quality, the fuel economy of the biogas vehicle alone will determine the driving distance. The losses of biogas while fuelling are negligible. The energy efficiency of a biogas vehicle powertrain is approximately 20 % [10], influenced foremost by energy losses in the internal combustion engine (ICE), friction losses throughout the mechanical powertrain and the total running resistance. The C-segment biogas vehicle utilise approximately 55 kWh/100 km [11], when operating in urban/semi-urban areas.

In 2030, the overall fuel economy of passenger vehicles is expected to improve in the order of 25-30 % [12], [13]. This paper will pessimistically assume a 25 % fuel economy improvement when assessing the vehicle technologies in year 2030. *Table 2* presents the available amount of biogas. *Table 3* show the results of the total number of kilometres generated by the produced amount of biogas and its corresponding numbers of biogas vehicles with an annual driving distance of 15 000 kilometres.

Table 3. Biogas – total propulsion and corresponding numbers of vehicles

	2009	2030
Promoted propulsion [100 km]	2 438 181	4 117 818
Numbers of vehicles	16 254	27 452

1.4 Electricity as road transport fuel

The other option considered in this paper is to utilise the produced biogas to generate renewable electricity for an electrified vehicle fleet, which may also increase the share of renewable fuels in the road transport system. As seen in *Figure 3*, there are additional steps (generation, distribution and fuelling) with coupled energy losses, see *Table 4*. Biogas may fuel either a gas turbine or an Otto engine, generating electricity. During assumed prevalent working conditions, approximately 10-14 MWh of biogas, these two energy conversion components acquire similar energy efficiency, as seen in *Table 4*. Energy losses during transmission and charging are small but not negligible.

Table 4. Energy efficiency of electricity generation, distribution and charging of vehicle

	Energy efficiency [%]	Reference:
Electricity generation	44 %	[14], [15]
Transmission and distribution	92 %	[16]
Conductive charging	99 %	[17]

Converting the energy carrier from biogas to electricity implies energy losses. By converting the energy input of biogas shown in *Table 2*, a conductive Electric Vehicle Supply Equipment (EVSE) may deliver the amount of electricity corresponding to *Table 5*.

Table 5. Potential renewable electricity originated from food waste in Stockholm County

	2009	**2030**
Electricity [GWh]	53,4	67,9

Within the category electric vehicles (EV's), the degree of powertrain electrification may vary from a conventional mechanical powertrain equipped with a powerful machine working as start engine, to a fully electrified powertrain. To utilise the generated electricity and charge from the grid, this paper distinguish between two different types of EV's:

- Battery Electric Vehicles (BEV) that have an electric engine and a battery as an energy storage unit. No internal combustion engine (ICE).
- Plug-in Hybrid Electric Vehicles (PHEV) that have both an ICE and an electric engine. The ICE generates electricity, via a generator mounted upon the ICE, to the electric powertrain. The energy storage in this case is also a battery.

This paper will only consider BEV since its sole fuel source is electricity, since the degree of electrical mileage may vary for a PHEV.

The electrical powertrain, compared to a conventional powertrain, is characterised by a high overall energy efficiency, about 80 % and includes charge/discharge cycle losses of the battery. The improved energy efficiency is predominantly the result from replacing the ICE by an electric engine (90 % energy efficiency compare to 30 % as for an ICE) and improvements due to electrical power transmission instead of mechanical [18]. A C-segment electric vehicle utilise approximately 20 kWh/100 km [19]. *Table 6* show the results of the total number of kilometres fuelled by generated electricity and its corresponding numbers of electric vehicles with an annual driving distance of 15 000 kilometres.

Table 6. Electricity – total propulsion and corresponding numbers of vehicles

	2009	2030
Promoted propulsion [100 km]	2 682 000	4 529 600
Numbers of vehicles	16 111	27 209

1.5 Food waste as a renewable resource for road transportation fuels

Comparing the promoted driving distance in *Table 3* and *Table 6*, it is shown that the overall energy efficiency in the case of electricity is 10 % higher then for utilising the biogas directly as a road transportation fuel.

The results may also be visualised using Sankey diagrams, see *Figure 4* and *Figure 5*. The Sankey diagram presents an average overview of the energy flows, and is not representative for a specific time during vehicle operation. The total energy input in both Sankey diagrams is the available amount of automotive quality biogas presented in *Table 2*.

The Sankey diagram illustrating the option of biogas as a road transport fuel, *Figure 4*, uses the input information given in section 1.3, which describes the energy efficiency of a biogas vehicle.

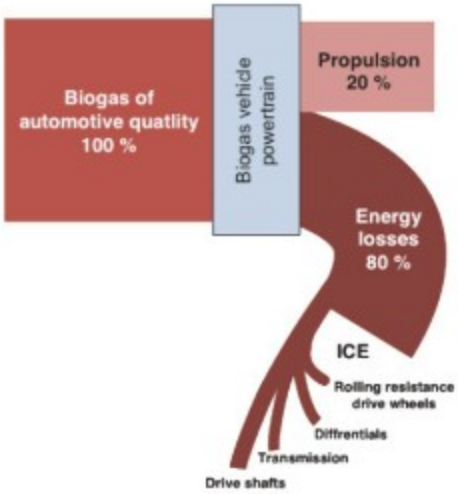

Figure 4. Sankey diagram of energy flows if utilising available biogas as road transport fuel

The Sankey diagram illustrating the option of utilising renewable electricity as road transport fuel, visualise the additional process steps associated with converting the energy carrier to electricity. Data given in *Table 4* is applied to each step, respectively, to express the coupled energy loss.

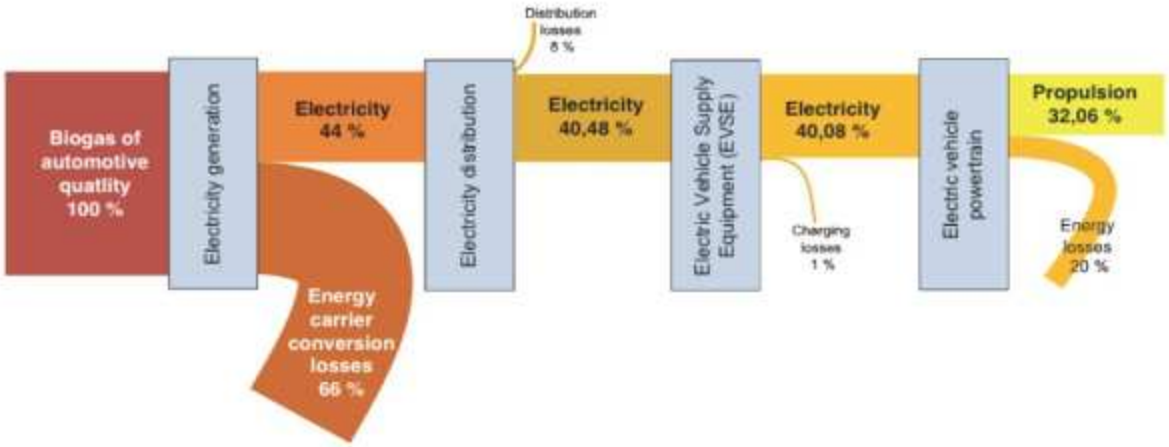

Figure 5. Sankey diagram of the energy flows if utilising the available biogas for power generation in order to obtain renewable electricity for an electrified vehicle fleet.

This paper have made the comparison of the corresponding number of vehicles each fuel option promote, found in *Table 3* and *Table 6*.In 2009, the number of passenger vehicles in the County of Stockholm was 800 534 [20]. Assessing the potential impact in fleet composition, the share of electric vehicles would run up to 2,2 % compared to the corresponding share of biogas vehicles that may be fuelled by the same resource that would be 2,0 %. Forecasting the vehicle fleet in the Stockholm County by 2030, it may be assumed that the potential impact might increase hence to intended governmental efforts to reduce the transport demand in the region [21], [22].

4. Discussion

The measure of energy efficiency used in this paper is total accumulated kilometres and corresponding number of vehicles caused by each fuel option derived from the equal amount of food waste originated biogas. In the case of biogas, produced amount of biogas is shown in *Table 3*. This amount of biogas is available for the end-consumer. In the case of electricity, the same amount

of biogas is combusted, generating electricity, which may be distributed and transmitted to a charging point. For end-consumer available electricity, in [GWh], is shown in *Table 5*. Converting the energy carrier from biogas to electricity results in energy losses, hence the reduced amount of energy input. When extending the analysis to include the vehicles it is notable how much more energy efficient the electric vehicle is compared to the biogas vehicle.

Using biogas for automotive applications demands additional purification steps to upgrade the raw gas obtained when digesting the food waste. Biogas that may be used for electricity generation does demand the same quality measures in order to operate efficient. This paper assumes automotive biogas, which in reality would not be necessary for power generation purposes, which implies additional benefits both in terms of energy efficiency and reduction in physical process step for electricity as an energy carrier.

To recognise other driving forces then the desire to optimise the resource efficiency of an energy carrier, it is much more profitable today in Sweden to produce, upgrade and sell automotive quality biogas compared to retail electricity. In a Swedish context, the most significant incentives, influencing the overall turnover for the producers are:

- Biogas: tax-exempted vehicle fuel [23] and investment grants [24]
- Renewable electricity: no energy or carbon dioxide tax[1] [23] and production plant may be rewarded "green certificates" [25]

Today, the relative benefit of selling automotive biogas is on average approximate 30 % higher, compared to selling electricity for a biogas producer [26]. This might contribute to decisions, comprising the energy- and material efficiency of the system, maximising monetary return.

To further extend the energy system analysis of the electricity production, to facilitate heat recovery may contribute to an even higher overall energy efficiency but also a sales possibility if integrated with, for example, a district heating system network.

5. Conclusion

Many factors may influence the utilisation of the limited renewable resources available, in this case food waste. The two options considered in this paper was to digest the food waste to biogas, then utilising the biogas either as a road transportation fuel or as fuel for renewable electricity generation. Including the vehicle and its powertrain in the analysis showed that the most energy efficient way of utilising the renewable resource was to fuel an electrified vehicle fleet. Converting the biogas from the food waste to electricity adds approximately another 10 % of driving distance. Assuming an annual driving distance of 15 000 kilometres, in 2030 this would imply either 27 450 biogas or 27 200 electric passenger cars in the county of Stockholm. Regarding food waste as a renewable resource, of course most desirable would be to minimise this source and instead enjoy the food before it becomes waste.

6. Acknowledgements

The work has been carried out under the auspices of The Energy Systems Programme – primarily financed by The Swedish Energy Agency.

[1] In 2011, the Swedish energy and carbon dioxide tax was 0,85 eurocents/kWh and 11,70 eurocents/kg CO_2, respectively [27].

7. References

[1] Kahn Ribeiro, S., S. Kobayashi, M. Beuthe, J. Gasca, D. Greene, D. S. Lee, Y. Muromachi, P. J. Newton, S. Plotkin, D. Sperling, R. Wit, P. J. Zhou, 2007: Transport and its infrastructure. In Climate Change 2007: Mitigation. Contribution of Working Group III to the Fourth Assessment Report of the Intergovernmental Panel on Climate Change. Cambridge University Press, Cambridge, United Kingdom and New York, NY, USA

[2] Swedish Energy Agency. Energy Outlook 2010 *(Energiläget 2010)*. Report no. ER 2010:45.

[3] European Parliament. Directive 2006/12/EC of the European Parliament and of the Council of 5 April 2006 on waste

[4] Stockholm County Administrative Board. Present and future 2011:2 Food waste provides new energy (*Nutid och framtid 2011:2.Matrester ger ny energi)*. Available at: http://www.lansstyrelsen.se/stockholm/Sv/publikationer/2011/Pages/nof-matrester-ger-ny-energi.aspx accessed: 2011-09-15

[5] Swedish Waste Management Association. Report 2008:02. The Swedish biogas potential from domestic raw materials (*Den svenska biogaspotentialen från inhemska råvaror)*. ISSN 1103-4092.

[6] European Parliament. Directive 2009/30/EC of the European Parliament and of the Council of 23 April 2009, amending Directive 98/70/EC as regards the specification of petrol, diesel and gas-oil and introducing a mechanism to monitor and reduce greenhouse gas emissions and amending Council Directive 1999/32/EC as regards the specification of fuel used by inland waterway vessels and repealing Directive 93/12/EEC.

[7] SPBI. Swedish Petroleum and Biofuel Institute. Fact sheet available at: http://spbi.se/faktadatabas/artiklar/berakningsmodeller accessed: 2011-09-28

[8] Euro NCAP. Technical report Development of the European new car assessment programme (EURO NCAP). Available at: http://www.euroncap.com/files/Development-of-Euro-NCAP-1998---0-7498ffa2-36b6-4328-8b6e-f44fe5d35563.pdf accessed: 2011-12-27

[9] Sweden Statistics. Transports and Communications. Driving distance and fuel consumption (*Transporter och Kommunikationer. Körsträckor och bränsleförbrukning*). 2009

[10] H Engerer, M Horn. Natural gas vehicles: An option for Europe. Energy Policy 38 (2010) 1017-1029

[11] Joint Research Centre of the European Commission (JRC). Tank-to-Wheel analysis of future automotive fuels and powertrains in a European context. Version 2c. JRC, EUCAR, CONCAWE. 2006. available at: http://iet.jrc.ec.europa.eu/sites/about-jec/files/documents/TTW_Report_010307.pdf accessed: 2011-12-30

[12] Duval M. Advanced Batteries for Electric Drive Vehicles – A technology and cost-effective assessment for battery electric vehicles, power assist hybrid electric vehicles and plug-in hybrid electric vehicles. EPRI. May 2004

[13] S E Plotkin. Examining fuel economy and carbon standards for light vehicles. Energy Policy. 37 (2009) 3843-3853

[14] A Poullikkas. An overview of current and future sustainable gas turbine technologies. Renewable and Sustainable Energy Reviews 9 (2005) 409-443

[15] M Edström, Å Nordberg. JTI – Swedish Institute of Agricultural and Environmental Engineering. Report no. 107. Producing biogas on the farm (Producera biogas på garden). 2004.

[16] Swedish Energy Agency. Energy in Sweden – facts and figures 2010. Report no. ET 2010.46. 2010

[17] Kågeson P. Nature Associates. The climate impact of electrified road transport. *Klimateffekten av elektrifierad vägtrafik*. 2010-06-29.

[18] Helms H, Pehnt M, Lambrecht U, Liebich A. Electric vehicle and plug-in hybrid energy efficiency and life cycle emissions. 18th International Symposium Transport and Air Pollution. Dübendorf. Switzerland. 18-19 May 2010

[19] Duval, M. Advanced Batteries for Electric Drive Vehicles – A technology and cost-effective assessment for battery electric vehicles, power assist hybrid electric vehicles, and plug-in hybrid electric vehicles. EPRI. May 2004

[20] Sweden Statistics. Vehicle statistics. Vehicles in counties and municipalities 2010/2011. (*Fordonsstatistik, Fordon i län och kommuner vid årsskiftet 2010/2011*). 2011

[21] Office of Regional Planning, Stockholm County Council. Report no. 5:2010. Regional development plan for the Stockholm region (*RUFS 2010 – Regional Utvecklingsplan För Stockholmsregionen*). 2010

[22] Office of Regional Planning, Stockholm County Council. Energy future of the Stockholm region 2010-2050: The way to reduce climate impact. 2010. Available at: http://www.tmr.sll.se/Global/Dokument/publ/2010/2010_r_energy_future_of_the_stockholm_region_2010-2050.pdf accessed: 2011-12-30

[23] Regulation (2010:178) on the taxation of energy (*Förordning (2010:178) om skatt på energi*). Stockholm. 2010. (SFS 2010:178)

[24] Regulation (2003:564) on public grants to promote efficient and environmental-friendly energy supply (*Förordning (2003:564) om bidrag till åtgärder för en effektiv och miljöanpassad energiförsörjning*). Stockholm. 2003. (SFS 2003:564)

[25] Regulation (2011:1480) on the electricity certificate system (Förordning 2011:1480 om elcertifikat). Stockholm. 2011. (SFS 2011:1480)

[26] M. Gunnarsson, T Lygnegård. Swedish Biogas International. Östergötland biogas production *(Östergötland biogasring*). 2008. Available at: http://www.energiost.se/content/images/energiost/pages/biogasring_ostergotland_081201.pdf accessed: 2011-12-30

[27] Swedenergy. Available at: http://www.svenskenergi.se/sv/Om-el/Miljo-och-klimat/Mal-och-styrmedel/ Accessed: 2011-12-29

Compressibility factor as evaluation parameter of expansion processes in Organic Rankine Cycles

Giovanni Manente[a] and Andrea Lazzaretto[b]

[a] *University of Padova, Padova, Italy, giovanni.manente@unipd.it,* ***CA***
[b] *University of Padova, Padova, Italy, andrea.lazzaretto@unipd.it*

Abstract:

In the conversion of low temperature heat sources into electricity using an Organic Rankine Cycle system the working fluid selection is a major design choice to maximize the overall performance. The placement of the power cycle on a T-s diagram depends on the fluid critical temperature. Several studies have shown that the power output can be maximized by using fluids with critical temperatures similar or lower than the inlet temperature of the heat source, which allow a better temperature profile match between the heat source and the working fluid. However, the choice of a fluid having a specific critical temperature also influences the fluid properties in the expansion process over a given temperature interval, as shown by the generalized compressibility chart. The aim of this paper is providing a better insight into the results of optimized ORCs through the analysis of the compressibility factor in the expansion process.

To this purpose the real enthalpy change in the expansion process is regarded as two separate terms associated with temperature and pressure drops, respectively. Starting from the analysis of different expansion processes in optimized cycles a correlation is obtained between the compressibility factor and the ratio between real enthalpy change and the enthalpy change term associated with temperature drop. Thus, the ratio between the former and the latter can be directly evaluated from the simple knowledge of pressure and temperature values along the expansion process and the observation of the compressibility chart.

Keywords:

Organic Rankine Cycle, Expansion Process, Real Gas, Compressibility Factor.

1. Introduction

In Organic Rankine Cycle systems low/medium temperature heat sources are used to evaporate a secondary working fluid with a low boiling point that expands through a turbine to generate power. The fluid is then discharged to the condenser where the condensing heat is transferred to a cooling water or cooling air flow. The liquid condensate is pumped into the evaporator completing the cycle. These systems, also known as binary cycle power plants [1], have found many applications in the recovery of waste heat from industrial plants and are playing a very important role in the modern geothermal electricity market [2].

The thermodynamic properties of the working fluid strongly influence the performance of these systems. In particular, the critical temperature plays a primary role in fixing the placement of the thermodynamic cycle on a T-s diagram [3]. The results of power-based performance comparisons show that the best fluids have critical temperatures similar or lower than the inlet temperature of the heat source ([4], [5]) so that the evaporation occurs at high subcritical reduced pressures ($p_R=p/p_{CR}$) or even at supercritical pressures that imply a good match between thermal profiles of the heat source and working fluid. At these conditions the ideal gas equation of state does not provide an acceptable representation of the *p-v-T* relationship, since the compressibility factor ($Z= pv/RT$) could assume values much lower than 1. An accurate knowledge of the *p-v-T* behavior is important in the evaluation of the specific enthalpy change that can be expressed in terms of p,v,T and c_P.

The "favourable" role of gas compressibility effects in reducing the work absorbed by the compression process in vapor refrigeration and heat pump cycles was studied in [6]. The same real gas effect is used to improve the conversion efficiency, through the minimization of the

compression work, in supercritical closed CO_2 Brayton cycles operating at moderate temperatures [7]. However, to the authors' knowledge, no studies are available about the relationship between the compressibility factor and the work obtained by the expansion process in organic Rankine cycles, with the exception of a very recent study [8] which only remarks that working fluids with higher compressibility factors at the turbine inlet result in higher turbine isentropic work.

In this paper the expansion process of four working fluids (CO_2, R125, R134a and isobutane) in optimized Organic Rankine Cycles ([9], [10]) is analyzed. The enthalpy change is divided into many intervals. At each interval the two terms that form the real enthalpy change are calculated. It is shown that the ratio between real enthalpy change and temperature related enthalpy change correlates well with the value of the compressibility factor. In particular, at low values of the compressibility factor (around 0.5-0.6) the real enthalpy change is only a small fraction of the enthalpy change calculated as the product of the fluid specific heat and the temperature drop. On the other hand, the generalized compressibility chart links the compressibility factor with reduced pressure (p_R) and reduced temperature ($T_R=T/T_{CR}$). So, it immediately shows thermodynamic states in the expansion process associated with low values of the compressibility factor, which imply a marked abatement of the real enthalpy change compared with that calculated from the temperature drop.

These findings suggest that the working fluid should be selected so that the expansion process occurs at temperatures and pressures associated with high values of the compressibility factor, which allow the real enthalpy change to approach the enthalpy change calculated from the temperature drop.

2. Evaluation of the specific enthalpy change in single-phase regions

2.1. Ideal gas

For a gas obeying the ideal gas model the specific enthalpy depends only on temperature, so the specific heat c_P, is also a function of temperature alone. That is:

$$c_P(T)=\frac{dh}{dT} \qquad (1)$$

Separating variables in (1):

$$dh=c_P(T)dT \qquad (2)$$

On integration:

$$h(T_2)-h(T_1)=\int_{T_1}^{T_2} c_P(T)dT \qquad (3)$$

When the specific heat is taken as constant (3) reduces to:

$$h(T_2)-h(T_1)=c_P(T_2-T_1) \qquad (4)$$

The constant value of c_P is a mean value calculated as follows:

$$c_P=\frac{\int_{T_1}^{T_2} c_P(T)dT}{T_2-T_1} \qquad (5)$$

However, when the variation of c_P over a given interval is slight, little error in normally introduced by taking the specific heat required by (4) as the arithmetic average of the specific heat values at the two end temperatures. Alternatively the specific heat at the average temperature over the interval can be used.

2.2. Real gas

For a real gas the specific enthalpy can be regarded as a function of temperature and pressure. That is:

$$h = h(T, p) \tag{6}$$

The differential of this function is:

$$dh = \left(\frac{\partial h}{\partial T}\right)_p dT + \left(\frac{\partial h}{\partial p}\right)_T dp \tag{7}$$

It can be shown [11] that (7) can be expressed in the following form:

$$dh = c_P\, dT + \left[v - T\left(\frac{\partial v}{\partial T}\right)_p\right] dp \tag{8}$$

where the right side of (8) depends solely on p,v,T and c_P.
Changes in specific enthalpy between two states are found by integrating (8):

$$h_2 - h_1 = \int_1^2 c_P\, dT + \int_1^2 \left[v - T\left(\frac{\partial v}{\partial T}\right)_p\right] dp \tag{9}$$

Integration of the second term on the right of (9) requires knowledge of the p-v-T behavior at the states of interest.

2.3. Compressibility factor

The relationship among pressure, specific volume and temperature is expressed by using the compressibility factor Z:

$$Z = \frac{pv}{RT} \tag{10}$$

The compressibility factor Z tends to unity as pressure tends to zero at fixed temperature. From (10) the specific volume can be expressed as:

$$v = \frac{ZRT}{p} \tag{11}$$

On differentiation:

$$\left(\frac{\partial v}{\partial T}\right)_p = \frac{RZ}{p} + \frac{RT}{p}\left(\frac{\partial Z}{\partial T}\right)_p \tag{12}$$

Using the previous two expressions, the second integrand on the right of (9) becomes:

$$v - T\left(\frac{\partial v}{\partial T}\right)_p = \frac{ZRT}{p} - T\left(\frac{RZ}{p} + \frac{RT}{p}\left(\frac{\partial Z}{\partial T}\right)_p\right) = -\frac{RT^2}{p}\left(\frac{\partial Z}{\partial T}\right)_p \tag{13}$$

Thus the change in specific enthalpy between two states can be evaluated by:

$$h_2 - h_1 = \int_1^2 c_P dT + \int_1^2 \left[-\frac{RT^2}{p}\left(\frac{\partial Z}{\partial T}\right)_p\right] dp \tag{14}$$

And assuming an infinitesimal change in enthalpy:

$$dh = c_P\,dT - \frac{RT^2}{p}\left(\frac{\partial Z}{\partial T}\right)_p dp \qquad (15)$$

That can be expressed as:

$$dh = dh_{dT} - dh_{dp} \qquad (16)$$

i.e., the real enthalpy change *dh* can be regarded as difference of two terms associated with the temperature drop (dh_{dT}) and pressure drop (dh_{dp}), respectively. The first term depends on the specific heat, the second one on pressure and temperature, and on the particular gas constant and partial derivative of the compressibility factor *Z* with respect to temperature. Note that the term dh_{dT} is not the enthalpy change calculated under the ideal gas model, being c_P dependent on both pressure and temperature.

3. Analysis of the expansion process in optimized ORCs

In this section the results of two optimization studies ([9], [10]) of ORCs are analyzed through the evaluation of the fluid properties along the expansion process. According to (15) the real enthalpy drop is composed by two components: the first related to the temperature change, the second to the pressure change. The calculation of these two terms shows that the real enthalpy drop is only a small fraction of the enthalpy drop related to the temperature change. Different cases are considered to understand how this fraction depends on the value of the compressibility factor, which in turn depends on the values of reduced pressure and temperature of the working fluids, as shown by the generalized compressibility chart. The examples presented in the following sections clearly show that the working fluid choice fixes the placement of the thermodynamic cycle in the *T-s* diagram and consequently the operating region in the compressibility chart.

3.1. Expansion processes analyzed

A brief summary of the thermodynamic optimization studies performed in ([9], [10]) is given to introduce the expansion processes that are analyzed in the following. Both optimization studies consider a thermodynamic objective function: the net power output in [9], the exergy recovery efficiency in [10], the latter being defined as the ratio between net power output and exergy available from the geothermal fluid. The mass flow rate of the heat source in [10] is 4000 times the mass flow rate in [9], which leads to net power outputs of around 3-3.5 MW in the first case and less than 1 kW in the second case. The isentropic efficiency of the turbine is 0.85 in the larger scale system and it was assumed equal to 0.80 in the smaller scale system. The larger system employs a dry cooling system with air cooled condensers (the specific consumption of which was assumed to be 0.15 kW per kg/s of air), whereas the smaller system includes a wet cooling system having a negligible power absorption.

In [9] the working fluids (CO_2 and R125) operating in transcritical cycles are compared assuming an inlet temperature of the heat source of 100°C. Given the low critical temperatures of both working fluids, supercritical cycles were obtained. Although the CO_2 turbine generates 28% more power than the R125 turbine, the R125 cycle results in a net power output 14% higher than the CO_2 cycle due to the high power absorbed by the CO_2 feed pump. In [10] isobutane and R134a are compared at geothermal fluid inlet temperatures between 130 and 180°C. The optimal R134a cycles are mainly supercritical whereas the isobutane ones are mainly subcritical. The R134a cycles provide more net power output than isobutane cycles in the whole temperature range considered for the heat source. At 150°C the R134a turbine generates 25% more power than the isobutane turbine, and the net power generated by the R134a cycle is 17% higher than the isobutane cycle. The 150°C case is analyzed here as representative of all cases presented in [10].

Table 1 shows the main working fluid properties and summarizes the optimal cycle parameters for the four expansion processes analyzed in this study. Note that the fluid critical temperatures vary in a large interval between 31°C and 135°C. The critical pressure of CO_2 is almost double the critical pressure of the other working fluids. In addition, the reduced pressure (p_R) at turbine inlet for CO_2 is the highest (around 1.7) among the fluids considered, which implies much higher evaporating pressure. The reduced temperature (T_R) at turbine inlet varies in the interval between 0.9 for isobutane and 1.2 for CO_2. The reduced pressure at turbine outlet is still high for CO_2 (just below 1), whereas it is much lower for isobutane and R134a. Only CO_2 has a turbine outlet temperature higher than the critical temperature.

Table 1. Fluid properties and optimal cycle parameters in the considered optimized ORCs.

	1	*2*	*3*	*4*
T_{heat_in} (°C)	100	100	150	150
m_{heat_in} (kg/s)	0.025	0.025	100	100
Working fluid	CO_2	R125	R134	Isobutane
T_{CR} (°C)	30.98	66.02	101.06	134.66
p_{CR} (bar)	73.77	36.18	40.59	36.29
Optimal turbine inlet and outlet states				
p_{turb_in} (bar)	123.32	44.56	47.97	18.85
t_{turb_in} (°C)	92.5	85.0	129.4	98.5
p_{turb_out} (bar)	69.04	16.37	8.323	4.376
t_{turb_out} (°C)	47.72	35.95	50.8	49.2
Optimal turbine inlet and outlet reduced states				
$p_{R_turb_in}$	1.67	1.23	1.18	0.52
$T_{R_turb_in}$	1.20	1.06	1.08	0.91
$p_{R_turb_out}$	0.94	0.45	0.21	0.12
$T_{R_turb_out}$	1.06	0.91	0.87	0.79
Power generated and absorbed				
P_{turb} (kW)	0.5863	0.4587	4822.9	3863.1
P_{pump} (kW)	0.2965	0.128	757.0	311.2
P_{ACC} (kW)	/	/	567.8	556.6
P_{net} (kW)	0.2898	0.3308	3498.1	2995.3

3.2. Calculation of the real enthalpy change

The EES software [12] is used to implement the equations of the expansion process. EES provides built-in thermophysical property data for many fluids, included those analyzed in this paper. The values of the thermodynamic properties calculated using the equations of state implemented in EES may slightly differ from those calculated using the REFPROP database in the original studies [9] and [10], shown in Table 1.

The expansion process between turbine inlet and outlet is divided into 100 intervals to approach the limiting condition of an infinitesimal enthalpy change. The elementary isentropic enthalpy change is therefore given by:

$$\Delta h_{IS_el} = \frac{\Delta h_{IS}}{100} \qquad (17)$$

The real elementary enthalpy change is calculated using the isentropic efficiency of the overall expansion process (η_{IS} = 0.80 for CO_2 and R125; η_{IS} = 0.85 for isobutane and R134a):

$$\Delta h_{el} = \Delta h_{IS_el} \cdot \eta_{IS} \qquad (18)$$

Equation (18) assumes that the polytropic efficiency (η_p) is equal to the isentropic efficiency, that is:

$$\frac{\eta_{IS}}{\eta_p} = \frac{\sum \Delta h_{IS_el}}{\Delta h_{IS}} \approx 1 \qquad (19)$$

which is quite well satisfied in the expansion processes considered.
For each interval the following parameters are evaluated using EES built-in fluid properties:

- Real enthalpy change, calculated from the temperature and pressure of the real gas at the inlet and outlet of each interval:

$$\Delta h = h_{in} - h_{out} \qquad (20)$$

- Enthalpy change associated with the temperature drop, where the specific heat is calculated as a function of temperature and pressure at the inlet of each interval:

$$\Delta h_{\Delta T} = c_{P_in} \cdot (T_{in} - T_{out}) \qquad (21)$$

- Ratio between real enthalpy change and enthalpy change term associated with temperature drop:

$$R_{\Delta h} = \frac{\Delta h}{\Delta h_{\Delta T}} \qquad (22)$$

- Enthalpy change associated with pressure drop:

$$\Delta h_{\Delta p} = \frac{R T_{in}^2}{p_{in}} \left(\frac{\partial Z_{in}}{\partial T} \right)_{p_{in}} \Delta p \qquad (23)$$

- Real enthalpy change calculated integrating (15) over an elementary expansion process. This value is an approximation of the real enthalpy change (20) because finite (and not infinitesimal), although small, enthalpy changes are considered:

$$\Delta h_{approx} = \Delta h_{\Delta T} - \Delta h_{\Delta p} \qquad (24)$$

- Percentage error between the enthalpy change calculated using (24) and the enthalpy change calculated from (20):

$$Err\% = \frac{\left| \Delta h_{approx} - \Delta h \right|}{\Delta h} \cdot 100 \qquad (25)$$

3.3. Evaluation of the enthalpy changes in the considered expansion processes

The fluid properties in the expansion process and the values of the parameters presented in the Section 3.2 are shown in Tables 2 to 5. For each fluid two Tables are included. Table *a* shows the fluid thermodynamic properties *p*, *T*, *h*, c_P, *Z* and the derivative $\left(\frac{\partial Z}{\partial T} \right)_p$ at inlet and outlet of intervals 1, 30, 60, 90 and 100, respectively called *I*, *II*, *III*, *IV*, *V*. The thermodynamic conditions at the outlet from the last interval (turbine outlet) may slightly differ from those in the original works shown in Table 1 due to the different property methods used and the assumption that the polytropic efficiency is equal to the isentropic efficiency. Table *b* shows, in the first three columns, the real enthalpy change (20), the enthalpy change associated with the temperature drop (21) and their ratio (22); in the last three columns the enthalpy change associated with the pressure drop calculated using (23), the approximated real enthalpy change (24) and the percentage error (25).

3.3.1. CO_2 expansion

In the optimized power cycle [9] CO_2 expands from 123.3 bar to about 69 bar. As shown in Table 2a, the specific heat of CO_2 remains almost constant along the expansion process. The compressibility factor varies within a narrow range between 0.655 and 0.663, whereas the derivative $(\partial Z/\partial T)_p$ increases from 4.7E-3 to 5.9E-3 from turbine inlet to outlet.

From Table 2b we see that the real enthalpy change over an elementary interval is 0.195 kJ/kg, whereas the enthalpy change associated with the temperature drop is about 4.5 times higher. The enthalpy change associated with pressure drop slightly increases from inlet to outlet, which leads to a slight reduction of the ratio $R_{\Delta h}$ from 0.237 to 0.217. The relative error introduced by using the approximate expression (24) is below 1%.

Figure 1 shows on a *T-s* diagram the expansion process of CO_2 in the optimized cycle. The expansion is divided into 10 intervals, having the same enthalpy drop. The values of the compressibility factor are shown near points 1, 4, 7 and 10. These points correspond to points 1, 31, 61 and 91 using a 100 intervals discretization (i.e. the inlet or outlet states of intervals *I*, *II*, *III* and *IV*). The temperature difference between two consecutive points (i.e. the vertical distance) is about the same along the whole expansion process since the specific heat is almost constant and the ratio between real enthalpy change and enthalpy change associated with temperature drop varies only slightly.

Table 2a. Thermodynamic conditions of CO_2 at inlet and outlet of intervals I, II, III, IV and V.

Interval	Points	p (bar)	T (°C)	h (kJ/kg)	c_P (kJ/kg-K)	Z	$(\partial Z/\partial T)_p$ (1/K)
I	1	123.3	92.50	-36.13	1.954	0.6630	0.004671
	2	122.7	92.08	-36.33	1.955	0.6628	0.004686
II	30	105.3	80.06	-41.79	1.972	0.6576	0.005080
	31	104.7	79.62	-41.98	1.973	0.6574	0.005093
III	60	88.83	66.79	-47.64	1.979	0.6557	0.005468
	61	88.32	66.34	-47.83	1.979	0.6557	0.005480
IV	90	74.41	53.23	-53.49	1.973	0.6573	0.005807
	91	73.97	52.78	-53.68	1.973	0.6574	0.005817
V	100	70.04	48.67	-55.44	1.969	0.6586	0.005906
	101	69.62	48.22	-55.63	1.968	0.6588	0.005916

Table 2b. Enthalpy changes of CO_2 calculated using Equations 21 to 26.

Interval	Δh (kJ/kg)	$\Delta h_{\Delta T}$ (kJ/kg)	$\Delta h/\Delta h_{\Delta T}$	$\Delta h_{\Delta p}$ (kJ/kg)	$\Delta h_{\Delta T}$ -$\Delta h_{\Delta p}$ (kJ/kg)	*Err%*
I	0.1950	0.8237	0.2368	0.6269	0.1968	0.91
II	0.1950	0.8608	0.2266	0.6639	0.1969	0.94
III	0.1950	0.8865	0.2200	0.6896	0.1969	0.96
IV	0.1950	0.8983	0.2171	0.7014	0.1969	0.97
V	0.1950	0.8989	0.2170	0.7020	0.1969	0.96

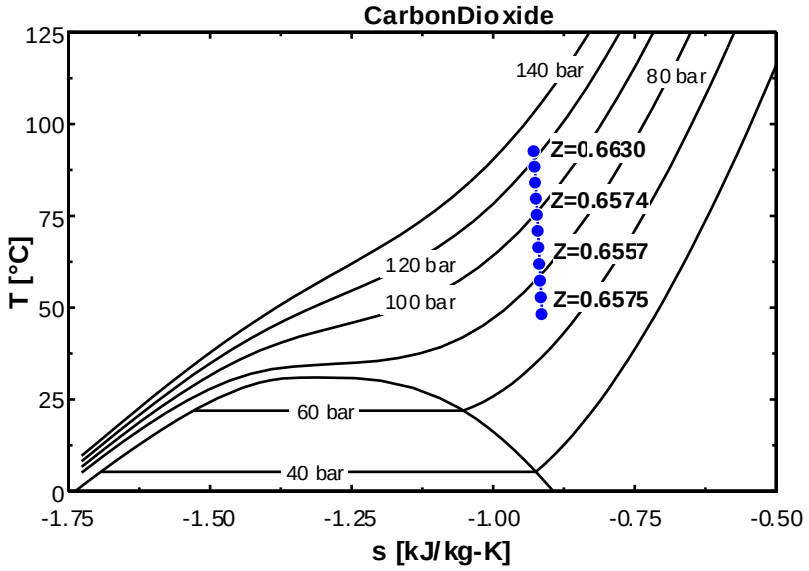

Fig. 1. Turbine expansion of CO_2 in the optimized cycle represented on a T-s diagram. Note that the values of the compressibility factor Z are almost constant along the expansion process.

3.3.2. R125 expansion

In the optimized power cycle [9] R125 expands from 44.5 to 16.5 bar. As shown in Table 3a the specific heat markedly changes during the expansion process, almost halving from turbine inlet to outlet. The compressibility factor is low, around 0.50, at turbine inlet and gradually increases up to 0.72. The derivative $(\partial Z/\partial T)_p$ decreases from 1.26E-2 to 5.3E-3.

The fourth column in Table 3b shows that at the beginning of the expansion process the real enthalpy change is less than 10% of the enthalpy change calculated from the temperature drop ($\Delta h_{\Delta T}$). As the expansion progresses the enthalpy term associated with pressure drop ($\Delta h_{\Delta p}$) gradually decreases so that the enthalpy drop ratio ($\Delta h/\Delta h_{\Delta T}$) reaches the value of 0.265. The relative error introduced by using (24) is variable, however in any case below 8%. This error is the highest among the cases considered and could be reduced using a discretization in a higher number of intervals, however it was considered acceptable for this analysis.

Figure 2 shows on a *T-s* diagram the expansion process of R125 in the optimized cycle. As already done for CO_2 in Fig. 1, the expansion line is divided into 10 intervals having the same enthalpy drop. The temperature difference between two consecutive points (i.e. the vertical distance) is lower at the end of the expansion than at the beginning. This is easily explained since the effect due to the decrease of the specific heat from turbine inlet to outlet is overcome by the increase of the ratio between real enthalpy change and enthalpy change associated with temperature drop.

Table 3a. Thermodynamic conditions of R125 at inlet and outlet of intervals I, II, III, IV and V.

Interval	Points	p (bar)	t (°C)	h (kJ/kg)	c_P (kJ/kg-K)	Z	$(\partial Z/\partial T)_p$ (1/K)
I	1	44.56	85.0	360.7	2.231	0.4959	0.01265
	2	44.06	84.39	360.6	2.223	0.4978	0.01267
II	30	32.56	67.84	357.6	1.817	0.5618	0.01089
	31	32.22	67.28	357.4	1.801	0.5642	0.01078
III	60	24.16	52.66	354.3	1.431	0.6346	0.007881
	61	23.93	52.20	354.2	1.421	0.6370	0.007795
IV	90	18.28	40.17	351.0	1.207	0.6983	0.005799
	91	18.12	39.79	350.9	1.202	0.7002	0.005744
V	100	16.71	36.47	349.9	1.156	0.7170	0.005282
	101	16.56	36.12	349.8	1.151	0.7188	0.005234

Table 3b. Enthalpy changes of R125 calculated using Equations 21 to 26.

Interval	Δh (kJ/kg)	$\Delta h_{\Delta T}$ (kJ/kg)	$\Delta h/\Delta h_{\Delta T}$	$\Delta h_{\Delta p}$ (kJ/kg)	$\Delta h_{\Delta T} - \Delta h_{\Delta p}$ (kJ/kg)	*Err%*
I	0.1097	1.363	0.08047	1.251	0.1116	1.8
II	0.1097	1.007	0.1089	0.9037	0.1030	6.1
III	0.1097	0.6526	0.1680	0.5515	0.1011	7.8
IV	0.1097	0.4576	0.2396	0.3555	0.1021	6.9
V	0.1097	0.4140	0.2649	0.3114	0.1025	6.5

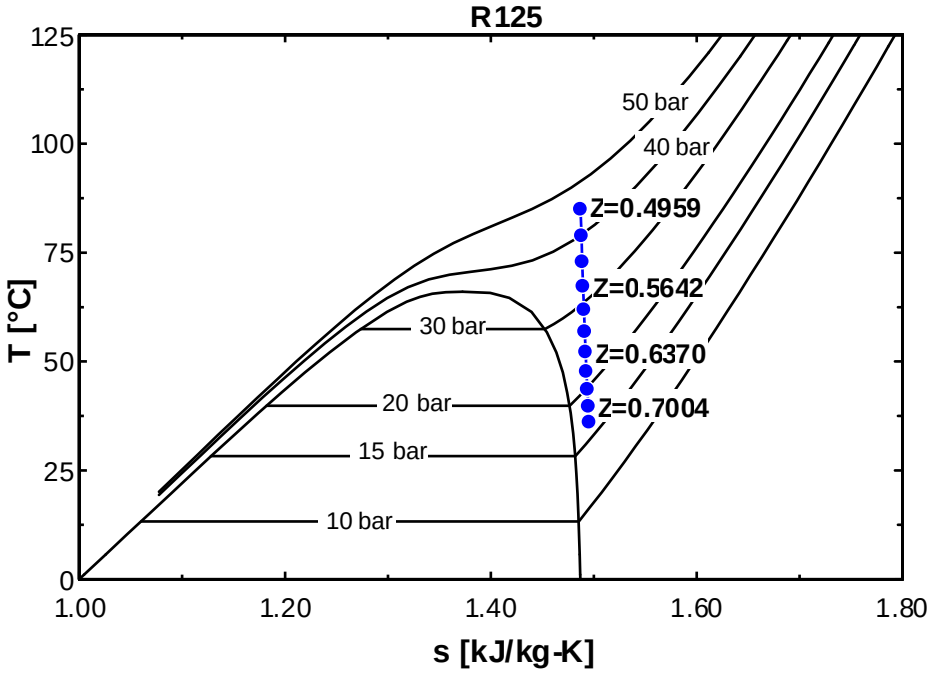

Fig. 2. Turbine expansion of R125 in the optimized cycle represented on a T-s diagram. Note the low value of the compressibility factor Z at turbine inlet.

3.3.3. R134a expansion

In the optimized power cycle [10] R134a expands from 48.0 to 8.5 bar. As in the previous case, the specific heat (Table 4a) decreases along the expansion line. At the beginning of the expansion process the compressibility factor is low, below 0.6, and gradually increases to around 0.85. The derivative $(\partial Z/\partial T)_p$ decreases by a factor 3.7 from inlet to outlet.

The results reported in Table 4b show that at the beginning of the expansion the real enthalpy change is only 0.15 times the enthalpy change calculated as the product of the specific heat and the temperature drop. Then it rapidly increases up to around 0.54 times in the final stage. The relative error introduced by using (24) decreases from about 5% to values well below 1%, and it was considered acceptable for this analysis.

As already seen for the other working fluids, Fig. 3 shows the expansion process of R134a on a *T-s* diagram where the expansion line is divided into 10 intervals of equal enthalpy change. At the beginning of the expansion the real enthalpy drop is only a small fraction of the enthalpy change calculated from the temperature drop, due to the high values of the enthalpy change associated with pressure drop shown in the fifth column of Table 4b. Thus, despite the higher specific heat values, a higher temperature change is needed in the first stages compared to the final stages, as clearly shown by the vertical distance between consecutive points in Fig. 3. The points get closer as the real gas approaches the ideal gas conditions.

Table 4a. Thermodynamic conditions of R134a at inlet and outlet of intervals I, II, III, IV and V.

Interval	Points	p (bar)	t (°C)	h (kJ/kg)	c_P (kJ/kg-K)	Z	$(\partial Z/\partial T)_p$ (1/K)
I	1	47.97	129.4	318.3	1.868	0.5837	0.006943
	2	47.05	128.3	318.0	1.852	0.5871	0.006891
II	30	28.05	100.2	309.2	1.440	0.6875	0.004788
	31	27.56	99.28	308.9	1.429	0.6909	0.004717
III	60	16.76	76.62	299.8	1.197	0.7766	0.003125
	61	16.48	75.92	299.4	1.192	0.7791	0.003084
IV	90	10.21	57.44	290.3	1.064	0.8407	0.002145
	91	10.04	56.85	290.0	1.061	0.8425	0.002120
V	100	8.669	51.67	287.2	1.032	0.8577	0.001908
	101	8.529	51.11	286.8	1.029	0.8593	0.001886

Table 4b. Enthalpy changes of R134a calculated using Equations 21 to 26.

Interval	Δh (kJ/kg)	$\Delta h_{\Delta T}$ (kJ/kg)	$\Delta h/\Delta h_{\Delta T}$	$\Delta h_{\Delta p}$ (kJ/kg)	$\Delta h_{\Delta T}$ - $\Delta h_{\Delta p}$ (kJ/kg)	*Err%*
I	0.315	2.084	0.1511	1.755	0.3295	4.6%
II	0.315	1.273	0.2475	0.9538	0.3190	1.3%
III	0.315	0.8339	0.3777	0.5171	0.3168	0.6%
IV	0.315	0.6262	0.5030	0.3100	0.3161	0.4%
V	0.315	0.5817	0.5415	0.2657	0.3160	0.3%

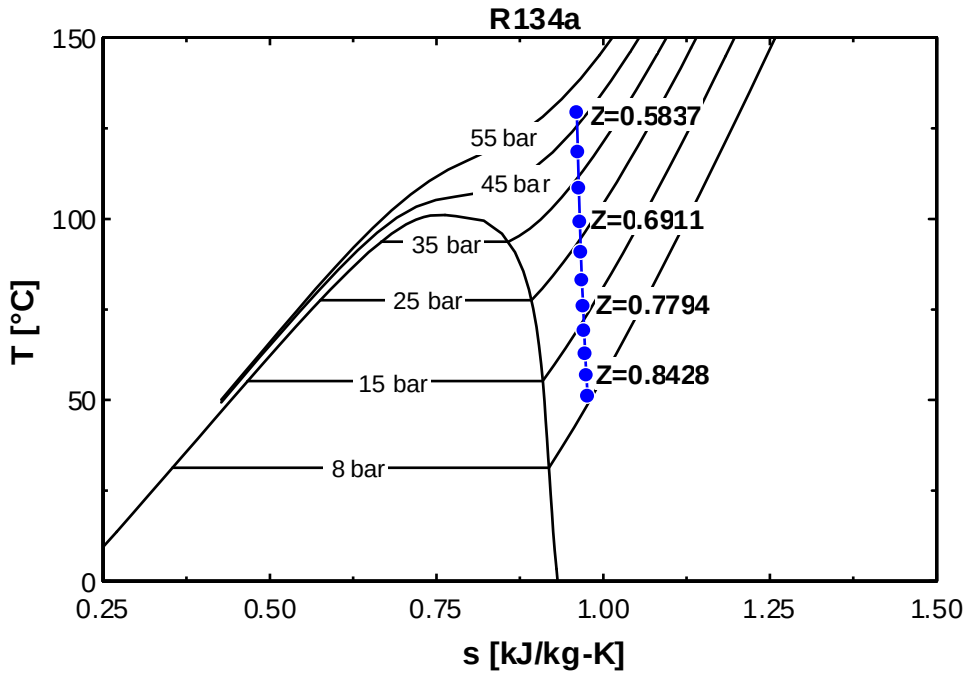

Fig. 3. Turbine expansion of R134a in the optimized cycle represented on a T-s diagram. Note the substantial increase of the compressibility factor Z from turbine inlet to turbine outlet.

3.3.4. Isobutane expansion

In the optimized power cycle [10] isobutane expands at subcritical pressures from 18.9 to 4.4 bar. The fluid thermodynamic properties are shown in Tables 5a and 5b. The specific heat markedly decreases from inlet to outlet conditions. As the expansion progresses, the compressibility factor increases from 0.675 to 0.90, while the derivative $(\partial Z/\partial T)_p$ becomes around 5 times smaller. At the beginning of the expansion the real enthalpy change is 0.23 times the enthalpy change associated with the temperature drop, then it rapidly increases reaching the value of 0.68 in the final stage. The

percentage error introduced by using (24) is in all cases well below 1%. According to the procedure followed in the previous cases, Fig. 4 shows on a *T-s* diagram the expansion process of isobutane divided into 10 identical enthalpy intervals. The values of the compressibility factor are reported near the inlet points of intervals 1, 4, 7 and 10. The points get closer toward the end of the expansion process: the effect due to the increase of the ratio $\Delta h/\Delta h_{\Delta T}$ is stronger than the decrease of the specific heat. In the final stages the real enthalpy drop is more than 65% the enthalpy drop at ideal gas conditions, which is the highest ratio among all cases considered in this study.

Table 5a. Thermodynamic conditions of isobutane at inlet and outlet of intervals I, II, III, IV and V.

Interval	Points	p (bar)	t (°C)	h (kJ/kg)	c_P (kJ/kg-K)	Z	$(\partial Z/\partial T)_p$ (1/K)
I	1	18.85	98.50	679.0	2.842	0.6754	0.005170
	2	18.55	97.75	678.5	2.812	0.6799	0.005043
II	30	12.09	80.29	664.7	2.324	0.7790	0.002874
	31	11.92	79.76	664.2	2.314	0.7817	0.002827
III	60	7.864	65.84	650.0	2.090	0.8461	0.001839
	61	7.754	65.40	649.5	2.084	0.8479	0.001815
IV	90	5.169	53.48	635.2	1.948	0.8909	0.001260
	91	5.098	53.09	634.7	1.944	0.8921	0.001245
V	100	4.499	49.64	630.3	1.911	0.9025	0.001121
	101	4.437	49.26	629.8	1.907	0.9035	0.001108

Table 5b. Enthalpy changes of isobutane calculated using Equations 21 to 26.

Interval	Δh (kJ/kg)	$\Delta h_{\Delta T}$ (kJ/kg)	$\Delta h/\Delta h_{\Delta T}$	$\Delta h_{\Delta p}$ (kJ/kg)	$\Delta h_{\Delta T}$ - $\Delta h_{\Delta p}$ (kJ/kg)	*Err%*
I	0.4917	2.121	0.2318	1.629	0.4923	0.12
II	0.4917	1.241	0.3961	0.7485	0.4927	0.20
III	0.4917	0.9156	0.5370	0.4231	0.4925	0.17
IV	0.4917	0.7579	0.6488	0.2655	0.4924	0.15
V	0.4917	0.7227	0.6803	0.2303	0.4924	0.14

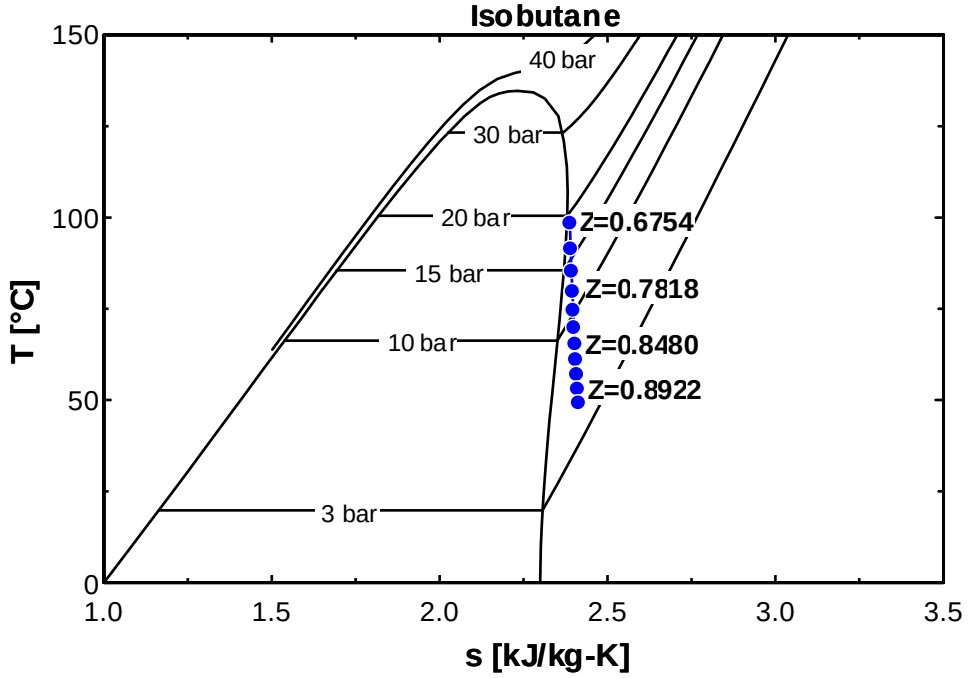

Fig. 4. Turbine expansion of isobutane in the optimized cycle represented on a T-s diagram. The values of the compressibility factor Z show that ideal gas conditions are nearly approached at turbine outlet.

4. Influence of the compressibility factor in the evaluation of the enthalpy change

The results presented in Section 3 have shown that the real enthalpy change is much lower than the enthalpy change calculated from the product of the specific heat and the temperature drop. While this difference is almost constant for CO_2, it gradually decreases from turbine inlet to turbine outlet for the other working fluids. The compressibility factor accounts for real gas effects and shows a similar trend of variation: it is roughly constant for CO_2 whereas it gradually increases from turbine inlet to turbine outlet conditions for the other working fluids. Starting from these findings, the ratio $R_{\Delta h}$ between real enthalpy change and enthalpy change associated with the temperature drop is correlated in the following sections with the compressibility factor.

4.1. Correlation between enthalpy change and compressibility factor

Figure 5 shows the ratio (22) between real enthalpy change and the term of the enthalpy change associated with temperature drop as a function of the compressibility factor *Z*. A good correlation is found for each working fluid. As the compressibility factor increases the real gas approaches the ideal gas behavior and the real enthalpy change approaches the enthalpy change calculated as the product of the specific heat and temperature drop (15, 16). Thus, the real gas effects associated with the second term on the right side of (15) can be easily correlated with the compressibility factor Z. These effects result in a decrease of the enthalpy change from the value calculated as the product of the specific heat and the temperature drop. Higher values of *Z* result in higher fractions of temperature related enthalpy change "converted" into real enthalpy change.

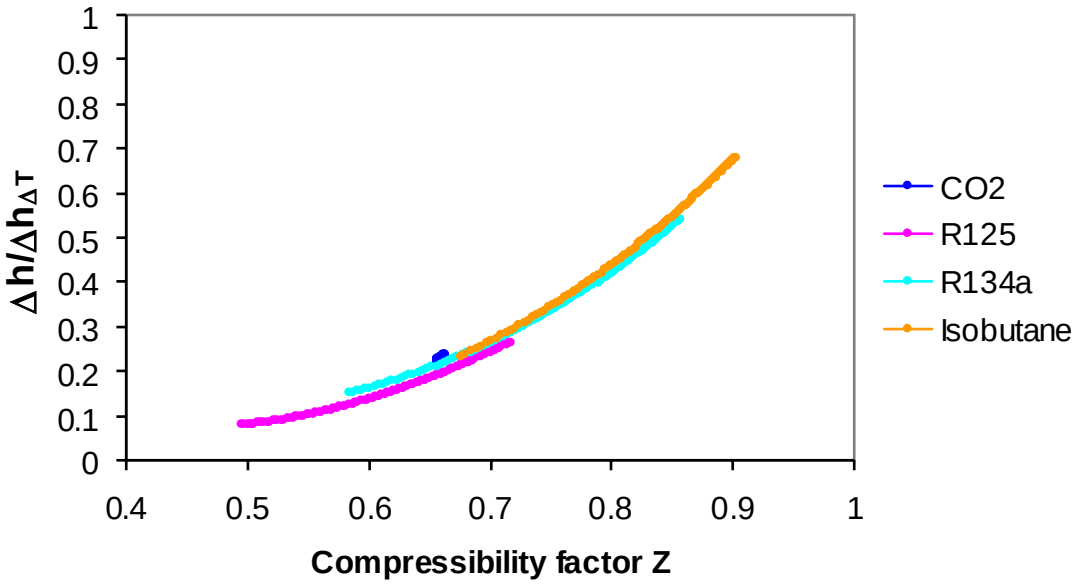

Fig. 5. Correlation obtained between compressibility factor Z and the ratio between real enthalpy change and enthalpy change evaluated from the temperature drop.

According to these findings, the real enthalpy change in an elementary expansion interval can be expressed as:

$$\Delta h \approx c_{P_in} \cdot (T_{in} - T_{out}) \cdot f(Z) \qquad (26)$$

where c_{P_in} is the specific heat of the working fluid at the inlet of the temperature interval (T_{in}-T_{out}) and *f(Z)* is a function that depends on the compressibility factor *Z*.

The functions $\Delta h / \Delta h_{\Delta T}$ obtained from the analysis of the considered expansion processes (see Section 3) undergone by different fluids, are shown in Fig. 5. These functions are interpolated using

the second order polynomials shown in Table 6. The expression of *f(Z)* for CO_2 is not shown since the expansion process of CO_2 spans a narrow range (almost constant) of *Z*. It is noteworthy that $\Delta h / \Delta h_{\Delta T}$ is a second order function of *Z*.

Table 6. Correlations between real enthalpy change and enthalpy change calculated from the temperature drop.

Working fluid	$f(Z)=\Delta h/\Delta h_{\Delta T}$
R125	$f(Z) = 2.4454 \cdot Z^2 - 2.1233 \cdot Z + 0.5304$
R134a	$f(Z) = 2.9650 \cdot Z^2 - 2.8602 \cdot Z + 0.8115$
Isobutane	$f(Z) = 3.2149 \cdot Z^2 - 3.1110 \cdot Z + 0.8682$

The turbine power output is:

$$\dot{W}_t = \dot{m}_{wf} \cdot \sum_n \Delta h \approx \dot{m}_{wf} \cdot \sum_n \left(c_{P_in} \cdot (T_{in} - T_{out}) \cdot f(Z) \right) \qquad (27)$$

where Δh is given by (26) and the sum is over all the temperature intervals (n).
The options to maximize the turbine power output consist in increasing all factors included in (27), that is: working fluid flow rate, temperature drop between turbine inlet and outlet, specific heat and *Z* along the expansion process. Accordingly:

- A good match between the thermal profiles of the heat source and the working fluid leads to both higher working fluid mass flow rates and to higher turbine inlet temperatures (close to the inlet temperature of the heat source).
- The use of a more effective cooling system allows the expansion to progress to lower temperature levels, which are also more effective in generating power due to the higher values of *Z*.
- The reduced pressures (p_R) and reduced temperatures (T_R) involved in the expansion process depend on the working fluid selection and fix the value of *Z* and *f(Z)*.
- Higher values of the specific heat increase the enthalpy drop ($\Delta h_{\Delta T}$), however they might result in lower working fluid mass flow rates evaporated by heat transfer with the heat source as well.

All these strategies contribute to the increase of turbine power output, but they do not affect the above conclusion that operating conditions involving high values of the compressibility factor are always suitable to maximize the enthalpy drop and, in turn, the turbine power output, according to (27).

4.2. Use of the generalized compressibility chart in the working fluid selection

Figure 6 shows the generalized compressibility chart in which the turbine inlet and outlet thermodynamic conditions of the considered expansion processes are superimposed. The choice of the working fluid and in turn the choice of the critical temperature fixes the operating conditions in terms of reduced pressure and reduced temperature in the expansion process. In the 100°C application the expansion process involves only supercritical states using CO_2, whereas it encompasses both supercritical and subcritical states in the case of R125. In the 150°C application the expansion process encompasses both supercritical and subcritical pressures using R134a, whereas it only involves subcritical pressures in the case of isobutane. These operating regions are associated with different values of the compressibility factor which, according to Fig. 5, imply different fractions between real enthalpy change and enthalpy change associated with the temperature drop. The compressibility factor becomes therefore an evaluation parameter of the quality of the expansion process.

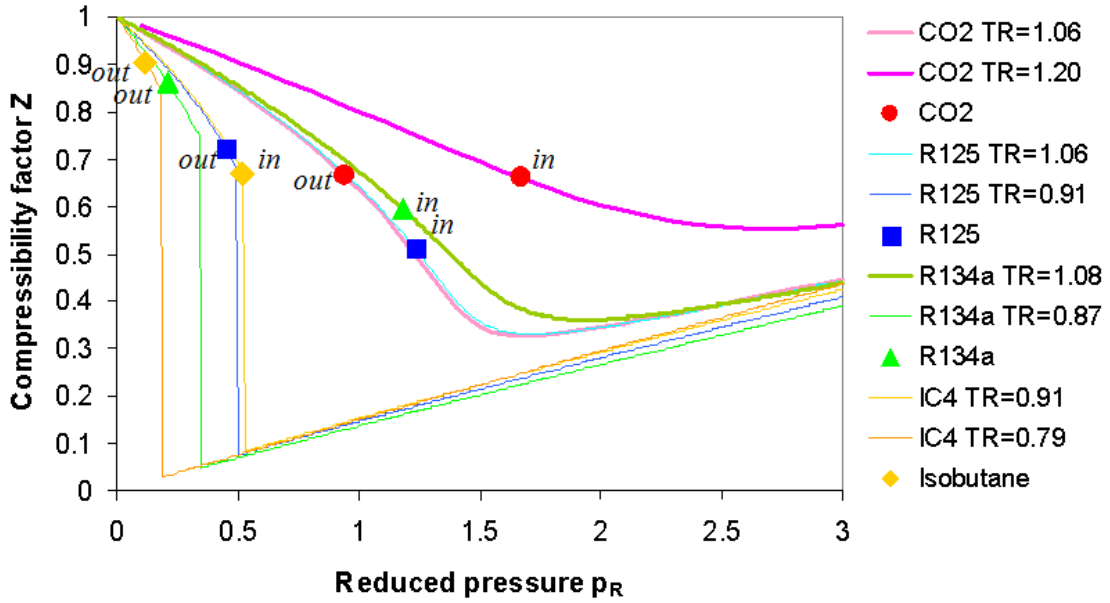

Fig. 6. Generalized compressibility chart with superimposed the turbine inlet and outlet conditions of the analyzed expansion processes.

5. Conclusions

This study analyzes the influence of the real gas effects in the calculation of the enthalpy change in an expansion process. The enthalpy change is regarded as the difference between two terms related with temperature and pressure drops, respectively. The study shows that the ratio between the real enthalpy change and the enthalpy change calculated as the product of the specific heat and the temperature drop can be easily correlated with the compressibility factor Z using a second order polynomial. As the compressibility factor increases, the real gas approaches the ideal gas behavior and the enthalpy term related with pressure drop gradually decreases.

The choice of the working fluid in an Organic Rankine cycle fixes the thermodynamic states in the expansion process in terms of reduced pressure and reduced temperature and, in turn, the values of the compressibility factor from the generalized compressibility chart. Thus, working fluids and operating conditions which lead to high values of the compressibility factor are always suitable to maximize the turbine power output.

This condition does not guarantee by itself the achievement of the highest turbine power output, which is the result of many concurring factors. Among them the optimal match between thermal profiles of heat source and working fluid, the work minimization in the compression process and features of the cooling system are the most important ones, and may "force" the expansion process where the compressibility factor is relatively low. Nevertheless, the information that can be inferred from this study may help both in the preliminary choice of the operating fluid and in the subsequent analysis of the ORC system performance.

Nomenclature

c_P	specific heat, kJ/kg-K
Err%	percentage error
h	specific enthalpy, kJ/kg
heat	heat source
$\dot{m}$	mass flow rate, kg/s
ORC	Organic Rankine Cycle
p	pressure, bar

R	specific gas constant, kJ/kg-K
R	ratio between enthalpy changes
s	specific entropy, kJ/kg-K
t	temperature, °C
T	temperature, K
v	specific volume, m^3/kg
Z	compressibility factor

Greek symbols

η	efficiency

Subscripts and superscripts

ACC	air cooled condenser
approx	approximated
CR	critical
dep	departure
Δt	related to temperature drop
Δp	related to pressure drop
el	elementary
idg	ideal gas
in	inlet
IS	isentropic
net	net
out	outlet
p	polytropic
pump	feed pump
R	reduced
rg	real gas
turb	turbine
wf	working fluid

References

[1] DiPippo R., Geothermal power plants: principles, applications, case studies and environmental impact. Butterworth-Heinemann, 2008, Burlington, MA, USA, Chap. 8.

[2] Bertani R., Geothermal power generation in the world 2005-2010 update report. Geothermics 2012; 41:1-29.

[3] Angelino G., Colonna di Paliano P., Multicomponent working fluids for Organic Rankine Cycles (ORCs). Energy 1998; 23:449-463.

[4] Shengjun Z., Huaixin W., Tao G., Performance comparison and parametric optimization of subcritical Organic Rankine Cycle (ORC) and transcritical power cycle system for low-temperature geothermal power generation. Applied Energy 2011;88:2740-2754.

[5] Dai Y., Wang J., Gao L., Parametric optimization and comparative study of organic Rankine cycle (ORC) for low grade waste heat recovery. Energy Conversion and Management 2009;50:576-582.

[6] De Monte F., Analysis of the gas compressibility effects on the constant-entropy reversible processes of refrigerants and refrigerant mixtures. International Journal of Refrigeration 2002;25:765-779.

[7] Utamura M., Tamaura Y., A solar gas turbine cycle with super-critical carbon dioxide as a working fluid. Proceedings of ASME Turbo Expo 2006.

[8] Stijepovic M.Z., Linke P., Papadopoulos A.I., Grujic A.S., On the role of working fluid properties in Organic Rankine Cycle performance. Applied Thermal Engineering 2012;36:406-413.

[9] Baik Y.-J., Kim M., Chang K.C., Kim S.J., Power-based performance comparison between carbon dioxide and R125 transcritical cycles for a low-grade heat source. Applied Energy 2011;88: 892-898.

[10] Toffolo A., Lazzaretto A., Manente G., Rossi N., 2010, Synthesis/Design Optimization of Organic Rankine Cycles for Low Temperature Geothermal Sources with the HEATSEP Method. ECOS2010: Proceedings of the 23rd International Conference on Efficiency, Cost, Optimization, Simulation and Environmental Impact of Energy Systems; 2010 June 14-17; Lausanne, Switzerland.

[11] Moran M.J., Shapiro H.N., Fundamentals of engineering thermodynamics. Wiley 2006, Fifth Edition.

[12] S.A.Klein, Engineering Equation Solver, F-Chart Software, Middleton, WI, 2010.

Design of Solar Heating System for Methane Generation

L. M. Gutiérrez Castro[a], P. Quinto Diez[a], L. R. Tovar Gálvez[b]

aSección de Estudios de Posgrado e Investigación, Escuela Superior de Ingeniería Mecánica y Eléctrica, Av. IPN s/n, UPALM Edif.5, 3er.Piso, C.P. 07738 México, D.F. Instituto Politécnico Nacional, moni-80-lgc@hotmail.com, pqd510@hotmail.com
bCentro Interdisciplinario de Investigaciones y Estudios sobre Medio Ambiente y Desarrollo, Calle 30 de Junio de 1520 s/n, Barrio. la Laguna Ticomán, C.P. 07340 México, D.F. Instituto Politécnico Nacional. luisraulto@gmail.com

Abstract:

In this paper the methodology carried out to design a solar heating system (SHS) is shown, it applies in a thermophilic process of anaerobic digestion for a new prototype of digester. The thermophilic process required to keep the mix into the digester between temperatures of 40 to 60°C. The optimal temperature to this process is 55°C. The SHS was designed with the "f" method and with the help of the selection program "Solar" carried out at the Instituto Politécnico Nacional. To meet the application needed, the SHS is integrated by flat plate solar collectors of parallel flow with a total collecting area of 12 m^2. In this project a new design of digester was needed. The most important parameters of design are rate and length of stirring and hydraulic retention time (HRT). Taking in account these parameters, the digester designed has a volume of 2 m^3, the feedstock, which is the organic fraction (OF) sorted at the source of the municipal solid waste (MSW) of Mexico City, is fed with centrifugal pumps and a heating exchange system was designed to achieve a more homogenous heat transmission in the digester. As a calculation tool, a computer program was developed in order to obtain the amount of energy required to several volumes of mix to heat into the thermophilic range. Improving the design and operation of an anaerobic digester can be result of an organic waste management more controlled and obtain the best design of anaerobic digester to applying it in rural zones. The SHS reduces fuel consumption in the process of methane generation. The advantages of this design are: reducing the time of methane generation and, thereby, improving the efficiency of the process, also reducing the solid retention time inside the digester and reducing its volume. Among the important achievements of this new design are: the deviation from landfilling of the OF since Mexico City, nowadays generates about 5,000 ton/day of it.

Keywords:

Anaerobic digestion, Digester design, Methane generation, Solar heating system, Thermophilic process.

1. Introduction

Among the most pressing global environmental challenges that faces humankind are the increase in emission of greenhouse gases causing the climatic change and the exponential generation of waste.

In Mexico the generation of solid municipal solid waste (MSW) is calculated in about 85,000 tons per day. Nowadays, the problematic has advanced, overcoming the common methods of recollection and its final disposal, in the specific case of México City (with a population of 8.9 millions of people), it generates about 11,000 tons per day of MSW [16]. It is known that 40% of MSW correspond to the organic fraction (OF) of this, therefore only in Mexico City, about 5,000 tons are generated on a daily basis, with a moisture content between 70% and 80%, which potentially could produces about 385,000 Nm^3 of methane (CH_4) per day. For the above, and since there is no treatment or method to avoid this methane to be released into the atmosphere, it is contributing to pollution, as methane is a powerful greenhouse gas [17].

The trouble of handling the MSW in Mexico has considerably increased due to the closure of an important landfill (Bordo Poniente stage IV). The Bordo Poniente stage IV received 4'872,300 tons of MSW in 2009 and a slightly higher quantity in 2010. At the time of the closure (December 31,

2011), it ended up with 69 million tonnes buried under an area of 375 ha, its emissions to the atmosphere are of about 1'068,384 m^3 of biogas per day [17].

Due to the dimensions of the problem, in this work an improvement to the method of anaerobic digestion is proposed using solar energy to work under the thermophilic range. The anaerobic digestion is a process to generate energy, which is carried out by managing the organic fraction of the MSW to obtain a stabilized product and thus, produce biogas. The biogas is made of methane and carbon dioxide (50 – 70% v/v), which can be used as fuel. The effectiveness in destructing pathogens, as well as higher production in biogas production, depends on the temperature range, in this case the thermophilic range (55 °C) that is more efficient than the mesophilic range (35 °C), [14],[7].

The thermophilic range needs an external energy source that in many cases is a conventional fuel which results in higher operation costs and does not avoid the problem of greenhouse gases emitted to the atmosphere, then using solar energy to heat the digester is a good alternative, because these sources are environmental friendly [18]. Therefore, the contribution of this work, is the design of a solar heating system (SHS) to provide the energy needed to maintain the thermophilic range in the process and to reduce costs. The obtained result was a new model of digester adapted with a heat transfer system to use the SHS and the methane produced. It was designed as well; a computer program to design digesters that calculates the energy needed to the process depending on the MSW quantity to convert it in methane.

2. Proceeding

According to El-Mashad et al. (2003) the use of solar energy for heating anaerobic reactor represent a kind of solar energy storage in the form of biogas. Hamed M. El-Mashad et al.(2002), present a design of a stirred tank reactor for anaerobic treatment of liquid cow manure under thermophilic conditions (50 °C), using a solar heating system mounted on the reactor roof, in this case a simulation models for two systems were developed.

In the present study, the solar thermophilic anaerobic digester (STAD) designed has been evaluated for different configurations the dimensions used a computer program. The STAD designed to obtain variable conditions which was used in the program is compound by 6 m^2 of solar collector area. The digester designed has a volume of 2 m^3; the feedstock is the organic fraction (OF) at thermophilic conditions (55 °C). The main objective was to design a STAD whit high energy efficiency including lower constructions costs, as well as a simple control system.

First, the design of solar heat transfer system was made. Second, the design of the digester was modified to maintain the temperature of thermophilic process about 55 °C. In the design all parameter was took in a count, such as the feed, the stirring and heating. Therefore, a new design of the digester was the result of analysis. Details of the procedure are below.

3. Design Methodology

3.1. Solar Heat Transfer System

The importance of the design is maintaining the mixture into the digester at 55 °C, so that several compounds are involved in the process to achieve it, [7]

Based on the energy's requirements of the thermophilic process to generate biogas, the solar heating system (SHS), with flat plate solar collectors was designed to apply to the "Solar" program [1]. This program was designed for flat plate solar collectors; it gives the solar collection area and storage of water per area of collection [10]. The solar collection area depends on the monthly radiation, on the installation zone of the SHS and also on the monthly heating loads needed.

The available measured data for solar energy were the monthly average daily solar radiation on a horizontal surface and the monthly average daily hours of bright sunshine [4].

The total solar radiation incident on a horizontal plane at the surface is the sum of direct and diffuse radiation. Also, it is necessary to determine the solar radiation on tilted surfaces such as flat solar collectors. Studies on the availability of solar resources in these FPSC have shown that the most appropriate orientation is north - south, which means that, if the FPSC are to be installed in the northern hemisphere, the collector should be oriented towards the geographical south and vice versa, [12]. The radiation is calculated by (1):

$$R_b = \frac{\cos\theta}{\cos\theta_Z} \tag{1}$$

To determine the total solar radiation on a tilted surface, based on solar radiation data on horizontal plane, it is necessary to define the coefficient R, which is the ratio of total radiation on the tilted surfaces in relation to radiation total surfaces in the horizontal plane it is shown in (2):

$$R = \frac{H_T}{H} \tag{2}$$

Therefore:

$$H_T = R * H \tag{3}$$

It can also be expressed as follows:

$$R = \frac{H_b}{H} R_b + \frac{H_d}{H} R_d \tag{4}$$

The total solar radiation on a horizontal plane (*H*) was measured for this study. Data measured are shown in the table 1 (see Appendix A, table A.1). These values were plotted as it shows in the Fig. 1.

The method used to both design and selecting is the "*f*" design method.

The "*f*" chart-method or "*f*" design method is used to estimate the annual thermic performance of the heating solar system activity by using a working fluid, by means of the calculus of the *f* energy fraction, supplied by the sun to meet the required heating load. The main design variable is the uptake area of solar energy. Among the secondary variables are: the type of collector, the storage capacity, the flow rate and the size of the heat exchangers. The *f* fraction is the relation between the useful energy delivered to the solar system (Q_t), which is the difference between the energy of the system only using conventional fuel (L_{aux}) and the heating load required by the system (L) [12]. For a given month, the reduction of the "*f*" fraction of the supplied solar energy is shown in (5):

$$f = \frac{L - L_{aux}}{L} = \frac{Q_t}{L} \tag{5}$$

The "*f*" fraction is the correlation obtained from results of hundreds of experiments in this area as well as simulations with solar heating systems operating under different circumstances. This fraction depends of two dimensionless parameters. The first one is related to the index of losses of heating load, *UL*, of the collector and the second one with the solar energy absorbed, *G*, and the heating load. Meteorological data of the zone are also required on a monthly basis.

The calculus of the "*f*" fraction is in function of two dimensionless parameters: X and Y. The procedure which Klein describes to determine these two variables is shown by the equations (6) and (7).

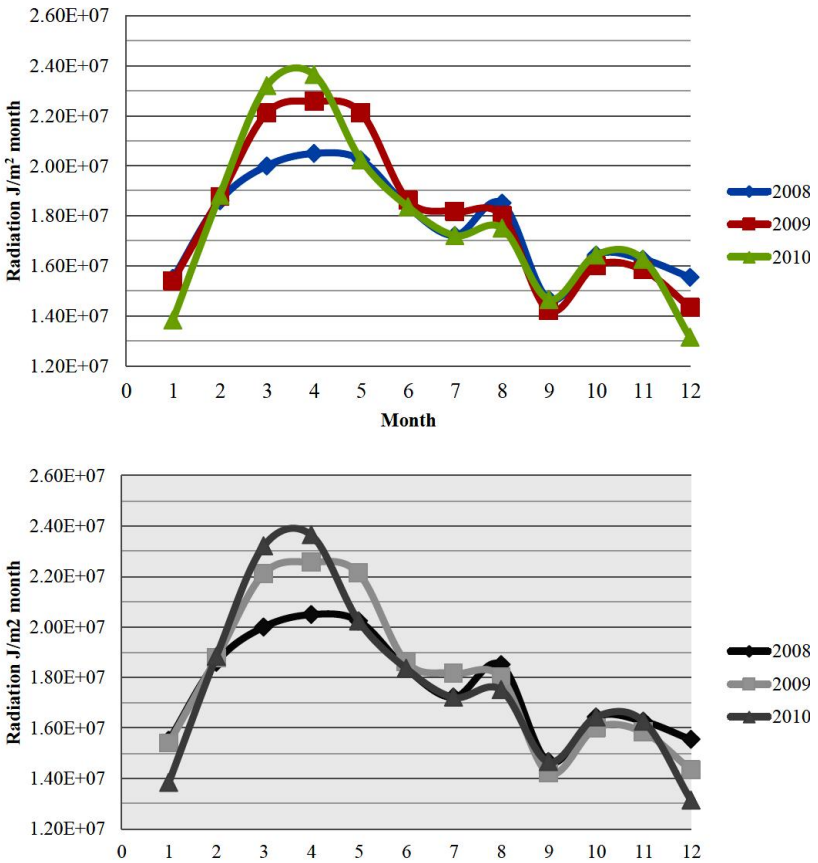

Fig. 1. Solar radiation on the study area from 2008 to 2010 [CINVESTAV, 2010]

$$\frac{F_R A_C}{L} = \int I_T(\tau\alpha)dt = \frac{F_R A_C}{L}\overline{H_*}(\overline{\tau\alpha})N = Y \qquad (6)$$

$$\frac{F_R A_C}{L} = \int^{\Delta t} U_L(T_{ref} - T_a)dt = \frac{F_R A_C}{L} U_L(T_{ref} - T_a)\Delta t = X \qquad (7)$$

The value *f* was obtained as a function of X and Y as it shows in the Fig. 2, [12].

The annual fraction of energy is provided for the solar heating system. This is the sum of contribution monthly that brings the system, divided by the annual thermal load of heating as it shown in equation (8):

$$f_{annual} = \frac{\sum_{i=1}^{12} Q_u}{L_{annual}} \qquad (8)$$

By means of experimental assays, design ranges of the variables used in the development of the "f" method for air and liquid systems have been obtained, which are the transmittance and absorbtance product (0.6 to 0.9), the collector-heat exchanger efficiency factor, (5 to 120 m^2), and the overall coefficient of heat losses, *UL* (2.1 to 8.3 W/m2-°C) [12].

The collector's heat transference efficiency factor or removed heat factor, FR, is defined as the relation between the actual energy available for the collector and the energy that would be available if the whole absorber plate of the flat solar collectors, FSC, was at the same temperature as that of the fluid's entrance to the flat plate solar collectors. [4].

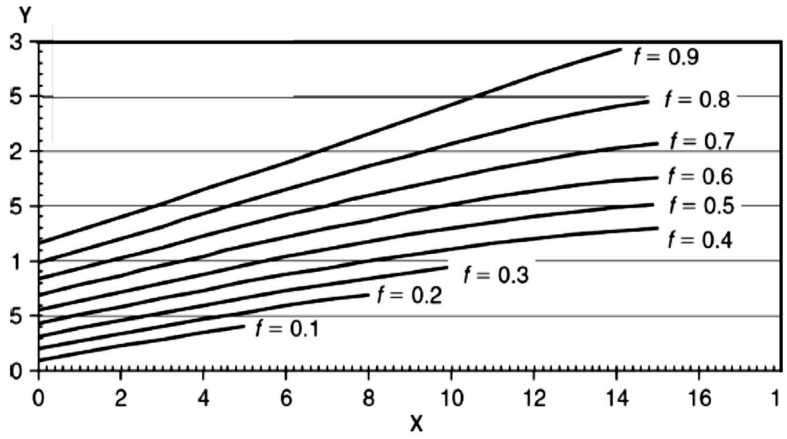

Fig. 2. The "f" chart to design of solar heating fluids systems

3.2. Application of the "Solar" Program

When the data that the "SOLAR" program requires are introduced [1], this determinates the provided amount for the sun at the system. The introduced data in the program are the next:

- Latitude of the place: 19.8°
- Product (*FR*)(*UL*): 3.75
- Product (*FR*)($\tau\alpha$): 0.68
- Collector's efficiency factor (*F'*): 1
- Number of collector's covers: 2
- Temperature of the supplied water: 18 °C
- Hot water temperature: 60 °C
- Volume of the water to be heated: 550 litters per day
- Collector's inclination: 20°

The total solar radiation in the zone and the average temperature are also introduced in the program. The Fig. 3 shows the results of the energy fraction to different radiation values.

For this design, the space available was 30 m2, hence we selected the storage capacity of 75 l / m 2. The storage capacity is also selected, taking into account the costs of installing the system. The value of the fraction of energy for the SSCP is approximately 43%, indicating the percentage of energy used by the solar system.

3.3. Determination of Net Thermal Energy Production Including Solar Energy

The quantity of overall energy needed to raise the temperature of water is shown in (9) [2]:

$$\dot{Q}_T = \dot{m}Cp\Delta T \qquad (9)$$

When the heat flow is obtained, the properties of the system are determined in order to dimension the heat transfer system of the mixture. In this case the heating is released by flat plate solar collectors. The exit temperature of the collectors is 60 °C. For the calculations, the convection and conduction losses of the digester were taken into account. The plus of the quantities of heat flows give to result the overall heating load (overall heat flow $\dot{Q}$), which is provided to the solar heating system by flat plate collectors.

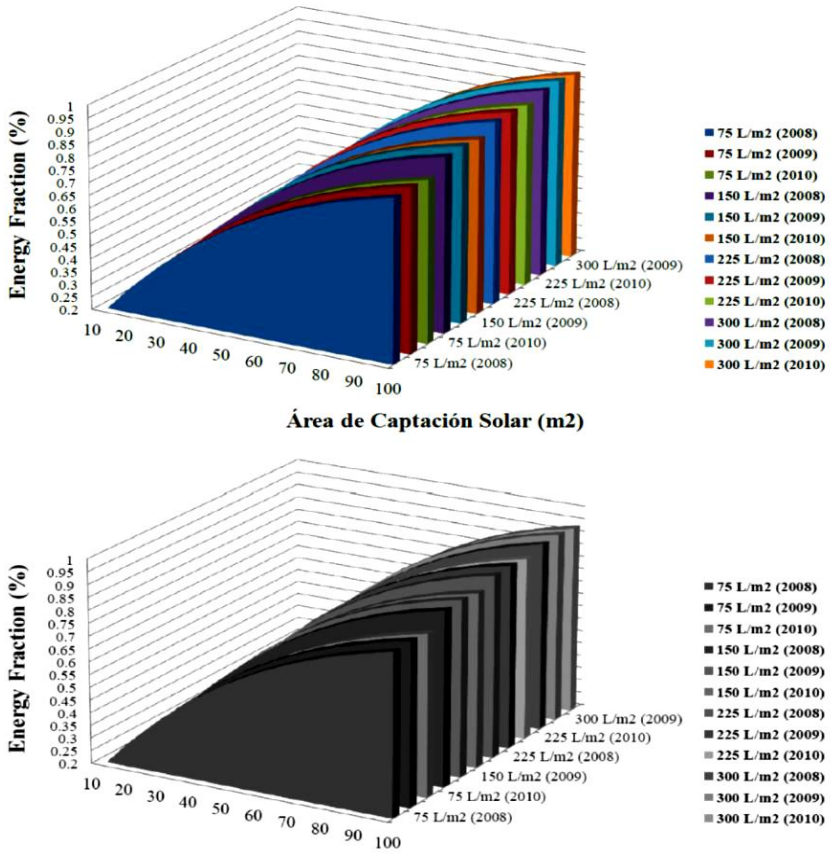

Fig. 3. Annual behaviour to the "f" energy fraction which is provided by the sun

The heat transfer in the heat exchanger involves convection in the fluid's side and conduction through the wall which separates it. The overall heat transfer coefficient (U), takes an account the contribution of this effects, as follows [2]:

$$U = \frac{1}{\frac{1}{h_{\text{int}}} + \frac{1}{h_{ext}}} \tag{10}$$

The overall heat transfer coefficient is used as follows:

$$Q_T = UA_s \Delta T_{lm} \tag{11}$$

The logarithmic mean temperature difference is calculated as depicted in (12):

$$\Delta T_{lm} = \frac{\Delta T_1 - \Delta T_2}{\ln \frac{\Delta T_1}{\Delta T_2}} \tag{12}$$

In this evaluation the overall heat balance including all temperatures and heat fluxes, such as T_{amb} ambient, T_{pch} air in pump chamber, T_b biogas and T_d digester temperatures. The heat fluxes that was considered are solar flux on a tilted surface I_T, top losses from the solar collector Q_{tlc}, sides losses from the solar collector Q_{lc}, bottom heat loss from the solar collector Q_{blc}, electrical energy consumption in agitation Q_{ecp}, heat losses from the liquid via biogas bubbles Q_{lbb}, heat losses by convection from the liquid to biogas Q_{lcb}, useful heat gain rate from the collector Q_u, auxiliary heat add to the digester Q_{aux}, rate of heat gain from the pumps Q_{rhp}, heat losses from the pump chamber to environment Q_{lche}, heat losses from the pump chamber to the reactor Q_{lcd}, heat recovered from the effluent Q_{re}.

The calculates was made more facility whit the development of a computer program in Math lab, in this program was considered all temperatures and heat fluxes, as well as the production of biogas. (see Apendix B, Table B.1). This program is easier tool to release the calculus.

4. Results

4.1. Digester Designed with the Solar Heating System

The amount of energy needed to heat the digester mixture to 55 ° C was previously determined, a value that is meet by means of solar energy. Therefore, the heating load for the SSCP is 7.2 x 109 J / month. The temperature of the exhaust manifold is 60 ° C. The digester is 1.8 m^3 with a height of 1.45 m. The heat exchanger is composed by 22 aluminium tubes, an arrangement of 6 flat plat solar collectors, a 150 l/m^2 storage tank, a 7 m^2 collection area. The design of this exchanger was made thinking about temperature uniform and more heat transfer of a fluid to another. The mixed is for two centrifugal pumps. The bottom on the digester has a conical shape to encourage the decantation of the sludge and avoid the passage of these through of the mixture's recirculation system. The heat exchanger is collocated in vertical position with its fixed outboard.

Into the digester the mixture is very corrosive due the corrosive components that are naturally formed in the process.

Control system: the control system is responsible for monitoring of system's functions; it controls the temperature into of the digester, the temperature of solar collectors, opening and closure of valves to solar and auxiliary heating system and on-off pumps system.

This new digester design was designed to build and industrial scale, below is shows the integral system to energy generation in Fig. 4 y Fig. 5.

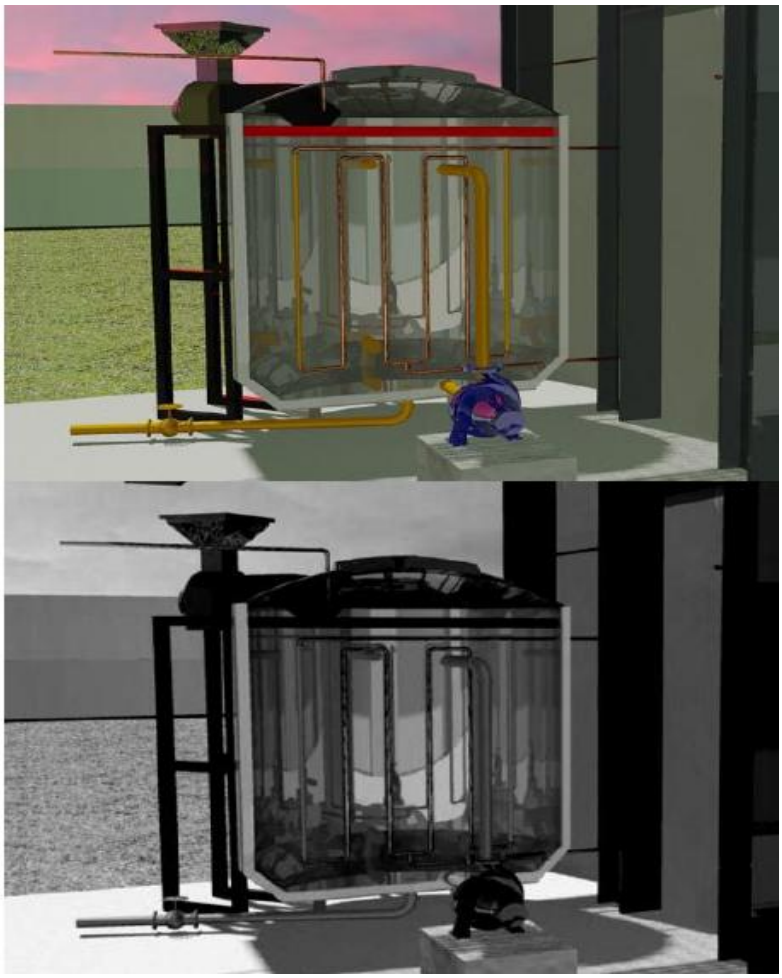

Fig. 4. Collector designed that shows heat exchanger

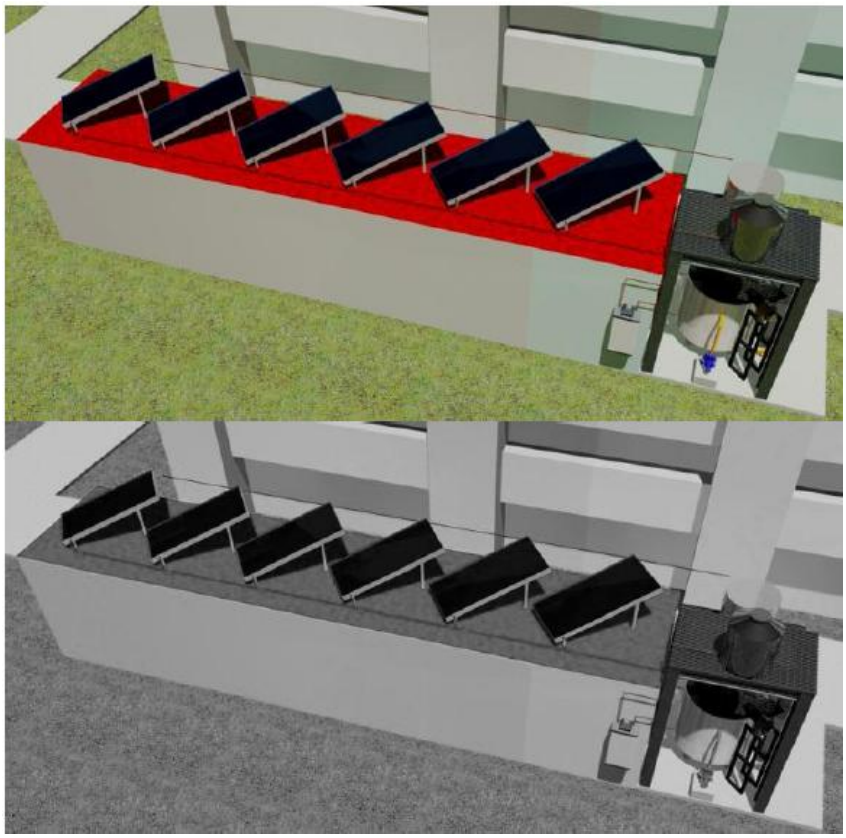

Fig. 5. Biogas generation system with the solar and auxiliary heating system

The result more important of computer program that was calculated is the generation of methane about the retention time. These values were determined taking in account standard conditions. In the Fig. 6 is shown a chart of generation of methane.

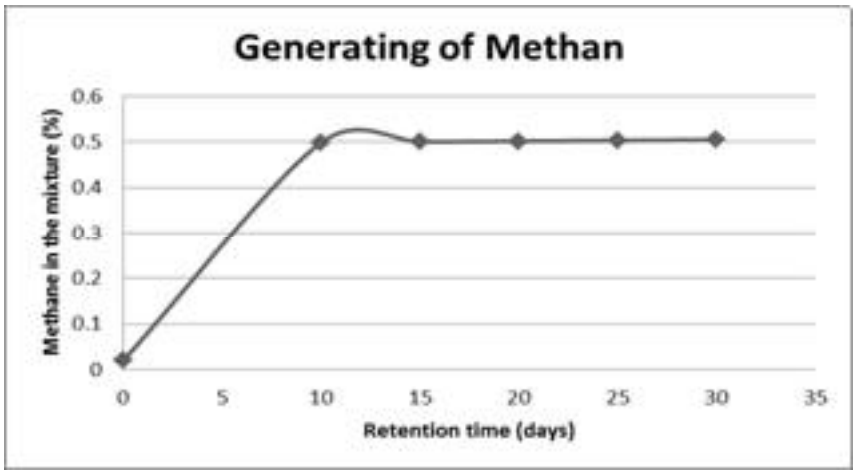

Fig. 6. This chart shows the generating methane from the digester design

The digesters of MSW are designed below the base to minimum retention time from 20 to 30 days.

6. Conclusions

The calculation methodology to the design of integral system called Digester-SHS was developed. Also the calculation tool was made which allows analysing of behaviour to volumes and loads different. The contribution of this study was an economic and environmentally friendly digester

model, as well as this digester can be used in the industry. The list following show the advantages of the digester designed:

- Higher speed of reaction to generate methane
- Lower solids retention time
- Lower volume of the digester
- Contribution to the final dispose of the SMW in the country
- Contribution to the reduction of greenhouse effect to the atmosphere

Appendix A

This table show the data of solar radiation that were plotted of 2008 to 2010 to obtain the behaviour of the radiation solar and can be consider whit the better option.

Table A.1. Data measurement of the total solar radiation on the zone

Year	2008	2009	2010	
Month	H [J/m^2-day]	H [J/m^2-day]	H [J/m^2-day]	Monthly average temperature (°C)
January	1.55E+07	1.54E+07	1.38E+07	14.3
February	1.87E+07	1.88E+07	1.88E+07	15.7
Marchs	2.00E+07	2.21E+07	2.42E+07	17.6
April	2.05E+07	2.26E+07	2.46E+07	19.8
May	2.02E+07	2.21E+07	2.02E+07	20.1
June	1.84E+07	1.86E+07	1.84E+07	19.8
July	1.72E+07	1.82E+07	1.72E+07	18.5
Augusth	1.85E+07	1.80E+07	1.75E+07	19.3
September	1.47E+07	1.42E+07	1.47E+07	18.3
October	1.64E+07	1.60E+07	1.64E+07	18.4
November	1.63E+07	1.58E+07	1.63E+07	15.6
December	1.55E+07	1.43E+07	1.31E+07	15.4

Appendix B

In this appendix an example of data calculated for the compute program is shown.

```
Choose 1, if knows amount of MSW
Choose 2, if knows volume of MSW
Choose 1 or 2
1
Enter the value of MSW daily load [kg]
60
Enter the retention time (10<rt<60) [days]
30
Enter the value of the digester height [m]
1.5
Enter the value of the temperature in the thermophilic range (40<T_termofi<55) [°C]
55
Digester volume (m^3):                          2.000
Digester diameter (m):                          0.800
Mass flow (kg/s):                               0.900
Energy to raise the temperature (W):            2615.000
-----------------------------------------------------------------
-THERMODYNAMIC VARIABLES-
Pipe diameter (m):                              0.0127          0.019           0.0254
External convective coefficient (W/m^2 K):      566.4541        552.6105        546.3759
Internal convective coefficient (W/m^2 K):      8566.8541       7291.912        6586.8296
Logarithmic temperatura difference:             13.9725         14.7782         15.034
-----------------------------------------------------------------
-Convective losses to the surroundings (W)-
Pipe diameter (m):                      0.0127          0.019           0.0254
Aluminum:                               24.0659         24.0658         24.0657
Carbon steel:                           24.0657         24.0656         24.0655
Stainless steel:                        24.0651         24.065          24.0649
Brick:                                  23.8336         23.8334         23.8334
-----------------------------------------------------------------
-Loss by evaporation (W)-:              5.651
-----------------------------------------------------------------
-Total heating load (W)-
Pipe diameter (m):                      0.0127          0.019           0.0254
Aluminum :                              2644.7169       2644.7168       2644.7167
Carbon steel:                           2644.7167       2644.7166       2644.7165
Stainless steel:                        2644.7161       2644.716        2644.7159
Brick:                                  2644.4846       2644.4845       2644.4844
-----------------------------------------------------------------
-HEAT TRANSFER SYSTEM-
Pipe diameter (m):                      0.0127          0.019           0.0254
Overall coefficient of heat transfer  (W/m^2 °C):
                                        531.3222        513.6816        504.5256
Logarithmic temperatura difference:
                                        13.9725         14.7782         15.034
Heat transfer area(m^2):
                                        0.35624         0.34839         0.34868
Lenght of pipe heat exchanger (m):
                                        8.9288          5.8366          4.5301
-----------------------------------------------------------------
-STIRRING SYSTEM-
Pipe diameter (m):                      0.0127          0.019           0.0254
Pump speed(rps):                        12.9496         3.8673          1.80373
Pump load (m):                          12.0726         1.61084         0.451844
Pump flow (m^3/s):                      0.11615         0.077636        0.060208
Pump power (W):                         13.7558         1.22683         0.266877
Pump power (Hp):                        18.4641         1.64676         0.358224
-----------------------------------------------------------------
-GENERATION OF METHANE-

Methane volume (m^3):                   24.5528

Volume of carbón dioxide (m^3):         20.981

Amount of methane in the mixture (%):   53.9222

Write the Word "OK" to repeat the calculation
```

Nomenclature

$\dot{m}$ mass flow rate, kg/s
c specific heat, J/(kg K)
h heat transfer coefficient, W/(m^2 K)
ΔT temperature difference within the digester, °C
$\dot{Q}$ heat flow rate, W
U overall heat transfer coefficient, W/(m^2 K)
U_L overall heat transfer coefficient of solar collectors; W/(m^2 K)
T_{ref} refence temperature; 100°C
$\overline{T_a}$ monthly overall temperature of the zone to evaluate; °C
A_c solar collector área; m^2
$\overline{H_t}$ Solar overall radiation on the solar collector area; W/m^2
$\overline{\tau\alpha}$ monthly overall of transmitance – absortance product of the collector
F_R collector-heat removed factor
N number of the day of the months
X relation between total energy loss for the solar collector to the environment and total heat load
Y relation between absorbed energy for the absorbed plat of the solar collector and total heat load

References

[1] Barbosa J. G. Método de diseño de sistemas solares para calentamiento de agua. Tesis de Maestría, 1999. Instituto Politécnico Nacional, SEPI. ESIME. 151p.

[2] Cengel Y. A. Transferencia de calo y masa. Tercera edición, 2007, 970p.

[3] Couper J. R., Fair J. R., Penney W. R. (2010). Chemical process equipment. Butterworth-Heinemann is an imprint of Elsevier, 166-164, 121, 134. 730 p.

[4] Duffie J. A., Beckman W. A. (2006). Solar engineering of thermal processes. Ed. Wiley Intersciencie publication, USA. 908 p.

[5] El-Mashad H. M., Van Loon WKP, Zeeman G.. A model of solar energy utilization in the anaerobic digestión of cattle manure. Biosystems Engineering, 2003. 84(2), 231-238.

[6] Foster C. T. (2005). Digestión anaerobia termofílica seca de residuos sólidos urbanos: estudio de las variables del proceso en el arranque y estabilización del bio-reactor. Tesis Doctoral. Universidad de Cádiz. 421 p.

[7] Guštin S., Marinšek-Logar R. Effect of PH, temperature and air flow rate on the continuos ammonia stripping of the anaerobic digestion effluent. Process Safety and Enviromental Protection 89 (2011) 61-66.

[8] Hamed M. El-Mashad; Wilko K.P. van Loon; Grietje Zeeman (2002). A model of solar energy utilization in the anaerobic digestion of cattle manure. Science Direct, 84 (2), 231–238.

[10] Hottel H. C. (1976). A simple model for estimating the transmitance of direct solar radiation trough clear atmospheres. Solar energy, 18, 129-134.

[11] Kaparaju P., Buendía I., Ellegoard L., Angelidakia I. Effects of mixing on methane production during thermophilic anaerobic digestion of manure: Lab-sacale and pilot-scale studies. Bioresurce Technology, 2008. 4919-4928.

[12] Klein S. A., Beckman W. A., Duffie J. A (1977). Solar heating design by the *f* chart method. Ed., Willey Intersciencie Publication, USA. 636 p.
[13] Mata-Álvarez, J., Macé, S., Llabrés, P. (2000). Anaerobic of organic solid wastes. An overview of research achievements and perspectives. Biores. Techn., 74:3-16.
[14] Romero L. I., Sales D., Galán M. A. Thermophilic anaerobic digestión of winery waste (vinasses): Kinetics and process optimization. Process Biochem 1988. 23 (4), 119-125.
[15] Soteris A. K. (2009). Solar energy engineering; processes and systems. Elsevier, USA, 760p.
[16] SEDESOL-INE. Informe de la situación general en materia de equilibrio ecológico y protección al ambiente. México, 1994. 220p.
[17] Tovar L. R., Castro R. A., Gutiérrez M. E., Estrada R. What if the organic fraction of the wholesale central market of Mexico city (Central de abastos del D.F.) is anaerobically digested?. Proceedings Venice 2010, Third International Symposium on Energy from Biomass and Waste Venice, Italy.
[18] Van Lier J. B. Thermophilic anaerobic waster water treatment; temperature aspects and process stability. PhD Thesis, 1995. Wageningen Agricultural University. Wageningen, The Netherlands.

Economic feasibility of PV systems in hotels in Mexico

Augusto Sánchez Cifuentes[a], Sergio Quezada García[b]

[a] *UNAM, Mexico, D. F., augsan@servidor.unam.mx, CA*
[b] *UNAM, Mexico, D. F., sequga@gmail.com*

Abstract:
In this study, the hotels located in Mexico, with energy demand over 100 kW are analyzed to determine the conditions for which it is profitable to produce their own electricity through photovoltaic panels. The electric tariff paid by hotels, has different prices for electricity during the day, i.e., is consider the hour of day in which electrical energy is consumed and the maximum demand that is taken in the month.
By using HOMER software, economic profitability is analyzed under different levels of solar radiation and demand curve to energy electricity in hotel.
The result shows that only for the hotels located in regions with higher solar radiation in Mexico the use of photovoltaic panels is profitable. During the study, one of the most important factors to profitability is the time of day that peak demand comes. However, when making a future projection of the electricity tariff, if they keep raising the price of electricity as in recent years, in early 2014 photovoltaic panels could be the best choice for hotels in most parts of the country.

Keywords:
Hotel, photovoltaic, Mexico

1. Introduction

Mexico has very favorable natural conditions for the application of photovoltaic systems. In many parts of its vast territory, the average solar radiation is twice that of European countries like Germany [1], which is now one of the largest PV markets in the world.

Given the limited information currently available, regarding the financial feasibility of PV systems connected to the grid in Mexico, in this paper examines whether the use of photovoltaic systems in hotels, with energy demand greater than 100 kW (kilo-watt), enables cost savings from the perspective of an investor, compared with the purchase of all electricity to the national grid.

To perform the analysis is used the Homer software.In this study, is limited to analysis of photovoltaic systems as an alternative to the purchase of electricity to the national grid.Other measures and technologies, such as energy efficiency or other renewable energy technologies are not considered.

2. Regulatory framework

In 2001 is approved by the *Regulatory Commission for Energy* (CRE - ComisiónReguladora de Energía) the "interconnection agreement for renewable energy source or system on a small scale cogeneration"that allows users to general use, install a maximum power generation of 30 kW produced by renewable energy source under the regime of *Net Metering* energy. In 2004 comes into force amendments to the *Law on Income Tax* (Ley del ImpuestoSobre la Renta), which states that taxpayers who invest in machinery and equipment for power generation from renewable sources, can deduct 100% of the investment in a single year [2].

3. Electric tariff H-M

The Tariff H-M (Horaria-Media Tensión, Time-MV), applies to energy services intended for any use, supplied at medium voltage, with a demand of 100 kW or greater [3]. This tariff is applied to hotels that are studied in this work.

The tariff has a charge by energy maximum demand (refers to the maximum power demanded, measured in kilowatt, it is considered from keeping it for 15 minutes) and charges for energy consumed in time: *peak*, *intermediate* and *base*; therefore, the energy does not have the same cost during the day.Table 1 shows the different fees for this tariff.

Table 1. Charges averages for tariff H-M for January 2012.

Charges for energy maximum demand ($/kW[1])	Charges for energy consumption in *peak*($/kWh[2])	Charges for energy consumption in *intermediate* ($/kWh)	Charges for energy consumption in *base* ($/kWh)
191.79	2.0206	1.2876	1.0332

The annual increase in maximum demand charges in the last three years is on average 4.12%,for energy in *top* is 8.33%, for energy in *middle* 12.61%, for energy in *base* 12.14%.

Figure 1 show the different periods of *peak*, *intermediate* and *base* for a long of the year, summer and not summer. The base period is from 00:00 hours until 06:00 throughout the year; the *peak* period, in not summer, is from 18:00 to 22:00 hours, while for summer season from 20:00 to 22:00; the rest are *intermediate* period.

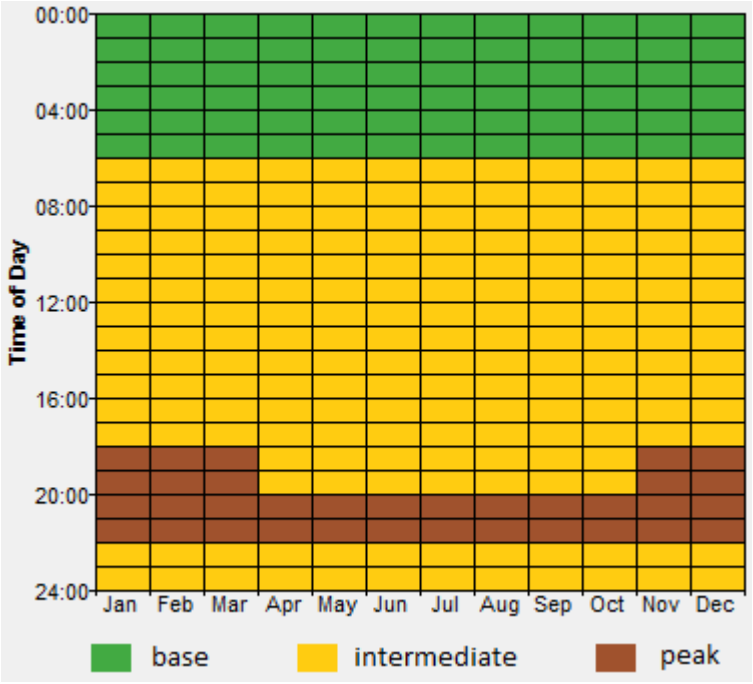

Fig. 1. Periods: peak, intermediate, and base, during the year.

[1]Mexican pesos/kilo-watt
[2]Mexican pesos/kilo-watt-hour

4. Methodological considerations and scenarios

Homer is energymodeling software for hybrid renewable energy systems, i.e., is a powerful tool for designing and analyzing hybrid power systems. In this work, Homer is used to analyze the financial viability of PV systems installed in hotels with electrical tariff H-M. Homer allows changing values such as: solar radiation, energy consumption, equipment price and equipment capacity, to name a few, is also possible to establish a minimum rate of return for consider financially feasible the installation of the photovoltaic system.

For the analysis is performed simulation in Homer by considering the following aspects:

- In the present study is considered financially feasible a PV system, if get an internal rate of return equal to or greater than 6%.
- Costs due to machinery and equipment in a PV system is about 65% of the total investment, therefore, this is the percentage that can be deducting with the Income Tax (Impuestosobre la renta – ISR).
- Radiation values are taken between 4 and 6 kw/m^2/day, since this radiation in the Mexican territory [4].
- PV system is 30 kW and is connected to the national grid.
- Interconnection is regulated by the principle of *Net Metering* energy, allows offset the cost of the electricity used by the energy supplied to the national grid.
- The price of installing a photovoltaic system is average 40 $/ W, identified in a market survey for the summer of 2011, if 65% is deducted from this price, the real price of the installation is 14 $/W.
- Lifetime of a solar panel is 25 years and the converter is 15 years.

When these values are introduced in Homer are obtained graphs showing the conditions under which it is profitable to install PVsystems.It is noteworthy that this study is valid only for buildings that have energy demand curves similar to those discussed below.

Some studies [1,5] shown that the financial viability of PV systems depend mainly on the energy consumption, solar radiation and PV system price; therefore the graphs made in this paper illustrate the behavior of these three variables.

We study two hotels with energy demand over 100 kW, for which two scenarios are taken:

Scenario 1 "present tariff": At current prices of PV systems,prices peak demand and energy by January 2012 for tariff H-M.

Scenario 2 "future tariff": With the price of photovoltaic systems for summer 2011 and prices for the tariff expected for January 2014, in Table 2 are reported these prices.

These scenarios are considered for study the economic viability of photovoltaic systems in the present (scenario 1) and for projection of economic viability with expected prices of electrical energy in near future (scenario 2).

Table 2. Tariff prices for the two scenarios

	Charges for energy demand ($/kW[3])	Charges for energy *peak* ($/kWh[4])	Charges for energy *intermediate* ($/kWh)	Charges for energy *base* ($/kWh)
Scenario 1	191.79	2.0206	1.2876	1.0332
Scenario 2	207.92	2.3711	1.6327	1.2993

5. Analysis of PV systems

We analyze two hotels which have different demand curves of electricity.Figure 2 shows the energy demand curves for each hotel, in the property ***a*** the peak demand of energy occurs from 16:00 to 18:00 hours, while for the property ***b*** the maximum demand of energy occurs from 17:00 to 19:00 hours, therefore the hotel ***a*** has no maximum demand in the peak hours, while for ***b***there is maximum demand in peak hours.

The energy demand curves for each hotel are formed from data measured on the property for a month every 20 minutes.The hotels are located in Mexico and were measured by the National Autonomous University of Mexico.

5.1. Scenario 1

Figure 3 shows the results of the simulation carried out in Homer,for hotel***a***,the right axis shows the maximum price that can be paid by the photovoltaic system to make it profitable to install,as seen with increasing solar radiation the price you can pay for the system is greater.

Figure 4 shows the results of the simulation carried out for the hotel***b***, the right axis shows the maximum price you can pay for the system for this is even profitable. As with the hotel***a***, with increasing solar radiation can be paid a higher price for the system, can also see that both hotels the consumption level of energy is not relevant to the study, because, for different energy consumption and the same solar radiation, the maximum price arrangement is the same.

Contrary to expectations, for these two hotels the level of energy consumption (x-axis) does not affect the financial viability of PV systems, i.e., the financial viability of PV systems is not a function of energy consumption, is depends mainly on solar radiation and the total price of the array.

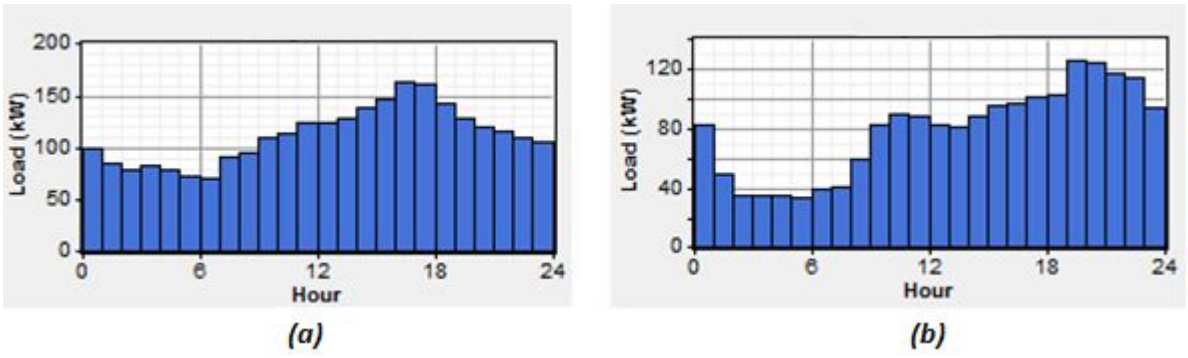

Fig. 2. Daily profile for each hotel.

[3]Mexican pesos/kilo-watt
[4]Mexacan pesos/kilo-watt-hour

The results for the two hotels are very similar, although it is a bit more profitable system in the hotel***a***, is due the peak demand of energy occurs earlierand may cover some of this demand with the PV system.

At current prices of PV systems,installation is profitable, if you subtract part of initial investment of the Income Tax (ISR) and has a solar radiation in the area greater than 4.65 kWh/m^2/day.

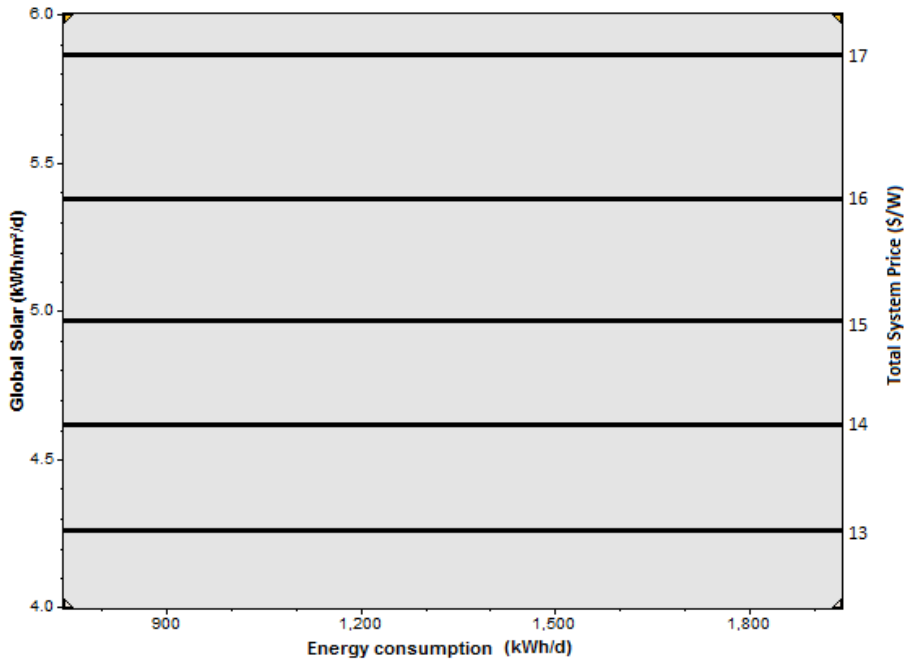

Fig. 3.Analysis of the photovoltaic system for the hotel ***a****.*

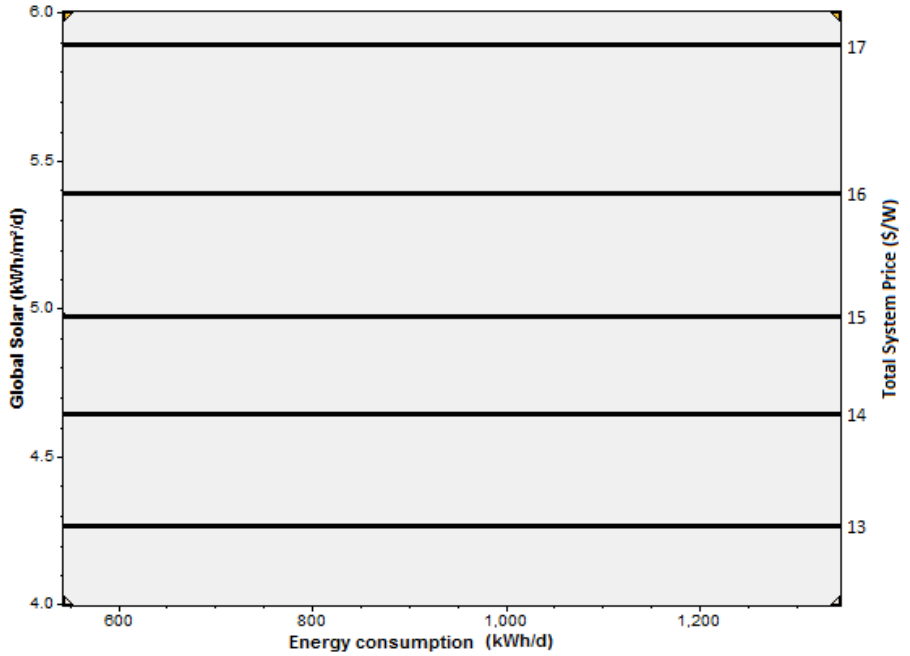

Fig. 4.Analysis of the photovoltaic system for the hotel ***b****.*

5.1. Scenario 2

Making a future projection is repeated the study for both hotelswith priced electrical tariffs that are expected for 2014.

Figures 5 and 6 show the results obtained in the simulation to the hotel ***a***and***b*** respectively.As in the previous scenario the results are similar for both hotels, does not influence the energy consumption in the project's profitabilityand as solar radiation increases the maximum price you can pay for the system increases.

If there is no change in the prices of the system and have no change in the Law of Income Tax,for hotels that subtract part of the investment with the Income Tax, the installation of systems photovoltaic will be profitable, area regardless of the country where they are located.

Comparing the two scenarios is clear that the financial viability of PV systems is affected by the price of energy in the electricity tariff, i.e., with increasing prices of energy also increases the maximum price of the PV system with which is profitable yet.

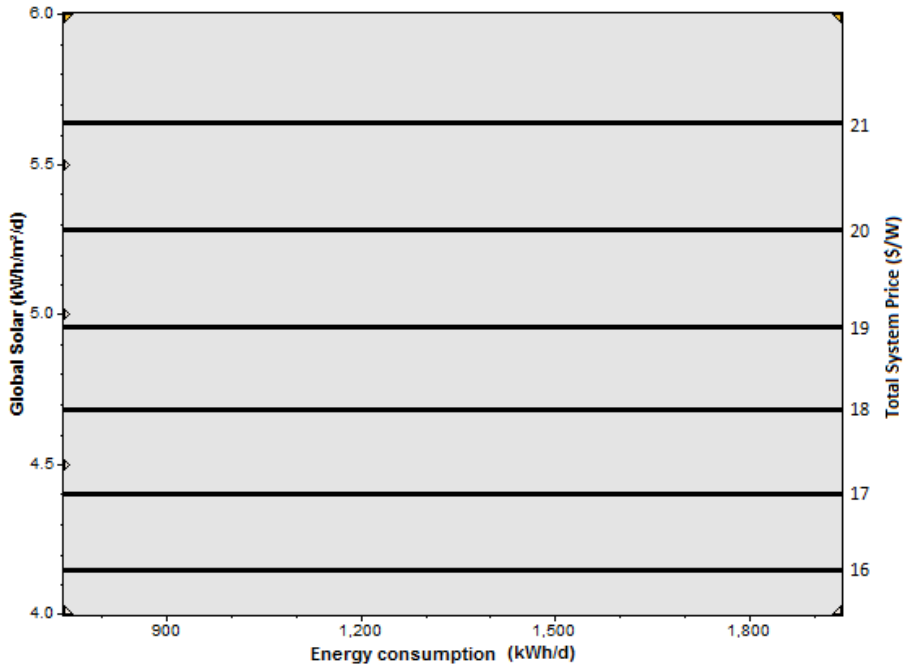

*Fig. 5.Analysis of the photovoltaic system for the hotel **a** with the expected electricity tariff in January 2014.*

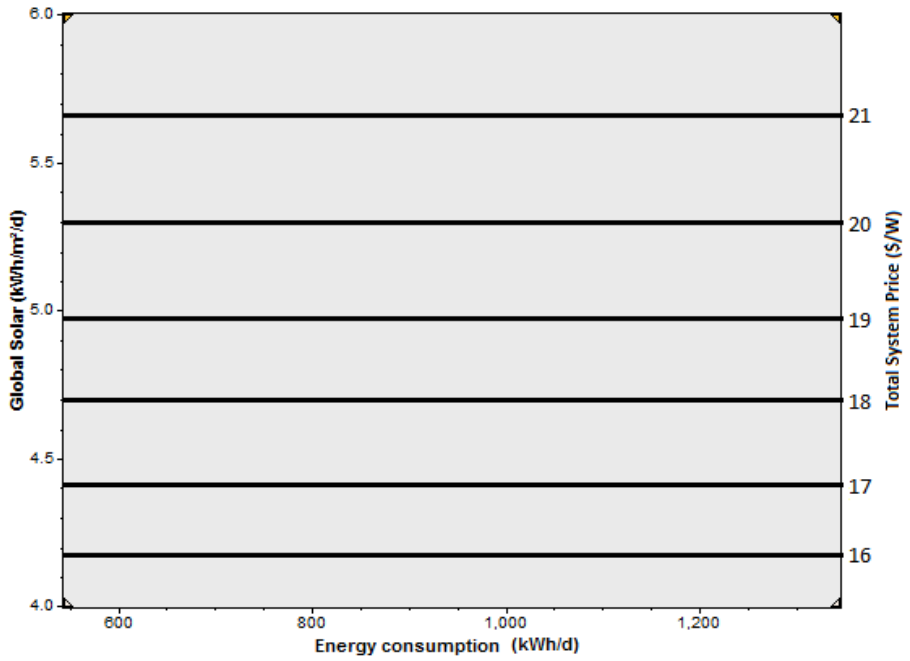

Figure 5.Analysis of the photovoltaic system for the hotel ***b*** *with the expected electricity tariff in January 2014.*

6. Conclusions

The financial viability of PV systems is not affected by the level of energy consumption in hotels, i.e., the financial viability of PV systems depends mainly on solar radiation in the area and the total system price.As seen in Figures 3 to 5, a given solar radiation has a maximum price of the system which remains constant for all levels of power consumption.This is true only for hotels with tariff H-M.

Comparing the two scenarios can be seen that as the price of energy from the grid grows the maximum price of the photovoltaic system can be greater and therefore becomes more viable economically, i.e., the price of electricity from the grid Electricity is directly proportional to the financial viability of PV systems.

At current prices of PV systemsis profitable installation in hotels that cover the tariff H-Mthat found in areas where average solar radiation in the year is higher than 4.65 kWh/m^2/day, regardless of the level of energy consumption, is a little more profitablefor those hotels that can meet peak demand of energy with the photovoltaic system.

If you continue the current trend in the electrical tariff increase,by January 2014, will be economically feasible to install photovoltaic systems in hotels located in any area of Mexico.

References

[1] CONUEE, *Nichos de mercado para sistemas fotovoltaicos en la conexión con la red eléctrica en México*, 2009

[2] Diario Oficial de la Federación(2004). Fracc. XII, Art. 40, *Ley del Impuesto sobre la Renta*, México.

[3] CFE - The official web site of the ComisiónNacional de Energía. Available at: <http://www.cfe.gob.mx/Paginas/Home.aspx>.[accessed 4.1.2012].

[4] ECOTEC – ECOTECSA S.A. de C.V. Available at: <http://www.ecotec2000.de/espanol/sun-7.htm> . [accessed 4.1.2012].

[5] Quezada S. Análisis de la rentabilidad económica de producir energía eléctrica en el sector residencial y comercial por medio de paneles solares y aerogeneradores en México. Tesis, Facultad de ingeniería. 2011.

Effect of a back surface roughness on annual performance of an air-cooled PV module

Riccardo Secchi[a], Duccio Tempesti[a], Jacek Smolka[b]

[a] Università degli Studi di Firenze, Dipartimento di Energetica "Sergio Stecco", Florence, Italy, riccardo.secchi@unifi.it
[b] Institute of Thermal Technology, Silesian University of Technology, Gliwice, Poland, jacek.smolka@polsl.pl

Abstract:

In this paper, a study of increasing a photovoltaic (PV) module efficiency via natural/forced cooling of the PV cell is presented. The PV module is cooled by the air flowing in a duct placed under a back surface of the PV panel. The cooling air is moved either by fan or naturally by the temperature difference generated from the heat transfer with a panel. The system could be applied on the roof of industrial facilities, with electrical and thermal energy needs. The presented 1-D model examines an already published thermal and electrical PV/T approach supplemented with a radiative heat transfer in the panel duct. In addition, an effect of the roughness of the panel back surface is also added to the model. The model coded in an Engineering Equation Software (EES) is capable of evaluating the PV module efficiency and other thermal parameters as the outlet air temperature and back surface temperature. As a result, the performance of the system in a typical winter and summer day is discussed. Furthermore, an annual simulation of the system is also analysed coupling the EES® model with the Trnsys software. The results of the annual simulation show that the raise of the relative roughness of the panel back surface from 0 to 0,05 leads to an increase of 0.25% of the average efficiency of the PV module in case of air moved by a fan. In terms of overall efficiency, this result means a relative improvement of 1.73%. Annual average thermal efficiency of the PV/T system of 28.6% is achieved for relative roughness of the panel back surface set to 0.05.

Keywords:

Solar photovoltaic thermal (PV/T) air collector, heat transfer, system optimization.

1. Introduction

In Europe, the solar photovoltaic (PV) electricity generation capacity has increased 160 times from 185 MW in 2000 to 29.5 GW in 2010 [1]. This is mainly due to the public support programs for renewable energies, which usually consist of feed-in tariffs for the new installed PV systems. Since only a small fraction of the incident solar radiation is used by the PV cells to generate electricity, the PV module efficiency is in the range of 4-17% depending on the type of solar cells and the working conditions. This means that at least 50% of the incident solar energy is mainly turned into heat in the cells and substrate, leading to two consequences: (a) a drop in cell efficiency (usually 0.4% per °C increase for c-Si cells) and (b) a permanent structural damage of the module if the thermal stress persists for extended period [2]. In solar photovoltaic thermal (PV/T) collector, the PV module is cooled by air or water, producing thermal and electrical energy simultaneously. The higher efficiency leads to a higher production of the system, which causes an increase in the economic incomes from the feed-in tariff for the PV system holder. In addition, the heated cooling flow rate (air or water) can be used both for domestic heating and production of hot water. For these reasons, in the last 40 years a lot of studies (theoretical as well as experimental) on the PV/T systems has been carried out. Kern and Russel [4] presented the design and the performance of water and air cooled PV/T systems, while Florschuetz [5] included the PV/T modelling in his

works. Garg and Adhikari [6] presented a variety of results regarding the effect of design and operational parameters on the performance of the air type PV/T systems. Hegazy [7] investigated glazed photovoltaic/thermal air system for a single and a double pass air heater for the space heating and drying purposes. Kalogirou [8] modelled the hybrid photovoltaic/thermal (water) solar energy system with TRNSYS and the simulations carried out for Nicosia (Cyprus) showed an increase of the mean annual efficiency of the PV solar system from 2.8% to 7.7% with the thermal efficiency of 49%. Zondag et al. [9] developed a range of steady–state and dynamic simulation models for the PV/T (water) energy performance analysis that included 1-D, 2-D and 3-D models of the serpentine PV/T collector (their accuracy was verified by experimental data). Tiwari et al. [10] validated the theoretical and experimental results for the photovoltaic (PV) module integrated with an air duct for a composite climate of India and concluded that the overall thermal efficiency of PV/T system is significantly increased due to utilisation of thermal energy from the PV module. Dubey et al. [14] studied different configurations of the glass-to-glass and the glass-to-tedlar PV modules. Analytical expressions for electrical efficiency with and without airflow were developed as a function of climatic and collector design parameters. Experiments that were performed at the Indian Institute of Technology, Delhi showed that the glass-to-glass type achieves higher supply air temperature and electrical efficiency. By the use of validated theoretical models, Tonui and Tripanagnostopoulos [16] studied a degree of improvement by adding suspended metal sheet at the middle of the air channel and the finned arrangements at the opposite wall of the air channel. It was found that these low-cost improvements are more effective at small collector length, and can be readily applied to PV/T (air) installations. On the other hand, an effect of the channel depth, mass flow rate or system length on the fan power consumption was found small.

In this study, on the basis of the PV models developed by Tiwari et al [10,15], and Tripanagnostopoulos and Tonui [16], a theoretical steady state 1-D model including a convective and radiative heat transfer in a panel duct is developed with the EES software [19]. In addition, the annual gain in energy production of the investigated system is modeled integrating the EES model with TRNSYS that is a transient simulation program, and using typical meteorological year (TMY) conditions data for the central Italy. Furthermore, an effect of the roughness of the back surface on the PV module effectiveness is also investigated. Finally, the results of the cooling of the PV module through air moved by fan or naturally flowing are presented.

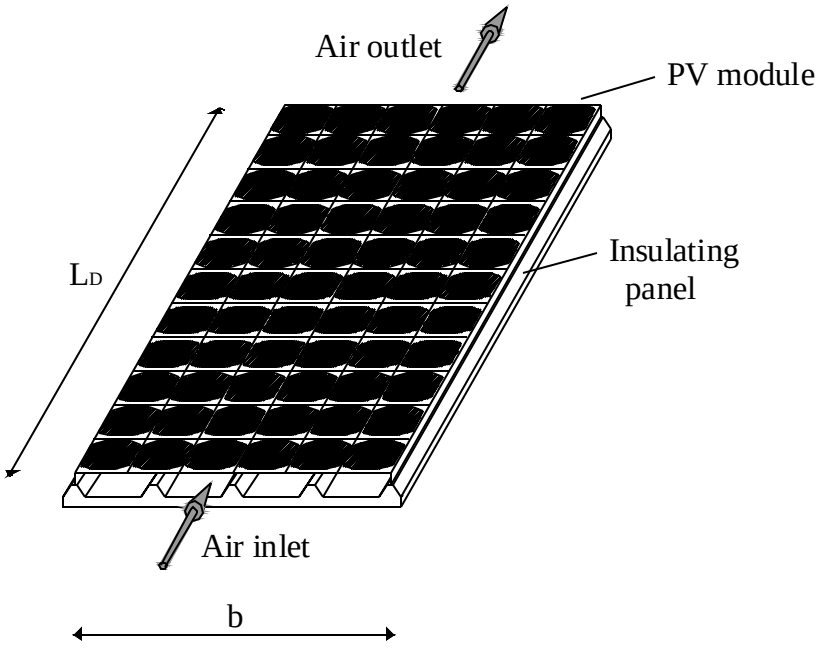

Fig.1 Perspective view of the hybrid PV/T system studied.

2. Configuration of PV/T hybrid system

The specific configuration of the hybrid PV/T system that has been studied consists of a photovoltaic module installed on industrial shed roof. A typical configuration of the system is shown in Fig.1. For such system, a 1-D thermal model was formulated based on a models reported in literature [10,11,13,14,15]. The energy balance equations have been modified taking into account the irradiation between the back surface of the PV module and the opposite wall of the duct.

Fig.2 shows a simplified cross-sectional view of the PV/T air collector that is composed of three layers. Furthermore, the equivalent thermal resistant circuit of the system discussed in Section 2.1 is also illustrated in Figure 2.

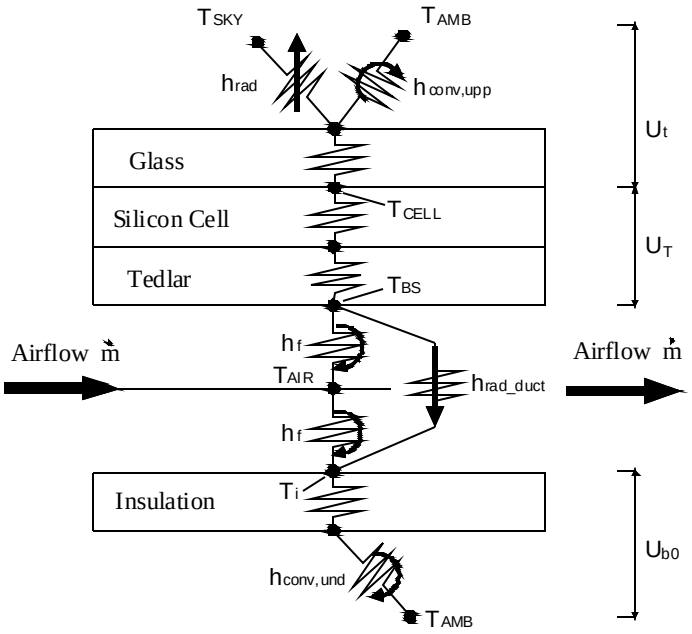

Fig.2 Thermal resistance circuit diagram for PV/T system.

2.1. Energy balance for PV/T hybrid system

In order to formulate the energy balance equations for each component of PV/T hybrid system, the following assumptions have been made:

- The heat conduction is one-dimensional (only along the height of the module).
- The temperature of the model layers is uniform.
- The system is in quasi-steady state.
- The ohmic losses in the solar cell are negligible.
- Air flow in the duct between a tedlar layer and insulating structure is one-dimensional.

To determine the temperatures of solar cells and then the efficiency of the considered system, four energy balance equations need to be written.

According to Fig.2, one can write the equation describing the overall heat transfer from the top of the module to the ambient below the insulation in a form:

$$\tau_G \cdot \left[\alpha_{CELL} \cdot p \cdot I + (1-p) \cdot \alpha_T \cdot I\right] \cdot b \cdot dx = \left[U_t \cdot (T_{CELL} - T_{AMB}) + U_T \cdot (T_{CELL} - T_{BS})\right] \cdot b \cdot dx + \alpha_{CELL} \cdot \eta_{CELL} \cdot p \cdot \tau_G \cdot I \cdot b \cdot dx \quad (1)$$

where the terms in Eq. (1) are the following:

$$\begin{bmatrix}\text{1 - The rate of solar}\\ \text{energy available}\\ \text{on solar cell}\end{bmatrix} = \begin{bmatrix}\text{2 - An overall heat}\\ \text{loss from top}\\ \text{surface of cell}\\ \text{to ambient}\end{bmatrix} + \begin{bmatrix}\text{3 - An overall heat}\\ \text{transfer from cell}\\ \text{to backsurfac e of tedlar}\end{bmatrix} + \begin{bmatrix}\text{4 - The rate of}\\ \text{electrical energy}\\ \text{produced}\end{bmatrix}$$

The second energy balance equation describes the heat transfer for back surface of tedlar:

$$U_T \cdot (T_{CELL} - T_{BS}) \cdot b \cdot dx = h_f \cdot (T_{BS} - T_{AIR}) \cdot b \cdot dx + h_{RAD_DUCT} \cdot (T_{BS} - T_I) \cdot b \cdot dx \quad (2)$$

where the terms in Eq. (2) are the following:

$$\begin{bmatrix}\text{3 - An overall heat}\\ \text{transfer from cell to}\\ \text{back surface of tedlar}\end{bmatrix} = \begin{bmatrix}\text{5 - The rate of heat trans fer}\\ \text{from back surface of the}\\ \text{tedlar to flowing fluid}\end{bmatrix} + \begin{bmatrix}\text{6 - The rate of heat}\\ \text{transfer from back surface of}\\ \text{tedlar to insulation upper surface}\end{bmatrix}$$

The next equation is the overall duct energy balance:

$$h_f \cdot (T_{BS} - T_{AIR}) \cdot b \cdot dx + h_{RAD_DUCT} \cdot (T_{BS} - T_I) \cdot b \cdot dx = \dot{m}_{AIR} \cdot C_{AIR} \cdot \frac{dT_{AIR}}{dx} \cdot dx + U_{b0} \cdot (T_I - T_{AMB}) \cdot b \cdot dx \quad (3)$$

where the terms in Eq. (3) are the following:

$$\begin{bmatrix}\text{5 - The rate of heat trans fer}\\ \text{from back surface of}\\ \text{the tedlar to flowing fluid}\end{bmatrix} + \begin{bmatrix}\text{6 - The rate of heat}\\ \text{transfer from back}\\ \text{surface of tedlar}\\ \text{to insulation}\\ \text{upper surface}\end{bmatrix} = \begin{bmatrix}\text{7 – The mass}\\ \text{flowrate of}\\ \text{flowing fluid}\end{bmatrix} + \begin{bmatrix}\text{8 – An overall heat}\\ \text{transfer from upper}\\ \text{surface of insulation}\\ \text{to ambient}\end{bmatrix}$$

Finally, the fourth energy balance equation for the upper surface of insulation can be written as:

$$h_{RAD_DUCT} \cdot (T_{BS} - T_I) \cdot b \cdot dx = U_{b0} \cdot (T_I - T_{AMB}) \cdot b \cdot dx + h_f \cdot (T_I - T_{AIR}) \cdot b \cdot dx \quad (4)$$

where the terms in Eq. (4) are the following:

$$\begin{bmatrix}\text{6 - The rate of heat trans fer}\\ \text{from back surface of tedlar}\\ \text{to insulation upper surface}\end{bmatrix} = \begin{bmatrix}\text{8 – An overall heat}\\ \text{transfer from upper surface}\\ \text{of insulation to ambient}\end{bmatrix} + \begin{bmatrix}\text{9 - The rate of heat trans fer}\\ \text{from upper surface of insulation}\\ \text{to flowing fluid}\end{bmatrix}$$

The mathematical transformations to obtain the explicit formulation for all temperatures are described in Appendix A. In addition, the relations used in Eqs (1)-(4) for the heat transfer

coefficients, and the assumptions adopted for the calculation of the radiative heat transfer coefficient are given in Appendix B.

In order to calculate the temperature-dependent electrical efficiency of the PV module, the following expression has been used [17,24]:

$$\eta_{CELL} = \eta_{REF} \cdot \left[1 - \beta \cdot \left(T_{CELL} - T_{REF}\right)\right] \quad (5)$$

The rate of thermal energy obtained from the hybrid system is:

$$\dot{Q}_U = \dot{m}_{AIR} \cdot C_{AIR} \cdot \left(T_{AIR}(L_D) - T_{AIR_IN}\right) \quad (6)$$

The thermal efficiency of the PV/T system has been calculated using the following equation:

$$\eta_{TH} = \frac{\dot{Q}_U}{b \cdot L_D \cdot I} \quad (7)$$

2.2 Roughness of back surface of PV panel

In order to obtain a larger temperature drop of photovoltaic cells, the heat transfer between the back surface of the PV module and the air flowing in the duct should be improved.

The convective heat transfer coefficient (h_f), which identifies the amount of heat exchanged between the module and the air flow rate, has been calculated by means of an internal function of the software EES called *"ductflow"* [19,21]. This function calculates the Nusselt number and the friction factor, and then uses these values to evaluate the pressure drop along the duct and the mentioned convective heat transfer coefficient. The input parameters of that function are: the size of the duct (width, height, length), the average airflow temperature, pressure, the air mass flow rate and Relative Roughness (RR).

The RR (roughness related to hydraulic diameter of the duct) can be between 0 and 0.05. The boundary of RR range (i.e. 0 and 0.05) have been considered to test a possible gain in terms of the net electrical efficiency of PV module, taking into account that the energy consumption to move the air flow rate raises at RR=0.05.

3. Results and discussion

3.1 Roughness influence

The governing equations have been initially computed with EES software to evaluate the behavior of the system in two steady-state weather reference conditions:

1. Italian Winter : I = 600 W/m^2 , T_{AMB} = 283 K.
2. Italian Summer : I =1000 W/m^2 , T_{AMB} = 308 K.

In order to simulate less advantageous heat removal conditions from the upper surface of PV/T system, in both cases the wind speed, that directly affects the convective heat transfer coefficient on upper surface of PV module, according to Equation B.2, has been considered to be zero (V_w = 0 m/s).

The aim of these simulations was to find the value of airflow velocity that would maximises the net power gain between RR=0 and RR=0.05.

The operating and design parameters of the PV/T air system used in the model simulations are described in Table 1. Fig.3 shows the electrical efficiency variation as a function of the air flow velocity in a duct for all the four cases considered (summer, winter, roughness considered or neglected).

Table 1. Design parameters of the PV/T air system [11].

PV/T air hybrid system parameters	***Value***
Length of PV module and air duct, L_D	2 m
Width of PV module, b	1.143 m
Thickness of glass cover, L_G	0.003 m
Conductivity of glass cover, K_G	1 W/(mK)
Transmittivity of glass cover, τ_G	0.95
Emissivity of glass cover, ε_G	0.88
Absorptivity of solar cell, α_{CELL}	0.85
Thickness of solar cells, L_{CELL}	300×10^{-6} m
Conductivity of solar cells, K_{CELL}	0.036 W/(mK)
Absorptivity of tedlar, α_T	0.5
Thickness of tedlar, L_T	0.5×10^{-3} m
Conductivity of tedlar, K_T	0.033 W/(mK)
Emissivity of tedlar, ε_T	0.87
Emissivity of insulation upper surface, ε_I	0.1
Thickness of tedlar, L_I	0.05 m
Conductivity of insulating panel, K_I	0.035 W/(mK)
Equivalent duct depth	0.0782 m
Packing factor of solar cells, p	0.83
Electrical efficiency at Standard Conditions, η_{REF}	0.1446
Solar cells temperature at Standard Conditions, T_{REF}	298 K
Solar radiation intensity at Standard Conditions, I_{REF}	1000 W/m^2

In winter reference conditions, the lower ambient temperature leads to a higher electrical efficiency. Furthermore, for RR=0.05, an air flow speed of 2 m/s is sufficient to obtain the maximum efficiency.

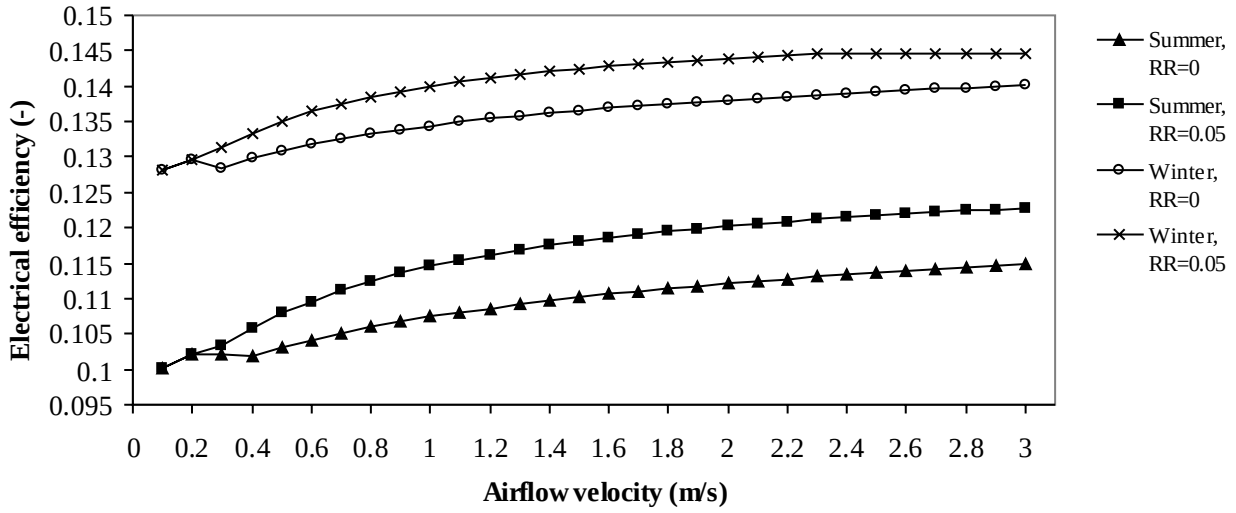

Fig. 3. Electrical efficiency for RR=0 and RR=0.05, for summer and winter weather reference conditions.

The effect of the roughness cannot be determined for average air flow speed lower than 0.2 m/s, because the Reynolds number is too low at that speed (see overlapped curves in Fig.3).

In Fig.4, the power gains between the configuration with RR=0 and RR=0.05 for both reference conditions are shown. The gap of power gains between summer and winter shown in Fig.4 include the power costs for ventilation, given by the total pressure drop in the duct, in accordance with the following equation:

$$W_{FAN} = \frac{1}{0.6} \cdot \frac{\dot{m}_{AIR}}{\rho_{AIR}} \cdot \Delta P \tag{8}$$

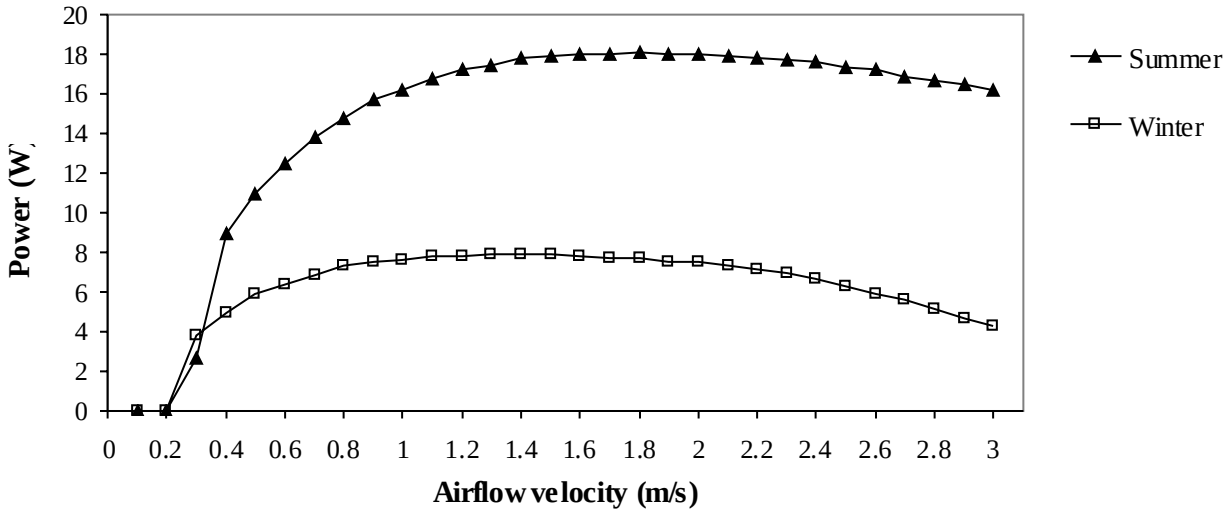

Fig. 4. Net power gains (in Watt) between RR=0 and RR=0.05 for summer and winter weather reference conditions.

An airflow velocity equal to 1.5 m/s, which is a mean value between the optimum of the single reference conditions, is considered the optimum value for the annual simulation.

The convective (h_f) and radiative (h_{RAD_DUCT}) heat transfer coefficients are the key parameters that affect the heat transfer inside the duct. For this reason, they are extracted from the results and shown in Table 2.

Table 2. Convective (h_f) and radiative (h_{RAD_DUCT}) heat transfer coefficients for RR=0 and RR=0.05 obtained for summer and winter weather reference conditions.

	Summer		*Winter*	
	RR=0	*RR=0.05*	*RR=0*	*RR=0.05*
h_f , W/(m^{2}K)	7.797	22.170	8.190	24.110
h_{RAD_DUCT} , W/(m^{2}K)	0.790	0.733	0.578	0.546

3.2 Comparison with the literature models

The differences between the proposed model and the two literature models used as a basis for this study are the following:

- Tripanagnostopoulos and Tonui - The upper layer of the model is considered to be composed of only glass and PV cells, which cover the entire surface. Thus, there is no distinction between the

fraction of solar radiation, which impacts the PV cells and the one that strikes the spaces between the cells. Furthermore, a consequence of this assumption concerns the calculation of temperatures in the different layers of the model: no distinction is made between the temperature of the PV cells and that of the back surface of Tedlar. As a result, the model one equation.

Another important assumption concerns the airflow temperature, which is assumed to vary linearly in the flow direction. Tan and Charters [18] correlation is used to compute Nusselt number and the resulting the forced convection heat transfer coefficient in the air channel. The friction factor that is needed for the calculation of the pressure drop along the duct, is calculated from the equations given by Incropera and DeWitt [23].

- Tiwari at al. - Radiative heat transfer in the air duct is neglected. In consequence, the temperature of the insulation upper surface is not calculated and the model is reduced by one equation. The convection heat transfer coefficient inside the duct has been originally assumed to be a constant value, but in recent works [11] is calculated according to flow regime and its Nusselt number (no information is given in [11] about the formulas used).

The three models have been tested with the design parameters of the present study in order to compare the values obtained for layer temperatures and other basic parameters of the PV/T system. The comparison is shown in Tables 4 and 5 for winter and summer reference conditions, respectively.

Table 4. Comparison of simulations results obtained with the three different models, for winter reference condition ($T_{AMB}=T_{AIR\ IN}=283$ K, $I=600$ W/m^2, $Vw=0$ m/s), Relative Roughness=0, and forced circulation with the airflow velocity of 1.5 m/s.

MODEL	$T_{AIR\ OUT}$ (K)	$\overline{T_{AIR}}$ (K)	T_{CELL} (K)	T_{BS} (K)	T_I (K)	h_f (W/(m^{2}K))	η_{EL} -	η_{TH} -	ΔP (Pa)
Tripanagnostopoulos	285.5	284.2	302.4	-	285.5	9.49	0.1417	0.3013	0.54
Tiwari et al.	285.5	284.2	310.8	306.5	-	8.19*	0.1361	0.3023	0.62*
Present work	285.5	284.3	310.1	305.7	285.1		0.1365	0.31	

Table 5. Comparison of simulations results obtained with the three different models, for summer reference condition ($T_{AMB}=T_{AIR\ IN}=308$ K, $I=1000$ W/m^2, $Vw=0$ m/s), Relative Roughness=0, and forced circulation with the airflow velocity of 1.5 m/s.

MODEL	$T_{AIR\ OUT}$ (K)	$\overline{T_{AIR}}$ (K)	T_{CELL} (K)	T_{BS} (K)	T_I (K)	h_f (W/(m^{2}K))	η_{EL} -	η_{TH} -	ΔP (Pa)
Tripanagnostopoulos	312.7	310.4	343.1	-	312.6	9.08	0.1146	0.3178	0.52
Tiwari et al.	312.0	310.0	350.9	344.6	-	7.79*	0.1094	0.2685	0.59*
Present work	312.1	310.1	349.8	343.1	312.8		0.1102	0.2792	

* Since Tiwari et al. [11] gives no information about the formulas used for convective heat transfer coefficient and pressure drop inside the duct, these values have been calculated by means of the EES function "ductflow" like in the present work.

3.3 Annual performance

The annual performance of the system have been simulated with the software TRNSYS, which allows the authors to test the system on the hourly averaged values of a solar radiation, ambient temperature and wind speed that characterize the annual weather conditions of one of many sets in

the software database. As an example, the weather data for *Rome* have been chosen in the present study.

In an annual simulation, the incident radiation on the PV module varies considerably depending on the position of the panel (azimuth, tilt to the horizontal) and the incoming radiation direction. In this simulation, the available radiation on the panel was calculated as a function of the angle of incidence of the three radiation components (direct, diffuse and reflected from the ground) in each time step. Incidence Angle Modifiers (IAM) of each radiation component was determined as a function of the Incidence Angle of the component [20,25].

The PV/T system has been considered oriented to the south with a slope of 30°.

Annual simulations have been performed for the following cases:

1. Natural circulation: the model has been modified so that the flow of air is generated by the temperature difference between the air inside the duct and the surrounding environment. For this configuration, only the simulation with RR=0 is considered.
2. Forced circulation (air average velocity of 1.5 m/s) with RR=0 and RR=0.05.

It is important to point out that in the annual simulations the wind speed values from the database have been used, while in the simulations in steady-state reference conditions the wind speed was fixed to zero. This leads to higher values of electrical efficiency due to the increased heat removal on the upper surface of a PV module. Moreover, the effects of wind are accentuated by the fact that the incoming direction is not accounted for.

The monthly net electrical energy generated by the PV module for all three cases considered is shown in Fig.5. According to this figure, it can be observed that the effects of the forced circulation and non-zero roughness lead to the maximum increase in energy produced that occurs in the months from May to September. Furthermore, Fig.5 shows a difference of the energy produced above 2 kWh between natural convection and convection with RR=0.05, and above 1 kWh between natural convection and forced convection with RR=0.

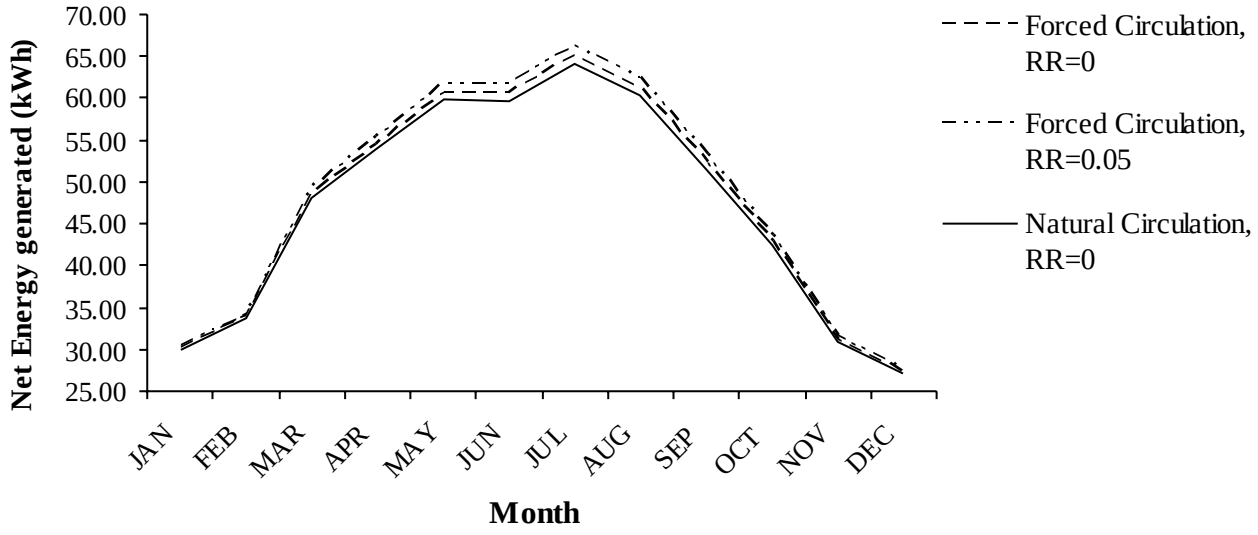

Fig. 5. Monthly Net Energy in kWh generated for natural circulation (RR=0) and forced circulation (RR=0 and RR=0.05).

Fig.6 presents the monthly averaged electrical energy efficiency for all three cases simulated. In this figure, it can be observed that an increase in the electrical efficiency obtained with a forced

circulation is higher in the months from May to September. The difference in the monthly averaged electrical efficiency between the forced convection cases and the natural convection case is shown in Table 3.

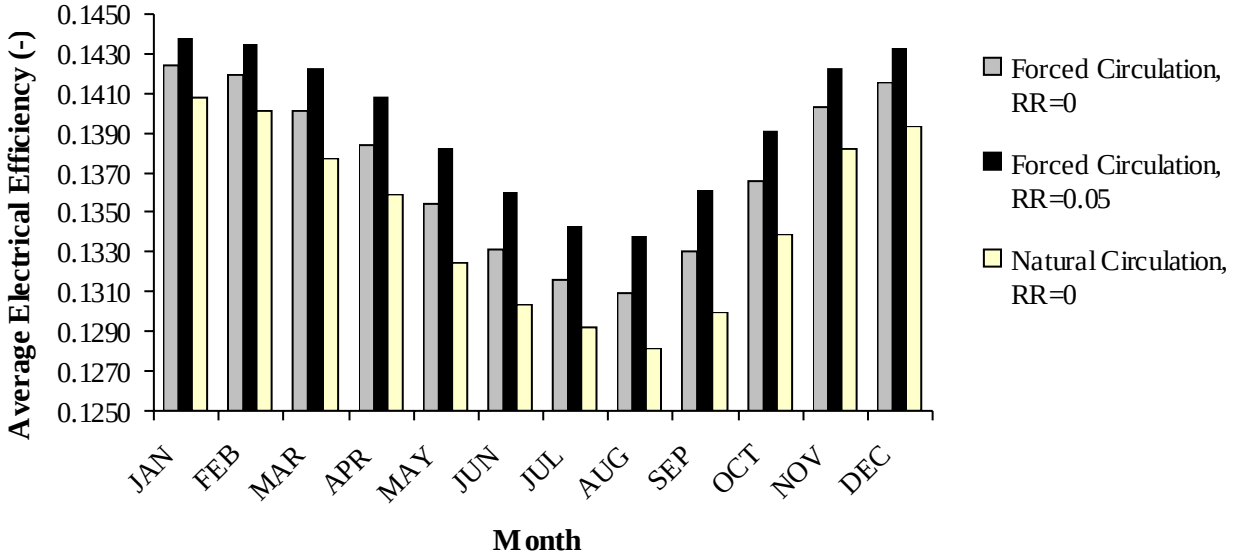

Fig. 6. Monthly averaged electrical efficiency for natural circulation (RR=0) and forced circulation (RR=0 and RR=0.05).

As already shown for the steady-state weather reference conditions, in winter months the increase in electrical efficiency of the PV module is limited, due to the low ambient temperature, which enables the module to naturally work close to its maximum efficiency.

The resulting annual average electrical efficiency are the following:

1. 13.35% for *Natural Circulation*
2. 13.60% for *Forced Circulation and RR=0*
3. 13.85% for *Forced Circulation and RR=0.05*

Table 3. Difference in monthly averaged electrical efficiency between the forced circulation (FC) cases with RR=0 and RR=0.05, and natural circulation (NC) case.

	JAN	*FEB*	*MAR*	*APR*	*MAY*	*JUN*	*JUL*	*AUG*	*SEP*	*OCT*	*NOV*	*DEC*
(FC, RR=0) - (NC)	0.16	0.18	0.25	0.25	0.29	0.28	0.24	0.28	0.31	0.26	0.21	0.22
(FC, RR=0.05) -(NC)	0.29	0.33	0.46	0.49	0.57	0.56	0.50	0.57	0.61	0.52	0.40	0.39

The monthly averaged thermal efficiency for all simulated cases is shown in Fig.7. The air flow velocity under natural circulation reaches the maximum value of 0.4 m/s. Then the thermal energy removed by the air flow results in the annual average thermal efficiency of about 8.3%. The annual average thermal efficiency of about 18.5% is achieved for the forced circulation simulations with

RR=0, due to the air flow velocity of 1.5 m/s. The third configuration (forced circulation, RR=0.05), leads to the maximum increase in annual average thermal efficiency of 28.6%.

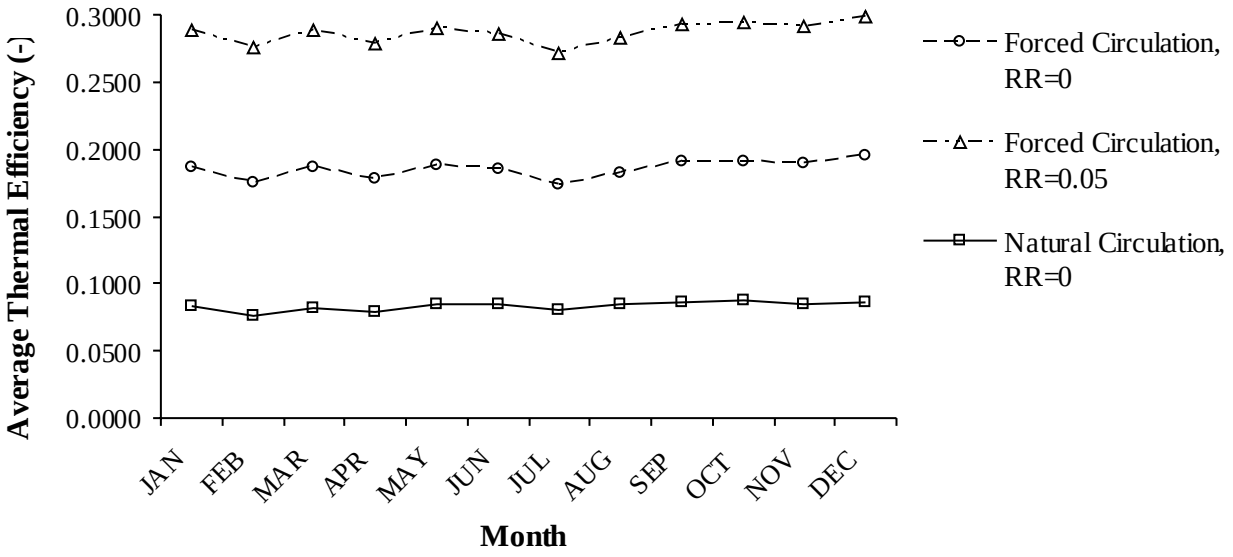

Fig. 7. Monthly averaged thermal efficiency for natural circulation (RR=0) and forced circulation (RR=0 and RR=0.05).

4. Conclusion

In this paper, the electrical and thermal performance of three different configurations of a hybrid PV/T system has been presented. A detailed one-dimensional thermal model was developed to calculate the thermal parameters of the system. The photovoltaic electrical efficiency was calculated using a linear correlation of the solar cell temperature. Numerical simulations concerning the evaluation of the optimal air flow velocity varying the roughness of the back surface of the module were carried out.

From the study the following conclusions can be drawn:

- The airflow velocity that maximizes the net power generated gains between RR=0 and RR=0.05 results is 1.5 m/s;
- For annual simulation, the raise of the relative roughness of the panel back surface from 0 to 0.05 leads to an increase of 0.25% of the annual average efficiency of the PV module in case of air moved by fan. In terms of overall efficiency, this result corresponds to a relative improvement of 1.73%.
- For RR=0, there is a difference of 0.25% in terms of the annual average electrical efficiency between forced and natural circulation configurations.
- The annual average thermal efficiency of the PV/T system increases by 10%, while a natural circulation is replaced with a forced circulation (both with RR=0). With a roughness of 0.05, there is an additional increase of 10%, which leads to an overall annual average thermal efficiency of 28.6%.

This preliminary assessment of the performance of the PV/T system here proposed will be used as a reference solution for the next planned experimental evaluation. However, in terms of power gain (and, finally, in terms of cash earnings from the feed in tariff) the PV/T system proposed is very interesting for industrial facilities with large roof surface, where it can easily be installed.

Appendix A

The mathematical steps for the explicit formulation of all model parameters are reported in this Appendix.

From Eq. (1), the expression for solar cell temperature is:

$$T_{CELL} = \frac{(\alpha\tau)_{EFF} \cdot I + U_t \cdot T_{AMB} + U_T \cdot T_{BS}}{U_t + U_T} \tag{A.1}$$

where

$$(\alpha\tau)_{EFF} = \tau_G \cdot \left(\alpha_{CELL} \cdot p + (1-p)\cdot \alpha_T + p \ \cdot \eta_{CELL}\right). \tag{A.2}$$

Using Eq. (1) and Eq. (2), the expression for the temperature of tedlar back surface is:

$$T_{BS} = \frac{h_{P1} \cdot (\alpha\tau)_{EFF} \cdot I + U_{tT} \cdot T_{AMB} + h_f \cdot T_{AIR} + h_{RAD_DUCT} \cdot T_I}{U_{tT} + h_f + h_{RAD_DUCT}} \tag{A.3}$$

where

$$h_{P1} = \frac{U_T}{U_t + U_T}, \quad U_{tT} = \frac{U_t \cdot U_T}{U_t + U_T}$$

Combining Eqs (1), (2) and (3), the following linear differential equation is obtained:

$$\frac{dT_{AIR}}{dx} + T_{AIR} \cdot \vartheta = \varsigma \tag{A.4}$$

where

$$\vartheta = \frac{(h_{P3})}{\dot{m}_{AIR} \cdot C_{AIR}} \cdot b \ , \ \varsigma = \left[T_{AIR} \cdot (U_{tf} + U_{b0}) + h_{P1} \cdot h_{P2} \cdot (\alpha\tau)_{EFF} \cdot I - T_I \cdot (h_{P4} + U_{b0})\right] \cdot \frac{b}{\dot{m}_{AIR} \cdot C_{AIR}} \ ,$$

$$h_{P2} = \frac{(h_f + h_{RAD_DUCT})}{(h_f + h_{RAD_DUCT} + U_{tT})} \ , \ h_{P3} = \frac{U_{tT} \cdot h_f}{(h_f + h_{RAD_DUCT} + U_{tT})}, \ h_{P4} = \frac{U_{tT} \cdot h_{RAD_DUCT}}{(h_f + h_{RAD_DUCT} + U_{tT})},$$

$$U_{tf} = \frac{U_{tT} \cdot (h_f + h_{RAD_DUCT})}{(h_f + h_{RAD_DUCT} + U_{tT})}.$$

Thus, solving Eq. (7) , with boundary conditions at $x = 0$, $T_{AIR}(x) = T_{AIR_IN} = T_{AMB}$, leads to:

$$T_{AIR}(x) = \frac{\varsigma}{\vartheta} + \left(T_{AIR_IN} - \frac{\varsigma}{\vartheta}\right) \cdot e^{-\vartheta \cdot x} \tag{A.5}$$

The temperature of the air leaving the duct (at a distance L_D form the entrance) can be obtained from Eq. (A.5) for $x=L_D$.

A fluid temperature can be averaged over the considered length and can be calculated as:

$$\overline{T_{AIR}} = \frac{1}{L_D} \int_0^{L_D} T_{AIR}(x) \cdot dx = \frac{\varsigma}{\vartheta} + \frac{1}{\vartheta \cdot L_D} \cdot \left(T_{AIR_IN} - \frac{\varsigma}{\vartheta}\right) \cdot \left(1 - e^{-\vartheta \cdot L_D}\right) \tag{A.6}$$

The expressions obtained in Eqs (A.5) and (A.6) for air temperature involves the value of T_I (temperature of the insulation upper surface), therefore, they can be solved using Eq. (4).

Appendix B

The heat transfer coefficients used in the modeling equations, are defined as follows:

$$h_{CONV,UPP} = 2.8 + 3 \cdot Vw \tag{B.1}$$

$$h_{CONV,UND} = 2.8 + 3 \cdot V_{A_UNDER_I} \tag{B.2}$$

$$h_{RAD} = \varepsilon_G \cdot \sigma \cdot \left(T_{SKY} + T_{CELL}\right) \cdot \left(T_{SKY}^{\ 2} + T_{CELL}^{\ 2}\right) \tag{B.3}$$

The radiative heat transfer coefficient inside the duct was calculated considering the formula for two infinitely long, gray, opaque, directly opposed parallel plates of the same finite width [22]. The emissivity of the back surface of PV module was set at 0.87 [26] and that of the insulation upper surface made of aluminum sheet was defined to be 0.1 [26].

$$h_{RAD_DUCT} = \left(\frac{1}{\frac{1}{\varepsilon_{BS}} + \frac{1}{\varepsilon_I} - 1} \right) \cdot \sigma \cdot \left(T_{BS} + T_I\right) \cdot \left(T_{BS}^{\ 2} + T_I^{\ 2}\right) \tag{B.4}$$

$$T_{SKY} = T_{AMB} - 6 \tag{B.5}$$

$$U_{b0} = \frac{1}{\left(\frac{L_I}{K_I} + \frac{1}{h_{CONV,UND}} \right)} \tag{B.6}$$

$$U_t = \frac{1}{\left(\frac{L_G}{K_G} + \frac{1}{h_{CONV,UPP} + h_{RAD}} \right)} \tag{B.7}$$

$$U_T = \frac{1}{\left(\frac{L_{CELL}}{K_{CELL}} + \frac{L_T}{K_T} \right)} \tag{B.8}$$

Nomenclature

b	width of PV module, m
L_D	length of PV module, m
C	specific heat, J/(kgK)
I	incident solar intensity, W/m^2
L	thickness, m

$\dot{m}$	mass flow rate, kg/s
h_{CONV_UPP}	convective heat transfer coefficient on upper surface of PV module, W/(m^{2}K)
h_{CONV_UND}	convective heat transfer coefficient on lower surface of insulating panel, W/(m^{2}K)
h_f	convective heat transfer coefficient inside the air duct, W/(m^{2}K)
h_{RAD}	radiative heat transfer coefficient from solar cells to ambient, W/(m^{2}K)
h_{RAD_DUCT}	radiative heat transfer coefficient inside the duct, W/(m^{2}K)
K	thermal conductivity, W/(mK)
$\dot{Q}_U$	rate of useful energy transfer, W
T	temperature, K
p	packing factor
ΔP	pressure drop, Pa
U_{b0}	overall back loss coefficient from upper surface of insulation to ambient, W/(m^{2}K)
U_t	overall heat transfer coefficient from solar cell to ambient ,W/(m^{2}K)
U_T	conductive heat transfer coefficient through solar cell and tedlar, W/(m^{2}K)
U_{tT}	overall heat transfer coefficient from glass to tedlar through solar cell, W/(m^{2}K)
V	velocity, m/s

Greek symbols

α	absorptivity
$(\alpha\,\tau)_{EFF}$	product of effective absorptivity and transmittivity
β	efficiency reduction coefficient
ε	emissivity
σ	Stefan–Boltzmann constant, W/(m^{2}K^4)
η	efficiency
ρ	density, kg/m^3
τ	transmittivity

Subscripts and superscripts

AIR	air
AMB	ambient
BS	back surface of PV module
CELL	solar cell
G	glass
I	insulating panel
REF	reference condition
T	tedlar
TH	thermal
w	wind

References

Journals:

[1] Jäger-Waldau A. The Photovoltaic Market – Appendix D. In: McEvoy A., Markvart T. and Castaner L., Practical Handbook of Photovoltaics (Second Edition) Fundamentals and Applications. Elsevier 2012, p. 1145-1151.

[2] Chow T.T. A review on photovoltaic/thermal hybrid solar technology. Applied Energy 2010;87:365–79.

[3] Wolf M. Performance analysis of combined heating and photovoltaic power systems for residences. Energy Conversion Management 1976;16:79–90.

[4] Kern Jr. E.C., Russell M.C. Combined photovoltaic and thermal hybrid collector systems. In: Proceedings of 13th IEEE photovoltaic specialists, 1978, Washington, DC,USA; 1153–7.

[5] Florschuetz L.W. Extension of the Hottel–Whiller model to the analysis of combined photovoltaic/thermal flat plate collectors. Solar Energy 1979;22:361–6.

[6] Garg H.P., Adhikari R.S. Conventional hybrid photovoltaic/thermal (PV/T) air heating collectors: steady-state simulation. Renewable Energy 1997;11:363–85.

[7] Hegazy A.A. Comparative study of the performances of four photovoltaic/thermal solar air collectors. Energy Conversion Management 2000;41:861–81.

[8] Kalogirou S.A. Use of TRYNSYS for modelling and simulation of a hybrid PV thermal solar system for Cyprus. Renewable Energy 2001;23:247–60.

[9] Zondag H.A., De Vries D.W., Van Helden W.G.J., Van Zolengen R.J.C., Van Steenhoven A.A. The thermal and electrical yield of a PV-thermal collector. Solar Energy 2002;72(2):113–28.

[10] Tiwari A., Sodha M.S., Chandra A., Joshi J.C. Performance evaluation of photovoltaic thermal solar air collector for composite climate of India. Solar Energy Material Solar Cells 2006;90(2):175–89.

[11] Sarhaddi F., Farahat S., Ajam H., Behzadmehr A., Adeli M.M. An improved thermal and electrical model for a solar photovoltaic thermal (PV/T) air collector. Applied Energy 2010;87:2328–39.

[12] Kumar R., Rosen M.A. A critical review of photovoltaic–thermal solar collectors for air heating, Applied Energy 2011;88:3603-3614.

[13] Dubey S., Tiwari G.N. Thermal modeling of a combined system of photovoltaic thermal (PV/T) solar water heater. Solar Energy 2008;82:602–12.

[14] Dubey S., Sandhu G.S., Tiwari G.N. Analytical expression for electrical efficiency of PV/T hybrid air collector. Applied Energy 2009;86(5):697–705.

[15] Joshi A.S., Tiwari A., Tiwari G.N., Dincer I., Reddy B.V. Performance evaluation of a hybrid photovoltaic thermal (PV/T) (glass-to-glass) system. Int J Therm Sci 2009;48:154–64.

[16] Tripanagnostopoulos Y., Tonui J.K. Air-cooled PV/T solar collectors with low cost performance improvements Solar Energy 2007;81:498–511.

[17] Evans D.L. Simplified method for predicting PV array output. Solar Energy 1981;27:555–60.

[18] Tan H.M., Charters W.W.S. Effect of thermal entrance region on turbulent forced-convective heat transfer for an asymmetrically rectangular duct with uniform heat flux. Solar Energy 1969;12,513–516.

Books:

[19] Klein S.A., Engineering Equation Solver, Academic Version V8.603, www.fchart.com

[20] Duffie J.A., Beckman W.A. Solar engineering of thermal processes. 3rd ed. New York, USA: Wiley; 2006.

[21] Nellis G.F, Klein S.A. Heat Transfer. Cambridge (UK): Cambridge University Press; 2009

[22] Cengel Y.A., Termodinamica e trasmissione del calore, McGraw-Hill,1998.

[23] Incropera F.B., DeWitt D.P.. Fundamentals of Heat and Mass Transfer. John Wiley & Sons, New York, 1996.

Conference Papers:

[24] Schott T. Operational temperatures of PV modules. In: Proceedings of 6th PV solar energy conference; 1985. p. 392–6.

[25] King, David L., Jay A. Kratochvil, and William E. Boyson. “Measuring the Solar Spectral and Angle-of-Incidence Effects on Photovoltaic Modules and Irradiance Sensors.” Proceedings of the 1994 IEEE Photovoltaics Specialists Conference. Sept 30-Oct 3, 1997. pp. 1113-1116.

Web references:

[26] Material Emissivity Properties : http://snap.fnal.gov/crshield/crs-mech/emissivity-eoi.htm

Energy and exergy analysis of the first hybrid solar-gas power plant in Algeria

Fouad Khaldi

Department of Physics, University of Batna, Batna, Algeria, fouadkhaldi@gmail.com

Abstract:

The first concentrating solar power plant in Algeria began to produce electricty in the middle of the last year. The hybridization solar-gas is realized by the integrating of parabolic trough collectors into a combined cycle power plant. The thermodynaic evaluation of the power plant performance at design running conditions is based on the exergy analysis. In this analysis, the exergy flow diagram is aideed by the value diagram which is used as a visualisation tool for identifying exergy degradation in heat transfer processes involved in the HRSG and the solar steam generator. The exergy destruction and the functional exergy efficiency are the key parameters in assessing the performance of every power plant component. In regard to the electrical power capacity of the power plant, 160 MW, the solar energy share is 14% (22 MW), while the solar exergy share is 12% (18.4 MW). The combustors and the solar field are the less efficient systems.The combustors destruct about one third of natural gas exergy and the solar field consumes about three quarters of solar exergy.

Keywords:

Integrated solar combined cycle, Concentrating solar power, Parabolic trough collector, Thermodynamic performance, Exergy analysis, Value diagram, Cycle-Tempo.

1. Introduction

In Algeria the total installed power generating capacity is over 9 GW, 98% of which is provided by gas-fired plants [1]. Algeria, located in the MENA region, has impressive solar resources [2-4]. The Algerian desert is exposed yearly to a direct sun irradiation higher than 2000 kWh/m^2 gained from 3500 hours of sunshine. These solar potential associated to huge land resources are suitable for the implementation of concentrating solar power plants (CSPPs) [5]. The Algerian authorities are planning to produce 6% of electricity from CSPPs by 2020 [1].This target should be reached through the building of four CSPPs totaling a solar installed capacity of 240 MW [1]. The first CSPP, at Hassi R'Mel, is already running since 2011. Since Algeria is a major producer and exporter of natural gas, hybrid solar-gas power plants are more appropriate; besides this option avoids the issues of storage systems. This choice is supported by the observation that in the last years the peak of electrical consumption in Algeria was recorded in summer and in day times [1]. That meets with the times of the day and the year when solar energy has the advantage to produce energy. The planned hybrid plants will contribute to save about 2.7 billion m^3 of natural gas. Similar projects are in progress in Morocco, Tunisia, Egypt, Jordan, and Iran [6-11] and elsewhere of MENA region [12].

The solar thermal power generated by CSPPs can be supplied at different temperature levels. Pure-solar power tower plants work at high temperature level (>500°C) [13-16]. CSP systems at low or medium temperature levels (250 to 400°C), based on trough or Fresnel collectors, are more suitable as options for solar repowering of new or existing fossil-fired power plants [17-22]. The parabolic trough collector (PTC) is the most common medium-temperature solar technology. It represents the most mature technology, from both commercial and technical viewpoints, for mid-to-large scale

grid connected power plants [23, 25]. Based on this technology a total installed electric capacity of 354 MW is generated from nine steam power plants in the California Mojave Desert [23].

In terms of cost and efficiency, integrated solar combined cycle systems (ISCCS) is the more appropriate cycle design for MENA's countries [26]. An ISCC consists on the integrating of the parabolic trough into a gas fired combined cycle composed of a gas topping cycle (GTC) and a steam bottoming cycle (SBC). The PTCs can supply a hot heat transfer fluid (HTF) at a temperature of about 400 °C. Thus, the thermal energy carried by the HTF becomes the hot source of generating additional steam to be sending to the SBC.

In last years, many studies had demonstrated the usefulness of exergy analysis in assessing the performance of power plants [27-30]. The methodology has been proven in analyzing gas turbine [31-33], steam turbine [34, 35] and combined cycle power plants [36-38].
In regard to CSPPs subjected to exergy analysis, the study [17] showed the benefits of a scenario proposed for the solar repowering of a coal fired steam turbine. In another work [19], the best options for solar boosting and fuel saving of two existing coal-fired power plants were determined. In analyzing the hybridization solar-gas in ISCCs [22], a detailed examination was paid to the solar collector, i.e. the linear Fresnel reflecting solar concentrator. The global optimal design of an ISCCS was carried out based on the exergoeconomic approach [20]. Reference [18] performed an exergy analysis of the first ISCCS in Iran. The plant is with full capacity 467 MW and the solar power is about 17 MW. The main results are that the solar collectors are the least efficient components in the plant and the combustors are the major destructors of exergy.

The present study presents the exergy analysis of the first ISCCS in Algeria. The Hassi R'Mel's plant has been lunched in operation few months ago. The analysis is based on the exergy flow diagram and the value diagram, the later is an unusual visualization tool for identifying exergy loss in heat transfer processes.
The thermodynamic simulations are performed by the flow-sheet program, "Cycle-Tempo". This software is a freeware advanced tool for the analysis and optimization of energy systems, developed at the Delft University of Technology [39].

2. Power plant description and operation

The hybrid power plant is located at the Algerian's largest natural gas field, Hassi R'Mel, province of Laghouat, in middle of Algeria, at about 500 km from Algiers. The site is at 33°7' latitude and 3°21'longittude, and its elevation above sea level is 750 m. The ambient temperature ranges between 21° C and 50°C in summer and ranges between -10° C and 20°C in winter. In summer the Direct Normal Irradiation (DNI) can reach 930 W/m^2. Based on yearly average value, the site is blessed daily by 9.5 sunny hours offering DNI estimated at 7,138 Wh/m^2/day. The design of the power plant considered air ambient at 0.928 bars and 35°C with relative humidity at 24%. The design solar output power is based on the average value of DNI considered as 751 W/m^2. This solar irradiation intensity is intended to produce some 50 MW of thermal energy. At design running conditions the full capacity of the plant is 160 MW.

The flow diagram of the plant is shown in Fig. 1. The plant is composed of a power block and a solar field. The power block is a conventional combined cycle power plant with two 40 MW SGT-800 gas turbine (GTs) [40] and an 80 MW SST-900 steam turbine (STs) [41]. The power block contains also two identical single-pressure HRSGs with supplementary firing and no reheats. The flow diagram shows the power block with only 1 GTPP and 1 HRSG. The HRSG is equipped by low pressures economizer and evaporator (DECO and DEVA), two super heaters (SHE1 and SHE2) and two duct burners (DBs). The first DB is integrated downstream of the GT exit to increase the temperature of the exhaust gas that passes through the SHE1. The second DB is integrated into the evaporator to compensate the deficit of solar steam in low sunny times. This DB is considered off

because the analysis is performed with the power plant running in design mode, with favourable sunny conditions.

The GTPP is fuelled with Hassi R'Mel's field natural gas. The gas is rich in CH_4 by about 85%, it has a LHV=45778 kJ/kg. The GTPP is supported by an inlet air cooling system to counter the adverse effect of air temperature during hot times on its performance. Therefore, 4 Sadinter chiller (CH) unites contribute to boost the GTPP by reducing intake air temperature to 15°C. Although, higher is the air temperature, higher is the power consumption of the chiller, this is usually synchronous with higher solar irradiation (higher solar power output). An air cooled condenser (ACC) is adopted as an option for condensing steam. This technology is preferable to the traditional water-cooled condenser when water availability is limited, notably in Hassi R'mel, characterized by an arid climate. The use of ACCs can reduce the plant water consumption by 90%; however, the plant efficiency suffers with the higher condensing pressure. The SPX cooling system with heat transfer duty of 147600 kW guaranteed by regrouping 15 fans, provides to the Hassi R'Mel power plant statured water at 52 °C and at about 0.14 bars. The design parameters of the power block are summarized in Table 1.

At 183,120 m^2 mirrors, the solar field comprises 224 parabolic collectors assembled in 56 loops, 4 collectors per loop. The collector is of ET-150 technology [24], aligned on a north-south line, it tracks sun from east to west by a single axis tracking system. The HTF circulating in loop in the solar field is synthetic oil; Therminol PV-1, its thermophysical properties versus temperature can be found in Reference [42]. Cycle-Tempo assumes 3^{rd} degree polynomial approximation for calculating heat capacity of the HTF at any temperature. The supplying of thermal energy from the solar field to the power block is performed when water/steam recovers the thermal energy from the HTF through the SSG.

The SSG is the assembling of an economizer (ECO), an evaporator (EVA) with a drum (DR) and a super heater (SHE).

The net output power of the plant is proportional to steam flow rate expanding in the ST, it is the sum of the flow rate of steam generated in the HRSG and that generated in the SSG. The operation of the hybrid plant is under the compulsory condition that the HTF circulates across the SSG at constant inlet temperature, 393°C, and at constant outlet temperature, 293°C, but it can be with variable mass flow rate. The high limit of temperature is imposed because the long-term exposure of the organic HTF beyond 400°C temperatures can lead to thermal decomposition of the fluid. Thermal fluid decomposition occurs when enough heat is applied to the fluid to cause the breaking of molecular bonds, which results degradation in the HTF's physical properties [43].

The solar steam flow rate is proportional to the HTF mass flow rate. The HTF mass flow rate varies following the DNI intensity, in other words, according to time during day and to climate conditions. The design value of the HTF mass flow rate is 200 kg/s, it is the resultant of DNI assumed at 751 W/m^2. This value of DNI is able to generate 22.6 kg/s of solar steam. Then, at the exit of the economizer, 22.6 kg/s of pressurized water is withdrawn from the HRSG and is sent to the SSG. After preheating and evaporating, the resultant saturated steam is superheated and resent to the HRSG at 372°C. The solar steam mixes with the steam exiting the SHE1, the whole steam passes through the SHE2 before expanding in the ST. At design load the ST, with about 70 kg/s of superheated steam at 560°C and 80 bars, delivers 80 MW of electric power.

3. Exergy analysis

The exergy analysis of the power plant is based on the results of the thermodynamic simulations performed by the flow-sheet program, "Cycle-Tempo". The calculations considered the simultaneous resolutions of mass equation and energy equation applied for each power plant component. Cycle-Tempo also calculates exergy values of all fluid flows of the cycle by using the ambient air (35°C and 0.928 bars) as the reference state. Furthermore, the program calculates exergy losses and efficiencies of all apparatuses. In the present study is used the functional exergy

definition where the exergy efficiency of any power plant component is determined as the ratio of the exergy flow rate considered to be the product of the power plant component and the exergy flow rate considered necessary for making this product [36].
Cycle-Tempo is able to draw *Q-T* diagrams and value diagrams.

Table 1. Design parameters of the power block.

	Value
GT	
Model	SGT-800
Ambient pressure	0.928
Ambient temperature	35°C
Intake compressor air temperature	15 °C
Compressor pressure ratio	20.2
Compressor isentropic efficiency	0.88
Inlet turbine temperature	1200°C
Turbine isentropic efficiency	0.88
Exhaust mass flow rate	120,20 Kg/S
Exhaust temperature	550 °C
LHV of natural gas	45778 kJ/kg
Net output power	40 MW
Thermal efficiency	35%
HRSG	
Type	Single pressure without reheat
Fuel mass flow rate in the DBs	0.66 kg/s
Approach temperature	25° C
Pinch temperature	25° C
Pressure losses in flue gas side	0.025
Pressure losses in water/steam side	16 bars
Inlet water temperature	60° C
Exit stack temperature	100° C
Thermal efficiency	98.50%
ST	
Model	SST-900
Inlet steam temperature	560°C
Inlet steam pressure	83 bars
Steam mass flow rate	70 kg/s
Condensate temperature	52°C
Isentropic efficiency	0.9
Full output capacity	80 MW
SSG	
Inlet water temperature	195°C
Inlet water pressure	93 bars
Exit steam temperature	372°C
Water/steam mass flow rate	22.60 kg/s
Inlet HTF temperature	392°C
Exit HTF temperature	292°C
HTF mass flow rate	205 kg/s
Pressure losses in water/steam side	5.8 bars
Pressure losses in HTF side	2 bars
Thermal efficiency	98 %

3.1. Value and exergy diagrams

In order to illustrate and to present heat transfer evolutions, for example, in the HRSG, it is common to use the so-called *Q-T* diagram. It shows profiles for the heat transfer process between exhaust gas and water/steam, using temperature on the ordinate axis and heat transferred on the abscissa axis.

A better insight into the exergy losses due to heat transfer in the HRSG can be derived from the value diagram [36].It is a graph that allows a simple presentation of how much is the recovering of the exergy of the flue gas by water/steam flow?

In the value diagram the temperature of the flows are also given as a function of the heat transferred to the water/steam flow; but the temperature at the vertical axis is replaced by the term $(1-T_0/T)$. As this axis begins at T_0 and goes up to ∞, the values on this axis can go from 0 to 1.

The term $(1-T_0/T)$ indicates which part of the considered heat can in principle be converted into work and can be seen as the exergy fraction of this amount of heat.

The total of exergy absorbed by water/steam flow is smaller than the exergy transferred from the flue gas flow. The difference is exergy that is lost due to the temperature difference necessary to transfer heat from the flue gas to water/steam flow.

The exergy flow diagram or Grassmann diagram is a convenient visualization tool to provide briefly an overview of the most important information with regard to magnitude and location of thermodynamic losses occurring through the power plant. It consists to plot out exergy flow, in the conversion of natural resources (coal, gas, solar irradiation) into electricity, on a line diagram of the flow system. This illustrates exactly the consumption or destruction of exergy in the power plant components.

3.2. Solar field efficiencies

The solar field receives the incident solar irradiation energy:

$$\dot{Q}_S = DNI.A \quad , \qquad (1)$$

where A is the total mirrors area.

The exergy input through this insolation is determined by the formula [19]:

$$\dot{E}x_s = \left[1 - \frac{4T_0}{3T_S}(1 - 0.28\ln(f))\right]\dot{Q}_s \quad , \qquad (2)$$

the symbols T_0 and T_s are, respectively, the ambient temperature and the temperature of the Sun (5777 K), and f is the dilution factor (1.3×10^{-5}).

The useful heat and the associated exergy transported by the HTF to the SSG are, respectively:

$$\dot{Q}_{HTF} = \dot{m}_{HTF}\Delta h, \qquad (3)$$

and

$$\dot{E}x_{HTF} = \dot{m}_{HTF}\Delta e_x \, . \qquad (4)$$

In these equations the symbols $\dot{m}_{HTF}$, Δh , and Δe_x, denote, respectively, the mass flow rate of the HTF and its mass enthalpy difference and exergy difference through the SSG.

The global energy and global exergy efficiencies of the solar field are defined, respectively, as follows:

$$\eta = \frac{\dot{Q}_{HTF}}{\dot{Q}_s} \quad , \qquad (5)$$

and

$$\eta_{ex} = \frac{\dot{E}x_{HTF}}{\dot{E}x_s} \quad . \qquad (6)$$

The global efficiency includes the optical and thermal efficiencies of the solar field, in other words, the efficiency of the global conversion of solar irradiation to heat to be injected into the SSG. The optical efficiency depends upon incident angle effects, solar field availability, collector tracking error and twist, geometric accuracy of the mirrors, mirror reflectivity, cleanliness of the mirrors, shadowing of the receiver, transmittance of the receiver glass envelope, cleanliness of the glass envelope, absorption of solar energy by the receiver, end losses, and row-to-row shadowing [44]. The thermal efficiency is function of receiver thermal losses and piping thermal losses. Receiver thermal losses are caused mainly by the thermal radiation of the receiver's selective coating. Piping thermal losses corresponds to the thermal losses from the solar field header piping and the HTF system piping.

4. Results and discussion

In Fig. 1, the flow diagram of the plant displays some important thermodynamic properties (pressure, temperature, mass flow rate and mass enthalpy) at both entry and exit of every apparatus at design running conditions. Cycle-Tempo calculations of absolute mass enthalpies of air, the flue gas and the HTF present some shifts relatively to the exact values, however the enthalpy differences are accurate because it is just a matter of the selection of the reference point. At design load, the Hassi R'Mel's power plant is able to deliver 160 MW of net output power, 80 MW from the GTPPs and 80 MW from the ST. The SSG supplies 49,906 kW of the total superheated steam, 179,758 kW, delivered by the HRSGs to the ST. The result is that the solar electric power is about 22 MW, and thus the solar share is about 14%. The thermal efficiency of the power plant is 56%, while, separately, the thermal efficiency of the GTPPS is 35 %. In reference to the conventional combined cycle (138 MW and 48%) the solar contribution increases the output electric power by about 16% and increases the thermal efficiency by 8 points. This fact is without computing the solar energy as input energy in the definition of the thermal efficiency, thanks to the fact that solar irradiation is free and inexhaustible; else, the thermal efficiency of the hybrid power plant is about 38%. That decrease in efficiency associated to solar boosting is related to the global efficiency of the SF limited at 78% (5), and to the thermal efficiency of the SSG, 98%.

For simplifying the analysis in the following, all of the apparatuses are categorized in four technology families, i.e. turbomachines (ACs, GTs and ST), heat exchangers (SSG and HRSGs), combustors (CCs and DBs) and the SF. The SSG and the HRSGs together have 17 heat exchangers (HXs), 7 HXs per 1 HRSG and 3 HXs in the SSG.

Based on the exergy flow diagram depicted in Fig. 2; it appears that the exergy efficiency of the plant is 53%; the efficiency of the GTPPs is about 34%. The solar exergy share in producing the 160 MW of electric power is about 12% (18.4 MW). Thus the solar exergy share is lower than the energy share. The explanation is that the HRSG supplies thermal power to the ST at 560°C while the SSG sends thermal power to the HRSG at lower temperature 372°C. From the exergy flow

diagram, the hybrid power plant is able to converting 397.4 MW of natural resources exergy, of gas and sun, in electrical power, 160 MW. The rest, 234.5 MW (60%), is lost.

The percentage of the solar exergy input is 24% (96.9 MW), that of natural gas is 76% (300.5 MW), from which 60% (237MW) are injected through the CCs and 16% (63.5 MW) are injected through the DBs.

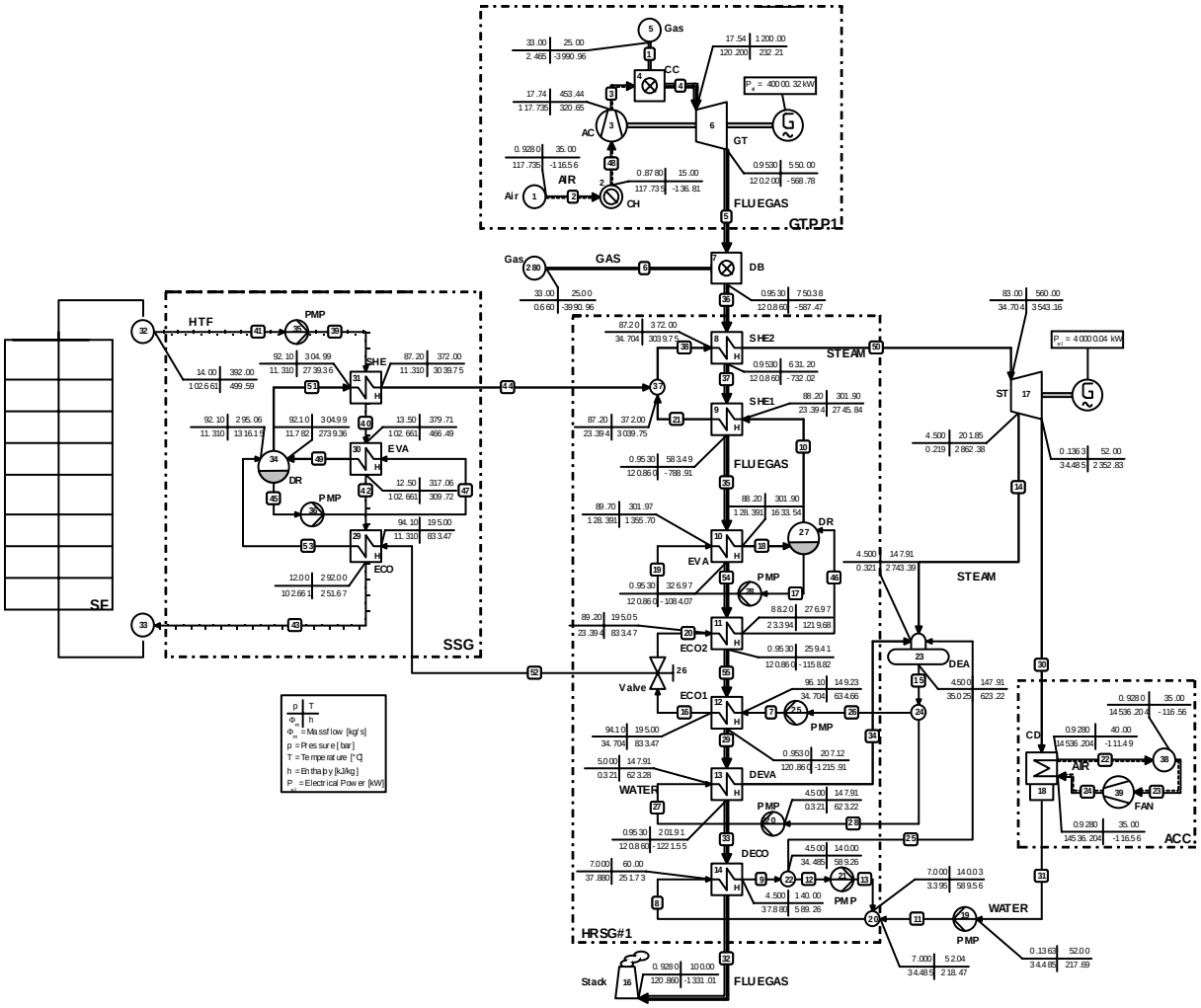

Fig.1. Flow diagram of the ISCCS.

The loss of exergy is caused by both internal thermodynamic irreversibilities occurring in the apparatuses and by exergy escaping into the environment.

The combustors are the major loser of exergy in the power block; they destruct 32% (95.7 MW) of natural gas exergy input (300.5 MW). The CCs are responsible of about 24% (73 MW) and the DBs of some 8% (22.7 MW). In regard to the total exergy input (397.4 MW), the turbomachines (ACs+GTs+ST) cause the destruction of around 9% (33.7 MW) of exergy. All of the heat exchangers (SSG+HRSG) consume 5% (21.9 MW) of exergy. The rest of exergy lost, 14. 5 MW (3%), is rejected as heat into environment through the ACC (7.82 MW) and the stack (6.71 MW). The lost in solar exergy is caused mainly by the SF which consumes about 74% (71.5 MW) of input solar exergy (96.9 MW), the SSG is responsible only of less than 3% (2.7 MW). Thus, in the whole 77% of solar exergy is lost before arriving at the HRSG. That explains why the solar energy increases the output electric power of the hybrid power plant but at lower efficiency (40%) when taken in consideration the solar exergy as an exergy input in the definition of the exergy efficiency. This definition of exergy efficiency is more pertinent when discussing the performance of the SF and the SSG.

Since the ACC has only the function to discharge heat to the environment, similarly to the stack, evaluating its performance does not have a significant importance.

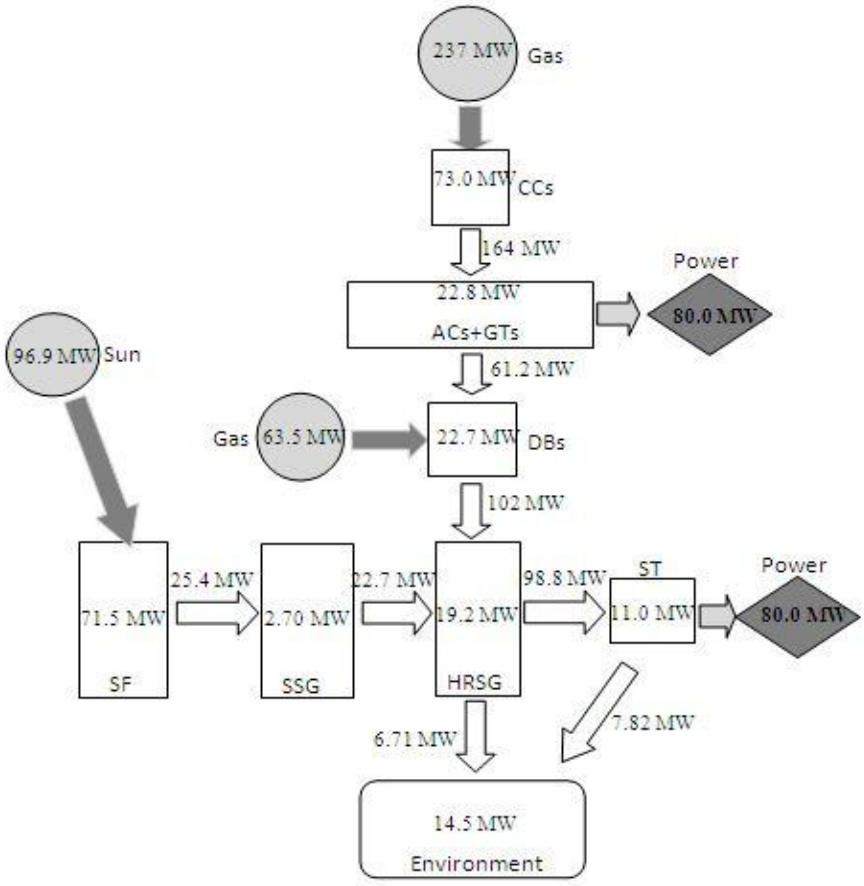

Fig. 2. Exergy flow diagram of the ISCCS

In terms of exergy efficiency, as shown in Fig. 3, the turbomachines are the most efficient components, theirs efficiencies are almost at the same level; they are between 90%, for the ST, and 94%, for the GTs, the ACs have 93%. In the second order appear the heat exchangers, but relatively at different levels, at all the SSG operates at 89 % and the HRSGs operate at 79%. The combustors are the least efficient systems in the power block, the CCs run at 68% and the DBs run at 64%. Far behind, the global exergy efficiency of the SF is about 25% (6). Although its reactants are hotter, the DBs are less efficient than the CCs. The explanation is that the combustion processes within the DBs results flue gases at low temperature (750°C), the consequence of being with air factor of 7.5, well far of the stochiometric mixture air/fuel where the air factor is around 1.On the other hand, with air factor estimated at 3 the flue gases leave the CCs at higher temperature (1200 °C).

Close look to the performance of the HXs is given in the following. The analysis is based on both the *Q-T* diagram and the value diagram which are combined in one graph. Figs. 4 and 5 show, respectively, the *Q-T/value* diagram for the SSG and the HRSG.

Considering the SSG, the sizes of the shaded areas reveal that the EVA is the most efficient HX while the ECO is the least efficient one, and the SHE is between both. The calculations confirm this order. The exergy efficiencies of the EVA, the SHE and the ECO are about, respectively, 92%, 88% and 79%. Any effort intending to enhance the performance of the SSG should be oriented in first priority to the ECO, then in less degree to the SHE. The value diagram helps to identify that the

temperature difference at the cold end of the ECO should be the pertinent location for increasing the efficiency. The potential of increasing the performance of the EVA is limited because its efficiency is yet relatively high and because it is common to heat transfers associated to phase change to be at lower efficiency.

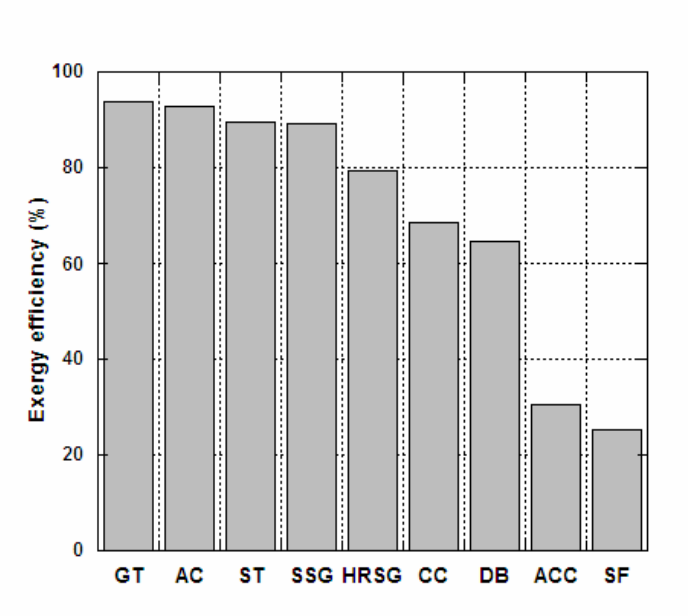

Fig. 3. Exergy efficiencies of ISCCS components.

Examining the HRSG, from Fig.5, supported by calculations, it comes out that the DECO has the smallest efficiency (56%). For the rest of HXs the efficiency ranges between 75 %, for the DEVA, and 87%, for the ECO2. A look at water/steam and the flue gas temperature profiles shows that the distance between both profiles varies slightly along the HRSG. Except for the EVA (phase change), increasing the efficiency of the HXs requires the narrowing of this distance. The magnitude of this distance can be related to the mass flow rates of both water/steam and the flue gas. In accordance to sunny conditions, the HRSG runs at different regimes, then at different mass flow rates. In consequence the shaded areas in the value diagram vary and the same for the exergy efficiency.

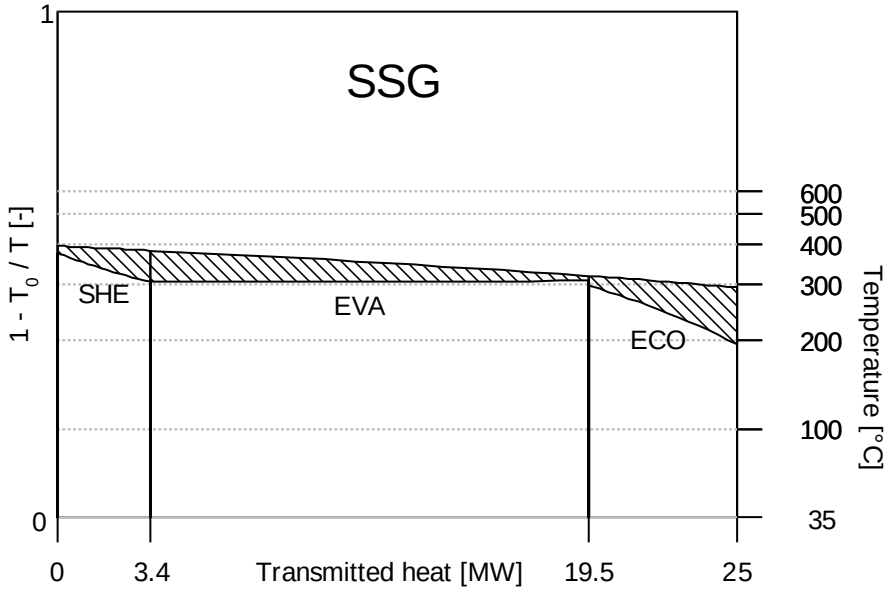

Fig. 4. Q-T/value diagram of the SSG.

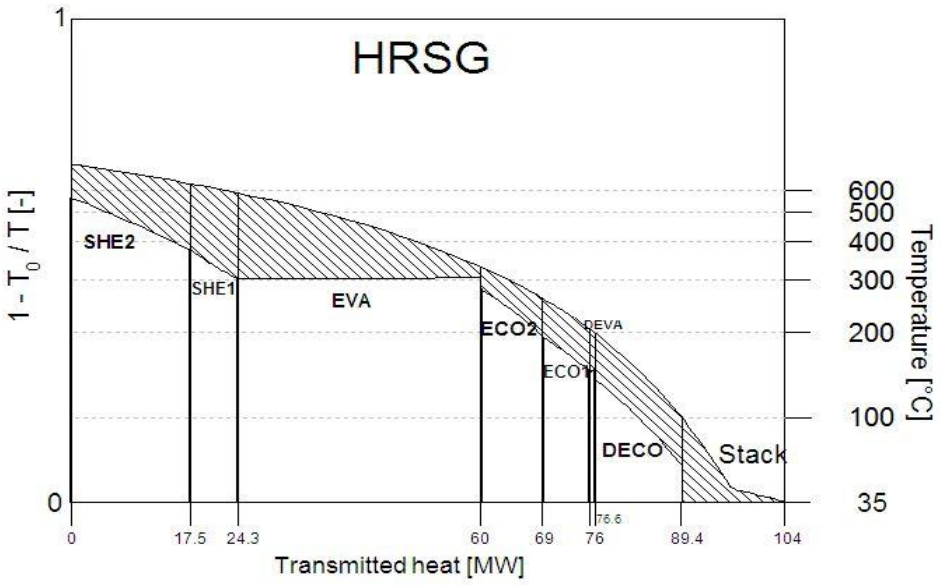

Fig. 5. Q-T/value diagram of the HRSG.

Conclusion

The purpose of the present study is the thermodynamic analysis of the first hybrid solar-gas power plant in Algeria. The Hassi R'Mel's power plant has been lunched in operation few months ago. The power block is composed of two SGT-800 gas turbines and a SST-900 steam turbine. The HRSG is of single-pressure with supplementary firing and no reheat. The solar field gathers ET-150 parabolic trough collectors, in which circulates the heat transfer fluid Therminol PV-1.

The exergy analysis is adopted as a methodology for evaluating the performance of every power plant component. The thermodynamic modelling and simulation, and also the post-processing of the results are performed by the flow-sheet program Cycle-Tempo.

At design load the capacity of the plant is 160 MW of electrical power, 80 MW from the two gas turbines and 80 MW from the steam turbine. Of this capacity the exergy solar share is lower than the solar energy one, 12% (18.4 MW) against 14% (22 MW). The reason is that the solar steam generator supplies about 50 MW of thermal power to the HRSG at 372 °C, which is lower the temperature of 560 °C, at which the HRSG sends superheated steam to the steam turbine.

The thermal efficiency of the plant is 56% whereas the exergy efficiency is 53%. The combustors, with efficiencies lower than 68%, are the least efficient components in the power block. They are the major destructors of exergy; they consume about 32% of gas natural exergy. The turbomachines (compressors, gas turbines and steam turbine) are the most efficient; their efficiencies are in the range of 90% to 94%. The HRSG and the solar steam generator, equipped together by 17 heat exchangers, have, receptively, the efficiencies 79% and 89%. With global exergy efficiency (optical and thermal) limited to 25%, the solar field loses 74% of solar exergy.

Acknowledgments

The author is grateful to the management and staff of New Energy Algeria (NEAL SpA) and he thanks especially Mr. Nordine Hamrene, Design Engineer, for providing the Hassi R'Mel's power plant data and for fruitful discussions. The author also thanks Mr. Teuss van der Stelt, from Delft University of Technology, for giving help about Cycle-Tempo.

Nomenclature

A	mirror area
e	mass exergy, J/kg
h	mass enthalpy, J/kg
$\dot{E}x$	exergy flow rate, W
LHV	Lower Heating Value, J/kg
$\dot{m}$	mass flow rate, kg/s
$\dot{Q}$	heat flow rate, W
T	temperature, °C

Greek symbols

η	efficiency

Subscripts and superscripts

0	Ambient
s	Solar

Acronyms

AC	Air Compressor
ACC	Air Cooled Condenser
CC	Combustion Chamber
CH	Chiller
CSPP	Concentrating Solar Power Plant
DB	Duct Burner
DEA	De-aerator
DECO	low pressure Economizer
DEVA	low pressure Evaporator
DNI	Direct Normal Irradiation
DR	Drum
ECO	Economizer
EVA	Evaporator
G	Generator
GT	Gas Turbine
GTC	Gas Topping Cycle
GTPP	Gas Turbine Power Plant
HRSG	Heat Recovery Steam Generator
HTF	Heat Transfer Fluid
HX	Heat Exchanger
ISCCS	Integrated Solar Combined Cycle System
MENA	Middle East and North Africa
PMP	Pump
PTC	Parabolic Trough Collector
SBC	Steam Bottoming Cycle
SF	Solar Field
SHE	Super Heater
SSG	Solar Steam Generator
ST	Steam Turbine

References

[1] Commission de Regulation de l'Electricité et du Gaz (Electricity and gas authority of Algeria). Annual Report 2010 (in French). Available at:<http://www.creg.org.dz> [accessed 12.6.2011].

[2] Himri Y., Arif S. Malik, Boudghene Stambouli A., Himri S., Draoui B., Review and use of the Algerian renewable energy for sustainable development, Renewable and Sustainable Energy Reviews 2009;13:1584-591.

[3] Boudghene Stambouli A., Promotion of renewable energies in Algeria: Strategies and perspectives. Renewable and Sustainable Energy Reviews 2011;15:1169–181.

[4] Boudghene Stambouli A., Algerian renewable energy assessment: The challenge of sustainability. Energy Policy 2011;39:4507-519.

[5] Quaschning V., Technical and economical system comparison of photovoltaic and concentrating solar thermal power systems depending on annual global irradiation. Solar Energy 2004;44:171-78.

[6] Kane M., Favrat D., Ziegler K., Allani Y., Thermoeconomic analysis of advanced solar-fossil combined power plants. Int. J. Applied Thermodynamics 2000;3(4):191-98.

[7] Horn M., Führing H., Rheinländer J., Economic analysis of integrated solar combined cycle power plants. A sample case: The economic feasibility of an ISCCS power plant in Egypt. Energy 2004;29:935-45.

[8] Dersch J., Geyer M., Herrmann U., Jones S. A., Kelly B., Kistner R., Ortmanns W., Pitz-Paal R., Price H., Trough integration into power plants-a study on the performance and economy of integrated solar combined cycle systems. Energy 2004;29:947-59.

[9] Hosseini R., Soltani M., Valizadeh G., Technical and economic assessment of the integrated solar combined cycle power plants in Iran. Renewable Energy 2005;30:1551-555.

[10] Al-Soud M. S., Hrayshat E. S., A 50 MW concentrating solar power plant for Jordan. Journal of Cleaner Production 2009;14:625-35.

[11] Tsikalakis A., Tomtsi T., Hatziargyriou N.D., Poullikkas A., Malamatenios Ch., Giakoumelos E., Cherkaoui Jaouad O., Chenak A., Fayek A., Matar T., Yasin A., Review of best practices of solar electricity resources applications in selected Middle East and North Africa (MENA) countries. Renewable and Sustainable Energy Reviews 2011;15:2838–849.

[12] Assessment of the World Bank/GEF strategy for the market development of concentrating solar thermal Power. Global Environment Facility Program. The World Bank; 2006. Available at <http://www.worldbank.org/gef > [accessed 12.6.2011].

[13] Heller P., Pfänder M., Denk T., Tellez F., Valverde A., Fernandez J., Ring A., Test and evaluation of a solar powered gas turbine system. Solar Energy 2006;80:1225-230.

[14] Schwarzbözl P., Buck R., Sugarmen C., Ring A., Crespo, M. J. M., Altwegg P., Enrile J., Solar gas turbine systems: Design, cost and perspectives. Solar Energy 2006;80:1231-240.

[15] Xu C., Wang Z., Li X., Sun F., Energy and exergy analysis of solar power plants. Applied Thermal Engineering 2011;31:3904-913.

[16] Spelling J., Favrat D., Martin A., Augsburger G., Thermoeconomic optimization of a combined-cycle solar tower power plant. Energy; *Available online 29 April 2011*.

[17] Hu E., Yang Y., Nishimura A., Yilmaz F., Kouzani A., Solar thermal aided power generation. Applied Energy 2009;87 (9):2881-885.

[18] Baghernejad A., Yaghoubi M., Exergy analysis of an integrated solar combined cycle system. Renewable Energy 2010;35:2157-164.

[19] Suresh M. V. J. J., Reddy K. S., Kolar A. K., 4-E (Energy, Exergy, Environment, and Economic) analysis of solar thermal aided coal-fired power plants. Energy for Sustainable Development, 2010;14 (4):267-79.

[20] Baghernejad A., Yaghoubi M., Exergoeconomic analysis and optimization of an Integrated Solar Combined Cycle System (ISCCS) using genetic algorithm. Energy Conversion and Management 2011;52:2193-203.

[21] Popov D., An option for solar thermal repowering of fossil fuel fired power plants. Solar Energy 2011;85:344-49.

[22] Siva Reddy V., Kaushik S. C., Tyagi S. K., Exergetic analysis of solar concentrator aided natural gas fired combined cycle power plant. Renewable Energy 2012;39:114-25.

[23] Price H., Lüpfert E., Zarza E., Cohen G., Gee R., Mahoney R., Advances in parabolic trough solar power technology. Journal of Solar Energy Engineering, 2002;124:109-25.

[24] Geyer M., Lüpfert E., Osuna R., Esteban A., Schiel W., Schweitzer A., Zarza E., Nava P., Langenkamp J., Mandelberg E., EUROTROUGH - Parabolic trough collector developed for cost efficient solar power generation. In: Steinfeld A., editor. Proceeding of 11th Int. Symposium on Concentrating Solar Power and Chemical Energy Technologies; 2002 September 4-6; Zurich, Switzerland. Published by Paul Scherrer Institut:1-7.

[25] Fernández-García A., Zarza E., Valenzuela L., Pérez M., Parabolic-trough solar collectors and their applications. Renewable and Sustainable Energy Reviews 2010;14:1695-721.

[26] Dersch J., Geyer M., Herrmann U., Jones S. A., Kelly B., Kistner R., Ortmanns W., Pitz-Paal R., Price H., Trough integration into power plants—a study on the performance and economy of integrated solar combined cycle systems. Energy 2004;29:947-59.

[27] Szargut J., Morris D. R., Steward F. R., Exergy analysis of thermal, chemical, and metallurgical processes. Springer ; 1988.

[28] Kotas T.J., The exergy method of thermal plant analysis. Reprint edition, Krieger, Malabar, FL, 1995.

[29] Bejan A, Tsatsaronis G, Moran M, Thermal design and optimization. New York: Wiley; 1996.

[30] Kaushik S.C., Siva Reddy V., Tyagi S.K., Energy and exergy analyses of thermal power plants: A review. Renewable and Sustainable Energy Reviews 2011;15:1857-872.

[31] Reddy B. V., Butcher C., Second law analysis of a natural gas-fired gas turbine cogeneration system. International Journal of Energy 2009;33(8):728-36.

[32] Ehyaei M.A., Mozafari A., Alibiglou M.H., Exergy, economic & environmental (3E) analysis of inlet fogging for gas turbine, power plant. Energy 2011;36:6851-861.

[33] Khaldi F., Adouane B., Energy and exergy analysis of a gas turbine power plant in Algeria. Int. J. Exergy, 2011;9(4):399-13.

[34] Al jundi I. H., Energy and exergy analysis of a steam power plant in Jordan. Applied Thermal Engineering 2009;29:324-28.

[35] Regulagadda P., Dincer I., Naterer G.F., Exergy analysis of a thermal power plant with measured boiler and turbine losses. Applied Thermal Engineering 2010;30:970-76.

[36] Woudstra N., Woudstra T., Pirone A., van der Stelt T., Thermodynamic evaluation of combined cycle plants. Energy Conversion and Management 2010;51:1099-110.

[37] Ahmadi P., Dincer I., Rosen M. A., Exergy, exergoeconomic and environmental analyses and evolutionary algorithm based multi-objective optimization of combined cycle power plants. Energy 2011;36:5886-898.

[38] Srinivas T., Reddy B. V., Gupta A. V. S. S. K. S., Parametric simulation of combined cycle power plant: A Case Study. Int. J. of Thermodynamics 2011;14 (1):29-36.

[39] Cycle-Tempo, Release 5.0., Delft University of Technology. 2007. Available at <http://www.cycle-tempo.nl.>

[40] Shukin S., Annerfeldt M., Bjorkman M., Siemens SGT-800 industrial gas turbine enhanced to 47MW. Design modifications and operation experience. ASME Turbo Expo 2008: Power for Land, Sea and Air GT2008; 2008 Jun 9-13; Berlin, Germany. Proceedings of ASME:65-70.

[41] Steam turbines for solar thermal power plants. Siemens AG; 2008. Order No. E50001-W410-A105-V1-4A00. Available at <http://www.siemens.com/ energy> [accessed 12.6.2011].

[42] Therminol-VP1. Technical Bulletin. Available at <http://www.therminol.com> [accessed 12.6.2011].

[43] Moens L., Blake D., Mechanism of hydrogen formation in solar parabolic trough receivers. National Renewable Energy Laboratory; 2008 Feb. Technical Report NREL/TP-510-42468. Available at<http://www.osti.gov/bridge> [accessed 12.4.2012].

[44] Assessment of parabolic trough and power tower solar technology cost and performance forecasts. National Renewable Energy Laboratory; 2003 Oct. Subcontractor Report No. NREL/SR-550-34440. Available at<http://www.osti.gov/bridge> [accessed 12.6.2011].

ENERGY RECOVERY FROM MSW TREATMENT BY GASIFICATION AND MELTING TECHNOLOGY

F. Strobino[a], A. Pini Prato[b], D. Ventura[c] and M. Damonte[d]

a Paul Wurth Italia S.p.A. Via di Francia 1, I-16149, Genova, Italy,
fabrizio.strobino@paulwurth.com,(CA)
b,c,d University of Genova, Department of Thermal Machines, Energy Systems and Transportation
Via Montallegro 1, I-16145, Genova, Italy, salabi@unige.it

Abstract:

The increase of waste production, joined to the difficulties concerning both the identification of new disposal sites and the construction of big conventional incinerators, hardly accepted by the communities, led in recent years to the development of new technologies for waste management.
The waste gasification and melting treatments, if compared with conventional incinerating methods, allow reducing significantly the burdens on final disposal sites. Therefore gasifying and melting technologies are attracting more and more the attention of academia and market operators.
Consequently, the possibility to introduce in the Italian context the "Direct Melting System" (DMS) technology, designed and manufactured by Nippon Steel Engineering Co. Ltd., has been taken into account for the scope of proposed work.
DMS technology consists in MSW gasification, slags melting and combustion of the syngas produced, with the consequent generation of electric energy through a steam cycle. The system does not simply treat wastes; in fact it minimizes environmental impact because there is an effective recycling of useful resources since the melted slags are vitrified and inert and then still reusable, particularly for the most demanding tasks in terms of leachability such as road pavement. DMS technology has also the real advantage of owning a modular design. This aspect allows greater degree of flexibility in terms of matching communities needs, bringing therefore a significant advantage during the phase of site identification.
The aim of this article is to consider different plant configurations in order to optimize the energy recovery downstream the DMS module.
As a case study also landfill gas exploitation integrated in the DMS plant will be considered as a typical situation that could occur in the Italian scenario. The energetic input provided by the biogas is generally interesting because it allows improving the thermo-economic performances also thanks to market incentives.

Keywords:

DMS, gasification, landfill gas, melting, municipal solid waste, recycling, slag.

1. Introduction

Disposal of municipal solid waste is a problem that every local government has to face. Waste volume annually produced has been increasing almost constantly in the various European States [1]. In densely populated areas proper disposal of a considerable mass of waste and the need of large areas dedicated to the disposal are two important problems.

The EU has ruled issuing directives under which the legislative authorities of each Member State should act with regard to waste management [2]. These principles address to the so-called "integrated waste management" that can be pursued by: reducing the amount of waste produced, increasing the recycling and reuse, recovering energy from the not recyclable fraction and reducing the volume of waste conferred to landfill without having undergone any treatment [3, 4]. In fact landfilling of unsorted waste represents both a waste of resources, and a potential source of environmental contamination.

On the one hand exists the energy recovery maximisation goal, which leads to the hypothesis of a few large size plants network able to reach an highly efficient electric conversion, on the other hand the ethical-economic-environmental principle of "zero kilometer waste" leads to the hypothesis of a smaller size distributed waste-treatment plants network.

In the field of the innovative technologies for the municipal waste treatment, DMS technology has attracted strong interest. The technology has been designed by Japanese Nippon Steel Engineering Co. Ltd. and "DMS" means "Direct Melting System".

DMS technology is very competitive because, due to modularization, allows small and medium size treatment plants construction, performing energy recovery with overall efficiencies in line with similar size conventional technology plants [5].

This article is reporting the preliminary study carried out on some technical improvements, starting from the DMS original solution designed by Nippon Steel Engineering, aiming to the increase of electricity production in order to suit better on a specific Italian case, suggested by Paul Wurth Italia S.p.A.

The case study represents a potentially typical plant scheme for the Italian scenario and therefore proposed solutions are expected to be generally implementable in order to match Italian electric market requirements.

2. Italian regulatory framework

The current Italian legislation [6] provides an incentive scheme for plants that produce electricity from renewable sources (IAFR) based on the awarding of green certificates (CV). The weighed average value of such CV for the year 2011 was of 80 €/MWh [7].

DMS technology is among the ones that can receive this incentive for the share of electricity produced by the biodegradable fraction of MSW and the said share currently is conventionally set by the law at 51% [6].

The Italian law also recognizes a so called "all-inclusive tariff", currently amounting to 180 €/MWh [6] and paid directly by the GSE, for electricity produced from renewable sources that do not exceed the annual average power of 1 MW with the exclusion of all plants that use the source of solar and wind energy for which the limit is 200 kW. This category includes many systems that exploit the landfill biogas.

Electricity production in the Italian context turns out to be an important item for the cash flow of waste to energy plants.
In this sense, the study focused on increasing the overall electric efficiency and therefore on the increase of electric power production.

3. DMS technology

The technology has been derived from a thermal process used so far in the metallurgical industry, which has been extended to the urban waste treatment. The process (Fig.1) consists in MSW gasification and slags melting in a shaft furnace. The system provides a high degree of flexibility in treating different types of wastes both combustible and incombustible. This includes wastes that cannot be recycled at the collection level and those unsuitable for conventional technology based waste to energy plants, such as incineration residues, sludge, automobile shredded residues, landfill reclamation waste, CFC gas and asbestos [8, 9]. This technology can be defined safe and reliable because 35 plants are nowadays in commercial operation (since the first installation in 1979) [10].

The process consists in a combined treatment of waste gasification, combustion of the syngas produced and slags melting. The gasification and melting occur within the same equipment that consists in a shaft furnace where waste is introduced from the top (after size reduction) together

with coke and limestone in percentage of around 4-5% of the waste input quantity (depending on the characteristics of the waste) [11]. The slags are discharged through the bottom of the furnace and granulated by a cooling system.

The syngas generated in the DMS is emitted from the top of the furnace and completely oxidized in the post-combustion chamber, by controlling the temperature, the turbulence and the residence time. Thanks to the homogeneous conditions of combustion which is taking place between gaseous phases, the pollutants generation is limited in comparison to conventional mass burn incineration and the plant, equipped with state-of-the-art flue gas treatment line, can achieve emissions into atmosphere that are by far lower than regulatory limits and fully in compliance with BREF both in terms of pollutants concentration and volume of flue gases [12].

The exhaust flue gas heat can be used to produce electricity by a recovery boiler and a steam cycle [13].

The system does not simply treat wastes; in fact it minimizes environmental impact because there is an effective recycling of useful resources since the melted slags are vitrified and inert and then still reusable, particularly for the most demanding tasks in terms of leachability such as road pavement. Even metal produced as final output of DMS can be reused as a resource [14]. At the end of the process, the only residue to landfill is made up from the fly ashes caught by the filters and generally it amounts at about the 2-3% of the waste input [14].

The system has generally a modular design, with multiple melting furnaces working in parallel, which allows flexibility and reliability, while the auxiliary systems can be grouped as a single module. Such an aspect allows greater degree of flexibility also in terms of matching communities needs, bringing therefore a significant advantage during the phase of site identification.

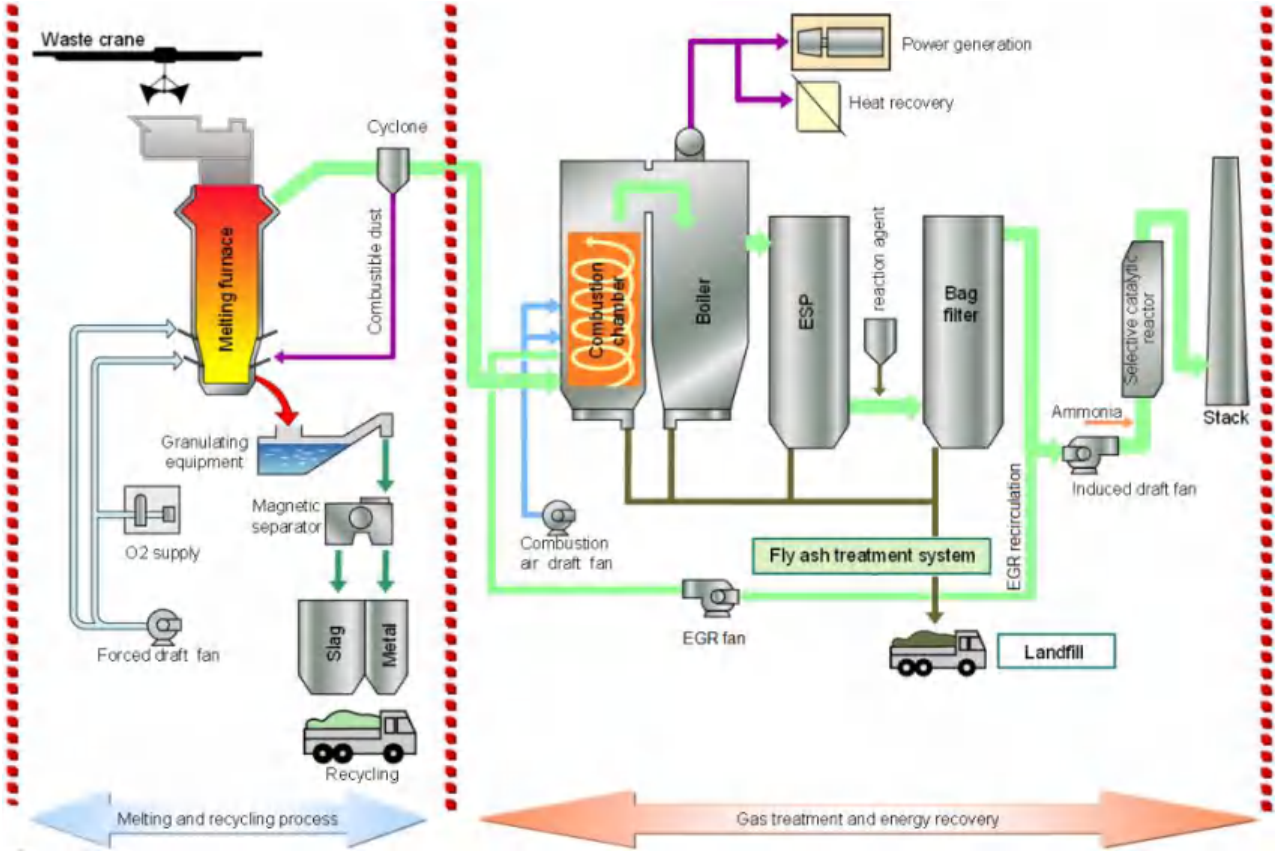

Fig. 1. Process diagram.

4. Case of study

The plant will have to treat 60,000 t/y and the average composition of wastes is reported in Table 1. The mean lower calorific value (LCV) of the feeding mixture is 10,691 kJ/kg and the heat flow diagram for the baseline solution is reported in Fig. 2. The area identified for the construction of the plant is located near to a landfill that provides a flow of biogas which should not be dispersed into the atmosphere and therefore has to be used for power generation. The average biogas mass composition consists of approximately 49.9% of methane, 27% carbon dioxide, 10.8% nitrogen, 9.5% moisture, 1.86% oxygen and argon, plus traces of other compounds.

Table 1. MSW average composition.

MSW average composition	C % d.b.	H % d.b.	O % d.b.	N % d.b.	S % d.b.	Ashes % d.b.	H_2O %w.b.	L.C.V. w.b. kJ/kg
Paper	44.80	6.00	43.30	0.24	0.16	5.50	15.00	12,100
Cardboard	43.85	6.00	45.00	0.25	0.20	4.70	12.50	13,100
Other cellulosic	52.24	7.70	37.83	0.15	0.09	1.99	20.00	11,500
Textiles	52.00	6.30	35.83	3.20	0.17	2.50	20.00	14,200
Wood	50.00	6.00	42.32	0.20	0.08	1.40	22.00	13,800
Plastic	61.60	8.50	17.40	2.30	0.20	10.00	6.00	28,300
Rubber	81.20	9.00	0.00	0.90	0.90	8.00	2.00	20,800
Glass and inerts	3.00	0.40	0.40	0.15	0.05	96.00	2.50	0
Metals	4.50	0.60	4.28	0.07	0.05	90.50	4.00	0
Domestic organic waste	48.00	6.00	34.00	2.18	0.32	9.50	70.00	2,100
Cuttings and prunings	47.00	6.20	37072	2.85	0.23	6.00	50.00	6,040
Organic waste	48.00	6.17	34.10	2.40	0.33	9.00	70.00	2,100
Undersize	26.35	5.50	30.50	2.50	0.15	35.00	30.00	5,400

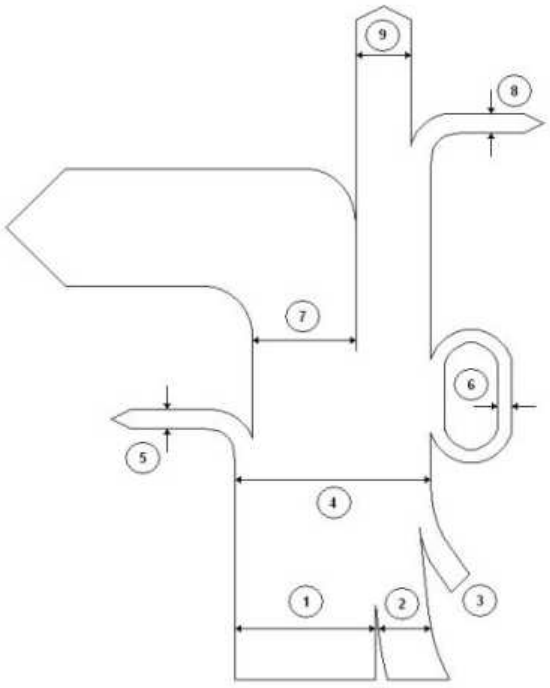

HEAT BALANCE		
ITEM	(MW)	(%)
1 – Waste-holding heat quantity	24.75	86.85
2 – Coke-holding heat quantity	2.82	9.89
3 – Supplied air sensible heat	0.93	3.26
4 – Total heat input	**28.50**	**100.00**
5 – Molten matter heat quantity	0.78	2.73
6 – EGR sensible heat	0.29	1.00
7 – Boiler recovery heat quantity	22.66	79.53
8 – Radiation heat loss	1.84	6.45
9 – Flue-gas sensible heat	3.22	11.29

Fig. 2. Heat flow diagram.

It can be noticed that the availability of the biogas will decrease from a value of 1,000 Nm^3/h till 406 Nm^3/h (Fig. 3). Both mean biogas and waste composition values are the result of experimental and statistical data processing.

In order to use the energy released by the combustion of biogas at high temperature, it was chosen to apply only external components outside DMS to avoid the redesign of the module and to maintain independent from the actual biogas availability the superheated steam output parameters outgoing the module.

Fig. 3. Estimated biogas production.

5. Plant solutions

The steam cycle shown in Fig. 4 is the basic configuration, designed for heat recovery from the flue gas coming out from the DMS. The boiler consists of an evaporator (EVA) a superheater (SH1) and an economizer (ECO). The steam generation does not occur only in the recovery boiler, but also in the bottom of the combustion chamber covered by boiler pipes.

The flow rate coming from the DMS is about 48,400 Nm^3/h and it is available at a temperature of 1,100°C and it exchanges heat with steam till 200°C.

In the superheater the steam reaches a maximum temperature of 428°C. The steam cycles subjected to DMS technology in Japan, reach a maximum temperature of 400°C [15] and this choice is mainly due to two reasons:

- in Japan there is only moderate interest in producing electricity from waste to energy plants because there are not incentives, hence the lack of need to reach high performances;
- steam temperatures above 430°C may cause problems of corrosion of pipe bundles [16].

In Italy electric generation efficiency must be maximized to exploit the beneficial contribution of market incentives.

Considering on the one hand minimum steam quality (in terms of water to vapour ratio) accepted by steam turbine manufacturer at the end of the expansion and on the other hand maximum temperature allowed by material resistance to corrosion, the implemented thermodynamic cycle optimization process has led to the selection of the steam condition equal to 428°C and 65 bar at turbine inlet.

The search for a further performance increase would lead to reach higher values of pressure, but this would necessarily require to adopt a reheater which is not justified given the small size of the plant [17].

In the gas treatment line, there are two heat exchangers which aim to preheat the feed water and at the same time to cool the flue gases coming from the DMS, before they are ejected from the stack.

With regard to the condenser, the choice falls on the air-cooled one for two main reasons:

- the use of water as coolant needs complicated path authorization;
- the air-cooled condenser is not tied to the availability of water.

Moreover the benefits, in terms of cycle efficiency, obtained by using water instead of air are negligible because, in each of the two cases, it is necessary to opt for a different cycle pressure. The maximum steam cycle pressure allowed when using water as coolant is 45 bar because the increase of this pressure would compromise the steam quality at the end of the expansion.

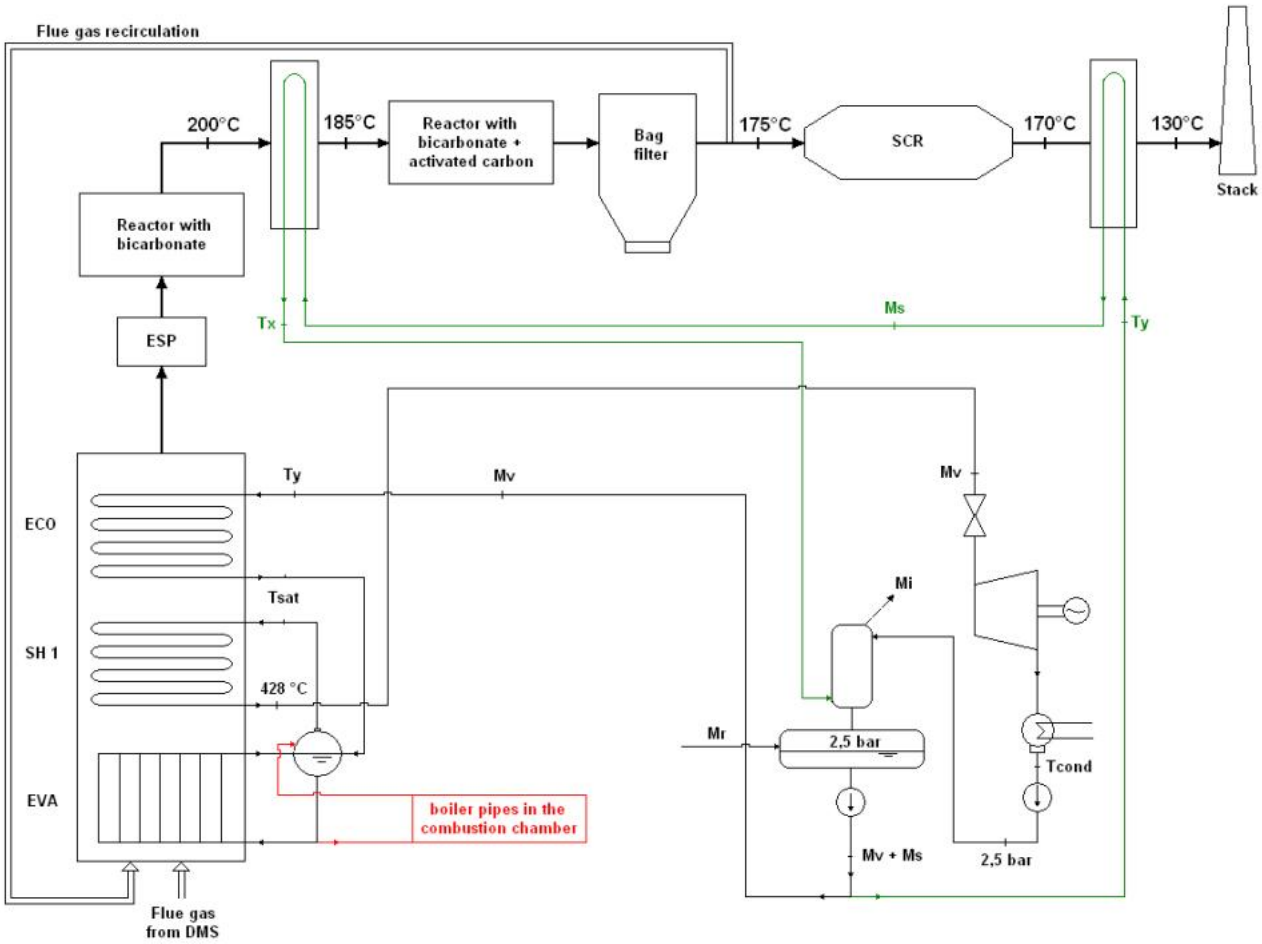

Fig. 4. Steam cycle – Basic configuration.

The second plant configuration (Fig. 5) aims to exploit the biogas produced in the landfill. The flue-gases generated by the biogas combustion are not critical with regard to pipes bundle corrosion as DMS ones, so it is possible to realize an external superheater (SH2) which can further increase the steam temperature above 428°C. Thus in an external component, i.e. separated from the main flue-gas stream proceeding from the DMS, it is possible to reach higher temperatures without any problems due to the pipe bundles corrosion.

Flue gases generated by biogas combustion are available at a temperature of about 680°C and they are cooled to 460°C. With this energetic input it is possible to reach a temperature of about 470°C (with an average biogas flow rate of 700 Nm^3/h); this value is far from the typical temperature of about 540°C which characterizes the steam cycle of fossil fuelled power plants, but that is because the biogas flue-gas flow rate is small if compared to the flow rate coming out from the DMS.

Heat remaining in the biogas flue gases is then used in a heat exchanger to preheat the feed water. The increase in temperature, both of the feed water and of the superheated steam, can increase the overall electric efficiency and the power production.

The possibility to exploit the biogas directly into the DMS module was discarded in principle because the post-combustion chamber and the boiler redesign and optimization would not be justified given the uncertainty about the availability of biogas, hence the need for the use of a configuration with an external component.

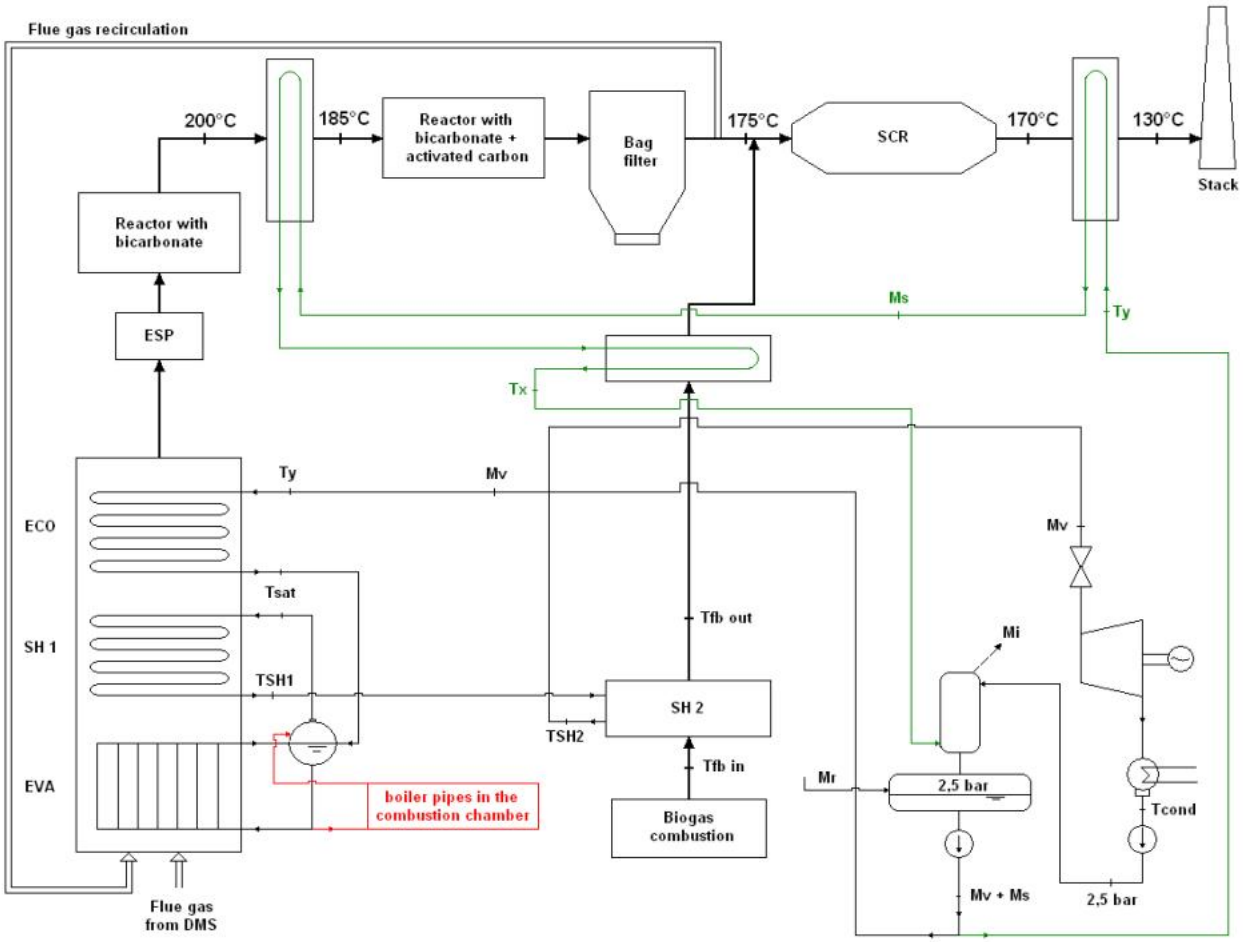

Fig. 5. Steam cycle – Configuration with external superheater.

Another plant solution with an external component (Fig. 6) has been taken into account. The biogas can be used in an external evaporator, to produce more steam. The flue gases coming from the DMS module are cooled till about 310°C and the maximum temperature reached from the steam is 428°C like the base configuration. Also with this configuration, is possible to use the heat remaining in the biogas flue gas coming from the external evaporator, to preheat the feed water.

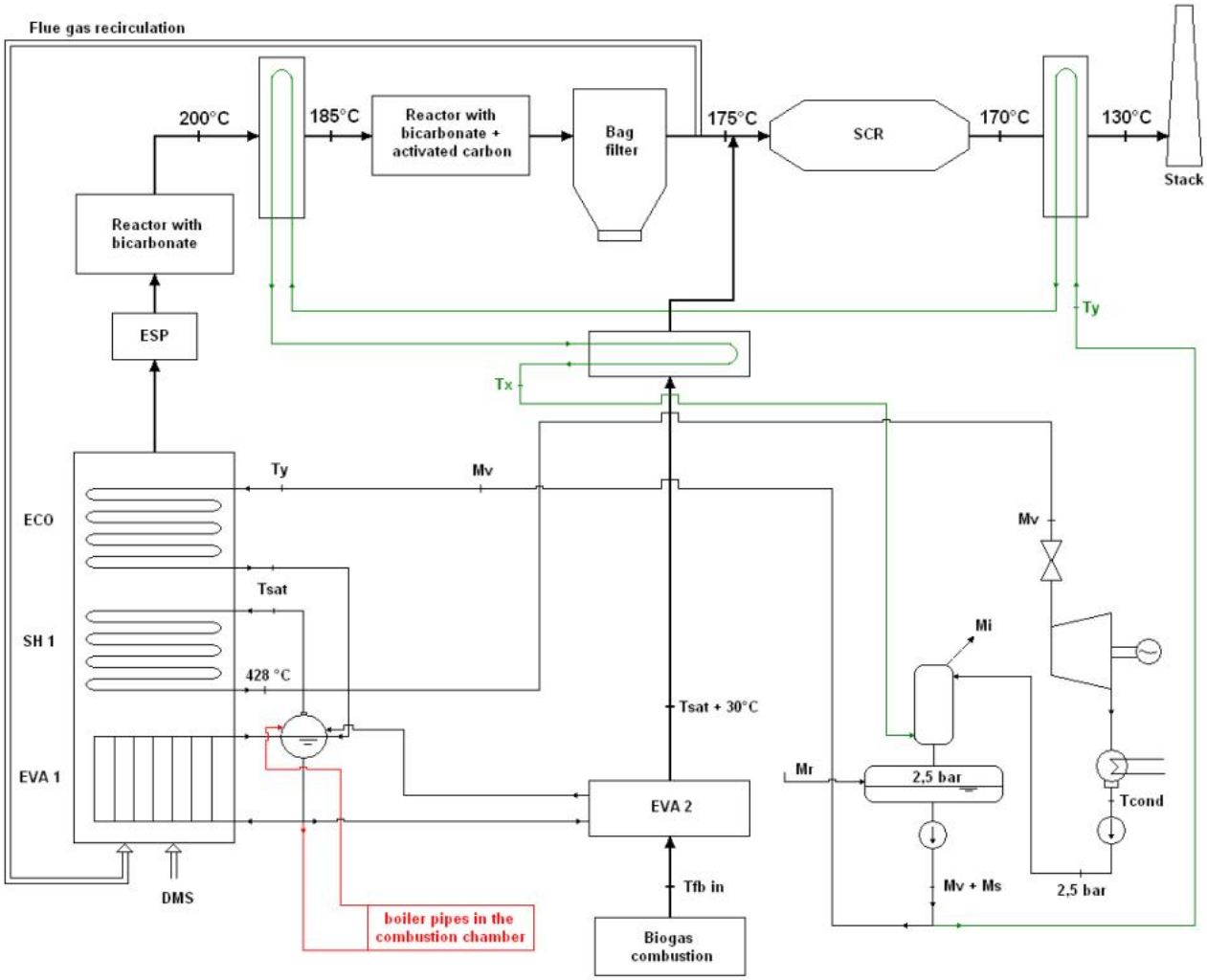

Fig. 6. Steam cycle – Configuration with external evaporator.

The last plant solution (Fig. 7), considered in present work, consists in coupling DMS plant with a biogas internal combustion engine. Part of the biogas (about 430 Nm^3/h) is burned in the engine with an electric efficiency of 33% and it is possible to produce about 700kW. The biogas flue gases, at a temperature of 500°C are still usable in a heat exchanger with the task to further preheat the feed water. The remaining part (about 280 Nm^3/h) can be recovered in the external component, evaporator or superheater. In this case, the plant solution is very flexible and also competitive from an economic point of view, because the electric power generated from the engine awards considerable incentives.

In most plants, the feed water degassing is made by means of a steam bled from the turbine. On the contrary, the plant here described proposes a solution that does not require to bleed any steam from the turbine, in order not to penalize the work obtained from the expansion with the aim to maximize the energy production. In this solution (Fig. 8), a portion of the feed water flow rate, is bled at a pressure of 65 bar (cycle pressure) and sent to a heat exchanger where it can exploit the heat of the flue gases coming from the recovery boiler. The water reaches a temperature T_x with an enthalpy $h_x=h_L(65\ bar, T_x)$; then it expands maintaining the same enthalpy. The steam produced in this way, at an enthalpy condition h_x can degas and preheat the water coming from the condenser.

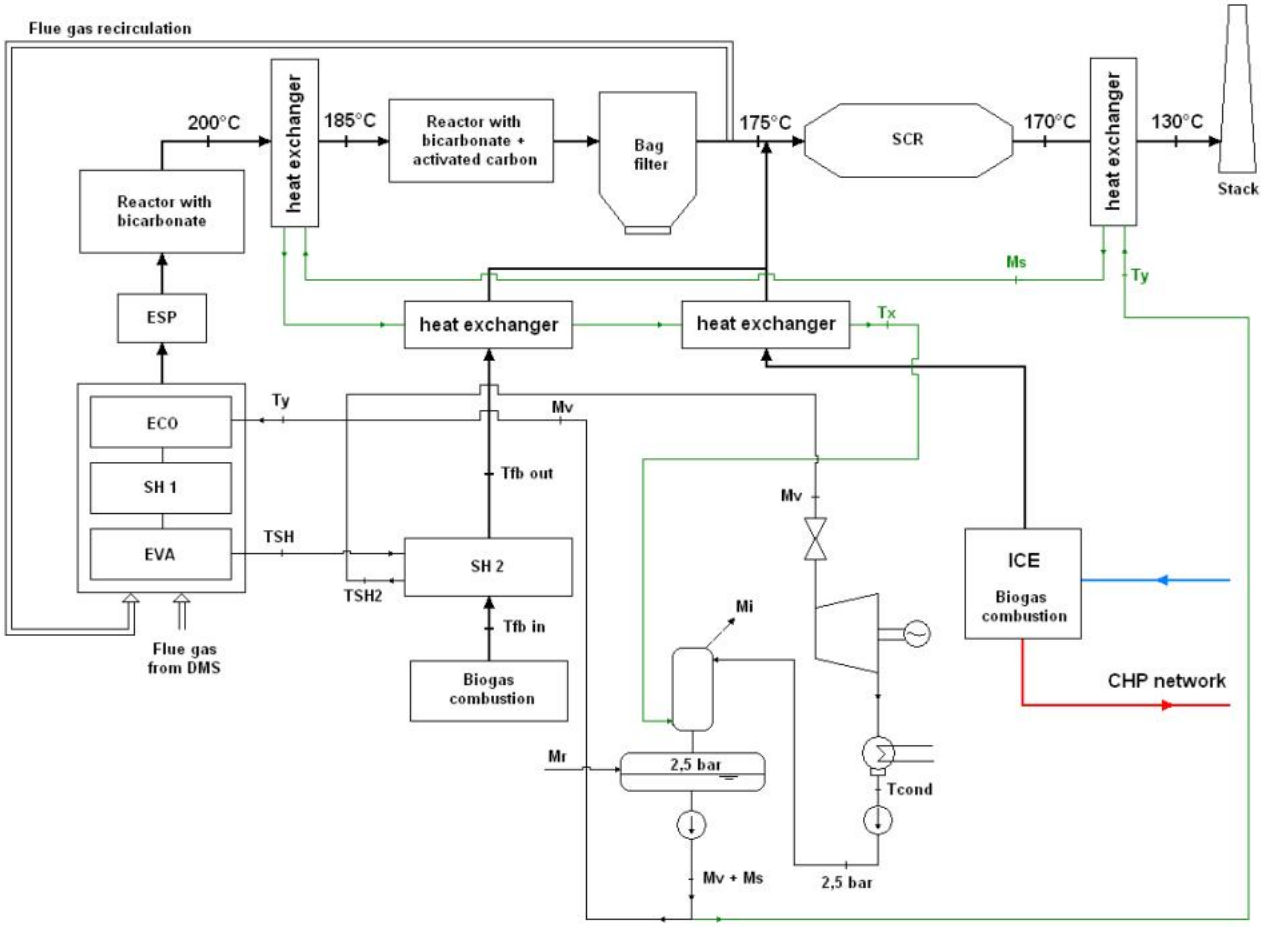

Fig. 7. Steam cycle – Configuration with external superheater coupled with ICE

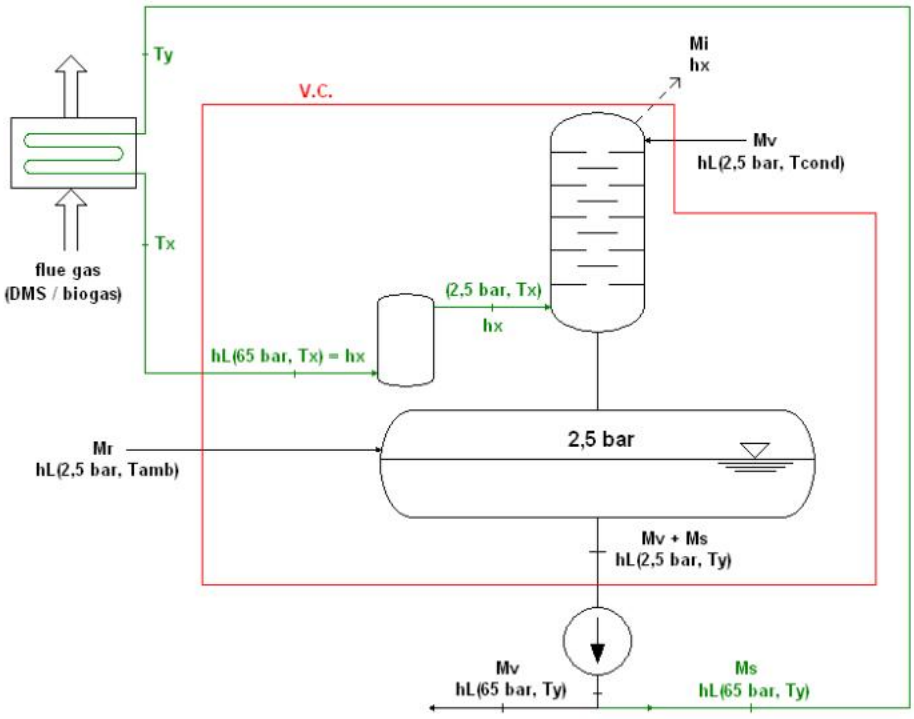

Fig. 8. Degassing system

6. Results

Results obtained from analysis are reported in Table 2. All results are referred only to the DMS plant, so in the case of presence of the internal combustion engine (ICE) (with a biogas flow rate of 430 Nm^3/h), the electrical power output has to be increased by 700 kWh_{el}.

Table 2.

Configurations	Biogas mass flow rate recovered by DMS [Nm^3/h]	DMS net electric power output [kWh_{el}/t_{MSW}]	DMS net overall electric efficiency[1] [%]
Basic configuration	-	626	18.52
Cycle with external SH	700	714	18.78
Cycle with external SH and ICE not coupled	270	663	18.66
Cycle with external SH and ICE coupled	270	686	18.91
Cycle with external EVA	700	701	18.43
Cycle with external EVA and ICE not coupled	270	657	18.49
Cycle with external EVA and ICE coupled	270	679	18.71

In the configurations with DMS and ICE coupled, the DMS net overall electric efficiency is better than the case of all biogas recovered in the external SH/EVA. In fact the largest part of biogas power input is exploited in a higher efficiency converter like ICE and DMS receives only as direct energy input the ICE waste heat and a little part of biogas flow.

Basic configuration results are included in the typical performance range of 400÷700 kWh_{el}/t_{MSW} for commercial gasification technologies [18]. Other solutions overcome this range up to +10% due to the landfill biogas combustion contribute (directly or indirectly). To note that steam cycles subjected to the DMS technology of Japanese operating plants, with steam at a pressure of 40 bar and a temperature of 400°C reach a net overall electric efficiency of approximately 16% (194,000 t_{MSW}/y) [12].

7. CHP option

Coupled DMS and biogas engine solutions can achieve the best electric performances, so it was interesting for these solutions to analyze the performance sensitivity versus the heat cogeneration. It was examined a solution using a steam bleed from the turbine at a pressure of 4 bar and a temperature of 146°C to heat a pressurized water flow from 80°C to 120°C which can feed a district heating network.

These coupled solutions allow to maximise the electric production even exploiting a thermal load.

In fact, owning to the electric production incentive frame that induce not to regulate, if the ICE works independently, it will dissipate part of the exhaust gas heat when the district-heating load is under the effective ICE production capacity. In this sense coupled solutions offer a more flexible ratio between electrical power output and thermal power output than not coupled ones by reason of the variable steam bleed.

[1] DMS net overall electric efficiency is obtained by the following ratio: $\frac{\text{Electric Power} - \text{Own consumptions}}{\text{Energy inputs (Waste, Coke, Biogas)}}$

Table 3.

Configurations	DMS electric production [%]	Net electric power [kWh_{el}/t_{MSW}]	Thermal power [kWh_{el}/t_{MSW}]	DMS net overall electric efficiency [%]
Cycle with external SH and ICE coupled	100	686	0	18.91
	90	617	278	17.01
	80	549	552	15.14
Cycle with external EVA and ICE coupled	100	679	0	18.71
	90	612	274	16.86
	80	544	548	14.98

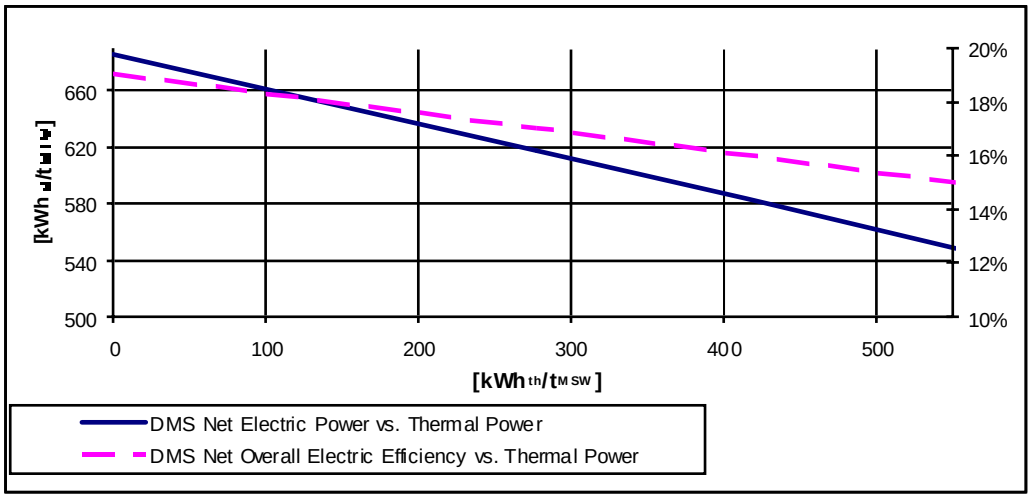

Fig. 9. DMS net electric power production and DMS net overall electric efficiency vs. Thermal power generation diagram for Cycle with external SH and ICE coupled

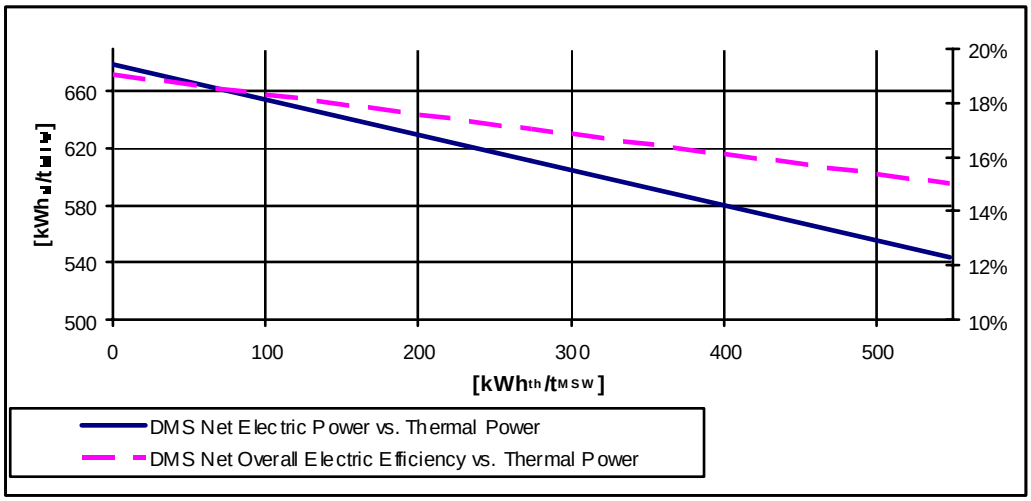

Fig. 10. DMS net electric power production and DMS net overall electric efficiency vs. Thermal power generation diagram for Cycle with external EVA and ICE coupled

According to the steam bleed progressive increase, electric performances decrease linearly with the increase of the heat production.

DMS CHP option is particularly suitable because if necessary it achieves up to 550 kWh/t_{MSW} of thermal power in respect of a reduction of overall electrical efficiency of only 4 percentage points.

CHP option is generally very suitable to improve environmental and economical performance of waste to energy plants compensating for their lower overall electric efficiency, caused by technical constraints, and their higher specific capital costs [19].

Furthermore, a significant aspect is that with a bleed of steam corresponding to a thermal power of about 440 kWh/t_{MSW} it is possible to produce approx. 26 GWh_{th}/y. This thermal energy corresponds to the heating requirements of 5,000 inhabitants in climatic zone E[2] with 2850 degree-days [20]. It thus demonstrates the versatility of the DMS in particular to serve small communities needs on the territory, while maintaining the electric standard efficiency usually accepted in Japan.

8. Conclusions

Italian and European laws prescribe to increase recycling and reuse and to decrease waste production and landfilling. The share of non-recyclable waste must be treated in plants for energy recovery in order to reduce volumes landfilled and reduce, as much as possible, danger of environmental contamination.

In Italy, the construction of these facilities is supported by an incentive that rewards the production of electricity.

The techniques to reach high conversion efficiencies to electricity require the realization of large size plants. These need during their life cycle to be fed with a waste flow that often comes from areas very far from the plant. This factor, together with the largest impact on the surrounding environment, often causes opposition of local people to their implementation.

Moreover recycling and reducing policy should ensure that the amount of unsorted waste decreases over the years, making difficult to operate the plant at design treatment capacity.

The present study considered the application of DMS technology in a particular Italian scenario requiring landfill biogas exploitation.

The results lead to say:

- DMS technology reaches high value of overall net efficiency (all solutions exceed 18%), considering a small plant size (60,000 t_{MSW}/y);
- coupling DMS with external SH or EVA and ICE can maximize revenue from electric energy production incentives even in CHP configuration.

More generally DMS technology energy recovery performances result aligned with other non conventional waste to energy technologies, while at the same time DMS features the peculiar advantage of minimizing the volume of material landfilled thanks to the slag and metal reuse. This fact represents a significant improvement in economical and in environmental terms. If the site chosen for construction offers a biogas flow rate, DMS technology can improve its performances by external components and if coupled with an ICE it can guarantee a very flexible electrical power vs. thermal power ratio in CHP configuration.

In particular, concerning environmental performances, the basic configuration examined in present work generates emissions into atmosphere that are by far lower than regulatory limits and analogous to those of modern conventional incinerators equipped with efficient flue gas cleaning systems according to BREF, both in terms of pollutants concentration and volume of flue gases [12].

At this stage of the study, as regards both the external evaporator configuration and the external superheater configuration, the pollutants incremental contribution to the DMS exhaust flow gases was not deemed significant, considering both biogas combustion gases small volume and low

[2] According to Law Decree D.P.R. N. 412 (1993) the Italian territory is divided into 6 climatic zones with the purpose of reference for the estimation of space heating systems average energy consumption. These climatic zones are named with letters from A to F in function of number of degree-days. Zone A includes the municipalities featuring a number of degree-days up to 600 whilst Zone F includes the municipalities featuring a number of degree-days greater than 3,000.

temperature due to cooling effect provided by high combustion air excess. In addition, these two conditions of combustion and heat exchange seem to have no more critical elements than ICE combustion that is deemed fully environmental acceptable in similar applications.

Finally, concerning the investment, previous studies have shown how, although the insertion of components such as external SH and EVA in addition to DMS baseline configuration or CHP option increase the initial investment amount, the Net Present Value and the Internal Rate of Return of the project are improved by the increase of revenue items [21].

Nevertheless economically best solution, among the ones discussed in this preliminary study, depends strongly on specific scenario and in particular on available biogas flow amount, heat demand and site characteristics.

Nomenclature

BREF	Reference Document on the Best Available Techniques for Waste Incineration (European Commission Integrated Pollution Prevention and Control)
CHP	Combined Heat and Power
CV	"Certificato verde" (Green Certificate)
DMS	Direct Melting System
d.b.	dry basis
ECO	Internal economizer
EGR	Exhaust gas recirculation
ESP	Electrostatic Precipitator
EVA	Internal evaporator
EVA1	Internal evaporator
EVA2	External evaporator
GSE	"Gestore Servizi Energetici", Italian state owned energy service company
h	enthalpy, kJ/kg
hL	enthalpy in liquid phase conditions, kJ/kg
IAFR	"Impianto Alimentato da Fonti Rinnovabili" (Plant Powered by Renewable Sources)
ICE	Internal Combustion Engine
LCV	Lower Calorific Value
mi	incondensable mass flow rate, equal to *mr*, kg/s
mr	reintegration mass flow rate, 2% of *mv*, kg/s
ms	feed water mass flow rate bled, kg/s
MSW	Municipal Solid Waste
mv	mass flow rate at turbine inlet, kg/s
SCR	Selective Catalytic Reactor
SH1	Internal superheater
SH2	External superheater
Tamb	ambient temperature, °C
Tcond	steam condensing temperature, °C
Tfb in	biogas flue gases temperature at external superheater inlet, °C
Tfb out	biogas flue gases temperature at external superheater outlet, °C
Tsat	steam saturation temperature, °C
TSH1	superheated steam temperature at boiler outlet, °C

TSH2 superheated steam temperature at external superheater outlet, °C

Tx degassing system inlet temperature

Ty ECO inlet steam temperature, °C

w.b. wet basis

References

[1] ISPRA, Rapporto rifiuti urbani edizione 2009, Roma, 2010 – Available at:<http://www.isprambiente.gov.it/site/it-IT/Pubblicazioni/Rapporti/> (in Italian).

[2] European Directive 2006/12/CE, 5/04/2006.

[3] Arena U., Gassificazione dei rifiuti solidi urbani: stato dell'arte dei principali processi e tecnologie. RS Rifiuti Solidi vol. XXVI n. 1 Gennaio-Febbraio 2012 (in Italian).

[4] Arena U., Advantage aspects of combustion and gasification processes for thermal treatment of municipal solid wastes, International waste management and landfill symposium, Sardinia, Italy; 2011.

[5] Belgiorno V., De Feo G., Della Rocca C., Napoli R.M.A., Energy from gasification of solid wastes. Waste Management 2003; 23: 1-15.

[6] Ministerial Decree, 18/12/2008, Incentivazione della produzione di energia elettrica da fonti rinnovabili, ai sensi dell'articolo 2, comma 150, della legge 24/12/2007 n. 244, Gazzetta ufficiale del 02/01/2009 (in Italian).

[7] Gestore dei mercati energetici, Market data available at < www.mercatoelettrico.org > (in Italian).

[8] Tanigaki, N., Motoyama K., Osada M., Jung B., Lee Y, Operating performance of gasification and melting facility in Korea, Proceedings of International conference on Combustion, Incineration/Pyrolysis and Emission Control (i-CIPEC 2008), Chiang Mai, Thailand; 16-19 December 2008: 416-421.

[9] Tanigaki N., Manako K., Osada M., Co-gasification of municipal solid waste and material recovery in a large-scale gasification and melting system. Waste Management 2012; 32: 667-675.

[10] <http://www.nsc-eng.co.jp>.

[11] Osada M., Murahashi K., Shibaike H., Characteristics of gasifying combustion in MSW Direct Melting System, Proceedings of International conference on Combustion, Incineration/Pyrolysis and Emission Control (i-CIPEC 2000), Seoul, Korea; 8-10 June 2000: 101-107.

[12] Genon G., Tedesco V., Urso P., Assessment of the feasibility of an innovative technology plant aimed at the energetic valorization of municipal waste in the province of Turin, Third Symposium on Energy from Biomass and Waste, Venice, Italy; November 2010.

[13] Chiappero A., La tecnologia DMS per la gassificazione dei rifiuti solidi urbani. Le tecnologie per il recupero di energia da rifiuti a confronto. Politecnico di Milano sede di Piacenza, 18 June 2008 (in Italian).

[14] Takamiya K., Osada M., Shibaike H., Kajiyama H., Reclamation waste treatment using a gasification and melting system, International waste management and landfill symposium, Sardinia, Italy; 2007.

[15] Manako K., Kashiwabara T., Kobata H., Osada M., Takeuti S., Mishima T., Dioxins control and high-efficiency power generation in a large-scale gasification and melting facility, Proceedings of 27th International Symposium on Halogenated Persistent Organic Pollutants (DIOXIN 2007), Tokyo, Japan; 2007.

[16] Berlo M. V., Simoes P, High efficiency waste-to-energy: Amsterdam's experiences after 4 years of operation, International waste management and landfill symposium, Sardinia, Italy; 2011.

[17] Genon G., Tedesco V., Urso P., Verifica della fattibilità di un impianto di trattamento termico dei rifiuti a tecnologia innovativa nella Provincia di Torino. Milan: CIPA Editore, 2010 (in Italian).

[18] Arena U., A critical assessment of municipal solid waste gasification, International waste management and landfill symposium, Sardinia, Italy; 2011.

[19] Consonni S., Giugliano M., Grosso M., Alternative strategies for energy recovery from municipal solid waste Part A: Mass and energy balances. Waste Management 2005; 25: 123-135.

[20] Pini Prato A., Strobino F., Broccardo M., Parodi Giusino L., Integrated management of cogeneration plants and district heating networks. Applied Energy 2012, article in press doi: 10.1016/j.apenergy.2012.02.038.

[21] Damonte M., Ventura D., Ottimizzazione del recupero energetico da RSU mediante tecnologia DMS. Master thesis. Università di Genova, Italy, March 2011 (in Italian).

Ethanol production by enzymatic hydrolysis from sugarcane biomass – the integration with the conventional process

Reynaldo Palacios-Bereche[a], Adriano Ensinas[b], Marcelo Modesto[c], and Silvia Nebra[d]

[a] Centre of Engineering, Modelling and Social Sciences, Federal University of ABC (CECS/UFABC), Santo André, SP, Brazil, reynaldo.palacios@ufabc.edu.br
[b] Centre of Engineering, Modelling and Social Sciences, Federal University of ABC (CECS/UFABC), Santo André, SP, Brazil, adriano.ensinas@ufabc.edu.br
[c] Centre of Engineering, Modelling and Social Sciences, Federal University of ABC (CECS/UFABC), Santo André, SP, Brazil, marcelo.modesto@ufabc.edu.br
[d] Centre of Engineering, Modelling and Social Sciences, Federal University of ABC (CECS/UFABC), Santo André, SP, Brazil, and Interdisciplinary Centre of Energy Planning, University of Campinas (NIPE/UNICAMP), Campinas, SP, Brazil, silvia.nebra@pq.cnpq.br

Abstract:

The aim of this study is to make an evaluation of the possibilities of ethanol production increase through the introduction of bagasse hydrolysis process in conventional distilleries, considering the limiting situation of bagasse use: it is the major by-product in sugar and ethanol production and is burnt in boilers to satisfy the steam and power requirements of the process. Simulations in ASPEN PLUS® software were performed, in order to evaluate the mass and energy balances, for the integrated process, considering the pre-treatment of sugarcane bagasse by steam explosion. The cogeneration system was also modelled and integrated with the ethanol production process. It consists of a steam cycle with backpressure steam turbines and parameters of live steam of 67 bar and 480°C. In all the cases studied it was considered that the steam flow used in the system was just that necessary to fulfil the process thermal needs, so, it was assumed that the surplus of bagasse was used to produce ethanol. The use of sugarcane trash was considered in order to accomplish the energetic needs of the overall process as well as lignin cake, which is a hydrolysis process residue. Several cases were evaluated, which include: the conventional ethanol production plant without hydrolysis (Case I), the conventional plant joint with hydrolysis process without thermal integration considering different solid contents in the hydrolysis reactor (Cases II, III and IV), and the conventional plant joint with the hydrolysis process considering thermal integration through Pinch method (Case V). The results shown a modest ethanol production increase of 9.7% for the situation without thermal integration and low solid content in the hydrolysis reactor, on the other hand, the case where thermal integration was applied presented an ethanol production increase of 17.4%.

Keywords:

Ethanol, sugarcane, enzymatic hydrolysis, thermal integration.

1. Introduction

Ethanol is produced in Brazil in large scale using sugarcane as raw material by fermentation of sugars and distillation. World consumption of ethanol tends to grow in the next years because of the growing interest of many countries by biofuels use, due to factors such as: environmental damage (avoided emissions of greenhouse gases) energy security (diversification of energy sources and reducing dependence on oil) and support to farmers [1]. The sugarcane bagasse is the major by-product in sugar and ethanol production and it is burnt in boilers to satisfy the steam and power requirements of the process. Sugarcane bagasse, as well as other lignocellulosic materials, can be also used for ethanol production but, the introduction of the bagasse hydrolysis process in the current ethanol production system is a real challenge, being bagasse the fuel of the current process and at the same time, raw material for the new one. Thus, the aim of this study is to make an evaluation of the possibilities of ethanol production increase through the bagasse hydrolysis

process, considering the limiting situation of bagasse use. Simulations in ASPEN PLUS® software were performed, in order to evaluate the mass and energy balances and Pinch Analysis was used to determine the minimum hot and cold utilities required by the integrated process in order to increase the ethanol production. The characteristics of the cogeneration system were adopted considering devices currently used in the new industrial plants, and prioritising the increase in ethanol production, and not electricity cogeneration.

2. Description and modelling of ethanol and electricity production process from sugarcane

2.1. Conventional ethanol and electricity production process from sugarcane

In this study, a plant producing anhydrous ethanol and electricity was considered, using sugarcane as raw material.

Sugarcane is composed essentially of juice and fibres. The juice is an aqueous solution of sugars (meanly sucrose and small fractions of fructose and glucose monosaccharaides) and other organic and inorganic substances (minerals and impurities). Fibre is defined as all insoluble material in cane. The composition of sugarcane stalks depends on a large number of factors, including the age of the cane, growing conditions, disease, while the composition of sugarcane delivered to the factory depends on stalk composition, cane variety, age, amount of tops and leaves and other exogenous matter carried in harvesting operation [2].

The sugarcane composition adopted in this study is shown in Table 1. Due to the fibre components cellulose, hemicellulose and lignin, are not in database of ASPEN PLUS® simulator, these components were created and their properties were specified using parameters reported in [3].

Table 1. Sugarcane composition specified in simulation [4]

Component	% Mass
Sucrose	13.85
Fibres	13.15
Reducing sugars	0.59
Minerals	0.20
Others non saccharides	1.79
Water	69.35
Soil	1.07

In sugarcane factory the process begins with the cleaning operation: the sugarcane that arrives to the factory contains some amount of soil that is carried in the harvesting operation; so, it must be cleaned upon reception. Dry cleaning was considered in the simulation. After that, cleaned sugarcane goes to the extraction system where sugarcane juice and bagasse are obtained; an extraction system with mills was considered. From specifications in the extraction system, the composition of bagasse obtained was (dry basis, wt.): cellulose 36.8% wt., hemicelluloses 35% wt., lignin 20.3% wt. and ashes 2.3%. The moisture content of bagasse (wet basis, wt.) was 50%.

Raw sugarcane juice goes to the physical-chemical treatment while bagasse goes to the cogeneration system. For juice treatment, the following operations were considered: screening, heating, liming, decantation and mud filtration. After that, the clarified juice goes to the concentration stage.

In conventional autonomous distilleries, the must for ethanol production is prepared from sugarcane juice, its concentration is necessary in order to obtain an adequate must sugar concentration for the fermentation process. Thus, a part of the clarified juice, with its original sucrose content of 11.8%,

is concentrated in an evaporation system of multiple effects to achieve a sucrose content of 55.4%. Then, the original clarified juice is mixed with the concentrated one, resulting in a must with a sucrose content of 17%.

In the evaporation system, part of the vapours, resulting from the concentration process, are used to satisfy heat duties in the plant and other part is used in the next evaporator body as heating source.

The must sterilization is done using a treatment type HTST (High Temperature Short Time). In this study it was adopted that must is heated until 130°C. After that, there is a fast cooling until a fermentation temperature of 32°C [5].

In this study, fermentation was based on the Melle Boinot process (batch fed fermentation with cell recycle), the most common system used in the local industry. Other fermentation by-products are considered in the simulation, such as glycerol, succinic acid, acetic acid, isoamyl alcohol and yeast, according to conversion data reported by [6]. At the end of the fermentation, the wine is centrifuged to recover most of the yeast. The yeast cream obtained is submitted to an acid treatment with H_2SO_4 to decrease the pH [7, 8]. An absorption column is considered in order to recovery the ethanol carried in fermentation gases.

After that, wine goes to distillation stage. A conventional distillation system was simulated considering the distillation and rectification columns, according to [8]. Ethanol content of hydrous ethanol is 93.7% while ethanol content of vinasse and phlegmasse is approximately 0.02%, according to [8].

Ethanol dehydration was simulated adopting the process of extractive distillation with monoethylene glycol (MEG), which considers the extractive column operating at atmospheric pressure and the recovery column at 0.2 bar [5,9]. Anhydrous ethanol is obtained with ethanol content of 99.4% mass basis.

The cogeneration system adopted in this simulation consists of a steam cycle with backpressure steam turbines and parameters of live steam of 67 bar and 480°C. The steam cycle with backpressure steam turbines was adopted in order to generate only the steam necessary for the process, therefore producing surplus bagasse that can be used in enzymatic hydrolysis process.

Table 2. Parameters adopted for the simulation of conventional ethanol production process [4]

Parameter	Value
Sugarcane crushing rate, t/h	500
Efficiency of soil removal in cleaning operation, %	70
Efficiency of sugar extraction in extraction system, %	97
Conversion yield from sugars to ethanol, %	89
Ethanol content in vinasse and phlegmasse, %	0.02
Ethanol content in anhydrous ethanol, wt %	99.4
Cogeneration system	
Pressure of boiler live steam, bar	67
Temperature of boiler live steam, °C	480
Isentropic efficiency of electricity generation in steam turbines, %	80
Alternator efficiency of turbine generator, %	97.6
Turbine mechanical efficiency, %	98.2
Isentropic efficiency of direct drive steam turbines, %	50
Pump isentropic efficiency, %	70
Boiler thermal efficiency, % (LHV base)	85
Mechanical power demand of cane preparation and extraction system, kWh/t of cane	16
Electric power demand of sugar and ethanol process, kWh/t of cane	12
Process steam pressure, bar	2.5
Process steam temperature, °C	127.4

Steam turbines have a bleed at 22 bar for mills direct drive turbines and at 6 bar for must sterilization process and ethanol dehydration requirements. The boiler was modelled according to previous studies [10] and [11].

Table 2 shows the mean parameters adopted in the simulation of conventional ethanol production process.

2.2. Ethanol production through enzymatic hydrolysis

The ethanol production through enzymatic hydrolysis begins with the pre-treatment of lignocellulosic material for the solubilisation of the hemicelluloses and for release the lignin in order to increase the porosity and contact area of the materials to let the cellulase enzymes gain access to the cellulose molecules [12].

There are several different pre-treatment methods proposed by researchers and engineering companies [13]: physical, physical-chemical, chemical and biological. In this study the steam explosion process was adopted because of its efficiency and low cost in comparison with other chemical pre-treatments.

The second step is the hydrolysis of cellulose, where cellulose chains are broken down in order to produce glucose for the fermentation step. Figure 1 shows the flow sheet of the ethanol production process by enzymatic hydrolysis considered in this study.

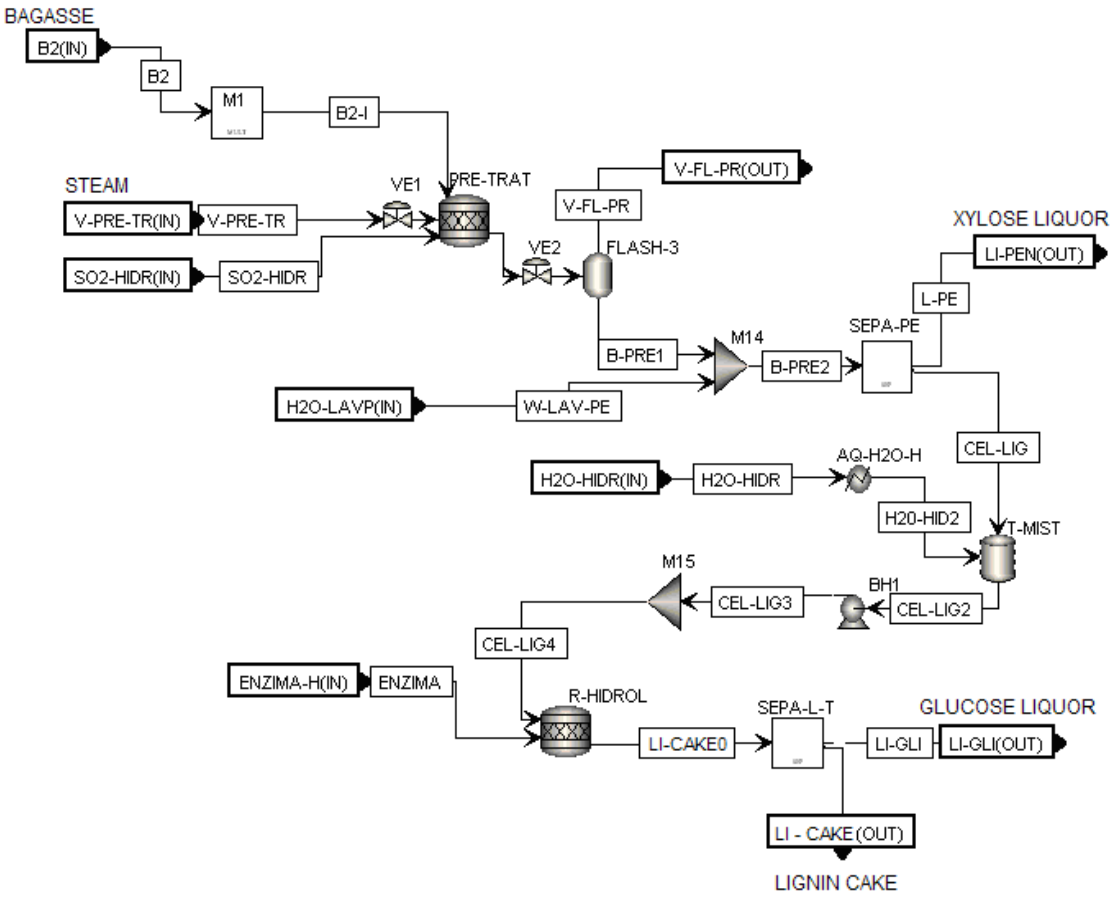

Fig. 1. Flow sheet of enzymatic hydrolysis process.

Sugarcane bagasse was considered as raw material for the hydrolysis process. Some authors [14] indicate the need of cleaning (washing) the raw material, before sending it to the pre-treatment

reactor, in order to remove impurities. This operation would reduce the amount of reactants in subsequent stages. As this study is an initial assessment, previous washing of bagasse and trash was not considered.

Thus, stream of bagasse B2 is sent to the pre-treatment reactor PRE-TRAT. Some studies indicate that it is not necessary the addition of a catalyst in the steam explosion reactor because it is an autocatalytic process: there is a dissociation of water molecules in their ions H^+ and OH^-, which hydrolyse hemicelluloses. The formation of acetic acid happens also, which catalyses the subsequent reactions. On the other hand, some researchers report that the addition of acid catalyst, such as SO_2 or H_2SO_4, is necessary in order to achieve higher yields of hemicellulose conversion. In this study, it was adopted the addition of SO_2 catalyst in the pre-treatment reactor in a rate of 2% w/w, according to [14].

In relation to the steam consumption by steam explosion pre-treatment, experimental data are reported in the range of 0.55 to 0.65 kg of steam /kg moist bagasse for moisture bagasse contents in the range of 38.6 to 65.5% [15].

In the pre-treatment reactor, the formation of xylose ($C_5H_{10}O_5$), acetic acid ($C_2H_4O_2$), furfural and glucose ($C_6H_{12}O_6$) was considered, according to [5]. Table 3 shows the reactions and conversion yields considered in pre-treatment reactor, according to [14].

Table 3. Yields considered for the reactions in pre-treatment reactor

Equation	Product	Yield (%)	From
$C_5H_8O_4 + H_2O \rightarrow C_5H_{10}O_5$	Xylose	61.4	Hemicellulose
$C_5H_8O_4 + H_2O \rightarrow 2.5\ C_2H_4O_2$	Acetic acid	9.2	Hemicellulose
$C_5H_{10}O_5 \rightarrow FURFURAL + 3\ H_2O$	Furfural	5.1	Xylose
$C_6H_{10}O_5 + H_2O \rightarrow C_6H_{12}O_6$	Glucose	4.1	Cellulose

The decompression in pre-treatment tank was represented by the expansion valve VE2 and the unitary block FLASH-3. Hence, there are the steam flashed V-FL-PR and the pre-treated material B-PRE1.

In order to remove xylose and other components that could inhibit the posterior processes of enzymatic hydrolysis and fermentation, pre-treated bagasse is washed in unit block SEPA-PE. After that, two fractions are present: the liquid fraction L-PE (xylose liquor) and the solid fraction CEL-LIG. In this first study, the use of xylose liquor was not considered.

For the next stage, water is added to the process (stream H2O-HIDR) in tank T-MIST, in order to achieve an appropriate concentration of water insoluble solids in the hydrolysis reactor. Three cases were considered in this study: solid contents of 5%, 8% and 10% in the hydrolysis reactor. In the next step, stream CEL-LIG4 goes to the hydrolysis reactor R-HIDROL, where enzymes (stream ENZIMA) are added to catalyze the hydrolysis reactions. After hydrolysis stage, the hydrolysate goes to a filter in order to separate the lignin cake (LI-CAKE) of the glucose hydrolysate (LI-GLI). Table 4 shows the yields adopted in the hydrolysis reactor calculated from [14] data

Table 4. Yields considered for the reactions in the hydrolysis reactor for different solid contents in the reactor (5%, 8% and 10%)

Reaction	From	Product	Yield (%)		
			5%	8%	10%
$C_6H_{10}O_5 + H_2O \rightarrow C_6H_{12}O_6$	Cellulose	Glucose	69.2	60.6	55.8
$C_5H_8O_4 + H_2O \rightarrow C_5H_{10}O_5$	Hemicellulose	Xylose	46.9	44.4	40.6

2.3. Insertion of enzymatic hydrolysis plant in the conventional distillery

To integrate the enzymatic hydrolysis process with the conventional distillery, it is necessary that the hydrolysate concentration (LI-GLI current) achieves appropriate glucose content for the fermentation process. After the concentration, the hydrolysate can be mixed with must of sugarcane juice to go to the fermentation process. Moreover, steam for pre-treatment (steam explosion) should be supplied from the cogeneration system. Lignin cake (LI-CAKE) should be prepared to be burnt in order to satisfy the heat requirements for steam generation.
Figure 2 shows the block diagram of the hydrolysis plant inserted in the conventional ethanol production process proposed.

2.3.1. Steam explosion pre-treatment

In this study, steam for pre-treatment is taken at the desuperheater outlet of direct drive turbines, in the cogeneration system. Then, part of the steam at 22 bar, 300°C is sent to the hydrolysis process, while the other part goes for direct drive turbines. The steam for hydrolysis pre-treatment passes through an expansion valve before to get into the pre-treatment reactor, to reduce its pressure until 12.5 bar, value adopted in this study [16].

2.3.2. Concentration of glucose hydrolysate

Glucose hydrolysate obtained at the outlet of the separator SEPA-L-T has very low glucose content, in the range of 1.8% to 3.4%, depending of the solid content adopted in the hydrolysis reactor. To match the concentration values needed in the fermentation step, this study assumed that the hydrolysate was concentrated in an appropriate plant, showed in Fig 3.

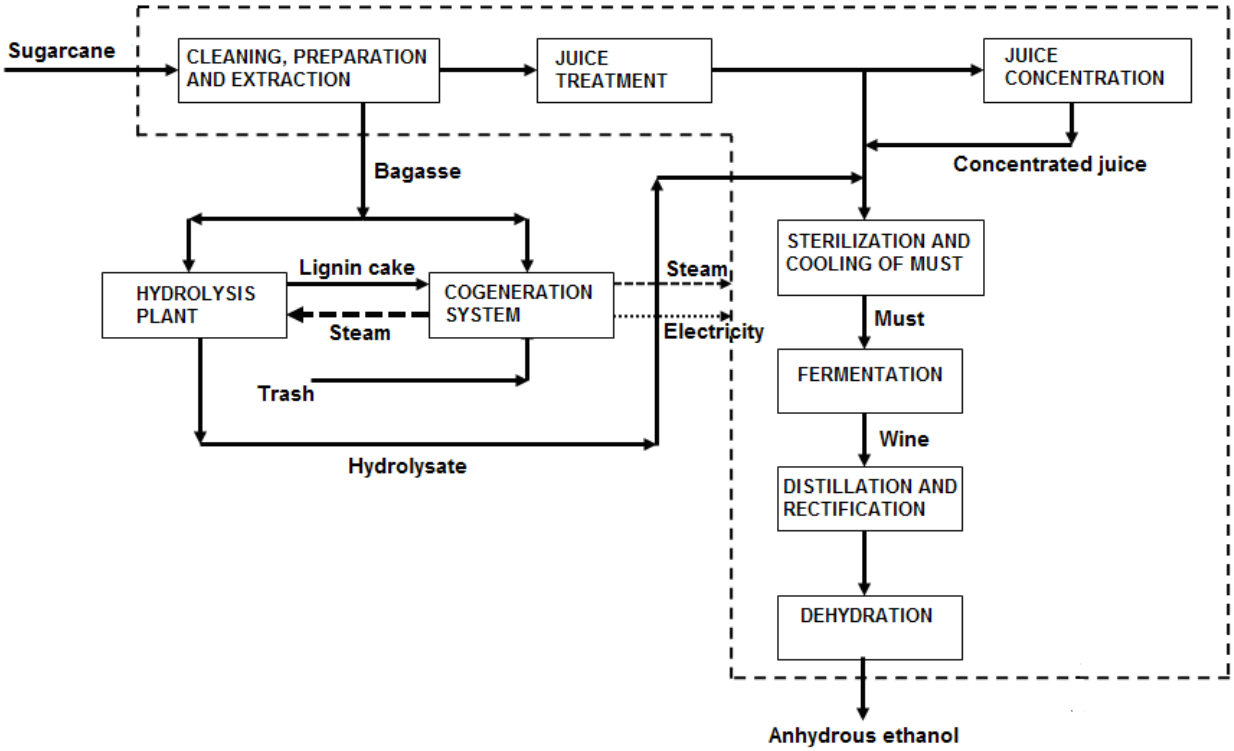

Fig. 2. Ethanol production process-Conventional process integrated with hydrolysis process.

Table 5 shows the mean parameters adopted for simulation of enzymatic hydrolysis process.

Table 5. Parameters adopted for the simulation of ethanol production through enzymatic hydrolysis

Parameter	Value
Pre-treatment reactor temperature, °C[a]	190
Pre-treatment reactor pressure, bar	12.5
Pre-treatment reactor steam consumption, kg of steam/kg of raw material[b]	0.55
Pressure at unitary block FLASH-3, bar	1.01
Efficiency of solid in solution removal in unit block SEPA-PE, %[a]	90
Loss of soluble lignin in unit block SEPA-PE, %[a]	6.3
Moisture content of solid fraction CEL-LIG, %[c]	60
Water for xylose washing, l/kg of dry material[c]	15
Hydrolysis reactor temperature, °C[d]	50
Enzymatic load – cellulose, FPU/g dry biomass[a]	53
Enzymatic load – b glucosidase, IU/g dry biomass[a]	83
Moisture content in solid fraction TORTA-LI0, %	70
Solid content in concentrate hydrolysate, %	19
Moisture content in sugarcane trash, % [e]	10.05
Trash lower heating value, MJ/kg [e]	13.9
Energy consumption in trash shredder, kWh/t of trash[e]	82.03
Energy consumption in cleaner station, kWh/t of trash[f]	13.6
Energy consumption in bagasse feeder, kWh/t of bagasse	0.459
Energy consumption in xylose separator SEPA-PE, kWh/t of material	2.3
Energy consumption in separator SEPA-L-T, kWh/m^3	0.4
Energy consumption in dewatering press of lignin cake, kWh/kg of dry matter	56.09

[a] Carrasco et al. (2010) [14]; [b] Kling et al. (1987) [15]; [c] Palacios-Bereche, (2011) [4]; [d] Galbe and Zacchi (2010) [25]; [e] Hassuani et al. (2005) [20]; [f] Cella (2010) [26]

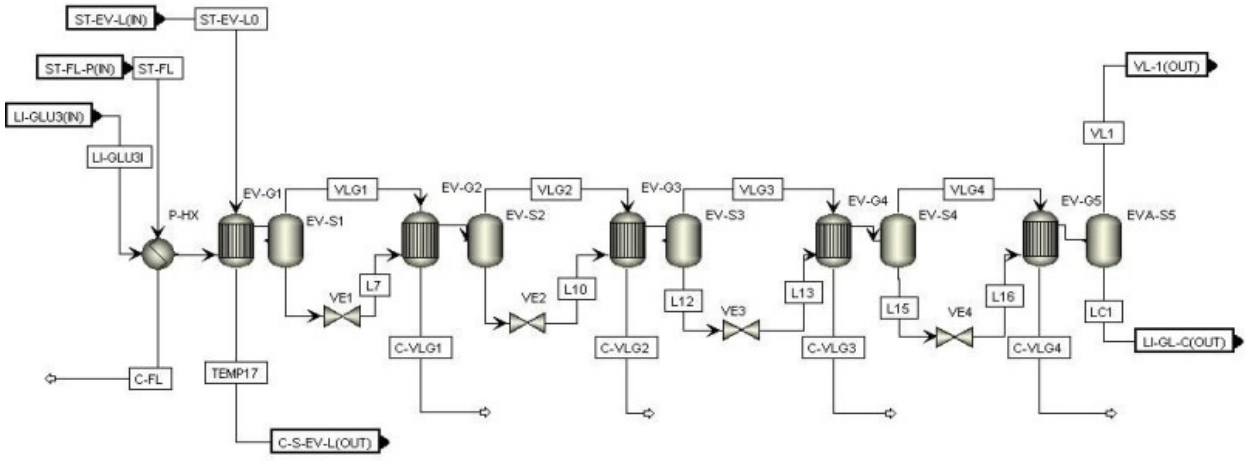

Fig. 3. Concentration of glucose hydrolysate.

According to the Fig. 3, glucose hydrolysate is preheated in the heat exchanger PHX with steam flash recuperated from the pre-treatment decompression (Fig. 1) before get into the evaporation system, which operates with exhaust steam at 2.5 bar. An evaporation system of five stages was considered in order to reduce the steam consumption. For the simulation in Aspen Plus software, each stage of the evaporation system was considered compounded by two unit operations: a heat exchanger and a flash separator, [9, 17]. It was assumed that the condensate of exhaust steam from this evaporation system C-S-EV-L returns to the cogeneration system.

Due to the possible presence of soluble lignin in glucose hydrolysate, as well as phenolic groups (they were not considered in this simulation), the detoxification of glucose hydrolysate is recommended before its mixture with must of sugarcane juice [18, 19]. In this simulation the removal of the components acetic acid, furfural and sulphurous acid was considered, before the mixture with must.

2.3.3. Use of lignin cake

In order to recuperate the heat value of the wet lignin cake, stream CAKE-LIG is sent to the dewatering press, where its moisture content is reduced to 50%. After that, the lignin cake is sent to the burner (stoichiometric reactor) where it is burned. In real installations, the lignin cake burning will happen in the boilers of the cogeneration plant. In this case, an independent burning was assumed with the unique purpose of simplifying the calculations. So, the gases stream of this burner block is conducted to the boiler. As no other date is available, the efficiency adopted for lignin boiler was the same than bagasse boilers.

2.3.4. Sugarcane trash utilization

The amount of residues from sugarcane harvesting depends on many factors such as: harvesting system, topping height, cane variety, age of crop, climate, soil and others. In this study, an average trash potential of 140 kg of dry residues per tonne of cane stalks was considered [1,20] and the amount of trash left in field was assumed as 50% of total, according to [21]. Thus 50 % of total trash was assumed available for use as fuel in the cogeneration system.
Sugarcane trash and lignin cake, are considered in order to satisfy the energetic requirements of the integrated process. In this way, it is possible to send a higher amount of bagasse to the hydrolysis process. Nevertheless, it is still necessary to burn part of the bagasse in the boilers to satisfy the energy requirements. The amount of bagasse for hydrolysis is defined after an iterative process, because the increase of raw material for hydrolysis increases the steam consumption of the plant; thus the amount of bagasse, trash and lignin cake for steam generation should be enough to satisfy the increase in energy requirements of the plant, and so on.
For the simulations, it was considered that trash and lignin cake are burned in the boiler with an efficiency of 86% (LHV base) [4].

3. Thermal integration applying Pinch-Point method

The Pinch Point method was used to analyse the streams of the process that are available for thermal integration. The minimum approach temperature difference (ΔT_{min}) adopted in this study was 10°C for the process and 4°C for the evaporation systems. As vapour bleedings of the concentration step are used to fulfil the process heating requirements, and these bleedings change depending on the process characteristics, the thermal integration procedure was accomplished following the next sequence:
Step 1. Calculation of the amounts of trash and bagasse to be burnt in the boiler, from an initial assumption of the steam consumption of the overall process.
Step 2. Thermal integration of the available process streams, excluding the evaporation systems (sugarcane juice and glucose liquor).
Step 3. Integration of both evaporation systems and calculation of the appropriate vapour bleeding demand according to the procedure of [22] and Grand Composite Curve construction.
Step 4. Re-calculation of the steam consumption of the overall process until the convergence is obtained.
In this study the thermal integration procedure was applied to the case of enzymatic hydrolysis with solid content 10% in the hydrolysis reactor. This value was selected because it presents the best results in terms of ethanol production [4].

From the iterative procedure explained before, the amount of bagasse for hydrolysis can be determined, moreover, thermal integration procedure permits to determine the targets of minimal energy consumption, maximizing, in this way, the production of ethanol from bagasse hydrolysis. Table 6 shows the streams considered for thermal integration, as well as the exchange heat and the initial and final temperature. Figure 6 shows the final Grand Composite Curve for the analyzed case.

Table 6. Streams considered for thermal integration, 10% of solid content in the hydrolysis reactor (Case V)

Heat streams	Ti °C	Tf °C	H MW	Cold streams	Ti °C	Tf °C	H MW
Sterilized juice	130.0	32	50.8	Treatment juice	34.2	105.0	44.9
Fermented wine	32.0	28	13.2	Pre-heating juice	98.1	115.0	2.8
Phlegmasse	103.8	35	3.7	Juice for sterilization	89	130.0	22.5
Vinasse	109.3	35	45.9	Final wine	31.2	90.0	41.4
Anhydrous ethanol	78.3	35	10.2	Reboiler column A	109.3	109.3	53
Vapour Condensates	83.2	35	16.8	Reboiler column B	103.4	103.8	35.4
Condenser column B	81.6	81.6	30.5	Reboiler extractive column	112.1	137.1	8.0
Condenser extractive column	78.3	78.3	8.7	Reboiler recovery column	149.6	149.6	2.9
Condenser column D	85.1	35	34.6	Hydrolysis water	25	50	9.7
Vapour steam explosion	100.7	100	17.9	Pre-heating glucose liquor	50	115	27.2
				Imbibition water	25	50	4.7

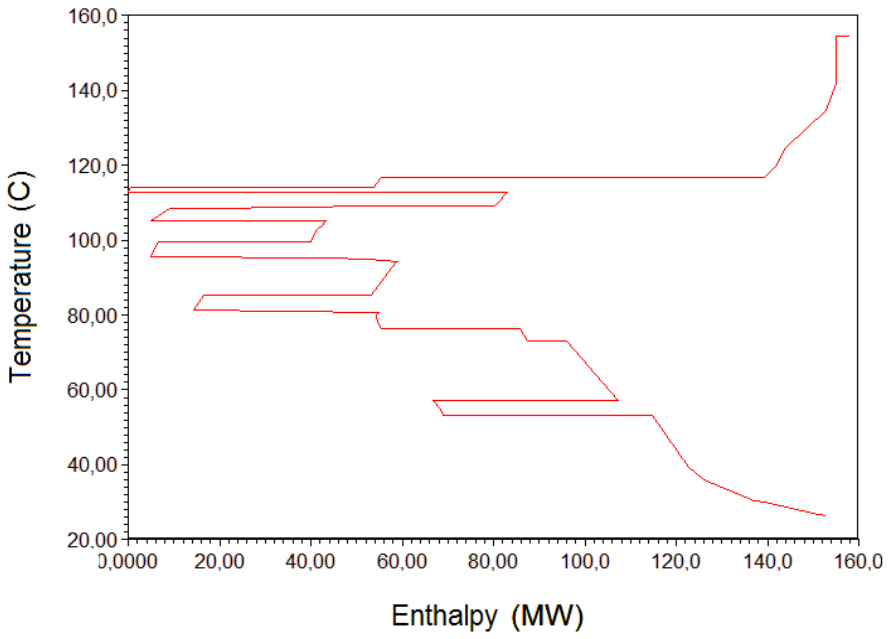

Fig. 4. Grand Composite Curve including the evaporation systems – GCC (Case V).

4. Results and discussion

Table 7 shows the results of the anhydrous ethanol production, electricity surplus, bagasse sent to the hydrolysis process and steam consumption for the evaluated cases. Case I corresponds to the

conventional distillery without hydrolysis, while cases II, III and IV correspond to the hydrolysis process coupled with the conventional distillery without thermal integration. Case V corresponds to the hydrolysis process integrated with the conventional process according to the method presented in item 3. A higher solids concentration in the hydrolysis process means lower steam consumption in the glucose liquor concentration step. This fact permits to assign higher amounts of bagasse for the hydrolysis process and consequently, to obtain higher increases in the ethanol production.

About electricity surplus, there is an increase of 47.9%, 29.3%, 21.3% in Cases II, III and IV respectively in comparison with Case I, these increases happen owing to an increase in steam consumption in the mentioned cases. On the other hand, in Case V there is a reduction of 27.9% in comparison with Case I, fact that is explained because in Case V, a reduction of steam consumption happens. In general, these results are due to the turbine configuration adopted in the cogeneration system (backpressure steam turbine) and the reduction of steam consumption for higher solid contents in the hydrolysis step.

From the thermal integration procedure, it can be observed a significant decrease in steam consumption in Case V. Steam consumption in Case V is 11.1% lower than the consumption in Case IV, while ethanol production in Case V is 4.6% higher than the production obtained in Case IV.

Table 7. Results of the simulation: Anhydrous ethanol production l/t of cane, electricity surplus kWh/t of cane and steam consumption kg/t of cane.

Parameter	**Case I**	**Case II**	**Case III**	**Case IV**	**Case V**
Solid content in hydrolysis reactor	--	5	8	10	10
Anhydrous ethanol, (l/t of cane)	79	86.7	88.1	88.7	92.8
Electricity surplus, (kWh/t of cane)	42.3	62.5	54.6	51.3	30.5
Bagasse for hydrolysis, (kg/t of cane)	0	110.3	149.5	172.7	239.7
Steam consumption, (kg/t of cane)	489.6	794.2	756.9	745.1	661.8
Increase in ethanol production, (%)		9.7	11.5	12.3	17.4
Increase in ethanol production, (l/t of cane)		7.7	9.1	9.7	13.7

In relation to vinasse production, there is an increase of 11.6%, 14.1%, 15.1% and 20.8% for Cases II, III, IV and V in comparison with Case I. It is due to the higher amount of must processed in distillation stage in comparison with Case I. In Brazilian current practice, the vinasse is used to irrigate the fields, where the nutrients are recuperated.

Figure 5 shows the bagasse balance for each case. Bagasse for hydrolysis increases from Case II to V, while bagasse for boiler decreases. The amount of trash for boiler is constant for all cases, 38.9 t/h considering a moisture content of 10%. The amount of lignin cake also increases from Case II to V, being a percentage of the bagasse for hydrolysis. Thus, the amount of lignin cake at 50% of moisture content was 0.43 and 0.46 kg/kg of bagasse for hydrolysis for Cases II and III respectively and 0.48 kg/kg of bagasse for Cases IV and V. The lower heating value of lignin cake was calculated through the simulator from their composition data. The lower heating values obtained for lignin cake were: 8563 kJ/kg for Case II, 8441 kJ/kg for Case III and 8373 kJ/kg for Cases IV and V. These differences occurred because of the conversion yields adopted in the hydrolysis reactor.

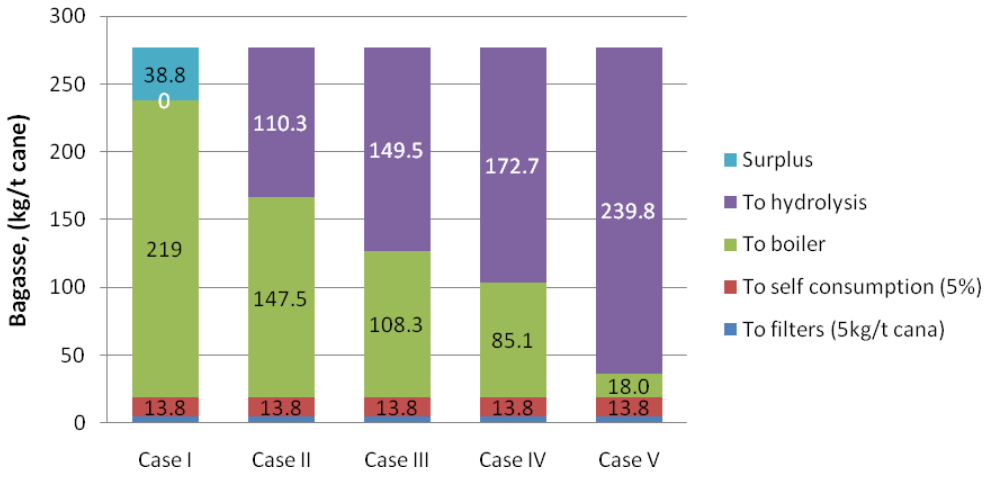

Fig. 5. Bagasse balance (kg/t of cane) for Cases I, II, III, IV and V.

Figure 6 shows the balance of electricity generated. A decrease in electricity surplus appear from Cases II to V due to the reduction in electricity produced in the cogeneration system, as a consequence of the decrease in the steam generated in boiler, and due to the consumption increase in the hydrolysis process.

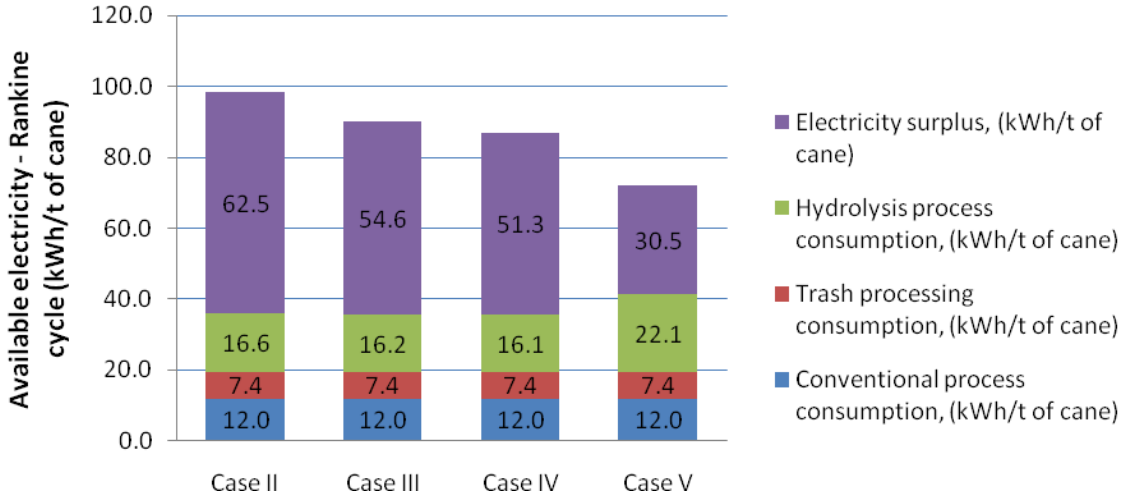

Fig. 6. Balance of electricity generated (kWh/t of cane) for Cases II, III, IV and V

The electricity consumed in the hydrolysis process was estimated from the data shown in Table 5. It was identified a significant electricity consumption in the agitators of the hydrolysis reactors, due to the large volume of the hydrolysis reactors. The reactor volume was calculated assuming reactors CSRT (Continuous Stirred Tank Reactors) and residence time of 48h, in agreement with data of Table 4. The total volume of reactors resulted in 20520 m^3, 17165 m^3, 15731 m^3 and 21835 m^3 respectively for the cases II, III, IV and V. The electricity consumption in the reactor agitators was determined from a scale up procedure based on the data reported in [23].

Results of the present study can be compared with others of the literature. Walter and Ensinas [19] indicated an increase in ethanol production of 25.6%, but in a future scenario and considering glucose and xylose fermentation. Dias et al. [24] indicated ethanol production increases of 18.3% and 20.3%, but considering an Organosolv hydrolysis process with diluted acid, while Leite [1] indicated an ethanol production increase, through enzymatic hydrolysis process, of 12.2% and 25.6%, for scenarios corresponding to the years of 2015 and 2025 respectively.

Dias et al. [27] also accomplished a simulation study considering the ethanol production by enzymatic hydrolysis and pre-treatment by steam explosion, and a reduction of 30.8% in steam consumption was obtained from thermal integration. These authors indicate an ethanol production in the integrated process in the range of 107.5 to 120.6 l/t of cane; these values represent an increase of 15.9% and 30% in comparison to their base case.

5. Conclusions

An evaluation of the mass balance and energy consumption for the ethanol production process by enzymatic hydrolysis was accomplished. Moreover, this study showed the potential ethanol production increase due to the introduction of the bagasse enzymatic hydrolysis in the conventional ethanol production process.

The results obtained for cases II, III an IV were modest because the study considers a conservative conventional factory with average technology, thus, in order to increase the ethanol production the optimization of the conventional process would be recommended, aiming an energy consumption reduction. Hence, the ethanol production increase for cases II, III and IV was 9.7%, 11.5% and 12.3%, respectively. These results showed that a higher ethanol production is obtained for higher solids concentrations in the hydrolysis process. They show that thermal energy consumption in the hydrolysate concentration stage is very significant, thus, other separation technologies with lower energy consumption should be studied. Reverse osmosis membranes in combination with evaporation systems can be tested for this application.

Case V showed the highest ethanol production of 92.8 l/t of cane, which represents an increase of 17.4%; however, this is a prospective study and pilot plant/industrial data would be necessary in order to adjust the modelling of the plant. The Pinch Analysis applied to this case showed to be a useful tool to evaluate the thermal integration potential.

There is an intrinsic vinasse increase due to the higher amount of must being processed with the introduction of the hydrolysis process; the highest vinasse production was 430.8 t/h for Case V which represents an increase of 20.8% in comparison with Case I. Currently, vinasse is used as fertirrigation in Brazilian sugarcane fields, however this practice is being regulated. Thus, the introduction of technologies to reduce the vinasse production becomes necessary.

The energy balance in the cogeneration system shows that the energy supplied by lignin cake is significant to operate the integrated process. For Case V, energy supplied by lignin cake represented 44.2% of total energy supplied to the cogeneration system. Hence, the study and characterization of lignin cake is important in order to enable the ethanol production by enzymatic hydrolysis process.

Acknowledgments

The authors wish to thank to CNPq (Process 304820/2009-1), FAPESP (Process 11/05718-1) and FINEP (Contract FINEP – FUNCAMP Nr. 01/06/004700) for the financial support.

References

[1] Leite R.C.C., Fuel bioethanol an opportunity to Brazil. Brasilia: Centro de Gestão e Estudos Estratégicos; 2009, (In Portuguese).

[2] Rein P., Cane Sugar Engineering. Berlin: Verlag Dr. Albert Bartens K. G.; 2007.

[3] Wooley R.J., Putsche V., Development of an ASPEN PLUS Physical Property Database for Biofuels Components", National Renewable Energy Laboratory, 1996. – Available at <www.p2pays.org/ref/22/21210.pdf> [accessed 12.11. 2007].

[4] Palacios-Bereche R., Modeling and energy integration of the ethanol production process from sugarcane biomass [PhD Thesis]. Campinas, Brazil: University of Campinas; 2011 (In Portuguese).

[5] Dias M.O.S., Simulation of ethanol production processes from sugar and sugarcane bagasse, aiming process integration and maximization of energy and bagasse surplus. [dissertation]. Campinas, Brazil: University of Campinas; 2008 (In Portuguese).

[6] Eijsberg R., The design and economic analysis of a modern bioethanol factory located in Brazil. [dissertation]. Delft, The Netherlands: University Delft; 2006.

[7] Rossell C.E.V., Sugarcane processing to ethanol for fuel purposes, In Chemistry and Processing of Sugarbeet and Sugarcane, edited by Clarke M. A. and Godshall M.A., Elsevier Science Publishers B. V., Amsterdam, 1988.

[8] Finguerut, et al., Fermentation, Hydrolysis and Distillation. In: Cortes et al. editors. Biomass for Energy. Campinas, Brazil: Ed. Unicamp. 2008. p. 436-474.

[9] Dias M.O.S., Modesto M., Ensinas A.V., Nebra S.A., Maciel Filho R., Rossell C.E.V., Improving bioethanol production from sugarcane: evaluation of distillation, thermal integration and cogeneration systems. Energy 2010; 36: 3691-3703.

[10] Palacios-Bereche R., Nebra S.A. Thermodynamic modeling of a cogeneration system for a sugarcane mill using ASPEN PLUS, difficulties and challenges. COBEM 2009: Proceedings of the 20th International Congress of Mechanical Engineering, 2009 Nov 15-20, Gramado, Brazil.

[11] Magnusson H., Process simulation in Aspen Plus of an integrated ethanol and CHP plant. [dissertation]. Sweden: Umea University. 2005.

[12] Sun Y., Cheng J., Hydrolysis of lignocellulosic materials for ethanol production: a review. Bioresource Technology 2002; 83: 1–11.

[13] Efe C., Technical and economical feasibility of production of ethanol from sugar cane and sugarcane bagasse. [dissertation], Delft, The Netherlands: TU-Delft; 2005.

[14] Carrasco C., Baudel H.M., Sendelius J., Modig T., Roslander C., Galbe M., Hahn-Hägerdal B., Zacchi G., Lidén G. SO_2-catalyzed steam pretreatment and fermentation of enzymatically hydrolyzed sugarcane bagasse. Enzyme and Microbial Technology 2010; 46: 64–73.

[15] Kling S.H., Carvalho Neto C., Ferrara M.A., Torres J.C.R., Magalhaes D.B., Ryu D.D.Y., Enhancements of enzymatic hydrolysis of sugar cane bagasse by steam explosion pretreatment. Biotechnology and Bioengineering 1987; 29: 1035 – 1039.

[16] Sanchez O.J., Cardona C.A., Trends in biotechnological production of fuel ethanol from different feedstocks. Bioresource Technology 2008; 99: 5270–5295.

[17] Jorge L.M.M, Righetto A.R., Polli P.A., Santos O.A.A., Maciel Filho R., Simulation and analysis of a sugarcane juice evaporation system. Journal of Food Engineering 2010; 99: 351–359.

[18] Cardona C.A., Sanchez O.J., Energy consumption analysis of integrated flowsheets for production of fuel ethanol from lignocellulosic biomass. Energy 2006; 31 (13): 2447-2559.

[19] Walter A., Ensinas A.V., Combined production of second – generation biofuels and electricity from sugar-cane residues. Energy 2010; 35: 874-879.

[20] Hassuani S.J., Leal M.R.L.V., Macedo I.C., Biomass power generation: Sugarcane bagasse and trash, Piracicaba, Brazil: Ed. PNUD and CTC, 2005.

[21] Michelazzo M.B., Sensitivity analysis of six systems for collection of sugarcane trash (Saccharum spp.). [dissertation]. Campinas, Brazil: University of Campinas, 2005 (In Portuguese).

[22] Westphalen D.L., Wolf Maciel M.R., Pinch Analysis of evaporation systems, Brazilian Journal of Chemical Engineering 2000; 17: 4-7.

[23] Pereira L.T.C., Teixeira R.S.S.T., Bom E.P.S., Freitas S.P. Sugarcane bagasse enzymatic hydrolysis: rheological data as criteria for impeller selection. Journal of Industrial Microbiology & Biotechnology 2010; DOI 10.1007/s10295-010-0857-8.

[24] Dias M.O.S., Ensinas A.V., Nebra S.A., Maciel Filho R., Rossell C.E.V., Production of bioethanol and other bio-based materials from sugarcane bagasse: Integration to conventional bioethanol production process. Chemical Engineering Research and Design 2009, 87: 1206-1216.

[25] Galbe, M., Zacchi, G. Ethanol production from lignocellulosic materials. In: CORTEZ, L.A.B. (Coord.). Bioethanol from sugarcane: R&D for productivity and sustainability. Sao Paulo: Blucher, 2010. Part. 4, Chap. 12, p. 697-716.

[26] Cella, N. Trash use as fuel in biomass boilers. Course Boilers, Environment and Renewable Energy. Ribeirao Preto, 23-24 de june 2010.

[27] Dias, M.O.S.; Cunha, M.P., Maciel Filho, R., Bonomi, A., Jesus, C.D. F., Rossell, C.E.V. Simulation of integrated first and second generation bioethanol production from sugarcane: comparison between different biomass pre-treatment methods. Journal of Industrial Microbiology & Biotechnology, 2011, 38: 955-966.

Evaluation of gas production in a industrial anaerobic digester by means of Biochemical Methane Potential of Organic Municipal Solid Waste Components

Isabella Pecorini[a], Tommaso Olivieri[b], Donata Bacchi[c], Alessandro Paradisi[d], Lidia Lombardi[e], Andrea Corti[f] and Ennio Carnevale[g]

[a] Dipartimento di Energetica "Sergio Stecco" - Università degli Studi di Firenze (CA), Florence, Italy, isabella.pecorini@unifi.it
[b] Dipartimento di Energetica "Sergio Stecco" - Università degli Studi di Firenze, Florence, Italy, tommaso.olivieri@unifi.it
[c] Dipartimento di Energetica "Sergio Stecco" - Università degli Studi di Firenze, Florence, Italy, donata.bacchi@unifi.it
[d] Dipartimento di Energetica "Sergio Stecco" - Università degli Studi di Firenze, Florence, Italy, alessandro.paradisi@unifi.it
[e] Dipartimento di Energetica "Sergio Stecco" - Università degli Studi di Firenze, Florence, Italy, lidia.lombardi@unifi.it
[f] Dipartimento di Ingegneria dell'Informazione - Università degli Studi di Siena, Florence, Italy, corti@dii.unisi.it
[g] Dipartimento di Energetica "Sergio Stecco" - Università degli Studi di Firenze, Florence, Italy, ennio.carnevale@unifi.it

Abstract:

The Biochemical Methane Potential (BMP) of several components of the Organic Fraction of the Municipal Solid Waste (OFMSW) were tested in order to assess the possibility to obtain a good estimate of the biogas production of a real scale anaerobic digestion plant. In particular, five different fractions and a mixed food waste sample were tested with batch anaerobic digesters at 37°C and both the BMP after 21 days (BMP21) and final BMP (BMPf) were measured. Regarding the mixed food waste substrate it was found an average BMP21 of about 405 NL/kgVS and a BMPf of 484 NL/kgVS with an average methane content of 57%. From the experimental results, some industrial potential biogas production were defined to compare them with data from real anaerobic digestion plants. In particular two different plants were considered: one located in a rural area that treats the source selected OFMSW from a public collection point, another located in a city area with a curbside collection system. Furthermore, studying the BMP of the pre-treatment reject of these plants, it was possible to study the pre-treatment efficiency and the difference performance of the two real plants.

Keywords:

Anaerobic Digestion, Biochemical Methane Potential, Biogas, Organic Fraction Municipal Solid Waste.

1. Introduction

In 2009, more than 10 million tons of waste, corresponding at the 33,6% of the whole amount of municipal solid waste (MSW) produced in Italy, were collected as source separated fractions. About the 35% of these fractions were organic fraction from kitchen and yard and garden waste and, since 2005, a constant increasing of 11% every year have been recorded. Moreover ISPRA [1] shows that most of them were treated in composting plants (about 281 facilities were registered in the 2009) and about 540'000 t where instead stabilized in anaerobic digestion plants, in particular 18 plants of which 15 working.

New strategies in MSW management, i.e., source-separate collection of the OFMSW and the need to reduce the biodegradable-MSW allocated in landfill, have favoured the development of composting and anaerobic digestion as useful biotechnologies for transforming organic waste into suitable agricultural products [2]. Moreover, given that the amount of OFMSW is still increasing and the attention to the environmental impacts is becoming all the time more important, the possibility to recover not only compost form waste but also energy could enhance the anaerobic digestion of OFMSW as way to provide a clean fuel from renewable energy [3]. In this way the quality of the OFMSW in terms of potential methane production becomes important in order to assess the biogas production expectation from the anaerobic treatment.

In the last years, several researches have been carried out for the analysis of biomethane potential of several waste substrates. In particular, most of these utilize BMP analysis as a possible way to characterize the biodegradability of the organic matter in order to assess its stability and the waste treatments efficiencies such as composting or anaerobic digestion. Others are instead interested in determining waste BMP as relevant in the context of treatment by anaerobic digestion and useful to determine the amount of organic carbon that can be anaerobic converted to methane. This research focus on this last purpose with the aim to understand how, by measuring the BMP of the main component of the OFMSW is possible to estimate the potential biogas production of real digestion plant. Moreover, to obtain more realistic results, this research focuses on how the pre-treatments and the operating environment could affect the biogas production of real plants.

2. Materials and methods

To study the BMP of the source-selected organic fraction, essentially kitchen and garden waste, several substrates were tested; in particular: proteins from meat and dairy products, carbohydrates from bread and pasta, fruit and vegetable, dirty paper from kitchen and other organic materials from yard and garden waste. Moreover, to assess the efficiency of a typical anaerobic digestion plant, it was also necessary to measure the BMP of the fractions rejected by the pre-treatment. In particular it has been possible to test the light fraction and the small heavy removed from the OFMSW by a specific treatment in two real industrial anaerobic digestion plant with different location: a rural and a urban area.

To estimate the biogas potential production of each fraction, the BMP analysis were carried out in duplicate and both the BMP21(biogas produced at 21 days) and the BMPf (when no significant biogas production is detected) were measured. For analysis a modified method of Ponsa et al. [4] was used and in the following, according with Angelidaki, Alves and Bolzonella et al. [5], the materials and the method used will be described.

2.1. Inoculum and substrates tested

Active inoculum from a mesophilic anaerobic digestion plant, that primarily treats organic fraction from MWS, was used. In order to deplete the residual biodegradable organic material present [5], the inoculum was pre-incubated for three day in a water bath at 37°C. Total Solid (TS) and Volatile Total Solid (VS) contents were about 3,9% on wet weight basis (w/w) and 64,1% on TS basis, respectively.

Table 1. Characterization of the substrates used

Substrate	*Experimental ID*	*TS, %FM*	*VS, %TS*
Proteins	Proteins	33,1±0,24	89,9±0,01
Carbohydrates	Carbohydrates	94,5±0,04	97,5±0,01
Fruit and vegetables	Fruit and Veget	14,0±0,05	98,1±0,06
Leafs	Yard and Garden waste	6,5±0,61	81,8±1,48
Cellulose	Dirty paper	40,3±0,02	90,4±0,04

The source selected OFMSW from curbside collection was used for the substrates tested in the batch assay. For each fractions water content and VS were measured in triplicate, in Table 1 only the mean value are shown.

Furthermore, a mixing of those fractions (Mixed Food Waste – MFW) was employed for the tests too; its composition is shown in Table 2. TS and VS contents, as the sum of each fractions, were about 42,4±0,38% (w/w) and 93,3±0,01% on TS basis respectively.

Table 2. Mixed food waste composition

Fraction	*Weight (g)*	*Percentage %(w/w)*
Fruit and vegetable	8	26,7
Proteins	8	26,7
Carbohydrates	8	26,7
Leafs	3	10
Cellulose	3	10

2.2. Set-up of measurement

The BMP was determined using 1L stainless steel bottles, incubated in a water bath at 37,5°C, tightly closed by special cap provided with a ball valve to enable the gas sampling. To ensure anaerobic conditions, the bottles were flushed with inert gas. All the equipment, 2 bar proof pressure, was specifically design and developed.

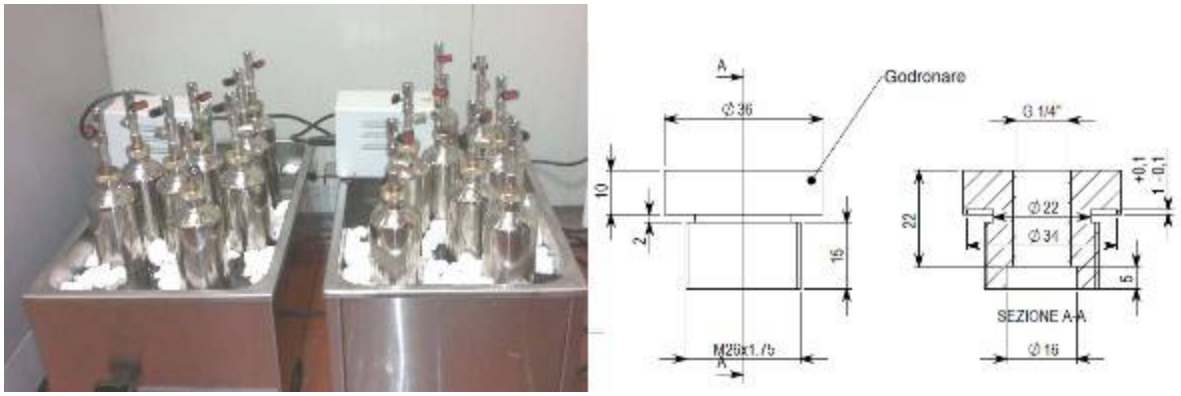

Fig 1. Batches and cap used

With the fractions described above, six sample and twelve batch reactors (the test was performed in duplicate) were prepared. Each reactor was loaded with different quantity of substrate, depending on the characteristics of the materials, to achieve a concentration of substrate in each batch of about 2gVS/100 mL solution, given that this concentration is a compromise of, one hand, the need to use a large sample to have good representativity and to get a high easy-to-measure gas production, and, on the other hand, to avoid too large and impractical volumes of reactors and gas production and keep the solution dilute to avoid inhibition from accumulation of volatile fatty acid (VFA) and ammonia [6].

Moreover, in every case, the inoculum to sample ratio was kept under 10:1 weight ratio, according with Ponsa et al. [4] for fresh feed-in substrate, and because it was demonstrated that the amount of inoculums should be enough to prevent the accumulation of volatile fatty acids and acid conditions[5].

To determine the background methane production, a blank assay with the only inoculum was done in duplicate.

According with the authors [7], biogas production was estimated by measuring the pressure in the head space of each reactor and then converting to volume by application of the ideal gas law.

Pressure was measured using a membrane pressure gauge (Model HD2304.0, Delta Ohm S.r.L., Italy). The values of pressure measured were converted into biogas volume as:

$$V_{biogas} = \frac{P_{measured} \cdot T_{NTP}}{P_{NTP} \cdot T_r} \cdot V_r$$

where:

V_{biogas}, volume of daily biogas production, expressed in Normal litre (NL);

$P_{measured}$, headspace pressure before the gas sampling (atm);

T_r and V_r, temperature (K) and volume (L) of the reactor;

T_{NTP} and P_{NTP}, Normal temperature and pressure, 273,15K and 1 atm respectively.

The headspace volume, calculated as the difference between the total volume of the batch and the volume occupied by the sample considering a sample density of 1g/mL, was about 600ml for each bottle.

The gas produced was routinely analyzed using an IR gas analyzer (ECOPROBE 5 - RS Dynamics). After every measurement the bottles were shaken to guarantee homogeneous conditions in the assay vessels [5].

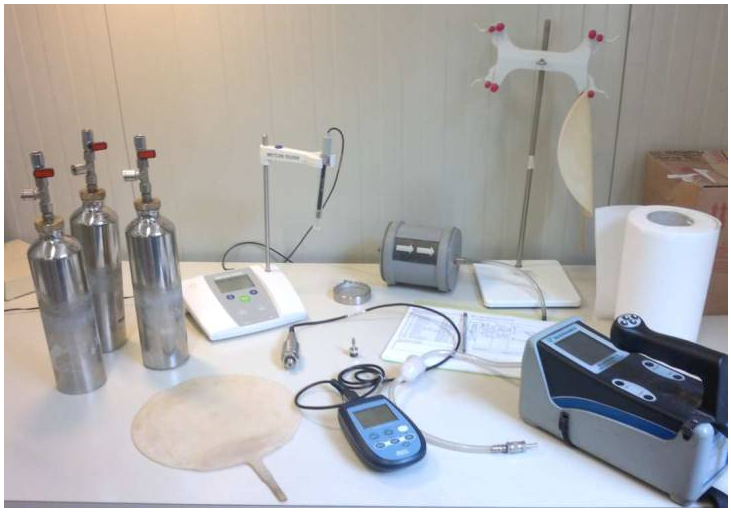

Fig 2. Laboratory equipments

The BMP was determined as the cumulate biogas production, calculated as the sum of the daily volumes, divided by the TS and the VS present in each batch. The results, reported in the Normal Temperature and Pressure (NTP), were obtained after 21 and about 90 days. After this period, in fact, the quantity of biogas produced by every sample was found to be lower than the blank production and no significant biogas volumes can be considered.

3. Results and Discussions

3.1. BMP assay

The results obtained for the biochemical methane potential at 21 days are shown in Table 3. In particular the quantity of biogas produced is referred to the TS and the VS and, in order to consider the inoculum biogas production, a percentage error is also shown. It was calculated as the ratio between the quantity of biogas produced by the inoculum and the total biogas produced from each fraction.

Table 3. BMP21

Experimental ID	*NL/kgTS*	*NL/kgVS*	*Error, %*
MFW (a)	413	542	14
MFW (b)	396	520	14
Proteins	386	528	14
Carbohydrates	91	109	67
Fruit and Veget	250	353	21
Yard and Garden waste	115	175	42
Dirty paper	315	422	17
Inoculum	47	74	-

Preliminary experiments on similar waste showed that 90 days of incubation at 35°C, after the lag period, was sufficient to insure the total gas production expression [8], therefore the values of BMP measured after 93 days has been considered as the final biogas produced by each substrate. The results obtained, deducted the inoculum yield, seem to be comparable to that obtained in other similar studies [9] and [10].

Table 4. BMPf

Experimental ID	*NL/kgTS*	*NL/kgVS*	*Error, %*
MFW (a)	501	657	31
MFW (b)	466	611	33
Proteins	452	617	33
Carbohydrates	101	120	168
Fruit and Veget	327	462	44
Yard and Garden waste	205	312	65
Dirty paper	377	504	40
Inoculum	130	203	-

The highest BMP value was obtained for the MFW, while, observing the calculated errors, it is clear that for charbohydrates some problem of acidification occurred.

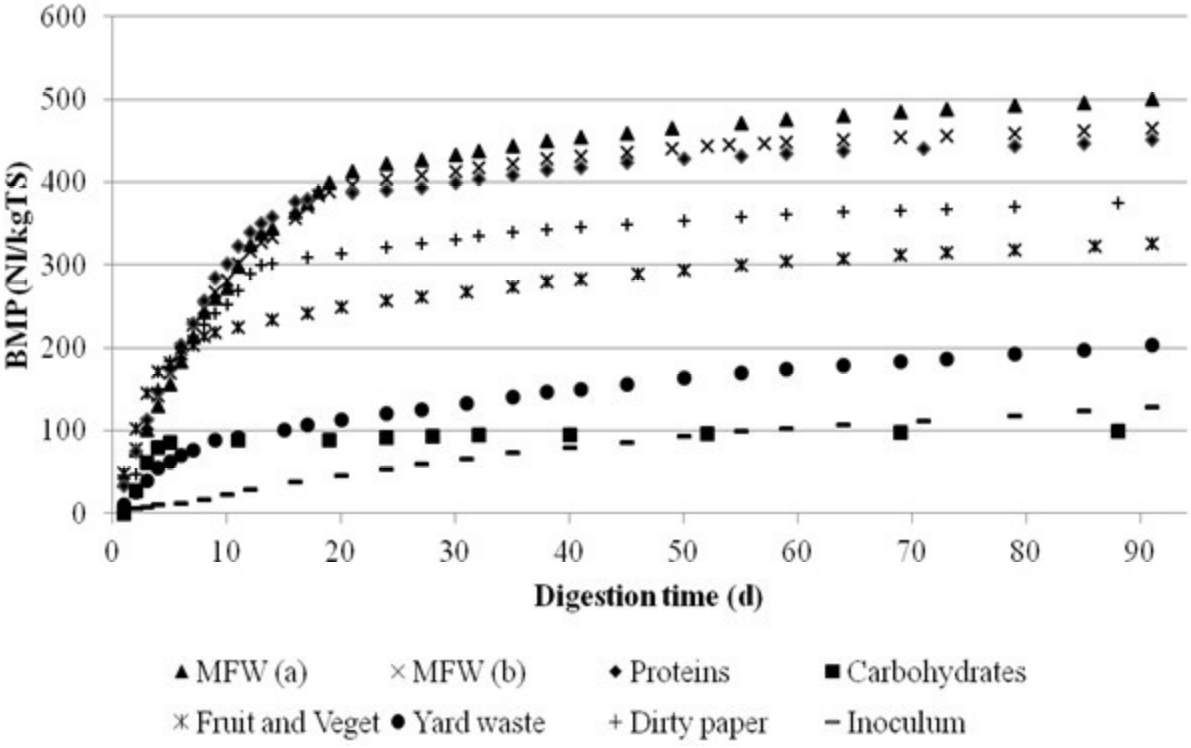

Fig. 3: Cumulative Biochemical methane production of the tested samples

This can be also noticed in the temporal plot of the average cumulative biochemical methane yields (Fig. 3): for the soon after few days, no significant methane production was detected.

With reference to Fig. 4, the correlation between the BMP21 and the BMPf has been studied [4]. As results from the chart, the biogas obtained at 21 days corresponds to the 89% of ultimate potential methane. In fact, as supported by the comparison between the cumulative and the daily MFW average BMP, the main part of the biogas totally produced was released during the first 20 days (Fig. 5).

Focusing on the MFW results, the peak value of daily biogas production was about 51 NL/d*kg VS, while the cumulative biogas were 542 and 520 NL/kgVS for the MFW (a) and (b) sample.

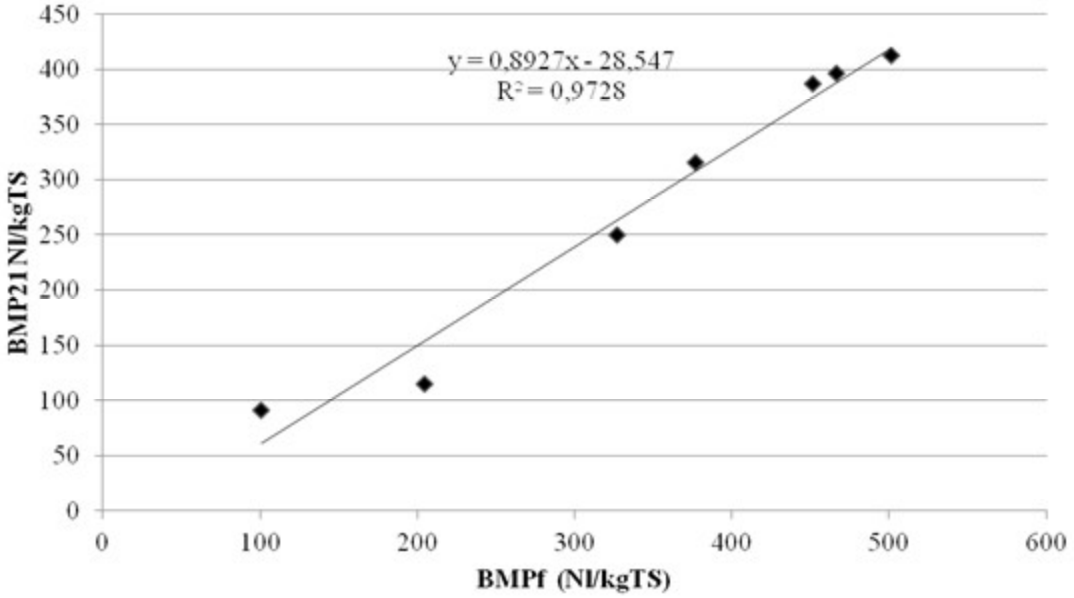

Fig. 4: BMP21 and BMPf correlation

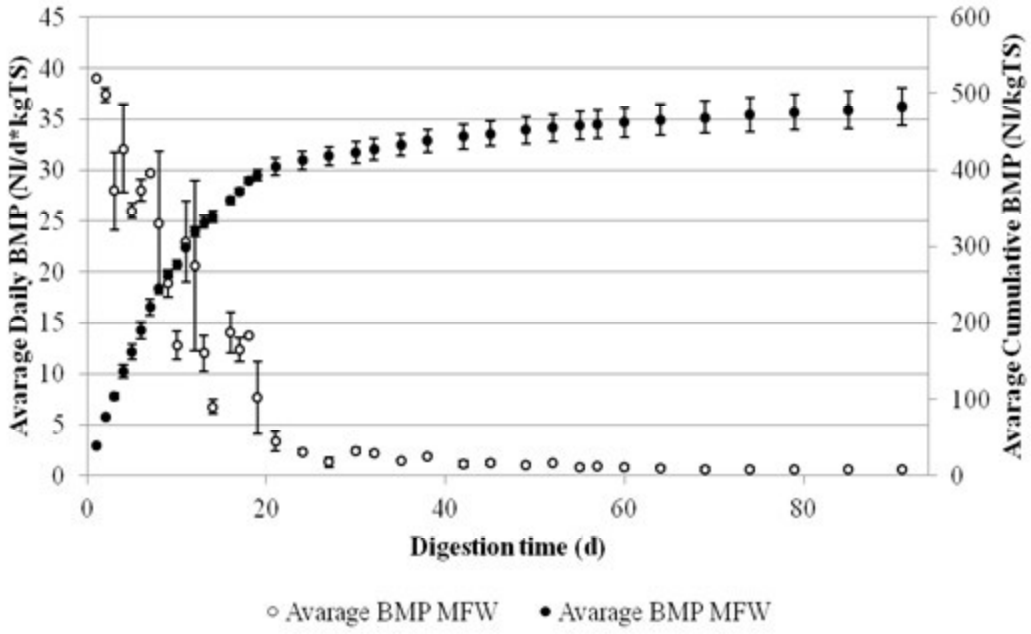

Fig. 5: Daily and cumulative BMP, Mixed Food Waste

As said before, the composition of the sampled biogas has been routinely analysed. As shown in Fig. 6, the methane content in the biogas produced by the MFW, increases from the 20% to 65% until the 20th day of digestion and from the 30th remains constant around the 60%.

Also for the other samples, the biogas composition was analysed in order to understand if the methanogenesis phase was correctly taking place during the digestion process.

From the biogas analysis it has also been possible to esteem the quantity of methane totally produced, simply as the product between the biogas released and the methane percentage of its composition (Fig. 7). Considering an average methane percentage of about the 57%, it was esteemed a methane yield of 309 and 296 $NLCH_4/kgVS$ for the sample MFW (a) and MFW (b) respectively.

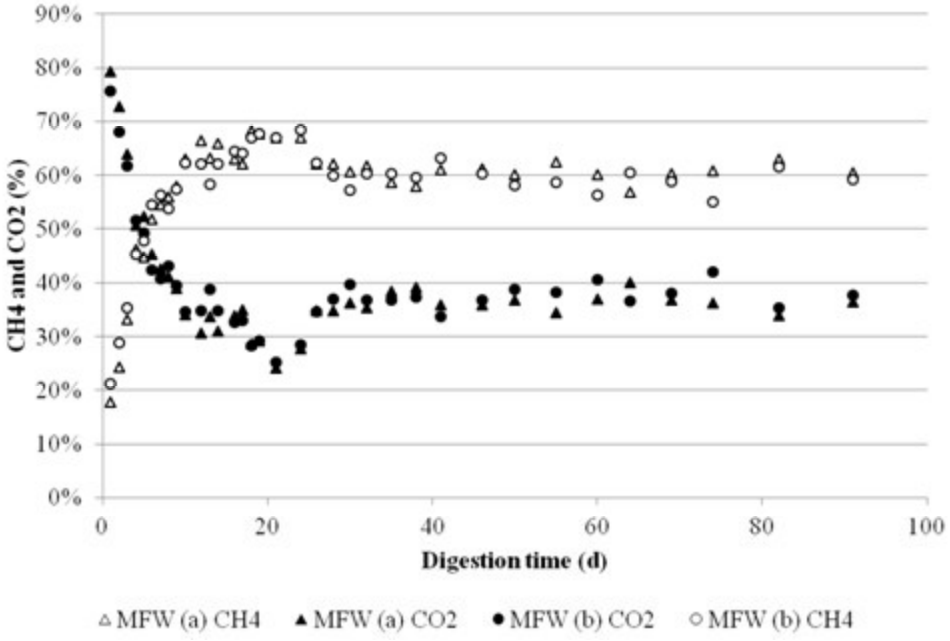

Fig. 6: MWF Sample biogas analysis

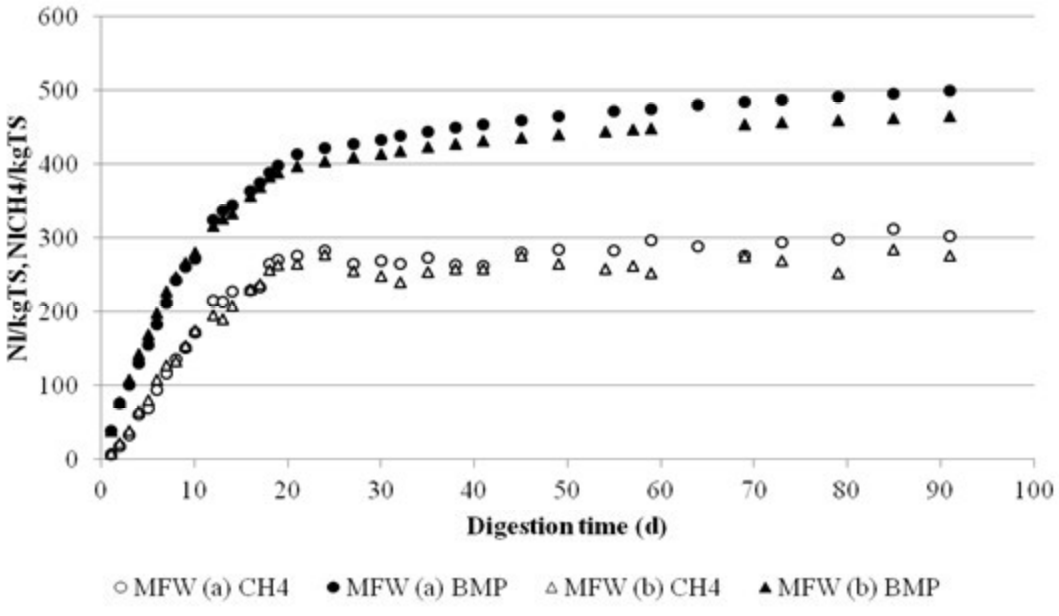

Fig. 7: MWF, BMP and CH4 production Comparison

As said before, the results obtained for the carbohydrates assay shows that the inhibition of the inoculum occurred. This is evident also looking at the errors behaviour (calculated as the ratio between the inoculums BMP and the BMP of each fraction) shown in Fig. 8. After 5 days, the biogas produced by the inoculums was the 20 % of the quantity produced by the sample, to become higher than the 120% at the 93rd day of digestion, which means a negligible biogas production from the substrate comparing with the one from the inoculums.

This is probably due to an accumulation of volatile fatty acid and acid conditions. In fact, in the preparation of the carbohydrates batches, too high concentrations of substrate were probably used, as well as the substrate to inoculums ratio was higher than 1,2, value suggested by the authors to avoid acidification[7] given that this ratio is recognised as one of the major parameter affecting the results of anaerobic assay[11].

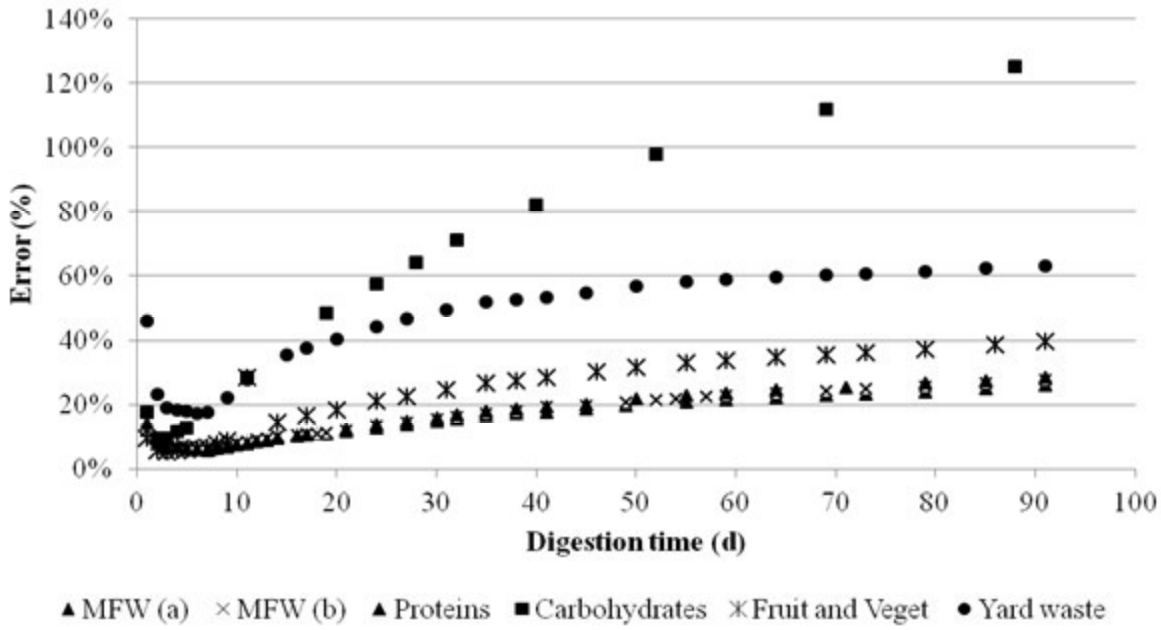

Fig. 8: Errors behaviour

Regarding the other substrates tested, the estimated errors were high too. After the 20th day of digestion, the BMP inoculum to BMP substrates ratio starts to increase until the 50th when all of them become higher than the 50%. This is probably due to a really high activity of the inoculum and an high VS content, as it is possible to observe in the average biomethane produced measured daily (Fig. 9): after 50 days the daily biogas production of all the substrates became comparable with the inoculum BMP.

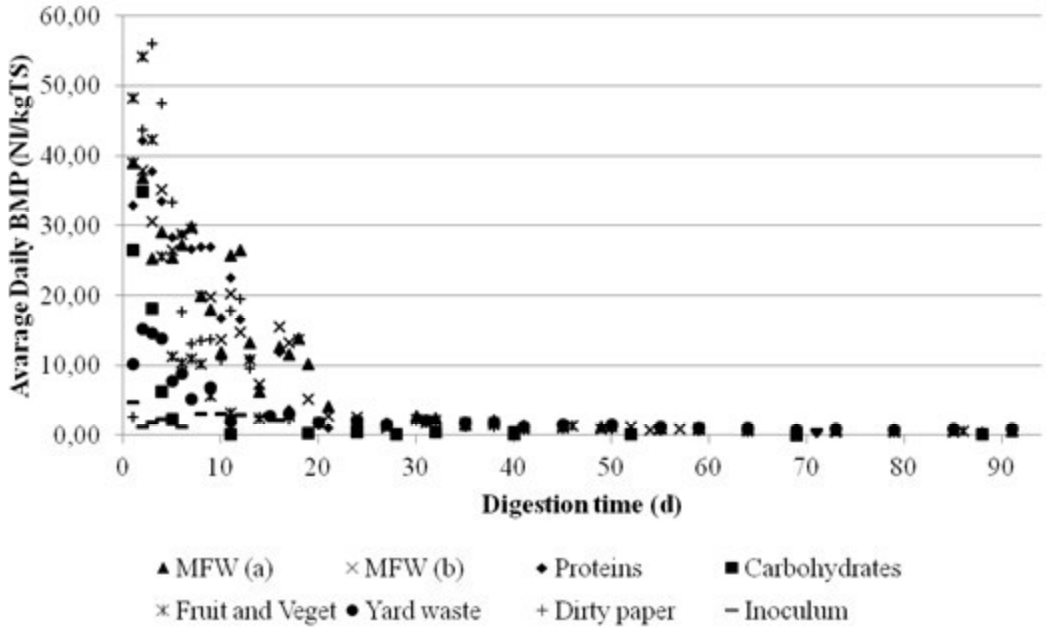

Fig. 9: Avarage Daily BMP comparison

As Fig. 5, the graphic in Fig. 9 shows that, comparing with the background methane production from the inoculum determined in blank assays, the biogas production after 40th day of digestion can be neglect and the most of the biogas was produced during the first 20th day of digestion. Furthermore, looking at the daily biogas pruduction,it can be noticed that, according with Zhu B., Gikas P. and Zhang R. et al. [7], the biogas production duration of food waste was prolunged, with initial daily biogas yields lower compare to others.

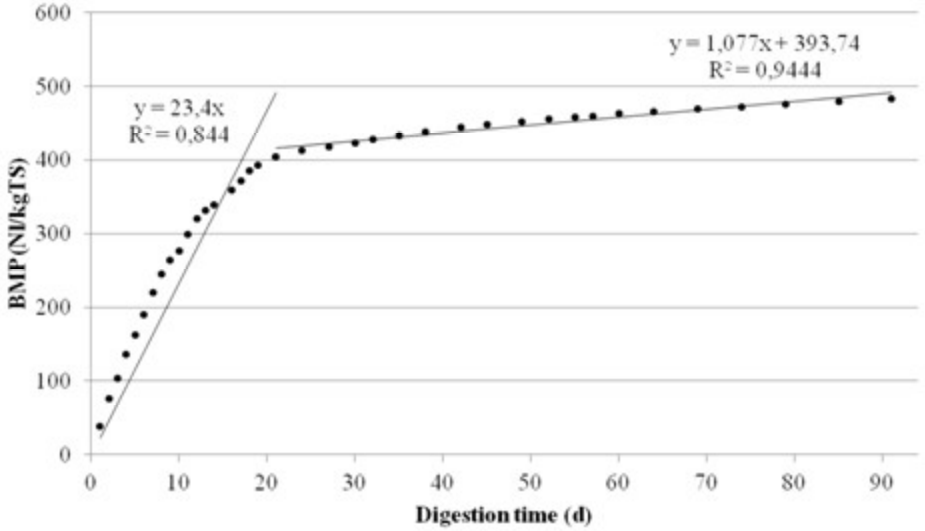

Fig. 10: MFW BMP schematization

With reference to the BMP measured for the mixed food waste samples, it is possible to find a good schematization of the biogas production. As show in Fig. 10, the curve could be well approximated by two lines with different slope. At the beginning the anaerobic digestion is faster and high biogas producing, but, after the meeting point of the two lines, anaerobic kinetics seems to be no more convenient given that the biogas production decreases and the biodegradation became really slow.

As suggested this raw model, for the first 20 days (first line) the anaerobic digestion seems to be a convenient treatment, after which (second line) aerobic stabilization process seems to be more suitable.

3.2. Industrial biogas production comparison

Moving from the results obtained from the tests, in order to compare the results with the biogas production from a real scale anaerobic digestion plant, it was calculated a specific BMP for a ton of input waste fraction (Table 5).

Table 5: BMP21 and BMPf for a ton of input waste

Experimental ID	*BMP21, Nm^3/t*	*BMPf, Nm^3/t*
MFW (a)	175	213
MFW (b)	168	198
Proteins	128	150
Carbohydrates	86	95
Fruit and Veget	35	46
Yard and Garden waste	7	13
Dirty paper	127	152
Inoculum	2	5

Adding up the BMP21 of each waste component and considering a typicall source selected OFMSW composition shown in Fig. 11, three potential industrial biogas production are define *(*Table 6):

- a maximum biogas production (GPmax), calculated assuming that the pre-treatment before the anaerobic digestion is able to remove only the undesired waste fractions with an efficiency of the 100%, i.e. wood packaging, plastic film and plastic packaging, other plastic, rubber, leather, ferrous and non ferrous metals, inert and hazardous waste;
- a potential production, in which is consider the 80% of pre-treatment efficiency and the 20% of biodegradable fraction removed wrongly (GP80%);
- another potential production defined as above but assuming an 75% removal efficiency and the 25% of organic fractions separate erroneously (GP75%).

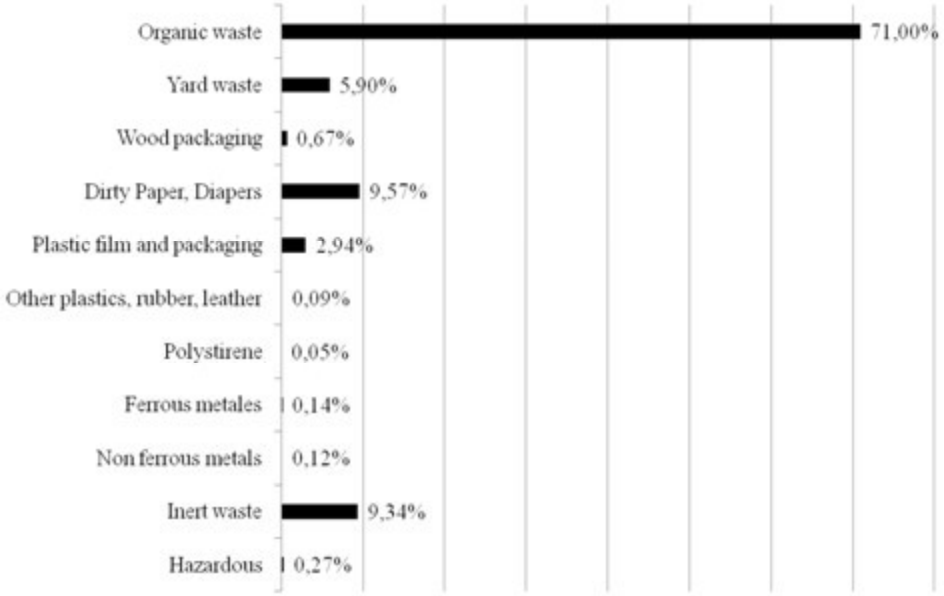

Fig. 11: OFMSW composition

Table 6: GPmax, GP80% and GP75% calculated values

Potential Industrial biogas production	*Removal efficiency, %*	*OF removed, %*	*Calculated value, Nm^3/t*
GPmax	100	0	134
GP80%	80	20	107
GP75%	75	25	100

These estimates could be compared with the biogas production of real anaerobic digestion plants (GPreal). In particular, two different anaerobic digestion plants are considered: one located in a rural area treating source selected OFMSW from a public collection point with a GP of 98 Nm^3/t, another located in a city area with a curbside collection system characterized by a higher GP (Table 7). It is possible to notice that the estimated biogas production (GP80% and GP75%) and the GPreal have similar values and that the rural area digester is characterized by the lowest biogas production.

Table 7: Biogas production, real industrial anaerobic digestion plant

Anaerobic digestion plant	*Collection system*	*GPreal, Nm^3/t*	*Data Source*
Rural Area	Public collection point	98	Management data
City Area	Curbside collection	108	Bozano Gandolfi P., [12]

As said before, during the experimental assay, it has been possible to measure also the BMP of the pre-treatment rejects. In particular the light fraction (LF) and the small heavy fraction (SHF) from the pre-treatment of the two anaerobic digesters were tested (Table 8).

Table 8: BMP21 of pre- treatment reject

Pre-treatment reject	*Provenience*	*BMP21, NL/kgVS*	*BMP21, Nm^3/t*
LF	Rural Area	240	57
SHF		261	8
LF	City Area	508	99
SHF		214	33

As before, also the BMP21 of both LF and SHF form the rural area digester were lower than the ones from the city area. This is probably due to an high presence of yard and garden waste in the rural waste composition, given that the yard and garden waste has a low BMP21 (with reference to Table 5, 7 Nm^3/t). On the other side, the rejects from the city area digestion plat are characterized by a high BMP21, probably because a considerable part of biodegradable fraction of input waste, with the highest BMP21, is wrongly removed by the pre-treatment.

5. Conclusions

The results of this study show that the biochemical methane potential assay could provide useful data to study the pre-treatment efficiency and the performance of real anaerobic digestion plant.

Focusing on the experimental work, the MFW had the highest biochemical methane potential, with an average BMP21 of 405 NL/kgTS and a BMPf of about 484 NL/kgTS and an average methane content of 57%. The laboratory equipments developed prove to be suitable to this kind of experimentation, given that no airtight problem occurred. However, the results obtained for the carbohydrates sample and the errors behaviour show that the measurement protocol and the sample preparation have to be improved in some parts. In particular more attention and specific evaluation have to be done for the substrate to inoculum ratio as well as for the inoculum characteristics. Actually, the estimates obtained with the experimental assay were comparable with the biogas production of real anaerobic digestion plant and it has been possible to assess the pre-treatment efficiency and the performance of some real cases. From the comparison results that: the GP of the rural plant is affected by the presence of yard and garden waste, as it is also supported by the BMP of the pre-treatment rejects; the pre-treatment reject of the city area plant, that treats OFMSW collected by a curbside system, has a high BMP probably because a considerable biodegradable fraction is removed by the pre-treatment.

Nomenclature

BMP Biochemical Methane Potential, NL/kgTS or NL/kgVS

BMP Biochemical Methane Potential after 21 days, NL/kgTS or NL/kgVS

BMPf Final Biochemical Methane Potential, NL/kgTS or NL/kgVS

GP80% Industrial biogas production, considering 80% of pre-treatment efficiency, Nm^3/t

GP75% Industrial biogas production, considering 75% of pre-treatment efficiency, Nm^3/t

GPmax Industrial biogas production, considering maximum pre-treatment efficiency, Nm^3/t

GPreal Industrial biogas production, considering existing real plants, Nm^3/t

LF Light Fraction, anaerobic digestion plant rejects

MFW Mixed Food Waste

MSW Municipal Solid Waste

NL Normal litre

NTP Normal Temperature and Pressure conditions, 273,15K and 1 atm respectively

OFMSW Organic Fraction from Municipal Solid Waste

SHF Small Heavy Fraction, anaerobic digestion plant rejects

TS Total Solid, % v/v on wet weight basis

VS Volatile Total solid, %v/v on TS basis

References

[1] Istituto Superiore per la Protezione e la Ricerca Ambientale. Rapporto Rifiuti Urbani Edizione 2009 – Available at: < http://www.apat.gov.it/site/it-it/apat/pubblicazioni/rapporti/documento/rapporto_108_2010_rifiuti.html>. [accessed 17.1.2012]

[2] Pognani M., BarrenaR., Font X., Scaglia B:, Adani F., and Sànchez A., Monitoring the organic matter properties in a combined anaerobic/aerobic full-scale municipal source-separated waste treatment plant. Bioresource Technol, 2010; 101:6873-6877

[3] Schievano A., Pognani M., D'Imporzano G., and Adani F., Predicting anaerobic biogassification potential of ingestates and digestates of a full-scale biogas plant using chemical and biological parameters. Bioresource Technol, 2008; 99:8112-8117

[4] Ponsa S., Gea T., Alerm L., Cerezo J., Sanchez A., Comparison of aerobic and anaerobic stability indices through a MSW biological treatment process. Waste Manage, 2008; 28:2735-2742

[5] Angelidaki I., Alves M., Bolzonella D., Borzacconi L., Campos J.L., Guwy A.J., Kalyuzhnyi S., Jenicek P and van Lier J.B., Defining the biomethane potential (BMP) of solid organic wastes and energy crops: a proposed protocol for batch assays. Water Sci Technol, 2009; 59:927-934

[6] Hansen L.T., Schmidt E.J., Angelidaki I., Marca E., Jansen J.L.C., Mosbæk H. and Christensen T.H., Method for determination of methane potentials of solid organic waste. Waste Manage, 2004; 24:393-400

[7] Zhu B., Gikas P., Zhang R., Lord J., Jenkins B. and Li X., Characteristics and production potential of municipal solid waste pretreated with a rotary drum reactor. Bioresource Technol, 2009; 100:1122-1129

[8] Bayard R., de Araùjo Morais J., Ducom G., Achour F., Rouez M. and Gourdon R., Assessment of the effectiveness of an industrial unit of mechanical-biological treatment of municipal solid waste, 2010; 175:23-32

[9] Lesteur M., Bellon-Maurel V., Gonzalez C., Latrille E., Roger J.M., Junqua G. and Steyer J.P., Alternative methods for determining anaerobic biodegradabilit: A review. Process Biochem, 2010; 45: 431-440

[10] Cho J.K. and Park S.C., Biochemical methane potential and solid state anaerobic digestion of Korean food waste. Bioresource Technol, 1995; 52: 245-253

[11] Neves L., Oliveira R. and Alves M. M., Influence of inoculum activity on the bio-methanization of a kitchen waste under different waste/inoculum ratios. Process Biochem, 2004, 39:2019-2024

[12] Bozano Gandolfi P., Pratical experiences in the production of biogas and energy from wastes – Available at: < http://bta-international.de/downloads.html?&lang=3>. [accessed 24.1.2012]

Exergy Analysis and Genetic Algorithms for the Optimization of Flat-Plate Solar Collectors

Soteris A. Kalogirou

Department of Mechanical Engineering and Materials Science and Engineering, Cyprus University of Technology, P. O. Box 50329, 3603, Limassol, Cyprus, email: Soteris.kalogirou@cut.ac.cy

Abstract:

This paper employs exergy analysis to derive a general equation for the exergy efficiency of flat plate collectors and thus optimize its design and operation. Exergy analysis of a flat-plate solar collector is a more effective method of finding the optimum relationship between flow rate and the collector area. The fixed parameters in this optimization are the collector inlet temperature, available solar radiation, the collector transmittance-absorptance product and the ambient temperature. The collector heat loss coefficient is estimated according to the collector plate temperature, wind convection loss, number of glass covers, collector indination, ambient temperature and emittance of collector plate and glass cover. In order to find the optimum value of this multivariable problem genetic algorithms are used which are based on the principles of genetics and survival of the fittest. The optimization parameter is exergy efficiency and the objective is to maximize this parameter. Genetic algorithms proved suitable and very quick in obtaining the required results. These results prove that the exergy efficiency of a flat-plate solar collector is maximized for small distances between the riser tubes and for very small diameter of these tubes. By using a more practical distance of 10 centimetres between the tubes, and excluding this parameter from the optimization procedure, very small differences are observed in maximum exergy efficiency and if the cost of the materials is accounted this is a more cost-effective solution. Other findings are that the exergy efficiency increases considerably at higher solar radiation and that the transmittance absorptance product affects to a great extent the exergy efficiency.

Keywords:

Exergy analysis, Genetic algorithms, Flat-plate collectors, Optimisation, Efficiency.

1. Introduction

Solar energy collectors are special kind of heat exchangers that transform solar radiation energy to internal energy of a transport fluid. Flat plate collectors are the most popular type of solar devises for low temperature applications. The main use of these collectors is in solar water heating systems operating at maximum temperatures of 80-90°C. Most of these systems are operating thermosiphonically at very small flow rate created by the small density differences between the hot and cold water. A number of researchers have used exergy analysis to design flat plate collectors. Badescu [1] optimized the width and thickness of the fins of a flat-plate collector by minimizing the cost per unit useful heat flux. The proposed procedure allows computation of the necessary collection surface area. A rather involved, but still simple, flat plate solar collector model is used in the calculations. Model implementation requires a specific geographical location with a detailed meteorological database available. Fins of both uniform and variable thickness were considered. The optimum fin cross section is very close to an isosceles triangle. The fin width is shorter and the seasonal influence is weaker at lower operation temperatures. Fin width and thickness at the base depend on the season. The optimum distance between the tubes is increased by increasing the inlet fluid temperature, and it is larger in the cold season than in the warm season.

Badescu [2] also considered the best operation strategies for open loop flat-plate solar collector systems. A direct optimal control method (the TOMP algorithm) is implemented. A detailed collector model and realistic meteorological data from both cold and warm seasons are used. The maximum exergetic efficiency is low (usually less than 3%), in good agreement with experimental

measurements reported in literature. The optimum mass-flow rate increases near sunrise and sunset and by increasing the fluid inlet temperature. The optimum mass-flow rate is well correlated with global solar irradiance during the warm season. Also, operation at a properly defined constant mass-flow rate may be close to the optimal operation.

Torres-Reyes et al. [3] presented a procedure to establish the optimal performance parameters for the minimum entropy generation during the collection of solar energy. The Entropy Generation Number, Ns, and the criterion for the optimal thermodynamic operation of a collector under non-isothermally, finite-time conditions, are reviewed. The Mass Flow Number, M, corresponding to the optimum flow of working fluid as a function of the solar collection area, is also considered. A general method for the preliminary solar collector design, based on Ns, M and the "Sun–Air" or stagnation temperature, is developed. This last concept is defined as the maximum temperature that the collector reaches at non-flow conditions for a given geographic location, geometry and construction materials. The thermodynamic optimization procedure was used to determine the optimal performance parameters of an experimental solar collector.

Torres-Reyes et al. [4] also presented the thermodynamic optimization of flat plate collectors based on the first and the second law, developed to determine the optimal performance parameters and to design a solar to thermal energy conversion system. An exergy analysis is presented to determine the optimum outlet temperature of the working fluid and the optimum path flow length of solar collectors with various configurations. The collectors used to heat the air flow during solar-to-thermal energy conversion are internally arranged in different ways with respect to the absorber plates and heat transfer elements. The exergy balance and the dimensionless exergy relationships are derived by taking into account the irreversibilities produced by the pressure drop in the flow of the working fluid through the collector. Design formulas for different air duct and absorber plate arrangements are obtained.

The use of genetic algorithms (GAs) for the optimal design of solar collectors is well known [5, 6]. Genetic algorithms have been used as a design support tool by Loomans and Visser [7] for the optimization of large hot water systems. The tool calculates the yield and the costs of solar hot water systems based on technical and financial data of the system components. The genetic algorithm allows for the optimization of separate variables as the collector type, the number of collectors, the heat storage capacity and the collector heat exchanger area.

Kalogirou [8] used also genetic algorithms together with a neural network for the optimization of the design of solar energy systems. The method is presented by means of an example referring to an industrial process heat system. The genetic algorithm is used to determine the optimum values of collector area and the storage tank size of the system which minimize the solar energy price. According to the author the solution reached is more accurate than the traditional trial and error method and the design time is reduced substantially.

Krause *et al.* [9] presented a study in which two solar domestic hot water systems in Germany have been optimized by employing validated TRNSYS models in combination with genetic algorithms. Three different optimization procedures are presented. The first concerns the planning phase. The second one concerns the operation of the systems and should be carried out after about one year of data is collected. The third one examines the daily performance by considering predictions of weather and hot water consumption and actual temperature level in the storage tank.

The objective of the present work is to maximize the exergy efficiency of flat-plate collectors. The fixed parameters in this optimization are the collector inlet temperature, available solar radiation, the collector transmittance-absorptance product and the ambient temperature. The collector heat loss coefficient is estimated according to the collector plate temperature, wind convection loss, number of glass covers, collector inclination, ambient temperature and emittance of collector plate and glass cover. For this purpose an evolution strategy based on genetic algorithms is used to determine the optimum solution.

2. Energy Analysis

In this section various relations that are required in order to determine the useful energy collected and the interaction of the various constructional parameters on the performance of a collector are presented.

The useful energy collected from a collector can be obtained from the following formula [10]:

$$Q_u = A_c F_R \left[G_t(\tau\alpha) - U_L \left(T_{f,i} - T_a \right) \right] = \dot{m} c_p \left(T_{f,o} - T_{f,i} \right) \quad (1)$$

where F_R is the heat removal factor given by [10]:

$$F_R = \frac{\dot{m} c_p}{A_c U_L} \left(1 - \mathrm{Exp}\left[\frac{U_L F' A_c}{\dot{m} c_p} \right] \right) \quad (2)$$

In (2) F´ is the collector efficiency factor which is calculated by considering the temperature distribution between two pipes of the collector absorber and by assuming that the temperature gradient in the flow direction is negligible [10]. This analysis can be performed by considering the sheet-tube configuration shown in Fig. 1, where the distance between the tubes is W, the tube diameter is D, and the sheet thickness is δ.

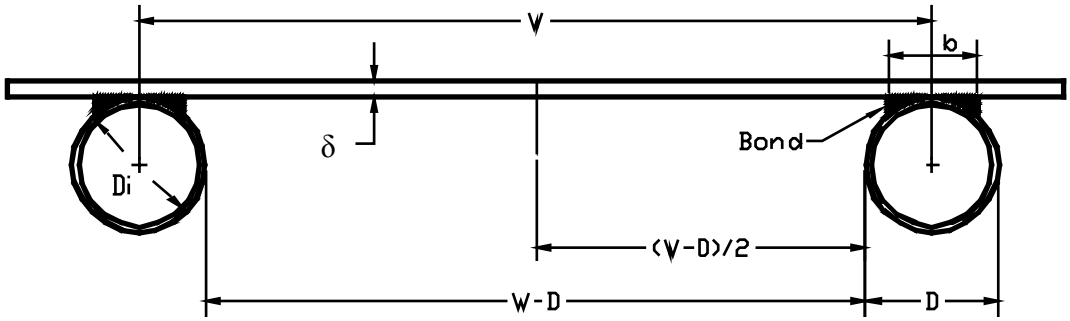

Fig. 1. Schematic diagram of a flat-plate sheet and tube configuration

As the sheet metal is usually made from copper or aluminum which are good conductors of heat, the temperature gradient through the sheet is negligible, therefore the region between the centerline separating the tubes and the tube base can be considered as a classical fin problem. By following this analysis the equation to estimate F´ is given by [10]:

$$F' = \frac{\dfrac{1}{U_L}}{W\left[\dfrac{1}{U_L\left[D + (W-D)F\right]} + \dfrac{1}{C_b} + \dfrac{1}{\pi D_i h_{fi}} \right]} \quad (3)$$

In (3), C_b is the bond conductance which can be estimated from knowledge of the bond thermal conductivity, the average bond thickness, and the bond width. The bond conductance can be very important in accurately describing the collector performance and generally it is necessary to have good metal-to-metal contact so that the bond conductance is greater that 30 W/mK and preferably the tube should be welded to the fin.

Factor F in (3) is the standard fin efficiency for straight fins with rectangular profile, obtained from:

$$F = \frac{\tanh\left[n(W-D)/2\right]}{n(W-D)/2} \quad (4)$$

where n is given by:

$$n = \sqrt{\frac{U_L}{k\delta}} \qquad (5)$$

The collector efficiency factor is essentially a constant factor for any collector design and fluid flow rate. The ratio of U_L to C_b, the ratio of U_L to h_{fi}, and the fin efficiency F are the only variables appearing in (3) that may be functions of temperature. For most collector designs F is the most important of these variables in determining F´. The factor F´ is a function of U_L and h_{fi}, each of which has some temperature dependence, but it is not a strong function of temperature. Additionally, the collector efficiency factor decreases with increased tube center-to-center distances and increases with increases in both material thicknesses and thermal conductivity. Increasing the overall loss coefficient decreases F´ while increasing the fluid-tube heat transfer coefficient increases F´.

Therefore it is obvious from the above analysis that by increasing F´ more energy can be intercepted by the collector. By keeping all other factors constant increase of F´ can be obtained by decreasing W. However, decrease in W means increased number of tubes and therefore extra cost would be required for the construction of the collector.

The collector efficiency is found by dividing Q_u given in (1), by the incident radiation A_cG_t. By doing so the following Equation is obtained:

$$\eta = F_R(\tau\alpha) - F_R U_L\left[\frac{T_{f,i} - T_a}{G_t}\right] = \frac{\dot{m}c_p\left(T_{f,o} - T_{f,i}\right)}{A_c G_t} \qquad (6)$$

By plotting η against $\Delta T/G_t$ a straight line is obtained with the slope equal to F_RU_L, called the loss coefficient and the intercept on the y-axis equal to $F_R(\tau\alpha)$, called optical efficiency.

Generally the efficiency of a solar thermal system increases by increasing the flow rate. This increase is asymptotic, i.e., the increase is rapid at small flow rates and becomes almost asymptotic to a certain maximum value at higher values of flow rate. In a similar way the collector outlet temperature increases with the collector area and decreases with increasing flow rate and vice versa. This creates difficulties in selecting appropriate values of flow rate and collector area.

In a real system the variation of the fluid inlet temperature depends to a great extent on the storage tank configuration, thermal load demand and the consequent make-up water to the storage tank which affects the fluid inlet temperature to the collector.

3. Exergy Analysis

According to Kalogirou [10] the temperature at any position y at a fluid inlet temperature $T_{f,i}$ is given by:

$$T_f - T_a = \frac{S}{U_L} + \left(T_{f,i} - T_a - \frac{S}{U_L}\right)\left(\mathrm{Exp}\left[-\frac{U_L F' N W y}{\dot{m}c_p}\right]\right) \qquad (7)$$

For y=L the collector area is given by A_c = NWL. If $T_{f,i} = T_a$ the fluid temperature variation at the exit from the solar collector is:

$$\Delta T = T_{f,o} - T_a = \left(\frac{S}{U_L}\right)\left(1 - \mathrm{Exp}\left[-\frac{U_L F'}{c_p}\frac{A_c}{\dot{m}}\right]\right) \qquad (8)$$

The flow rate of exergy transferred from the sun to the fluid that is heated while crossing the riser pipe is:

$$\dot{E}_f = \dot{m}e_f = \dot{m}\left[\left(h_{f,o} - h_{f,i}\right) - T_a\left(s_{f,o} - s_{f,i}\right)\right] \qquad (9)$$

Where $h_{f,o} - h_{f,i} = c_p(T_{f,o} - T_{f,i})$ is the variation of specific enthalpy. The variation of the specific entropy is:

$$s_{f,o} - s_{f,i} = c_p \ln\left(\frac{T_{f,o}}{T_{f,i}}\right) \tag{10}$$

Therefore:

$$\dot{E}_f = \dot{m}c_p\left(\Delta T - T_a \ln\left(\frac{T_{f,o}}{T_{f,i}}\right)\right) \tag{11}$$

And the exergy efficiency is given by dividing $\dot{E}_f$ by the available solar radiation $Q_{s,in}$ which is equal to $A_c G_t$:

$$\eta_{ex} = \frac{\dot{E}_f}{\dot{Q}_{S,in}} = \dot{m}c_p\left(\frac{\Delta T - T_a \ln\left(\frac{T_{f,o}}{T_{f,i}}\right)}{A_c G_t}\right) \tag{12}$$

Replacing ΔT given by (8) in (12), the following relation for the exergy efficiency can be obtained:

$$\eta_{ex} = \frac{\dot{m}c_p}{A_c G_t}\left\{\frac{S}{U_L}\left(1 - \mathrm{Exp}\left[-\frac{U_L F' A_c}{\dot{m}c_p}\right]\right) - T_a \ln\left(1 + \frac{S}{T_a U_L}\left(1 - \mathrm{Exp}\left[-\frac{U_L F' A_c}{\dot{m}c_p}\right]\right)\right)\right\} \tag{13}$$

As can be seen from the exergy analysis, a general equation for the exergy efficiency of flat plate collectors is derived. This efficiency depends on the values of flow rate, collector area and collector efficiency factor. The latter depends on the distance between consequent riser tubes, the diameter of the riser tubes, the collector fin efficiency, the internal riser tube diameter (depends on outside tube diameter) and the convection coefficient inside the tube - which depends on the mass flow rate and tube inside diameter, which affect the Reynolds number and thus the Nusselt number.

4. Method Description

The objective of this work is to find the parameters that maximize the exergy efficiency. In order to do this a numbers of parameters need to be considered as constants. These are shown in Table 1.

Table 1. Constant parameters used in exergy optimization

Parameter	Value
Fluid specific heat, c_p	4185 J/kg-K
Available solar radiation, G_t	500-1000 W/m^2
Transmittance-absorptance product, ($\tau\alpha$)	0.60-0.90
Ambient temperature, T_a	25°C
Bond conductance, C_b	100 W/m^2-K
Absorbing plate thickness, δ	0.5 mm
Thermal conductivity of fluid, k	410 W/m-K

From these constant parameters a number of other parameters are evaluated. These are:

1. Heat loss coefficient, U_L, estimated from [10]:

$$U_L = \frac{1}{\dfrac{N_g}{\dfrac{C}{T_p}\left[\dfrac{T_p - T_a}{N_g + f}\right]^{0.33}} + \dfrac{1}{h_w}} + \frac{\sigma\left(T_p^2 + T_a^2\right)\left(T_p + T_a\right)}{\dfrac{1}{\varepsilon_p + 0.05N_g\left(1-\varepsilon_p\right)} + \dfrac{2N_g + f - 1}{\varepsilon_g} - N_g} \quad (14)$$

Where:

$$f = \left(1 - 0.04h_w + 0.0005h_w^2\right)\left(1 + 0.091N_g\right) \quad (15)$$

$$C = 365.9\left(1 - 0.00883\beta + 0.0001298\beta^2\right) \quad (16)$$

$$h_w = \frac{8.6V^{0.6}}{L^{0.4}} \quad (17)$$

This estimation ignores the bottom and edge losses and considers the wind velocity to be 1 m/s, collector slope, β, equal to 45°, one glass cover and emittance values of 0.8. The estimation is also done at a plate temperature T_p to be 20°C above the mean collector fluid temperature.

2. Factor n estimated from (5)
3. Fin efficiency F, estimated from (4)
4. The convection heat transfer coefficient inside the pipe, $h_{f,i}$, estimated from the principles of heat transfer and according to the type of flow, turbulent or laminar according to the mass flow rate and the riser tube diameter.
5. The collector efficiency factor F´, estimated from (3)

For the above parameters the inputs required are the distance between successive riser tubes, W, the riser tube diameter, D, and the collector mass flow rate. These are varied during the optimization process until the exergy efficiency is maximized using a genetic algorithm described in the following section.

It should be noted that a "proper" exergy optimization should include optimization of both the process parameters and the size of equipment by considering two key parameters, i.e., exergy efficiency and cost, which include the capital investment (proportional to the collector area) and operating cost due to the pressure drop. However, in this work the pressure drop is not included as the collector is assumed to operate at very small flow rate (similar to the thermosyphonic one), therefore, no exergy consumption for the fluid pumping is included in the analysis and this should shift the optimum to the smaller diameters of tubes and distances between the tubes. This assumption will be proved by the obtained results. Additionally, no other cost-connected parameter is included in the optimization, such as exergy cost of equipment, so the optimization related to the collector area only affects the amount of radiation collected by the system.

5. Genetic Algorithm

The genetic algorithm (GA) is a model of machine learning, which derives its behavior from a representation of the processes of evolution in nature. This is done by the creation within a machine/computer of a population of individuals represented by chromosomes. Essentially these are a set of character strings that are analogous to the chromosomes that we see in the DNA of human beings. The individuals in the population then go through a process of evolution.

It should be noted that evolution as occurring in nature or elsewhere is not a purposive or directed process, i.e., there is no evidence to support the assertion that the goal of evolution is to produce Mankind. Indeed, the processes of nature seem to end to different individuals competing for resources in the environment. Some are better than others are, those that are better are more likely to survive and propagate their genetic material.

In nature, the encoding for the genetic information is done in a way that admits asexual reproduction, which typically results in offspring that are genetically identical to the parent. Sexual reproduction allows the creation of genetically radically different offspring that are still of the same general species.

In an over simplified consideration, at the molecular level what happens is that a pair of chromosomes bump into one another, exchange chunks of genetic information and drift apart. This is the recombination operation, which in GAs is generally referred to as crossover because of the way that genetic material crosses over from one chromosome to another.

The crossover operation happens in an environment where the selection of who gets to mate is a function of the fitness of the individual, i.e., how good the individual is at competing in its environment. Some GAs use a simple function of the fitness measure to select individuals (probabilistically) to undergo genetic operations such as crossover or asexual reproduction, i.e., the propagation of genetic material remains unaltered. This is fitness - proportionate selection. Other implementations use a model in which certain randomly selected individuals in a subgroup compete and the fittest is selected. This is called tournament selection. The two processes that most contribute to evolution are crossover and fitness based selection/reproduction. Mutation also plays a role in this process.

GAs are used for a number of different application areas. An example of this would be multidimensional optimization problems in which the character string of the chromosome can be used to encode the values for the different parameters being optimized.

In practice, this genetic model of computation can be implemented by having arrays of bits or characters to represent the chromosomes. Simple bit manipulation operations allow the implementation of crossover, mutation and other operations.

When the GA is executed, it is usually done in a manner that involves the following cycle [11]:

- Evaluate the fitness of all of the individuals in the population.
- Create a new population by performing operations such as crossover, fitness-proportionate reproduction and mutation on the individuals whose fitness has just been measured.
- Discard the old population and iterate using the new population.

One iteration of this loop is referred to as a generation. More details on genetic algorithms can be found in Goldberg [12].

The first generation of this process operates on a population of randomly generated individuals. From there on, the genetic operations, in concert with the fitness measure, operate to improve the population. Genetic algorithms (GA) are suitable for finding the optimum solution in problems where a fitness function is present. Genetic algorithms use a “fitness” measure to determine which of the individuals in the population survive and reproduce. Thus, survival of the fittest causes good solutions to progress. A genetic algorithm works by selective breeding of a population of “individuals”, each of which could be a potential solution to the problem. The genetic algorithm is seeking to breed an individual, which either maximizes, minimizes or it is focused on a particular solution of a problem. In this case, the genetic algorithm is seeking to breed an individual that maximizes the exergy efficiency of the solar collector.

The larger the breeding pool size, the greater the potential of it producing a better individual. However, the fitness value produced by every individual must be compared with all other fitness values of all the other individuals on every reproductive cycle, so larger breeding pools take longer time. After testing all of the individuals in the pool, a new “generation” of individuals is produced for testing.

A genetic algorithm is not gradient based, and uses an implicitly parallel sampling of the solutions space. The population approach and multiple sampling means that it is less subject to becoming trapped to local minima than traditional direct approaches, and can navigate a large solution space with a highly efficient number of samples. Although not guaranteed to provide a globally optimum

solution, GAs have been shown to be highly efficient at reaching a very near optimum solution in a computationally efficient manner.

During the setting up of the GA the user has to specify the adjustable chromosomes, i.e. the parameters that would be modified during evolution to obtain the maximum or minimum values of the fitness functions. In this work, the fitness function is exergy efficiency given by (13). Additionally the user has to specify the range of the input parameters called constraints.

The genetic algorithm parameters used in the present work are:

- Population size=50

Population size is the size of the genetic breeding pool, i.e., the number of individuals contained in the pool. If this parameter is set to a low value, there would not be enough different kinds of individuals to solve the problem satisfactorily. On the other hand, if there are too many in the population, a good solution will take longer to be found because the fitness function must be calculated for every individual in every generation.

- Crossover rate=90%

Crossover rate determines the probability that the crossover operator will be applied to a particular chromosome during a generation.

- Mutation rate=1%

Mutation rate determines the probability that the mutation operator will be applied to a particular chromosome during a generation.

- Generation gap=96%

Generation gap determines the fraction of those individuals that do not go into the next generation. It is sometimes desirable that individuals in the population be allowed to go into next generation. This is especially important if individuals selected are the most fit ones in the population.

- Chromosome type=continuous

Populations are composed of individuals, and individuals are composed of chromosomes, which are equivalent to variables. Chromosomes are composed of smaller units called genes. There are two types of chromosomes, continuous and enumerated. Continuous are implemented in the computer as binary bits. The two distinct values of a gene, 0 and 1, are called alleles. Multiple chromosomes make up the individual. Each partition is one chromosome, each binary bit is a gene, and the value of each bit (1, 0, 0, 1, 1, 0) is an allele. Enumerated chromosomes consist of genes, which can have more allele values than just 0 and 1.

The genetic algorithm is usually stopped after best fitness remained unchanged for a number of generations or when the optimum solution is reached. In this work the genetic algorithm was stopped after best fitness remained unchanged for 75 generations.

6. Results

The input parameters (adjustable chromosomes) were used in a genetic algorithm program to find the values that maximize collector exergy efficiency. The whole model was set – up in a spreadsheet program in which the various parameters are entered into different cells. The optimum values of the various parameters were used in (13) to estimate the collector exergy efficiency which is the fitness function that needs to be maximized. The various input parameters are constrained to vary between certain values. The ones used in this work are shown in Table 2.

Table 2. Constrains of the input parameters

Parameter	Symbol	Range
Mass flow rate	$\dot{m}$	0.001-0.08 kg/s
Collector area	A_c	1-10 m^2
Distance between riser tubes	W	0.03-0.15 m
Riser tube diameter	D	0.004-0.022 m

The optimum results can be presented graphically or in tables. Here the table presentation is preferred so as to show the exact values obtained. The results are shown in Tables 3-5. It should be noted that for each run of the program the optimum solution was reached in less than 5 seconds on a Pentium 3.2 GHz machine, which is very fast.

Table 3 presents the results of the optimization process with respect to the effect of inlet temperature and radiation.

Table 3. Results of the optimization process-effect of inlet temperature and radiation

G_t (W/m^2)	(τα)	T_{in} (°C)	W (m)	D (m)	η_{ex} (%)	T_{out} (°C)	A_c (m^2)	$\dot{m}$ (kg/s)
500	0.8	25	0.03	0.004	3.07	66.02	7.49	0.0106
		27	0.03	0.004	4.85	59.86	9.98	0.0196
		30	0.03	0.004	7.90	52.24	9.61	0.0304
		35	0.03	0.013	13.77	43.27	8.76	0.0797

According to the results shown in Table 3 by increasing the collector inlet temperature the collector outlet temperature reduces, the optimum flow rate increases and the exergy efficiency increases. As can be seen the distance between the riser tubes remains to the minimum value, same as the riser tube diameter except the last value which differs from the minimum value possible, determined by the constrains. It is apparent that the optimum collector area reaches a maximum value at the inlet temperature of 27°C and then drops for bigger values. The effect of solar radiation is shown in Table 4.

Table 4. Results of the optimization process-effect of solar radiation

G_t (W/m^2)	(τα)	T_{in} (°C)	W (m)	D (m)	η_{ex} (%)	T_{out} (°C)	A_c (m^2)	$\dot{m}$ (kg/s)
500	0.8	25	0.03	0.004	3.07	66.02	7.49	0.0106
500		27	0.03	0.004	4.85	59.86	9.98	0.0196
1000		25	0.03	0.004	5.19	95.88	8.24	0.0140
1000		27	0.03	0.004	6.21	92.22	9.93	0.0190

As can be seen from Table 4 by increasing the solar radiation and keeping the other parameters constant, the collector outlet temperature increases, as expected, and the same applies to the optimum collector area and the optimum mass flow rate. Both the riser tube spacing, W, and diameter, D, remain at their minimum values. The effect of solar radiation and the value of the transmittance-absorptance product are presented in Table 5.

Table 5. Results of the optimization process-effect of radiation and transmittance absorptance product

G_t (W/m^2)	(τα)	T_{in} (°C)	W (m)	D (m)	η_{ex} (%)	T_{out} (°C)	A_c (m^2)	$\dot{m}$ (kg/s)
500	0.6	27	0.03	0.004	3.57	49.56	10.0	0.0224
500	0.9		0.03	0.004	5.60	64.56	9.96	0.0190
1000	0.6		0.03	0.004	4.10	77.32	9.68	0.0180
1000	0.9		0.03	0.004	7.39	99.03	9.26	0.0180

The results presented in Table 5 reveal that the increase of the transmittance-absorptance product causes increase in the collector outlet temperature, and a slight decrease in the optimum collector

area and the optimum mass flow rate. The exergy efficiency however almost doubles. It is thus required to achieve a high value of ($\tau\alpha$) as possible in flat-plate collectors. Again both, the riser tube spacing, W, and diameter, D, remain at their minimum values.

As seen from the above tables the distance between the riser tubes, W, is very small. In fact it could be zero but was stuck to the minimum value specified as a constrain. For this reason a more practical distance of 10 centimetres between the tubes is used and this parameter is excluded from the optimization procedure. By doing so the results shown in Table 6 are obtained.

Table 6. Optimization results for a fixed distance between riser tubes of 10cm

G_t (W/m^2)	($\tau\alpha$)	T_{in} (°C)	D (m)	η_{ex} (%)	T_{out} (°C)	A_c (m^2)	$\dot{m}$ (kg/s)
500	0.8	27	0.004	4.72	59.6	9.98	0.0193
1000	0.8	27	0.004	6.02	92.1	8.38	0.0156

As can be seen for this more practical case, and by comparing the values shown with the values presented in previous tables, the exergy efficiency is not affected too much. This case however is much more cost effective because the minimum the distance between the riser tubes the maximum would be the number of tubes and the collector will cost more.

Another practical case that needs to be investigated is the effect of riser pipe diameter on the exergy efficiency. For this exercise the distance between the riser pipes is kept to 10 cm and the other parameters, like optimum collector area and mass flow rate, as the ones presented in Table 6. The results of this exercise are shown in Table 7.

Table 7. Effect of pipe diameter for a fixed distance between riser tubes of 10 cm

G_t (W/m^2)	($\tau\alpha$)	T_{in} (°C)	A_c (m^2)	$\dot{m}$ (kg/s)	D (m)	η_{ex} (%)
500	0.8	27	9.98	0.0193	0.004	4.72
					0.008	4.71
					0.012	4.70
					0.015	4.69
1000	0.8	27	8.38	0.0156	0.004	6.02
					0.008	6.01
					0.012	5.99
					0.015	5.99

As can be seen the pipe diameter can be increased from the optimum small diameter without any problem as the exergy efficiency is marginally affected for the bigger sizes. So this needs to be decided solely on cost, which increases for bigger diameter pipes and the friction factor imposed by the smaller diameter pipe, which needs to be kept as small as possible in order not to block the thermosiphonic flow.

It should be noted that in all results presented in Tables 3-7 a very small flow rate is given as the optimum and the actual value approaches the thermosiphonically created one which is the most frequently used operation mode for flat-plate collectors. So the assumption made earlier about the small flow rate and the exclusion of fluid pumping from the analysis is proved.

7. Conclusions

It is proved in this paper that exergy analysis and genetic algorithms are very suitable for obtaining the required results quickly. These results prove that the exergy efficiency of a flat-plate solar collector is maximized for small distances between the riser tubes and for very small diameter of these tubes. By using a more practical distance of 10 centimeters between the tubes, and excluding this parameter from the optimization procedure, very small differences are observed in maximum exergy efficiency and if the cost of the materials is accounted this is a more cost-effective solution. The exergy efficiency it is also insensitive to the size of the riser pipe diameter. Other findings

prove that exergy efficiency increases considerably at higher solar radiation and that the transmittance absorptance product affects to a great extent the exergy efficiency.

Nomenclature

A_c collector area, m^2
B bond width , m
C factor given by (16)
C_b bond conductance, W/(mK)
c_p specific heat capacity, J/(kgK)
D riser tube outside diameter, m
D_i riser tube inside diameter, m
$\dot{E}_f$ exergy flow rate, W
e specific exergy, J/kg
F´ collector efficiency factor
F fin efficiency
f factor given by (15)
F_R heat removal factor
G_t solar radiation, W/m^2
h specific enthalpy, J/kg
h_{fi} heat transfer coefficient inside absorber tube, $W/(m^2K)$
h_w wind loss coefficient, $W/(m^2K)$
I solar radiation, W/m^2
k absorber plate thermal conductivity, W/(mK)
k_b bond thermal conductivity, W/(mK)
L collector length, m
$\dot{m}$ mass flow rate, kg/s
n factor given by (5)
N number of riser tubes
N_g number of glass covers
$Q_{s,in}$ available solar radiation, W/m^2
Q_u rate of useful energy collected, W
s specific entropy, J/(kgK)
S power absorbed per unit area of collector, W/m^2
T_a ambient temperature, K
T_f fluid temperature, K
$T_{f,i}$ collector inlet temperature, K
$T_{f,o}$ collector outlet temperature, K
T_p plate temperature, K
U_L overall heat loss coefficient, $W/(m^2K)$
V wind speed, m/s
W distance between riser tubes, m

Greek symbols

β collector slope, degrees

δ absorber (fin) thickness, m

ε_p plate emittance

ε_g glass cover emittance

ΔT temperature difference, K

$\tau\alpha$ transmittance-absorptance product

References

[1] Badescu V., Optimum fin geometry in flat plate solar collector systems, Energy Conversion and Management 2006; 47(15-16): 2397-413.

[2] Badescu V., Optimal control of flow in solar collectors for maximum exergy extraction, International Journal of Heat and Mass Transfer 2007; 50: 4311-22.

[3] Torres-Reyes E., Cervantes-de Gortari J.G., Ibarra-Salazar B.A., Picon-Nuñez M., A design method of flat-plate solar collectors based on minimum entropy generation, Exergy the International Journal 2001; 1(1): 46-52.

[4] Torres-Reyes E., Navarrete-Gonzalez J.J., Zaleta-Aguilar A., Cervantes-de Gortari J.G., Optimal process of solar to thermal energy conversion and design of irreversible flat-plate solar collectors, Energy 2003; 28(2): 99-113.

[5] Kalogirou S.A., Use of genetic algorithms for the optimal design of flat plate solar collectors, Proceedings of the ISES 2003 Solar World Congress on Solar energy for a sustainable future, 2003 June 14-19; Goteborg, Sweden, on CD ROM.

[6] Kalogirou S.A., Artificial neural networks and genetic algorithms for the optimisation of solar thermal systems**,** In: Sayigh, A.S., Editor, WREC IX: Proceedings of the IX World Renewable Energy Congress on CD-ROM, 2006; Florence, Italy.

[7] Loomans M., Visser H., Application of the genetic algorithm for the optimisation of large solar hot water systems, Solar Energy 2002; 72: 427-39.

[8] Kalogirou, S.A., Use of artificial intelligence for the optimisation of solar systems, International Journal of Renewable Energy Engineering 2002; 4: 499-505.

[9] Krause M., Valen K., Wiese F., Ackermann H., Investigations on optimizing large solar thermal systems, Solar Energy 2002; 73: 217-25.

[10] Kalogirou S.A., Solar Energy Engineering: Processes and Systems, New York: Academic Press, Elsevier Science; 2009.

[11] Zalzala A., Fleming P., Genetic Algorithms in Engineering Systems, London, UK: The Institution of Electrical Engineers; 1997.

[12] Goldberg D.E., Genetic Algorithms in Search Optimisation and Machine Learning, Reading, MA: Addison-Wesley; 1989.

Experimental study of tar and particles content of the produced gas in a double stage downdraft gasifier

Ana Lisbeth Galindo[a], Sandra Yamile Giraldo[b], Rene Lesme-Jaén[c], Vladimir Melian Cobas[d], Rubenildo Viera Andrade[e] and Electo Silva Lora[f]

[a]Federal university of Itajubá (UNIFEI), Itajuba, Brazil, lisbethgn37@hotmail.com
[b]Federal university of Itajubá (UNIFEI), Itajuba, Brazil, sayagire@yahoo.com
[c]University of Oriente, Cuba, lesme3258@yahoocom
[d]Federal university of Itajubá (UNIFEI), Itajubá, Brazil, vlad@unifei.edu.br
[e]Federal university of Itajubá (UNIFEI), Itajubá, Brazil, ruben@unifei.edu.br
[e]Federal university of Itajubá (UNIFEI), Itajubá, Brazil, esl43@yahoo.com

Abstract:

Biomass gasification is not a new technology, but there is a renewed interest in its further development, mainly to produce power and heat as part of locally based combined heat and power plants. The produced gas mainly consists of H_2, CO, CO_2, CH_4, H_2O and some trace impurities such as H_2S, COS, NH_3, HCN, HCl, alkali, tar and particulate matter. These impurities are the responsible for clogging, corrosing, poisoning and carbon deposition on different elements of the power systems, like alternative internal combustion engines, gas turbines, also in fuel cells and auxiliary equipments, being necessary their removal or the adjusting of its concentration level, depending on the final application.

This work presents the experimental evaluation of the tar and particle content in the produced gas from fixed bed downdraft gasifier with two stages of air supply. A very widely considered technology for the biomass gasification is the downdraft fixed-bed reactor, because had shown to produce a gas with lower tar level, compared with other gasifiers. The experiments were carried out varying the amount of air supplied to the reactor and the air ratio between the two stages (AR). The temperatures in different points along of gasifier and the gas compositions were also measured. The results show that there is an operational point where there is a coincidence of the highest conversion of the gasifier and the better quality of the gas, (higher calorific and lower tar content) and also that the use of a second stage can reduce the gas tar content up to 87%.

Keywords:

Biomass gasification, Double stage downdraft gasifier, Produced gas, Tar content, particle content.

1. Introduction

Biomass has been considered as a promising source of energy for the partial substitution of fossil fuels, not only because its global potential, but as a neutral source of CO_2; its thermal conversion generates low emissions of SO_2 and NOx, it is cheap and relatively fast-growing, can be grown on marginal land, without affecting food crops and helps the retention of water and fertilizers in the soil. The possibility to produce fuels from biomass on a large scale reduces the greenhouse effect, the environmental pollution and also increases the security and energetic independence of the countries, but its challenging complexity lies on the need to implement all the stages of the technological biomass production chain, for the conversion into biofuels and chemicals or in electrical generation. There are several processes to transform chemical energy from biomass into thermal energy (combustion, gasification and pyrolysis), of which, gasification is the one with greatest perspectives, because it offers advantages as: a higher efficiency of conversion, compared with combustion and pyrolysis. In the practice, the gasification can convert from 60 to 90% of the

biomass energy conversion in gas energy [1,2]. The produced gas by biomass gasification is composed mainly of H_2, CO, CO_2, H_2O, CH_4, light hydrocarbons (C_xH_y) and some impurities, as heavy hydrocarbons (tar), nitrogen compounds (NH_3, HCN), sulphur compounds (H_2S, COS) and solid particles. This gas can be used for energy production in internal combustion engines, gas turbines and fuel cells or for the production of synthetic natural gas (SNG) and liquid fuels or chemicals through the Fischer Tropsch synthetic path [3-7]. Each application needs a specific quality of the gas used, especially in terms of impurities concentration, which depend on the characteristics of biomass, the type of the reactor used and the operational conditions [8-12].

Tar formation are one of the biggest problems that occurs during the gasification of biomass, it can cause blockade, fouling of pipes and valves and operation problems in the equipments where the gas is used, increasing the maintenance cost of equipments. Thus, it is necessary a gas cleaning system for the removal of tar, whose complexity depends on the concentration limits for these pollutants according to the final application [13,14].

Double stage gasification is being used as an economical primary method to reduce the tar content in the produced gas from biomass [15-16]. The basic concept of a two-stage gasification process is the separation of the two zones the pyrolysis zone and the combustion zone, with the air injection in each stage, which may occur in a same reactor or in separate reactors. Recently, experimental evaluations of the tar content in two and three stage downdraft gasifiers had been reported. These gasifiers are distinguished by their constructive characteristics, where different biomasses had been used (composition and shape) and different experimental conditions had been evaluated (temperature, ratio of the air supplied between the stages), getting different results in terms of tar and particle content of the gas [17-20], as it is shown in Table 1.

Table 1. Tar content in gas from downdraft gasifiers.

Biomass	Operation Temperature (^oC)	Tar (mg/ Nm^3)	Air injection	Reactor size	Ref.
Eucalyptus Pelets (2 cm)	800	43.2	Two inlets. Zone of pyrolysis, mixed air - gas.	25 cm diameter, 100 cm height	[17]
Yang and Pará wood 10-15 mm in length	950	10	Primary and secondary air preheated up to 210 ^0C	25cm diameter, 190 cm height,	[18]
Coconut husk	700-900	28	Three air inlets.	20 cm diameter,	[19]
Pine wood chips of 5x5x25mm	780-850	100	Two air inlet, internal pyrolysis gas recirculation.		[20]

Jaojaruek et al [17] made an experimental study and evaluated the relation between the tar content of the gas and the gasifier operational parameters, conducted in three conditions: a) the reactor working with a single stage, b) with two stages and c) two stages, with an air-gas mixture fided at the second stage. The results showed that the second stage reduces the gas tar content in the gas. Additionally, using an air-gas mixture for the second stage an increase in the calorific value of the gas was achieved. Bhattacharya and Dutta [18], tested a two stage gasifier and with a layer of coal for the start up of the reactor. The influence of the level of the coal layer, type of biomass and moisture content over the tar content and gas composition were checked. It was possible to find out

that during the start-up and warming of the gasifier, due to low temperatures, there was a large tar production; to reduce this period it´s recommended to use a layer of charcoal, with a height of the layer slightly above the primary air inlet and adjusting combustion conditions at the second air stage. They also concluded that, for a constant airflow at the primary stage, increasing the airflow through the secondary stage leads to a decrease of the tar content and increase the CO and H_2 content. Regardless of the results achieved, there is not always a charcoal availability for the operation of the gasifiers and warming of the air up to 210 ^oC requires an additional heat source.

Bhattacharya et al [19] tested a three stage gasifier. During the start up of the reactor a layer of charcoal was also used and was possible observe that the airflow distribution of 40% at the first stage, 28 % at the second, and 30% at 3rd stage, getting a significant decrease of tar content.

As a conclusion, the decreasing of tar formation is achieved when: a) preheating the air is made, b) use dual stages of air injection, c) air-gas mixture in the second stage, d) optimal parameter of operation as ER of 0.3-0.4 and moisture content of 6-20%. The tar content in these gasifiers is in the range of 10-100 mg/Nm^3, values lower than those obtained in other types of gasifiers.

The objective of this work is to evaluate the tar and particulate content from the produced gas in a downdraft gasifier with two-stage air injection, analyzing the influence of the total air inlet and the ratio between stage one and stage two in these pollutants. The tested biomass was eucalyptus wood, charcoal was not used during the start up of the gasifier and the air supplied was not heated.

2. Materials and methods

2.1. Biomass used in the tests

Eucalyptus wood with a size smaller than 5 cm in length and diameter was used; its proximate composition (ash, volatile and fixed carbon content), ultimate composition (carbon, nitrogen, hydrogen, sulphur and oxygen content), low heating value and moisture are shown in Table 2.

Table 2. Analyses of the biomass (dry basis)

Parameter	Value
Proximate analysis (wt %)	
Ash	1.34
Volatile	83.27
Fixed carbon	15.66
Ultimate analysis (wt %)	
Carbon	45.78
Nitrogen	5.92
Hydrogen	3.21
Sulphur	0.093
Oxygen	42.83
Moisture (%)	12.23
LHV (kJ/kg)	18432.67

2.2. Downdraft gasifier

A double stage downdraft gasifier, manufactured by the Brazilian Company “Termoquip Energy Alternative Ltda”, was used. It has an internal diameter of 0.3 m and a height (from the reactor top to the grate) of 1.06 m. The gasifier is built of carbon steel with an internal coating of refractory material. Six K-type thermocouples were installed along the reactor that recorded the temperature at different points. Two thermocouples measure the inlet air temperature and other thermocouple

measures the temperature of the gas at the gasifier exhaust. The air is supplied by a blower (1900 mmH_2O). The gases generated in the reactor go out by the lower section, after crossing the gasification zone and the grid and pass finally by a cyclone where the larger solid particles are removed.

The biomass gasification starts by burning the wood layer by and external heat source, by this way the reactor is heated up to 150 ^oC (temperature at the combustion zone in the inner wall of the reactor). Once this temperature is attained, air is fed into the gasifier. Quasi-stoichiometric combustion conditions are adjusted reaching a bed temperature (in the combustion zone) of around 600 ^oC. Air flow values are measured through an orifice plate, according to the methodology given in ISO 5167-2 [21]. After reaching the steady state (no significant variations in temperature and gas concentrations are observed) the operating conditions are fixed, the sampling of tar and particles are made.

Previous experimental tests [22] showed that the condition of the higher gasifier cold efficiency (η) is 68%. That corresponds to 20 Nm^3/h of total airflow, ratio air/biomass (ER) of 0.4, with air flow ratio between the first and second stage (AR) of 80%. Under these conditions the concentrations of CO and H_2 was 19.04% and 16.83% respectively, and low heating value of the gas was 4.53 MJ/Nm^3. These conditions were take for the experimental planning. The details of the experimental installation and termocouples position in the gasifier are shown in Figure 1.

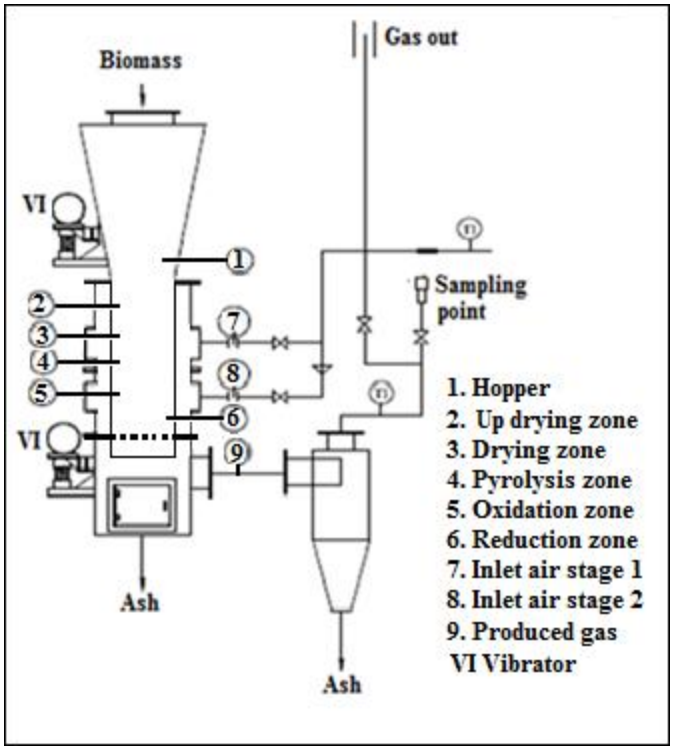

Figure 1. Diagram of the experimental installation and termocouples in the gasifier.

2.3. Experimental planning

Gasification variables that influences tar and particles content in the produced gas and were considered in this study are the total air flow and the ratio between the primary and secondary stage air flow (AR) according to the Equation (1).

$$AR = \frac{(V_a)_{1est}}{(V_a)_{2est}}.100\% \qquad (1)$$

Where:

$(V_a)_{1est}$: Air flow through stage 1 (Nm^3/h)

$(V_a)_{2est}$: Air flow through stage 2 (Nm^3/h)

During the tests the temperatures along the gasifier height, the CO, CH_4, H_2 and CO_2 concentrations of the produced gas were measured using a BINOS 100, HYDROS 100 and MaMos gas analyzer system. The precission of the equipment is ±0.1 for the BINOS 100, ±0.01 for the HYDROS 100 and ±0.01 for the MaMos. The concentrations were measured at the cyclone outlet. Nine experimental runs with three variations of the total air flow and three values of AR, were carried out. Values are showed in Table 3.

Table 3. Experimental Conditions for the gasification tests

No.	AR (%)	Airflow (Nm^3/h)		
		$(V_a)_{1est}$	$(V_a)_{2est}$	Total air
1		0	18	18
2	0	0	20	20
3		0	22	22
4		5,14	12,86	18
5	40	5,71	14,29	20
6		6,28	15,72	22
7		8	10	18
8	80	8,88	11,12	20
9		9,77	12,23	22

2.4. Tar and particles sampling and measurement

2.4.1. Sampling set and analytical procedure

The tar and particles sampling were carried out based on European Fifth Framework Programme report [23], that consist in an isokinetic sampling of gas, solid filtration and tar absorption in a solvent contained in bottles that are kept at low temperature. The diagram of the sampling line is shown in Figure 2.

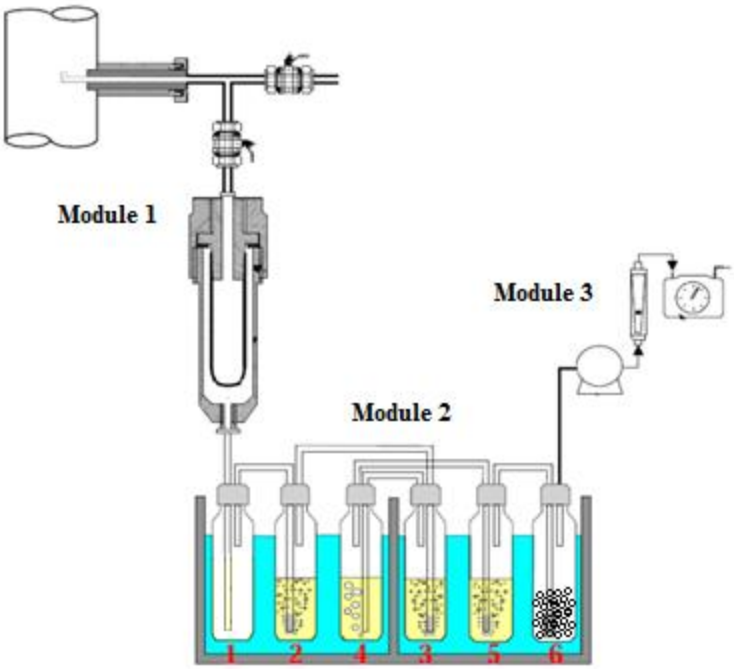

Figure 2. Diagram of tar and particle sampling line [23].

The module one is the pre-conditioning stage of gas and particle collection, consists of an isokinetic tube connected to the gas line, heated with an electrical resistance to prevent condensation of the tar inside of the tube and the vessel that contains the filter for the particles collection. Thimble quartz filter Advantec® No. 86R was used. The tube and the port filter are heated up to 250 ^{o}C. The module two, six impingers bottles for tar dilution. The first impinger that is empty, acts as moisture collector; the others four impinger filled with Isopropanol, in which water and tar are condensed from the produced gas and the last impinger with silica to dry the gas. Salt/ice/water mixture to keep the impingers at low temperature was used. The module three contains the vacuum pump to extract the gas, flow meter and temperature indicator.

The sample is taken during an hour after established operational conditions. After the sampling, a gravimetric analysis to determine the tar and particles content is made. The filter is weight before of sampling. After the sampling, the filter that not only retains particle but also a part of the tar is placed in a soxhlet extraction system, where the residual tar from the particles is separated using isopropanol. Them, the filter is dried and the particles mass is obtained for weight difference. The bottles content and the liquid produced in the soxhlet extraction are evaporated by rotavaporation to remove the solvent and the tar mass is obtained. An analytical balance model BL 210S to determine the mass of particles and tar in the sample was used. Finally, the tar and particles content per volume of gas sampled is reported (mg/Nm^3).

3. Results and discussions

3.1 Temperatures behaviour inside the gasifier

During the development of the experimental runs, a data acquisition system was used to register the temperatures at different section of the reactor. The Figure 2 and 3 shows the typical variation of temperature over time for different sections of the reactor for total air of 20Nm^3/h. Figure 2 for AR of 0% (unique stage air inlet) and Figure 3 for AR of 80% (two stage of air inlet).

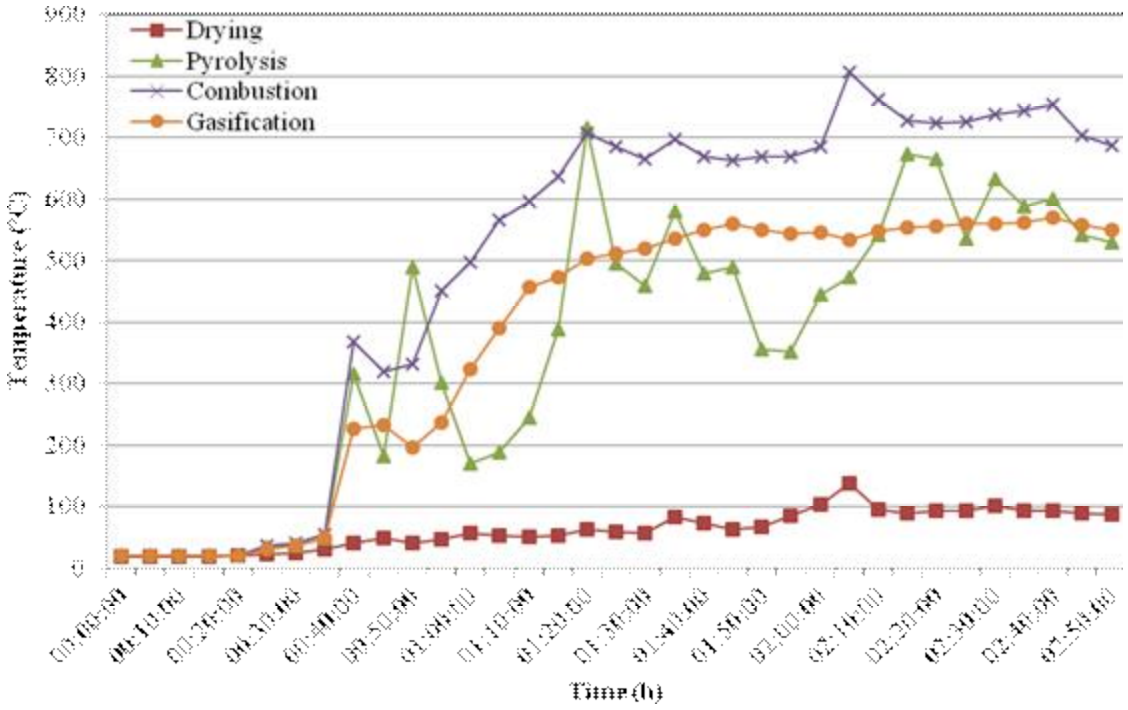

Figure 2. Temperature profile of the gasifier for AR of 0% and total airflow of 20 Nm^3/h

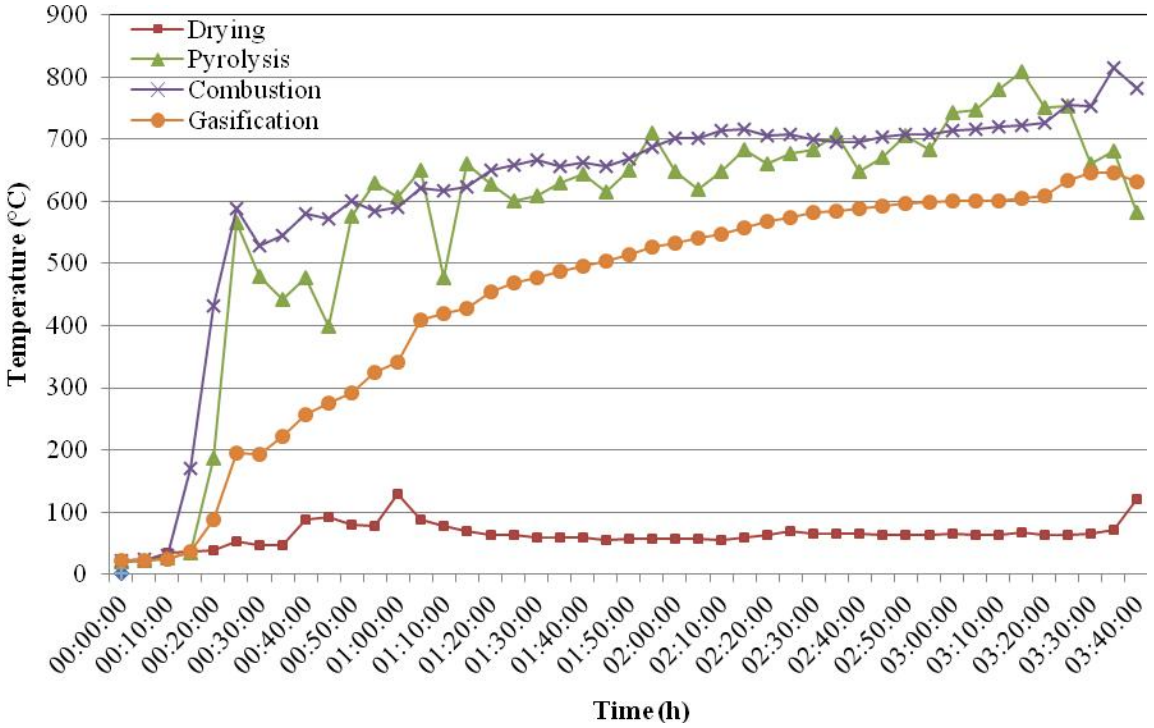

Figure 3. Temperature profile of the gasifier for AR of 80% and total airflow of 20 Nm^3/h

In Figures 2 and 3 it's shown that 20 minutes after ignition begins a sudden rise in gasifier temperatures, is possible to observe how the use of a second stage of air supply increases the pyrolysis zone temperature, bringing it closer to the temperature of the combustion zone in the reactor. According of Figure 2 and 3, the average temperature in the pyrolysis zone was 539 ^oC and 661 ^oC, and the difference with respect to average temperature in the combustion zone was 174 ^oC and 40 ^oC for one stage and two stages respectively. This behavior reduces the amount of tar because a high temperature inside the reactor induces the tar destruction. Figure 4 shows the average temperature of different zone in the gasifier depending of the total air flow.

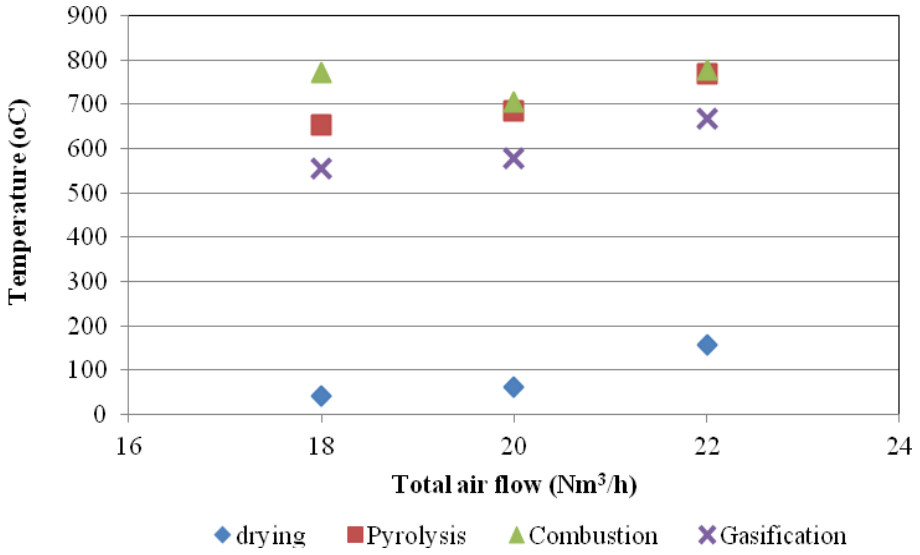

Figure 4. Average temperature inside of the gasifier for AR of 80% and different airflow.

As it's shown in the Figure 4, it´s possible to confirm that in a two stage downdraft gasifier, the temperature in the pyrolysis zone is closer to the temperature in the combustion zone, being highly differentiated at high air flows.

3.2. Composition and low heating value of the produced gas

During the development of the experimental runs, a data acquisition system was used to register CO, CO_2, H_2, CH_4 concentrations. The low heating value (LHV) of gas is obtained from the fuel gases concentration of CO, CH_4 and H_2, and their energy contents as shown in Equation (2). Those experimental results for AR of 80% are presented in Figure 5.

$$LHV = 10790.(\%H_2) + 12630.(\%CO) + 35800.(\%CH_4) \quad (2)$$

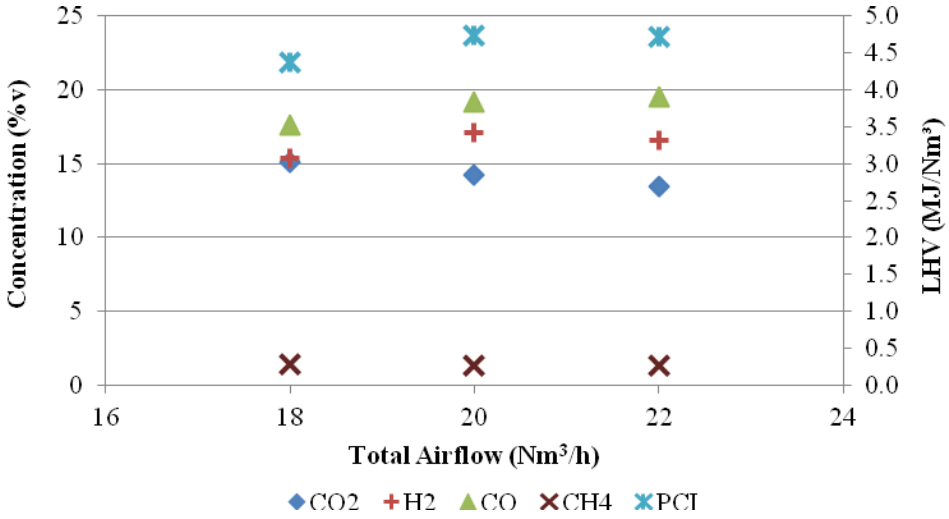

Figure 5. Composition and LHV of gas for AR=80%.

Figure 5 shows the CO, CO_2, CH_4, H_2 concentration of the produced gas for AR of 80% for runs 7 to 9. It also shows LHV, as a function of the total airflow fed to the gasifier. At 20 Nm^3/h^1 of total air flow (run 8) the highest H_2 concentration was 17.14 %v and the LHV of 4738 kJ/Nm^3 in the produced gas is reached. At 22 Nm^3/h (run 9), the H_2 concentration and the LHV showed a slight decrease reaching 16.56 %v and 4714 kJ/Nm^3 respectively. From this total airflow, the process begins to be favored by combustion given the temperature increase along the gasifier. The higher concentrations at these conditions are also attributed to the good stability and performance of the combustion and pyrolysis zones.

3.3. Tar and particles content in the produced gas

The tar and particles content of the produced gas are presented in Table 4 and the influence of different parameters on the results are shown in Figures 6-7.

Table 4. Tar and particles content of the gas.

Parameters	Units	Results								
		Run 1	Run 2	Run 3	Run 4	Run 5	Run 6	Run 7	Run 8	Run 9
AR	(%)	0	0	0	40	40	40	80	80	80
Total air flow	Nm^3/h	18	20	22	18	20	22	18	20	22
Tar	mg/Nm^3	1269.70	418.95	179.86	76.09	104.99	78.57	171.49	54.09	99.61
Particles	mg/Nm^3	216.45	146.04	176.04	142.39	107.16	164.99	97.19	22.69	292.2

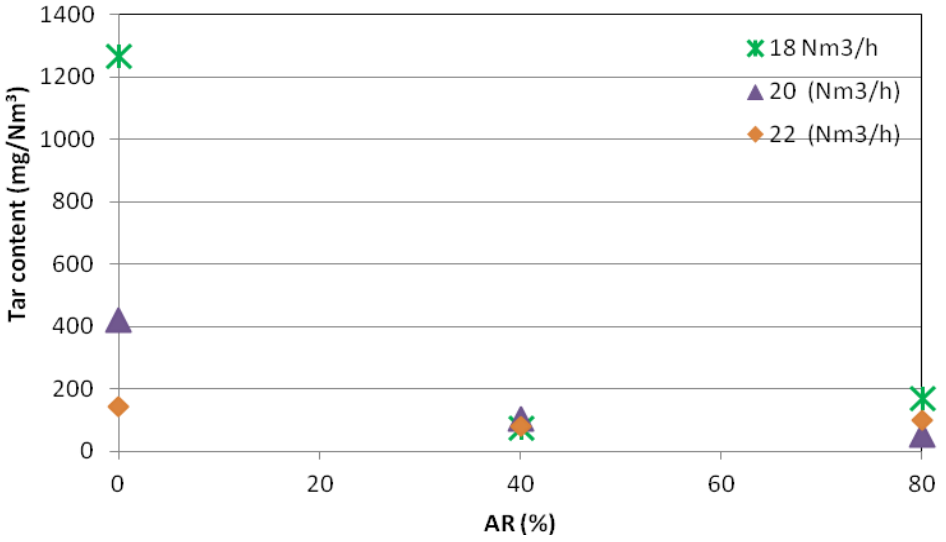

Figure 6. Influence of AR over the tar content at different total airflows..

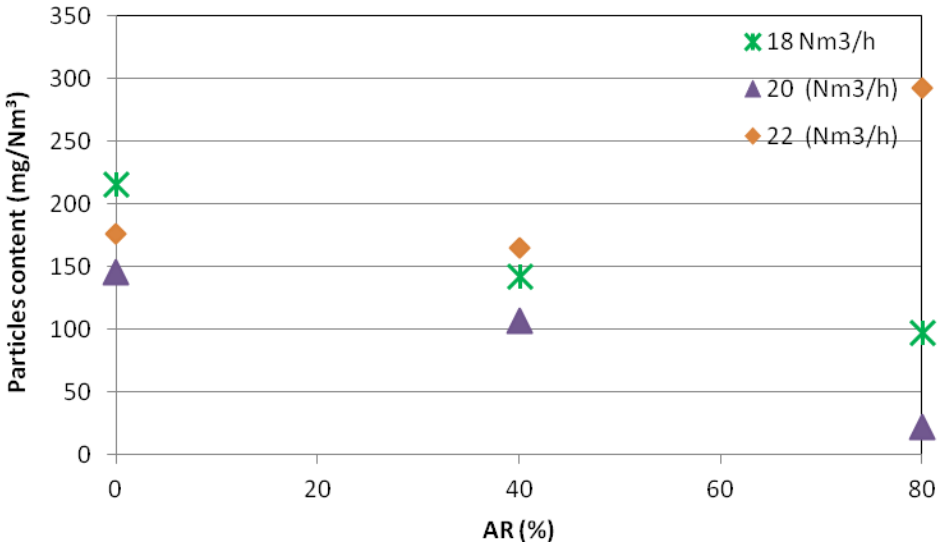

Figure 7. Influence of AR on the gas particles content at different total airflow.

According to Figure 6, at the point of higher efficiency of the gasifier when AR is 80% and total air flow is 20 Nm^3/h, the tar content of 54.09 mg/Nm^3 is within the range and even lower than values reported in Table 1 for other two stage downdraft gasifiers, and without the use of an air-gas mixture through the second stage. As it is observed in Figure 7, at same conditions, the particles content presents it's lower value of 22.69 mg/Nm^3. The increase of the total airflow and of the AR values decrease the tar and particles contents in the gas as it's observed in Table 4 and confirmed in Figures 6 and 7. Specifically, this suggests that when an 80% of the total air is entering into the first stage, the biomass volatization is favored, allowing the formation of lighter compounds that are more easily cracked when the gas stream pass through the combustion zone, and in this way reducing the tar content of the produced gas.

4. Conclusions

For the gasifier used in this study with operational conditions of 20 Nm^3/h of total air flow, ER of 0.4 and AR of 80%, a fuel gas with levels of CO, CH_4, CO_2, H_2 contents of 19.2, 1.34, 14.21 and 17.14 %v was obtained, at these conditions the low heating value of the gas was 4738.4 kJ/Nm^3 and the tar content decrease to 54.09 mg/Nm^3, compared with CO, CH_4, CO_2, H_2 contents and LHV of 17.90, 1.72, 13.90, 15.71 %v and 5103 kJ/Nm^3 respectively, and 418.95 mg/Nm^3 tar content obtained at AR of 0% and 20 Nm^3/h. These results showed a decreasing in the tar content of 87%.

The results suggest a relationship between the CH_4 concentration with the tar content in the produced gas. In this way, increasing the air supply and use of a second stage decrease the tar content and the CH_4 concentration. This suggest advantages for the biomass devolatilization in the pyrolysis zone, by production of lighter compounds that are easily cracked when the gas passes through the combustion zone.

The use of a second stage of air supply increases the temperature at the pyrolysis zone. This allows to reducing from four to three temperature zones inside the reactor: drying, the first zone, pyrolysis-combustion, the second one and gasification, the third one. This behavior leads to a decrease of the tar content in the produced gas, so this method is considered an efficient and economic primary method for tar conversion without air/gas mixture o preheated air as was reported in literature.

Acknowledgments

The authors would like thank the Energy Company of Minas Gerais (CEMIG) and the Secretary of Science and Technology (SECTES) for the financial support received for the development of this project. Also to thank the Committee on Coordination of Improvements in Higher Education (CAPES), the National Research Council of Brazil (CNPq) and the Foundation for Research Support of Minas Gerais State (FAPEMIG) for the graduate and research productivity grants allocations.

References

[1] Marsh R, Hewlett S, Griffiths T, Williams K. Advanced thermal treatment for solid waste – a waste manager's guide. Proceeding of the 22nd international conference on solid waste management and technology. Philadelphia (USA); 2007

[2] Kristina Difs, Elisabeth Wetterlund, Louise Trygg, Mats Söderström. Biomass gasification opportunities in a district heating system. Biomass and Bioenergy. 2010: 34: 637–651.

[3] Kurkela E, Simell P, mckeough P, Kurkela M. Production of synthesis gas and clean fuel gas [synteesikaasun ja puhtaan polttokaasun valmistus]. In: VTT Publications, vol. 682. Technical Research Centre of Finland, VTT; 2008.

[4] Goyal HB, Seal D, Saxena RC. Bio-fuels from thermochemical conversion of renewable resources: a review. Renew Sust Energy Rev 2008: 12: 504–17.

[5] K.D. Panopoulos, L. Fryda, J. Karl, S. Poulou, E. Kakaras. High temperature solid oxide fuel cell integrated with novel allothermal biomass gasification Part II: Exergy analysis. Journal of Power Sources 2006: 159: 586–594

[6] H. Moritaa, F. Yoshibaa, N. Woudstrab, K. Hemmesc, H. Spliethoff. Feasibility study of wood biomass gasification/molten carbonate fuel cell power system—comparative characterization of fuel cell and gas turbine systems. Journal of Power Sources 2004: 138: 31–40.

[7] Anastasia A. Zabaniotou, Vasiliki K. Skoulou, Dimitris P. Mertzis, George S. Koufodimos, and Zissis C. Samaras. Mobile Gasification Units for Sustainable Electricity Production in Rural Areas: The smart-CHP Project. Ind. Eng. Chem. Res. 2011: 50: 602–608.

[8] José Corella, José Manuel Toledo and Gregorio Molina. Biomass gasification with pure steam in fluidised bed: 12 variables that affect the effectiveness of the biomass gasifier. Int. J. Oil, Gas and Coal Technology 2008: 1: 194-207.

[9] Li, C.-Z. Some recent advances in the understanding of the pyrolysis and gasification behavior of Victorian brown coal. Fuel 2007: 86: 1664–1683.

[10] Hong Cui, Scott Q. Turn, Vheissu Keffer, Donald Evans, Thai Tran, and Michael Foley. Contaminant Estimates and Removal in Product Gas from Biomass Steam Gasification. Energy Fuels 2010: 24: 1222–1233.

[11] S. Monteiro Nunes, N. Paterson, D. R. Dugwell, and R. Kandiyoti. Tar Formation and Destruction in a Simulated Downdraft, Fixed-Bed Gasifier: Reactor Design and Initial Results. Energy & Fuels 2007: 21: 3028-3035.

[12] Takashi Yamazaki, Hirokazu Kozu, Sadamu Yamagata, Naoto Murao, Sachio Ohta, Satoru Shiya and Tatsuo Ohba. Effect of Superficial Velocity on Tar from Downdraft Gasification of Biomass. Energy & Fuels 2005: 19: 1186-1191

[13] Yan Cao, Yang Wang b, John T. Riley, Wei-Ping Pan. A novel biomass air gasification process for producing tar-free higher heating value fuel gas. Fuel Processing Technology 2006: 87: 343 – 353.

[14] Devi L, Ptasinski KJ, Janssen FJJG. A review of the primary measures for tar elimination in biomass gasification processes. Biomass Bioenergy 2003: 24: 125-1240.

[15] Abu El-Rub Z, Bramer EA, Brem G. Review of catalysts for tar elimination in biomass gasification processes. Ind Eng Chem Res 2004: 43: 6911-6919

[16] Han J, Kim H. The reduction and control technology of tar during biomass gasification/pyrolysis: an overview. Renew Sust Energy Rev 2008: 12: 397-416.

[17] Kitipong Jaojaruek, Sompop Jarungthammachote, Maria Kathrina B. Gratuito , Hataitep Wongsuwan, Suwan Homhual. Experimental study of wood downdraft gasification for an improved produced gas quality through an innovative two-stage air and premixed air/gas supply approach. Bioresource Technology 2011: 102: 4834–4840.

[18] S. C. Bhattacharya and Animesh Dutta. Two-stage gasification of wood with preheated air supply: a promising technique for producing gas of low tar content. Energy Program, Asian Institute of technology, P O Box 4, Klong Luang, Pathumthani 12120, Thailand.

[19] S.C. Bhattacharya, San Shwe Hla, Hoang-Luang phamm. A study on a multi-stage hybrid gasifer-engine system. Biomass and Bioenergy 2001: 21: 445-460

[20] Susanto H, Beenackers AACM. A moving-bed gasifier with internal recycle of pyrolysis gas. Fuel 1996: 75: 1339-47.

[21] ISO 5167-2. Measurement of fluid flow by means of pressure differential devices inserted in circular cross-section conduits running full. Part 2: Orifice plates. European standard. 2003.

[22] Martínez J. D, Silva L. E. E, Viera A. R, Lesme J. R. Experimental study on biomass gasification in a double air stage downdraft reactor. Biomass and Bioenergy. 2011: 35: 3465-3480.

[23] Neeft J, Knoef H, Zielke U, Sjöström K, Hasler, P, Simell P. Guideline for sampling and anaysis of Tar and particles in Biomass produced gases (Tar protocol). Energy Project ERKG-CT1999-2002

FEASIBILITY STUDY TO REALIZE AN ANAEROBC DIGESTER FED WITH VEGETABLES MATRICES IN CENTRAL ITALY

Umberto Desideri[a], Francesco Zepparelli[a] (CA), Livia Arcioni[a], Ornella Calderini[b], Francesco Panara[b] and Matteo Todini

[a] *University of Perugia, Dept. of Industrial Engineering, Perugia, Italy, zepparelli@tre-eng.com*
[b] *CNR IGV Perugia, Italy, ornella.calderini@igv.cnr.it*

Abstract

In the present paper we have analysed the possibility to realize an anaerobic digester in a bio-Energy Park located in Città della Pieve, a small town in Central Italy. The use of anaerobic digesters is quite common in Europe for reducing the environmental impact of manure in a co-digestion procedure with vegetables materials. In addition, for several areas of Central Italy there is the need to find alternative productions to improve farmer's incomes, as traditional cropping systems are loosing convenience. An interesting alternative seems to be cultivation of energy crops because of the favourable conditions of the electric energy market. We are suggesting a low input cropping system to be implemented in areas where low input food/feed crops are no more profitable.

In particular our case-study is an example based on the use of a forage legume, alfalfa (Medicago sativa L.), together with other crops, like sorghum, to realize small-size bio-digesters plants.

Alfalfa: is a highly sustainable crop as it is able to fix nitrogen and therefore it does not require this fertilization with the consequence of avoiding underground water pollution. Moreover alfalfa residual products are nitrogen rich thus improving soil structure and fertility more than popular graminaceous energy crops such as corn. Beside, alfalfa mostly does not need irrigation in the typical Central Italy environment, all these traits make it one of the species with the lowest energy needs for growing.

The aims of this feasibility study are: i) optimization of plant materials feeding the bio-digester, ii) typology of bio-digester, iii) size of bio-digester in relation with land availability for growing energetic cultures, iv) the utilization of bio-gas produced by bio-digester plant to produce electric and thermal energy using cogeneration engines, vi) disposal of waste-water produced according to regional and national laws.

The final aim of this study is to verify the possibility to develop an alternative economical use of marginal soils in relatively dry areas of Central Italy that would be replicable in other European areas with a similar climatic situation.

Keywords:

Alfalfa, Anaerobic digestion, Digestate, Silage, Sorghum.

1. Introduction

Anaerobic digestion is an appropriate technique for converting biomass such as ensiled energy crops into renewable energy. In addition, since the digested residue can be used as a fertilizer, a cropping system based on energy crops has favourable traits of sustainability.

The interest in using ensiled crops for anaerobic digestion is increasing. In Europe the development of anaerobic digestion began in the sector of civil sewage treatment plants for the stabilization of sludge and currently it is estimated that there are more than 1600 operational digesters.

At the moment this technique is considered to be one of the best for the treatment of the wastewater from agro-industrial complexes with high organic content. As early as 1994 there were about 400 business and consortium biogas units while now there are more than 3500 anaerobic digesters operating on livestock effluent in all countries of the European Union. The highest number is in Germany followed by United Kingdom and Italy. There are currently about 450 active plants for the recovery of biogas from MSW landfills with a high concentration in Great Britain. This type of

treatment is being increasingly supplemented in recent years by the treatment of the organic fraction deriving from the differentiated collection of municipal waste (bio waste), digested with other organic industrial waste and livestock slurries. In Denmark alone there are now 21 centralized co-digestion plants of this type, treating about 1,750,000 tons of livestock slurry and 450,000 tons of organic industrial waste and bio waste.

In 2010, primary energy production from biogas had an impressive increase of 31,3%. Biogas produced more than 10.9 Mtoe in 2010, which is an additional 2.6 Mtoe in just twelve months, and energy was primarily channeled into electricity production. The power output from this source should be as much as 30.3 TWh in 2010, which is 20.9% more than 2009 [1].

The country that developed anaerobic digestion at the highest degree in the last ten years is Germany, particularly in the livestock sector: the German biogas association reports that the country had 7,100 methanation plants in 2010 with 2,780 MW of electrical capacity. [1]

In 2010 Italy should become Europe's number three biogas producer, with primary energy production estimated at 478.5 ktoe. This is the result of the policy of incentives adopted by the national government which, in addition to providing a contribution for the investment, pays a price for electrical energy from biogas which may reach 0.28 €/kWh over a period of 15 years.

Central Italy is characterized by a great percentage of farmland localized in marginal areas. These kinds of areas are suffering to a greater extent of the general crisis of the primary sector due to lowering of incomes, abandoning of farms and the scarce appeal to the new generations. Eurostat reports a reduction of farmer's income of 3.3% in Italy. Energy from biomasses has become an interesting alternative to food/fodder crop production in the last years. The majority of power plants settled in Italy are based on biogas production in medium-large scale farms with animal husbandry. Because of the general Italian condition for farming this occurs mostly in Northern Italy. Anyway due to constant loss of income for traditional crops, farmers from marginal areas in central Italy are seeking an alternative to improve the profitability of their land. The present study analyse the possibility to suggest a model for biogas production in typical medium-small size farm in marginal areas where animal husbandry is not as common as it used to be. We are suggesting the use of two low/modest input crops with a special emphasis on alfalfa. Calculations are based on literature data but experimental analysis is in progress to test crop yield and biogas profitability in our conditions.

The present work takes into account the *"Regolamento regionale 4 maggio 2011, n. 4"* of Regione Umbria, concerning the management of facilities for the treatment of livestock manure and biomass for biogas production and utilization [2]. The new regional framework, in twenty articles, establishes: 1) the requirements for operation and management of anaerobic digestion plants and company, 2) inter-treating livestock manure and/or biomass to produce electricity and heat from biogas power up to 1 MW, 3) the terms of the agronomic use of the resulting digestate from anaerobic digestion.

In particular, the regulation sets that the materials to be treated must not come from more than thirty kilometres from the plant and that the same distance should be respected for the transport of digestate from the plant to the land of the company (art. 9). With articles 10 and 11 regulates the management and agronomic use of digestate and possible further treatment.

2. The anaerobic digestion process

Anaerobic digestion is an appropriate technique for converting biomass such as ensiled energy crops into renewable energy. The system proves its sustainability also because the digested residue can be used as a fertilizer.

Methane can be produced from biomass by either thermal gasification or biological gasification: biological gasification is commonly referred to as anaerobic digestion. A consortium of several different anaerobic bacteria carries out the process using a wide range of temperatures from 10°C to

over 100°C and at a variety of moisture contents from around 50% to more than 99%.. Bacteria living optimally at temperatures between 35 – 40 °C are called mesophiles, those surviving warmer and more hostile conditions at 55–60 °C are called thermophiles.
In the absence of oxygen, anaerobic bacteria ferment biodegradable matter into methane and carbon dioxide, a mixture called biogas. Biogas contains 60–70% methane and 30–40% carbon dioxide depending on the feedstock type [3]. Trace amounts of hydrogen sulfide, ammonia, hydrogen, nitrogen, carbon monoxide, oxygen and siloxanes are occasionally present in the biogas. Usually, the mixed gas is saturated with water vapor.
Anaerobic digestion takes place in basically three stages. In the first stage, complex organic macromolecules are hydrolyzed into simpler soluble molecules. In the second stage these molecules are converted by acid forming bacteria to simple organic acids, carbon dioxide and hydrogen; the principal acids produced are acetic acid, propionic acid, butyric acid and ethanol. In the third stage, methanogen bacteria form methane, either by breaking down the acids to methane and carbon dioxide, or by reducing carbon dioxide with hydrogen [4].
The biogas produced in an anaerobic digestion energy plant consists of 55–80% CH_4, 20–45% CO_2, 0.0–1.0% H_2S, and 0.0–0.05% NH_3, and it is saturated with water [5].

2.1. Digester Technology in Europe

In Europe digesters are mainly made of concrete with a steel skeleton or just steel. Their sizes vary between 500 and 3,000 m³, although there are still smaller units for small users. The digesters have usually a cylindrical form standing upright in most cases. Not only because of the climatic conditions in Europe but also in order to control temperature conditions inside the digester tanks are equipped with an insulation and a heating system. Digesters are also equipped with a system to agitate or to stir the digesting slurry. There are many systems available to stir the system: some with slow moving propellers stirring for longer periods or such with fast turning propellers switched on only for short periods. The biogas is collected either in an external plastic bag or in the space above the slurry covered with a plastic membrane [6].
The digesters are flow through systems, which are fed several times per day. In the case of agricultural biogas plants the slurry comes directly from the stables or is collected in small storages before entering the digester. There is often a premixing pit where other feedstock can be added to the slurry. Sometimes the bulk feedstock can be added directly to the digester through an extra input system. The outlet works in parallel to the inlet. The digested slurry is often pumped to a post digester and/or to a storage tank. These storage tanks must have the capacity to store the slurry for several, often six to nine, months [6].
The average retention time in the main digester is usually approximately 28 days, but it can be easily demonstrated that, especially if crops and crop residues were added, biogas production can be detected still after 90 days. Therefore many biogas plants work with a post digester and/or the slurry storage tank is also covered with a foil, which works as gas storage. During post-digesting process and storage, approximately 30% of the total biogas evaluation is captured [6].
In addition to the described technology of wet anaerobic digestion there is a growing interest in dry anaerobic digestion [7]. The wet technology works with slurries of less than 12% dry matter content whereas the dry process can handle dry matter contents of 30% and more which would enable the user to use mainly crops and crop residues as feedstock. In the past dry anaerobic digestion was limited to waste processing biogas plants. Dry continuous-flow systems are very expensive and the income from waste disposal fees was necessary for an economic business.

2.2. Crops characteristics

Different crops are being used for bioenergy production; in our system we want to stress the presence of low input crops to be able to enhance production of energy from biomasses in agricultural areas where cash crops are not profitable anymore. This will avoid competition with food/fodder cultivation and at the same time it will sustain farmer's income. We are focusing on alfalfa and sorghum, two commonly cultivated crops in Italy.

Alfalfa is a polyannual (2-5 years) plant species used as forage crop. In the last year work from different laboratories suggested its alternative use as a source of biomass for biofuel production [5]. On average its dry matter yield is 8-10 tons/ha, which is rather competitive with other crops more widely used for bioenergy such as giant cane (Arundo donax) or Mischantus. In fact the input needed by an alfalfa field is very limited in terms of irrigation and fertilization, in particular, due to its ability to fix nitrogen, it has a widely acknowledged ability to improve the organic matter content and structure of the soil. Therefore alfalfa can be suggested as a highly sustainable alternative to commonly used grasses for bioenergy production, in particular in Italy where it is a well-adapted crop more than the mentioned grasses.

The initial establishment of the field that depends on the soil preparation and the availability of deep ground water, enhance alfalfa productivity. Anyway according to literature, a satisfactory productivity can be obtained also in low rainfall regimes. It has to be considered that maximum productivity generally occurs in the second and third year of establishment. An average dry matter yield that is considered in our system for this period is 8-10 tons/ha. To provide a continuous supply to the biodigestor we assume the storage of plant biomass as silage. Data from literature suggest that alfalfa silage provides a dry matter yield of 11.5 t/ha [9], with 69.5% moisture, 5.7g protein, 1g fat, 8.8g fiber, 2.4g ash.

The study conducted by Heiermann et al. [3, 10], investigates the suitability of various field crops for anaerobic digestion included alfalfa, thanks to laboratory scale batch anaerobic digestion tests under mesophilic condition.

Production on a continuous basis and an almost homogeneous feedstock is indispensable to enable an uninterrupted supply of crops for anaerobic digestion. Focusing on biogas production ensiling is the favorable and common method of whole crop preservation.

Legumes such as alfalfa have been ensiled but ensiling has relatively recently become a common means of conservation (Albrecht and Beauchemin, 2003).

Considering that chemical composition and structure of crops change during their growth, harvest time also plays a major role with regard to silage quality and maximum yield per hectare.

Fiber and sugar sorghum has been suggested as well suited for energy production. Sorghum itself is another low requirement crop and it is particularly interesting for its high resistance to drought and parasites. It is characterized by a high level of rusticity, growing well in different types of soil with a vegetative cycle of 95 - 120 days. Its dry matter yield on average is around 12-18 t/ha. Sorghum silage DM yields is 18 t/ha [2].

Energy outcome of the two crops is considered to be on average 530 l/kg biogas/organic DM for alfalfa silage ([5, 6], P. Weiland pers. comm) and 610 l/kg biogas/organic DM for sorghum silage (P. Weiland pers. comm).

We have considered cultural cost for the two crops as in the following table (sorghum data are from Contagraf, University of Padova, 2010, alfalfa data referred to a 4 years cycle, are from Rinaldi, 2005).

Table 1. Sorghum and alfalfa cultural costs

	sorghum, €/ha	*alfalfa*, €/ha
Seed bed preparation	230.00 – 250.00	90.00 – 100.00
Seed and sowing	160.00 – 170.00	50.00 – 60.00
Fertilization	130.00 – 150.00	50.00 – 60.00
Weed control	50.00 – 60.00	60.00 – 70.00
Harvest/ensiling	350.00 – 400.00	250.00 – 300.00
Total	930.00 – 1,030.00	500.00 – 600.00

As equipment for harvesting of sorghum, a combined forage harvester (mowing, chopping, loading) was accounted, for alfalfa swathing, raking, chopping of windrows and loading operations were considered.
We have used a combination of data from different literature sources to proceed with the calculations reported in the following parts of the paper.

4. Feasibility study

The chain for producing methane through anaerobic digestion from energy crops is presented in Fig. 1, from the production and harvest of crop biomass, to storage and pre-treatment of the biomass, production and utilization of biogas, storage, post-methanation and post-treatment of the digestate, and finally returning the digestate back to the crop production areas as fertilizer and soil-improvement medium [12].

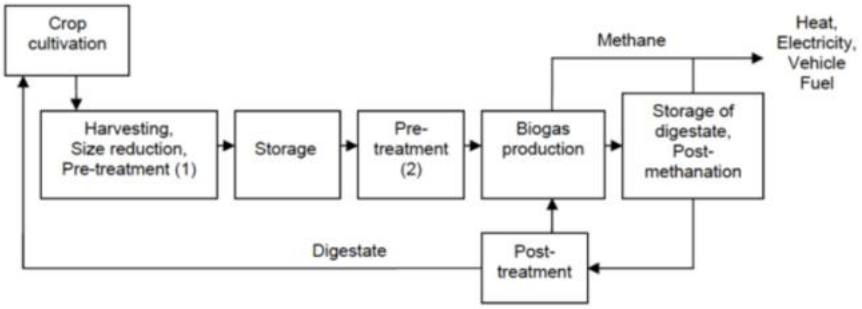

Fig. 1. Biogas production chain

Energy crops and crop residues can be digested either alone or in co-digestion with other materials, employing either wet or dry processes. In the agricultural sector one possible solution to processing crop biomass is co-digestion together with animal manures, the largest agricultural waste stream. In addition to the production of renewable energy, controlled anaerobic digestion of animal manures reduces emissions of greenhouse gases, nitrogen and odors from manure management, and intensifies the recycling of nutrients within agriculture. Animal manures typically have low solids content (<10% TS), and thus, the anaerobic digestion technology applied in manure processing is mostly based on wet processes, mainly on the use of continuously stirred tank reactors (CSTRs).
In co-digestion of vegetable matrices and manures, manures provide buffering capacity and a wide range of nutrients, while the addition of plant material with high carbon content balances the carbon to nitrogen (C/N) ratio of the feedstock, thereby decreasing the risk of ammonia inhibition. The positive synergy effects often observed in codigestion, due to the balancing of several parameters in the co-substrate mixture, have offered potential for higher methane yields.

The most important parameter in choosing crops for methane production is the net energy yield per hectare, which is defined mainly by biomass yield and convertibility of the biomass to methane, as well as cultivation inputs. Energy crops should be easy to cultivate, harvest and store, tolerant to weeds, pests, diseases, drought and frost, have good winter hardiness and be able to grow on soil of poor quality with low nutrient input.
Due to the problems related to the animal manure management, the present feasibility study concerns a co-digestion of vegetable matrices, in particular alfalfa and sorghum.
The co-digestion of two vegetable matrices may create problems in regard to the activation of the anaerobic digestion process. Because of this it may be necessary to make an inoculum of slurry to help the activation process.

Table 2. Methane and gross energy potentials of energy crops and crops residues

Substrate	*Methane potential*			*Gross energy potential*		*Ref.*
	($m^3 CH_4 kg^{-1} VS_{added}$)	*($m^3 CH_4 kg^{-1} TS_{added}$)*	*($m^3 CH_4 t^{-1}$ ww)*	*(m^3 CH_4 ha^{-1} a^{-1})*		
Forage beet	0.46	n.r.	n.r.	5800[a]	56[ac]	1
“	0.36	0.32[c]	55[c]	3240[b]	34[b]	2
Alfalfa	0.41	n.r.	n.r.	3965[a]	38[ac]	1
“	0.32	0.28[c]	56[c]	2304[b]	24[b]	2
Potato	0.28	n.r.	n.r.	2280[a]	22[ac]	1
Maize	0.41	n.r.	n.r.	5780[a]	56[ac]	1
Wheat	0.39	n.r.	n.r.	2960[a]	28[ac]	1
Barley	0.36	n.r.	n.r.	2030[a]	20[ac]	1
Rape	0.34	n.r.	n.r.	1190[a]	12[ac]	1
Grass	0.41	n.r.	n.r.	4060[a]	39[ac]	1
“	0.27	0.24[c]	46[c]	1908[b]	20[b]	2
“	0.27-0.35	0.25-0.32	64-83	n.r.	n.r.	3
Clover	0.35	n.r.	n.r.	2530[a]	25[ac]	1
“	0.14-0.21	0.12-0.19	24-36	n.r.	n.r.	3
Marrow	0.26	n.r.	n.r.	1680[a]	16[ac]	1
kale	0.32	0.28[c]	42[c]	2304[b]	24[b]	2
Jerusalem artichoke	0.27	0.24[c]	49[c]	2862[b]	30[b]	2
Sugar beet	0.23	0.19[c]	n.r.	n.r.	n.r.	4
tops	0.36-0.38	0.29-0.31[c]	36-38[c]	n.r.	n.r.	5
Straw	0.25-0.26	0.23-0.24	139-145	n.r.	n.r.	3
“	0.30[c]	0.25[c]	n.r.	n.r.	n.r.	6

[a] in Germany, [b] in Sweden, [c] Values calculated from the data reported, a = year, n.r. = not reported. 1: Weiland 2003, 2: Brolin et al. 1988, 3: Kaparaju et al. 2002, 4: Gunaseelan 2004, 5: Zubr 1986, 6: Badger et al. 1979.

This study assesses the sizing of the anaerobic digestion dimension plant, the quantification of the necessary agricultural area for the crops cultivation and for the agronomic utilization of the digested produced by the anaerobic digestion process.

We have considered a size of the CHP engine of 250 kW, which is a power that fits the needs of a typical medium-small size farm. In addition the following technical parameters are assumed:

- Mesophilic temperature range;
- Hydraulic retention time (HRT) equal to 28 days;
- Co-digestion of alfalfa and sorghum.

Following these assumptions, we have determined the amount of alfalfa and sorghum necessary to feed the 250 kW CHP engine. Considering a lower heating value of the biogas equal to 6.8 kWh/m^3, an efficiency of the engine equal to 36% and 7,500 operating hours for year, we obtain an amount of biogas equal to 766,544 m^3 per year.
In order to evaluate the amount of alfalfa and sorghum necessary for the production of biogas amount stated above, we have considered the parameters reported in table 3 (regarding alfalfa) and table 4 (regarding sorghum).

Table 3. Alfalfa silage parameters

Alfalfa silage	
Dry matter, DM	40%
Organic dry matter, ODM	85%
Biogas yield	0,55 m^3 biogas/kg ODM

Table 4. Sorghum silage parameters

Sorghum silage	
Dry matter, DM	30%
Organic dry matter, ODM	85%
Biogas yield	0,60 m^3 biogas/kg ODM

We have also assumed that anaerobic digestion of alfalfa produces 60% of the biogas, while 40% is produced by sorghum digestion.
The volume of the digester is calculated based on the following equation, given the amounts of the vegetable matrices and the hydraulic retention time:
V = HRT * Q
The necessary volume of the digester resulted of 407 m^3.
Given the vegetable yield/ha of the vegetable matrices it is possible to evaluate the amount of areas necessary to produce enough supply for the digester. Assuming alfalfa silage yield equal to 10.92 t/ha*year, and sorghum silage yield equal to 16.91 t/ha*year, and we have obtained that 225.23 ha are required for the production of alfalfa silage, and 118.51 for production of sorghum to feed the digester.

4.1. Digestate management

Digestate is a solid material remaining after the anaerobic digestion of a biodegradable feedstock and it is produced both by acidogenesis and methanogenesis with different characteristics.
Digestate is an easy product to handle and to apply and it can be used successfully as a substitute of mineral fertilizers. The fertilizer value of digestate depends on the nutrients present in the feedstock. However, digestate is the result of a living process and therefore has characteristics that are specific to each digester tank.
In the present study we have assumed that the digestate produced by the digester is stored in a specific waterproof lagoon, that as to be dimensioned to contain the amount of digestate produced in 150 days. The storage device of the digestate also envisages a frank minimum safety of at least

fifty centimeters. The design must include all the necessary measures to minimize odorous emissions [2].
In fact, the application of digestate at times of the year when there is little plant uptake, for instance autumn and winter, can result in nutrient leaching and runoff into ground and surface waters (e.g. of N and P). Digestate must therefore be stored until the correct time of application.
Digestate applications should be matched with crop nutrient requirements; this will minimize any unintended negative impact to the environment and also maximize farmers' profits. Table 5 reports application rates (especially for nitrogen), length of storage periods, and timings for applications that must also comply with national limits.

Table 5. National limits regulating nitrogen loading on farmland, required storage capacity and its spreading season

	Maximum nutrient load	*Required storage capacity*	*Compulsory season for spreading*
Austria	170 kg N/ha/year	6 months	28 feb – 5 oct
Denmark	170 kg N/ha/year (cattle) 140 kg N/ha/year (pig)	9 months	1 feb – harvest
Italy	170 - 340 kg N/ha/year	150 days	depends on the weather conditions
Sweden	170 kg N/ha/year	6 – 10 months	1 feb – 1 dec
Northern Ireland	170 kg N/ha/year	4 months	1 feb – 14 oct
Germany	170 kg N/ha/year	6 months	1 feb – 31 oct arable land 1 feb – 14 nov grassland

5. Conclusions

This study has assessed the opportunity to realize an anaerobic digester in a bio-Energy Park located in Città della Pieve, a small town in Central Italy.
We have chose to evaluate the anaerobic co-digestion of vegetable matrices such as alfalfa and sorghum silage and we have evaluated the principal process parameters.
In particular, assuming a 250 kW CHP engine, we have determined the biogas necessary, the volume of the digester, the amount of alfalfa silage and sorghum, and also the areas required to their production.
The area requested seems to be rather relevant, depending on the lower productivity of the crops chosen as alternative to the largely used energy crops for biogas production, such as maize. The economic feasibility is being currently investigated also taking into account smaller digester size and that marginal lands should be used. Further analysis including other low-input energy crops as suggested by latest literature in the field will be carried out.
Finally we have reported some important consideration about the digestate management, that could be a great opportunity but also a critical point of the system.

Nomenclature

CSTRs	Continuously Stirred Tank Reactors
HRT	Hydraulic Retention Time
ODM	Organic Dry Matter
TS	Total Solids
TVFA	Total Volatile Fatty Acids
VFA	Volatile Fatty Acids

VS	Volatile Solids
ww	wet weight

References

[1] Eurobserv'er, "The state of renewable energies in Europe". 2011 edition.

[2] Regolamento regionale 4 maggio 2011, n. 4 "Norme di attuazione dell'articolo 4, comma 1, lettera e) della legge regionale 10 dicembre 2009, n. 25 concernente la gestione degli impianti per il trattamento degli effluenti di allevamento e delle biomasse per la produzione di biogas e l'utilizzazione agronomica delle frazioni palabili e non palabili" Bollettino Ufficiale della Regione Umbria n. 21 del 11 Maggio 2011.

[3] M. Plöchl, M. Heiermann, B. Linke, H. Schelle. "Biogas Crops – Part II: Balance of Greenhouse Gas Emissions and Energy from Using Field Crops for Anaerobic Digestion". Agricultural Engineering International: the CIGR Ejournal 2009. Manuscript number 1086. Vol. XI. Month.

[4] R. M. Jingura, R. Matengaifa, Optimization of biogas production by anaerobic digestion for sustainable energy development in Zimbabwe, Renewable and Sustainable Energy Reviews 13 (2009) 1116–1120.

[5] L. Xiaohui, N. Sugiura, F. Chuanping, M. Takaaki, Pretreatment of anaerobic digestion effluent with ammonia stripping and biogas purification, Bioresource Technology 100 (2009) 5478–5484.

[6] Plöch M., Heiermann M. "Biogas Farming in Central and Northern Europe: A Strategy for Developing Countries?". Agricultural Engineering International: the CIGR Ejournal. Invited Overview No. 8. Vol. VIII. March, 2006.

[7] Köttner M., Dry fermentation – a new method for biological treatment in ecological sanitation systems (ECOSAN) for biogas and fertilizer production from stackable biomass suitable for semiarid climates. In Proc. 3rd International Conference on Environmental Management, pp 16. Johannesburg, South Africa 2002.

[8] Chen F., Dixon RA Lignin modification improves fermentable sugar yields for biofuel production Nat Biotechnol 2007. 25(7):759-61.

[9] Borreani G, Tabacco E. Insilamento dell'erba medica per valorizzare le proteine. Terra e vita 2008, 14: 80-82.

[10] M. Heiermann, M. Plöchl, B. Linke, H. Schelle, C. Herrmann. "Biogas Crops – Part I: Specifications and Suitability of Field Crops for Anaerobic Digestion". Agricultural Engineering International: the CIGR Ejournal. Manuscript 1087 2009. Vol. XI. June.

[11] Candolo G. "Energia dalle biomasse vegetali: le opportunità per le aziende agricole" Agronomica 2006, 4:26-35.

[12] A. Nordberg, A. Jarvis, B. Stenberg, B. Mathisen, B. H. Svensson. "Anaerobic digestion of alfalfa silage with recirculation of process liquid". 2006.

Investigations on the Use of Biogas for Small Scale Decentralized CHP Applications with a Focus on Stability and Emissions

Steven MacLean[a], Eren Tali[a], Anne Giese[a], Jörg Leicher[a]

[a] *Gaswärme-Institut e.V, Essen, Germany, maclean@gwi-essen.de*

Abstract:

For both environmental and economic reasons, the use of biogas for heat and power generation (CHP), especially on a small and decentralized scale, is predicted to increase dramatically in the years to come. However, these unconventional fuel gases present new challenges to manufacturers of combustion systems as their properties differ from natural gas. In general, their calorific values (LCV) are much lower than those of natural gas, as they contain large amounts of inert species such as CO_2 or N_2. Also, their chemical compositions may vary significantly over time and they may contain species such as HCN or NH_3, leading to increased NO_x formation during combustion due to fuel-bound nitrogen. While NO_x formation due to fuel-bound nitrogen is common in coal combustion, NO_x reduction measures for the combustion of gaseous fuels are usually aimed towards the reduction of thermal NO_x formation and are thus not able to prevent the conversion of chemically bound nitrogen in biogas into nitrogen oxides.

In the course of several research projects, Gaswärme-Institut e.V. Essen (GWI) investigated on how to best make use of these renewable fuels in future combustion systems. Using both numerical and experimental techniques, several burner systems were developed which can achieve a stable combustion of different types of biogases with a minimum of NO_x formation. Using CFD simulations, burners based on the COSTAIR and flameless oxidation (FLOX®) principles were modified to operate with low calorific value fuel gases. The performance of these burners was then further investigated by experimental investigations in GWI's semi-industrial test rigs where a satisfactory agreement between numerical and experimental data was observed.

In a further step, the COSTAIR burner was then mounted into a commercially available 100 kW micro gas turbine (MGT) and tested under real operating conditions. It was shown that the combustion system was able to operate in a stable manner while producing only a minimum of NO_x-emissions, making the combination of a MGT and a burner system optimized for low calorific value gases an ideal choice for small scale decentralized combined heat and power applications.

Keywords:

Low Calorific Gases, Alternative Fuels, Simulation, Fuel-Bound Nitrogen, COSTAIR, Flameless Oxidation, Product Gases formed from Biomass, NO_x-Emissions

1. Introduction

Product gases formed in biomass gasification plants usually have a fluctuating lower heating value and contain several different chemical species, depending on the type of process and biomass being used. The gasified biomass produces a low calorific value gas that can be used in a similar manner as natural gas. Generally some of the more common chemical species of low calorific value product gas are e.g. methane (CH_4), carbon monoxide (CO), hydrogen (H_2), carbon dioxide (CO_2), nitrogen (N_2) and traces of benzol, toluol and tars. Low calorific product gases are defined as gases with lower heating values (LCV) less then < 3 kWh/m_N^3. The large percentage of N_2 and CO_2 and the low CH_4 contents of many (LCV) product gases are the reason why the lower heating value decreases significantly compared to natural gas. However the term low calorific value gas is not solely restricted to product gases formed in gasification processes, but in a broader sense sums up various types of product gases produced in steel mills, chemical processing facilities or landfills. An

overview of typical chemical compositions and properties of some common low calorific gases is listed in table 1.

Table 1. Compositions and Properties of various Low Calorific Value Gas

No.	Reference	Composition [Vol. - %]						LCV H_i [kWh/m^3]
		CH_4	CO	H_2	CO_2	N_2	NH_3	
1	Landfill Gas	10 –30	0	0	0	70 - 90		1 - 3
2	Bio Gas	5	20	15	10	50	<0.1	ca. 1.5
3	Mine Gas	25	0	0	10	65		ca. 2.5
4	Wood Gas	5	15	15	15	50		ca. 1
5	Sewage Gas	35	0	0	55	10		ca. 3.5

H_i (Natural Gas)= 10-12 kWh/m^3

At present, the majority of biogas is produced in biogas fermentation plants. In the future,gasification of biomass may pose an alternative to increase the generation of low calorific product biogas and pave the way for sustainable use of biomass in numerous industrial heat and power applications.

Burning low calorific product gases with conventional burners is difficult because of the large amounts of inert species (mainly N_2 and/or CO_2), tar particles and low LHVs of these gases. However, another challenge with burning these fuel gases is fuel-bound nitrogen, an issue that is normally not a problem with gaseous fuels. Fuel-bound nitrogen in fuel gases leads to a considerable increase of NO_x-emissions during combustion. Nitrous oxides are toxic greenhouse gases which cause nitric acid to form in the atmosphere and the deplete Earth's ozone layer. Furthermore, NO_x-emissions have a 310 times more environmentally damaging impact than CO_2 with regards to global warming. Therefore, advanced burner systems specifically designed to prevent the formation of NO_x during combustion are needed. Fuel-bound nitrogen in gases normally consists up to 95 % out of ammonia compounds, for example when saw dust, chicken manure and various types of biomass are gasified at 1000°C.

The intermediate species formed from the fuel-bound nitrogen tend to convert to NO molecules when a surplus of oxygen due to over-stochiometric conditions is available in the combustion zone . A simplified diagram such a NO-formation mechanism is shown in Fig. 1. Several research activities have focused on exploiting this NO-mechanism to develop a low NO_X combustion system for low calorific biogases containing fuel-bound nitrogen [1].

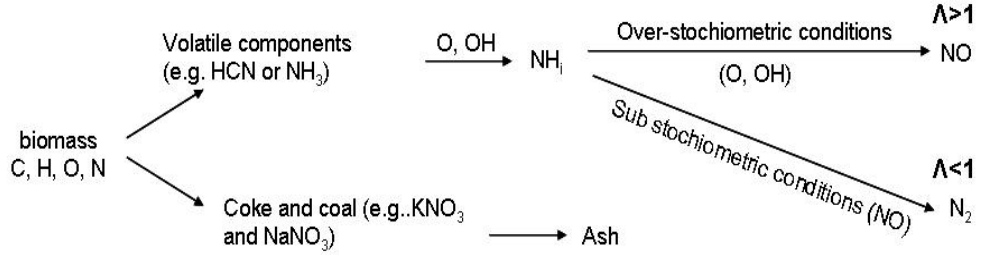

Fig. 1. Simplified NO-Mechanism of Fuel-Bound Nitrogen

In a recent research project conducted by the Gaswärme-Institut e. V. Essen, two burners based on the different concepts of FLameless OXidation (FLOX^{TM}) and COntinuously STaged Air with Internal Recirculation (COSTAIR) were subject to extensive numerical and experimental investigations. The main goal of the project was to develop a method to reduce the NO_x-emission levels during combustion of biogases containing fuel-bound nitrogen. In past research projects, both burner concepts have proven to be low NO_x-emission technologies capable of handling fluctuating fuel gas qualities and low calorific values [2]. The prototype burners were developed in three steps. As a first step, the unmodified burners were simulated with CFD FLUENT with regards to their predicted NO_x-emission levels while combusting low calorific product gas containing fuel-bound nitrogen. In the next step of the project several geometric modifications and improvements to the burners were simulated, again applying the same gases and simulation parameters. Finally, both burners were built and experimentally tested at GWI. The aim of this paper is to give readers a greater insight into the numerical and experimental results as well as the approaches taken to develop a low NO_x combustion system for low calorific gases containing fuel-bound nitrogen.

2. Numerical Development

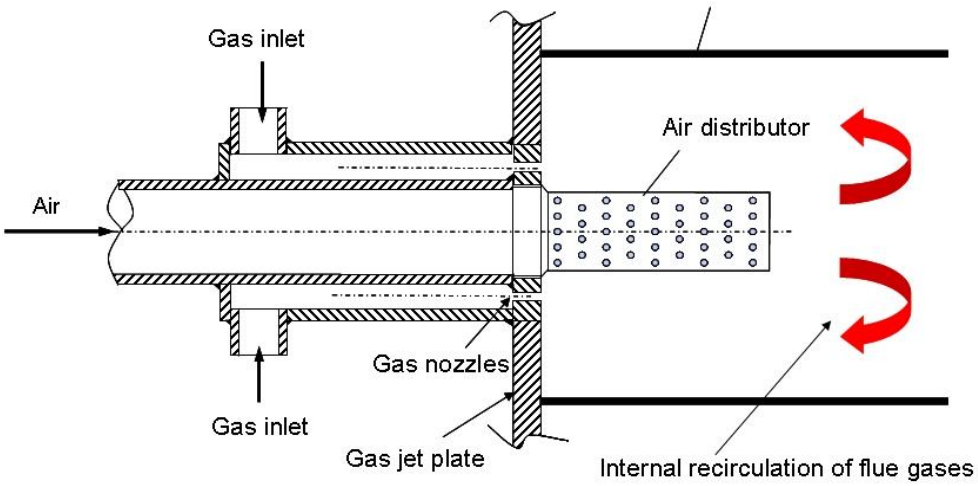

Fig. 2. COSTAIR Burner Concept

The COSTAIR burner concept applies continuously staged air with internal recirculation of flue gases to achieve a stable combustion with low NO_X- and CO- emission levels. Air is injected perpendicularly to the main flow by means over a large number of small nozzles on the surface of the air distributor, thus continuously varying the local air ratio. The internal recirculation of the flue gas helps to produce a stable, uniform combustion that minimizes peak flame temperatures and pockets of oxygen in the combustion reaction zone [3]. The fuel gas nozzles are equally spaced around the central air distributor to ensure that the combustion products mix appropriately with the continuously staged air. In Fig. 2 a simplified sketch of the COSTAIR burner is given.

Throughout the course of this project, CFD simulations played an important role in the development and optimization of COSTAIR burner s. The main idea behind reducing the high NO_x-emission levels of product gases with fuel-bound nitrogen was to stage the air in such a manner that the combustion reaction zone is globally split into a sub-stochiometric ($\lambda < 1$) reduction zone followed by over-stochiometric ($\lambda < 1$) burnout region. The gases simulated in the numerical models consisted of the chemical species CO, H_2, CH_4, CO_2 and N_2. By injecting small amounts of ammonia gas (NH_3) into the product gas,the presence of fuel-bound nitrogen was emulated. The simulation results show that adding small amounts of NH_3 to the fuel gas, caused the NO_x emission levels to increase drastically during combustion since the fuel NOx formation pathway yields much

more nitric oxides than the thermal NOx production pathway which is usually dominant in the combustion of gaseous fuels.. During the development of the COSTAIR burner a strong emphasis was focused on the design of the air distributor. The initial CFD results showed that the positioning and size of the air jets on the air distributor had a tremendous impact on the stability of the combustion zone and and the increase of NO_x emissions levels. The results also confirm that sectioning the air jets on the air distributor causes the reaction zone to shift within the combustion chamber. If for instance the reaction zone is shifted behind the air distributor a considerable rise in NO_x-emission levels is calculated. After determining the basic design of the modified COSTAIR burner, further optimization of the burner and air distributor geometries was required in order to effectively burn low calorific value gas containing fuel-bound nitrogen. A promising approach taken was to extend the length of the air distributor in order to divide the reaction zone more clearly into a sub-stochiometric and over-stochiometric reaction zone. Another important aspect during the development of the prototype burners was the size and positioning of the fuel gas nozzles. Therefore the optimum distance and angle of the fuel jets to the air distributor were numerically determined as well. In Fig. 3 the simulated velocity and temperature distributions of both COSTAIR burner variants are shown. The temperature and velocity distributions confirm that a stable combustion is possible with both COSTAIR variants. By extending the length of the air distributor the combustion reaction zone is clearly divided into two regions with different air ratios. Most importantly, the CFD results confirm that a reduction of NO_x emissions from fuel-bound nitrogen can be achieved with the optimized air distributor.

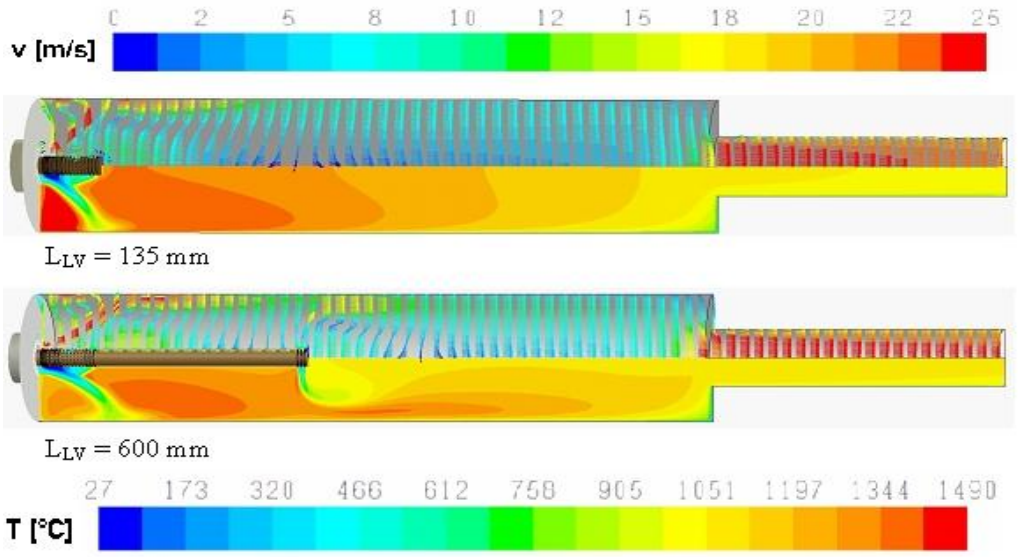

Fig. 3. Temperature and Velocity Distributions of the COSTAIR Burner Variants

FLOX^{TM} burners are low NO_x-emission combustion systems used in various clean energy processes. The term FLOX^{TM} implies that during combustion the flame appears invisible. This is achieved by injecting both fuel gas and oxidizer at high velocities into the combustion reaction zone. The high momentum injection causes the flue gases to be entrained into the reaction zone, thus reducing peak flame temperatures and hence NO_x emissions [4]. The internal recirculation of the flue gases also dilutes and stabilizes the combustion reaction zone. In Fig. 4 a schematic drawing of the FLOX® concept is presented. The FLOX® burner investigated in this project was originally designed to burn natural gas with pre heated air. Since the LCVs of product gases are considerably lower than that of natural gas, a larger gas flow is required to deliver an equal amount of thermal energy. Therefore, several modifications to the air and fuel nozzles were made in order to burn low calorific product gas with an optimized FLOX® burner variant. Prior to the

experimental tests performed at GWI's testing facilities, the same CFD models and boundary conditions used to investigate the COSTAIR burner were applied to adapt a FLOX® burner system to low calorific product gas. The cross sections of the fuel and air nozzles were increased in order to generate the required gas velocities for flameless oxidation.

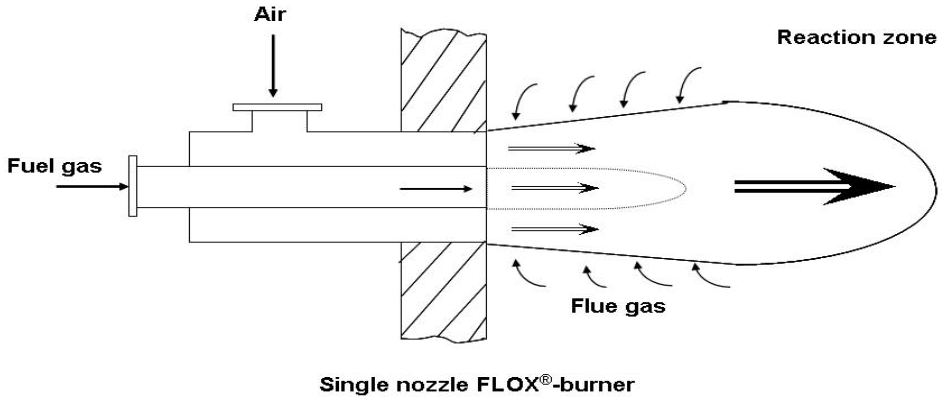

Fig 4. Flameless Oxidation Burner Concept

Further evaluation of the results showed that placing the secondary air inlets behind the combustion reaction zone leads to a considerable decrease in NO_x-emission levels. The temperature and velocity distributions shown in Fig. 5., illustrates that the injection of secondary air does not influence the recirculation of flue gases in the combustion reaction zone. The maximum peak flame temperature of the FLOX® burner is 250 °C lower compared to the COSTAIR burner. The largest reduction of NO_x-emissions was achieved when the primary and secondary air inlets were spaced 1000 mm apart. Injecting the secondary air behind the main combustion reaction zone causes the maximum flame temperatures to decrease while simultaneously the primary reaction zone is divided into two different reaction regions with different air ratios, thus leading to a decline of NO_x- and CO emission during the combustion of low calorific product gas containing gaseous ammonia.

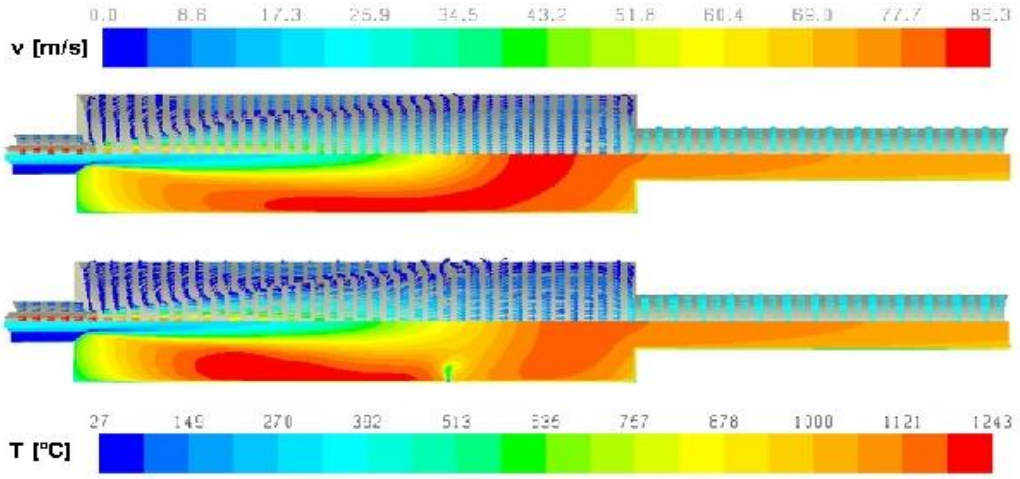

Fig. 5. Temperature and Velocity Distributions of the FLOX® Burner Variants

3. Experimental Investigations

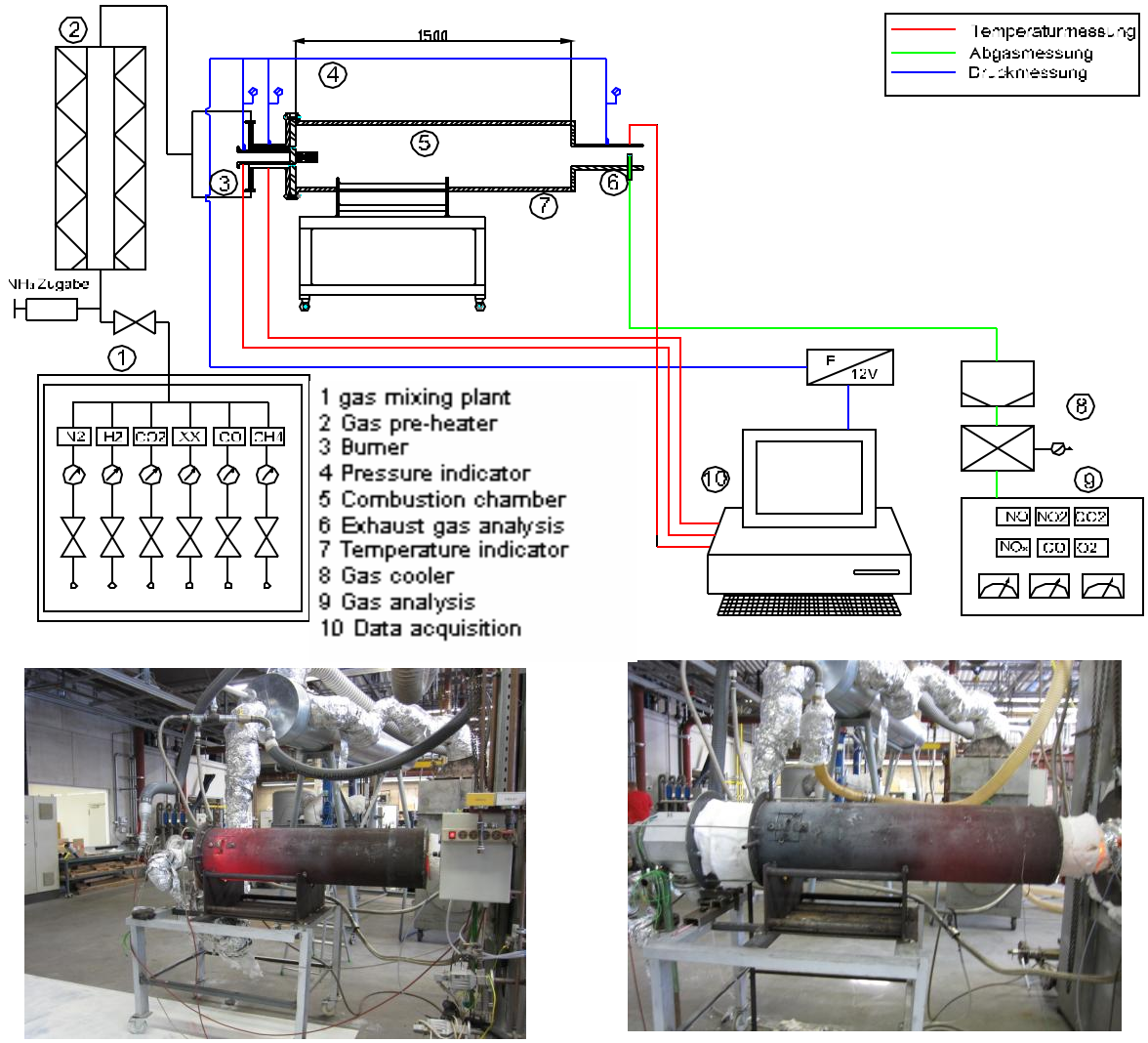

Fig. 6. Layout of the Test Rig (bottom left COSTAIR Burner, bottom right FLOX® Burner)

A schematic drawing of the test rig along with images of the FLOX® and COSTAIR burners are presented in Fig. 6. The experimental investigations of the COSTAIR and FLOX® prototype burners were conducted in two testing stages. During the first phase the original COSTAIR and FLOX® burners were tested without modifying the original burner geometries and secondary air staging inlets. During the second stage of testing the air staging concepts developed for the both burner prototypes were investigated and evaluated. The testing conditions for both burners were kept constant throughout the course of the experimental investigations in order to directly compare the testing results. The low calorific gases used in the experimental tests at GWI were synthetically produced with a gas mixing station, while a gas pre-heater warmed up the gas mixtures to 350°C in order to simulate the actual operating temperatures of a variety of product gases formed in landfills or gasification processes. One of the fuel gases used was seeded with small amounts of ammonia gas (NH_3) in order to investigate the impact of fuel-bound nitrogen on NO_x-emissions. The ammonia gas was added to the fuel gas in increments of 1000, 3000 and 5000 ppm. The composition of the flue gas was measured with an exhaust probe to determine concentrations of CO, CO_2, O_2, NO and NO_2. Moreover, the pressures of the fuel gas and air along with the temperature of the flue gas were recorded.

3.1 COSTAIR Burner Tests

After the final simulations of the COSTAIR variants were completed, experimental testing of both COSTAIR burner variants began. In Fig. 7 the bar graphs of the recorded NO_x-emission levels of the unmodified and optimized burner designs prove that air staging is an effective method to decrease NO_x-emissions. The graph also illustrates that adding 1000, 3000 and 5000 ppm of ammonia to the product gas causes the NO_X-emission levels to almost double in value when air staging is not applied, as in the case of the unmodified COSTAIR burner variant.

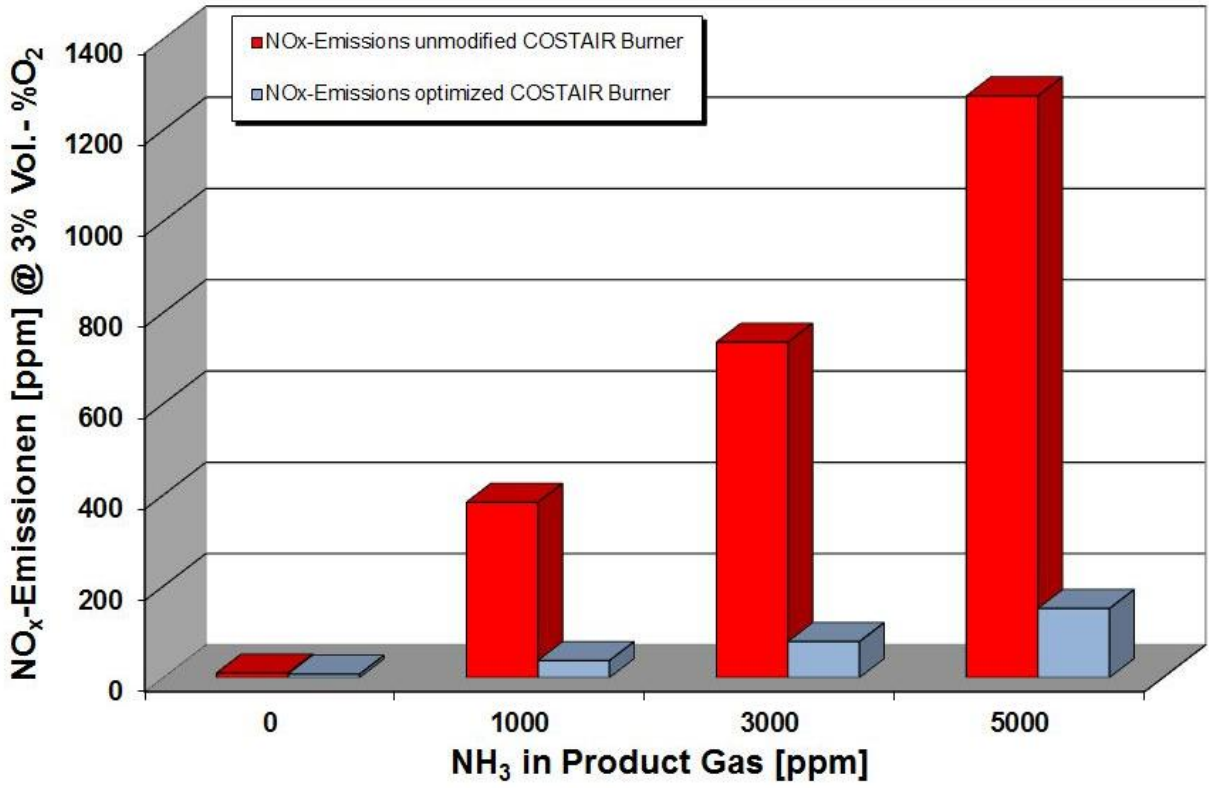

Fig. 7. Experimental Results of Both COSTAIR Burner Variants (NO_x-Emissions)

The results in table 2 show that nearly a 90 % reduction of NO_x-emission levels was possible with the optimized COSTAIR air distributor.

Table 2. Overview of NO_x Emissions for Both COSTAIR Burner Variants

Air Ratio λ	NH_3 in Fuel Gas [ppm]	Unmodified COSTAIR NO_x [ppm] @ 3 Vol.-% O_2	Optimized COSTAIR NO_x [ppm] @ 3 Vol.-% O_2	NO_x Reduction [%]
1.2	0	9.77	7.51	23.13
1.2	1000	384.45	37.45	90.26
1.2	3000	735.44	78.93	89.27
1.2	5000	1275.33	151.42	88.13

The data collected during the first set of burner tests served as points of reference in order to determine the total reduction of NO_x-emissions and the effectiveness of the optimized air distributor on NO_x-emissions during the second stage of testing. A tremendous decline in NO_x-emissions was demonstrated by imposing a strong gradient of the local air ratio along the distributor length of the COSTAIR burner while burning product gases containing fuel-bound nitrogen.

3.2 FLOX® Burner Tests

The results of the experimental tests reveal that the NO_x-emissions from fuel-bound nitrogen are slashed by nearly 50% with the optimized FLOX® burner. The bar graph of the testing results in Fig. 8. confirm that in general, the NO_x-emissions produced by the FLOX® system are remarkably low.

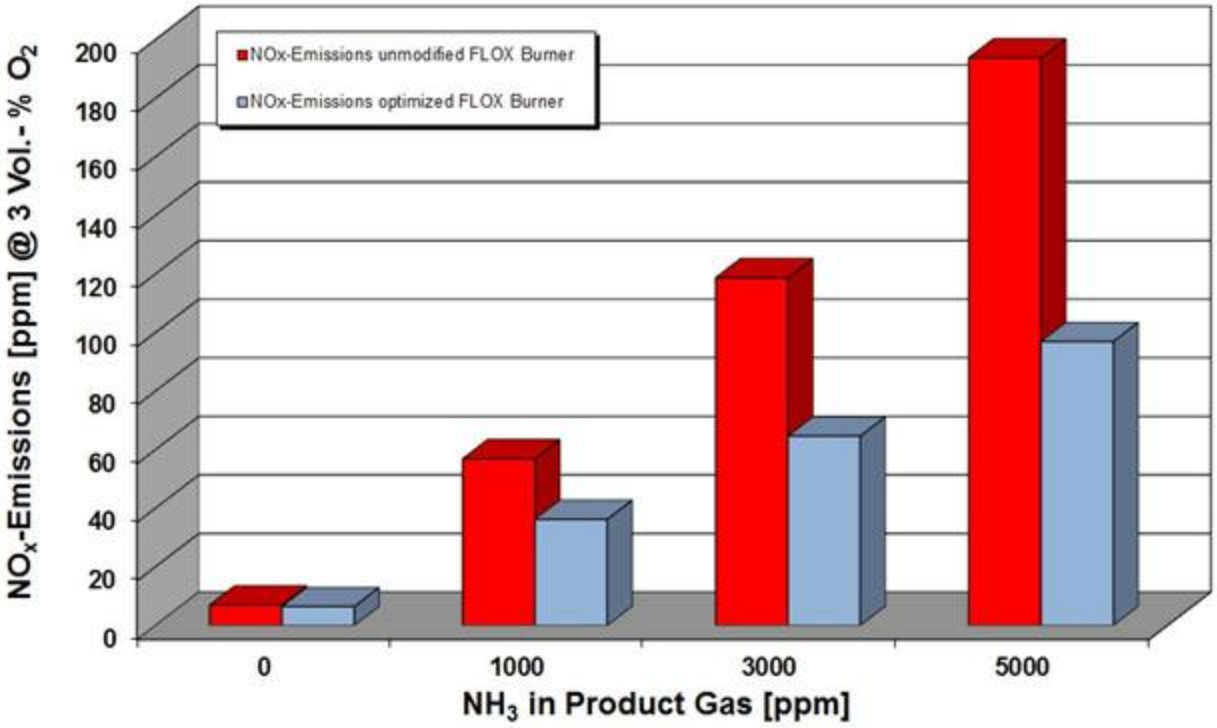

Fig. 8. Experimental Results of both FLOX® Burner Variants (NO_x-Emissions)

An overview of the NO_x reduction of the FLOX® combustion system is provided in table 3.

Table 3. Overview of NO_x Emissions for Both FLOX® Burner Variants

Air Ratio λ	NH_3 in fuel gas [ppm]	Unmodified FLOX® NO_x [ppm] @ 3 Vol.-% O_2	optimized FLOX® NO_x [ppm] @ 3 Vol.-% O_2	NO_x Reduction [%]
1.2	0	6.91	6.38	7.67
1.2	1000	56.85	36.18	36.36
1.2	3000	118.66	64.62	45.54
1.2	5000	193.74	96.88	50.01

The measurements of the basic FLOX® burner variant reveal that less NO_x-emissions are formed when compared to the basic COSTAIR burner. However the use of optimized air distributor had

greater impact on reducing NO_x-emissions compared to the secondary air used with the FLOX® system. A direct comparison of the optimized burners generally shows that a reduction of NO_x-emissions is achieved equally well with both combustion concepts. The results confirm that nearly a 50% reduction of NO_x-emissions from product gases containing fuel-bound nitrogen is possible with the FLOX® burner when the combustion air is staged.

4. CHP Applications for Low Calorific Gases

Micro gas turbines are a beneficial and profitable alternative to utilize low calorific gases in CHP processes, due to their simple design, low CO and NO_x-emissions, operating and maintenance costs as well as noise emissions and adaptability to changing gas qualities compared to gas-powered engines. Within the scope of a prior research project [5], GWI in collaboration with several research and industrial partners optimized and experimentally investigated the burner concepts of flameless oxidation „FLOX® " and continuously staged air „COSTAIR" for low calorific gases under micro gas turbine conditions. Furthermore, the COSTAIR burner was validated on an actual landfill during continuous operation, using a gas with a CH_4 content below 30 vol-%. The first set of results describing the methodology, burner design, burner optimization as well as experimental burner tests were already published in [5].

The initial experimental tests under atmospheric conditions at GWI indicate that the optimized COSTAIR burner operates steadily without causing high emissions. To assure a stable operation mode during testing, the positioning of the pilot burner and the spark ignition were determined numerically with the CFD-program FLUENT. These fluid flow investigations were carried out by the Department of Energy Plant Technology of the Ruhr-University Bochum. The pilot gas nozzle is aligned in between two of the main gas nozzles as shown in Fig. 9. In Fig. 10 a side view of the pilot burner‘s exit velocities is shown. The recirculation zone (highlighted red circle) formed above the gas jet, improves the stability of the flame once the pilot gas ignites. The radially injected air stream collides with the axially flowing pilot gas jet improving the overall mixture and ignition of the pilot burner. A front view of the burner in Fig. 11 clearly illustrates the radial recirculation zone located above the fuel gas nozzle.

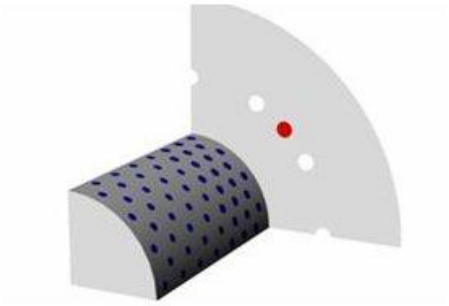

Fig. 9. Close Up View of the MGT COSTAIR Burner

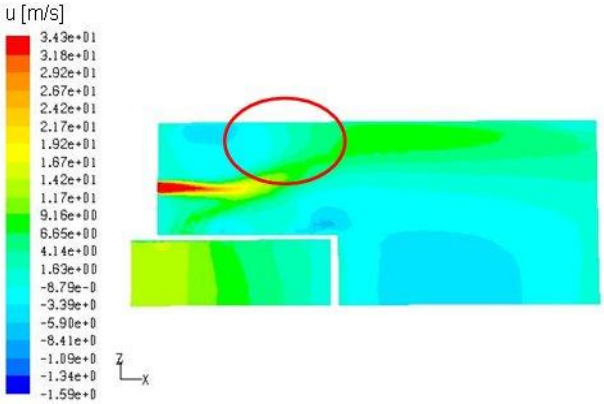

Fig. 10. Simulation of the Exit Velocities of the Pilot Burner Nozzle

Further evaluation of the numerical results concluded that a small area circa 30 mm above the gas jet forms a low velocity field containing an ignitable gas/air mixture. Corresponding to the numerical results a new burner flange plate was constructed and installed in the MGT T100 for

validation testing. In Fig. 12 the optimized COSTAIR burner is shown (please note the position of the pilot gas nozzle and spark ignition). In the adjacent images the entire COSTAIR burner including the head pipe of the MGT T100 is displayed.

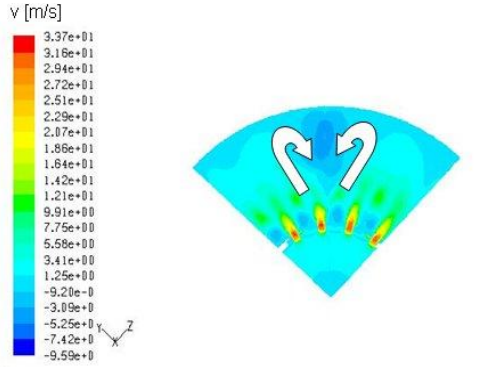

Fig. 11. Radial Velocities 30 mm above the Gas Nozzle

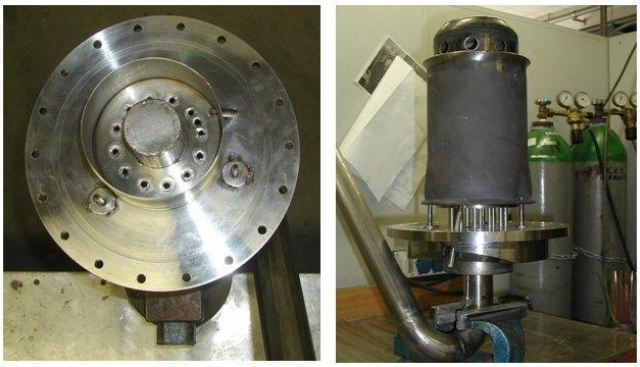

Fig. 12. Adjusted Burner Geometry(left) and Head Pipe Mounted to the Burner (right)

5. Conclusion

Throughout the course of this project, the suitability and optimization of the COSTAIR and FLOX® combustion systems using low calorific product gases containing fuel-bound nitrogen were investigated. One of the first steps taken in this project was to develop two burner systems for low calorific product gases. The influence of different fuel gas compositions and properties was simulated with CFD FLUENT under realistic burner operating conditions. During the second stage of development, both burner designs were optimized to efficiently burn low calorific value gases and reduce NO_x -emissions of product gas containing fuel bound nitrogen. A variety of NO_x-reduction methods were considered and simulated in numerous simulation approaches. Finally, both prototype burners were installed and tested in a GWI test rig. The results show that secondary air staging is an effective method to reduce NO_x- emissions due to fuel-bound nitrogen. Also both burners responded stably to fluctuations of the fuel gas composition and maintained low emissions over a wide range of operating conditions.

The outcome of these projects shows that applying secondary air staging to FLOX® and COSTAIR burner systems leads to a considerable decline in NO_x-emission levels. Yet a further conclusion is that small traces of fuel bound nitrogen in product gases causes the NO_x-emission levels to increase immensely. The developments and combustion concepts investigated in this project, may soon pave the way for new and innovative CHP applications such as micro gas turbines, fuel cells, gas powered engines to utilize low calorific product gases containing fuel-bound nitrogen in an economically feasible manner. The developed burner is able to combust low calorific fuel gases with LHVs as low as 1.25 kWh/Nm^3 (corresponding to a CH_4 concentration of about 12.5 vol-%) without releasing high NO_x-emissions. Furthermore, the necessity to treat product gases containing fuel-bound nitrogen can be reduced considerably using both combustion concepts as primary measures to reduce NO_X formation in the combustion space. The use of alternative fuels combined with innovative burner systems may give industrial plant operators a technical advantage to react in a more competitive and flexible manner to fuel price fluctuations. On behalf of all the corresponding authors, we thank the Department of Energy Plant Technology, Ruhr-University of Bochum, Germany.

References

[1] Brink, A., Huppa, M., Kurkela, E., Suomalainen, M.: Nitric oxide yield from combustion of a low calorific gasification product gas: numerical and experimental results, Progress in Computational Fluid Dynamics, Vol. 6, No. 4/5, 2006

[2] AiF-Projekt MGT: Neue Brennersysteme zur dezentralen Nutzung von schwachkalorigen Gasen in Mikro-Gasturbinen. AiF-Vorhaben Nr.: 13216 N, Projektdauer: 01.03.2002 bis 31.08.2004

[3] Al-Halbouni, A.: Entwicklung NO_x-emissionsminimierter Heizkesselfeuerungen. Habilitation, Otto-von-Guericke-Universität Magdeburg, Shaker Verlag 2001

[4] Maclean, S., Tali, E., Giese, A., Leicher, J., Görner, K.: Investigations on the Reduction of NO_x Emissions of Product Gases containing Fuel Bound Nitrogen in Thermal Processing Plants, 9th European Conference on Industrial Furnaces and Boilers, Porto, Portugal, 2011

[5] Leicher, J., Giese, A., Görner, K., Scherer, V., Schulzke, T.: Development of a Burner System for Use of Low Calorific Fuel Gases in Micro Gas Turbines, Proceedings of the European Combustion Meeting, Cardiff, England 2011 .

Kinetic energy recovery system for sailing yachts

G.L. Guizzi[a] and M. Manno[b]

[a] *Università degli Studi di Roma Tor Vergata, Roma, Italia, guizzi@ing.uniroma2.it*
[b] *Università degli Studi di Roma Tor Vergata, Roma, Italia, michele.manno@uniroma2.it*

Abstract:

SEAKERS (SEA Kinetic Energy Recovery System) is a research project, funded within the 7th EU Framework Programme and officially started on January 1st, 2011, whose goal is to develop an innovative device consisting in a kinetic energy recovery system for sailing yachts based on the conversion of boat oscillations (heave, pitch and roll) caused by the sea into electric energy by means of a linear generator.
Therefore, SEAKERS addresses a well known unsatisfied requirement of yacht owners, since energy is a resource of primary importance in a boat, especially in a sailing one: it is well known that during a one day cruise, electricity consumption has to be carefully managed (for instance the refrigerator is switched off), so as not to be short of energy at night. It often happens that, after one day of sail cruise, it is necessary to recharge the batteries through the onboard generator, which means keeping it on for hours, producing very annoying noise, smoke and pollution.
The device that is going to be developed aims at recovering as much kinetic energy as possible from the natural movements of a sailing yacht on the sea, therefore taking the view of a boat as a moving wave energy converter with energy harvesting capacity. The boat's motions can be vertical oscillations due to the buoyancy in the presence of sea waves, both when the boat is still or sailing, and rolling and pitching motions originated both by sailing in wavy waters and by the normal boat dynamics due to the sails' propulsion. Linear generators will convert kinetic energy into electrical energy to be used as "green" electricity for any possible application on board.
Preliminary calculations show that a properly configured system could be able to recover 100-400 W under most sea conditions, which can be an extremely attractive result since an electric energy availability of 1-2 kWh on a sailing yacht is of significant interest.

Keywords:

Wave Energy Recovery, Linear Generator, Sail Yacht.

1. Introduction

This paper presents some preliminary results obtained in the SEAKERS project, whose aim is to design and test a kinetic energy recovery system to be used on board of sail yachts in order to recover energy from the wave-induced boat's vertical motion.

Such a system is able to recover actual free energy, as opposed to other devices, already commercially available, that subtracts energy from the propulsion offered by the wind's lift on the sails, as in the case of micro-wind turbines installed on the boat, which are set into motion by the apparent wind originating from the yacht's motion.

In practical terms, the SEAKERS device is intended to be a linear oscillator, with a mass oscillating vertically inside a prismatic guide and gaining kinetic energy; if the mass is the moving element of a linear generator, the resulting mechanical energy can be extracted and converted into electricity. The oscillating mass incorporates permanent magnets which, moving in proximity of stator windings, generate electric power due to electromagnetic induction.

The SEAKERS device addresses a well known unsatisfied requirement of yacht owners, since energy is a resource of primary importance in a boat, especially in a sailing one: it is well known that during a one day cruise, electricity consumption has to be carefully managed (for instance the refrigerator is switched off), so as not to be short of energy at night. It often happens that, after one

day of sail cruise, it is necessary to recharge the batteries through the onboard generator, which means keeping it on for hours, producing very annoying noise, smoke and pollution.

The idea of a linear generator originates from work carried out at the University of Uppsala [1-4], where such devices have been designed and tested in order to recover wave energy from a buoy, oscillating on the sea surface, connected to a rope that makes a piston move inside a generator placed on the seafloor. In the SEAKERS project, the oscillating mass is set into motion not directly by the sea waves but by its inertia as the yacht is subject to heave, pitch and roll motions.

In order to design the test-bed for testing the generator, it is necessary to set up a reliable model of different sea conditions that could be of practical interest for a normal cruise on a sail yacht (thus there is no need to consider extreme, stormy waves) and of the ship motion due to such sea states. Furthermore, it is interesting to find out, by means of a very simple mechanical model of the linear generator, how much power could be extracted under these simplifying assumptions, in order to decide whether the project's outcome could in principle be commercially viable, and quickly to provide data against which results from more detailed analytical models and experimental tests could later be compared.

This paper presents the results obtained in this first stage of the project, detailing first the model of sea conditions (section 2), then the outcome of simulations on the yacht's motion carried out by means a commercial software (section 3), and finally the results of the analysis carried out on a linear mechanical system located on the boat (section 4).

2. Wave excitation

2.1. Wave spectra

The main characteristic of sea waves is randomness. Indeed, by checking even a short a time series, two characteristics arise: height and period of a wave are different from height and period of another wave. For this reason, the free surface elevation of sea waves is modelled as a stochastic process and is assumed to be a random, Gaussian, ergodic process in the time domain [5-8].

Mathematically, sea elevation can be reconstructed in one dimension as a Fourier series as follows:

$$\zeta(x,t) = \sum_{j=1}^{n} Z_j \cos\left(\omega_j t - k_j x + \vartheta_j\right) \qquad (1)$$

In this equation, Z_j is the wave amplitude for the j-th wave form of circular frequency ω_j, k_j its wave number (dependent on ω_j through the dispersion relation) and ϑ_j its phase shift. The *dispersion relation* defines the relationship between wave frequency and wave number; in deep water it is expressed as [5-8]:

$$\omega^2 = kg \qquad (2)$$

where g is the acceleration of gravity. (It may be useful to recall that wave number and wave length are mutually dependent: $k = 2\pi / \lambda$).

Given a sea elevation time pattern ζ for a given spatial coordinate x, the amplitudes Z_j of its Fourier series may be evaluated as Fourier transforms of ζ:

$$Z_j = \frac{1}{T}\int_{-\frac{T}{2}}^{\frac{T}{2}} \zeta(t)\exp\left(-i\,2\pi\,\omega_j t\right)\mathrm{d}t \qquad (3)$$

The most meaningful representation from a statistical point of view of a particular sea state is given in the frequency domain by means of the wave spectrum $S(\omega)$, which is defined as:

$$S(\omega_j)\mathrm{d}\omega = Z_j Z_j^* = \left|Z_j\right|^2 \qquad (4)$$

Z_j^* being the complex conjugate of Z_j. Therefore, the spectrum $S(\omega_j)$ is proportional to the energy content of the j-th wave form of circular frequency ω_j, while the area under the spectrum s proportional to the overall energy content of the sea state described by sea elevation $\zeta(t)$:

$$\int_{-\infty}^{\infty} S(\omega)\mathrm{d}\omega = \sum_{j=1}^{n} |Z_j|^2 \qquad (5)$$

Since $S(\omega)$ is an even function, that is, $S(-\omega) = S(\omega)$, and taking also into account that negative angular frequencies have no physical meaning beyond that of the corresponding positive values, it is frequently adopted an alternative definition of the energy spectrum (S_ζ), which is defined for positive angular frequencies only:

$$2\int_0^{\infty} S_\zeta(\omega)\mathrm{d}\omega = \int_{-\infty}^{\infty} S(\omega)\mathrm{d}\omega \qquad (6)$$

By virtue of equation (5), the energy spectrum is correlated to the overall energy content of the sea state, because the energy content of a single sinusoidal wave is proportional to the square of its height. Furthermore, statistical data that can be gleaned from the energy spectrum correspond to important parameters for the description of a sea state. Of particular importance is the 0-th spectrum moment, which is equivalent to the area under the wave spectrum curve:

$$m_0 = \int_0^{\infty} S_\zeta(\omega)\mathrm{d}\omega \qquad (7)$$

For a narrow band spectrum, it can be demonstrated that the root mean square (RMS) wave amplitude is given by $\sqrt{m_0}$, and the RMS value of wave height (crest to trough) is therefore:

$$H_{RMS} = 2\sqrt{m_0} \qquad (8)$$

One of the most useful parameter to represent the sea state is the *significant wave height*, which is the mean of highest third wave heights, and for narrow band spectrum it is given by [5-8]:

$$H_s = 4\sqrt{m_0} \qquad (9)$$

Significant wave amplitude is by definition half the corresponding wave height:

$$\zeta_{0s} = 2\sqrt{m_0} \qquad (10)$$

2.2. Simulation assumptions

The simulations that will be presented in the following sections were carried out taking into account statistical wave data for the Mediterranean Sea, with particular reference to the measurements taken at Capo Linaro (Civitavecchia, Italy)[1].

In the case of random waves, it is possible to find a particular set of parameters that make the JONSWAP spectrum suitable to represent sea conditions in the location of interest (the above mentioned Capo Linaro near Civitavecchia).

The JONSWAP spectrum was developed from extensive field measurements in the context of the Joint North Sea Wave Project [5-8]. This formulation is suitable for wind-generated waves in fetch limited locations. The inputs are the wind speed and the fetch length. The mathematical formulation is given by equation:

[1] Personal communications with Prof. Felice Arena, University of Reggio Calabria, 2011.

$$S_\zeta(\omega) = \alpha g^2 \omega_p^{-5} \exp\left[-\frac{5}{4}\left(\frac{\omega}{\omega_p}\right)^{-4}\right] \exp\left\{\ln(\gamma)\exp\left[-\frac{(\omega-\omega_p)^2}{2\sigma^2\omega_p^2}\right]\right\} \quad (11)$$

In the above equation, $\omega_p = 2\pi/T_p$ is the peak circular frequency, α is the Phillips' parameter given by $\alpha = 0.0076(gx/\overline{U}^2)^{-0.22}$, where x is the fetch length and $\overline{U}$ the mean wind speed, and γ is the peak-shape parameter. For practical applications, σ can be assumed equal to 0.08 in the whole frequency domain.

In deep water, wave period and length are correlated by the dispersion relation (2), which may be rewritten as follows:

$$\lambda = gT^2/(2\pi) \quad (12)$$

Wave velocity is given by:

$$c = \lambda/T = gT/(2\pi) \quad (13)$$

Furthermore, wave period is also related to the significant wave height through parameters α and γ:

$$T_p = f(\alpha,\gamma)\sqrt{H_s/g} \quad (14)$$

Thus, higher waves are longer (12), propagate faster (13) and are less frequent (14). The JONSWAP spectrum is completely defined when the significant wave height H_s and parameters α and γ are specified.

In order to represent correctly sea conditions at Capo Linaro, values of α, γ, f and T_p are chosen according to the following table. The corresponding wave spectra are illustrated in fig. 1.

Table 1. Parameters used to represent random sea waves at Capo Linaro near Civitavecchia, Italy.

H_s [m]	α	γ	$f(\alpha,\gamma)$	T_p [s]
0.5	0.016	1.0	13.2	2.98
1.0	0.008	2.0	14.9	4.75
1.5	0.010	0.5	15.5	6.06
2.0	0.008	0.5	16.4	7.40

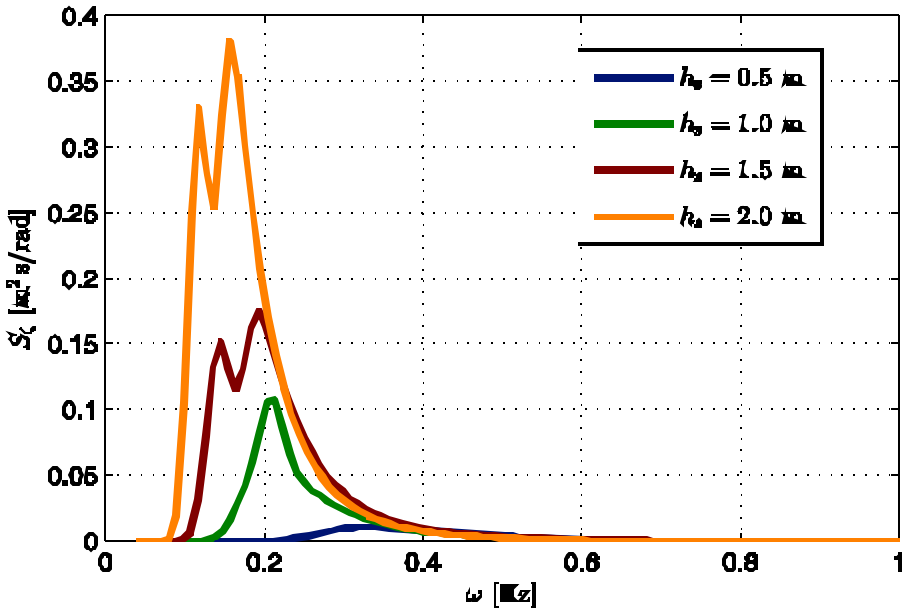

Fig. 1. Wave spectra representing sea conditions at Capo Linaro near Civitavecchia, Italy.

3. Yacht's response

3.1. Encounter frequency

Due to its forward speed *V*, the wave spectrum for the ship is different than for a fixed observer. When studying the ship's response it is therefore necessary to take into account the frequency at which it actually encounters the waves (*encounter frequency*). The encounter frequency depends on wave velocity and ship speed and relative direction with respect to waves μ. Angle μ is defined between the forward directions of wave and ship: thus for bow waves $\mu = \pi$, for transverse waves $\mu = \pi/2$, and for aft waves $\mu = 0$.

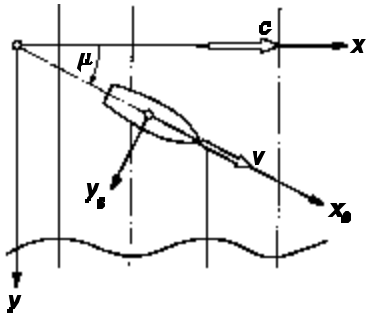

Fig. 2. Definition of angle of encounter [5].

Encounter frequency[2] must be evaluated taking into account the velocity component of the ship in the direction of the waves, subtracting wave velocity *c*. The relative velocity is given by:

$$V_{rel} = c - V\cos\mu \tag{15}$$

Thus the encounter period is:

$$T_e = \frac{\lambda}{V_{rel}} = \frac{\lambda}{c - V\cos\mu} \tag{16}$$

The encounter frequency is thus given by:

$$\omega_e = \frac{2\pi}{\lambda}\left(c - V\cos\mu\right) \tag{17}$$

For seakeeping purposes, the assumption of deep water may be applied; in this case, taking into account the dispersion relation (2), the encounter frequency can be finally derived as:

$$\omega_e = \omega - \frac{\omega^2 V}{g}\cos\mu \tag{18}$$

The wave energy spectrum must also be modified according to the encounter frequency (it is practically a Doppler shift of the spectrum). Since the energy content of a spectrum must be the same for any observer, fixed or moving with the ship, the 0-th momentum must be the same:

$$m_0 = \int_0^\infty S(\omega)\mathrm{d}\omega = \int_0^\infty S_e(\omega_e)\mathrm{d}\omega_e \tag{19}$$

Therefore, the relation between wave spectrum and encounter spectrum is the following:

$$S_e(\omega_e)\mathrm{d}\omega_e = S(\omega)\mathrm{d}\omega \tag{20}$$

[2] In this paper, the term "frequency" will be used indifferently to identify both frequency *f*, measured in Hz, or angular (circular) frequency ω, measured in rad/s.

which becomes, taking into account that $\mathrm{d}\omega_e = \left|1 - 2\omega V \cos\mu / g\right| \mathrm{d}\omega$:

$$S_e(\omega_e) = \frac{S(\omega)}{\left|1 - 2\frac{\omega V}{g}\cos\mu\right|} \tag{21}$$

3.2. Response amplitude operators

The ship response is usually described in terms of transfer functions (RAO, Response Amplitude Operator), which give the normalised amplitude of the resulting ship's motion for a sinusoidal excitation of frequency ω_e, the normalization factor being the wave amplitude ζ_0 for linear motions, the wave slope $k\zeta_0 = 2\pi\zeta_0/\lambda$ for angular motions and the wave acceleration $\omega_e^2\zeta_0$ for accelerations:

$$\mathrm{RAO}_z(\omega_e) = \frac{z_0}{\zeta_0} \tag{22}$$

$$\mathrm{RAO}_\vartheta(\omega_e) = \frac{\vartheta_0}{k\zeta_0} \tag{23}$$

$$\mathrm{RAO}_a(\omega_e) = \frac{a_0}{\omega_e^2\zeta_0} \tag{24}$$

Obviously, equally important are the phase shifts α of each motion with respect to the wave excitation. With the knowledge of RAOs and phase shifts, it is possible to reconstruct heave (z), pitch (ϑ) and roll (η) motions from a sinusoidal wave excitation $\zeta(t) = \zeta_0 \exp(i\omega_e t)$ as follows:

$$z(t) = z_0 \exp\left[i\left(\omega_e t + \alpha_z\right)\right] \tag{25}$$

$$\vartheta(t) = \vartheta_0 \exp\left[i\left(\omega_e t + \alpha_\vartheta\right)\right] \tag{26}$$

$$\eta(t) = \eta_0 \exp\left[i\left(\omega_e t + \alpha_\eta\right)\right] \tag{27}$$

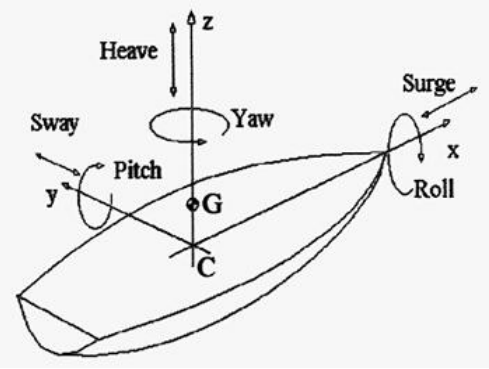

Figure 3. Coordinate system and definition of motion [9].

Therefore, vertical oscillations for any point on the ship may be calculated as follows (fig. 3):

$$y(t) = z(t) - L\sin\left(\vartheta(t)\right) + B\sin\left(\eta(t)\right) \tag{28}$$

where L and B are the longitudinal and lateral distance of the point of interest from the center of gravity. Since angular motions (pitch and roll) are usually small, it is possible to approximate the above expression:

$$y(t) \cong z(t) - L\vartheta(t) + B\eta(t) \qquad (29)$$

Therefore, being the sum of harmonic motions (phasors), the vertical oscillation $y(t)$ is also represented by a harmonic oscillation:

$$y(t) = y_0 \exp\left[i\left(\omega_e t + \alpha_y\right)\right] \qquad (30)$$

and it is possible to define a RAO for the particular point of interest on the ship:

$$\mathrm{RAO}_y(\omega_e) = \frac{y_0}{\zeta_0} \qquad (31)$$

In case of a random wave excitation, with the assumption that the response is a linear function of wave amplitude and applying the superposition principle, vertical motion can be reconstructed as:

$$y(t) = \sum_{j=1}^{n} y_{0,j} \cos\left(\omega_{e,j} t + \alpha_{y,j}\right) \qquad (32)$$

where each oscillation amplitude $y_{0,j}$ is a function of frequency and amplitude of the j-th harmonic, according to (31).

Furthermore, it is possible to demonstrate that the ship's response energy spectrum is given by the product of the square of the RAO and the wave energy spectrum. Thus, heave motion's energy spectrum is:

$$S_z(\omega_e) = \mathrm{RAO}_z^2(\omega_e) S_\zeta(\omega_e) \qquad (33)$$

and analogous equations hold for the other motions, while for any point on the ship the energy spectrum associated to its wave-induced motion is:

$$S_y(\omega_e) = \mathrm{RAO}_y^2(\omega_e) S_\zeta(\omega_e) \qquad (34)$$

3.3. Simulation results

The foundation for the commercial software package *Seakeeper*[3], which was used to carry out the computation of the yacht's motions under different wave conditions, is the linear strip theory based on the work of Salvesen [10], which is used to calculate the coupled heave and pitch response of the vessel; the roll response is calculated using linear roll damping theory [11].

The main purpose of the kinematic model presented is to provide reasonable data about the response of a generic yacht to different sea conditions, in order to have reliable information on the motion which the SEAKERS device is subjected to. Since the project does not address a particular yacht model, nor even a specific size of boat, there was no point in developing a focused *in-house* software: hence the choice of adopting a commercial software that has a proven record of reliability, using it to simulate the response of a yacht of adequate length included in the extensive library provided.

The yacht's model used in the numerical simulations is one of the library models that can be found in Seakeeper's library, since it has geometric and mass properties comparable to those of commercial sail yachts of interest for the SEAKERS project.

The most relevant hydrostatic properties of this yacht are given in table 2. The generator considered in the simulations presented is placed at bow on the longitudinal axis ($B = 0$) at a distance L = 5.17 m from the center of gravity.

[3] *Seakeeper* is a software by Formation Design Systems Pty Ltd (trading as FormSys); website: http://www.formsys.com/maxsurf/msproducts/seakeeper.

Figure 4 gives an overview of 21 two-dimensional sections used in the Seakeeper software to evaluate sectional hydrodynamic masses, damping coefficients, and all other data needed in the context of the strip theory [5-9].

Table 2. Yacht's hydrostatic properties.

	Value	*UoM*
Displacement	6.531	t
Volume (displaced)	6.372	t
Overall length	11.5	m
Draft amidships	2.475	m
Immersed depth	3.054	m
Waterline length	10.64	m
Max beam on waterline	2.866	m
Max section area	1.213	m^2
Waterplane area	21.21	m^2
Prismatic coefficient (Cp)	0.494	
Block coefficient (Cb)	0.068	

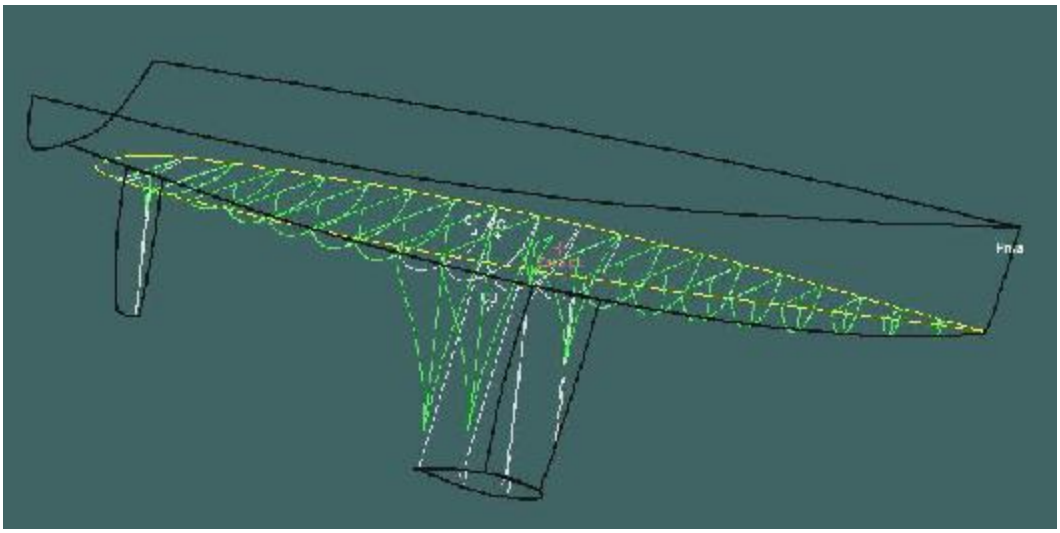

Fig. 4. Yacht's mapped sections used to evaluate hydrodynamic coefficients in the equations of motion by the Seakeeper software.

As illustrated in section 3.2, the ship's response is defined by means of Response Amplitude Operators (RAO) and phase shifts, with reference to a sinusoidal wave excitation. Figures 5 and 7 show values of RAO for each motion (heave, pitch and roll) for two different speeds (V = 5 knt and V = 8 knt respectively), while figs. 6 and 8 show the phase shifts, as obtained by means of the *Seakeeper* software. For the roll motion, the default value of non-dimensional damping factor proposed by the software has been taken into account.

The response to random waves is illustrated in figs. 9 and 10 in terms of energy spectra of the vertical oscillations (34). The significant oscillation amplitudes are obtained from these spectra in the same way as the significant wave amplitude (10) is calculated from the wave spectrum:

$$y_{0s} = 2\sqrt{m_{0y}} = 2\sqrt{\int_0^\infty S_y(\omega_e)\mathrm{d}\omega_e} \qquad (35)$$

Values of significant vertical oscillation amplitudes, corresponding to the energy spectra of figs. 9 and 10, are given in table 3.

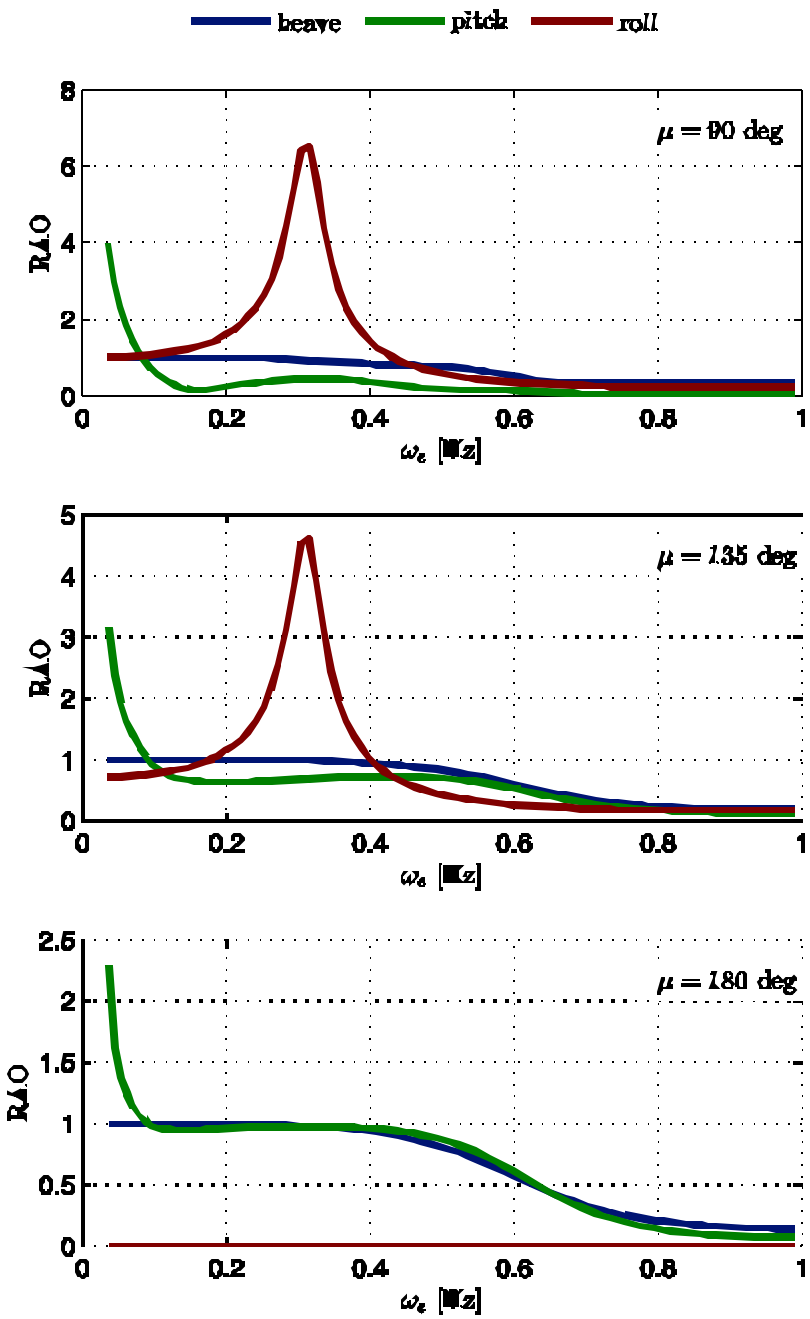

Fig. 5. Yacht's response: response amplitude operators (RAO) at speed V = 5 knt.

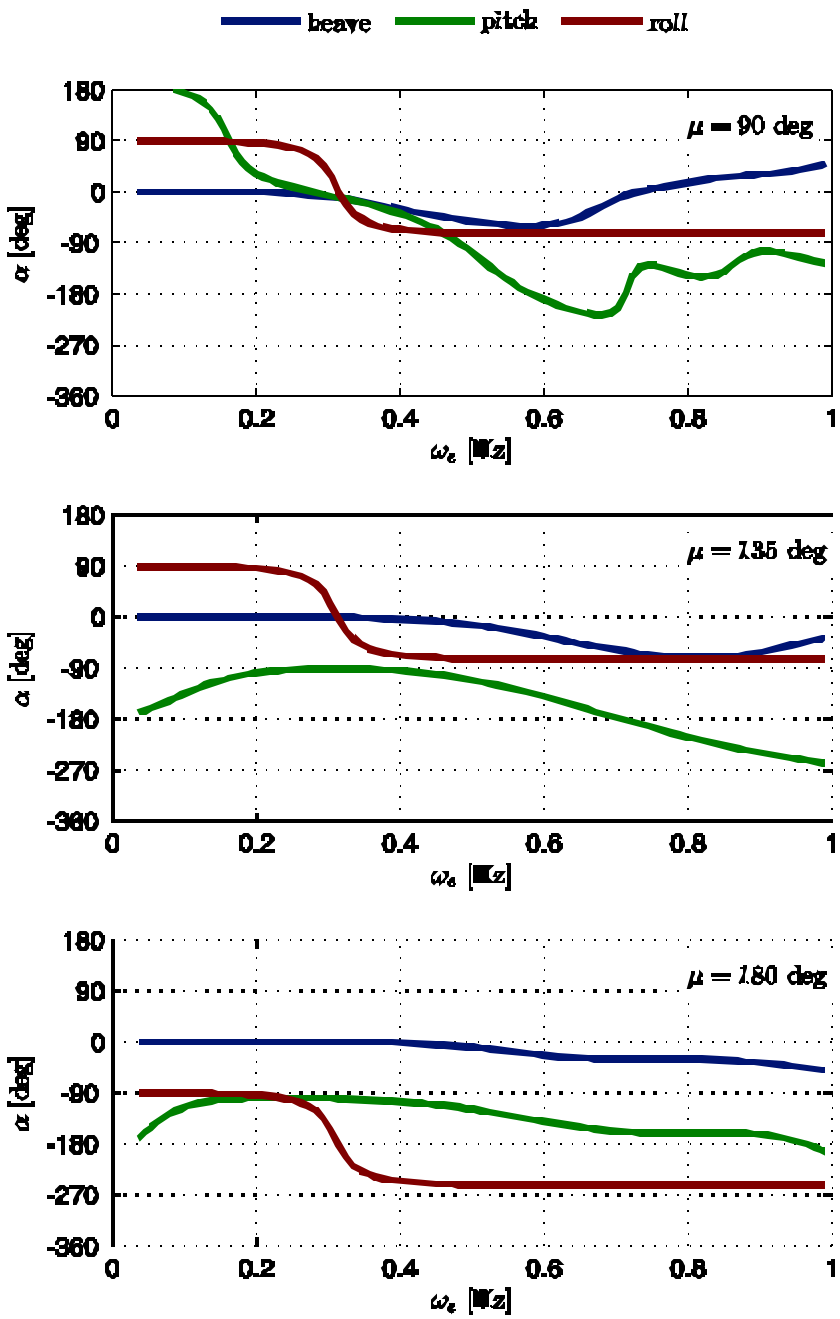

Fig. 6. Yacht's response: phase shifts at speed V = 5 knt.

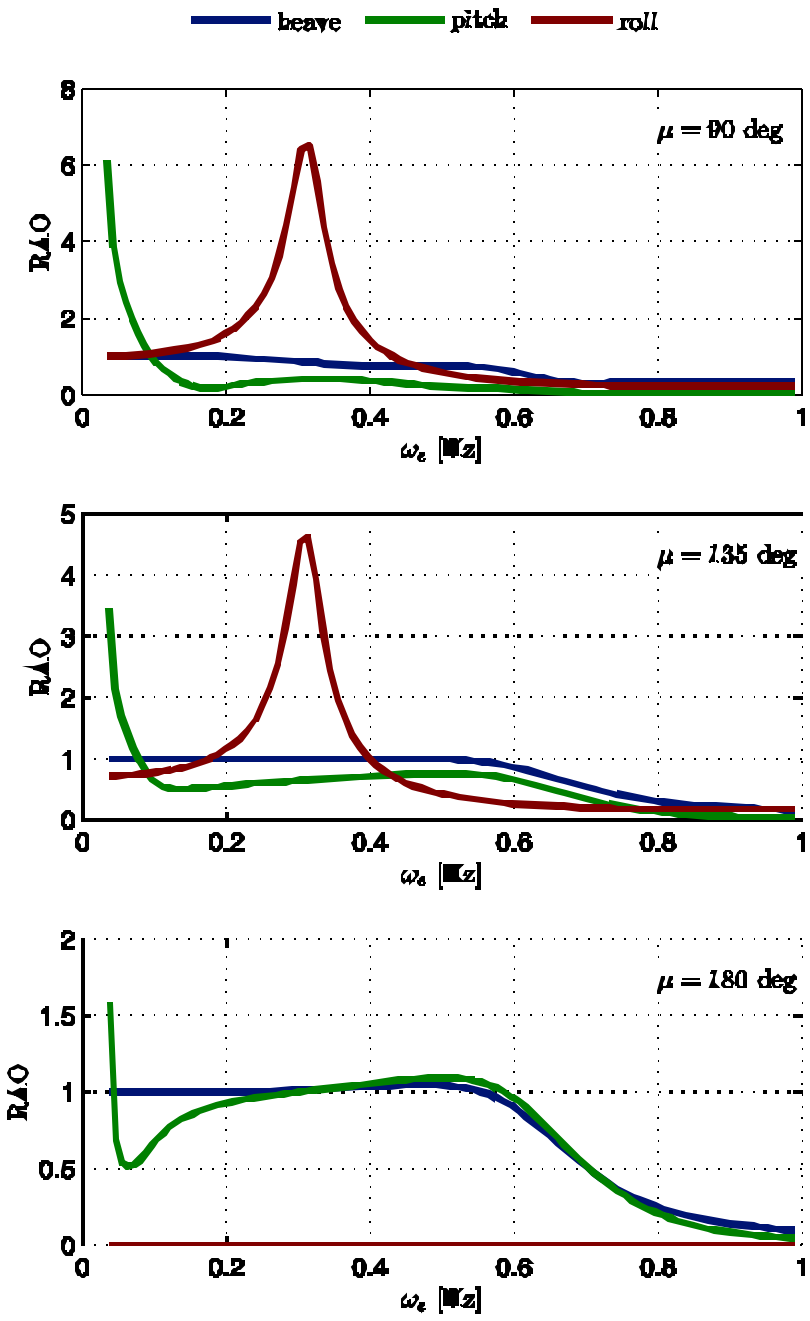

Fig. 7. Yacht's response: response amplitude operators (RAOs) at speed V = 8 knt.

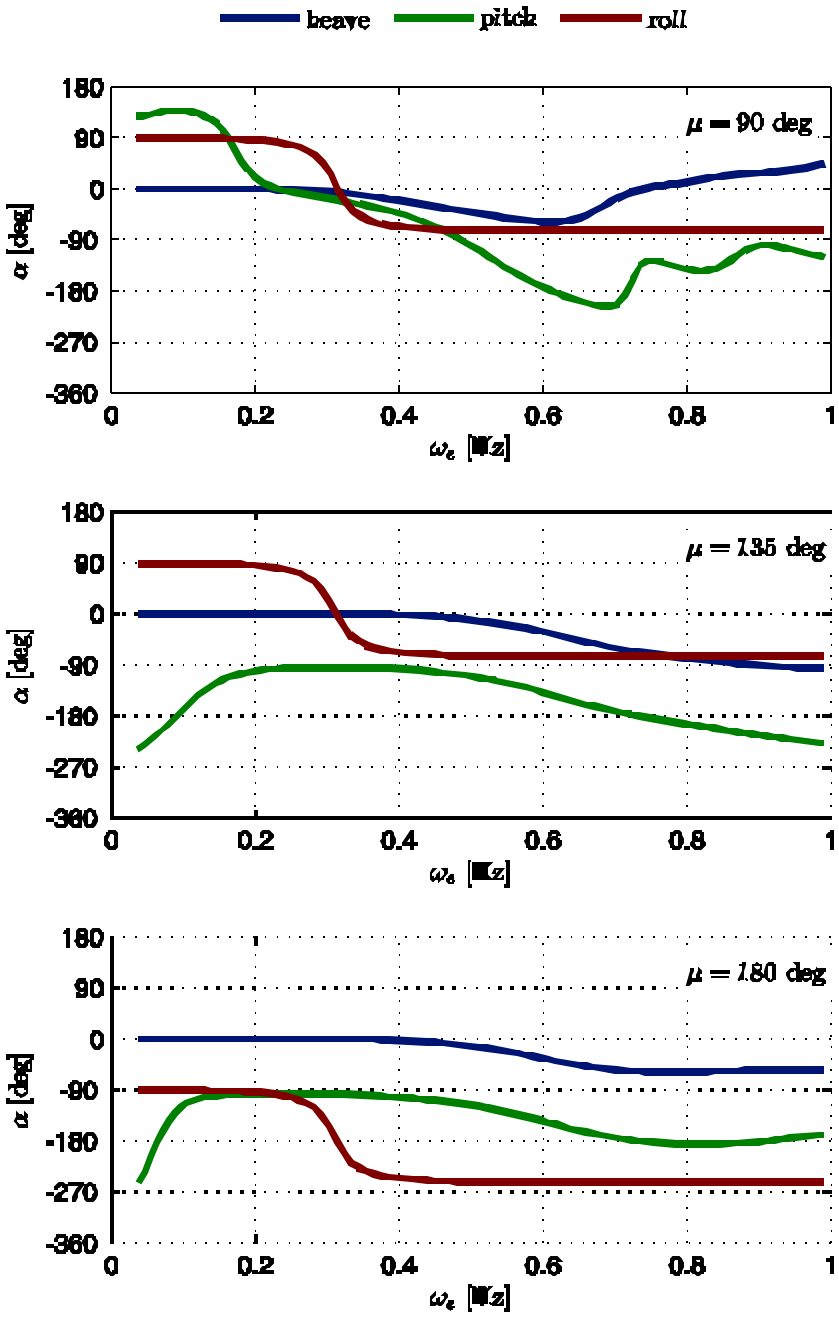

Fig. 8. Yacht's response: phase shifts at speed V = 8 knt.

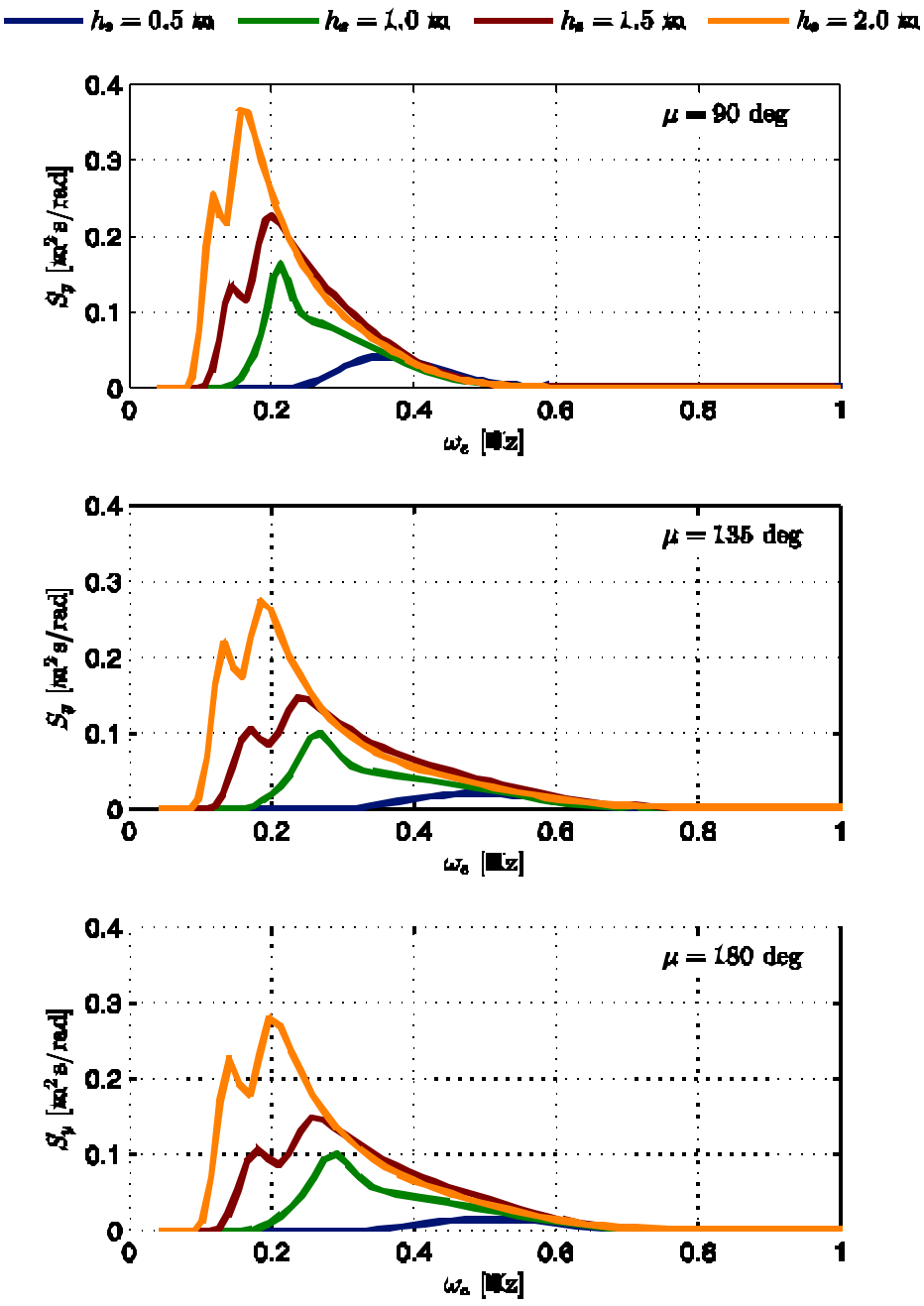

Fig. 9. Energy spectrum of vertical oscillations at the generator's location at speed V = 5 knt.

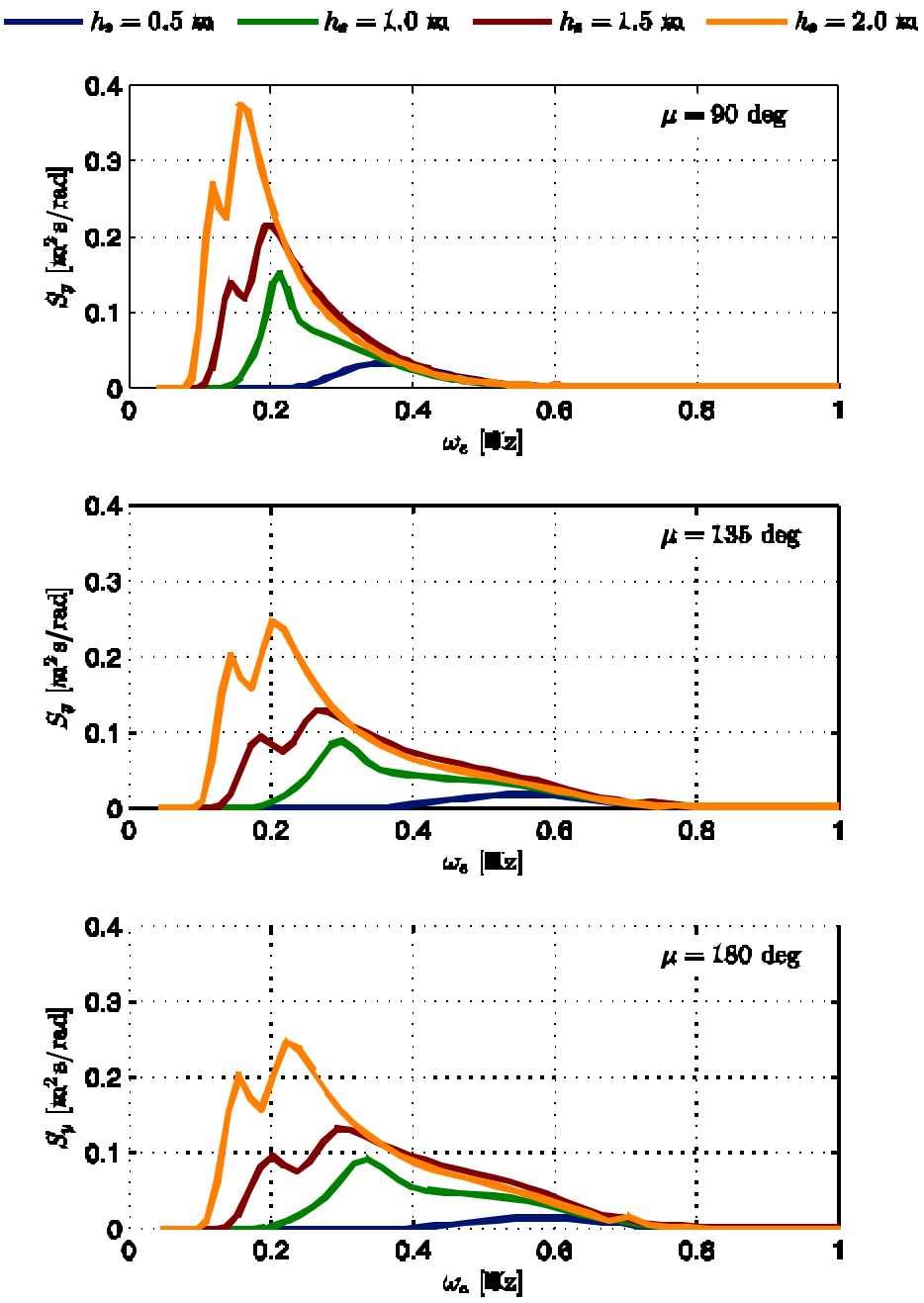

Fig. 10. Energy spectrum of vertical oscillations at the generator's location at speed V = 8 knt.

Table 3. Yacht's significant vertical oscillation amplitudes at the bow generator's location.

	y_{0s} [m]					
	V = 5 knt			V = 8 knt		
H_s [m]	μ = 90 deg	μ = 135 deg	μ = 180 deg	μ = 90 deg	μ = 135 deg	μ = 180 deg
0.5	0.433	0.383	0.322	0.405	0.366	0.318
1.0	0.721	0.684	0.688	0.680	0.697	0.732
1.5	0.980	0.943	0.967	0.937	0.964	1.024
2.0	1.147	1.127	1.175	1.120	1.152	1.233

4. Linear oscillator

4.1. General remarks

The linear generator that will be used in the SEAKERS device to recover energy from the wave-induced motions of the yacht is analysed and approximated in this paper as a simple linear mechanical oscillator, where the damping element represents a linear approximation of the effect of the electromagnetic force exerted by the generator as it provides a voltage difference proportional to the square of its relative velocity with respect to its basement, and the spring represents the stiffness of the generator's support. It is further assumed that the damping coefficient can be dynamically varied depending on sea conditions: this could be achieved in the final system by means of a variation of some electrical parameters in the associated circuit. The equation of motion is thus:

$$m\ddot{x} + c(\dot{x} - \dot{y}) + K(x - y) = -mg + F_s \qquad (36)$$

where m is the generator's mass, x its position in an inertial frame of reference, y is the basement's position, c is the damping coefficient, K the spring's stiffness, g the acceleration of gravity, F_s a static force provided by the support in order to balance the weight mg such that $F_s = mg$.

It is assumed here that the support can exert such a static force in order to balance the mass' weight; it can be seen that mechanical springs alone cannot play such a role, because the resulting stiffness would be too high for the typical forcing frequencies. Indeed, if the spring were to counterbalance the weight with a limited elongation at rest l = 0.05 m, the resulting natural frequency would be $\omega_n = \sqrt{g/l} \approx 2.2$ Hz, which is much larger than the forcing frequency of sea waves: as the following section explains, this would make the system too stiff, i.e. the mass would move rigidly with the basement, with no relative motion between the two and, thus, no power extracted.

Equation (36) can thus be rewritten eliminating all static forces and introducing the relative position $s = x-y$ of the mass in a frame of reference moving with the basement:

$$m\ddot{s} + c\dot{s} + Ks = -m\ddot{y} \qquad (37)$$

which becomes the well-known second order ordinary differential equation for an oscillating body:

$$\ddot{s} + 2\beta\omega_n\dot{s} + \omega_n^2 s = -\ddot{y} \qquad (38)$$

with the introduction of the natural frequency of the oscillator:

$$\omega_n = \sqrt{K/m} \qquad (39)$$

and of the damping ratio:

$$\beta = c/\left(2\sqrt{Km}\right) = c/(2m\omega_n) \qquad (40)$$

4.2. Response to sinusoidal waves

The steady-state response of the linear mechanical system to a harmonic forcing of the type $y(t) = y_0 \exp(i\omega_e t)$ is itself harmonic:

$$s(t) = \sigma_0 \exp(i\omega_e t) \qquad (41)$$

with a complex amplitude σ_0 given by:

$$\frac{\sigma_0}{y_0} = \frac{n^2}{n^2 - 1 - i\,2\beta n} \qquad (42)$$

where n is the ratio of forcing and natural frequency:

$$n = \omega_e/\omega_n \qquad (43)$$

The magnitude of σ_0 gives the amplitude s_0 of the harmonic motion of the generator (fig. 11, top), and its ratio with the ship's oscillation amplitude is the response amplitude operator for the generator's relative motion:

$$\frac{s_0}{y_0} = \mathrm{RAO}_s(\beta, \omega_n, \omega_e) = \frac{n^2}{\sqrt{(1-n^2)^2 + (2\beta n)^2}} \qquad (44)$$

while its argument α gives the phase of the generator's motion with respect to the forcing oscillation (fig. 11, bottom):

$$\alpha = \arctan\frac{2\beta n}{n^2 - 1} \qquad (45)$$

The resulting harmonic motion can therefore be expressed as:

$$s(t) = s_0 \exp(i\omega_e t + \alpha) \qquad (46)$$

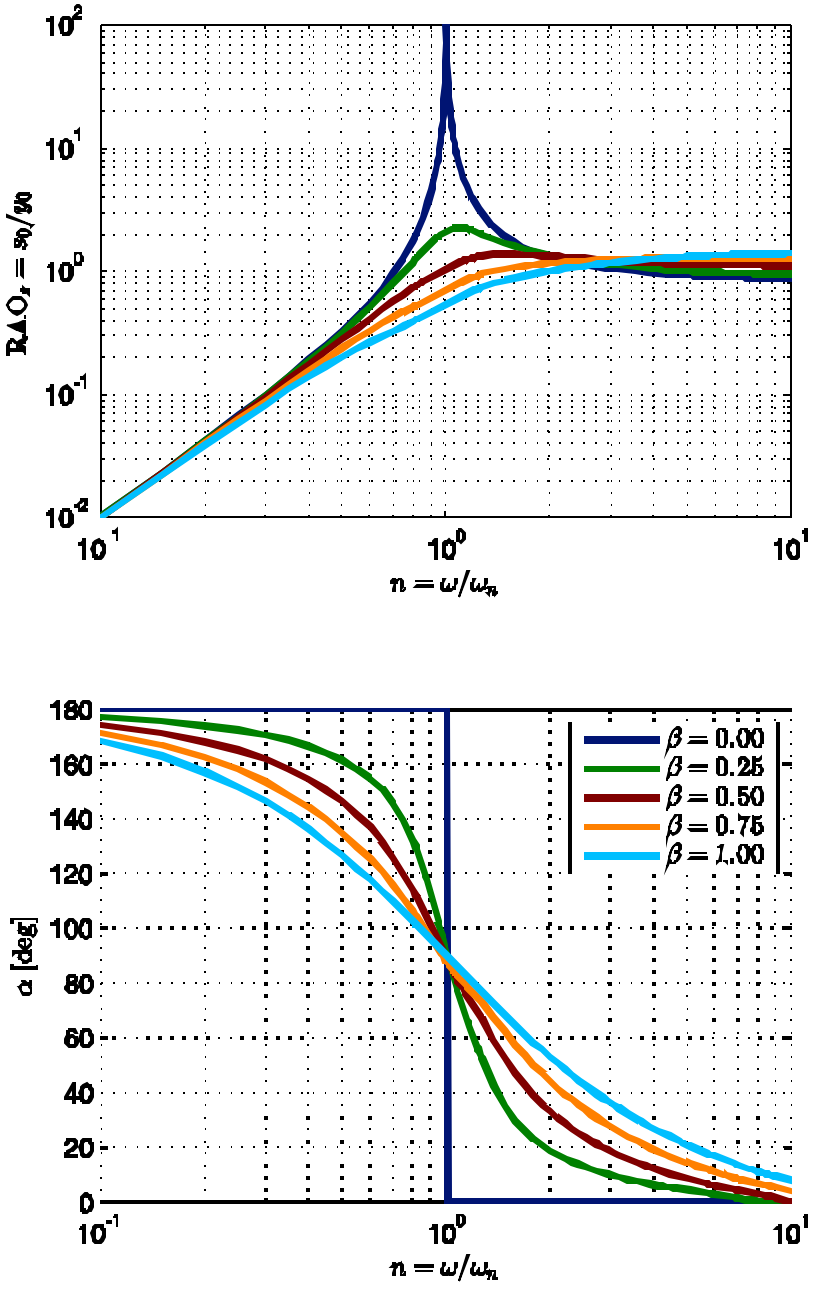

Fig. 11. Frequency response of the harmonic oscillator: amplitude (top) and phase (bottom).

In this model, damping the oscillations in the linear mechanical system provides the mean to extract energy from the wave excitation; thus, it is interesting to identify optimal values for the damping coefficient c in order to extract the maximum power. The power absorbed is given by:

$$P(t) = c\dot{s}^2 \tag{47}$$

and its average value over one cycle (which will be indicated as Π) is:

$$\Pi = \frac{1}{T}\int_0^T P(t)\mathrm{d}t = \frac{1}{2}c\omega_e^2 s_0^2 \tag{48}$$

the above expression, taking into account (40) and (44), becomes:

$$\Pi = m\omega_e^3 y_0^2 \frac{n^3\beta}{\left(1-n^2\right)^2 + \left(2\beta n\right)^2} \tag{49}$$

Since the oscillations are constrained by the size of the generator, two different scenarios must be considered. In the first one, let us imagine that the undamped oscillations do not reach the maximum range allowed s_{max}: in this case, increasing the damping coefficient from 0 initially yields higher values of Π even though s_0 decreases according to (44), until a maximum for Π is reached, beyond which it decreases. The optimum value of β can thus be found when $\mathrm{d}\Pi/\mathrm{d}\beta = 0$:

$$\beta_{\mathrm{opt}} = \frac{1}{2}\frac{\left|1-n^2\right|}{n} \tag{50}$$

with corresponding optimum damping coefficient, maximum average power and oscillation amplitude given by:

$$c_{\mathrm{opt}} = m\omega\left|1-\frac{1}{n^2}\right| \tag{51}$$

$$\Pi_{\max} = \frac{1}{4}m\omega_e^3 y_0^2\left|1-\frac{1}{n^2}\right|^{-1} \tag{52}$$

$$s_0 = y_0\frac{1}{\sqrt{2}}\left|1-\frac{1}{n^2}\right|^{-1} \tag{53}$$

In the second case, the undamped oscillations would be larger than the maximum allowed range s_{max}: then it is possible to extract more power by increasing the damping coefficient while the oscillation amplitude y_0 remains at its maximum permissible level s_{max}. It is possible to show that the maximum power is obtained when the damping coefficient is such that the oscillation given by (44) is exactly equal to the stroke ($s_0 = s_{max}$):

$$\beta_{\mathrm{opt}} = \frac{n}{2}\sqrt{\left(\frac{y_0}{s_{\max}}\right)^2 - \left(1-\frac{1}{n^2}\right)^2} \tag{54}$$

$$c_{\mathrm{opt}} = m\omega\sqrt{\left(\frac{y_0}{s_{\max}}\right)^2 - \left(1-\frac{1}{n^2}\right)^2} \tag{55}$$

and the corresponding maximum average power is:

$$\Pi_{\max} = \frac{1}{4}m\omega_e^3 s_{\max}^2\sqrt{\left(\frac{y_0}{s_{\max}}\right)^2 - \left(1-\frac{1}{n^2}\right)^2} \tag{56}$$

If the mechanical system is "tuned" to the forcing wave condition ($n \cong 1$), then the above expression can be simplified as follows:

$$\Pi_{max} \cong \frac{1}{4} m \omega_e^3 s_{max} y_0 \quad \text{if } n \cong 1 \tag{57}$$

It is possible to find out which wave excitations make the system reach its maximum stroke s_{max} by setting the oscillation amplitude given by (53) equal to s_{max}, yielding:

$$\frac{y_0}{s_{max}} = \sqrt{2}\left|1 - \frac{1}{n^2}\right| \tag{58}$$

Thus, for wave amplitudes originating boat oscillations lower than the limit set by the above equation, the system oscillates "freely" and equations (51)-(53) apply, while for higher waves more damping, and thus more power, is available, in order to constrain the system within the maximum stroke allowed, and (55)-(56) apply.

It is worth to point out that in both cases the optimum value for the damping coefficient is directly proportional to the oscillator's mass and to the forcing frequency: the average power absorbed is therefore proportional to mass m and to the third power of forcing frequency (ω_e^3), as shown by (52) and (56).

In particular, the linear dependence on the oscillating mass m is, on the one hand, almost obvious because energy recovery depends on inertia and kinetic energy, but on the other hand it is an important property to be taken into account because it allows to design, test and prototype modular systems of relatively low mass, with the overall power extracted given by the sum of power available from different modules. For this reason, the results discussed in section 4.4 will be given with reference to a unit mass m = 1 kg.

4.3. Response to random waves

The frequency response of the harmonic oscillator can also be used when the external forcing is not harmonic (as in the case of real wave excitation): if $S_y(\omega_e)$ is the energy spectrum associated to the vertical oscillations of a particular point of interest, which can be evaluated from the wave energy spectrum by means of (34), then the energy spectrum associated to the relative motion s of a linear system such as the one described in the previous section is given by:

$$S_s(\beta, \omega_n, \omega_e) = \mathrm{RAO}_s(\beta, \omega_n, \omega_e)^2 S_y(\omega_e) \tag{59}$$

In the following considerations the dependence of relative motion and its spectrum on natural frequency ω_n will be implicitly assumed, so that $S_s(\beta,\omega_e) \equiv S_s(\beta,\omega_n,\omega_e)$.

The spectrum of relative motion allows the evaluation of the *significant oscillation amplitude* as follows:

$$s_{0s} = 2\sqrt{m_{0s}} = 2\sqrt{\int_0^\infty S_s(\beta, \omega_e)\mathrm{d}\omega_e} \tag{60}$$

Since power generation depends on the square of the generator's velocity (47), the energy spectrum related to relative velocity must be introduced. This is simply given by:

$$S_{\dot{s}}(\beta, \omega_e) = \omega_e^2 S_s(\beta, \omega_e) = \omega_e^2 \mathrm{RAO}_s(\beta, \omega_e)^2 S_y(\omega_e) \tag{61}$$

The 0-th moment of the velocity spectrum gives velocity's root mean square (RMS), which is related to average power generation:

$$\dot{s}_{\mathrm{RMS}}(\beta) = \sqrt{m_{0\dot{s}}} = \sqrt{\int_0^\infty S_{\dot{s}}(\beta, \omega_e)\mathrm{d}\omega_e} \tag{62}$$

$$\Pi_{\mathrm{RMS}}(\beta) = \frac{c}{m}\dot{s}_{\mathrm{RMS}}(\beta)^2 = 2\beta\omega_n \dot{s}_{\mathrm{RMS}}(\beta)^2 \qquad (63)$$

As in the case of sinusoidal waves, for a given natural frequency the generator's motion depends on the choice of the damping coefficient β, for which an optimum value is found by maximizing power output (63) with the constraint that the significant oscillation amplitude is lower than the maximum allowed range $s_{\max}$ (for this non-linear optimization procedure the MATLAB® function `fmincon` has been used):

$$\left.\frac{\mathrm{d}\Pi_{\mathrm{RMS}}}{\mathrm{d}\beta}\right|_{\beta_{\mathrm{opt}}} = 0 \quad \text{with} \quad s_{0s}(\beta_{\mathrm{opt}}) \le s_{\max} \qquad (64)$$

4.4. Simulation results

In this section, results obtained with the mechanical model of the linear generator subject to random wave excitations for two different speeds (V = 5 knt and V = 8 knt) are discussed. As detailed in section 3.3, the yacht's oscillation is described by energy spectra represented in figs. 9 and 10.

The maximum stroke taken into consideration in the simulations is $s_{\max}$ = 0.5 m, since this value is about the highest possible on sail yachts of length from 10 to 14 m, which are the main target for the SEAKERS project. The natural frequency ω_n is taken as 0.25 Hz, in order to make the mechanical system almost resonant with most sea conditions that may be encountered.

Figures 12 and 13 show the energy spectra associated to the generator's relative motion and RMS power generation for different speeds and directions. Power generation values are also given in table 4, while table 5 gives calculated values of significant oscillation amplitudes.

From table 5 it is possible to see that for wave heights higher than 0.5 m, the generator's oscillation is always limited to the maximum range $s_{\max}$: in order to analyze the results, it is thus useful to consider the simplified equation for average power generation (57), which shows that, if the mechanical system is "tuned" to the forcing wave condition ($n \cong 1$), average power is proportional to the third power of the encounter frequency, and to the product of boat's vertical oscillation y_0 and maximum range $s_{\max}$.

Therefore, an increase in significant wave height gives rise to two opposite effects on power generation: on the one hand it increases due to its dependence on y_0, but on the other hand the wave energy spectrum shifts towards lower frequencies (fig. 1), resulting in a decrease in power generation. Clearly, this gives rise to a maximum power generation for a particular sea state, that under the assumptions taken into account in this paper correspond to a significant wave height of 1.5 m, as figs. 12 and 13, along with table 4 show.

In other words, even with high values of significant wave height, which correspond to rather low values of peak frequencies (table 1), if the full spectrum is taken into account significant contributions to the excitation can be found also at frequencies higher than the peak one, and these contributions increase average velocities and, consequently, power generation. Nonetheless, it is still possible to find that increasing wave heights beyond a certain threshold decreases the power output, because in this case significant contributions can indeed be found only at low frequencies.

Tables 6 and 7 report values of optimum damping coefficients and damping ratios as defined by the optimization procedure (64).

Table 4. Average power generation.

	Π_{RMS}/m [W/kg]					
	V = 5 knt			V = 8 knt		
H_s [m]	μ = 90 deg	μ = 135 deg	μ = 180 deg	μ = 90 deg	μ = 135 deg	μ = 180 deg
0.5	0.552	0.401	0.247	0.500	0.352	0.230
1.0	0.617	0.620	0.546	0.572	0.644	0.630
1.5	0.753	0.807	0.721	0.704	0.852	0.848
2.0	0.664	0.715	0.656	0.619	0.757	0.789

Table 5. Significant oscillation amplitudes for the linear mechanical system.

	s_{0s} [m]					
	V = 5 knt			V = 8 knt		
H_s [m]	μ = 90 deg	μ = 135 deg	μ = 180 deg	μ = 90 deg	μ = 135 deg	μ = 180 deg
0.5	0.500	0.332	0.281	0.477	0.303	0.263
1.0	0.500	0.500	0.500	0.500	0.500	0.500
1.5	0.500	0.500	0.500	0.500	0.500	0.500
2.0	0.500	0.500	0.500	0.500	0.500	0.500

Table 6. Optimum damping coefficients.

	c/m [N s/(m kg)]					
	V = 5 knt			V = 8 knt		
H_s [m]	μ = 90 deg	μ = 135 deg	μ = 180 deg	μ = 90 deg	μ = 135 deg	μ = 180 deg
0.5	1.522	2.709	2.724	1.469	3.142	3.228
1.0	2.410	2.729	2.816	2.232	3.036	3.413
1.5	3.096	3.665	3.851	2.894	4.139	4.725
2.0	3.107	3.732	4.017	2.934	4.223	4.922

Table 7. Optimum damping ratios.

	β					
	V = 5 knt			V = 8 knt		
H_s [m]	μ = 90 deg	μ = 135 deg	μ = 180 deg	μ = 90 deg	μ = 135 deg	μ = 180 deg
0.5	0.484	0.862	0.867	0.468	1.000	1.027
1.0	0.767	0.869	0.896	0.710	0.967	1.086
1.5	0.986	1.167	1.226	0.921	1.317	1.504
2.0	0.989	1.188	1.279	0.934	1.344	1.567

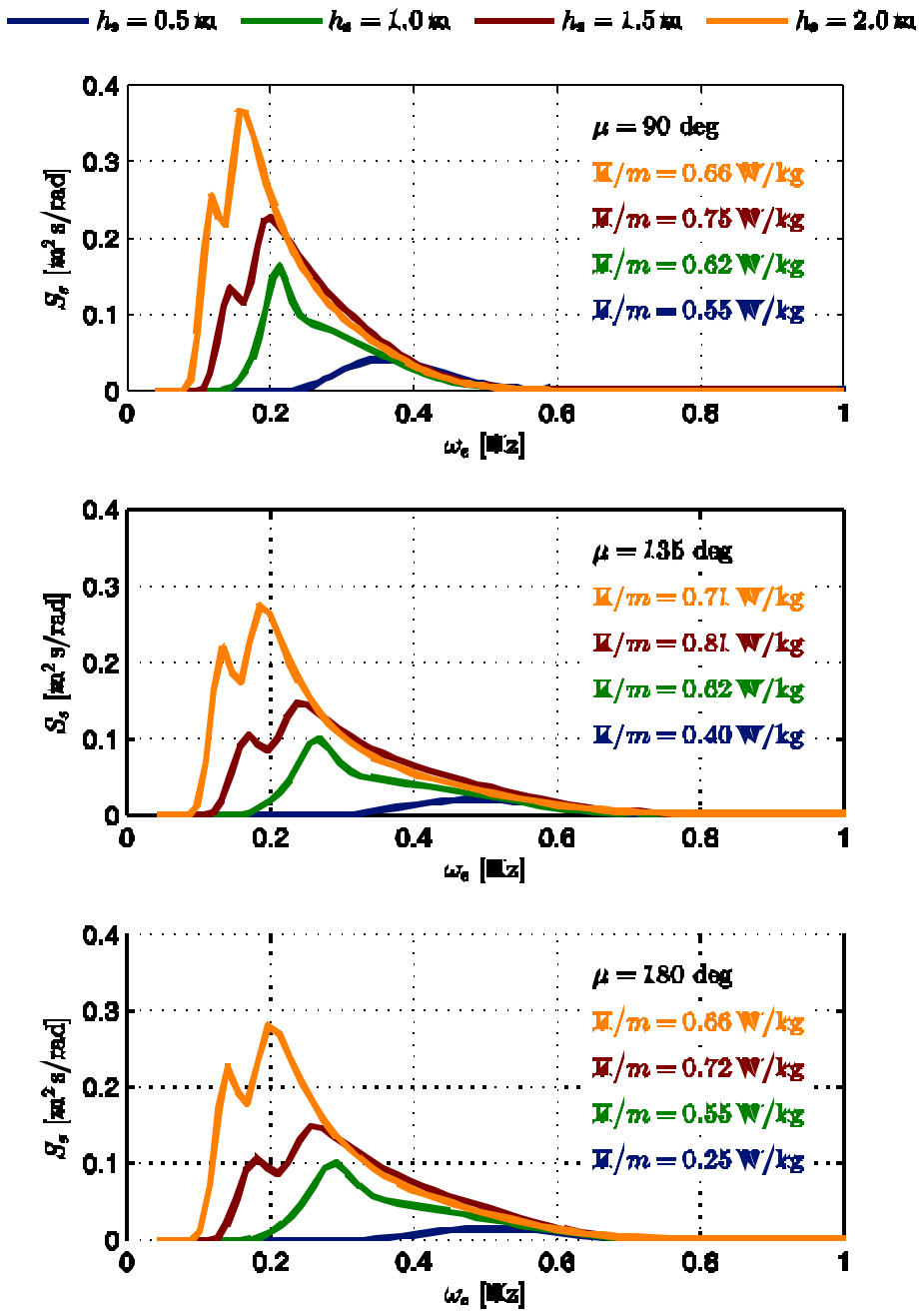

Fig. 12. Energy spectra associated to the linear mechanical system's motion at speed V = 5 knt.

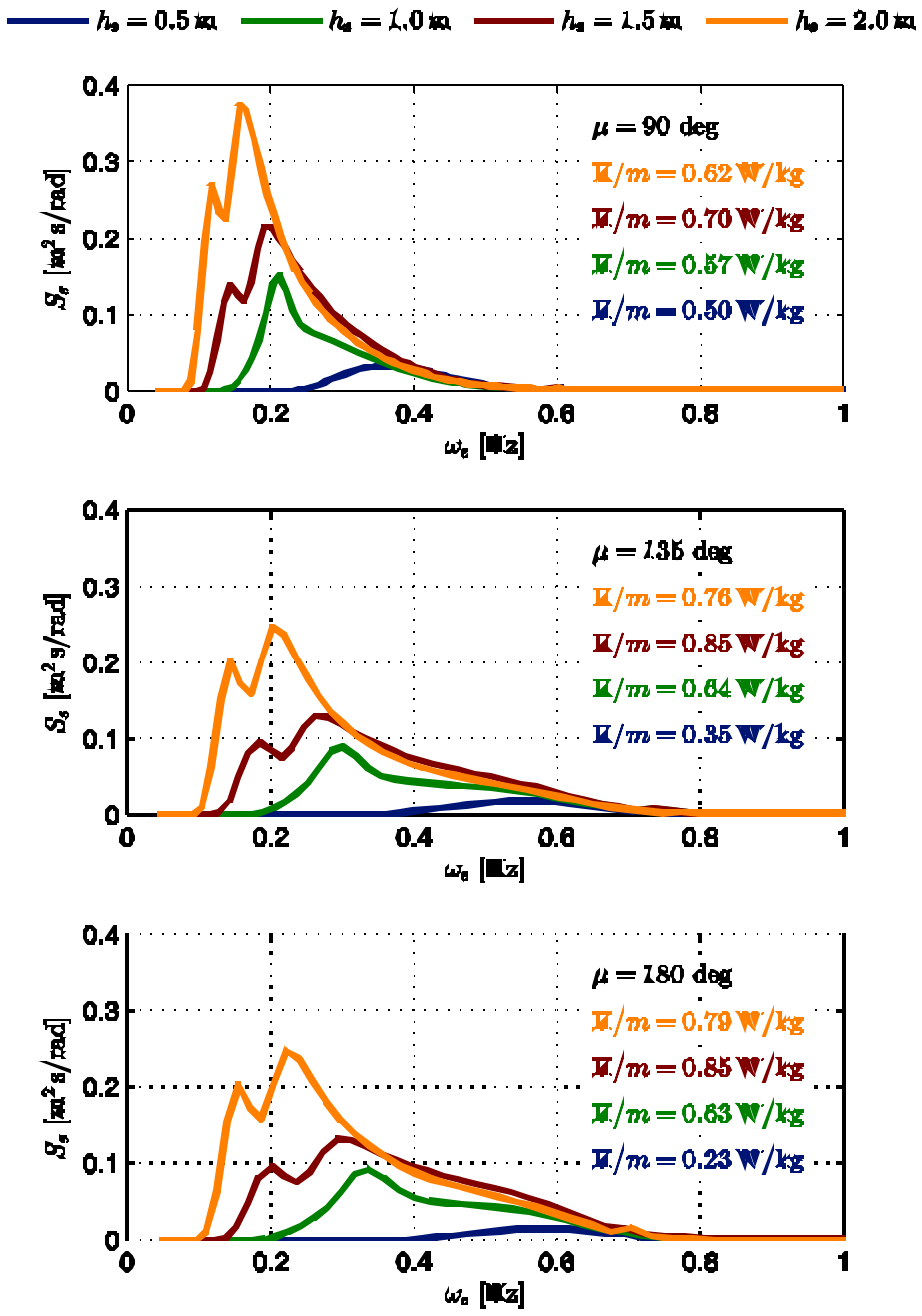

Fig. 13. Energy spectra associated to the linear mechanical system's motion at speed V = 8 knt.

5. Conclusions

This paper has provided an overview of the results obtained with the kinematic and mechanical models of the yacht's response to different wave excitations, and of the linear generator taken as a simple mechanical linear system which extracts power from the wave-induced motion by means of an ideal linear damping.

These preliminary evaluations, even though based on a rather simplified model of the generator, have produced some important insights on system dynamics and on the range of values to be assigned to several significant parameters, such as mechanical stiffness and damping ratio.

In particular, given the particular range of forcing frequencies, the mechanical stiffness must be chosen so as to obtain a natural frequency within the range of most forcing frequencies: a value of 0.25 Hz has been considered in this paper, with a resulting stiffness around 2.5 N/(m kg).

The choice of damping ratios is based on the maximisation of power output for a given natural frequency for different wave excitation conditions. Values of damping coefficients in the range 1.5-5.0 N s/(m kg) have been found, and this result will be useful in the definition of the electric circuit's physical parameters associated to the linear generator.

Power generation of up to 0.85 W/kg have been obtained in the most favourable sea conditions, and anyway values higher than 0.5 W/kg are available in most cases, which represent an interesting result for this particular application. Indeed, a total weight for the SEAKERS device of up to 200 kg can be considered acceptable on sail yachts with length in the range 12-14 m, especially in the case of a first equipment (as opposed to retrofitting an already existing yacht, because in this case many more design constraints should be addressed). With an optimized design, it is conceivable from preliminary evaluations that up to 50% of this weight (100 kg) could be allocated to the oscillating masses; in this case, an average power generation of almost 100 W is feasible, which could make possible to recover at least 1 kWh at the end of a day-long cruise. This amount of energy generation could indeed be interesting for this particular application.

Obviously, the issue related to the influence of this moving mass on sailing performance should be addressed: but specific calculations, which have not been reported here for brevity's sake, show that the inertial forces generated by the mass' motion are at least two orders of magnitude lower than the forces exerted by the sea on the boat. After all, this must be the case because the energy absorbed by the linear system is but a small fraction of the total energy of the incoming waves. Therefore, in all probability the impact of the added mass due to the generator on sailing performance can be safely deemed negligible.

It should be observed that the concept of "power availability" (or "availability factor") routinely used to appreciate the performance of a system based on renewable energy, is much less useful for this particular application, because the final goal is not the generation of electricity *per se* on a continuous basis but, rather, only on the particular occasion when the yacht is used for a cruise. An availability factor should therefore be considered only with reference to a single cruise, and it would take into account the time frequency of encountered wave height during a typical cruise of a sailing boat, because this is the main parameter influencing average power output. However, it is rather difficult to make any prediction about this probability, other than saying that sail cruises are most common when wind (and, consequently, wave) conditions are not extreme (i.e. with moderate winds and waves, while it is safe to assume that calm or stormy seas are avoided); furthermore, a leisure cruise usually requires stable weather conditions. In the end, it is reasonable to infer that in most cases sea conditions encountered on a leisure cruise are reasonably constant and marked by a significant wave height within the range 0.5-1.5 m. Under these assumptions, average power generation is expected to be almost constant during the whole cruise.

The next activities in the SEAKERS project will be focused on the implementation of a non-linear electro-mechanical model of the generator, in order to define suitable ranges for the most important

electrical parameters in the system, and to narrow down the set of possible runs of the more detailed 2D and 3D models that have been set up.

Acknowledgments

The research leading to these results has received funding from the European Union Seventh Framework Programme (FP7/2007-2011) under grant agreement n° 262591. The authors would also like to acknowledge the invaluable effort provided by all the staff of Labor srl, the projects' coordinator, as well as the contribution of the SMEs and RTD performers involved in the project.

References

[1] Ivanova I.A., Bernhoff H., Ågren O., Leijon M., Simulated generator for wave energy extracction in deep water. Ocean Engineering 2005;32(14-15):1664-1678.

[2] Thorburn K., Leijon M., Farm size comparison with analytical model of linear generator wave energy converters. Ocean Engineering 2007;34(5-6):908-916.

[3] Eriksson M., Isberg J., Leijon M., Hydrodynamic modelling of a direct drive wave energy converter. International Journal of Engineering Science 2005;43(17-18):1377-1387.

[4] Leijon M., Danielsson O., Eriksson M., Thorburn K., Bernhoff H., Isberg J., Sundberg J., Ivanova I., Sjöstedt E., Ågren O., Karlsson K.E., Wolfbrandt A., An electrical approach to wave energy conversion. Renewable Energy 2006;31(9):1309-1319.

[5] Bertram V., Practical ship hydrodynamics, Oxford, UK: Butterworth-Heinemann; 1999.

[6] Biran A., Ship hydrostatics and stability, Oxford, UK: Butterworth-Heinemann; 2003.

[7] Jensen J.J., Load and global response of ships, Oxford, UK: Elsevier; 2001.

[8] Rawson K.J., Tupper E.C., Basic ship theory, Oxford, UK: Butterworth-Heinemann; 2001.

[9] Perez N.A., Sanguinetti C.F.O., Scale model tests of a fishing vessel in roll motion parametric resonance. Síntesis Tecnológica 2006;3(1):33-37. ISSN 0718-025X. Available at <http://mingaonline.uach.cl/scielo.php?pid=S0718-025X2006000100004&script=sci_arttext>.

[10] Salvesen N., Tuck O.E., Faltinsen O., Ship motions and sea loads. Transactions, Society of Naval Architects and Marine Engineers 1970;78:250-287.

[11] Formation Design Systems Ltd. Seakeeper Manual – Available at: <www.formsys.com/extras/FDS/webhelp/seakeeper/skmanual.htm> [accessed 3.2.2012].

Mirrors in the sky: Status and some supporting materials experiments

Noam Lior

University of Pennsylvania, Philadelphia, USA, lior@seas.upenn.edu

Abstract:
This paper critically reviews the state of the art of an approach to supply energy to earth from space mirrors that would be placed in orbit with angle control to reflect solar radiation to specific sites on earth for illumination. These mirrors would be of the order of a square kilometer or more, planned to be made of thin plastic reflective films, which are launched to some optimal orbit around the Earth. One could, for example, thereby provide night or emergency illumination to cities and other locations, or illuminate agricultural production areas to lengthen the growing season, or to illuminate photovoltaic or thermal collectors on earth for producing electricity or heat. Proposals were also made for using such mirrors for weather modification, and we added here the possibility of using the space mirrors for shading the earth to reduce global warming. Experiments with space mirrors were conducted in the past by the former Soviet Union. In addition, thin film aluminized Kapton mirrors were manufactured and optically an mechanically tested to examine their property changes when exposed to a cryogenic temperature, an economic analysis related to several applications was performed, and leading issues that must be taken into account in the sustainability analysis of the concept were described. Our experiments with thin film mirror have shown that the reflectance at 77K is always higher (about 1.7 fold) than that at 300K, and the ultimate tensile strength and modulus increased at the cryogenic temperature. Without (yet) consideration of environmental and social impact externalities, our economic analysis agrees with past studies that if transportation costs to mirror orbit are reduced to a few hundred $/kg, as planned, the use of orbiting space mirrors for providing energy to earth is an investment with a good rate of return and a cost effective alternative to other power sources. This energy concept is very appealing relative to other options for addressing the severe energy and global warming problems that we face, and deserves much and urgent R&D attention.

Keywords:
Space mirrors, Space energy, Solar mirrors, Mirrors, Cryogenic mirrors, Illumination

1. Objectives and general background

This paper critically reviews the status and potential of space-based solar mirrors that reflect solar energy (light) for use on earth, as well as our experiments with manufacturing and testing a prototype thin-film mirror intended for that purpose.

Escalating problems of energy, environment and increased and more demanding population make it increasingly difficult to generate power, heat, light and food on earth [1,2]. As described in the publications by Glaser and co-workers (e.g. [3,4]), Mankins [5,6], Criswel and co-workers [7], Brown [8], Woodcock [9], NASA [10], Lior and co-workers [11-13] and many others. Space has many desirable attributes for serving as the location for supplying energy to earth by constructing space satellite or moon-based power generation stations where the power is beamed to earth by microwave or laser for use. This topic has received significant support by the U.S. NASA during the late 1970-s till the early 1990-s, and beginning somewhat later but to some extent still continuing by several European countries and Japan. A web site of the National Space Society [14] keeps at this time a record of developments, an important recent update report "Space Solar Power: The First International Assessment of Space Solar Power: Opportunities, Issues and Potential Pathways Forward" edited by Mankins and Kaya having been published in 2011 [6].

The other space energy approach, which is the subject of this paper, is the construction and deployment of space mirrors that would be placed in orbit with orbit, angle and altitude control to reflect solar radiation to specific sites on earth for illumination. These mirrors would be very large,

typically of the order of a square kilometer or more each, highly reflective, planned to be made of thin plastic reflective films to minimize weight and cost, mounted in an appropriate light frame. They would be launched to one or more orbits around the earth. One could, for example, thereby provide night illumination to cities and other locations and for emergency lighting, or provide sunshine for agricultural production in some areas to enable or lengthen the growing season, or for applications such as crop drying ad water desalination, or to illuminate photovoltaic (PV) and thermal collectors (including salt-gradient solar ponds) on earth for producing electricity or for heating. This approach was originally briefly proposed by the space science pioneer H. Oberth in 1928 [15]. This concept seems to have laid dormant and was then advanced most notably by Buckingham and Watson (in 1968, 60 years later [16]), NASA (Billman, Gilbreath and Bowen) [17-19], Ehricke [20-22], and others [23-25]. The review portion in this paper relies strongly on [16-21] in recognition of the pioneering work of these authors.

When considering space power generation, the major advantages of the space mirrors approach are: (1) instead of PV collectors on the energy source spacecraft there are only mirrors (optical reflectors), planned to be made from very thin film coated polymers (microns thick); (2) the energy is transmitted directly to earth in the form of solar light, without need for conversion of the collected solar energy to microwave or laser beams and their transmission through the atmosphere to earth; (3) sunlight is less threatening environmentally than the transmission of microwave or laser radiation; (4) no requirement for power management and distribution or thermal management systems on the spacecraft; (5) constructed of light thin (μm order) films, mirrors are easier to bring to orbit and deploy than the equivalent PV cells; (6) if used for power generation, it would probably need smaller collector and energy conversion fields on earth because of the safety-dictated need to make microwave beams diffuse when PV satellites are used; (7) no need for technical energy conversion systems on earth when the reflected sunlight is used for lighting, agriculture or bio-enrichment. There are, however, also a number of significant technical challenges: (1) the reflected sunlight arriving at the earth surface is more subject to the effects of weather, such as overcast, haze and atmospheric refraction, than microwave or laser beams; (2) amounts of sunshine reflected to earth that are sufficient to help supply significant fractions of needed global energy, and to be commercially viable, would require very large (order of 1 km^2 or more) mirrors, that must be optically flat (to a fraction of a wavelength of light) over these huge areas, and durable both mechanically and optically; (3) environmental effects, such as associated glitter and other "light pollution". These challenges have contributed to the fact that significantly less has been done so far, or planned to be done, on space mirrors, when compared with PV solar satellites.

A significant albeit brief step in the development of space mirrors was the Russian Space Mirror Project "Znamya" (banner) developed by the "Space Regatta Consortium" (SRC) [24] established in 1990 by the Russian space agency and the corporation Energia [26] (which specializes in space and launch vehicles and rocket boosters). The purpose of SRC in project Znamya, according to their official website, was the development of thin sheet technologies for solar reflection and solar sails and then for illuminating high latitude earth regions during winter months.

Detailed information about the Znamya experiments (Fig. 1) is somewhat sparse [24,26-28] , and the following is available. The first SRC to be tested in space was "Znamya-2", on February 4, 1993. The mirror was a 20 m diameter circular 5 μm-thick aluminized PETF (Mylar) film, with an estimated aerial density of 22 g/cm2 that was composed of 8 sections with radial gaps between them. It was installed together with the unfolding mechanism inside the docking compartment of the cargo space vehicle Progress M-15 which disengaged from the MIR space station. The deployment test was successful. According to the SRC website, the spot of light produced by the mirror was about 5 km in diameter and moved across the earth's surface (starting in France and through Eastern Europe and Asia) at a speed of around 8 km/s. The brightness of the mirror as seen from the earth was reported to have been similar to that of a single full moon (<1 lux).

"Znamya 2.5" was the second attempt to launch a space mirror, as a continuation of SRC's space

reflector experiments that hopefully will lead to the deployment of 200-m-diameter reflectors. The reflector was 25-m-diameter and was constructed of materials and design similar to Znamya 2. Deployment of Znamya 2.5 was attempted on February 4, 1999. As the sail unfurled it collided with and wrapped around the docking antenna, and the whole apparatus crashed into the ocean. Since then, there have been no attempts to launch a solar mirror. The Znamya experiments received much attention from the media, including criticisms about light pollution that such space mirrors may create [29-31].

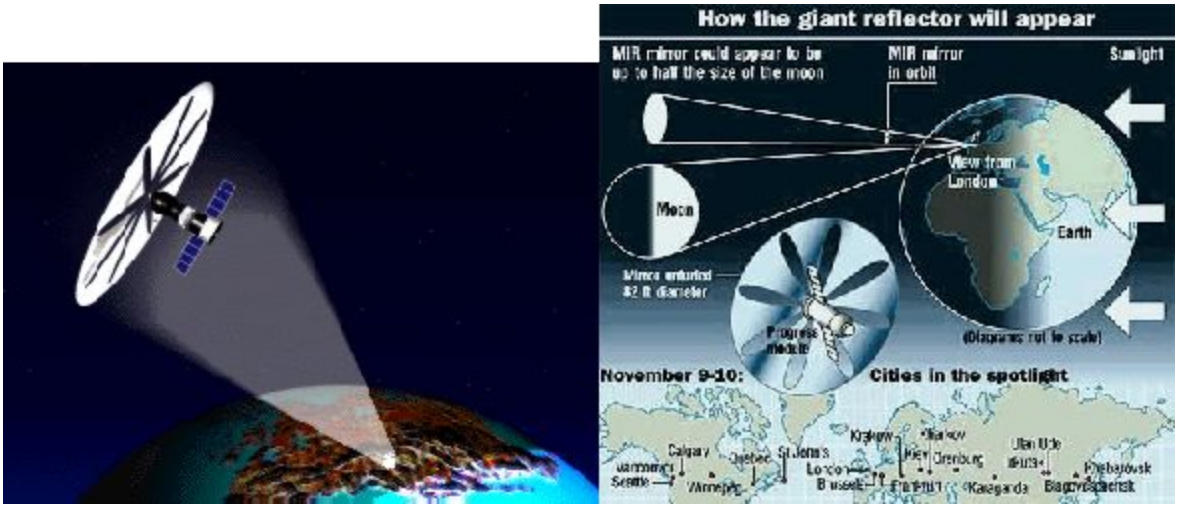

a. *b.*

Figure 1. Artists' illustrations of the Znamya Solar Reflector a. [24], b. [27]

It appears that NASA has dedicated very small resources to research and development of space-based solar mirrors. It did perform some fundamental studies describe in Section 3 below and performed some slightly related experiments [32,33].

In the rest of the paper we show the basic equations for molar light reflection to earth, the different space mirror system concepts proposed, reflector configurations, energy considerations, our work on mirror materials and coatings, system economics and system sustainability considerations.

2. A few key equations for space mirrors [16-19,21]

The basic reflection optics are shown in Fig. 2.

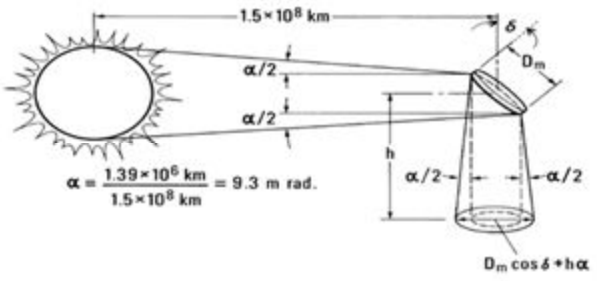

Fig. 2 The illuminated ground area as a function of the space mirror orbit altitude h [17].

For mirrors of diameters considered in the studies so far, the illumination I_e at the earth's surface by a space reflector in terms of solar illuminance I_s. reflectance ρ, cloudiness factor C ($C = 1$ for cloudless sky), reflecting area A_r (of single or cluster of reflectors), angle of incidence δ between the

reflected beam and the illuminated earth spot, and angle θ at the reflector between the incident and reflected light beam, is given by

$$\frac{I_e}{I_s} = \rho C \frac{A_r}{A_e} f(\varepsilon) \cos\delta \cos\frac{\theta}{2} \tag{1}$$

where $f(\varepsilon)$ is a function representing the intensity extinction, due to haze and zenith distance (that increases the beam's path length through the atmosphere) and ε is the elevation angle of the reflector above the horizon; for $\varepsilon = 0^0$, $f(\varepsilon) = 1$.

Equation (1) shows that he earth spot illumination intensity (I_e) increases in proportion to the reflector area (A_r).

If the solar reflector is above the atmosphere, as typically planned for such space mirrors, the solar radiation intensity at the reflector is at the atmosphere's edge, I_{sc} the Luminous Solar Constant is 133,334 lx or 134,108 lx and the Solar Constant = 1,366.1 kW/m². If it is within the atmosphere, the illuminance I_s at the reflector is diminished by effects of air molecules, dust and water vapor along the beam path, with this diminution expressed by C_o, the overall coefficient of absorption ad reflection in a cloudless atmosphere, so

$$\frac{I_s}{I_{sc}} = C_o \tag{2}$$

The image area on the earth of an orbiting mirror of area A_r positioned at a height h above that image is expressed by

$$\begin{aligned} A_e &= A_r + \frac{\pi}{4}(\alpha h)^2 \quad \text{for a non-focusing reflector, and} \\ A_e &= \frac{\pi}{4}(\alpha h)^2 \quad \text{for a focusing reflector or point sources} \end{aligned} \tag{3}$$

where α is the angular subtense of the Sun, α = 1.39xl0^6 km/l.5xl0^8 km = 9.27 mrad, $h = r - r_{earth}$, r is the radial distance between the orbiting mirror and the center of the earth, and r_{earth} is the earth radius. The area illuminated on the ground is an ellipse with major axis ($D_m + \alpha h \cos\delta$) and minor axis ($D_m + \alpha h$). Equation (3) shows that the illuminated earth area becomes gradually independent of the reflector area as the orbit altitude increases.

Very significantly, the overall reflectance of the mirror depends not only the surface specular reflectance but also on its flatness to within a small fraction of the sun's angular diameter *a*. This means that all parts of the mirror's surface must point in the same direction to within 1 or 2 mrad.

The reflector diameter influences the sharpness of the image. For a reflector of diameter D_r, the earth spot image will have a penumbra region of shadow of the same diameter, which thus does not practically affect the spot size.

For a synchronous orbit of h = 22,400 miles (36,049 km), the diameter of the illuminated spot on earth is then 208 miles (~335 km). Obviously, if a smaller illumination area is needed the satellite can be placed in lower orbits but then, as shown by Eq. (4), the illumination will take place for shorter periods of time. This can be remedied by using a number of mirrors in the same or similar orbits.

The period of a satellite (T) and the mean distance from the earth (h) are related by the

$$\text{equation: } T = \frac{2\pi}{3600}\left(\frac{h^3}{K}\right)^{1/2} \tag{4}$$

where $K \equiv GM_{earth}$, G is the Universal Gravitational Constant, G = 6.673 x 10^{-11} N m^2/kg^2, and M_{earth} = 5.9742 x 10^{24} kg, so K = 398,659 km^2/s^2.

3. Space mirror concepts and proposed applications

Buckingham and Watson have in 1968 published a paper in which they described a system, shown in Fig. 3, in which a synchronous altitude satellite with a large reflecting surface is used to reflect the sun's rays to earth [16]. The reflector is required to continuously change its angle of incidence with respect to the sun-line to illuminate continuously a given spot on the earth. They provided equations to calculate the illuminated area and illuminance with effects of cloud cover, and proposed structural methods for frames to construct such thin film mirrors, as that shown in Fig. 3.

They concluded that reflector satellites are technically feasible but quite expensive for illumination levels of 0.1 lx and higher, but may be economical for low levels of illumination of the order of 10^{-3} to 10^{-2} lx (less than 1/10 of brilliant moon light), useful for low-light-level sensors and could thus roughly double their utility for night use.

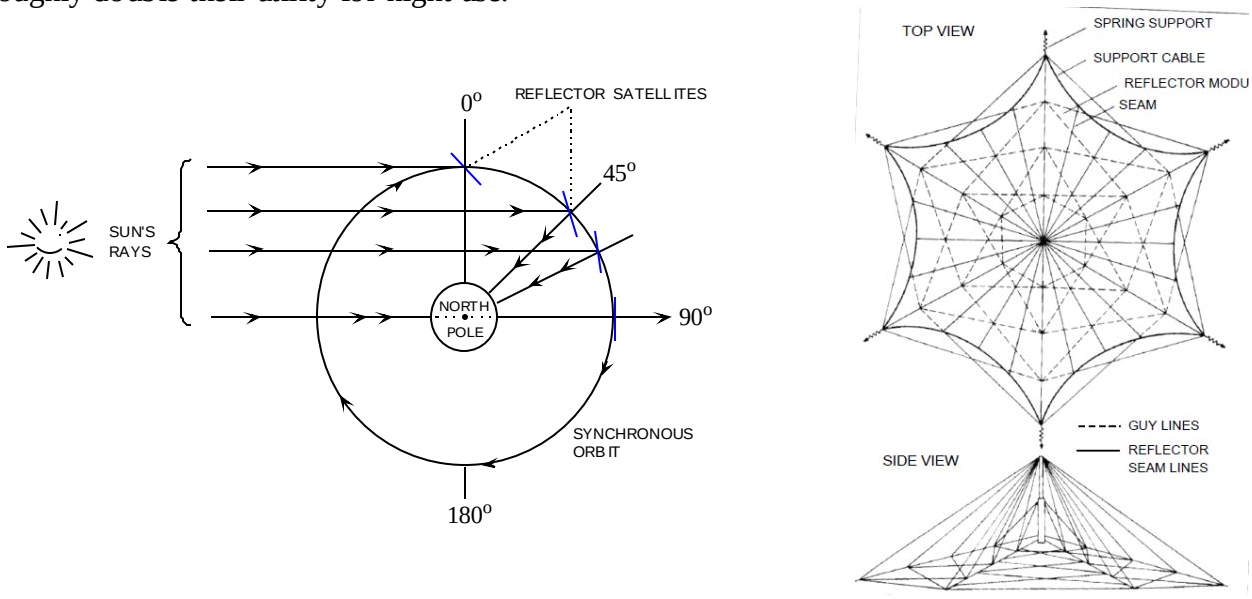

Fig. 3 Buckingham and Watson's basic concept of a reflector satellite and structure for supporting the thin-film mirror [16].

A very comprehensive conceptual, technical and socio economic study and exposition of space mirrors as conducted by the space visionary Krafft Ehricke [20-22]. He proposed and analyzed in some detail a number of generic applications for providing lunar-type night illumination service ("Lunetta"). solar type light energy services ("Soletta"), insolation for bio-production enhancement ("Biosoletta") to produce food and biomass, insolation for agricultural weather stabilization, precipitation management, crop drying and desalination ("Agrisoletta"), and insolation for generating electricity on earth ("Powersoletta"). He made an economic feasibility study and predicted that very competitive electricity generation costs can be obtained; for example he predicted that Powersoletta with a PV energy conversion on earth can produce electricity at 4.8c/kWh.

He added a number of new concepts [21] beyond past considerations:

- use of a variety of sub-geosynchronous orbits, particularly, sun-synchronous ones,
- "splitting" of large single reflectors into a number of smaller reflectors operating in clusters and, to reduce the size of the individual reflector, lower cost, increase system robustness. The illumination pattern in this configuration is determined by the number of co-orbits, the time position of their maximum latitude passage, and the lighting power (number of reflector units) assigned to each co-orbit.

- splitting of one orbit into several *co-orbits* (Fig. 4) which is particularly advantageous for urban night illumination where multi-directional illumination creates a more diffuse and uniform lighting effect;
- More possible applications;
- the concept of retro-reflection (called by some others "relay mirrors"), i.e. reflecting light from a mirror that does not have direct optical sight line to an area on earth that needs to be illuminated, to one in orbit that does (Fig. 5; thus enabling day and night operation raises the system's utilization factor.

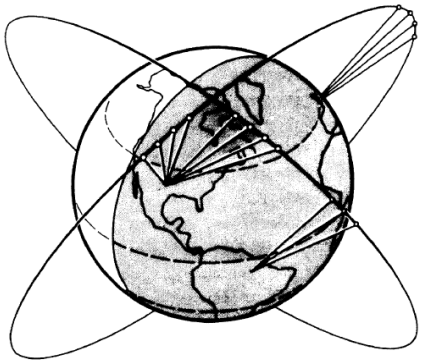

Fig. 4 The NASA SOLARES multiple orbiting mirror concept. Note 2 co-orbits and that several mirrors exposed to the sun at the same time are reflecting to the same earth spot [19].

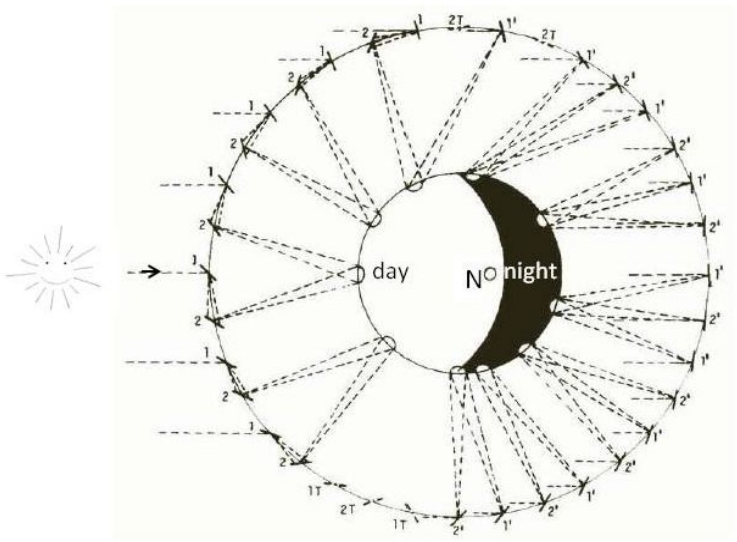

Fig. 5. Retro-reflection technique for daytime use of space light (adapted from [21]). Primary reflectors (marked 1) are those that face the Sun and reflect the light to secondary (2) reflectors that beam to the ground service area. Reflectors numbered with a prime beam solar radiation directly to the ground service area without retro-reflection.

We add, without further analysis, the possibility of using the space mirrors for shading the earth, a possibly useful application that may be locally useful for a number of obvious reasons, or as a geo-engineering way to reduce global warming, a concern that did not exist when the early researchers did their studies of solar mirrors in the 1970-s. In the extreme case, the mirrors, or some of them, could be turned towards the sun and thus prevent the solar radiation reaching the atmosphere and earth area that are that is now in the mirrors' shadow.

NASA performed some detailed preliminary feasibility studies of the design, deployment and use of space mirrors, published in the late 1970-s [17-19][1], and concluded that "The use of orbiting mirrors for providing energy to ground conversion stations to produce electrical power is shown to be a viable, cost effective and environmentally sound alternative to satellite solar power stations and conventional power sources."

Their proposal, which they called SOLARES, was to use a cluster of free-flying very lightweight (10 g/m^2) metal-coated polymeric film mirrors, optimally 1 km^2 each which, after deployment at altitude of 800 km, are placed in operational orbit and controlled by solar radiation pressure, to almost continuously illuminate a chosen surface on earth an intensity of I_e~ 1kW/m^2 ("at a fairly constant level", which, however, must take into account atmospheric variability with time). This would increase the available insolation at the earth energy collection and conversion station about 4-fold, and, if the insolation is uniform enough over time would also eliminate or reduce the need for energy storage.

They developed equations showing the influence of a number of parameters - mirror altitude, orbit inclination, period, mirror size and number, and atmospheric effects - on the reflected insolation that may be received by a round spot as a function of location. In their economic analysis they found that generated electricity costs range may be as low as about 1.6 c/kWh (in 1977/8 US cents). At the same time, as discussed in more detail in Section 7 below, they used extremely low costs for transportation into orbit, which make the costs of electricity and heat generated they determined much too low when considering current technology. As the environmental issues of principal concern they identified the perpetual twilight that neighboring communities might experience and the land area required, and felt that atmospheric effects are minimal and to their opinion perhaps beneficial. More details about their economic and environmental study can be found in Sections 7 and 8. They expressed the opinion that SOLARES could supply the entire global energy requirement.

Other authors have proposed mirror deployment at geostationary orbits (GEO), but Eq. (3) shows that at this altitude of h = 35,800 km the area illuminated on earth would have the huge diameter of about 3,329 km. At the chosen ground intensity of 1 kW/m^2 the mirror area would then have to have an area of about 150,000 km^2. The annual energy generated at one such location with 15% ground conversion efficiency would be, if atmospheric solar radiation transmission effects are ignored, up to about 41,200 EJ, 82 fold of the current world usage of 500 EJ. To achieve a practical ground area size with realistic capital investment and energy output, to provide energy to more than a single ground station, and to be able to employ the enhanced insolation for nonelectrical applications if desired, they postulated the use of a large number of flat1-km diameter reflectors in lower orbits (Fig. 4). Such configuration would allow each selected ground site could be insolated at all times (excluding eclipse and inclement periods), and any given mirror could be used for other tasks, including the insolation of other sites. The use of many and small reflectors clearly also allows the desirable feature capability of incremental implementation and easier repair and replacement.

Smaller reflector areas also require much lower torque for their control, since their moment of inertia scales as $I_i \sim \sigma A R_i^2$ t where σ is the average areal mass density, A is the mirror area and R_i is the characteristic radial dimension along the i^{th} rotational axis.

These NASA studies also calculated the daily and annual variation in the solar flux, both the natural one and that supplied by the orbital mirror system, and it is shown in Fig. 6. The most impressive feature *is* that although the direct solar input varies seasonally by more than a factor of two, the mirror input *is* constant to about 10%, making the system suitable for baseload electricity generation use.

[1] It is noteworthy that while these NASA publications all had the same objective and focus, the assumptions and results changed with the publication time, probably indicating an evolution of the concept.

Thorough techno-economic analysis is required to find the optimal system, so they only considered an example of the mirrors at an altitude of 4,146 km in a 3-hr periodic orbit with inclination of 45° relative to the equatorial plane (or several inclined orbits separated by latitude). The mirrors would be deployed or erected at an altitude of approximately 800 km. From this altitude, where the solar radiation pressure is much larger than the drag force, it is possible to "solar sail" the mirrors to their operational orbit (i.e. 4,146 km), requiring about a 3-mo transit time.

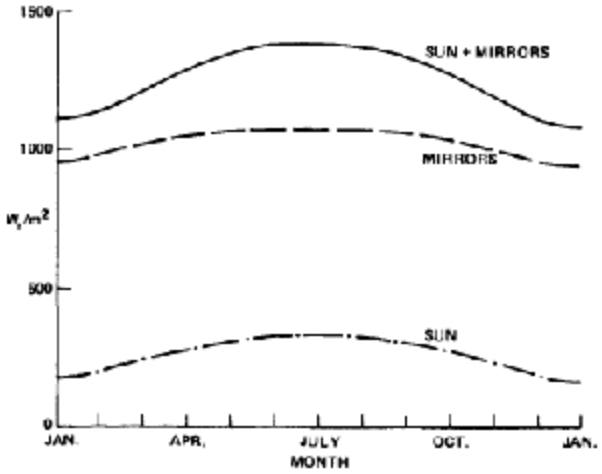

Fig. 6 The annual variation of the solar flux at the area illuminated on earth by the sun alone, by the proposed mirror system, and by their combination [19]

Using Eqs. (1) and (3), and as best it can be concluded from [17-19] assuming 23% losses and geometric spreading due to the sun-mirror-site angle, eclipsing, non-zenith mean apparent reflector location and atmospheric effects, 62,800 km^2 of mirror area was stated to be required to deliver an average 1.25 kW/m^2 (0.25 kW/m^2 from regular solar incidence + 1 kW/m^2 from the mirrors) to ground stations at 30° latitude. With their proposal to build individual mirrors of 1 km diameter each, this translates to the need for 80,000 orbiting mirrors having a total mass of about 6.3×10^8 kg. This mirror system was estimated to be able to supply this flux to at least 5 (of a theoretical 13) ground sites around the world. For each site, about 70% of the incident insolation falls within area of diameter $h\alpha$ (38.4 km, A_e = 1,167 km^2) and 99% within 2 $h\alpha$ (76.8 km, A_e = 2,334 km^2). We note that a conclusion from [19] appears to be that the ratio of the mirror area and the ground area steadily insolated with the added 1 kW/m^2 from the mirrors is 62,800/(5x1,167) = 10.76. With 15% conversion of just the $h\alpha$ insolation to the five ground stations, up to 27.6 EJ of electricity can be generated, amounting to about the electricity generated globally in 1977 (at the time of the NASA studies) and 36% of the electricity generated in 2010. After deducting the energy converted in the PV system, the remaining 85% of the energy at $h\alpha$, as well as the energy in the annulus between $h\alpha$ and $2h\alpha$ could additionally constitute a large usable energy resource.

4. Some reflector configurations

The reflector may be of any geometry, usually dictated by structural and weight considerations, and the mirrored surface may be flat, as proposed in most of the studies, or curved for concentration. If the reflector is so large that its size may no longer be regarded as a negligible fraction of its image size a curved concentrating surface is needed. It is noteworthy that it may be possible to vary the concentration (curvature) as needed during the orbital motion of the reflector.

Based on such a concept, the NASA [20] study proposed that the additional insolation from the space mirrors can be significantly greater than average ambient sunlight, and they have chosen to supply an earth surface and additional solar intensity of I_e ~ 1kW/m^2 (total of ~1.25 kW/m^2 including the natural, unreflected, insolation) for sizing the space system and ground stations and for deriving costs. They point out that the maximal average U.S. value of normal sunlight is about 0.25 kW/m^2, and therefore this increase intensity should reduce the area-related terrestrial solar converter system costs (for collectors, converters, land preparation, etc.) fivefold [(1 + 0.25)/0.25 - 5] from that of a solar power generation system of equal output that operates without the space mirrors.

The NASA study [18-20] has shown that for a given orbital inclination the number of mirrors needed to provide continuous insolation at a given ground site increases with decreasing altitude, and thus the total mirror area for a fixed ground site intensity decreases. However, several factors place a limit on the lowest usable altitude. First, atmospheric drag necessitates an altitude above 1,500 km for the 15 g/m^2 structure they proposed to allow a system life of 30 years. A remedy is to employ solar sailing for countering drag, thus perhaps providing the desire system life down to altitudes of 1,000 km. Second, the angular acceleration needed for the mirror to insolate a given spot during its transit varies approximately inversely with the third power of the altitude, thus creating significantly tougher demands on structural characteristics and control at lower altitudes. Third, lower orbits increase the fraction of time the mirror is eclipsed by the Earth. They thus conclude that the lower bound for an operational reflector system is probably not less than 1000 km.

5. The energies: generation and embodied

As stated above, the reflected insolation to a ground area can be augmented by using the space mirrors as a Fresnel field. For various environmental and social reasons it is safer to limit the $I_{e,m}$ reflected from the mirrors to approximately maximal natural levels and in the NASA study [17-19] it was proposed to make it 1 kW/m^2. This would be suitable for agricultural as well as heating and power generation purposes. Atmospheric radiation-loss effects have been considered in the estimation of the required mirrors' area, and to avoid the important losses due to persistent cloudiness (scattered clouds were indicated to have minimal effect), it is recommended to install the mirror-illuminated ground stations in sunny regions that experience least cloudiness. It is important to keep in mind that the space mirrors eliminate the diurnal and seasonal periodicities due to the rotation of the earth and the sun. Based on global insolation data, it was assumed that the time-averaged insolation without the mirrors is 0.25 kW/m^2, for a total ground insolation of 1.25 kW/m^2.

On this assumption The NASA study found that the total energy used to produce the SOLARES space system (mining through turn-on) was about 1.5×10^{12} kWh. With the above assumption of I_e = 1.25 W/m^2 and a 15% ground conversion efficiency, this embodied energy is equivalent to only 10 weeks of energy production at the five ground sites. Inclusion of the ground system added from 4 to 15 weeks to this number, depending on the conversion technique.

6. The space mirrors

6.1 Materials and optics

The design of the mirror needs to provide maximal specific power reflected with very low weight and payload volume. Its surface must have a reflectance (ρ) that is as close as possible to 1.0, it must be accurate enough to ensure that most of the solar radiation reflected from its surface arrives at the earth site area dictated by the fully-planar mirror optic, it must be durable and easily deployed and the material needs to withstand years of solar winds, radiation, and the extreme temperatures and their variations in space. Importantly, the mirror is exposed to micro-meteorites/ space debris, electromagnetic radiation from sunlight [34], including solar wind, comprised of streams of

particles originating from the sun and propelled by the Earth's magnetic field. The composition of solar wind includes approximately $2x10^8$ H^+/cm^2s protons (96%), of about $6x10^6$ alpha particles/cm^2s (3-4%) and a few 10^5 ions/cm^2s of higher mass with average velocities of about 400 km/h (corresponding to energies of 0.85, 3.4, and 10 keV, respectively) as well as 3-30 keV electrons. There are also some occasionally emitted particles as the result of solar flares or storms.

Studies in [35] have shown a rapid worsening in the optical properties, including loss of reflectivity and defocusing due to blistering, due to the effects of solar wind, affecting the very beginning of a solar mirror's operation. They suggest the mirror's film thickness should be at least 0.1 μm, which is the maximum penetration depth of the solar particles. As discussed below, this is also the same minimal thickness required for the metallic thin film to remain opaque to visible light and to other low frequencies of electromagnetic radiation. Another type of radiation is the ultraviolet (UV) part of sunlight with wavelengths between 4 and 400nm. Two UV bands are particularly relevant to materials degradation, the near UV range (200 – 400nm) and vacuum UV range (100 – 200nm) [36]. This type of radiation causes the greatest material degradation to polymers and most of this damage is sustained by the first 0.3 microns from the surface.

A commonly used mirror substrate is polyethyleneglycolterepthalat (PETP) with the net composition $(C_{10}H_8O_4)_n$, known as Mylar, Hostaphan, etc., and are produced by companies like Bayer, and Du Pont, and Kapton, which is poly(4,4'-oxydiphenylene-pyromellitimide) made by DuPont. They are coated with a thin film metallic surface by chemical vapor deposition (CVD) to provide high reflection. The most common metal is aluminum due to its good reflectance and low cost, but gold and silver were also used for small mirrors due to their stability or higher reflectance.

It is generally agreed that the film mirrors should be maintained periodically, say once in 10 years, by applying a thin fresh Al (or other reflective material) layer in situ, which could be accomplished by flying a furnace with evaporating Al along the foil surface at a certain distance [34]. This was expected to restore the initial reflectivity (smoothing of the blistered flaked areas), and sintering together the eventual brittle foil surface areas (flakes) by the freshly evaporated material. to prolong the mirror reflectivity to the order of a 100 years. Such maintenance would also be needed to repair possible holes due to meteorite impact, or for replacement of part or all of the reflector film. It was estimated, however, that meteoroid damage would be very small, 3% for 30 years in orbit [17].

The solar mirror must have mechanical properties that can withstand its temperature in space, that goes down to 3K (with the associated embrittlement) but also rises to much higher values especially on its non-reflecting parts which are intermittently exposed to the sun. The mirrored surface substrate has the leading role in the mirror's overall structural integrity.

6.2 Our reflective thin film mirrors construction and experiments

We have investigated the fabrication of thin film mirrors akin to those that were considered suitable for space mirror application (Sections 1, 3, 6.1), and then examined their microscopic surface quality and measured their reflectance, tensile strength, creep (fatigue) at both room and cryogenic temperatures, i.e. 300K and 77K, respectively.

Based on a list of the most common space materials used by NASA, the polymer substrate was chosen to be the polyimide Kapton HN (Dupont) because of its much greater tolerance – by as much as three orders of magnitude – to radiation, such as UV and soft X-Ray, in comparison with another commonly used polymer, Mylar (PET), and because of its proven performance in temperatures near 0 K and greater resistance to high temperatures, and its higher tensile strength [37]. Aluminum was chosen as the reflective thin film because it is a commonly used reflective material for thin film mirrors, primarily because its density is an order of magnitude and its cost is two orders of magnitude lower than silver, which is often used for mirrors.

The thickness of the Kapton film substrate was 7.6 μm, as thin as Dupont had commercially available. The thickness of the aluminum coating was chosen to be 100 nm, again as done by

NASA. The size of the available vacuum evaporator dictated the diameter of the mirror film to be 134.6 mm. The pure aluminum coating was done by vapor deposition, and the manufactured film mirror supported by a ring structure is shown In Fig. 7.

Fig. 7: Our manufactured reflective thin film

The film reflectivity was measured as a function of wavelength in the visible light range (300-1000 nm), at ambient and cryogenic temperatures, by using a spectrophotometer, using as reflector reference a commercially available reflective mirror film (Mylar with Ag coating) made by 3M.The cryogenic temperature was obtained by immersion in liquid nitrogen (~77K) for 60 min. While the absolute values of the measure reflectance are subject to large experimental error, the trends are consistent: the reflectance at 77K is always higher than that at 300K. For example, at the median wavelength of 450 nm, where solar radiation has maximal intensity, the reflectance at 77K is about 1.68 fold higher than at 300K for our sample and 7% higher for the 3M film. Also consistently, the reflectance of our film is about 16% lower than that of the reference 3M one. The film transmittance was measured too, in the same wavelength range and was found to be zero for all films tested, at both temperatures.

While surface contraction at the cryogenic temperature, resulting in contraction of pinhole and other defects may partially explain the increased reflectance, much more detailed examination of the films is needed for full understanding of the reasons for that reflectance-temperature relationship. Samples from the test, of both the mirror film we manufactured and the commercial 3M reference sample, were examined by an optical microscope. The first set of these two samples were kept at ambient temperature (approximately 300 K), and the second set was exposed to at least 60 minutes in an isothermal container with liquid nitrogen (~77K). Once the samples were removed from the nitrogen bath, they were rapidly cleaned and observed and photographed at a magnification of 500. The surface photographs are shown in Fig. 8.

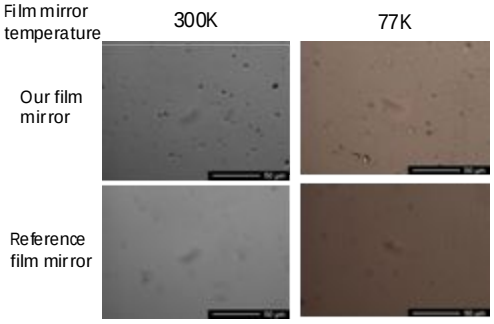

Fig. 8. 500X microscope surface photos of our thin film mirror and of the reference one, at 300K and 77K. Note: the bean-shaped dark area in the center of each photograph is a smudge on the microscope lens, not a defect.

Figure 8 shows that the number of defects/imperfections per unit area (i.e. surface defect density) is higher for our film mirror than for the reference one. These defects include mostly pitting for the samples and spits in the standard, typical of using a vapor deposition. This may therefore be the reason for the measured lower reflectance of our mirror. Since the vapor deposition process we used can be improved significantly, there is no doubt that better reflectance can be obtained, as shown by many.

An interesting observation is that for both films the imperfection surface density is lower for the cryogenic temperature, perhaps thus justifying the higher reflectance at this temperature. Another interesting observation is that nevertheless, the reference film experience significantly higher degradation when exposed to the low temperature, as shown by lines the along the vertical direction of the image that appear to be micro-cracks that formed after exposure to liquid nitrogen (~77 K). In fact, when the reference film was placed into the liquid nitrogen it made a loud crackling noise that lasted for a few seconds, while no sound was heard for our film. In contrast, the sample did not exhibit any sounds at all when placed inside the container. No micro-cracks developed in our film. The likely explanation is that the thermal expansion coefficients of silver and Mylar (the reference film) differ by 6-fold, while those between Aluminum and Kapton (our film) differ by only ~15%. Table 2 below shows the experimental values for ultimate tensile strength and Young's modulus from our mechanical tests.

Table 2: Measured Mechanical Properties for our film mirrors exposed to 300K and 77K

Film temperature, K	**Ultimate Tensile Strength, MPa**	**Young's Modulus, MPa**
300	9.9	129
77	13.3	448

The observed trends are consistent with the behavior of thermoset polymers, like polyamides, which are characterized by a high tensile strength and modulus with a small total elongation, prior to failure, brittle behavior, and an increase of the ultimate tensile strength and tensile modulus at lower temperatures.

6.3 Mirror Mounting Structures

The structure must of course support the reflective mirror film, but must also provide the necessary tension for maintain its shape, as well as the control mechanism for adjusting its orientation during flight as needed. It was proposed that the control devices (thrusters) be momentum flywheel pairs (Fig. 9), which can change their relative speeds to provide turning torques and steering corrections, and which could be charged with small motors powered by solar cells or by radiation pressure.

The huge size of these mirrors mandates assembly in space, with the components ferried to the location by a cargo space vehicle, and then constructing the frame from its component and unfurling the reflective film and attaching it to the frame. As described in Section 3, the NASA plan was to do the assembly at an altitude of 800 km and then ferry the mirror into its final orbit by solar sailing.

For the SOLARES concept, NASA's study [17,19] proposed mirror structures, shown in Fig. 9, which, although not yet optimized, "can work". The aluminized film was assumed to have an areal density of 4.0 g/m^2. The film is tensioned onto a supportive structure consisting of an outer torus with radial-segmented spokes and concentric rings. Such tensioning is necessary to maintain the reflector planarity at 0.01 rad (deemed as adequate to maintain a flatness that will not increase the spot size by more than 5% over that of a perfectly planar mirror) despite the perturbing radiation pressure, gravitational gradient, and angular acceleration forces acting on it. The rim torus must have sufficient buckling strength to provide this tension. They proposed that the support structure would be fabricated from a high-modulus carbon-fiber-epoxy (or polyimide) matrix composite.

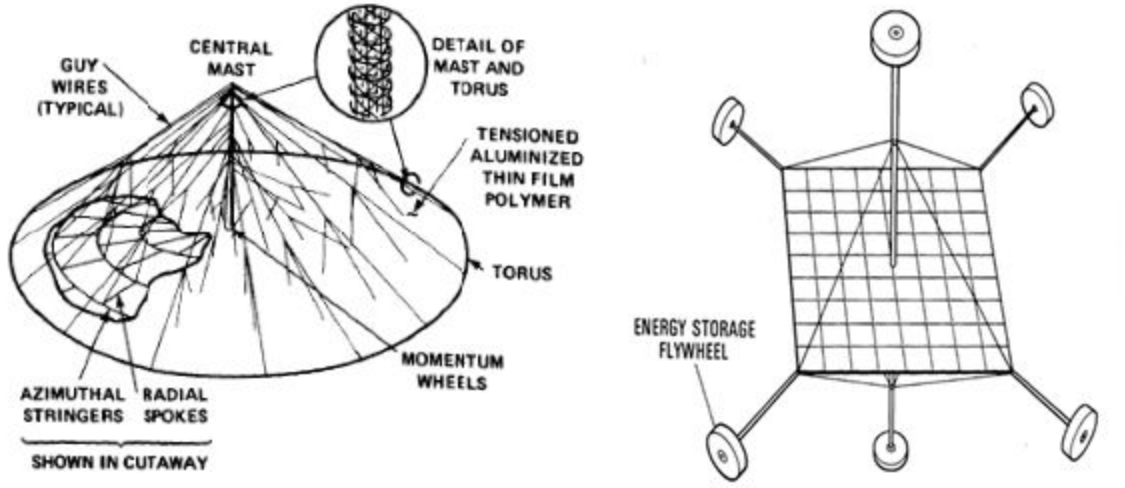

Fig. 9 Proposed structural configuration of a space mirror and its flywheel control system [17,19].

The design draws on interest in constructing and using solar sailing for transporting payloads in deep space exploration, in one case of which an ultralight truss mast that can be deployed to kilometer lengths was designed, and a means to fabricate a large quadrant of sail material and stow it without material creasing or trapped air were proposed [28,38,39]. Sailcraft areal densities ranging from 8.9g/m^2 down to 4.6g/m^2 were proposed by NASA as a goal, and since the sail material used in NASA experiments had an areal density of 3g/m^2, this leaves 1.6g/m^2 for the supporting structure, bus and payload.

Parallel applications of more immediate interest are high-precision space reflectors for communications, earth observation, or radio-astronomy. At a few tens of meters in diameter, the ones considered are orders of magnitude smaller than space mirrors and they can afford an order of magnitude higher areal mass of typically 0.5 kg/m^2, but some of the goals and technology are synergistic. Here we mention the work by Datashvilli, Baier and co-workers [40,41], with a small model of their design shown folded and then deployed in Fig. 10.

Fig. 10. Deployment of membrane reflector model (0.6m diameter), a) stowed, b) deploying, c) (scaled) deployed [40].

7. System Economics

While it is obviously extremely difficult to predict the costs of generated energy by space mirrors, because of the novelty of the concept, uncertainties about developments that will arise during the

decades needed for its materialization, as well as about all of the externalities that will accompany it, several economics analyses were conducted to at least provide an initial prediction.

A study by Ehricke in 1979 [21] estimated that the investment for Biosoletta is of the order of $1,200 billion, that is about $80 billion/year for the 15 yr construction time he predicted.

The NASA economic analysis of their SOLARES space mirror concept [19] see also Section 3) to supply approximately the global electricity demand at that time (32 EJ, which in 2010 is 77 EJ [2]) based on a desired 15% capital return, 30-year system life, and a load factor which takes into account eclipse and inclement periods, found that generated electricity costs range from about 2.5 c/kWh to less than 16 c/kWh (in 1977 US cents), and that the ground station for converting the solar radiation received from the mirrors to electricity by using PV is the major component of the total system investment, since the cost of reflectors in space is much lower. We note that this was based on PV system costs of $\$5/W_{peak}$ that have since then dropped in some favorable cases up to less than $\$2/W_{peak}$ [42], but that is likely to have also been true for other components of the space mirror system. The same study states that if the solar radiation incident on earth from SOLARES was used just as heat, the cost would be about 1 c/100MJ thermal.

In that analysis, performed on the assumption of making 80,000 space mirrors of 1 km diameter each to be placed in a 4,146 km altitude orbit, they assumed the use of a thin film mirror made of a 0.1 μm Al reflector on 2.5 μm polymer substrate weighing 4 gr/m^2, and the structure made from HM graphite-epoxy. The total mirror weight, including also controls, instrumentation and growth allowance, was estimated to be 10.01 gr/m^2, i.e. 7,860 kg/mirror, and the total cost of the mirror including prorated R&D costs excluding transportation costs into orbit was $1,654,000 per mirror, i.e. $\$2.11/m^2$. Including the transportation they came up with a total price of $2 million per mirror, i.e. $\$2.55/m^2$. They estimated the cost of the total system to supply approximately the entire world 1977 electricity demand of about 32 EJ to be about $500 billion or an average of nearly $40 billion/year with their assumption of a 15-year implementation period.

A major problem with their economic analysis is that they used a cost of $44/kg for transportation into the needed orbit, assuming the existence of the planned Heavy Lift Vehicle. This is an areal mirror cost of $\$0.44/m^2$. A vehicle that can transport at such a cost has never materialized, in fact the current space transportation costs acan at best be around $3,000/kg and are more likely around $10,000/kg [43]. Conservatively assuming the latter cost and keeping all the NASA assumptions the same, the price of a 1 km diameter orbiting mirror would rise to $80.3 million, i.e. $\$102.30/m^2$ (40.1 times higher) and would thus raise the price of generated electricity in similar proportion and make it highly uncompetitive. It is noteworthy that the cost of transportation to orbit is also the major obstacle for economic deployment and use of the SPS, and the only way to have competitive space power generation is to reduce the transportation costs to about $200/kg, i.e. by nearly 2 orders of magnitude, achievable by frequently planned but never commercially produced reusable launch vehicles (RLV) [10,11,14] and other methods.

We have also conducted an economic feasibility analysis of the use of a space solar mirror system by approximating life time costs, profits and resulting revenues for three separate applications: (1) 24hr farm lighting, (2) Night-time illumination in Polar Regions, and (3) Greenhouse produce growing in Polar Regions.

The mirror aerial weight we determined was 11 gr/m^2 (an aluminized 7.62μm Kapton mirror reflector),which turned out to be close to the 10 gr/m^2 used in the NASA study [19], and considering all of the reflector components the reflector cost was estimated at $\$2.05/m^2$. Using the NASA data that show that reflector cost is about 48% of the total mirror cost without transportation, our estimate of the mirror area cost was thus $\$4.27/m^2$.

For transportation costs, we used those for the Falcon 9 rocket in [44], at $7,143/kg. i.e $\$78.57/m^2$ of mirror. Like in NASA's analysis we assumed a functional life of the mirror as 30 years and a discount rate of 15% but also calculated for a 5% discount rate to provide a range of values that

come closer to present conditions. A lifetime maintenance cost of \$1.27/m^2 (4.25 c/(m^2yr) was added. Summing the mirror and its launch costs, the total areal investment cost comes to \$82.84/m^2 (\$65.03 million per mirror) and the 4.25 c/(m^2yr) recurring maintenance costs.

From Eqs. (1) and (3) and as following NASA's estimates of the mirror area shown above and in Section 3, each m^2 of the mirror illuminates 0.093 m^2 of ground site area, at the planed insolation of 1.25 kW/m^2. This amounts to 116.2 W per m^2 of the space mirror. The annual solar energy incidences are thus 39.4 GJ per m^2 ground area, or 3.67 GJ per m^2 of the space mirror.

If the energy is used for PV electricity generation at 15% conversion efficiency and normal incidence, this would steadily generate 187.5 W electricity per m^2 of the illuminated ground area, and thus 17.4 W electricity per m^2 of the space mirror, i.e. 150 kWh/yr (0.55 GJ/yr) per m^2 of the space mirror. At the typical US electricity price of \$0.012/kWh, this should generate an annual revenue of \$18 per m^2 of the space mirror. The cost of the PV system is estimated to be \$4/W_{peak} [42,45], and considering the above result that the power generation is 17.4 W per m^2 of the space mirror, this would be i.e. \$69.60 per m^2 of the space mirror and is added to the \$82.84/m^2 space mirror cost for a total areal investment cost of \$152.44 per m^2 of the space mirror.

The present value of the initial investment into the solar space mirror system for a discount rate of 5% is \$276.05 and the NPV = \$276.05 – \$152.44 = \$123.61, and the internal rate of return (*IRR*) is 11%, indicating a financially rather viable investment. The *NPV* –based payback period is 14 years. If the discount rate was 15%, as assumed in the prior NASA study, then the *NPV* becomes negative, -\$34.53, i.e. not financially viable. Discount rates up to 11% produce positive *NPV*.

Since transportation into orbit is in this analysis 52% of the needed capital investment, and since it is the cost item most likely to decrease significantly in the future, the same economic analysis was performed for the transportation costs of \$200/kg, amounting to \$2.22/m^2 and resulting in an overall mirror system cost of \$6.51/m^2 and to total mirror+PV system cost of \$76.11/m^2. Now the investment achieves an *IRR* of 24% and becomes very viable even under the 15% discount rate, and we note that the mirror system becomes only 8.6% of the total cost.

Using the solar radiation from the mirror to grow agricultural products in Polar Regions allows an extension of the growing season from the current 4 months [46] to 12 months per year. The benefit is obviously avoidance of the need for importation of expensive produce in the off seasons, and the amount saving by growing locally is US\$4.50/lb or \$45.52 per m^2 of the space mirror. This creates annual revenues that are 2.5-fold higher than those estimated above for electricity generation. Furthermore, while not calculated here, the investment into a tomato growing greenhouse system may also be lower than the installation of a PV energy conversion system, with all of this pointing to the recommendation that such agricultural use is financially most viable.

Nighttime municipal illumination failed in this analysis to break even over the lifetime of the mirror, because of the relatively low density of needed streetlights in the selected northern regions, but it may be a rather viable application for both civilian and limitary purposes, when the demand justifies it.

It is noteworthy that the space mirror designs considered in the NASA analysis and also used here were not optimized. Furthermore, the costs of materials, of space deployment and of PV electricity generation are dropping. The economics can thus only improve, unless some unknown technical or environmental problem arises during the more detailed system development and testing,

The estimated very high needed investments, of the order of more than \$600 billion (about \$40 billion per year for about 15 years), for the space mirror system become more acceptable and appealing when compared with the expected accomplishment of providing renewable and relatively clean energy for satisfying energy of the order of the entire global demand, with relatively minimal global warming effects. These investments should also be compared with some other global financial values: in 2010 the annual world and OECD GDPs were about \$63,000 billion [48] and \$42,000 billion [49], respectively, and the world defense budgets were \$1,437 billion (2.3% of

GDP) [50]. The estimated annual expenditure for the space mirrors project are thus 0.06% of the World GDP, of the order of the World Bank subscribed capital of $44 billion for 2010.

Some other proposed high magnitude global renewable energy projects were estimated for the Space Power Satellite (SPS) [5,9] at $908 to $15,000/kWe, which for generating the current global power capacity of 4.4 TWe [2] would require an investment of $4,000 to $65,000 billion f, and for the DESERTEC project at close to $600 billion to supply by 2050 “only” 700 TWh per year of electricity from the Saharan deserts [51]. The space mirror concept is predicted to incur much lower costs.

8. System Sustainability

A huge and basically untested project like this one requires a very careful formal scientific sustainability analysis from the very start. Founded on the commonly used economic, environmental, and social pillars of sustainability, such an analysis in quantitative form is beyond the scope of this paper, but some major issues are identified and discussed, as follows.

8.1 The environmental pillar

- On the positive side:
  - the concept promises the satisfaction of a good part of the global energy demand from renewable energy,
  - alleviation by orders of magnitude of emissions and global warming, and
  - preservation of the remaining fossil fuels/hydrocarbons for other uses.
- Negative impacts are not minor and must be carefully considered and alleviated:
  - Emissions and noise from the launch vehicles; a current space launch typically produces 28 tons of CO_2, and 23 tons of toxic particulate matter[
  - Embodied emissions in the space mirror materials and construction
  - Effects on the atmosphere from the passage of the launch vehicles
  - Effects on the atmosphere from the added sunlight reflected to earth, including possible photochemical effects; these may be accelerate global warming if greenhouse gas concentrations in the atmosphere continue rising, but may ultimately reduce global warming as fossil fuels are replaced by solar space mirror system.
  - The associated light glint (global) and scattering (near conversion sites) may add to the “ecological light pollution", a phenomenon well know among ecological and health hazards, is one that alters natural light regimes in terrestrial and aquatic ecosystems, and some of the catastrophic consequences of light for certain taxonomic groups are well known, such as the deaths of migratory birds around tall lighted structures, and those of hatchling sea turtles disoriented by lights on their natal beaches. The more subtle influences of artificial night lighting on the behavior and community ecology of species are still less well recognized and should be studied [52]. Light pollution also has detrimental effects on human lives possibly impairing vision [53] and altering the production of melatonin, the hormone that makes us sleep as it is released during darkness, and thus altering human circadian clock whose disruption has been linked to depression, insomnia, cardiovascular disease, and cancer. Also, according to the “First World Atlas of the Artificial Night Sky Brightness,” two thirds of the US population and about half of the European Population can no longer see the Milky Way, thus destroying the aesthetic value of the night sky and impeding human connection to nature [54].
  - The additional light at night is an especially serious problem for astronomy since it prevents, or at the least makes very difficult to conduct astronomical observations and studies. At the

same time, the associated launch capabilities developed for the space mirror system should advances possibilities for space astronomical laboratories [19]. A response to the strong criticisms about the effects of light that projects like "Novey Svet" ([24-26], Section1) may create was posted by the Russian Space Regatta [24]; they indicate that the problem must indeed be studied and any projects were and should be implemented with minimal damaging impact, but also list the large advantages that such lighting can provide.

- Generation of a large amount of space debris, and possible risks of their fall to earth

8.2 The economic pillar

- As with any energy endeavor, the economics of the system metrics focused on the magnitude of the investment, and on the cost of the generated energy for use, all in comparison with alternatives methods for meeting the same objectives, are key. These were discussed in Section 7, and show some promise that the system can provide much of the global energy needs at a reasonable cost, especially if the cost of transportation to space is reduced to a few hundred $/kg. This reduction is included in the planning by several national space organizations and private businesses and is synergistic with the need for low-cost space transport for other commercial applications..
- To move towards sustainable development of the concept, the economic analysis must include monetization of all externalities, some of them negative and some positive, many of which are mentioned under the discussion of the environmental and social pillars in this Section.
- The magnitude of the needed capital investment, of above $600 billion over about 15 years, should naturally be considered relative to other alternatives and to global economic conditions.
- In such a novel and large project the risks play a key role. Gradual, incremental, introduction of the system, with careful preparation and monitoring would be necessary.

8.3 The social pillar

- Some human impacts
  - Those related to health and aesthetics are described under the above-discussion of the Environmental Pillar
  - Public anxiety due to large number of satellites in orbit; self destruction of failing mirrors to safe levels would be a way to alleviate this problem somewhat
  - It is very likely that the project would make significantly positive contributions to employment, education, and creativity with associated beneficial spinoffs
  - Generation of adequate energy to about 1/6 of the world population which lacks it will certainly improve their health and education and improve chances for reducing poverty.
- International space stewardship: There is considerable and very justified concern about assuring internationally fair and safe use of space. This certainly would apply to the massive proposed space mirrors project, which in the case of NASA's SOLARES proposes to place 80,000 1-km diameter mirrors in the sky, with all the associated impacts. The Outer Space Treaty ratified by the UN in 1967 [55] provides the basic framework on international space law, including the following principles:
  - "the exploration and use of outer space shall be carried out for the benefit and in the interests of all countries and shall be the province of all mankind;
  - outer space shall be free for exploration and use by all States;
  - outer space is not subject to national appropriation by claim of sovereignty, by means of use or occupation, or by any other means;
  - States shall not place nuclear weapons or other weapons of mass destruction in orbit or on celestial bodies or station them in outer space in any other manner;

- the Moon and other celestial bodies shall be used exclusively for peaceful purposes;
- astronauts shall be regarded as the envoys of mankind;
- States shall be responsible for national space activities whether carried out by governmental or non-governmental entities;
- States shall be liable for damage caused by their space objects; and
- States shall avoid harmful contamination of space and celestial bodies."

As of October 2011, 100 countries and states are parties to the treaty, while another 26 have signed the treaty but have not completed ratification. The treaty remains, however, very incomplete and lacks some essential detail and clearly effective enforcement measures. Amongst the obvious omissions are intellectual property of space research, and space pollution [56,57]. A much more solid treaty must be developed to ensure internationally fair and safe deployment and use of the space mirrors project.

9. Conclusions and recommendation

A critical review of the current status of the space mirrors concept was conducted, thin film aluminized Kapton mirrors were manufactured and optically an mechanically tested to examine their property changes when exposed to a cryogenic temperature, an economic analysis related to several applications was performed, and leading issues that must be taken into account in the sustainability analysis of the concept were described. We add, without analysis, the possibility of using the space mirrors for shading the earth: if needed, the mirrors, or some of them, could be turned towards the sun and thus prevent the solar radiation from reaching the atmosphere and earth area that is then placed in the mirrors' shadow.

Our experiments with thin film mirror have shown that the reflectance at 77 K is higher than that at 300 K, about 1.68 fold at the peak solar intensity wavelength of 450 nm. The imperfection surface density is lower for the cryogenic temperature. The ultimate tensile strength and tensile modulus increased at the cryogenic temperature, consistent with the behavior of polymers like Kapton.

As in any large energy development endeavor, it is impossible to eliminate all negative impacts, just to render them tolerable and sustainable, especially relative to other available options. The overall concept sustainability, especially taking into account the environmental and social impacts and their associated costs, must be analyzed carefully and quantitatively, and all externalities must be included in its future evaluations.

Without consideration of these externalities, our economic analysis agrees with NASA's Ehricke's, published in the late 1970-s [18-22], that if transportation costs to mirror orbit are reduced to a few hundred $/kg, as planned, the use of orbiting space mirrors for providing energy to earth is an investment with a good rate of return and a cost effective alternative to satellite solar power stations (SPS) and terrestrial renewable and conventional power sources.

This energy concept is very appealing relative to other options for addressing the severe energy and global warming problems that we face, and deserves much and urgent R&D attention.

Acknowledgments

My former students Kamal Shair, Betsy Rosenblatt, and Travis Schlegel have conducted the experiments presented in Section 6.2 and contributed to other parts of this paper. I am grateful to William P. Gilbreath and Stuart W. Bowen, authors of some the seminal NASA papers on space mirrors, for their answers to my questions. Iris Chu and Eri Mizukane have been very helpful in the literature search for this study.

References

[1] Lior, N. The ECOS 2009 World Energy Panel: An introduction to the Panel and to the present (2009) situation in sustainable energy development, Energy 36 (2011) 3620-3628.

[2] Lior, N. Sustainable energy development: A brief introduction to the present (May 2011) situation", accepted for publication in Energy, 2012,

[3] Glaser, P.E. Power from the Sun: Its Future, Science, 162 (1968) 857-861.

[4] Glaser, PE, Davidson, FP, Csigi, KI, editors. Solar power satellites, the emerging energy option. New York: Ellis Horwood, 1993.

[5] Mankins JC. Space solar power: a major new energy option? Journal of Aerospace Engineering 2001;14(2):38-45.

[6] Mankins, J.C. (USA), Kaya, N. (Japan), Editors. Space Solar Power: The First International Assessment of Space Solar Power: Opportunities, Issues and Potential Pathways Forward. August 2011, International Academy of Astronautics, 6 rue Galilée, BP 1268-16, 75766 Paris Cedex 16, France, ISBN/EAN 978-2-917761-11-3

[7] Criswell DR, Thompson RG. Data envelopment analysis of space and terrestrially-based large scale commercial power systems for earth: a prototype analysis of their relative economic advantages. Solar Energy 1996;56:119-31.

[8] Brown WC. The history of wireless power transmission. Solar Energy 1996;56:4-21.

[9] Woodcock, G.R. Solar Satellites - space key to our power future. Astronautics and Aeronautics, Vol. 15, July-Aug 1977, 30-43

[10] NASA, Solar Power Satellite Concept Evaluation. vol. 1, NASA JSC-12973, July 1977

[11] Lior, N. Power from space. Energy Conversion & Management J. 2001;42(15-17):1769-1805.

[12] Tarlecki Jason, Lior Noam, Zhang Na. Analysis of thermal cycles and working fluids for power generation in space. Energy Conversion & Management2007;48:2864-78.

[13] Zidanšek, A., Ambrožić, M. Milfelner, M. Blinc, R. Lior, N. Solar orbital power: Sustainability analysis. Energy 36 (2011) 1986-1995.

[14] National Space Society, http://www.nss.org/settlement/ssp/index.htm [accessed 2/19/2012].

[15] Oberth, H. *Wege zur Raumschiffahrt*. Berlin: Oldenburg Verlag, 1929 (Translation, NASA TT-F-662).

[16] Buckingham, A.G, Watson, H.M. Basic Concepts of Orbiting Reflectors," J. Spacecraft, vol. 5, May 1968, pp. 852-853.

[17] Billman, K.W., Gilbreath, W. P., Bowen, S.W. Introductory Assessment of Orbiting Reflectors for Terrestrial Power Generation. NASA TM X-73,230, 1977.

[18] Billman, K.W., Gilbreath, W. P., Bowen, S.W. Satellite Mirror Systems for Providing Terrestrial Power: System Concept. Paper AAS-77-240, 23rd Meeting of the AAS, San Francisco, Calif., Oct. 1977.

[19] Billman, K.W., Gilbreath, W. P., Bowen, S.W. SOLARES-A New Hope for Solar Energy? Alternative energy sources; Proceedings of the Miami International Conference, Miami Beach, Fla., December 5-7, 1977. Volume 1. (A79-33984 13-44) Washington, D.C., Hemisphere Publishing Corp., 1978, p. 233-255. IISSN: 0278-1662

[20] Gilbreath, W. P, Billman, K.W. Bowen, S.W. Enhanced solar energy options using earth-orbiting mirrors. Proc. 13th Intersociety Energy Conversion Engineering Conf. San Diego, California August 20 - 25, 1978, Paper 789186, Vol. 2, 1528-1534 Published by the Society of Automotive Engineers, Inc. 400 Commonwealth Drive, Warrendale, PA 15096.

[21] Ehricke, Krafft A. Kraftsoletta - eine Industrie-Sonne fur Europa - Moglichkeiten kostenrealistischer Solarenergie. Astronautik, vol. 3, 1977, 85-87.

[22] Ehricke, Krafft A. Space light: space industrial enhancement of the solar option. Acta *Astronautica* Vol. 6. pp. 1515_1633, 1979.

[23] Krafftehricke.com Krafft A. Ehricke and America in Space. [http://www.krafftaehricke.com/ehricke_power_relay_satellite_2.php] [accessed 2/19/2012].

[24] Sistach, L. A. The moon orbital mirror.The International Academy of Astronautics, and the International Institute of Space Law, 54th International Astronautical Congress of the International Astronautical Federation, 29 Sept. 2003, Bremen, Germany.
[25] Space Regatta Consortium. An open letter to astronomers professional and amateur. http://src.space.ru/page_30e.htm [accessed 2/19/2012].
[26] Ashurly, M.Z. Space-based mirror reflector of solar radiation. J. Opt. Technol. 67 (6), June 2000 577-579.
[27] S.P. Korolev Rocket and Space Corporation «Energia». http://www.energia.ru/english/ [accessed 2/19/2012].
[28] Shpakovsky, N. "Space Mirror." Space Mirror. The TRIZ Journal. <http://www.triz-journal.com/archives/2002/06/e/index.htm>. [accessed 2/19/2012].
[29] Garner, C., Diedrich, D., Leipold, M. A Summary of Solar Sail Technology Developments and Proposed Demonstration Missions, Jet Propulsion Laboratory report JPC·99·2697.
[30] Freiman, Chana. "Mirror, Mirror, up in Space? - Space Mirror for Providing Light." CBS Interactive, 3 Dec. 1993. Web. 10 Dec. 2011. <http://findarticles.com/p/articles/mi_m1590/is_n7_v50/ai_14719235/>. [accessed 2/19/2012].
[31] Steen, M. (1999, August 2). UK Astronomers Attack Russian Space Mirror Plan. http://www.planetark.com/avantgo/dailynewsstory.cfm?newsid=1073 [accessed 2/19/2012].
[32] NASA. History: Glenn Contributions to Deep Space 1. May 21, 2008 update, NASA. <http://www.nasa.gov/centers/glenn/about/history/ds1.html>. [accessed 2/19/2012].
[33] Wong, Wayne. "SBIR Inflatable Concentrator Tested for Space." Aerospace Technology Innovation. Sept.-Oct. 2001. NASA. http://nctn.hq.nasa.gov/innovation/innovation95/6-smallbiz3.html [accessed 2/19/2011]..
[34] Fink, D. Biersack, J. P., Städele, M. On the performance and lifetime of solar mirror foils in space. Space Solar Power Review. Vol. 5, pp. 91-100, 1985.
[35] Gulino, D.A. The Survivability of Large Space-Borne Reflectors Under Atomic Oxygen and Micrometeoroid Impact. NASA Technical Memorandum 88914, Prepared for the 25th Aerospace Sciences Meeting sponsored by the American Institute of Aeronautics and Astronautics, Reno, Nevada, January 12-15, 1987
[36] Kutz, Myer. Handbook of Environmental Degradation of Materials. (pp. 479-487). William Andrew Publishing. 2005.
[37] Griffin, Michael D.; French, J. R. Space Vehicle Design (2nd Edition). (pp. 80, Table 3.5 on p. 87, p.431). American Institute of Aeronautics and Astronautics. <http://knovel.com/web/portal/browse/display?_EXT_KNOVEL_DISPLAY_bookid=1597&VerticalID=0>. [accessed 2/19/2012].
[38] Lichodziejewski, D., Derbès, B., West, J., Reinert, R., Belvin, K., Pappa, R. Bringing an Effective Solar Sail Design Toward TRL 6. Paper AIAA 2003-4659, 39th AIAA Joint Propulsion Conference, 2003.
[39] Brown, M.A. Mechanical Design of a Kilometer-Sized Solar Sail AIAA 2010-2586 12 ·15 April 2010, Orlando, Florida 1010-1023
[40] Datashvili, L., Baier, H. Building blocks of large deployable precision membrane reflectors", Proceedings of the 42nd AIAA/ASME Structures, Structural Dynamics and Materials Conference, AIAA paper no. 2001-1478, April 2001, Seattle
[41] Datashvili, L., Baier, H. Wehrle, E., Kuhn, T., Hoffmann, J. Large Shell-Membrane Space Reflectors. 51st AIAAlASME/ASCE/AHS/ASC Structures, Structural Dynamics, and Materials Conference, 18th AIAA 2010-2504 12 ·15 April 2010, Orlando, Florida.
[42] Solarbuzz, Module prices - Retail Price Summary - February 2012 Update. http://solarbuzz.com/facts-and-figures/retail-price-environment/module-prices [accessed 2/19/2012].
[43] Koelle, D.E. Cost efficiency as design and selection criterion for future launch vehicles Acta Astronautica Volume 57, Issues 2–8, July–October 2005, Pages 623–629
[44] Spacex Space Exploration Technologies. Falcon 9 Overview. March 2009. http://www.spacex.com/falcon9.php [accessed 2/19/2012].

[45] REN 21 (Renewable Energy Policy Network for the 21st Century). Renewables Global Status Report 2011 Update, http://www.ren21.net/default.aspx?tabid=5434 [accessed 2/19/2011].
[46] Nield, Jeff. Growing Food in the Arctic Circle. August 29, 2008. http://www.treehugger.com/files/2008/08/growing-food-in-the-arctic-circle.php [accessed 2/19/2012].
[47] Cook, Roberta, Calvin, Linda. North American Greenhouse Tomatoes Emerge as a Major Market Force. Amber Waves. April 2005. http://www.ers.usda.gov/Amberwaves/April05/Features/GreenhouseTomatoes.htm [accessed 2/19/2012].
[48] World Bank. World GDP. http://data.worldbank.org/indicator/NY.GDP.MKTP.CD/countries/1W?display=graph [accessed 2/19/2011].
[49] OECD. Gross domestic product in US dollars. OECD 2012. http://www.oecd-ilibrary.org/sites/gdp-cusd-table-2012-1-en/index.html;jsessionid=cld88aof9i8.delta?contentType=&itemId=/content/table/gdp-cusd-table-2012-1-en&containerItemId=/content/table/gdp-cusd-table-2012-1-en&accessItemIds=&mimeType=text/html [accessed 2/19/2012].
[50] Stockholm International Peace Research Institute (SIPRI). http://milexdata.sipri.org/ [accessed 2/19/2012].
[51] DESERTEC Foundation, Clean power from deserts. http://www.desertec.org/ [accessed 2/19/2012].
[52] Longcore, T., Rich, C. Ecological light pollution. Frontiers in Ecology and the Environment, Vol. 2, No. 4, May, 2004, 191-198.
[53] Laframboise, J. G., Chou, B. R.. Space Mirror Experiments: A Potential Threat to Human Eyes. *Journal of the Royal Astronomical Society of Canada*, 94, 237-240, 2000, June 27.
[54] Chepesiuk R 2009. Missing the Dark: Health Effects of Light Pollution. Environ Health Perspect 117:A20-A27. http://dx.doi.org/10.1289/ehp.117-a20
[55] U.N. The outer space treaty, http://www.oosa.unvienna.org/oosa/SpaceLaw/outerspt.html [accessed 2/19/2012].
[56] European Centre for Space Law (ECSL). Space policy documents and useful readings on regional and national space legislations. http://www.esa.int/SPECIALS/ECSL/SEMDTNLTRJG_0.html [accessed 2/19/2012].
[57] Oosterlinck, Rene <"Who owns and regulates space and why are space laws necessary?". European Space Agency (ESA) http://www.youtube.com/watch?v=ADTg5CfNNUA [accessed 2/19/2012].

Numerical parametric study for different cold storage designs and strategies of a solar driven thermoacoustic cooler system

Maxime Perier-Muzet[a], Pascal Stouffs[b], Jean-Pierre Bedecarrats[c] and Jean Castaing-Lasvignottes[d]

[a] *Université de Pau et des Pays de l'Adour, LaTEP, Pau, France, maxime.perier-muzet@etud.univ-pau.fr (**CA**)*
[b] *Université de Pau et des Pays de l'Adour, LaTEP, Pau, France, pascal.stouffs@univ-pau.fr*
[c] *Université de Pau et des Pays de l'Adour, LaTEP, Pau, France, jean-pierre.bedecarrats@univ-pau.fr*
[d] *Laboratoire de Physique Et Ingénierie Mathématique pour l'Energie et l'environnemeNT (PIMENT), Ile de la Réunion, France, jean.castaing-lasvignottes@univ-reunion.fr*

Abstract:

A heat driven thermoacoustic cooler consists of a thermoacoustic engine that converts heat into acoustic waves, coupled to a thermoacoustic cooler that converts this acoustic energy into cooling effect. These machines have simple structures without moving parts. The coupling of a solar concentrator and a heat driven thermoacoustic cooler seems to be an interesting alternative to the electrically driven compression vapour cycle. As the other solar refrigeration systems, even if the cooling demand generally increases with the intensity of the solar radiation, one of the major difficulties is to insure a frigorific power supply when there is no or low solar radiation. In our prototype, in order to guarantee a sufficient cooling capacity to face to refrigeration loads in spite of the production fluctuations, a latent cold storage has been considered. The aim of the work presented here is to investigate the behaviour of this key element under several design and operative conditions. A description of the future prototype is done insisting on the thermoacoustic refrigeration and the cold storage system. A modelling of the main elements of the prototype is developed. The results of simulations under real solar radiation as well as a parametric study considering the main design and operative parameters of the cold thermal storage system are presented.

Keywords:

Solar energy, Solar refrigeration, Thermoacoustic refrigerator, Cold latent thermal storage.

1. Introduction

Energy use for refrigeration has risen sharply in recent years. Nowadays, the major part of this production is provided by electrically driven vapour compression machines. Globally, the refrigeration devices consumed roughly 15% of the world electricity production. The forecasts for the refrigeration indicate an increase in the number of units in operation over the coming years. To ensure the refrigerating production in the next years while responding to environmental challenges (emissions of greenhouse gases and ozone layer) the future cooling machines should not be primary energy intensive and should use environmentally friendly refrigerants [1, 2].

Thanks to numerous possible combinations between solar thermal collectors and heat driven cooling machines, solar cooling equipment seems to be an interesting alternative [3]. Among these possibilities, the coupling of a solar concentrator with a heat driven thermoacoustic refrigerator is a promising technology. Compared to the other refrigeration technologies, heat driven thermoacoustic machines have several advantages with no moving part and environmentally friendly gas as working fluid like helium, argon or air [4]. During the last decades, experimental investigations have been carried out on these machines. They have proven their ability to reach very low temperatures compatible with the liquefaction of gases such as, natural gas, nitrogen or hydrogen [5-7]. Other studies have demonstrated the possibility to uses thermoacoustic refrigeration for higher temperature applications like for food refrigeration [8]. The couplings of thermodriven

thermoacoustic refrigerators and solar concentrators have also already been experimentally studied thanks to low power prototypes [9, 10].

Although the cooling demand is generally higher when the sun is shining, the intermittent nature of solar energy is one of the major constraints for using solar cooling systems. To meet the time-dependency of the primary energy supply and end-use requirement, a thermal energy storage has to be used. Various configurations of the energy storage can be achieved; storing the hot energy for continuously supply the refrigeration system or storing the produced cool energy. This energy can be stored in the form of sensible heat (in liquid or in solid), latent heat of a Phase Change Material (PCM), or by chemical reaction. The choice of the storage system depends on various criteria like the amount of energy that has to be stored or the storage temperature. However for cooling application, the latent storages have numerous advantages: the technology is well known with a high energy storage density; the stored and retrieved energy is at a quasi constant temperature which corresponds to the phase change transition of the PCM [11].

The studied prototype consists in a one kW scale solar thermodriven thermoacoustic refrigerator supplied in primary energy by a solar dish concentrator. To ensure a low variability of the availability of refrigerating capacity, a cold latent thermal storage is coupled to the refrigerator.

In the first part of this paper the project and the main parts of its development are presented. Secondly, the lumped model that has been built is described. Then, the first simulation results for a long period including days with various solar radiation conditions are presented and discussed. Finally, the results of the parametric study are presented, considering the above-mentioned different cold storage design characteristics and storage strategies.

2. Prototype description

The device considered here consists in a solar concentrator, a solar flux modulator, a solar receiver, a thermoacoustic machine composed firstly of a thermoacoustic prime mover linked to an acoustic resonator and secondly of a thermoacoustic refrigerator linked to a cool thermal energy storage (Fig. 1).

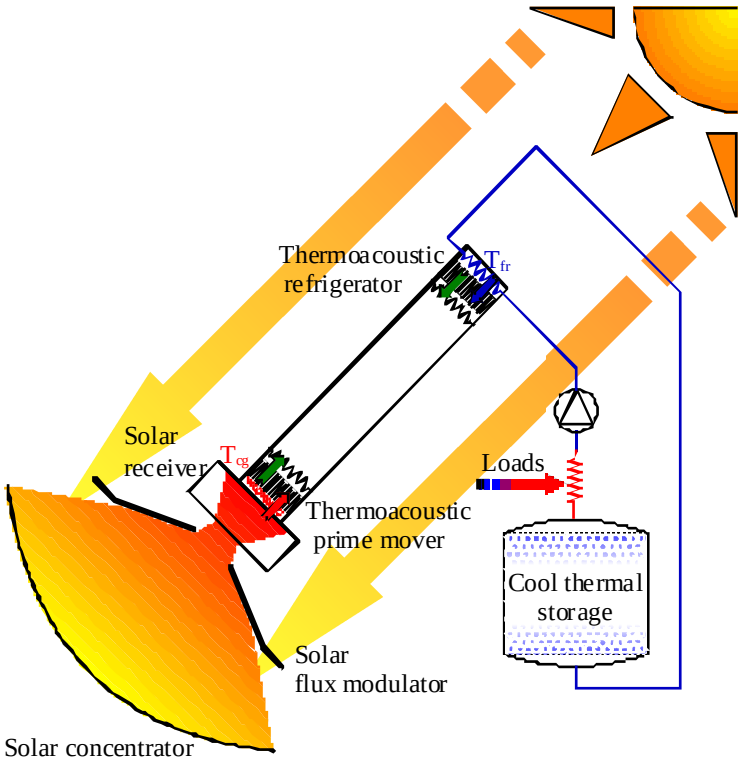

Fig. 1. Solar driven thermoacoustic refrigerator experimental plant

The solar driven thermoacoustic refrigerator heat fluxes represented in Fig. 2 are described in the following sections. The direct solar radiation is collected, reflected and concentrated by a parabolic mirror. More details on this element can be found in [12]. A solar flux modulator is placed between the concentrator and the receiver cavity. This element regulates the solar power entering in the absorbing cavity; it thus allows controlling the temperature of this latter. The concentrated solar radiation is collected by an absorber situated in the receiver cavity. This latter transfers approximately 4 kW to the working fluid (helium at about 4 MPa), while being at a temperature close to 500°C. More details on this component can be found in [13, 14].

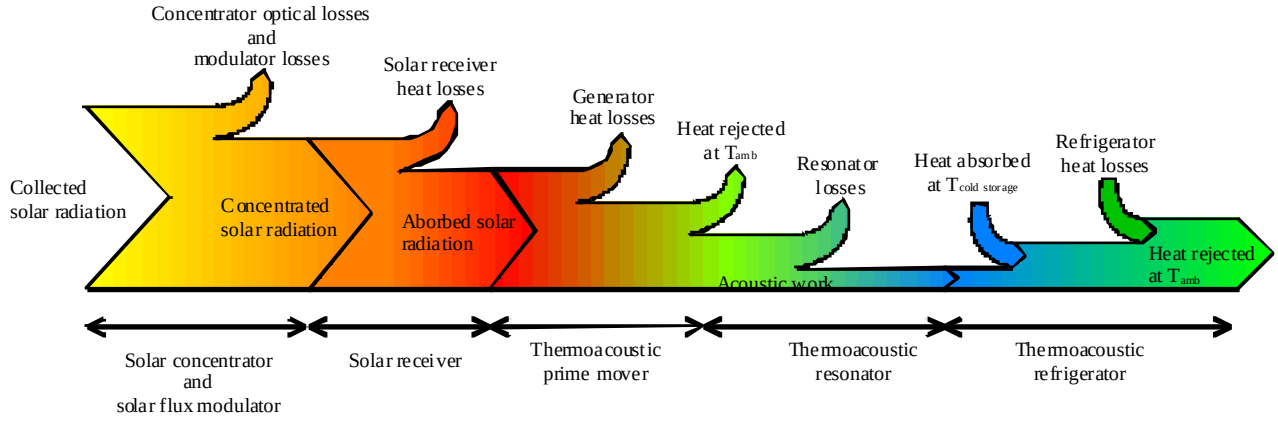

Fig. 2. Solar driven thermoacoustic refrigerator heat fluxes

The thermoacoustic cooler is composed of a wave generator, an acoustic resonator and a thermoacoustic refrigerator. Thank to the solar heat absorbed, the thermoacoustic prime mover generates a traveling wave with large acoustic power. This power is used into the thermoacoustic refrigerator to pump approximately 800 W of heat from the cold heat exchanger and reject it at the intermediate temperature exchanger of the refrigerator. A detailed explanation of the way these coolers work is given in [15].

To ensure a constant power supply at the cold exchanger, a latent storage is intended to be used. This later uses encapsulated nodules filled with an eutectic Phase Change Material (PCM). The storage tank is filled with these nodules and the cold transfer fluid which circulates in the tank ensures the heat exchange between the PCM and the cold production unit [16]. During the time where the tank is being cooled, the crystallization of nodules allows the storage of the energy.

To produce a controlled thermal load, an electrical fluid circulation heater is placed between the storage tank and the cold heat exchanger. The power regulation of this latter allows generating different consumption and storage strategies.

3. Modelling

To predict the future performance of the prototype a lumped model of the entire plant has been developed. The time variation of the energy source and the frigorific power consumption imposes a transient approach. The solar part and the cold storage are treated by simplified transient models. For the thermodriven thermoacoustic refrigerator, a quasi-stationary approach it used. We describe the equations and the principal assumptions of this model in the following sections.

3.1. The solar concentrator and the solar flux modulator

The solar concentrator consists in a 8.5 m diameter parabolic mirror. For this prototype, the aperture of the dish is reduced at 13.5 m² by using non reflective bands at the concentrator periphery. Thanks to the sun tracking system, solar rays are always perpendicular to the collector aperture. The collecting solar power is calculated as following:

$$\dot{Q}_{sol_collect} = A_{collector_aperture} . DNI \,, \qquad (1)$$

Where *DNI* is the Direct Normal Irradiation and $A_{collector_aperture}$ is the collector aperture area.

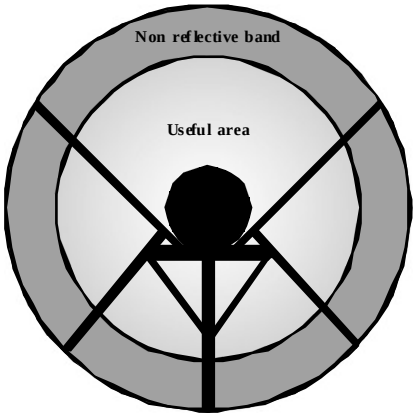

Fig. 3. Concentrator aperture

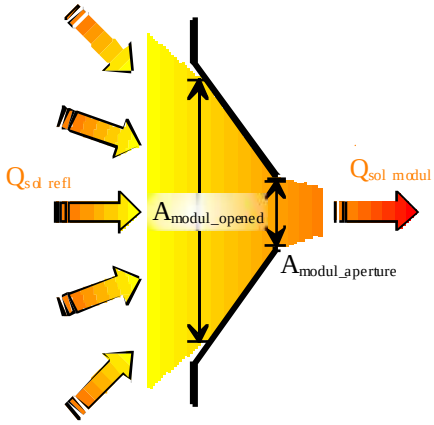

Fig. 4. Modulator geometry

The Thermoacoustic machine, the flow pipes, the frame of the concentrator, etc… shadow a part of the dish (Fig. 3). The sun tracking system is considered to be accurate so that the useful area of the concentrator remains constant all along the day. A constant and uniform mirror reflectivity is assumed. According these hypotheses, the reflected solar power is expressed by:

$$\dot{Q}_{sol_reflect} = A_{collector_useful} \cdot \chi . DNI \,, \qquad (2)$$

Where $A_{collector_useful}$ is the useful area of the concentrator aperture calculated by $A_{collector_useful} = A_{collector_aperture} - A_{shadow}$, and χ is the mirror reflectivity.

A uniform solar concentrated flux is assumed in the modulator plan (Fig. 4). It is also considered that it has no impact if it is totally opened. The solar modulated power is determined by:

$$\dot{Q}_{sol_modul} = \dot{Q}_{sol_reflect} \frac{A_{modul_aperture}}{A_{modul_opened}}, \qquad (3)$$

Where $A_{modul_aperture}$ is the area of the modulator aperture and A_{modul_opened} is the area of the modulator aperture when it is totally opened.

3.2. The solar driven thermoacoustic refrigerator

We consider in this modelling, a uniform wall and fluid temperature in all heat exchangers of the thermoacoustic device. The temperature of the hot exchanger of the thermoacoustic generator is also assumed to be equal to the temperature of the solar receiver cavity wall.

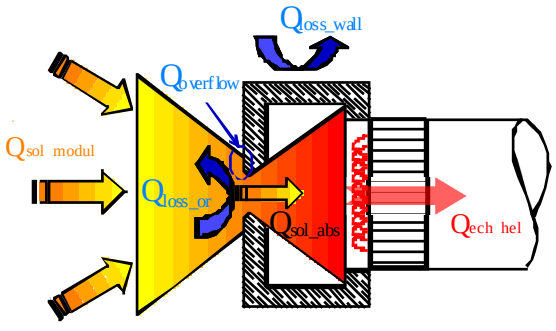

Fig. 5. Absorber cavity and hot exchanger heat fluxes

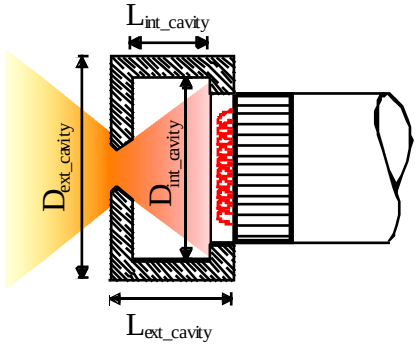

Fig. 6. Absorber cavity geometry

The cavity absorbs the solar concentrated flux. Thanks to the hot exchanger, a large part of this heat flux is transferred to the working fluid, the rest is exchanged with the surroundings (Fig. 5). The

cavity walls are considered as an equivalent mass of the hot exchanger. The energy balance of these elements can be written as:

$$\frac{dU_{cavity+hg}}{dt} = \dot{Q}_{sol_abs} + \dot{Q}_{loss_cavity} + \dot{Q}_{hel-wall_hg}, \qquad (4)$$

Where $\dot{Q}_{sol_abs}$ is the absorbed solar power. The absorber cavity absorbs the major part of the solar power which passes through the solar flux modulator. The rest is the solar loss by overflow. This loss is due to the diameter difference between the solar focus point and the cavity orifice. If the diameter of the focal point is larger than the one of the cavity aperture (as it is the case for the studied prototype, in order to limit the thermal losses through the orifice) a part of the solar radiation cannot enter in this later. In this model, the solar overflow losses are evaluated considering a solar overflow rate ($\tau_{sol_overflow}$). This rate is equal to a constant value when the solar flux modulator is totally opened and equal to zero when the modulator is partially closed. The absorbed solar power is calculated by:

$$\dot{Q}_{sol_abs} = \dot{Q}_{sol_modul}.\left(1-\tau_{overflow}\right), \qquad (5)$$

The cavity exchanges with the surrounding by the orifice, the lateral wall and the back wall. The cavity thermal losses $\dot{Q}_{loss_cavity}$ can be determined by:

$$\dot{Q}_{loss_cavity} = \dot{Q}_{loss_or} + \dot{Q}_{loss_lateral_wall} + \dot{Q}_{loss_back_wall}, \qquad (6)$$

$\dot{Q}_{loss_lateral_wall}$ and $\dot{Q}_{loss_back_wall}$ are calculated considering that radiative heat exchanges are negligible compared to convective ones from the insulating material surface. The convective heat exchange coefficient between the orifice and the surrounding is estimated from [17].

The two others cavity losses are determined using the various thermal resistances except the thermal resistance of contact between the cavity wall and the insulation which is neglected.

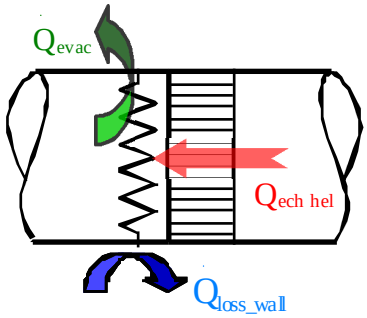

Fig. 7. Heat fluxes in the ambient and cold heat exchangers

The cold exchanger of the refrigerator as well as the heat exchangers at intermediate temperature, (Fig. 7) transfer on one side with the helium and on the other with a heat transfer fluid. The cold one is submitted to heat transfer with surroundings while such an exchange is neglected for the other ones because of the low temperature difference between these exchangers and ambient air. Applying the first law to the wall and to the heat transfer fluid of these elements gives:

$$\begin{cases} \frac{dU_{wall_exch}}{dt} = \dot{Q}_{fluid-wall_exch} + \dot{Q}_{hel-wall_exch} + \dot{Q}_{loss_exch} \\ \frac{dU_{fluid_exch}}{dt} = \dot{Q}_{wall-fluid_exch} + \dot{m}_{fluid_exch}\left(h_{fluid_input_exch} - h_{fluid_output_exch}\right) + \dot{Q}_{visco_exch} \end{cases}, \qquad (7)$$

The convective heat transfers between the heat exchanger walls and the fluids are given by:

$$\dot{Q}_{fluid-wall_exch} = \alpha_{fluid-wall}.A_{fluid-wall}\left(T_{fluid} - T_{wall_exch}\right), \qquad (8)$$

Where the heat exchange coefficients ($\alpha_{fluid\text{-}wall}$) are calculated thanks to a correlation for a fluid flowing across a bank of tubes proposed in [18].

The viscous dissipation inside the exchanger is calculated by:

$$\dot{Q}_{visco_exch} = \Delta P_{exch} \frac{\dot{m}_{fluid_exch}}{\rho_{fluid}}, \quad (9)$$

Where ΔP_{exch} are the pressure drops inside the exchangers. They are calculated thanks to a correlation for a fluid flowing across a bank of tubes determined by [18] and ρ_{fluid} is the density of the fluid.

Each equation relative to the exchanger walls has a term of transfer with helium. A stationary model is used to determine these heat fluxes at each calculation time step of the quasi-stationary model [19].

3.3. The cool loop and cool thermal energy storage

The cool loop is mainly composed of flow pipes, an electrical load, a pump and a cool thermal storage.

3.3.1. Flow pipes

The flow pipes insure the connection between the elements. For this model, only the two longer pipes are considered (between the pump and the cold exchanger and between the cold exchanger and the cool storage). The temperatures of the fluid and the wall are assumed uniform inside the pipes. They are also considered perfectly insulated. The pipe walls are considered as an equivalent mass of fluid. With these hypotheses the energy balance on these elements is:

$$\frac{dU_{fluid+wall_pipe}}{dt} = \dot{m}_{fluid_cool_circuit}\left(h_{fluid_input_pipe} - h_{fluid_output_pipe}\right) + \dot{Q}_{visco_pipe}, \quad (10)$$

The viscous dissipations $\dot{Q}_{visco_pipe}$, are calculated by (11) with the pressure drop determined by:

$$\Delta P_{pipe} = \rho_{fluid} \frac{V_{fluid}^2}{2}\left[\sum K + \lambda \frac{L_{pipe}}{D_{int_pipe}}\right], \quad (11)$$

With K the local coefficients of pressure drop for valves, changes of direction, …and λ the linear coefficient of pressure drop.

3.3.3. Circulating pump and electrical fluid circulation heater

We assumed that there is no variation of the internal energy of these elements. They are also considered adiabatic.

Applying the first law to the heat transfer fluid of these elements under these hypothesis gives:

$$\dot{Q}_{elec_heater} = \dot{m}_{fluid_cool_circuit}\left(h_{fluid_output_heater} - h_{fluid_input_heater}\right), \quad (12)$$

Where $\dot{Q}_{elec_heater}$ is the electrical power which feeds the heater.

A constant efficiency (η_{pump}) is considered for the pump. Considering these limitations, the energy balance of the fluid inside the circulating pump is expressed by:

$$h_{fluid_output_pump} - h_{fluid_input_pump} = \frac{\Delta P_{circuit}}{\rho_{fluid}}\left(1 - \eta_{pump}\right), \quad (13)$$

Where $\Delta P_{circuit}$ are the total pressure drops of the circuit.

3.3.3. The cool thermal energy storage

The model which has been already described in detail in a previous paper [20], considers the aspects of both the surrounding heat transfer fluid and the phase change material packed inside the nodules in the charge mode as well as in the discharge mode. Only the main hypotheses and equations are presented here with a special adaptation to the selected configuration.

In order to simplify the physical model of the latent heat storage, the following assumptions were made:

- The tank is vertical with flow from the bottom to the top for the charge mode and the discharge mode;
- The flow in the tank is axial and incompressible;
- Variation of temperature of the heat transfer fluid occurs only along the axial direction, i.e. as checked experimentally [16], the temperature is independent of the radial position;
- The insulation of the tank is considered perfect;
- Heat transfer by conduction is neglected in the heat transfer fluid;
- Kinetic and potential energy changes are negligible;
- The tank is divided in several control volumes according to the height (Fig. 9);
- The nodules are considered as exchangers. The energy flux exchanged is proportional to the difference of temperature between the fluid and the interior of the spherical nodule;
- The supercooling phenomenon is taken into account.
- The variation of the internal energy of the tank elements (metal wall pipe, flow diffusers, etc..) is neglected.
- The pressure losses are considered for the flow inlet and outlet, the flow diffusers and the nodule bed thank to local coefficients of pressure drops.
-

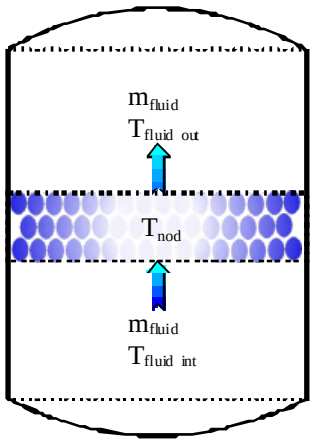

Fig. 9. Tank control volume.

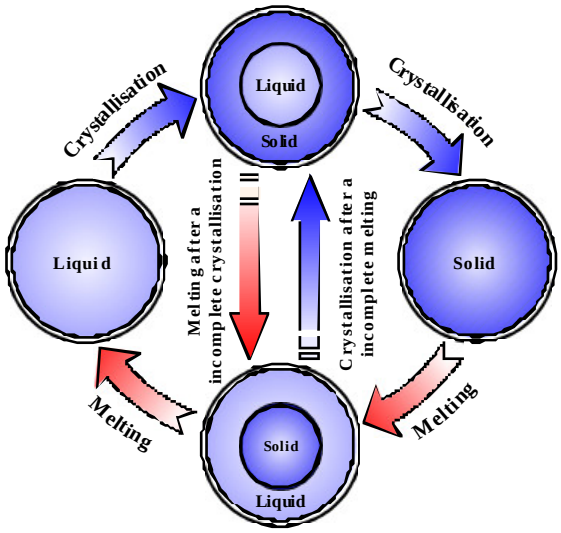

Fig. 10. State of nodule and way of crystallisation and melting

Based on these assumptions the energy balance equations in transient state in each control volume for the heat transfer fluid and each spherical nodule *i* are:

$$\frac{dU_{fluid}}{dt} = \dot{m}_{fluid}\left(h_{fluid\ in} - h_{fluid\ out}\right) + \sum_{i=1}^{N_{nod}} \dot{Q}_{nod-fluid,i} + \dot{Q}_{visco_storage} \quad (14)$$

$$\frac{dU_{nod,i}}{dt} = m_{nod}\frac{du_{nod,i}}{dt} = \dot{Q}_{nod-fluid,i} \quad (15)$$

With

$$u_{nod,i} = \begin{cases} u_{ref} + Cv_{PCM\ solid}\left(T_{nod,i} - T_{ref}\right) & if \quad x_{nod,i} = 1 \\ u_{ref} + Cv_{PCM\ solid}\left(T_{melt} - T_{ref}\right) + x_{solid}\ L & if \quad 0 < x_{nod,i} < 1 \\ u_{ref} + Cv_{PCM\ solid}\left(T_{melt} - T_{ref}\right) + L + Cv_{PCM\ liq}\left(T_{nod,i} - T_{ref}\right) & if \quad x_{nod,i} = 0 \end{cases} \tag{16}$$

Even when the heat transfer fluid temperature is considered uniform in each layer, all the nodules of each layer do not simultaneously pass through the phase change at the melting temperature T_{melt} during cooling because of the supercooling and the erratic character of the crystallisation. The nodules can be in different states (non-crystallised, entirely crystallised or partly crystallised) according to their own value of the beginning of the crystallization (Fig. 10).

Applying the nucleation laws, the number of new crystallisations and the corresponding fluxes can be calculated at each time t [20].

Considering a nodule of inner radius r_{int} (Fig. 11). Uniform cooling of its surface will result in a spherically symmetric crystallisation-front, $r = r_{interface}(t)$ the inner radius of solid PCM, propagating inwards from $r = r_{int}$ with liquid at T_{melt} for $0 \le r \le r_{interface}(t)$ and solid for $r_{interface}(t) \le r \le r_{int}$. Assuming constant thermal properties in each phase, the steady-state solution of the heat conduction in the solid phase has the form (θ is the temperature of the solid PCM):

$$\theta(r,t) = T_{melt} + \left[T_{fluid}(t) - T_{melt}\right] \frac{1 - \frac{r_{interface}(t)}{r}}{\left(\frac{k_{PCMsolid}}{k_{env}} - 1\right)\frac{r_{interface}(t)}{r_{int}} + \left(\frac{k_{PCMsolid}}{\alpha_{ext} r_{ext}} - \frac{k_{PCMsolid}}{k_{env}}\right)\frac{r_{interface}}{r_{ext}} + 1} \tag{17}$$

The interface conditions here have the standard form:

$$k_{PCMsolid}\left[\frac{\partial\theta(r,t)}{\partial r}\right]_{r=r_{interface}(t)} = \frac{-\dot{Q}_{nod-fluid,i}}{4\pi r_{interface}^2(t)} \tag{18}$$

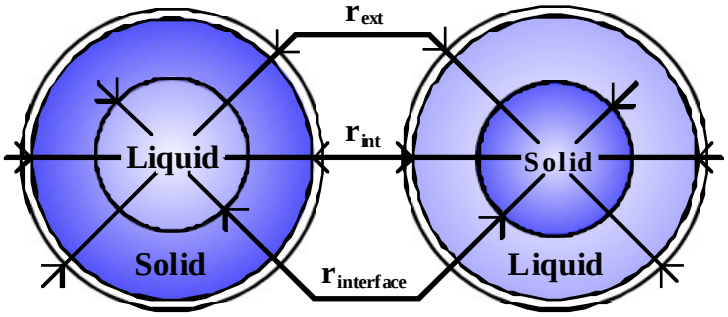

Fig. 11. Crystallization inside a nodule (left) and melting inside the nodule (right).

The determination of $\dot{Q}_{nod-fluid}$ before crystallisation starts and after crystallisation is finished is done considering the uniform PCM temperature and it is possible to write that the internal energy variation in the PCM is equal to the flux that leaves the nodule.

The heat transfer coefficient between the nodule and the fluid is determined by a correlation [20] and so depends on the flow rate and on the fluid temperature.

Supercooling occurs only upon crystallisation but never upon melting. So, all the nodules from each layer simultaneously pass through the phase change at the melting temperature T_{melt}.

According to a simplifying assumption, the melting-front is considered to be concentric (Fig. 11) and equations for $\dot{Q}_{nod-fluid}$ are the same than for crystallisation. During the melting process, heat is transfered by natural convection and conduction. Only the heat conduction equation is kept into consideration but an apparent thermal conductivity [21] is used in order to take the natural convection into account.

4. Results

From the model described in the previous section, numerical simulations of the experimental plant have been carried out assuming a constant ambient temperature of 20°C. The solar radiation conditions that have been used are the DNI measured between the 1st and the 7th of July 2006 by PROMES laboratory at Odeillo (South of France) (Fig. 12). The main parameters that have been considered for this simulation are summarised in Table 1.

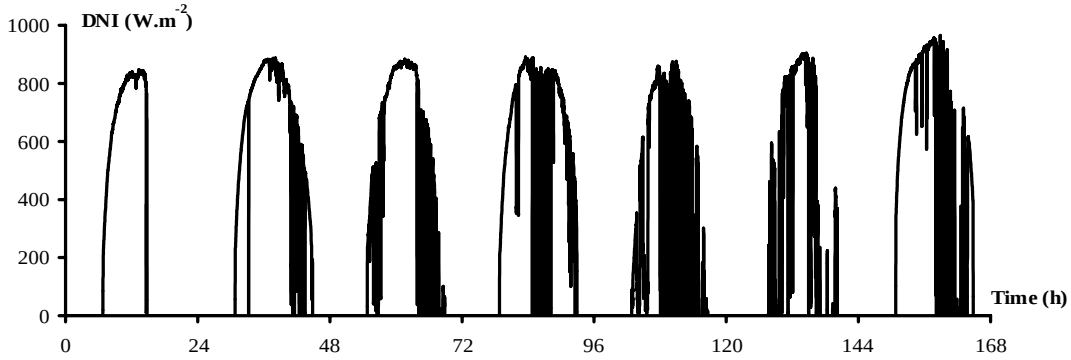

Fig 12. DNI

Table 1. Main simulation parameters

Solar concentrator aperture area (m²)	13.5	Hot heat exchanger mass (kg)	30
Shadow area on the concentrator (m²)	3.5	Ambient heat exchanger mass (kg)	1
Reflectivity of the concentrator	0.92	Cold heat exchanger mass (kg)	1
Cavity orifice diameter (m)	0.1	Electrical power of the heater (W)	350
Solar overflow rate	0.1	MCP nodule diameter (mm)	77

4.1. Standard case

A standard case for design and operating parameter of the cool storage has been considered (Table 2). The simulation results of this case are presented in this section.

Table 2. Main storage tank design and operative parameters

	Standard case	Variation for parametric study
Tank volume (m^3)	0.2	0.15 and 0.25
Masse flow rate ($kg.s^{-1}$)	0.1	0.05 and 0.2
PCM melting temperature (°C)	-21.3	-18.8 and -26.2

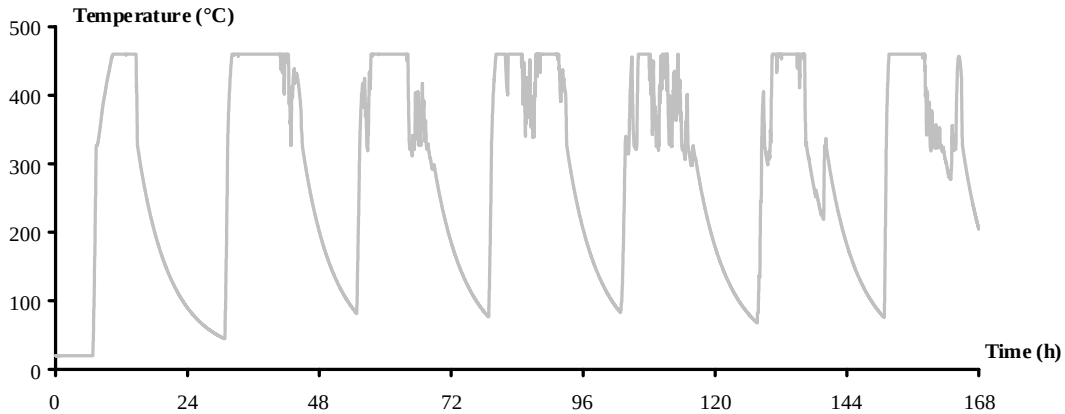

Fig 13. Temperature of the hot exchanger of the generator

As shown in Fig. 13, when the sun is shining, the temperature of the hot exchanger of the generator increases extremely rapidly to reach the temperature threshold for wave generation. Actually the machine starts only if a sufficient temperature gradient exists between the two heat exchangers of the engine cycle. According to previous experiences, the starting hot temperature (and also stop temperature when the exchanger temperature decreases) of the generator has been set at 600 K. The solar power available is very large compared to the one consumed by the acoustic wave generation and the thermal losses so that the temperature of the hot exchanger continues to grow rapidly to reach the regulating temperature. This regulation is ensured by the control of the absorbed solar radiation thank to the solar flux modulator. When the DNI is important, it can shut up to 45% of the reflected solar power. At the end of the day or during cloudy periods, the hot exchanger is cooled due to the power consumed by the acoustic wave generation (if its temperature is higher than 600 K) and due to the radiative and convective heat losses. The hot exchanger behaviour is roughly the same for each simulated days with variations in function of the solar radiation fluctuations.

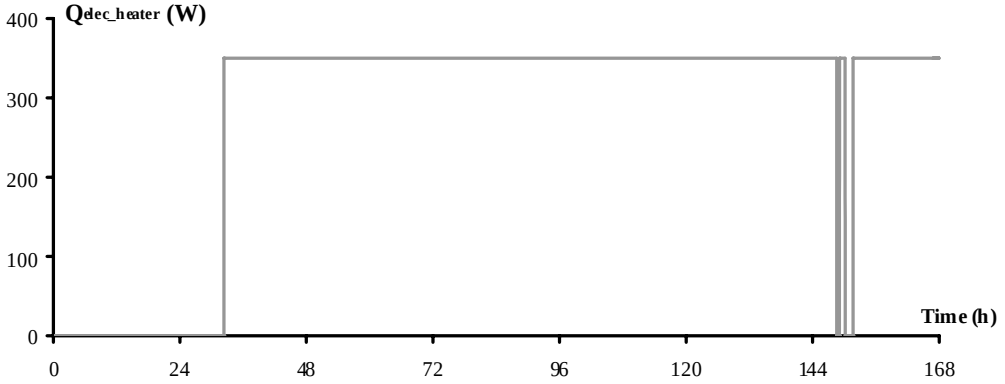

Fig 14. Electrical power of the fluid heater

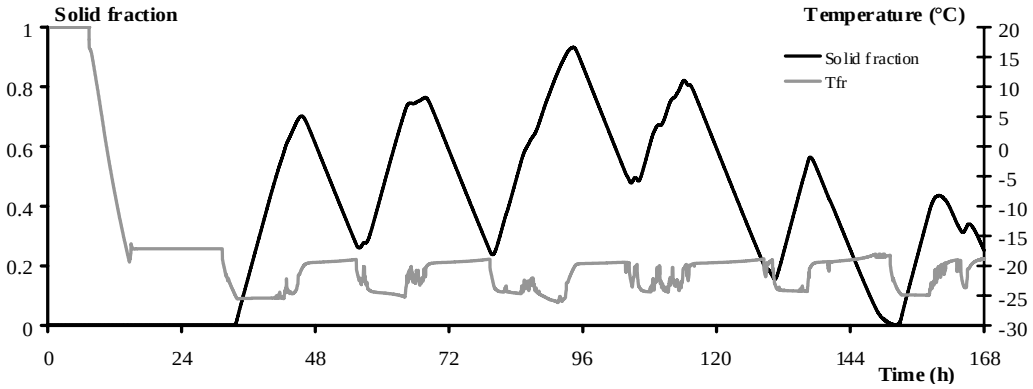

Fig 15. Solid fraction in the storage tank and temperature of the cold exchanger of the refrigerator

The operative conditions corresponding to the frigorific loads have been set as follows: a constant heating power if the fluid temperature at its outlet stays lower than -18°C and no heating power if this temperature is higher than this limit. To ensure the cooldown of the storage and the loop elements the heater is turned off during the first 30 hours (Fig. 14 and 15). During this period, when the refrigerator works, the temperature of the cold exchanger of the refrigerator decreases to reach a temperature close to the melting temperature of the PCM (Fig. 15). Due to the adiabatic assumption and no heating power, the temperature of the storage remains constant during the first night. At the beginning of the second day (close to 32 hours after the beginning of the simulated experimentation) the tank temperature continues to decrease below the melting temperature of the PCM. Due to thermal resistances between the fluid and the nodule and due to the supercooling

effect, the temperature of the fluid has to be a few degrees lower than the melting temperature to initiate the crystallisation. Even if the refrigerator continues to produce a frigorific power, the temperature of the cold exchanger remains quasi constant after the initiation of the crystallisation thank to the isothermal behaviour of the nodules during this phase. At the end of the second day, the majority of the PCM is solid. During the following night, a large part of the solid PCM is melting to supply the loads. During the next four days, the system reaches a quasi periodically steady state condition, the storage tank solid fraction evolves between the same levels from one day to the other and the temperature of the cold loop stays close to the melting temperature of PCM. Due to a low insolation during the two last days, the solid fraction of the tank decreases and there are periods where the storage cannot provide the cooling capacity within the imposed temperature condition.

4.2. Parametric study

From the standard case described previously, we consider the effects of the variation of the principal parameters of the cold thermal energy storage on the temperature of this storage and on the global performance of the experimental plant. The effect of the supercooling is firstly analyzed. Then the effect of the storage tank volume, the melting temperature of the PCM and the fluid mass flow rate, are successively considered (Table 2).

Supercooling effect: A simulation has been made considering no supercooling effect. As expected the lack of supercooling allows the initiation of crystallization of the PCM at a temperature higher than when this effect is considered. This temperature difference can be observed (Fig. 16) during the first crystallization stage. During the next four days, no difference can be observed because a large number of nodules remain constantly partially crystallized. Because of the total discharge of the stock during the night preceding, this phenomenon is again perceptible on the last day.

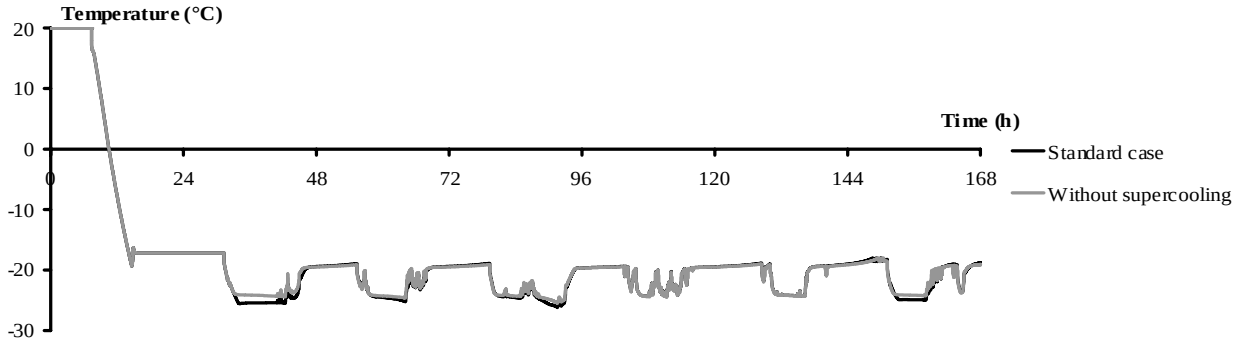

Fig. 16. Temperature of the cold exchanger of the refrigerator with and without PCM supercooling

Volume of the storage tank: The variations of the tank volume have significant impact on the cold exchanger temperature (Fig 17) and the PCM solid fraction (Fig 18). With the smallest tank there are periods where all the PCM into the tank is solid, thus the residual energy have to be stored as sensible heat. This generates very low temperatures in the cold circuit. Considering the largest tank, due to higher mass of fluid and PCM, a larger part of the energy is stored as sensible heat. The solid fractions are thus in this case lower than the other one. Due to this, with this configuration, there is a large period of time between the two last days where the storage cannot provide the cooling capacity.

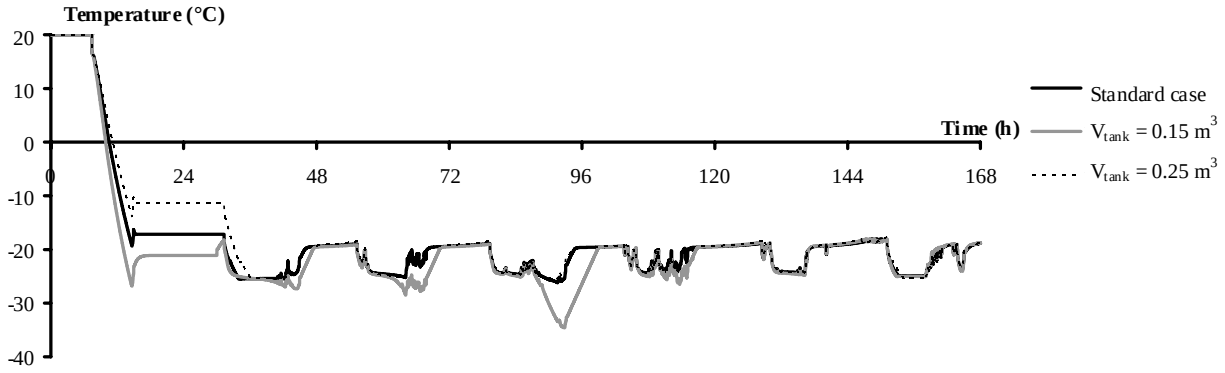

Fig. 17. Temperature of the cold exchanger of the refrigerator for different tank volumes

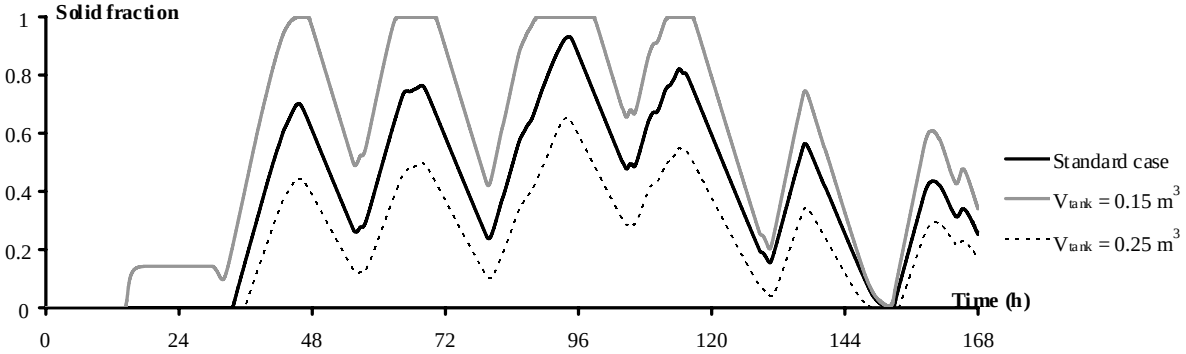

Fig. 18. Solid fraction in the storage tank for different tank volumes

Heat transfer fluid mass flow rate: Simulations have been made for different heat transfer fluid mass flow rates. The obtained results show that in the simulation conditions, this parameter has only a slight effect on the operation of the cold circuit (Fig. 19).

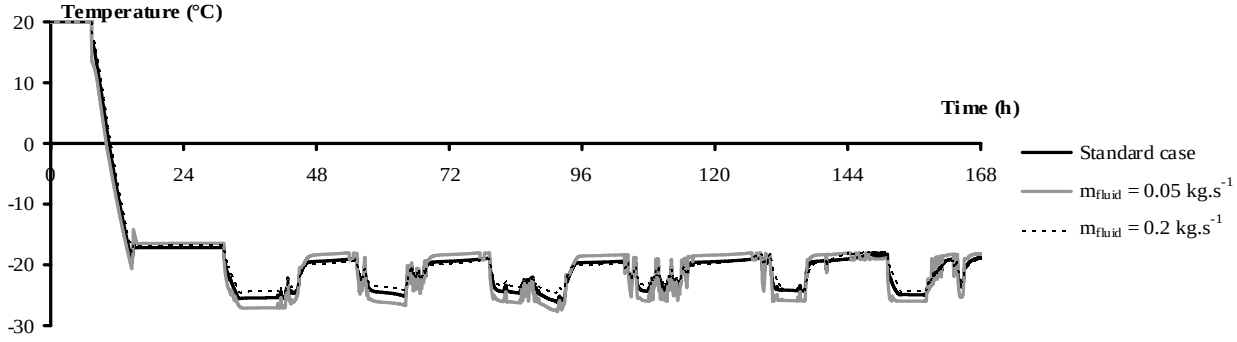

Fig 19. Temperature of the cold exchanger of the refrigerator for different mass flow rates

Melting temperature of the PCM: For these simulations the thermophysical properties of the PCM (except the melting temperature) are considered identical. Because of the low temperature difference between the expected temperature at the heater and the melting temperature of the highest PCM melting temperature, the major part of the energy is stored as sensible heat (Fig. 20. and Fig. 21). Due to the difficulty of the refrigerator to reach a low temperature to initiate the crystallisation of the lowest melting temperature PCM, the variation of the solid fraction in this case is low. In these two cases the temperature stabilisation which is expected with latent energy storage is not assured (Fig 21).

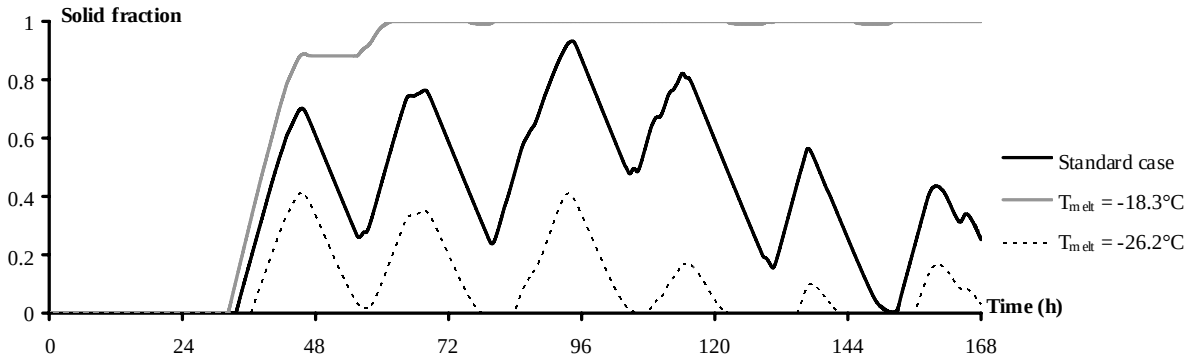

Fig 20. Solid fraction in the storage tank for different PCM melting temperatures

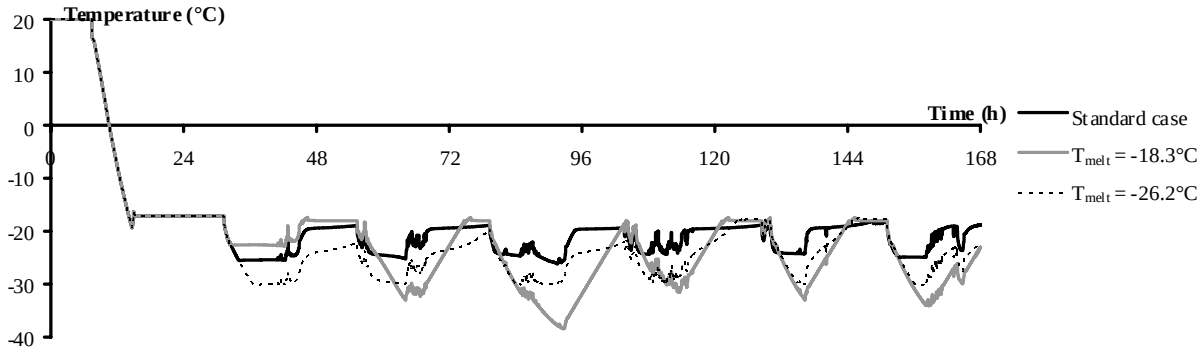

Fig 21. Temperature of the cold exchanger of the refrigerator for different PCM melting temperatures

4. Conclusion

A solar driven thermoacoustic cooler which consists of a thermoacoustic engine that converts solar energy into acoustic waves, coupled to a thermoacoustic cooler that converts this acoustic energy into cooling effect, has been studied using a numerical model. The designed prototype would be able to deliver a refrigerating capacity of about 1 kW at -30°C.

In order to guarantee a sufficient cooling capacity to face to refrigeration loads in spite of the production fluctuations, a cold storage using encapsulated PCM has been considered. It stores the excess cooling power when the sun is highly shining and restitutes it at night or during cloudy hours.

The developed model permits to determine the future performances of the prototype but also to choose the best configuration of the storage tank which has to be adapted to the loads. The main design parameters for the cool storage are the tank volume, the crystallization and melting temperature of the PCM and the mass flow rate of the heat transfer fluid.

Acknowledgments

This work was carried out within the framework of the TACSOL project. It is funded by the ANR PRECODD. We would like to thank our project partners, S. Cordillet (PROMES), P. Duthil (IPNO), M.X. François (Hekyom), T. Le Polles (Hekyom), G. Olalde (PROMES), M. Pierens (IPNO), J.P. Thermeau (IPNO), for their help.

Nomenclature

A area, m²

C specific heat, J kg^{-1} K^{-1}

DNI Direct Normal Irradiation, W m^{-2}

h enthalpy, J kg^{-1}

k thermal conductivity, W m^{-1} K^{-1}

K local coefficient of pressure drop

L length, m

L latent heat of the PCM, J kg^{-1}

$\dot{m}$ mass flow rate, kg s^{-1}

N number of nodules in the tank layer

ΔP pressure drop, Pa

$\dot{Q}$ heat flux, W

r radius, m

t time, s

T temperature, K

u specific internal energy, J kg^{-1}

U internal energy, J

x solid fraction of PCM

Greek symbols

α *convective* heat transfer coefficient, W m^{-2} K^{-1}

ε *emissivity*

χ reflectivity of the concentrator

λ linear coefficient of pressure drop

ρ density, kg m^{-3}

σ Stefan–Boltzmann constant, W m^{-2} K^{-4}

τ rate

η efficiency

Subscripts and superscripts

abs absorbed

amb ambient

collect collected

collector solar collector

env nodules envelope

exch exchanger

ext external

fluid heat transfer fluid

hg hot exchanger of the generator

hel-wall exchange between the helium and the exchanger wall

int internal

interface interface liquid/solid of the PCM

liq liquid phase of the PCM

loss yhermal losses

melt melting of the PCM

modul modulated or solar flux modulator

nod nodule
or orifice
PCM Phase Change Material
ref reference
reflect reflected
sol solar
solid solid phase of the PCM
visco viscous

References

[1] J. M. Calm, « Emissions and environmental impacts from air-conditioning and refrigeration systems », International Journal of Refrigeration 2002; 25 (3): 293-305.

[2] C. James M., « The next generation of refrigerants – Historical review, considerations, and outlook », International Journal of Refrigeration 2008; 31(7): 1123-1133.

[3] D. S. Kim et C. A. Infante Ferreira, « Solar refrigeration options - a state-of-the-art review », International Journal of Refrigeration 2008;31(1): 3-15.

[4] F. Zink, J. S. Vipperman, et L. A. Schaefer, « Environmental motivation to switch to thermoacoustic refrigeration », Applied Thermal Engineering 2010; 30(2–3): 119-126.

[5] J. J. Wollan, G. W. Swift, S. Backhaus, et D. L. Gardner, « Development of a thermoacoustic natural gas liquefier », presented at the AIChE New Orleans Meeting, New Orleans, 2002.

[6] G. Yu, E. Luo, et W. Dai, « Advances in a 300 Hz thermoacoustic cooler system working within liquid nitrogen temperature range », Cryogenics, vol. 50, n°. 8, p. 472-475, Aug. 2010.

[7] J. Y. Hu, E. C. Luo, S. F. Li, B. Yu, et W. Dai, « Heat-driven thermoacoustic cryocooler operating at liquid hydrogen temperature with a unique coupler », Journal of Applied Physics, vol. 103, p. 104906, 2008.

[8] M. E. Poese, R. W. M. Smith, S. L. Garrett, R. van Gerwen, et P. Gosselin, « Thermoacoustic refrigeration for ice cream sales », in Proceedings of 6th IIR Gustav Lorentzen Conference, Glasgow, UK, 2004.

[9] J. A. Adeff et T. J. Hofler, « Design and construction of a solar-powdered, thermoacoustically driven, thermoacoustic refrigerator », The Journal of the Acoustical Society of America, vol. 107, n°. 6, p. L37-L42, 2000.

[10] C. Shen, Y. He, Y. Li, H. Ke, D. Zhang, et Y. Liu, « Performance of solar powered thermoacoustic engine at different tilted angles », Applied Thermal Engineering, vol. 29, n°. 13, p. 2745-2756, Sept. 2009.

[11] A. Sharma, V. V. Tyagi, C. R. Chen, et D. Buddhi, « Review on thermal energy storage with phase change materials and applications », Renewable and Sustainable Energy Reviews, vol. 13, n°. 2, p. 318-345, Febr. 2009.

[12] F. Nepveu, A. Ferrière, et F. Bataille, « Thermal model of a dish/Stirling systems », Solar Energy, n°. 83, p. 81-89, 2009.

[13] S. Cordillet, P. Duthil, F. Nepveu, T. Le Polles, G. Olalde, A. Salome, et J.-P. Thermeau, « Theoretical proof of concept of an optimal solar receiver to produce low-temperature (-40°C) cooling using a thermoacoustic tri-thermal machine », in Proceedings of SolarPACES 2010, Perpignan, 2010.

[14] S. Cordillet, P. Duthil, E. Guillot, G. Olalde, et C. Gueymard, « Potential effects of rapid incident flux variations on the design of a solar thermoacoustic receiver », in Proceedings of SolarPACES 2010, Perpignan, 2010.

[15] G. Swift et Acoustical Society of America., Thermoacoustics: a unifying perspective for some engines and refrigerators. Melville NY: Acoustical Society of America through the American Institute of Physics, 2002.

[16] J. P. Bédécarrats, J. Castaing-Lasvignottes, F. Strub, et J. P. Dumas, « Study of a phase change energy storage using spherical capsules. Part I: Experimental results », Energy Conversion and Management, vol. 50, n°. 10, 2527-2536, oct. 2009.
[17] F. Nepveu, « Production décentralisée d'électricité et de chaleur par système Parabole/Stirling: Application au système EURODISH », Université de Perpignan, Odeillo, France, 2008.
[18] Y. A. Çengel, Heat transfer: a practical approach. Boston: McGraw-Hill, 2003.
[19] M. Perier-Muzet, J. Castaing-Lasvignottes, P. Stouffs, P. Duthil, J.-P. Thermeau, G. Olalde, S. Cordillet, et M.-X. François, Modélisation et simulation transitoire d'un refrigerateur thermoacoustique, in Actes Congrès Français de Thermique 2010, Le Touquet, (2): 851-856.
[20] J. P. Bédécarrats, J. Castaing-Lasvignottes, F. Strub, et J. P. Dumas, « Study of a phase change energy storage using spherical capsules. Part II: Numerical modelling », Energy Conversion and Management, vol. 50, n°. 10, p. 2537-2546, Oct. 2009.
[21] S. Fukusako et M. Yamada, « Recent advances in research on melting heat transfer problems », presented at the 10th Int Heat Transfer Conf, Brighton, Brighton, 1994, 313-331.

Parabolic Trough Photovoltaic/ Thermal Collectors. Part 1: Design and Simulation model

Francesco Calise[a], Laura Vanoli[b]

[a] *DETEC- Univ. of Naples Federico II, P.le Tecchio 80, 80125 Naples, Italy, frcalise@unina.it*
[b] *DIT – Univ. of Naples "Parthenope" C. D. IS.5, 80143 Naples, Italy, laura.vanoli@uniparthenope.it*

Abstract:
Photovoltaic/thermal (PVT) solar collectors are based on a combination of solar thermal and solar photovoltaic collectors. PVT systems allow one to produce simultaneously electrical energy and thermal energy by solar irradiation. Different PVT arrangements are presently under investigation. The most common configuration is the "tube and sheet" one in which a photovoltaic layer is encapsulated in the absorber of a conventional flat plate solar thermal collector. PVT electrical efficiency may be even higher than the one of a similar PV system when the fluid average temperature is relatively low. Therefore, the majority of PVT systems presently under development produce hot streams at temperatures lower than 45 °C. However, in the last few years different types of high temperature PVT systems are also under investigation. In fact, rising PVT fluid outlet temperature would dramatically increase the range of possible thermal applications. This paper is focused on this specific technology and presents a design procedure and a simulation model of a novel concentrating PVT collector. The layout of the PVT system under investigation was derived from a prototype recently presented in literature and commercially available in order to improve its electrical performance. The prototype consisted in a parabolic trough concentrator and a linear triangular receiver. The bottom surfaces of the receiver are equipped with mono-crystalline silicon cells whereas the top surface is covered by an absorbing surface. The aperture area of the parabola was covered by a glass in order to improve the thermal efficiency of the system. In the modified version of the collector considered in this paper, two changes are implemented: the cover glass was eliminated and the mono-crystalline silicon cells were replaced by triple-junction cells. These modifications allow one to increase significantly the electrical efficiency of the system especially in case of high operating temperatures. In order to analyze the performance of the modified Concentrating PVT (CPVT) collector a detailed mathematical model was implemented. This model is based on zero-dimensional energy balances on the control volumes of the system. The simulation model allows one to calculate in detail the temperatures of the main components of the system (PV layer, concentrator, fluid inlet and outlet and metallic substrate) and the main energy flows (electrical energy, useful thermal energy, radiative losses, convective losses). Results showed that the performance of the system is excellent even when the fluid temperature is very high (>100 °C). Conversely, both electrical and thermal efficiencies dramatically decrease when the incident beam radiation decreases

Keywords:
PVT, triple-junction, solar energy

1. Introduction

In the last few years, special attention has been paid to the renewable energy sources as a consequence of the dramatic decrease of the availability of conventional fossil fuels and the related increase of their costs. Among the available renewable technologies (solar, wind, hydro, geothermal, etc.), solar energy is commonly considered one of the most viable options. This is due to large availability of solar radiation for the all over the world and to the recent development of its conversion technologies. On the other hand, solar energy technology is still suffering of high capital costs and low power density. However, during the last few years the capital cost of solar collectors significantly decreased - specially in case of electrical ones - and their cost is expected to further decrease during the next few years. Conversely, dramatic improvements of the power density are not realistically expected since this parameter could be increased only by raising the conversion efficiency of the solar collectors. The solar energy can be exploited for producing both electricity

(by photovoltaic collectors, PV) and heat (by thermal solar collectors, SC). From this point of view, different commercial devices are available since several decades [1-2]. However, a possible improvement of both PV and SC technologies consists in a combination of their effects. This occurs in photovoltaic/thermal collectors (PVT) which simultaneously provide electricity and heat. The basic principle of a PVT collector is simple, since it can be obtained by a conventional thermal collector whose absorber is covered by a suitable PV layer [3]. The absorbed thermal energy is distributed to a fluid (typically air or water), whereas the PV produces electricity [1-2]. The final result of this arrangement is the combined production of electricity and heat and a possible improvement of PV efficiency. In fact, the PV electrical efficiency is strongly dependent on the system operating temperature, linearly decreasing with high values of such parameter [4]. Therefore, if the PV layer operating temperature is reduced by a cooling fluid, the system efficiency will be higher than the one of conventional PV [1-2, 4]. In order to achieve this result, the outlet temperature of the cooling fluid should be sufficiently low (usually < 40 °C). For this reason, the heat available from PVT systems can be used only for low-temperature heat demand (e.g., domestic hot water, floor heating, etc.). From this point of view, an interesting application is the desiccant cooling [5-6]. The selection of the PVT operating temperature is an important key-point in the system design. In fact, while higher operating temperatures increase the potential use of the cogenerative heat, they decrease the electricity production [1-2, 4]. As a consequence, researchers are performing a special effort seeking to realise a PVT collector providing medium-temperature heat (60 ÷ 80 °C) at high electrical efficiency [7]. A possible alternative for increasing fluid PVT outlet temperature without decreasing PV electrical efficiency, may consist in the use of a heat pump (driven by PV electricity) [1-2, 7]. Although the basic idea of the PVT was developed about 40 years ago, this product is still far from a mature commercialization [8]. Thus, several researchers are investigating several novel PVT arrangements [8-11]. For example, Zhao et al. investigated a novel PVT where thermal and electrical sections are separated [12]. One of the key points in the design of a PVT system is the eventual selection of a transparent cover. In fact, the covering can improve the thermal performance (higher insulation) but reduces the electrical one (higher reflection). This topic is still under investigation by a number of researchers analyzing different types of covers (tedlar, DEA, glass-to-glass, etc) [13]. Similarly, different studies investigated the optimal design of fluid channels. Different options are under investigation: the cooling fluid may flow between the PV and the absorber or between the absorber and the insulation (as usual in SC) [1-2]. Usually, the adopted PVT cooling fluid is water [10]. However, several studies are focused on the use of air [11] or in a combination of air and water [9]. The use of air as cooling fluid is very attractive in case of building integration. In fact, some companies and researchers are developing new prototypes of PVT facades or Building Integrated PVT (BIPVT) [14] which can: i) produce electricity; ii) provide space heating during the winter; iii) shade from the solar radiation in summer; iv) act as a ventilated façade in summer for reducing the cooling load [1-2]. In this case, the appropriate selection of PV technology is crucial for maximizing system overall performance [14]. Anyhow, the majority of the studies regarding PVT are focused on the development of devices that reduce capital costs and improve the system reliability. In this framework, a possible system configuration consists in the adoption of Concentrating PVT collectors (CPVT). Basically, they are simple PVT collectors placed in the focus of some reflectors (Fresnel, parabolic, dish, etc.) [1-2, 7, 15]. Obviously, the specific cost of this system is dramatically lower than the flat plate PVT one; this is due to the lower amount of PV employed per unit area. On the other hand, it must be considered that concentrating solar radiation devices determine an increase of radiative flux on PV, increasing its operating temperature and therefore decreasing its electrical efficiency. Usually, this drop off is not too high (typically, 0.45%/K for silicon cells), if the increase of temperature is fair (a silicon cell having an efficiency of 15 % at 25 °C, will show an efficiency of 11.6 % at 75 °C). Conversely, for high concentration ratios, the PVT operating temperature and the corresponding inefficiencies may significantly increase (for silicon cells, the voltage drops to zero at 270 °C) [4]. Therefore, the use of CPVT may be improved adopting novel PV materials, such as multi-junction solar cells which can approach a nominal

efficiency of 40% [15-16]. The adoption of such materials in CPVT may lead to a system operating up to 240 °C at reasonable conversion efficiency (slightly lower than 20%) [15]. The perspective of using high temperature PVT is very interesting since it extends the number of possible applications. An example consists in the use of the high-temperature heat provided by the PVT to drive a heat engine [17] or an Organic Rankine Cycle (ORC) [18] or a Solar Heating and Cooling system [15].

However, commercially or pre-commercially available CPVT systems are typically a small amount of the PVT under development [8]. Similarly, the availability of theoretical and experimental studies investigating CPVT performance is scarce. In particular, Mittelman et al [15, 19-20] performed some experimental and theoretical works dealing with CPVT systems. In reference [20] presented a novel miniature CPVT based on a dish concentrator (0.95 m^2) and a silicon PV cell. A thermal model for that system was developed in order to predict its performance. The system provides 140-180 W of electricity and 400-500 W of heat. The cost of the system was evaluated at 2.5 $ per peak electric Watt. The operation at high temperature of similar CPVT systems was also analyzed both for solar cooling [15] and water desalination [19] applications. A Parabolic Trough CPVT prototype was experimentally investigated by Coventry [21]. In this work the author pointed out that one of the major challenges in designing CPVT systems is to achieve an acceptable radiation flux distribution. The concentration ratio of the system under investigation was 37, thermal and electrical efficiencies were rated respectively at 58 % and 11 %. In this study the author also concluded that the thermal efficiency of CPVT is higher than the one of flat plate solar collectors only when radiation is scarce and/or ambient temperature is low. In fact, flat plate collectors convert both beam and diffuse radiation, whereas CPVT can only convert the beam one. Parabolic Trough CPVT were also investigated by Li et al. [22-24] comparing the electrical and thermal efficiencies of the system varying the PV technology, for different concentration ratio. Authors concluded that GeAs cells increase electrical efficiency with respect to silicon cells. However, the thermal efficiency of GeAs results lower than the one of silicon cells. Authors also pointed out that the cost of unit area of the GeAs is 3067.16 $/$m^2$ versus the 131.34 $/$m^2$ of the silicon cell. A similar work was performed by Bernardo et al. analyzing a low concentrating parabolic trough CPVT for the Swedish climate [25]. This study presents a thermal model of the PVT subsequently validated by experimental data. The system is based on a combination of a one axis tracking parabolic concentrator and silicon cells. This prototype is distributed by the Swedish company Absolicon. Additional specific applications of CPVT technology are also investigated in literature. Xu et al. [26] analyzed the integration of CPVT in the evaporator of an heat pump system. Al-Alilli et al. [27] investigated the use of a CPVT in a desiccant cooling system. Finally, Rosell [28] et al. investigated a low concentrating PVT system based on a linear Fresnel receiver. the system was analyzed by a mathematical model subsequently validated by experimental data. The rated thermal efficiency was about 60 %.

This paper is focused on the technology of concentrating parabolic trough PVT solar collectors and it presents a design procedure and a simulation model of a novel concentrating PVT collector. The layout of the PVT system under investigation was derived from a prototype recently presented in literature and commercially available [25]. The design of this prototype was modified with the scope to improve its electrical performance and it consists in a parabolic trough concentrator and a linear triangular receiver. The bottom surfaces of the receiver are equipped with mono-crystalline silicon cells whereas the top surface is covered by an absorbing surface. The aperture area of the parabola was covered by a glass in order to improve the thermal efficiency of the system. In the modified version of the collector considered in this paper, two modifications are implemented: the cover glass was eliminated and the mono-crystalline silicon cells were replaced by triple-junction cells allowing one to increase significantly the electrical efficiency of the system especially in case of high operating temperature. In order to analyze the performance of the modified Concentrating PVT (CPVT) collector a detailed mathematical model based on zero-dimensional energy balances on the control volumes of the system was implemented. The simulation model calculates in detail the temperatures of the main components of the system (PV layer, concentrator, fluid inlet and outlet and metallic substrate) and the main energy flows (electrical energy, useful thermal energy,

radiative losses, convective losses). The input parameters of the model include all the weather conditions (temperature, insolation, wind velocity, etc) and the geometrical/material parameters of the systems (lengths, thermal resistances, thicknesses, etc.). The model was used in order to evaluate both electrical and thermal efficiency curves related to the beam incident radiation, fluid inlet temperature and external temperature.

2. CPVT simulation model

The idea of CPVT considered in this study is based on the work performed by Bernardo et al [25, 29] and on the prototype recently commercialized by Absolicon [8, 25, 29]. The CPVT (Fig. 1) consists in a parabolic trough concentrator, equipped with a one-axis tracking system using the same operating principle of the solar thermal Parabolic Trough Collectors (PTC) [30-32]. The collector is horizontal and its axis is North-South oriented, whereas the tracking system follows the solar azimuth angle. However, while in solar thermal PTC at the focus of the parabola is installed an evacuated tube for heating the fluid, in the considered CPVT system the focus of the parabola is equipped with a triangular receiver (Fig. 1). A metallic substrate is used between the circular fluid channel and external surfaces (PV layer and top surface) in order to promote conductive heat transfer.

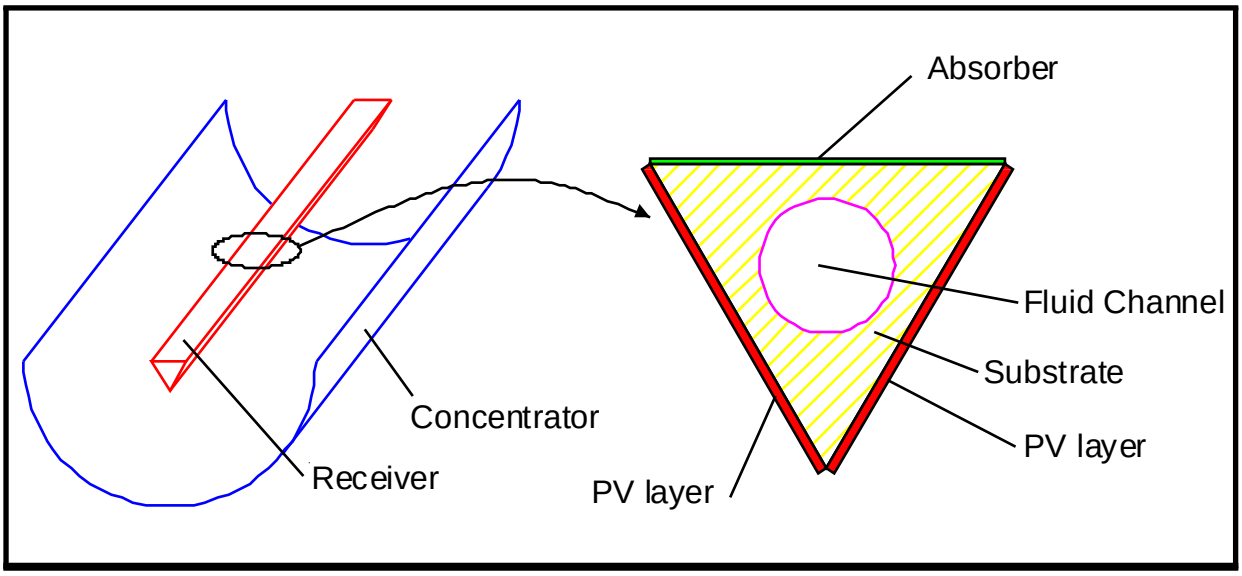

Fig. 1 - CPVT layout

The two sides of the triangle facing the parabolic concentrator are equipped with triple-junction PV layers, whereas the top side of the receiver is equipped with a thermal absorber. The triangular receiver includes an inner channel where the fluid to be heated flows. Therefore, the concentrated solar irradiation is converted simultaneously in electricity by the PV layer and in thermal energy by the cooling fluid. Note also that the top side of the triangular receiver is capable to absorb both beam and diffuse radiation, whereas PV layers can only convert the concentrated beam radiation. In summary, the system is basically the same as the one shown in references [25, 29] differing from that for two reason: i) there is no covering glass; ii) the PV layer is based on InGaP/InGaAs/Ge triple-junction solar cells [16]. These two modifications allow one to increase significantly the electrical efficiency of the system with respect to the values rated in references [25, 29]. In fact, the covering glass is used to increase the thermal efficiency of the system since it reduces convection and radiation losses. However, the glass also reduces the radiation incident on the PV layer, determining a decrease of the electrical efficiency of the system. Then, the triple-junction cells are significantly more efficient than silicon ones and they are also less sensitive to the variation of the operating temperature.

Although simplified models for the calculation of CPVT performance are available in literature [33], they cannot be applied to the system under investigation due to the use of concentrating systems and triple junction cells. Therefore, an appropriate model, based on energy balances, has been developed in order to design and simulate the CPVT under investigation. This is a 0-D model since the final scope of this work is to create a new Type to integrate in TRNSYS environment. Therefore, the model should be sufficiently fast for being used in a quasi-stationary yearly simulation. Therefore, 1-D models have not been considered since they are too computational-intensive for the scope of that work.

The general assumptions adopted for the model are: thermodynamic equilibrium, steady state, kinetic and gravitational terms negligible in the energy balances, radiation uniformly concentrated along PV area. In addition the small thickness of the PV layer and the high conductivity in the metal substrate allow one to assume negligible temperature gradients in the PV film and in the substrate. In other words PV and substrate temperature are assumed uniform.

The system was assumed to operate below 100 °C, since it is safer for the reliability of PV cells, although the system can theoretically operate up to 240 °C [15]. In this case, the CPVT could drive a double effect ACH, significantly increasing the overall efficiency of the system. However, this possibility must still be explored by experimental tests. Therefore, water was assumed as cooling fluid. Nevertheless, several types of cooling fluids can be implemented in the model. The thermodynamic and thermo-physical properties of the fluids, namely air and water, were calculated using the appropriate routine included in TRNSYS.

The concentration ratio is defined as the ratio between the area of the receiver, A_{PVT}, namely the two PV triangular sides, and the aperture area, A_{ap}, of the concentrator:

$$C_{PVT} = \frac{A_{PVT}}{A_{ap}} \qquad (1)$$

The optical efficiency (η_{opt}) of the concentrator is assumed being constant [15]. Therefore, the radiation indent on the PV surface is:

$$G_{PVT} = A_{PVT} I_b C_{PVT} \eta_{opt} IAM_{th} \qquad (2)$$

As usual in concentrating systems, in the previous equation only the beam incident radiation (I_b) is considered. Such radiation is also corrected considering both the optical efficiency of the receiver and the Incidence Angle Modifier (IAM) [34], the last considering that the radiation decreases when the angle of incidence increases. The IAM, related to the thermal production is evaluated on the basis of the data experimentally calculated by Bernardo et al.[25, 29]:

$$\begin{aligned} &\vartheta < 60 && IAM_{th} = 1 - b_{0,th}\left(\frac{1}{\cos\vartheta} - 1\right) \\ &\vartheta \geq 60 && IAM_{th} = \left[1 - b_{0,th}\left(\frac{1}{\cos\vartheta} - 1\right)\right]\left(1 - \frac{\vartheta - 60}{30}\right) \end{aligned} \qquad (3)$$

Simultaneously, additional thermal energy is absorbed by the top thermal absorber.

$$Q_{top} = A_{top} I_{tot} \alpha_{top} \qquad (4)$$

In this case, the top surface area, A_{top}, can convert both beam and diffuse radiation, i.e. the total radiation (I_{tot}) since the insolation incident on that surface is not concentrated.

Assuming the top surface area as gray surface and considering that the area of the top surface is much lower than the one of the sky, the radiative heat transfer between the top absorber and the sky can be calculated as follows [34]:

$$Q_{top-sky} = A_{top}\varepsilon_{top}\sigma\left(T_{top}^4 - T_{sky}^4\right) \qquad (5)$$

Here, the sky equivalent temperature (T_{sky}) is calculated using TRNSYS routine. T_{top} is the temperature of the top surface.

Similarly, assuming the area of the concentrator much larger than the one of the PVT receiver and assuming both PVT and concentrator as gray surfaces, the radiative heat transfer between the PVT and the concentrator [34]:

$$Q_{PVT-conc} = A_{PVT}\sigma\varepsilon_{PVT}\left(T_{PVT}^4 - T_{conc}^4\right) \qquad (6)$$

T_{PVT} and T_{conc} are respectively PVT and concentrator surfaces temperatures.

The convective heat transfer between the PVT and the air is calculated as follows [35]:

$$Q_{conv,PVT} = A_{PVT}h_{c,PVT}\left(T_{PVT} - T_a\right) \qquad (7)$$

The convective heat transfer coefficient, $h_{c,PVT}$, is calculated taking into account that the wind velocity is typically around 4-5 m/s. Therefore, the convection mechanism is definitively a forced convection. Therefore, the corresponding heat transfer coefficient is calculated using the following correlation, relating the Nusselt, Reynolds and Prandtl numbers [35]:

$$Nu = 0.664\,\mathrm{Pr}^{\frac{1}{3}}\,\mathrm{Re}^{\frac{1}{2}} \qquad (8)$$

In this equation the characteristic length is the length of the surface in the wind direction, assumed parallel to the CPVT longitudinal axis, i.e. L_{tube}. The same correlation is used to calculate the heat transfer coefficient for the forced convection between the top absorber and the air, $h_{c,top}$. The corresponding heat flow is [35]:

$$Q_{conv,top} = A_{top}h_{c,top}\left(T_{top} - T_a\right) \qquad (9)$$

The gross electrical power produced by the PV layer is:

$$P_{PVT,gross} = C_{PVT}A_{PVT}I_b\eta_{opt}\eta_{PV}IAM_{el} \qquad (10)$$

Note that this energy is calculated considering the concentrated beam radiation (corrected by the concentrator optical efficiency and by the IAM coefficient) incident on the PV layer, corrected by the electrical efficiency of the PV, η_{PV}. The electrical efficiency of the triple-junction PV (η_{PV}) is experimentally related to the concentration ratio and to the temperature [15].

$$\eta_{PV} = 0.298 + 0.0142\ln\left(C_{PVT}\right) + \left[-0.000715 + 0.0000697\ln\left(C_{PVT}\right)\right]\left(T_{PVT} - 298\right) \qquad (11)$$

Note that this equation returns ultra-high values of electrical efficiency, also approaching 40 %, as usual in III-V PV cells. The IAM_{el} is also evaluated on the basis of the experimental data provided by Bernardo et al.[25, 29]:

$$\begin{aligned} &\vartheta < 60 \qquad IAM_{el} = 1 - b_{0,el}\left(\frac{1}{\cos\vartheta} - 1\right) \\ &\vartheta \geq 60 \quad IAM_{el} = \left[1 - b_{0,el}\left(\frac{1}{\cos\vartheta} - 1\right)\right]\left(1 - \frac{\vartheta - 60}{30}\right) \end{aligned} \tag{12}$$

The net power produced by the system is reduced of the amount of electricity lost in the module connections and in the inverter, considering the corresponding conversion efficiencies (η_{mod} and η_{inv}) [15].

$$P_{PVT,net} = P_{PVT,gross}\eta_{mod}\eta_{inv} \tag{13}$$

Finally, the heat absorbed by the cooling fluid is:

$$Q_f = \dot{m}_f\left(h_{out} - h_{in}\right) \tag{14}$$

In the previous equation, the enthalpies of the inlet and outlet cooling fluid (h_{in} and h_{out}) are calculated by the thermo-physical property subroutine discussed above.

Therefore, the overall energy balance on a control volume including the entire triangular receiver is:

$$\begin{aligned} &A_{PVT}I_bC_{PVT}\eta_{opt}IAM_{th} + A_{top}I_{tot}\alpha_{top} = \dot{m}_f\left(h_{out} - h_{in}\right) + C_{PVT}A_{PVT}I_b\eta_{opt}\eta_{PV}IAM_{el} \\ &+A_{PVT}I_bC_{PVT}\eta_{opt}IAM_{th}\rho_{PVT} + A_{top}\varepsilon_{top}\sigma\left(T_{top}^4 - T_{sky}^4\right) + A_{PVT}\sigma\varepsilon_{PVT}\left(T_{PVT}^4 - T_{conc}^4\right) \\ &+A_{PVT}h_{c,PVT}\left(T_{PVT} - T_a\right) + A_{top}h_{c,top}\left(T_{top} - T_a\right) \end{aligned} \tag{15}$$

Note that in this energy balance the left side is representative of the energy flows entering the control volume, whereas the terms at the right side of the equation are the energy flows exiting the control volume. Among these terms at the right side, the first one is the useful thermal energy, the second one is the electrical power produced and all the remaining terms are losses. As discussed in the following section, this energy balance is dominated by the radiative terms being the convection losses low, due to the low receiver area, as typical in concentrating solar collectors

A second energy balance considers the control volume including the metallic substrate and the fluid channel (also including the fluid flowing inside). In this study, this control volume can be considered as a heat exchanger. In particular, it is here assumed that the temperature of the metallic substrate is homogeneous along both radial and circumferential directions. In this case, the primary side of the heat exchanger is at constant temperature equal to the temperature of the metallic substrate. This assumption can be considered acceptable as a consequence of the high thermal conductivity of the metallic substrate [15, 19-20, 25, 29] and allows one to develop a 0-D model of the CPVT. According to the 0-D approach here implemented, the performance of the heat exchanger can be calculated using the well-known ε-NTU technique [36]. For the case under consideration, the NTU number is:

$$NTU = \frac{\frac{1}{\frac{1}{h_{fluid}} + r_{sub}} A_{HEX}}{\dot{m}_f c_f} \quad (16)$$

The heat exchange area, A_{HEX}, is the lateral area of the fluid channel. The thermal resistance of the metallic substrate, r_{sub}, is typically orders of magnitude lower than the one of the fluid. The fluid heat transfer coefficient, h_{fluid}, is calculated using the following correlation [35]:

$$Nu_f = 0.023 \mathrm{Re}_f^{\frac{4}{5}} \mathrm{Pr}_f^{\frac{2}{5}} \quad (17)$$

Finally, the heat transfer effectiveness is [36]:

$$\varepsilon = 1 - e^{-NTU} \quad (18)$$

Defined T_{sub} the temperature of the metallic substrate, the energy balance for the considered heat exchanger is:

$$\dot{m}_f \left(h_{out} - h_{in} \right) = \varepsilon \dot{m}_f c_f \left(T_{sub} - T_{in} \right) \quad (19)$$

Note that, for the given boundary conditions (inlet temperature and mass flow rate, beam and total radiations and relative angle of incidence, ambient and sky temperature, ambient pressure and wind velocity), the unknowns are five, namely: PVT temperature, substrate temperature, fluid outlet temperature, temperature of top receiver surface (facing the sky) and temperature of the concentrator. Therefore, three further equations, in addition to eqs. (15) and (19), must be considered.

The third of the required five equations is derived from an energy balance on a control volume including the PVT layer, and the metallic substrate.

$$A_{PVT} \frac{T_{PVT} - T_{sub}}{r_{PVT-sub}} = \dot{m}_f \left(h_{out} - h_{in} \right) + A_{top} \frac{T_{sub} - T_{top}}{r_{top}} \quad (20)$$

In other words, the previous equation is showing that the conductive thermal flow coming from the PVT layer is partly used to increase the outlet temperature of the cooling fluid and partly is conductively exchanged with the top side of the triangular receiver. Note that the top thermal resistance, r_{top}, is the conductive resistance calculated considering both the metallic substrate and the top absorbing surface included between the fluid channel and the top surface.

A fourth energy balance can be considered with respect to the control volume including the top side of the substrate and the top surface of the triangular receiver:

$$A_{top} \frac{T_{sub} - T_{top}}{r_{top}} + A_{top} I_{top} = A_{top} I_{top} \rho_{top} + A_{top} \varepsilon_{top} \sigma \left(T_{top}^4 - T_{sky}^4 \right) + A_{top} h_{c,top} \left(T_{top} - T_a \right) \quad (21)$$

Finally, the last energy balance considers the control volume including only the parabolic concentrator.

$$A_{PVT}\sigma\varepsilon_{PVT}\left(T_{PVT}^4 - T_{conc}^4\right) + I_{tot}A_{conc}\alpha_{conc} = A_{conc}\sigma\varepsilon_{conc,back}\left(T_{conc}^4 - T_{sky}^4\right) + A_{conc}h_{c,conc,front}\left(T_{conc} - T_a\right) + A_{conc}h_{c,conc,back}\left(T_{conc} - T_a\right) \quad (22)$$

In this case, the left side of the energy balance includes the radiative heat transfer with the PVT and the radiative energy absorbed by the concentrator surface. Conversely, the terms at the right side of the equations are respectively: the radiative heat transfer of the back surface (external side of the parabola) of the concentrator, the convective losses at the front surface (facing the sun) of the concentrator, and the convective heat loss at the back surface.

Eqs (15), (19), (20), (21), (22) are a system of five equations in the above mentioned five unknowns. This system of equations is highly non linear as a consequence of the radiative terms included in the energy balances and of the correlations for the calculations of heat transfer coefficients. This system must be solved by conventional numerical iterative techniques.

Note also that the model discussed above lies on the assumption of steady state. However, this assumption can be easily removed, simply adding the capacitive terms in the five energy balances described above. In that case, the algebraic system of equations turns in a system of differential equations that can be easily solved using the tool included in TRNSYS package.

Table 1- CPVT design parameters

Parameter	Symbol	Value	Unit
CPVT aperture area	A_{ap}	12	m^2
Top absorber area	A_{top}	0.60	m^2
PV layer area	A_{PVT}	0.12	m^2
Fluid channel diameter	d	0.03	m
Fluid specific heat	c_f	4.1877	kJ/ kg K
Rated fluid flow rate	m_f	0.15	kg/s
Top surface absorptance	α_{top}	0.90	
Concentrator absorptance	α_{conc}	0.03	
Back surface concentrator emissivity	ε_{conc}	0.30	
Top surface emissivity	ε_{top}	0.20	
PV reflectance	ρ_{PVT}	0.03	
PV emissivity	ε_{PVT}	0.20	
IAM electrical coefficient	b_{0el}	0.28	
IAM thermal coefficient	b_{0th}	0.14	

The overall performance of the CPVT is often evaluated using the well-known thermal and electrical efficiencies, which are conventionally related to the incident beam radiation and to the collector aperture area:

$$\eta_{CPVT,th} = \frac{\dot{m}_f\left(h_{out} - h_{in}\right)}{A_{ap}I_b} \quad (23)$$

$$\eta_{CPVT,el} = \frac{C_{PVT}A_{PVT}I_b\eta_{opt}\eta_{PV}IAM_{el}}{A_{ap}I_b} \quad (24)$$

CPVT design parameters are reported in Table 1[15, 19-20, 25, 29]. For the design parameters assumed in this table, the concentration ratio is 10.

3. Results and Discussion

On the basis of the model of the CPVT discussed in the previous section, the curves of the electrical and thermal efficiencies were analyzed as a function of the well-known parameter [34].

$$\frac{\left(\frac{T_{in}+T_{out}}{2}\right)-T_a}{I_b}=\frac{T_{f,avg}-T_a}{I_b} \qquad (25)$$

The result of this analysis is shown in Fig. 2. Here, it is clearly shown that the correlation between the thermal efficiency and the above mentioned parameter is very good. In fact, the value of the correlation index is very high even using a linear interpolating curve. However, it is also clear that the markers are not perfectly aligned on the interpolating curve. In fact, the thermal efficiency curve of a solar thermal collector is a second-order polynomial when constant heat transfer coefficients are considered [34]. Therefore, the deviation of the performance calculated by the model discussed in the previous section and the interpolating curve is basically due to the fact that, in the proposed model, the overall heat transfer coefficients is not constant and varies with the CPVT operating conditions.

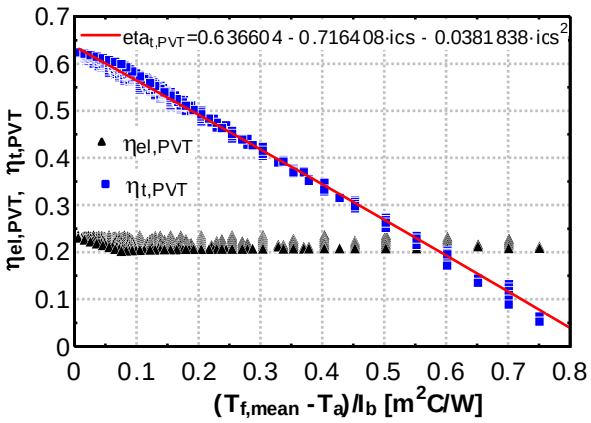

Fig. 2- CPVT electrical and thermal efficiency

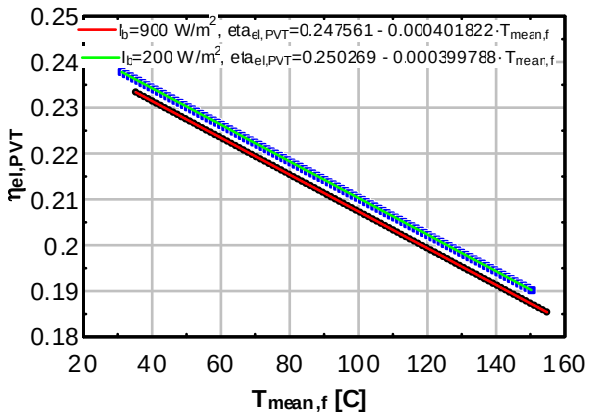

Fig. 3 - CPVT electrical efficiency vs fluid mean temperature

Conversely, there is not any good correlation between the electrical efficiency and the parameter shown in eq. (25). In fact, the electrical efficiency of the CPVT basically depends on the operating temperature of the PV layer and on the concentration ratio, as shown in eq. (11). In the case of the electrical efficiency it is a common use to show this parameter as a function of fluid average temperature [21, 25, 29]. This graph is shown in Fig. 3 where the linear interpolating curve is also displayed. Such Figure shows that the electrical efficiency basically linearly depends on the fluid mean temperature since such temperature directly affects the PV layer temperature. Note also that the electrical efficiency scarcely depends on the incident beam radiation. In fact, a reduction of the beam radiation, for a given fluid average temperature, only determines a slight decrease of PV layer temperature, consequently causing a slight increase in CPVT electrical efficiency. The plots of Fig. 2 and Fig. 3 also show that the efficiency curve of the proposed CPVT is slightly different from the original model of the Bernardo et al. [25, 29] due to: the use of triple-junction PV and to the absence of the covering glass. As a consequence, the optical and the electrical efficiencies are higher. In fact, this last efficiency ranges between 20 % and 25 % for the considered operating points. The use of a covering glass reduces the amount of radiation available for both electrical and

thermal conversions but also reduce thermal losses. Note also that a higher electrical efficiency is often counterbalanced by a lower value of the thermal efficiency. However, the thermal performance of the CPVT considered in this work is also very good due to the excellent radiative properties of the considered surfaces. Therefore, it can be concluded that the modifications in the layout of the CPVT considered in this work, allow one to increase both thermal and electrical efficiency with respect to the values published by Bernardo et al. [25, 29]. Obviously, this increase in efficiency is counterbalanced by a significantly higher capital cost due to the use of triple-junction PV layer. Therefore, the system considered in this work may be considered a suitable option for the next future when the cost of triple-junction PV is expected to dramatically decrease. In the following paragraphs a brief parametric study is performed, with the scope to analyze the performance of the CPVT under different operating condition and varying some of its main design parameters. The study was performed considering the set of boundary conditions shown in Table 2 This parametric analysis aims at evaluating the effect of the variation of the design parameters on the CPVT thermal and electrical performance.

Table 2- CPVT boundary conditions

Parameter	Value	Unit	Parameter	Value	Unit
T_{in}	70	°C	w_a	5	m/s
T_{sky}	25	°C	I_{tot}	1000	W/m^2
T_a	25	°C	I_b	800	W/m^2
p_a	101	kPa	θ	0	deg

As mentioned above, the layout of the system under investigation was derived by some prototypes previously developed and discussed in literature [8, 21, 25, 29] and has been here modified in order to improve the electrical performance of the system and to achieve a good thermal performance at operating temperatures up to 90-100 °C. To this scope, in the following figures some of the main geometrical parameters were varied from the initial configuration, in order to assess their impact on the overall performance of the system. First, the axial length - L_{tube} - of the CPVT (including the axial lengths of the triangular receiver and of the parabolic concentrator) was varied in very large range. Fig. 4 shows both thermal and electrical efficiencies as a function of this parameter. Here, it is clearly displayed that both efficiencies are very slightly affected by the increase of CPVT length, showing a slight decrease for higher CPVT length. However, thermal and electrical efficiencies drops are lower than 1%. Obviously, an increase of CPVT length also determines a proportional increase of CPVT aperture area and of PV layer area. This linear relationship is clearly shown in Fig. 5, where both thermal and electrical powers are plotted as a function of the CPVT length. Note also that the slight decrease of efficiencies shown in Fig. 4 also determines a deviation of the plots of Fig. 5 from an ideal proportional relationship. In fact, for a CPVT length of 4 m, thermal and electrical powers are respectively 8320 kJ/h and 4531 kJ/h, whereas at 16 m these values increase up to 33403 kJ/h and 15178 kJ/h, which are values slightly lower than the ones expected in case of constant thermal and electrical efficiencies. The reason of this decrease may be explained by the temperature profiles shown in Fig. 6. Here, it is shown that higher lengths of the CPVT system also determine a slight increase of all the temperatures. In fact, an increase in the length also causes an increase of fluid outlet temperature that consequently determines an overall increase of the temperatures of the system. In particular, the increase in PV temperature determines the decrease of the electrical efficiency. Moreover, the increase of PV and top side temperatures also determines an increase of both convective and radiative losses causing the slight reduction of thermal efficiency shown in the previous figure. Therefore, from this analysis it could be concluded that, for maximizing the efficiency of the CPVT the length of the system should be small and the temperature increase of the fluid should be also small. This result is in accordance with the expected behaviour of the system since an increase of the fluid mean temperature generally determines a decrease of both thermal and electrical performances.

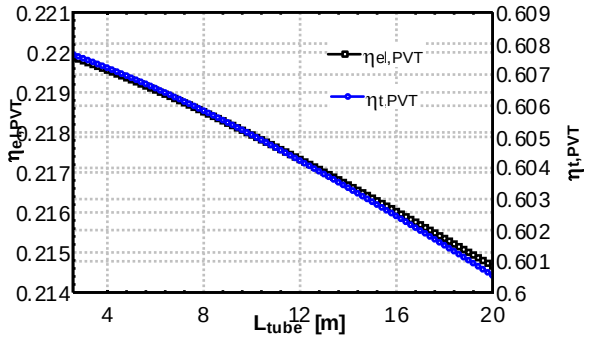

Fig. 4 - CPVT thermal and electrical efficiency vs L_{tube}

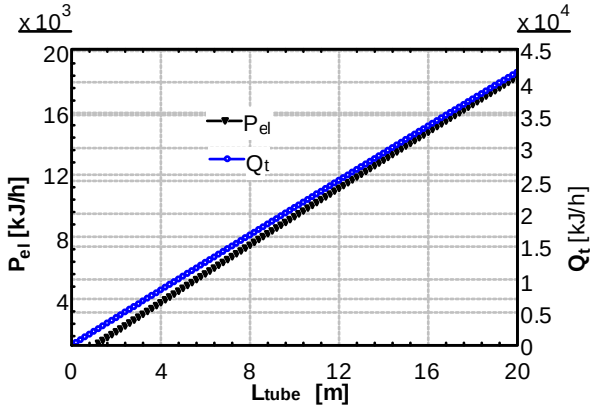

Fig. 5 - CPVT Electrical and Thermal Power vs L_{tube}

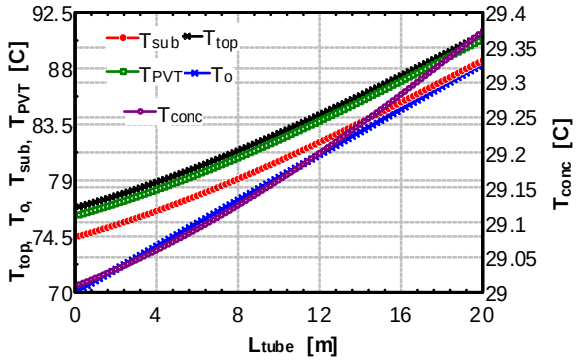

Fig. 6 - CPVT Temperatures vs L_{tube}

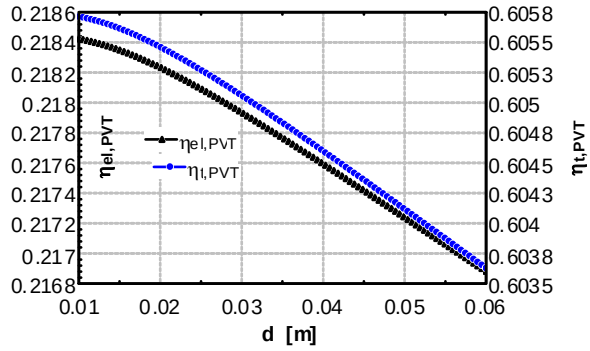

Fig. 7- CPVT thermal and electrical efficiency vs channel diameter

The variation of the diameter of the fluid channel does not significantly affect the overall performance of the system, being important only for the internal balance of the system. In fact, Fig. 7 and Fig. 8 clearly show that an increase in channel diameter determines a slight decrease of electrical and thermal efficiencies. A similar decrease is also observed for both thermal and electrical powers produced by the CPVT. Conversely a variation in the diameter shows a significant impact on the temperatures of the layers of the CPVT, as shown in Fig. 9. Here, it is clearly shown that an increase of the diameter determines a general increase of the temperature of all the solid layers of the CPVT, whereas the outlet temperature of the fluid does not significantly vary. In fact, the lower the diameter, the higher the velocity of the fluid also determining a corresponding increase of its heat transfer coefficient. Simultaneously, the higher the diameter, the higher the heat exchange area. The two contrasting effects determine the temperature plot shown in Fig. 9.

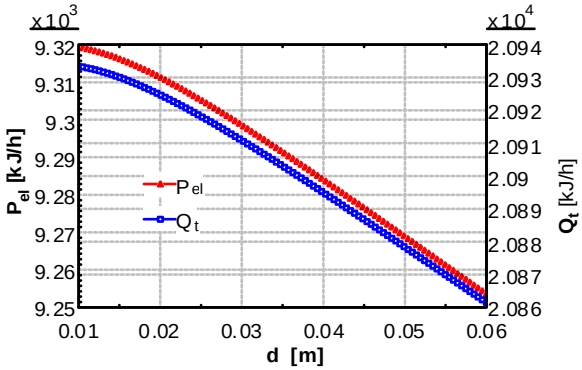

Fig. 8 - CPVT Electrical and Thermal Power vs channel diameter

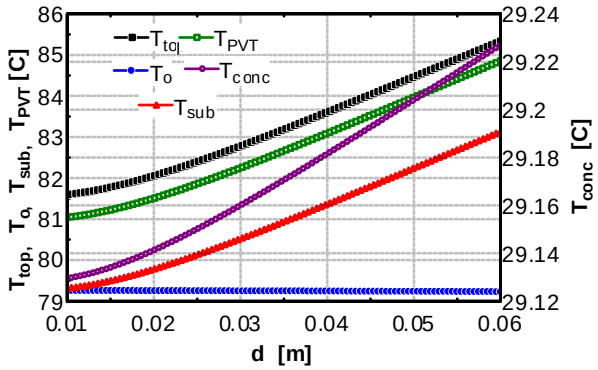

Fig. 9 - CPVT Temperatures vs channel diameter

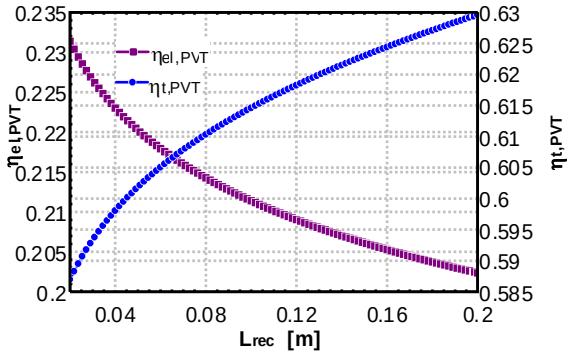

Fig. 10- CPVT thermal and electrical efficiency vs receiver length

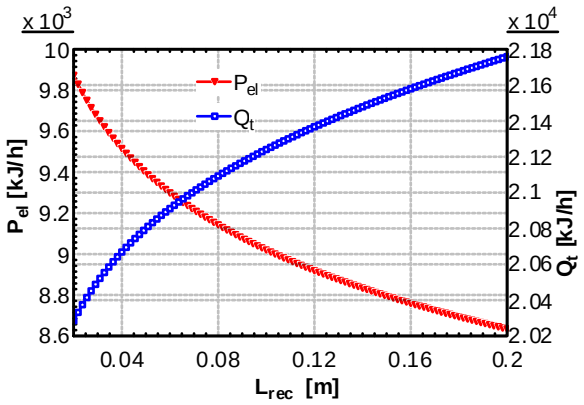

Fig. 11 - CPVT Electrical and Thermal Power vs receiver length

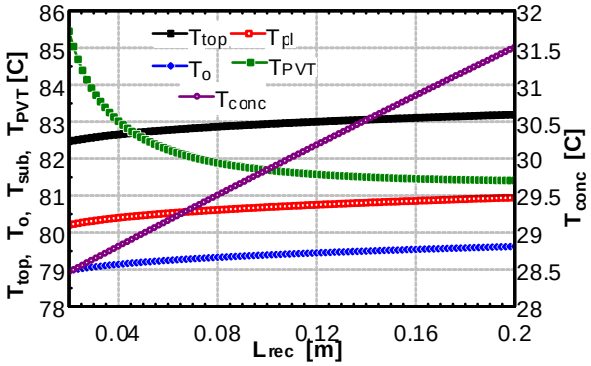

Fig. 12 - CPVT Temperatures vs receiver length

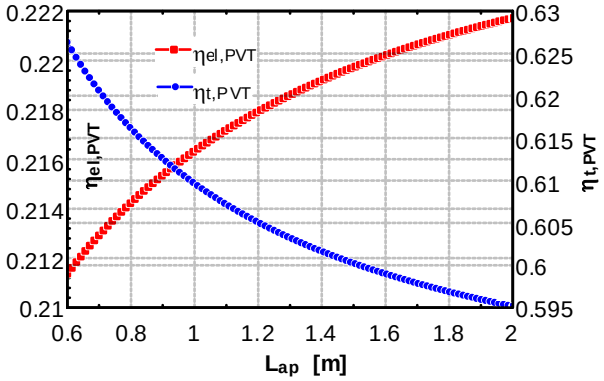

Fig. 13- CPVT thermal and electrical efficiency vs aperture length

A further design parameter is the length of each of the three sides of the triangular receiver, L_{rec}. The variation of such parameter is very important since affects: the concentration ratio, PV area and top absorber area. The length of the receiver significantly affects both thermal and electrical efficiencies, as shown in Fig. 10 displaying that an increase in receiver length determines a decrease of the electrical efficiency and a simultaneous increase of the thermal efficiency. Similar trends are also shown for the thermal and electrical powers (Fig. 11). An increase of the length of the receiver determines a proportional decrease of the concentration ratio, reducing the radiative flow incident on the PV layer. Such phenomenon determines, as expected, a decrease of PV layer temperature (Fig. 12). A reduction of the PVT temperature would suggest an increase of the electrical efficiency, in contrast to the trend shown in Fig. 10. This is due to the fact that the electrical efficiency of the triple-junction PV layer also depends on the concentration ratio, as shown in eq. (11). In particular, a reduction of the concentration ratio also determines a decrease of the of the PV electrical efficiency. This effect is dominant over the decrease of PV temperature, determining the overall result of a significant decrease of PV electrical efficiency, as shown in Fig. 10. Conversely, the thermal efficiency increases faster than the electrical efficiency decreases. In fact, the thermal efficiency increases for two simultaneous effects: i) a lower electrical efficiency makes more heat available for thermal conversion; ii) an increase of top absorber area improves the utilization of the total radiation. This is also clear by Fig. 12, showing that an increase of the temperature length determines an increase of the top surface temperature, causing also an increase of the outlet temperature of the fluid. Therefore, it may be concluded that the length of the receivers plays an important role in the design of the CPVT system. In case the goal is the maximization of the electrical efficiency this parameter should be as low as possible. Conversely, it should very high if the goal is the increase of the thermal efficiency.

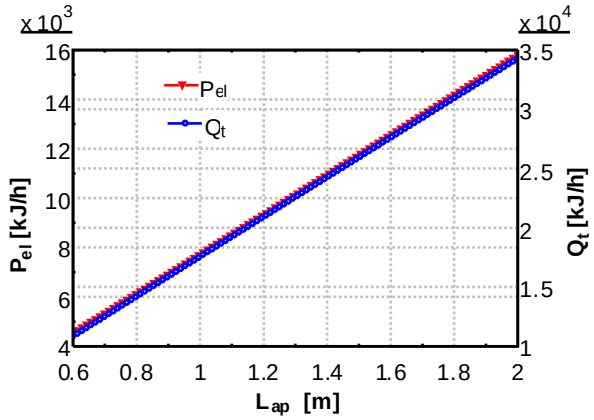

Fig. 14 - CPVT Electrical and Thermal Power vs aperture length

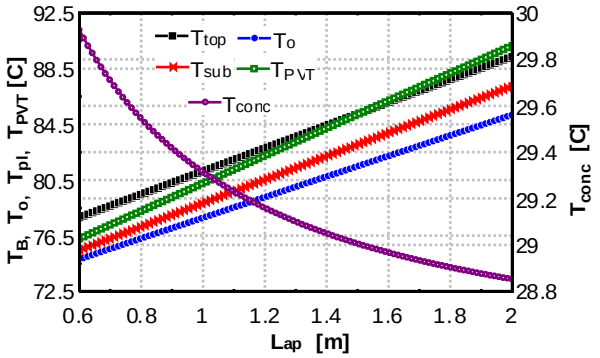

Fig. 15 - CPVT Temperatures vs aperture length

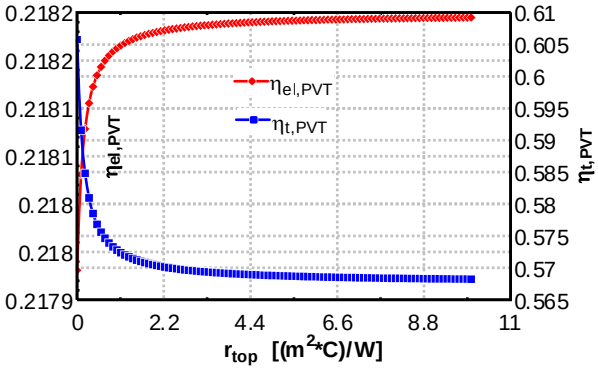

Fig. 16- CPVT thermal and electrical efficiency vs top thermal resistance

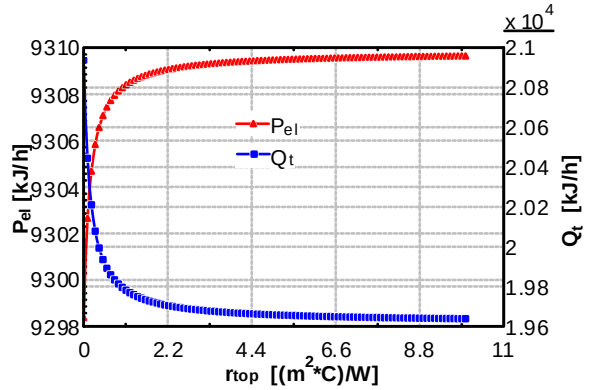

Fig. 17 - CPVT Electrical and Thermal Power vs top thermal resistance

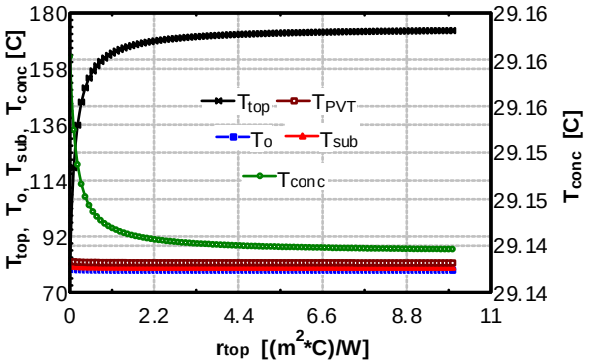

Fig. 18 - CPVT Temperatures vs top thermal resistance

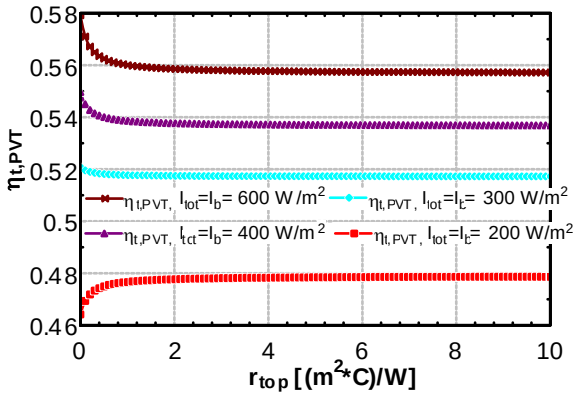

Fig. 19 - Thermal efficiency vs top thermal resistance and radiation

Opposite results are achieved varying the aperture length, i.e. the length of the aperture area in the radial direction. In fact, an increase of the aperture length determines a decrease of the thermal efficiency and a simultaneous increase of the electrical efficiency (Fig. 13). In addition, both thermal and electrical powers increase proportionally with the aperture length (Fig. 14). Note that the decrease of the thermal efficiency is much larger than the increase in the electrical one. In fact, the thermal efficiency basically decreases as a consequence of the significant increase of both radiative and convective losses, due to the increase of both PV and top temperatures (Fig. 15). A temperature increase of the layers of the CPVT receiver is due to the increase of the radiative flow to the higher concentration ratio. This increase of the concentration ratio would also determine an increase of the electrical efficiency, as discussed before. However, this positive effect is partly

counterbalanced by the increase in PVT temperature (Fig. 15), resulting in a slight overall increase of the electrical efficiency. Note also that this particular trend is achieved as a consequence of the high efficiency PV layer considered in this work. If a conventional silicon PV layer would be considered, the electrical efficiency would have dramatically reduced.

A possible alternative to the CPVT layout discussed in this paper may consist in a thermal insulation of the top surface of the receiver [20]. This arrangement could reduce thermal losses but would also reduce the radiative heat absorbed by that surface. In order to analyze this possibility, the top thermal resistance was varied in a very wide range, whose lower bound could be representative of no insulation, whereas the upper bound is achieved only in case of good thermal insulation. The results of this analysis showed that both thermal efficiency and thermal power dramatically decrease with higher insulation (Fig. 16 and Fig. 17). Conversely, the variations of electrical efficiency and electrical powers are marginal (Fig. 16 and Fig. 17). This is due to the fact that an increase of top insulation determines a dramatic increase of top surface temperature (Fig. 18) whereas the temperatures of the remaining layers of the CPVT do not significantly vary (Fig. 18 shows only a slight decrease). In fact, a higher insulation inhibits the heat transfer from top surface to the cooling fluid, determining only an increase of the top surface temperature. As a consequence, increasing the insulation, the fluid is not capable to absorb the radiative heat coming from the top surface. This results in a local increase of the temperature in the top surface and in a general decrease of the CPVT temperatures (including the fluid outlet temperature) determining the decrease of thermal efficiency shown in Fig. 16. Therefore, the results of this study would suggest that, for the boundary conditions assumed in this study, the option of insulating the top surface is not profitable for the layout under investigation. However, these results dramatically change if different values of irradiation are considered. This is clearly shown in Fig. 19, where the thermal efficiency is plotted for different values of radiation and top resistance. Here, it is clearly shown that for low irradiation, the thermal efficiency increases in case of higher insulation whereas the opposite trend occurs in case of higher solar radiation. However, this type of CPVT is typically used for locations in which the average solar radiation is high, where the top insulation would not be profitable.

4. Conclusions

The results of the case study presented prove the technical feasibility of the novel arrangement of a concentrating parabolic trough PVT solar collector based on triple-junction technology. Results showed that:

- Both thermal and electrical efficiencies are very high for a wide range of operating conditions.
- The system is particularly sensitive to the available beam radiation since both thermal and electrical efficiencies dramatically decrease for low beam insolation. Therefore, the results of the model suggest that this kind of device can be profitably adopted for the locations in which the average beam radiation is sufficiently high.
- An increase in CPVT length and/or in fluid channel diameter determines a decrease in both thermal and electrical efficiencies, due to the increase of CPVT operating temperature, causing an increase of thermal losses and in PVT electrical efficiencies.
- Decreasing receiver length and/or increasing aperture length determine an increase of the concentration ratio. This is favourable for the electrical efficiency which increases for higher concentration ratios. Conversely, such modification also determines a general increase in CPVT operating temperature, negatively affecting its thermal efficiency.
- Insulating the top surface rather than using a high-absorbitivity surface is recommended for increasing the CPVT electrical efficiency. On the other hand, a simultaneous decrease of the

thermal efficiency must be taken also into account, due to lower radiation absorbed by the collector.

The analysis has been performed by a simulation model which allows one to change the design parameters of the system and to evaluate the corresponding thermodynamic performance. The model also allows one to perform dynamic simulations and system optimization, defining the set of the design parameters maximizing system performance.

On the other hand, it must be pointed out that the system investigated in this study is very expensive due to the use of triple-junction PV cells. Therefore, the use of this technology is presently scarcely profitable from an economic point of view. However, a possible market penetration of this technology would make this CPVT an excellent system for providing electricity and heat for several applications, such as: industry, residential, solar heating and cooling, integration in ORC cycles, etc.

In the Part II of this paper a specific application of this system will be investigated, i.e. the integration of the CPVT in a Solar Heating and Cooling systems providing space heating, space cooling, domestic hot water and electricity to the user.

Future developments of this work will include the investigation of dish concentrating PVT systems for higher temperature applications.

Nomenclature

A	Area [m^2]
c	Specific Heat [J/kg/K]
C_{PVT}	Concentration ratio
D	Fluid channel diameter [m]
G_{PVT}	Incident radiative Flow [W]
h_c	Convective heat transfer coefficient [W/m^2/K]
h_f	Fluid specific Enthalpy [J/kg]
I_b	Beam radiation [W/m^2]
I_{tot}	Total radiation [W/m^2]
IAM	Incidence Angle Modifier
k	Conductivity [W/m/K]
L	Length [W/m^2]
$\dot{m}_f$	Fluid mass flow rate [kg/s]
Nu	Nusselt Number
p	Pressure [kPa]
P_{PVT}	PVT Electrical Power [W]
Pr	Prandtl Number
$\dot{Q}$	Thermal Power [W]
r	Area specific thermal resistance [m^{2}K/W]
Re	Reynolds Number
t	Temperature [°C]

T	Temperature [K]
UA	Overall heat transfer coefficient [W/K]
w	velocity [m/s]

Greek Symbols

α	Absorptance
ε	Emittance
ρ	Density [kg/m^3]
ρ_{PVT}	PVT Reflectance
σ	Stephan-Botzmann constant
μ	Viscosity [kg/m/s]
η_{inv}	Inverter efficiency
η_{mod}	Module efficiency
η_{PV}	PV efficiency
η_{opt}	Optical efficiency
η_{th}	Thermal efficiency
η_{el}	Electrical efficiency
η_{ex}	Exergetic efficiency

Subscripts

a	Ambient
ap	Aperture
atm	Atmospheric
$conc$	Concentrator
el	Electrical
f	Fluid
hor	Horizontal
in	Inlet
out	Outlet
rec	Receiver
top	Top surface
th	Thermal

References

[1] Chow, T.T., *A review on photovoltaic/thermal hybrid solar technology* Applied Energy, 2010. **87**(2): p. 365-379.

[2] Zondag, H.A., *Flat-plate PV-Thermal collectors and systems: A review* Renewable and Sustainable Energy Reviews, 2008. **12**(4): p. 891-895.

[3] Calise, F., Palombo, A., Vanoli, L., , *Design and dynamic simulation of a novel solar trigeneration system based on photovoltaic/thermal collectors*, in *ECOS 2011*. 2011: Novi Sad, Serbia.

[4] Skoplaki, E., Palyvos, J.A. , *On the temperature dependence of photovoltaic module electrical performance: A review of efficiency/power correlations* Solar Energy, 2009. **83**: p. 614-624.

[5] Fong, K.F., Chow, T.T., Lee, C.K., Lin, Z., Chan, L.S., *Advancement of solar desiccant cooling system for building use in subtropical Hong Kong* Energy and Buildings, 2010. **42**: p. 2386-2399.
[6] Beccali, M., Finocchiaro, P., Nocke, B., *Energy and economic assessment of desiccant cooling systems coupled with single glazed air and hybrid PV/thermal solar collectors for applications in hot and humid climate* Solar Energy, 2009. **83**: p. 1828-1846.
[7] Ibrahim, A., Othman, M., Ruslan, M.H.,/ Mat, S., Sopian, K., *Recent advances in flat plate photovoltaic/thermal (PV/T) solar collectors* Renewable and Sustainable Energy Reviews, 2011. **15**: p. 352-365.
[8] Zhang, Xingxing, Zhao, Xudong, Smith, Stefan, Xu, Jihuan, Yu, Xiaotong, *Review of R&D progress and practical application of the solar photovoltaic/thermal (PV/T) technologies* Renewable and Sustainable Energy Reviews, 2011. **In Press, Corrected Proof,Sep 2011**
[9] Tripanagnostopoulos, Y., *Aspects and improvements of hybrid photovoltaic/thermal solar energy systems* Solar Energy, 2007. **81**(9): p. 1117-1131.
[10] Daghigh, R. , Ruslan, M.H. ,Sopian, K., , *Advances in liquid based photovoltaic/thermal (PV/T) collectors* Renewable and Sustainable Energy Reviews, 2011. **15**(8): p. 4156-4170.
[11] Kumar, Rakesh, Rosen, Marc A., , *A critical review of photovoltaic–thermal solar collectors for air heating* Applied Energy, 2011. **88**(11): p. 3603-3614.
[12] Zhao, J., Song, Y., Lam, W.H., Liu, W., Liu, Y., Zhang, Y., Wang, D.Y., *Solar radiation transfer and performance analysis of an optimum photovoltaic/thermal system* Energy Conversion and Management, 2011. **52**: p. 1343-1353.
[13] Joshi, A.S., Tiwari, A., Tiwari, G.N., Dincer, I., Reddy, B.V., *Performance evaluation of a hybrid photovoltaic thermal (PV/T) (glass-to-glass) system* International Journal of Thermal Sciences, 2009. **48**: p. 154-164.
[14] Daghigh, Ronak, Ibrahim, Adnan, Jin, Goh Li, Ruslan, Mohd Hafidz , Sopian, Kamaruzzaman, *Predicting the performance of amorphous and crystalline silicon based photovoltaic solar thermal collectors* Energy Conversion and Management, 2011. **52**(3): p. 41-1747.
[15] Mittelman, G., Kribus, A., Dayan, A., *Solar cooling with concentrating photovoltaic/thermal (CPVT) systems* Energy Conversion and Management, 2007. **48**: p. 2481-2490.
[16] Nishioka, K., Takamoto, T., Agui, T., Kaneiwa, M., Uraoka, Y., Fuyuki, T., *Annual output estimation of concentrator photovoltaic systems using high-efficiency InGaP/InGaAs/Ge triple-junction solar cells based on experimental solar cell's characteristics and field-test meteorological data.* Solar Energy Materials and Solar Cells, 2006. **90**: p. 57-67.
[17] Vorobiev, Y. , González-Hernández, J. , Vorobiev, P. , Bulat, L., *Thermal-photovoltaic solar hybrid system for efficient solar energy conversion* Solar Energy, 2006. **80**: p. 170-176.
[18] Kosmadakis, G. / Manolakos, D. / Papadakis, G., *Simulation and economic analysis of a CPV/thermal system coupled with an organic Rankine cycle for increased power generation* Solar Energy, 2011. **85**: p. 308-324.
[19] Mittelman, Gur / Kribus, Abraham / Mouchtar, Ornit / Dayan, Abraham, *Water desalination with concentrating photovoltaic/thermal (CPVT) systems* Solar Energy, 2007. **83**(8): p. 1322-1334.
[20] Kribus, Abraham / Kaftori, Daniel / Mittelman, Gur / Hirshfeld, Amir / Flitsanov, Yuri / Dayan, Abraham, *A miniature concentrating photovoltaic and thermal system* Energy Conversion and Management, 2006. **47**(20): p. 3582-3590.
[21] Coventry, Joe S., *Performance of a concentrating photovoltaic/thermal solar collector* Solar Energy, 2005. **78**(2): p. 211-222.
[22] Li, M., Li, G.L. , Ji, X. ,Yin, F. , Xu, L., *The performance analysis of the Trough Concentrating Solar Photovoltaic/Thermal system* Energy Conversion and Management, 2011. **52**(6): p. 2378-2383.

[23] Li, Ming, Ji, Xu , Li, Guoliang,Wei, Shengxian , Li, YingFeng , Shi, Feng, *Performance study of solar cell arrays based on a Trough Concentrating Photovoltaic/Thermal system* Applied Energy, 2011. **88**(9): p. 3218-3227.

[24] Li, M. , Ji, X. , Li, G.L., Yang, Z.M. , Wei, S.X. , Wang, L.L, *Performance investigation and optimization of the Trough Concentrating Photovoltaic/Thermal system* Solar Energy, 2011. **85**(5): p. 1028-1034.

[25] Bernardo, L.R., Perers, B.,Håkansson, H. ,Karlsson, B., *Performance evaluation of low concentrating photovoltaic/thermal systems: A case study from Sweden* Solar Energy, 2011. **85**(7): p. 1499-1510.

[26] Xu, Guoying / Zhang, Xiaosong / Deng, Shiming, *Experimental study on the operating characteristics of a novel low-concentrating solar photovoltaic/thermal integrated heat pump water heating system* Applied Thermal Engineering, 2011. **31**(17-18): p. 3689-3695.

[27] Al-Alili, A., Hwang, Y., Radermacher, R. / Kubo, I., *A high efficiency solar air conditioner using concentrating photovoltaic/thermal collectors* Applied Energy, 2011. **In Press, Corrected Proof,May 2011**.

[28] Rosell, J.I. / Vallverdú, X. / Lechón, M.A. / Ibáñez, M., , *Design and simulation of a low concentrating photovoltaic/thermal system* Energy Conversion and Management, 2005. **46**(18-19): p. 3034-3046.

[29] Bernardo, Ricardo., *Retrofitted Solar Thermal System for Domestic Hot Water for Single Family Electrically Heated Houses, Development and Testing*, in *Faculty of Engineering*. 2010, Lund University.

[30] Calise, F., *Design Of A Hybrid Polygeneration System With Solar Collectors And A Solid Oxide Fuel Cell: Dynamic Simulation And Economic Assessment.* International Journal of Hydrogen Energy, 2011. **36**(10): p. 6128-6150

[31] Calise, F., *High Temperature Solar Heating and Cooling Systems for Different Mediterranean Climates: dynamic simulation and economic assessment* Applied Thermal Engineering, 2011. **32**: p. 108-124.

[32] Calise F., Dentice d'Accadia M., Palombo, A., Vanoli L., *Dynamic Simulation Of High Temperature Solar Heating And Cooling Systems*, in *Eurosun 2010*. 2010: Graz (AU).

[33] Florschuetz, L. W. , *Extension of the Hottel-Whillier model to the analysis of combined photovoltaic/thermal flat plate collectors.* Solar Energy, 1979. **22**: p. 361-366.

[34] Duffie, J.A., Backman, W.A, *Solar engineering of thermal processes*, ed. John Wiley and sons. 1980.

[35] Incropera, F.P., DeWitt , D.P., *Fundamentals of Heat and Mass Transfer, 5th Edition* ed. Inc. John Wiley & Sons. 2001.

[36] Kakac, S., Liu, H., *Heat Exchanger Selection, Rating, And Thermal Design.*, ed. CRC Press. 1998.

Parabolic Trough Photovoltaic/ Thermal Collectors. Part II: Dynamic Simulation of a Solar Trigeneration System

Francesco Calise[a], Laura Vanoli[b]

[a] *DETEC- Univ. of Naples Federico II, P.le Tecchio 80, 80125 Naples, Italy, frcalise@unina.it*
[b] *DIT – Univ. of Naples "Parthenope" C. D. IS.5, 80143 Naples, Italy, laura.vanoli@uniparthenope.it*

Abstract:
During the last few years, the technology of photovoltaic/thermal (PVT) solar collectors is becoming more and more attractive. In fact, these systems allow one to produce simultaneously electrical energy and thermal energy by solar irradiation. In particular, PVT systems are very attractive when they are able to produce medium-temperature heat. The majority of PVT systems presently under development produce hot stream at temperatures lower than 45 °C. This is determined by the fact the electrical efficiency of the PVT dramatically decreases for higher operating temperatures. However, medium-temperature PVT systems can be designed using two technical devices: i) multi-junction PV collectors which can achieve very high electrical efficiencies even when their operating temperature is high; ii) concentrating devices which can concentrate the beam radiation on the PV panel. The combination of these two devices allows one to design an efficient medium-temperature PVT solar collector. In particular, in this work the collector considered, consisted in a parabolic-trough concentrator and a triangular receiver, placed on the focus of the parabola, on which a multi-junction PV panel is laminated. The triangular receiver is equipped with an internal tube for the cooling fluid. The system is also equipped with a one-axis tracking system, typical of Parabolic-Trough Solar Thermal Collectors. The system was accurately simulated by means of detailed energy balances and calculations of heat transfer coefficients. The model of this innovative device was subsequently integrated with a transient model of a solar tri-generation system based on PVT collectors and solar heating and cooling technologies, previously developed by the authors. Although concentrating PVT collectors are also capable to produce hot streams up to 240 °C, while maintaining reasonable electrical efficiency, in this study an operating temperature below 100 °C was considered, since presently no PVT collector operating at higher temperature is commercially available. The peculiarities of concentrating PVT are specially attractive for integration in Solar Heating and Cooling system (SHC), where PVT can be used as an auxiliary system driving the absorption chiller. The combination of concentrating PVT and SHC are studied in this work, implementing a novel virtually zero-emission polygeneration system able to produce electricity, space heating and cooling and domestic hot water. The polygeneration system is based on the following main components: concentrating parabolic PVT collectors, a single-stage LiBr-H_2O absorption chiller, tanks, auxiliary heaters, balance of plant devices and the building. The PVT produces electrical energy which is in part consumed by the building lights and equipments, in part is used by the system parasitic loads and the rest is eventually sold to the grid. Simultaneously, the PVT provides the heat required to drive the absorption chiller. The system was designed and then simulated by means of a zero-dimensional transient simulation model. The economic results show that the system under investigation can be profitable, if a proper funding policy is available. In any case, the overall energetic and economic results are more encouraging than the ones previously published in literature for similar polygeneration systems

Keywords:
PVT, solar heating and cooling, solar energy, TRNSYS

1. Introduction

The Part I of this paper presents the technology of Photovoltaic Thermal (PVT) solar collectors, producing simultaneously thermal and electrical energy. In particular, Part I of the paper presents a simulation model of a novel concentrating PVT (CPVT) based on parabolic trough concentrators and triple-junction photovoltaic (PV) receiver. The Part II of the paper investigates a very interesting application of the CPVT collector presented in Part I, consisting in its integration in a

Solar Trigeneration system. In fact, the final scope of this work is the analysis of the possible integration of PVT in Solar Heating and Cooling (SHC) systems, designing a novel solar trigeneration system producing heat, cool and electricity for an educational building.

A SHC system is conventionally based on solar thermal collectors producing heat. This heat is used during the winter for space heating and domestic hot water, whereas in the summer it is converted in cooling energy by a thermally-driven (absorption, adsorption, etc.) chiller [1-6]. The majority of the SHC systems investigated in literature are based on the combination of evacuated tube solar collectors and single-stage absorption chillers [1-16]. However, in the last few years, the combination of concentrating solar collectors and double-stage chillers is becoming more and more attractive [17-22]. Replacing solar thermal by PVT collectors caused an additional production of electricity by the PVT.

As discussed above and in Part I, literature review showed a large number of papers investigating separately PVT and SHC systems. However, the analysis of these two technologies in a single polygeneration system is scarcely investigated. In particular, the literature review revealed only two works investigating the theoretical feasibility of the integration of SHC and PVT. The first work was presented by Vokas et al. [23]. Here, the theoretical feasibility of flat plate PVT, producing both space heating and cooling (by an absorption chiller), for a domestic user is investigated. This preliminary work was based on a simplified approach (F-charts) for the system simulation; in addition, suitable system layout and control strategies are not applied. Anyway, the considered system may cover a significant amount of domestic heating and cooling demand [23]. A second work on this topic was recently presented by Mittelman et al. [24]. The authors of this study investigated the theoretical feasibility of integrating concentrating PVT, based on triple-junction cells, with SHC based on a single-effect LiBr-H_2O absorption chiller. The presented system layout is very simple and it does not include storage tank, auxiliary heater and/or control equipments. The electrical efficiency ranged approximately between 19 and 23% (in function of PVT operating temperature, varying between 65 and 120 °C). On the other hand, the thermal efficiency of the PVT was stably slightly lower than 60%. The authors concluded that the reduction of PVT electrical efficiency, due to the increase in its operating temperature, was not significant. They also showed that the system was economically profitable (under certain conditions) and improvable optimizing the system layout (e.g. including a storage tank) or performing a sensitivity analysis in function of the climatic area and energy costs [24]. An additional paper about this topic was recently presented by the authors [25], investigating the possibility of integrating "tube and sheet" flat PVT system in previously developed SHC layouts [19, 26]. The results of the simulations, developed TRNSYS environment [27], showed that the selected type of PVT dramatically suffer of the high operating temperature required to drive to absorption chiller. Therefore, the authors concluded that a possible improvement of that layout may consist in CPVT system, based on multi-junction PV modules, which are less sensitive to the increase of temperature. The use of a concentrating system is recommended in order to reduce the high capital cost per unit area of the multi-junction modules. This is improvement has been here implemented by the authors, aiming at designing and analysing a novel trigeneration solar system based on CPVT technology equipped with multi-junction PV modules. In fact, apart from the works of Mittelman [24] and the one recently presented by the authors [25], none of the papers found in literature analyze the possibility of integrating CPVT or PVT in SHC systems. In particular, this work is an improvement of the one recently presented by the authors [25], in which the flat plate tube and sheet PVT has been replaced by a parabolic CPVT including multi-junction PV cells, with the scope to improve its thermal and electrical performance at the operating temperature demanded by the SHC. As discussed in Part I, a new thermodynamic model, based on mass and energy balances, has been implemented by the authors for the simulation of a novel configuration of parabolic CPVT. This model has been integrating in TRNSYS environment creating a new type that is included in the layout discussed in reference [25]. Finally,

the study also includes energy and cost analyses in order to evaluate the conditions for system convenience.

2. System Layout

In the following, for sake of brevity, the investigated polygeneration system is named PVSHC. The considered system layout is schematically shown in Fig. 1. Here six different loops are shown for the considered fluids: Solar Collector Fluid, SCF (water); Hot Fluid, HF (water); Hot Water, HW; Cooling Water, CW; Domestic Hot Water, DHW; Chilled or Hot Water, CHW.

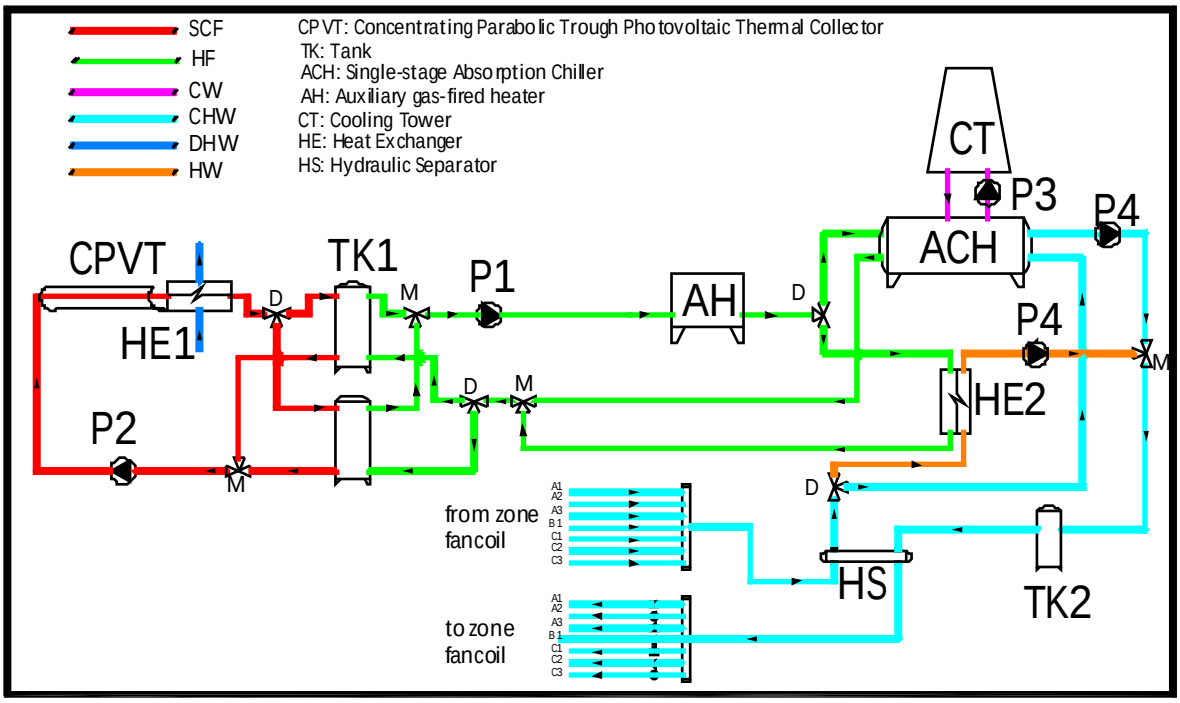

Fig. 1 – PVSHC layout

The system includes the following main components:

- a Solar Collector field, CPVT, consisting of concentrating parabolic trough solar collectors whose absorber is covered by a triple-junction PV layer;
- a Thermal Storage system (TK1), consisting of a set of two vertical hot storage tanks, equipped with mixers, diverters and a controller (the subsystem consists of two tanks, one large and one small, managed by a controller which may enable the first, the second or both, according to the thermal storage demand);
- a LiBr-H_2O single-effect absorption chiller (ACH), whose generator is fed by the hot fluid (HF), heated up by the solar field; the condenser and the absorber of the ACH are cooled by the cooling water loop (CW) provided by the cooling tower;
- a closed-circuit Cooling Tower (CT), providing cooled water (CW) to the condenser and absorber of ACH;
- a gas-fired Auxiliary Heater (AH), providing auxiliary thermal energy;
- a fixed-volume pump (P1) for the HW loop; a variable-speed pump (P2) for the SCF loop; a fixed-volume pump (P3) for the CW loop; a fixed-volume pump (P4) for the CHW loop;
- an inertial chilled/hot water storage tank (TK2), adopted in order to reduce the number of start-up and shut-down events for the absorption chiller ACH;
- an hydraulic separator (HS), balancing the flows between the primary and secondary hydraulic circuits;

- a plate-fin heat exchanger (HE2) in the HW loop, transferring the heat from the HF to the hot water (CHW) to be supplied to the fan-coils during the winter;
- a plate-fin heat exchanger in the solar loop, used to produce Domestic Hot Water (HE1) when the solar irradiation is higher than ACH (or HE2) thermal demand;
- some Balance of the Plant (BOP) equipments (the majority not displayed in Fig. 1, for sake of simplicity), such as pipes, mixers, diverters, valves, and controllers required for the system operations.

A number of additional mandatory components (not displayed in Fig. 1) have been also implemented in order to run the simulations and to process the data, such as: controllers (feedback, proportional and on/off), schedulers (daily and seasonal), weather databases, printers, integrators, etc.

Details regarding the operating principle and the controls strategies of the system are extensively provided in [25]. Note also that the system investigated in this paper is based on a Parabolic Trough CPVT equipped with a single axis system, similar to the one discussed in references [19, 26, 28]. Note also that this is a concentrating system. Therefore, it can convert only the beam fraction of the total solar insolation. This is only partially compensated by the one axis tracking system [19, 26, 28].

The considered PVSHC provides electricity, space heating and cooling and domestic hot water to the building. The same building test case (university building with thermal demand for a fitness centre) used in previous analyses [4, 26, 29] was here considered. Thus, it is possible to compare the results of this study with those achieved by the previously analyzed systems [4, 26, 29]. Data regarding building walls, occupancy, equipments and loads are diffusely discussed in reference [4], whereas the design data of the components are given in reference [19]. The duration curve of the building electric load is given in reference [29]. The considered DHW daily demand was set at 25 m^3/day at 45 °C.

3. Simulation model

The PVSHC polygeneration system described in the previous section was dynamically simulated by TRNSYS, which is a well-known software diffusely adopted for both commercial and academic purposes. The TRNSYS software includes a large library of built-in components, often validated by experimental data [27]. As above mentioned, the PVSHC layout investigated in this paper was originated from the layout developed in previous works [3-5, 19, 26, 29], where the models of both built-in and user-developed components are described in detail. As discussed in references [1-5, 19, 29], the majority of the models of the components (e.g. pumps, mixers, diverters, valves, controllers, auxiliary heater, absorption chiller, cooling tower, plate-fin heat exchanger, building, etc.) were taken from TRNSYS library whereas some new models (defined types, in TRNSYS) were developed by the authors in Fortran and then linked to TRNSYS (e.g. DHW heat exchangers, Hydraulic Separator, Fan coils, Primary Energy Calculator, Economic Costs Calculator, CPVT, etc). In particular, a new TRNSYS type has been created by the authors in order to simulate the CPVT under investigation. This new model of the CPVT is discussed in detail in Part I of the paper where details regarding the modelling approach are also provided. As regards the remaining new TRNSYS types developed by the authors, the reader is referred to references [3-5, 19, 26, 29] for further details. Conversely, the present part of the paper (Part II) is focused on the integration of the CPVT in a SHC layout.

A complete validation of the whole trigeneration system is not possible since, in authors' knowledge, a similar prototype has never been experimented. However, all models of the components included in the systems are very reliable. In fact, the components included in TRNSYS

library are validated against experimental data. Similarly, all the components previously developed by the authors are based on experimental data provided by the manufacturers.

3. Results and Discussion

A case study was developed for a university building located in Naples, South of Italy. It is the same building investigated by the authors in reference [4] and assumed as test case in several further studies [3-5, 19, 29]. The building consists in 7 classes, a common area and is located close to a university fitness center, so that the produced DHW can be delivered to that user. The building is utilised from Monday to Saturday, from 8.00 a.m. to 6.00 p.m., all year long. The solar trigeneration system presented in reference [25] will be assumed as reference case and the results of the PVSHC under investigation will be compared with those achieved in reference [25]. The total cooling capacity of the PVSHC system is set at 325 kW. The total CPVT aperture area was set at 996 m^2 - corresponding to a solar field consisting of 83 CPVT modules - which is significantly higher than the area adopted for thermal solar collectors in previous studies [3-5, 19, 26, 29] in which thermal loads were also covered by additional devices. Conversely, this value is very close to the one adopted for the simulation of the solar trigeneration system, based on tube and sheet PVT, analyzed in reference [25]. In fact, in polygeneration system based on photovoltaic/thermal technology, PVT or CPVT collectors must also provide electricity and the use of the auxiliary heater must be limited as much as possible, since the combination of AH and single stage ACH is not competitive with the EHP of the Reference System, as shown in references [1, 3, 5]. Note also that the system simulated in this work and the one analyzed in reference [25] differ only for the technology of PVT considered. In this work a concentrating parabolic trough PVT is considered instead of the flat tube and sheet configuration considered in reference [25]. Therefore, the results between these two studies can be usefully compared in order to evaluate the differences in energetic and economic performances between the two technologies. In reference [25] the methodology for the calculation of energetic and economic balances is diffusely discussed.

Table 1- Annual results: thermal energy (kJ/year)

Q_{HE1}	Q_{AH}	Q_{PVT}	ΔPE	Q_{rej}	Q_h
1.47E+09	1.78E+08	2.25E+09	2.95E+09	7.77E+08	7.50E+07
Q_c	$Q_{c,ACH}$	$Q_{AH,s}$	Q_{HE2}	Q_{CT}	$Q_{PVT,s}$
6.36E+08	6.48E+08	1.35E+08	8.85E+07	1.46E+09	1.85E+09

As mentioned in the previous sections, the simulation tool can provide results on whatever time basis. In particular, yearly results are graphically reported from Table 1 to Table 3. Table 1 shows some important annual energy flows. Here, the total amount of thermal energy produced by the CPVT (Q_{PVT}) is 2.25 10^9 kJ/year. Such thermal energy is basically produced during the summer period ($Q_{PVT,s}$:1.85 10^9 kJ/year) when the thermal performance of the CPVT is significantly better as a consequence of the higher availability of beam radiation. Note that the thermal performance of the CPVT is slightly better than the one of the PVT considered in reference [25] which produced a total thermal energy of 1.84 10^9 kJ/year (in summer 1.39 10^9 kJ/year). It could be argued that the better performance of the CPVT is due to the one-axis tracking system which allows one to pick up a higher amount of irradiation. In fact, the flat plate PVT (South, 30 deg slope) can convert 6.23 kJ/m^2 year of total insolation (3.64 kJ/m^2 year of beam radiation), whereas the total radiation incident on the CPVT is 6.93 kJ/m^2 year (4.23 kJ/m^2 year of beam radiation). However, it must be considered that CPVT can convert only the beam radiation (except for the small top absorber area) whereas the flat plate PVT collectors can convert the total radiation. Therefore, it can be concluded the insolation available for conversion is lower for the case of the CPVT. Thus, the higher thermal production by the CPVT is basically due to its high thermal efficiency which is significantly better than the one of flat plate PVT. This circumstance is well known in literature and it is due to the

lower surface per unit thermal power of the CPVT (lower thermal losses) and to the lower average angle of incidence occurring in the CPVT due to the one-axis tracking system. This better thermal performance also determines a lower demand of thermal energy by the auxiliary heater AH. In fact, the thermal energy produced by the AH (Q_{AH}) is 1.78 10^8 kJ/year (1.35 10^8 kJ/year in summer, $Q_{AH,s}$), which is significantly lower than the value calculated in reference [25] (2.31 10^8 kJ/year). As a consequence, a better primary energy saving (2.95 10^9 kJ/year, ΔPE) is achieved with respect to the value calculated in [25] (2.29 10^9 kJ/year). Note also that this increase in energy saving is lower than expected since the additional thermal energy produced by the CPVT is not completely consumed since a large amount of this heat must be rejected. This is basically due to the phase shift between solar radiation and space heating/cooling demand. This phase shift also determines a large amount of heat (Q_{HE1}) produced by the CPVT field and employed for DHW. In fact, HE1 produces DHW only when PVT outlet temperature is higher than the set point. In other words, HE1 produces DHW when CPVT thermal energy is not demanded by the building and when TK1 storage tank is full. The system equipped with CPVT produces a larger amount of DHW (Q_{HE1}) with respect to the flat plate PVT (1.47 10^9 kJ/year vs 1.11 10^9 kJ/year). However, this additional DHW is generally dissipated. In fact, the amount of heat rejected (Q_{rej}) by the CPVT (7.77 10^8 kJ/year) is significantly higher than the one calculated in [25] (4.22 10^8 kJ/year). Finally, as expected, the calculated values of space cooling (Q_c) and heating (Q_h) demand, Cooling Tower thermal energy (Q_{CT}), ACH cooling energy ($Q_{c,ACH}$) and HE2 thermal energy (Q_{HE2}) are the same as the ones calculated in reference [25]

Table 2- Annual results: electrical energy (kJ/year)

$E_{el,PVT}$	$E_{el,aux}$	$E_{el,+}$	$E_{el,-}$	$E_{el,+,F1}$	$E_{el,+,F2}$	$E_{el,+,F3}$	$E_{el,-,F1}$	$E_{el,-,F2}$	$E_{el,-,F3}$
8.79E+08	6.98E+07	4.60E+08	3.11E+08	2.28E+08	1.12E+08	1.20E+08	2.76E+08	3.48E+07	6.28E+04

The electricity annual balance is shown in Table 2. Here, it is clearly displayed that the electricity produced by the PVT ($E_{el,PVT}$) is very high (8.79 10^8 kJ/year), also determining a large amount of electricity in excess and sold to the grid ($E_{el,+}$). The overall electrical energy produced by the CPVT is significantly higher than the one produced by the flat plate PVT (6.04 10^8 kJ/year) [25], as a consequence of the high nominal efficiency of the triple-junction PV included in the CPVT collector. Consequently, the electrical energy in excess ($E_{el,+}$) produced by the CPVT is larger than one calculated in reference [25] (4.60 10^8 kJ/year vs 2.01 10^8 kJ/year). Similarly, in case of CPVT collectors, the electrical energy bought from the grid ($E_{el,-}$) decreases (3.11 10^8 kJ/year vs 3.24 10^8 kJ/year).

Table 3- Annual results: performance indexes

PES	$\eta_{t,PVT}$	$\eta_{el,PVT}$	$\eta^*_{t,PVT}$	$\eta^*_{el,PVT}$	$F_{sol,el}$	$F_{sol,s}$	$F_{sol,w}$	F_{DHW}
7.70E-01	3.26E-01	1.27E-01	5.29E-01	2.07E-01	7.39E-01	9.32E-01	9.01E-01	6.56E-01

The overall thermal and electric energy balances can be summarized by some indexes, shown in Table 3. The Primary Energy Saving ratio (PES) was significantly higher than the one achieved by the flat plate system (77.0 % vs 70.2 %). This is mainly due to the higher values of both thermal and electrical efficiencies of the CPVT compared with the flat plate PVT. In fact, the CPVT thermal efficiency ($\eta_{t,PVT}$), calculated on the basis of the total incident radiation, is 32.6 % whereas the same value was about 29.4 % in case of flat plate PVT. This is typical of concentrating systems whose heat transfer area is significantly lower than the one of non-concentrating systems, determining lower losses toward the environment. This is much clear if the efficiency is calculated with respect of the sole beam radiation ($\eta^*_{t,PVT}$): in this case the thermal efficiency is slightly lower than 53 %. Similarly, the use of high performance triple-junction PV layer allows one to achieve ultra-high electrical efficiency. In fact, the electrical efficiency, calculated with respect to the total radiation

($\eta_{el,PVT}$), is 12.7 %, whereas the value increases up to 20.7 % ($\eta^*_{el,PVT}$) when the sole beam radiation is considered. Such values are significantly high, considering the typical operating temperature of the PV layer. In fact, the electrical efficiency calculated in [25] was 9.7%. As a consequence, the electrical solar fraction, $F_{sol,el}$, i.e. the ratio of the overall electrical energy demand produced by the PVT, is significantly higher than one rated in [25] (73.9 % vs 65%). Similar results are also achieved for the summer solar fraction, $F_{sol,s}$ (93.2 % vs 88.2 %). Conversely, the winter solar fraction, $F_{sol,w}$,of the CPVT is slightly lower than the one calculated in [25] (90.1 % vs 90.8%). This is also typical of concentrating systems whose thermal performance dramatically decreases during the winter as a consequence of the lower availability of beam radiation. Finally, Table 3 shows that the about 65.6 % (F_{DWH}) of the heat produced by PVT is used by HE1 for the production of DHW. This high value is not surprising since the PVT area is significantly high and the TK volume relatively low. Therefore, there are long periods in which the PVT thermal production is higher than system space cooling/heating demand and the storage capacity of TK is full. In addition, PVT thermal energy is always used exclusively for DHW during the Sundays and during the periods in which both space cooling and heating systems are switched off [4].

Table 4- Annual results: costs (€/year)

ΔC_{op}	C_{DHW}	$C_{el,-}$	$C_{el,+}$	$C_{el,+,RS}$	C_{rej}	$C_{ft,ee}$	$C_{ft,pe}$	ΔI_0/FA
4.29E+04	1.45E+04	1.18E+04	9.38E+03	1.53E+04	1.62E+04	1.10E+05	2.13E+05	6.37E+04

From the energetic point of view the system equipped with CPVT collectors shows a better performance than the one based on planar PVT. This was a quite trivial result due to higher technological level of CPVT. However, this energetic performance must be evaluated simultaneously with the economic one. In this study, according with the literature review discussed in the Part I of the paper, a capital cost of 600 € per m^2 of aperture area of CPVT was assumed. This cost could be achieved in the next future due to the increasing commercialization of triple junction PV layers. In spite of this optimistic assumption, the capital cost of the whole system is dramatically high, due to the high capital cost of CPVT collector. In fact, Table 4 shows that the annual owning cost (ΔI_0/FA), defined in [25], of the PVSHC system is dramatically higher than the one calculated for flat PVT (6370 €/year vs 47910 €/year). On the other hand, CPVT based system can achieve better values for all the cash flows (ΔC_{op}) and eventual feed-in tariffs ($C_{ft,pe}$ and $C_{ft,ee}$, proportional respectively to the primary energy saved and to the electrical energy produced). The overall result is a lower economic performance with respect to the ones of reference [25]. In fact,

Table 5 shows that all the Simple Pay Back Periods are slightly higher the ones of reference [25] (respectively 16.8, 11.7, 5.4 and 3.6 years). Therefore, it can be concluded that the cost assumed for the CPVT is still high to recover the higher energetic performance shown by this kind of photovoltaic system. Note that in

Table 5 four different Simple Pay Back Periods were considered [25]:

- SPB: no public funding
- SPB_{cc}: Capital cost contribution of 30% of the extra cost of the PVSHC with respect to the cost of the RS
- $SPB_{ft,ee}$: Feed-in tariff equal to 0.45 € per electricity kWh (similar to the one presently adopted for PV in Italy) produced by the PVT
- $SPB_{ft,pe}$: Feed-in tariff equal to 0.207 € per primary kWh saved by the PVSHC with respect to the RS

Table 5- Annual results: SPB

SPB	SPB_{cc}	$SPB_{ft,ee}$	$SPB_{ft,PE}$
1.85E+01	1.30E+01	5.21E+00	3.74E+00

The tool also allows one to display the trends of the state-points temperatures and components energy flows, during the dynamic simulation. The related plots can be displayed in whatever time basis multiple of the simulation time step (0.040 hours). For example yearly plots are useful for detecting the general trends whereas daily or weekly plots can display in detail the typical dynamic oscillations of temperatures and energy flows. Some of these analyses, regarding both building and system performances, were presented and discussed in previous works [4, 25-26, 28, 30]. Therefore, in the following the discussion will be focused only on the differences of the CPVT system considered in this work with respect to the layouts previously analyzed. *Fig. 2* and *Fig. 3* display some key-points temperatures of the system under investigation. Similarly, *Fig. 4* and *Fig. 5* show respectively the thermal and electrical energy flows, whereas PVT thermal and electrical efficiencies are shown in *Fig. 6*. Such Figures are useful to detect the general trends of the thermodynamic parameters. However, for a better interpretation of the results it is more convenient to consider a random winter and summer week to analyse in detail the trends of the thermodynamic parameters.

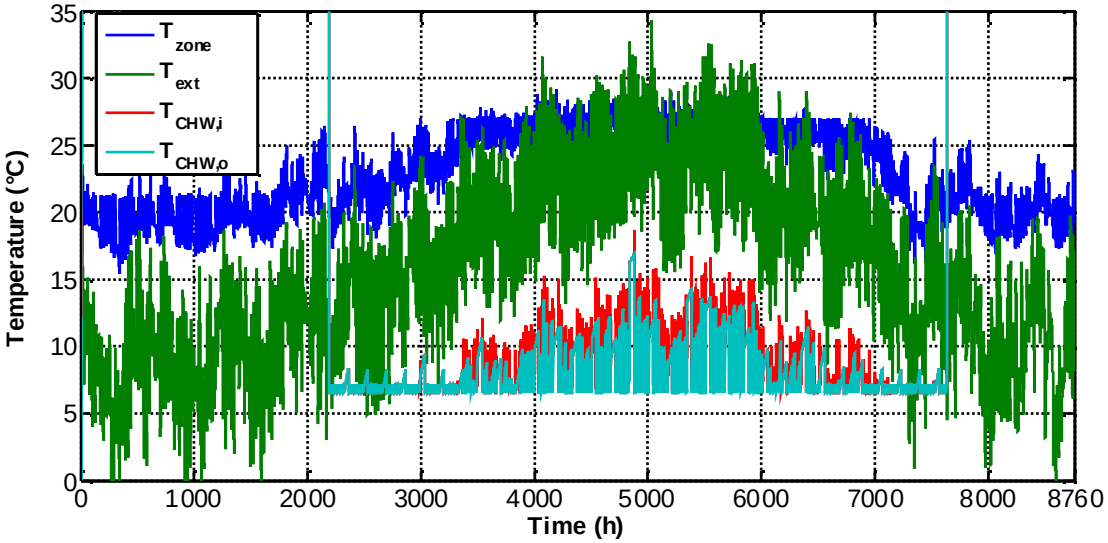

Fig. 2 - Dynamic simulation: Temperatures (1)

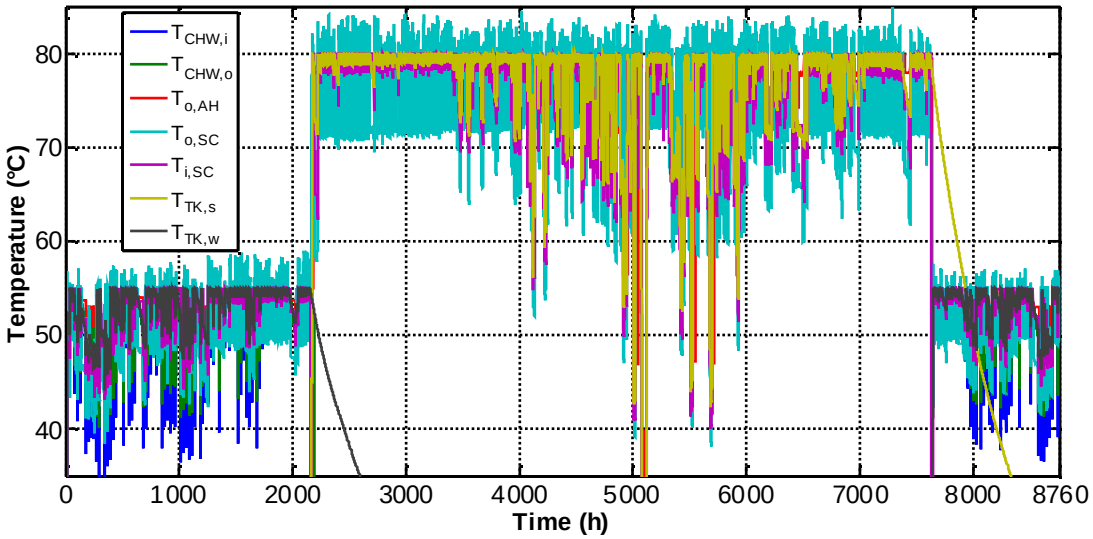

Fig. 3- Dynamic simulation: Temperatures (2)

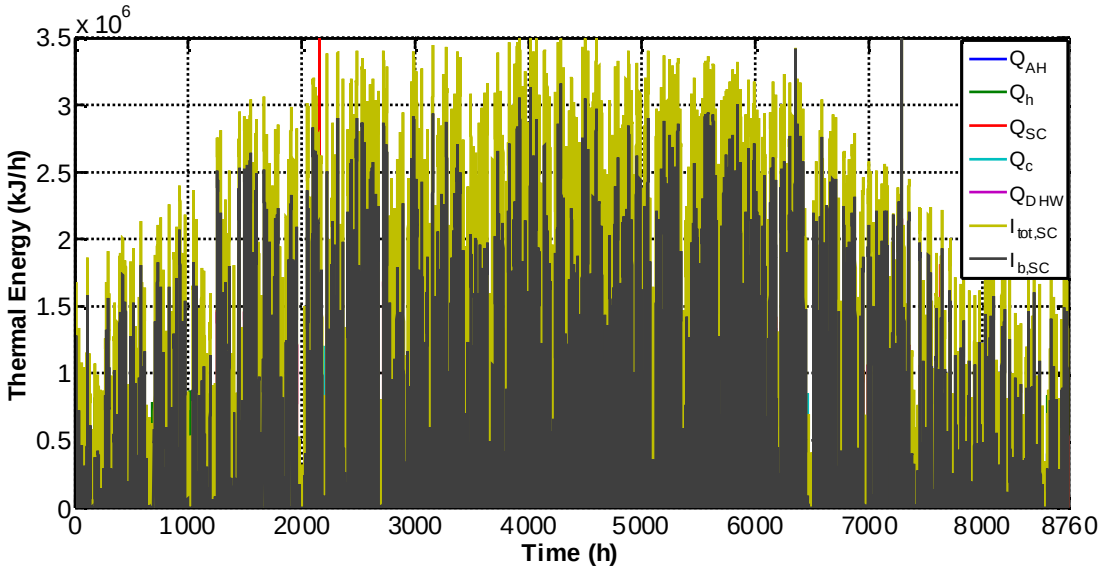

Fig. 4 - Thermal Energy

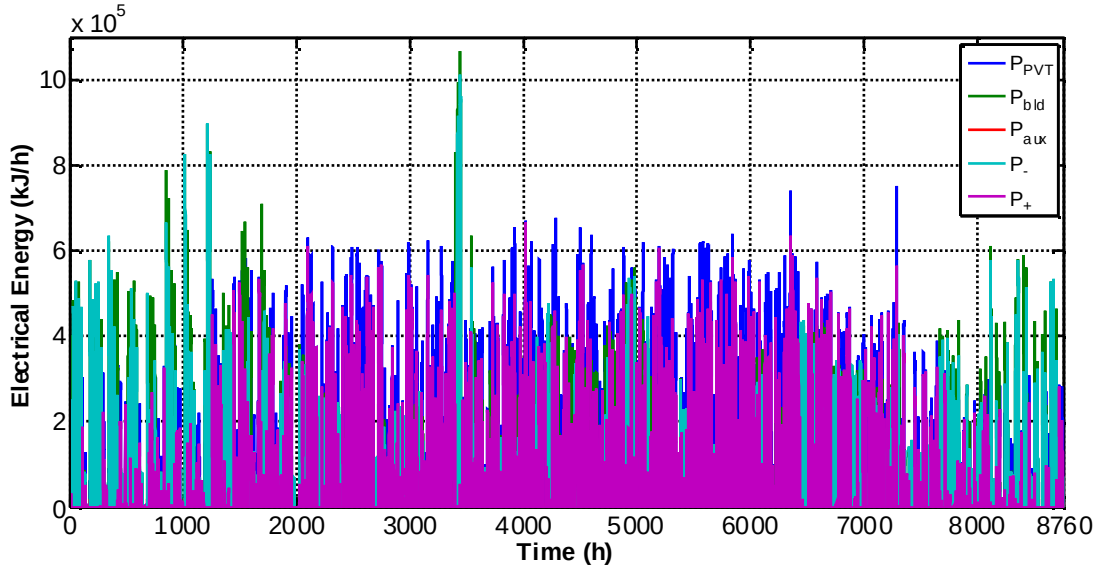

Fig. 5 - Dynamic simulation: Electrical Energy

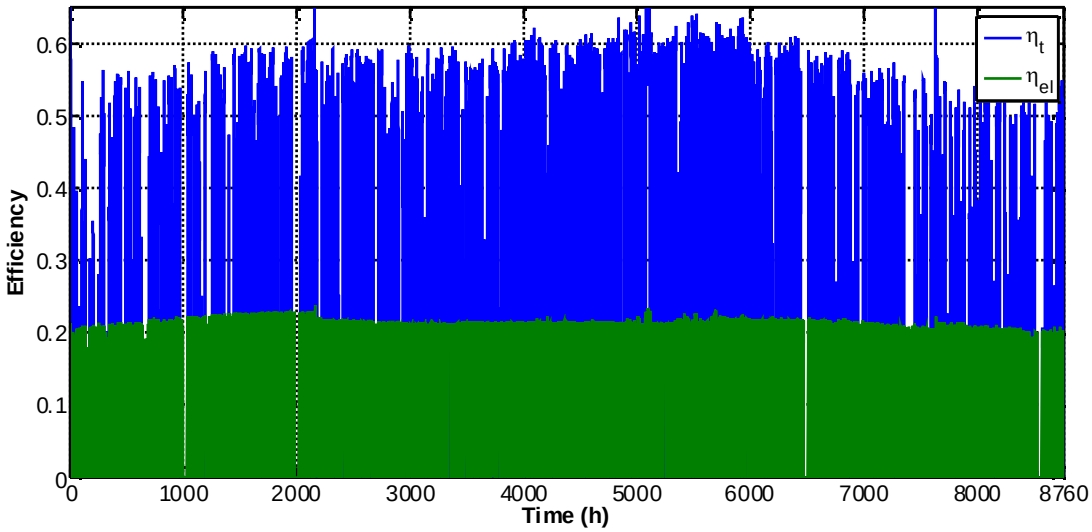

Fig. 6 - Dynamic simulation: Thermal and electrical efficiencies

In particular, the corresponding summer plots are shown from *Fig. 7* to *Fig. 11*, whereas the winter week is shown from *Fig. 12* to *Fig. 16*. *Fig. 7* and *Fig. 8* show some key-point temperatures for the considered summer week. Here, it is clearly shown the typical oscillating trend of the internal zone air temperature due to the operation of the on/off thermostat. The internal temperature is controlled for the first six days of the week since during the Sunday the building is not used. *Fig. 7* also shows that ACH outlet temperature is often equal to corresponding set-point except for the central hours of the Tuesday. Conversely, the CHW inlet temperature significantly varies as a consequence of the variations of cooling demands of the building. *Fig. 8* shows the temperatures of the solar loop. Here, it is clearly displayed that the CPVT outlet temperature is stably over its set point temperature. PVT outlet temperature is often even higher than the summer set-point (80 °C). This often occurs when the inlet temperature is also high. In fact, the variable speed pump cannot increase the fuel flow up to its maximum capacity (0.333 kg/s per CPVT module), determining the increase of CPVT outlet temperature shown in *Fig. 7*. Note that *Fig. 7* also shows that TK average temperature is often close to 80 °C: only during the first two days of the week TK temperature significantly decreases. This trend can be better interpreted analyzing *Fig. 9*. Here, it is clearly shown that the thermal energy produced by the PVT is significantly low during the first two days as a consequence of the reduction of solar beam radiation. As a consequence, during these days the AH must provide additional thermal energy to achieve the temperature of the hot fluid required to drive the ACH. Obviously, in those days there is no DHW production since there is no heat in excess from solar loop. Conversely, during the other days of the week the PVT thermal energy is significantly higher than the one demanded by the ACH and a lot of thermal energy in excess is converted in DHW by HE1. This trend could be mitigated using larger TK storage systems, balancing positive and negative energy flows in the solar loop. However, larger systems would also determine larger thermal losses and a longer response of the system to the user demand. Therefore, a possible solution to this problem could consist in a variable volume storage system which is an option that the authors are going to explore in forthcoming studies. *Fig. 10* shows the electricity flows for the same summer week. Here, it is clearly displayed that the electrical power produced by the PVT is generally higher than the overall electrical energy demand (CPVT auxiliary devices, building equipments and lights). Therefore, the electrical energy in excess is typically a large amount of the PVT production, whereas the integration from the grid is required only in case of low beam radiation.

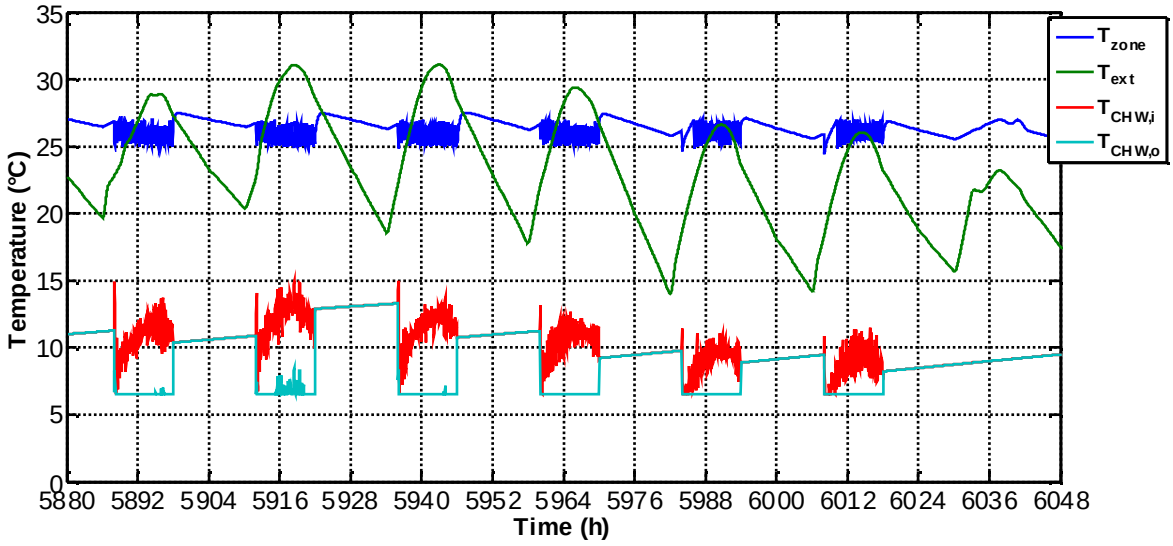

Fig. 7- Summer week: Temperatures (1)

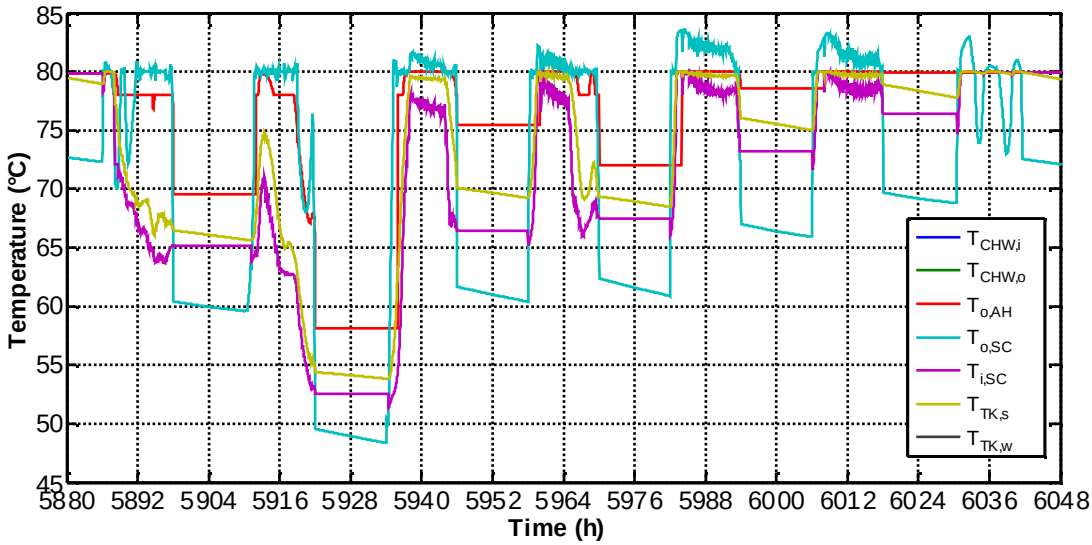

Fig. 8- Summer week: Temperatures (2)

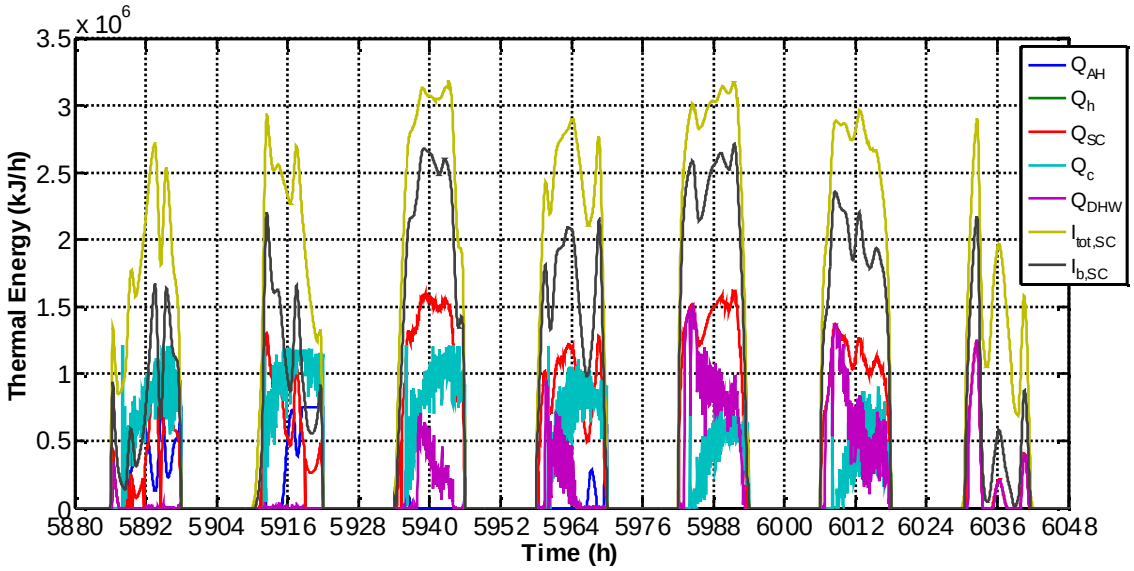

Fig. 9- Summer week: Thermal Energy

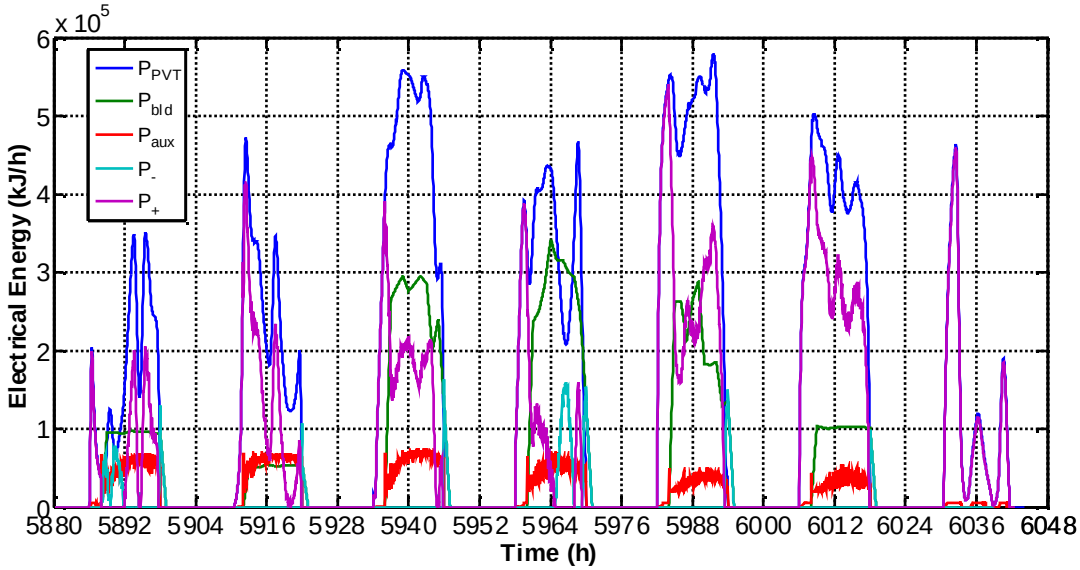

Fig. 10 - Summer week: Electrical Energy

Finally, Fig. 11 shows that the electrical efficiency of the PVT is stably higher than 20 % and it slightly decreases during the central hours of the day due to a corresponding increase of PV layer temperature. The thermal performance of the CPVT is also very good being typically higher than 50 % for highly insolated days. Note that both the efficiencies shown in figure are calculated with respect to the incident beam solar radiation.

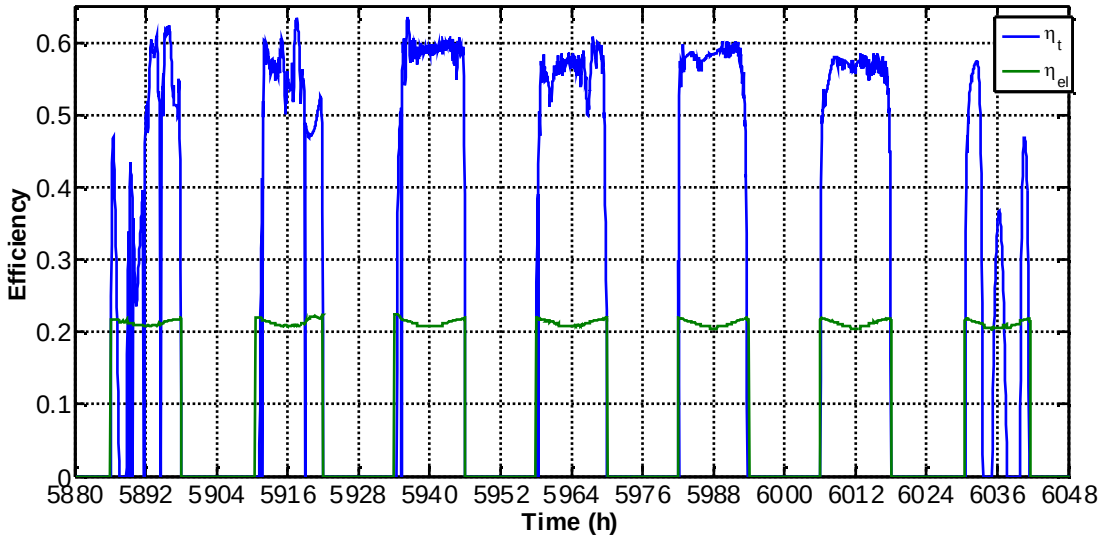

Fig. 11 - Summer week: Thermal and electrical efficiencies

The winter operation of the system is dramatically different from the summer one. For the considered winter week, temperatures are shown in *Fig. 12* and *Fig. 13*. Here, it shown that the temperature of the internal zone oscillates around 20 °C (winter set point) only during the first hours of the day. Then the temperature overcomes the set-point only driven by the internal loads (equipment and people) of the building. Therefore, the thermal energy is required only during the first hours of the day when unfortunately beam radiation is scarce and external temperature is low. In fact, for the selected week PVT outlet temperature is significantly lower of the corresponding set point in the 3rd and 4th day when the beam radiation is very low (*Fig. 14*).

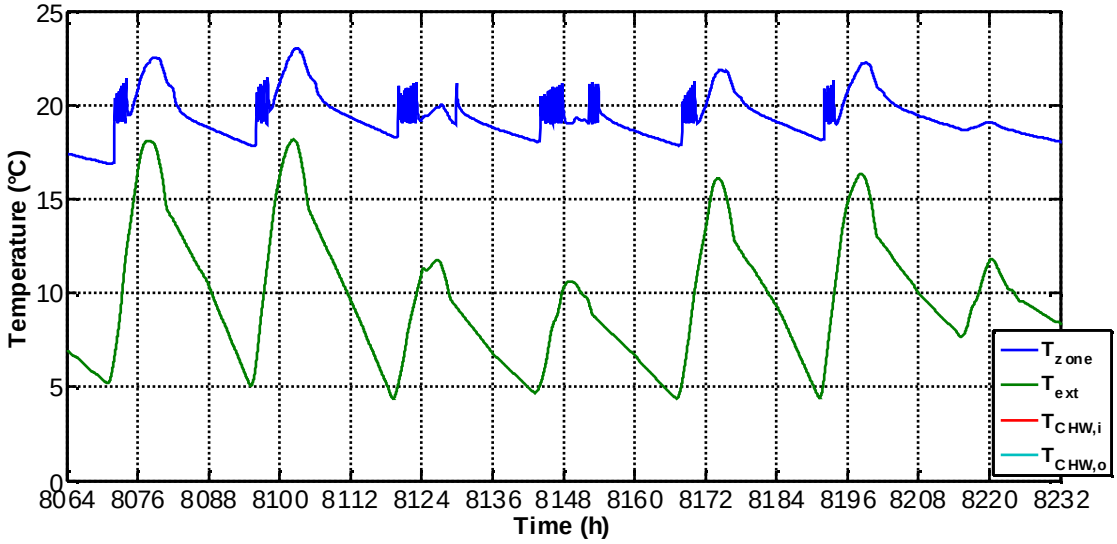

Fig. 12 - Winter week: Temperatures (1)

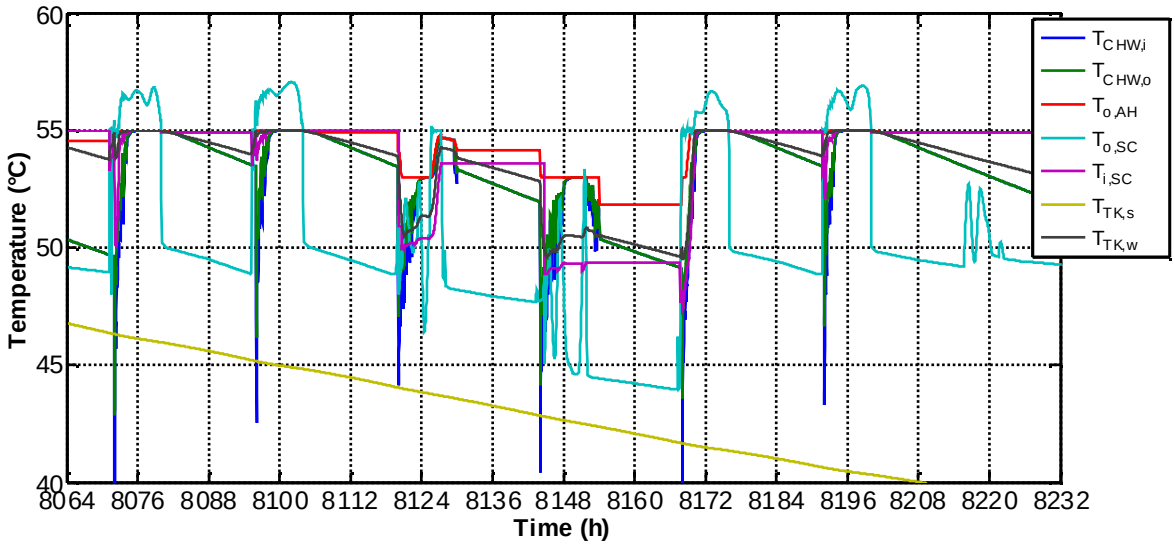

Fig. 13 - Winter week: Temperatures (2)

Fig. 14 also shows that the thermal energy produced by the solar field is basically used for DHW since for the majority of the day there is no space heating demand. The winter plot of the electrical energy flows (Fig. 15) is completely different from the summer one. In fact, the electrical energy produced by the PVT is very often lower than building and auxiliaries demand, determining a larger amount of electrical energy bought from the grid. This is also determined by the lower PVT electrical efficiency shown in Fig. 16 which is stably lower than 20 %. Such lower values - compared to the summer ones- are basically determined by the lower availability of solar radiation which also overcomes the positive effect of the lower operating temperature of the winter operation. This lower availability of beam radiation also affects the thermal performance of the CPVT whose thermal efficiency is significantly lower than 50 %.

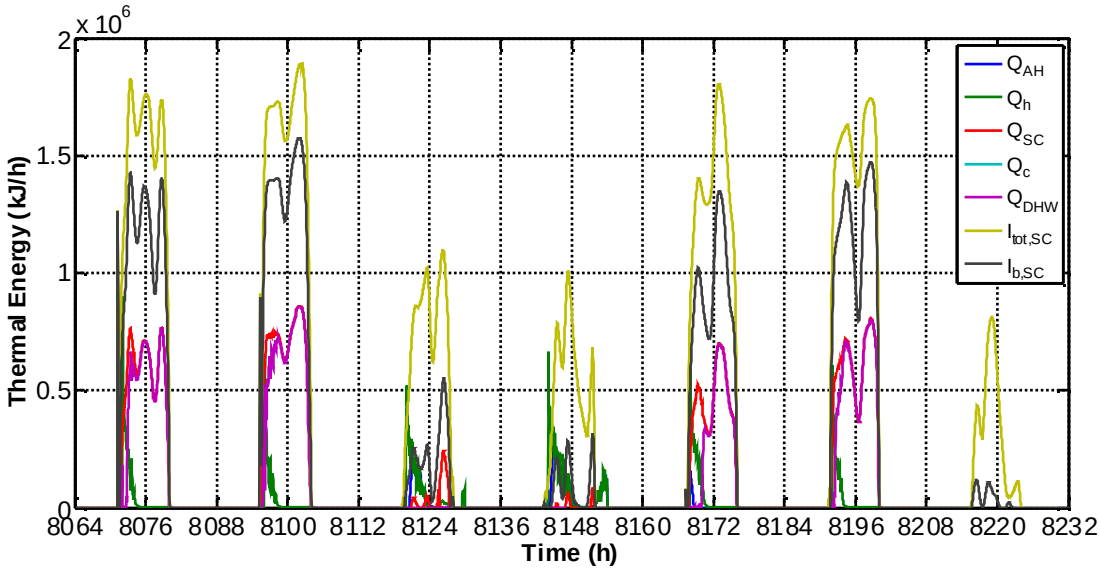

Fig. 14 - Winter week: Thermal Energy

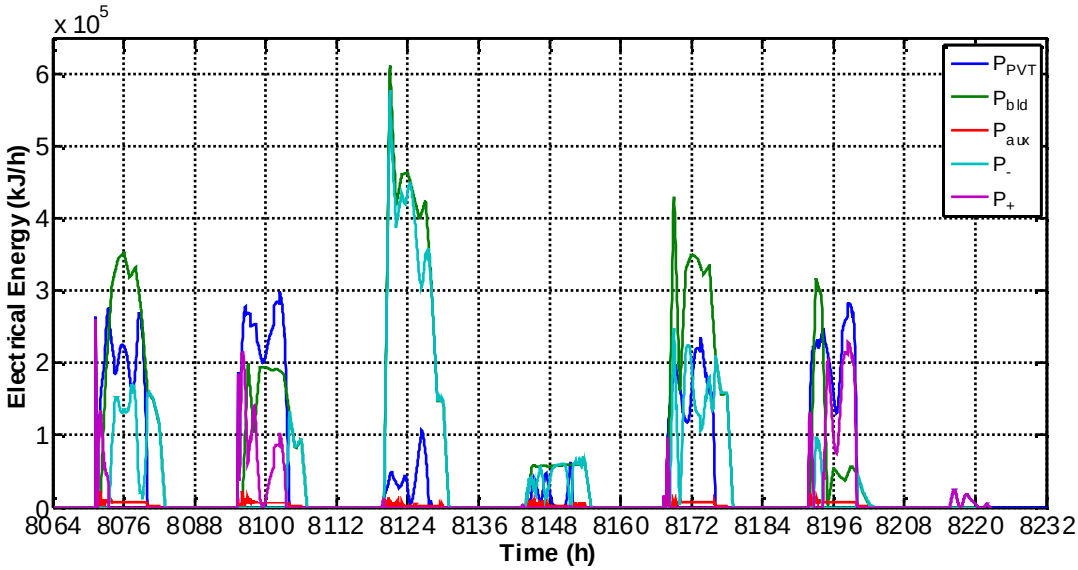

Fig. 15 - Winter week: Electrical Energy

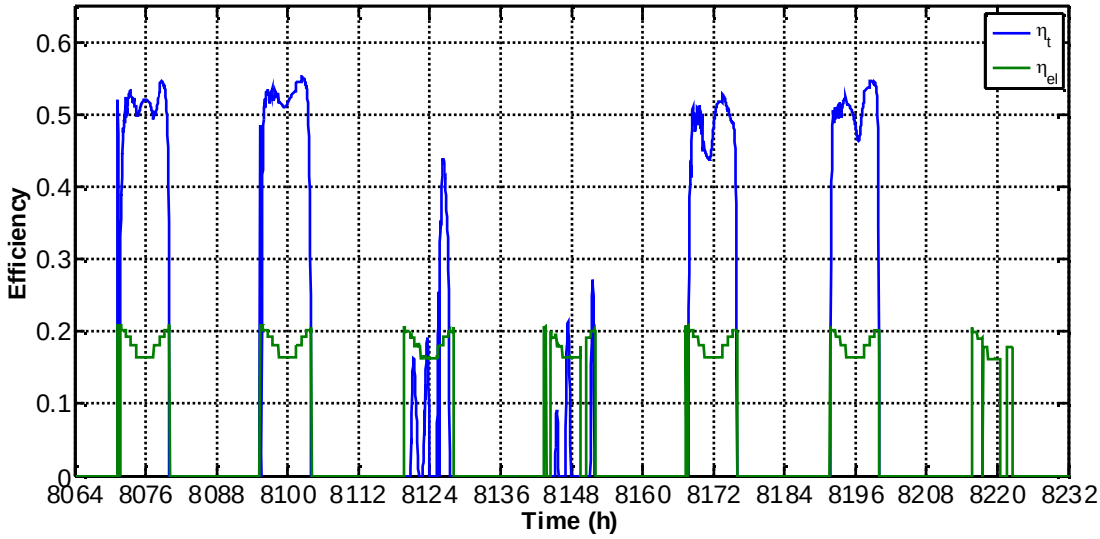

Fig. 16 - Winter week: Efficiency

The study was also completed by a parametric analysis with the scope to analyze the variation of PVSHC performance in function of the following variables: PVT Area (A_{SC}), P2 flow rate per PVT area; PVT summer outlet fluid set point temperature ($T_{set,PVT,s}$); PVT winter outlet fluid set point temperature ($T_{set,PVT,w}$); TK1 summer volume per PVT Area ($v_{TK1,s}$); TK1 winter volume per PVT Area ($v_{TK1,w}$). As expected, the results are dramatically sensitive to the variations of PVT area. In fact, in Fig. 17 it is clearly shown the heat produced by the PVT linearly increases with PVT area. However, it must be considered that the higher the PVT area, the higher the amount of solar heat used for DHW (Q_{HE1}). In addition, for large PVT fields, the majority of the DHW produced by the PVT, is in excess vs. the building demand and it is rejected (Q_{rej}). This is also clear by the trend of the AH heat (Q_{AH}) which decreases very slowly. In fact, a larger PVT area cannot eliminate the amount of auxiliary heat demanded to the AH in case of scarce solar radiation. In fact, the slope of the primary energy saving curve (ΔPE) is significantly lower than the one of the heat produced by the PVT: the difference is due to the increase in heat rejection. PVT area also affects the electricity production.

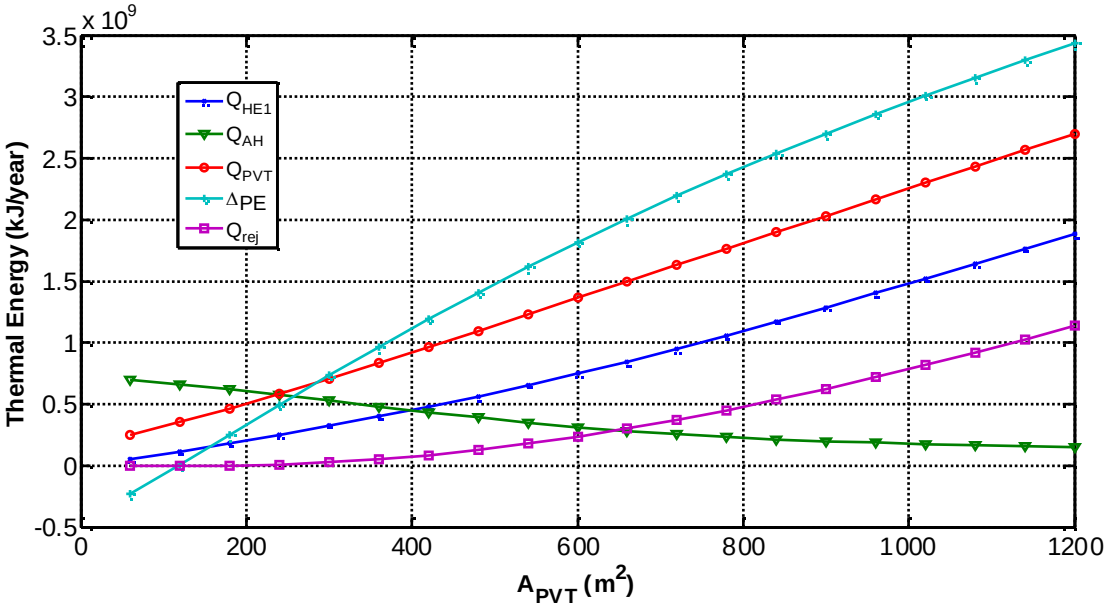

Fig. 17 - Sensitivity analysis: Thermal energy vs PVT area

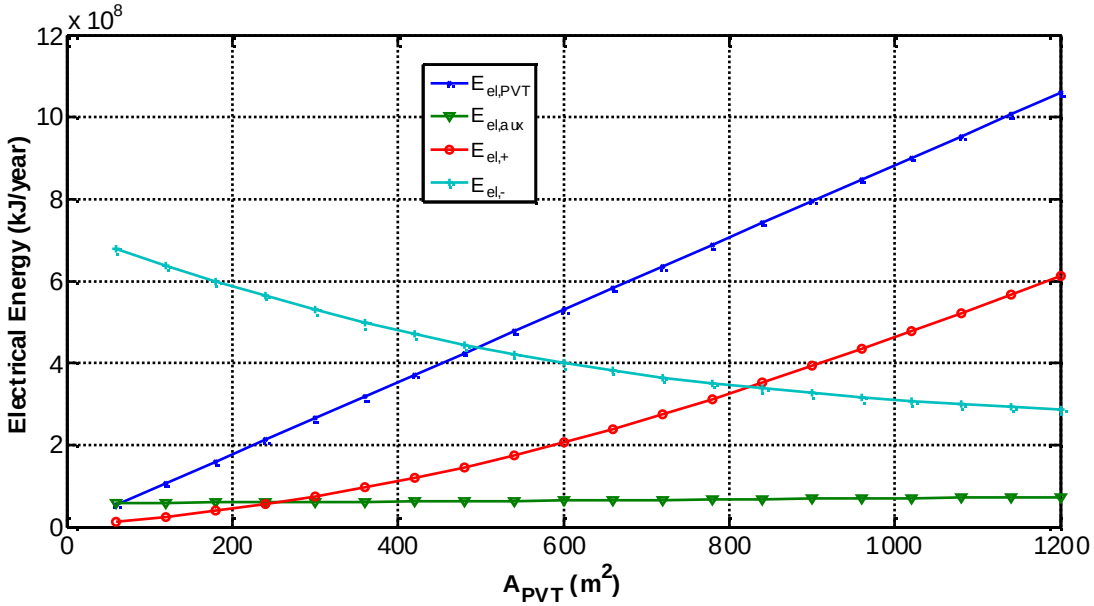

Fig. 18 - Sensitivity analysis: Electrical energy vs PVT area

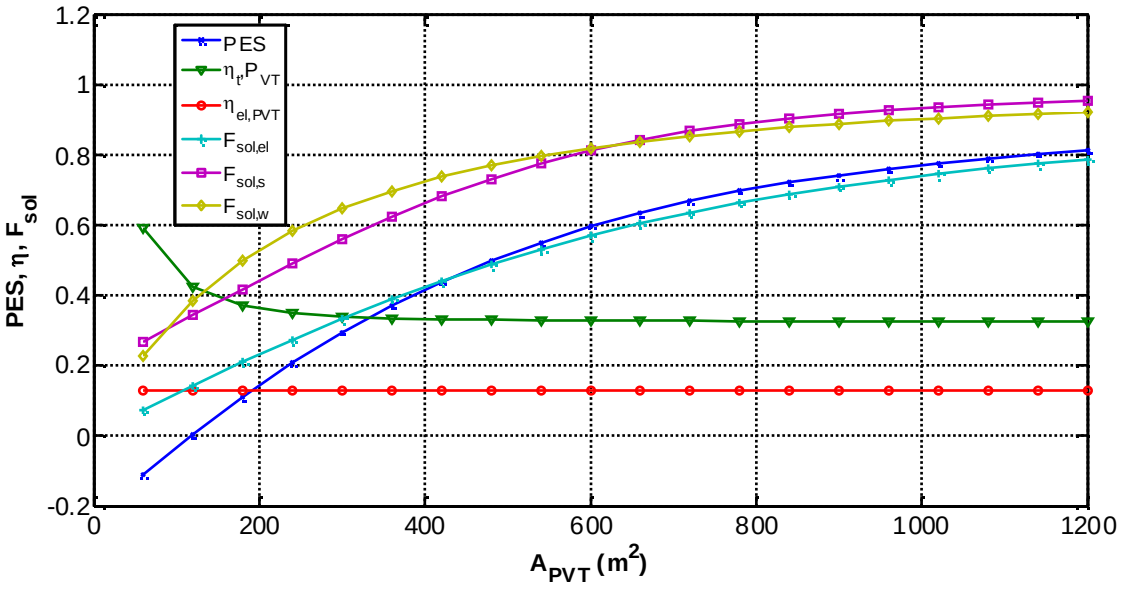

Fig. 19 - Sensitivity analysis: PES, efficiencies and Solar Fractions vs PVT area

As expected, Fig. 18 shows that PVT electricity production ($E_{el,PVT}$) linearly increases with PVT area. This increase also determines a larger amount of electricity sold to the grid ($E_{el,+}$) whereas the one bought from the grid ($E_{el,-}$) obviously decreases. Fig. 19 shows that PES and all the solar fractions increase less then proportionally with PVT area. In fact, the higher the PVT area is, the higher the PES. In fact, for larger solar fields, the amount of thermal and electrical energy produced by the auxiliary devices (heater or grid) reduces, also increasing the PES. Conversely, as typically occurs, PVT thermal efficiency decreases for higher PVT area whereas the electrical efficiency is only very slightly affected by the variation of the PVT area.

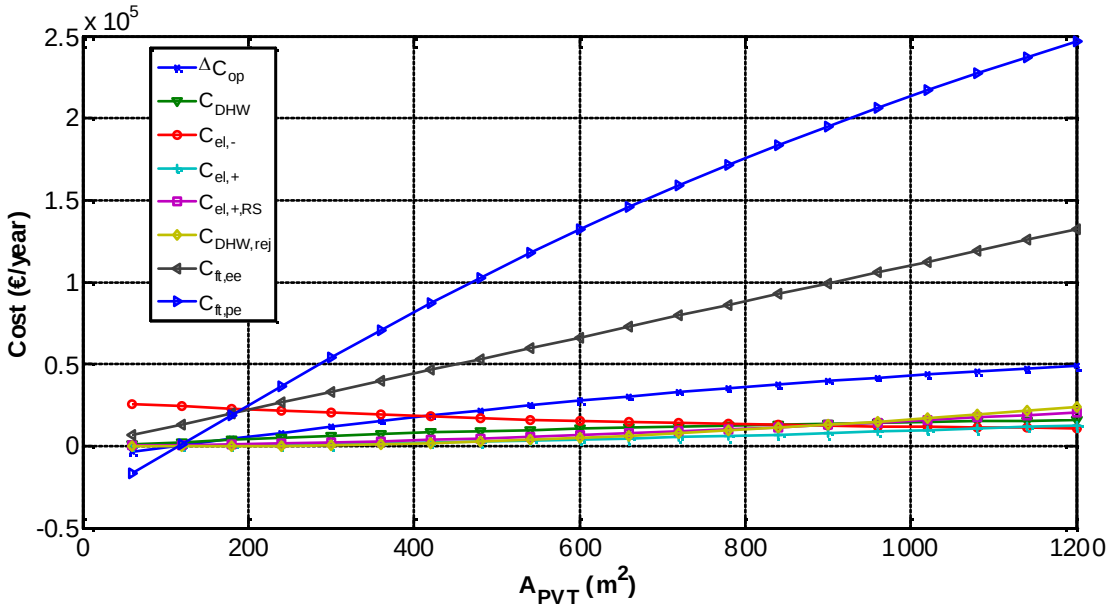

Fig. 20 - Sensitivity analysis: Costs vs PVT area

The thermal and electrical flows also affect the annual costs, as shown in Fig. 20. Note that the annual operating cost savings (ΔC_{op}) reproduce the same trend of the one shown by the primary energy saving (ΔPE). This is mainly due to the incomes of the DHW production. In fact, this cash flow is almost constant in the range 60 ÷ 1200 m^2, because the additional DHW produced by the HE1 is rejected since the daily DHW is still supplied. As expected, the feed-in tariff based on the

electricity production, linearly increases with PVT area (the electricity production is a linear function of the PVT area). Conversely, the feed-in tariff proportional to the PE savings, shows the same shape of the ΔPE curve. Both feed-in tariffs are dramatically higher than all the remaining cash flows for whatever PVT area is considered. Note also that cash flow due to the selling of the exceeding electricity ($C_{el,+}$) is significantly lower than the corresponding purchase cost by the RS ($C_{+,RS}$). This is due to the differences between electricity costs and prices discussed in the previous section.

The economic performance of the system under investigation is calculated using Simple Pay Back, SPB (Fig. 21), Net Present Value (Fig. 22) and Profit index (Fig. 23). The minimum SPB is achieved at 960 m^2 except for the case of $SPB_{ft,ee}$ whose minimum occurs at 1200 m^2. However, the system is never profitable without incentive since PI and NPV are always negative for whatever PVT area. Conversely, NPV increases with PVT area considering both feed-in tariffs. The corresponding Profit Indexes are maximum respectively at 960 m^2 (PI_{ftpe}) and 1200 m^2 (PI_{ftee}).

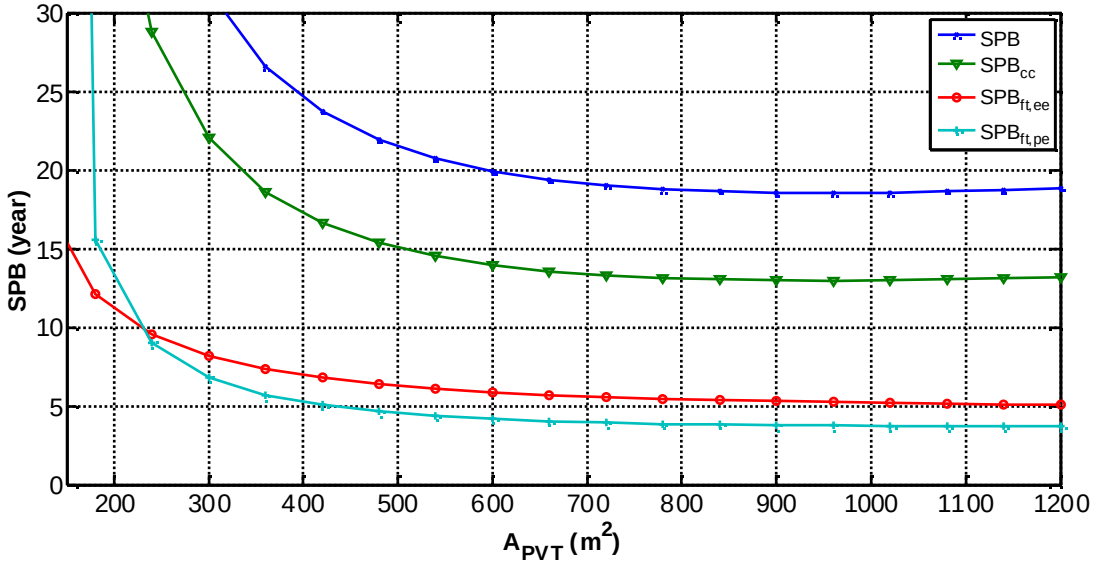

Fig. 21 - Sensitivity analysis: SPB vs PVT area

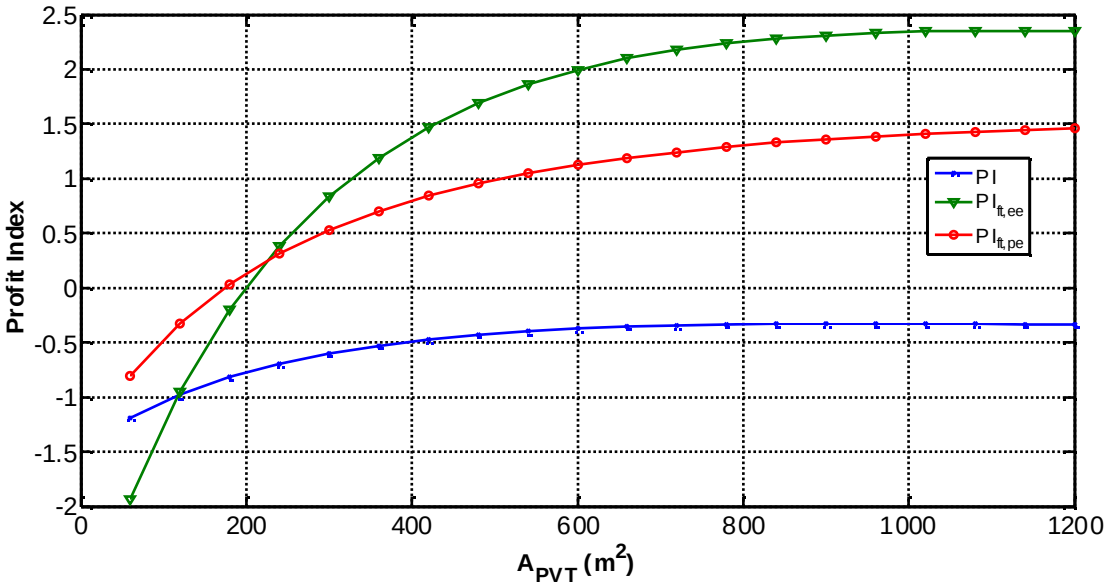

Fig. 22 - Sensitivity analysis: PI vs PVT area

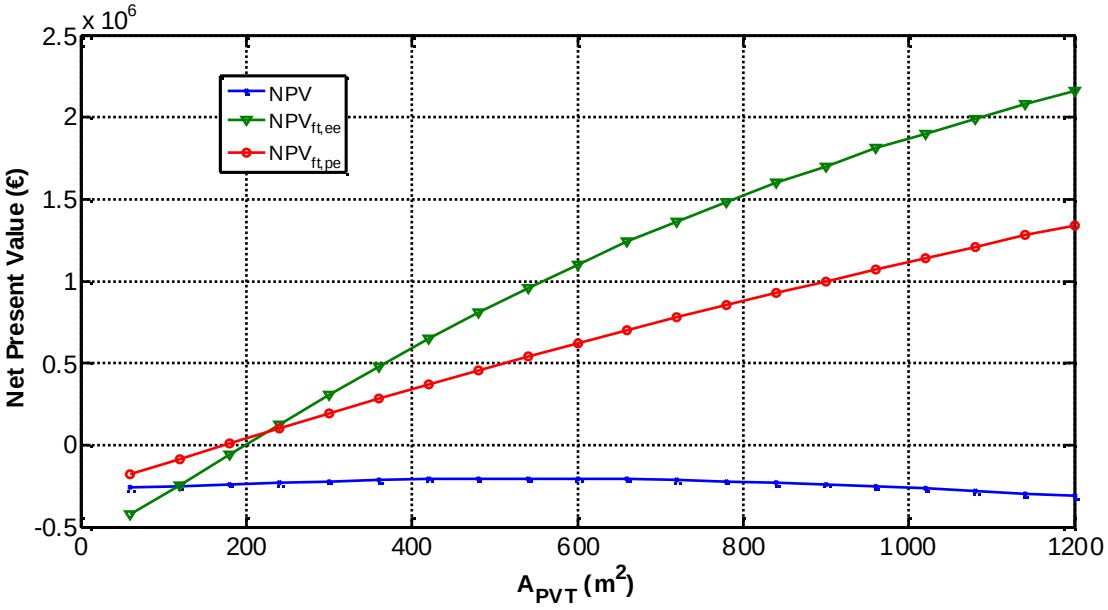

Fig. 23 - Sensitivity analysis: NPV vs PVT area

In this analysis a key parameter is the capital cost of the CPVT. Fig. 24 and Fig. 25 show the variation of NPV and PI indexes as a function of both PVT area and PVT capital costs. Results show that both NPV and PI (without incentive) become positive only when the capital cost falls below 200 €/m^2 and the PVT area is higher than 600 m^2. Conversely, in case of feed-in tariffs capital costs up to 1200 €/m^2 may lead to good profitability if PVT area is higher than 400 m^2. Fig. 24 also shows that PI index initially linearly increase with PVT area and then becomes almost insensitive to that parameter.

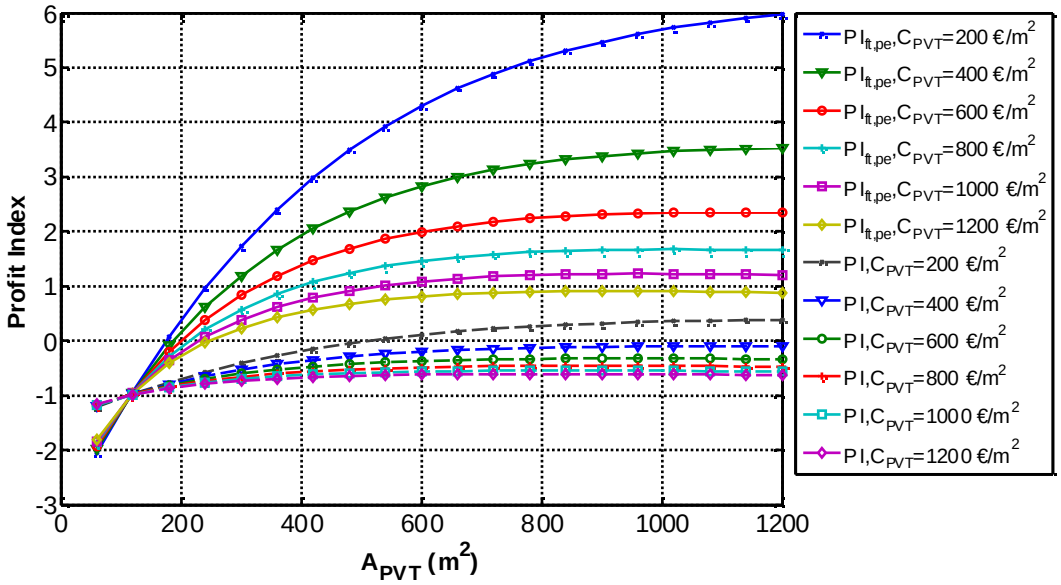

Fig. 24 - Sensitivity analysis: $PI_{ft,pe}$ vs PVT area and PVT capital cost

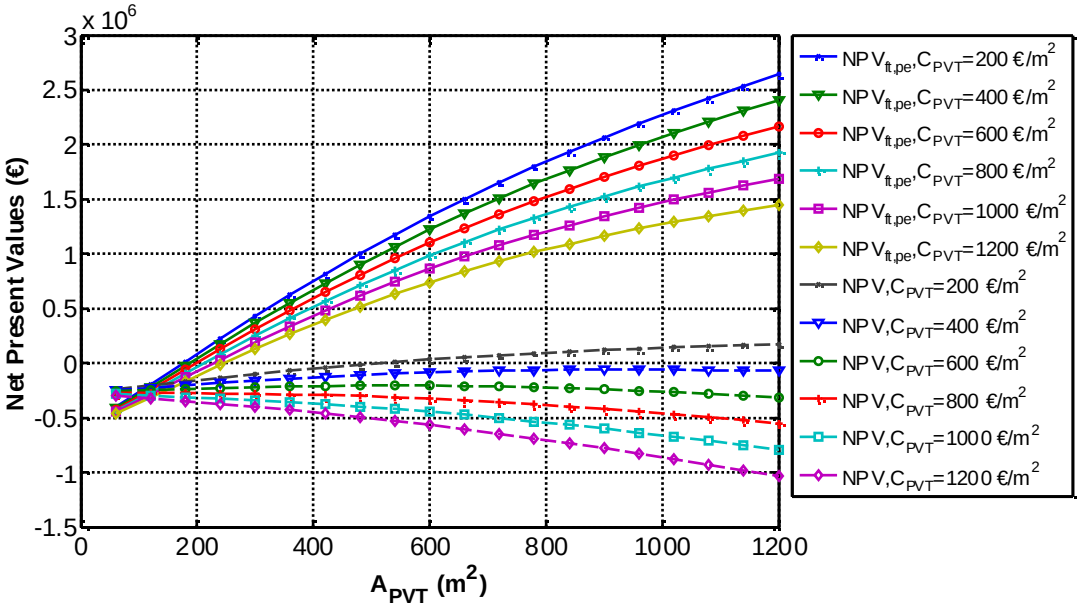

Fig. 25 - Sensitivity analysis: $NPV_{ft,pe}$ vs PVT area and PVT capital cost

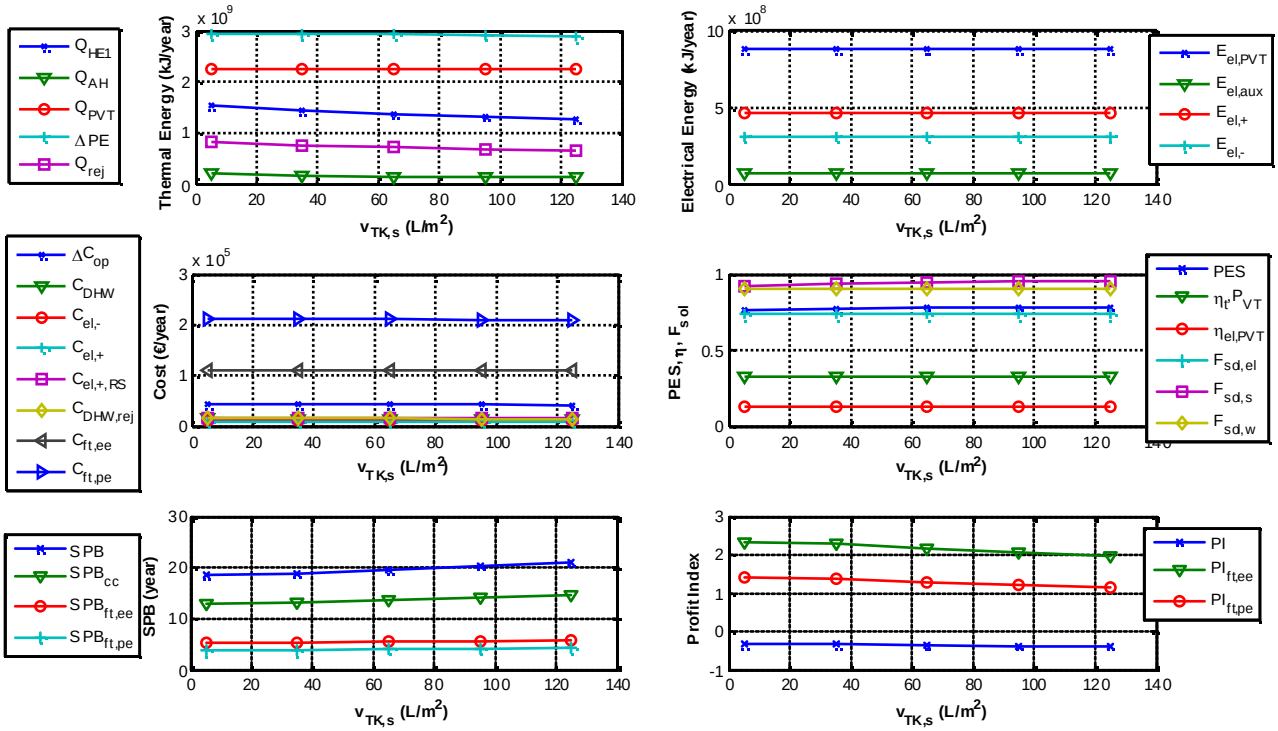

Fig. 26 - Sensitivity analysis: TK1 volume per PVT area (summer)

The energetic and economic parameters are slightly affected by the variation of the PVT outlet set point temperatures. The corresponding parametric analyses - not displayed in Figures for brevity - show that the PVT outlet set point temperatures (summer and winter) must be as low as possible since their increase determines a slight decrease in PVT thermal and electrical efficiencies. As a consequence, lower PES are achieved and all the economic indexes get worse. An increase in TK summer volume (Fig. 26) improves the storage capacity of the system determining a corresponding increase of all the solar fractions and consequently the PES also increases. However, these savings are very low and they determine operating costs savings significantly lower than the corresponding increase in capital costs, due to the larger TK volumes. Therefore, all the economic indexes improve for low TK summer volume. Conversely, during the winter (Fig. 27) small TK volumes are

preferable also from the energetic point of view. In fact, the time shift between solar radiation and energy demand is lower and the het losses toward the environment are higher. Therefore, low TK winter volumes should be considered according both energetic and economic criteria.

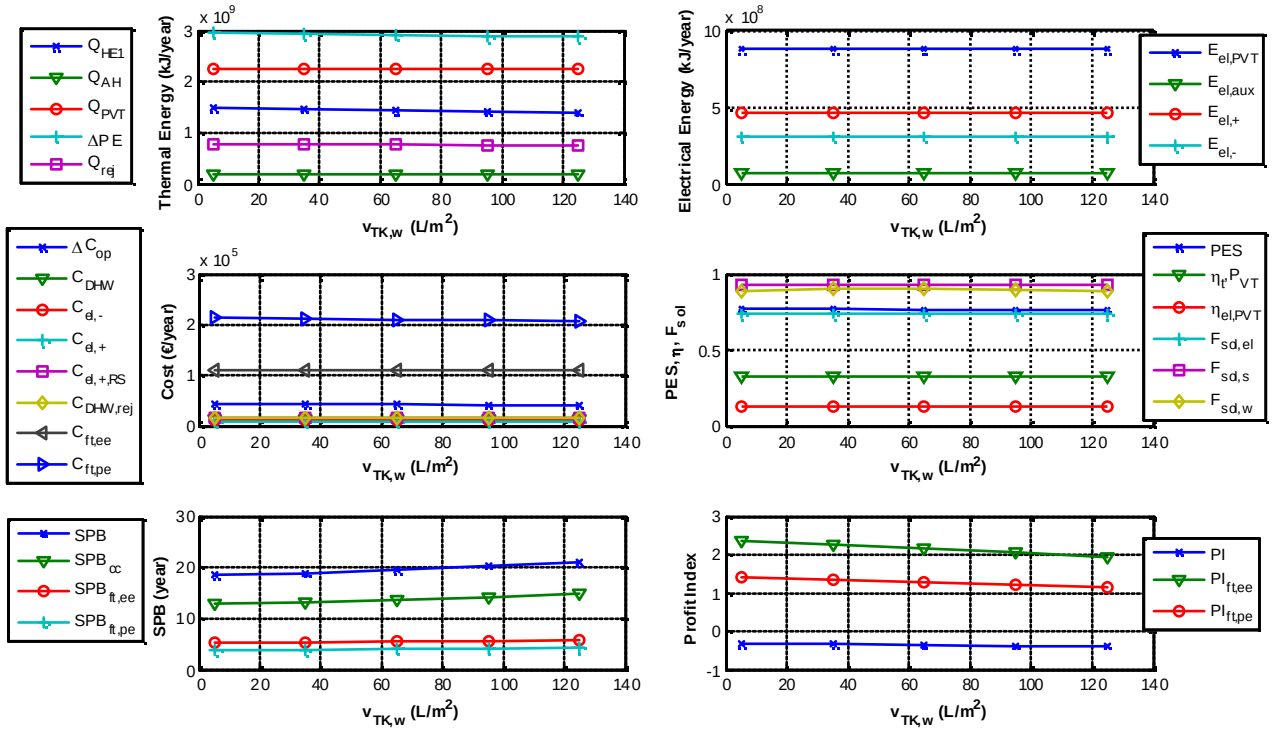

Fig. 27 - Sensitivity analysis: TK1 volume per PVT area (winter)

4. Conclusions

The results of the case study presented prove the technical feasibility of the PVSHC polygeneration system analyzed in the paper, based on photovoltaic/thermal solar collectors. The dynamic simulation showed that the system is capable to produce electricity, space heating, space cooling and domestic hot water all year long. The results of the dynamic simulations showed the significant potential of energy savings of CPVT, specially when they are coupled with an absorption chiller for the production of cooling energy. The combination of CPVT and SHC allows one to maximize the utilization of the thermal energy produced by the CPVT, particularly during the summer. On the other hand, results showed that CPVT thermal and electrical productions are very fluctuating in function of external radiation and temperature. Therefore an auxiliary system is always mandatory for a safe operation of the system. In addition, such fluctuations also determine a large amount of peak thermal energy which cannot be stored in storage tanks. Therefore, in order to maximize energy utilization, the simultaneous demand of DHW is crucial, since this DHW can be produced using the peak thermal energy of CPVT, exceeding building space heating and cooling demand. Finally, results also showed that CPVT are particularly sensitive to the ambient temperature: during the cold winter days their outlet temperature is often significantly lower than the corresponding set-point.

The economic analysis showed a profitability of the PVSHC considered of the same order of magnitude than other SHC systems. In particular, the system is not profitable without public funding policies and becomes extremely convenient in case of feed-in tariffs comparable to the ones presently adopted for PV collectors in UE.

The overall energetic performance of the CPVT system under investigation is better than the one based on flat plate CPVT previously investigated by the authors. Conversely, the economic indexes of the system based on concentrating PVT are slightly worse than the ones of flat plate PVT. This is mainly due to the high capital cost of triple-junction PV cells which is not adequately balanced by the increase in its overall electrical efficiency

Future developments of this work will focus on the possibility to increase CPVT operating temperature in order to drive a double effect absorption chiller. The aim of this improvement is to improve the summer performance of the system, reducing the PVT area required to drive the absorption chiller.

References

[1] Calise F., Dentice d'Accadia M., Vanoli L., *Thermoeconomic optimization of solar heating and cooling systems*. Energy Conversion an Management, 2010. **In Press**.

[2] Calise F., Dentice d'Accadia M., Vanoli R., *Dynamic simulation and parametric optimization of a solar-assisted heating and cooling system*. International Journal of Ambient Energy, 2010. **31**(4): p. 173-194.

[3] Calise, F., M. Dentice d'Accadia, and A. Palombo, *Transient analysis and energy optimization of solar heating and cooling systems in various configurations*. Solar Energy, 2010. **84**(3): p. 432-449.

[4] Calise, F., *Thermoeconomic analysis and optimization of high efficiency solar heating and cooling systems for different Italian school buildings and climates*. Energy and Buildings, 2010. **42**: p. 992-1003.

[5] Calise, F., A. Palombo, and L. Vanoli, *Maximization of primary energy savings of solar heating and cooling systems by transient simulations and computer design of experiments*. Applied Energy, 2010. **87**: p. 524-540.

[6] Calise, F., M. Dentice d' Accadia, A. Palombo, and L. Vanoli. *Simulation model and analysis of a small solar-assisted refrigeration system: dynamic simulation and optimization*. in *Proceedings of the ASME International Mechanical Engineering Congress & Exposition 2008 IMECE08*. 2008. Boston, USA.

[7] Ardehali, M.M., Shaharestani, M., Adams C.C., *Energy simulation of solar assisted absorption system and examination of clearness index effects on auxiliary heating*. Energy Conversion and Management, 2007. **48**: p. 864-870.

[8] Assilzadeh, F., S.A. Kalogirou, Y. Ali, and K. Sopian, *Simulation and optimization of a LiBr solar absorption cooling system with evacuated tube collectors*. Renewable Energy, 2005. **30**: p. 1143-1159.

[9] Folrides, G.A., Kalogirou, S.A., Tassou, S.A., Wrobel, L.C., *Modelling and simulation of an absorption solar cooling system for Cyprus*. Solar Energy, 2001. **72**(1): p. 43-51.

[10] Folrides, G.A., Kalogirou, S.A., Tassou, S.A., Wrobel, L.C., *Modelling, simulation and warming impact assessment of a domestic-size absorption solar cooling system*. Applied Thermal Engineering, 2002. **22**: p. 1313-1325.

[11] Garcia-Casals, X., *Solar absorption cooling in Spain: Perspectives and outcomes from the simulation of recent installations*. Renewable Energy, 2006. **31**: p. 1371-1389.

[12] Ghaddar, N.K., Shihab, M., Bdeir, F., *Modeling and simulation of solar absorption system performance in Beirut*. Renewable Energy, 1996. **10**(4): p. 539-558.

[13] A.Joudi, Khalid and J. Abdul-Ghafour Qussai, *Development of design charts for solar cooling systems. Part I: computer simulation for a solar cooling system and development of solar cooling charts*. Energy Conversion and Management, 2003. **44**: p. 313-339.

[14] A.Joudi, Khalid and Qussai J. Abdul-Ghafour, *Development of design charts for solar cooling systems. Part II: Application of the cooling f-chart*. Energy Conversion and Management, 2003. **44**: p. 341-355.

[15] Mateus, T. and A.C. Oliveira, *Energy and economic analysis of an integrated solar absorption cooling and heating system in different building types and climates*. Applied Energy, 2009. **86**: p. 949-957.
[16] U. Desideri, S. Proietti, *Analysis of energy consumption in the high schools of a province in central Italy* Energy and Buildings, 2002. **34**: p. 1003-1016.
[17] A. El Fadar, A. Mimet and M. Pérez-García, *Modelling and performance study of a continuous adsorption refrigeration system driven by parabolic trough solar collector* SOlar Energy, 2009. **83**(6): p. 850-861.
[18] Ahmet Lokurlu, Fritz Richarts, Dirk Kruger, *High efficient utilisation of solar energy with newly developed parabolic trough collectors (SOLITEM PTC) for chilling and steam production in a hotel at the Mediterranean coast of Turkey*. International Journal of Energy Technology and Policy, 2005. **3**(1-2): p. 137-146.
[19] Calise F., Dentice d'Accadia M., Palombo, A., Vanoli L., *Dynamic Simulation Of High Temperature Solar Heating And Cooling Systems*, in *Eurosun 2010*. 2010: Graz (AU).
[20] M. Mazloumi, M. Naghashzadegan, and K. Javaherdeh, *Simulation of solar lithium bromide–water absorption cooling system with parabolic trough collector* Energy Conversion an Management, 2008. **49**(10): p. 2820-2832.
[21] Ming Qu, Hongxi Yin, David H. Archer, *A solar thermal cooling and heating system for a building: Experimental and model based performance analysis*. Solar Energy, 2009. **84**(2).
[22] Tierney, M.J., *Options for solar-assisted refrigeration—Trough collectors and double-effect chillers*. Renewable Energy, 2007. **32**(2): p. 183-199.
[23] Vokas, G., N. Christandonis, and F. Skittides, *Hybrid photovoltaic–thermal systems for domestic heating and cooling—A theoretical approach* Solar Energy, 2006. **80**(5): p. 607.
[24] Mittelman, G., A. Kribus, and A. Dayan, *Solar cooling with concentrating photovoltaic/thermal (CPVT) systems* Energy Conversion and Management, 2007. **48**: p. 2481-2490.
[25] Calise, Francesco, Adolfo Palombo, and Laura Vanoli, *Design and dynamic simulation of a novel solar trigeneration system based on photovoltaic/thermal collectors*, in *ECOS 2011*. 2011: Novi Sad, Serbia.
[26] Calise, F., *Design Of A Hybrid Polygeneration System With Solar Collectors And A Solid Oxide Fuel Cell: Dynamic Simulation And Economic Assessment*. International Journal of Hydrogen Energy, 2011. **36**(10): p. 6128-6150
[27] Klein, S.A. et al., Solar Energy Laboratory, , *TRNSYS. A transient system simulation program*. 2006: University of Wisconsin, Madison.
[28] Calise, F., *High Temperature Solar Heating and Cooling Systems for Different Mediterranean Climates: dynamic simulation and economic assessment* Applied Thermal Engineering, 2011. **32**: p. 108-124.
[29] F. Calise, Ferruzzi G., Vanoli L., *Transient Simulation of Polygeneration Systems Based on Fuel Cells and Solar Cooling Technologies* in *ECOS 2010*. 2010: Lousanne, CH.
[30] Calise, F., G. Ferruzzi, and L. Vanoli, *Transient simulation of polygeneration systems based on PEM fuel cells and solar heating and cooling technologies*. Energy, 2011. **In Press, Corrected Proof,Jun 2011**

Performance analysis of downdraft gasifier - reciprocating engine biomass fired small-scale cogeneration system

Jacek Kalina

Silesian University of Technology, Gliwice, Poland, e-mail: jacek.kalina@polsl.pl

Abstract:

Energy and environmental performances of a small-scale cogeneration system composed of downdraft wood gasifier and reciprocating engine is theoretically examined in the paper. The gasifier is modelled using a non-stoichiometric thermodynamic quasi equilibrium approach. Achievable power and efficiency of the gas engine is estimated using a method based on analysis of the engine thermodynamic fuel-air theoretical cycle. It is assumed that the relative changes of operating parameters of a selected machine are proportional to the relative changes of the cycle parameters after the change of fuel. It is taken into account that the gasification agent can be composed of ambient air and recirculated exhaust gas from the engine. The proposed configuration of the system is examined in the aspect of electricity generation efficiency, total fuel energy utilization, potential for primary energy savings and global CO_2 emission reduction. It was found that the proposed modification of a typical downdraft reactor – gas engine system, that runs at a given reactor temperature, reduces the heating value of the producer gas. Consequently the electric power output of the engine module is derated. However, the recirculation of exhaust gas from the engine improves the cold gas efficiency and the performance of the whole system.

Keywords:

Renewable Energy, Biomass, Gasification, Gas Engines, Energy Conversion, Cogeneration.

1. Introduction

Reductions of CO_2 emission and consumption of fossil fuels are nowadays the main driving forces for using biomass in the energy sector. It is usually assumed that the traditional, fossil fuel based generation technologies are replaced if renewable energy sources are introduced. The electricity from renewable sources as well as from cogeneration is nowadays supported by different legal and financial means. Consequently, it can be assumed that with a high probability the power replaced within the national system will be the one from the coal fired plants. Therefore the potential for fuel energy savings and emission reduction can be evaluated with respect to coal.

In order to demonstrate emission and primary energy saving potential of the biomass based cogeneration two indices can be used. The first is the global reduction of CO_2 emission (under assumption that the firing of biomass is CO_2 emission neutral). The second one is the Energy Replacement Index (ERI), that shows the amount of non-renewable energy saved within the regional energy system by using biomass energy in a cogeneration plant (in GJ of non-renewable energy saved per GJ of biomass energy input).

$$\Delta m_{CO_2} = \frac{\Delta m_{coal} LHV_{coal} WE_{coal} + E_{el} WE_{ref}}{m_{bio} LHV_{bio}} = \frac{EUF - \eta_{el}}{\eta_b} WE_{coal} + \eta_{el} \frac{WE_{ref}}{3.6}, \tag{1}$$

$$ERI = \frac{\Delta m_{coal} LHV_{coal} + \dfrac{3.6 E_{el}}{\eta_{ref}}}{m_{bio} LHV_{bio}} = \frac{EUF - \eta_{el}}{\eta_b} + \frac{\eta_{el}}{\eta_{ref}}, \tag{2}$$

Where the characteristics of an energy conversion plant is given by net electricity production E_{el}, generation efficiency η_{el}, fuel energy utilization factor EUF and cogeneration index σ:

$$E_{el} = E_{el,gen}(1-\alpha) - E_{el,fss}, \tag{3}$$

$$\eta_{el} = \frac{3.6E_{el}}{m_{bio}LHV_{bio}}, \tag{4}$$

$$EUF = \frac{3.6E_{el} + Q}{m_{bio}LHV_{bio}}, \tag{5}$$

$$\sigma = \frac{3.6E_{el}}{Q} = \frac{\eta_{el}}{EUF - \eta_{el}}, \tag{6}$$

It can be concluded from Equations (1) and (2) that a good performance of a conversion technology depends not only on the power generation efficiency (usually lower than the reference system efficiency) but also on the cogeneration mode. In the Fig. 1 there are presented results obtained under the following assumptions: reference efficiency of power generation $\eta_{ref,system}$ = 0.36 [1], reference efficiency of a heating boiler η_b = 0.86 [2], CO_2 emission from the system power plant WE_{ref} = 936.36 kg/MWh and from a coal fired heating boiler WE_{coal} = 94.85 kg/GJ [1]. It can be noticed that starting from relatively low values of performance parameters of biomass fired cogeneration plant (η_{el} at the level of 0.26 and EUF at the level of 0.5) savings of non-renewable energy (loco plant) are bigger than the amount of biomass energy used (ERI > 1.0). Additionally there are expected lower values of cumulative energy consumption and cumulative emission of CO_2 in the fuel production and delivery processes.

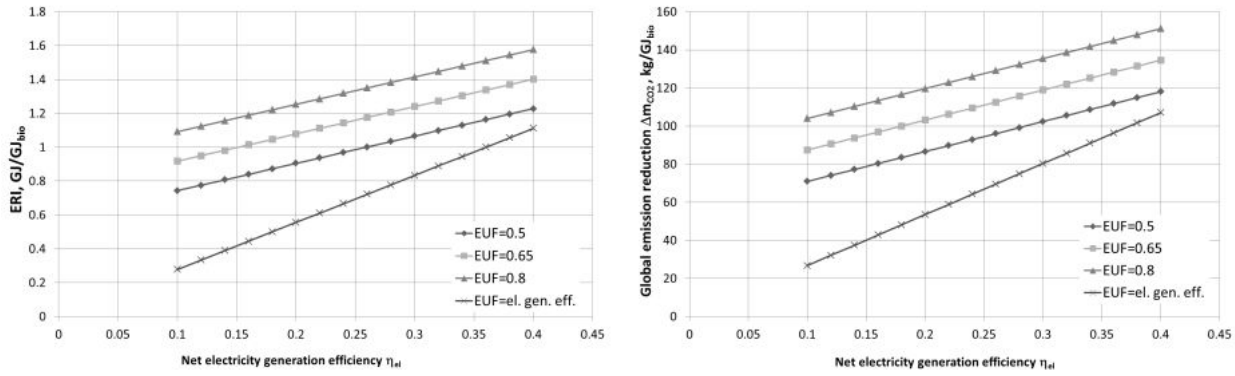

Fig. 1. ERI and global CO_2 emission reduction resulted from biomass fired cogeneration

Gasification based cogeneration is an important technological alternative for biomass fired distributed generation plants of small and medium scale electric outputs. Reciprocating engines integrated with gasification reactors and gas cleaning devices can be widely applied in this field. On the other hand there are no engines manufactured for producer gas utilization. Natural gas or diesel engines are usually used. Despite this fact there is little information available in the published literature about the effects of fuelling an engine with the producer gas. Due to the complexity of in-cylinder processes there are not many analytical tools available to estimate the parameters of a machine running in the producer gas mode.

In this paper there is presented the study of a downdraft gasifier - gas engine cogeneration system integrated with biomass gasification. The gasification process is analyzed using a non-stoichiometric approach with minimization of the Gibbs free energy. Such approach is reported in the literature as a satisfactory for general plant studies (Baggio et al.[3], Schuster et al.[4], Ruggiero

et al.[5]). In this work the quasi-equilibrium approach is used. The performance of a piston engine after the change of fuel there is estimated using the model based on the spark-ignition engine fuel-air theoretical thermodynamic cycle.

2. Plant configuration

The cogeneration plant consists of typical fixed bed downdraft gasifier, gas cleaning equipment and gas engine. The scheme of the plant is shown in Fig. 2.

Biomass is converted into a combustible gas in the reactor using a mixture of air and engine exhaust gas as the gasifying agent. The temperature of the agent can be elevated using waste heat from the raw producer gas. The exhaust gas from the engine is recirculated into the gasifier as well as it is used for feedstock drying and network water heating. Scheme of the drying system is given in Fig. 3. The low temperature heat from engine cooling cycle is used for water heating.

The prime mover selected for the analysis is the GE J320 GS gas lean fuel-air mixture burn engine. The operation of this type of engine fuelled with producer gas has been already demonstrated by Papagiannakis et al. [33]. According to Herdin et al. [6] many problems have been so far encountered in this type of plants. The biggest one is currently a low reliability. The authors claim that a great research and development work must be done to improve the performance. There are also required commercial applications to demonstrate the economic effectiveness. Nevertheless the technology is available and it can be applied in many locations [7].

The type of feedstock is spruce in the form of chips. Characteristics of the wood is given in Table 1.

Table 1. Characteristics of the feedstock (spruce chips)

Proximate analysis (%wt, dry basis)		Ultimate analysis (%wt, dry basis)	
Fixed carbon	28.3%	Carbon *C*	51.2%
Volatile mater	70.2%	Hydrogen *H*	6.1%
Ash	1.5%	Oxygen *O*	40.9%
HHV, MJ/kg	20.1	Nitrogen *N*	0.3%

3. Biomass drying

It is assumed that the initial biomass water content is 40% (wet basis). The feedstock is dried to 10% of water content using a rotary drum drier. The drying medium is a mixture of the engine exhaust gas after the heat recovery boiler and ambient air. If it is necessary a small amount of producer gas can be burned in order to provide the heat required for drying. The temperature of the drying medium at the inlet of the drier is 140°C. According to Bolhàr-Nordenkampf et al. [8] using a low temperature heat source gives the significant advantage of a low exergetic input into the dryer as well as low organic emissions.

The total mass balance of the drying process takes the form:

$$\dot{m}_{wood,db}\left(1+w_{db}\right)+\dot{m}_{dm}\left(1+X_{dm,in}\right)=\dot{m}_{wood,db}\left(1+w_{db,\max}\right)+\dot{m}_{dm}\left(1+X_{dm,out}\right), \tag{7}$$

The balance of moisture is as follows:

$$\dot{m}_{bio,db}w_{db}+\dot{m}_{dm}X_{dm,in}=\dot{m}_{bio,db}w_{db,\max}+\dot{m}_{dm}X_{dm,out}, \tag{8}$$

Finally the energy balance of the drying process can be written:

$$\begin{aligned}&\dot{H}_{bio,in}+\dot{m}_{dm}\left(\sum_{i=1}^{4}g_i\Delta h_i\Big|_{T_0}^{T_{exh}}+X_{dm,in}h_{H_2O}\Big|_{T_{dm},\left(z_{H_2O}\right)_{in}p_{dm}}\right)=\\&\dot{H}_{bio,out}+\dot{m}_{dm}\left(\sum_{i=1}^{4}g_i\Delta h_i\Big|_{T_0}^{T_{out}}+X_{dm,out}h_{H_2O}\Big|_{T_{out},\left(z_{H_2O}\right)_{out}p_{dm}}\right)+\dot{Q}_{out}\end{aligned}, \tag{9}$$

Where the enthalpy of wet wood chips is calculated using formula:

$$\dot{H}_{bio} = \dot{m}_{bio,db}(1+w_{db})c_{wet}(T_{bio}-T_0), \tag{10}$$

The dry drying medium is assumed to be composed of N_2, O_2, CO_2 and Ar. The heat capacity of wet wood is calculated using correlation given by Regland et al. [9]:

$$c_{wet} = \frac{(c_{dry}+4.19w_{db})}{1+w_{db}} + (0.02355T_{wood} - 1.32w_{db} - 6.191)w_{db}, \tag{11}$$

$$c_{dry} = 0.1031 + 0.003867T_{wood}, \tag{12}$$

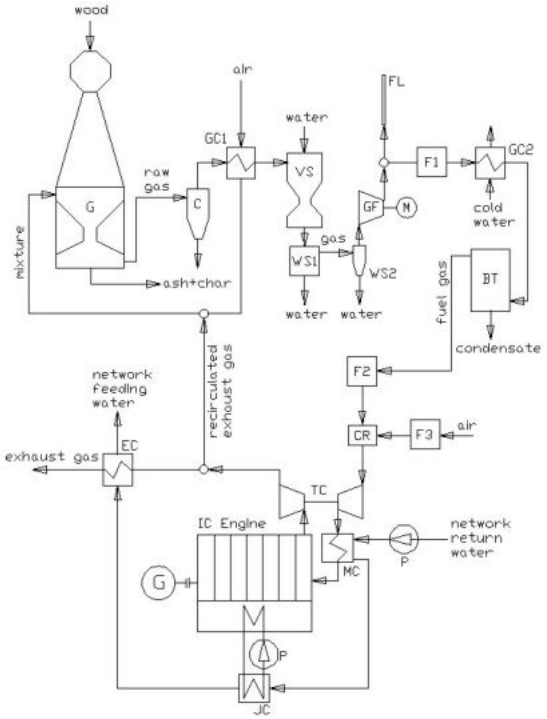

Fig. 2. Scheme of the proposed downdraft gasifier-gas engine cogeneration plant (G - gasifier; C - cyclone; GC1 - raw gas cooler; VS - Venturi scrubber; WS1, WS2 - water separators; GF - producer gas fan, FL - flare; F1, F2, F3 - filters; GC2 - final cooler; BT - buffer tank; CR - carburetor; TC - turbocharger; MC - mixture cooler; JC - jacket water cooler; EC - exhaust gas cooler; G - electric power generator; P - pump)

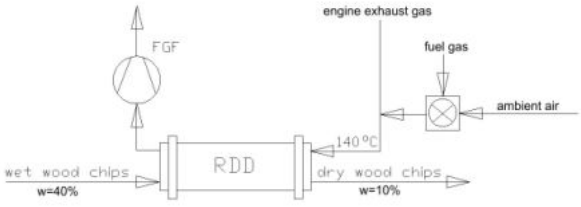

Fig.3. Schematic diagram of drier system (FGF – flue gas fan; RDD – rotary drum drier)

It is assumed that the temperature of wood at the outlet of the drier is equal to the dew point temperature for the given partial pressure of water. Heat loss from the drier is assumed to be 3% of the total inlet enthalpy. Relative humidity of the drier outlet gas is controlled to be lower than 100%. From this condition the demand for an additional heating using a portion of producer gas is calculated. Emission of organic compounds and corresponding loss of carbon are, basing on [8], neglected due to a relatively big size of wood chips and low temperature of the heating medium.

4. Modeling of gasification process

There have been several mathematical models of the fixed bed downdraft gasification process presented in the published literature. The models can be divided into three groups: simplified [10], equilibrium [11, 12, 13, 14, 15, 16] and combined kinetically modified [17]. In this study it was decided to use a model based on thermodynamic equilibrium calculations. To a certain extend such model is independent on the gasifier design and can be used to estimate the thermodynamic limits of the technology [18].

An example of using a single-compartment equilibrium model based on minimization of Gibbs free energy was presented by Altafini et al. [11]. Despite the model was calibrated with experimental data, the calculation resulted in overestimated H_2 content (20.06% versus 14.00% measured) and underestimated CH_4 content (negligible versus 2,31% measured). The calculated higher heating value of the gas was 5042 kJ/Nm^3 versus the measured 5276 kJ/Nm^3. Another simulation made using Cycle-Tempo software resulted in even higher differences in producer gas composition.

Zainal et al. [13] proposed stoichiometric equilibrium model based on a global gasification reaction. They assumed that the products of pyrolysis are totally oxidized and the equilibrium is reached within the reduction zone. The set of nonlinear equations is solved at a specified bed temperature. The modeled composition of the gas was again different from an experimental data.

Similar models were presented by Babu et al. [14], Melgar et al. [15] and Jarungthammachote et al. [16]. They all claim that the equilibrium models can be used for modeling of the downdraft gasifiers due to the fact that the pyrolysis occurs before combustion reactions. This assures combustion and cracking of pyrolysis products at high temperature before gasification reactions. The residence time of the reactants in the reactor's bed is assumed to be high enough to reach the chemical equilibrium. Göbel et al. [19] claim on the basis of their measurements and the results obtained by other researchers that the thermodynamic state of the gas phase in the reduction zone is very close to the state equilibrium between the components CO, CO_2, H_2 and H_2O.

In this study it was decided to use a two-zone equilibrium model. The first zone includes heating the charge, drying, pyrolysis and oxidation. The second zone includes the reduction phase. It is assumed that there is a typical temperature profile along the axis of the reactor. Such profile is presented in [12, 20]. The maximum process temperature of about 1000 - 1200 ºC is reached within a slight distance after the throat. Both measured as well as calculated temperature drop in the reduction zone is 300 - 500 K [12, 19].

The following assumptions have been made:

- Total quantity of volatile matter is released in the pyrolysis, that ends in the combustion zone.
- Pyrolysis takes place with simultaneous combustion of the gas phase ("flaming pyrolysis").
- Gas-phase oxidation process, due to high temperature and high reaction rate reaches a state of thermodynamic equilibrium. Gaseous products passing from first to second zone are CO, CO_2, H_2, CH_4, H_2O, N_2 and SO2 (if sulphur is present in the fuel).
- There is a temperature gradient between solid phase and gas phase at the beginning of the reduction zone. It can be concluded from the literature [19, 21] that the temperature difference is about 350 - 500 K. In this study the average value of 425 K was used in calculations.
- Inside a solid particle temperature is uniform. This corresponds to the assumption that the thermal resistance of heat conduction inside the particle is small when compared to convection on the outer surface.
- Gasification in the reduction zone achieves a state of thermodynamic equilibrium at final temperature and pressure of the process. Pure carbon in the form of graphite is assumed to be the only solid product of the process.
- Tar (C_xH_y where $x \geq 6$ [22]) is a non-equilibrium product present at the reactor outlet. The tar content in the raw gas form a downdraft gasifier is typically within the range of 0.3 to 5.0 g/Nm^3 [22]. In the model the tar content is defined in g/kg of wet biomass input. The specified amount of tar does not take part in the equilibrium calculations.

- As presented by Gerun et al. [23] the tar is modeled as a mixture of benzene C_6H_6 and naphthalene $C_{10}H_8$. The ratio of benzene to naphthalene is 0.35/0.65 [23].
- Mass flow of carbon passing into the reduction zone is equal the flow of fixed carbon indicated by the proximate analysis.
- Gaseous products of the process are: CO, CO_2, H_2, CH_4, H_2O, N_2, SO_2.
- Methane from the pyrolysis is partially converted in oxidation zone. Remaining CH_4 stays inactive in reduction reactions and passes to products of the process.
- Pressure losses in the gasifier bed can be neglected [19].

The assumed global stoichiometric reaction of the process is:

$$\begin{aligned} &n'_C CH_aO_bN_cS_d + n'_{H_2O} H_2O(l) + n_{H_2O} H_2O(g) + \lambda n_{O_2,\min} O_2 + n_{CO_2} CO_2 + n_{N_2} N_2 = \\ &n''_{CO} CO + n''_{CO_2} CO_2 + n''_{H_2} H_2 + n''_{CH_4} CH_4 + n''_{H_2O} H_2O(g) + n''_{N_2} N_2 + n''_{SO_2} SO_2 + n''_{tar} C_xH_y \end{aligned}, \quad (13)$$

The process involves also ash and argon from the atmospheric air, that are regarded as inert substances. The total mass composition of biomass is:

$$C + H + O + S + N + w + ash = 1, \quad (14)$$

The stoichiometric formula of biomass in (13) can is determined from the ultimate analysis:

$$a = \frac{2n'_{H_2}}{n'_C},\ b = \frac{2n'_{O_2}}{n'_C},\ c = \frac{2n'_{N_2}}{n'_C},\ d = \frac{2n'_S}{n'_C}, \quad (15)$$

The composition of gas phase after oxidation and reduction respectively is determined assuming the state of thermodynamic equilibrium in which the Gibbs free energy reaches its minimum. The objective function takes the following form:

$$\sum_{i=1}^{ls}\sum_{j=1}^{lf} n_{ji}\left[h^0_{ji}(T) - Ts^0_{ji}(T,p) + RT\ln z_{ji}\right] \to \min, \quad (16)$$

The constraints are substance balances of components *C*, *H* and *O*:

$$b_1:\ n'_C + n_{CO_2} - n''_C - n''_{CO_2} - n''_{CO} - n''_{CH_4} - xn''_{tar} = 0, \quad (17)$$

$$b_2:\ n'_{H_2} + n'_{H_2O} + n_{H_2O} - n''_{H_2} - n''_{H_2O} - 2n''_{CH_4} - yn''_{tar} = 0, \quad (18)$$

$$b_3:\ n'_{O_2} + \lambda n_{O_2,\min} + n_{CO_2} + \frac{1}{2}\left(n'_{H_2O} + n_{H_2O}\right) - n''_{CO_2} - n''_{SO_2} - \frac{1}{2}\left(n''_{CO} + n''_{H_2O}\right) = 0, \quad (19)$$

In order to estimate the amount of methane from pyrolysis the assumptions made by Ratnadhariya et al. [10] have been initially adopted. It was however found that if half of the hydrogen, that is not associated with oxygen, is released as CH_4 and then it is not involved in the calculation of equilibrium, the final content of methane in producer gas is to high in comparison with experimental results. It was found that the additional assumption that 50% of CH_4 from pyrolysis is involved in calculation of equilibrium in oxidation zone leads to a reasonable level of accuracy.

The total number of moles of the raw producer gas at the output of the gasifier is:

$$n''_g = n''_{H_2} + n''_{CO} + n''_{CH_4} + n''_{CO_2} + n''_{H_2O} + n''_{N_2} + n''_{SO_2} + n''_{Ar} + n''_{tar}, \quad (20)$$

Experimental studies show that a small amount of char leaves the gasifier unconverted. Therefore the carbon conversion efficiency is defined:

$$\varepsilon_C = \frac{n'_C - n''_C}{n'_C}, \quad (21)$$

Where n''_C contains two sources of carbon. The first one is the assumed value of n''_{C_1} that is not available for the calculation of equilibrium. Remaining carbon n''_{C_2} results from the equilbrium:

$$n''_C = n''_{C_1} + n''_{C_2}, \tag{22}$$

Construction of the solid particle removal system of downdraft reactors limits the maximum value of ε_C. In this study it is assumed that the achievable carbon conversion efficiency is 0.95.

Minimization of the objective function (16) can be performed by the method of Lagrange multipliers [24]. The modified objective function to be minimized takes the form:

$$F = \sum_{i=1}^{ls_g} n''_i \left[\frac{g_i^0(T,p)}{RT} + \ln n''_i - \ln n''_g \right] + n''_{C_2} \frac{g_C^0(T,p)}{RT} + \sum_{k=1}^{3} \lambda_k b_k \rightarrow \min, \tag{23}$$

Minimization procedure requires a solution of eight equations with eight unknowns (n''_{H2}, n''_{CO}, n''_{CH4}, n''_{CO2}, n''_{H2O}, λ_1, λ_2, λ_3). Five equations result from the condition of zeroing the partial derivatives of function F with respect to unknowns:

$$\frac{\partial F}{\partial n''_i} = 0, \tag{24}$$

The final form of Equations (24) for the gas components takes the form:

$$n''_i = n''_g \exp\left[-\frac{g_i^0(T,p)}{RT} - \sum_{k=1}^{3} \sum_{j=1}^{ls_g} \lambda_k a_{kj} \right], \tag{25}$$

For solid carbon present in reduction zone Equation (24) takes the form:

$$g_C^0(T,p) - \lambda_1 = 0, \tag{26}$$

The remaining three equations are substance balances (17), (18) and (19).

The procedure is solved twice - for first and second respectively. This approach allows control of the temperature after the oxidation process. As the equilibrium calculations are justified for high temperatures, the temperature at the outlet of the first zone is controlled to be equal 1273 K.

The process temperature T is determined from the energy balance of the individual zones. For 1 kg of wet biomass at input temperature 298 K the balance of the first zone takes the form:

$$\begin{aligned} &LHV_{db}(1-w) - wr + \sum_i n_i \Delta h_i \Big|_{298K}^{T_i} = \\ &\sum_j n''_j \left(LHV_j + \Delta h_j \Big|_{298K}^{T_I} \right) + m_{fc} LHV_C + m_{char} c_{char} \left(T_I - \Delta T_{g-s} \right) + Q_{out} \end{aligned}, \tag{27}$$

Heat capacity of char passing from first to second zone is modeled using formula [25]:

$$c_p = 1430 + 0.355T - 7.32 * 10^{-7} T^2, \left[\frac{kJ}{kgK} \right], \tag{28}$$

In the second zone the energy balance takes the form:

$$\begin{aligned} &\sum_j n''_j \left(LHV_j + \Delta h_j \Big|_{298K}^{T_I} \right) + m_{fc} LHV_C + m_{char} c_{char} \left(T_I - \Delta T_{g-s} \right) = \\ &\sum_{j,II} n''_{j,II} \left(LHV_j + \Delta h_j \Big|_{298K}^{T_{II}} \right) + n'_C (1-\varepsilon_C) M_C \left(LHV_C + \Delta h_C \Big|_{298K}^{T_{II}} \right) + m_{ash} c_{ash} T_{II} + Q_{out} \end{aligned}, \tag{29}$$

Heat capacity of ash is modeled using Kirov's correlation [26], that for ash takes the form:

$$c_{ash} = 0.18 + 1.4 \times 10^{-4} T, \left[\frac{kJ}{kgK} \right], \tag{30}$$

Finally the cold gas efficiency of the gasification process is defined as follows:

$$\eta_{cold_gas} = \frac{\dot{V}_g LHV_g}{\dot{m}_{db} LHV_{db}}, \tag{31}$$

For solving the reactor model an in-house code was written in FORTRAN. The problem of Gibbs function minimization is of the type that in many cases is difficult to converge. There are however procedures available to solve the task. In this study there are applied the procedures of the program CEA (Chemical Equilibrium with Applications) [24]. Thermodynamic properties of substances are determined using the JANAF tables.

The model has been verified against experimental data presented in the published literature [20, 27]. All the conditions of the process applied for the verification of the model are the same as given in the cited papers. A representative example of results of the validation is given in Table 2. It was found that the model generates typical results reported for equilibrium based approach. It can be noticed in Table 2 that in comparison with the experiment there are overestimated carbon conversion efficiency, product gas flow, yields of hydrogen and carbon dioxide. The yields of carbon oxide and nitrogen are significantly underestimated while the yield of methane is in relatively good agreement with the measured data. It was finally concluded that the model generates the results that are over optimistic. Therefore the modified approach has been tested. It has been assumed in the modified model that a certain amount of H_2O present at the reduction zone is not available for the calculation of the equilibrium. It was found that if it is at the level of 25 - 35% the model gives better results of carbon conversion efficiency and product gas flow. Also composition of the gas is corrected.

Table 2. Verification of the model against experimental data

	Experiment (run 8) [20]	Experiment (run 9) [20]	Model (run 8)	Model (run 9)	Model modified (run 8)	Model modified (run 9)
Input data						
Air excess ratio λ	0.339	0.323	0.339	0.323	0.339	0.323
Total heat loss, % of chemical energy input	n.a.	n.a.	8.8	2.7	8.8	2.7
Tar yield, g/kg_{wb}	6	5	5	5	5	5
Results:						
Throat temperature, °C	1130	1206	1129	1208	1129	1208
Product gas flow, Nm^3/h	9.18	9.48	9.86	10.37	9.18	9.48
Product gas composition, %vol						
N_2	53.95	54.24	44.20	41.98	47.44	45.97
H_2	11.86	13.83	18.94	20.16	16.15	16.41
CO	19.89	18.41	12.76	15.38	15.22	18.96
CH_4	2.47	1.98	2.2	2.0	1.55	1.35
CO_2	11.25	11.12	17.04	15.59	14.68	12.35
Ar	n.a.	n.a	0.56	0.54	0.61	0.59
C_2H_2	0.26	0.19	0	0	0	0
C_2H_6	0.12	0.02	0	0	0	0
Carbon conversion ε_C	89.1	88.9	93.39	96.61	85.72	87.52

5. Engine performance estimation

The crucial issue of the analysis of the gasifier - gas engine system is the estimation of a gas engine performance. In a typical gas engine that was designed for natural gas operation, the achievable electric output is reduced when the machine is fueled with the producer gas. Sidhar et al. [28] presented the results of the tests where the de-rating was observed at the level of 29.4% and 28.5% for the engines with compression ratios of CR = 12 and CR = 10. In another paper Sidhar et al. [29] presented results of tests conducted on modified Kirloskar RB-33 compression-ignition engine. The engine was able to run at different compression ratios (CR = 11.5, 13.5, 14.5 and 17.0 respectively). The original electric power of the module was 21 kW and efficiency was 31%. Maximum electric power of the module fueled with producer gas (4.65±0.15 MJ/Nm^3) was 17.5 kW while efficiency was 21%. These parameters were reached at CR = 17. Both power and efficiency decreased with a reduction of CR.

Different methods are used nowadays in order to predict the engine operating parameters. The most simple approach to this problem was presented by Baratieri et al. [30] who have just assumed thermal and electrical efficiencies of a machine. Tinaut et al. [31] proposed an index called the Engine Fuel Quality (EFQ). The index is the ratio of the volumetric heating value of a mixture under specified thermodynamic conditions to the reference air density under intake manifold pressure and temperature. The effective power of the machine can be estimated using reference power and ratio of EFQ indices calculated for producer gas and reference fuel respectively.

Another simplified method of assessment of the engine power was presented by Dasappa [32]. The method is based on a set of dimensionless correction factors that take into account change of the most important parameters of the engine cycle. The author claims that the approach, though simplified, gives results close to an experimental measurements.

Centeno et al. [17] presented the model based on the spark ignition engine fuel-air thermodynamic cycle. The model takes into account formation of burned and unburned mixtures, cycle heat and mass losses through the walls of the cylinder and due to the gas blow by. The model was validated against the experimental results. In experiments the achievable electric power was 5 kW while the original LPG fired engine gave 10 kW. The de-rating of power in producer gas mode was about 50%. The comparison of calculated and measured power revealed that at the higher loads the predicted values of the electrical power output are greater than experimental data. It was also found that the results of modeling are very sensitive to the amount of air/fuel mixture in the cylinder at the beginning of the compression process.

Papagiannakis et al. [33] presented a comparison between experimental and computed results for a conventional multi-cylinder, four-stroke, turbocharged, spark-ignition, natural gas GE J320 GS engine fuelled with syngas. It can be concluded from graphical representation of the results that the engine fuelled with the syngas (of LHV = 6.84 MJ/Nm^3) generated slightly higher power than the one computed for natural gas operation. In the same case the heat release curves showed that more heat was delivered into the cycle with the syngas-air mixture [33]. There was also reported a little reduction of the engine efficiency.

In this paper it is proposed to estimate the performance of an engine after the change of fuel using the spark-ignition engine fuel-air theoretical cycle analysis. The cycle is presented in Fig. 4.

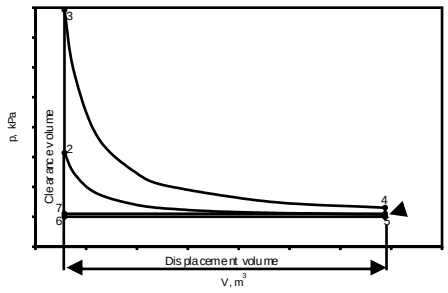

Fig. 4. Spark ignition engine theoretical thermodynamic cycle

According to Heywood [34] such cycle can be composed of the following processes: reversible adiabatic compression of mixture of air, fuel and cylinder residual gas; combustion at constant volume without heat loss, to burned gas in chemical equilibrium; reversible adiabatic expansion of the burned gas; ideal adiabatic exhaust gas blowdown and ideal intake with adiabatic mixing between residual gas and fresh mixture. This approach takes into account:

- variations of density of the mixture and volumetric efficiency that result from mixing with a residual amount of gas in the cylinder,
- variations of maximum temperature and pressure of the cycle,
- different properties of working fluid in compression and expansion processes due to combustion.

It is assumed that the engine is turbocharged and intercooled. A working fluid is a mixture of ideal gases. Compression of fresh mixture in turbocharger is described by an isentropic process equation:

$$\int_{T_0}^{T_{TC,out,s}} c_{p,m}(T)\frac{dT}{T} = \int_{T_0}^{T_{TC,in}} c_{p,m}(T)\frac{dT}{T} + R\ln\frac{p_{TC,out}}{p_{TC,in}}, \tag{32}$$

At the beginning of the in-cylinder compression (point 1 of the cycle) the fluid is composed of fresh mixture and cylinder residual gas:

$$n_1 = n_m + n_r, \tag{33}$$

The amount n_1 of the fluid in cylinder is calculated from the equation of state:

$$n_1 = \frac{p_1 V_1}{R T_1}, \tag{34}$$

Where pressure p_1 results from turbocharger outlet pressure and pressure loss in the intake manifold

$$p_1 = p_{TC,out} - \Delta p_m, \tag{35}$$

The temperature T_1 is calculated from an energy balance of the intake process:

$$n_1 c_{v,u}\big|_{T_1} T_1 = n_m c_{p,m}\big|_{T_m} T_m + n_r c_{v,b}\big|_{T_5} T_5 + p_1(V_1 - V_6), \tag{36}$$

Reversible adiabatic compression of mixture in cylinder is calculated using equation:

$$\int_{T_0}^{T_{2s}} c_{v,u}(T)\frac{dT}{T} = \int_{T_0}^{T_1} c_{v,u}(T)\frac{dT}{T} - R\ln\frac{1}{CR}, \tag{37}$$

Where CR is the engine compression ratio:

$$CR = \frac{V_1}{V_2}, \tag{38}$$

Pressure of the fluid after the ideal adiabatic compression is calculated using the equation of state:

$$p_2 = p_1 \frac{T_{2s}}{T_1} CR, \tag{39}$$

After the compression the mixture is burned at constant volume $V_2 = V_3$ ($v_2 = v_3$) to the state of thermodynamic equilibrium. Non-stoichiometric approach using minimization of Gibbs free enthalpy is applied:

$$U_3 + p_3 V_3 - T_3 S_3 \rightarrow \min, \tag{40}$$

The mass of each chemical element remains unchanged before and after the combustion. The mass balances are the constraints of the equilibrium.

The peak temperature T_3 is calculated from the energy balance of the adiabatic combustion process at constant volume:

$$n_1\left(LHV_u + c_{v,u}\Big|_{T_2} T_2\right) = n_3\left(LHV_b + c_{v,b}\Big|_{T_3} T_3\right), \tag{41}$$

Maximum pressure of the cycle is calculated from the equation of state.

Temperature T_4 after ideal adiabatic expansion of burned mixture is calculated from the equation:

$$\int_{T_0}^{T_{4s}} c_{v,b}(T)\frac{dT}{T} = \int_{T_0}^{T_3} c_{v,b}(T)\frac{dT}{T} - R\ln CR, \tag{42}$$

Pressure at the end of expansion is:

$$p_4 = p_3 \frac{T_{4s}}{T_3}\frac{1}{CR}, \tag{43}$$

Parameters of the residual gas result from the pressure of the blowdown process, that is limited by turbocharger operation. Residual gas pressure p_r is calculated due to current power demand for compression of the fresh mixture. From the mass balance of the engine the flow of exhaust gas can be calculated:

$$n_{ex} = n_m \frac{M_m}{M_b}, \tag{44}$$

The expansion of exhaust gas in the cylinder from pressure p_4 to the final pressure $p_5 = p_6$ is assumed to be also an isentropic process. Final temperature after adiabatic reversible expansion from point 4 to the final exhaust pressure is calculated from equation:

$$\int_{T_0}^{T_{ex,s}} c_{p,b}(T)\frac{dT}{T} = \int_{T_0}^{T_4} c_{p,b}(T)\frac{dT}{T} + R\ln\frac{p_{ex,TC,out}}{p_4}, \tag{45}$$

Then the energy balance of the turbocharger together with the equations of internal work of fresh mixture compression and exhaust gas expansion within turbocharger assuming irreversible process lead to the temperature T_5:

$$n_{ex}\left(c_{p,b}\Big|_{T_5} T_5 - c_{p,b}\Big|_{T_{ex,s}} T_{ex,s}\right)\eta_{i,T}\eta_{mech,T} = \frac{n_m\left(c_{p,m}\Big|_{TC,out,s} T_{TC,out,s} - c_{p,m}\Big|_{TC,in} T_{TC,in}\right)}{\eta_{i,C}\eta_{m,C}}, \tag{46}$$

Finally pressure p_5 is calculated from the equation:

$$\int_{T_0}^{T_5} c_{p,b}(T)\frac{dT}{T} = \int_{T_0}^{T_4} c_{p,b}(T)\frac{dT}{T} + R\ln\frac{p_5}{p_4}, \tag{47}$$

The mass ratio of residual gas to total charge in the cylinder at the beginning of compression is calculated assuming constant thermodynamic state of the gas between points 5 and 6 [34]:

$$x_r = \frac{m_r}{m_1} = \frac{n_r M_b}{n_m M_m + n_r M_r} = \frac{v_2}{v_5}, \tag{48}$$

Therefore the amount of residual gas in cylinder is:

$$n_r = \frac{p_5 V_2}{R T_5}, \tag{49}$$

Calculation of the cycle parameters is an iterative process. Once it is completed the cycle work is calculated:

$$W_{cycle} = W_{3-4} - W_{1-2} = m_1 \left(c_{v,b}\Big|_{T_3} T_3 - c_{v,b}\Big|_{T_4} T_4 - c_{v,u}\Big|_{T_2} T_2 + c_{v,u}\Big|_{T_1} T_1 \right), \tag{50}$$

For a given displacement volume the volumetric efficiency can be estimated:

$$\eta_v = \frac{m_m}{\rho_m (V_1 - V_2)} = \frac{\rho_1 CR(1 - x_r)}{\rho_m (CR - 1)}, \tag{51}$$

The cycle efficiency is:

$$\eta_{cycle} = \frac{W_{cycle}}{m_m LHV_m} = \frac{c_{v,b}\Big|_{T_3} T_3 - c_{v,b}\Big|_{T_4} T_4 - c_{v,u}\Big|_{T_2} T_2 + c_{v,u}\Big|_{T_1} T}{1 - x_r}, \tag{52}$$

Assuming that mechanical efficiency η_m and electricity generator efficiency η_g remain unchanged after the change of fuel the following formulas are used for estimation of electric power, efficiency and exhaust gas temperature of an ICE module fueled with producer gas:

$$P_{el} = P_{el,ref} \frac{W_{cycle}}{W_{cycle,ref}} = P_{el,ref} C_P, \tag{53}$$

$$\eta_{el} = \eta_{el,ref} \frac{\eta_{cycle}}{\eta_{cycle,ref}} = \eta_{el,ref} C_{Eff}, \tag{54}$$

$$T_{ex} = T_{ex,ref} \frac{T_{ex,cycle}}{T_{ex,cycle,ref}} = T_{ex,ref} C_T, \tag{55}$$

Where the engine cycle exhaust gas temperature $T_{ex,cycle}$ is:

$$T_{ex,cycle} = \frac{c_{p,b}\Big|_{T_5} T_5 - \left(c_{p,b}\Big|_{T_5} T_5 - c_{p,b}\Big|_{T_{ex,s}} T_{ex,s} \right) \eta_{i,T}}{c_{p,b}\Big|_{T_{ex,cycle}}}, \tag{56}$$

It is also assumed that the ratio of exhaust gas heat to total available engine heat remains constant in the producer gas mode. Therefore the available jacket water heat $\dot{Q}_{CC}$ can be estimated:

$$\dot{Q}_{CC} = \dot{Q}_{CC,ref} \frac{\Delta H_{ex}\Big|_{393K}^{T_{ex}}}{\Delta H_{ex,ref}\Big|_{393K}^{T_{ex,ref}}}, \tag{57}$$

Where 393 K is the engine exhaust outlet temperature given in the technical specification.

Engine simulation has been performed using in-house built Fortran code. Properties of working fluids were calculated using JANAF tables. As there are no detailed experimental data available in the literature, validation of the model was performed using the specification data of the JMS 320 GS engine [36] in natural gas and biogas mode respectively. The calculated values of correcting factors in biogas mode are as follows: C_P= 1.003; C_{Eff} = 0.982; C_T = 1.022. If these factors are calculated from the data given in Table 3 the values are: C_P=1.000 ; C_{Eff} = 1.000; C_T = 1.033. Another validation was made using data from tests of commercial GAS-250 power pack system purchased from Ankur Scientific Energy Technologies Ltd. (India) [35]. The of engine used within

this system is Cummins GTA-1710-G. The electric power generated in producer gas mode was within the range of 240 - 250 kW and the efficiency was 27.52% - 28.67%. It gives the range of relative power C_P is 0.789 - 0,822 while the model estimated value is C_P = 0.794. Efficiency correction factor C_{Eff} is 0.917 - 0.955 while the model gave C_{Eff} = 0.919. Finally it was concluded that the modeling results are in relatively good agreement with the measured parameters.

Table 3. Technical specification of GE J320 GS engine [36]

Engine manufacturer	GE Jenbacher	
Engine fuel	Natural gas	Biogas
Fuel gas LHV, kJ/Nm^3	34200	23040
Bore, mm	135	
Stroke, mm	170	
Number of cylinders	20	
Compression Ratio CR	12.5	
Aspiration	Turbocharged-intercooled	
Electric power (at p.f. = 0.8), kW	1054	
Fuel energy input (LHV based), kW	2607	
Max cooling water intercooler inlet temperature, ºC	40	50
Combustion air flow rate, Nm^3/h	4249	4006
Exhaust gas flow rate, Nm^3/h	4491	4389
λ^*	1.695	1.603
Exhaust gas temperature at 100% load, ºC	427	450
Recoverable thermal output** (water; 90/70ºC), kW	1197	1147
Electricity generation efficiency (at p.f. = 0.8),%	40.4	
EUF in cogeneration mode	0.863	0.844
Reference fuel LHV	36.2 MJ/Nm^3	

* value calculated; ** Natural gas - exhaust to 120 ºC, Biogas - exhaust to 150 ºC.

6. Cogeneration system performance

There were several simulations performed to estimate performance of the system. In natural gas mode the λ coefficient in the engine is almost 1.7 (Table 3). However, in the producer gas mode it is assumed that the fuel-air mixture is enriched and the value of λ is 1.5. Simulations were run for different parameters of the gasification agent. In the base case the gasification agent is composed of unheated atmospheric air (at 298 K) and engine exhaust gas. The heat of the product gas cooling is used for the network water heating. In the second case the air is preheated to 700 K in the raw producer gas cooler GC1. The temperature of the raw producer gas after the cooler must be high enough to prevent condensation of tar in the gas duct. Therefore the value of 500 K is assumed.

The excess oxygen coefficient λ at the gasification reactor is calculated assuming constant throat temperature equal 1000ºC. There are also assumed: heat loss from the gasifier equal 3% of biomass chemical energy input and tar yield equal 5 g/kg of wet biomass. The gasification process is modeled using the modified approach assuming that 30% of H_2O present in the reduction zone does is not available for the calculation of equilibrium. The temperature of the fuel gas at the buffer tank BT is assumed equal 30 ºC.

It was found that in each case the engine exhaust gas contains enough energy for the biomass drying process. No recirculation of the producer gas was required. The results of simulations are given in fig. 5, 6 and 7. For the calculations of net electricity generation efficiency and EUF the onsite power consumption was assumed equal 15% of the generator output power.

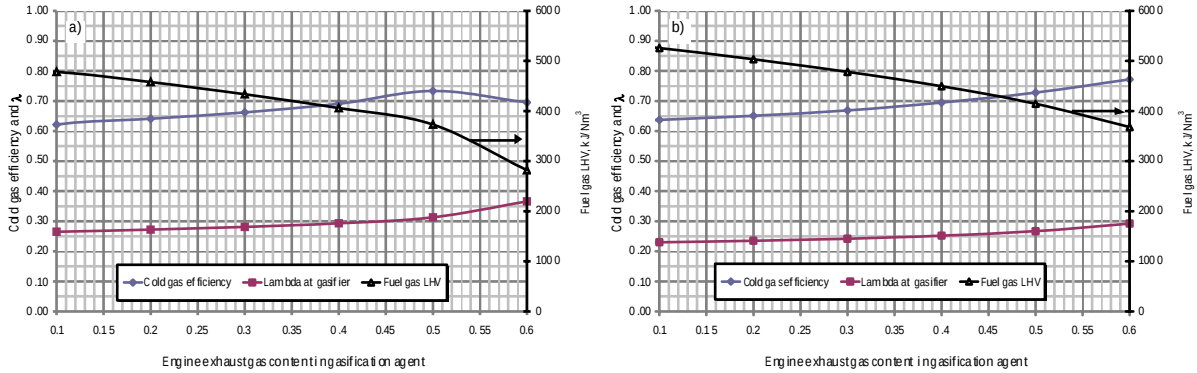

Fig. 5. Gasification system performance; a) air at 298 K, b) air preheated to 700 K

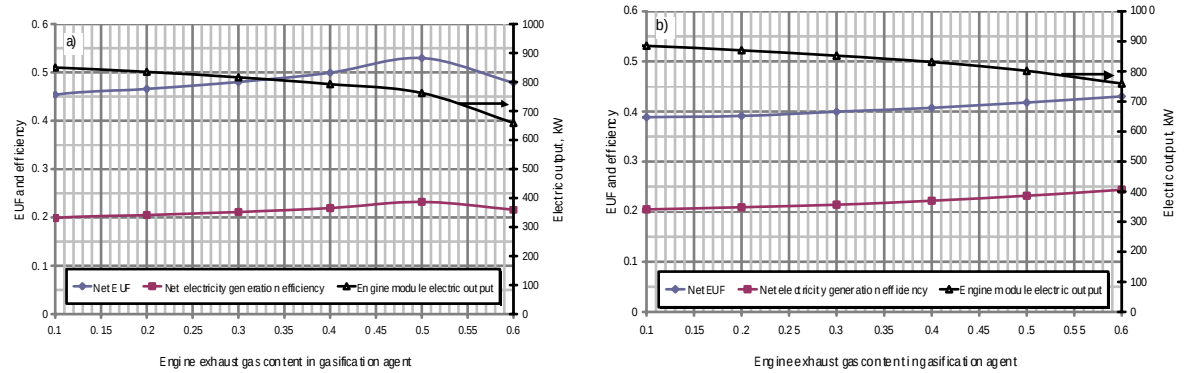

Fig. 6. Gasification system performance; a) air at 298 K, b) air preheated to 700 K

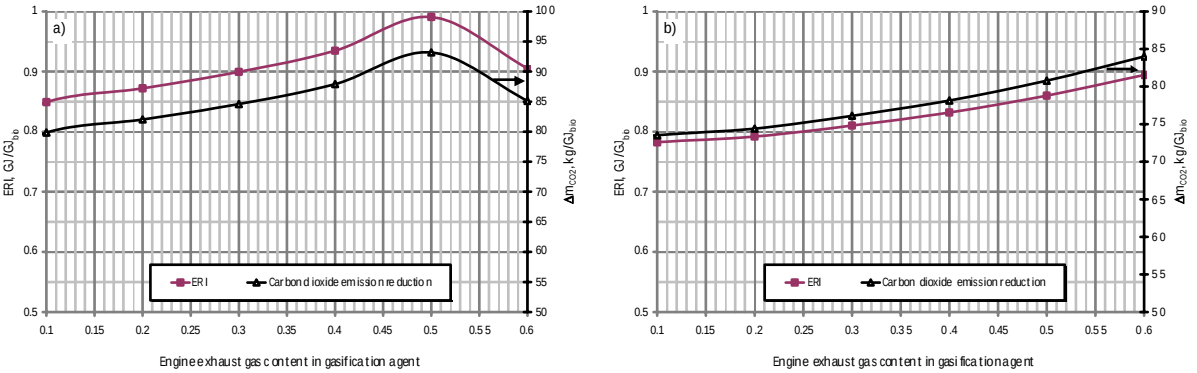

Fig. 7. Gasification system performance; a) air at 298 K, b) air preheated to 700 K

The most interesting findings of the analysis relate to the gasification process. The proposed recirculation of the engine exhaust gas into the gasification rector reduces combustible components contents of the producer gas as well as its heating value. In order to sustain the constant value of process temperature the value of λ must increase together with the exhaust gas content in the gasification agent. Therefore the flow of the gas increases and thus the cold gas efficiency of the process. Consequently the degree of derating of the engine module electric is higher with exhaust gas recirculation but the net efficiency of the system is being noticeably improved.

If preheated air is used as the gasification agent both calorific value of the gas and cold gas efficiency of the process are better. On the other side the preheating of air eliminates a possibility of the network water heating in the raw gas cooler GC1. It reduces the value of EUF for the system and thus the global performance indices ERI and are slightly worse.

The achievable level of the net electric generation efficiency of downdraft gasifier – gas engine system is a little higher than the one of conventional combustion boiler and steam turbine based

solutions. The best value obtained in the analysis is 24.4%. On the other hand the demand for biomass drying reduces the value EUF for the gasification based technology. Therefore the global non-renewable energy saving and CO_2 emission reduction are lower than expected in the case of plant with combustion boiler, where EUF is usually higher than 0.8 (see Fig. 1). The advantage of the integrated gasification technology is a smaller power range that makes the technology a potential candidate for distributed plants, if there are no offers for small steam boilers.

7. Conclusions

The complex analysis of downdraft biomass gasifier – reciprocating engine system is presented in the paper. Two mathematical models of gasification and engine processes have been developed. The models though relatively simple and based only on thermodynamic calculations give results of a relatively good quality. Therefore these have been used in order to examine the effectiveness of modification of a typical reactor-engine system, that assumes recirculation of the engine exhaust gas back into the gasification process. The model gave an encouraging results that need an experimental verification. There is also an economic analysis required in order to judge a financial attractiveness of the technology. The profitability of a potential investment projects is nowadays the most important decision parameter of distributed generation plants.

Acknowledgments

This work was carried out within the frame of research project no. N N513 004036, titled: *Analysis and optimization of distributed energy conversion plants integrated with gasification of biomass*. The project is financed by the Polish Ministry of Science.

The paper has been also supported by the RECENT project (REsearch Center for Energy and New Technologies) supported by 7th Framework Programme, Theme 4, Capacities.

Nomenclature

ash ash content in wet biomass

a number of particles of element (C, O, H) in gas component

b constraint equation identifier

c specific heat, J/(kmolK)

C carbon; mass content of carbon in biomass

E energy

EUF fuel energy utilization factor

ERI energy replacement index

g partial free enthalpy of pure component, kJ/kmolK

h specific enthalpy, kJ/kmol

H hydrogen; mass content of hydrogen in biomass; enthalpy, kJ

$\dot{H}$ enthalpy flow, kW

m mass, kg

$\dot{m}$ mass flow rate, kg/s

LHV lower heating value, kJ/kg,

ls number of components,

ls_g number of gaseous compounds

lf number of phases,

M molecular mass, kg/kmol.

n number of moles of substrate

n' number of moles of a substrate in biomass
n'' number of moles of reaction product
N nitrogen; mass content of nitrogen in biomass
O oxygen; mass content of oxygen in biomass
p pressure, kPa
P power, kW
Q heat, kJ
r heat of evaporation, kJ/kg H2O
R universal gas constant, 8,314 kJ/kmolK,
s specific entropy, kJ/kmolK
S sulphur; entropy, kJ/K
T temperature, K
U internal energy, kJ
$\dot{V}$ volumetric flow rate, m3/s
WE CO_2 emission index, kg/GJ, kg/MWh
w mass content liquid water in wet biomass,
W work, *kJ*
X mass content of water in drying medium, kg/kg
z molar share of component in mixture.

Greek symbols

α own power demand factor
Δ difference
ε conversion efficicency
η efficiency
λ excess oxygen coefficient; Lagrange multiplier
σ cogeneration index (power to heat ratio)

Subscripts and superscripts

ash related to ash
b combustion boiler; burned mixture
bio biomass
C compressor; carbon
CC cooling cycle
C_xH_y tar
char related to char
coal related to coal
cycle calculated from engine theoretical cycle
db dry basis
dm drying medium
Eff efficiency
el electric
ex exhaust gas
fc fixed carbon

fss related to fuel supply system

g related to gas

gen at generator output

g-s temperature difference between gas and solid phases

i component identifier; internal

in input

j phase identifier

m mixture; mechanical

out output; loss

p at constant pressure

P power

r residual gas

ref reference value

T temperature, turbine

TC turbocharger

u unburned mixture

v at constant volume

wb wet basis

0 standard state

References

[1] National Fund for Environmental Protection and Water Management: Methodology for calculation of CO_2 emission reduction in the action 9.1 of the EU Operating Program Infrastructure and Environment 2007 - 2013. Report prepared by National Agency for Energy Savings KAPE S.A. (in Polish, available at: http://pois.nfosigw.gov.pl).

[2] Decree of the Minister of Economy issued on 26 September 2007 in the matter of calculation of data within the application form for the certificate of electricity origin from cogeneration... Journal of Law no. 185/2007 pos. 1314. (in Polish).

[3] Baggio P., Baratieri M., Grigiante M.: Equilibrium simulation of small-scale gasification biomass CHP plant. Proceedings of 3rd Int. Conference "Bioenergy 2007". Jyväskylä, Finland.

[4] Schuster G., Löffler G., Weigl K., Hofbauer H.: Biomass steam gasification - an extensive parametric modeling study. Bioresource Technology 77 (2001), pp. 71-79

[5] Ruggiero M., Manfrida G.: An equilibrium model for biomass gasification process. Renewable Energy Vol. 16 (1999), pp. 1106-1109.

[6] Herdin G., Robitschko R., Klausner J., Wagner M.: GEJ Experience with Wood Gas Plants. Printed materials of GE Jenbacher AG, Jenbach, Austria, 2003, <media.godashboard.com/gti/IEA/9revGEJenbacherRauschengl.PDF> accessed 17.02.2011.

[7] Warren T.J.B., Poulter R., Parfitt R.I.: Converting Biomass to Electricity on a Farm-Scale using Downdraft Gasification and Spark-ignition Engine. Bioresource Technology Vol. 52, 95 - 98.

[8] Bolhàr-Nordenkampf M., Hofbauer H.: Biomass gasification combined cycle thermodynamic optimisation using integrated drying. Proceedings of ASME Turbo Expo 2004: Power for Land, Sea, and Air. June 14–17, 2004, Vienna, Austria. ASME Paper GT2004-53269.

[9] Ragland K. W., Aerts D. J., Baker A. J.: Properties of Wood for Combustion Analysis. Bioresource Technology Vol. 37 (1991) 161-168.

[10] Ratnadhariya J.K., Channiwala S.A.: Three zone equilibrium and kinetic free modeling of biomass gasifier – a novel approach. Renewable Energy 34 (2009) 1050–1058.

[11] Altafini C.R., Wander P.R. Barreto R.M.: Prediction of the working parameters of a wood waste gasifier through an equilibrium model. Energy Conversion and Management 44 (2003) 2763–2777.

[12] Sharma A.Kr.: Equilibrium modeling of global reduction reactions for a downdraft (biomass) gasifier. Energy Conversion and Management Vol. 49 (2008), pp. 832 – 842.

[13] Zainal Z.A., Ali R., Lean C.H., Seetharamu K.N.: Prediction of performance of a downdraft gasifier using equilibrium modeling for different biomass materials. Energy Conversion and Management 42 (2001) 1499-1515.

[14] Babu B.V., Sheth P.N.: Modeling and Simulation of Downdraft Biomass Gasifier. Proceedings of ChemCon'04. Mumbai, India 2004.

[15] Melgar A., Perez J.F., Laget H, Horillo A.: Thermochemical equilibrium modelling of a gasifying process. Energy Conversion and Management 48 (2007), 59–67.

[16] Jarungthammachote S., Dutta A.: Thermodynamic equilibrium model and second law analysis of a downdraft waste gasifier. Energy, 2007, vol. 32, no. 9, pp. 1660-1669.

[17] Centeno F., Mahkamov K., Silva Lora E.E., Andrade R.V.: Theoretical and experimental investigations of a downdraft biomass gasifier-spark ignition engine power system. Renewable Energy 37 (2012) 97-108.

[18] Baratieri M., Baggio P., Fiori L., Grigiante M., Biomass as an energy source: Thermodynamic constraints on the performance of the conversion process. Bioresource Technology, Volume 99, Issue 15, October 2008, 7063-7073.

[19] Göbel B., Henriksen U., Jensen T.K., Qvale B., Houbak H.: The development of a computer model for a fixed bed gasifier and its use for optimization and control. Bioresource Technology 98 (2007), 2043–2052.

[20] Dogru M., Howarth C.R., Akay G., Keskinler B., Malik A.A.: Gasification of hazelnut shells in a downdraft gasifier. Energy 27 (2002), 415–427.

[21] Tinaut F.V., Melgar A., Pérez J.F., Horrillo A.: Effect of biomass particle size and air superficial velocity on the gasification process in a downdraft fixed bed gasifier. An experimental and modelling study. Fuel Processing Tech. Vol. 89 (2008), 1076 – 1089.

[22] Milne T.A., Evans R.J., Abatzoglou N.: Biomass Gasifier "Tars": Their Nature, Formation, and Conversion. Report prepared under Task No. BP811010. NREL/TP-570-25357, National Renewable Energy Laboratory, Golden, Colorado, November 1998.

[23] Gerun L., Bellettre J., Tazerout M., Gobel B., Henriksen U.: Investigation of the Oxidation Zone in a Biomass two-Stage Downdraft Gasifier, Conférence ECOS 2005, 1525-1532 (Trondheim, 20-23 June 2005).

[24] Gordon S., McBride B. J.: Computer Program for the Calculation of Complex Chemical Equilibrium Compositions with Applications; I. Analysis. NASA Reference Publication 1311 (1994) (available at: http://www.grc.nasa.gov/WWW/CEAWeb/RP-1311.pdf)

[25] Larfeldt J., Leckner B., Melaaen M.C.: Modelling and measurements of the pyrolysis of large wood particles. Fuel 79 (2000) 1637-1643.

[26] Kirov N.Y.: Specific Heath and Total Contents of Coals and Related Materiale At Elevated Temperatures. BCURA Monthly Bulletin 1965, pp. 29 – 33.

[27] Jayah T.H., Aye L., Fuller R.J., Stewart D.F.: Computer simulation of a downdraft wood gasifier for tea drying. Biomass and Bioenergy 25 (2003), pp. 459 – 469.

[28] Sridhar G., Sridhar H.V., Dasappa S., Paul P.J., Rajan N.K.S., Mukunda H.S. Development of producer gas engines. Proceedings of the Institution of Mechanical Engineers, Part D: Journal of Automobile Engineering 219 (2005) 423-438.

[29] Sridhar G., Paul P.J., Mukunda H.S.: Biomass derived producer gas as a reciprocating engine fuel - an experimental analysis. Biomass and Bioenergy 21 (2001) 61–72.

[30] Baratieri M., Baggio P., Bosio B., Grigiante M., Longo G.A.: The use of biomass syngas in IC engines and CCGT plants: A comparative analysis. Applied Th. Eng. 29 (2009) 3309–3318.

[31] Tinaut F.V., Melgar A., Horrillo A., Diez de la Rosa A.: Method for predicting the performance of an internal combustion engine fuelled by producer gas and other low heating value gases. Fuel Processing Technology 87 (2006) 135 – 142.

[32] Dasappa S.: On the estimation of power from a diesel engine converted for gas operation – a simple analysis, Proceedings of the Seventeenth National Conference on IC Engines and Combustion. India. December 2001 <cgpl.iisc.ernet.in> accessed 17.02.2011.

[33] Papagiannakis, R.G., Rakopoulos, C.D., Hountalas, D.T. and Giakoumis, E.G.: Study of the performance and exhaust emissions of a spark-ignited engine operating on syngas fuel', Int. J. Alternative Propulsion, Vol. 1 (2007), No. 2/3, pp.190–215.

[34] Heywood J.B.: Internal Combustion Engine Fundamentals. McGraw-Hill International Editions. Automotive Technology Series. USA 1988. ISBN 0-07-100499-8.

[35] Ankur Scientific Energy Technologies Pvt. Ltd. (www.ankurscientific.com): Results of test measurements of commercial Gas-250 power pack system. Baroda, India, 2006.

[36] Jenbacher AG: Technical specifications of JMS 320 GS-N.L Natural gas engine module of 1.065kWel and JMS 320 GS-B.L Biogas engine module of 1.065kWel. Jenbach, Austria, 22 January 2003.

Proposing offshore photovoltaic (PV) technology to the energy mix of the Maltese islands

Kim Trapani[a,b] and Dean L. Millar[a,b]

[a]Laurentian University, Sudbury, Canada, ktrapani@mirarco.org (CA)
[b]Mining Innovation, Rehabilitation, and Applied Research Corporation, Sudbury, Canada, dmillar@mirarco.org

Abstract:

The islands of Malta are located in the Mediterranean basin enjoying 5.3kWh/m^2/day of solar insolation, at a latitude of 35° 50N. Electricity generation for the islands is dependent upon imported fossil fuels for combustion. The available solar resource could be exploited to offset the current generation of electricity using solar photovoltaic technology (PV). Due to the limited land availability onshore, the offshore environment surrounding the Maltese islands could be considered for the installation of PV floating on the sea surface. The output from such an installation would have to be integrated with the existing conventional electricity generation infrastructure, which relies on gas and steam turbine technology. Gas and steam turbines have a variable efficiency output depending on the load which they have to deliver, with highest efficiency delivered at the specified full load of the turbine. Displacing fossil fuel derived electricity with that from variable and intermittent photovoltaic systems reduces the former's load factors and hence efficiency, which must be taken account of in feasibility studies.

To assess the feasibility of floating PV being integrated with the existing fossil plant, monthly trend consumption data for Malta were analysed. The change in gasoil and heavy fuel oil (HFO) consumption resulting from the part load efficiency variation and the displacement of electricity generation from the PVs were estimated. A cost analysis was prepared for the system integration analysis specifically accounting for the reduction in combustion of fossil fuels at the power station and the capital expenditures and operating costs due to the floating PV installation. Aside from the basic cost-benefit of a floating PV installation, CO_2 are also considered.

Keywords:

Floating PV, Offshore solar, Malta PV.

1. Introduction

The islands of Malta are located in the Mediterranean basin enjoying an average daily insolation of 5.29kWh/m^2, at a latitude of 35° 50 N, with minimal land space availability due to its 316km^2 small size.Electricity generation for the island is solely dependent upon fossil fuels which are high in CO_2 emissions. According to the EU Directive [1] of the European Parliament and of the Council,on the promotion of the use of energy from renewable energy sources, it requires member states to achieve a share of energy of the gross final consumption from renewable energy. As per Annex I of this directive, Malta is required to produce 10% of its energy from renewable energy sources by 2020. Malta must find alternative feasible solutions for production of electricity, which is challenging because the amount of land that can be allocated to energy production is low due to the high population density.

Solar energy is the primary source of renewable energy available in Malta. Two methods of generating electricity from solar energy are 1) through concentration of direct sunlight to generate superheated fluid which is then passed through a heat engine power cycle, and 2) using photoelectric properties of P-N junctions within photovoltaic (PV) panels. Solar thermal electricity generation relies on direct sunlight suited to climates with high proportion of clear skies. PV panels

convert both direct and diffuse sunlight into electricity, potentially making it more appropriate for the site.

For high performance of solar energy resource dependent technology such as PV, maximum exposure to the sun is necessary. This requires a large open space for multi MW installations, approximately 6,500m^2 area for a 1MW crystalline array. This is not easily attainable in a small country such as Malta, where the land resources are so restricted that uses alternative to power production, for example agriculture, may take higher priority. PV installed offshore, may offer an attractive alternative in such situations.

1.1. Maltese Islands

Malta is made up of three islands (Malta, Gozo and Comino), totalling 316km^2 in area. This archipelago is situated right in the middle of the Mediterranean Sea, just beneath Sicily, with a population 410,567 according to the latest consensus of 2007; with the majority of the people living on the biggest of the islands Malta. The main economy of the country is tourism and Malta depends almost entirely on importation for the supply of natural resources and consumer goods.

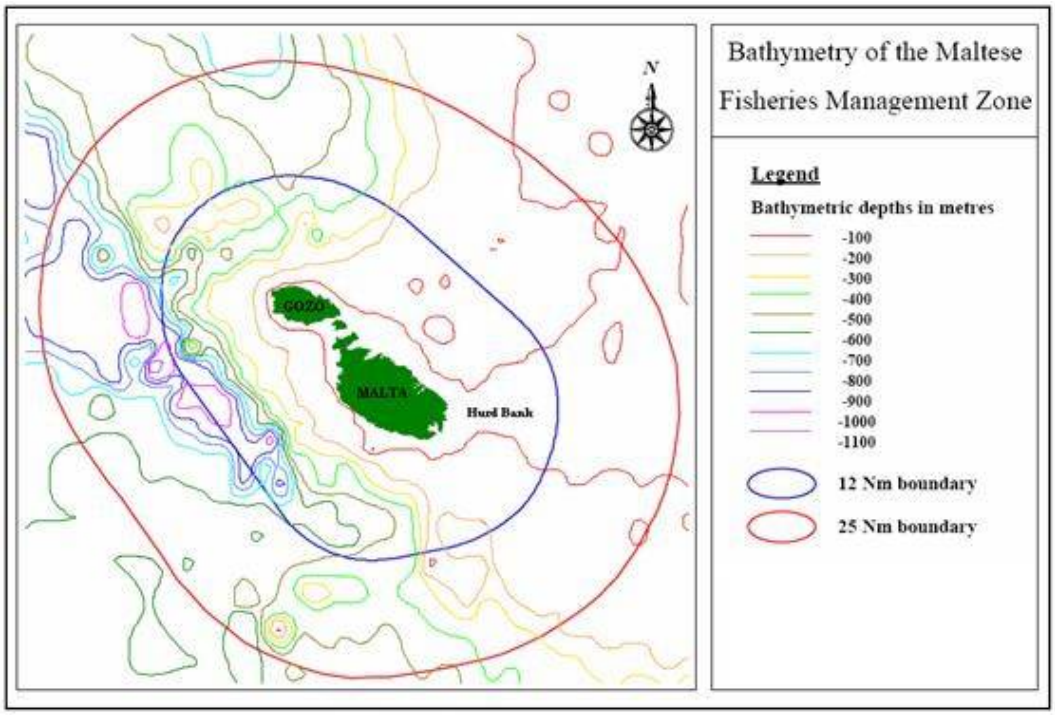

Figure 1: Map of the Maltese Islands showing Territorial Waters (Blue) and Fishing Zone (Red) [2]

There are no pipeline or cable connections yet available with any neighbouring countries (e.g. Italy, Libya). Plans are in place for a cable interconnection to Sicily commencing 2013 [3]. Malta has territorial waters spanning over 3,000 km^2 and control over approximately 61,000 km^2 of the Mediterranean Sea [4]. The ratio of area of territorial waters to area of land mass for Malta is approximately 10, implying that the resource potential from solar electricity generation is significantly larger offshore than it is onshore.

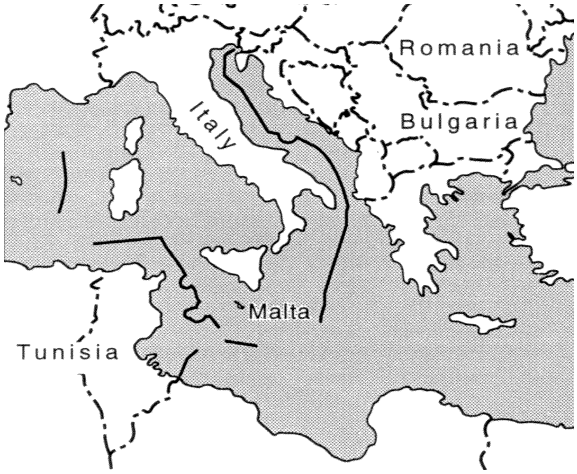

Figure 2: Map of the central Mediterranean showing the southern and western maritime boundaries of Malta [4]

The waters surrounding the island are almost landlocked by the countries surrounding the Mediterranean Sea, with ocean access through the Suez Canal and the Strait of Gibraltar water level variation due to the tidal is negligible around the Maltese coastline and tidal currents are slight. Also the characteristic waves within the Mediterranean basin tend to be of less destructive nature compared to ocean waves, due to the shorter fetches over which the wind acts.

1.2. Floating PV Array Concept

In Malta, the introduction of energy policy targeted at increasing the renewable energy share of the generated national electricity (through feed-in tariffs, quota mechanisms and tendering) has resulted in significant increases in production of photovoltaic (PV) panels, amongst other renewable energy technologies. Other than in a few isolated cases, reported in section 1.2.1, research involving array deployment of thin film, a-Si and crystalline, mono-Si and poly-Si, in offshore environments is limited (although some research has been focused in offshore deployment for concentrated solar photovoltaics, due to the technology's requirement for cooling).

1.2.1. Existing Floating PV Projects

The recent initial movers in the field of floating PVs were SPG Solar of Novato, California, and Thompson Technologies Industries (TTi), Inc. of Novato, California, through collaboration on a 175kWp project in May, 2007 at Far Niente Winery in Napa Valley, California. The offshore array is mounted on pontoons in the irrigation pond of the winery, and was proposed to satisfy the sustainability practices employed at the winery while not displacing any profitable land required for their grape harvest. Following this in 2011, SPG Solar installed a prototype 350kWp array in Petaluma, California as an intermediate step to a 1MW full scale array [5].

In August 2007,8,500km away in Aichi, Japan, an alternative scheme for a floating PV prototype was being tested by the National Institute of Advanced Industrial Science and Technology[6]. This research was focused on reporting the advantages of a water cooled PV system, compared to one which was not cooled. Hence, two 10kWp systems where installed on two separate floats, one with a cooling system integrated, and both having the PV panels installed horizontally – with results reported by Ueda et al [6] indicating higher efficiency of the cooled panels. In 2009, Enerdaiet, installed a 20kWp array in Solarolo, Italy deployed a biogically inspired floating PV array designed to resemble *Nelumbo nucifera* (lotus plant), and with proposals that such modules be scalable to large scale installations. Similar to the installations in California and Japan, the "Lotus" project was mounted on pontoons in a reservoir, with air ducts maintained underneath the panels to allow air cooling.

Figure 3: Existing floating PV projects

In contrast to the installations of SPG Solar, the systems at Solarolo and Aichi were installed at an almost horizontal angle, rather at the optimal solar tilt, in order to support a higher power density on the water surface. The specific rated power (according to the project's installed occupation area) is 0.067kWp/m^2, 0.074kWp/m^2 and 0.057kWp/m^2 for the installations in California, Japan and Italy respectively. The installation in Japan comprised of mono-crystalline PV modules while those of California and Italy comprised of polycrystalline modules. Monocrystalline modules tend to have higher electricity conversion efficiency due to the higher silicon purity. Between 2010 and 2011 the University of Pisa and the University of Catania, Italy, in collaboration with Terra Moretti Holdings plc. constructed another two floating PV systems one in Suverto, Livorno and the other in Colignola, Pisa. The panels were mounted on a horizontal platform, with mirrors positioned on either side of the panel to reflect light onto the PV panel as illustrated in Figure 3 (bottom right).

All of these installations were mounted on lakes or reservoirs with pontoon or rigid structures to support the panels. For the marine environment, the designs would be subjected to further challenges arising from the sea water and the wave climates.

2. Resource, Infrastructure and Demand

2.1. Solar Resource

The total annual solar radiation on the horizontal surface in the waters offshore of the Maltese islands (at a Lat. 35.9 and Long. 14.6) is 1932.9kWh/m^2(5.29kWh.m^2/d x 265d) according to the data given in Table 1.

Table 1: Malta solar and technical PV (for horizontal oriented panels) resource averages including climatic conditions [7]

Month	Solar radiation[1] - horizontal	Yield Thin Film PV Panels (η = 8%)	Yield Crystalline PV Panels (η = 14%)
	kWh/m^2/d	*kWh/m^2*	*kWh/m^2*
Jan	2.67	6.62	11.59
Feb	3.70	8.29	14.50
Mar	5.00	12.40	21.70
Apr	6.36	15.26	26.71
May	7.29	18.08	31.64
Jun	8.02	19.25	33.68
Jul	8.11	20.11	35.20
Aug	7.21	17.88	31.29
Sept	5.76	13.82	24.19
Oct	4.18	10.37	18.14
Nov	2.84	6.82	11.93
Dec	2.31	5.73	10.03
Annual	5.29 (Avg.)	154.47 (Total)	270.60 (Total)

The calculations undertaken in preparation of Table 1assume that the panels lie perfectly horizontal on the surface of the lake and that the PV panels generate electricity all year round. Yield estimates in Table 1 assumed miscellaneous losses of 10% and depict an efficiency of 8% for thin film arrays and 14% for crystalline arrays as reported by RETScreen [8] and packing density is not accounted for when calculating the specific yield from either technology.

2.2. Existing Electricity Generation Infrastructure

Enemalta is the public entity which is responsible for the electricity generation and distribution to consumers in Malta. It operates two power stations, including five generating stations: two of which produce steam for electricity generation through the combustion of heavy fuel oil (HFO) with 0.7%S and the other three combust gas oil with 0.1% S. The open cycle gas turbines (OCGT) are mainly utilised as peaking plants, with the base load being supplied by the steam turbines from the HFO plants. The combined installed generating capacity for Malta is 562.5MW, as indicated in Table 2.

Table 2: Electricity generating power stations Malta [3]

	Generating Stations	Generating Units	Installed Capacity (MW)
MPS	Marsa Station(Steam)	7	220
DPS	Delimara Station(Steam)	2	120
GTs	Marsa Station(Gas)	1	37.5
	Delimara Station(Gas)	2	75
CC	Delimara Station(CCGT)	1	110
	Total	13	562.5

A 100km inter-connector power line with Sicily is planned for and is expected to be operational by the end of 2013, which will increase the available capacity by 200MW and provide opportunity for

[1] Accounts for variation in solar insolation arising from overcast conditions and variability.

electricity export (although it primarily designed for electricity importation)[9]. As of 2005, Enemalta also committed itself to purchase all renewable energy generated on the islands.

2.3. Load Demand

Table 3: Base and peak loads for monthly weekday and weekend demand profiles based on Enemalta monthly demand profiles for 2010 [3]

		Jan	Feb	Mar	Apr	May	Jun	Jul	Aug	Sep	Oct	Nov	Dec
WD	Base Load (MW)	162	163	161	158	165	181	235	230	216	189	164	168
	Peak Load (MW)	293	294	302	271	268	293	352	350	335	316	286	323
WE	Base Load (MW)	156	165	148	162	167	184	226	203	208	194	165	165
	Peak Load (MW)	259	290	272	242	238	271	305	291	282	286	276	308

From recorded load data supplied by Enemalta [3], the base load for the Maltese power system can be seen to be in the early morning hours, between 1 – 5am. The main trend for the demand profile in winter is an increase in electricity consumption until 8am (at which time a plateau is achieved), an increase to peak conditions in the evening (~ 6pm) and then a decrease back to the base load. In summer, the peak is shifted to morning hours, reflecting usage of air conditioning systems. The base load is higher in summer (c. 225MW) than it is in winter (c. 170MW), when the greatest influx of tourists is measured on the islands. For the weekends, the base load is generally lower, with two peaks occurring, the first just before noon and the second in the evening.

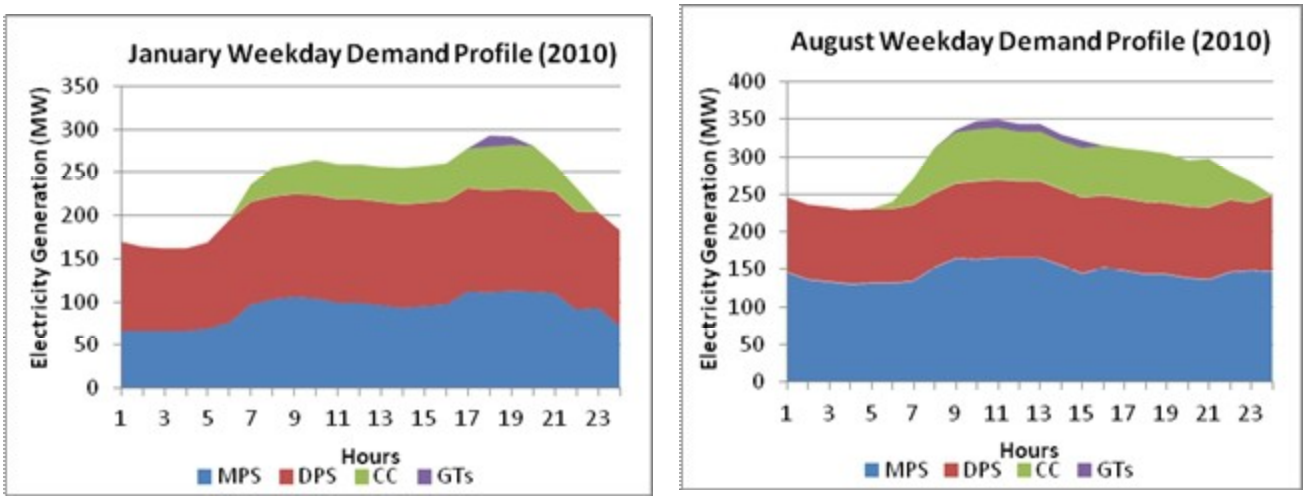

Figure 4: Weekday (2010) demand profiles – January and August, for Malta [3]

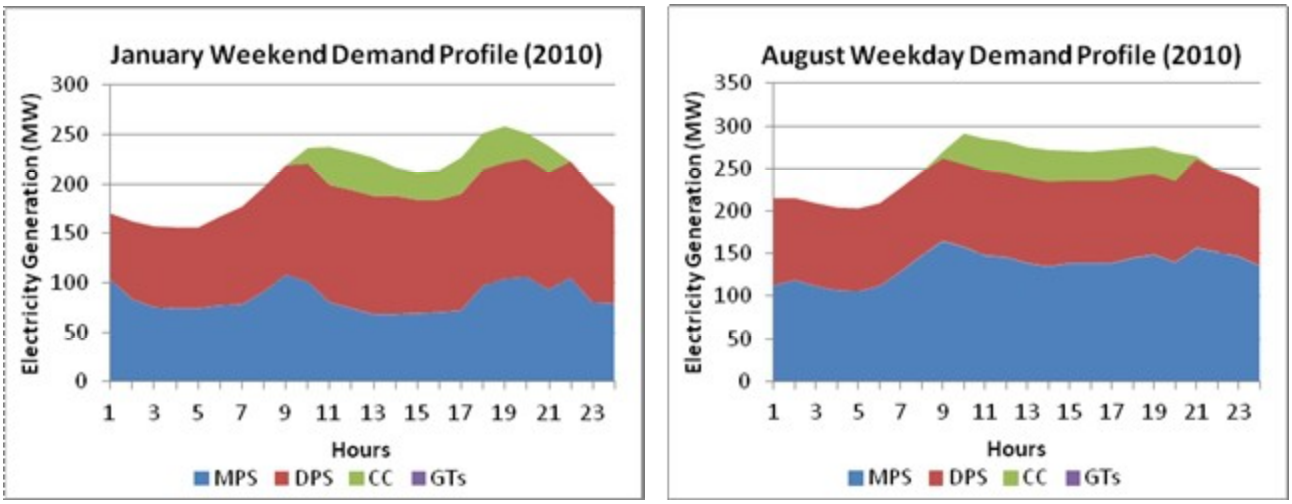

Figure 5: Weekend (2010) demand profiles – January and August, for Malta [3]

For the analysis of integration of PV, the demand profiles are based on a typical weekday and weekend profiles for each month. Collectively these represent an annual electrical consumption for the Maltese Islands of 2,158,817 MWh (Table 4), implying an aggregate load factor for the islands' power stations of 43.8%, where this is considered the ratio of the actual electricity generated to the maximum possible electricity that could be produced.

$$\text{Capacity Factor, } C_p = \frac{\text{Actual } P_{out}}{\text{Max } P_{out}} = \frac{2{,}158{,}817\text{MWh/year}}{562.5\text{MW} \times 8760\text{hrs/year}}$$

Table 4: Representative monthly electricity consumption data according to demand profiles for 2010 [3]

	Days		MWh/Day		Total
Month	*WEs*	*WDs*	*WEs*	*WDs*	*(MWh)*
Jan	10	21	4966	5604	167344
Feb	8	20	5369	5656	156072
Mar	8	23	5028	5647	170105
Apr	8	22	5060	5415	159610
May	10	21	5078	5593	168233
Jun	8	22	5657	6019	177674
Jul	9	22	6579	7193	217457
Aug	9	22	6015	7002	208179
Sep	8	22	5991	6700	195328
Oct	10	21	5787	6389	192039
Nov	8	22	5252	5510	163236
Dec	8	23	5589	6036	183540
			Total (MWh)		**2,158,817**

3. Solar and Fossil Fuel Electricity Generation Integration

3.1. Part Load Efficiency of Turbines

The power stations employed in Malta use three different technologies to produce electricity: i) steam turbine, ii) gas turbine (GT), and iii) a combined cycle gas turbine (CCGT) which is a combination of i) and ii). Although all turbine generating units permit variable speed adjustments to modulate the specific production of electricity, the gas turbines are the most controllable. This controllability comes with the consequence of reduced efficiency at part load (Figure 6 – left).

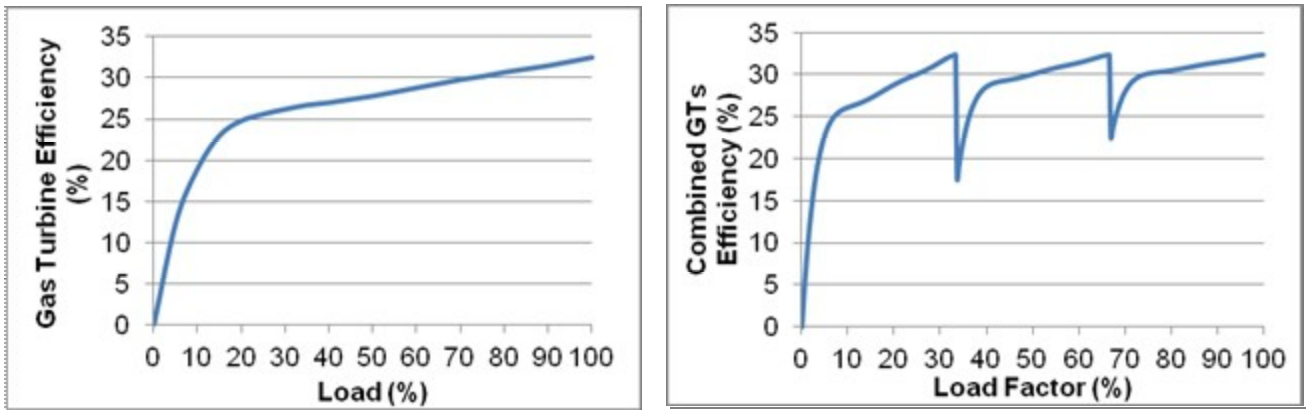

Figure 6: Efficiency curve for a single unit 37.5MW gas turbine with part load range 19 – 32% (left); aggregate efficiency curve for 3 such 37.5MW gas turbines units (right)

The 37.5MW gas turbine units have efficiency ranging from 19% at minimum load to 32% at maximum load [3]. Using this range as a baseline, a curve representing the varying performance of the turbine with the load could be depicted (Figure 6 - right).

For three of these units running in a coordinated fashion, with maximum output of 112.5MW, the part load efficiency calculation was split into three stages:

i) Load: 0 – 37.5MW : 1 unit working
ii) Load: 37.5 – 76MW : 2 units working, 1 at full load (η = 32%)
iii) Load: >76MW : 3 units working, 2 at full load (η = 32%)

Table 5: CCGT and GTs peak loads for monthly weekday and weekend demand profiles based on Enemalta monthly demand profiles for 2010 [3]

CC + GTs	**Jan**	**Feb**	**Mar**	**Apr**	**May**	**Jun**	**Jul**	**Aug**	**Sep**	**Oct**	**Nov**	**Dec**
Weekday (MW)	64	95	118	100	118	85	90	100	111	74	51	69
Weekend (MW)	39	55	95	86	89	78	68	68	73	39	51	58

The 8 steam turbine (ST) generators producingelectricity have three different installed capacities and part load efficiencies (60, 30 and 10MW turbines). The resulting combined steam turbine part load efficiency is illustrated in Figure 7.

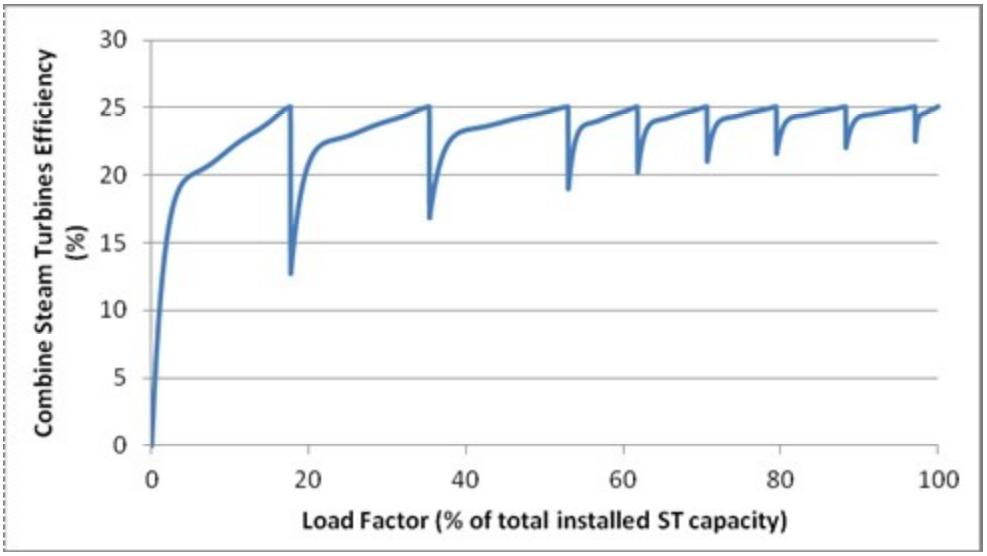

Figure 7: Efficiency curve for an 8 series combination of 10, 30 and 60MW unit steam turbines with part load efficiency range from 20to 25%

3.2. PV and Oil-fired Power Station Integration

Due to the part load efficiency characteristics of the conventional generators on the islands, offsetting electricity otherwise generated from these technologieswith that from PV has direct economic effect. Every MW supplied by an array of PV devices will increase the cost of the remaining MW produced conventionally, if an individual unit operates at part load. Thus apart from the offsetted electricity in the case of the CCGT and the GTs, the part load efficiency has to be compiled accordingly.

The units of electricity displaced from the fossil fuel stations are highlighted in Table 6. Applying the part load efficiency curve for the loads of the GTs and CCGT both before and after integration, the change in fuel consumption could be estimated and hence the added/reduced fuel consumption could be calculated accordingly. Considering two scenarios for which the installed capacity of photovoltaics are set at 4 and 8MW, for Scenario 1 and 2 respectively,the corresponding fuel

consumption for the conventional generators the PV array integration could be compiled, which is also indicated in Table 6.The scenarios are the set at 4 and 8MW, in order to allow large scale integration of the offshore PV technology and hence applicability for commercial economics – also 8MW is the threshold at which crystalline PV is somewhat economical.

Table 6: Integration summary for Scenario 1 and 2

	Scenario 1 – 4MW Installed PV Capacity:			**Scenario 2 – 8MW Installed PV Capacity:**		
	PV Electricity Generation	7221	MWh	PV Electricity Generation	14442	MWh
GTs Power Station	Power Generation (Prior PV)	29334	MWh	Power Generation (Prior PV)	29334	MWh
	Power Generation (After PV)	25921	MWh	Power Generation (After PV)	23956	MWh
	Difference (Before – After)	3413	MWh	Difference (Before – After)	5378	MWh
	Total Fuel Consumed (Prior PV)	10673	MT	Total Fuel Consumed (Prior PV)	10673	MT
	Total Fuel Consumed (After PV)	7822	MT	Total Fuel Consumed (After PV)	7499	MT
	Change in Fuel Consumed	2851	MT	Difference (Before – After)	3173	MT
CCGT Power Station	Power Generation (Prior PVs)	408658	MWh	Power Generation (Prior PV)	408658	MWh
	Power Generation (After PVs)	403722	MWh	Power Generation (After PV)	398529	MWh
	Difference (Before – After)	4935	MWh	Difference (Before – After)	10128	MWh
	Total Fuel Consumed (Prior PVs)	82967	MT	Total Fuel Consumed (Prior PV)	82967	MT
	Total Fuel Consumed (After PV)	82085	MT	Total Fuel Consumed (After PV)	82092	MT
	Difference (Before – After)	882	MT	Difference (Before – After)	875	MT
Steam Power Station	Power Generation (Prior PV)	1744373	MWh	Power Generation (Prior PV)	1744373	MWh
	Power Generation (After PV)	1745500	MWh	Power Generation (After PV)	1745437	MWh
	Difference (Before – After)	-1127	MWh	Difference (Before – After)	-1064	MWh
	Total Fuel Consumed (Prior PV)	506430	MT	Total Fuel Consumed (Prior PV)	506430	MT
	Total Fuel Consumed (After PV)	506270	MT	Total Fuel Consumed (After PV)	506286	MT
	Difference (Before – After)	161	MT	Difference (Before – After)	145	MT

3.3. Economic Analysis of Scenarios

The generating cost of electricity can be estimated for each scenario by accounting for the total annual costs (including the annuitized capital costs, O&M and the fuel costs) of electricity generated throughout that year. According to a report published by Enemalta [10], for 2005 the generating cost (excluding the fuel costs) for the two power stations was equivalent to €4.15c/kWh, where total production was 2,263,145 MWh. The split between the annuitized capital expenditures (CAPEX) and the operation and maintenance (O&M) costs was at 49.43% and 50.57% respectively. This implies that the cost per MW for the power stations was €100,373 and €82,473 for the CAPEX and O&M respectively. These costs were inflated to 2010 costs using an index figure of 0.72987 for 2010 and 0.66289 for 2005 [11]. A discount rate of 10% was taken throughout the economic analysis. The resulting costs for the power stations are illustrated in Table 7. With the gas oil and HFO fuel prices taken to be €570/MTon and €366/MTon respectively, according to trading data for the central Mediterranean region [12] in 2010.

With regards to the offshore PV installation, if an offshore PV device was to replace a wave energy converter in a wave farm, the infrastructure required would be the same for both. The cost per 750kW Pelamis[2] wave energy device was estimated to be $3.05M [13], which when inflated to

[2]This wave energy converter (WEC) was used as a reference in compiling the economic case, due to it being the only commercial WEC installation to date and would signify expected costs for mooring arrangements of an offshore large scale PV installation.

current prices, means the cost of a 2.25MW wave park would be $12.38M. Moorings, installation, grid connection and project management account for a total of 24% of the total investment [14] in a wave farm. Hence the infrastructural and installation costs can be taken to be approximately $1320/kWp for a marine floating PV array of the same rating. The cost per Wp for crystalline PV are taken to be $2.07 and $1.03 for the thin film [15]. Thus the specificCAPEX was estimated to be $3390/kWp and $2350/kWp for crystalline and thin film floating PV systemsrespectively. For the operating and maintenance costs of the project, US $2700/MW/year and US $1800/MW/year were taken to apply for both the crystalline and the thin film technologies as indicated in research comparing large scale application of PV technologies [16]. Using an average conversion rate of 0.7533 $/€ for 2010, these rates were converted to those shown in Table 7.

Table 7: Capital expenditures and O&M costs for the power station and PVs

		Annuitized Costs (*i = 10%*)	Inc. Fuel Costs
Year	**Generating Station**	**CAPEX**per MW/year	**O&M**per MW/year
2010	Malta Power Stations	€131,334	€107,912
2010	Offshore Crystalline	€290,625	€1,971
2010	Offshore Thin Film	€201,466	€1,314

Thesecosts for the thin film and crystalline PV were taken together with those for conventional power generating capacity to estimate the average annual cost per unit of electricity for Scenario 1 and 2 operating in an integrated fashion. The results are illustrated in Table 10 calculated using the costs of investment and operation in Table 8 and Table 9.

Table 8: Investment and operation cost estimates for Scenario 1 and 2

		Installed Capacities		**Power Station Costs**		**PV Costs**	
		Power Stations	PVs	CAPEX	O&M	CAPEX	O&M
		(MW)	*(MW)*	*Million EUR/year*	*Million EUR/year*	*Million EUR/year*	*Million EUR/year*
	W/O PV Integration	562.5	-	73.88	60.70	-	-
1	W Thin Film PV	562.5	4.00	73.88	60.70	0.81	0.0053
	W Crystalline PV	562.5	4.00	73.88	60.70	1.16	0.0079
2	W Thin Film PV	562.5	8.00	73.88	60.70	1.61	0.0105
	W Crystalline PV	562.5	8.00	73.88	60.70	2.33	0.0158

Table 9: Electricity and fuel distribution generation for Scenario 1 and 2

		Electricity Generation				**Fuel Consumed**		
		GTs	CCGT	Steam	PV	GTs	CCGT	Steam
		MWh	*MWh*	*MWh*	*MWh*	*Mtonnes*	*Mtonnes*	*Mtonnes*
	W/O PV Integration	29,334.0	408,657.5	1,744,373.0	-	10,672.5	82,966.8	506,430.2
1	W Thin Film PV	25,920.9	403,722.4	1,745,500.0	7,221.2	7,821.6	82,084.9	506,269.6
	W Crystalline PV	25,920.9	403,722.4	1,745,500.0	7,221.2	7,821.6	82,084.9	506,269.6
2	W Thin Film PV	23,955.9	398,529.2	1,745,437.0	14,442.4	7,499.0	82,091.7	506,285.6
	W Crystalline PV	23,955.9	398,529.2	1,745,437.0	14,442.4	7,499.0	82,091.7	506,285.6

Table 10: Economical cost analysis of Scenario 1 and 2

		Annual Fuel Cost			Cost of Electricity
		GTs	CCGT	Steam	(Total)
		Million EUR	*Million EUR*	*Million EUR*	*EUR c/kWh*
	W/O PV Integration	6.09	47.31	185.53	17.114
1	W Thin Film PV	4.46	46.81	185.47	17.051
	W Crystalline PV	4.46	46.81	185.47	17.068
2	W Thin Film PV	4.28	46.81	185.48	17.081
	W Crystalline PV	4.28	46.81	185.48	17.113

The costs of electricity reported in Table 10 show the averaged cost per unit of electricity at the power stations when integrated with the two scenarios analysed. For scenario 1 using thin film, which has the lowest cost of electricity for the scenarios considered, the annual savings which could be made through the offsetting of fossil fuel generation is of $1.376 million. For higher installed capacities of offshore PVs investigated the demand variability faced by the integrated system implied that more fuel was being consumed to balance off the system utilising only part load efficiency, and this was not compensated for by electricity generated from the PV arrays. This limited the techno-economical viability of offshore PVs to approximately 14-15MW, at which point the cost of electricity from the integrated PV - power station generation would be equal to the cost of electricity from the power station alone.

3.4. CO_2 Balance

The net gain/loss of CO_2 from the installation of renewable energy technology depends on the quality of fossil fuel which is offsetted and how much CO_2 was required to manufacture, install and deliver the PV array to site. The considered installations would occupy a footprint of 0.100km^2, 0.200km^2, 0.057km^2 and 0.114km^2, for thin film PV scenario 1 & 2 and crystalline PV scenario 1 & 2 respectively, at a specific rated power of 0.04kWp/m^2 for thin film and 0.07kWp/m^2.

Table 11: Embedded carbon in crystalline [17] and thin film PV [18]

	Crystalline PV	Thin Film PV
Process	*kgCO_2/m^2*	*kgCO_2/m^2*
Manufacturing Process	51.1	21.3
Panels	20.1	20.1
Inverter	2.3	2.3
Support	19.9	19.9
Balance of System (BOS)	2.3	2.3
Capital Inputs	18.4	18.4
Transportation	0.53	0.13
Total	**114.63**	**84.43**

Table 11 presents the list of processes which emit CO_2 during the manufacturing, installation and transportation of the PV arrays. According to the International Energy Agency [19] the CO_2 emissions from the generation of a kW in Malta was at 850g CO_2/kWh for 2009, which reflectsthe average 3.09 g CO_2/Tonne of fuel combusted at the power stations in Malta. For the installed capacities specified by Scenario 1 and 2, carbon savings are over twenty times higher the embedded PV carbon for thin film and crystalline installations in both scenarios.

4. Conclusion

New renewable energy generating capacity in Malta must consider variable demand in techno-economic studies, offshore PV is no exception. This paper has shown that PV integration will lead to an overall reduction of generating costs across the system.With the inter-connector (Malta to Sicily) in place, by the end 2013, it could provide more flexibility in the system with ability to absorb some further excess generation from either renewable energy technologies or to operate the current system more efficiently at full load.

The carbon savings through the adaptation of offshore PVs are considerable and a 12MW installation would be able of providing 1% of the electricity generation in Malta, equivalent to 10% of the total 2020 electrical renewable target as specified by the EU. Future work will address environmental implications of such a development, as well as the actual electrical yield from a similar system.

Acknowledgments

The authors acknowledge the provision of data supporting this research by Enemalta, as well as valuable contributions regarding plant operation. MIRARCO is also acknowledged for its financial support for the lead author's research.

References

[1] European Comission (EC), Directive 2009/28/EC of the European Parliament and of the Council. Official Journal of the European Union; 2009.

[2] UoM, PJS – BENSPEFISH, University of Malta, Malta. Available at: <http://www.um.edu.mt/science/biology/staff/profpatrickschembri/fisheries_management_zone_fmz> [accessed 13.2.2012]

[3] Enemalta Corporation, Plant system load and operation data. Personal Communication: 2011 Oct 12th.

[4] Blake, G., Coastal state sovereignty in the Mediterranean sea: the case of Malta. GeoJournal 1997; 14(2):173 – 180.

[5] Woody, T., Solar on the water. New York, US: The New York Times; 2011 April 20th.

[6] Ueda, Y., Sakurai, T., Tatebe, S., Itoh, A., Kurokawa, K., Performance analysis of PV systems on the water. Proceedings of the 23rd European Photovoltaic Solar Energy Conference; 2008 Sep 1-5; Valencia, Spain. 2670-2673.

[7] NASA. Surface meteorology and solar energy. Atmospheric Science Data Center. Available at: <http://eosweb.larc.nasa.gov/sse/RETScreen> [accessed 28.9.2011].

[8] RETScreen. RETScreen clean energy project analysis software. Natural Resources Canada: PV4 Module, 2010.

[9] Alstom, Alstom partners with Nexans for Malta-Sicily submarine electrical interconnection. Available at: <http://www.alstom.com/grid/news-and-events/press-releases/Nexans-Malta-Sicily/>[accessed 20.1.2012].

[10] Enemalta Corporation, Electricity generation plan: 2006 – 2015. Marsa, Malta. Available at: <http://www.enemalta.com.mt/enemaltastorage/images/files/archived%20news/generation%20plan%20%2821.06.06%29.pdf> [accessed 19.1.2011].

[11] CEPCI. Chemical engineering plant cost index. Available at: <http://www.che.com/pcritical/> [accessed 15.2.2011]

[12] Platts, European marketscan – January release. 2011; 43 (1).

[13] Burman, K., Ocean Energy Technology Overview. Energy Efficiency & Renewable Energy: US Department of Energy, 2009.

[14] Callaghan, J., Results of the marine energy challenge: cost competitiveness and the growth of wave and tidal stream energy. London, UK: Carbon Trust, 2006.

[15] SunElectronics, Solar panels and inverter price comparison. Available at: <http://sunelec.com/> [accessed 21.11.2010].
[16] M. Ito, K. Kato, K. Komoto, T. Kichimi, K. Kurokawa, A Comparative Study on Cost and Life-Cycle Analysis for 100MW Very Large PV Systems in Deserts Using m-Si, a -Si, CdTe and CIS Modules, Progress in Photovoltaics: Research and Applications, 2008; 16: 17 - 30.
[17] Myrans, K., Comparative energy and green carbon assessment of three green technologies for a Toronto roof [dissertation]. Toronto, Canada: University of Toronto; 2009.
[18] Pacca, S., Silvraman, D., Keolelan, G. A., Life cycle assessment of the 33kW photovoltaic system on the Dana building at the University of Michigan: Thin film laminates, multi-crystalline modules and a balance of system components. Michigan, US: University of Michigan. Available at: <http://css.snre.umich.edu/> [accessed 8.3.2011].
[19] IEA, CO_2 fuel emissions from fuel combustion highlights – 2011 edition. International Energy Agency. Available at: <http://www.iea.org/co2highlights> [accessed 18.1.2011].
[20] Cazzaniga, R., Rosa-Clot, M., Tina, G. M., Floating tracking cooling concentrating (FTCC) system. Scienza Industria Technologia. Available at: <http://www.scintec.it/ricerca/energia/ftcE.html>[accessed 11.12.2011].
[21] Campbell, H., Solar power proposed for remote mines. Sudbury, Canada: Sudbury Mining Solutions Journal; 2011: 8.
[22] Cangini, E., Loto progetto energia. Consorzio di bonifica della Romagna occidentale. Available at: <http://www.bonificalugo.it/uploads/ba/60/ba60299310a79a5d6325208235d3ecf4/LOTO-progetto-energia.pdf>[accessed 22.12.2012].

Research of Integrated Biomass Gasification System with a Piston Engine

Janusz Kotowicz[a], Aleksander Sobolewski[b], Tomasz Iluk[b]

[a] *Institute of Power Engineering and Turbomachinery, Silesian University of Technology, ul. Konarskiego 18 44-100 Gliwice, Poland*
[b] *Institute for Chemical Processing of Coal, Zabrze, Poland, tomasz.iluk@polsl.pl, CA*

Abstract:

The article presents the issue related to power production from gas received during biomass gasification process and advantages of biomass gasification technology use in cogeneration systems. Research installation for power production from biomass (~ 60 kW_t), developed at the Institute for Chemical Processing of Coal in Zabrze, is characterized. The installation consists of a fuel supply system, gas generator with fixed-bed, dry gas cleaning system and the system used to produce electricity. The artide describes installation development process which was divided in three staged. The influence of four different biomass available on polish market, on quality of received process gas is presented as well as received reduction efficiencies of dust and organic contaminations in proposed new conception of dry purification of gas system. Power generation system supplied by process gas, equipped with dual fuel combustion engine with rated power of 25 kW is presented. The artide presents results of work of power generation system for production of 8 and 15 kW of electricity, by engine supplied with diesel oil and process gas.

Keywords:

Biomass, Gasification, Research installation, Double-fuel piston engine, Electricity

1. Introduction

The process of producing electrical energy and heat in the coming years will be connected with the taking up of, with a more intensive effort, the aim of lowering the harmful influences of the energy industry in man's natural environment [1]. One of the interesting directions, which may bring the desired ecological effects, may be the use of renewable sources of energy, biomass in particular. Because of the specific properties of biomass there is the possibility of it becoming an interesting solution in gasification technology [2,3,4]. The conversion of chemical energy contained in biomass for energy of combustible gas is meaningful for a larger area of energetics used in biomass. The use of processed gas as a fuel for diffused and average co-generation systems of the production of electrical energy and heat may result in the achievement of the minimal established value of the OZE system in the general balance of used fuel. Furthermore, these systems allow the use of local sources of fuel in the places where they occur, which thus eliminates the cost of transport. An important asset of these systems, based on biomass gasification technology, is likewise the possibility of using solid fuel, often waste products e.g. from the wood or food industry.

2. Research installation

The introduction of new technological solutions onto the energy sector are usually preceded by a series of well-used research tests on a smaller scale of the proposed technology of innovative equipment [5, 6]. On a lesser scale it allows one to check the accuracy of the applied solution. A similar method of proceedings was adopted in the case of the development of the installation of biomass gasification with an innovative gas generator called GazEla [7].

The experimental installation was built, started up and tested by The Institute for Chemical Processing of Coal in Zabrze.

During the research there appeared a gradual development of the position, which was connected with, among other things, the accepted schedule of the experimental work. There also occurred during the process of research the necessity of making changes in the construction with the aim of improving reliability and the efficiency of both particular parts of the apparatus and of the equipment in the composition of the installation.

The conducted research of the development of the installation may be detailed in three stages:
- Stage I - the starting of the gas reactor together with the biomass measurement system in the processed gas combustion chamber.
- Stage II - extension of the installation in stages, through the biomass drying system of gas purification,
- Stage III - the integration of a double-fuel piston engine with the installation of biomass gasification equipped within the gas purification system.

Stage I: Research of the experimental installation of biomass gasification involved work connected with the starting up and examining of the GazEla gas generator - fig. 1 [8].

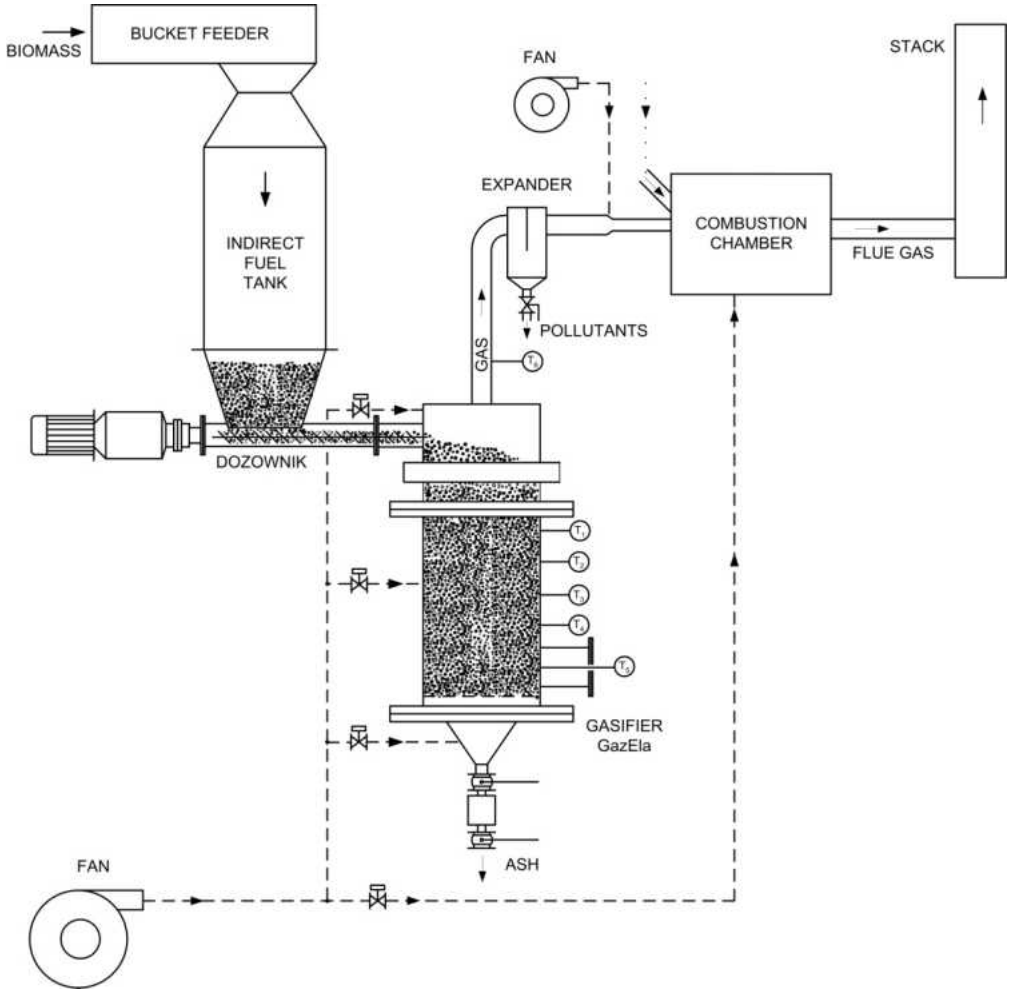

Fig. 1. Outline of the examined installation during the first stage of experimental research

Stage II is the introduction of the researched concept of the system of the purification of drying gas produced in the GazEla generator with the aim of attaining a level of purified gas which allows for its combustion in a piston engine.

Processed gas is generated in the reactor in the first stage of purification which is then directed to an inertial flash vessel. The next is the transportation of the gas to the cyclone separator with the aim of removing minute particles of dust contamination. Initially, purified gas is directed to the gas cooler where it undergoes the process of reducing the temperature from approx. 120°C to approx. 30 ÷ 40°C with the aim of condensation contained in the organically contaminated gas and steam from water. The condensed damp and contamination are gathered in lower exchanger collector. In the next stage of purification, the gas flows to two coke filters. The filters determine the rinsing of the coke of granulation 10 ÷ 20 mm. The purified gas is then burnt in the combustion chamber, and the remaining combustion is emitted through the chimney into the atmosphere [9].

After achieving a satisfactory level of purified gas we move on to stage III, which depends on the integration with the previously described system of the piston engine with the aim of practically examining the possibilities of creating in the system co-generated electrical energy together with heat.

A current-generating system from the firm Andoria from Andrychow was used during the experimental tests. The adaptation of the engine in the research was carried out by The Institution of Combustion Engines, Department of Environmental Engineering and Energetics of the Polytechnic of Silesia, Gliwice. This engine has a strength of 24,6 kW (33,5KM), 3620 cm^3 and also 1500 rev./min. The engine was produced in 1971.

During this research there was used an engine with an automatic mixed ignition working in a two-stroke system. During the setting in motion phases of the engine there was used only diesel fuel. The produced electrical energy collected of the generator was with the help of a resonance system of power collection, a cooled air flow. The work of the engine is dependent on the load of the collecting system of electric power. The forced thrust of electric power on the load current-generating aggregate causes an automatic change in the flow of the collected fuel with the help of a regulator of the internal engine.

After achieving the nominal work parameters of the gas generator and also the purification system there followed on the starting up of the current-generating aggregate. The next step was the opening of the shutter which allowed the entrance of the processed gas, together with the inducted air, to the process of combustion in the engine. In figure 2 we have presented the final outline of the gas purification system integrated with a two-stroke piston engine.

The final appearance of the biomass gasification system integrated with the drying system of gas purification and an internal combustion engine consists of a bucket feeder, a biomass intermediary tank, a conveyor worm, a GazEla gas generator, an inertial pressure reducing valve, a cyclone, a gas cooler, a water processing tank, a cox filter, a fabric filter, a combustion chamber and a two-stroke piston engine.

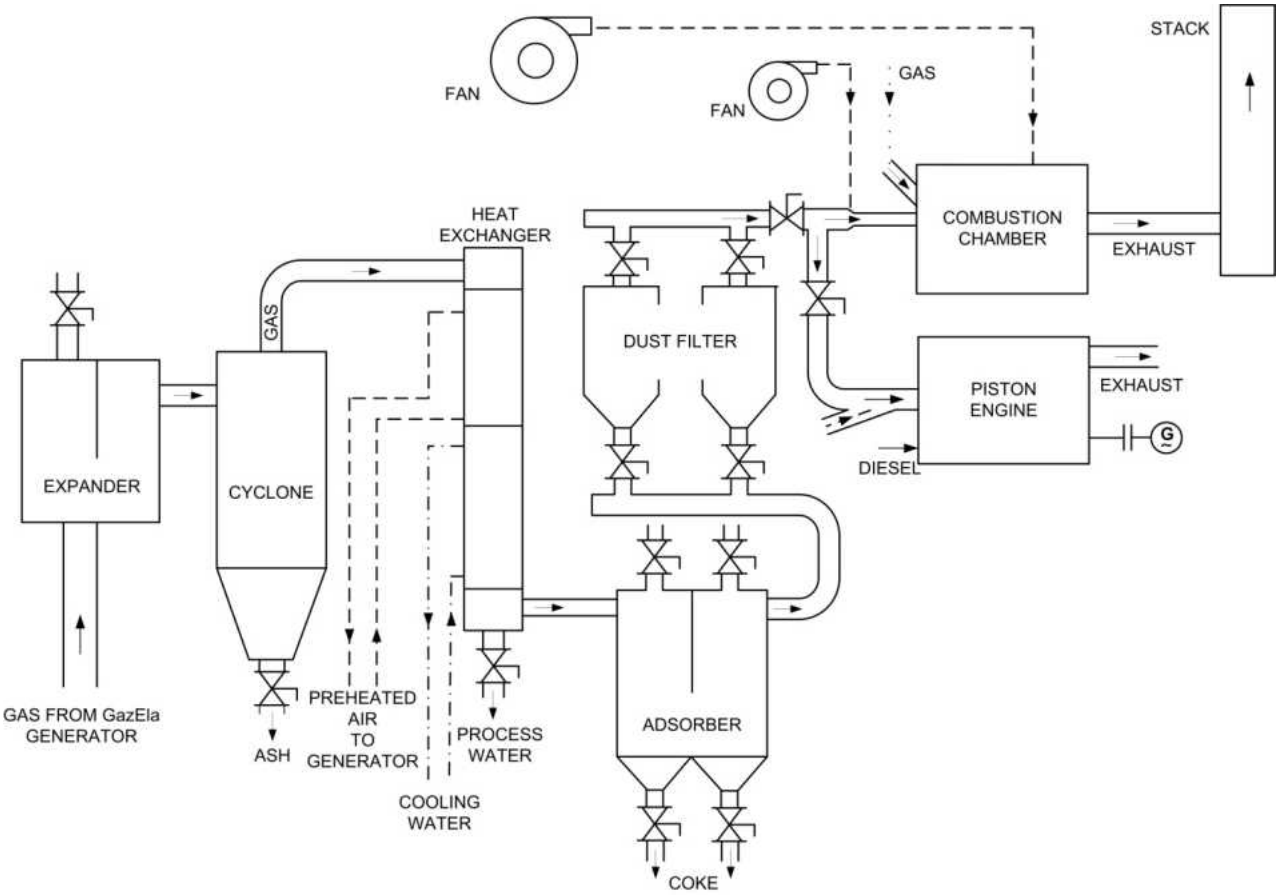

Fig. 2. Outline of the gas purification system integrated with a two-stroke piston engine

3. The influence of the type of biomass on the composition containing the gas

In the area of research the influence of the type of biomass used characterises the generator gas. A various range of tests were carried out. In order to conduct a deeper analysis four tests of biomass gasification were chosen and presented, which are briefly described in table 1. Both the parameters and the fuel used are further highlighted as being nominal for the GazEla generator in agreement with Test I.

Table 1. The main assumptions for four chosen tests

Test Designation	Fuel
Test I	Chips II
Test II	Pellets II
Test III	Pellets I
Test IV	Chips I

Fig. 3. Observations of the researched biomass

From among many groups available on the biomass market the following were chosen: wood chip pieces (Chips II) and wood fibres (Chips I), pellets made from wood waste (Pellets I) and wheat straw (Pellets II) - fig. 3. From among the four types of biomass used as fuel for the reactor, alder wood chips were chosen. In figure 4 there is shown the rate of progress of the main ingredients of processed gas during the gasification of alder chips. It has also be shown how it effects the dry gas.

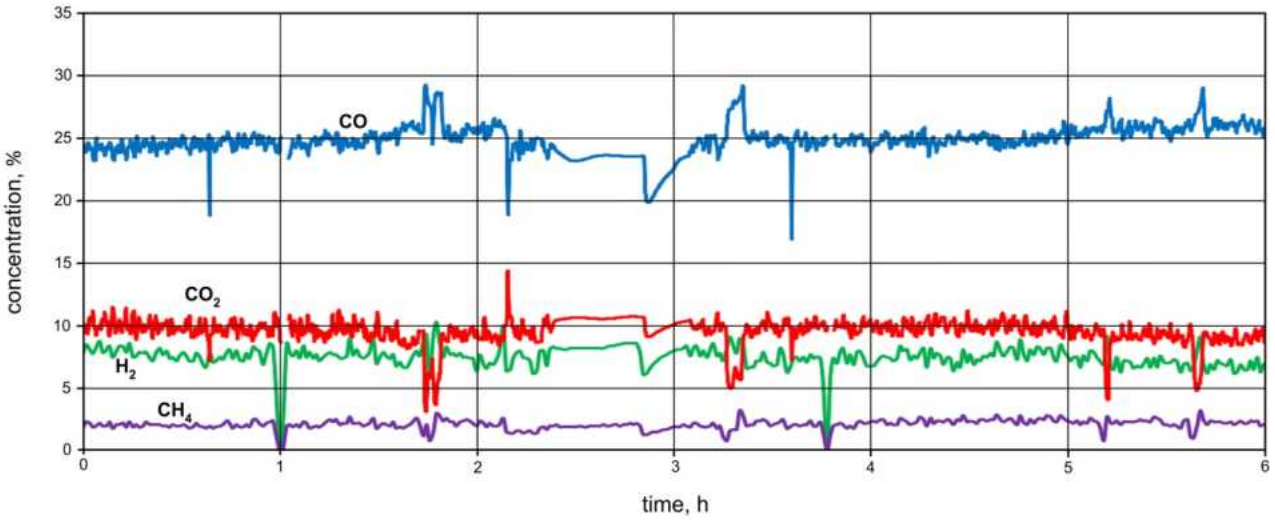

Fig. 4. The rate of progress of the main ingredients of processed gas for chips II - Test I

The rate of progress of the internal temperature of the reactor is shown in figure 5.

It is noticeable that there is greater intermittent fluctuation of the gas contribution brought out by the prescribed measurement of the fuel to the reactor and also a temporary growth in the governing pressure inside the generator. In figure 4 there appears less fluctuations during the depicted six

hours of work and this is a normal phenomenon for this type of equipment. A similar situation took place on the scale shown in figure 5.

During the test conducted with the generator, the flow of processed air was distributed to a particular zone of the equipment. The average value sum of three flows was approx. 21,6 m^3_n/h.

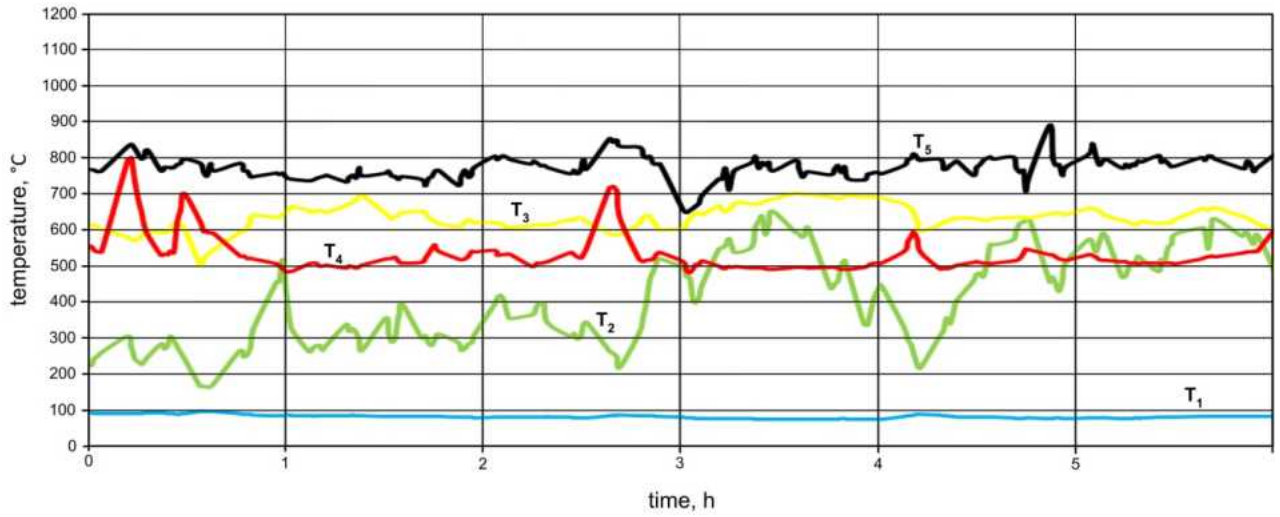

Fig. 5. The rate of temperature progress in the reactor - Test I

In table 2 there are given the average values of the contribution of dry gas from the analysis in figure 4. The values obtained are from these integrally measured temporal processes. For the introduced contribution of the gas, the fuel value is 4,72 MJ/m^3_n.

The average temperature in the gasification zone was approx. 784°C. An additional measured temperature in the combustion carbonised zone was at the level of 1134°C. This was the highest temperature within the reactor. On the other hand the observed average temperature of processed gas exiting the generator was 590°C.

The results shown in table 2, observed during the research of the installation, confirm the possibility of using these raw materials in the strengthening of biomass gasification systems.

Table 2 The change of the composition of processed gas depending on the type of biomass used

Type of gas	Unit	Chips II (Test I)	Chips I (Test IV)	Wood I pellets (Test III)	Straw II pellets (Test II)
H_2	%	7,5	6,1	6,7	8,9
CH_4	%	2,1	2,5	0,9	2,6
CO	%	25,0	19,5	22,0	20,3
CO_2	%	9,5	11,8	12,9	12,8
O_2	%	0,0	0,0	0,0	0,0
N_2	%	55,9	60,1	57,5	55,4
W_d	MJ/m^3_n	4,72	4,01	3,82	4,45

It is likewise important to notice that for some types of biomass it is essential to modify the manner of conducting the gasification process. This is particularly important in the case of straw, for which it was essential during the research to reduce the load in the combustion carbonised zone with the

aim of lowering the resulting high temperatures or the essential minimalising of the amount of remaining ash crust. The appearance of high temperatures in the deposit of fuel during the gasification tests of straw pellets led to the appearance of crusts in the lower parts of the system. This was particularly problematic in the exploitation of the system resulting in the appearance of slag. This appears in areas characterised by the highest temperatures, namely, in the area of the suction chamber and also in the grate. The next problem then was the exceeding of temperatures; softening; melting and the flow of slag, which confirmed the analysis conducted in the laboratory.

4. Purification of process gas

The research carried out during the realisation of the below-detailed work depended likewise on the choice of relevant processed parameters and the configuration of the system of drying purified gas with the aim of allowing the strengthening of the piston engine with processed gas.

The demands of the products of the new piston engines concerning the purification of gas strengthening the engine is respectively: 5 mg/m3n for ash contamination and 50 mg/m3n for organic contamination [2]. This, at the same time, particularly concerns modern solutions. The older constructions are characterised by a much larger "toleration" for contaminated fuel.

The main aim of this presented concept of a drying purifying system of gas is the reduction of ash contaminates to under 100 mg/m3n. In the case of organic contaminates it was assumed that most of their parts will be combusted in the engine and thus the use of this current-generating unit in research will not cause a problem. Presented above are the working assumptions, bearing in mind the possibilities of using gas in engines of older construction, which are not so rigorous concerning fuel purity and will thus result in a lessened performance.

The obtained average performance of the purifying process of gas for the last configuration of the purifying system from a pressure reducing valve, a cyclone dust - collector, a gas cooler, a coke adsorber and a dust filter was:

- gas contamination approx. 95% - from 1500 mg/m3n to 70 mg/m3n,
- organic contamination approx. 47% - from 3600 mg/m3n to 1900 mg/m3n.

The presented average value of the gas purification process obtained from contamination on the basis of the arithmetic amount of contamination from a few tests of biomass gasification.

5. Research of a biomass gasification system integrated with an internal combustion engine

In the field of research of biomass gasification systems with a GazEla gas generator, combustion tests of the production of processed gas have been conducted with a two-stroke piston engine. The directing of the amount of produced electrical power through the current-generating unit realised was with the assistance of a power collection system. This system consisted of an electric heater, which was cooled by an air flow. This amount from the heater forced the aggregate load of current-generation and in the process of this research variants of 8 and 15 kW_{el} were achieved.

The dimensions were measured during the tests of the combustion of processed gas in the unit of the engine to: electrical power created in the power-generating aggregate N_{el} and the flow of used diesel fuel $\dot{m}_{ol.}$. The quality and thickness of the diesel fuel were accepted on the basis of the data of the fuel products, which was respectively $W_{d\,ol.}$=43 MJ/kg and ρ=0,84 kg/dm^3.
The flow of damp processed gas was received on the basis of a primary estimated balance for gasification tests of alder chips, described in Test I. In agreement with calculation the flow $\dot{m}_{gazs}$

was at a of level 36,2 kg/h. The observed average value of fuel for the used dry gas was 3858,5 kJ/kg.

The performance of producing electrical energy was observed with the aim of grading the effects of the energy of the work of the system η_{el}.

In describing the performance of producing electrical energy in the research of the current-generating unit we may highlight it using the following contingents:

$$\eta_{el} = \frac{N_{el}}{\dot{E}_{ch}} \qquad (1)$$

where: N_{el} - created electrical power,

$\dot{E}_{ch}$ - the flow of the chemical energy of the fuel.

The exploitation research of the combustion of processed gas in a two-stroke piston engine conducted with three variants:
- **variant A** - The engine output on the basis of fuel (i.e. diesel fuel), and electrical power was level at 8 kW_{el},
- **variant B** - The engine output on the basis of a mixed substance consisting of diesel and processed gas of 8,3 kW_{el},
- **variant C** - The engine output on the basis of diesel and processed gas of 15,5 kW_{el}.

In variants B and C the directed flow of processed gas to the piston engine was always 100% of the value of the created flow in the gas generator (i.e. used permanent value of 42,45 kg/h)

During the work of the current-generating unit only on the basis of fuel (variant A) the contribution of diesel in the fuel used was 100%. The collected flow through the fuel engine was level at 4,05 l/h during the production of electrical power at a level of 8 kW_{el}. The temporary performance of the chosen system with contingents (1) was 16,54%, at the same time the value gained for the arranging of the angle of the injection for optimal fuel for the combustion process was a mix of processed gas and diesel. In the case of variant B the flow of diesel was level at 1,42 l/h, and the observed electrical performance was 15,62%. For nominal conditions of the work of the engine (variant C) with electric power at 15,5 kW_{el} the flow of diesel was formed at a level of 2,4 l/h. The performance of the creation of electrical energy in this case was 24,61%.

From the above results we may notice that the highest performance of the system is gained by the burning of a mixture of processed gas and diesel fuel with the dominating advantage being from the first of these ingredients and with nominal power from a current-generating unit.

6. Summary

The development of biomass gasification is currently possible depending on the solving of some key problems. These are connected with its technology. Among other things, the improvement of the gas generator reliability, the development of gas purification systems characterised by low levels of complication, connected directly with the lowering of investment costs and the exploitation of the installation. The level of gas purity, directly after the value of fuel, determines one of the fundamental parameters in deciding about the possibility of the further use of the gas process, e.g. in internal combustion engines. A vital aspect in the resolving of the above issues is experimental research conducted on the installations characterised by a semi-technical scale (exploitation) piloting and then a demonstration. Such research would permit the creation of a mature technological solution, which would then allow commercial application of the above-described technology.

During the development of the installation there were many hours of testing with the aim of controlling the output of the whole installation. Particular attention was given to the gas generator in order to achieve the output of the equipment without any difficulties. The value of fuel gained from the drying gas process with a GazEla generator contained in the compartment from 3,82 to 4,72 MJ/m^3_n which was appropriate to its value and which is presented with the assistance of national or international publications. For a wood chip composition of drying gas contained within the following ranges: H2=6,1÷7,5%, CH4=2,1÷2,5%, CO=19,5÷25,0%, CO2=9,5÷11,8%, N2=55,9÷60,1%. In the case of pellets being the main ingredients of gas, the results were respectively: H2=6,7÷8,9%, CH4=0,9÷2,6%, CO=20,3÷22,0%, CO2=12,8÷12,9%, N2=55,4÷57,5%. The change of the main ingredients of gas are not great and the acquired concentration process of the specific ingredients are stable. The nominal flow of added fuel to the testing reactor was measured at a level of approx. 14 ÷ 15 kg/h. The experimental generator is characterised by a power nominal of approx. 62 kW_t.

The presented development of the dry-purifying system of the gas process and also its final configuration allows for the achieving of an average performance of the removal of ash contamination of approx. 95%, and of organic contamination of approx. 47%. Further development of this installation will issue from the requirements of specific products of the internal-combustion engine.

Purified gas is used as a source of chemical energy in a two-stroke piston engine in the creation of electrical energy and also heated in the form of hot combustion gas. The flow of obtained electrical energy during the tests depended on the load of the system's collection of power, approx. 8,3 or 15,5 kW_{el}. This was adapted to the research of the engine, of which the basic fuel was diesel during the gas-burning process and liquid fuel was characterised by obtaining it in relation to a low performance in comparison with the present commercial solutions. The optimum achieved efficiency of created electrical energy for the nominal parameters of the engine output (i.e. for electrical power 15,5 kW_{el}) was approx. 24,6%. At the same time gas processes determined 61,8% of chemical energy fed into the engine, and diesel fuel 38,2%.

Acknowledgements

The strategic program of scientific research and experimental development of the National (Polish) Centre for Research and Development: „Advances Technologies for Energy Generation”; Task 4. „Elaboration of Integrated Technologies for the Production of Fuels and Energy from Biomass as well as from Agricultural and other Waste Materials’’.

References

[1] [1] Chmielniak T.: Role of different types of Technologies in achieving emission target up to 2050, Rynek Energii (Energy Market), 92 (2011), 3-9.

[2] [2] Chmielniak T., Skorek J., Kalina J., Lepszy S.: Integrated power systems with biomass gasification. Gliwice, 2008. Wydawnictwo Politechniki Śląskiej.

[3] [3] McKendry P.: Energy production from biomass (part 3): gasification technologies. Bioresource Technology, 83 (2002), 55-63.

[4] [4] Kirkels A.F, Verbong G.P.J.: Biomass gasification: Still promising? A 30-year global overview. Renewable and Sustainable Energy Reviews, 15 (2011), 471-481.

[5] [5] Najser J., Ochodek T., Chłond R.: Character of operations of the biomass gasification installation and economic aspects of electricity generation. Rynek Energii (Energy Market), 85 (2009), 68-74.

[6] [6] Plis P., Wilk K. R.: Theoretical and experimental investigation of biomass gasification process in a fixed bed gasifier , Energy, 36 (2010), 3838-3845.

[7] [7] Polish Patent application: P-383541 (2007).

[8] [8] Sobolewski A., Kotowicz J., Iluk T, Matuszek K.: Influence of biomass type on operating parameters of the gas generator with fixed bed, Rynek Energii (Energy Market), 82 (2009), 53-58.

[9] [9] Kotowicz J., Sobolewski A., Iluk T.: Parametric Analysis of Biomass Gasification Installation Integrated with a Combustion Engine, Proceedings of the 24rd International Conference ECOS 2011, 04-07th July 2011, Novi Sad, Serbia, s.3658-3667.

Start Up of a Pre-Industrial Scale Solid State Anaerobic Digestion Cell for the Co-Treatment of Animal and Agricultural Residues

Francesco Di Maria[a],Giovanni Gigliotti[b], Alessio Sordi[a], Caterina Micale[a], Luisa Massaccesi[b]

[a] *Dipartimento di Ingegneria Industriale, Perugia, Italy, fdm@unipg.it*
[b] *Dipartimento di Scienze Agrarie ed Ambientali, Perugia, Italy, gigliott@unipg.it*

Abstract:

A Pre-Industrial Scale Anaerobic Digestion Cell, working in batch mode in the Solid State (*i.e.* Total Solids content higher than 25% w/w) was built for the co-treatment of Animal and Agricultural Residues.
The anaerobic cell has a total volume of about 170m^3 and is able to treat about 95 tonnes of biomass per cycle. The aim is to perform the Anaerobic Digestion process with a high solids content to reduce, or completely eliminate, the waste liquid fraction usually produced by other types of Anaerobic Digestion technology. This could lead to the production of renewable electrical energy from animal manure and other agricultural residues in a more sustainable way.
The cell was built on an existing Italian farm that raises about 135 tonnes per year of live weight swine, and also produces other agricultural residues.
The problem of the starting the Anaerobic Digestion inside the cell without inoculum was analysed and different strategies were evaluated. The one based on aerobic pre-treatment of the mixture before the anaerobic process inside the cell seems to give interesting results both for the rapidity of starting the methanogens phase as well as for the quality of the biogas produced.
The results show that 15 days of aerobic pre-treatment led to the production of a biogas with a biomethane concentration of about 50%v/v after 10 days of anaerobic treatment. Further, the whole anaerobic process can be considered practically finished after about 65 days.

Keywords:

Agricultural Residues, Biogas, Renewable Energy, Solid State Anaerobic Digestion, Swine manure co-treatment

1. Introduction

The production of energy from renewable sources is one of the most crucial issues to be pursued in the EU [1], in order to achieve a more sustainable and environmentally sound development [2]. Among the different renewable sources, biogas, a biological gas rich in methane, is the one that gives a relevant contribution to the total energy demand of different European countries, and the one that shows a very high potential for growth in the near future [3]. Sources of biogas may be energy crops [4], [5], various biodegradable residues, livestock manure [6], [7] and the organic fraction of municipal solid waste [8], [9]. From the energy and ethical points of view, the most suitable sources are from waste and residues. In particular, the exploitation of livestock manure in Anaerobic Digestion (AD) facilities has a very high potential for spreading in the different countries of the EU 27. The most diffused AD technologies work with a TS content generally less than 15% w/w, causing the production of a large amount of digestate. This digestate has a high concentration of compounds with a high COD (Chemical Oxygen Demand) and N, together with other potentially polluting compounds such as P, S, Cu Zn and pathogens. Due to the high liquid phase in which these compounds are dissolved, they are a serious threat both for the ground and surface water as well as for the air (*i.e.* gaseous emissions) and for agricultural fields (*i.e.* heavy metal content). For

these reasons, the common practice of spreading livestock manure on agricultural fields is becoming more difficult, also as a consequence of the last EU Directive 91/676/CEE on water resource protection. A possible solution to the aforementioned problems could be the adoption of an AD process able to operate at a high TS content, to reduce the amount of the liquid fraction discharged by the process. The solid fraction arising from AD can be quite easily managed by aerobic stabilization, to obtain, at least, a high quality organic fertilizer, hence becoming a resource for the environment. This aim can be pursued by Solid State Anaerobic Digestion (SSAD), which is a batch static anaerobic digestion process [8], able to work with a TS content from 25% up to 50% w/w. The amount of liquid fraction discharged by this process is usually less than 10% w/w of the treated mass. Livestock manure generally have a low TS content, <15%w/w, not compatible for use in SSAD. Hence, to achieve a suitable moisture level, it is necessary to mix the manure with other materials that come from agricultural and pruning residues. For this reason a pre-industrial scale SSAD cell was built on an existing swine farm of about 135 tonnes/year of live weight swine. Before co-treatment in this SSAD cell, the manure produced by the swine was first mixed with other crop and trimming residues to reach a suitable moisture level. Another problem concerning the SSAD cell is the production of suitable inoculums to activate the process [10], [11]. In this study, the problem concerning the start-up of the SSAD cell and the amount and quality of the biogas able to be generated from the mixture produced on the farm was analysed both from the theoretical and experimental points of view.

2. System description and Methods

2.1. The existing farm

The farm analysed raises about 11,000 swine from 6 up to 25 kg, in about 6 cycles per year (Table 1). The manure production is on average about 0.075 litres per day per kg of live weight. The total daily manure production increases as the swine weight increases.

Table 1. Main features of swine rearing.

Parameter	*Value*	*Unit*
Swine per cycle	11,000	-
Swine initial weight	6	kg
Swine final weight	25	kg
Length of cycle	50+10	day
Manure production	0.075	litres/day per kg[(1)]

[(1)]kg of live weight.

Currently manure is managed by mixing it with other agricultural and trimming residues, to obtain a mixture with a TS content of about 20-25% w/w. Then the mixture is aerobically treated in a dedicated facility for the production of an organic fertilizer. The facility consists of a concrete trench in which moves a crane bridge with screws able to mix and aerate the mass under treatment (Fig. 1). At the end, the stabilized material is spread on fields for agricultural needs. All the agricultural and trimming residues, along with the swine manure, have a high BP that is currently completely unexploited. Hence they could be an important source of renewable energy for increasing the efficiency and environmental sustainability of the farm.

For this aim a pre-industrial scale cell able to perform the SSAD process was built and now it needs to be activated (Fig. 2). The total volume of the cell is about 170 m^3. This means that at full operating conditions it will be able to treat about 90 tonnes of biomass per cycle. For this reason the problem of generating a suitable amount of inoculum able to allow a rapid production of high methane rate is crucial. The correct inoculum is fundamental for making the process start in as short a time as possible, together with the production of a high-energy content biogas. Furthermore, the inoculum has to be generated by material that is produced on the farm and is classified as biomass.

Using inoculums from other AD facilities seems to be complicated and costly, considering that in the area there are no AD facilities operating by the SSAD process.

Fig. 1. Aerobic treatment facility.

Fig. 2. SSAD cell during construction.

2.2. Biomass characterization

Currently the management of swine manure requires mixing it with materials such as agricultural and trimming residues, coming from the area considered. Even if there are some changes at particular times of the year, the proportions used in the mixture should be more or less constant. For this reason characterization of the biomass was performed on the mean mixture, instead of analyzing the different substrates separately.

The TS were determined by measuring the weight loss, on a wet basis, of three different samples of the mixture before and after heating at 378.14 K for 24 h. The Volatile Solids (VS) content was determined by weight loss, by heating the TS samples obtained from the previous analysis at 823.14 K for 24 h. The Total Organic Carbon (TOC) content of the mixture was determined by the Springer and Klee wet dichromate oxidation method, while Total Nitrogen (TN) was obtained by the Kjeldahl method. Phosphorus assimilated was extracted with a 0.5 M $NaHCO_3$ solution at pH

8.5, followed by spectrophotometric detection. For heavy metals, samples were digested according to the US EPA 3050B method [12]. Heavy metal concentrations were determined by flame atomic absorption spectrophotometry using a Shimadzu AA-6800 apparatus.

2.3. Experimental tests

The experimental tests were performed by making a typical mixture using the three different types of biomass (Table 2) usually employed for the aerobic process, for achieving an adequate level of TS.

Table 2. Mixture characteristics.

Substrate	*Fraction*	*Unit*
Straw	7.10	% w/w
Trimmings	17.6	% w/w
Swine manure	75.3	% w/w

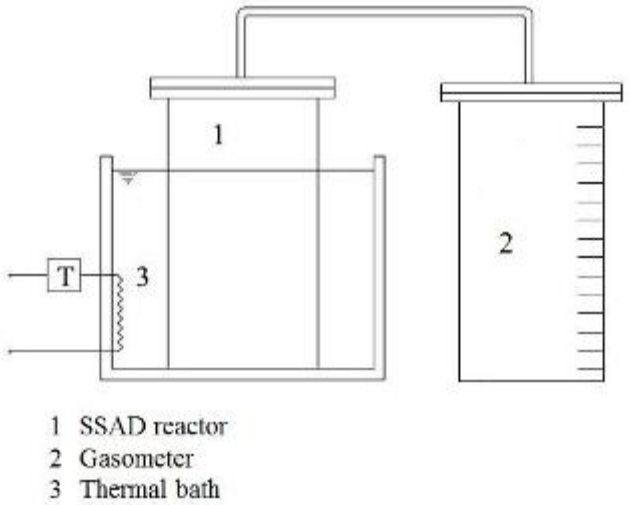

Fig. 3. Scheme of the experimental SSAD apparatus.

The mixture was treated aerobically from 0 to 15 days, and every three days a SSAD process was activated. The SSAD process was simulated in cylindrical, gastight reactors, of about 12 litres each, able to process about 5 kg of the mixture with no inoculum (Fig. 3). The SSAD process temperature was kept at mesophilic conditions (308±2°K) by the aid of a thermal bath. The biogas produced during the SSAD test was stored in a gasometer device for volume and composition determination. The CH_4 and CO_2 content (%v/v) of the biogas was determined by infrared sensors (±1%), whereas the H_2S and O_2 content (%v/v) was determined by electrochemical cell sensors (±2%). Other biogas components, such as ammonium, chlorine, and others, were included in a balance term.

The BP and BMP of the mixture were determined by a triplicate mesophilic test using a 10%TS mixture inoculated with cow manure digestate produced in mesophilic laboratory tests. A blank test was used to determine the contribution of the inoculum to the BP and BMP values.

3. Main preliminary results and discussion

The analyses performed on the mixture (Table 3) show that the moisture content was about 72%, with VS about 89% of the TS. The pH was slight acidic, whereas the C/N ratio was about 25, which is close to the optimal value of around 30-40.

The BP runs (Fig. 4) show a lag phase of about 20 days and a total biogas production of about 85 Nl/kg VS, calculated on the average of the three BP runs even if after about 120 days the runs had not yet finished. There was a similar trend for the biomethane production curve (Fig. 5) that reached a maximum value of about 55 Nl/kgVS, about 65% v/v of the entire biogas production. After about 130 days, the SSAD runs gave different results that were to some extent and in some cases greatly influenced by the duration of the aerobic pre-treatment (Fig. 6).

Table 3. Chemical and physical characterization of the mixture.

Parameter	*Value*	*Unit*
moisture	72.0	% w/w
VS	88.7	% TS
pH	6.56	-
EC	4.30	mS/cm
C	39.1	% TS
N	1.55	% TS

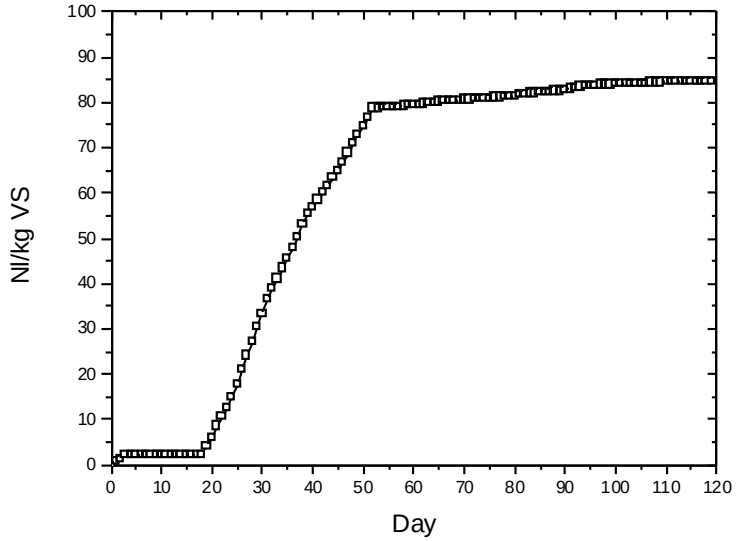

Fig. 4. Average BP curves for the three runs.

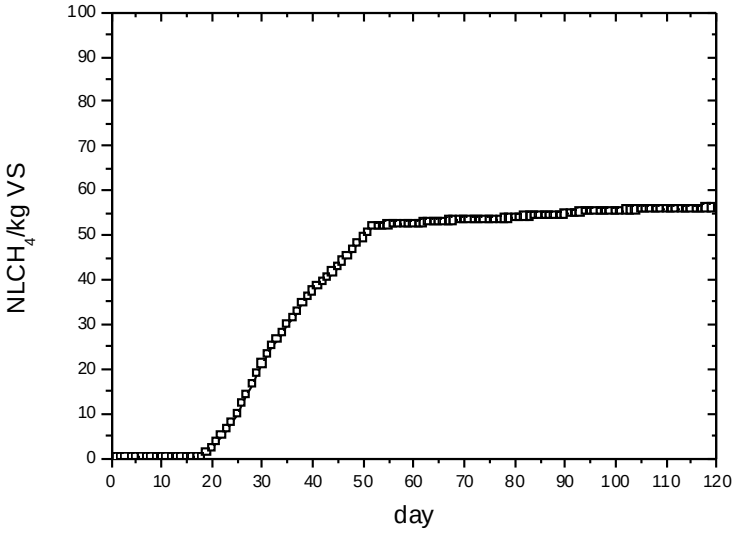

Fig. 5. Average BMP curves for the three runs.

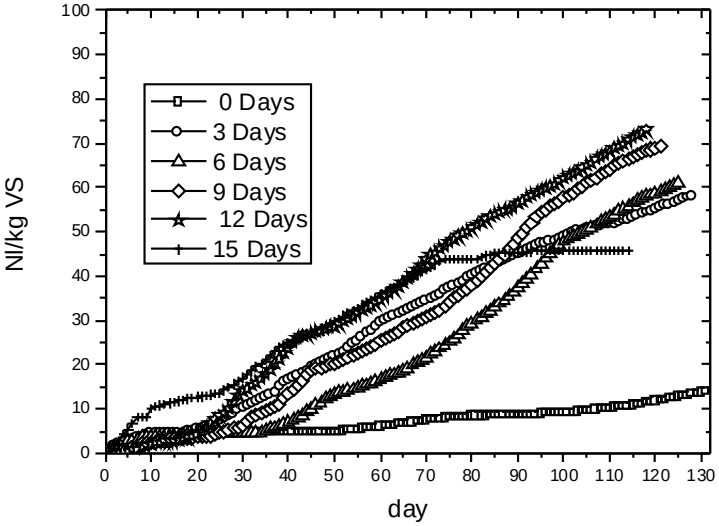

Fig. 6. Cumulative biogas production curve for SSAD runs.

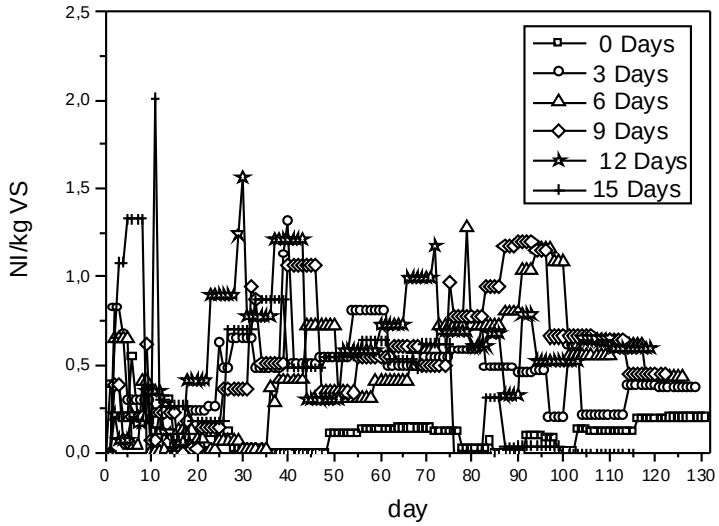

Fig.7. Daily biogas production curves for SSAD runs.

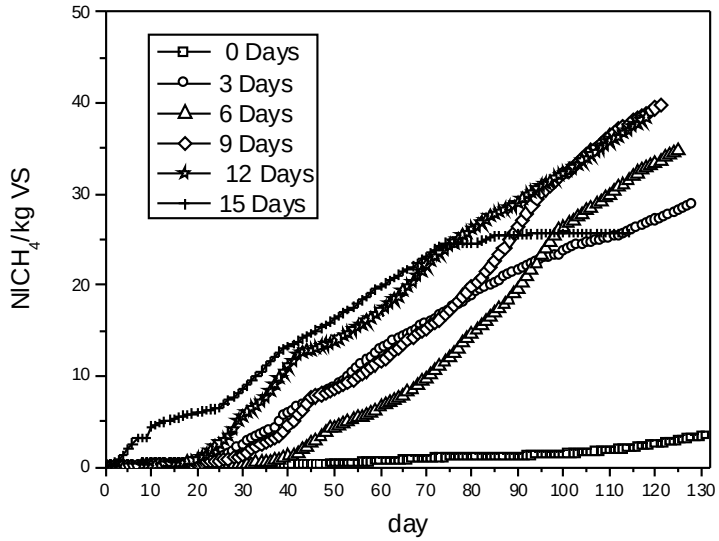

Fig. 8. Cumulative biomethane production curves for SSAD runs.

As expected the SSAD run of the sample with 0 days of pre-treatment had a very low biogas and biomethane production. This is a consequence of strong inhibition phenomena due to the high VS concentration causing an Organic Load of the process of about 280 gVS/kg. Hydrolysis and successive alcoholic fermentation cause a high production of volatile fatty acids, leading to an organic overload along with a reduction in pH. As a consequence the methanogens bacteria are greatly inhibited and biomethane production was practically null in the first 60 days of the process.

The runs on samples with longer pre-treatment times showed a higher production of biogas and biomethane. In particular, a longer aerobic pre-treatment is able to reduce inhibition during the methanogens phase, leading to a higher production of biogas and biomethane in the first days of the SSAD process (Figs. 7 and 8). The higher biomethane production also indicates that the methanogens bacteria were operating in rather favourable conditions. The sample with 15 days of pre-treatment was able to produce a biogas with a methane concentration of 50% v/v after about 10 days from the start of the process, whereas the other SSAD runs reached a comparable biomethane concentration after about 25 to 50 days from the start of the process. Further, the biomethane production phase of the sample with 15 days of pre-treatment can be considered practically finished after about 65 days from the start of the SSAD process. From that time, the resulting digestate could be used as inoculum for starting a new SSAD process.

4. Conclusion

The problem of the start up phase of the pre-industrial scale Solid State Anaerobic Digestion cell can be solved by the approach investigated in the present work. The mixture used gave a BP of about 85 Nl/kgVS and a BMP of about 55 Nl/kgVS. The aerobic pre-treatment gave a very positive effect on the anaerobic phase and in particular the methanogens phase, when operating with SSAD runs without inoculum. The longer is the aerobic pre-treatment time, the faster is the start of methanogens activity. After 130 days the sample with no aerobic pre-treatment gave a very low biogas production and almost no biomethane. For the samples with longer aerobic pre-treatment, both the biogas and biomethane production were quite high, from 45 to 70 Nl/kgVS and from 25 to 40 Nl/kgVS, respectively. Fifteen days of aerobic pre-treatment was the most suitable for use in starting up the SSAD process. In this case, the biomethane reaches a concentration of about 50%v/v in about 10 days and the anaerobic process can be considered concluded in about 65 days.

Acknowledgments

The authors would like to acknowledge the Agricultural Office of the Umbria Region for the economic support given for this study.

Nomenclature

AD	Anaerobic Digestion
BMP	BioMethane Potential (Nl/kgVS)
BP	Biogas Potential (Nl/kgVS)
C	Carbon
EC	Electrical Conductivity (mS/cm)
SSAD	Solid State Anaerobic Digestion
T	Temperature (K)
TS	Total Solids (%w/w)
VS	Volatile Solids (% TS)

References

[1] Directive 2001/77/CE of the European Parliament and of the Council of 27 September 2001 on the promotion of the electricity produced from renewable energy sources in the internal electricity market. Official Journal of the European Communities 27.10.2001.

[2] EUROPA- the official web site of the European Commission. Climate Action – Available at: < http://ec.europa.eu/clima/policies/package/index_en.htm>.[accessed 28.12.2011].

[3] Beurskens L.W.M., Hekkenberg M., Vethman P., ECN – Renewable Energy Projection as Published in the National Renewable Energy Action Plans of the European Members States – Available at: < http://www.ecn.nl/docs/library/report/2010/e10069.pdf>.[accessed 24.12.2011].

[4] Amon T., Amon B., Kryvoruchko V., Machmuller A., Hopfner-Sixt K., Bodiroza V., Hrbek R., Firedel J., Potsch E., Wagentristl H., Schreiner M., Zollotsch W., Methane production through anaerobic digestion of various energy crops grow in sustainable crop rotations. Bioresource Technology 2007; 98: 3204-3212.

[5] Murphy JD, Power N. Technical and economical analysis of biogas production in Ireland utilising three different crop rotations. Applied Energy 2009; 86: 25-36.

[6] Gebrezgabher S.A., Meuwissen M.P.M., Prins B.A.M., Lansink A.G.J.M.O., Economic analysis of anaerobic digestion – A case of Green power biogas plant in The Netherlands. NJAS Wageningen Journal of Life Sciences 2010; 57: 109-115.

[7] Di Maria F., Pavesi G., Leombruni S., Improvement of an existing anaerobic digestion plant: technical and economic analysis. ORBIT 2008: Proceeding of the 6th International Conference on Moving Organic Waste Recycling towards Resource Management and for the Bio-based Economy; 2008 October 13-15; Wageningen, The Netherlands.

[8] Di Maria F., Sordi A., Micale C., Energy production from mechanical biological treatment and composting plants exploiting solid anaerobic digestion batch: an Italian case study. Energy Conversion and Management 2012; 56: 112-120.

[9] Murphy J.D., McKeogh E., Technical, economic and environmental analysis of energy production from municipal solid waste. Renewable Energy 2004; 28: 1043-1057.

[10] Forster-Carneiro T., Perez M., Romero L.I., Sales D., Dry-thermophilic anaerobic digestion of organic fraction of the municipal solid waste: Focusing on the inoculum sources. Bioresource Technology 2007; 98: 3195-3203.

[11] Fdez-Guelfo L.A., Alvarez-Gallego C., Maruqez D.S., Romero Garcia L.I., Start-up of thermophilic-dry anaerobic digestion of OFMSW using adapted modified SEBAC inoculum. Bioresource Technology 2010; 101: 9031-9039.

[12] US EPA 3050 B (1996), Environmental Protection Agency.

The Role of Biomass in the Renewable Energy System

Ruben Laleman[a], Ludovico Balduccio[b], Johan Albrecht[c]

[a] *Ghent University, department of economics, Belgium, Ruben.Laleman@ugent.be*
[b] *Ghent University, department of economics, Belgium, Ludovico.Balduccio@ugent.be*
[c] *Ghent University, department of economics, Belgium, Johan.Albrecht@ugent.be*

Abstract:

Europe is striving for zero carbon electricity production by 2050 in order to avoid dangerous climate change. To meet this target a large variety of options is being explored. Biomass is such an option and should be given serious consideration. In this paper the potential role of biomass in a NW-European electricity mix is analyzed. The situation in NW-Europe is unique since it is a region which is a fore runner in renewable technology promotion but also an area with little sun, almost no potential for hydro and a lot of wind. This will result in a substantial need for non-intermittent low-carbon options such as biomass. The benefits and issues related to biomass are discussed in detail from both an environmental and an economic perspective. The former will focus on the life cycle of a biomass pellet supply chain, from the growth of the trees down to the burning of the pellets on site. The latter will provide detailed insights on the levelized cost of electricity for biomass and the role of biomass as a grid stabilizer in high intermittent scenarios. During the discussion, biomass will be compared to other competing electricity technologies to have a full understanding of its advantages and drawbacks. We find that biomass can play a very important role in the future low carbon electricity mix, the main bottleneck being the supply of large amounts of sustainably produced feedstock.

Keywords:
Biomass, Renewable Energy, Sustainability, Economics, Learning Rate.

1. Introduction

Biomass as a renewable energy source has been used by humans for many centuries. Today, it is still a very important source of energy in developing countries. In 2011, biomass had a share of about 10% in global energy demand, however, only a small amount of biomass is used for electricity production. Globally, about 62 GW of biomass power capacity was estimated to be installed by the end of 2010. This is slightly higher than the installed capacity of PV, but significantly smaller compared to global wind capacity (1). In the EU-27, biomass has been used for energy purposes for a long time, mainly by Scandinavian countries. Today, Sweden and Finland together account for 18.4 TWh of electricity production from solid biomass, namely 30% of the total EU-27 solid biomass electricity production. This is almost entirely due to the use of CHP plants (17.5 TWh)(2). Similarly, other countries are now looking at biomass technology too, in order to reach their renewable energy targets imposed by the European commission (3). Especially countries like Belgium, the Netherlands, Germany and the U.K. are trying to tap into this energy source for renewable electricity production. Together, these four countries produced 21.1 TWh of electricity from solid biomass in 2009, which is about 34% of the total amount of solid biomass electricity production in the EU (2). Unlike the Scandinavian countries, NW-European (NW-E) member states mainly use biomass for “electricity-only” purposes (15 TWh), in increasingly larger power plants.

Despite the growing interest by governments to use biomass for electricity production in large scale power plants, the scientific world has not focused much on this subject. Most literature is targeting biomass use for transport (4-6). Authors that did focus on the use of biomass for electricity

production have often only considered small scale installations, mainly CHP (7-9), which is not so common in NW-E. Furthermore, most papers limit the analysis to the environmental implications of biomass use (5, 10, 11), and neglect economic aspects.

This paper aims to assess the potential role of large scale biomass pellet power plants in NW-E from an environmental and economic perspective. The environmental assessment is based on the Life Cycle Assessment (LCA) methodology. For the economic analysis, the Levelized Cost of Electricity (LCOE) methodology is applied to evaluate the cost competitiveness of the technology. Finally, the potential of biomass electricity as a backup for variable renewables in the electricity mix is studied.

Most of the data, such as energy prices and investment costs, on which the assessments in this study are based, were obtained from a combination of a vast literature review and long discussions with the industry. In the first part of this paper, the environmental impact of biomass use will be discussed. The second part will consist of the economic analysis. We will conclude with an overall discussion on the implications of increasing the role of large scale biomass in the future electricity mix in NW-E. Even though this study is focusing on NW-E, the findings can be interesting for policymakers, energy companies and investors worldwide.

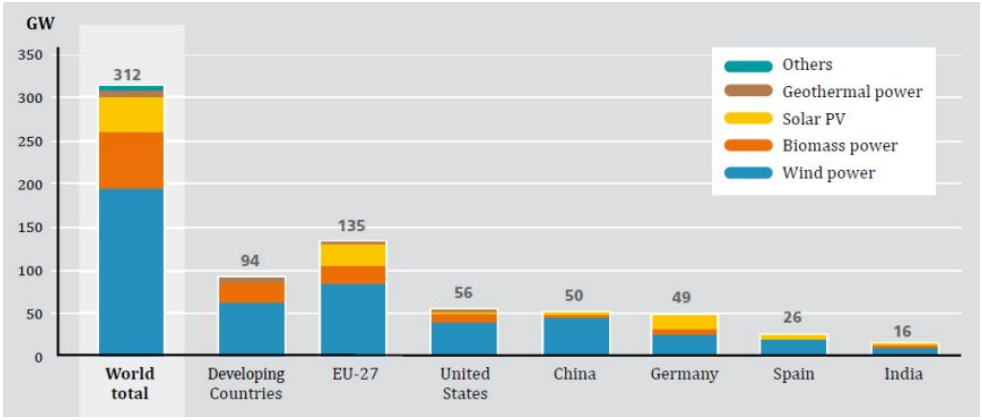

Figure 1: Renewable capacity; globally, in developing countries, the EU-27 and top 5 regions (1)

2. Environmental analysis

2.1. Introduction

A life cycle assessment (LCA) is considered to be the most comprehensive and credible method to evaluate the environmental impact of a good or service. In an LCA the whole lifecycle of a technology is considered. Many scientists have used the LCA methodology to evaluate the environmental impact of renewable and non-renewable energy technologies (5, 12-17). The lifecycle of an energy technology typically consists of construction, fuel use, operation and maintenance (O&M) and decommissioning. Various perspectives such as land use change, water use, mineral extraction, energy use and human health can be included in an LCA (18). However, due to increasing concerns about climate change, current research is mainly focusing on greenhouse gas (GHG) emissions (17, 19-21).

Recently, biomass has received a lot of attention and is widely considered to be an essential part of the sustainable or “green” economy (22, 23). This growing interest is unfortunately matched by a rise in criticism. The impact of the development of a bio-based economy on the environment in general, and on land use and food prices in particular is causing great concern (24). This resulted in an abundance of studies that have primarily shown that the afore-mentioned issues are complex and the sustainability of biomass strongly depends on specific circumstances (5, 14, 18).

The debate on the merits and problems surrounding biomass benefits from improved knowledge on the life cycle of biomass in the green economy. LCAs can provide important insights in the

environmental impact of a biomass energy chain and help locate the most critical steps in that chain. This information should help developers and policymakers to increase the sustainability of biomass production and its use, and to possibly overcome some of the current issues. This study will focus specifically on the life cycle of large scale (> 300MW) biomass power plants in NW-Europe using Canadian wood pellets.

2.2. Methods

The environmental impact of biomass usage for energy purposes has been studied extensively. Unfortunately, assumptions regarding type of biomass, land use change, fertilizer usage, pesticide usage, transport and final combustion technology vary immensely (18). It is thus difficult to find studies that focus specifically on the life cycle of large scale combustion plants using pellets. In fact, only one such paper was found in the literature (25). The main steps of the biomass life cycle are shown in Figure 1. Each of these steps will be described in more detail below (see next paragraph "The NWE Case").

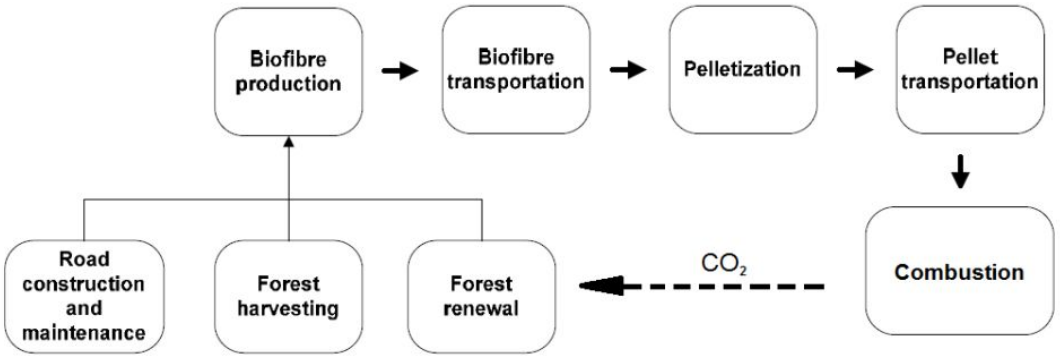

Figure 2: Boundaries of the large scale biomass lifecycle (based on Zhang et al. 2010)

An assumption which is crucial for this LCA is that the wood from Canadian forests is sustainably grown which allows us to state that the emission of GHGs at the plant site are balanced by the uptake of GHGs in the growth phase of the biomass. In other words, the net GHG emissions are considered to be equal to zero. We chose not to consider the possible effects of biomass production on land use or on carbon stocks, even though these two aspects could have a very big influence (14, 18, 26, 27). It is therefore important to note that if the sustainability assumption does not hold, the results presented below will not be valid. If not sustainably produced, the use of biomass is neither environmentally nor socially desirable.

2.2.1. The NW-European Case

In order to fit with a NW-European situation, we adapted the data from the literature (25). To this end, we split up the biomass pellets production chain into four phases:

1. Harvest and pellet production in Canada
2. Transport from pellet plant to harbour in Canada
3. Transport from harbour in Canada to a harbour in NW-Europe
4. Burning of pellets in a NW-European biomass plant

GHG and NOx emissions were calculated in every phase and adapted to the NW-European situation if needed. The harvest and pellet production phase were assumed to be similar. Also, the transport distance from pellet plant to harbour is likely to be in the same range as the transport distance from the pellet plant to a power plant (+/- 1000 km by train or boat, comparable to the 750 km by train estimated by industry). In other words, we made no changes in phases one and two, but, from the third phase onwards, the data was adapted. In phase three, the emissions during transport from Canada to NW-Europe were calculated for a distance of 3500 miles (+/- 6000 km). GHG and NOx emissions due to this transport are considered to be around 5.89-12.5 g/(ton*mile) and 0.22-0.36

g/(ton∗mile) respectively (21, 28). Finally, in phase four, NOx emissions from the NW-E power plant were estimated to be equal to the European limit for new large scale biomass power plants (>300 MW), namely150 mg/Nm³ at 6% O_2, or 0.55 g/kWh (29). The GHG emissions on site are considered to be compensated by the growth of new biomass, and thus they were assumed to be zero.

2.3. Results and Discussion

2.3.1. Biomass plants in NW-Europe

The results in Figure 3 show that total life cycle GHG and NOx emissions for a NW-E biomass pellet plant are estimated to be 109.5 and 1.6 g/kWh respectively. Focusing on GHG emissions, we find that the majority is released during the growth, harvest and pellet production phase in Canada. GHG emissions related to Canada/NW-E sea transport are relatively low. As mentioned above, GHG emissions on site are assumed to be equal to zero. Unsustainable forestry practices could however result in GHG emissions exceeding 300 g/kWh (18).

For NOx emissions, things are very different. These are emitted in every step of the production chain, in relatively equal amounts. Pellet production accounts for 32% of the total NOx emission, sea transport for 33% and on site emissions account for the remaining 35%. Be aware that NOx emissions on site are assumed to be equal to the European emission limit value (0.55 g/kWh). Since this is a legal upper limit, it is very likely that these emissions will be lower in practice. One should also keep in mind that individual member states, or regions, can have lower emission standards than those imposed by the EU. In Flanders, for example, the NOx norm for large scale biomass plants is 90 mg/m³ at 6% O_2, or 0.33 g/kWh. In other words, a Flemish biomass power plant would have NOx combustion emissions below 0.33 g/kWh. Therefore, the NOx emissions presented here are considered to be an upper limit for NW-Europe.

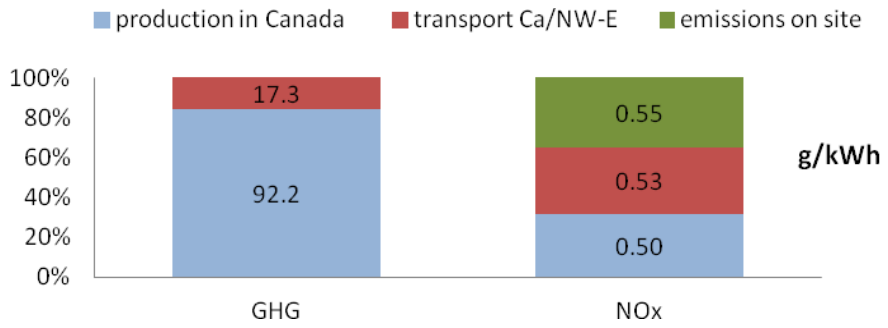

Figure 3: Estimated GHG and NOx emissions for a NW-E biomass plant fired with Canadian pellets (calculations based on (21, 25, 28, 29))

2.3.2. Literature review

The results in Table 1 present recent findings in LCA literature. The data contains a mix of both old and new technologies currently used in developed countries (EU, N-America). The "NW-E biomass plant" case is, however, an exception as this refers to a specific type of biomass power plant, subject to European NOx emission laws. In other words, the table indicates how GHG and NOx emissions of a new biomass power plant (including the biomass life cycle) differ from average power plants and other energy technologies currently in operation.

2.3.2.1 Combustion emissions

The GHG combustion emissions from an average gas fired power plant and coal plant are around 400 and 950 gCO_2-eq/kWh respectively, which is much higher than biomass combustion emissions, since the latter are assumed to be zero. Focusing on NOx, we find that the NW-E biomass plants have NOx emissions of only (maximum) 554 mg/kWh, which is considerably lower than emissions coming from average coal or gas fired power plants. However, new coal plants in the EU will also

be subjected to the EU norm of 150 mg/Nm³ at 6% O_2, gas plants will even have lower norms (100 mg/Nm³ at 6% O_2).

2.3.2.2 Life cycle emissions

For gas and coal, lifecycle GHG and NOx emissions are similar to combustion emissions[1] (Table 1). In the case of biomass this is quite different; life cycle emissions for biomass are markedly higher than combustion emissions. Nevertheless, over the whole lifecycle, biomass power plants emit less GHG compared to coal and gas. For life cycle NOx emissions, biomass is similar to gas, but much lower than coal.

The last row of Table 1 shows the estimated results for a future coal powered plant (2025) with CCS technology. According to the literature (21), current biomass technology emits less GHGs than possible future CCS technology, while NOx emissions are similar. However, by 2025, better NOx removal technology could be in place for biomass too, which is likely to result in NOx emissions lower than coal + CCS.

Compared to PV technology, biomass emits similar amounts of GHGs over its lifecycle, although the NOx emissions of PV-systems are significantly lower. Overall, wind onshore and offshore emit the lowest amount of polluting substances during the entire life cycle of all the energy technologies considered here.

Table 1: Combustion and LCA emissions for GHG and NOx of various energy technologies (5, 10, 17, 18, 21, 25, 30-37)

Combustion emissions

		GHG (g/kWh)			NOx (mg/kWh)		
		min	average	max	min	average	max
100% biomass	*New >300 MW (NW-E)*		*0*			*554*	
Gas		318	454	636	54	1208	2361
Coal	no CCS (today)	780	953	1044	1162	2642	4122

Life Cycle emissions

		GHG (g/kWh)			NOx (mg/kWh)		
		min	average	max	min	average	max
100% biomass	Mixed types	2	66	122	781	923	1064
	Canada pellets		92			1000	
	New >300 MW (NW-E)	*103*	*110*	*116*	*1473*	*1587*	*1702*
PV		50	99	160		340	
Wind	onshore	4	17	40		31	
	offshore	9	13	17		21	
Gas		360	466	720	77	1782	4268
Coal	no CCS (today)	800	1024	1800	1285	2842	4399
	with CCS (2025)	130	190	280	863	1251	1639

2.3.2.3 Particulate Matter

The emission of fine dust particles (particulate matter or PM) is an important issue from a human health perspective, which is, unfortunately, not well documented in LCA literature. A recent report by Greenpeace (2011) indicated that PM combustion emissions from biomass power plants (560 mg/kWh) are higher than PM released by fossil-based technologies, such as coal, gas or oil. However, it is important to keep in mind that their data are only valid for small scale biomass power

[1] For LNG gas this is different, since a lot of energy is needed for compression/transport/decompression

plants (<70 MW), which typically use relatively inefficient flue gas filtering technologies. These emissions can be reduced drastically by using the most advanced equipment.

The upper limit of dust combustion emissions for large scale biomass plants in Europe can be calculated starting from the legal PM-emission limit which is 20 mg dust/Nm³ at 6% of O_2, or about 67 mg/kWh (29). This is considerably lower than the emissions mentioned in the Greenpeace report. Furthermore, since 20 mg dust/Nm³ at 6% of O_2 is the legal limit in the EU, we can safely state that in practice emissions are likely to be lower than 67 mg/kWh. However, over the whole lifecycle the dust emissions will be higher, especially due to transport by truck and ship.

2.4. Conclusions

In general, considering GHG and NOx emissions, biomass is more environmentally friendly than coal or gas. However, this statement is only valid if the biomass is produced sustainably. If this is not the case, GHG and NOx emissions can be much higher than presented here. When compared to other renewables, biomass appears to have a relatively high impact on the environment. The life cycle GHG emissions of biomass are comparable to those of PV systems but about a tenfold higher than the amount of GHGs emitted when using wind energy. The results for NOx are even worse, with biomass releasing roughly five times as much as PV and 50 times more than wind. However, some issues should be kept in mind. Firstly, the environmental impact of biomass could decrease if power plants became more efficient or transport was organized in a more sustainable way. Secondly, comparing biomass to intermittent renewables is not really fair, since the latter will not be able to achieve high penetration as long as cheap storage technology is unavailable. Biomass LCAs should be considered from a holistic, system wide perspective. Unfortunately, this is far from easy since the specific properties of the electricity infrastructure need to be taken into account.

Finally, it should be stressed that the scope of this study is rather limited. Other important aspects of the environmental impact of the power technologies would also be interesting to compare. Data on life cycle particulate matter emissions, fossil fuel depletion or energy efficiency would result in a broader understanding of the environmental impact of biomass electricity production. Unfortunately, data on these issues is currently not available for large scale biomass power plants. Further research is necessary to have a better understanding of all the steps in the whole lifecycle and how these affect the environment.

3. Economic analysis

When comparing energy technologies many criteria need to be considered. For example, the type of demand for which new capacity is needed – base, intermediate or peaking load – will determine the most economically effective technology to supply electricity. Electricity might be a standardized commodity, behind it lays a segmented supply side, with each segment functioning on different economic parameters. Due to the expected growth of intermittent generation, the boundaries between the different demand types will become less explicit in the coming years and many assets will have multiple load purposes (even during one single day).

3.1. Levelized Cost of Electricity (LCOE)

3.1.1 Introduction

The LCOE (levelized cost of electricity) methodology is an interesting tool to compare the cost of producing a unit of electricity with various technologies. According to the International Energy Agency “LCOE remains the most transparent consensus measure of generation costs and remains a widely used tool for comparing the costs of different power generation technologies in modelling and policy discussions” (38). The levelized cost of electricity (LCOE) represents the present value of the total costs of building and operating a generation plant or a generation asset over its financial life. In principle, the LCOE is calculated for *new* generation assets. As a consequence, the

production cost per MWh of *existing* assets should not be compared to LCOE results, as the investment cost per MWh is not included.

However, the LCOE methodology has some limitations; as it does not evaluate the aspect of risk, which is very important when taking investment decisions, in addition, it looks at the different technologies from a "stand alone" perspective. The LCOE is calculated at the plant level and excludes system costs and system externalities. The latter factor is a major issue for variable (non-dispatchable) renewable energy technologies (38) because demand and supply need to be balanced literally every second. Basically, direct system costs should be added to the plant-level LCOE of all technologies but this proves to be very challenging. In order to overcome this issue, a broader, system-wide, economic assessment will complement the LCOE analysis (see section 3.2).

Finally, the LCOE should be interpreted as a social cost or the cost for society of building and operating the generation plants. The financial impact of taxes, subsidies, portfolio standards or other incentive schemes is therefore not considered. In this section, eight technologies will be compared: 100% biomass using pellets, biomass co-firing (50% co-firing, see Appendix A), PV, wind onshore, wind offshore, coal, nuclear and gas.

3.1.2. Methodology

3.1.2.1. LCOE calculation

The LCOE takes into account the annualized investment cost, the operation and maintenance (O&M) cost, fuel cost and carbon cost:

$$LCOE = I + O\&M + F + C \quad (1)$$

With I = annualised investment cost [EUR/MWh]
O & M = operation and maintenance cost [EUR/MWh]
F = fuel cost [EUR/MWh]
C = carbon cost [EUR/MWh]

And

$$I = Itot / \left(AF_i^n \cdot FLEOH \right) \quad (2)$$

With Itot = total investment cost/MW [EUR/MW]
AF_i^n = annuity factor
FLEOH = full load equivalent operating hours [h]

The annuity factor for a given lifetime and discount rate has been calculated as follows[2]:

$$AF_i^n = \left[1 - (1+i)^{-n} \right] / i \quad (3)$$

With n = lifetime
i = discount rate

The assumptions regarding fuel cost, lifetime and O&M costs are based on data found in the literature and discussions with the industry. They can be found in Appendix A.

Essential for estimating the full load equivalent operating hours (FLEOH) is the load factor (LF). This indicates the percentage of time that a technology produces electricity at maximal capacity. It shows how much electricity can be produced with an installation of a certain capacity in one year.

[2] Annuity factor is commonly used to calculate the present value of future series of cash flows (Richard et al, Quantitative Investment Analysis, 2007).

$$LF = \frac{FLEOH}{24h \cdot 365d} \quad (4)$$

With LF = load factor [%]
FLEOH = full load equivalent operating hours [h]

Unlike fossil fuelled technologies, renewable intermittent technologies such as wind and PV have the disadvantage of only producing electricity when the weather is favorable. Luckily, the NW-E region is blessed with respect to wind, having relatively high average annual wind speeds compared to the rest of Europe. Onshore wind turbines operate at full load for about 2200 hours annually (39), which is equal to a load factor of about 25% (2200/24/365 = 25%), offshore wind turbines have higher load factor (35%). For PV, on the other hand, NW-E is not a favorable region. In fact, the LF for PV decreases with declining yearly average solar irradiation. A PV system in London, for example, produces roughly half the amount of electricity compared to a PV system in Malta, for a given capacity (30). Therefore, the LF for a PV system in NW-E is very low (12%). By contrast, the load factor of fossil fuelled power plants is much higher. In this study, the 2012 LFs were estimated to be 85%, 75% and 60% respectively for nuclear, coal and gas.

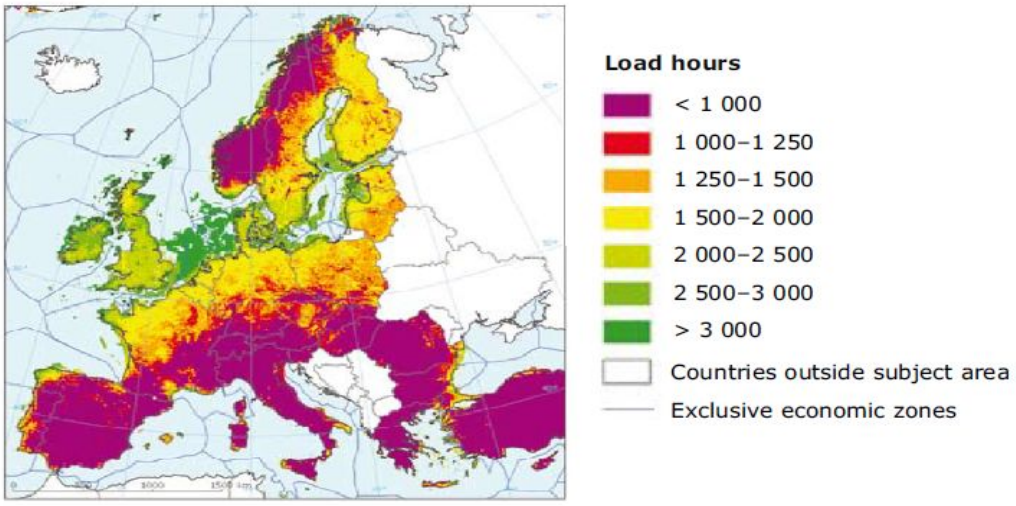

Figure 4: Full load hours for wind turbines in Europe (39)

3.1.2.2 Learning Rate

The economic theory of learning rates (LRs) (40-46) states that due to learning effects the cost of a specific technology will decrease as cumulative production increases according to the following mathematical relationship (based on (47) and (48)):

$$I_t = I_0 \cdot CC^a \quad (5)$$

With I_t = investment cost at time t [EUR/MW]
I_0 = cost of the first unit produced (theoretically) [EUR/MW]
CC = cumulative capacity [MW]
a = learning elasticity

From this the learning rate can be calculated as follows:

$$PR = 2^a \ \ and \ \ 1 - LR = PR \ \ \ thus \ \ LR = 1 - 2^a \quad (6)$$

With LR = learning rate
PR = progress ratio

This formula indicates how the cost will decrease with each doubling of production. For example, if the LR for a given technology is 20% and the installed capacity is 1 GW, the costs are assumed to be 20% lower when capacity has reached 2 GW. The LRs for the various technologies were found in the literature. More information is available in Appendix A.

Although a broad literature on technology learning exists, there is no consensus on the typical and prospective learning rates for the considered generation technologies. However, the learning rates presented here are in line with the literature (49). To address the uncertainty in estimating learning rates, a sensitivity analysis was carried out to illustrate the impact of changes in learning rates.

3.1.2.3. Discount rate

The discount rate reflects the return on capital for an investor in the absence of specific market or technology risks. In the energy sector, relatively high discount rates can be expected due to the uncertain market environment of today with the ongoing liberalization, multiple CO_2 policies, subsidies for new technologies (such as offshore wind and CCS) and the challenge of integrating a growing share of intermittent generation. Furthermore, LCOE methodology assumes a single set of future fuel prices but mostly neglects the impact of higher fuel prices and investment costs (e.g. steel and concrete prices should follow fuel prices). In our calculations, a 10% discount rate was used. This is complemented by a sensitivity analysis with discount rates of 7% and 13%.

3.1.2.4. Fuel and CO_2 prices

The cost evolution of pellets (in bulk) between now and 2030 is probably the most difficult parameter to project. In order to cope with this problem, three pellet price scenarios were evaluated. Next to a standard scenario, with the price of biomass pellets rising at a rate of 1% each year, two other scenarios were added: an optimistic and a pessimistic scenario. In the optimistic scenario, the supply is assumed to be able to keep up with demand and due to improved logistics and better technologies, this would result in a stable pellet price (73 €/MWh), from now to 2030. In the pessimistic case, the supply will have a hard time to keep up with a very sharp increase in pellet demand, resulting in a doubling of the pellet price by 2030. Not surprisingly, the pellet price will have a major impact on the LCOE of a biomass produced MWh of electricity.

Regarding fossil-based technologies, the price of gas and coal is likely to rise with time. Also the CO_2 price is likely to increase between now and 2030. The estimated gas and coal fuel costs were calculated based on the averages of the recent price trends. Biomass pellets costs for 2012 were estimated based on recent literature. However, all the fuels cost estimates have been adapted after discussion with the energy industry. Information on these assumptions can be found in Appendix B.

3.1.3. Results and discussion

The LCOE for the generation technologies between 2011 and 2030 was estimated based on the assumptions found in Appendices A and B. For simplicity the learning rates were kept constant over the period 2011-2030.

3.1.3.1. Standard Scenario

Figure 5 shows the evolution of the LCOE for new generation investments between 2011 and 2030 upon the condition that the load factors in Appendix A are kept stable over the period. Since we assume that fuel costs will increase in the next decades the LCOE of generation technologies depending on fuels (gas, coal, biomass) will increase, with the exception of nuclear for which the fuel cost remains constant along the period. Only the intermittent – fuel free – generation technologies benefit from decreasing investment costs, due to the learning effect. Wind and PV will experience significant LCOE reductions. However, keep in mind that the price of steel and other constructing materials might mitigate the learning effect under certain circumstances and hence reduce the gap between fuel-based technologies and steel-intensive assets.

As illustrated in Figure 5, the LCOE of PV electricity significantly exceeds the cost of other generation technologies. However, by 2030 PV should be close to 120 €/MWh and able to compete

with coal, gas and biomass technologies. Keep in mind that we have assumed low irradiation and very conservative learning rates.

In order to provide a better picture of the LCOE for the other technologies, next to Figure 5, we present Figure 6, which is the same figure with the exclusion of PV.

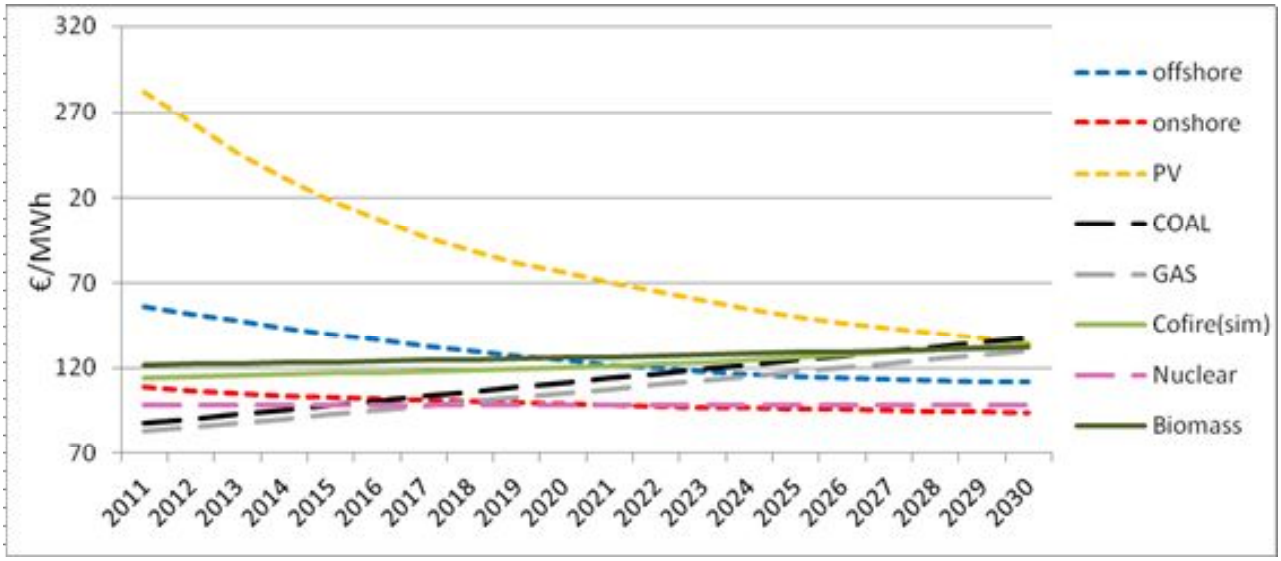

Figure 5: LCOE of new generation assets – standard pellet price scenario

Figure 6 clearly shows that the cost gap between biomass and fossil-based technologies is high in 2012 but declines with time. At the end of the period, the LCOE of biomass is similar to the LCOE of coal and gas. The cost gap between 100% biomass and co-firing is small and decreases over time; by 2030 the LCOE of these technologies is about 132 €/MWh.

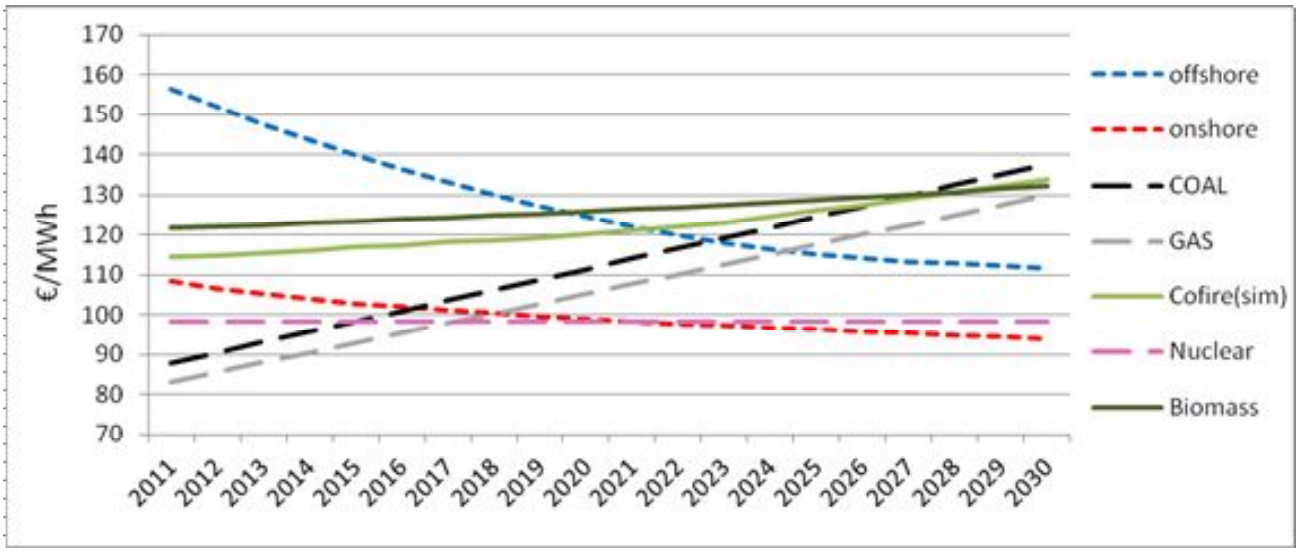

Figure 6: LCOE of new generation assets (PV excluded) – standard pellet price scenario

Since nuclear does not emit CO_2 and uranium prices were assumed to be constant, the cost of nuclear does not evolve in the selected time span, making it one of the cheapest technologies from 2017 onwards. However, from 2022 onwards, the LCOE of wind onshore is lower than the LCOE of nuclear, thus becoming the cheapest technology. Despite having higher investment and maintenance costs, offshore wind benefits from higher load factors than onshore wind (39), also, in this analysis, offshore benefits from the relatively high growth in installed capacity between 2012 and 2030, therefore, due to the bigger learning effect its cost will decrease more than onshore wind.

3.1.3.2. Pessimistic Scenario

Figure 7 presents the results under the assumption that biomass pellet prices double between 2011 and 2030. In this scenario, the LCOE of biomass technologies always exceeds the LCOE of all the non-intermittent technologies.

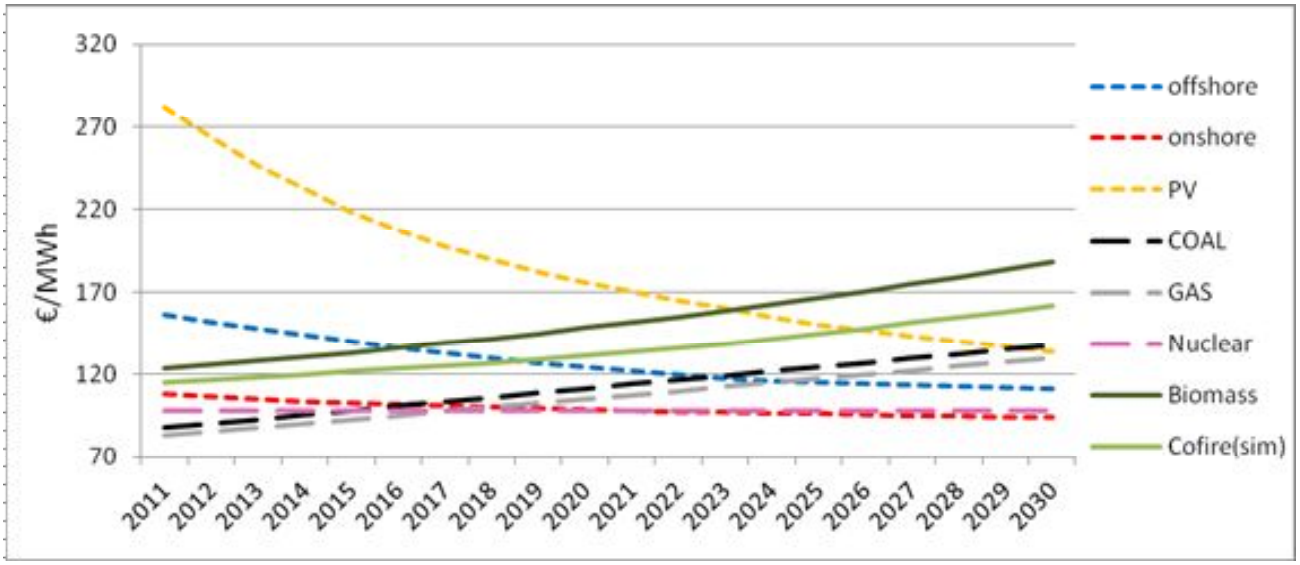

Figure 7: LCOE of new generation assets – pessimistic pellet price scenario

Assuming high pellet prices, the LCOE of the biomass co-firing plant is below the LCOE of the dedicated biomass plant over the whole period, furthermore, the cost gap increases with time, in contrast to the standard pellet price scenario. By 2030, the LCOE of biomass is some 90% higher than the LCOE of wind and nuclear technologies. This means that in case of a considerable pellet price increase, biomass technologies will be uncompetitive compared to the other generation technologies.

3.1.3.3. Optimistic Scenario

Under the optimistic pellet price scenario – with a constant fuel cost for a dedicated biomass plant of 73 €/MWh – the outlook for biomass technologies becomes completely different (Figure 8). In this scenario, biomass technologies become competitive with coal and gas from 2024 onwards. Furthermore, the results in Figure 8 illustrate that in the long term biomass technologies have a lower LCOE then coal, PV and gas.

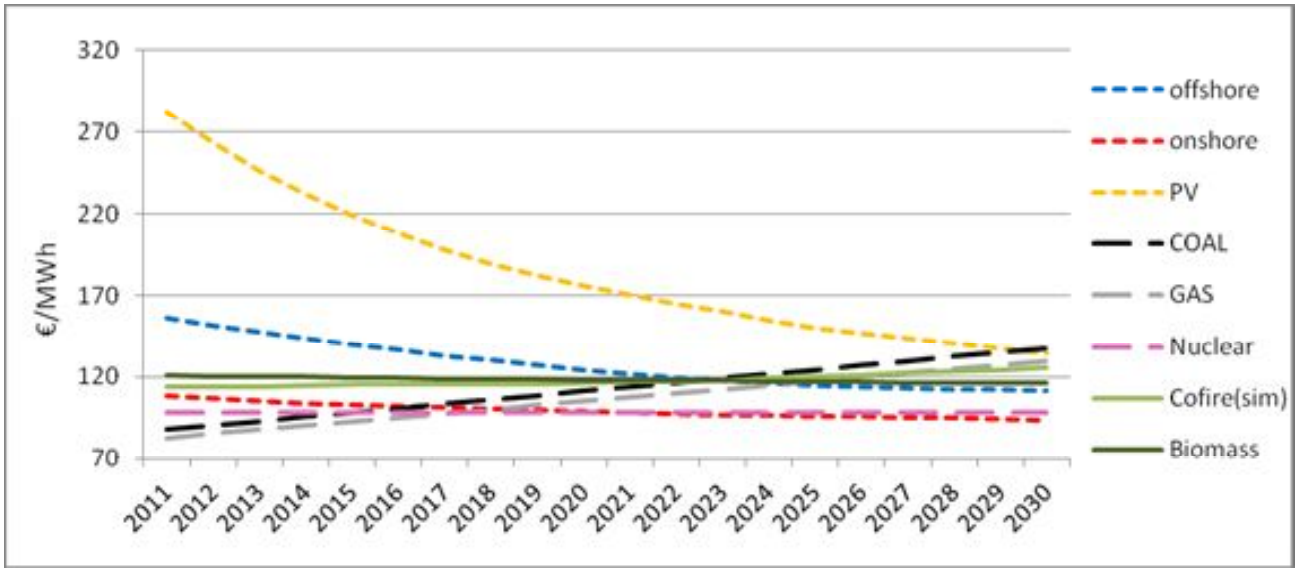

Figure 8: LCOE of new generation assets – optimistic pellet price scenario

On the other hand, the gap with nuclear and onshore wind remains substantial. The LCOE of co-firing lies above that of biomass from 2023 onwards, but below gas, PV and coal. The latter becoming the most expensive technology from 2030 onwards in this scenario.

3.1.3.3. Discussion

The three scenarios with stable load factors – 80% for both biomass technologies – confirm that the economic attractiveness of biomass technologies is highly sensitive to the expectations about the pellet price evolution. In the pessimistic pellet price scenario, the LCOE of biomass technologies is significantly higher than the LCOE of PV, coal and gas. Investing in biomass is moderately attractive in the standard pellet price scenario and even very attractive in the optimistic pellet price scenario. If pellet prices were to evolve as assumed in the standard or the pessimistic scenario, then biomass will roughly be as expensive as fossil-based technologies in the long run. From an investment perspective, policy measures to ensure a sufficient supply of biomass are of utmost importance to trigger significant investments in new biomass generation capacity. However, it should be pointed out that finding this cheap supply – considering the sustainability issues mentioned in the first chapter – will be far from easy. Policymakers should be cautious in promoting biomass overnight, without a clear sustainability framework.

3.1.4. Sensitivity analyses

3.1.4.1. Load factor

The expected growth of intermittent generation is likely to have a significant impact on the load factors of other generation technologies. Consequently, lower load factors will increase the capital cost per MWh and hence augment LCOEs (see equations 1-3). In order to calculate the total cost of non-intermittent technologies under these assumptions, we assume that load factors gradually decline along the period. The evolution of the load factors in our simulation is presented in Appendix B. In Table 2, we compare the LCOE in 2030 for the two load factor scenarios ('full' and 'reduced'). The intermittent technologies are not included in this table, but, as a benchmark, it is useful to mention that the LCOE of onshore wind (the cheapest technology) is estimated to be 94 €/MWh in 2030.

Table 2: LCOE (2030) in €/MWh of new generation assets with reduced load factors

Load Factor	Biomass P	Biomass S	Biomass O	Cofiring P	Cofiring S	Cofiring O	Coal	Gas	Nuclear
Full	188	132	116	162	134	126	138	130	98
Reduced	193	136	120	165	137	129	146	136	120

In general, the reduced load factors do not significantly impact the gap between biomass technologies and coal and gas. Only nuclear is subjected to a high impact under the conditions of the reduced load factor scenario. In fact, the LCOE of nuclear increases from 98 to 120 €/MWh, therefore the gap with the other non-intermittent technologies is reduced slightly. Nevertheless, it remains the most attractive non-intermittent technology.

The lower load factors obviously increase the 2030 LCOE-gap between wind and all the non-intermittent technologies. With the reduced load factor, the high pellet price scenario leads to a 100% biomass LCOE that is about double the LCOE of wind in 2030. When we compare the latter pellet price scenario to the LCOE of coal, we find a 'worst case' cost-disadvantage of biomass of some 32% (€ 193 vs. € 146). On the other hand, under the optimistic pellet price scenario with the reduced load factors, the LCOE of 100% biomass is only 20 € above the LCOE of wind onshore. With standard pellet prices, the 2030 cost gap of 100% biomass technologies with wind onshore increases from 35%, under the full load scenario, to 39%, under the reduced load scenario. In short, the reduced load factor scenario illustrates that the 2030 LCOE differences between biomass-based technologies and the other non-intermittent assets remain roughly the same, while wind onshore

(the most competitive technologies) slightly increases its competitiveness against all the non-intermittent technologies.

3.1.4.2 Learning Rate

The presented results depend on many assumptions and have intrinsic limitations. As we assumed that future investment cost reductions depend on learning efforts, higher or lower learning rates are likely to influence our findings. Figure 9 illustrates the learning rate sensitivity of our results in the standard pellet price scenario with stable load factors. This figure projects the LCOE with the assumed learning rate (see Table 1) together with the alternative LCOE when we increased and reduced this learning rate by 2%.

Figure 9 shows that the variation in the learning rates mainly influences the LCOE of PV, offshore and onshore wind and biomass co-firing. Not surprisingly, the technologies with the biggest growth potential are more influenced by a change in the learning rate. For biomass co-firing, the difference in LCOE with the extreme levels of the learning rates is limited to some € 6/MWh. For PV technologies, a 2% change in the learning rate can result in a LCOE variation of € 15/MWh. Nuclear is not depicted in Figure 9 since it was assumed that, due to increasing safety measures, costs for nuclear plants would not decrease in the future. The learning effect is thus, according to us, not applicable to nuclear.

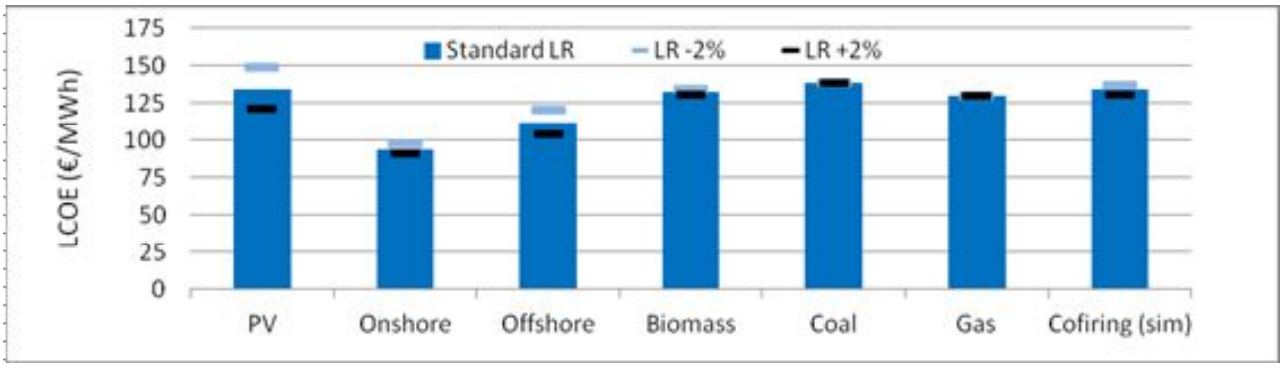

Figure 9: Learning rate sensitivity of 2030 LCOE (standard pellet price scenario)

3.1.4.3. Discount Rate

Another important parameter for the calculation of the LCOE is the discount rate. We used a 10% discount rate and present in Figure 10 alternative results with discount rates of 7 and 13%. As expected, the variation in the discount rate significantly impacts the results.

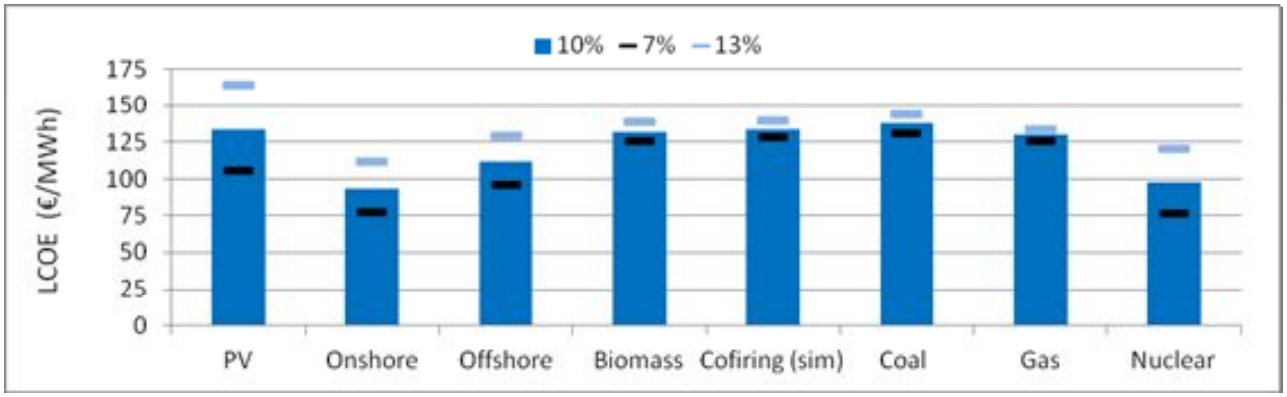

Figure 10: Discount rate sensitivity of 2030 LCOE (standard pellet price scenario)

A 3% variation in the discount rate markedly changes the LCOE-ranking in the standard scenario. With a 7% discount rate, nuclear technologies offer the lowest LCOE in 2030, followed by onshore wind, offshore wind, PV, 100% biomass and gas, biomass co-firing and coal. Lower discount rates increase the LCOE-gap between wind onshore and biomass technologies. A discount factor of 13% leads to a scenario where the gap between nuclear and wind technologies and biomass technologies is significantly reduced if compared both with the 7 and 10% discount rate scenarios. Higher discount factors reduce the LCOE-gap between wind and nuclear and biomass technologies.

3.1.5 Conclusion

From a LCOE-perspective, including a pragmatic carbon cost and a discount rate of 10%, we can conclude that today gas offers the least expensive generation opportunity with full production costs of around € 86 per MWh. The LCOE of biomass technologies – 100% biomass and 50% co-firing – is respectively some 48 and 38% higher than the LCOE of gas, which represents the 2012 benchmark. Without a CO_2 cost, biomass technologies are some 68% (100%) and 56% (50% co-fire) more expensive than gas. Onshore wind today (2012) has a LCOE slightly below our estimates for biomass technologies.

To explore the opportunity of biomass technologies from a stand-alone perspective – excluding all external costs for the electricity system at large – we compared three pellet price scenarios and two load factor scenarios for the period 2012-2030. Table 3 summarizes our findings. We compare both (100% and 50% co-fire) biomass technologies together – by averaging their LCOE in 2030 – to the LCOE of coal, gas and wind technologies in 2030. From Table 3 we can conclude that biomass technologies offer attractive investment opportunities from an LCOE-perspective in 2030. Only with high pellet prices, the LCOE of biomass technologies is 27-35% higher than the LCOE of coal and gas technologies. Compared to wind technologies, biomass faces a LCOE-disadvantage of 70 to 74% in 2030 under the pessimistic pellet price scenario.

With the standard pellet price scenario, biomass technologies are less expensive in 2030 than coal and as expensive as gas, and the LCOE-disadvantage to wind technologies is between 29 and 32%. With low pellet prices, biomass technologies have a significant LCOE-advantage over coal and gas technologies – between 9 and 15% – while wind technologies still offer a better investment opportunity.

Table 3: Competitiveness of biomass considering six scenarios in 2030

	Pessimistic pellet price	Standard pellet price	Optimistic pellet price
LCOE biomass / LCOE coal			
Full load	1.27	0.96	0.88
Reduced load	1.23	0.93	0.85
LCOE biomass / LCOE gas			
Full load	1.35	1.02	0.93
Reduced load	1.32	1.00	0.91
LCOE biomass / LCOE wind			
Full load	1.70	1.29	1.17
Reduced load	1.74	1.32	1.21

3.2. Economics from a system perspective

3.2.1. Introduction

LCOE analyses only provide information on production costs per MWh for different energy technologies on a ‘stand-alone’ basis. However, as all technologies need to be integrated into a system continuously balancing demand and supply, we need to consider the system dynamics and its boundary conditions. Further investments in some generation technologies can directly or indirectly increase total system costs, while investing in other technologies can eventually lead to

lower system costs and thus generate system benefits. Also, it needs to be acknowledged that the impact of a given technology on system dynamics varies over time.

3.2.2. Towards a new system

In the electricity system of today, most production is generated with highly controllable assets which have guaranteed availability and predictable production. The production of electricity generally responds to changes in the electricity price. However, some technologies do not directly respond to price signals and continue to generate electricity, even when market prices are very low. For example, nuclear plants continue to produce irrespective of prices. Additionally, renewable electricity production is also insensitive to market prices, given the current incentive schemes in Europe (FIT or GSC).

The overview given in Table 4 is based on the assumption that in the world of tomorrow renewable production from wind, solar and biomass technologies will be much more important than today. As a consequence, assets with a limited availability and a limited predictability (wind and solar) need to be integrated. In this respect, biomass technologies offer the significant advantage of a high availability as well as a high predictability. On the other hand, biomass technologies face a resource scarcity just like fossil and nuclear technologies. If the share of renewable generation is high and nuclear capacity remains operational, the electricity system will contain many assets that do not respond to price signals, a situation which is not optimal from an economic perspective.

Prices have two dimensions; firstly, they reflect the economic cost of a commodity and secondly they provide information on the economic value of the produced commodities. Economic activities not responding to transparent and complete price information risk to create suboptimal allocations (e.g. excess production or shortages).

In the coming years, generation will become less responsive to price signals but will increasingly depend on weather patterns. In line with the limited predictability of weather patterns – especially on the medium and the long term – generation assets will also become increasingly unpredictable and their availability will decline.

Table 4: Comparison of electricity generation technologies from a system perspective

	Gas/Coal	Nuclear	Wind	Solar	Biomass	Hydro
Available when needed?	Yes	Yes	No	No	Yes	Yes
Predictable?	Yes	Yes	No	No	Yes	Yes
Input scarcity?	Yes	Yes	No	No	Yes	Variable
Sensitive to electricity price?	Yes	No, not flexible	No, subsidized	No, subsidized	No, subsidized	Yes
Current world	X	X				X
Future world	X	X	X	X	X	X

The above discussion indicates that biomass technologies can provide important system benefits. Only biomass and hydro plants offer the potential for renewable base-load and mid-merit/ intermediate generation. As it is very unlikely to develop a 100% renewable electricity system without renewable base-load and mid-merit production, biomass and hydro should play a pivotal role in energy transition scenarios. In the next decades, flexible biomass and hydro plants can also play a role in balancing the production from the intermittent renewable technologies.

The debate on the adaptation of the system to accommodate a growing intermittent production is far from settled. A more flexible system requires significant investments in transmission, distribution and smart grids to facilitate balancing and to accommodate changes in supply and demand. The need to foresee back-up and the long-term impact on loading factors and shedding should equally be considered given their potential impact on investment decisions. As biomass offers the potential

for renewable generation without the typical system challenges of intermittent renewables, estimates of the system implications of additional intermittent generation can provide indications of the economic value of biomass in 'high intermittency' scenarios. In the next sections, we elaborate the system benefits of biomass starting from 'high intermittency' perspectives on future generation.

3.2.3. Back-up requirement

The typical availability of conventional plants is about 95%, however, on average only 4% of the total installed wind capacity in Spain and Germany has a comparable level of firmness (50). Around 17% of the total installed wind capacity has a level of firmness of 60%. This implies that wind's firm contribution to available capacity of the system is around 10% (or less). The intermittent renewables should therefore be considered as energy sources but not as capacity suppliers (50).

The following example sheds light on the diverse needed back-up of wind and biomass technologies. When 10,000 MW wind capacity is installed in a system with a peak demand of 30,000 MW and 30,000 MW of fossil capacity, less than 1000 MW of this wind capacity is always available. To meet the peak demand of 30,000 MW in this system, 29,000 MW of the fossil capacity needs to be used. The development of 10,000 MW wind capacity does not make it possible to close down 10,000 MW of the available fossil capacity. According to Eurelectric (50), every MW of wind capacity generally requires a 1MW of back-up firm capacity to ensure 90% availability. Total capacity will evolve differently if we replace in this same system the 10,000 MW wind capacity with biomass capacity. As the biomass capacity is available at peak demand moments, it is indeed possible to close down fossil plants.

In Table 5, the back-up need per 100 MW generation assets is calculated starting from the typical "firm availability" for the NW European context. When assuming a 70% firm availability for biomass capacity, the addition of 100 MW biomass assets requires the provision of 30 MW back-up. In the basic system of Table 5, there are back-up needs for 3 generation technologies. The back-up needs for wind significantly exceed the back-up needs for biomass and for coal capacity. However, the total back-up for a generation portfolio is lower than the sum of back-up requirements per technology.

Table 5: Back-up needs per technology from a stand-alone perspective

100 MW Frontline	Firm availability	Back-up need	Back-up addition (relative to coal)
Coal	90%	10 MW	
Wind	10%	90 MW	80 MW
Biomass	70%	30 MW	20 MW

In Table 6, we present an example of how a future generation mix could look like in a NW-European region without hydro. Such a region could have a generation portfolio of 15,000 MW, of which 7000 MW is intermittent capacity (5000 MW wind + 2000 MW solar PV). In addition, there is 3000 MW biomass together with 2000 MW nuclear. The fossil capacity is limited to 3000 MW. The required back-up capacity depends on all the assets in the generation mix. Starting from base-load assets, the back-up need for 2000 MW nuclear capacity is around 100 MW. Adding 2000 MW gas will increase the total back-up needs to 250 MW, which is below 300 MW because the correlation of the non-availabilities of nuclear and gas assets is rather low. Adding 1000 MW coal further increases the back-up needs to 300 MW. The 3000 MW biomass capacity requires a back-up of 900 MW but 300 MW back-up is already established (in response to investments in nuclear, gas and coal capacity). As the correlation between the non-availabilities of biomass and the other assets is low, we do not need to increase the total back-up pool by 900 MW. We assume that an additional back-up investment of 700 MW is sufficient. With respect to the 5000 MW wind capacity, a back-up need of 4500 MW emerges from a stand-alone perspective. As already 1000 MW back-up assets are provided, total back-up provision will not increase by 4500 MW but by e.g. 3700 MW. Finally, the back-up needs for 2000 MW solar PV are 1900 MW from a stand-alone perspective but as already 4700 MW back-up is foreseen, a modest increase of the total back-up can be sufficient. In

the example of Table 6 we end up with a total back-up need of 5000 MW or 33% of total installed capacity. With only nuclear, gas and coal capacity the back-up requirement would be only 6% of total installed capacity.

Table 6: Back-up needs for a portfolio of 15,000 MW with 7000 MW intermittent capacity

Frontline generation portfolio (15000 MW capacity)	Firm availability (capacity credit)	Back-up needed per asset	Cumulative Required back-up (nuclear ◊ PV)	% of installed capacity	Increase of back-up need due to RES
2000 MW nuclear	95%	100 MW	100 MW	5%	
2000 MW gas	90%	200 MW	250 MW	6.25%	
1000 MW coal	90%	100 MW	300 MW	6 %	
3000 MW biomass	70%	900 MW	1000 MW	12.5%	+ 700 MW
5000 MW wind	10%	4500 MW	4700 MW	36%	+ 3700 MW
2000 MW solar PV	5%	1900 MW	5000 MW	33%	+ 300 MW
Total: 15000 MW		**7700 MW**	**5000 MW**		**+ 4700 MW**
Alternative portfolio with only changes in RES capacity (nuclear, gas and coal unchanged)					
6000 MW biomass	70%	1800 MW	1900 MW	17%	+ 1600 MW
3000 MW wind	10%	2700 MW	2900 MW	20%	+ 1000 MW
1000 MW solar PV	5%	950 MW	3100 MW	20%	+ 200 MW
Total: 15000 MW		**5850 MW**	**3100 MW**		**+ 2800 MW**

In an alternative portfolio in Table 6 ('*Alternative portfolio with only changes in RES capacity*') we increase total biomass capacity up to 6000 MW (+ 3000 MW) and lower the intermittent assets by 3000 MW. In this second example, the maximal generation on a given moment is identical to the maximal generation with the upper panel of Table 6 (under the assumption of strong wind and a high solar irradiation). With the alternative portfolio, total back-up needs are lower and the increase of back-up due to renewables is also much lower than in the upper panel. With 6000 MW of biomass, total back-up needs are 'only' 20% of total installed capacity. 3000 MW additional biomass capacity lowers total back-up needs by 1900 MW (while replacing 3000 MW intermittent capacity). In this example, trading 1 MW wind capacity for 1 MW biomass capacity lowers back-up needs by 0.6 MW per additional MW biomass.

From an environmental perspective, the back-up pool in the example of Table 6 should consist of very efficient assets. If not, the environmental benefits of a low-carbon generation system risk to be lowered by frequent use of inefficient high-carbon back-up plants. In principle, part of the back-up challenge could be met by integrating the regional market of Table 6 into a larger European market. In case of sufficient transmission and interconnection capacity, some of the needed back-up generation can be provided for by the excess production of wind electricity in neighboring countries. The ability to import electricity is sometimes presented as an alternative to the local provision of back-up capacity. The most comprehensive historical weather models however conclude that total wind and solar output in NW-E will be highly correlated and will not 'average out' over regions (51). In fact, when there is no wind in Belgium, there is probably no massive production of wind electricity in the Netherlands, Germany or France either.

As local back-up is essential to guarantee generation capacity, we can observe a massive expansion of total generation capacity in all scenarios with a high penetration of intermittent renewables in the next decades. As mentioned before, investments in additional wind capacity do not lead to equivalent reductions of fossil or nuclear capacity. When the UK would like to increase the share of intermittent renewables up to 50% by 2030, total installed capacity would have to increase from 80 GW today to 125 GW in 2030 (or increase by 56%). To further strongly increase the share of intermittent generation between 2030 and 2050, total generation capacity in the UK has to increase

from 125 GW in 2030 to 230 GW in 2050. The latter increases by 85% between 2030 and 2050 will lead to a rise in electricity production of some 33% (52).

3.2.4. Load factors and shedding

In scenarios which combine a strong increase of installed capacity and only a slight – or perhaps no – increase in electricity demand, the use of capital can only decrease. The high penetration of intermittent renewables will lower the load factors of all other energy technologies, including low-carbon generation. It is to be expected that fossil and nuclear load factors will decrease. However, in extreme scenarios where wind capacity is maximized, the high penetration of intermittent renewables will even result in lower load factors for offshore wind (52).

In Table 7, we present projected load factors in several high intermittency scenarios developed by Pöyry for the UK (52). The results are striking; load factors for many technologies risk to become too low to trigger new investments as long as markets reward investors for produced MWh and not for the availability of capacity (irrespective of the use of this capacity). In the most extreme scenarios with the highest intermittent production, biomass plants – not a priority so far in the UK – will operate with load factors between 30 and 40%.

The high share of intermittent generation automatically results in underutilisation of other low-carbon assets. From an environmental perspective, the gains from replacing biomass by wind are marginal when compared to replacing an old fossil plant by wind. Shedding or shutting down efficient low-carbon generation can therefore be interpreted as indication of overinvestments in low-carbon capacity. In the high intermittency scenarios of Pöyry for the UK, shedding will become important by 2050. In both the High and Very High scenarios, shedding amounts to 7% of total electricity demand by 2050. In the Max scenario, shedding is 20% of total electricity demand and some 80 TWh of offshore wind generation is shed. Pöyry concludes that '*given our assumptions about flexibility and the renewable mix, the system struggles to accommodate renewable penetration above 80%* (52)'

Table 7: Load factors in high intermittency scenarios for the UK (52)

Scenario	% RES	LF offshore	LF biomass	LF nuclear	LF CCGT	LF peakers	Shedding (% of demand)	Shedding (TWh)
2010	4%	40%	65%	88%	50%	5%	-	-
High 2030	51%	40%	51%	88%	19%	0%	1%	6
High 2050	60%	40%	42%	75%	12%	5%	1%	6
Very High 2030	64%	40%	50%	81%	18%	0%	7%	38
Very High 2050	80%	40%	40%	62%	12%	3%	7%	41
Max 2050 or later	+90%	36%	30%	0%	19%	9%	20%	120

Massive investments in intermittent renewables can thus produce high external costs in terms of lower load factors, lower investment opportunities in other generation assets and significant shedding of low-carbon generation. These costs should be interpreted as uncompensated external costs: not the investors in intermittent generation but investors in other assests and society at large will have to bear these costs. The investors in intermittent generation will not compensate the owners of other generation assets for the reductions in load factors. Only in the extreme Max scenario with very significant shedding of offshore wind capacity, investors in intermittent generation will bear themselves part of load factor and shedding losses.

As a reduction of the load factor increases the LCOE of a technology, final consumers will face higher prices because of the increasing intermittency of the electricity system. According to models by Mott MacDonald, the levelized cost of nuclear and coal CCS would triple when the load factors would fall from 70% to 30%. For flexible gas plants, the levelized cost would only increase strongly once load factors are below 15% (53).

Investing in biomass plants can lead to lower shares of intermittent renewable and hence lower external load factor and shedding costs from high penetration rates of intermittent renewables. However, investors in biomass capacity will not be rewarded for their contribution to lower external costs while investors in intermittent generation are not held responsible for these external costs.

3.2.5. System flexibility costs

In addition to the costs in the preceding paragraphs, we still have to consider the general cost of system flexibility in terms of new transmission and distribution capacity. To accommodate high intermittency, it is essential to move demand within the day and within longer periods. The cost to move demand should also be considered a part of the general cost of system flexibility. Modern energy systems have a significant potential for demand-side flexibility but there is a significant cost of harnessing this potential. Without smart grids, washing machines will not start working at the optimal moment and batteries of electric cars will not be charged at times with a high flexible supply but a low fixed demand. In the Pöyry analysis for the UK (52), it is assumed that movable demand can increase to about 15% of total demand in 2030 to become close to 200 TWh (one third of total demand in 2050). From a methodological perspective, it is challenging to calculate the full cost of moving demand in the electricity system. In order to connect a washing machine to the smart grid, some hardware changes need to be provided by the producers of washing machines and this brings a cost for users. Furthermore, strong price incentives need to be provided in order to stimulate users and producers to consider moving demand. These costs for final users are generally not included in estimates of system flexibility[3].

Table 8 presents the annualized costs of system flexibility in the UK for several 'high intermittency' scenarios developed by Pöyry (High 2030, High 2050, Very High 2030, Very High 2050 and Max). In this study, the cost of system flexibility is limited to the costs of transmission, distribution, interconnection, bulk storage, smart meters/grids and peaking capacity. Not surprisingly, the annualized cost of system flexibility is very sensitive to the share of intermittent renewables in total electricity generation. When comparing the 'High 2030' scenario and the 'Very High 2030' scenario, the results show that, amazingly, an additional capacity of 9 GW of wind and 22 GW of solar leads to an increase of annualized costs of system flexibility by £ 3.1 billion per year. By 2050, the annualized flexibility cost with 'High 2050' is £ 5.9 billion while 'Very High 2050' implies an annualized flexibility cost of £ 10 billion. This flexibility cost difference of £ 4.1 billion per year is the consequence of an additional wind capacity of 17 GW and a solar capacity investment of 35 GW.

Table 8: Intermittency scenarios for the UK and the annualized flexibility cost (AFC) in 2030 and 2050 (52)

Scenario	Cons (TWh)	Cap (GW)	% ren	Installed capacity (GW)						AFC (£bn/a)
				Wind on+off	Solar	Marine	Hydro + BM	CCGT	Peaker	
High 2030	409	125	51%	59	3	4	6	30	0	5.4
High 2050	551	171	60%	102	3	4	6	9	6	5.9
Very High 2030	409	158	64%	68	25	8	6	35	1	8.5
Very High 2050	551	230	80%	119	38	23	6	9	10	10.0
Max	611	298	+95%	191	38	31	6	13	21	16.6

Pöyry stresses that the high intermittency scenarios have not been selected from a cost-effectiveness perspective, as the main goal of the analysis was to find out whether high intermittency can be technically accommodated. It is thus possible to lower the high flexibility cost estimates in the left column of Table 8 by replacing wind and solar capacity with hydro and biomass capacity. The potential to increase hydro capacity is however limited in the UK. A strong increase of biomass is

[3] To include the cost of all assets to move electricity demand would imply that the upfront investment cost of electric vehicles is part of the flexibility cost.

not integrated in the Pöyry scenarios as the goal was to assess high intermittency. Furthermore, the UK currently adopts a 'holding position' with respect to bio-energy at large. No significant increase in bio-energy use is assumed in official documents such as Renewable Energy Review '*given concerns over sustainability and questions over the best long-term use for this limited resource*' (executive summary, p16, (54)).

In an effort to lower the flexibility cost of the system, we have to consider the replacement potential of biomass. With a load factor for biomass of 60% in 2030, 8 GW of additional biomass capacity can replace 16 GW wind capacity (with an average load factor of 30% for onshore together with offshore) or 9 GW wind and 21 GW solar (LF 10%). With a load factor of 75% for biomass plants in 2030, much more intermittent capacity can be replaced. The difference between High 2030 and Very High 2030 also includes more tidal energy capacity (+4 GW), more CCGT capacity (+5 GW) and more peaking capacity (+1 GW). As especially the CCGT and peaking capacity is related to the increasing intermittency between High 2030 and Very High 2030, 8 GW additional biomass capacity can partly replace the additional CCGT and peaking needs in Very High 2030.

Although the comparison is simplified and not complete, we can conclude that the investment in 8 GW biomass capacities by 2030 can prevent most of the projected increase of annualized flexibility cost in the shift from the High 2030 scenario to the Very High 2030 scenario. Based on the Pöyry assessment for the UK (52), investing in 8 GW of biomass capacity avoids an increase of system flexibility costs close to £ 3 billion per year. By 2050, more biomass capacity can be developed but the (much) lower load factors will make it difficult to replace much more wind and solar capacity.

Summarized, in this framework with an electricity system of 400 TWh we have to distinguish two pathways to a high share of renewable generation (50 to 60% share of renewable in generation): the massive deployment of intermittent generation will lead to high system flexibility costs while the alternative with a lower – but still very important – deployment of intermittent renewables is complemented by investments in additional biomass capacity. We estimate that the annual flexibility cost from mainly intermittent renewables can be reduced by roughly one third (£ 3.1 bn / £ 8.5 bn) when intermittent capacity is lowered by 15% in response to additional biomass investments.

It is important to realize that these findings are mainly indicative and based on the rather radical deployment scenarios for the UK (52). These scenarios should however not be interpreted as unique 'island' scenarios since increased interconnection with Ireland, NW-E and Norway is included, as well as powerful active demand management systems – that move up to 30% of total demand – and bulk storage possibilities.

3.3. Conclusions

In this electricity system overview we focused on back-up needs, load factors, shedding, cost-efficient RES targets and the general system flexibility costs. We can identify that biomass capacity offers several important benefits. Most of them will however only become visible in the next decades – assuming that the share of intermittent renewables will indeed strongly increase – although there are also benefits to be experienced as of today;

1. In high intermittency scenarios, biomass capacity can significantly lower total back-up needs; in our example, trading 1 MW wind capacity for 1 MW biomass capacity lowers back-up needs by 0.6 MW per additional MW biomass
2. In high intermittency scenarios, biomass capacity can limit the projected reduction of load factors
3. In high intermittency scenarios, biomass capacity can avoid massive shedding of low-carbon generation (up to 30% of demand in extreme scenarios)
4. In high intermittency scenarios, massive deployment of biomass capacity can lower system flexibility costs by 30%

From a societal perspective, additional biomass capacity lowers the system investment needs. Also, biomass capacity limits the expected price increases from a system that becomes more capital-intensive but has lower load factors and requires increasing shedding of efficient low-carbon generation. For the final consumer, the electricity bill will increase with every additional euro invested in new assets. Although we can only estimate the system benefits of additional biomass capacity, it is obvious that all these positive externalities from biomass use are currently not considered in our policy frameworks. In the market configuration of today, there are no incentives to consider the external cost and benefits of generation technologies. The debate on externalities is much wider than the conventional focus on negative externalities such as pollution and CO_2 costs. Renewable energy frameworks are dominated by flat production incentives for all generation technologies irrespective of their system consequences. In optimal incentive frameworks targeting high shares of renewable energy sources (RES), assets with the potential to significantly limit system costs should be favored over assets that not only generate renewable electricity but high system costs as well.

From a public policy perspective, the existence of positive system externalities typically leads to underinvestments in the assets producing these externalities. To correct for negative externalities, the underlying activity should be supported, leading to incentive schemes that internalize the external benefits for investors. In the context of support for biomass assets, an optimal support framework should internalize the system benefits of biomass to trigger additional investments in biomass capacity.

4. Conclusion

Biomass electricity production has the potential to become a very important piece in the energy puzzle of tomorrow. It comes with many interesting benefits which are currently underestimated and thus unrewarded. Some of these are already visible; others will become prominent in coming decades. Today, biomass can be used as a low-carbon source for electricity, and can help member states in the EU to reach their 20/20/20 targets efficiently. In the world of tomorrow, biomass power plants can become a crucial part of the electricity mix, as a grid stabilizer and a renewable source of back-up power supply. This is especially true for NW-Europe, since this region does not have sufficient hydro capacity to balance weather dependent, intermittent renewables, such as solar and wind.

Society as a whole can strongly benefit from the use of biomass for electricity production; however, in order to reach this goal, some conditions need to be met. The primary condition is that sufficient supplies of sustainably produced biomass need to be available. Failing to meet this condition will result in either high, non-competitive electricity production costs or in producing electricity with a high carbon footprint, or, in the worst case, both. This can be avoided by investing in both sustainable forest management – to ensure the sustainability – and reliable biomass supply chains – to avoid shortages. Since the likelihood of reaching the 2°C target has only decreased in recent years, these investments should start as soon as possible.

Acknowledgments

The authors would like to thank GDF Suez, Electrabel and Laborelec for their cooperation and support in the making of this paper.

Appendix A

In Table A. 1, we present an overview of the LCOE for new investments in different generation technologies in 2011/2012. The cost figures in this table should be interpreted as averages for the period 2011-2012. We opted for average cost figures to avoid that our results strongly depend on temporary price movements. Table A. 1 is based on the international literature while the load factors are set in line with the NW European context. We added a CO_2 cost of 30 US$ per ton (or € 23/tCO_2) to reflect the cost of climate policy measures for electricity producers. This CO_2 cost is above the ETS price of January 2011, but is an adequate illustration of the resource cost of climate measures. The total cost per technology in €/MWh should be interpreted as the average cost (in present value) per MWh for an investor who invests today in a particular technology and uses a discount factor of 10%.

In Table A. 1, we included two biomass technologies. The first – 100% Biomass – is a dedicated biomass plant of significant scale (>300 MW) which only burns wood pellets. As biomass is mostly co-fired in coal plants with co-firing rates between 5 and 10%, we also wanted to include co-firing in our overview. Today, an investor will however not build a new coal plant with the purpose of 5% or 10% biomass co-firing. A typical co-firing plant therefore does not fit in the LCOE methodology for new projects. To accommodate the co-firing technology to the LCOE philosophy, we assume that co-firing technologies evolve in way that 50% co-firing of biomass becomes possible in the next years. As this 50% co-firing does not yet exist, we refer to it as Cofire(sim) in our simulations. We want to emphasize that the latter plant should not be confused to the co-firing practice of today in most countries. In our approach, we estimate the investment cost of a 50% co-firing plant to be around € 2300 per kW and use this value as a starting position in our analysis. From an investment perspective, flexible coal plants with the ability of 50% biomass co-firing offer the benefit of flexible generation in response to the relative prices of coal and pellets. The insurance against feedstock price spikes can compensate the higher investment cost for this type of plant.

Once the CO_2 cost is included, Table A. 1 shows that coal and gas offer the least expensive generation opportunities with production cost of some € 100 per MWh. The LCOE with biomass technologies is some 35% above the LCOE with coal and gas technologies. Without a CO_2 cost, biomass technologies are some 60% more expensive than coal and gas technologies. Onshore wind technologies have a LCOE that is close to the estimates for biomass technologies. Offshore wind is some 20% more expensive than onshore wind while the LCOE of PV is still prohibitive. The LCOE of nuclear technologies is between the LCOE of biomass and the LCOA of gas and coal technologies. We opted for a high investment cost for nuclear capacity in response to post-Fukushima concerns and cost overruns for new nuclear in France and Finland[4].

[4] http://www.guardian.co.uk/environment/damian-carrington-blog/2011/jul/22/nuclear-power-cost-delay-edf and http://www.nytimes.com/2009/05/29/business/energy-environment/29nuke.html?pagewanted=al

	World Capacity	Lifespan	Load Factor	Learning Rate	Investment. Cost	O&M	Feedstock Cost	Carbon Cost	Total Costs
	GW	Years	%	%	€/kW	€/MWh	€/MWh	€/MWh	€/MWh
PV	61[a,b]	25[o]	12[f,e,k]	15[h,i]	2600[b]	10[f]	0	0	264[a]
Wind onshore	286[c,g]	25[e]	25[f,e,k]	8[h,i]	1800[j]	18[j]	0	0	107[a]
Wind offshore	5[c]	20[e]	35[f,e]	8-10[h,i]	3300[f,j]	30[j,f]	0	0	152[a]
100% Biomass	64[a,c]	25[f]	80[f]	7[a,i]	2100[f,m]	15[f]	73[l,a]	0	122[a]
Co-firing (sim)	3[a]	30[f]	80[f]	8[a,f]	2300[f]	15[f]	54[a]	11.5[e,a]	115[a]
Coal	1513[c,d]	35[f]	80[f,k]	7[h]	1700[d,e,f]	7[f,e,a]	30[a]	23[e]	90[a]
Gas	1308[c,d]	30[e]	70[f,k]	10[h,i]	900[d,e,f]	5[f,e,a]	50[a]	10[e]	86[a]
Nuclear	388[c,d,n]	50	85[e,k,n]	0[i]	5700[e,p,q]	13[e,a]	8[e,a]	0	98[a]

Table A. 1: LCOE of new generation technologies in 2011-2012 (first quarter) with starting assumptions for simulation up to 2030

a) our calculation; b) EPIA, 2010 (55); c) REN21, 2011 (1); d) IEA ETSAP, 2010 (56); e) IEA, 2010 (57); f) discussion with the industry; g) EWEA, 2011 (58); h) Weiss et al., 2010 (49); i) Neij, 2008 (42); j) IEA, 2009 (59); k) Lenzen, 2010 (60); l) Sikkema et al., 2011 (61); m) Faaij, 2006 (62); n) World Nuclear Association (63); o) Laleman et al., 2011. (30); p) NY times (64); q) Guardian (65)

Appendix B

In Table B. 1, the projected evolution of fuel and carbon costs is summarized. In our simulations, we also considered the impact of lower load factors for non-intermittent generation technologies in response to an increasing share of intermittent generation. The two left columns of Table B. 1 present the load factors of Table A. 1 used in the 'stable load factor' scenarios and the reduced load factors used in the 'reduced load factor' scenarios (see further). The three fuel cost levels for biomass technologies by 2030 in Table B. 1 refer to the three pellet price scenarios; optimistic (O), standard (S) and pessimistic (P).

	2010 Fuel Cost	2030 Fuel Cost	2010 CO_2 Price	2030 CO_2 Price	2030 Stable LF	2030 Reduced
	€/MWh	€/MWh	€/MWh	€/MWh	%	%
100% Biomass	73	73 - 89 - 145 (O – S – P)	0	0	80	70
Cofiring(Sim)	54	66 - 75 - 103 (O – S – P)	11.5	23	80	70
Coal	30	60	23	46	80	60
Gas	50	90	10	20	70	50
Nuclear	8	6	0	0	85	65

Table B. 1 Fuel and CO_2 price assumptions (2010-2030) per technology

The fuel costs in Table B. 1 can be considered as minimal marginal production costs for the considered generation technologies. Market prices below these minimal marginal production costs will produce marginal losses. The rather low market prices in NW Europe since 2008 significantly complicate investment decisions in new generation technologies with high marginal production costs such as biomass and gas technologies.

References

[1] REN21. Renewables 2011, Global status report. 2011.

[2] EurObserv'ER. The state of renewable energies in Europe, 10th EurObserver Report. 2010.

[3] Commission E. SEC(2008) 85 Impact assessment. 2008.

[4] Bravi M, Coppola F, Ciampalini F, Pulselli FM. Comparing renewable energies: estimating area requirement for biodiesel and photovoltaic solar energy. Energy and Sustainability. 2007;105:187-96.

[5] Cherubini F, Bird N, Cowie A, Jungmeier G, Schlamadinger B, Woess-Gallasch S. Energy- and greenhouse gas-based LCA of biofuel and bioenergy systems: Key issues, ranges and recommendations. Resources Conservation and Recycling. 2009;53(8):434-47.

[6] Forsberg G. Biomass energy transport - Analysis of bioenergy transport chains using life cycle inventory method. Biomass & Bioenergy. 2000;19(1):17-30.

[7] Eriksson O, Finnveden G, Ekvall T, Bjorklund A. Life cycle assessment of fuels for district heating: A comparison of waste incineration, biomass- and natural gas combustion. Energy Policy. 2007;35(2):1346-62.

[8] Kaliyan N, Morey R, Tiffany D. Reducing life cycle greenhouse gas emissions of corn ethanol by integrating biomass to produce heat and power at ethanol plants. Biomass & Bioenergy. 2011;35(3):1103-13.

[9] Kimming M, Sundberg C, Nordberg A, Baky A, Bernesson S, Noren O, et al. Biomass from agriculture in small-scale combined heat and power plants - A comparative life cycle assessment. Biomass & Bioenergy. 2011;35(4):1572-81.

[10] The Environment Agency. Minimizing greenhouse gas emissions from biomass energy generation. 2009.

[11] Heller M, Keoleian G, Mann M, Volk T. Life cycle energy and environmental benefits of generating electricity from willow biomass. Renewable Energy. 2004;29(7):1023-42.

[12] Ardente F, Beccali G, Cellura M, Lo Brano V. Life cycle assessment of a solar thermal collector. Renewable Energy. 2005;30(7):1031-54.

[13] Bizzarri G, Morini GL. A life cycle analysis of roof integrated photovoltaic systems. International Journal of Environmental Technology and Management|International Journal of Environmental Technology and Management. 2007:134-46.

[14] Brandão M, Milà i Canals L, Clift R. Soil organic carbon changes in the cultivation of energy crops: Implications for GHG balances and soil quality for use in LCA. Biomass and Bioenergy. 2011;35(6):2323-36.

[15] De Wild-Scholten MJ, Alsema EA. Environmental life cycle inventory of crystalline silicon photovoltaic module production. Life-Cycle Analysis Tools for Green Materials and Process Selection. 2006;895:59-71.

[16] Varun, Bhat IK, Prakash R. LCA of renewable energy for electricity generation systems-A review. Renewable & Sustainable Energy Reviews. 2009;13(5):1067-73.

[17] Weisser D. A guide to life-cycle greenhouse gas (GHG) emissions from electric supply technologies. Energy. 2007;32(9):1543-59.

[18] IPCC. Special Report Renewable Energy Resources2011. Available from: http://srren.ipcc-wg3.de/report.

[19] Cherubini F. GHG balances of bioenergy systems - Overview of key steps in the production chain and methodological concerns. Renewable Energy. 2010;35(7):1565-73.

[20] Hillier J, Whittaker C, Dailey G, Aylott M, Casella E, Richter G, et al. Greenhouse gas emissions from four bioenergy crops in England and Wales: Integrating spatial estimates of

yield and soil carbon balance in life cycle analyses. Global Change Biology Bioenergy. 2009;1(4):267-81.

[21] Jaramillo P, Griffin W, Matthews H. Comparative life-cycle air emissions of coal, domestic natural gas, LNG, and SNG for electricity generation. Environmental Science & Technology. 2007;41(17):6290-6.

[22] IEA. Energy Technology Perspectives 2010: International Energy Agency; 2010.

[23] Junginger M, Bolkesjo T, Bradley D, Dolzan P, Faaij A, Heinimo J, et al. Developments in international bioenergy trade. Biomass & Bioenergy. 2008;32(8):717-29.

[24] Greenpeace. Fuelling a biomess2011. Available from: http://www.greenpeace.org/canada/en/campaigns/boreal/Resources/Reports/Fuelling-a-Biomess/.

[25] Zhang Y, Mckechnie J, Cormier D, Lyng R, Mabee W, Ogino A, et al. Life Cycle Emissions and Cost of Producing Electricity from Coal, Natural Gas, and Wood Pellets in Ontario, Canada. Environmental Science & Technology. 2010;44(1):538-44.

[26] Brandão M, Clift R, Milà i Canals L, Basson L. A Life-Cycle Approach to Characterising Environmental and Economic Impacts of Multifunctional Land-Use Systems: An Integrated Assessment in the UK. *Sustainability*. 2010;10(2):3747-76.

[27] Lettens S, Muys B, Ceulemans R, Moons E, Garcia J, Coppin P. Energy budget and greenhouse gas balance evaluation of sustainable coppice systems for electricity production. Biomass & Bioenergy. 2003;24(3):179-97.

[28] Spielmann M, Bauer C, Dones R, Tuchschmid M. Transport services. ecoinvent report n° 17 Swiss center for life cycle invertories,. Dübendorf: 2007.

[29] DIRECTIVE 2010/75/EU OF THE EUROPEAN PARLIAMENT AND OF THE COUNCILof 24 November 2010on industrial emissions (integrated pollution prevention and control) [database on the Internet]. 2010. Available from: http://eur-lex.europa.eu/LexUriServ/LexUriServ.do?uri=OJ:L:2001:309:0001:0021:EN:PDF.

[30] Laleman R, Albrecht J, Dewulf J. Life Cycle Analysis to estimate the environmental impact of residential photovoltaic systems in regions with a low solar irradiation. Renewable & Sustainable Energy Reviews. 2011;15(1):267-81.

[31] Martinez E, Sanz F, Pellegrini S, Jimenez E, Blanco J. Life cycle assessment of a multi-megawatt wind turbine. Renewable Energy. 2009;34(3):667-73.

[32] Azapagic A, editor. Sustaining Future Ecosystem Services. 2009; London.

[33] Pehnt M. Dynamic life cycle assessment (LCA) of renewable energy technologies. Renewable Energy. 2006;31(1):55-71.

[34] Djomo S, El Kasmioui O, Ceulemans R. Energy and greenhouse gas balance of bioenergy production from poplar and willow: a review. Global Change Biology Bioenergy. 2011;3(3):181-97.

[35] Manish S, Pillai IR, Banerjee R. Sustainability analysis of renewables for climate change mitigation. Energy for Sustainable Development. 2006;10(4):25-36.

[36] Odeh NA, Cockerill TT. Life cycle analysis of UK coal fired power plants. Energy Conversion and Management. 2008;49(2):212-20.

[37] Lenzen M, Munksgaard J. Energy and CO2 life-cycle analyses of wind turbines - review and applications. Renewable Energy. 2002;26(3):339-62.

[38] International Energy Agency. Projected costs of generating electricity. 2010.

[39] EEA. Europe's onshore and offshore wind energy potential. European Environment Agency, 2009.

[40] Kobos PH, Erickson JD, Drennen TE. Technological learning and renewable energy costs: implications for US renewable energy policy. Energy Policy. 2006;34:1645-58.

[41] McDonald A, Schrattenholzer L. Learning rates for energy technologies. Energy Policy. 2001;29(4):255-61.

[42] Neij L. Cost development of future technologies for power generation - A study based on experience curves and complementary bottom-up assessments. Energy Policy. 2008;36(6):2200-11.

[43] Nemet GF. Beyond the learning curve: factors influencing cost reductions in photovoltaics. Energy Policy. 2006;34(17):3218-32.

[44] Pan H, Kohler J, editors. Technological change in energy systems: Learning curves, logistic curves and input-output coefficients. Forum on Sustainability Well Being and Environmental Protection; 2005 Dec 02; Washington, DC.

[45] Rout UK, Blesl M, Fahl U, Remme U, Voss A. Uncertainty in the learning rates of energy technologies: An experiment in a global multi-regional energy system model. Energy Policy. 2009;37(11):4927-42.

[46] Soderholm P, Sundqvist T. Empirical challenges in the use of learning curves for assessing the economic prospects of renewable energy technologies. Renewable Energy. 2007;32(15):2559-78.

[47] van der Zwaan B, Rabl A. The learning potential of photovoltaïcs: implications for energy policy. Energy Policy. 2004:1545-54.

[48] Albrecht J. The future role of photovoltaics: A learning curve versus portfolio perspective. Energy Policy. 2007;35(4):2296-304.

[49] Weiss M, Junginger M, Patel MK, Blok K. A review of experience curve analyses for energy demand technologies. Technological Forecasting and Social Change. 2010;77(3):411-28.

[50] Eurelectric. Integrating intermittent renewables sources into theEU electricity system by 2020: challenges and solutions2010. Available from: http://www.eurelectric.org/PublicDoc.asp?ID=63539.

[51] Pöyry. The challenges of intermittency inNorth West European power markets2011. Available from: http://www.poyry.com/linked/en/press/NEWSIS.pdf.

[52] Pöyry. Analysis technical constraints on renewable generation to 2050: A report to the Committee on Climate Change2011. Available from: http://hmccc.s3.amazonaws.com/Renewables%20Review/232_Report_Analysing%20the%20technical%20constraints%20on%20renewable%20generation_v8_0.pdf.

[53] Mott MacDonald. Costs of low-carbon technologies2011. Available from: http://hmccc.s3.amazonaws.com/Renewables%20Review/MML%20final%20report%20for%20CCC%209%20may%202011.pdf.

[54] Committee on Climate Change. Renewable energy review2011. Available from: http://www.theccc.org.uk/reports/renewable-energy-review.

[55] EPIA. Global Market outlook for photovoltaics until 2014. 2010.

[56] International Energy Agency. Energy Technology System Analysis Program. 2010; Available from: http://www.iea-etsap.org/web/Supply.asp.

[57] International Energy Agency. Energy Technology Perspectives 2010. Paris: IEA; 2010.

[58] EWEA. Pure Power, wind energy targets up to 2020 and 2030. 2011.

[59] International Energy Agency. Technology Roadmap: Wind energy. International Energy Agency [Internet]. 2009. Available from: http://www.ieawind.org/wnd_info/IEA_Paris/Wind_Roadmap.pdf.

[60] Lenzen M. Current State of Development of Electricity Generating Technologies: A Literature Review. 2010;2010(3):462-591.

[61] Sikkema R, Steiner M, Junginger M, Hiegl W, Hansen M, Faaij A. The European wood pellet markets: current status and prospects for 2020. Biofuels Bioproducts & Biorefining-Biofpr. 2011;5(3):250-78.

[62] Faaij A. Modern Biomass Conversion Technologies. Mitigation and Adaptation Strategies for Global Change. 2006;11(2):335-67.

[63] World Nuclear Association. Available from: http://www.world-nuclear.org/.

[64] Kanter J. In Finland, Nuclear Renaissance Runs Into Trouble. New York Times; 2009; Available from: http://www.nytimes.com/2009/05/29/business/energy-environment/29nuke.html?pagewanted=all.

[65] Carrington D. Nuclear power's real chain reaction: spiralling costs. The Guardian; 2011; Available from: http://www.guardian.co.uk/environment/damian-carrington-blog/2011/jul/22/nuclear-power-cost-delay-edf.

Vegetable Oils of Soybean, Sunflower and Tung as Alternative Fuels for Compression Ignition Engines

Ricardo Morel Hartmann[a], Nury Nieto Garzon[a], Eduardo Morel Hartmann[a], Amir A. M. Oliveira[a], Edson Bazzo[a] , Bruno Shimabukuro Okuda[b] and Josélia E. A. Piluski[b]

[a] *Federal University of Santa Catarina, Florianópolis-SC, Brazil, ricardo@labcet.ufsc.br.*
[b] *Eletrobrás Eletrosul Centrais Elétricas S.A, Florianópolis-SC, Brazil, joselia@eletrosul.gov.br.*

Abstract:

This paper deals with the use of straight vegetable oil as fuel for compression ignition engine applied to distributed electric generation. It was studied three typical oils from southern of the Brazil, soybean oil, sunflower oil and tung oil. For this purpose it was designed and assembled two conversion kits that allow the use of the selected oils directly in the engine. The first kit preheats the fuel to a temperature where their physical properties, mainly viscosity, reaches the diesel oil levels. The other kit is an electronic injection mobile bench that allows controlling the timing, the pressure and the mass of injected fuel. Both kits are electronic controlled and it was used standardized measurements of some physical properties of the fuels, for the design of their control software. The straight vegetables oils, its blends 50/50 v/v with petrodiesel fuel and neat petrodiesel fuel were tested in dynamometer bench. It was obtained results of brake power, torque, specific fuel consumption and emissions as function of the rotation of the engine. The discussions about the results in terms of efficiency first law showed the technical feasibility of the using of straight vegetable oils and the effectiveness of the developed conversion kits.

Keywords:
Renewable energy, Vegetable Oils, Biofuels, Compression Ignition Engine.

1. Introduction

The use of complementary sources for the Brazilian energetic matrix has been sought by government and corporative stakeholders. Biofuels are the choice for transportation, either as a neat fuel or as an additive to petroleum derived fuels (Martines-Filho et al. [47], Pousa et al. [57]). Ethanol has been used in automobiles mixed with gasoline in volumetric fraction from 20% to 100%. Biodiesel has also been mixed to diesel oil in a 5% volumetric basis. This has led to reduction of sulphur content in fuels for CI engines, higher octane rating fuel for SI engines and to a more sustainable transportation energy matrix. There are also applications in which the presence of biofuels could increase. For example, isolated communities in the Brazil northern areas shall use diesel oil for electrical energy generation. This diesel consumption could be displaced by a more environmentally friendly and economical fuel mix (Andrade and Miccolis [9]). Rural areas can also benefit from the use of locally produced fuels. In this scenario, oil from vegetable and animal sources could provide alternative solutions.

One of the routes for the use of vegetable oil and fats is the transesterification that leads to monoalkyl esters known as biodiesel (Shahid and Jamal [72]). Several studies have shown that biodiesel can displace diesel oil without the need for any modifications in CI engines, both for transportation or stationary applications (see references in Agarwal [2], Dwivedi et al. [25]). However, this requires an industrial transesterification process that carries its own intrinsic complexities and costs. A more direct approach would be the use of straight vegetable oil in CI

engines, obtained after filtration only, with a minimum of modification of the engine's hardware (Sidibé et al. [68]).

Table 1. List of the literature reporting tests in CI engines fuelled with raw vegetable oils and their mixtures with diesel oil.

Character	Common name (Botanical name)	References
Edible	Soybean (*Glycine max*)	Engelman et al. [27], Pryor et al. [61], Altin et al. [6]
	Rapeseed (or, canola) (*Brassica napus*)	Peterson et al. [56], Nwafor [51], Bialkovski et al. [18], Hazar and Aydin [33], Kleinova et al. [42], Yilmaz and Morton [79]
	Palm (*Elaeis guineensis)*	Sapaun et al. [70], Bari et al. [12], Almeida et al. [5], Belchior and Pimentel [15], Antwi [10]
	Coconut (*Cocos nucifera*)	Thaddeus [74], Kalam et al. [41], Antwi [10]
	Cottonseed (*Gossypium hirsutum and Gossypium herbaceum*)	Altin et al. [6], Amba and Rama [8], He and Bao [34], Fontaras et al. [29], Siva et al. [73], Sarada et al. [67], Martin and Prithviraj [46]
	Corn (*Zea mays*)	Altin et al. [6]
	Olive (*Olea europaea*)	Rakopoulos et al. [66]
	Sunflower (*Helianthus annuus)*	Karaosmanoglu et al. [39], Altin et al. [6], Maziero et al. [48], Yilmaz and Morton [79]
	Peanut (*Arachis hypogaea*)	Barsic and Humke (1981), Yilmaz and Morton (2011)
	Safflower (*Carthamus tinctorius*)	Bettis et al. [14], Isigigur et al. [38]
	Sesame (*Sesamum indicum)*	Altun et al. [7]
	Rice bran (O*ryza sativa)*	Bari and Roy [12], Agarwal et al. [2], Raghu et al. [64]
	Linseed (or flaxseed) (*Linum usitatissimum*)	Agarwal et al. [2]
	Castor seed (*Ricinus communis)*	Naga et al. [49]
	Hazelnut (*Corylus avellana)*	Çetin and Yüksel [21]
	Poppy seed (*Papaver somniferum*)	Aksoy [4]
	Clove stem (*Syzygium aromaticum*)	Mbarawa [47]
	Mahua (*Madhuca longifolia*)	Agarwal et al. [1], Pugazhvadivu and Sankaranarayanan [62]
	Neem (*Azadirachta indica* or *Antelaea azadirachta)*	Sivalakshmi and Balusamy [69]
Nonedible	Jatropha (*Jatropha curcas*)	Kumar et al. [44], Pramanik [60], Forson et al. [30], Agarwal and Agarwal [1], Antwi [10], Chauhan et al. [23], Yadong et al. [78], Chalatlon et al. [20]
	Pongam (or, indian beech, karanja, karanj, honge) (*Pongamia pinnata*)	Agarwal and Rajamanoharan [3], Venkanna et al. [75]
	Tobacco seed (*Nicotiana tabacum*)	Giannelos et al. [31]
	Tung (*Aleurites fordii)*	Chan and Wan [22]

It is well accepted that Rudolph Diesel used peanut oil in a public demonstration of his engine (Knothe [40]). Times of war and the petroleum crises in the seventies have spurred modern developments in the use of raw vegetable oils in diesel engines. Chan and Wan [22] report studies carried out in continental China during the Second World War using tung oil as fuel for compression ignition engine. In that work they presented the performance of a compression ignition engine fuelled with diesel oil, cotton seed oil, rapeseed oil and tung oil. Recent reviews may be

found in Bhattacharya and Reddy [17], Sinha and Misra [71], Babu and Devaradjane [11], Mondal at al. [49] and No [50].

It is estimated that there are in Brazil more than 20 varieties of crops for the production of vegetable oils. Among them, the varieties that have national or regional interest are soybean, castor beans, sunflower, peanut, cottonseed, babassu, palm, jatropha and canola (CONAB [24]). Most of them (and others) have already been tested as neat fuels for CI engines. Table 1 lists oil producing crops that have been used as straight vegetable oil (SVO) fuel in CI engines in recent years. The references for their use as biodiesel far outnumber those shown and are omitted.

Vegetable oils present, comparatively to diesel oil, lower LHV (from 10% to 17% lower, leading to lower energy release per mass burned), higher viscosity (leading to poor atomization), higher boiling temperatures (delaying evaporation and formation of a combustible mixture), higher bulk modulus (causing injector to open earlier), higher flash point (delaying mixture ignition), higher oxidation instability (leading to higher tendency to degradation during storage) and a tendency for thickening with time (Babu and Devaradjane[11], Franco and Nguyen [28]). When using the same injectors and settings adjusted for diesel fuel, the higher viscosity, surface tension and density of the vegetable oils result in changes in injected oil volumes, injection delay after injector opening, spray patterns (cone and penetration) and atomization (droplet size distribution) (Bialkowski et al. [18]). As a result of poor atomization, mixing and ignition there are:

(a) longer ignition delay, smaller pressure rise, lower cylinder peak pressure and a longer combustion duration (Venkanna et al. [75]), resulting in 5% to 25% (Chalatlon et al. [20]) reduction in thermal efficiency at maximum power when compared to pure diesel oil,
(b) the formation of carbon deposits on fuel injectors, ring landings, exhaust valves, and contamination of the lubricating oil by vegetable oil. These effects can severely limit the engine lifespan.
(c) a reduction in the formation of NOx, but a possible increase in smoke, CO and HC (Pimentel et al. [58], Belchior and Pimentel [15]).

Tests with long term operation (> 60 hours) with neat sunflower oil (Maziero et al. [48]) have reported obstruction of the lubricating oil flow galleries, damage of piston rings and gaskets, presence of tar in the exhaust manifolds and the presence of elevated concentration of copper, chromium, iron and lead in the lubricating oil. Bialkowski et al. [18] (working with Elsbett, Germany) reported coking, spray obstruction by lacquer formation at spray tip and engine deterioration. They also reported problems with slow flow along oil lines, filter clogging and engine oil deterioration.

Since the pioneering work, a few solutions have been proposed and implemented:

(a) The viscosity of the vegetable oil can be reduced by heating (Forson et al. [30], Venkanna et al. [75], Kleinova et al. [49], Aksoi [4]). The oil temperature before injection has been regulated from 20^{o}C (Bialkowski et al. [18]) to 160^{o}C (Raghu and Ramadoss [64]). Most authors preheat the SVO such as to bring the physical properties closer to those of diesel oil. Most commonly, the oil temperature does not exceed 130^{o}C (Pugazhvadivu and Sankaranarayanan [62]).
(b) Blending vegetable oil with diesel also decreases viscosity and improves volatility. These improved properties result in better mixture formation and spray penetration. A number of investigators tried the vegetable oils in varying proportions with diesel. Most remarkably, few studies (Forson et al. [30]) show engine performance even above that of operation with neat diesel oil.

(c) Advanced injection timing compensates the effects of the longer delay period and slower burning rate that is exhibited by vegetable oils (Nwafor and Rice [52]). Staged injection may not lead to improvement in fuel/air mixing when it occurs too late along the expansion cycle (Bialkowski et al. [18]).

Most of the recent work was developed using low power single cylinder CI engines fuelled by mechanical pumps (Altin et al. [6], Forson et al. [30], Venkanna et al. [75], Pugazhvadivu and Sankaranarayanan [62], Sarada et al. [67], Aksoi [4], Martin and Prithviraja [46], Raghu and Ramadoss [64], Sivalakshmi and Balusamy [69]) in the context of the application of small engines for rural and remote areas. Fewer works were developed with larger engines for general use (Bialkowski et al. [18]), for use in agriculture (Maziero et al. [48]), and for transportation (Kleinova et al. [42], Chalatlo et al.[20]). Usually, large IDI (indirect injection compression ignition) operate better during long duration tests while small IDI and DI engines present problems (He and Bao [34], Bialkowski et al. [18]). Only Kleinova et al. [42] and Bialkowski et al. [18]) have developed their studies using common rail injection systems. Most modern CI engines nowadays employ common rail injection. The use of a central electronic unit and the common rail has enabled great advances in performance and in-cylinder emissions control using diesel oil and these improvements could also be expected when using straight vegetable oils. For example, Venkanna et al. [75] investigated the effect of the injection pressure in a mechanical system, varying the injection pressure from 200 bar to 280 bar. Even in this small range they measured differences in thermal efficiency that point out to an optimum operation pressure for a given combustion chamber, injector and oil temperature. They argue that, for their engine, a further increase in pressure would cause an excessive diminution of droplet sizes and insufficient spray penetration. They also noticed that smoke reduces continually with the increase in pressure. This indicates the need to explore further the effects of injection pressure, injection timing, and split injection.

This work is part of a larger project including engine test in a dynamometric bench, measurement of spray parameters in an interferometric laser bench and studies of maintainability of the engine when applied to stationary electricity generation. The main project is supported by the Southern Brazilian Power Plants Company through its Research and Development Fund. Here, the initial tests of a mechanical injected engine in a dynamometric bench operating with straight vegetable oils of Soybean, Sunflower and Tung and their mixtures with diesel oil are reported. This work relies on the assumption that oil heating and higher injection pressure contribute to a better spray development and atomization, leading to better performance, efficiency and smaller emission of smoke. The basic strategy for pre-heating consists in bringing the straight vegetable oil before the injector to a temperature in which the viscosity of the oil approaches that of the diesel oil at ambient temperature. To allow for the control of the fuel heating an electronically controlled heating unit was developed and adapted to the engine. This set up is described next.

2. Materials and Methods

2.1. Engine and equipments

The study was carried out in a single cylinder, 4 strokes direct injection diesel engine. The engine was coupled to a Schenck W70, Eddie Current dynamometer. The torque was measured with an Hbm Wagezelle extensometer type load cell and the speed was measured with an incremental encoder with resolution of 360 steps. The temperature of the exhaust gases was measured in the exhaustion manifold, close to the exhaustion valve. The concentration of the exhaust gases were measured with a Testo Portable Gas Analyzer, model 350-XL. The mass of the fuel was measured with a Shimadzu electronic balance model UX 8200S. The entire experimental operation was

controlled using a student version of the LabVIEW software. Table 2 lists the main characteristics of the engine.

Table 2. Engine basic characteristics.

Manufacturer	Yanmar
Model	YT22
Bore [mm]	115
Stroke [mm]	115
Compression Ratio	17.3:1
Volume [cm³]	1194
Nominal conditions:	
Speed [rpm]	2000
Power [kW]	14,7
BSFC [g (kWh)-1]	238
Injection pressure [bar]	200
Injection timing [°BTDC]	18

The engine had a mechanical speed control system that uses a mechanism called *governor*. To adjust the engine to full load, the handle load is set to its maximum. This load handle is connected to an arm that directly acts in the engine injection pump, controlling the fuel flowing to the combustion chamber. Between the handle and the arm there is a spring. Also connected to the arm, there is a centrifugal regulator that acts towards diminishing the fuel flowing if the engine speed increases. The engine subsystem formed by the arm, the spring and the centrifugal regulator is called *governor*. The governor has the function of keeping the engine in the same speed set by the operator, when the engine is subject to variable loads. Figure 1 pictures the governor.

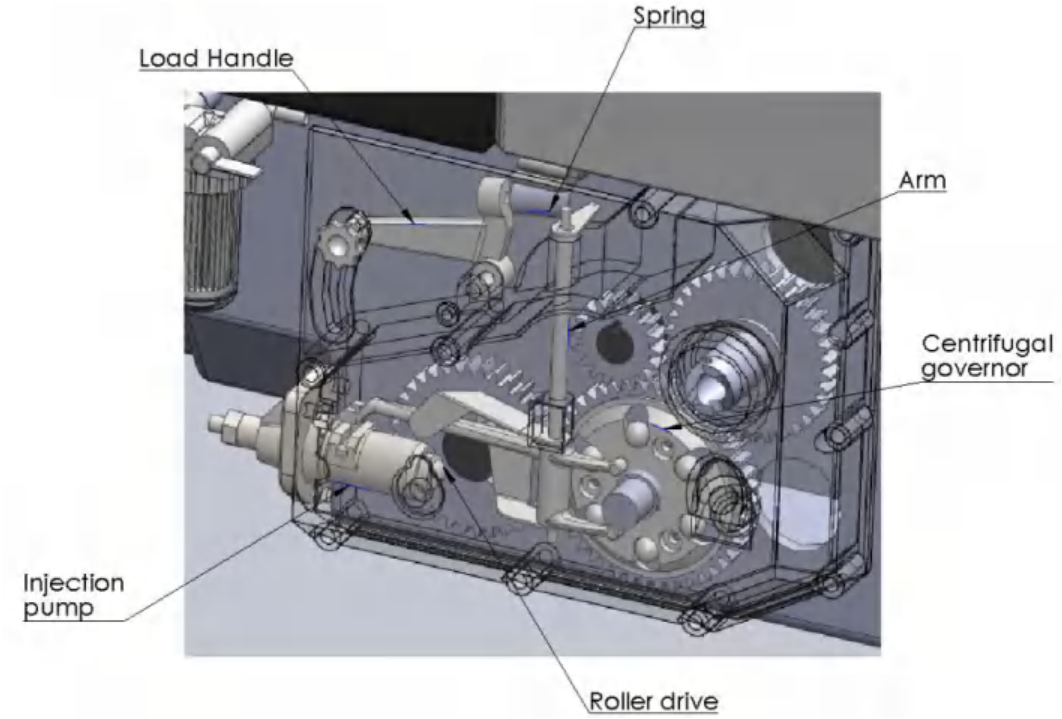

Fig. 1. Drawing of the governor subsystem and synchronizer gears.

The constant speed range is possible for a limited range of load. To obtain a constant speed range, the spring is initially partially unstretched. When the engine is started at a low load, this regulation establishes a given rotation speed. Then, when the dynamometer breaks the engine increasing the load, the engine speed tends to decrease. But, the springs pulls the arm back increasing the fuel flow

to the engine, bringing back the speed to the initially value set. In this regime, the speed remains approximately constant, as presented in the high speed range (> 2000 rpm) in figure 2. This process continues until the spring is totally stretched. When this occurs, any subsequent increase in the dynamometer load result in the decrease of the engine speed, completing the remaining of the characteristic curves, as showed for the lower speeds (< 2000 rpm) in figure 2.

2.2. Test Procedure

The experimental procedure starts with the engine warm up at full load using neat regular diesel oil until the temperature of its coolant reaches 70°C. Then, the fuel is switched to the fuel of interest and the engine operation at full load is allowed to stabilize for 10 min. After stabilizing at full load, the brake is applied and the speed is allowed to change from 2200 rpm to 1500 rpm in about 10 steps.

Each complete run takes about 2 hour and leads to the full load curve of the engine. The data acquisition is synchronized and rotation, torque, engine coolant temperature, instantaneous fuel mass, fuel temperature, inlet air humidity and temperature, exhaust gas temperature and concentration of CO, CO_2 and NO_x are recorded. Each complete run was repeated at least three times, until statistical repeatability was observed.

2.3. Measurement uncertainties

The uncertainty of the reported measurements was estimated based on the uncertainty of each equipment used for the measurement of the base variables and with the statistical uncertainty related to the number of experiments. Table 3 summarizes the expanded uncertainties. It can be observed that the measurement of emissions has the greater expanded uncertainty while the results obtained in the dynamometric bench are associated to smaller uncertainties.

Table 3. Expanded uncertainty of each measurement.*

Measurements	***Expanded Uncertainty [%]***
Engine Speed	± 2.5
Break Torque	± 2.8
Power	± 2
Fuel Mass Rate	± 6.3
Specific Fule Consumption	± 6.1
Efficiency Fisrt Law	± 6.1
CO	± 9
CO_2	± 13
NO_x	± 8
Exhaust gas temperature	± 0.8

*Expanded uncertainty as a percentage of the mean value for a probability of 95%.

3. Fuels

The three vegetable oils and their blends with commercial Brazilian agricultural diesel oil were used. Brazilian diesel oil has a volumetric addition of 5% of biodiesel, as required by law and regulated by ANP, the National Petroleum Agency. The fuels used are labelled as presented in Table 4.

The straight vegetable oils and their respective mixtures were preheated before injection in the engine. The strategy was to bring the fuel properties close to those of diesel oil. For that, the viscosities of the fuel mixtures were measured as a function of temperature by standardized

viscosity experiments carried out in the National Institute of Technology (INT [37]) at Rio de Janeiro. Table 5 summarizes the injection temperature, the kinematic viscosity and the specific mass of the fuel blends. The specific mass was measured using Archimedes principle with a Kern electronic balance model EW 220 – 3 NW. The fuel temperature was kept sufficiently low to avoid thermal degradation.

Table 4. Nomenclature for the fuel mixtures used.

100% SW	Straight Sunflower Oil
100% SY	Straight Soybean Oil
100% TG	Straight Tung Oil
50%SW-50%D	Volumetric Mixture between Sunflower Oil and diesel oil
50%SY-50%D	Volumetric Mixture between Soybean Oil and diesel oil
50%TG-50%D	Volumetric Mixture between Tung Oil and diesel oil
100% D	Brazilian Commercial (countrifield) diesel oil

Table 5. Injection temperatures and kinematic viscosity measured (INT [37]).

Fuel	***Injection Temperature [°C]***	***Kinematic Viscosity [mm²/s]***	***Specific mass [kg/m^3]***
100% SW	85	10.52	863.2
100% SY	85	8,48	859.8
100% TG	95	16.33	869.1
50%SW-50%D	65	5.45	857.4
50%SY-50%D	65	5.53	856.1
50%TG-50%D	85	8,26	854.9
100% D	25	4.52	846.4

Table 6 summarizes the energy content of the fuel blends. It is observed that the diesel oil has the higher lower heating value (LHV), which is about 15% greater than that of the straight vegetable oils. For completeness, Table 7 shows the results for an elemental analysis of the vegetable oils. For comparison, for an alkane with sixteen carbon atoms, the percentage mass of carbon is near 85% and of hydrogen is 15%.

Table 6. Energy content of the fuel blends (INT [37]).

Fuel	***LHV (kcal/kg)***	***% diff. in respect to diesel***	***Method***
100% SW	8649 ±7	*14.9*	*ASTM D 4809*
100% SY	8678 ±5	*13.6*	*ASTM D 4809*
100% TG	*8553*	*13.9*	*ASTM D 4809*
100% D	*10047*	*0*	*Estimated by ANP Standards*

Table 7. Elemental analysis of the straight vegetable oils (INT [37]).

	Soybean	***Sunflower***	***Tung***	***Method***
Carbon (%m/m)	76.91	*77.61*	*77.51*	*ASTM D 5291*
Hydrogen (%m/m)	11.40	11.29	11.40	*ASTM D 5291*
Nitrogen (%m/m)	2.03	*0*	*0*	*ASTM D 5291*
Total sulphur (mg/kg)	1.24	1.49	*0.60*	*ASTM D 5453*

The main technical development in this project is the conversion kit to control the preheating of the straight vegetable oils and blends to the temperatures showed in table 3. It is important that besides preheating the fuels, the temperature must be controlled within a narrow range. The electronic control unit – ECU was developed and assembled in the lab. The main component of the ECU is a microcontroller model dsPIC. The conversion kit preheats the vegetable oil using the rejected heat of the engine. This heat is recovered from the exhaust gases by a heat exchanger that uses a solution of water and mono-ethylene glycol as thermal fluid. The solution is then pumped to another heat exchanger, where the vegetable oils are heated to the selected temperature. The temperature of the vegetable oil is measured at the outlet of the heat exchanger. This value is sent to the ECU that controls the temperature of the vegetable oils by controlling the flow of the thermal fluid. A second conversion kit that will allow the use of a *common rail* system is under development. The results reported here were obtained with a mechanical control of injection, as it will be explained below.

4. Results

In this section, the results obtained in the dynamometric bench are shown. Figures 2 and 3 present power. Figure 4 presents the thermal efficiency. Figures 5 and 6 present fuel consumption. Figures 7 to 9 present emissions and exhaust gas temperature.

In figure 2, the region for speed higher than 2000 rpm corresponds to the spring-controlled regime. In this region, the curves for all fuels are similar. This is supposed to occur, since the governor will allow for the fuel needed to sustain a constant speed. The fact that this is observed in the results indicates that no accidental event occurred. In the following, each curve is analyzed separately.

4.1. Engine performance

Figure 2 presents power as a function of engine speed for the 3 oils and their blends with diesel oil. At all speeds, the tendency for higher power follows tung, soybean, sunflower and diesel oil. This is the same behaviour commonly reported in the literature (Altin et al. [6], Venkanna et al. [75], Pugazhvadivu and Sankaranarayanan [62], Sarada et al. [67], Aksoi [4], Martin and Prithviraja [46], 2011; Raghu and Ramadoss, 2011; Sivalakshmi and Balusamy, 2011; Tripathi and Sahoo, 2011; Maziero et al. [48], Kleinova et al. [42], Chalatlo et al. [20],). As an exception for this behavior, Balafoutis et al. [15], using cottonseed, rapeseed and sunflower in a Case-New Holland compression ignition engine, with 4 cylinders, turbo charged (bore of 104 mm, displacement of 132 mm), reported that all oils resulted in higher power when compared to diesel oil, being the largest value of 10% provided by rapeseed.

Here, tung oil resulted in the lower power, which is 14% smaller than the power produced by the diesel oil at the speed of 2000 rpm, the speed for maximum power. This is the same relation that exists between the LHV of both fuels, according to Table 6. However, although the other fuels also present an approximate 14% reduction in LHV, the reduction in maximum power is smaller. This indicates that either the specific fuel consumption will be higher, or a better thermal efficiency will be achieved. For all fuels, the blending with diesel oil increased the power, but it remained still smaller than that for neat diesel oil. Both blends of sunflower and soybean equally approximate the power delivered by neat diesel oil, with only a 4% decrease at 2000 rpm. These percentage differences can be seemed in figure 3.

Reporting back to Table 4, we observe that the viscosity increase in the sequence diesel oil, soybean oil, sunflower oil and tung oil. The peak power presented in Figure 2 also decreases in the same sequence. Also, the curves could be separated in three groups formed by, respectively, (1) the blends of soybean and sunflower oils, (2) the straight soybean, sunflower and the blend of tung oil and (3) the straight tung oil. This is also in accordance with the distribution of viscosities showed in Table 6.

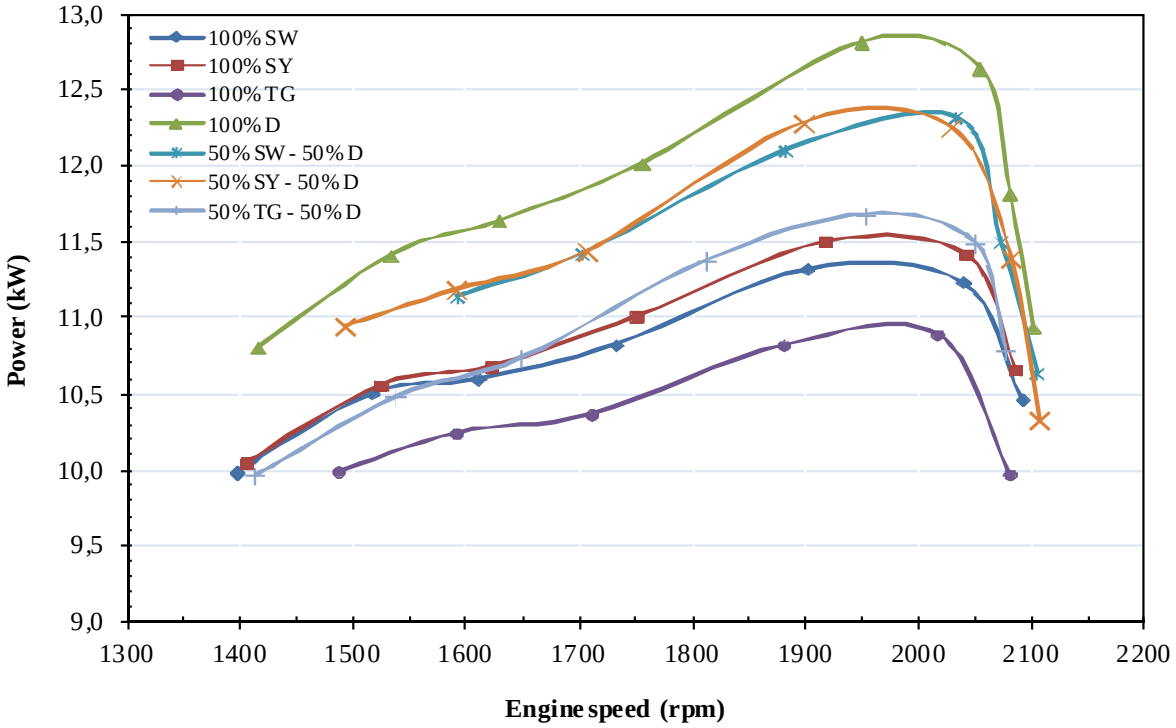

Fig. 2. Power versus engine speed.

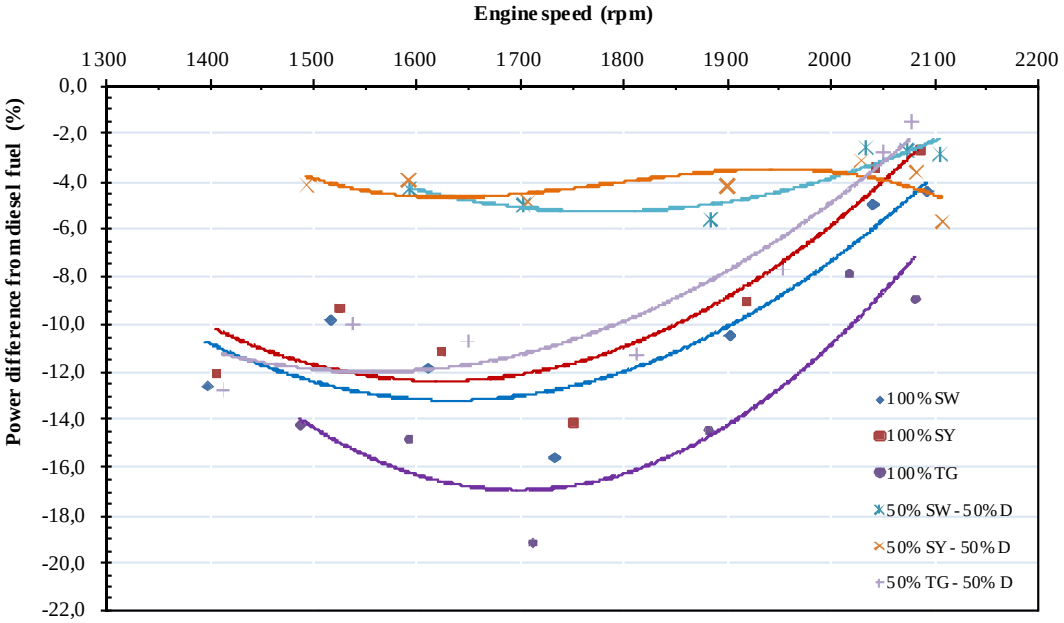

Fig. 3. Percentage delivered power difference versus engine speed. The lines represent 2nd degree polynomial curve fits.

Figure 4 presents the mean value of fuel mass injected per cycle as a function of engine speed. The amount of fuel injected increases as the speed decreases for all fuels. This occurs because when the speed decreases, the roller that drives the injection pump actually stays longer pressing the pump, thus injecting a larger amount of fuel. Notice that this increase in fuel injected per cycle may not mean an increase in fuel mass flow rate.

Since the engine speed is decreasing and the load handle and the spring are both promoting the maximum pump injector aperture, i.e. the set volumetric flow rate to the injection pump is the same for the range since 2000 rpm to lower speeds, the volumetric fuel flow increases with the decrease of the engine speed. It is interesting to note that, again, the vegetable oils delivered lower torque than diesel oil, as can be obtained through the analysis of figure 2.

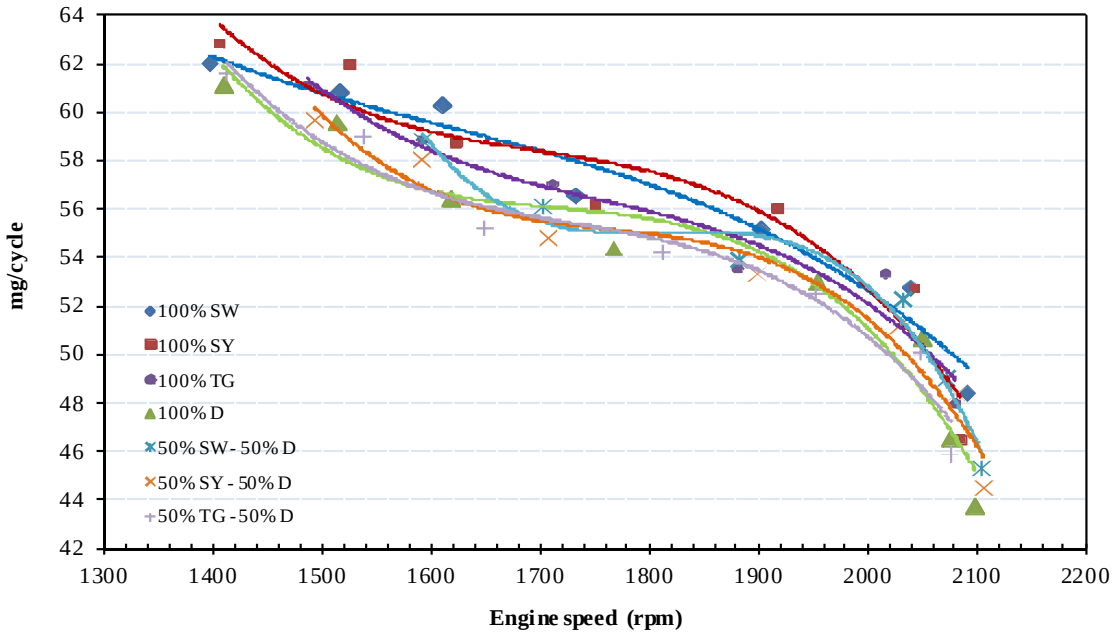

Fig. 4. Mean fuel mass flow per engine cycle versus engine speed. The lines represent 2nd degree polynomial curve fits.

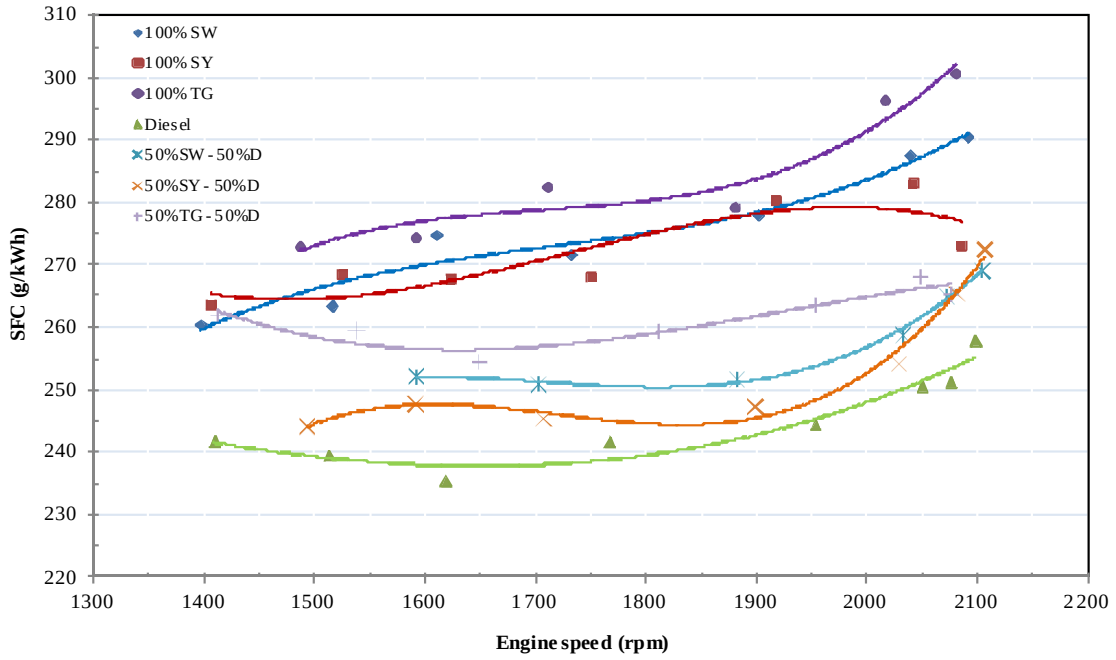

Fig. 5. Specific fuel consumption - BSFC versus engine speed. The lines represent 2nd degree polynomial curve fits.

Figure 5 presents the brake specific fuel consumption (BSFC) as a function of engine speed for the different oils and their blends. The BSFC increases with speed. All vegetable oils and blends result in higher BSFC when compared to diesel oil. The BSFC for tung oil at 2000 rpm is approximately 18% higher than that for diesel oil. The blend with 50% soybean oil approximates more the BSFC of the diesel oil than the BSFC of the pure soybean oil, resulting in a 2% increase only at 2000 rpm. We note that the BSFC for diesel oil at the nominal speed matches the value listed in Table 2.

4.2. First law thermal efficiency

Figure 6 presents the first law efficiency as a function of engine speed. The efficiency remains approximately constant up to 1800 rpm, where it falls about 4%. The thermal efficiency for tung oil and its blend is smaller than that for diesel oil, but the efficiency of all the other fuels is in fact higher. Balafoutis et al. [15] have reported an increase of 8% over the efficiency of neat diesel oil when neat rapeseed oil is used (reaching 39% thermal efficiency), 2% with cotton seed and a drop of 3% for sunflower. Here, best efficiencies (around 37.5%) are achieved by the 50% blend of soybean, which are about 6% higher than that for neat diesel at 2000 rpm. The blends of soy and sunflower present thermal efficiencies that are higher than the neat fuels themselves. Remarkably, Forson et al. (2004) reported a 33% increase in thermal efficiency over neat diesel for a 2.6% jatropha oil blend (reaching 20% thermal efficiency). Somehow, there is some improvement when the fuels are mixed.

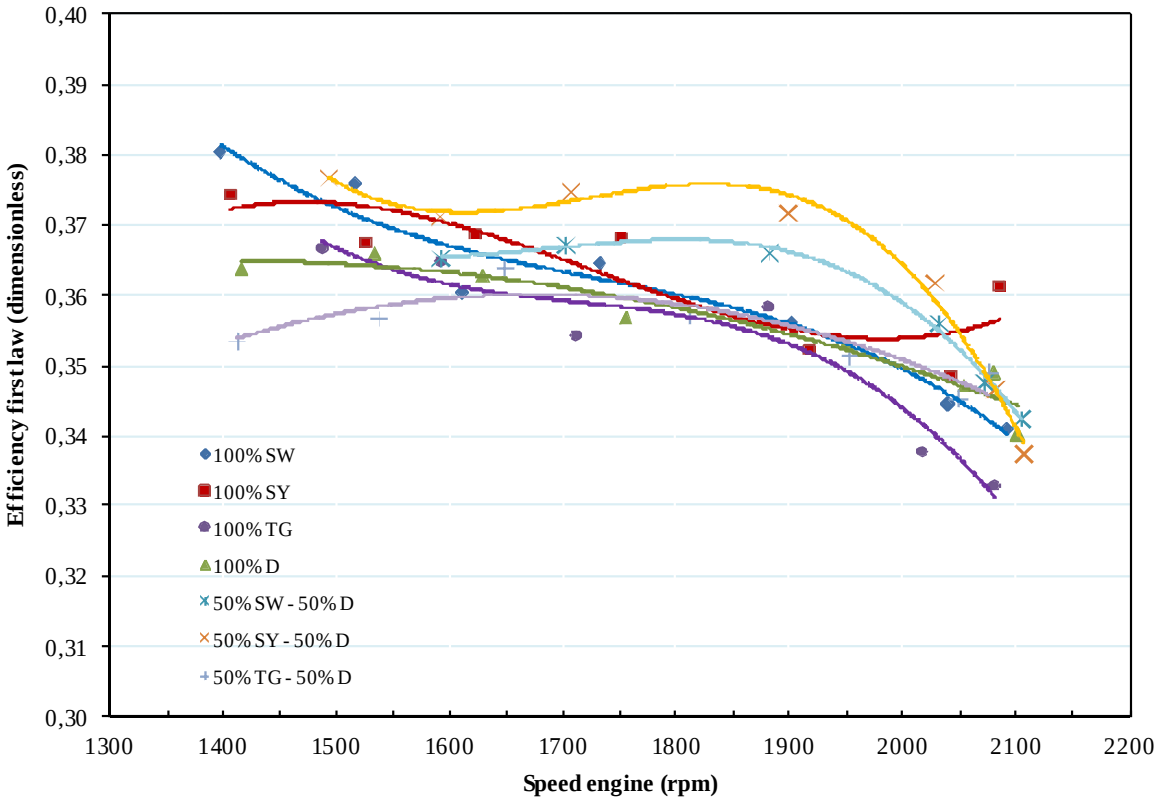

Fig.6. First law efficiency versus engine speed. The lines represent 2nd degree polynomial curve fits.

4.3. Emission of gas pollutants

Figure 7 presents the volumetric CO fraction in the exhaust gases as a function of engine speed. The CO emissions are related with the combustion efficiency. The CO increases as the speed is reduced as a result of excessive enrichment of the fuel/air mixture, as indicated in figure 4. Tung, soybean and the blend with tung resulted in higher emission of CO. Neat sunflower is equivalent to diesel oil. While the blend with sunflower increase the emission of CO, the blend with soybean decrease the emission of CO, becoming actually equivalent to the emission of diesel oil.

Figure 8 presents the volumetric NO_x fraction in the exhaust gases as a function of engine speed. The operation with soybean and tung resulted in smaller emission of NOx. Sunflower resulted in a mirrored higher emission of NOx. It was noted that sunflower and soybean resulted both in approximately the same values of power and BSFC, but sunflower emitted less CO than soybean.

Figure 9 presents the temperature of the exhaust gases as a function of engine speed. All vegetable oils and their blends present lower exhaust gas temperature than diesel oil. Sunflower and tung present the same exhaust temperature while soybean present the higher temperature.

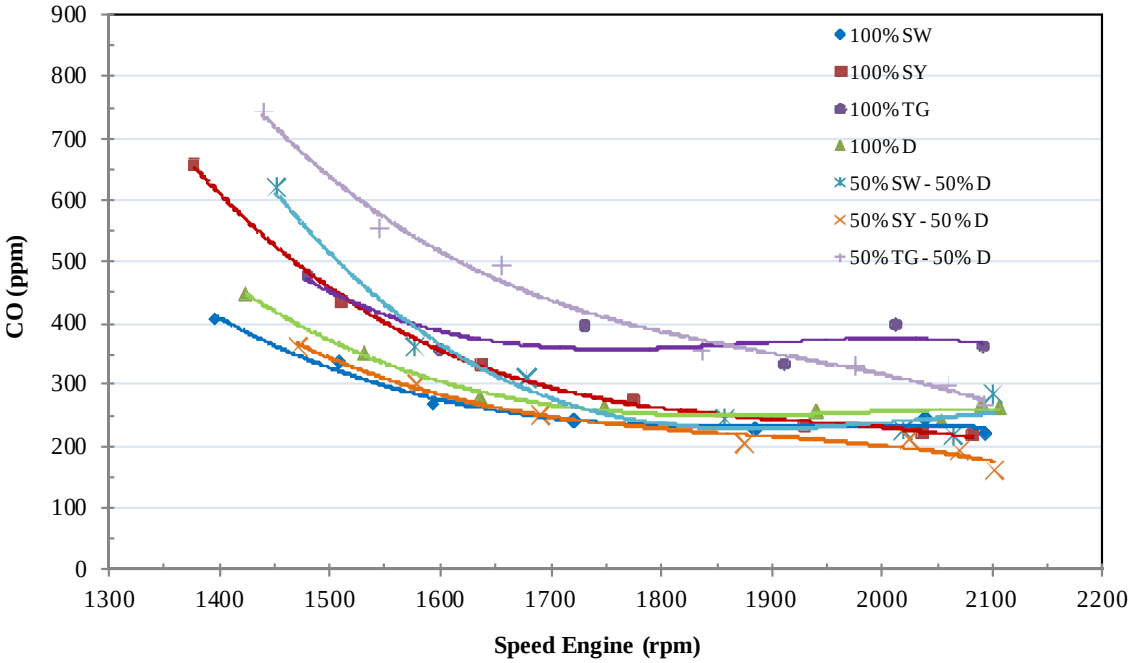

Fig. 7. Fraction of CO in exhausted gases versus engine speed.

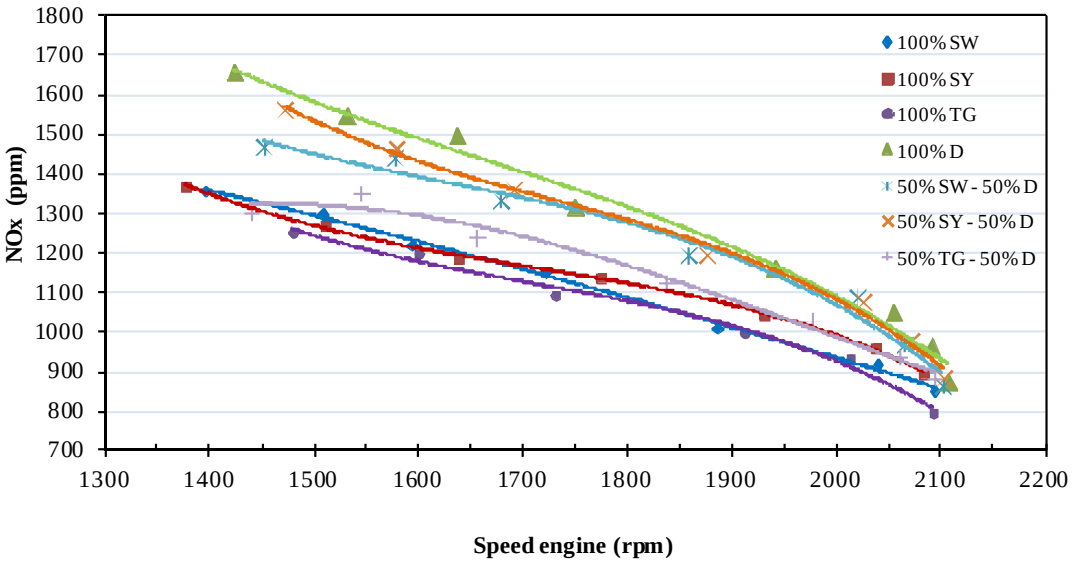

Fig. 8. Fraction of NOx in exhausted gases versus engine speed. The lines represent 2nd degree polynomial curve fits

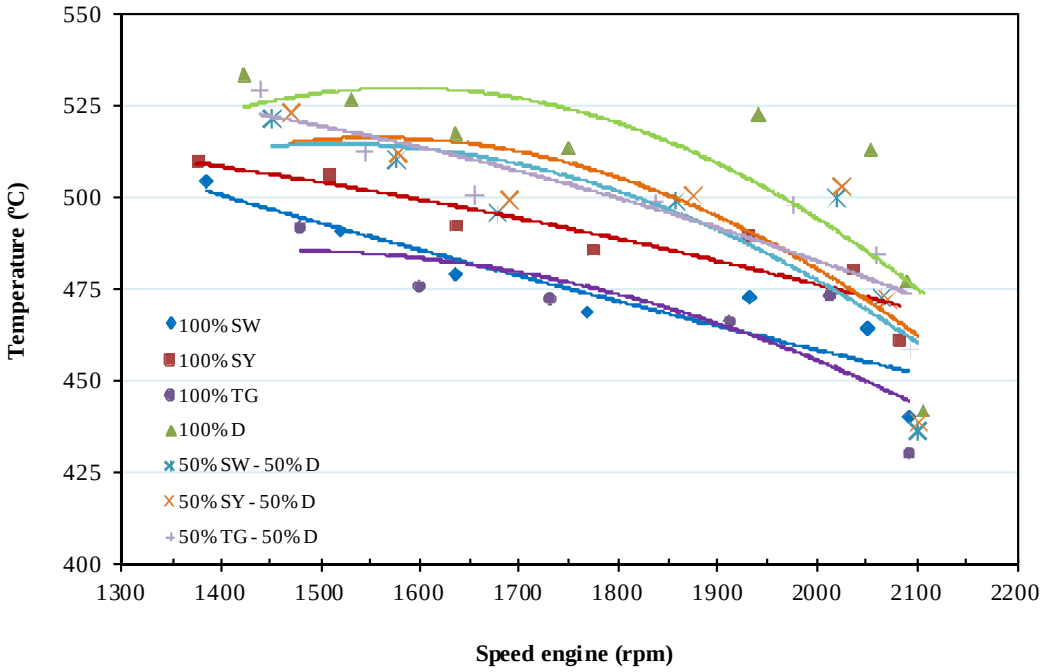

Fig. 9. Temperature of the exhaust gases versus engine speed. The lines represent 2nd degree polynomial curve fits.

The lower exhaust temperature is consistent with the higher efficiency, since more of the fuel energy is being transformed into useful work.

5. Conclusions

The results show that the engine and heating system worked reasonably well for the straight vegetable oils and their blends used.

The curves of power and specific fuel consumption as a function of engine speed behaved in accordance with the values of LHV and specific mass of vegetable oils and their blends. The lower LHV and higher specific mass of the SVO fuel tested led to a decrease in power as well as to an increase in specific fuel consumption when compared to the operation with neat diesel oil.

The results for thermal efficiency were particularly interesting. They showed that the thermal efficiency for sunflower and soybean oils are higher than that for the neat diesel oil. Besides, the best efficiencies (around 37.5%) were achieved by the 50% blend of soybean, which are about 6% higher than that for neat diesel at the same power output of 11 kW, at 1500 rpm. Also, the blends of soybean and sunflower presented thermal efficiencies that were higher than the diesel oil and the neat fuels themselves. Somehow, there is some improvement when the fuels are mixed. The reason for this behaviour is not clear at the moment. This is encouraging from the point of view of increasing the efficiency of the electrical energy generation systems.

The CO emitted by the engine increased as the engine speed decreased. This occurred because the mechanical control of injection results in higher amount of fuel injected per cycle as the speed is reduced. Since the volumetric efficiency remains constant or decreases (it was not measured), the mixture might become richer for lower speeds and burn over a longer combustion period. The emission of NOx is also higher at lower speeds, as a result probably of a longer residence time at lower speeds. The exhaust gas temperature was lower for the vegetable oils and their blends when compared to neat diesel, indicating that there is room to improve atomization and combustion.

In order to improve atomization, a common rail system will be adapted to the engine to provide injection pressures up to 800 bar. Also, the use of an electronically controlled injection system will

allow for a more systematic study of the effect of the advance in the injection timing and the use of a pre-injection. This will be reported later, in a future paper.

Acknowledgments

To Eletrobrás Eletrosul Centrais Elétricas S. A. for the financial support.

Abbreviations and Acronyms

ANP	Agência Nacional de Petróleo
BSFC	Brake Specific Fuel Consumption
CI	Compression Ignition
DI	Direct Injection
ECU	Electronic Control Unit
IDI	Indirect Injection
INT	National Institute of Technology
LHV	Lower Heating Value
SVO	Straight Vegetable Oil

References

[1] Agarwal D., Agarwal A. K. Performance and emissions characteristics of Jatropha oil (preheated and blends) in a direct injection compression ignition engine. Appl. Therm. Eng., 27: 2314-223, 2007.

[2] Agarwal, A. K., Biofuels (alcohols and biodiesel) applications as fuels for internal combustion engines, Progress in Energy and Combustion Science, Volume 33, Issue 3, pp 233-271, 2007.

[3] Agarwal, A. K., Rajamanoharan K., Experimental investigations of performance and emissions of Karanja oil and its blends in a single cylinder agricultural diesel engine. Appl. Energy, 86(1): 106-112, 2009.

[4] Aksoy, F., The effect of opium poppy oil diesel fuel mixture on engine performance and emissions International Journal of Environment Science and Technology, Vol. 8, No. 1, pp. 57-62, 2010.

[5] Almeida, S. C.A., Belchior C. R., Nascimento M.V. G., Vieira L. Dos S. R., Fleury G. Performance of a Diesel Generator Fuelled with Palm Oil. Fuel 81, PP 2097-2102, 2002.

[6] Altin, R. Cetinkaya, S., and Yucesu, H. S., The potential of using vegetable oil fuels as fuel for diesel engines, International Journal of Energy conversion and management Vol. 42, pp 529-538, 2001.

[7] Altun, S., Oner, C., Biodiesel production from inedible animal tallow and an experimental investigation of its use as alternative fuel in a direct diesel engine, Applied Energy, 86, pp 2114 - 2120, 2009.

[8] Amba, P. R. G. and Rama, M.P., Effect of Supercharging on performance of DI Diesel engine with cotton seed oil, Energy Conversion and Management, 44, pp. 937 – 944, 2003.

[9] Andrade, R. M. T., and Miccolis A., Biodiesel in the Amazon. ICRAF Working Paper no. 113. Nairobi, Kenya: World Agroforestry Centre, 2010.

[10] Antwi, E., Experimental analysis of vegetable oil blends in a compression ignition (CI) engine, Master Thesis, Mechanical Engineering, Kwame Nkrumah University of Science and Technology, Ghana, 2008.

[11] Babu, A. K. and Devaradjane, G., Vegetable Oils And Their Derivatives As Fuels For CI Engines: An Overview, SAE Technical Paper 2003-01-0767, 2003.
[12] Bari, S., Roy, M. M., Prospect of rice bran oil as an alternative to diesel, Proc. of the Fifth Int. Conf. on small engines, their fuels and the environment. The Universty of Reading, UK, pp. 31-36, 1995.
[13] Bari, S., Lim T. H. and Yu, C. W. , Effect of preheating crude palm oil on injection system performance and emissions of a diesel engine. Renew. Energy. 77, 339-351, 2002.
[14] Barsic, N. J and Humke, A. L., Performance and emissions characteristics of a naturally aspirated diesel engine with vegetable oil fuels. SAE. 810262, 1173-1187, 1981.
[15] Belchior, C. R. P., Pimentel, V. S. B., The use of palm oil in diesel engine, 18th International Congress of Mechanical Engineering, Ouro Preto – MG – Brasil, 2005.
[16] Bettis, B. L., Peterson, C. L., Auld, D. L. , Driscoll, D. J., and Peterson, E. D. ,Fuel characteristics of vegetable oil from oilseed crops in the Pacific Northwest. Agronomy Journal, 74(March/April) pp 335-39,1982.
[17] Bhattacharya, .S and Reddy, C.S, Vegetable oils as Fuel for Internal combustion Engines: A Review, Journal of Agricultural, Engineering Research. 57, pp. 157-166, 1994.
[18] Bialkowski, M.T.; Pekdemir, T.; Reuben, R.; Brautsch, M.; Towers, D. P.; Elsbett, G., Preliminary Approach Towards a CDI System Modification Operating on Neat Rapeseed Oil Journal of KONES, vol 12 Issue 1, 2005.
[19] Bialkowski, M. T., Theoretical And Experimental Investigation Of A Cdi Injection System Operating On Neat Rapeseed Oil - Feasibility And Operational Studies, Ph.D. Thesis, Heriot-Watt University, 2009.
[20] Chalatlon, V., Roy, M. M., Dutta, A., Kumar, S., Jatropha oil production and an experimental investigation of its use as an alternative fuel in a DI diesel engine, JPTAF, 2(issue 5), pp 76-85, 2011.
[21] Chandra, V. M. R., Experimental investigations on a four stroke compression ignition engine using Eco friendly Non edible vegetable oils, PhD Thesis, Jawaharlal Nehru Technological University, 2011.
[22] Chang, C. C., Wan, S. W., China's Motor Fuels from Tung Oil, Ind. Eng. Chem. 39, pp 1543-1548, 1947.
[23] Chauhan, B. S., Kumar N., Jun Y. D. , Lee K. B., Performance and emission study of preheated Jatropha oil on medium capacity diesel engine. Energy, 35, pp 2484-2492, 2010.
[24] CONAB, Brazilian Crop Assessment: Grain, National Company of Food Supply, Third Assessment, Brasilia, December, 2011.
[25] Dwivedi, D., Agarwal, A. K. and Sharma, M., Particulate Emission Characterization of a Biodiesel vs. Diesel-Fuelled Compression Ignition Transport Engine: A Comparative Study, Atmo-
[26] spheric Environment, 40, 5586-5595, 2006.
[27] Engelman, H. W., Guenther, D. A., and Silvis, T. W., Vegetable oil as a diesel fuel. Diesel and Gas Engine Power Division of ASME Paper Number 78-DGP-19. New York, NY: ASME, 1978.
[28] Franco, Z., Q.D. Nguyen, Flow properties of vegetable oil–diesel fuel blends, Fuel, Volume 90, Issue 2, Pages 838-843, 2011.
[29] Fontaras, G., Samaras, Z., Miltsios, G., Experimental evaluation of cottonseed oil- diesel blends as automotive fuels via vehicle and engine measurements. SAE paper, No. 2007-24-0126, 2007.
[30] Forson, F. K., Oduro, E. K., Hammond-Donkoh, E., Performance of Jatropha oil blends in a diesel engine. Renew. Energ. 29(7): 1135-45, 2004.
[31] Giannelos, P. N., Zannikos, F., Stournas, S., Anastopoulos, G., Tobacco seed oil as an alternative diesel fuel: physical and chemical properties, Industrial Crops and Products, 16, pp. 1– 9, 2002.

[32] Haldar, S. K., Ghosh BB, Nag A. Studies on the comparison of performance and emission characteristics of a diesel engine using three degummed non-edible vegetable oils. Biomass Bioenerg. 33: 1013-1018, 2009.
[33] Hazar, H., Aydin, H., Performance and emission evaluation of a CI engine fuelled with preheated raw rapeseed oil (RRO)-diesel blends. Appl. Energy, 87(3): 786-790, 2010.
[34] He, Y., and Bao, Y. D., Study on cottonseed oil as a partial substitute for diesel oil in fuel for single-cylinder diesel engine. Renewable Energy, 30: 805-813, 2005.
[35] Herchel, T., Machacon, C., Matsumoto, Y., Ohkawara, C., Shiga, S.,Nakamura, H. The effect of coconut oil and diesel fuel blends on diesel engine performance and exhaust emissions, JSAE Review, Volume: 22, Issue: 3, Pages: 349-355, 2001.
[36] Heywood, J. B., Internal Combustion Engine Fundamentals. New York, USA: McGraw-Hill Inc, 1988.
[37] INT, Experiment Report 00300/2011, National Institute of Technology, Rio de Janeiro-RJ, 2011.
[38] Isigigur, A. , F. Karaosmanoglu, H. A. Aksoy, Hamdullahpur, F. and Gulder, O. L. , Safflower seed oil of Turkish origin as a diesel fuel alternative, Applied Biochemistry and Biotechnology, Volume 39-40, Number 1, 89-105, 1993.
[39] Karaosmanoglu, F., Kurt, G., Özaktaş, T., Long term CI engine test of sunflower oil, Renewable EnergyVolume 19, Issues 1–2, Pages 219–221, 2000.
[40] Knothe, G., Historical Perspectives on Vegetable Oil-Based Diesel Fuels, Inform, Volume 12, pp. 103-1107, 2001.
[41] Kalam, M. A. , Husnawan, M., Masjuki, M. H., Exhaust emission and combustion evaluation of coconut oil-powered indirect injection diesel engine. Renewable Energy, 28: 2405–2415, 2003.
[42] Kleinova, A., Vailing I., Franta, R., Mikulec, J., Cvengroš, J., Vegetable oils as diesel fuels for rebuilt vehicles, 44th International Petroleum Conference, Bratislava, Slovak Republic, September 21-22, 2009.
[43] Knothe, G. H. Hictorical Perspectives on Vegetable Oil-Based Diesel Fuels. 2001. Available at: http://www.ars.usda.gov. [Acessed 24.8.2011].
[44] Kumar, M. S., Ramesh, A., Nagalingam, B., An experimental comparison of methods to use methanol and Jatropha oil in a compression ignition engine, Biomass Bioenerg., 25: 309-318, 2003.
[45] Lefebvre A. H., Atomization and Sprays. Boca Raton/FL, USA: Routledge Taylor and Francis Group, 1989.
[46] Martin, M. and Prithviraj, D., Performance of Pre-heated Cottonseed Oil and Diesel Fuel Blends in a Compression Ignition Engine, Jordan Journal of Mechanical and Industrial Engineering, Volume 5, Number 3, pps 235 – 240, 2011.
[47] Martines-Filho, J., Heloisa L. Burnquist, and Carlos E. F. Vian, Bioenergy and the Rise of Sugarcane-Based Ethanol in Brazil, CHOICES, 2nd Quarter, 21(2), 2006.
[48] Maziero, J. V. G., Corrêa, M., Úngaro, M. R., Bernardi, J. A., Storino, M., Diesel Engine Performance With Raw Sunflower Oil Fuel, R. Bras. Agrociência, Pelotas, v. 13, n. 2, p. 249-255, abr-jun, 2007.
[49] Naga, P. Ch. S, Vijaya, K.R.K, Kumar, B.S.P., Ramjee., E., Hebbel, O.D. and Nivendg,i M.C., Performance and emission characteristics of a diesel engine with castor oil, Indian Journal of Science and Technology, 2 (No.10), pp.25-31, 2009.
[50] No, S. Y., Inedible vegetable oils and their derivatives for alternative diesel fuels in CI engines: A review. Renewable Sustain. Energy Rev., 15: 131-14, 2011.
[51] Nwafor, O. M. I., The effect of elevated fuel inlet temperature on performance of diesel engine running on neat vegetable oil at constant sspeed conditions. Renewable Energy 28, pp 171-181, 2003.
[52] Nwafor, O. M. I., Emission Characteristics of Diesel Engine Running on Vegetable Oil With Elevated Fuel Inlet Temperature. Biomass and Bioenergy 27, PP 507-511, 2004.

[53] Nwafor, O. M. I. and Rice, G., "Performance of rapeseed oil blends in a diesel engine", International Journal of Applied Energy, Vol.54, No.4, 1996, 345-354.
[54] Park, H. S., Kim, H. J., Suh, H. K., Lee, C. S., Experimental and numerical analysis of spray-atomization characteristicas of biodiesel fuel in various fuel and ambient temperatures conditions, International Journal of Heat and Fluid Flow 30, pp960-970, 2009.
[55] P. K. Devan and N. V. Mahalakshmi, "Performance, emission and combustion characteristics of poon oil and its diesel blends in a DI diesel engine", Fuel, Vol. 88, 2009, 861-867.
[56] Peterson, C. L., Auld, D. L., Korus, R. A., Winter rape oil fuel for diesel engines: Recovery and utilization, Journal of the American Oil Chemists' Society, Volume 60, Number 8, 1579-1587, 1983.
[57] Pousa, G. P.A.G., André L.F. Santos, Paulo A.Z. Suarez, History and policy of biodiesel in Brazil, Energy Policy, Volume 35, Issue 11, Pages 5393–5398, 2007.
[58] Pimentel, V. S. De B., Belchior, C. R. P. , Pereira, P. P., Avaliação Experimental do Desempenho e Emissões de Motores Diesel Usando Misturas de Óleo de Mamona e Óleo Diesel. AGRENER 2004: Proceedings of the 16Th Conference on Rural Energy. Brasilia-DF, Brasil. PP 504-513, 2004.
[59] Mondal, P., Basu, M.,Balasubramanian, N., Direct use of vegetable oil and animal fat as alternative fuel in internal combustion engine, Biofuels, Bioproducts and Biorefining, Volume 2, Issue 2, pp 155–174, 2008.
[60] Pramanik K. (2003). Properties and use of Jatropha oil and diesel blends in compression ignition engine. Renewable Energy, 28: 239-248.
[61] Pryor, R. W., Hanna, M. A., Schinstock, J. L. and Bashford, L. L., Soybean oil fuel in a small diesel engine. Transactions of the ASAE 26(2): 333-337, 1983.
[62] Pugazhvadivu, M., and Sankaranarayanan, G., Experimental studies on a diesel engine using mahua oil as fuel, Indian Journal of Science and Technology Vol. 3 No. 7 ISSN: 0974-6846, 2010.
[63] Quick G. R. (1980). Developments in use of vegetable oils as fuel for diesel engines. ASAE Paper, No. 80-1525.
[64] Raghu, R., Ramadoss, G., Sairam, K., Arulkumar, A., Experimental Investigation on the Performance and Emission Characteristics of a DI Diesel Engine Fueled with Preheated Rice Bran Oil European Journal of Scientific Research, Vol.64 No.3, pp. 400-414, 2011.
[65] Rakopoulos, C. D., Olive oil as a fuel supplement in DI and IDI diesel engines, Energy, Volume 17, Issue 8, August 1992, Pages 787–790.
[66] Rakopoulos, D. C., Rakopoulos, C.D., E.G. Giakoumis, A.M. Dimaratos, M.A. Founti, Comparative environmental behaviour of bus engine operating on blends of diesel fuel with four straight vegetable oils of Greek origin: Sunflower, cottonseed, corn and olive, Fuel, Volume 90, Issue 11, November 2011, Pages 3439-3446.
[67] Sarada, S. N., Shailaja, M., K. Kalyani Radha, Optimization of injection pressure for a compression ignition engine with cotton seed oil as an alternate fuel, International Journal of Engineering, Science and Technology, Vol. 2, No. 6, pp. 142-149, 2010.
[68] Sidibé, S.S., Blin, J. , Vaitilingom, G., Azoumah, Y., Use of crude filtered vegetable oil as a fuel in diesel engines state of the art: Literature review, Renewable and Sustainable Energy Reviews, Volume 14, Issue 9, Pp 2748-2759, 2010.
[69] Sivalakshmi, S., Balusamy, T.,Experimental investigation on a diesel engine using neem oil and its methyl ester, Thermal Science Year, Volume 15, Issue 4, pp 1193 - 1204, 2011.
[70] Sapaun, S. M., Masjuki, H. H., Azlan, A., The use of palm oil as diesel substitute. Power Energy (Part A) 210: 47-53, 1996.
[71] Sinha, S., Misra, N. C., Diesel fuel alternative from vegetable oils. Chem. Eng. World, 32(10), pp 77-80, 1997.
[72] Shahid, E. M., Jamal, Y., Production of Biodiesel: A Technical Review, Renewable and Sustainble Energy Reviwes (15): 4732-4745, 2011.

[73] Siva, K.A, Maheswar, D., V. Kumar, R. K., Comparison of diesel engine performance and emissions from neat, IJAEST (11), pp 121-128, 2009.
[74] Thaddeus, H. C. M., Asuyuki, S., Okobatae, T., Operation and Combustion Characteristics ofa a DI Diesel Engine Fueled with Biomass Oil-Diesel, SAE Technical Paper 2001-28-0030, 2001.
[75] Venkanna, B. K., Swati, B., and Reddy, C. V., Effect of Injection Pressure on Performance, Emission and Combustion Characteristics of Direct Injection Diesel Engine Running on Blends of Pongamia Pinnata Linn Oil (Honge oil) and Diesel Fuel. Agricultural Engineering International: The CIGR Ejournal. Manuscript number 1316. Vol. XI. May, 2009.
[76] Wang, Y. D., An experimental investigation of the performance and gaseous exhaust emissions of a diesel engine using blends of a vegetable oil, Applied Thermal Engineering, Volume: 26, 2006, Pages: 1684-1691.
[77] Yoshimoto, Y., Onodera, M., Tamaki, H. "Performance and emission characteristics of diesel engines fueled by vegetable oils", SAE Technical Paper Series , Paper No. 2001-01-1807/4227.
[78] Yaodong, W., Huang, Y., Roskilly, A. P., Ding, Y., Hewitt, N., Trigeneration running with raw jatropha oil, Fuel Processing Technology, Volume 91, Issue 3, pp 348–353, 2010.
[79] Yilmaz, N, Morton, B., Effects of preheating vegetable oils on performance and emission characteristics of two diesel engines. Biomass Bioenerg., 35: 2028-2033.
[80] Ziejewski M, Goettler H and Pratt GL (1986) Influence of vegetable oil based alternative fuels on residue deposits and components wear in a diesel engine. SAE. 860302, 297– 307.
[81] Zimmerman, J., Brazil Oilseeds and Products Annual Oilseeds Report, USDA Foreign Agricultural Service, 2011.

WIND ENERGY CONVERSION PERFORMANCE AND ATMOSPHERIC STABILITY

Francesco Castellani[a],Emanuele Piccioni[b], Lorenzo Biondi[c] and Marcello Marconi[d]

[a] Università degli Studi di Perugia -Dipartimento di Ingegneria Industriale, Perugia, Italy, castellani@unipg.it
[b] Università degli Studi di Perugia -Dipartimento di Ingegneria Industriale, Perugia, Italy, piccioni@mec.dii.unipg.it
[c] Università degli Studi Guglielmo Marconi Telematica, Dipartimento di Meccanica, Impianti e Infrastrutture - D.M.I.I., Roma, Italy l.biondi@unimarconi.it
[d] Università degli Studi Guglielmo Marconi Telematica, Dipartimento di Meccanica, Impianti e Infrastrutture - D.M.I.I., Roma, Italy m.marconi@unimarconi.it

Abstract:

Wind energy conversion technology is by now fully developed on an industrial scale; commercial wind turbines capacity factors have reached very good values and now the scientific community is engaged in understanding in details all the phenomena which can affect the power performances of an aerogenerator.
Among them atmospheric stability is still not well investigated comparing to others environmental conditions; this is partially due to the low incidence of non-neutral conditions on the actual productive periods.
Usually the wind energy assessment studies were generally performed referring to neutral stability; this was considered acceptable because neutral conditions prevail on the high wind situations.
Anyway, especially on coastal and offshore sites, stability can induce meaningful effect on power production both directly on the net power output and on the wakes.
The wind energy industry is now producing wind turbines with a high ratio of the rotor surface by the nominal power; in this way producing energy even with low wind regimes and non-neutral conditions can involve significant periods. In such situations the variations of the vertical wind shear can affect the energy production and it could be fundamental to investigate how atmospheric stability can affect the overall power conversion efficiency.
In present work the effect of atmospheric stability was investigated analysing the production data of a small wind farm operating in flat terrain in southern Italy; in the site only two turbines with a very high ratio of rotor surface by nominal power are operating under a low-medium wind regime.
Results demonstrate that atmospheric stability can have a meaningful impact on power production especially for unstable conditions
Furthermore a good overall agreement was discovered between the results from the experimental dataset and from numerical simulations of different thermal conditions through a CFD (Computational Fluid Dynamics) code and the actuator disc model.

Keywords:

Wind Energy conversion, Atmospheric stability, CFD.

1. Introduction

This work deals with the production and wind data of a little wind farm located in the south of Italy; power performances were analyzed in order to investigate the influence of thermal stratification on the overall production. On the site, located in a quite flat land, there are two turbines with a specific rated power of 1000 kW, a hub height of 65 m and a rotor diameter of 77 m. The site altitude is between 40 and 55 m over the sea level. A 50 m anemometer is located on the site 315 m (4.06 diameters) south-east from turbine nr. 2 and 670 m (8.07 diameters) south-west from turbine nr. 1. The distance between the turbines is 720 m (9.35 diameters). The relative locations are shown in Fig. 1:

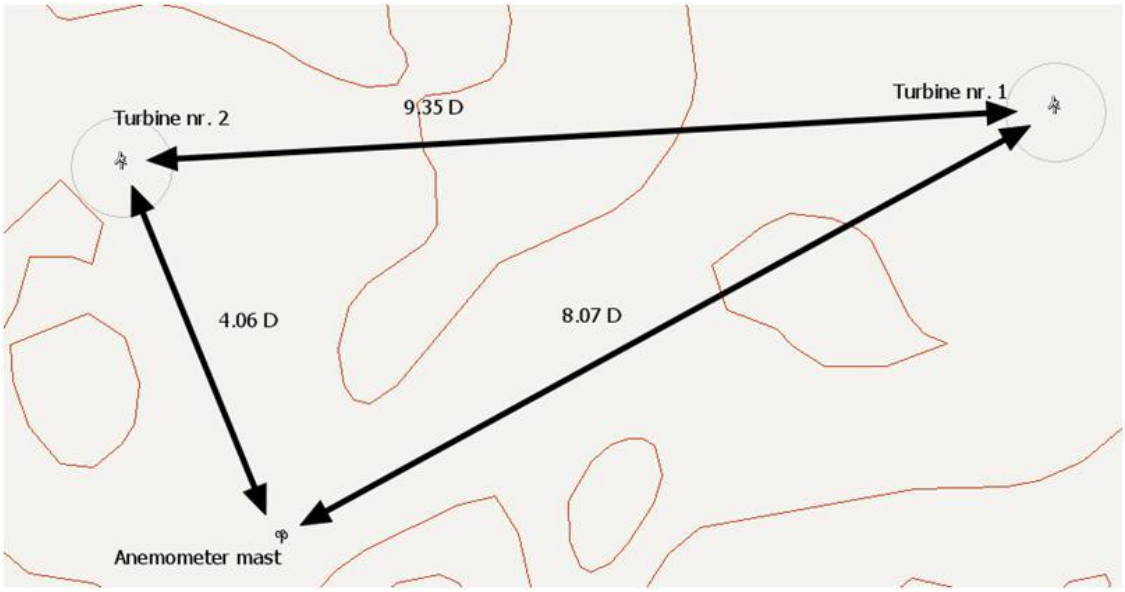

Fig. 1. Layout for the two wind turbines and the anemometer mast.

Experimental data from the SCADA (supervisory control and data acquisition) system was available and analyzed for the first yearly period of operation for the two aerogenerators from 01/01/2010 to 31/12/2010; at the same time also measurements from the anemometer mast were used. All the meaningful signals were aggregated on a synchronized dataset with 10 minutes averaged values. Atmospheric stratification analysis was performed using the insolation, the radiation and other meteorological data calculated by the numerical model WRF (Weather Research and Forecasting); such data were provided by LAMMA laboratory (http://www.lamma.rete.toscana.it). The WRF data are hourly averaged. Production, insolation and anemometer data were synchronized to split them into stability classes.

The influence of thermal stratification was investigated using the following databases:

- the production time history of the two aerogenerators (10 minutes averaged);
- the wind database (10 minutes averaged) of the met mast placed in the wind farm area;
- the hourly meteorological time history calculated by the WRF (Weather Research & Forecasting) model.

All the sources of data were synchronized in order to select the production periods according to different direction sectors and different thermal conditions; for the atmospheric stability analysis the Pasquill classification was used.
In each different situation the upstream turbine production time history was used to reproduce the wind turbine's power curve normalizing the reference wind speed according to the IEC standard.

Better results were obtained through the nacelle anemometry included in the production dataset.

2. Theory and methods

2.1. The experimental dataset

The anemometer data were available for the period from 01/01/2010 to 12/12/2010 averaged on 10 minutes. The anemometer mast height is 50 m above ground level (a.g.l.) and it has three sensors for wind speed measurement (at 50, 40 and 30 m a.g.l.) and two sensors for direction measurement (at 50 and 30 m a.g.l.).

The wind rose measured at 50 m is show in figure 2:

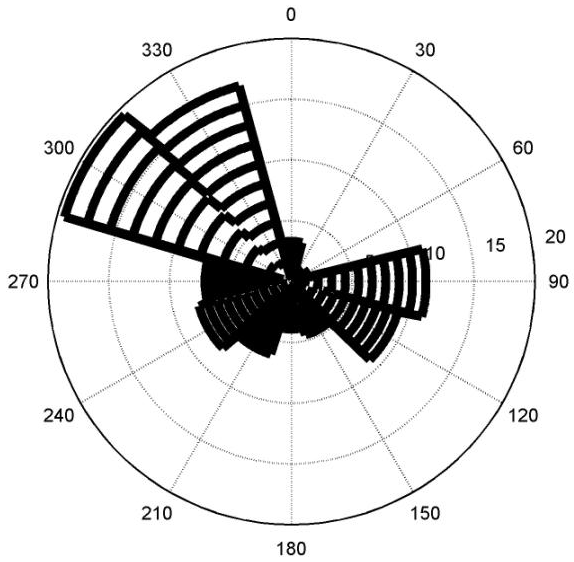

Fig. 2. Wind rose measured at the anemometer position 50 m a.g.l. for the yearly period.

The most populated sectors are 300° and 330°, but in these sectors the anemometer is downstream the turbine nr. 2 and data from these sectors cannot be used for the power curve evaluation due to wake effects. The third most populated sector is 90°.In this sector turbine nr. 2 is in the wake of turbine nr. 1; looking at production data an energy loss for turbine nr. 2 can be estimated for this sector. As a consequence only the production time history of turbine nr. 1 in the 90° sector was used for the power performance analysis.

Production data available from the SCADA were used to assess the power performance of the turbines in different atmospheric conditions. From the overall dataset only the following parameters were extensively analyzed for the present work:

- the turbine power output (kW);
- the nacelle anemometer wind speed (m/s);
- the nacelle orientation (°).

A lot of work was done to filter the dataset in order to exclude all invalid data; especially in the early period of operation of the turbine there were some problems with the power control so that production data were useless for the present study.

Another important issue was the choice of the wind speed reference value for the power curve evaluation. IEC standards [1] recommend measuring the power curve using an anemometer mast placed at a distance of 2.5 rotor diameters (D) from the turbine in the upstream direction.

The nearest turbine to the anemometer mast on the site under investigation is placed 4.06 D (a bit more of the maximum allowable distance of 4 D) and looking at the wind rose of figure 2 the anemometer is frequently affected by the wake of such turbine.

The only meaningful direction sector for which the anemometer is not affected by turbine's wakes is 90°; for this direction the upstream undisturbed turbine is placed 8.07 D from the mast.

Plotting the power output of turbine nr. 1 versus the anemometer wind speed for the 90° sector (figure 3) reveals that, in this way, the power curve of the aerogenerator cannot be assessed.

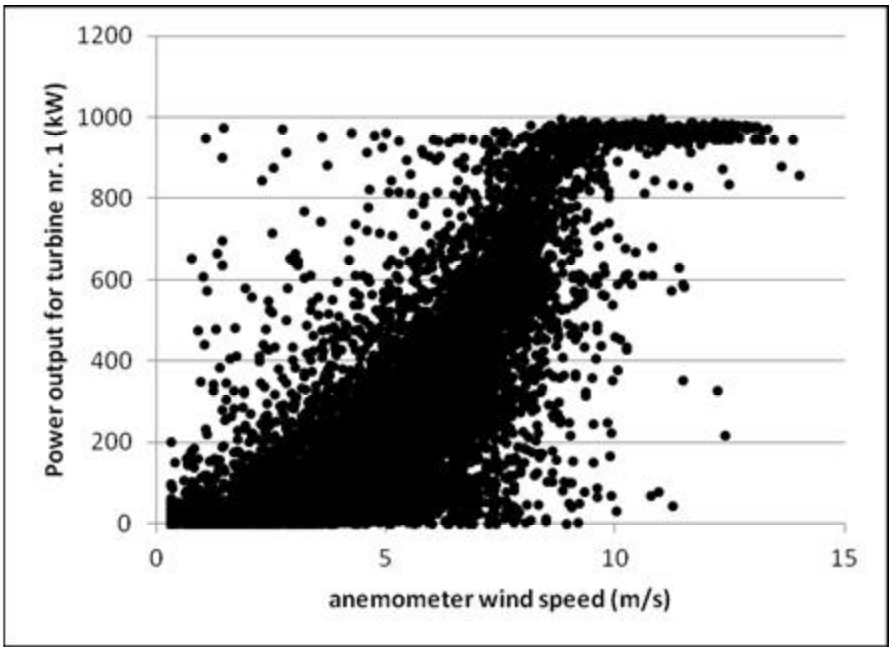

Fig. 3. Power output for turbine nr. 1 versus the wind speed at the anemometer position (50 m a.g.l.).

The power curve of a wind turbine can also be estimated using the nacelle anemometry; this procedure cannot be used when measuring the power curve for certification purpose but can be very useful when assessing the power performance of the machine in different weather conditions or in different time periods.

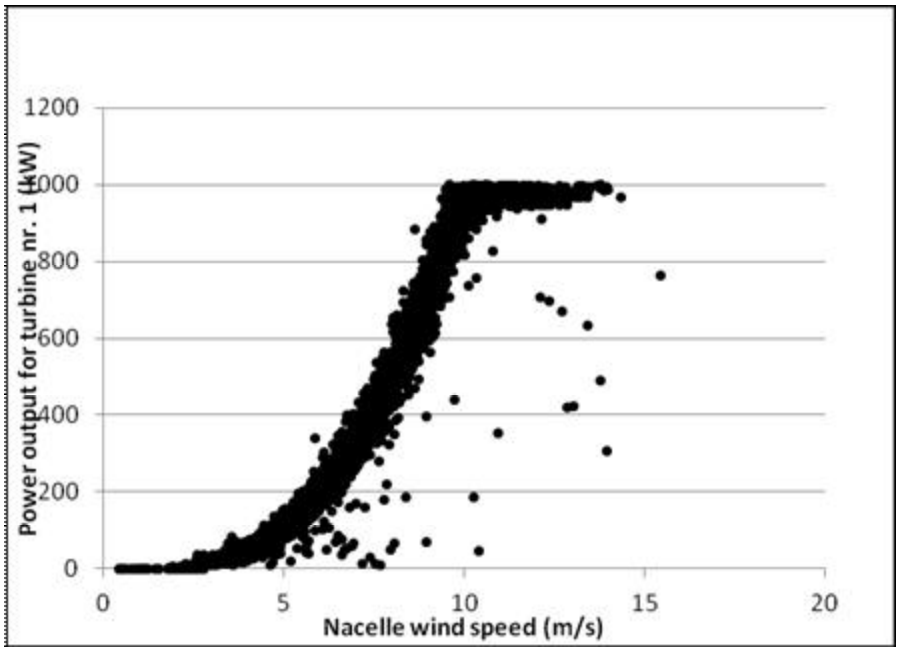

Fig. 4. Power output for turbine nr. 1 versus the nacelle wind speed.

Comparing figure nr. 3 and nr. 4 it is possible to assess the improvement of the power curve representation when using nacelle anemometry; for this reason in present work such technique was applied and data from anemometer mast were retained to assess the boundary layer conditions and to define the wind direction. The wind direction could have been also estimated using the nacelle position from the SCADA dataset; anyway direction data from the anemometer vane were discovered to be more reliable and representative.

Following the IEC standard [1] the production data need to be normalized to the standard air density conditions. For this purpose the 10 minutes averaged air density was calculated in each time steps using the following formulation:

$$\rho_{10min} = \frac{P_{10min}}{R\,T_{10\min}} \quad (1)$$

where:

- $\rho_{10\min}$ is the calculated air density, averaged over 10 min.,
- $\mathbf{T}_{10\min}$ is the air absolute temperature averaged over 10 min.,
- $P_{10\min}$ is the air pressure averaged over 10 min. and R is the gas constant $(287.05\ J/KgK)$.

For modern wind turbines with a full-pitch control system the power curve referred to the standard air density can be evaluated using the normalized wind speed:

$$V_n = V_{10\min}\left(\frac{\rho_{10min}}{\rho_0}\right)^{\frac{1}{3}} \quad (2)$$

where V_n is the normalized wind speed and $V_{10\min}$ is the 10 minutes averaged speed.

The production dataset was also filtered to exclude malfunction periods; to do this also the manufacturer theoretical power curve was used to reproduce the expected power history calculated from the nacelle wind speed. If the ratio between the expected power and the actual power was outside the range between 0.8 to 1.2 for the upstream turbine the data of the specific timestep were disregarded. In figure nr. 5 it is possible to verify how the experimental power curve is very close to the expected one.

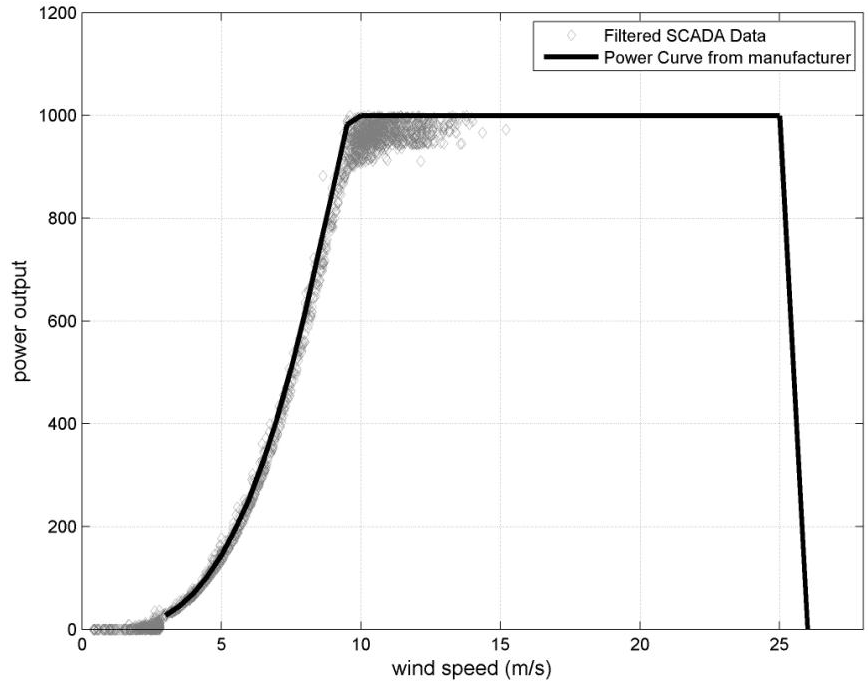

Fig. 5. Comparison of the manufacturer's power curve and the experimental one for the direction sectors from east (0-180°) for turbine nr. 1.

2.2. The atmospheric stability analysis

On the boundary layer the behavior of the wind is affected by roughness, geostrophic wind, Coriolis force and thermal effects. The thermal effects can modify the wind flow; the different conditions induce different stability characteristics that can be divided in 3 classes: stable, unstable and neutral cases.

The unstable conditions are characterized by strong superficial warming that means that the air expand and the pressure go down. If the equilibrium is not found, the air expand and form convection cells. On the boundary layer often there are turbulent vortices on large scale and a lot of vertical mixing of momentum. With the high there is a little change in wind speed (little wind shear).

On the stable conditions there is an adiabatic cooling effect on the night that induces that the rising air become colder than the surroundings and the vertical motion is stopped. The turbulence is dominated by friction and there is a big change of wind speed with air (large wind shear).

On the neutral conditions the adiabatic cooling is such that the air is in equilibrium with the surroundings. In this case there are strong winds and the turbulence due to the roughness causes mixing of momentum on the boundary layer. This case is the most important for the energy production because it is more frequent for high wind conditions; in such situation the load of the turbulent wind on the turbine is the largest.

The atmospheric stability analysis was carried out using the meteorological database available from WRF model; such data were provided by La.M.M.A. Laboratory (http://www.lamma.rete.toscana.it/). The WRF (Weather Research and Forecast) model is a mesoscale meteorological numerical code that is used both for weather forecasting and atmospheric research activities; La.M.M.A. is running WRF for weather forecasting on a domain which covers all Italy with a grid resolution of 10 km. The stability class can be calculated according to the Pasquill classification (Table 1) [2] using historical data from the nearest node to the site.

Table 1. The Pasquill atmospheric stability classification (RT is the global radiation and RN is the net radiation)..

	Wind speed 10 m a.g.l.					
Radiation (W/m^2)	$V<2$	$2\le V<3$	$3\le V<4$	$4\le V<5$	$5\le V<6$	$V\ge 6$
Day						
$RT\ge 700$	A	A	B	B	C	C
$540\le RT<700$	A	B	B	B	C	C
$400\le RT<540$	B	B	B	C	C	D
$270\le RT<400$	B	B	C	C	C	D
$140\le RT<270$	C	C	C	D	D	D
$RT<140$	D	D	D	D	D	D
Nigth						
$RN\ge -20$	D	D	D	D	D	D
$-40\le RN<-20$	F	E	D	D	D	D
$RN\le -40$	F	F	E	E	D	D

A: Extremely unstable conditions	D: Neutral conditions
B: Moderately unstable conditions	E: Slightly stable conditions
C: Slightly unstable conditions	F: Moderately stable conditions

Analyzing all the hourly 2010 WRF dataset calculated for the nearest node it was possible, for each timestep, to give an estimation of the Pasquill class.

The distribution of such calculus is shown in table 2 from which it is possible to assess how the neutral conditions prevails on stable and unstable conditions.

Table 2. Results for the stability classification of the site.

Atmospheric conditions	*frequency* %
NEUTRAL	41
STABLE	32
UNSTABLE	27

These results were used to characterize the power performances of turbine nr. 1 in the three different stability conditions; the Pasquill classes were aggregated in only three groups in order to reach a good power curve data population.

Atmospheric stability was also considered, in an easier way, in the numerical model of the wind farm.

The initialization of thermal conditions within the numerical code can be done in different way: in present work a rough comparison of the numerical and the experimental power performances of the wind farm was done using the initialization with the Monin-Obukhov length L. In order to obtain good results with a full convergence of the code only slightly stable and unstable conditions were simulated. The Monin-Obukhov length can be estimated from the surface roughness length Z_0 [3] and the Pasquill classes using the following formula:

$$\frac{1}{L} = aZ_0^{\,b} \qquad (3)$$

where a and b are coefficients that can be estimated from the following table:

Table 3. Different values for a and b coefficients.

Pasquill Class	*a*	*b*
A	-0.0875	-0.1029
B	-0.03849	-0.1714
C	-0.00807	-0.3049
D	0	0
E	0.00807	-0.3049
F	0.03849	-0.1714

2.3. The numerical model

The numerical study of the wind farm was performed using a CFD (Computational Fluid Dynamics) code and the actuator disc model. Such kind of numerical tool models the power extraction applying only the axial forces on the rotor swept area of the aerogenerator. Such model was developed to study not only wind turbines but also propellers and rotors [4]; even if it disregards many detailed characteristics of the rotor aerodynamics such the wake rotation and meandering [5,6], despite its simplicity, it is able to reproduce the wind deficit and the wake losses only through the axial energy exchanges.

Recently the actuator disc is often used to model multiple wakes and it can give a reliable description of the far wake [7] and its interaction with the main wind field as well as the other wakes.

With the actuator disc model the streamlines passing through the disc are affected by the power extraction so that a wind velocity deficit is generated and the wind speed on the rotor v_r is lower

than the undisturbed one v_∞ . According to the 1D momentum theory the following formulation is to be considered introducing the axial induction factor a :

$$v_r = (1 - a) * v_\infty \quad (4)$$

The axial force to be applied on the rotor S_a can be estimated using the thrust coefficient C_T that is generally provided with the power curve of the aerogenerator:

$$C_T = \frac{S_a}{\frac{1}{2}\rho \cdot v_\infty^2 \cdot A} \quad (5)$$

where A is the rotor area.

The 1D momentum theory also gives the following equation relating the thrust coefficient with the axial induction factor:

$$C_T = 4a(1 - a) \quad (6)$$

The numerical model was used to simulate the wind field and finally calculate the power output P multiplying the pressure drop dP across the rotor and the local axial component of the wind speed v_{ra} on the disc. Such calculation was done in the post processing approximating on the discrete domain the following integral formulation:

$$\mathbf{P} = \int_A (v_{ra} \cdot dP \cdot dA) \quad (7)$$

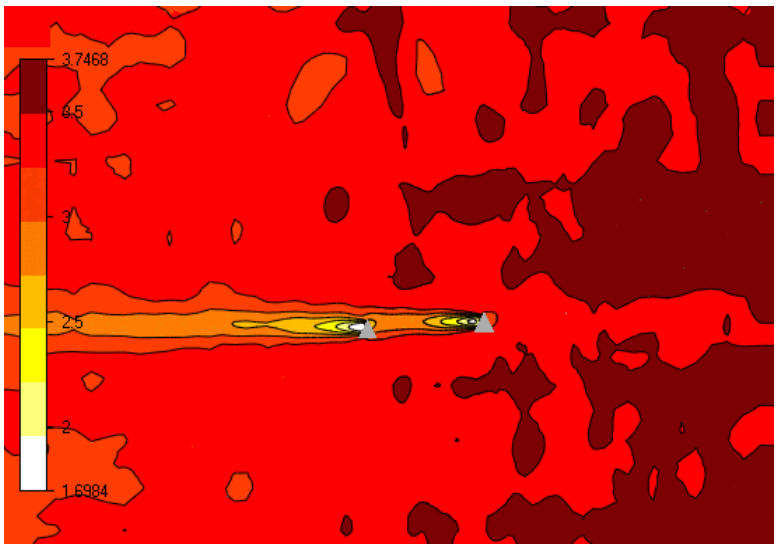

Fig. 6. Calculated wind field (Speed 2D) at the turbine's hub height (65 m a.g.l.) for the 90° sector in neutral condition.

In figure 6 the simulated wind field is shown for the neutral condition case.

The CFD model domain is approximately 5x3 kilometres with a grid horizontal resolution varying from 6 up to 120 m; the overall number of cells is 331958. Simulations for neutral and stable conditions were performed using the standard k-ε turbulence model while the for unstable conditions the RNG k-ε model was used in order to achieve a better convergence.

The boundary conditions were tuned to reach quite similar conditions of wind speed on the rotor for the three thermal conditions (figure 7).

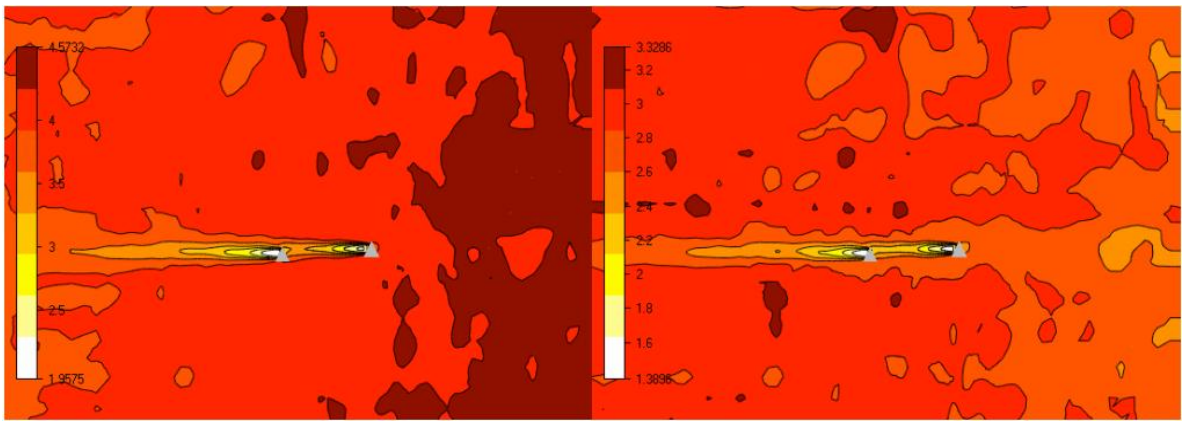

(a) (b)

Fig. 7. Calculated wind field (Speed 2D) at the turbine's hub height (65 m a.g.l.) for the 90° sector in unstable (a) and stable (b) condition.

3. Results

Using the stability classes time history obtained through the WRF model dataset it was possible to split, for turbine nr. 1 in the eastern sectors (0-180°), the power curve obtained in neutral, stable and unstable conditions. Unfortunately the filtered database was poor especially for stable conditions events and an extensive analysis of the power curve was not possible. Moreover, as can be deduced from table 1, non neutral conditions occurs especially in low-wind regimes so that a reliable comparison between the power performances in the three different stability conditions was possible only in the early part of the power curve (from 3 to 6.5 m/s) and a comparison for all the analyzed dataset is quite useless (figure 8).

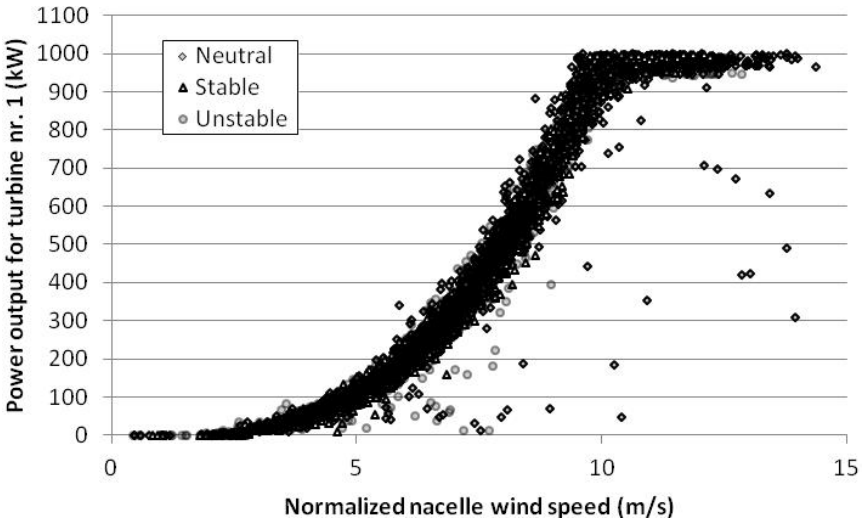

Fig. 8. Comparison of the power curve in the different thermal conditions.

More interesting information can be found looking at the power curve obtained calculating the mean values within bin intervals of 0.5 m/s width for wind speeds from 3 to 6.5 m/s (figure 9).

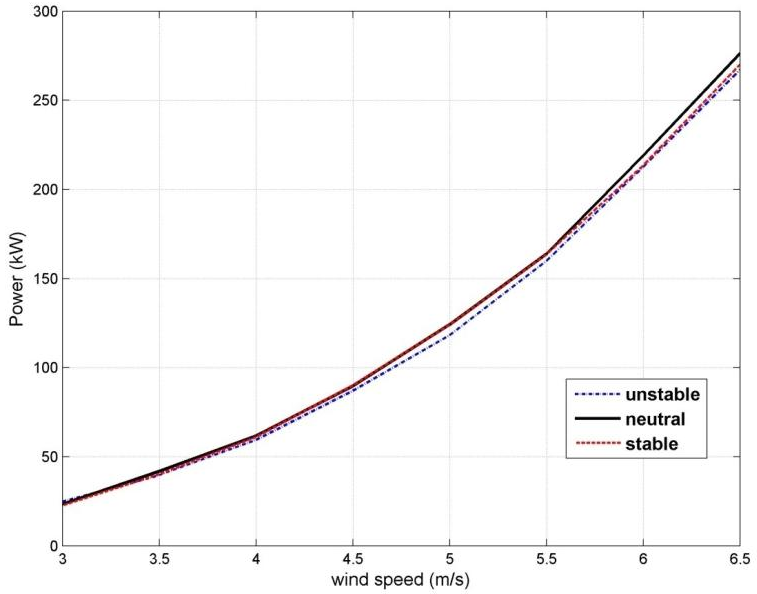

Fig. 9. Comparison of the "binned" power curves for turbine nr. 1 in the eastern sectors (0-180°) for different atmospheric stability conditions.

Unfortunately the poor quality of the available experimental dataset allowed only a weak comparison of the conversion efficiency in the different thermal conditions.

In figure 10 it is represented the standard deviation of the power output (expressed in percentage of the mean value) and the maximum difference observed between the productions in the three different thermal conditions (expressed in percentage of the mean value as well).

The maximum difference is higher and comparable with the standard deviation only for a wind regime of 9 m/s; in such conditions the possible intervention of the turbine control make the comparison not significant.

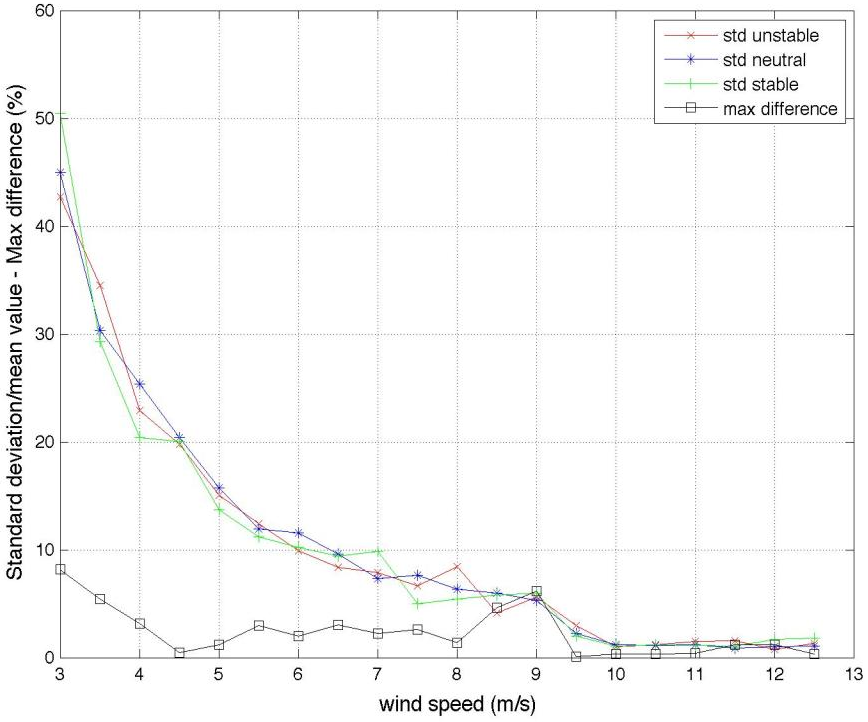

Fig. 10. Comparison of the standard deviation of power output with the maximum difference observed for the analysed thermal conditions.

Anyway the mean values of figure 9 (even if affected by high uncertainties) give a first estimation of how conversion efficiency can be affected by thermal stratification: in unstable conditions the turbine seems to work with a lower power even with the same normalized nacelle wind speed. This is consistent with some previous numerical investigations [8] and can be addressed to the poorest energy content of the wind profile.

Using the anemometer dataset a different coefficient α of the power law profile was estimated in the three thermal conditions: 0.167 in the neutral case, 0.191 in the stable case and 0.0827 in the unstable case.

Results from the power output estimation in the numerical model for the same turbine nr. 1 are in good agreement with the experimental results. The numerical model solves the wind field using the Reynolds Average method (RANS solution) and a comparison with the experimental data can be done mainly in a qualitative way. The numerical values of the calculated power output in the three stability conditions were used to estimate the power coefficient defined as:

$$C_p = \frac{P}{\frac{1}{2}\rho \cdot v_\infty^3 \cdot A} \tag{8}$$

where the undisturbed wind speed was calculated using the axial induction factor that can be estimated through the wind speed on the disc and the thrust coefficient curve.

At the same time the power coefficient can also be estimated from the axial induction factor using the formula from the 1D momentum theory:

$$C_p = 4a(1-a)^2 \tag{9}$$

This is the theoretical value of the power coefficient that derives from 1D momentum theory and is generally higher than the numerical power coefficients due to three-dimensional effects and to the boundary layer effects.

Table 4. Theoretical and numerical power coefficients..

	Power Coefficients	
	1 D Momentum Theory	Numerical
Neutral	0.5786079	0.4273396
Stable	0.5786079	0.4602921
Unstable	0.5815354	0.4254921

In the numerical wind field both the upstream wind speed as well as the rotor wind speed can be estimated so that the value of the axial induction factor can be calculated. Using that value and equation 9 an estimation of the power coefficient according to the 1D momentum theory is possible.

At the same time the numerical pressure drop on the rotor can be calculated and, using equation 7, a second estimation (numerical) of the power output can be extrapolated; in this second estimations also the three-dimensional effect are numerically considered and the obtained values are comparable with the actual power coefficient of a real operating turbine,

As can be deduced from table 4 in the three different atmospheric stability conditions the gap between the numerical and theoretical power coefficients can vary due to the influence of the boundary layer conditions.

In unstable conditions the gap is higher and the power performances are poor while the power efficiency is higher in neutral and stable conditions.

3. Conclusions

In present work an analysis of the impact of atmospheric stability on the wind energy conversion efficiency was done through numerical and experimental investigations. Results demonstrate that poor efficiency is to be addressed especially to unstable thermal stratification.

An improvement of the numerical model can give very useful information in order to optimize the overall production and the turbine lifetime in wind sites where non neutral conditions can involve relevant operational periods.

Acknowledgments

The authors acknowledge the Italian company Calypso Engineering spa who provided all data treated and analyzed in present work.

Nomenclature

ρ_{10min}	calculated air density averaged over 10', $\frac{kg}{m^3}$
$\mathbf{T_{10min}}$	air absolute temperature averaged over 10', $^{\circ}K$
P_{10min}	air pressure averaged over 10' min, Pa
R	gas constant, $287.05\ \frac{J}{KgK}$
V_n	normalized wind speed, $\frac{m}{s}$
V_{10min}	10' averaged speed, $\frac{m}{s}$
ρ_0	standard air density, $1.225\frac{kg}{m^3}$
RT	global radiation, $\frac{W}{m^2}$
RN	net radiation, $\frac{W}{m^2}$
L	Monin-Obukhov length, m
Z_0	surface roughness length, m
v_r	wind speed on the rotor, $\frac{m}{s}$
v_{ra}	local axial component of the wind speed on the rotor, $\frac{m}{s}$
v_∞	undisturbed speed, $\frac{m}{s}$
a	axial induction factor
S_a	axial force applied on the rotor, N
C_T	thrust coefficient
A	rotor area, m^2
P	pressure, Pa

C_p power coefficient

References

[1] IEC 61400-12 WIND TURBINES – Part 12-1: “Power performance of electricity producing wind turbines”, 2006

[2] A. Venkatram, 1996, An examination of the Pasquill-Gifford-Turner dispersion scheme. Atmospheric. Environment, 30:1283-1290

[3] A. Capanni, G. Gualtieri, 1999: “Sodar application for estimating boundary layer parameters”. In: Proc. EUROPTO series: Optics in atmospheric propagation and adaptive systems III. Florence, Italy, Sept., 23-24.

[4] Van Kuik GAM., 1991, "On the limitations of Froude’s actuator disc concept." PhD Thesis, Technical University of Eindhoven Doctoral Thesis, 1991.

[5] Vermeer L.J.,Sørensen J.A., Crespo A., 2003, “Wind turbine wake aerodynamics.” – Progress in Aerospace Sciences – 39 (2003) 467–510

[6] B. Sanderse - ‘Aerodynamics of wind turbine wakes – Literature review’, Energy research centre of the Netherlands http://www.ecn.nl/docs/library/report/2009/e09016.pdf

[7] Rèthoré P.E.,Sørensen N. N., Zahle F. – "Validation of an Actuator Disc Model." - European Wind Energy Conference & Exhibition Proceedings - Tuesday 20 - Friday 23 April 2010, Warsaw, Poland

[8] Castellani F., Vignaroli A., Piccioni E. - "Wind shear investigation for site-specific wind turbine performance assessment" - Journal of Energy and Power Engineering ISSN 1934-8975, USA

Comparison Study on different SOFC hybrid Systems with Zero-CO_2 emission

Liqiang DUAN [a], Kexin Huang[a], Xiaoyuan Zhang[a] and Yongping Yang[a]

[a] *School of Energy, Power and Mechanical Engineering, Beijing Key lab of Energy Safety and Clean Utilization, Key Laboratory of Condition Monitoring and Control for Power Plant Equipment of Ministry of Education, North China Electric Power University, Beijing, 102206, China,*

E-mail: dlq@ncepu.edu.cn

Abstract:

Based on a traditional SOFC (Solid Oxide Fuel Cell) hybrid power system, three different SOFC hybrid power systems with zero-CO2 emission are proposed in this paper and their performances are analyzed and compared. The exhausted gas from the anode of SOFC is burned with pure oxygen and the concentration of CO2 gas is greatly increased. Because the combustion produce gas is only composed of CO2 and H2O , the separation of CO2 hardly consume any energy. At the same time, three different methods (steam injection, CO2 gas injection, heat exchange layout) are taken to maintain the proper turbine inlet temperature. With the exergy analysis method, this paper studied the exergy loss distribution of every unit of SOFC hybrid systems with CO2 capture and revealed the rules of exergy loss distribution. The effects of main operating parameters on the overall SOFC hybrid system with CO2 capture are also investigated.

The research results show that the zero-CO2 SOFC hybrid systems proposed in this paper still have higher efficiencies when compared with the SOFC hybrid system without CO2 capture. Their efficiencies only decreases about 3-4 percentage points compared with the basic SOFC hybrid system without CO2 capture. The research achievements obtained from this paper will provide the new idea and method for further study on zero emission CO2 system with high efficiency.

Keywords:

SOFC, Hybrid power system, Zero CO_2 emission, Steam injection, Exergy analysis.

1. Introduction

Now, climate change due to the emission of greenhouse gases, especially the emission of CO2, is becoming more and more serious. Though many countries have taken some measures to control and reduce the emission of CO2, in the short term, CO2 emission is still maintaining the rapid growth trend. Power industry is the biggest CO2 emission sector. So, there exists the greatest CO2 emission reduction potential in the power industry [1]. Now, many kinds of fossil fuel power generation systems with CO2 recovery are usually based on the chemical absorption method or the oxygen combustion method. The former demands a chemical absorption and separation unit to recover CO2 from the exhaust combustion gas. The latter demands the special oxygen combustion technology, the special equipment and larger ASU (air separation unit). And these technologies all consume great energy and result in the huge equipment investment and higher operating costs [2]. Now, people are eager to develop the high-efficiency power generation technology with the less energy consumption for CO2 capture. Fuel cell can satisfy the above requirements, with the higher energy conversion efficiency and less CO2 capture energy consumption, so it has attracted considerable interest in recent years.

Solid Oxide Fuel Cell (SOFC) is an attractive power-generation technology that can convert the chemical energy of fuel directly into electricity while causing little pollution. Because the anode fuel gas is naturally separated from the cathode air by the solid electrolyte, the CO2 gas with the higher concentration can be obtained in the anode exhaust gas. In addition, SOFC can employ all kinds of fuels, including various hydrocarbon fuels. Compared with the traditional power generation system, the SOFC hybrid system power plant has the higher overall system efficiency (LHV). Even

after CO2 is captured, the efficiency of SOFC hybrid system still can be higher or equal to that of the traditional power system without CO2 capture. In order to further improve the CO2 concentration of anode exhaust gas, SOFC can employ the O2/CO2 combustion mode in the afterburner. Because the required mass flow of pure O2 is less, the energy consumption is lower. After capturing the CO2, the SOFC hybrid system does not result in the bigger efficiency reduce. So the SOFC hybrid power system with zero CO2 emission becomes a new way which can simultaneously solve the problem of efficient energy utilization and lower pollution emission.

In the last decades, many researchers were involved in study of SOFC stack and the hybrid power system with CO2 capture. Y.Inui proposed and investigated two types of carbon dioxide recovering SOFC/GT combined power generation systems in which a gas turbine with carbon dioxide recycle or water vapor injection is adopted at the bottoming cycle system [2]. The overall efficiency of the system with carbon dioxide recycle reaches 63.87% (HHV) or 70.88% (LHV), and that of the system with water vapor injection reaches 65% (HHV) or 72.13% (LHV). A. Franzoni considered two different technologies for the same base system to obtain a low CO2 emission plant [3]. The first technology employed a fuel decarbonization and CO2 separation process placed before the system feed, while the second integrated the CO2 separation and the energy cycle. The result showed that the thermodynamic and economic impact of the adoption of zero emission cycle layouts based on hybrid systems was relevant. Philippe Mathieu presented the integration of a solid oxide fuel cell operating at a high temperature (900–1000℃, 55–60% efficiency) in a near-zero emission O2/ CO2 cycle [4]. Takeshi Kuramochi compared and evaluated the techno-economic performance of CO2 capture from industrial SOFC-combined heat and power plant (CHP) [5]. CO2 is captured by using an oxyfuel afterburner and conventional air separation technology. The results were compared to both SOFC-CHP plants without CO2 capture and conventional gas engines CHP without CO2 capture. B.Fredriksson Moller examined the SOFC/GT configuration with and without a tail-end CO2 separation plant and based on a genetic algorithm, selected the key parameters of the hybirid system[6]. The result of the optimization procedure shows that the SOFC/GT system with part capture of the CO2 exhibits an electrical efficiency above 60%. Some researchers also studied the performance parameters of the different SOFC hybrid power systems from the thermoeconomic or exergy efficiency point [7-9]. For example, Ali Volkan Akkaya proposed a new criterion-exergetic performance coefficient (EPC), then applied it in the SOFC stack and SOFC/GT CHP system[10-11]. F. Calisa discussed the simulation and exergy analysis of a hybrid SOFC-GT power system. The result showed that the SOFC stack was the most important sources of exergy destruction [12].

In this paper, three kinds of zero-CO2 emission SOFC hybrid power systems are proposed. Using exergy analysis method, the exergy loss distributions of every unit of zero-CO2 emission SOFC hybrid system are revealed. The effects of different operating parameters on exergy loss of every unit, as well as the overall system performance, are also investigated. The results obtained in this paper provide useful reference for further study on high-efficient zero emission CO2 power system.

2. SOFC system modelling

The models developed in the paper are all based on the following general assumptions:

1) All components are sealed-in and the systems operate under steady-state conditions.
2) The cathode gas consists of 79% nitrogen and 21% oxygen, and all gases are assumed ideal.
3) The mass flow of the input fuel, gas and all the reaction products are stable, the fluid kinetic energy and potential energy changes are neglected.
4) The unreacted gases are assumed to be fully oxidized in the after-burner of the SOFC stack, and the after-burner is assumed to be insulation , the heat loss of all heat exchangers are assumed as 2% .The pressure drops of the components are assumed as 2%.
5) The temperature of the anode and cathode outlet gases are equal to the cell stack operating temperature, the current and voltage of every cell unit are the same [13].

2.1. The analysis and simulation of SOFC stack

SOFC system model is selected by reference to the literature [14].The natural gas feed tubular SOFC system process is implemented by using Aspen Plus software. The Aspen Plus contains rigorous thermodynamic and physical property database and provides comprehensive built-in process models, thus offering a convenient and time saving means for chemical process studies, including system modelling, integration and optimization. The simulated SOFC flowsheet is shown in Figure 1. It includes all the components and functions contained in the SOFC stack, such as ejector, pre-reformer, fuel cell (anode and cathode) and afterburner.

Firstly, the preheated fuel (stream 1) mixes with the recycling anode exhausted gas (stream 6), and then the mixed fuel gas (stream 2) is sent to the pre-reformer where the steam reform reaction takes place. After that, the stream (4) enters the anode of SOFC in which the electrochemical reaction of fuel and oxygen from the anode occurs. The reaction product and unreacted flue mixture (stream 5) is separated into two parts. One part (stream 6) is recycled to mix with fuel to meet the specified ratio of steam to carbon (S/C), which is 2.5 in this paper, and the recycled gas also provide the heat for reforming reaction to enhance the pre-reformer temperature and get more H_2. Another part enters the afterburner and mixes with the nitrogen-rich air (stream 13) from the anode. After the combustion reaction, the exhausted gas from the afterburner (stream 14) is introduced into the regenerator to preheat the air (stream 9) for the anode.

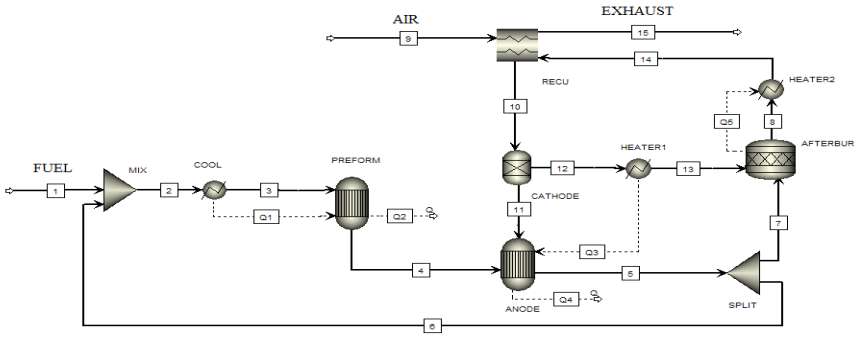

Figure 1 The model flowsheet of SOFC stack

2.2 Mathematical model of SOFC stack

The cell voltage is the core of the fuel cell modeling. The voltage is consisted of two parts: 1).the reference voltage, 2). the loss of SOFC real operating parameters. The experimental data of V_{ref} at standard operating conditions (fuel composition: 67% H_2, 22% CO, 11% H_2O, fuel utilization factor U_f =85%, air utilization factor U_a= 25%, P_{ref} = 1 bar ; T_{ref} = 1000℃;) can be obtained from literatures [14-16]. The actual cell voltage value, V_c, is then calculated by semiempirical correlation [14-16] accounting for the differences between the real operating conditions and the standard operating conditions as follows:

$$\Delta V_p(\mathrm{mV}) = 76\log(\frac{p}{p_{ref}}) \tag{1}$$

$$\Delta V_T(\mathrm{mV}) = 0.008(T - T_{ref}) \times i_c \tag{2}$$

$$\Delta V_{an}(mV) = 172\log\frac{p_{H_2}/p_{H_2O}}{(p_{H_2}/p_{H_2O})_{ref}} \tag{3}$$

$$\Delta V_{cat}(mV) = 92\log(\frac{p_{O_2}}{(p_{O_2})_{ref}}) \tag{4}$$

Where i_c is the current density; p_{H_2} / p_{H_2O} is the ratio of H_2 and steam partial pressure; P_{O_2} is the average oxygen partial pressure at the cathode for the actual case; V_c is the actual cell voltage; the subscribe "ref" is the reference case.

P_{ref} = 1 bar ; T_{ref} = 1000℃; $(p_{O_2})_{ref}$ = 0.164; $(p_{H_2} / p_{H_2O})_{ref}$ = 0.15.

The current density (i_c) is calculated by the following equation:

$$i_c = \frac{zn_eF}{NA} \tag{5}$$

Where A is the active area of single cell, cm^2 , F is Faraday constant, 96487 C/mol , n_e is electrons transferred per reaction , N is Number of single cells , z is the mole flow of reacted H_2;

By summing the above five equations (1)-(5) , the actual voltage V_c can be calculated as:

$$V_c = V_{ref} + \Delta V_p + \Delta V_T + \Delta V_{cat} + \Delta V_{an} \tag{6}$$

The fuel cell power output is the product of the cell voltage and current.

$$Power = i_c(A) \times V_c(V) \tag{7}$$

The cell electrical efficiency is calculated according to

$$\eta = \frac{\text{Power}}{G_f \times LHV_f} \tag{8}$$

Where G_f is the flow rate of fuel, mol/s, LHV_f is the low heating value of fuel, kJ/mol;

In the process of modelling the SOFC hybrid power system, the accuracy of the fuel cell stack model is critical for the overall system. So this paper firstly checked the accuracy of SOFC stack model. With the same input parameters of the literature [17-20], the simulation result of this paper is compared with those of the literature [17-20] (as shown in Table 1). The results show that this paper's simulation results are very close to the literature results which are close to the experimental data [18-20]. So the model of SOFC stack is feasible and reliable, it can be applied to simulate the overall SOFC hybrid system.

Table 1 The Simulation Results of SOFC Stack (120kW DC output)

Parameter (unit)	Literature Data [17]	Literature Data [18-20]	Simulation data of this paper
Voltage (V)	0.70	-	0.70
Current Density (mA/cm^2)	178	180	179.1
Air utilization factor	19%	-	18.2%
Pre-reformer Outlet Temperature (℃)	536	550	537.2
Stack exhaust composition (EXHAUST)	77.3%N_2 15.9%O_2 4.5%H_2O 2.3%CO_2	77%N_2 16%O_2 5%H_2O 2%CO_2	77.5%N_2 16.4%O_2 4 %H_2O 2.1%CO_2
Anode outlet composition (stream5)	50.9% H_2O 24.9%CO_2 11.6%H_2 7.4%CO 5.1%N_2	48% H_2O 28%CO_2 14%H_2 5%CO 5%N_2	50.9% H_2O 24.9% CO_2 11.6%H_2 7.4%CO 5.1%N_2
Stack exhaust temperature (℃)	834	847	832
Stack efficiency (AC)	52%	50%	51.99%

2.3. Description of the basic SOFC hybrid system without CO_2 capture

The basic SOFC hybrid system is a tubular SOFC stack with higher operating temperature. Figure 2 shows the flowsheet of the system. The fuel is compressed and preheated, then is put into pre-reformer to generate the required H_2, CO and CO_2. Air is supplied by a blower and preheated prior to entering the SOFC stack. Then air participates an electrochemical reaction with fuel in the fuel cell stack. Because the pre-reformer needs a larger amount of water vapor, a hot recycled stream from the anode outlet is directed to the pre-reformer. The outlet stream of SOFC anode is mainly composed of H_2O, CO_2 and unconverted fuel (H_2 and CO). Part of this stream is injected into the after-burner, then the hot outlet gas with high pressure expands in gas turbine, the rest is recycled and mixed with the compressed and preheated fuel. The recirculation fraction is calculated to meet a given steam/carbon (S/C) ratio. In this way, the system can prevent from the carbon deposition phenomenon, enhance the pre-reformer temperature and get more H_2. Finally, the product gas of SOFC is sent into the after-burner, where the unreacted fuel is burnt with part of the excess air from the cathode. After expansion of the hot gas in gas turbine, it is sent into heat exchangers to heat the inputted fuel and air. Then, it enters into the heat recovery steam generator and steam turbine system to produce addition power.

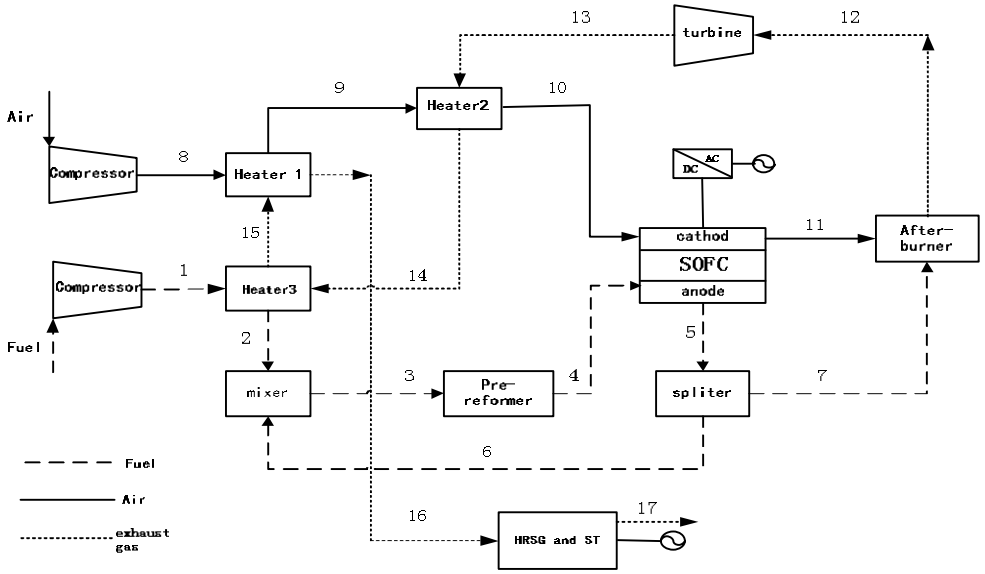

Figure 2 Flowchart of SOFC hybrid power system without CO_2 capture

Although SOFC hybrid power system has realized energy conversion with higher efficiency, the hybrid system still emits greenhouse gas when the fossil fuel is used. In addition, the exhausted gas from the afterburner contains a large number of N_2 that will greatly impact the energy consumption of capturing CO_2. The paper proposed three kinds of zero CO_2 emission SOFC hybrid power systems and made the detailed exergy analysis on them.

3. Three kinds of SOFC hybrid systems with CO_2 capture

The new systems and the basic system's primary processes are the same, but the new systems employ O_2/CO_2 combustion mode. Pure oxygen from air separation unit (ASU) is fed into the combustion chamber to burn with the anode exhaust gas. The product gas only contains steam and CO_2. CO_2 can be separated by condensation, which does not consume extra energy. In order to reduce the penalties of CO_2 capture in system efficiency and cost, it is fed to the multi-stage compressor and makes CO_2 liquefied for transportation.

Because the temperature of afterburner is very high after employing the O_2/CO_2 combustion mode, in order to maintain the proper turbine inlet temperature, three different methods (steam injection, CO_2 injection, and heat exchanger layout) are proposed.

3.1. Zero CO_2 emissions SOFC hybrid power systems with steam injection (case a)

The system flowchart is shown in Figure 3. The compressed and preheated nature gas and air are sent into the SOFC anode and cathode, respectively. Then the electrochemical reaction takes place at the three-phase boundaries of both electrodes to generate electricity. The depleted air out from the cathode expands in the turbine and finally is channelled to HRSG to produce steam. The steam produced from the heater4 is injected into the oxy-fuel burner to control temperature not exceed the maximum allowed turbine inlet temperature. The exhausted flue gas from the afterburner firstly expand in turbine1, then enters into a serial of heaters to exchange heat with flue and air, finally, the exhausted flue gas is introduced into heater4 to produce steam for the afterburner. The flue gas from the heater4 enters into the CO_2 compression and liquefaction unit. The cathode outlet gas firstly expands in turbine2, and then enters into HRSG and ST system to produce additional electricity.

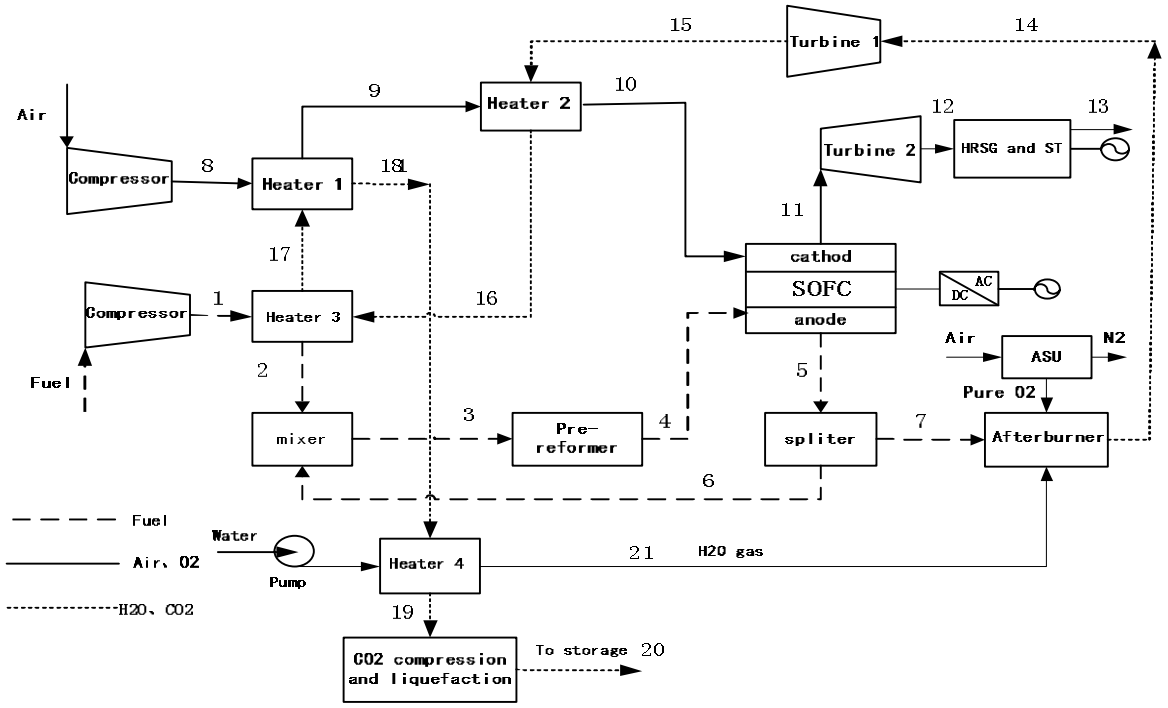

Figure 3 Flowchart of zero CO_2 emission hybrid system case (a)

3.2. Zero CO_2 emissions SOFC hybrid power system with CO_2 gas injection (case b)

The system flowchart of case b is shown in Figure 4. Compared with case a, the main difference is that CO_2 gas, not steam, is injected into the oxy-fuel burner, which can further increase the concentration of CO_2. After the heat transfer with the fuel and air through a series of heat exchangers, the combustion product gas is channelled into the HRSG to produce steam to generate more power. Then, the flue gas (mainly CO_2 and steam) exhausted from the HRSG is split into two parts. One part is compressed and injected into the O_2/CO_2 afterburner, while the other part is exhausted from the system and liquefied.

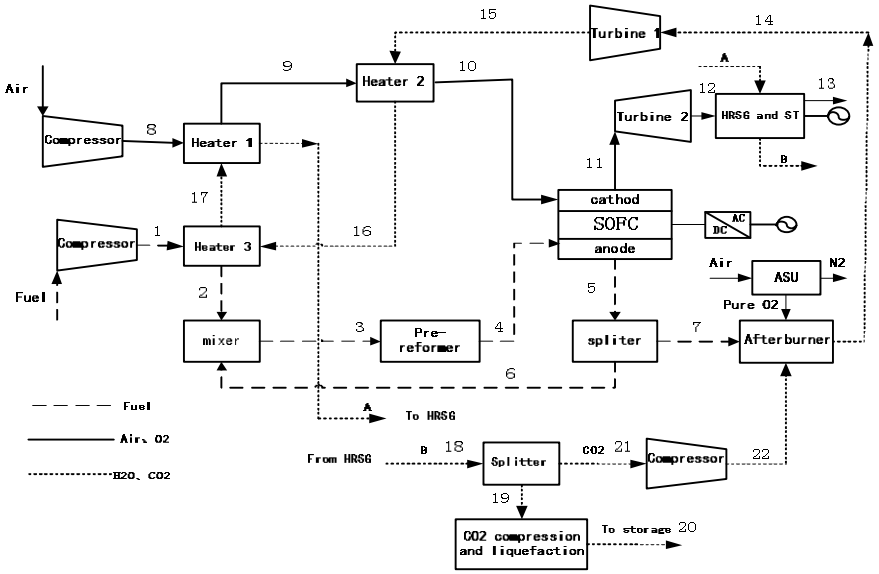

Figure 4 Flowchart of zero CO_2 emission hybrid system case (b)

3.3. Zero CO_2 emissions SOFC hybrid power system (case c)

The system flowchart of case c is shown in Figure 5. Compared with case a and b, neither steam nor CO_2 gas is injected into the O_2/CO_2 afterburner. The combustion product gas with high temperature exchanges the heat with the cathode outlet gas in heater4, and cathode inlet air in heater2 respectively. Then, the cathode outlet gas enters into turbine2 to produce power, while the flue gas exited from the heater2 enters into turbine1 to expand. After heating the air and fuel, the flue gas is introduced to HRSG and steam turbine system to produce additional power. The exhausted flue gas from HRSG enters into CO_2 compression and liquefaction unit to liquefy CO_2 for storage. The exhausted O_2-depleted air from turbine2 firstly enters into HRSG and steam turbine system to produce power, and then exits into the air.

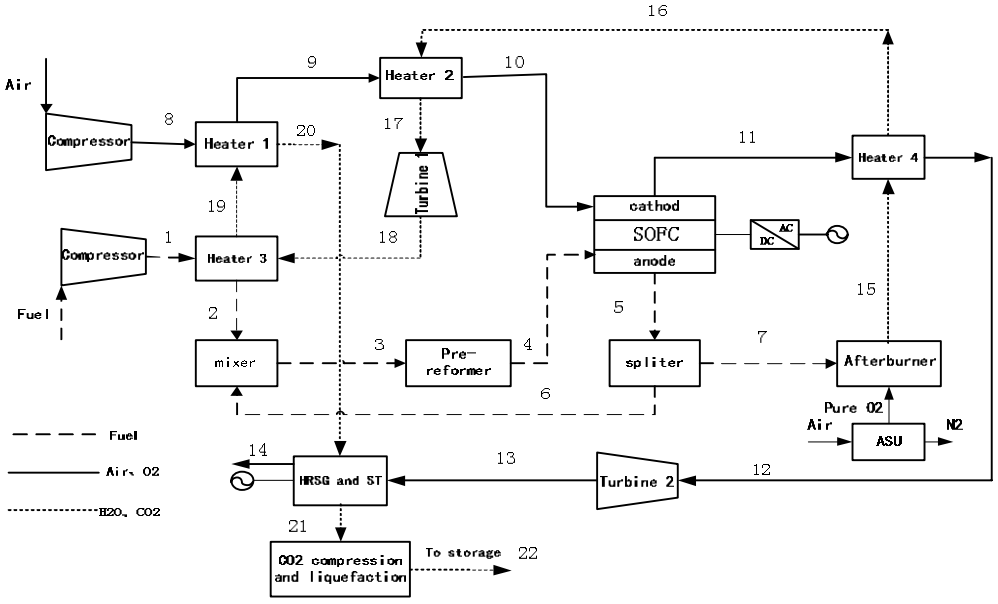

Figure 5 Flowchart of zero CO_2 emission hybrid system case (c)

All the three systems include the cryogenic air separation unit and CO_2 capture unit. The CO_2 is compressed by 6 stages intercooled compressor and the discharge pressure is 80 atm. Then it is cooled to 25℃ again after compression. The operating pressure of the cryogenic air separation unit is 0.6MPa, and the purity of oxygen is assumed as 100%.

4. Exergy analysis method

The exergy analysis method is applied for the three systems. These systems basically are composed of pre-reformer, SOFC stack, afterburner, turbine, fuel compressor, air compressor, recuperators, HRSG, CO_2 compression unit and some heaters. Exergy analysis method is used to calculate the thermodynamic losses in each unit and to assess the energy saving potentials of the systems[21-24].

Here, exergy destruction rate (σ_i) is defined as the ratio of the exergy destruction ($E_{X_{D,I}}$)in a specific unit to total exergy destruction($E_{X_{D,tot}}$) of system, it **c**an be calculated using the following formula:

$$\sigma_i = \frac{E_{X_{D,i}}}{E_{X_{D,tot}}} \times 100\% \qquad (9)$$

It means the ratio of local exergy destruction to total exergy destruction. This coefficient can be used to show the distribution of each unit's exergy destruction, which will help to assess the energy-saving potentials of the systems**.** To highlight exergy variation rule of the system with the change of key parameters, exergy destruction coefficient R_a as another evaluation index is defined as follow:

$$R_a = \frac{E_{X_{D.tot}}}{E_{X_{tot}}} \times 100\% \qquad (10)$$

It means the ratio of total exergy destruction ($E_{X_{D,tot}}$) to the output exergy of the system ($E_{X_{tot}}$). For a given system, the smaller R_a is , the smaller the exergy destruction is , the better the system with more output exergy is .

5 Simulation and analysis of SOFC hybrid power systems

5.1 Simulation results of systems

The initial simulation condition of system is shown in Table 2. For ensuring the rationality of the comparisons of all the systems, the input fuel, the inlet temperature of cathode and the active area of SOFC stack are the same among the three systems**.** Table 3 shows the detailed data of different systems. Table 4 shows the comparison results of the different SOFC hybrid power systems with CO_2 capture.

Table 2 Simulation parameters of system

Fuel Inlet Composition	CH_4 93.6%, C_2H_6 4.9%, C_3H_8 0.4%, C_4H_{10} 0.2%, CO 0. 9%。		
S/C ratio	2.5	DC to AC inverter efficiency (%)	92
Overall fuel utilization factor (%)	85	Air utilization factor (%)	25
Cell operating temperature (℃)	910	Cell operating pressure (MPa)	0.3
Inlet fuel temperature (℃)	15	Inlet air temperature (℃)	15
SOFC thermal losses (%)	5	Isentropic efficiency of turbine (%)	80
Isentropic efficiency of compressor (%)	80	Mechanical efficiency of compressor (%)	98
Generator efficiency (%)	99	Mechanical efficiency of generator (%)	98

Table 3 Detail data of main streams of different SOFC hybrid systems

Basic	T	P	Mole Flow	Mole Fraction									
system	℃	bar	kmol/hr	H2	O2	N2	CO	CO2	H2O	C2H6	C3H8	C4H10	CH4
1	117.7	3.24	1281	0	0	0	0.01	0	0	0.05	0	0	0.94
2	336.9	3.21	1281	0	0	0	0.01	0	0	0.05	0	0	0.94
3	544	3.19	7581.93	0.1	0	0	0.07	0.22	0.45	0.01	0	0	0.16
4	586.9	3.14	8343.12	0.26	0	0	0.07	0.24	0.32	0	0	0	0.12
5	910	3.04	10282.27	0.12	0	0	0.08	0.26	0.54	0	0	0	0
6	910	3.19	6300.93	0.12	0	0	0.08	0.26	0.54	0	0	0	0
7	910	3.04	3981.34	0.12	0	0	0.08	0.26	0.54	0	0	0	0
8	149.6	3.1	17892.02	0	0.21	0.79	0	0	0	0	0	0	0
9	326.9	3.1	17892.02	0	0.21	0.79	0	0	0	0	0	0	0
10	526.9	3.06	17892.02	0	0.21	0.79	0	0	0	0	0	0	0
11	910	3.04	15626.13	0	0.1	0.9	0	0	0	0	0	0	0
12	1200.7	3.04	19207.61	0	0.06	0.74	0	0.07	0.14	0	0	0	0
13	946.3	1.08	19207.61	0	0.06	0.74	0	0.07	0.14	0	0	0	0
14	783.3	1.06	19207.61	0	0.06	0.74	0	0.07	0.14	0	0	0	0
15	763.2	1.04	19207.61	0	0.06	0.74	0	0.07	0.14	0	0	0	0
16	619.7	1.02	19207.61	0	0.06	0.74	0	0.07	0.14	0	0	0	0
17	110.3	1.01	19207.61	0	0.06	0.74	0	0.07	0.14	0	0	0	0
Air	15	1.01	17892.02	0	0.21	0.79	0	0	0	0	0	0	0
Fuel	15	1.01	1281	0	0	0	0.01	0	0	0.05	0	0	0.94

Case a	T	P	Mole Flow	Mole Fraction									
	℃	bar	kmol/hr	H2	O2	N2	CO	CO2	H2O	C2H6	C3H8	C4H10	CH4
1	117.7	3.24	1281	0	0	0	0.01	0	0	0.05	0	0	0.94
2	336.9	3.21	1281	0	0	0	0.01	0	0	0.05	0	0	0.94
3	544	3.19	7581.93	0.1	0	0	0.07	0.22	0.45	0.01	0	0	0.16
4	586.9	3.14	8343.12	0.26	0	0	0.07	0.24	0.32	0	0	0	0.12
5	910	3.04	10282.27	0.12	0	0	0.08	0.26	0.54	0	0	0	0
6	910	3.19	6300.93	0.12	0	0	0.08	0.26	0.54	0	0	0	0
7	910	3.04	3981.34	0.12	0	0	0.08	0.26	0.54	0	0	0	0
8	149.6	3.1	17892.03	0	0.21	0.79	0	0	0	0	0	0	0
9	326.9	3.1	17892.03	0	0.21	0.79	0	0	0	0	0	0	0
10	526.9	3.06	17892.03	0	0.21	0.79	0	0	0	0	0	0	0
11	910	3.04	15626.13	0	0.1	0.9	0	0	0	0	0	0	0
12	682.7	1.03	15626.13	0	0.1	0.9	0	0	0	0	0	0	0
13	90.55	1.01	15626.13	0	0.1	0.9	0	0	0	0	0	0	0
14	1226.3	3.04	7041.41	0	0	0	0	0.19	0.81	0	0	0	0
15	1019.5	1.08	7041.41	0	0	0	0	0.19	0.81	0	0	0	0
16	668.3	1.06	7041.41	0	0	0	0	0.19	0.81	0	0	0	0
17	623	1.04	7041.41	0	0	0	0	0.19	0.81	0	0	0	0
18	286.7	1.02	7041.41	0	0	0	0	0.19	0.81	0	0	0	0
19	110	1.01	7041.41	0	0	0	0	0.19	0.81	0	0	0	0
20	25	80	1361.7	0	0	0	0	1	0	0	0	0	0
21	146.8	3.55	5679.65	0	0	0	0	0	0.18	0	0	0	0
Air	15	1.01	17892.03	0	0.21	0.79	0	0	0	0	0	0	0
Fuel	15	1.01	1281	0	0	0	0.01	0	0	0.05	0	0	0.94

Case b	T	P	Mole Flow	Mole Fraction									
	℃	bar	kmol/hr	H2	O2	N2	CO	CO2	H2O	C2H6	C3H8	C4H10	CH4
1	117.7	3.24	1281	0	0	0	0.01	0	0	0.05	0	0	0.94
2	336.9	3.21	1281	0	0	0	0.01	0	0	0.05	0	0	0.94
3	544	3.19	7581.93	0.1	0	0	0.07	0.22	0.45	0.01	0	0	0.16
4	586.9	3.14	8343.12	0.26	0	0	0.07	0.24	0.32	0	0	0	0.12
5	910	3.04	10282.27	0.12	0	0	0.08	0.26	0.54	0	0	0	0
6	910	3.19	6300.93	0.12	0	0	0.08	0.26	0.54	0	0	0	0
7	910	3.04	3981.34	0.12	0	0	0.08	0.26	0.54	0	0	0	0
8	149.6	3.1	17892.03	0	0.21	0.79	0	0	0	0	0	0	0
9	326.9	3.1	17892.03	0	0.21	0.79	0	0	0	0	0	0	0
10	526.9	3.06	17892.03	0	0.21	0.79	0	0	0	0	0	0	0
11	910	3.04	15626.13	0	0.1	0.9	0	0	0	0	0	0	0
12	682.7	1.01	15626.13	0	0.1	0.9	0	0	0	0	0	0	0
13	90	1.01	15626.13	0	0.1	0.9	0	0	0	0	0	0	0
14	1187.2	3.04	6783.62	0	0	0	0	0.61	0.39	0	0	0	0
15	1002.5	1.08	6783.62	0	0	0	0	0.61	0.39	0	0	0	0
16	669.4	1.06	6783.62	0	0	0	0	0.61	0.39	0	0	0	0
17	626.9	1.04	6783.62	0	0	0	0	0.61	0.39	0	0	0	0
18	110.3	1.01	6783.62	0	0	0	0	0.61	0.39	0	0	0	0
19	24.85	1.01	1361.73	0	0	0	0	1	0	0	0	0	0
20	24.85	80	1361.73	0	0	0	0	1	0	0	0	0	0
21	24.85	1.01	2802.19	0	0	0	0	1	0	0	0	0	0
22	122.44	3.04	2802.21	0	0	0	0	1	0	0	0	0	0
A	311.7	1.02	6783.62	0	0	0	0	0.61	0.39	0	0	0	0
Air	15	1.01	17892.03	0	0.21	0.79	0	0	0	0	0	0	0
Fuel	15	1.01	1281	0	0	0	0.01	0	0	0.05	0	0	0.94

Case c	T	P	Mole Flow	Mole Fraction									
	℃	bar	kmol/hr	H2	O2	N2	CO	CO2	H2O	C2H6	C3H8	C4H10	CH4
1	117.7	3.24	1281	0	0	0	0.01	0	0	0.05	0	0	0.94
2	336.85	3.21	1281	0	0	0	0.01	0	0	0.05	0	0	0.94
3	544	3.19	7581.93	0.1	0	0	0.07	0.22	0.45	0.01	0	0	0.16
4	585.64	3.14	8348.01	0.26	0	0	0.07	0.24	0.32	0	0	0	0.12
5	910	3.04	10282.27	0.12	0	0	0.08	0.26	0.54	0	0	0	0
6	910	3.19	6300.93	0.12	0	0	0.08	0.26	0.54	0	0	0	0
7	910	3.04	3981.34	0.12	0	0	0.08	0.26	0.54	0	0	0	0
8	149.63	3.1	17892.03	0	0.21	0.79	0	0	0	0	0	0	0
9	326.85	3.1	17892.03	0	0.21	0.79	0	0	0	0	0	0	0
10	526.85	3.06	17892.03	0	0.21	0.79	0	0	0	0	0	0	0
11	910	3.04	15626.13	0	0.1	0.9	0	0	0	0	0	0	0
12	1034.65	3.04	15626.13	0	0.1	0.9	0	0	0	0	0	0	0
13	787.03	1.01	15626.13	0	0.1	0.9	0	0	0	0	0	0	0
14	90	1.01	15626.13	0	0.1	0.9	0	0	0	0	0	0	0
15	1863.45	3.04	3981.41	0	0	0	0	0.34	0.66	0	0	0	0
16	1550	3.02	3981.41	0	0	0	0	0.34	0.66	0	0	0	0
17	992.06	3	3981.41	0	0	0	0	0.34	0.66	0	0	0	0
18	815.88	1.08	3981.41	0	0	0	0	0.34	0.66	0	0	0	0
19	740.56	1.06	3981.41	0	0	0	0	0.34	0.66	0	0	0	0
20	157.4	1.04	3981.41	0	0	0	0	0.34	0.66	0	0	0	0
21	110.53	1.01	3981.41	0	0	0	0	0.34	0.66	0	0	0	0
22	25	80	1361.7	0	0	0	0	1	0	0	0	0	0
Air	15	1.01	17892.03	0	0.21	0.79	0	0	0	0	0	0	0
Fuel	15	1.01	1281	0	0	0	0.01	0	0	0.05	0	0	0.94

Table 4 Simulation results of different systems

Parameters	Basic system	Case a	Case b	Case c
Fuel intake rate (kg/s)	6.06	6.06	6.06	6.06
Air intake rate (kmol/s)	4.97	4.97	4.97	4.97
ASU outlet oxygen (kg/s)	-	3.55	3.55	3.55
Voltage (V)	0.635	0.635	0.635	0.635
Current density (mA/cm^2)	177.31	177.31	177.31	177.31
Cell stack power (MW)	141.96	141.96	141.96	141.96
Turbine power(MW)	50.03	48.27	50.30	44.78
Power output of HSRG(MW)	26.14	24.36	29.35	31.21
Air and fuel compressor energy consumption (MW)	21.44	21.15	21.44	21.44
oxygen energy consumption (MW)	-	3.296	3.296	3.296
CO_2 capture energy consumption (MW)	-	5.219	8.228	5.217
Total power (MW)	196.69	184.93	188.65	187.99
Cell stack efficiency（AC）(%)	47.65	47.65	47.65	47.65
Net efficiency (%)	66.02	62.07	63.32	63.10

Three different zero CO_2 emission SOFC hybrid power systems are about 3-4 percentage points lower than the basic SOFC hybrid power system without CO_2 capture. The differences of output power and power consumption in other units lead to disparity of system efficiencies among three systems. The efficiency of case b is the highest as shown in table 4.

The comparison results show that turbine power of Case c has the lowest power output than those of other systems because of the mass rate of turbines input gas (cathode outlet gas and combustion product gas), other reason for it is that the temperature of turbine 1 inlet gas is reduced after transferring heat in heater 4 and heater 2.

After exchanging heat with the fuel and air through a series of heat exchanger, the combustion product gas has higher temperature to produce steam to generate more power in the HRSG in case c, so case c has the biggest power output from HSRG among all three systems.

Before injecting the H_2O or CO_2 gas into the oxy-fuel burner, the gas must be compressed firstly with additional equipment and power consumption. For case a, pump is used to enhance the pressure of H_2O. For case b, gas compressor is employed to compress the injected CO_2 gas. It is clear that the power consumption of case b for CO_2 capture is higher than that of case a and case c.

In a word, the different performances of the system configurations bring about different system efficiency among three systems. The system efficiency of case b is 2.7 percentage points lower than that of the traditional SOFC hybrid power system and 1.25% and 0.22% higher than that of case a and case c, respectively.

5.2 Exergy analysis of SOFC hybrid power systems

According to the simulation result and exergy balance equation, it is possible to obtain the exergy destruction distribution in each unit of systems as shown in Fig.6. Results show that SOFC stack, afterburner and HSRG are responsible for the major exergy destruction in the system. In order to improve the system exergy efficiency, the exergy destructions of these units should be firstly considered and further reduced.

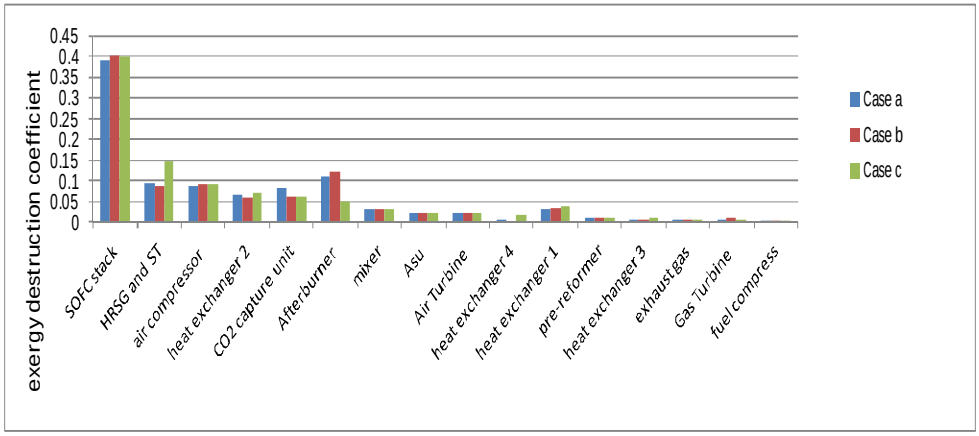

Figure 6 The exergy destruction distributions of every unit

As shown in Figure 6, the exergy destruction ratio of SOFC stack is above 35%. As the inlet air of SOFC stack has a significant cooling effect in fuel cell stack, the irreversibly lost is caused. Meanwhile in order to heat the air, some of the fuel chemical energy must convert to heat energy, which further increases the irreversible loss. The exergy destruction of afterburner relates to the pressure and temperature of the inlet and the outlet gas. In order to keep the temperature not exceed the maximum allowed turbine inlet temperature, it is necessary to reduce the temperature of the gas out from the afterburner greatly by employing different cooling method, therefore the exergy destruction of afterburner is rather huge.

Based on the second law of thermodynamics, the dissipative phenomena (friction, chemical reaction, heat transfer, thermal losses) lead to irreversibly exergy destruction. The HRSG is the biggest heat exchanger in the system which also has a rather larger exergy destruction, it is necessary to design the pattern of heat exchange reasonably.

As shown in the Figure 6, it is clear that in case c the exergy destruction of HRSG and ST system is larger, while the exergy destruction of afterburner is lower than those of other two systems. For case c, the depleted fuel burns with pure O_2 in the afterburner without any injected cooling working media. On one hand, the combustion product gas has the higher temperature and the exergy destruction of afterburner is lower, on the other hand, after exchanging heat with the outlet gas from the cathode of SOFC stack, the temperature of gas channelled into HRSG is increased greatly, which increase the temperature difference between gas and the steam and results in the bigger exergy destruction. The exergy destruction of HRSG and ST is larger than that of others obviously.

5.3 The effects of operating parameters on the performance of systems

5.3.1 Effect of the operating temperature

When the mass flow of input fuel keeps constant, with the increase of the operating temperature of SOFC, the efficiencies of all systems increase and exergy destruction coefficients reduce except case a. As the operating temperature of SOFC increase, the required air for cell stack decreases. The activity of cell stack also enhances, the exergy destructions of systems except for case a reduce and the total output powers of system increase as shown in Figure 7. For case a, although the output power of SOFC stack increases, its increment is less than the decrement of the turbine and HRSG output power due to the decreasing of the inlet air with the increase of the operating temperature, which results in the variation tendency of system efficiency and exergy destruction coefficient are opposite to that of other systems as shown in Figure 8 and Figure 9. Therefore, in the practical situation, the system should operate in the proper temperature [25-26].

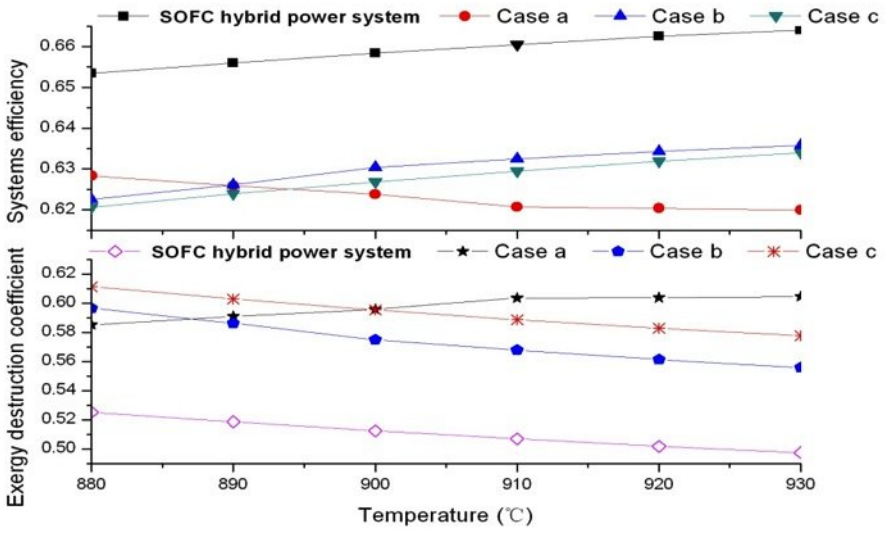

Figure 7 Effect of the operating temperature on system exergy destruction

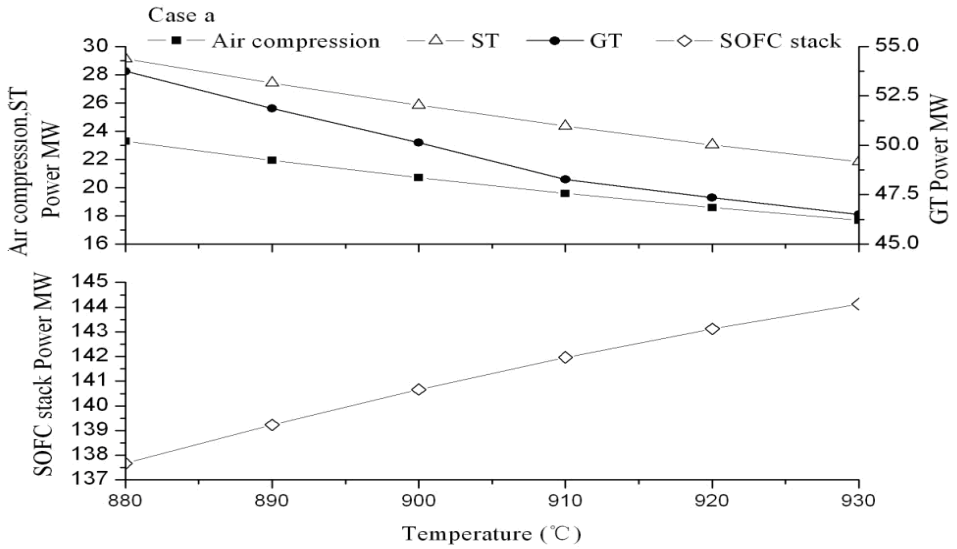

Figure 8 Effect of the operating temperature on unit output power (case a)

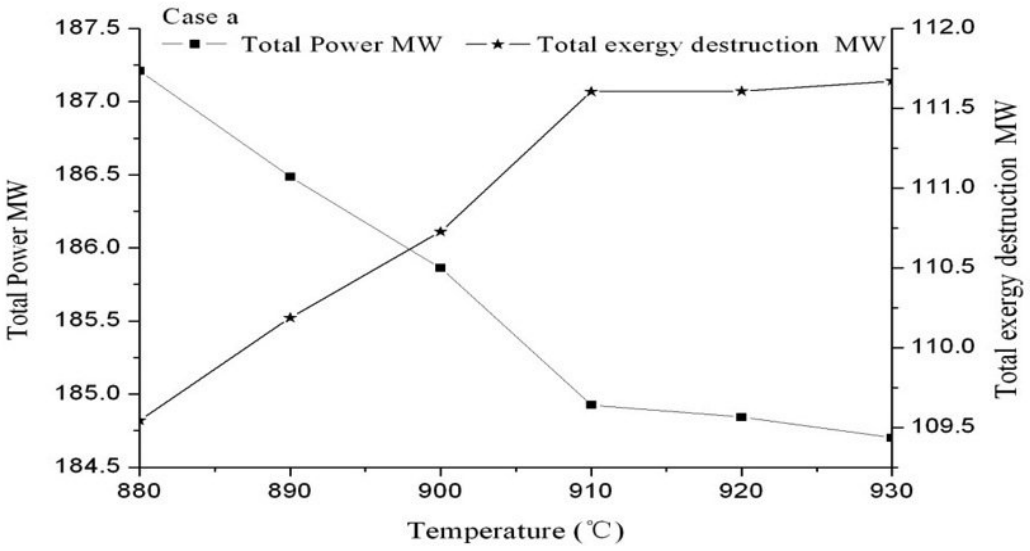

Figure 9 Effect of the operating temperature on system total power and exergy destruction (case a)

5.3.2 Effect of the operating pressure

The operating pressure is another key variable to the system performance. Improving the operating pressure of SOFC stack, the SOFC voltage will increase because the H_2 amount and H_2 partial pressure increase which increase the output power of the SOFC stack. The high pressure also be beneficial to increasing the output power of turbine and HRSG .

As shown in Figure 10, as the operating pressure increases, the exergy loss of SOFC stack reduces and the total system output exergy increases. The system efficiency increases meanwhile the exergy destruction coefficient reduces. However, the growth rate of efficiency becomes less and less with the increase of the operating pressure. In addition, the higher pressure will results in the increase the cost of system investment. So it is necessary to choose the proper operating pressure when designing the SOFC.

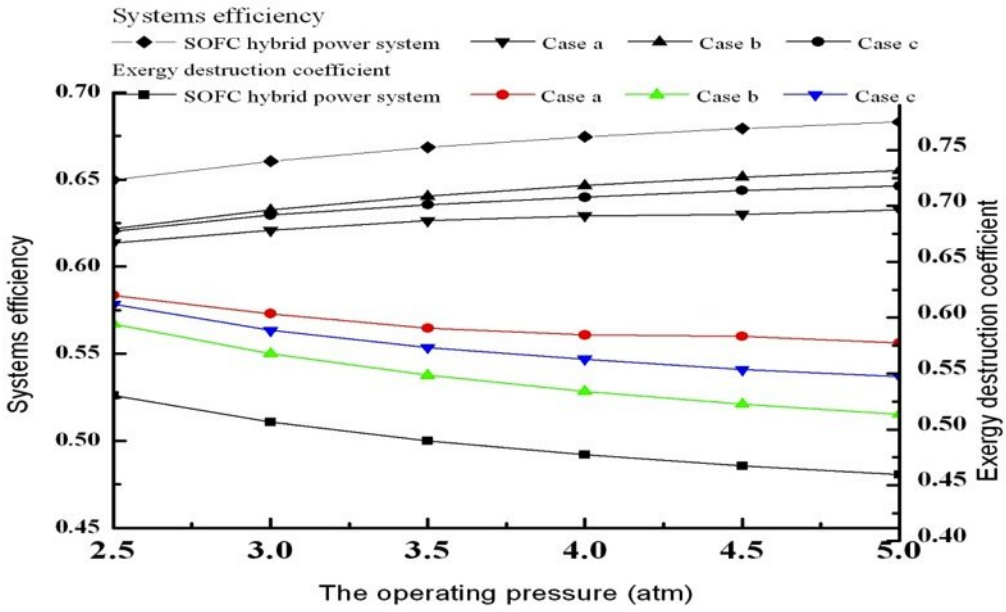

Figure 10 Effect of the operating pressure on system exergy destruction

5.3.3 Effect of fuel utilization factor (U_f)

The fuel utilization factor (U_f) has a significant effect on the cell voltage and efficiency. With the increase of U_f from 0.83 to 0.87, the current density will increase, which will result in the decrease of the cell voltage. All the systems efficiency increase until achieve the biggest value then begin decrease with the increase of U_f, although different systems reach their biggest system efficiency at different U_f. And U_f also has a significant impact on the composition of the anode exhausted gas. The CO_2 concentration at the anode outlet increases when U_f is increased because the fuel is more depleted by the electrochemical reaction in the SOFC(less CO and H_2), which will result in the change of the system unit exergy loss as shown in Figure 11.

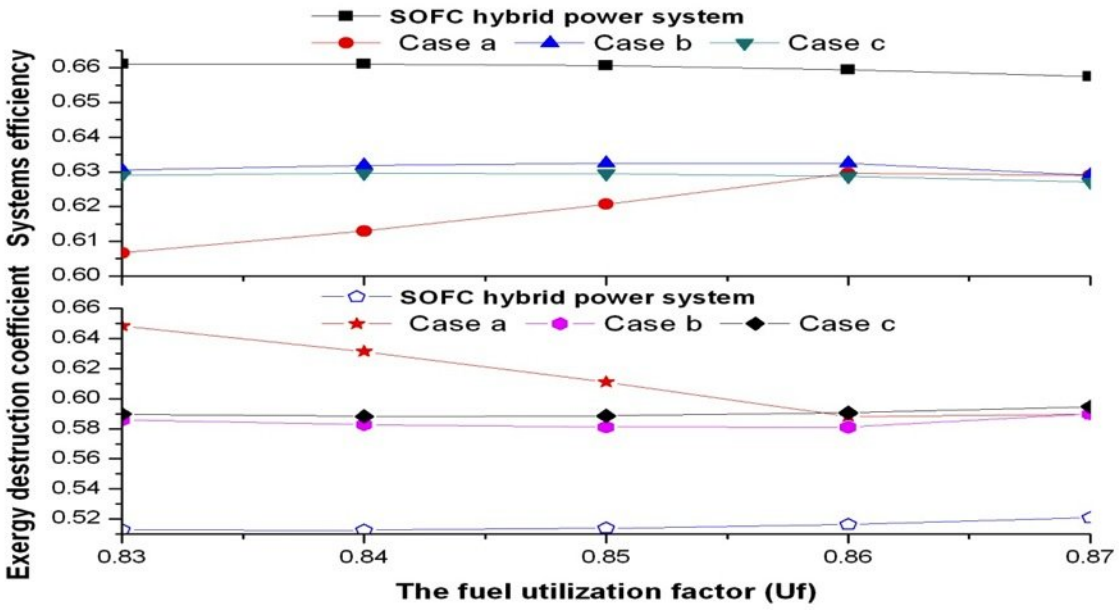

Figure 11 Effect of the fuel utilization factor (U_f) on system exergy destruction

6 Conclusions

This paper proposed three kinds of SOFC hybrid systems with CO_2 capture. The research results show that the new SOFC hybrid system still has a higher efficiency even with the CO_2 capture. Their efficiencies only decrease 3-4 percentage points compared with the basic SOFC hybrid system without CO_2 capture. The system efficiency of case b is 1.25 and 0.22 percentage points higher than that of case a and case c respectively.

The O_2/CO_2 combustion mode can fully burn the anode's fuel gas, and increase the concentration of CO_2 gas; at the same time with the steam injection and the combustion products are channelled into turbine, the efficiency of system greatly increases. The liquefaction of CO_2 by the mode of multi-stage compression and intermediate cooling can also greatly reduce the energy consumption.

Exergy analysis of SOFC hybrid power systems provides better understanding of losses and draws ones attention to the most important sections. It is clear that SOFC stack, afterburner and the HSRG are responsible for the major exergy destruction in the system. Consequently, some appropriate measures should be adopted to lower exergy destruction to enhance the overall system efficiency. The operating temperature, the operating pressure and the fuel utilization factor as key variables influence the overall system performance greatly, which should be taken into account for the systems to achieve the optimal condition. Above research achievements will provide the new idea and method for further study on zero emission CO_2 system with high efficiency.

Acknowledgments

This study has been supported by the Fundamental Research Funds for the Central Universities (No.10ZG03), National Nature Science Foundation Project (No. 50606010 and No. 51025624), the National Basic Research Program of China (No. 2009CB219801), the Scientific Research Foundation for the Returned Overseas Chinese Scholars, State Education Ministry and by the 111 Project（B12034）.

References

[1] Kartha S, Grimes P. Fuel cells: energy conversion for the next century. Physics Today, 1994 (11) : 54–61

[2] Y.Inui, T.Matsumae, H.Koga, K.Nishiura. High performance SOFC/GT combined power generation system with CO_2 recovery by oxygen combustion method. Energy Conversion and Management, 2005, 46, pp: 1837–1847

[3] A. Franzoni, L. Magistri, A. Traverso, A.F. Massardo. Thermoeconomic analysis of pressurized hybrid SOFC systems with CO_2 separation. Energy,2008, 33, pp: 311–320

[4] Philippe Mathieu. Towards the hydrogen era using near-zero CO_2 emissions energy systems. Energy, 2004, 29 , pp: 1993–2002

[5] Takeshi Kuramochi, Hao Wu, Andrea Ramirez, Andre Faaij and Wim Turkenburg. Techno-economic prospects for CO_2 capture from a Solid Oxide Fuel Cell – Combined Heat and Power plant. Preliminary results. Energy Procedia, 2009,1, pp: 3843–3850

[6] B. Fredriksson Möller, J. Arriagada, M. Assadi, I. Potts. Optimisation of an SOFC/GT system with CO_2-capture. Journal of Power Sources, 2004, 131, pp: 320–326

[7] Bozzolo M, Brandani M, Traverso A, Massardo AF. Thermoeconomic analysis of gas turbine plants with fuel decarbonization and carbon dioxide sequestration, ASME transactions. J Eng Gas Turbines Power, 2003, 125 (4) : 947–53.

[8] Asle Lygre, Matteo Ce. Solid Oxide Fuel Cell Power with Integrated CO_2 capture. Second Nordic Minisymposium on Carbon Dioxide Capture and Storage, Goteborg, October 26, 2001

[9] Takuto Araki, Takuya Taniuchi, Daisuke Daisuke Sunakawa. Cycle analysis of low and high H_2 utilization SOFC/gas turbine combined cycle for CO_2 recovery, Journal of Power Sources. 2007, 171, pp: 464–470

[10]Ali Volkan Akkaya, Bahri Sahin , Hasan Huseyin Erdem. Thermodynamic model for exergetic performance of a tubular SOFC module. Renewable Energy, Volume 34, Issue 7, July 2009, pp: 1863–1870

[11]Ali Volkan Akkaya, Bahri Sahin, Hasan Huseyin Erdem. Exergetic performance coefficient analysis of a simple fuel cell system. International Journal of Hydrogen Energy, 2007, 32, pp:4600– 4609

[12] F. Calisea, M. Dentice d'Accadiaa, A. Palomboa, L. Vanoli. Simulation and exergy analysis of a hybrid Solid Oxide Fuel Cell (SOFC)–Gas Turbine System. Energy, 2006, 31, pp: 3278–3299

[13] Akkaya AV, et al. Exergetic performance coeffcient analysis of a simple fuel cell system. International Journal of Hydrogen energy, 2007: 1–10

[14] J.H. Hirschenhofer, D.B. Stauffer, R.R. Engleman, Fuel Cells, A Handbook (Rev.3), Commonwealth Inc. for US Department of Energy (DOE) , Gilbert , 1994.

[15] H. Ide, et al., Natural gas reformed fuel cell power generation systemsÐa comparison of three system efficiencies, Proceedings of the 24th IECEC , Washington , 1989.

[16] N.F. Bessette, R.A. George , Electrical performance of Westinghouse's AES solid oxide fuel cell, Proceedings of the Second International Fuel Cell Conference , Japan , 1996.

[17]W. Zhang, E. Croiset, P.L.Douglas, M.W.Fowler, E.Entchev. Simulation of a tubular solid oxide fuel cell stack using AspenPlus^{TM} unit operation models. Energy Conversion and Management, 2005,(46): 181-196.

[18]Veyo SE, Forbes CA. Demonstractions based on Westinghouse's prototype commercial AES design. In: Proceedings of the Third European Solid Oxide Fuel Cell Forum, 1998, pp: 79-86.
[19]Veyo SE. The Westinghouse solid oxide fuel cell programe—a status report. In: Proceedings of the 31st IECEC, No. 96570, 1996, p. 1138-43.
[20]Veyo S, Lundberg W. Solid oxide fuel cell power system cycles. ASME Paper 99-GT-356, International Gas Turbine and Aeroengine Congress and Exhibition, Indianapolis, June 1999
[21]Wang Jiaxuan, Zhang Shufang. Exergy method and its application in power plants, China Water Power Press, 1993.87–121
[22]Lu Lining. Calculation and optimization study on the performance of a Combined Power Generation System Incorporating a Solid-oxide Fuel Cell and a Gas Turbine. Master's thesis, Dalian University of Technology, 2004
[23]JIA Junxi. Study of Model Heat and Mass Transfer in Solid Oxide Fuel Cell, Doctor's thesis, Dalian University of Technology, 2006
[24]Calise F, d'Accadia MD, Palombo A, Vanoli L. Simulation and exergy analysis of a hybrid solid oxide fuel cell (SOFC)– gas turbine system. Energy, 2006, 31, pp:78—99
[25]Meng Ni, Michael K.H. Leung, Dennis Y.C. Leung. Parametric study of solid oxide fuel cell performance. Energy Conversion and Management, 2007, 48, pp:1525–1535
[26]Li Xiaolin. Study on heat/power ratio of SOFC-GT hybrid system, Master's thesis, Central South University. 2008

Exergy analysis and optimisation of a steam methane pre-reforming system

George G. Dimopoulos[a], Jason C. Stefanatos[b] and Nikolaos M.P. Kakalis[c]

[a] *Det Norske Veritas, Research & Innovation, Piraeus, Greece, George.Dimopoulos@dnv.com*
[b] *Det Norske Veritas, Research & Innovation, Piraeus, Greece, Jason.Stefanatos@dnv.com*
[c] *Det Norske Veritas, Research & Innovation, Piraeus, Greece, Nikolaos.Kakalis@dnv.com* ***CA***

Abstract:

In this paper we present the exergetic analysis and optimisation of a steam methane pre-reformer system for marine fuel cells. Hybrid marine energy systems combining conventional power generation with fuel cells can offer significant reductions in emissions and overall efficiency gains, promote the shift to more environmentally-friendly fuels, such as LNG, and can increase the operational flexibility of a vessel. High temperature molten carbonate fuel cells (MCFC) is a promising option for marine use due to their high efficiency and high energy content exhaust gasses. A key component of this technology is the steam methane pre-reformer which reforms completely higher-chain hydrocarbons contained in LNG and partly reforms methane to hydrogen in order to assist the internal reforming process within the fuel cell stack. We consider a pre-reformer system concept consisting of a water evaporator, a steam/methane heater and a catalytic tubular packed-bed reformer. The water evaporation and steam/methane heat exchangers utilise the high temperature exhaust gases of the fuel cell stack, while the pre-reformer uses the heat input of the process stream. The pre-reformer system uses about 39% of the exhaust gas exergy, which amounts to about 10% of the chemical exergy of the overall system's fuel. Therefore, there is considerable potential for improving the design in terms of energy efficiency that will achieve higher performance and applicability for the overall fuel cell unit.

In this work we present a three-step approach. First, we develop a dynamic mathematical model that describes the physical/chemical behaviour of the pre-reformer system. Second, we perform exergy analysis, and third, we optimise the reformer with respect to its exergetic performance. Our methodology is based on the thermofluid and chemical reactions modelling of the system components, using a generic and reconfigurable process modelling framework. The developed models are spatially distributed in order to account for, and give insight on, the internal process characteristics of each individual component. In addition, spatially distributed exergy balances are considered within the component models, to capture the interrelation of the local exergy destruction (irreversibility) with component design geometry, configuration and process phenomena. A design optimisation problem is then formulated that minimises the total irreversibility of the steam methane reforming system, subject to design, technical, operational and space constraints.

Our approach was applied to a standard marine MCFC pre-reformer system and the exergy analysis and optimisation results have successfully yielded the sources of irreversibility, and provided a low irreversibility optimal design with more than 50% less exergy destruction. The exergy analysis and optimisation proved to be particularly suited for this chemically reacting and heat exchanging system since traditional energy (first-law) and pinch-point calculations have certain shortcomings in their usage, which often fail to reveal the full picture of losses within the system. The results will be subsequently used to improve an existing marine system design and serve as the basis for the integrated optimisation of the entire fuel cell-based unit.

Keywords:

Marine fuel cells, Steam methane reformer, Exergy analysis, Modelling, Optimisation.

1. Introduction

The rising fuel costs, increased environmental concerns and forthcoming emissions regulations impose a pressure on ship energy conversion systems to become more efficient, cost-effective and environmentally friendly. In that context, hybrid marine energy systems combining conventional power generation with fuel cells emerge as promising future solutions offering reductions in

emissions and overall efficiency gains, promoting the shift to more environmentally-friendly fuels, such as LNG, and increasing the operational flexibility of a vessel. High temperature molten carbonate fuel cells (MCFC) is a promising option for marine use due to their high efficiency and high energy content exhaust gasses. This technology has already been installed onboard the offshore supply vessel Viking Lady (Eidesvik Offshore ASA) as an auxiliary power unit during the research demonstration project FellowSHIP [1, 2]. A key component of the MCFC plant is the steam methane pre-reformer (SMR) which is used to completely reform higher-chain hydrocarbons contained in the liquefied natural gas (LNG) fuel of the MCFC and partly reform methane to hydrogen in order to assist the internal reforming process within the fuel cell stack.

Steam methane reformers (SMR) are widely used for hydrogen production from hydrocarbon and alcohol fuels, like natural gas and methanol [3, 4]. In this work we present the modelling, exergetic analysis and optimisation of a SMR fuel pre-processing system for marine MCFC modules. The purpose of this study is to gain insight on the internal process characteristics of the SMR system components, identify the sources of exergy losses and to optimise the system with respect to its exergetic performance. Exergy analysis and optimisation is particularly suited for this chemically reacting and heat exchanging system since traditional energy (first-law) and pinch-point calculations have certain shortcomings in their usage, often failing to reveal the full picture of losses within such systems [5-8]. In previous studies, exergy analysis approaches have been successfully used to assess and improve fuel cell systems [7-16] and steam methane reformers [6, 17, 18]. This work combines exergy analysis and optimisation at a system level [6, 17] with spatially distributed exergy balances within components [7, 12, 18] in order to investigate the interrelation of the local exergy destruction (irreversibility) with the component design geometry, configuration and process phenomena. Subsequently, a design optimisation problem is formulated that minimises the total irreversibility of the SMR system, subject to design, technical, operational and space constraints.

The following sections present the SMR system description, the mathematical formulation of the individual component models and the optimisation problem formulation. Finally, the results of the exergy analysis and optimisation are given and discussed.

2. System description

We consider a marine MCFC unit with a MCFC stack and a SMR sub-system [2], Fig. 1. The MCFC stack is a low-pressure module with direct internal reforming (DIR). The SMR system mainly consists of a cross flow water evaporator, a cross flow steam/methane heater and an adiabatic catalytic tubular packed-bed reformer. These components constitute a fuel pre-processing / reforming module with main mission the complete reform of higher-chain hydrocarbons contained in the natural gas and the partial reforming of methane to hydrogen in order to produce the suitable operating conditions for the internal reformers of the MCFC-DIR stack. This is the main difference of the SMR of Fig. 1 with SMR concepts examined in other studies [6, 17], where the reformers are used for the bulk production of hydrogen. Literature results indicate that this MCFC-DIR concept has an improved exergetic performance compared to the complete external reforming solutions [4, 19].

The heat exchange process takes place on the water evaporator and the steam/methane heater, utilising the high temperature exhaust gases of the fuel cell stack. These were selected to be of a cross flow arrangement in order to minimise their footprint and simplify the layout. The adiabatic steam methane reformer utilises the heat input of the feed process stream. This heat input is required to initiate and drive the endothermic reforming reactions within the reactor. The main reactions taking place in the reforming process are the water gas shift and the methane reforming. Apart from the heat input, a catalyst material is also required. Usually the catalyst materials are in the form of a Nikel-based active metal packing with a porous $MgAl_2O_4$ support surface [20, 21]. The structure of the packing material can be either structured or random. In this concept a random

packing material of pellets is considered. Finally, the adiabatic operation of the pre-reformer and the heat exchangers is achieved via external layers of heat insulation.

In terms of operational boundaries, the fuel pre-processing system must supply the MCFC stack a fuel mixture with a steam-to-carbon (S/C) ratio of 2.0 to 2.1 and a hydrogen molar fraction between 10 and 15%, so as the MCFC stack to operate within the operational limits given by the manufacturer [2]. In addition, the complete fuel pre-processing system must be able to be enclosed in a standard 20 feet container. The aforementioned boundaries and space constraints have been used in the optimisation problem formulation of Section 4.

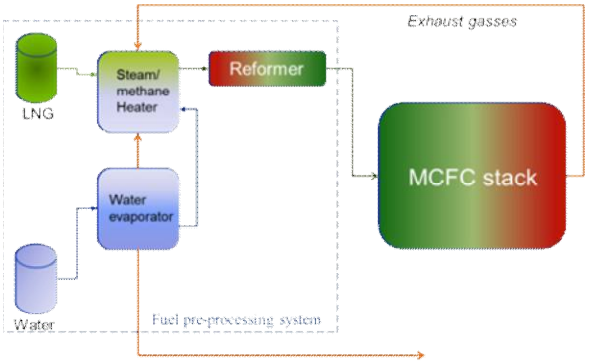

Fig. 1. Marine MCFC module: Fuel pre-processing system and Fuel cell stack.

3. Mathematical model formulation

3.1. Modelling framework

A generic model of the SMR system of Fig. 1 has been developed in our in house modelling framework DNV COSSMOS. COSSMOS is an acronym for Complex Ship Systems MOdelling and Simulation. We have developed a modular library of reconfigurable generic component models suitable for design, performance and transient operation analyses, and optimisation of integrated ship machinery systems [22-24]. Our methodology is based on the mathematical modelling of the steady-state and dynamic thermofluid behaviour of ship machinery components. This approach results in large systems of non-linear Partial Differential and Algebraic Equations (PDAE), subject to initial and boundary conditions. The steady-state versions of the PDAE systems are derived by supplying appropriate initial conditions equations, stating that the time derivatives of all differential variables, at the start of simulation, are equal to zero. With this approach, the same mathematical formulation and set of equations are used for both dynamic and steady-state simulations.

The SMR system process model in the COSSMOS platform is shown in Fig. 2, along with the numbering of process stream nodes and short names of system components. In the following paragraphs the mathematical formulation of the key system component models is presented.

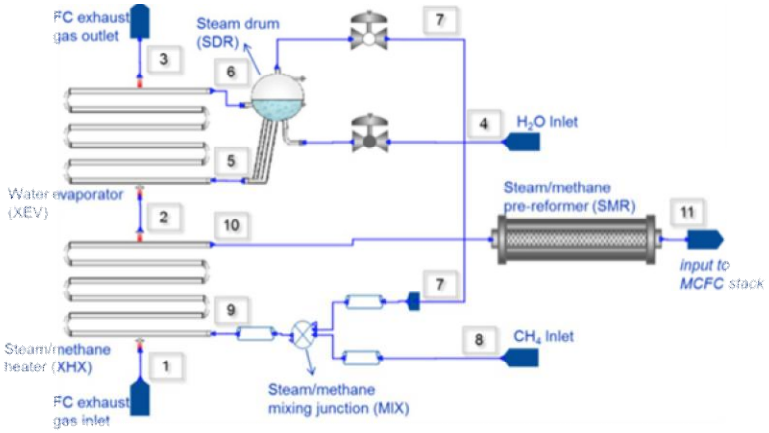

Fig. 2. SMR system process model flowsheet.

3.2. Cross flow heat exchanger & evaporator

Cross flow heat exchangers have, in general, high effectiveness and low footprint. Therefore, they are suitable for high efficiency and compact heat exchange solutions. A typical cross flow heat exchanger (or evaporator) consists of serpentine tube bundles arranged in vertical panels in series. The tubes can be either bare or finned. The cross flow heat exchanger model geometry is shown in Fig. 3. There are many studies in the literature that consider the modelling, simulation and optimisation of cross flow heat exchangers [25-29]. Our approach is further enhanced by developing a spatially distributed dynamic model with advanced heat transfer modelling [30].

The tube-side energy conservation equations and their associated boundary conditions are formulated according to the direction of the flow; from right to left (odd tube rows) and from left to right (even tube rows), following the serpentine configuration (Fig. 3):

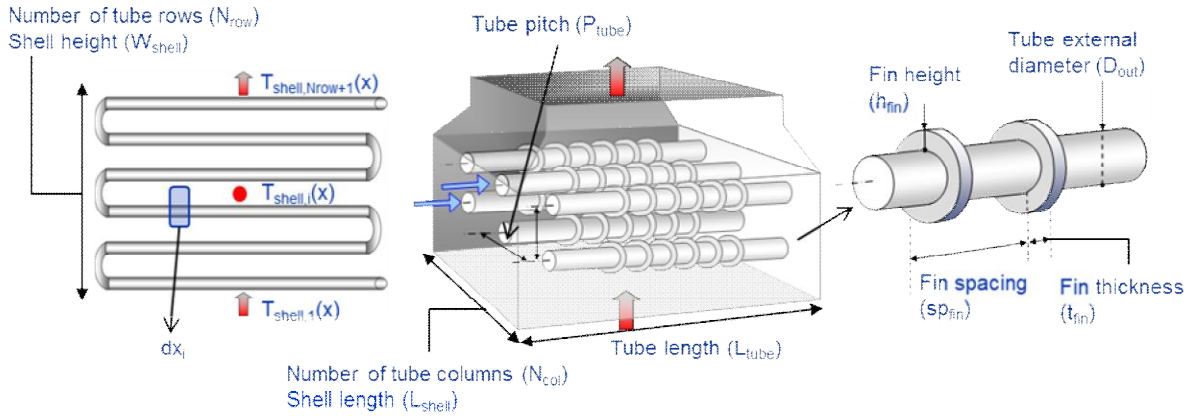

Fig. 3. Cross flow heat exchanger geometry.

$$A_{x,tube}\cdot\frac{d}{dt}\left[u_{tube,2i-1}(x)\right]+\frac{1}{L_{tube}}\cdot\frac{\partial}{\partial x}\left[\dot{H}_{tube,2i-1}(x)\right]=-\frac{A_{h,tube}}{L_{tube}}\cdot k_{tube,2i-1}(x)\cdot\left[T_{tube,2i-1}(x)-T_{metal,2i-1}(x)\right] \quad (1)$$

$$\forall x\in(0,1],\quad i=1,2...N_{row}$$

$$A_{x,tube}\cdot\frac{d}{dt}\left[u_{tube,2i}(x)\right]-\frac{1}{L_{tube}}\cdot\frac{\partial}{\partial x}\left[\dot{H}_{tube,2i}(x)\right]=-\frac{A_{h,tube}}{L_{tube}}\cdot k_{tube,2i}(x)\cdot\left[T_{tube,2i}(x)-T_{metal,2i}(x)\right] \quad (2)$$

$$\forall x\in[0,1),\quad i=1,2...N_{row}$$

It is noted that the equations are formulated for a non-dimensional domain along the tube length. This facilitates significantly the numerical treatment of design studies, in which the tube length may vary. In addition, in the gas flow direction, $N_{row}+1$ nodes are considered (index i), representing the tube metal conditions exposed in the shell-side temperature profile in the in-between locations of tube rows (Fig. 3).

The shell-side energy conservation equation is:

$$A_{x,shell}\cdot\frac{d}{dt}\left[u_{shell,i}(x)\right]+\frac{\dot{H}_{shell,i}(x)-\dot{H}_{shell,i-1}(x)}{L_{tube}}=-\frac{A_{h,shell}}{L_{tube}}\cdot k_{shell,i}(x)\cdot\left[T_{shell,i}(x)-T_{metal,i-1}(x)\right] \quad (3)$$

$$\forall x\in[0,1],\ i=2,...,N_{row}+1$$

The tube side heat transfer and pressure drop correlations depend on the phase of the fluid. In single phase flow (i.e. cross flow heat exchanger) the heat transfer and pressure drop correlations of Gnielinski are used [31]. In the case of the cross flow evaporator model, where boiling (two-phase flow) inside the tubes takes place, the heat transfer correlation of Kandlikar [31, 32] is used.

For the shell side, two different correlations are used: one for bare tubes and another for finned tubes [30]. The first heat transfer correlation (for no fins) was developed by Zhukauskas and is modelled as presented in [30]. The second heat transfer correlation of Briggs and Young for finned tube bundles in cross flow is employed, as presented and further adapted in [30].

The energy balance for the metal mass interface is given as:

$$c_p \cdot \rho_{metal} \cdot A_{metal} \cdot \frac{dT_{metal,i}(x)}{dt} =$$
$$\left(\frac{A_{h,tube}}{L_{tube}}\right) \cdot k_{tube,i}(x) \cdot \left(T_{tube,i}(x) - T_{metal,i}(x)\right) + \left(\frac{A_{h,shell}}{L_{tube}}\right) \cdot k_{shell,i}(x) \cdot \left(T_{shell,i}(x) - T_{metal,i}(x)\right) \quad (4)$$
$$\forall x \in [0,1],\ i = 1,2....N_{row}$$

Especially for the cross flow evaporator model the two-phase flow regime is characterised by the vapour fraction:

$$\alpha_{vp,tube,i}(x) = \frac{h_{tube,i}(x) - h_{sat,liq}}{h_{sat,vap} - h_{sat,liq}} \quad (5)$$

It is noted that all partial differential equations (1) to (4) are completed by appropriate boundary and initial conditions. In addition, thermodynamic and physical properties are calculated using appropriate equations of state, already implemented in DNV COSSMOS [23].

3.3. Steam methane reformer

Steam methane reformer modelling is widely addressed in the literature [33-39]. In this work, the modelling of the SMR component follows a generic approach for packed-bed tubular reactors employing reaction kinetics, one-dimensional (1-D) formulation of mass and energy conservation along the reactor tube length, semi-empirical heat transfer modelling, 1-D quasi steady-state momentum conservation (pressure drop) and use of packing material properties.

The key steam methane reforming reactions are [35, 38]:

$$CH_4 + H_2O \leftrightarrow CO + 3H_2 \quad \text{(I)} \quad (6)$$

$$CH_4 + 2H_2O \leftrightarrow CO_2 + 4H_2 \quad \text{(II)} \quad (7)$$

$$CO + H_2O \leftrightarrow CO_2 + H_2 \quad \text{(III)} \quad (8)$$

The reforming reactions (I) and (II) are strongly endothermic, and thus, high temperatures are required to obtain the forward reaction. The water-gas shift reaction (III) is moderately exothermic, so is favoured by low temperatures. This trade-off limits the temperature range for efficient reforming of CH_4. In addition, the reforming reactions are also favoured by low pressures. On the other hand, the water-gas shift reaction is not significantly affected by pressure.

The SMR is modelled as a tubular reactor consisting of a N_{tubes} tubes. Since the reformer is considered to be adiabatic without external heat input or extraction, it can be represented by an equivalent tube having the same thermochemical/physical regime of the entire tube bundle.

The conservation of mass for each individual species, considering an axial distribution domain along the tube length is [35, 36, 39]:

$$MW_i \frac{dc_i(x)}{dt} = -\frac{\partial \dot{m}_i(x)}{\partial x} \cdot \frac{1}{L \cdot A_{tube}} + \frac{MW_i}{L \cdot A_{tube}} \cdot \sum_{j=I}^{III} v_{ij} \cdot r_j(x) \quad (9)$$
$$\forall x \in (0,1],\ i = 1,2,...,N_{species},\ j = I, II, III$$

The reaction kinetic model of Xu and Froment [35, 36, 38] is used to obtain the molar reaction rates:

$$r_I(x) = L \cdot A_{tube} \cdot \rho_{pack} \cdot A_{CH_4} \cdot e^{-\frac{E_{a,CH_4}}{R \cdot T(x)}} \cdot p_{H_2}^{-2.5} \cdot \left(p_{CH_4} \cdot p_{H_2O} - \frac{p_{CO} \cdot p_{H_2}^3}{10266.76 \cdot 10^6 \cdot e^{-\frac{26830}{T(x)}+30.11}} \right) \cdot \frac{1}{DEN^2(x)} \quad (10)$$

$$r_{II}(x) = L \cdot A_{tube} \cdot \rho_{pack} \cdot A_{H_2O} \cdot e^{-\frac{E_{a,H_2O}}{R \cdot T(x)}} \cdot p_{H_2}^{-1} \cdot \left(p_{CO} \cdot p_{H_2O} - \frac{p_{CO_2} \cdot p_{H_2}}{e^{-\frac{4400}{T(x)}-4.063}} \right) \cdot \frac{1}{DEN^2(x)} \quad (11)$$

$$r_{III}(x) = L A_{tube} \rho_{pack} A_{CO} e^{-\frac{E_{a,CO}}{R \cdot T(x)}} p_{H_2}^{-3.5} \left(p_{CH_4} p_{H_2O}^2 - \frac{p_{CO_2} p_{H_2}^4}{10266.76 \cdot 10^6 e^{-\frac{26830}{T(x)}-30.11} \cdot e^{-\frac{4400}{T(x)}-4.063}} \right) \frac{1}{DEN^2(x)} \quad (12)$$

with:

$$\begin{aligned} DEN(x) = {} & p_{CH_4}(x) \cdot \left(6.65 \cdot 10^{-9} \cdot e^{\frac{4604.28}{T(x)}} \right) + p_{H_2}(x) \cdot \left(6.12 \cdot 10^{-14} \cdot e^{\frac{9971.13}{T(x)}} \right) + \\ & + p_{CO}(x) \cdot \left(8.23 \cdot 10^{-9} \cdot e^{\frac{8497.71}{T(x)}} \right) + \frac{p_{H_2O}(x)}{p_{H_2}(x)} \cdot \left(1.77 \cdot 10^5 \cdot e^{\frac{-10666.35}{T(x)}} \right) \end{aligned} \quad (13)$$

The energy conservation along the tube length is:

$$\frac{du(x)}{dt} = -\frac{1}{A_{tube} \cdot L} \frac{\partial \dot{H}(x)}{\partial x} + \frac{\dot{q}(x)}{A_{tube}} \qquad \forall x \in (0,1] \quad (14)$$

$$u(x)/\rho(x) = h(x) + \sum_{i=1}^{N_{species}} \left(y_i(x) \cdot \Delta h_f \right) - p(x)/\rho(x) \quad \forall x \in [0,1] \text{ and } i = 1,2,\ldots,N_{species} \quad (15)$$

$$\dot{H}(x) = \dot{m}(x) \cdot \left(h(x) + \sum_{i=1}^{N_{species}} \left(y_i(x) \cdot \Delta h_f \right) \right) \quad \forall x \in [0,1] \text{ and } i = 1,2,\ldots,N_{species} \quad (16)$$

$$\dot{q}(x) = k(x) \cdot \pi \cdot D_{in} \cdot (T_{metal} - T(x)) \quad \forall x \in [0,1] \quad (17)$$

The heat balance across the adiabatic metal surface of the tube is:

$$m_{metal} \cdot C_{p,metal} \cdot \frac{dT_{metal}}{dt} = -L \cdot \int_0^1 \dot{q}(x) dx + \frac{\dot{Q}_{ext}}{N_{tubes}} \qquad \forall x \in [0,1] \quad (18)$$

where $\dot{Q}_{ext}$ is an external heat addition or heat rejection term which in the perfect, insulated, case is equal to zero.

The heat transfer coefficient k, appearing in Eq. (17), is calculated using the semi-empirical heat transfer correlations of [34, 37] for packed bed columns with spherical packing material, which are widely applied in the literature [35, 37, 39, 40]:

$$k(x) = 2.03 \cdot \frac{\lambda}{D_{in}} \cdot \mathrm{Re}^{0.8}(x) \cdot e^{-6 \cdot \frac{D_{pack}}{D_{in}}} \qquad for \ \mathrm{Re} \geq 20 \quad (19a)$$

$$k(x) = 6.15 \cdot \frac{\lambda}{D_{in}} \cdot \left(e_{void} + \frac{1 - e_{void}}{0.139 \cdot e_{void} - 0.0339 + \frac{2}{3} \cdot \lambda} \right) \qquad for\ \mathrm{Re} < 20 \tag{19b}$$

with the Reynolds number defined as:

$$\mathrm{Re}(x) = \frac{\upsilon(x) \cdot e_{void} \cdot D_{pack}}{\nu(x)} \tag{20}$$

The momentum conservation is expressed by the steady-state Ergun spatial pressure drop correlation, which is a standard approach for packed tubular columns [33, 35, 36, 39, 40]:

$$-\frac{1}{L}\frac{\partial p(x)}{\partial x} = u(x) \cdot \left(\frac{C_{flow,1} \cdot \nu(x) \cdot (1 - e_{void})^2}{e_{void} \cdot D_{pack}^2} + \frac{C_{flow,2} \cdot \rho(x) \cdot |\upsilon(x)| \cdot (1 - e_{void})}{e_{void} \cdot D_{pack}} \right) \quad \forall x \in [0,1) \tag{21}$$

Finally, the SMR model is complemented by the necessary boundary and initial conditions.

3.4. Exergy analysis

The exergy evaluation is performed at two levels: a) the system level in which the component contributions synthesise the overall SMR system exergy losses and efficiency [6, 17], and, b) the component level in which spatially distributed exergy balances are considered within the components in order to identify the sources of local exergy destruction [7, 12, 18].

The specific physical and chemical exergy are calculated at every node of the process streams and at every spatial location within the distribution domains of the SMR system components (Fig. 2):

$$\varepsilon_{ph} = h - h_0 - T_0 \cdot (s - s_0) \tag{22}$$

$$\varepsilon_{ch} = \left[\sum_{i=1}^{N_{species}} x_i \cdot \varepsilon_{ch,0} + RT_0 \cdot \sum_{i=1}^{N_{species}} x_i \cdot \ln(x_i) \right] / MW \quad \forall i = 1,...,N_{species} \tag{23}$$

The specific chemical exergy is calculated under the assumption of perfect gas mixtures [5]. The reference state is set at a pressure of p_0 = 1.013 bar and temperature T_0 = 298.15 K.

The exergy rate at each node and /or spatial position is then calculated:

$$\dot{E} = \dot{m} \cdot (\varepsilon_{ph} + \varepsilon_{ch}) \tag{24}$$

Within the major system components, namely XHX, XEV and SMR (c.f. Fig. 2) spatially distributed exergy balances are derived for infinitesimal control volumes. The equations are formulated under the assumption of steady-state conditions, which are well-suited for normal MCFC operation [2].

For the SMR component the local exergy balance at each location along the tube length is:

$$i_{SMR}(x) = \frac{1}{L_{tube}} \cdot \frac{\partial \dot{E}_{SMR}(x)}{\partial x} + \dot{\varepsilon}^{q}_{SMR}(x), \ \forall x \in [0,1] \tag{25}$$

The exergy of the heat flux appearing in Eq. (25) is calculated:

$$\dot{\varepsilon}^{q}_{SMR}(x) = \dot{q}_{SMR}(x) \cdot \left(1 - \frac{T_0}{T_{SMR}(x)} \right), \ \forall x \in [0,1] \tag{26}$$

The irreversibility rate of SMR results from the integration of the unit irreversibility rate:

$$\dot{I}_{SMR} = N_{tubes} \cdot L_{tube} \cdot \int_0^1 i_{SMR}(x) \cdot dx \tag{27}$$

The exergetic efficiency of the SMR component is:

$$\zeta_{SMR} = 1 - \frac{\dot{I}_{SMR}}{\dot{E}_{10}} \tag{28}$$

For the XHX and XEV the following expression for the local exergy balance is derived:

$$i_{Y,i}(x) = \frac{1}{L_{tube}} \cdot \left[\left(\dot{E}_{shell,i}(x) - \dot{E}_{shell,i+1}(x) \right) - \left(-(-1)^i \cdot \frac{\partial}{\partial x} \left(\dot{E}_{tube,i}(x) \right) \right) \right]_{Y=XHX,XEV} \tag{29}$$

$\forall x \in [0,1]$ and $i = 1,2,..., N_{row}$

The irreversibility rate and the exergetic efficiency of XHX and XEV are:

$$\dot{I}_{Y=XHX,XEV} = N_{col} \cdot L_{tube} \sum_{i=1}^{N_{row}} \left[\int_0^1 i_{Y,i}(x) \cdot dx \right] \tag{30}$$

$$\zeta_{XHX} = 1 - \frac{\dot{I}_{XHX}}{\dot{E}_1 - \dot{E}_2} \text{ and } \zeta_{XEV} = 1 - \frac{\dot{I}_{XEV}}{\dot{E}_2 - \dot{E}_3} \tag{31}$$

For the steam drum (SDR) the irreversibility rate and exergetic efficiency are:

$$\dot{I}_{SDR} = \left(\dot{E}_6 - \dot{E}_5 \right) - \left(\dot{E}_7 - \dot{E}_4 \right) \tag{32}$$

$$\zeta_{SDR} = \left(\dot{E}_7 - \dot{E}_4 \right) / \left(\dot{E}_6 - \dot{E}_5 \right) \tag{33}$$

For the steam/ methane mixing junction (MIX) the irreversibility rate and exergetic efficiency are:

$$\dot{I}_{MIX} = \dot{E}_7 + \dot{E}_8 - \dot{E}_9 \tag{34}$$

$$\zeta_{MIX} = \dot{E}_9 / \left(\dot{E}_7 + \dot{E}_8 \right) \tag{35}$$

The irreversibility and the exergetic efficiency of the SMR system are:

$$\dot{I}_{TOT} = \dot{I}_{XHX} + \dot{I}_{HEV} + \dot{I}_{SDR} + \dot{I}_{MIX} + \dot{I}_{SMR} \tag{36}$$

$$\zeta_{TOT} = 1 - \frac{\dot{I}_{TOT}}{\dot{E}_1 + \dot{E}_3} \tag{37}$$

Finally, the component contributions to the overall SMR system irreversibility and to the whole MCFC system, as parts of the fuel input, are:

$$\delta_Y = \dot{I}_Y / \dot{I}_{TOT} \ , \ \text{Y = XHX, XEV, SDR, MIX, SMR} \tag{38}$$

$$\delta_{Y,f} = \dot{I}_Y / \dot{E}_8 \ , \ \text{Y = XHX, XEV, SDR, MIX, SMR, TOT} \tag{39}$$

4. Optimisation problem formulation

A system design optimisation problem is formulated for the minimisation of the total SMR system irreversibility at nominal operating conditions. Here, only the SMR sub-system optimisation is considered, having appropriate boundary constraints to maintain the inputs to the MCFC stack at

the pre-defined ranges set by the manufacturer. The total irreversibility of the SMR system is an explicit performance criterion that is particularly suited for chemical reacting and heat exchanging systems, since energetic (first-law) approaches do not reveal adequately the full picture of losses within such systems [5-8]. The problem formulation is:

$$\min_{\mathbf{x}}\left(\dot{I}_{TOT}\right) \tag{40}$$

with independent decision variables the geometry characteristics of the key system components:

$$\mathbf{X}=\begin{Bmatrix} N_{col,XHX}, D_{in,XHX}, L_{tube,XHX}, P_{tube,XHX}, N_{col,XEV}, D_{in,XEV}, L_{tube,XEV}, P_{tube,XEV}, \\ N_{tubes,SMR}, D_{in,SMR}, L_{tube,SMR} \end{Bmatrix} \tag{41}$$

The optimisation problem is subject to space, design, and operability constraints. The space constraints mandate that the SMR system must be able to fit in a standard 20 feet container, resulting in:

$$\left\{W_{shell,XHX}, W_{shell,XEV}\right\} \le 2.5m \tag{42}$$

$$Height_{TOT} = \left(L_{shell,XHX} + L_{shell,XEV}\right) \le 2.4m \tag{43}$$

The design constraints involve the allowable tube pitch to diameter ratios for the heat exchangers:

$$1.25 \le \left\{\frac{P_{tube}}{D_{out}}\right\}_{XHX,XEV} \le 3.0 \tag{44}$$

In order to ensure safe and uninterrupted operation and nominal feed conditions to the MCFC system, a set of operability constraints is imposed. The velocities in the heat exchangers must be within allowable limits:

$$5m/s \le \left\{\upsilon_{in}, \upsilon_{out}\right\}_{XHX,XEV} \le 60m/s \tag{45}$$

The inlet and outlet velocities of the SMR reactor must be sufficiently low to avoid catalyst flooding conditions:

$$0.03m/s \le \upsilon_{SMR}(x)\Big|_{\substack{x=0\\x=1}} \le 0.38m/s \tag{46}$$

The (S/C) at the SMR reactor inlet is set to a near constant value to ensure optimum operation of the MCFC stack. This entails that for a given fuel flow a respective water flow is derived.

$$2.0 \le S/C = \frac{x_{H2O}}{x_{CH4} + x_{CO} + x_{XO2}} \le 2.12 \tag{47}$$

There is a minimum inlet temperature to the SMR reactor to ensure that the reactions will occur:

$$T_{10} \ge 640K \tag{48}$$

A minimum pressure is required in the MCFC stack inlet to ensure flow within the stack:

$$p_{11} \ge 1.032bar \tag{49}$$

The hydrogen content at the MCFC stack inlet must be within a certain range:

$$0.10 \le x_{H2}\Big|_{SMR,x=1} \le 0.15 \tag{50}$$

Finally, the overall pressure drop in the fuel cell exhaust gas path must be under a limit to ensure sufficient exhaust back-pressure to the MCFC stack:

$$\Delta p_{TOT} = p_1 - p_3 \leq 1400Pa \quad (51)$$

The problem formulation is completed with the specification of the system design parameters, the assignment of the independent optimisation variables bounds and the introduction of the boundary conditions to integrate the SMR system with the MCFC stack. These are presented in Table 1.

Table 1. SMR system design parameters and boundary values.

Optimisation variables			Geometry / design parameters	Operational boundaries
Variable	LB	UB		
$N_{col,XHX,XEV}$	1	50	$N_{row,XHX,XEV} = 10$	$p_1 = 1.035bar$
$D_{in,XHX,XEV}$	0.01 m	0.09 m	$h_{fin,XHX,XEV} = 0.m$	$T_1 = 800K$
$L_{tube,XHX,XEV}$	0.5 m	2.0 m	$t_{fin,XHX,XEV} = 0.m$	$\dot{m}_1 = 0.9203$kg/s
$P_{tube,XHX,XEV}$	0.05 m	0.15 m	$sp_{fin,XHX,XEV} = 0.m$	$p_4 = p_{H2O} = 1.4bar$
$N_{tubes,SMR}$	1	300	$t_{tube,XHX,XEV,SMR} = 0.003m$	$T_4 = T_{H2O} = 298K$
$D_{in,SMR}$	0.01 m	0.10 m	$D_{pack,SMR} = 0.003m$	$p_5 = p_{SDR} = 1.3bar$
$L_{tube,SMR}$	0.5 m	2.4 m	$\rho_{pack,SMR} = 139kg/m^3$	$p_8 = p_{CH4} = 1.3bar$
	N.B.: LB: lower bound and UB upper bound.		$e_{void,SMR} = 0.5$	$T_8 = T_{CH4} = 298K$
				$\dot{m}_8 = \dot{m}_{CH4} = 0.0146$kg/s

5. Results

The optimisation problem of Eqs. (40) – (51) consists of 11 independent variables, 3 of which are integer, and 13 inequality constraints. The PDAE system of the SMR system process model flowsheet, depicted in Fig. 2, consists of 19,040 equations, implemented in the gPROMS process modelling environment [41]. The optimisation problem was solved in approximately 111 CPU sec on an Intel® Core Duo @ 2.53GHz with 3.5 GB of RAM.

The optimisation algorithm started from an initial feasible design point of minimum footprint and progressed towards the minimum total irreversibility optimum. The initial and optimal SMR system design results are shown in Table 2. The optimal SMR system design offers a significant reduction of the total system irreversibility of about 50%. It is noted that this efficiency improvement can only be produced via second-law exergy considerations. The SMR system exergy losses amount to 10% in the initial and 5% in the optimal design of the chemical exergy of the overall system's fuel. This formally justifies the need for exergetic optimisation of the SMR system. The improved heat recovery of the optimal system allows for a higher hydrogen production of 13.7% compared to 10% of the initial design, due to the increased temperature/ heat input to the reformer. In addition, the exhaust gas exergy rate and temperature leaving the SMR system are higher than the initial design, which can be subsequently exploited via heat recovery e.g. for additional power production. The optimal SMR system design has a higher than the initial height and footprint, however, the 20 feet container enclosure constraints are still satisfied.

At a component level, the contributions of XHX, XEV, SDR, MIX and SMR to the overall exergy losses are depicted in Fig. 4. The biggest sources of exergy losses are the water evaporation and steam/ methane mixing processes. Through the exergetic optimisation the evaporator losses can be reduced by 67%. On the other hand, the mixing process irreversibility is not affected by the optimisation and can be considered as an unavoidable source of losses. In the optimal solution, the mixing process contributes 21.5% to the overall system irreversibility. The steam/ methane heater contributes 9.8 and 6.6% to the initial and optimal design, respectively. This is another component that its irreversibility is significantly reduced, by 66%, via optimisation. The SMR contributes roughly 6% to the overall system irreversibility. The SMR irreversibility in the optimal solution is

higher than the initial design due to the higher temperature profile within the reformer. Finally, the steam drum has a nearly constant irreversibility in both designs, with a contribution from 1.5 to 3%.

Table 2. SMR system optimisation results.

Figure	Initial	Optimal	Figure	Initial	Optimal
$N_{col,XHX}$ (-)	5	35	*H*eight (m)	2.340	1.202
$D_{in,XHX}$ (m)	0.0349	0.0340	Footprint (m^2)	0.854	1.969
$L_{tube,XHX}$ (m)	2.000	1.125	$T_{SMR,in} = T_{10}$ (K)	717.4	763.3
$P_{tube,XHX}$ (m)	0.0854	0.0500	$T_{SMR,out} = T_{11}$ (K)	616.9	651.4
$N_{col,XEV}$ (-)	1	9	$P_{SMR,out} = P_{11}$ (bar)	1.0511	1.2214
$D_{in,XEV}$ (m)	0.0900	0.0213	$x_{H2,SMR,out}$ (%)	10.092	13.744
$L_{tube,XEV}$ (m)	2.000	0.500	*S*/C (-)	2.12	2.11
$P_{tube,XEV}$ (m)	0.1485	0.0702	$\Delta p_{exh} = p_1 - p_3$ (Pa)	134	1400
$N_{tubes,SMR}$ (-)	141	300	$T_{exh,out} = T_3$ (K)	653.0	709.2
$D_{in,SMR}$ (m)	0.1000	0.1000	$\dot{E}_{exh,out} = \dot{E}_3$ (W)	142334	175301
$L_{tube,SMR}$ (m)	0.500	2.400	$\delta_{TOT,f}$ (%)	10.01	5.05
$\dot{I}_{TOT}$ (W)	75445	38076	ζ_{TOT} (%)	17.39	35.33

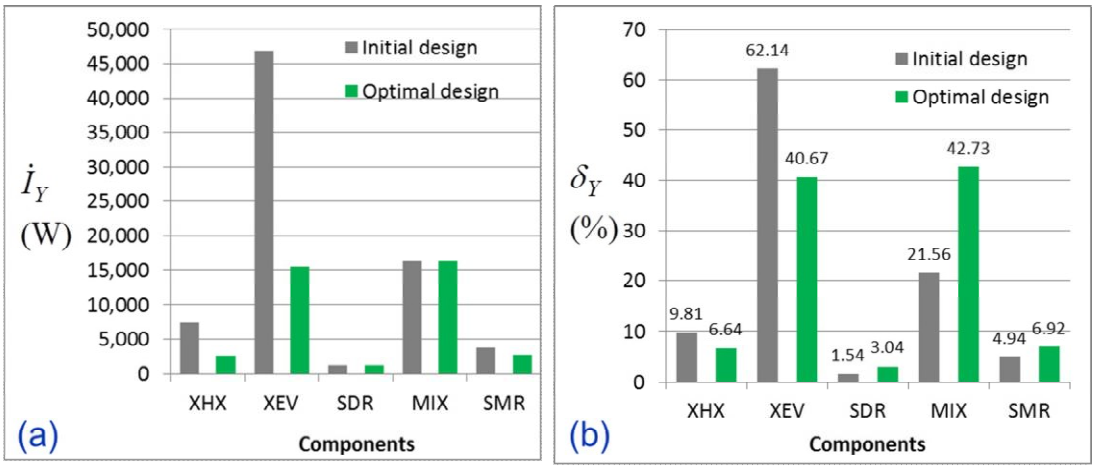

Fig. 4. Component irreversibilities (a) and contributions to the system irreversibility (b).

Zooming further to the spatially distributed properties within the system major components, the exergy losses mechanisms are revealed. In Fig. 5 the unit irreversibility rate and water vapour fraction profiles of XEV are depicted. Due to the evaporation process, the unit irreversibility rate along the XEV is high, resulting in the high overall irreversibility rate of the component. The variance of the unit irreversibility with tube row and distance are moderate resulting also in a smooth profile in the vapour fraction (latent heat conversion).

In Fig. 6 the unit irreversibility rate and tube temperature profiles along the XHX tubes are shown. Due to the high temperature regime of the exhaust gasses the unit irreversibility profiles are steep. There is a significant reduction of the unit irreversibility in the first three tubes. From this row and on there are only marginal changes in the unit irreversibility. Therefore, the bulk of the heat addition and temperature increase occurs at the first tube rows of the XHX.

Finally, in Fig. 7 the unit irreversibility, temperature and molar fraction profiles of the SMR are given. The unit irreversibility exhibits a very steep decrease within the first 20% of the total SMR length. Therefore, the main heat addition and reactions take place within that distance. This is due

to the fact that the SMR operates with the heat input of its incoming stream and there is no other heat addition across its length. Since the reactions consume heat, the temperature drops quickly in the first 10% of the total tube length and the hydrogen conversion slows down significantly. For the rest of the tube distance the hydrogen conversion, temperature decrease and unit irreversibility contributions progress very slow, having only incremental changes over the length. This is mainly due to the adiabatic operation of the SMR.

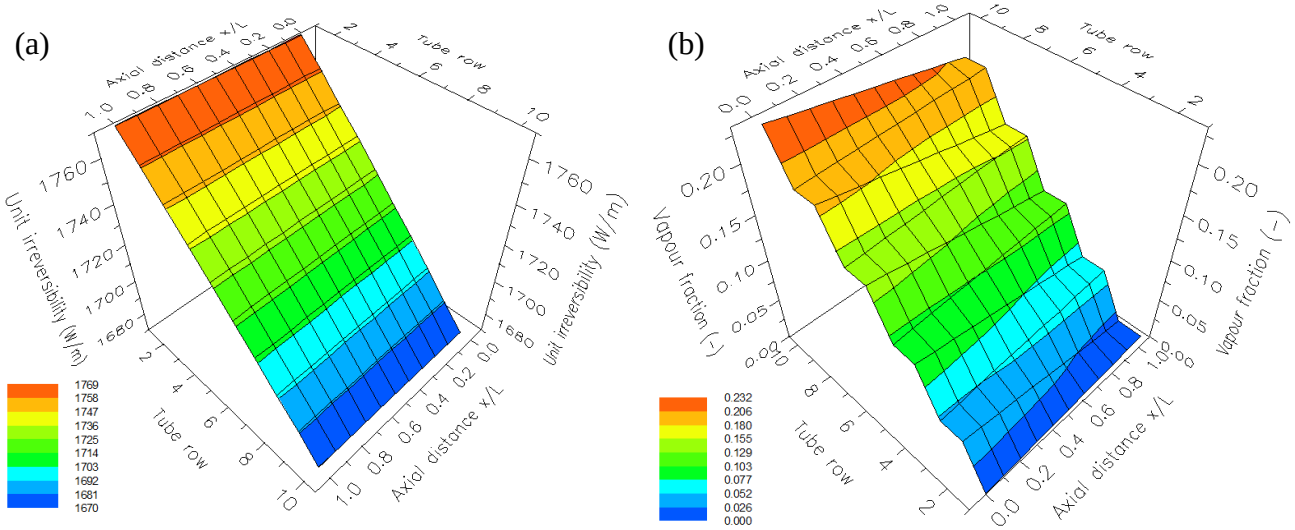

Fig. 5. Unit irreversibility rate (a) and vapour fraction (b) profiles within XEV.

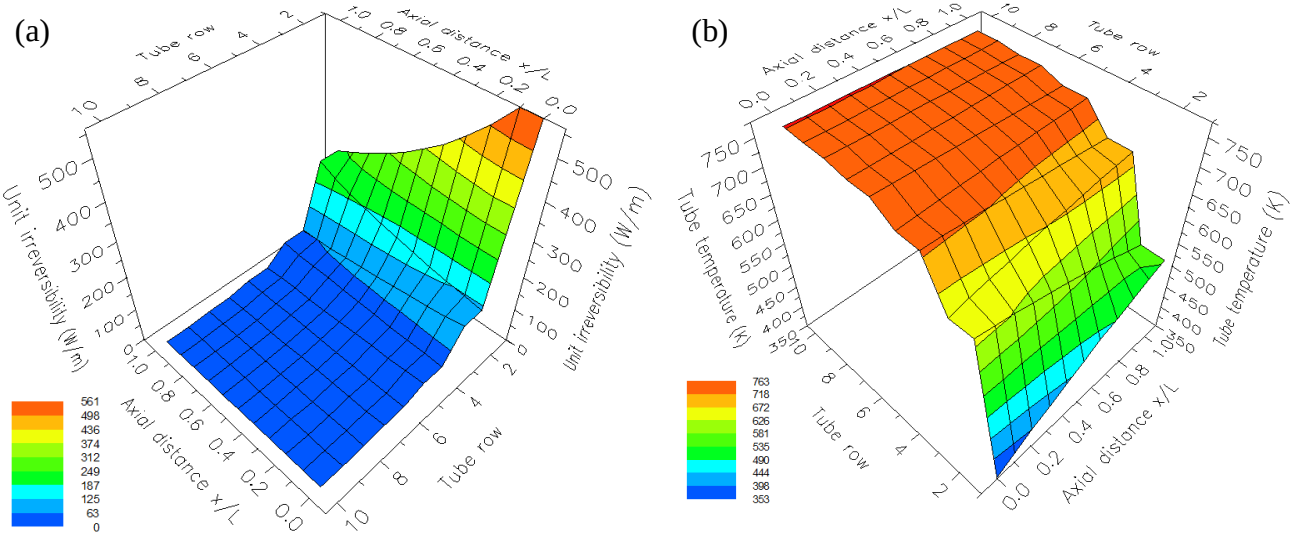

Fig. 6. Unit irreversibility rate (a) and tube temperature (b) profiles within XHX.

6. Conclusions

In this paper the exergetic analysis and design optimisation of a steam methane pre-reformer system for marine fuel cells was presented. With the aid of exergy analysis the internal sources of irreversibility were identified and minimised through exergetic optimisation. The exergetic optimisation resulted in a system design with 50% less exergy losses compared to the initial – low footprint design. The exergy analysis identified the water evaporation and mixing processes as the main sources of exergy losses. A step further to the exergy analysis was the formulation of spatially distributed exergy balances within components. Through this analysis, the propagation of the local irreversibility within components was identified and the system-level contributions were revealed.

The exergy analysis and optimisation proved to be particularly successful for assessing and improving this chemically reacting and heat exchanging system. It is noted that the energy (first-law) and pinch-point calculations have certain shortcomings in their usage, that are not able to adequately identify the true losses within such systems. The results of this study will serve as the starting point for the integrated optimisation of the entire fuel cell-based unit.

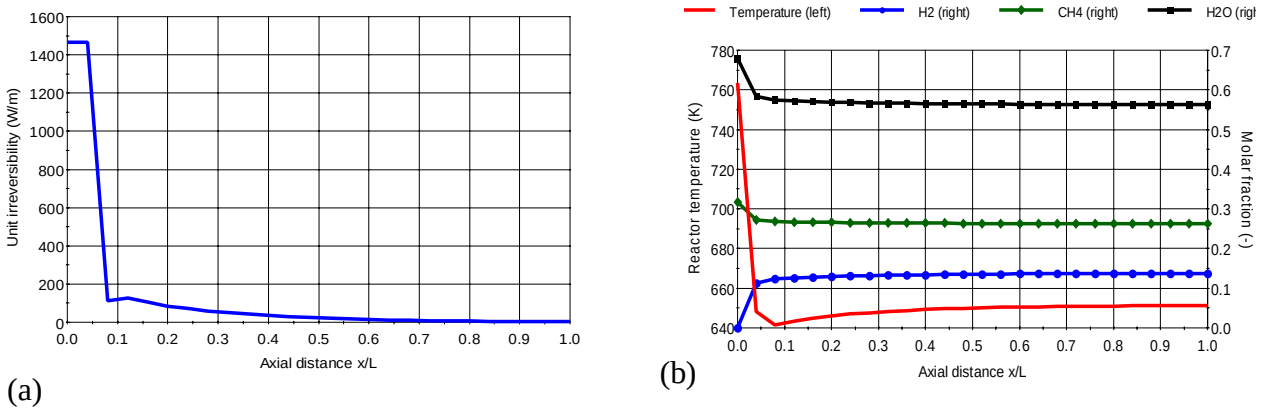

(a) (b)

Fig. 7. Unit irreversibility rate (a) and temperature / molar fractions (b) profiles within SMR.

Nomenclature

A_i	Pre-exponential Arrhenius factor
A_h	Heat transfer area, (m^2)
A_x	Cross-sectional area, (m^2)
c_i	Molar concentration, (mol/m^3)
C_{flow}	Flow coefficient, (-)
c_p	Specific heat capacity (J / kgK)
D_{in}	Inner tube diameter, (m)
D_{out}	Outer tube diameter, (m)
D_{pack}	Packing material diameter, (m)
$\dot{E}$	Exergy rate, W
$E_{a,i}$	Reaction activation energy, (J/mol)
e_{void}	Packing material void fraction
h	Specific enthalpy, (J/kg)
$\dot{H}$	Enthalpy rate, (J/s – W)
h_{fin}	Fin height, (m)
$\dot{I}$	Irreversibility rate, W
k	Heat transfer coefficient, (W/m^2K)
L	Length, (m)
$\dot{m}$	Mass flow rate, (kg/s)
MW	Molecular weight, (kg/mol)
N_{col}	Number of columns of tubes, (-)
$N_{reaction}$	Number of reactions, (-)
N_{row}	Number of rows of tubes, (-)
$N_{species}$	Number of species, (-)
Nu	Nusselt number, (-)
p	Pressure, (Pa)
P	Pitch, (m)
$\dot{q}$	Heat flux, (W/m)
R	Universal gas constant, (J/molK)
r_j	Molar reaction rate, (mol/s)
Re	Reynolds number, (-)
s	Specific entropy, J/(kgK)
sp_{fin}	Fin spacing, (m)
T	Temperature, (K)
t_{fin}	Fin thickness, (m)
t_{tube}	Tube thickness, (m)
u	Volume specific int. energy, (J/m^3)
υ	Velocity, (m/s)
W_{shell}	Width of shell, (m)
$\mathbf{X}$	Independent optimisation variables
x_i	Molar fraction
y_i	Mass fraction

Greek letters

a_{vp}	Vapour fraction (-)
δ	Ratio of irreversibilities
Δh_f	Enthalpy of formation, (J/kg)
ε	Specific exergy, (J/kg)

$\dot{\varepsilon}^q$	Heat exergy flux (W/m)
ζ	Exergy efficiency
i	Unit irreversibility rate, (W/m)
λ	Thermal conductivity (J / mK)
μ	Kinematic viscosity, (m^2/s)
v	Dynamic viscosity , (Pa s)
$v_{i,j}$	Stoichiometry reaction coefficients
ρ	Density, (kg/m^3)

Subscripts

0	Reference state
ch	Chemical
col	Column
f	Fuel
liq	Liquid
mean	Mean
metal	Metal interface
out	Outlet
pack	Packing material
ph	Physical
row	Row
shell	Shell-side
tot	Total
tube	Tube-side
vap	vapour

References

[1] FellowSHIP project web page, Available at: < http://www.VikingLady.no >, [accessed 15/01/2012].

[2] E. Ovrum and G. Dimopoulos, 2012, A validated dynamic model of the first marine molten carbonate fuel cell, *Applied thermal engineering*, Vol. 35, No. 1, pp. 15-28.

[3] M. A. Rosen, 1991, Thermodynamic investigation of hydrogen production by steam-methane reforming, *International Journal of Hydrogen Energy*, Vol. 16, No. 3, pp. 207-217.

[4] J. R. Rostrup-Nielsen, 2001, Conversion of hydrocarbons and alcohols for fuel cells, *Physical Chemistry Chemical Physics*, Vol. 3, No. 3, pp. 283-288.

[5] A. Bejan, G. Tsatsaronis and M. J. Moran, 1996, *Thermal design and optimization*, John Wiley, New York ; Chichester.

[6] A. Boyano, A. M. Blanco-Marigorta, T. Morosuk and G. Tsatsaronis, 2010, Advanced exergetic analysis of a steam methane reforming system for hydrogen production, *Proceedings of The 23rd International Conference on Efficiency, Cost, Optimization, Simulation and Environmental Impact of Energy Systems (ECOS)*, Lausanne

[7] N. Hotz, S. M. Senn and D. Poulikakos, 2006, Exergy analysis of a solid oxide fuel cell micropowerplant, *Journal of power sources*, Vol. 158, No. 1, pp. 333-347.

[8] M. A. Rosen, 1990, Comparison based on energy and exergy analyses of the potential cogeneration efficiencies for fuel cells and other electricity generation devices, *International Journal of Hydrogen Energy*, Vol. 15, No. 4, pp. 267-274.

[9] K. Ayoub, 2004, Exergy analysis of a PEM fuel cell at variable operating conditions, *Energy conversion and management*, Vol. 45, No. 11–12, pp. 1949-1961.

[10] F. Calise, M. Dentice d'Accadia, A. Palombo and L. Vanoli, 2006, Simulation and exergy analysis of a hybrid Solid Oxide Fuel Cell (SOFC)–Gas Turbine System, *Energy*, Vol. 31, No. 15, pp. 3278-3299.

[11] E. R. Delsman, C. U. Uju, M. H. J. M. de Croon, J. C. Schouten and K. J. Ptasinski, 2006, Exergy analysis of an integrated fuel processor and fuel cell (FP–FC) system, *Energy*, Vol. 31, No. 15, pp. 3300-3309.

[12] N. Hotz, M.-T. Lee, C. P. Grigoropoulos, S. M. Senn and D. Poulikakos, 2006, Exergetic analysis of fuel cell micropowerplants fed by methanol, *International Journal of Heat and Mass Transfer*, Vol. 49, No. 15–16, pp. 2397-2411.

[13] A. Ishihara, S. Mitsushima, N. Kamiya and K.-i. Ota, 2004, Exergy analysis of polymer electrolyte fuel cell systems using methanol, *Journal of power sources*, Vol. 126, No. 1–2, pp. 34-40.

[14] B. Pegah Ghanbari, 2007, Energy and exergy analysis of internal reforming solid oxide fuel cell–gas turbine hybrid system, *International Journal of Hydrogen Energy*, Vol. 32, No. 17, pp. 4591-4599.
[15] A. Sciacovelli and V. Verda, 2010, Entropy Generation Minimization for the Optimal Design of the Fluid Distribution System in a Circular MCFC, *Proceedings of The 23rd International Conference on Efficiency, Cost, Optimization, Simulation and Environmental Impact of Energy Systems (ECOS)*, Lausanne
[16] C. Ciano, M. Calì and V. Verda, 2009, Analysis of Entropy Generation for the Performance Improvement of a Tubular Solid Oxide Fuel Cell Stack, *International Journal of Thermodynamics*, Vol. 12, No. 1, pp. 1-8.
[17] A. Boyano, A. M. Blanco-Marigorta, T. Morosuk and G. Tsatsaronis, 2011, Exergoenvironmental analysis of a steam methane reforming process for hydrogen production, *Energy*, Vol. 36, No. 4, pp. 2202-2214.
[18] M. J. Stutz, N. Hotz and D. Poulikakos, 2006, Optimization of methane reforming in a microreactor—effects of catalyst loading and geometry, *Chemical engineering science*, Vol. 61, No. 12, pp. 4027-4040.
[19] J. R. Rostrup-Nielsen, K. Aasberg-Petersen and P. S. Schoubye, 1997, The role of catalysis in the conversion of natural gas for power generation, *Studies in Surface Science and Catalysis*, Vol. 107, pp. 473-488.
[20] K. Johnsen, 2006, Sorption-Enhanced Steam Methane Reforming in Fluidized Bed Reactors, PhD Thesis, Norwegian University of Science and Technology, Trondheim, Norway.
[21] Topsøe, 2010, AR-401 Pre-reforming catalyst brochure, Haldor Topsøe A.S., (available at: www.topsoe.com).
[22] G. G. Dimopoulos, C. A. Georgopoulou and N. M. P. Kakalis, 2011, Modelling and optimisation of an integrated marine combined cycle system, *Proceedings of 24th International Conference on Energy, Cost, Optimization, Simulation and Environmental Impact of Energy Systems (ECOS)*, Novi-Sad, Serbia.
[23] G. G. Dimopoulos and N. M. P. Kakalis, 2010, An integrated modelling framework for the design, operation and control of marine energy systems, *Proceedings of 26th CIMAC World Congress*, Bergen, Norway.
[24] N. M. P. Kakalis and G. Dimopoulos, 2012, Managing the complexity of marine energy systems, Position Paper 11/2012, Det Norske Veritas, Research & Innovation, (available at: www.dnv.com).
[25] A. Alebrahim and A. Bejan, 1999, Entropy Generation Minimization in a Ram-Air Cross-Flow Heat Exchanger, *International Journal of Thermodynamics*, Vol. 2, No. 4, pp. 145-158.
[26] W. A. Khan, J. R. Culham and M. M. Yovanovich, 2007, Optimal design of tube banks in crossflow using entropy generation minimization method, *Journal of thermophysics and heat transfer*, Vol. 21, No. 2, pp. 372-378.
[27] M. Mishra, P. K. Das and S. Sarangi, 2004, Optimum Design of Crossflow Plate-Fin Heat Exchangers Through Genetic Algorithm, *International Journal of Heat Exchangers*, Vol. 5, No. 2, pp. 379-402.
[28] M. Mishra, P. K. Das and S. Sarangi, 2009, Second law based optimisation of crossflow plate-fin heat exchanger design using genetic algorithm, *Applied thermal engineering*, Vol. 29, No. 14-15, pp. 2983-2989.
[29] J. V. C. Vargas and A. Bejan, 2001, Thermodynamic optimization of finned crossflow heat exchangers for aircraft environmental control systems, *International Journal of Heat and Fluid Flow*, Vol. 22, No. 6, pp. 657-665.
[30] R. K. Shah and D. P. Sekulić, 2007, *Fundamentals of Heat Exchanger Design*, John Wiley & Sons, Inc., Hoboken, New Jersey.

[31] A. Bejan and A. D. Kraus, 2003, *Heat transfer handbook*, John Wiley & Sons, Inc., Hoboken, New Jersey.
[32] S. G. Kandlikar, 1990, A general correlation for saturated two-phase flow boiling heat transfer inside horizontal and vertical tubes, *Transactions of the ASME, Journal of Heat Transfer,* Vol. 112, No. 1, pp. 219-228.
[33] M. E. E. Abashar, 2004, Coupling of steam and dry reforming of methane in catalytic fluidized bed membrane reactors, *International Journal of Hydrogen Energy*, Vol. 29, No. 8, pp. 799-808.
[34] A. P. de Wasch and G. F. Froment, 1972, Heat transfer in packed beds, *Chemical engineering science*, Vol. 27, No. 3, pp. 567-576.
[35] Y. Ding and E. Alpay, 2000, Adsorption-enhanced steam–methane reforming, *Chemical engineering science*, Vol. 55, No. 18, pp. 3929-3940.
[36] K. Kim, M. Wang, M. R. v. Spakovsky and D. J. Nelson, 2008, Stochastic Modeling and Uncertainty Analysis With Multi-Objective Optimization Strategies for the Synthesis/Design and Operation/Control of a PEMFC Fuel Processing Subsystem, *ASME Conference Proceedings*, Vol. 2008, No. 48692, pp. 667-678.
[37] C.-H. Li and B. A. Finlayson, 1977, Heat transfer in packed beds—a reevaluation, *Chemical engineering science*, Vol. 32, No. 9, pp. 1055-1066.
[38] J. Xu and G. F. Froment, 1989, Methane steam reforming, methanation and water-gas shift: I. Intrinsic kinetics, *AIChE journal*, Vol. 35, No. 1, pp. 88-96.
[39] H. Zhang, L. Wang, S. Weng and M. Su, 2008, Performance research on the compact heat exchange reformer used for high temperature fuel cell systems, *Journal of power sources*, Vol. 183, No. 1, pp. 282-294.
[40] D. F. Rancruel, 2005, Dynamic Synthesis/Design and Operation/Control Optimization Approach applied to a Solid Oxide Fuel Cell based Auxiliary Power Unit under Transient Conditions, PhD Thesis, Virginia Institute of Technology, Blacksburg, VA, USA.
[41] PSE, 2009, Process Systems Enterprise, gPROMS, www.psenterprise.com/gproms, 1997-2009.

Modelling of a CHP SOFC power system fed with biogas from anaerobic digestion of municipal wastes integrated with a solar collector and storage units

Domenico Borello [a], Sara Evangelisti[b] and Eileen Tortora[c]

[a]DIMA Sapienza Università di Roma , Roma,Italy, domenico.borello@uniroma1.it
[b] CIRPS Sapienza Università di Roma, Roma, Italy,sara.evangelisti@uniroma1.it,
[c]DIMA Sapienza Università di Roma , Roma,Italy, eileen.tortora@uniroma1.it

Abstract

The paradigm of the sustainable energy community is recognized as the future energy approach due to its economical, technical and environmental benefits. Future systems should integrate renewable energy systems applying a "community-scale" approach to maximize energy performances, while minimizing environmental impacts. Efforts have to be directed toward the promotion of integrated technical systems needed to expand the use of renewable energy resources, to build sustainable local and national energy networks, to guarantee distribution systems for urban facilities and to reduce pollution. In this framework poly-generation is a promising design perspective, for building and district scale applications, in particular where different types of energy demand are simultaneously present and when sufficient energy intensity justifies investments in smart grids and district heating networks.
In situ anaerobic digestion of biomass and organic waste has the potential to provide sustainable distributed generation of electric power together with a viable solution for the disposal of municipal solid wastes. A thermal recovery system can provide the heat required for district-heating.
The system analysed is a waste-to-energy combined heat and power (CHP) generation plant that perfectly fits in the sustainable energy community paradigm. The power system is divided in the following sections: a) a mesophilic - single phase anaerobic digestion of Organic Fraction of Municipal Solid Waste for biogas production; b) a fuel treatment section with desulphurizer and pre-reformer units; c) a Solid Oxide Fuel Cell (SOFC) for CHP production; d) a solar collector integrated system(integrated storage system - ISS).
An integrated TRNSYS/ASPEN Plus model for simulating the power system behaviour during a typical reference period (day or year) was developed and presented. The proposed ISS consists of a solar collector integrated with storage systems system designed to continuously provide the thermal power required by the anaerobic digester.
The net thermal energy production as a function of reactor volume, thermal insulation and additional pre-heating is evaluated.

Keywords:

Distributed Generation, Anaerobic Digestion, Fuel Cells, Transient Model, Waste-to-energy, Integrated TRNSYS/ASPEN Plus model

1. Introduction

In the last years, the new trend in power generation drives toward distributed power generation [1]. The term distributed generation (DG) [2] indicates that the energy conversion units are situated close to energy consumers using small power unit when compared to the usual plants used for large scale production. Several definitions of distributed generation power unit rating exist: from 1 W to 300 MW of capacity, depending of the number of units connected in a modular form. Based on the classification of [3], the system rating here analyzed is a small capacity (5 kW÷5 MW).DG approach should be recognized as the new future power paradigm due to the economic, technical and environmental benefits it achieves [4]. Application of DG means that single urban districts could be, in the future, self-supported in terms of electricity, heat and cooling energy.

This is in contrast with the facilities present to date, which concentrate the production of goods, thermal and electrical energy in large plants operating in a central location and connected with the final users via transmission and distribution networks. The centralized generation paradigm shows strong limitations due to the vulnerability of complex systems and the scarcity of the fossil fuels commonly used in large scale plants. On the other hand, small scale plant can advantageously use fuels locally available, often produced by Renewable Energy Sources (RES), e.g. biogas from wastes and wood biomass, improving the sustainability of the power generation.
In the European Union, the path toward future energy systems has been clearly underlined with several directives [5-7], research initiatives [8-10], and short terms energy initiatives (cutting greenhouse gases emissions by 20%, 20% share of RES in UE energy consumption, cutting energy consumption through improved energy efficiency by 20%). The success of DG systems is strongly subjected to their ability to use the waste heat from electricity generation as a heat source, obtaining total system efficiencies up to 90% [11]. These applications, commonly called Combined Heat and Power (CHP) can lead to significant reductions of CO_2 emissions.
Here a local community scale approach will be applied. It means that, following the definition of [12], settlements of various types (residential, commercial, industrial) will be considered, in which, through a mix of technological solutions, the interaction between fuel production and local electric and thermal energy generation will be optimized, reducing fossil fuel consumption and applying renewable sources. Poly-generation is then a possible solution, especially when different types of energy are requested at the same time and different sources – such as solar power and waste in this case - are available.
The system presented in this paper is based on the use of Organic Fraction of Municipal Solid Waste (OFMSW, [13]) for the generation of biogas, through an anaerobic digestion process integrated with the heat produced by an array of solar collectors as cycle pre-heating, in order to feed Solid Oxide Fuel Cell stacks for the electric and thermal power generation. This enhances the system sustainability in terms of use of renewable sources and of efficient waste management. Production and collection of OFMSW takes place at district level where energy demands occur, making it a potential non-seasonal energy feedstock [14]. Moreover, using OFMSW for energy reduces land demands for waste disposal sites near urban areas where land pressures are high. The biogas can then be used as fuel for energy production, through several energy systems. Furthermore biogas is an alternative to natural gas and reduces the amount of greenhouse gas (GHG), since the carbon dioxide produced by the combustion of biogas is considered biogenic and does not to the global warming [15].
The biogas can be efficiently used to feed an internal combustion engine for CHP. However, the need to increase the electrical efficiency of the system leads to the adoption of equipment with higher conversion efficiency.
Fuel cells are very promising energy conversion devices: they show a very high electrical efficiency, no moving parts and – important for the sustainability – zero emissions at the point of use. Among the different types of fuel cells commercially available, low temperature Polymeric Electrolyte Membrane Fuel Cell (PEMFC) and high temperature Solid Oxide Fuel Cells (SOFC) are considered reliable to be applicable for DG [16]. Despite a very low capital cost, PEMFC requires pure hydrogen to be fed. Therefore biogas must be converted to H_2-rich gas before feeding the PEMFC, using reformer and CO removal, dramatically increasing system complexity and decreasing the overall electrical efficiency. On the other hand, SOFC are very flexible in burning several type of fuels due to the high working temperatures (700-1000°C) that allow them to convert hydrocarbons into hydrogen internally, with an overall electrical efficiency of about 55-60 % even when fed by methane [17, 18], the absence of moving component (reducing mechanical stresses, noises and vibrations) and small efficiency reduction when working in off-design conditions. Moreover this efficiency can be even higher- up to 70% [19] - when SOFCs are coupled with gas turbine or organic Rankin cycle turbine in hybrid cycles. Due to their modularity, SOFC can be easily integrated in combine heat and power plants (CHP), reaching very high global efficiency (around 80 %) [20].

On the other hand, technology of fuel cells (and of SOFC in particular), is far to be mature and many developments have to be done to increase reliability of such equipment before it will be possible that SOFC can become economically competitive with ICE alternatives.
This paper aims at analysing a community scale poly-generation energy system, through an integrated TRNSYS/ASPEN Plus model. The system is composed by four main units: a) a mesophile - single phase anaerobic digestion of Organic Fraction of Municipal Solid Waste for biogas production; b) a fuel treatment section with fuel steam reforming; c) a Solid Oxide Fuel Cell (SOFC) for CHP production; d) a solar collector systems to supply heat to the anaerobic digester. The anaerobic digester process needs a constant temperature in order to maximize the biogas production. The heat demand can be supplied in different ways, generally with a furnace that uses the biogas as fuel source. The low price of solar collectors and the sun availability as energy source in the Mediterranean area supports the idea to use solar thermal collectors to maintain the desired constant temperature inside the digester.

2. Case study description

The studied scenario is representative of a community-scale plant, serving a hypothetical urban group of 50 families. The estimated electric power is set equal to 150 kW and it is delivered by a SOFC fed with biogas from anaerobic digestion.
In order to reach higher biogas production, the temperature of the digester has to be controlled. Here it is considered an equipment working in the mesophilic range (35-45°C). To compensate the heat losses and to heat up the substrate, a continuous feed of heat to the digester is required. No waste pre-treatment processes before the anaerobic digestion phase are considered in this analysis.
In the elaborated scenario, a poly-generation system is designed and solar thermal collectors are considered as complementary heat source for the digester [21, 22]. This heat feeds a thermal energy storage (TES), eventually integrated with heat produced by a biomass furnace, that deliveries the required heat also during the winter or the night periods.
The heat power obtained from the conversion process, about 318 kW, is primarily used by the same SOFC for maintaining the reformer temperature (12.90%) heating the fuel inlet stream at the anode side (10.73%) and the air inlet stream at the cathode (74.38%). Finally, a remain of 12.57kW is delivered to the final user to integrate a district heating system (not specified here).

3. Methodology

In order to evaluate the time-dependent behaviour and the performance of the proposed system a transient model is developed in the TRNSYS framework [23].To the best of the author knowledge few studies have appeared to date in the open literature, that propose the use of TRNSYS-framed models for complex energy systems. Some of the exceptions deal with studies on renewable energy system integration in grid-connected or stand-alone power systems [24, 25]. Some studies deal with the integration of fuel cells in buildings energy systems [26] and poly-generation systems with solar collectors [27].

The transient system layout is schematically shown in Figure 1. Besides the standard TRNSYS library components, the transient model also includes in-house made types for the digester, the biogas storage, the SOFC system (derived from Aspen Plus model) and the output temperature and thermal power controls. The simulation is performed with a hourly time step over a reference year period.

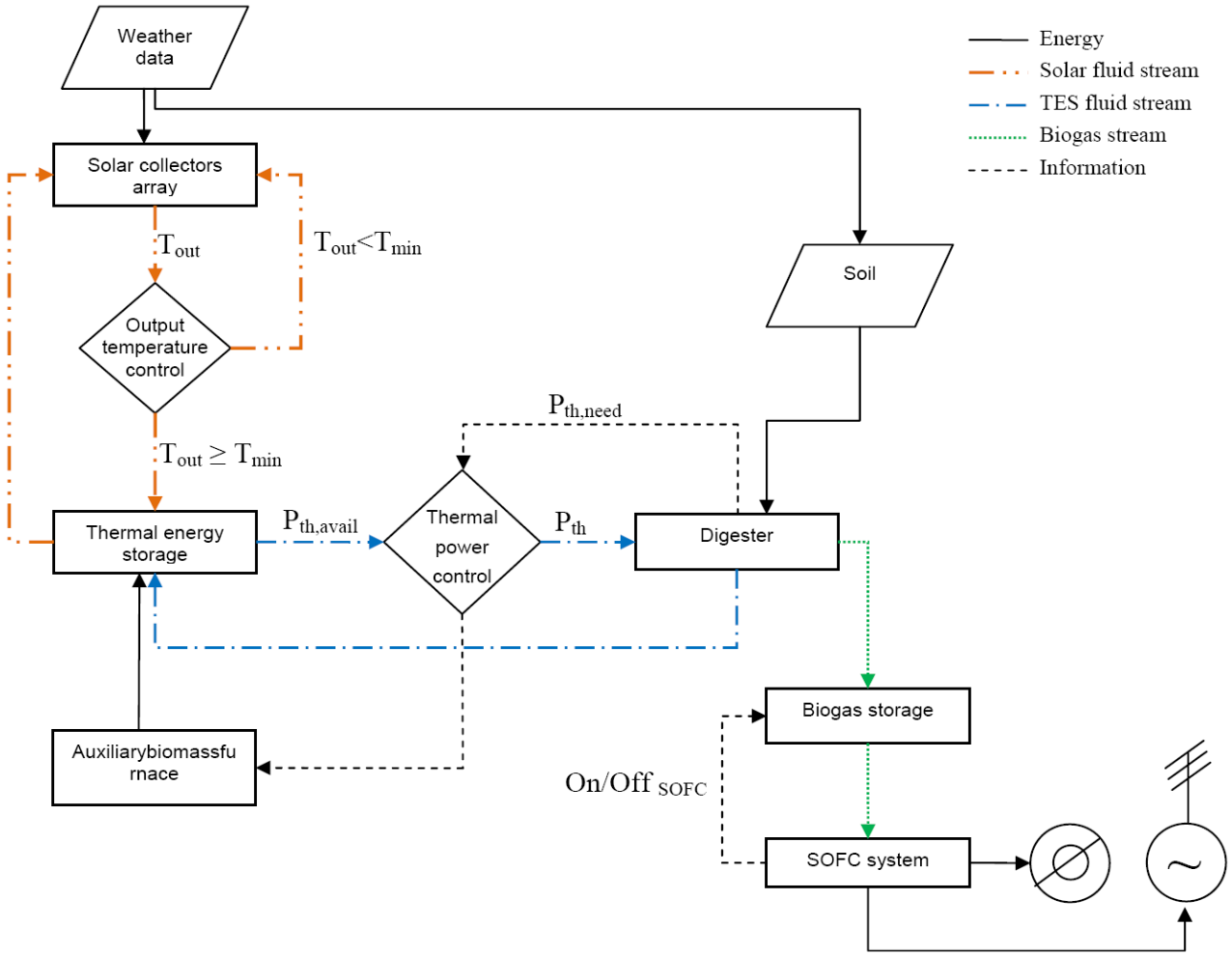

Figure 1.Flow diagram of the modelled transient energy conversion system.

The weather data provide the solar radiation information to the solar collector array, which supplies the converted thermal energy to the TES. The operating conditions inside the digester require a constant inner temperature of 35 °C irrespective of the climate conditions that also influence the soil temperature. The digester needs to be warmed-up feeding thermal power from the TES to compensate the heat losses through the walls and to warm-up the substrate entering at environment (lower) temperature. As the solar section and the digester behaviour depend on the local meteorological conditions, their working results may differ from the design. To this end a control was made on the temperature output of the solar collectors array and one on the digester. In particular, the temperature control checks the exit temperature from the collectors at each time step, giving rise to two possible situations:

1. the outlet temperature (T_{out}) undergoes the fixed minimum temperature (T_{min}), starting the flow recirculation into the solar field until it reaches a proper temperature;
2. the outlet temperature is higher than the fixed minimum temperature, allowing the flow to pass into the thermal energy storage.

Finally, the thermal power control determines the fluid flow to be withdrawn from the TES and sent to the digester for maintaining mesophilic conditions..

Moreover, when the thermal power control indicates that TES is getting too cold (temperature lower than 60°C), a biogas furnace is switched on to supply the required heat.

The digester subroutine was designed following the hypothesis already described in [28], thus giving the geometrical parameters, the feeding material characteristics, the working temperature and

the ambient temperature. It calculates the biogas production, the thermal losses and the thermal energy need to maintain the inner design operating temperature.

The biogas storage subroutine takes the SOFC duty information and the input biogas flow-rate and manages the biogas supply to the SOFC system in order to return a constant flow-rate.

The SOFC system subroutine takes into account all the pre-treatment elements described above and the SOFC itself.

4. Components description

The energy system is composed by a solar collector array equipped with a thermal energy storage, supplying thermal energy to maintain the digester at a constant inner temperature of 35°C. The digester needs to be warmed-up feeding thermal power from the TES to compensate the heat losses and to warm-up the substrate .The fuel obtained from anaerobic digestion is sent to a biogas storage and then fed the SOFC system in order to deliver heat and power to the final users.
A brief description of the main components follows. The main components sizes are summarized in Table 1.

Table 1. Main components description and nominal size.

Solar collectors array	280 collectors, 560 m^2
Thermal energy storage	15 m^3 max energy supply 345 kWh
Digester	317.93m^3 volume
Biogas storage	42,800 kg biogas
Auxiliary TES heater (biomass furnace)	72,000 kJ/h (20 kW)

Input data

The input data [29] used for the simulation of the solar collectors are based on a hourly time step over a year period, referring to Rome's latitude, i.e. 41°54'39"24 N, as indicative of a central Italian location. The direct normal insulation (DNI) data show an annual cumulative irradiation of 5760 MJ/m^2, with a maximum value of 733.68 MJ/m^2 in July and a minimum value of 253.04 MJ/m^2 in December. The weather data are read in TRNSYS by type 89 of the standard TRNSYS library [23]. The monthly average environmental temperature, required to determine the heat losses of the digester is reported in Figure 2.

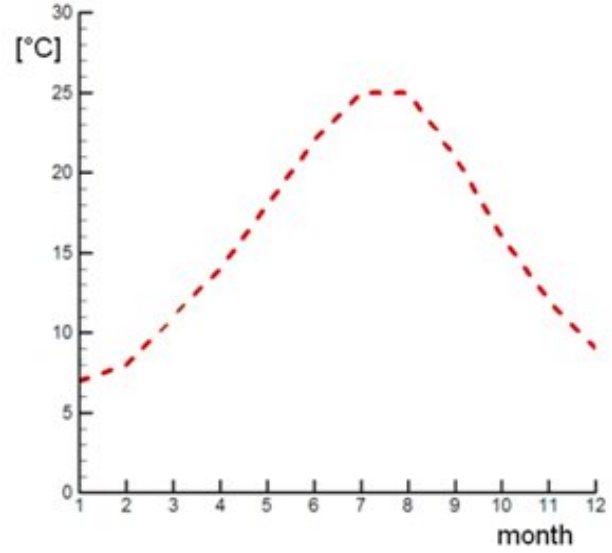

Figure 2. Ambient monthly average temperature behaviour [28].

The waste considered in this study for the digestion process is the organic fraction of municipal solid waste. The organic substrate is defined by its Total Solid (TS) and Volatile Solid (VS) concentrations. In the present study a 15%TS and 80%VS substrate of a food industry-sorted organic waste is considered, following the study of Sans [28]. A continuous feeding schedule is set, with a loading rate of 7.27 t/d of OFMSW.

Solar Field

The solar field is composed by 280 collectors distributed over 7 strings of 40 collectors each. The total collector area is of 560 m^2. The fluid flowing through the solar circuit is water, with an overall flow rate of 700 kg/h. The thermal storage is a tank 4 m high with a volume of 15 m^3. It is equipped with an auxiliary biomass furnace of 20 kW to face the solar source fluctuations and maintain a minimum fluid temperature of 60 °C inside the tank.
The solar field is modelled by using the elements available in the standard TRNSYS library [23], in particular type 73 for the parabolic troughs, type 60 for the thermal energy storage.

Anaerobic Digester

The Anaerobic Digester reactor (AD) is designed for a mesophilic temperature of 35°C. The process considered is a single stage continuous-flow stirred tank reactor (CSTR), operating in wet regime, with total solids concentration less than 10%, with an organic load equal to 5 kgVS/m^3d and a hydraulic retention time (HRT) of 15 days [30]. The digester is a concrete reactor, with a polyurethane external insulation and steel internal layers, partially placed underground (4.5 m). The top of the reactor consists of an elastic polyurethane surface. Table 2 shows the values used to design the reactor. Due to some uncertainty in the design process a safety factor equal to 1.2 is assumed. Then, the final volume of the digester is set equal to about 320 m^3.

Table 2. Design parameters of anaerobic digester.

Diameter	9m
Overall height	7 m
Organic Load Rate (OLR)	5kgVS/ m^3d
HRT	15days
Safety factor	1.2

The AD heat demand is evaluated considering the heat for warming-up the inlet organic substrate assuming a specific heat of 1000 kcal/m^3°C, and the heat losses through the side walls. The top surface is considered adiabatic, while heat losses are present through the lateral and lower walls.
Table 3 shows the parameters used and the heat losses evaluated in the digester through the bottom and lateral surfaces.

The digester is modelled in TRNSYS with an in-house made type which asks for the ambient and soil temperature and the OFMSW flow rate, returning the produced biogas flow rate and the needed heat to maintain the digester inner temperature of 35°C. The soil temperature is obtained by type 501, which is the soil temperature profile component of the TESS Trnsys library [31].

Table 3. Parameters and power loss in the digester.

Ground surfaces heat transfer coefficient	0.22 W/m^2°C
Air surfaces heat transfer coefficient	0.5W/m^2°C
Overall power losses	2,684W

Biogas storage

The biogas storage is inserted into the system with the aim to decouple the biogas production from the fuel consumption inside the SOFC. In fact, the digester process is continuously working producing biogas (except for small maintenance periods) due to the need to treat the OFMSW.
On the other hand, the SOFC requires more frequent stops for maintenance and then the storage has to be designed in order to compensate the difference in biogas production and consumption. To guarantee safe operating conditions the storage is designed to allow biogas accumulation for 1000h during the SOFC inactivity period and to gradually return it during the SOFC activity period, in order to feed the SOFC with a constant biogas flow-rate. The biogas storage allows accumulating 42,800 kg of biogas.
The biogas storage is modeled in TRNSYS with an in-house made type, which just computes the amount of biogas stored in the tank in relation with the SOFC duty.

SOFC

The energy system used for electricity and thermal power source consists of a SOFC of 150 kW_{el} size. The mass and energy flows into the SOFC are analysed by using the AspenPlus™ software, successfully used for simulating fuel cells based energy systems [32, 33]. Referring to SOFC systems, in Aspen Plus the most are simulated by user models [34 - 36] and only a few are modelled using standard library elements of Aspen Plus [24, 37].
The system is fed by a biogas with a mole based composition of 8 % H_2, 60 % CH_4 and 32 % $CO_2$and a low heating value of 21,600 kJ/m^3.
The SOFC model flow sheet, Figure 3, includes all the components and functions contained in the system. It is worth noting that the software does not have the fuel cell component and then all the processes and reactions occurring in a SOFC are modelled separately.
The fuel coming from the biogas storage is mixed with recirculating fluid coming from the fuel cell (see blue dashed box) for obtaining a steam to carbon ratio equal to 2.5 that is considered optimal for SOFC [32].
The red box shows the reforming process. This process occurs at a temperature of 600 °C (steam reforming). A constant temperature is imposed in the reformer to control the process and then two heat exchangers are introduced to give the correct temperature to the fuel before and after the reformer and to feed the digester with the heat needed for performing the endothermic reforming reaction. Most of the needed heat comes from the SOFC cooling (thermal stream Q3). Out from the reformer the fuel is mainly composed by H_2, CO and CO_2, with traces of methane, butane and propane.
The blocks inside the black box are used to model the SOFC. The reaction occurs at 1000 °C. A flux of oxygen flows through stream 6 from cathode to anode and it reacts here with the CO and H_2. Energy stream Q_2 contains both the electricity produced and the waste heat. The flow exiting the anode contains some fuel not burned in order to guarantee safe operating working conditions to the cell (if all the fuel is consumed near the cell exits the reaction does not occur anymore and then the voltage becomes rapidly zero).
In the split component (green circle) the fluid leaving the SOFC is split in two streams: the first one mixes with the inlet fuel and it is calibrated to guarantee a S/C ratio of 2.5; the second one, having some fuel remaining is sent to an afterburner (purple circle) devoted to increase the exhaust outlet temperature. The high energetic content of the exhausts is then used to pre-heat the air entering the cathode and to feed the thermal user, i.e. district heating (turquoise circle).

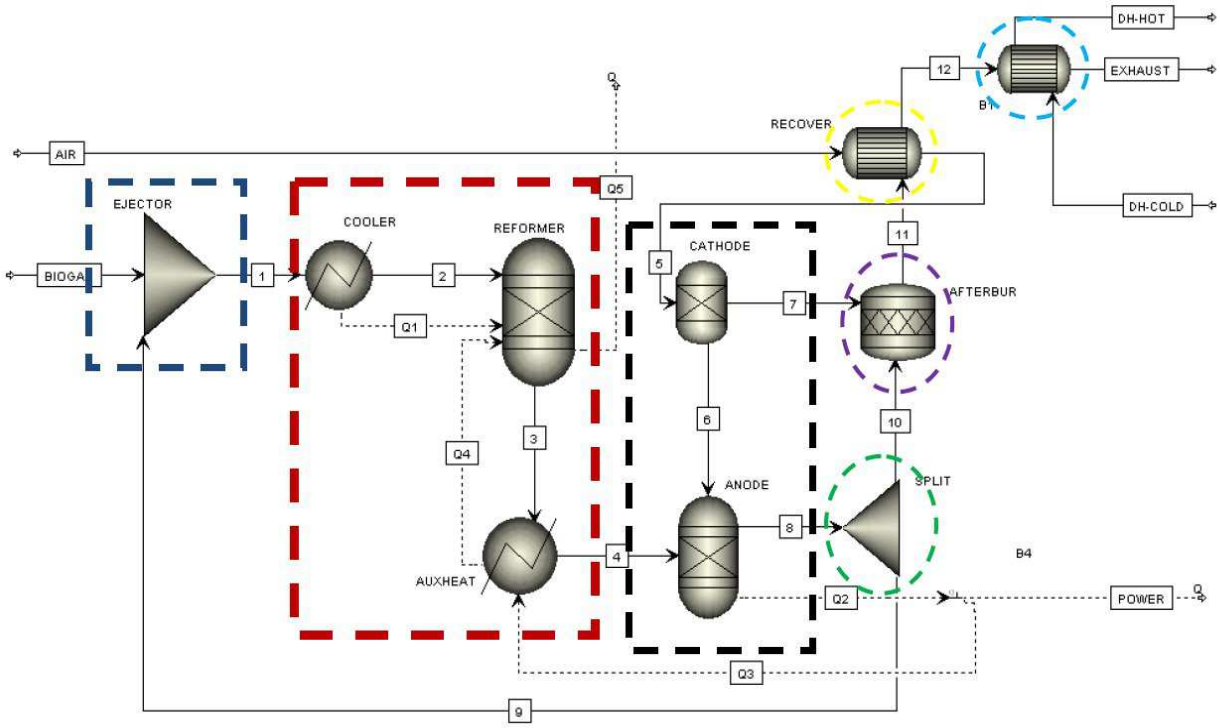

Figure 3. AspenPlus™ SOFC model flow sheet.

The in-house made TRNSYS model of the SOFC system takes into account the entire Aspen Plus model in a single type, based on an empirical relationship, obtained by a sensitivity analysis simulation of the ASPEN Plus SOFC model. The sensitivity analysis are conducted with the hypothesis of a 12.57 kW constant heat power output available for the district heating. In particular the obtained relations give the values of the hydrogen utilization factor (Uf) at the SOFC and the electric power output (P_{el}) related to the biogas flow rate (m_b) supplied to the SOFC system inlet:

$$Uf = 0.607\, m_b$$

$$P_{el} = 76606.42\, m_b^2$$

5. Results

Overall hourly results

The global results of the transient simulation are shown in Table 4. As can be seen, the solar field receives about 3550 GJ/y with a global solar energy availability of 4679 hours. The heat effectively supplied to the TES from the solar field amounts to 134.62 GJ/y which is about 3.8% of the incident solar energy. Such a low percentage of supplied energy is an effect of the fluid recirculation into the collectors when the solar radiation is not high enough to determine a fluid temperature that is adequate to feed the TES (i.e. greater than 70°C). In a successive step the solar field will be leaved without the recirculation and it will pass through the auxiliary heater to be eventually heated up to the TES inlet temperature.

Assuming that the solar contribution is available only on daytime the TES requires an auxiliary heat of 194.98 GJ/y during 3652 duty hours (including hours when both systems are working). Taking into account the variable heat supply and withdrawal to the TES, the average TES temperature at the tank top and bottom amount respectively to 82.58°C and 63.28°C.

The heat to be supplied to the digester to maintain the temperature of 35°C required from the mesophilic digestion is equal to269.03 GJ/y.

The produced biogas is about 240 ton/y, with a constant hourly output of 27.39 kg/h.

During the SOFC off-duty time the biogas output from the digester is sent to a biogas storage which, during the SOFC on-duty time releases an hourly rate of 6 kg/h to the SOFC.

The SOFC is fed with 233.75 ton/year of biogas with a constant hourly delivery, during the on-duty time, of 33.39 kg/h deriving partly from the digester and partly from the biogas storage.

The SOFC output is of about 317 GJ/y of thermal energy and 3,780 GJ/y of electric energy.

Table4. Overall results.

Solar field	Incident solarenergy [GJ/y]	3,552.51
	Hours with incident solar energy [h/y]	4679
	Solar energy exchanged with the TES [GJ/y]	134.62
	Hours of thermal energy supply to the TES [h/y]	1513
TES	Auxiliary TES heat [GJ/y]	194.98
	Auxiliary TES heater duty hours [h/y]	3652
	Energy supplied to the digester by the TES [GJ/y]	269.03
	Average tank temperature [°C]	75.39
	Average top tank temperature [°C]	82.58
	Average bottom tank temperature [°C]	63.28
Digester	Heat loss of the digester [GJ/y]	37.39
	Heat need of the substrate[GJ/y]	231.61
	Global heat demand of the digester [GJ/y]	269.03
	Biogas production [ton/y]	239.96
SOFC system	Biogas supply to SOFC [ton/y]	233.75
	SOFC duty hours [h/y]	7,000
	SOFC thermal energy output [GJ/y]	316.77
	SOFC electric energy output [GJ/y]	3,779.51
	SOFC electrical efficiency	55%

Hourly results

To better understand the behaviour of the system, the focus is now on the hourly time-steps. According to the system design hypothesis, the only sections which behave in a transient fashion are those directly linked to the solar collectors field, thus the collectors field itself, the TES, the biomass furnace and the digester.

Figure 4 shows the thermal power requested by the digester on an hourly-based time. The requested thermal energy is obviously higher in the winter period, when the difference between the design temperature and the ambient temperature is higher, reaching power needs of about 20 kW. In some hours of the summer period the temperature difference leads to power request lower than 1 kW. Nevertheless, there is a continuous variation of the request during the whole year, corresponding to the alternation of day and night time.

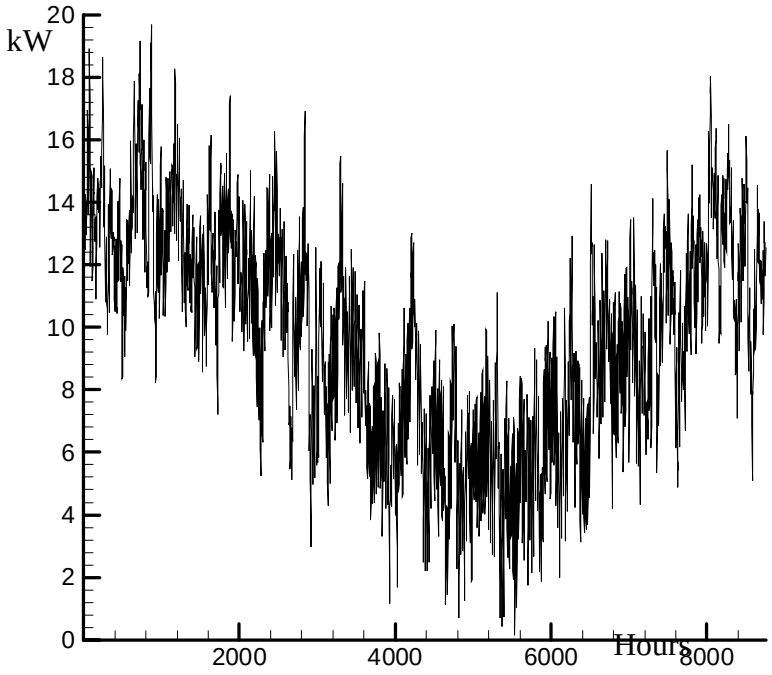

Figure 4. Thermal power request fromthe digester.

Such a variable request, matched with the transient behaviour of the solar thermal energy supply (which is higher during the summer period) leads to a continuous variation of the temperatures in the TES tank. Figure 5 shows the pattern of the top and bottom temperature of the tank. At the bottom of the tank, the minimum temperature is always higher than 59.40°C and the maximum is equal to 82.88°C. At the top of the tank, the minimum temperature is 68.46°C ant the maximum is 100°C.

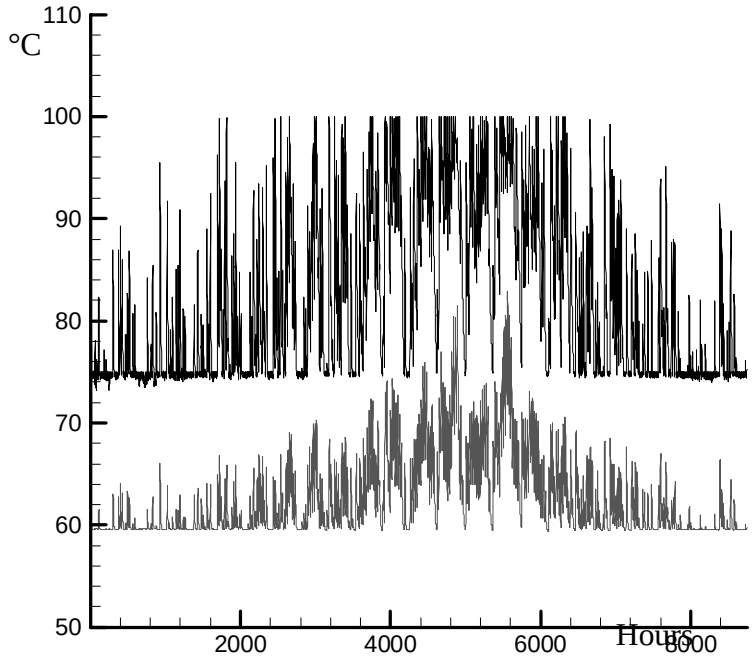

Figure 5. TES top tank temperature (black line) and bottom temperature (grey line).

Figure 6 shows the thermal energy balance of the TES. As already stated, the digester needs a lower amount of thermal energy during the summer period with respect to the winter one. The thermal energy supplied by the TES (Q_{sup}) follows the request of thermal energy from the digester. Moreover, the seasonal behaviour of the solar energy supply (Q_{RES}) influences the auxiliary thermal supply Q_{aux} (i.e. the biomass furnace) performance, which shows an inverted seasonal pattern. It is worth noting that the sum of the thermal energy delivered to the TES (i.e. Q_{RES} and Q_{aux}) is higher than the supplied thermal energy to the digester from the TES (Q_{sup}). This is due to the need to maintain the minimum temperature of 60°C in the TES itself in order to assure the thermal supply when needed. During the summer period, in the months of July and August, the solar collectors field thermal energy supply is able to almost fulfil the thermal request of the digester.

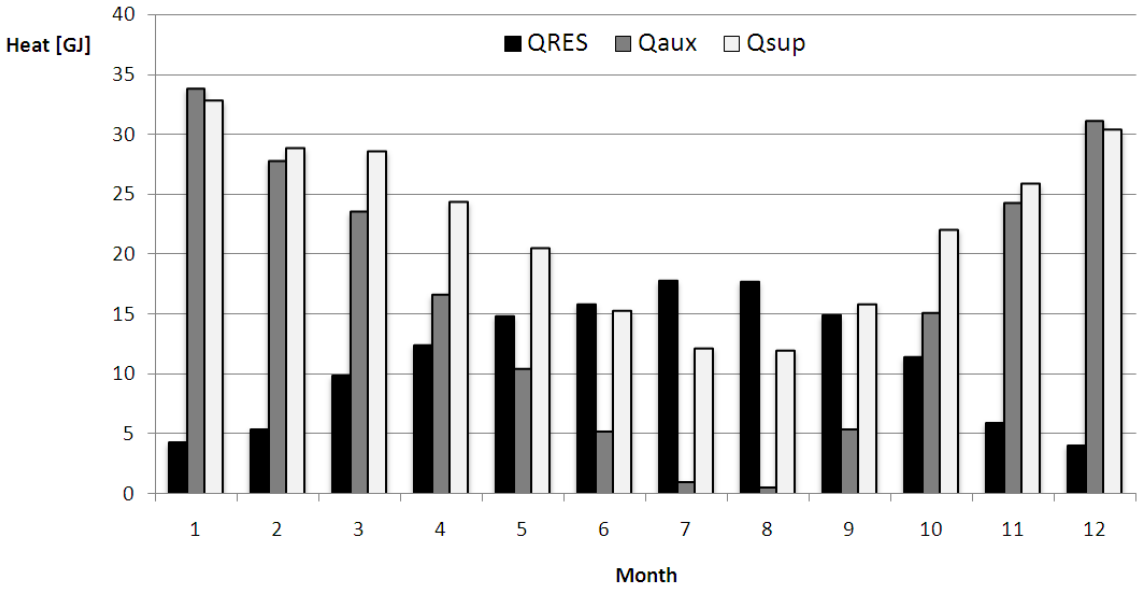

Figure 6.TES thermal energy contribution.

6. Conclusions

A transient model for the simulation of a biogas fuelled CHP 150 kW_{el} plant was presented. The integrated renewable sources power plant here described has the potential to achieve high generation efficiencies as well as important environmental benefits through the mitigation of greenhouse gas emissions.

The biogas is produced by an anaerobic digester processing OFMSW. The heat required to warm the substrate and to compensate losses is obtained by a solar field integrated by an auxiliary biomass furnace. The biogas produced is sent to a SOFC for co-generation of electricity and heat for possible use in a district heating (not modelled here). A large fraction of the produced heat is used for pre-heating the SOFC plant, so only 10% of the available heat is available for end users.

The transient model shows that the heat supplied to the digester by the solar field allows a saving of 7.63 ton/y of biogas – or the 4% of the total biogas production, equal to 131 GJ/y of electricity energy produced by the SOFC. Further improvements are in progress. A positioning of the solar field on the top of the digester as cover for the gas holder will allow a more efficient heat supply system for the digester. Moreover different type of solar collectors with a higher energy efficiency could totally substitute the biogas furnace, with considerable economic saving. .

The whole system adopts a mix of renewable technologies to produce electricity and thermal power. Furthermore this approach indicates a ‘smart’ solution for the disposal of organic fraction of municipal solid waste, allowing to define a fully sustainable chain from waste to energy.

Bibliography

[1] Alanne, K. and Saari, A., Distributed energy generation and sustainable development, *Renewable and Sustainable Energy Reviews*, 2006, 10: 539–558.

[2] Ackermann T., Andersson G., Sode, L., Distributed generation: a definition, *Electric Power Systems Research* 2001, 57: 195–204.

[3] Elkhattam W. and Salama M. M. A., Distributed generation technologies, definitions and benefits, *Electric Power Systems Research*, 2004, 71 (2): 119-128.

[4] Manfren M., Caputo P. and Costa G., Paradigm shift in urban energy systems through distributed generation: Methods and models, *Applied Energy*, 2011, 88:1032–1048

[5] Directive 2002/91/EC, Directive 2002/91/EC of the European Parliament and of the Council of 16 December 2002 on the energy performance of buildings.

[6] Directive 2006/32/EC, Directive 2006/32/EC of the European Parliament and of the Council of 5 April 2006 on energy end-use efficiency and energy services and repealing Council Directive 93/76/EEC.

[7] Directive 2009/28/EC, Directive 2009/28/EC of the European Parliament and of the Council of 23 April 2009 on the promotion of the use of energy from renewable sources and amending and subsequently repealing Directives 2001/77/EC and 2003/30/EC

[8] European Commission C(2011)9493 of 20 December 2011, Work Programme, Theme 5 – Energy

[9] Commission of the European Community, Investing in the Development of Low Carbon Technologies(SET-Plan), October 2009, COM (2009) 519

[10] Commission of the European Community, A European Strategic Energy Technology Plan (SET-PLAN): 'Towards a low carbon future', November 2007, COM (2007) 723

[11] Strachan, N. and Farrell A., Emissions from distributed vs. centralized generation: The importance of system performance, *Energy Policy*, 2006, 34: 2677–2689.

[12] VV.AA., Dall'eco-building al distretto energetico: la proposta ENEA per un modello di sviluppo fondato su eco-edifici e generazione distribuita, *ENEA Workshop*,2007, Roma (in Italian).

[13] Eriksson, O., Bisaillon, M., Haraldsson, M., Sundberg, J., Integrated waste management as a mean to promote renewable energy, *World Renewable Energy Congress* 2011, 8-11 May 2011, Sweden.

[14] Gregg. J., National and regional generation of municipal residue biomass and the future potential for waste-to-energy implementation, *Biomass and Bioenergy*, 2010, 34 (3): 379-388.

[15] Morin, P., Marcos, B., Moresoli, C. and Laflamme C.B., Economic and environmental assessment on the energetic valorisation of organic material for a municipality in Quebec, Canada, *Applied Energy*, 2010, 87 (1): 275-283.

[16] Calise, F., Design of a hybrid polygeneration system with solar collectors and a Solid Oxide Fuel Cell: Dynamic simulation and economic assessment, *International Journal of Hydrogen Energy*, 2011, 35: 6128- 6150.

[17] Larminie, J. and Dicks, A., Fuel cell system explained. *John Wiley & Sons Ltd*; 2004.

[18] Shiratori Y., Oshima T. and Sasaki K., Feasibility of direct-biogas SOFC, *International Journal of Hydrogen Energy*, 2008, 33 (21): 6316-6321

[19] Calise F., Dentice D'Accadia M., Palombo A., and Vanoli L., Simulation and exergy analysis of a hybrid Solid Oxide Fuel Cell (SOFC)–Gas Turbine System, *Energy*, 2006, 31 (15): 3278-3299

[20] Liso V., Zhao Y., Brandon N., Nielsen M. P., and KærS. K., Analysis of the impact of heat-to-power ratio for a SOFC-based mCHP system for residential application under different

climate regions in Europe, *International Journal of Hydrogen Energy*, 2011, 36 (21): 13715-13726

[21] Axaopoulos, P., Panagakis, P., Tsavdaris, A., Georgakakis, D., Simulation and experimental performance of a solarheated anaerobic digester, *Solar Energy*, 2001, 70 (2): 155–164.

[22] Alkhamis, T.M., El-khazali, R., Kablan, M.M. and Alhusein, M.A., Heating of a biogas reactor using a solar energy system with temperature control unit, *Solar Energy*, 2001, 69 (3): 239-247.

[23] Klein, S.A., Beckam, W.A., Mitchell, J.W., Braun, J.E., Evans B.L., Kummert J.P., et al., 2000, "TRNSYS – a transient system simulation program. Version 15.1", Madison: Solar Energy Laboratory, University of Wisconsin; 2000.

[24] Quesada B., Sánchez C., Cañada J., Royo R., PayáJ., Experimental results and simulation with TRNSYS of a 7.2kWp grid-connected photovoltaic system, Applied Energy Volume 88, Issue 5, May 2011, Pages 1772–1783.

[25] Corsini, A., Rispoli, F., Gamberale, M., and Tortora, E., 2009, "Assessment of H2- and H2O-based renewable energy-buffering systems in minor islands", Renewable Energy 34 (2009) 279–288.

[26] Dorer V., Weber R., Weber A., Performance assessment of fuel cell micro-cogeneration systems for residential buildings, Energy and Buildings, Volume37, Issue 11, November 2005, Pages 1132–1146.

[27] Calise F., Design of a hybrid poly-generation system with solar collectors and a Solid Oxide Fuel Cell: Dynamic simulation and economic assessment, International Journal of Hydrogen Energy Volume 36, Issue 10, May 2011, Pages 6128–6150.

[28] Sans, C., Mata-Alvarez, J., Cecchi, F., Pavan, P. and Bassetti, A., Volatile fatty acids production by mesophilic fermentation of mechanically sorted urban organic wastes in a plug flow reactor, *Bioresource Technology*, 1995,51: 89-96.

[29] Solar Energy Laboratory (NREL), University of Wisconsin-Madison, 2003, Generated hourly weather data.

[30] Laraia R., Il trattamento anaerobico dei rifiuti, *Manuali e Linee Guida 13 – ANPA Unita' Normativa Tecnica*, 2002, (in Italian).

[31] Thermal Energy System Specialists, LLC, TESS COMPONENT LIBRARIES General Descriptions, www.trnsys.com.

[32] Zhang, W., Croiset, E., Douglas, P.L., Fowler, M.W., Entchev, E., Simulation of a tubular solid oxide fuel cell stack using ASPEN Plus™ unit operation models, *Energy Conversion and Management* 46 (2005) 181-196.

[33] Borello, D., Del Prete, Z., Marchegiani, A., Rispoli, F. and Tortora, E., Analysis of an integrated PEMFC/ORC power system using ammonia for hydrogen storage, *ASME TurboExpo 2012, GT2012-68599*, Copenhagen, 11-15 June, 2012.

[34] Doherty W., Reynolds A., Kennedy D., Computer simulation of a biomass gasification-solid oxide fuel cell power system using Aspen Plus, Energy 35 (2010) 4545e4555.

[35] Kim Y., Hong S., Nam S., Seo S., Yoo Y., Lee S., Development of 1 kW SOFC power package for dual-fuel operation, international journal of hydrogen energy 36 (2011) 10247-10254.

[36] Kuchonthara P., Bhattacharya S., Tsutsumi A., Energy recuperation in solid oxide fuel cell (SOFC) and gas turbine (GT) combined system, Journal of Power Sources volume 117, Issues 1-2, 15 May 2003, Pages 7-13.

[37] Barelli L., Bidini G., Gallorini F., Ottaviano A., An energetic-exergetic comparison between PEMFC and SOFC-based micro-CHP systems, International Journal of Hydrogen Energy, Volume 36, Issue 4, February 2011, pages 3206-3214.

ECOS 2012

The 25th International Conference on Efficiency, Cost, Optimization and Simulation of Energy Conversion Systems and Processes

(Perugia, June 26th-June 29th, 2012)

edited by
Umberto Desideri, Giampaolo Manfrida,
Enrico Sciubba

firenze university press
2012

ECOS 2012 : the 25th International Conference on Efficiency, Cost, Optimization and Simulation of Energy Conversion Systems and Processes (Perugia, June 26th-June 29th, 2012) / edited by Umberto Desideri, Giampaolo Manfrida, Enrico Sciubba. – Firenze : Firenze University Press, 2012.
(Proceedings e report ; 90)

http://digital.casalini.it/9788866553229

ISBN 978-88-6655-322-9 (online)

Progetto grafico di copertina Alberto Pizarro, Pagina Maestra snc
Immagine di copertina: © Kts | Dreamstime.com

Peer Review Process
All publications are submitted to an external refereeing process under the responsibility of the FUP Editorial Board and the Scientific Committees of the individual series. The works published in the FUP catalogue are evaluated and approved by the Editorial Board of the publishing house. For a more detailed description of the refereeing process we refer to the official documents published on the website and in the online catalogue of the FUP (http://www.fupress.com).

Firenze University Press Editorial Board
G. Nigro (Co-ordinator), M.T. Bartoli, M. Boddi, F. Cambi, R. Casalbuoni, C. Ciappei, R. Del Punta, A. Dolfi, V. Fargion, S. Ferrone, M. Garzaniti, P. Guarnieri, G. Mari, M. Marini, M. Verga, A. Zorzi.

© 2012 Firenze University Press
Università degli Studi di Firenze
Firenze University Press
Borgo Albizi, 28, 50122 Firenze, Italy
http://www.fupress.com/
Printed in Italy

ECOS 2012

The 25th International Conference on

Efficiency, Cost, Optimization and Simulation
of Energy Conversion Systems and Processes

Perugia, June 26th-June 29th, 2012

Book of Proceedings - Volume VI

Edited by:
Umberto Desideri, Università degli Studi di Perugia
Giampaolo Manfrida, Università degli Studi di Firenze
Enrico Sciubba, Università degli Studi di Roma "Sapienza"

ECOS 2012 - THE 25TH INTERNATIONAL CONFERENCE ON
EFFICIENCY, COST, OPTIMIZATION, SIMULATION AND ENVIRONMENTAL IMPACT OF ENERGY SYSTEMS
JUNE 26-29, 2012, PERUGIA, ITALY
EDITED BY UMBERTO DESIDERI, GIAMPAOLO MANFRIDA, ENRICO SCIUBBA
FIRENZE UNIVERSITY PRESS, 2012, ISBN ONLINE : 978-88-6655-322-9

Advisory Committee (Track Organizers)

Building, Urban and Complex Energy Systems
V. Ismet Ugursal
Dalhousie University, Nova Scotia, Canada

Combustion, Chemical Reactors, Carbon Capture and Sequestration
Giuseppe Girardi
ENEA-Casaccia, Italy

Energy Systems: Environmental and Sustainability Issues
Christos A. Frangopoulos
National Technical University of Athens, Greece

Exergy Analysis and Second Law Analysis
Silvio de Oliveira Junior
Polytechnical University of Sao Paulo, Sao Paulo, Brazil

Fluid Dynamics and Power Plant Components
Sotirios Karellas
National Technical University of Athens, Athens, Greece

Fuel Cells
Umberto Desideri
University of Perugia, Perugia, Italy

Heat and Mass Transfer
Francesco Asdrubali, **Cinzia Buratti**
University of Perugia, Perugia, Italy

Industrial Ecology
Stefan Goessling-Reisemann
University of Bremen, Germany

Poster Session
Enrico Sciubba
University Roma 1 “Sapienza”, Italy

Process Integration and Heat Exchanger Networks
Francois Marechal
EPFL, Lausanne, *Switzerland*

Renewable Energy Conversion Systems
David Chiaramonti
University of Firenze, Firenze, Italy

Simulation of Energy Conversion Systems
Marcin Liszka
Polytechnica Slaska, Gliwice, Poland

System Operation, Control, Diagnosis and Prognosis
Vittorio Verda
Politecnico di Torino, Italy

Thermodynamics
A. Özer Arnas
United States Military Academy at West Point, U.S.A.

Thermo-Economic Analysis and Optimisation
Andrea Lazzaretto
University of Padova, Padova, Italy

Water Desalination and Use of Water Resources
Corrado Sommariva
ILF Consulting M.E., U.K

Scientific Committee

Riccardo Basosi, University of Siena, Italy
Gino Bella, University of Roma Tor Vergata, Italy
Asfaw Beyene, San Diego State University, United States
Ryszard Bialecki, Silesian Institute of Tecnology, Poland
Gianni Bidini, University of Perugia, Italy
Ana M. Blanco-Marigorta, University of Las Palmas de Gran Canaria, Spain
Olav Bolland, University of Science and Technology (NTNU), Norway
Renè Cornelissen, Cornelissen Consulting, The Netherlands
Franco Cotana, University of Perugia, Italy
Alexandru Dobrovicescu, Polytechnical University of Bucharest, Romania
Gheorghe Dumitrascu, Technical University of Iasi, Romania
Brian Elmegaard, Technical University of Denmark , Denmark
Daniel Favrat, EPFL, Switzerland
Michel Feidt, ENSEM - LEMTA University Henri Poincaré, France
Daniele Fiaschi, University of Florence, Italy
Marco Frey, Scuola Superiore S. Anna, Italy
Richard A Gaggioli, Marquette University, USA
Carlo N. Grimaldi, University of Perugia, Italy
Simon Harvey, Chalmers University of Technology, Sweden
Hasan Heperkan, Yildiz Technical University, Turkey
Abel Abel Hernandez-Guerrero, University of Guanajuato, Mexico
Jiri Jaromir Klemeš, University of Pannonia, Hungary
Zornitza V. Kirova-Yordanova, University "Prof. Assen Zlatarov", Bulgaria
Noam Lior, University of Pennsylvania, United States
Francesco Martelli, University of Florence, Italy
Aristide Massardo, University of Genova, Italy
Jim McGovern, Dublin Institute of Technology, Ireland
Alberto Mirandola, University of Padova, Italy
Michael J. Moran, The Ohio State University, United States
Tatiana Morosuk, Technical University of Berlin, Germany
Pericles Pilidis, University of Cranfield, United Kingdom
Constantine D. Rakopoulos, National Technical University of Athens, Greece
Predrag Raskovic, University of Nis, Serbia and Montenegro
Mauro Reini, University of Trieste, Italy
Gianfranco Rizzo, University of Salerno, Italy
Marc A. Rosen, University of Ontario, Canada
Luis M. Serra, University of Zaragoza, Spain
Gordana Stefanovic, University of Nis, Serbia and Montenegro
Andrea Toffolo, Luleå University of Technology, Sweden
Wojciech Stanek, Silesian University of Technology, Poland
George Tsatsaronis, Technical University Berlin, Germany
Antonio Valero, University of Zaragoza, Spain
Michael R. von Spakovsky, Virginia Tech, USA
Stefano Ubertini, Parthenope University of Naples, Italy
Sergio Ulgiati, Parthenope University of Naples, Italy
Sergio Usón, Universidad de Zaragoza, Spain
Roman Weber, Clausthal University of Technology, Germany
Ryohei Yokoyama, Osaka Prefecture University, Japan
Na Zhang, Institute of Engineering Thermophysics, Chinese Academy of Sciences, China

The 25th ECOS Conference 1987-2012: leaving a mark

The introduction to the ECOS series of Conferences states that "ECOS is a series of international conferences that focus on all aspects of Thermal Sciences, with particular emphasis on Thermodynamics and its applications in energy conversion systems and processes". Well, ECOS is much more than that, and its history proves it!

The idea of starting a series of such conferences was put forth at an informal meeting of the Advanced Energy Systems Division of the American Society of Mechanical Engineers (ASME) at the November 1985 Winter Annual Meeting (WAM), in Miami Beach, Florida, then chaired by Richard Gaggioli. The resolution was to organize an annual Symposium on the Analysis and Design of Thermal Systems at each ASME WAM, and to try to involve a larger number of scientists and engineers worldwide by organizing conferences outside of the United States. Besides Rich other participants were Ozer Arnas, Adrian Bejan, Yehia El-Sayed, Robert Evans, Francis Huang, Mike Moran, Gordon Reistad, Enrico Sciubba and George Tsatsaronis.

Ever since 1985, a Symposium of 8-16 sessions has been organized by the Systems Analysis Technical Committee every year, at the ASME Winter Annual Meeting (now ASME-IMECE). The first overseas conference took place in Rome, twenty-five years ago (in July 1987), with the support of the U.S. National Science Foundation and of the Italian National Research Council. In that occasion, Christos Frangopoulos, Yalcin Gogus, Elias Gyftopoulos, Dominick Sama, Sergio Stecco, Antonio Valero, and many others, already active at the ASME meetings, joined the core-group.

The name ECOS was used for the first time in Zaragoza, in 1992: it is an acronym for **Efficiency, Cost, Optimization and Simulation** (of energy conversion systems and processes), keywords that best describe the contents of the presentations and discussions taking place in these conferences. Some years ago, Christos Frangopoulos inserted in the official website the note that "ècos" ('οικος) means "home" in Greek and it ought to be attributed the very same meaning as the prefix "Eco-" in environmental sciences.
The last 25 years have witnessed an almost incredible growth of the ECOS community: more and more Colleagues are actively participating in our meetings, several international Journals routinely publish selected papers from our Proceedings, fruitful interdisciplinary and international cooperation projects have blossomed from our meetings. Meetings that have spanned three continents (Africa and Australia ought to be our next targets, perhaps!) and influenced in a way or another much of modern Engineering Thermodynamics.
After 25 years, if we do not want to become embalmed in our own success and lose momentum, it is mandatory to aim our efforts in two directions: first, encourage the participation of younger academicians to our meetings, and second, stimulate creative and useful discussions in our sessions. Looking at this years' registration roster (250 papers of which 50 authored or co-authored by junior Authors), the first objective seems to have been attained, and thus we have just to continue in that direction; the second one involves allowing space to "voices that sing out of the choir", fostering new methods and approaches, and establishing or reinforcing connections to other scientific communities. It is important that our technical sessions represent a place of active confrontation, rather than academic "lecturing".
In this spirit, we welcome you in Perugia, and wish you a scientifically stimulating, touristically interesting, and culinarily rewarding experience. In line with our 25 years old scientific excellency and friendship!

Umberto Desideri, Giampaolo Manfrida, Enrico Sciubba

CONTENT MANAGEMENT

The index lists all the papers contained all the eight volumes of the Proceedings of the ECOS 2012 International Conference.
Page numbers are listed only for papers within the Volume you are looking at. The ID code allows to trace back the identification number assigned to the paper within the Conference submission, review and track organization processes.

CONTENT

VOLUME VI

VI. 1 CARBON CAPTURE AND SEQUESTRATION

» A novel coal-based polygeneration system cogenerating power, natural gas and liquid fuel with CO2 capture (ID 96) ……..... *Pag. 1*
Sheng Li, Hongguang Jin, Lin Gao

» Analysis and optimization of CO2 capture in a China's existing coal-fired power plant (ID 532) ……..... *Pag. 18*
Gang Xu, Yongping Yang, Shoucheng Li, Wenyi Liu and Ying Wu

» Analysys of four-end high temperature membrane air separator in a supercritical power plant with oxy-type pulverized fuel boiler (ID 442) ……..... *Pag. 35*
Janusz Kotowicz, Sebastian Stanisław Michalski

» Analysis of potential improvements to the lignite-fired oxy-fuel power unit (ID 413) ……..... *Pag. 45*
Marcin Liszka, Jakub Tuka, Grzegorz Nowak, Grzegorz Szapajko

» Biogas Upgrading: Global Warming Potential of Conventional and Innovative Technologies (ID 240) ……..... *Pag. 61*
Katherine Starr, Xavier Gabarrell Durany, Gara Villalba Mendez, Laura Talens Peiro, Lidia Lombardi

» Capture of carbon dioxide using gas hydrate technology (ID 103) ……..... *Pag. 73*
Beatrice Castellani, Mirko Filipponi, Sara Rinaldi, Federico Rossi

» Carbon dioxide mineralisation and integration with flue gas desulphurisation applied to a modern coal-fired power plant (ID 179) ……..... *Pag. 83*
Ron Zevenhoven, Johan Fagerlund, Thomas Björklöf, Magdalena Mäkelä, Olav Eklund

» Carbon dioxide storage by mineralisation applied to a lime kiln (ID 226) ……..... *Pag. 103*
Inês Sofia Soares Romão, Matias Eriksson, Experience Nduagu, Johan Fagerlund, Licínio Manuel Gando-Ferreira, Ron Zevenhoven

» Comparison of IGCC and CFB cogeneration plants equipped with CO2 removal (ID 380) ……..... *Pag. 116*
Marcin Liszka, Tomasz Malik, Michał Budnik, Andrzej Ziębik

» Concept of a "capture ready" combined heat and power plant (ID 231) ……..... *Pag. 133*
Piotr Henryk Lukowicz, Lukasz Bartela

» Cryogenic method for H2 and CH4 recovery from a rich CO2 stream in pre-combustion CCS schemes (ID 508) ……..... *Pag. 145*
Konstantinos Atsonios, Kyriakos D. Panopoulos, Angelos Doukelis, Antonis Koumanakos, Emmanuel Kakaras

» Design and optimization of ITM oxy-combustion power plant (ID 495) ……..... *Pag. 158*
Surekha Gunasekaran, Nicholas David Mancini, Alexander Mitsos

» Implementation of a CCS technology: the ZECOMIX experimental platform (ID 222) ……..... *Pag. 169*
Antonio Calabrò, Stefano Cassani, Leandro Pagliari, Stefano Stendardo

» Influence of regeneration condition on cyclic CO2 capture using pre-treated dispersed CaO as high temperature sorbent (ID 221) ……..... *Pag. 175*
Stefano Stendardo, Antonio Calabrò

ECOS 2012 – THE 25TH INTERNATIONAL CONFERENCE ON
EFFICIENCY, COST, OPTIMIZATION, SIMULATION AND ENVIRONMENTAL IMPACT OF ENERGY SYSTEMS
JUNE 26-29, 2012, PERUGIA, ITALY
EDITED BY UMBERTO DESIDERI, GIAMPAOLO MANFRIDA, ENRICO SCIUBBA
FIRENZE UNIVERSITY PRESS, 2012, ISBN ONLINE : 978-88-6655-322-9

» **Investigation of an innovative process for biogas up-grading – pilot plant preliminary results (ID 56)** ……..... *Pag. 185*
Lidia Lombardi, Renato Baciocchi, Ennio Antonio Carnevale, Andrea Corti, Giulia Costa, Tommaso Olivieri, Alessandro Paradisi, Daniela Zingaretti

» **Method of increasing the efficiency of a supercritical lignite-fired oxy-type fluidized bed boiler and high-temperature three - end membrane for air separation (ID 438)** ……..... *Pag. 197*
Janusz Kotowicz, Adrian Balicki

» **Monitoring of carbon dioxide uptake in accelerated carbonation processes applied to air pollution control residues (ID 539)** ……..... *Pag. 205*
Felice Alfieri, Peter J Gunning, Michela Gallo, Adriana Del Borghi, Colin D Hills

» **Process efficiency and optimization of precipitated calcium carbonate (PCC) production from steel converter slag (ID 114)** ……..... *Pag. 218*
Hannu-Petteri Mattila, Inga Grigaliūnaitė, Arshe Said, Sami Filppula, Carl-Johan Fogelholm, Ron Zevenhoven

» **Production of Mg(OH)2 for CO2 Emissions Removal Applications: Parametric and Process Evaluation (ID 245)** ……..... *Pag. 233*
Experience Ikechukwu Nduagu, Inês Romão, Ron Zevenhoven

» **Thermodynamic analysis of a supercritical power plant with oxy type pulverized fuel boiler, carbon dioxide capture system (CC) and four-end high temperature membrane air seprator (ID 411)** ……..... *Pag. 251*
Janusz Kotowicz, Sebastian Stanisław Michalski

VI. 2 PROCESS INTEGRATION AND HEAT EXCHANGER NETWORKS

» **A multi-objective optimization technique for co- processing in the cement production (ID 42)** ……..... *Pag. 261*
Maria Luiza Grillo Renó, Rogério José da Silva, Mirian de Lourdes Noronha Motta Melo, José Joaquim Conceição Soares Santos

» **Comparison of options for debottlenecking the recovery boiler at kraft pulp mills – Economic performance and CO2 emissions (ID 449)** ……..... *Pag. 270*
Johanna Jönsson, Karin Pettersson, Simon Harvey, Thore Berntsson

» **Demonstrating an integral approach for industrial energy saving (ID 541)** ……..... *Pag. 287*
René Cornelissen, Geert van Rens, Jos Sentjens, Henk Akse, Ton Backx, Arjan van der Weiden, Jo Vandenbroucke

» **Maximising the use of renewables with variable availability (ID 494)** ……..... *Pag. 297*
Andreja Nemet, Jiri Jaromír Klemeš, Petar Sabev Varbanov, Zdravko Kravanja

» **Methodology for the improvement of large district heating networks (ID 46)** ……..... *Pag. 314*
Anna Volkova, Vladislav Mashatin, Aleksander Hlebnikov, Andres Siirde

» **Optimal mine site energy supply (ID 306)** ……..... *Pag. 327*
Monica Carvalho, Dean Lee Millar

» **Simulation of synthesis gas production from steam oxygen gasification of Colombian bituminous coal using Aspen Plus® (ID 395)** ……..... *Pag. 340*
John Jairo Ortiz, Juan Camilo González, Jorge Enrique Preciado, Rocío Sierra, Gerardo Gordillo

CONTENTS OF ALL THE VOLUMES

VOLUME I

I . 1 – SIMULATION OF ENERGY CONVERSION SYSTEMS

» A novel hybrid-fuel compressed air energy storage system for China's situation (ID 531)
Wenyi Liu, Yongping Yang, Weide Zhang, Gang Xu,and Ying Wu

» A review of Stirling engine technologies applied to micro-cogeneration systems (ID 338)
Ana C Ferreira, Manuel L Nunes, Luís B Martins, Senhorinha F Teixeira

» An organic Rankine cycle off-design model for the search of the optimal control strategy (ID 295)
Andrea Toffolo, Andrea Lazzaretto, Giovanni Manente, Marco Paci

» Automated superstructure generation and optimization of distributed energy supply systems (ID 518)
Philip Voll, Carsten Klaffke, Maike Hennen, André Bardow

» Characterisation and classification of solid recovered fuels (SRF) and model development of a novel thermal utilization concept through air- gasification (ID 506)
Panagiotis Vounatsos, Konstantinos Atsonios, Mihalis Agraniotis, Kyriakos D. Panopoulos, George Koufodimos,Panagiotis Grammelis, Emmanuel Kakaras

» Design and modelling of a novel compact power cycle for low temperature heat sources (ID 177)
Jorrit Wronski, Morten Juel Skovrup, Brian Elmegaard, Harald Nes Rislå, Fredrik Haglind

» Dynamic simulation of combined cycles operating in transient conditions: an innovative approach to determine the steam drums life consumption (ID 439)
Stefano Bracco

» Effect of auxiliary electrical power consumptions on organic Rankine cycle system with low-temperature waste heat source (ID 235)
Samer Maalouf, Elias Boulawz Ksayer, Denis Clodic

» Energetic and exergetic analysis of waste heat recovery systems in the cement industry (ID 228)
Sotirios Karellas, Aris Dimitrios Leontaritis, Georgios Panousis, Evangelos Bellos, Emmanuel Kakaras

» Energy and exergy analysis of repowering options for Greek lignite-fired power plants (ID 230)
Sotirios Karellas, Aggelos Doukelis, Grammatiki Zanni, Emmanuel Kakaras

» Energy saving by a simple solar collector with reflective panels and boiler (ID 366)
Anna Stoppato, Renzo Tosato

» Exergetic analysis of biomass fired double-stage Organic Rankine Cycle (ORC) (ID 37)
Markus Preißinger, Florian Heberle, Dieter Brüggemann

» Experimental tests and modelization of a domestic-scale organic Rankine cycle (ID 156)
Roberto Bracco, Stefano Clemente, Diego Micheli, Mauro Reini

» Model of a small steam engine for renewable domestic CHP system (ID 31)
Giampaolo Manfrida, Giovanni Ferrara, Alessandro Pescioni

» Model of vacuum glass heat pipe solar collectors (ID 312)
Daniele Fiaschi, Giampaolo Manfrida

» Modelling and exergy analysis of a plasma furnace for aluminum melting process (ID 254)
Luis Enrique Acevedo, Sergio Usón, Javier Uche, Patxi Rodríguez

» Modelling and experimental validation of a solar cooling installation (ID 296)
Guillaume Anies, Pascal Stouffs, Jean Castaing-Lasvignottes

» The influence of operating parameters and occupancy rate of thermoelectric modules on the electricity generation (ID 314)
Camille Favarel, Jean-Pierre Bédécarrats, Tarik Kousksou, Daniel Champier

» Thermodynamic and heat transfer analysis of rice straw co-firing in a Brazilian pulverised coal boiler (ID 236)
Raphael Miyake, Alvaro Restrepo, Fábio Kleveston Edson Bazzo, Marcelo Bzuneck

» Thermophotovoltaic generation: A state of the art review (ID 88)
Matteo Bosi, Claudio Ferrari, Francesco Melino, Michele Pinelli, Pier Ruggero Spina, Mauro Venturini

I . 2 – HEAT AND MASS TRANSFER

» A DNS method for particle motion to establish boundary conditions in coal gasifiers (ID 49)
Efstathios E Michaelides, Zhigang Feng

» Effective thermal conductivity with convection and radiation in packed bed (ID 60)
Yusuke Asakuma

» Experimental and CFD study of a single phase cone-shaped helical coiled heat exchanger: an empirical correlation (ID 375)
Daniel Flórez-Orrego, Walter Arias, Diego López, Héctor Velásquez

» Thermofluiddynamic model for control analysis of latent heat thermal storage system (ID 207)
Adriano Sciacovelli, Vittorio Verda, Flavio Gagliardi

» Towards the development of an efficient immersed particle heat exchanger: particle transfer from low to high pressure (ID 202)
Luciano A. Catalano, Riccardo Amirante, Stefano Copertino, Paolo Tamburrano, Fabio De Bellis

I . 3 – INDUSTRIAL ECOLOGY

» Anthropogenic heat and exergy balance of the atmosphere (ID 122)
Asfaw Beyene, David MacPhee, Ron Zevenhoven

» Determination of environmental remediation cost of municipal waste in terms of extended exergy (ID 63)
Candeniz Seckin, Ahmet R. Bayulken

» Development of product category rules for the application of life cycle assessment to carbon capture and storage (537)
Carlo Strazza, Adriana Del Borghi, Michela Gallo

» Electricity production from renewable and non-renewable energy sources: a comparison of environmental, economic and social sustainability indicators with exergy losses throughout the supply chain (ID 247)
Lydia Stougie, Hedzer van der Kooi, Rob Stikkelman

» Exergy analysis of the industrial symbiosis model in Kalundborg (ID 218)
Alicia Valero Delgado, Sergio Usón, Jorge Costa

» Global gold mining: is technological learning overcoming the declining in ore grades? (ID 277)
Adriana Domínguez, Alicia Valero

» Personal transportation energy consumption (ID305)
Matteo Muratori, Emmanuele Serra, Vincenzo Marano, Michael Moran

» Resource use evaluation of Turkish transportation sector via the extended exergy accounting method (ID 43)
Candeniz Seckin, Enrico Sciubba, Ahmet R. Bayulken

» The impact of higher energy prices on socio-economic inequalities of German social groups (ID 80)
Holger Schlör, Wolfgang Fischer, Jürgen-Friedrich Hake

VOLUME II

II . 1 – EXERGY ANALYSIS AND 2ND LAW ANALYSIS

» A comparative analysis of cryogenic recuperative heat exchangers based on exergy destruction (ID 129)
Adina Teodora Gheorghian, Alexandru Dobrovicescu, Lavinia Grosu, Bogdan Popescu, Claudia Ionita

» A critical exploration of the usefulness of rational efficiency as a performance parameter for heat exchangers (ID 307)
Jim McGovern, Georgiana Tirca-Dragomirescu, Michel Feidt, Alexandru Dobrovicescu

» A new procedure for the design of LNG processes by combining exergy and pinch analyses (ID 238)
Danahe Marmolejo-Correa, Truls Gundersen

» Advances in the distribution of environmental cost of water bodies through the exergy concept in the Ebro river (ID 258)
Javier Uche Marcuello, Amaya Martínez Gracia, Beatriz Carrasquer Álvarez, Antonio Valero Capilla

» Application of the entropy generation minimization method to a solar heat exchanger: a pseudo-optimization design process based on the analysis of the local entropy generation maps (ID 357)
Giorgio Giangaspero, Enrico Sciubba

» Comparative analysis of ammonia and carbon dioxide two-stage cycles for simultaneous cooling and heating (ID 84)
Alexandru Dobrovicescu, Ciprian Filipoiu, Emilia Cerna Mladin, Valentin Apostol, Liviu Drughean

» Comparison between traditional methodologies and advanced exergy analyses for evaluating efficiency and externalities of energy systems (ID 515)
Gabriele Cassetti, Emanuela Colombo

» Comparison of entropy generation figures using entropy maps and entropy transport equation for an air cooled gas turbine blade (ID 468)
Omer Emre Orhan, Oguz Uzol

» Conventional and advanced exergetic evaluation of a supercritical coal-fired power plant (ID 377)
Ligang Wang, Yongping Yang, Tatiana Morosuk, George Tsatsaronis

» Energy and exergy analyses of the charging process in encapsulted ice thermal energy storage (ID 164)
David MacPhee, Ibrahim Dincer, Asfaw Beyene

» Energy integration and cogeneration in nitrogen fertilizers industry: thermodynamic estimation of the efficiency, potentials, limitations and environmental impact. Part 1: energy integration in ammonia production plants (ID 303)
Zornitza Vassileva Kirova-Yordanova

» Evaluation of the oil and gas processing at a real production day on a North Sea oil platform using exergy analysis (ID 260)
Mari Voldsund, Wei He, Audun Røsjorde, Ivar Ståle Ertesvåg, Signe Kjelstrup

» Exergetic and economic analysis of Kalina cycle for low temperature geothermal sources in Brazil (ID 345)
Carlos Eymel Campos Rodriguez, José Carlos Escobar Palacios, Cesar Adolfo Rodríguez Sotomonte, Marcio Leme, Osvaldo José Venturini, Electo Eduardo Silva Lora, Vladimir Melián Cobasa, Daniel Marques dos Santos, Fábio R. Lofrano Dotto, Vernei Gialluca

» Exergy analysis and comparison of CO2 heat pumps (ID 242)
Argyro Papadaki, Athina Stegou - Sagia

» Exergy analysis of a CO2 Recovery plant for a brewery (ID 72)
Daniel Rønne Nielsen, Brian Elmegaard, C. Bang-Møller

» Exergy analysis of the silicon production process (ID 118)
Marit Takla, Leiv Kolbeinsen, Halvard Tveit, Signe Kjelstrup

» Exergy based indicators for cardiopulmonary exercise test evaluation (ID 159)
Carlos Eduardo Keutenedjian Mady, Cyro Albuquerque Neto, Tiago Lazzaretti Fernandes, Arnaldo Jose Hernandez, Paulo Hilário Nascimento Saldiva, Jurandir Itizo Yanagihara, Silvio de Oliveira Junior

» Exergy disaggregation as an alternative for system disaggregation in thermoeconomics (ID 483)
José Joaquim Conceição Soares Santos, Atilio Lourenço, Julio Mendes da Silva, João Donatelli, José Escobar Palacio

» Exergy intensity of petroleum derived fuels (ID 117)
Julio Augusto Mendes da Silva, Maurício Sugiyama, Claudio Rucker, Silvio de Oliveira Junior

» Exergy-based sustainability evaluation of a wind power generation system (ID 542)
Jin Yang, B. Chen, Enrico Sciubba

» Human body exergy metabolism (ID 160)
Carlos Eduardo Keutenedjian Mady, Silvio de Oliveira Junior

» Integrating an ORC into a natural gas expansion plant supplied with a co-generation unit (ID 273)
Sergio Usón, Wojciech Juliusz Kostowski

» One-dimensional model of an optimal ejector and parametric study of ejector efficiency (ID 323)
Ronan Killian McGovern, Kartik Bulusu, Mohammed Antar, John H. Lienhard

» Optimization and design of pin-fin heat sinks based on minimum entropy generation (ID 6)
Jose-Luis Zuniga-Cerroblanco, Abel Hernandez-Guerrero, Carlos A. Rubio-Jimenez, Cuauhtemoc Rubio-Arana, Sosimo E. Diaz-Mendez

» Performance analysis of a district heating system (ID 271)
Andrej Ljubenko, Alojz Poredoš, Tatiana Morosuk, George Tsatsaronis

» System analysis of exergy losses in an integrated oxy-fuel combustion power plant (ID 64)
Andrzej Ziębik, Paweł Gładysz

» What is the cost of losing irreversibly the mineral capital on Earth? (ID 220)
Alicia Valero Delgado, Antonio Valero

II . 2 – THERMODYNAMICS

» A new polygeneration system for methanol and power based on coke oven gas and coal gas (ID 252)
Hu Lin, Hongguang Jin, Lin Gao, Rumou Li

» Argon-Water closed gas cycle (ID 67)
Federico Fionelli, Giovanni Molinari

» Binary alkane mixtures as fluids in Rankine cycles (ID 246)
M. Aslam Siddiqi, Burak Atakan

» Excess enthalpies of second generation biofuels (ID 308)
Alejandro Moreau, José Juan Segovia, M. Carmen Martín, Miguel Ángel Villamañán, César R. Chamorro, Rosa M. Villamañán
» Local stability analysis of a Curzon-Ahlborn engine considering the Van der Waals equation state in the maximum ecological regime (ID 281)
Ricardo Richard Páez-Hernández, Pedro Portillo-Díaz, Delfino Ladino-Luna, Marco Antonio Barranco-Jiménez

» Some remarks on the Carnot's theorem (ID 325)
Julian Gonzalez Ayala, Fernando Angulo-Brown

» The Dead State (ID 340)
Richard A. Gaggioli

» The magnetocaloric energy conversion (ID 97)
Andrej Kitanovski, Jaka Tusek, Alojz Poredos

VOLUME III

THERMO-ECONOMIC ANALYSIS AND OPTIMIZATION

» A comparison of optimal operation of residential energy systems using clustered demand patterns based on Kullback-Leibler divergence (ID 142)
Akira Yoshida, Yoshiharu Amano, Noboru Murata, Koichi Ito, Takumi Hashizume

» A Model for Simulation and Optimal Design of a Solar Heating System with Seasonal Storage (ID 51)
Gianfranco Rizzo

» A thermodynamic and economic comparative analysis of combined gas-steam and gas turbine air bottoming cycle (ID 232)
Tadeusz Chmielniak, Daniel Czaja, Sebastian Lepszy

» Application of an alternative thermoeconomic approach to a two-stage vapor compression refrigeration cycle with intercooling (ID 135)
Atilio Barbosa Lourenço, José Joaquim Conceição Soares Santos, João Luiz Marcon Donatelli

» Comparative performance of advanced power cycles for low temperature heat sources (ID 109)
Guillaume Becquin, Sebastian Freund

» Comparison of nuclear steam power plant and conventional steam power plant through energy level and thermoeconomic analysis (ID 251)
S. Khamis Abadi, Mohammad Hasan Khoshgoftar Manesh, M. Baghestani, H. Ghalami, Majid Amidpour

» Economic and exergoeconomic analysis of micro GT and ORC cogeneration systems (ID 87)
Audrius Bagdanavicius, Robert Sansom, Nick Jenkins, Goran Strbac

» Exergoeconomic comparison of wet and dry cooling technologies for the Rankine cycle of a solar thermal power plant (ID 300)
Philipp Habl, Ana M. Blanco-Marigorta, Berit Erlach

» Influence of renewable generators on the thermo-economic multi-level optimization of a poly-generation smart grid (101)
Massimo Rivarolo, Andrea Greco, Francesca Travi, Aristide F. Massardo

» Local stability analysis of a thermoeconomic model of an irreversible heat engine working at different criteria of performance (ID 289)
Marco A. Barranco-Jiménez, Norma Sánchez-Salas, Israel Reyes-Ramírez, Lev Guzmán-Vargas

» Multicriteria optimization of a distributed trigeneration system in an industrial area (ID 154)
Dario Buoro, Melchiorre Casisi, Alberto de Nardi, Piero Pinamonti, Mauro Reini

» On the effect of eco-indicator selection on the conclusions obtained from an exergoenvironmental analysis (ID 275)
Tatiana Morosuk, George Tsatsaronis, Christopher Koroneos

» Optimisation of supply temperature and mass flow rate for a district heating network (ID 104)
Marouf Pirouti, Audrius Bagdanavicius, Jianzhong Wu, Janaka Ekanayake

» Optimization of energy supply systems in consideration of hierarchical relationship between design and operation (ID 389)
Ryohei Yokoyama, Shuhei Ose

» The fuel impact formula revisited (ID 279)
Cesar Torres, Antonio Valero

» The introduction of exergy analysis to the thermo-economic modelling and optimisation of a marine combined cycle system (ID 61)
George G. Dimopoulos, Chariklia A. Georgopoulou, Nikolaos M.P. Kakalis

» The relationship between costs and environmental impacts in power plants: an exergy-based study (ID 272)
Fontina Petrakopoulou, Yolanda Lara, Tatiana Morosuk, Alicia Boyano, George Tsatsaronis

» Thermo-ecological evaluation of biomass integrated gasification gas turbine based cogeneration technology (ID 441)
Wojciech Stanek, Lucyna Czarnowska, Jacek Kalina

» Thermo-ecological optimization of a heat exchanger through empirical modeling (ID 501)
Ireneusz Szczygieł, Wojciech Stanek, Lucyna Czarnowska, Marek Rojczyk

» Thermoeconomic analysis and optimization in a combined cycle power plant including a heat transformer for energy saving (ID 399)
Elizabeth Cortés Rodríguez, José Luis Castilla Carrillo, Claudia A. Ruiz Mercado, Wilfrido Rivera Gómez-Franco

» Thermoeconomic analysis and optimization of a hybrid solar-electric heating in a fluidized bed dryer (ID 400)
Elizabeth Cortés Rodríguez, Felipe de Jesús Ojeda Cámara, Isaac Pilatowsky Figueroa

» Thermoeconomic approach for the analysis of low temperature district heating systems (ID 208)
Vittorio Verda, Albana Kona

» Thermo-economic assessment of a micro CHP systems fuelled by geothermal and solar energy (ID 166)
Duccio Tempesti, Daniele Fiaschi, Filippo Gabuzzini

» Thermo-economic evaluation and optimization of the thermo-chemical conversion of biomass into methanol (ID 194)
Emanuela Peduzzi, Laurence Tock, Guillaume Boissonnet, François Marechal

» Thermoeconomic fuel impact approach for assessing resources savings in industrial symbiosis: application to Kalundborg Eco-industrial Park (ID 256)
Sergio Usón, Antonio Valero, Alicia Valero, Jorge Costa

» Thermoeconomics of a ground-based CAES plant for peak-load energy production system (ID 32)
Simon Kemble, Giampaolo Manfrida, Adriano Milazzo, Francesco Buffa

VOLUME IV

IV . 1 – FLUID DYNAMICS AND POWER PLANT COMPONENTS

» A control oriented simulation model of a multistage axial compressor (ID 444)
Lorenzo Damiani, Giampaolo Crosa, Angela Trucco

» A flexible and simple device for in-cylinder flow measurements: experimental and numerical validation (ID 181)
Andrea Dai Zotti, Massimo Masi, Marco Antonello

» CFD Simulation of Entropy Generation in Pipeline for Steam Transport in Real Industrial Plant (ID 543)
Goran Vučković, Gradimir Ilić, Mića Vukić, Milan Banić, Gordana Stefanović

» Feasibility Study of Turbo expander Installation in City Gate Station (ID 168)
Navid Zehtabiyan Rezaie, Majid Saffar-Avval

» GTL and RME combustion analysis in a transparent CI engine by means of IR digital imaging (ID 460)
Ezio Mancaruso, Luigi Sequino, Bianca Maria Vaglieco

» Some aspects concerning fluid flow and turbulence modeling in 4-valve engines (ID 116)
Zoran Stevan Jovanovic, Zoran Masonicic, Miroljub Tomic

IV . 2 – SYSTEM OPERATION CONTROL DIAGNOSIS AND PROGNOSIS

» Adapting the operation regimes of trigeneration systems to renewable energy systems integration (ID 188)
Liviu Ruieneanu, Mihai Paul Mircea

» Advanced electromagnetic sensors for sustainable monitoring of industrial processes (ID 145)
Uroš Puc, Andreja Abina, Anton Jeglič, Pavel Cevc, Aleksander Zidanšek

» Assessment of stresses and residual life of plant components in view of life-time extension of power plants (ID 453)
Anna Stoppato, Alberto Benato and Alberto Mirandola

» Control strategy for minimizing the electric power consumption of hybrid ground source heat pump system (ID 244)
Zoi Sagia, Constantinos Rakopoulos

» Exergetic evaluation of heat pump booster configurations in a low temperature district heating network (ID 148)
Torben Ommen, Brian Elmegaard

» Exergoeconomic diagnosis: a thermo-characterization method by using irreversibility analysis (ID 523)
Abraham Olivares-Arriaga, Alejandro Zaleta-Aguilar, Rangel-Hernández V. H, Juan Manuel Belman-Flores

» Optimal structural design of residential cogeneration systems considering their operational restrictions (ID 224)
Tetsuya Wakui, Ryohei Yokoyama

» Performance estimation and optimal operation of a CO2 heat pump water heating system (ID 344)
Ryohei Yokoyama, Ryosuke Kato, Tetsuya Wakui, Kazuhisa Takemura

» Performances of a common-rail Diesel engine fuelled with rapeseed and waste cooking oils (ID 213)
Alessandro Corsini, Valerio Giovannoni, Stefano Nardecchia, Franco Rispoli, Fabrizio Sciulli, Paolo Venturini

» Reduced energy cost through the furnace pressure control in power plants (ID 367)
Vojislav Filipović, Novak Nedić, Saša Prodanović

» Short-term scheduling model for a wind-hydro-thermal electricity system (ID 464)
Sérgio Pereira, Paula Ferreira, A. Ismael Freitas Vaz

VOLUME V

V . 1 – RENEWABLE ENERGY CONVERSION SYSTEMS

» A co-powered concentrated solar power Rankine cycle concept for small size combined heat and power (ID 276)
Alessandro Corsini, Domenico Borello, Franco Rispoli, Eileen Tortora

» A novel non-tracking solar collector for high temperature application (ID 466)
Wattana Ratismith, Anusorn Inthongkhum

» Absorption heat transformers (AHT) as a way to enhance low enthalpy geothermal resources (ID 311)
Daniele Fiaschi, Duccio Tempesti, Giampaolo Manfrida, Daniele Di Rosa

» Alternative feedstock for the biodiesel and energy production: the OVEST project (ID 98)
Matteo Prussi, David Chiaramonti, Lucia Recchia, Francesco Martelli, Fabio Guidotti

» Assessing repowering and update scenarios for wind energy converters (ID 158)
Till Zimmermann

» Biogas from mechanical pulping industry – potential improvement for increased biomass vehicle fuels (ID 54)
Mimmi Magnusson, Per Alvfors

» Biogas or electricity as vehicle fuels derived from food waste - the case of Stockholm (ID 27)
Martina Wikström, Per Alvfors

» Compressibility factor as evaluation parameter of expansion processes in organic Rankine cycles (ID 292)
Giovanni Manente, Andrea Lazzaretto

» Design of solar heating system for methane generation (ID 445)
Lucía Mónica Gutiérrez, P. Quinto Diez, L. R. Tovar Gálvez

» Economic feasibility of PV systems in hotels in Mexico (ID 346)
Augusto Sanchez, Sergio Quezada

» Effect of a back surface roughness on annual performance of an air-cooled PV module (ID 193)
Riccardo Secchi, Duccio Tempesti, Jacek Smolka

» Energy and exergy analysis of the first hybrid solar-gas power plant in Algeria (ID 176)
Fouad Khaldi

» Energy recovery from MSW treatment by gasification and melting technology (ID 393)
Fabrizio Strobino, Alessandro Pini Prato, Diego Ventura, Marco Damonte

» Ethanol production by enzymatic hydrolysis process from sugarcane biomass - the integration with the conventional process (ID 189)
Reynaldo Palacios-Bereche, Adriano Ensinas, Marcelo Modesto, Silvia Azucena Nebra

» Evaluation of gas in an industrial anaerobic digester by means of biochemical methane potential of organic municipal solid waste components (ID 57)
Isabella Pecorini, Tommaso Olivieri, Donata Bacchi, Alessandro Paradisi, Lidia Lombardi, Andrea Corti, Ennio Carnevale

» Exergy analysis and genetic algorithms for the optimization of flat-plate solar collectors (ID 423)
Soteris A. Kalogirou

» Experimental study of tar and particles content of the produced gas in a double stage downdraft gasifier (ID 487)
Ana Lisbeth Galindo Noguera, Sandra Yamile Giraldo, Rene Lesme-Jaén, Vladimir Melian Cobas, Rubenildo Viera Andrade, Electo Silva Lora

» Feasibility study to realize an anaerobic digester fed with vegetables matrices in central Italy (ID 425)
Umberto Desideri, Francesco Zepparelli, Livia Arcioni, Ornella Calderini, Francesco Panara, Matteo Todini

» Investigations on the use of biogas for small scale decentralized CHP applications with a focus on stability and emissions (ID 140)
Steven MacLean, Eren Tali, Anne Giese, Jörg Leicher

» Kinetic energy recovery system for sailing yachts (ID 427)
Giuseppe Leo Guizzi, Michele Manno

» Mirrors in the sky: status and some supporting materials experiments (ID 184)
Noam Lior

» Numerical parametric study for different cold storage designs and strategies of a solar driven thermoacoustic cooler system (ID 284)
Maxime Perier-Muzet, Pascal Stouffs, Jean-Pierre Bedecarrats, Jean Castaing-Lasvignottes

» Parabolic trough photovoltaic/thermal collectors. Part I: design and simulation model (ID 102)
Francesco Calise, Laura Vanoli

» Parabolic trough photovoltaic/thermal collectors. Part II: dynamic simulation of a solar trigeneration system (ID 488)
Francesco Calise, Laura Vanoli

» Performance analysis of downdraft gasifier - reciprocating engine biomass fired small-scale cogeneration system (ID 368)
Jacek Kalina

» Proposing offshore photovoltaic (PV) technology to the energy mix of the Maltese islands (ID 262)
Kim Trapani, Dean Lee Millar

» Research of integrated biomass gasification system with a piston engine (ID 414)
Janusz Kotowicz, Aleksander Sobolewski, Tomasz Iluk

» Start up of a pre-industrial scale solid state anaerobic digestion cell for the co-treatment of animal and agricultural residues (ID 34)
Francesco Di Maria, Giovanni Gigliotti, Alessio Sordi, Caterina Micale, Luisa Massaccesi

» The role of biomass in the renewable energy system (ID 390)
Ruben Laleman, Ludovico Balduccio, Johan Albrecht

» Vegetable oils of soybean, sunflower and tung as alternative fuels for compression ignition engines (ID 500)
Ricardo Morel Hartmann, Nury Nieto Garzón, Eduardo Morel Hartmann, Amir Antonio Martins Oliveira Jr, Edson Bazzo, Bruno Okuda, Joselia Piluski

» Wind energy conversion performance and atmosphere stability (ID 283)
Francesco Castellani, Emanuele Piccioni, Lorenzo Biondi, Marcello Marconi

V. 2 – FUEL CELLS

» Comparison study on different SOFC hybrid systems with zero-CO2 emission (ID 196)
Liqiang Duan, Kexin Huang, Xiaoyuan Zhang and Yongping Yang

» **Exergy analysis and optimisation of a steam methane pre-reforming system (ID 62)**
George G. Dimopoulos, Iason C. Stefanatos, Nikolaos M.P. Kakalis

» **Modelling of a CHP SOFC power system fed with biogas from anaerobic digestion of municipal wastes integrated with a solar collector and storage units (ID 491)**
Domenico Borello, Sara Evangelisti, Eileen Tortora

VOLUME VII

VII . 1 – BUILDING, URBAN AND COMPLEX ENERGY SYSTEMS

» **A linear programming model for the optimal assessment of sustainable energy action plans (ID 398)**
Gianfranco Rizzo, Giancarlo Savino

» **A natural gas fuelled 10 kW electric power unit based on a Diesel automotive internal combustion engine and suitable for cogeneration (ID 477)**
Pietro Capaldi

» **Adjustment of envelopes characteristics to climatic conditions for saving heating and cooling energy in buildings (ID 430)**
Christos Tzivanidis, Kimon Antonopoulos, Foteini Gioti

» **An exergy based method for the optimal integration of a building and its heating plant. Part 1: comparison of domestic heating systems based on renewable sources (ID 81)**
Marta Cianfrini, Enrico Sciubba, Claudia Toro

» **Analysis of different typologies of natural insulation materials with economic and performances evaluation of the same buildings (ID 28)**
Umberto Desideri, Daniela Leonardi, Livia Arcioni

» **Complex networks approach to the Italian photovoltaic energy distribution system (ID 470)**
Luca Valori, Giovanni Luca Giannuzzi, Tiziano Squartini, Diego Garlaschelli, Riccardo Basosi

» **Design of a multi-purpose building "to zero energy consumption" according to European Directive 2010/31/CE: Architectural and plant solutions (ID 29)**
Umberto Desideri, Livia Arcioni, Daniela Leonardi, Luca Cesaretti ,Perla Perugini, Elena Agabitini, Nicola Evangelisti

» **Effect of initial systems on the renewal planning of energy supply systems for a hospital (ID 107)**
Shu Yoshida, Koichi Ito, Yoshiharu Amano, Shintaro Ishikawa, Takahiro Sushi, Takumi Hashizume

» **Effects of insulation and phase change materials (PCM) combinations on the energy consumption for buildings indoor thermal comfort (ID 387)**
Christos Tzivanidis, Kimon Antonopoulos, Eleutherios Kravvaritis

» **Energetic evaluation of a smart controlled greenhouse for tomato cultivation (ID 150)**
Nickey Van den Bulck, Mathias Coomans, Lieve Wittemans, Kris Goen, Jochen Hanssens, Kathy Steppe, Herman Marien, Johan Desmedt

» **Energy networks in sustainable cities: temperature and energy consumption monitoring in urban area (ID 190)**
Luca Giaccone, Alessandra Guerrisi, Paolo Lazzeroni and Michele Tartaglia

» **Extended exergy analysis of the economy of Nova Scotia, Canada (ID 215)**
David C Bligh, V.Ismet Ugursal

» **Feasibility study and design of a low-energy residential unit in Sagarmatha Park (Nepal) for envirnomental impact reduction of high altitude buildings (ID 223)**
Umberto Desideri, Stefania Proietti, Paolo Sdringola, Elisa Vuillermoz

» **Fire and smoke spread in low-income housing in Mexico (ID 379)**
Raul R. Flores-Rodriguez, Abel Hernandez-Guerrero, Cuauhtemoc Rubio-Arana, Consuelo A. Caldera-Briseño

» Optimal lighting control strategies in supermarkets for energy efficiency applications via digital dimmable technology (ID 136)
Salvador Acha, Nilay Shah, Jon Ashford, David Penfold

» Optimising the arrangement of finance towards large scale refurbishment of housing stock using mathematical programming and optimisationg (ID 127)
Mark Gerard Jennings, Nilay Shah, David Fisk

» Optimization of thermal insulation to save energy in buildings (ID 174)
Milorad Bojić, Marko Miletić, Vesna Marjanović, Danijela Nikolić, Jasmina Skerlić

» Residential solar-based seasonal thermal storage system in cold climate: building envelope and thermal storage (ID 342)
Alexandre Hugo and Radu Zmeureanu

» Simultaneous production of domestic hot water and space cooling with a heat pump in a Swedish Passive House (ID 55)
Johannes Persson, Mats Westermark

» SOFC micro-CHP integration in residential buildings (ID 201)
Umberto Desideri, Giovanni Cinti, Gabriele Discepoli, Elena Sisani, Daniele Penchini

» The effect of shading of building integrated photovoltaics on roof surface temperature and heat transfer in buildings (ID 83)
Eftychios Vardoulakis, Dimitrios Karamanis

» The influence of glazing systems on energy performance and thermal comfort in non-residential buildings (ID 206)
Cinzia Buratti, Elisa Moretti, Elisa Belloni

» Thermal analysis of a greenhouse heated by solar energy and seasonal thermal energy storage in soil (ID 405)
Yong Li, Jin Xu, Ru-Zhu Wang

» Thermodynamic analysis of a combined cooling, heating and power system under part load condition (ID 476)
Qiang Chen, Jianjiao Zheng, Wei Han, Jun Sui, Hong-guang Jin

VII . 2 – COMBUSTION, CHEMICAL REACTORS

» Baffle as a cost-effective design improvement for volatile combustion rate increase in biomass boilers of simple construction (ID 233)
Borivoj Stepanov, Ivan Pešenjanski, Biljana Miljković

» Characterization of CH4-H2-air mixtures in the high-pressure DHARMA reactor (ID 287)
Vincenzo Moccia, Jacopo D'Alessio

» Development of a concept for efficiency improvement and decreased NOx production for natural gas-fired glass melting furnaces by switching to a propane exhaust gas fired process (ID 146)
Jörn Benthin, Anne Giese

» Experimental analysis of inhibition phenomenon management for Solid Anaerobic Digestion Batch process (ID 348)
Francesco Di Maria, Giovanni Gigliotti, Alessio Sordi, Caterina Micale, Claudia Zadra, Luisa Massaccesi

» Experimental investigations of the combustion process of n-butanol/diesel blend in an optical high swirl CI engine (ID 85)
Simona Silvia Merola, G. Valentino, C. Tornatore, L. Marchitto , F. E. Corcione

» Flameless oxidation as a means to reduce NOx emissions in glass melting furnaces (ID 141)
Jörg Leicher, Anne Giese

» Mechanism of damage by high temperature of the tubes, exposed to the atmosphere characteristic of a furnace of pyrolysis of ethane for ethylene production in the petrochemical industry (ID 65)
Jaqueline Saavedra Rueda, Francisco Javier Perez Trujillo, Lourdes Isabel Meriño Stand, Harbey Alexi Escobar, Luis Eduardo Navas, Juan Carlos Amezquita

» Steam reforming of methane over Pt/Rh based wire mesh catalyst in single channel reformer for small scale syngas production (ID 317)
Haftor Orn Sigurdsson, Søren Knudsen Kær

VOLUME VIII

VIII . 1 - ENERGY SYSTEMS : ENVIRONMENTAL AND SUSTAINABILITY ISSUES

» A multi-criteria decision analysis tool to support electricity planning (ID 467)
Fernando Ribeiro, Paula Ferreira, Madalena Araújo

» Comparison of sophisticated life cycle impact assessment methods for assessing environmental impacts in a LCA study of electricity production (ID 259)
Jens Buchgeister

» Defossilisation assessment of biodiesel life cycle production using the ExROI indicator (ID 304)
Emilio Font de Mora, César Torres, Antonio Valero, David Zambrana

» Design strategy of geothermal plants for water dominant medium-low temperature reservoirs based on sustainability issues (ID 99)
Alessandro Franco, Maurizio Vaccaro

» Energetic and environmental benefits from waste management: experimental analysis of the sustainable landfill (ID 33)
Francesco Di Maria, Alessandro Canovai, Federico Valentini, Alessio Sordi, Caterina Micale

» Environmental assessment of energy recovery technologies for the treatment and disposal of municipal solid waste using life cycle assessment (LCA): a case study of Brazil (ID 512)
Marcio Montagnana Vicente Leme, Mateus Henrique Rocha, Electo Eduardo Silva Lora,Osvaldo José Venturini, Bruno Marciano Lopes, Claudio Homero Ferreira

» How will renewable power generation be affected by climate change? – The case of a metropolitan region in Northwest Germany (ID 503)
Jakob Wachsmuth, Andrew Blohm, Stefan Gößling-Reisemann, Tobias Eickemeier, Rebecca Gasper, Matthias Ruth, Sönke Stührmann

» Impact of nuclear power plant on Thailand power development plan (ID 474)
Raksanai Nidhiritdhikrai, Bundhit Eua-arporn

» Improving sustainability of maritime transport through utilization of liquefied natural gas (LNG) for propulsion (ID 496)
Fabio Burel, Rodolfo Taccani, Nicola Zuliani

» Life cycle assessment of thin film non conventional photovoltaics: the case of dye sensitized solar cells (ID 471)
Maria Laura Parisi, Adalgisa Sinicropi, Riccardo Basosi

» Low CO2 emission hybrid solar CC power system (ID 175)
Yuanyuan Li, Na Zhang, Ruixian Cai

» Low exergy solutions as a contribution to climate adapted and resilient power supply (ID 489)
Stefan Goessling-Reisemann, Thomas Bloethe

» On the use of MPT to derive optimal RES electricity generation mixes (ID 459)
Paula Ferreira, Jorge Cunha

» Stability and limit cycles in an exergy-based model of population dynamics (ID 128)
Enrico Sciubba, Federico Zullo

» The influence of primary measures for reducing NOx emissions on energy steam boiler efficiency (ID 125)
Goran Stupar, Dragan Tucaković, Titoslav Živanović, Miloš Banjac, Srđan Belošević,Vladimir Beljanski, Ivan Tomanović, Nenad Crnomarković, Miroslav Sijerčić

» The Lethe city car of the University of Roma 1: final proposed configuration (ID 45)
Roberto Capata, Enrico Sciubba

VIII . 2 - POSTER SESSION

» A variational optimization of a finite-time thermal cycle with a Stefan-Boltzmann heat transfer law (ID 333)
Juan C.Chimal-Eguia, Norma Sanchez-Salas

» Modeling and simulation of a boiler unit for steam power plants (ID 545)
Luca Moliterno, Claudia Toro

» Numerical Modelling of straw combustion in a moving bed combustor (ID 412)
Biljana Miljkoviü, Ivan Pešenjanski, Borivoj Stepanov, Vladimir Milosavljeviü, Vladimir Rajs

» Physicochemical evaluation of the properties of the coke formed at radiation area of light hydrocarbons pyrolysis furnace in petrochemical industry (ID 10)
Jaqueline Saavedra Rueda , Angélica María Carreño Parra, María del Rosario Pérez Trejos, Dionisio Laverde Cataño, Diego Bonilla Duarte, Jorge Leonardo Rodríguez Jiménez, Laura María Díaz Burgos

» Rotor TG cooled (ID 121)
Chiara Durastante, Paolo Petroni, Michela Spagnoli, Vincenzo Rizzica, Jörg Helge Wirfs

» Study of the phase change in binary alloy (ID 534)
Aroussia Jaouahdou, Mohamed J. Safi, Herve Muhr

» Technip initiatives in renewable energies and sustainable technologies (ID 527)
Pierfrancesco Palazzo, Corrado Pigna

ECOS 2012

VOLUME VI

A NOVEL COAL-BASED POLYGENERATION SYSTEM COGENERATING POWER, NATURAL GAS AND LIQUID FUEL WITH CO2 CAPTURE

Sheng Li[a,b], Hongguang Jin[a,*], Lin Gao[a]

[a] Institute of Engineering Thermophysics, Chinese Academy of Sciences, Beijing, China, 100190
[b] Graduate school of Chinese Academy of Sciences, Beijing, China, 100049
**the corresponding author: hgjin@mail.etp.ac.cn*

Abstract:

In this paper, a novel coal-based polygeneration system has been proposed, in which power, natural gas and liquid fuel are cogenerated and 62% of carbon is captured. Through proper adjustment instead of full adjustment of the syngas component, the CO/H_2 of the unreacted gas in methanol synthesis unit can exactly meet the CO/H_2 requirement for SNG synthesis, and thus cogeneration of methanol and SNG can be realized easily. By adopting partial recycle instead of full recycle of the unreacted gas in chemical island, the sharp increase of energy consumption for chemical synthesis can be avoided. On the other hand, part of the unreacted gas from methanol synthesis unit, which is hard to be converted, together with the recovery gas in chemical islands will be sent to combustion for power generation efficiently. At the same time, 62% of the carbon has been captured by low-temperature methanol wash method (LTMW) after concentration. As a result, the thermal efficiency of the novel system is around 54.9%, and the exergy efficiency is about 57.3%, which is much higher than the IGCC system, or single methanol synthesis system. Compared with the conventional single product systems, primary energy saving ratio of this novel polygeneration system can reach as high as 10.8 percent. Based on the graphical exergy analysis, the key processes of the new system are disclosed and the internal phenomena for high performance are revealed. The promising results obtained in this coal-based system may realize both the low-energy-penalty decarburization of coal and high-efficient coal utilization, and will possibly provide a new option to enforce the safety of energy supply for countries with abundant coal resources but lack of natural gas and oils.

Keywords:

Polygeneration system, CO_2 capture, SNG, Liquid fuel.

1. Introduction

Coal plays an important role in the energy supply of the world, especially for countries with abundant coal resources. For example, coal supplies over 70% of energy demand in China currently [1]. In the foreseeable future, coal will still remain the major resource of energy supply for a long time in China [2]. The most challenging environment issue of today is to slow down the accumulation of CO_2 in the atmosphere, which is the prime criminal of the climate change. At present, 22 billion tons of CO_2 per year is emitted as a result of the use of fossil fuel, most of which come from the combustion of coal [3-6]. How to abate CO_2 emission during the coal utilization becomes a huge challenging for coal-rich countries.

Until now, three typical technologic options for CO_2 capture in power plants are developed, which are famous as pre-combustion, post-combustion and oxy-fuel combustion. There are many studies have investigated about these options. For example, the pre-combustion capture option has been studied by Consonni and Chiesa, Lozza and Chiesa [7-9]. Oxy-fuel combustion has been studied by Chiesa and Lozza, Inui et.al, Yang and Lin [10-12]. And post-combustion for CO_2 capture using membranes and amine has been studied by Bounaceur et.al and Romeo et.al [13-14] respectively. Some other options, such as the integration of polygenration systems with CO_2 capture has been studied by Jin et.al [6, 15-16], biomass-based energy system with negative CO_2 emissions has been

studied by Möllersten et.al, Obersteiner et.al [17-19], and chemical-looping combustion systems have been investigated by Jin and Ishida [20].

However, great energy penalty must be paid for CO_2 capture in most of the above systems except for few polygeneration systems or chemical combustion systems et.al, which usually lead to an overall thermal efficiency decrease by nearly 7.0~15.0 percent points. Thus, how to reduce the energy penalty for CO_2 capture in coal-based energy systems is of significant importance.

Meanwhile, for countries with abundant coal but lack of natural gas and oil, energy security is another big issue that needs to be considered. For these counties, production of SNG or alternative liquid fuel from coal may be a more wise strategy instead of increasing import increasingly. For example, in China, with the rapid economic growth, the liquid fuel demand is increasing sharply as a result of the up burst of the number of cars. It is predicted that the demand for liquid fuel will soar to 0.45~0.61 billion tons [21-22] whereas the supply of liquid fuel can only keep at about 0.2 billion per year [22]. Huge gap exists between liquid fuel demand and supply in China.

Aiming at the two big issues including CO_2 abatement and energy security, the purpose of this paper is (1) to integrate a novel coal-based polygeneration system in which power, natural gas and liquid fuel are cogenerated and CO_2 is captured with low energy penalty; (2) to reveal the internal phenomena of key processes in the new system by exergy analysis; (3) and to provide an option for production of SNG and alternative liquid fuel from coal to enforce energy security.

2. PROPOSAL OF THE NEW POLYGENERATION SYSTEM

2.1. Basic concept of system integration

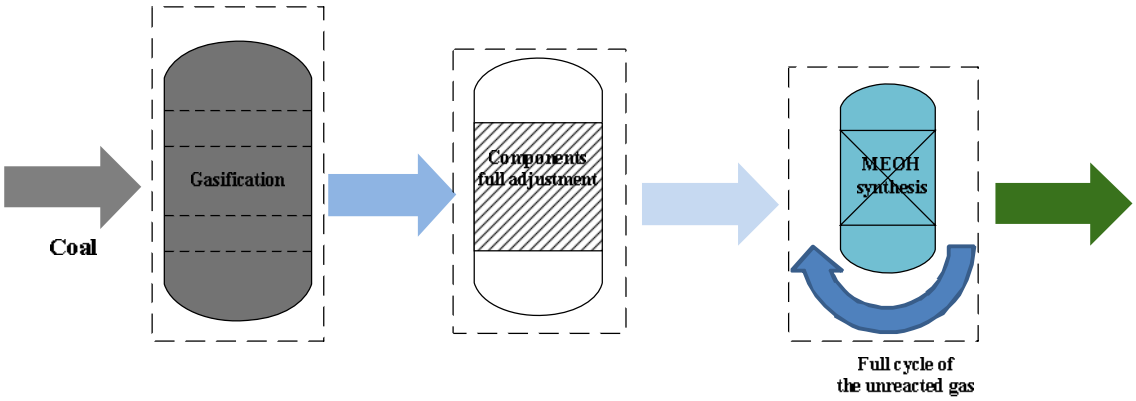

Fig. 1. Single methanol production process

For single methanol production process, it is the main target to convert the raw material into products to the maximum extent. To achieve this target, the H_2/CO in the syngas must be adjusted to be 2:1 and the unreacted gas should be fully recycled. Whereas, the component adjustment of the syngas will lead to great portion of exergy destruction and the full recycle of the unreacted gas will also requires large amount of work. When the conversion ratio exceeds a certain value, the exergy destruction for methanol synthesis will increase sharply if we purely pursue higher conversion of the raw material, as shown in Figure 2. This concept that “exhaustion of the active composition of the material” causes great energy consumption for methanol production in some way, which is about 45GJ/t.

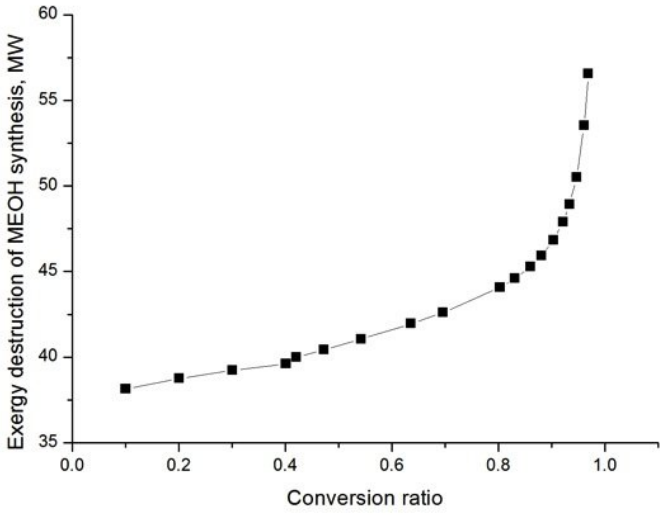

Fig. 2. The exergy destruction of MEOH synthesis with the conversion ratio (circulation ratio)

Aiming at the lacks of the conventional single methanol production process, by proper adjustment instead of full adjustment of the component of the syngas, the CO/H_2 of the unreacted gas in methanol synthesis unit can exactly satisfy the CO/H_2 requirement for SNG synthesis and thus the component adjustment for SNG synthesis can be avoided. On the other hand, part of the unreacted gas, which is hard to be converted, will be sent to combustion for power. This concept of system integration for polygeneration system is part of the principle "Cascade utilization of chemical and thermal energy", which is interrupted in Figure 3.

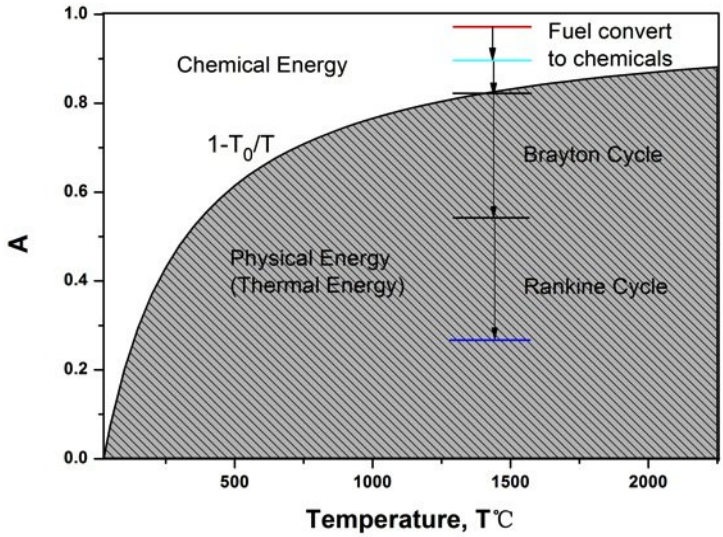

Fig. 3. The principle of system integration for polygeneration systems

In Figure 3, A on the vertical coordinate represents the energy level. The fossil fuel with high energy level is first converted to chemicals according to its component in cascade. And then, the unreacted, which is hard to be converted, is sent to generate high temperature by combustion for high-efficiency combined cycle. By such cascade utilization of fossil fuels, energy systems with high efficiency would be expected.

2.2. System integration and innovation

A conceptual flowsheet of the new polygeneration system is shown in Figure 4. The syngas produced in a Texaco gasifier is sent to a Waste Heat Boiler (WHB) to recover its sensible heat from 1346℃ to 231℃, in which the steam at 120bar will be superheated to 535℃ and then enters the steam turbine. After heat recovery, the syngas together with a 230℃ steam at 30bar enters the shift reactor for component adjustment, in which the mole ratio of H_2/CO is adjusted to 2.65. Then the syngas leaving the shift reactor is cooled down to 40℃ after two heat exchangers, in which steams of 230℃ at 9.8bar and 180℃ at 5bar are generated and will be sent to the sequential clean-up unit. In the clean-up unit, most of the sulfides and CO_2 in the syngas will be removed through the low-temperature methanol wash process. The CO_2 from the clean-up unit is high concentrated (mole fraction is typically over 99%). Then, the purified syngas, in which the mole content of H_2S is lower than 10^{-6}, with CO and H_2 will be sent to the methanol synthesis unit sequentially.

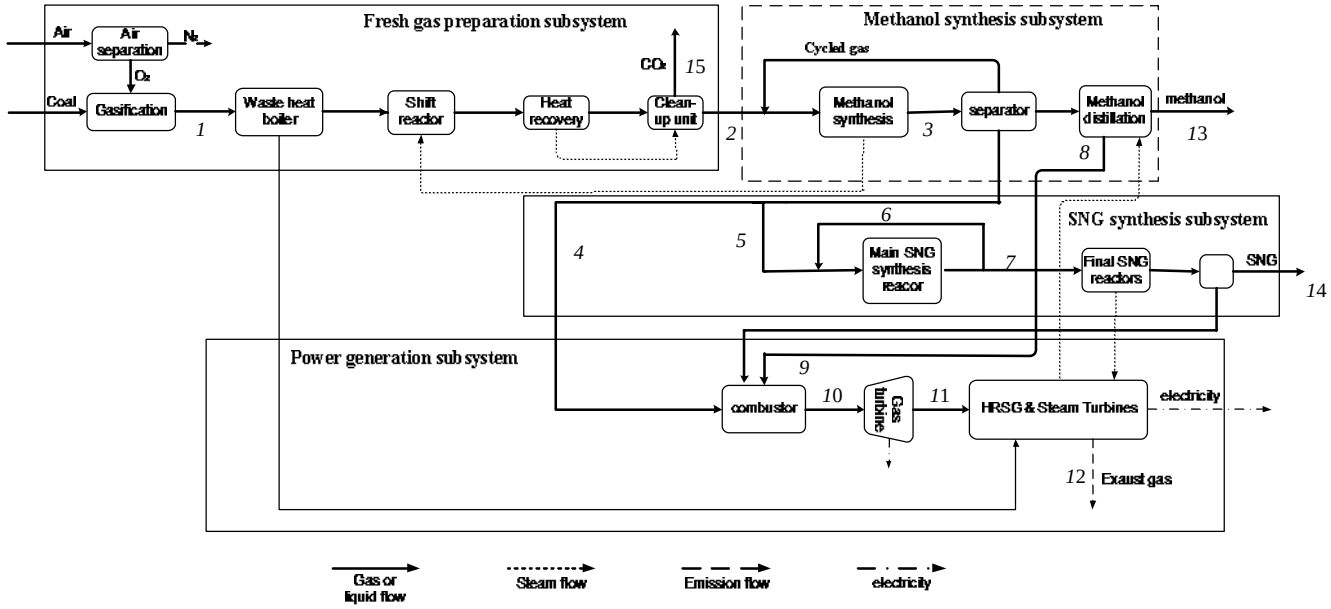

1-raw syngas; 2-fresh gas; 3-crude methanol; 4-unrecycled gas for power; 5-unrecycled gas for SNG synthesis; 6-cycled gas for SNG synthesis; 7-crude SNG; 8-recovered methanol; 9-distillation waste; 10-inlet gas for gas turbine; 11- inlet gas for HRSG; 12- flue; 13-methanol product; 14-SNG product; 15-CO_2 product

Fig. 4. New polygeneration system adopting proper composition adjustment and partial-recycle scheme with CO_2 capture

Liquid Phase Methanol synthesis (LPMEOH) technology is adopted. The reaction occurs at 76bar, and the temperature of the reactor is kept by the evaporation process of cooling water at about 200 ℃. After the reactor, the crude products will be cooled down to 40℃ through two heat exchangers, in which the steam for shift reaction and a steam saturated at 3.75bar are generated. Then, the crude methanol and the unreacted gas will be separated by flash. Crude methanol is sent to a flash drum to remove the dissolved gas, and then fed into a three-stage distillation unit. The unreacted gas will be divided into three streams: the recycled gas, which will be recycled back to the methanol synthesis reactor, the reacting gas for SNG synthesis, and the unrecycled gas, which will be sent to the combined cycle subsystem for power.

High Pressure SNG synthesis technology is adopted in this polygeneration system. The reacting gas for SNG synthesis from the methanol synthesis unit is sent to three sequential adiabatic reactors at about 79bar. Nickel-based catalyst MCR-2X developed by Topsoe company is used for SNG synthesis, which can keep high activity in the range of 300-700℃. Between each reactor, exchangers are placed to recover the high-temperature heat of the products to avoid the

ineffectiveness of the catalyst, in which steam at 535℃ and 120bar is generated and sent to combined cycle subsystem for power. After the three reactors, the products is cooled down to 25℃ to remove water and then sent to a flash drum to separate a spot of methanol which is mixed in the SNG. SNG of over 93% CH_4 (mole basis) is produced and the separated mixed methanol is sent for combustion in the combined cycle subsystem for power.

As shown in Figure 4, the new system applies the serial connection between the chemical production process and power generation system: all of the syngas produced by gasifier enters the chemical production process at first, and after methanol production and SNG production, the unreacted gas is then sent to power generation subsystem.

Compared with the single methanol and SNG synthesis production process, the new system has the following key features: (1) Adopting partial adjustment of composition of the fresh gas instead of full adjustment to satisfy the H_2/CO for both methanol synthesis and SNG synthesis, and thus avoiding greater exergy destruction for individual adjustment of composition of fresh gas in single production systems; (2) Instead of total recycle of the unreacted gas in methanol synthesis unit, partial-recycle scheme is adopted in the polygeneration system, avoiding the sharp increase of energy consumption for methanol synthesis, and at the same time realizing the SNG synthesis with no adjustment of the composition and efficient power generation; (3) recovery of the sensible heat of the syngas and recovery of gases released in chemical synthesis process for power.

2.3. Description of the reference systems

For performance comparison, a system of integrated gasification combined cycle (IGCC) for power generation is selected as a reference for the application of power generation. A coal-based methanol production process which adopts the low-pressure Lurgi methanol synthesis technology is selected as the reference for single methanol production system. And a coal-based SNG synthesis process, in which High Pressure SNG synthesis technology is applied, is selected as the reference system for SNG production.

Figure 5(a) shows the flowsheet of IGCC system, including the air separation unit (ASU), a Texaco slurry-feed and O_2-blown gasification unit, clean up unit adopting Selexol process to remove sulfids, and a combined cycle unit.

Figure 5(b) shows the flow sheet of single methanol product process, which can be identified into fresh gas preparation subsystem and methanol synthesis subsystem. An ASU unit, a Texaco gasifier, and a cleanup unit are included in fresh gas preparation unit. The composition adjustment unit for producing fresh gas with proper CO/H_2, which can meet the synthesis of methanol, is also included in fresh gas preparation subsystem. The methanol synthesis subsystem includes the synthesis unit and distillation unit. In methanol synthesis unit, nearly all of the unreacted gas is sent back to the reactor to pursue highest conversion of materials. In the distillation unit, the crude methanol will be refined as the final product. The steam and work requirements in single methanol product process are supplied by a captive power plant with coal-fired boiler, and by recovering the surplus heat of the chemical reaction.

The single SNG product process is shown in Figure 5(c), which can also be divided into fresh gas preparation subsystem and SNG synthesis subsystem. Different from the single methanol process, in the cleanup unit CO_2 and sulfids will be removed by low-temperature methanol wash method. In SNG synthesis unit, three sequential reactors adopting TREMP process designed by Haldor Topsoe are placed, in which synthesis reaction occurs at about 80bar, above 300℃. Between reactors, steam with high parameters, usually 120bar, 535℃, will be generated to recover heat from the products in case the catalyst was burnt. The superheated steam will supply the work requirement of the single SNG product process, the insufficient of which will be provided by a captive power plant with coal-fired boiler if necessary.

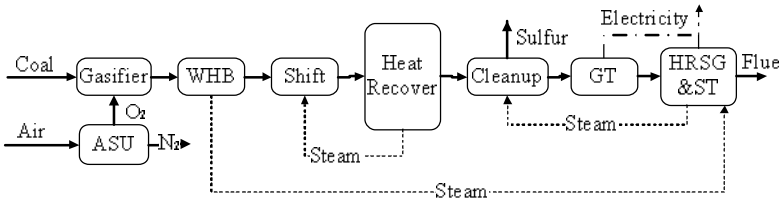

(a)

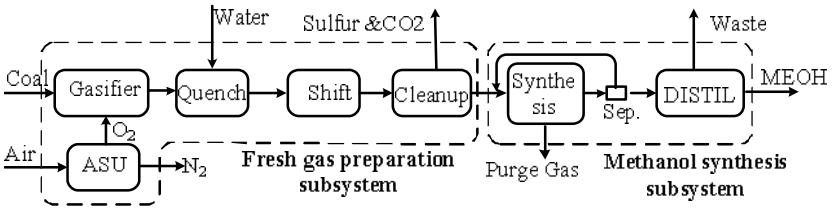

(b)

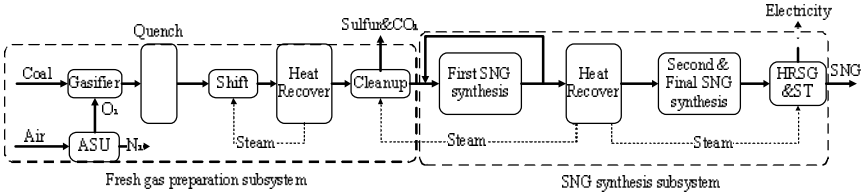

(c)

Fig. 5. Flow diagrams of single product systems: (a) IGCC system (b) single methanol product process (c) single SNG product process

3. PERMORMANCE ANALYSIS OF THE NEW SYSTEM

For evaluating the performance improvement of the polygeneration system, a criterion of Energy Saving Ratio (ESR) is defined as follows:

$$ESR = \frac{[P/\eta_C + G_{mth} \cdot C_{mth} + G_{SNG} \cdot C_{SNG}] - F}{P/\eta_C + G_{mth} \cdot C_{mth} + G_{SNG} \cdot C_{SNG}} \quad (1)$$

where P represents the net power output of the polygeneration system, kW; η_C represents the thermal efficiency of the power reference system (IGCC); G represents the mass flow rate (kg/s); C_{mth} represents the energy consumption for unit methanol production in a single methanol production process, kJ/kg; C_{mth} is the energy consumption for unit SNG production in a single SNG production process, kJ/kg; F represents the lower heating value (LHV) of total fuel input for the polygeneration system, kW. The *ESR* denotes that how much fossil fuel will be saved if the same products are produced in the polygeneration system as that in the reference systems.

The thermal efficiency and exergy efficiency are defined in formula (2) and (3).

$$ESR = \frac{[P + E_{mth} + E_{SNG}]}{F} \quad (2)$$

where E_{mth} and E_{SNG} represents the energy output of methanol and SNG respectively, kW.

$$ESR = \frac{[P + EX_{mth} + EX_{SNG}]}{F} \quad (3)$$

where EX_{mth} and EX_{SNG} represents the exergy output of methanol and SNG respectively, kW.

The performance of the new polygeneration system and the reference systems is simulated by Aspen Plus software. The thermodynamic properties of syngas and chemicals are calculated by the Peng-Robinson and Redlich-Kwong equations respectively. The key parameters in the polygeneration system are selected to agree with the reference systems. For example, the inlet temperature of gas turbine is 1200℃, the pressure ratio is 16.5, and the isentropic efficiency for gas turbine, high-pressure, middle-pressure and low-pressure steam turbines are selected to be 0.9, 0.88, 0.89 and 0.86 respectively. Datong coal was assumed as the basis for this study, whose LHV is 26,710 kJ/kg. The coal analysis data along with some other basic conditions for simulation are listed in table 1.

Table 1. Basic condition for simulation

Coal component analysis (weight %)				
C^f	H^f	O^f	N^f	S^f
68.54	3.97	6.85	0.74	1.08
Ash^f	W^f			
9.98	8.84			
Condition for gas turbine				
parameter				value
Inlet temperature (℃)				1200
Pressure ratio				16.5
Isentropic efficiency				0.9
Condition for steam cycle				
Inlet temperature (℃)				535
Inlet pressure High/Middle/Low (bar)				120/39/3.75
Isentropic efficiency High/Middle/Low pressure				0.88/0.89/0.86
Pinch temperature difference of HRSG (℃)				17

The stream data corresponding to the points indicated in Figure 4 is listed in Table 2. The simulation results of the polygeneration system and its reference systems are summarized in Table 3.

Table 2. Stream data for the flow sheet in Figure 4

	1	**2**	**3**	**4**	**5**	**6**	**7**	**8**	**9**	**10**	**13**	**14**	**15**
Pressure(bar)	68.0	27.4	74.5	74.5	74.5	80.0	77.7	77.7	4.9	16.4	1.1	77.7	30.0
Temperature(℃)	1346	51	40	40	40	423	25	25	92	1200	66	25	40
Flow rate (mol/s)	2763	2088	169	523	1045	5301	279	6	2.8	4967	163	273	957
Mole fraction,%													
CO	44.0	27.0	0.3	24.3	24.3	4.3	0.1		1.5			0.1	
CO_2	11.7	0.9	0.7	1.6	1.6	2.9	5.4	2.2	34.1	3.0		5.5	99.9
H_2	30.5	71.6	0.3	73.4	73.4	14.1	0.2		0.7			0.2	
CH_4						38.7	91.4	4.3				93.2	
COS	0.6												
H_2S	0.3												
H_2O	12.6	0.4	1.7			38.7	0.1	6.0	0.2	8.2	0.1		
N_2	0.3						0.2			74.5		0.2	
O_2										14.3			
CH_4O			97	0.6	0.6	1.1	2.4	87.3	58.7		99.8	0.7	
C_2H_6O			0.1				0.1	0.2	4.7			0.1	
Others													0.1

Table 3. The performance of the polygeneration (PG) system

Items	**PG with CO_2 capture**	**Reference systems**		
		IGCC	**Single methanol process**	**Single SNG process**

Fuel input（kW）	728221	203771	237719	374571
SNG output				
Flow rate（kg/s)	4.9			4.9
LHV（kJ/kg)	42228			42164
SNG output(kW）	206918			206918
Methanol output				
Flow rate（kg/s)	5.2		5.2	
LHV（kJ/kg)	19938		19938	
Methanol output（kW）	103679		103679	
Electricity output(kW）	89456	89456		
Energy consumption for the polygeneration system（kW）				
Air&O_2 compression in ASU	36461			
Air compressor for combustion	58070			
Fresh gas compressor	9395			
Electricity needs for clean-up unit	518			
Coal cracker	3090			
Pumps	915			
The compressor of recycled gas in methanol synthesis unit	67			
The compressor of recycled gas in SNG synthesis unit	592			
Work output in gas turbine	-111652			
Work output in steam turbine	-86912			

Net work output	-89456		
Thermal efficiency	54.9%	43.9%	55.2%
ESR	10.8%		

With 62% of carbon captured in chemical production process, the CO_2 emission rate in the new polygeneration system is 0.278kg/kWh, which is much lower than 0.763kg/kWh in IGCC system. Moreover, compared with the single methanol product process, single SNG product process and IGCC system, the thermal efficiency of this polygeneration system is as high as 54.9% and can save 10.8 percent points of fuel input. This indicates that the new polygeneration system has obvious advantages at CO_2 capture over the single product systems.

What most attractive is that the new polygeneration system with CO_2 capture even performances better than most energy systems without CO_2 capture. For example, the thermal efficiency of IGCC without CO_2 capture is about 43.9%, much lower than 54.9% of the new polygeneration system with 62% of carbon captured.

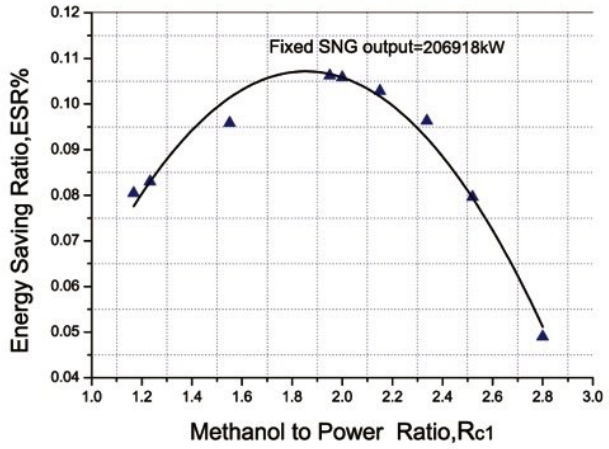

Fig. 6. The thermal performance of the novel system at different Rc1 (methanol to power ratio)

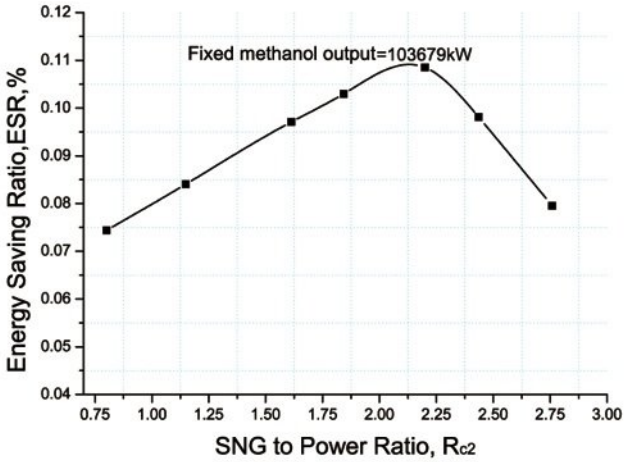

Fig. 7. The thermal performance of the novel system at different Rc2 (SNG to power ratio)

Not only at desined R_c (the ratio of chemical products to power) does the new polygeneration system performance well, but also at other variable R_c. Results show that when R_c varies from 0.5 to 3, this new polygeneration system can always save primary energy compared with single product systems. And an optimal R_c exists to make the thermal performance of the new polygeneration system highest, as shown in Figure 6 and Figure 7. The results illustrated in figures 6 and 7 show that the polygeneration system achieve best performance by adopting partial recycle instead of full recycle of the unreacted gas.

To disclose the key process of energy saving and to reveal the high performance of the polygeneration system, exergy analysis is applied and listed in Table 4 (at designed R_c). Compared with the single product systems, the exergy destruction in the new polygeneration system can decrease by 89.2MW assuming the same product output. In the new polygeneration system, the internal power consumption, for example the work for compressors is supplied by steam turbines and gas turbines instead of the captive power plant of single product systems, and this change can decrease exergy destruction by 38.2MW. This is because coal-based steam system is adopted in captive power plant, and the huge temperature difference between the combustion temperature of coal, as high as 1600℃, and the 600℃ steam leads to large amount of exergy destruction of the captive power plant. Whereas, in this polygeneration system, the difference between the inlet temperature of gas turbine, as high as 1200℃, and the combustion temperature of fuel is much smaller, and thus the exergy destruction is much less. By adopting proper component adjustment instead of full adjustment of syngas and abolishing the component adjustment in SNG process, the shift process can decrease exergy destruction by 3.1MW. Waste heat boiler instead of quench to recover sensible heat of the raw syngas can decrease exergy destruction by 6.0MW. And recovery of the chemical emissions to combustion for power can decrease exergy destruction by 15.6MW. Other processes, like the ASU or gasification process, can also decrease the exergy destruction for the less input of fuel in the new polygeneration system.

Table 4. The exergy analysis for polygeneration system and reference systems

Items	Polygeneration system with CO_2 capture		Single product systems			
			Total of ref	IGCC	MEOH	SNG
	MW	%	**MW**	**MW**	**MW**	**MW**
Fuel exergy	739.1	100	828.3	206.8	241.3	380.2
Exergy output						
SNG	215.9	29.2	215.9			215.9
Methanol	118.4	16.0	118.4		118.4	
Electricity	89.5	12.1	89.5	89.5		
Exergy destruction						
ASU	18.8	2.5	21.0	5.6	5.3	10.1

Gasification	100.6	13.6	113.0	31.4	27.0	54.6
Cooling of syngas	29.3	4.0	35.3	5.0	10.6	19.7
Shift of syngas	16.7	2.3	19.8		7.7	12.1
Cleanup	19.0	2.6	23.3	2.1	10.2	11.0
MEOH synthesis	6.7	0.9	4.1		4.1	
MEOH distillation	4.3	0.6	5.8		5.8	
SNG synthesis	27.8	3.8	20.2			20.2
Captive power plant			38.2		29.4	8.8
Air compression & combustion	42.0	6.2	36.4	36.4		
Gas turbine	4.6	0.6	9.1	9.1		
Steam turbine& pumps	9.4	1.3	15.5	10.5		5.0
HRSG	3.6	0.5	5.4	5.4		
Exergy emission						
Exhaust emission	4.0	0.5	7.0	7.0		
ASU N_2 emission	6.5	0.9	11.3	1.2	1.2	8.9
Emission of cleanup unit	22.0	3.0	23.5	3.6	6.0	13.9
Emission of chemical island			15.6		15.6	
Exergy efficiency %	57.3					

4. DISCUSSION

The graphic exergy analysis (EUD methodology) for the key processes in the polygeneration system is adopted to reveal the internal phenomena of high performance of the key processes. A represents for the energy level, and ΔH represents for the enthalpy change. Figure 8(a) illustrates the Energy Utilization Diagram for combustion of coal in boiler of captive power plant of single product systems. The oxidation of coal (curve A_{ed1}) and the heat recovery in coal economizer (curve A_{ed2}) act as the energy donor. The energy acceptors include preheating of air (curve A_{ea1}), the preheating of fuel (curve A_{ea2}), preheating (from 90℃ to 351.6℃), evaporation, superheating (from 351.6℃ to 540℃) of water in boiler (curve A_{ea3}), and the water preheating in boiler economizer (from 50℃ to 90℃, curve A_{ea4}). The shaded area between energy donor and acceptor represents for the exergy destruction of the process. The area $\Delta\varepsilon_1$ in Figure 8(a) represents the exergy destruction in boiler, and $\Delta\varepsilon_2$ for exergy destruction in coal economizer. The average energy level of coal is about 1.03, but the average energy level of superheating steam is no more than 0.65. This indicates that huge difference exists between the energy level of energy donor and acceptor, which causes large amount of exergy destruction in captive power plant of single product systems.

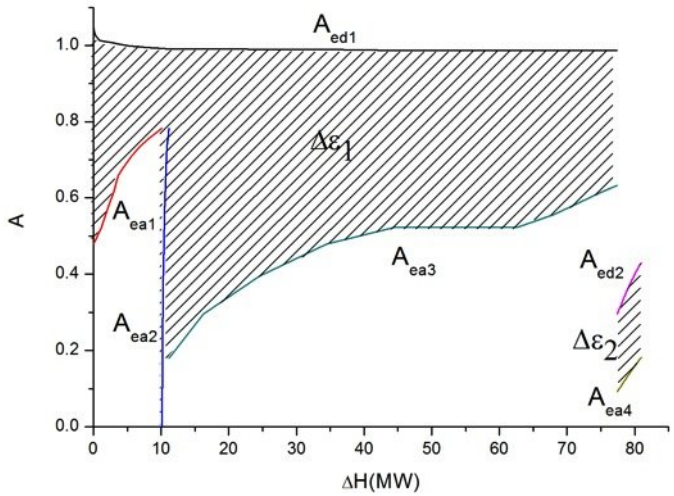

(a)

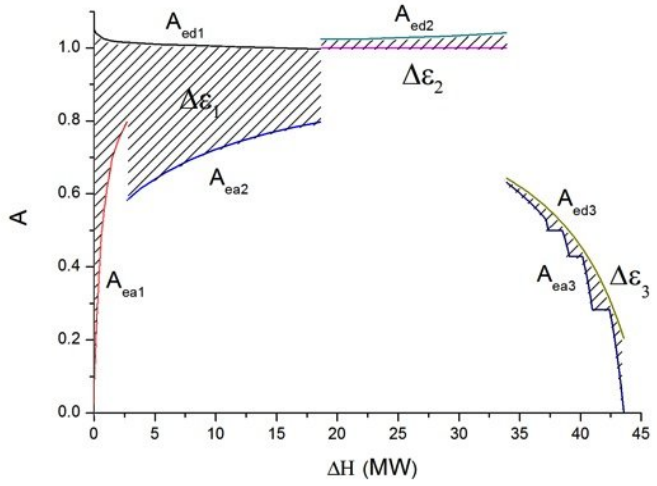

(b)

Fig. 8. (a) EUD for combustion of coal in boiler of captive power plant of single product systems; and (b) EUD for the combined cycle in the new polygeneration system

Figure 8(b) discloses the exergy utilization of combined cycle in the novel polygeneration system. The energy donor includes the oxidation of unreacted gas and recovery gas (curve A_{ed1}), the gas turbine (curve A_{ed2}) and the heat recovery of gas in HRSG (curve A_{ed3}). The energy acceptors are the preheating of fuel gas (curve A_{ea1}), the preheating of air (curve A_{ea2}), and the water heating in HRSG (from 30℃ to 535℃, curve A_{ea3}).

Comparing Figure 8(a) with Figure 8(b), the difference of energy level between energy donor and acceptors in the polygeneration is much smaller for the adoption of gas turbine and HRSG, and that resulted in sharp decrease of exergy destruction in the novel polygeneration system. And this example is exactly coincided with the general principle of system integration "Cascade utilization of chemical and physical energy".

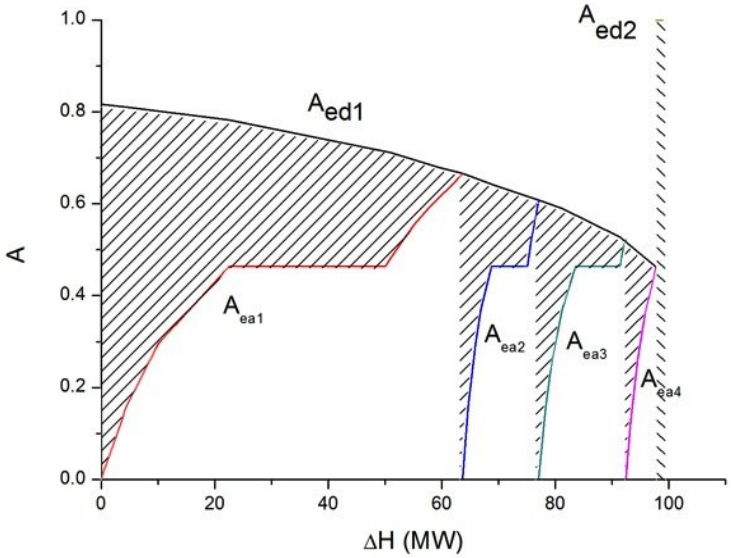

(a)

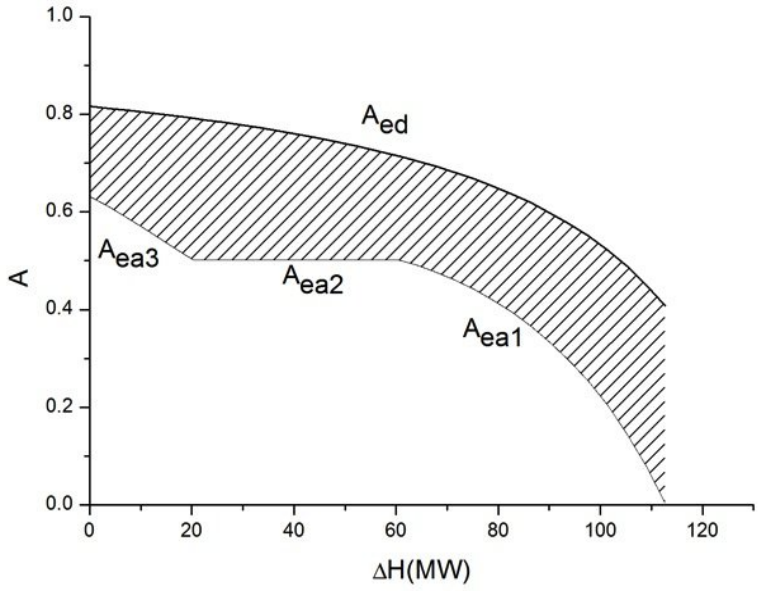

(b)

Fig. 9. (a) EUD for quench process in single product systems; and (b) EUD for heat recovery of sensible heat of syngas

Figure 9(a) illustrates the energy utilization of quench process in single product systems, in which cooling water of about 30℃ will be jet to mix with the hot syngas continuously to lower the temperature of the syngas very quickly. Figure 9(b) illustrates the energy utilization of recovery of sensible heat of syngas in the novel polygeneration system. In both Figure 9(a) and 9(b), the cooling down of syngas (curve A_{ed1}) acts as the energy donor and the heat absorption of water acts as the acceptor (curve A_{eas}). It can be found that the average energy level of the acceptor in the novel polygeneration system has been increased for just one jet of water in WHB is adopted, whereas the average energy level of the acceptor in single product systems has been decreased for the adding of the cold water continuously, and thus the exergy destruction in the novel system has been decreased by 6.0MW for such process.

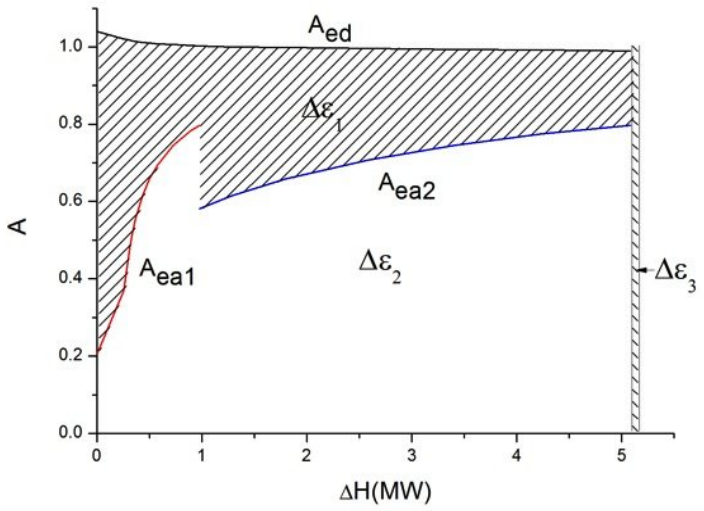

Fig. 10. EUD for recovery of chemical emissions

Figure 10 discloses exergy utilization in the process of recovery of chemical emissions. Curve A_{ed} represents for the oxidation of the recovery chemical emissions. Curve A_{ea1} represents for the fuel heating process, and cure A_{ea2} represents for the air heating process. In single product systems, the chemical emissions will be emitted to atmosphere directly after combustion, whose exergy destruction is represented by the area between curve A_{ed} and the horizontal ordinate. Whereas, in the novel polygeneration system, the chemical emissions will be recovered for power, and the shaded area $\Delta\varepsilon_1$ represents for the exergy destruction of this process, which is much smaller than that in single product systems.

5. CONCLUSIONS

In this paper, a novel coal-based polygeneration system with CO_2 capture, which cogenerates power, natural gas and liquid fuel, has been proposed. With 54.9% of thermal efficiency and 62% of carbon captured, the primary energy saving ratio of this novel polygeneration system can reach as high as 10.8 percent compared with the single product systems. Based on the graphical exergy analysis, it is disclosed that abolishing captive power plant, converting the unreacted gas from methanol synthesis unit into SNG without composition adjustment, and recovering chemical emissions for power play an important role in decreasing exergy destruction in the novel system.

This novel system has realized “the cascade utilization of chemical and thermal energy of the coal” and realized the CO_2 separation with low energy penalty. The promissing results obtained in this coal-based polygeneration system can realize both the coal decarbonization with low energy penalty

and the clean utilization of coal, and will possibly provide a new path to enforce the safety of energy supply.

ACKNOWLEDGEMENTS

This work has been supported by Supported by the major international cooperation projects of the National Natural Science Foundation of China (Grant No. 50520140517) and supported by NFSC Projects (No. 50706052).

REFERENCES

[1] BP (British Petroleum), 2009. BP statistical review of world energy 2009. Available from: <http://bp.com/statisticalreview>.

[2] X.M. Ou, X.Y. Yan, X. L. Zhang, 2010. Using coal for transportation in China: Life cycle GHG of coal-based fuel and electric vehicle and policy implications, International Journal of Greenhouse Gas Control, 4(2010), pp. 878-887.

[3] IEA (International Energy Agency), 2003. CO_2 emissions from fuel combustion 1997-2001, IEA/OECD, Paris, France, 2003.

[4] IPCC (Intergovernmental Panel on Climate Change), 2001. Climate Change 2001, 3rd assessment report of the Intergovernmental Panel on Climate Change, Cambridge University Press, Cambridge, UK, 2001.

[5] IPCC (Intergovernmental Panel on Climate Change), 2005. Special Report on Carbon dioxide Capture and Storage, Eighth Session of IPCC Working Group III, Montreal, Canada, 2005.

[6] H. G. Jin, L. Gao, W. Han, 2007. A NOVEL COAL-BASED POLYGENERATION SYSTEM OF POWER AND LIQUID FUEL WITH CO_2 CAPTURE, Proceedings of GT2007 ASME TURBO EXPO 2007: Power for Land, Sea and Air May 14-17, 2007, Montreal, Canada.

[7] Chiesa, P. and Consonni, S., 1999. Shift reactors and physical absorption for low-CO_2 emission IGCCs, ASME Trans., Journal of Engineering for gas turbines and power, 121, pp. 295-305.

[8] Lozza, G. and Chiesa, P., 2002. Natural gas decarbonization to reduce CO_2 emission from combined cycles-part I: partial oxidation, ASME Trans., Journal of Engineering for gas turbines and power, 124, pp. 82-88.

[9] Lozza, G. and Chiesa, P., 2002. Natural gas decarbonization to reduce CO_2 emission from combined cycles-part II: steam-methane reforming, ASME Trans., Journal of Engineering for gas turbines and power, 124, pp. 89-95.

[10] Chiesa, P. and Lozza, G., 1998. CO_2 Emission Abatement in IGCC Power Plants by Semi-closed Cycles, Part A: With Oxygen-blown Combustion. ASME, 98-GT-384.

[11] Y. Inui, T. Matsumae, H. Koga, K. Nishiura, 2005. High performance SOFC/GT combined power generation system with CO_2 recovery by oxygen combustion method. Energy Conversion and Management 46 (2005), pp. 1837-1847.

[12] Q. Yang, Jerry Y.S. Lin, 2006. Fixed-bed performance for production of oxygen-enriched carbon dioxide stream by perovskite-type ceramic sorbent., Separation and Purification Technology 49 (2006), pp.27–35.

[13] Roda Bounaceur, Nancy Lape, Denis Roizard, Ce′ cile Vallieres, Eric Favre, 2006. Membrane processes for post-combustion carbon dioxide capture: A parametric study, Energy 31 (2006), pp. 2556–2570.

[14] Luis M. Romeo, Irene Bolea, Jesu′ s M. Escosa, 2008. Integration of power plant and amine scrubbing to reduce CO_2 capture costs, Applied Thermal Engineering 28 (2008), pp. 1039–1046.

[15] H.G. Jin, S.E. Sun, W. Han, L. Gao, 2007. A Novel Multi-functional Energy System for Co-producing Coke, Hydrogen and Power, Proceedings of the ASME 2007 International Design

Engineering Technical Conferences & Computers and Information in Engineering Conference IDETC/CIE 2007 September 4-7, 2007, Las Vegas, Nevada, USA.

[16] H.G Jin, W. Han, L. Gao, 2007. A NOVEL MULTI-FUNCTIONAL ENERGY SYSTEM (MES) FOR CO_2 REMOVAL WITH ZERO ENERGY PENALTY, Proceedings of GT2007 ASME Turbo Expo 2007: Power for Land, Sea, and Air May 14-17, 2007, Montreal, Canada GT-2007-27680.

[17] Möllersten K., Yan J., 2001. Economic evaluation of biomass-based energy systems with CO_2 capture and sequestration—The influence of the price of CO_2 emission quota, World Resour Rev, 13(4), pp. 509-525.

[18] Möllersten K., Yan J., Moreira JR., 2003. Potential market niches for biomass energy with CO_2 capture and storage—opportunities for energy supply with negative CO_2 emissions. Biomass and Bioenergy, 25(3), pp. 273-285.

[19] Obersteiner M., Azar Ch., Kauppi P., Möllersten K., Moreira J., Nilsson S., Read P., Riahi K., Schlamadinger B., Yamagata Y., Yan J., Van Ypersele J.-P., 2001. Managing Climate Risk, Science, 294(2001), pp. 786-787.

[20] IEA (International Energy Agency), 2001. Key World Energy Statistics from the IEA, 2001 Edition.

[21] H.G. Jin., Ishida M., 1997. A New Advanced IGCC Power Plant with Chemical-Looping Combustion, Proc. of TAIES'97, pp. 548-553, Beijing, 1997.

[22] W. D. Ni, H.S. Zhen, Z. Li, N. Jiang, 2003. Polygeneration : A Very Important Way to Overcome Five Challenges in Energy Field of China, POW ER ENGINEERING, (3)2003, pp. 2245-2251.

Analysis and Optimization of CO_2 Capture in a China's Existing Coal-fired Power Plant

Gang Xu[a], Yongping Yang[b], Shoucheng Li[c], Wenyi Liu[d] and Ying Wu[e]

a North China Electric Power University, Beijing, China, xg2008@ncepu.edu.cn
b North China Electric Power University, Beijing, China, yyp@ncepu.edu.cn
c North China Electric Power University, Beijing, China, lishoucheng6363@126.com
d North China Electric Power University, Beijing, China, lwy@ncepu.edu.cn
e North China Electric Power University, Beijing, China, 837469236@qq.com

Abstract:

In China, pulverized coal-fired power plants provide over 70% of the total electricity, on the other side, make up nearly half of the total CO2 emission volume of the whole country. Thus, CO2 capture in these coal fired power plants will be extremely important to the effort of CO2 reduction made worldwide. However, to retrofit existing power plant for CO2 capture may encounter many constrains from the layout of original process and the structure of existing equipments, causing a lot of special problems in process design and bringing deep influence on system performance, which in turn requiring special considerations in system integration. In view of these factors, this paper carried out the process simulation, characteristics analysis and system integration of CO2 capture based on a typical China's existing coal-fired power plant with supercritical parameters. The paper analyzes main constrains encountered in retrofitting existing power plant with CO2 capture using monoethanolamine (MEA) solution and puts forward several special system integration schemes for CO2 capture in an existing 600MW unit of China. The results revealed that, due to the constrains of the layout of original process and the structure of existing equipments, efficiency penalty of CO2 capture in a existing power plant will be even higher than a re-design new power plant by 3-5%-points. However, through the special system integrations, the efficiency of such retrofitting existing power plant can increase by 2-4%-points. The research of this paper may provide a feasible technology solution for decarburization retrofits of existing power plants, and promote CCS technologies into application.

Keywords:

CO_2 Capture, Existing Coal-fired Power Plant, Retrofit, Thermal Energy Integration.

1. Introduction

Increasing concentration of CO_2 and other greenhouse gases (GHG) is the main reason behind alarming environmental phenomena, such as global warming and sea level rising [1-2]. China, one of the world's largest producers of CO_2 emissions, is responsible for approximately one fifth of global CO_2 emissions [3].

Different from many industrialized countries, China's main primary energy is coal, which is a kind of cheap but carbon-intensive energy resources. And in China, pulverized coal fired power plants, whose total installed capacity is over 700GW, provide nearly 80% of the total electricity, however, make up almost half of the total CO_2 emission volume of the whole country [4]. Thus, the reduction of CO_2 emissions in the electricity supply sector of China, especially in these pulverized coal fired power plants, will make a significant contribution to the country and even to the whole world.

Though suffering of high energy and cost penalty, CO_2 capture and storage (CCS) is commonly considered as a technically feasible method of making deep reductions in carbon dioxide emissions from sources such as energy utilization systems, and attracted great attentions worldwide [5-11]. At present, there are three basic technologies for capturing CO_2 from energy systems: post-combustion capture, oxy-fuel combustion capture, and pre-combustion capture. As for CO_2 separation process,

generally there are four kinds of methods, that is, absorption (including chemical and physical absorption), adsorption, membrane and cryogenic separation [1,12]. For pulverized coal fired power plant, post-combustion capture with chemical absorption using an aqueous solution, such as monoethanolamine (MEA), is recognized as one of the most feasible technologies for the sake that it is suitable for removing CO_2 at low concentration, quite mature in technology, and easy to make great improvements. [7-8,12-15].

During the past few decades, recovering CO_2 by chemical absorption has been investigated by many researchers [8-9, 16-26]. For example, Alie et al. presented a detailed simulation method for a typical CO_2 capture process using MEA solvent, and carried out the optimization of key process operating variables [8]. Jean-Marc and Pellegrini respectively analyzed the influence of different absorbents (MDEA-TETA and ammonia) for regeneration energy [9,16]. Mohammad et al. investigated the technical and economic performance of CO_2 capture from power plants in detail [17,18]. Hetland et al. integrated a full carbon capture scheme onto a 450MW nature gas combined cycle power station [19]. Huang et al. conducted the industrial test and techno-economic analysis of CO_2 capture in Huaneng Beijing coal-fired power station. These researches disclosed the basic characteristics of the coal-fired power plants with chemical CO_2 absorption process and revealed that post-combustion is a good option for the capture of CO_2 produced by commercial coal-fired power plants [20].

Besides, a few researchers are also paying attention to the system integration of CO_2 capture process with power generation system [21-26]. For example, Sanpasertparnich et al. integrated post-combustion capture and storage into a pulverized coal-fired power plant [23]. Gibbins et al. put forward the CO_2 capture ready(CCR) plant, They focus on newly-built plant and propose three different turbine options for CCR plant [25]. However, most of such integration researches neglect the restrictions of the existing power generation assembly and make great modification in the steam system of plant, which may be possible in a newly-built plant with thoroughly redesign but not suitable for the existing power plant. In fact, to retrofit existing power plant for CO_2 capture may encounter many constrains from the layout of original process and the structure of existing equipments, causing a lot of special problems in process design and bringing deep influence on system performance, which in turn requiring special considerations in system integration. However, few studies pay much attention to these special phenomena in the research of large scale CO_2 capture in existing power plants

In view of the importance of the CO_2 reduction of China's enormous existing power plants, this paper carries out the process simulation, characteristics analysis and system integration of CO_2 capture based on an existing supercritical power plant in China. Through this study, the paper achieves the following targets: (1) to reveal main constrains encountered in retrofitting existing power plant with CO_2 capture. (2) to put forward several special system integration schemes for CO_2 capture in the typical existing power generation unit of China. (3) to provide feasible technology solutions for decarburization retrofits of existing power plants, and promote CCS technologies into application.

2. Particularity of CO_2 capture in existing power plant

For the coal-fired power plant which uses chemical absorption method to reduce CO_2 emissions, its thermal efficiency will decrease by 10-15%-points [23-24,27], to achieve a 90% CO_2 recovery ratio. Most of such efficiency penalty comes from the energy consumption of CO_2 capture process, particularly the heat requirement of solvent regeneration. For example, in the amine scrubbing process, an energy demand between 3.5 and 4.2 $MJ/kgCO_2$ has been reported for solvent regeneration [17,23-24]. For CO_2 capture in power plant, such huge amount of heat provided for

solvent regeneration mainly comes from the condensation of the steam extracted from steam turbine.

However, retrofitting of the existing power plant for CO_2 capture would encounter many constrains and be more complex. Compared with the virtual plant or redesigned newly-built plant, the steam/water cycle of an existing power plant can not be made great changes due to the restriction of process and devices.

2.1. Restrictions of steam extraction parameters

In a chemical absorption process for CO_2 capture, the solvent desorption temperature would vary with different absorbents. However, most chemical absorption methods need to provide thermal energy with temperature in the range of 100°C and 150°C for stripping process. Take MEA for example, the CO_2-rich amine stream, leaving from the absorber bottom, is regenerated by thermal treatment at 100°C up to 140°C in the stripper, releasing CO_2 [17,24-25,28]. The stripper makes use of steam extracted from the steam/water cycle of the power plant. As economic consideration, the extracted steam at 2.1-3.4bar is suitable to provide the solvent regeneration heat.

Besides, the amount of extraction steam is enormous, which can be half of the total steam flow of LP turbine cylinders[24-25], due to the extensive heat demand of solvent desorption. However, in the existing power plant, it is impossible to extract too much steam within low-pressure turbines (LPT) due to the constraint of the structure of turbines. The only feasible steam extraction point for an existing power plant may be located at the crossover pipe between the intermediate pressure (IP) and low pressure (LP) cylinders of the steam turbine, [23,25]. And the crossover pipe is also the quite place to extract a large amount of steam for heat supply in many combined heat-and-power units[29-32].

In most supercritical or ultra supercritical units, the pressure of steam extracted from the IP/LP steam turbine can be as high as 9-12 bar [23,33-34], this is far higher than the required parameters of stripper for absorbent regeneration, which will bring extra power loss due to steam extraction. Figure1 shows the relationship of power loss per kg extracted steam with its pressure. As is shown in Fig. 1, the higher the extracted pressure, the higher the specific power loss. When the pressure of extracted steam reaches 9-12 bar, its power loss will be almost twice as much as that of the steam extracted at 2.1bar.

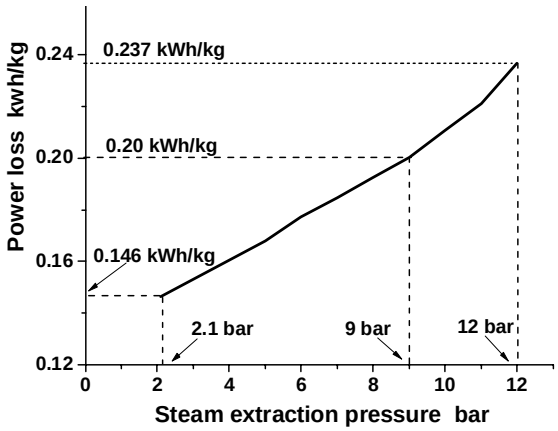

Fig. 1. Relationship between power loss and steam extraction pressure

2.2. Off-design conditions of LP turbine due to huge extraction steam

As is mentioned above, a large amount of heating steam will be extracted from the crossover pipe between IP and LP turbines in CO_2 capture retrofitting of existing power plants, which leads to LP cylinders operating under off-design conditions. In this situation, the steam mass flow rate of LP cylinders will drop deeply, which leads to the substantial deviation of steam parameters from the rated values.

However, even under the off-design conditions, the performance characteristics of steam parameters within turbine will still comply with certain rules. If the steam velocity in a stage of a given stage group becomes equal to or greater than the critical velocity, the pressure behind that stage will influence the steam parameters in the preceding stages and, with the same clear cross-sectional area, the flow rate will depend, only on the steam parameters before the blade cascades of the preceding stages and will be determined by the equation $G = A\sqrt{p/\nu}$. The ratio of an arbitrary steam flow rate through a group of stages to the rated flow rate can be represented in the form:

$$\frac{G}{G_0} \cong \frac{p_{01}}{p_{00}}\sqrt{\frac{T_{00}}{T_{01}}}\sqrt{\frac{x_{00}}{x_{01}}} = \varepsilon_1\sqrt{\frac{T_{00}}{T_{01}}}\sqrt{\frac{x_{00}}{x_{01}}} \qquad (1)$$

Where p_{00}, T_{00} and x_{00} are the pressure, temperature and dryness fraction of steam at the rated flow rate G_0, and p_{01}, T_{01} and x_{01} are those under the changed conditions with a new flow rate G. For superheated steam, the equation (1) with $x_{01} = x_{00} = 1$ can be simplified:

$$\frac{G}{G_0} \cong \frac{p_{01}}{p_{00}}\sqrt{\frac{T_{00}}{T_{01}}} = \varepsilon_1\sqrt{\frac{T_{00}}{T_{01}}} \qquad (2)$$

In many cases, it can be taken approximately that the steam temperature in intermediate turbine stages remains constant on a change of flow rate. Thus until the steam velocity in a stage remains critical, the steam pressure in all preceding stages varies in direct proportion to steam flow rate.

For cases when none of the stages of a group reach the critical velocity, the relationship between pressures and flow rate for an i-th stage under the assumption that $T_{01} = T_{00}$=constant can be given the following form:

$$\left(\frac{G}{G_0}\right)^2 [(p_{00})_i^2 - (p_{20})_i^2] = (p_{01})_i^2 - (p_{21})_i^2 \qquad (3)$$

Writing similar equations for all stages of the group considered and noting that the relative change of steam mass flow rate G/G_0 is the same in all stages, we can sum the left-and right-hand parts of these equations:

$$\left(\frac{G}{G_0}\right)^2 \sum_1^z [(p_{00})_i^2 - (p_{20})_i^2] = \sum_1^z [(p_{01})_i^2 - (p_{21})_i^2] \quad (4)$$

Since the final pressure of the i-th stage is equal to the initial pressure of the (i+1)-th stage, all intermediate values of pressure are cancelled and we have for a group of stages:

$$\frac{G}{G_0} = \sqrt{\frac{p_{01}^2 - p_{z1}^2}{p_{00}^2 - p_{z0}^2}} = \sqrt{\frac{\varepsilon_{01}^2 - \varepsilon_{z1}^2}{1 - \varepsilon_{z0}^2}} \qquad (5)$$

Where $\varepsilon_{01} = p_{01}/p_{00}$ are the relative pressure before the group of stages, and $\varepsilon_z = p_z/p_{00}$ is the relative pressure behind it.

Let us introduce a correction factor equal to $\sqrt{T_{00}/T_{01}}$ in order to account for a probable temperature change before the group of stages. Then, the following formula is obtained for a group of stages operating with sub-critical velocities of superheated steam:

$$\frac{G}{G_0} = \sqrt{\frac{\varepsilon_{01}^2 - \varepsilon_{z1}^2}{1 - \varepsilon_{z0}^2}}\sqrt{\frac{T_{00}}{T_{01}}} \qquad (6)$$

In conclusion, if a group of turbine stages operates with steam velocities above the critical value, the steam flow rate on a change of steam state or one of the steam parameters on a change of flow rate can be found by formula (2); if steam velocities of all stages are subsonic, formula (6) is applicable.

Fig. 2 shows the performance curves under different steam extraction proportion. Dotted line represents the conditions without consideration of pressure loss, which means that the inlet pressure of LP turbine will keep constant with part of steam extracted (see dotted line in Fig. 2a)), and the power loss of LP turbine is only caused by the fact that extraction steam doesn't do any work. (see dotted line in Fig. 2b)). Obviously, it is a kind of assumptive operation status and impossible in a existing power plant.

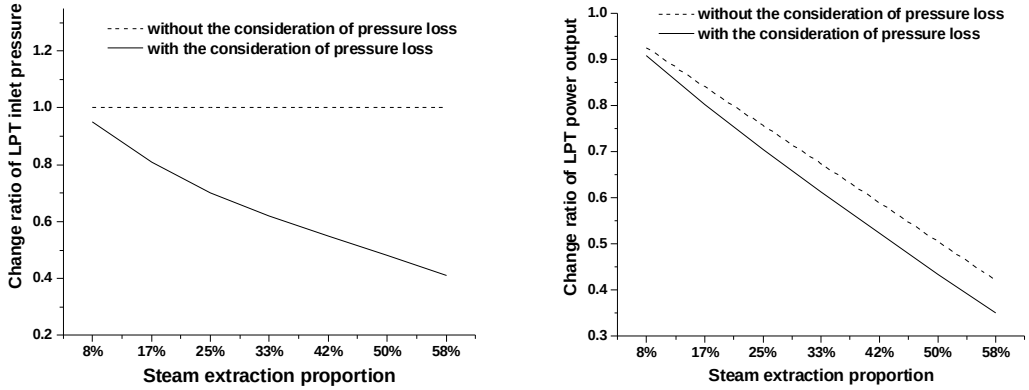

(a) *(b)*

Fig. 2. Variation trends of LPT performances with different steam extraction proportion: a) LPT inlet steam pressure, b) LPT power output.

On the contrary, the solid line stands for practical operation conditions, that is, the steam turbines operate under the off-design condition when part of steam is extracted from the system, complying with formula (6). Here, the inlet pressure of LP turbine will decrease with the increase of steam extraction proportion (see the solid line in Fig. 2a)), which leads to more power loss of LP turbine(see the solid line in Fig. 2b)). This means that the pressure loss of extraction steam will bring an additional power loss. (see space between the solid and dotted line in Fig. 2b)). For example, when the steam extraction proportion is 50% of total steam flow LP cylinder, its pressure loss is approximately 50%(Fig. 2a)), and the power output of LP turbine is only 42%(Fig. 2a)). The power loss caused by the fact that the extracted steam doesn't do work, accounts for nearly 50%. Meanwhile, additional power loss caused by pressure loss of extraction steam covers about 8%. In a word, large amount of steam extraction not only brings significant reduction of steam flow in LP cylinder, but also cause LP cylinder operation to deviate from design condition greatly, leading to additional power loss and further decrease of power plant efficiency.

3. Case study based on existing 600MW Supercritical Unit

3.1. Base Case: a typical 600MW Supercritical Unit in China

A typical 600MW coal-fired power generation unit without CO_2 capture in China is selected as base case. It is a pulverized coal fired power generating unit with a 600MW output adopting a supercritical pressure steam/water cycle, and the bituminous coal is selected as fuel. A Schematic diagram of the supercritical coal-fired power plant without CO_2 capture is shown in Fig. 3.

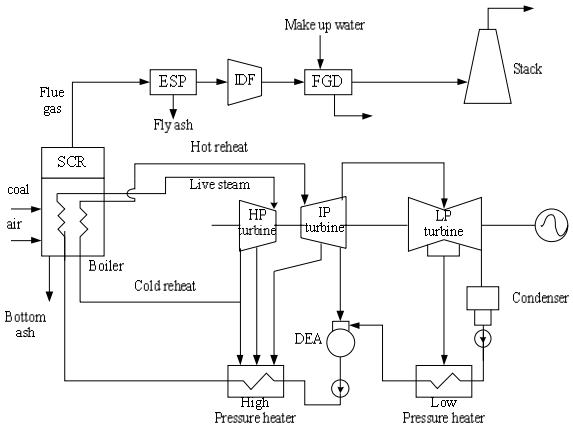

Fig. 3. 600MW supercritical coal-fired power plant without CO_2 capture process

The selected steam turbine process flow diagram is shown in Fig. 4. The turbine consists of a HP, IP and LP sections all connected to the generator with a common shaft. Steam from the exhaust of the HP turbine is returned to the boiler for reheating and then sent to the double flow IP turbine. Exhaust steam form the IP turbines then flows into the double cylinders/four flows LP turbine system.

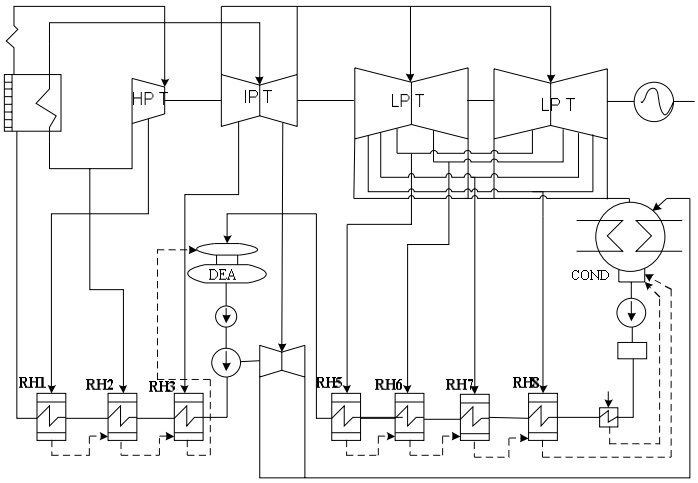

Fig. 4. Steam/water cycle of the 600MW supercritical power unit

And the overall performances of the unit is summarized in Table 1. Besides, the unit is designed to generate about 1677.5t/h of steam at nominal conditions of 24.2MPa and 566^{o}C with reheat steam heated to 566^{o}C, and the exhaust steam pressure of the steam turbine is 5.88kPa. These represent the typical parameters of China's existing power generation unit.

Table 1. Overall performance of Base Case

Fuel Parameters		
Coal Heat Input (HHV)	MJ/kg, $_{ar}$	23.92
Coal Heat Input (LHV)	MJ/kg, $_{ar}$	22.76
Steam/Water Cycle Parameters		
Existing Steam Turbine Generator Output	MW	604.3
Total Auxiliary Power	MW	30.22
Net Output	MW	573.8
Overall Plant Performance Parameters		
Net Efficiency	%	40.28

Net Coal Consumption Rate	g/kWh	305
Net Heat Rate	kJ/kWh	8937.1
Overall Plant CO_2 Emissions		
Carbon Dioxide Emissions	g/kWh	867.8

3.2. Amine scrubbing process for post-combustion CO_2 capture

In this study, the process design of CO2 capture was based on a standard monoethanolamine (MEA) absorption-desorption method. Fig. 5 shows the process of the CO2 separation unit. As is shown in Fig. 5, flue gas from the power plant is first cooled (down to a temperature of 40-50oC)and desulphurized in a flue gas desulfurization unit (FGD). Then, after passing through a booster fan, flue gas is absorbed by MEA in an absorber. The treated flue gas, from which most of the CO2 gas has been separated, is vented to the atmosphere. Rich solvent from the bottom of CO2 absorber is delivered to a cross heat exchanger by a pump (P1). Having been heated in the heat exchanger, it is delivered to a stripper to desorb CO2 by thermal treatment at 100oC up to 140oC. The CO2-H2O stream desorbed from the stripper is condensed and the moisture is removed to get more pure CO2 in a condenser and a separator (Sp). The lean solvent is delivered to the cross heat exchanger by a pump (P2), and then to the absorber after cooling the stream to the designed temperature by a cooler (C1). Considering the degradation and volatilization of MEA, makeup of MEA solvent is also added to the absorber. Usually the CO2 separated from the stripper is compressed to the required pressure and temperature by the multistage compressor (CP) for CO2 transportation.

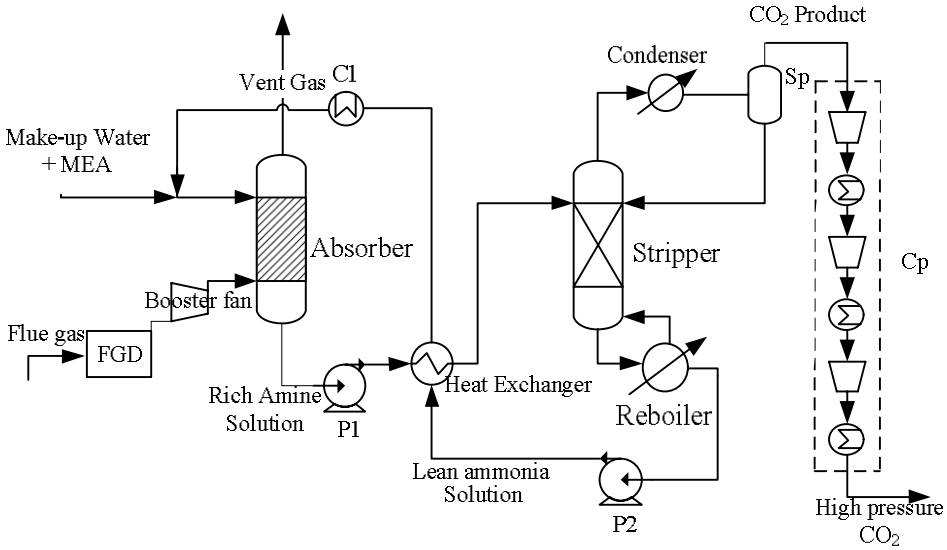

Fig. 5. The typical CO_2 capture process based on MEA

The main parameters of the absorption process based on MEA are listed in Table 2. The pressure of the stripper is set as 2.1bar, and the stripper temperature is 115oC. The entire flue gas stream enters the absorber tower and the CO2 recovery ratio can reach over 90%. And the mass purity of CO2 can reach 99.8%, which is high enough for CO2 storage or many industrial applications.

Table 2. Main performance parameters with MEA-based CO_2 capture process

Title	Number
Desorber Pressure (bar)	2.1
Temperature of reboiler (°C)	115
CO_2 recovery ratio (%)	90
CO_2 lean loading(molCO_2/molMEA)	0.3

CO_2 rich loading(molCO_2/molMEA)	0.45
Energy consumption of reboiler (MJ/t CO_2)	3404
Energy consumption of condenser (MJ/t CO_2)	-684
Mass purity of CO_2 (%)	99.8
Mole purity of CO_2 (%)	99.6

3.3. Capture Case 1: CO_2 capture case without considering the constraint of existing power plant

Case 1 is a typical 600MW coal-fired power generation unit combined with CO2 capture system. A simplified process flow diagram of Case1 is shown in Fig. 6. As it can be seen from this figure, flue gas of the generation unit directly enters the absorber of the capture process, and the thermal energy consumed by stripper reboiler is supplied by the steam extracted from the steam turbine subsystem. Fig. 6 illustrates the extraction scheme of the water/steam system. Thus, steam with pressure of 2.1 bar is directly extracted from the IP cylinder of the turbine, supplying thermal energy with temperature of 115oC for stripper reboiler. The pressure selected can ensure a reasonable temperature differential in the reboiler. However, this scheme neglects the constraint of existing power plant.

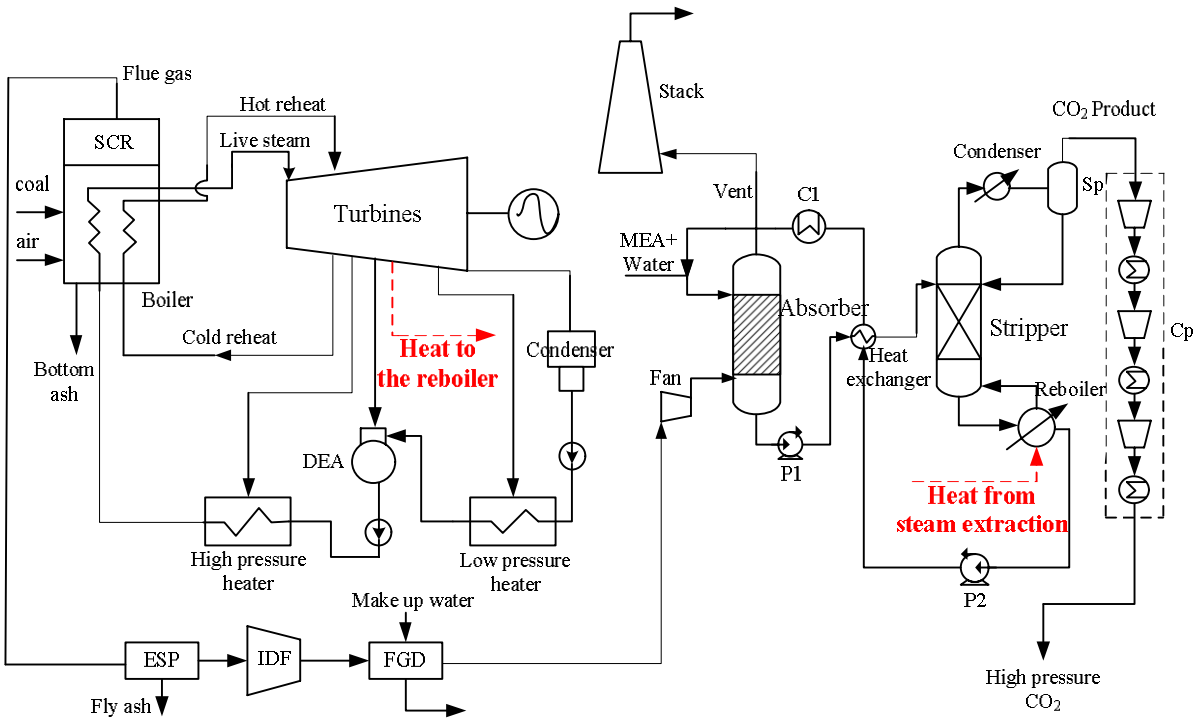

Fig. 6. 600MW supercritical coal-fired power plant with CO_2 capture

The power generation in Case 1 is the same as that of base case. Besides, its input fuel, boiler capacity, main steam and reheated steam flow rate also equal to that of base case. Neglecting the constraint of existing power plant, large amounts of 2.1 bar steam is directly extracted from the turbine system to provide heat and energy for MEA regeneration in the stripper without consideration of the pressure change in the IP cylinder after the large-scale extraction.

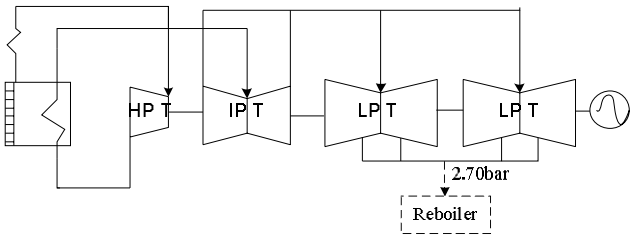

Fig. 7. Steam extraction scheme of Case 1

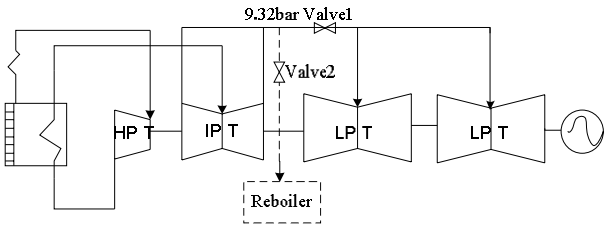

Fig. 8. Steam extraction scheme of Case 2

3.4. Capture Case 2: CO_2 capture case with consideration of the constraint of existing power plant

Case 2 is generally similar to Case 1 in the process flow. (see Fig. 6 for details). However, Case 2 makes adequate consideration of the constraint of existing power plant. For example, as shown in Fig. 8, the steam extraction point of Case 2 is located at the crossover pipe between the intermediate pressure (IP) and low pressure (LP) cylinders of the steam turbine, which may be the only feasible point to achieve large amount steam extraction in an existing power plant. Here, the steam pressure of the crossover pipe between the IP and LP cylinders can reach 9.32bar, much higher than the required steam pressure for absorbent regeneration (about 2.1bar), which will bring extra power loss due to steam extraction. Furthermore, the extra pressure loss due to the large amount steam extraction and the additional power loss resulted from the extraction are also be well considered in Case 2.

Besides, the steam extraction for amine absorption process can account for approximately 50% of the total steam flow exhausted from HP turbine cylinder. It may lead to unstable operation conditions and bring about some safety problems. For example, the pressure at the exhaust of the existing IP turbine would be dropped to a low level, which results in increased mechanical loading of the IP blades, especially the last stages of IP cylinder. Besides, because the flow area of the LP turbine cylinder is not variable, such a large decrease in the steam flow may lead to an unstable operation condition in the LP turbine.

3.5. Performance analysis

The performance analysis of three cases is listed in Table 3, the three cases include:

- Base Case: A typical 600MW supercritical power generation unit, as discussed in Section 3.1;
- Case 1: CO_2 capture case without considering the constraint of existing power plant, as discussed in Section 3.3;
- Case 2: CO_2 capture case with consideration of the constraint of existing power plant, as discussed in Section 3.4;

Table 3. Performance analysis of Base Case and Case 1-2

	Base Case	**Case1**	**Case2**
Coal input rate (kg/s)	46.66	46.66	46.66
CO_2 capture amount (kg/hr)	-	447423	447423
CO_2 capture rate (%)	-	90	90
Reboiler heat duty (MW)	-	420.83	420.83
Extracted steam flow (kg steam/kg CO_2)	-	1.489	1.439
CO_2 compression work (kWhe/tonne CO_2)	-	39.91	39.91
Power output of steam turbine (MW)	604	517.09	461.57
Auxiliary work (MW)	30.22	85.66	85.44
Net power output	573.8	431.43	376.13

Net efficiency (%)	40.28	30.29	26.40
Efficiency penalty(%-points)	-	9.99	13.88

As is shown in Table 3, due to the fact that Case 1 and Case 2 adopt the same MEA CO_2 capture process illustrated in the same Base Case, the process configuration and several basic parameters of these two cases are similar to each other, such as coal input rate, reboiler heat duty, CO_2 capture amount and CO_2 compression work.

However, because of the difference of the two capture cases in the extracted locations, the flow rate and the parameters of extraction steam, the great differences lie in the power output of steam turbine, net power output and net efficiency. In fact, on account of the high extraction pressure and large power loss of IP cylinder after steam extraction in Case 2, its steam turbine output is only 461.57MW, 55.52MW less than that of Case 1, which in turn leads to the obvious drop of net power output and net efficiency of Case 2 when compared with Case 1. Eventually, efficiency penalty of Case 2 reaches 13.88% points, nearly 4% points higher than that of Case 1.

Though performance of Case 2 seems worse, more attention are paid to the production process of power station in this case, which is closer to the practice. In fact, even for a newly-built power station, the same constraints in CO_2 capture process will be confronted if it uses the traditional station design. In other words, in terms of a practical pulverised coal power plant which adopts the chemical absorption method to achieve large-scale decarbonisation, the practical efficiency penalty will be much higher than the theoretical analysis if no specific optimization is made.

In a word, specific optimization in the retrofit scheme for CO_2 capture in a pulverised coal power plants will be very helpful to control the penalty of CO_2 capture at a low level, which will be discussed in the following section.

4. Special integration for CO_2 capture in existing power plant

4.1. Add a new letdown steam turbine generator (LSTG)

Since the steam pressure of the IP-LP crossover pipe (9.32bar) are much higher than the required steam pressure for solvent regeneration (about 2.1bar), a new letdown steam turbine generator is proposed to utilize the surplus pressure for power generation, as is shown in Fig. 9.

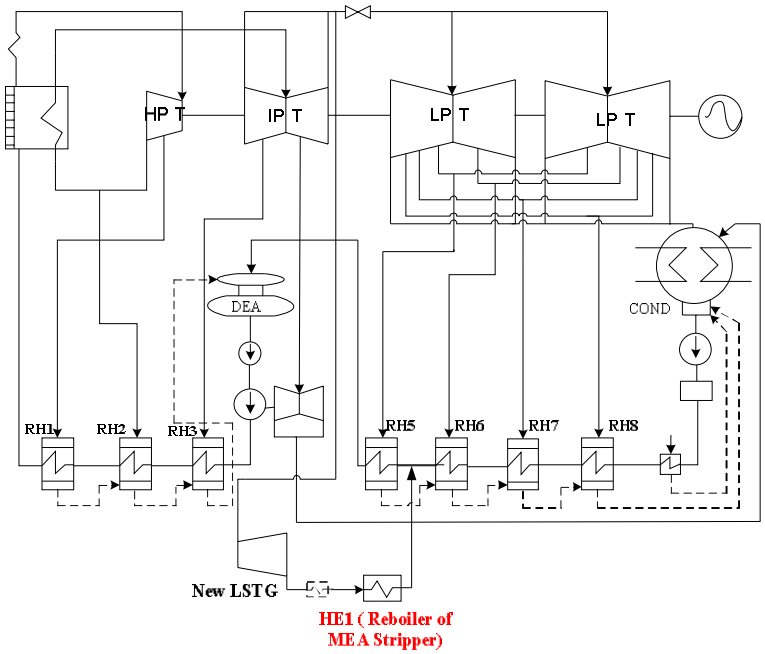

Fig. 9. The structure of adding a new letdown steam turbine generator

Such improvement is really simple and easy to implement, however, it is very effective to retrieve the surplus pressure, which can also make the power plant efficiency increase greatly. Fig.9 gives the variation trend of the power output and the extraction steam flow, with LSTG outlet pressure of the small turbine changed. As is shown in Fig. 10, with the decline of LSTG outlet pressure, the power output of LSTG will increase quickly, while the flow of the extracted steam is also increasing. The reason lies in that the temperature and enthalpy of the exhaust steam of LSTG will decrease with the drop of LSTG outlet pressure. As a consequence, it needs more extraction steam flow so as to provide the same energy. However, the enlargement of extraction steam flow and the pressure ratio caused by outlet pressure decrease will contribute to the increase of power output of LSTG.

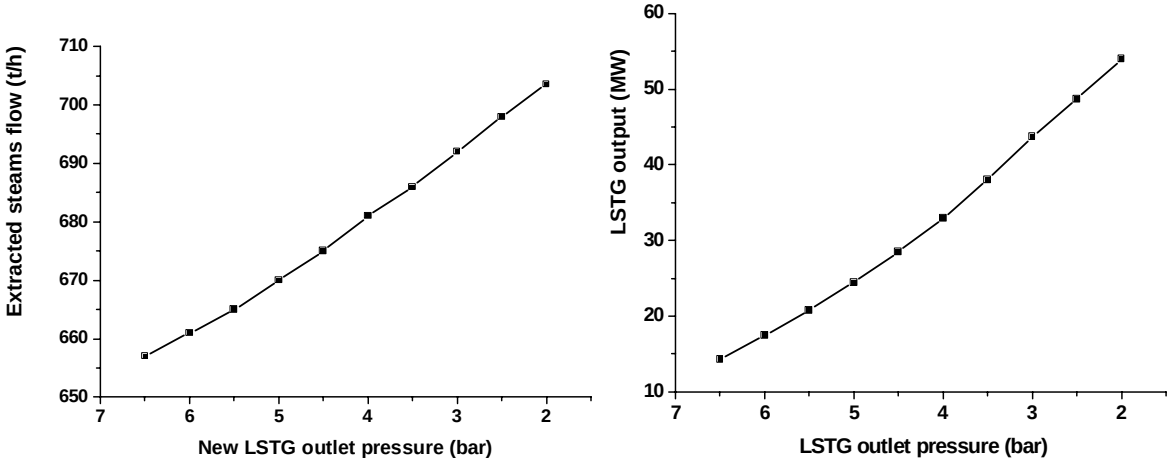

(a) *(b)*

Fig. 10. Variation trends of steam cycle performances with different LSTG outlet pressures: a) Extracted steam flow, b) Power output of new LSTG.

4.2. Thermal energy integration

For MEA-based CO2 capture process, on the one hand, the CO2 separation unit needs a lot of intermediate temperature steam extracted from steam turbine cycle to regenerate the solvent. On the other hand, the CO2 separation unit will also release a large amount of low temperature heat, such as the heat released by the CO2-H2O condenser of stripper and the intercooler of CO2 multistage compressor (Fig. 6). If these heat can be well employed, the energy consumption of CO2 capture will dramatically be reduced.

Fig. 11 reports the basic information of the heat integration of steam turbine cycle with CO2 capture process. As is shown in Fig. 11, the main integration measures are:

(1) the thermal energy released by CO2 cooler of MEA stripper are used for condensed water heating (HE3);

(2) the thermal energy released by CO2 compressor intercoolers are used for condensed water heating (HE4);

(3) After recovered surplus pressure within LSTG, the extracted steam is first sent to heat the condensed water (HE2), then sent to the reboiler of stripper (HE1).

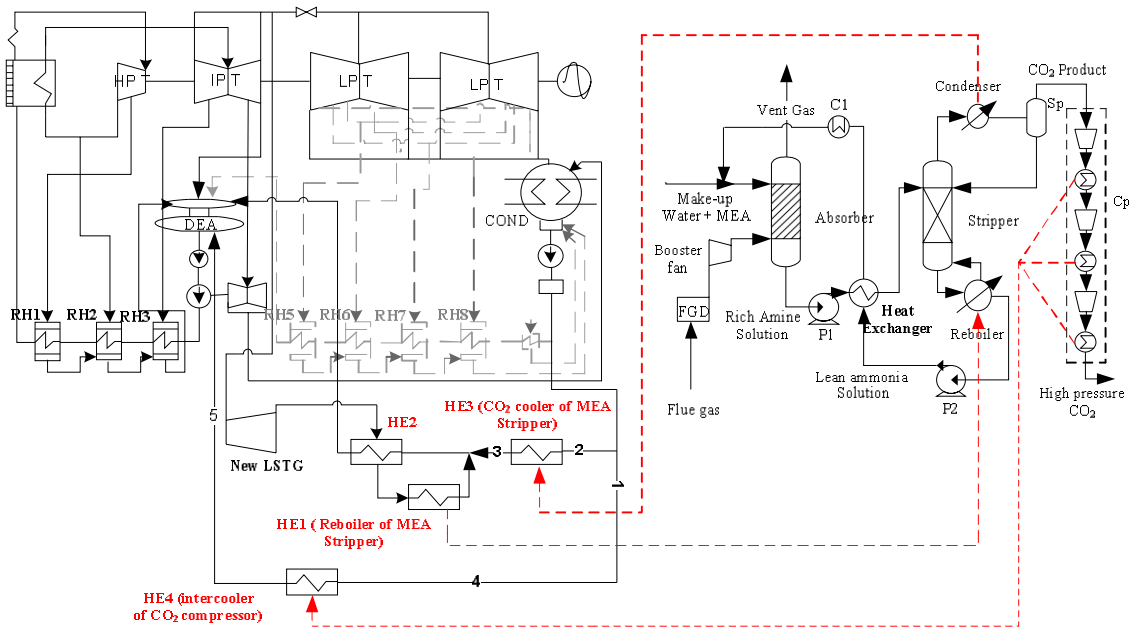

Fig. 11. Schematic diagram of heat integration of steam turbine cycle with CO_2 capture process

As mentioned above, steam extracted from the IP-LP crossover pipe is 9.32bar, 695t/hr. And at the outlet of LSTG, the extracted steam is 3 bar, 244℃. However, the reboiler temperature should not exceed 135℃, otherwise the degradation of MEA and corrosion will be sharply aggravated. Therefore, the surplus heat of the extracted steam can be used to heat the condensed water (HE2), before it is sent to the reboiler of stripper (HE1).

To recover the thermal energy of the CO_2 capture system, the condensed water out of condenser is divided into two parts. One part, which accounts for about 45% of total flow, is sent to absorb the heat of CO_2 cooler (HE3). The other part is used for recovering the inter-cooling heat of CO_2 compression (HE4). Such an integration scheme can totally replace the original low-pressure regenerative heater system to raise the temperature of the condensed water up to approximately 155℃, before it enters the deaerator (DEA).

4.3. Throttling one of LP cylinder of steam turbine (Case 5)

As mentioned above, the flow rate of steam extraction for MEA solvent regeneration is almost half of the total inlet steam flow of original LP cylinder. In other words, the flow rate of low pressure steam after extraction is approximately equal to one of the two IP cylinder in design conditions.

In view of this, if we let the low pressure steam after extraction flow into one LP cylinder, the LP cylinder can be considered to operate under design conditions and the flow rate similarly equals the design flow, as a result of which, the large-scale extra pressure drop caused by steam extraction can be avoided.

However, for a conventional existing power plant, all of the turbine cylinder rotors are connected in the same shaft and it is impossible to completely clutch them from machine. Thus, we propose that through throttling, most of steam flow into one of the LP cylinders while only a small amount of steam enters the other cylinder for heat dissipation. Fig. 12 shows the process scheme. As it can be seen in the figure, the huge pressure drop of the LP cylinder can be avoided, which can ensure the increment of the power output of steam turbine as well as the net efficiency.

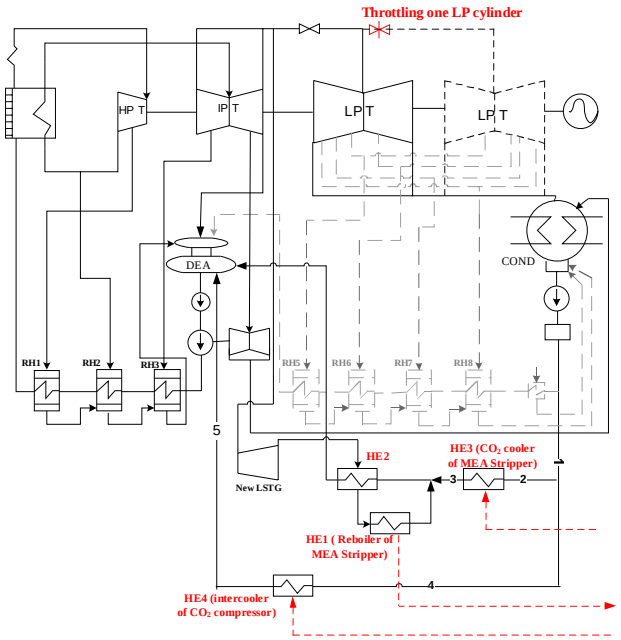

Fig. 12. The structure of clutched LP turbine option

4.4. Results analysis

The performance analysis of three cases of this section is listed in Table 4, the three cases include:

- Case 3: based on Case 2, Add a new letdown steam turbine generator (LSTG), as discussed in Section 4.1;
- Case 4: based on Case 3, adopting thermal energy integration, as discussed in Section 4.2;
- Case 5: based on Case 4, Throttling one of LP cylinder, as discussed in Section 4.3;

Table 4. Performance analysis of Case 3-5

	Base Case	**Case 3**	**Case 4**	**Case 5**
Coal input rate (kg/s)	46.66	46.66	46.66	46.66
CO_2 capture amount (kg/hr)	-	447423	447423	447423
CO_2 capture rate (%)	-	90	90	90
Reboiler heat duty (MW)	-	420.83	420.83	420.83
CO_2 compression work (MW)	-	39.91	39.91	39.91
Outlet pressure of LSTG (bar)	-	3.0	3.0	3.0
Extracted steam flow (kg steam/kg CO_2)	-	1.553	1.553	1.553
Heat recovery from CO_2 capture(MW)	-	0	73.05	73.05
Power output of steam turbine (MW)	604	450.18	459.9	474.23
Power output of LSTG (MW)	-	43.69	44.59	44.59
gross power output (MW)		493.87	504.49	518.82
Auxiliary work (MW)	30.22	85.51	85.51	85.51
Net power output	573.8	408.36	418.97	433.31
Net efficiency of plant (%)	40.28	28.67	29.41	30.42
Efficiency penalty (%-points)	-	11.61	10.87	9.86

As is shown in Table 4, compared with Case 2, when a new letdown steam turbine generator was added, the net efficiency of Case 3 can be increased by 2.27%-points, rising from 26.40% to

28.67%. In addition, through heat integration of steam turbine cycle with CO_2 capture process, the net efficiency of Case 4 can be further increased by 0.74%-points compared with Case 2, rising from 28.67% to 29.41%. Furthermore, if one of LP cylinder of steam turbine can be throttled to let most of steam entering the other LP cylinder, the huge pressure drop of the LP cylinder can be avoided, which can make system net efficiency further increase by 1.01%-points, rising from 29.41% to 30.42%. And through adopting all of three system integration measures, Case 5 presents the best performance. Compared with Base Case, the efficiency penalty of Case 5 is only 9.86%-points, even less than that of Case 2.

5. Exergy analysis

To reveal the internal phenomena of the new integration system, an exergy analysis is performed for both Case 5 and Case 2 with CO_2 capture. The results are listed in Table 5. The exergy analysis is also based on the assumption that the same quantity of coal was consumed in all of the Cases.

As shown in Table 5, the exergy efficiency of Case 5 is 30.42%, which is 4.02% points higher than that of Case 2, 9.86% lower than that of Base Case. Comparing the exergy distributions of Case 5 and Case 2, we find that the exergy of the net electricity has increased by 57.18 MW and the total exergy loss of the CO_2 capture unit is obviously decreased. Otherwise, the exergy loss of power generation system is also reduced. And the detailed distribution of exergy loss of these two units is given in Table 5.

Compared with the Case 2, the exergy loss of the CO_2 capture unit of Case 5 is decreased remarkably 30.25MW. The reason lies in thermal utilization of CO_2 capture, it makes heat exergy utilization rate improve greatly. In comparison, the exergy loss of power generation system of Case 2 is 24.88 MW higher than Case 5.

From the above analysis, we conclude that through thermodynamic system integration of steam/water system and CO_2 recovery and cascade utilization of energy, the key problem of high energy penalty for CO_2 capture may be improved in the Case 5 and favorable thermal and environment performances can be achieved. However, some challenges still exist, such as the complexity of the system, as well as the possible high investment of the system, which will be further studied in our following work.

Table 5. Exergy analysis of Case 2-5 and Base Case

	BaseCase		Case2		Case3		Case4		Case5	
	MW		MW		MW		MW		MW	
Exergy input of coal	1424.53		1424.53		1424.53		1424.53		1424.53	
Exergy output										
Net electricity	573.80	40.28%	376.13	26.40%	408.36	28.67%	418.97	29.41%	433.31	30.42%
Separated CO2			84.89	5.96%	84.89	5.96%	84.89	5.96%	84.89	5.96%
Exergy loss										
CO2 recovery unit:										
CO2 separation			71.60	5.03%	71.60	5.03%	71.60	5.03%	71.60	5.03%
CO2 compression			5.16	0.36%	5.16	0.36%	5.16	0.36%	5.16	0.36%
Heat exergy			36.85	2.59%	36.85	2.59%	6.61	0.46%	6.61	0.46%
Subtotal			113.61	7.98%	113.61	7.98%	83.36	5.85%	83.36	5.85%
Power generation system:										
Boiler(Fuel combustion)	749.97	52.65%	749.97	52.65%	749.97	52.65%	749.97	52.65%	749.97	52.65%
HTP	14.31	1.00%	14.31	1.00%	14.31	1.00%	14.31	1.00%	14.31	1.00%
IPT	8.46	0.59%	8.27	0.58%	8.27	0.58%	8.27	0.58%	8.27	0.58%
LPT	25.12	1.76%	12.16	0.85%	8.87	0.62%	12.17	0.85%	10.99	0.77%
High temperature heater	5.23	0.37%	5.27	0.37%	5.27	0.37%	5.27	0.37%	5.27	0.37%
Low temperature heater	6.00	0.42%	13.23	0.93%	4.82	0.34%	3.93	0.28%	4.36	0.31%
Condenser	30.08	2.11%	20.93	1.47%	17.05	1.20%	21.94	1.54%	19.80	1.39%
Throttling			15.82	1.11%	11.29	0.79%	16.29	1.14%	4.51	0.32%
Other equipments	7.57	0.53%	5.60	0.39%	3.11	0.22%	3.20	0.22%	3.20	0.22%
Subtotal	846.74	59.44%	845.56	59.36%	822.98	57.77%	835.37	58.64%	820.68	57.61%
Exergy efficiency	40.28%		26.40%		28.67%		29.41%		30.42%	

6. Conclusions

The process simulation, characteristics analysis and system integration of CO_2 capture based on a typical China's existing coal-fired power plant with supercritical parameters are carried out in this paper. From the work completed in this study, some important conclusions can be drawn out and a few of interesting integration measures are put forward.

(1) When an existing power plant is transformed into a CO_2 capture plant using chemical absorption methods, some special problems will be met with, which is very different from the virtual plant. On the one hand, it will be difficult to find a suitable extraction point for the large amount of steam which has to be supplied to the CO_2 capture process. On the other hand, some component of the existing power plant, especially the steam turbine, will significantly deviate from their original design conditions because of a large amount of steam extracted from steam/water cycle, resulting in a large efficiency penalty.

(2) When retrofitting existing power plant, due to the constraint of existing equipments, the energy penalty of CO_2 capture will tend to be even higher. For example, because the parameters of extraction steam doesn't match with the steam parameters for CO_2 capture process, it will be certain to bring additional power loss. Eventually, efficiency penalty of CO_2 capture in an existing power plant (Case 2) can be 4% points higher than that of a redesigned new power plant(Case 1).

(3) In this study, through the special (unique) system integrations(Case 3, Case 4, Case 5), the efficiency of existing 600MW supercritical power plant increased by 4.02%, rising from 26.40%(Case 2) to 30.42%(Case 5). The overall studies in this report show that if MEA absorption is adopted to recover CO_2 from flue gas of a power plant, with a CO_2 recovery ratio of 90% the efficiency penalty for the power plant will be 9.86% points, and the extraction steams flow is 1.553 kg steams/kg CO_2.

Acknowledgments:

The paper is supported by National Nature Science Fund of China (No. 51006034, No. 51025624), and the National Major Fundamental Research Program of China (No. 2009CB219801, No. 2011CB710706).

Reference

[1] Working Group III of the Intergovernmental Panel on Climate Change (IPCC), IPCC Special Report on Carbon Dioxide Capture and Storage. Cambridge, United Kingdom: Cambridge University Press; 2005.

[2] Ralph EH, Simsa, Rogner HH, Gregory K. Carbon emission and mitigation cost comparisons between fossil fuel, nuclear and renewable energy resources for electricity generation. Energy Policy 2003;31(13):1315-1326.

[3] United Nations Statistics Division, Greenhouse Gas Emissions, August 2009. Available at: http://unstats.un.org/unsd/environment/air_CO_2_emissions.htm.

[4] China Electricity Council. The Current status of air pollution control for coal-fired power plants in China 2009. China Electric Power Press, Beijing; 2009.

[5] Park SK, Kim TS, Sohn JL, Lee YD. An integrated power generation system combining solid oxide fuel cell and oxy-fuel combustion for high performance and CO_2 capture. Applied Energy 2011;88:1187–1196.

[6] Sun R, Yingjie L, Hongling L, Shuimu W, Chunmei L. CO_2 capture performance of calcium-based sorbent doped with manganese salts during calcium looping cycle. Applied Energy 2011.

[7] Kanniche M, Gros-Bonnivard R, Jaud P, Valle-Marcos J, Amann JM, Bouallou C. Pre-combustion, post-combustion and oxy-combustion in thermal power plant for CO_2 capture.

Applied Thermal Engineering 2010;30:53–62.

[8] Alie C, Backham L, Croiset E, Douglas PL. Simulation of CO_2 capture using MEA scrubbing: a flowsheet decomposition method. Energy Convers Manage 2005;46(3):475–87.

[9] Jean-Marc G. Amann, Bouallou C. CO_2 Capture from Power Stations Running with Natural Gas (NGCC) and Pulverized Coal (PC): Assessment of a New Chemical Solvent Based on Aqueous Solutions of N-MethylDiEthanolAmine + TriEthylene TetrAmine. Energy Procedia. 2009. p. 909-916.

[10] Yukun H, Jinyue Y. Characterization of flue gas in oxy-coal combustion processes for CO_2 capture. Applied Energy 2011.

[11] Hao L, Yingjuan S. Predictions of the impurities in the CO_2 stream of an oxy-coal combustion plant. Applied Energy 2010;87:3162–3170.

[12] Parsons Infrastructure & Technology Group, 2002, Updated cost and performance estimates for fossil fuel power plants with CO_2 removal. Report under Contract No. DE-AM26-99FT40465, USA.

[13] Rao AB, Rubin ES. A technical, economic, and environmental assessment of amine based CO_2 capture technology for power plant greenhouse gas control. Environmental Science and Technology 2002;36(20):4467-4475.

[14] Singh D, Croiset E, Douglas PL, Douglas MA. Techno-economic study of CO_2 capture from an existing coal-fired power plant: MEA scrubbing vs. O_2/CO_2 recycle combustion. Energy Conversion and Management. 2003. p. 3073-3091.

[15] Alstom Power Inc., ABB Lummus Global Inc., Alstom Power Environmental Systems and American Electric Power, 2001, Engineering feasibility and economics of CO_2 capture on an existing coal-fired power plant. Report under Contract No. PPL-01-CT-09, USA.

[16] Pellegrini G, Strube R, Manfrida G. Comparative study of chemical absorbents in post-combustion CO_2 capture. Energy 2011;35:851–857.

[17] Mohammad RM, Abu-Zahra, Schneiders LHJ. CO_2 capture from power plants Part I. A parametric study of the technical performance based on monoethanolamine. International journal of greenhouse gas control. 2007. p. 37– 46.

[18] Mohammad RM, Abu-Zahra, Niederer JPM, Feron PHM, Versteeg GF. CO_2 capture from power plants Part II. A parametric study of the economical performance based on monoethanolamine. International journal of greenhouse gas control. 2007. p. 135– 142.

[19] Hetland J, Kvamsdal HM, Haugen G, Major F, Karstad V, Tjellander G. Integrating a full carbon capture scheme onto a 450 MWe NGCC electric power generation hub for offshore operations: Presenting the Sevan GTW concept. Applied Energy 2009;86:2298–2307.

[20] Bin H, Shisen X, Shiwang G, Lianbo L, Jiye T, Hongwei N, Ming C, Cheng Jian. Industrial test and techno-economic analysis of CO_2 capture in Huaneng Beijing coal-fired power station. Applied Energy 2010;87:3347–3354.

[21] Doukelis A, Vorrias I, Grammelis P, Kakaras E. Partial O_2-fired coal power plant with post-combustion CO_2 capture: A retrofitting option for CO2 capture ready plants. Fuel 2009;88: 2428–2436.

[22] Yu YS, Li Y, Li Q, Jiang J, Zhang ZX. An innovative process for simultaneous removal of CO_2 and SO_2 from flue gas of a power plant by energy integration. Energy Conversion and Management 2009;50:2885–2892.

[23] Sanpasertparnich T, Idem R, Bolea I, deMontigny D, Tontiwachwuthikul P. Integration of post-combustion capture and storage into a pulverized coal-fired power plant. International Journal of Greenhouse Gas Control 2010;14:499–510.

[24] Cifre PG, Brechtel K, Hoch S, Garcia H, Asprion N, Hasse H, Scheffknecht G. Integration of a chemical process model in a power plant modelling tool for the simulation of an amine based

CO_2 scrubber. Fuel 2009;88:2481–2488.

[25]Lucquiaud M, Gibbins J. Retrofitting CO_2 capture ready fossil plants with post-combustion capture. Part 1: requirements for supercritical pulverized coal plants using solvent-based flue gas scrubbing. Power and Energy. 2009. p. 213-226.

[26]National Energy Technology Laboratory of USA. Carbon Dioxide Capture from Existing Coal-Fired Power Plants. DOE/NETL-401/110907, Final Report; 2007.

[27]Göttlicher G., Pruschek R. COMPARISON OF CO_2 REMOVAL SYSTEMS FOR FOSSIL-FUELLED POWER PLANT PROCESSES. Energy Conversion and Management 1997;38: S173-S178.

[28]Hanna K, Hallvard FS, Mikko A. CO2 capture from coal-fired power plants based on sodium carbonate slurry; a systems feasibility and sensitivity study. International Journal of Greenhouse Gas Control 2009;3:143-151.

[29]Boleslaw Z, Radoslaw S. Energy analysis of technological systems of natural gas fired combined heat-and-power plants. Applied Energy 2003;75:43-50.

[30]Bjorn R. Combined heat-and-power plants and district heating in a deregulated electricity market. Applied Energy 2004;78:37-52.

[31]Jianye Z, Shu X. Type Selection and Parameter Determination Method for Unit of Cogeneration Project. Electrical Equipment 2008;9(1):72-75.

[32]Yongxiu H, Peiji Z, Yixing Z. Cost study of heat supply and electricity supply of cogeneration project. Electric Power 2004;37(6):63-66.

[33]Jianqun X, Gang L, Ling L, Keyi Z, Yongfeng S. Thermodynamic model of HP-IP leakage and IP tuibine efficiency. Applied Thermal Engineering 2011;31:311-318.

[34]Shintaro I, Yasushi M, Yasuyoshi K, Satoshi N, Takumi H, Yasunobu N. Study of steam, helium and supercritical CO2 turbine power generations in prototype fusion power reactor. Nuclear Energy 2008;50:325-332.

Analysis of four end high temperature membrane air separator in a supercritical power plant with oxy type pulverized fuel boiler

***Janusz Kotowicz*[a], *Sebastian Michalski*[b]**

[a] *Silesian University of Technology, Poland, janusz.kotowicz@polsl.pl*
[b] *Silesian University of Technology, Poland, sebastian.michalski@polsl.pl,*

Abstract:

In this article computational algorithm and exemplary results for a model of an air separation unit (ASU) with "four end" high temperature membrane (HTM) were presented. First, the software environment for building of a "four end" membrane separator model was chosen. Then, a model of an air separation unit was created and preliminary calculations were made on that model. The air separation unit structure consists of a "four end" membrane, heat exchanger, electrical generator, air compressor and expander. Parameter that determines all flows in the ASU model is the oxygen mass flow rate. This mass flow rate is approximately the same as oxygen mass flow rate feeding oxy boiler working in a 460 MW power plant. The most important step of this paper was the integration of a model of pulverized fuel boiler in the oxy-combustion technology and the air separation unit model by sending flue gas from boiler to ASU. The characteristics of ASU such as power and efficiency as a function of the oxygen recovery rate were made. Maximal value of oxygen recovery rate was calculated. The difference between optimal compressor pressure ratio of the autonomic gas turbine and of the air separation unit are presented in this paper.

Keywords:

Pulverized fuel boiler, oxy-combustion technology, "four end" membrane separator

1. Introduction

Currently appearing world trend to reduce emissions of harmful substances such as greenhouse gases into the environment is changing a direction of the energy technologies [1]. Particularly important is the development of low emission coal technologies that play a significant role in the balance sheets of many countries including Poland, in which a significant part of electricity is generated in coal-fueled power plants. Additionally, during the production of electricity in coal-fueled power plants carbon dioxide emission per produced electricity unit is higher than in other power generation technologies, for example, about 2.5 times more than in gas-steam blocks fueled with natural gas. The two most important directions of research aiming to reduce the emissions from coal-fueled power plants may be mentioned. The first one is the optimization of a power plant within its structure and work parameters. The second direction of development of low emission coal technologies is finding new and optimization of the already known low-energy carbon capture technologies [2]. The currently developed carbon capture technologies are as follows:

- pre-combustion technology
- post-combustion technology
- oxy-combustion technology

Oxy-combustion technology is based on fuel combustion in an atmosphere with increased oxygen concentration in order to eliminate nitrogen from the flue gas. In this technology, flue gas that

leaves boiler is composed mainly of carbon dioxide and steam, so the separation of carbon dioxide from flue gas is based on the low energy-consuming condensation process [3÷4]. The oxy-combustion technology is now the most promising solution for carbon energetic technologies [5÷7]. Currently, most advanced is a cryogenic air separation technology. Membrane air separation technologies are also considered, in particular air separation units (ASU) with high temperature membranes (HTM) [8].

Among the currently investigated high-temperature separation membranes, a "three-end" and "four end" membrane-types should be distinguished [9]. The oxygen flow through the membrane is caused by the oxygen partial pressure difference on both sides of a membrane. "four-end" type membrane used for air separation is immersed on one side by compressed air, while the other side of a membrane is immersed by flue gas from boiler. Oxygen mass flow rate permeating through the membrane depends on a membrane constant (C), oxygen partial pressure on the feed side of the membrane (p_{O2_F}) and oxygen partial pressure on the permeate side (p_{O2_Per}). The relationship between these quantities is expressed by the following formula:

$$j_{O2} = C \cdot \ln\left(\frac{p_{O2_F}}{p_{O2_Per}}\right), \text{mol/sm}^2 \qquad (1)$$

The membrane constant (C) in (1) depends, among other, on the thickness of the membrane and the membrane working temperature.

Figure 1 shows a power plant diagram with average integration with air separation unit (ASU) that contains "four end" high temperature membrane for air separation. It should be noted that for the increase of the oxygen partial pressure on the feed side of membrane the compressor with pressure ratio β_k is used. Steam cycle of this power plant is composed of a steam turbine, four low pressure and three high pressure feed-water heaters, condenser, deaerator, condensate pump, feed-water pump, one low-pressure and one high-pressure flue gas-water heat exchangers and one low pressure retentate-water heat exchanger. The steam turbine consist of three parts: high-pressure, intermediate-pressure and low-pressure. Between the intermediate and high-pressure part of the steam turbine steam is reheated. Water heated in steam cycle is directed first to the two parallel economizers and then the water is directed to the boiler. One of the economizers is fed with the flue gas and second with the permeate. Flue gas with the temperature at 850 ^{o}C leaving the boiler are subjected to high temperature filtration. Then, part of the flue gas is supplied to the air separation unit. The remaining flue gas is cooled by water and then compressed. The air separation unit is composed of the "four-end" high temperature separation membrane, counter-flow permeate-air heat exchanger, economizer, permeate fan, air compressor, expander and electric generator. The flue gas supplied to ASU is flowing to the separation membrane, where is enriched in oxygen. The gas leaving the membrane (called permeate) heats compressed air in a counter-current permeate-air heat exchanger. Then, the permeate is cooled to a temperature of 320 ^{o}C in the economizer and is supplied by the fan as an oxidant to the boiler`s combustion chamber. The air drawn to the ASU is compressed and then heated to a temperature of 750 ^{o}C in permeate-air heat exchanger. Then, the air flows to the separation membrane (feed) where the oxygen is separated. The gas leaving the membrane, that consists mostly of nitrogen, is called retentate. The retentate enters the expander and then is cooled by a feed water in the steam cycle. Expander drives the air compressor, and the excess of the mechanical power is used to generate electricity.

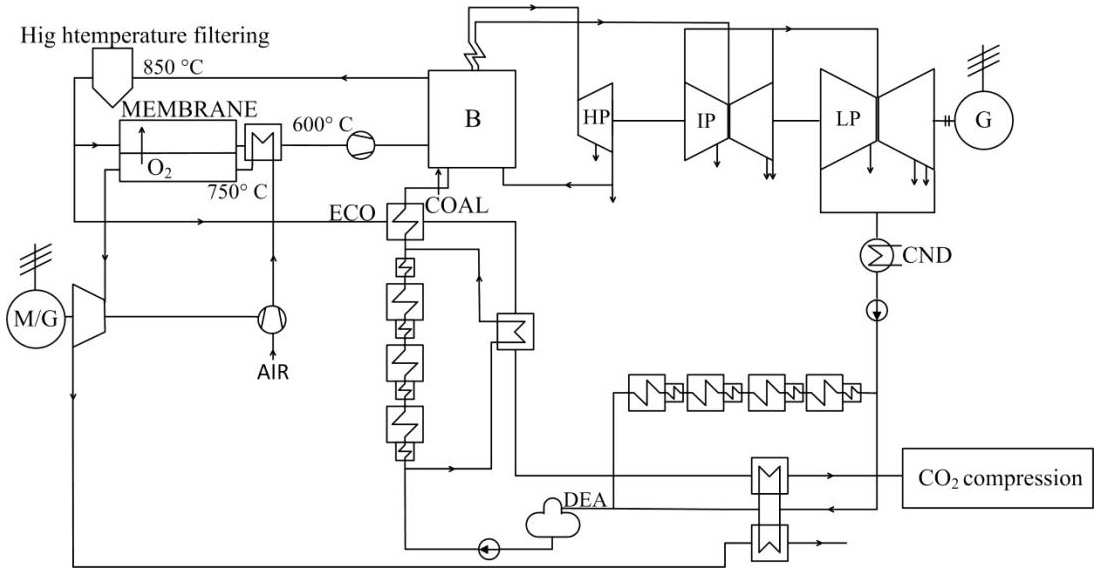

Fig. 1. Solution diagram of „four end", average integration [9]

The paper includes the analysis and comparison with a classic gas turbine of an air separation unit (ASU). The computations results obtained with ASU model were compared with the results obtained using an autonomous gas turbine model. The air separation model will be used to build the models of oxy-combustion power plants.

2. Model of the air separation unit (ASU) and assumptions for calculations

Air separation unit structure consists of: counter-flow air heater (APH), air compressor (C), expander (EX), electric generator (G) and "four-end" type membrane (M). The expander drives the air compressor. Depending on the assumed quantities the expander and compressor can give or take electricity from the grid. The structure of the air separation unit is shown in Figure 2. The characteristic basic quantities of the air separation unit and autonomous gas turbine are gathered in Table 1.

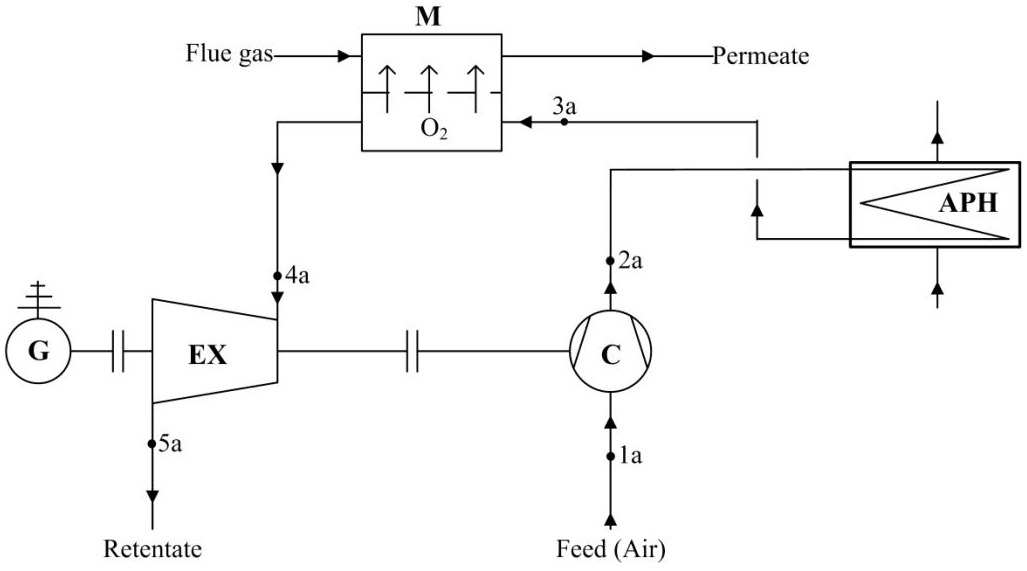

Fig. 2. Scheme of the air separation unit (ASU)

Table 1. Characteristic quantities for investigated air separation unit (ASU)

Name	Symbol	Value	Unit
Ambient pressure	p_{ot}	101.3	kPa
Ambient temperature	t_{ot}	20	^{o}C
Membrane working temperature	t_{mem}	750;850	^{o}C
Stream of separated oxygen	$\dot{m}_{O2}$	107.56	kg/s
Oxygen recovery rate	R	40÷100	%
Compressor pressure ratio	β_k	2÷30	-
Compressor isentropic efficiency	η_{iS}	0.88	-
Expander isentropic efficiency	η_{iT}	0.9	-
Generator efficiency	η_g	0.99	-

It was assumed for the calculations that the air taken from environment is a dry gas consisting of 21% oxygen and 79% nitrogen (volumetric composition).

The characteristic quantities gathered in Table 1 were used for computations performed on a "four-end" membrane air separation unit model, made in GateCycle^{TM} software. The built-in components were used to build the air separation unit model. The quantity that determinates the value of the mass flow rate in the entire ASU model is a mass flow rate of oxygen. This mass flow rate is approximately the same as the oxygen mass flow rate feeding an oxy boiler working in a 460 MW power plant. It was assumed that through the membrane flows pure oxygen.

The structure of an autonomous gas turbine as opposed to a structure of ASU shown in Figure 2 does not contain a "four-end" type membrane. In the autonomous gas turbine model the assumption concerning a compressor, expander and air heater are the same as in the ASU model. The air mass flow rate in both models are the same, the difference is only in the mass flow rate and composition of gas flowing into the expander. In the ASU model the composition and mass flow rate of the gas is different from air because some oxygen is separated from air in the membrane. In the autonomous gas turbine model the mass flow rate and composition of gas flowing into the expander is the same as mass flow rate and composition of air leaving the air heater.

3. The results of calculations of air separation unit and autonomous gas turbine

The air mass flow rate depends on the separated in membrane oxygen mass flow rate ($\dot{m}_{O2}$), oxygen recovery rate (R) and mass content of oxygen in the air (g_{O2-air}). The relationship between these quantities is as follows:

$$\dot{m}_{1a} = \frac{\dot{m}_{O2}}{R \cdot g_{O2-air}}, \qquad (2)$$

Next the air is compressed by the compressor. Effective power required to drive the compressor depends on the air mass flow rate ($\dot{m}_{1a}$), the air temperature (T_{1a}), the average specific heat ($\left(\tilde{c}_p\right)_K$), the compressor pressure ratio (β_K), the heat capacity ratio contained in the factor ($\mu_K = \left(\frac{\chi-1}{\chi}\right)_K$), the compressor isentropic efficiency (η_{iK}) and the compressor mechanical efficiency (η_{mK}). The equation showing the relationship between these quantities is as follows:

$$N_{eK} = \dot{m}_{1a} \cdot \left(\tilde{c}_p\right)_K \cdot T_{1a} \cdot \left(\frac{\beta_K{}^{\mu_K} - 1}{\eta_{iK} \cdot \eta_{mK}} \right), \qquad (3)$$

The mass flow rate flowing through the expander is lower than the oxygen mass flow rate separated in the membrane by the mass flow rate flowing through the compressor. This mass flow rate depends on the oxygen mass flow rate separated from the air in the membrane ($\dot{m}_{O2}$) and the air flow rate ($\dot{m}_{1a}$). The relationship between these quantities is as follows:

$$\dot{m}_{4a} = \dot{m}_{1a} - \dot{m}_{O2}, \qquad (4)$$

The expander effective power depends on the retentate mass flow rate ($\dot{m}_{4a}$), the retentate temperature (T_{4a}), the average specific heat ($\left(\tilde{c}_p\right)_K$), the compressor pressure ratio (β_K),the reduction factor of compressor pressure ratio (σ), the heat capacity ratio contained in the factor ($\mu_T = \left(\frac{\chi - 1}{\chi} \right)_T$), the expander isentropic efficiency (η_{iT}) and the expander mechanical efficiency (η_{mT}). The equation showing the relationship between these quantities is as follows:

$$N_{eT} = \dot{m}_{4a} \cdot \left(\tilde{c}_p\right)_T \cdot T_{4a} \cdot \left[1 - (\sigma \cdot \beta_K)^{-\mu_T}\right] \cdot \eta_{iT} \cdot \eta_{mT}, \qquad (5)$$

Figure 3 shows computed gross electric power as a function of oxygen recovery rate. The curve in this figure is determined for β_K=20 and t_{3a}=750 ^oC. The gross electrical power depends on the expander gross power (N_{eT}), the compressor gross power (N_{eK}) and the generator efficiency (η_g). The relationship between these quantities is as follows:

$$N_{elTG} = \left(N_{eT} - N_{eK}\right) \cdot \eta_g, \qquad (6)$$

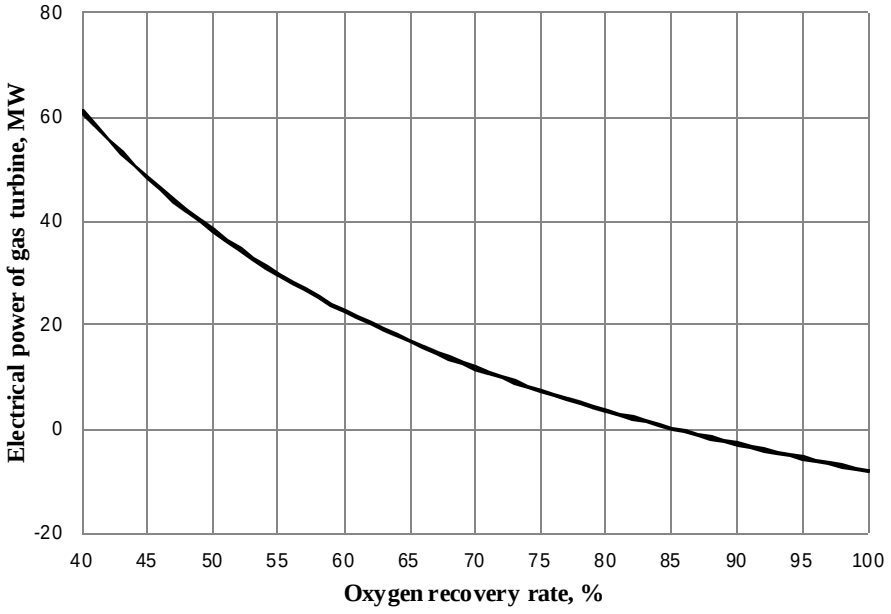

Fig. 3. Electrical power achieved or required for power the turbine set in ASU model as a function of oxygen recovery rate for β_K =20 and t_{3a} =750^oC

Figure 4 shows a graph of the electric power generation efficiency for β_K=20 and t_{3a}=750°C. This efficiency depends on the gross electrical power (N_{elTG}) and the heat supplied to the unit (Q_d). The relationship between these quantities is as follows:

$$\eta_{el} = \frac{N_{elTG}}{Q_d}, \qquad (7)$$

The heat supplied to the unit depends on the air mass flow rate ($\dot{m}_{2a}$), the air enthalpy (h_{2a}), the retentate mass flow rate ($\dot{m}_{4a}$) and retentate enthalpy (h_{4a}). The relationship between these quantities is as follows:

$$Q_d = \dot{m}_{4a} \cdot h_{4a} - \dot{m}_{2a} \cdot h_{2a}, \qquad (8)$$

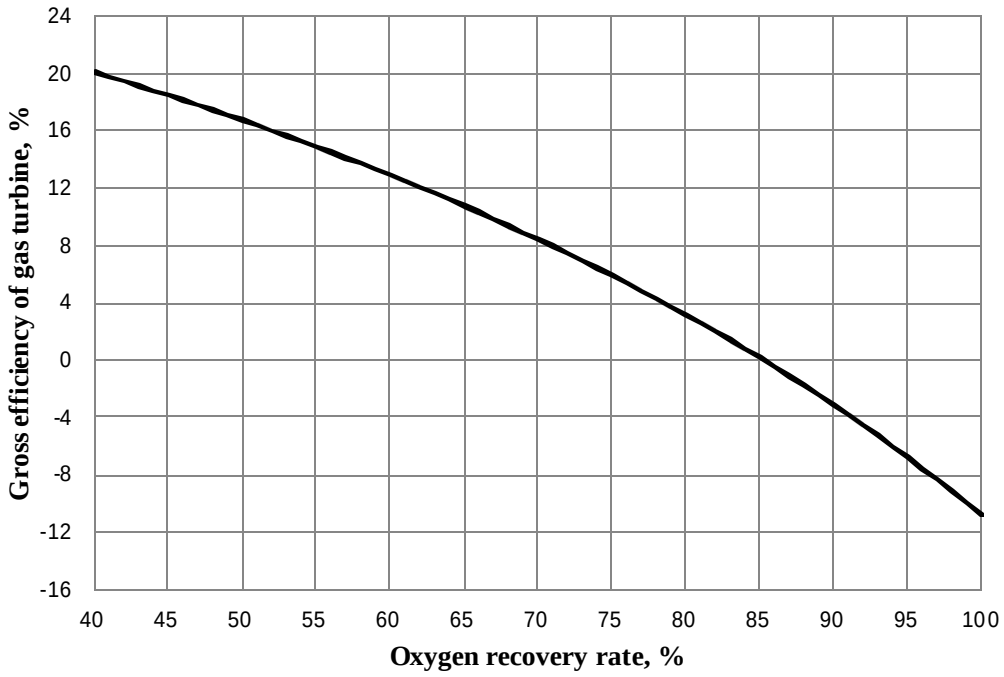

Fig. 4. Gross efficiency of ASU model as a function of oxygen recovery rate for β_K =20 and t_{3a} =750°C

It should be noted that the gross electrical power (Fig. 3) at a large oxygen recovery rate is below zero. Equation for the maximal oxygen recovery rate using (2) and (5) is as follows:

$$R_{gr} \le \frac{1}{g_{O2}}\left[1 - \frac{T_{1a}}{T_{3a}} \cdot \frac{1}{\eta_{iK} \cdot \eta_{iT} \cdot \eta_{mK} \cdot \eta_{mT}} \cdot \frac{\left(\tilde{c}_p\right)_K}{\left(\tilde{c}_p\right)_T} \cdot \frac{\beta_K{}^{\mu_K} - 1}{1 - (\sigma \cdot \beta_K)^{-\mu_T}}\right], \qquad (9)$$

Figure 5 shows graph of maximal oxygen recovery rate as a function of a compressor pressure ratio. Computations made for this graph were carried out with the use of GateCycle™ software for the two different membrane working temperature (t_{3a}=750 °C and t_{3a}=850 °C).

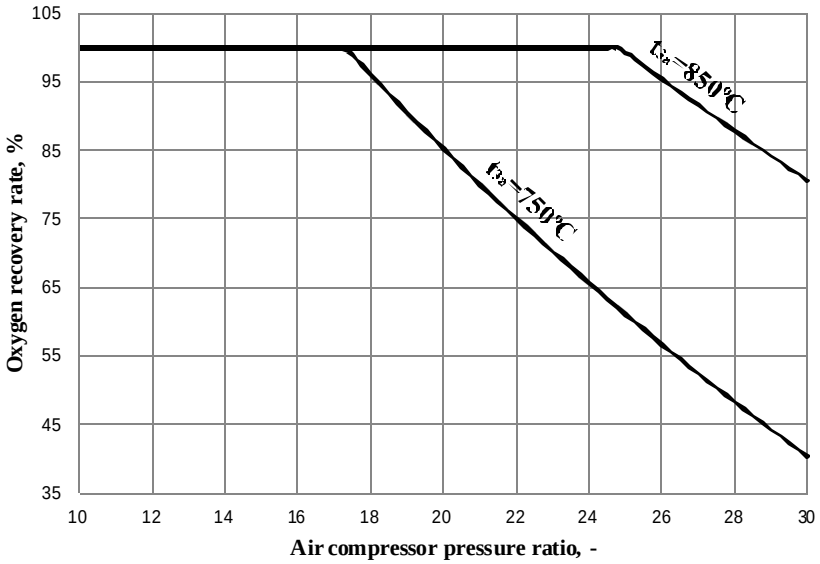

Fig. 5. Maximal oxygen recovery rate in the ASU model as a function of the compressor pressure rate for two different membrane work temperature

Figure 6 shows a graph of gross electric power of the air separation unit (marked as "ASU" on a graph) as a function of the compressor pressure ratio for the two different oxygen recovery rate (50% and 90%). The same figure also shows the gross electric power of the autonomous gas turbine (marked as "TG" on graph) as a function of the compressor pressure ratio for the same oxygen recovery rate.

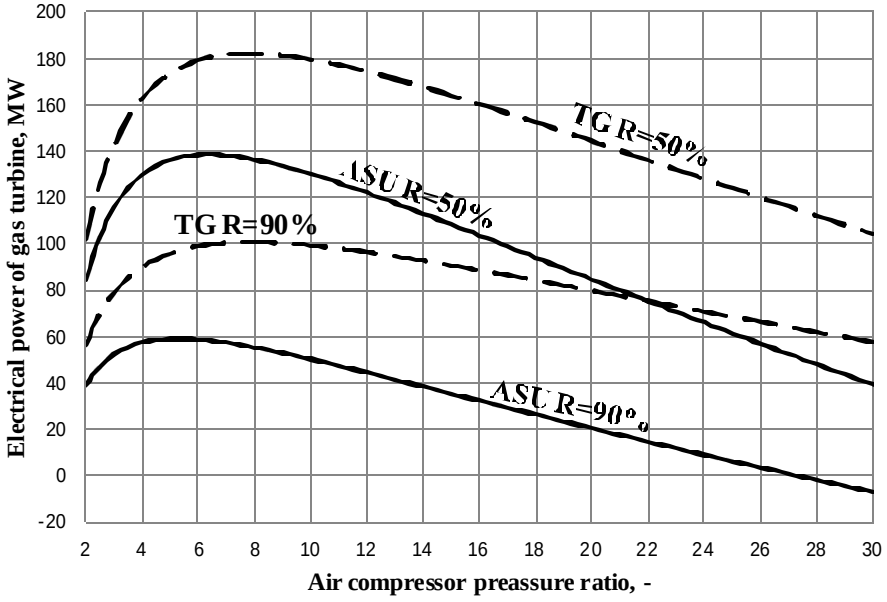

Fig 6. Gross electrical power for both units as a function of compressor pressure ratio for two different oxygen recovery rate

It should be noted that the optimal compressor pressure ratio in the air separation unit and the autonomous gas turbine are not equal. Using (3) and (5) the optimal compressor pressure ratio in air separation unit can easily be determined:

$$\beta_k^{opt(N_{eTG})} = \left[\beta_k^{opt(N_{eTG})}\right]_{kl} \cdot (1 - g_{O2} \cdot R)^{\frac{1}{\mu_K + \mu_T}}, \quad (10)$$

In the (8) optimal compressor pressure ratio ($\left[\beta_k^{opt(N_{eTG})}\right]_{kl}$) is determined in the same way as for a classic gas turbine. Calculated optimal compressor pressure ratio values, due to generated electricity from the turbine set are gathered in Table 2.

Table 2. The optimal compressor pressure ratio values, due to generated electricity from turbine set

Name	Symbol	Value		
The oxygen recovery rate	R, %	50	70	90
Optimal compressor pressure ratio for ASU	β_{k_ASUopt}, -	6.4	5.8	5.3
Optimal compressor pressure ratio for TG	β_{k_TGopt}, -	7.8	7.8	7.8

The optimal compressor pressure ratio values, due to the gross efficiency as well as for the autonomous gas turbine depends on the optimal compressor pressure ratio values, due to electricity generated from the turbine set ($\beta_k^{opt(N_{eTG})}$) and the gross efficiency of the electricity generation of the unit (η_{elTG}). The relationship between these quantities is as follows:

$$\beta_k^{opt(\eta_{eTG})} = \beta_k^{opt(N_{eTG})} \cdot \left(\frac{1}{1 - \eta_{elTG} \cdot \eta_{mK}}\right)^{\frac{1}{\mu_K + \mu_T}}, \quad (11)$$

Equation (11) was determined using (3), (5) and (7), with the condition $\frac{d\eta_{elTG}}{d\beta_k} = 0$.

Figure 7 shows a graph of gross efficiency of electricity generation as a function of the compressor pressure ratio for the two different oxygen recovery rates in the air separation unit (50% and 90%) and for autonomous gas turbine.

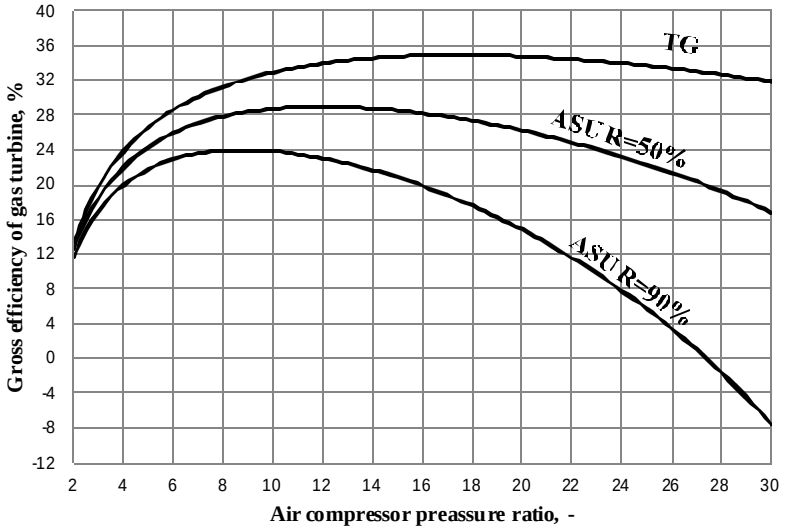

Fig. 7. Gross efficiency of both units as a function of compressor pressure ratio for two different oxygen recovery rate

Calculated optimal compressor pressure ratio values, due to the gross efficiency are gathered in Table 3.

Table 3. The optimal compressor pressure ratio values, due to gross efficiency of both units

Name	Symbol	Value		
Oxygen recovery rate	R, %	50	70	90
Optimal compressor pressure ratio for ASU	β_{k_ASUopt}, -	11.9	10.2	8.8
Optimal compressor pressure ratio for TG	β_{k_TGopt}, -	17.6	17.6	17.6

4. Summary

In this paper the air separation unit with "four-end" high-temperature membrane (HTM) was analyzed.

For the analysis of the air separation unit and of the autonomous gas turbine power and efficiency characteristic as a function of oxygen recovery rate and compressor pressure ratio were determined. The characteristics for both units are summarized and compared in the figures 6 and 7.

The maximal oxygen recovery rate as a function of the compressor pressure ratio for the two different membrane work temperature were determined. This quantity separates the area of work in which we get the extra power from expander in the air separation unit from the area of work in which we must deliver additional power to drive the compressor.

The optimal compressors pressure ratio due to a power of turbine set and due to the efficiency of electricity generation for different oxygen recovery rates in the air separation unit and in the autonomous gas turbine were determined. The optimal values of compressor pressure ratio in the air separation unit are decreasing with the increase of the oxygen recovery rate. In the case of the autonomous gas turbine, these values are constant.

Acknowledgements

The results presented in this paper were obtained from research work co-financed by the National Centre for Research and Development within a framework of Contract SP/E/2/66420/10 – Strategic Research Programme – Advanced Technologies for Energy Generation: Development of a technology for oxy-combustion pulverized-fuel and fluid boilers integrated with CO_2 capture.

LITERATURE

[1] Chmielniak T., The role of various technologies in achieving emissions objectives in the perspective of the years up to 2050. Rynek Energii, 2011;92:3-9

[2] Chmielniak T., Łukowicz H., Kochaniewicz A., Trends of modern power units efficiency growth. Rynek Energii, Nr 6(79), 2008, 14-20.

[3] Kotowicz J., Janusz-Szymańska K., Influence of CO_2 separation on the efficiency of the supercritical coal fired power plant. Rynek Energii, 2011, 2 (93), 8-12.

[4] Liszka M., Ziębik A.: Coal – fired oxy – fuel power unit – Process and system analysis. Energy, 35 (2010), 943 – 951.

[5] Toftegaard M.B., Brix J., Jensen P.A., Glarborg P., Jensen A.D., Oxy-fuel combustion of solid fuels. Progress in Energy and Combustion Science, 2010;36:581-625

[6] Dillon D.J., White.V., Allam R.J., Wall R.A., Gibbins J., Oxy-combustion Process for CO2 Capture from Power Plant. Mitsui Babcock Energy Limited,2005

[7] Buhre B.J.P., Elliott L.K., Sheng C.D., Gupta R.P. and Wall T.F., Oxy-fuel combustion technology for coal-fired power generation. Progress in Energy and Combustion Science, 2005;31:283-307

[8] Pfaff I., Kather A., Comparative thermodynamic analysis and integration issues of CCS steam power plants based on oxy-combustion with cryogenic or membrane based air separation. Energy Procedia 1 (2009) 495-502.

[9] Stadler H. et al.: Oxyfuel coal combustion by efficient integration of oxygen transport membranes. International Journal of Greenhouse Gas Control 5 (2011) 7-15.

Analysis of potential improvements to the lignite-fired oxy-fuel power unit

Marcin Liszka[a], Jakub Tuka[b], Grzegorz T. Nowak[c], Grzegorz Szapajko[d]

[a] Institute of Thermal Technology, Silesian University of Technology, 44-100 Gliwice, Konarskiego 22, Poland, marcin.liszka@polsl.pl
[b] Institute of Thermal Technology, Silesian University of Technology, 44-100 Gliwice, Konarskiego 22, Poland, jakub.tuka@polsl.pl, CA
[c] Institute of Thermal Technology, Silesian University of Technology, 44-100 Gliwice, Konarskiego 22, Poland, grzegorz.t.nowak@polsl.pl
[d] Institute of Thermal Technology, Silesian University of Technology, 44-100 Gliwice, Konarskiego 22, Poland, grzegorz.szapajko@polsl.pl

Abstract:
One of the most promising technologies for coal-to-electricity conversion considering CO2 removal is the oxy-fuel process. As the energy efficiency of oxy-fuel system is ca. 10 percentage points lower than traditional pulverized-coal power unit, it is desirable to look for ways to partial recovery of efficiency loss due to CO2 capture. The main goal of the presented paper is the energy analysis of several structural improvements of the oxy-fuel power unit based on waste energy recovery and waste product (nitrogen) utilization. Five case studies have been proposed and analysed. First, the reference lignite-fired, oxy-fuel power unit have been proposed and simulated. It is composed of boiler, flue gas recirculation loop, steam cycle, air separation unit and CO2 purification and compression system. The subsystems are however only slightly integrated representing the state of the art for oxy-fuel systems proposed in recently published pre-feasibility studies. Remaining cases are focused on ideas for efficiency improvements like heat recovery from the flue gas to combusted oxygen, heat recovery from the flue gas compression train to steam cycle, as well as, lignite drying by waste nitrogen leaving the air separation unit. First two of these ideas have been already investigated in the literature, while the use of waste nitrogen for coal drying seems to be innovative and promising. As the nitrogen leaving air separation unit is completely dry, its potential for lignite drying is higher than for ambient air. Moreover, the risk of ignition and explosion in the dryer is minimised. The last, fifth case is the summarize of all structural improvements. The Thermoflex software has been used as simulation tool for all analysed cases. The proposed improvements based on waste heat recovery within the oxy-fuel power unit may bring substantial rise of the net electric efficiency. The reference, not thermally integrated plant, achieves the efficiency of 29.55%, while in case of highly integrated plant (almost all waste heat is utilized) the efficiency increases to 32,98%.

Keywords:
Oxy-fuel, CCS, integration, lignite, drying

1. Introduction

One of the most promising technologies for coal-to-electricity conversion considering CO2 removal is the oxy-fuel process. As the energy efficiency of oxy-fuel system is ca. 10 percentage points lower than traditional pulverized-coal power unit [1, 2], it is desirable to look for ways to partial recovery of efficiency loss due to CO2 capture. The CCS-related drop of efficiency is mainly caused by the necessity of ASU and CO2 purification and compression system installation. On the other hand, the utilisation of waste energy generated within these subsystems is possible.

The main goal of the presented paper is thus the energy analysis of several structural improvements of the oxy-fuel power unit based on waste energy recovery and waste product

(nitrogen) utilization. Five case studies have been proposed and analyzed. The first one is a reference, lignite-fired oxy-fuel power unit. It is composed of boiler, flue gas recirculation loop, steam cycle, air separation unit and CO2 purification and compression system. The subsystems within the reference case have been only slightly integrated. It represents therefore, the state of the art for oxy-fuel systems proposed in recently published prefeasibility studies [3, 4]. Remaining cases are focused on ideas for efficiency improvements like heat recovery from the flue gas to combusted oxygen, heat recovery from the flue gas compression train to steam cycle, as well as, lignite drying by waste nitrogen leaving the air separation unit. First two of these ideas have been already investigated in the literature, while the use of waste nitrogen for coal drying seems to be innovative and promising. The results dealing with heat recovery from the flue gas to combusted oxygen have been presented in [2]. Authors concluded that it is better to use the waste heat to preheat boiler feed water than oxidizer.

Considering the ASU-waste nitrogen as drying agent for lignite, it is important to mention, that this gas is completely dry and have therefore higher potential for moisture absorption than ambient air. Moreover, the risk of ignition and explosion in the dryer is minimized.

The last, fifth case summarize all structural improvements applied in previous cases.

2. Case studies

General assumptions for all analysed cases have been summarized in Table 1. As it has been already mentioned case no. 1 is the reference.

Table 1. Analyzed case studies

	Heat recovery from the flue gas to combustion oxygen	Heat recovery from the flue gas compression train to steam cycle	Lignite drying by waste nitrogen
Case 1	NO	NO	NO
Case 2	YES	NO	NO
Case 3	NO	YES	NO
Case 4	NO	NO	YES
Case 5	YES	YES	YES

2.1 Reference case (Case 1)

The flow sheet of the reference case has been presented in Fig. A1a and A1b in the appendix A. The reference case structure composes of boiler, flue gas treatment and conditioning line, CO2 compression system, ASU and supercritical steam cycle. The recirculation loop is of hot and wet type which means that part of the flue gas which goes back to the furnace to control the flame temperature has not been cooled down and the moisture has not been condensed. In accordance to [2], oxy-fuel power units equipped in hot or cold recirculation loop do not differ in energy efficiency.

Main parameters of the reference case plant have been presented in Table 2. Volumetric content of oxygen in oxidizer entering the combustion chamber has been assumed to 23,5% which enables for keeping similar adiabatic flame temperature and heat exchange rates in the boiler furnace as for conventional air-combustion system [5].

The net amount of the flue gas leaving the boiler island is of high CO2 concentration (ca 82,5 %vol), however further inert gas separation (mainly O2 and N2) is necessary. Inert gas separation line is of cryogenic type. The inert gas separation line has not been physically modelled within the current paper as it is not related to the analysed waste heat recovery systems. After [3], it has been just assumed that there is some required flue gas pressure before the cryogenic separation unit. The flue gas pressure drop within the separation installation, as well as, separation effectiveness have also been assumed as constant values. The auxiliary power consumption related to inert gas separation is determined as power of flue gas compressors. Finally, the CO2 content in flue gas leaving the oxy-fuel system is nearly 96% and is the same as reported in [3].

The steam cycle is of single reheat supercritical design. Its structure and parameters represent the best available technology for today plants – the parameters of live / reheated steam are: 600OC, 28,5MPa / 620OC, 5MPa.

2.2 Heat recovery from the flue gas to combustion oxygen (Case 2)

The idea of case 2 has been shown in Fig. 1, where the oxygen heater has been added between ASU and boiler. The oxygen taken from ASU exhaust is preheated up to 260^{0}C by the flue gas flowing within the main recirculation loop. The detailed flow sheet of Case 2 has been presented in Fig. A2 in appendix A. The steam cycle is the same as for the reference case, so the Fig. A1b in appendix A refers also to case 2.

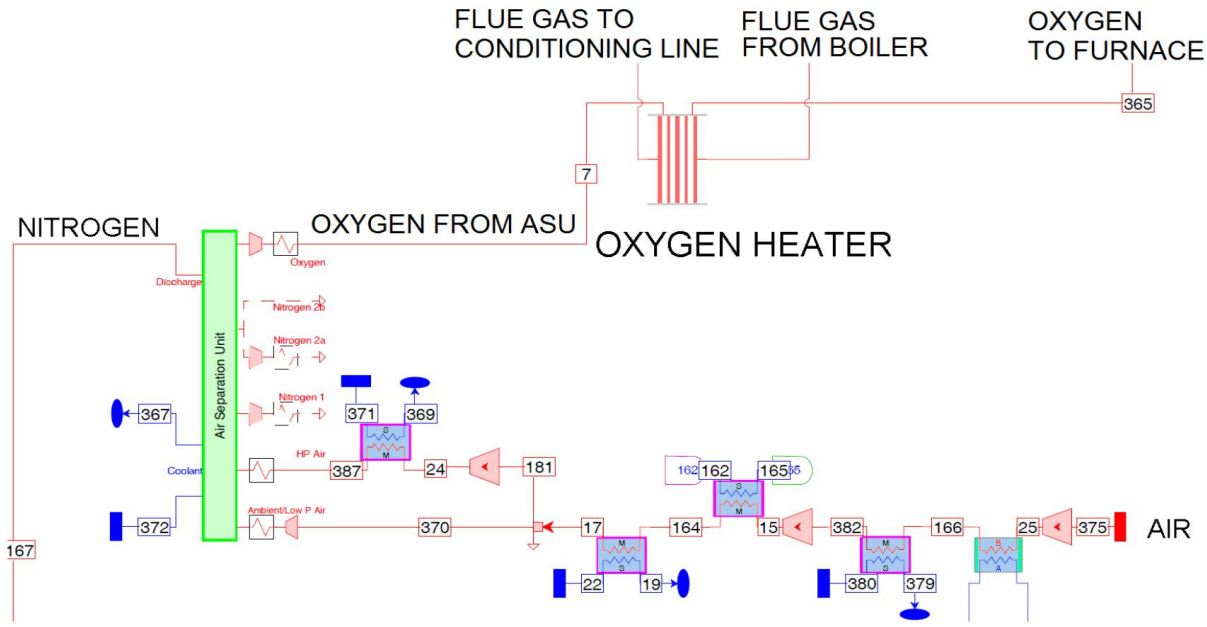

Figure 1. Idea for heat recovery from the flue gas to combustion oxygen (case 2)

2.3 Heat recovery from the flue gas compression train to steam cycle (Case 3)

The idea for heat recovery from the flue gas compression train to steam cycle which is the essence of case 3 is presented in Fig. 2. Recovered heat replaces the LP heat regeneration within the steam cycle in ca 70%. The detailed flow sheet of Case 3 has been presented in Fig. A3a and A3b in appendix A.

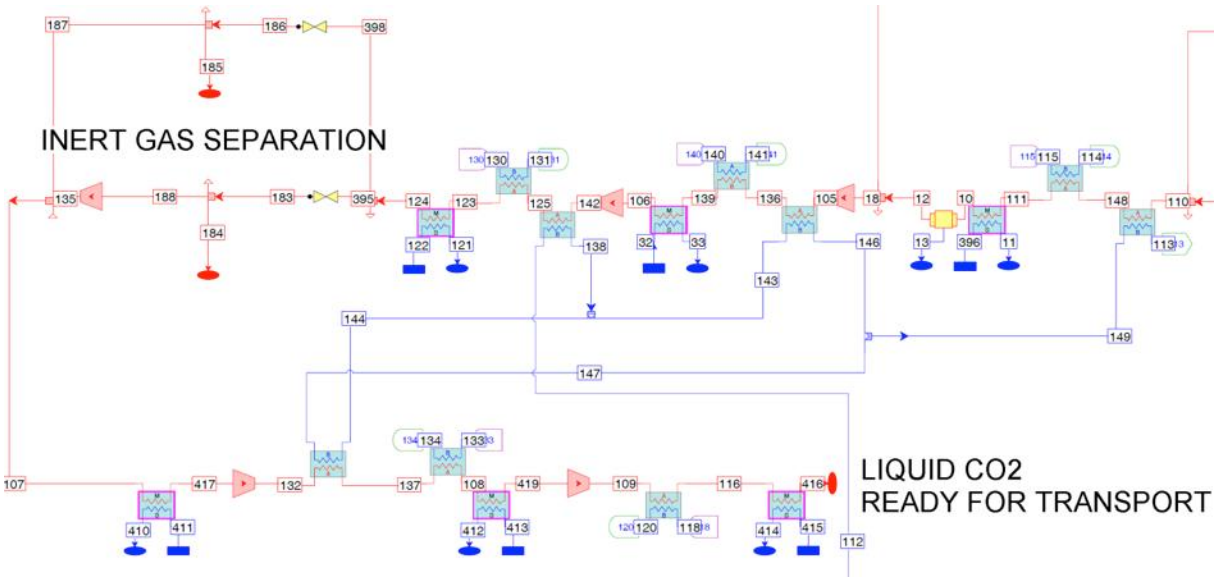

Figure 2. Idea for heat recovery from the flue gas compression train to steam cycle (case 3)

Comparing to the reference case, the additional flue gas coolers located behind appropriate compression stages have been added. The cooling media within these new coolers is steam cycle condensate. The flue gas is finally cooled to the required, possible lowest temperature before following compression stage by cooling water as for the reference case.

2.4 Lignite drying by ASU-waste nitrogen (Case 4)

The idea for lignite drying by ASU-waste nitrogen (case 4) is presented in Fig. 3. The plant structure includes fluidized-bed lignite dryer fed by dry nitrogen taken from ASU exhaust. Additionally, the heat exchanger is located inside the bed to enhance the heat transfer to the fuel being dried. Such a technology has been tuned for utilization of low-temperature waste heat and follows the commercially proved idea presented in [6]. The coal dryer applied within power system presented in [6] uses however air as drying agent and assumes integration with conventional air-firing boiler.

It has been assumed, that the dry nitrogen and water for the in-bed heat exchanger are preheated by the compressed air from the ASU air compression line. The detailed flow sheet of Case 4 has been presented in Fig. A4 in appendix A. The steam cycle is the same as for the reference case, so the Fig. A1b in appendix A refers also to Case 4. Detailed information about streams entering fuel drier has been shown in Table 2.

Table 2. Detailed information about streams entering fuel dryer

Stream (No at Fig.3)	Temperature, ^{0}C	Mass flow, kg/s
Nitrogen entering preheater (158)	30	566,9
Nitrogen entering fuel dryer (161)	70	566,9
Nitrogen leaving fuel dryer (155)	35	575,3
Lignite entering fuel dryer (159)	25	219,2
Lignite leaving fuel dryer (2)	30	204,5

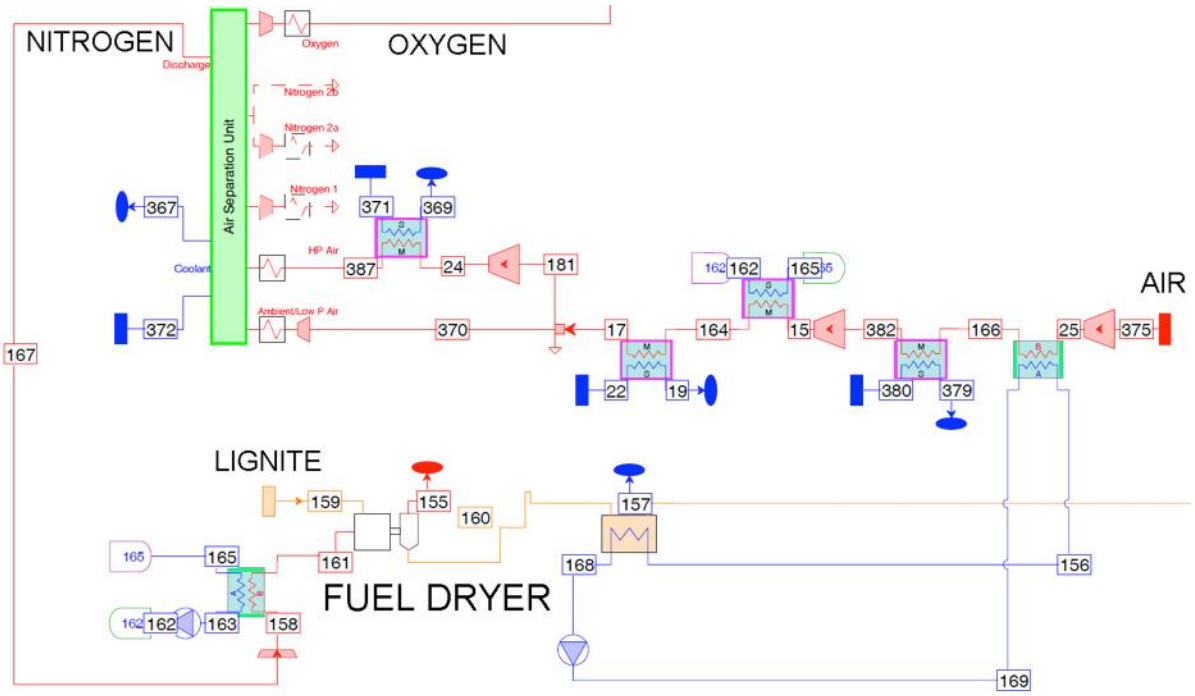

Figure 3. Idea for lignite drying by ASU-waste nitrogen (case 4)

3. Simulation model

All the analysed cases have been modelled using the Thermoflex software [7]. The schemes used for modelling purposes follow structural configurations presented in Figs A1-A4 in appendix A.

Selected assumed parameters of analysed power units have been reported in Table 3. Fuel specification has been shown in Table 4. Parameters presented in Tables 2 and 3 are kept constant for all analyzed cases.

Table 3. Assumed design parameters for simulation modelling

Cooling water temperature rise at each cooler (ASU air, CO2-rich flue gas) and in ST condenser	K	10
Minimal temperature difference (pinch) at each cooler	K	20
Live (HP) steam pressure	MPa	28,5
Live (HP) steam flow rate	kg/s	620
Live (HP) steam temperature	^{0}C	600
Reheated (MP) steam temperature	^{0}C	620
ST condenser pressure	kPa	5
ST polytrophic efficiency	%	89
ASU compressors polytrophic efficiency	%	86
CO2-rich flue gas compressors polytrophic efficiency	%	92
Content of oxygen in oxidizer entering the boiler combustion chamber	% (vol)	23,5
ASU oxygen purity	% (vol)	95
Final CO2 pressure for transport pipeline	MPa	13
Ambient parameters:		
Temperature	^{0}C	15
Pressure	MPa	0,1013
relative humidity	%	60

Table 4. Assumed lignite parameters (as received, mass shares)

Total moisture	%	45,00
Ash	%	20,00
Carbon	%	23,80
Hydrogen	%	2,17
Nitrogen	%	0,25
Sulphur	%	0,70
Oxygen	%	8,08
LHV	kJ/kg	8340

4. Results

The energy efficiency calculated for a whole oxy-fuel power unit has been selected as a main assessment factor of the proposed improvements. Calculated efficiencies have been presented in Fig. 4. Moreover, the more detailed results of simulation have been collected in Table 6. Temperature profiles for waste heat utilizing units have been shown in Figs 5 and 6.

Table 5. Lignite parameters after drying (mass shares)

Total moisture	%	41,05
Ash	%	21,44
Carbon	%	25,51
Hydrogen	%	2,321
Nitrogen	%	0,268
Sulphur	%	0,750
Oxygen	%	8,661
LHV	kJ/kg	9116

Table 6. Results of simulation

Parameter	Unit	Case 1 (reference)	Case 2	Case 3	Case 4	Case 5 (cumulative)
Live steam flow rate	kg/s	620	620	620	620	620
Chemical energy flow rate (LHV based)	MW	1875,9	1856,2	1875,9	1816,5	1798,6
Generator terminal power	MW	842,5	842,5	879,7	842,5	872,7
Net power output	MW	554,3	558,8	590,2	560,7	593,2
Auxiliary power consumption	MW	288,2	283,8	289,5	281,8	279,5
including:						
- ASU	MW	130,7	129,3	130,7	127,3	125,7
- CO2 compression and purification line	MW	86,1	87,6	88,6	86,3	85,2
- steam cycle	MW	6,0	6,0	6,9	6,0	6,8
- others	MW	65,6	60,8	63,3	62,2	61,8
Total waste heat recovered	MW	0,0	40,2	187,5	30,4	240,3
Net plant efficiency	%	29,55	30,10	31,46	30,87	32,98

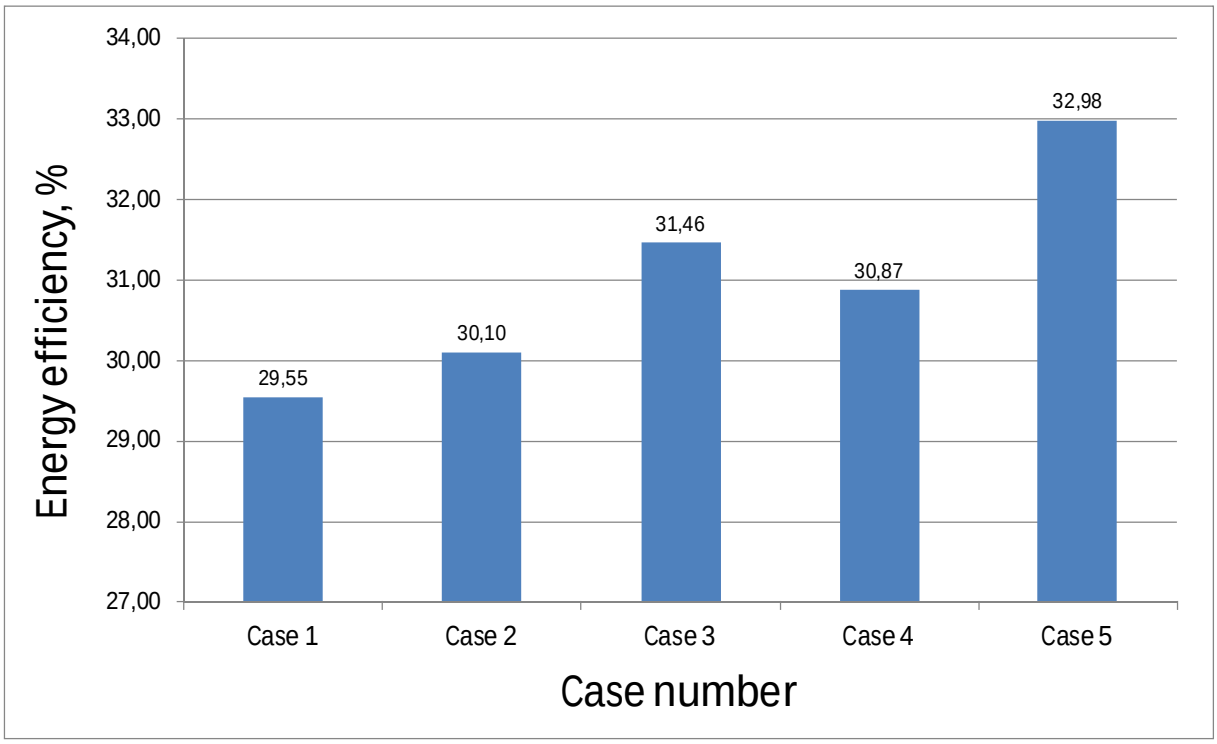

Fig. 4. Energy efficiency of oxy-fuel power unit

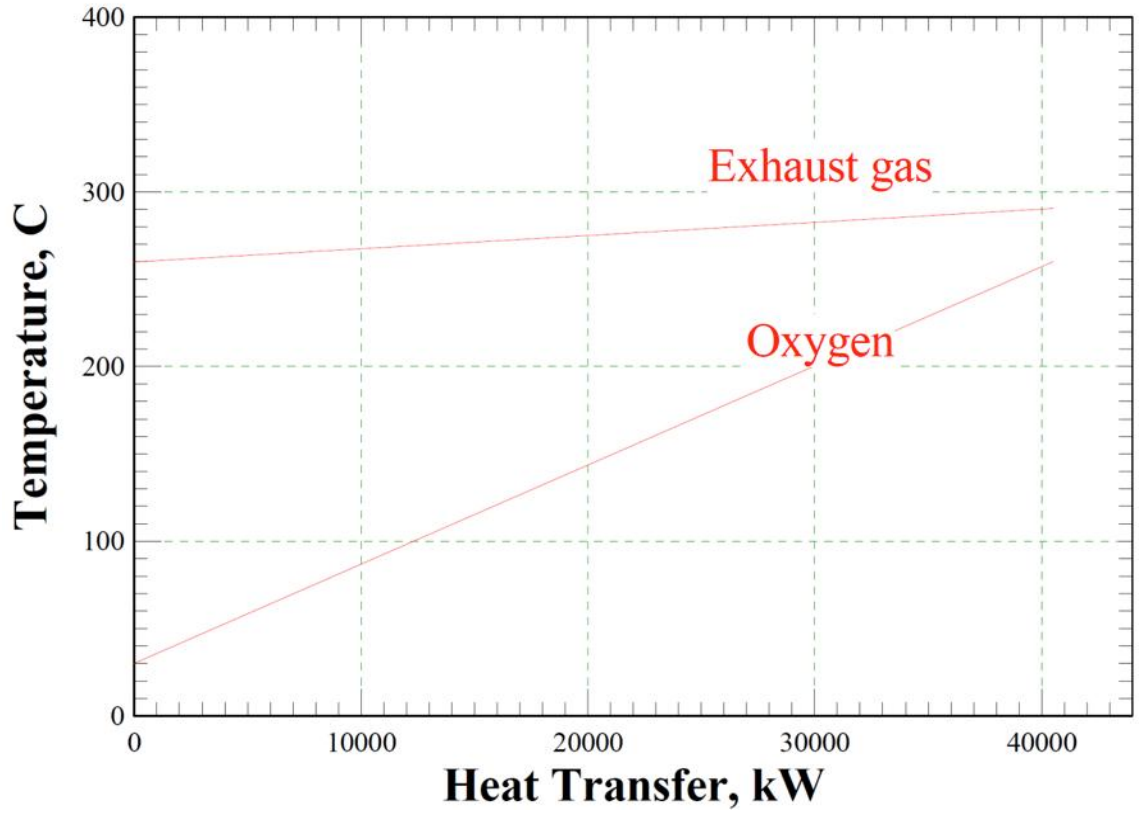

Fig. 5. Temperature profiles in oxygen preheater (case 2)

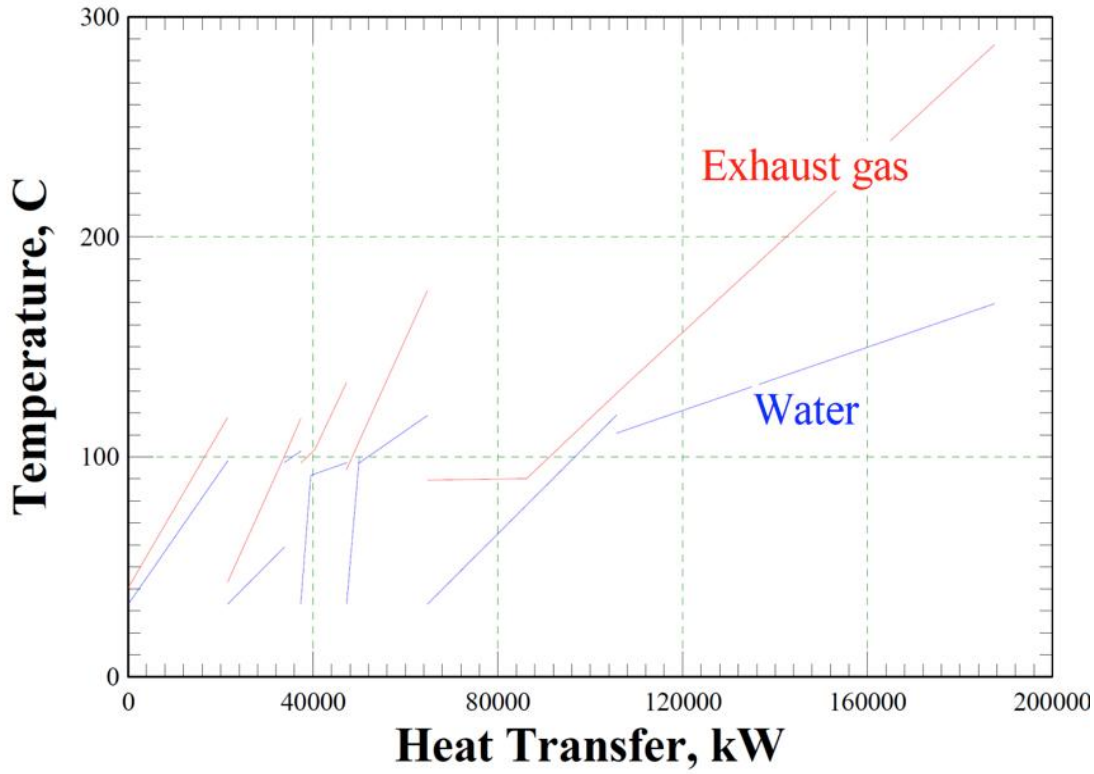

Fig. 6. Temperature profiles in compressors intercoolers preheating steam cycle condensate (case 3)

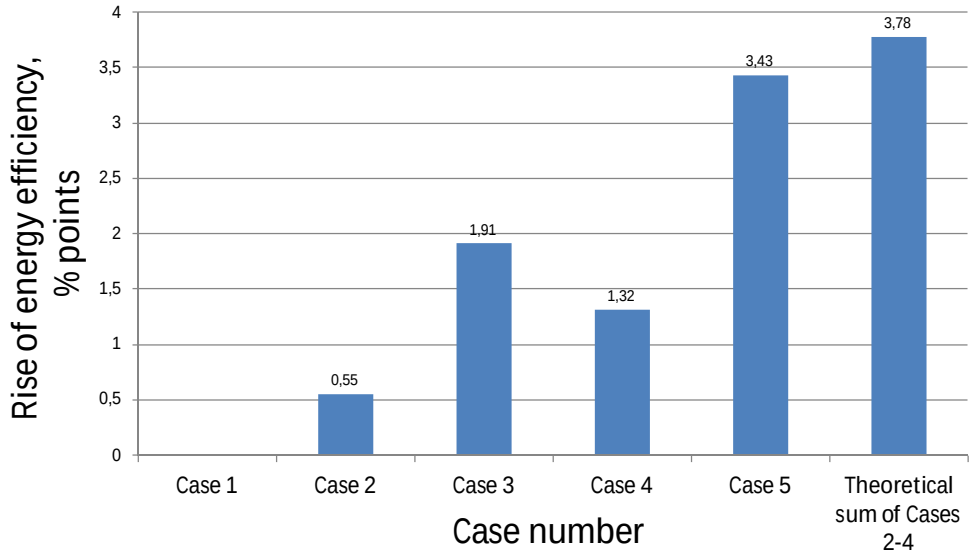

Fig. 7. Increase of energy efficiency related to the reference case

The influence of proposed improvements on the energy efficiency of analysed oxy-fuel power unit is clearly visible. The highest increase, nearly 2 percentage points, brings heat recovery from the flue gas compression train to steam cycle (case 3). The substantial increase of efficiency (1.3 % point) is caused also by lignite drying (case 4). The parameters of lignite after dryer have been presented in Table 5. Heat recovery from the flue gas to combustion oxygen (case 2) provides relatively low (0.5 % point) increase of plant efficiency. Case no 5 which includes all proposed modifications is, as expected the best one, achieving the 3.4%

points efficiency increase related to the reference plant. This increase is however lower than sum of efficiency changes obtained for cases 2, 3 and 4.

5. Conclusions

The proposed improvements based on waste heat recovery within the oxy-fuel power unit may bring substantial rise of the net electric efficiency. The reference, not thermally integrated plant, achieves the efficiency of 29.55%, while in case of highly integrated plant (almost all waste heat is utilized) the efficiency increases to 32,98%.

As results from the temperature profiles in heat exchangers where waste heat is recovered, there is still some potential for increase of waste energy use by e.g. replacing also part of the high-pressure steam regeneration.

Comparing to literature studies, the conclusion drawn in [2] on better results obtained by preheating the steam cycle condensate comparing to preheating of oxidizer has been confirmed within the current research.

The proposed lignite drying by ASU-waste nitrogen is promising technology from the energy efficiency and exploitation safety (explosion risk) points of view. Considering practical aspects presented in [6] for similar air-fed dryers, the verification of dryer dimensions and capital cost will be crucial for final assessment of this technology.

It is important to mention, that the efficiency increase in case no. 5 (relative to the reference plant – case no 1) which simultaneously cumulates all improvements introduced in cases 2, 3, and 4 is less than the sum of efficiency increases obtained in cases 2, 3 and 4. The reason is that each single improvement causes decrease of waste heat production. Moreover, single cases are partially using the same waste heat of the flue gas which is not possible within the cumulated case no 5.

Acknowledgments

This work has been prepared in framework of the task of research: "Development of oxy-combustion technologies for pulverized-coal and fluidized bed boilers integrated with carbon dioxide capture" funded by the Polish National Centre for Research and Development within the strategic program of research and development: "Advanced energy generation technologies".

Nomenclature

ASU	air separation unit
CCS	carbon capture and storage
$\dot{E}_{chfuel}$	chemical energy of lignite, calculated on LHV basis, MW
HP	high pressure
LHV	lower heating value, kJ/kg
MP	medium pressure
LP	low pressure
N_{elN}	net electric power of the system, MW
ST	steam turbine

Appendix A

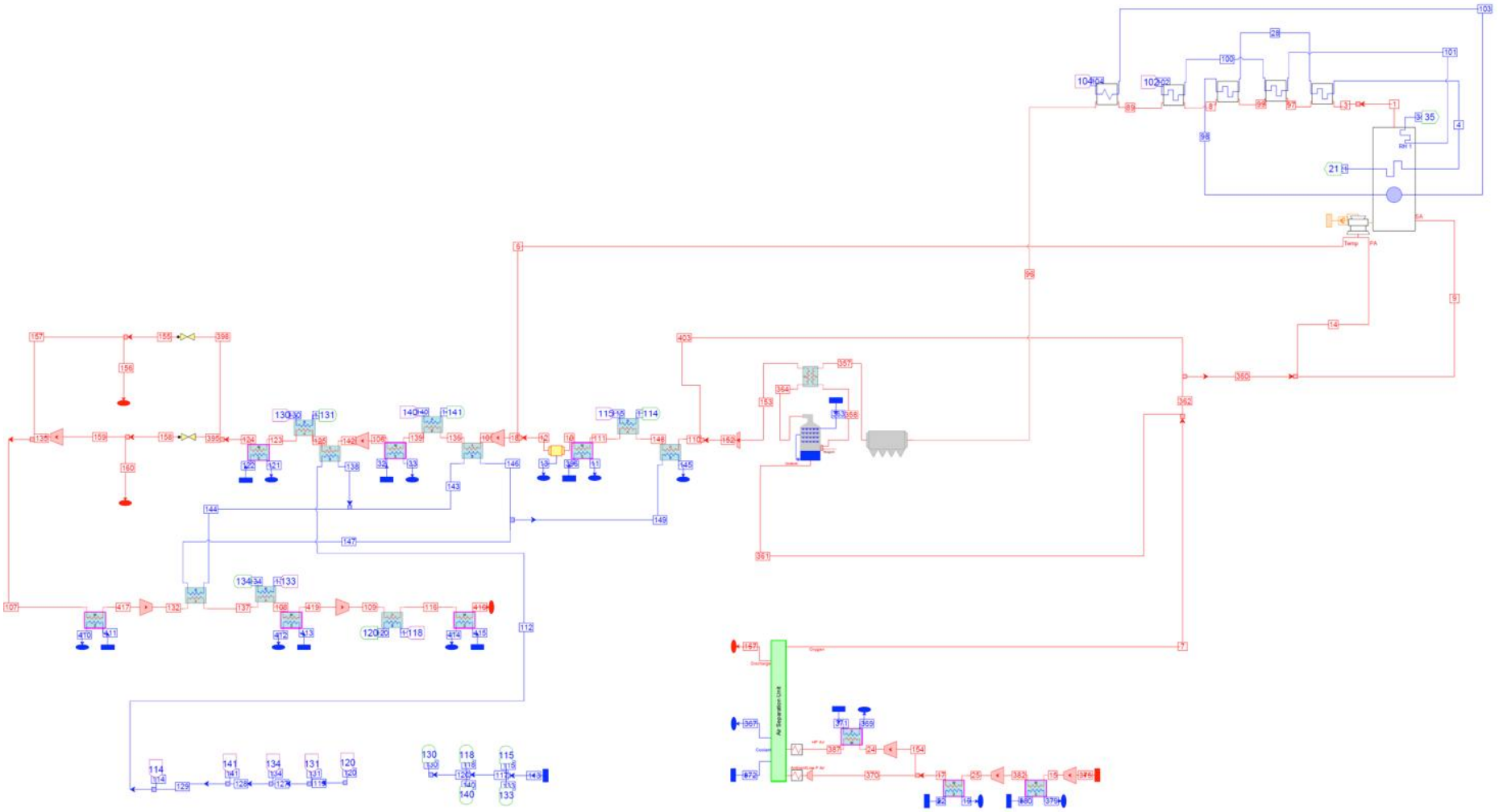

Figure A1a. Thermoflex flow sheet of the reference plant (case no. 1) including boiler, flue gas treatment and conditioning line, CO2 compression system and ASU

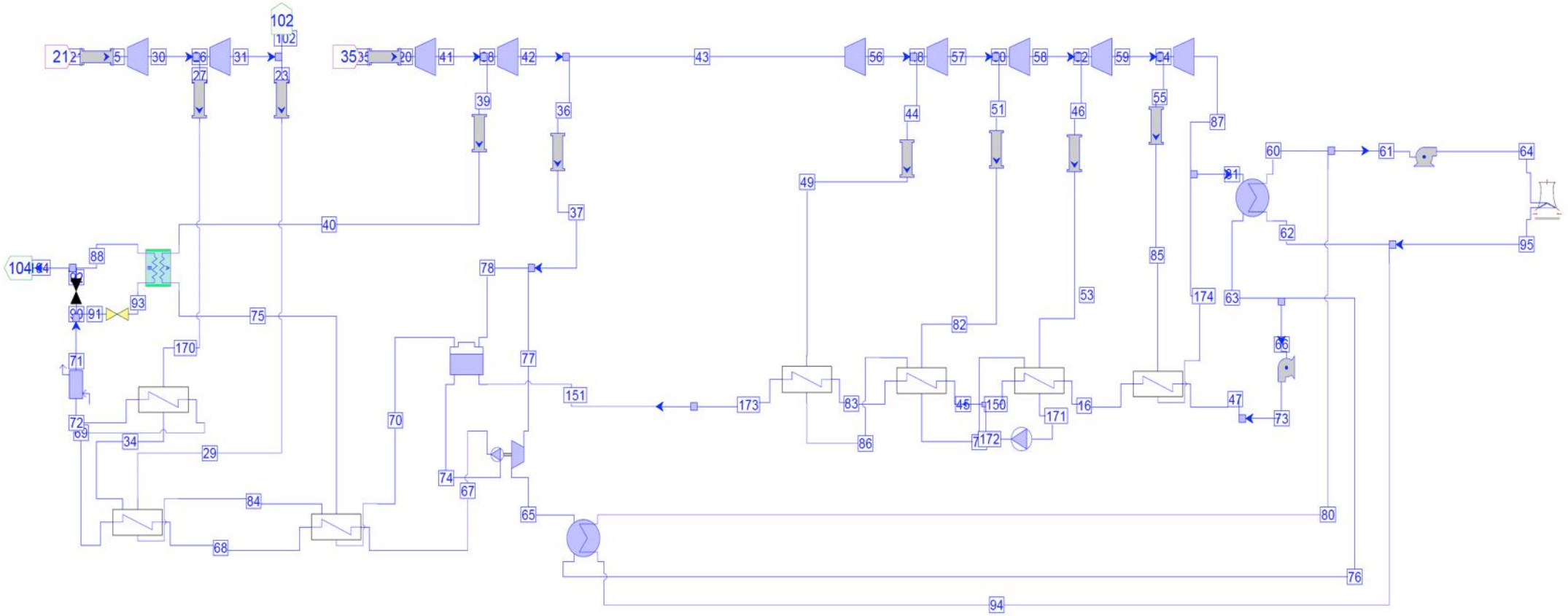

Figure A1b. Thermoflex flow sheet of reference steam cycle (the same for cases no. 1, 2 and 4)

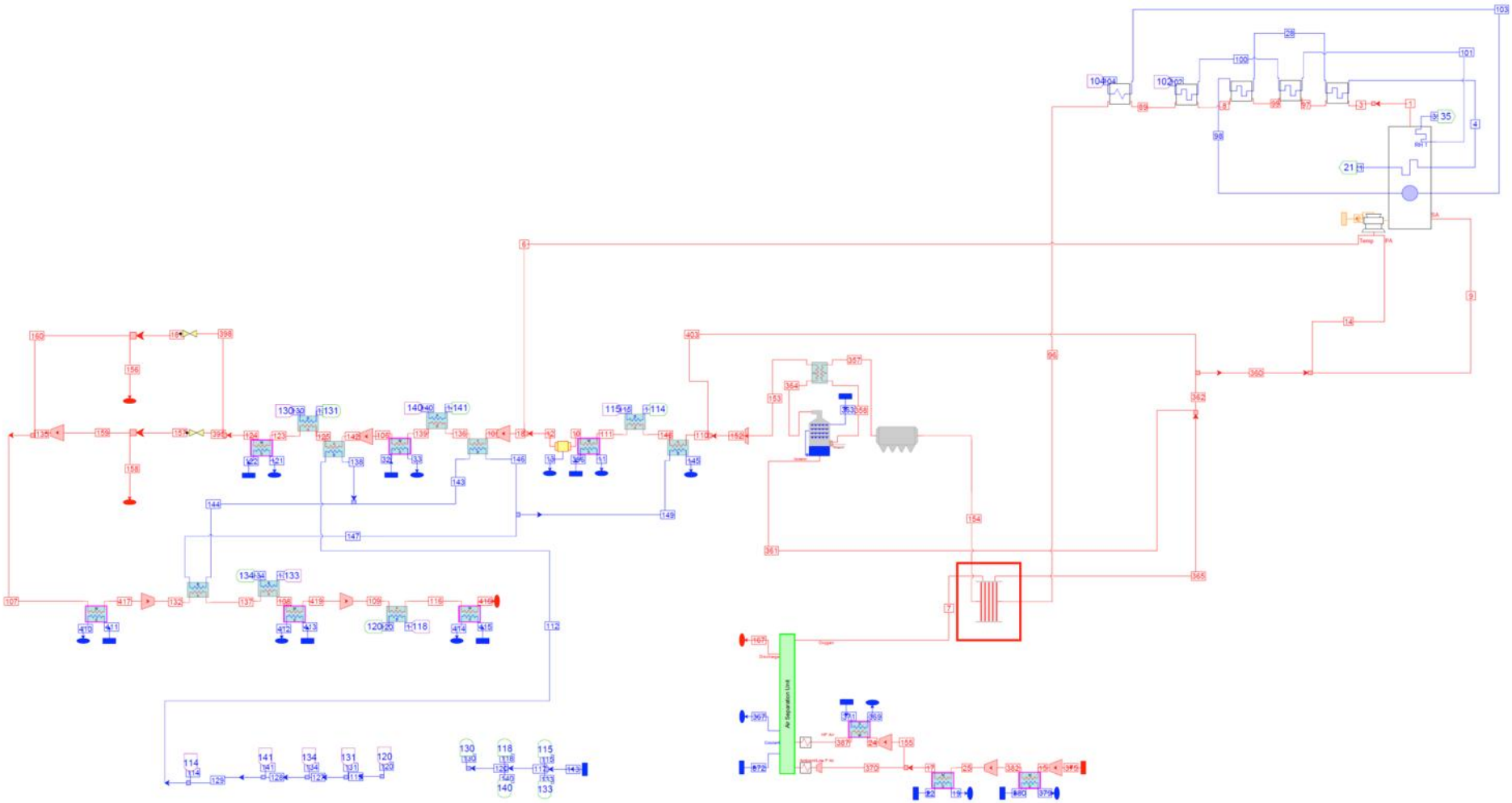

Figure A2. Thermoflex flow sheet of case no. 2 including boiler, flue gas treatment and conditioning line, CO2 compression system, ASU and oxygen preheater (red box)

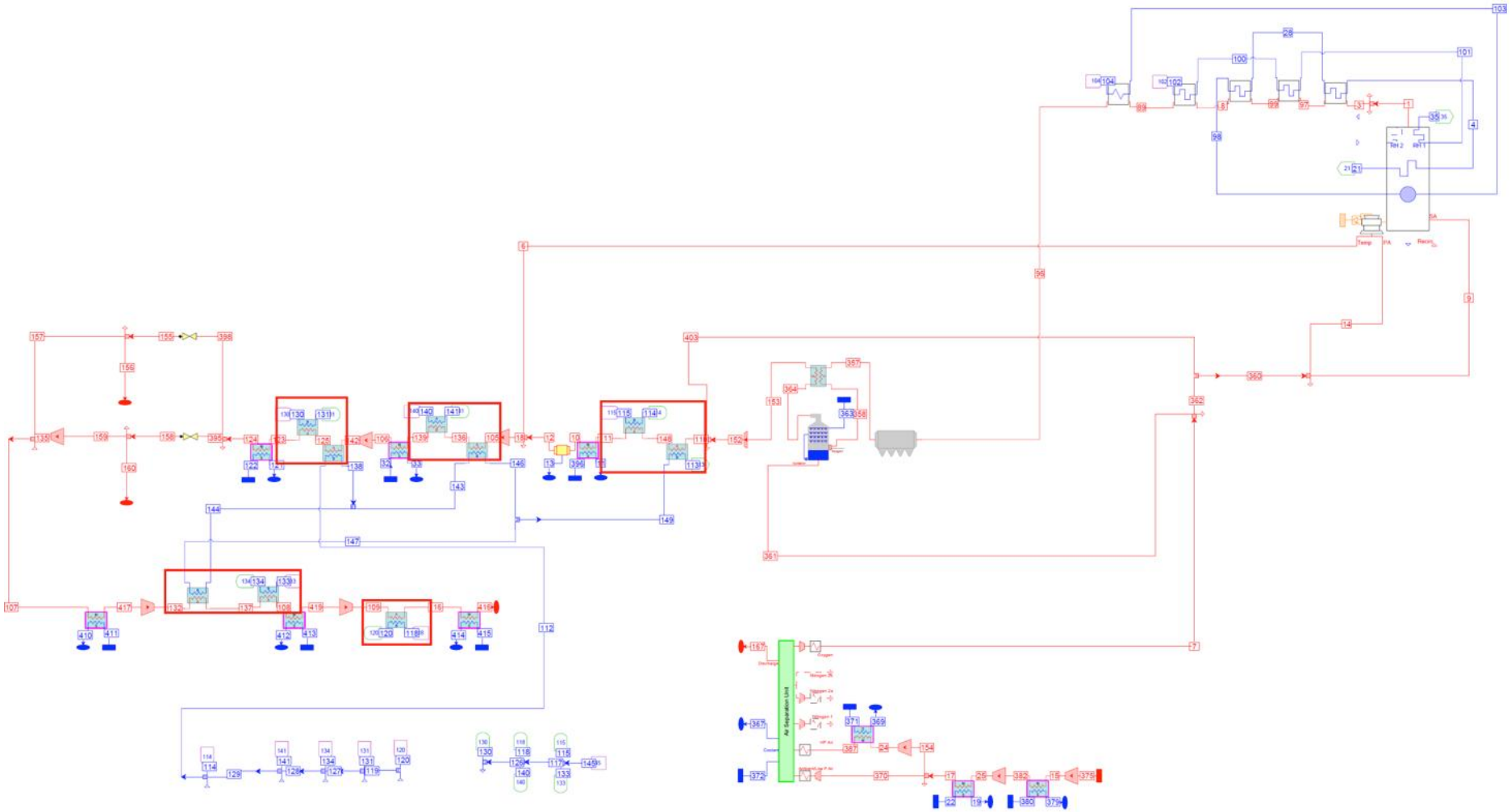

Figure A3a. Thermoflex flow sheet of case no. 3 including boiler, flue gas treatment and conditioning line, CO2 compression system, ASU and heat recovery exchangers (red boxes)

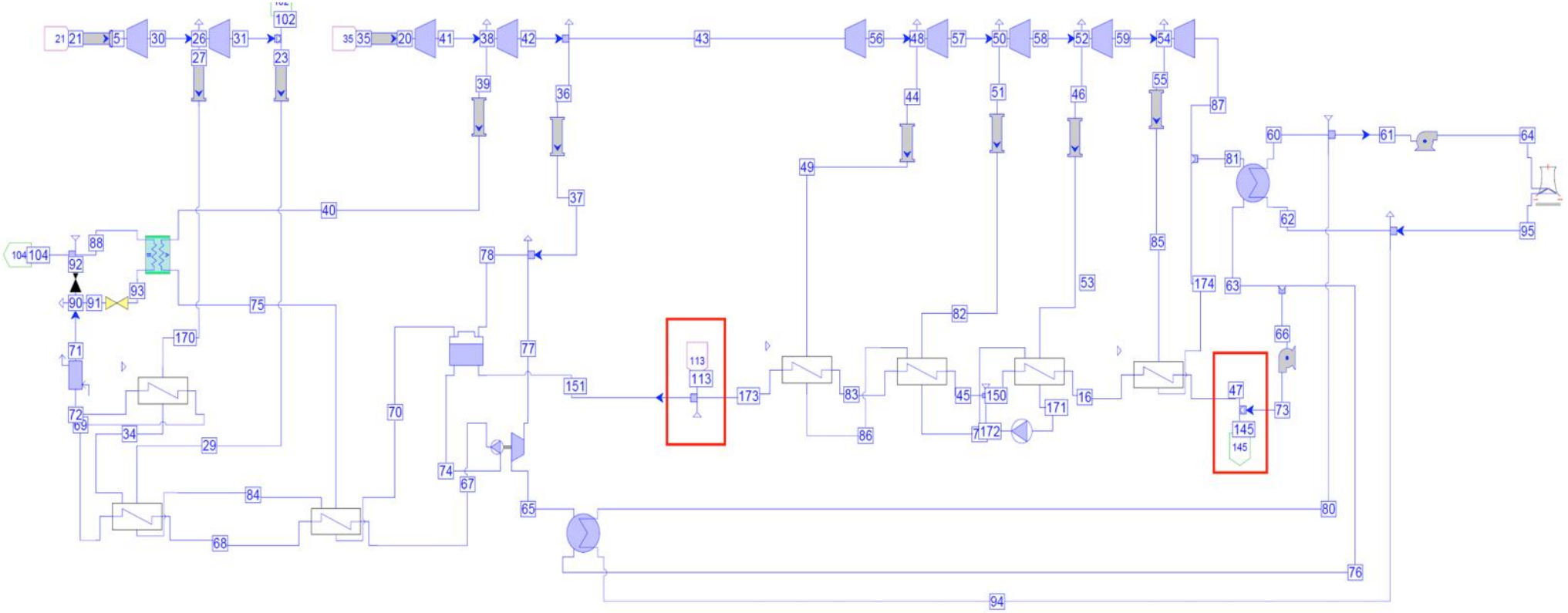

Figure A3b. Thermoflex flow sheet of steam cycle in case no. 3

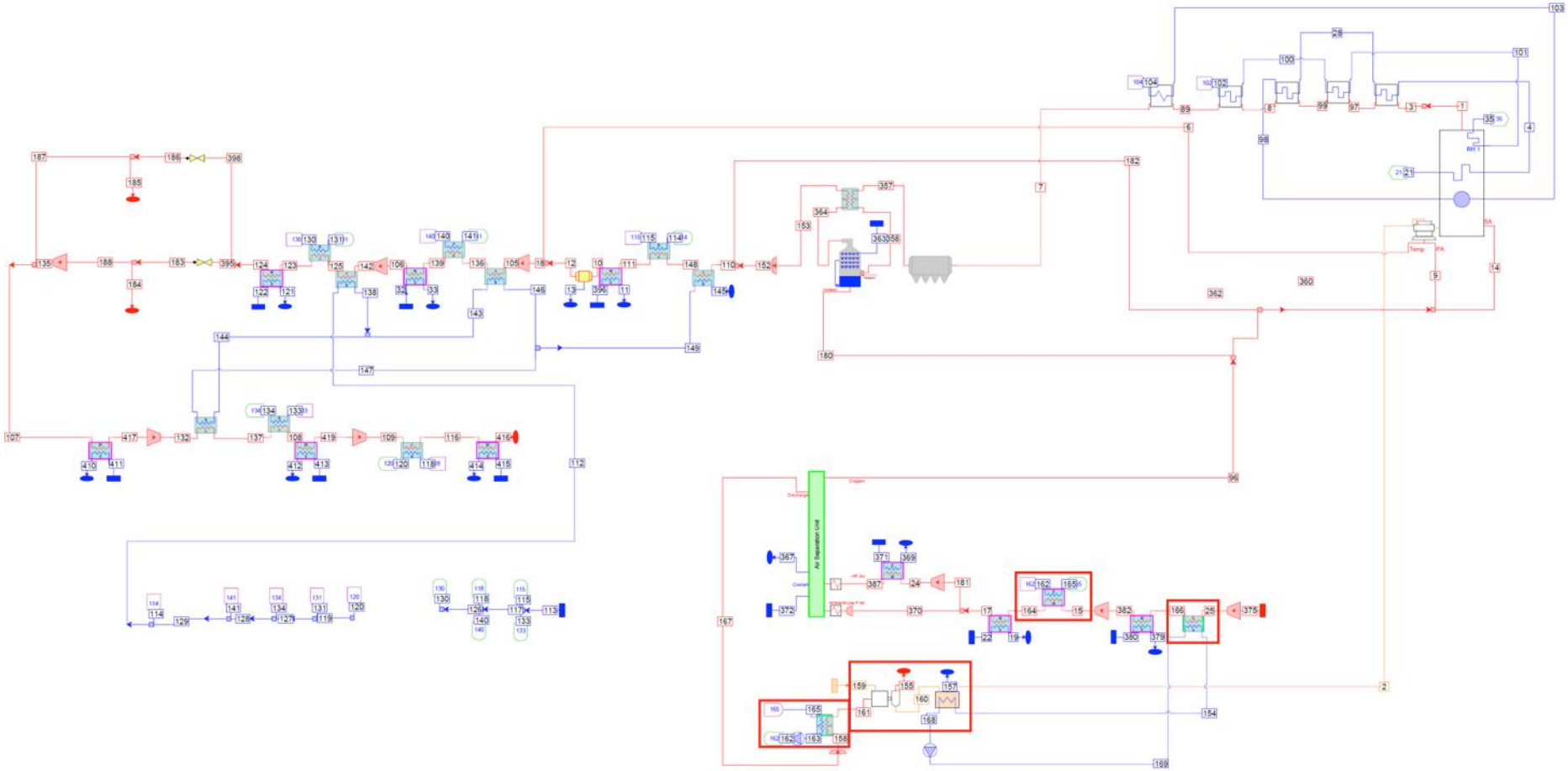

Figure A4. Thermoflex flow sheet of case no. 4 including boiler, flue gas treatment and conditioning line, CO2 compression system, ASU and fuel dryer with heat exchangers (red boxex)

References

[1] CO_2 Capture Ready, IEA Report Number 2007/4, May 2007

[2] Eriksson T., Sippu O., Hotta A., Oxyfuel CFB Boiler as a Route to Near Zero CO_2 Emission Coal. Foster Wheeler

[3] Oxy Combustion Processes for CO2 Capture from Power Plant, IEA Report Number 2005/9, July 2005

[4] Pulverized Coal Oxycombustion Power Plants, DOE/NETL-2007/1291, Final Report August 2008

[5] Hack H., Fan Z., Seltzer A., Eriksson T., Sippu O., Hotta A., Development of Integrated Flexi-Burn Dual Oxidant CFB Power Plant. The 33rd International Technical Conference on Coal Utilization & Fuel Systems, June 1 - 5, 2008 – Clearwater, Florida, USA

[6] Bullinger Ch.W., Sarunac N., Lignite Fuel Enhancement. Final Technical Report Great River Energy, 2010

[7] Thermoflow, Inc., 29 Hudson Road , Sudbury, MA 01776 USA, http://www.thermoflow.com

Biogas Upgrading: Global Warming Potential of Conventional and Innovative Technologies

Katherine Starr[a], Xavier Gabarrell Durany[b], Gara Villalba Mendez[b] , Laura Talens Peiro[c] and Lidia Lombardi[d]

[a] Sostenipra, Department of Chemical Engineering, Xarxa de Referència en Biotechnologia (XRB) de Catalunya, Universitat Autònoma de Barcelona, Bellaterra, Spain, Katherine.starr@uab.cat, CA
[b] Sostenipra, Institute de Ciència i Technologua Ambientals (ICTA), Department of Chemical Engineering, Xarxa de Referència en Biotechnologia (XRB) de Catalunya, Universitat Autònoma de Barcelona, Bellaterra, Spain, Xavier.gabarrell@uab.cat, gara.villalba@uab.cat,
[c] INSEAD - Campus Europe, Fontainebleau, France, laura.talenspeiro@insead.edu
[d] Dipartimento di Energetica, Universita delgi Studi di Firenze, Firenze, Italy lidia.lombardi@unifi.it

Abstract:

Biogas upgrading technologies provides an alternative source of methane and their implementation in waste management systems can help reduce the greenhouse effect. This paper uses a life cycle assessment (LCA) to study eight technologies, six of which are already on the market and the two others are novel technologies that use carbon mineralization in their process in order to not only remove CO2 but also store it. The two technologies are under development in the frame of the UPGAS-LOWCO2 LIFE08/ENV/IT/000429 project (upgas.eu) and include alkaline with regeneration (AwR) and bottom ash upgrading (BABIU). These technologies utilize waste from municipal solid waste incinerators rich in calcium to store CO2 from biogas. Among all conventional technologies, high pressure water scrubbing and chemical scrubbing with amine had the lowest CO2 impacts. The results of the two novel technologies show that BABIU saves 10% more CO2 than AwR. An uncertainty analysis and a material flow analysis showed that the placement of these two novel technologies is an important factor (for CO2 emissions and availability of waste) and therefore they should be located close to a MSWI that produces sufficient waste.

Keywords:

Biogas, Carbon Capture, Carbon Mineralization, Life Cycle Assessment, Sustainability.

1. Introduction

Among the renewables, the biogas industry in the EU is growing, reaching about 8.3 Mtoe in 2009 with more than 6000 biogas plants. The main source is agriculture (52%), then landfills (36%) and sewage plants (12%) [1].

Biogas can be fed with a variety of bio-materials which can be waste or energy crops. Biogas produced in anaerobic digestion plants (AD-plants) or landfill sites is primarily composed of methane (CH_4) and carbon dioxide (CO_2) with smaller amounts of hydrogen sulphide (H_2S) and ammonia (NH_3). Trace amounts of hydrogen (H_2), saturated or halogenated carbohydrates and oxygen (O_2) are occasionally present in the biogas. Usually the gas is saturated with water vapour and may contain dust particles and organic silicon compounds (e.g. siloxanes).

Biogas from anaerobic digestion plants (AD-plants) or landfill sites can be directly used for the production of heat and steam, electricity, vehicle fuels and chemicals. Alternatively, it can be further upgraded to increase the methane concentration, by removing CO_2 and other impurities, in order to be suitable as a substitute for natural gas in the already established distribution grid. This gas can now be regarded as biomethane and is of a quality where it can fed into the natural gas distribution grid or be used as a vehicle fuel. This option is gaining more interest throughout Europe

and there are currently several different commercial technologies for reducing the concentration of CO_2 in biogas.

There are four different types of upgrading technologies which removes CO_2 and they include absorption, adsorption, membrane separation and cryogenic separation. For the absorption processes a reagent is used to absorb CO_2. Within absorption one can find high pressure water scrubbing (HPWS) which uses water, chemical scrubbing (AS) which uses an amine based solvent such as diethanolamine (DEA), and organic physical scrubbing (OPS) which uses a commercial blend of polyethylene glycol. Under adsorption CO_2 is normally adsorbed onto a medium such as activated carbon and then removed through changes in pressure, as in the case of pressure swing adsorption (PSA). For membrane separation (MS) a selective membrane is used to separate CO_2 from the biogas. Cryogenic separation (Cry) separates CH_4 and CO_2 through a decrease in temperature which causes a change in the physical state of the gases [2]. The marketed technologies use varying techniques to process the gas but what they do have in common is that they do not permanently store the CO_2, instead it is sent back into the atmosphere or used for industrial purposes if it meets quality requirements [3].

Currently, under the framework of the UPGAS-LOWCO2 LIFE08/ENV/IT/000429 project, there are two novel upgrading technologies under development additionally storing the separated CO_2 through carbon mineralization. These technologies use wastes from municipal solid waste incinerators (MSWI) rich in calcium compounds to fix CO_2 and thus form calcium carbonate ($CaCO_3$). The two technologies that are being developed, and are currently in the pilot plant stage, are alkaline with regeneration (AwR) – developed jointly "Tor Vergata" in Italy [4,5] - and the bottom ash for biogas upgrading (BABIU) – developed by the University of Natural Resources and Life Sciences in Austria [6,7]. The AwR process, which is a continuous process, absorbs the CO_2 using an alkaline solution of potassium hydroxide (KOH). This solution is regenerated at a rate of 70% when put into contact with air pollution control residues (APC) which is rich in calcium. Once the CO_2 is adsorbed into the APC the biogas (from here referred to as biomethane) is free of impurities. BABIU, which is a batch process, uses a direct solid-gas phase interaction. Biogas is pumped through a column containing bottom ash (BA) rich in calcium, CO_2 is absorbed in the BA and thus the resulting biomethane has a high concentration of CH_4.

In this study the amount of greenhouse gases created and saved by implementing these technologies is analyzed through a life cycle assessment (LCA). Eight technologies that were described above are examined and they include AwR, BABIU, PSA, HPWS, OPS, Cry, MS, and AS. LCA is a useful tool to determine the environmental impact of technologies. While it is often applied to technologies that are on the market, it is often used during the development phase in order to help create a more environmentally sound process [8]. While LCAs have various indicators that can be selected, the Global Warming Potential was chosen as the focus of the study as one of the roles of biogas upgrading technologies could be considered to be reducing CO_2 emissions from anaerobic digesters or landfills.

These results are then compared with a Material Flow Analysis (MFA), which quantifies the flows and stocks of a system, in order to determine the applicability of the novel technologies.

2. Methodology

A life cycle assessment (LCA) was run according to the ISO 14040 [9]. A material flow analysis (MFA) was conducted for the waste flow of Spain as a complement to the LCA.

2.1. Life Cycle Assessment

2.1.1. Goal and Scope

The goal of this study is to determine the global warming potential (GWP) of biogas upgrading technologies. By accounting the GWP, we can identify the process that diverts the highest amount of greenhouse gases from being emitted into the atmosphere.

2.1.2. Functional Unit

The functional unit used for this study is 1 kWh of biomethane upgraded from biogas which is composed of 50% CH_4 and 50% CO_2. This hypothetical composition is applied as it allows one to disregard any prior gas treatment.

2.1.3. System Boundaries

The system boundaries include the electricity used to treat the gas, the production of any reagents used, the amount of biogas that is upgraded, the amount of methane lost during the process either through the treatment (know as methane slip) or lost within the waste gas. Fig. 1 demonstrates the boundaries for the LCA and the uncertainty analysis.

— — LCA

– – – Uncertainty Analysis, transport

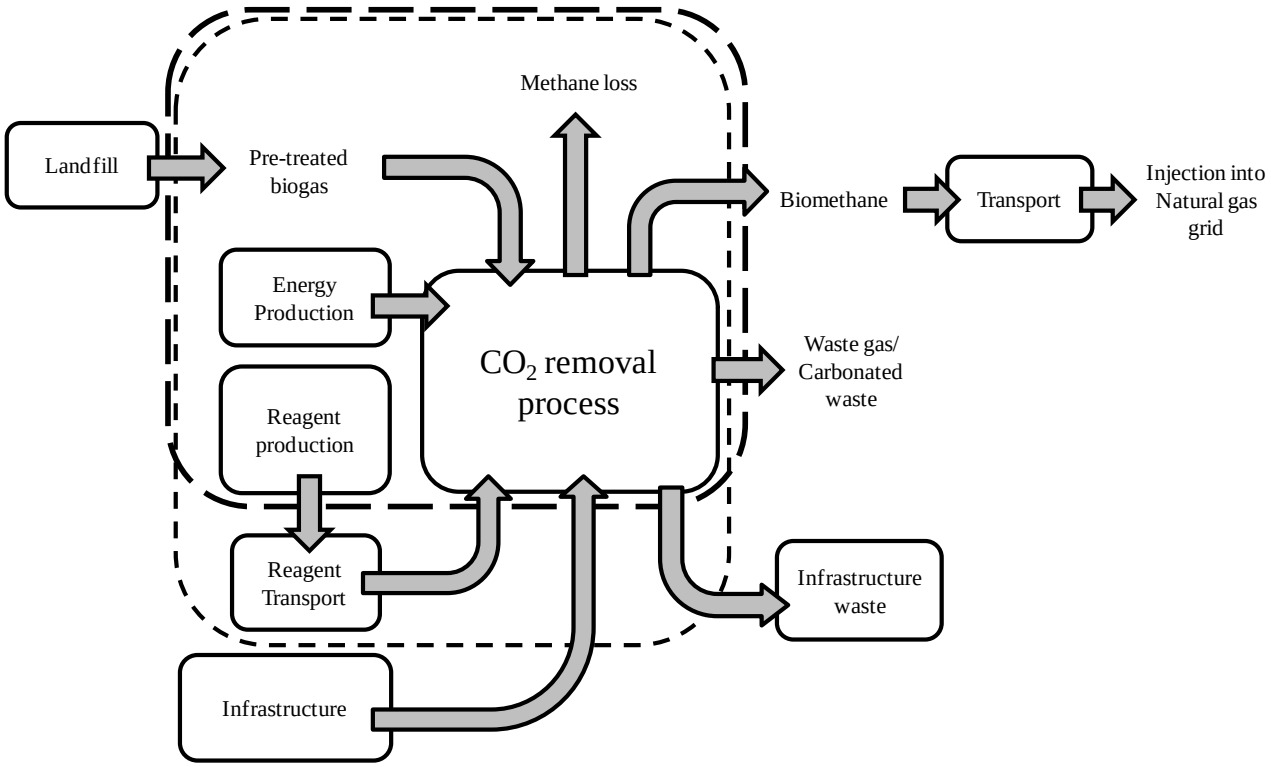

Fig. 1. System boundaries

The processes excluded for the LCA and the uncertainty analyses are the generation of the biogas in landfills and its pre-treatment, and the infrastructure for the CO_2 removal process and to manage the waste generated. The transport of the reagents was excluded from the LCA study, but it was included in an uncertainty analysis discussed in section 3.3.2.

2.1.4. Literature Review

The technologies that were chosen for the study are: AwR, BABIU, HPWS, PSA, AS, Cry, MS and OPS [10].

2.2. Life Cycle Inventory

A life cycle inventory was conducted on the eight chosen technologies. Information on the AwR and BABIU process was obtained through direct email communication and information request forms sent to the Universities developing these technologies, in the framework of the ongoing Life project. Actually, the information for the AwR and BABIU have to be considered preliminary as it is the results of the laboratory analysis phase of the project and has been upscaled to industry size.

Information for the HPWS was obtained through email communications and questionnaires received from representatives of two manufacturers, Greenlane Biogas (part of the Flotech Group) and DMT Environmental Technologies. Information for the other technologies was obtained through literature review. The median point was chosen for information that had more than one value.

Information for reagents used in certain processes was not obtainable and therefore was not included in the study, as in these cases their impact could be considered negligible [10].

Data for the LCA was complemented by the Ecoinvent 2.2 [11] and GaBi PE databases [12] and inventory data for Spain was used. The inventory data used can be found in Table 1.

Table 1. Life cycle inventory data for biogas upgrading technologies per 1 kWh of biomethane (functional unit)

		BABIU	AwR	HPWS	PSA	OPS	AS	MS	Cry	reference
Inputs	Electricity (kWh) [11]	0.017	0.009	0.042	0.051	0.060	0.024	0.068	0.070	[2,3,13-22]
	KOH (kg) [11]		0.087							[19]
	H_2O (kg) [11]		1.468	0.025						[19,21,22]
	N_2 (kg) [12]	0.015								[20]
	DEA (kg) [11]						0.0002			[23]
	BA (kg)	8.890								[20]
	APC (kg)		1.018							[19]
	Diesel (kg) [11]	0.002								[20]
	Biogas (m3)	0.203	0.206	0.203	0.209	0.210	0.202	0.233	0.203	
	Heat (kWh) [11]					0.031	0.109			[14,17,24]
Properties	Biomethane purity (%)	90.3	96.7	98	97.5	97	99	85	98	[2,3,14,16-22,25]
	Methane loss (%)	0.78	2.3	1	3.5	4	0.1	13.5	0.65	[2,3,13-16,18-22,25]

2.3. Life Cycle Impact Assessment

The LCA was run using the program GaBi 4.4. The impact indicator selected for this study is the Global Warming Potential, 100 years [g CO_2 equiv.] from the CML 2001 method [26]. For this impact indicator positive values mean that CO_2 is being emitted and therefore is considered as a negative impact on the environment. Meanwhile negative values mean that CO_2 is removed from the environment and therefore is seen as a positive impact to the environment, or as a CO_2 savings.

The following assumptions were taken into consideration. The methane that is upgraded (also referred to as biomethane) and used as a substitute for natural gas down the line is considered as a CO_2 savings. The CO_2 originally contained in the biogas can either be considered CO_2 neutral if it is released back into the environment or as a savings if it is stored. The methane slip (methane loss) of each process is considered as a CO_2 emission.

As the methane slip and the final biomethane concentration is a property that is inherent to each technology, a sensitivity analysis was performed to ensure that the end results were independent of

these factors. A sensitivity analysis was also preformed to evaluate possible changes once the novel technologies reach industrial scale. As well, two uncertainty analyses were also performed to explore the effects on CO_2 emissions in: the regeneration rate in AwR, the distance between a municipal solid waste incinerator and AwR and BABIU facilities, and the effect of the country where the upgrading plant is located.

2.4 Material Flow Analysis

BABIU and AwR are currently being developed with the goal of applying it to waste treatment processes (Anaerobic Digesters (AD) and landfills) while using waste from another waste treatment process (MSWI). Therefore it is important to study the flows of waste to see whether there would be enough Bottom ash (BA) and air pollution control (APC) residues from MSWI for BABIU and AwR, respectively.

Therefore a MFA was conducted on the municipal waste flows of Spain in 2008. This data was obtained through literature reviews and personal communications with people in the field [27-31]. Once the waste flow was determined three scenarios were planted and explored.

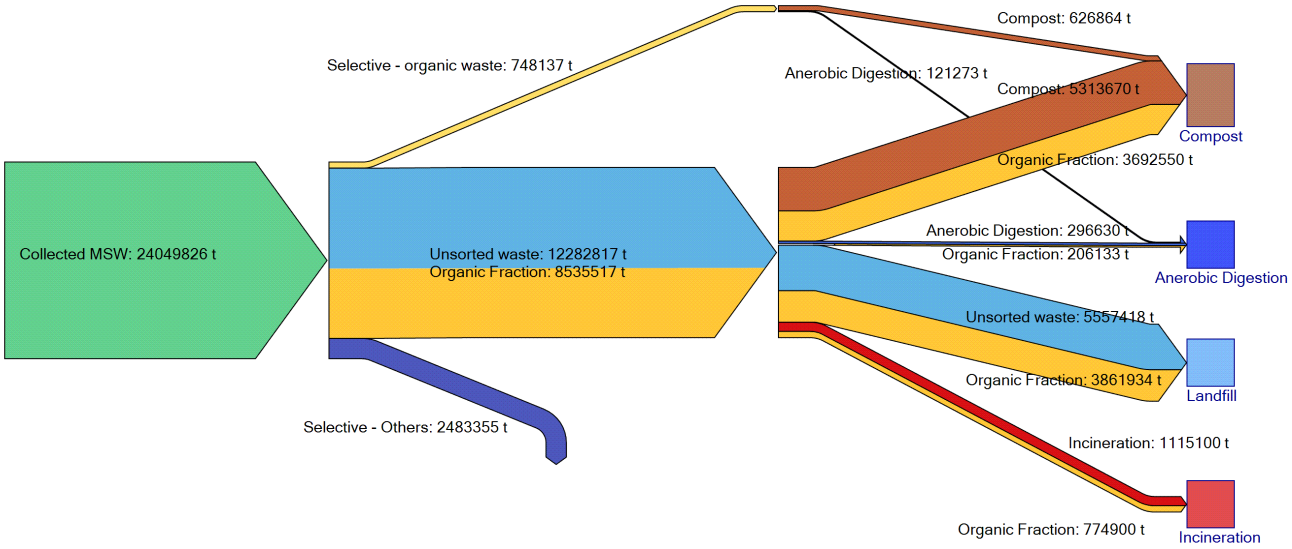

Fig. 2. Urban waste flow of Spain for2008

The amount of organic matter (OM) within the flow of unsorted waste was calculated at 41% [27]. For the potential amount of biogas generated the following assumptions were made: AD generates 115m^3 of biogas per t of OM [32], with a capture rate of 100%; and landfills generate 170 m^3 of CH_4 per t of OM [33], with a capture rate of 30%. The potential amount of BA produced was calculated as 20% of the total waste in MSWI. The potential electricity that can be generated in MSWI was estimated to be around 0.52 MWh/t of waste and was determined based on information provided for a MSWI in Barcelona in 2008 [34].

3. Results and Discussion

3.1. Life Cycle Assessment

Table 2 shows the g of CO_2 saving by each of the technologies under study. The amount of CO_2 saved varies from 1400 g to almost 2000 g. The BABIU process has the lowest global warming potential (GWP) and actually the largest potential CO_2 savings, 1980 g of CO_2 eq. In general all the other processes generate about 10% more CO_2 emissions than BABIU, except for OPS and MS which generate 15% and 25% more emissions, respectively.

Table 2. Global warming potential of biogas upgrading technologies

Upgrading process	Global Warming Potential (g of CO_2 Eqv.)
BABIU	-1977
AwR	-1794
HPWS	-1766
AS	-1761
Cry	-1758
PSA	-1714
OPS	-1691
MS	-1489

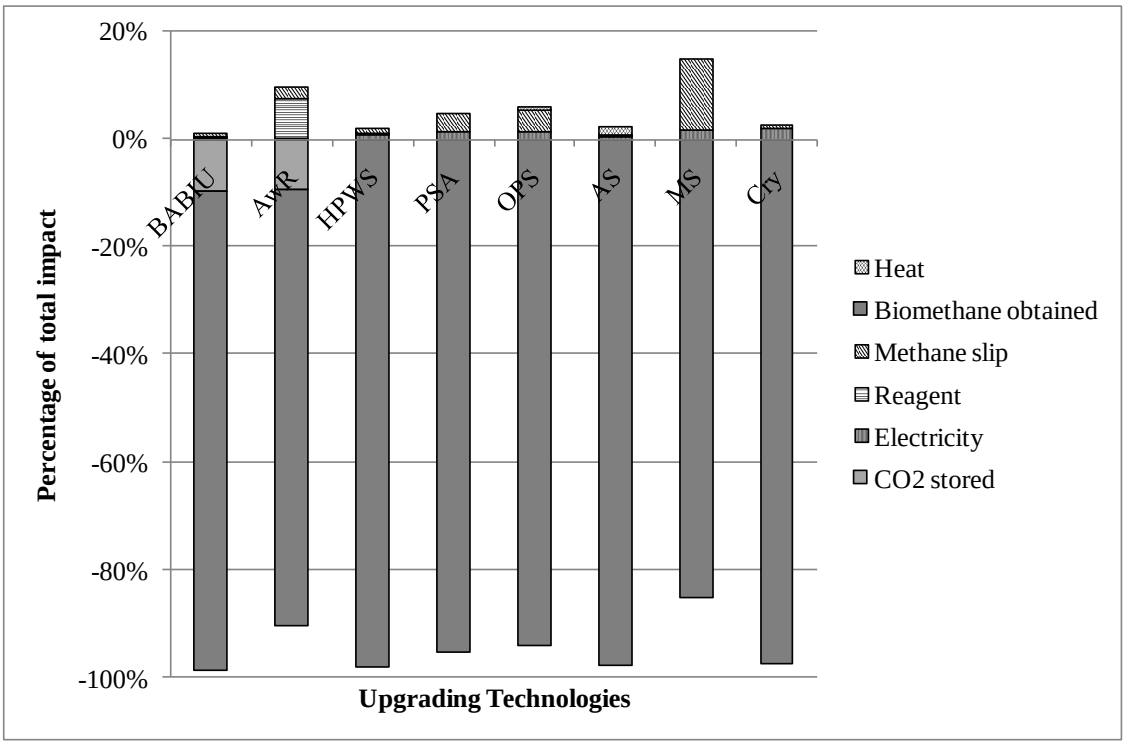

Fig. 3. Breakdown of the global warming impact of biogas upgrading technologies

Fig. 3 demonstrates the role that each component plays in the carbon balance of each technology. The biomethane processed and the CO_2 stored account for the CO_2 savings while the production of reagents, electricity and any methane slip contribute to CO_2 emissions.

The amount of CH_4 processed and turned into biomethane saves the largest amount and accounts for the fact that these technologies overall save CO_2 rather than contribute to climate change, as was demonstrated in Table 2. All the processes do emit CO_2 but the amount saved compensates for this impact. Both the BABIU and the AwR process store CO_2 and therefore this contributes to an extra savings of 198 g and 204 g of CO_2 respectively. The BABIU process had the greatest savings as it not only processes a large amount of biogas but it also produces a relatively small amount of CO_2. While AwR stores more CO_2 than BABIU it doesn't have as high of an overall CO_2 savings due to the production of KOH which counts for 8% of AwR's GWP.

For only two of the upgrading technologies, HPWS and Cry, the electricity used produced the largest amount of CO_2 emissions. For AS the production of required heat was the largest source of emissions. Meanwhile, for all the other technologies BABIU, PSA, OPS and MS, the methane slip that occurs during the upgrading process had the highest negative impact. In the case of MS, the

methane slip contributes to 13% of the overall impact. For these technologies if the methane loss is reduced then their GWP would improve.

3.2. Sensitivity Analysis

Each technology has a final biomethane concentration and methane slip that is inherent to each process. It is therefore of interest to determine whether these characteristics affect their CO_2 balance. A sensitivity analysis done for all the 8 technologies showed that there is no correlation between the GWP of the technologies and the percentage of methane loss nor the final biomethane concentration.

The data obtained for the two novel technologies, BABIU and AwR consist of laboratory scale data that was scaled up to industrial scale. Therefore one can rightfully assume that once these technologies are developed to the industrial level that the data may not be the same. Though in Table 1 it is possible to see that values such as biogas input, electricity use, biomethane purity and methane loss for BABIU and AwR fall within the range established by the other six technologies that are currently on the market. From Fig. 3 one can see that the electricity use and methane loss in play a small role in the overall CO_2 impact of the technologies. Therefore one can assume that while there may be changes once the technologies are commercialized, the effect on the GWP would not be significant. This assumption is supported by a sensitivity analysis conducted where the amount of electricity used by both AwR and BABIU was increased to 0.07 kWh (which is the higher end of the electricity use by commercialized technologies). Applying this new value only reduced the CO_2 savings by less than 1.5 %.

3.3. Uncertainty Analysis

3.3.1. Reagent use in AwR

As was seen in Fig. 3, one of the largest sources of CO_2 for the AwR is the production of the alkaline reagent KOH. Currently, the regeneration rate is around 70%, therefore it was decided to study if improving the regeneration rate would improve the technology enough so that it could be comparable to BABIU and others on the market. As well NaOH is another base that is of interest for this process therefore it was also used in this comparison. The AwR using each base at different regeneration rates were compared to BABIU, AS and HPWS.

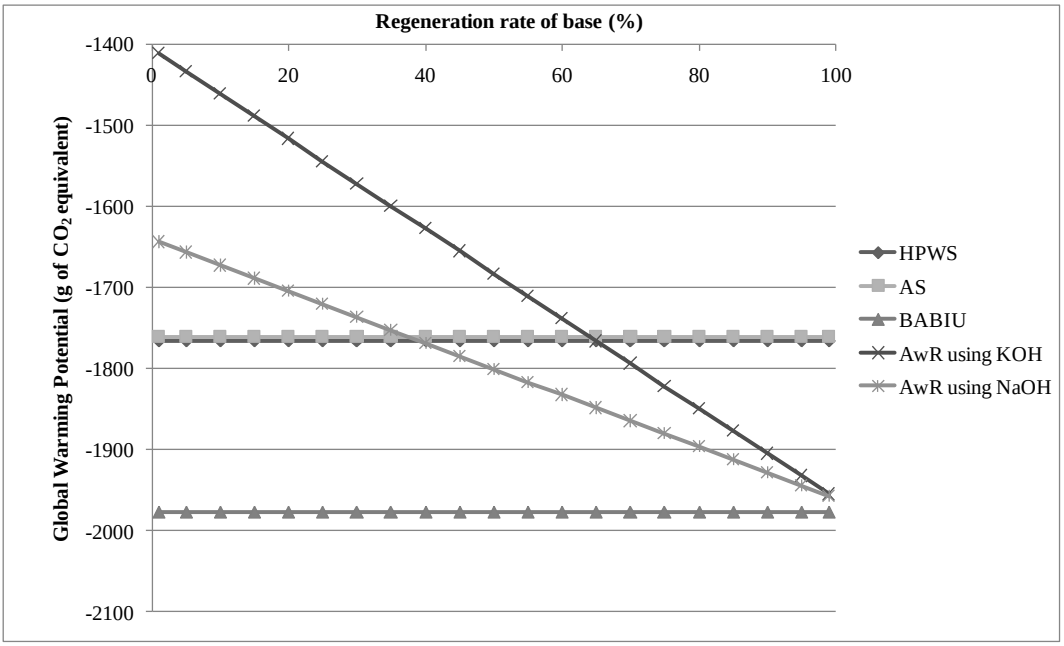

Fig. 4. Comparison of the global warming potential of using KOH and NaOH at varying regeneration rates in AwR

As can be seen in Fig. 4 even if for AwR the regeneration rate of both KOH and NaOH is improved to 99%, BABIU is still the technology with the greatest CO_2 savings. This is due to the fact that the AwR process has a slightly higher methane slip than BABIU. Though, since both of these technologies are in the development stage the methane slip may improve for both before commercialization.

Using NaOH instead of KOH will result in a greater CO_2 savings for AwR. While using KOH, AwR passed HPWS at a 65% regeneration rate but NaOH passed HPWS at a 40% regeneration rate. If the regeneration rates of either bases is improved a greater CO_2 savings is achieved, though if the regeneration rate is not improved and NaOH is substituted for KOH then an additional savings of 71 g can be achieved.

3.3.2. Transport distance and location of technology

A variable in the implementation of the novel technologies that could affect the final CO_2 emissions generated is the location of where the technology is installed. This pertains to both the distance between the upgrading plant and a municipal solid waste incinerator (MSWI), and the country where the upgrading plant is located.

As the novel technologies depend on waste coming from MSWI it is important to determine how the distance between the MSWI and the location of the upgrading technology affects the GWP. As well, large amounts of the waste are needed to run the system, for BABIU it requires 9 kg of bottom ash (BA) and 1 kg of air pollution control residues (APC) for AwR, per functional unit of 1 kWh of biomethane. It was decided to explore the impact related to transport by truck on a small scale with a distance up to 300km.

The electricity production mix of the country where the technology is installed could have an effect on the GWP. For the LCA study the inventory data used was for Spain. We decided to use also the electricity production mix for Italy as the pilot plant of BABIU and AwR are presently located there.

BABIU and AwR were compared to HPWS and AS which are the marketed technologies that showed the greatest CO_2 savings. Though to ensure proper comparability, the energy mixes of both Spain and Italy were used for all four technologies. As well a travel of 50km by truck was applied to any additional reagents used for AwR, BABIU and the amine used in AS.

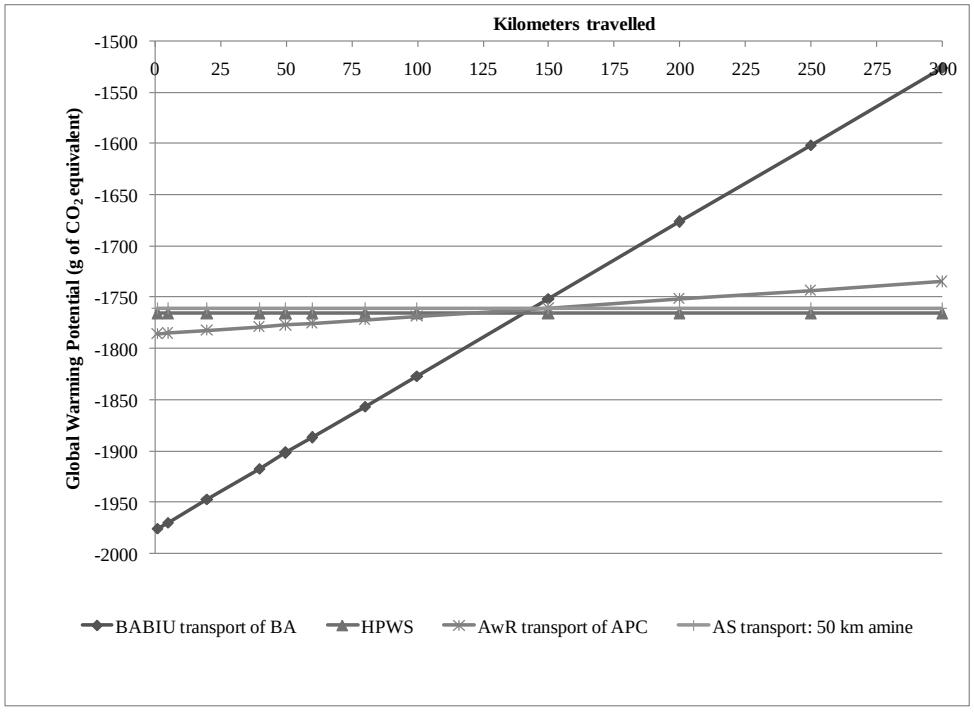

Fig. 5. Comparison of global warming potential of distance of transport of bottom ash for BABIU and APC of AwR.

As can be seen in Fig. 5 the impact of the distance travelled becomes increasingly significant when the amount of waste (APC for AwR and BA for BABIU) transported is increased. From 0 to 125 km the BABIU process still shows the greatest CO_2 savings. At around 145 km the AwR process and the BABIU process have the same CO_2 savings. At distances greater than 145 km the AwR achieves a greater CO_2 savings than BABIU, but at the same time they both have a lower CO_2 savings than HPWS and AS. When the distance between the MSWI and a BABIU plant reaches around 1315 km the impact from transport becomes higher than any CO_2 savings and the process begins to have a negative impact on the environment. For AwR, this point is reach at a much further distance of around 10475 km.

As the other part of the study, it was determined that comparatively the country where the system is implemented does not have a large effect on the GWP. Overall Spain has a greater CO_2 savings than Italy but one could state that the effect is negligible. This difference exists due to the fact that Spain uses more nuclear and solar energy than Italy [11]. Only in HPWS is it possible to note a difference and that is because out of all the 4 technologies the HPWS uses the most energy, therefore highlighting better the difference between the two.

3.4 Material Flow Analysis

Both BABIU and AwR use waste coming from MSWI in order to remove CO_2 from biogas which comes from landfills or anaerobic digesters (AD). Therefore it is of interest to determine how much BA and APC would be needed and whether enough could be generated. To obtain a general idea, the waste flow of Spain in all of 2008 was studied and the hypothetical situation was applied where all of the biogas generated was upgraded through either BABIU or AwR. This was considered as scenario 1.

Fig. 2, which demonstrates the waste flow in Spain, highlights the fact that most of the unsorted waste goes to either the landfill or for composting. On the other hand, Spain currently does not treat a lot of its waste through AD or MSWI.

Table 2. Scenarios for implementation of BABIU and AwR based on municipal waste flow of Spain in 2008

	Waste received (t)	Estimated biogas production (m3)	Estimated electricity production potential (MWh)			BA from MSWI needed for BABIU (t)	APC from MSWI needed for AwR (t)	Possible BA production (t)
			MSWI	BABIU	AwR			
Scenario 1								
Anaerobic digester	624,036	37,651,670		185,476	182,570	1,648,882	185,857	
Landfill	9,419,352	393,917,300		1,940,447	1,910,077	17,250,844	1,944,459	
MSWI	1,890,000		984,007					378,000
Scenario 2								
Anaerobic digester	9,283,654	1,067,620,203		5,259,207	5,176,815	46,754,354	5,269,998	
MSWI	6,672,517		3,473,970					1,334,503
Scenario 3								
Anaerobic digester	624,036	37,651,670		185,476	182,570	1,648,882	185,857	
MSWI	11,309,352		5,888,085					2,261,870

From Table 2 it can be seen that under scenario 1 not enough waste is treated through MSWI to supply sufficient BA or APC to treat all of the biogas emitted from AD and landfills. It might be possible to have enough APC to treat biogas from AD using AwR, but there would not be enough to

treat the biogas from landfills and in both cases there would not be enough BA to treat the biogas using the BABIU process.

In an ideal situation countries would have citizen that are engaged enough to ensure that all organic material (OM) is selectively collected. In scenario 2 all of this OM is treated in the AD and all unsorted non OM waste would be sent to the MSWI. While in this scenario the production of biogas is around 2.5x higher, this would in turn require almost 47,000,000 t of BA for the BABIU process and 5,000,000 t of APC for the AwR, which could not be satisfied as only 6,000,000 t of waste would be treated through MSWI.

Scenario 3 therefore focuses on increasing the amount of BA and APC generated by sending the unsorted waste that would have gone to the landfill to the MSWI instead. In this case there would only be biogas coming from AD. Applying this scenario could generate enough APC for AwR and even enough BA for BABIU. As well, the potential electricity generated through MSWI is greater than the potential electricity from biomethane obtained through upgrading landfill biogas. While this situation seems like the best possible choice, given the current infrastructure of waste management in Spain, it would not be feasible to implement. Currently there are not enough MSWI plants to handle the additional waste.

4. Conclusion

Out of the technologies that are currently on the market the HPWS and AS showed the greatest potential CO_2 savings followed by Cry. In the former and later processes the impact of electricity used plays the largest role in the CO_2 emissions generated, while for AS the production of heat played this role. In the lower end of the spectrum are located PSA, OPS and at last place MS. For all of these three technologies the impact due to the methane slip plays the largest role. If the technologies are improved in these areas then its potential CO_2 savings could possibly be improved.

The BABIU process showed the overall greatest potential CO_2 savings. Though if one starts to factor in the distance between the MSWI and the location where the technology is installed, then it rapidly decreases in CO_2 savings due to the high amount of BA that must be transported. Therefore in order for the BABIU technology to keep its position as best technology, it must be installed within 125 km of a MSWI. As well since BABIU requires a large amount of BA it was found that applying it as a biogas upgrading solution for all of Spain is not realistic. Therefore based on these two studies the installation of BABIU should be applied at a local scale where an AD plant or landfill can be found close to a MSWI. Therefore it is dependent on whether or not there is a MSWI close enough that produces sufficient BA. Meanwhile AwR, which uses less APC per functional unit, has more of a leeway in both the distance from a MSWI and the production capacity of the MSWI.

The production of the KOH used in AwR plays a large role in its CO_2 impact. If the KOH is changed to NaOH then its impact is reduced. AwR can currently obtain a base regeneration rate of 70%, if this is improved then the GWP is improved as well, though it cannot yet achieve the same CO_2 savings as for BABIU.

These novel technologies show a great potential savings mainly due to the fact that they also store the CO_2 from the biogas. If the CO_2 removed from the current technologies is stored then they may also show similar savings, though it would be necessary to factor in the impact of the storage technology as well.

Acknowledgments

The authors of this study would like to thank the Life + 2008 programme for its financial support.

References

[1] Eurobserv'er, The State of Renewable Energies in Europe. Liébard A., Editor; 2010. Technical report: 10th EurOberv'ER Report.

[2] Petersson A., Wellinger A., Biogas upgrading technologies – developments and innovations. IEA Bioenergy; 2009 Oct.

[3] Lems R., Dirkse E., Making pressurized water scrubbing the ultimate biogas upgrading technology with the DMT TS-PWS system. DMT Dirkse Milieutechniek Environmental Technology. 2009.

[4] Baciocchi R., Corti A., Costa G., Lombardi L., Zingaretti D., Storage of carbon dioxide captured in pilot-scale biogas upgrading plant by accelerated carbonation of industrial residues. Energy Procedia 2011; 4: 4985-4992.

[5] Baciocchi R., Costa G., Faraoni G., Lombardi L., Olivieri T., and Zingaretti D., Pilot-Scale Carbonation of APC Residues for CO_2 Storage and Alkali Regeneration Downstream and Absorption Column. Thirteenth International Waste Management and Landfill Symposium; 2011 Oct 3-7; Cagliari, Italy.

[6] Mostbauer P., Lenz S., Upgrading of lean landfill gas using MSWI bottom ash. Proceedings of Eleventh International Waste Management and Landfill Symposium; 2007 Oct 1-5; Sardinia, Italy. CISA publisher.

[7] Olivieri T., Lombardi L., Mostbauer P., Demonstration Scale Upgrading of Landfill Gas with the Use of Bottom Ash –BABIU Process Design and Preliminary Results. Thirteenth International Waste Management and Landfill Symposium; 2011 Oct 3-7; Cagliari, Italy.

[8] Gabarrell X., Font M., Vicent T., Caminal G., Sarra M., Blanquez P., A comparative life cycle assessment of two treatment technologies for Grey Lanaset G textile dye : biodegradation by Trametes versicolor and granular activated carbon adsorption. International Journal of Life Cycle Assessment 2012. In press.

[9] ISO 14040 Environmental management - Life cycle assessment - Principles and framework. 2006.

[10] Starr K., Gabarrell X., Villalba G., Talens L., Lombardi L., Life cycle assessment of biogas upgrading technologies. Waste Management 2012; 32(5): 991-9.

[11] Swiss Center for Life Cycle Inventories. Ecoinvent Data, The Life Cycle Inventory Data. Version 2.2. 2010

[12] PE international, PE international database. Extensions: Ib Inorganic Intermediates, XIV Construction Materials. Last updated: 2010

[13] MT- BIOMETHAN. Gas Treatments, Efficiency - Available at:<http://en.mt-biomethan.com/gasaufbereitung/efficiency> [accessed 02.12.2010]

[14] Badger G., Zach C., Biogasaufbereitungssysteme zur Einspeisung in das Erdgasnetz - ein Praxisvergleich. Munich, Germany: BASE Technologies GmbH, Fraunhofer-Institut für Umwelt-, Sicherheits- und Energietechnik, Bavarian Association for the Promotion of Solar Energy; 2008 Technical Report No: 02

[15] Pertl A., Mostbauer P., Obersteiner G. Climate balance of biogas upgrading systems. Waste Manage. 2010; 30:92-99.

[16] Urban, W., Biogas upgrading to pipeline quality - technology and costs. Presentation at Connecting Clean Mobility conference; 2007 Nov 14-15; Arnhem, Netherlands.

[17] Bekkering J., Broekhuis A.A., van Gemert W.J.T., Optimisation of a green gas supply chain – A review. Bioresour. Technol. 2010; 101; 450-456.

[18] de Arespacochaga N., Bouchy L., Cortina J., Larrotcha E., Sanchez M., Peregrina C., Sewage biogas to biomethane for grid injection: challenges and opportunities in Europe. ORBIT 2010 (Organic Resources for the Carbon Economy) Conference; 2010 Jun 29 –Jul 3; Crete, Greece.

[19] Olivieri, T., Lombardi, L., Costa, G., Upgas environmental assessment forms. 2010, personal communications.

[20] Mostbauer, P., BABIU LCI data. 2010, personal communications.

[21] Rowntree, S., High pressure water scrubber - request for information, GreenLane Biogas. 2010, personal communications.

[22] Kruit, J., PWS - Request for information, DMT Dirkse Milieutechniek Environmental Technology. 2010, personal communications.

[23] Bailey D.W., Feron P.H.M., Post-combustion Decarbonisation Process. Oil & Gas Science and Technology - Rev. IFP 2005; 60:461-474.

[24] Beil M., Beyrich W., Holzhammer U., Krause T. BIOMETHAN. Fraunhofer-Institut für Windenergie und Energiesystemtechnik IWES/ Bereich Bioenergie-Systemtechnik. Fachagentur Nachwachsende Rohstoffe e. V. (FNR). Gülzow-Prüzen, Germany. 2012

[25] de Hull J., Maassen J.I.W., van Meel P.A., Shazad S., Vaessen J.M.P., Comparing different biogas upgrading techniques. Eindhoven, Netherlands: Eindhoven University of Technology and DMT Dirkse Milieutechniek; 2008 Jul 3.

[26] Guinée J.B., Gorrée M., Heijungs R., Huppes G., Kleijn R., Koning A.d., Oers L.v., Wegener Sleeswijk A., Suh S., Udo de Haes H.A., Bruijn H.d., Duin R.v., Huijbregts M.A.J., Handbook on Life Cycle Assessment. Operational Guide to the ISO Standards. Dordrecht: Kluwer Academic Publishers; 2002.

[27] Farreny R., Huella de carbono del sector residuos panel de control / escenario actual. Inèdit Innovació per la sostenibilitat. 2011 Nov, Personal Communications.

[28] Ministerio de Medio Ambiente, y Medio Rural y Marino, Perfil Ambiental de España 2010. Ch 2.7 Residuos. Gobierno de España. 2010; Spain. Technical report: 770-11-221-7

[29] Instituto Nacional de Estadística, Encuesta sobre recogida y tratamiento de residuos. Residuos urbanos. 2008; Madrid, Spain. <http://www.ine.es/jaxi/tabla.do?path=/t26/e068/p01/a2008/l0/&file=02003.px&type=pcaxis&L=0#nogo> [accessed 22.11.2011]

[30] Observatorio de la Sostenibilidad en España, Sostenibilidad en España, 2010. Capítulo 13. Residuos urbanos. 2010; Spain. Technical Report: 770-10-275-3

[31] Ministerio de Medio Ambiente, y Medio Rural y Marino, Plan Nacional Integrado de Residuos (PNIR). Gobierno de España. 2008 Dec; Spain.

[32] Vicent T. 2011 Nov 18, Personal Communications.

[33] USEPA, LandGEM- Landfill gas Emissions Model, Version 3.02. U.S. Environmental Protection Agency, Office of Research and Development, National Risk Management and Research Laboratory, and Clean Air technology Center. 2005 May.

[34] Tersa (Tractament i selecció de residus), Memoria 2008 Anexos. Datos de producción. 2009; Barcelona

CAPTURE OF CARBON DIOXIDE USING GAS HYDRATE TECHNOLOGY

Beatrice Castellani[a], Mirko Filipponi[b], Sara Rinaldi[a] and Federico Rossi[b]

[a] CRB Biomass Research Center, University of Perugia, Perugia, Italy, castellani@ipassnet.it
[b] CIRIAF, University of Perugia, Perugia, Italy, filipponi.unipg@ciriaf.it CA

Abstract:

According to IPCC Fourth Report, carbon dioxide emissions from the combustion of fossil fuels have been identified as the major contributor to global warming and climate change. To reduce these environmental concerns, there is a considerable R&D effort in all technical fields to capture carbon dioxide and subsequently lower the emissions.
One of the new approaches for capturing carbon dioxide is based on gas hydrate crystallization. Gas hydrates have a large capacity for the storage of gases which also resemble an attractive method for gas filtration.
Gas hydrates are crystalline solids, in which low molecular weight guest molecules are trapped inside cages of hydrogen-bonded water molecules. These crystals are stable under high pressures and low temperatures. The basis of the separation is the selective partition of the target component between the hydrate phase and the gaseous phase. It is expected that carbon dioxide is preferentially encaged into the hydrate crystal phase compared to the other components.
In the present paper, after a comparison of gas hydrates with existing capture technologies, a novel apparatus for gas hydrate production is illustrated and results of a first set of experimental applications of the reactor for CO2 hydrate formation and separation are presented. Results are a basis for setting up a procedure for CO2 separation and capture.

Keywords:

Carbon dioxide capture, Gas hydrate, Gas separation, Promoters, Water spraying.

1. Introduction

Carbon capture and sequestration (or storage) - known as CCS - has attracted interest as a measure for mitigating global climate change because large amounts of carbon dioxide emitted from fossil fuel use are potentially available to be captured and stored or prevented from reaching the atmosphere.

A variety of capture processes have been developed for removing or isolating carbon dioxide from a gaseous stream. These processes include absorption, adsorption, membrane separation, cryogenic fractionation [1-3].

After separation, the captured carbon dioxide must be definitely stored: methods under study include storage in depleted oil reserves, salt formations, terrestrial ecosystems and geological formations or direct injection into the deep ocean [4]. To be considered viable, a storage method must provide stable and long-term storage, be environmentally safe and cost-effective.

One of the biggest issues is the high energy consumption for CO_2 separation. It has been estimated that, the cost of separation and disposal of CO_2 from existing coal-fired, air-blown boilers would increase the cost of electricity by about 75% [5]. The cost of CO_2 separation may reduce the power generation efficiency from 38 to 26% [6].

Therefore, the major research interest is in the development of new less energy intensive processes.

Several works on estimation of energy consumption for CCS processes are available in literature. In every CCS process, separation of CO_2 from a flue gas mixture and its compression are the largest contributors to the cost [2,6,7].

Aaron and Tsouris [8] reviewed in detail all processes available for recovery of CO_2 from a flue gas mixture including some which are still at the laboratory stage and concluded that the absorption with monoethaolamine (MEA) is the best method. However the regeneration of the solvent makes the absorption process energy-intensive.

The need to reduce costs motivates further research into the subject. One of the novel separation techniques for subsequent storage or utilization of CO_2 is through gas hydrate formation [8]. Hydrate technology for gas separation seems to be cheaper in case of a CO_2 rich source gas and gas separation by hydrate technology will be competitive in application fields where the inlet gas has a high pressure such as the oil and gas industry [9].

Gas hydrates are crystalline solids, in which low molecular weight guest molecules are trapped inside cages of hydrogen-bonded water molecules.

The three most commonly occurring hydrate structures are Structure I (sI), Structure II (sII) and Structure H (sH), all with individual crystal structures (see Fig.1). The three structures are formed by five different water cavities, the 5^{12}, $5^{12}6^2$, $5^{12}6^4$, $5^{12}6^8$ and the $4^35^66^3$ [10]. In its pure form, the unit cell of the sI hydrate contains two 5^{12} and six $5^{12}6^2$ cavities while a unit cell of the sII hydrate contains sixteen 5^{12} and eight $5^{12}6^4$ cavities. Both of these unit cell lattice structures belong to the cubic type. The sH hydrate structure is more complex and contains three 5^{12}, two $4^35^66^3$ and one $5^{12}6^8$ cavities [10]. This hydrate structure forms a hexagonal unit cell.

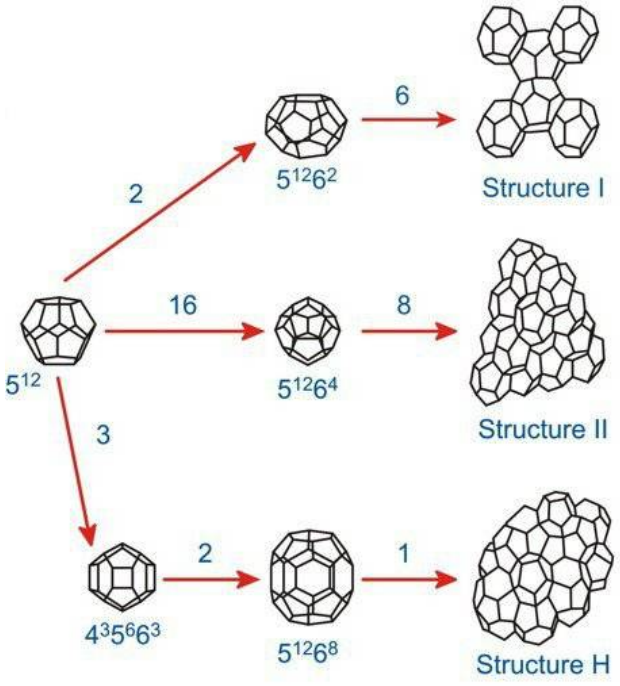

Fig. 1. Hydrate structures.

A given hydrate structure is typically determined by the size and shape of the guest molecule. Carbon dioxide is known to form structure I. Each cavity may encapsulate one - or in rare cases more - guest molecules of proper sizes. It is the presence of the guest molecule that stabilizes the crystalline water structure at temperatures well above the normal freezing point.

Gas hydrate technology may be used as a CO_2 separation method but also in marine sequestration applications, where the replacement of CO_2 in marine methane hydrate fields is carried out. Results of this process will be sequestration of CO_2 and release of methane for energetic purposes [4].

As a separation method, gas hydrates may be used with treated flue gas from power plants in which CO_2 is separated from N_2 and O_2; with synthesis gas from integrated coal gasification power plants,

in which CO_2 is separated from H_2, but also in biogas upgrading processes, in which CO_2 must be separated from biomethane [1;9;11].

The basis of the separation is the selective partition of the target component between the hydrate phase and the gaseous phase. It is expected that CO_2 is preferentially encaged into the hydrate crystal phase compared to the other components. For instance, the equilibrium pressure of N_2 hydrate is three times greater than that of CO_2. This difference allows to separate CO_2 from treated flue gas, that is a CO_2-N_2 mixture [12].

Flue gas from power plants usually contains from 15% to 20% mol. of CO_2 and are released at atmospheric pressure. The gas/hydrate equilibrium pressure for this kind of gas mixture is relatively high. For example, the equilibrium pressures for a gas mixture containing CO_2 at 17.61% mol. are 7.6 MPa and 11.0 MPa at 274 K and 277 K, respectively [13]. These pressures are not compatible with the industrial reality, since the operative cost will be expensive if it is necessary to compress the gas to the hydrate formation pressure.

In addition, evaluations of energy consumption for gas separation processes by the clathrate hydrate formation indicate that hydrate separation process is competitive – compared to other conventional separation processes - under lower pressure conditions, as well as in case of lower hydrate formation heat [14].

Consequently, the main challenge is to obtain a decrease in the operating pressure. This task can be achieved using specific compounds called promoters that allows to reach milder conditions for hydrate formation. A suitable promoter is essential to help in reducing the hydrate formation pressure and the energy consumption.

Conventionally, water-soluble additives are classified either as kinetic or as thermodynamic additives. Thermodynamic additives consist of organic compounds and have the tendency to displace the equilibrium conditions towards higher temperatures or lower pressures. Kinetic additives consist typically of surfactant molecules and have the effect to accelerate hydrate formation [10,12].

Several studies report a significant reduction of hydrate equilibrium pressures at a given temperature by adding small amounts of tetrahydrofuran (THF) in the aqueous phase. Kang et al. [13] and Linga et al. [15] found that the equilibrium pressure of hydrates in the presence of this additive is considerably lower than the case without the additive.

Another promoter is Sodium dodecyl sulfate (SDS), which seems the best commercially available surfactant to be used for enhancement of hydrate formation [16] and has already been investigated in various works [17-20]. It was found that a small concentration of SDS added to the aqueous phase drastically increases the kinetics of hydrate formation.

Recently, Liu et al. [21] and Torré et al. [22] showed that THF and SDS used in combination are efficient additives for promoting CO_2 hydrate formation.

According to previous works [23-26] a continuous production of hydrates is feasible, provided that the technology assures an optimal contact between gas and liquid phases.

The choice of the correct gas-liquid mixing method, together with the proper promoter, is crucial for producing hydrates in a continuous manner suitable for scale-up to industrial settings.

The apparatus described in the present work allows the use of aqueous solutions with additives for rapid hydrate production.

In particular, the reactor was designed to maximize interfacial area between reactants. A first set of hydrate formation experiments indicated that mass transfer barriers and thermal effects that negatively affect conversion of reactants into hydrate are minimized, resulting in fast hydrate production and good storage capacity [20].

In the present paper, an improved configuration of the apparatus and its application to CO_2 hydrate formation are presented and discussed. Experiments on formation of hydrates from pure CO_2 are

preparatory to further applications, such as biogas upgrading and CO_2 replacement in methane hydrates.

2. Experimental apparatus

The experimental apparatus consists of a high-pressure cylindrical AISI 304 stainless steel vessel with internal diameter of 200 mm, an internal length of 800 mm and a total internal volume of 25 l. It has been designed for pressure values up to 120 bar and provided with a safety valve (Fig. 2).

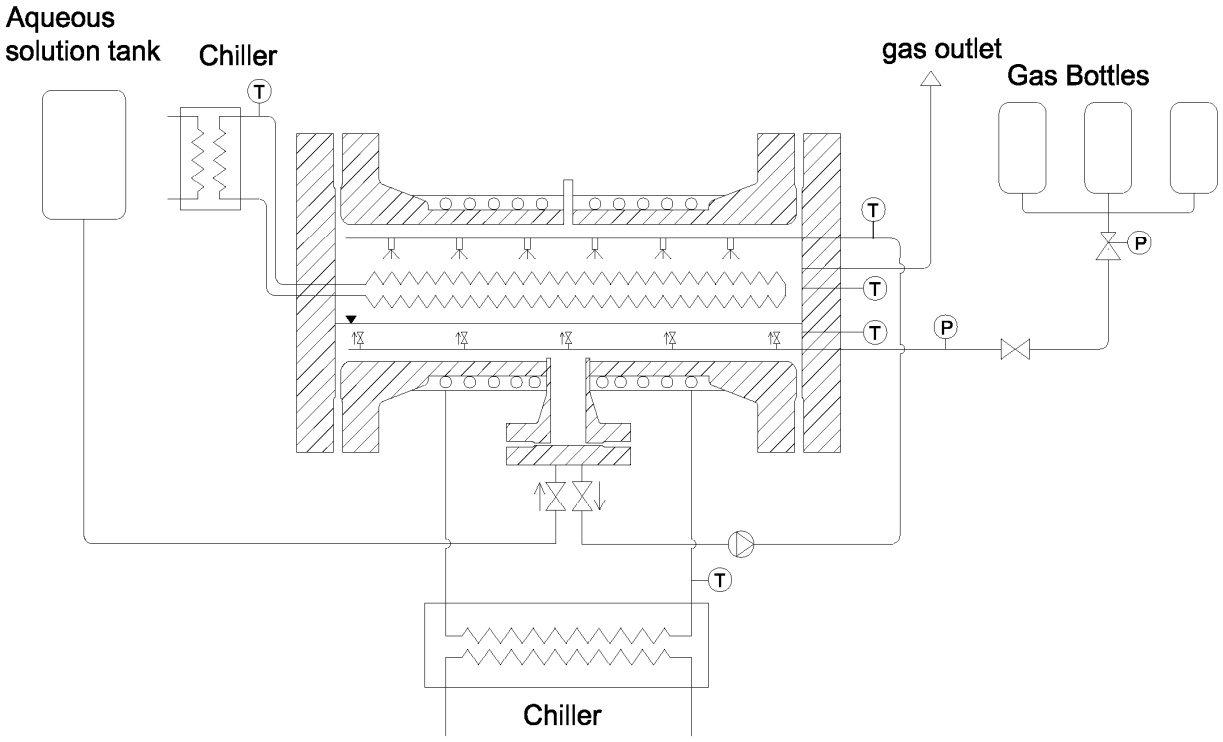

Fig. 2. Schematic diagram of the experimental apparatus.

To remove reaction heat and to ensure a rather constant internal temperature, the reactor was provided with copper cooling coils wrapped around the outside of its vessel wall and with an internal heat exchanger constituted by a finned tube.

The external cooling coils were coated with a thermally insulating paste and a metallic sheet to minimize thermal dispersion from coils to external environment. The cooling medium is ethylene glycol – water solution supplied by an air-cooled chiller (GC-LT Eurochiller).

Two side flanges and a bottom- smaller - flange are used to seal the reactor. One side flange has appropriate ports for access to the interior. The five ports are used for inserting 2 temperature sensors, for gas inlet and outlet and for pressurized aqueous solution recirculation. The temperature sensors are mineral insulated type T thermocouples (accuracy class 1) and measure the temperature inside the vessel in the lower part and in the upper part, near spray nozzles (see Fig. 1). The gas inlet line is equipped with a pressure sensor, that is a digital piezo-resistive manometer (Kobold - accuracy class 0.5) and a mass flow meter (Bronkhorst Hi-Tech) to measure flow rate of gas injected in the reactor. Gas is supplied directly by gas bottles through a pressure-reducing valve, that provides adjustment of the pressure to the gas injection line. Gas is injected through a manifold on which five check valves are mounted.

The bottom flange has two ports, the former is used for the initial aqueous solution uploading and the latter is connected to a pump for recirculation. The pump flows the aqueous solution, previously uploaded inside the reactor, to the atomizing manifold. Water is atomized by six hydraulic nozzles mounted on the internal part of the manifold itself. Such devices for water spraying allow control of

dimensions of water droplets and water flow. The manifold is equipped with pressure gauge for the measure of differential pressure and with a thermocouple for the measure of recirculated solution temperature.

Voltage signals from pressure transducers and temperature sensors are collected by a software for data acquisition on a personal computer. The installation of the apparatus is shown in Fig. 3.

Fig. 3. Installation of the experimental apparatus.

2.2. Materials

Carbon dioxide (99% purity) was supplied by Air Liquide Italia Service. Tap water was used to prepare solutions. SDS (purity >99%) and THF (purity >99.8%) were from Sigma-Aldrich.

2.3. Procedure for hydrate formation

The reactor was designed to produce hydrates in a rapid manner, with hydrate formation times of few minutes. Moreover the new - improved - configuration is suitable for hydrate formation both through bubbling gas into the liquid phase and through spraying aqueous solution into the gas phase. In this set of experiments, the reactor was used to produce carbon dioxide hydrates through spraying aqueous solution into the gas phase according to the procedure described below.

The established amount of aqueous solution is firstly uploaded and the reactor is filled with carbon dioxide from gas bottles until the internal pressure equals the experimental pressure and then cooled. Gas is bubbled into the liquid phase through 5 check valves. The temperature is controlled in order to achieve relatively uniform values inside the reactor. When the experimental conditions are reached, aqueous solution is flowed by the recirculation pump through the nozzles.

Since the flow rate of aqueous solution through the nozzles depends on the differential pressure on nozzles themselves, the water spraying is continued for several minutes until the established total amount of aqueous solution is injected. During the experiment pressure and temperature data are collected every 5 seconds.

Each experiment is carried out with a constant internal pressure. When the internal pressure decreases because of hydrate formation, gas is injected into the reactor to re-establish the correct pressure value.

Investigations were carried out in batch conditions. Therefore, at the end of each experiment, gas is vented out from gas outlet port. Flange is opened both for visual observations and for taking hydrate samples out.

In fact, several samples are taken directly out from the reactor. Hydrate storage capacity is determined putting hydrate samples inside a custom built dissociation vessel. It is a cylindrical AISI 304 stainless steel vessel with a volume of 1.4 lt. It was designed and built to carry out the dissociation of samples of gas hydrate formed.

After sealing the vessel, the dissociation starts and gas pressure and temperature after dissociation are measured. To calculate number of gas moles Eq.(1) was used:

$$P V = Z n R T \qquad (1)$$

where P is the gas partial pressure in the vessel at the end of dissociation, V is the volume of gas in the vessel, n is number of the gas moles, T is the temperature in K at the end of dissociation, R is the universal gas constant, and Z is the compressibility factor, which can be calculated using Benedict-Webb-Rubin equation of state.

As the number of gas moles is calculated, hydrate storage capacity, measured both in %wt of CO_2 and in Nm^3/m^3, can be determined, since hydrate density is known.

In the calculation of hydrate storage capacity, the contribute of CO_2 solubility in water was also taken into account.

3. Results and discussion

A first set of experimental runs were carried out for CO_2 hydrate production. Effects of additives, such as THF and SDS, were tested. The amount of additives was chosen according to the optimal ranges of concentration found in literature [15, 18, 19].

Typical profiles of internal pressure and temperature for an experimental run of 15 minutes are shown in Fig. 3. Those profiles are for experimental run 2 in Table 1.

In particular, internal temperature is calculated as the average of the two temperature values measured by two thermocouples in two different positions.

All experimental runs were carried out with an internal pressure of 3 MPa and with initial temperature values of ca. 3 °C. With an experimental pressure of 3 MPa, the equilibrium temperature of carbon dioxide hydrates is ca. 280 K [27], therefore experiments were carried out with a not negligible subcooling as a driving force for the process.

Before starting aqueous solution recirculation and spraying, a slight decrease in pressure values was observed and ascribed to carbon dioxide solubility. Therefore, only when constant values of temperature and pressure were reached, recirculation started and continued for 15 minutes (runs 1,2,3 in Table 1) or 30 minutes (Runs 4,5 in Table 1).

As a result of the hydrate formation, which is an exothermic process, internal temperature increases after ca. four minutes. Heat removal and temperature control is an issue, especially for applications in scaled-up systems, in which constancy and uniformity of internal temperature are difficult to achieve. With the improvements brought to the temperature control system, variations were kept within 1 °C, as shown in the temperature profile.

Moreover, internal and external heat exchangers of the apparatus allow to achieve also relatively uniform values of temperature inside the entire internal volume.

In Fig.4 it can be noted that internal pressure is constant for the first minute and then decreases smoothly for 6-7 minutes. This can be ascribed to gas consumption due to hydrate formation. The following four peaks result from gas injection for re-establishing the fixed experimental pressure. After each peak, a rapid decrease in internal pressure, due to formation of gas hydrates, is observable.

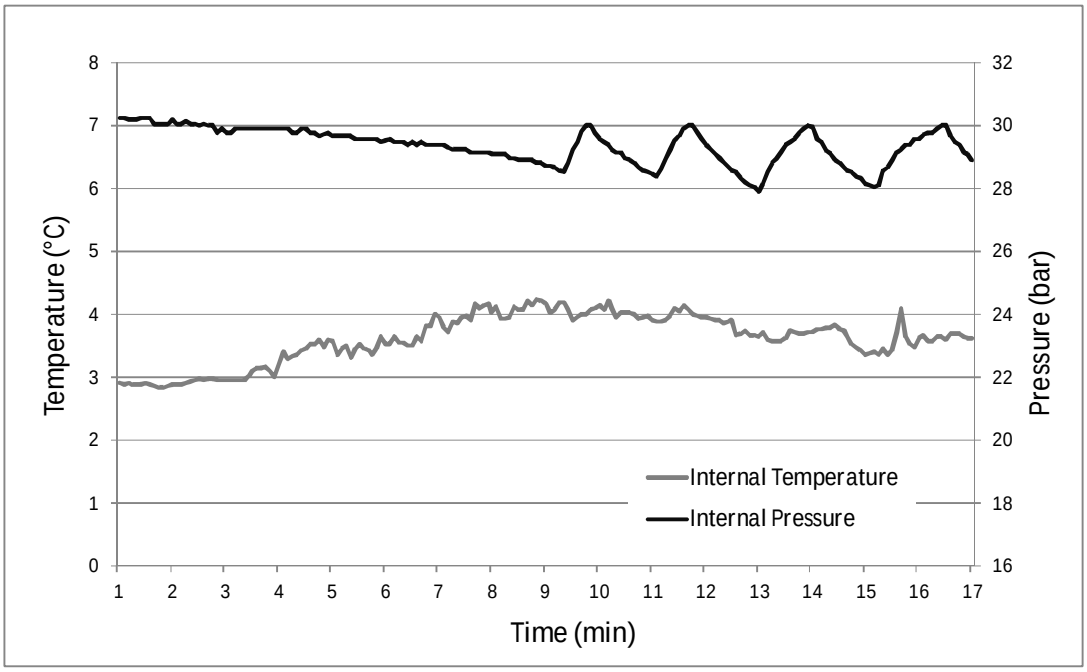

Fig. 4. Pressure and temperature profile with elapsing time for CO_2 hydrate formation in SDS 300 ppm- experimental run 2 in Table 1. Water spraying starts at t = 2 min.

In Fig. 5 pressure profiles for runs 1, 2, 3 in Table 1 are reported. These three runs help to determine the effects of two different promoters (SDS and THF). It is evident that in absence of promoter, pressure decreases, due to gas capture in the hydrate structure, are not observable. On the other hand, in presence of promotor, pressure starts decreasing after 4-5 minutes, with an induction time shorter than those observed in other experiments described in literature, as already proved in our previous applications [20].

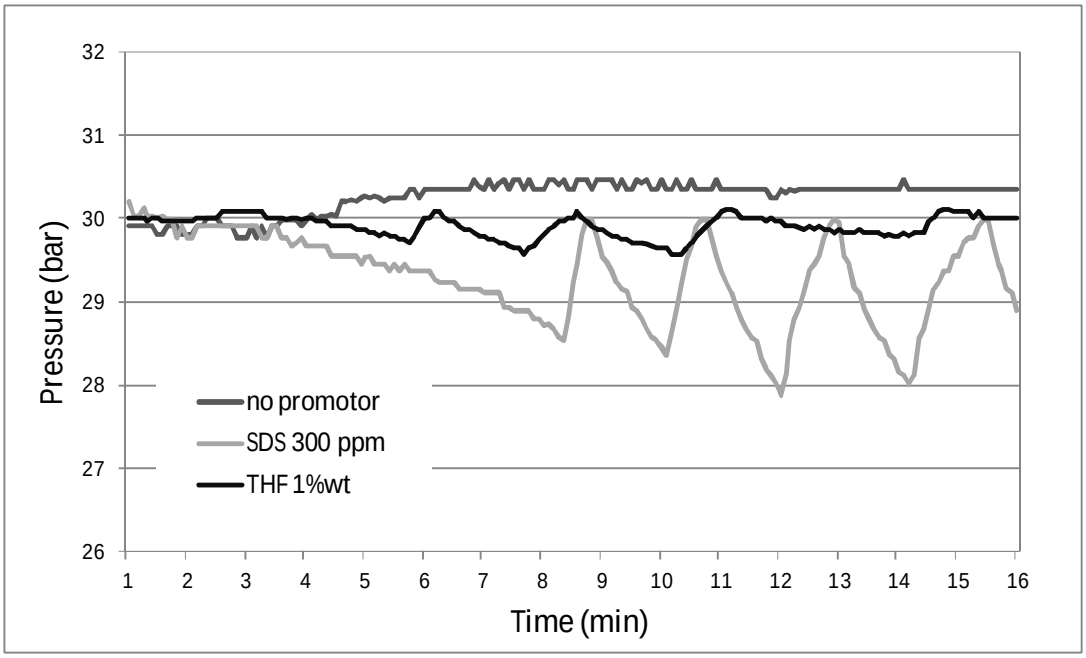

Fig. 5. Pressure profiles with elapsing time for CO_2 hydrate formation with and without promotors- experimental runs 1-2-3 in Table 1. Water spraying starts at t = 1 min.

Several samples were taken directly from the reactor. Hydrate storage capacity was determined putting hydrate samples inside a custom-built dissociation vessel, as described in section 2.3.

Hydrate storage capacity was measured in CO_2wt% (weight percentage) and in Nm^3/m^3 (Nm^3 of gas entrapped in 1 m^3 of hydrates), since these two parameters represent, in a macroscopic and engineering approach, the capability of hydrates to entrap gases in their structure.

Results of experimental applications are reported in Table 1. Initial temperature is calculated as the mean value of those measured in the lower and upper part of the reactor, before starting recirculation and spraying.

Table 1. Results of experimental applications for CO_2 hydrate formation.

Run	*T initial, °C*	*Promotor*	*Water spraying time, min*	*CO_2 Wt%*	*Storage capacity Nm^3/m^3*
1	1.7	-	15	1.3	6.4
2	3.0	SDS 300 ppm	15	8.0	47.4
3	2.2	THF 1%wt	15	5.3	30.9
4	4.0	SDS 300 ppm	30	9.2	62.3
5	3.8	THF 1%wt	30	7.5	44.6

For comparison, a first experiment without additives was carried out (Run1). Results show that in this case gas content is very small and the effect of gas solubility is not negligible.
Both SDS and THF promote formation of gas hydrates with a short reaction time, suitable for industrial in-continuo applications (Run 2-3). Fig. 6 shows the picture of the hydrates formed in Run 2.

Fig. 6. Carbon dioxide hydrates on the internal heat exchanger.

Gas storage increased of 15%, in case of SDS, and 41%, in case of THF, if the spraying time was doubled (Run 4-5).
Gas storage capacity values are consistent with or rather greater - in case of SDS - than that observed by other authors [9].

4. Conclusions

In the present paper, a novel apparatus for gas hydrate production is illustrated and results of a first set of experimental applications of the reactor for CO_2 hydrate formation are presented.

Improvements on reactor design allowed to overcome issues relating to thermal effects and mass transfer barriers, resulting in a rapid CO_2 hydrate formation with reaction times of even 15 minutes with additive promotion.

Carbon dioxide hydrate formation was carried out in mild operating conditions, such as pressure values of 30 bar and temperature of 2-3 °C. The maximum value of storage capacity was 62.3 Nm^3/m^3 in presence of SDS with a reaction time of 30 minutes. Gas storage capacity values are consistent with or rather greater - in case of SDS - than that observed by other authors.

Results on CO_2 hydrate formation are preparatory to investigation on other applications of industrial interest. In particular, our research activities will focus on CO_2 separation from gas mixture, especially in case of biogas upgrading, and CO_2 replacement in methane hydrates.

Acknowledgments

The authors would like to thank Consorzio IPASS Scarl, Italy for providing laboratory personnel and materials.

References

[1] A. Scondo, A. Sinquin, Effect of additives on CO2 capture from simulated flue gas by hydrates formation in emulsion –Proceedings of the 7th International Conference on Gas Hydrates (ICGH 2011), Edinburgh, Scotland, United Kingdom, July 17-21, 2011.

[2] Davison J, Thambimuthu K, Technolgies for Capture of Carbondioxide. In: 7th International Conference on Greenhouse Gas Control Technologies (GHGT-7); Vancouver, 2004.

[3] E.S. Kikkinides, R.T. Yang, S.H. Cho, Concentration and recovery of CO2 from flue-gas by pressure swing adsorption, Ind. Eng. Chem. Res. 1993;32:2714–2720.

[4] R. Sivaraman, The Potential Role of Hydrate Technology in Sequestering Carbon Dioxide. Gas Tips, 2003

[5] C.A. Hendriks, K. Blok,W.C. Turkenburg, The Recovery of Carbon Dioxide from Power Plants in Climate and Energy, Kluwer Academic Publishers, Dordrecht, The Netherlands, 1989.

[6] A. Chakma, A.K. Mehrotra, B. Nielsen, Comparison of chemical solvents for mitigating CO_2 emissions from coal-fired power-plants, Heat Recovery Syst 1995; 15:231–240.

[7] Herzog HJ, Drake E, Adams E, CO_2 Capture, Reuse, and Storage Technologies for Mitigating Global Climate Change, White Paper Final Report 1997 DOE: 66.

[8] Aaron D, Tsouris C, Separation of CO2 from flue gas: A review. Separation Science and Technology 2005; 40:321-348.

[9] Nguyen Hong Duc, F. Chauvy, J.M. Herry - CO2 capture by hydrate crystallization – A potential solution for gas emission of steelmaking industry – Energy conversion and management 2007, 48:1313-1322.

[10] Sum, A. K., Koh, C. A., Sloan, E. D. Clathrate Hydrates: From Laboratory Science to Engineering Practice. Ind. Eng. Chem. Res. 2009; 48: 7457-7465.

[11] S. Arca, L. Poletti, R. Poletti, E. D'Alessandro. Upgrading of biogas technology through the application of gas hydrates. Proceedings of the 7th International Conference on Gas Hydrates (ICGH 2011), Edinburgh, Scotland, United Kingdom, July 17-21, 2011.

[12] Sloan, E. D., Koh, C.A., 2008. Clathrate hydrates of natural gases, third ed. CRC Press, Taylor &Francis Group, Boca Raton.

[13] Kang S.P., Lee H., Lee C.S., Sung W.M. Hydrate phase equilibria of the guest mixtures containing CO2, N2 and tetrahydrofuran. Fluid Phase Equilibria, 2001;85(1-2):101-109.

[14] H. Tajima, A. Yamasaki, F. Kiyono, Energy consumption estimation for greenhouse gas separation processes by clathrate hydrate formation, Energy 2004; 29:1713–1729

[15] Linga P., Adeyemo A. and Englezos P. Medium-pressure clathrate hydrate/membrane hybrid process for postcombustion capture of carbon dioxide. Environmental Science & Technology, 2008;42(1):315-320.

[16] Di Profio, P., Arca, S., Germani, R., Savelli, G., 2005. Surfactant promoting effect on clathrate hydrate formation: are micelles really involved? Chemical Engineering Science 60, 4141-4145.

[17] Kalogerakis N, Jamaluddin AKM, Dholabhai PD, Bishnoi PR. Effect of surfactants on hydrate formation kinetics. (SPE 25188). Proceedings of SPE International Symposium on Oilfield Chemistry, New Orleands, 1993.

[18] Zhong, Y., Rogers, R.E., 2000. Surfactant effects on gas hydrate formation. Chemical Engineering Science 55, 4175-4187.

[19] Ganji, H., Manteghian, M., Sadaghiani Zadeh, K., Omidkhah, M.R., Rahimi Mofrad, H., 2007. Effect of different surfactants on methane hydrate formation rate, stability and storage capacity. Fuel 86, 434-441.

[20] L. Brinchi, B. Castellani, M. Filipponi, F. Rossi, G. Savelli – Investigation on a novel reactor for gas hydrate production - Proceedings of the 7th International Conference on Gas Hydrates (ICGH 2011), Edinburgh, Scotland, United Kingdom, July 17-21, 2011.

[21] Liu N, Gong G, Liu D, Xie Y. Effect of additives on carbon dioxide hydrate formation. Proceedings of the 6th International Conference on Gas Hydrates (ICGH 2008); Vancouver, 2008.

[22] Torré JP, Dicharry C, Ricaurte M, Daniel-David D, Broseta D. CO_2 capture by hydrate formation in quiescent conditions: in search of efficient kinetic additives. Energy Procedia 2011;4:621-628.

[23] M. Mork, Gudmundsson. Hydrate crystallization rate in a continuous stirred reactor: experimental results and a bubble-to-crystal model. In: Proceedings of the 4th international conference on gas hydrates, vol. 2; 2002. p. 813–8.

[24] Iwasaki et al. Continuous natural gas hydrate pellet production by process development unit. - Proceedings of the 5th international conference on gas hydrates, vol. 4; 2005. p. 4003.

[25] Hideo Tajima, et al. Continuous gas hydrate crystallization process by static mixing of fluids. - Proceedings of the 5th international conference on gas hydrates, vol. 1; 2005. p. 1010.

[26] Dwain F. Spencer. US Patent: methods of selectively separating CO_2 from a multicomponent gaseous stream; 2000.

[27] G. K. Anderson, Enthalpy of dissociation and hydratation number of carbon dioxide hydrate from the Clapeyron equation – J. Chem. Thermodynamics 2003;35:1171-1183

Carbon dioxide mineralisation and integration with flue gas desulphurisation applied to a modern coal-fired power plant

Ron Zevenhoven [a], Johan Fagerlund [a], Thomas Björklöf [a,b], Magdalena Mäkelä [c], Olav Eklund [c]

[a] Åbo Akademi University, Dept. of Chemical Engineering, Åbo / Turku, Finland, ron.zevenhoven@abo.fi (CA), johan.fagerlund@abo.fi (presenter)
[b] currently with Neste Jacobs, Porvoo, Finland
[c] Åbo Akademi University, Dept. of Geology & Mineralogy, Åbo / Turku, Finland, magma@abo.fi, oleklund@abo.fi

Abstract:

For Finland, carbon dioxide mineralisation was identified as the only option for CCS (carbon dioxide capture and storage) application. Unfortunately it has not been embraced by the power sector, partly because the most suitable mineral resources are found in central and northern Finland while most fossil-fuel fired electricity production is located in southern Finland. One interesting source-sink combination, however, is formed by the magnesium silicate resources at Vammala, located ~ 85 km east of the 565 MWe coal-fired Meri-Pori power plant on the country's southwest coast, producing 2.5 Mt/y CO2. Between 2008 and 2010 the companies Fortum and TVO considered retrofitting the Meri-Pori power plant with CCS. Due to absence of geological storage options within Finland, the CO2 would be shipped to the North Sea for injection into saline aquifers. The project was, however, discontinued. This paper assesses sequestration of Meri-Pori power plant CO2 by mineralisation, using the Vammala mineral resources and the mineralisation process under development at Åbo Akademi University. That process implies Mg(OH)2 production from magnesium silicate-based rock, followed by gas/solid carbonation of the Mg(OH)2 in a pressurised fluidised bed. Included here are results on experimental work, i.e Mg(OH)2 production, with rock material from locations close to Meri-Pori. Results suggest a total CO2 fixation capacity ~ 50 Mt CO2 for the Vammala site, although production of Mg(OH)2 from rock from the site is challenging as a result of varying magnesium silicate mineral types (serpentine, amphibole, pyroxene). Finally, as carbon dioxide mineralisation without CO2 pre-capture could be directly applied to flue gases that contain sulphur oxides, we report from experimental work where carbonation of Mg(OH)2 with CO2 is compared with CO2-SO2-O2 gas mixtures. Results show that SO2 readily reacts with Mg(OH)2, providing an opportunity to simultaneously capture SO2 and CO2. Ideally, this could make separate flue gas desulphurisation redundant.

Keywords:

CO2 mineral sequestration, Large-scale application, Coal-fired power plant, Desulphurisation

1. Introduction

Between 2008 and 2010 Fortum and TVO explored the possibility of retrofitting the Meri-Pori coal combustion power plant with CO_2 capture technology. Due to a lack of geological storage options within Finland, the CO_2 was to be shipped to the Danish North Sea, by ship, for injection into saline aquifers. The project was, however, discontinued in October 2010 [1-5]. The Meri-Pori power plant (1994) is a 565 MWe coal fired power plant with a thermal efficiency of 43%, producing 2.5 Mt/y CO_2, or 820 kgCO_2/MWh. The plan was to capture and store 1.2 Mt/y of this. For the capture, both oxy-fuel combustion and amino acid salt technology (Siemens) were considered, the latter being deemed more convenient (easier to retrofit). The CO_2 would have been transported, as a cooled liquid (-50 ºC, ~7 bar), with two or three tanker ships over a distance of 1000 km to the closest storage site.

The biggest obstacle on Meri-Pori's path to CCGS (carbon capture and geological storage) was considered to be the energy demand of the capture process. Post-combustion capture required 2-4

GJ/tCO_2 during pilot scale tests, with 90% capture efficiency. Apart from the capture, other cost factors considered are:

- Compression and cooling of the CO_2
- Shipping
- Intermediate storage facilities
- Injection into underground storage (including pressurisation to 120 bar)

This would lower the efficiency of the power plant by 10-13 percentage units. In terms of cost (and by deduction, energy), the capture was estimated to account for the largest part, with 50 – 80% of the total costs related to CCGS. Transporting the CO_2 was estimated to account for 5 – 35% of the total costs, and storage for 5 – 25%.

This paper explores another possibility for sequestering the CO_2 emitted by the Meri-Pori power plant, namely CO_2 mineralisation, using mineral resources located not too far from the power plant. There are several motivations for this:

- It is known for quite some time (and repeatedly confirmed) that underground storage capacity is not available in Finland [e.g., 6,7], while the same appears to hold for the Baltic region in general (apart from CCGS capacity in Poland, a country with a lot of coal-derived CO_2 emissions) [8]
- Finland has vast resources of magnesium silicate-based mineral resources; assessments by the Geological Survey of Finland typically mention 2-3 Gt CO_2 storage capacity in minerals of the Outokumpu-Kainuu region of central Finland alone [9-11]
- Underground storage capacity in west-Russia may seem attractive but export of CO_2 to outside the European Economic Area is prohibited under the EU directive on CCS (which in fact addresses only CCGS) [12]
- Implementation of the above-mentioned EU directive on CCS in Finnish legislation is ongoing and may result in CO_2 underground storage being forbidden within Finland's borders [13,14]
- A five-year (2011-2015) research program on CCS is commencing in Finland coordinated by Cleen Oy [15]. (The work reported here is outside that program, however.)
- Finland (and at the moment primarily Åbo Akademi University, ÅA) has an extensive track record on CO_2 mineral sequestration R&D, with process routes that use either both magnesium silicate-containing rock [e.g. 16,17, based on presentations at ECOS2010] or steelmaking slags moving from lab-scale to demonstration scale [18].

Below, the feasibility of CO_2 mineralisation applied to CO_2 produced at the Meri-Pori power plant using four types of minerals and the staged process route that is under development at ÅA is assessed. Moreover, the combined removal and trapping of SO_2 and CO_2 from the flue gas is investigated in an experimental study at the end of this paper. CO_2 pre-capture would be omitted from the CCS chain.

2. Considering the mineralisation option

Given that Finland does not possess underground storage sites, CCGS will always entail large transport distances and export of the CO_2 to Norway, Denmark or Poland. The location of the Meri-Pori plant is indicated in Fig. 1.

Onshore pipeline transport of CO_2 is significantly cheaper than shipping, for distances up to 1500 km (see Fig. 4.6 in [19]). With proven Mg-rich serpentine ($Mg_3Si_2O_5(OH)_4$) deposits as close as ~85 km from Meri-Pori, in Vammala, and olivine-type material located at Meri-Pori itself, not only could transport costs be minimised, but the whole capture process could potentially be omitted if the carbonation can be applied to the flue gas directly. Current CO_2 mineral sequestration R&D focuses more and more on direct carbonation with the CO_2 containing gas, removing the expensive and complicated (especially for gases that contain oxygen) capture step from the CCS chain. Compared to pumping CO_2 into saline aquifers, current mineralisation technology comes with an energy

penalty, but without separate capture and long transport distances the energy use should at least be comparable to the capture step of CCGS, of the order of 2-5 GJ/ton CO_2 (mainly heat).

In recent years, research into CO_2 mineralisation has taken a giant leap forward as demonstrated by the rate at which new process routes are suggested, patented and in several promising cases developed to large-scale application [20]. Many of these processes do not require pure CO_2, but can be run with flue gases directly, such as the process routes suggested by Nottingham University [21], Hunwick [22] and also the ÅA route, to be described below in more detail.

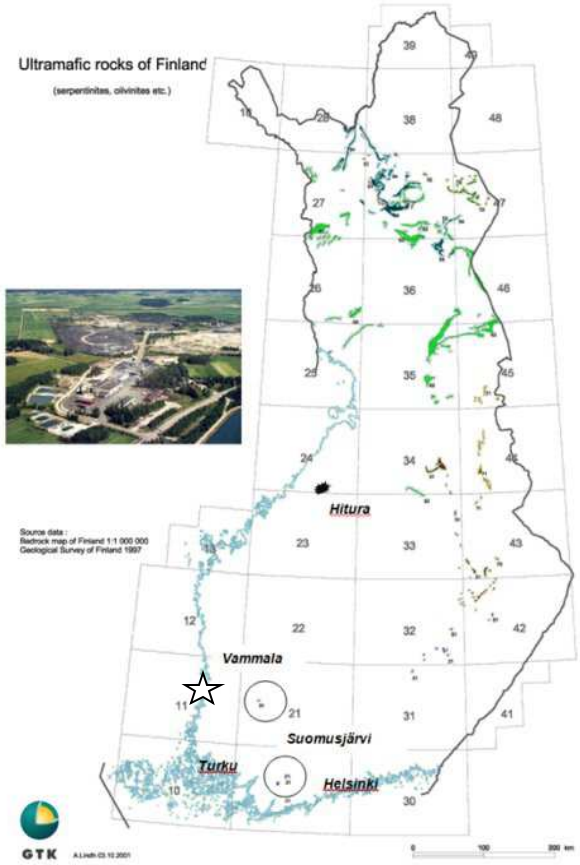

Fig 1. The location of the Meri-Pori power plant, indicated as , ☆ and ultramafic rock in Finland. Also shown a photo of the nickel mine at Hitura and its location, and ultramafic rock findings in southern Finland at Vammala and Suomusjärvi (circled).

3. Mineralisation of CO_2

3.1 - General

Carbon dioxide mineralisation is the general term describing the sequestration of CO_2 by reacting it with Mg- or Ca-containing compounds, to produce stable carbonates. Magnesium in particular is abundant in the earth's crust, as silicates such as serpentinite and olivine. Calcium also has a potential to store significant amounts of CO_2, although calcium silicates are not as abundant as magnesium silicates. In general, the exothermic reaction between magnesium or calcium silicates and CO_2 can be described by reaction 1.

$$(Mg,Ca)_xSi_yO_{x+2y+z}H_{2z}(s) + xCO_2(g) \leftrightarrow x(Mg,Ca)CO_3(s) + ySiO_2(s) + zH_2O(l/g) \quad (1)$$

These reactions occur in nature over geological timescales (hundreds of thousands of years). Research has focused on improving the reaction rates by treating the mineral rock by thermal, mechanical or chemical means (Chapter 7 in [19], [20], [23]). Due to the exceptionally large scale of CCS processes, all additives must be recovered, and the energy input minimised. Strong acids, such as HCl and H_2SO_4 are able to dissolve the rock rapidly, but are difficult to recover. Hence, most promising processes incorporate a combination of weaker acids or ammonium salts and thermal and/or mechanical treatment to produce more reactive magnesium containing species. Examples of such processes can be found in the literature.

Both the process developed by Hunwick [22] and a similar one by Maroto-Valer and co-workers [21] utilise ammonia to capture CO_2. Hunwick claims to react ammonium bicarbonate directly with serpentinite, whereas Maroto-Valer extracts magnesium from mineral with ammonium bisulfate, before carbonating the $MgSO_4$ with ammonium bicarbonate. The latter reports over 90% conversion of Mg to carbonates.

A process under development at ÅA uses recoverable ammonium sulphate (AS) salt to extract Mg from grinded serpentinite rock, under elevated temperatures. The extraction has been shown conversions of up to 70% of Mg into either reactive $Mg(OH)_2$ or $MgSO_4$, depending on the desired intermediate. $Mg(OH)_2$ reacts directly with CO_2 under elevated temperature and pressure, whereas $MgSO_4$ can be reacted with aqueous ammonium (bi-) carbonate, in both cases producing magnesium carbonates. Here, the route that involves $Mg(OH)_2$ carbonation in a pressurised fluidised bed, aiming at obtaining the reaction heat from the carbonation step at a useful temperature level is considered – see Fig. 2 for an overview of the process route.

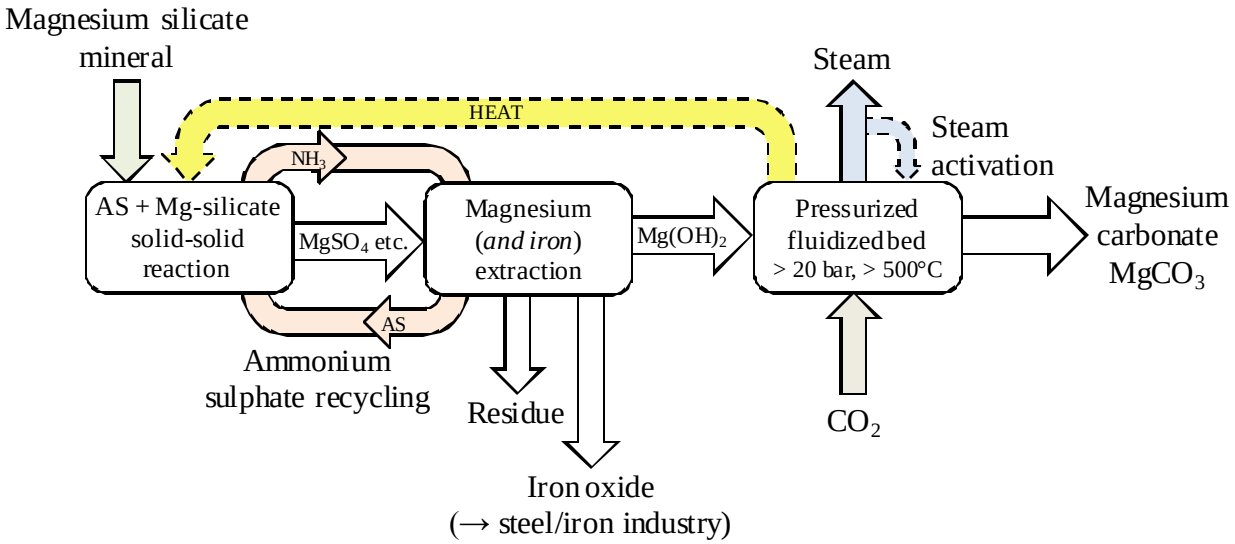

Fig. 2. A schematic illustration of the mineral carbonation process under development at ÅA.

3.2 – The ÅA process route

3.2.1. $Mg(OH)_2$ production

In the first process step, (preheated) serpentinite rock is thermally treated with ammonium sulphate (AS) at 400 – 500 °C and atmospheric pressure for 10 – 60 minutes. A significant amount of the magnesium, Mg, in the rock is thus converted to sulphate, $MgSO_4$, which is highly soluble in water. Unfortunately, $MgSO_4$ cannot be directly converted with CO_2 to $MgCO_3$, but in an aqueous solution it can be converted to $Mg(OH)_2$. After cooling, the solid from the reaction with AS is slurried in water, leaving behind unreacted mineral and insoluble reaction products, e.g., silica. The pH of the filtrate solution is raised to 8 – 9, precipitating iron and calcium (from the mineral, see Table 1 below) as FeOOH and $Ca(OH)_2$, respectively, while increasing the pH further to 10 – 11 precipitates $Mg(OH)_2$. For the Finnish Hitura mineral, the preferable conditions for extraction of Mg (and Fe) to $MgSO_4$ (and $FeSO_4$) are temperatures 400 – 440 °C, for 30 – 60 minutes at S/AS =

0.5 – 0.7 kg/kg, resulting typically in 60 – 66% extraction of Mg. Lower temperatures and longer reaction times give a higher (relative) extraction of iron. Ammonia vapour, NH_3, released during the thermal step is collected and used to give the necessary pH increases for precipitation. It is thereafter recovered for regeneration of the AS salt downstream, using heat from another process step. Nonetheless, the recovery of solid ammonium sulphate from the aqueous form incurs a not insubstantial energy penalty. More detail on the procedure is given by Nduagu et al. [24,25].

3.2.2. $Mg(OH)_2$ carbonation

The $Mg(OH)_2$ produced as described above is converted into $MgCO_3$ in a pressurised fluidised bed (PFB) reactor at pressures > 20 bar and temperatures 450 – 600 °C. (Some more detail on the set-up is given in section 7.2). Results on conversion levels obtained under varying conditions (temperature, pressure, water content of the gas, time, fluidisation velocity) are reported elsewhere [16,26,27] for both a synthetic, commercial $Mg(OH)_2$ material and $Mg(OH)_2$ produced from Finnish or Lithuanian serpentinites. (A few tests were made under supercritical CO_2 conditions, pressure > 74 bar, which showed significantly lower conversion levels and rates, suggesting that little benefit should be expected from operating at such pressure levels.) It was found that the $Mg(OH)_2$ materials produced from the serpentinites are much more reactive (as a result of a ~10× larger specific surface of ~45 m^2/g vs. ~5 m^2/g), giving conversion levels of 50% within 15 minutes for ~300 μm particles.

The product gas from the carbonator is a hot, pressurised mixture of CO_2 and H_2O, the solids obtained will be partly recycled for further carbonation conversion. Unfortunately, although the carbonation reaction is rapid it levels off at carbonation levels up to 65% (the best result obtained so far) [27], which appears to be the result of calcination of $Mg(OH)_2$ to MgO. However, it is noted that in order for $Mg(OH)_2$ to carbonate, dehydroxylation (i.e. calcination) has to occur. Apparently, carbonation at some point becomes slower than dehydroxylation, resulting in a partially calcined and carbonated product. Thus, below it is assumed that with ~2/3 of the $Mg(OH)_2$ produced also being carbonated the necessary amount of it is 150% of the stoichiometric amount.

3.2.3. Process energy input requirements

Since CCS is one of the solutions to what is in fact an energy problem, routes that lead to the production of large amounts of CO_2 while producing the power and heat for the CCS process are obviously not viable. The Meri-Pori plant produces 820 g CO_2/kWh electricity, thus CCS with an electricity consumption of 1/0.82 = 1.22 kWh = 4.39 MJ/kg CO_2 would have a zero net output of both electricity and CO_2. The use of electricity in CCS processes should be avoided although some power consumption will follow from gas compression and crushing/grinding of solid material. Fortunately, part of the energy input of a CCS processes would be in the form of heat and at ~ 43% thermal efficiency the Meri-Pori plant produces similar amounts of electricity and (waste) heat.

CCS routes based on CO_2 mineralisation appear to be more dependent on heat as energy input than the "conventional" route that involves underground storage of CO_2, while – as done in the ÅA route – the heat output from the carbonation reaction can be benefitted from. (Therefore the higher temperature of the carbonation step in the ÅA route, ~500 °C, compared to the earlier suggested process route from the Albany Research Center (ARC), currently NETL Albany, in the US, results in a better LCA (life cycle assessment) performance of the ÅA route compared to the ARC route [28]. The ARC route is based on one-step carbonation in pressurised aqueous solutions at ~150 bar, ~185 °C [29,30].) At the same time, CO_2 mineralisation routes that involve electrochemical steps (electrolysis, fuel cells) are very unlikely to have a net CO_2 fixation effect [31].

As presented at ECOS2010 [17] a quick assessment of energy input requirements for the ÅA route can be made based on the reaction heat Q_E or ΔH_E needed for Mg extraction from rock and the heat Q_C or ΔH_C released by $Mg(OH)_2$ carbonation. Besides this, crushing/grinding of rock contributes to only a few % of the energy input requirements while process integration and optimisation will result in improvements to the energy efficiency [17].

With Mg extraction conversion $X_E = X_{Mg(OH)2prod}$ and $Mg(OH)_2$ carbonation conversion $X_C = X_{Mg(OH)2carb}$ the net heat input requirements is equal to

$$Q\,(\text{MJ/kg } CO_2) = \frac{\Delta H_E}{X_E} - X_C \cdot \Delta H_C \qquad (2)$$

with ΔH_E = 234.6 kJ/mol Mg extracted (value for 480 °C) and ΔH_C = -59.5 kJ/mol Mg carbonated (value for 550 °C) as in [17]. For serpentinite (rock mainly composed of serpentine) found at Hitura composed of ~84%-wt serpentine, ~13%-wt iron oxides as FeO and ~3%-wt calcium silicates the heat input requirements are given in Table 1 for X_E and X_C ranging from 25 to 100% [17].

Table 1. Process energy input requirements (MJ/ kg CO_2) according to (2)

	$Mg(OH)_2$ carbonation efficiency					
Mg extraction efficiency	25%	50%	75%	90%	95%	100%
25%	21.33	20.65	20.32	20.11	20.05	19.98
50%	10.66	9.99	9.65	9.45	9.38	9.31
75%	7.11	6.43	6.10	5.89	5.83	5.76
90%	5.92	5.25	4.91	4.71	4.64	4.57
95%	5.61	4.94	4.60	4.40	4.33	4.26
100%	5.33	4.66	4.32	4.12	4.05	3.98

Of course, incomplete Mg extraction would not have a heat penalty (an endothermic reaction that doesn't occur won't give an energy penalty) and thus only the last row of Table 1 would apply. At the same time, if Mg extraction conversion X_E << 100% then crushing and grinding of what is then mainly inert material will give excessive costs and the material must still be heated to > 400 °C. Also, temperatures > 400 °C give increased thermal decomposition of the AS salt, with an energy penalty. Therefore for a case with X_E = 0.75 and X_C = 0.75 the heat input requirements for a Hitura serpentinite-type material (see below) are 4.32 < Q < 6.10 MJ/kg CO_2, and presumably closer to the higher value Note that this is heat of ~ T = 450 °C = 723 K: for surroundings temperature T° = 15 °C = 288 K this corresponds to exergy equal to Ex(Q) = (1-T/T°)·Q = 2.6 – 3.7 MJ/kg. Using the exergy of heat allows for comparing it in calculations with power input requirement P, for which the exergy Ex(P) = P.

3.2.4. CO2 mineralisation applied directly on power plant flue gas

The capture of CO_2 from flue gases that contain oxygen and other problematic species is more complicated than CO_2 (and H_2S) stripping from natural gas, and is hard to accomplish against an energy penalty lower than 3 – 4 MJ/kg CO_2 captured [32]. This is one main reason why CO_2 mineralisation R&D increasingly focuses on avoiding CO_2 separation and would operate on the CO_2-containing gas directly. Energy input requirements for CSM (carbon storage by mineralisation) would be of the same order as those for only the capture step of "conventional" CCS. (An LCA study on this approach for CO_2 mineralisation applied to natural gas – fired electricity production in Singapore, using the ÅA route with serpentinite rock purchased from Australia, and considering both CO_2 capture and operating with the flue gas directly was recently reported [33].) In that case a gas with Y%-vol CO_2 must be compressed to a total pressure of ~ 20 / (Y/100) bar, which is integrated with expansion of a carbonation product gas mixture (in which CO_2 is replace by H_2O) at the same 20 / (Y/100) bar, at ~500 °C, to atmospheric pressure.

Moreover, the mineralisation of CO_2 from a flue gas may be combined with sulphur capture: $Mg(OH)_2$ may also react with SO_2 (and SO_3) present in the flue gas which would then allow for removing the FGD unit from a power plant that uses a sulphur-containing fuel. This is addressed in sections 7 and 8 below.

3.3 – Utilising waste heat

All existing mineralisation processes require significant amounts of energy (usually as heat) in order to achieve sufficient reaction kinetics and/or favourable thermodynamic circumstances. Especially those processes, where large amounts of low quality heat are required, could benefit from access to sources of waste heat. Such sources may be low quality steam or flue gas from the very power plant the CO_2 would be extracted from.

In the relative vicinity of Pori (at ~ 60 km to the south), the Olkiluoto nuclear power plant is located, which produces large amounts of waste heat. Presently this waste heat is rejected into the sea as 29500 kg/s of cooling water used to condense low quality steam at a temperature of around 200 °C, from each of the two reactors already in operation. The heat carried off with the cooling water amounts to approximately 1600 MW per reactor. A fraction of that waste heat would be enough to carbonate all the CO_2 emissions from the Meri-Pori power plant [34]. Unit 3 is under construction, for operation in 2014 to generate 2700 MW waste heat besides 1600 MW electricity.

The ÅA mineralisation process requires heat at above 400 °C. But even with a heat source of a lower than required temperature, significant savings could be achieved using a heat pump. This, of course, would require that the mineralisation could be performed close to the heat source.

4. Mineral resources and characterisation

4.1 – The rock resources considered suitable

Finland has large amounts of serpentine available. The suitability of any given mining site as a source of mineral for carbonation depends on the magnesium (and calcium) contents of the rock. In addition, the distance from the power plant and total amount of rock, as well as possible nearby sources of waste heat are of importance. Many mines in relative proximity to Meri-Pori are in operation or have previously been in operation producing large amounts of serpentinite as mine tailings and overburden. Table 2 presents a shortlist of sites with their respective rock compositions.

Table 2. Composition (as oxides) of the Finnish rock considered for mineralisation

Location	MgO %-wt	CaO %-wt	*Fe_2O_3 %-wt	SiO_2 %-wt	Al_2O_3 %-wt	Other %-wt
Suomusjärvi	16.2	8.6	11.4	47.6	10	6.2
Hyvinkää / Mäntsälä**	9.8	11.4	13.2	45.9	13.6	6.1
Lammi / Asikkala**	4.9	6.8	8.0	58.0	15.6	6.7
Kaipola / Kuhmoinen**	7.2	7.5	7.7	55.2	14.9	7.5
Vammala	14.5	5.6	12.5	49.5	8.8	9.1
Hitura	38.1	0.5	14.8	32.6	0.4	13.6

* Calculated, presumably a mixture of FeO and Fe_2O_3, partly (?) Fe_3O_4. ** Not a mining site

The Suomusjärvi and Vammala rock and, for comparison with a "better" material, the Hitura nickel mine mining tailings are central for this work – see the locations of these in Fig. 1. The other southern-Finland rock types (Hyvinkää, Lammi and Kaipola) won't be further addressed here [35]. For the work reported here the materials and chemical compositions as given in Table 3 are used.

Table 3. Composition (as oxides) of the Finnish rocks for mineralisation as tested

Working names	MgO %-wt	CaO %-wt	*Fe_2O_3 %-wt	SiO_2 %-wt	Al_2O_3 %-wt	Other %-wt
Hitura[#]	36.2	0.5	14.4	24.8	<0.1	24.1
Vammala-1[¤]	19.2	9.0	15.4	45.0	3.5	7.9
Vammala-2[¤]	28.0	1.4	18.4	39.3	1.3	11.6
Satakunta[§] olivine	5.5	8.7	15.3	46.9	16.1	7.5
Suomusjärvi-1[¤]	13.5	7.8	10.9	50.2	10.8	6.8
Suomusjärvi-2[¤]	20.9	8.3	11.9	44.3	7.0	7.6

[#] Ref. [24], [§] Ref [25], [¤] Ref. [35] * Calculated, presumably a mixture of FeO and Fe_2O_3, partly (?) Fe_3O_4.

4.2 – Hitura mine rock

The Hitura mine is an operational nickel mine in the province of Oulu, around 350 km (in north-east direction) from Meri-Pori. Rocks from Hitura, tested at ÅA, have been shown to contain ~ 83% serpentine mineral, which constitutes a MgO content of ~ 36%. The continuous transport cost by pipeline, for pure CO_2, would amount to less than 5 €/tCO_2. However, should the transported gas be the total (dried) flue gas, the costs can be expected to rise by a factor of three to five, depending on the CO_2 content [19].

The Hitura ultramafic complex consists mainly of serpentinite, with a volume of an estimated 1300 m × 300 m × 1000 m, i.e. 0.39 km^3 = $390 \cdot 10^6$ m^3 [36]. With an assumed density ~ 3000 kg/m^3 it corresponds to ~ 1170 Mt material. Given the rock composition with ~ 36%-wt MgO (Table 3), this amount of rock has a theoretical capacity to sequester more than 400 Mt CO_2.

4.3 – Vammala (Stormi-Vammala) nickel mine rock

The Stormi ultramafic complex in the Vammala nickel belt is a 1500 m × 600 m × 300 m large volume, with an upper layer of 70 m of serpentinite [37]. This gives a volume of 0.063 km^3 = $63 \cdot 10^6$ m^3 with an assumed density ~ 3000 kg/m^3 this corresponds to ~ 200 Mt material. Given the rock composition with 20 ~ 25%-wt MgO (Table 3), theoretically around 44 ~ 55 Mt of CO_2 could be sequestered with the upper layer minerals.

On one hand, the MgO content in the Vammala upper layer serpentinites necessitates the processing of larger amounts of rock (4 ton/ton CO_2 compared to ~3 ton/ton CO_2 for Hitura material), but Vammala, on the other hand, is significantly closer to Meri-Pori compared to Hitura. At a distance of only 75-85 km both pipeline transport costs and capital costs could be kept at a minimum.

The Vammala mine is no longer being mined for nickel, but still produces gold. However, nickel deposits are generally found in ultramafic rock formations, whereas gold tends to be present in quartz formations. There is nonetheless the possibility that the overburden from mining contains serpentinite material. Another option is to reconsider nickel mining in the light of new uses for the mine tailings, or to mine for serpentine without specific regard for nickel altogether. It does however appear that Belvedere Resources, the company operating in Hitura, were, at least in 2008, exploring the possibility to start mining nickel in Vammala again [38]. The rocks collected and analysed are from a rock mass nearby, not at, the Stormi mine [35].

4.4 – Pori olivine deposits rock

Only a few kilometres south-east of Pori, in the region around Nakkila and Harjavalta, olivine deposits can be found [39]. Historically nickel has been mined in Harjavalta, but presently the only mining activity in the region is copper mining [40]. The chemical composition of olivine favours its use as a source of magnesium due to stoichiometrically higher ratio of Mg to rock, compared to serpentine. Nduagu et al. [25] argued that due to lower surface area and porosity, as well as being harder than serpentine, olivine cannot be used for extracting magnesium, according to the method described in section 3.2.1.

4.5 – Suomusjärvi olivine deposits rock

Two samples for testing were taken from the region around Suomusjärvi, located roughly half-way between Turku and Helsinki – see Fig.1. This is at the south end of the Vammala nickel belt [41]. One sample (Suomusjärvi-1) is a side-material from the Salittu quarry where macadam is mined for roadmaking. The other sample (Suomusjärvi-2) is an olivine-hornblendite actually from Nummi-Pusula (~20 km east of Suomusjärvi), containing ~50% olivine $(Mg,Fe)_2SiO_4$ [35]. Data on amounts of material is not yet available.

5. Production of $Mg(OH)_2$ from the rocks considered suitable

Table 4 summarises the results of $Mg(OH)_2$ production from the materials listed in Table 3, using the procedure described in section 3.2.1. For most tests, 2 g rock + 3 g ammonium sulphate powder were mixed, with rock particle size 75-125 µm and using an Al sample cup.

Table 4. Production efficiency of $Mg(OH)_2$ and FeOOH from the Finnish rocks tested

	T °C	Time min	pH levels - / -	FeOOH g/g rock	% Fe extracted	$Mg(OH)_2$ g/g rock	%Mg extracted
Hitura[#,§]	400 - 440	30 – 60	8-9 / 11-12			~ 0.34	~ 65
"	480			0.006	4	0.23	44
"	440	30		0.037	23	0.39	74
"	550			0.008	5	0.13	25
Vammala-1[¤]	420	40	9.5 / 11.5	0.02	13	0.005	3
"	460	30	9.5 / 11.5	0.02	13	0.035	18
"	520	20	9.5 / 11.7	0.09	58	0.035	18
Vammala-2[¤]	420	40	9.5 / 11.5	0.04	22	0.075	27
"	460	30	9.1 / 11.5	0.04	20	0.070	25
"	520	20	9.1 / 11.5	0.055	30	0.070	25
Satakunta[§]	480	< 30			2		14
olivine	550	< 30			3		1
Suomusjärvi-1[¤]	520	20	9.9 / 11.9	0.025	23	-	0
Suomusjärvi-2[¤]	520	20	9.5 / 11.9	0.055	46	0.03	14

[#] Ref. [23], [§] Ref [24], [¤] Ref. [35], * Calculated, presumably a mixture of FeO and Fe_2O_3, i.e. Fe_3O_4.

The amount of rock, m_{rock}, needed to sequester a unit mass of CO_2 can be calculated from the MgO content of the rock (%MgO) and the extraction of the magnesium from it, producing $Mg(OH)_2$, $X_{Mg(OH)2\ prod}(\%)$:

$$\frac{m_{rock}}{m_{CO2}}(kg/kg) = \frac{40.3}{44}\cdot\frac{1}{\%MgO/100}\cdot\frac{1}{X_{Mg(OH)2\,prod}(\%)/100} = 0.916\cdot\frac{1}{\%MgO/100}\cdot\frac{1}{X_{Mg(OH)2\,prod}(\%)/100} \quad (3)$$

(The values 40.3 and 44 give the molar masses (kg/kmol) of MgO and CO_2, respectively.) This assumes complete carbonation of $Mg(OH)_2$ to $MgCO_3$; as the best experimental result obtained for that so far is 65% ≈ 2/3, also the requirement of 1½× the amount calculated with (3) is given in the results presented below.

The number of years it would take to consume the suitable rock material m_{site} at a certain location can be calculated for the sites mentioned above, for a CO_2 sequestration rate of 1.2 Mt/year (as was the plan with the Fortum / TVO project):

$$t\,(year) = \frac{m_{site}}{m_{rock}\,/\,year} = \frac{m_{site}}{\frac{m_{rock}}{m_{CO2}} \cdot m_{CO2}\,/\,year} = \frac{m_{site}}{\frac{m_{rock}}{m_{CO2}} \cdot 1.2\,\mathrm{Mt\,CO_2}\,/\,year} \qquad (4)$$

where m_{rock}/m_{CO2} (kg(kg) is given by (3).

6. Feasibility of the considered deposits for Meri-Pori CO_2

6.1 – Hitura mine rock

As noted in section 4.2, the rock available at Hitura has a theoretical capacity to sequester more than 400 Mt CO_2. Figure 3 shows the amount of rock needed to carbonate 1 t CO_2 as a function of Mg extraction, for full and partial (65%) carbonation extent. With $Mg(OH)_2$ production levels of the order of 65- 70% obtained for the rock processing according to Nduagu et al., the process would require ~ 5 ton rock / ton CO_2 and could sequester 1.2 Mt CO_2/y during a period of ~150 years with 65% Mg/OH) carbonation. According to Romão et al. [17] - see also Table 1 – the heat requirements would be ~ 6 GJ/t CO_2 which can be reduced somewhat by heat integration. It would be reduced to ~ 4 GJ/t CO_2 if extraction and carbonation levels > 90% can be realised.

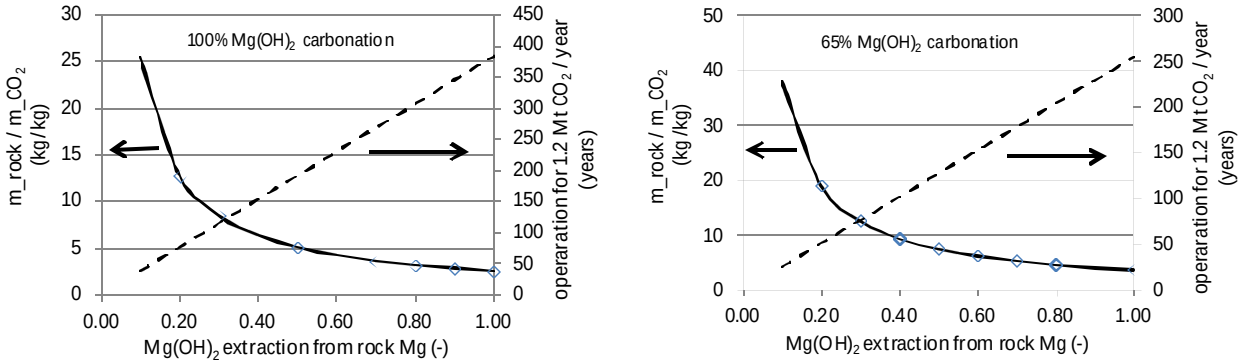

Fig. 3 Rock consumption rate and availability at Hitura depending on extraction of Mg from the rock, for full (left) or partial (right) carbonation of the $Mg(OH)_2$ produced.

The distance of around 300 km from Meri-Pori to the Hitura site would add a few €/t (on-shore pipeline) transport costs to this CCS option, making a site like Stormi-Vammala more attractive.

6.2 – Vammala (Stormi-Vammala) nickel mine rock

As presented in section 4.3, the rock available at Stormi-Vammala has a theoretical capacity to sequester ~50 Mt CO_2. Figure 4 shows the amount of rock needed to carbonate 1 t CO_2 as a function of Mg extraction, for full and partial (65%) carbonation extent. With $Mg(OH)_2$ production levels of ~ 25% obtained for the rock processing [35] the process would require ~ 12 ton rock / ton CO_2 and could fix 1.2 Mt/y during a period of < 10 years only, with 65% $Mg(OH)_2$ carbonation. The heat requirements would be in the range of 4.5 – 20 GJ/t CO_2 depending on whether non-reactive material behaves as inert or not. These values can be reduced somewhat by heat integration but the most urgent need for improvement is the extraction of Mg and producing more $Mg(OH)_2$ from the rock material. With the current result the contribution of crushing and grinding the rock

material will change from a few % to a significant energy penalty. Again, note that the rocks collected and analysed are from a rock mass nearby, not at, the Stormi mine [35].

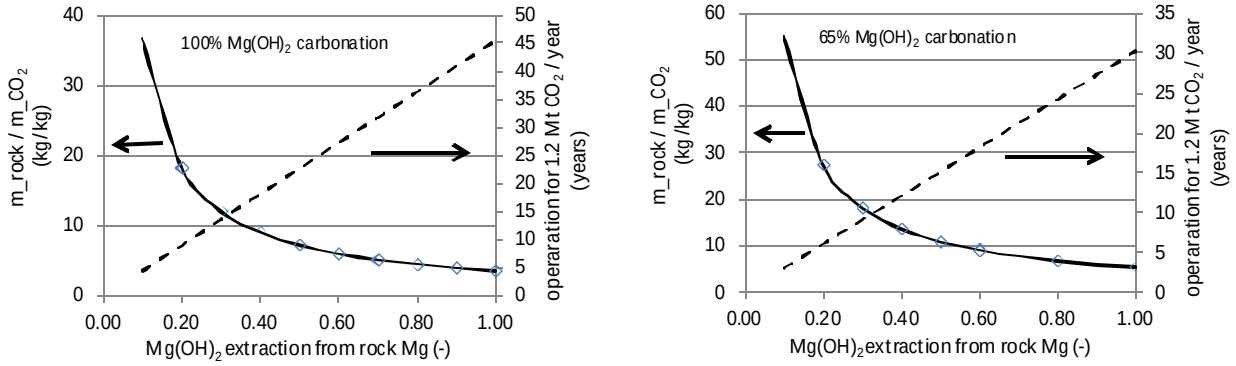

Fig. 4 Rock consumption rate and availability at Stormi-Vammala depending on extraction of Mg from the rock, for full (left) or partial (right) carbonation of the $Mg(OH)_2$ produced.

6.3 – Pori olivine deposits rock

A small number of experiments were carried out with olivine from Åheim in Norway, which confirmed (with < 10% of present Mg extracted) the hypothesis that the method developed by Nduagu et al. is not well applicable to olivines. Tests on the Satakunta olivine diabase gave no good result: Mg extraction was a disappointing 15% of the material's Mg content which is already quite low at only 5.5%. Work at ÅA is ongoing to further analyse the application of the $Mg(OH)_2$ production method on minerals like olivine and enstatite, besides serpentine.

6.4 – Suomusjärvi olivine deposits rock

The experimental results showed that $Mg(OH)_2$ could be produced only from the rock material Suomusjärvi-2, (Nummi-Pusula), at an extraction of ~14% of the ~21%-wt of MgO in the material. This implies that ~ 3 t $Mg(OH)_2$ can be produced from ~100 t of rock, which is ~10-15× the amount of rock needed compared to a Hitura-type serpentinite and crushing / grinding energy needs become a significant cost factor. As noted above, more work is needed on extending the capabilities of the Nduagu et al. route to $Mg(OH)_2$ production from "low quality" (< 20%-wt MgO) type of rock.

7. Combined SO_2 capture and CO_2 mineralisation: scope

7.1 – Background

Very few studies have been conducted using $Mg(OH)_2$ for sulphur and/or CO_2 capture, mainly due to its limited operational temperature range [42,43], but there are some studies that consider the use of MgO based sorbents [44,45]. Still, a similar material that has been much more studied is calcium oxide (e.g. [42,43,46-48]). Although calcium-based species are considered not abundant enough for large scale CO_2 sequestration at levels that mitigate global warming and climate change [49], it is being widely studied for the use of separating CO_2 from flue gases by means thermal cycling (see e.g. a review by Stanmore and Gilot [50]). The idea is to carbonate CaO in one fluidised bed (FB) reactor and then decompose the formed $CaCO_3$ in another FB releasing a pure stream of CO_2, while simultaneously recovering the CaO for re-use in the first reactor. In contrary to these studies, carbonation of $Mg(OH)_2$ for CO_2 sequestration purposes does not require the recycling of the reactant, and the product from the carbonation unit is ready for re-use or final disposal. This is beneficial as the continuous carbonation-calcination cycling has been shown to reduce (often quickly) the performance of the used material (CaO, in most cases) [50].

In the case of simultaneous sulphation and carbonation experiments, sulphate formation has been found to dominate when $Ca(OH)_2$ or CaO is exposed to a SO_2 (1 ppm) and CO_2 (6 ppm) containing gas [47]. Although, the conditions were different from those studied here, it was also noted that, SO_2 readily reacts with Ca species at dry conditions, while some humidity was needed to form carbonate. On the other hand, Stanmore and Gilot [50] commented in a review article that carbonation is initially much faster than sulphation and only in the longer run does sulphation become the principal reaction. In contrast to this study, however, it should be noted that the sorbents considered were Ca-based and that the conditions did not incorporate elevated pressures.

Despite the fact that SO_2 readily reacts with various Ca-based sorbents, the conversion levels obtained are typically in the range of 30–50% [42,50] leaving room for considerable improvement. The reason for the low conversion levels has been attributed to the closing of pores at the surface of the reacting particles due to the larger molar volume of calcium sulphate than that of either calcium oxide or –carbonate [50].

To date, most of the experiments using the ÅA mineral carbonation process have only considered the use of pure pressurised CO_2. However, in order for the process to become a realistic alternative, it is apparent that it needs to work with diluted CO_2 streams as well, such as industrial flue gases. In this paper we present the results from a number of experiments using CO_2 containing a small amount of sulphur dioxide and oxygen, both of which are common components in typical industrial flue gases. If successful, simultaneous carbonation and sulphation may motivate the removal of flue gas desulphurisation (FGD) equipment from sulphur-containing fossil fuel-fired power plants.

7.2 – Materials and methods

The materials used for the gas-solid carbonation experiments consists of two different types of $Mg(OH)_2$, one commercially obtained (Dead Sea Periclase Ltd.) and one derived from Finnish serpentinite according the ÅA process described briefly above. From here on, these will be referred to as DSP-$Mg(OH)_2$ and serp-$Mg(OH)_2$ respectively.

DSP-$Mg(OH)_2$ has already been studied extensively [27] and is also used for reference purposes in this paper. However, the difference between serpentinite-derived $Mg(OH)_2$ and DSP-$Mg(OH)_2$ is apparent from surface analysis and typically serp-$Mg(OH)_2$ has a much higher specific surface area (~50 vs. ~5 m^2/g) and porosity (0.24 cm^3/g vs. 0.024 cm^3/g) than DSP-$Mg(OH)_2$. For this reason, serp-$Mg(OH)_2$ offers a much greater potential in form of reactivity and reaction extent than DSP-$Mg(OH)_2$.

The gas used in the carbonation experiments has been a high purity (99.999%-vol) CO_2 bottle and a pre-mixed CO_2-O_2-SO_2 bottle with 90%, 8% and 2%-vol of each component respectively. For some experiments steam was added to the gas stream. The amount of SO_2 in the gas-mixture was varied between 0 and 20 000 ppmv (parts per million, volumetric).

A more thorough description of the methods used to carbonate $Mg(OH)_2$ can be found elsewhere [26,27], but for purposes of continuity, a short summary is also given here.

The experimental setup for gas/solid carbonation at ÅA, see Fig 5, consists of a small (height ~0.5 m, inner diameter ~1.5 cm) pressurised fluidised bed (PFB) that is operated by preheating the incoming fluidisation gas and by maintaining the reactor at the target conditions during each experiment. The PFB is operated as a bubbling fluidised bed and run in batch mode (max. temp. ~600 °C, max pressure ~100 bar). After each experiment the particles are blown out and collected by a cyclone for easy removal.

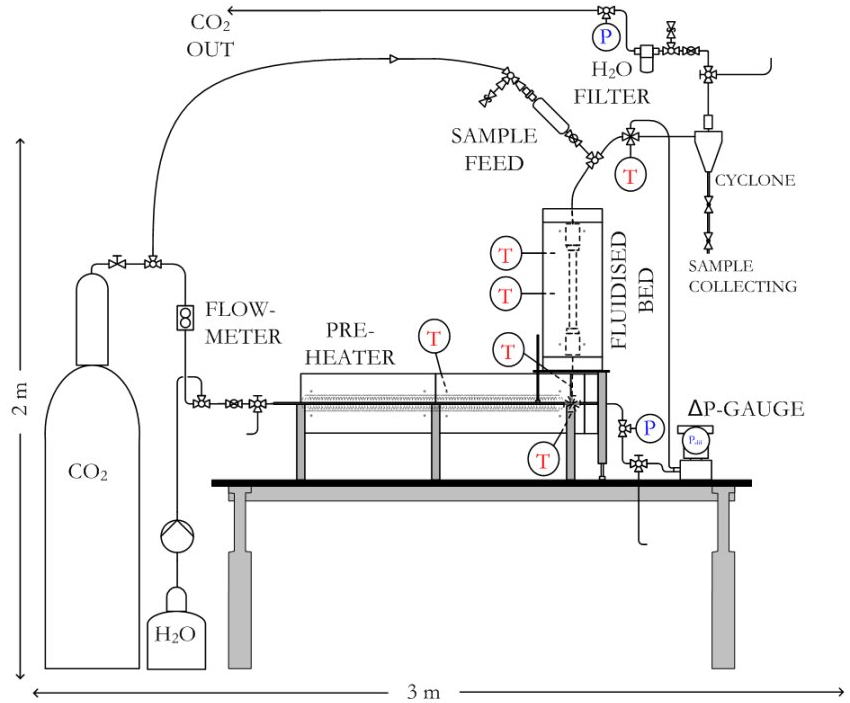

Fig. 5 Schematic diagram of the PFB setup at ÅA [26,27].

The appropriate fluid velocity is regulated/maintained by two flow controllers that allow for the mixing of two gas streams. In addition a HPLC-pump is used for adding water to the system prior to the preheater when steam is required in the reaction gas.

In contrary to previous studies, where a simple method of reacting the carbonated product with hydrochloric acid could be used for determining the carbonate content [51], the now both carbonated and sulphated $Mg(OH)_2$ samples were analysed for elemental carbon and sulphur using an ELTRA elemental analyser.

7.3 – Thermodynamics

We have recently concluded that the reaction between $Mg(OH)_2$ and CO_2 is likely taking place in accordance to the following overall equations [27]:

$$Mg(OH)_2 \longleftrightarrow MgO \cdot H_2O^* \longleftrightarrow MgO + H_2O(g) \quad (5)$$

$$MgO \cdot H_2O^* + CO_2(g) \longleftrightarrow MgCO_3 + H_2O(g) \quad (6)$$

The equations have been simplified to emphasize the importance of H_2O, but it is clear that the elementary reactions taking place on the surface of $Mg(OH)_2$ particles are more complex than what the simple direct carbonation of $Mg(OH)_2$ would suggest. To further highlight the role of H_2O, the assumed intermediate product of $Mg(OH)_2$ dehydroxylation is $MgO \cdot H_2O^*$, which corresponds to magnesium capable of forming carbonate. In the absence of water the reaction between MgO and CO_2 is slow and likewise if the temperature for $Mg(OH)_2$ dehydroxylation is not exceeded very little carbonation will take place [52]. Adding sulphur dioxide to the reaction gas will compete with the formation of magnesium carbonate, but to what extent is highly dependent on the SO_2 concentration. In any case, a SO_2 concentration at < 0.5%-vol is much lower than that of CO_2 in a typical flue gas. Similar conclusions have also been established for calcium-based species [53].

In a study by Hartman and Svoboda [44] a number of alternative reaction mechanisms between magnesium species and SO_2 were suggested. However, in the reaction conditions investigated here,

the formation of $MgSO_3$ is found thermodynamically infeasible [44] (see also Fig.), but in the presence of oxygen the following reaction has been suggested [44,47]:

$$MgO + SO_2(g) + \frac{1}{2}O_2(g) \longleftrightarrow MgSO_4 \quad (7)$$

Increasing the concentration of oxygen further, increases the amount of sulphur trioxide in the gas and thus the reaction between MgO and SO_3 also needs to be considered [44]:

$$MgO + SO_3(g) \longleftrightarrow MgSO_4 \quad (8)$$

In addition to the reactions above, the possibility of $MgCO_3$ reacting with SO_2 (or SO_3) to form $MgSO_4$ cannot be ignored. The conversion of $MgCO_3$ to $MgSO_4$ is given by the equation below:

$$MgCO_3 + SO_2(g) + \frac{1}{2}O_2(g) \longleftrightarrow MgSO_4 + CO_2(g) \quad (9)$$

From thermodynamic equilibrium calculations (HSC Chemistry 5.11 software) it can be concluded that both Reactions (8) and (9) are thermodynamically favoured under the experimental conditions investigated here. It appears that $MgSO_4$ is stable up to 640 °C for SO_2 and SO_3 concentrations above 0.1 ppmv. Furthermore, as long as the CO_2/SO_2 ratio is below 10^{10}, sulphation of $MgCO_3$ is also feasible as can be seen from Fig. 6. In other words, even if the concentration of SO_2 is only 0.1 ppbv (parts per billion, volumetric) in CO_2, sulphate is stable. In order to perform the equilibrium calculations, the amount of oxygen in the gas was arbitrarily chosen to be 3.5%-vol.

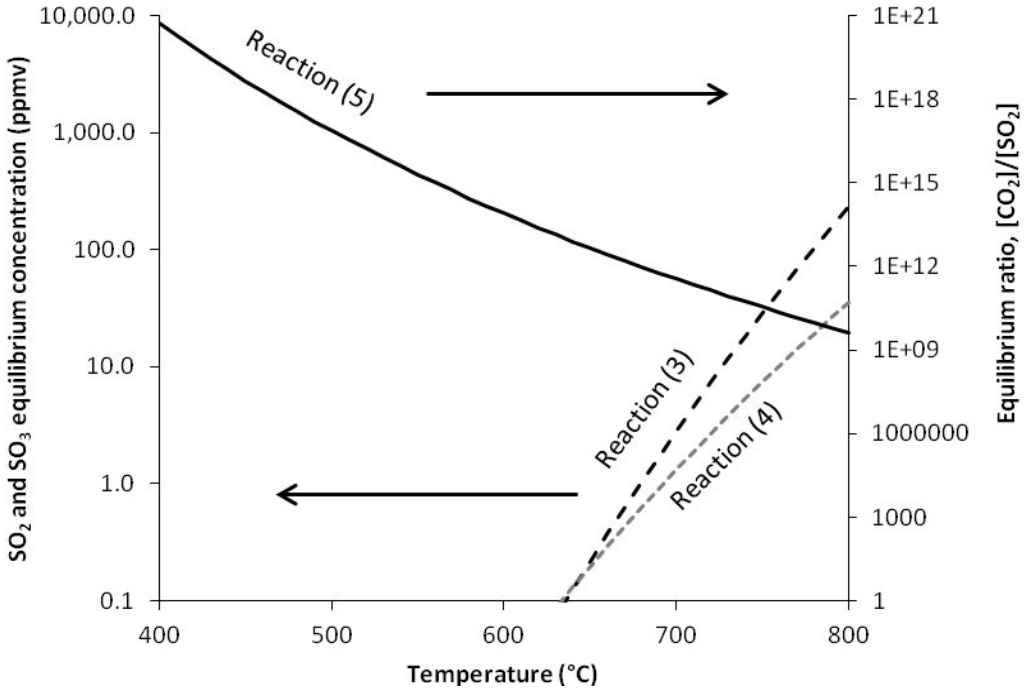

Fig. 6. Equilibrium concentrations of SO_2 (Reaction 3) and SO_3 (Reaction 4), together with the equilibrium ratio, CO_2/SO_2 (Reaction 5) as a function of temperature based on Gibbs energy minimisation calculations (HSC Chemistry 5.11). O_2 (arbitrarily chosen) in the gas phase: 3.5%-vol.

8. Combined SO_2 capture and CO_2 mineralisation: results

8.1 – Test results with DSP-$Mg(OH)_2$

In accordance with results from experiments with similar calcium-based species [46,47] and the thermodynamic calculations shown in Fig. 8, the reactivity of $Mg(OH)_2$ towards SO_2 (and SO_3) is significant as seen in Fig. 7. Typically, the concentration of SO_2 in a flue gas is much lower than 20 000 ppmv, hence the most interesting result in Fig. 7 are the ones showing the influence of SO_2 concentrations below 5 000 ppm (= 0.5%-vol).

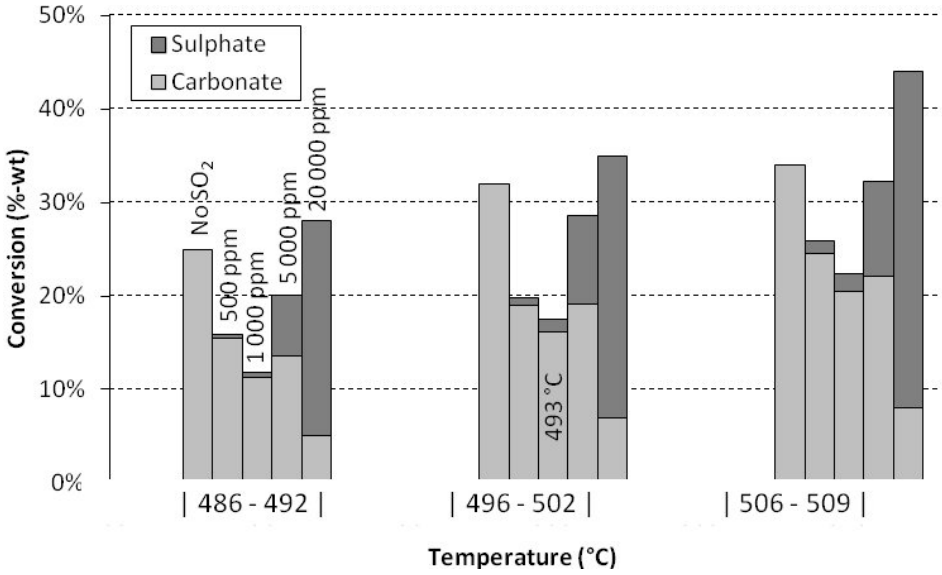

Fig. 7. The influence of SO_2 concentration (0–20 000 ppmv) on the reactivity of DSP-$Mg(OH)_2$ (125–212 μm) under a total pressure of 25 bar. The experiment time was 15 minutes. $P_{O_2} = 4 \cdot P_{SO_2}$ in dry CO_2.

Interestingly the influence of SO_2 is much stronger than that of CO_2, although it was present in much lower concentrations (90%-vol CO_2 vs. 2%-vol SO_2). However, it should be noted that SO_2 is a much stronger acid than CO_2 [53] and likely has a stronger affinity for the basic surface of the $Mg(OH)_2$ particles. The reason why carbonation is inhibited considerably in the presence of even small amounts (500 ppmv) of SO_2 is unclear, but evident from the data shown in Fig. 7.

In addition, the small increase in carbonate formation between experiments performed under 1 000 and 5 000 ppmv SO_2 is interesting, but could be the result of slightly differing temperature conditions inside the fluidised bed.

Because all of the experiments shown in Fig. 7 were performed for 15 minutes, the results represent a kind of steady state and product layer diffusion (much slower than the initial kinetics) is necessary for further reactivity. The initial reactivity of DSP-$Mg(OH)_2$ is comparatively fast and can be seen in Fig. 8 from a set of experiments performed under similar conditions (510 °C, 25 bar), but for different durations. However, it should be noted that 2%-vol SO_2 in the gas-phase is very high compared to industrial standards.

Although the influence of temperature can be seen from Fig 7, it is easier to compare its effect on both carbonation and sulphation from Fig. 9. Increasing the temperature beyond 520 °C, results in the decomposition of $MgCO_3$, which is why this is the maximum temperature in the graphs below.

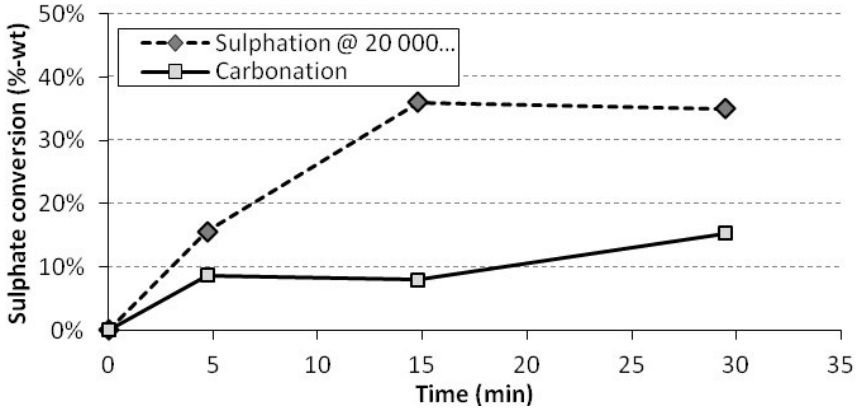

Fig. 8. Reactivity of DSP-Mg(OH)$_2$ at 510 °C, 25 bar. SO_2 concentration 20 000 ppmv (=2%-vol).

It is likely that a further increase in temperature would result in a slightly higher sulphation degree after which pore closure is expected. The porosity of the used DSP-Mg(OH)$_2$ material is relatively low (0.024 cm^3/g) and it has been noted to limit the overall conversion attainable during carbonation experiments [27].

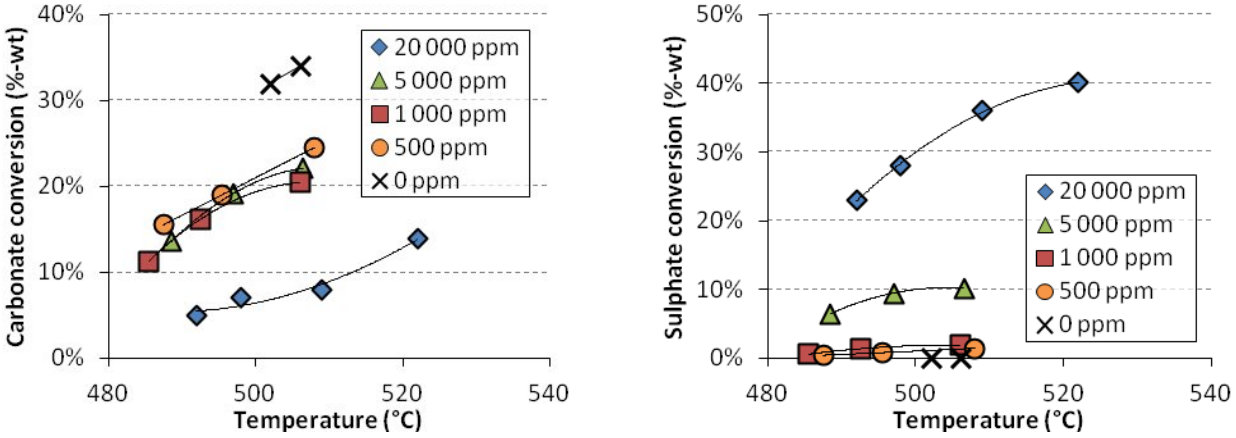

Fig. 9. Carbonate- (left) and sulphate (right) conversion using DSP-Mg(OH)$_2$ as a function of temperature at 25 bar and $P_{O_2} = 4 \cdot P_{SO_2}$ in dry CO_2.

It can be noted that sulphur contents between 500 and 5 000 ppmv resulted in similar carbonation extents, but not sulphation extents. Clearly the formation of sulphates is primarily driven by reactions (3) and (4), while the transformation of carbonate to sulphate, reaction (5), is less pronounced. A similar conclusion was reached by Wang et al. [54], who studied the simultaneous sulphation and carbonation of CaO in a CO_2 rich gas (oxy-fule combustion) in the presence and absence of steam at temperatures between 600–800 °C.

8.2 – Test results with serpentinite-derived Mg(OH)$_2$

In order to investigate the effect of pore closure another Mg(OH)$_2$ material was used for the experiments. This material (serpentinite-derived) is more porous and has a higher surface area than that of DSP-Mg(OH)$_2$. The results from only three such experiments, shown in Fig. 10, indicated that both carbonation and sulphation increased, likely due to the increased particle surface area. However, more experiments are required before any further conclusions from the data can be made.

In addition, two experiments with steam in the gas-phase were performed, but both experiments (1%-vol, 2%-vol steam) resulted in lower overall conversion of the material. Thus it seems that, dehydroxylation is a necessary precursor to both carbonation and sulphation (as also suggested by Reactions 5 and 6). This is a topic for future work, while scale-up tests are ongoing on producing larger batches of serp-Mg(OH)$_2$.

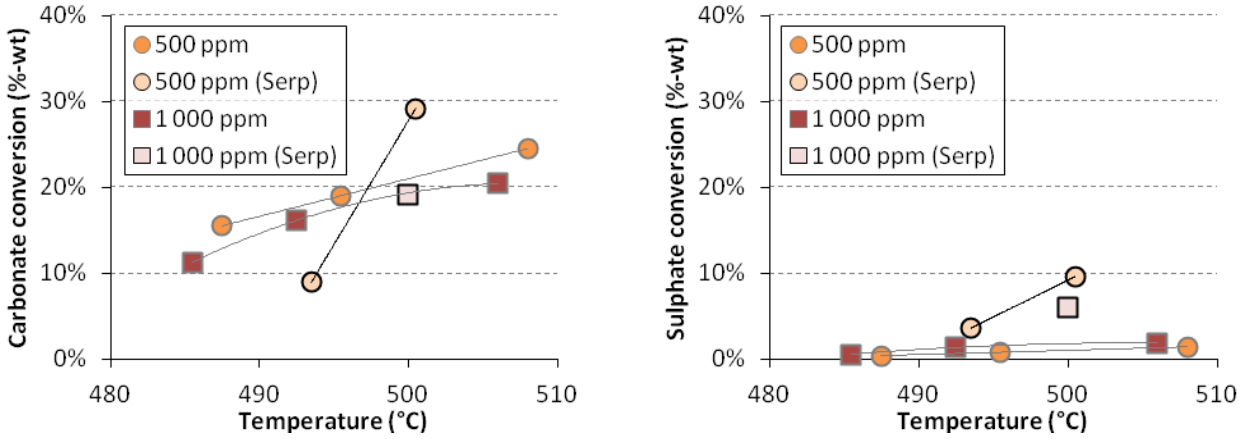

Fig. 10 Carbonate- (left) and sulphate (right) conversion using serpentinite-derived $Mg(OH)_2$ as a function of temperature at 25 bar and $P_{O_2} = 4 \cdot P_{SO_2}$ in dry CO_2. For reference purposes, the results using DSP-$Mg(OH)_2$ at similar conditions (500 and 1 000 ppmv SO_2) have also been included.

9. Conclusions

A study was made on the application of CO_2 mineral carbonation for the sequestration of CO_2 from the Meri-Pori power plant in Finland, after a plan for "convential" CCS, (or rather CCE, carbon capture and export, to Norway/Denmark) was cancelled. Serpentinite rock at Hitura, a nickel mine at ~ 300 km from Meri-Pori would be useful, with good and well-defined process chemistry and energy efficiency, and is available in much more than sufficient amounts. Serpentinite rock available at a shorter distance of ~70-80 km at Vammala appears to be available in a reasonably sufficient amount but the production of $Mg(OH)_2$ for subsequent carbonation must be improved before it can be considered. Still more improvement and R&D work is needed on olivine-containing dunites (>90% olivine), peridotites (60-100% olivine) and olivine diabase – type rock: the latter is available in the immediate surroundings of the Meri-Pori power plant but the $Mg(OH)_2$ production method isn't (so far) able to extract more than a few % of the materials Mg content, which is also much lower than for the serpentinites considered. Also the possibility to co-capture SO_2 and CO_2 was evaluated. It was found that the reactivity of $Mg(OH)_2$ towards SO_2 in the presence of CO_2 at pressurised conditions is significant even under low SO_2 partial pressures. As a consequence, the possibility to replace a conventional flue gas desulphurisation unit with a combined CO_2 and SO_2 scrubber could be considered. However, in order to be more conclusive, additional experiments are required.

Acknowledgments

This work was supported by KH Renlund's Foundation funding 2010 for project "Large scale CO_2 mineralisation in Finland: broadening the mineral resources horizon". Vilija Vaijegaite and Agne Babarskaite, visiting from Kaunas University of Technology, Lithuania, are acknowledged for the experimental work on the Vammala and Suomusjärvi rocks. Experience Nduagu and Inês Romão of ÅA are acknowledged for comments and feedback. The authors would also like to acknowledge Nordkalk and in particular Thomas Nyberg for the analysis of carbonated/sulphated samples.

Nomenclature

AS ammonium sulphate

Ex exergy, J or W

H enthalpy, J/mol

m mass, kg

P power, J or W

Q heat, J or W

t time, year

T remperature, °C or K

X degree of conversion, -

y year

Y %-vol CO_2 in flue gas

Δ difference

Subscripts and superscripts

C Carbonation

E Extraction (of Mg)

Mg(OH)2carb $Mg(OH)_2$ carbonation

Mg(OH)2prod $Mg(OH)_2$ production

site rock deposit site

References

[1] Fortum and Polish PGE cooperate on CCS technology. Carbon Capture and Storage Journal, on-line version, April 17, 2009, Available at: <http://www.carboncapturejournal.com/> [Accessed: 25.1.2012]

[2] Siemens, Fortum and TVO cooperate on Finnish project. Carbon Capture and Storage Journal, on-line version, October 23, 2009, Available at: <http://www.carboncapturejournal.com/> [Accessed: 25.1.2012]

[3] Fortum, TVO and Maersk join for Finnish project. Carbon Capture and Storage Journal, on-line version, October 23, 2009, Available at: <http://www.carboncapturejournal.com/> [Accessed: 25.1.2012]

[4] Fortum scraps CCS project in Finland. Carbon Capture and Storage Journal, on-line version, November, 2010, Available at: <http://www.carboncapturejournal.com/> [Accessed: 25.1.2012]

[5] Iso-Trykkäri, M., Meri-Pori CCS project. Presented at the ClimBus seminar on CCS, Espoo, Finland, Nov. 11, 2010. Avialable at: <http://www.vtt.fi/files/projects/ccsfinland/ seminaari2010/12-iso-tryykari.pdf> [Accessed: 25.1.2012]

[6] Koljonen, T., Siikavirta, H., Zevenhoven, R., Savolainen. I. CO_2 capture, storage and reuse potential in Finland, Energy 2004; 29:1521-1527

[7] Teir, S. et al. Potential for carbon capture and storage (CCS) in the Nordic region, VTT Research notes 2556, 2010 (223 p). Available at: <http://www.vtt.fi/inf/pdf/tiedotteet/ 2010/T2556.pdf> [Accessed: 25.1.2012]

[8] Shogenova, A. Insight into storage of CO_2. Presentation at the Cleen CCSP kick-off seminar, Espoo, Finland, Sept. 6, 2011.

[9] Aatos S., Sorjonen-Ward, P., Kontinen, A., Kuivasaari, T., Outlooks for utilisation of serpentine and serpentinite *(in Finnish: Serpentiinin ja serpentiniitin hyötykäyttönäkymiä)* Geological Survey of Finland (GSF), Report No. M10.1/2006/3, Kuopio, Finland (2006).

[10] Teir, S., Aatos, S., Kontinen, A., Zevenhoven, R., Isomäki, O.-P. 2006. Silicate mineral carbonation as a possible sequestration method of carbon dioxide in Finland. *(in Finnish, English summary): Silikaattimineraalien karbonoiminen hiilidioksidin loppusijoitus-menetelmänä Suomen oloissa)* Materia 2006;63 (1):40-46.

[11] Aatos, S., Kujanpää, L., Teir, S. CO_2 capture and geological storage applications in Finland. Geological Survey of Finland, 2011; Special Paper 49, 187-193

[12] Directive 2009/31/EC of the European Parliament and of the Council of 23 April 2009 on the geological storage of carbon dioxide. Available at: <http://eur-lex.europa.eu/LexUriServ/ LexUriServ.do?uri=OJ:L:2009:140:0114:0135:EN:PDF> [Accessed: 25.1.2012]

[13] Ekdahl, E., Idman, H. Statement on the applicability of Directive 2009/31/EC in Finland for Finnish Ministry of the Environment, K/468/42/2010, March 14, 2011.

[14] Proposal for implementation of legislation on CCS, Finnish Ministry of the Environment, (in Finnish and in Swedish), July 12, 2011, Available at < http://www.ymparisto.fi/ default.asp?node=3662&lan=fi#a1> [Accessed: 25.1.2012]

[15] Finlands Cleen Oy CCSP (Carbon Capture and Storage Program). Available at: <http://www.cleen.fi/en/program_overviews/ccsp_carbon_capture_and_storage_program> [Accessed: 25.1.2012]

[16] Fagerlund, J., Nduagu, E., Romão. I., Zevenhoven, R. CO_2 fixation using magnesium silicate minerals. Part 1: Process description and performance. Energy 2012;41:184-191

[17] Romão, I., Nduagu, E., Fagerlund, J., M. Gando-Ferreira, L., Zevenhoven, R. CO_2 Fixation Using Magnesium Silicate Minerals. Part 2: Energy Efficiency and Integration with Iron-and Steelmaking. Energy, 2012;41:203-2011

[18] Mattila, H.-P., Grigaliūnaitė, I, Said, A., Filppula, S., Fogelholm, C.-J., Zevenhoven, R. Process efficiency and optimization of precipitated calcium carbonate (PCC) production from steel converter slag. Submitted to ECOS2012, Perugia, Italy, June 2012; *resubmitted after minor revision*

[19] IPCC Special Report on Carbon Dioxide Capture and Storage B. Metz, O. Davidson, H. de Coninck, M. Loos, L. Meyer, Working Group III of the IPCC, Cambridge Univ. Press (2005) Available at: <http://ipcc.ch/publications_and_data/publications_and_data_reports.shtml>

[20] Zevenhoven, R., Fagerlund, J., Songok, J.K. CO_2 mineral sequestration - developments towards large-scale application. Greenhouse Gases: Science and Technology. 2011; 1:48-57

[21] Wang, X, Maroto-Valer, M. Dissolution of Serpentine using recyclable ammonium salts for CO_2 mineral carbonation. FUEL 2011; 90(3): 1229-1237

[22] Hunwick, R.J. A new, integrated approach to mineralisation-based CCS, Modern Power Systems, 2009; November:25-28

[23] Sipilä, J., Teir, S., Zevenhoven, R. Carbon dioxide sequestration by mineral carbonation – Literature Review Update 2005-2007. Åbo Akademi Univ., Heat Engineering Lab. report VT 2008-1, Turku, Finland (2008). Available at: <http://users.abo.fi/rzevenho/ MineralCarbonationLiteratureReview05-07.pdf >

[24] Nduagu, E., Björklöf, T., Fagerlund, J., Wärnå, J., Geerlings, H., Zevenhoven, R. Production of reactive magnesium from magnesium silicate for the purpose of CO_2 mineralization. Part 1. Application to Finnish serpentinite. Minerals Engineering, 2012;30:75 - 86

[25] Nduagu, E., Björklöf, T., Fagerlund, J., Mäkelä, E., Salonen, J., Geerlings, H., Zevenhoven, R. Production of reactive magnesium from magnesium silicate for the purpose of CO_2 mineralization. Part 2. Mg extraction modeling and application to different Mg silicate rocks. Minerals Engineering, 2012, 2012;30:87-94

[26] Fagerlund, J., Zevenhoven, R. An experimental study of $Mg(OH)_2$ carbonation. Int. J. of Greenhouse Gas Control 2011; 5:1406-1412

[27] Fagerlund, J., Carbonation of $Mg(OH)_2$ in a pressurised fluidised bed for CO_2 sequestration [PhD thesis], Turku, Finland: Åbo Akademi University / Chemical Engineering (2012) Available at: <http://www.doria.fi/handle/10024/74477> [Accessed: 1.5.2012]

[28] Nduagu E, Bergerson, J., Zevenhoven, R. Life cycle assessment of CO_2 sequestration in magnesium silicate rock - a comparative study. Energy Conv. & Manage. 2012; 55:116-126

[29] O'Connor, W.K., Dahlin, D.C., Rush, G.E., Gerdemann, S.J., Penner, L.R., Nilsen, R.P., Aqueous mineral carbonation: Mineral availability, pretreatment, reaction parametrics, and process studies, DOE/ARC-TR-04-002, Albany Research Center, Albany, (OR) USA (2005)

[30] Gerdemann, S.J., O'Connor, W.K., Dahlin, D.C., Penner, L.R., Rush, H. 2007. Ex Situ Aqueous Mineral Carbonation Environ. Sci. Technol. 2007;41:2587-2593

[31] Björklöf, T., Zevenhoven, R. Energy efficiency analysis of CO_2 mineral sequestration in magnesium silicate rock using electrochemical steps. Chem. Eng. Res. & Des. 2012; *accepted / in press*, available on-line: doi: 10.1016/j.cherd.2012.02.001

[32] Zahra, A. Carbon dioxide capture from flue gas: Development and evaluation of existing and novel process concepts [PhD Thesis] Delft, the Netherlands: Delft University of Technology2009.

[33] Khoo, H.H., Sharatt, P.N., Bu, J., Borgna, A., Yeo, T.Y., Highfield, J., Björklöf, T.G., Zevenhoven, R. Carbon capture and mineralization in Singapore: preliminary environmental impacts and costs via LCA. Ind. & Eng. Chem Res. 2011; 50:11350 - 11357

[34] Nuclear plant units Olkiluoto 1 and Olkiluoto 2 *(in Finnish: Ydinvoimalaitos yksiköt Olkiluoto 1 ja Olkiluoto2)* Available at: <http://www.tvo.fi/uploads/File/yksikot-OL1-OL2%281%29.pdf> [Accessed: 2.2.2012]

[35] Mäkelä, M. Storing of carbon dioxide by mineral carbonation in Southern Finland *(in Finnish; Hiilidioksidin sitominen mineraalikarbonaatiolla Etelä-Suomessa)* [MSc thesis]. Turku, Finland: University of Turku / Geology and Mineralogy; 2011.

[36] Hitura - Nickel Database Available at: <http://en.gtk.fi/ExplorationFinland/Commodities/ Nickel/hitura.html> [Accessed: 25.1.2012]

[37] Stormi - Nickel Database Available at: <http://en.gtk.fi/ExplorationFinland/Commodities/ Nickel/stormi.html> [Accessed: 25.1.2012]

[38] Belvedere Resources Ltd, A European Nickel Producer Available at: <http://www.belvedere-resources.com/assets/ files/Mar%2008web.pdf> [Accessed: 2.2.2012]

[39] Hamalainen, Arja,. The Postjotnian diabases of Satakunta. *(in Finnish, English summary): Satakunnan Postjotuniset Diabaasit)* Geological Survey of Finland, Report of Investigation 1987; 76:173-178. Available at: < http://arkisto.gtk.fi/tr/tr76/tr76_pages_173_178.pdf >

[40] Norilsk Nickel Harjavalta *(in Finnish only)* Available at: <http://www.nornik.fi/> [Accessed: 2.2.2012]

[41] Nickel in Finland. Available at: <http://en.gtk.fi/ExplorationFinland/Commodities/Nickel/ gtk_ni_map.html> [Accessed: 25.1.2012]

[42] Anthony, E. J., and Granatstein, D. L., Sulfation phenomena in fluidized bed combustion systems, Progress in Energy and Combustion Science, 2001;27(2): 215-236.

[43] Gupta, H., and Fan, L., Carbonation-Calcination Cycle Using High Reactivity Calcium Oxide for Carbon Dioxide Separation from Flue Gas, Ind Eng Chem Res, 2002;41(16): 4035-4042.

[44] Hartman, M., and Svoboda, K., Physical properties of magnesite calcines and their reactivity with sulfur dioxide, Ind. Eng. Chem. Proc. Des. Dev., 1985; 24(3):613-621.

[45] Han, K. K., et al., Efficient MgO-based mesoporous CO_2 trapper and its performance at high temperature, J. Hazard. Mater., 2012; 203–204: 341-347.

[46] Snow, M. J. H., Longwell, J. P., and Sarofim, A. F., Direct sulfation of calcium carbonate, Ind Eng Chem Res, 1988:27(2): 268-273.

[47] Elfving, P., Panas, I., and Lindqvist, O., In situ IR study on the initial sulphition and carbonation of $Ca(OH)_2$ and CaO by SO_2 polluted air, Atmos. Environ., 1996:30(23): 4085-4089.

[48] Chen, H., and Zhao, C., Development of a CaO-based sorbent with improved cyclic stability for CO_2 capture in pressurized carbonation, Chem. Eng. J., 2011;171(1): 197-205.

[49] Lackner, K. S., Butt, D. P., and Wendt, C. H., Progress on binding CO_2 in mineral substrates, Energy Convers. Mgmt., 1997;38(Supplement 1): 259-264.

[50] Stanmore, B. R., and Gilot, P., Review — calcination and carbonation of limestone during thermal cycling for CO_2 sequestration, Fuel Process Technol, 2005; 86(16): 1707-1743.

[51] Fagerlund, J., et al., Gasometric Determination of CO_2 Released from Carbonate Materials, J. Chem. Educ., 2010:87(12): 1372-1376.

[52] Highfield, J., et al., The promoter effect of steam in gas-solid CO_2 mineralisation, Proc. ICCDU-XI, Dijon, France, June 2011.

[53] Lu, H., and Smirniotis, P. G., Calcium Oxide Doped Sorbents for CO_2 Uptake in the Presence of SO_2 at High Temperatures, Ind Eng Chem Res, 2009;48(11):5454-5459.

[54] Wang, C., Jia, L., and Tan, Y., 2011, Simultaneous Carbonation and Sulfation of CaO in Oxy-Fuel CFB Combustion, Chem. Eng. Technol., 2011;34(10): 1685-1690.

Carbon dioxide storage by mineralisation applied to a lime kiln

Inês Romão[a,b], Matias Eriksson[c,d], Experience Nduagu[a], Johan Fagerlund[a], Licínio M. Gando-Ferreira[b] and Ron Zevenhoven[a]

[a] Åbo Akademi University, Dept. of Chemical Engineering, Åbo / Turku, Finland, iromao@abo.fi (CA)
[b] University of Coimbra, Dept. of Chemical Engineering, Coimbra, Portugal
[c] Nordkalk Corporation, Pargas / Parainen, Finland
[d] Umeå University, Sweden

Abstract:

This paper describes a design, for a pilot-scale application, of a two-staged process that is under study at Åbo Akademi University (ÅA), for Carbon dioxide Storage by Mineralisation (CSM). The ÅA route implies the production of brucite (besides Ca- and Fe- based by-products) from a magnesium/calcium silicate rock, using recoverable ammonium sulphate (AS), followed by carbonation of the Mg(OH)2 in a pressurised fluidised bed at ~ 500°C, 20-30 bar CO2 partial pressure. An assessment is reported for operating the CSM process on waste heat from a limekiln (lime production: 210 t/day) in Pargas, Southwest Finland, i.e. without external energy input apart from what is needed for crushing the rock to the required particle size (a few % of the overall CSM process energy requirement) and compressing the flue gas to be treated. Part of the off-gas from the limekiln (CO2 content ~21%-vol) will be processed without a CO2 separation step. The feature of operating without CO2 separation makes CSM an attractive and cost-competitive option when compared to conventional CCS involving underground storage of CO2. An exergy analysis is used to optimise process layout and energy efficiency, and at the same time maximise the amount of CO2 that can be bound to MgCO3 given the amount of waste heat available from the kiln. Also, experimental results are reported for producing Mg(OH)2 (and Fe,Ca(OH)2) from local rock material.

Keywords:

CO_2 mineral sequestration, Scale-up, Lime kiln.

1. Introduction

1.1 CO_2 mineralisation

For Finland, carbon dioxide storage by mineralisation (CSM) was identified as the only option for CCS (carbon dioxide capture and storage) application. It is a permanent storage option and has an estimated storage potential that is much larger than underground storage as pressurized CO_2 [1-2], the currently most intensively studied option for CO_2 disposal. The purpose of CSM is to promote CO_2 fixation by metal oxides into thermodynamically stable carbonates while benefiting of the exothermicity of the carbonation reaction:

$$(Ca,Mg)*ySiO_2*zH_2O\ (s) + CO_2\ (g) \rightarrow (Ca,Mg)CO_3\ (s) + ySiO_2\ (s) + z\ H_2O\ (g) + HEAT \qquad (R1)$$

Magnesium in particular is abundant in the earth's crust, as silicates such as serpentinite and olivine. These reactions occur in nature over geological timescales (hundreds of thousands of years). Research has focused on improving the reaction rates by treating the mineral rock by thermal, mechanical or chemical means [1-4]. Due to the exceptionally large scale of CCS processes, all additives must be recovered, and the energy input minimised.

A process under development at ÅA uses recoverable ammonium sulphate (AS) salt to extract Mg from grinded serpentinite rock, at elevated temperatures. The extraction has shown conversions of up to 70 % of Mg into either reactive $Mg(OH)_2$ or $MgSO_4$, depending on the desired intermediate. $Mg(OH)_2$ reacts directly with CO_2 under elevated temperature in a pressurised fluidised bed. The ÅA process may also be used as a scheme to capture the CO_2 directly from a flue gas stream. The direct mineralisation of flue gas instead of separated and compressed CO_2, eliminates the need of expensive and energy intensive processes to isolate and compress CO_2, thus significantly lowering the materials and energy requirements for the overall CCS process chain. Besides, the simultaneous CO_2 separation and capture avoids the main risks associated with geological storage (potential leakage of CO_2 into the atmosphere) and the costs associated with monitoring [5]. Hence, CSM is a promising, safe and permanent CO_2 fixation route and for that reason has been studied at ÅA since 2006.

In addition, metal and mineral processing and papermaking sectors (but not the power sector) have shown much interest in using CSM for CO_2 emissions mitigation. The prospect of simultaneously making use of and (in some cases) upgrading/stabilising process' by-products and waste materials (ashes e.g) is another interesting benefit [6,7].

This paper explores the possibility of running the ÅA CSM process on waste heat provided by a limekiln (lime production: 210 t/day) in Pargas, Southwest Finland (Nordkalk Corporation) and assess the performance of a pilot plant, with direct mineralisation of flue gases. Nordkalk is one of the European leading producers of lime emitting a total of 0.79 $MtCO_2/a$ [8]. Along with the limestone mining comes significant amounts of diopside. The use/upgrading of this by-product by CSM is discussed at the end of this paper.

The serpentinite rock material, used in this particular simulation, comes from a nickel mine located in Hitura, Central Finland, 500 km from Pargas. This mine has significant resources of magnesium silicate rocks (<1000 Mt) and experimental tests show that its serpentinite material is suitable for the ÅA process [9].

1.2 – Process description

The serpentinite rock reacts with ammonium sulphate (AS) and water at 450°C and atmospheric pressure in order to produce XSO_4 salts (X=Mg,Ca,Fe), as first described by Nduagu [9-11]. During the reaction considerable amounts of NH_3, SO_3 and water are released. The solids are put in water and the insoluble fraction (mainly unreacted serpentinite and SiO_2) is discarded. The NH_3 produced in the first step is used to raise the pH of the aqueous solution to ~8-9 in order to precipitate the iron and calcium in the form of hydroxides. These are separated and possibly redirected to the steelmaking industry creating the opportunity to reduce the net CO_2 emissions and replace raw materials [12]. Once more, using the NH_3 produced in the first step, the pH of the aqueous solution is raised to ~10-12 and the magnesium precipitates to form $Mg(OH)_2$. AS is recovered from the residual solution and the $Mg(OH)_2$ is carbonated at 500°C and 20 bar of CO_2 partial pressure, in a pressurised fluidised bed (PFB) reactor. The carbonation method is described in more detail by Fagerlund [13-15]. The gas entering the carbonator may be a pure stream of CO_2 but may also be the whole flue gas from a process. The heat released in the carbonation reactor may provide some of the energy needed to heat the serpentinite rock, aiming at an auto-thermal process.

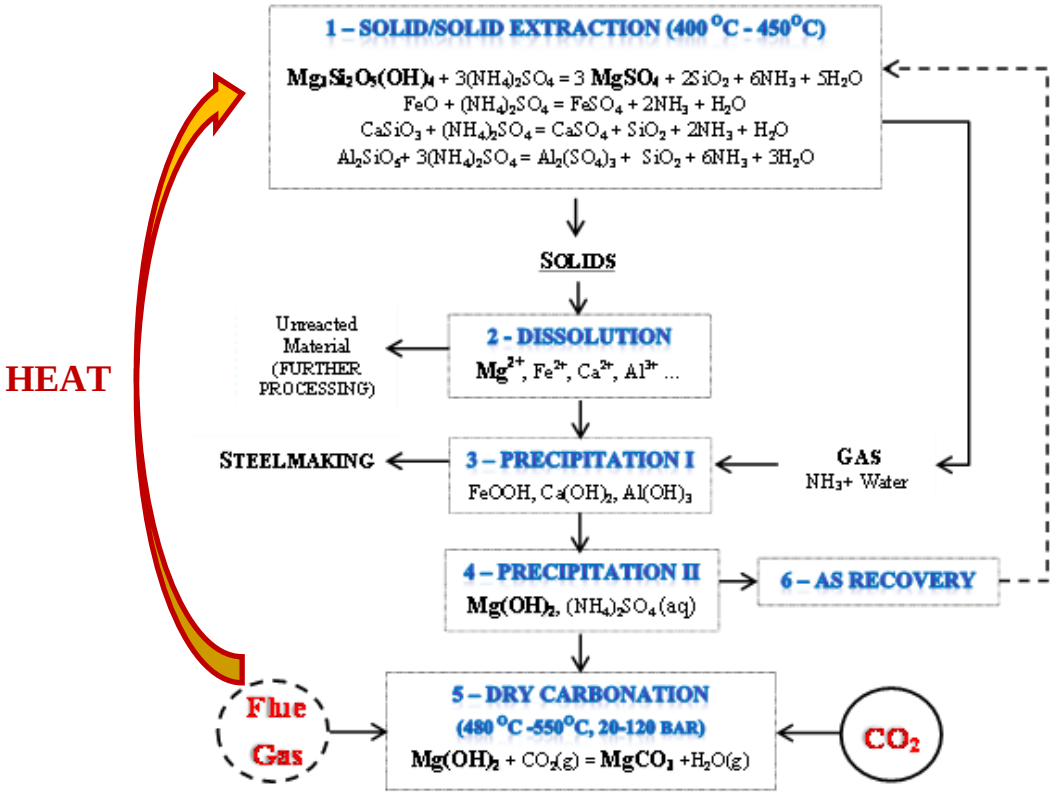

Fig. 1. Scheme and main reactions of the magnesium silicates' carbonation process. Adapted from [15]

2. Aspen Plus ® simulations – Mineralisation of serpentine with flue gas

2.1. Aspen Plus ® model – Hitura's (Finland) serpentine

The ÅA CSM process was simulated using Aspen Plus® Software. The model follows the same scheme as the ones presented in earlier publications [12,16-17] but differs on the CO_2 inlet stream of the carbonation step and on the source of heat supplied to the endothermic stages.

The S-DECOMP block represented in the Aspen Plus model (Figure 3) simulates the Solid/Solid extraction reactor. It operates at 440ºC and atmospheric pressure. Experimental results, on Portuguese samples, show that the presence of water greatly enhances the rate of magnesium extraction and lowers the temperature by ≈50°C compared to reacting dry matter. [16-17].

In this block, AS is mixed with Hitura's serpentinite (86% $Mg_3Si_2O_5(OH)_4$, 13% FeO, 1% $CaSiO_3$) and water at a ratio of 3:2:1. In the simulations 80% of Magnesium[1], 60% of iron and 100% of calcium are assumed to be extracted.

It is expected that, under the referred operating conditions, the following reactions occur:

$$Mg_3Si_2O_5(OH)_4 + 3\ (NH_4)_2SO_4 = 3\ MgSO_4 + 2\ SiO_2 + 6\ NH_3\ (g) + 5\ H_2O\ (g) \quad (R1)$$

$$FeO + (NH_4)_2SO_4 = FeSO_4 + 2\ NH_3\ (g) + H_2O\ (g) \quad (R2)$$

[1] Although experimental results with Hitura's samples so far had a maximum of 74% of Mg extraction.

$$CaSiO_3 + (NH_4)_2SO_4 = CaSO_4 + SiO_2 + 2\ NH_3\ (g) + H_2O\ (g) \quad (R3)$$

$$(NH_4)_2SO_4\ (s) \rightarrow 2NH_3(g) + SO_3\ (g) + H_2O(g) \quad (R4)$$

As the large amounts of NH_3 and water released are cooled, the NH_3 dissolves in the water to produce a 30-40% solution of NH_4OH (Block TANK 1). A small make-up stream of NH_3 or NH_4OH will be necessary due to possible losses in the overall process. The appropriate temperature for this vessel depends on the amount of water present in the gases and, in this case, it was estimated to be ~40°C (roughly the boiling temperature of an aqueous solution with ≈30% NH_3). The NH_4OH produced in this vessel is later used to cautiously raise the pH in both precipitation steps (blocks PPI and PPII). After cooling, the hot solid from the S-DECOMP block is dissolved in water (block DISSOLUT). Unreacted serpentine, iron oxide, wollastonite and insoluble reaction products (silica, e.g) settle and are separated, most likely by a filtration process, forming the RESIDUE. In the aqueous solution at ~80^{0}C, the XSO_4 salts formed in the first step are converted to X^{2+} species.

For the sequential precipitations, pH is the most important operation parameter. The solution must be rigorously kept at pH=9-9,5 (block PPI) so that only iron and calcium are precipitated and, consequentially, magnesium recovery is maximised in the second precipitation stage (block PPII) at a pH of ~9,5-11,5. This pH may slightly vary depending on the mineral and reaction conditions. The iron is precipitated in the form of FeOOH (goethite), (although in the simulation $Fe(OH)_2$ is used due to some database problems in Aspen Plus®) calcium as $Ca(OH)_2$ and magnesium as $Mg(OH)_2$. The NH_3 present in the gases from the Solid/Solid Reactor may not be enough to increase the pH of the second precipitation stage to 11,5. For that reason it may be necessary to add NH_3 to the block PPII.

Although AS is a cheap chemical (cheaper than ammonia or sulphuric acid) its recovery is compulsory, not only for environmental reasons but also to make the process economically viable. After being separated from the precipitated $Mg(OH)_2$, the AS is recovered from the aqueous solution through a concentration/crystallisation process (block EVAPORAT). The recovered wet AS is then fed back to S-DECOMP reactor, thereby closing the AS cycle and process loop.

The $Mg(OH)_2$ is directly carbonated with flue gas from the limekiln, in a pressurised fluidised bed (block CARBONAT). In order to achieve a CO_2 partial pressure of ~ 20 bar, the flue gas, with ~21%-vol CO_2, must be compressed to at least 80 bar. The block MSCOMPRESS (multistage compressor) represents a series of 6 polytropic compressors with 80% of efficiency. $Mg(OH)_2$ reacts with gaseous CO_2 to form $MgCO_3$ and water vapour at 500°C and a total pressure of 80 bar. The stream leaving the CARBONAT reactor contains $MgCO_3$(s), H_2O(g), O_2, N_2 and unreacted $Mg(OH)_2$(s) and CO_2(g). The gases are separated from the solids (most likely) by a cyclone. The $MgCO_3$/$Mg(OH)_2$ solid product mix may be re-circulated until the $Mg(OH)_2$ content becomes sufficiently low (few %). Decompressing and cooling the gaseous stream leaving the separation unit allows for the recovery of some of the energy input for the initial flue gas compression. This stream contains water vapour, produced in the carbonation reaction.

$$Mg(OH)_2\ (s) + CO_2\ (g) \rightarrow MgCO_3\ (s) + H_2O(g) \quad (R4)$$

In order to avoid the presence of a liquid phase inside the isentropic expansion turbine, the decompression cannot go under ~5.6 bar. The rest of stream's exergy/heat content is recovered in a heat exchanger. The main assumptions taken to design the Aspen model are summarized in Table 1.

In this simulation, the heat required for this process is provided by ~10.3 m^3n [7] of flue gases coming from the limekiln located in Pargas. Currently, the heat content of those gases is utilised to supply district heating for the city of Pargas. In the Aspen Plus® model the flue gas is defined as two different utilities. Utility FG500 is the flue gas leaving the limekiln at 500^{0}C and is used to provide heat for the Mg, Ca and Fe elements extraction and to pre-heat the CO_2 rich gas entering the carbonator. After cooling to 440^{0}C, the flue gas FG440 is then used to provide heat for the

(raw) materials pre-heating and AS recovery. The specifications for these two utilities are listed in Table 2.

Table 1. Main assumptions taken in the Aspen Plus ® model

Block	Assumption
S-SDECOM	Operating conditions: T= 440ºC, P=1bar AS/S/W=3:2:1 Extraction %: Mg = 80%, Fe = 60%, Ca = 100%
DISSOLUT	T=80ºC; Total conversion of XSO_4 species to X^{2+}
TANK 1	T=40ºC; Complete dissolution of NH_3 into water producing a 30~40% solution of NH_4OH
PPI	Total precipitation of Fe and Ca as $Fe(OH)_2$ and $Ca(OH)_2$ pH =9-9.5; T=30ºC
PPII	Precipitation of Fe and Ca as $Fe(OH)_2$ and $Ca(OH)_2$ pH =9.5-11.5; T=30ºC
CRYST	Water is evaporated so that the recovered product has 75% -w/w of AS and 25 %-w/w of water.
CARBONAT	Carbonation with Flue Gas from the limekiln p_{CO2}~=20 bar, P=80 bar 90% of $Mg(OH)_2$ carbonation according to reaction R4
MSCOMPRE	6 polytropic compressors with 80% efficiency and intercoolers
TURBINE	Isentropic; Decompression to ~5.6 bar

Table 2. Data for the limekiln's flue gas defined as a utility in the Aspen Plus ® model

Utility ID	Composition (mol %)	T_{IN} (°C)	T_{OUT} (°C)
FG500	H_2O 5.9 CO_2 21.7	500	460
FG440	O_2 6.9 N_2 65.5	440	350

2.2. Results – Mass and exergy

The aim of this simulation is to evaluate the performance of a pilot scale mineral carbonation plant running on waste heat from the limekiln. In order to process 600 kg/hr of flue gas (7 m^3 at 500 ^{0}C and 80 bar) i.e, ~190 kg of CO_2, 500 kg/hr of serpentinite and 750 kg/hr (later recovered) of AS are required. The amounts of residue produced are quite significant, 298 kg/hr. However, this material is very rich in SiO_2 (>70%) making its future processing for Si recovery an auspicious possibility. Ideally, the ~36 kg/hr of iron and calcium hydroxide products are redirected to the steelmaking industry. Although this appears to be a modest quantity of by-product, note that, at a larger scale, the mineralisation of, e.g., all the CO_2 emissions of a single steel company operating in Finland (Ruukki), is enough to replace up to 18% of iron ore raw material with FeOOH [12].

Out of the 500 kg/hr of processed serpentinite it is possible to produce 275.3 kg/hr of $Mg(OH)_2$. Assuming a 90% carbonation efficiency, 275 kg/hr of $MgCO_3/Mg(OH)_2$, with a content of 90% $MgCO_3$, are produced. Figure 2 presents a schematic diagram of the process including mass balance results.

Table 3 presents the detailed exergy results for each block simulated in Aspen Plus®. Flue gas provides heat to all endothermic units (including AS recovery) making the process auto-thermal while not compromising the district heating supply to Pargas. Partly this is because the ÅA route generates itself significant amounts of low temperature heat suitable for district heating.

Clearly, the most energy intensive block is the extraction of the various (Mg, Ca, Fe…) elements from serpentinite. The heat needed for the Mg extraction is supplied by gas leaving the limekiln at 500ºC. After this, the flue gas is further used to pre-heat (raw) materials and provide heat for the AS recovery.

The energy needed for crushing the rock was estimated using a Bond index of 19 kWh/t [18] and equation (1):

$$E_0 = W_i \cdot \left(\frac{\sqrt{F} - \sqrt{P}}{\sqrt{F}} \right) \cdot \sqrt{\frac{100}{P}} \quad (1)$$

where:

- E_0: energy required for pulverisation [kWh/t];
- W_i: work index [kWh/t];
- F: size of feed particles [μm], assumed to be 2 cm;
- P: size of the pulverized particles [μm], assumed to be the average particle size of the samples used in earlier experiments, 100 μm [8-10,14-16].

The main drawback in this process is the energy required for the flue gas compression, even though ~66% of this energy input may be recovered later on while decompressing gaseous products from the carbonator (CARBONAT), where the CO_2^{gas} is converted to H_2O^{vapor}. Table 2 presents the overall exergy input needed for flue gas compression and crushing of the serpentinite rock. The final value for the overall exergy input for this is 0.71MJ/kg CO_2 captured.

Table 2. Exergy input for the gases compression and raw materials crushing.

	MJ/hr	**MJ/kg CO_2**
Compressor	280	1.52
Turbine	-185	-1.01
Crushing	35	0.19
Total	**131**	**0.71**

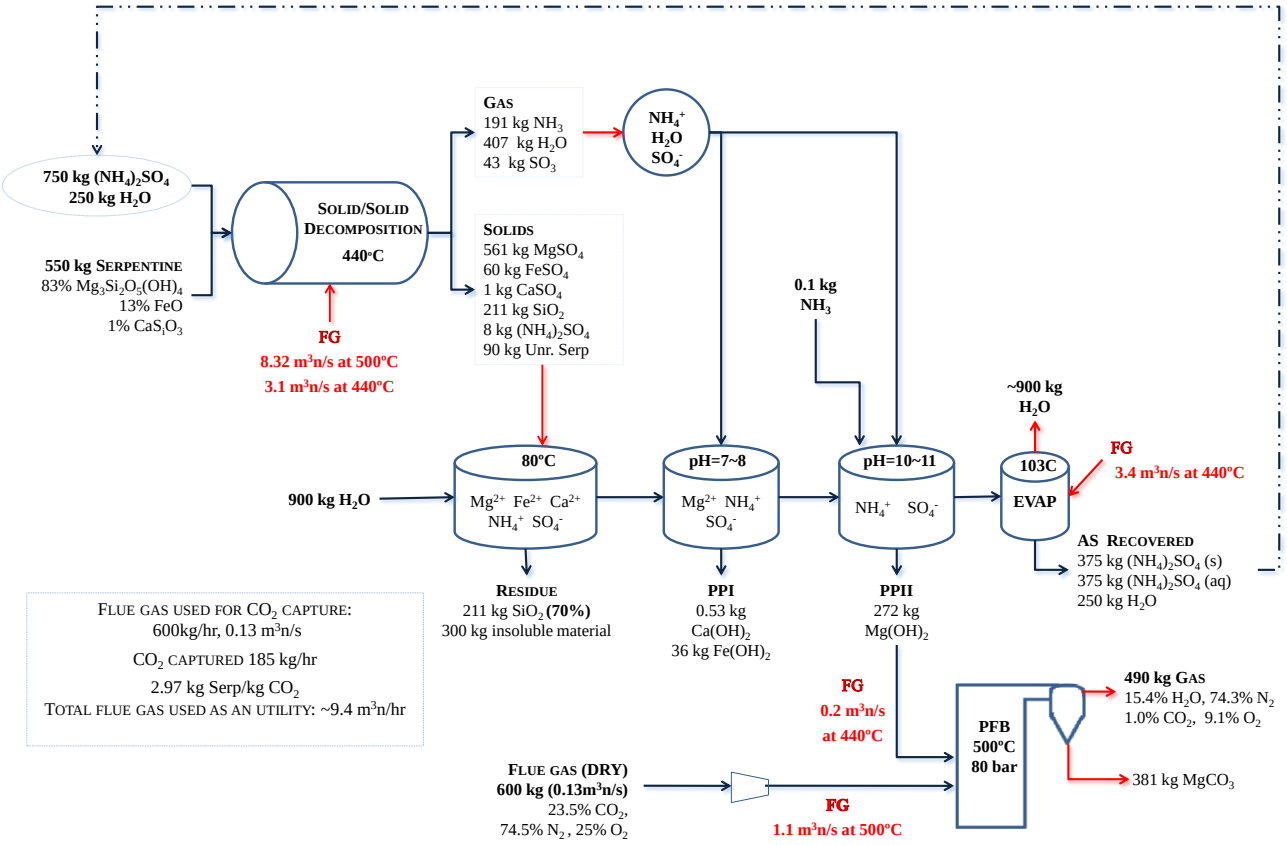

Fig. 2. Mass results for 80% magnesium extraction and 90% $Mg(OH)_2$ carbonation using Hitura nickel mine serpentinite rock (kg values are for one hour operation).

3. Mineralisation of diopside with flue gas

This section assesses the applicability of the ÅA process using the in-site available diopside as the metal oxide source, instead of nickel mine tailing from Hitura (500 km from Pargas). The Aspen Plus® model presented in section 2 simulates a case where serpentinite rock is used as the mineral source for Mg. An alternative would be to use a diopside material that is produced by Nordkalk as by-product from its limestone quarry. Therefore the reactivity of this material was assessed by the performing of some experimental tests using the same experimental procedure developed by Nduagu [9], before embarking on furthers Aspens Plus® simulations.

3.1. Diopside characterisation and experimental work

A sample of diopside provided by the Nordkalk's facility located in Pargas, was ground to obtain a size distribution of 125-250 µm and analysed using X-ray Diffraction (XRD) and X-ray Fluorescence (XRF). The results are reported in Table 4.

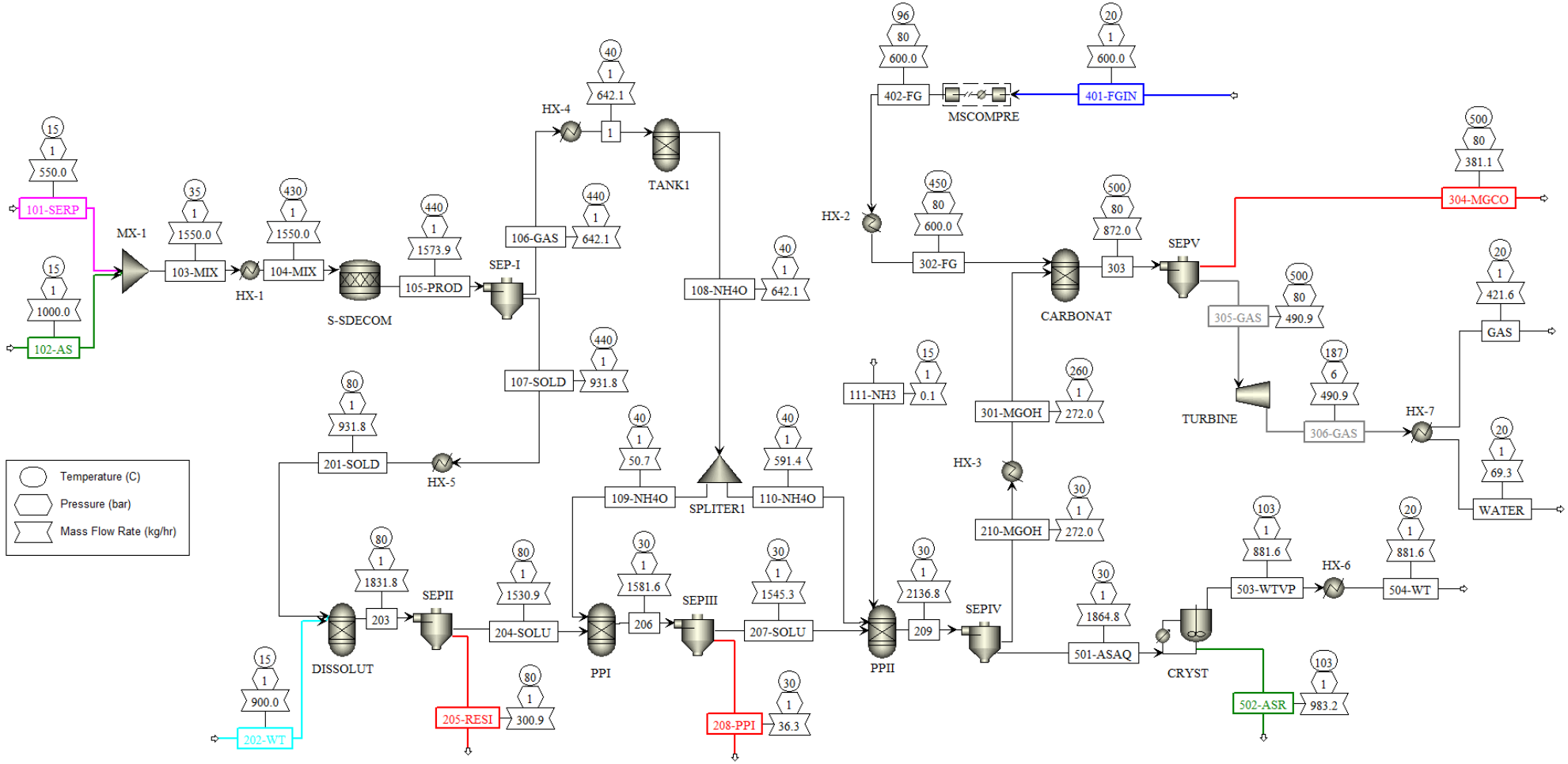

Fig 3- Aspen Plus® model

Table 3. Summary of the process' exergy.

EQUIPMENT	Energy	T	Exergy as heat			Flue Gas (kg/hr)		Flue Gas NTP (m^3n/s)	
	Q (J/s)	(°C)	(MJ/hr)	$MJ/kgCO_2$		FG500	FG440	FG500	FG440
SS DECOMPOSITION	463146	450	1003	5.44		37442		8.32	
DISSOLUTION	-52259	80	-35	-0.19			11235		3.40
PPI	-52455	30	-9	-0.05		4992		1.11	
PP2	-14218	30	-3	-0.01			13723		3.08
TANK 1	-82000	40	-137	-0.74			891		0.20
EVAPORAT	630066	103	532	2.88					
CARBONATOR	-5500	500	-12	-0.07					
HX-1 (S+AS+WT pre-heat)	434378	430	923	5.01					
HX-2 (FG pre-heat)	65050	450	141	0.76					
HX-3 ($Mg(OH)_2$ pre-heat)	27517	260	46	0.25					
HX-4 (Gaseous Products)	-472663	440	-1014	-5.50					
HX-5 (solid Products)	-93161	440	-200	-1.08					
HX-6 (wt from AS recovery)	-612765	103	-517	-2.80					
HX-7 (gas from turbine)	-73507	187	-99	-0.54					
Utilities Multistage Compressor (Water [15–90] °C)									
stage 1	-30105	90	-22	-0.12					
stage 2	-23328	90	-17	-0.09					
stage 3	-23512	90	-18	-0.09					
stage 4	-23878	90	-18	-0.10					
stage 5	-24599	90	-18	-0.10					
Total Exergy Process [2]			525	**2.85**	Total	42434	24958	9.42	6.65
Exergy provided by the FG [3]			2645	**14.34**					
Exergy Process + FG [4]			-2120	**-11.49**					

[2] Total exergy as heat (120~450^{0}C) needed to run the process, without integration with flue gas. [3] Exergy that the flue gas provides to the endothermic blocks. [4] Total exergy of the process when flue gas provides heat to all the endothermic stages. This final value may lead to the erroneous conclusion that the heat content of the flue gas is enough to process more serpentine. This "surplus" of exergy comes from streams at T ≤ 400^{0}C making its heat content unsuitable for the processing of rock material at ~440^{0}C. On the other hand this heat is appropriate for district heating.

Table 4. Elemental and XRD analysis of the diopside sample.

Elemental Analysis (%)									Structural Analysis (XRD)
CaO	SiO_2	TiO_2	Al_2O_3	Fe_2O_3	MgO	K_2O	Na_2O	Others	
15.6	50.9	0.4	12.2	4.5	4.9	3.1	2.1	6.3	Hedenbergite, Orthoclase, Albite (Calcium), Muscovite, Clinochlore

A total of twelve experiments were done in order to determine the reactivity of the rock. The diopside (D) was mixed with solid ammonium sulphate (D:AS=2g:3g) and placed in an oven at different temperatures, 250-500°C, for 30 minutes. The products of this extraction step were dissolved in water and the concentrations of magnesium, iron, aluminium, calcium, sodium, potassium and sulphur in the solution were measured by an ICP-OES analysis. In six of the experiments, the influence of water was studied by adding 3 ml of water to the diopside/AS mixture (D:AS:W=2g:3g:1ml).

3.2 Experimental results

À priori, the composition of the diopside does not seem to be very suitable for direct application of the ÅA procedure mainly due to its dramatically low content of MgO, but also due to its high percentage of aluminium and other alkaline elements. In earlier experiments [16] the increase of aluminium content did not appear to favour the extraction reactions.

Disappointingly, also the extraction results are very discouraging. Besides its low Mg content, the diopside's reactivity is extremely low making the upgrading of this material doubtful. Water does not appear to play a key role on the materials reactivity. In fact, contrary to what occurs with the serpentine minerals [17], the evolution of the extraction rates with temperature is quite similar both in the presence and absence of water.

Even if it was possible to extract all the X elements of the rock material, the applicability of the ÅA route presents several challenges. The extraction of all the magnesium is energy consuming due to the presence (in greater percentages) of other elements (mainly Al, Fe, Na, K, and Ca). In fact, a quick calculation allows for concluding that only 1/4 of the overall reactions' heat is used for Mg extraction. A successful extraction of Ca would imply a second carbonation stage (probably in an aqueous solution). And finally, the presence of alkali metals (which are highly water soluble and do not precipitate) would make the AS recovery very difficult implying the application of extra separation stages to preclude the recirculation/accumulation of those unwanted elements. In Table 5 a brief comparison of the pros and cons of using serpentinite vs diopside for CO_2 mineralisation is presented. As these results show that the diopside seems not to be a suitable material, no Aspen Plus simulations were made for that.

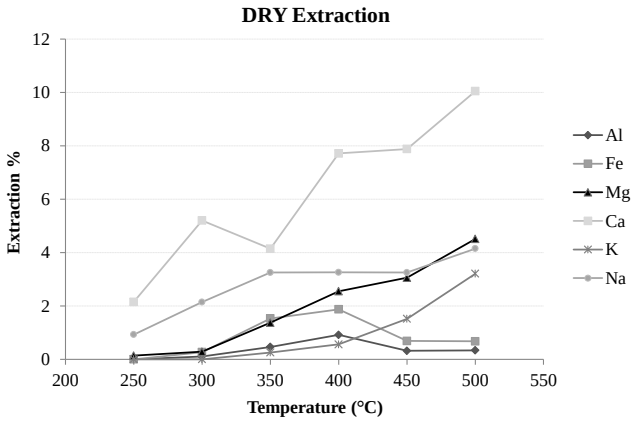

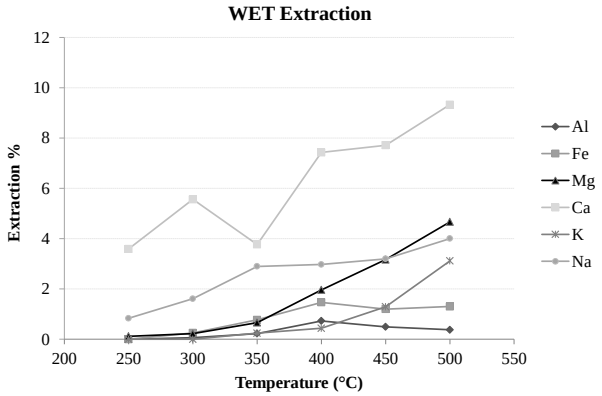

Fig.4 Experimental results concerning the extraction *Fig.5 Experimental results concerning the*

of six X elements from the diopside material in absence of water.

extraction of six X elements from the diopside material in presence of water.

Table 5 – Pros and cons of utilising serpentinite or diopside as raw materials in the ÅA CSM process.

	Serpentinite	Diopside
Availability	Must be purchased (500 km away)	Available at the plant site
Extraction temperature	~400 – 440 °C	≥ 500°C making the use of waste heat questionable.
Reactivity	Good reactivity (So far ~60 – 70 % of Mg extraction but with good potential for 80%)	Very low reactivity (<5% of Mg extraction)
Iron/Calcium/ Aluminium by-product	Low content of Al hydroxides Suitable for the steel-making industry.	High content of Al making it unsuitable to the steel making industry. An extra carbonation step needed to carbonate the by-products coming from the first precipitation stage.
$Mg(OH)_2$ product	~0.5kg$Mg(OH)_2$/kg of serpentinite processed (89% Mg extraction) Crushing energy is ~12% of the exergy input (as electricity): 0.19MJ/kgCO_2 captured	~0.087 kg$Mg(OH)_2$/kg of diopside processed (if 100% Mg extraction is achieved) To produce an equal amount of $Mg(OH)_2$ (as when serpentine is used) it's necessary to process at least 5.75x more rock. Excessive energy consumption for milling the raw materials which escalates to 1.09MJ/tCO_2 (~73% of the exergy input as electricity) In this case, the waste heat available from the limekiln will be insufficient to achieve an auto-thermal process while processing such amounts of rock in the solid/solid decomposition stage.
AS recovery	Final solution contains NH_4^+, SO_4^{2-} and water	Presence of alkali elements (Na^+ & K^+) in the remaining solution make the AS recovery and recycling problematic.

4. Conclusions

The waste heat available from a limekiln located at Pargas, Southwest Finland is enough to process 550 kg/hr of serpentinite coming from Hitura, (western central Finland) with a capture potential of ~190 kg/hr of CO_2, for 80% of Mg extraction and 90% of $Mg(OH)_2$ carbonation. Even though the integration with flue gas allows for an auto-thermal process, a total of 0.71 MJ/kg CO_2 captured is needed, as an electrical input, for materials crushing/grinding and compression of gases.

Although it would be interesting to carbonate the diopside (by-product from the limestone quarry) available at Pargas, this material does not possess the required composition and reactivity to apply

the ÅA CSM route. The content of Mg and Ca in the material make it unsuitable for CO_2 mineralisation in general because the large amounts of material needed will give rise to excessive crushing and grinding costs.

The energy penalty on the district heating supply, which arises from CO_2 capture, may be reduced by running this during low demand hours, for example during the summer. The same integration concept may be applied to other industries, making use of steam, at the right temperature, from a steam cycle of a power plant or some other nearby process which could supply most of the heat needed for CSM.

Acknowledgements

The authors want to acknowledge Cleen Ltd. and Tekes (the Finnish Funding Agency for Technology and Innovation) for their financial support for the research via the Cleen CCSP project (2011-2015)

Nomenclature

AS – Ammonium Sulphate

CCS – Carbon Capture and Storage

CSM – Carbon storage by Mineralisation

D – Diopside

E_0 – Energy required for pulverisation [kWh/t]

F – Size of feed particles [μm]

MC – Mineral Carbonation

PFB – Pressurised Fluidised Bed (reactor)

P – Size of the pulverized particles [μm]

W – Water

W_i– work index [kWh/t]

X – Mg, Ca, Fe, Al, Na, K

References

[1] IPCC Special Report on Carbon Dioxide Capture and Storage B. Metz, O. Davidson, H. de Coninck, M. Loos, L. Meyer, Working Group III of the IPCC, Cambridge Univ. Press (2005) Available at: <http://ipcc.ch/publications_and_data/publications_and_data_reports.shtml>

[2] Lackner, K.S., A guide to CO_2 sequestration, Science Vol 300, 1677-1678, 13 June 2003

[3] Zevenhoven, R., Fagerlund, J., Songok, J.K. CO_2 mineral sequestration - developments towards large-scale application. Greenhouse Gases: Science and Technology. 2011; 1:48-57

[4] Sipilä, J., Teir, S., Zevenhoven, R. Carbon dioxide sequestration by mineral carbonation – Literature Review Update 2005-2007. Åbo Akademi Univ., Heat Engineering Lab. report VT 2008-1, Turku, Finland (2008). Available at: <http://users.abo.fi/rzevenho/ MineralCarbonationLiteratureReview05-07.pdf >

[5] Zevenhoven, R., Fagerlund, J., Songok, J.K. CO_2 mineral sequestration - developments towards large-scale application. Greenhouse Gases: Science and Technology. 2011; 1:48-57

[6] Teir, S. Fixation of carbon dioxide by producing carbonations from minerals and steelmaking slags. PhD thesis, Helsinki Univerisity of Technology, Espoo Finland, 2008

[7] Eloneva, S., Teir, S., Revitzer, H., Salminen, J., Said, A., Fogelholm, C.-J., Zevenhoven, R. Reduction of CO_2 emissions from steel plants by using steelmaking slags for production of marketable calcium carbonate. Steel Research International 2009; 80:415-421

[8] Confidential Report on Lime Production, Nordkalk, May 2011

[9] Nduagu, E. Mineral carbonation: preparation of magnesium hydroxide [$Mg(OH)_2$] from serpentinite rock. M.Sc. (Eng.) Thesis, Åbo Akademi University, Finland, 2008

[10] Nduagu, E., Björklöf, T., Fagerlund, J., Wärnå, J., Geerlings, H., Zevenhoven, R. Production of reactive magnesium from magnesium silicate for the purpose of CO_2 mineralization. Part 1. Application to Finnish serpentinite. Minerals Engineering, 2012; 30:75-86

[11] Nduagu, E., Björklöf, T., Fagerlund, J., Mäkelä, E., Salonen, J., Geerlings, H., Zevenhoven, R. Production of reactive magnesium from magnesium silicate for the purpose of CO_2 mineralization. Part 2. Mg extraction modeling and application to different Mg silicate rocks. Minerals Engineering, 2012; 30:87-94

[12] Fagerlund, J., Zevenhoven, R. An experimental study of $Mg(OH)_2$ carbonation. Int. J. of Greenhouse Gas Control 2011; 5:1406-1412

[13] Fagerlund, J., Carbonation of $Mg(OH)_2$ in a pressurised fluidised bed for CO_2 sequestration PhD thesis, Åbo Akademi University, Turku Finland (2012) Available at: <www.doria.fi/handle/10024/74477>

[14] Fagerlund, J., Zevenhoven, R. The effect of SO_2 on CO_2 mineral sequestration applied directly to a flue gas. Submitted to ECOS2012, Perugia, Italy, June 2012; *paper under review*

[15] Romão, I., Nduagu, E., Fagerlund, J., M. Gando-Ferreira, L., Zevenhoven, R. CO_2 Fixation Using Magnesium Silicate Minerals. Part 2: Energy Efficiency and Integration with Iron-and Steelmaking. Energy, 2012; 41:203-211

[16] Romão, I., Fagerlund, J., Gando-Ferreira, L. M., Zevenhoven, R. CO_2 Sequestration with Portuguese serpentine. Proceedings of 3rd International Conference on Accelerated Carbonation for Environmental and Materials Engineering – ACEME10, 29 Nov - 1 Dec, 2010, Turku, Finland; 77-87; Ed. Ron Zevenhoven

[17] Romão, I., Gando-Ferreira, L. M, Morais, I., Silva, M.V.G., Fagerlund, J., Zevenhoven, R., CO_2 sequestration with Portuguese serpentinite and metaperidotite. 11th International Conference on Energy for a clean environment – CLEAN AIR 2011, 5-8th July

[18] Bond, F:C:, The third Theory Communition, Trans AIME, 1952; 193: 484-494

Comparison of IGCC and CFB cogeneration plants equipped with CO2 removal

Marcin Liszka[a], Tomasz Malik[b], Michał Budnik[c], Andrzej Ziębik[d]

[a] *Institute of Thermal Technology, Silesian University of Technology, 44-100 Gliwice, Konarskiego 22, Poland, marcin.liszka@polsl.pl,*
[b] *Institute of Thermal Technology, Silesian University of Technology, 44-100 Gliwice, Konarskiego 22, Poland, tomasz.malik@polsl.pl,* ***CA***
[c] *Institute of Thermal Technology, Silesian University of Technology, 44-100 Gliwice, Konarskiego 22, Poland, michal.budnik@polsl.pl,*
[d] *Institute of Thermal Technology, Silesian University of Technology, 44-100 Gliwice, Konarskiego 22, Poland, andrzej.ziebik@polsl.pl*

Abstract:

The introduction of CO2 removal processes into coal-fired power units causes usually generation of waste heat which is not possible to utilize within steam cycle. Normally, the waste heat is rejected to cooling water and then to the environment. As the temperature of waste heat carriers is usually moderately high (ca. 80 - 100˚C), there is a potential possibility for using them in district heating systems. The main goal of the present paper is thus the energy and CO2 emission analysis of large-scale CHP plants equipped with CO2 removal and utilizing waste heat generated within the plant. Two case studies have been formulated. First of them is dealing with the CFB plant equipped with a tap-backpressure steam turbine and post-combustion chemical CO2 absorption. The steam necessary for CO2 solvent (MEA) regeneration is taken from the steam turbine exhaust, while district heat is produced mainly in CO2 dehumidifier and CO2 compression train. The second case is dealing with an IGCC equipped with the pre-combustion CO2 removal by physical absorption. The district heat is then produced using classical final flue gas cooler located in HRSG, syngas cooler, as well as, compression trains of ASU air, nitrogen and CO2 product. For both analyzed cases, the peak-load district heat production using steam turbine extraction is also possible. Both CFB and IGCC plants have been modelled on the Thermoflex software. The reference, CFB-based CHP plant without CO2 removal has also been modelled. The district heat production and district water parameters have been fixed for all analyzed cases to the same values. The energy utilization factor, exergy efficiency and electricity-to-heat ratio have been calculated for both plants as main assessment factors. The methodology of alternative electricity production (equivalent power unit) has been involved for calculation of CO2 emissions. The obtained results indicates, that IGCC plant has better thermodynamic indicators than CFB-based unit. Moreover, the CO2 emission considering system interconnections within the electricity production network is negative for both the CFB and IGCC plants equipped with CCS. When comparing exergy efficiency, the highest value is achieved for the reference CFB plant (without CO2 capture). The decrease of exergy efficiency caused by CO2 capture and compression is ca. 8 percentage points, but in case of IGCC CHP plant the exergy efficiency plant is only 3 points lower than for the reference system.

Keywords:

IGCC, CFB, CHP, CCS, waste heat

1. Introduction

The CO2 removal processes integrated with coal-fired power units cause significant drop of energy efficiency and economic profitability of the overall power generation process. The decrease of power generation efficiency is externalized usually by increased amount of waste heat rejected to the environment. The waste heat coming from the CO2 removal and compression installations is often of moderate temperature (ca. 80-100˚C), and therefore its utilization within the power cycle or for external purposes could be possible. On the other hand, the decrease of CO2 emission without its removal is also possible. The combined heat and power production (CHP) is a good example

where the thermodynamic integration of processes leads inherently to higher effectiveness, fuel saving and therefore decrease of CO2 emission.

Combining the availability of a moderate-temperature waste heat at the CO2 removal facility with inherently high effectiveness of the coal-fired CHP plant, the idea for the CHP system equipped with CCS unit and utilizing waste energy for district heat production has been proposed and analysed within the current paper. It was expected, that the high-level integration of power cycle with CO2 removal unit and district water heat exchangers will the partial recovery of CCS energy expenses make possible.

Within the current paper two different CHP plants incorporating presented idea have been proposed and investigated. First is the classical Rankine-based steam unit equipped with back-pressure steam turbine, circulated fluidized-bed boiler and CO2 removal unit based on chemical absorption in monethanolamine. Second plant configuration is based on IGCC structure equipped with pre-combustion CO2 removal based on physical absorption in Selexol. Both plants have been scaled to the same rated district heat production (110 MW_t).

The idea for rather small CHP units equipped with CO2 removal and waste heat recovery is relatively new. There is a lot of literature references for CHP systems (non CCS) based on CFB boilers, as well as, for large coal-fired power units equipped with post-combustion CCS. The problem of waste heat recovery from the chemical CO2 absorption units is discussed e.g. in [1]

In case of IGCC CHP system, described in literature installations use biomass mostly. Experience gained in IGCC CHP plants based on biomass gasification may be however transferred into similar plants based on coal. Several IGCC CHP plants do exist, however usually biomass or wastes are gasified, there is no plant which uses hard coal as a main feedstock. The SVZ plant in Schwarze Pumpe is one of such installations where coal and municipal wastes mix is gasified in BGL (British Gas and Lurgi) gasifier [2]. Installation produces electricity and methanol. This installation was however unprofitable, which caused that in year 2007 has been closed [2]. Another example of IGCC CHP plant is installation in Varnamo in Sweden. This biomass-based unit reaches 6MW_e electric and 9MW_{th} thermal power, while the energy efficiency in cogeneration mode is 83% [3]. Plant in Varnamo was operating since 1996 till 2000, then it was closed for the same reason as SVZ plant [3]. Plant which uses lignite as a main feedstock for IGCC has been built in Versova (Czech Republic) [4]. There are 26 Lurgi and 1 Siemens gasifier in operation. Electricity and liquid fuels are the main products of this installation, however hot flue gas is used for district heat production [4]. In all recognized IGGC CHP installations district heat is produced in conventionally as for combined cycles – using flue gas from the heat recovery steam generator (HRSG) exhaust or steam turbine extraction.

2. Case studies

Two case studies of CCS-integrated CHP units have been analyzed:

- IGCC CHP plant with waste heat recovery equipped with Selexol-based CO2 absorption,
- CFB CHP plant with waste heat recovery equipped with tap-backpressure steam turbine and MEA-based CO2 absorption.

For comparison purposes the same fuel parameters have been used for both analysed systems. Fuel composition has been presented in Table 1.

Table 1. Fuel composition

Coal parameters (as received)		
c, carbon	-	0,5263
h, hydrogen	-	0,0343
o, oxygen	-	0,1102
n, nitrogen	-	0,0075
s, sulphur	-	0,0104

moisture	-	0,2237
ash	-	0,0876
LHV	MJ/kg	20,16

2.1 IGCC plant

IGCC plants are usually designed as electricity or chemicals production plants, however they have a high potential for district heat production. Present IGCC units (especially with CO_2 capture) give an opportunity for recovering waste heat at levels suitable for district heat production as well as for using classical heat sources e.g. tap-steam turbine or outlet of HRSG.

Proposed IGCC CHP plant configuration is schematically presented in Fig.1. The system is based on that presented in [5] which has been optimized and redesigned towards IGCC CHP plant. It is composed of cryogenic air separation unit (ASU), dry-feed gasifier with syngas cooler, water gas shift reactors (WGSR), acid gas removal (AGR) unit and finally the combined cycle.

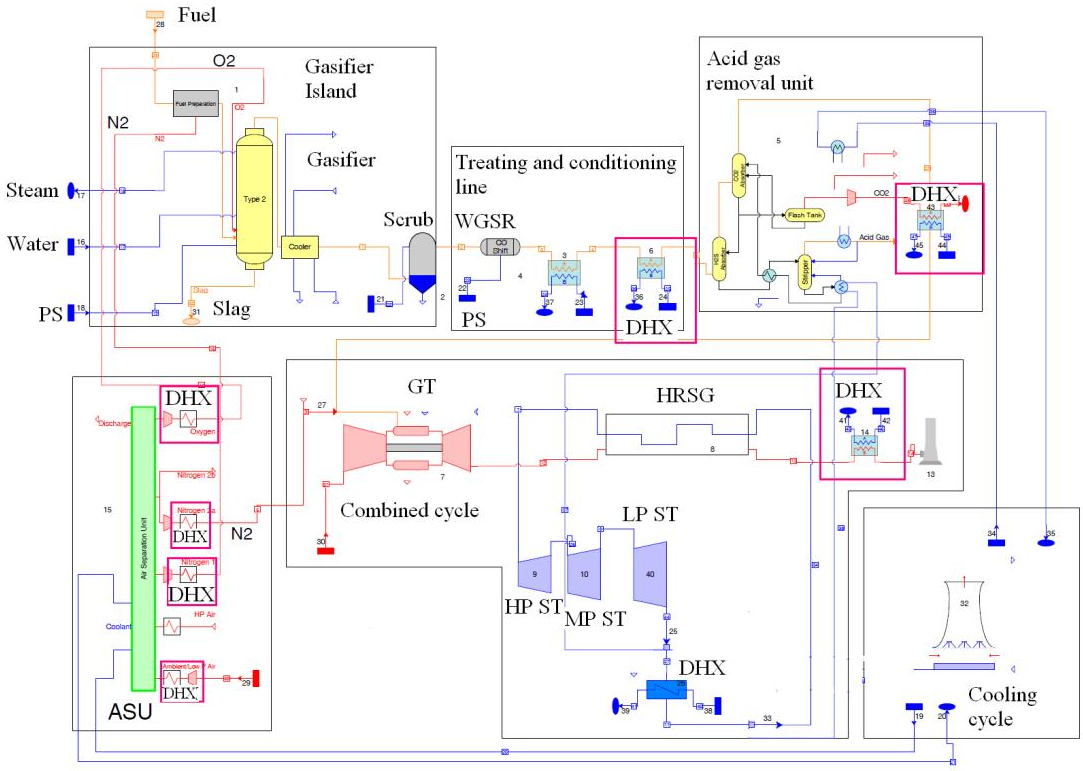

Fig. 1. Concept of IGCC CHP plant

The entrained flow dry-feed gasifier has been chosen for syngas production. Its operating pressure has been set to 4,238 MPa. The temperature of the syngas leaving the reactor reaches 1639°C. The syngas is cooled down primarily by its partial recirculation and then by the production of high pressure steam in a radiant/convection heat exchanger. The temperature of the syngas leaving the cooler and entering the scrubber is equal to 335˚C. The gasification reactor consumes oxygen of 95% purity. The coal feeding system is based on ASU nitrogen. The syngas treating and conditioning line is composed of an inter-cooled WGSR reactor. The syngas temperature after the first WGSR reactor has been assumed to 460˚C while behind the second one to 360˚C.

The heat rejected from the syngas during the conditioning processes is recovered to the steam cycle and for district heat production. The AGR unit is based on a two-stage Selexol process. The syngas stream leaving the second WGSR is cooled down, dehydrated and supplied to the first stage of AGR unit, where 99% of H_2S is stripped. The separated H_2S is then sent to the Claus plant for

conversion to elemental sulphur. The H2S-free gas is supplied to the second stage of AGR where it is brought in contact with a low-temperature lean Selexol solvent for CO2 absorption. The reverse CO2 desorption process occurs in flash drums operating on 3 different pressure steps. Desorbed CO2 is compressed and pumped into the transportation pipeline.

The hydrogen-rich (ca 90%) syngas leaving the AGR is diluted by ASU nitrogen and used as a gas turbine (GT) fuel. An F-class GT has been selected. As already mentioned, the steam turbine receives steam from both the HRSG and syngas cooling equipment. All compressors within the ASU and AGR islands have been assumed as electric motor – driven machines. Table 2 summarizes the assumptions/specifications concerning the input/output for the system.

Waste heat recovery concept involves final flue gas cooler located in the HRSG, syngas cooler in syngas treating and conditioning line prior to AGR unit, as well as, intercoolers in compression trains of ASU air, nitrogen and CO2 product. All waste heat recovery exchangers are marked in red boxes in Fig.1.

For further transportation, the CO2 stream is compressed to 13 MPa.

Table 2. Assumed parameters for IGCC CHP Plant

Parameter		IGCC CHP plant
Pressure in the reactor	MPa	4,238
Temperature of syngas at scrubber outlet	^{O}C	180
Nitrogen to fuel ratio (for fuel transportation), mass basis	-	0,175
Steam to fuel ratio, mass basis	-	0,005
Oxygen to fuel ratio, mass basis	-	0,66
Specific electricity consumption	kWh/Mg_{fuel}	67
Syngas treating and conditioning line		
CO conversion ratio at 1st WGSR	%	63,6
CO conversion ratio at 2nd WGSR	%	86,2
H2O to CO ratio at 1st WGSR	-	2,34
H2O to CO ratio at 2nd WGSR	-	4
Syngas temperature prior to AGR	^{O}C	35
Acid gas removal and CO2 compression		
Effectiveness of H2S removal	%	99
Effectiveness of CO2 removal	%	90
Process steam consumption	kg/s	1,81
CO2 capture miscellaneous auxiliary load	kWh/Mg_{CO2}	60
Gas turbine		
Combustor exit temperature	^{O}C	1300
Compressor pressure ratio	-	15,5
Steam cycle		
Live (HP) steam temperature	^{O}C	565
Live (HP) steam pressure	MPa	12,8
MP steam pressure	MPa	3,95

2.2 CFB plant

For the current moment, one of the closest to commercial application method for CO2 capture in classic coal-fed CHP units is post-combustion absorption using MEA or similar solvent. The main energy requirement for this type of process is heat demand for desorption of CO2 from the amine solution.

Proposed CHP plant with CO2 capture is equipped with CFB boiler, tap-backpressure steam turbine and CO2 capture unit – Fig. 2. CFB boiler produces live steam which has typical parameters for modern CFB boilers installed recently in Poland (560˚C, 16,1MPa). Boiler is equipped with economizer, convective and radiant superheater. Steam expands in tap-backpressure steam turbine. Steam cycle is equipped with four heat recovery exchangers The heat necessary for the CO2 removal unit is taken from the steam turbine exhaust as a back-pressure steam. The rest of steam flow available at the turbine outlet is supplied to the district water heater which operates in parallel with other heaters utilizing waste heat from the CO2 absorption and compression units - district water is preheated basically in CO2 dehumidifier and CO2 compression train (inter-coolers).

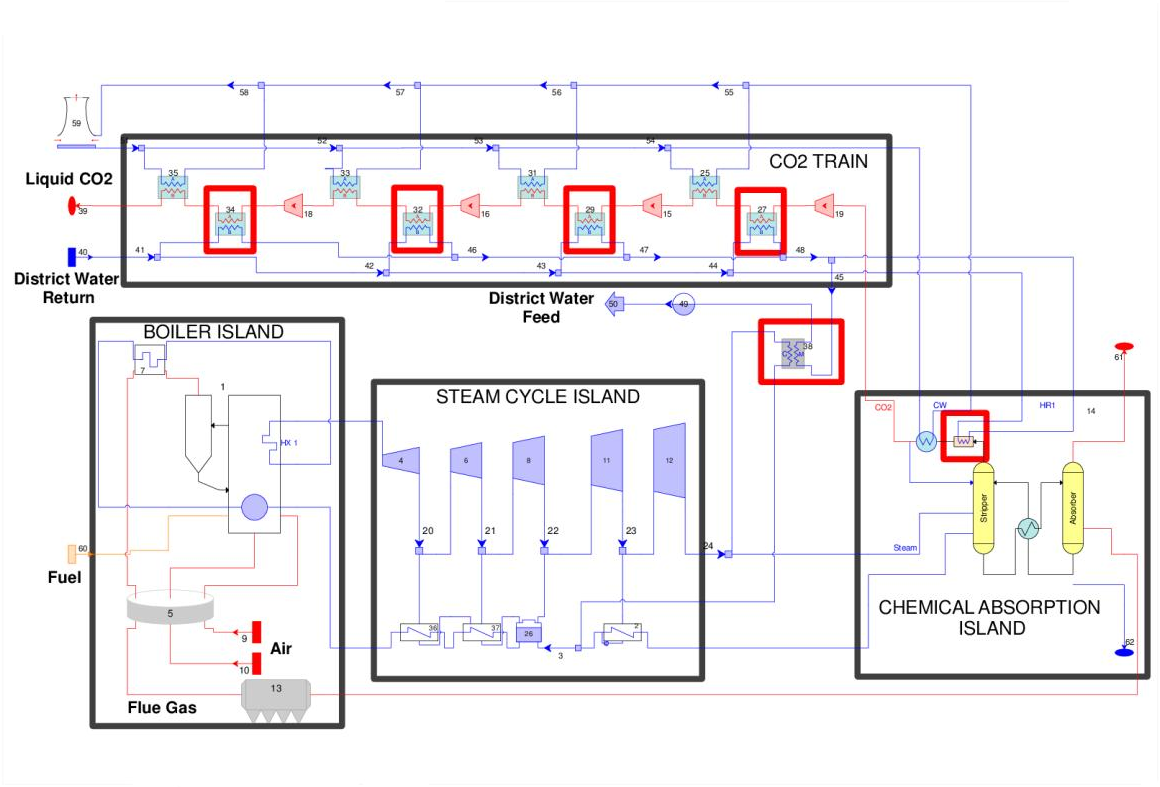

Fig. 2. Concept of CFB CHP plant

Hot flue gas leaving the economiser is primarily cooled down in rotating heat exchanger, where combustion air is preheated. Then in electrostatic precipitator fly ash is removed and finally prior to CO2 absorption process, flue gas is cooled down to 40˚C and desulphurized for final required SO2 concentration (10 ppmv). Absorption unit is composed of absorber and stripper columns. In absorber column flue gases are brought in contact with MEA solvent, rich solvent is then injected into a stripper column where occurs its regeneration and CO2 is separated. For further transportation, the CO2 stream is compressed to 13 MPa.

For comparison purposes, the typical CFB-based CHP plant without CCS has also been studied. The district heat production within the non-CCS CFB CHP plant takes place in two heat exchangers connected to steam turbine outlet (base load) and extraction (peak-load). The structure and thermal

parameters within the boiler island and steam cycle are the same expecting the stem turbine outlet, where steam pressure is lower than for the CCS case, as the required temperature for district heat exchanger is lower than for CO2 desorption process.

Crucial parameters of both considered CFB CHP plants have been presented in Table 3.

Table 3. Assumed parameters for CHP Plants with CFB boiler

Parameter	Unit	CHP plant without CO2 capture	CHP plant with CO2 capture
Boiler type		Natural circulation	Natural circulation
Live steam pressure	MPa	16,1	16,1
Live steam temperature	˚C	560	560
Dry step efficiency of steam turbine (HP, MP)	%	91	91
Dry step efficiency of steam turbine (LP)	%	85	85
Temperature of flue gases behind rotary air heater	˚C	130	130
Temperature of preheated air	˚C	260	260
Furnace exit temperature	˚C	850	850
Excess air ratio	%	20	20
Steam pressure at steam turbine exhaust	MPa	0,084	0,24
Heat demand for the CO2 absorption unit (per 1 kg of CO2 removed)	kJ	-	4000
CO2 removal effectiveness	%	-	90

3. Assessment factors

For the comparison purposes, each of three analysed units (IGCC with CCS, CFB with CCS and CFB reference – without CCS) has been evaluated from the energy, exergy and CO2 emission points of view.

Energy utilization factor has been calculated as defined in (1), representing the proportions of energy balance rather than a true thermodynamic assessment.

$$EUF = \frac{\dot{Q}_{dh} + N_{elN}}{\dot{E}_{chfuel}} \qquad (1)$$

Energy analysis does not take into account different quality of products. Exergy is a measure of energy quality or thermodynamic irreversibility related to the isolated devices or whole analyzed system [6-8]. Exergy analysis is suitable for the thermodynamic comparison of co-product or multi-product systems. The exergy efficiency of each analyzed CHP system has been calculated in accordance to (2).

$$\eta_X = \frac{\dot{X}_{dh} + N_{elN}}{\dot{X}_{fuel}} \qquad (2)$$

The exergy of produced heat is expressed by increase of exergy of district water as presented in (3) where subscript “II” characterize hot water, while subscript “I” characterize cold water.

$$\dot{X}_{dh} = \dot{m}_{dh}\left[h_{II} - h_I - T_a(s_{II} - s_I)\right] \qquad (3)$$

The CO2 emission factor which indicates the net CO2 emission per 1 GJ of produced heat has also been calculated in accordance with (4). Considering dual product situation (heat and electricity) it has been assumed that the main product is heat and the emission assigned to heat is calculated as difference between total emission from the CHP unit and emission avoided in other power stations due to production of specified amount of electricity in considered CHP unit. The scheme for avoided emission calculus has been illustrated in Fig. 3. The equivalent power plant is assumed to be coal-fired, non-CCS, supercritical unit of net electric efficiency equal to 44%.

$$\varepsilon = \frac{\dot{m}_{CO2} - \dot{m}_{CO2_avoid}}{\dot{Q}_{dh}} \qquad (4)$$

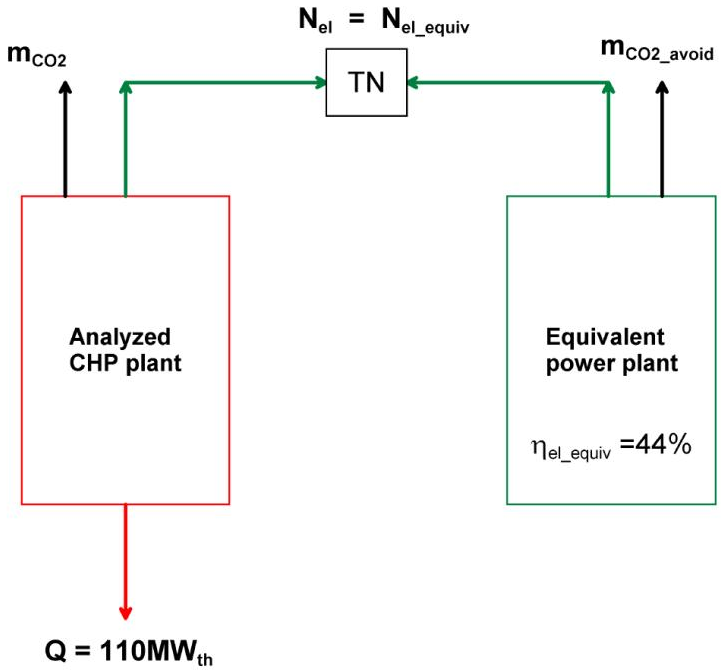

Fig. 3. Scheme for calculus of avoided CO2 emission

4. Simulation model

All analyzed CHP systems have been modelled using the Thermoflex software [9]. Thermoflex contains models of typical energy conversion devices like compressors, turbines or heat exchangers, as well as, agglomerated multi-device models such as steam boiler or gasifier islands. The modeling approach combines the physical and empirical modeling.

The flow sheets of analyzed IGCC, CFB and CFB reference systems used for simulation purposes are presented in Figs A.1, A.2 and A.3 in appendix A.

Main assumptions taken for the simulation process for all considered systems are as follows:

- the same district heat power (ca. 110MW_{th}),
- the same parameters of district water 62,6˚C/37˚C (annual average),
- the same feedstock (hard coal),
- CO2 stream compressed to 13 MPa for both CO2 capture installations,
- the same temperature of cooling water at battery limits (20˚C).

The calculated parameters in characteristic points of the analyzed systems are presented in Tables A.1, A.2, A.3 in appendix A.

5. Results

The crucial calculated parameters at system boundaries of each analysed CHP unit have been presented in Table 3.

For the same district heat production, obtained net and gross electricity production is the highest for IGCC unit. The CO2 emission for both plants equipped with CO2 capture is relatively low. Lack of energy consumption for the CO2 capture installation in case of reference CFB plant results in the highest value of energy utilization factor achieved. EUF indicator for the IGCC CHP plant is lower than for other systems as it does not take into account different quality of products.

When comparing exergy efficiency, the highest value is achieved for the reference CFB plant (without CO2 capture). The decrease of exergy efficiency caused by CO2 capture and compression is ca. 8 percentage points, but in case of IGCC CHP plant the exergy efficiency plant is only 3 points lower than for the reference system.

Table 3. Results of simulation analysis

Parameter	Unit	CFB CHP plant without CO2 capture (reference)	CFB CHP plant with CO2 capture	IGCC CHP plant with CO2 capture
Total district heat production	MW_{th}	**110,22**	**110,26**	**110,14**
including:				
- waste heat	MW_{th}	**0**	**53,24**	**29,22**
- steam-fed heat exchangers	MW_{th}	**110,22**	**57,02**	**80,92**
Fuel flow rate	kg/s	9,34	10,40	13,02
Fuel chemical energy (LHV-based)	MW	188,29	209,66	262,48
Gross electricity production	MW_e	64,70	64,10	113,30
Net electricity production	MW_e	**60,10**	**50,80**	**78,40**
Electric power consumption for CO2 compressors	MW	-	6,10	7,00
CO2 emission from CHP plant (total)	kg/s	18,46	2,06	2,52
CO2 mass flow rate for transportation (captured)	kg/s	-	18,49	22,20
EUF (Eq. 1)	%	**0,90**	**0,77**	**0,72**
Fuel exergy input	MW	205,24	228,53	286,11
District water exergy increase (Eq. 3)	MW	10,36	10,36	10,36
Exergy efficiency (Eq. 2)	-	**0,35**	**0,27**	**0,32**
CO2 emission factor per GJ of produced district heat (Eq. 4)	$kgCO2/GJ_t$	**48,86**	**-81,59**	**-131,95**

The CO2 emission factor calculated in accordance with (4) is below zero for both cases with CO2 capture due to effect of coupling CO2 capture and cogeneration effectiveness. Better values has been obtained for IGCC CHP plant. Values of emission factor have been achieved for assumed net electric efficiency of equivalent power station equal to 44%. For better recognition of the impact of equivalent plant efficiency on CO2 emission, sensitivity analysis has been prepared as presented in Fig. 4.

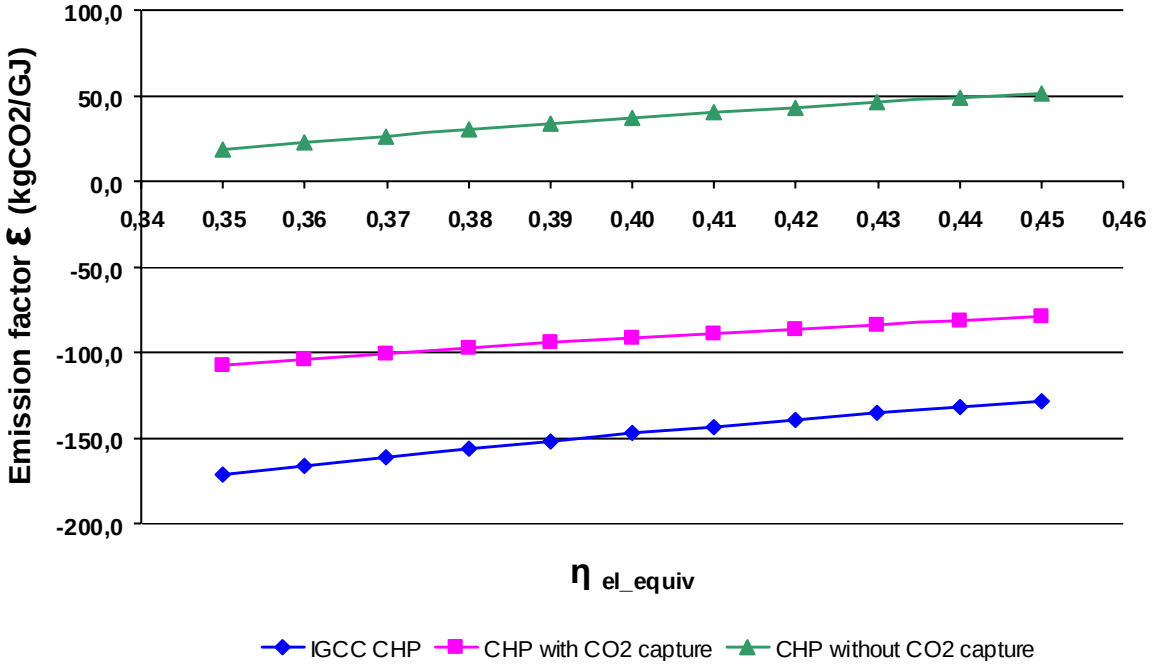

Fig. 4. Sensitivity analysis of equivalent power station efficiency on CHP emission factor.

6. Concluding remarks

Two configurations of coal-fed CHP plants with massive CO2 removal and waste heat recovery systems have been proposed and analysed assuming constant district heat demand.

Obtained results of exergy analysis indicate, that the drop of efficiency due to CO2 removal and compression (ca. 8 % points for CFB CHP) is lower than for large-scale coal-fired power units (ca. 10-12 % points for similar CCS heat demand as reported in [10,11]), as the waste heat recovery lets for partial cancellation of negative impact of CCS on overall plant efficiency.

An IGCC CHP unit with CO2 capture has significantly better emission factors and thermodynamic excellence when comparing to CHP plant with CFB boiler and post-combustion CO2 capture process. Advantages of IGCC CHP unit are mainly due to commonly known effect of Brayton and Rankine cycles integration, as well as, due to advantage of pre-combustion CO2 removal over post-combustion system (referring to assumed in this paper energy demands for both installations).

Negative value of CO2 emission factor which arises from applied CO2 removal processes and substituting of electricity produced in other power stations (system advantage of cogeneration), enables potentially for substituting emission from power facilities, where decreasing emission is economically ineffective or impossible (e.g. peak-load boilers).

Future work should be focused on off-design analysis of both proposed CHP systems to evaluate change of supply of waste heat as function of variable ambient temperature and district heat demand. The comparative economic analysis reflecting the costs of district heat production, as well as, costs of avoiding the CO2 emission should also be done.

Acknowledgments

This work has been prepared in framework of the task of research, "Development of coal gasification technology for high efficient production of fuels and electricity" funded by the Polish National Centre for Research and Development within the strategic program of research and development: "Advanced energy generation technologies".

The results presented in this paper were obtained from research work co-financed by the National Centre of Research and Development in the framework of Contract SP/E/1/67484/10 – Strategic Research Program – Advanced technologies for energy generation: Development of a technology for highly efficient zero-emission coal-fired power units integrated with CO2 capture.

Nomenclature

AGR Acid gas removal

ASU Air separation unit

$\dot{E}_{chfuel}$ chemical energy of coal, calculated on LHV basis, W

EUF Energy utilization factor

DHX District heat exchanger

GT Gas turbine

h specific enthalpy, kJ/kg

h_a specific enthalpy at ambient parameters, kJ/kg

HP High pressure

HRSG Heat recovery steam generation

IGCC Integrated gasification combined cycle

LHV Lower heating value

$\dot{m}$ mass flow rate, kg/s

MP Medium pressure

N_{elN} net electric power of the system, W

N_{elG} gross electric power of the system, W

$\dot{Q}_{dh}$ district heat flow rate, W

r enthalpy of vaporization, kJ/kg

s specific entropy, kJ/kgK

s_a specific entropy at ambient parameters, kJ/kgK

ST Steam turbine

T_a ambient temperature, K

WGSR Water gas shift reactor

$\dot{X}_{fuel}$ chemical exergy of coal, W

$\dot{X}_{dh}$ exergy of produced district heat, W

z_i molar share of *i-th* compound

η_X exergy efficiency

Appendix A

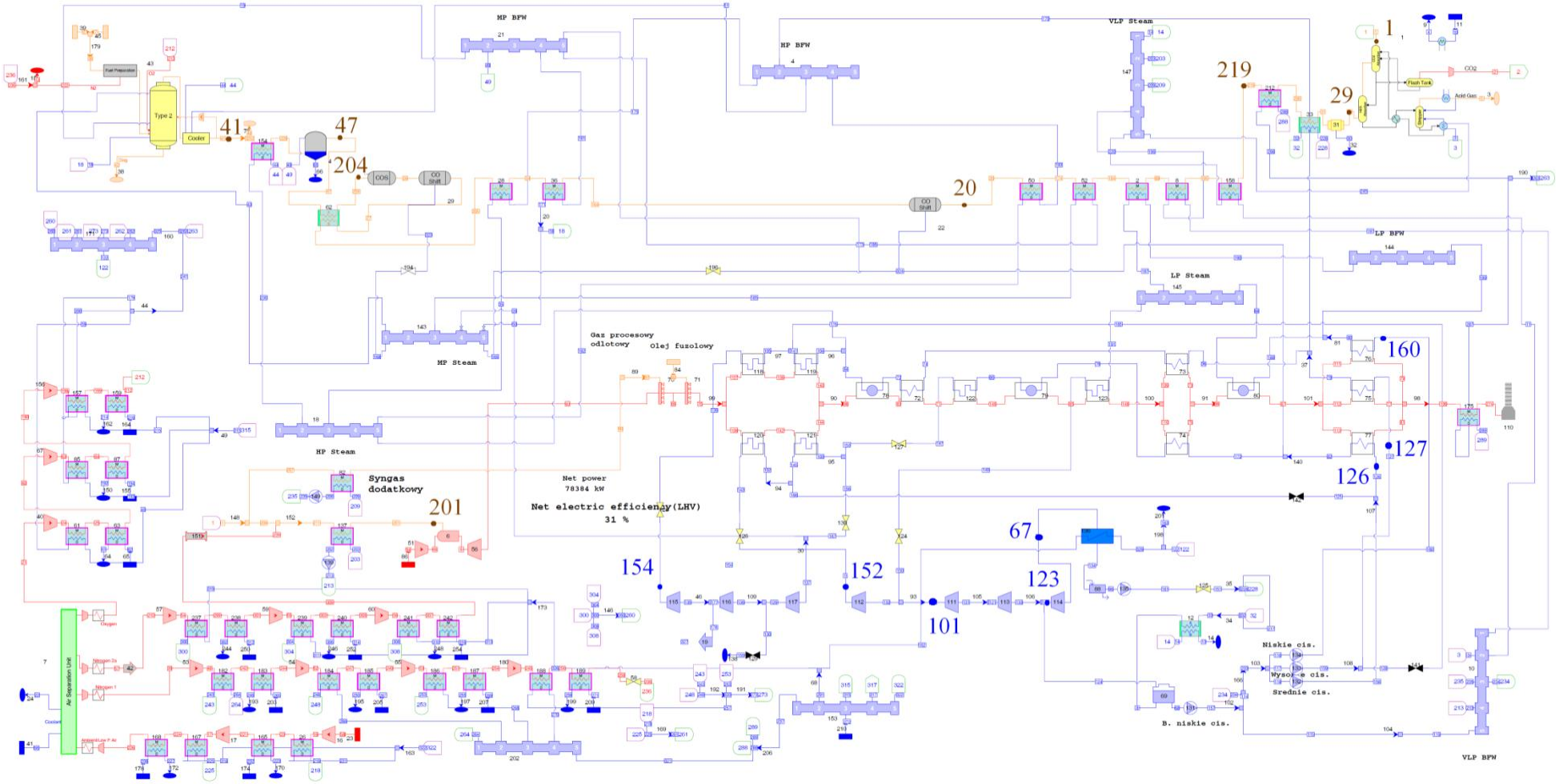

Fig A.1. Simulation model of IGCC CHP unit with waste heat recovery (Thermoflex)

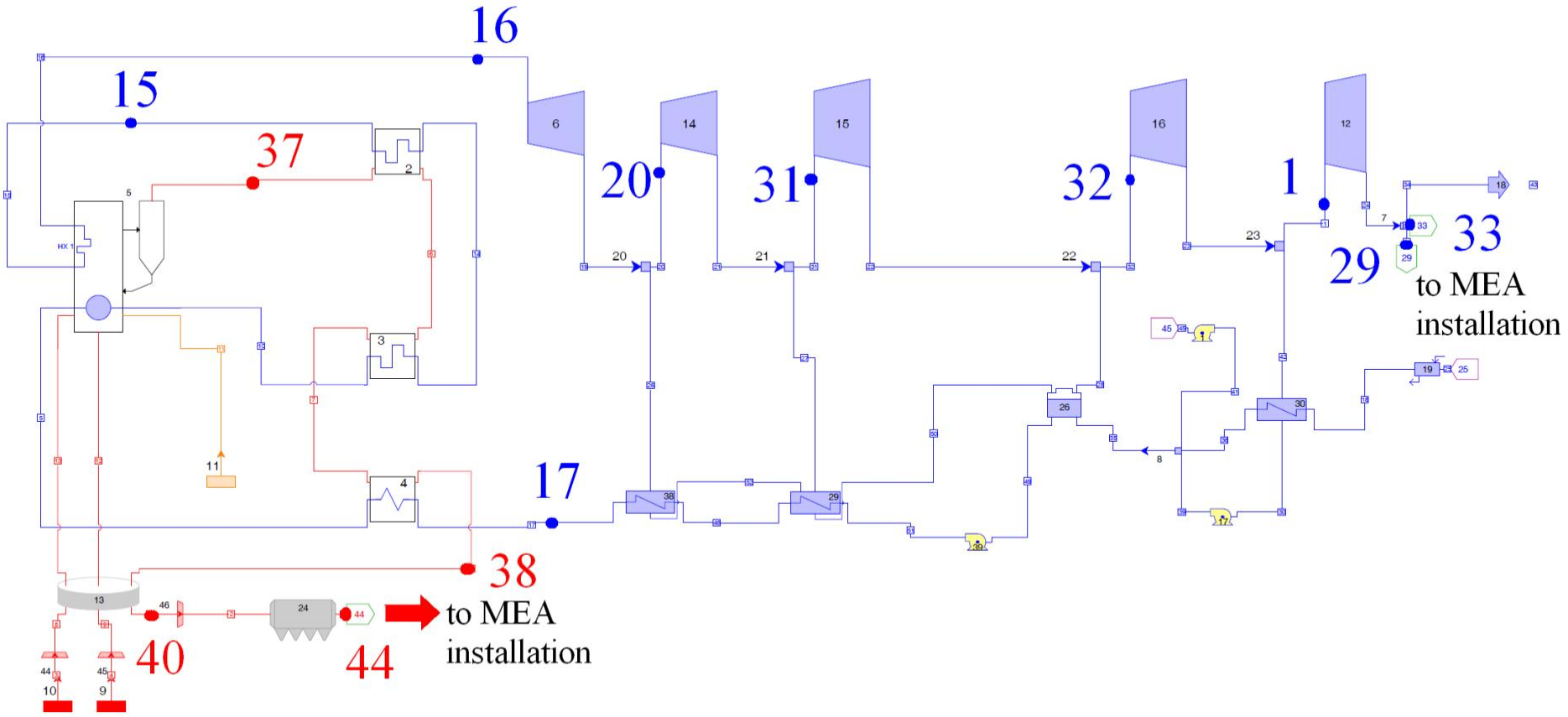
16
15
37
20
31
32
1
29
33
to MEA
installation
17
38
to MEA
installation
40
44

(a)

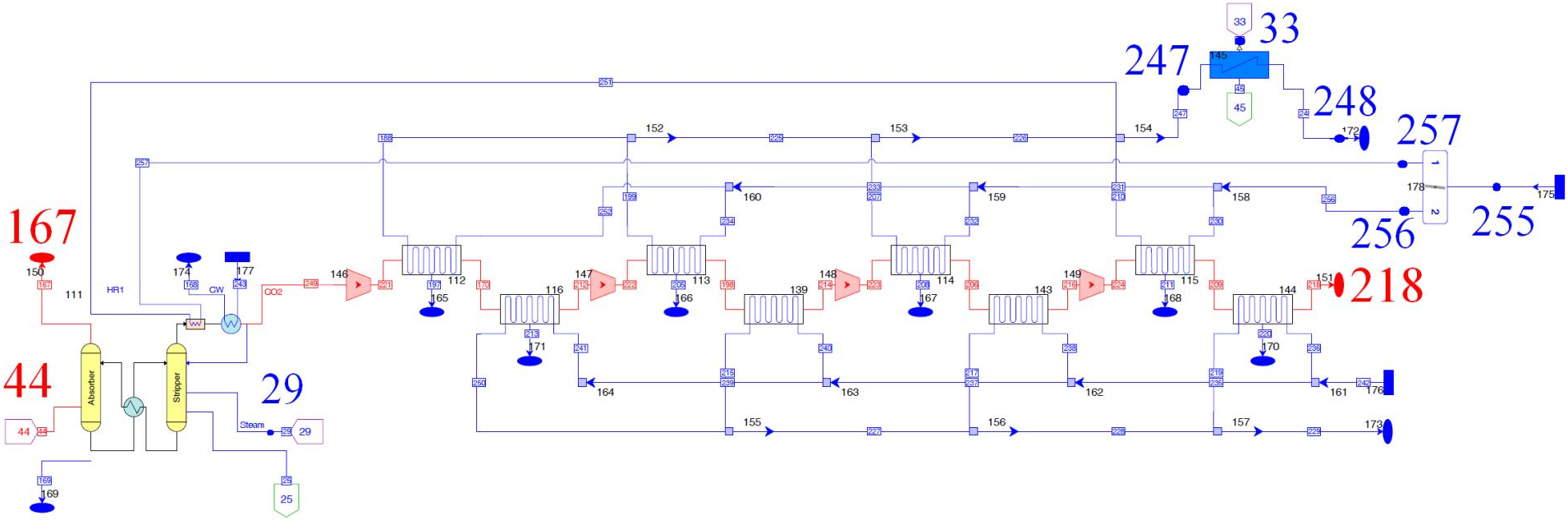

(b)

Fig. A.2. Simulation model of CFB CHP plant with CO2 capture (Thermoflex): a) boiler and power cycle, b) CO2 capture and compression installation

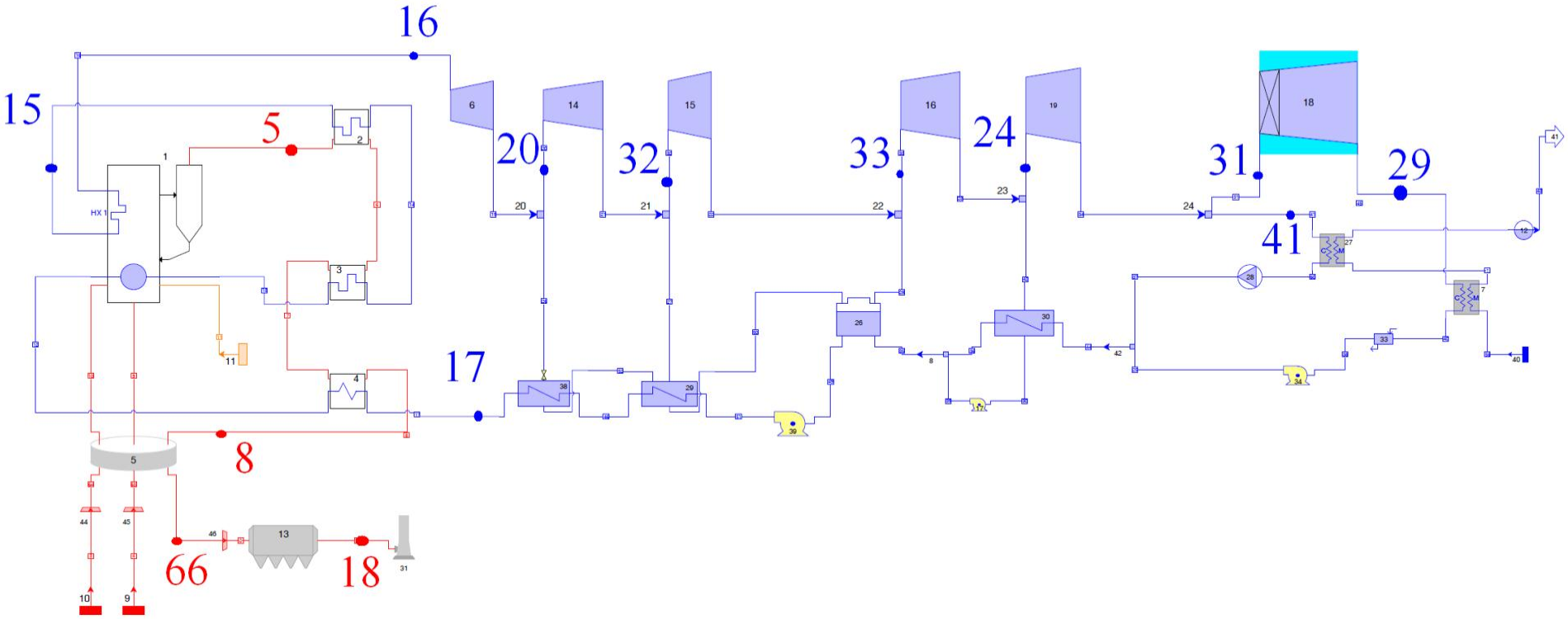

Fig. A.3. Simulation model of CFB CHP plant, without CO2 capture (Thermoflex)

*Table A.1. Calculated parameters at selected points of the plant structure for **IGCC CHP** case (point numbers correspond to those in Fig. A.1)*

Water/Steam *Stream number*	***T, ˚C***	***p, bar***	***m, kg/s***	***Quality***
154	565	128	40,26	Superheated 235,4˚C
152	565	39,5	35,02	Superheated 315,4˚C
101	321,92	8	39,93	Superheated 151,5˚C
123	211,96	3	35,67	Superheated 78,4˚C
67	72,53	0,3478	35,67	0,9703
126	122,8	43,16	8,52	Sub cooled 132,1˚C
127	125,38	154,06	40,34	Sub cooled 218,9˚C
160	122,06	11,22	4,92	Sub cooled 62,9˚C

Syngas *Stream number*	***T, ˚C***	***p, bar***	***m, kg/s***	***H2***	***CO2***	***CO***	***N2***	***H2O***	***H2S***	***COS***	***Ar***	***Other***
				mole fractions								
41	600	41,17	22,74	21,73	6,64	47,80	8,18	15,2	0,38	0,031	0,03	0,009
47	179,88	40,44	24,44	19,29	5,9	42,44	7,26	24,73	0,33	0,0275	0,02	0,0025
204	220	38,89	24,44	19,29	5,9	42,44	7,26	24,73	0,33	0,0275	0,02	0,0025
20	358,39	35,06	35,82	38,31	29,72	1,37	4,67	25,68	0,23	0,0004	0,01	0,0096
219	149,61	30,24	35,82	38,31	29,72	1,37	4,67	25,68	0,23	0,0004	0,01	0,0096
29	58,9	28,79	27,79	51,21	39,73	1,83	6,23	0,66	0,31	0,0005	0,02	0,0095
1	27,22	27,03	5,12	84,5	2,11	3,02	10,29	0,042	0,0005	0,0008	0,03	0,0067
201	143,73	26,5	17,33	53,3	1,33	1,91	42,59	0,03	0,0003	0,0275	0,03	0,7822

*Table A.2. Calculated parameters at selected points of the plant structure for **CHP plant with CO2 capture** case*
(point numbers correspond to those in Fig. A.2a and Fig. A.2b)

Water/Steam *Stream number*	***T, ˚C***	***p, bar***	***m, kg/s***	***Quality***
16	560	161	81,14	Superheated 212,1˚C
20	344,8	39,8	76,54	Superheated 94,8˚C
31	287,1	25,3	71,59	Superheated 62,6˚C
32	194,6	10,9	63,32	Superheated 10,9˚C
1	158,8	6	61,19	0,977
29	126,1	2,4	35,99	0,936
33	126,1	2,4	25,09	0,936
17	245	172,6	81,34	Sub cooled 108,5˚C
15	470	162,6	81,14	Superheated 121,3˚C

255	37	20	1030	Sub cooled 175,4˚C
256	37	20	42,3	Sub cooled 175,4˚C
257	37	20	987,7	Sub cooled 175,4˚C
247	49,35	20	1030	Sub cooled 163˚C
248	62,6	20	1030	Sub cooled 149,8˚C

Flue Gas *Stream number*	***T, ˚C***	***p, bar***	***m, kg/s***	***m_{ash}, kg/s***	***CO2***	***N2***	***H2O***	***SO2***	***Ar***	***O2***
					mole fractions					
37	850	1,0427	95,41	1,241	14,44	71,11	10,40	0,007	0,86	3,18
38	323,13	1,0353	95,41	1,241	14,44	71,11	10,40	0,007	0,86	3,18
40	130,3	1,0328	98,83	1,241	13,93	71,34	10,06	0,007	0,86	3,8
44	130,3	1,0132	98,83	0,002	13,93	71,34	10,06	0,007	0,86	3,8
167	35	1,0132	76,65	0	1,71	87,68	4,88	0	1,06	4,67
218	30	130	18,49	0	99,97	0	0,03	0	0	0

Table A.3. Calculated parameters at selected points of the plant structure for ***reference CHP plant without CO2 capture*** *case*
(point numbers correspond to those in Fig. A.3)

Water/Steam *Stream number*	***T, ˚C***	***p, bar***	***m, kg/s***	***Quality***
16	560	161	72,7	Superheated 212,1˚C
20	344,8	39,8	68,6	Superheated 94,8˚C
32	287,1	25,3	64,2	Superheated 62,6˚C
33	194,6	10,9	60,5	Superheated 10,9˚C
24	158,8	6	53,9	0,977
31	105,6	1,2	53,7	0,913
29	95	0,85	53,7	0,901
41	105,6	1,2	0,2	0,913
17	245	172,6	72,9	Sub cooled 108,5˚C
15	470	162,6	72,7	Superheated 121,3˚C

Flue Gas *Stream number*	***T, ˚C***	***p, bar***	***m, kg/s***	***m_{ash}, kg/s***	***CO2***	***N2***	***H2O***	***SO2***	***Ar***	***O2***
					mole fractions					
5	850	1,0378	85,73	1,134	14,44	71,1	10,41	0,007	0,86	3,18
8	329	1,0303	85,73	1,134	14,44	71,1	10,41	0,007	0,86	3,18
66	130	1,0228	94,97	1,134	13,01	71,71	9,49	0,007	0,86	4,92
18	130	1,0132	94,97	0,002	13,01	71,71	9,49	0,007	0,86	4,92

References

[1] Pfaff I., Oexmann J., Kather A., Optimised integration of post-combustion CO2 capture process in greenfield power plants. Energy 2010;35:4030-4041

[2] Rakowski J., Przegląd zagadnień technologicznych związanych ze zgazowaniem paliw stałych dla potrzeb energetycznych. Energetyka 2003 September (in Polish)

[3] Stahl K., Neergaard M., IGCC Power Plant for Biomass Utilisation, Värnamo, Sweden, Biomass and Bioenergy 1998:15(7):205-211.

[4] Report from Vresova: 12 years of operating experience with the world's largest coal-fuelled IGCC. (PLANT OPERATING EXPERIENCE). Available at: < http://goliath.ecnext.com/coms2/gi_0199-9669125/Report-from-Vresova-12-years.html> [accessed 1.10.2008]

[5] Liszka M., Malik T., Manfrida G., Energy and Exergy Analysis of Hydrogen-Oriented Coal Gasification with CO_2 Capture. Proceedings of the 24th International Conference on Efficiency, Cost, Optimization, Simulation, and Environmental Impact of Energy Systems; 2011 Jul 4-7; Novi Sad, Serbia.

[6] Szargut J., Exergy Method. Technical and Ecological Applications, WIT Press, Southampton-Boston 2005.

[7] Uson S., Valero A., Thermoeconomic Diagnosis of Energy Systems, Prensas Universitarias de Zaragoza 2010.

[8] Bejan A., Tsatsaronis G., Moran M., Thermal Design & Optimisation, John Wiley & Sons, New York 1996.

[9] Thermoflow, Inc., 29 Hudson Road , Sudbury, MA 01776 USA, Available at:<http://www.thermoflow.com>

[10] Davison J., Performance and costs of power plants with capture and storage of CO2. Energy 2007;32:1163-1176

[11] Liszka M., Ziębik A., Thermoeconomic comparison of coal-based oxy-fuel and post-combustion CO2 capture - case study for Polish conditions. Proceedings of 25th Annual International Pittsburgh Coal Conference; 2008 Sep 29 - Oct 2; Pittsburgh, PA, USA.

Concept of a "capture ready" combined heat and power plant

Piotr Lukowicz[a], Lukasz Bartela[b]

[a] *Silesian University of Technology, Gliwice, Poland, piotr.lukowicz@polsl.pl*
[b] *Silesian University of Technology, Gliwice, Poland, lukasz.bartela@polsl.pl*

Abstract:

In case of the CHP plants with backpressure turbines and auxiliary condensing units, there is no possibility of an additional steam extraction for CO2 chemical sequestration. This is due to the fact that those turbines are designed to operate in conditions where the mass flow rate directed to district heating heat exchangers varies from 0 to 90 percent. Such plants require an additional heat source to be installed to cover the heat consumption of the CO2 sorbent regeneration system. It is possible to build an additional power unit with a backpressure turbine to heat the sorbent up. However one must consider high costs of such an operation and must provide additional space for the installation. The paper presents an analysis of a CHP (Combined Heat and Power) plant with the increased steam flow rate by the amount needed for the sequestration process.

Advantages of this solution would be an increased efficiency through increased blade length and higher heat power until integration with CO2 sequestration plant. Two variants are analyzed, one with a single low-pressure unit, second with two parallel connected LP units. In the second case, a possibility of removing one of the LP parts after integration with CO2 installation.

A parametric study of the units efficiency as a function of sorbents energy consumption ratio is carried out.

Keywords:

Combined Heat and Power, Carbon Capture and Storage.

1. Introduction

Sorbent regeneration process requires amount of heat that depends on the type of used chemical agent. The heat is carried by steam extracted from a turbine bleed, Fig. 1. In CHP plans with extraction-condensing turbines there exists no possibility of an extra steam extraction for the chemical absorption process due to the construction reasons of those turbines, for which it is usually assumed that the steam flow rate varies, depending on the needed heating power, from 0 to 95% of the steam supplied to an inlet of a LP (Low Pressure) turbine unit. As a result, there is an insufficient amount of steam that could feed an absorber column. Therefore, such a CHP plant does not meet the requirements of a "capture ready" plant, which state that a "capture ready" plant should be designed in the way that will allow it to be equipped with an CO2 capture installation as soon as commercial technology is available. In practice it all comes to the providence of the required space needed to build the installation. The lack of an extra steam extraction, in case of the typical plants, implies an introduction of an additional heat source that will provide the required heat to the sorption process. One of the mostly considered options is an introduction of an additional small CHP plant with an backpressure turbine to heat the sorbent in a CCS (Carbon Capture and Storage) unit, Fig.1. However, such a solution is costly, and needs some extra space for the installation itself. Furthermore it will also emit CO2. Most probably coal would be used here as fuel, since only-biomass boiler would not provide enough steam. Such concepts should be considered, however the most reasonable solution seems to be such a design of a plant that would include the heating needs of a CC (Carbon Capture) installation from the very beginning. Which means, the plant would be capable of producing more steam that is required only for district heating and electrical power production. Thus, any bigger modifications of an existing plant to couple it

with a CC installation could be avoided. Most practical would be an available additional steam extraction with parameters desired for the adsorption process. Such a solution could also be economically beneficial. Flow rate of steam feeding the turbine results from a CC installation heat consumption and desired electric and district heating power production.

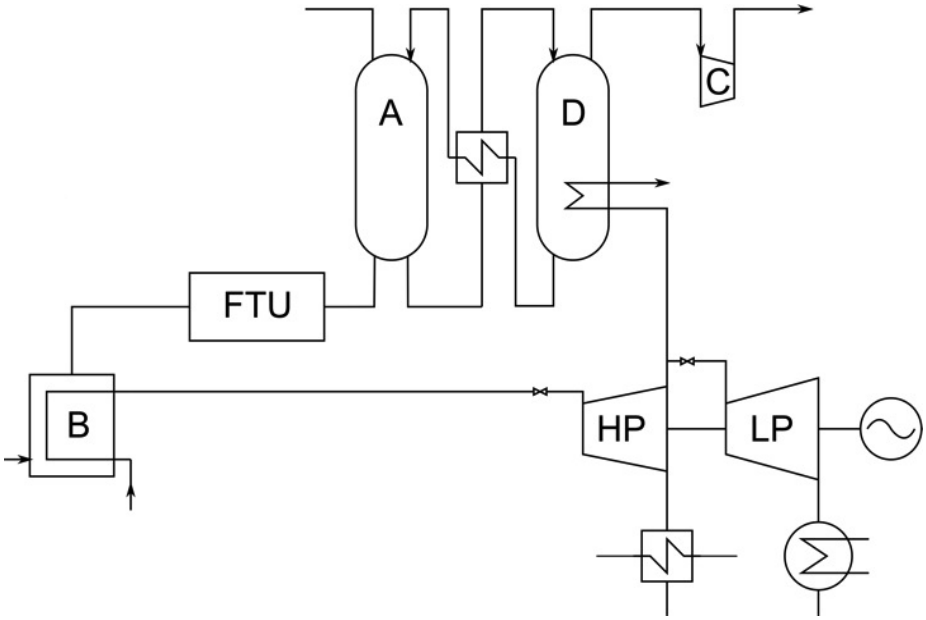

Fig. 1. Scheme of CHP plant integration with a CO2 capture unit. A - absorption column, D - desorption column, C - compressor, HP – high pressure turbine, LP – low pressure turbine, B – boiler, FTU – flue gas treatment unit

2. Design calculations

2.1. Basic thermal parameters of steam in the cycle

The higher the steam parameters that feeds a turbine are, the higher the cycle efficiency is and also the CO2 emitted to the atmosphere shrinks. A steam boiler of given below parameters is considered in the project:

Table 1. Steam and water thermal parameters in the cycle

	Unit	Value
Fresh steam pressure at boilers outlet	MPa	30.3
Fresh steam temperature at boilers outlet	℃	653
Fresh steam pressure at turbines inlet	MPa	30
Fresh steam temperature at turbines inlet	℃	650
Reheated steam pressure at boilers outlet	MPa	6
Reheated steam temperature at boilers outlet	℃	672
Reheated steam temperature at turbines inlet	℃	670
Boilers feeding water temperature	℃	310

Coal of composition c=0.599, h=0.038, s=0,01, n=0,012, o=0,05, p=0.2, w=0.09 and LHV of 23 MJ/kg was considered as fuel.

2.2. Design Cases

Aim of this research is to design a CHP plant that will meet the requirement of the UE parliament directive 2001/80/WE. According to which any fossil fired power unit of electric power of 300MW and above has to undergo an analysis of CO2 storage possibility, economical and technical aspects of CO2 transport as well as modernization towards CC installation coupling to a power unit. Therefore it was assumed that the CHP plant will have 305MWe power. Electric power of currently working polish CHP units does not exceed 145MWe. For an assumed nominal electric power, heating power depends on the amount of steam that can be directed to a heating station. Two design cases for a CHP plant were considered:

1. A "capture-ready" plant. Its design allows to build on an CC unit in future.
2. A plant that will be equipped with a CC unit already from the beginning.

Fig. 2 shows a scheme of CHP plant with an extraction point intended to feed a CC unit. Steam used for district heating purposes is taken from the outlet of the IP part of turbine which also supplies the CC unit.

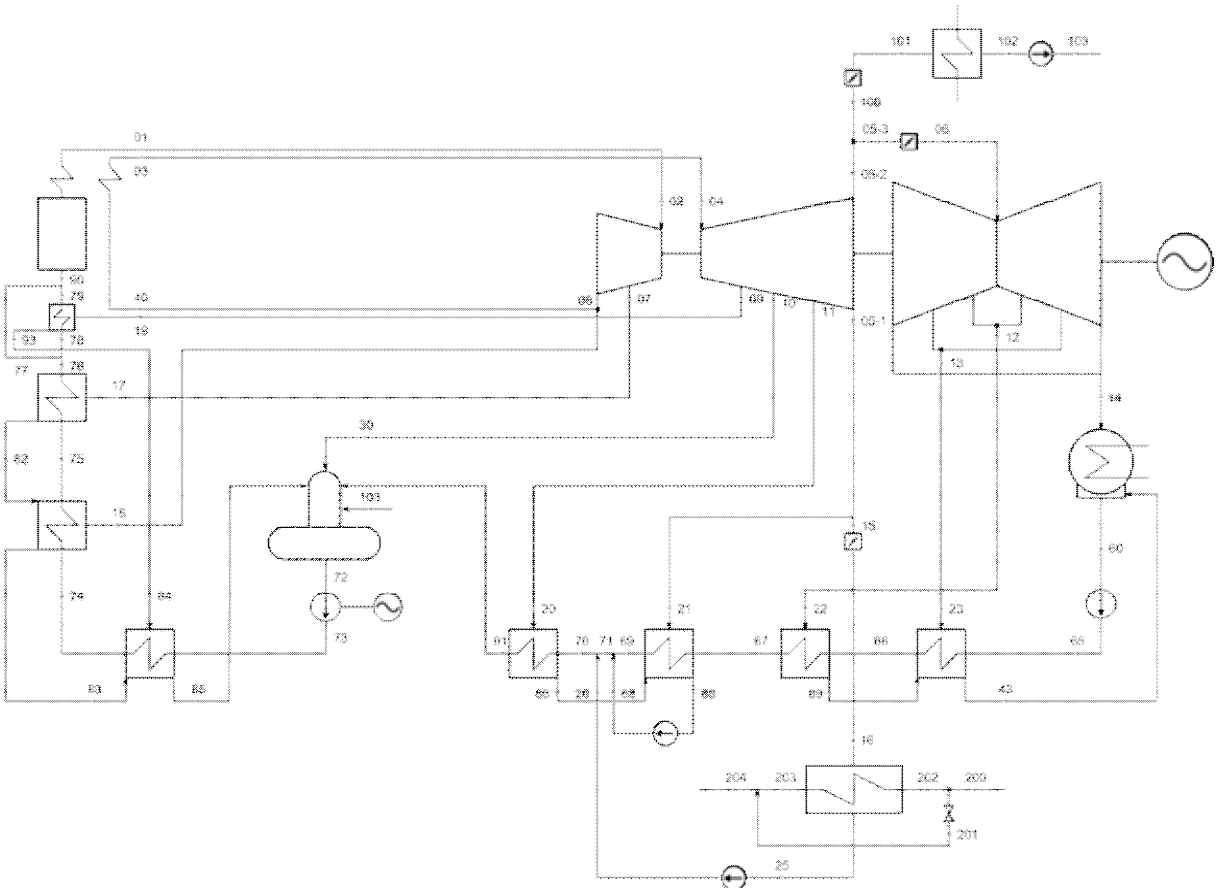

Fig. 2. Scheme of CHP plant with a steam extraction point for CO2 capture purposes

An important role plays here the appropriate choice of the structure of a plant. There are various possibilities like i.e.:

1. With a single-flow IP and one single-flow LP part of turbine.
2. With a symmetric double-flow IP and one or two connected parallel LP parts of turbine.

The second option allows shutting down one of the LP parts, after integration with a CC unit. The chosen structure was selected on the basis of an analysis of different LP regeneration configurations.

2.3. Basic CHP plant indices.

The basic indices are based upon following equation:

Cycle efficiency:

$$\eta_c = \frac{\dot{Q}_1 - \dot{Q}_2}{\dot{Q}_1} \quad (1)$$

Where: $\dot{Q}_1$ - heat delivered to the cycle, $\dot{Q}_2$ – heat extracted from cycle

Plant gross efficiency:

$$\eta_{el}^b = \frac{N_{el}^b}{\dot{B} W_d} \quad (2)$$

Where: N_{el}^b – gross electric power, $\dot{B}$ – fuel flow, W_d - lower heating value

Plant net efficiency:

$$\eta_{el}^n = \frac{N_{el}^b - N_{pw}}{\dot{B} W_d} \quad (3)$$

Where: N_{pw} – in-house load (auxiliaries)

Heat rate:

$$q = \frac{Q_1}{N_{el}^b} \quad (4)$$

CHP plant efficiency:

$$\eta_{EC} = \frac{N_{el}^b + N_t}{\dot{B} W_d} \quad (5)$$

Where: N_t - heating capacity

2.4. Selection of steam extraction point for CO2 separation process.

The appropriate placing of an extraction point is dictated by the heat consumption of a given sorbent and the required temperature for the sorbent regeneration.

There are currently studies carried out on new types of sorbents in order to decrease their regeneration heat consumption (i.e. for MEA from 4,5 MJ/kg CO2 to 3 MJ/kg [2]). Because of large amount of steam required it is only possible to extract it from IP to LP line. Thermal parameters at this point should fulfill sorbents regeneration process requirements and on the other hand be low enough to avoid thermal degeneration of the sorbent. The desired pressure should be then equal to $p=ps(T+\Delta Ts)/(1-\zeta)$

Where: T – Sorbent upper temperature, ΔTs – upper temperature difference, ζ – pressure loss coefficient.

If one decides to use amine sorbents, then it is necessary to heat them to ca. T = 127 °C. If $\Delta Ts = 5$ K and $\zeta = 0.02$, then steam of pressure p = 0.3 MPa is needed to feed the sorption unit.

2.5. Results of the design calculations.

It was assumed in computations that the plants nominal working conditions is pure condensation, which means no steam is provided for district heating. Table 2 shows calculated results for considered variants of nominal electric power of 305 MW each. Computations were carried out under assumption that the house load is equal to 7.5 % of plants gross power. They were also performed for two values of sorbents heat consumption.

Table 2. Results of design calculations

	Only condensation	**With CC unit steam consumption**	
Fresh steam flow rate, kg/s	209	245,2	231,5
Sorbents energy consumption, MJ/kgCO2	-	3,89	2,83
CO2 separation steam flow rate, kg/s	0	101,3	70,298
Steam feeding LP turbine flow rate, kg/s	140,12	69,48	90,916
Cycle efficiency, %	51,23	43,48	46,14
Gross cycle efficiency, %	49,35	42,09	44,59
Net cycle efficiency, %	45,65	38,94	41,24
Boiler efficiency, %	94,41	94,41	94,41
Heat rate, kJ/kWh	6886,6	8074,1	7711,8
Fuel flow rate, kg/s	26,87	31,524	30,06
CO2 flow rate, kg/s	59,398	69,686	65,793
Percentage of removed CO2, %	0	90	90

Steam mass flow rate produced in boiler depends on the chosen variant. In case of a “capure-ready” CHP plant it is smaller than that in case of a plant already equipped with a CC installation. It is related to the bigger mass flow rate through LP turbine compared to that in the previous case, which is responsible for generating more mechanical power. Sorbents heat consumption has high impact on work indices of a CHP plant that is already build with a CCS installation. Its reduction by 1 MJ/kgCO2 causes an efficiency growth of 2% points. Whereas in case of “capture-ready” plant the efficiency is higher by 4.5 % points compared to a plat with CC unit of sorbents energy consumption equal to 2.83 MJ/kgCO2 and about 6.5 % points of sorbents energy consumption equal to 3.89 MJ/kgCO2. Calculations included only sorbents energy needs and left out sorbent pump losses and CO2 compressors work.

3. Off-design calculations

The main task of off-design calculations is to analyze their working conditions for different thermal and electrical load. Examinations were carried out under assumption that plants operate under nominal boiler load (table 2). Results of the calculations for the different variants are shown in Fig. 3. Fig. 3 shows electric power of a CHP plant with an operating CC unit of CO2 capture efficiency 90 % and with a turned off district heating unit. Gross electric power of the first variant plant will decrease after integration with a CC unit from 305 to 256 MW for sorbents energy consumption of 3,89 MJ/kgCO2 and to 269 MW for sorbents of 2,83 MJ/kgCO2 energy consumption. Fig. 4 illustrates values of the gross efficiency of the plants, corresponding to their design points. Gross efficiency value of variant W1-2,8 and W1-3,89 is the expected efficiency of plant after its integration with the CC unit. Fig. 5 shows peak heating capacities of the discussed variants and decrease in electric power resulting from lower steam flow rate in the LP turbine, which is to be directed to the district heating heat exchanger. Fig.6 illustrates the influence of the sorbents heat consumption rate on the efficiency of CHP plants by their peak heating capacities. A simple relation can be seen here: the smaller the heat consumption of a sorbent is the more heat (steam) can be directed to the district heating heat exchanger and is then considered as useful.

One of the most important characteristic values of CHP plant is electric power produced in co-generation and in condensation, while they play an important role in economic effectiveness of a CHP plant. In case of a CHP plant integrated with a CC unit it is also advisable to include power generated by the steam used in the CC unit. Fig. 7-12 show shares of each steam flow (for heating, sorbent regeneration and condensation) in power generation.

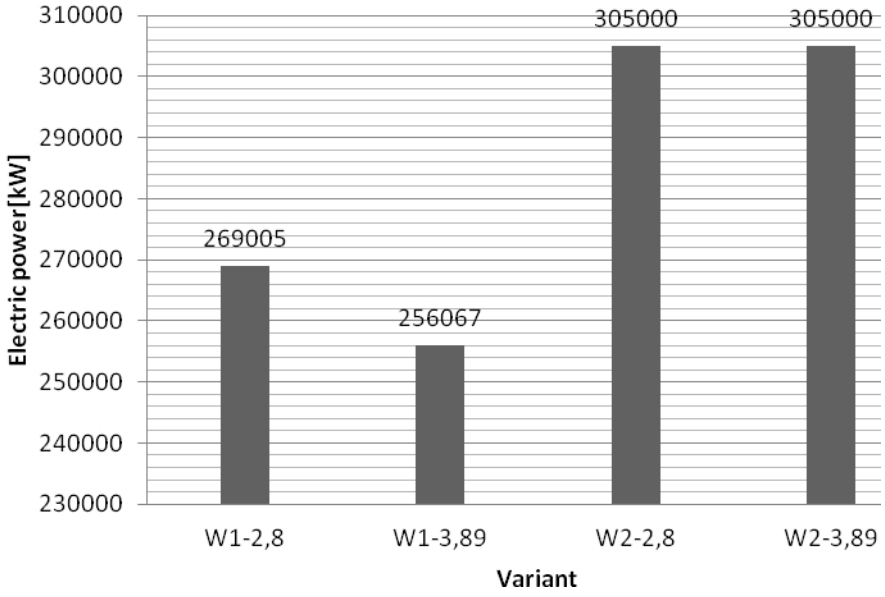

Fig. 3. Electric power

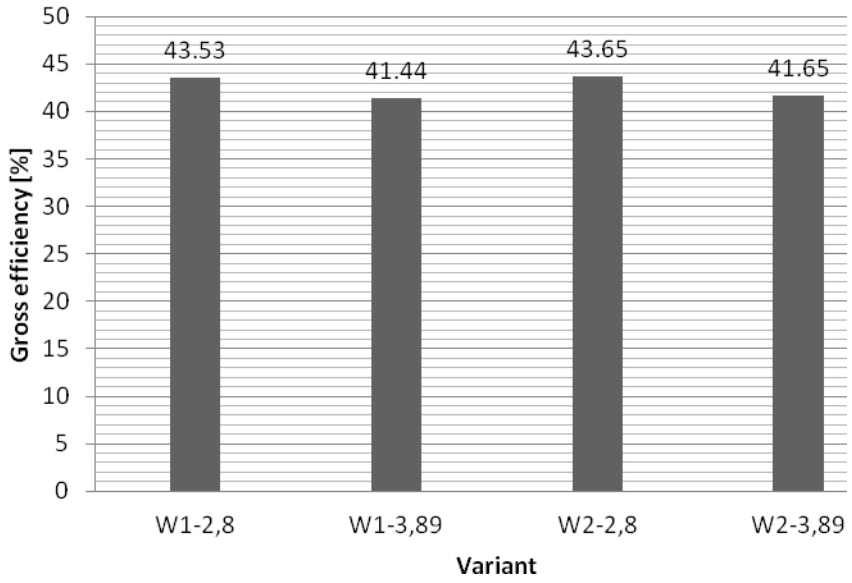

Fig. 4. Gross efficiency of plants

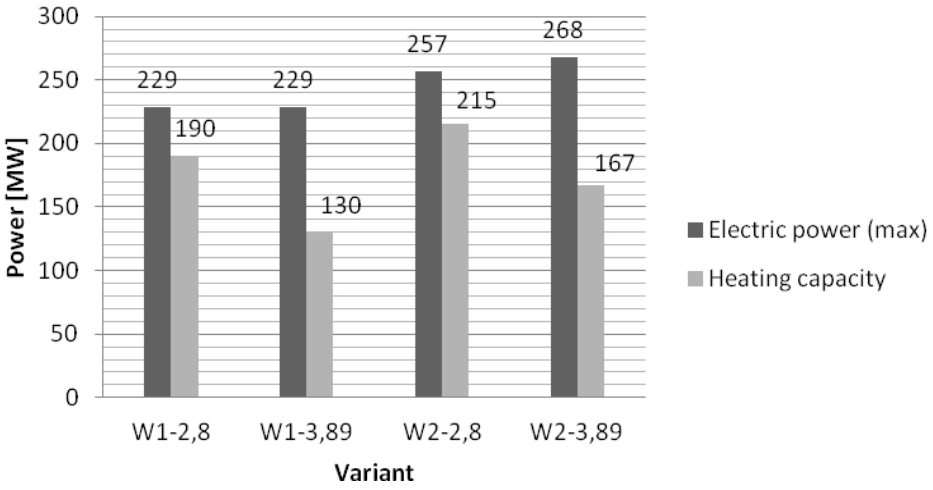

Fig. 5. Electric power at peak heating capacities

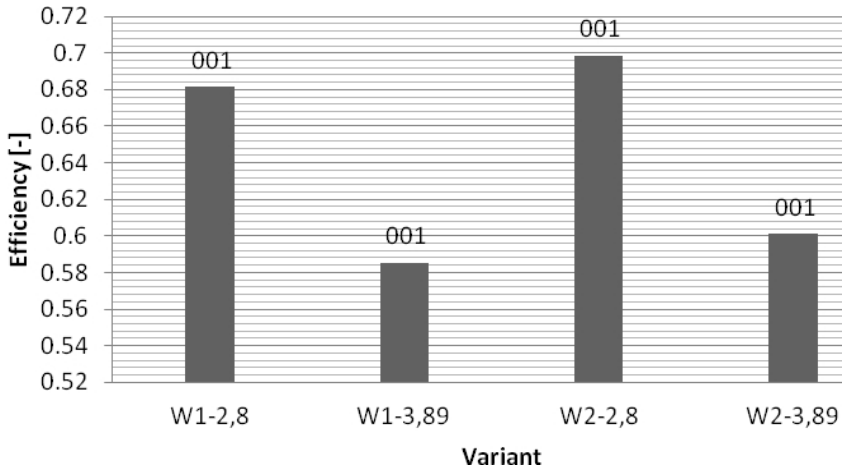

Fig. 6. CHP plant efficiency

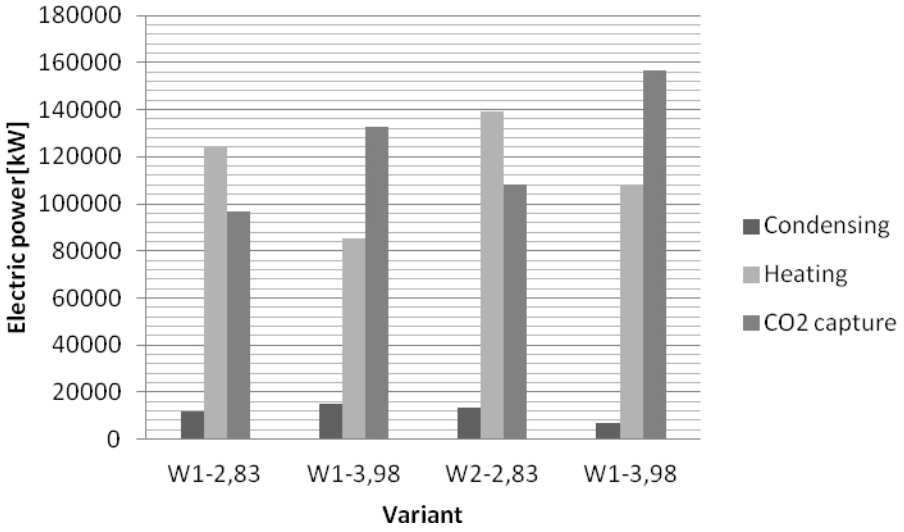

Fig. 7. Electric power produced by steam used for: condensation, heating and CO2 absorption

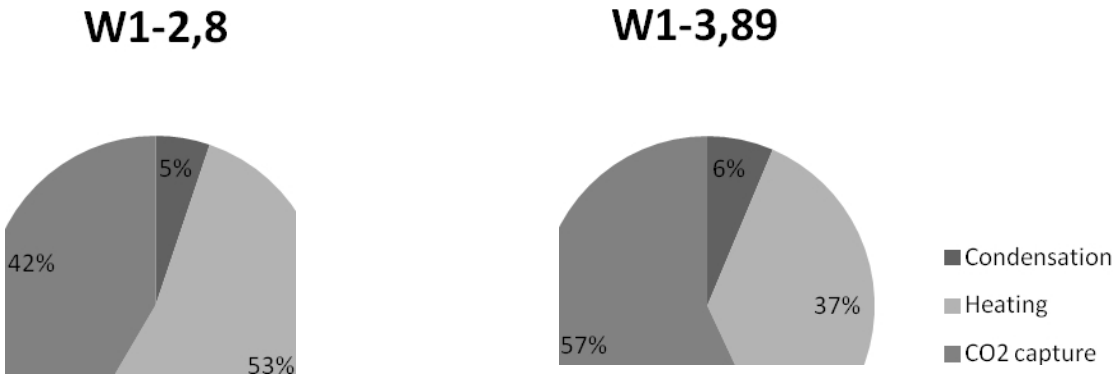

Fig. 8. Percentage share of electric power produced by steam directed to condenser, district heating and CO2 capture purposes for the first variant – W1 by different energy consumption rates of sorbent (2,8 MJ/kgCO2 and 3,89 MJ/kgCO2).

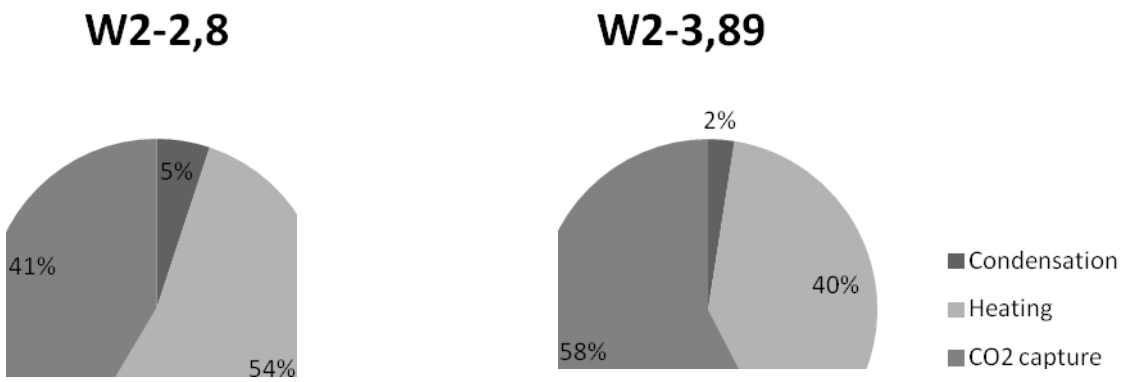

Fig. 9. Percentage share of electric power produced by steam directed to condenser, district heating and CO2 capture purposes for the second variant – W2 by different energy consumption rates of sorbent (2,8 MJ/kgCO2 and 3,89 MJ/kgCO2).

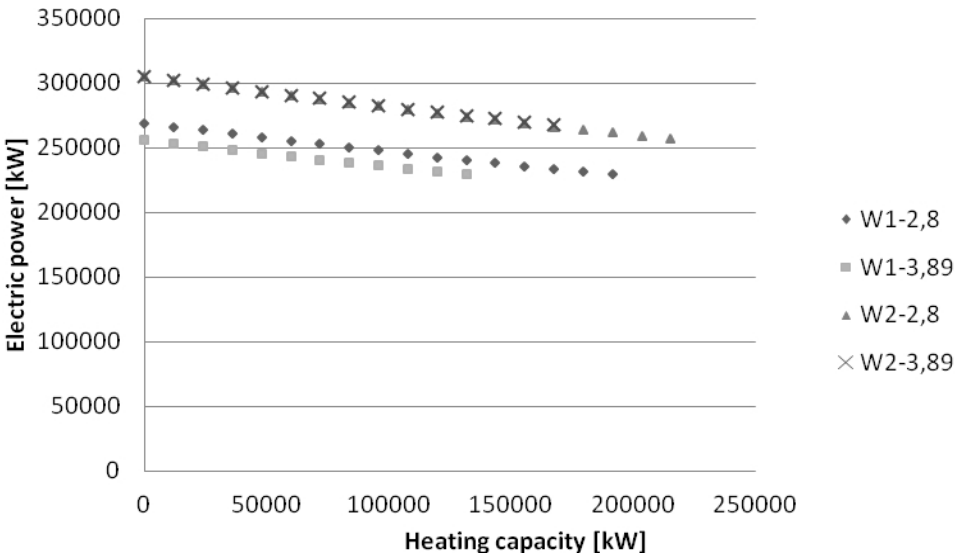

Fig. 10. Electric power as function of heating capacity

3.1. Heating unit operation

Heating unit is fed from the intermediate pressure turbine outlet. Before integration with a CC unit outlet water temperature can be regulated only by means of steam throttling at the low pressure turbines inlet. After integration, pressure at the intermediate turbines outlet has to be kept on a level that will provide proper temperature for sorbents regeneration. Regulation is realized then by

amount of steam delivered to the heating unit, adjusted by a throttling valve and a by-pass on the heated water side.

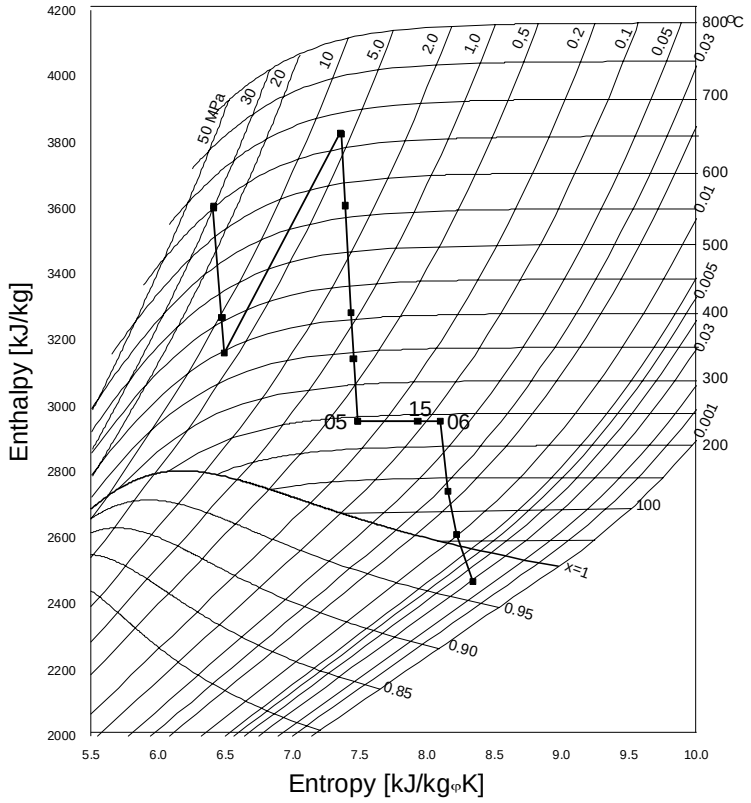

Fig. 11. Expansion line in the turbine

Table 3 contains results of a "capture-ready" CHP plant off-design calculations after integration with a CC unit with sorbent of 2.83 MJ/kgCO2. Computations were carried out for the nominal steam flow of fresh steam and two types of heated water outlet temperature regulation by thermal power equal to 108400 kW, which is 57% of its maximal value. In case of steam throttling regulation the regulation valve remains closed. Throttling starts at point 05 and continues towards point 15, Fig. 11. During by-pass regulation no throttling is used so water is heated by steam of parameters at point 05. Division of water stream between the heat exchanger and by-pass results from the desired water temperature.

Table 3. Steam and water parameters at the heating unit

Quantity	**Unit**	**Regulation method**	
		throttling	bypass
Heating capacity	kW	108400.	108400.
Fresh steam flow rate	kg/s	209.0	209.0
Steam flow rate m_{15}	kg/s	43.245	45.511
Steam pressure p_{15}	MPa	0.300	0.300
Steam pressure p_{16}	MPa	0.116	0.297
Water temperature T_{200}	^{o}C	55.8	55.800
Water temperature T_{203}	^{o}C	98.7	128.216
Water temperature T_{204}	^{o}C	98.7	98.7
Water flow rate m_{200}	kg/s	602.877	602.877
Watre flow rate m_{201}	kg/s	0	247.178

Gross electric power	kW	244619.	244962.
CHP plant efficiency	%	57.13	57.19

Results of performed analysis show that the efficiency of the CHP plant is only slightly influenced by the way of regulation. By-pass regulation provides higher electric power by 1.4 per mill and efficiency by 0.06 percentage point higher than that obtained when using throttling.
This kind of regulation is also used in the second variant.

4. Modernization of the power plant after its integration with a CO2 capture facility

A CHP plant will need to be modernized after being coupled with a CO2 capture unit. This problem is covered in [3 - 6]. It concerns especially turbine, regeneration system and condensers cooling [3 - 5]. Therefore, machinery and utilities of such a plant should be chosen appropriately during the design stage taking those changes into consideration. Considered structure (first variant) of a CHP plant was chosen in the way that will reduce required after the integration changes as much as possible. In fact, they are limited to the low pressure turbine, which will be mostly affected by changed operation conditions.

5. Conclusions and remarks

Aim of this work was a design of a CHP plant structure, that will meet the requirements of the UE Parliament and Council directive UE 2001/80/WE.
Presented structure of a "capture ready" CHP plant will work with possibly high efficiency before and after the integration with a CO2 capture unit, providing costs of modernization to be low as possible.
By decreasing the sorbents energy consumption by 1 MJ/CO2 one can raise the efficiency by ca. 2 percentage points.
Peak power of the heating unit is limited by the sorbents energy consumption rate.
Calculation results show that the heating unit regulation method does not affect the plants efficiency significantly.
Performed analysis includes only the sorbents energy consumption rate and omits other auxiliary power needs.

Acknowledgments

The results presented in this paper were obtained from research work co-financed by the National Centre of Research and Development in the framework of Contract SP/E/1/67484/10 – „Strategic Research Programme – Advanced Technologies for obtaining energy: Development of a technology for highly efficient zero-emission coal-fired Power units integrated with CO_2 capture".

References

[1] Duan L., Zhao M., Xu G., Yang Y.: Integration and optimization on the coal fired power plant with CO_2 capture using MEA. 24th International Conference ECOS 2011, Novy Sad, 4-7.07.2011, Conference papers, p. 582-593.

[2] Abu-Zahra M.R.M., Schneiders L.H.J., Niederer J.P.M., Feron P.H.M., Versteeg G.F., CO_2 capture from power plants. A parametric study of the technical performance based on monoethanolamine. Part I. International Journal of Greenhouse Gas Control 2007; p. 47-46

[3] IEA Greenhouse Gas R&D Programme (IEA GHG), "CO_2 capture ready plants", 2007/4, May 2007.

[4] Lucquiaud M., Chalmers H., Gibbins J.: Capture-ready supercritical coal-fired power plants and flexible post-combustion CO_2 capture. Energy Procedia 1(2009), p. 1411-1418.

[5] Lukowicz H., Mroncz M.: Analysis of the possibilities of steam extraction from a condensing turbine 900 MW for the carbon dioxide separation system. Archiwum Energetyki, vol. XLII(2012), nr. 1, p.1–13.

Cryogenic Method for H2 and CH4 recovery from a rich CO_2 stream in pre-combustion CCS schemes

K. Atsonios [1,2], K. D. Panopoulos [2], A. Doukelis [1], A. Koumanakos [1], E. Kakaras [1,2]

1 Laboratory of Steam Boilers and Thermal Plants, National Technical University of Athens, Heroon Polytechniou 9, 15780, Athens, Greece, atsonios@central.ntua.gr, adoukel@central.ntua.gr, akouman@central.ntua.gr, ekak@central.ntua.gr

2 Institute for Solid Fuels Technology and Applications, Centre for Research and Technology Hellas, 4th km. N.R. Ptolemais – Kozani, 50200 Ptolemais, Greece, panopoulos@certh.gr

Abstract:

Pre-combustion carbon capture technology based on coal gasification or methane reforming followed by water gas shift reactors assisted with Pd-alloys membranes (WGS-MR) is considered very promising for the production of a rich hydrogen stream that can be combusted in combined cycles.
However, the recovery of the total H2 content is not feasible and a part of it remains in the retentate side. The requirement for upstream high pressure operation of the necessary reforming step has a drawback: complete reforming of the CH4 is not allowed; thus small but significant amounts of it remain in the rich CO2 stream. These CH4 amounts not only affect the efficiency of the process but also are against regulations for the allowed composition of carbon dioxide for storage. Therefore an efficient purification step before its compression is of high importance. This work models a cryogenic method for combustibles separation from a rich-CO2 stream and evaluates its effects on pre-combustion carbon capture systems' efficiency. The modeling study is performed in AspenPlusTM. An investigation of the operating parameters is presented as well as how other parameters of the Purification & Compression Unit (PCU) affect performance.

Keywords:

Hydrogen production, ATR, WGS Membrane Reactor, CO2 purification, cryogenic separation

1. Introduction

Pre-combustion capture is one of the proposed options for carbon dioxide removal for which great interest has been shown lately [1, 2]. Having sequestrated carbon in the form of CO2 before the fuel combustion and at high pressures, enables using the resulting fuel gas in various applications like the production of power, pure hydrogen or other chemicals.

In CO_2 pre-combustion capture schemes based on Combined Cycles using Natural Gas (NGCC) or Integrated with Coal Gasification (IGCC) the main strategy is to reform or gasify the original fuel towards a reformate fuel. The standard proposed method for this carbon reduction is then to perform water gas shift, transform CO into CO_2 and use amine absorption for capture. An alternative is to employ H_2 permeable reactors assisting the shift reaction: this option has advantages, such as high hydrogen recovery by pushing the shift reaction and high H_2 purity. A schematic of such an operation is shown in Figure 1: the reformate gas stream is fed to the reactor, CO is shifted with simultaneous H_2 recovery on the permeate side through Pd-alloys membranes. The permeation mechanism of Pd-alloys is through the disassociation of H_2 on the membrane surface and transportation through the metal structure as atomic hydrogen [9, 10]. Some of the main disadvantages of this technique are the high costs, potential poisoning at low temperatures and the fact that the hydrogen recovery is not perfect and considerable amounts of hydrogen remain at the retentate side (from 2 to 10% of the total hydrogen [11]). Besides hydrogen, other combustibles are present such as residual CH4 that was not reformed, as well as CO traces that have not been shifted. Since the retentate stream contains the whole amount of CO2 that is led to storage, it is essential to increase CO2 purity by removing the other species, like H2O, H2, CH4, CO, etc. On one hand,

water removal is feasible by cooling the stream under the dew point so that the water is condensed. On the other hand, special attention is paid to the other species. The conventional suggestion in order to eliminate these compounds is to combust them [12], but this has to be accomplished with pure oxygen as the oxidant agent. Technically this would require the use of catalysts to achieve high combustion rates with such a lean fuel and stoichiometric ratio very close to 1.
In all carbon capture schemes, it is of paramount importance that the internal energetic consumption of the CO2 compression train is minimised [3-8] by purifying the rich-CO2 stream. Huang et al. [6] and Posch et al. [8] adopted a cryogenic method for CO2 purification for oxy fuel capture schemes, which was proven to be energetically and costly inefficient because of high energy consumptions due to the cooling loads, while the recovered gas could not be further utilized and was directed to the stack. It was also shown that applying a distillation column rather than flash separators provided better CO2 stream purification, accompanied by a higher energy penalty.
The present study suggests an alternative choice to handling the combustibles by recovering them with cryogenic separation techniques. Based on differences in thermodynamic properties as far as the dew point of each component is concerned, the retentate stream is cooled down and the CO2 is separated in flash separators or a distillation column. A parametric investigation for the best operation of the plant is performed and a comparison is made with the conventional option for purification with oxy combustion.

2. Plant Description

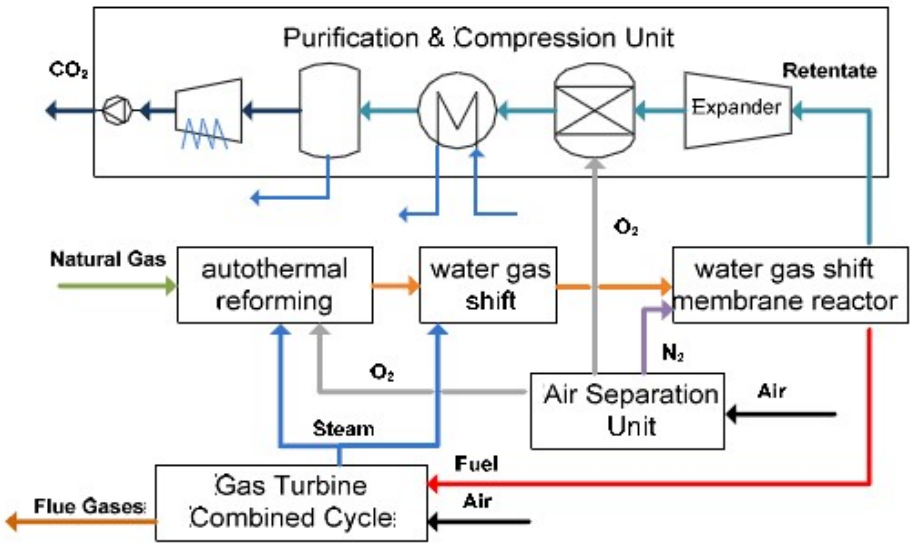

Figure 1. Process flowsheet diagram of the total power system

The outline of the system is presented in Figure 1. A H_2 rich fuel is produced from natural gas reforming in an Autothermal Reactor (ATR), and CO is further shifted in a High Temperature Water Gas Shift Reactor (HT-WGS). The autothermal conditions are met using a rich oxygen stream (95% purity) which is produced in an Air Separation Unit (ASU). The maximization of hydrogen production and purification is performed in Water Gas Shift -Membrane Reactor where it is assumed that the Hydrogen Recovery Factor (*HRF*) is equal to 98% and the operating temperature 400°C is (base case). The nitrogen stream that is produced from the ASU is utilized as sweep gas, increasing the hydrogen recovery driving force in the membranes. The H2-fuel mixture is fed to the power plant island, which consists of a Gas Turbine combined with a Heat Recovery Steam Generator (HRSG). A more detailed description of the process can be found in a previous study [13].

The base case for the CO_2 purification and compression option is also shown in Figure 1: The retentate stream after the membranes is expanded and catalytically combusted in an oxy-fired combustor. Chemical equilibrium predicts that complete combustion of the remaining combustible species is feasible with almost no oxygen surplus [13] but this is not practically easily achievable. The required oxygen depends on how the upsteam units (ATR and WGS performance) are operated: for example assuming *TATR*=1050°C and *S/CATR*=1.5 for the base case, the required amount of oxygen for the post combustor increases the total oxygen production in the ASU by 17.5%. The hot flue gases deliver heat in a secondary Heat Recovery Steam Generator where the feedwater is transformed to high-pressure superheated steam. Next, the water content of the flue gases is removed in a flash separator, and the almost pure CO_2 is then compressed and pumped. The operating parameters of the ATR and WGSMR play an important role in the amount of heat present in the retentate stream. The present study is focused in the CO2 stream purification and compression block based on two separation methods, (a) flash separator and (b) distillation column (see Fig. 2). Apart from CO_2, the retentate stream mainly consists of H_2O, H_2, CH_4, N_2 and Ar (see Table 1).

Table 1. Retentate stream T, P and composition

stream	*T* (°C)	*p* (bar)	*M* (kg/s)	*molar fraction (%)*						
				CO_2	*CO*	H_2	CH_4	N_2	*Ar*	H_2O
retentate	400.0	46.0	67.82	*52.92*	*0.03*	*3.14*	*1.92*	*0.72*	*0.89*	*40.40*

This gas stream is firstly expanded and then is cooled down to around 220°C. Some of the heat is recovered for generating superheated intermediate pressure steam at 315°C. Expanding the gas has a triple positive effect: firstly, the mixture is separated more easily at lower pressures. Secondly, the manufacturing cost of equipment such as the evaporator is significantly lower if they operate at lower pressures. Thirdly, as the content of water in the retentate stream is about 25% w/w, the CO_2 rich mass flow rate that is compressed is less than the corresponding stream that is expanded, contributing positively to the total power balance.

After that, cooling water is used to bring the stream to water condensation conditions at 28°C. The next part of the Purification and Compression Units differs for the two proposed schemes:

2.1 Scheme 1: Double flash separation – internal cooling

This system is auto-refrigerated with no additional cooling system required (Figure 2). Flash separations are performed at two different temperatures, and at the same pressure level. Before each flash, there is a Heat Exchanger that cools the inlet stream. The required cooling loads are taken from the final steams as can be seen in Figure 2a. The rich-CO_2 liquid steams are throttled adiabatically and their temperature is reduced (Joule–Thomson effect). The level of throttling has been set so as to permit heat transfer at the two Heat Exchangers, without temperature crossovers, assuming a minimum temperature approach ΔT =3°C. The final streams come out of the Purification Unit at the temperature of 18°C and the rich-CO_2 stream enters the Compression Unit, where it is compressed in a three stage inter-cooled compressor up to 80 bar to supercritical conditions. Then, it is cooled, liquefied and pumped up to 28°C/110bar and is transported for storage.

Since the temperature at the 2nd Flash is -54.5°C, (near the triple point of CO_2) the parameters that determine the system's efficiency are the expander outlet pressure and the temperature of the 1st flash separation.

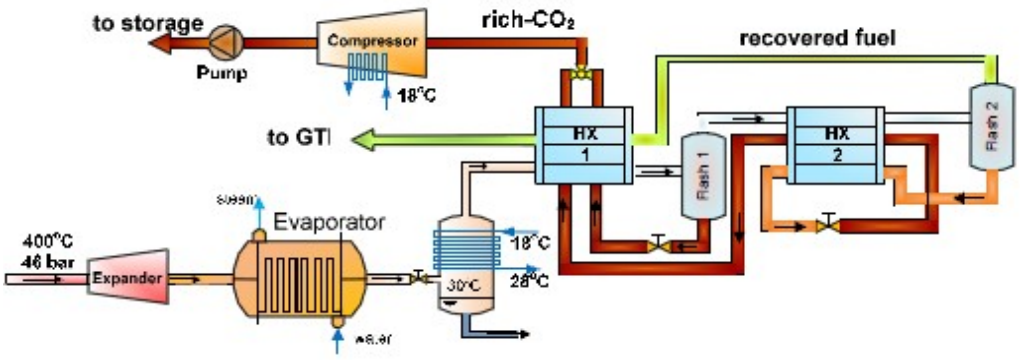

Figure 2. Sketch of the suggested Purification and Compression Unit with cryogenic fuel recovery with flash separators.

The expander outlet pressure determines the CO_2 capture rate: Lower outlet pressures result in better CO_2 recovery rate. On the other hand, if the pressure outlet of the rich CO_2 stream is low, the energy duty for compression is considerable.

2.2 Scheme 2: Separation by distillation column – external & internal cooling

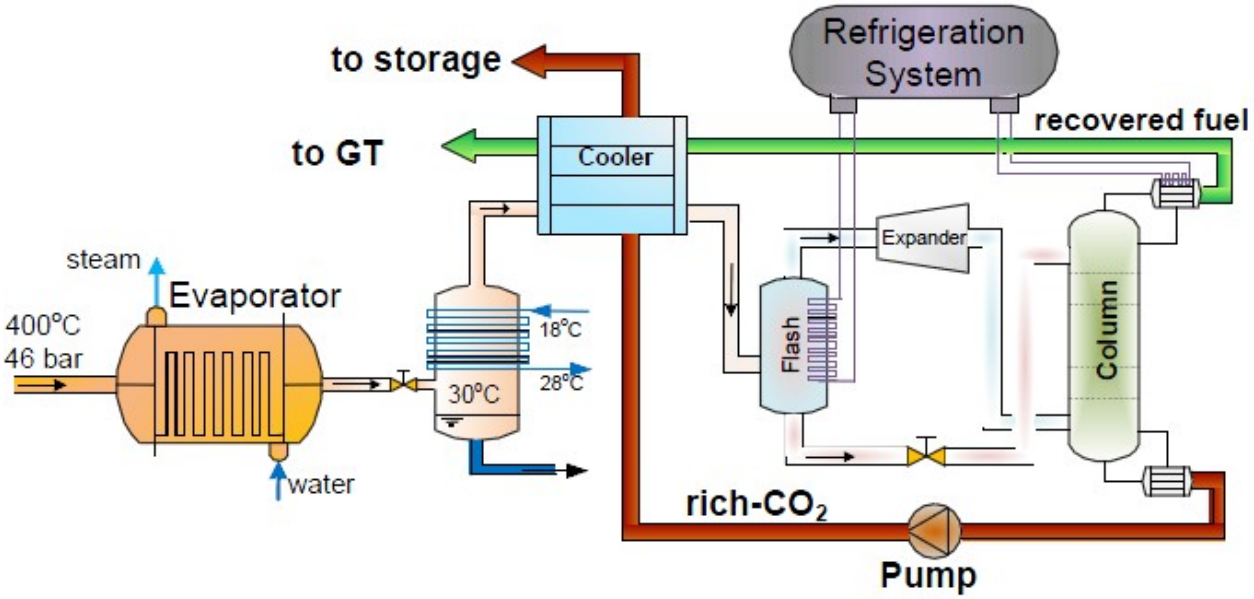

Figure 3. Schematic of the suggested Purification and Compression Unit with cryogenic fuel recovery with distillation column.

The concept of combustibles recovery with distillation mainly consists of a distillation column, a heat exchanger, a flash separator and an external refrigeration system (Figure 3).

After the Heat Exchanger, the inlet stream is partly condensed and is separated at the flash separator. The liquid stream is further cooled by means of an expansion Joule–Thomson effect, while the gas stream is cooled through expansion. Both streams enter the distillation column to make combustibles separation more effective. The cooling loads for the column's condenser are obtained from an external refrigerant and are dependent to the desirable rate of Carbon Capture Efficiency. The corresponding heat at the reboiler can be obtained by the refrigerant inter-cooling

while it is compressed. The distillation column outlet streams can be used to assist the cooling of the retentate stream after water removal (reducing energy consumption).

The refrigeration system comprises a two stage compressor in order to provide cooling loads at two different temperatures: at -20°C for the retentate stream cooling and at around -65°C (depending on recovery rate that determines the dew point of the outlet gas stream) to fulfil the condenser duties at the distillation column. The most suitable cooling medium that is employed in the modelling is R1150 (ethylene – C_2H_4). Assuming that the temperature approach of all heat exchangers is 3°C, the pressure levels of the evaporation are 2.26 and 23.47 bar and that for condensing is 27 bar. Finally, the compressor's polytropic efficiency is assumed to be equal to 0.82. Since the present cooling medium cannot reject its heat directly to the ambient while it is condensed, a secondary auxiliary cooling cycle is required. The cooling medium in this refrigerant cycle is the commercial R134a and the *COP* of this cycle is assumed 3.59.

The thermochemical properties of the PCU block are calculated according to the Peng- Robinson equation of state [8]. The technical data of the system are presented at the Table 1.

Table 1. Process model specifications

compressors polytropic efficiency, η_p (%)	82.0
expander isentropic efficiency, η_{is} (%)	80.0
mechanical efficiency, η_m (%)	99.6
pressure drop in the column (bar)	0.50
heat exchangers minimum temperature approach (°C)	3.0
column stages, N	5

3. Results and Discussion

3.1 Process parameters investigation

In order to come up with concluding remarks about the efficiency of the proposed systems, the comparison of exergetic efficiencies of the schemes is performed. The exergy balance of the PCU block is shown in Figure 5a. The exergy input comes from the retentate stream while any power or heat duties are considered as part of the exergy outputs.

The exergy dissipation for the cases under investigation is depicted by Grassmann diagrams, which are displayed in Figures 5b-d. Arrows that are at the upper side of the main exergy arrow correspond to exergy that is not lost (power production or heat recovery at the steam cycle) whereas the remaining arrows refer to exergy losses (irreversibilities). As far as the process of the oxy-combustion option is concerned, heat recovery and power generation are exergy that is not lost.

The retentate stream at the exit of the burner is at high temperature and a large fraction of the exergy input is utilised for high enthalpy superheated steam generation.

The ASU consumption for extra oxygen production is not taken into account in the exergy balance and its effect on total efficiency is investigated below. On the other hand, both separation options can recover almost half of the total exergy by recovering the combustible content.

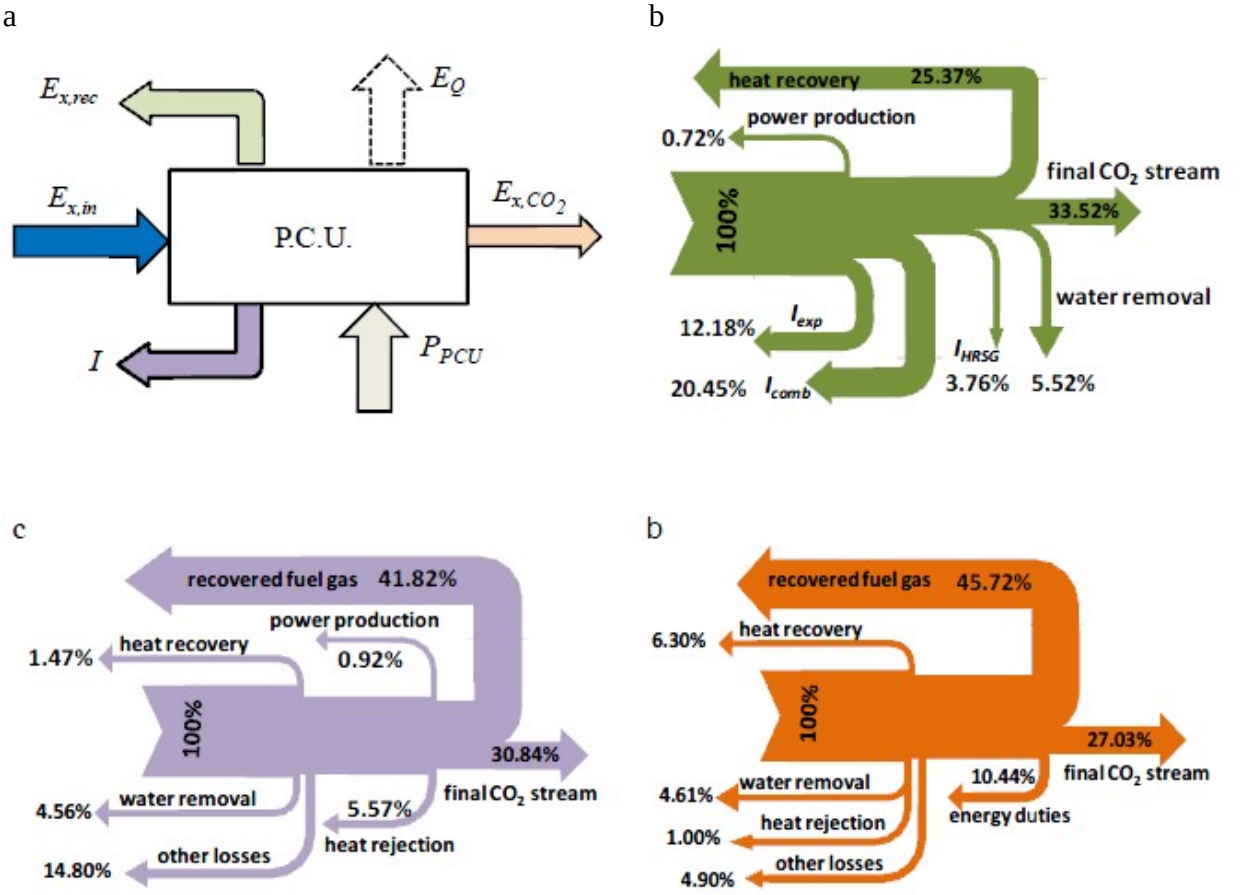

Figure 5. a) Exergy balance of the PCU and Grassmann diagram of PCU with b) expander and post combustor, c) flash separation and d) distillation column.

The corresponding gains from heat recovery are lower in the combustibles separation cases, as the temperature inlet at the heat exchanger is 400°C instead of 708°C in the oxycombustion case. Consequently, the steam quality differs from case to case, as well as the corresponding exergy utilisation. The final CO_2 stream in the oxy-combustion case has larger exergy fraction than the separation options, due to increased CO_2 content from CH_4 combustion. Other losses correspond to irreversibilities from various processes like heat exchanger, valves, expanders, separators etc. According to Figure 5a, the exergetic efficiency of the Unit can be defined as:

$$\eta_{ex,PCU} = \frac{E_{x,rec} + E_{Q,useful} + P_{PCU}}{E_{x,in}} \quad (1)$$

where, $P_{PCU}>0$ when the Unit operation yields power and $P_{PCU}<0$ when the Unit consumes power. The ability of combustibles' recovery and re-usage can also be quantified by the following factor:

$$\eta_{rec} = \frac{LHV_{rec}[kW]}{LHV_{in}[kW]} \quad (2)$$

which stands for the fraction of combustibles heat input in terms of LHV entering the *PCU* that is recovered. The corresponding values of these parameters for each *PCU* case are presented in Table 2. Provided that the initial PCU scheme is technically feasible, CO_2 is completely captured, compressed and stored, while electrical power is generated.

Table 2. Comparison of the three CO_2 purification and compression options

	with post combustor	with flash separation	with distillation column
power consumption (kJ_{PCU}/kg_{CO2})	+87.65	+2.46	-92.13
$\eta_{ex,PCU}$, (%)	27.5	31.9	42.45
η_{rec} (%)	-	62.6	99.2
max. CO_2 capture efficiency (*CCE*) (%)	100.0	98.0	99.0

The most important streams of the process are shown in Table 3. The second method of separation is more efficient as far as η_{rec} is concerned, resulting in higher purity CO_2-rich stream. What is more, in this case, the CO2 content in the recovered gas stream is lower.

Table 3. Outlet streams from PCU for the three purification methods

separation method		flash separator		distillation column		post combustor
stream		rich CO_2	recovered combustibles	rich CO_2	recovered combustibles	rich CO_2
T (°C)		18.0	-29.2	18.0	16.7	18.0
p (bar)		110.0	25.0	110.0	25.0	110.0
M (kg/s)		49.96	2.21	49.66	2.52	46.70
% mole fraction	CO_2	96.28	18.65	99.77	7.74	96.59
	CO	0.01	0.23	0.00	0.26	0.00
	H_2	0.62	47.95	0.00	43.50	0.00
	CH_4	1.80	16.20	0.04	26.25	0.00
	N_2	0.40	8.68	0.00	10.03	1.38
	Ar	0.75	8.29	0.01	12.22	1.89
	H_2O	0.14	0.00	0.18	0.00	0.13

It should be mentioned that high recovery rates do not mean high efficiency of the total plant. The way that the recovered combustibles are exploited plays significant role on the choice of the most suitable technique. To this end, the thermodynamic comparison of the purification options under investigation is completed by the process integration and the investigation of their effects on total plant operation.

3.2 Effect of purification methods on total plant operation

Unlike other cryogenic CCS applications, due to the fact that the recovered gas stream has a considerable amount of chemical energy, it can be fed back to the system for increased energy efficiency. The proposed alternatives for its utilisation are either to reform or to burn it.

Although returning them to the ATR would decrease fuel consumption, the inert compounds that are contained in the stream (mainly N_2 and Ar) would accumulate in the reactor since there is no way to escape from the system. Given that there is not an available method to remove them, this option is abandoned. The alternative choice suggests the injection to the GT combustor. In this case, the carbon capture rate of the system is less than the capture rate at the PCU due to the produced CO_2 from the combusted CH_4 in the GT. Given that the system under investigation is aimed to the maximization of the final H_2 rich fuel and not the maximization of electrical power production, a different approach concerning the recovered fuel should be adopted.

The basis of comparison of each method from performance perspective can be the parameter named *SPECCA* (Specific Energy Consumption for CO2 Avoided). It expresses the additional fuel energy in MJ that is required to avoid 1 kg of CO2:

$$SPECCA = \frac{3600 \cdot \left(\frac{1}{\eta} - \frac{1}{\eta_{REF}} \right)}{E_{REF} - E}, \left[kJ_{LHV} / g_{CO_2} \right] \quad (3)$$

where E is the CO2 emission rate, in kgCO2/kWh$_{el}$, and η the net electrical efficiency of the plants. The reference plant (*REF*) is referred to the corresponding NGCC plant without Carbon Capture. The net efficiency of the reference plant is η_{REF}=58.3% with specific CO_2 emission rate *E*REF=354.3gr$_{CO2}$/kWh.

Among the most important parameters for total plant specification are the operating parameters of the ATR and the WGS-MR. Table 4 summarizes the characteristics of the base case model for the three purification methods under investigation:

Table 4. Base case results for the three purification methods (CCR=90%)

separation method	flash separator	distillation column	oxy combustor
specific H_2 production (kg_{H2}/kg_{NG})	0.328	0.328	0.291
specific O_2 production (kg_{O2}/kg_{NG})	0.89	0.89	0.99
GT power production (% kW_{GT}/LHV)	39.64	39.99	38.06
ST power production (% kW_{ST}/LHV)	15.53	15.72	17.75
specific PCU power (% kW_{PCU}/LHV)	+0.01	-0.49	+0.45
specific ASU power (% kW_{PCU}/LHV)	-5.37	-5.37	-5.94
net efficiency (%)	**50.74**	**50.77**	**51.36**
specific CO_2 emissions (g_{CO2}/ kWh_{el})	42.4	42.4	42.1
SPECCA (kJ_{LHV}/g_{CO2})	2.95	2.94	2.67

It is clear from Table 4 that oxy combustion of the retained combustibles (namely CH4 that is not reformed, CO that is not shifted and H_2 not recovered at the membranes) is the most efficient method for the CO_2-rich gas treatment in terms of energy efficiency. However, the specific quantity of the produced H2 that enters the GT combustor is increased by 11% in the cases of cryogenic separation. In other words, for systems dedicated to H_2 production, cryogenic separation methods are considered to be more efficient in terms of H_2 production yield. Additionally, the oxygen demand is reduced by 10% in these cases, implying a smaller ASU. However, the more complex purification system compensates this feature. The high heat recovery rate in the oxy-combustion case results in the increased power production in the ST (c. 2% increase).

3.2.1 Effect of Carbon Capture Rate (*CCR*)

It should be mentioned that Carbon Capture Efficiency (*CCE*) does not coincide with the Carbon Capture Rate (*CCR*) of the total plant because it is independent of the final usage of the recovered gases. In this study, this stream is fed to the GT to be combusted. As a result, the CCR is also dependent on the recovered CH_4 and CO.

Figure 6 provides useful information about the effect of Carbon Capture Rate on the plant performance.

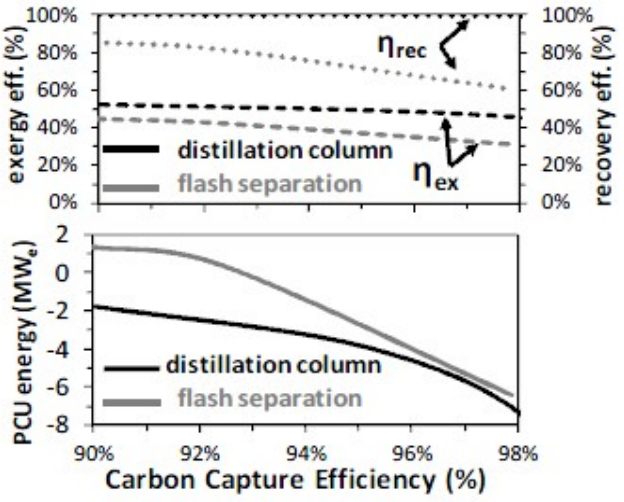

Figure 6a. Impact of CCE on PCU performance for the two purification methods.

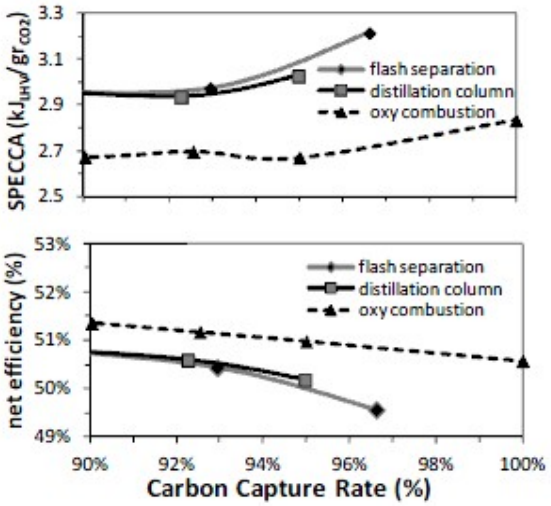

Figure 6b. Effect of CCR on the power plant for the two purification methods.

For low *CCE* the flash separation method has positive effect on energy balance as the *PCU* produces electrical power instead of consuming (Figure 6a). This is owed to the expansion of the CO2-rich stream. However, the combustibles are not recovered as effectively as in the case of the distillation column method and therefore the latter is exergetically more efficient. As the *CCE* approaches 100%, energy duties for both methods tend to be equal and the divergence of the corresponding exergy efficiency increases. The effect of *CCR* on the overall plant efficiency and the corresponding *SPECCA* (Figure 6b) is the same for both combustibles separation options (especially for *CCR*<95%). According to the process specifications adopted (more specifically the methane rate that is assumed not having been reformed) the maximum *CCR* for the distillation column and flash separator options is 96% and 97% respectively, for maximum CH_4 recovery. For lower CH_4 recovery rates, a large part of the methane would remain at the CO_2 stream and the total efficiency would drop considerably. If a higher *CCR* is preferable, process specifications at the *ATR* which are related to methane conversion should be changed. On the other hand, at the oxy combustion case, since the *CCR* correlates with the fraction of NG that is by-passed and not reformed, the efficiency variation drops linearly as *CCR* increases.

The parametric investigations that follow are conducted for *CCR*=90% for all cases.

3.2.2 Effect of Steam to Carbon Ratio of the ATR (S/CATR)

The amount of steam that is injected in the ATR plays a significant role in methane reforming. The higher hydrocarbons that are in the Natural Gas (NG) are easily reformed at the prereforming stage at lower temperatures and hence, a reforming efficiency equal to 100% is assumed for them. High S/C_{ATR} ratios benefit CH4 reforming and lower the energy consumption for its recovery at the PCU. On the other hand, electrical power derived from steam turbines is decreased when *S/CATR* increases as more of the produced steam is extracted instead of being expanded. According to Figure 7b, the optimum value for plant efficiency is 1.5 for all cases. For high *S/CATR* ratios, the flash separation method is slightly better, as the exergy efficiencies are almost the same and the power gain from this method is quite high. What is more, for low *S/CATR* ratios, where steam extraction is less, an efficient recovery of the unreformed CH4 is rather preferable and approaches oxy-combustion case.

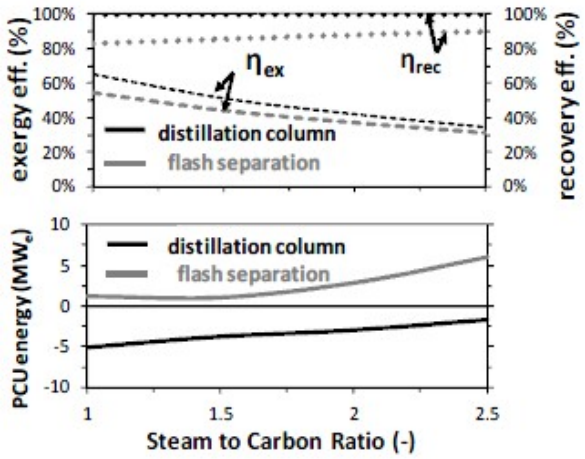

Figure 7a. Impact of S/C$_{ATR}$ on PCU performance for the two purification methods (CCE=90%).

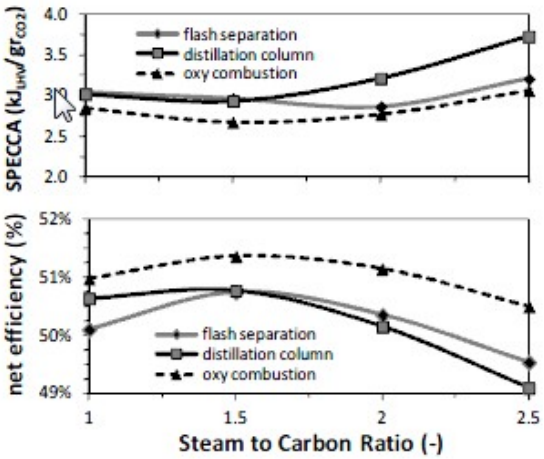

Figure 7b. Effect of S/C$_{ATR}$ on the power plant for the two purification methods.

3.2.3 Effect of Hydrogen Recovery Factor (*HRF*) of the WGS-MR

This parameter refers to the ability of the reactor to make hydrogen available at the opposite side (permeate side), where the H_2-rich fuel is produced. Recent developments at Pd-alloys membranes combined with WGS catalysts showed that hydrogen recovery is achievable at rates greater than 90% [14] and in some cases even close to 100% [11]. Hydrogen recovery factor strongly affects membranes cost as the higher the hydrogen recovery the larger membrane area required [15].

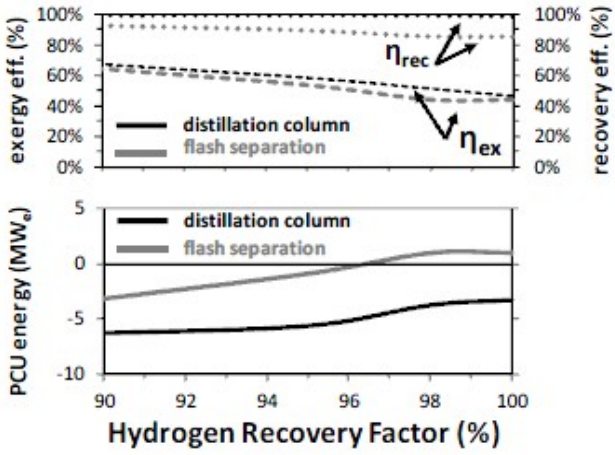

Figure 8a. Impact of HRF on PCU performance for the two purification methods (CCE=90%).

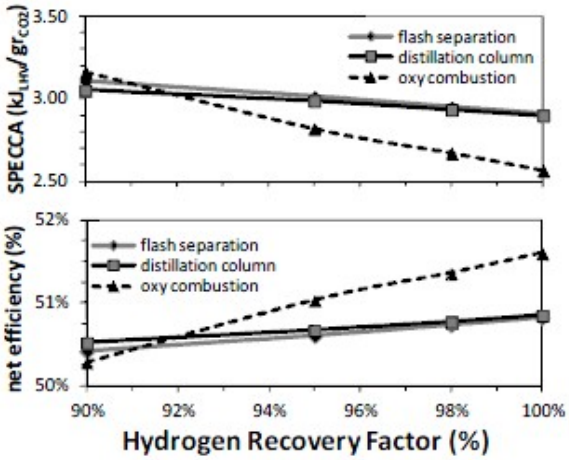

Figure 8b. Effect of HRF on the power plant for the two purification methods.

Figure 8b shows that cryogenic methods may be beneficial for membranes with low *HRF* (>90%) as the variation of this parameter does not affect the total efficiency, unlike the oxy combustion option. Membranes with high *HRF* favor the application of oxy combustor instead of combustibles recovery.

3.2.4 Effect of the ATR operational temperature (T_{ATR})

The ATR operating temperature is of high importance as it plays significant role on the syngas quality: according to the chemical equilibrium, the higher the temperature, the higher the methane conversion rate. On the other hand, in order to secure the autothermal conditions in the reactor, more oxidant agent is required in the case that the temperature is high.

Furthermore, materials stability limits the maximum operating temperature to around 1100°C.

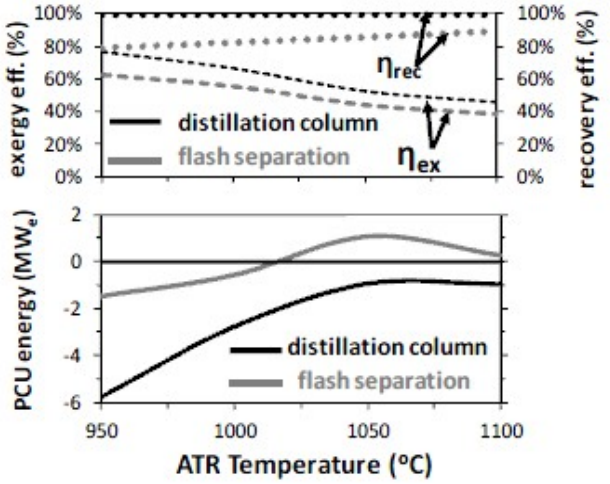

Figure 9a. Impact of T_{ATR} on PCU performance for the two purification methods (CCE=90%).

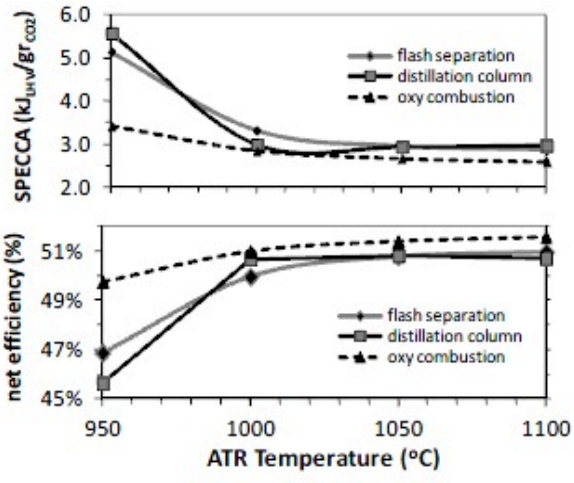

Figure 9b. Effect of T_{ATR} on the power plant for the two purification methods (CCR=90%).

The ATR operating temperature is of high importance as it plays significant role on the syngas quality: according to the chemical equilibrium, the higher the temperature, the higher the methane conversion rate. On the other hand, in order to secure the autothermal conditions in the reactor, more oxidant agent is required in the case that the temperature is high.

Furthermore, materials stability limits the maximum operating temperature to around 1100°C.

As is shown in Figure 9a, at low ATR temperatures, cryogenic systems consume more energy for CO_2 purification due to the increased presence of methane in the retentate stream.

Recovery and exergy efficiencies for separation with a distillation column are greater than those of the corresponding flash separation method. This feature has a positive effect on the total system when the combustion of the recovered fuel satisfies the required CO_2 capture rate. In this case, for T_{ATR} = 950°C, part of the methane is selected not to be recovered in order to meet the goal of *CCR*=90%. Consequently, the net efficiency drops considerably, (Figure 9b). At high temperatures, the oxy combustion option is more efficient than the cryogenic options by ca. 1%.

4. Conclusions

This study investigates the cryogenic method as an alternative choice for the rich-CO2 stream purification after membrane separation, instead of simply combusting the retained combustibles. Two proposed cryogenic systems are investigated: flash separation with internal cooling and separation with distillation column. In the first case, electrical power is produced while the separation efficiency is quite high, as 62.6% of the combustibles heat input is recovered. On the other hand, separation by a distillation column may result in the complete separation of combustibles, providing high purity in the final CO2 stream (>99%).

However, more energy duty is required due to the external cooling system.

The sensitivity analysis showed that the cryogenic methods can overbalance any 'weak' operating mode of the hydrogen block, such us low methane conversion rates at the ATR and low hydrogen recovery rates at the membranes. Nevertheless, as far as the total system efficiency is concerned, the oxy combustion option is preferable as it can combine both high capture rates and performance.

Future work that correlates membrane area and investment cost of the whole plant would finally determine under which conditions a cryogenic recovery system is required.

Acknowledgments

The authors would like to gratefully acknowledge the support of the European Commission (CACHET II, FP7 Project No. 241342).

Abbreviations

ASU	Air Separation Unit
ATR	Autothermal Reformer reactor
COP	Coefficient of performance
GT	Gas Turbine
HRSG	Heat Recovery Steam Generator
HRF	Hydrogen Recovery Factor
HT-WGS	High Temperature Water Gas Shift reactor
LHV	Lower Heating Value
NG	Natural Gas
PCU	Purification & Compression Unit
ST	Steam Turbine(s)
S/C$_{ATR}$	Steam-to-Carbon Ratio in ATR
WGS-MR	Water Gas Shift Membrane Reactor

References

[1] Olajire A. CO2 capture and separation technologies for end-of-pipe applications - A review. Energy 2010;35: 2610-2628.

[2] Kanniche M., Gros-Bonnivard R., Jaud P., Valle-Marcos J., Amann J.M., Bouallou H. Precombustion, post-combustion and oxy-combustion in thermal power plant for CO2 capture. Applied Thermal Engineering 2010;30:53–62.

[3] Romeo L.M., Lara Y., González A, Reducing energy penalties in carbon capture with Organic Rankine Cycles, Applied Thermal Engineering 31 (2011) 2928-2935

[4] Zanganeh K.E., Shafeen A., Salvador C., Beigzadeh A. Abbassi M., CO2 processing and multipollutant control for oxy-fuel combustion systems using an advanced CO2 capture and compression unit (CO2CCU), Energy Procedia 4 (2011) 1018–1025

[5] Kakaras E., Koumanakos A., Doukelis A., Giannakopoulos D., Vorrias I., Oxyfuel boiler design in a lignite-fired power plant, Fuel 86 (2007) 2144–2150

[6] Huang Y., Wang M., Stephenson P., Rezvania S., McIlveen-Wright D., Minchener A., Hewitt N., Dave A., Fleche A., Hybrid coal-fired power plants with CO2 capture: A technical and economic evaluation based on computational simulations, Fuel paper in press

[7] Romeo L. M., Bolea I., Lara Y., Escosa J. M., Optimization of intercooling compression in CO2 capture systems, Applied Thermal Engineering 29 (2009) 1744–1751

[8] Posch S., Haider M., Optimization of CO2 compression and purification units (CO2CPU) for CCS power plants, Fuel paper in press

[9] Colin A. Scholes, Kathryn H. Smith, Sandra E. Kentish, Geoff W. Stevens, CO2 capture from pre-combustion processes - Strategies for membrane gas separation, International Journal of Greenhouse Gas Control 2010;4:739–755.

[10] John J. Marano, Jared P. Ciferino, Integration of Gas Separation Membranes with IGCC - Identifying the right membrane for the right job, Energy Procedia 1 (2009) 361–368

[11] Mendes D., Chibante V., Zheng J.M., Tosti S., Borgognoni F., Mendes A., Madeira L. M., Enhancing the production of hydrogen via water gas shift reaction using Pd-based membrane reactors, J Membrane Sci 35 (2010) 12596- 12608

[12] Dijkstra J.W., Jansen D., Novel concepts for CO2 capture, Energy 29 (2004) 1249–1257 (In: 6th International Conference on Greenhouse Gas Control Technologies).

[13] Atsonios K., Panopoulos K., Doukelis A., Kakaras E., Exergy Analysis of a Hydrogen fired combined cycle with natural gas reforming and membrane assisted shift reactors for CO2 capture, presented in ECOS 2011 in Novi Sad, Serbia, July 4-7 2011.

[14] Jan Wilco Dijkstra, Johannis A.Z. Pieterse, Hui Li, Jurriaan Boon, Yvonne C. van Delft, Gunabalan Raju, Gerard Peppink, Ruud W. van den Brink, Daniel Jansen. Development of membrane reactor technology for power production with pre-combustion CO2 capture. Energy Procedia 2001;4:715–722

[15] Criscuoli A., Basile A., Drioli E., Loiacono O., An economic feasibility study for water gas shift membrane reactor. Journal of Membrane Science 181 (2001) 21–27

Design and Optimization of ITM Oxy-Combustion Power Plants

Surekha Gunasekaran[a], Nicholas D. Mancini[a] and Alexander Mitsos[a]

[a] Massachusetts Institute of Technology, Cambridge, United States
surekhag@mit.edu, mancini@mit.edu, amitsos@alum.mit.edu (CA)

Abstract:

Oxy-fuel combustion using an oxygen ion-transport membrane (ITM) is a promising alternative to the existing cryogenic air separation method, which incurs heavy thermodynamic and economic penalties. The performance of ITM-based power plant systems depends on the operating conditions, geometric structure of the reactor and the integration approach of ITM to the existing power plant system. A detailed study of these factors is required to perform an optimization analysis. In this paper, an intermediate-fidelity ITM model is used to study the performance of ITM reactors under different operating conditions and flow configurations. Using this model, ITM-based oxy-combustion power cycles are investigated. This article focuses on the results of an optimization analysis of the AZEP 100 cycle, which consists of a Brayton-like topping cycle and a triple pressure heat recovery steam generation bottoming cycle. The effects of power plant operating parameters are analyzed, namely the outlet pressure of pumps, turbines, valves and de-aerator, the split fractions of splitters, flow rates, and the outlet temperatures of heat exchangers. The optimization study has resulted in an increase of 2.92 percentage points which is important with respect to the feasibility of ITM-based oxy-combustion power plants compared to alternatives.

Keywords:

Oxy-fuel combustion, Ion-transport membrane, Zero-emission power cycle, Power cycle efficiency.

1. CCS and ITM Technology

Global warming and anthropogenic emissions of CO_2 have motivated the search for more efficient and economically feasible environment-friendly technologies for power generation, which contributes to about 65% of total anthropogenic CO_2 emissions [1]. Carbon-dioxide capture and sequestration (CCS) allows for the use of fossil fuels for power generation without the detrimental effects of associated CO_2 emissions. The most conventional CCS technique is post-combustion capture, which is energy-intensive and expensive [2].

In the oxy-combustion method, O_2 is separated from air prior to the combustion of the fuel-air mixture and fuel oxidation occurs in a nitrogen free environment, typically with large recirculation of exhaust gases to control the temperature. The flue gas consists only of CO_2 and H_2O, from which CO_2 can be separated simply by condensation. Thus, the penalty associated with separation of CO_2 from the flue gas is greatly reduced [3]. At present, large scale separation of O_2 from air is done using cryogenic air separation methods. The major disadvantages of this method are that it is energy intensive, and has low second law efficiency [4]. A promising alternative is the use of ion-transport membranes (ITM), which operate based on chemical potential differences, and use a high temperature mixed-conducting (ionic and electronic) ceramic membrane [5]. This technology is motivated by the fact that the penalties incurred are much lower than the additional power requirement for cryogenic air separation [6].

2. Assessment of flow configurations

2.1. Intermediate-Fidelity ITM Modelling

A spatially-distributed quasi two dimensional model developed based on the fundamental conservation laws (mass and energy balance), semi empirical oxygen transport equations and fuel oxidation kinetics is used in this work. Reference [7] gives a detailed description of this model. A brief overview of the results obtained using this model is presented here.

2.1. Separation-Only Flow Configuration

Co-current and counter-current mode separation-only ITMs are compared for various flow rates, while keeping the sweep ratio the same for a fixed ITM size [8].

The partial pressure difference between feed and permeate steam along the length of the reactor remains constant for counter-current flow, but decreases for co-current flow. One major advantage of the counter-current arrangement is that it has a higher recovery ratio due mostly to a higher average wall temperature. Heat transfer coefficient and wall temperature distribution are important factors for the optimization of an ITM power plant.

2.2. Reactive Separation

The reactive mode arrangement combines the separation of O_2 from air with combustion. The main promise is to increase the driving force by maintaining a very low partial pressure of O_2 on the permeate side. In principle, this can eliminate the thermodynamic penalty for separation: the reaction drives the separation.

Reference [8] discusses important co-current simulation results. Initially, the temperature rises slowly due to the slow oxygen transport, which is the rate-determining step for the oxidation of the fuel. The values of the permeate, feed stream, and membrane temperatures are close to each other because of the high heat transfer coefficient between the permeate and feed streams. As the temperature increases gradually, the chemical reaction speeds up, accelerating the increase of the local temperature. This ultimately results in hot spots, i.e., locations with high temperatures. Since ITM membranes have maximum allowed temperature limits, the combustion process needs to be controlled by manipulating the diluent to fuel flow ratio in order to ensure membrane stability.

Although partial pressure difference of O_2 between permeate and feed sides is higher for a reactive-mode arrangement when compared to the separation-only mode, the diffusive flux of O_2 does not increase significantly. This is due to the greater dependence of the diffusive flux on temperature than on the partial pressure difference. Results of counter-current reactive mode simulations show that the counter-current arrangement increases localized heating effects. The temperature overshoot occurs because the local heat release rate due to combustion exceeds the local heat transfer capacity.

It is interesting to note that the flow direction does not affect the main driving force (partial pressure difference across the membrane) of reactive type ITM. Analogous to a single stream heat exchanger, in which one of the temperatures is independent of flow direction, the partial pressure of the permeate side is zero irrespective of the flow arrangement.

3. ITM Oxy-Combustion Power Cycles

An optimization analysis of ITM and a study of its thermodynamic performance require an understanding of the effect of power plant operating conditions, geometric structure of the reactor and the specific way in which ITM is integrated with the power plant system, on its performance. In particular, the ITM model must predict the effect of ITM size, flow configuration and operation on performance (e.g., recovery ratio of oxygen) and constraints (e.g., maximal temperature); moreover, it is essential to accurately calculate the pressure drop in the ITM. In this section, the implementation of the ITM model used is described along with the optimization formulation.

3.1. JACOBIAN-ASPEN Interface

ASPEN Plus® and JACOBIAN are used to simulate an ITM integrated power cycle. A power plant flow sheet is constructed using ASPEN Plus®, which has pre-defined unit operation models for heat exchangers, turbo-machines, splitters, chemical reactors, etc. JACOBIAN [9] is an equation-oriented modelling and simulation program that is used to model the ITM. JACOBIAN and ASPEN Plus® are linked using the USER2 model block in ASPEN Plus® as shown in Fig. 1.

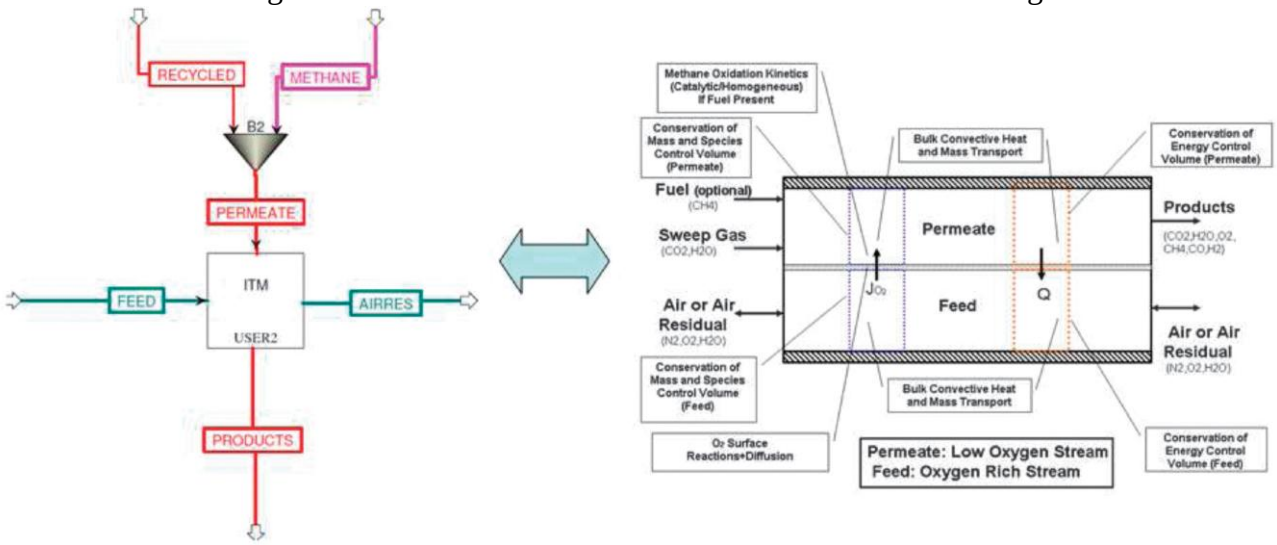

Fig. 1. JACOBIAN -Based ITM Model in ASPEN Plus® using USER 2 Block [10]

3.2. ITM-Power Cycle Flow Sheet

Due to its high performance and compatibility, the advanced zero emission power plant (AZEP) is the most commonly studied ITM-based power plant in the literature [6, 12, 13, 15]. The AZEP concept can be used for both (essentially) zero emission cycles and partial emissions cycles [6, 13, 15]. Partial emissions cycles have an additional afterburner which increases the efficiency, but also increases the CO_2 emissions.

The focus of this article is optimization of an AZEP 100 power cycle [6, 10, 13, 15]. The cycle is sized to produce a net electric power of 500 MW. For partial emission cycles, the base flow sheet is the same as the AZEP 100 with the exception of the inclusion of an afterburner after the high-temperature heat exchanger in order to increase the gas turbine inlet temperature to the maximum possible limit (assumed) of 1573 K. Reference [10] gives a detailed description of various ITM-power cycles and the assumptions.

3.3. AZEP 100

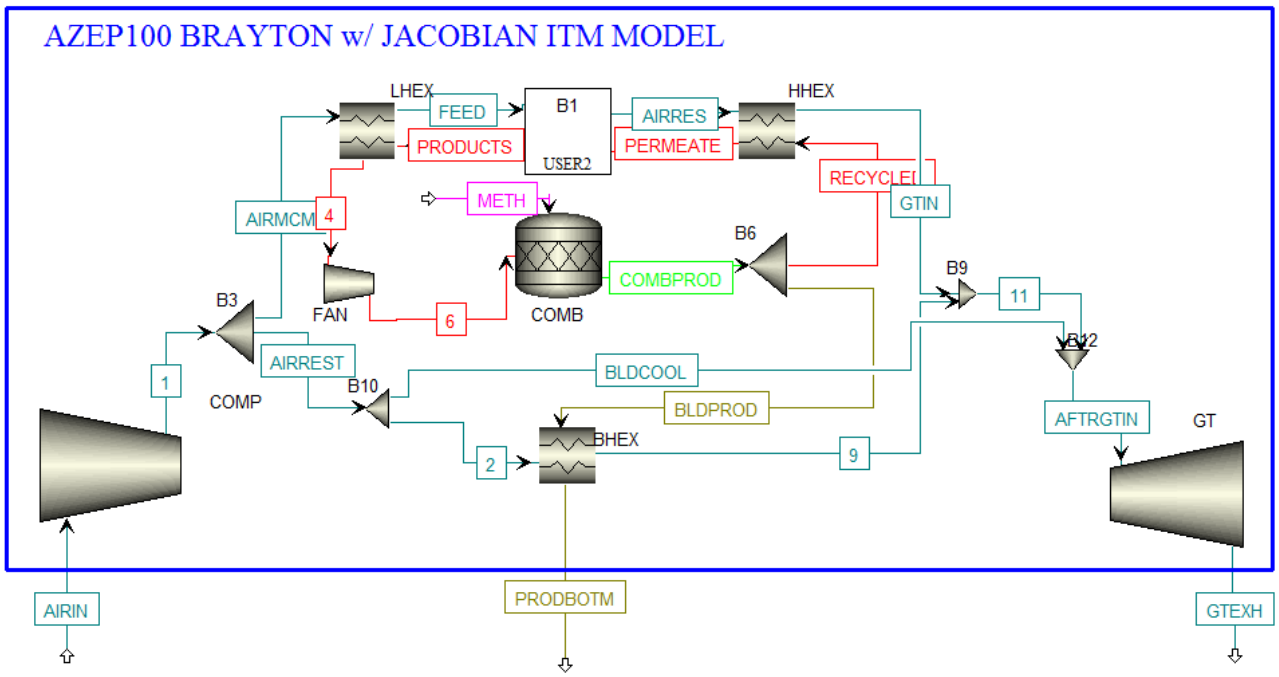

Fig. 2. AZEP 100 Top Cycle Process Flow Diagram in ASPEN Plus® with a JACOBIAN based ITM model [10]

The topping cycle of the AZEP 100 is a Brayton-like cycle with an ITM air separation unit and a combustor. The air is compressed and split into two streams - "AIRMCM" and "AIRREST". The feed stream to the ITM is preheated by the recycled combustion products with a heat exchanger network (see "LHEX-ITM-HHEX" shown in Fig. 2). "AIRMCM" is preheated to 973 K in the heat exchanger "LHEX". This preheated feed stream provides oxygen to the permeate stream in the ITM. The "AIRRES" exiting the ITM (O_2 depleted stream) is further heated by the combustion products "RECYCLED" (which serves as the permeate stream in the ITM) and is expanded in the gas turbine. A part of "AIRREST" is used to cool the gas turbine and a part is used to regenerate thermal energy from the combustion products in the heat exchanger "BHEX". The permeate stream contains O_2 (from the feed stream) necessary to burn the required amount of fuel.

The temperature of combustion products is limited by the temperature limit of the high temperature heat exchanger "HHEX". A design specification control loop is implemented to maintain the temperature of the combustion products at 1473 K by varying the split fraction of the compressed air (splitter "B3"). Another design specification control loop varies the recycle ratio (split fraction of splitter "B6") to maintain a minimum approach temperature in "LHEX" without any temperature cross over in the heat exchanger network "LHEX-ITM-HHEX". The degrees of freedom for the topping cycle include the inlet flow rates and ITM size.

The "PRODBOTM" stream after extraction of thermal energy in "BHEX" and the "GTEXH" (outlet from the turbine) are fed to the bottoming cycle for extraction of work from the thermal energy of these streams. A standard triple pressure stream generator cycle with pressure levels at 100, 25 and 5 bars is used as bottoming cycle for the AZEP 100 (Fig. 3). The outlet stream "TOCPU" is fed to the compression and purification unit to separate H_2O and CO_2.

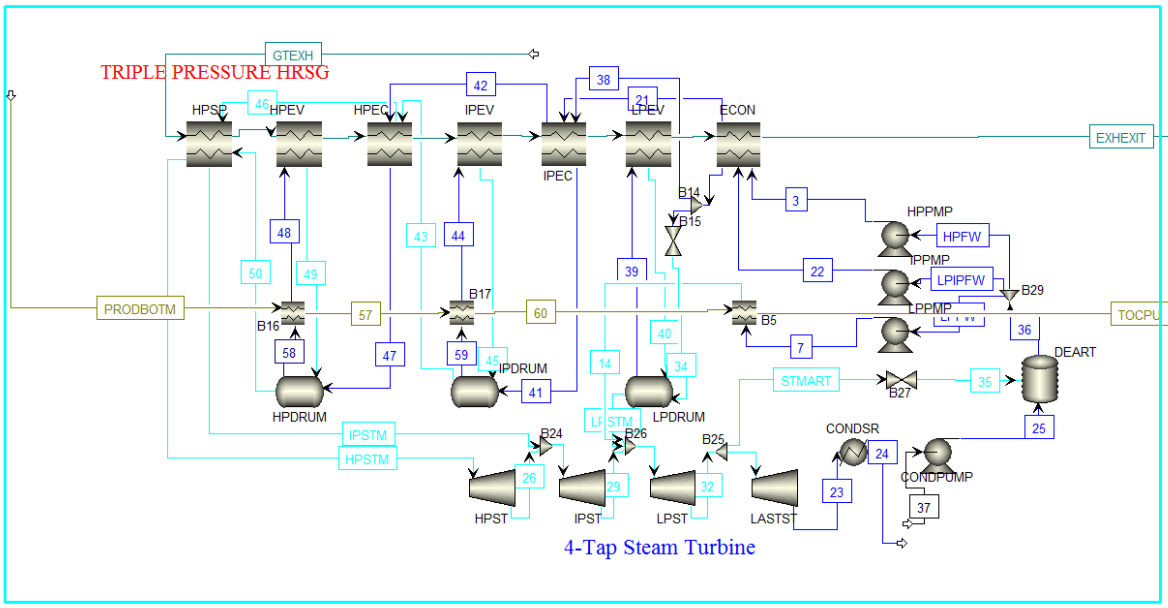

Fig. 3. Triple Pressure Bottoming Steam cycle: Pressure Levels are 100, 25, 5 bar [10]

3.4. Optimization of AZEP 100

A local optimum is determined with sequential quadratic programming (SQP) using the inbuilt ASPEN Plus® Optimizer. Overall, the objective is maximal efficiency keeping the ITM size fixed. The power cycle has 14 optimization variables – 5 variables for the topping cycle, and 9 for the bottoming cycle. To overcome numerical difficulties and limitations of ASPEN Plus®, the power cycle is optimized in two steps. First, only the topping cycle is optimized. Then, only the bottoming cycle is optimized using the inlet streams to the bottoming cycle – "GTEXH" and "PRODBOTM" – as input specifications, fixed to the optimum operating condition of the topping cycle. In principle, this two-stage method does not guarantee local optimization of the entire cycle [25]. However, as the efficiency of the gas turbine "GT" in the top cycle is higher than that of the bottoming cycle, it is more efficient to extract work through the gas turbine in the topping cycle than the bottoming cycle. In other words, to attain maximum efficiency of the total power plant, maximum possible power extraction should take place in the top cycle, transporting minimum thermal energy to the bottoming cycle. Thus, sequential optimization of the topping cycle followed by the bottoming cycle is believed to give the optimum of the entire power cycle.

3.4.1. Optimization of Top Cycle

The one-dimensional intermediate fidelity ITM model makes it impossible to optimize the ITM geometry. Attempting to minimize the pressure drop would result in an infinite number of permeate and feed channels, which are extremely small in length. Moreover, the ITM is an expensive component, so optimization of the ITM size would require accurate estimates for its cost which are not available since ITM is a very new technology. Hence, the topping cycle is optimized by varying operational parameters such as mass flow rate, temperature and split fractions, while the ITM size is kept fixed. More specifically, the degrees of freedom are the mass flow rates of "AIRMCM" and "AIRREST", the split fraction of "B10", and the cold side outlet temperature of "BHEX". Varying "AIRMCM" varies fuel flow rate since flue flow rate is stoichiometrically related to the amount of O_2 separated in ITM to ensure complete combustion.

As the mass flow rate of "AIRMCM" increases, the amount of oxygen separated by a fixed size ITM also increases. This corresponds to an increase in fuel flow rate and greater compressor power (decrease in efficiency). At the same time, the power output from the turbine increases (increase in efficiency). The combination of these opposing effects provides scope for optimization.

As the mass flow rate of "AIRREST" increases, the compressor power and flow rate through the turbine increase, thus increasing the power output from gas turbine "GT". At the same time, increase in "AIRREST" flow rate, keeping the "B10" split fraction constant, decreases the input temperature to the turbine, which decreases the output power. A similar effect is seen for the variation of the "B10" split fraction. For fixed "AIRREST" flow rate, increased direct flow through the gas turbine results in lower gas turbine "GT" inlet temperatures. However, this results in smaller flow rates through "BHEX" and thus, the maximum energy in the heat exchanger is not extracted. When the flow to the heat exchanger is large, the air inlet flow temperature to the gas turbine decreases. The interplay of these effects emphasizes the importance of optimization.

As aforementioned, it is advantageous to extract the maximum possible power from the gas turbine and transport less thermal energy to the bottoming cycle. Therefore, the air outlet temperature from the heat exchanger "BHEX" must be the maximum possible, while satisfying the minimum pinch. Fixing the pinch which occurs at the hot end to 10 K, for inlet temperature of combustion products 1473.15 K, the outlet temperature of air must be 1463.15 K. However, it is seen that as air flow rate through the heat exchanger "BHEX" is increased, air outlet temperature begins to decrease after a point. Though larger air-flow through "BHEX" is expected to produce more power in gas turbine "GT", other deteriorative factors such as a higher air compression power required, and lower air outlet temperature in "BHEX" also come into play. It is seen from the optimization results of Table 1, the local optimum occurs at lower flow rates, with maximum possible air outlet temperature from "BHEX".

The amount of "GT" turbine blade cooling required is chosen according to performance maps [11 Chart 5.16] and is specified as an optimization constraint. Performance maps specify the amount of cooling air required based on the turbine inlet temperature. As the optimizer searches for a local optimum, the turbine inlet temperature varies. Therefore, a constraint is added to meet the turbine blade cooling requirements. The average of the lower and upper limit of this range is chosen for our optimization studies.

Based on the performance map:

For faster convergence of the ASPEN Plus® optimizer, the design specifications of the topping cycle have been implemented as optimization constraints. The split fractions of "B6" and "B3", which are treated as design specification variables earlier, are now treated as optimization variables. This means, in addition to the actual optimization constraints, design specifications also become optimization constraints, and in the process, design specification variables now become optimization variables. The minimum approach temperature for "BHEX" is also treated as an optimization variable.

Table 1. Results of Optimization of Topping cycle

Variables	*Units*	*Before Optimization*	*After Optimization*
Molar flow rate of AIRREST	kmol/s	5.665	9.28
Molar flow rate of AIRMCM	kmol/s	37.335	49.18
Split fraction of B6 (BLDPROP)		0.1267	0.1189
Split fraction of B10 (Stream 2)		0.73	0.7169
Air outlet temperature from BHEX	K	1463.15	1463.15
ITM ΔP feed/permeate (%)		1.1/0.6	1.5/0.9
ITM Recovery ratio		29.1	30.51
Efficiency		25.33 %	26.07%

As seen from Table 1, the mass flow rates of both "AIRMCM" and "AIRREST" have decreased. This implies lesser oxygen separation across the ITM and lower fuel intake. Split fractions of "B6" vary to attain minimum approach temperature in heat exchanger "LHEX" without any temperature crossover in the heat exchanger network "LHEX-ITM-HHEX" (implemented as one of the constraints). The air outlet temperature of "BHEX" does not change as 1463.15 K is the maximum temperature of air that can be reached for the specified minimum approach temperature of "BHEX". The first law efficiency, which is defined as the ratio of power output to the product of heating value of the fuel and the fuel flow rate, increases by 0.74 percentage points (from 25.33 % to 26.07 %) as a result of the optimization.

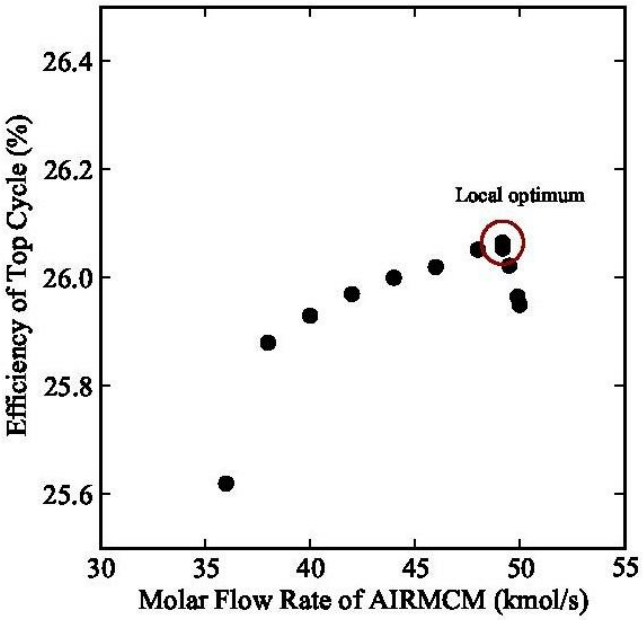

Fig. 4. Variation of efficiency with air mass flow rate through "LHEX"

Fig. 4 shows the effect of varying the air flow rate through the heat exchanger "LHEX" on the efficiency of the topping cycle, while the topping cycle is optimized by changing the other variables with the solution of the previous run as the initial guess value for the present run. Clearly, in the range 30 - 55 kmol/sec, only one local optimum exits and hence the point that has been reported has the maximum efficiency, although this does not prove that it is the global optimum. Thus global optimization is capable of improving the cycle efficiency even higher.

3.4.2. Optimization of Bottoming Cycle

The bottoming cycle is a triple pressure HRSG. The input specifications of the streams "GTEHX" and "PRODBOTM" are specified using the results obtained from the optimized top cycle, and the bottoming cycle is then independently optimized.

The variables considered for optimization of the bottoming cycle include the three pressure levels, the discharge pressure of the turbine and the condenser pump, and the split fraction of the three splitters. Lowering the temperature of stream "EXHEXIT" which leaves the heat exchanger "ECON" and increasing the temperature of streams "HPSTM" and "IPSTM" which exits the heat exchanger "HPSP" increases the efficiency as the heat input to the bottoming cycle increases. Thus, the outlet temperature of the heat exchangers "ECON" (stream "EXHEXIT") and "HPSP" (streams "HPSTM" and "IPSTM") are increased and decreased respectively, to the maximum possible extent such that there are no temperature crossovers in any of the heat exchangers. At the optimal point, the pinch value for heat exchangers "ECON" and "HPSP" are observed to be 4.8 K and 4.4 K respectively. This can be done only for the AZEP 100 as "GTEXH" is pure air without any CO_2 emissions. This is not true in the case of partial emission cycles. For partial emission cycles, there is a limit on "ECON" outlet temperature since low temperatures can cause acid condensations.

The discharge pressure of "LASTST" is fixed to be equal to the saturation pressure for an atmospheric temperature which is assumed to be 25 °C.

Unlike the topping cycle, implementing design specifications as constraints does not work well for the bottoming cycle. It is found that implementing design specifications and optimization constraints separately for the bottoming cycle makes the optimizer convergence easy. The optimization constraints include vapor quality of the outlet stream from the de-aerator be equal to zero and the inlet pressure of the valve "B27" be greater than its outlet pressure.

Table 2. Results of Optimization of Bottoming cycle

Variables	*Units*	*Before Optimization*	*After Optimization*
Outlet pressure of HPPMP	bar	100	104.9
Outlet pressure of IPPMP	bar	25	24.5
Outlet pressure of LPPMP	bar	5	8.6
Discharge pressure of LPST	bar	0.3	0.33
Outlet pressure of CONDPUMP	bar	0.2	0.29
Split fraction of B29 (LPFW)		0.1663	0.2025
Split fraction of B29 (LPIPFW)		0.083	0.060
Split fraction of B14 (Stream 30)		0.3	0.2
Split fraction of B25 (Stream 33)		0.95	0.94
Outlet Temperature of air from ECON	K	400.4	381.15
Outlet Temperature of HPSTM from HPSP	K	460	501
Outlet Temperature of IPSTM from HPSP	K	460	485
Efficiency		23.47 %	25.65 %

Optimization of the bottoming cycle increases its efficiency (bottoming cycle efficiency is defined as the ratio of power output from the bottoming cycle to the product of fuel flow rate and heating value) from 23.47 % to 25.65 % - an increase of 2.18 percentage points. The total efficiency of the power plant thus increases by 2.92 percentage points. This is a significant improvement in the efficiency, which plays an important role in determining the feasibility of AZEP cycles, see also the discussion in the next section. A summary of results from the optimization of the topping and bottoming cycles is shown in Table 3.

Table 3. Summary of Optimization of Top and Bottoming cycle

Efficiency	*Before Optimization*	*After Optimization*	*Increment in Percentage points*
Top cycle	25.33 %	26.07 %	0.74
Bottoming cycle	23.47 %	25.65 %	2.18
Entire power plant	48.8 %	51.72 %	2.92

4. Conclusion

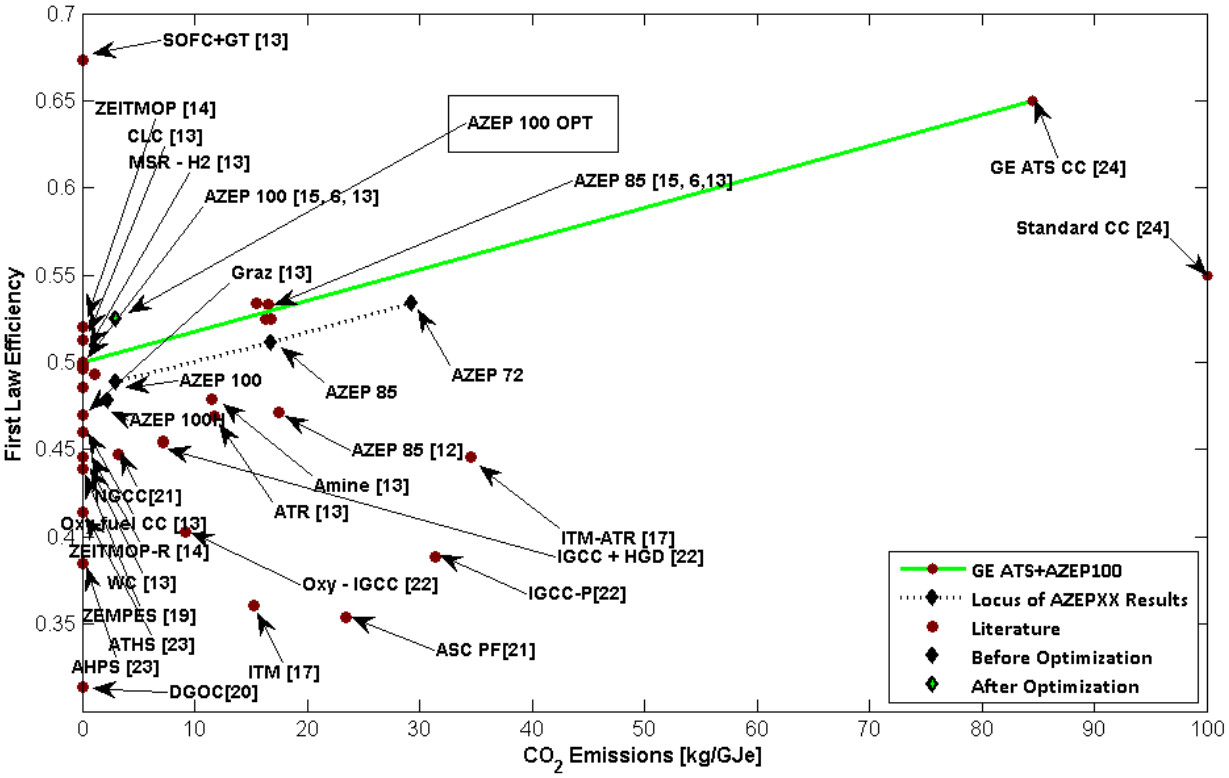

Fig. 5. Partial Emission ITM cycle analysis

Reference [10] gives a detailed analysis of partial emission cycles along with a new metric (see Fig. 5) which compares plants at the fleet level. Different variations of partial emission ITM cycles have been proposed to increase the efficiency. Improving the efficiency of a partial emission cycle by a small fraction is not very useful if the CO_2 emissions simultaneously increase by a large amount. Fig. 5 shows the first law efficiency and specific CO_2 emissions for different cycles which have been studied in the literature [6, 12-24]. Theoretically it is possible to get 100% CO_2 separation for AZEP 100 cycle with large number of compression and cooling stages in the CO_2 compression and purification unit, but this involves unreasonable capital costs. Therefore, practically, CO_2 compression and purification units are not 100% efficient as seen in Fig. 5, which shows a small CO_2 emission for the AZEP 100 cycle simulation result. A linear combination of the AZEP 100 and a combined cycle is also shown for comparison. In Fig. 5, AZEP 100 cycles from literature assume 100% CO_2 separation and hence have zero CO_2 emissions .The black dotted line represents the stipulated locus of partial emission cycles from AZEP 100 to AZEP 72 [10]. The green solid line represents the linear combination of a zero emission cycle and a combined cycle with an efficiency of 65 %. The green line shows the efficiency and the specific CO_2 emission for different combinations of the AZEP 100 and the best efficiency reported for a combined cycle without carbon capture. For the partial emission cycle to be feasible, it should have better efficiency than the combination of an AZEP 100 and a combined cycle for the same specific CO_2 emission [10]. This implies that for the partial emission cycles to be considered feasible, they must lie above the green line, which is not the case for virtually all partial emission cycles proposed. As can be seen from Fig. 5, after optimization the AZEP 100 cycle lies above the green line. This means after optimization the AZEP 100 cycle which nominally has complete capture (zero CO_2 emission) is viable even after the imperfections of the CO_2-H_2O separation is accounted for this cycle, but not for the literature results. Note that fuel-cell based processes can achieve substantially higher performance, but require completely different technology. The improvements obtained for the nominally zero emissions cycle herein, suggest that optimization of partial emission cycles may increase their efficiency to a significant extent and make them viable.

Acknowledgments

The authors would like to thank the King Fahd University of Petroleum and Minerals (KFUPM) in Dhahran, Saudi Arabia, for funding the research reported in this article through the Center for Clean Water and Energy at Massachusetts Institute of Technology (MIT) and KFUPM under project R2-CE-08.

References

[1] I.E.A., CO_2 emissions from fuel combustion, IEA Statistics, 2011.

[2] Steenveldt R., Berger B, Torp T., CO_2 capture and storage: closing the knowing-doing gap. Chemical Engineering Research and Design 2006;84(9):739-63.

[3] Wall TF., Combustion processes for carbon capture. Proceedings of the Combustion Institute 2007;31(1):31-47.

[4] Pfaff I., Kather A., Comparative thermodynamic analysis and integration issues of CCS steam power plants based on oxy-combustion with cryogenic or membrane based air separation. Energy Procedia 2009;1(1):495e502.

[5] Gellings PJ., Bouwmeester HM., The CRC handbook of solid state electrochemistry. CRC Press; 1997. Ch. 14, pp. 16-30.

[6] Sundhvist S., Julsrud S., Viegeland B., Naas T., Budd M., Winkler D., Development and testing of AZEP reactor components. In proceedings of International Journal of Greenhouse Gas Control, 2007,1,180 -187.

[7] Mancini ND., Mitsos A., Ion transport membrane reactors for oxy-combustion-Part I: intermediate fidelity modeling. Energy 2011;36(8):4701-20

[8] Mancini ND., Mitsos A., Ion transport membrane reactors for oxy-combustion-Part II: analysis and comparison of alternatives. Energy 2011;36(8):4721-39

[9] Numerica Technology, JACOBIAN Modeling and Optimization Software – Available at: <http://www.numercatech.com > [accessed 8.01.2009].

[10] Mancini ND, Mitsos A., Conceptual design and analysis of ITM oxy-combustion power cycles. Phys. Chem. Chem. Phys., 2011, 13, 21351-21361

[11] P. P. Walsh, P. Fletcher, Gas turbine performance, Blackwell Science, Malden Mass., 2004

[12] Colombo, K.E., Bolland, O., Kharton, V.V., Stiller, C., Simulation of an oxygen membrane based combined cycle power plant: Part-load operation with operational and material constraints, Energy and Environmental Science 2009, 2 (12), pp. 1310-1324.

[13] Kvamsdal H., Jordal K., Bolland O., A quantitative comparison of gas turbine cycles with CO_2 capture Energy, 2007, 32, 10–24.

[14] Liu S., Gavalas GR., Membr J., Oxygen selective ceramic hollow fiber membrane. Journal of Menbrane Science., 2005, 246, 103–108.

[15] Anantharaman R., Bolland O., Asen K., Novel cycles for power generation with CO_2 capture using OMCM technology. Energy Procedia, 2009, 1, 335-342.

[16] Yantovski E., Gorski J., Smyth B., J. Elshof., Zero-emission fuel-fired power plants with ion transport membrane. Energy, 2004, 29, 2077-2088.

[17] Fiaschi D., Gamberi F., Bartlett M., Griffin T., The air membrane -ATR integrated gas turbine power cycle: A method for producing electricity with low CO_2 emissions. Energy Conversation and Management, 2005, 46, 2514-2529.

[18] Pfaff I and Kathe A., Comparative thermodynamic analysis and integration issues of CCS steam power plants based on oxy-combustion with cryogenic or membrane based air separation. Energy Procedia, 2009, 1, 495–502.

[19] Yantovski E., Shokotov M., Shokotov V., McGovern J., Kirsten Foy., Elaboration of Zero Emissions Membrane Piston Engine System (ZEMPES) for Propane Fuelling. Proceedings of Fourth Annual Conference on Carbon Capture and Sequestration DOE/NETL; 2005, May 2-5.

[20] Walker ME., Abbasian J., Chmielewski DJ., Castaldi MJ., Dry Gasification Oxy-combustion Power cycle. Energy Fuels 2011, 25, 2258-2266.

[21] Dillon DJ., Panesar RS., Wall RA., Allam RJ., WhiteV., Gibbins J., Haines MR., Oxy-combustion processes for CO_2 capture from advanced supercritical PF and NGCC plant. Proceedings of seventh conference on greenhouse gas control technologies (CHGT-7), Vancouver, BC, Canada, 2004

[22] Lozza G., Romano M., Giuffrida A., Thermodynamic Performance of IGCC with Oxy-Combustion CO_2 capture. In proceedings of First International Conference on Sustainable Fossil Fuels for Future Energy - S4FE 2009.

[23] Gou C., Cai R., Hong Hui., A novel hybrid oxy-fuel power cycle utilizing solar thermal energy. Energy 32 (2007) 1707-1714

[24] Tan. X., Wang Z., Meng B., Meng X., Li K., Pilot-scale production of oxygen from air using perovskite hollow fiber membranes. J. Membr. Sci., 2010, 352, 189-196

[25] Bertsekas DP., Nonlinear Programming. Athena Scientific; 1999.

[26] Petrakopoulou F., Tsatsaronis G., Morosuk T., Exergoeconomic Analysis of an Advanced Zero Emission Plant. Journal of Engineering for Gas Turbines and Power , 2011, 133, 113001-12

Implementation of a CCS technology: the ZECOMIX experimental platform

Calabrò Antonio[a], Cassani Stefano[a], Pagliari Leandro[a]
Stendardo Stefano[a]

[a] ENEA, Italian National Agency for New Technologies, Energy, and the Sustainable Economic Development Via Anguillarese, 301, S. Maria di Galeria, 00123, Rome, Italy

Abstract:

One of the key challenges for the implementation of CO2 Capture and Storage (CCS) is the reduction of the CO2 capture costs derived by their applications in actual power plants. The research of new technologies based on more efficient materials and more efficient design for integration of CO2 capture technologies in power cycles, is a promising way to ensure, in the medium term, costs and energy performances comparable to the actual power plant without CCS. ZECOMIX experimental platform represents the ENEA proposal for this challenge and it can be count among the Research Infrastructures more innovative in Europe. The aim of this work is to present the first results of commissioning plant tests. Therefore this work is focused on the planning of future experimental activities in order to demonstrate the feasibility of the high temperature solid sorbent CO2 sorption process, applied to a syngas derived from coal gasification.

Keywords:

Keywords: Ca-based sorbent, carbon capture, solid chemical looping, gasification.

1. Introduction

In July 2005 the activities of the project ZECOMIX (Zero Emission Coal Mixed Technology) started officially, within the framework of a program funded by the Italian University and Research Minister. The main aim of the project is to demonstrate, through a series of modelling and experimental activities, the feasibility of a new innovative process for production of electricity and hydrogen "zero emission" by coal. In the ZECOMIX project different processes (e.g. coal gasification, clean-up of syngas, capture and sequestration of CO_2, combustion of hydrogen in gas turbine) have been coupled. The integration of these processes is the key factor to achieve higher cycle performance and optimization (fig.1) of the platform at hand. Preliminary studies on high temperature decarbonization syngas [1-3] and thermodynamic H_2/O_2 cycle [4,5] as led us to propose ZECOMIX cycle with a net electrical efficiency close to 50% [6]. The analysis was subsequently refined with the cooperation of major Italian Universities and Research Institutes, and the results have fully confirmed the encouraging prospects that the cycle had announced: at least ten-point performance higher than a current post-combustion capture technology coal plant [4,5]. The design and realization of a complex experimental platform to test new process for CO_2 capture and hydrogen production was certainly the more challenging tasks from a technical and financial point of view. A large numbers of advanced research issues is related to the proposed platform (coal hydro-gasification, simultaneous high temperature CO_2 and H_2S capture with solid sorbents, hydrogen/steam fuelled micro-turbine). Preliminary studies have permitted us the commencement of several research lines in the fields of advanced system modelling [2,6] for testing coal gasification, and the study of materials for CO_2 capturing [1-2]. On the other hand the great know-how gained with years allows us to enter with a leading role in the most important European scientific organizations, in order to coordinate the research on CCS technologies considered the most promising option for sustainable use of fossil fuels in the near future. The experimental ZECOMIX pilot plant has been designed and constructed to test each single unit integrated in the platform. It is an advanced and flexible facility particularly oriented to the experimental

investigation and the developing of process and component modeling. The plant has been presented in an international framework (e.g. CSLF, ZEP, ECCSEL, EERA) and consistent with advanced technological initiatives of the European and worldwide scientific community. Moreover ZECOMIX plant has been evaluated and inserted in the first Italian Roadmap towards the Large research Facilities conceived by the Ministry of Research.

2. Conceptual description of the ZECOMIX platform

Details of the ZECOMIX concept are presented in [6] whereas alternative configurations are proposed in [4,5] . In Fig 1(a) we have reported the main areas of the platform and how they are connected each other; in Fig 1(b) the layout of the platform constructed is showed. This work highlights our efforts in the realisation of the plant layout showed in Fig 1(b). The plant (see Fig 2(a)) can be broken into :

- Unit based on a 50 kg/h coal fluidised bed;
- Syngas decarbonising reactor. It has been conceived as a fluidised bed and designed in order to decarbonise 100 Nm3/h of coal syngas leaving the gasifier or a gaseous mixture produced by means adequate cylinders;
- 100 kWe micro-turbine modified to accommodate a mixture of H_2 and H_2O.

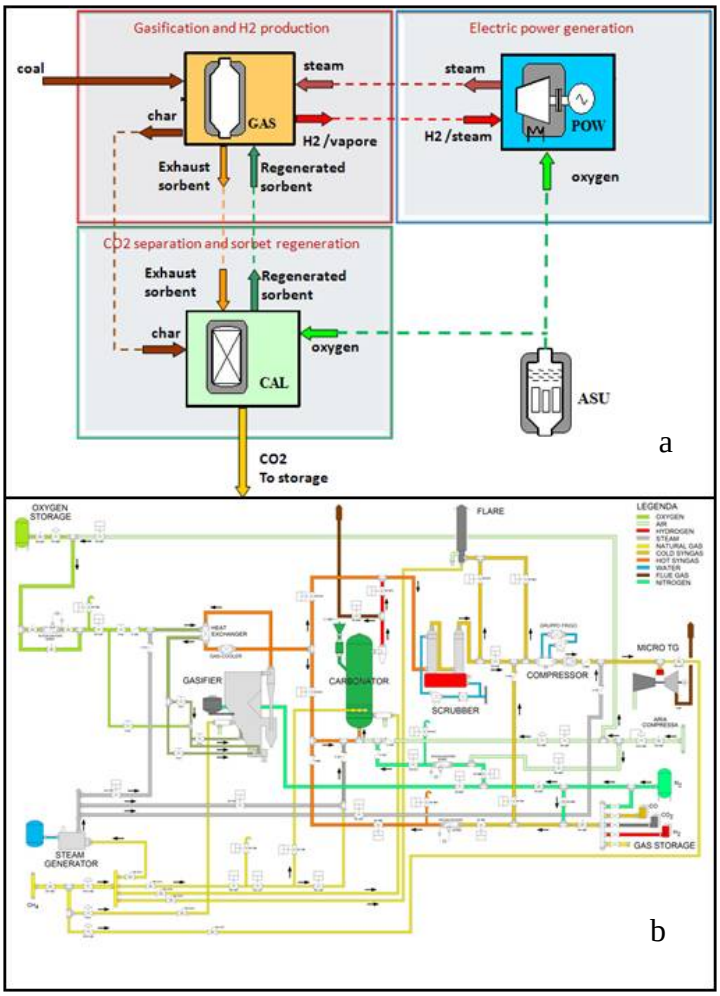

Fig. 1. (a) Simplified schematic of the ZECOMIX concept; (b) Layout of the ZECOMIX platform.

A number of devices are installed to further treat the syngas (e.g. scrubbing, drying and compression) to make it suitable as fuel for the micro-turbine. Moreover a steam generator has been

envisaged for operating the gasifier, the carbonator and the micro-turbine as well. The plant has been designed to test several experimental configurations:

- Gasification test: the yielded syngas is diverted directly to the scrubbing device and then to the flare stack;
- Carbonator test: the syngas is produced by mixing pure gases leaving bottles. This test allows us to investigate the decarbonising process over a number of syngases or flue gases; the inlet temperature of the syngas could be set up to 600 °C by means an adequate electric heater;
- Micro-turbine test: in this test the turbine is fuelled with the syngas produced at the mixing unit;
- Base-case test: such a test is carried out with the syngas produced by means of the gasifier and driven to the carbonator. Having completed the decarbonising process the syngas undergoes a scrubbing process and fed the micro-turbine or burnt in the flare stack. When the micro-turbine runs the syngas is compressed up to 6 bar by means of a compressing device and an amount of water steam is injected into the micro-turbine's combustion chamber to moderate operating temperature. Such a device has been already tested by the Italian company "Ansaldo Ricerche" retrofitting an existing micro-turbine named Turbec T100;
- Regeneration test: in this configuration the carbonator operates in regeneration mode firing by a number of adequate burners placed at the bottom of the reaction chamber to heat the sorbent up to the regeneration temperature.

The layout of experimental configuration and the control of the whole plant is carried on by a particular Distributed Control System (DSC) interfaced software through several synoptic schemes with regard to the plant configuration (Fig 2(b)).

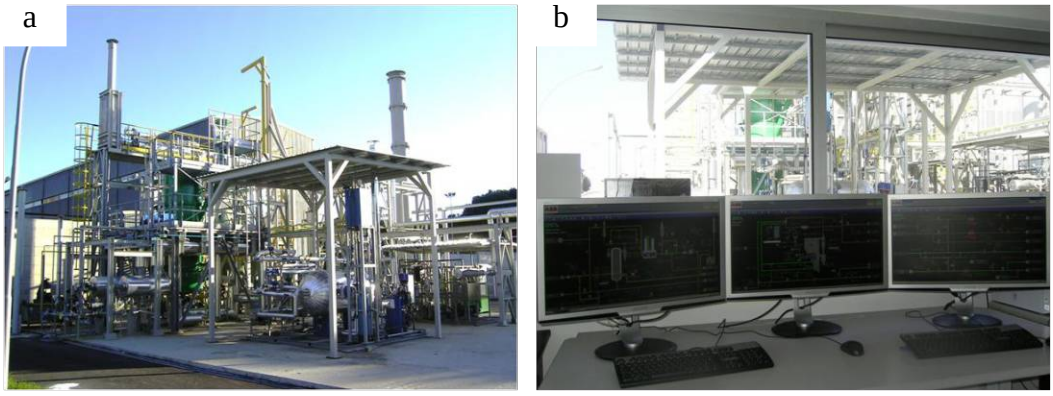

Fig. 2. (a) Picture of the ZECOMIX platform; (b) Control station of the platform.

3. General description of the platform main components.

The detailed design of the plant started in early 2007 and it was realized with the help of Ansaldo Energy, and the first supply contracts were launched in April 2008. Civil infrastructures are composed of plant foundations, storage for solid material (dolomite, catalyst and coal), security bunker for H_2 and CO gas cylinders, platforms of CO_2, N_2 and O_2 gas tanks, and the basement of gas mixing station. Moreover, a control room building has been realized which includes the electrical cabinets of main equipments and the DCS. Simultaneously to the progress of civil works, the order of main equipments of the plant were carried out: carbonation reactor, fluidized bed gasifier, steam generator, syngas compressor, gas pre-heaters, gas clean up scrubber, flare stack, and, a micro-turbine adapted to high content hydrogen syngas.

Gasifier: Hydrogasification reactor as presented in [6] operates at pressure up to 60 bar, incompatible with the project design atmospheric pressure; thus, it has been replaced by an oxygen/steam atmospheric gasifier, more robust and flexible than hydro-gasification reactor (see Fig 3(a)). The coal gasifier is a fluidized bubbling bed reactor designed in collaboration with

University of L'Aquila and Germanà&Co. Engineering. The coal feed system has been design in order to feed a nominal load of 50 kg/h of coal. The system is formed by a 2 m^3 coal silo, which permits a stationary operation up to 36 hours, and two worm drives: a dosage worm drive in order to control the coal mass flow, and a second one to introduce mechanically the coal to the interior of gasifier. Steam and oxygen are feed on different points of the reactor, in order to control the solids hydrodynamics, and the reaction rate all over the reactor. Dolomite is added to the coal enhancing the fluidization, controlling temperature and capturing the H_2S formed in the coal gasification. A syngas composed of H_2, CO, CO_2 and steam at temperature of 800°C is obtained. This syngas is sent to a regenerative heat exchanger reducing its temperature around 600°C. After this point can be introduced into the carbonation reactor, or can be clean-up in a scrubber, after a second cooling step to 350°C. Methane is mixed with the yielded syngas in order to emulate syngas composition of a syngas leaving hydro-gasification reactor. Moreover water is injected into this gaseous mixture in order to carry on steam methane reforming and CO-shift reactions

Carbonator: The carbonation reactor is a cylinder with 1 m diameter and 4.5 m height cylindrical chamber (Fig. 3(b)). Reactor wall have 30 cm thickness and two layers refractory enclosure. At the bottom of the reactor there are two burners in order to calcine the sorbent in the regeneration phase at 900 °C. The distributor gas plate is situated above the burners and realized as a series of tubes placed perpendicularly to the orifices in order to broke the gas jets producing a quasi-homogenous velocity field. Moreover, this design allows us to reduce the attrition of nozzles and particles, and prevent the clogging of the particles in the orifice. The fluidized bed reactor is loaded with Ni-based catalyst, necessary for the steam methane reforming, and Ca-based sorbent in order to capture CO_2. The addition of the sorbents serves to decarbonize the flue gas and to enhanced the steam methane reforming. This process is called Sorption Enhanced-Steam Methane Reforming and allows us to obtain a very high hydrogen content syngas, improving the methane conversion at relatively low temperatures (550-600°C). When the solid sorbent reaches at its ultimate conversion it is sent back to the regeneration step. Regeneration is done by means of oxy-combustion of methane in order to calcine the spent sorbent. High-concentrated CO_2 stream is released and sent to final disposal. Subsequently, a cooling process is accomplished in order to return to initial carbonation condition starting another CO_2 capture cycle.

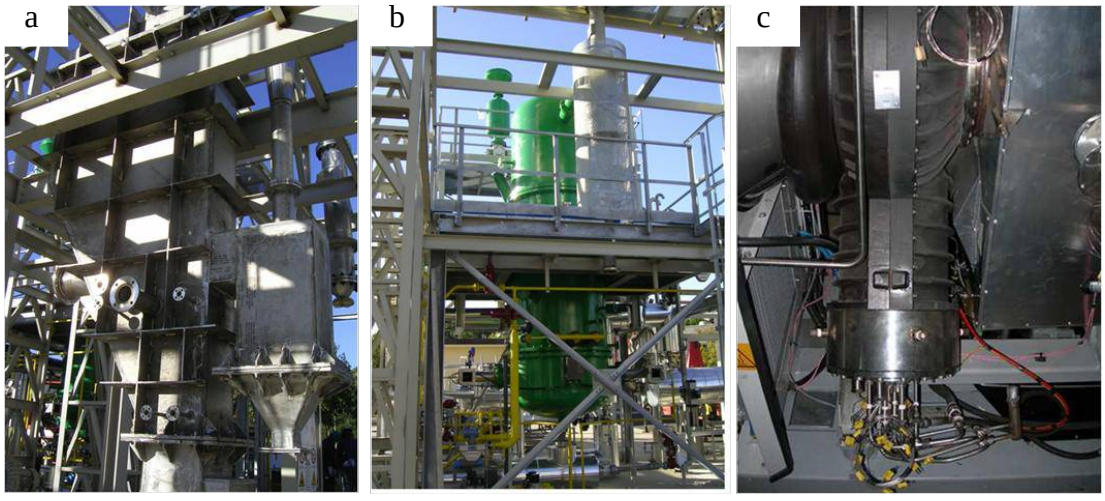

Fig. 3. (a) Fluidised bed gasifier; (b) Carbonator; (c) Turbec T100 micro-turbine with the modified burner.

Micro-turbine and syngas scrubbing unit: The power generation is produced by means a micro-turbine adapted to high content hydrogen syngas (Fig. 3(c)). Original turbine is a Turbec T100, with 100 kWe of power output, retrofitting with a hydrogen burner ARI100T2 developed by Ansaldo Energy. Flue gas in the turbine outlet are mainly nitrogen and steam, achieving the " carbon zero

emission" scope of the cycle. Micro-turbine is very sensible to the impurities. Then syngas scrubbing unit is fitted upstream the micro-turbine. Therefore, the scrubber is able to treat 400 Nm3/h in three stages: a Venturi scrubber, a spray tower wet scrubber, and a packed tower wet scrubber. The outlet particle diameter is lower than 1 ●m. The flare stack has been designed to the correct combustion of syngas from carbonator reactor or gasifier.

Steam generator: The steam generator have 200kWt power output, and it is provided with an accumulator which permits a high flexibility mass flow production as a function of the configuration tests. It is possible to obtain three different mass flows at different pressure for every equipment: 30 kg/h at 1 atm for the coal gasification, 90 kg/h at 1 atm to the carbonatator, and 60 kg/h at 6 bar to the micro-turbine.

Syngas compressor: The syngas compressor has three intercool centrifugal stages in order to maintain hydrogen under 130°C and water is drained. Then hydrogen stream is pre-heated and mixed with steam to the turbine conditions.

Heaters: Three heaters are installed in the platform. An oxygen heater has been fitted in order to prevent condensation of water in the oxygen/steam mix. A nitrogen heater is needed to control the temperature in the heating/cooling processes in carbonation reactor between carbonation/calcination reactions. A heater of the syngas entering the carbonator is installed. Such a component is needed when synthetic gas is produced in the mixing station and send to the carbonator. In this case the syngas has to be heated from environmental temperature up to the carbonation temperature (600 °C).

The platform is being commissioning. Several tests has been carried out in order to prove DCS system, steam generator, hydrogen compressor, pre-heater and flare. The main objectives which have been accomplished are mainly related to coal gasification, high temperature CO_2 capture by means of solid sorbents, fluidynamics of bubbling bed, combustion of hydrogen.

4. Future activities in the framework of the ZECOMIX project

In order to supply the experimental platform with a number of solid fuels (e.g. biomass and a blend of coal) a feeding system as flexible as possible is envisaged. Such a technological option will permit us to study the performances of the hydrogen production from solid fuels by varying the ratio of the different blends. Particularly the co-gasification of coal and biomass could be experienced and the main parameters affecting such a process will be studied. Such an experimental investigation will give information on how to mix coal and biomass and how the quality of the feedstock affects the production of electricity from hydrogen. Implementation of new sensors and probes (thermocouples and flux-meters) are envisaged. This improvement will permit us to increase the potential of the acquisition system and then the remote control of the process at hand with on-line monitoring and dynamic measurement. Particularly during the warm up of decarbonisation reactor the control of the refractory temperature is needed in order to know the evolution of the temperature profile into the refractory wall of the reactor and the characteristic time for heating up the reactor. In order to manage the energetic system at hand in an economically viable way, optimization of hydrogen and electricity production should be taken into account. These outputs of the experimental platform strongly depend on the correct blend of both feedstock and energy inputs (e.g quality and quantity of the solid fuel to be gasified and heat demand of calciner for sorbent regeneration as well). There is a lack of dependable economic and operative parameters, due to the intrinsic novelty of the proposed process. A valuable tool for addressing such a problem could be modeling each single main component (gasifier, carbonator, micro-turbine) to simulate and optimize ZECOMIX system. When thermo-economic constraints are included the optimization problem will increase significantly. Moreover if the number of variables governing the hydrogen and power production is relatively low an adequate and accurate DoE (design of experiment) is suggested as a valuable tool to determine how the main parameters affect the electricity production. Finally, the activities scheduled for the power unit at hand have been proposed in order to test the

hydrogen combustion technology at different scale levels and grades of integration with the whole experimental platform. In particular a dynamic model of the micro-turbine has been developed and integrated in a commercial power plant simulator. Such a model is a valuable tool for the simulation of a the micro-turbine in a number of operative conditions. Numerical simulation are needed to estimate the dynamic behavior of the power unit when the fuel supply switches from natural gas to hydrogen during full and half load as well. The experimental programmed activities have been enthusiastically welcomed by a number of European projects and research alliances to promote the co-operation between researchers. ZECOMIX project is involved in the ECCSEL initiative in the framework of CCS research facilities to share knowledge through network of researchers with the common interest to improve the assessment methodology for decarbonised energy production. Moreover the platform is involved in the EERA sub-programme for developing a methodology and comparing process performances in the field of CO_2 capture.A complete schedule of activities has been planned are:

1. hot tests on carbonator in order to study heat transfer in the gas-particle-wall system and start-up procedure. Modeling activities are planned to predict the thermal behavior of the carbonator reactor. Start-up of H_2 micro-turbine will be performed as well.
2. tests of SE-SMR reactor fed with synthetic syngas from cylinders. Performance of CO_2 capture sorbents and catalyst. Study of instabilities in the process between calcination and carbonation phase. Integration with micro-turbine. Optimizing of operational conditions.
3. carbonation/calcination cycling with gasification integration. Studies of influence of gasification on flue gas composition. Effect of gasification on hydrogen production. Optimization of the process. Study of loss efficiency due to clean-up of gases.

Acknowledgment

The authors are grateful to Prof. Pier Ugo Foscolo and Prof. Antonino Germanà, of University of L'Aquila, for carbonator and gasifier design, and SO.IM.I. company for constructing the experimental platform.

References

[1] Stendardo S., Calabrò A., Experiments on CaO–CaCO3 loop for high temperature CO_2 capture. ENEA Technical Report 2008 No.: EHE08039 TER-ENEIMP.

[2] Stendardo S., Foscolo P.U., Carbon dioxide capture with dolomite: A model for gas–solid reaction within the grains of a particulate sorbent. Chem Eng Science 2009;64:2343-2352.

[3] Stendardo S., Di Felice L., Gallucci K., Foscolo P.U., CO_2 capture with calcined dolomite: the effect of sorbent particle size. Biomass Conv and Biorefinery 2011;1(3):149-161.

[4] Galeno G., Spazzafumo G., ZECOMIX: Performance of alternative layouts. International Journal of Hydrogen Energy 2010;35:9845-9850.

[5] Romano MC, Lozza G. 2010. Long-term coal gasification-based power plants with near-zero emissions. Part A: Zecomix cycle. Int Journal of Greenhouse Gas Control 2010;4:459-468.

[6] Calabrò A., Deiana P., Fiorini P., Girardi G., Stendardo S., Possible optimal configurations for the ZECOMIX high efficiency zero emission hydrogen and power plant. Energy 2008;33:952-962.

Influence of regeneration condition on cyclic CO_2 capture using pre-treated dispersed CaO as high temperature sorbent

Stendardo Stefano[a], Calabrò Antonio[a]

[a] ENEA, Italian National Agency for New Technologies, Energy, and the Sustainable Economic Development Via Anguillarese, 301, S. Maria di Galeria, 00123, Rome, Italy

Abstract:

In this experimental investigation the effect of calcination temperature and atmosphere composition on CO_2 uptake of a solid sorbent have been analysed. The sorbent were synthesized by means of a CaO hydrolysis technique to generate sorbents with 75% and 85% of active phase CaO. The material at hand also contains a calcium aluminate phase acting as a binder of the active phase. Pre-treatment was accomplished in a thermo-gravimetric analyser (TGA) exposed in an atmosphere of 86% N_2 and 14% CO_2 under 600 °C. The as-synthesised sorbent and the pre-treated sorbent have been characterised by scanning electron microscope, nitrogen physic-sorption tests, and multi-cycling carbonation-calcination test in TGA (160 cycles). Here, the CO_2 uptake took place at programmed temperature (600 °C) with three different regeneration condition tested:

a) mild condition: regeneration under 900 °C with 14% CO_2 and 86 % N_2;

b)moderately severe condition: regeneration under 1000 °C with 14% CO_2 and 86 % N_2;

c) severe condition: regeneration under 1000 °C with 86% CO_2 and 14 % N_2.

The experimental results show significant improvement in the stability of the CO_2 uptake capacity over multiple cycles when comparing the synthetic sorbents to natural dolomite. For an instance, the 75% CaO synthetic sorbent shows a good reversibility for the CO_2 uptake (0.13 g-CO_2/g-sor) up to 150th cycle under severe condition.

Keywords:

Keywords: solid sorbent, carbon capture, carbonate chemical looping, self-reactivation.

1. Introduction

Carbon capture technologies are expected to be a promising route to meet the objective of a low carbon electricity production and the increasing of coal foreseen by the scientific and industrial community. Hydrogen production from renewable energy sources, coal and biomass is a priority for Italian medium and long term energy policy. Thus, in Italy technologies for CO_2 capture are considered a main topic to be studied and demonstrated, and represent a significant opportunity for industries. In order to promote carbon capture technologies, ENEA has constructed an experimental platform, named ZECOMIX, to investigate both the gasification of coal and the separation of CO_2 from synthetic gas fuel or flue gas. Particularly the decarbonisation of the gaseous stream happens by means of a carbonate looping (CaL) technology with a CaO based solid sorbent. When the CaO is converted to the calcium carbonate, the spent solid sorbent is sent back to the regeneration process where an active sorbent is regenerated for a new carbonate looping. As reported in the scientific literature: [1-4], when naturally occurring material as calcite or dolomite are used as CO_2 acceptor in a CaL, there is a decay of reversibility. The ideal CO_2 sorbent in a CaL should show a number of properties: high and stable CO_2 uptake capacity throughout continuous decarbonising-regeneration cycling, fast reaction kinetics, uptake capacity and kinetics close to theoretical maximum values, and also mechanical stability and sintering resistance. In an attempt to achieve this goal, researchers have developed novel synthetic sorbents based on e.g. CaO dispersed on calcium aluminate ceramic supports. [5]. In this work a number of experimental results on the

reversibility of a pre-treated synthetic solid sorbent are reported. In particular the uptake of CO_2 through a multi-cycling carbonation-regeneration has been evaluated. The main goal of this work is analysing the influence of regeneration of the tailored material on its performance. Recent papers [6-7] have demonstrated that pre-treating dolomite or calcite increases stability and reversibility of the material. However those experimental tests were focused on pre-treating naturally occurring sorbent while material regeneration occurs in 100% nitrogen atmosphere. As the aim of CO_2 capture is obtaining a high-concentrated CO_2 stream, there is a need to investigate the behaviour of solid sorbent when the regeneration step is conducted in presence of carbon dioxide. Then the material at hand was regenerated in high concentration of CO_2 near to realistic condition required for CCS technologies and compared with that regenerated in low concentration of CO_2. Besides the influence of regeneration condition on the subsequently CO_2 uptake, the aim of this work is to see whether the positive effect of heating pre-treatment persists also for the synthetic sorbent presented here.

2. Material and method

2.1. Synthesis of solid sorbent

The synthesis was performed according to [5] where powdered CaO (about 99.8%, after calcination) and aluminum nitrate $Al(NO_3)_3 \cdot 9H_2O$ (> 98%) were used as precursors in the synthesis of the CaO-$Ca_{12}Al_{14}O_{33}$ sorbent. A wet method was used to ensure an intimate mixing of starting materials: Distilled water was used containing 2-propanol as surfactant. CaO was calcined at 900°C for 2 h in the presence of air to remove humidity and decompose any traces of $CaCO_3$ into CaO. The amounts of CaO and aluminium nitrate were chosen such that the mass ratio of CaO to binder phase was 75:25 and 85:15. The compounds were added to the water and the mixture was stirred at 75 °C and 700 rpm. After 60 minutes stirring, the solution was dried at 120 °C for 18 h to obtain a dried cake. In order to form the binder $Ca_{12}Al_{14}O_{33}$ the material was ground and heated up to 850 °C. Before reaching the temperature for $Ca_{12}Al_{14}O_{33}$ formation the sorbent precursor was maintained at 500 °C for 180 minutes to evaporate nitric oxides and produce Al_2O_3 in a controlled mode. After cooling to room temperature the material was ground again in a mortar (at this stage some water could be added) and heated up to 850 °C for 90 minutes in order to react Al_2O_3 with CaO to form $Ca_{12}Al_{14}O_{33}$. The solid-solid reaction to form $Ca_{12}Al_{14}O_{33}$ will require several hours, but the reaction rate can be improved by second grinding of the manufactured material as specific surface area is maintained higher and fresh surface is brought in contact. After having completed the final calcination and the subsequent cooling to the room temperature the sorbent material was grounded and sieved. The powder used in this investigation had particle sizes in the range 180 to 500 μm.

2.2. Characterisation of solid sorbent

A number of experimental investigation at a lab scale have been performing to characterise a synthetic solid sorbent to accomplish the uptake of CO_2 from a gaseous mixture. The reactivity and CO_2 uptake capacity during cycling of the sorbent were analysed by using a GC-10 Mettler-Toledo thermo-gravimetric analyzer (TGA). This apparatus can measure minute mass changes of solid samples placed in a furnace with a variable and well-controlled temperature and gas atmosphere. Blank runs were conducted with an empty crucible to record the disturbances in the mass change readings when moving the experiment from calcinations to carbonation process. To avoid the effect of the sample size on carbonation and regeneration processes, such as the external mass transfer resistance of CO_2 through the sample, a ~2.90 mg samples were used. The experimental protocol used for performing the solid chemical looping consisted of three steps:

1) **Regeneration phase**. This phase is conducted by heating the sample up to a programmed temperature at 100 °C/min rate (maximum heat rate allowed by this experimental apparatus). A mixture of nitrogen and carbon dioxide flows over the sample. During this phase the $CaCO_3$ is

decomposed into CaO. The sample dwells for 15 min at 1000 °C. Three representative regeneration condition were used:

- *Mild condition*: temperature 900 °C, atmosphere composition 14/86 %v (CO_2/ N_2);
- *Moderately severe:* temperature 1000 °C, atmosphere composition 14/86 %v (CO_2/ N_2);
- *Severe:* temperature 1000 °C; atmosphere composition 86/14 %v (CO_2/ N_2);

2) **Cooling and carbonation phase**. The temperature is then lowered with the rate of 100 °C/min to reach 600 °C selected for CO_2 sorption. The atmosphere remains 84% v/v nitrogen and 16% carbon dioxide. When the temperature goes below 700-750 °C the CO_2 begins reacting with CaO to form $CaCO_3$.
3) **Isotherm carbonation phase**. Having completed the cooling phase, the temperature is maintained constant at 600 °C for 20 min exposing the solid specimen to a reacting atmosphere composed of 25 % CO_2 and 75 % N_2.

As reported earlier here, the synthesised material was thermal pretreated to see whether the advantage found for the dolomite and calcite [6-7] persists on the investigated material. Thus solid specimens have been dwelling at 600 °C for 80 minutes, exposing it to a controlled atmosphere composed of 14 % O_2 and 86 %N_2. Then the sample was pre-treated in the TGA and subsequently undergone the multi-cycling regeneration-carbonation process to avoid influences on the investigated specimen (e.g reaction between sample and CO_2 in the room atmosphere). Comparison between as synthesised sorbent and thermal pretreated sorbent are presented in this work. Particularly the capacity to retain carbon was investigated by cycling the material up to 150 cycles.

3. Results and discussion

Fig. 1 (a-b) show conversion-time curves for different numbers of regeneration-carbonation cycles regenerated in moderately severe condition. At the beginning of each single cycle, besides a short nucleation period, a linear kinetically-controlled mass growth was found followed by a transition to a much slower reaction rate. This transition was found to be smoother when compared with that occurred during the carbonation of naturally occurring sorbent investigated in [3]. In other words, no plateau is reached during the last slower phase and the surface reaction continues to play a key role in the whole process. Such a smooth transition was found in [6] where experimental test on CO_2 capture for pre-treated limestone were presented. Moreover, Fig 1(b) shows that with increase in cycle number the initial slope of the conversion-time curves increases from the first to the tenth cycle. The augment of the slope could likely be explained with the migration of the CaO grains from the core of the sorbent particle to the outer. As a consequence more specific calcium oxide surface would be exposed enhancing the reaction between active phase (CaO) and CO_2. The increase of the sample weight with first cycles could likely explained with the phenomenon, named self-reactivation, previously found in [6]. Analogous effect was observed also in the field of chemical looping combustion where a particular O_2-carrier showed a gain in reactivity during reduction/oxidation cycle performed in a thermo gravimetric analyzer. After the 10^{th} cycle the linear growth shows the same slope up to the 80^{th} cycle carbonation-regeneration loop of the experimental test. Moreover After that cycle, as reported in Fig 1(a), TG curves were found to be similar denoting a good reversibility through the multi-cycling CO_2 capture. In addition, Fig 1(a) shows that with the increase of cycling up to 10^{th} carbonation-regeneration step the sample mass achieved after each single loop was increased when compared with the previous loop. In Fig 2 the self-reactivation phenomenon is presented in term of the uptake of CO_2 referred to the initial sample weight. In order to compare the self reactivation of synthetic sorbent to the performance of naturally occurring sorbent, dolomite sample (Bianchi dolomite: 55.6% $CaCO_3$ and 44.2% $MgCO_3$) was selected and exposed to the same condition reported in Fig. 1.

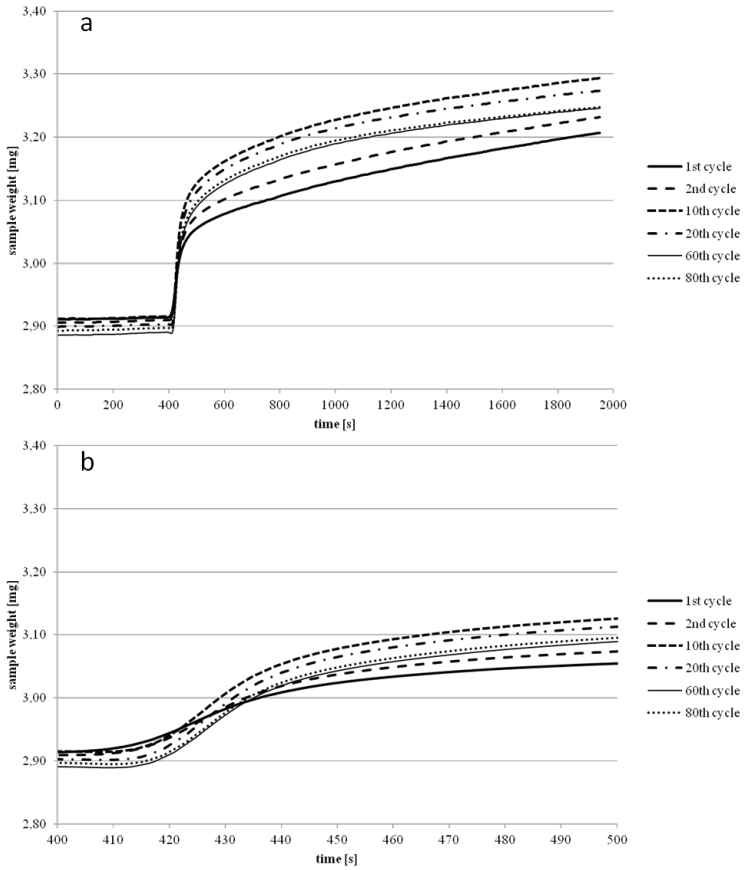

Fig. 1. TG curves collected for specimens subjected to moderately severe regeneration up to 80 cycles: (a) mass growth shows no plateau; (b) self reactivation effect: the slope of initial linear mass growth increases with the number cycle.

In particular, the uptake of the two sorbents for each single cycle was evaluated according to the following ratio:

$$CO_2\ uptake = \Delta m_{Nth} / m_0 \qquad (1)$$

where Δm_{Nth} represents the mass augment of the solid specimen at each the N-th cycle and m_0 represents the weight of the sample inserted in TGA.

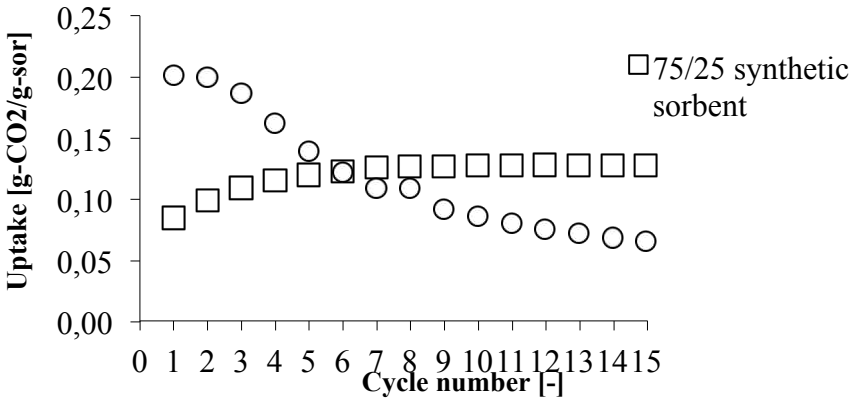

Fig. 2. Comparison between 75 % CaO synthetic sorbent and "Bianchi" dolomite in term of carbon retain capacity.

Even if the dolomite shows a larger uptake when compared to that of synthetic sorbent, a decay in the capacity to retain carbon during the first few cycles was found for Bianchi dolomite whereas the synthetic sorbent shows higher uptake while the material is cycled during CO_2 capture tests. As shown in Fig 3, the self reactivation was observed also for the 85% CaO sorbent. Interestingly, during the first cycles the uptake of CO_2 for the 85% CaO sorbent is greater to that of 75% CaO sorbent because there is more active phase (CaO). But as the cycling runs the pore plugging occurs likely due to the reduced amount (15%) of binder leading to more CaO being less dispersed and thus more inaccessible to CO_2.

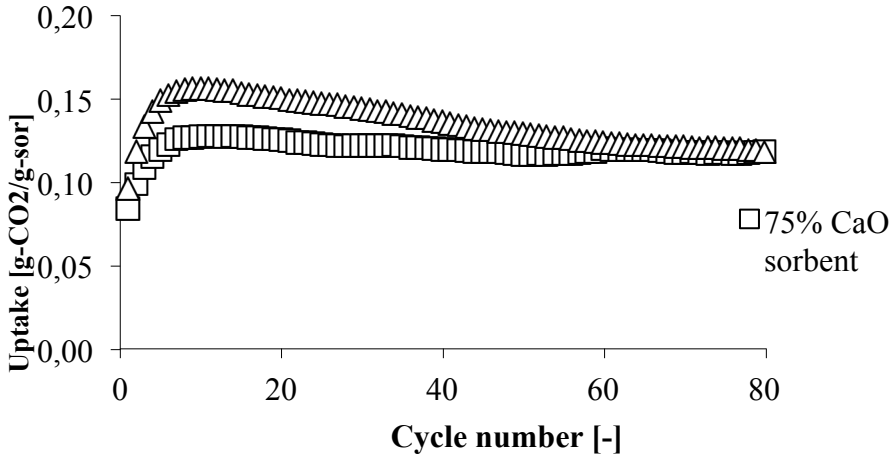

Fig. 3. Effect of CaO load: increasing the load of active phase a decreasing of capacity was observed

In fact during repeated cycling the grains grow and sinter together via formed 'necks' as reported in Fig 4. You can see the genesis of a neck structure for a 75% CaO sorbent. The circle (a) focuses the neck between two different bodies, at a later stage the neck increases its cross section (b) and when the neck reaches at its maximum size the two bodies merge together in a single body (c). This structural alteration could lead the blockage of pores and the formation of isolated volumes throughout the particle and it is likely an important factor leading to reduced uptake kinetics and capacity.

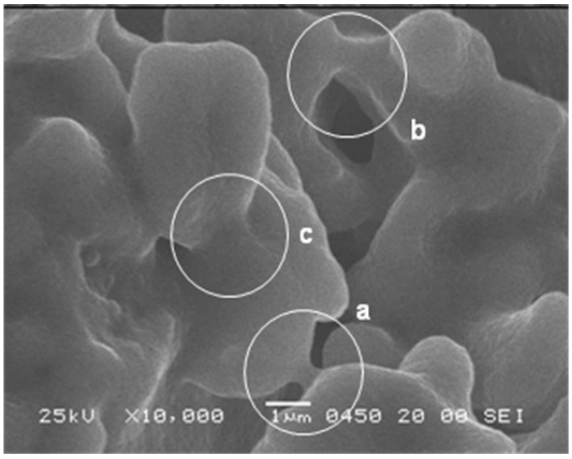

Fig. 4. Micrograph of sorbent after 60 carbonation/regeneration cycle

Improvement of sorbent activity was also observed for the sorbent obtained by chemical pretreatment of the sorbent precursor. By adding water after the second grinding (see Sec 2.1) the obtained sorbent shows greater uptake when compared with the sorbent whose precursor was dry

(see Fig 5). Carbon dioxide uptake of the former sorbent was ~94% higher that the latter at the second cycle. In subsequent cycles the uptake was at least ~60% higher than that obtained with dry precursor.

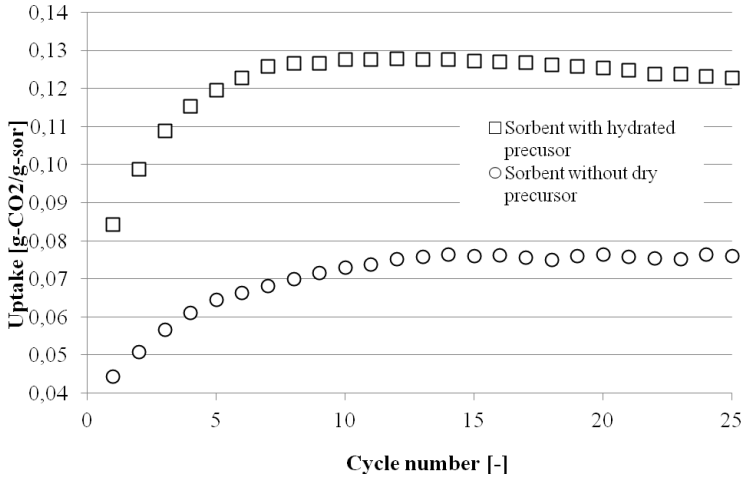

Fig. 5. Comparison between material obtained with hydrated precursor and dry precursor when subjected to moderately severe regeneration.

Such an improvement could be likely be explained with the formation of calcium hydroxide in the sorbent precursor due to the presence of water and the subsequently calcination (for the binder formation see Sec 2.1) leaving more pore volume. In fact the molar volume of Ca(OH)2 is greater than that of CaO. Thus when the hydrated precursor would undergo calcination process water vapor would be formed and it would leave the particle producing extra pore volume. Moreover the migration of water vapor towards the outer part could likely create cracks throughout the sorbent particle exposing more specific surface area to the carbon dioxide. Consequently the specific surface area is higher and more CaO surface is brought in contact with the CO_2. Moreover as Fig 6 suggests the chemical treatment of the sorbent precursor leads to a major change in the pore size distribution. The formation of larger and smaller pores was indeed found as reported in Fig. 6 where the BJH curves for the two kinds of sorbent are presented

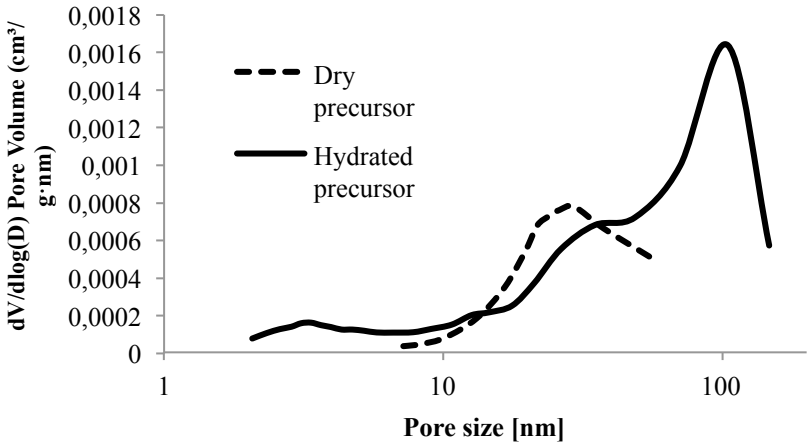

Fig. 6. Pore size distribution of material obtained with hydrated precursor and dry precursor.

As you can see the sorbent synthesized with dry precursor shows an uni-modal pore size distribution (average size 30 nm) whereas for the material obtained from hydrated precursor a wider

pore size distribution was observed. Particularly, the formation of larger pores (100 nm) were detected which permits CO_2 to get the inner core of the particle with a major CaO utilization whereas smaller pores play a key role to the rapid carbonation of the sorbent material. Then the experimental results presented in the remainder of this work are collected from the sorbent obtained from the hydrated precursor.

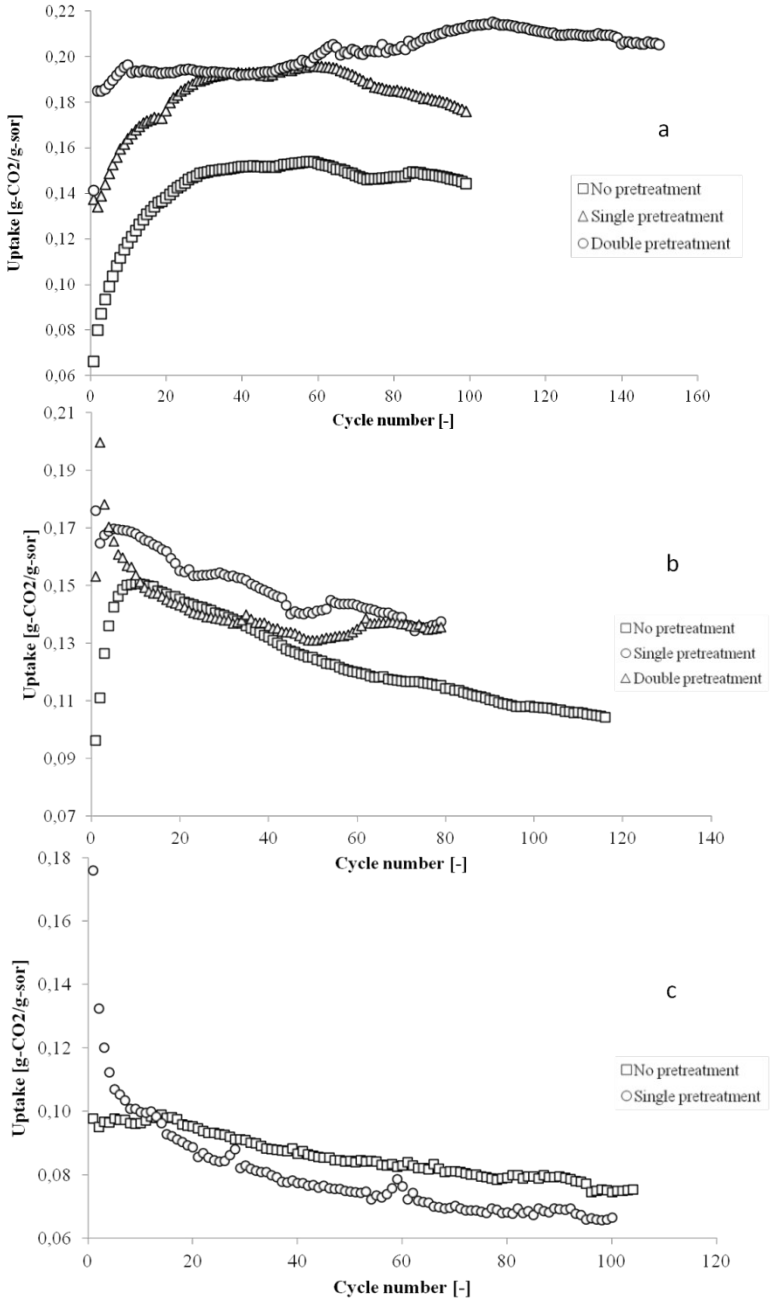

Fig. 7. Carbon capture capacity of 85% CaO sorbent when subjected to different regeneration condition: (a) mild regeneration: 900 °C, 14/86 %v (CO_2/ N_2); (b) moderately severe regeneration: 1000 °C, 14/86 %v (CO_2/ N_2); (c) severe regeneration: 1000 °C, 86/14 %v (CO_2/ N_2).

Fig 7 shows the influence of regeneration condition on the 85% CaO sorbent activity. In particular, you can see that with the increase of both temperature and the amount of CO_2 in the atmosphere during the sorbent regeneration the self reactivation period decreases. When the sorbent is regenerated with mild condition, the self reactivation period is extended up to ~60th (Fig 7 (a)). As reported in Fig. 7 (b), if the regeneration temperature is increased up to 1000 °C the self reactivation

period is reduced to the first 15 cycles. When the presence of CO_2 is increased up to 86% as in the severe condition, the material did not present considerable self reactivation period (see Fig 7 (c)). In addition while the regeneration temperature and the CO_2 content in the atmosphere are increased the ability to retain carbon decreases in later cycles.

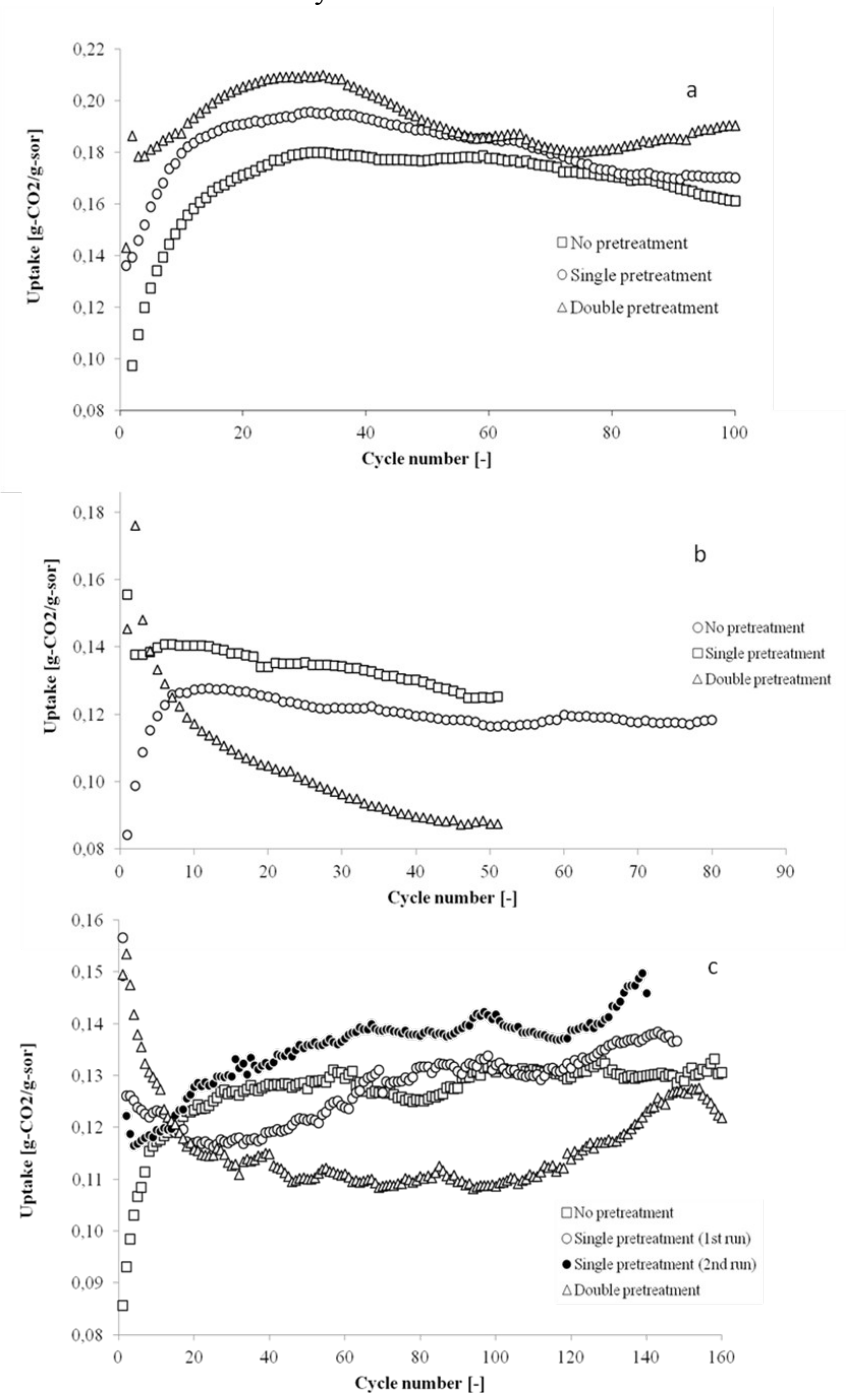

Fig. 8. Carbon capture capacity of 75% CaO sorbent when subjected to different regeneration condition: (a) mild regeneration: 900 °C, 14/86 %v (CO_2/ N_2); (b) moderately severe regeneration: 1000 °C, 14/86 %v (CO_2/ N_2); (c) severe regeneration: 1000 °C, 86/14 %v (CO_2/ N_2).

Moreover Fig 7 shows improvement of sorbent activity due to the thermal pretreatment confirming results published elsewhere [6-7] where naturally occurring sorbents (limestone, dolomite) showed better uptake capacity when exposed to thermal pretreatment. Here, thermal pretreatment of the manufactured sorbent with a short carbonation period (80 minutes at 600 °C under 14/86 % v/v

CO_2/N_2), indeed, leads to some improvement in the CO_2 uptake in subsequent cycles. Moreover CO_2 uptake for sorbent treated with a further carbonation period and a previous calcination step are presented as well. As reported in Fig 7 (a) the single pretreated sorbent shows a self reactivation period as for the untreated material but the ability of reacting with the carbon dioxide is superior to the latter one. Particularly for the single pretreated sorbent a ~68 % higher uptake when compared to the as synthesized sorbent was observed at the second cycle. In consequent carbonation/regeneration cycles the uptake was at least ~22% higher than that without thermal pretreatment. Instead a loss of activity was found for the untreated and single treated material at the later cycles (beyond the 60^{th} cycle). The double treated sorbent shows no significant self reactivation period but a very good reversibility for 150 cycles was detected. The increase of activity was found to be maximum at the third cycle, ~110%, whereas in later cycles the augment was ~26% higher than the untreated sorbent. With the increase in the regeneration temperature sorbent material shows a decreasing activity with cycling and an increase in the loss of reversibility. On the contrary, the positive effect of thermal treatment persists: ~49 % higher uptake when compared to the as synthesized sorbent was found at the second cycle whereas the performance was at least ~8% higher with respect to the untreated sorbent (Fig 7 (a)). The double treated material shows neither positive effect of thermal treatment at later cycles nor self activation at the beginning: even if a small self reactivation effect was detected at later cycles (in particular beyond 70^{th} cycle). Finally, Fig 7 (c) shows the performance of the material subjected to severe regeneration condition. When the molar fraction of CO_2 is increased up to 86% the investigated material did not show self regeneration at all. Besides an initial short period where the material shows stability in CO_2 capturing, thermal treatment did not influence positively the reversibility through the material cycling particularly beyond the 20^{th} cycle.

Finally, Fig 8 shows the influence of regeneration condition on the 75% CaO sorbent activity. As for the 85 % CaO sorbent, self reactivation effect is reduced when increasing both temperature and carbon dioxide during the regeneration step. When the material is regenerated at lower temperature (900 °C) and low CO_2 content (14 % CO_2) the self reactivation stage is expanded up to ~60^{th} cycle for the as synthesized sorbent and up to ~30^{th} cycle for the single and double treated sorbent (see Fig 8 (a)). As for the 85 % CaO sorbent, when the regeneration temperature is increased up to 1000 °C the self reactivation period was observed up to ~15^{th} cycle (Fig 8 (b)). It is worth to note that, on the contrary of 85 % CaO sorbent, when the untreated material is regenerated in severe condition self reactivation effect was observed (Fig 8 (c)). The positive effect of thermal pretreatment was also confirmed for the 75 % CaO sorbent. As reported in Fig 8 (a) the capability of reacting with CO_2 is greater when compared to the as synthesized material. For the single pretreated specimen a ~43 % higher uptake when compared to the as synthesized sorbent was observed at the second cycle. In later cycles the performance was at least ~1% higher than that without thermal pretreatment. A loss of activity was observed for the single and double pretreated specimen beyond ~30^{th} cycle, even if a minor self reactivation effect was found for the double treated sorbent beyond ~70^{th} cycle (as observed earlier here for the 75 % CaO sorbent in Fig 7 (b)). For the double treated sorbent the augment of activity was found to be maximum at the third cycle, ~63%, whereas in later cycles the augment was at least ~4% higher than the untreated sorbent. When the temperature is increase from 900 °C to 1000 °C at the same CO_2 molar fraction (16 %) the self reactivation period was found to shrink to 15^{th} cycle. Thermal treatment confirms its positive effect on increasing the CO_2 capture capability: ~39 % higher capacity at the second stage whereas the uptake was at least ~6 % in the remainder of the cycling when compared to as synthesized sorbent. The double treated sorbent has instead a negative influence on the material: the CO_2 uptake decreases drastically below the performance of the untreated material. Perhaps the most remarkable result is reported in Fig 8 (c) where the sorbent activity subjected to severe regeneration condition is showed. On the contrary of 85 % CaO sorbent, the as synthesized 75 % CaO sorbent shows self reactivation period at the beginning of the cycling test when severe regeneration condition are used. Besides an initial decrease of the performance, the single pretreated sorbent shows a continuously increment of its

CO_2 capture capacity up to 150th cycle. In order to confirm such an unexpected behavior another experimental run has been accomplished confirming the previous observation (see black dots in Fig 8 (c)) with a good reproducibility. Finally for the double treated specimen no self reactivation period was found at the beginning where a loss of activity was observed followed by a period of good reversibility; beyond such a period a self reactivation was observed reaching a maximum at ~150th cycle.

4. Conclusion

The multi-cycling CO_2 sorption-desorption tests on synthetic CaO-$Ca_{12}Al_{14}O_{33}$ sorbent show that the reversibility of the CO_2 uptake in repeated cycles is significantly improved compared that of dolomite. Preliminary experiments aimed at increasing the capacity to retain carbon show that exposing the material to carbon dioxide at 600 °C for 80 minutes prior the multi-cycling experiments the sorbent activity is increased. Self reactivation period is found at the beginning of the multi-cycling experiments or at later cycles reaching a maximum or a plateau in CO_2 uptake. Unexpected results are detected for the 75 % CaO sorbent which shows a continuously increase in CO_2 capture up to 150th cycle under severe regeneration condition. The good reversibility showed by this material in severe regeneration condition make it as a good candidate for CO_2 acceptor in a carbonate looping. In fact, in such a technology option a high concentrated CO_2 stream is required for final disposal [8]. In fact, carbon dioxide is collected at the outlet of the calciner where regeneration of the sorbent happens. As a consequence the ideal CO_2 acceptor should withstand high CO_2 concentration in the calciner to achieve a good regeneration extent to begin properly another carbon capture cycle.

References

[1] Abanades J.C., Anthony E.J., Lu D.Y., Salvador C., Alvarez D., Capture of CO_2 from combustion gases in a Fluidized Bed of CaO. American Institute of Chemical Engineers Journal 2004, 50(7): 1614-1622.

[2] Grasa GS, Abanades JC.,CO_2 capture capacity of CaO in long series of carbonation/calcination cycles. Ind Eng Chem Res 2006; 45:8846-8851.

[3] Gallucci K., Stendardo S., Foscolo P.U., CO_2 capture by means of dolomite in hydrogen production from syn gas. Int J Hydrogen Energy 2008;33:3049-3055.

[4] Delgado J., Aznar M.P., Corella J., Calcined dolomite, magnesite, and calcite for cleaning hot gas from a fluidized bed biomass gasifier with steam: life and usefulness. Ind Eng Chem Res 1996;35:3637-3643.

[5] Li Z., Cai N., Huang Y., Han H., Synthesis, Experimental Studies, and Analysis of a New Calcium-Based Carbon Dioxide Absorbent. Energy Fuels 2005;19:1447-1452.

[6] Manovic V., Anthony E.J., Thermal Activation of CaO-Based Sorbent and Self-Reactivation during CO_2 Capture Looping Cycles. Environ. Sci. Technol. 2008;42:4170–4174.

[7] Chen Z., Song H.S., Portillo M., Lim C.J., Grace J.R., Anthony E.J., Long-Term Calcination/Carbonation Cycling and Thermal Pretreatment for CO2 Capture by Limestone and Dolomite. Energy & Fuels 2009;23:1437-1444.

[8] Calabro`A., Deiana P., Fiorini P., Girardi G., Stendardo S., Possible optimal configurations for the ZECOMIX high efficiency zero emission hydrogen and power plant. Energy 2008;(33) 952–962.

Investigation of an innovative process for biogas up-grading – pilot plant preliminary results

Lidia Lombardi[a], Renato Baciocchi[b], Ennio Carnevale[a], Andrea Corti[c], Giulia Costa[b], Tommaso Olivieri[a], Alessandro Paradisi[a] and Daniela Zingaretti[b]

[a]Dipartimento di Energetica, Università degli Studi di Firenze - Firenze, Italy, lidia.lombardi@unifi.it
[b]Dipartimento di Ingegneria Civile – University of Roma Tor Vergata - Roma, Italy, baciocchi@ing.uniroma2.it
[c]Dipartimento di Ingegneria dell'Informazione,Università degli Studi di Siena - Siena, Italy, corti@dii.unisi.it

Abstract:

Biogas up-grading treatments aimed at producing biomethane to fuel vehicles or to inject into the gas grid, are applications that are gaining increasing interest throughout Europe. Several different commercial methods are available for separating carbon dioxide from biogas. In this work an innovative carbon dioxide removal method that, differently fromthe currently employed commercial techniques, allows also to capture and store the separated $CO_2$is investigated.This process, named Alkali absorption with Regeneration (AwR),consists in a first step in which $CO_2$is separated from the biogas by chemical absorption with an alkali aqueous solution followed by a second step in which the spent absorption solution is regeneratedfor reuse in the first step of the upgrading process and the captured $CO_2$is stored in a solid and thermodynamically stable form. The latter process is carried outcontacting the spent absorption solution, rich in carbonate and bicarbonate ions, with a waste material characterized by a high content of calcium hydroxide andleads to the precipitation of calcium carbonate and to the regeneration of the alkali hydroxide content of the solution.The proposed processes werefirst investigated by preliminary laboratory and simulation analysis. On the basis of the results of these tests, air pollution control (APC) residues from Waste-to-Energy plants were selected as the waste material to use for the regeneration step and a pilot-scale regeneration plant to place downstream of an existing absorption column installed at a landfill site was designed and built.In this paper the layout of the plants, their operating conditions and the results obtained bypreliminary pilot-plant tests are reported.This study was conducted in the framework of theUPGAS-LOWCO2 (LIFE08/ENV/IT/000429) Life+ project.

Keywords:

Biogas upgrading, carbon dioxide capture, accelerated carbonation, air pollution control residues,alkali absorption.

1. Introduction

Among renewable energy sources, the biogas industry is growingin the EU, reaching about 8,3 Mtoe in 2009 with more than 6.000 biogas plants. The main source is agriculture (52%), then landfills (36%) and sewage plants (12%)[1].

Biogas produced in AD-plants – fed with a variety of bio-materials such as waste or energy crops - or landfill sites is primarily composed of methane (CH_4) and carbon dioxide (CO_2) with smaller amounts of hydrogen sulphide (H_2S) and ammonia (NH_3). Trace amounts of hydrogen (H_2), nitrogen (N_2), saturated or halogenated carbohydrates and oxygen (O_2) are also occasionally present in biogas. Usually, the gas is saturated with water vapour and may contain dust particles and organic silicon compounds (e.g.:siloxanes).The heating value of biogas is determined mainly by the methane content of the gas.

There are four basic ways of biogas utilization:heat and steam production, electricity production and/or co-generation, use asvehicle fuel andproduction of chemicals. Biogasutilisation strategies may vary depending on National factors such astaxation, subsidies, availability of gas and heat grids. Worldwide, biogas is mainly used for electricity production whereas in Sweden and in Switzerland a growing amountof biogas is used in the transport sector. The major driver defining

the way for biogas utilisation is the compensation of the energy, i.e. electricity or (upgraded) biogas. Most of the European countries have increased feed-in tariffs for electricity. However, using biogas as vehicle fuel or injecting the gas into the gas grid are applications that are gaining more and more interest. After proper upgrading - i.e. removal of carbon dioxide and tracecontaminants - biogas canbefed into the natural gas distribution grid. The deregulation of the natural gas market in Europe has opened the possibility to find new customers for upgraded biogas via the gas grid. There is no international technical standard for biogas injection but some countries have developed national standards and procedures for biogas injectioninto the natural gas grid, such Sweden, Switzerland, Germany and France [2]. The standards have been set to avoid contamination of the gas grid or atend use. In the standards requirements onWobbe index values and limits on the concentration of certain components such as sulphur, oxygen, dustand the water dew point, as well asaminimum methane concentration of 96% are reported. These demands are in most cases achievable applying existing upgrading processes. In some cases landfill gas can be difficult to upgrade to sufficient quality due to highnitrogen contents.

There are several different commercial methods for reducing the carbon dioxide content of biogas[3]. The most common are High Pressure Water Scrubbing (HPWS), amine scrubbing, and Pressure Swing Adsorption (PSA) on activated carbon. New technologies are, for example, cryogenic upgrading, molecular sieves and separation membranes. When removing carbon dioxide from the biogas stream small amounts of methane are also removed. It is important to keep these methane losses low for economical and environmental reasons and to maximize thegasenergy content.

The commercial technologies available for biogas upgrading have the common feature of removing carbon dioxide from biogas without focusing on the fate of the separated carbon dioxide, which is usually re-emitted into the atmosphere during the system regeneration phase. For example, when CO_2 removal is achieved by means of absorption with a liquid solution, the load solution containing the absorbed CO_2 is regenerated emitting CO_2 to the atmosphere. The same happens during theregeneration of activated carbon when PSA is applied. In thecases in which absorption takes place using water without regeneration, CO_2 is discharged with the spent solution and released to the atmosphere. It should be anyhow pointed out that these CO_2emissions are of biogenic originand should hence not be accounted for as an effective contribution to greenhouse gas emissions.

As a matter of fact, the innovative aspect proposed in this work, developed in the framework of the European Life+ project UPgrading of landfillGAS for LOWeringCO_2 emissions (UGAS-LOWCO2), is to develop a biogasupgrading process that can not only capture but also definitely store the separated CO_2in a solid form [4]. The subtraction of carbon dioxide of biogenic origin from the atmosphere can contribute as a negative emission (sink) to the overall greenhouse gases balance. In addition, the proposed method may allow to achieve also other specific environmental benefits that will be highlighted in the following paragraphs.

2. Alkali absorption with regeneration process concept

This method – named Alkali absorption with Regeneration (AwR) - is based on CO_2 chemical absorption by means of an alkali aqueous solution followed by regenerationof the spent solution using Air Pollution Control (APC) residues.

CO_2 is first physically absorbed in the liquid solution and here it reacts with the alkaline compound producing carbonate (CO_3^{2-}) and bicarbonate ions (HCO_3^-) (chemical absorption) [5][6][7]. The alkaline reactants that can be used in the absorption process are potassium hydroxide (KOH) or sodium hydroxide (NaOH). The reactions that take place during the absorption step are the following:

$$2\ KOH + CO_2 \rightarrow K_2CO_3 + H_2O \quad (1)$$

or

$$2\ NaOH + CO_2 \rightarrow Na_2CO_3 + H_2O \quad (2)$$

The load solution – i.e. the solution containing the carbonate/bicarbonate ions – can be chemically regenerated by contacting it withcalcium hydroxide ($Ca(OH)_2$) in solid form. In this step, poorly soluble calciumcarbonate($CaCO_3$) precipitation takes place (carbonation reaction), thus the CO_2separated from the biogas can be permanently storedin a chemically inert and thermodynamically stable form, whereas KOH or NaOH is recovered for the first step of the upgrading process. The basic reactions that take place during the regeneration phase are the following:

$$Ca(OH)_2 + K_2CO_3 \rightarrow CaCO_3(\downarrow) + 2KOH \quad (3)$$

or

$$Ca(OH)2 + Na2CO3 \rightarrow CaCO3(\downarrow) + 2NaOH \quad (4)$$

Since the use of calcium hydroxide for such a process would not make sense from a carbon dioxide mitigation perspective, as it is manufactured by calcination of limestone releasing carbon dioxide into the atmosphere, in order to obtain a net reduction of carbon dioxide emissions, in this project industrial waste residues were chosen as alternative alkalinity sources. Several studies have in fact shown the feasibility of using different types of industrial residues, characterized by a high content of calcium hydroxide phases, such as bottom ash and air pollution control (APC) residues from waste incineration or steel slag, to sequester CO_2. Such a capture process is known as accelerated carbonation of natural minerals or industrial residues [8][9][10]. In case of using industrial residues, the accelerated carbonation allows also improving the leaching behaviour of the residues [11][12][][].

From preliminary investigations, APC residues, which are the product of incineration flue gas treatment with calcium-based products, were selected for the regeneration process owing to their chemical, physical and mineralogical composition [][][]. Figure 1 shows the schematic layout ofthe AwR process.

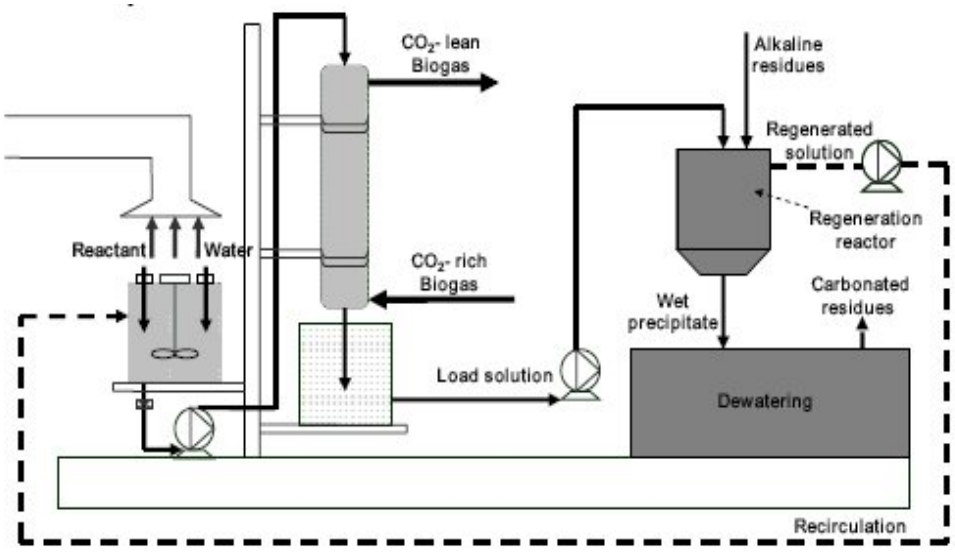

Fig. 1. Conceptual layout of the AwR process.

3. Results of the preliminary investigation phase

At a preliminary level the two steps of the AwR process were studied separately. In particular, the absorption step was first investigated by means of computer simulations and carrying out some absorption tests on the pilot plant – which was already available from a previous research

projectand is described in the following[]. The regeneration step was instead investigated by laboratory testing [][].

One of the main outcomesof the preliminary analysis concerned the definition of the maximum concentrations of the alkali compoundsto use in the absorption process. In fact,for increasing initial concentrations of KOH or NaOHin the absorption solution and hence of K_2CO_3 or Na_2CO_3 in the solution resulting from the absorption treatment, the yield of the regeneration process showed to decrease owing to the combination of two negative effects: a decrease in KOH or NaOH regeneration efficiency and an increase in solution losses during the solid separation process after regeneration []. So it was concluded that a maximum of 4 eq/l of carbonate ionscould be acceptable in the solution to be regenerated in order to allow for high regeneration yields during the second stage of the process[]. Hence, assuming a complete conversion of KOH or NaOH during the absorption step, the above mentioned condition would correspond to an absorption solution with a 18-20 % wt. concentration of KOH or NaOH. As a matter of fact, such concentration values are definitely lower than those used in previous pilot-scale absorption experiments aimed at treating 20 Nm^3/h of landfill gas in which mass concentrations ofover 50%wt. of KOH were adopted[][]. Under those conditions with a liquid flow rate of 60 l/h characterized by a KOH concentration of 48-53% wt, CO_2 removal efficiencies of 83-97% were achieved[][].At least 97% CO_2 removal efficiency is required to obtain an acceptable upgraded biogas quality (CH_4> 98%) starting from 50% in vol. CH_4 and 50% in vol. CO_2.Consequently - keeping the same landfill gas and solution flow rates as those defined in the original design of the pilot plant - the achievable CO_2 removal efficiency obtained using alkali concentration values of 12-25% would be far lower than the target value, as is evident in Table 1, where the results obtained by both the simulations and the pilot plant tests are compared. In this case the simplified simulations of the absorption process were carried out using Aspen Plus[25]. The layout of the simulation was based on one absorption column, modeled using a radfrac unit, with two entering streams (biogas and absorbing solution) and two exiting streams (CH_4 enriched biogas and load solution).

Then the simulation layout was modified, considering more than one absorption column, with the aim of evaluating the number of consecutive absorption stages, required to reach the biomethane quality in output, according to the German standards [2]. From these simulations, it was estimated that to reach the required removal efficiency, three absorption stages, with an entering solution flow rate of 60 l/h and KOH or NaOHconcentrations of 12-14% wt. would be required to process 20 Nm^3/h of landfill gas.

The existing pilot absorption column represents the first absorption stage of the three stage process.For this reason, the results ofthe pilot tests that will be reported in the following paragraphs are to be considered representative, for the moment, only of the first of the three absorption stages.

Table 1. CO_2 removal efficiency obtained from simulations and pilot plant tests, considering 20 Nm^3/h entering landfill gas with 50% CH_4 and 50% CO_2 in vol.; absorption solution flow rate 60 l/h.

Mass concentration	CO_2 removal efficiency % - Simulation	CO_2 removal efficiency % - Pilot plant test
	KOH	
11,9	35,8	29,7±1,45
17,0	51,9	41,8±3,5
25,5	78,5	60,5±4,9
	NaOH	
11,0	35,7	32,9±1,1
20,0	59,4	56,0±3,7

Concerning the regeneration step, specificlaboratory experiments were preliminarily carried out to characterize the APC residues and to investigate their capability of regeneratingthe spent absorptionsolution rich in carbonate/bicarbonate ions[].The amount of calcium phases available for the regeneration reaction was estimated as the difference between the total Ca and the Ca as $CaCO_3$ content of the ash, and consisted mainly of $Ca(OH)_2$ and CaClOH[]. The quite high chloride content (around22% by weight) of the ash, mainly as calcium hydroxychlorideproved to hinder the regeneration reaction. As a matter of fact, for every mole of CaOHCl, as shown in Eq. (5), only 1 mol of KOH can be produced, differently from calcium hydroxide thatallows to regenerate 2 mol of potassium hydroxide (see Eq. (3)):

$$CaOHCl + K_2CO_3 \rightarrow KCl + KOH + CaCO_3 \quad (5)$$

Since CaOHCl is more soluble than $Ca(OH)_2$, it is more readilyavailable for reacting with potassium carbonate than $Ca(OH)_2$;hence an increase in the amount of ashes added to the solution produceda reduction of the efficiency of the regeneration reaction[].To improve the alkali regeneration yield, a washing pretreatmentof the APC residues was hence tested in order to remove mostof the phases responsible of decreasing the total buffering capacityof the solution.

Furthermore, in order to improve the overall leaching behavior of the solidmaterial so to comply with the disposal criteria for non hazardouswaste landfilling, the effects of a second washing treatment appliedto the residues after the regeneration step were investigated. In this case, due tothe removal of part of the KOH contained in the ash, the pH of theresidues decreased, but remained still well above values indicatingsolubility control by calcite. The mobility of most of the testedcompounds (Zn, Pb, Sb, Cr and SO_4^{2-}) appeared anyhow to decreaseafter this latter treatment, resulting lower than the limit values fornon hazardous waste disposal[].

The appropriate operating conditions able to maximize KOH or NaOHregenerationwere defined[][], including pre- and post-washing of the residues, as reported in Table 2. The APC residues were added to the solution to be regenerated on the basis of their calcium content as $Ca(OH)_2$, applyinga 1,2 ratio with respect to the carbonate ions content of thesolution.In this way it was possible to reach a 90% efficiency of the reaction in terms of KOH or NaOH regeneration. In addition, the solid product showed to be mainly made up by calcite and a CO_2 storagecapacity of above 300 g/kg solid product was obtained.It should be noted however, that after the regeneration reaction the liquid solution must be separated from the solid product and that disregarding the type of method useda complete recovery of the solution is not possible and therefore a lower overallfinal recovery of KOH or NaOH should be anticipated.

Table 2. Operating conditions selected for the regeneration step.

Pre-treatment		
Type	Washing	
L/S	5	l/kg
Time	15	min
Regeneration		
Ca/CO_3^{2-} ratio	1,2	mol Ca/mol CO_3^{2-}
Temperature	55	°C
Time	60	min
Post-treatment		
Type	Washing	
L/S	5	l/kg
Time	15	min

4. Pilot plant tests

In order to demonstrate the technical feasibility of the proposed process, an integrated pilot plant for CO_2absorption and regeneration of the spent solution with CO_2 storage was designed and built. The pilot plant is located at the research laboratory of the University of Florence hosted at the landfill site managed by one of the partnersof the UPGAS-LOWCO2 project.

4.1. Absorption pilot plant

The absorption pilot plant (Figure 2 (i)) consists of a packed column where an aqueous solution of KOH or NaOH reacts with the carbon dioxide contained in the landfill gas, which is directly extracted from the landfill [][][][][].

The alkali compound aqueous solution is fed to the column top, while the landfill gas is fed to the bottom of the column. The landfill gas is extracted from a collection station in the landfill and flows into the column by means of a side channel blower. The column fillingconsistsofSulzerlaboratoryDX packing, with a diameter of80mmandoverall heightof990cm, in stainlesssteel. The column was originally designed to process about 20-25 Nm^3/h of landfill gas and 40-60 l/h of absorbingsolution.

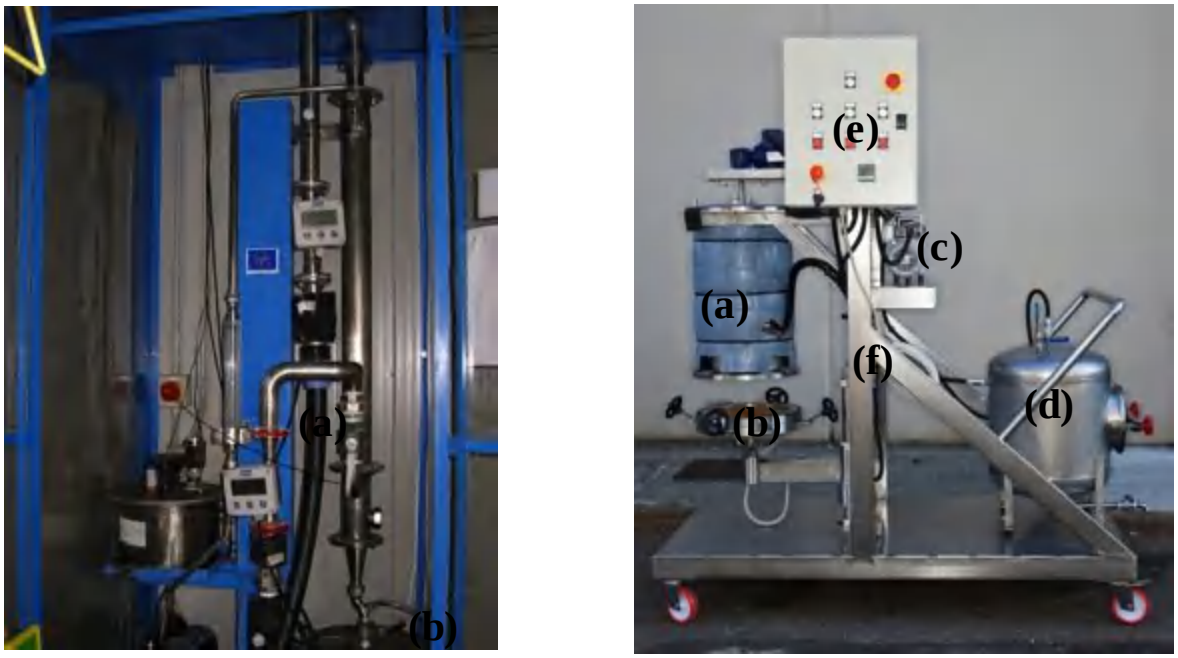

(i) (ii)

Fig. 2. Pictures of the pilot plant: i) absorption column; ii) regeneration reactor and its main components: a) regeneration reactor with mixer and heating jacket, b) bottom section of the reactor with filter tensioning system, c) vacuum filtration pump, d) liquid collection tank, e) control panel and f) steel frame.

4.1.1. Monitoring equipment

Input and output gas flow ratesaremeasured by means of a volumetric flow meter (Fluidwell – F110) able to work in the range from 2,5 to 35 m^3/h.Input and output volumetric gas composition is measured too by means of a portable gas analyzer (input with Geotechnical Instruments - GA 94- and output with Geotechnical Instruments-GA2000) which measures $CH_4$and $CO_2$by infra-red absorption and O_2 by internal electro-chemical cells.Input and output differential pressure is measured by a diaphragm pressure transducer (Delta Ohm-HD 408T 100MBG) able to work in the range from -100 to +100 mbar relative to the atmospheric pressure. Atmospheric pressure is measured by means of a barometric pressure transducer (Delta Ohm HD 9908 BARO) able to work

in the range from 700 to 1100 mbar. Input and output gas temperature is measured by means of K-typethermocouples. Gas flow rate, pressure and temperature are measured and registered in a quasi-continuous manner (every 10 seconds). The measurement instruments are controlled by a programmable automation controller (Compact Field Point – National Instrument) composed by rugged I/O modules and intelligent communication interfaces. The composition is measured every 60 seconds and is directly registered by the gas analyzers.

4.2. Regenerationpilot plant

The regeneration pilot plant was designed and built with the aim of using the same reactor to perform in batch mode the pre-washingtreatment of the residues, the regeneration/carbonation reaction and the post-washing treatment, as well as the liquid/solid separation step after each of the three operations. For the separation step it was decided to apply vacuum filtration, the same method adopted for the lab-scale experiments. As shown in Figure 2 (ii), the plant is made up by: the regeneration reactor, which includes a paddle type mixer and an external heating jacket; the filter medium, which is fitted on the bottom of the reactor in a custom made tensioning system; the vacuum filtration system, made up by the pump and filtered liquid collection tank; the control panel with switches for activating all equipment (mixer, heating system and vacuum pump) and a display for setting the heating temperature; a stainless steel support system on wheels on which all units and equipment are placed and manoeuvred.

The APC residues and the liquid medium (distilled water for the pre- and post-washing treatments and the spent solution exiting from the absorption step for the carbonation process) are mixed in the regeneration reactor tank. In the first step of pre-washing, distilled water and APC residues are mixed and kept in the tank for the required time; then filtration starts and at the end of this process a solid cake remains at the bottom of the reactor, while the filtered water is collected in the liquid collection tank and, from there, discharged. In the second step, the solution coming from the absorber is added to the cake previously formed at the bottom of the reactor. The slurry is mixed and after the required reaction time the filtration starts again. The liquid phase which accumulates in the collection tank is the regenerated solution, which is reused – after proper make up addition – in the absorption column. The carbonated cake remaining at the bottom of the reactor after the second filtration step is washed with distilled water and after a third filtration step, the final solid product is extracted from the bottom of the reactor while the filtration liquid is removed from the collection tank and disposed of.

4.3. AwR operation test: procedure and preliminary results

In this paragraph the procedure adopted and the results obtained from the preliminary operational tests carried out on the pilot-scale AwR plant are described. The operating conditions selected for these tests are reported in Table 3.

Table 3. Operating conditions selected for the preliminary AwR pilot plant tests.

Alkali compound	KOH
Absorbing solution flow rate [l/h]	60
Absorption operation time [min]	10
Volume of load solution to be regenerated[1] [l]	8
Alkali mass concentration [%]	11,9%
Alkali normality [eq/l]	2,35
Reactive Ca to CO_3^{--} ratio [Camol /CO_3^{2-}mol]	1,2

[1]The volume of liquid produced by the column during a 10 minutes absorption operation, discarding the solution generated during the first 2 minutes, in order to consider steady functioning.

Concerning the absorption reaction, after the preparation of the absorbing solution – obtained mixing the appropriate amount of KOH and water - the experiment was started. Temperature, pressure, flow rate and composition were continuously measured and recorded for the inflow and outflow gas. The average flow rate of entering landfill gas was 18,03 Nm^3/h, while the average exiting flow was 15,07 Nm^3/h. Entering average concentration in vol. of CH_4 was 50,66% while CO_2 was 37,48% in vol. In the exiting gas the average CH_4concentration was 60,61%, while the average CO_2content was 28,76%. The calculated CO_2 removal efficiency was about 35,86%.

The spent solution was collected at the outlet of the column in a bucket after the first two minutes of the reaction. After ten minutes the absorption experiment was stopped.

The spent solution sample was titrated, showing a complete conversion of KOH to K_2CO_3 with a total concentration of 2,35 eq./l (Figure 3 (ii)).

Before the testing phase, the properties of the APC residues to use for the test were assessed by laboratory analysis. Basically this characterisation was necessary to determine the amount of APC residues to be used for the regeneration experiments. Specifically the total $Ca(OH)_2$ content of the washed ash was estimated as 55,5% wt, while the weight loss of the material measured upon the washing pre-treatment (mainly due to NaCl and CaClOH dissolution) was of 43,2 % by weight.

Based on the above mentioned characteristics and the conditions reported in Table 3, the required amount of washed APC residues for the regeneration test was calculated to be equal to 1,5 kg; hence considering the weight loss of the material consequent to the washing pre-treatment, it was estimated that 2,64 kg of untreated APC ash would be necessary for the complete regeneration test. Based on this, the amount of distilled water required for the washing pre-treatment with a L/S ratio of 5 l/kg was calculated (13,23 l).

Prior to the beginning of the experiment the reactor was washed and dried and the filtering material was substituted. The valve at the bottom of the reactor was closed and the required amounts of APC residues and of distilled water were weighed and fed into the reactor.

After the introduction of the residues and distilled water into the reactor, the mixer was activated. The mixing was maintained for 15 minutes at ambient temperature (internal temperature 24,3 °C), then the vacuum pump was turned on and connected to the liquid collection tank and the valve at the bottom of the reactor was opened. During the liquid separation phase the mixing of the solution was continued in order to help the filtration process. After about 100 minutes the mixer was stopped since the liquid separation appeared to be complete. The filtered washing solution was collected from the tank, which was then cleaned and dried and samples of the washing solution were taken.

The absorption spent solution (8 l)wasthen poured into the reactor and mixed with the washed APC residues cake. After 1 hour of reaction time at 55°C, the vacuum pump was turned on and connected to the liquid collection tank and the valve at the bottom of the reactor was opened. Also during this liquid separation phase the mixing of the solution was continued in order to help the filtration process. This separation step proved faster than the previous one and after 45 minutes the filtration appeared to be complete (Figure 3 (i)). Samples of the solid product of the regeneration process were taken and right after that the final washing treatment was performed. At the same time the regenerated solution was emptied from the collection tank and a sample of it was directly titrated. Around 1 eq./l of KOH were regenerated out of a total buffering capacity of 1,6[2]eq/l, hence the regeneration yield(ability of the reaction to obtain again the initial compound) was about 62,5%. This value was quite lower than the one measured in the lab scale tests (78-92%)[][]. Through a preliminary mass balance it is possible to estimate the overall regeneration efficiency (mass of recovered KOH with respect to the initial amount of KOH entering in the absorption column) which resulted of about 41%. This overall regeneration efficiency is quite low and needs to be increased in

[2] Due to dilution with the humidity of the washed cake, the total buffering capacity of the regenerated solution was lower than the spent solution one(1,6 vs. 2,35 eq./l) as shown in Figure 3 (ii).

order to increase the competitiveness of this method compared to other upgrading processes from an environmental and economical point of view[][][].

The amount of distilled water necessary for the final washing treatment was estimated assuming that the product of the regeneration phase had a humidity of 50% wt. and a weight increase of 40% compared to the washed residues characterized by a density of 0,99 kg/l (data determined in the lab-scale tests). On the basis of these assumptions, the amount of water required to set the L/S ratio to 5 l/kg was calculated to be 8,42 kg. The distilled water was poured into the reactor and the mixer was switched on. After 15 minutes the vacuum pump was turned on and connected to the liquid collection tank and the valve at the bottom of the reactor was opened. During the liquid separation phase the mixing of the solution was continued in order to help the filtration process. The liquid/solid separation appeared to be complete after 45 minutes. The bottom of the reactor was then opened and the solid cake was collected: roughly 2,64 kg of solid humid product were recovered.

In conclusion, the outcome of this preliminary pilot-scale test was considered satisfactory, since no great operating difficulties were encountered and all three steps of the regeneration process were carried out. The liquid/solid separation step after the first washing treatment proved to be as expected the most critical one in terms of time; in addition some ash particles were found in the liquid collection tank, hence it was decided to check if other types of filtering materials could be used to optimize this process. As for the outcome of the regeneration process, the lower regeneration yield was ascribed to the less constant temperature and especially to poor mixing at the bottom of the tank that did not allow the complete reaction of $Ca(OH)_2$. To improve this aspect it was decided to try to verify if the shape of the mixer could be modified.

Finally, the amount of CO_2 stored per unit of mass of solid product after the regeneration process was of about 220 g/kg solid material, and showed to increase after the final washing treatment owing to the dissolution of residual soluble phases.

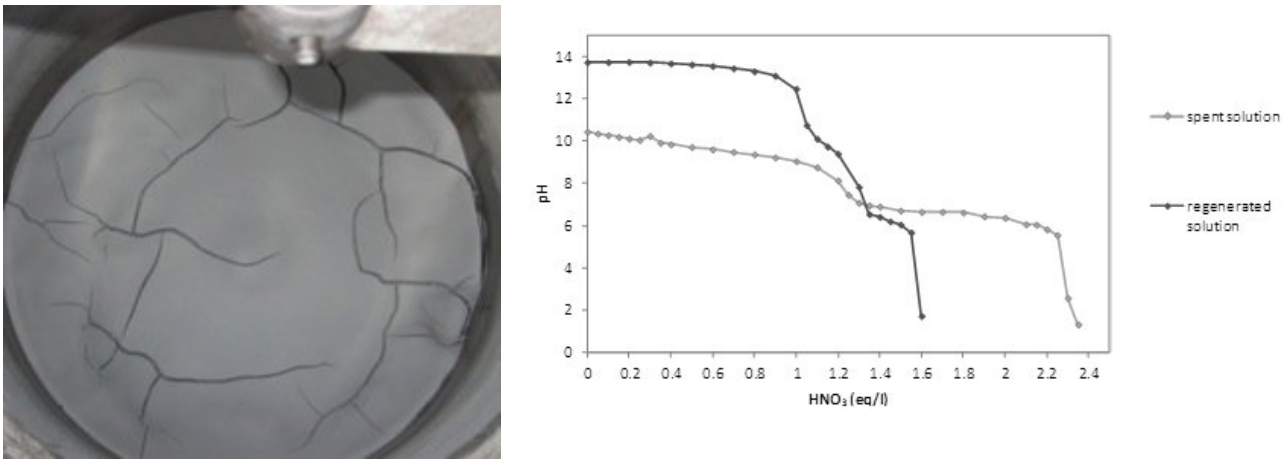

(i) (ii)

Fig. 3. Picture of the solid cake obtained at the end of the filtration process after the regeneration/carbonation reaction (i); titration curves of the spent and regenerated solution (ii).

5. Conclusions

An innovative method for removing carbon dioxide from landfill gas – with the final aim of upgrading its quality to that of natural gas– was proposed and investigated. With respect to commercial methods for biogas upgrading, the proposed process presents two additional environmental benefits: i) the carbon dioxide separated from the methane is permanently stored by accelerated carbonation of an alkaline waste material(air pollution control residues from waste incineration flue gas treatment), ii) the series of treatments applied during the regeneration process has shown to improve the leaching behaviour of the residues. This process, named Alkali absorption

with Regeneration (AwR), consists in a first step in which CO_2 is separated from the biogas by chemical absorption with an alkali aqueous solution followed by a second step in which the spent absorption solution is regenerated for reuse in the first step of the upgrading process and the captured CO_2 is stored in a solid and thermodynamically stable form. The processes were investigated first by simulations and laboratory testing and then in order to verify the feasibility of the method at a larger scale, a pilot-scale AwR plant for treating 20 Nm^3/h of biogas was designed, built and installed at a landfill site. From the results of preliminary tests, the regeneration yield achieved at pilot scale appeared to be lower than the yields obtained in the laboratory, so the main efforts for the next testing phase will focus on the optimization of plant operation in order to increase the overall efficiency of KOH or NaOH recovery and possibly allow to improve the competitiveness of this process compared to traditional commercial biogas upgrading methods.

Acknowledgments

The authors wish to acknowledge the Life+ Programme and European Commission for co-funding the activities of the UPGAS-LOWCO_2 project (LIFE08/ENV/IT/000429) www.upgas.eu.

References

[1] Eurobserv'er. Biogas Barometer. November 2010. Available at <http://www.eurobserv-er.org/downloads.asp> [accessed 10.02.2012].

[2] Persson M., Jönsson O. and Wellinger A. (2006). Biogas Upgrading to Vehicle Fuel Standards and Grid Injection. IEA Bioenergy. Available at <http://www.iea-biogas.net/_content/publications/publications.php> [accessed 10.02.2012].

[3] Petersson A. and Wellinger A. (2009). Biogas upgrading technologies – developments and innovations. IEA Bioenergy. Available at <http://www.iea-biogas.net/_content/publications/publications.php> [accessed 10.02.2012].

[4] Lombardi, L., Baciocchi R., Carnevale E., Corti A., Costa G., Gabarrell X., Mostbauer P., Olivieri F., Olivieri T., Paradisi A., Starr K., Villalba G., Zingaretti D.. Innovative processes for biogas upgrading. In Proceedings of Sardinia 2011 Thirteenth International Waste Management and Landfill Symposium 3 - 7 October 2011 S. Margherita di Pula (Cagliari), Sardinia, Italy. ISBN 978-88-6265-000-7

[5] Corti A. (2004). Thermoeconomic evaluation of CO_2 alkali absorption system applied to semi-closed gas turbine combined cycle, Energy 29 (3) march 2004, 415-426, Elsevier ldt.

[6] Corti A., Beconi B.M., Lombardi L. (2001). Alkali absorbing for CO_2 removal: thermo-economic comparison between carbonate and sodium hydroxide based processes. InProceedings of IcheaP-5 The Fifth Italian Conference on Chemical and Process Engineering, Firenze, Italy - 20-23 May, 2001, AIDIC, Milano

[7] Baciocchi R., Storti G., Mazzotti M. (2006). Process design and energy requirements for the capture of carbon dioxide from air. Chemical Engineering and Processing; 45(12):1047-1058.

[8] Huijgen W.J.J. (2007). Carbon dioxide sequestration by mineral carbonation. Thesis, Energy research Centre of the Netherlands, The Netherlands.

[9] Huijgen, W. J. J., Witkamp, G. J., &Comans, R. N. J. (2005). Mineral CO2 sequestration by steel slag carbonation. Environmental Science and Technology, 39, 9676–9682.

[10] Li X., FernándezBertos M., Hills C.D., Carey P.J., Simon S. (2007). Accelerated carbonation of municipal solid waste incineration fly ashes. Waste Management, 27, 1200–1206

[11] Huijgen, W. J. J., &Comans, R. N. J. (2006). Carbonation of steel slag for CO2 sequestration: leaching of products and reaction mechanisms. Environmental Science and Technology, 40, 2790–2796.

[12] Van GervenT.,VanKeer, ArickxS.,Jaspers M., Wauters G., Vandecasteele C. (2005).Carbonation of MSWI-bottom ash to decrease heavy metal leaching, in view of recycling. Waste Management, 25, 291–300

[13] Costa G., Baciocchi R., Polettini A., Pomi R., Hills C.D., Carey P.J. (2007). Current status and perspectives of accelerated carbonation processes on municipal waste combustion residues, Environmental Monitoring and Assessment, 135:55-75.

[14] Baciocchi R., Costa G., Polettini A., Pomi R. (2008). An insight into the effect of accelerated carbonation on metal release from incinerator ash. In Proceedings of the 2nd International Conference on Accelerated Carbonation for Environmental and Materials Engineering, Rome 1-3 October 2008.

[15] Baciocchi R. Corti A., Costa G., Lombardi L., Zingaretti D. (2010). Storage of carbon dioxide captured in a pilot-scale biogas upgrading plant by accelerated carbonation of industrial residues. International Conference on Greenhouse Gas Technologies (GHGT-10). 19th-23rd September 2010, RAI, Amsterdam, The Netherlands. Energy Procedia (2011) 4: 4985–4992.

[16] Baciocchi R., Costa G., Lombardi L., Verginelli I., Zingaretti D. (2010). Storage of carbon dioxide captured in a pilot-scale biogas upgrading plant by accelerated carbonation of industrial residues. In Proceedings of the Third International Conference on Accelerated Carbonation for Environmental and Material Engineering. ACEME10. Turku, Finland, Nov. 29 – Dec. 1 2010. ISBN 978-952-12-2505-5 - ISBN 978-952-12-2506-2 (pdf version).

[17] Baciocchi R. Costa G., Lombardi L., Zingaretti D. (2010). Storage of carbon dioxide captured in a pilot-scale biogas upgrading plant by accelerated carbonation of industrial residues. In Proceedings of Venice 2010, Third International Symposium on Energy from Biomass and Waste. Venice, Italy; 8-11 November 2010. CISA, Environmental Sanitary Engineering Centre, Italy. ISBN 978-88-6265-008-3.

[18] Lombardi L., Carnevale E., Corti A., Olivieri T.. Biogas up-grading through carbon dioxide absorption with alkali solution. In Proceedings of Sardinia 2011 Thirteenth International Waste Management and Landfill Symposium 3 - 7 October 2011 S. Margherita di Pula (Cagliari), Sardinia, Italy. ISBN 978-88-6265-000-7.

[19] Baciocchi R., Costa G., Gavasci R., Lombardi L., Zingaretti D.. Regeneration of a spent alkaline solution from a biogas upgrading unit by carbonation of APC residues. ChemicalEngineering Journal; 179:63– 71.

[20] Baciocchi R., Costa G., Faraoni G., Lombardi L., Olivieri T., Zingaretti D.. Pilot-scale carbonation of APC residues for CO_2 storage and alkali regeneration downstream an absorption column for biogas upgrading. In Proceedings of Sardinia 2011 Thirteenth International Waste Management and Landfill Symposium 3 - 7 October 2011 S. Margherita di Pula (Cagliari), Sardinia, Italy. ISBN 978-88-6265-000-7.

[21] Lombardi L. and Corti A. (2009). Carbon Dioxide Capture: Technical Review and Proposal of an Alternative Absorption Process. In: Theodore B.N. (ed.), Flue Gases – Research, Technology and Economics, Chapter 8, Nova Science Publishers (ISBN 978-1-60692-449-5).

[22] Lombardi L., Corti A. Carnevale E., (2008). Carbon Dioxide Capture from Landfill Gas. In Proceedings of Second International Conference on Accelerated Carbonation for Environmental and Materials Engineering. Rome (Italy) 1-3 October 2008 (pp. 17-26).

[23] Lombardi L., Carnevale E., Corti A. (2008). Landfill gas quality up-grading through carbon dioxide capture: environmental and economic evaluations. In Proceedings of 16th European Biomass Conference and Exhibition. Valencia (SP) 2-6 June 2008.

[24] Lombardi L. Corti A. Carnevale E. Baciocchi R. Zingaretti D. (2010). Carbon dioxide removal and capture for lanfill gas up-grading. International Conference on Greenhouse Gas Technologies (GHGT-10). 19th-23rd September 2010, RAI, Amsterdam, The Netherlands. Energy Procedia (2011) 4:465–472.

[25] Aspen Plus 2004.1. Cambridge, MA, USA: Aspen Technology Inc.; 2005
[26] Lombardi L, Carnevale E, Carpentieri M, Corti A (2007). Carbon dioxide capture from landfill gas. In Proceedings of ISWA/NRVD World Congress 2007, Amsterdam, The Netherlands, 24-27 September, 2007.

[27] Starr K., GabarrellDurany X., Villalba Mendez G., TalensPeiró L., Lombardi L.. Life cycle assessment of biogas upgrading technologies. Waste Management (2012), doi:10.1016/ j.wasman.2011.12.016

[28] Starr K., GabarrellDurany X., Villalba Mendez G., TalensPeiró L., Lombardi L.. CO2 balance of biogas upgrading technologies. In Proceedings of Sardinia 2011 Thirteenth International Waste Management and Landfill Symposium 3 - 7 October 2011 S. Margherita di Pula (Cagliari), Sardinia, Italy. ISBN 978-88-6265-000-7

[29] Starr K., GabarrellDurany X., Villalba Mendez G., TalensPeiro L., Lombardi L., Biogas Upgrading: Environmental Comparison of Conventional and Innovative Technologies. Submitted to ECOS 2012.

Method of increasing the efficiency of a supercritical lignite-fired oxy-type fluidized bed boiler and high-temperature three - end membrane for air separation

Janusz Kotowicz[a], Adrian Balicki[a]

[a] *Institute of Power Engineering and Turbomachinery, Silesian University of Technology, ul. Konarskiego 18 44-100 Gliwice, Poland, adrian.balicki@polsl.pl*

Abstract:

In this paper a thermodynamic analysis of a supercritical power plant supplied with lignite was made. The power plant consists of: a steam cycle at constant power of 600 MW, live steam parameters at 600 °C/29 MPa and reheated steam parameters at 620 °C/5 MPa; supercritical OXY type circulating fluidized bed boiler and air separation unit. An air separation unit is based on a three – end type high temperature membrane. Models of the steam cycle, circulating fluidized bed boiler and air separation unit were built using a commercial computer program GateCycle™ and inhouse codes. After the integration of the listed above models, CFB boiler thermal efficiency as a function of the oxygen recovery ratio in the high temperature membrane for the variant without and with fuel drying were determined. The calculated thermal efficiency for the variant with fuel drying increases from 76% to 87% with increasing oxygen recovery ratio from 0.45 to 0.9.

Keywords:

Thermodynamic analysis, Supercritical oxy-fuel boiler, High temperature membranes, Oxy-combustion, Lignite drying

1. Introduction

The necessity of meeting the standards of flue gas emissions, introduced by both, EU and national legislators, requires the continuous development of the technologies, which allow for maximum limitation of the greenhouse gases emission. The group of these technologies includes oxy–combustion technology, which, thanks to an almost complete elimination of nitrogen from the process, substantially limits the flue gas stream generated by the power unit [1]. For uninterrupted operation of the OXY type boiler it is necessary to provide a constant stream of oxidizer with the highest possible oxygen content, which mixed with a stream of recirculated exhaust gas as an oxidizing is mixture fed to the combustion chamber. The production of the technical oxygen with the use of both currently available on an industrial scale cryogenic technology and considered alternative technologies, is associated with the significant power consumption of the process, and thus also with a decrease of the efficiency of the block [2]. For boilers fed with lignite, just like in classical solutions, a possible way to improve the efficiency of electricity generation is to pre-dry the fuel prior to the injection into the combustion chamber. The presence of large amounts of water in the fuel reduces the lower heating value, enforces necessity to provide greater fuel mass flow to the boiler and, which is particularly important in systems with wet type recirculation, increases the probability of condensation of moisture from the flue gases. The drying process requires the delivery of large quantities of the drying medium, of which a function is to raise the temperature and the evaporation of the greatest possible amount of moisture from the fuel. In the classical solutions as a drying medium hot air or exhaust gases leaving the boiler is used. In OXY type

systems for fuel drying waste stream of a mixture of nitrogen and oxygen from the air separation unit can be used.

2. Assumptions

A model of a supercritical boiler with circulating fluidized bed working in oxy - combustion technology was built using commercially available computer program GateCycle™ and in-house codes. Scheme of the model built (with ideological scheme of steam cycle) is shown in Figure 1.

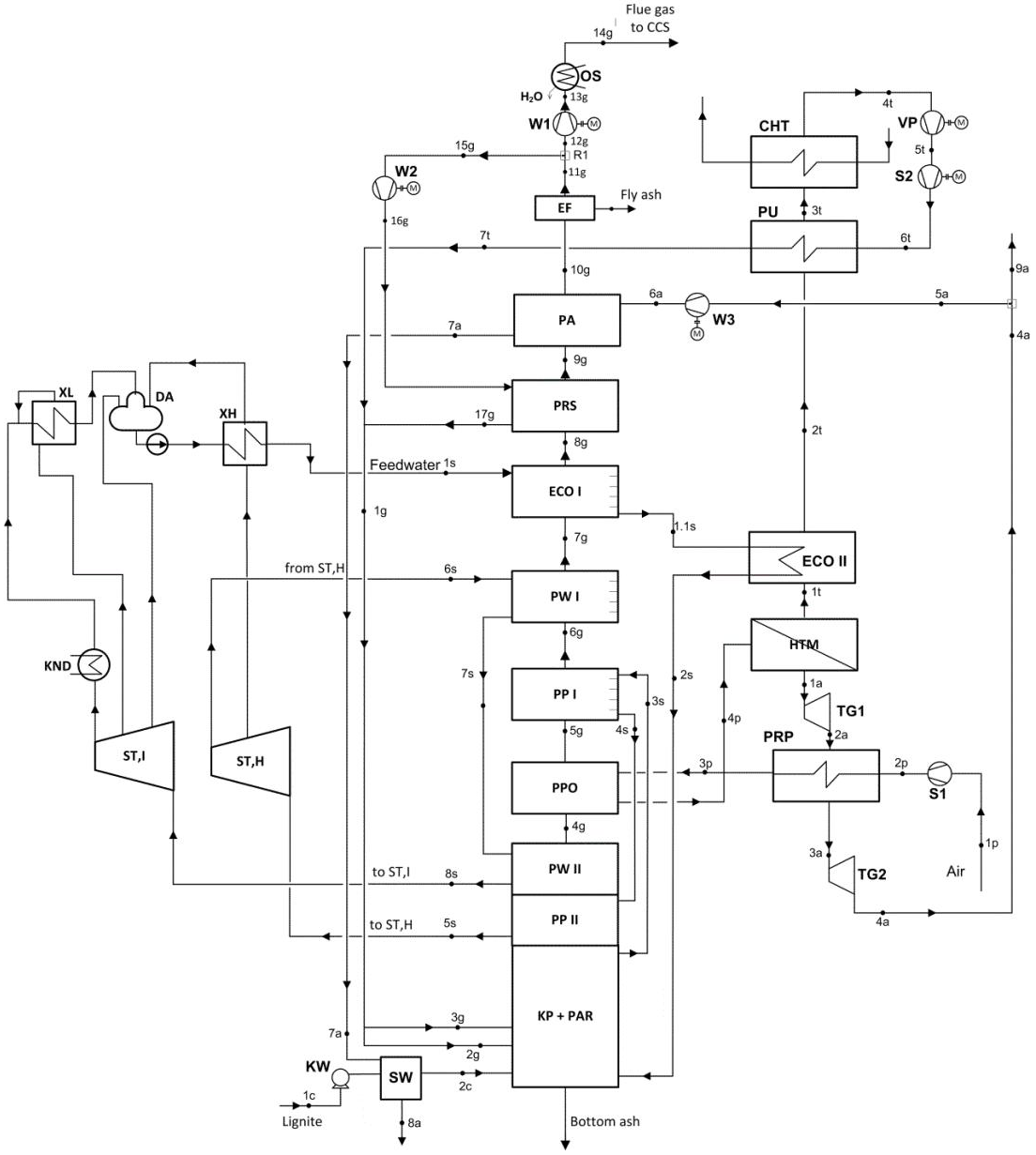

Fig. 1. Scheme of the CFB boiler integrated with lignite dryer, steam cycle, ASU and CCS installations

At the stage of adopting assumption for its construction it was decided to use provided by the GateCycle™ program the fluidized bed boiler block, which consists of: furnace chamber (AC), evaporator (EVAP) and last sections of the live steam superheater (PP II) and reheated steam superheater (PW II). In the direction of flue gas flow this block ends with particle separator (cyclone). After the cyclone gas/gas type heat exchanger (PPO), in which air from ASU installation is heated to the temperature of 850°C, was placed. Subsequently following exchangers were placed: live steam superheater (PP I), reheated steam superheater (PW I), economizer (ECO), recirculated

exhaust gas heater (PRS) and nitrogen heater (PA). The last devices in the direction of flue gas flow are: electrostatic precipitator (EF), flue gas fan (W1) and the flue gas dryer (OS) [3,4].

Table. 1. Main assumptions for OXY type CFB boiler

Lower Heating Value	kJ/kg	9960
Feedwater flow	kg/s	431.02
Feedwater temperature	ºC	297
Feedwater temperature at the outlet of ECO II	°C	340
Steam temperature at the outlet of the evaporator	°C	480
Live steam temperature at the outlet of the boiler	ºC	604.9
Live steam pressure at the outlet of the boiler	MPa	30.1
Reheated steam flow at the outlet of the boiler	kg/s	364.82
Reheated steam temperature at the outlet of the boiler	ºC	622.4
Reheated steam pressure at the outlet of the boiler	MPa	5.12
Temperature difference at the cold side of ECO I	K	55
Oxidant excess ratio	-	1.2
Oxygen content in oxidizer fed to the boiler	%	30
Temperature difference at the hot end of recirculated flue gas heater PRS	K	30
Ambient pressure	kPa	101.32
Ambient temperature	ºC	15

The boiler is supplied with lignite composed of: C - 28.60%, S - 0.95%, N - 0.25%, H - 2.20%, O - 8.00%, ash – 17.50%, moisture – 42,5% [3]. Main assumptions for the CFB boiler adopted for the calculations are shown in Table 1.

In the present model a three – end type high temperature membrane was treated as a black box, where at a given composition of the permeate (in this case 100% composed of oxygen) the recovery ratio of oxygen was a decision variable [2,5,6]. Recovery ratio of oxygen during the calculation was changed from the value of 45% to 90%. Heat losses were not included, so each of the streams within the membrane has a temperature of 850°C. The pressure losses within the same membrane were not assumed as well. Chosen assumptions for the calculations for an air separation unit are shown in Table 2.

Oxygen recovery ratio is defined as the ratio of oxygen in the stream which permeated through the membrane (permeate) to a stream of oxygen contained in the air feeding the membrane (feed).

Table. 2. Main assumptions for ASU

Air pressure at the outlet of compressor	kPa	1400
Feed temperature	°C	850
Permeate pressure	kPa	42.5
Oxygen content in the permeate	%	100
Permeate temperature	°C	850
Retentate temperature	°C	850
Oxygen temperature at the inlet to the vacuum pump	°C	20
Air compressor isentropic efficiency	-	0.88
Expanders isentropic efficiency	-	0.90
Vacuum pump isentropic efficiency	-	0.88
Temperature difference at the hot end of oxygen heater PU	K	40

Lignite dryer model was built as a simple heat exchanger in which the fuel stream is dried by the drying medium (a mixture of nitrogen and the oxygen derived from ASU). Drying medium is pre-

heated in a heat exchanger placed in the path of exhaust gas within the convective pass of the CFB boiler. Chosen assumptions for a lignite dryer are shown in Table 3.

Table. 3. Main assumptions for lignite dryer

Lignite temperature at the inlet to the dryer	°C	15
Drying medium temperature at the outlet of the dryer	°C	130
Minimum temperature difference between lignite and drying medium	K	20
Temperature difference at the hot end of drying medium heater PA	K	30
Drying medium pressure at the outlet of the drying medium fan	kPa	108

3. Methodology and computational algorithm

Lower heating value of lignite with a given in section 2 of this paper composition was calculated using the following Dulong formula variant:

$$W_{\mathrm{d}} = 340.80 \cdot \mathrm{c} + 1427.70 \cdot \left(h - \frac{\mathrm{o}}{8} \right) + 92.90 \cdot \mathrm{s} - 25.50 \cdot \left(\mathrm{w} + 9 \cdot \mathrm{h} \right) \quad \frac{\mathrm{kJ}}{\mathrm{kg}} \tag{1}$$

where: c, s, o, h, p, w - mass fractions of: carbon, sulfur, oxygen, hydrogen, nitrogen, ash and moisture in the fuel.

In the calculation process for lignite dryer it was necessary to determine the specific heat of coal before and after drying. For this purpose the following correlation was used:

$$c_{\mathrm{w}} = c \cdot c_{\mathrm{c}} + s \cdot c_{\mathrm{s}} + o \cdot c_{\mathrm{o}} + h \cdot c_{\mathrm{h}} + n \cdot c_{\mathrm{n}} + p \cdot c_{\mathrm{p}} + w \cdot c_{\mathrm{H_2O}} \tag{2}$$

where: c_{c} - specific heat of carbon (0.71 kJ·kg^{-1}·K^{-1}),

c_{s} - specific heat of sulfur (0.71 kJ·kg^{-1}·K^{-1}),

c_{o} - specific heat of oxygen (0.92 kJ·kg-1·K^{-1}),

c_{h} - specific heat of hydrogen (14.304 kJ·kg-1·K^{-1}),

c_{n} - specific heat of nitrogen (1.04 kJ·kg-1·K^{-1}),

c_{p} - specific heat of ash (0.8 kJ·kg-1·K^{-1}),

$c_{\mathrm{H_2O}}$ - specific heat of moisture (4.19 kJ·kg-1·K^{-1}).

The amount of heat that can be used to evaporate the moisture was determined from the formula:

$$\dot{Q}_{\mathrm{odp}} = \dot{Q}_{7\mathrm{a}} - \dot{Q}_{8\mathrm{a}} + \dot{I}_{1\mathrm{c}} - \dot{I}_{2\mathrm{c}} \tag{3}$$

where: $\dot{Q}_{7\mathrm{a}}$, $\dot{Q}_{8\mathrm{a}}$ - heat flux of drying medium feeding and leaving lignite dryer,

$\dot{I}_{1\mathrm{c}}$, $\dot{I}_{2\mathrm{c}}$ - physical enthalpy flux of raw lignite and lignite leaving dryer.

The mass flow of moisture evaporated in the drying process from the fuel is determined by the formula:

$$\dot{m}_{\mathrm{H_2O_odp}} = \frac{\dot{Q}_{\mathrm{odp}}}{(r + c_{\mathrm{p}} \cdot \Delta T)} \tag{4}$$

where: r - enthalpy of vaporization, kJ·kg^{-1},

c_p - specific heat of water vapor, (1.88 kJ·kg^{-1}·K^{-1}),

ΔT - temperature increase of water vapor derived from the lignite.

After evaporation of the moisture contained in the fuel the new lower heating value of the fuel must be determined:

$$W_{d_2c} = W_{d_1c} \cdot \left(\frac{1 - w_{2c}}{1 - w_{1c}} \right) + \left(\frac{w_{1c} - w_{2c}}{1 - w_{1c}} \right) \cdot r \tag{5}$$

where: W_d - lignite lower heating value, kJ·kg^{-1},

w - moisture content in lignite, kg H_2O·kg lignite^{-1}.

The whole computational process aims at setting a new stream of lignite fed to the boiler, that it was possible to determine the thermal efficiency of the boiler [7]:

$$\eta_k = \frac{\dot{m}_{5s} \cdot (h_{5s} - h_{1s}) + \dot{m}_{8s} \cdot (h_{8sl} - h_{6s})}{\dot{m}_{1c} \cdot W_{d_1c}} \tag{6}$$

where: $\dot{m}_{5s}, \dot{m}_{8s}$ – streams of live and reheated steam, kg·s^{-1},

h_{5s} – live steam enthalpy at the outlet of the boiler, kJ□kg^{-1},

h_{1s} – feedwater enthalpy at the inlet to the boiler, kJ□kg^{-1},

$h_{8s} - h_{6s}$ – reheated steam enthalpy at the inlet and outlet of the boiler, kJ□kg^{-1},

$\dot{m}_{1c}$ – raw lignite stream fed to the boiler, kg□s^{-1},

W_{d_1c} – lower heating value of lignite fed to the boiler, kJ□kg^{-1}.

4. Results of calculations

Using a model with the assumptions that were made for calculations the impact of drying of lignite supplied to the boiler on selected characteristics of the system were determined.

The first stage of the calculations was to determine the characteristics of the calculated lower heating value of fuel as a function of the changing oxygen recovery ratio at high temperature membrane. The results of this analysis are shown in figure 2. For the variant without drying the fuel heating value is maintained at a constant level of 9960 kJ/kg. In a variant with fuel drying the whole stream of the available nitrogen – oxygen mixture was used for drying. The amount of the drying medium flow varies inversely to changes in oxygen recovery ratio. That means that the lower oxygen recovery ratio the greater the flow of drying medium, and thus a greater degree of fuel drying. As it can be seen, the highest lower heating value of the fuel equal to 18210 kJ/kg was obtained for oxygen recovery ratio 0.45, then the lower heating value decreases to reach the value 12911 kJ/kg for the oxygen recovery ratio equal to 0.90.

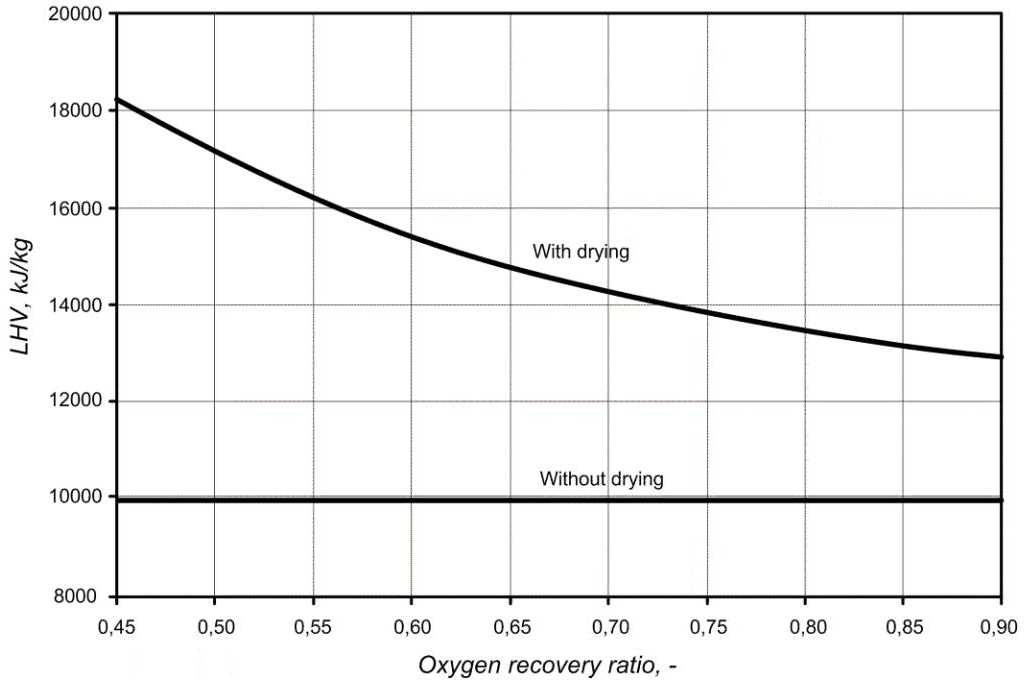

Fig. 2. Lower heating value of fuel as a function of the oxygen recovery ratio in the membrane

The next step was to examine how the flow of the lignite supplied to the boiler changes as a function of the oxygen recovery ratio at high temperature membrane. The lignite stream fed to the boiler, at constant parameters of the circulating agent, is significantly influenced by the load of the heat exchanger, in which air stream delivered to the high-temperature membrane is heated.

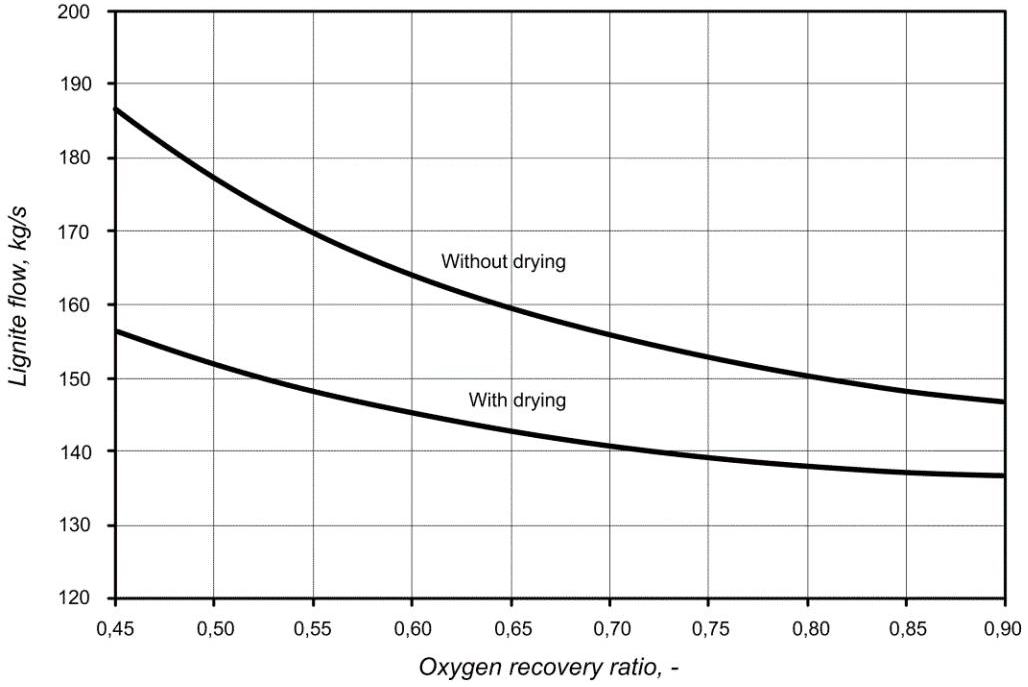

Fig. 3. Lignite stream supplied to the boiler as a function of the oxygen recovery ratio in the membrane

The lower the oxygen recovery ratio in the membrane the greater the intake air stream needed to keep the assumed excess air ratio in the combustion chamber and hence, a greater load on the heat exchanger. As it can be seen in figure 3, for the variant without drying the amount of the supplied coal for the oxygen recovery ratio from 0.45 to 0.9 it decreases from 186 kg/s to 147 kg/s, while in

the case of the drying of the fuel in the same range of oxygen recovery ratio stream of coal decreases from 156 kg/s to 136 kg/s.

As a result of the process of producing technical oxygen in the air separation unit based on three - end type high-temperature membrane in comparison with the classic coal boiler, a significant reduction in thermal efficiency of the boiler can be observed. The results of the analysis of the impact of the oxygen recovery ratio in the membrane on the boiler thermal efficiency are shown in figure 4. In the variant without drying of the fuel for the oxygen recovery ratio equal to 0.45 boiler thermal efficiency is only 63.6%. When drying of the lignite was implemented, for the same oxygen recovery ratio thermal efficiency of the boiler increased by over twelve percentage points, to 75.8%.

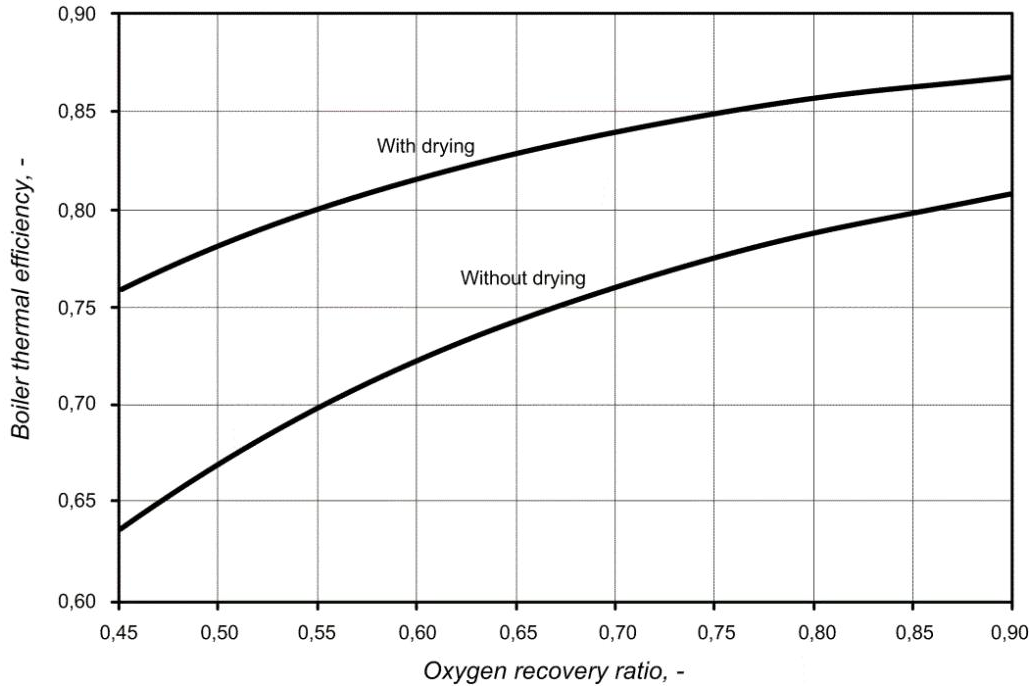

Fig. 4. Boiler thermal efficiency as a function of the oxygen recovery ratio in the membrane.

For the variant with fuel drying, despite a higher LHV of fuel for low volumes of recovery of oxygen recovery ratios in the membrane, the boiler thermal efficiency increases with the oxygen recovery ratio up to the value of 86.8%. For the oxygen recovery ratio equal to 0.9 in the variant with fuel drying an increase in thermal efficiency of the boiler compared to the variant without drying by six percentage points was observed.

Summary

This paper presents a model of the supercritical circulating fluidized bed OXY type boiler integrated with the air separation unit based on three - end type high temperature membrane and the installation of fuel drying and results of studies of the impact of lignite drying on a number of characteristics, such as mass flow of fuel supplied to the boiler and boiler thermal efficiency. A Sensitivity analysis of a built model shows that a change of oxygen recovery ratio at a high temperature membrane causes an increase in thermal efficiency of the boiler. For oxygen recovery ratio from 0.45 to 0.9 for the installation with a working lignite dryer, the boiler thermal efficiency increases from 75.8% to 86.8%. The increase in thermal efficiency of the boiler in comparison to the installation without lignite dryer ranges from 12 percentage points for the oxygen recovery ratio equal to 0.45 to 6 percentage points for the oxygen recovery ratio equal to 0.9. Basing on the outcome results it can be concluded that the fuel drying in OXY type systems fed by lignite leads to a significant increase in the boiler thermal efficiency. In addition to an increase in efficiency, the use of fuel drying leads to a reduction of water stream supplied to the system and thus helps to reduce the likelihood of condensation of moisture from the exhaust gases.

Acknowledgements

The results presented in this paper were obtained from research work co-financed by the National Centre for Research and Development within a framework of Contract SP/E/2/66420/10 – Strategic Research Programme – Advanced Technologies for Energy Generation: Development of a technology for oxy-combustion pulverized-fuel and fluid boilers integrated with CO_2 capture.

References

[1] Chmielniak T., Kosman G., Łukowicz H., Integracja instalacji wychwytu CO_2 z kondensacyjnymi blokami energetycznymi. Rynek Energii, 2008, 6 (79), 75-81.

[2] Pfaff I., Kather A.: Comparative thermodynamic analysis and integration issues of CCS steam power plants based on oxy-combustion with cryogenic or membrane based air separation. Energy Procedia, 1 (2009), 495-502.

[3] The technical report of step 6.1 in research topic: "Numerical simulations and systemic analysis of oxy - burning," the research task 2 " Development of a technology for oxy-combustion pulverized-fuel and fluid boilers integrated with CO_2 capture." in the strategic program of research and development, "Advanced Technologies for Energy Generation ".

[4] Skorek – Osikowska A., Bartela Ł.: Model of a supercritical oxy-boiler - analysis of the selected parameters. Rynek Energii, 2010, 5 (90), 69 – 75.

[5] Castillo R.: Thermodynamic analysis of a hard coal oxyfuel power plant with high temperature three-end membrane for air separation. Applied Energy, 88 (2011), 1480-1493.

[6] Stadler H. et al.: Oxyfuel coal combustion by efficient integration of oxygen transport membranes. International Journal of Greenhouse Gas Control, 5 (2011), 7-15.

[7] Liszka M., Ziębik A.: Coal – fired oxy – fuel power unit – Process and system analysis. Energy, 35 (2010), 943 – 951.

Monitoring of carbon dioxide uptake in accelerated carbonation processes applied to air pollution control residues

Felice Alfieri[a], Peter J. Gunning[b], Michela Gallo[c], Adriana Del Borghi[d], Colin D. Hills[e]

[a] Department of Chemical and Process Engineering "G.B. Bonino", University of Genoa, Genoa, Italy, felice.alfieri@unige.it (CA)
[b] Centre for Contaminated Land Remediation, University of Greenwich, Medway, Chatham Maritime, United Kingdom, peter@c8s.co.uk
[c] Department of Chemical and Process Engineering "G, B, Bonino", University of Genoa, Genoa, Italy, michela.gallo@unige.it
[d] Department of Chemical and Process Engineering "G, B, Bonino", University of Genoa, Genoa, Italy, adry@unige.it
[e] Centre for Contaminated Land Remediation, University of Greenwich, Medway, Chatham Maritime, United Kingdom, c.d.hills@greenwich.ac.uk

Abstract:

The application of Accelerated Carbonation Technology (ACT) has potential for the sequestration of carbon in waste and geological materials. ACT also has potential to be supported by carbon credit mechanisms based upon the amount of carbon sequestered from industrial emissions. For this to happen, the routine monitoring of CO2 sequestered into the solid phase is required for the planning and operation of any accelerated carbonation plant. The present paper reports the preliminary results from an assessment of existing methods for measuring CO2 imbibed into a solid by an accelerated carbonation processes. Laboratory-scale experiments were carried out to evaluate the accuracy of methodologies for measuring mineralised carbon including: loss on ignition, acid digestion and total carbon analysis. The CO2 reactivity of several wastes from municipal incineration known as Air Pollution Control residues (APCr) were also included in the study. A detailed characterisation of the materials being carbonated, using X-ray diffraction (XRD), X-ray fluorescence (XRF), thermogravimetric analysis (TGA) and ion chromatography was carried out. The results of this study showed that monitoring CO2 during accelerated carbonation is made difficult by the complex mineralogy of materials such as APCrs. As such, the presence of calcium bearing species and polymorphs of calcium carbonate formed varied between the materials investigated. The use of an acid digestion technique was not subject to interference from the chemistry or mineralogy of an ash. Among the investigated methods, acid digestion gives the most promising results as it provided robust data on the amount of carbon imbibed during processing.

Keywords:

Accelerated carbonation technology (ACT), Air pollution control residues (APCr), CO_2 uptake.

1. Introduction

Carbonation is a natural phenomenon occurring when gaseous carbon dioxide (CO_2) reacts with substrate materials, resulting in the production of carbonate salts. Carbonation can be accelerated using management techniques such as accelerated carbonation technology (ACT) working under a gaseous, carbon dioxide (CO_2)-rich environment [1]. Chemical stability and leaching behaviour of materials such as alkaline combustion residues is improved and carbonated materials can be diverted from landfill into beneficial use as engineering media [1-4].

The accelerated carbonation of alkaline combustion residues is an attractive Carbon Capture and Storage (CCS) option. These residues such as Air Pollution Control residues (APCr), are capable of combining with significant amounts of CO_2, and are often generated by processes also producing

large amount of CO_2 [1,5-7]. APCr are produced from dry and semi-dry scrubber systems fitted to municipal incinerator flue stacks, which involve the injection of an alkaline powder or slurry to remove acid gases, particulates and condensation/reaction products. Fabric filters in baghouses are used after the scrubber systems to remove fine particulates (baghouse filter dust). APCr also include the solid phase generated by wet scrubber systems (scrubber sludge) [4]. These particulates residues can contain large amounts of reactive calcium species coming from the alkaline sorbents commonly used [8,9].

The amount of CO_2 sequestered during industrial-scale carbonation has potential to be traded as a commodity. Companies, governments, or other entities buy carbon offsets in order to comply with caps on the total amount of carbon dioxide they are allowed to emit. This market exists in order to achieve compliance with obligations of Annex 1 Parties under the Kyoto Protocol, and of liable entities under the European Emissions Trading Scheme (EU-ETS). Carbon Capture and Storage is being introduced in the EU-ETS in 2013, initially for geological storage [10, 11]. It is anticipated that a carbon market will eventually provide a financial incentive for the minimization of CO_2 emissions from a wider range of industrial processes. In addition to geological storage of carbon, processes that encourage the beneficial re-use of captured carbon (e.g. in solid materials) by technologies such as ACT, will be supported.

The monitoring of the amount of carbon sequestered by carbonation processes, also known as CO_2 uptake, is a key aspect of process planning and operation. Different methods to measure the CO_2 uptake by accelerated carbonation are reported in literature. In several works the CO_2 uptake was assessed by calcimetry [12, 13], by thermo-gravimetric analysis [1, 14, 15, 16], or by gravimetric methods [14, 16, 18].

In order to ensure that the emission reductions claimed during the life time of an accelerated carbonation plant are verifiable and permanent, reliable methods for the monitoring of CO_2 uptake are currently needed that are both accurate and economical. This investigation evaluates the suitability of three methods: loss on ignition, acid digestion and total carbon analysis. A validation of these analytical methods has been carried out and presented in to ensure that future measurements in routine analysis will be close enough to the unknown true value for the CO_2 uptake.

2. Material and methods

2.1. Accelerated Carbonation of APCr

An accelerated carbonation treatment was applied to seven APCr samples (APCr 1-7) supplied by different incinerators in the UK. About 100 g of each APCrs were mixed with water (30% to 40% w/w) and treated with 100% CO_2 in static reaction vessels (20 x 10 cm) held at atmospheric pressure for 72 hours.

In order to investigate the effect of the accelerated carbonation on mineralogy, the APCrs were analysed by X-ray diffraction (XRD). A Siemens D500 diffractometer with a CuKα radiation source at 40 kV and 30 mA was used for analysis. The APCr samples were prepared as powder tablets and scanned between 5° and 65° 2θ, with a step size of 0.02° each lasting 1.2 seconds. Peak identification and interpretation of the X-ray diffractograms was achieved using DIFFRACplus EVA software (Bruker AXS).

Thermo-gravimetric analysis (TGA) and differential thermo analyses (DTA) was performed on both untreated and carbonated APCrs using a Stanton-Redcroft STA-780 Series analyser. Approximately 10 mg of material were placed in an alumina crucible (4mm of diameter). The temperature was raised between 20 °C and 1000 °C at a constant heating rate of 10 °C/min.

2.2. Synthetic standards

To test the accuracy of the three methods, ten synthetic standards (STD1-10) representative of the mineralogical composition of APCr were formulated. Analytical grade reagents; calcium carbonate ($CaCO_3$), portlandite ($Ca(OH)_2$), lime (CaO), anhydrite ($CaSO_4$), gypsum ($CaSO_4.2H_2O$), bassanite ($CaSO_4.0.5H_2O$), halite (NaCl), sylvite (KCl) and quartz (SiO_2) were combined according to Table 1. The produced synthetic standards were stored in a desiccated environment to avoid possible alteration due to atmospheric humidity.

STD1 to STD4 were formulated with a high percentage of reactive calcium phases (portlandite and lime) and a low content of calcium carbonate, simulating the composition of an untreated APCr. Other standards (STD7, STD9 and STD10) were formulated without reactive calcium species and with higher percentage of calcium carbonate, simulating the composition of a carbonated APCr. The influence of the other phases including gypsum and anhydrite were also investigated.

Table 1. Percentage mineralogical composition of synthetic standards

Standard ID	$CaCO_3$ (Calcite)	$Ca(OH)_2$ (Portlandite)	CaO (Lime)	$CaSO_4$ (Anhydrite)	$CaSO_4.2H_2O$ Gypsum	$CaSO_4.0.5H_2O$ Bassanite	NaCl Halite	KCl Sylvite	SiO_2 Quartz
STD1	0.2	-	20.8	6.5	14.1	14.9	22.3	6.1	15.1
STD2	14.1	21.9	10.4	18.8	-	-	20.0	9.9	5.0
STD3	20.7	37.2	-	-	10.0	-	15.9	5.6	10.6
STD4	20.6	24.4	-	6.5	-	6.2	31.8	10.5	-
STD5	24.7	5.0	-	-	-	9.5	14.6	17.1	29.3
STD6	40.0	6.9	9.9	5.4	3.9	17.1	4.9	9.2	2.7
STD7	36.1	-	-	4.5	-	14.8	26.9	17.8	-
STD8	50.9	4.3	5.1	4.0	15.9	19.8	-	-	-
STD9	51.3	-	-	8.2	5.3	10.1	14.9	10.2	-
STD10	55.6	-	-	19.9	-	-	14.6	-	9.9

The synthetic standards were tested using the three methods to assess their carbon dioxide content [CO_2 (%)]. All tests were conducted in triplicate for each material. The carbon dioxide uptake [$CO_{2,uptake}$ (%)] can be calculated as difference between carbon dioxide content of treated sample [$CO_{2,treated}$ (%)] minus the carbon dioxide content of untreated sample [$CO_{2,untreated}$ (%)] according to eq. (1).

$$CO_{2,uptake}(\%) = CO_{2,treated}(\%) - CO_{2,untreateted}(\%) \quad (1)$$

A validation process was carried out. Carbon dioxide content [CO_2(%)] in synthetic standards was measured and compared with the expected values. The accuracy and precision of the methods was evaluated. Equation (2) was used to assess the relative error of mean (RE_m) [19]:

$$RE_m = \frac{|Z - T|}{T} \quad (2)$$

where Z is the analytical result and T is the calculated true value. Precision was assessed by sample standard error of the mean (SE_m) (3), where σ is the standard deviation according to (4), n is the number of measurements and x_i are the observed value for the sample and x_m is the mean value of these measurements:

$$SE_m = \frac{\sigma}{\sqrt{n}} \quad (3)$$

$$\sigma = \sqrt{\frac{\sum_{i=1}^{N}(x_i - x_m)}{n-1}} \quad (4)$$

2.3. Carbonation measuring methods

Three different experimental methods were used to assess the CO_2 content of the synthetic standards. These are summarised in figure 1.

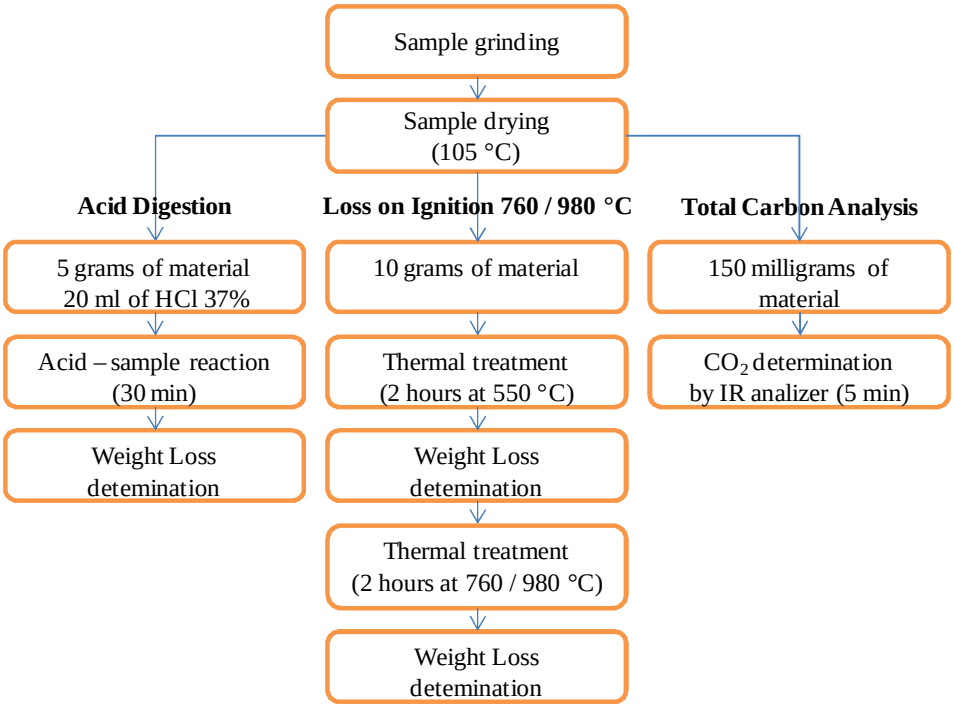

Fig. 1. Experimental methods

2.3.1. Loss on ignition (LOI)

About 10 grams of <125µm oven dried material were accurately weighed (2 d.p.) into a ceramic crucible. The crucible was placed in a temperature-controlled furnace at 550 °C for two hours. After cooling in a desiccator the mass was re-determined. LOI was determined by two further ignition cycles at 760 °C and 980 °C, being the two main decomposition ranges identified by thermogravimetric analysis. LOI was determined according to equations 6 and 7:

$$LOI(\%)_{760} = \frac{W_{550} - W_{760}}{W_{Sample}} x100 \quad (5)$$

$$LOI(\%)_{980} = \frac{W_{550} - W_{980}}{W_{Sample}} x100 \quad (6)$$

Where W_{550} is the mass of the sample after heating to 550ºC, W_{760} is the mass of the sample after heating to 760ºC, W_{980} is the mass of the sample after heating to 980ºC, and W_{sample} is the mass of the sample after heating to 105ºC.

2.3.2. Acid digestion (AD)

About 5 grams of <125µm oven dried material were accurately weighed (2 d.p.) into a 250ml plastic pot with a screw top. A connection port was fitted to lid to hold a 20 ml syringes filled with

a dilute hydrochloric acid solution (37% w/w). The pots were tightly closed and a tiny hole was drilled in the lid to allow the liberated gaseous CO_2 to escape. The entire apparatus was reweighed, before the contents of the syringe were flushed into the pot. Reweighing the apparatus continued until a constant value was achieved.

$$AD(\%) = \frac{W_{Before} - W_{After}}{W_{Sample}} x100 \quad (7)$$

Where W_{Before} is the mass of the apparatus before digestion, W_{After} is the mass of the sample after digestion, and W_{sample} is the mass of the oven dried material.

2.3.3. Total carbon analysis (TCA)

TCA was determined using a Hach Lange TOC IL-550 analyser. In the analyser, the sample is heated in a tube furnace under a stream of oxygen. Carbon present is converted to carbon dioxide, and the concentration carried in the exhaust gas leaving the furnace is quantified. Analytical grade calcium carbonate was used for the calibration of the instrument.

3. Results and discussions

3.1. APCr characterization

X-Ray Diffraction was used to analyse the seven APCrs, which were composed of eight main phases (see table 2). XRD analysis confirms the presence of calcite ($CaCO_3$) for all the residues. Portlandite ($Ca(OH)_2$) was detected in four APCrs, which was found to correlate with the TGA observation. Similarly, a unique thermal interval was found in the six APCrs for the presence of calcium hydroxide-chloride (CaClOH). Halite (NaCl), sylvite (KCl), lime (CaO), anhydrite ($CaSO_4$) and quartz (SiO_2) were also identified. Accelerated carbonation of the APCrs resulted in mineralogical change (see table 3). The disappearance of the carbon dioxide-reactive phases (portlandite, lime, CaClOH) was observed, with the formation of new calcium carbonate in the form of vaterite.

Table 2. Mineralogical composition of untreated APCrs

	$Ca(OH)_2$ (Portlandite)	CaO (Lime)	CaClOH	$CaCO_3$ (Calcite)	$CaCO_3$ (Vaterite)	NaCl (Halite)	KCl (Sylvite)	$CaSO_4$ (Anhydrite)	SiO_2 (Quartz)
APCr1			•	•		•	•	•	•
APCr2		•	•	•		•	•	•	
APCr3		•	•	•		•	•	•	•
APCr4	•			•		•	•	•	•
APCr5	•	•	•	•		•	•	•	•
APCr6	•		•	•		•	•	•	
APCr7	•		•	•		•	•	•	•

Table 3. Mineralogical composition of accelerated carbonated APCrs

	$Ca(OH)_2$ (Portlandite)	CaO (Lime)	CaClOH	$CaCO_3$ (Calcite)	$CaCO_3$ (Vaterite)	NaCl (Halite)	KCl (Sylvite)	$CaSO_4$ (Anhydrite)	SiO_2 (Quartz)
APCr1				•	•	•	•	•	•
APCr2				•	•	•	•	•	
APCr3				•	•	•	•	•	•
APCr4				•	•	•	•	•	•
APCr5				•	•	•	•	•	•
APCr6				•	•	•	•	•	
APCr7				•	•	•	•	•	•

DTA analysis of the untreated APCrs show three clear events occurring between 400 – 440 °C, 465 – 550 °C, and 550 – 760 °C. This is illustrated in the DTA curves for APCr7 (see figure 2). According to Bodenan and Deniard [8] the peak in the 400 – 440 °C interval corresponds to $Ca(OH)_2$ decomposition and the peak in the 465– 550 °C interval is related to that of calcium hydroxide-chloride (CaClOH).The 550–760 °C interval corresponds to $CaCO_3$ decomposition.

In the accelerated carbonated APCrs, the $Ca(OH)_2$ and CaClOH signatures are absent, and there is an increase in the $CaCO_3$ peak. DTA was used to assess the calcium phases present in the remaining six untreated and accelerated carbonated APCrs (see tables 4 and 5).

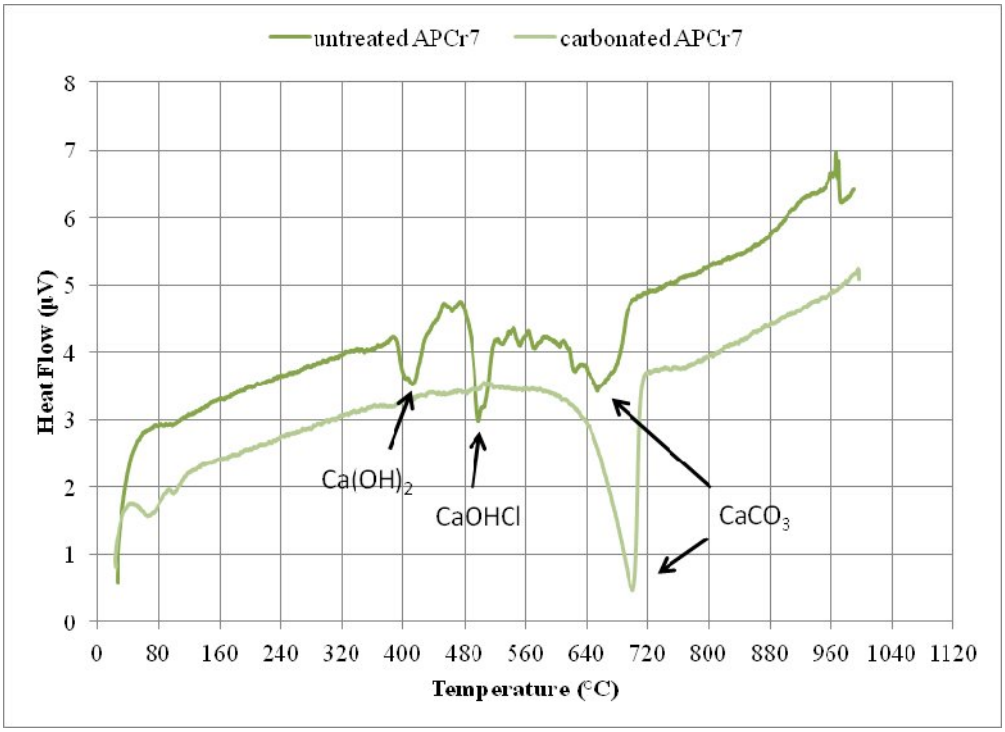

Fig. 2. DTA of untreated and accelerated carbonated APCr7

Table 4. Calcium phases of the untreated APCrs by DTA analysis

	$Ca(OH)_2$ (Portlandite)	CaClOH (calcium hydroxide-chloride)	$CaCO_3$
APCr1		•	•
APCr2		•	•
APCr3		•	•
APCr4	•		•
APCr5	•	•	
APCr6	•	•	
APCr7	•	•	

TGA analyses of APCrs show slightly differing behaviours between untreated and treated materials up to 500 °C. These differences are due to the portlandite and calcium hydroxide chloride that were found to be present only in untreated APCrs. They are responsible for two small decomposition steps at 400 °C and 500 °C respectively, due to bound water loss. In accelerated carbonated APCrs these steps are not present, although a gradual decomposition process starts at temperatures lower than 300 °C. Most significant is a sudden change in mass in the region 550–760 °C. This mass

change is significantly greater in the accelerated carbonated APCrs. A second major event begins at 800 °C (see figure 3).

Table 5. Calcium phases of the accelerated carbonated APCrs by DTA analysis

	$Ca(OH)_2$ (Portlandite)	CaClOH (calcium hydroxide-chloride)	$CaCO_3$
APCr1			•
APCr2			•
APCr3			•
APCr4			•
APCr5			•
APCr6			•
APCr7			•

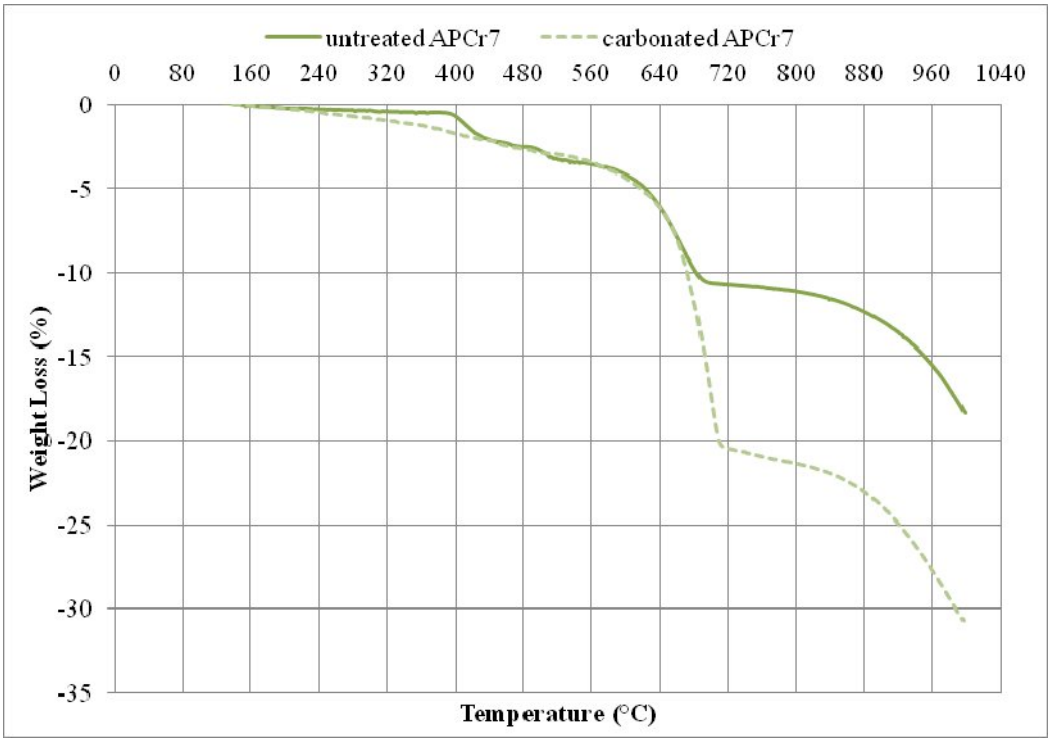

Fig. 3. TGA of untreated and accelerated carbonated APCr7

3.2. Carbonation Measuring Methods

The CO_2 content of the synthetic standards was measured by AD, TCA, LOI 550-760 °C and LOI 550-980 °C and compared with known compositions. SE_m and RE_m for all the developed methods and for all the tested standards are summarised in Table 4 and Table 5.

Table 4. Relative Error (%) of the mean (RE_m) of carbon content determination for synthetic standards.

	| Z –T | / T									
	STD1	STD2	STD3	STD4	STD5	STD6	STD7	STD8	STD9	STD10
AD	2991	32,1	7,6	6,8	5,6	1,2	3,4	5,3	4,7	13,5
TCA	515	37,75	39,70	35,2	15,0	21,8	6,8	19,7	16,5	7,1
LOI 550-760 °C	1420	125,3	107,4	94,6	70,8	68,5	43,6	51,7	25,9	62,4
LOI 550-980 °C	10919	132,3	82,9	83,8	89,2	31,8	360,7	3,1	35,8	6,1

Table 5. Standard Error (%) of the mean (SE_m) of carbon content determination for synthetic standards.

	SE_m										
	STD1	STD2	STD3	STD4	STD5	STD6	STD7	STD8	STD9	STD10	N
AD	0,4	0,2	0,9	1,2	0,8	0,9	1,1	0,1	0,9	0,2	3
TCA	0,2	0,2	0,5	0,7	0,5	0,5	0,6	0,1	0,5	0,1	3
LOI 550-760 °C	0,2	0,4	0,8	0,7	1,3	2,6	2,7	2,7	0,6	4,2	4
LOI 550-980 °C	0,3	0,8	0,1	1,3	2,4	0,9	0,4	0,2	0,8	0,9	3

3.2.1 Loss on ignition (LOI) results

The results of the LOI analyses are shown in figure 4. LOI methods were found to have a poor degree of accuracy (see table 4) and a weak linear relationship between observed and calculated CO_2 content (see figure 4). Overlaps with thermal events associated with other phases, or the presence of CO_2 bound as different polymorphs with the effect of broadening the decomposition temperature range, can be considered as possible mechanisms of affecting the measurement.

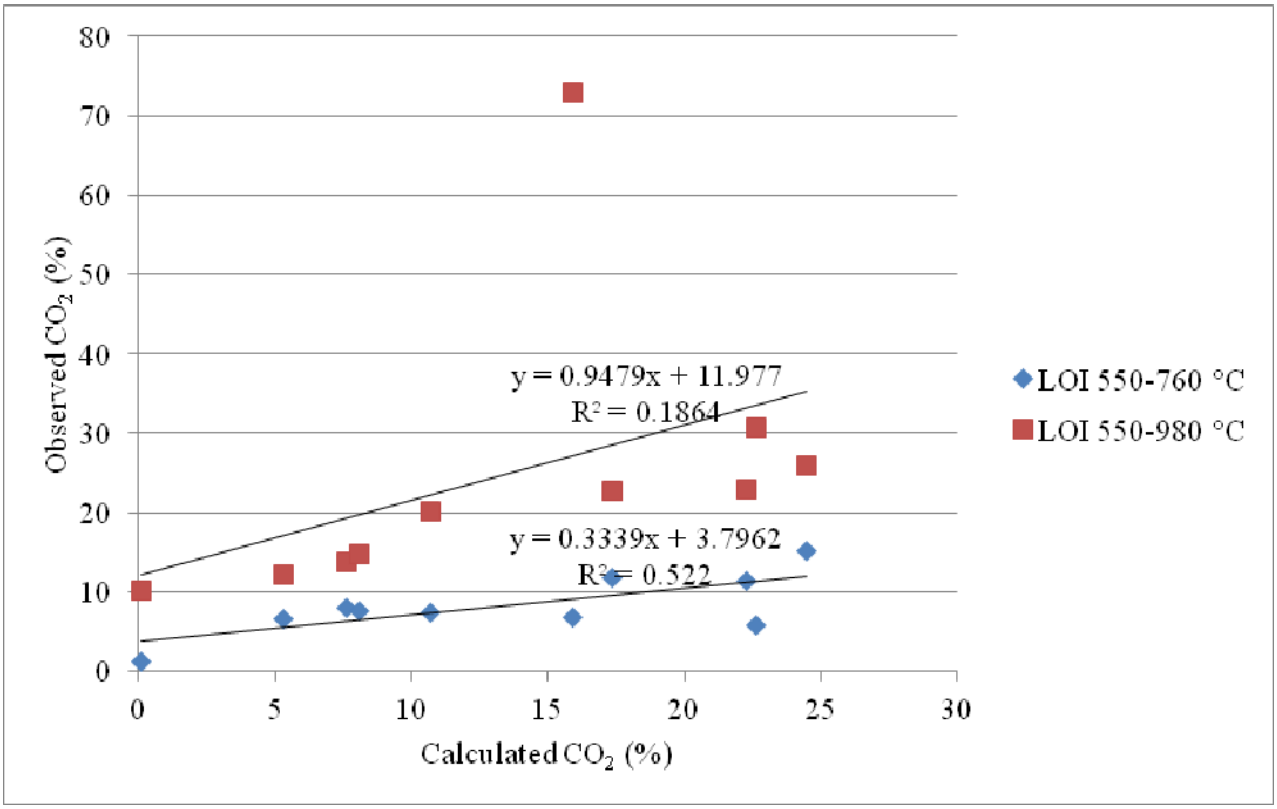

Fig. 4. CO_2(%) in synthetic standards measured by LOI (550-760) and LOI (550-980).

The significant endothermic event occurring in the range 550 – 760 °C is due to calcium carbonate decomposition.

Treated APCrs have different thermal behaviours compared to untreated APCrs. The first decomposition step starts slower and at a lower temperature (Fig. 6), affecting the accuracy of the tested LOI methods. This decomposition step could be due to decomposition of amorphous or finely divided vaterite. This polymorph of calcium carbonate is the main mineralogical product of the accelerated carbonation process. One study [20] conducted by TGA-TDA coupled with an on-line gas chromatography confirms CO_2 leaving the carbonated APCr samples at temperatures lower than 500 °C.

TGA analysis of STD7 identified further events in the 760 – 980 °C range (see figure 3). Analysis of Analar grade NaCl and KCl shows that decomposition of these minerals takes place within this range (see figure 5). Consequently, the presence of NaCl and KCl together with $CaCO_3$ can result in the overestimation of CO_2(%) by LOI 550-980 °C. $CaSO_4$ and his hydrated forms ($CaSO_4.0.5H_2O$ and $CaSO_4.2H_2O$), does not affect the LOI measurements. $CaSO_4.H_2O$ profile shows weight loss below 500 °C, related to the bound-water loss (see figure 5).

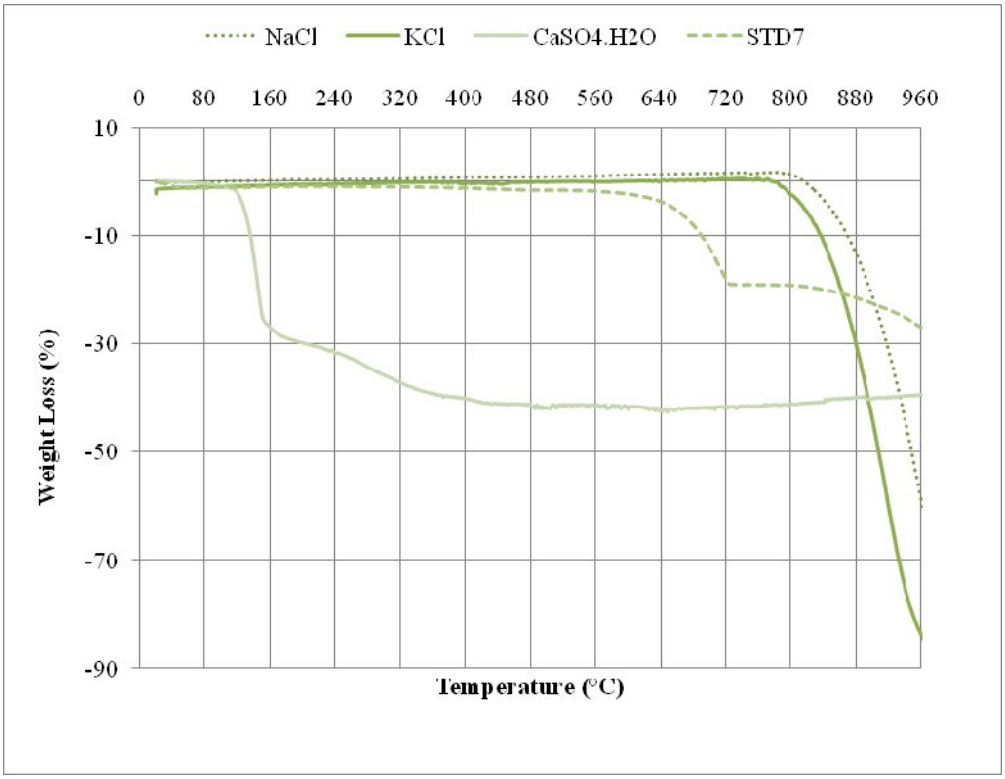

Fig. 5. Thermo-gravimetric profiles of STD7 compared to 100% NaCl and 100% KCl.

3.2.2 Acid digestion (AD) results

The results of the AD analyses are shown in figure 6. AD results show a very good linear relationship between observed and calculated CO_2 content (R^2 value 0.9824), low values of SE_m (Table 5), and low values of RE_m (Table 4) except for STD1 and STD2 characterized by a low CO_2 content (less than 5%).

During the digestion process, a 'rebound' in the weight of the sample is observed (see figure 7), which may be ascribed to evaporation of the dilute acid, followed by condensation. Hydrochloric acid can produce three different exothermic reactions with the APCr or synthetic standards (8, 9, 10). Particularly when using concentrated acid, a heating of the samples occurs due to the exothermic neutralization reactions.

$$CaO_{(s)} + 2HCl_{(aq)} \rightarrow CaCl_{2(aq)} + H_2O_{(l)} \qquad \Delta H_{reaction} = -193 kJ/mol \qquad (8)$$

$$CaOH_{2(s)} + 2HCl_{(aq)} \rightarrow CaCl_{2(aq)} + 2H_2O_{(l)} \qquad \Delta H_{reaction} = -127.9 kJ/mol \qquad (9)$$

$$CaCO_{3(s)} + 2HCl_{(aq)} \rightarrow CaCl_{2(aq)} + 2CO_{2(s)} + 2H_2O_{(l)} \qquad \Delta H_{reaction} = -15.3 kJ/mol \qquad (10)$$

In order to minimize any loss by evaporation, the acid must be diluted to 30% w/w to minimise heating of the system.

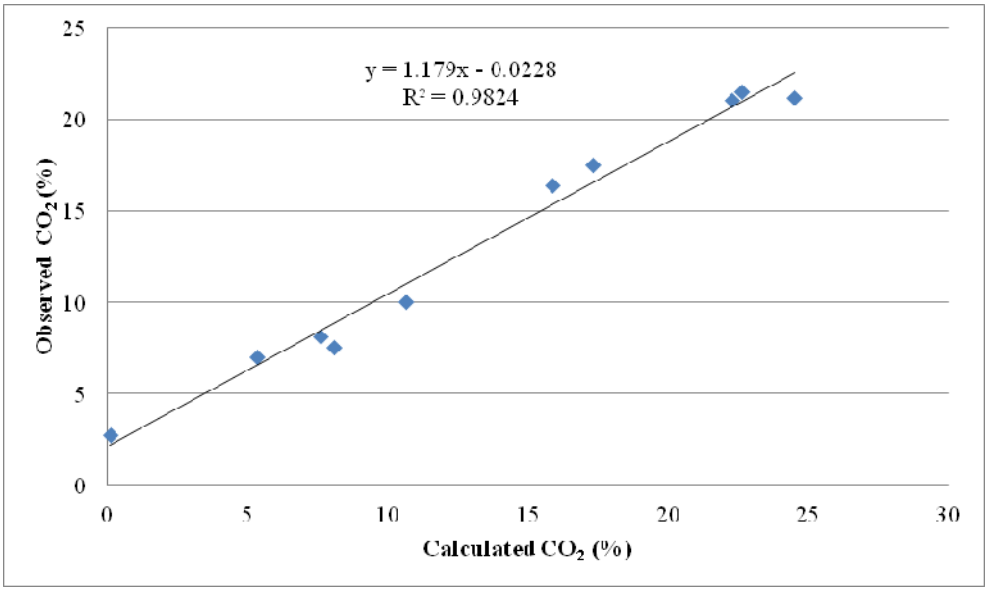

Fig. 6. CO_2(%) in synthetic standards measured by AD.

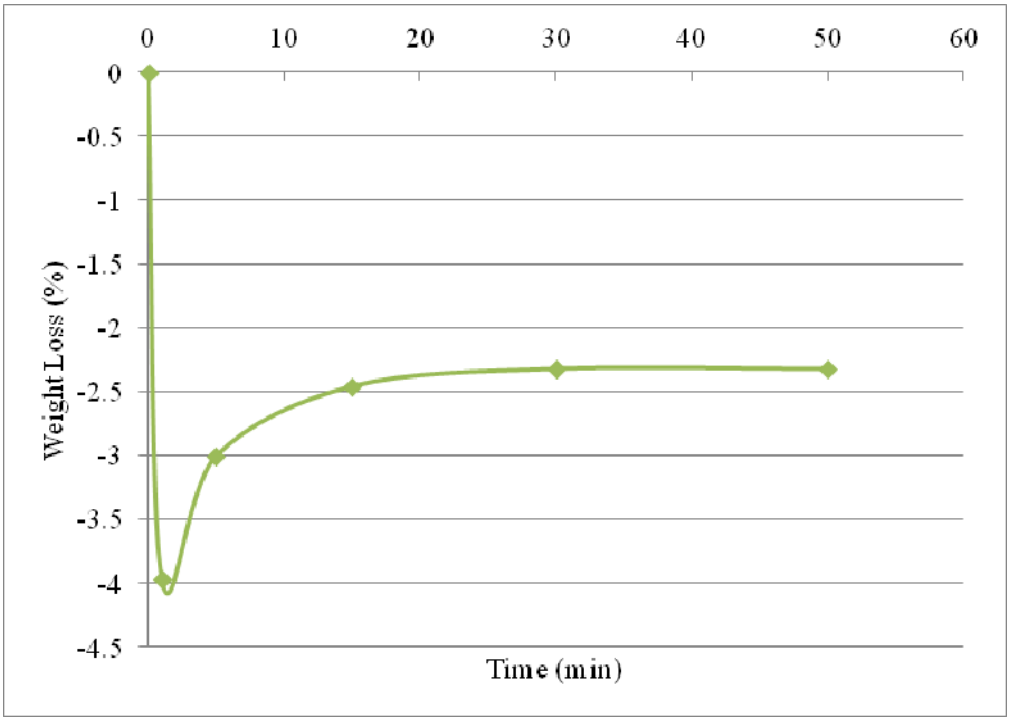

Fig. 7. Rebound effect in AD measurements.

3.2.3 Total Carbon Analysis (TCA) results

The results of the TCA analyses are shown in figure 10. The correlation coefficient shows a good relationship between the observed and calculated values. However, the accuracy of the TCA results were found to be lower than those for AD (see table 4).

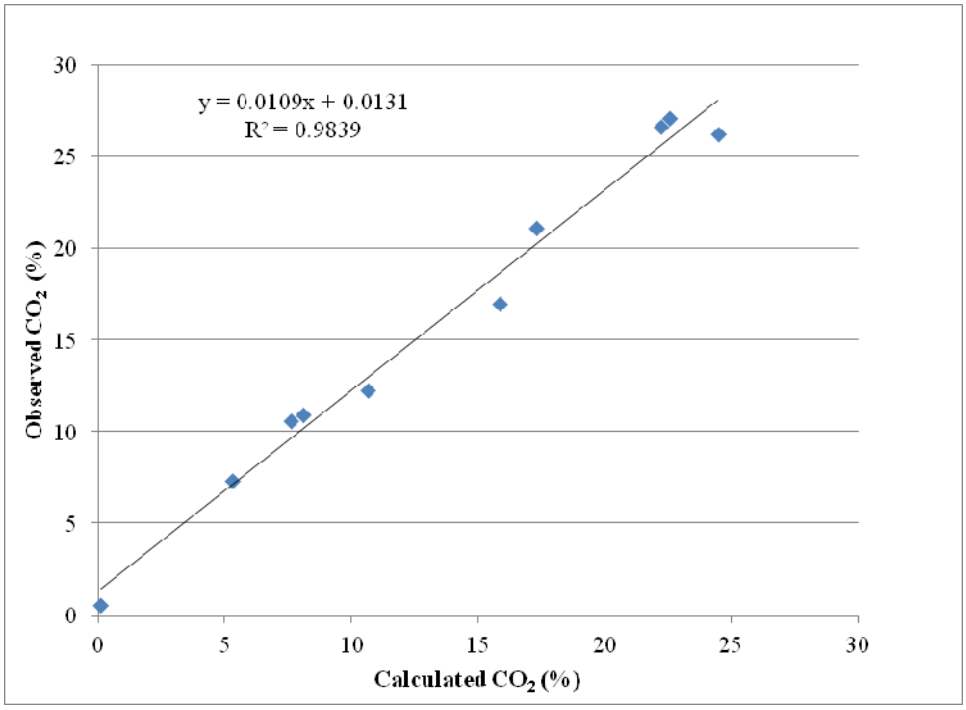

Fig. 8. CO_2 (%) in synthetic standards measured by TCA.

4. Conclusions

The accurate measurement of bound carbon dioxide in reactive materials, including wastes, is important for the purposes of assessing Carbon Capture and Storage. Municipal incineration APC residues are mineralogically complex materials. XRD and TGA-DTA have identified the presence of calcium-bearing minerals e.g. lime, portlandite, calcium hydroxide-chloride and calcium carbonate. Since different reaction mechanisms and carbonation pathways can be involved, the accurate measurement of imbibed carbon dioxide becomes challenging.

APCrs subjected to accelerated carbonation show a decrease in the minimum temperature and a broadening of the range at which calcium carbonate decomposes. TGA-DTA analyses have shown that calcium carbonate decomposition starts at temperatures lower than 500°C for treated APCr, at which point overlap with thermal events associated with calcium hydroxide and calcium hydroxide chloride occurs. Consequently, this has a significant effect upon the measured values obtained with thermo-gravimetric methods using fixed temperature ranges.

Among the tested methods, acid digestion has been shown to have good precision and a linear correlation between measured and calculated CO_2 contents. Total carbon analysis measurements show a good linear correlation with calculated results, but overall accuracy is lower while loss on ignition was found to be unreliable due to different thermal behaviour between APC residues before and after carbonation.

Obtained CO_2 uptake values, corrected for the mass balance (input/output) of the carbonation process, can be integrated during the operational life of the plant through a continuous monitoring process. This gives the opportunity of monitoring the total amount of CO_2 sequestered and the related amount of potential carbon credits.

References

[1] M. Fernández Bertos, S.J.R. Simons, C.D. Hills, P.J. Carey, A review of accelerated carbonation technology in the treatment of cement-based materials and sequestration of CO_2, Journal of Hazardous Materials 2004;B112:193–205

[2] Peter J. Gunning, Colin D. Hills, Paula J. Carey, Accelerated carbonation treatment of industrial wastes, Waste Management 2010;30:1081–1090.

[3] M. Fernández-Bertos, X. Li, S. J. R. Simons, C. D. Hills and P. J. Carey, Investigation of accelerated carbonation for the stabilisation of MSW incinerator ashes and the sequestration of CO_2, Green Chem. 2004;6:428-436.

[4] D. Amutha Rani, A.R. Boccaccini, D. Deegan, C.R. Cheeseman, Air pollution control residues from waste incineration: Current UK situation and assessment of alternative technologies, Waste Management 2008;28:2279–2292

[5] E.-E. Chang, Shu-Yuan Pan, Yi-Hung Chen, Hsiao-Wen Chu, Chu-Fang Wang, Pen-Chi Chiang (2011), CO_2 sequestration by carbonation of steelmaking slags in an autoclave reactor, Journal of Hazardous Materials 2011;186(1):558-564.

[6] Renato Baciocchi, Andrea Corti, Giulia Costa, Lidia Lombardi, Daniela Zingaretti, Storage of carbon dioxide captured in a pilot-scale biogas upgrading plant by accelerated carbonation of industrial residues, Energy Procedia 2011;4:4985–4992.

[7] Valentina Prigiobbe, Alessandra Polettini, Renato Baciocchi, Gas–solid carbonation kinetics of Air Pollution Control residues for CO_2 storage, Chemical Engineering Journal 2009;148:270–278.

[8] F. Bodenan, Ph. Deniard, Characterization of flue gas cleaning residues from European solid waste incinerators: assessment of various Ca-based sorbent processes, Chemosphere 2003;51:335–347.

[9] T. Van Gerven, D. Geysen, L. Stoffels, M. Jaspers, G. Wauters, C. Vandecasteele, Management of incinerator residues in Flanders (Belgium) and in neighbouring countries. Waste Management 2005;25:75–87

[10] EUROPA- the official web site of the European Union. Official Journal of the European Communities. Directive 2009/29/EC of the European Parliament available at: http://eurlex.europa.eu/LexUriServ/LexUriServ.do?uri=OJ:L:2009:140:0063:0087:en:PDF. [accessed 24.01.2012].

[11] UNFCCC, CMP 6 - Cancun: Carbon dioxide capture and storage in geological formations as clean development mechanism project activities http://unfccc.int/files/meetings/cop_16/application/pdf/cop16_cmp_ccs.pdf . [accessed 24.01.2012].

[12] G. Cappai, S.Cara, A.Muntoni, M.Piredda, Application of accelerated carbonation on MSW combustion APC residues for metal immobilization and CO_2 sequestration. Journal of Hazardous Materials Article in Press (2011).

[13] R. Baciocchi, G. Costa, E. Di Bartolomeo, A. Polettini, R. Pomi, Comparison of different process routes for stainless steel slag carbonation. Energy Procedia 2009;1:4851–4858

[14] Deborah N. Huntzinger, John S. Gierke, Lawrence L. Sutter, S. Komar Kawatra, Timothy C. Eisele, Mineral carbonation for carbon sequestration in cement kiln dust from waste piles. Journal of Hazardous Materials 2009;168:31–37.

[15] V. Morales-Flórez, A. Santos, A. Lemus, L. Esquivias, Artificial weathering pools of calcium-rich industrial waste for CO_2 sequestration, Chemical Engineering Journal 2011;166:132–137.

[16] Xiaomin Li, Marta Fernandez Bertos, Colin D. Hills, Paula J. Carey, Stef Simon, Accelerated carbonation of municipal solid waste incineration fly ashes Waste Management 2007;27:1200–1206

[17] Lei Wanga, Yiying Jin, Yongfeng Nie, An investigation of accelerated and natural carbonation of MSWI fly ash with a high content of Ca, Journal of Hazardous Materials 2010;174:334–343

[18] Frederic Clarens, Fidel Grandia, Sandra Meca, Lara Duro, Joan de Pablo. Determination of CO_2 sequestration capacity and stabilization of MSWI fly ash through accelerated carbonation. Proceedings of the third international conference on Accelerated Carbonation for Environmental and Materials Engineering, Turku (Finland), 29 November - 1 December 2010

[19] A. Gustavo Gonzalez, M. Angeles Herrador, A practical guide to analytical method validation, including measurement uncertainty and accuracy profiles, Trends in Analytical Chemistry 2007;26(3):227-238.

[20] Renato Baciocchi, Alessandra Polettini, Raffaella Pomi, Valentina Prigiobbe, Viktoria Nikulshina Von Zedwitz and Aldo Steinfeld (2006). CO_2 Sequestration by Direct Gas-Solid Carbonation of Air Pollution Control (APC) Residues. Energy & Fuels; 2006(20):1933-1940.

Process efficiency and optimisation of precipitated calcium carbonate (PCC) production from steel converter slag

Hannu-Petteri Mattila[a], Inga Grigaliūnaitė[b], Arshe Said[c], Sami Filppula[d], Carl-Johan Fogelholm[e] and Ron Zevenhoven[f]

*[a] Thermal and Flow Engineering Laboratory, Åbo Akademi University, Turku, Finland, hmattila@abo.fi, **CA***
[b] Thermal and Flow Engineering Laboratory, Åbo Akademi University, Turku, Finland, currently at Feyecon, Weesp, The Netherlands, ingagrigaliunaite@feyecon.com
[c] Department of Energy Technology, School of Engineering, Aalto University, Espoo, Finland, arshe.said@aalto.fi
[d] Thermal and Flow Engineering Laboratory, Åbo Akademi University, Turku, Finland, sfilppul@abo.fi
[e] Department of Energy Technology, School of Engineering, Aalto University, Espoo, Finland, carl-johan.fogelholm@aalto.fi
[f] Thermal and Flow Engineering Laboratory, Åbo Akademi University, Turku, Finland, rzevenho@abo.fi

Abstract:

CO_2 emissions could be reduced with capture and storage (CCS) methods. CCS causes costs for the industry, creating an extra barrier for implementation of these techniques. A recently developed mineral carbonation process producing a valuable product covering process implementation costs is advanced towards commercial scale. In this two-step process, calcium-rich steel converter slag is treated with an aqueous ammonium salt solution to selectively extract the calcium. Then the dissolved calcium is removed from the process liquid as pure precipitated calcium carbonate (PCC) by introducing gaseous CO_2 to the system. This concept would utilise waste material from steel industry, and spare the natural resources used for conventional PCC production. Experimental results have shown that papermaking grade PCC can be produced with ammonium nitrate, chloride or acetate solvents. The used solvent has also been regenerated and recycled between the process stages, which reduces the need for fresh solvent and lowers the process costs. To maximise the PCC production in a continuous process, a thermodynamic process model in Aspen Plus is now constructed. The modelling results are validated with a series of semi-continuous experiments. It is found that by using staged carbonate precipitation the yield of pure product is increased. Ammonium nitrate is observed to enable the highest conversion of calcium from steel slag to calcium carbonate also in continuous operation. At ambient conditions the process steps generate heat but this low temperature heat cannot be utilised. The mixing and pumping energies for process operation are small in comparison to the heat duties in chemical reactors. Preliminary results on solid-liquid separation studies, on washing of the solid outlet streams, as well as on recovery and make-up needs of process chemicals are discussed. The work is a continuation of work presented by Said et al. at 22nd ECOS in Brazil 2009.

Keywords:

Ammonium salt solution, Chemical thermodynamics, Mineral carbonation, pH swing process, Steel converter slag.

1. Introduction

It is a widely accepted fact that the climate on Earth is changing because of human activities. One major factor causing global warming is the high emission rate of so-called greenhouse gases. Of these, carbon dioxide is an especially problematic one, since modern economies are based on combustion of fossil, carbon-based fuels. Thus the amount of CO_2 emissions is also high compared to other greenhouse gas emissions like N_2O that are possibly more harmful to the climate calculated per mass only [1].

Various methods have been proposed to diminish CO_2 emissions. Apart from improving the efficiencies of existing combustion processes, choosing CO_2 neutral fuels and decreasing the need

of power and electricity on global scale, carbon capture and storage (CCS) technologies are seen as one means of reducing carbon dioxide emissions. In CCS, carbon is removed from the gases at different stages in combustion or gasification processes depending on the chosen technology. The capture techniques are already on a relatively mature level, especially for oxygen-free gases, since they have during several decades been applied for industrial processes to produce pure CO_2 [2]. Thus, one major threshold in CCS applications is currently the lack of a permanent, leakage-free storage [1].

Mineral carbonation, where the carbon dioxide gas is reacted directly with some magnesium or calcium containing compounds, is one option for safe storage. Simultaneously it offers the possibility of removing the separate capture stage. However, the mineralization reactions with natural materials are very slow by their nature, and thus development is still needed before industrial applications [3].

Apart from this, there are industrial waste materials, in which calcium or magnesium is present in more reactive forms [3-7]. For example, steel slags from steelmaking plants have been found to react with suitable solvents in such a way that calcium is selectively extracted from the slag matrix. This selective reaction enables the utilization of the produced carbonates in other industrial processes. Thus, two waste streams, CO_2 in flue gases and calcium in steel slags can be used for generating a marketable calcium carbonate product [3, 6, 7].

In this paper, a two-step pH swing process (Fig. 1) operating at ambient temperature and pressure is discussed. In this concept, calcium from steel converter slag is first leached out with ammonium chloride, nitrate or acetate solution under slightly acidic conditions, and then, after separating the slag residue, the dissolved calcium is carbonated in a separate reaction vessel with a feed of gaseous CO_2. This CO_2 gas could be absorbed to the process liquid directly from the flue gas stream from e.g. a lime kiln or a steel plant, and thus there would be no need for a separate capture unit. Naturally, the concentration of CO_2 in the flue gas would be a crucial factor for the process kinetics. In the carbonation step the ammonium salt solvent is regenerated and can be recycled back to the extraction reactor after the precipitated carbonate product has been separated.

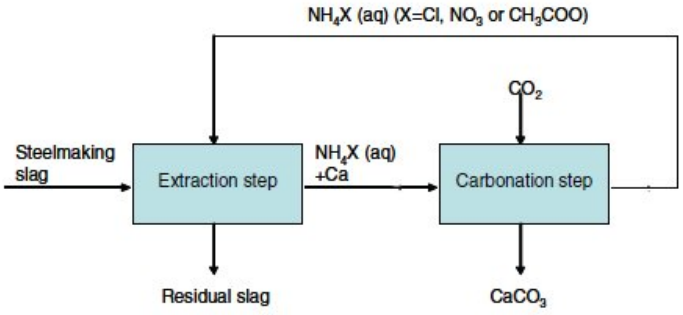

Fig. 1. A principal process scheme of the two-step pH swing process.

In this text especially the efficiencies and losses of different process steps are evaluated based on both thermodynamic modelling and experimental work. The development and scale-up of the process from laboratory scale batch tests towards industrial applications is discussed too [8-9].

The general target of the current study is to produce calcium carbonate that would meet the demands of papermaking applications; if the product could be utilised as filler or a coating pigment, Precipitated Calcium Carbonate (PCC), the profits of selling this material would according to preliminary calculations cover the costs of the carbonation process. This in turn would remove or lower the financial threshold of the utilization of CCS technologies, which usually bring large costs to CO_2 generating industries or power plants. Also, the financial incentive would enable a larger scale demonstration of this mineral carbonation concept [3, 6, 9]. To ensure a high quality product, the CO_2 feed should be free of sulphur and particulate matter.

2. Process development

2.1. Background

During earlier studies [6, 10, 11], several batch experiments have been performed to verify the effects of different process changes such as temperature and CO_2 pressure on the process chemistry. It was found that the reaction steps, which both generate some heat (see Section 4), could be performed at room temperature (20–30 °C). An increase in temperature to 70 °C had hardly any effect on the extraction stage kinetics. In carbonation the shape of the precipitated particles changes with the temperature. This restricts the applicable carbonation temperatures below 30–40 °C. The effect of carbon dioxide pressure was limited to changes in process kinetics, the precipitation rate being slower at lower partial pressures of CO_2. Thus, 20–30 °C was chosen as a suitable process operation temperature interval. At these temperatures the kinetic reaction rates are acceptable [10] and solubility and volatility of gaseous components such as NH_3 and CO_2 are beneficial for the process.

Steel converter slag was reported to contain calcium as free lime (CaO), larnite (Ca_2SiO_4) and various calcium-iron compounds that seem not to react with ammonium salt solvents. The dissolution reactions of lime and larnite are presented as (R1) and (R2). Carbonate precipitation chemistry can be summarised as (R3) and (R4). X in the reaction equations represents Cl^-, NO_3^- or CH_3COO^- (acetate), depending on the chosen salt.

$$CaO(s) + 2NH_4X(aq) + H_2O(l) \rightarrow CaX_2(aq) + 2NH_4OH(aq) \quad \text{(R1)}$$

$$2CaO*SiO_2(s) + 2NH_4X(aq) + H_2O(l) \rightarrow CaX_2(aq) + CaO*SiO_2(s) + 2NH_4OH(aq) \quad \text{(R2)}$$

$$2NH_4OH(aq) + CO_2(g) \leftrightarrow (NH_4)_2CO_3(aq) + H_2O(l) \quad \text{(R3)}$$

$$(NH_4)_2CO_3(aq) + CaX_2(aq) \leftrightarrow CaCO_3(s) + 2NH_4X(aq) \quad \text{(R4)}$$

In the batch experiments it was also observed that if solvents with molarities higher than 1.0 mol/L or solid-to-liquid ratios higher than 100 g/L were used, also some iron and manganese was extracted from the steel slag, decreasing the purity and whiteness of the process solution and the produced carbonates [10-12]. Thus, these specifications were used in the current work. Mainly ammonium chloride solutions were used, both in modelling work and in experiments, since the available data were most complete for this solvent, and also because it is cheaper than the other two ammonium salts. Some observations of experimental work with ammonium nitrate will be presented in later sections.

In larger scale, the process should preferably be operated on continuous basis to achieve presumably lower operational costs and better adaptability to changes in feedstock quality. Problems arising especially from the continuous operation as identified already by [9, 13] are the losses of solvent components (NH_3 and water vapour, ammonium and calcium salt precipitates) and dissolution of excess carbon dioxide as bicarbonate and carbonate ions in the carbonation step. The solvent losses cause an unnecessary increase in process costs, both as a need of a solvent make-up but also as a need for purification of precipitates and purged gases. On the other hand, if excess dissolved carbon species are recycled from carbonation to the extraction unit, solid calcium carbonate is precipitated on the slag particles, lowering the overall production rate of pure carbonate product (PCC). These problems exist to some extent also in a batch type process.

2.2. Process modelling

Thermodynamic modelling and simulation software Aspen Plus 7.2 were utilised to study the possibilities to decrease losses of both carbonate product and solvent components. The software

also provided information on sizes and compositions of different process streams. The model design is shown in Fig. 2. It consists of one extraction step “EXTRACTO”, and two carbonation steps, “CARBONAT” and “SETTLER”. All these reactors are so called RGIBBS units, which calculate the output by minimizing Gibbs’ free energy of the system. Carbonation is divided in two stages to enhance the precipitation rate of calcium (see Section 3.1.).

25 ton/h dry steel converter slag, containing 5%-wt CaO and 59%-wt Ca_2SiO_4, the remaining 36%-wt consisting of inert compounds, is fed to the extraction reactor together with an ammonium salt solution (~1 mol/L NH_4Cl). The solid-to-liquid ratio used in modelling is approximately 100 g slag in one litre of solvent [10-11].

In the first carbonate precipitation unit, “CARBONAT”, 85-100% of the calcium-rich solution from extraction unit is put in contact with 25 ton/h flue gas containing 20% CO_2 and 80% N_2, being approximately the composition of lime kiln flue gases. The 300 °C flue gas is fed to the process via a cooling unit to estimate the released heat, when the gas is brought down to room temperature (20°C). The flue gas feed amount is adjusted so that approximately 5% of the CO_2 gas leaves the system unreacted. After the first step the solution is flashed to 0.5 bar in “VAPORSEP”, thus removing the non-reacted gases. Re-pressurisation to 1.0 bar is done by a separate “PUMP” unit. The “SETTLER” unit is used to increase the pH of the once carbonated solution, so that the chemical equilibrium can be shifted to favour additional precipitation of calcium carbonate. This is done by introducing 0-15% of the calcium-rich solution coming from the extraction unit directly to “SETTLER” as a bypass stream of “CARBONAT”. At the same also some calcium is added to the “SETTLER” reactor, shifting the equilibrium even further towards carbonate. After this second precipitation unit the solution is again flashed to 0.5 bar in “VAPORSE2” and pressurised to 1.0 bar with “PUMP2” to remove dissolved gases.

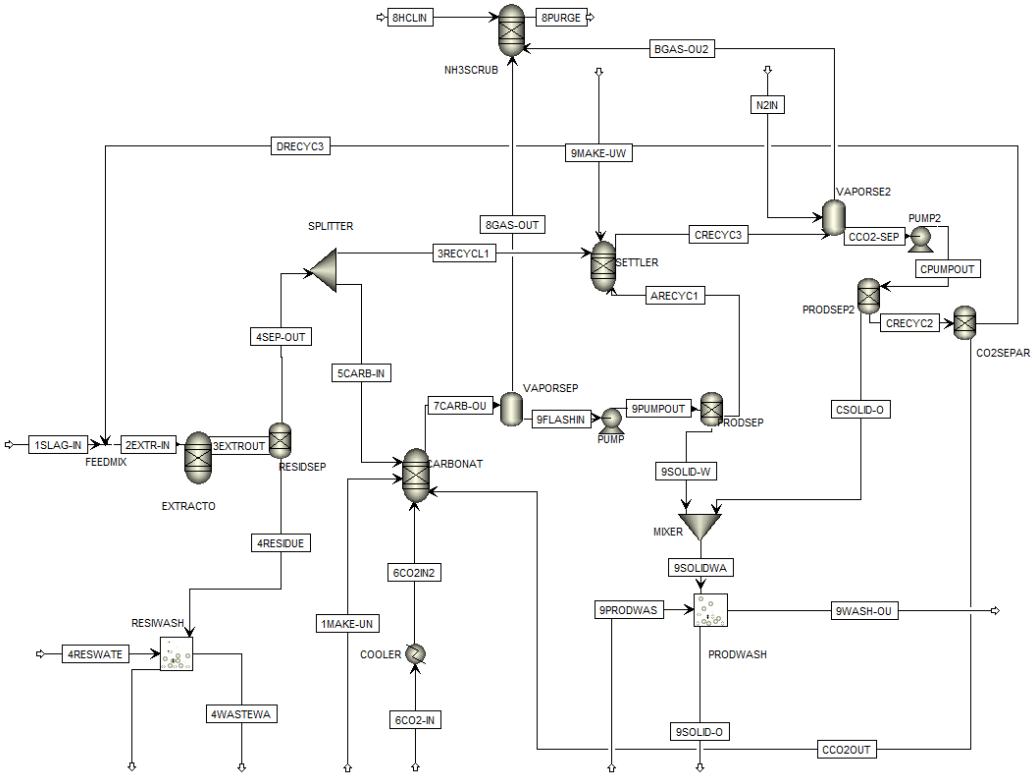

Fig. 2. A detailed process scheme of the pH swing process as simulated with Aspen Plus.

Solids are separated from the process solution with “RESIDSEP” for slag residue and “PRODSEP” and “PRODSEP2” for carbonate product. These units are based plainly on percentages of separation efficiency specified for each component. They can be thickeners, filters, hydrocyclones and combinations of these. Later in this paper some studies on gravitational separation of steel slag are presented. Both the slag residue (“RESIWASH”) and produced PCC (“PRODWASH”) are washed

to dissolve the chloride salts precipitated on these particles. To demonstrate the recovery of vaporised ammonia from the carbonation steps, an additional RGIBBS unit, "NH3SCRUB" is introduced to the model. In this unit an HCl solution is reacted with NH_3 vapour to produce aqueous NH_4Cl. These aspects are discussed in more detail in Section 5.

The solvent liquid is recycled in the process. Also make-up streams for ammonia and water are included in the model to maintain the balance with vaporization losses. The "CO2SEPAR" unit is not active in this model, although it could be used to artificially decrease the concentrations of carbon species in the recycled stream.

2.3. Experimental work

A set of five experiments was performed to provide information that could not be obtained from the modelling work, but also to confirm that the modelling results can be applied for predicting the behaviour of the process in practice. Thus, the product yields and conversion rates from the Gibbs energy minimization performed in Aspen Plus software and experimental work could be compared with each other, but also the purity and crystal shape of PCC product, properties that are difficult to model, were studied in experiments. In future, the exact experimental result values may be used in modelling work to get better estimates for the large scale stream sizes and energy needs of the process.

The tests were done at ambient conditions (20°C, 1 bar), with a mechanical stirrer (170 rpm) in the extraction reactor, using 1 mol/L ammonium chloride or ammonium nitrate solution, and maintaining the slag-to-liquid ratio at approximately 100 g/L during extraction. After each experiment the process equipment was modified according to the obtained results before the next experiment (Tables 1 and 2).

Table 1. Experimental parameters

Experiment	1	2	3	4	5
Reaction time, min	75	135	180	255	255
Ammonium salt	NH_4Cl	NH_4Cl	NH_4Cl	NH_4Cl	NH_4NO_3
Volume of ammonium salt, ml	750	1500	2500	3500	2500
System filled in the beginning	No	No	Yes	Yes	Yes
Initial slag amount, g	50	50	50	50	50
Total slag amount used, g	50	70	90	110	110

Table 2. Amount of equipment used in experimental set-ups

Experiment	1	2	3	4	5
Filters	2	4	4	4	4
Settlers	0	1	0	1	0
Pumps	2	4	5	4	4
H_2O lock	0	1	1	1	1
pH adjustment unit	0	0	1	1	1
CO_2 removal unit	0	0	1	1	1

Table 3. Volumes, volume flows and residence times in experiments 4 and 5

Unit	Volume, ml	Volume flow, ml/min	Residence time, min
Extraction	500	20	25
Carbonation	300	15	20
pH adjustment	500	20	25
CO_2 removal	500	20	25
Filter equipment	600	N/A	N/A

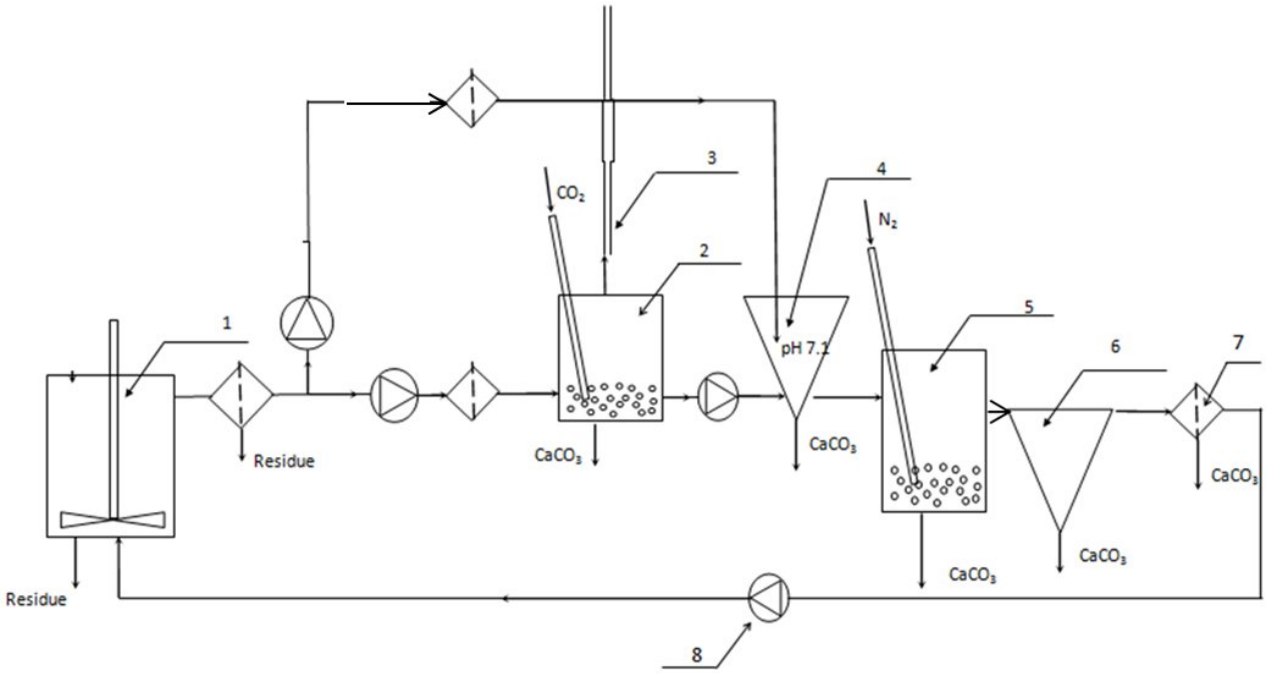

Fig. 3. Process scheme for experiments 4 and 5. 1 – Extraction step; 2 – Carbonation step; 3 – water lock; 4 – pH adjustment unit; 5 – CO_2 removal unit; 6 – Settler (not used in experiment 5); 7 – Filtration step; 8 – Pump.

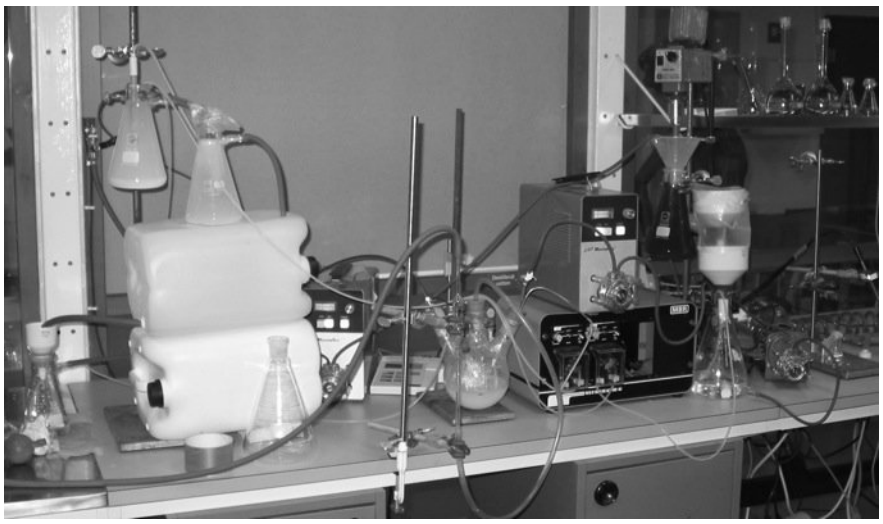

Fig. 4. Process equipment used in experiments 4 and 5.

Figs. 3 and 4 represent the process equipment of experiments 4 and 5, for which the most successful and advanced setup was constructed. Volume flows and residence times for these tests are shown in Table 3. In experiment 4 the whole system was filled with ammonium chloride solution, of which 0.5 L with 50 g steel converter slag (size fraction 125-250 µm) was fed to the extraction reactor. 5 g slag was added to the extractor with 15 minutes interval during the whole experiment. To allow for the calcium concentration in the extractor to increase towards a constant level, the solution was allowed to react 5 minutes before the pumps were switched on. Fine particles were continuously removed from extraction reactor via an overflow of 20 ml/min. The overflow was filtered to prevent solid particles from entering the carbonation stages. 75% of the filtrate (15 ml/min) was pumped to the 1st carbonation reactor, where a small overpressure (0.02 bar) of carbon dioxide (99.9996%, Oy Aga Ab) was maintained with a water lock. CO_2 was introduced through a Waters 10 micron Hplc solvent inlet filter (WAT025531) to provide an even gas distribution. Pure CO_2 gas was used because of the impracticality of actual flue gas, but as mentioned above, this has been found to mainly affect the process kinetics, if the flue gas is sulphur-free and contains no solid particles.

The remaining 25% (5 ml/min) of the filtrate from extraction was fed to the 2nd precipitation stage to adjust the pH of this step to approximately 7. The neutralised solution was transferred by gravimetric flow into a vessel, where 99.9999% nitrogen (Oy Aga Ab, 0.5 L/min) was bubbled through the liquid to remove the unreacted CO_2. Finally, the slurry was allowed to settle in another vessel, after which the overflow was filtered with 0.45µm/47mm membrane (Pall Life Sciences, Supor-450) and the particle-free solution (20 ml/min) was recycled back to the extraction reactor. Since the product was not continuously removed from the system, this process can be described as semi-continuous. For comparison, the experiment was repeated with ammonium nitrate solvent, other parameters unchanged. The settler, however, was not used in the nitrate experiment, since it was observed to have no effect in experiment 4.

Samples were taken of both the slag residue and the produced PCC. They were dried overnight at 105°C and analysed with SEM/EDX to get an approximate elemental composition. The concentrations of dissolved calcium ions were measured after each step with an ion selective electrode (NICO 2000).

3. Conversion efficiencies of calcium and CO_2 to PCC

3.1. Modelling results

Theoretically, based on presented assumptions on extraction chemistry and slag composition, 44.7% of the calcium present in the feed can be extracted. However, if only one carbonation unit is used, almost 7% of this extracted calcium will precipitate as a mixture with slag residue in the extraction reactor. Table 4 represents the effect of different bypass fractions on the efficiencies of both calcium and carbon dioxide conversions. As can be seen, according to the model already a 5% bypass stream is enough to reduce the losses by 40%. With a 15% bypass practically all extracted calcium could be utilised as marketable product. On the other hand, the amount of sequestered CO_2 remains constant, since the total amount of $CaCO_3$ precipitate is not changing.

Table 4. Modelled conversion efficiency calculations of calcium and CO_2 to PCC with various process configurations

Bypass fraction	%	0	5	10	15
Reactive calcium feed	kmol/h (ton/h)	108 (4.3)			
PCC product	kmol/h (ton/h)	101(10.1)	104(10.4)	107(10.7)	108(10.8)
PCC in residue	kmol/h (ton/h)	7(0.7)	4(0.4)	1(0.1)	0(0)
Loss of marketable calcium	% of reactive input	6.5	3.7	0.9	0.0
Conversion of total Ca to PCC	%	42	43	44	45
CO_2 feed	kmol/h (ton/h)	114 (5.0)			
CO_2 not sequestered	kmol/h (ton/h)	6 (0.3)			
	%	5.3			

Table 5. Modelled changes in solution pH values at different stages of the process

Bypass fraction	%	0	5	10	15
pH after extraction		10.61	10.70	10.83	11.13
pH after 1st carbonation		7.68	7.64	7.61	7.61
pH after 2nd carbonation		7.71	7.87	8.18	8.68

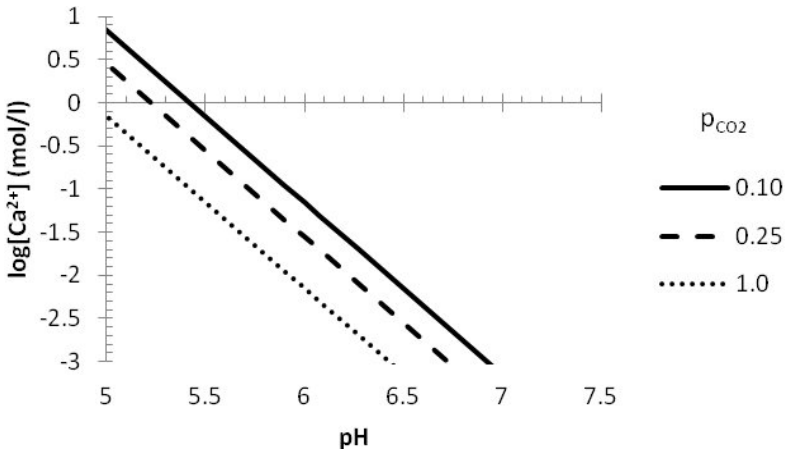

Fig. 5. Theoretical dependency of dissolved Ca^{2+} equilibrium concentration at 20°C on pH and CO_2 pressure modified from [14].

The chemical explanation for this behaviour can be summarised in Table 5 and Fig. 5. When the pH of solution is increased, the concentration of dissolved calcium at thermodynamic equilibrium is decreased. Consequently, the precipitation of $CaCO_3$ is favoured at higher pH values. In the Aspen model, the increase of pH after both carbonation steps at different bypass rates is almost one pH unit from 0 to 15% bypass, resulting in the above described shift in marketable carbonate production efficiency. Thus, pH measurement and adjustment can be used for process control purposes.

3.2. Experimental results

Experimentally obtained conversion rates (Table 6) are remarkably lower than modelling results (Table 4). This can be partially explained by experimental inaccuracies, the main reason being the lower extraction efficiency from the used steel converter slag. As discussed in [10], this might be due to a long storage time in laboratory conditions. However, in general it can be observed that by introducing the pH adjustment unit with a 25% bypass stream passing the first carbonation unit, the total conversion of calcium from slag to precipitated product can be enhanced. Compared to a case with only two reactors, one extractor and one carbonator (Experiment 1), the setup described in Figs. 3 and 4 (Experiment 4) was able to increase the conversion efficiency by 13 %-units. By changing the ammonium chloride solvent to ammonium nitrate an additional increase of 7 %-units was measured (Experiment 5). When carbon dioxide concentration was decreased before the pH adjustment unit (Experiment 3), the calcium conversion was 5 %-units lower than in experiment 4.

Nevertheless, results from experiment 2 show that only by introducing an additional settler unit, compared to experiment 1, a similar conversion efficiency as with the pH adjustment system can be obtained. From the measured calcium concentrations (Table 7) it can be seen that this is actually due to a more efficient extraction conversion, depending on the variation of the input slag composition and on the different operation of pumps during the experiments, which resulted in longer residence times during extraction.

Fig. 6 shows the recorded pH values from experiments 3-5, where the pH adjustment unit was used. It can be seen that the levels are stabilising quite well to constant values both in extraction and in carbonation, especially in experiments 4 and 5. Still, the extraction pH is slightly decreasing with time, indicating carbonate precipitation also in this reactor. The stable carbonation pH at approximately 6.3 with a calcium concentration of 0.004-0.007 mol/L is quite well corresponding to the theoretical values of Fig. 5 (pH 6.3 gives 0.002 mol/L), when the experimental inaccuracy is taken into account as well. Also, the pH values obtained from Aspen Plus are systematically 1.3-2 units too high compared to the experimental results.

Table 6. Experimental conversions of steel slag into PCC

Experiment		1	2	3	4	5
Reactive calcium feed	g/h	5.8	4.5	4.3	3.7	3.7
PCC product (carbonator)	g/h(% of total)	2.5(100)	4.2(75)	1.9(51)	1.4(31)	2.0(35)
PCC product (pH adjustment)	g/h(% of total)	-	-	0.8(20)	2.3(51)	3.5(60)
$CaCO_3$ (other system)	g/h(% of total)	-	1.4(25)	1.1(29)	0.8(18)	0.3(5)
$CaCO_3$ (total)	g/h	2.5	5.6	3.8	4.5	5.8
Conversion of reactive Ca	%	17	49	35	48	62
Conversion of total Ca	%	8	22	16	21	28

Table 7. Experimental Ca^{2+} concentrations after and before extraction reactor

Experiment		1	2	3	4	5
Ca^{2+} after extraction reactor	mol/L	0.026	0.041	0.012	0.015	0.018
Ca^{2+} before extraction reactor	mol/L	0.007	0.019	0.004	0.007	0.004

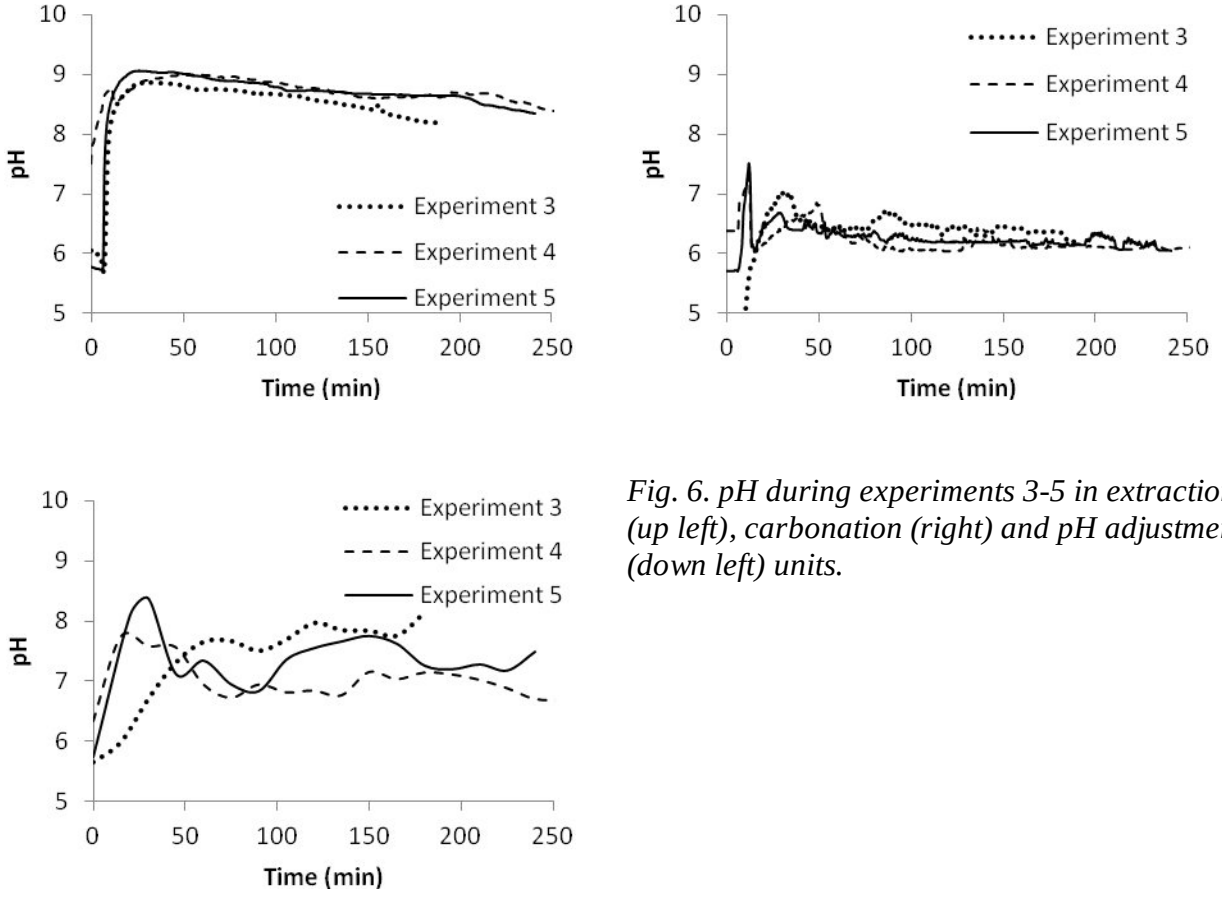

Fig. 6. pH during experiments 3-5 in extraction (up left), carbonation (right) and pH adjustment (down left) units.

A remark that can be made based on Fig. 6 is that the pH in the pH adjustment unit has been quite unstable during the experiments. Thus, applying a process control device to steer the bypass rate as proposed in the previous section would improve the performance of the experimental setup.

4. Energetic properties of the process

Based on the presented Aspen model, heat duties of different process steps can be estimated. In Table 8 values are shown for the case with a 15% bypass, which was in above discussion found to result in highest production rate of pure PCC. It can be observed that all process steps, except for the flashing units, are exothermic, i.e. release heat. However, as the process is operated at low

temperature, this heat can in practice not be utilised. Only exception is the cooling unit for flue gas, where the gas is cooled from 300°C to 20°C. The maximum amount of reversible work from these process steps, when the ambient temperature is assumed to be 20°C, is shown as exergy in Table 8. Calculations were made using (1) for heat Q [15].

$$Exergy(Q) = (1 - \frac{T^0}{T}) * Q \quad (1)$$

Table 8. Heat duties, inlet temperatures and pressures as well as exergies of heat in different process steps according to Aspen Plus model (Fig. 2) with 25 ton/h slag feed and a 15% bypass

Process unit	Q(kW)	Θ_{in}(°C)	p(bar)	*Exergy* (Q)@T^0=293.15K(kW)
EXTRACTO	-1638	20	1	0
CARBONAT	-2614	20	1	0
COOLER	-2010	300	1	982
VAPORSEP	258	20	0.5	-
SETTLER	-62	20	1	0
VAPORSE2	215	20	0.5	-
SUM	-5851			982

It must also be noted that the heat duties for process units where gas absorption into process solution, or vaporization of solvent liquid is occurring, include also these values, besides of the actual heats of chemical reactions. If the results are presented as specific values, the result becomes 66 W/kg slag for the extraction step. During carbonation, 390 W/kg PCC is generated. This value is a sum of all units listed in Table 8, excluding the extractor.

Two energy-related topics not yet discussed are the energy inputs needed for pumping the process liquids and mixing the contents of the reactor units, especially during extraction, where a large amount of solids is blended with a liquid stream. From the presented Aspen model the power consumption of the two pumps to pressurise the liquid streams after flashing is 2.8 kW for "PUMP" and 3.4 kW for "PUMP2", calculated according to $P=\Delta p*\dot{V}$, where Δp is the pressure change (0.5 bar) and $\dot{V}$ is the volume flow. Compared to heat duties in reactors, these are quite small numbers. In general, also other pumping equipment will be needed for the process, but since the pressure losses can be assumed to remain low with small distances and height differences, even for flows of 200-250 m^3/h.

For mixing, the energy dissipation ε from the stirrer can be calculated with (2) [16], where Po is Power number, n is the frequency of rotation for the mixer (1/s), d is the diameter of the mixer (m), and V is the total volume (m^3).

$$\varepsilon = \frac{Po * n^3 * d^5}{V} \quad (2)$$

Power number can be estimated from Reynolds number of mixing according to (3) [16], where ρ is the density of the solution and η is the viscosity of slag-ammonium salt solution mixture, calculated from (4) [17] with ε_p as the volume fraction of slag (m^3/m^3) and η_p the viscosity of the dispersed material. Also is assumed that the viscosity of ammonium salt solution will not differ noticeably from viscosity of pure water.

$$\mathrm{Re}_v = \frac{\rho n d^2}{\eta_{mixture}} \quad (3)$$

$$\eta_{mixture} = \frac{1+1.5\dfrac{\eta_p \varepsilon_p}{\eta_p + \eta_{H_2O}}}{1-\varepsilon_p}\eta_{H_2O} \approx \frac{1+1.5\varepsilon_p}{1-\varepsilon_p}\eta_{H_2O}, \text{using } \eta_p >> \eta_{H_2O} \quad (4)$$

With input values η_{H2O} = 1002.7*10^{-6} Pa*s, ρ_{slag}=2604 kg/m^{3}and $\rho_{solvent}$ =1008 kg/m^3, (4) yields $\eta_{mixture}$= 1102*10^{-6} Pa*s. Together with ρ=1074 kg/m^3, and with experimental values n=5 1/s and d=0.09 m, Re$_v$ =39471. In other words, the mixing situation is clearly turbulent. Power number in a vessel without baffles for a turbine stirrer is then estimated to 1.25, resulting finally to energy dissipation of 0.076 W/kg$_{solution}$. In a fully baffled reactor, resulting to better mixing, the power number would be approximately 6, yielding to 0.369 W/kg$_{solution}$ [16].

If it is further assumed that the ratio of mixer diameter and vessel volume is maintained constant in scale-up, this means that plainly mixing of slag and ammonium salt solvent in extraction requires 20.8 kW/25 ton slag, or 0.8 kW/ton slag. Related to PCC production, this equals to 1.9 kW/ton PCC. If the experimental residence times (Table 3) would be used for the larger scale, this would mean 0.8 kW/ton slag * (25/60) h = 0.33 kWh/ton slag. However, these numbers do not include the electrical losses of the system (90% efficiency would yield to 23.1 kW/ 25 ton slag), nor they are optimised considering the mixer dimensions and reactor size relation. When compared to heat duties of the different reactors (Table 8), it can be seen that also the mixing energy has a small, yet significant role for the overall energy balance of the process.

For the carbonation reactor, the energy dissipation in mixing would be lower since the high gas flow through the reactor lowers the solution density and viscosity. Also, depending on the gas inlet arrangement, the mixing caused by the gas flow itself could be sufficient to obtain the required dispersion of solution components.

5. Studies on additional process units

5.1. Separation equipment

As mentioned in Section 2.2, various options exist for continuous separation of solids from the aqueous streams. For steel slag separation, a gravitational settling tube (Fig. 7) was tested experimentally [18]. The utilised plastic tube with a circular cross-section had a volume of 8.64 L (*length 110 cm, diameter 10 cm*), and it was used with a feed flow of 40 L/h. The underflow was maintained at ~7 L/h, a value high enough to guarantee a steady stream for the concentrated particle suspension, resulting thus to an overflow of 33 L/h.

The feasibility of using the settling tube was tested with spherical Ballotini glass beads (ρ_p = 2634 kg/m^3, $\bar{d}_p$ = 163 µm) in water. Tests were performed with the settling tube positioned horizontally (0°) and at an angle of 10°. The beads settled within 0-22 cm from the feed orifice on the horizontal tube and approximately within the same range in the tube with 10° angle. The distances where the settling occurred were observed visually during the experiments. Because of the large size and high density of the glass beads the separation efficiency was ~100%.

To obtain an estimate with separation efficiencies with the actual steel slag, tests were performed with the steel converter slag (ρ_p = 2604 kg/m^3, $\bar{d}_p$ = 96 µm) that was used also as an input material for the modelling work described in Section 2. Angles of 30° and 45° were used with water as the liquid phase, but 45° was tested also with 1 mol/L NH_4Cl. Sedimentation was observed between 0-83 cm (0-80 cm for 45°), although the determination was quite challenging due to a very turbid suspension.

After the process had reached a steady-state, a sample was taken from the outflow to determine the concentration of particles. The samples were filtrated, dried in an oven at 105 °C and weighed. Calculated from (5), the separation efficiencies were 99.9% for both 30° and 45° experiments.

$$\eta = \frac{c_{in} - c_{out}}{c_{in}} * 100\% \quad (5)$$

However, a SEM picture taken of an overflow sample revealed that the particle size in this fraction was approximately 1-2 μm, indicating thus that for the actual slag particles the separation efficiency had been 100%, in accordance with the glass particle experiments. Only a fraction of small particles released from the slag was leaving the separation unit through the overflow. Thus, according to these tests, a gravitational settler could be utilised for steel slag separation in a continuous process, but it should be accompanied with a filter to remove also the fraction of dissolved, micrometre scale particles. At the same, this filter could also be used to protect the pump needed to transport the process liquid from extraction to carbonation. In a larger scale process, the height of the settler tube would directly affect the needed pumping effect. Optimisation of the required tube dimensions and angle for particles of a known size and density with a known flow is on-going.

Fig. 7. A 30° inclined settling tube 0 minutes (left) and 2 minutes (right) from the start of the test.

5.2. Washing steps

As discussed above, losses of ammonia and water vapour as well as ammonium chloride precipitate, mixed with slag residue or the PCC product, should be minimised to increase the profitability of the process. During the described experiments it has been measured that residual slag exiting the process had moisture content of approximately 10%. Moreover, the chlorine level in dry residue was 5.5%-wt according to SEM/EDX measurements. For the modelled process, this would mean that 1670 kg/h ammonium chloride (~0.15 kg per kg PCC product) would be lost with the residue, assuming that all chlorine is bound with ammonia.

However, from the experimental results of applying one washing stage for the residue, with washing water amount of 0.50 m^3/t residue, the reduction in calcium content was found to be 0.65 mol, while approximately 1.5 mol chlorine was dissolved. Thus, it would mean that only 14% of the chlorine would have been bound as NH_4Cl, the rest being $CaCl_2$. In other words, 230 kg/h ammonium chloride and 1485 kg/h calcium chloride would be lost with the slag residue.

According to experimental results the one-stage wash would lower the chlorine level in the residue to 0.7%-wt, corresponding to 28 kg/h NH_4Cl and 177 kg/h $CaCl_2$, if calculated with the same distribution as above. The used washing liquid of 10 m^3/h would then contain 0.003 mol/L Cl^-, 0.001 mol/L Ca^{2+} and 0.0004 mol/L NH_4^+, that could be re-utilised in the process by evaporating the water in such extent that the need for make-up water for the process would be satisfied at the same. This, however, would bring an extra energy penalty to the process.

Regarding the produced PCC, washing tests will be done as a part of future work. It can be mentioned, that for unwashed PCC produced with 1 mol/L ammonium chloride, the experimental chlorine levels have been below 1 %-wt, being still too high for a marketable product. Using ammonium nitrate solvent instead of ammonium chloride would remove the problem of chlorine precipitates.

Calculating from the Aspen Plus model with 15% bypass of the 1st carbonation unit, the vaporization losses of ammonia would be 18 kg/h (1.1 kmol/h) with PCC production of 10795 kg/h. This amount, 0.4% of the total ammonium species present, is of the same order of magnitude what has been obtained experimentally by FTIR measurements [13]. However, also this ammonia could be captured, e.g. by using an HCl-based scrubber for the flue gas stream leaving the system (Fig. 2).

The need for make-up water to replace the moisture lost with streams of solid matter and water vapour flashed from the separation units depends on many variables, and has not yet been quantitavely studied. However, assuming a 20% moisture content for the PCC product and 10% for slag residue, the need for make-up water for the above discussed process would be 5830 kg/h. This amount could easily be taken from washing units, but it requires further optimisation. In general, all the values presented in this section are based on preliminary studies, and thus need to be verified by additional experimental studies and analysis as a central part of future work. Only then can the usage of fresh make-up chemicals be optimised too.

6.Conclusions

The studied pH swing process possesses potential for commercial application. Based on both modelling and experimental work, precipitated calcium carbonate can be produced with a continuously operating system instead of batch reactors. By choosing the solvent with highest conversion efficiency (ammonium nitrate) and by dividing the precipitation step in two stages, the conversion of calcium in the input material to a valuable product can be enhanced. Energetically the process will require some mixing and pumping power, but the chemical reaction steps are exothermic. The recovery and separation units for process chemicals and for solids need to be studied in more detail in future work, but it seems to be possible to use a gravitational settler to separate slag residues from the process liquid. Also, washing the output streams will aid the recovery of chemicals, and thus decrease the need for make-up material. However, additional studies on particle quality, shape, purity and whiteness of the produced PCC must be performed to guarantee that a marketable product is manufactured.

Acknowledgements

The authors want to acknowledge Cleen Ltd. and Tekes (the Finnish Funding Agency for Technology and Innovation) for their financial support for the research via the Cleen CCSP project (2011-2015). H.-P. Mattila also acknowledges the Graduate School in Chemical Engineering for support for his work.

Nomenclature

c	concentration, g/L
d	diameter of the mixer, m
$\bar{d}$	mean diameter, μm
n	frequency of rotation, 1/s
P	power, kW
p	pressure, bar
Po	power number, –
Q	heat duty, kW
Re_v	Reynolds number of mixing
T	temperature, K
T^0	ambient temperature, K
V	volume, m^3
$\dot{V}$	volume flow, m^3/h

Abbreviations

CCS	Carbon Capture and Storage
FTIR	Fourier Transform Infrared Spectroscopy
PCC	Precipitated Calcium Carbonate
SEM/EDX	Scanning Electron Microscopy – Energy Dispersive X-ray

Greek symbols

Δ	difference
ε	energy dissipation, $W/kg_{solution}$
η	viscosity, Pa·s; efficiency, %
Θ	temperature, °C
ρ	density, kg/m^3

Subscripts and superscripts

in	at inlet
p	particle

References

[1] IPCC, IPCC Special Report on Carbon Dioxide Capture and Storage, Cambridge University Press, New York, 2005.

[2] Herzog, H., An Introduction to CO_2 Separation and Capture Technologies, MIT Energy Laboratory, 1999. Available at: <http://sequestration.mit.edu/pdf/introduction_to_capture.pdf> [accessed 27.1.2012].

[3] Teir, S., Fixation of carbon dioxide by producing carbonates from minerals and steelmaking slags. [Dissertation]. Espoo, Finland: Helsinki University of Technology; 2008.

[4] Baciocchi, R., Costa, G., Polettini, A., Pomi, R., Prigiobbe, V., Comparison of different reaction routes for carbonation of APC residues, Energy Procedia 2009;1: 4851-4858.

[5] Velts, O., Uibu, M., Kallas, J., Kuusik, R., CO_2 mineral trapping: Modeling of calcium carbonate precipitation in a semi-batch reactor. Energy Procedia 2011;4: 771-778.

[6] Eloneva, S., Reduction of CO_2 Emissions by Mineral Carbonation: Steelmaking Slags as Raw Material with a Pure Calcium Carbonate End Product. [Dissertation]. Espoo, Finland: Aalto University, School of Science and Technology; 2010.

[7] Kodama, S., Nishimoto, T., Yamamoto, N., Yogo, K., Yamada, K., Development of a new pH-swing CO_2 mineralization process with a recyclable reaction solution. Energy 2008;33: 776-784.

[8] Eloneva, S., Teir, S., Savolahti, J., Fogelholm, C.-J., Zevenhoven, R., Co-utilization of CO_2 and calcium silicate-rich slags for precipitated calcium carbonate production (Part II). In: Mirandola, A., Arnas, O., Lazzaretto, A., editors. ECOS 2007: Proceedings of the 20th International Conference on Efficiency, Cost, Optimization, Simulation and Environmental Impact of Energy Systems; 2007 Jun 25-28; Padova, Italy. Volume II:1389-1396.

[9] Said, A., Eloneva, S., Fogelholm, C.-J., Mattila, H.-P., Zevenhoven, R., Process simulation of utilization CO_2 and steelmaking slags to form Precipitated Calcium Carbonate (PCC). In: ECOS 2009: Proceedings of the 22nd International Conference on Efficiency, Cost, Optimization, Simulation and Environmental Impact of Energy Systems; 2009 Aug 31- Sep 3; Foz du Iguacu, Brazil. pp. 1261-1270.

[10] Mattila, H.-P., Grigaliūnaitė, I., Zevenhoven, R., Chemical kinetics modeling and process parameter sensitivity for precipitated calcium carbonate production from steelmaking slags. Chem. Eng. J. 2012;192: 77-89.

[11] Mattila, H.-P., Experimental studies and process modeling of aqueous two-stage steel slag carbonation. M.Sc. Thesis. Turku, Finland: Åbo Akademi University; 2009.

[12] Mattila, H.-P., Grigaliūnaitė, I., Said, A., Fogelholm, C.-J., Zevenhoven, R., Production of papermaking grade calcium carbonate from steelmaking slag – product quality and development of a larger scale process. Accepted to be presented at SCANMET IV conference, Luleå, Sweden, Jun 2012.

[13] Eloneva, S., Mannisto, P., Said, A., Fogelholm, C.-J., Zevenhoven, R., Ammonium salt-based steelmaking slag carbonation: Precipitation of $CaCO_3$ and ammonia losses assessment. Greenhouse Gases: Science and Technology 2011;1(4): 305-311.

[14] Wiklund, A., Sipilä, J., Eloneva, S., Zevenhoven, R., Assessment of Shell work on carbonation of calcium based materials. Åbo Akademi University, Heat Engineering Laboratory; 2008. Report.

[15] Szargut, J., Exergy Method: Technical and Ecological Applications. Southampton, UK: WIT Press; 2005.

[16] Beek, W. J., Muttzall, K. M. K., van Heuven, J. W., Transport Phenomena, 2nd edition. Guildford, UK: Biddles Ltd; 2000.

[17] Kunitz, M., An empirical formula for the relation between viscosity of solution and volume of solute. J.Gen.Physiol. 1926, 9:715-25.

[18] Davis, R. H., Gecol, H., Classification of concentrated suspensions using inclined settlers. International Journal of Multiphase Flow 1996; 22(3): 563-574.

Production of $Mg(OH)_2$ for CO_2 emissions removal applications: parametric and process evaluation

Experience Nduagu[a*], Inês Romão[a,b], Ron Zevenhoven[a]

[a] *Åbo Akademi University, Åbo/Turku, Finland, enduagu@abo.fi. CA*
[b] *University of Coimbra, Coimbra, Portugal*

Abstract:

Technological processes that accelerate natural and geochemical weathering of abundantly available Mg-silicate minerals have the potential for large-scale, safe and permanent storage of CO2. One of these CO2 sequestration routes involves as a first step the production of reactive Mg(OH)2 from Mg-silicates using recoverable ammonium sulfate (AS) salt. This route avoids the very slow kinetics of carbonating magnesium silicates. A recently identified Mg(OH)2 production process involves a closed loop, staged process of Mg extraction followed by Mg(OH)2 precipitation and reagent (AS) recovery. This process has been applied to different Mg-silicate (serpentinite and olivine rocks in particular) minerals from worldwide locations, having varying physical and chemical properties. Experimental results showed some dependence of Mg extraction and mass of the Mg(OH)2 product on the reaction parameters: mass ratio of Mg-silicate mineral (S) to AS salt reacted, reaction temperature (T) and time (t). This paper statistically evaluates the contribution of these effects and their interactions using a 2n-1 factorial experimental design. Both Mg(OH)2 production and carbonation were simulated using Aspen Plus® software while process heat integration was done by pinch analysis. Process energy evaluation, on an exergy basis, gives 3.88 GJ of energy requirement for 1t-CO2 sequestered (for Finnish serpentinite). This value is ~ 0.5 GJ/t-CO2 (10 % points) less than the energy requirement of the process in a previous model. The results of this analysis would be beneficial for optimization and pilot scale studies of this process.

Keywords:

Mg-silicates, Magnesium hydroxide, CO_2 mineralization, Process evaluation.

1. Introduction

Weathering of alkaline silicate rocks plays a significant role in absorbing atmospheric CO_2 [1]. Alkaline and alkaline-earth silicate mineral deposits are abundant and larger than fossil resources[2]. A resource of this magnitude, over 300,000 Gt of Mg-based silicate minerals[3] provides significant amounts of base ions for the natural process of neutralizing atmospheric CO_2 emissions. However, natural weathering has very slow kinetics and occurs on geological (multimillion-year) timescales [4]. So, it becomes foolhardy to rely on natural weathering in reducing or stabilizing atmospheric CO_2 emissions. The goal of meeting both current and future energy demands in a "carbon neutral" manner has therefore spurred research that aims at accelerating the kinetics of the reaction of mineral silicates and CO_2. This geochemical option of carbon (dioxide) capture and storage is known as CO_2 mineralization or mineral carbonation.

The direct carbonation chemistry of Mg silicates is exothermic, and potentially allows for a process with a zero or negative overall energy input [5]. Mg silicates, for example, serpentine and olivine which are abundantly available (with a combined capacity of ~ 200,000 Gt[3]) reacts with CO_2 according to (1) and (2)[6].

$Mg_2SiO_4(s) + 2CO_2(g) \rightarrow 2MgCO_3(s) + SiO_2(s)$,

ΔH (298 K)= - 69...-109 kJ/mol CO_2 (1)

$Mg_3Si_2O_5(OH)_4 + 3CO_2(g) \rightarrow 3MgCO_3(s) + 2SiO_2(s) + 2H_2O(l)$,

ΔH (298 K) = -46… -64 kJ/mol CO_2 (2)

Direct gas/solid carbonation of Mg-silicates appears simple but suffers from slow chemical kinetics and poor energy economy even at elevated temperatures and pressures. Surprisingly, most of the routes presented in the literature do not take benefit of the exothermic nature of the overall mineral carbonation chemistry. A staged process of CO_2 mineralization via production of $Mg(OH)_2$ followed by gas/solid carbonation is the major focus of the mineralization research at Åbo Akademi University (hereafter ÅA), Finland. This route allows for a good process heat integration utilizing the exothermic heat produced from $Mg(OH)_2$ carbonation to drive the upstream $Mg(OH)_2$ process. $Mg(OH)_2$ produced in the first step can be used to capture and store CO_2 via the following ways:

i. carbonation using a high temperature pressurized fluidized bed (FB) reactor (480-600 ^oC, <50 bars)[7, 8]. Recent developments[9, 10] involve applying CO_2 mineralization to flue (or other CO_2-containing) gases directly. This would eliminate the very expensive and CO_2 capture step from the CCS process chain.
ii. direct aqueous reaction with CO_2 from air at near ambient temperature and pressure conditions[11].
iii. application in oceans (and water bodies) to capture atmospheric CO_2 as well as to reduce alkalinity of oceans[3, 12].

In spite of the abundance and global spread of Mg-silicate minerals (which are raw materials for $Mg(OH)_2$ production) and the potential applications of $Mg(OH)_2$ in removing CO_2 emissions, very few studies aim at producing $Mg(OH)_2$ for this purpose. This paper intends to bridge this gap by studying various factors affecting Mg extraction and $Mg(OH)_2$ production from olivine and serpentinite rocks. These mineral-containing rocks tested possess different chemical and physical characteristics: elemental compositions (Table A1 in the Appendix section), porosity and hardness[6].

2. Experimental

2.1 Mg-silicate rocks preparation and characterization

The mineral rocks tested in this study are Finnish serpentinite (Finnish serp.) from the Hitura nickel mine owned by Finn Nickel Oy; Australian serpentinite (N.S. Wales serp.) from the Great Serpentinite Belt of New South Wales; serpentinite from the Varena region of Southeast Lithuania (Lithuania serp.); serpentinites from Bragança, northeast Portugal (Bragança serp, Donai serp., 7 Fontes serp.); olivine from Åheim (Åheim olivine), Norway and olivine minerals from Finland (labeled Satakunta olivine, Vammala-1, Vammala-2, Suomusjärvi-1 and Suomusjärvi-2). Details of composition of these minerals can be found in the Appendix section (Table 1A). The composition of the rocks were in most cases determined from the results of a combination of two of the following analytical tools: X-ray fluorescence (XRF), X-Ray diffraction (XRD) or inductively coupled plasma optical emission spectrometry (ICP-OES). Aside the high Mg content, most of the minerals also contain significant amounts of iron compounds and silica (SiO_2). The form in which iron (FeO, Fe_2O_3 or Fe_3O_4?) exists in these rocks is yet to be completely ascertained. For example, there is conflicting information on the form that iron appears in the Finnish serpentinite rock used. Teir *et al.*[13] reported an XRD analysis which shows that iron is present in serpentinite as magnetite (Fe_3O_4), constituting 14 wt.% of this serpentinite. On the other hand, Rinne [14] reported

an XRD analysis showing that a combination of FeO and Fe_2O_3 compounds (which of course could be summed up to be Fe_3O_4) is present in the same rock sample.

2.2. Method for producing $Mg(OH)_2$ from Mg-silicate minerals

This section describes the method for producing $Mg(OH)_2$ from Mg-silicate minerals, a procedure that has been previously reported in literature[6, 15, 16]. The process route of producing $Mg(OH)_2$ involves a staged, closed loop process of Mg extraction using recoverable *AS* salt. The process schematic is presented in Fig.1.

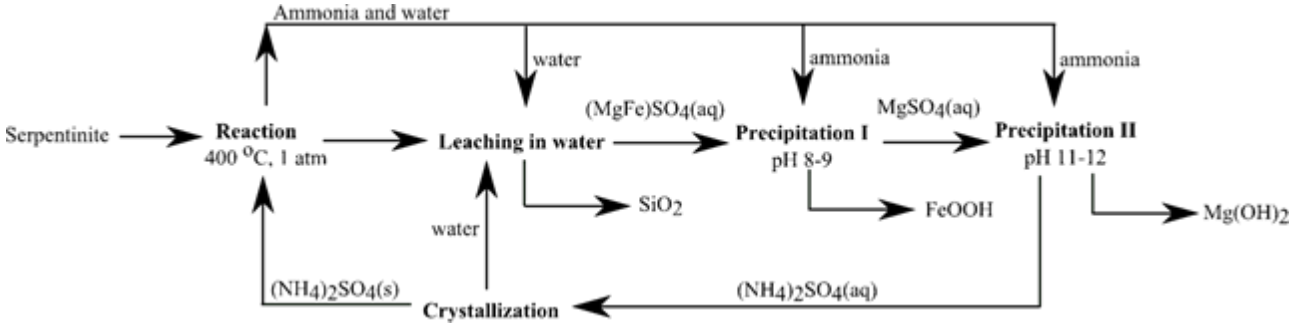

Figure 1. Schematic of process route for the production of $Mg(OH)_2$ from Mg-silicate minerals. After Nduagu et al.[17].

Mg is extracted from the reaction of Mg-silicate rocks and *AS* salt at 270-550 °C (depending on the rock type) in an oven/reactor. Information on the ranges of reaction parameters tested is presented in Table 1. The reaction in the oven produces $MgSO_4$, SiO_2, water vapor and recoverable gaseous NH_3. For details of the reactions and thermodynamics of the (Mg/Fe/Ca) extraction, refer to the Appendix section (Table A2 and Fig. A1). Mg/Fe/Ca sulfates obtained from the extraction reaction are leached in water at room temperature and pressure conditions. The elemental amounts of Mg, Fe and Ca and other metals extracted were determined by ICP-OES analysis.

Increasing the pH of (Mg/Fe/Ca) sulfates-rich solution (using the recovered ammonia) results in the precipitation of hydroxides or oxy-hydroxides. Of major interest are Fe, which is precipitated as goethite (FeOOH) and Mg, precipitated as $Mg(OH)_2$[16]. At pH ranges of 8–9 and 11–12 Fe and Mg respectively precipitate out of the solution. FeOOH by-product could be a useful raw material in the iron- and steelmaking industry. Due to the high concentration of iron compounds in these minerals (in different oxide forms), iron oxide by-product stream may be a useful raw material for the iron- and steel-making industry[17-19]. In Finland, for instance, the iron and steel sector is the largest point-source CO_2 producer. Thus, integrating steel industry's CO_2 emissions with mineralization is crucial and would result in emissions reduction, and in the replacement of raw materials (iron ore) using the iron oxide by-products. However, we have shown earlier[17] that the processing of Fe together with Mg in a CO_2 sequestration process comes with a significant energy penalty. The results showed that the contribution of iron to the energy requirement of CO_2 sequestration increases by 70%, 30% and 16% points for rocks containing Fe as Fe_3O_4, Fe_2O_3 and FeO compounds respectively as compared to an iron-free rock.

After filtering precipitated Fe/Mg/Ca (oxy)hydroxides from the solution, *AS* salt is then recovered via crystallization. The following crystallization techniques may suffice: evaporative, mechanical vapor recompression (*MVR*) or anti-solvents (especially alcohols)[17]. This study focuses on *MVR*. The $Mg(OH)_2$ thus produced from Mg-silicate mineral rocks is then used to sequester CO_2 in the form of thermodynamically stable magnesium carbonates.

3. Parametric evaluation by 2^{n-1} experimental design

This section studied the extent to which the reaction parameters affect Mg extraction, and in extension their effects on $Mg(OH)_2$ production. These parameters include elemental Mg to Fe ratio

(*Mg/Fe*) of the mineral rock, Mg-silicate to *AS* mass ratio (*S/AS*), reaction temperature (*T*), time (*t*), and the interaction of these effects.

It is important to point out the nature of the test data (statistical details are presented in Table 1). The initial batch of tests were done using mostly Finnish serpentinite between 2008 and 2009, and were reported in [15] and [16]. The aim at that time was to prove that $Mg(OH)_2$ can be produced from Finnish serpentinite, and efficiently too. After this, efforts were channeled towards applying the method to different Mg-silicate rocks from worldwide locations[6, 20-22].

Table 1. Statistical overview of the parameter values tested in 82 experiments.

Parameters	Minimum	Maximum	Median	Average	Standard Deviation
Mg/Fe (kg/kg)	0.31	5.90	2.16	2.81	1.32
S/AS (kg/kg)	0.40	4.0	0.67	0.85	0.6
T (^{o}C)	270	550	475	457	63
t (min)	10	120	22	32	27

Clearly, earlier tests did not focus on identifying reaction trends as experiments were performed at varying reaction conditions chosen almost at random - targeting to cover a broad range of each parameter. However, after testing a range of values of each of the factors, it now becomes necessary to identify which parameters have the most significant effects on Mg extraction and $Mg(OH)_2$ production. More so, parameter cross-correlation effects would be determined as well. A better understanding of these effects and their interactions is essential for optimization of $Mg(OH)_2$ production from Mg-silicate minerals for the purposes of fixing CO_2 as carbonate(s).

Due to the range of values parameters considered (Table 1) the choice of a reasonable reference point was important in order to design a two-level fractional factorial design. We used a reference level "0" condition to classify each factor according to levels: *high* (*+1*) or *low* (*-1*) (in Table 2). The first "0" level was chosen to reflect the median value of the parameters while a second "0" level was chosen at values of the parameters at near optimal conditions. The response parameter (dependent variable) in this analysis is % Mg extraction (% Mg ext). The % Mg extraction is the amount of Mg (grams) extracted from the Mg-silicate rock divided by the total amount of Mg (grams) present in the Mg-silicate, expressed as percentage. The motivation for focusing on the parametric analysis of Mg extraction is the fact that the amount of $Mg(OH)_2$ produced from the process strongly correlates with values for Mg extraction[16].

Table 2. Reference level "0" conditions for evaluation of factors and their interactions.

Parameters	Mg/Fe (kg/kg) A		S/AS (kg/kg) B		T (^{o}C) C		t (min) D	
Levels	high (+1)	low (-1)	high (+1)	low (-1)	high (+1)	low (-1)	high (+1)	low (-1)
Condition I	> 2.16	≤ 2.16	≤ 1	> 1	≥ 480	< 480	> 25	≤ 25
Condition II	> 2.16	≤ 2.16	≤ 0.67	> 0.67	≥ 440	< 440	> 60	≤ 60

 Condition I reflects the median of the data. Condition II is chosen at near optimal experimental conditions. "*+1*" and "*-1*" are the *high* and *low* levels respectively.

3.1 Fractional factorial design

Fractional factorial design (2^{n-1}, where *n* represents the number of parameters) enables the analysis of only a subset of treatment combinations, while still obtaining a meaningful result that is statistically representative of the entire data set. In this analysis *n*=4 (*A*, *B*, *C* and *D* in Table 3) and the objective function is *Y* which represents % Mg extraction. The fractional factorial design is constructed by partitioning the runs into two blocks; one block, which is a contrast of the other, is completely sacrificed [23]. Instead of using a full 2^n design with 16 design points, the 2^{n-1} design

with only 8 design points was chosen at points *ABCD=I* (*1*, *ab*, *ac*, *ad*, *bc*, *bd*, *ad* and *abcd*). Design points having *ABCD=-I* (*a*, *b*, *c*, *d*, *abc*, *abd* and *bcd*) which are considered as complementary to the points with *ABCD=I* were excluded in the 2^{n-1} factorial design (as illustrated in Table 3). At this stage, the third and fourth order interaction effects of the parameters (*ABC*, *ABD*, *ACD*, *BCD* and *ABCD*) were also neglected in order to avoid ambiguity.

Table 3. 2^{4-1} factorial design.

Treatment	Effects and interactions								Observation
	Mg/Fe (*A*)	*S/AS* (*B*)	*T* (*C*)	*t* (*D=BCD*)	*AB* (*=CD*)	*AC* (*=BD*)	*AD* (*=BC*)	*ABCD* (*=I*)	*Y*
1	−	−	−	−	+	+	+	+	---
ab	+	+	−	−	+	−	−	+	---
ac	+	−	+	−	−	+	−	+	---
ad	+	−	−	+	−	−	+	+	---
bc	−	+	+	−	−	−	+	+	---
bd	−	+	−	+	−	+	−	+	---
cd	−	−	+	+	+	−	−	+	---
abcd	+	+	+	+	+	+	+	+	---

The estimated effect (see (3)) of each design factor is represented mathematically as the average at the *high* level (+) of the factor minus the average at the *low* level (-) of the factor.

$$Effect=Contrast/(n' 2^{n-1}) \quad (3)$$

Where *n and n'* are the number of factors and replicates respectively, and *Contrast* is the sum of the values of each factor at its *high* level minus the sum of the values of the same factor at its *low* level. The significance of any parameter or the interaction of parameters was determined at 95 % (α=0.05) confidence level. This value is determined by using a student *t*-test to obtain *t*-values and assessing that with the probability (*p* value) associated with the test statistic. MINITAB® statistical software [24] was used to analyze the data from experimental tests using the 2^{n-1} (and a 2-level) factorial design.

3.2. Mg extraction: parametric effects and interactions

3.2.1 Effect of *Mg/Fe* ratio of rock types

Thirteen different Mg-silicate minerals (nine serpentinite and four olivine rocks) were studied in a total of eighty-four tests performed at varying reaction conditions. The results showed a huge difference in reactivity of serpentinites and olivines using the method applied in this study. Based on maximum extraction values obtained so far for each rock type, serpentinite is about 5x as reactive as olivine (see Fig.2). This confirms previous results for two olivine-containing rocks (from Åheim, Norway and Satakunta, Finland) samples tested and found not to be suitable for Mg extraction[6]. It was observed that the olivine rocks tested had a harder texture, smaller internal Brunauer, Emmett and Teller (BET) surface area as well as pore volume. The range of % Mg extraction between the maximum (Max.) and minimum (Min.) in Fig.2 is due to results obtained at wide range of reaction conditions.

At varying reaction conditions the factors and interactions that have a significant effect on the extent of Mg extraction were obtained (see Table 4). While keeping constant some parameters and varying others, the effects of changing levels of each parameter was determined. This sensitivity analysis was performed in order to determine if the parameters are important or not. If any parameter was found to contribute significantly to Mg extraction, it was important to determine the levels to which that factor is significant.

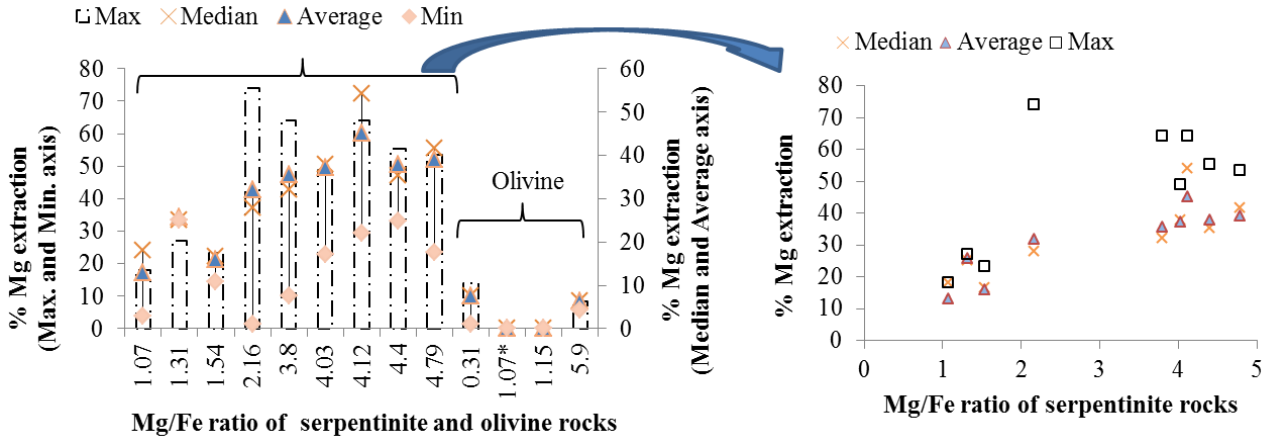

Figure 2. Effect of Mg/Fe ratio of the Mg-silicate rocks on % Mg extraction. The figure on the left shows results from both serpentinite and olivine rocks while the one on the right is for only serpentinite rocks.

Table 4. Sensitivity analysis for the factors affecting Mg extraction by varying the conditions.

#	Selected conditions	Factors				Interactions			
		Mg/Fe (g/g) *A*	*S/AS* (g/g) *B*	T (^{o}C) *C*	T (min) *D*	*AB*	*AC*	*AD*	R^2
1	A>2.16 g/g, B≤1 g/g, C>480 ^{o}C, D>60 min				√				27%
2	A>2.16 g/g, B≤1 g/g, C>440 ^{o}C, D>60 min				√				31%
3	A>2.16 g/g, B≤0.67 g/g, C>480 ^{o}C, D>60 min								22%
4	A>2.16 g/g, B≤0.67 g/g, C>440 ^{o}C, D>60 min								25%
5	A>2.16 g/g, B≤1 g/g, C>480^{o}C, D>25 min		√	$\sqrt{}^{\beta}$	√				47%
6	A>2.16 g/g, B≤1 g/g, C>440^{o}C, D>25 min		√		√	√			52%
7	A>2.16 g/g, B≤0.67 g/g, C>480^{o}C, D>25 min	√	√		√				45%
8	A>2.16 g/g, B≤0.67 g/g, C>440^{o}C, D>25 min	√	√		√				50%

√ and $\sqrt{}^{\beta}$ represent positive and negative effect of the factors/interactions respectively. R^2 is the regression coefficient obtained for each condition.

It is obvious from Fig. 2 that serpentinite rocks with a *Mg/Fe* ratio ≥ 2.16 show an exceptionally (>2x) higher % Mg extraction than others. This was the reason why *Mg/Fe* ratio level was benchmarked at > 2.16 (Table 4) in the sensitivity analysis. Given the information deductible from Fig. 2, it was more interesting to understand the effects and interaction effects of the more reactive minerals with *Mg/Fe* ratio > 2.16.

Our goal is to obtain a process condition that allows us to design a Mg extraction reactor that operates at optimal reaction conditions. The reactor should be able to process different types of serpentinite minerals with varying Mg/Fe ratios, minimal amounts of *AS salt* reagent (slightly less than 1 g/g), temperatures < 440 ^{o}C and reaction time ≤ 60 min. The combination of parameters in Table 4 which mostly suits this goal is condition 6 which also has the highest regression coefficient (R^2=52%). It is arguable that the R^2 value obtained is not sufficient enough to describe a process; however, it is not surprising that a system as complicated as the one simulated here would give a

comparatively low R^2. The results reported here contain tests performed on the reaction of solids (solid state reaction) with multivariate parameters. Solid state reactions are less predictable than those involving other states/phases. We assume that not all the factors contributing to Mg extraction have been identified and studied. Some other factors like particle size difference between the reacting Mg-silicate mineral and *AS* salt, heat and mass transfer, geometry and size of the reactants and their containers may affect solid/solid reactions. These are the main subjects of ongoing investigation as we embark on the next stage - pilot scale development.

3.2.2 Effect of amount of reagents (*S/AS* ratio)

By varying *S/AS* ratio of the tests between ≤0.67 g/g and ≤1 g/g, its effect on the extent of Mg extraction was evaluated. For conditions 5-8 (Table 4), at 95 % (α = 0.05) significance level, *S/AS* ratio has a significant positive effect on Mg extraction. The results obtained show that an increase in *S/AS* salt ratio above both the level of 0.67 g/g or 1 g/g does not significantly affect Mg extraction beyond a reaction time of 60 min (see conditions 1 to 4 in Table). In other words, a change in the amount of *AS* salt reagent levels is more important when the reaction time is less than 60 min. Increasing *S/AS* salt from *low* (-1) to *high* (+1) levels results in a 10% point increase in Mg extraction. The effects of *S/AS* ratio, those of the parameters and their interactions can be visualized from Fig.3 which is plotted for condition 6.

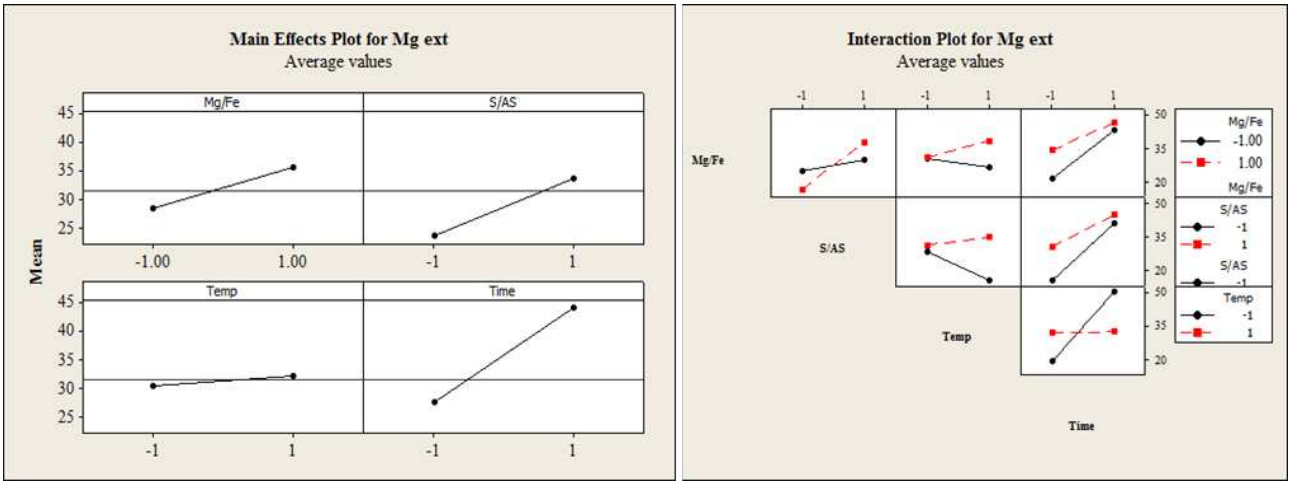

Figure 3.Main effects and interaction for Mg extraction under Condition I

3.2.3 Effect of reaction temperature and time

The effect of reaction temperature is not important under most of the conditions evaluated, but shows negative dependence on Mg extraction above 480 ^{o}C (condition 4 in Table 4).

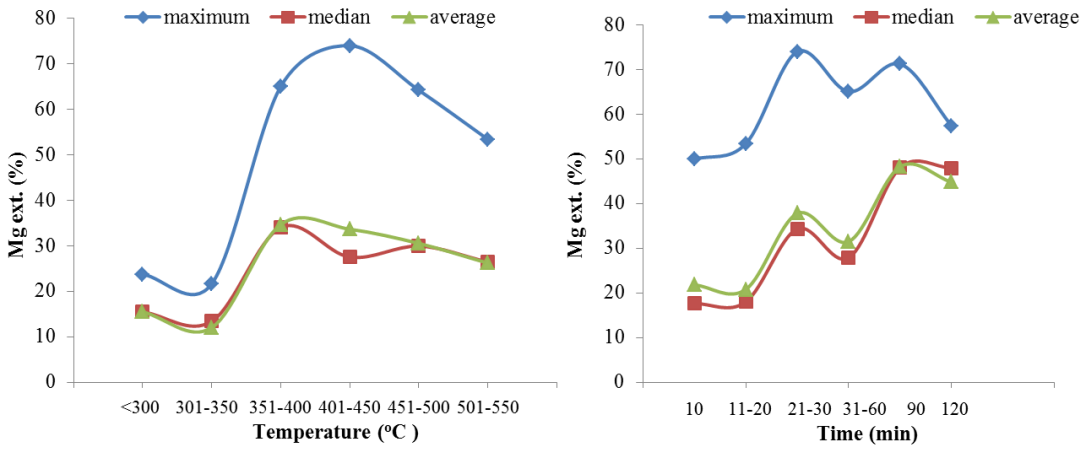

Figure 4. Effect of temperature (left) and time (right) on Mg extraction

Figure 4 shows that an increase in temperature results in a reduction in % Mg extraction is already at 440 ^{o}C (i.e. within the 401-450 ^{o}C temperature range). For the selected reaction condition 6, the effect due to temperature is almost flat (see Fig.3). However, reaction time has a significant effect on magnesium extraction; an increase in reaction time from *low* (*-1*) to *high* (*+1*) levels leads to a 15 percent points' increase in magnesium extraction. More so, reaction time significantly affects Mg extraction at all the conditions modeled except when $t > 60$ min and *S/AS* ≤ 0.67 g/g (conditions 3 and 4). Besides, this effect of reaction time on *Mg ext* seems not straightforward from Fig.4; more investigation is needed.

3.2.4 Interaction effects

Under the conditions modeled, the interaction effects of *Mg/Fe-S/AS* ratios and *T-t* are significant at 95 % significance level. The interaction effects presented in Fig.3 show that increasing the reaction time from *high* (*+1*) to *low* (*-1*) (above 25 min) levels significantly increases (by 30 % point) the value for Mg extraction if the reaction temperature are kept below 480 ^{o}C. Above this temperature, no increase in Mg extraction is possible, presumably due to thermal decomposition of AS above at high temperatures leading to the formation of sulfur trioxide gas, which could alter the thermodynamics [16]. On the other hand, increasing S*/AS* ratio levels from *high* (+1) to *low* (-1) ($\leq$1 g/g) at both *high* (+1) and *low* (-1) levels *Mg/*Fe leads to a significant increase in % *Mg ext*. But, the % *Mg ext* values obtained with *high* (+1) level of *Mg/*Fe (>2.16 g/g) are higher. This confirms previous results which showed that rocks with high Mg/Fe ratios respond better to Mg extraction than those with low Mg/Fe ratios[6].

4. Process evaluation using exergy and pinch analysis

4.1 Process simulation

The $Mg(OH)_2$ production, *AS* recovery and $Mg(OH)_2$ carbonation were modeled using Aspen Plus® software. The process flow diagram is presented in Fig.5. Pinch analysis was done using Aspen Energy Analyzer®.

4.1.1 Mg, Fe and Ca extraction

The base property method used for this simulation is the ELECTRTL method. The solid state reaction of serpentinite and AS salt was simulated using a stoichiometric reactor (REACTOR) with the extraction equations and thermodynamics specified as presented in the Appendix section ((R1), (R3) and (R5) in Table A2). The serpentinite feed has its composition simulated after the Finnish serpentinite which contains ~83 %-wt $Mg_3Si_2O_5(OH)_4$, ~14 %-wt Fe_2O_3 and ~1 %-wt $CaSiO_3$. The *AS* feed (AS-1) is a product from the *MVR* section, where *AS* salt is crystallized. The specified conversion of this reactor is 100% – meaning that serpentine and *AS* feed react completely to form products. This assumption is based on the best case scenario of the extraction reaction which is the aim of an ongoing optimization study. However, all the scenarios have previously been explored using life cycle analysis (LCA)[25].

4.1.2 Dissolution of extraction products

The product stream from the reactor (*PRDTS*) was separated in a solid/gas separator (*SEP-1*) into a solid stream (*SOLIDS-1*) and a gas stream (*GASES*) before cooling. The dissolution of the solid products was modeled using a stoichiometric reactor (*CONVTR*) and an *RGibbs* reactor (*DISSOLUT*) respectively. At the *CONVTR* the solid compounds were converted to aqueous compounds before dissociating into anions and cations at the *DISSOLUT*. The *DISSOLUT* simulated the dissolution reactions of $MgSO_4$, $FeSO_4$, $Fe_2(SO_4)_3$ and $CaSO_4$ in water streams at 40 °C by calculating both the phase and chemical equilibrium based on Gibbs free energy minimization. The water stream (*DISS-H2O*) used for dissolution is made up of the following: a recycled water stream (*MVR-H2O*) from the *MVR* section, a water stream (*WATER*) recovered from the separation of the *GASES* stream into H_2O and NH_3 gas. After dissolution, the mixture is

separated by filtration into a solid stream (*SIO2*), containing mainly silica and a liquid stream (*DIS-PRDT*) of mainly Fe- and Mg-sulfate compounds.

4.1.3 Precipitation of FeOOH and $Mg(OH)_2$

The stoichiometric reactors, *PREP-1* and *PREP-2* were used for precipitation of FeOOH and $Mg(OH)_2$ respectively, and the following reactions and thermodynamics (4) - (5) specified:

Table 5. Chemical reactions and thermodynamics of the precipitation stage

#	**Precipitation reactions**	**ΔHr (T=313K)**
4	$Fe_2(SO_4)_3(s)+6NH_3(g)+4H_2O(l)\rightarrow 2FeOOH(s)+3(NH_4)_2SO_4(aq)$	-720 kJ/mol Fe
5	$MgSO_4(s)+2NH_3(g)+2H_2O(l) \rightarrow Mg(OH)_2(s)+(NH_4)_2SO_4(aq)$	-85 kJ/mol Mg

The pH of Fe- and Mg-rich solution stream (*DIS-PRDT*) was increased (using the recovered NH_3 gas from the flash separator *SEP-4*) in stages of 8–9 and 11–12 to precipitate hydroxides of iron and magnesium respectively. $Ca(OH)_2$ precipitates together with Fe in the first precipitation stage. Aqueous *AS* is formed at both precipitation stages (see (4) and (5)). Products of the precipitation stages, FeOOH and $Mg(OH)_2$ were separated by filtration while aqueous *AS* passes through a converter (*CONVTR-2*) to the *MVR* section for crystallization before it is recycled. The role of the *CONVTR-2* was to combine anions and cations in stoichiometric amounts into aqueous compounds.

The application of the *MVR* crystallization method to this process has been reported earlier [17, 26]; however, this paper revisits the *MVR* crystallization application in the pinch analysis section (section 4.2).

4.1.4 $Mg(OH)_2$ carbonation

The reaction of CO_2 and $Mg(OH)_2$ is exothermic, and at suitable conditions forms thermodynamically stable $MgCO_3$ and superheated steam. Sequestration of CO_2 using the gas/solid route as being developed at ÅA [7, 8, 27] provides utilizable energy at high temperatures (480- 550 ^oC, ΔH ~ -59.5 kJ/mol Mg) and pressure conditions. Pressures can vary from 20 bars to 80 bars depending on the concentration of CO_2 – pure and concentrated or in flue gas stream [9, 10] . For simulation purposes, it was assumed that the sequestration plant stores 1 ton/h CO_2 (~ 8000 t/y).

As shown in Figs. 5 and 6, at high carbonation conversion (> 90%) the exothermic heat of carbonation makes the temperature of outlet stream of the reactor hotter than those of the inlet streams (according to (6)). This energy is at the same time sufficient enough to heat up the reactants ($Mg(OH)_2$ and CO_2) and as well provide energy to the process (heat or power depending on what it is designed to achieve). The carbonation section in Fig. 5 produces both heat and power while that of Fig.6 produces only heat.

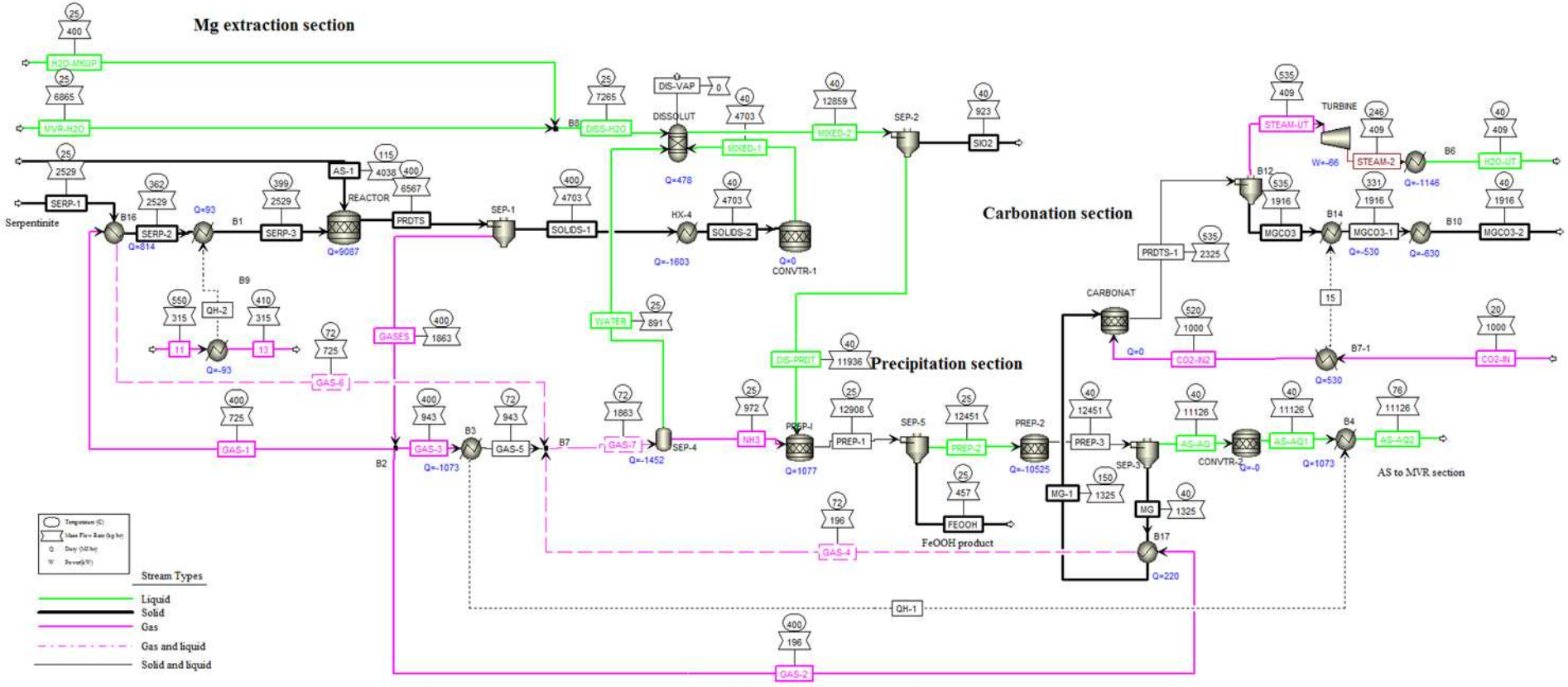

Figure 5. Process flow diagram of $Mg(OH)_2$ production and carbonation simulated using ASPEN PLUS software.

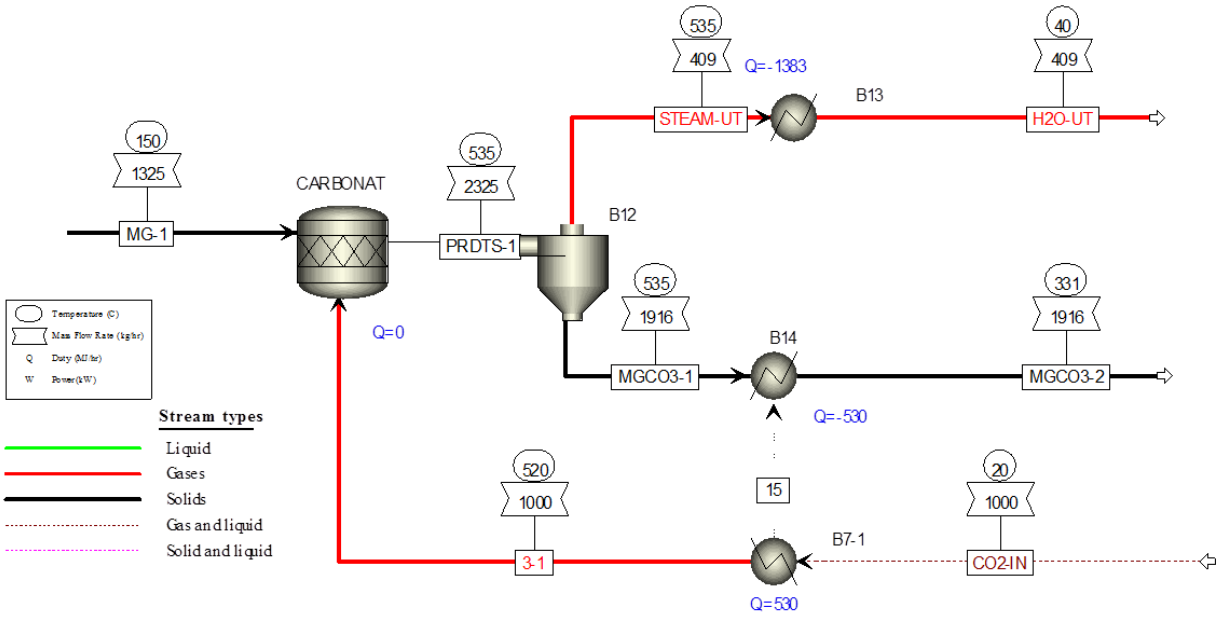

Figure 6. $Mg(OH)_2$ carbonation flow sheet producing utilizable heat.

$$\text{———————————} \quad , \qquad (T_2 > T1_x, T1_y) \qquad (6)$$

where *z* - $MgCO_3$, *s* - H_2O, *x* - $Mg(OH)_2$, *y* - CO_2, - heat of formation, $\dot{n}$ - molar amount of compound, *Cp* - specific heat capacity, T1- inlet temperature and T_2 - outlet temperature. In this case, the molar amounts associated with each term on the left side of (6) cancel out (since they are equal). If the inlet temperatures of the reactants are same (i.e. $T1_x=T1_y=T_1$), (6) reduces to (7).

$$\text{————————} \quad , \qquad (T_2 > T_1) \qquad (7)$$

It was assumed that CO_2 was delivered at 20°C, 20 bars from stream *CO2-IN*. The CO_2 pressure of this stream looks optimistic; however, this value was based upon the fact that the CO_2 capture and purification unit would be located nearby the CO_2 sequestration site. This in essence provides compressor power savings that are required for CO_2 compression to pipeline transport pressures of ~ 150 bars. The $Mg(OH)_2$ product separated by filtration in *SEP-3* was dried by heating to 150 °C before entering the carbonation reactor (*CARBONAT*). The CO_2 stream (*CO2-IN*) was heated to 520 °C before entering the *CARBONAT*. The exothermic nature of carbonation reaction led to a higher temperature of the products than that of the reactants. This was beneficial since power and heat were intended to be extracted from the steam and $MgCO_3$ products using a turbine (*TURBINE*) and heat exchangers respectively. More importantly, given the resulting temperature difference, the outlet streams of the reactor can then be used to heat up the inlet streams.

4.2 Pinch analysis

Pinch analysis has become a useful energy targeting and design tool for thermal and chemical processes and utilities[28]. This method enables the plotting of composite and grand composite curves using temperature versus enthalpy axes[29]. These curves provide an insight on the process heat availability and requirements.

These basic rules were followed while applying the pinch analysis[28]:

1. Separate the system into two independent sections – above and below the pinch, and do not transfer heat across the pinch.

2. Only cold utility is needed below the pinch. Heating of streams at the section below the pinch incurs a heat penalty.
3. Only hot utility is needed above the pinch. Cooling of streams at the section above the pinch incurs an energy penalty.

Table 6. Heating and cooling requirements of the process implemented using Pinch Analysis

Streams		Inlet T ^{o}C	Outlet T ^{o}C	Flow rate kg/h	Enthalpy MJ/h	mCP MJ/ ^{o}C-h
Cold Streams						
SERP-1		25	400	2529	909	2.4
AS-AQ1	Stream 1	40	107	10926	8413	125.6
	Stream 2	107	115	10926	9381	1173
CO2-IN		20	520	1000	530	1.06
MG		40	150	1325	220	2
Hot streams						
SOLIDS-1		400	40	4703	1603	4.45
GASES		400	25	1863	3559	9.49
MGCO3		532	40	1916	1160	2.36
STEAM - UT		246	40	520	1146	5.56

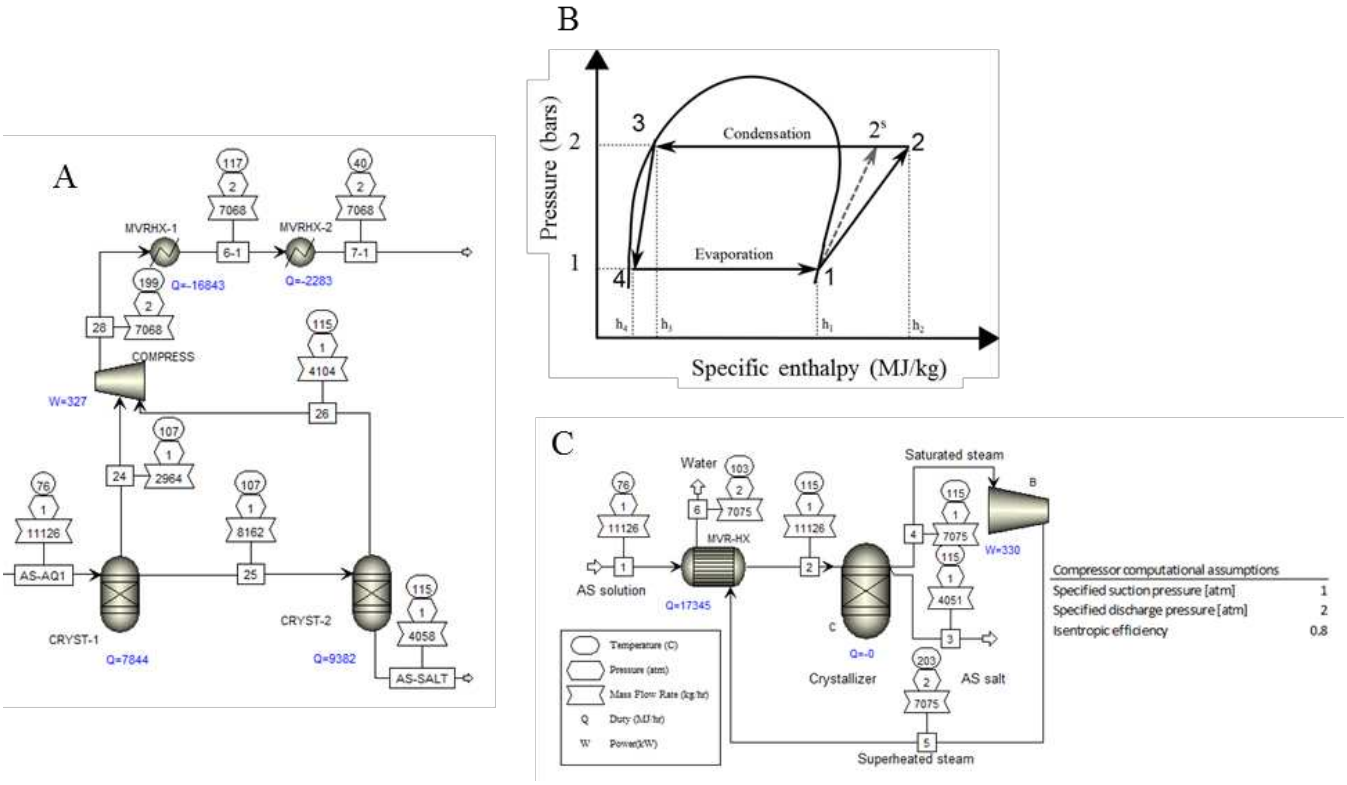

Figure 7. Working cycle (B) and Aspen process flow sheets (A&B) of mechanical vapor recompression (MVR) crystallization of AS salt. Modified after Nduagu et. al[17].

More rules were applied during designing of an optimal heat exchanger network as implemented using the Aspen Plus model in Fig.5. These include:

1. For pinch matches, above the pinch the $CP_{cold} \geq CP_{Hot}$ while below the pinch $CP_{Hot} \geq CP_{cold}$. CP is a value calculated by dividing the enthalpy of a stream by the difference in temperatures of the outlet and the inlet streams (see Table 6).

2. ΔT of 10 °C was the set minimum temperature difference.
3. Solid streams were not matched with solid stream as solid/solid heat exchange may be problematic.

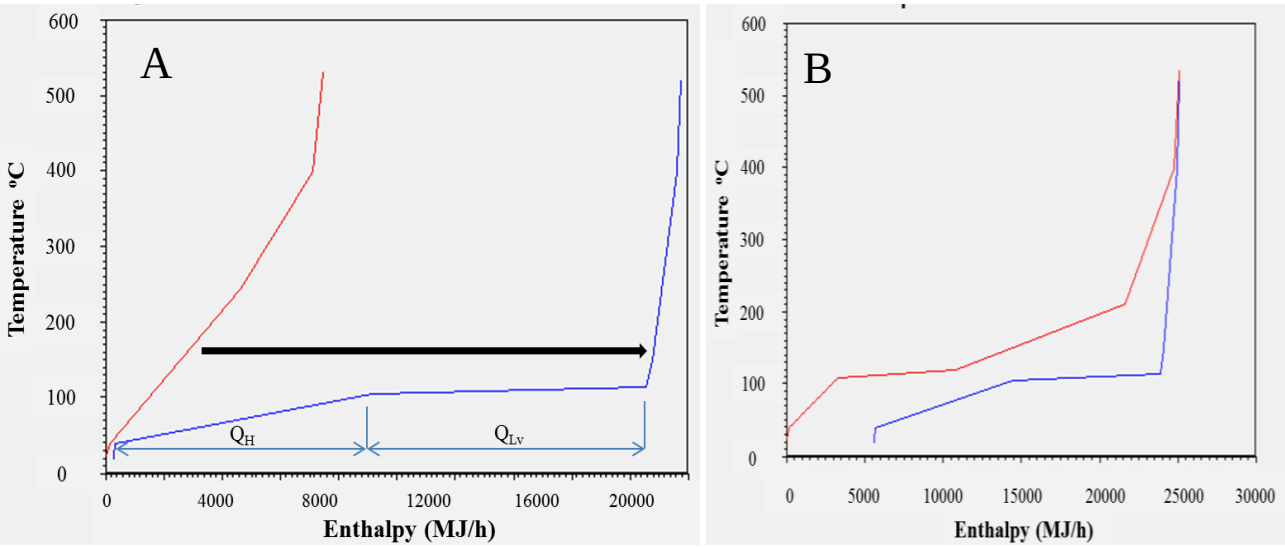

Fig 8. Hot and cold composite curves of the process shown in red and blue colors respectively

Two scenarios, with and without the *MVR* crystallization were compared. In the case of without *MRV*, the *AS*-water stream (*AS-AQ1* in Fig. 5, Fig.7A) was heated step-wisely, 40 °C →76 °C → 115 °C. At 115 °C, all the water in the stream was evaporated with virtually no heat recovery. In Fig. 7A the *MVR* was simulated with two crystallization vessels, allowing for an operation in two different temperature regimes (107 and 115 °C) while Fig.7C used only one crystallizer. However, compressing the water vapor stream from 1 to 2 bars (points 1→2 in Fig. 7) increases the enthalpy as well as the temperature of the stream to a level it can transfer heat to saturated water at 100 °C. The temperature-enthalpy plot (composite curve) of the process was first plotted (in Fig. 8A), assuming that a complete evaporative crystallization of the *AS* salt was carried out. The upper and lower pinch points are 40 °C and 50 °C. In this case, the latent heat added to evaporate water from *AS*-water mixture would be lost as low grade heat. Most part of that heat is represented in Fig.8A as Q_{Lv} (~ 9.4 GJ/h). Q_H is the value of other low temperature heating (sensible heat) required. The thick black arrow in the Fig. 8A pointing towards the cold composite curve (in blue color) gives an insight to the temperature and enthalpy values of the hot utility required. The gap between the hot and cold steams needs to be closed in order to optimize heat recovery. In order to achieve this, the temperature and the enthalpy of the hot stream must be such that allows for a heat transfer to the cold stream (saturated water at about 100 °C) while maintaining a minimum ΔT of 10 °C. Applying MVR closes the gap by compressing low grade steam, consequently increasing its enthalpy and temperature and forming superheated steam. The heat from the superheated steam is then used to produce more saturated steam. This modification changes the pinch point from 40 - 50 °C to 400 - 410 °C (Fig. 8) and reduces the hot utility requirements from 12290 MJ to 93 MJ. In achieving this, however, a power penalty of 330 kWh/t-CO_2 is incurred.

4.3 Exergy analysis

Exergy analysis was used to evaluate the process modeled based on the results from heat exchanger network implemented through pinch analysis. At any specified surroundings temperature (here T_0 = 15°C = 288 K), using exergy provides a standard basis for calculating the amount of valuable energy[30] that can be extracted from a heat stream and comparing heat with power input requirement P, for which the exergy Ex(P) = P. For example, ~ 9.1 Gt/t-CO_2 heat requirement of the

extraction process at 400 °C (~ 623 K) corresponds to an exergy equal to $Ex(Q) = (1-T/T_0)\cdot Q = 9.1 – 3.9$ GJ/t-CO_2. $(T/T_0)\cdot Q$ is the exergy destruction, E_D.

Table 7. Energy (Q), exergy destruction (E_D) and requirement (E_Q) of the process in GJ/t-CO_2

	Q	**E_D**	**E_Q**
$Mg(OH)_2$ production			
Kiln	9.09	3.89	5.20
DISS	0.48	0.46	0.02
PREP1	1.10	1.06	0.04
PREP 2	-10.5	-9.70	-0.84
MVR Compressor	1.18		1.18
Sep-4	-0.89	-0.65	-0.24
Heat exchangers	-2.40	-1.73	-0.67
Total	-1.99	-6.67	4.68[#]
$Mg(OH)_2$ Carbonation			
Turbine	-0.24		-0.24
Heat exchangers	-1.78	-1.22	-0.55
Total	-2.02	-1.22	-0.79
Net			**3.88[#]**

[#]These values are lowered by ~0.45 GJ/t-CO_2 if the Fe form in mineral is assumed to be FeO instead of the Fe_2O_3 used here.

The exergy destruction of a system, which is the measure of the amount by which the value of the resource is consumed or degraded, is shown as (8) while the exergy flow is presented in (9);

(8)

(9)

where $(S-S_0)$ is the entropy change, T_0 is the ambient temperature and $(H-H_0)$ the enthalpy change. The results obtained here are compared with the results of a previous model [17] where no pinch analysis was done.

The application of pinch analysis and the heat exchanger network as implemented in the Aspen Plus model (Fig.5) resulted in a ~ 0.5 Gt/t-CO_2 (~ 10% points) reduction in the exergy requirement of producing $Mg(OH)_2$. $Mg(OH)_2$ carbonation unit provides ~ 17% points energy offset to the process. When the $Mg(OH)_2$ production and carbonation units are integrated, the process requirements of the process becomes 3.88 Gt/t-CO_2. This value becomes 3.4 GJ/t-CO_2 (reducing by another ~0.5 GJ/t-CO_2) if the compound form of Fe in mineral is assumed to be FeO instead of the Fe_2O_3 used here.

5. Conclusions

This paper investigated the influence that reaction parameters has on the production of $Mg(OH)_2$ by analyzing the effects of *Mg/Fe* ratio, *S/AS* ratio, *T* and *t* on Mg extraction. Once produced $Mg(OH)_2$ could be used to sequester carbon by direct reaction with flue gases or CO_2 derived from power or chemical plants. Notable among the results presented in this paper is the fact that olivine rocks are 5x less as reactive as their serpentinite counterparts. It was also obvious that serpentinite rocks with Mg/Fe < 2.16 were less (>2x) reactive than others. This validates previous results which showed that an increase in Mg/Fe ratio increases Mg extraction. Reaction time has a significant effect on magnesium extraction as an increase in *t* above 25 minutes results in a 15 percent points' increase in Mg extraction, but this effect tends to diminish after 60 min. On the other hand, Mg extraction shows a negative dependence on reaction temperature; $T > 440$ °C do not favor Mg extraction. This

appears to be due to thermal decomposition of ammonium sulfate leading to the formation of sulfur oxide(s), which could alter the thermodynamics of the extraction reactions.

The application of pinch analysis and the heat exchanger network as implemented in an Aspen Plus model resulted in a ~ 0.5 Gt/t-CO_2 (~ 10% points) reduction in the exergy requirement of producing $Mg(OH)_2$. When the $Mg(OH)_2$ production and carbonation units are integrated the process requirements of the process becomes 3.88 Gt/t-CO_2. Carbonating $Mg(OH)_2$ in the carbonation unit provides a ~17% points energy offset to the entire process. The overall energy requirement of the process reduces by another ~0.5 GJ/t-CO_2 if the compound form of Fe in mineral is assumed to be FeO instead of the Fe_2O_3 used here.

Acknowledgements

This work was supported by the Academy of Finland program "Sustainable Energy" (2008-2011). Further support came from KH Renlund Foundation (2007-2009). Financial support from Åbo Akademi University's Graduate School for Chemical Engineering (GSCE) is also acknowledged.

Appendix

Apendix A - Tables

Table A1 . Composition of magnesium silicate minerals tested.

	Elemental composition (%-wt)					Mg/Fe
Rock type and locations	**Mg**	**Fe**	**Si**	**Ca**	**Al**	**(kg/kg)**
Serpentinite rocks						
N.S. Wales serp. (Aus)	23.0	4.80	19.5	0.00	0.50	4.8
Donia serp. (Portugal)	22.0	5.01	19.4	0.18	0.88	4.4
7 Fontes serp. (Portugal)	23.3	5.77	19.5	0.09	1.02	4.0
Bragança serp. (Portugal)	21.6	5.70	19.6	0.00	0.60	3.8
Finnish serp. (Fin)	21.8	10.1	11.6	0.30	0.00	2.2
Lithuania serp. (Lit)	18.9	12.3	15.9	0.90	0.10	1.5
Olivine rocks						
Åheim olivine (Nor)	29.6	5.00	19.5	0.10	2.80	5.9
Suomusjärvi-2 (Fin)	12.60	8.32	20.71	5.93	3.71	1.5
Vammala-2 (Fin)	16.88	12.87	18.37	1.00	0.69	1.3
Vammala-1 (Fin)	11.58	10.77	21.03	6.43	1.85	1.1
Suomusjärvi-1(Fin)	8.14	7.62	23.46	5.57	5.72	1.1
Satakunta olivine (Fin)	3.30	10.7	21.9	6.30	8.50	0.3

Reactions (A1)-(A5) represent the thermodynamics of reactions involving $Mg_3Si_2O_5(OH)_4$, Fe- and Ca-based compounds; iron could be found as FeO/Fe_2O_3/Fe_3O_4 and calcium is present as $CaSiO_3$[16, 17]. It can be seen from the thermodynamic compositions of possible products of the reactions (see also Fig.B1) that MgSO4 is the dominant solid product of the reaction.

Table A2. Extraction equations and thermodynamics

#	Extraction reactions	T (K) ΔG <0	ΔHr T=873 K
(A1)		472	222 kJ/mol Mg
(A2)		447	167 kJ/mol Fe
(A3)		622	360 kJ/mol Fe
(A4)		614	818 kJ/mol Fe
(A5)		318	116 kJ/mol Ca

Appendix B – Figures

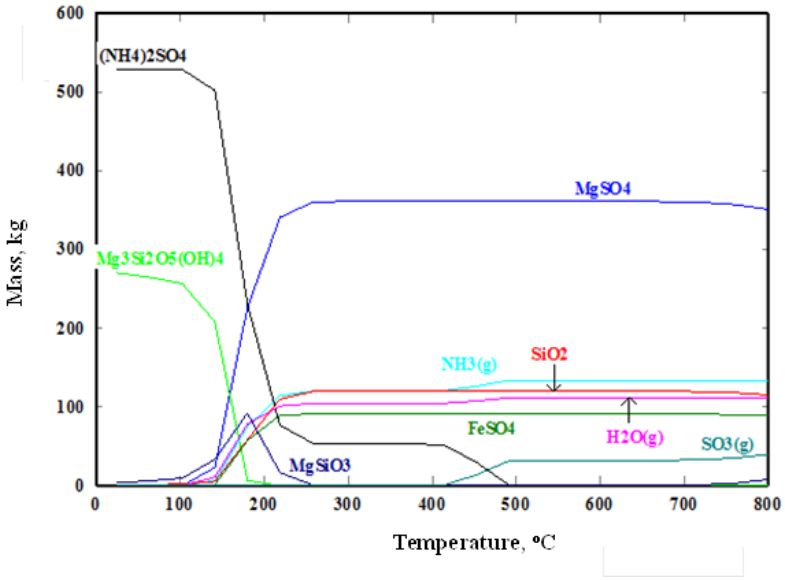

Figure B1. Thermodynamic compositions of the reaction of Finnish serpentinite rock and AS salt[16].

Nomenclature

ÅA	Åbo Akademi University
AS	Ammonium sulfate salt
E	Exergy, J
FB	Fluidized bed
G	Gibbs free energy, J/mol
GJ	Gigajoule
GJ/t-CO_2	Gigajoule per ton CO_2
H	Enthalpy, J/mol
kWh/t-CO_2	kilowatt hour per ton CO_2
Mg/Fe	Elemental Mg to Fe ratio of Mg-silicate rock

Mg-silicate	Magnesium silicate mineral.
MVR	Mechanical vapor recompression
P	Pressure, atm
Q	Heat, J
R&D	Research and development
T	Temperature, K
t	time
S	Magnesium silicate mineral
S/AS	Mg-silicate to ammonium sulfate ratio
ΔS	Change in entropy, J/mol-K
W	Work, J/s
Greek symbols	
Δ	difference
∑	sum

References

[1] Kojima T, Nagamine A, Ueno N, Uemiya S. Absorption and fixation of carbon dioxide by rock weathering. Energy Conversion and Management. 1997;38:S461-S6.

[2] Lackner K. Climate change: a guide to CO2 sequestration. Science. 2003;300(5626):1677.

[3] Lackner K. Carbonate chemistry for sequestering fossil carbon. Annu Rev Energy Environ. 2002;27:193–232.

[4] Hilley GE, Porder S. A framework for predicting global silicate weathering and CO2 drawdown rates over geologic time-scales. Proceedings of the National Academy of Sciences. 2008;105(44):16855-9.

[5] Zevenhoven R, Teir S, Eloneva S. Heat optimisation of a staged gas-solid mineral carbonation process for long-term CO2 storage. Energy. 2008;33(2):362-70.

[6] Nduagu E, Björklöf T, Fagerlund J, Mäkilä E, Salonen J, Geerlings H, et al. Production of magnesium hydroxide from magnesium silicate for the purpose of CO_2 mineralization – Part 2: Mg extraction modeling and application to different Mg silicate rocks. Minerals Engineering. 2012;30:87-94.

[7] Fagerlund J, Nduagu E, Romão I, Zevenhoven R. A stepwise process for carbon dioxide sequestration using magnesium silicates. Frontiers of Chemical Engineering in China. 2010;4(2):133-41.

[8] Fagerlund J, Teir S, Nduagu E, Zevenhoven R. Carbonation of magnesium silicate mineral using a pressurised gas/solid process. Energy Procedia. 2009;1(1):4907-14.

[9] Romão I, Eriksson M, Nduagu E, Fagerlund J, Gando-Ferreira L, Zevenhoven R. Carbon dioxide storage by mineralisation applied to an industrial-scale lime kiln. 25th International Conference on Efficieny, Costs, Optimisation, Simulation and Environmental Impact of Energy Systems (ECOS 2012). Perugia, Italy.2012.

[10] Fagerlund J, Zevenhoven R. The effect of SO_2 on CO_2 mineral sequestration applied directly to a flue gas. 25th International Conference on Efficieny, Costs, Optimisation, Simulation and Environmental Impact of Energy Systems (ECOS 2012). Perugia, Italy.2012.

[11] Zhao L, Sang L, Chen J, Ji J, Teng HH. Aqueous Carbonation of Natural Brucite: Relevance to CO2 Sequestration. Environmental Science & Technology. 2009;44(1):406-11.

[12] Kheshgi HS. Sequestering atmospheric carbon dioxide by increasing ocean alkalinity. Energy. 1995;20(9):915-22.

[13] Teir S, Kuusik R, Fogelholm CJ, Zevenhoven R. Production of magnesium carbonates from serpentinite for long-term storage of CO_2. International Journal of Mineral Processing. 2007;85(1-3):1-15.

[14] Rinne J. CO_2 sequestration potential of industrial by-products and waste materials in Finland [M.Sc.(Eng) Thesis]: Helsinki University of Technology, Finland, 2008.

[15] Nduagu E. Mineral carbonation: preparation of magnesium hydroxide [$Mg(OH)_2$] from serpentinite rock [MSc. (Eng) Thesis]. Turku: Åbo Akademi University, Finland, 2008.

[16] Nduagu E, Björklöf T, Fagerlund J, Wärnå J, Geerlings H, Zevenhoven R. Production of magnesium hydroxide from magnesium silicate for the purpose of CO_2 mineralisation – Part 1: Application to Finnish serpentinite. Minerals Engineering. 2012;30:75-87.

[17] Nduagu E, Fagerlund J, Zevenhoven R. Contribution of iron to the energetics of CO_2 sequestration in Mg–silicates-based rock. Energy Conversion and Management. 2012;55(0):178-86.

[18] Romão I, Nduagu E, Fagerlund J, Gando-Ferreira LM, Zevenhoven R. CO_2 Fixation Using Magnesium Silicate Minerals. Part 2: Process Energy Efficiency and Integration with iron-and steelmaking. Energy – the Int J (special edition ECOS2010). 2012;41 203-11

[19] Lackner K, Doby P, Yegulalp T, Krevor S, Graves C. Integrating Steel Production with Mineral Carbon Sequestration. New York, NY: Columbia University, Department of Earth and Environmental Engineering, New York, NY; 2008. p. Medium: ED; Size: 75 pages, 1914 KB.

[20] Romão I, Ferreira LMG, Fagerlund J, Zevenhoven R. CO_2 sequestration with Portuguese serpentinite. Conference CO_2 sequestration with Portuguese serpentinite, Turku, Finland. p. 77-87.

[21] Stasiulaitiene I, Fagerlund J, Nduagu E, Denafas G, Zevenhoven R. Carbonation of serpentinite rock from Lithuania and Finland. Energy Procedia. 2011;4(0):2963-70.

[22] Nduagu E, Zevenhoven R. Production of magnesium hydroxide from magnesium silicate for the purpose of CO_2 mineralisation and increasing ocean alkalinity: effect of reaction parameters. Accelerated Carbonation for Environmental and Materials Engineering (ACEME10). Turku, Finland 2010. p. 31-40.

[23] Montgomery D. Design and analysis of experiments. Wiley New York; 1997.

[24] MINITAB®. MINITAB statistical software, Release 16 for windows, State College, Pennsylvania. MINITAB®, is a registered trademark of Minitab Inc2010.

[25] Nduagu E, Bergerson J, Zevenhoven R. Life cycle assessment of CO_2 sequestration in magnesium silicate rock – A comparative study. Energy Conversion and Management. 2012;55(0):116-26.

[26] Björklöf T. An Energy Efficiency Study of Carbon Dioxide Mineralization [MSc. (Eng) Thesis]. Turku: Åbo Akademi University, Finland, 2010.

[27] Fagerlund J, Nduagu E, Romão I, Zevenhoven R. CO_2 fixation using magnesium silicate minerals. Part 1: Process description and performance. Energy – the Int J (special edition ECOS2010). 2012;41:184-91.

[28] Kemp IC. Pinch analysis and process integration: a user guide on process integration for the efficient use of energy. Oxford, UK.: Butterworth-Heinemann, 2007.

[29] Linnhoff B. Pinch analysis: a state-of-the-art overview: Techno-economic analysis. Chemical engineering research & design. 1993;71(5):503-22.

[30] Kotas TJ. The exergy method of thermal plant analysis. Stoneham, MA, US.: Butterworth Publishers, 1985.

Thermodynamic analysis of a supercritical power plant with oxy type pulverized fuel boiler, carbon dioxide capture system (cc) and four-end high temperature membrane air separator

Janusz Kotowicz[a], Sebastian Michalski[b]

[a] *Silesian University of Technology, Poland, janusz.kotowicz@polsl.pl,*
[b] *Silesian University of Technology, Poland, sebastian.michalski@polsl.pl,*

Abstract:

In this paper the analysis of a supercritical power plant was made. Power of the power plant is 460 MW. The parameters of life steam are at 29 MPa/600 oC and of the reheated steam 4.8 MPa/600 oC. Power plant is equipped with the following units: oxy type pulverized fuel boiler, "four-end" high temperature membrane (HTM) air separator and carbon dioxide capture system (CC). With the assumption of a constant gross power of the analyzed power plant the thermal efficiency of the boiler and power consumption of all mentioned above units were calculated. These parameters were designated as a function of the recovery rate of oxygen in the HTM. This allowed to make the characteristic of efficiency as a function of recovery rate. The net efficiency increased from 34.8% to 36.7% with a change of oxygen recovery rate from 0.45 to 0.9. The effect of membrane working temperature on the efficiency characteristics was also analyzed. Integration of CC, HTM air separator and steam cycle was proposed for the increase of the efficiency of a power plant. The theoretical analysis was carried out and appropriate calculations were made for this integration.

Keywords:

OXY type pulverized fuel boiler, air separation, four-end HTM (High Temperature Membrane)

1. Introduction

Currently observed in the world trend in efforts to reduce emissions, especially of greenhouse gases, contributes to significant changes in the direction of the development of energy technologies [1]. This is very important for the development of coal technologies, due to importance of these fuels in the energy balances of many countries, including Poland, as well as due to significant emission of CO_2 per electricity production unit. In the area of coal technology there are two main research directions aiming to bring down the reduction of CO_2 unit emission, thus, in consequences, to the reduction of global emission:

- search of low-energy consuming carbon capture technologies (including searching for new technologies, optimization of known technologies, also in the area of integration of the CCS unit with a power plant),
- increasing the efficiency of electricity generation, including optimization of a power plant, both in the area of its structure, as well as in area of operation parameters [2].

Among carbon capture technologies three directions are developed:

- pre-combustion technology,
- post-combustion technology,
- oxy-combustion technology.

In the area of coal technologies all of these solutions can be used. However, the first solution is predisposed for IGCC systems [3], in which there is the possibility of generating carbon dioxide before combustion of synthesis gas. The fuel before entering the combustion chamber is subjected to a carbon sequestration. Due to the lower gas stream from which the carbon dioxide is removed such a separation process is connected with less energy consumption. The next technology is based on removing carbon dioxide from flue gases leaving the power system. The post-combustion technology is predisposed for the conventional coal-fired power plants. In the area of post-combustion technology, as in the case of pre-combustion, the research on absorption and adsorption techniques, as well as membrane and cryogenic separation are realized [4÷5]. Among of clean coal technology large hopes are associated with oxy-combustion technology, of which the principal purpose is combustion of coal in the oxygen-rich atmosphere in order to eliminate from the exhaust gases the inert gas (nitrogen). In this case the exhaust gases leaving the steam boiler consists mainly of carbon dioxide and steam, so the carbon capture process is much less energy intensive. Currently in the research area of oxy-combustion technology, the solutions aiming for decreasing the energy consumption connected with oxygen production in the air separation unit are searched for [6÷10].

The results presented in the paper were realized within the framework of the Strategic Project ”Advanced Technologies for Energy Generation: Oxy-combustion technology for PC and FBC boilers with CO_2 capture”. In the paper the results of the analysis of the steam cycles of energy generation units are shown. These steam cycles will be the basis for creation of the models of the whole oxy-combustion power plants. In the paper the results of analysis including the influence of different solutions of steam cycles, and thus their assumed parameters, on the energy effectiveness evaluation indicators are shown.

2. Model of the air separation unit integrated with the oxy type pulverized boiler and assumptions for calculations

Air separation unit structure consists of: a counter-current air heater (APH), an air compressor (C), an expander (EX), a generator (G) and a "four end" type membrane (M). The expander drives the air compressor. Depending on the assumed quantities the expander and compressor can give or take electricity from the grid. The structure of the air separation unit is shown in Figure 1.

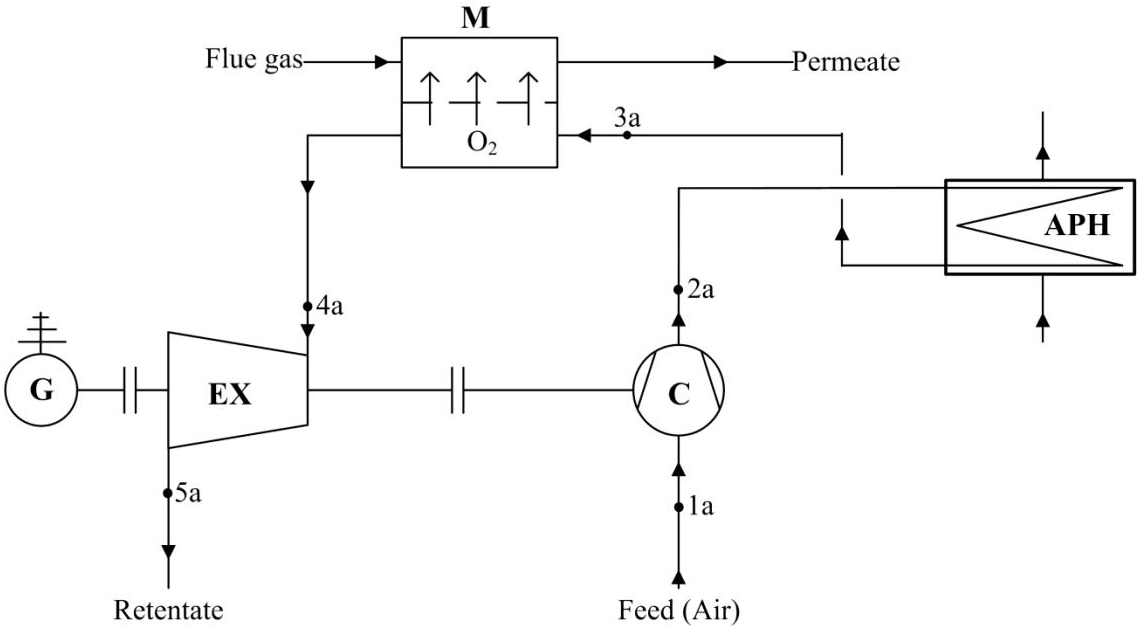

Fig. 1. Scheme of the air separation unit (ASU)

Oxy type pulverized boiler structure consist of: a combustion chamber (CC), an evaporator divided into two parts (EVAP), a counter-current air heater (APH), three recirculated flue gas heaters (RHX1, RHX2 and RHX3), a live steam superheater (LSSH), a reheated steam superheater (RSSH), an economizer (ECO), an electrostatic precipitator (EP), a flue gas extractor fan (F1), a flue gas dryer (FGD) and a recirculated flue gas fan (F2). The structure of air separation unit integrated with the oxy type pulverized boiler is shown in Figure 1. The basic characteristic quantities of integrated models are gathered in Table 1.

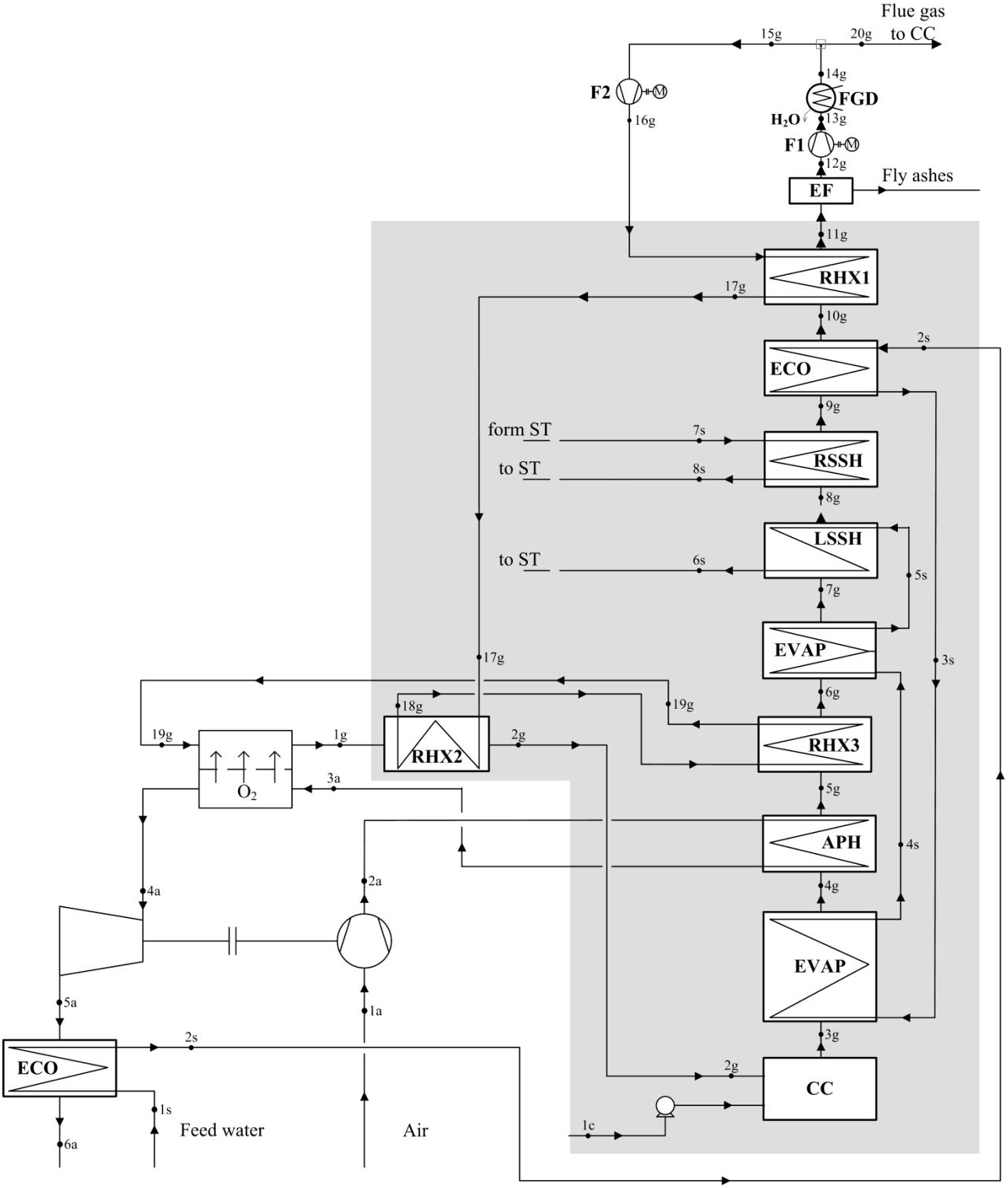

Fig.2. Scheme of air the separation unit (ASU) integrated with OXY type pulverized boiler

Tabel 1. Characteristics quantities for considered air separation unit integrated with the oxy type pulverized boiler

Name	Symbol	Value	Unit
Excess air coefficient	λ	1.2	-
Live steam flow rate, Reheated steam flow rate	$\dot{m}_{6s}, \dot{m}_{8s}$	336.05, 284.42	kg/s
Temperature, Pressure of live steam leaving the boiler	t_{6s}, p_{6s}	604.90, 30100.00	°C, kPa
Temperature, Pressure of reheated steam leaving the boiler	t_{8s}, p_{8s}	602.40, 4918.03	°C, kPa
Temperature of feed water	t_{1s}	297.00	°C
Temperature of recycled feed gas leaving PRS	t_{17g}	320	°C
Efficiency of heat exchangers in the boiler heat	η_{wck}	99.8	%
Moisture content in the flue gas leaving flue gas dryer	$(H_2O)_{14g}$	10	%
Share of oxygen in the mixture of the recycled flue gas and oxygen from ASU supplied to the combustion chamber	$x_{O2,per}$	0.3	$\frac{\text{kmol, O}_2}{\text{kmol, gw}}$
Ambient pressure, Pressure of flue gas supplied to the carbon dioxide capture unit	p_{ot} , p_{16g}	101.325	kPa
Ambient temperature	t_{ot}	20	^{o}C
Fan isentropic efficiency, Compressor isentropic efficiency	η_{iF}, η_{iS}	0.88	-
Expander isentropic efficiency	η_{iT}	0.9	-
Generator efficiency	η_g	0.99	-
Share of slag in the ash	$u_{ż}$	40	%
Share of fly ash in the ash	u_{pl}	60	%
Share of carbon element from coal in the ash	$c_{ż}$	0.5	%
Membrane work temperature, Temperature of flue gas at the inlet to the separation membrane	t_{mem} , t_{19g}	850	^{o}C
Specific temperature difference of the permeate-recycled flue gas heat exchanger	$\Delta T_{sP\text{-}S}=t_{1g}$-$t_{18g}$	50	K
Oxygen recovery rate	R	40÷100	-
Compressor pressure ratio	β_k	15	-
Energy consumption of electrostatic precipitator	-	1	kJ/kg, fg
Energy consumption of coal mill	-	64.8	kJ/kg, fuel
Energy consumption of carbon dioxide capture unit	-	316.03	kJ/kg, fg

It was assumed that the air taken from environment is a dry gas consisting of 21% oxygen and 79% nitrogen (volumetric composition).

The characteristic quantities gathered in Table 1 were used for computations performed on the model of the oxy-type pulverized boiler integrated with the air separation unit, made in the

GateCycle^{TM} software. The built-in components were used to build the integrated model. It was assumed that through the membrane flows pure oxygen. The auxiliary power rate of steam cycle, the live steam thermodynamic parameters, reheated steam thermodynamic parameters, mass flow rates of live steam and reheated steam were assumed as for a 460 MW power plant. The gross power of steam turbine is constant, despite electricity generated in the air separation unit.

Energy consumption of the carbon dioxide capture unit was calculated with use of the model of carbon dioxide capture unit. The structure of this model is shown in Figure 3. The energy consumption value is correct for the specific composition of the flue gas.

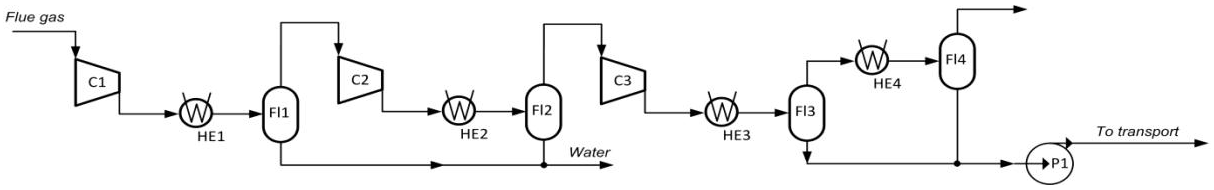

Rys.3. Scheme of the carbon dioxide capture unit (CC)

3. The results of calculations of air separation unit integrated with the oxy type pulverized boiler

The air mass flow rate depends on the separated in membrane oxygen mass flow rate ($\dot{m}_{O2}$), oxygen recovery rate (R) and mass content of oxygen in the air (g_{O2-air}). The relationship between these quantities is as follows:

$$\dot{m}_{1a} = \frac{\dot{m}_{O2}}{R \cdot g_{O2-air}} \qquad (1)$$

Next the air is flowing to the compressor. Effective power required to drive the compressor depends on the air mass flow rate ($\dot{m}_{1a}$), the air temperature (T_{1a}), the average specific heat ($\left(\tilde{c}_p\right)_K$), the compressor pressure ratio (β_K), the heat capacity ratio contained in the factor ($\mu_K = \left(\frac{\chi-1}{\chi}\right)_K$), the compressor isentropic efficiency (η_{iK}) and the compressor mechanical efficiency (η_{mK}). The equation showing the relationship between these quantities is as follows:

$$N_{eK} = \dot{m}_{1a} \cdot \left(\tilde{c}_p\right)_K \cdot T_{1a} \cdot \left(\frac{\beta_K{}^{\mu_K} - 1}{\eta_{iK} \cdot \eta_{mK}}\right) \qquad (2)$$

The mass flow rate of gas flowing through the expander is lower than the mass flow rate of gas flowing through the compressor. This mass flow rate depends on the oxygen mass flow rate separated from the air in the membrane ($\dot{m}_{O2}$) and the air flow rate ($\dot{m}_{1a}$).The relationship between these quantities is as follows:

$$\dot{m}_{4a} = \dot{m}_{1a} - \dot{m}_{O2} \qquad (3)$$

The expander effective power depends on the retentate mass flow rate ($\dot{m}_{4a}$), the retentate temperature (T_{4a}), the average specific heat ($\left(\tilde{c}_p\right)_K$), the compressor pressure ratio (β_K), the reduction factor of compressor pressure ratio (σ), the heat capacity ratio contained in the factor ($\mu_T = \left(\frac{\chi-1}{\chi}\right)_T$), the expander isentropic efficiency (η_{iT}) and the expander mechanical efficiency (η_{mT}). The equation showing the relationship between these quantities is as follows:

$$N_{eT} = \dot{m}_{4a} \cdot \left(\tilde{c}_p\right)_T \cdot T_{4a} \cdot \left[1-(\sigma \cdot \beta_K)^{-\mu_T}\right] \cdot \eta_{iT} \cdot \eta_{mT} \qquad (4)$$

The gross electrical power of the air separation unit depends on the expander gross power (N_{eT}), the compressor gross power (N_{eK}) and the generator efficiency (η_g). The relationship between these quantities is as follows:

$$N_{elTG} = \left(N_{eT} - N_{eK}\right) \cdot \eta_g \qquad (5)$$

Figure 4 shows a graph of boiler thermal efficiency as a function of oxygen recovery rate of the air separation unit. It should be noted that the boiler thermal efficiency increases from about 55% for low oxygen recovery rates to about 83% for high recovery rates. The boiler thermal efficiency depends on the live steam flow rate ($\dot{m}_{6s}$), the reheated steam flow rate ($\dot{m}_{8s}$), the enthalpy of live seam leaving the boiler (h_{6s}), the enthalpy of feed water at inlet to the boiler (h_{2s}), the enthalpy of reheated steam leaving the boiler (h_{8s}),the enthalpy of reheated steam at the inlet to the boiler (h_{7s}), the fuel mass flow rate ($\dot{m}_{1c}$) and fuel lower heating value (W_{dp}). The equation showing the relationship between these quantities can be written as:

$$\eta_k = \frac{\dot{m}_{6s} \cdot \left(h_{6s} - h_{2s}\right) + \dot{m}_{8s} \cdot \left(h_{8s} - h_{7s}\right)}{\dot{m}_{1c} \cdot W_{dp}} \qquad (6)$$

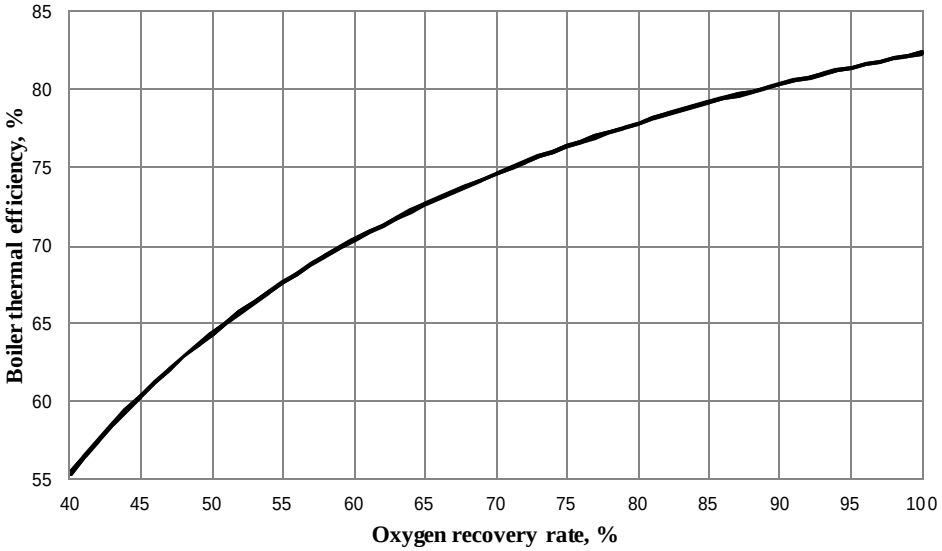

Fig.4. Thermal efficiency of the oxy type boiler as a function of the air separation unit oxygen recovery rate

The thermal efficiency of steam cycle depends on the heat supplied to the steam cycle ($\dot{Q}_d$) and the heat discharged from the steam cycle ($\dot{Q}_w$).The relationship between these quantities is as follows:

$$\eta_{obp} = \frac{\dot{Q}_d - \dot{Q}_w}{\dot{Q}_d} \qquad (7)$$

The gross efficiency of electricity generation is calculated in terms of the generator electrical power driven by the steam turbine. The electricity generated in other units is included in their auxiliary recovery rates. The gross efficiency of electricity generation depends on the steam turbine electrical power (N_{el}), the fuel flow rate ($\dot{m}_{1c}$) and lower heating value (W_{dp}).The equation showing the relationship between these quantities can be written as:

$$\eta_{\text{el,brutto}} = \frac{N_{\text{el}}}{m_{1c} \cdot W_{\text{dp}}} \qquad (8)$$

The net efficiency of electricity generation depends on the gross efficiency of electricity generation ($\eta_{\text{el,brutto}}$), the auxiliary power rate of air separation unit ($\delta_{\text{pw,ASU}}$), the auxiliary power rate of carbon dioxide capture unit ($\delta_{\text{pw,CCS}}$), the auxiliary power rate of steam cycle ($\delta_{\text{pw,bloku}}$) and the auxiliary power rate of the boiler ($\delta_{\text{pw,kotła}}$). The equation showing the relationship between these quantities is as follows:

$$\eta_{\text{el,netto}} = \eta_{\text{el,brutto}} \cdot (1 - \delta_{\text{pw,ASU}} - \delta_{\text{pw,CCS}} - \delta_{\text{pw,bloku}} - \delta_{\text{pw,kotła}}) \qquad (9)$$

Auxiliary power rates except the auxiliary power rate of the air separation unit, depends on auxiliary power of unit ($N_{\text{pw,i}}$) and the steam turbine electric power (N_{el}).The equation showing the relationship between these quantities can be written as:

$$\delta_{\text{pw,i}} = N_{\text{pw,i}} / N_{\text{el}} \qquad (10)$$

The auxiliary power rate of the air separation unit depends on the mechanical power used to drive the compressor (N_{SN}), the mechanical power generated in expander (N_{TR}) and the steam turbine electrical power (N_{el}).The equation showing the relationship between these quantities is as follows:

$$\delta_{\text{pw,ASU}} = \frac{N_{\text{SN}} - N_{\text{TG}}}{N_{\text{el}}} \qquad (11)$$

Figure 5 shows a graph of auxiliary power rates of the boiler, steam cycle and carbon dioxide capture unit as a function of oxygen recovery rate. Figure 6 shows a graph of the auxiliary power rate of the air separation unit. It should be noted that the auxiliary power rate of the air separation unit, unlike the other auxiliary power rates, has a negative value in the studied range of oxygen recovery rate.

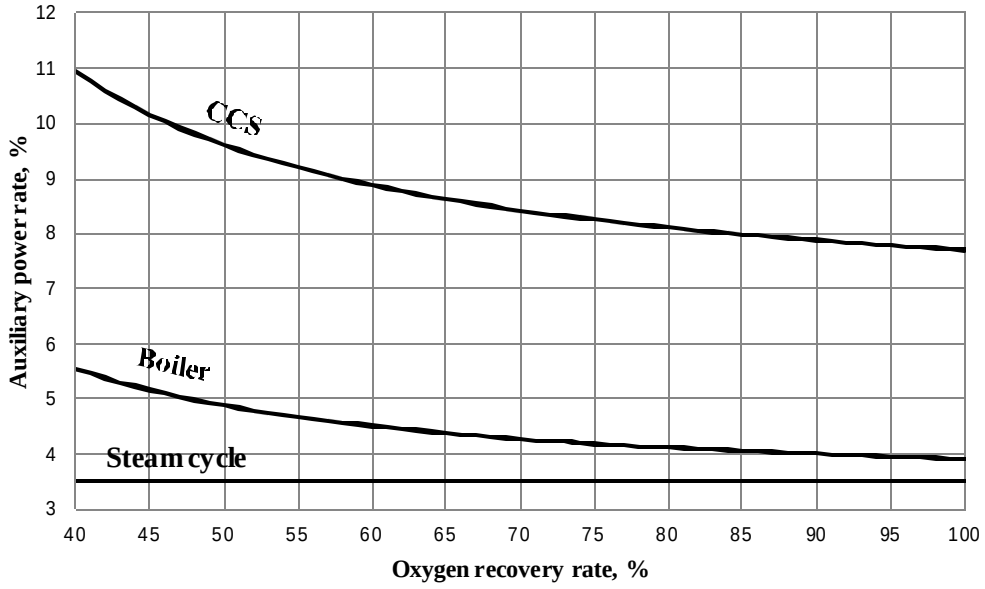

Fig.5. The auxiliary power rates of the carbon dioxide capture unit (CCS), boiler and steam cycle as a function of the oxygen recovery rate

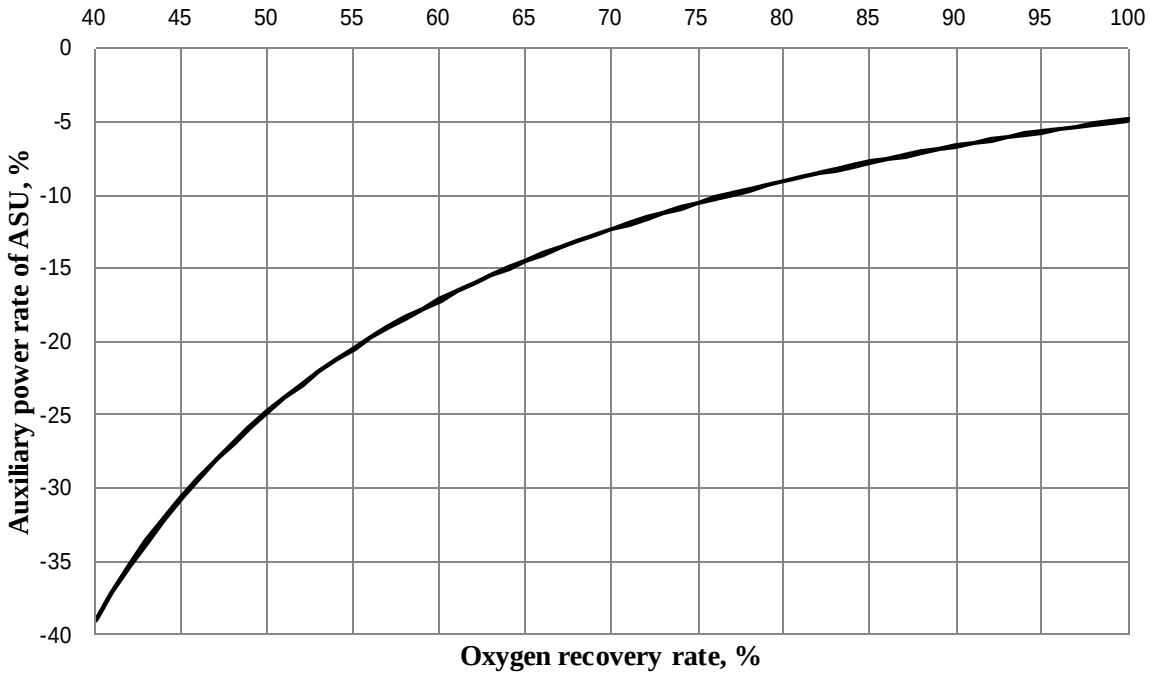

Fig.6. The auxiliary power rate of the air separation unit as a function of the oxygen recovery rate

Figure 7 shows a graph of the gross and net efficiency of electricity generation as a function of oxygen recovery rate. This characteristics were determined with the use of equations (8) and (9).

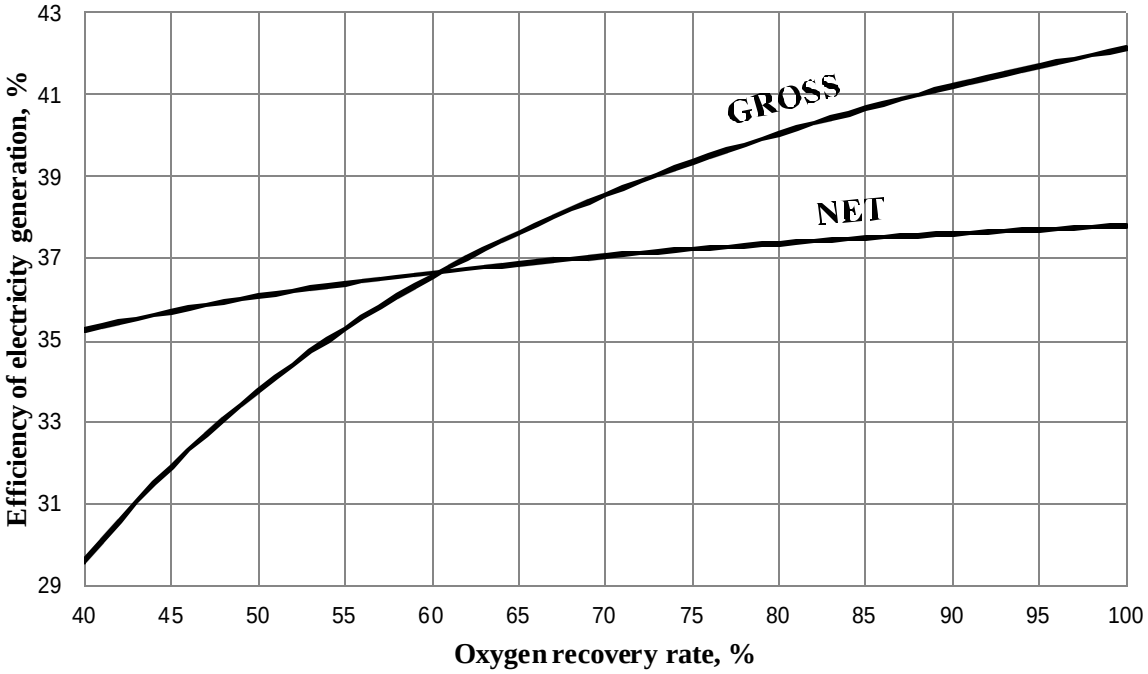

Fig.7. Gross and net efficiency of electricity generation as a function of the air separation unit oxygen recovery rate

Summary

In this paper the air separation unit integrated with the oxy type pulverized boiler was analyzed. The oxy type boiler supplies the live steam and the reheated stem to the steam cycle. The gross power of the steam turbine generator of the steam cycle is equal to 460 MW.

For the analysis the characteristics of the boiler thermal efficiency, auxiliary power rate of the steam cycle, carbon dioxide capture unit and air separation unit as a function of oxygen recovery rate in the "four-end" type separation membrane were determined.

It should be noticed that the value of the boiler thermal efficiency shown in Figure 4 is increasing from about 55% (for 40% of the oxygen recovery rate) to about 83% (for 100% of the oxygen recovery rate). This characteristic is nonlinear and the acceleration of growth of the boiler thermal efficiency decreases with increasing oxygen recovery rate.

The auxiliary power rate of the carbon dioxide capture unit and the auxiliary power rate of the oxy-type pulverized boiler shown in Figure 5 decreases with increasing the oxygen recovery rate. This characteristics are nonlinear. The auxiliary power rate of steam cycle is the same for all oxygen recovery rates, because the power of steam turbine is held at a constant level. The auxiliary power rate of the air separation unit shown in Figure 6 unlike the other auxiliary power rates has a negative value in the studied range of oxygen recovery rate. This means that the expander generates more power than the power needed to drive the compressor. The auxiliary power rate of the air separation unit increases with the increase of the oxygen recovery rate.

It should be noticed that the value of the net efficiency of electricity generation shown in Figure 7 is increasing from about 35% (for 40% of the oxygen recovery rate) to about 38% (for 100% of the oxygen recovery rate). This characteristic is nonlinear and the acceleration of growth of net efficiency of electricity generation decreases with increasing the oxygen recovery rate. This graph indicates that the studied integrated models have the highest net overall efficiency for the oxygen recovery value equal to 100%.

Acknowledgements

The results presented in this paper were obtained from research work co-financed by the National Centre for Research and Development within a framework of Contract SP/E/2/66420/10 – Strategic Research Programme – Advanced Technologies for Energy Generation: Development of a technology for oxy-combustion pulverized-fuel and fluid boilers integrated with CO_2 capture.

LITERATURE

[1] Chmielniak T., The role of various technologies in achieving emissions objectives in the perspective of the years up to 2050. Rynek Energii, 2011;92:3-9

[2] Chmielniak T., Łukowicz H., Kochaniewicz A., Trends of modern power units efficiency growth. Rynek Energii, Nr 6(79), 2008, 14-20.

[3] Badyda K., Kupecki J., Milewski J., Modelling of integrated gasification hybrid power systems. Rynek Energii, 2010;88:74-79.

[4] Kotowicz J., Janusz-Szymańska K., Influence of CO_2 separation on the efficiency of the supercritical coal fired power plant. Rynek Energii, 2011, 2 (93), 8-12.

[5] Liszka M., Ziębik A.: Coal – fired oxy – fuel power unit – Process and system analysis. Energy, 35 (2010), 943 – 951.

[6] Toftegaard M.B., Brix J., Jensen P.A., Glarborg P., Jensen A.D., Oxy-fuel combustion of solid fuels. Progress in Energy and Combustion Science, 2010;36:581-625

[7] Dillon D.J., White.V., Allam R.J., Wall R.A., Gibbins J., Oxy-combustion Process for CO2 Capture from Power Plant. Mitsui Babcock Energy Limited,2005

[8] Buhre B.J.P., Elliott L.K., Sheng C.D., Gupta R.P. and Wall T.F., Oxy-fuel combustion technology for coal-fired power generation. Progress in Energy and Combustion Science, 2005;31:283-307

[9] Pfaff I., Kather A., Comparative thermodynamic analysis and integration issues of CCS steam power plants based on oxy-combustion with cryogenic or membrane based air separation. Energy Procedia 1 (2009) 495-502.

[10] Stadler H. et al.: Oxyfuel coal combustion by efficient integration of oxygen transport membranes. International Journal of Greenhouse Gas Control 5 (2011) 7-15.

A multi-objective optimization technique for co-processing in the cement production

Maria Luiza Grillo Renó[a], Rogério José da Silva [b], Mirian de Lourdes Noronha Motta Melo[c] , José Joaquim Conceição Soares Santos[d]

[a] Federal University of Itajubá, Itajubá, Brazil, malureno@yahoo.com.br
[b] Federal University of Itajubá, Itajubá, Brazil, rogeriojs@unifei.edu.br
[c] Federal University of Itajubá, Itajubá, Brazil, mirianmottamelo@unifei.edu.br
[d]Federal University of Espírito Santo, Vitória, Brazil, jose.j.santos@ufes.br

Abstract:

Cement is produced by blending different raw materials and by burning them at high temperatures. The Portland cement production is a process that demands high energy consumption; therefore the process needs a great amount of fuel. Moreover, industrial waste has been used by Portland cement industries as a secondary fuel through a technique called co-processing. For energy conservation in this work, mineralizers are added into the clinker formation. The mineralizers promote the decrease the temperature in the kiln and improve the quality of the clinker. The purpose of the present work is to provide an analysis of an optimal production point through an optimization technique with multiple objective functions, in which genetic algorithms, sequential quadratic programming are applied.

Keywords:

Optimization, Portland cement, Co-processing, Mineralizers.

1. Introduction

The cement industry is connected to the environment. The production process requires energy and this causes to emissions. Information on energy consumption including secondary fuels in the cement industry is relatively well known. Fossil fuels (e.g. coal, oil or natural gas) are the predominant fuels used in the cement industries. However, low-grade fuels such as petrol coke and waste derived fuels have been increasingly utilised in the recent years.

The use of waste derived fuels, as alternative secondary fuels, has been showed itself as a possible path so that the cement industries reduce its production costs and reduce the consumption of fossil fuels. Moreover, for the residues industries generators is the expected solution for the disposition demanded by the environmental legislation. Now the spectrum of residues co-processed in the cement industry is varied being added the list of alternative fuels used since the decade of eighty: used oils, waste of the re-refining process of lubricating oils, used tyres, shavings of tyres, residues of solvents, dregs of paintings, urban residues and treatment muds and others.

Besides, it is well known that the most energy-demanding phases of cement manufacturing is the clinkering process, which consumes 80% of the total energy for pyro processing. Thus a potential for energy conservation, which could be rapidly and economically accomplished by promoting the clinker formation at lower temperature in the kiln by using mineralizers that promote certain reactions and fluxes that lower the melting point of clinker liquid phase. Then this work proposes the combination of mineralizers and alternative fuel in cement production with main to reduce the production costs and environmental impacts.

1.1 - Cement Manufacturing

The cement manufacturing process consists broadly of quarrying, crushing and grinding, burning, and grinding with gypsum. Two basic processes, the wet process and the dry process, are used for cement manufacturing. In the wet process, proper proportions of the raw materials are mixed with water. The mixture is called slurry. While in the dry process there is not water with raw materials.

Both processes of the raw materials are proportioned, mixed, grounded and pulverized, and then pumped into a rotary kiln. Inside the kiln, the raw materials are subjected to a thermal treatment process consisting of consecutive steps of drying/preheating, calcination, and sintering (or clinkerisation, at temperatures up to 1450°C).

The burnt product "clinker" is cooled down with air to 100-200°C and is transported to intermediate storage. After, a few percentage of natural or industrial gypsum is added to clinker to regulate the setting time of cement. Finally, the finished product, known as the Portland cement, is stored in large storage bins called silos, from which is fed to an automatic packing machine.

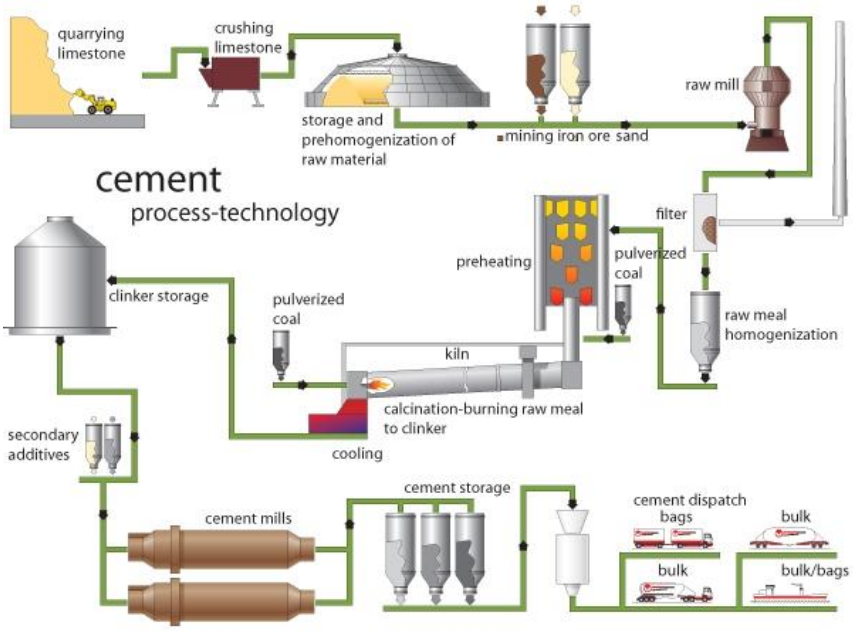

Fig. 1 – Cement manufacturing process [1]

1.2 – Emissions of cement production

The atmospheric emission of the cement plant includes particles, NO_x, SO_2, CO_2 and lower amounts of CO, organic compounds such as metals (mainly adhered to particles), as well as other minor pollutants [2].

The SO_2 emissions are primarily determined by the content of volatile sulphur in raw materials and fuel used. Sulphur dioxide emissions result from the combustion of fuel and raw materials. In addition, SO_2 emissions can result from decomposition of alkali or calcium sulphates that are trapped within the volatile cycles of the kiln [3].

Sulphur input is usually absorbed within a range of 50-90 % of input. Modern kiln system of preheat and pre-calciner types tend to have higher rates of SO_2 absorption. The unabsorbed portion of the sulphur input is emitted from the kiln system as SO_2 and SO_3.

NO_x emissions from cement kilns depend on both the kiln type and the fuel type. In general, pre-heater and precalciner kilns have lower NO_x emission rates than long dry and wet kilns, due to the higher fuel efficiency and lower firing rates in the kiln firing zone [4].

NO_x is formed during fuel combustion by oxidation of molecular nitrogen of combustion air as well as nitrogen compounds of the fuel. Significant oxidation of molecular nitrogen of combustion air takes place in oxidizing flames with a temperature above 1200°C. The NO_x formed in this way is named thermal NO_x, otherside the NO_x formed by oxidation of nitrogen compounds in the fuel which is named fuel NO_x.

1.3 – Co-processing

Cement companies are introducing the industrial waste co-processing from a perspective that combines environmental policies with the interests of companies. Industrial wastes with residual energy and low content of chlorides and heavy metals can be appropriate to provide part of the energy required to make cement.

The process of clinker burning in rotary kiln creates favourable conditions for the use of industrial waste like alternative fuel. These conditions are high temperature, alkaline environment, oxidizing atmosphere, large heat-exchange surface, good mixture of gases and products, and sufficient time (over 2 seconds) for the disposal of hazardous wastes [5]. The Table 1 presents examples of alternative fuels used in cement industry.

Table 1 – Examples of Alternative Fuels

Alternative Fuel	**Examples**
gaseous	Landfill gas, pyrolysis gas
Liquid	Pasty wastes, solvents, waste oils, greases
Solid	Paper, used tires, rubber wastes, plastics

The used tires are material residual special, based on higher heating value (28–32 MJ/kg of tyres), they are excellent sources of energy, mainly when used as secondary fuels. The high temperature, the high time of residence, the high effect of absorption of the raw material in the pre-heating and the incorporation of the ashes generated to the clinker, are favourable conditions for burning of tyres in rotary kilns of clinker production, so that, is an adequate form to final disposition for these wastes. Besides, due to the high calorific value of the tires, the co-processing contributes to a decrease in consumption of others fossil fuels utilized (as coal, petroleum coke and fuel oil), saving the natural resources [6].

1.4 – Mineralizers

The use of mineralizers in the cement industry is widely known. The incorporation of compounds other than those usual in low proportions improves the clinkering conditions as well as decreases the maximum clinkering temperature or improves the phase formation in the clinker without altering the final properties of the product [7]. The mineralizing properties of the compounds CaF_2 and $CaSO_4$ have already been described in the literature. Their properties are different when they are added separately or jointly in the raw materials.

It has been verified that the combined addition of CaF_2 and $CaSO_4$ to raw clinker materials results in a decrease of the maximum clinkering temperature to approximately 1350°C, in a clinker with a good proportion of alit and a cement with satisfactory mechanical properties [7]. The reduction of temperature by 100°C is expected to result in a saving of fuel by 80-100 kcal/kg of clinker [8].

2. Numerical model

The purpose of this section is to provide an analysis of an optimal production point through optimization problem with multi-objective functions and constraints. The multi-objective functions are the clinker production cost, NO_x and SO_2 emissions. The constraints refer to operational parameters and clinker quality.

2.1. Objective functions

Clinker production cost function:

The clinker production cost taking into consideration raw materials cost as well the energy consumption requested for grinding. This last can be written with respect to the specific surface of the cement, silica modulus and electricity cost (Eq. (1)).

$$E = ce \times A\exp^{(BS)} \tag{1}$$

Where:

$A = 5,76(SM) - 5,82$

$B = -0,2(SM) + 0,98$

SM = Silica Modulus; *ce* = electricity cost; *S* = specific surface of cement

Silica modulus (SM) is the ratio of the silicates oxide with the sum of the ferric oxide and alumina oxide in the clinker. The Silica Modulus has influence on the burning of raw materials, clinker granulometry and liquid phase. The raw materials and fuel costs are written as linear combination, Eq. (2):

$$C = \sum_{i=1}^{n} p_i \times (x_i) \tag{2}$$

Where:

p_i = raw materials and fuels medium cost.

x_i = raw materials and fuel quantity.

The raw materials of clinker production are limestone (x_1), clay (x_2), sand (x_3), and iron ore (x_4). The fuels used are mineral coal (x_5), petroleum coke (x_6), and the alternative fuel used is the scrap tires (x_7). The mineralizers applied in this work are CaF_2 (x_8) and $CaSO_4$ (x_9), these mineralizers proceed from industrial wastes and it is considered as revenue for the cement industry, with a symbolic income of US$ 1/ton. The final cost equation (clinker production cost) is presented in Eq. (3):

$$f_1(x) = 1.25x_1 + 1.45x_2 + 0.87x_3 + 10x_4 + 63.11x_5 + 40x_6 - 1x_7 - 1x_8 - 1x_9 + ce * \{(5.76(SM) - 5.82) * e^{(-0.2(SM)+0.98)*S}\} \tag{3}$$

Where

$$SM = \frac{0.61x_1 + 58.86x_2 + 83.67x_3 + 4.4x_4 + 4.03x_5 + 1.97x_7 + 18.80x_8 + 1.41x_9}{0.32x_1 + 21.31x_2 + 5.6x_3 + 92.58x_4 + 6.975x_5 + 0.9207x_7 + 0.09x_9} \qquad S = 4\ cm^2 / kg$$

SO_2 and NO_x emissions functions:

In this optimization model the SO_2 and NO_x emissions functions refer to S and N contained in fuels (mineral coal, petroleum coke and used tires). Table 2 shows the composition of S and N in fuels used. Eq. (4) and (5) represent the SO_2 and NO_x emissions functions respectively. The composition is obtained in [9], [10], [11].

Table 2 – N and S composition in the fuels

	Mineral coal (%)	**Petroleum coke (%)**	**Tires used (%)**
N	1.2	1.5	0.36
S	5.5	5	1.23

$$f_2(x) = 0.055x_5 + 0.05x_6 + 0.0123x_7 \quad (4)$$

$$f_3(x) = 0.012x_5 + 0.015x_6 + 0.0036x_7 \quad (5)$$

2.2. Constraints

Equation (6) up to Eq. (8) represents the operational order restrictions for SiO_2, Al_2O_3 and Fe_2O_3 content, respectively. The data were obtained in Brazil cement industry.

$$0.0061x_1 + 0.59x_2 + 0.837x_3 + 0.044x_4 + 0.0403x_5 + 0.0192x_7 + 0.188x_8 + 0.0141x_9 = 0.216 \quad (6)$$

$$0.0015x_1 + 0.171x_2 + 0.047x_3 + 0.027x_4 + 0.017x_5 + 0.0079x_7 + 0.0009x_9 = 0.062 \quad (7)$$

$$0.0017x_1 + 0.042x_2 + 0.0095x_3 + 0.90x_4 + 0.053x_5 + 0.0013x_7 = 0.025 \quad (8)$$

Equation (9) and Eq. (10) represent the silica modulus that present an adequate value for interval between 2.3 and 2.7. Eq. (11) and Eq. (12) relate to alumina modulus. This modulus influences mainly on the burning process by acting on speed of the reaction of limestone and silica. The values for this modulus are within the range of 1.3 and 2.7. Eq. (13) and Eq. (14) refer to the lime saturation factor. A high factor of lime saturation causes burning difficulties. Acceptable values for this factor are between 0.9 and 1.

$$-0.216x_1 + 9.85x_2 + 70.8x_3 - 208.53x_4 - 12.01x_5 - 0.20x_7 + 18.80x_8 + 1.20x_9 > 0 \quad (9)$$

$$-0.254x_1 + 1.32x_2 + 68.55x_3 - 245.57x_4 - 14.8x_5 - 0.57x_7 + 18.80x_8 - 1.17x_9 < 0 \quad (10)$$

$$-0.071x_1 + 11.65x_2 + 3.42x_3 - 114.12x_4 - 5.146x_5 + 0.63x_7 + 0.09x_9 > 0 \quad (11)$$

$$-0.309x_1 + 5.77x_2 + 2.085x_3 - 240x_4 - 12.53x_5 + 0.452x_7 + 0.09x_9 < 0 \quad (12)$$

$$51.57x_1 - 157.1x_2 - 210.64x_3 - 70.33x_4 - 13.69x_5 - 4.77x_7 - 34x_8 + 29.3x_9 > 0 \quad (13)$$

$$51.37x_1 - 175.71x_2 - 234.65x_3 - 78.15x_4 - 15.37x_5 - 5.41x_7 - 39.21x_8 + 28.9x_9 < 0 \quad (14)$$

The total feeding of fuel must satisfy the specific heat consumption. This value would be 3600 kJ/kg clinker, but the additions of mineralizers reduce to 3181 kJ/kg clinker. Eq. (15) presents the specific heat consumption; the coefficients of equation are Lower Heating Value of fuels. Eq. (16) denotes the consumption of used tires. Eq. (17) and (18) are the mineralizers' limits for CaF_2 and $CaSO_4$. These limits are obtained in work [8] that established 1 % (mass) of each mineralizer.

$$27670x_5 + 36425x_6 + 32100x_7 = 3181 \quad (15)$$

$$32100x_7 \leq 795 \quad (16)$$

$$x_8 \leq 0.01634 \quad (17)$$

$$x_9 \leq 0.01634 \quad (18)$$

3. Optimization techniques

In this work, the nonlinear problem defined with multi-objective functions and constraints was solved using Genetic Algorithms (GAs) and Sequential Quadratic Programming (SQP).

3.1. Genetic Algorithms (GAs)

Genetic algorithms (GAs) work on the principle of "survival of the fittest". They have been extensively applied by many optimization problems. In GAs, the decision variables are encoded in a string form. The encoded solutions are called chromosomes and the elements of the chromosomes are called genes.

Depending on the nature of the problem the encoded solution may include binary digits or real numbers. An initial population is created and the fitness (the objective function value) of the population members is evaluated. Genetic operators (mutation and crossover) are applied to keep the gene pool diverse that aids the inclusion of better fitted members for quick convergence [12].

3.2. Sequential Quadratic Programming (SQP)

The main idea in SQP is to obtain a search direction by solving a quadratic program, that is, a problem with a quadratic objective function and linear constraints. This approach is a generalization of Newton's method for unconstrained minimization [13], and it is used to solve a nonlinear program in the following form:

$$\begin{aligned} &Minimize\ f(x) \\ &Subject\ to\ g(x) = 0 \end{aligned} \quad (19)$$

Where g is a vector of m constraint functions gi. Applying Newton's method to the corresponding optimality conditions, the Lagrange for this problem is obtained as:

$$L(x,\lambda) = f(x) - \lambda^T g(x) \tag{20}$$

Thus, the formula for Newton's method is:

$$\begin{pmatrix} x_{k+1} \\ \lambda_{k+1} \end{pmatrix} = \begin{pmatrix} x_k \\ \lambda_k \end{pmatrix} + \begin{pmatrix} p_k \\ v_k \end{pmatrix} \tag{21}$$

where p_k and v_k are obtained as the solution to the following linear system:

$$\nabla^2 L(x_k, \lambda_k) \begin{pmatrix} p_k \\ v_k \end{pmatrix} = -\nabla L(x_k, \lambda_k) \tag{22}$$

This linear system has the form:

$$\begin{pmatrix} \nabla^2_{xx} L(x_k, \lambda_k) & -\nabla g(x_k) \\ -\nabla g(x_k)^T & 0 \end{pmatrix} \begin{pmatrix} p_k \\ v_k \end{pmatrix} = \begin{pmatrix} \nabla_x L(x_k, \lambda_k) \\ g(x_k) \end{pmatrix} \tag{23}$$

These formulas are used in the method for constrained optimization. This system of equations represents the first-order optimality conditions for the optimization problem:

$$\begin{aligned} &\textit{Minimize} \quad \frac{1}{2} p^T \left[\nabla^2_{xx} L(x_k, \lambda_k) \right] p + p^T \left[\nabla_x L(x_k, \lambda_k) \right] \\ &\textit{subject to} \quad \left[\nabla g(x_k) \right]^T p + g(x_k) = 0 \end{aligned} \tag{24}$$

With v_k is the vector of Lagrange multipliers. This optimization problem is a quadratic program, where the quadratic function is a Taylor series approximation to the Lagrange at (x_k, λ_k), and the constraints are a linear approximation to $g(x_k + p) = 0$. In the SQP method, at each iteration a quadratic program is solved to obtain (p_k,v_k), which are used to update (x_k,λ_k), and the process repeats at the new point.

4. Results

Numerical results for SQP and GA are obtained using the SQP function GA function from optimization toolboxes in a computer package [14]. The SQP algorithm shows fast convergence rates. Nevertheless the GA has a computer time of 10 seconds. The GA obtain a global optimal, and the SQP a local optimal. The results of objective functions and optimal points are presented in Table 4.

Table 4 – Results of the optimization model

	Functions (US$/ton clinker)		
GA	$f_1 = 8,54$	$f_2 = 0,0047$	$f_3 = 0,00125$
SQP	$f_1 = 8,39$	$f_2 = 0,0038$	$f_3 = 0,0011$
	Variables (kg/kg clinker)		
GA	$x_1 = 0,823$	$x_4 = 0,0801$	$x_7 = 0,0082$
	$x_2 = 0,1149$	$x_5 = 0,03369$	$x_8 = 0,5284$
	$x_3 = 0,1115$	$x_6 = 0,05448$	$x_9 = 0,8534$
SQP	$x_1 = 1,0783$	$x_4 = 0,0094$	$x_7 = 0,0192$
	$x_2 = 0,3505$	$x_5 = 0$	$x_8 = 0,0088$
	$x_3 = 0$	$x_6 = 0,0704$	$x_9 = 0,0163$

The numerical results for SQP and GA conclude that the SQP method presents better solutions since the objective functions present minor values. Moreover, the GA did not attend all restrictions as well as the restrictions regarding the quantity of mineralizers

Therefore, the optimization technique mostly applied for this optimization problem is the SQP because of minor results and it attends all restrictions. Both techniques showed emissions values (SO_2 and NO_x) smaller than the ones in European laws. The European laws values are:

- SO_2 : 0,02 – 7,00 kg/ton clinker [15]
- NO_x : 0,4 – 6 kg/ton clinker [15].

5. Conclusions

In this work were presented a multi-objective optimization technique for co-processing in the cement production. SQP and GA optimizations were applied in order to obtain optimal point and objective functions.

The results of SO_2 and NO_x emissions, as well as the cost function were better when it was applied the Sequential Quadratic Programming method. Besides the emissions were smaller than the values that regulates in Europe.

Future works can be developed focusing the reduction of others emissions, mainly the carbon dioxide and heavy metal provide of co-processing. The application of others mineralizers e its influence in energy consumption is also important for cement production that looking for reducing the fossil fuel consumption and production costs.

Acknowledgments

The authors would like to acknowledge FAPEMIG – Fundação de Amparo à Pesquisa do Estado de Minas Gerais, CNPq – Conselho Nacional de Pesquisa and CAPES – Coordenação de Aperfeiçoamento de Pessoal de Nível Superior for the finanacial support that allowed to conduct this study.

References

[1] SAMAC, Sand & Cement Cogeneration Plant – Available at: <http://crushersouthafrica.com/> [accessed 12.16.2011].

[2] Schuhmacher M., Doming J.L., Garreta, J., Pollutants emitted by a cement plant: health risks for the population living in the neighborhood. Environmental Research 2004; 95:198-206.

[3] Greer, W.L., SO_2/NO_x Control Compliance with Environmental Regulations. IEE Transactions on Industry Applications 1989; 25:475-485.

[4] McQueen, A.T., Bortz, S.J., Hatch, M.S., Leonard, R.L., Cement Kiln NO_x Control. IEE Transactions on Industry Applications 1995; 31:36-44.

[5] Mokrzycki, E., Uliasz-Bochénczyk, A., Alternative Fuels for the Cement Industry. Applied Energy 2003; 74:95-100.

[6] Souza F.A., Utilização de Pneus Pós-Consumo como Combustível em Fornos de Cimento. In: CETESB, Seminário Nacional Sobre Reuso/Reciclagem de Resíduos Sólidos Industriais; 2000; São Paulo.

[7] Giménez-Molina, S., Blanco-Varela, M.T., Solid state phases relationship in the CaO-SiO, Al_2O, CaF_2-$CaSO_4$ system. Cement and Concrete Research 1995; 25:870-882.

[8] Raina, K., Janakiraman, L.K., Use of Mineralizer in Black Meal Process for Improved Clinkerization and Conservation of Energy. Cement and Concrete Research 1998; 28:1093-1099.

[9] Lawrence, L.B., Joseph, R.H., Chemical Analyses of Middle and Upper Pennsylvanian Coals form south eastern Kansas – Available at: <http://www.kgs.ku.edu> [accessed 3.16.2006].

[10] Salomon V.G., Evaluation of the Effects of the Presence of Heavy Metals in Waste Co-processed when Used as Alternative Fuels and Raw Materials in Cement Industry [dissertation]. Itajubá, Brazil: Universidade Federal de Itajubá; 2002.

[11] Kaplan E., Nedder N., Petroleum Coke Utilization for Cement Kiln Firing. In: Cement Industry Technical Conference, IEEE-IAS/PCA; 2001 29 Abr – 03 Mai; Vancouver, Canada. Academic Press: 251-263.

[12] Jha, M.K., Abdullah, J., A Markovian approach for optimization highway life-cycle with genetic algorithms by considering maintenance of roadside appurtenances. Journal of the Franklin Institute 2006; 343:404-419.

[13] Nash S.G., Sofer, A., A Linear and Nonlinear programming. McGraw-Hill, NY: 1996.

[14] MatLab 7.0, MathWorks, USA – Available at: <http://www.mathworks.com> [accessed 6.22.2004].

[15] Carpio R.C., Optimization in Co-processing Waste in Cement Industry involving Costs, Quality and Environmental Impact [Thesis]. Itajubá, Brazil: Universidade Federal de Itajubá; 2005.

Comparison of options for debottlenecking the recovery boiler at kraft pulp mills – Economic performance and CO_2 emissions

Johanna Jönsson[a], Karin Pettersson[b], Simon Harvey[c] and Thore Berntsson[d]

[a]Div. of Heat and Power Technology, Dept. of Energy and Environment, Chalmers University of Technology, Göteborg, Sweden, johanna.jonsson@chalmers.se
[b]Div. of Heat and Power Technology, Dept. of Energy and Environment, Chalmers University of Technology, Göteborg, Sweden, karin.pettersson@chalmers.se,
[c]Div. of Heat and Power Technology, Dept. of Energy and Environment, Chalmers University of Technology, Göteborg, Sweden, simon.harvey@chalmers.se
[d]Div. of Heat and Power Technology, Dept. of Energy and Environment, Chalmers University of Technology, Göteborg, Sweden, thore.berntsson@chalmers.se

Abstract:

The trend in the European pulp and paper industry is toward fewer mills with larger capacity. As a result, a number of existing mills will increase their production capacity. For increased production capacity in kraft pulp mills, the recovery boiler is often a bottleneck.This paper compares three different options for debottlenecking the recovery boiler and utilizing a potential mill steam surplus at a typical Scandinavian kraft pulp mill, when increasing the production capacity by 25%:1) Upgrading the recovery boiler, 2) Lignin extraction and 3) Black liquor gasification (as a booster). For black liquor gasification (BLG) two options for using the product gas are considered: production of electricity or DME motor fuel. Furthermore, both BLG and upgrading of the recovery boiler are assumed to be possible to combine with carbon capture and storage (CCS). The extracted lignin is assumed to either be valued as wood fuel or as oil. The different options are evaluated and compared with respect to annual net profit and global CO_2 emissions for four different future energy market scenarios.The results show that, generally, BLG with motor fuels production and lignin extraction with lignin valued as oil achieve the best economic performance. Upgrading the recovery boiler and capture and store CO_2 from the boiler flue gases gives the highest CO_2 emissions reduction but is only an economically attractive option in scenarios with a high CO_2 emissions charge.

Keywords:

Kraft pulp mill, Biorefinery, Black liquor gasification, Lignin extraction, Carbon capture and storage, Energy market scenarios.

1. Introduction

With increased concern for climate change and increasing energy prices, the need for energy efficiency measures is high on the agenda for both industrial and political decision makers. The industry sector, which stands for almost 30% of the energy use in Europe [1], is a key player in the transition towards a more sustainable European energy system. The pulp and paper industry is the sixth largest industrial energy user in Europe, using approximately 121 TWh of electricity and 365 TWh of thermal energy during 2007 [2]. Due to its high use of biomass and possibility to achieve an energy surplus, the kraft pulp industry has the potential to become a major contributor in reducing global CO_2 emissions through increased delivery of energy products[3-10].

The potential for reduced process steam demand in the kraft pulp industry through improved process integration and by installing new efficient equipment has in previous research shown to be up to approximately 30-35%[11-14]. For most market kraft pulp mills implementation of such measures would lead to a significant steam surplus that can be utilized in different

ways. It could for example be used to cover the heat demand of production processes for additional products (such as electricity production or capture of CO_2)or it permits the introduction of processes which reduces the steam production whilst producing new products (such as extraction of lignin or black liquor gasification where the product gas is used to produce motor fuels or electricity). Throughout this paper these two options are referred to as "utilisation of a potential steam surplus".In a previous study by the authors [18], it was shown that making investments in steam saving measures and thereby enabling production of additional products generally is very profitable and contributes to reduction of global CO_2 emissions.

The trend in the pulp and paper industry is toward fewer mills with larger capacity. This means that some mills will be closed down, while the remaining mills will increase their production capacity [15]. For increased production capacity in pulp mills, the recovery boiler is often a bottleneck. In a study by Axelsson et al.[16], lignin extraction was found to be an economically attractive alternative for debottlenecking the recovery boiler, in comparison to upgrading the recovery boiler (and steam turbines) at a kraft pulp mill. The economic performance of lignin extraction compared to increased electricity generationfor utilization of a potential steam surplus is better for mills investigating investment options in connection with increased production capacity [8, 16]. Another approach to achieve debottlenecking of the recovery boiler is to introduce a black liquor gasifier as a booster. This approach has been investigated by for example Berglin and Andersson[17], who concluded that a black liquor gasifier using the product gas for steam generation yields a better economic return than investing in a new recovery boiler (it was assumed that the existing recovery boiler could not be rebuilt).

2. Objective

This paper compares three different options for debottlenecking the recovery boiler and utilizing a potential steam surplus at a typical Scandinavian kraft pulp mill when increasing the production capacity by 25%:

1. Upgrading the recovery boiler
2. Lignin extraction
3. Black liquor gasification (as a booster)

For black liquor gasification two options for the product gas are considered; production of electricity (black liquor gasification combined cycle, BLGCC) or DME motor fuel (black liquor gasification with motor fuel production, BLGMF). Furthermore, both black liquor gasification and upgrading of the recovery boiler are assumed to be possible to combine with carbon capture and storage (CCS),where excess steam is used to cover the heat demand of the capture process. The extracted lignin is assumed to either be valued as wood fuel or as oil.

The different options are evaluated and compared with respect to annual net profit and global CO_2 emissions for four different future energy market scenarios. A further analysis of how different parameters such as policy instruments and investment costs affect the different technologies is also included. The results are compared with the results from the previous study by the authors where no production increase was considered; see [18].

3. Methodology

This work follows a methodology previously developed and described by one of the authors [6, 9]. The methodology enables changes in a studied energy system to be analyzed in a systematic way. The main steps in this methodology are briefly described below:

1. Define the studied system (in this case the kraft pulp mill).
2. Define possible system changes to be evaluated (in this case the investments in energy efficiency measures together with the different options for debottlenecking the recovery boiler).
3. Define the surrounding system used for evaluation of the studied system (in this case the different energy market scenarios describing energy market prices, policy instruments and associated CO_2 emissions for marginal use of energy carriers).
4. Construct a model for simulation of energy flows in the overall system defined in steps 1-3 (in this case the simulation model is constructed using the energy systems modelling tool reMIND).
5. Define the performance indicator(s) to be used for evaluating the system changes considered (in this case the net annual profit and global CO_2 emissions).
6. Use the simulation model to optimize the system based on the selected performance indicator for given settings in the surrounding system (defined by the aim of the study in question).
7. Vary key settings in the surrounding system to see how/whether the optimal solution is affected by these changes (in this study we calculate the optimal solution for a number of possible energy market conditions defined by energy market scenarios).
8. Fix certain parameters in order to investigate how close other solutions of interest are to the optimal solution (in this case solutions for all of the studied energy related technologies are obtained together with a sensitivity analysis showing the effect of changes in different system parameters)
9. Analyze the results in relation to the aim of the study (as defined by steps 1-3).

For constructing the model of the studied system and the surrounding system (described in step 3 above) the energy systems modelling tool reMIND, based on mixed-integer linear programming, is used. The reMIND tool has previously been used and described by e.g. Karlsson [19]. With this tool a simulation model of an energy system can be specified using a graphical interfaceand pre-defined equations. The constructed model can then be used for optimization purposes. In this study the objective is to minimize the total annual system cost of the studied energy system (the mill), assuming given conditions in the surrounding system (the energy market, including policy instruments) and the objective function can be defined as follows:

$$\min Z = rI_{tot} - B_{tot} + C_{tot} \quad (1)$$

where r = *Capital recovery factor (0.2)*

I_{tot} = *Total investment cost (energy efficiency measures and technologiesfor utilizing the steam surplus and debottlenecking the recovery boiler)*

B_{tot} = *Revenue of sold energy products including policy instruments (electricity, district heating, bark, captured CO_2, biofuels etc.)*

C_{tot} = *Running costs (electricity, chemicals etc.)*

For the system studied in this paper the different parameters, that is the investment costs, running costs and revenues for the different technologies, are described in Section 4. Asdescribed above, reMIND is constructed for minimization of the annual system cost. The different investment options studied in this paper are profitable when the annual system cost, Z, is negative. Hereafter the annual system cost is therefore referred to as the system's annual net profit.

4. The studied system and input data

The studied system consists of a kraft pulp that is planning to increase its production capacity and has the possibility to invest in energy efficiency measures that reduce the mill steam demand. The mill is further described in Section 4.1. The studied system is connected to a surrounding system in which the imported and exported energy and material streams are priced and the CO_2 emissions associated with the imported and exported energy products are calculated. Section 4.2 presents the data for the surrounding system (energy market scenarios). Fig. 1 shows a schematic representation of the studied energy system and the surrounding system.

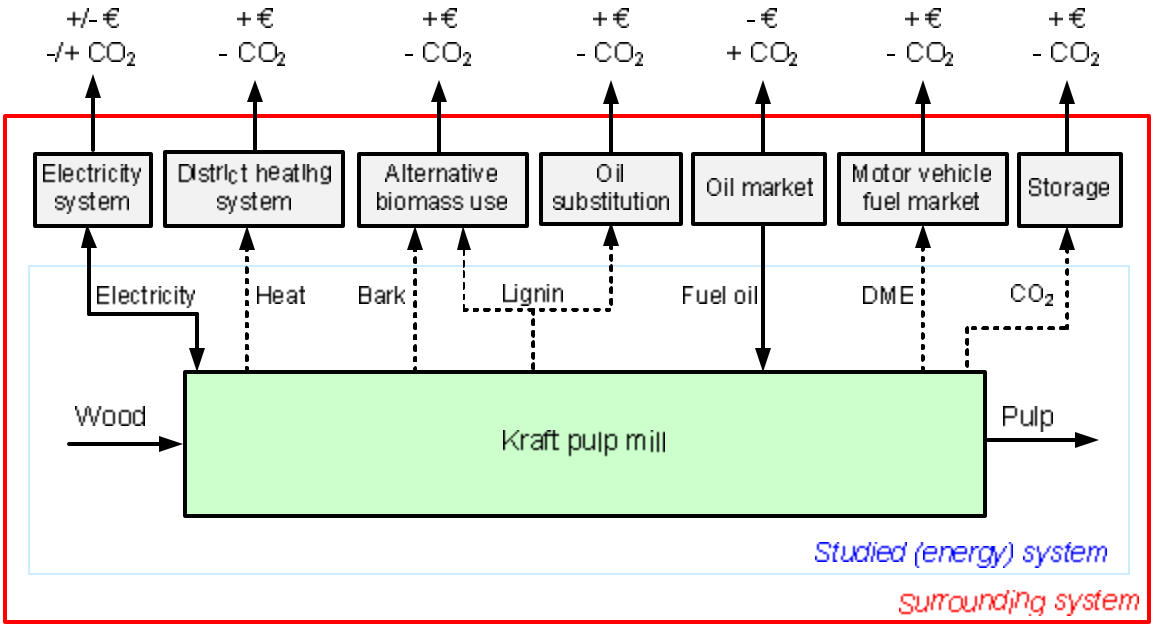

Fig. 1.A schematic representation of the studied system and surrounding system. Solid lines represent flows that are relevant for all studied cases, whereas dotted lines represent possible flows.

4.1. The studied system

The studied mill is a model mill, developed within the national Swedish research programme "Future Resource Adapted pulp Mill" (FRAM), representing an average Scandinavian market kraft pulp mill[20]. Table 1 presents an overview of key mill data. Axelsson et al. [11]have shown that the mill can achieve a steam surplus through investments in process integration and new efficient equipment, hereafter denoted energy efficiency measures. The energy efficiency measures in which the studied mill can invest in order to achieve the steam surplus are described in e.g. [6, 18]. The steam savings of MP and LP steam are approximately 0-20 % and 35-50 % respectively (depending on which energy efficiency measures are chosen) at a total cost of approximately 10-17 MEUR.

In this study, the mill is assumed to increase its production by 25% (typical number used in other studies, e.g. Axelsson et al. [16]) to 1250 ADt/d. The use of steam, electricity and oil is assumed to increase in direct proportion to the production. It is assumed that the recovery boiler is the bottleneck and to handle the increased amount of black liquor, the mill has to invest in either a black liquor gasifier (connected to a DME plant or a gas turbine combined

cycle) or a lignin extraction plant, or upgrade the recovery boiler.Fig. 2 shows the main energy and material streams for the mill with a 25% increased pulp production.

Table 1.Key mill data.

		Original design[a]	25% production increase
Kraft pulp production, design	[ADt/d]	1000	1250
Process thermal energy use[b]	[GJ/ADt]	14.3	17.9
Steam use MP/LP	[t/h]	69/190	86/238
Electricity use/production	[MW]	33/24	41/[c]
Oil use in lime kiln	[MW]	22	28[d]
Biomass surplus (bark sold)	[MW]	31	39

[a]*Earlier work by the authors compare different energy-related technologies for utilisation of excess steam and heat for the mill in its original design, not considering any production increase, see Jönsson et al. [18].*
[b]*Excluding steam conversion to electricity in the back-pressure turbine.*
[c]*Depends on which option that is used for debottlenecking the recovery boiler.*
[d] *In case of black liquor gasification, the oil usage increases.*

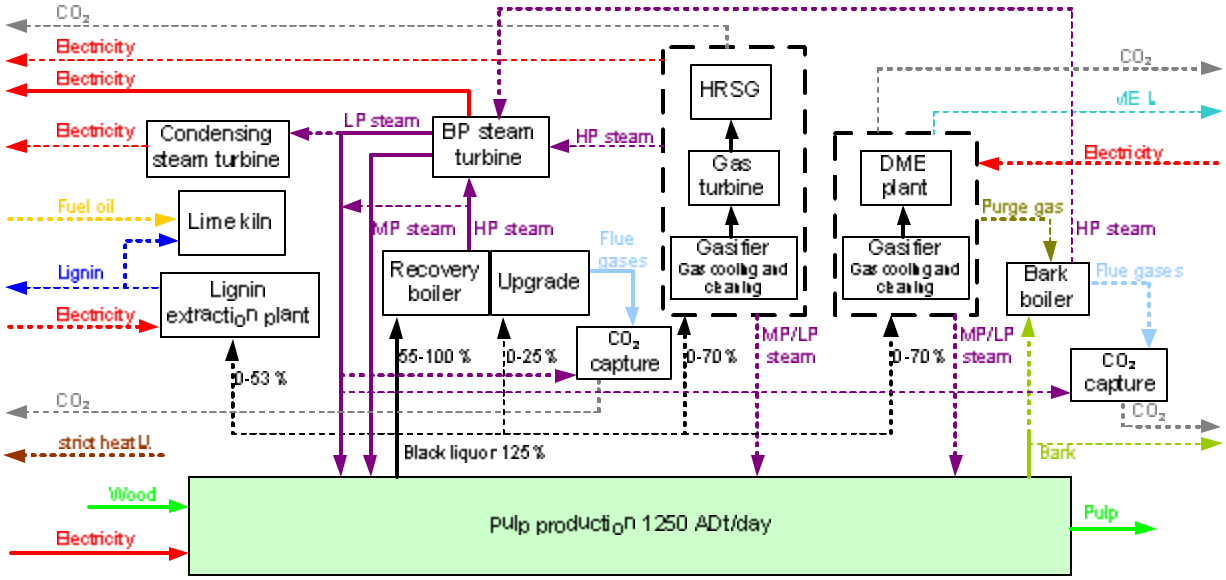

Fig. 2. A schematic representation of the main energy and material streams for the mill with a 25% increased pulp production. Solid lines represent flows that are relevant for all studied cases, whereas dotted lines represent possible flows.

Table 2 presents the different possible outcomes studied (cases). The option to invest in a new mini-recovery boiler has not been included, because it is always more expensive than the option to rebuild the recovery boiler (which gives the same result, increased capacity for burning the black liquor). In theory, all of the considered investment alternatives could be adopted at the same time. In practice, however, this will not be the case since the investment costs for the technologies are scale-dependent (see Table 3). Thus, the optimal solution will most likely consist of investments in energy efficiency measures together with only one of the investment alternatives for debottlenecking the recovery boiler.

Table 2. Presentation of the different possible outcomes (cases) including case code, case description and references.

	Case code	Case description	Key data from
Black liquor gasification	BLGMF	70% of the BL to the BLGMF/DME plant.	[21]
	BLGMF:CCS	70% of the BL to the BLGMF/DME plant. The removed CO_2 (part of the BLGMF process) is compressed and sent for storage. If profitable, a part of the CO_2 from the recovery boiler (and bark boiler) flue gases can also be captured by absorption.	[21], own calculations
	BLGCC	70% of the BL to the BLGCC plant. Possible investment in a new back-pressure steam turbine and/or a condensing steam turbine.	[22, 23]
	BLGCC:CCS	70% of the BL to the BLGCC plant. Possible investment in a new back-pressure steam turbine and/or a condensing steam turbine. The BLGCC plant is modified to include CO_2 capture (different gas cleaning including a water gas shift reactor). If profitable, a part of the CO_2 from the recovery boiler (and bark boiler) flue gases can also be captured by absorption.	[21-23], own calculations
Lignin extraction	Lignin:Wood fuel	Lignin is extracted from the black liquor, which leads to a decrease of the energy content in the BL to the RB (max 53%). The lignin is sold as fuel priced as wood chips.	[8]
	Lignin:Oil	Lignin is extracted from the black liquor, which leads to a decrease of the energy content in the BL to the RB (max 53%). The lignin is sold as fuel or feedstock priced as fuel oil.	[8]
Recovery boiler upgrade	RBU:Electricity	The RB is upgraded so it can handle the total amount of BL, 125%. Investment in a new back-pressure steam turbine and a condensing steam turbine.	[16]
	RBU:CCS	The RB is upgraded so it can handle the total amount of BL, 125%. Investment in a CO_2 capture plant connected to the recovery boiler flue gases and a new back-pressure steam turbine.	[24]

For all cases, there is also a possibility to invest in heat exchangers and/or heat pumps for district heating production (DH). It is assumed to be possible to deliver between 10 and 50 MW of district heating depending on season[1]. The falling bark can be fired in an existing bark boiler and/or be sold. The possibility to import external wood fuel is not considered; the steam use has to be met by internal resources. Thus, this study shows what can be done at a kraft pulp mill without importing external biomass, something that could be of interest in the future when the supply of biomass may be low due to its limited availability.

For technical reasons, the minimum load of the recovery boiler is set to 55% of the maximum load. For both of the cases with black liquor gasification, the mill's steam balance is not the

[1] The district heating demand that can be supplied with mill excess heat varies according to a duration heat load curve with a top load of 50 MW.

limiting factor for the maximum size of the plants – this factor is the minimum load of the recovery boiler (in the BLGMF case, however, the maximum size set by the minimum load of the recovery boiler is close to the maximum size set by the steam balance). However, for lignin extraction the steam balance limits the size of the plant. Black liquor gasification leads to an increased consumption of fuel oil in the lime kiln[2].

Extracted lignin can be used in the lime kiln to replace fossil fuel oil, or be sold as a wood fuel or oil replacement (both for replacement of oil as a fuel and for replacement of oil as a feedstock in production of materials and chemicals). Therefore, two different lignin cases are considered: one where lignin is valued as wood chips and one where it is valued as fuel oil. The captured (green) CO_2 is compressed and delivered to a storage location (for costs, see Table 3). It is assumed to generate an income corresponding to the charge for emitting fossil CO_2. Table 3presents the cost related to the different investment options.The investment cost for the not yet commercial technologies, that is black liquor gasification, lignin extraction and CO_2 capture and storage, are assumed to be for the "N^{th} plant". Energy-related operating costs have been omitted in the table, since they vary depending on energy market scenario. The capitalrecovery factor is set to 0.2[3].

Table 3. Investment and operating costs for different units needed for implementation of the different cases studied.

	Investment and operating costs[a]	**Based on**
BLGMF/BLGMF with CO_2separation[b]	$7055BL^{0,6}$ M€, 9.7 k€/yr/BL	[21]
BLGCC[b,c]	$5952BL^{0,6}$ M€, 1.0 k€/yr/BL	[22]
BLGCC[b,c] with CO_2 separation	$6365BL^{0,6}$ M€, 1.0 k€/yr/BL	[21, 22]
Lignin extraction plant[d]	$7.2LR^{0,6}$ M€, 5.8 €/MWh	[8]
Recovery boiler upgrade including cost for lost production	35.4 M€	[16]
Back-pressure steam turbine[e]	$1.3P^{0,6}$ M€	[8]
Condensing steam turbine[e]	$2.4P^{0,6}$ M€	
CO_2 separation plant for RB flue gases[f, g]	$2.3CO_2{}^{0.7}$, 4% of investment cost	[24]
CO_2compressor[f, h]	$1.1P^{0.7}$, 4% of investment cost	
Transportation and storage of CO_2	8 €/tonne	
Heat pump for DH[i]	0.11Q M€	[25]
Heat exchanger steam-DH[i]	0.68+0.033Q M€	[6]
Heat exchanger heat-DH[i]	0.059+0.042Q M€	

[a] *All values in 2008 money value. All investment costs have been recalculated to 2008 money value using Chemical Engineering's Plant Cost Index (CEPCI).*
[b] *BL refers to the flow of black liquor in MW.*
[c] *Excluding the steam turbine/s.*
[d] *LR refers to the lignin extraction rate in kg/s.*
[e] *P refers to the power output in MW.*
[f] *Operating cost CO_2 absorber and CO_2 compressor: 4% of investment cost.*
[g] *CO_2 refers to the CO_2 capture rate in kg/s.*
[h] *P is the compressor electricity demand.*
[i] *Q refers to the heat supplied by the heat pump or heat exchanged in the heat exchanger in MW.*

[2]Due to a different composition of the green liquor, the load of the lime kiln increases.

[3]A capital recovery factor of 0.2 is equivalent to e.g. an economic lifetime of 10 years and an interest rate of 15% or an economic lifetime of 6 years and an interest rate of 5%.

4.2. Energy market scenarios

The future economic performance, as well as the global emissions of CO_2, associated with the different cases studied is dependent on the development of the energy market. Consequently, to identify robust investment options, their performance should be evaluated for varying future energy market conditions. Here, energy market scenarios are used to reflect a variety of possible future energy market conditions. To achieve reliable results from an evaluation using energy market scenarios, the energy market parameters within a given scenario must be consistent, i.e. the energy prices must be related to each other (i.e. accounting for energy conversion technology characteristics and applying suitable substitution principles). Consequently, a systematic approach for constructing such consistent scenarios is facilitated by the use of a suitable calculation tool. In this work the Energy Price and Carbon Balance Scenarios tool (the ENPAC tool) developed by Axelsson and Harvey [26] was used. The scenarios reflect different future energy market conditions for the "average" years 2020 and 2030 and are based on two fossil fuel price levels (low and high) and two CO_2 emission charge levels (low and high).The big difference between the two time periods is that for the period with 2020 as its average year, it is assumed that infrastructure for CCS is not established, and therefore the options for CCS are excluded. Tables 4 and 5 present scenario data used. A further description of the ENPAC tool and the scenarios used in this work can be found in Jönsson et al. [18].

Table 4. Key data for the four energy market scenarios used for 2020.

Scenario input data	**1**	**2**	**3**	**4**
Fossil fuel price level[a]	Low	Low	High	High
CO_2 charge level	Low	High	Low	High
CO_2 charge [€/tonne CO_2]	26	67	26	67
Green electricity policy instrument [€/MWh]	26	26	26	26
Resulting prices and values of policy instruments [€/MWh]				
Electricity	63	85	66	95
DME	47	58	70	81
Bark/by-products/wood chips[b]	22	37	23	38
Heavy fuel oil (incl. CO_2)	37	49	53	65
District heating	15	28	18	28
Biofuel policy instrument	49	61	28	41
Resulting marginal/alternative technologies and their CO_2 emissions [kg/MWh]				
Electricity	722	345	722	722
marginal production of electricity	CP	NGCC	CP	CP
Biomass	225	237	225	225
marginal user of biomass	CP/DME	CP/DME	CP/DME	CP/DME
District heating production	224	380	224	224
alternative heat supply technology	CCHP/GB	CCHP/GB	CCHP/GB	CCHP/GB
Transportation	273	273	273	273
alternative transportation technology	Diesel	Diesel	Diesel	Diesel

[a] *Oil prices: Low: 62 USD/barrel, High: 100 USD/barrel.*
[b] *In the past years the prices of wood by-products and chips have been very similar.*

Table 5. Key data for the four energy market scenarios used for 2030.

Scenario input data	**1**	**2**	**3**	**4**
Fossil fuel price level[a]	Low	Low	High	High
CO_2 charge level	Low	High	Low	High
CO_2 charge [€/tonne CO_2]	35	109	35	109
Green electricity policy instrument [€/MWh]	26	26	26	26
Resulting prices and values of policy instruments [€/MWh]				
Electricity	68	90	74	98
DME	57	77	88	109
Bark/by-products/wood chips[b]	27	52	30	56
Heavy fuel oil (incl. CO_2)	45	67	67	89
District heating	19	49	27	56
Biofuel policy instrument	46	67	20	41
Resulting marginal/alternative technologies and their CO_2 emissions [kg/MWh]				
Electricity	679	129	679	129
marginal production of electricity	CP	CP CCS	CP	CP CCS
Biomass	227	244	227	244
marginal user of biomass	CP/DME	CP/DME	CP/DME	CP/DME
District heating production	242	468	242	468
alternative heat supply technology	CCHP/GB	CCHP/GB	CCHP/GB	CCHP/GB
Transportation	273	273	273	273
alternative transportation technology	Diesel	Diesel	Diesel	Diesel

[a] *Oil prices: Low: 74 USD/barrel, High: 126 USD/barrel.*
[b] *In the past years the prices of wood by-products and chips have been very similar.*

4.3. Sensitivity analysis

Table 6 presents the parameters included in the sensitivity analysis.

Table 6. Parameters included in the sensitivity analysis.

Parameter	**Denotation**	**Cases**
District heating production	a	1. The amount of district heating possible to deliver is increased by 100%, to between 20-100 MW depending on season. 2. No possibility to deliver district heat.
Capital recovery factor	b	The capital recovery factor is changed from 0.2 to 0.1.
Investment costs for non-commercial technologies	c	The investment costs for the non-commercial technologies, i.e. BLG, lignin extraction and CO_2 capture and storage, are increased by 25%.
Green electricity policy instrument support level	d	1. The support is increased by 50%. 2. The support is decreased by 50%. 3. No support is considered.
Biofuel policy instrument support level	e	1. The support is decreased by 50%. 2. No support is considered.
Recovery boiler upgrade cost	f	The investment cost for upgrading the recovery boiler is lowered from 35.4 to 27.4 M€.

By using the described energy market scenarios, a sensitivity analysis regarding energy and CO_2 prices is automatically carried out. It is, however, difficult to include all parameters affecting the results, for example the level of different policy instruments in the scenarios and the effect of the estimate of the investment cost. Therefore an extended sensitivity analysis is performed in addition to that inherent in using the scenarios for some key parameters to identify their impact on investment decision variables. The variation of the policy instruments are performed without considering the relationship between these parameters, and other parameters, within the scenarios.

5. Results and discussion

Figs 3 and 4 present a comparison of the different studied options for debottlenecking the recovery boiler and utilise pulp mill excess steam and heat for the energy market of 2020 and 2030. Each technology option is represented by a shaded area where the larger focal point show the original solution gained for the technology and the smaller points show the solutions gained from the sensitivity analysis. Since non-energy related costs and revenues (e.g. raw material costs and sales of pulp) are omitted in this study no information can be found in the absolute values; it is only the comparisons between the different cases that are interesting.RBU:Electricity is used as a baseline for the comparison, represented by the intersection by the x- and y-axises. Consequently, solutions positioned in the lower right quadrant both have a better economic performance and are associated with lower global CO_2 emissions thanRBU:Electricity.

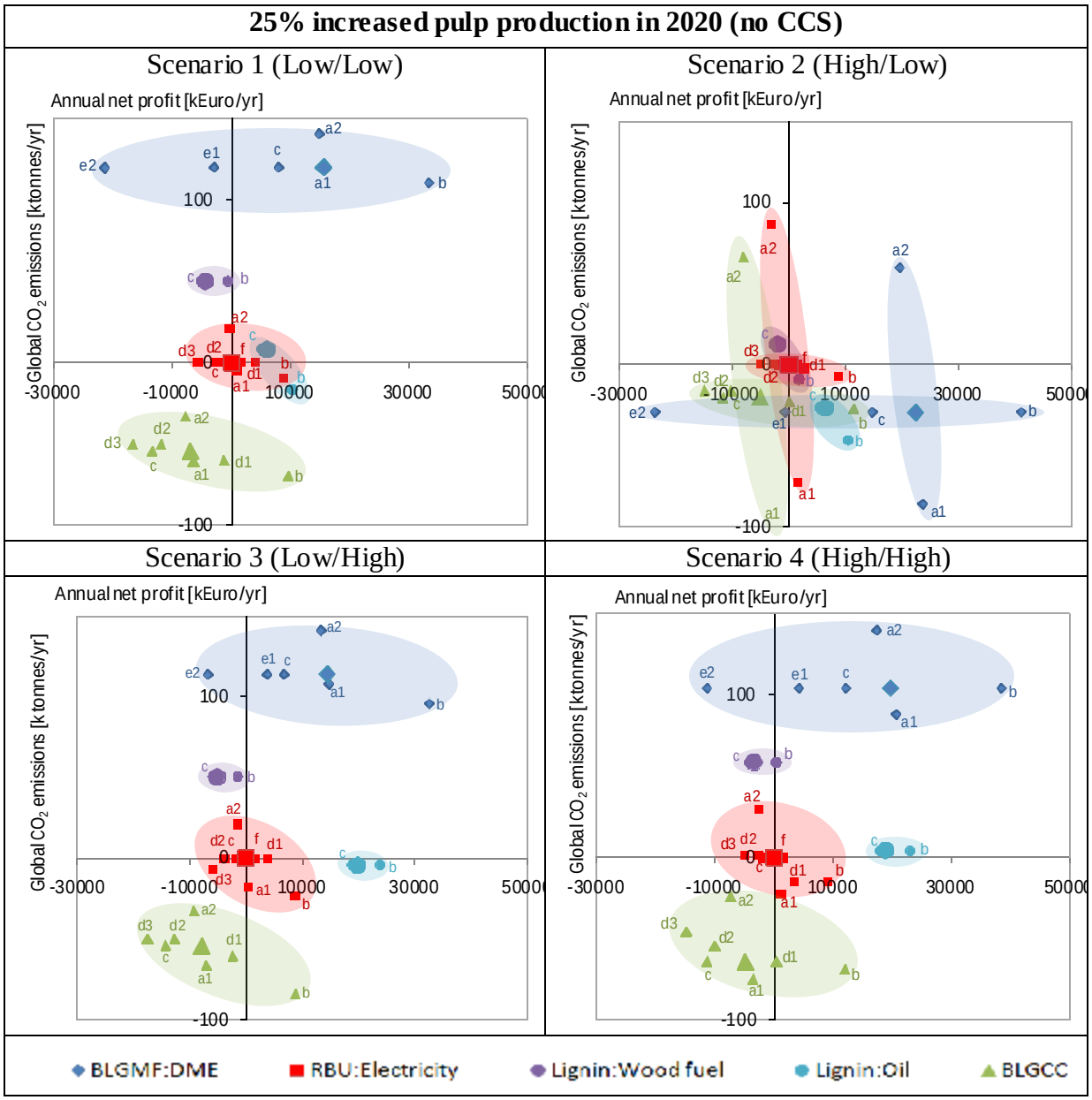

Fig. 3. Results for the different studied cases and the sensitivity analysis for the average year of 2020.For each studied case, the larger centre point represents the optimal solution for that case given the energy market scenario prices. The smaller points show how the optimal solution shifts when changing certain parameters in the sensitivity analysis. The shaded areas show the span between the solutions given in the sensitivity analysis.RBU:Electricity is used as a baseline for the comparison, represented by the intersection by the x- and y-axises.

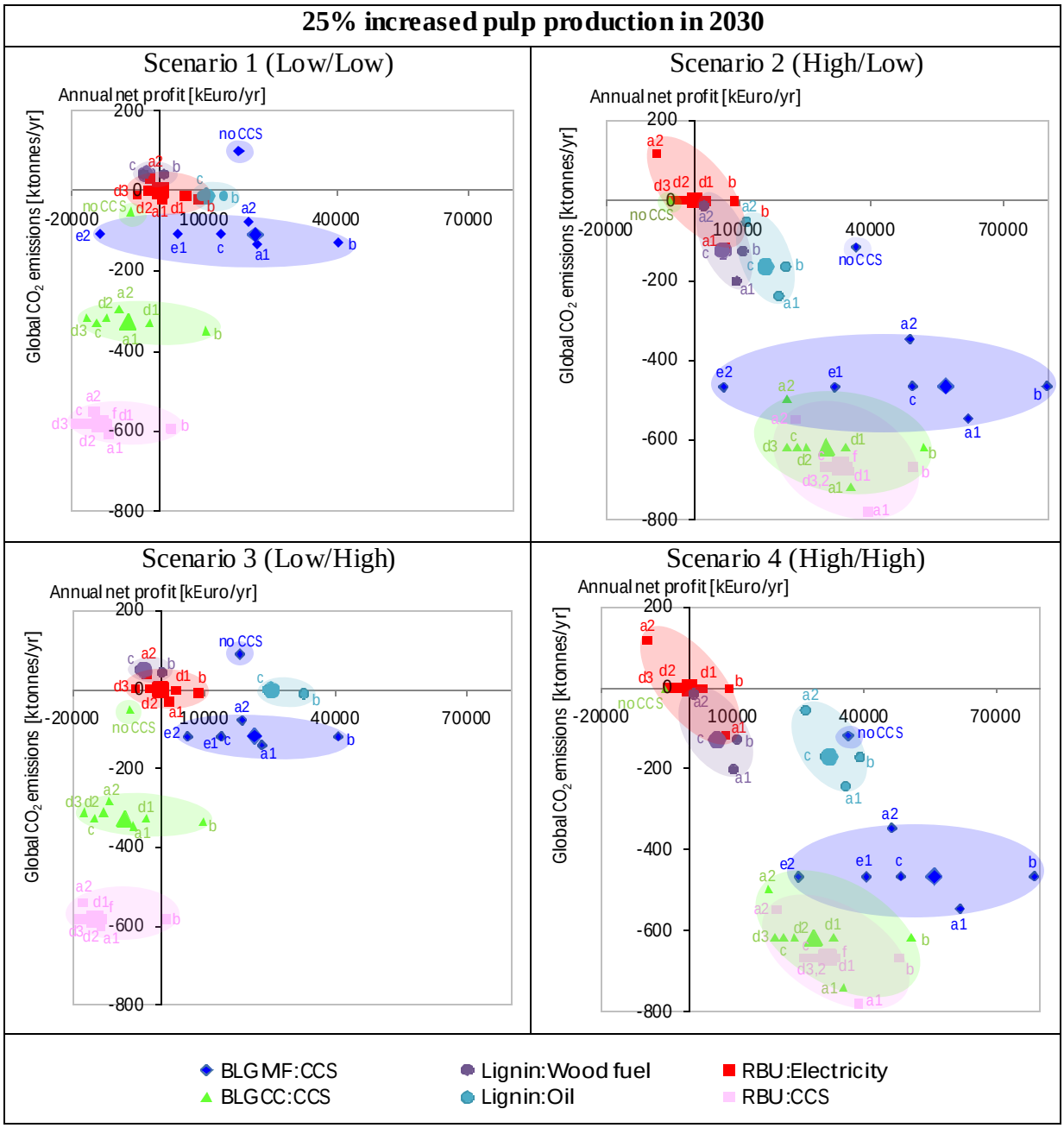

Fig.4. Results for the different studied cases and the sensitivity analysis for the average year of 2030. For each studied case, the larger centre point represents the optimal solution for that case given the energy market scenario prices. The smaller points show how the optimal solution shifts when changing certain parameters in the sensitivity analysis. The shaded areas show the span between the solutions given in the sensitivity analysis.RBU:Electricity is used as a baseline for the comparison, represented by the intersection by the x- and y-axises.

5.1. General characteristics for, and comparison of, the studied alternatives (cases)

Using a BLG booster as a means of debottlenecking the recovery boiler yields very different results for both economic performance and global CO_2 emissions depending on whether the product gas is used for electricity or motor fuel production. The BLGMF case shows the best economic performance of the two cases but is very sensitive to changes of the level of support

for biofuels and the investment cost. Fairly large amounts of CO_2 can, however,be separated at a low cost. This has a positive effect on both the global CO_2 emissions and the economic performance for BLGMF 2030 (where it is assumed that an infrastructure for CCS is established). The BLGCC case is considerably less profitable compared to BLGMF, but also less profitable than RBU:Electricity due to a large investment cost in relation to the additional amount of electricity produced. BLGCC shows the greatest global CO_2 emission reduction potential in all scenarios for the year 2020. However, for the year 2030 RBU:CCS shows the greatest CO_2 emission reduction potential in all scenarios.

For the cases of lignin extraction as a means to debottleneck the recovery boiler, lignin valued as wood fuel shows a poor economic performance with the exception of Scenarios 2 and 4 (with high wood fuel prices). Lignin valued as oil, however, has a very good economic performance, even in the scenarios with a low oil price (Scenarios 1 and 2). Furthermore, it is not highly influenced by any of the parameters studied outside the scenarios, and can therefore be said to be a fairly robust investment. As stated, lignin can replace oil both as a fuel and as a feedstock for production of material or chemicals. If, for example, lignin is upgraded to a material at the mill, it is of course possible to get an evenhigher price than the oil price depending on the type of material. However, the cost and energy demand for upgrading will then also have to be taken into consideration.

Investing in a recovery boiler upgrade and new turbines gives quite similar results for both global CO_2 emissions and net annual profit in the different scenarios. The possibility to capture CO_2 from the boiler flue gases yields a large CO_2 reduction potential. However, the profitability of capturing the CO_2 is strongly dependent on the CO_2 charge – e.g. it is only for the scenarios having the highest CO_2 charge, Scenarios 2 and 4, that RBU:CCS is more profitable than RBU:Electricity.

5.2. Levels of support for green electricity and biofuels

From the results it can be concluded that the level of the green electricity support does not significantly affect the economic performance of RBU:Electricity. For BLGCC the effect is more pronounced, but is small compared to the effects of other parameter changes such as the level of annuity factor. The relatively small effects are partly due to the assumed design of the green electricity support system where only new production capacity is entitled to support.

The support for biofuels varies between the scenarios and is set at a level so that a stand-alone biofuel production plant has the same willingness to pay for wood fuel as a coal power plant, which is assumed to be a large volume price-setting user of wood fuel. This results in very substantial levels of support for biofuels in Scenarios 1 and 2, which of course is questionable. The resulting CO_2 emission reduction in relation to the cost for society is relatively low, and the money might be better used elsewhere. The sensitivity analysis (point e1) shows for example the consequences of a 50% reduction of the level of support, which in Scenarios 1 and 2 results in a more reasonable level of the support. At this level, BLGMF is only the most profitable option in Scenario 4 2030.

5.4. CCS

For 2030 CCS was assumed to be commercially available. The possibility to capture CO_2 both from the recovery boiler flue gases and, if in operation, from the bark boiler flue gases gives a large CO_2 reduction potential. However, the profitability of capturing the CO_2 is strongly dependent on the CO_2 charge; e.g. it is only for the scenarios having the highest CO_2 charge, Scenarios 2 and 4, that RBU:CCS is more profitable than RBU:Electricity. If CCS is available, this improves the global CO_2 emissions effect and the economic performance for BLGMF both in absolute terms and in relation to the other technologies. For Scenarios 2 and

4 the CO_2 emissions effect for BLGMF is further improved due to the occurrence of CCS on the margin in the power sector. If CCS is available, BLGCC gives almost as large CO_2 emission reductions as RBU:CCS, however, due to a higher capital intensity it always shows a poorer economic performance.

5.5. Comparison with results for unchanged production capacity

Here, the results of this paper are compared with the results from a previous study of the same mill where the production capacity remained unchanged (presented in [18]). Comparing the results from this paper with those previous results it becomes clear that the BLG cases, BLGMF and BLGCC (both with and without CCS), benefit from economy of scale. Thus, they have a better economic performance when increasing the production capacity than when the production capacity remains unchanged. For the BLGMF case, this means that if the production capacity is increased, BLGMF becomes more profitable than Lignin:Oil for some of the scenarios where lignin prices as oil were more profitable in case of unchanged production. For the RBU:Electricity and RBU:CCS cases, the production capacity increase affects the economic performance in a negative way. This is due to the fact that an additional investment in an upgrading of the recovery boiler *has* to be made. Thus, a production capacity increase benefits lignin extraction and BLG since these technologies unload the existing recovery boiler and thereby an investment in an upgrade of the recovery boiler can be avoided.

6. Conclusions

This paper compares different technologies for utilisation of a potential steam surplus and debottlenecking the recovery boiler of a typical Scandinavian kraft pulp mill assuming a pulp production increase of 25%. The technologies are compared with respect to annual net profit and global CO_2 emissions for four different energy market scenarios using two time frames, 2020 (where CCS is not available, neither for the mill nor in the surrounding power system) and 2030. Based on the results and discussion the following main conclusions can be drawn:

- For all energy market scenarios, both year 2020 and 2030, BLGMF and lignin extraction where the lignin is priced as oil have a better economic performance than upgrading the recovery boiler (and existing steam turbines).
- The BLGMF case generally has the best economic performance, but is contrary to lignin extraction very sensitive to changes of several parameters, especially the level of support for biofuels and the investment cost.
- Extraction of lignin that can be priced as oil has a very good economic performance and it is not highly influenced by any of the parameters studied outside the scenarios and can therefore be said to be a fairly robust investment. The CO_2 emissions reduction from lignin extraction is also fairly stable between the scenarios.
- For the year 2020, where there are assumed to be no possibilities for CCS, BLGCC generally gives the highest CO_2reduction potential. For the year 2030, where there is assumed to be an established infrastructure for CCS, upgrading the recovery boiler and investing in CCS coupled to the boiler flue gases render the highest CO_2 reduction potential, followed by BLGCC and BLGMF, where CCS also can be included.

- The possibility to capture CO_2 from the recovery boiler flue gases gives a large CO_2 reduction potential. However, the profitability of capturing the CO_2 is strongly dependent on the CO_2 charge – e.g. it is only for the scenarios with a high CO_2 charge that CCS coupled to the boiler flue gases is more profitable than investments in new turbines (in connection to upgrading the recovery boiler). CCS decreases the global CO_2 emissions and increases the economic performance for BLGMF and BLGCC both in absolute terms and in relation to the other technologies.
- BLGMF and BLGCC benefit from economy of scale and thus have a better economic performance when increasing the production capacity than when the production capacity remains unchanged. For the BLGMF case this means that for some of the scenarios with increased production BLGMF becomes more profitable than extracting lignin that can be priced as oil, which was the most profitable choice if the production was unchanged. For increased electricity production and CCS in connection with the recovery boiler, the production capacity increase affects the economic performance in a negative way due to the fact that an additional investment in an upgrading of the recovery boiler *has* to be made.

Nomenclature

ADt	Air Dried tonne
BL	Black Liquor
BLG	Black Liquor Gasification
BLGCC	Black Liquor Gasification Combined Cycle
BLGMF	Black Liquor Gasification with Motor Fuel production
CCS	Carbon Capture and Storage
CHP	Combined Heat and Power
CCHP	Coal Combined Heat and Power
CP	Coal Power
DH	District Heat
DME	Dimethyl Ether
GB	Gas Boiler
HP	High Pressure (steam)
LP	Low Pressure (steam)
MP	Medium Pressure (steam)
NGCC	Natural Gas Combined Cycle
RB	Recovery Boiler
RBU	Recovery Boiler Upgrade

Acknowledgements

The work has been carried out under the auspices of the Energy Systems Programme, which is financed by the Swedish Energy Agency (SEA). The work was co-funded by the Black Liquor Gasification Programme, which is financed by SEA, MISTRA, Chemrec, Smurfit Kappa, Södra Cell, SCA Packaging, Sveaskog and the County Administrative Board

of Norrbotten. The work was also co-funded by the Södra Foundation for Research, Development and Education.

References

[1] Eurostat. Energy, transport and environment indicators. Eurostat pocketbooks. Luxembourg, 2009.

[2] CEPI. Key Statistics 2008 -European Pulp and Paper Industry. Brussels: Confederation of European Paper Industries, 2009.

[3] Costa A, Bakhtiari B, Schuster S, Paris J. Integration of absorption heat pumps in a Kraft pulp process for enhanced energy efficiency. Energy. 2009;34(3):254-60.

[4] Costa A, Paris J, Towers M, Browne T. Economics of trigeneration in a kraft pulp mill for enhanced energy efficiency and reduced GHG emissions. Energy. 2007;32(4):474-81.

[5] Consonni S, Katofsky RE, Larson ED. A gasification-based biorefinery for the pulp and paper industry. Chemical Engineering Research and Design. 2009;87(9):1293-317.

[6] Jönsson J, Algehed J. Pathways to a sustainable European kraft pulp industry: Trade-offs between economy and CO_2emissions for different technologies and system solutions. Applied Thermal Engineering. 2010;30(16):2315-25.

[7] Marinova M, Mateos-Espejel E, Jemaa N, Paris J. Addressing the increased energy demand of a Kraft mill biorefinery: The hemicellulose extraction case. Chemical Engineering Research and Design. 2009;87(9):1269-75.

[8] Olsson MR, Axelsson E, Berntsson T. Exporting lignin or power from heat-integrated kraft pulp mills: A technoeconomic comparison using model mills. Nordic Pulp and Paper Researsh Journal. 2006;21(4):476-84.

[9] Jönsson J, Svensson I-L, Berntsson T, Moshfegh B. Excess heat from kraft pulp mills: Trade-offs between internal and external use in the case of Sweden--Part 2: Results for future energy market scenarios. Energy Policy. 2008;36(11):4186-97.

[10] Andersson E, Harvey S. System analysis of hydrogen production from gasified black liquor. Energy. 2006;31(15):3426-34.

[11] Axelsson E, Olsson MR, Berntsson T. Heat Integration Opportunities in Average Scandinavian Kraft Pulp Mills: Pinch Analysis of Model Mills. Nordic Pulp and Paper Research Journal. 2006;4(21):466-74.

[12] Laaksometsä C, Axelsson E, Berntsson T, Lundström A. Energy savings combined with lignin extraction for production increase: Case study at a eucalyptus mill in Portugal. Clean Technologies and Environmental Policy. 2009;11(1):77-82.

[13] Wising U, Berntsson T, Stuart P. The potential for energy savings when reducing the water consumption in a Kraft Pulp Mill. Applied Thermal Engineering. 2005;25(7):1057-66.

[14] Axelsson E, Olsson MR, Berntsson T. Opportunities for process-integrated evaporation in a hardwood pulp mill and comparison with a softwood model mill study. Applied Thermal Engineering. 2008;28(16):2100-7.

[15] CEPI. Annual Statistics 2007 -European Pulp and Paper Industry. Brussels: Confederation of European Paper Industries, 2008.

[16] Axelsson E, Olsson MR, Berntsson T. Increased capacity in kraft pulp mills: Lignin separation and reduced steam demand compared with recovery boiler upgrade. Nordic Pulp and Paper Research Journal. 2006;21(4):485-92.

[17] Berglin N, Andersson L. Process Integration of Black Liquor Gasification for Incremental Recovery Capacity. Conference Process Integration of Black Liquor Gasification for Incremental Recovery Capacity, Whistler, B.C., Canada, June 11-14, 2001.

[18] Jönsson J, Pettersson K, Harvey S, Berntsson T. Comparison of options for utilization of a potential steam surplus at kraft pulp mills – Economic performance and CO_2 emissions. International Journal of Energy Reseach. Accepted for publication.

[19] Karlsson M. The MIND method: A decision support for optimization of industrial energy systems - Principles and case studies. Applied Energy. 2011;88(3):577-89.

[20] FRAM. FRAM Final report – Application area: Model mills and system analysis. FRAM report No 70, 2005.

[21] Ekbom T, Berglin N, Lögdberg S. Black Liquor Gasification with Motor Fuel Production - BLGMF II Nykomb Synergetics, 2005.

[22] KAM. Ecocyclic Pulp Mill -"KAM", Final Report 1996-2002. In: STFI, editor. KAM-report A100. Stockholm, 2003.

[23] Berglin N, Lindblom M, Ekbom T. Preliminary economics of black liquor gasification with motor fuels production. Colloquium on Black Liquor Combustion and Gasification, Park City, Utah, May13-16, 2003.

[24] Hektor E, Berntsson T. Future CO_2 removal from pulp mills - Process integration consequences. Energy Conversion and Management. 2007;48(11):3025-33.

[25] Bengtsson C. Novel Process Integration Opportunities in Existing Kraft Pulp Mills with Low Water Consumption. Göteborg: Chalmers University of Technology, 2004.

[26] Axelsson E, Harvey S. Scenarios for assessing profitability and carbon balances of energy investments in industry. AGS Pathways report 2010:EU1. Göteborg, Sweden: AGS, The alliance for global sustainability. Pathways to sustainable european energy systems, 2010.

Demonstrating an integral approach for industrial energy saving

René Cornelissen[a], Geert van Rens[b], Jos Sentjens[c] , Henk Akse[d], Ton Backx[e], Arjan van der Weiden[f], Jo Vandenbroucke[g]

[a] CCS B.V., Deventer, The Netherlands, cornelissen@cocos.nl,
[b] CCS B.V., Deventer, The Netherlands, vanrens@cocos.nl, ***CA***
[c] Jacobs consultancy, Leiden,The Netherlands, Jos.Sentjens@jacobs.com
[d] Traxxys, Woerden, The Netherlands, henk.akse@traxxys.com
[e]Eindhoven University of Technology, Eindhoven, The Netherlands, a.c.p.m.backx@tue.nl
[f] NL Agency,Utrecht, The Netherlands, arjan.vanderweiden@agentschapnl.nl
[g]Nyrstar, Budel, The Netherlands, Jo.Vandenbroucke@nyrstar.com

Abstract:

The reduction of energy consumption in industry is getting increasingly more difficult. In this article an integral approach is used to perform an industrial energy saving study at a Zinc manufacturing plant. The approach is a combination of exergy analysis, pinch analysis, process intensification and control engineering. It was found that exergy analysis at the level of process functions can act as a focal point for more detailed studies, like process intensification, control engineering and exergy itself. Optimising on control engineering as a part of an energy saving study has the advantage of tackling process control issues, while saving energy. It was found that the structured method of the integral approach ensures a broad range of solutions for both the short term and the long term, of which 12 were elaborated into simple business cases.

Keywords:

Integral approach, Energy, Exergy, Pinch, Industry.

1. Introduction

Natural resources are becoming increasingly scarce. Oil prices are fluctuating, but have an upward tendency. Furthermore, many oil reserves are located in countries which are not always politically stable. Income from oil can increase the political instability. Therefore, a shift away from oil is required. Coal could be an alternative, as coal reserves are distributed more widely over the world. However, consumption of coal leads to more polluting emissions, like CO_2, which is believed to cause the greenhouse effect.

Instead of focussing on alternative fuels to replace fossil fuels, this paper focuses on the reduction of energy use; to be more precise on the reduction of energy consumption in industrial processes. Companies with a long history of energy saving, find it increasingly difficult to come up with additional measures for energy saving with an attractive pay-back period. The conventional analyses focus on optimisation based on energy balances, however, other tools are available for energy optimisation as well. When these tools are used, they are often applied haphazardly, in parts of the process that are expected to cause the biggest losses, or expected to achieve the biggest gains. A systematic approach to energy saving is generally not used.

Therefore NL Agency (an agency of the Dutch ministry of Economic affairs, agriculture and innovation) supported an approach that uses a multitude of disciplines. This may lead to new ideas, and more clever ways of saving energy. This approach consists of an exergy analysis, a pinch analysis, a process intensification scan and an analysis of the control system of the process. This approach was used in a number of pilot projects. The approach is illustrated using one of those pilot projects, being a Zinc-manufacturing plant.

2. Methodology

2.1. Overview of the approach

The integral approach used aspects in the field of process engineering, systems and control engineering and heat integration. The project partners were selected for complimentary knowledge, and each partner had their own way of evaluating a process. CCS was selected for its knowledge in the field of exergy, Jacobs Consultancy for its experience in the field of pinch-analysis, Traxxys for the process intensification, and Eindhoven University of Technology for the systems and control engineering. To enhance the knowledge transfer, several plenary meetings were held to discuss the process and generate solutions for the brainstorm session.

The project was split in five phases:

1. The analysis of the process
2. Generation of solutions
3. Selection of the solutions
4. Technical elaboration of selected solutions
5. Making business cases of selected solutions

The integral approach is characterised by a relatively thorough analysis phase. About half of the man-hours were spent in the analysis phase. Without a proper and profound evaluation of the process, no proper solutions are expected. In the analysis phase Nyrstar provided the project partners with a mass and energy balance of the plant and indicated bottlenecks within the process. This formed the base for the analyses on exergy and pinch.

In this case exergy was used at a functional level of a group of devices and not at the level of every single device or process unit. This enabled the use of exergy as a focal point. The exergy analysis identified opportunities for process improvement and improvement for thermal integration. This is why an exergy analysis may serve as an indicator for the need for a pinch-analysis. In this study it was used as a focal point for the process intensification options. Both during the pinch-analysis and the process intensification scan (PI-scan) the process was studied in detail. Pinch-analysis is a way of improving heat-integration of the plant. The PI-scan looks at improvement of the process, by the application of new technology or by using different (more energy-friendly) production methods.

The used method is indicated in Fig. 1. For more simple processes, the pinch-analysis, exergy-analysis and PI-scan could be performed in parallel.

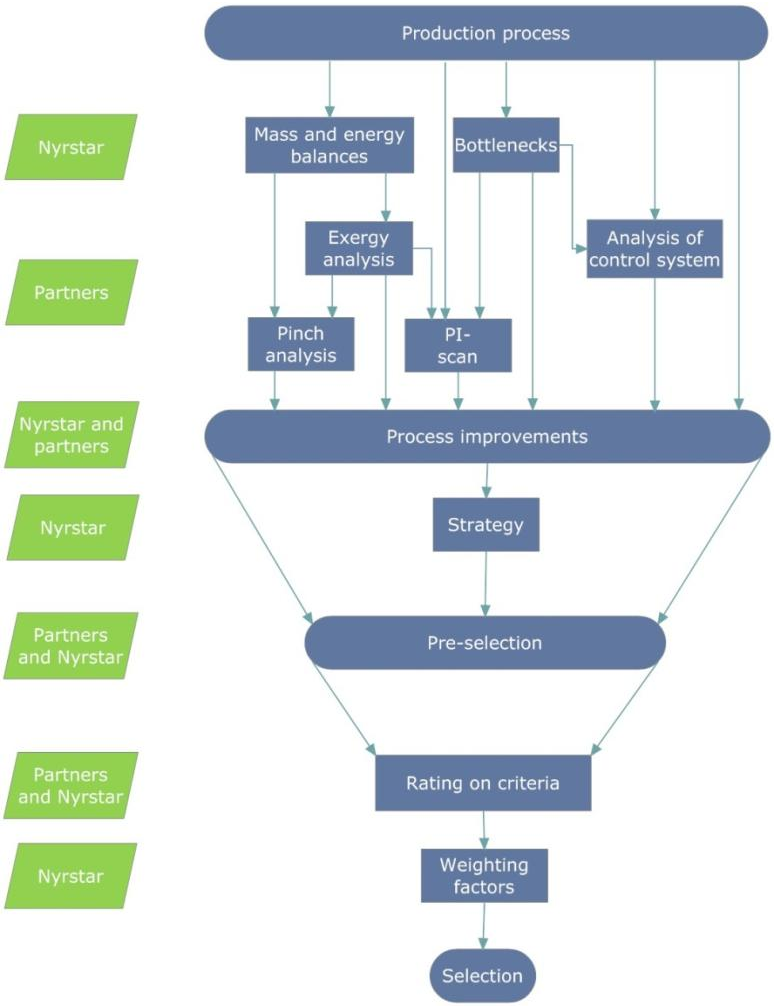

Fig. 1. Schematic overview of the Integral Approach

2.2. Analysis phase

2.2.1. Exergy analysis

Exergy is known for more than 50 years. Rant was the first to introduce the term exergy [1]. The approach was further developed by amongst others Szargut [1,2] and Kotas [3]. Amongst others Tsatsaronis and Valero [4-6] took the concept one step further by focussing on thermo-economic costs.

Although the concept of exergy is widely known in the academic world and the chemical industry, its use is rather limited outside the academic world and new chemical plants. This is in our opinion partly caused by the limited availability of data, which makes it difficult to make an energy balance, let alone one that closes, and as a result makes it difficult to perform an exergy analysis. However in industry, and specifically for existing plants the use of exergy may lead to new insights too.

In this specific example it was opted to use an exergy analysis on a function level, and use exergy as a tool to pinpoint the process steps with the biggest losses and destruction of exergy. These process steps are then subsequently studied in more detail, by for example the process intensification scan. The analysis was performed by using the software tool OptiJoule, which is in-house developed by CCS.

2.2.2. Pinch analysis

Pinch analysis is a method to find the ideal way of integrating excess heat and heat demand. For more information on the pinch analysis method, please refer to literature, for example [7]. It has been used in many industrial plants, see e.g. [8,9] as examples of recent publications. The analysis consists of the following stages:

- Data extraction, including evaluation of the heat and mass balances
- Creating the 'Composite Curves' and 'Grand Composite Curves', resulting in design targets. This gives insight in the present heat situation and the possibilities for improvement.
- Analysis of the heat exchangers network and identification of new heat integration measures.

2.2.3. Process intensification scan

The process intensification scan addresses perceived bottlenecks within the process, and attempts to solve them using process intensification options. The performed PI-scan is a 3-phase entity, which is described in more detail in [10]. The first phase is a quick scan which identifies the current bottlenecks in the process and delivers a list with possible spots where PI may solve the bottleneck. The second phase is a more detailed study, which develops into business cases. The third phase is the actual contracting phase. In the Netherlands 42 of these quick scans (i.e. phase 1) have been performed up to 2011 [10]. In the present approach loss of exergy is added as a bottleneck to phase 1. The result of the process intensification scan should be a substantial saving of the fuel and feedstock use. For new installations or refurbishment of an existing plant, the investment cost may be reduced significantly as well by using PI. By using process intensification, options can be discovered that require a complete redesign of the installation or even R&D, which are more long-term solutions, and solutions that can be implemented immediately.

2.2.4. Analysis of control system

The analysis of the control system is performed to examine where in the production process fuel and feedstock can be saved by using more advanced control systems. Additionally, difficulties in the present operation of the process were taken into account. More advance control systems that improve both energy use and process operation were preferred. In the analysis the focus was on fast control systems that require a limited amount of calculation power and on the development of estimation routines for control systems if a limited amount of measured data was available.

2.3. Solution and Selection phase

In the solution phase, process improvements were generated during a brainstorm session. During this brainstorm session employees of Nyrstar participated as well. Ideally this brainstorm session takes place after the pinch-analysis and the PI-scan and after the detailed analysis of the control system. In this case the approach slightly deviated from the ideal approach in order to reduce the number of plenary meetings. The additional options for process improvement were added later to the list of process improvements. Other ideas of participants that came up after the brainstorm session were added to the list as well.

The brainstorm session led to a rather long list of ideas for process improvement. The list contained 132 ideas in total. Rating all ideas on selection criteria would have been a tedious job, as all 132 ideas need to be discussed. Therefore the long-list was reduced. To reduce the long list every technical expert including the technical experts of Nyrstar was asked to list their 7 favourite ideas independently, based on their experience and the strategy of Nyrstar. The number of 7 was chosen to ensure that the list was on one hand not too long, and on the other hand sufficiently long, to still include less likely candidates, that might prove to be interesting. The mix of backgrounds ensured

sufficient diversity of the ideas in terms of disciplines and also meant that the less likely ideas could be filtered out before rating all the ideas.

Given the 7 technical experts, the longest possible list was 49 options. Because some solutions were selected twice or more, this resulted in a shorter list of 39 ideas. These ideas were rated on a number of ranking criteria.

The chosen ranking criteria were:

- magnitude of the (expected) energy saving
- exergy level of the energy saving
- a qualitative estimate of the required investment
- the influence on the operation of the production process
- the extent of modifications needed within the process
- the timeframe in which the solution is expected to be technically feasible.

Rating based on the ranking criteria was done by discussing the merits of the solutions within the entire project team. The scoring possibilities and criteria are given in Table 1. Note that the quantitative units need to be different for each study, as these savings are clearly not possible for a smaller plant.

Table. 1. Schematic overview of the ranking criteria

Magnitude (expected) energy saving			
<0.1 MW	0.1MW -0.5 MW	0.5 MW - 2 MW	> 2MW
0	3	6	9
Exergy level (expected) energy saving			
Heat (<100°C)	Steam (>100°C)	Electricity and gas	
3	6	9	
Required investment (estimate)			
<50 k€	50 -500 k€	500 - 2.000 k€	> 2.000 k€
10	7	4	1
Influence on operation of production process			
Positive (more stable)	No influence	Slightly more complex	Loss of robustness
13	10	7	4
Extent of modifications needed within the process			
Easy modifications	Slight modifications	Significant modifications	Major modifications
10	7	4	1
Time horizon within which the solution can be implemented			
Direct (<2 year)	2 to 5 years	5 to 10 years	>10 years
10	7	4	1

Each ranking criterion had a weight factor accompanying it. In this way the ranking criteria can be matched to the company's strategy. The magnitude of the expected energy saving for example had a higher weight factor than the timeframe in which the solution is expected to be technically feasible, i.e. long-term solutions with big energy savings would be rated higher than short-term solutions with mediocre energy savings. The weight factors varied from 1 to 5. The score for each criterion was multiplied by the weight factor. All scores were added up to find the best scoring solutions. Based on available capacity and similarity of solutions, the twelve highest ranking ideas were elaborated into business case.

3. Case study

3.1. Plant and process

The plant under consideration is the Budel Plant of Nyrstar. The main products of the plant are high-purity zinc (SHG-zinc), zinc alloys and sulphuric acid. A side product is Budel Leach Product; a product containing silver and lead, that was present in the zinc ore, which is used for the production of silver. The plant uses the so-called Roasting, Leaching, Electrolysis process. The scheme is given below.

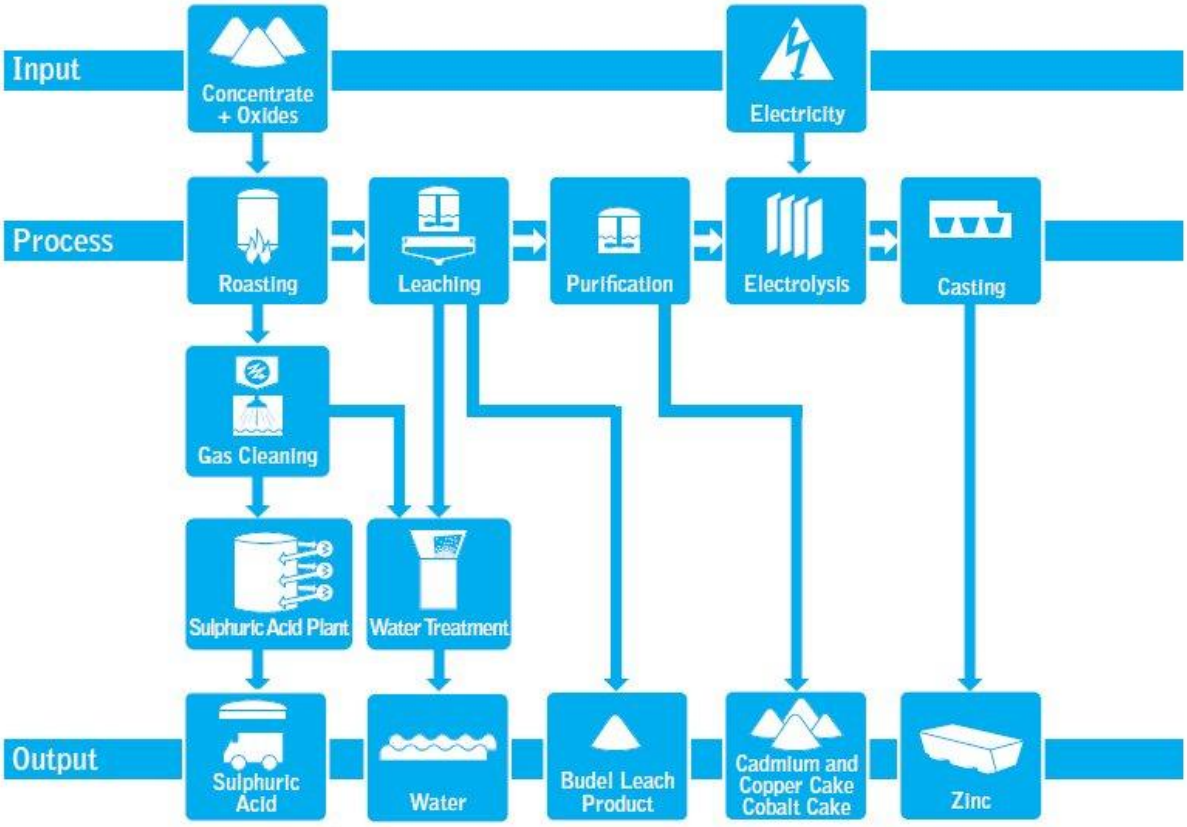

Fig 2. Roasting-Leaching Electrolysis Zinc production process at Budel plant. Reproduced with permission from [11]

The zinc ore is roasted in an air-blown furnace, thereby converting ZnS into ZnO and SOx. The zinc-oxide is cooled and subsequently leached in sulphuric acid, thereby forming $ZnSO_4$ (solute) and water. Other metals are removed from the liquor of H_2SO_4 and Zn. The main metals are contained in the Budel Leach Product, but also pure cadmium, and copper and cobalt containing cakes are removed from the process. Very pure zinc is formed on electrodes in the electrolysis process, where $ZnSO_4$ (solute) and water are converted into Zn, O_2 and H_2SO_4.

The heat in the SOx-containing roast gas is first used to produce steam. Solids and other impurities are removed, and subsequently sulphuric acid is produced. Additional process units are a water purification plant and the melting and casting process.

The majority of the consumed energy is electricity. The majority of the electricity is consumed in the electrolysis section. The primary energy use of the entire plant is about 8000 TJ per year.

3.2. Results

3.2.1. Exergy analysis

The process can be characterised as a process with excess heat that becomes available at (relatively) low temperatures. Because of the location of the Budel plant the heat cannot be used elsewhere. From the exergy analysis it can be concluded that all the additional energy is not required from exergy point of view. The exergy present in the zinc ore is in theory sufficient to fuel the entire process. The destruction of exergy and the losses are illustrated in Fig 3.

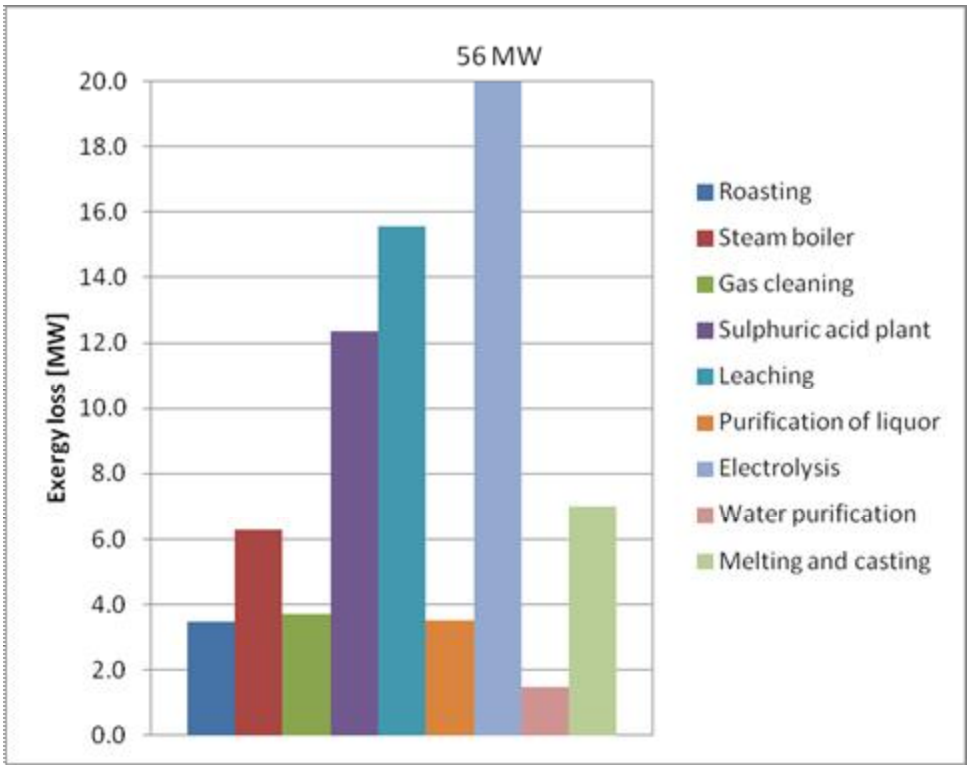

Fig 3. Exergy destruction and exergy losses for each section of the plant

Clearly the biggest exergy loss is the electrolysis section. The loss is mainly caused by resistance and overpotential in the electrolysis section, which leads to the generation of low-temperature heat. However the losses in the leaching section and the sulphuric acid plant are significant as well. The losses in the leach section are caused by the exothermic reactions. The heat is released to the cooling water. Additionally steam is used to fulfil a low-temperature heat demand. This indicates that there should be opportunities to optimise the heat consumption, which was confirmed during the pinch analysis. The losses in the sulphuric acid plant are caused by the low temperature heat (80°C), that is released during the exothermic reaction. The exergy loss in the steam boiler and roasting section are in part caused by the suboptimal operation of the roasting process (from exergy point of view), and in part by the fact that any combustion process results in exergy loss.

3.2.2. Pinch analysis

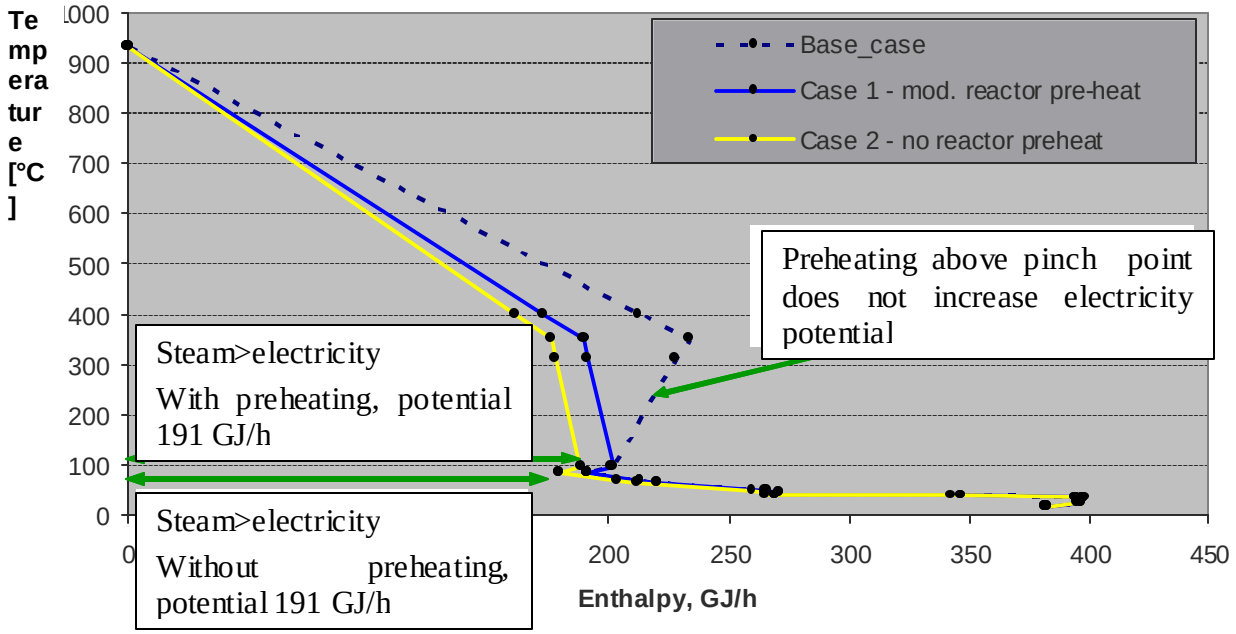

Fig 4. Grand composite curve of the pinch analysis

The pinch analysis learns that there is an excess of heat. No heat source is required except for the zinc ore. The aim of the pinch analysis is, therefore, to maximise the amount of steam that can be used for power production. Nyrstar has a high power consumption, which is required during the entire year. The potential for energy saving is 180 GJ per hour without reactor preheating or 191 GJ per hour if the reactor is preheated.

Two scenarios for heat integration have been made. In scenario 1 the thermal energy saving is 73 GJ per hour leading to an electrical potential of 4.6 MWe and an investment of € 1.8 million. In scenario 2 the thermal energy saving is 92 GJ per hour leading to an electrical potential of 5.3 MWe with an associated investment of € 2.1 million

3.2.3. Process intensification

The results of the process intensification scan are solutions or solution directions, and thereby differ from regular analyses.

The process intensification scan suggests to increase the understanding of the processes in the boiler, by completing the mass and energy balances, making a chemical analysis of the scaling in the bed and determining the effect of the process parameters on the bed. On the basis of this information an improved redesign of the roaster and boiler can be made.

For the gas cleaning section a process simulation study is suggested. For the long term new technologies can be considered. The leaching and purification section have different steps, which occur at different pH. It is proposed to investigate the possibilities of using membranes to extract water, when the pH needs to be decreased, i.e. acidity increased. It is expected that the process will become more stable and easier to control. Demands on the material of the membrane will be an important research parameter.

In the electrolysis the $ZnSO_4$-solution is transformed into Zn metal. This is one of the large energy consuming steps. The recommendations from the process intensification study, have led to renewed thinking on the electrolysis process.

3.2.4. Process control

The present process control system is mainly by hand and quasi static, i.e. the process is automatically controlled on the level of a single process unit for which a desired value is manually set, but the process is not automatically controlled for a combination of process units that interact with each other. There is no feedback from the output to the input and the systems to be controlled have a very complex interaction. It is suggested to apply a process controller that incorporates feedback by application of an Advanced Process Controller. Additionally it is suggested to use a planning system and a real-time optimizer to determine the optimal operation points of the plant.

In the electrolysis section the production capacity is proportional to the power requirement, and therefore it is desirable to adjust the production capacity with the electricity price. Because of this, the production capacity in the leaching and purification section may have to vary. The present control systems have controllers which have relative large steps, which means that a small deviation will lead to bigger changes in the input than required. This can be changed easily by using filters, that allow the process to operate more smoothly.

3.3. Selected measures

From the proposed measures, twelve have been selected to be worked out in business cases. About half of the measures were in the area of improved heat integration. The pay-back period for each solution ranges between 4.5 and 30 years (including steam turbine), basically because heat integration itself does not lead to energy efficiency, because heat is available in excess and no steam turbine is present to convert the saved steam. It is demonstrated that the present system of direct coupling between the steam turbine and SO_2-blower is not ideal. When revision of the blowers is required an investment in a steam turbine is strongly recommended. If the steam turbine would be dimensioned for a larger steam flow than present, or alternatively is supported by a gas boiler, the presence of the steam turbine will act as a catalyst for further reduction in heat consumption, as in this case heat or steam will have a monetary value.

Other plans focused on the improvement of the roaster oven and electrolysis section. Interesting opportunities could be created by improvement of the process control systems. These solutions potentially could be used at more sites. Further study should show the feasibility of these ideas.

It is noteworthy, that the exergy losses in the gas cleaning system are significant, even though the removal of SOx from the exhaust gas is state of the art. Further process development is required.

4. Conclusions

The integral approach, is a well-structured method for performing energy saving studies. The relatively long analysis phase gives additional insight in the process regarding the loss of the quality of energy, which is often a precursor to the actual energy loss. The exergy analysis and pinch analysis were used on the level of process functions. The exergy analysis acted as a focus for more detailed analyses. On the detailed level, a process intensification scan and a process control analysis were performed. Exergy can be applied on the detailed level as well, and thereby indicate where the losses are taking place, but in this study it was opted not to.

Application of the approach led to a list of 132 possible process improvement options. It included options which could be implemented immediately, but it also provided options for long term improvement. Of these improvement options 12 were elaborated into business cases, of which several are now under consideration.

Acknowledgments

We acknowledge AgentschapNL, division energy and climate for the financial support of and participation in this project.

References

[1] Szargut J., Morris D.R., Steward F.R., Exergy analysis of thermal, chemical and metallurgical processes. New York: Hemisphere Publ. Corp; 1988.

[2] Szargut J., Exergy Method, Technical and ecological applications, Southampton, UK: Wittpress; 2005

[3] Kotas T.J., The Exergy Method of Thermal Plant Analysis. London, UK: Butterworths; 1985

[4] Tsatsaronis G., 1993, Thermoeconomic analysis and optimization of energy systems. Prog. Energy Combust, Vol 19, pp. 227-257.

[5] Valero A., Lozano M.A. and Munoz M., A general theory of exergy saving I. On the exergetic Cost. In: Gaggioli R.A. Computer-aided engineering and energy systems Vol. 3: Second Law Analysis and Modelling, AES Vol 2-3, The American Society of mechanical engineers, New York, USA.

[6] Morusuk T. and Tsatsaronis G. How to calculate the parts of exergy destruction in an advanced exergetic analysis. In: Ziębik A., Kolenda Z. and Stanek W., editors. ECOS 2008: Proceedings of the 21st International Conference on Efficiency, Cost, Optimization, Simulation and Environmental Impact of Energy Systems; 2008 Jun 24-27; Cracow-Gliwice, Poland.

[7] Linhoff B., Townsend D.W, Boland D., Hewitt G.F., Thomas B.E.A., Guy A.R., Marsland R.H., A user guide on Process integration for the efficient use of energy. Revised first edition, Rugby, UK: Institution of Chemical engineers; 1994.

[8] Martinez-Patiño J., Verda V., Serra L.M., Picón-Núñez N. and Hernández-Figueroa M.A., Composite curves in direct and indirect heat exchange network for simultaneous heat and mass transfer system: Analysis and applications. In: ECOS 2010: Proceedings of the 23rd international conference on efficiency, cost, optimization, simulation and environmental impact of energy systems; 2010 Jun 14-17; Lausanne, Switzerland

[9] Dubliauskaite M., Becker H., Maréchal, F. Utility optimization in a brewery process based on energy integration methodology. In: ECOS 2010: Proceedings of the 23rd international conference on efficiency, cost, optimization, simulation and environmental impact of energy systems; 2010 Jun 14-17; Lausanne, Switzerland

[10] Akse H.N., Technology Outlook. Woerden, The Netherlands: Traxxys Innovation & Sustainability, Technical Report No.: 2011 008 2 20-07-11. Available at:< http://traxxys.com/downloads/Files/Technology%20Outlook%20-%20Traxxys%20Report%202011%20008%202%2020-7-11.pdf> [accessed 04.05.2012].

[11] Nyrstar, Budel Fact Sheet Available at http://www.nyrstar.com/operations/Documents/NYR1288%20BUDEL%20230911.pdf [accessed 04.05.2012].

Maximising the Use of Renewables with Variable Availability

Andreja Nemet[a], Jiří Jaromír Klemeš[a]*, Petar Sabev Varbanov[a], Zdravko Kravanja[b]

*[a]Centre for Process Integration and Intensification - CPI[2], Research Institute of Chemical and Process Engineering, Faculty of Information Technology, University of Pannonia, Veszprém, Hungary, klemes@cpi.uni-pannon.hu (**CA**)*
[b]Faculty of Chemistry and Chemical Engineering, University of Maribor, Maribor, Slovenia,

Abstract:
A problem connected with the exploitation of renewable energy sources, such as wind and sun is, their fluctuating availability. The accelerating development has been very substantial for techniques, methodologies and equipment for exploiting solar energy [1]. The integration of renewables into an energy system needs an approach that accounts for the variations in energy supply availability, as well as for those of the demands. Dynamic models could be used for modelling precisely is intermittency. They are usually employed to solve servo- and regulatory tasks in process control. Dynamic models have been used to model solar thermal plants [2-4], but only a few models have been dedicated to estimating available energy from solar sources [5] and they usually evaluate only a part of the whole capture system – e.g. the thermal storage [6]. However, dynamic models are unsuitable for design or long-horizon operational optimisation.
In the present work, the Heat Integration [7] for batch processes based on Time Slices [8, 9] is extended to the integration of solar thermal energy with certain variations. The main steps involve partitioning the measured/forecasted heat availability profile using a large number of candidate time boundaries and then approximating it by a piecewise-constant profile using high-precision. The approximation profile is obtained by subjecting the candidate superset of time-boundaries to MILP optimisation thus minimising the integral inaccuracy. The integration of solar thermal energy can be performed for each Time Slice, after the optimal number of Time Slices has been selected with approximated constant load. Using heat storage, the heat can then be transferred between Time Slices.

Keywords:
Variations of Renewables, Renewable Availability Curve, Solar Thermal Energy Integration, Time Slices, Heat Integration

1. Introduction

An accelerated development of techniques, methodologies and equipment for exploiting solar energy has been taking place recently. This helps to improve the existing technology. An example is solar-based water desalination [1]. A lot of attention has been focused on photovoltaic panels for producing electricity. There is also a significant potential for utilising solar irradiation as heat. Generally, thermal solar capture offers a higher efficiency compared to photovoltaic panels.

The integration of renewables into a process system needs a specific approach due to the variations in energy supply availability from renewable sources, and fluctuations in the users' energy demands. Two approaches can be used for integrating renewables and accounting for this variability:

(i) A dynamic model formulation, followed by dynamic optimisation

(ii) A multi-period model involving steady-states, associated with time intervals.

The advantage of dynamic models is that they accurately describe the system behaviour. They are usually employed to solve servo- and regulatory tasks during process control. There are dynamic models that describe plants using solar thermal-energy as a utility [2]. Several other models estimate solar irradiation [3, 4], and just a few models estimating the available solar thermal-energy and available electricity [5]. Typically, such models only evaluate a part of the whole capture system, for example, just thermal-energy storage [6]. The main drawback of dynamic models is that they are not favourable for design or long-horizon operational optimisation since these models are complex and presently computationally intensive.

Models assuming steady-states are simpler and yet still capable of describing the systems with acceptable accuracy. As some of the variables are discretised, the computational time becomes much shorter.

During batch processes, energy demands vary over time. In order to account for these variations, Batch Process Integration was formulated by Kemp and Deakin [7] who developed two models: (i) The Time Average Model, where the heat-loads are averaged throughout the time horizon, and (ii) The Time Slice Model, where the Time Slices are obtained by combining the starting and ending time points of the involved process streams. During each Time Slices Heat Integration is performed in the same manner as the continuous processes. A detailed description can be found in [8]. The batch process scheduling method using the MILP formulation with heat integration was another step in exploiting batch process heat integration [9]. A similar formulation of the problem was also used to design a HEN [10]. In addition, a different, more combinatorial approach has been developed for batch process scheduling based on the S graph, [11] where also scheduling influence is presented on the HEN synthesis. To enable the integration of heat-storage into the system design, combined with pinch analysis, another combinatorial approach was subsequently introduced using time decompositions of the processes [12]. Majozi [13] developed a mathematical model for optimising energy usage for a multi-purpose batch plant. The evolution of a batch heat exchanger network was described by Foo et al. [14]. The methodology of time decomposition was recently extended by Varbanov and Klemeš [15] for analysing Total Sites using the integration of renewables. A Comprehensive review of Process Integration, including batch, has been presented by Friedler [16, 17].

Muster-Slawitsch et al. [18] presented the annual load curve for a renewable energy source. While adequate for that work, the approach is not appropriate for the integration of solar thermal energy as developed in this work. The reason is that clustering of the loads leaves the temporal sequence out of consideration, accounting only for the load horizon. It lumps loads from different time intervals within the overall horizon (one year) at certain temperature and load levels. For the current problem accounting for the temporal sequence is essential, as the heat supply and demand streams may be active during different time intervals, since a batch process is considered.

Ludig et al. [19] modelled a power system, investigating 14 different technologies for producing electricity. They evaluated optimal technology-mix from the viewpoint of cost. An interesting part of this work was how they dealt with the variations of renewable energy sources e.g. wind, hydro, solar. They created equal-length time slices and averaged the load of supply within each time slice.

In contrast, in the present work the time durations of the TSs and the supply load are the result of a two-stage optimisation. It is a systematic approach compared to the heuristic used previously.

The focus of previous work in the field of varying heat supply and demand was either on a variation of the process demand or the energy availability from renewable sources. This current work accounts for both aspects. An analogy from batch process integration is used. TSs, with loads assumed to be constant, was developed for varying the availability of solar thermal-energy. The procedure for integrating solar thermal-energy covers several steps:

- Heat recovery within batch processes
- Identifying the number of TSs and the values of the TS boundaries for solar irradiation
- Estimation of the supply loads

- Combination of TSs for process demand and solar thermal-energy
- Integration of solar thermal-energy within each combined TS
- Estimation of storage size

The trade-off between the inaccuracy and number of TSs should be evaluated, in order to determine the number of TSs.

2. Determining the number of time slices

2.1. Problem formulation

The approximation inaccuracy decreases with an increasing number of TSs. On the other hand, the aim is to minimise the number of TSs, in order to simplify the computations during the following steps of the integration procedure. Therefore, the task can be defined as obtaining the minimum number of TSs with acceptable accuracy. The solar irradiation (G) measurements or the temporal variation of the captured heat flow could be used to identify the TS for solar energy availability.

2.2. Approximation of the irradiation profile

This procedure is based on optimising the load-levels and selecting items from a discrete superset of candidate time boundaries. These represent the measured Solar Irradiation – G data in dependence of time, t[h], by constructing a high-precision piecewise-constant profile [20] (Fig 1).

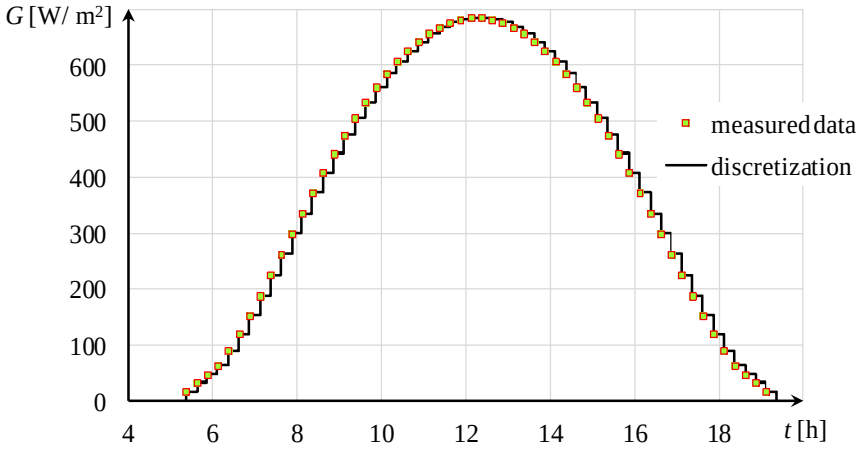

Fig 1: Discretisation of the measured profile/ input data for optimising the number of TSs

When using a large number of time-intervals, the inaccuracy of this transformation is minimised and can be ignored. However, such high-accuracy would require very intensive computation Therefore, the piecewise–constant load profile to be obtained has to contain a significantly smaller number of TSs. The supply is approximated separately at each time-interval by the minimisation of any inaccuracy represented by those areas occurring between the approximated and real input-supply profiles (Fig 2).

The boundaries of the time-intervals are the candidate boundaries for the final TSs. If there is a difference between two consecutively approximated supply levels, the time-boundary is also a TS boundary. When two time-intervals are joined into one TS, the approximated supply-levels should

be equal at both time intervals and the time-interval period boundary candidate is deselected as a TS boundary (Fig 3).

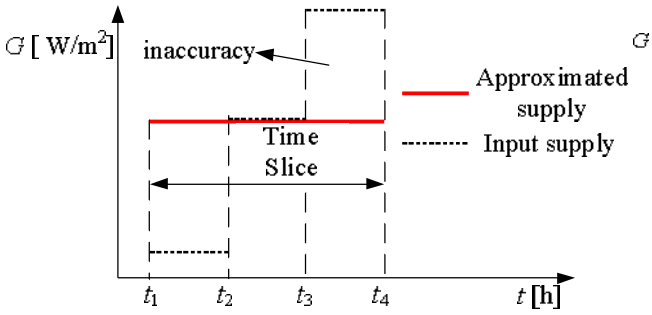

Fig 2: Determining the inaccuracy between the input and approximated supply

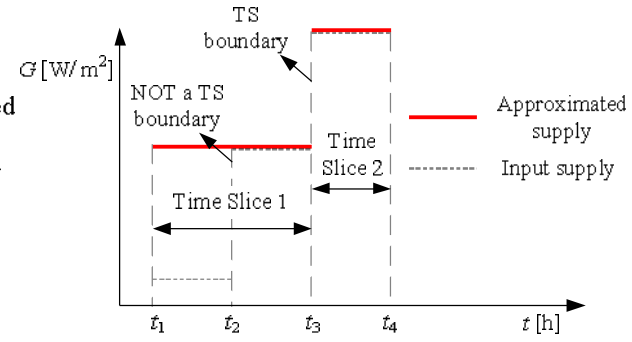

Fig 3: Acceptance/ rejection of the candidate time period boundary as a TS boundary

2.3. MILP model formulation

A two-stage MILP model has been developed for minimising the number of TSs at acceptable inaccuracy. During the first stage, the number of TSs is minimised, depending on the tolerance of inaccuracy specified by the models' users. During the second stage, the inaccuracy is minimised at a fixed minimum number of TSs, determined during the first optimisation stage.

Initially there is N_I number of time-intervals and, hence, N_I+1 boundaries of time-intervals indexed by the following index and set: i for the time-boundaries of the time-intervals, $i \in I$.

The difference between the real input-supply and approximated-supply is calculated during each time period separately:

$$SD_i = RS_i - AS_i, \forall i \in I, \qquad (1)$$

Because the difference, SD_i can have a positive or negative value, it can be represented as the difference between the positive variables PD_i and ND_i:

$$SD_i = PD_i - ND_i, \forall i \in I, \qquad (2)$$

Note that, when the SD_i has a positive value, the ND_i is zero, as a result of minimising the inaccuracy. When SD_i has a negative value, the PD_i is zero. For minimal inaccuracy the difference between the real and approximated supply should be the lowest possible.

$$ED_i = PD_i + ND_i, \forall i \in I, \qquad (3)$$

In (3) the positive value is obtained for the difference between real and approximated supply load. Further equations relate to the accepting / rejecting of the time-interval boundary as a TS boundary. The decision is made by the binary variable y_i. When there is a positive (4) or negative difference (5) between the two consecutively-approximated supply loads, there is a TS boundary and the value of y_i is 1. If there is no difference between these supplies, there is no TS boundary and the value of y_i is 0.

$$AS_{i+1} \le AS_i + LV \cdot y_i, \forall i \in I, i \ne N_I + 1, \qquad (4)$$

$$AS_{i+1} \ge AS_i - LV \cdot y_i, \forall i \in I, i \ne N_I + 1, \qquad (5)$$

In order to present the selected TS boundaries, the binary variable is multiplied by the observed time-period boundary:

$$TS_i = y_i \cdot t_{i+1}, \forall i \in I, i \neq N_I + 1, \quad (6)$$

The number of TSs is obtained from (7). One is added to the sum of the selected TS boundaries, as the TS boundaries at the beginning and end of the observed time-horizon were excluded within the model:

$$NTS = \sum_{i \in I, i \neq N_I + 1} y_i + 1, \quad (7)$$

The inaccuracy during each time-interval is determined by multiplying the positive difference between the real and approximated supplies with the time-horizon of the time-interval.

$$IN_i = ED_i \cdot (t_i - t_{i-1}), \forall i \in I, i \neq N_I + 1, \quad (8)$$

The overall inaccuracy is a result of summating the inaccuracies over the time-intervals:

$$INA = \sum_{i \in I, i \neq N_I + 1} IN_i, \quad (9)$$

and this overall inaccuracy is constrained and should be less than or equal to the ε fraction of the initial amount of solar irradiation presented as an area (A_0) below the measured profile of Fig 1:

$$INA \leq \varepsilon \cdot A_0, \quad (10)$$

$$A_0 = \sum_{i \in I, i \neq N_I + 1} ((t_{i+1} - t_i) \cdot RS_i), \quad (11)$$

2.4. Optimisation procedure

Optimisation is performed over two stages. During the first stage of optimisation, Equations (1-11) are used with the objective of minimising the number of TSs as follows:

$$\min z_{\mathrm{I}} = NTS, \quad (12)$$

This step requires specifying the acceptable error-level (tolerance) ε. The procedure applies multi-objective optimisation by the ε–constraint method, where one objective is considered in the objective function and the other is inserted in the model as an ε–constraint. The result from optimisation is the minimal number of TSs, min NTS_I required to meet any constraint about the inaccuracy limit (10).

However, after the first stage, the inaccuracy is not optimal. In order to obtain a further reduction in inaccuracy, in the second stage of optimisation the same model using equations (1–11) is used together with an additional equation (13), which fixes the number of TSs, and the objective as expressed in (14) ,

$$NTS = \min NTS_I, \quad (13)$$

$$\min z_{\mathrm{II}} = INA, \quad (14)$$

Multi-objective optimisation could also be performed over one stage, with the so called weighted sum method as sometimes this is faster. In this case, the objective function would be a weighted sum of *NTS* and *INA* with a high enough weight *w* (e.g. 10,000) for *NTS*, in order for the minimised *NTS* to have priority over the minimum of *INA*.

$$z = w \cdot NTS + INA, \quad (15)$$

2.5. Selecting the number of TSs

Selecting the number of TSs depends on the accuracy required. Fig 4 presents the obtained Pareto results from the multi-objective optimisation, where minimal numbers of TSs are shown vs. different tolerances selected.

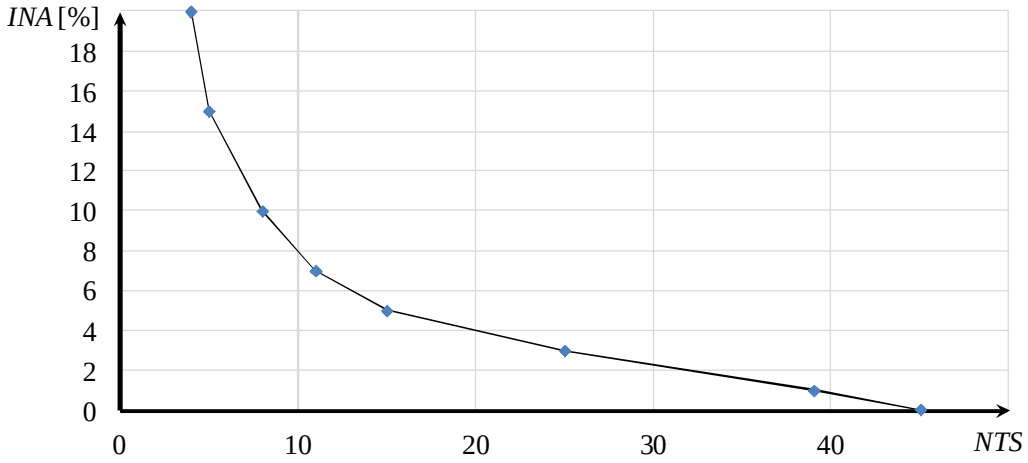

Fig. 4: Selecting an acceptable inaccuracy

As can be seen from Fig 4, by increasing the tolerance the number of TSs decreases but, however, the inaccuracy becomes too high. On the other hand, if the tolerance is too small, the number of TSs might become too high and, hence, the further steps of integration would be too complex; however, no significant improvement may be achieved. The exact trade-off between the number of *NTS* and *INA* depends on the users *INA* tolerance. As can be seen from Fig 4, generally, a tolerance of between 5 and 10 % should be acceptable as with increase *NTS* the inaccuracy is not increased significantly.

3. Estimating the supply-loads

The supply of the loads is determined separately in each TS. Estimation of the supply-loads depends on the capture system. Different kinds of systems are possible, or even a system coupled with a heat pump [21]. A simplified scheme for capturing was assumed during this work (Fig 5). The heat-transfer from the collectors in this model can be (i) direct or (ii) indirect. Direct heat-transfer is feasible when solar thermal-energy is available and there is a demand within the evaluated TS. If the amount of heat is higher than the demand or the heat-transfer is unfeasible in one TS, then the heat is transferred to storage. This heat will be available for covering any heat-demand in the following TSs. The indirect heat-transfer is the described transfer through storage.

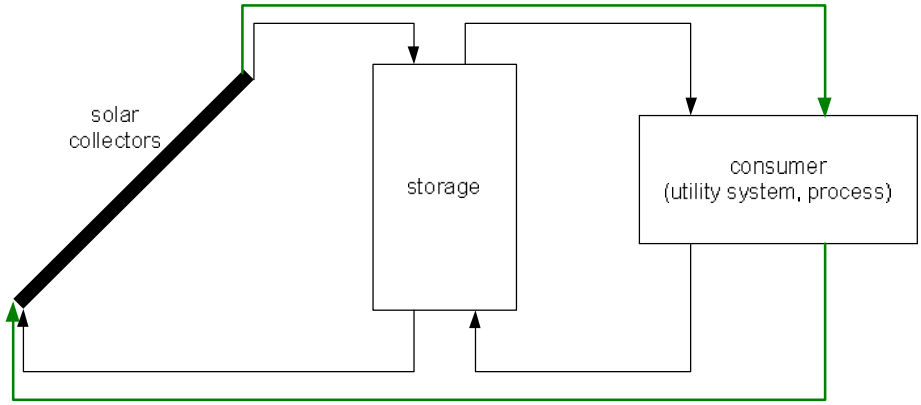

Fig 5: Simplified scheme for the integration of solar thermal-energy

In order to determine the heat-load for the direct transfer of solar thermal-energy to the process, the irradiation load was multiplied by:

- The area of collectors and
- The efficiency of the solar collector system.

The area usually depends on the investment and the available area of the collectors.

Solar collector-efficiency varies significantly with changes in the quantities of solar radiation (G), ambient air temperature (T_A), and the average internal fluid temperature (T_C) [22]:

$$\eta_C = \eta_O - \frac{a_1(T_C - T_A) + a_2(T_C - T_A)^2}{G}, \qquad (16)$$

when η_O is the optical efficiency of the collector and a_1 and a_2 are the solar collector thermal loss coefficients, which are usually determined experimentally. During the first stage of the evaluation the average fluid temperature can be assumed to be the arithmetic average of the collectors' inlet and outlet temperatures [22]:

$$T_C = \frac{T_{in} + T_{out}}{2}, \qquad (17)$$

The efficiency also depends on the ambient air temperature. It is the average temperature of the air in each TS separately.

4. Integration of solar thermal-energy

4.1. Combining the supply and demand

The first step when combining the supply and demand is determining the TSs for any fluctuating load of solar thermal-energy. However, many processes have fluctuating demands. Therefore the solution is to also create TSs, as developed for the batch processes [7]. A combination of these two types of TSs can be seen in Fig 6.

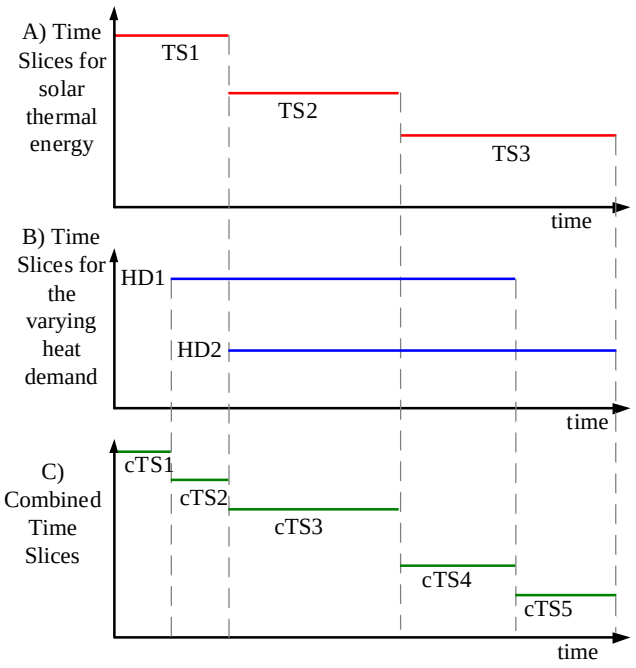

Fig 6: A Gantt chart for those TSs for supplying A) Solar thermal-energy, B) Heat demand and C) A combination of for both.

The TS boundaries for solar thermal-energy and those processes with varying demand are joined together into combined TS boundaries.

4.2. Integration with the Grand Composite Curve

Integration of the solar thermal-energy should be performed after the combined Time Slices (cTSs) are obtained. The Grand Composite Curve [23, 24] can be used for the integration of solar-thermal energy (Fig 7).

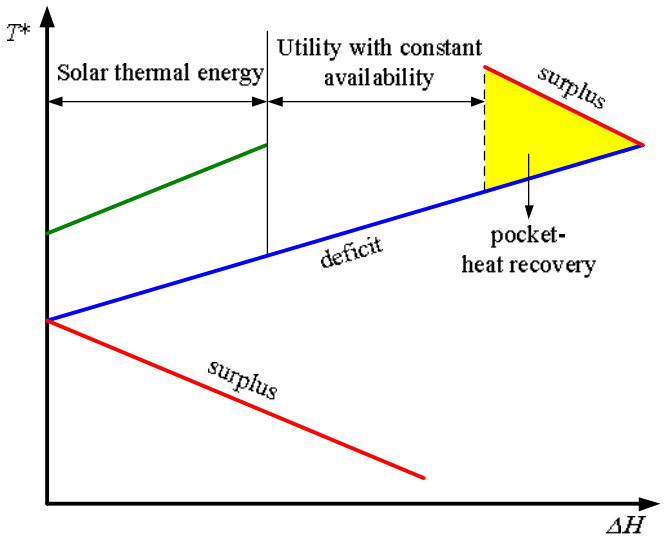

Fig 7: Integration of solar thermal energy in one combined TS [23, 24]

This is not, however, the only option. The use of Total Site analysis [25] and especially a Total Site with renewable sources of energy, including solar thermal-energy [26, 27], would be an efficient approach when analysing heat recovery and the integration of solar thermal energy.

4.3. Hierarchy for covering heat demand

Within each Time Slice, there are three different sources regarding utilities. The following hierarchy [26, 27] should be followed in order to cover the heat demand:

i) Heat recovery should be maximised.
ii) The use of solar thermal energy via direct heat-transfer from collectors – immediately, when available.
iii) Usage of the energy from the storage-indirect heat-transfer of solar thermal energy.
iv) A backup utility with constant availability is required.

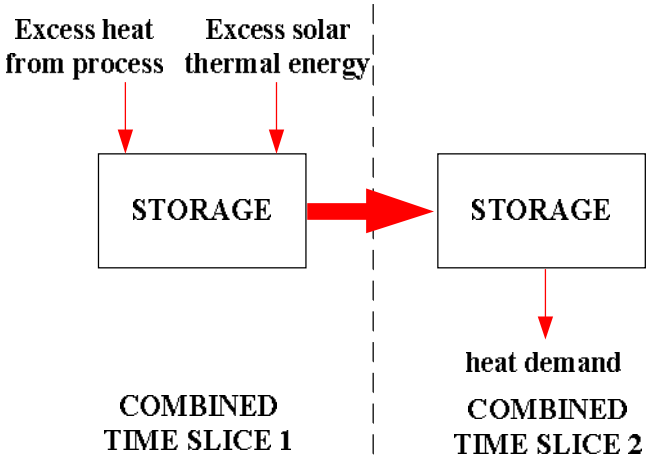

Fig 8: Transferring solar heat from one combined TS to another [7, 27]

Integration using the direct transfer of solar thermal-energy within TS is then performed after heat recovery. If there is unused heat from the solar-source, it is transferred to storage. The solar thermal-energy can be unused for different reasons. One is a surplus and the other is a higher demanded temperature than the temperature of the heat available from the solar-source. The stored heat will be available in other TSs (Fig 8). This is an indirect way of using the solar thermal-energy.

When all the available solar thermal heat from the direct and indirect transfers is integrated, the rest of the demand should be covered by those utilities with constant availability.

5. Case Study

5.1. Heat recovery

In this case study, the varying demand was presented by the batch process [7]. The streams are presented in Table 1. The Time Slices from the heat demand were the starting and ending times of the streams or changes in the loads for heat demand.

Table 1: Streams for Case Study [7]

Stream No and type	T_S [°C]	T_T [°C]	CP [kW/°C]	t_{start} [h]	t_{end} [h]
1 Cold	25	110	10	12	16
2 Cold	55	115	8	6	24
3 Hot	140	35	4	0	12
4 Hot	130	15	3	6	19

The first step of procedure is to perform heat recovery within the batch process using a Problem Table Algorithm. The Grand Composite Curves for each TS obtained separately are presented in Fig 9.

In the first TS there was an excess of heat, which could be used in the following TS. In the second TS there was a heat recovery pocket (Fig 9). There was also an excess of heat; however the temperature of the available heat was quite low, below 60 °C. There was a significant heat demand in the TS of between 12 h and 16 h. There was also some heat surplus; however, its temperature was too low, 10 °C, to be usable in the following TS. In the TS of between 16 h and 19 h, the demand was also significant and there was also an opportunity to store the heat, but the temperature was low. In the last TS, there was only heat demand and no heat surplus. Only after maximising the heat recovery a solar thermal energy should be integrated to the process.

5.2. Creating a TS for solar thermal-energy

The input real-supply profile is presented in Fig 1 (in section 2.2). This presents the daily irradiation. The data was taken as for a typical summer day in Central Europe. The time-period of the irradiation was from 5-22 to 19-22 as there was no irradiation before or after this period. It was a 14 h time-horizon and the measurements were taken every 15 mins. This resulted in 56 measurements [25]. The discretisation of the irradiation can be seen in Fig 1. The results were obtained in 49 s on Intel(R) Core (TIM) i3 CPU processor.

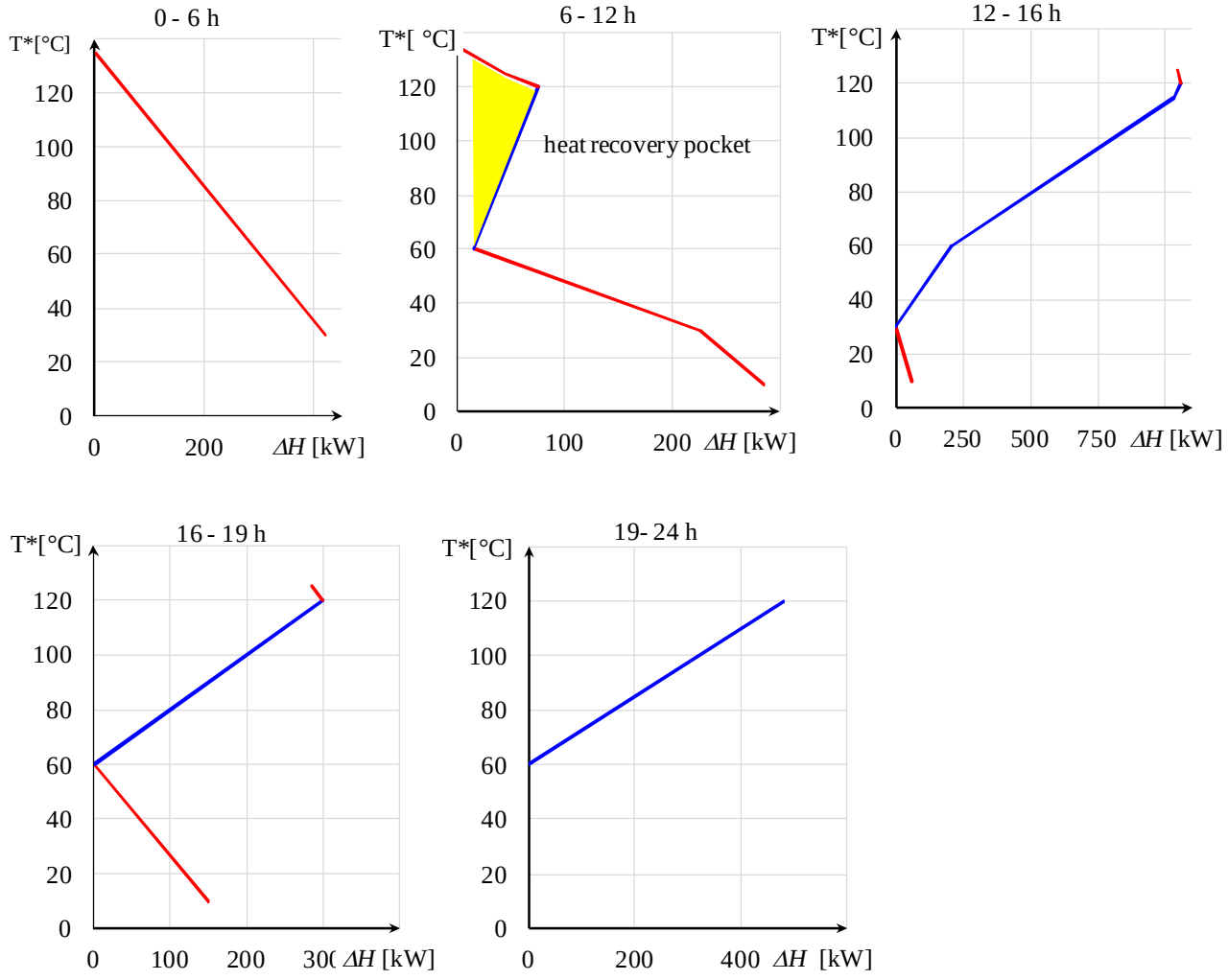

Fig 9: GCCs for each TS separately

The optical efficiency of the tube collectors was η_0=76 %, the coefficients a_1=1.53 W °C^{-1} m^{-2} and a_2=0.0003 W °C^{-2}m^{-2} [22], the inlet and the outlet temperatures of the solar collector media were 70 and 90 °C, and the area of the solar collectors was 150 m^2.

The selected acceptable tolerance in this Case Study was 10 %. The optimal number of TSs, obtained by the proposed MILP model, was 8. It was an important achievement, as the initial number of time-intervals from the measurements was 56. The minimal inaccuracy at this number of TSs was 9.4 %. The TS determined for the irradiation can be seen in Fig 10.

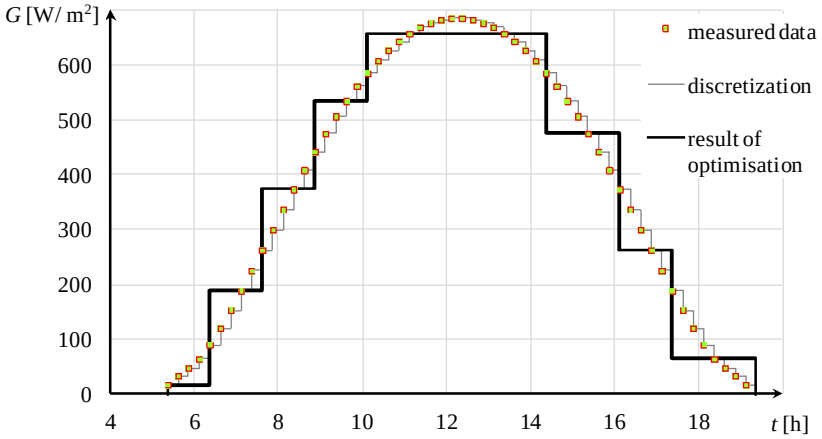

Fig 10: TS boundaries for irradiation.

The results, obtained for TS for irradiation, suggested 8 TSs. However, capture of the heat was impossible when determining the efficiency of the capture system in the first and last TSs, as the irradiation was too low. For this reason the number of TSs with a constant load of supply was, in this case, 6. Fig 11 presents the final approximated load-profile for the supply of solar thermal-energy, and the TS boundaries.

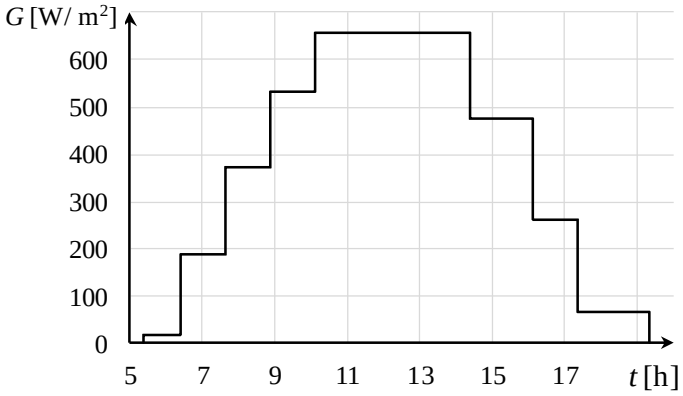

Fig 11: TSs and approximated loads for solar thermal energy

5.3. Combining the TSs

After obtaining TSs the (i) heat demand variations and (ii) solar thermal energy supply were joined. In order to combine them, the time-boundaries from both TSs were listed and any duplicates (if existing) were eliminated. As can be seen in Fig 12, in this case study there were 5 TSs (with 6 time boundaries) from the heat demand and 6 (with 7 time boundaries) from the solar thermal energy supply. Combining them resulted in 12 cTSs (with 13 time boundaries). This case study clearly showed how important it is to reduce the number of TSs for solar thermal-energy supply.

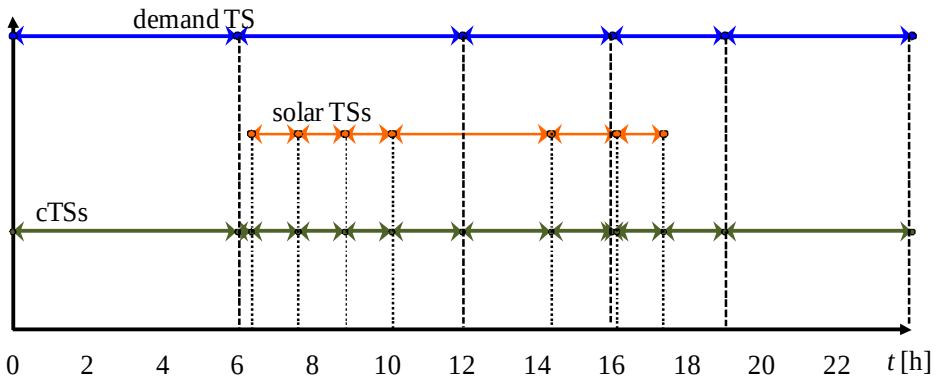

Fig 12: Combining the TS together from the Solar TSs and heat demand TSs

5.4. Integration of solar thermal energy

In all the cTSs the heat recovery was done first, as described in the hierarchy for covering heat demand (section 4.3). The hot utility requirement after heat recovery, ΔH_{UR}, and the excess of heat, ΔH_E, are shown in Table 2. The next step was to integrate the available solar thermal-energy, ΔH_{STE}, within the observed TS in order to determine the load of the direct heat-transfer of the solar thermal energy, ΔH_{DTE}. The load of heat demand at the feasible temperature of the heat- transfer was also obtained. From these two calculated loads, the amount of exchanged heat and the heat load transferred to or from the storage of solar thermal-energy could have been also be specified. Another source of heat could have been also be excess-heat, which could have also been stored if the temperature allowed for it. For simplicity, an isothermal storage was assumed. As the time-horizon when using the storage was short, it was not far from a real situation. As backup, at least one hot, ΔH_{HU}, and one cold, ΔH_{CU}, utility were required, with constant availability.

Table 2: Determining the load of solar thermal energy supply and the utility with constant load

cTS	After recovery		Solar thermal energy		Storage from		Constant available utility	
Duration h	ΔH_{UR} kW	ΔH_E kW	ΔH_{STE} kW	ΔH_{DHT} kW	ΔH_E kW	ΔH_{STE} kW	ΔH_{HU} kW	ΔH_{CU} kW
0:00-6:00	-	420	-	-	220		-	200
6:00-6:22	-	285	-	-	-	-	-	285
6:22-7:37	-	285	57.1	-	-	57.1	-	285
7:37-8:52	-	285	273	-	-	273	-	285
8:52-10:07	-	285	461	-	-	461	-	285
10:07-12:00	-	285	607	-	-	607	-	285
12:00-14:22	1045	60	607	510	-	97	535	60
14:22-16:00	1045	60	402	402	-	-108	535	60
16:00-16:07	285	150	402.1	100	-	302.1	185	150
16:07-17:22	285	150	157.4	100	-	57.4	185	150
17:22-19:00	285	150	-	-	-	-100	185	150
19:00-24:00	480	-	-	-	-	-160	320	-

As can be seen from Table 2, not all of the heat demand could have been covered from solar thermal-energy, because the temperature of the capture was often lower than some of the heat demands. This was also a reason for using a utility with constant availability. The amount of hot utility needed after the recovery was 7,435 kWh. This amount was calculated by multiplying the

load by the time horizon of the TS. 2,000 kWh could have been covered by direct heat-transfer from solar thermal-energy and 1,140 kWh could have been covered from indirect heat-transfer using storage. This means that the demand 3,140 kWh could have been covered by solar thermal-energy, which is 42.2% of the overall heat demand. The rest of the demand, 4,295 kWh, should still been covered from the utility with constant availability. However, the dependency on fossil fuels should be decreased as much as possible, since this energy source has an impact on the environment.

5.5. Determination of storage size

In order to estimate the storage size, the amount of the heat stored or used should be determined in each cTS separately e.g. the heat stored at the cTS1 is ΔH = 220 kW··6 h=1320 kWh (Table 2, storage column and Fig 13). These calculated amounts of heat are presented in the boxes of Fig 13. The cumulative amount of stored heat is represented by the numbers outside the boxes (Fig 13). Fig 13A presents the initial cumulative heat stored. As can be seen, in the last cTS12 the amount of stored heat is more than zero. This indicates that smaller storage would also be sufficient. The smallest storage, at which the heat recovery remains the same, would be when the cumulative amount stored at the last cTS is equal to zero (Fig 13B).

The storage from this case study should be large enough to store 1,032.4 kWh of heat. The result was determined by the maximal amount of heat within the cascade. However, in order to obtain a proper trade-off besides the rate of heat recovery, also the investment of the storage should be analysed.

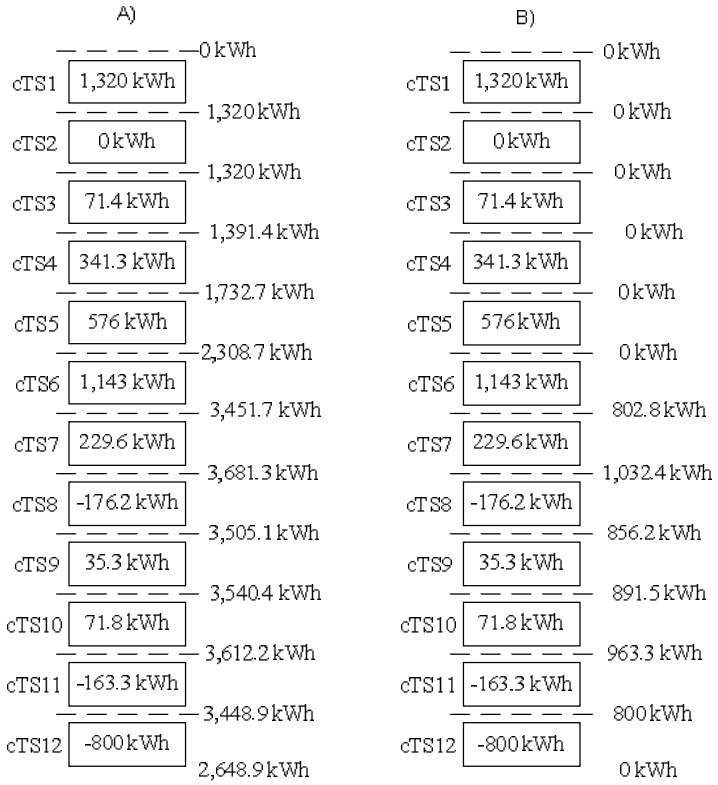

Fig 13: Cascading the amount of heat in storage through different Time Slices at A) maximal storage and B) reduced storage

6. Conclusions and future work

In the presented paper a framework for the integration of solar thermal-energy with processes featuring varying demand was developed. By applying this framework, the amount of solar thermal-energy can be determined, which can be potentially used within the process.

As part of the algorithm, the current work offers a systematic procedure capable of identifying Time Slices with an assumed constant solar thermal-energy supply. It is an important step because, to date, Time Slices have mostly been detected heuristically, usually with equal lengths. However, the solar irradiation varies unevenly and the inaccuracy in such a model is high. This current model enables the user to set the accuracy wanted at the stage of analysis. Higher accuracy will result in a larger number of TSs.

The presented case study used utility demand as a base case. It illustrated that the demand for a utility with constant availability (usually a fossil fuel) can be reduced by up to 27 % by utilising solar thermal-energy directly, without any storage. A further decrease of up to 15 % (on the same basis) can be achieved by introducing thermal-energy storage. The combined reduction in hot utility resulting from these two steps is about 42 %. This is a significant decrease, which should be encouraging enough taking solar thermal-energy in consideration, during the designing of a utility system.

The formulated algorithm offers a simple and fast approach with the accuracy openly available as a degree of freedom for the user. Another important step for achieving better solutions is the simultaneous evaluation of heat supply and demand.

As future work, the computer-aided synthesis of the developed framework will be pursued. As a further methodological development, shifting process operations in time (rescheduling) should be considered, in order to achieve as high a usage of direct transfer from solar thermal-energy as possible.

7. Nomenclature

ΔH_{CU}	cold utility requirement, with constant availability, kW
ΔH_{DTE}	direct heat-transfer the solar thermal energy to process, kW
ΔH_{E}	excess of heat after heat recovery, kW
ΔH_{HU}	hot utility requirement, with constant availability, kW
ΔH_{STE}	available solar thermal energy, kW
ΔH_{UR}	utility requirement after heat recovery, kW
A_0	initial overall amount of irradiation, kWh m^{-2}
a_1	solar collector thermal loss coefficients, W $°C^{-1}$ m^{-2}
a_2	solar collector thermal loss coefficients, W $°C^{-2}$ m^{-2}
AS_i	approximated supply over time-interval i, W m^{-2}
CP	heat capacity flowrate, kW $°C^{-1}$
cTS	combined time slice
ED_i	the positive and negative difference between the real and approximated supplies together over time-interval i, W m^{-2}
G	solar irradiation, W m^{-2}
I	set of time boundaries
i	time boundaries of time intervals
INA	overall inaccuracy, kWh
IN_i	inaccuracy within time-interval i, kWh

LV large value, maximum difference between real and approximated supplies

ND_i positive differences between the real and approximated supplies over time-interval i, W m^{-2}

N_I number of time-intervals

NTS number of Time Slices

PD_i positive differences between the real and approximated supplies over time-interval i, W m^{-2}

RS_i real supply irradiation over time-interval i, W m^{-2}

SD_i supply difference over time-interval i, W m^{-2}

t time, h

T_A ambient air temperature, °C

T_C average internal fluid temperature, °C

t_{end} ending time of the heat demand, h

t_i time period boundary of time-interval i, h

T_{in} inlet temperature for collectors, °C

T_{out} outlet temperature for collectors, °C

TS Time Slice

T_S supply temperature of streams, °C

TS_i Time Slice boundary, h

t_{start} starting time of the heat demand, h

T_T target temperature of streams, °C

y_i binary variable, selection as to whether the time period boundary is a TS boundary

z objective function

z_I first-stage objective function

z_{II} second-stage objective function

ε tolerance, %

η_0 optical efficiency of the collector, %

η_C efficiency of the collector, %

Acknowledgements

Financial support is gratefully acknowledged from the EC FP7 project "Intensified Heat Transfer Technologies for Enhanced Heat Recovery - INTHEAT", Grant Agreement No. 262205 and Társadalmi Megújulás Operatív Program (TÁMOP-4.2.2/B-10/1-2010-0025).

References

[1] Gude VG, Nirmalakhandan N, Deng S. Desalination using solar energy: Towards sustainability. Energy 2011; 36: 78 – 85.

[2] Chaabene M, Annabi M. Dynamic thermal model for predicting solar plant adequate energy management. Energy Conversion and Management 1998; 39: 349 – 355.

[3] GeoModel Solar s.r.o. <solargis.info> ; 2011 [Accessed 28/9/2011].

[4] KGA Associates, <www.pvoptimize.com> ; 2011 [Accessed 28/9/2011].

[5] Erdil E, Ilkan M, Egelioglu F. An experimental study on energy generation with a photovoltaic (PV)– solar thermal hybrid system. Energy 2008; 33: 1241– 1245.

[6] Mawire A, McPherson M, van den Heetkamp RRJ. Simulated energy and exergy analyses of the charging of an oil–pebble bed thermal energy storage system for a solar cooker. Solar Energy Materials & Solar Cells 2008; 92: 1668–1676.

[7] Kemp IC, Deakin AW. The Cascade Analysis for Energy and Process Integration of Batch Processes, Part 1: Calculation of Energy Targets. Chem Eng & D 1989; 67: 495-509.

[8] Klemeš J, Linnhoff B, Kotjabasakis E, Zhelev TK, Gremouti I, Kaliventzeff B, et al. Design and Operation of Energy Efficient Batch Processes, EC Project EURO BATCH Final Report, EC Brussels; 1994.

[9] Zhao XG, O'Neill BK, Roach JR, Wood RM, Heat integration for batch processes Part 1: Process Scheduling Based on Cascade Analysis. Trans IChemE 1998; 76: 685 – 699.

[10] Zhao XG, O'Neill BK, Roach JR, Wood RM. Heat integration for batch processes Part 2: Heat Exchanger Network Design. Trans IChemE 1998; 76: 700 – 710.

[11] Adonyi R, Romero J, Puigjaner L, Friedler F. Incorporating heat integration in batch process scheduling. Applied Thermal Engineering 2003; 23: 1743–1762.

[12] Pourali O, Amidpour M, Rashtchian D., Time decomposition in batch process integration, Chemical Engineering and Processing 2006; 45: 14 – 21.

[13] Majozi T. Minimization of energy use in multipurpose batch plants using heat storage: an aspect of cleaner production. Journal of Cleaner Production, 2009; 17: 945 – 950.

[14] Foo DCY, Chew YH, Lee CT. Minimum units targeting and network evolution for batch heat exchanger network, Applied Thermal Engineering, 2008; 28: 2089-2099.

[15] Varbanov P, Klemeš J. 2010, Total Sites Integrating Renewables with Extended Heat Transfer and Recovery. Heat Transfer Engineering, 31(9), 733-741.

[16] Friedler F. Process integration, modelling and optimisation for energy saving and pollution reduction, Chemical Engineering Transactions 2009; 18: 1-26.

[17] Friedler F. Process integration, modelling and optimisation for energy saving and pollution reduction. Applied Thermal Engineering 2010; 30: 2270-2280.

[18] Muster-Slawitsch B, Weiss W, Schnitzer H, Brunner C. The green brewery concept e Energy efficiency and the use of renewable energy sources in breweries. Applied Thermal Engineering 2011, 31, 2123-2134.

[19] Ludig S, Haller M, Schmid E, Bauer N. Fluctuating renewables in a long-term climate change mitigation strategy. Energy 2011, 36 (11) 6674-6685

[20] European Commission, <re.jrc.ec.europa.eu/pvgis/apps4/pvest.php> [Accessed: 23/08/2011].

[21] Xi C, Hongxing Y, Lin L, Jinggang W, Liu W. Experimental studies on a ground coupled heat pump with solar thermal collectors for space heating. Energy 2011; 36: 5292 – 5300.

[22] Atkins MJ, Walmsley MRW, Morrison AS. Integration of solar thermal for improved energy efficiency in low-temperature-pinch industrial processes. Energy2010; 35: 1867 – 1873.

[23] Townsend DW, Linnhoff B. Heat and power networks in process design. Part II: Design procedure for equipment selection and process matching. AIChE Journal 1983; 29(5): 748-771.

[24] Linnhoff B, Townsend DW, Boland D., Hewitt GF, Thomas BEA, Guy AR, Marsland RH. A user guide on process integration for the efficient use of energy. IChemE, Rugby UK;1982, last edition 1994.

[25] Klemeš J, Dhole VR, Raissi K, Perry SJ, Puigjaner L. Targeting and Design Methodology for Reduction of Fuel, Power and CO_2 on Total Sites. Appl Therm Eng 1997; 17: 993 – 1003.

[26] Perry S, Klemeš J, Bulatov I. Integrating waste and renewable energy to reduce the carbon footprint of locally integrated energy sectors. Energy 2008; 33: 1489-1497.

[27] Varbanov PS, Klemeš JJ. Integration and management of renewables into Total Sites with variable supply and demand. Computers and Chemical Engineering 2011; 35: 1815 – 1826.

Methodology for the Improvement of Large District Heating Networks

Anna Volkova[a], Vladislav Mashatin[b], Aleksander Hlebnikov[c] and Andres Siirde[d]

*[a]Tallinn University of Technology, Estonia, anna.volkova@ttu.ee, **CA***
[b]Tallinn University of Technology, Estonia, vladislav.mashatin@dalkia.ee
[c]Tallinn University of Technology, Estonia, aleksandr.hlebnikov@ttu.ee
[d]Tallinn University of Technology, Estonia, andres.siirde@ttu.ee

Abstract:

The purpose of this paper is to offer a methodology for the evaluation of large district heating networks. The methodology includes an analysis of heat generation and distribution based on the models created in the TERMIS and EnergyPro environment. For the approbation of proposed methodology the data on large-scale Tallinn district heating system was used as a basis of case study. The effective operation of district heating system, both at the stage of heat generation and heat distribution, can reduce the cost and price of heat supplied to the consumers. It can become an important factor for increasing the number of district heating consumers and demand for the heat load, which in turn will allow installing new cogeneration plants, using renewable energy sources and heat pump technologies.

Keywords:

District heating, DH, energy efficiency, energy systems, simulation, pipes, cogeneration

1. Introduction

The properly operating district heating systems can provide possible improvement of energy efficiency, reduce emissions, improve energy security and competitiveness and creating of new jobs. A district heating network includes the infrastructure for centralised heat production and distribution to the consumers for providing space heating and hot tap water in a wider area. The district heating system can be considered energy efficient and cost-effective only at optimal operation conditions and minimum heat loss.

One of the actions mentioned in the EU strategy Energy 2020 is to increase the uptake of high efficiency district heating systems. A high efficiency district heating system can only be provided when efforts are concentrated on the whole energy chain, from energy production, via distribution, to final consumption [1].

There are more than 5000 district heating systems in Europe, currently supplying more than 9% of total European heat demand. District heating systems are mainly used in the northern European countries, such as Sweden and Finland [2]. As regards to Latvia, Lithuania and Estonia, the percentage of district-heated households is around 60-75%.

The main advantages of district heating are efficiency, reliability and cleanness compared to the individual heating systems. Efficiency can be reached when heat is produced simultaneously with electricity in the cogeneration process. For larger heat generation units there are more options of flue gas cleaning available than for small scale boilers. District heating is a good solution for the areas with high population density and multiplied welling houses, because the investments per household can be reduced. Due to the fact that the connection to a single-family house is rather expensive, district heating is a less attractive solution for the countryside.

Large district heating networks supply heat usually in big cities, since the level of heat consumption in large areas is high. Large district heating systems are typical for Estonia. District heating is used in all bigger cities in Estonia, including the capital Tallinn [3].

The purpose of this paper is to offer a methodology for the improvement of large district heating networks. For the approbation of the offered methodology, the data on Tallinn district heating system was used as a basis of the case study.

District heating systems offer a potential for renewable heat generation technologies. The most popular renewable energy source for heat generation is biomass, which includes agricultural, forest, and manure residues and in extent, urban and industrial wastes, which under controlled burning conditions, can generate energy, with limited environmental impacts [4-6]. Geothermal as renewable energy can be used for district heating system and geothermal district heating has been given increasing attention in many countries during the last decade [7]. The expansion of district heating will help utilize heat production from above mentioned renewable energy sources [8].

The developed district heating systems promote cogeneration development. When cogeneration plant supplies heat to district heating system, its capacity is defined by maximum heat load of this system [9, 10]. In some cases thermal storage unit is attached to cogeneration plant for efficient operation of district heating system [11]. Cogeneration plant with district heating provides an alternative energy production and delivery mechanism that is less resource intensive, more efficient and provides greater energy security than many popular alternatives [12].

2. Methodology

As it was mentioned before only an optimally operated district heating system can be considered energy efficient. The efficiency of operation should be evaluated both relative to heat generation (boiler houses and cogeneration plants) and heat distribution networks (pre-insulated pipes).

2.1. Evaluation and improvement of heat distribution

Improvement of district heating network is a complex task where many parameters should be taken into account. There are three ways to improve a district heating system by reducing the heat loss:

The low investment scenario assumes reduction of supply temperature and increased water flow. This can be possible only in case the network pipe dimensions are larger than required. In this case the pressure will grow, which means that the number of damaged pipes may increase. The increased pressure can also be a problem for the customer systems. Additional pumping capacity is required in power plants.

The medium investment scenario assumes replacement of pipe insulation. The insulation can be replaced when the steel casing of pipe is in good condition, otherwise the pipe should be fully replaced. Selection of insulation thickness is a complex task where many parameters should be taken into account: material and work cost, thermal conductivity of new and old insulation, pipe diameter, environmental temperature and water temperature and so on.

The high investment scenario assumes reconstruction of pipelines with the installation of pre-insulated pipes and increasing or decreasing their diameter, if needed. The new diameter should be selected very carefully whereas considering the future network development possibility. As a matter of fact, it is possible to replace all the pipes only in small networks; otherwise the project cost will be too high.

It is not possible to carry out such improvement without creating a virtual model and trying all possible scenarios, especially in large networks where many heat suppliers can work together in different combinations. For the evaluation of heat distribution, a special model was created using the commercial TERMIS software [13]. Simulation can be done using other software like Bently sis HYD or Zulu Thermo, but TERMIS is considered to be the most advanced, powerful and extensive

district energy network simulation platform for improving system design and operation. Different types of improvement of European district heating systems were made using commercial TERMIS [13-15]. TERMIS is a hydraulic modelling software tool, which gives an overview and control of district energy network by simulating the flow, pressure and thermal behaviour. With TERMIS, it is possible to reduce energy loss and reduce the CO2 emission [13].
Before creating the model, it is necessary to create a database, which should include the data on all the pipes with their dimension, insulation, coordinates, roughness and single pressure loss description; the consumer data like seasonal consumption of heat and tap water; environmental data like the air temperature for overhead pipelines and soil temperature for subsurface pipelining to calculate the heat loss.

2.2. Evaluation and improvement of heat production

Usually in large-scale district heating systems various energy sources are used: large and small boiler houses and cogeneration plants. Both fossil fuel and wood fuel can be used for heat production. The operation efficiency of boiler houses depends on the age of installed equipment. The renovated or new boiler houses have higher efficiency and are easily operated.

As regards to cogeneration plants, especially those based on wood fuel, the efficiency begins to fall when the load is less than 70 %. Besides, the investments in cogeneration plants operation are much higher than in boiler houses. That is why, it is more important to operate the cogeneration plants at the maximum load. The boiler houses are often used as peak demand covering units.

The following indicators should be used for the evaluation of heat production: type of production unit (boiler house or cogeneration plant), heat capacity (for cogeneration plant the electrical capacity, additionally), age of a heat production unit, fuel type (fossil fuel of renewable fuel), energy efficiency, and shut-downs.

It is important to find a right solution in the operation strategy for all heat production units. Priority should be given to CHP production. Boiler houses are used only in case the heat supplied from a cogeneration plant is insufficient.

Different types of modelling tools for the economic analysis and optimal operation of cogeneration plants have been developed in recent years. As the examples SEA/RENUE, CHP sizer, Ready Reckoner, EnergyPro can be mentioned [16]. EnergyPRO was chosen for evaluation of heat production in the district heating system, because it is modelling software which allows carrying out detailed technical and financial analyses of energy projects. For the optimisation of cogeneration plants, the priority in EnergyPRO software tool is that the cogeneration plant meets the heat demand for the period being analysed [17].

A simple model, which was created using the EnergyPro software, can be applied to determine the optimal operating strategy. The current situation and development scenarios can be compared, using the following parameters: heat production, fuel consumption, electricity production, operation time.

3. Case Study

3.1. Tallinn Municipality District Heating System

Tallinn is the capital of Estonia located on the northern coast of the country. Tallinn is the largest city in the country with about 415,000 inhabitants.

District heating networks in Estonia are mostly old and in poor condition. The state of the district heating networks of Tallinn is typical for the rest of Estonian district heating systems. In Tallinn the heat is supplied to the consumers through a 429-kilometre long heating network including 119 km of pre-insulated pipes (27.7%), 22.2km is a pipeline with the renovated PUR insulation; 46% of the

whole pipeline network is canal pipes and 8.2 % overhead pipeline. Other pipelines are in tunnels and undergrounds. The diameter of main pipeline is up to 1200mm. The peak heat load of Tallinn district heating system was 640 MW (-22.6 C) in the 2010/2011 heating season while in the 2009/2010 heating season it had been higher reaching 695 MW (-23.4 C). The minimum heat load during the summer period is 55-65 MW [3]. The district heating systems of Tallinn were mostly constructed in 1960-1980 and their average age is 23 years as of 2012. The district heating systems of Tallinn consist of three connected districts of central heat supply where one of them is divided into two smaller districts, and 26 local boiler houses. Currently two cogeneration plants and three large-scale boiler houses supply heat to the districts of Tallinn. Almost the whole district heating network belongs to the Tallinna Küte company[18]. The Tallinn district heating network is shown in Fig. 1.

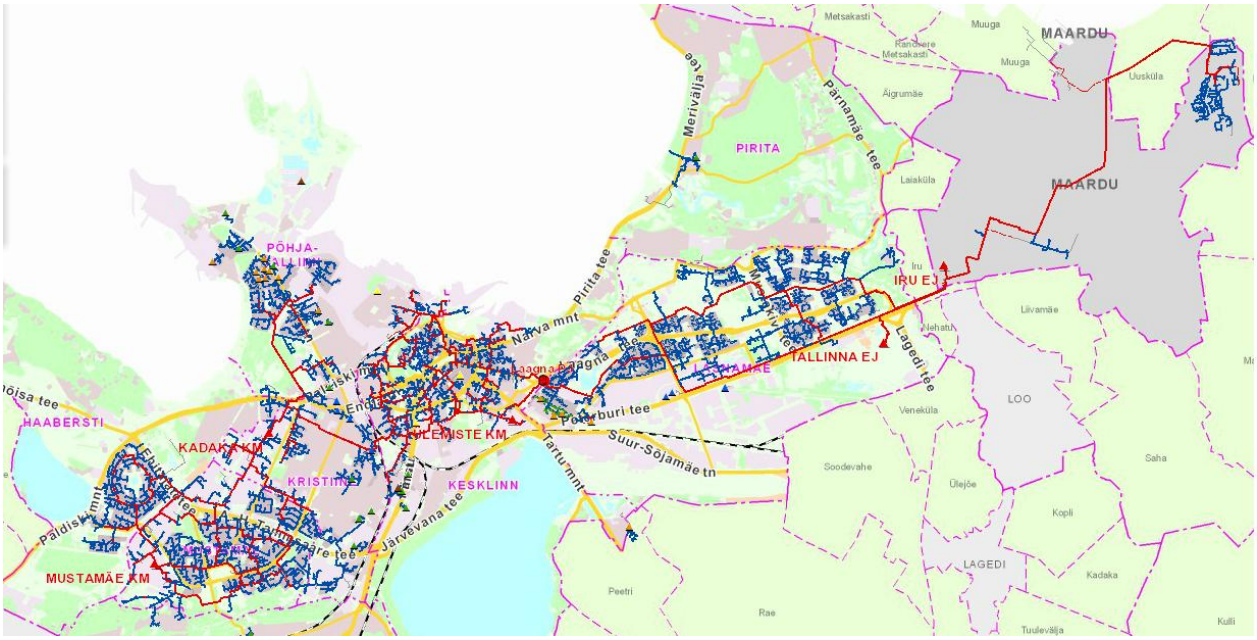

Fig.1. Tallinn district heating network.

Most of the pipelines were built during the rapid industrial growth of the city and thus the pipelines were oversized with a view of future development. After the collapse of Soviet Union many industries were closed. At the moment there are two main problems in the network: bad insulation and oversized pipelines; as a result, heath losses are high. According to the Tallinna Küte AS development plans, the relative heat loss should be reduced by 20%.

3.1. Heat distribution

3.1.1. Model description

A model was created for the Tallinn district heating network. The model was designed for 9868 pipes, over 3658 consumers and 9800 nodes with the geographic information included.

Different scenarios were simulated for the hydraulic and heat loss analyses:

-current consumption and temperature schedule;

-current consumption and maximum temperature decrease by 15 ℃;

- consumption reduced by 20% and current temperature schedule;

- consumption reduced by 20% and maximum temperature decrease by 20 ℃.

In the fourth scenario the temperature is decreased by 20°C and due to the reduced consumption, the water flow can be increased further. For the heat loss analysis the average seasonal temperatures

were decreased by 10°C.All scenarios were calculated twice: for the maximum consumption at -22°C to analyse the hydraulics and for the average seasonal parameters to analyse the heat loss.

3.1.2. Input data and assumptions

All the data has been taken from the Tallinna Küte GIS and converted to fit the TERMIS model. Tallinna Küte has also a large statistical database on different parameters in the critical points and consumption of each household during the last ten years. The parameters in critical points are required for model tuning; the number of points depends on the network. The GIS data and other databases can easily be interconnected by using Model Manager. Depending on the model, the estimated or average seasonal consumption can be used while the average seasonal consumption is more justified in most cases. First simulation can be made when the plant parameters like water flow, pressure and temperature are given. After first simulation with the adjustment factors applied, the simulation results should be identical to the known parameters in critical points. Only in this case the input parameters can be changed and it can be assumed that the simulation result is correct.

3.1.3. Results

The results of model simulation are shown in Tables 1 to 2. Table 1 shows the results at the maximum consumption and should be used for hydraulic parameters analysis, the Table 2 shows the seasonal average results and should be used for heat loss analysis.

Table 1. Simulation results for the maximum consumption at -22°C

Outdoor temp. -22°C	today	-15°C	-20%	-20°C /-20%
Production, MW	678	670	558	546
Consumption, MW	600	600	480	480
Heat loss, MW	78	70	78	66
Heat loss, %	11.5%	10.4%	14.0%	12.1%
Water flow, t/h	11180	14070	8920	11890

As it can be seen in Table 2,with changing the yearly average temperature by 10°C, it is possible to reduce the average relative heat loss for a heating season by 1.1% points that makes about 23.2GWh (for the 5800h heating season) or over 4200t/CO_2 in case the consumption stays at the same level as today. In case the consumption will be reduced for 20% in the future, the relative heat loss can be reduced by 1.3% compared to the current temperature schedule. However, the relative loss would be higher compared with the present consumption. A possible solution in this case the temperature lowering could be higher, especially, as it can be seen, water flow is only 6,5%.

Table 2. Simulation results for average seasonal parameters

Season average	today	-10°C	-20%	-10°C /-20%
Production, MW	324	320	267	263
Consumption, MW	279	279	223	223
Heat loss, MW	45	41	44	40
Heat loss, %	13.9%	12.8%	16.5%	15.2%
Water flow, t/h	7280	9260	5800	7340

It should be mentioned that the total water flow and pressure difference in the network will grow. It means that more powerful pumps should be used. Electricity consumption will grow, but the heat savings will be bigger than the increase of pumping cost. Besides, in case of Tallinn, most of the pipes are oversized and the growth of pressure difference is not so rapid.

3.2. Heat production

3.2.1. Model description

The model of current situation was built using the EnergyPro software. The components included in this model are shown in the Table 3. The model consists of three sites. Site 1includes 2 boiler houses operated during the heating season and a heat consumer. Site 2 includes a heat consumer, which is supplied by the heat produced in Site 1 and Site 3. Site 3 includes 2 energy units: the Tallinn CHPP where heat and electricity are cogenerated and Iru Plant where only two boilers are operated with no electricity generation. Besides, a heat consumer is included in Site 3. During the summer period only the Tallinn CHPP is operated supplying heat for hot water production to the whole district heating system. During the winter period all energy units are operated while the heat produced in Sites 1 and 3 is used to cover the heat demand of these sites and supplied to Site 2 also. The description of the model components is presented in Table 3.

Table 3. Components of the Tallinn DH model

Site 1		
Heat sources	Mustamäe boiler house	Natural gas, heat capacity 100 MW, fuel input 106, working time, 15/09-15/05
	Kadaka boiler house	Natural gas, heat capacity 129 MW, fuel input 138, working time, 15/09-15/05
	Site 2	When the boiler houses in Site 1 are shut down, heat is supplied via Site 2
Heat load	Demand in Mustamäe District	Annual heat demand is 693 GWh, 11% of the demand is hot water heating load, 89% of the demand depends linearly on ambient temperature during the heating period. The data on the ambient temperature in Tallinn for 2010 were used for simulation
	Site 2	During the heating period the heat produced in Mustamäe and Kadaka boiler houses is supplied to Site 2
Site 2		
Heat sources	Site 1	Heat produced in Site 1 (by Mustamäe and Kadaka boiler houses) during the heating season is supplied to Site 2
	Site 3	Heat produced in Site 3 (by the Tallinn CHPP and Iru Plant) during the heating season and in summer supplied to Site 2
Heat load	Demand in Kesklinna District	Annual heat demand is 380 GWh, 11% of the demand is hot water heating load and 89% of the demand has a linear dependence on the ambient temperature during the heating period. The data on the ambient temperature in Tallinn for 2010 were used for the simulation.

	Site 1	During the summer period, the heat supplied from Site 3 is distributed in Site 1
Site 3		
Heat sources	Tallinn CHPP	Wood, heat capacity 65 MW, electrical capacity 25 MW, fuel input 125, working time year-round supply
	Iru Plant	Natural gas, 353 MW
Heat load	Demand in Lasnamäe District	Annual heat demand is 561 GWh, 11% of the demand is hot water heating load and 89% of the demand has a linear dependence on the ambient temperature during the heating period. The data on the ambient temperature in Tallinn for 2010 were used for simulation.
	Site 2	During the heating period and in summer the heat produced in Tallinn CHPP and Iru Plant is supplied to Site 2, during the summer time when other heat generation units are shut down, the heat is supplied via Site 2 to Site 3
Transmissions		
Transmission 1	Heat from Site 1 can be supplied to Site 2 and from Site 2 to Site 1, the maximum capacity 200 MW, loss 10%	
Transmission 2	Heat from Site 3 can be supplied to Site 2 and from Site 2 to Site 3, the maximum capacity 173 MW, loss 10%	

The sites of the model are shown in Figs 2 to 4.

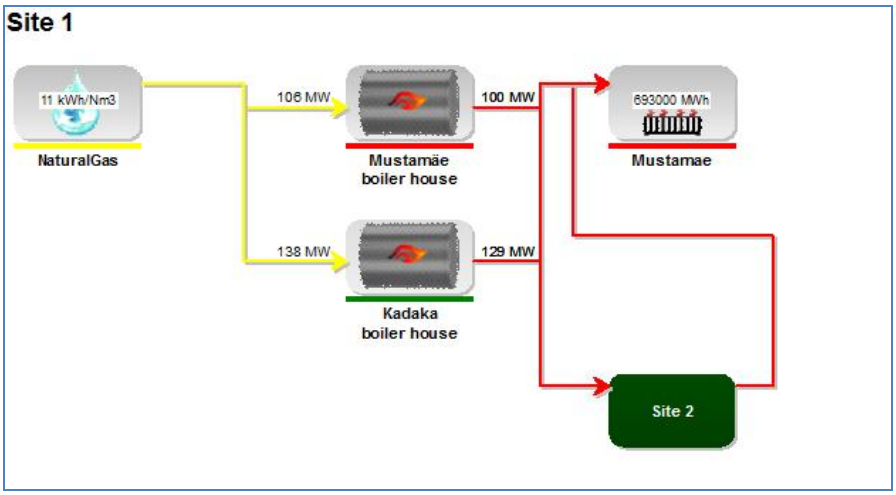

Fig. 2. Model of Tallinn district heating system, Site 1.

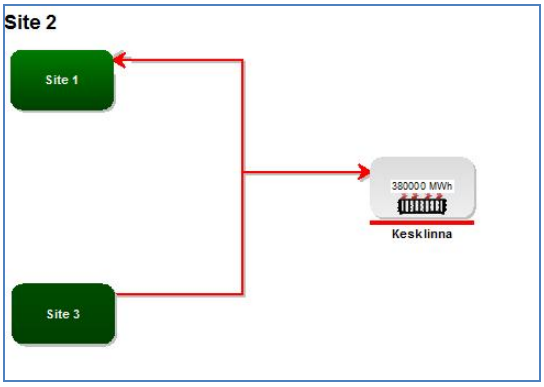

Fig. 3. Model of Tallinn district heating system, Site 2.

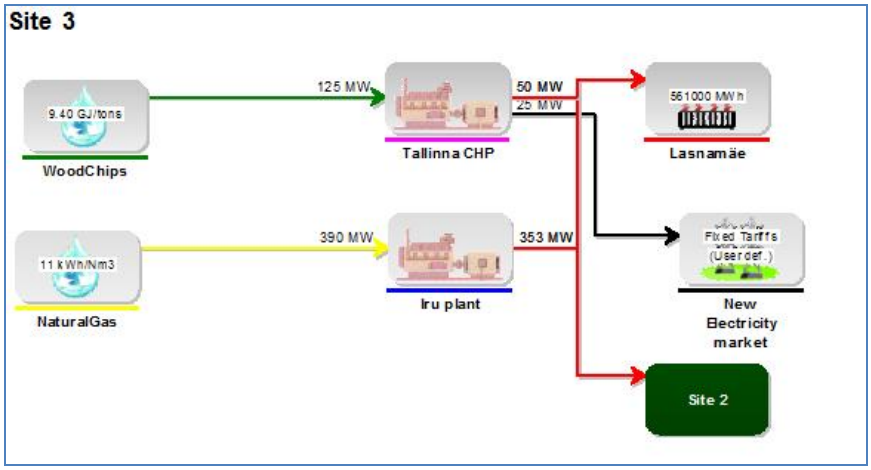

Fig. 4. Model of Tallinn district heating system, Site 3.

On the territory of Iru Plant a waste incineration plant is planned to be built where electricity and heat will be generated from the municipal waste (Site 3). To forecast the possible operating process, two scenarios were simulated, with and without a new incineration unit.

The future changes in Site 3 are shown in Fig. 5.

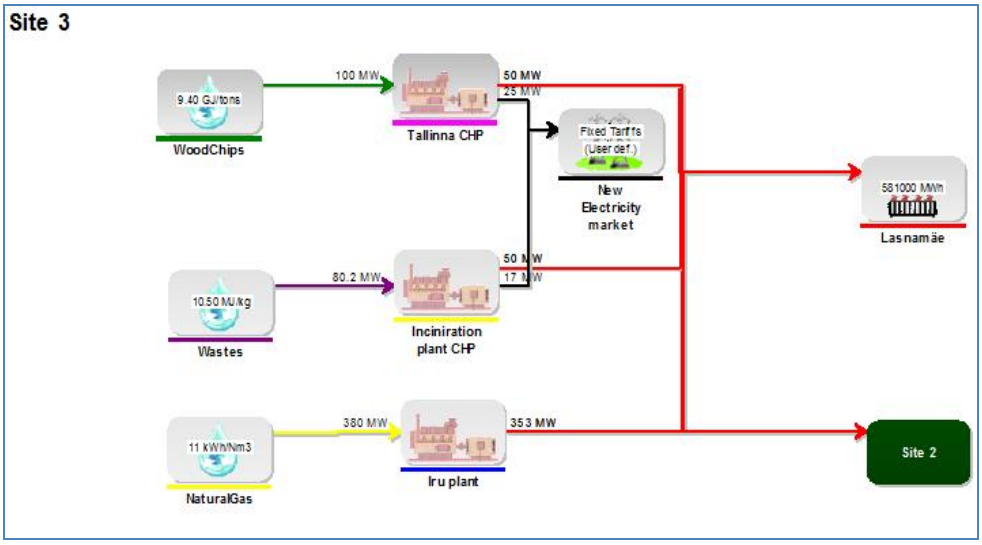

Fig. 5. Model of Tallinn district heating system, Site 3 (with an incineration plant).

Data about the new unit are presented in Section 3.2.2.

3.2.2. Input data and assumptions

Actual data on operating heating plants were used (Table3). For the heat demand simulation, it was assumed that 89% of heat demand is linearly dependent on ambient temperatures and 11% of the demand goes to cover the hot water consumption. The average annual heat demand for last three years (2008-2010),which is 1691 GWh, was taken as a basis for the calculation

As it was mentioned above, the simulation was made for two scenarios: with and without a new waste incineration plant. The data on the waste incineration plant used in the simulation are shown in Table 4.

Table 4.Parameters of waste incineration plant [19, 20]

Waste incineration plant	
Fuel	Waste
Heat value of fuel	10.5 MJ/kg
Fuel input	80.5 MW
Heat capacity	50 MW
Electricity capacity	17 MW

For simulating the operation, one more indicator should be included. This indicator is the priority of unit operation. The assumed priorities according to the operation strategy are shown in Table 5.

In both cases the highest priority is the Tallinn CHPP. Tallinn CHPP is a plant, which was launched in cogeneration mode in 2009. Wood chips are used as a fuel for electricity and heat production.

The Mustamäe and Kadaka boilers have almost the same parameters and that is why they have the same priority. The Iru Plant is owned by another company and will be bought from the owner.

When the incineration plant will start to operate, its priority will be very high, because it is an environmentally friendly and energy efficient technology.

Table 5.Operation strategy priorities

Unit	Priority (current situation)	Priority (with the incineration plant)	Partial load allowed
Tallinn CHPP	1	1	yes
Iru Plant (boiler)	4	4	yes
Mustamäe boiler	2	3	yes
Kadaka boiler	2	3	yes
Incineration plant (CHP)	-	2	yes

3.2.3. Results

The results of simulation are shown in Table 6.

The simulation showed that in case the incineration plant is used additionally, electricity generation will increase by 43 %. The consumption of fossil fuel - natural gas will decrease by 20%.

Table 6.Simulation results for heat production

Indicators	Without the incineration plant	With incineration plant

Heat production (GWh)	1,854.60	1,857.30
Tallinn CHPP	438.00	438.00
Incineration plant CHP		278.40
Mustamäe boiler house	711.00	667.10
Kadaka boiler house	394.40	354.70
Iru Plant	311.20	119.10
Electricity production (GWh)	219.00	313.60
Tallinn CHPP	219.00	219.00
Incineration plant CHP		94.66
Fuel consumption (GWh)	2,314.00	2,467.40
Natural gas	1,438.00	1,144.80
Wood	876.00	876.00
Waste		446.60
Working hours		
Tallinn CHPP	8760	8760
Incineration plant CHP		5568
Mustamäe boiler house	5616	5616
Kadaka boiler house	5064	4008
Iru Plant	5136	2544

The year-round operation of the system is shown graphically in Fig. 6. Fig. 6 shows that Tallinn CHPP operates all year round. The Mustamäe boiler house operates during all the heating period, but Kadaka boiler house and Iru Plant are used for peak loads.

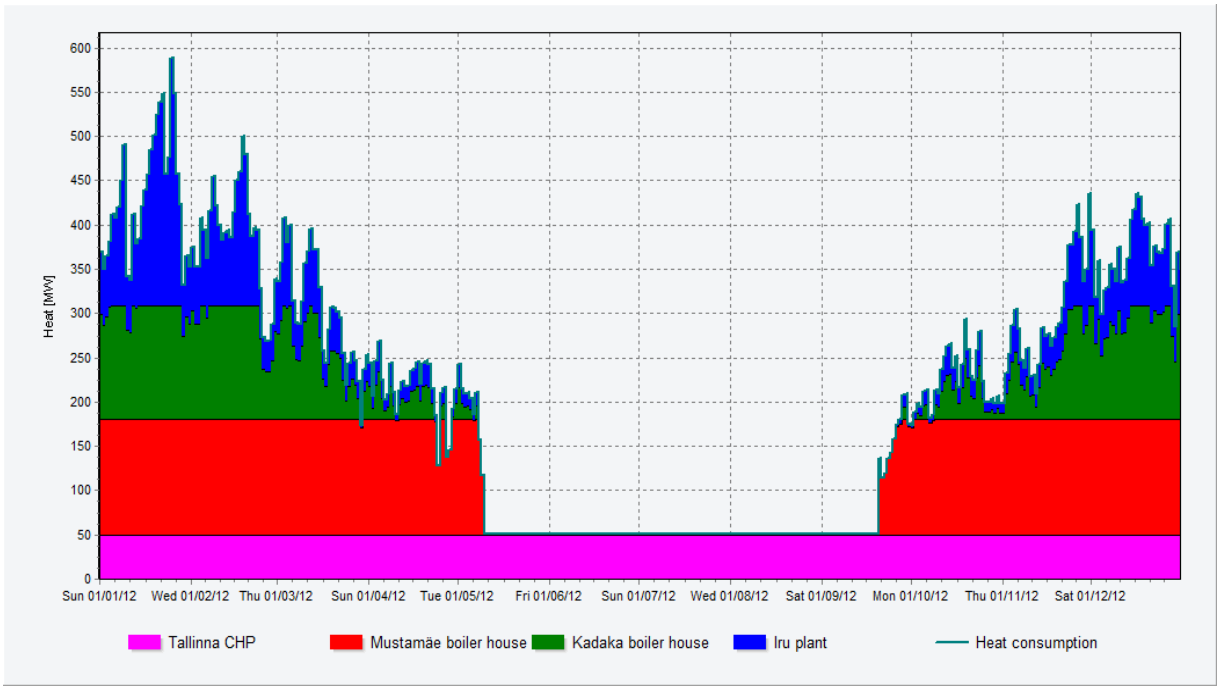

Fig. 6. Heat load of Tallinn District Heating Network. Simulation of the current situation.

Fig.7 shows the operation forecast for the second scenario when the incineration plant is added. The Tallinn CHPP operates all year round. The incineration plant works during all the heating period at full load. The Mustamäe boiler house operates during all the heating period, but at partial load. The Kadaka boiler house and Iru Plant work less than in the first scenario.

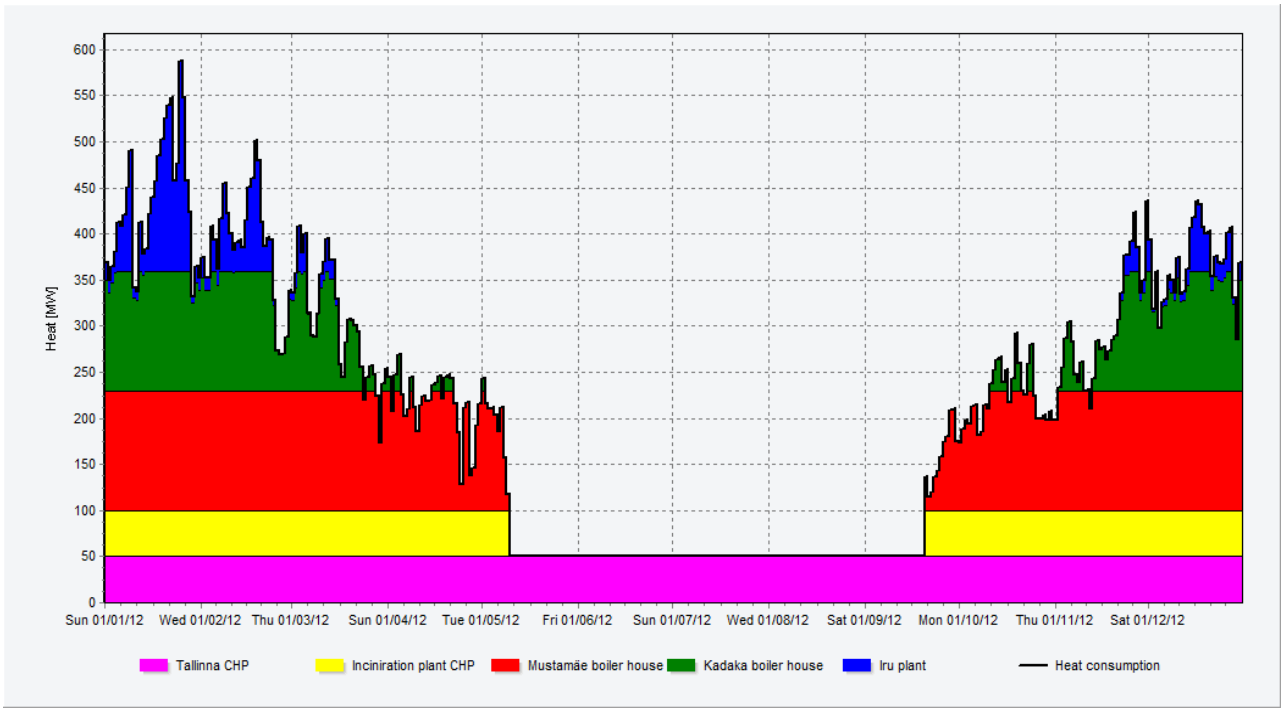

Fig.7. Heat load of Tallinn District Heating Network. Simulation of the scenario with an additional waste incineration plant.

Conclusion

The reliability and cost-efficiency of district heating depends on the efficiency of its operation. In this paper a methodology for the assessment and efficiency increasing of heat production and distribution was offered.

As a case study, the Tallinn district heating system was analysed. The Tallinn district heating system includes 4 heat plants, which cover the heat demand in 3 districts. For the evaluation of district heating network, a model was created using the TERMIS software. For the heat loss analysis and hydraulic analysis, four different scenarios were simulated: the current situation, decreased maximum flow temperature by 15°C, decreased consumption by 20% and decreased temperature by 20°C with the decreased consumption by 20%. As a result, the decreasing of relative heat loss by 23.2GWh during the heating season compared to the current situation was gained.

For the evaluation of energy production, a model was created using the EnergyPro software. The system was split into three sites. This model was used for the simulation of two scenarios: the current situation and the case where anew incineration cogeneration plant will be installed. The actual data for the last years were used for the simulation. The results of simulation showed that according to the current situation, the cogeneration plant should work all year round, the boiler houses should operate during the heating period and the Iru Plant boiler should be used only for the peak heat load. In case when the incineration plant is added, it can operate at full load during more than 5500 hours per year. Heat generation in this plant will decrease the consumption of natural gas

by 20%. The amount of electricity production in cogeneration mode will increase by 43%. The evaluation of district heating demand was made mainly from the technical point of view.

The effective operation of district heating system, both at the stage of heat generation and heat distribution, can reduce the cost and price of heat supplied to the consumers. It can become an important factor for increasing the number of district heating consumers and demand for the heat load, which in turn will allow installing new cogeneration plants, using renewable energy sources and heat pump technologies.

Acknowledgments

This work has been partly supported by the European Social Fund within the researcher mobility program MOBILITAS (2008-2015), MJD10 and DoRa program.

References

[1] EUROPA- the official web site of the European Union [internet]. Brussels, Belgium: Communication from the Commission to the European Parliament, the Council, the European Economic and Social Committee and the Committee of the Regions. Energy 2020. A strategy for competitive, sustainable and secure energy. Available at <http://www.energy.eu/directives/com-2010-0639.pdf>>. [accessed 01.12.2011].

[2] Rezaie B, Rosen MA. District heating and cooling: Review of technology and potential enhancements. Applied Energy 2012; 93: 2-10.

[3] Hlebnikov A., Volkova A., Džuba O., Poobus A., Kask U. Damages of the Tallinn District Heating Networks and indicative parameters for an estimation of the networks general condition In:Proceedings of 12th International Symposium on District Heating and Cooling , Estonia, Tallinn, 5.-7. September, 2010. - 277.-282. pp

[4] Vallios I., Tsoutsos T., Papadakis G. Design of biomass district heating systems. Biomass and Bioenergy 2009; 33(4): 659-678

[5] Difs K., Wetterlund E., Trygg L., Söderström M. Biomass gasification opportunities in a district heating system. Biomass and Bioenergy 2010, 34(5): 637-651

[6] Holmgren K., Gebremedhin A. Modelling a district heating system: Introduction of waste incineration, policy instruments and co-operation with an industry. Energy Policy 2004; 32(16): 1807-1817

[7] Hepbasli A. A review on energetic, exergetic and exergoeconomic aspects of geothermal district heating systems (GDHSs) Energy Conversion and Management 2010; 51(10): 2041-2061

[8] Lund H., Möller B., Mathiesen B.V., Dyrelund A. The role of district heating in future renewable energy systems. Energy 2010; 35(3):1381-1390

[9] Tveit T.-M., Savola T., Gebremedhin A., Fogelholm C.-J. Multi-period MINLP model for optimising operation and structural changes to CHP plants in district heating networks with long-term thermal storage. Energy Conversion and Management 2009;50(3):639-647

[10] Volkova A., Hlebnikov A., Siirde A. Methodology for defining of eligible capacity for wood fuel based cogeneration plants in small towns in Estonia. Journal of Energy and Power Engineering: 2011; 5(6):481 – 489

[11] Barelli L., Bidini G., Pinchi E.M. Implementation of a cogenerative district heating system: Dimensioning of the production plant Energy and Buildings:2007;39(6):658-664

[12] Kelly S., Pollitt M. An assessment of the present and future opportunities for combined heat and power with district heating (CHP-DH) in the United Kingdom Energy Policy 2010, 38(11):6936-6945

[13] TERMIS Operation User Guide, 7-Technologies, 2011

[14] Tol H.I., Svendsen S. Improving the dimensioning of piping networks and network layouts in low-energy district heating systems connected to low-energy buildings: A case study in Roskilde, Denmark, Energy 2012: 38(1):276–290

[15] Li H., Dalla Rosa A., Svendsen S. Design of low temperature district heating network with supply water recirculation, In: Proceedings of 12th International Symposium on District Heating and Cooling , Estonia, Tallinn, 5.-7. September, 2010:73-80

[16] Hinojosa L.R., Day A.R., Maidment G.G., Dunham C. A Comparison of combined heat and power feasibility models, Applied Thermal Engineering 2007;27 (13): 2166–2172

[17] User's Guide energyPRO, EMD, 2008

[18] Tallina Küte www.soojus.ee

[19] Report of environmental assessment. Waste use for combined heat and power production on the territory of Iru Plant. (Kütusena jäätmeid kasutava soojus- ja elektrienergia koostootmisploki rajamine Iru elektrijaama territooriumile, KMH hindamise aruanne), EestiEnergia 2007

[20] IRU WtE - technical overview Jäätme energia plokk WTE, 2010, CNIM

Optimal mine site energy supply

Monica Carvalho[a], Dean Millar[b]

*[a] (**CA**) Energy Renewables & Carbon Management Group, Mining Innovation Rehabilitation and Applied Research Corporation (MIRARCO), Sudbury, Ontario, Canada. {mcarvalho@mirarco.org}*

[a,b] Bharti School of Engineering, Laurentian University, Sudbury, Ontario, Canada. {dmillar@mirarco.org}

Abstract:

This paper reports on early work and concept development for Optimal Mine Site Energy Supply, where the specific energy supply requirements and constraints for mineral production operations are considered against methodologies that have been applied for other sectors and in other energy policy regimes. The primary motivation for this research is to help ensure that Canadian mineral producers will achieve reduced production costs through improvements in the efficiency with which they consume energy resources. Heat has not yet been considered for the mining sector in an integrated manner, which makes polygeneration of great interest. Through extension of proven methodologies, the 'most adequate' configurations of energy supply equipment that satisfice the energy requirements of mine sites both on and off transmission and distribution systems are identified by the optimization process. The methodology that optimizes configuration of polygeneration systems for mine sites has not been reported before. The variety of mining circumstances, temporal variations in energy prices, institutional inertia, and conservatism in design for mines are some of the reasons. This paper reviews some aspects of precedent energy management practice in mineral operations, which highlights energy challenges characteristic of the sector and sets out the initial formulation of optimal mine site energy supply. The review indicates the additional benefits of energy supply systems for mine sites that concurrently meet all utilities.

Keywords:

Polygeneration, renewable energy, heat integration, energy management, mineral sector.

1. Introduction

Mining is first and foremost a source of mineral commodities that all countries find essential for maintaining their economies and improving their standards of living. Mined materials are needed to construct roads and hospitals, to build automobiles and houses, to make computers and satellites, to generate electricity, and to provide many other goods and services [1]. Both energy consumption within the mining industry and energy prices, are rising and thus there increased need to reduce consumption, and improve primary energy utilization to maintain competitiveness within the mining sector by reducing input costs. Generally, energy supply security and reduced emissions can be achieved through [2]: i) improvement in energy efficiency; ii) energy savings; iii) higher proportion of renewable energy in supply systems; and iv) process-wide integration.

Given the significance of energy costs in operating expenses, efficiency of energy production and use must be improved in the energy-intensive mining sector [3]. Governments and mining associations recognize the importance of improving energy efficiency, and are working together to implement more energy-efficient technologies. Energy efficiency makes sense for mining operations because it can reduce production cost while simultaneously realizing additional benefits including reduction in the greenhouse gas emissions. While not yet well utilized, process integration and polygeneration are promising tools which reach the double objective of increasing the efficiency of utilization of natural resources, and also of reducing the environmental impact [4].

Polygeneration is a term used to describe a generalization of the cogeneration concept where two (co-generation) or more (poly-generation) energy services are simultaneously provided through use of highly-integrated energy systems. An immediate advantage of polygeneration is its thermodynamically efficient use of fuel. Polygeneration systems utilize otherwise wasted thermal energy, and can use it for space heating, industrial process needs, or as an energy source for another system component. This "cascading" use of energy is what distinguishes polygeneration systems from conventional separate electric and thermal energy systems (e.g., a powerplant and a lowpressure boiler), and from simple heat recovery strategies [5].

The deployment of polygeneration systems in mine sites aims at increasing the efficient use of natural resources by combining different technologies, process integration, and energy resources, an objective which may render mineral production operations compliant with the new energy management standard, ISO 50001 [6].

Advantages of polygeneration systems have been demonstrated in literature [7] [8], as energy efficiency is associated with economic savings and sparing of the environment, as less fuel is consumed and consequently less pollution is generated. Such integrated energy systems could play an important role in the gap between fossil fuel-based energy systems and renewable energy-based systems. Polygeneration is a fully developed technology that has a long history of use in many types of industry, particularly in pulp and paper, petroleum and chemical industries, where there is a large demand for both heat and electricity at each site [9]. In recent years, the greater availability and choice of suitable technology options means that polygeneration can become an attractive and practical business proposition.

In recent years, the analysis and design tools for energy systems and energy management have undergone development. In particular, the synthesis and design of energy systems for the industrial sector has become increasingly elaborate, with numerous possibilities for energy sources and technological options. This increase in complexity allows for more flexible systems but at the same time increases difficulties when designing the polygeneration system itself.

This paper reports on early work and concept development for Optimal Mine Site Energy Supply, where the specific requirements and constraints of mineral production operations are considered against methodologies that have been applied for other sectors and in other energy policy regimes. Through these extensions, the 'most adequate' configurations of energy supply equipment that *satisfice* (as coined by Herbert Simon [10]) the energy requirements of mine sites in different scenarios and conditions of constraint can be identified.

This paper also presents a critical review of precedent energy management practice in mineral operations, where the thrust has been independent deployment of beneficial technologies. The review indicates the additional benefits of energy supply systems for mine sites that concurrently meet all utilities.

2. Energy in mineral operations

South Africa's Department of Minerals and Energy estimates that the mining industry uses 6% of all the energy consumed in South Africa. In Brazil, the largest single energy consumer is mining giant Vale, which accounts for around 4% of all energy used in the country. In the US State of Colorado, mining has been estimated to account for 18% of total industrial sector energy use, while overall in the US it is calculated that the mining industry uses 3% of industry energy [11]. A secure and reliable supply of energy is thus critical for all mining operators to meet their production requirements. For most, energy constitutes a major operating expense and its generation and distribution requires substantial capital investment. To minimize costs, it is important to recognize that energy is a controllable operating cost [12].

Canada is one of the world's leading mining countries and ranks among the largest producers of minerals and metals [13]. Mines, quarries, and primary metal and mineral manufacturing facilities (the mining sector) are distributed across every province and territory [14]. Industrial energy prices increased 58% for electricity and 310% for heavy fuel oil in Canada, from 1990 to 2008 [15]; these increases partly illustrate the financial incentive for energy management which aims to allow companies to reduce economic risks resulting from rising energy costs balanced against a need for security of energy supply to ensure continuous production [16]. Between 1990 and 2008, total energy use in Canada has risen by 25.7%, with the mining industry increasing its energy consumption by 137.7% in the same period [15].

It has been reported [17] that the metal mining industry in the United States has the potential to reduce energy consumption by about 61% from current practice to the best-estimated practical minimum energy consumption. This reduction was made up of a 21% reduction by implementing best practices and a 40% reduction from research and development that improves energy efficiency of mining and mineral processing technologies. Governments, especially in countries with large mining sectors, are imposing standards for energy efficiency. Australia's miners are obliged to comply with the Equipment Energy Efficiency program for energy efficiency. In South Africa, the DME set a target in 2007 for the mining industry to reduce energy demand by 15% by 2015 [11]. In China, a vigorous program was launched in 2004 aimed at reducing energy intensity by 20% over the period between 2006 and 2010 [18].

Energy management is the judicious and effective use of energy to maximize profits (and minimize costs) and enhance competitive positions [19], while meeting energy demand when and where it is needed (the energy utility). This can be achieved by adjusting and optimizing energy systems and procedures so as to reduce energy requirements per unit of output while maintaining or reducing total costs of producing the output from these systems [20].

Energy management activities are often categorized into supply side management or demand side management activities. As mineral production businesses are frequently vertically integrated businesses that hold their own generation [21] and/or transmission [22] and/or distribution assets, as well as maintaining control of their own demand centers, both sides of the energy system (supply and demand) are of concern in energy management practice.

Demand Side Management (DSM) can be defined [23] as the planning, implementation, and monitoring of distribution network utility activities designed to influence customer use of electricity in ways that will produce desired changes in the load shape. The goal of DSM is to smooth out peaks and valleys in energy demand to make better use of energy resources and defer the need to build new power plants.

Supply-side management (SSM) refers to actions taken to ensure the generation, transmission and distribution of energy are conducted efficiently [24]. Effective SSM actions will usually increase the efficiency with which demand centers are supplied, allowing installed generating capacity to provide electricity at lower cost (permitting lower prices to be offered to consumers) and reducing environmental emissions per unit of end-use electricity provided.

The potential economic benefits of a high energy consumption intensity for mineral production (see for example [25]) lead to consideration of local (mine site) elements of supply side energy management. One example of supply side energy management is the adoption of energy supply technologies including renewable energy and polygeneration. As heat has not yet been considered for the mining sector in an integrated manner, polygeneration is of great interest for the sector. Renewables and polygeneration options are the new pathways that are subject to the current investigations.

3. Polygeneration technology

The increase in energy utilization efficiency is, without doubt, the main advantage of producing different energy services (heating, coolth, and electricity) in one installation from the same energy source. Furthermore, polygeneration schemes can generate many configurations and thus allow for ample design flexibility that accommodates specific regional conditions [26]. However, choosing the correct size and design of a polygeneration system is a key factor for the success of the project: undersized systems do not realize the profit of exploiting the whole polygeneration potential of the site, and if the system is oversized low or negative primary energy savings may be obtained [27].

In the case that the energy supply system has already been built, the optimization procedure will encompass only the operational strategy. However, if external conditions change (energy demands, utility prices, etc.), a retrofit adopting additional equipment is added to the existing system (the configuration of which then comprises a constraint on optimization). For new systems, in addition to the optimal dispatch of energy supply plant the optimal system configuration must also be identified (essentially the specification of equipment in rating and number) [28] [29].

A general framework has been established [30] [31] [32] [33] [34] to identify optimal combinations of energy conversion and delivery technologies, as well as operating rules for systems installed in tertiary sector buildings. A reference system for production of electricity, heating and coolth to attend the demands of a hospital is shown in Figure 1, where all electricity is purchased from a utility company owned electricity distribution grid to either meet the electricity demand directly or produce cooling in mechanical chillers driven by electrical motors, and heating demand is produced by a natural gas boiler. The aforementioned framework described as an *energy superstructure* [30] is shown in Figure 2, containing all technology alternatives that may be adopted (but not their ratings or numbers). D, S, P and W refer to, respectively, demand, sale, purchase and waste (loss) of a utility. Within Figure 1 and 2, the horizontal or vertical lines essentially represent physical distribution systems into which the technologies indicated can feed in energy of a specific form. Site loads for energy in that specific form (a specific energy utility) are supplied from that distribution system, including further energy conversion technologies that convert the supplied utility into another form (which in turn supplies another distribution required by the site loads).

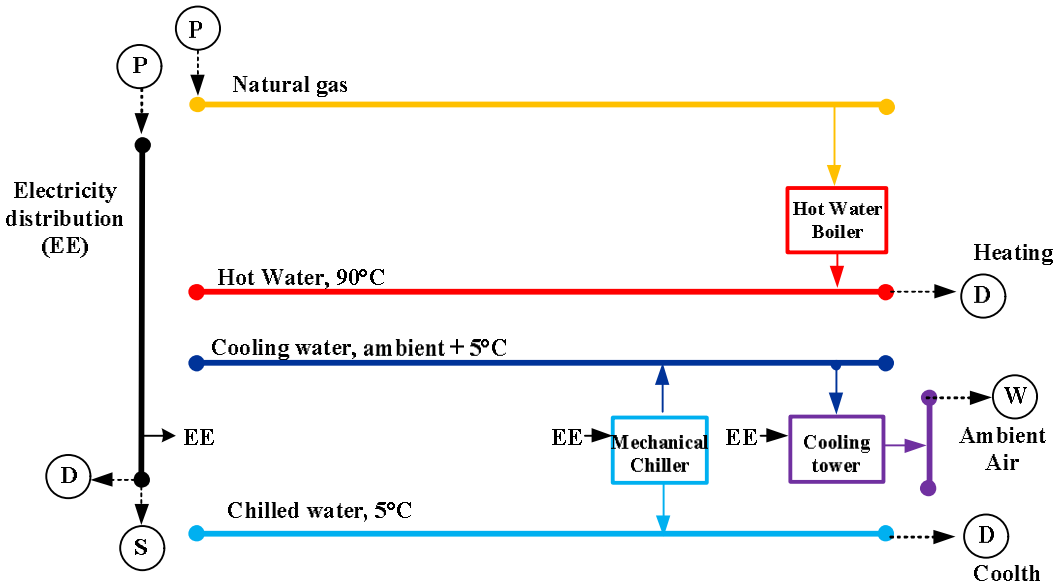

Figure 1 Reference system.

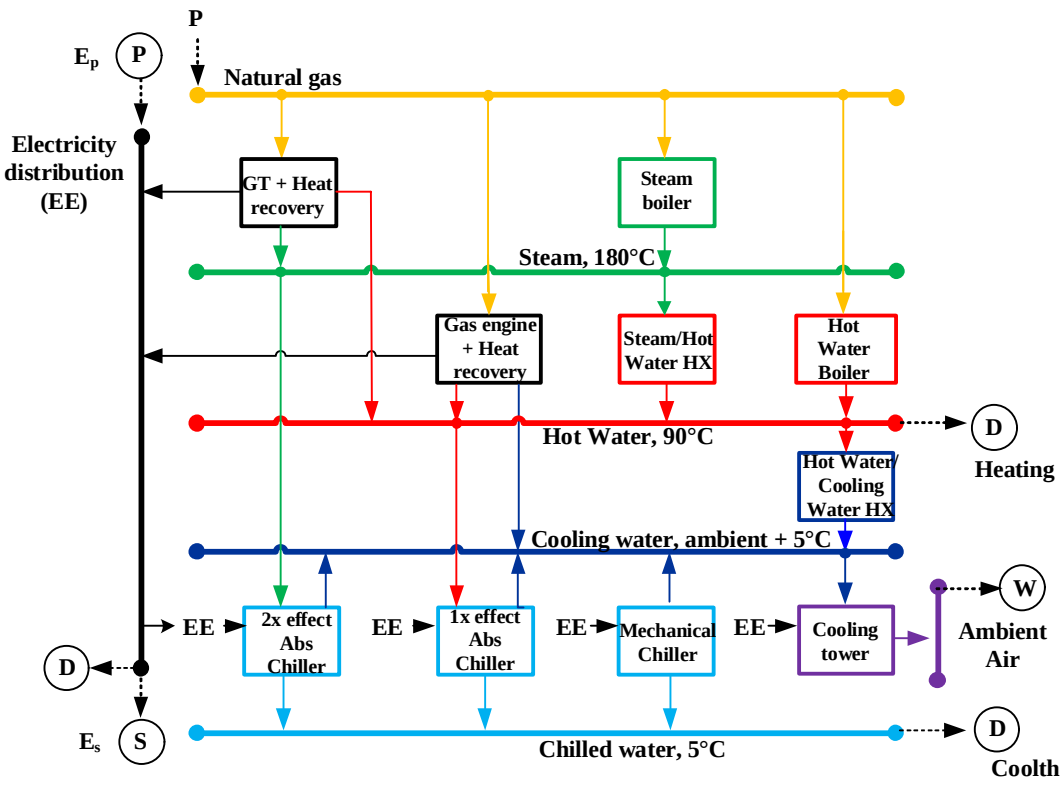

Figure 2 Superstructure of energy supply system for a hospital.

4. Optimal Mine Site Energy Supply – OMSES initial formulation

For energy services superstructures such as those presented in Figures 1 and 2, following precedent practices [32] [34]], the decision variables for an optimization problem formulated to determine the optimal mine site energy supply may be characterized as follows:

i) binary variables (denoting whether a technology is/is not installed);

ii) integer variables (denoting the number of installed units of a technology);

iii) continuous variables (denoting the energy flows between utilities). The latter include connections to distribution systems across the site boundary (to the utility company's electrical and natural gas distribution systems – where appropriate) and energy flows between distributions and site loads.

The constraints that may be taken to apply to the optimization process are manifold:

1. Energy conversion technology constraints. These are constraints that reflect an energy conversion mass and energy balance across each technology of a specific type. A graphical example representation of such a constraint is presented in Figure 3 which shows the energy (and inferred mass) balance across a gas turbine equipped with a heat recovery unit.
2. Technology installation limit constraints. These constraints apply a threshold on the maximum number of units of a given technology type that may be installed. Such a constraint is useful to reflect practical considerations such as the amount of land footprint available to accommodate technology of a specific type. This also articulates a capacity constraint for the specific technologies.
3. Utility balancing off constraints. These are constraints that ensure that the net sums of energy flows from each of the indicated distributions are zero, which also ensure that energy supply (in all its forms) meets on-site demand. In the event that hourly on-site demand data

are available for an entire year, 8760 such constraints feature in the problem formulation, for a specific utility. In practice, various heuristics may be deployed to reduce the number of these constraints (e.g., considering only 12, 24 hour periods, each representative of a typical day in a typical month – see Figure 4).

4. Carbon dioxide equivalent emissions constraints. These are constraints that express the idea that the total emissions associated with the production of energy from the energy services system falls below a given threshold. In prior formulations [e.g., [32] [33]], such emissions include those attributable to the materials (manufacture and installation of the technologies at the site) and operation of the system.
5. Energy market constraints. These include *inter alia* thresholds on the quantities of energy that may be procured externally, exported off-site, or wasted.

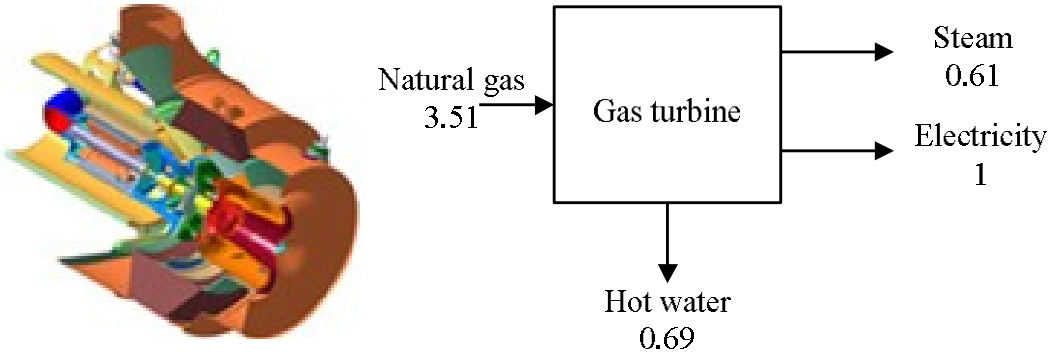

Figure 3: Showing (LHS) a cut-away diagram of a Capstone C600 gas turbine [35] and (RHS) the energy flows for this technology normalized to the electrical energy output.

The objective function for the optimization process is defined in economic terms, expressed as a minimum total cost of meeting the on-site energy demand. Various components are considered in its formulation. Principally, the total cost is decomposed into an annuitized fixed cost element and a variable cost element.

The fixed cost element thus accounts for the discounting process and the time value of money, as well as the replacement / major overhaul interval of the technology. The variable cost element is primarily expressed in terms of the unit cost of procurement of energy in a particular form, supplied to the site, multiplied by the volume of that energy used in a specified time period. Through constraints taken to apply in the optimization process, this cost element may reflect particular operational strategies imposed, for example, a user-defined decision to operate bespoke co-generation plant components at full load.

As it is within the scope of the energy services infrastructure to export energy in various forms off the site, revenues arising from any such sales are treated as negative costs.

Given the nature of the decision variables indicated, in prior deployments Mixed Integer Programming (MIP) has been found effective in establishing optimal configurations and equipment operating strategies, this technique having been broadly applied in production planning, sequencing processes, distribution and logistics problems, refinery planning, power plant scheduling, and process design. MIP captures the complexity of polygeneration systems in synthesis problems such as that described for optimal on-site energy supply. Formulation of the problem in MIP compatible terms presents opportunities to benefit from significant recent advances in the mathematical programming field such as those found in [36].

5. Characteristic challenges of OMSES

Mining operations in Northern Canada can also face a particular energy challenge given the lack of grid (electric and gas) capacity and limited infrastructure. In addition, it is typical for underground mines that they require progressively more energy to access and extract the minerals as they mine deeper. Deep mines (nominally >2000 m) acquire substantial cooling loads as they age, and meeting such important energy demands is becoming economically and technically important.

Opportunities for savings offered by adoption of polygeneration have not been investigated in depth previously for the specific cases of mine sites, possibly for the following reasons: i) wide variety of technology options for the provision of energy services; ii) temporal variations (diurnal, seasonal and inter-annual) in energy prices; iii) temporal variations (diurnal, seasonal) in climate; iv) temporal variation (diurnal, seasonal and inter-annual) in energy demand; and v) institutional inertia, and conservatism in mine design for mines.

Diurnal, seasonal and inter-annual variability of thermal loads in the mining sector in Canada increase the complexity of a generic energy supply systems and solutions of high sophistication are required for operation to be economically attractive. Mine air heating and cooling loads are seasonally complementary (see Figure 4). The timing of the highest cooling loads in summer seasons, if serviced by a mechanical chiller system, is at odds with electricity tariff peak times.

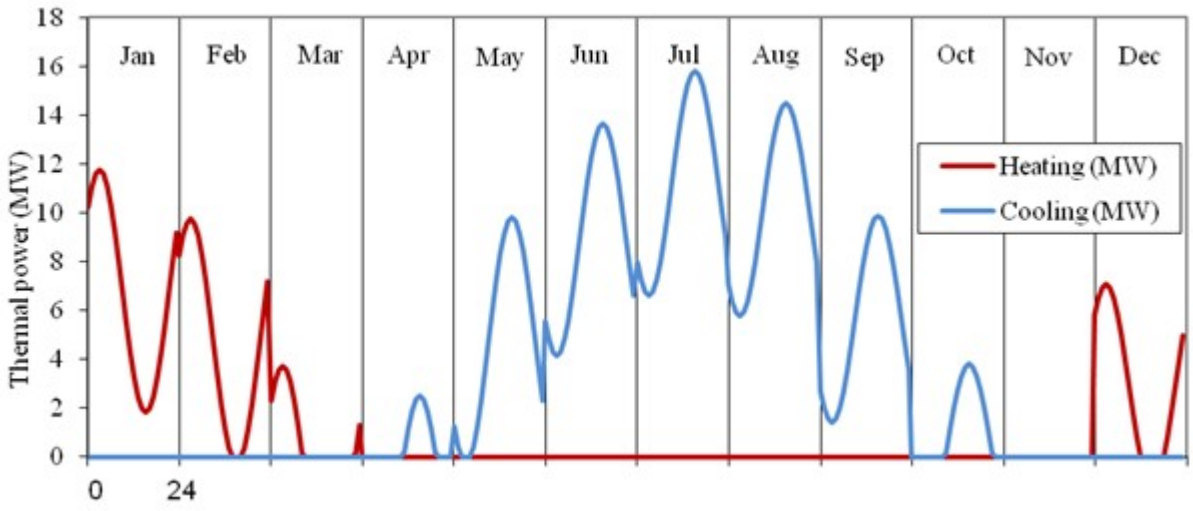

Figure 4 Heating and cooling demand profile projections for a 2500 m deep mine located in Canada at latitude 46° North.

In Figure 4, thermal demand profile projections are illustrated for a study period of one year, distributed in 12, each day taken as typical for each month and divided into 24 hourly periods (at 2500 m depth, base temperatures were: for heating = 18°C; for cooling = 30°C).

Applying optimization techniques to the problem of mine-site energy supply presents some unique challenges: variability of energy loads which will always remain variable, but may be highly predictable (*e.g.*, those due to winding and groundwater pumping activity in the case of electricity), the need to produce from deeper, hotter levels, as in Canadian climates with extreme climatic variation, and in remote areas with no connection to the electric or gas grids. These characteristics are not seen as insurmountable and offer potential for innovation as indicated below.

6. Extensions to core methodology

6.1 Integration of renewable energy technologies

Primary energy inputs from new and renewable energy resources and technologies are considered, with characteristics of intermittency and variability, alongside conventional energy supply technologies, as shown in Figure 5. Potential advantages are set out by Trapani & Millar in [37], for remote mining operations. Renewable energies are introduced as available utilities in the synthesis, design and operation of energy systems, which is generically applicable to renewable energy integration studies for other industries too.

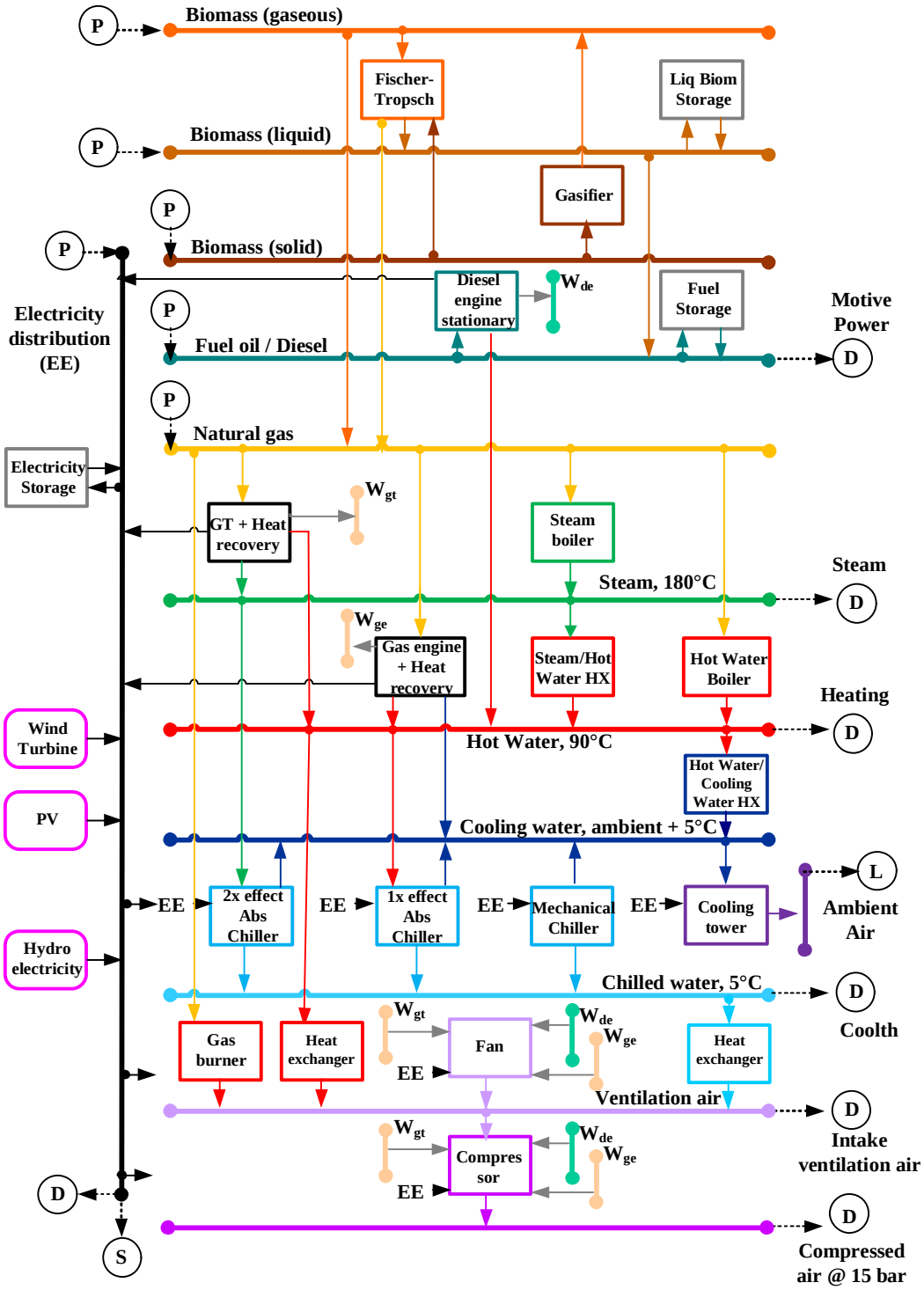

Figure 5 Superstructure of an energy supply system for a mine.

6.2 Integration of energy storage technologies

Energy storage systems will also be considered as utilities on the supply side and as dispatchable loads on the demand side. On-site energy storage technologies are included to compensate for the variable and intermitent characteristics of renewable energy sources. Integration of storage technologies into the energy supply optimization process may introduce less constraint into the resulting energy supply system, and consequently could lower energy supply cost, equivalent CO_2 emissions, or both. Many of the technical challenges in reformulating the mathematical optimization procedures to accommodate intermittent and variable renewable energy supply utilities, may be reapplied in consideration of energy stores acting as energy supply components.

6.3 Part load operation of all technologies

A common practice to facilitate the operation of a system is to consider that cogeneration modules operate at full load when in service. This study will go a step further by considering that energy balance data varies with load conditions for all technologies. As a consequence of considering part load operation, a more heterogeneous range of technologies may emerge in optimal solutions.

6.4 Consideration of work from prime movers as a new utility

On mineral production sites, some processes that form part of the electricity base load fundamentally constitute a demand for energy in the form of work (W_{de}, W_{gt}, and W_{ge} in Figure 5) , which could be met by the prime mover of a polygeneration system. Examples of the latter could include surface pumping, production of compressed air, and the running of main ventilation fans on surface.

6.5 Work in progress

A database and models of the potentially installable equipment is currently being adapted through the addition of equipment with larger rating (commensurate with that needed for large industrial applications, such as mining). It contains investment, operation, performance and environmental information on each technology that may be considered. The latter informs Life Cycle Analysis that sets and coordinates criteria in the multiobjective optimization (economic/environmental trade-off).

Energy demands are characterized for mine sites, and the collaborators will also supply data on the purchase/sale tariffs of the different utilities (when available). The exemplar consumer centers to be used in this extension are located in Northern Ontario (Canada), with energy demands varying seasonally and diurnally. The consumer centers are mineral productions operations that are connected to energy supply infrastructure and those that are not.

7. Closure

This contribution outlines the priorities of investigation, development and demonstration of new concepts and technologies to improve energy efficiency and reduce final consumption of primary energy in the mining sector, considering the life cycle holistically. Due to the energy-intensive nature of mining operations, energy is a significant component of total operating costs and a reduction in energy consumption may directly result in cost savings. It is expected that energy procurement costs will increase in the future adding to the incentive to effectively manage energy [12] in the sector.

The analysis of thermal process integration has contributed to the improvement of the efficiency of cogeneration systems used in the industry sector, and its application to polygeneration systems with

thermal storage and possible support of renewable energies will reveal the most cost effective or low carbon configuration and operational strategy. Scenarios with substantial economic potential in which renewables are advantageous, alone or in combination with cogeneration systems have been identified, while *a priori* both are energy production systems that compete.

The design techniques developed will facilitate the collaboration of equipment manufacturers in the development and commercialization of modular systems. The development of new products (modular systems) and the techniques involved will contribute to a greater competitiveness of the participating companies and, what is equally important, to decrease the energy costs of the consumer center.

Although the research is applied and has a Canada focus, in terms of the case studies adopted, the work is of global scientific importance. The local dimension, even the specific industry focus, is just a way in which the relevance of the science will be demonstrated. Theoretical extensions (storage, renewables) are of generic applicability for all integration studies. The mining sector is just used as an example to drive and exemplify the methodological development process.

Acknowledgments

This work was developed within the framework of research projects **S**mart **U**nderground **M**onitoring and **I**ntegrated **T**echnologies for Deep Mining (SUMIT, funded by Ontario Research Fund for Research Excellence Funding - Round 5), **O**ptimal **M**ine **S**ite **E**nergy **S**upply (OMSES, funded by **N**atural **S**ciences and **E**ngineering **R**esearch **C**ouncil of Canada through an Industrial Research & Development Fellowship), and **Low Carb**on Mine Site Energy Initiatives (LOWCARB, funded by the Research Fund for Coal & Steel - European Commission). Thanks are extended to DeBeers Canada, Hearst Community, and the Ontario Geological Survey (unit of Ministry of Northern Development and Mines).

References

1. NRC. Evolutionary and revolutionary technologies for mining. National Research Council, Committee on Technologies for the Mining Industries. Washington, U.S. 2001.
2. LIU, P.; GEORGIADIS, M. C.; PISTIKOPOULOS, E. N. Advances in Energy Systems Engineering. Ind. Eng. Chem. Res., v. 50, n. 9, p. 4915–4926, 2011.
3. MILLAR, D. L. et al. Enabling advanced energy management practice for minerals operations. Montreal: Proceedings of the Annual Canadian Institute of Mining, Metallurgy and Petroleum (CIM) Conference and Exhibition. 2011.
4. SERRA, L. M. et al. Polygeneration and efficient use of natural resources. Energy, v. 34, p. 575-586, 2009.
5. STUICKEL, J. J. Industrial and Commercial Cogeneration. Office of Technology Assessment Arquive, 1983. See also: <http://www.fas.org/ota/reports/8311.pdf>. Accessed on: 11 Jan 2012.
6. ISO50001. Energy Management Systems - requirements with guidance. International Organization for Standardization (ISO). Geneva. 2011.
7. MAGLORIE, P.; HETEU, T.; BOLLE, L. Economie d´énergie en trigénération. International Journal of Thermal Sciences, v. 41, p. 1151-1159, 2002.
8. CHICCO, G.; MANCARELLA, P. Distributed multi-generation: A comprehensive review. Renewable and Sustainable Energy Reviews, v. 13, p. 535-551, 2007.

9. LOZANO, M. A.; CARVALHO, M.; SERRA, L. M. Allocation of economic costs in trigeneration systems at variable load conditions. Energy and Buildings, v. 43, n. 10, p. 2869-2881.

10. CARMEL, Y.; BEN-HAIM, Y. Info-gap robust-satisficing model of foraging behavior: do foragers optimize or satisfice? American Naturalist, v. 166, p. 633-641, 2005.

11. MCIVOR, A. Energy in Mining. Cleantech (special edition fuel cells), v. 5, p. 16-19, 2010.

12. EA. Energy efficiency & greenhouse gas reduction. Environment Australia, 2002. See also:: <http://commdev.org/content/document/detail/822/>. Accessed on: 06 Jan 2012.

13. MAC. http://www.miningworks.mining.ca/miningworks/media_lib/documents/Facts_Figures_2007_E.pdf. Mining Association of Canada - Facts & Figures. A report on the state of the Canadian Mining Industry., 2007. Acesso em: 5 jan. 2012.

14. NRC. Mining sector performance. Natural Resources Canada - Final report of the Federal, Provincial and Territorial social licence task group., 2010. See also:: <http://www.nrcan.gc.ca/sites/www.nrcan.gc.ca.minerals-metals/files/pdf/mms-smm/pubr-pubr/pdf/EMMC_english.pdf>. Accessed on: 05 jan. 2012.

15. NRC. Industrial energy prices and background indicators. Natural Resources Canada, 2010. See also: <http://oee.nrcan.gc.ca/corporate/statistics/neud/dpa/tableshandbook2/agg_00_7_e_4.cfm>. Accessed on: 10 Jan 2012.

16. LEVESQUE, M. Understanding mine heat. M.A.Sc. dissertation (Natural Resources Engineering). School of Graduate Studies, Laurentian University. Sudbury, Canada, p. 140. 2011.

17. NORGATE, T.; HAQUEA, N. Energy and greenhouse gas impacts of mining and mineral processing operations. Journal of Cleaner Production., v. 18, p. 266-274, 2010.

18. FANG, H.; WU, J.; ZENG, C. Comparative study on efficiency performance of listed coal mining companies in China and the US. Energy Policy, v. 37, n. 12, p. 5140-5148, 2009.

19. CAPEHART, B.; TURNER, W. C.; KENNEDY, W. J. Guide to energy management. 5th edition. ed. [S.l.]: The Fairmont Press, 2005.

20. ABDELAZIZ, E. A.; SAIDUR, R.; MEKHILEF, S. A review on energy saving strategies in industrial sector. Renewable and Sustainable Energy Reviews., v. 15, n. 1, p. 150-168, 2011.

21. INCO, V. Vale Inco Limited. 100 years of Clean Renewable Power. See also:: <http://www.greatersudbury.ca/cms/index.cfm?app=div_earthcare&lang=en&currID=6855>. Accessed on: 23 Jan 2012.

22. LARMOUR, A. Empowering remote communities. Northern Ontario Business, v. 27, n. 4, p. 9, 2007.

23. QURESHI, W. A.; NAIR, N. C.; FARID, M. M. Impact of energy storage in buildings on electricity demand side management. Energy Conversion and Management., v. 52, n. 5, p. 2110-2120, 2011.

24. UNIDO. Suply-side management. United Nations Industrial Development Organization - Sustainable energy regulation and policymaking for Africa. See also: <http://africa-toolkit.reeep.org/modules/Module13.pdf>. Accessed on: 10 Jan 2012.

25. MUDD, G. M. Global trends and environmental issues in nickel mining: Sulfides versus

laterites. Ore Geology Reviews, v. 38, n. 1-2, p. 9-26, 2010.

26. LIU, P.; GEROGIORGIS, D. I.; PISTIKOPOULOS, E. N. Modeling and optimization of polygeneration energy systems. Catalysis Today, v. 127, p. 347-359, 2007.

27. EUROPE, C. Deploying large-scale polygeneration in industry (D-PLOY), 2008. See also:: <http://eaci-projects.eu/iee/page/Page.jsp?op=project_detail&prid=1506>. Accessed on: 11 Jan 2012.

28. YOKOYAMA, R. et al. Development of a General-Purpose Optimal Operational Planning System for Energy Supply Plants. Journal of Energy Resources Technology, v. 16, p. 290-296, 1994.

29. LOZANO, M. A.; RAMOS, J. C.; SERRA, L. M. Cost optimization of the design of CHCP. Energy , v. 35, n. 2, p. 794 - 805, 2010.

30. CARVALHO, M. Thermoeconomic and environmental analyses for the synthesis of polygeneration systems in the residential-commercial sector. Zaragoza: PhD thesis; Department of Mechanical Engineering, University of Zaragoza, Spain, 2011.

31. CARVALHO, M.; LOZANO, M. A.; SERRA, L. M. Multicriteria synthesis of trigeneration systems considering economic and environmental aspects. Applied Energy, v. 91, n. 1, p. 245-254, 2012.

32. CARVALHO, M.; SERRA, L. M.; LOZANO, M. A. Optimal synthesis of trigeneration systems subject to environmental constraints. Energy, v. 36, n. 6, p. 3779-3790, 2011.

33. CARVALHO, M.; SERRA, L. M.; LOZANO, M. A. Geographic evaluation of trigeneration systems in the tertiary sector. Effect of climatic and electricity supply conditions. Energy, v. 36, n. 4, p. 1931-1939, 2011.

34. LOZANO, M. A. et al. Structure optimization of energy supply systems in tertiary sector buildings. Energy and Buildings, v. 41, n. 10, p. 1063-1075, 2009.

35. CORPORATION, C. T. Capstone product catalog, P0112 CAP11. Chatsworth, CA, U.S. 2010.

36. GROSSMANN, I. E.; CABALLERO, J. A.; YEOMANS, H. Advances in mathematical programming for the synthesis of process systems. Latin American Applied Research, v. 30, n. 4, p. 263-284, 2000.

37. TRAPANI, K.; MILLAR, D. L. Powering mines in the McFauls lake area using large scale arrays of floating PV panels. Proceedings of the Mining and Environment V Conference. Sudbury, Canada: 2011.

38. WUA, L.; KANEKOB, S.; MATSUOKAB, S. Dynamics of energy-related CO2 emissions in China during 1980 to 2002: The relative importance of energy supply-side and demand-side effects. Energy Policy, v. 34, n. 18, p. 3549–3572, 2006.

39. STRICKLAND, C.; NYBOER, J. Cogeneration Potential in Canada Phase 2. Natural Resources Canada. Ottawa. 2002.

40. MCKINSEY&CO. Reducing US greenhouse gas emissions: How much at what cost? McKinsey & Company, 2007. See also: <http://www.mckinsey.com/Client_Service/Sustainability/Latest_thinking/Reducing_US_greenhouse_gas_emissions>. Accessed on: 11 Jan 2012.

41. IEA. Cogeneration and District Energy. International Energy Agency. Paris, p. 60. 2009.

42. HOUWING, M. et al. Uncertainties in the design and operation of distributed energy resources: The case of micro-CHP systems. Energy, v. 33, p. 1518-1536, 2008.

43. FISKEL, J. Designing Resilient, Sustainable Systems. Environmental Science and Technology,

v. 37, p. 5330-5339, 2003.

44. DOE. International Energy Outlook 2011. U.S. Department of Energy - U.S. Energy Information Administration, 2011. See also: <http://www.eia.gov/forecasts/ieo/pdf/0484(2011).pdf>. Accessed on: 11 Jan 2012.

Simulation of Synthesis Gas Production from Steam Oxygen Gasification of Colombian Bituminous Coal using Aspen Plus®

John Ortiz[a], Juan González[b], Jorge Preciado[c], Rocío Sierra[d] and Gerardo Gordillo[e]

[a] *Universidad de los Andes, Bogotá, Colombia: jj.ortiz24@uniandes.edu.co,*
[b] *Universidad de los Andes, Bogotá, Colombia, jc.gonzalez141@uniandes.edu.co*
[c] *Universidad de los Andes, Bogotá, Colombia, je.preciado40@uniandes.edu.co*
[d] *Universidad de los Andes, Bogotá, Colombia, rsierra@uniandes.edu.co*
[e] *Universidad de los Andes, Bogotá, Colombia, g.gordillo43@uniandes.edu.co*

Abstract:

The growing energy demand, sustained increase in fossil fuel prices, and need for environmental protection have forced to consider alternatives to the traditionally energy resources employed. Synthesis gas (syngas) produced by gasification of coal, biomass, petroleum coke, or solid waste has proven to be a useful clean fuel due to its lower emissions of sulfurs and nitrous oxides compared to other fuels. In this work, a simulation of syngas production from a Steam-Oxygen Gasification (SOG) process that uses the GE/Texaco technology was performed using Aspen Plus®. For the simulation, the average proximate and ultimate compositions of bituminous coal obtained from the Colombian Andean region were employed. The obtained simulation was applied to conduct sensitivity analyses in key parameters. The information obtained allows the selection of critical operating conditions leading to improve system efficiency and environmental performance. The results of the parameter analysis indicate that the oxygen to carbon ratio is a key variable as it affects significantly both the LHV and thermal efficiency of the process. On the other hand, the process becomes almost insensitive to SDG values higher than 2. Finally, a thermal efficiency of 62.2% can be reached. This result corresponds to a slurry solid concentration of 0.65, a WGS process SDG of 0.59, and a LTS reactor operating temperature of 473 K. At these fixed variables, a syngas with H_2 molar composition of 92.2% and LHV of 12 MJ N m^{-3} was attained.

Keywords:
Aspen Plus® Simulation, Coal, Steam-Oxygen Gasification, Synthesis Gas.

1. Introduction

Currently, in a world of high and growing energy demands and increasing oil prices, alternative and sustainable raw material resources are being sought. Ideally, these sources would be used for either energy generation or as valuable chemical feedstocks for variety of chemical processes and synthesis. Among different alternatives, syngas has shown to be a favorable option. Syngas is considered a clean fuel with environmental advantages compared to other fossil fuels because the sulfur oxides (SO_X), nitrous oxides (NO_X) and CO_2 emissions are considerably lower [1, 2].

Syngas is an important building block in chemical, oil and energy industries due to its applications: 1) as a feedstock for the production of several chemicals such as hydrogen, ammonia, methanol, and Fischer-Tropsch products [3], 2) as a fuel in a gas turbine to produce electricity [4], 3) as a cell fuel for mobile sources [5], 4) as an electricity supplier through solid oxide fuel cells [3], and 5) as a primary fuel. Syngas, which is mainly a mixture of hydrogen (H_2) and carbon monoxide (CO), is mainly used as a chemical substance rather than a fuel, representing 50 billion US$ market for 40 Tg (40 Mt) annual production nowadays [6]. Hydrogen could help to satisfy the world energy demand. Recent reports show that global energy consumption grew 5.6% in 2010, the largest yearly increase since 1973 [7].

There are many alternatives for hydrogen production from liquid and gaseous hydrocarbons such as thermo-catalytic cracking, steam reforming and plasma arc decomposition [6]. Moreover, from solid feedstocks, H_2 can be produced through the gasification of coal, biomass, petroleum coke, or solid waste. Nearly 50% of the global hydrogen is generated through natural gas reforming, 30% from oil/naphtha reforming, 18% from gasification, 3.9% from water electrolysis and 0.1% from other sources [6]. Coal gasification is a promising way to obtain H_2 because the production techniques have achieved maturity and are commercially available. Moreover, the relatively high global resources of coal and its widespread availability worldwide make his resource a promising option [8]. In addition, this process has environmental advantages: 1) SO_X can be processed into a marketable by-product, 2) ash can be liquefied into a slag that passes toxicity issues, 3) CO_2 can be held and recovered in the loops of gasifiers for remediation/reuse, and 4) gasifiers can be modified such that wide product flexibility is easily obtained [9].

The steam-oxygen gasification (SOG) process is the only commercialized method of gasification used to manufacture several chemicals from coal. The Wabash River Coal Gasification Repowering Plant, near to West Terre Haute, Indiana (USA), has proven since November of 1995 the successful application of H_2 production by coal gasification. This plant uses H_2, from SOG process, in a gas combustion turbine generator to produce electricity. It generates around 292 MW of electric power. With this production, this plant is one of the largest single-train gasification combined cycle plants operating commercially in the world [10].

Table 1. Ultimate and proximal analysis of Guaduas Formation's coal (HHV = 30,634 kJ kg^{-1}) data taken from [11]

	w/w (%)
Proximate analysis	
Moisture	4.12
Ash	5.61
Fixed carbon	67.8
Volatiles	22.4
Ultimate analysis*	
Carbon	70.7
Hydrogen	5.29
Nitrogen	1.58
Chloride	2.35
Sulfur	1.57
Ash	5.61
Oxygen	7.91

*dry basis

Two thirds of the total fuel fossil reserves in the world are coal and will last for more than 150 years [12]. Coal is in fact one of the main resources in Colombia. It is estimated that 0.7% of the world proved coal reserves, which corresponds to 6.7 Pg (6700 Mt), are in Colombian territory [11]. Colombia has several coal formations over its territory. The main ones are: Cerrejón, Los Cuervos, Guaduas, Umir, Cerrito, and Amagá. The Guaduas formation's coal, located in the center of Colombia, is characterized by a bituminous coal with high volatiles and low sulfur and ash content (Table 1). which is advantageous for a gasification use [13]. Therefore, coal from Guaduas formation was selected for this study.

Aspen Plus® has been widely employed to simulate chemical processes in a wide number of fields including but not limiting to the petroleum industry, chemical processes and biomass gasification. It also can be used to model steady state processes handling solid carbons materials in multiple unit operations. Therefore, many coal and biomass conversion processes have been simulated using Aspen Plus as integrated coal gasification combined cycle (IGCC) power plant [14], biomass

gasification [15], hybrid biomass gasification [16], hydrogen production from biomass gasification [17], and coal combustion [18]. Additionally, proximate and ultimate analysis properties of solid coal are specified to provide a fairly rigorous simulation of the gasifier performance [19].

The purpose of this study is to simulate and analyze through Aspen Plus the coal gasification process and subsequent processing for the hydrogen-rich syngas production, using the most commercialized and referenced available technologies. A sensitive analysis of the variables with high impact over the key process parameters is performed to identify important process efficiency improvements (yield and energy) and environmental performance.

1.1. Gasification Technologies

There are three main types of coal gasification technologies: fixed-bed, fluidized-bed, and entrained-flow gasification. Table 2 summarizes key parameters for these gasification technologies. Among these processes, entrained-flow gasification is the commercially preferred technology due to its versatility and lower environmental impact [4, 13, 14, 20] .

Table 2. Main features of industrial gasifiers

Gasifier type	Main features
Entrained-flow	Particle size below 0.1 mm High operating temperature (> 1473 K) High operating pressure (3 to 12 MPa) High oxidant demand Short residence time (0.5 to 10 s) Ash is removed as molten slag
Fluidized-bed	Particle size between 6 and 10 mm Uniform temperature distribution High operating temperature (1073 to 1323 K) Lower carbon conversion Ash is removed as slag or dry
Fixed-bed	Coarse particles (6 to 50 mm) Low operating temperature (698 to 1088 K) Low oxidant demand Resident time above 600 s Ash is removed as slag or dry

Many commercial technologies in entrained-flow gasification reactors are available nowadays such as: GE/Texaco, Shell, and ConocoPhillips. GE/Texaco and Shell entrained-flow gasification reactors are used in about 75% of the gasification plants throughout the world [13]. In this study, the GE/Texaco gasifier has been selected because: 1) it is profusely discussed in the literature, 2) high coal conversion is reported, and 3) the resulting syngas is free of tars, phenols and paraffins. Additionally, the GE/Texaco gasifier is leader worldwide with 145 reactors in commercial operation and 85 in planning, engineering, or under contract agreements in 15 different countries [21].

2. Process Description

In the SOG process, coal-water slurry is gasified with O_2 from the air separation unit (ASU) to produce a gas mainly composed by CO and H_2. It is necessary to increase the H_2 concentration by a

sour water-gas shift (WGS) process followed by an acid gas removal. H_2-rich syngas is obtained after water condensation in the resulting gas. The SOG simplified process flow diagram is shown in Fig. 1:

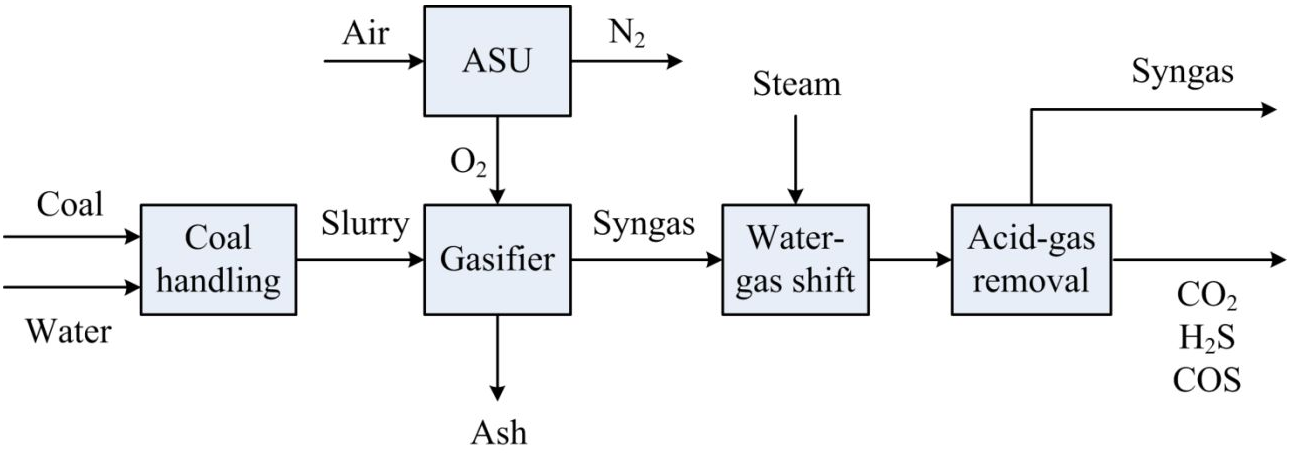

Fig. 1. SOG simplified process flow diagram.

There are many technologies for separating air into its main components. The application of either one depends on the process requirements. For lower volumes of O_2 and/or N_2 (< 1.6 kg s^{-1}), pressure swing adsorption or membrane processes are preferred [22]; whereas, for producing large quantities of gaseous products, cryogenic air separation technology is currently the most efficient, especially when high purity products are required [23].

The cryogenic process consists on several unit operations that compress, purify and separate air into its principal components. First, impurities (H_2O, CO_2, among others) are removed in a pre-purification unit, located downstream of the air compression. Secondly, the air is cooled down to cryogenic temperatures (from 123 K to 463 K, depending on the operating pressure [24]) and goes into the air separation unit. Then, a multi-column cryogenic distillation is usually used for separating O_2 and N_2 [22]. Several configurations of rectifying columns and heat exchangers are made according to the requirements of the process [25].

A double column system is widely used in air separation processes. Air enters into the high pressure column (HPC) and provides two reflux streams that feed the low pressure column (LPC) [26]. At the top of the LPC, a pure gaseous nitrogen stream is obtained while liquid oxygen is evaporated at the bottom of this column to deliver a pure oxygen stream [25]. The two columns are built in a single tower for the commercial application, considering the use of a condenser-reboiler as a heat exchange unit [24].

The gasification process is developed using a GE gasifier with a gas-water quench system. Guaduas formation coal is wet-milled to a particle size about 100 μm and mixed with water to produce slurry. Coal slurry and O_2 stream from the ASU unit are fed in the top of the pressurized reactor through burners. The coal reacts exothermally with O_2 at high temperature (> 1473 K) and high pressure (> 7 MPa) to produce syngas and slag [27]. The hot gas is contacted directly with water where the slag is solidified. The quenching process cools the syngas and generates a water-saturated gas product, leaving the quench chamber at a temperature between 473 K and 573 K. The resulting syngas is mainly free of particulate matter and water-soluble contaminants such as NH_3, HCN and chlorides [20].

To increase the H_2 concentration, the WGS process is employed to convert mostly CO into H_2. This process consists of two reactors in series with intercooling. A high temperature (HTS) reactor (573 K - 873 K) as an initial stage followed by a low temperature (LTS) reactor (453 K – 523 K). The HTS reactor feed is heated by the effluent of the LTS to control the operating temperature. Additionally, the effluent of the HTS is cooled producing high pressure steam and then it is fed in

the second reactor. In this unit, syngas and steam are mixed with a steam to dry gas ratio (SDG) depending on the feed syngas water content and the required H_2 to CO ratio.

In the WGS reaction, chemical equilibrium favors products at low temperature; therefore, a catalyst is required to enhance the reaction rate. A catalyst typically made of sulfided Co/Mo on aluminum support reacts with the sulfurs, producing metal sulfides which activates the catalyst [28, 29]. Carbonyl sulfide (COS) is converted to H_2S making the sulfur removal easier due to the WGS process location before the acid-gas removal process.

For conditioning of the gas leaving the LTS, the Rectisol process is used. It employs methanol (CH_3OH) as solvent to clean up the syngas. The high selectivity of methanol for H_2S over CO_2 at low temperatures (211 K to 233 K) and the ability to remove COS are the main advantages of the process. Besides, it allows a deep sulfur removal (< 0.1 ppmv H_2S + COS) [30].

There are many possible process configurations for Rectisol, depending on the process requirements. A selective H_2S removal configuration was used in the simulation. In this configuration, the raw syngas feeds up the main absorber in which CH_3OH absorbs most of the impurities produced in gasification process such as CO_2, H_2S, COS, HCN and NH_3 [31]. Thereafter, the solvent passes through a regeneration process, where these components are desorbed by reducing the pressure, stripping and/or boiling up the solvent. The regenerated and recirculated solvent is free of sulfur compounds but still contains some CO_2. The acid gas leaving the solvent regeneration units is suitable for the Claus process [32].

3. ASPEN PLUS® Simulation Model

In order to model the process, the following assumptions were considered: 1) the process is in steady state, 2) the coal feed flow rate is 12500 (kg h^{-1}), 3) the reactors are perfectly insulated, 4) heat losses are neglected, and 5) coal tar is not modeled; char only contains carbon and ash. Main unit operations modeled in Aspen Plus® are shown in Table 3:

Table 3 Main blocks used in the process

Unit operation	Aspen Plus model	Comments/specifications
ASU	RadFrac	LPC: Rigurous distillation model, first stage to separate N_2 and O_2. SN 40, RR 12.3, BR 41.3, partial-vapor condenser, TSP 0.14 MPa, CPD 0.005 MPa. HPC: Rigurous distillation model, second stage to separate N_2 and O_2. SN 26, RR 0.5, BR 1.0, partial-vapor condenser, TSP 0.6 MPa, CPD 0.05 MPa.
Coal Gasification	RGibbs	Specification of the possible products: CO, CO_2, C, H_2, H_2O, CH_4, SO_2, H_2S, S, CS_2, COS, N_2, NH_3, HCN, O_2, NO_2, NO_3.
HTS reactor	REquil	Specification of the stoichometric reactions. OP 3.8 MPa, OT 623 K.
LTS reactor	REquil	Specification of the stoichometric reactions. OP 0.5 MPa, OT 473 K.
CH_3OH absorber	Radfrac	Rigorous absorption of H_2S, SO_2, COS, NH_3, HCN. SN 10, TSP 3.2 MPa.

SN: Stage number; RR: Reflux ratio; BR: Boil up ratio; TSP: Top stage pressure; CPD: Column pressure drop; OT: Operating temperature; OP: Operating pressure.

3.1. Physical Property Method

The Soave-Redlich-Kwong equation of state with Kabali-Danner mixing rules (SRKKB) was selected to calculate all thermodynamic properties for the conventional components in the overall process. Additionally, the HCOALGEN and DCOALIGT models were used to calculate enthalpy and density for coal and ash (non-conventional components) [14].

3.2. Chemical Reactions

Gasification reactions occur above 873 K; at this temperature or higher, the kinetic barrier is minimized and reactor products are found around equilibrium. Therefore, in the simulation, a free kinetics model was implemented [33]. In this model, the equilibrium approach was employed by neglecting the hydrodynamic complexity of the gasifier. Gasification products are estimated employing the RGibbs model which uses Gibbs free energy minimization to calculate the chemical equilibrium of a list of conventional components. The gasification products are taken from the most important coal gasification reactions (Table 4) [18]. As RGibbs only estimate chemical equilibrium of conventional compounds, it is necessary to decompound solid coal (a nonconventional compound) on its constituting components. This is done by using the RYield model and specifying the yield distribution according to the Guaduas coal ultimate analysis. By this approach, satisfactory results have been obtained for many researchers from gasification simulation using Aspen Plus® [14, 16, 34, 35].

The HTS and LTS reactors are simulated using the REquil model. The WGS reaction (R4) and COS hydrolysis (R14) are obtained specifying the stoichiometric reactions [4].

Table 4. Main process reactions

Reaction	Reaction name	Heat of reaction (kJ mol^{-1})	Reaction number
$C + O_2 \rightarrow CO_2$	Carbon combustion	-393	R1
$2C + O_2 \rightarrow 2CO$	Carbon combustion	-221	R2
$C + CO_2 \leftrightarrow 2CO$	Boudouard	+173	R3
$C + H_2O \leftrightarrow CO + H_2$	Steam gasification	+131	R4
$CO + H_2O \leftrightarrow CO_2 + H_2$	Water gas Shift	-412	R5
$CO + 3H_2 \leftrightarrow CH_4 + H_2O$	Steam reforming	- 206	R6
$CO_2 + 4H_2 \leftrightarrow CH_4 + 2H_2O$,	Methanation	-165	R7
$S + O_2 \rightarrow SO_2$	Sulfur combustion	- 297	R8
$SO_2 + 3H_2 \leftrightarrow H_2S + 2H_2O$	H_2S formation	-207	R9
$C + 2S \leftrightarrow CS_2$	CS_2 formation	+115	R10
$CO + S \leftrightarrow COS$	COS formation	+63	R11
$N_2 + 3H_2 \leftrightarrow 2NH_3$	NH_3 formation	-46	R12
$N_2 + 2O_2 \leftrightarrow 2NO_2$	NO_2 formation	+66	R13
$COS + H_2O \rightarrow H_2S + CO_2$	COS hydrolysis	-34	R14

4.Sensitivity Analysis

Sensitivity analysis was performed with the aim to analyze and optimize overall operating conditions in the process.

The chosen variables were: 1) O_2 to coal mass ratio, 2) mass solid concentration in coal slurry, 3) LTS reactor operating temperature, and 4) steam to dry gas molar ratio (SDG) in the WGS process.

The variables effect was evaluated over the next key process parameters: 1) syngas molar composition upstream and downstream the WGS process, 2) overall CO conversion in the WGS reactors, 3) lower heating value (LHV) of H_2 rich-syngas, and 4) thermal efficiency (η_{TE}).

4.1. Thermal efficiency

As the best performance, which is also the most economic option, is sought; this discussion starts showing the results obtained during the sensitivity analysis for thermal efficiency (η_{TE}). This is an indicator of the overall process performance [14]. Thermal efficiency was calculated considering the hydrogen-rich syngas output energy divided by the thermal energy of the coal used as raw material and the energy requirements for auxiliary equipment (ASU, Rectisol, etc) as follows:

$$\eta_{TE}(\%) = 100 \cdot \frac{M_{Syn} \cdot LHV_{Syn}}{[(M)_{Coal} \cdot LHV_{Coal} + Q_{Aux})} \quad (1)$$

Table 5. Variables effect on η_{TE} and H_2-rich syngas LHV

Variable	η_{TE}, %	LHV, MJ kg^{-1}	LHV, MJ Nm^{-3}	H_2 molar fraction in H_2-rich syngas
O_2 to carbon ratio[†]				
0,160	34,1	55,5	20,9	0,561
0,320	42,2	69,0	15,1	0,806
0,480	52,0	79,8	13,0	0,895
0,640	62,6	83,4	12,0	0,922
0,800	60,1	92,7	10,8	0,977
0,960	54,5	97,3	10,7	0,983
Coal slurry concentration (% w/w)[‡]				
86,21	61,3	61,8	10,8	0,926
75,47	60,4	87,0	10,8	0,971
65,01	59,9	95,1	10,8	0,979
56,34	59,2	97,0	11,0	0,974
50,00	58,4	93,4	11,5	0,958
LTS reactor temperature (K)**				
453,15	59,5	99,3	10,7	0,983
473,15	59,9	95,1	10,8	0,979
473,25	59,9	95,0	10,8	0,979
498,15	60,4	88,6	10,8	0,971
523,15	61,5	81,5	10,8	0,962
SDG gas molar ratio in WGS[††]				
0,694	59.9	95,1	10,8	0,979
0,972	58.6	102,5	10,8	0,986
1,768	55.3	106,3	10,8	0,989
2,564	52.4	107,3	10,8	0,990
3,360	49.8	107,7	10,8	0,990
3,917	48.2	107,9	10,8	0,991

[†]Solid concentration in coal slurry: 0.65, WGS process SDG : 0.59, LTS reactor operating temperature: 473 K and HTS reactor operating temperature: 623 K.

[‡]O_2 to coal ratio: 0.8, WGS process SDG : 0.59, LTS reactor operating temperature: 473 K and HTS reactor operating temperature: 623 K as fixed variables.

[**]O_2 to coal ratio: 0.8, solid concentration in coal slurry: 0.65, WGS process SDG : 0.59, and HTS reactor operating temperature: 623 K as fixed variables.

††O_2 to coal ratio: 0.8, solid concentration in coal slurry: 0.65, LTS reactor operating temperature: 473 K and HTS reactor operating temperature: 623 K as fixed variables.

According to Chen and co-workers [34], the LHV of syngas (kJ N m^{-3}) can be defined as:

$$\mathbf{LHV} = \left(\mathbf{119950.4} \cdot \mathbf{n_{H_2}} + \mathbf{10103.9} \cdot \mathbf{n_{CO}} + \mathbf{50009.3} \cdot \mathbf{n_{CH_4}}\right) \cdot \rho \quad (2)$$

Table 5 summarizes the results obtained from the sensitivity analysis of the variables which presents higher effect on the η_{TE} and LHV of the H2-rich syngas. Additionally, the H_2 molar fraction in the final process stream is reported. The effect of those variables will be analyzed individually in the next subsections:

4.2. Oxygen to Carbon Mass Ratio Effect

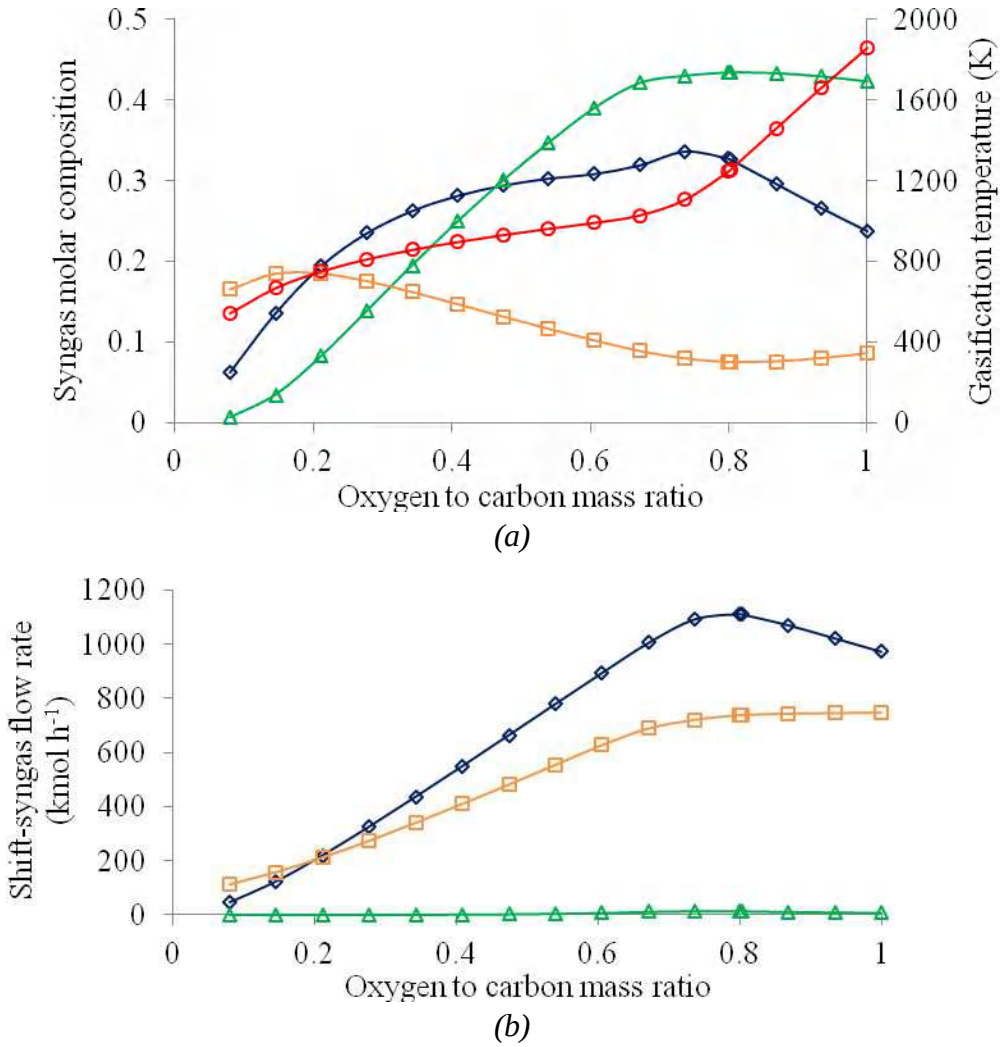

Fig. 2. Effect of the O_2 to carbon ratio on (a) the syngas molar composition upstream WGS reactors and (b) molar flow rate downstream WGS reactors: CO (△), H_2 (◇), CO_2 (□), and adiabatic temperature (○) with solid concentration in coal slurry: 0.65, WGS process SDG : 0.59, LTS reactor operating temperature: 473 K and HTS reactor operating temperature: 623 K as fixed variables.

Fig. 2 (a) and (b) summarizes the results obtained in the syngas molar composition and the gasification temperature in the gasifier as functions of a wide variation of the O_2 to carbon mass

ratio, as well as the shift-syngas flow rate after WGS. As expected, the increase in O_2 to coal ratio favors exothermic reactions, therefore, an increase in gasifier operating temperature is achieved. However, as shown Fig. 2(a), there is a turning point in the operating gasifier temperature at an O_2 to carbon ratio close to 0.8. This is due to the differences in the heat released from partial combustion and complete combustion [33]. This turning point appears when the maximum CO and H_2 concentration is reached. Beyond this point the CO_2 increases because of the complete combustion while the CO and H_2 compositions decrease.

As shown in Fig. 2(b), the maximum H_2 flow rate downstream the WGS reactors was obtained with an O_2 to carbon ratio of 0.8. At this rate, CO concentration in the syngas leaving the gasifier is maximized while CO_2 concentration is minimized. As a consequence, H_2 production is favored in the WGS reactors.

Surprisingly, the maximum thermal efficiency was 62.6% and was obtained for an O_2 to carbon ratio of 0.64 (see Table 5). When O_2 to carbon ratio was fixed at 0.8, the thermal efficiency was 60.0%, decreasing 17% with respect to the maximum. That efficiency fall is caused by the increment in O_2 flow rate. As a result, energy requirements for ASU process penalize the η_{TE} despite LHV increment.

As suggested by the results presented in Table 5, there is a linear correlation between the syngas H_2 composition and its LHV. As the H_2 composition is raised LHV also increases. This is because H_2 is the main contributor, over CH_4 and CO, to the syngas heating value.

4.3. Coal Slurry Concentration Effect

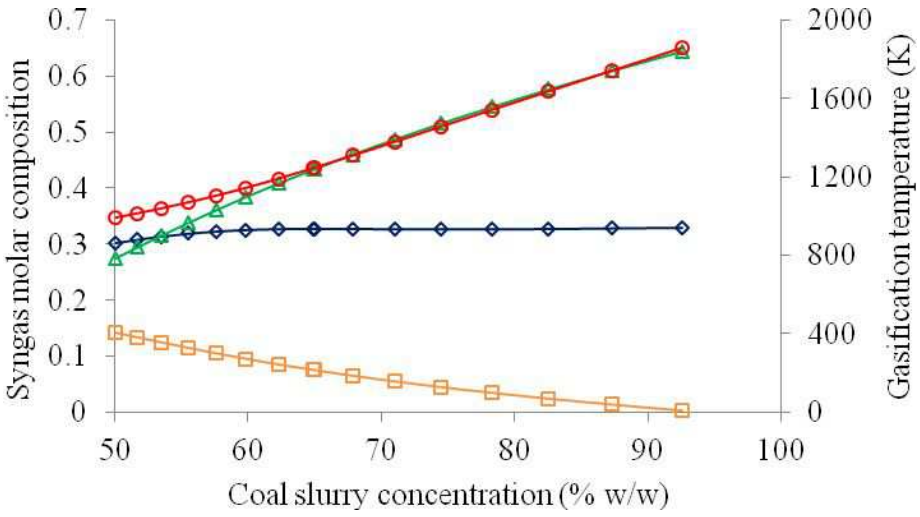

(a)

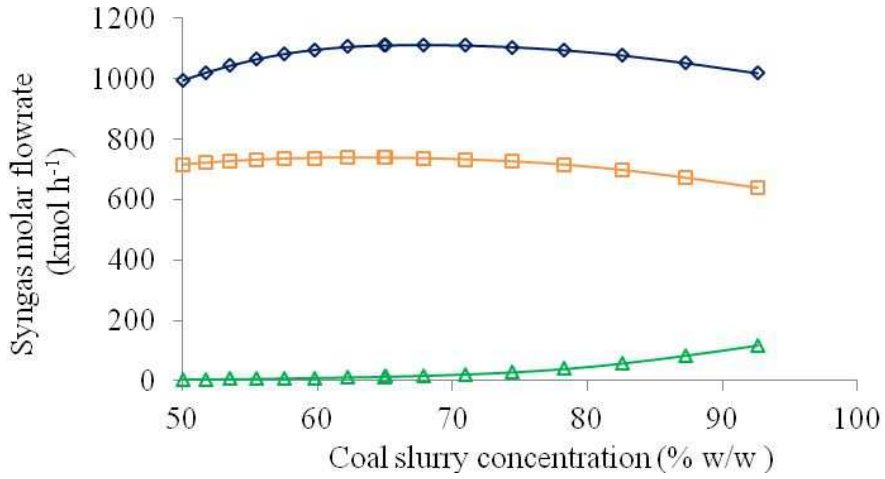

(b)

Fig. 3. Effect of the coal slurry concentration on (a) the syngas composition upstream WGS reactor and (b) molar flow rate downstream the WGS reactors: CO (△), H_2 (◇), CO_2 (□) and the adiabatic temperature (○) with O_2 to coal ratio: 0.8, WGS process SDG : 0.59, LTS reactor operating temperature: 473 K and HTS reactor operating temperature: 623 K as fixed variables

Fig. 3 (a) and (b) summarizes the results obtained in the syngas molar composition and the gasification temperature in the gasifier as functions of a wide variation of the coal slurry concentration, as well as the shift-syngas flow rate after WGS. Fig. 3(a) shows that lower steam flow leads to a slight raise in H_2 concentration and a significant increment of CO at the gasifier downstream. An increase in solid concentration results in a higher gasifier temperature. Hence, at higher temperatures Boudouard reaction (R3) and steam gasification (R4) are favored and CO production is increased. Downstream the WGS reactors, the H_2 maximum flow is obtained with a solid concentration of 65% approximately, as shown in Fig. 3(b). Beyond this value, the H_2 flow decreases because the CO conversion in the WGS reactors is limited by the steam flow rate.

As shown in Table 5, the coal slurry concentration has slight effect on the η_{TE} (< 5% change within the range). Nevertheless, higher solid concentration does affect the LHV, as the WGS conversion is decreased and final H_2 composition decrease moderately.

4.4. WGS reactor operating temperature effect

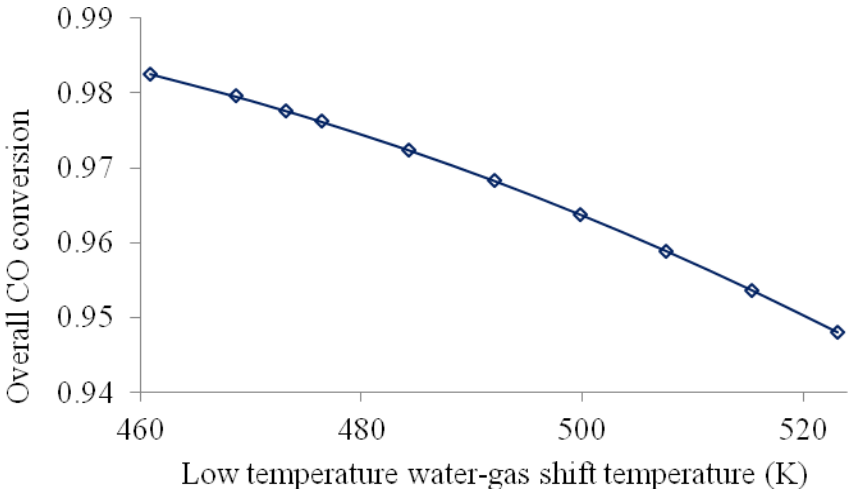

Fig. 4. Effect of operating temperature on overall CO conversion in the shift reactors with O_2 to coal ratio: 0.8, solid concentration in coal slurry: 0.65, WGS process SDG : 0.59, and HTS reactor operating temperature: 623 K as fixed variables.

As shown in Fig. 4, when the LTS reactor is operated at low temperatures, the CO conversion is promoted due to the exothermic nature of the WGS reaction (R5). Low operating temperatures are preferred to obtain higher CO to H_2 conversion but it implies a decrease in the reaction rate and catalytic activity.

When the LTS reactor operating temperature was raised from 473 K to 523 K, the cleaned-syngas LHV felt from 99.33 MJ kg^{-1} to 81.54 MJ N kg^{-1}. This is a decrease of 18% (Table 5). Nevertheless, the η_{TE} increases 3.3%. The CO_2 flow in the shift-syngas drops as the LTS reactor temperature is increased (from 7.43 Mg h^{-1} to 7.19 Mg h^{-1}). Therefore, less acid gas is removed in the Rectisol absorber from the shift-syngas. The energy requirement necessary to achieve the CH_3OH recuperation is lower compared with higher CO_2 concentration downstream the LTS reactor (from 4.20 GJ h^{-1} to 4.16 GJ h^{-1}).

4.5. Effect of steam to dry gas molar ratio.

As shown in Fig. 5, the total CO conversion grows inversely exponential with the steam to dry gas ratio (SDG), approaching asymptotically to an extent of CO conversion of 1. Besides, the SDG is dependent of the operating temperature. At lower temperatures, higher conversion with lower steam flow fed to the HTS reactor is reached. The maximum conversion of 0.999 was achieved when a 3.9 SDG was set at 473 K. However, the CO conversion keeps mainly constant after a SDG of 2, whilst a 0.996 conversion was attained. Past this value, to increase the CO conversion 0.12%, it is required to raise the SDG by 40%. Therefore, to get a conversion over 0.996 is preferred to manipulate other variables as it becomes almost insensitive to the SDG in ratios greater than 2.

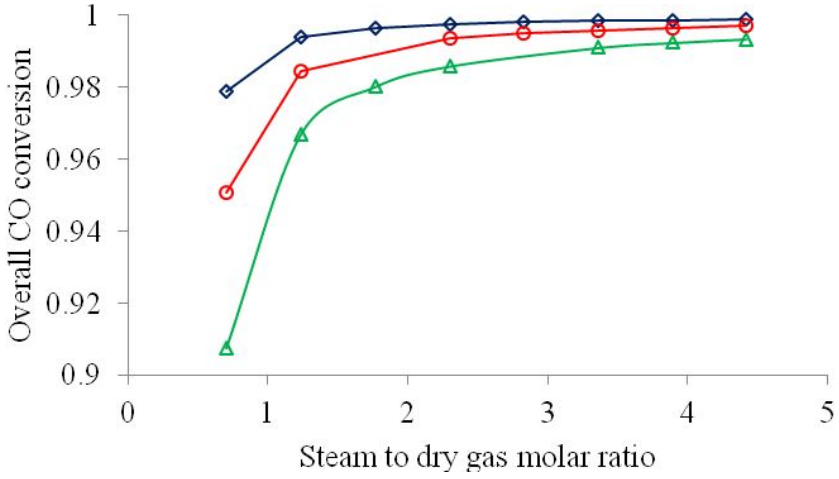

Fig. 5. Effect of the steam to dry gas molar ratio over overall CO conversion, when an operating temperature of 473 K (◇), 523 K (○) and 573 K (△) is established in the LT-WGS reactor with O_2 to coal ratio: 0.8, solid concentration in coal slurry: 0.65, and HTS reactor operating temperature: 623 K as fixed variables.

Cleaned-syngas LHV and η_{TE}, increases inversely exponential and decreases lineally respectively with an increasing of the SDG at a LTS operating temperature of 473 K (Table 5). Cleaned-syngas LHV increment is due to the CO conversion raising. Therefore, as in the CO conversion, after a SDG of 2 the LHV is almost constant. On the other hand, η_{TE} drop is caused by the steam flow

feed increment in WGS process. As a result, in the Rectisol process higher acid gas flow required to be treated increasing the energy consumption.

4.6. Optimal Syngas composition

According to Table 5, the highest efficiency is reached at a slurry solid concentration of 0.65, a O_2 to carbon ratio of 0.64, a WGS process SDG of 0.59, a LTS reactor operating temperature of 473 K. Table 6 shows the H_2-rich syngas composition at these conditions.

Table 6. H2-rich syngas molar fraction

Component	H_2-rich syngas molar fraction
H_2O	$6{,}47x10^{-11}$
H_2	0,922
N_2	$7{,}13x10^{-3}$
CL_2	$3{,}77x10^{-24}$
CO	$9{,}58x10^{-3}$
CO_2	$6{,}00x10^{-6}$
CH_4	0,062
H_2S	$3{,}53x10^{-20}$
COS	$2{,}89x10^{-20}$
NH_3	$1{,}74x10^{-7}$
HCN	$2{,}20x10^{-42}$
CH_4OH	$4{,}15x10^{-6}$

As shown in Table 6, the syngas product is suitable for gas turbines since H_2 molar fraction is 92.2%. The operation of gas turbines using syngas with hydrogen fuel concentrations (>90%) has been demonstrated at several facilities in the United States [36]. Nevertheless, the co-sequestration of CO_2 and H_2S with the Rectisol process has proven to be a success as a high CO_2 + H_2S capture is obtained. The CO_2 composition in the H_2-rich syngas is 6 ppm as well as H_2S and COS are found as traces. Furthermore, tail gas CO_2 molar fraction is over 98% with a H_2S concentration is 0.26% mol. As a result, this tail gas can be advantageous for enhanced oil production in sour fields as the environmental impact and processing costs will not be significant [37].

5. Conclusions

In this paper, a SOG simulation was proposed using Aspen Plus® to estimate syngas production by coal gasification. Sensitivity of the process for different operating variables was then analyzed. As a result, a maximum thermal efficiency of 62.6% was reached. This maximum corresponds to a slurry solid concentration of 0.65, a O2 to carbon ratio of 0.64, a WGS process SDG of 0.59, a LTS reactor operating temperature of 473 K. At these fixed conditions, a H2-rich syngas of 92.2% molar composition and LHV of 12 MJ N m^{-3} was attained.

The thermal efficiency is found to be (1) insensitive to coal slurry concentration and LTS reactor operating temperature, (2) moderately sensitive to SDG in the WGS process and (3) most sensitive to oxygen to carbon ratio. An excessive increase in the O2 flow rate causes a fall in thermal efficiency. This behavior is caused as the energy requirements for ASU process and Rectisol process penalized the η_{TE} despite LHV increment.

The lower heating value of the H2-rich syngas results to be (1) moderately sensitive to the LTS reactor temperature and coal slurry concentration, (2) most sensitive to O2 to carbon ratio. Nonetheless, a SDG higher than 2 is necessary for a complete CO conversion. Beyond this ratio, the

SDG has slight effect on the syngas composition (<0.12% within range) and the LHV remains constant.

Environmentally, simulation results shown that the Rectisol process is an effective method for CO_2 and H_2S capture as these compounds concentrations in the H_2-rich syngas were very low. Besides, the by-product tail gas can be used for enhanced oil production in sour fields.

6. Nomenclature

ASU air separation unit

HPC high pressure column

HTS high temperature reactor

LHV lower heating value, MJ N m^{-3}

LPC low pressure column

LTS low temperature reactor

$\mathbf{M}$ mass flow rate, kg h^{-1}

$\mathbf{n}$ mass fraction

$\mathbf{Q_{Aux}}$ auxiliary power required, MJ h^{-1}

SOG steam-oxygen gasification

SDG steam to dry gas ratio

WGS water-gas shift

Greek symbols

η_{TE} thermal efficiency, %

ρ syngas density, kg m^{-3}

Subscripts and superscripts

Coal coal

Syn syngas

References

[1.] Jin H, Lu Y, Liao B, Guo L, Zhang X. Hydrogen production by coal gasification in supercritical water with a fluidized bed reactor. International Journal of Hydrogen Energy. 2010;35(13):7151-60.

[2.] Ramos IAC, Montini T, Lorenzut B, Troiani H, Gennari FC, Graziani M, et al. Hydrogen production from ethanol steam reforming on M/CeO2/YSZ (M = Ru, Pd, Ag) nanocomposites. Catalysis Today. 2012;180(1):96-104.

[3.] Higman C, van der Burgt M. Chapter 7 - Applications. Gasification (Second Edition). Burlington: Gulf Professional Publishing; 2008. p. 257-321.

[4.] Liu K, Cui Z, Fletcher TH. Coal Gasification. Hydrogen and Syngas Production and Purification Technologies: John Wiley & Sons, Inc.; 2009. p. 156-218.

[5.] Giunta P, Amadeo N, Laborde M. Simulation of a low temperature water gas shift reactor using the heterogeneous model/application to a pem fuel cell. Journal of power sources. 2006;156(2):489-96.

[6.] Dincer I. Green methods for hydrogen production. International Journal of Hydrogen Energy. 2012;37(2):1954-71.

[7.] BP. BP Statistical Review of World Energy June 2011. 2011 Available at: http://www.bp.com/statisticalreview. [accessed 10.02.2012].

[8.] Stańczyk K, Kapusta K, Wiatowski M, Świądrowski J, Smoliński A, Rogut J, et al. Experimental simulation of hard coal underground gasification for hydrogen production. Fuel. 2012;91(1):40-50.

[9.] Jones RH, Thomas GJ. Materials for the Hydrogen Economy: CRC; 2007.

[10.] Energy USDo. Pioneering Gasification Plants. 2011 Available at: http://www.fossil.energy.gov/programs/powersystems/gasification/gasificationpioneer.html. [accessed 10.02.2012].

[11.] Colombia MdMyEad. El carbón Colombiano; Recursos, Reservas y Calidad 2004.

[12.] Kopyscinski J, Schildhauer TJ, Biollaz SMA. Methanation in a fluidized bed reactor with high initial CO partial pressure: Part II— Modeling and sensitivity study. Chemical Engineering Science. 2011;66(8):1612-21.

[13.] Minchener AJ. Coal gasification for advanced power generation. Fuel. 2005;84(17):2222-35.

[14.] Emun F, Gadalla M, Majozi T, Boer D. Integrated gasification combined cycle (IGCC) process simulation and optimization. Computers & Chemical Engineering. 2010;34(3):331-8.

[15.] Nikoo MB, Mahinpey N. Simulation of biomass gasification in fluidized bed reactor using ASPEN PLUS. Biomass and Bioenergy. 2008;32(12):1245-54.

[16.] Ramzan N, Ashraf A, Naveed S, Malik A. Simulation of hybrid biomass gasification using Aspen plus: A comparative performance analysis for food, municipal solid and poultry waste. Biomass and Bioenergy. 2011;35(9):3962-9.

[17.] Shen L, Gao Y, Xiao J. Simulation of hydrogen production from biomass gasification in interconnected fluidized beds. Biomass and Bioenergy. 2008;32(2):120-7.

[18.] Liu B, Yang X, Song W, Lin W. Process Simulation Development of Coal Combustion in a Circulating Fluidized Bed Combustor Based on Aspen Plus. Energy & Fuels. 2011;25(4):1721-30.

[19.] Robinson PJ, Luyben WL. Simple Dynamic Gasifier Model That Runs in Aspen Dynamics. Industrial & Engineering Chemistry Research. 2008;47(20):7784-92.

[20.] Chiesa P, Consonni S, Kreutz T, Robert W. Co-production of hydrogen, electricity and CO2 from coal with commercially ready technology. Part A: Performance and emissions. International Journal of Hydrogen Energy. 2005;30(7):747-67.

[21.] Davison TY. GE Gasification Project Update. Gasification 11 Conference: GE Energy; 2012.

[22.] Smith AR, Klosek J. A review of air separation technologies and their integration with energy conversion processes. Fuel Processing Technology. 2001;70(2):115-34.

[23.] Vinson DR. Air separation control technology. Computers & Chemical Engineering. 2006;30(10–12):1436-46.

[24.] AG L. Cryogenic Air Separation, History and Technological progress. Pullach: 2009 Available at: http://www.linde-le.de/process_plants/air_separation_plants/documents/L_2_1_e_09_150dpi.pdf. [accessed 10.02.2012].

[25.] Chen P-C, Chiu H-M, Chyou Y-P, Yu C-S. Processes Simulation Study of Coal to Methanol Based on Gasification Technology. Engineering and Technology. 2010;65:988-96.

[26.] Castle WF. Air separation and liquefaction: recent developments and prospects for the beginning of the new millennium. International Journal of Refrigeration. 2002;25(1):158-72.

[27.] Damartzis T, Zabaniotou A. Thermochemical conversion of biomass to second generation biofuels through integrated process design—A review. Renewable and Sustainable Energy Reviews. 2011;15(1):366-78.

[28.] Topsøe H. Sulphur resistant/sour water-gas shift catalyst. Lyngby 2009.

[29.] Bell D, Towler B. Coal Gasification and Its Applications: ELSEVIER; 2010.

[30.] Korens N, Simbeck D, Wilhelm D. Process screening analysis of alternative gas treating and sulfur removal for gasification. Prepared for DOE/NETL. 2002.

[31.] Heil S, Brunhuber C, Link K, Kittel J, Meyer B. Dynamic Modelling of CO2-removal units for an IGCC power plant. Proceedings 7th Modelica Conference; Sep. 20-22; Como, Italy: The Modelica Association; 2009. p. 77-85.

[32.] Larson ED, Consonni S, Katofsky RE, Consulting N, Burlington I, Iisa K, et al. A Cost-Benefit Assessment of Gasification-Based Biorefining in the Kraft Pulp and Paper Industry Volume 1 Main Report. Princeton University, Princeton, NJ. 2006.

[33.] Yuehong Z, Hao W, Zhihong X. Conceptual design and simulation study of a co-gasification technology. Energy Conversion and Management. 2006;47(11–12):1416-28.

[34.] Chen C, Jin Y-Q, Yan J-H, Chi Y. Simulation of municipal solid waste gasification in two different types of fixed bed reactors. Fuel. [Available online 24 August 2011]. 2011.

[35.] Wang Y, Dong W, Dong L, Yue J, Gao S, Suda T, et al. Production of Middle Caloric Fuel Gas from Coal by Dual-Bed Gasification Technology. Energy & Fuels. 2010 2010/05/20;24(5):2985-90.

[36.] Walton SM, He X, Zigler BT, Wooldridge MS. An experimental investigation of the ignition properties of hydrogen and carbon monoxide mixtures for syngas turbine applications. Proceedings of the Combustion Institute. 2007;31:3147-54.

[37.] Davison J, Bressan L, Domenichini R. CO2 capture in coal-based IGCC power plants. 7th International Conference in Greenhouse Gas Control Technologies; Vancouver2004.

ECOS 2012

The 25th International Conference on Efficiency, Cost, Optimization and Simulation of Energy Conversion Systems and Processes

(Perugia, June 26th-June 29th, 2012)

edited by
Umberto Desideri, Giampaolo Manfrida,
Enrico Sciubba

firenze university press
2012

ECOS 2012 : the 25th International Conference on Efficiency, Cost, Optimization and Simulation of Energy Conversion Systems and Processes (Perugia, June 26th-June 29th, 2012) / edited by Umberto Desideri, Giampaolo Manfrida, Enrico Sciubba. – Firenze : Firenze University Press, 2012.
(Proceedings e report ; 90)

http://digital.casalini.it/9788866553229

ISBN 978-88-6655-322-9 (online)

Progetto grafico di copertina Alberto Pizarro, Pagina Maestra snc
Immagine di copertina: © Kts | Dreamstime.com

Peer Review Process
All publications are submitted to an external refereeing process under the responsibility of the FUP Editorial Board and the Scientific Committees of the individual series. The works published in the FUP catalogue are evaluated and approved by the Editorial Board of the publishing house. For a more detailed description of the refereeing process we refer to the official documents published on the website and in the online catalogue of the FUP (http://www.fupress.com).

Firenze University Press Editorial Board
G. Nigro (Co-ordinator), M.T. Bartoli, M. Boddi, F. Cambi, R. Casalbuoni, C. Ciappei, R. Del Punta, A. Dolfi, V. Fargion, S. Ferrone, M. Garzaniti, P. Guarnieri, G. Mari, M. Marini, M. Verga, A. Zorzi.

© 2012 Firenze University Press
Università degli Studi di Firenze
Firenze University Press
Borgo Albizi, 28, 50122 Firenze, Italy
http://www.fupress.com/
Printed in Italy

ECOS 2012

The 25th International Conference on

Efficiency, Cost, Optimization and Simulation
of Energy Conversion Systems and Processes

Perugia, June 26th-June 29th, 2012

Book of Proceedings - Volume VII

Edited by:
Umberto Desideri, Università degli Studi di Perugia
Giampaolo Manfrida, Università degli Studi di Firenze
Enrico Sciubba, Università degli Studi di Roma "Sapienza"

ECOS 2012 - THE 25TH INTERNATIONAL CONFERENCE ON
EFFICIENCY, COST, OPTIMIZATION, SIMULATION AND ENVIRONMENTAL IMPACT OF ENERGY SYSTEMS
JUNE 26-29, 2012, PERUGIA, ITALY
EDITED BY UMBERTO DESIDERI, GIAMPAOLO MANFRIDA, ENRICO SCIUBBA
FIRENZE UNIVERSITY PRESS, 2012, ISBN ONLINE : 978-88-6655-322-9

Advisory Committee (Track Organizers)

Building, Urban and Complex Energy Systems
V. Ismet Ugursal
Dalhousie University, Nova Scotia, Canada

Combustion, Chemical Reactors, Carbon Capture and Sequestration
Giuseppe Girardi
ENEA-Casaccia, Italy

Energy Systems: Environmental and Sustainability Issues
Christos A. Frangopoulos
National Technical University of Athens, Greece

Exergy Analysis and Second Law Analysis
Silvio de Oliveira Junior
Polytechnical University of Sao Paulo, Sao Paulo, Brazil

Fluid Dynamics and Power Plant Components
Sotirios Karellas
National Technical University of Athens, Athens, Greece

Fuel Cells
Umberto Desideri
University of Perugia, Perugia, Italy

Heat and Mass Transfer
Francesco Asdrubali, **Cinzia Buratti**
University of Perugia, Perugia, Italy

Industrial Ecology
Stefan Goessling-Reisemann
University of Bremen, Germany

Poster Session
Enrico Sciubba
University Roma 1 “Sapienza”, Italy

Process Integration and Heat Exchanger Networks
Francois Marechal
EPFL, Lausanne, *Switzerland*

Renewable Energy Conversion Systems
David Chiaramonti
University of Firenze, Firenze, Italy

Simulation of Energy Conversion Systems
Marcin Liszka
Polytechnica Slaska, Gliwice, Poland

System Operation, Control, Diagnosis and Prognosis
Vittorio Verda
Politecnico di Torino, Italy

Thermodynamics
A. Özer Arnas
United States Military Academy at West Point, U.S.A.

Thermo-Economic Analysis and Optimisation
Andrea Lazzaretto
University of Padova, Padova, Italy

Water Desalination and Use of Water Resources
Corrado Sommariva
ILF Consulting M.E., U.K

Scientific Committee

Riccardo Basosi, University of Siena, Italy
Gino Bella, University of Roma Tor Vergata, Italy
Asfaw Beyene, San Diego State University, United States
Ryszard Bialecki, Silesian Institute of Tecnology, Poland
Gianni Bidini, University of Perugia, Italy
Ana M. Blanco-Marigorta, University of Las Palmas de Gran Canaria, Spain
Olav Bolland, University of Science and Technology (NTNU), Norway
Renè Cornelissen, Cornelissen Consulting, The Netherlands
Franco Cotana, University of Perugia, Italy
Alexandru Dobrovicescu, Polytechnical University of Bucharest, Romania
Gheorghe Dumitrascu, Technical University of Iasi, Romania
Brian Elmegaard, Technical University of Denmark , Denmark
Daniel Favrat, EPFL, Switzerland
Michel Feidt, ENSEM - LEMTA University Henri Poincaré, France
Daniele Fiaschi, University of Florence, Italy
Marco Frey, Scuola Superiore S. Anna, Italy
Richard A Gaggioli, Marquette University, USA
Carlo N. Grimaldi, University of Perugia, Italy
Simon Harvey, Chalmers University of Technology, Sweden
Hasan Heperkan, Yildiz Technical University, Turkey
Abel Abel Hernandez-Guerrero, University of Guanajuato, Mexico
Jiri Jaromir Klemeš, University of Pannonia, Hungary
Zornitza V. Kirova-Yordanova, University "Prof. Assen Zlatarov", Bulgaria
Noam Lior, University of Pennsylvania, United States
Francesco Martelli, University of Florence, Italy
Aristide Massardo, University of Genova, Italy
Jim McGovern, Dublin Institute of Technology, Ireland
Alberto Mirandola, University of Padova, Italy
Michael J. Moran, The Ohio State University, United States
Tatiana Morosuk, Technical University of Berlin, Germany
Pericles Pilidis, University of Cranfield, United Kingdom
Constantine D. Rakopoulos, National Technical University of Athens, Greece
Predrag Raskovic, University of Nis, Serbia and Montenegro
Mauro Reini, University of Trieste, Italy
Gianfranco Rizzo, University of Salerno, Italy
Marc A. Rosen, University of Ontario, Canada
Luis M. Serra, University of Zaragoza, Spain
Gordana Stefanovic, University of Nis, Serbia and Montenegro
Andrea Toffolo, Luleå University of Technology, Sweden
Wojciech Stanek, Silesian University of Technology, Poland
George Tsatsaronis, Technical University Berlin, Germany
Antonio Valero, University of Zaragoza, Spain
Michael R. von Spakovsky, Virginia Tech, USA
Stefano Ubertini, Parthenope University of Naples, Italy
Sergio Ulgiati, Parthenope University of Naples, Italy
Sergio Usón, Universidad de Zaragoza, Spain
Roman Weber, Clausthal University of Technology, Germany
Ryohei Yokoyama, Osaka Prefecture University, Japan
Na Zhang, Institute of Engineering Thermophysics, Chinese Academy of Sciences, China

The 25th ECOS Conference 1987-2012: leaving a mark

The introduction to the ECOS series of Conferences states that "ECOS is a series of international conferences that focus on all aspects of Thermal Sciences, with particular emphasis on Thermodynamics and its applications in energy conversion systems and processes". Well, ECOS is much more than that, and its history proves it!

The idea of starting a series of such conferences was put forth at an informal meeting of the Advanced Energy Systems Division of the American Society of Mechanical Engineers (ASME) at the November 1985 Winter Annual Meeting (WAM), in Miami Beach, Florida, then chaired by Richard Gaggioli. The resolution was to organize an annual Symposium on the Analysis and Design of Thermal Systems at each ASME WAM, and to try to involve a larger number of scientists and engineers worldwide by organizing conferences outside of the United States. Besides Rich other participants were Ozer Arnas, Adrian Bejan, Yehia El-Sayed, Robert Evans, Francis Huang, Mike Moran, Gordon Reistad, Enrico Sciubba and George Tsatsaronis.

Ever since 1985, a Symposium of 8-16 sessions has been organized by the Systems Analysis Technical Committee every year, at the ASME Winter Annual Meeting (now ASME-IMECE). The first overseas conference took place in Rome, twenty-five years ago (in July 1987), with the support of the U.S. National Science Foundation and of the Italian National Research Council. In that occasion, Christos Frangopoulos, Yalcin Gogus, Elias Gyftopoulos, Dominick Sama, Sergio Stecco, Antonio Valero, and many others, already active at the ASME meetings, joined the core-group.

The name ECOS was used for the first time in Zaragoza, in 1992: it is an acronym for **Efficiency, Cost, Optimization and Simulation** (of energy conversion systems and processes), keywords that best describe the contents of the presentations and discussions taking place in these conferences. Some years ago, Christos Frangopoulos inserted in the official website the note that "ècos" ('οικος) means "home" in Greek and it ought to be attributed the very same meaning as the prefix "Eco-" in environmental sciences.
The last 25 years have witnessed an almost incredible growth of the ECOS community: more and more Colleagues are actively participating in our meetings, several international Journals routinely publish selected papers from our Proceedings, fruitful interdisciplinary and international cooperation projects have blossomed from our meetings. Meetings that have spanned three continents (Africa and Australia ought to be our next targets, perhaps!) and influenced in a way or another much of modern Engineering Thermodynamics.
After 25 years, if we do not want to become embalmed in our own success and lose momentum, it is mandatory to aim our efforts in two directions: first, encourage the participation of younger academicians to our meetings, and second, stimulate creative and useful discussions in our sessions. Looking at this years' registration roster (250 papers of which 50 authored or co-authored by junior Authors), the first objective seems to have been attained, and thus we have just to continue in that direction; the second one involves allowing space to "voices that sing out of the choir", fostering new methods and approaches, and establishing or reinforcing connections to other scientific communities. It is important that our technical sessions represent a place of active confrontation, rather than academic "lecturing".
In this spirit, we welcome you in Perugia, and wish you a scientifically stimulating, touristically interesting, and culinarily rewarding experience. In line with our 25 years old scientific excellency and friendship!

Umberto Desideri, Giampaolo Manfrida, Enrico Sciubba

CONTENT MANAGEMENT

The index lists all the papers contained all the eight volumes of the Proceedings of the ECOS 2012 International Conference.
Page numbers are listed only for papers within the Volume you are looking at. The ID code allows to trace back the identification number assigned to the paper within the Conference submission, review and track organization processes.

CONTENT

VOLUME VII

VII. 1 BUILDING, URBAN AND COMPLEX ENERGY SYSTEMS

» A linear programming model for the optimal assessment of sustainable energy action plans (ID 398) ……..... *Pag. 1*
Gianfranco Rizzo, Giancarlo Savino

» A natural gas fuelled 10 kW electric power unit based on a Diesel automotive internal combustion engine and suitable for cogeneration (ID 477) ……..... *Pag. 14*
Pietro Capaldi

» Adjustment of envelopes characteristics to climatic conditions for saving heating and cooling energy in buildings (ID 430) ……..... *Pag. 24*
Christos Tzivanidis, Kimon Antonopoulos, Foteini Gioti

» An exergy based method for the optimal integration of a building and its heating plant. Part 1: comparison of domestic heating systems based on renewable sources (ID 81) ……..... *Pag. 40*
Marta Cianfrini, Enrico Sciubba, Claudia Toro

» Analysis of different typologies of natural insulation materials with economic and performances evaluation of the same buildings (ID 28) ……..... *Pag. 54*
Umberto Desideri, Daniela Leonardi, Livia Arcioni

» Complex networks approach to the Italian photovoltaic energy distribution system (ID 470) ……..... *Pag. 72*
Luca Valori, Giovanni Luca Giannuzzi, Tiziano Squartini, Diego Garlaschelli, Riccardo Basosi

» Design of a multi-purpose building "to zero energy consumption" according to European Directive 2010/31/CE: Architectural and plant solutions (ID 29) ……..... *Pag. 90*
Umberto Desideri, Livia Arcioni, Daniela Leonardi, Luca Cesaretti ,Perla Perugini, Elena Agabitini, Nicola Evangelisti

» Effect of initial systems on the renewal planning of energy supply systems for a hospital (ID 107) ……..... *Pag. 107*
Shu Yoshida, Koichi Ito, Yoshiharu Amano, Shintaro Ishikawa, Takahiro Sushi, Takumi Hashizume

» Effects of insulation and phase change materials (PCM) combinations on the energy consumption for buildings indoor thermal comfort (ID 387) ……..... *Pag. 119*
Christos Tzivanidis, Kimon Antonopoulos, Eleutherios Kravvaritis

» Energetic evaluation of a smart controlled greenhouse for tomato cultivation (ID 150) ……..... *Pag. 134*
Nickey Van den Bulck, Mathias Coomans, Lieve Wittemans, Kris Goen, Jochen Hanssens, Kathy Steppe, Herman Marien, Johan Desmedt

» Energy networks in sustainable cities: temperature and energy consumption monitoring in urban area (ID 190) ……..... *Pag. 146*
Luca Giaccone, Alessandra Guerrisi, Paolo Lazzeroni and Michele Tartaglia

» Extended exergy analysis of the economy of Nova Scotia, Canada (ID 215) ……..... *Pag. 160*
David C Bligh, V.Ismet Ugursal

FIRENZE UNIVERSITY PRESS, 2012, ISBN ONLINE : 978-88-6655-322-9

» **Feasibility study and design of a low-energy residential unit in Sagarmatha Park (Nepal) for envirnomental impact reduction of high altitude buildings (ID 223)** ..... *Pag. 173*
Umberto Desideri, Stefania Proietti, Paolo Sdringola, Elisa Vuillermoz

» **Fire and smoke spread in low-income housing in Mexico (ID 379)** ..... *Pag. 186*
Raul R. Flores-Rodriguez, Abel Hernandez-Guerrero, Cuauhtemoc Rubio-Arana, Consuelo A. Caldera-Briseño

» **Optimal lighting control strategies in supermarkets for energy efficiency applications via digital dimmable technology (ID 136)** ..... *Pag. 196*
Salvador Acha, Nilay Shah, Jon Ashford, David Penfold

» **Optimising the arrangement of finance towards large scale refurbishment of housing stock using mathematical programming and optimisationg (ID 127)** ..... *Pag. 213*
Mark Gerard Jennings, Nilay Shah, David Fisk

» **Optimization of thermal insulation to save energy in buildings (ID 174)** ..... *Pag. 229*
Milorad Bojić, Marko Miletić, Vesna Marjanović, Danijela Nikolić, Jasmina Skerlić

» **Residential solar-based seasonal thermal storage system in cold climate: building envelope and thermal storage (ID 342)** ..... *Pag. 239*
Alexandre Hugo and Radu Zmeureanu

» **Simultaneous production of domestic hot water and space cooling with a heat pump in a Swedish Passive House (ID 55)** ..... *Pag. 251*
Johannes Persson, Mats Westermark

» **SOFC micro-CHP integration in residential buildings (ID 201)** ..... *Pag. 261*
Umberto Desideri, Giovanni Cinti, Gabriele Discepoli, Elena Sisani, Daniele Penchini

» **The effect of shading of building integrated photovoltaics on roof surface temperature and heat transfer in buildings (ID 83)** ..... *Pag. 273*
Eftychios Vardoulakis, Dimitrios Karamanis

» **The influence of glazing systems on energy performance and thermal comfort in non-residential buildings (ID 206)** ..... *Pag. 281*
Cinzia Buratti, Elisa Moretti, Elisa Belloni

» **Thermal analysis of a greenhouse heated by solar energy and seasonal thermal energy storage in soil (ID 405)** ..... *Pag. 295*
Yong Li, Jin Xu, Ru-Zhu Wang

» **Thermodynamic analysis of a combined cooling, heating and power system under part load condition (ID 476)** ..... *Pag. 304*
Qiang Chen, Jianjiao Zheng, Wei Han, Jun Sui, Hong-guang Jin

VII. 2 COMBUSTION, CHEMICAL REACTORS

» **Baffle as a cost-effective design improvement for volatile combustion rate increase in biomass boilers of simple construction (ID 233)** ..... *Pag. 321*
Borivoj Stepanov, Ivan Pešenjanski, Biljana Miljković

» **Characterization of CH4-H2-air mixtures in the high-pressure DHARMA reactor (ID 287)** ..... *Pag. 331*
Vincenzo Moccia, Jacopo D'Alessio

» **Development of a concept for efficiency improvement and decreased NOx production for natural gas-fired glass melting furnaces by switching to a propane exhaust gas fired process (ID 146)** ..... *Pag. 343*
Jörn Benthin, Anne Giese

» **Experimental analysis of inhibition phenomenon management for Solid Anaerobic Digestion Batch process (ID 348)** ……..... *Pag. 349*
Francesco Di Maria, Giovanni Gigliotti, Alessio Sordi, Caterina Micale, Claudia Zadra, Luisa Massaccesi

» **Experimental investigations of the combustion process of n-butanol/diesel blend in an optical high swirl CI engine (ID 85)** ……..... *Pag. 358*
Simona Silvia Merola, G. Valentino, C. Tornatore, L. Marchitto , F. E. Corcione

» **Flameless oxidation as a means to reduce NOx emissions in glass melting furnaces (ID 141)** ……..... *Pag. 372*
Jörg Leicher, Anne Giese

» **Mechanism of damage by high temperature of the tubes, exposed to the atmosphere characteristic of a furnace of pyrolysis of ethane for ethylene production in the petrochemical industry (ID 65)** ……..... *Pag. 381*
Jaqueline Saavedra Rueda, Francisco Javier Perez Trujillo, Lourdes Isabel Meriño Stand, Harbey Alexi Escobar, Luis Eduardo Navas, Juan Carlos Amezquita

» **Steam reforming of methane over Pt/Rh based wire mesh catalyst in single channel reformer for small scale syngas production (ID 317)** ……..... *Pag. 388*
Haftor Orn Sigurdsson, Søren Knudsen Kær

CONTENTS OF ALL THE VOLUMES

VOLUME I

I . 1 – SIMULATION OF ENERGY CONVERSION SYSTEMS

» **A novel hybrid-fuel compressed air energy storage system for China's situation (ID 531)**
Wenyi Liu, Yongping Yang, Weide Zhang, Gang Xu,and Ying Wu

» **A review of Stirling engine technologies applied to micro-cogeneration systems (ID 338)**
Ana C Ferreira, Manuel L Nunes, Luís B Martins, Senhorinha F Teixeira

» **An organic Rankine cycle off-design model for the search of the optimal control strategy (ID 295)**
Andrea Toffolo, Andrea Lazzaretto, Giovanni Manente, Marco Paci

» **Automated superstructure generation and optimization of distributed energy supply systems (ID 518)**
Philip Voll, Carsten Klaffke, Maike Hennen, André Bardow

» **Characterisation and classification of solid recovered fuels (SRF) and model development of a novel thermal utilization concept through air- gasification (ID 506)**
Panagiotis Vounatsos, Konstantinos Atsonios, Mihalis Agraniotis, Kyriakos D. Panopoulos, George Koufodimos,Panagiotis Grammelis, Emmanuel Kakaras

» **Design and modelling of a novel compact power cycle for low temperature heat sources (ID 177)**
Jorrit Wronski, Morten Juel Skovrup, Brian Elmegaard, Harald Nes Rislå, Fredrik Haglind

» **Dynamic simulation of combined cycles operating in transient conditions: an innovative approach to determine the steam drums life consumption (ID 439)**
Stefano Bracco

» Effect of auxiliary electrical power consumptions on organic Rankine cycle system with low-temperature waste heat source (ID 235)
Samer Maalouf, Elias Boulawz Ksayer, Denis Clodic

» Energetic and exergetic analysis of waste heat recovery systems in the cement industry (ID 228)
Sotirios Karellas, Aris Dimitrios Leontaritis, Georgios Panousis, Evangelos Bellos, Emmanuel Kakaras

» Energy and exergy analysis of repowering options for Greek lignite-fired power plants (ID 230)
Sotirios Karellas, Aggelos Doukelis, Grammatiki Zanni, Emmanuel Kakaras

» Energy saving by a simple solar collector with reflective panels and boiler (ID 366)
Anna Stoppato, Renzo Tosato

» Exergetic analysis of biomass fired double-stage Organic Rankine Cycle (ORC) (ID 37)
Markus Preißinger, Florian Heberle, Dieter Brüggemann

» Experimental tests and modelization of a domestic-scale organic Rankine cycle (ID 156)
Roberto Bracco, Stefano Clemente, Diego Micheli, Mauro Reini

» Model of a small steam engine for renewable domestic CHP system (ID 31)
Giampaolo Manfrida, Giovanni Ferrara, Alessandro Pescioni

» Model of vacuum glass heat pipe solar collectors (ID 312)
Daniele Fiaschi, Giampaolo Manfrida

» Modelling and exergy analysis of a plasma furnace for aluminum melting process (ID 254)
Luis Enrique Acevedo, Sergio Usón, Javier Uche, Patxi Rodríguez

» Modelling and experimental validation of a solar cooling installation (ID 296)
Guillaume Anies, Pascal Stouffs, Jean Castaing-Lasvignottes

» The influence of operating parameters and occupancy rate of thermoelectric modules on the electricity generation (ID 314)
Camille Favarel, Jean-Pierre Bédécarrats, Tarik Kousksou, Daniel Champier

» Thermodynamic and heat transfer analysis of rice straw co-firing in a Brazilian pulverised coal boiler (ID 236)
Raphael Miyake, Alvaro Restrepo, Fábio Kleveston Edson Bazzo, Marcelo Bzuneck

» Thermophotovoltaic generation: A state of the art review (ID 88)
Matteo Bosi, Claudio Ferrari, Francesco Melino, Michele Pinelli, Pier Ruggero Spina, Mauro Venturini

I . 2 – HEAT AND MASS TRANSFER

» A DNS method for particle motion to establish boundary conditions in coal gasifiers (ID 49)
Efstathios E Michaelides, Zhigang Feng

» Effective thermal conductivity with convection and radiation in packed bed (ID 60)
Yusuke Asakuma

» Experimental and CFD study of a single phase cone-shaped helical coiled heat exchanger: an empirical correlation (ID 375)
Daniel Flórez-Orrego, Walter Arias, Diego López, Héctor Velásquez

» Thermofluiddynamic model for control analysis of latent heat thermal storage system (ID 207)
Adriano Sciacovelli, Vittorio Verda, Flavio Gagliardi

» Towards the development of an efficient immersed particle heat exchanger: particle transfer from low to high pressure (ID 202)
Luciano A. Catalano, Riccardo Amirante, Stefano Copertino, Paolo Tamburrano, Fabio De Bellis

I . 3 – INDUSTRIAL ECOLOGY

» Anthropogenic heat and exergy balance of the atmosphere (ID 122)
Asfaw Beyene, David MacPhee, Ron Zevenhoven

» Determination of environmental remediation cost of municipal waste in terms of extended exergy (ID 63)
Candeniz Seckin, Ahmet R. Bayulken

» Development of product category rules for the application of life cycle assessment to carbon capture and storage (537)
Carlo Strazza, Adriana Del Borghi, Michela Gallo

» Electricity production from renewable and non-renewable energy sources: a comparison of environmental, economic and social sustainability indicators with exergy losses throughout the supply chain (ID 247)
Lydia Stougie, Hedzer van der Kooi, Rob Stikkelman
» Exergy analysis of the industrial symbiosis model in Kalundborg (ID 218)
Alicia Valero Delgado, Sergio Usón, Jorge Costa

» Global gold mining: is technological learning overcoming the declining in ore grades? (ID 277)
Adriana Domínguez, Alicia Valero

» Personal transportation energy consumption (ID305)
Matteo Muratori, Emmanuele Serra, Vincenzo Marano, Michael Moran

» Resource use evaluation of Turkish transportation sector via the extended exergy accounting method (ID 43)
Candeniz Seckin, Enrico Sciubba, Ahmet R. Bayulken

» The impact of higher energy prices on socio-economic inequalities of German social groups (ID 80)
Holger Schlör, Wolfgang Fischer, Jürgen-Friedrich Hake

VOLUME II

II . 1 – EXERGY ANALYSIS AND 2ND LAW ANALYSIS

» A comparative analysis of cryogenic recuperative heat exchangers based on exergy destruction (ID 129)
Adina Teodora Gheorghian, Alexandru Dobrovicescu, Lavinia Grosu, Bogdan Popescu, Claudia Ionita

» A critical exploration of the usefulness of rational efficiency as a performance parameter for heat exchangers (ID 307)
Jim McGovern, Georgiana Tirca-Dragomirescu, Michel Feidt, Alexandru Dobrovicescu

» A new procedure for the design of LNG processes by combining exergy and pinch analyses (ID 238)
Danahe Marmolejo-Correa, Truls Gundersen

» Advances in the distribution of environmental cost of water bodies through the exergy concept in the Ebro river (ID 258)
Javier Uche Marcuello, Amaya Martínez Gracia, Beatriz Carrasquer Álvarez, Antonio Valero Capilla

» Application of the entropy generation minimization method to a solar heat exchanger: a pseudo-optimization design process based on the analysis of the local entropy generation maps (ID 357)
Giorgio Giangaspero, Enrico Sciubba

» Comparative analysis of ammonia and carbon dioxide two-stage cycles for simultaneous cooling and heating (ID 84)
Alexandru Dobrovicescu, Ciprian Filipoiu, Emilia Cerna Mladin, Valentin Apostol, Liviu Drughean

» Comparison between traditional methodologies and advanced exergy analyses for evaluating efficiency and externalities of energy systems (ID 515)
Gabriele Cassetti, Emanuela Colombo

» Comparison of entropy generation figures using entropy maps and entropy transport equation for an air cooled gas turbine blade (ID 468)
Omer Emre Orhan, Oguz Uzol

» Conventional and advanced exergetic evaluation of a supercritical coal-fired power plant (ID 377)
Ligang Wang, Yongping Yang, Tatiana Morosuk, George Tsatsaronis

» Energy and exergy analyses of the charging process in encapsulted ice thermal energy storage (ID 164)
David MacPhee, Ibrahim Dincer, Asfaw Beyene

» Energy integration and cogeneration in nitrogen fertilizers industry: thermodynamic estimation of the efficiency, potentials, limitations and environmental impact. Part 1: energy integration in ammonia production plants (ID 303)
Zornitza Vassileva Kirova-Yordanova

» Evaluation of the oil and gas processing at a real production day on a North Sea oil platform using exergy analysis (ID 260)
Mari Voldsund, Wei He, Audun Røsjorde, Ivar Ståle Ertesvåg, Signe Kjelstrup

» Exergetic and economic analysis of Kalina cycle for low temperature geothermal sources in Brazil (ID 345)
Carlos Eymel Campos Rodriguez, José Carlos Escobar Palacios, Cesar Adolfo Rodríguez Sotomonte, Marcio Leme, Osvaldo José Venturini, Electo Eduardo Silva Lora, Vladimir Melián Cobasa, Daniel Marques dos Santos, Fábio R. Lofrano Dotto, Vernei Gialluca

» Exergy analysis and comparison of CO2 heat pumps (ID 242)
Argyro Papadaki, Athina Stegou - Sagia

» Exergy analysis of a CO2 Recovery plant for a brewery (ID 72)
Daniel Rønne Nielsen, Brian Elmegaard, C. Bang-Møller

» Exergy analysis of the silicon production process (ID 118)
Marit Takla, Leiv Kolbeinsen, Halvard Tveit, Signe Kjelstrup

» Exergy based indicators for cardiopulmonary exercise test evaluation (ID 159)
Carlos Eduardo Keutenedjian Mady, Cyro Albuquerque Neto, Tiago Lazzaretti Fernandes, Arnaldo Jose Hernandez, Paulo Hilário Nascimento Saldiva, Jurandir Itizo Yanagihara, Silvio de Oliveira Junior

» Exergy disaggregation as an alternative for system disaggregation in thermoeconomics (ID 483)
José Joaquim Conceição Soares Santos, Atilio Lourenço, Julio Mendes da Silva, João Donatelli, José Escobar Palacio

» Exergy intensity of petroleum derived fuels (ID 117)
Julio Augusto Mendes da Silva, Maurício Sugiyama, Claudio Rucker, Silvio de Oliveira Junior

» Exergy-based sustainability evaluation of a wind power generation system (ID 542)
Jin Yang, B. Chen, Enrico Sciubba

» Human body exergy metabolism (ID 160)
Carlos Eduardo Keutenedjian Mady, Silvio de Oliveira Junior

» Integrating an ORC into a natural gas expansion plant supplied with a co-generation unit (ID 273)
Sergio Usón, Wojciech Juliusz Kostowski

» One-dimensional model of an optimal ejector and parametric study of ejector efficiency (ID 323)
Ronan Killian McGovern, Kartik Bulusu, Mohammed Antar, John H. Lienhard

» Optimization and design of pin-fin heat sinks based on minimum entropy generation (ID 6)
Jose-Luis Zuniga-Cerroblanco, Abel Hernandez-Guerrero, Carlos A. Rubio-Jimenez, Cuauhtemoc Rubio-Arana, Sosimo E. Diaz-Mendez

» Performance analysis of a district heating system (ID 271)
Andrej Ljubenko, Alojz Poredoš, Tatiana Morosuk, George Tsatsaronis

» System analysis of exergy losses in an integrated oxy-fuel combustion power plant (ID 64)
Andrzej Ziębik, Paweł Gładysz

» What is the cost of losing irreversibly the mineral capital on Earth? (ID 220)
Alicia Valero Delgado, Antonio Valero

II . 2 – THERMODYNAMICS

» A new polygeneration system for methanol and power based on coke oven gas and coal gas (ID 252)
Hu Lin, Hongguang Jin, Lin Gao, Rumou Li

» Argon-Water closed gas cycle (ID 67)
Federico Fionelli, Giovanni Molinari

» Binary alkane mixtures as fluids in Rankine cycles (ID 246)
M. Aslam Siddiqi, Burak Atakan

» Excess enthalpies of second generation biofuels (ID 308)
Alejandro Moreau, José Juan Segovia, M. Carmen Martín, Miguel Ángel Villamañán, César R. Chamorro, Rosa M. Villamañán

» Local stability analysis of a Curzon-Ahlborn engine considering the Van der Waals equation state in the maximum ecological regime (ID 281)
Ricardo Richard Páez-Hernández, Pedro Portillo-Díaz, Delfino Ladino-Luna, Marco Antonio Barranco-Jiménez

» Some remarks on the Carnot's theorem (ID 325)
Julian Gonzalez Ayala, Fernando Angulo-Brown

» The Dead State (ID 340)
Richard A. Gaggioli

» The magnetocaloric energy conversion (ID 97)
Andrej Kitanovski, Jaka Tusek, Alojz Poredos

VOLUME III

THERMO-ECONOMIC ANALYSIS AND OPTIMIZATION

» A comparison of optimal operation of residential energy systems using clustered demand patterns based on Kullback-Leibler divergence (ID 142)
Akira Yoshida, Yoshiharu Amano, Noboru Murata, Koichi Ito, Takumi Hashizume

» A Model for Simulation and Optimal Design of a Solar Heating System with Seasonal Storage (ID 51)
Gianfranco Rizzo

» A thermodynamic and economic comparative analysis of combined gas-steam and gas turbine air bottoming cycle (ID 232)
Tadeusz Chmielniak, Daniel Czaja, Sebastian Lepszy

» Application of an alternative thermoeconomic approach to a two-stage vapor compression refrigeration cycle with intercooling (ID 135)
Atilio Barbosa Lourenço, José Joaquim Conceição Soares Santos, João Luiz Marcon Donatelli

» Comparative performance of advanced power cycles for low temperature heat sources (ID 109)
Guillaume Becquin, Sebastian Freund

» Comparison of nuclear steam power plant and conventional steam power plant through energy level and thermoeconomic analysis (ID 251)
S. Khamis Abadi, Mohammad Hasan Khoshgoftar Manesh, M. Baghestani, H. Ghalami, Majid Amidpour

» Economic and exergoeconomic analysis of micro GT and ORC cogeneration systems (ID 87)
Audrius Bagdanavicius, Robert Sansom, Nick Jenkins, Goran Strbac

» Exergoeconomic comparison of wet and dry cooling technologies for the Rankine cycle of a solar thermal power plant (ID 300)
Philipp Habl, Ana M. Blanco-Marigorta, Berit Erlach

» Influence of renewable generators on the thermo-economic multi-level optimization of a poly-generation smart grid (101)
Massimo Rivarolo, Andrea Greco, Francesca Travi, Aristide F. Massardo

» Local stability analysis of a thermoeconomic model of an irreversible heat engine working at different criteria of performance (ID 289)
Marco A. Barranco-Jiménez, Norma Sánchez-Salas, Israel Reyes-Ramírez, Lev Guzmán-Vargas

» Multicriteria optimization of a distributed trigeneration system in an industrial area (ID 154)
Dario Buoro, Melchiorre Casisi, Alberto de Nardi, Piero Pinamonti, Mauro Reini

» On the effect of eco-indicator selection on the conclusions obtained from an exergoenvironmental analysis (ID 275)
Tatiana Morosuk, George Tsatsaronis, Christopher Koroneos

» Optimisation of supply temperature and mass flow rate for a district heating network (ID 104)
Marouf Pirouti, Audrius Bagdanavicius, Jianzhong Wu, Janaka Ekanayake

» Optimization of energy supply systems in consideration of hierarchical relationship between design and operation (ID 389)
Ryohei Yokoyama, Shuhei Ose

» The fuel impact formula revisited (ID 279)
Cesar Torres, Antonio Valero

» The introduction of exergy analysis to the thermo-economic modelling and optimisation of a marine combined cycle system (ID 61)
George G. Dimopoulos, Chariklia A. Georgopoulou, Nikolaos M.P. Kakalis

» The relationship between costs and environmental impacts in power plants: an exergy-based study (ID 272)
Fontina Petrakopoulou, Yolanda Lara, Tatiana Morosuk, Alicia Boyano, George Tsatsaronis

» Thermo-ecological evaluation of biomass integrated gasification gas turbine based cogeneration technology (ID 441)
Wojciech Stanek, Lucyna Czarnowska, Jacek Kalina

» Thermo-ecological optimization of a heat exchanger through empirical modeling (ID 501)
Ireneusz Szczygieł, Wojciech Stanek, Lucyna Czarnowska, Marek Rojczyk

» Thermoeconomic analysis and optimization in a combined cycle power plant including a heat transformer for energy saving (ID 399)
Elizabeth Cortés Rodríguez, José Luis Castilla Carrillo, Claudia A. Ruiz Mercado, Wilfrido Rivera Gómez-Franco

» Thermoeconomic analysis and optimization of a hybrid solar-electric heating in a fluidized bed dryer (ID 400)
Elizabeth Cortés Rodríguez, Felipe de Jesús Ojeda Cámara, Isaac Pilatowsky Figueroa

» Thermoeconomic approach for the analysis of low temperature district heating systems (ID 208)
Vittorio Verda, Albana Kona

» Thermo-economic assessment of a micro CHP systems fuelled by geothermal and solar energy (ID 166)
Duccio Tempesti, Daniele Fiaschi, Filippo Gabuzzini

» Thermo-economic evaluation and optimization of the thermo-chemical conversion of biomass into methanol (ID 194)
Emanuela Peduzzi, Laurence Tock, Guillaume Boissonnet, François Marechal

» Thermoeconomic fuel impact approach for assessing resources savings in industrial symbiosis: application to Kalundborg Eco-industrial Park (ID 256)
Sergio Usón, Antonio Valero, Alicia Valero, Jorge Costa

» Thermoeconomics of a ground-based CAES plant for peak-load energy production system (ID 32)
Simon Kemble, Giampaolo Manfrida, Adriano Milazzo, Francesco Buffa

VOLUME IV

IV . 1 – FLUID DYNAMICS AND POWER PLANT COMPONENTS

» A control oriented simulation model of a multistage axial compressor (ID 444)
Lorenzo Damiani, Giampaolo Crosa, Angela Trucco

» A flexible and simple device for in-cylinder flow measurements: experimental and numerical validation (ID 181)
Andrea Dai Zotti, Massimo Masi, Marco Antonello

» CFD Simulation of Entropy Generation in Pipeline for Steam Transport in Real Industrial Plant (ID 543)
Goran Vučković, Gradimir Ilić, Mića Vukić, Milan Banić, Gordana Stefanović

» Feasibility Study of Turbo expander Installation in City Gate Station (ID 168)
Navid Zehtabiyan Rezaie, Majid Saffar-Avval

» GTL and RME combustion analysis in a transparent CI engine by means of IR digital imaging (ID 460)
Ezio Mancaruso, Luigi Sequino, Bianca Maria Vaglieco

» Some aspects concerning fluid flow and turbulence modeling in 4-valve engines (ID 116)
Zoran Stevan Jovanovic, Zoran Masonicic, Miroljub Tomic

IV . 2 – SYSTEM OPERATION CONTROL DIAGNOSIS AND PROGNOSIS

» Adapting the operation regimes of trigeneration systems to renewable energy systems integration (ID 188)
Liviu Ruieneanu, Mihai Paul Mircea

» Advanced electromagnetic sensors for sustainable monitoring of industrial processes (ID 145)
Uroš Puc, Andreja Abina, Anton Jeglič, Pavel Cevc, Aleksander Zidanšek

» Assessment of stresses and residual life of plant components in view of life-time extension of power plants (ID 453)
Anna Stoppato, Alberto Benato and Alberto Mirandola

» Control strategy for minimizing the electric power consumption of hybrid ground source heat pump system (ID 244)
Zoi Sagia, Constantinos Rakopoulos

» **Exergetic evaluation of heat pump booster configurations in a low temperature district heating network (ID 148)**
Torben Ommen, Brian Elmegaard

» **Exergoeconomic diagnosis: a thermo-characterization method by using irreversibility analysis (ID 523)**
Abraham Olivares-Arriaga, Alejandro Zaleta-Aguilar, Rangel-Hernández V. H, Juan Manuel Belman-Flores

» **Optimal structural design of residential cogeneration systems considering their operational restrictions (ID 224)**
Tetsuya Wakui, Ryohei Yokoyama

» **Performance estimation and optimal operation of a CO2 heat pump water heating system (ID 344)**
Ryohei Yokoyama, Ryosuke Kato, Tetsuya Wakui, Kazuhisa Takemura

» **Performances of a common-rail Diesel engine fuelled with rapeseed and waste cooking oils (ID 213)**
Alessandro Corsini, Valerio Giovannoni, Stefano Nardecchia, Franco Rispoli, Fabrizio Sciulli, Paolo Venturini

» **Reduced energy cost through the furnace pressure control in power plants (ID 367)**
Vojislav Filipović, Novak Nedić, Saša Prodanović

» **Short-term scheduling model for a wind-hydro-thermal electricity system (ID 464)**
Sérgio Pereira, Paula Ferreira, A. Ismael Freitas Vaz

VOLUME V

V . 1 – RENEWABLE ENERGY CONVERSION SYSTEMS

» **A co-powered concentrated solar power Rankine cycle concept for small size combined heat and power (ID 276)**
Alessandro Corsini, Domenico Borello, Franco Rispoli, Eileen Tortora

» **A novel non-tracking solar collector for high temperature application (ID 466)**
Wattana Ratismith, Anusorn Inthongkhum

» **Absorption heat transformers (AHT) as a way to enhance low enthalpy geothermal resources (ID 311)**
Daniele Fiaschi, Duccio Tempesti, Giampaolo Manfrida, Daniele Di Rosa

» **Alternative feedstock for the biodiesel and energy production: the OVEST project (ID 98)**
Matteo Prussi, David Chiaramonti, Lucia Recchia, Francesco Martelli, Fabio Guidotti

» **Assessing repowering and update scenarios for wind energy converters (ID 158)**
Till Zimmermann

» **Biogas from mechanical pulping industry – potential improvement for increased biomass vehicle fuels (ID 54)**
Mimmi Magnusson, Per Alvfors

» **Biogas or electricity as vehicle fuels derived from food waste - the case of Stockholm (ID 27)**
Martina Wikström, Per Alvfors

» **Compressibility factor as evaluation parameter of expansion processes in organic Rankine cycles (ID 292)**
Giovanni Manente, Andrea Lazzaretto

» **Design of solar heating system for methane generation (ID 445)**
Lucía Mónica Gutiérrez, P. Quinto Diez, L. R. Tovar Gálvez

» Economic feasibility of PV systems in hotels in Mexico (ID 346)
Augusto Sanchez, Sergio Quezada

» Effect of a back surface roughness on annual performance of an air-cooled PV module (ID 193)
Riccardo Secchi, Duccio Tempesti, Jacek Smolka

» Energy and exergy analysis of the first hybrid solar-gas power plant in Algeria (ID 176)
Fouad Khaldi

» Energy recovery from MSW treatment by gasification and melting technology (ID 393)
Fabrizio Strobino, Alessandro Pini Prato, Diego Ventura, Marco Damonte

» Ethanol production by enzymatic hydrolysis process from sugarcane biomass - the integration with the conventional process (ID 189)
Reynaldo Palacios-Bereche, Adriano Ensinas, Marcelo Modesto, Silvia Azucena Nebra

» Evaluation of gas in an industrial anaerobic digester by means of biochemical methane potential of organic municipal solid waste components (ID 57)
Isabella Pecorini, Tommaso Olivieri, Donata Bacchi, Alessandro Paradisi, Lidia Lombardi, Andrea Corti, Ennio Carnevale

» Exergy analysis and genetic algorithms for the optimization of flat-plate solar collectors (ID 423)
Soteris A. Kalogirou

» Experimental study of tar and particles content of the produced gas in a double stage downdraft gasifier (ID 487)
Ana Lisbeth Galindo Noguera, Sandra Yamile Giraldo, Rene Lesme-Jaén, Vladimir Melian Cobas, Rubenildo Viera Andrade, Electo Silva Lora

» Feasibility study to realize an anaerobic digester fed with vegetables matrices in central Italy (ID 425)
Umberto Desideri, Francesco Zepparelli, Livia Arcioni, Ornella Calderini, Francesco Panara, Matteo Todini

» Investigations on the use of biogas for small scale decentralized CHP applications with a focus on stability and emissions (ID 140)
Steven MacLean, Eren Tali, Anne Giese, Jörg Leicher

» Kinetic energy recovery system for sailing yachts (ID 427)
Giuseppe Leo Guizzi, Michele Manno

» Mirrors in the sky: status and some supporting materials experiments (ID 184)
Noam Lior

» Numerical parametric study for different cold storage designs and strategies of a solar driven thermoacoustic cooler system (ID 284)
Maxime Perier-Muzet, Pascal Stouffs, Jean-Pierre Bedecarrats, Jean Castaing-Lasvignottes

» Parabolic trough photovoltaic/thermal collectors. Part I: design and simulation model (ID 102)
Francesco Calise, Laura Vanoli

» Parabolic trough photovoltaic/thermal collectors. Part II: dynamic simulation of a solar trigeneration system (ID 488)
Francesco Calise, Laura Vanoli

» Performance analysis of downdraft gasifier - reciprocating engine biomass fired small-scale cogeneration system (ID 368)
Jacek Kalina

» Proposing offshore photovoltaic (PV) technology to the energy mix of the Maltese islands (ID 262)
Kim Trapani, Dean Lee Millar

» Research of integrated biomass gasification system with a piston engine (ID 414)
Janusz Kotowicz, Aleksander Sobolewski, Tomasz Iluk

» Start up of a pre-industrial scale solid state anaerobic digestion cell for the co-treatment of animal and agricultural residues (ID 34)
Francesco Di Maria, Giovanni Gigliotti, Alessio Sordi, Caterina Micale, Luisa Massaccesi

» The role of biomass in the renewable energy system (ID 390)
Ruben Laleman, Ludovico Balduccio, Johan Albrecht

» Vegetable oils of soybean, sunflower and tung as alternative fuels for compression ignition engines (ID 500)
Ricardo Morel Hartmann, Nury Nieto Garzón, Eduardo Morel Hartmann, Amir Antonio Martins Oliveira Jr, Edson Bazzo, Bruno Okuda, Joselia Piluski
» Wind energy conversion performance and atmosphere stability (ID 283)
Francesco Castellani, Emanuele Piccioni, Lorenzo Biondi, Marcello Marconi

V. 2 – FUEL CELLS

» Comparison study on different SOFC hybrid systems with zero-CO2 emission (ID 196)
Liqiang Duan, Kexin Huang, Xiaoyuan Zhang and Yongping Yang

» Exergy analysis and optimisation of a steam methane pre-reforming system (ID 62)
George G. Dimopoulos, Iason C. Stefanatos, Nikolaos M.P. Kakalis

» Modelling of a CHP SOFC power system fed with biogas from anaerobic digestion of municipal wastes integrated with a solar collector and storage units (ID 491)
Domenico Borello, Sara Evangelisti, Eileen Tortora

VOLUME VI

VI . 1 – CARBON CAPTURE AND SEQUESTRATION

» A novel coal-based polygeneration system cogenerating power, natural gas and liquid fuel with CO2 capture (ID 96)
Sheng Li, Hongguang Jin, Lin Gao

» Analysis and optimization of CO2 capture in a China's existing coal-fired power plant (ID 532)
Gang Xu, Yongping Yang, Shoucheng Li, Wenyi Liu and Ying Wu

» Analysys of four-end high temperature membrane air separator in a supercritical power plant with oxy-type pulverized fuel boiler (ID 442)
Janusz Kotowicz, Sebastian Stanisław Michalski

» Analysis of potential improvements to the lignite-fired oxy-fuel power unit (ID 413)
Marcin Liszka, Jakub Tuka, Grzegorz Nowak, Grzegorz Szapajko
» Biogas Upgrading: Global Warming Potential of Conventional and Innovative Technologies (ID 240)
Katherine Starr, Xavier Gabarrell Durany, Gara Villalba Mendez, Laura Talens Peiro, Lidia Lombardi

» Capture of carbon dioxide using gas hydrate technology (ID 103)
Beatrice Castellani, Mirko Filipponi, Sara Rinaldi, Federico Rossi

» Carbon dioxide mineralisation and integration with flue gas desulphurisation applied to a modern coal-fired power plant (ID 179)
Ron Zevenhoven, Johan Fagerlund, Thomas Björklöf, Magdalena Mäkelä, Olav Eklund

» Carbon dioxide storage by mineralisation applied to a lime kiln (ID 226)
Inês Sofia Soares Romão, Matias Eriksson, Experience Nduagu, Johan Fagerlund, Licínio Manuel Gando-Ferreira, Ron Zevenhoven

» Comparison of IGCC and CFB cogeneration plants equipped with CO2 removal (ID 380)
Marcin Liszka, Tomasz Malik, Michał Budnik, Andrzej Ziębik

» Concept of a "capture ready" combined heat and power plant (ID 231)
Piotr Henryk Lukowicz, Lukasz Bartela

» Cryogenic method for H2 and CH4 recovery from a rich CO2 stream in pre-combustion CCS schemes (ID 508)
Konstantinos Atsonios, Kyriakos D. Panopoulos, Angelos Doukelis, Antonis Koumanakos, Emmanuel Kakaras

» Design and optimization of ITM oxy-combustion power plant (ID 495)
Surekha Gunasekaran, Nicholas David Mancini, Alexander Mitsos

» Implementation of a CCS technology: the ZECOMIX experimental platform (ID 222)
Antonio Calabrò, Stefano Cassani, Leandro Pagliari, Stefano Stendardo

» Influence of regeneration condition on cyclic CO2 capture using pre-treated dispersed CaO as high temperature sorbent (ID 221)
Stefano Stendardo, Antonio Calabrò

» Investigation of an innovative process for biogas up-grading – pilot plant preliminary results (ID 56)
Lidia Lombardi, Renato Baciocchi, Ennio Antonio Carnevale, Andrea Corti, Giulia Costa, Tommaso Olivieri, Alessandro Paradisi, Daniela Zingaretti

» Method of increasing the efficiency of a supercritical lignite-fired oxy-type fluidized bed boiler and high-temperature three - end membrane for air separation (ID 438)
Janusz Kotowicz, Adrian Balicki

» Monitoring of carbon dioxide uptake in accelerated carbonation processes applied to air pollution control residues (ID 539)
Felice Alfieri, Peter J Gunning, Michela Gallo, Adriana Del Borghi, Colin D Hills

» Process efficiency and optimization of precipitated calcium carbonate (PCC) production from steel converter slag (ID 114)
Hannu-Petteri Mattila, Inga Grigaliūnaitė, Arshe Said, Sami Filppula, Carl-Johan Fogelholm, Ron Zevenhoven

» Production of Mg(OH)2 for CO2 Emissions Removal Applications: Parametric and Process Evaluation (ID 245)
Experience Ikechukwu Nduagu, Inês Romão, Ron Zevenhoven

» Thermodynamic analysis of a supercritical power plant with oxy type pulverized fuel boiler, carbon dioxide capture system (CC) and four-end high temperature membrane air seprator (ID 411)
Janusz Kotowicz, Sebastian Stanisław Michalski

VI . 2 – PROCESS INTEGRATION AND HEAT EXCHANGER NETWORKS

» A multi-objective optimization technique for co- processing in the cement production (ID 42)
Maria Luiza Grillo Renó, Rogério José da Silva, Mirian de Lourdes Noronha Motta Melo, José Joaquim Conceição Soares Santos

» Comparison of options for debottlenecking the recovery boiler at kraft pulp mills – Economic performance and CO2 emissions (ID 449)
Johanna Jönsson, Karin Pettersson, Simon Harvey, Thore Berntsson

» Demonstrating an integral approach for industrial energy saving (ID 541)
René Cornelissen, Geert van Rens, Jos Sentjens, Henk Akse, Ton Backx, Arjan van der Weiden, Jo Vandenbroucke

» Maximising the use of renewables with variable availability (ID 494)
Andreja Nemet, Jiri Jaromír Klemeš, Petar Sabev Varbanov, Zdravko Kravanja

» Methodology for the improvement of large district heating networks (ID 46)
Anna Volkova, Vladislav Mashatin, Aleksander Hlebnikov, Andres Siirde

» Optimal mine site energy supply (ID 306)
Monica Carvalho, Dean Lee Millar

» Simulation of synthesis gas production from steam oxygen gasification of Colombian bituminous coal using Aspen Plus® (ID 395)
John Jairo Ortiz, Juan Camilo González, Jorge Enrique Preciado, Rocío Sierra, Gerardo Gordillo

VOLUME VIII

VIII . 1 - ENERGY SYSTEMS : ENVIRONMENTAL AND SUSTAINABILITY ISSUES

» A multi-criteria decision analysis tool to support electricity planning (ID 467)
Fernando Ribeiro, Paula Ferreira, Madalena Araújo

» Comparison of sophisticated life cycle impact assessment methods for assessing environmental impacts in a LCA study of electricity production (ID 259)
Jens Buchgeister

» Defossilisation assessment of biodiesel life cycle production using the ExROI indicator (ID 304)
Emilio Font de Mora, César Torres, Antonio Valero, David Zambrana

» Design strategy of geothermal plants for water dominant medium-low temperature reservoirs based on sustainability issues (ID 99)
Alessandro Franco, Maurizio Vaccaro

» Energetic and environmental benefits from waste management: experimental analysis of the sustainable landfill (ID 33)
Francesco Di Maria, Alessandro Canovai, Federico Valentini, Alessio Sordi, Caterina Micale

» Environmental assessment of energy recovery technologies for the treatment and disposal of municipal solid waste using life cycle assessment (LCA): a case study of Brazil (ID 512)
Marcio Montagnana Vicente Leme, Mateus Henrique Rocha, Electo Eduardo Silva Lora,Osvaldo José Venturini, Bruno Marciano Lopes, Claudio Homero Ferreira

» How will renewable power generation be affected by climate change? – The case of a metropolitan region in Northwest Germany (ID 503)
Jakob Wachsmuth, Andrew Blohm, Stefan Gößling-Reisemann, Tobias Eickemeier, Rebecca Gasper, Matthias Ruth, Sönke Stührmann

» Impact of nuclear power plant on Thailand power development plan (ID 474)
Raksanai Nidhiritdhikrai, Bundhit Eua-arporn

» Improving sustainability of maritime transport through utilization of liquefied natural gas (LNG) for propulsion (ID 496)
Fabio Burel, Rodolfo Taccani, Nicola Zuliani

» Life cycle assessment of thin film non conventional photovoltaics: the case of dye sensitized solar cells (ID 471)
Maria Laura Parisi, Adalgisa Sinicropi, Riccardo Basosi

» Low CO2 emission hybrid solar CC power system (ID 175)
Yuanyuan Li, Na Zhang, Ruixian Cai

» Low exergy solutions as a contribution to climate adapted and resilient power supply (ID 489)
Stefan Goessling-Reisemann, Thomas Bloethe

» On the use of MPT to derive optimal RES electricity generation mixes (ID 459)
Paula Ferreira, Jorge Cunha

» Stability and limit cycles in an exergy-based model of population dynamics (ID 128)
Enrico Sciubba, Federico Zullo

» The influence of primary measures for reducing NOx emissions on energy steam boiler efficiency (ID 125)
Goran Stupar, Dragan Tucaković, Titoslav Živanović, Miloš Banjac, Srđan Belošević,Vladimir Beljanski, Ivan Tomanović, Nenad Crnomarković, Miroslav Sijerčić

» The Lethe city car of the University of Roma 1: final proposed configuration (ID 45)
Roberto Capata, Enrico Sciubba

VIII . 2 - POSTER SESSION

» A variational optimization of a finite-time thermal cycle with a Stefan-Boltzmann heat transfer law (ID 333)
Juan C.Chimal-Eguia, Norma Sanchez-Salas

» Modeling and simulation of a boiler unit for steam power plants (ID 545)
Luca Moliterno, Claudia Toro

» Numerical Modelling of straw combustion in a moving bed combustor (ID 412)
Biljana Miljkoviü, Ivan Pešenjanski, Borivoj Stepanov, Vladimir Milosavljeviü, Vladimir Rajs

» Physicochemical evaluation of the properties of the coke formed at radiation area of light hydrocarbons pyrolysis furnace in petrochemical industry (ID 10)
Jaqueline Saavedra Rueda , Angélica María Carreño Parra, María del Rosario Pérez Trejos, Dionisio Laverde Cataño, Diego Bonilla Duarte, Jorge Leonardo Rodríguez Jiménez, Laura María Díaz Burgos

» Rotor TG cooled (ID 121)
Chiara Durastante, Paolo Petroni, Michela Spagnoli, Vincenzo Rizzica, Jörg Helge Wirfs

» Study of the phase change in binary alloy (ID 534)
Aroussia Jaouahdou, Mohamed J. Safi, Herve Muhr

» Technip initiatives in renewable energies and sustainable technologies (ID 527)
Pierfrancesco Palazzo, Corrado Pigna

ECOS 2012

VOLUME VII

A Linear Programming model for the optimal assessment of Sustainable Energy Action Plans.

Gianfranco Rizzo[a], Giancarlo Savino[b]

[a] Department of Industrial Engineering, University of Salerno,Fisciano (SA), Italy, grizzo@unisa.it
[b] Energy Manager, City of Salerno, Italy, g.savino@comune.salerno.it

Abstract:

A relevant effort is being spent to reach the EU climate and energy goals by involving European cities and towns in sustainable energy planning. Many Italian and European cities are now involved in the development of Sustainable Energy Action Plans (SEAP), presenting in detailed way the actions finalized to the reduction of CO_2 emissions. In most cases, a large number of actions are proposed, ranging from renewable energy production to energy saving and to information and communication actions. It therefore emerges the need of methodologies for guiding the administrators to the selection of the most effective actions for the achievement of the desired emission reduction, compatibly with budget and resource availability.
A Linear Programming model for the optimal selection of the actions and of their priorities is presented. The model allows to allocate in optimal way the economic resources among different actions to achieve a given level of CO_2 emissions reduction, considering resource constraints. The model has a user-friendly interface, and a complexity compatible with applications to municipal level. An example of application of the model to a school is presented and discussed.

Keywords:

Model, Linear Programming, Energy Plan.

1. Introduction

In last decades there are growing concerns about fossil fuel reserve depletion, greenhouse effect and related climate changes. After ratification of the Kyoto protocol [1], a relevant effort is being spent by Europe to enhance renewable energy production and to promote energy efficiency. In December 2008, the EU adopted an integrated energy and climate change policy (20/20/20), with ambitious targets for 2020: cutting greenhouse gases by 20%; reducing energy consumption by 20% through increased energy efficiency; meeting 20% of energy needs from renewable sources [2].

In order to reach these goals, an active participation of European cities and towns in sustainable energy planning has been stimulated by the European institutions. Many European cities are now involved in the development of Sustainable Energy Action Plans (SEAP), presenting in a detailed way the actions finalized to the reduction of CO_2 emissions [3]. In Italy, 1225 municipalities have joined the Covenant of Major, while only 16% of them have already produced the SEAP (January 2012) [5]. Most of them are located in the North of Italy (***Fig. 1***).

A study on a set of SEAP produced in eight representative Italian cities (Alessandria, Bergamo, Cesena, Modena, Padova, Piacenza, Torino, Udine) is being carried out by the authors, within the studies to develop the SEAP for the city of Salerno [26] [28]. In most cases, a large number of actions are proposed, ranging from renewable energy production to energy saving, to information and communication actions and to stakeholders involvement. The analysis has demonstrated a certain lack of quantitative data in part of the proposed actions.

Moreover, when quantitative evaluations of costs and benefits in terms of CO_2 reduction and/or energy savings of each proposed action are provided (***Table 1***), any indication of priorities or selection criteria among them is missing. Actually, most of the planned actions have quite different cost effectiveness in terms of CO_2 reductions and energy savings, as evidenced by the graphs

reported in Fig. 2, representing: i) the avoided CO_2 versus energy savings (upper part) and ii) their unit costs (lower part) for a set of actions and cities (listed in the legend). The analysis of the data shows that there is more than one order of magnitude between the unit costs related to different actions. Moreover, a significant spread between the unit costs of same actions for different cities also occurs [26].

Fig. 1. Number of Italian cities that have completed the SEAP

Table 1. Analysis of a group of Italian SEAPs. Actions and Cities.

	Alessandria	Bergamo	Cesena	Modena	Padova	Piacenza	Torino	Udine	Total
Biomass	1	0	1	0	0	0	0	1	3
PV plants	0	1	1	1	1	0	0	1	5
LED for traffic lights	0	1	0	1	1	1	1	1	6
Street lighting optimization	0	1	0	1	1	1	1	1	6
Private Building Optimization	0	1	1	1	0	0	1	0	4
Public Building Optimization	0	1	0	0	0	0	1	1	3
RSU	0	0	0	0	0	0	1	0	1
Thermal Solar Plants	1	0	1	0	0	0	1	1	4
District Heating	1	1	0	0	0	1	0	1	4
Public Transportation	1	0	0	0	1	0	1	0	3
Total	4	6	4	4	4	3	7	7	39

Therefore, it is apparent that a selection criteria between different actions could be needed, at least in case of partial availability of financial resources. Moreover, some of these actions could be mutually exclusive or subject to some common constraints: for instance, space heating requirements could be satisfied by use of solar thermal panels or cogeneration plants, but also reduced by proper building insulation; similarly, the installation of solar thermal panels or photovoltaic panels on building roofs cannot exceed the available surface. It is evident that, in many cases, the decisions about possible alternative actions are somewhat interrelated and not independent of each other.

The above considerations evidence the need of methodologies for guiding the administrators to the selection of the most effective actions for the achievement of the desired emission reduction, compatibly with budget and resource availability.

A review on the models available in literature for energy and environmental planning is summarized in next chapter, while a model based on Linear Programming, particularly suitable for

small scale and municipal level, is presented in the following chapters, and some results are discussed.

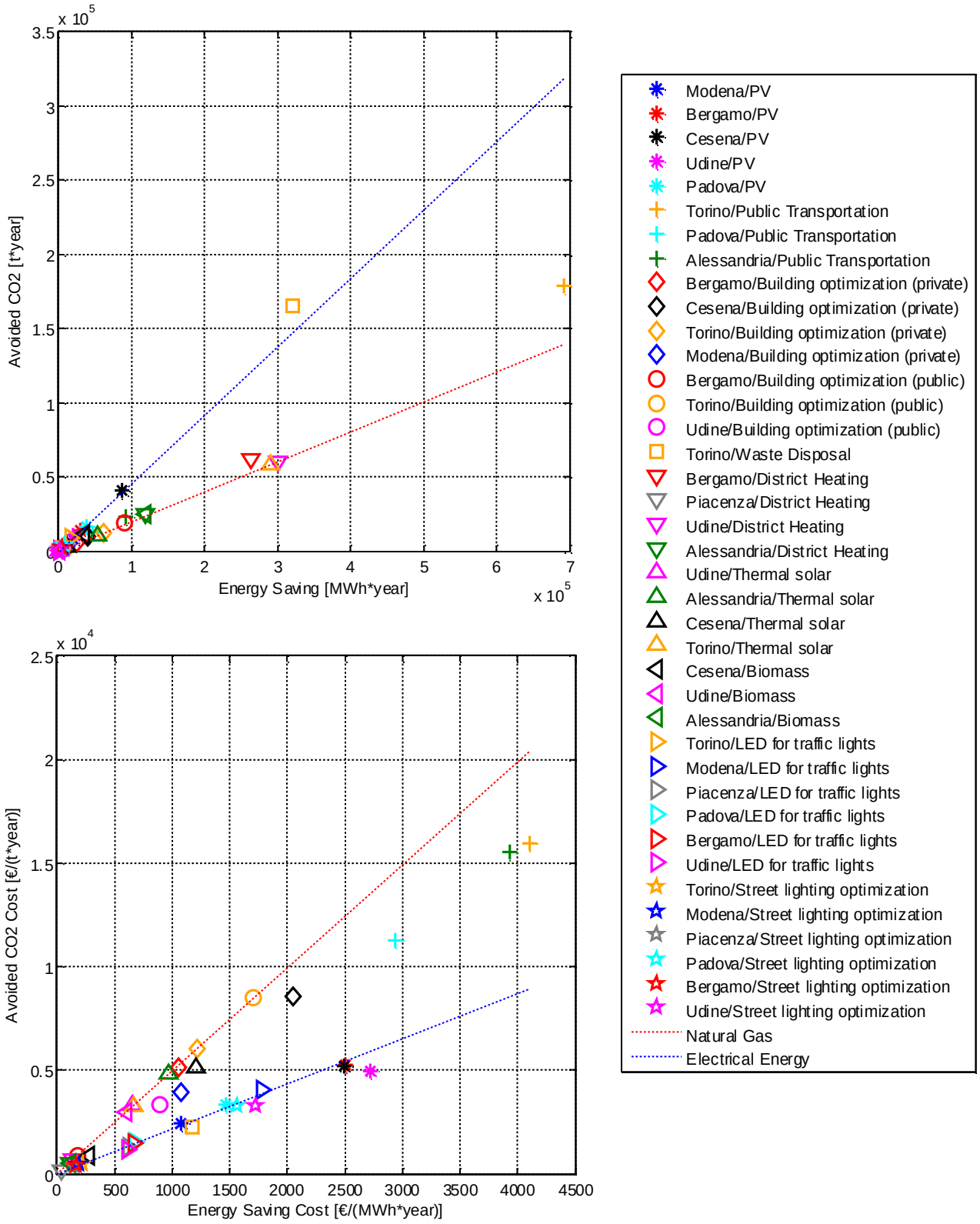

Fig. 2. Analysis of a group of Italian SEAPs. Avoided CO_2 vs Energy savings (up) - Avoided CO_2 Unit Cost vs Energy savings unit cost (down)

2. Models for Energy Systems

Several models have been developed to study and plan the evolution of complex systems involving interaction of economic, energetic and environmental aspects. A large review of models used for energy studies, at different levels and approaches, is available in [20]. In the early '70s, the model WORLD3 was used to model the interactions between population, industrial growth, food production and limits in the ecosystems of the Earth [6].

Some years later, the MARKAL models generator was developed by a consortium of 14 countries under the aegis of an IEA committee (Energy Technology Systems Analysis Development Programme, ETSAP), with a specific focus on energy system analysis [7]. Starting from the original formulation, further implementations have been carried out to account for different situation and purposes. A short overview of MARKAL models is presented in ***Table 2***. The mathematical approach is mainly based on Linear Programming (LP), while Non-Linear Programming (NLP), Multiple Integer Programming (MIP) and Stochastic Programming (SP) are also used. Further details, with reference to selected bibliography, is available in [8]. The MARKAL models are now widely used in many countries to support energy-environmental planning at national and local scale [9][10][11].

Specific tools have also been developed at the Environmental Protection Agency (EPA) in U.S.. The "Integrated Planning Model" (IPM) allows to analyze the impact of air emissions policies on the U.S. electric power sector. EPA has used multiple iterations of the IPM model in various analyses of regulations and legislative proposals [13].

Table 2. Overview of the MARKAL family of models (from[8]).

Member /Version	Type of Model	Short Description
MARKAL	**LP**	Standard model. Exogenous energy demand
MARKAL-MACRO	**NLP**	Coupling to macro-economic model energy demand endogenous.
MARKAL-MICRO	**NLP**	Coupling to micro-economic model, energy demand endogenous, responsive to price changes.
MARKAL-ED (MED)	**LP**	As MARKAL-MICRO but with step-wise linear representation of demand function.
MARKAL	**NLP**	Linkage of multiple countries specific MARKAL-MED With multiple regions and MARKAL-MACRO, including trade of emission Permits.
MARKAL	**LP**	Besides energy flows (electricity, heat) material flows with material flows and recycling of materials can be modeled in the RES.
MARKAL	**SP**	Stochastic Programming. Only with standard model. With Uncertainties
MARKAL – ETL	**MIP**	Endogenous technology learning based on learning-by-doing curve. Specific cost decreases as function of cumulative experience.

Some models address specifically the energy plans at municipal level [21]-[25]. Both general models [21] [22] [25] and specific models, i.e. for Solid Waste Management [23], have been developed. However, in some cases the term 'municipal' may be misleading, being referred to very large communities as Beijing [21].

The MARKAL and IPM models, in their numerous versions, can cover most, if not all, of the possible cases occurring in the study of an energy and environmental system, and could certainly be adapted to study actions at municipality level, as considered by SEAP. However, their modelling structure is quite complex, and their use is probably more suitable in academic and government agencies context rather than at municipal level, in particular for a small or medium size town or city. On the other hand, at a local level interactions with macro-economic aspects, material flows

and prices changes, representing the distinctive features of the MARKAL or IPM models, are of course less relevant than at regional or national level. In next chapter a simpler LP model will be presented, specifically tailored to the exigencies of small scale systems, as for a SEAP at municipal level.

3. The proposed LP model

The proposed methodology is based on the solution of an optimal resource allocation problem by means of a Linear Programming (LP) approach. The classical LP problem consists of the determination of the decision variable vector x minimizing a linear objective function $F(x)$:

$$min_x F(x) = \sum_{i=1}^{n} f_i * x_i \quad (1)$$

subject to linear equality constraints:

$$A_{eq,i} x = B_{eq} \quad (2)$$

and to linear inequality constraints:

$$A_i x \leq B \quad (3)$$

Starting from its basic formulation from Dantzig [15], several different versions of LP methods have been proposed, for the solution of different problems. In the present case, the solution is obtained by means of the Simplex method, as implemented in the Matlab function 'linprog' [16].

The decisions variables x_i represent a measure of the investment in each action. Their units vary according to the specific action considered, as specified in ***Table 3***. Regarding their nature, x_i are real and non-negative numbers. In case of LED, x_3 should be indeed an integer number, representing the optimal number of lamps. However, it is treated as a real number, being its value quite large (particularly in applications at municipal level). The result of the optimization problem is therefore approximated to the nearest integer number.

The objective function $F(x)$ (1) is expressed as a linear combination of the product of decision variables x_i and terms f_i:

$$f_i = i_i - r_i T \quad (4)$$

where i_i is the yearly unit investment and r_i is the yearly unit revenue associated to the i-th action, while T is the time horizon, in years. The objective function therefore represents the global investment needed by the decision maker (the municipality) to achieve a given level of CO_2 emissions, minus the possible revenues associated to the actions, achieved in the given time horizon. Both short and long terms strategies can be examined by varying T.

In particular, if T is set to zero, no revenues are considered. Therefore, the solutions corresponding to the minimum investment needed to achieve the given level of CO_2 reduction are sought. This solution would then represent the minimum cost strategy to achieve the given emissions reduction, regardless of future revenues.

The variable B_{eq} in the equality constraint (2) represents the global reduction of CO_2 emission, while the diagonal terms of the matrix A_{eq} contain the unit impact factors of the actions x_i on CO_2 emissions.

The inequality constraints (3) express the availability of resources to be allocated to the actions x, where variable B is the maximum available resource for each group of actions, and the matrix A indicates the correspondence between each action and a group of resources.

An additional inequality constraint (5) expresses the conditions that the total required investment I must be not greater than the available economic resource I_{max}:

$$\sum_{i=1}^{n} x_i i_i \leq I_{max} \quad (5)$$

The solution of the problem is achieved for two scenario's with different time horizon, i.e. Short Term (T=0) and Long Term (T=20). In the former case, the solutions corresponding to the minimum investment compatible with the given emission reduction are obtained, regardless the long term result. In the second case, the maximum long term results are obtained, of course with a greater initial investment. The results corresponding to intermediate investment values between these two limit cases are also investigated, by imposing suitable values to the maximum allowed investment in (5).

For each scenario, the whole range of emissions reduction B_{eq} is examined. Therefore, a complete picture of the required actions, of their priorities and of the needed investment is provided, both in tabular and in graphical form.

Some general comments on the linear assumption of the model seem necessary. As shown in ***Table 2*** and in literature review presented in the previous chapter, Linear Programming is one of the most used techniques for energy planning problems. Although most physical systems involved in such problems are inherently non-linear in nature, the relationship between the decision variables and the output variables can often be approximated by linear relationships. With reference to the actions considered in this paper and in the on-going applications to municipal level, there are certainly some scale effects related to the size of the plant, affecting unit costs, and possibly efficiencies and CO_2 emissions. In case that these effects are relevant, they could be treated by non-linear relationships, so leading to a non-linear optimization problem, characterized by a significant increase in complexity and computational burden with respect to a LP problem. Another way to tackle the problem is to consider separately the actions referring to small, medium or large plants, where each class of plants can be characterized by (approximate) linear relationships between decision variables and output variables. This approach, that seems more suitable at small or medium scale energy systems, could allow to maintain the advantages of Linear Programming with only a moderate increase in problem dimensionality.

4. An example of application

In order to check the operation of the model on a small scale example, the case of a school has been considered. The energy required is for space heating (in the period from November 15 to April 30) and electricity and hot water (all the year, except August), while no air conditioning is required. Different solutions have been considered:

A. Solar thermal collectors for hot water and space heating, with seasonal storage.
B. Photovoltaic (PV) panels (the surplus electricity is sold to the grid).
C. Reduction of electricity demand by adopting LED.
D. Cogeneration plant (CHP), fueled with natural gas (the surplus electricity is sold to the grid).
E. Reduction of thermal energy demand by building insulation.

Investment costs, yearly savings and avoided CO_2 per unit are reported in Table 3, for each action. They represent respectively the terms i and r in equations (4) and (5), and the terms A_{eq} in equation (2). For instance, in case of PV panels (second row) the decision variable x_2 is represented by panel surface in m^2, the term f_2 (4) is equal to 300-50·T, while 70 is the estimated yearly avoided CO_2 per unit (square meter), representing the term $A_{eq2,2}$ in the equality constraint (2).

Table 3. Actions, unit cost, savings and avoided CO_2.

Actions	Unit	Unit cost €	Savings €/year/unit	Avoided CO_2 kg/year*unit
Thermal Solar + Seasonal Storage	m^2	750	50	300
PV panels	m^2	300	40	70
LED	No. of lamps	100	20	50
CHP with methane	kWe	2000	680	1600
Building insulation	€	1	0,24	0,45

The links between actions and resources are summarized in ***Table 4***. In the second row the maximum available resource for each action is reported, representing the terms *B* in equation (3). They express the maximum allowed surface for solar panels (the sum of thermal and photovoltaic), the maximum number of LED lamps, the maximum electric power for co-generator and the actual thermal load of the building. The correspondence between each action and the resources, representing matrix A in (3), is also presented in the lower part of the table. In this case, the matrix expresses a link between solar thermal panels and PV panels (second column), whose surface cannot exceed the total available surface of 200 m^2. A further constraint (last column) connects thermal panels, CHP plant and building insulation, since their effect cannot exceed the given yearly thermal load, estimated in 91500 kWh. In other words, their effects are additive, and should not exceed the required thermal load to avoid energy waste. The use of LED lamps, instead, is not linked to the other actions related to electrical energy production (PV panels and CHP), since it is assumed that the excess electrical energy can be sold to the grid.

Table 4. Actions and available resources.

Resource	Panel Surface [m^2]	N lamps [/]	CHP [kWe]	Thermal load [kWht/year]
Availability	200	80	100	91500
Actions				
Thermal Solar + Seasonal Storage	1	0	0	450
PV panels	1	0	0	0
LED	0	1	0	0
CHP with methane	0	0	1	17520
Building insulation	0	0	0	2,25

The data in the tables have been estimated starting from average producibility of solar plant, cost of natural gas and of electricity in Italy, studies on thermal solar plants with seasonal storage and literature data on building insulation costs and performance. It has to be remarked, however, that the main purpose of this calculation is to check and illustrate the features of the proposed method, rather than to design in detailed way the best energy system for a school. Of course, more precise and complex methods exist for thermal design and optimization of buildings, also including non-linear and transient effects, that are not considered in this analysis [17], [18], [19].

4.1. Results

A global picture of the results, in terms of investment, costs and CO_2 reduction, is provided in Fig. 3. The optimal size of investment and the related profit for each action is shown in Fig. 4, for the two scenarios (short term and long term). It is timely to remark that, both in short and long term scenarios, profits are evaluated after the same time horizon (i.e.20 years). However, while in long term scenario profit coincides with the objective function (1), in the short term case (T=0) the long term profit corresponding to the minimum investment is computed.

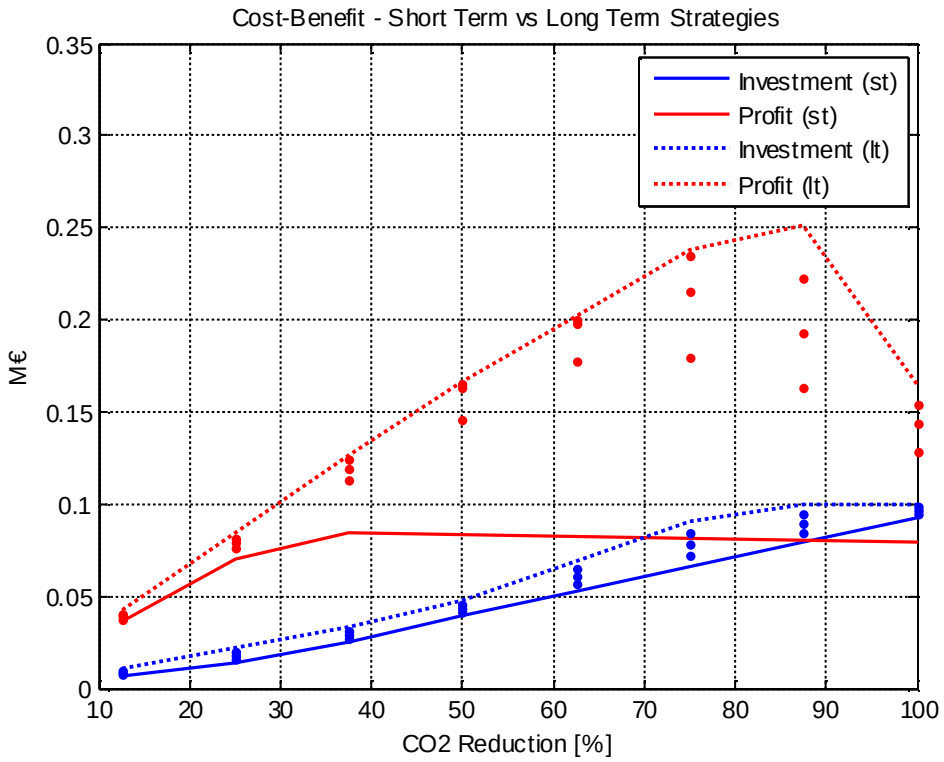

Fig. 3. Optimal results - Investment Costs and Profit vs CO_2 reduction

In Fig. 3, the short term scenario is indicated by continuous lines, while dotted lines represent the long term scenario. To achieve a given CO_2 reduction, different solutions are available, with investment costs ranging from a minimum value (continuous blue line) to a maximum value (dotted blue line). In correspondence, profit also ranges from a minimum value (red continuous line) to a maximum value (red dotted line). Intermediate results are indicated by blue and red stars.

It can be observed that the investment costs (blue lines) are always increasing with CO_2 reduction. The dotted line stops at 0.1 M€, representing the maximum allowed investment I_{max}. The slope of profit (red lines), instead, tends to decrease, and to become negative. This tendency is much more evident for the dotted line (long term). In this case (upper part of Fig. 4), the actions corresponding to higher profit per avoided emission unit are first selected (building insulation, in this case), then the other actions (PV panels, LED and thermal panels). It can be observed that, when the emission reduction increases, a gradual substitution between PV and thermal panels occurs, due to the constraint on maximum available surface. Similarly, the investment in building insulation decreases when thermal solar panels are adopted. For the actions not conflicting with others (i.e. LED lamps), the investment gradually increases until the saturation level is reached.

For the short term scenario (lower part of Fig. 4) the most convenient solutions in terms of initial investment versus CO_2 reduction are first selected. In this case, the suggested actions are CHP, LED and thermal solar panels. It can be also observed that, when investment for thermal solar panel increases, the size of CHP plant is reduced, to satisfy the constraint on the thermal load.

It can be observed that there is a large difference between the minimum and the maximum profit, corresponding to short and long term scenarios. The difference is small at lower investment values, growths to their maximum at about 87% of CO_2 reduction, when the maximum allowed investment (blue dotted line) reaches the limit value of 0.1 M€ (Fig. 3). After this value, the differences between short and long terms scenarios tend to decrease again. It emerges, therefore, that, for a large range of CO_2 emissions, even small differences in investment costs (blue) may produce large differences in profit, at the same level of CO_2 emissions. An analysis limited only to investment costs and related CO_2 emissions could therefore strongly penalize the long term results, while much better profits could be obtained with only a slight increase in initial investment.

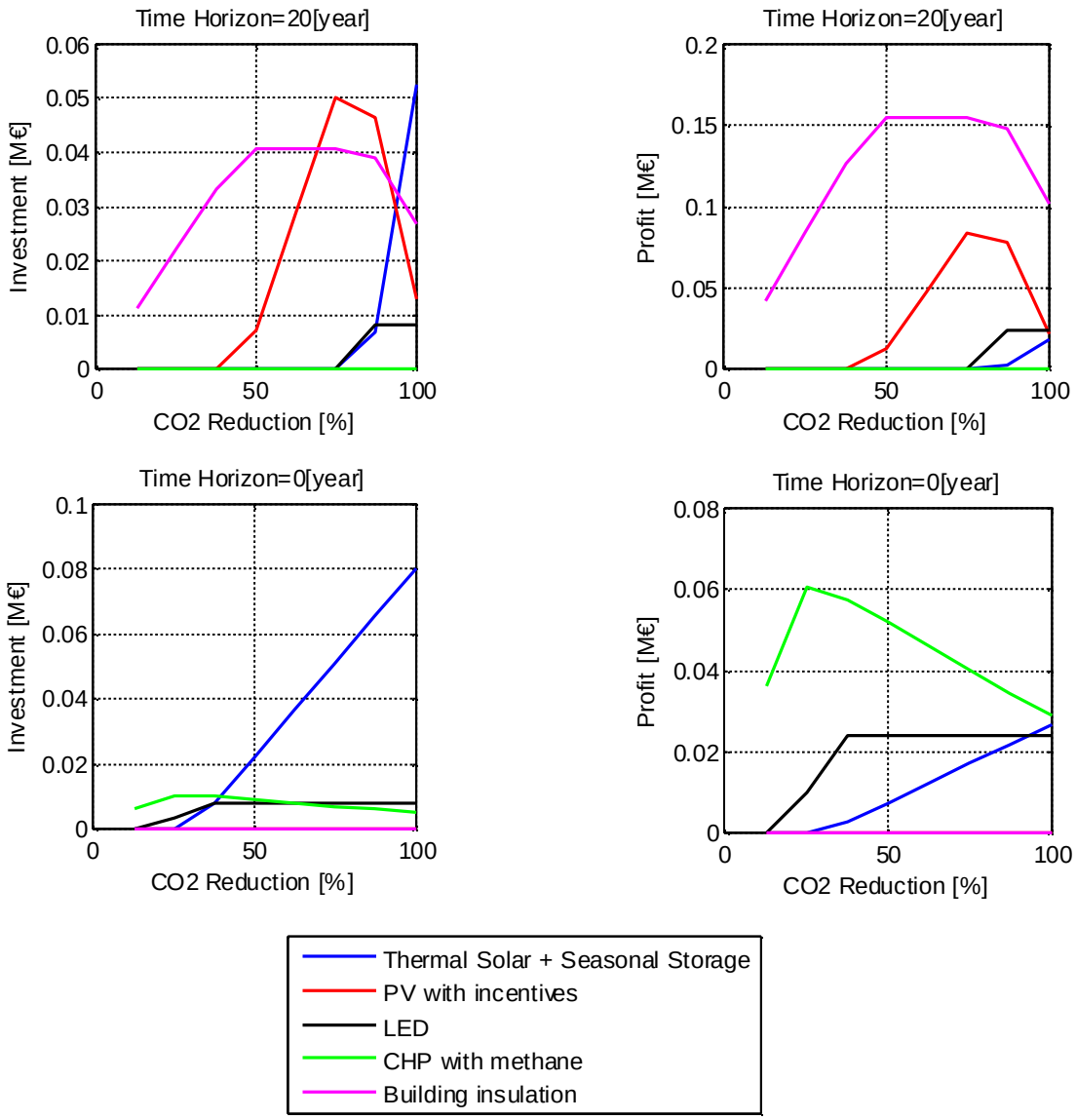

Fig. 4. Optimal results - Investment and profit for each action vs CO_2 reduction

It is worth noting that the CO_2 reduction can even exceed 100% of the original CO_2 emissions. In fact, the production of electrical energy via CHP and PV panels is not necessarily limited to the electrical load of the school, since it can be sold to the grid.

A graph with the ratio between profit and investment is presented in ***Fig. 5***. This ratio ranges between 1 and 5,5, approximately. Similar graphs are obtained to describe the optimal size of the proposed actions, versus CO_2 reduction and investment. Two graphs refer to optimal surface of PV plant, reaching their maximum value at a CO_2 reduction of about 75% (***Fig. 6***), and to optimal number of LED lamps, that tend to be selected only for CO_2 reduction greater than 30% (***Fig. 7***). Similar graphs, not reported in the paper due to space constraints, are obtained for the other planned actions.

The set of results presented above has been obtained by solving the LP problem (1)-(5) 45 times, for different values of constraints on CO_2 level and maximum allowed investment. About 100 graphs and several tables in Excel were automatically generated. Computational time is about 50 seconds on a Desktop PC (CPU Intel® Core™ i3, 4 GB RAM, 3.07 GHz).

These results demonstrate that, even considering a relatively simple energy system as a school, a rather complex picture emerges and articulate strategies are needed to achieve the best results in

terms of CO_2 reduction, with limited economic resources and in presence of constraints between the different actions.

The best mix of solutions depends on the target emission reduction, and therefore on the available financial resources. Moreover, even if provided by a linear model, the solutions are not linear with respect to the output (CO_2 emissions reduction): in other words, the best solution to achieve 100% reduction of CO_2 is not simply obtainable (i.e. doubling each action) from the solution corresponding to 50% reduction, as clearly shown in ***Fig. 4***. In fact, passing from 50% to 100% reduction, the best solution is obtained not only incrementing some actions, but also reducing some others.

This implies that a clear picture of objectives and of available resources is required at the start of the project, since the best strategy to enhance system performance (i.e. increase CO_2 reduction) could not be simply obtained by additional investments on an existing plant, even if starting from an optimal solution.

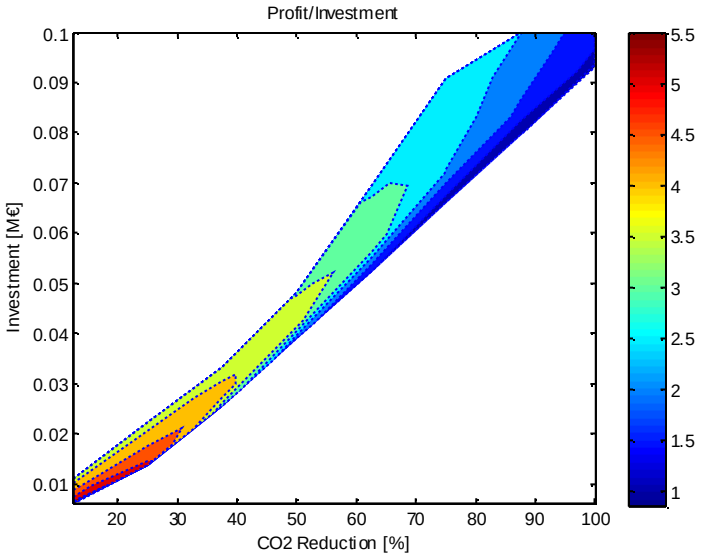

Fig. 5. Optimal results – Ratio between profit and investment vs. CO_2 reduction.

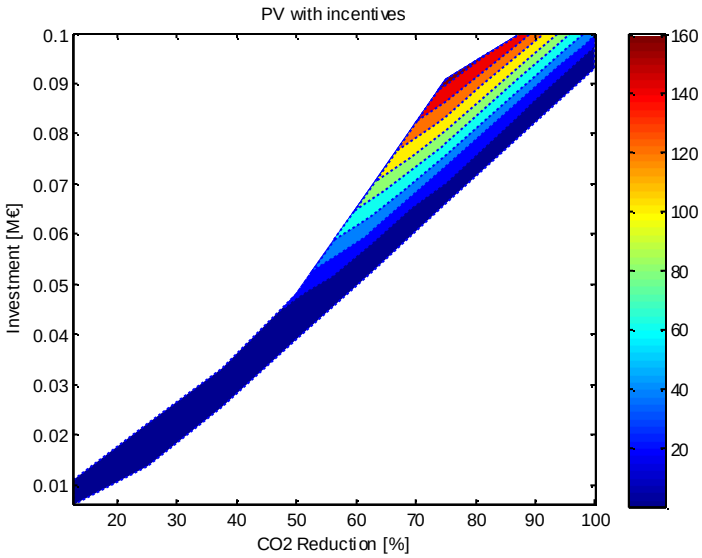

Fig. 6. Optimal results – Optimal surface of PV panels (m^2) vs. CO_2 reduction.

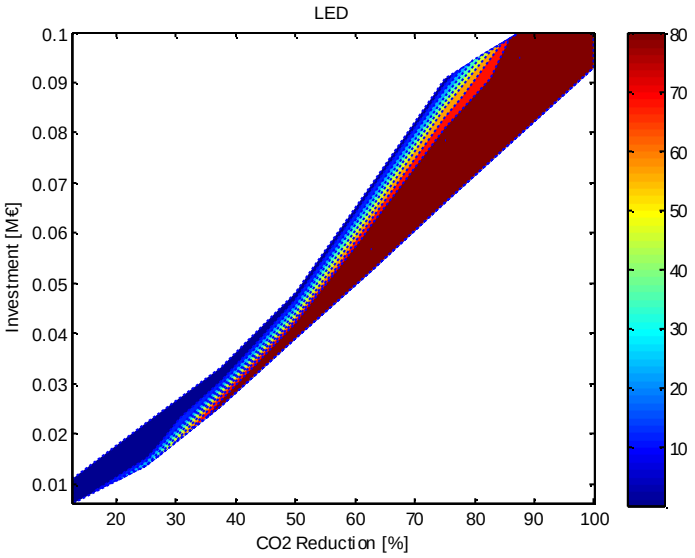

Fig. 7. Optimal results – Number of LED lamps vs. CO_2 reduction.

5. Conclusions

A methodology to assess the optimal combination of actions to achieve given CO_2 emission reduction, considering their effectiveness and costs, has been presented. The proposed procedure is particularly suitable at a municipality level, to assist the development of Sustainable Energy Action Plans.

The methodology, based on a Linear Programming approach, provides the optimal selection of the actions and of their priorities in order to achieve the best environmental benefits in presence of limited economic resources and of constraints between the different actions. The results, obtained by application of the model to a school, have evidenced that not straightforward strategies can be required to achieve the best mix of the planned actions in order to maximize the environmental benefits, for different availability of economic resources. It has also been shown that the analysis cannot be limited to the minimization of investment costs for given emission reduction, since long term effects could be significantly penalized by this approach. This result is of practical relevance for the assessment of the Sustainable Energy Action Plans, since in most of the analyzed cases only investment costs and impact on CO_2 emissions were provided in the documents, regardless of their long term economic impact. This approach could lead into significant inefficiencies in terms of allocation of financial resources.

The procedure is actually in course of application to the development of Sustainable Energy Action Plan for the city of Salerno, in South Italy. In this case, the actions are being treated at aggregate levels (i.e. buildings are not described individually, but as clusters of homogeneous cases; the same happens for infrastructures and transport systems). A study on SEAP of different Italian cities [5] [26] [28] has shown that the number of different actions considered is of the order of ten (***Table 1***). It is therefore expected that the total number of actions will be not very large, and that it will compatible with the proposed method, in terms of computational burden and of robustness.

References

[1] The Kyoto Protocol, available at <http://unfccc.int/kyoto_protocol/items/2830.php>

[2] European Commission, Climate Action Documents and Publications, available at <http://ec.europa.eu/climateaction/key_documents/index_en.htm>

[3] P.Bertoldi, D.Bornás Cayuela, S.Monni, R.Piers de Raveschoot, Existing Methodologies and Tools for the Development and Implementation of Sustainable Energy Action Plans (SEAP),

Publications Office of the European Union, 2010, JRC56513, ISBN: 978-92-79-14852-1, ISSN: 1018-5593.

[4] Convenant of Majors, available at <http://www.eumayors.eu>

[5] Italian Cities belonging to Convenant of Majors, available at <http://www.campagnaseeitalia.it/il-patto-dei-sindaci>

[6] D.H. Meadows, D.L. Meadows, J.Randers, and W.W. Behrens III. (1972), The Limits to Growth. New York: Universe Books. ISBN 0-87663-165-0.

[7] Fishbone LG, Abilock H., MARKAL - A linear-programming model for energy system analysis: technical description of the BNL version. Int J Energy Res 1981;5:353–75.

[8] Mohammad Reza Faraji Zonooz, Z.M. Nopiah, Ahmad Mohd Yusof, Kamaruzzaman Sopian, "A Review of MARKAL Energy Modeling", European Journal of Scientific Research, ISSN 1450-216X Vol.26 No.3 (2009), pp.352-361

[9] E. Endoa, M. Ichinoheb, Analysis on market deployment of photovoltaics in Japan by using energy system model MARKAL, Solar Energy Materials & Solar Cells 90 (2006) 3061–3067

[10] M. Salvia, C. Cosmi, M. Macchiato, L. Mangiamele, Waste management system optimisation for Southern Italy with MARKAL model, Resources, Conservation and Recycling, 34 (2002) 91–106.

[11] Johnsson J, Bjorkqvist O, Wene C-O. Integrated energy-emissions control planning in the community of Uppsala. Int J Energy Res 1992;16:173–95.

[12] ETSAP, Energy Technology Systems Analysis Program, available at <http://www.iea-etsap.org>

[13] EPA Integrated Planning Model, available at <http://www.epa.gov/airmarkt/progsregs/epa-ipm/index.html>

[14] City Energy Plan, Salerno (in Italian), available at <http://www.dimec.unisa.it/PEC_Salerno>

[15] G.B Dantzig, Maximization of a linear function of variables subject to linear inequalities, 1947. Published pp. 339–347 in T.C. Koopmans (ed.):Activity Analysis of Production and Allocation, New York-London 1951 (Wiley & Chapman-Hall).

[16] Linear Programming on Matlab, available at <http://www.mathworks.it/help/toolbox/optim/ug/linprog.html>

[17] D.B. Crawley, L.K. Lawrie, F.C. Winkelmann, W.F. Buhl, Y.J. Huang, C.O. Pedersen, R.K. Strand, R.J. Liesen, D.E. Fisher, M.J. Witte, J. Glazer, EnergyPlus: creating a new-generation building energy simulation program, Energy and Buildings, pp. 319-331, vol. 33, 2001

[18] J. A. Clarke, J. Cockroft, S. Conner, J. W. Hand, N. J. Kelly, R. Moore, T. O'Brien, P. Strachan, Simulation-assisted control in building energy management systems, Energy and Buildings, pp. 933-940, vol. 34, 2002.

[19] Building Energy Software Tools Directory, US Dept. Of Energy, available on http://apps1.eere.energy.gov/buildings/tools_directory/subjects_sub.cfm

[20] S. Jebaraja, S. Iniyanb, A review of energy models, Renewable and Sustainable Energy Reviews, 10 (2006) 281–311

[21] Q.G. Lin, G.H. Huang, Planning of energy system management and GHG emission control in the Municipality of Beijing - An inexact-dynamic stochastic programming model, Energy Policy 37(2009) 4463–4473.

[22] Clas-Otto Wene, Bo Rydén, A comprehensive energy model in the municipal energy planning process, European Journal of Operational Research, Volume 33, Issue 2, January 1988, Pages 212–222

[23] Guohe Huang, Brian W. Baetz and Gilles G. Patry, A Grey Linear Programming Approach for Municipal Solid Waste Management Planning under Uncertainty, Civil Engineering Systems, Volume 9, Issue 4, 1992

[24] Jenny Ivner, Municipal Energy Planning – Scope and Method Development, PhD Thesis, Linköping Studies in Science and Technology, Dissertation no. 1234

[25] Dag Henning, MODEST—An energy-system optimisation model applicable to local utilities and countries, Energy, Volume 22, Issue 12, December 1997, Pages 1135–1150

[26] Daniele Galdi, Piani d'Azione per l'Energia Sostenibile: analisi quantitativa delle azioni proposte, Bachelor Thesis in Mechanical Engineering, University of Salerno, February 2012, in Italian.

[27] Gabriele Orlando, Modelli per la pianificazione energetica ed ambientale, Bachelor Thesis in Mechanical Engineering, University of Salerno, February 2012, in Italian.

[28] Vito Di Guida, Analisi comparata dei Piani d'Azione per l'Energia Sostenibile, Bachelor Thesis in Mechanical Engineering, University of Salerno, February 2012, in Italian.

Acknowledgments

The contributions given to the present analysis by Vito Di Guida, Daniele Galdi and Gabriele Orlando during their Master Thesis in Mechanical Engineering at the University of Salerno are gratefully acknowledged.

A natural gas fuelled 10 kw electric power unit suitable for distributed energy conversion based on an automotive internal combustion engine

Pietro Capaldi

CNR-Istituto Motori, Naples, Italy, pietro.capaldi@cnr.it

Abstract

The paper discusses the concept and the overall performance of an auxiliary power unit, suitable for distributed energy conversion, based on a wide-spread automotive supercharged Diesel internal combustion engine. The latter has been converted into a spark ignition methane/natural gas unit by Istituto Motori CNR of Italy and it has been specifically chosen among many other engines as a reliable, high efficiency, cost effective unit, suitable for energy conversion systems (such as microcogeneration for residential or commercial applications). The paper starts by defining the ratio which leaded to the adoption of an automotive four cylinders, Diesel internal combustion engine, in order to produce the above mentioned electric power. This is followed by a explanation of the main modifications adopted to convert the former Diesel engine in a spark ignited stoichiometric unit, with a discussion over the most significant element and technical solution that could give the system a high efficiency, low gaseous emissions and long endurance. The unit has been coupled with a liquid cooled induction generator and then tested as an electricity and heat production system, ready for grid connection and to become a base for a future microcogeneration system, thanks to a new designed management/control system. During field test a complete report of its running behavior has been reported.

Keywords:

Distributed generation, Microcogeneration, Micro-grids, Natural gas.

Introduction

Micro-cogeneration plants seem to be a interesting solution to become a smart way of energy supplying for single houses, buildings and commercial activities; moreover it's considered a simple and immediate form to enhance the full utilization of fuel energy and, consequently, a reduction for CO_2 emissions, especially when natural gas is used as fuel. Actually there are some plants available on the European market, able to produce an electric power of about 15 kW (such as. Tandem [1], Energy-Werkestatt [2], EC-Power [3], Energ-Co [4]), offering interesting overall performances in terms of electric efficiency (between 25% and 31%) and Primary Energy Ratio (i.e. the energy utilization rate of fuel, comprised between 85% and 90%). However these units still have some disadvantages if compared to a conventional electricity and heat supply (i.e. by grid distribution and conventional gas heater), such as high cost, bulk and electric efficiency; for these reasons micro-cogeneration could be still far from high volume production, waiting for new solutions capable of reducing the effect of the above mentioned disadvantages, while still taking benefits deriving from full utilization of energy.

A first definition for a new 10 kw electric power unit

In its simplest form, a 10 kW electric power unit could be conceived as a multicylinder internal combustion engine coupled to an electric generator and a number of heat exchangers, in order to recover as much heat as possible from cooling fluid and exhaust gas. The rated speed for these units is

normally set between 1500 rpm and 1800 rpm, depending on the specific electric generator (normally 4-poles synchronous or asynchronous generators) and/or grid frequency (50 or 60 Hz); this choice is made in order to keep both mean piston speed and noise as low as possible and get a longer expected life. It's to be underlined that the last aspect is a basilar theme as regards microcogeneration units, as most of them are expected for a 40.000 hours running period. Based on these same elements, the Author focused his attention over a number of engines which could led to the required electric power, among some small industrial multipurpose units and several automotive engines, taking into account that the unit must produce a mechanical power comprised between 11 and 12 kW, considering the efficiency of a generic electric generator. Of course, just gas fuelled units have been considered, as Diesel or gasoline engine were both too far from European limits regarding low emissions and fuel economy.
As regards industrial units, small scale gas engines are not very typical (as most of them are Diesel engine) as just higher power systems (> 50 kW) are today available on the market. So, another class of engines has been analyzed, i.e. the automotive engines. In this case, these units are close to the required power at the rated speed of 1500 rpm, showing quite interesting performances in terms of global efficiency, low noise and vibration. But at the same time they cannot be compared to the industrial units in terms of durability and reliability, as they have not been designed for heavy-duty service, but simply as mass-production spark-ignited automotive units. For this reason the Author concluded that, in order to reach a longer endurance even for small cogenerative engine, another kind of units should be considered. From this point of view, a modern automotive Diesel engine converted into a spark ignited unit results more similarly designed to large industrial engine, because it results more robustly constructed, as it has to undergo to much higher pressures. But another important aspect of this philosophy is that such kind of engine can run at higher loads (in terms of higher b.m.e.p. brake mean effective pressure) without reliability problems, while most of other spark ignited micro-cogenerators normally work under lower loads, in order to keep long term durability; so, in the first case, a higher mechanical efficiency can be expected, giving to this solution a higher potential in terms of global efficiency. In order to achieve a first definition of displacement for this unit, it can be observed that most of modern spark ignited internal combustion engine can express a specific torque of 80 Nm/liter around their highest volumetric efficiency. In order to reach a mechanical power of 12,5 kW at the rated speed of 1500 rpm (taking into account an electric efficiency of 0,80 to get the required electric power of 10 kW), a torque of about 80 Nm is needed: so, having fixed a (conservative) value of 65 Nm/liter for the engine at 1500 rpm, a 1200 cc displacement would be necessary.

The electric generating system

The final aim of a microcogeneration unit suitable for domestic and commercial applications in Europe is the production of a single phase 230 VAC (Voltage in Alternating Current), characterized by a grid-equivalent power quality; this could be obtained by a three-phase 400 VAC asynchronous machine (as most of the models cited in the introduction), together with some active power factor control systems and line filters, each different phase serving three different utility groups. The choice of the electric generator was made among some different units available on the European market, each of them capable of producing the required power at the rated tension, torque and speed. After some analysis it was clear that the required performances could only be assured by a water cooled unit, because of its high specific power and efficiency, but especially because of its intrinsic low noise, (due to the absence of cooling fan and fins) and the possibility to be placed, together with the internal combustion engine, into a completely closed containing case. Moreover, compactness was taken into account because a

significant volume and weight reduction could be obtained with this solution. So it was decided to design and make a water cooled generator (in collaboration with an Italian electric machine producer), with the aim of arrange not only a prototype, but a pre-industrial component.

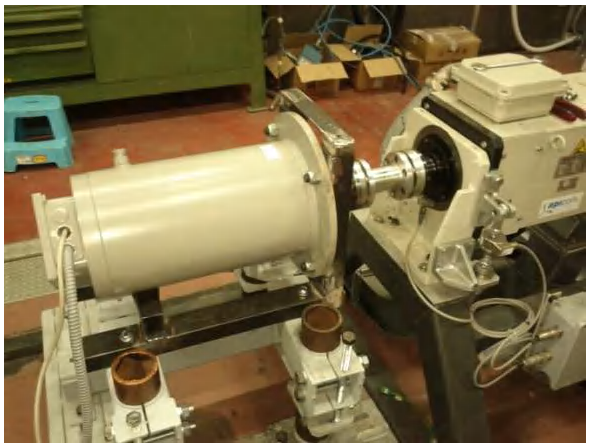

Figure 1 – Water cooled asynchronous generator on the test bench

This unit has been examined on a test bench as first and it has been characterized by varying the external torque; water temperature was fixed at 50°C, i.e. the same set as the incoming water-flow temperature into the future micro-cogenerator; a set of experimental data was produced and then reported in the following Table. 1;

Load (%)	Power (kW)	Current (A)	Power factor	Efficiency (%)	Speed (rpm)	Voltage (V)	Mech. power	Losses
100	11,04	19	0,82	87,33	1565	388	12,6	1,606
75	8,28	16	0,75	88,5	1545	388	9,4	1,076
50	5,52	13	0,62	88,1	1532	388	6,3	0,746
25	2,67	10	0,38	83	1516	388	3,3	0,565

Table 1 – Asynchronous generator experimental data characteristic

The recorded data show an interesting behavior expressed by the prototype generator, with an efficiency of about 88% in most of its functioning curve, and higher than planned in the previous calculations where an electric efficiency of 80% was fixed. However the Author consider that some diminution in the generating efficiency of asynchronous machine will occur when the unit would be coupled with an internal combustion engine, because of its intrinsic torque and speed fluctuation [7].

The internal combustion engine

After having known the behavior of the electric generator, as regard global performances, it can be better defined the engine displacement and the needed torque to move the electric machine. Several automotive Diesel has been considered during this analysis; at the end the chosen unit was a Fiat 1250 cm^3 of displacement, turbocharged Diesel engine, even known as 1,3 MultiJet. This engine represents one of the most advanced unit today available on the market, owing to its double overhead cams with hydraulic lifters and integrated rocker-arms, four cross-valve with high turbulence intake design. This

unit has been transformed in a stoichiometric spark ignited engine, atmospheric pressure charged and natural gas fuelled, representing the very first 1,3 MultiJet Diesel unit to be transformed into a methane prototype. The high turbulence deriving from intake ducts (very typical for a Diesel unit) was considered to be an important issue by the Author, this aspect in order to sustain the flame propagation and avoiding knocking at the low speed of 1500 rpm even with an high compression ratio (12:1). As regards combustion chamber, the previous Saurer type has been replaced with a large central bowl with a very limited squish area, (similar to a Heron type) in order to give the combustion chamber an high volume/surface ratio (to improve thermal efficiency), to reduce HC formation and to avoid the swirl enhancing. This aspect must be controlled, in order to reduce heat transfer to chamber walls and it will be no doubt part of further developments of the engine in the future (together with compression ratio optimization), by means of CFD and combustion simulation programs; the internal piston shape can be easily seen in the following Fig 2.

Fig.2 Modified pistons with enlarged bowl

In Fig.3 it can be seen the flat head with the four valves and the central spark plug; the glow plug hole of the original Diesel engine has been used to install a pressure sensor.

Fig. 3 Four valve head with spark plug

As underlined before, another important issue for this prototype was reliability and endurance, being the same engine an important work-bench to test technical solutions in the future, especially regarding surface hardening and special lubricants. The most critical parts, as regards wear and friction, are some

mechanical couples, i.e. liners and pistons, valve and seat and finally rocker-arms and camshaft. So, as first step, the valve springs have been reduced in their pre-load and stiffness (if compared to the original engine version) in order to reduce friction [6], thanks to the lower rotational speed performed by this new unit. Moreover, special exhaust valve with Stellite coating have been adopted, together with hardened valve seat. Further developments will consider hardened liners (by PVD coatings) associated with new formulated fullurene added lubricants. As regards lubrication system, an auxiliary apparatus has been installed, made up of a large capacity oil-tank (21 liters) and of a constant oil-level device, which permits to fix the optimal lubricant amount in the sump. The oil circulation is forced by an external electric pump without any particular modification of the original lubricating system. The auxiliary tank has been dimensioned on the average oil consumption showed by this engine, this permitting to make oil change intervals longer than the standard engine (so reducing global costs).
As regards the control and management system, the engine is provided with an especially designed integrated electronic platform, which has been conceived as a global control system (both of electric and thermal power) especially suitable for cogeneration plants. This equipment has been designed to perform different load strategies, such as electric load driven or heat load driven. As regards the first strategy, it makes the energy produced by the generating group just follow the energy requirement from a generic utility, through the control of an automotive electric driven throttle; in this way no energy flow can be delivered to the grid. At the same time, the system can control a straight stoichiometric operation, managing natural gas flow by means of a step motor valve put on the feeding line and thanks to two different oxygen sensors (before and after the three-way catalytic converter), in order to control both steady and transient load conditions. Other features of this system are an active cooling apparatus control (through an electric pump) and the active control of oil consumption and circulation. The system architecture has been conceived as very flexible, in order to permit future up-grades of the same through the installation of other sub-modules, in order to control more engine/system functions, such as ignition system, EGR control, power factor and other thermal regulating apparatuses. In the following Fig.4 and the prototype control system is shown, while in Fig.5 the engine with the catalytic converter and double oxygen sensor can be seen.

Fig. 4 Prototype cogenerator control/management system

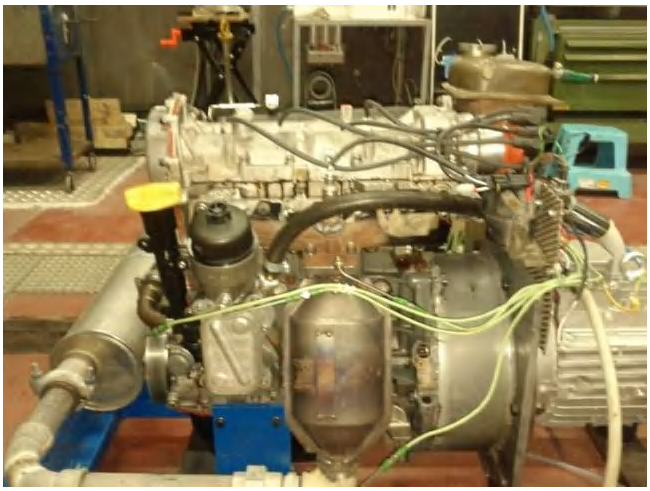

Fig.5 The prototype with catalyst and double oxygen sensor

In order to reduce NOx emissions an exhaust gas recirculation (EGR) has been set up. An important difference between the EGR system of the original Diesel engine and the one introduced in this prototype stands in the different achievable cooling of exhaust gas. In this prototype they are spilled at the end of the last stage of the heat recovery system, where a maximum temperature of 80°C can be reached at full load; this condition is very important in a spark ignited engine, in order to avoid knocking and obtain a higher global efficiency. The EGR mass flow is still not controlled by any adjustable valve, having been optimized just for full load conditions; as reported before, further development of global management system will consider a special module for active EGR control.
As regards the ignition system, the global management platform was not fitted with an ignition module; so an automotive based component was adopted and modified in order to improve life cycle of the whole ignition apparatus. With this aim, an electronic ignition system (with high voltage distributor), coupled with a single special high voltage coil was employed. The latter was used to meet the heavy load conditions of high compression, natural gas fuelled engines, where sparks need a higher voltage to take place. The distributor, provided with an internal electronic pick-up, was put on the camshaft (in place of the Diesel high pressure pump), with the aim of getting a one-spark per cycle strategy, instead of a one-spark per round; in this way a significant excess load on the whole system was avoided, for a better durability and maintenance cost reduction, because of the lesser plug electrodes erosion.

The system as an electric and heat generator

The two systems, separately analyzed before, have been finally coupled and tested, in order to get the global performance as electric and heat generator. The unit was tested with four different throttle openings, just connected to the electric grid and without any passive electric load to simulate a generic utility during the experiment. All tests have been performed with natural gas from the Italian distribution network, with a declared average LHV (Lower Heating Value) of 34.400 kJ/Sm^3.
As regards laboratory setup, the apparatus which has been used to characterize the behavior of the electric generator was an API-COM motor/brake system, equipped with a low-inertia asynchronous machine. As regards the air and fuel flow metering, a hot wire flow meter (by VSE) has been adopted, together with a Coriolis fuel flow meter (by Emerson MicroMotion). As regards emissions, raw

exhaust gas has been analyzed with an API-COM measurement system (Mod. S-5000), consisting of the following analyzers: NDIR (Non-Dispersive Infrared Detector), CLD (Chemiluminescence Detector) and FID (Flame Ionization Detector) all by Emerson.
The engine performances regarding electric and thermal output are showed below in Table 2, while global emissions (before and after catalyst) are reported in following Table 3.

Load (%)	Electric Power (kW)	Speed (rpm)	Current (A)	Power factor	Primary Energy (kW)	Electric efficiency (%)	Thermal power (kW)	Thermal Efficiency (%)	Primary Energy Ratio
100	11,45	1570	21,1	0,84	41,55	27,5	24,7	59,5	0,87
75	8,20	1548	17,3	0,74	32,6	25,1	20,8	63,9	0,89
50	5,35	1534	13,5	0,60	25,4	21,0	17,8	68,0	0,89
25	2,55	1518	10,8	0,35	18,6	14,2	13,1	75,8	0,90

Table 2: Global electric and thermal performance

Load [%]	THC (bef. Kat) [p.p.m.]	NOx (bef. Kat) [p.p.m.]	CO (bef. Kat) [%]	Exhaust Temp. [°C]	THC (aft. Kat) [p.p.m.]	NOx (aft. Kat) [p.p.m.]	CO (aft. Kat) [%]	Exhaust Temp. [°C]
100	910	1270	0,18	525	110	130	0,02	520
75	1020	940	0,20	466	140	80	0,02	460
50	1190	510	0,21	398	150	65	0,02	395
25	1200	290	0,23	313	150	55	0,02	307

Table 3: Global emissions before and after catalyst

The obtained results are quite interesting if referred to an experimental unit; as regards the overall efficiency, the system showed an interesting 27,5%, with a net power generation of 11,5 kW and a thermal power generation of 19,7 kW, corresponding to a global Primary Energy Ratio (i.e. the sum of heat and electric power vs. potential fuel power) of 87% at full load. The electric power is higher than required, but capable of compensating the performance drop when very low pollution emissions are mandatory (especially regarding NOx), or in case of high wear and aging of the unit. Regarding thermal efficiency, global performances are very interesting if compared to other units, also because the system was not yet provided with a containing case; so that a significant amount of convective and irradiative heat was lost, with higher value for the higher loads because of the surface temperature rise. However, the system showed these results also because the external cooling fluid was kept at 50°C (because of the required maximum temperature for the electric generator), this causing water condensation in the exhaust gas and giving the system an extra heat amount. As regards the electric generating efficiency, it can be observed that generator behavior doesn't seem to be much affected by torque variability of the internal combustion engine [7], this also because of a special elastic coupling between the generator and the I.C.E., the latter provided with a high inertia flywheel (as can be seen in the following Fig.9), which limited the rotational speed fluctuation of the whole system.

Fig.9 Elastic coupling with high inertia flywheel

As regards emissions, the overall behavior reflects quite low global levels, owing to the stoichiometric setting and to the a methane optimized three-way catalyst. The NOx production before catalyst could be limited even more with a higher rate of exhaust gas recirculation (EGR), in order to meet the most stringent European limitation [5] and reduce, at the same time, both catalyst dimension and cost. In this case, a powered EGR valve is needed (controlled by the managing/control device), because of performance instability showed by I.C.E. at partial load conditions. The internal combustion engine coupled with the electric generator can be seen in the following. Fig.10.

Fig.10: The 10 kW power unit during endurance test

Conclusions

The 10 kW power unit developed by Istituto Motori - CNR showed interesting global performances, similar to other commercial competitors and capable of being improved in many aspects in the future. The final goal of 10 kW electric power has been overlapped and it can even increase in the future

owing to further developments of the internal combustion engine, such as higher compression ratio (obtained with a new design combustion chamber and piston) and optimized intake ducts, being all these aspect capable of increasing global efficiency too. As regards thermal efficiency, a better result could be reached by mean of a containing case for the whole system and another cooling stage inside of the same volume, in order to control the internal temperature and perform a higher heat recovery [7]. The CNR system also showed to be an interesting prototype for the testing and the evaluation of technical solutions applied to microcogeneration in general, especially for further developments in the field of durability (materials and lubrication), noise and vibration reduction (silencers, suspension devices, noise absorbing panels), electric efficiency (different generators, flywheels an inverters) and other solutions to obtain higher Primary Energy Ratio (unconventional heat-exchangers). Finally, this unit, constructed with low cost industrial elements, showed that the introduction on the market of a reliable and cost-effective system could be no-doubt carried out by industry in a next future, being most of its components absolutely widespread in the automotive and domestic heater production.

Nomenclature

$\eta_{E.E}$ Electric efficiency of microcogenerator;

$\eta_{T.E}$ Thermal efficiency of microcogenerator;

$\eta_{O.E}$ Overall efficiency of the internal combustion engine;

η_{gen} Electric efficiency of generator;

Nm Newton-meter (Torque unit);

cc cubic centimeters (displacement unit);

LHV Lower Heating Value;

I.C.E. Internal combustion engine

b.m.e.p. Brake mean effective pressure

References

[1] http://www.energianova.it

[2] http://www.energiewerkstatt.de

[3] http://www.ecpower.co.uk

[4] http://www.energ.co.uk

[5] Bernd Thomas “Benchmark testing of Micro-CHP units” Applied thermal engineering, Volume 28, Issue 16, November 2008, pages 2049-2054

[6] Shigeto Suzuki, Tooru Maeda; “Development of a car-based, low NOx, highly reliable GHP engine” Small Engine Technology Conference (SETC), Vol 2, Pisa December1993;

[7] P.Capaldi, A. DelPizzo, L. Piegari, R.Rizzo, “Prototype Of A Small Cogeneration Unit Suitable For Low Power Industrial Applications” EETI 2004, Rio de Janeiro

Adjustment of envelopes characteristics to climatic conditions for saving heating and cooling energy in buildings

C. Tzivanidis[a],K.A. Antonopoulos[b],F. Gioti[c]

[a]Lecturer, National Technical University of Athens (N.T.U.A.),
School of Mechanical Engineering, Thermal Engineering Department,
Refrigeration and Air-Conditioning Laboratory, Solar Energy Laboratory
9, Heroon Polytechniou, Zografou 157 73, Athens, Greece
ctzivan@central.ntua.gr, CA
[b]Professor, N.T.U.A., kanton@central.ntua.gr
[c]Ph. D. Candidate, N.T.U.A., fgioti@yahoo.gr

Abstract

Among buildings envelope elements, fenestration and insulation exert the most intense influence on heating and cooling energy consumption. Fenestration permits entrance into the indoor space of large amounts of solar radiation, which are desired only during the heating period. The values combinations of fenestration and insulation characteristics for obtaining a "quasi-adiabatic" envelope, on a daily basis, have been predicted. It was found that such values combinations (a) depend strongly on the climatic conditions and they exist for the months from November to March and only for buildings with energetic heating systems, and (b) they are different for each one of these months. Therefore, for buildings operating during a specified period, the corresponding "quasi-adiabatic" envelope values may be used for minimizing heating energy consumption while for all year operating buildings, the yearly energy consumption, which is predicted in terms of the main envelope parameters, may be used for energy saving. A critical value of the fenestration heat transfer coefficient has been detected, for each level of insulation effectiveness, for which the yearly energy consumption becomes independent of fenestration percentage, thus providing the means to reduce the often undesired limitations concerning the size of fenestration area. The present analysis is based on a developed implicit finite-difference solution of a set of differential equations, which describe the transient thermal behavior of buildings. Although the findings and conclusions of the analysis refer to the Greek Typical Reference Building (GTRB) under the Athens typical weather conditions, they have a considerable degree of generality and may, therefore, be used not only for the thermal analysis of similar buildings under similar climates, but also for cases with different conditions and requirements. Apart from its theoretical relevance, the information provided may be used by the consulting engineer for making preliminary energy consumption estimations for the values combinations of the main envelope parameters, for selecting those which satisfy energy saving, low initial cost and aesthetic requirements.

Keywords:
buildings envelope parameters, fenestration, building insulation, quasi-adiabatic buildings envelope, thermal comfort energy saving

1. Introduction

The effects of envelopes characteristics on the energy consumed for obtaining indoor thermal comfort of buildings have been studied in a large number of publications, for example refs [1-9]. In most of these, attention is focused on the envelopes elements with the lowest and highest thermal resistance, i.e. the fenestration and the insulation.

Recent examples from the former class of studies may be found in refs [1-4]: In ref. [1] a fenestration heat a transfer model is developed on the basis of experimental and theoretical analysis of fenestration thermal behavior. In ref. [2] a simulation procedure is developed and used for the evaluation of the contribution of windows in buildings energy balance in Amman. Applications of advanced glazing and overhangs are proposed and the resulting shading effects on their overall

behavior are analysed in ref. [3]. Improvements of fenestration solar heat gain measurement systems are presented in ref. [4].

Recent examples from the latter class of studies, i.e. those related to the effects of insulation on heating energy consumption may be found in refs. [5-9], in most of which the insulation thickness is optimized using various criteria, i.e. the kind of energy source [5], the electricity tariff [6], or the life cycle cost [7]. A correlation between insulation thickness and thermal conductivity, for obtaining the optimum result, is developed in ref. [8]. In ref. [9] a case study on the influence of insulation in regions for extreme weather conditions is presented.

The above studies represent only a small part from the large number of studies on the effects of envelope characteristics on energy consumption for buildings heating and cooling. However, little work has been done on the effects of envelope parameters combinations [10,11] and in particular on the combined effects of fenestration and insulation, which are the envelope elements with the strongest influence on building heating and cooling energy consumption. An effort towards this direction has been done in our recent studies [12-14], where the effect of fenestration and insulation parameters combinations on the heating energy consumption was predicted. In the first of the above publications [12] the concept of "quasi-adiabatic" or "pseudo-adiabatic" wall was introduced, while in the second [13] the analysis was extended to the "quasi-adiabatic" or "pseudo-adiabatic" envelope. In these studies the required fenestration and insulation parameters combinations for obtaining quasi-adiabatic walls and envelopes were predicted for specified weather conditions. The analysis refers only to buildings with energetic heating systems.

In the present study, both energetic and passive systems are considered and the parameters of weather conditions are introduced. The required fenestration and insulation parameters combinations for quasi-adiabatic envelopes are predicted for various weather conditions, thus enabling consulting engineers to select the appropriate values combinations of fenestration and insulation parameters for obtaining minimization of the consumed energy for indoor thermal comfort at any specified climatic conditions or any month of the year. The corresponding values of the yearly energy consumed are also predicted for use in the case of buildings operating throughout the year. The analysis is based on a developed implicit finite-difference solution of a set of differential equations, which describe the transient thermal behavior of buildings.

2. Thermal behavior simulation of a Greek Typical Reference Building (GTRB)

Existing computer codes, which are suitable for the simulation of buildings transient thermal behavior, as for example refs. [15,16], require extensive modifications for the purposes of the present study. Therefore, a new simulation procedure was developed, based on an implicit finite-difference solution of a set of differential equations, which describe the transient thermal behavior of a Greek Typical Reference Building (GTRB).

GTRB characteristics have been defined by examining the Athens and other Greek cities buildings in conjunction with the related Hellenic Directive published in the official Government Gazette Issue 407/9-4-2010, which is based on the European Union Directive 91/2000 on the energy performance of buildings. The typical year weather data used have been obtained by statistical processing of 20 years hourly measurements of ambient temperature [17] and solar radiation [18,19] in the Athens area.

Although GTRB characteristics may be found in our previous articles on related subjects [12,13], they are repeated below very briefly for the sake of completeness: 100 m^2 detached one-storey house of square shape with exterior walls composed of 2 cm exterior finishing layer, 9 cm brickwork, 4 cm insulation with specific thermal conductivity k_i=0.038 W/mK, 9 cm brickwork and 2 cm interior finishing layer; roof composed of 2 cm interior finishing layer, 14 cm reinforced concrete slab, 4 cm insulation and 10 cm of usual exterior waterproof and concrete mixtures layers; floor constructed from 10 cm upper floor tiles with cement mixture sub-layers, 4 cm insulation layer

and 10 cm reinforced concrete slab directly in contact with the ground; indoor walls of 30 m length made of single bricks with finishing layers on both sides; the four sides of the house are oriented towards the four main orientations and each one is composed of 25% fenestration with overall heat transfer coefficient 3.2 W/m^2 K; outdoor and indoor convection coefficients 16 W/m^2 ^{o}C and 8 W/m^2 ^{o}C, respectively; light-coloured exterior envelope surface with absorption coefficient for solar radiation 0.44; constant ventilation of 1 indoor air changes per hour. The developed procedure for the simulation of the GTRB described above is based on previous procedures [20-26], presented and tested against experimental data and other numerical predictions in previous studies [27-29]. Therefore, only a very brief description will be given below, containing mainly the new points introduced. The thermal behaviour of the multilayer GTRB envelope elements e (i.e. exterior walls, fenestration, ceiling and floor) is expressed by the transient one-dimensional heat conduction differential equation:

$$\rho_{ej} C_{ej} \partial T_{ej}(t,x) / \partial t = k_{ej} \partial^2 T_{ej}(t,x) / \partial x^2 \quad , \quad x_j \le x \le x_j + B_{ej} \quad , \quad j = 1, 2, \ldots, J \qquad (1)$$

as only the direction x normal to the walls and other extended surfaces present significant temperature variations. In the above equation $T_{ej}(t,x)$ is the temperature of any layer j of multilayer envelope element e at time t and depth x, measured from its outdoor surface; J is the number of layers each envelope element is composed of; ρ_{ej}, C_{ej}, k_{ej} and B_{ej} are the density, thermal capacity, thermal conductivity and thickness of each layer j of multilayer element e, respectively; and x_j, x_j+B_{ej} are the coordinates of the jth layer surfaces of element e.

The boundary conditions for the exterior walls may be written as

$$q_{o,e}(t) = h_o[\, T_o(t) - T_{e1}(t,x) \,] \quad , \quad x = 0 \qquad (2)$$

$$q_{i,e}(t) = h_i[T_{eJ}(t,x) - T_i(t)] + \Sigma_v g_{e,v}[\, T_{eJ}(t,x) - T_v(t)] + R_e(t) \quad , \quad x = x_J + B_{eJ} \qquad (3)$$

where $q_{i,e}(t)$ and h_i are the heat flow and the convection coefficient at the indoor surface, respectively, while $q_{o,e}(t)$ and h_o denote the corresponding quantities for the outdoor wall surface; $T_i(t)$ and $T_o(t)$ are the indoor and the equivalent outdoor air temperature, which includes the effect of the incident solar radiation, according to the related ASHRAE [30] model; Σ_v denotes summation over indoor surfaces v; $g_{e,v}$ is the radiation heat-transfer factor between indoor surface of element e and any other indoor surface v of temperature $T_v(t)$; and $R_e(t)$ expresses the part of solar radiation transmitted through any opposite fenestration, and the parts of the radiative loads from lighting, equipment and people, which are absorbed by the indoor surface of exterior walls. The same equations (2) and (3) express the boundary conditions for the outdoor and indoor fenestration surfaces, respectively, where $T_o(t)$ now expresses the real ambient temperature $T_{amb}(t)$ and the term $R_e(t)$ is omitted. The percentage of solar radiation absorbed by fenestration is taken as a source term in the corresponding transient heat conduction equation (1).

Table 1. Greek Typical Reference Building (GTRB) parameters

Area	100 m^2 (square shape).
External Wall	2cm finishing layer, 9cm brickwork, 4cm insulation, 9cm brickwork, 2cm finishing layer.
Roof	2cm interior finishing layer, 14cm reinforced concrete slab, 4cm insulation, 10cm exterior waterproof and concrete mixtures layers.
Floor	10cm upper floor tiles with cement mixture sub-layers, 4cm insulation layer, 10cm reinforced concrete slab.
Indoor Wall	2cm finishing layer, 9cm brickwork, 2cm finishing layer.
Fenestration	25% of each external's wall orientation, U=3.2 W/m^{2}K
Outdoor convection coefficient	8 W/m^2^{o}C
Indoor convection coefficient	16 W/m^2^{o}C

Roof surfaces are treated in the same way as exterior walls, surfaces, i.e. eqs (2) and (3), are used as boundary conditions for the upper and lower roof surfaces, respectively. Adiabatic boundary conditions are imposed to the lower surface of floors directly in contact with the ground, or over an underground non-ventilated basement [30]. Equation (2) is imposed as boundary condition if the floors lower surface is in contact with the ambient. Boundary condition expressed by eq. (3) is imposed on the upper floors surface.

The transient one-dimensional heat conduction equation (1) with subscript e replaced by p is used for the calculation of the temperature distribution $T_{pj}(t,x)$ within any indoor multilayer partition p (indoor wall, ceiling or floor), composed of j=1,2,…,J layers, each one of thickness B_{pj}. Boundary conditions at the two sides of any partition p may be expressed as

$$q_{p1}(t) = h_i[T_{p1}(t,0) - T_i(t)] + \Sigma_v g_{p,v}[T_{p1}(t,0) - T_v(t)] + R_{p1}(t) \quad (4)$$

$$q_{pJ}(t) = h_i[T_{pJ}(t, x_J+B_{pJ}) - T_i(t)] + \Sigma_v g_{p,v}[T_{pJ}(t, x_J+B_{pJ}) - T_v(t)] + R_{pJ}(t) \quad (5)$$

where $T_{p1}(t,0)$ and $T_{pJ}(t, x_J+B_{pJ})$ denote the temperatures at the two sides (first and last layers j=1 and j=J) of partition p at time t, respectively; $q_{p1}(t)$ and $q_{pJ}(t)$ stand for the heat flows at the corresponding sides of the partition; $T_i(t)$ and h_i are the indoor air temperature and the convection heat-transfer coefficient at partition surfaces, respectively; $g_{p,v}$ is the radiation heat-transfer factor between surfaces of partition p and any other indoor surface v of temperature $T_v(t)$. The parts of solar radiation, transmitted through any opposite fenestration, and the parts of the radiative loads from lighting, equipment and people, which are absorbed by the two partitions sides 1 and J are expressed by terms $R_{p1}(t)$ and $R_{pJ}(t)$, respectively.

Same equations as those for the indoor partitions, with subscript p replaced by f, are used to calculate the temperature distribution $T_{fj}(t,x)$ within furniture, which is simulated by equivalent multilayer slabs composed of the usual furnishings materials, i.e. wood, plastics, glass, textile mater, metal, etc.

The sum of heat flows from envelope indoor surface, partitions and equivalent furnishing slabs may be expressed as

$$Q_1(t) = \Sigma_e q_{i,e}(t)A_e + \Sigma_p [q_{p1}(t) + q_{pJ}(t)]A_p + \Sigma_f[q_{f1}(t) + q_{fJ}(t)]A_f \quad (6)$$

where summation Σ_e refers to the e (=1,2,…) elements of building envelope, with corresponding indoor heat-transfer surfaces A_e and heat flows $q_{i,e}(t)$; summations Σ_p and Σ_f refer to the p(=1,2,..) indoor partitions and to the f (=1,2,..) equivalent furnishings slabs, respectively, with corresponding heat-transfer surfaces A_p and A_f and heat flows at either sides (q_{p1}, q_{pJ}) and (q_{f1}, q_{fJ}).

The parts of radiation from lighting, equipment, people and transmitted solar radiation through fenestration, which are directly or after reflection absorbed by the indoor air, as well as ventilation and infiltration, provide the indoor environment with a load $Q_2(t)$. An additional load $Q_o(t) \geq 0$ or $Q_o(t) < 0$ is also provided by the heating or cooling equipment, respectively.

The above mentioned loads $Q_1(t)$, $Q_2(t)$ and $Q_o(t)$ may be used to express the indoor air thermal energy balance, i.e.

$$m_a c_a \partial T_i(t)/\partial t = Q_1(t) + Q_2(t) + Q_o(t) \quad (7)$$

where $T_i(t)$, m_a and c_a are the temperature at time t, the mass and the thermal capacity of indoor air, respectively.

Differential equations for envelope elements, indoor partitions, furnishings and indoor air thermal energy balance form a set of equations, which is solved by the finite difference procedure described

in detail in Ref. [31]. Therefore, a very brief outline of the solution procedure is given here for completeness reasons: Initial conditions (for $t=t_o$) are first prescribed for all temperature fields $T_{ej}(t_o,x)$, $T_{pj}(t_o,x)$, $T_{fj}(t_o,x)$ and for the indoor air temperature $T_i(t_o)$. Then, the temperature fields $T_{ej}(t_o+\Delta t, x)$, $T_{pj}(t_o+\Delta t, x)$ and $T_{fj}(t_o+\Delta t, x)$ at the next time level $t=t_o+\Delta t$ are calculated by solving the transient one-dimensional heat conduction differential equations for the above variables, which are of the form of eq.(1), by employing a usual implicit finite-difference procedure [32]. The indoor air temperature $T_i(t+\Delta t)$ at any time level $t+\Delta t$ is calculated from the discretized form of differential equation (7), i.e.

$$T_i(t+\Delta t) = T_i(t) + [\, Q_1(t) + Q_2(t) + Q_o(t) \,]\, \Delta t / (m_a c_a) \qquad (8)$$

Solution is repeated for consecutive days with identical outdoor conditions until convergence to the periodic steady-state, in which solution repeats itself every 24 hours. Convergence criterion was set to 0.01^oC and the grid dependence study performed defined time and space grid finesses $\Delta t=60$ s and $\Delta x = 0.002$ m, respectively, apart from the insulation for which $\Delta x=0.001$ m was taken. Grid dependence tests were performed using 40%, 70%, 100% and 130% of the above mentioned grid node numbers. The maximum temperature difference between the latter two cases was 0.06%, which was considered sufficiently small. Therefore, the 100% case was selected.

3. Main envelope characteristics

Buildings envelope parameters affecting heating and cooling energy consumption are numerous. However, their number can be considerably reduced, because:
(a) The values of a considerable number of envelope parameters are determined by state laws and directives, as for example is the European Union Directive 91/2000 on the energy performance of buildings or, for the case of Greece, the Hellenic Directive published in the Official Government Gazette Issue 407/9-4-2010.
(b) A large number of envelope parameters either should be fixed to nearly constant values for physical, technical or construction reasons, or their values have very small effect on the heating and cooling energy consumption.

A related analysis using the developed computer code described in Section 2, showed that the most important envelope parameters are those related to the envelope elements with the highest and lowest thermal resistance, i.e. the insulation with characteristics its thickness W_i and specific thermal conductivity k_i, and the fenestration with characteristics its overall heat transfer coefficient U_f , the percentage P_f (with respect to the envelope surface), the orientation and degree of shading E_f.

4. Pseudo-adiabatic or quasi-adiabatic envelopes for energetic and passive systems

In our previous publications concerning the effects of envelope parameters on the transient heating energy consumption of buildings [12,13], we have analysed the favourable and adverse effects of fenestration and we have introduced the concepts of “quasi-adiabatic” or “pseudo-adiabatic” wall [12] and envelope [13] as described in brief below.

Daily heat gain and loss through buildings envelope is composed of:
(a) Solar heat gain through fenestration, F_S.
(b) Conducted envelope heat loss E_C, composed of the conducted solar heat gain through the envelope (excluding fenestration), E_{CS}, and the conducted heat loss through the envelope (including fenestration), owing to temperature difference, E_{CT}.
Therefore, the net daily heat flow through buildings envelope is

$$F_S - E_C = F_S - (E_{CS} - E_{CT}) \qquad (9)$$

and the condition for a quasi-adiabatic or pseudo-adiabatic envelope may be written as

$$F_S - E_C = F_S - (E_{CS} - E_{CT}) = 0 \qquad (10)$$

Further analysis in the present study showed that for climatic conditions similar to those of Greece, quasi-adiabatic envelopes can be obtained only in buildings with energetic heating systems, which retain thermal comfort levels. In the case of passive heating systems a quasi-adiabatic envelope cannot be obtained. These findings are illustrated in Figs. 1 and 2 for the cases of buildings with energetic and passive heating systems, respectively, as follows. Both figures correspond to the typical Athens 21 January for insulation thermal conductivity k_i= 0.03 W/mK and thickness W_i= 3 cm.

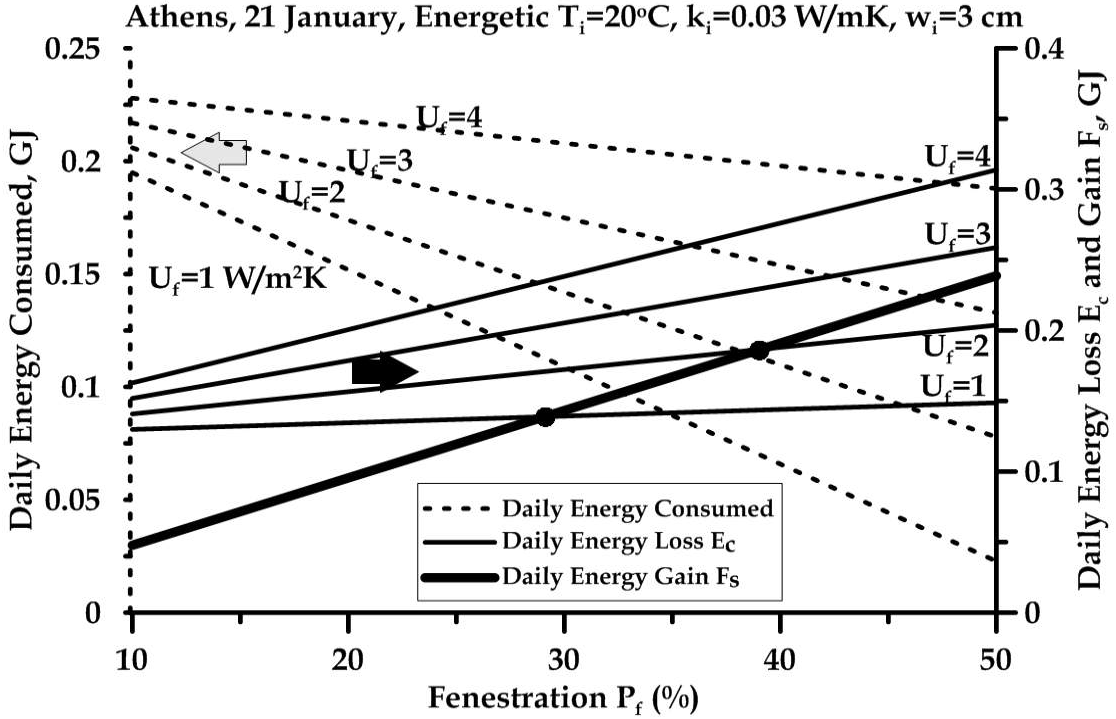

Fig. 1 Predicted daily energy consumed, envelope heat loss E_C and fenestration solar heat gain F_S in terms of fenestration percentage P_f for various values of the fenestration heat transfer coefficient U_f, for the energetic GTRB during the typical Athens 21 January. Intersection points of curves $E_C(P_f)$ and $F_S(P_f)$ represent the quasi-adiabatic envelope conditions.

Dash lines in Fig. 1 show in the left axis the energy consumed daily by the building heating system for retaining 20°C indoor temperature (energetic system) in terms of fenestration percentage P_f for various values of fenestration overall heat transfer coefficient U_f. The thin solid lines show in the right axis the daily conducted heat loss E_C in terms of fenestration percentage P_f for various values of U_f, while the thick solid line represents (right axis again) the daily solar heat gain F_S in terms of P_f. The intersection points of the solar heat gain line $F_S(P_f)$ and the heat loss lines $E_C(P_f)$ correspond to quasi-adiabatic envelopes, since at these points, the net daily envelope heat flow becomes zero, according to eq.(10).

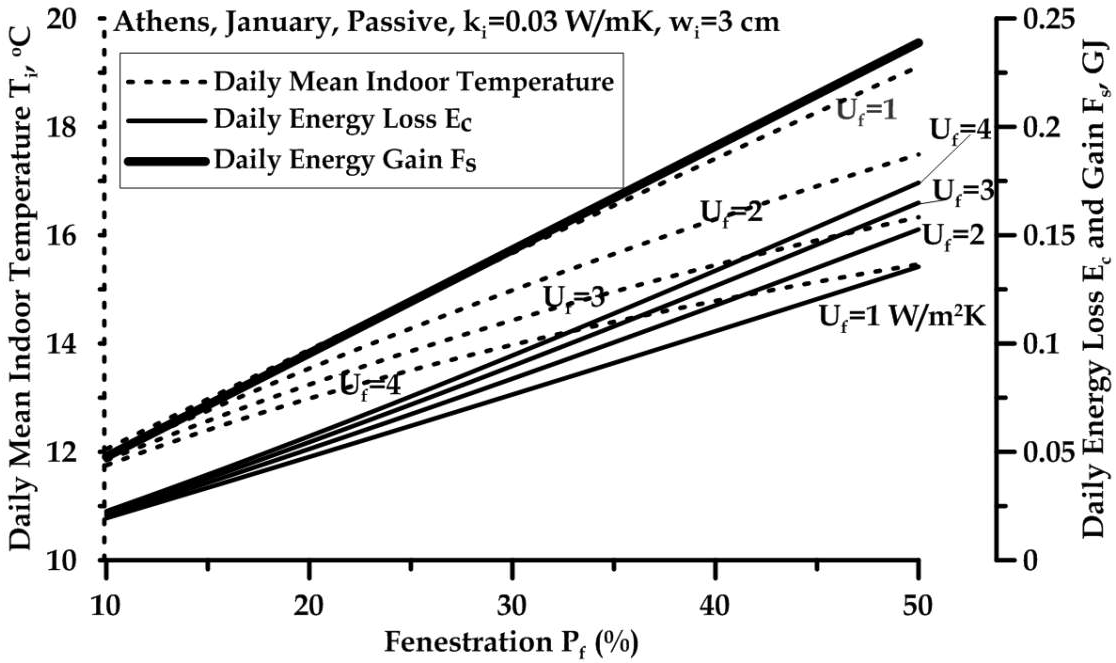

Fig. 2 Predicted daily mean indoor temperature, daily heat loss E_C and fenestration solar heat gain F_S in terms of fenestration percentage P_f for various values of the fenestration heat transfer coefficient U_f, for the passive GTRB during the typical Athens 21 January. Intersection points of curves $E_C(P_f)$ and $F_S(P_f)$ do not appear and therefore a quasi-adiabatic envelope does not exist.

Dash lines in Fig. 2 show in the left axis the daily mean indoor temperature T_i (passive system, no energy consumed) in terms of fenestration percentage P_f for various values of fenestration overall heat transfer coefficient U_f. The thin solid lines show in the right axis the daily conducted heat loss E_C in terms of fenestration percentage P_f for various values of U_f, while the thick solid line represents (right axis again) the daily solar heat gain F_S in terms of P_f. Intersection points of the solar heat gain line $F_S(P_f)$ and the heat loss lines $E_C(P_f)$ are not observed. Therefore, a quasi-adiabatic envelope cannot be obtained. Extensive tests showed that combinations of envelope parameters (k_i , W_i , P_f , U_f) which give a quasi-adiabatic envelope do not exist for passive heating systems, for the Athens and all other locations of a similar climate.

5. Values combinations of envelope parameters for quasi-adiabatic envelopes during the heating period for energetic systems

In our previous article, where the concept of quasi-adiabatic envelope was introduced [13], the values combinations of the main envelope parameters (k_i , W_i , P_f , U_f) for which quasi-adiabatic envelopes are obtained, were given but only for the climatic conditions of the typical Athens January. Here, the effect of weather conditions is examined, i.e. calculations are extended to the whole heating period (from November to March). The calculated values combinations are given in Fig. 3 for the typical Athens November and December and in Fig. 4 for January, February and March. The above figures show the fenestration heat transfer coefficient U_f in terms of the fenestration percentage P_f for insulation thicknesses W_i=3, 4, 5 and 6 cm and insulation specific thermal conductivities k_i=0.02 W/mK (Figs. 3(a) and 4(a)), k_i=0.03 W/mK (Figs. 3(b) and 4(b)), k_i=0.04 W/mK (Figs. 3(c) and 4(c)) and k_i=0.05 W/mK (Figs. 3(d) and 4(d)). The above results correspond to the GTRB but without indoor partitions and for 20°C indoor temperature, ventilation of 1 change per hour and fenestration percentage P_f distributed to percentages 50% , 0% , 25% and 25% to the south, north, east and west walls, respectively. The following comments may be made on the interdependence of parameters values of Figs 3 and 4 during the entire heating period (i.e. from November to March).

(a) When insulation effectiveness decreases (i.e. k_i increases and/or W_i decreases) under constant fenestration heat transfer coefficient U_f, a quasi-adiabatic envelope is obtained by increasing fenestration percentage P_f. This happens because the increase of P_f allows higher solar heat gain F_S, which counteracts the higher conduction heat loss E_{CT} provoked by the decrease of insulation effectiveness. This effect is more pronounced during the months with the lower solar radiation (i.e. January in comparison with March), for obvious reasons.

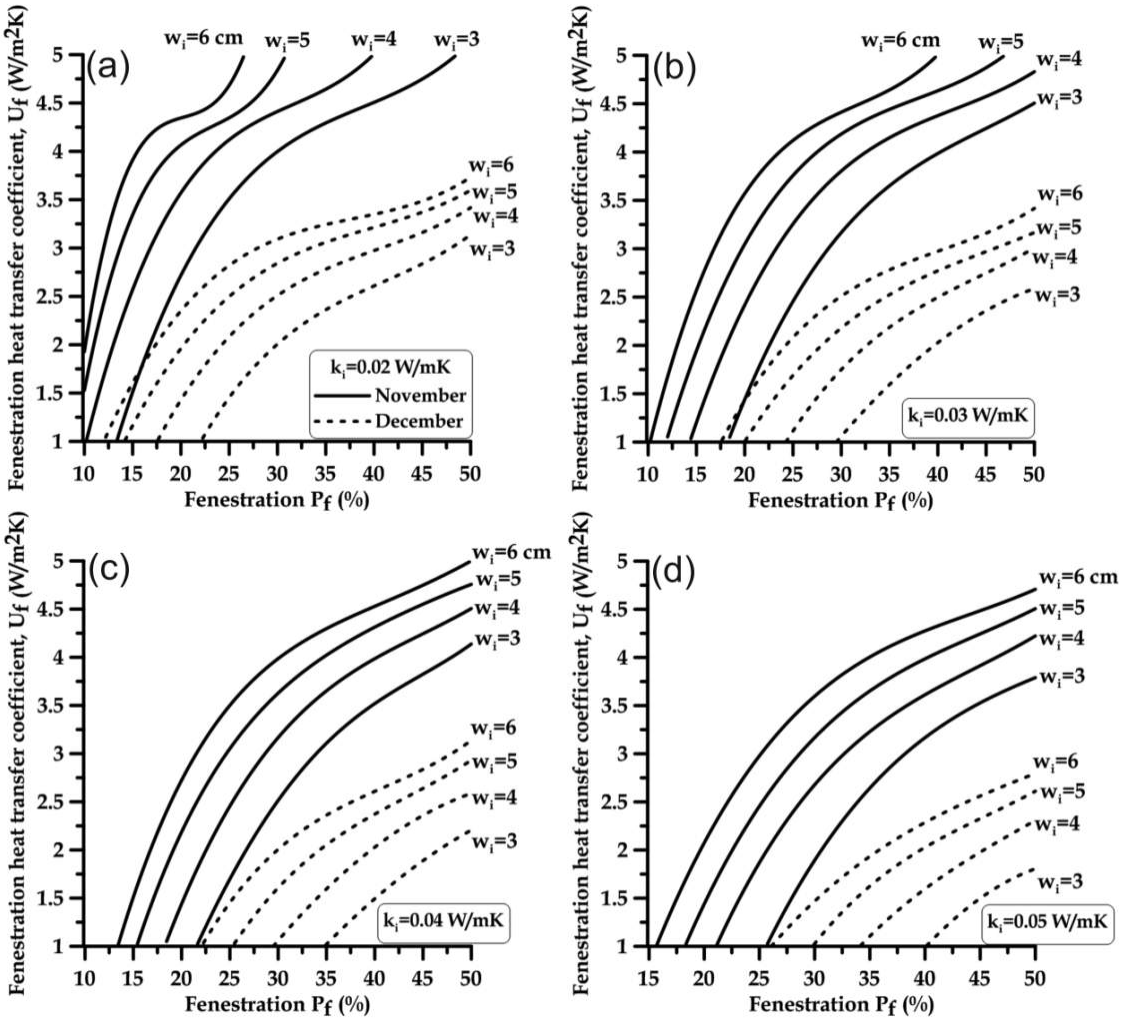

Fig. 3 Predicted combinations of envelope parameters (k_i, W_i, U_f, P_f), for which quasi-adiabatic envelopes are obtained for the energetic GTRB during the typical Athens 21 November and December, and for insulation specific thermal conductivities: (a) k_i=0.02 W/mK, (b) k_i=0.03 W/mK, (c) k_i=0.04 W/mK, (d) k_i=0.05 W/mK.

(b) When fenestration heat transfer coefficient U_f increases under constant insulation characteristics (i.e. k_i=const., W_i=const.), a quasi-adiabatic envelope may be obtained by increasing fenestration percentage P_f, in order to increase the incoming solar radiation, which will counteract the higher fenestration heat loss. Obviously for the low solar radiation months (for example January in comparison with March) the required P_f increase is higher.

(c) When insulation effectiveness decreases (i.e. k_i increases and/or W_i decreases), under constant fenestration percentage P_f, envelope heat loss increases. This increase will be eliminated by decreasing fenestration heat transfer coefficient U_f, thus obtaining a quasi-adiabatic envelope. Here, because of the constant value of fenestration percentage P_f, fenestration solar heat gain remains constant and therefore only a small effect of the month is observed related to the "wall solar heat gain".

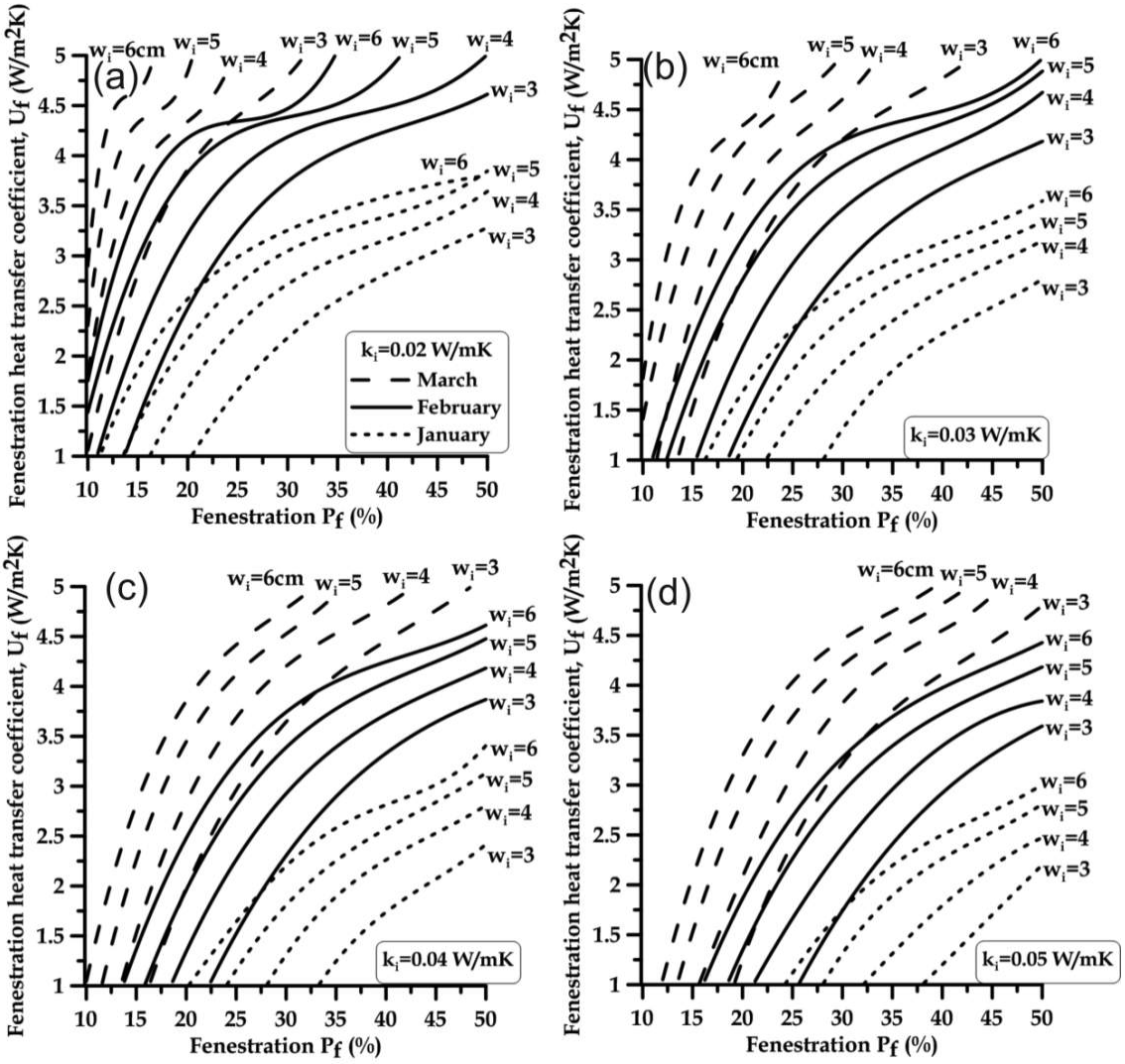

Fig. 4 Predicted combinations of envelope parameters (k_i , W_i , U_f , P_f), for which quasi-adiabatic envelopes are obtained for the energetic GTRB during the typical Athens 21 January, February and March and for insulation specific thermal conductivities: (a) k_i=0.02 WmK, (b) k_i=0.03 WmK, (c) k_i=0.04 WmK, (d) k_i=0.05 WmK.

(d) When fenestration percentage P_f decreases, solar heat again F_S also decreases. Therefore, a quasi-adiabatic envelope will be obtained by provoking an equal decrease of envelope heat loss, which is obtained by decreasing insulation thermal conductivity k_i and/or increasing insulation thickness W_i and/or decreasing fenestration heat transfer coefficient U_f. This effect is more pronounced during the months with the higher solar radiation.

(e) Figures 3 and 4 show clearly that the effect of the month on the values combinations of envelope parameters (k_i, W_i, P_f, U_f) for quasi-adiabatic envelopes along the heating period for energetic systems is very strong.

6. Values combinations of envelope parameters for quasi-adiabatic envelopes during the cooling period for energetic systems

Extensive tests for the main cooling period, as well as for spring and autumn months (i.e. from April to October) showed that for the Athens and for all other similar climate locations, values combinations of envelope parameters (k_i , W_i , P_f , U_f), which give a quasi-adiabatic envelope, do

not exist. This is an expected result, as during the above period eq.(10) does not hold because of the high daily values of solar heat gain.

7. Yearly energy consumption for indoor thermal comfort

The above analysis shows that the values combinations of the main envelope parameters (k_i , W_i , P_f , U_f) for which the desired quasi-adiabatic envelope is obtained, depends on the climatic conditions. A related example linking some of the values combinations of quasi-adiabatic envelope parameters (contained in Figs. 3 and 4 for the months from November to March) to the energy consumed yearly for indoor thermal comfort is given in Fig. 5. This figure shows the calculated values of the yearly energy consumption E_y in terms of fenestration percentage P_f for various values of the fenestration heat transfer coefficient U_f with insulation characteristics fixed to k_i=0.03 W/mK and W_i=3 cm. The basic conclusion of the above figure is that for buildings operating only during a specified heating period of the year, the appropriate combination for obtaining the lowest energy consumption may be selected from Figs. 3 and 4, while for all year operating buildings, the yearly energy consumption level for indoor thermal comfort should be used as the energy saving criterion.

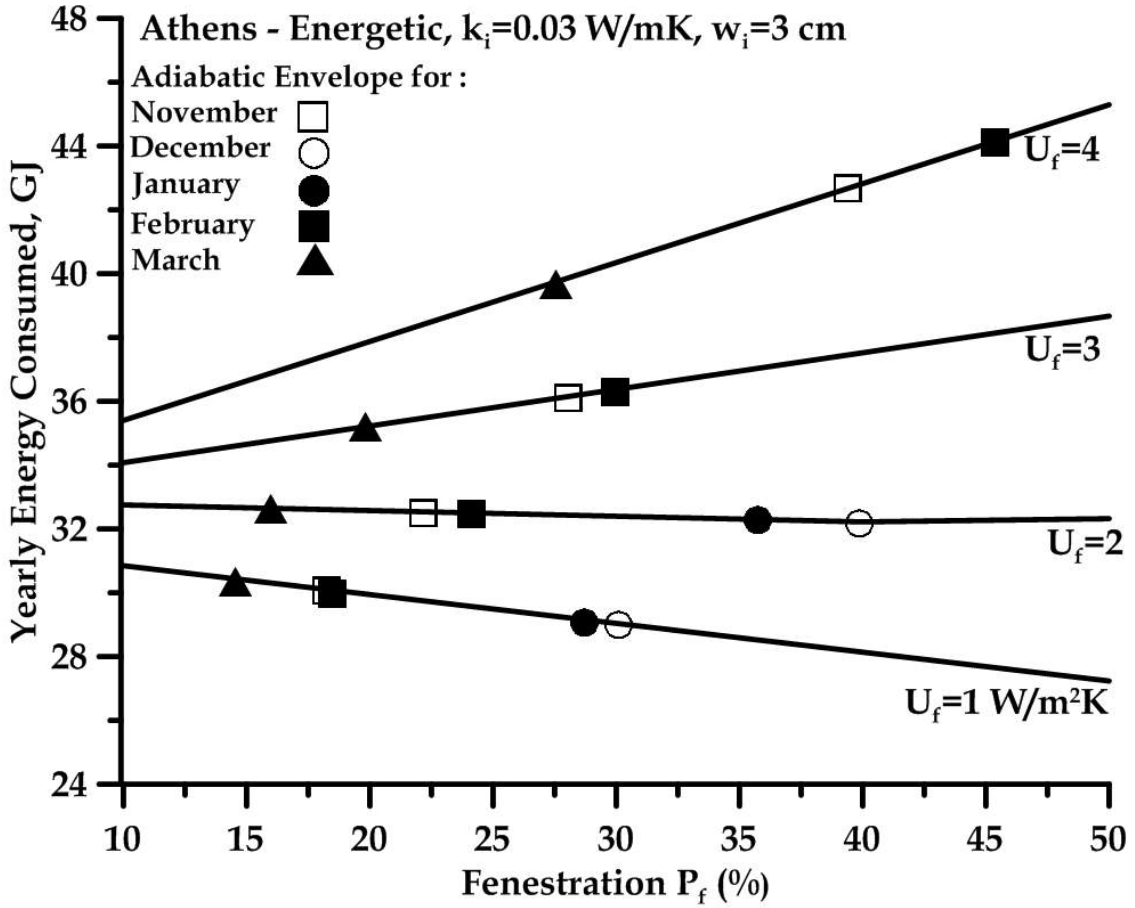

Fig. 5 Predicted values of the yearly energy consumption E_y in terms of fenestration percentage P_f for various values of the fenestration heat transfer coefficient U_f, for the energetic GTRB. Some combinations of parameters (k_i , W_i , U_f , P_f) for quasi-adiabatic envelopes corresponding to the months from November to March are also shown as examples.

Figure 6 provides the predicted yearly energy consumption for indoor thermal comfort (T_i = 20°C for the heating period and T_i = 26°C for the cooling period) corresponding to an extended range of envelope parameters values combinations (k_i , W_i , P_f , U_f) for the energetic GTRB, under the climatic conditions of the Athens typical year. In the above figure, the yearly energy consumption E_y is given in terms of the fenestration percentage P_f for fenestration heat transfer coefficient U_f=1, 2, 3 and 4 W/m^{2}K and insulation characteristics (k_i in W/mK, W_i in cm) as follows: (0.02 , 3) ,

(0.02 , 4) , (0.03 , 3) , (0.03 , 4) , (0.04 , 3) and (0.04 , 4) in Figs. 6(a) , (b) , (c) , (d) , (e) and (f), respectively.

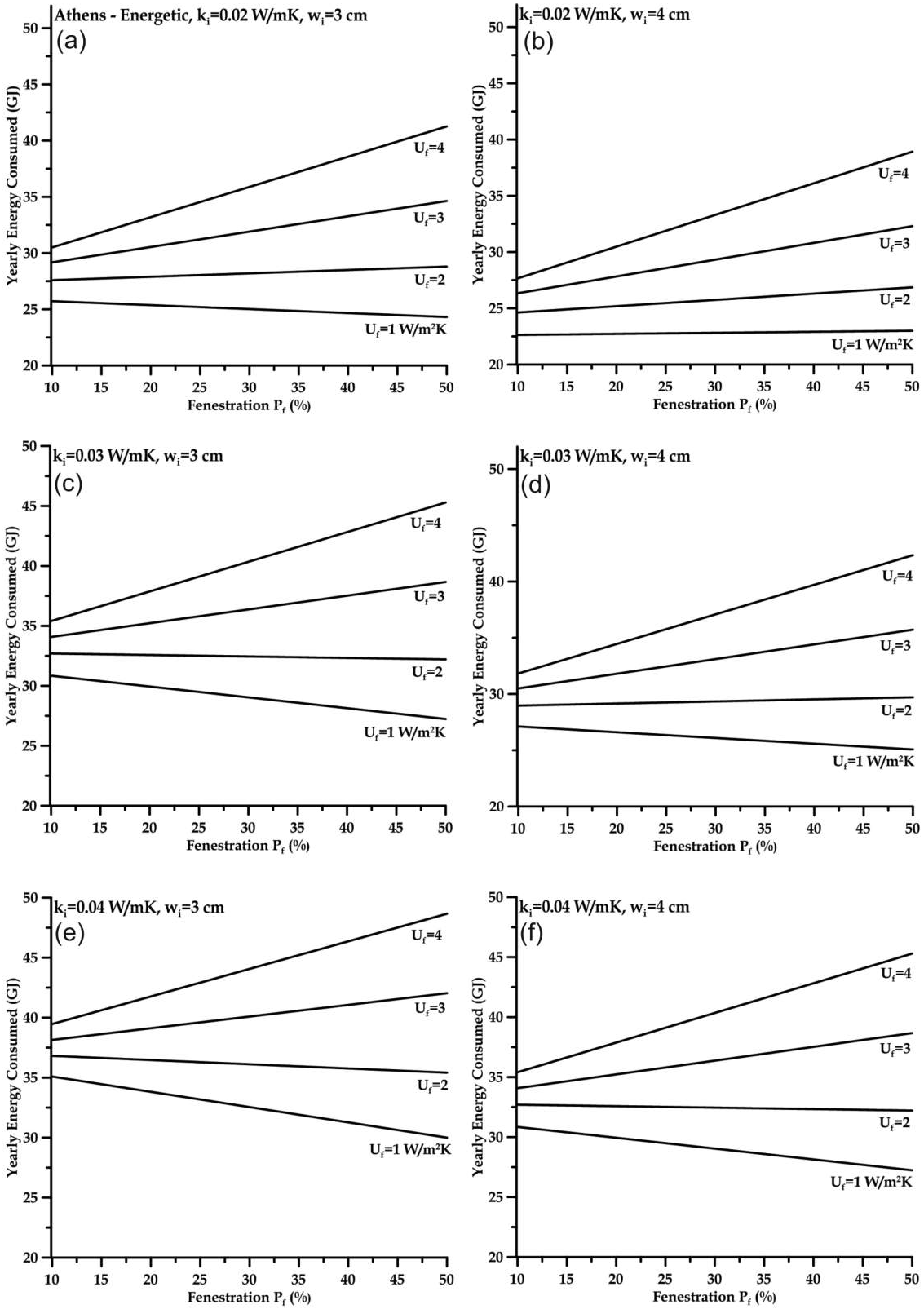

Fig. 6 Predicted yearly energy consumption E_y in terms of fenestration percentage P_f for various values of fenestration heat transfer coefficient U_f for the energetic GTRB during the Athens typical year and for insulation characteristics (k_i in W/mK , W_i in cm): (a) (0.02 , 3), (b) (0.02 , 4), (c) (0.03 , 3), (d) (0.03 , 4), (e) (0.04 , 3), (f) (0.04 , 4).

The following conclusions on the interdependence of envelope parameters values in relation to the yearly building heating and cooling energy consumption may be drawn from Fig. 6.

(a) For the higher values of the fenestration heat transfer coefficient U_f, the yearly energy consumption E_y increases with increasing fenestration percentage P_f, while for the lower values of U_f, E_y decreases with increasing P_f. The explanation lies on the fact that solar heat gain, which is desired only during the heating period, is strongly connected to the fenestration percentage P_f.

(b) Because of the above behavior there is a value U_{fo} of the fenestration heat transfer coefficient U_f for which the yearly energy consumption E_y becomes independent of the fenestration percentage P_f. This critical value U_{fo} is a function of the insulation characteristics k_i and W_i, i.e.

$$E_y = \text{const.} \qquad \text{for} \quad U_f = U_{fo}\,(k_i\,,\, W_i) \tag{11}$$

Therefore, each pair of insulation characteristics (k_i , W_i) defines a value U_{fo} of U_f for which E_y becomes independent of P_f. The significance of this finding, in practice, lies on the fact that the critical value U_{fo} allows the selection (without any increase of E_y) of the fenestration size, which satisfies architectural criteria (aesthetics, natural lighting, panoramic view, etc). Also, the increased natural lighting obtained by increased fenestration size reduces the artificial lighting and the associated energy consumption, thus obtaining energy saving.

(c) For the higher values of fenestration heat transfer coefficient U_f, the rate of increase of the yearly energy consumption E_y with increasing fenestration percentage P_f is high, while for the lower values of U_f the rate of decrease of E_y with increasing P_f is low.

(d) For constant fenestration heat transfer coefficient U_f , when insulation effectiveness decreases (i.e. k_i increases and/or W_i decreases) the yearly energy consumption variation rate with fenestration percentage P_f increases for the low values of U_f and remains practically constant for the high U_f.

(e) The effect of fenestration heat transfer coefficient U_f on the yearly energy consumption E_y increases with fenestration percentage P_f, as expected.

Apart from the theoretical relevance of Fig. 6 concerning the analysis of the envelope parameters effects on the yearly energy consumption for buildings heating and cooling, the above figure may also be used in practice by the consulting engineer for making preliminary energy consumption estimations for various values combinations of the main envelope parameters (k_i , W_i , P_f , U_f) in order to select those combinations which satisfy energy saving, low initial cost, aesthetic requirements, etc.

8. Discussion and Conclusion

Among buildings envelope elements, fenestration and insulation exert the most intense influence on heating and cooling energy consumption, as they present the lowest and highest thermal resistance, respectively. Moreover, fenestration permits entrance into the indoor space of large amounts of solar radiation, which are desired only during the heating period. Literature survey revealed that a large number of studies has been published on the effects either of fenestration or of envelope insulation on building heating and cooling energy consumption. However, the combined effects of insulation and fenestration parameters have been analysed only in a small number of articles. The effort towards this direction, which was made in our previous studies [12-14] for buildings with energetic heating systems and the weather conditions of the typical Athens January, has been extended in the present analysis to include weather conditions of all months of the year for buildings with both energetic and passive heating and cooling systems.

According to our analysis, main envelope parameters are the insulation and fenestration characteristics, i.e. the insulation specific thermal conductivity ki and layer thickness Wi, and the

fenestration percentage Pf and heat transfer coefficient Uf. The values combinations of the above parameters (ki, Wi , Pf , Uf) for obtaining a quasi-adiabatic envelope on a daily basis have been calculated for the Athens climate and their interdependence has been analysed. It has been found that the values combinations of (ki, Wi , Pf , Uf) for obtaining a quasi-adiabatic envelope (a) depend strongly on the climatic conditions, (b) they exist only for buildings with energetic heating systems, (c) they exist only for the months from November to March, and (e) they are different for each of these months and therefore for buildings operating only during a specified period, the corresponding quasi-adiabatic envelope values may be used for minimizing heating energy consumption. For all year operating buildings the yearly energy consumption for indoor thermal comfort Ey should be used as the energy saving criterion. The values of Ey for the Athens climate have been calculated in terms of the main envelope parameters (ki, Wi , Pf , Uf).

Among the various conclusions on the interdepence of the above envelope parameters is that for each pair of insulation characteristics (ki, Wi) a critical value Ufo of the fenestration heat transfer coefficient Uf exists, for which the yearly energy consumption Ey becomes independent of the fenestration percentage Pf. This finding has considerable practical significance as it reduces the often undesired limitations concerning the size of fenestration area. Thus, by taking Uf = Ufo, selection is allowed (without any Ey increase) of that fenestration size, which satisfies architectural criteria (aesthetics, natural lighting, panoramic view, etc). Also, the increased natural lighting obtained by increased fenestration size reduces the artificial lighting and the associated energy consumption, thus obtaining energy saving.

The conducted analysis for the envelope parameters effects on the yearly energy consumption for obtaining buildings indoor thermal comfort has theoretical as well as considerable practical relevance, since the related diagrams provided may be used by the consulting engineer for making preliminary energy consumption estimations for the values combinations of the main envelope parameters (ki, Wi , Pf , Uf) in order to select those combinations which satisfy energy saving, low initial cost and aesthetic requirements.

Although the findings and conclusions of the present study refer to the Greek Typical Reference Building (GTRB) under the Athens typical climatological conditions, they have a considerable degree of generality. Therefore, they may be useful not only for the thermal analysis of similar buildings under similar climates, but also for cases with different conditions and requirements.

Nomenclature

A Area (m^2)

C Specific heat at constant pressure (J/kg K)

E_C Conducted envelope heat loss (W)

E_{CS} Conducted solar heat gain through buildings envelope (excluding fenestration) (W)

E_{CT} Conducted heat loss through buildings envelope (including fenestration) (W)

Ed Daily heating energy consumption (J/day)

E_f Fenestration degree of shading (%)

F_S Solar heat gain through fenestration (W)

g Radiation heat-transfer factor (W/m^2K)

h Heat transfer coefficient (W/m^2K)

k Specific thermal conductivity (W/mK)

k_i Insulation specific thermal conductivity (W/mK)

P_f Fenestration area percentage with respect to the envelope surface (%)

P_{fo} Critical value of Pf (%)

T Temperature (K or oC)

T_{in} Indoor air comfort temperature (K or oC)

T_o Equivalent (sol-air) outdoor temperature (K or oC)

t Time (s)

U_f Fenestration overall heat-transfer coefficient (W/m2K)

v Volume (m^3)

W_i Insulation thickness (m)

W Layer thickness (m)

x Cartesian coordinate (m)

Subscripts

a Air

amb Ambient

e Element of building envelope

f Equivalent furniture slabs

i Indoor

J Total number of layers of a multilayer building element

j Layer of a multilayer building element

o Outdoor

p Partition

v Indoor surfaces of building envelope, partitions or equivalent furniture slabs

References

[1] S. Pal, B. Roy, S. Neogi, Heat transfer modeling on windows and glazing under the exposure of solar radiation, Energy and Buildings 41 (2009) 654-661.

[2] K. Hasouneh, A. Alshboul, A. Al-Salaymeh, Influence of windows on the energy balance of apartment buildings in Amman, Energy Conversion and Management 51 (2010) 1583-1591.

[3] A. Ebrahimpour, M. Maerefat, Application of advanced glazing and overhangs in residential buildings, Energy Conversion and Management 52 (2011) 212-219

[4] D.L. Marinoski, S. Guths, F. O.R. Pereira, R. Lamberts, Improvement of a measurement system for solar heat gain through fenestrations, Energy and Buildings 39 (2007) 478-487.

[5] O.A. Dombayci, M. Golcu, Y. Panca, Optimization of insulation thickness for external walls using different energy-sources, Applied Energy 83 (2006) 921-928.

[6] S.A. Al-Sanea, M.F. Zedan, S.A. Al-Ajlan, Effect of electricity tariff on the optimum insulation-thickness in building walls as determined by a dynamic heat-transfer model, Applied Energy 82 (2005) 313-330.

[7] A. Hasan, Optimizing insulation thickness for buildings using life cycle cost, Applied Energy 63 (1999) 115-124.

[8] T.M.I. Mahlia, B.N. Taufiq, Ismail, H.H. Masjuki, Correlation between thermal conductivity and the thickness of selected insulation materials for building wall, Energy and Buildings 39 (2007) 182-187.
[9] M.A. Aktacir, O. Buyukalaca, T. Yilmaz, A case study for influence of building thermal insulation on cooling load and air-conditioning system in the hot and humid regions, Applied Energy 87 (2010) 599-607.
[10] J. Yu, C. Yang, L. Tian, Low-energy envelope design of residential building in hot summer and cold winter zone in China, Energy and Buildings 40 (2008) 1536-1546.
[11] R. Fayaz, B.M. Kari, Comparison of energy conservation building codes of Iran, Turkey, Germany, China, ISO 9164 and EN 832, Applied Energy 86 (2009) 1949-1955.
[12] C. Tzivanidis, K.A. Antonopoulos, F. Gioti, Numerical simulation of the favourable and adverse effects of fenestration characteristics on the transient heating energy consumption of buildings, 4th IC-EpsMsO, International Conference on Experimental/Process/System Modeling/Simulation/ Optimization, Athens, Greece, 6-9 July 2011.
[13] C. Tzivanidis, K.A. Antonopoulos, F. Gioti, Computational analysis of the envelope parameters effects on the transient heating energy consumption of buildings, 24th Int. Conf. ECOS 2011, Novi Sad, Serbia, pp. 1894-1908.
[14] C. Tzivanidis, F. Gioti, K.A. Antonopoulos, Effect of insulation and fenestration combination on the transient energy consumption of buildings (in Greek), Energy Institute of South East Europe (IENE), 15th National Energy Congress, "Energy and Development 2010" , Athens 2011.
[15] TRANSYS, A transient simulation program, solar energy laboratory, University of Wisconsin, Madison, WI, U.S.A., 1990.
[16] EPS-r, A transient simulation program, Energy Systems Research Unit (ESRU), Strathclycle University, Glascow, 1998.
[17] Kouremenos DA, Antonopoulos KA, Rogdakis E. Performance of solar NH_3/H_2O absorption cycles in the Athens area. Solar Energy 1987;39:187-195.
[18] Kouremenos DA, Antonopoulos KA, Domazakis ES. Solar radiation correlations for the Athens, Greece, area. Solar Energy. 1985;35:259-269.
[19] Kouremenos DA, Antonopoulos KA, Doulgerakis S. Direct and diffuse solar radiation correlations for tilted surfaces in the Athens, Greece. Solar Energy, 1987;38:203-217.
[20] K.A. Antonopoulos, C. Tzivanidis, Finite difference prediction of transient indoor temperature and related correlation based on the building time constant, Int. J. of Energy Research, 20 (1996) 507-520.
[21] K.A. Antonopoulos, C. Tzivanidis, Numerical solution of unsteady three-dimensional heat transfer during space cooling using ceiling embedded piping, Energy -The Int. Journal 22 (1997) 59-67.
[22] C. Tzivanidis, K.A. Antonopoulos, E.D. Kravvaritis, Transient three-dimensional numerical solution of night ceiling cooling using PCM-embedded piping. J. of Energy Engineering, under publication, 2011.
[23] K.A. Antonopoulos, E. Koronaki, Envelope and indoor thermal capacitance buildings, Applied Thermal Engineering 19 (1999), 743-756
[24] K.A. Antonopoulos, E. Koronaki, Effect of indoor mass on the time constant and thermal delay of buildings, Int. J. of Energy Research, 24 (2000) 391-402.
[25] C. Tzivanidis, K.A. Antonopoulos, E.D. Kravvaritis, Parametric analysis of space cooling systems based on night ceiling cooling with PCM-embedded piping. Int. Journal of Energy Research, under publication, 2011, Wiley on line Library DOI:10.1002/er.1777.
[26] C. Tzivanidis, K.A. Antonopoulos, F. Gioti, Numerical simulation of cooling energy consumption in connection with thermostat operation mode and comfort requirements for the Athens buildings, Applied Energy, under publication, 2012.
[27] Kuznik F, Virgone J, Roux JJ. Energetic efficiency of room wall containing PCM wallboard: A full-scale experimental investigation. Energy and Buildings 2008;40:148-156.

[28] E.D. Kravvaritis, K.A. Antonopoulos, C. Tzivanidis, Solar energy management using PCM passive systems in the Athens area buildings, Energy Conversion & Management, under publication 2012.
[29] K.A. Antonopoulos, M. Vrachopoulos, C. Tzivanidis, Experimental and theoretical studies of space cooling using ceiling-embedded piping, Applied Thermal Engineering 17 (1997) 351-367.
[30] "American Society of Heating, Refrigerating and Air-Conditioning Engineers. ASHRAE Fundamentals, Atlanta, GA, 1993"
[31] C. Tzivanidis, K.A. Antonopoulos, F. Gioti, Numerical simulation of cooling energy consumption in connection with thermostat operation mode and comfort requirements for the Athens buildings, Applied Energy, under publication 2012.
[32] S.V. Patankar, Numerical heat transfer and fluid flow, Hemisphere Publishing Corporation, McGraw-Hill Book Company, 1980.

An exergy based method for the optimal integration of a building and its heating plant. Part 1: comparison of domestic heating systems based on renewable sources

Marta Cianfrini[a], Enrico Sciubba[b], Claudia Toro[b]

[a] *Dept. of Mechanical and Aerospace Engineering, U. of Roma –Sapienza, claudia.toro@uniroma1.it*
[b] *Dept. of Electrical Engineering, U. of Roma – Sapienza,*

Abstract:

In all developed Countries, the residential space conditioning sector is one of the highest exergy consumers and least efficient from the point of view of primary-to-end-use matching. Such an unsatisfactory situation can be cured by a systematic analysis of the conditioning system of a building that takes into correct account the thermodynamics of primary-to-final energy conversion chain.

The present study analytically and critically compares different domestic heating systems based on renewable energy resources. Specifically, solar and hybrid photovoltaic-thermal (PV/T) panels coupled with radiative heating panels and ground-source (closed and open loop) heat pumps coupled with fan coils and radiative heating panels are analyzed in detail from an exergy point of view.

The main objective of the study is the development and implementation of a general systemic procedure for the optimal integration of the building and its heating plant (heating element + primary energy supply system): the "optimality" -intended here as the most convenient choice among a finite set of alternative processes- is reached by identifying the thermodynamically most convenient heating configuration for the building under examination. The method combines a CFD modeling of the thermal building dissipation, a simulation of the system that makes up for the thermal consumption and finally a calculation of the global (well-to-final use) exergy efficiency.

Keywords:

space conditioning, green buildings, exergy efficiency, renewable resources, source/end-use matching.

1. Introduction

The sustainable energy conversion in building heating/cooling systems has become an urgent issue on the energy agendas of most developed countries. Worldwide energy use by HVAC equipment in buildings accounts for 16–50% of the total final energy use, depending on the countries and their sectorial energy use patterns; and, more than half of this energy is typically used for heating [5]. Therefore, a reduction in the energy demand for building conditioning is very important for the large-scale improvement of the energy resources management.

While a wide literature exists on the exergy analysis of power plants, the application of the exergy approach to the built environment may be still considered at an earlier stage.

Most of the energy use in a building is related to near-environmental temperature thermal uses for space heating/cooling and for domestic hot water production. These low exergy demands are mainly satisfied with high exergy sources (e.g. fossil fuels), and thus a wide margin for exergy saving exists.

Renewable energy sources may give an essential contribution to the CO_2 emissions reduction. Although some of them may be considered purely renewable (e.g. solar energy), others are not

endlessly available (e.g. biomass), since their availability depends on the ratio between their consumption and regeneration timescales.

Therefore, it is proper to apply exergy analysis to renewable energy-based systems to identify the most efficient use of the available renewable sources in space conditioning: in fact, some recent studies [14] stress the need for providing such an assessment.

Balta et al. [1]evaluated a low exergy heating system from the primary exergy source through the ground-source heat pump to the building envelope and showed that the largest exergy destruction rate of the system occurred in the primary energy conversion. Shukuya and Hammache [12] compared three numerical examples of exergy consumption for space heating from the external source, through the boiler to the building envelope in steady state conditions. More than 20 case studies of "low exergy" buildings from 11 countries were presented in the Lowex guidebook [8]. Shukuya [11] described an exergetic approach to the assessment of future buildings equipped with low-exergy heating and cooling systems. Sakulpipatsin et al. [9] presented an extended method for the exergy analysis of buildings and HVAC systems by using a commercial building simulation tool, TRNSYS, for a reference building and its HVAC systems. Balta et al. [1] conducted an energy and exergy analyses of four building heating options driven by renewable and fossil-fuel sources and compared their energy and exergy efficiencies.

Scope of present study is to develop and test a general systemic procedure [3] for the optimal integration of buildings and their conditioning plants. First, a thermal building dissipation modelling is applied to compute the actual thermal demand of a living space, and a process simulator is then used to identify the most exergetically suitable energy plant.

The "optimal" configuration depends on the thermal characteristics of the building, the type of internal heating element (fan coil, ceiling or floor radiant panel in this study, since the example of application is limited to the winter mode of operation) and the type of primary energy conversion system (solar collector, PVT and ground source, closed-loop, heat pump).

In detail, the proposed procedure, that we plan to completely incorporate within an automatic computational procedure in the second part of this project, consists of an initial thermo-fluiddynamic phase, in which the detailed temperature maps within the building are obtained by means of a CFD simulation, followed by a calculation, for each type of heating element, of the actual thermal power required to meet the environmental comfort standards. This second step is performed by means of a process simulator that uses as input the data extracted from the CFD results. In this step, all the feasible different combinations of internal and external systems providing the prescribed thermal power are simulated by means of the process simulator CAMEL-Pro™ and the flow sheet of the primary-to-final use energy conversion chain is completely quantified. Finally, the individual systems are evaluated on the basis of the global exergy efficiency of the conversion chain to identify the most convenient pairings, i.e., those that consume the least primary resources for the same comfort level of the inside space.

2. 2. The numerical tools

In the selection of the "optimal" integration of the building and its energy plant, it is necessary to examine three main aspects: the heat demand of the building, the type of heating element and the type of the primary energy conversion system.

In this work, the first point consists of a detailed analysis of the thermal characteristics of the building and its temperature map, to obtain a more accurate calculation of the convective and radiative heat transfer on the inner surfaces and therefore to a better prediction of the thermal load. Notice that such thermal maps depend substantially on the type of the installed heating/cooling device: therefore, the calculations must be repeated for each one of the possible/feasible

configurations. All thermo-fluid dynamic simulations presented in this work have been performed via a commercial CFD code (Fluent® [4]). The pre-processing software Gambit, embedded in Fluent, has been used to create the geometry and generate the grid. The procedure, consisting of geometry modelling, creation of the mesh and its automatic acquisition by Fluent, can be easily translated into a systematic methodology for all type of heating elements.

Since the internal flows are likely to be turbulent, the Navier-Stokes equations have been solved here by a modified version of the Hanjalic/Launder/Spalding k_e-ε model [6]. This well established model is based on transport equations for the turbulence kinetic energy (k_e) and its dissipation rate (ε): the equation for k_e is derived by modelling its exact counterpart, while the equation for ε is obtained by using flow similarity and energy balance considerations, and bears little resemblance to its exact counterpart. In the derivation of the k_e-ε model, the assumption is that the flow is fully turbulent, and the effects of molecular viscosity are negligible. The model is therefore valid only for fully turbulent flows.

The pressure-velocity coupling is handled through the SIMPLE-C algorithm described by Van Doormaal and Raithby [15]. The advection fluxes are evaluated by the QUICK discretization scheme proposed by Leonard [7]. The computational spatial domain is filled with a non-uniform grid, with a higher concentration of grid lines near the boundary walls and other high-gradient areas, and a coarser uniform spacing throughout the remainder of the domain. After convergence of the velocity and temperature fields, the amount of thermal power transferred to the enclosure is calculated. As stated above, the results of the CFD simulations provide the thermal maps of the interior, that are then used to:

a) verify that the comfort zone fits well with the usual occupancy areas;

b) calculate the actual thermal load of the building.

The next step is the process simulation of each type of building conditioning system, to calculate the power consumption and exergy efficiency of each configuration. To this purpose, models [3] of external and internal sub-units have been implemented and integrated in an existing process simulator, CAMEL-Pro™[17].

In CAMEL the system is represented as a network of components connected by material and energy streams; each component is characterized by its own set of equations describing the thermodynamic changes imposed on the streams. The solver algorithm is based on the "equation system" concept; each component of the plant has its own transfer function, based on a "local" equation system and a similarly "local" array of variables. When the simulation is launched, the first step CAMEL performs is to assemble the overall (typically non-linear) system: it does so by collecting together all the components equations and renumbering/reshuffling the unknowns, to form a single, global, equations system that describes the whole plant behaviour. An optimized iterative Newton-Raphson algorithm is used to solve the global equation system. The main feature of CAMEL-Pro™ is in fact its modularity that enables users to expand the code by adding new components or by modifying the model of the existing ones: we exploited these capabilities to introduce the proper process equations for heating (internal and external) and cooling component models as described with more details in [3] and [2]. Clearly, the proposed procedure is to a large extent independent of the process simulator employed: any commercial code may be used, provided it contains the proper functions and utilities required by the computation of the local and global parameters of the energy conversion chain.

3. 3. The concept of exergy

The introduction of exergy as a thermodynamic analysis tool can help achieve the objective of reducing the degree of unsustainability of modern buildings.

The exergy of a system in a given environment is defined as the maximum work obtainable by the system when it is brought to a state of stable (possibly dynamic) equilibrium with the reference environment by means of ideally reversible transformations in which it exchanges heat only with the environment at a fixed reference temperature T_0 [13]. Exergy analysis has been applied to energy conversion systems since the early 1970s with the aim of encouraging the rational use of energy, which means in essence to strive for a better matching of the quality levels of the energy supply and demand. For each component of a plant, the outlet exergy is always less than the inlet exergy because of irreversible entropy generation. When calculating the exergy of a process component, the difference between the exergy losses and exergy destruction are recorded. Exergy losses include the exergy flowing to the surroundings, whereas exergy destruction indicates the exergy destruction within the system boundary due to irreversibility.

The exergy of a stream of matter can be divided into different "component exergies". In the absence of nuclear, magnetic, electrical and surface tension effects, exergy is calculated as the sum of :

$$Ex = Ex_K + Ex_P + Ex_{Ph} + Ex_{Ch} \quad (1)$$

where Ex_K, Ex_P , Ex_{Ph} and Ex_{Ch} are the kinetic, potential, physical and chemical exergy respectively: in the present study, the changes in kinetic and gravitational potential energies are neglected.

Physical exergy has been defined above, whereas chemical exergy is defined as the maximum amount of work which can be obtained when a stream of matter is brought from the environment state to the total dead (unrestricted) state as a result of heat transfer and exchange of substances only with the environment.

$$Ex_{Ph} = (h - h_0) - T_0 \cdot (s - s_0) \quad (2)$$

$$Ex_{Ch} = R \cdot T_0 \cdot \sum x_i \cdot \ln x_i + \sum x_i ex_{ch,i}{}^0 \quad (3)$$

where x_i is the mole fraction of the species i in the flow and exch,i_0 is the molar chemical exergy of the i^{th} species.

To perform an exergy analysis of the heating plants studied in this work, we need to calculate first the mass- and energy flows of each process. The process simulator (CAMEL-Pro™) calculates the exergy of each (material and immaterial) stream and displays the values of the exergy destruction, $Ex_{\square}$ and of the exergy efficiency, η_{ex}, of each component.

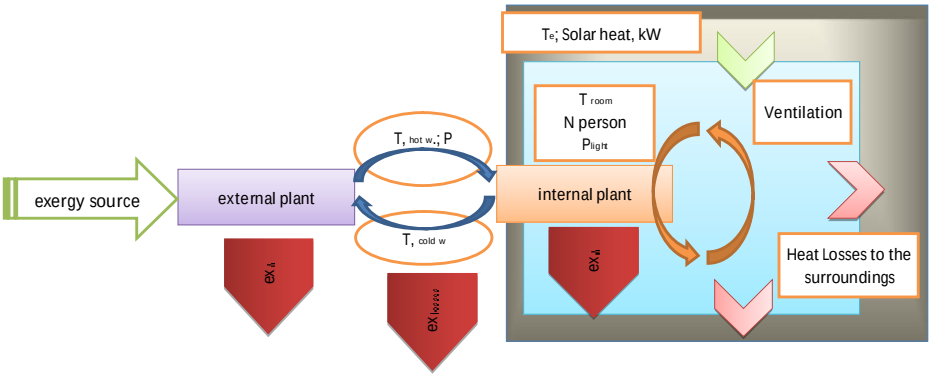

Figure 1 Exergy flows within the "building" system

3.1 - Internal system exergy analysis

The distribution of warm and cold air by ventilation, heat transfer through the walls and fixtures, and solar heat gain within the building envelope are calculated by a CFD simulation, which results in a more accurate determination of the actual thermal demand for space conditioning.

This newly calculated thermal load is then used to design the heating/cooling surface of the internal plant, which leads in turn to the calculation of the hot/cold water flow rate and its inlet temperature

and pressure. These parameters, together with the hardware characteristics of the space conditioning devices, allow to calculate the exergetic destruction and exergy efficiency of the internal system.

The exergy exchanged between a heating surface and the room is calculated as

$$\dot{E}_Q = \dot{Q} \cdot \left(1 - \frac{T_0}{T_{av}}\right) \tag{4}$$

where $\dot{Q}$ is the heat transfer rate of the device, T_0 is the environment temperature taken as 273 K, T_{av} is the average temperature of the exchange, calculated here as the room temperature plus the log mean temperature difference of the exchange, T_{LMTD}.

$$T_{av} = T_0 + T_{LMTD} \tag{5}$$

The LMTD is given by:

$$T_{LMTD} = \frac{(T_{in} - T_0) - (T_{out} - T_0)}{ln\left[(T_{in} - T_0)/(T_{out} - T_0)\right]} \tag{6}$$

The exergy destruction rate general formulation for the internal plant is then calculated as:

$$\dot{E}x_\delta = P_{el} + \dot{m} \cdot (ex_{in} - ex_{out}) - \dot{E}_Q \tag{7}$$

where the first term on the right represents the electrical input to the internal system (only in case of a fan coil), the second term is the exergy "input" provided by the hot water, $\dot{m}$ being the water mass flowrate and ex_{in} and ex_{out} the water specific exergy in the respective states.

The exergy efficiency of the internal plant is finally calculated by:

$$\eta_{ex} = \frac{\dot{E}_Q}{\dot{m} \cdot (ex_{in} - ex_{out}) + P_{el}} \tag{8}$$

3.2 - Intermediate system exergy analysis

The storage subsystem is represented by a water tank and piping system. The former is assumed to operate at steady state and is affected by a pre-assigned thermal loss (2% in the present analysis). The piping system leads to both thermal and pressure losses, allocated here to the water tank. The circulation pumps (and, where present, the air circulation fans) consume additional electrical power, the value of which is added to the exergy consumption of the system. In this case we assume that every unit of electrical energy is fully converted to exergy, therefore for electrical devices the electricity/exergy conversion coefficient is equal to 1 (but each device is assigned its own mechanical efficiency).

The exergy destruction within the auxiliary devices is:

$$\dot{E}x_\delta = \dot{E}x_{in} - \dot{E}x_{out}$$

$$\dot{E}x_{in,out} = \dot{m} \cdot (ex_{hot} - ex_{cold})$$

$$\dot{E}x_{in} = P_{el} \tag{9}$$

where $\dot{E}x_{in}$ and $\dot{E}x_{out}$ are the exergy content of the working fluid at the inlet and outlet of the device, $\dot{m}$ stands for the mass flow rate, exhot and excold are the specific exergies of the fluid calculated at the highest and lowest temperature within the subsystem respectively, P_{el} is the electric power absorbed by pumps and fans.

.

3.3 - External generation system exergy analysis

The external plant satisfies the global demand of all "downstream" subsystems. It may do so by using electrical energy, natural gas or other fuels, and/or solar irradiation or ground heat to heat the working fluid. The exergy destruction for the external plant is calculated by the same formulae as for the intermediate subsystems. In the present study, the exergy factor for solar radiation is calculated with Petela's formula [9] and posited constant and equal to 0.95.

For all electrically powered devices the national average conversion efficiency factor equal to 0.45 is applied, which represents the efficiency of the primary resources conversion into electrical power for the italian mix in year 2009 [16]: lacking a sufficiently detailed database, this was taken also equal to the average exergy resource-to-electricity conversion factor, though it is likely that substantial adjustments may be necessary in this case [13].

The results of the calculations are reported in Section 6.

4. 4. Description of the case studies

4.1 Layout

To show the potential of the proposed methodology, sevencase studies will be presented here. All deal solely with the "winter mode" operation, in which the building is heated against a pre-specified lower ambient temperature.

Several different domestic heating systems based on renewable energy resources have been simulated here. Specifically, solar and hybrid PV/T panels coupled with radiative heating panel and ground-source (closed and open loop) heat pumps coupled with fan coils and radiative heating panels are analyzed in detail from an exergy point of view.

The analyzed cases are:

CASE A: floor heating panel coupled with a solar collector;

CASE B: radiant ceiling panels coupled with a solar collector;

CASE C: floor heating panel coupled with PVT collector;

CASE D: radiant ceiling panels coupled with PVT collector;

CASE E: floor heating panel coupled with ground-source heat pump;

CASE F: radiant ceiling panel coupled with ground-source heat pump;

CASE G: fan coil coupled with ground-source heat pump.

Inlet and outlet stream for each case are reported in Table 1

Table 1. Input and output streams of simulated cases

CASE	*Description*	*Inputs*	*Outputs*
A	Floor heating panel + solar collector	Water pumps electrical power Solar irradiance	Heating load of the building
B	Radiant ceiling panels + solar collector	Water pumps electrical power Solar irradiance	Heating load of the building

C	Floor heating panel + PVT collector	Water pumps electrical power Solar irradiance	Heating load of the building PVT Electrical Power
D	Radiant ceiling panels + PVT collector	Water pumps electrical power Solar irradiance	Heating load of the building PVT Electrical Power
E	Floor heating panel + ground-source heat pump	Water pumps electrical power Ground heat	Heating load of the building
F	Radiant ceiling panel + ground-source heat pump	Water pumps electrical power Heat to ground heat exchanger	Heating load of the building
G	Fan coil + ground-source heat pump	Water pumps electrical power Fan coil electrical power Heat to ground heat exchanger	Heating load of the building

5. 5. Input data

5.1 CFD simulations

The object of the simulations is a simple two-levels house. The ground floor consists of a single room, while the first floor consists of two rooms, so that the building consists of three enclosed spaces which have a strong thermal interaction, Fig.2 and Table 2. The wall separating the two floors is thermal insulating and is characterized by a thermal conductivity of 0.03 W/mK. The wall separating the two rooms on first floor is an ordinary partition characterized by a thermal conductivity value of 0.3 W/mK. All remaining horizontal and vertical walls have a thermal conductivity value of 0.6 W/mK. The heating devices examined in this work are floor and radiant panels and fan coil units. In each simulation, the building is heated by a single type of device. The heated floor or ceiling is considered isothermal, at a temperature of 300K and 303K, respectively. The mass flow rate through the fan coil units, two at the ceiling of the main floor and one at the bottom, is 0.16kg/s each and the outlet air temperature is 302K (this value is necessary to compensate heat losses). The outdoor temperature is 0°C and the solar radiation is 500W/m^2, Table 3. The buoyancy-induced air flow inside the enclosures is assumed to be steady and incompressible.

The grid generator Gambit is used to create a mesh in the fluid domain. An unstructured mesh is used in entire domain except around the walls, where a boundary layer mesh is used. A proper mesh sensitivity analysis has been performed. The accuracy of the mesh results could be increased by refining the mesh, but the additional refinement is expensive in both computation cost and solution time. As a result, the number of nodal points used for computations for the three heating configurations is shown in Table 4. The optimal grid-size values, those used for computations, are such that further refinements do not produce noticeable modifications in the heat transfer rates.

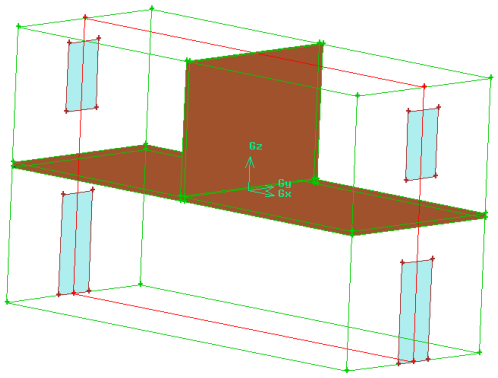

Figure 2 Building geometry

Table 2. Building geometry

	Dimension (m)
Building	10(w)x4(d)x6(h)
Ground floor-Room 0	10(w)x4(d)x3(h)
First floor-Room 1	5(w)x4(d)x3(h)
First floor-Room 2	5(w)x4(d)x3(h)
Floor radiant panel (ground floor)	10(w)x4(d)
Floor radiant panel (first floor-Room 1)	5(w)x4(d)
Floor radiant panel (first floor-Room 2)	5(w)x4(d)
Ceiling radiant panel (ground floor)	10(w)x4(d)
Ceiling radiant panel (first floor-Room 1)	5(w)x4(d)
Ceiling radiant panel (first floor-Room 2)	5(w)x4(d)
Window (ground floor)	0.9(w)x2.2(h)
Window (first floor)	0.9(w)x1.5(h)

Table 3. CFD simulations data input

	Mass flow rate (kg/s)	*Temperature(K)*	*Internal emissivity (at ~ 300K)*	*Outdoor temperature (K)*	*Solar radiation (W/m^2)*
Floor radiant panel	-	300	0.96	273	500
Ceiling radiant panel	-	303	0.96	273	500
Fan Coil Unit	0.16	302	-	273	500

Table 4. Mesh sensitivity analysis

	Floor radiant panel	*Ceiling radiant panel*	*Fan Coil Unit*
Number of nodal points per meter	*Heat transfer rate (W/m^2)*	*Heat transfer rate (W/m^2)*	*Heating capacity (W)*
70	57.9	85.3	1463
80	60.5	91.8	1516
90	65.4	96.4	1599
100	67.6	100.1	1649
120	67.9	100.5	1663

5.2 Building energy systems simulations

The main parameters assigned in CAMEL-Pro™ process simulations are reported in Table 5

Table 5 Process simulation input parameters

Parameter	Description [3]	Value	Units
η_0	SCconstant	0.819	-
k1	SCconstant	3.125	W/m2K
k2	SCconstant	0.022	W/m2K2
η_P	Pumps hydraulic efficiency	0.9	-
$\eta_{P.m}$	Pumps mechanic efficiency	0.98	-
ΔpRH	RHpressure losses	2	%
kA (Floor Panels)	RH upward thermal transmittance	0.00872	kW/m^2K
kA (Ceiling Panels)	RH upward thermal transmittance	0.00174	kW/m^2K
kB (Floor Panels)	RH downward thermal transmittance	0.001395	kW/m^2K
kB (Ceiling Panels)	RH downward thermal transmittance	0.006978	kW/m^2K
λ	thermal conductivity	0.0015	W/mK
$\eta_{Comp,HP}$	Heat Pump compressor efficiency	0.8	-
$\eta_{mecc,HP}$	Heat Pump mechanical efficiency	0.98	-
T_{soil}	Ground temperature	15	°C
$\eta_{Comp,HP}$	Ground heat exchanger efficiency	90	%
Δp_{FCU}	FCU pressure losses (water side)	5	kPa
$\Delta T_{w,FCU}$	FCU Water temperature difference	10	K

For each configuration simulations have been performed the heat demand value calculated from the CFD simulations,depending on the type of heating device selected (Table 6) .

Table6. Process simulation main data inputs: heat demands and characteristic temperatures for each case.

Parameter	Units	A	B	C	D	E	F	G

Heat Demand	W	4350	6500	4350	6500	4350	6500	6600
RH Inlet water T	K	318	313	318	313	318	313	-
RH Outlet water T	K	310	310	310	310	310	310	-
HP Inlet ground water T	K	-	-	-	-	285	285	285
HP Outlet ground water T	K	-		-		281	281	281
FCU inlet water	K	-	-	-				307
FCU air outlet T	K	-	-	-				303

6. 6. Results

6.1 Results of the CFD simulations

The results of the CFD simulations are shown in Figures 3 to 5 were the flow and temperature patterns for all configurations are shown in terms of isotherm contours and stream function, plotted on the central section of the building. The streamlines are coloured by their respective mass flow rates, which are proportional in each point to the local velocity vector. The heat transfer rate required to meet the environmental comfort standards for floor and ceiling radiant panel configuration is 67.6W/m^2 and 100.1 W/m^2, respectively. The actual thermal power required to meet the environmental comfort standards for each fan coil heating is 1649W.

The ideal standard for thermal comfort can be defined by the operating temperature, which is the average of the air dry-bulb temperature and of the mean radiant temperature at a given place in a room. The operating temperature intervals vary depending on the type of indoor location. They also vary by the time of year. ASHRAE [20] has lists of suggested temperatures, in different types of buildings and different environmental conditions. For a single room in a building, with an occupancy ration per square meter of 0.1, the recommended winter operating temperature is between 21 °C and 24°C. From this point of view, the best heating device, which also provides an homogeneous temperature distribution, is the floor radiant panel. In addition, this configuration provides a greater improvement because it generates circulation cells so that stagnation zones, which are the cause of mold and moisture in buildings, are avoided.

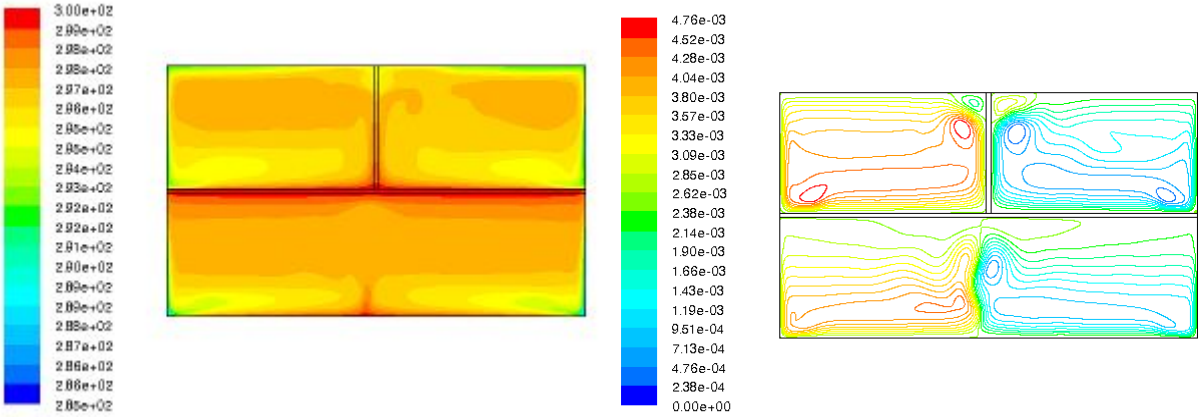

Figure 3 Isotherms (K) and stream function (kg/s) for floor radiant panel configuration

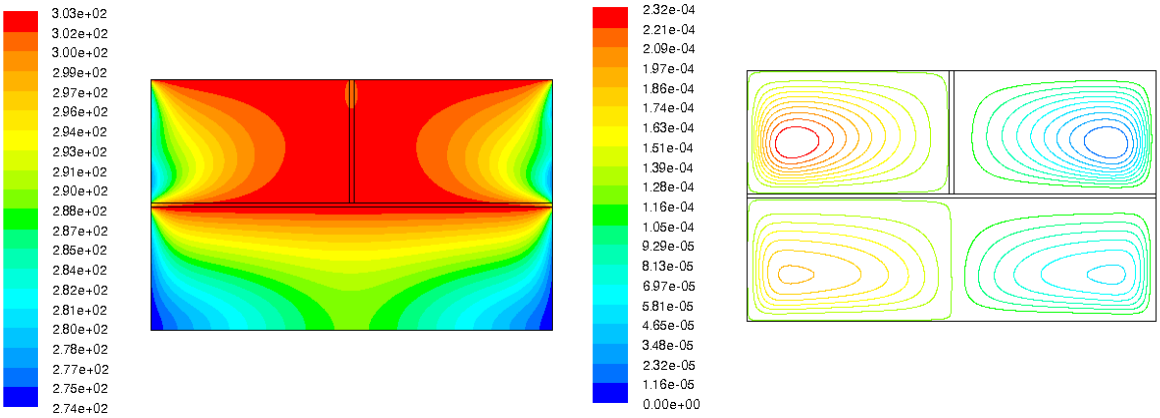

Figure 4 Isotherms (K) and stream function(kg/s) for ceiling radiant panel configuration

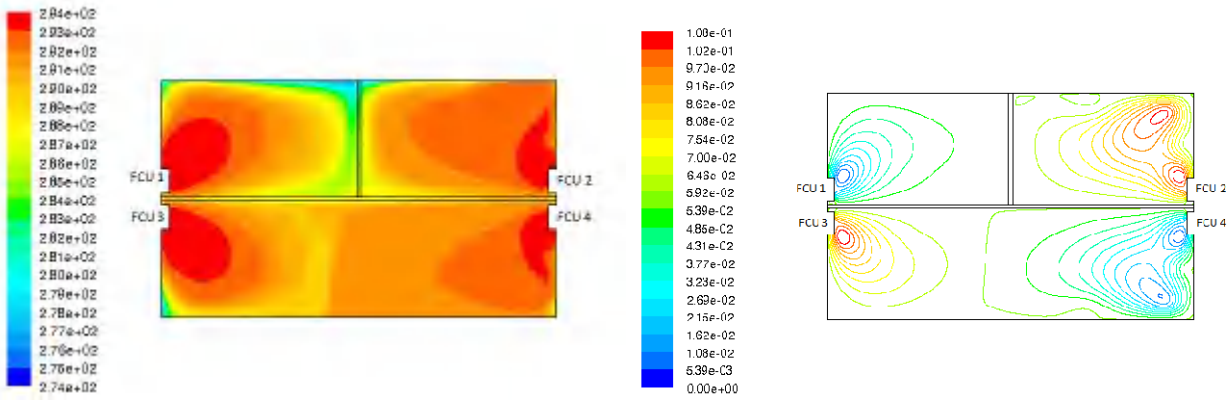

Figure 5 Isotherms (K) and stream function(kg/s) for Fan Coil Units configuration

6.2 Exergy analysis

The main results of the exergy calculations are reported in Figure 6. The exergy input represents the total "exergy load" in our simplified building model. It is the total "external" power required by the heating system to obtain the desirable user's comfort. The exergy output is for all practical purposes the exergy of the heat load calculated at some proper average temperature (we used the LMTD of the heating device). The exergy efficiency is the ratio of the latter to the former (in exergy terms, of the "product" to the "fuel").

The system that presents the best exergetic performance is Case C (floor heating panel coupled with PVT) with an overall exergy efficiency of 12,11%.

The results show (see Figs 7 and 8) that -under the conditions assumed in these experiments- the best external system performer is the GSHP that uses less exergy than the solar thermal panel to deliver the same heat load. It is not surprising that solar thermal collectors have a lower efficiency as hot water generators: they have an intrinsically low exergy efficiency (on the average, their exergy destruction amounts to 65-80%).

With the new generation of hybrid solar collectors – PVT (Cases C and D), which, besides the heated water, co-generate electrical power, the values of exergy efficiency are 12,11% for Case C and 11,52% for Case D, 2% higher than that of the solar collector. Therefore, applying solar collectors for a space heating purposes (hot water generation) remains the worst scenario.

The internal heating elements have also different exergetic performances: the floor panel is more efficient because the natural air circulation it generates improves the heat convection in the room and reduces the overall thermal load (more uniform inside temperature), the worst is the fan coil that uses direct external electrical power.

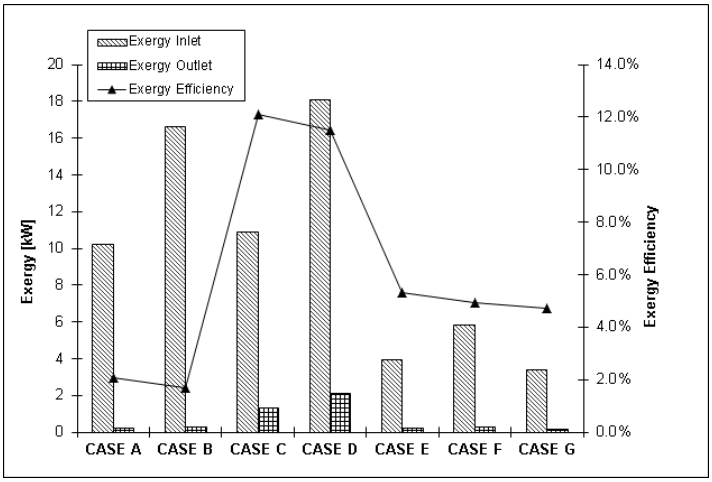

Figure 6 Exergy analysis results: Exergy Inlet, Outlet and Exergy Efficiency for each case.

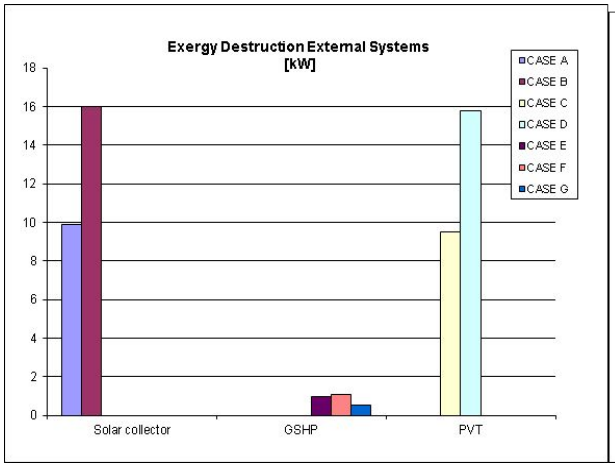

Figure 7

Exergy destruction within external components

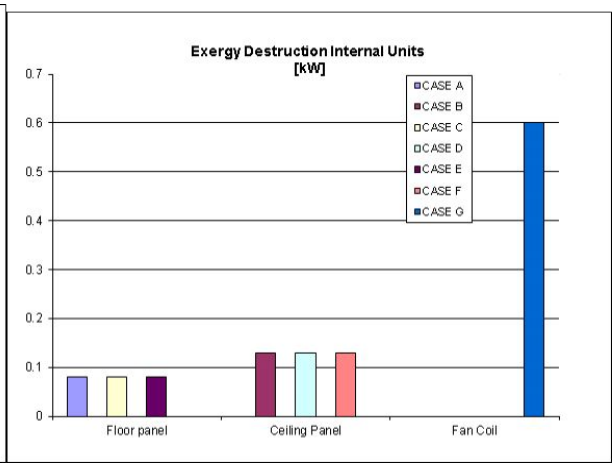

Figure 8

Exergy destruction within internal components

Conclusions

Scope of this study was to test a novel systemic approach to the joint design-and-analysis of space conditioning. In order to identify more thermodynamically efficient configurations, and using only

commercially available devices, the proposed procedure is developed along the following steps: first, a refined estimate for the thermal power requirements for a given heating system inserted into a prescribed residential space is obtained by CFD simulations. Then, the data thus obtained are elaborated by a process simulator in order to calculate the total exergy demand for the (steady) operation of the space heating system. Finally, the exergy efficiency of each configuration is calculated and the tested configurations are ranked accordingly.

Seven study cases are presented and discussed. The results show that the heating plant consisting of floor heating panel coupled with PVT is the most efficient solution, since it covers the same thermal load with the best overall exergy efficiency.

The present paper demonstrates the feasibility of the proposed approach. More complex building envelopes and different combinations of internal/external heating devices can be tested. Cooling loads can be taken into account as well, and so on. The final goal is to develop an application to the entire (seasonal) operational curve of the "building+plant" system, including inertia effects. A systematic application of the procedure outlined in this study will help design less exergy-destroying buildings, and reduce the exergy intensity of the Domestic and Tertiary sectors.

Nomenclature

ex	specific exergy , kJ/kg
Ex	Exergy flow, kJ/s
$\dot{Ex}_{\delta}$	destroyed exergy , kW
ε	turbulence dissipation rate, m^2/s^3
η	exergy efficiency
I	Solar Irradiance , W/m2
h	specific enthalpy, J/kg
k	thermal transmittance, W/m2K
k_e	turbulence kinetic energy, $m^{2/}s^2$
$\dot{\boldsymbol{m}}$	mass flow rate, kg/s
P	Electric power, kW
$\dot{\boldsymbol{Q}}$	thermal power, kW
R	universal gas constant, J/(mol K)
s	specific entropy, J/(kg K)
T	temperature, K
η_{ex}	exergy efficiency, %

References

[1] Balta M.T, Dincer I., Hepbasli A., Performance and sustainability assessment of energy options for building HVAC applications, Energy and Buildings, v. 42, 1320–1328, 2010.

[2] Cheremnykh E., Cianfrini M., Toro C., A general procedure for the optimal integration of buildings and their energy plants, Proc. WEC2011, Geneva, Swiss, September 4–9, 2011.

[3] Cheremnykh E., Cianfrini M., Sciubba E., Toro C., A Novel Integrated Exergetic Approach for the Optimization of Building Conditioning Systems, Proc. ECOS2011, Novi Sad, Serbia, July 4–7, 2011.

[4] Fluent 6.2.3 Manual, Fluent Inc./Ansys

[5] International Energy Agency, Key World Energy Statistics, 2011.

[6] Launder B.E., Spalding D.B., Lectures in Mathematical Models of Turbulence, Academic Press, London, 1972

[7] Leonard B.P., A stable and accurate convective modelling procedure based on quadratic upstream interpolation, Comp. Meth. in Appl. Mech. Eng., v. 19, 59-78, 1979.

[8] LOWEX guide book, Low exergy systems for heating and cooling of buildings guide book, examples of lowEx buildings, http://www.lowex.net/guidebook/index.htm

[9] Petela, R. , Engineering Thermodynamics of Thermal Radiationfor Solar Power Utilization McGraw-Hill, 2010,

[10] Sakulpipatsina P. Itardc L.C.M., van der Kooia H.J., Boelmana E.C., Luscuerea P.G., An exergy application for analysis of buildings and HVAC systems, Energy and Buildings, V. 42, N. 1, January 2010, Pages 90-99.

[11] Shukuya M., The exergy concept and its application to the built environment, Building and Environment, V.44,.1545–1550, 2009.

[12] Shukuya M., Hammache A., Introduction to the Concept of Exergy—For a Better Understanding of Low-Temperature-Heating and High-Temperature-Cooling Systems, VTT research notes, Espoo, Finland, 2002.

[13] Szargut J., Morris D. H., Steward F. R., Exergy Analysis of Thermal, Chemical, and Metallurgical Processes, Springer-Verlag, 1988

[14] Torío H., Angelotti A., Schmidt D., Exergy analysis of renewable energy-based climatisation systems for buildings: A critical view, Energy Conversion and Management, v. 50, n. 2, February 2009, 387-392.

[15] Van Doormaal J.P., Raithby G.D., Enhancements of the simple method for predicting incompressible fluid flows, Num. Heat Transfer, v. 11, 147-163, 1984.

[16] www.autorita.energia.it

[17] www.turbomachinery.it, 2010, CAMEL-Pro Users Manual, rev. 4.

Analysis of different typologies of natural insulation materials with economic and performances evaluation of the same in building

Umberto Desideri[a], Daniela Leonardi[b], Livia Arcioni[c]

[a] Perugia University, Industrial Engineering Dept., Perugia, Italy, umberto.desideri@unipg.it
[b] Perugia University, Industrial Engineering Dept., Perugia, Italy, daniela.leonardi@unipg.it
[c] TREE Srl, Perugia, Italy, arcioni@tre-eng.com

Abstract:

Considering the significant impact that the residential sector has on energy consumption, it is particularly important to implement policies aimed at improving energy efficiency in buildings for saving primary energy, and also to spread the concept of sustainable development through the use of appropriate technology and proper project criteria both for new constructions and for the rehabilitation of existing ones. It is in this context and in an attempt to reduce as much as possible the consumption of resources that fits the possibility of utilizing "natural" materials for the insulation of buildings.
In this work they have been analyzed the natural insulation materials present on the Italian building market, where for "natural" it is meant the ones that are derived from renewable materials, which emit no pollutants and that are recyclable or biodegradable. Then it has been created a database which highlights the physical and thermohygrometrical characteristics (density, conductivity, specific heat, vapor permeability, etc.), as well as the possible applications (ceiling, wall, roof).
Then it has been carried out a performing and economic comparison related to the replacement of the traditional insulation of a residential building located in Perugia (Central Italy) with the majority of the insulating materials identified in relation to its type of use. The synthetic insulating materials have been replaced in order to reach, for the analysed building, the same thermal performances obtained with the application of traditional insulators. From the analysis of dynamic thermal parameters has been deduced that the building envelope insulated with natural products has better thermal summer performances compared to the same insulated with traditional materials such as XPS, with the same thermal winter performances. This improvement is mainly due to the high value of the specific heat characteristic of the natural insulators.
Finally, it has been carried out an economic comparison between the two types of insulation from which it has been possible to deduce that the utilize of natural insulation products have meant an increase in the costs which is widely variable depending on the type of natural insulator used.

Keywords:

sustainability, building, insulation materials, energetic performances

1. Introduction

The slowdown which hit the world economy and trade have played an important role in the decrease of overall energy consumption, especially in countries, such as Italy, where the manufacturing sector still plays an important role.

In 2009, energy consumption decreased by 5,6% compared to 2008, even though domestic consumption grew by 3,6% [1].

In this context, the implementation of policies aimed at improving energy efficiency in buildings is particularly important, with the subsequent saving of primary energy and the dissemination of the concept of sustainable development, through the use of appropriate technologies and project criteria both for new constructions and for renovation of existing buildings.

The insulation of buildings through the use of "natural" materials falls into this category, in an attempt to reduce as much as possible the consumption of resources.

A new approach has made its way in the construction industry, where the main goal is to realize buildings which provide maximum living comforts and maximum energy efficiency in a strict respect of the environment, through the use of building materials made by predominantly natural and renewable raw materials, which are characterized by a reduced environmental impact in terms of consumption of natural resources and energy.

The building envelope regulates the contacts and exchanges of matter and energy with the exterior. A very important aspect in the construction of a building envelope aimed at minimizing heat loss is the insulation of the same, obtained with a high degree of thermal insulation. The thickness increase of the insulating material layer in walls and roofs is therefore an essential solution, as is the importance of paying maximum attention to discontinuity points in the insulating layer, i.e. thermal bridges, where in addition to the risk of substantial losses of energy there is also the risk of condensation and mould [2].

In the light of these considerations, both the importance of knowing the performance characteristics of the "natural" materials and the importance of assessing their application within the building envelope become evident; the reason being that only an appropriate project of the structural elements and a proper placement and installation of the insulating material, according to its characteristics, can provide a long and efficient duration of the material inside the building.

This choice must take into account not only the quantitative aspects, but also the quality of the building and the environment. The assessment of the materials' characteristics becomes thus fundamental to evaluation of their impact on the environment

To this end, a number of product certifications exist, such as the EPD (Environmental Product Declaration) and the Ecolabel that span every product category, but also specific certifications for building products., For example, the Natureplus label, promoted by a European group consisting of the major institutions working in the field of quality control of products for green building, and the ANAB (National Association for Bioecological Architecture) - the only institution in Italy that has developed standards for assessing the sustainability of the building industry products - bioecological label, are among those [3].

In addition to the environmental impact, monetary cost is essential in the choice of a material, while taking into account that the additional spending due to the realization of a good thermal insulation is offset in a short time by cost savings of climate control.

In this article, a database of natural insulation materials available on the Italian market is presented, divided according to their main applications.

Furthermore, through a specific calculation software (MC4), which complies to the UNI TS 11300:2008 standards parts 1 and 2, as according to D.P.R. 2 April 2009 n.59, a building used for residential purposes located in the city of Perugia has been analyzed from an energy consumption point of view. This was done in order to carry out an efficiency and economic comparison analysis between the use of traditional insulating materials and natural insulating materials. The thicknesses of the natural insulations were chosen so that they could achieve the same energy performance of the building's envelope obtainable with traditional materials.

2. Development of a natural insulating materials database

Insulation materials can be classified according to various aspects, for example in relation to their origin, (synthetic, mineral, plant or animal), and according to their structure, (fibrous or cellular). In particular, one might have[4-5]:

- *totally synthetic materials,* mainly polyester fiber, expanded polystyrene, extruded polystyrene foam, polyurethane foam and polyethylene foam, which are thermosetting or thermoplastic polymers obtained by a long and complex processing of petroleum oil, raw material base;
- *totally mineral materials,* mainly natural granular materials (pumice) and expanded (clay, perlite, vermiculite and glass granular), cellular limestone-cement insulation and cellular glass, derived

from the processing of raw materials such as clay minerals , limestone, volcanic rocks, quartz sands, recycled glass, without the addition of binders and resins;

- *totally plant-based materials*, like cork, reed, wood fiber, coir, jute, maize, and some products in kenaf and flax, in which the plant material undergoes a process that does not require the addition of binders and synthetic support .

There are also a wide range of mixed materials that arise from the combination of different raw materials, in order to improve their performance:

- *mixed-synthetic minerals*, in particular mineral wools (glass wool and rockwool), in which the mineral raw materials (quartz sand, recycled glass, rocks of volcanic origin) is added a percentage of synthetic resins functioning as binder;
- *mixed plant-synthetics and animal-synthetics*, in particular soft fibre panels (cellulose fibers, hemp, sheep wool, and in some cases kenaf and flax) to which a synthetic fiber is added (usually the extent of 10-15 %, in some cases even 30-50%) that links the material and gives greater stability;
- *mixed vegetable-mineral*, in particular mineralized wood wool, in which a percentage of mineral binder (Portland cement or magnesite) is added to the plant raw material, to give greater strength to the material.

This division, however, does not provide an exhaustive description of the wide range of materials on the market today. A further subdivision is based on the production process:

- *natural materials*: used as they are offered by nature, without substantial transformations, although they are also subject, before the installation, to a certain degree of processing in order to provide them with the appropriate requirements for a particular use (cutting, washing, etc..);
- *man-made (artificial) materials*: they are obtained by the specific production process which tends to give a mixture of properly dosed raw materials, certain characteristics.

Therefore, in most cases it is not correct to speak of natural materials, as all insulation materials must undergo a process of more or less complex transformation; and depending on the consistency, it is possible to identify panels, mattresses, mats, strands, flakes and granules .

In this paper, the insulation materials have been analyzed taking into account their main features and applications with an emphasis on vertical walls, roof, floors between storeys and floors on the ground, in order to create a repertoire of insulation products available on the Italian market.

In particular, the following rules for the installation/laying of insulating materials have been taken into consideration [6-7]:

Laying of insulating materials on vertical walls (Table 1):

1. *Outer Coat:* the insulation is placed on the outer walls of the building, so as to remove the thermal bridges and reduce the induced effects in the structures and wall surfaces of rapid or significant changes in outside temperature.
2. *Interior Coat*: panels are placed on the interior surface of the wall. They consist of a layer of insulating material, a vapour barrier and a plaster slab. Unlike the outer coat, this technique does not correct the thermal bridges and it does not allow to maintain the perimeter walls at a higher temperature.
3. *Ventilated Wall*: the insulation layer is installed in direct contact with the wall and is separated from the lining by a special structure, so that, the ventilation layer reduces the risk of condensation on the interior surfaces of the building.
4. *Gap Insulation*: A gap is placed between two vertical elements, filled with air or insulating materials. Two types of insulating materials may be used:
   - paneled insulating materials, which can be fibrous panels or foam materials.
   - injected insulating materials, usually into granules, which are injected into the cavity to fill it up.

Table 1: Insulation materials on vertical wall

N.	Wall Stratigrafy	Materials
1)	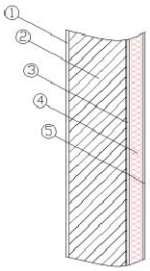	1 : 1.5-cm thick Plaster.; 2 : Masonry; 3 : 1-cm thick Mortar; 4 : Insulation; 5 : Smoothing layer in which a 0.5-cm thick fiberglass net is embedded, plus an additional 0.5-cm thick smoothing compound.
2)	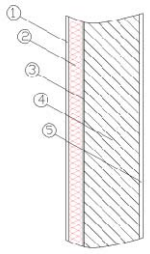	1 : 1,3-cm thick Plasterboard; 2 : Insulation; 3 : Metal framework; 4 : Masonry; 5 : 1.5-cm thick Plaster.
3)	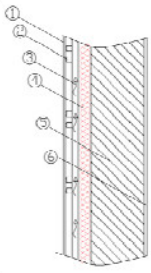	1 : External coat; 2 : Fixing system; 3 : Air vent; 4 : Insulation; 5 : Masonry; 6 : 1.5-cm thick Plaster.
4)	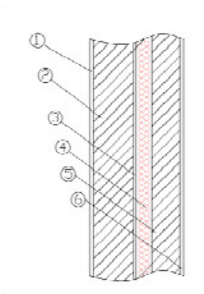	1 : 1.5-cm thick Plaster; 2 : Brick; 3 : 1.5-cm thick Rough coat; 4 : Insulation; 5 : 8–12 cm thick Air Brick; 6 : 1.5-cm thick Plaster.

Laying of insulating materials in floors (Table 2):

1. *Floors on the ground (also known as slab on-grade) and vented crawl spaces*: the insulation of floors on the ground or on crawl space involves the application of an insulating layer on the extrados of the floor. Having to bear the weight of the screed above, the insulation must have a mechanical strength suitable for this purpose.
2. *Insulation of floor intrados (or lower surface) with coating system*: referring to the insulation of the floor which looks out onto porticoes or open spaces, it provides the placement of the insulation at the underside of the slab floor.
3. *Insulation of floor extrados (or upper surface):* it refers to the insulation of floor covering open spaces or basements, and it provides the placement of the insulation at the top face of the slab floor.

Table 2: Insulation materials on floor

N.	Floor Stratigrafy	Materials
1)	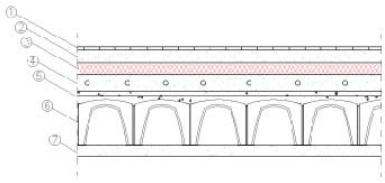	1 : 1-cm thick Floor; 2 : 4-6 cm thick Screed; 3 : Insulation; 4: Lightened screed; 5 : about 5-cm thick Slab; 6 : Vented crawl space; 7 : 10-cm thick Lean concrete.
2)	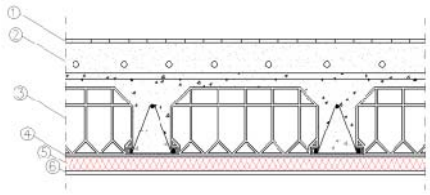	1 : 1-cm thick Floor; 2 : 4-cm thick Screed; 3 : 20+4 cm thick Floor; 4 : Mortar; 5: Insulation; 6 : 1.5-cm thick Plaster.
3)	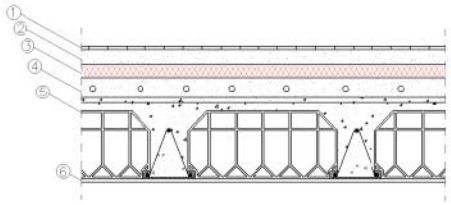	1 : 1-cm thick Floor; 2 : 4-cm thick Screed; 3 : Insulation 4 : 6-cm thick Lightened screed; 5 : 20+4 cm thick Floor; 6 : 1.5-cm thick Plaster.

Application of insulating materials in roofs (Table 3):

1. *Insulation at the roof intrados:* it is used with pitched roofs, that have a live-in attic, and the insulation is placed directly on the pitch structure (which can be in strips of wood, iron or precast joists).
2. *Insulation under the outer skin,or "warm roof"*: the insulation is placed just below tiles, pantiles or slabs, and is supported by the sloped pitch. It is a good rule that the insulations are laid with a sheet on the underside, which acts as a vapor barrier. Fig 2.a) shows the stratigraphy of a "warm roof" in masonry, while in (Table 3 Figure 2.b) the stratigraphy of a timber "warm roof" is shown.
3. *Insulation under the outer skin, "vented roof"*: in order to build a vented roof, a "blade" of air must be created between the covering mantle of tiles and the underneath insulating panels, so as to obtain an upward air flux. Fig 3.a) describes the stratigraphy of a "vented roof" in masonry, while in Fig 3.b) the stratigraphy of a timber "vented roof" is shown.

Table 3: Insulation materials on roof

N.	Roof Stratigrafy	Materials
1)	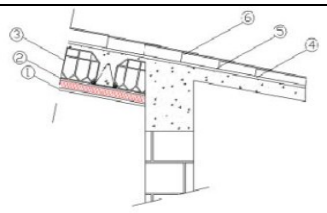	1 : 1.5-cm thick Plaster; 2 : Insulation; 3 : 20+4 cm thick Floor; 4 : 1,2 cm Planking; 5 : Waterproof sheath; 6 : Outer skin.

2.a)	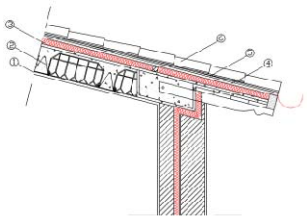	1 : 1.5-cm thick Plaster; 2 : 20+4 cm thick Floor; 3 : Insulation; 4 : 1,2 cm thick Planking; 5 : Waterproof sheath; 6 : Outer skin.
2.b)	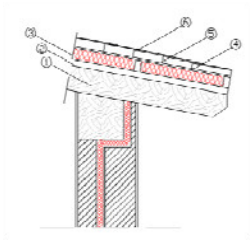	1 : 10 x 20 cm timber tables; 2 : 3 cm thick Planking; 3 : Insulation; 4 : 1,2 cm thick Plywood planking; 5 : Waterproof sheath ; 6 : Outer skin.
3.a)	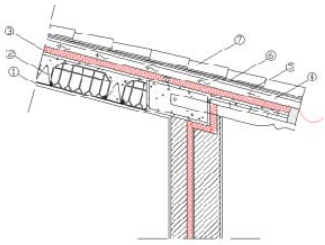	1 : 1.5-cm thick Plaster; 2 : 20+4 cm thick Floor; 3 : Insulation; 4 : 5 cm thick Air vent; 5 : 1,2 cm Planking; 6 : Waterproof sheath; 7 : Outer skin.
3.b)	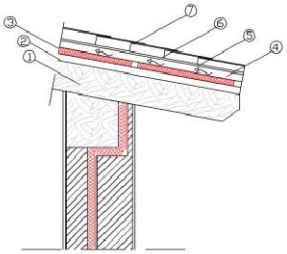	1 : 10 x 20 cm timber tables; 2 : 3 cm thick Planking; 3 : Insulation; 4: 5 cm thick Air vent; 5 : 1,2 cm Planking 6 : Waterproof sheath 7 : Outer skin.

On the basis of the main applications of the natural insulating materials described above, a Microsoft Office Excel database of insulating products available on the Italian market was created, based on the manufacturing companies [8-9].

In particular, for each structure destination (floor, wall and roof) and for each typology of installation, a range of products divided on the basis of their origin (plant, animal and mineral) was been chosen. In addition, for each insulating material, the data template shown in Table 4 was included into the database.

Table 4: Data classification in the Database

Data	Units of Measurement
Product name	
Manufacturing or distributing company	
Price (2010 price list)	€/m^2
Using typologies	
Description	
Thickness	mm
Density (ρ)	kg/m^3

Thermal conductivity (λ)	W/m·K
Specific heat (Cp)	kJ/kg·K
Water vapor diffusion resistance (μ)	

The present work does not consider any products made of natural materials coupled with panels of petrochemical origin (expanded polystyrene, extruded polystyrene, polyurethane, etc.).

Commercial products included in the database are 100% natural or they contain a small percentage of synthetic binder in polyester fiber. The polyester fiber is an innovative material that derives largely from recycled PET bottles. In this way, the eco-sustainability of the selected insulating materials was been guaranteed.

The following is an excerpt of the database related to vertical walls, on the ground and perimetral, This analysis indicates the possible applications of natural insulating materials both in new constructions and in renovation and recovery of existing buildings. The proposed construction details summarize the instructions of use suggested by the manufacturers based on green building design evaluations.

Criteria for choosing between different insulating materials are clearly identifiable on the basis of the prevailing and/or specific application requirements that materials must meet.

In order to make the most appropriate choice, it is necessary to know the materials' performance characteristics and assess materials in relation to their application type within the building envelope. Finally, an economic assessment is also required to properly choose the right insulating material. with gap insulation.

3. Economic evaluation of natural insulating materials utilization in a building in Central Italy

A residential building located in the municipality of Perugia was assessed in energetic terms by using the software MC4. The objective was to carry out an economic and efficiency assessment of the selected building realized with conventional insulation materials in comparison with the same building constructed by using natural insulation.

3.1. Case Study

The single-family house has three floors consisting of an attic that is not heated nor air-conditioned, a garage in the basement, and a heated apartment. The building envelope dimensional characteristics are presented in Table 5.

Table 5 Building envelope data

Data	
Vertical closures area	233 m^2
Transparent surfaces area	25,57 m^2
Effective surface area (unheated)	122 m^2
Effective surface area (heated)	94,67 m^2
Gross surface area	388,95 m^2
Heated gross volume	378,38 m^3
S/V	1,0147 m^{-1}

Inside the building two different heating zones were outlined, a heated area (Figure 1) and an unheated area (Figure 2).

Extruded polystyrene foam XPS, was selected to insulate the building envelope, a widely-used material of petrochemical origin. Different currently available insulating panels XPS (Table 6) were chosen, depending on their application typology.

Table 6: Selected Building Insulations

Insulation typology	ρ (kg/m^3)	λ (W/m K)	C_p (kJ/kgK)	μ	Laying
XPS_styrodur 250 CNL	28	0,034	1,45	100	Vertical walls gap
XPS_expandit	33	0,0304	1,6	100	Under the roof outer skin
XPS_styrodur 2800 CS	30	0,032	1,45	100	Floor estrados

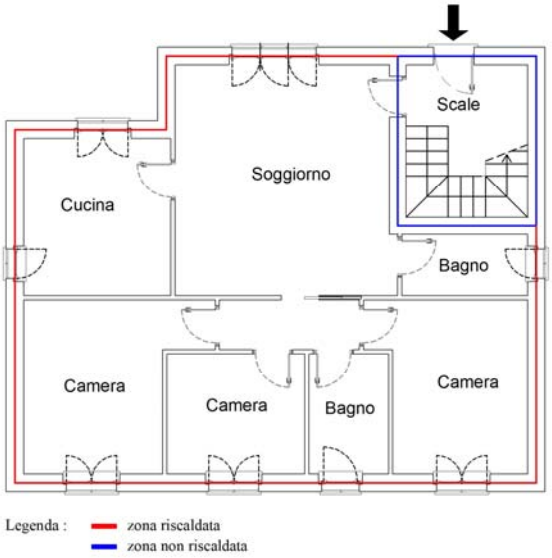

Figure 1: Ground floor thermal zone

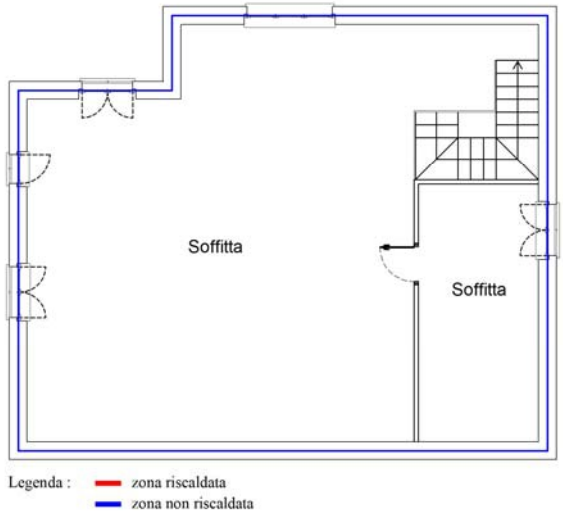

Figure 2: Attic thermal zone

Stratigraphies of the opaque components used in the case study are reported as follows.

1. *Perimeter separation wall between heated zone and unheated staircase*; starting from the outside, the wall is composed of the following layers: plaster, Poroton thermal brick, rough coat of plaster, cavity filled with insulation panels 5 cm. thick, hollow bricks, plaster. Table 7 shows the stratigraphy, while in Table 8 the thermal characteristics are presented.

Table 7: Perimeter wall stratigraphy

Layer Description	S (cm)	λ (W/m°C)	C (W/m²°C)	ρ (kg/m^3)
Lime and gypsum plaster	1,50	0,700		1.400
Air brick F120	12,00		2,28	775
XPS styrodur_250 CNL	5,00	0,034		28
Cement mortar	1,00	1,400		2.000
POROTON	20,00		1,04	845
Lime mortar or cement lime	1,50	0,900		1.800

Table 8: Thermal and inertial characteristic

Total thickness (cm)	41,00	Superficial mass (kg/m²)	263,40
Unit conductance		**Unit resistance**	
Internal surface [W/(m²·K)]	7,69	Internal surface [(m²·K)/W]:	0,13
External surface [W/(m²·K)]:	25,00	External surface [(m²·K)/W]:	0,04
Transmittance		**Thermal resistance**	
Tot. [W/(m²·K)]:	0,32	Tot. [(m²·K)/W]:	3,09

2. *Ground floor on crawl space with igloos*; the floor is composed of a lean concrete layer, crawl space of 30 cm igloos, 5 cm reinforced concrete slab, cellular concrete lightened substrate, XPS insulating layer, preformed panel in EPS for floor heating, high thermal conductivity screed layer where a 2 cm. diametre pipe of the radiating heating system is embedded and, finally, the upper surface of floor. Tables 9 and Table 10 respectively show stratigraphy and transmittance values.

Table 9: Stratigraphy of Ground floor on vented crawl space with igloos

Layer Description	S (cm)	λ (W/m°C)	C (W/m²°C)	ρ (kg/m^3)
Clay tile	2,00	0,720		1.800,00
Heating plant screed	6,00	1,830		2.000,00
EPS performed panel	2,00	0,035		30,00
XPS styrodur_2800 CS	6,00	0,032		30,00
Cellular concrete	5,00	0,090		400,00
Common concrete	5,00	1,280		2.200,00

Table 10: Thermal and inertial characteristic

Total thickness (cm)	26,00	Superficial mass (kg/m²)	288,40
Unit conductance		**Unit resistance**	
Internal surface [W/(m²·K)]	5,88	Internal surface [(m²·K)/W]:	0,17
External surface [W/(m²·K)]:	25,00	External surface [(m²·K)/W]:	0,04
Transmittance		**Thermal resistance**	
Tot. [W/(m²·K)]:	0,30	Tot. [(m²·K)/W]:	3,31

3. *Vented covering in masonry*; the covering is made of a 1,5 cm plaster layer, 20 cm of masonry floor, 4 cm. of reinforced concrete slab, 6 cm. of XPS Expandit insulating layer, a 5 cm. ventilation cavity/gap, 1.2 cm of planks, a waterproof membrane and a covering mantle. Stratigraphy and trasmittance values are shown in Tables 11 and 12.

Table 11: Covering stratigraphy

Layer Description	S (cm)	λ (W/m°C)	C (W/m²°C)	ρ (kg/m^3)
Lime mortar or cement lime	1,50	0,900		1.800,00
Floor 20cm	20,00		3,33	950,00
Common concrete	4,00	1,280		2.200,00
XPS expandit	6,00	0,030		33,00

Table 12: Thermal and inertial characteristic

Total thickness (cm)	31,50	Superficial mass (kg/m²)	280,13
Unit conductance		**Unit resistance**	
Internal surface [W/(m²·K)]	10,00	Internal surface [(m²·K)/W]:	0,10
External surface [W/(m²·K)]:	25,00	External surface [(m²·K)/W]:	0,04
Transmittance		**Thermal resistance**	
Tot. [W/(m²·K)]:	0,40	Tot. [(m²·K)/W]:	2,49

4. *Separation floor between attic and heated zone*; the floor is formed of a plaster layer, a 24 cm thick supporting structure in masonry, cellular concrete lightened substrate, insulation layer, finishing screed layer and floor. Stratigraphy and transmittance value are given in Tables 13 and 14.

Table 13: Separation floor stratigraphy

Layer description	S (cm)	λ (W/m°C)	C (W/m²°C)	ρ (kg/m^3)
Lime mortar or cement lime	1,00	0,900		1.800,00
Floor 20cm	20,00		3,33	950,00
Common concrete	4,00	1,280		2.200,00
Cellular concrete	8,00	0,090		400,00
XPS styrodur_2800 CS	7,00	0,032		30,00
Finishing screed	4,00	1,350		2.000,00
Clay tile	2,00	0,720		1.800,00

Table 14: Thermal and inertial characteristic

Total thickness (cm)	46,00	Superficial mss (kg/m²)	428,10
Unit conductance		**Unit resistance**	
Internal surface [W/(m²·K)]	10,00	Internal surface [(m²·K)/W]	0,10
External surface [W/(m²·K)]:	25,00	External surface [(m²·K)/W]	0,04
Transmittance		**Thermal resistance**	
Tot. [W/(m²·K)]:	0,28	Tot. [(m²·K)/W]:	3,62

5. *Separation floor between heated area and garage*: this floor is composed of plaster, 24 cm thick masonry supporting structure, cellular concrete lightened substrate, XPS insulation, preformed panel in EPS for floor heating , high thermal conductivity screed layer where a 2 cm. pipe of

radiating heating system is embedded and the floor. Stratigraphy and transmittance values shown in Tables 15 and 16.

Table 15: Stratigraphy of separation floor between heated area and garage

Layer description	S (cm)	λ (W/m°C)	C (W/m²°C)	ρ (kg/m^3)
Clay tile	2,00	0,720		1.800
Heating system screed	6,00	1,830		2.000
EPS preformed panel	2,00	0,035		30,00
XPS styrodur_2800 CS	5,00	0,032		30,00
Cellular concrete	5,00	0,090		400,00
Ordinary concrete	4,00	1,280		2.200
20cm Floor	20,00		3,33	950,00
Lime mortar or cement lime	1,00	0,900		1.800

Table 16: Thermal and inertial characteristic

Total thickness (cm)	45,00	Superficial mss (kg/m²)	456,10
Unit conductance		**Unit resistance**	
Internal surface [W/(m²·K)]	5,88	Internal surface [(m²·K)/W]	0,17
External surface [W/(m²·K)]:	25,00	External surface [(m²·K)/W]	0,04
Transmittance		**Thermal resistance**	
Tot. [W/(m²·K)]:	0,30	Tot. [(m²·K)/W]:	3,30

Once materials and design building packages were defined, a three-dimensional model of the studied building was created in the software environment.

This analysis established that the building is in energy class C with a global energy performance index of 110.09 kWh/m2/year, which is very close to the legal limit of 111.86 kWh/m2/year. Its partial energy performances are reported as follows (Table 17).

Table 17: Energy partial performance

Cooling		Heating		Sanytary hot water	
Primary energy index (EPe)	-	Primary energy index (EPi)	77,72	Primary energy index (EPacs)	32,37
Primary energy index law limit	-	Primary energy index law limit (d.lgs. 192/05)	93,86		
Envelope index (EPe,invol)	12,43	Envelope index (EPi,invol)	62,46	Renewable sources	-
Plant output	-	Plant season average output (η_g)	76,39		
Renewable sources	-	Renewable sources	-		

An economic analysis was then carried out by calculating the surfaces of different structural design typologies and subsequently determining the total price of the insulation for each project structure.

Table 18: Insulation materials economic assessment

Structure	Price €/m^2	Surface m^2	Total cost €
External wall	11,75	233	**2.737,75**

Wall close to unheated Staircase zone	11,75	16,97	**199,3975**
Staircase zone			
Masonry vented roof	13,2	176,37	**2.328,084**
Attic floor	17,01	111,45	**1.895,7645**
Floor on garage	12,15	51,5	**625,725**
Floor on vented crawl space with igloos	14,58	59,95	**874,071**

Following this analysis, low environment impact, eco-sustainable, unconventional insulating materials were selected in the database, based on the type of installation.. The objective was to obtain a building envelope with the same energy performance of the envelope analyzed in the first part of the study, realized with conventional insulation materials (extruded polystyrene XPS), leaving unchanged all the other materials. For each structural package, the insulation thickness necessary to obtain a thermal transmittance as close as possible to that obtained with the extruded polystyrene XPS was then calculated, admitting a 5% margin of error. Finally, the cost per square meter of both the insulations, natural and traditional (XPS), were determined and compared in terms of percentages [10].

The calculations results are reported below.

1. *Perimeter separation wall between heated zone and unheated staircase.*

Table 19: Walls thermal characteristics

Material	Insulation	S	Price	External wall cost	Perimeter wall cost
		Cm	€/m^2	€	€
	celenit FL120	6	17,2	4008	292
Timber fiber	hofatex therm	6	15,24	3551	259
	flytherm	6	11,4	2656	193
Wood wool and	PLS 120	12	25,2	5872	428
Mineral binders	celenit N	9	24,58	5727	417
	eraclit	10	35,3	8225	599
	corktherm 040	6	22,5	5243	382
Cork	corkpan	6	30,8	7176	523
	celenit LSC	6	20,18	4702	342
	vital celenit	5	15,69	3656	266
Cellulose fibre	flex CL	6	11	2563	187
	homatherm flex 040	6	14,8	3448	251
	isolmant BIO FK	5	19	4427	322
Kenaf fibre	kennevo	6	11,2	2610	190
	tecnokenaf	6	22	5126	373
	celenit LC30	6	11,53	2686	196

Hemp fibre	isolcanapa pan	6	11,08	2582	188
	canaton 35	6	19,8	4613	336
Maize fibre	biofiber	5	14,5	3379	246
Coir fibre	coccotherm	6	35,25	8213	598
	rotolo ennat	6	19,6	4567	333
Sheep wool	woolin	6	14,1	3285	239
	lankot	6	13,95	3250	237
	idroperalit	7	13,23	3083	225
Expanded perlite	biosfloor	7	10,85	2528	184
	pavaself	7	12,46	2903	211
Vermiculite	vermiculite BPB	8	14,4	3355	244

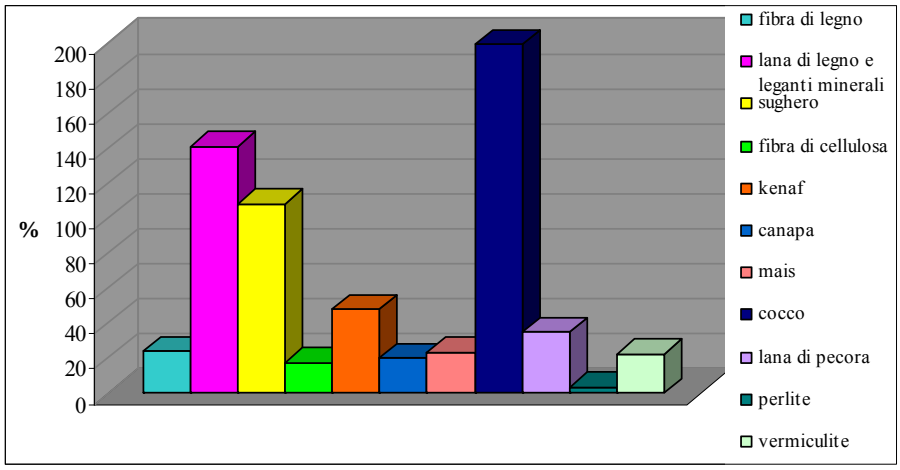

Figure 3: Chart of Percentage increase in walls cost

2. Ground floor on vented crawl space with igloos

Table 20:Vented floor thermal characteristics

Material	Insulation	S Cm	Price €/m^2	Floor cost €
	3therm naturel	7	16,31	978
Timber fibre	flytherm 100	8	21,7	1301
	Pavatex Pavaboard	9	25,59	1534
Wood wool	eraclit	14	49	2938
And mineral	celenit N	12	32,7	1960
bindings	novolit NL	12	27,04	1621
	celenit LSC	8	26,92	1614
Cork	selva kork	7	14	839
	natural kork	8	14,4	863

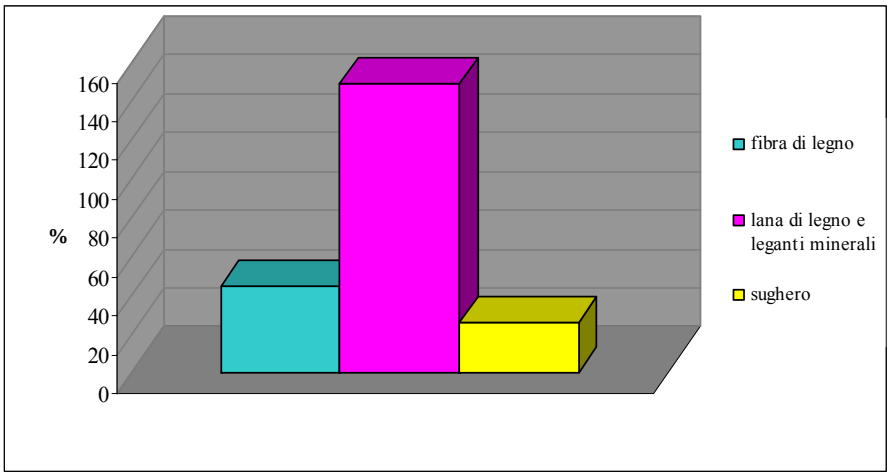

Figure 4: Chart of Percentage Growth in vented floors cost

3. Vented covering in masonry

Table 21: Vented covering thermal characteristics

Material	Insulation	S Cm	Price €/m^2	Covering cost €
	3therm naturel	8	18,64	3288
Timber fibre	flytherm	8	15,2	2681
	Pavatex Pavatherm	8	17,68	3118
Wood wool and	Eraclit	15	53	9348
Mineral bindings	Euchonit K	12	34,56	6095
	novolit NL	12	27,04	4769
	celenit LSC	9	30,28	5340
Cork	Corkpan	8	41,1	7249
	natural kork	9	16,2	2857
	flex CL	8	13,95	2460
Cellulose fibre	homatherm flex 040	8	19,7	3474
	Isolcel	8	21,6	3810
	Nafcotherm	7	13,41	2365
Kenaf fibre	Tecnokenaf	9	27,9	4921
	Isolkenaf	8	16,8	2963
	canaton 35	8	26	4586
Hemp fibre	isolcanapa pan	8	14,77	2605
Maize fibre	Biofiber	7	20,3	3580
	Coccotherm	9	52	9171
Coir fibre	cocco R	9	29,7	5238
	Lankot	7	16,3	2875
Sheep wool	isolana 100	6	13,4	2363
	wallen dach	7	14,31	1995

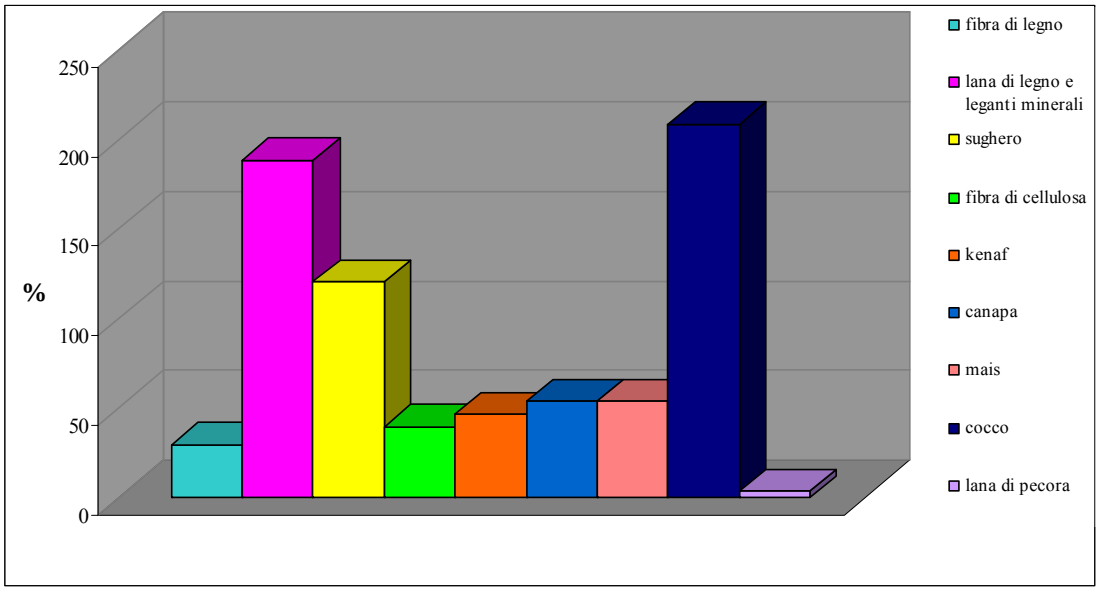

Figure 5: Chart of Percentage growth in vented covering cost per square meter

4. Separation floor between attic and heated zone

Tabella 22: Walls thermal characteristics

Material	Insulation	S cm	Price €/m^2	Floor cost €
	3therm naturel	8	18,64	2077
Timber fibre	flytherm 1000	9	24,4	2719
	Pavatex Pavaboard	9	25,59	2852
Wood wool and	eraclit	15	53	5907
Mineral bindings	celenit N	14	38,24	4262
	novolit NL	14	31,5	3511
	celenit LSC	9	30,28	3375
Cork	selva kork	8	16	1783
	natural kork	10	18	2006
	Kennevo	8	16,3	1560
Kenaf fibre	tecnokenaf	9	27,9	3109
	isolkenaf	8	16,8	1872
Flax fibre	naturaflax	8	18,06	2013
Maize fibre	biofiber	8	23,2	2586

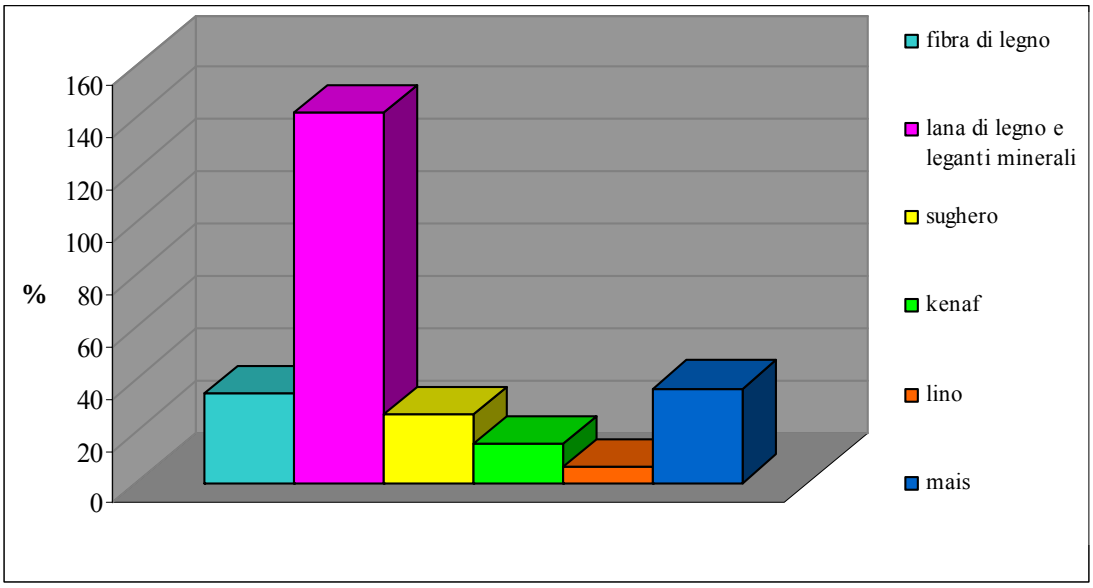

Figure 6: Chart of Percentage increase in separation floor cost

5. Separation floor between heated area and garage

Tabella 23: Walls thermal characteristics

Material	Insulation	S Cm	Price €/m^2	Floor cost €
	3therm naturel	6	13,98	720
Timber fibre	flytherm 1000	7	18,99	978
	Pavatex Pavaboard	7	19,9	1025
Wood wool and	eraclit	11	38,8	1998
Mineral bindings	celenit N	10	28,56	1471
	novolit NL	10	27,6	1421
	celenit LSC	7	23,55	1213
Cork	selva kork	6	12	618
	natural kork	7	12,6	649
	Kennevo	6	11,2	577
Kenaf fibre	tecnokenaf	7	25,6	1318
	isolkenaf	6	12,6	649
Flax fibre	naturaflax	6	13,54	697
Maize fibre	biofiber	6	17,4	896

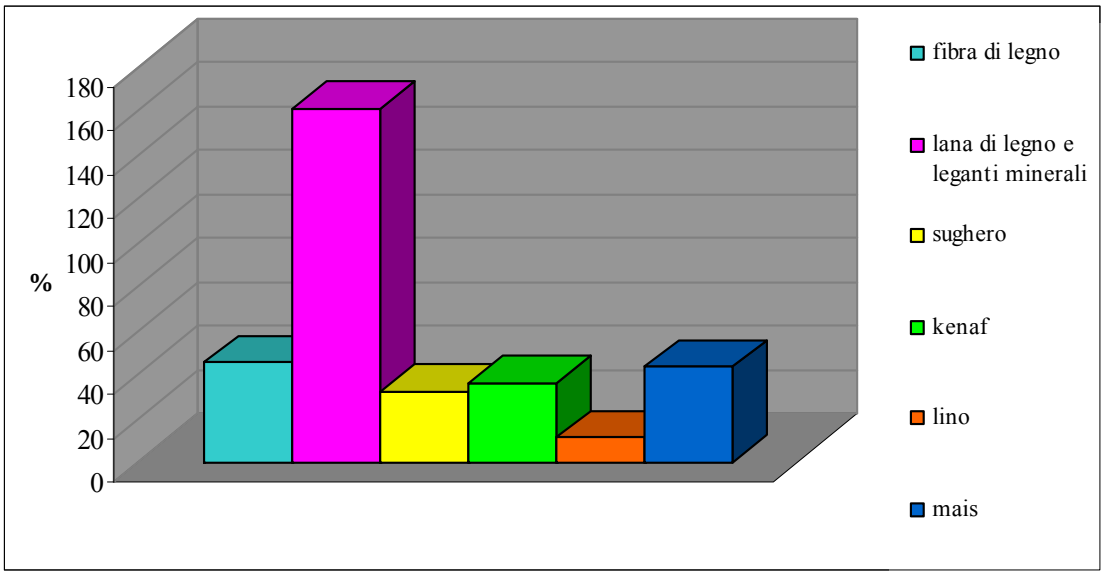

Figure 7: Chart of Percentage increase in separation floor cost

The article title appears centred at the top of the first page. To format the title authors should use the "Title" style from the formatting menu. The use of acronyms and abbreviations in the title should be avoided, unless they are widely understood, or they are accompanied by the expanded expression.

4. Conclusions

The economic assessment of ecologically sustainable materials show that, as expected, their utilization involves a cost increase, when considering an equal thermal performance of a building's envelope. In particular, the percentage increase in the cost per square meter, compared to the XPS cost, was more important for some insulation typologies, such as wood wool with mineral binders (up to a maximum increase of 189% for the roof), coir fiber (up to a maximum increase of 209% for the roof) and cork (up to a maximum increase of 121% for the roof). In particular, for wood, wool, and mineral binders, the increase in cost is due to the considerable increase in thickness which is necessary to achieve the same insulation performances of XPS, while the considerable increase for cork and coir fiber is caused by the high cost per square meter of the insulations, considering an equal thickness.

Among the great variety of products available on market, there are nevertheless a number which offer very satisfactory performances in respect of a modest cost increase. This is particularly true for some, such as sheep wool, which has an increase in the cost per square meter of 4% when considering roof insulation, and also wood fiber with a 24% increase for perimetral walls and, finally, flax fiber with an increase of 6% for the floor of the attic. The economic analysis even demonstrates that some products cost less than the XPS given the same thermal performance of the project structure. Among these, for example, the "flytherm" wood fiber panel, which costs 0,35 €/m2 (- 2,9%) less than the XPS, and also the "kennevo" kenaf fiber panel with a lower cost of € 0,55/m2 (- 4,6%), and the "kork forest" cork panel with a lower cost of 0,15 € / m2 (-1,2%) compared to the XPS. Despite the lower cost of the aforementioned insulation products, the average cost by product typology is always higher than XPS cost. As a result, it is possible to conclude that within the range of ecologically sustainable insulation materials there is considerable cost variability.

In light of these considerations, it is clear that in order to make a proper choice, it is necessary to know the materials' performance characteristics and assess them in relation to the building envelope installation/laying typology. The reason being that only a correct design of structural elements and a

proper placement and installation/laying of the insulating material, on the basis of its characteristics, can ensure a long and efficient life of that material inside the building.

It is also necessary to take into account aspects which are not easily quantifiable, such as building and environmental quality, by examining the materials' ecological characteristics. Even the material price strongly influences the choice, but it must not be the main aspect, namely because of the additional expenditure due to a good thermal insulation application is quickly offset by saving on heating and air conditioning costs, and secondly, because the cost of an insulating material with low impact on the environment contributes, even though in small part, to environmental cost savings.

References

[1] CRESME, Secondo Rapporto su ENERGIA e COSTRUZIONI, Bologna, Italy, SAIEenrgia 2010.

[2] B. Berge, The Ecology of Building Materials, Second ed., 2009, ISBN 978-1-85617-537-1.

[3] The Waste & Resources Action Programme and AMA Research Ltd, Guide to the recycled content of mainstream construction products, Banbury, Oxon, WRAP, 2008.

[4] E. Oleotto Guida agli isolanti naturali, Edicom Edizioni (2007)

[5] C. Benedetti Materiali isolanti, Bozen-Bolzano University Press (2010)

[6] V. Lattanzi Certificazione energetica degli edifici – progettazione e guida, Legislazione Tecnica (2010)

[7] V. Lattanzi Certificazione energetica degli edifici – esempi pratici, Legislazione Tecnica (2010)

[8] Korjenic A., Petranek V., Zach J., Hroudova J., Development and performance evaluation of natural thermal-insulation materials composed of renewable resources, Energy and Buildings 43 (2011) 2518−2523;

[9] Thormark C. The effect of material choice on the total energy need and recycling potential of a building. Building and Environment 2006;41(8):1019−26.

[10] Ekici BB., Gulten AA., Aksoy UT., A study on the optimum insulation thicknesses of various types of external walls with respect to different materials, fuels and climate zones in Turkey, Applied Energy 92 (2012) 211−217

Complex Networks Approach to the Italian Photovoltaic Energy Distribution System

Luca Valori[a,b], Giovanni Luca Giannuzzi[a], Tiziano Squartini[b,c], Diego Garlaschelli[c] & Riccardo Basosi[a,b]

[a] *Department of Chemistry, Università degli Studi di Siena, Siena, Italy, riccardo.basosi@unisi.it (CA)*
[b] *Centro per lo Studio dei sistemi Complessi (C.S.C.), Siena, Italy, valoril@unisi.it*
[c] *Leiden Institute for Theoretical Physics, University of Leiden, Leiden, The Netherlands, garlaschelli@lorentz.leidenuniv.nl*

Abstract:

One problem in the study of the Italian electric energy supply scenario is determining the ability of photovoltaic production to provide a constant and stable energy background over space and time. Knowing how the photovoltaic energy produced in a given node diffuses on the power grid is of crucial importance. A smart grid able to face peaks of load must be designed. Approached here from a complex systems point of view, the network of energy supply might be represented by a graph in which nodes are Italian municipalities and edges cross the administrative boundaries from a municipality to its first neighbours. Using datasets from ISTAT, GSE and ENEA, the node production and attraction of photovoltaic energy have been estimated with high accuracy. The attraction index was built using demographic data, in accordance with medium per capita energy consumption data. Moreover, the energy produced in each node could be determined using data on the installed photovoltaic power and on local solar radiation. The available energy on each node was calculated by running a distributive model assuming that the energy produced in one node which diffuses to its first neighbours is proportional to the attraction index of the latter. Therefore the available energy at each node is the sum of many contributions, coming from topological paths involving all the other nodes across the network. The availability of cross temporal data on the photovoltaic power installed on the Italian territory also make it possible to understand the evolution of the available photovoltaic energy landscape over time.

Keywords:

Complex Systems, Energy Networks, Optimization methods, Renewable energies, Smart grids.

1. Introduction

The scarcity of fossil energy sources will become a more serious problem as the energy demand from developing nations as China, India and Brazil grows. New energy sources will become of strategic relevance politically from the viewpoint of restraining international tensions arising from the market of the energy produced by the use of fossil fuels. Approaching the global energy crisis from the perspective of proposing new ways to generate energy could be the first step in changing the existing energy production paradigm, and consequentially positively influence the international political balances and the sustainable development of countries all around the planet.

Renewable energies can solve these problems, because of their following important features:

- they are unlimited, because in large part they are ascribable to the solar elemental source;
- they produce electrical energy, which is extremely valuable, because it is easily convertible in mechanical energy and heat, and may be instantaneously transported from the place of production to the utilization place.

A closer look at the international landscape of energy production shows large growth of the field of renewable energy systems, in particular wind, hydraulic and photovoltaic. Aside from the environmental group strain, the scarcity of fossil fuels has convinced governments to search for new energy sources. As an additional debating point, the *green economy* proposes new opportunities for economic and occupational revitalization, as confirmed by the results which were obtained by the countries which decided to invest in wind and photovoltaic compartments, i.e. Germany and China (14).

The scarcity of fossil energy sources also forces an investment in electric energy generation to satisfy branches of consumption which traditionally have been considered as "off grid," as house heating or transport on wheels. For an improvement in the energetic efficiency it is desirable to consider new technologies such as heat-pumps and electric engines.

Focusing on a solar photovoltaic source, one can appreciate the opportunity to recover very large and unused surfaces for energy production, i.e. deserts and urbanized-areas aerial surfaces. The notion of sustainable development imposes a rational plan for this occupation to match the needs of the "local factors" to the need for a shared social acceptance. One half of the planet surface is constantly hit by solar radiation; this make it possible to have a substantial continuity in photovoltaic energy production.

Fortunately, photovoltaic technology exhibits features which facilitate its introduction into the Italian electric power grid. In fact energy production occurs only in daytime, when the electrical energy requirement is higher (16), with geographically diffused inputs and in a way which is predictable[1]. Also in the short run, (72 hours is the typical precision of weather forecasting). However, seasonal, daily and meteorological variability in solar irradiation make optimization of the power grid infrastructure indispensable to gain the required efficiency of the system and to minimize the probability of supply failures. On the other hand, it is necessary to develop new regulation and monitoring protocols which can exploit these variable energy contributions. Both kinds of intervention require a deep understanding of the system. This necessitates an accurate estimate of the photovoltaic energy landscape across Italy over both space and time.

In particular, photovoltaic energy turns to be a very promising form of renewable energy in the Italian power generation scenario (17). Due to the high modularity of solar installations and of the Italian incentive system *Conto Energia*, investments on photovoltaic energy became attractive also for private citizens and, from 2007 on, the total nominal power installed on Italian territory grew dramatically (13). This growth seems to be destined to go on after the transient regime of fares. In fact, with high solar irradiation, the gradual lowering of solar panel supply and installation costs, the continuous rising of the cost for the electric energy produced by means of fossil fuels, are factors which contribute to a rapid reaching of the so called "grid parity." This parity is supposed to be obtained in 2012 for the south of Italy. In other words, the profit will be guaranteed by the "asset" energy, with or without fares.

One could look at the power grid as a huge, high performance, battery accumulator able to receive, transfer and exchange instantaneously large amounts of electric energy. The development, adaptation and managerial revision of the global network of electric energy transmission, represent necessary conditions for the rise of a new paradigm: the renewable energy generation model. At present, TERNA S.p.a., the Italian electric power grid administrator, is working on the development of a new concept of grid (15), able to minimize the risk for energy wastes and cascade failures. This is accomplished by the use of an integrated platform based on information technology, for the control and remote management of the electric connections, called SCTI (Plant Control and Remote Management System). This "Smart Grid" will be able to manage in real time the offer and demand of electric energy from diffused generation by renewable energy installations.

[1] It should be noticed that this statement is true for Italy, but other countries exists in which the peak of load occurs in early night.

In view of the above depicted scenario It will be very important to know how electric energy generated by photovoltaic installations flows from the site of production to the final users and how this energy propagates on the network in the absence of specific control systems.

Because of the structural complexity of the Italian power grid, in order to define a good model, able to describe the system properly, it is necessary to assume a complex systems perspective. The power grid, under a reasonable hypothesis, could be depicted as a complex network. This schematization allows one to employ useful mathematical methods and algorithms from complex systems theory.

1.1 – Networks

In physics, a network is any real system that can be represented by mathematical objects called *graphs*. A graph is defined by a set of *vertices* (also called *nodes*) and a set of connections, between them, called *edges* (or *links*). Edges connecting vertices can be alternatively undirected, if there is not a preferential direction defined on them, or directed, if there is a preferential orientation.

A graph built by directed edges is called a directed graph. One can also associate a certain value to an edge to take into account the "load" carried by that edge; in this case we speak of a *weighted graph*.

To indicate a graph composed by n vertices and m edges one usually writes $G(n,m)$. The two quantities n and m are called *order* and *size* of the graph respectively, and they are not independent of each other: for an undirected graph one has that the maximum value of the size is $m = n(n-1)/2$ while $m = n(n-1)$ for a directed one. The structure of a graph $G(n,m)$ can be captured by an *adjacency matrix* $A(n, n)$, that is a matrix whose entries a_{ij} are 1 if there is an edge from i to j and 0 otherwise. In a weighted graph, the entries different from 0 are real numbers which account for the weight associated to the edge. For undirected graphs, the adjacency matrix is symmetrical.

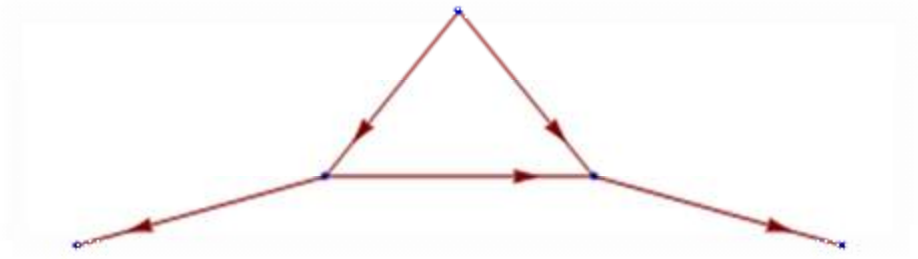

Figure 1: Example of a directed graph *G(5,5)* of *order* 5 and *size* 5. The arrows show the edge directions.

In Fig. 1 is showed a graph of *order* 5 and *size* 5. As one can see the graph is directed and the direction of the edges is indicated by an arrow. The adjacency matrix for the mentioned graph is:

$$a_{ij} \equiv \begin{pmatrix} 0 & 0 & 0 & 1 & 1 \\ 1 & 0 & 0 & 1 & 0 \\ 0 & 0 & 0 & 0 & 0 \\ 0 & 0 & 1 & 0 & 0 \\ 0 & 0 & 0 & 0 & 0 \end{pmatrix}$$

One can obtain an undirected graph from a directed one by making the adjacency matrix symmetrical.

If in a graph of order *n* all possible edges are drawn, the graph is *complete* and it is indicated by K_n while, if no edge is drawn the graph is empty and one can refer to it as E_n.

It is straightforward to define some basic properties of a graph:

- the *degree* k_i of a vertex *i* is the number of edges attached to it; in an undirected graph any edge contributes to the degree of each of the two vertices it connects; it is not the same for directed graphs, where one can define an *in-degree* and an *out-degree* with an obvious meaning; the list of the degrees of all vertices present in a graph is called a *degree sequence*.
- in the case of weighted graphs, one can define also a generalization of the concept of degree, which is the *strength* or *weighted degree* of a vertex, k^w_i : it is calculated as the sum of the weights "carried" by the edges attached to the node. The definitions of *in-strength*, *out-strength* and *strength sequence* are straightforward;
- in an *undirected graph* two vertices are connected if there is a *path* (i.e. a sequence of edges) between them. If for every couple of vertices there is a path, the graph is connected. A *connected component* (CC) is a connected sub-graph of maximum size in a graph. In a directed graph one can have *strongly* and *weakly connected components* (SCC and WCC respectively). In the former case directed paths exist for every pair of vertices, while in the latter case paths exist only when considering the edges as undirected.

Here we presented only a small number of all the topological properties of a graph that one can determine by starting from the adjacency matrix. For an exhaustive picture on complex networks we recommend the review article by R. Albert and A. L. Barabási (1) and the book by G. Caldarelli (2).

1.2 – Available data

The present scenario of photovoltaic installations in Italy is implemented in the on-line atlas *Atlasole* (7) developed by the *Gestore dei Servizi Energetici* (GSE), which reports the up-to-date number of installations, collecting them by nominal (peak) power, date of installation and geographic location, reaching the resolution of single municipalities.

The GSE atlas shows that the current number of photovoltaic installations in Italy exceeds *322,000* units, with a total nominal installed power of about *12,500 MW*, which, by comparison, is more than *2.5* times the aggregated nominal power of the four nuclear reactors operating in *Fukushima Dai-ichi* installation, before the March 2011 earthquake. Most installations, around *283,000*, are small installations with a nominal power under *20 kW*, while about *11,400* have a nominal power between *20* and *50 kW*, and about *28,800* have a power which exceeds *50 kW*. The three classes of installations contribute respectively *13%*, *4%* and *83%* to the total power from photovoltaic generation.

The capability to freely access data from *Atlasole* makes it possible to approach the Italian photovoltaic generation scenario from an evolutionary perspective both over space and time. However to have a picture of the consumption scenario, we need highly detailed data on the per capita electric requirements also. Referred data are freely available in the section *Dati Statistici* of the website of *Terna S.p.a* (8); the *Consumi* file reports Italian electric consumption statistics both in aggregated form and under different user typologies.

An estimate of the energy production of solar installations also is useful to obtain irradiation data with the best resolution possible, or at the least with the same resolution of solar installation data. A useful resource to this purpose is the section on solar radiation of the *Archivio Climatico DBT* (9) of the *Ente per le Nuove tecnologie, l'Energia e l'Ambiente (ENEA)*. This archive collects

the results of the activity performed by ENEA for estimating the solar radiation normal to the horizontal surface in Italy. Data on irradiation are computed by means of the images transmitted by *Meteosat* satellites on the visible spectrum. Estimated values associated with an error of 6-7% and are computed for *1614* of the *8092* Italian municipalities (9). Data tables report mean daily solar radiation for the twelve months and for years between 1994 and 1999.

For the purpose of our analysis it is essential to gain socio-demographic data, data on the administrative boundaries of the Italian municipalities and geographic coordinates of the municipality territory centre. In order to acquire this data, we have referred to the *Istituto Nazionale di Statistica* (ISTAT) datasets (10), which are updated to 30 June 2011 and contain data on population and municipality territory areas, to the whole dataset of *Comuniverso* (11) and to the dataset of municipality centroid geographic coordinates of ENEA (12). The last dataset gives information on minimum and maximum altitudes for each municipality making it possible, if needed, to provide a correction to irradiation data

2. A distributive model for generation and attraction of photovoltaic energy

In this work, we propose a useful model for estimating the amount z_j of photovoltaic electric energy which can be available for each municipality of the Italian territory at a given time t. The model is, in some sense, similar to "generation-attraction models" developed in road traffic management engineering: in particular, to that class of models which estimate the distribution of road traffic in urban road networks (4).

The highly complex structure of the Italian power grid makes impossible to have a precise picture of the entire network, therefore in building our model, it is necessary to make appropriate simplifications. Our first hypothesis is that the network by which photovoltaic energy is delivered might be reduced to a graph in which nodes are municipalities and the edges crosses the administrative boundaries between a municipality and its first neighbours. The graph is drawn with undirected links and self-looping is allowed, *i.e.* the diagonal entries of the adjacency matrix are all ones. Moreover we do not know either the exact geographic localization of the solar installations or the list of the *Points of Delivery* (POD), which are the points where the energy is provided to the customer, or the real structure of the power grid. Even if that data were available, we have chosen to aggregate them to the scale of the single municipality, in order to fit the need for a high accuracy for a global vision of the results at a national scale.

Italian territory is characterized by a medium high demographic density which, whit respect to other European countries, is uniformly distributed. The power grid is capillary structured to serve the large number of users. On this basis it is plausible to depict the network (Fig. 2) with the above mentioned graph; it is unlikely to think that the electric energy flowing from a node could "skip" each one of its first neighbours if they exhibit lack of energy.

To build the graph, we downloaded the *Comuniverso* data-files which for each municipality gives the administrative boundaries. In a small number of cases it was necessary to edit the data-files adding municipalities which are not physically but only topologically adjacent to the one under observation: for example this is the case for the electric connection between the municipalities of *Nettuno* and *Porto Torres*, which are connected by the S.A.P.E.I. underwater cable (6) and for *Scilla* and *Villafranca Tirrenica*.

The energy $P_j(t)$ generated at one node is a function of the total nominal amount of installed photovoltaic power and of the local solar irradiation. It diffuses from the production node to its first neighbours in proportion to an attraction parameter α_{ij} which is in a direct proportion with the population and with the local per capita energy consumption of the attracting node. As mentioned

above, we allow the presence of self-loops, as it is reasonable to think that a significant portion of the photovoltaic energy is used *in situ*.

The model we propose gives an algorithm for re-distributing the energy produced in a node *j* to the other nodes in a way useful to obtain the available energy in each of the 8092 Italian municipalities.

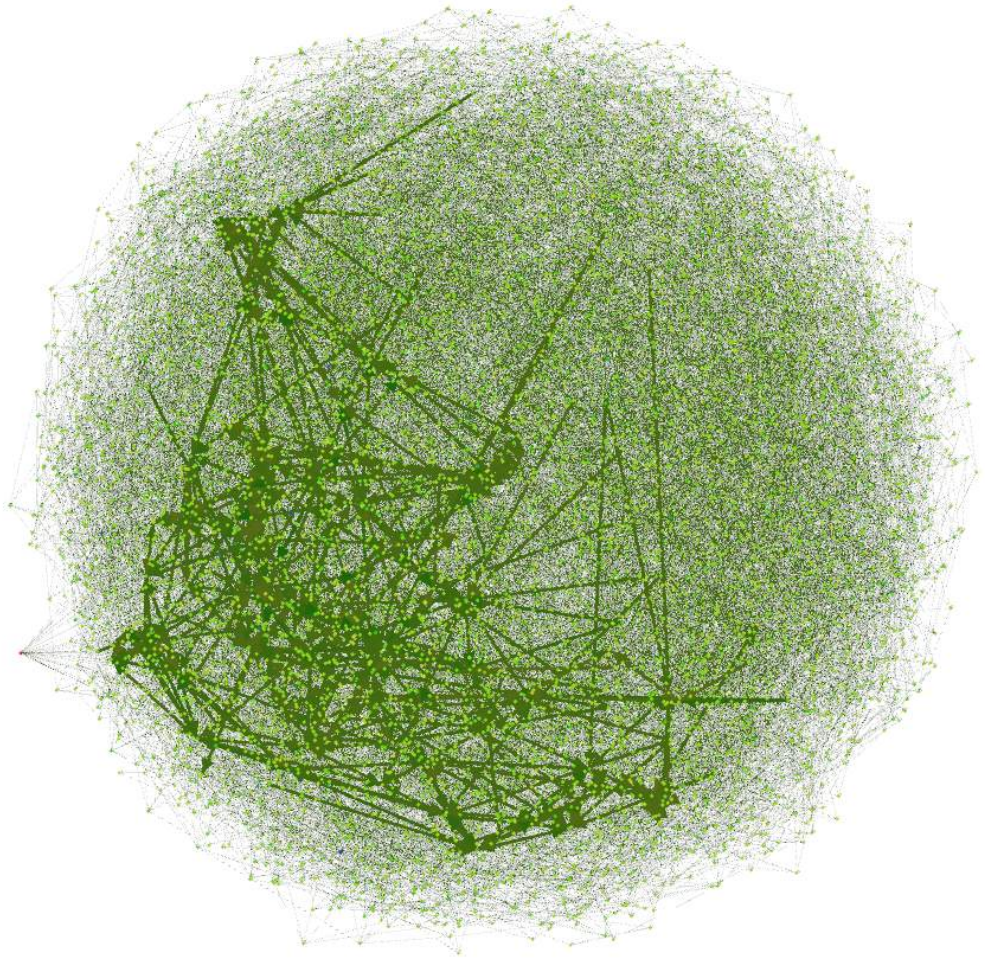

Figure 2: Graph showing the Italian photovoltaic energy distribution network topology, as implemented in our model, *i.e.* with nodes placed in the municipal territory centroids and the links crossing the administrative boundaries from a municipality to its first neighbours. Node colour intensity is proportional to node degree *k*.

A preliminary step in the calculation of the solar irradiation in each municipality of the Italian territory. For this purpose we developed a spherical trigonometric algorithm which, starting from the ENEA database of the municipal centroid coordinates, computes the geodetic distance from each pair of municipalities. We obtained a upper triangular square matrix of size 8092 housing the outputs. Then to each municipality we attributed the irradiation data of the nearest one for which ENEA had estimated it. This is a very good approximation. Indeed, the maximum value of the above mentioned distance, excluding isolated cases (*e.g.* the distance from the municipalities of *Lipari and Linosa* and the nearest municipality in the ENEA database), is less than 30 km. For such a small distance it is unlikely that solar irradiation could change in a significant way.

Irradiation data were used to compute an accurate estimate of the produced energy at every node of the network in which solar installations are present. We defined eight temporal sampling intervals, multiples of 251 days, starting from 25 December 2005 (switch on of the first Italian solar installation). The outputs were geo-referred.

As an example we show bubble plots of the generated energy data for the municipalities of *Treviso*, *Perugia* and *Lecce* provinces and for the largest sampling interval. In the pictures (Fig. 3-5) the size of the red bubbles is directly proportional to the amount of generated energy. The referred data are updated to 30 June 2011. We give data tables in appendix A.

The energy $P_j(t)$ produced in a given municipality is the sum of the energy produced by the solar installations which are present in the territory of the municipality j. Single installation production is computed by multiplying the solar irradiation data $x_j(t)$ by the nominal power $q_j(t)$ of the installation. So one has:

$$P_j(t) \equiv \sum_{i \in j} p_i(t) = \gamma \frac{x_j(t)}{I_{SPT}} \sum_{i \in j} q_i(t). \qquad (1)$$

Where γ is the *performance ratio* and I_{STC} is the *irradiance*[2]. The performance ratio, for a given solar installation, is given by the product of the non-photovoltaic equipment efficiency (*e.g.* conversion losses, etc.) with a reduction factor which takes into account solar panel overheating, partial reflection of incident radiation, spectral dependence of the energy conversion and accumulation of dust on protection glass. In this work we assume for the performance ratio a value of 0.75, which is the same value assumed by the Photovoltaic Geographical Information System of the European Union (18).

Figure 3: Bubble representation of the generated energy per year in *Treviso* province: the size of the spheres is proportional to the produced photovoltaic energy. To make a comparison among the size of different bubbles, the energy that is yearly produced in *Treviso* municipality is *3,320.2 MWh/y*; a complete numerical data-table for all the municipalities of the province is available in Appendix (see Appendix A, Table A.1).

The energy $P_j(t)$ is attracted by a neighbouring municipality i proportionally to an attraction parameter α_{ji} which is defined as:

[2] The irradiance value in Standard Test Conditions (*i.e.* at an air mass of 1.5 and a cell junction temperature of 25 °C) is $I_{STC} = 1\ kW/m^2$.

$$\alpha_{ji} \equiv \frac{a_{ji} C_i}{\sum_k a_{jk} C_k}, \quad (2)$$

where c_i is the average consumption (obtained as the product of population size and average per-capita consumption data) in the municipality *i*, and a_{ij} is the *ij* element of the symmetric adjacency matrix of the graph. Because of the presence of self-loops this matrix has all the entries of the principal diagonal equals to *1*. The attraction parameter is normalized with respect to the cumulated energy consumption in the surrounding area of *i*.

As stated above, the ENEA atlas on solar irradiation reports monthly averaged per day data, while the energy exchange on the power-grid occurs at the speed of light.

Figure 4: Bubble representation of the generated energy per year in *Perugia* province: the size of the spheres is proportional to the produced photovoltaic energy. To make a comparison among different bubbles, the energy that is yearly produced in *Perugia* municipality is *27,116.9 MWh/y*; a complete numerical data-table for all the municipalities of the province is available in Appendix (see Appendix A, Table A.2).

In other words, the time-scale of the energy exchange is much smaller than the resolution of our data. A method to compute energy exchanges on this very short time-scale is needed. From the perspective of a distributive model able to estimate the sum of the energy accumulated in a given municipality, the average daily produced energy will be divided by an integer factor *M*. This operation produces a time discretization in which any time sample corresponds to an *M-th* fraction of the daily produced energy. The model proceeds with a discrete clock.

Given *T* as a set of *n* natural numbers higher than *0* and lower than *M+1*, we have that for each *n* in *T*, the energy that has been accumulated is:

$$z_i(n) = P_i(n) + \sum_j \alpha_{ji}\, z_j(n-1) \quad . \tag{3}$$

Put into words, the accumulated energy at the *n-th* clock on node *i* is the sum of the amount of energy produced by that municipality at that clock plus a fraction of the energy accumulated from its first neighbours at the *(n-1)-th* clock (recall that by allowing self-looping, in our picture a node is, in some sense, a first neighbour of itself).

Starting from (3) and substituting recursively the same expression to $z_j(n-1)$ one can deduce the lower value of *M* which allows one to simulate the distribution of the energy to the whole network.

$$z_i(n) = P_i(n) + \sum_j \alpha_{ji}\, P_j(n) + \sum_k \left(\sum_j [\![\alpha_{kj}\alpha_{ji}]\!] \right) z_k(n-2) \tag{4}$$

The sum over the index *j* in the third summand, on the right hand side of the expression, is a sum of attraction indices over all the paths from *i* to *j*. Therefore the model succeeds in mimicing the distribution of the energy to the whole network. This is an almost instantaneous process which rapidly spans the entire system, only if the number *M* of steps is larger than the order of the graph (i.e. than the number of municipalities).

Figure 5: Bubble representation of the generated energy per year in *Lecce* province: the size of the spheres is proportional to the produced photovoltaic energy. To make a comparison among different bubbles, the energy that is yearly produced in *Lecce* municipality is *42,566.5 MWh/y*; a complete numerical data-table for all the municipalities of the province is available in Appendix (see Appendix A, Table A.3).

To have a real picture of the energy landscape across Italy after the re-distribution on the network, one has to find the stationary state of the process. There are two ways to accomplish this

task: the first one is to iterate the above proposed algorithm a very large number of times and to compute the available energy, for each vertex, till $z_i\ (n)$ is equal to $z_i\ (n\text{-}1)$. This is, in some sense, a "brute force" method which requires large computational resources and a lot of time. The other way might work by noticing that the transposed of the attraction matrix $\boldsymbol{\alpha}^T$ (which has elements α_{ij}) satisfy the condition:

$$\sum_j \alpha_{ij} = \mathbf{1} \tag{5}$$

The entries of this matrix, instead of representing the percentage of energy flowing in the sense of the attraction, represent the percentage of energy which, after leaving the production node, flows through the edges, pointing to its first neighbours.

The matrix $\boldsymbol{\alpha}^T$ has the same form of the *transition matrix* of a *Markov chain* and, if we restrict our analysis to the connected components of the network, the corresponding sub-matrices are irreducible and so *ergodic*; in other words, in a large enough number of steps, the energy can flow from a starting node to any other node of the connected sub-graph to which it belongs. With little effort one can demonstrate that the sub-matrix representing a given connected component is also regular, *i.e.* there exists a power of it which has all strictly positive entries.

A well known property of regular Markov chains states that for a given process with transition matrix $\boldsymbol{\alpha}^{\mathbf{T}}$ there is a unique vector $\boldsymbol{V}$ such that, for any starting energy distribution represented by the row-vector $\boldsymbol{v}$ and for large values of n, satisfy:

$$\boldsymbol{v} \cdot (\boldsymbol{\alpha}^{\mathbf{T}})^{\boldsymbol{n}} \approx \boldsymbol{V} \tag{6}$$

Vector $\boldsymbol{V}$ represents the equilibrium state of the system and it is called the *fixed vector*. It is demonstrated that in dealing with regular Markov chains there exists a probability vector $\boldsymbol{V}$ such that:

$$\boldsymbol{V}(\boldsymbol{\alpha}^{\mathbf{T}})^{\mathbf{n}} = \boldsymbol{V} \tag{7}$$

Vector **V** gives the long-range trend for the proportion of the re-distributed energy which reaches each one node of the distribution network and can be found by solving the system.

$$\begin{cases} \boldsymbol{V}(\boldsymbol{\alpha}^{\mathbf{T}})^{\mathbf{n}} = \boldsymbol{V} \\ \sum_i V_i = \mathbf{1} \end{cases} \tag{8}$$

This elegant and simple formulation of the problem of finding the stationary state of the re-distribution process can be solved very quickly by the use of modern numerical analysis software.

The energy in the final equilibrium state is given by the vector **Z** which has entries:

$$Z_i = V_i \left(\sum_i P_i \right) \tag{9}$$

where the index *i* runs over all the vertices which belong to a given connected sub-graph.

For the sake of simplicity, in this work, we restrict the analysis to the largest connected component (LCC) of the Italian photovoltaic energy distribution network, has hypothesised above (Fig. 6).

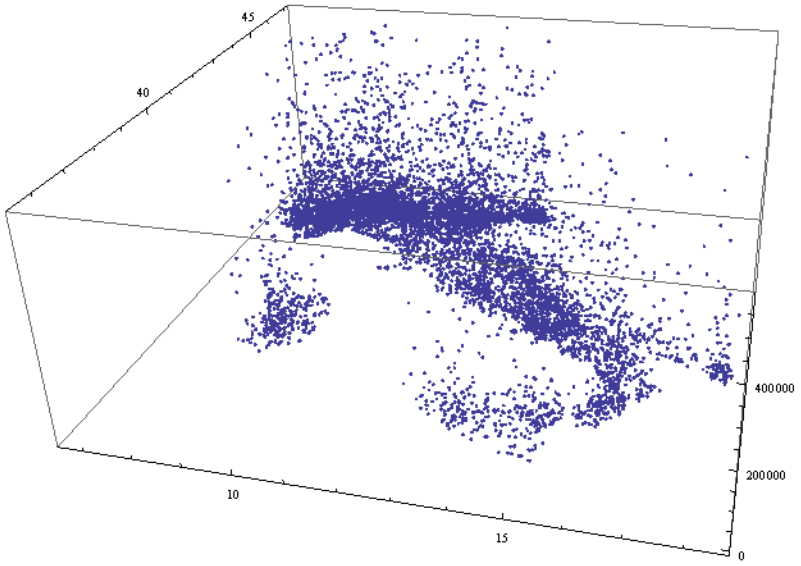

Figure 6: The 3D plot shows (on the vertical axis) the available energy z_i, expressed in kWh/y, after the redistribution process, when the stationary state is reached. It was computed for each node belonging to the LCC of the network. Data are geo-referred.

After the redistribution on the network photovoltaic energy also reaches nodes in which there are not solar installations. Referring to the report on electric energy consumptions in Italy for the years 2005-2010, compiled by TERNA S.p.a., and to cross-temporal data on photovoltaic power installed, available in GSE Atlasole, we plotted the variation in available energy Δz_i versus the increase in energy consumption ΔC_i (Fig. 7).

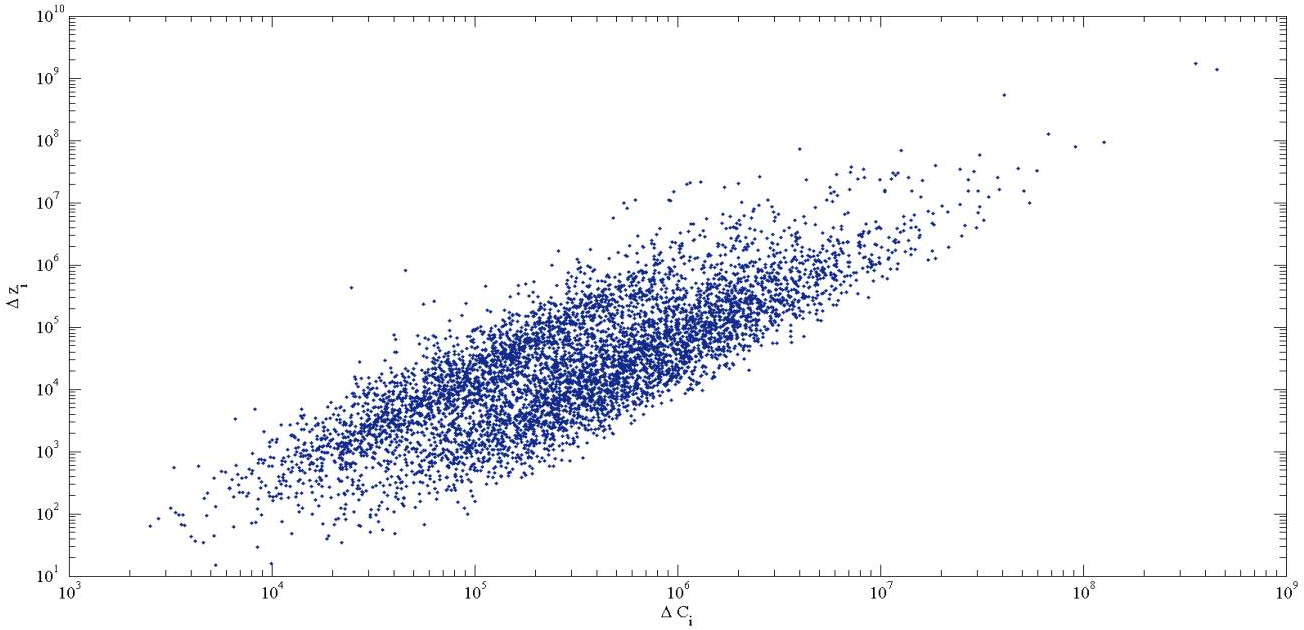

Figure 7: Growth in the available energy at the stationary state Δz_i versus the increase in energy consumption ΔC_i during the period 2006 to 2011 for the LCC of the network.

For *2425* municipalities, *i.e.* about *30%* of the LCC order, and for the *2006-2011* time interval, the growth of available energy is higher than the increase in energy consumption. We would like to stress that, in the proposed picture, photovoltaic energy represents a buffer to growth of consumption as well for those nodes that have low or null installed photovoltaic power.

As an emerging effect arising from the complex dynamics of energy exchanges, large amounts of photovoltaic energy flows to nodes such as Roma, Milano, Torino, Napoli and Bologna. These nodes, which present high degrees and large values of the attraction index, if compared to their neighbourhood, operate as massive attractors (Fig. 8).

The last evidence demonstrates that the effect of the weighted network structure is not merely that of averaging out the differences between municipalities which produce photovoltaic energy and ones that do not host solar installations. Diffusion of photovoltaic energy in the power-grid, driven by the attraction matrix, turns in producing a stationary state energy landscape which is completely different from the production scenario. While the diffused energy production is carried out by a large number of small installations, massive attractors capture amounts of energy which are at most two orders of magnitude higher than those of small (lowly connected and sparsely populated) municipalities.

3. Conclusions

One could look at the Italian power grid as a huge, high performance, battery accumulator able to receive, transfer and exchange instantaneously large amounts of electric energy. The development, adaptation and managerial revision of the global network of electric energy transmission, represent necessary conditions for the raise of a new paradigm: the renewable energy generation model.

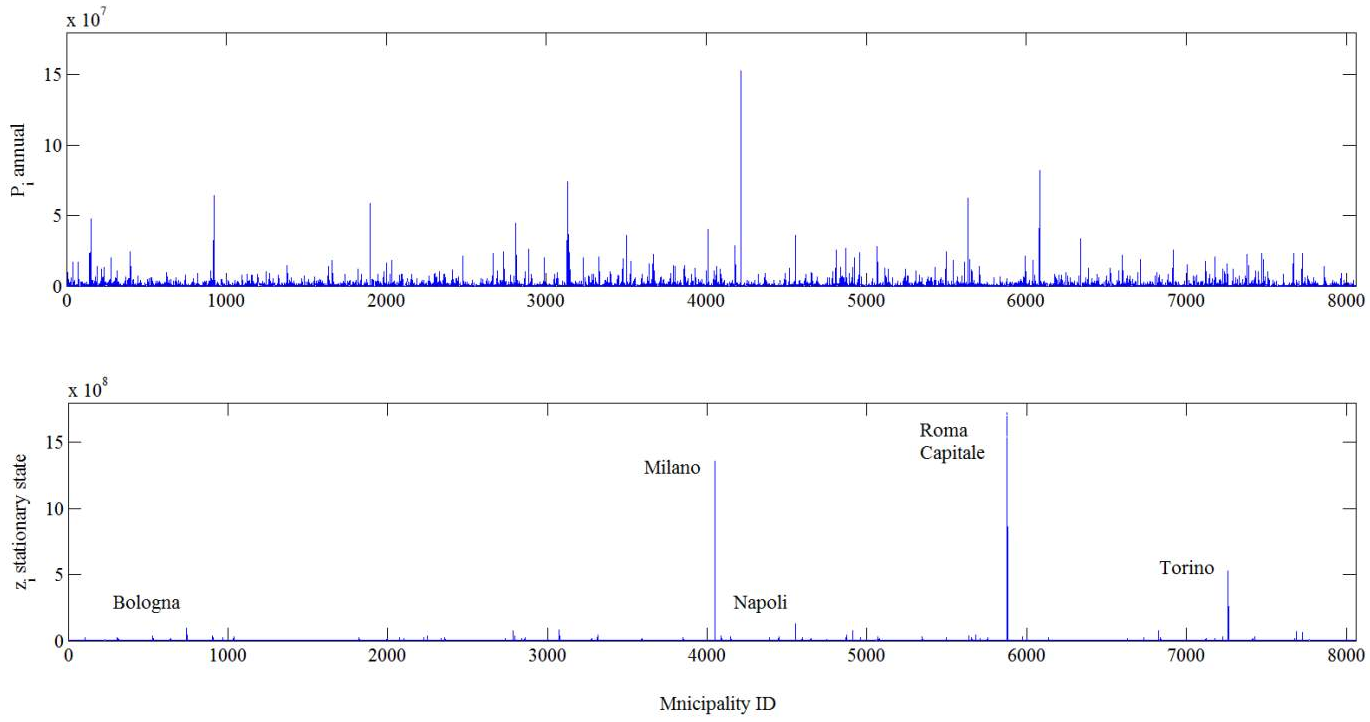

Figure 8: Upper plot: energy generated by photovoltaic installations for each one of the Italian municipalities. Lower plot: available energy at the stationary state at each node of the network.

In order to propose an efficient way to optimize the system of photovoltaic installations and manage the intrinsic complexity of the energy exchange it is necessary to understand how the photovoltaic energy is distributed from the production municipalities to the entire network.

Here we approached the above-mentioned problem from a complex systems point of view, assuming that the network of energy supply might be schematized by an undirected graph in which nodes are Italian municipalities and the edges cross the administrative boundaries from a municipality to its first neighbours, allowing also the presence of self-loops.

Using datasets from ISTAT, GSE and ENEA, we estimated the node production and attraction of photovoltaic energy with high accuracy.

In order to establish the ability of the Italian system of photovoltaic installations to provide a constant and stable energy background over space and time, we developed a model able to estimate the energy generated and attracted by each one of the Italian municipalities. To that scope we defined an attraction index by the use of demographic data, in accordance with medium per capita energy consumption data. Implementing discrete time-steps, the model mimics energy exchanges happening on a time-scale that is very short if compared to the daily resolution of the available irradiation data. The energy produced in the *i-th* node diffuses to its *j-th* first neighbour proportionally to the attraction index of the latter. By noting that the attraction matrix, if transposed, has the same form of the transition matrix of a Markov chain, we found the stationary state, represented by a fixed vector. At this state the flux of energy in every edge of the network is constant.

The availability of cross-temporal data on the photovoltaic power installed on the Italian territory allows us to understand the evolution of the available photovoltaic energy landscape over time. Computing the growth in the available energy at the stationary state for the time interval *2006-2010* and for each node of the network, we found that photovoltaic energy is efficient as a buffer in mitigating the increase in consumption.

The effect on the energy landscape of the redistribution at the equilibrium state is not merely that of averaging out the differences in available energy, but results in a new scenario in which few massive attractors pick up a large portion of the photovoltaic energy coming by diffused production.

Acknowledgements

The authors want to acknowledge Francesco Mancini, Project Manager at Xenesys S.r.l., who provided support for the use of the software QlikView (Copyright by QlikTech International AB© 1994–2011) and for the fruitful discussions too. Careful reading and revising of the manuscript by Professor Emeritus Les Brooks, Sonoma State University, is gratefully acknowledged.

Appendix A

Table 1. Theoretical photovoltaic energy production for municipalities of Treviso province. It was computed using data on the total photovoltaic power installed in every one of the Italian municipality; Referred data are updated to 30 June 2011. It must be said that the Atlasole database is constantly updated by the GSE.

Photovoltaic Energy (*KWh/y*) in Treviso province municipalities		
Follina: 573080,6576	Gorgo al Monticano: 544670,885	Montebelluna: 2868976,5368

Resana: 2160255,0288	Giavera del Montello: 974623,9822	Motta di Livenza: 2527787,2994
Ponte di Piave: 791220,9778	Asolo: 704458,667	Volpago del Montello: 1510711,125
Trevignano: 821378,668	Maser: 264460,1366	San Zenone degli Ezzelini: 1202145,6084
Caerano di San Marco: 1048791,304	Borso del Grappa: 378549,4482	Ormelle: 359205,2156
San Polo di Piave: 1019326,2618	Crocetta del Montello: 1330823,3092	Spresiano: 1172480,9206
Meduna di Livenza: 358277,271	Nervesa della Battaglia: 2782819,2744	Oderzo: 1912483,6346
Mareno di Piave: 1088789,6888	Paderno del Grappa: 291552,8594	Fonte: 535086,8776
Valdobbiadene: 1252951,3392	Crespano del Grappa: 241328,7492	Arcade: 399183,2284
Orsago: 439583,9602	Fontanelle: 1502586,7714	Zenson di Piave: 326247,394
Colle Umberto: 1031921,2508	Monfumo: 67916,1736	Istrana: 859223,7324
Mogliano Veneto: 1458842,9944	Cornuda: 558426,0594	Carbonera: 1725000,1186
Casale sul Sile: 1457118,5046	Castelcucco: 800506,5354	San Biagio di Callalta: 906793,371
Zero Branco: 1585091,3342	Vazzola: 971910,4318	Vedelago: 3123654,039
Preganziol: 1221363,5346	Santa Lucia di Piave: 321879,6372	Castello di Godego: 1289155,439
Roncade: 1298105,8772	Susegana: 736859,3144	Salgareda: 963963,3146
Casier: 840738,1796	Possagno: 382550,509	Villorba: 2286396,4156
Morgano: 411870,91	Pederobba: 732829,7328	Cessalto: 548989,749
Quinto di Treviso: 921693,4518	Cavaso del Tomba: 339821,2576	Ponzano Veneto: 2391523,0658
Monastier di Treviso: 481009,4036	Vidor: 875281,9614	Breda di Piave: 906385,931
Silea: 864474,6154	Moriago della Battaglia: 684566,4276	Chiarano: 548241,078
Treviso: 3320145,0348	Sernaglia della Battaglia: 817190,1848	Riese Pio X: 1867008,2376
Castelfranco Veneto: 3522677,3472	Gaiarine: 2574585,8578	Loria: 1162093,2378
Paese: 5245329,5928	Conegliano: 1720958,3138	Altivole: 2236252,7748
Revine Lago: 731583,985	San Vendemiano: 902205,5966	Maserada sul Piave: 654684,778
Fregona: 305781,6828	Pieve di Soligo: 1617355,4892	Povegliano: 599359,519
Tarzo: 494907,182	Farra di Soligo: 947745,1654	Tarzo: 494907,182

Sarmede: 482445,6296	San Pietro di Feletto: 445014,1168	Sarmede: 482445,6296
Vittorio Veneto: 4191583,8184	Segusino: 254568,512	Vittorio Veneto: 4191583,8184
Godega di Sant'Urbano: 1167439,8692	Cordignano: 1884252,117	San Fior: 712031,958
Miane: 315684,512	Cappella Maggiore: 539039,0456	Refrontolo: 373649,9822
Godega di Sant'Urbano: 1167439,8692	Cison di Valmarino: 174471,9196	

Table 2. Theoretical photovoltaic energy production for municipalities of Perugia province. It was computed using data on the total photovoltaic power installed in every one of the Italian municipality; Referred data are updated to 30 June 2011. It must be said that the Atlasole database is constantly updated by the GSE.

Photovoltaic Energy (*KWh/y*) in Perugia province municipalities		
Castel Ritaldi: 790553,517	Sellano: 6009,3696	Torgiano: 952229,876
Foligno: 4097071,9062	Montefalco: 255921,861	Valtopina: 135481,671
Monteleone di Spoleto: 8865,987	Collazzone: 992933,9654	Assisi: 3732579,3232
Scheggino: 10569,364	Marsciano: 15001231,947	Nocera Umbra: 825307,223
Cascia: 52196,768	Gualdo Cattaneo: 575676,4208	Perugia: 27116869,8242
Sant'Anatolia di Narco: 15775,799	Bevagna: 1728524,382	Castiglione del Lago: 2895145,019
Spoleto: 3392623,7956	Piegaro: 187609,8224	Magione: 2707824,1086
Vallo di Nera: 7042,23	Deruta: 4414680,0906	Passignano sul Trasimeno: 198193,632
Massa Martana: 1602992,118	Spello: 3449817,5374	Tuoro sul Trasimeno: 140839,7848
Todi: 1176124,638	Cannara: 2251751,2368	Gualdo Tadino: 5339601,7636
Norcia: 39930,046	Panicale: 2007845,7074	Lisciano Niccone: 112838,193
Campello sul Clitunno: 159375,8972	Corciano: 4373177,8818	Fossato di Vico: 2830977,6638
Cerreto di Spoleto: 10792,067	Valfabbrica: 2002809,0082	Umbertide: 2590082,8382
Giano dell'Umbria: 247748,059	Costacciaro: 1205124,18	Sigillo: 150125,898
Monte Castello di Vibio: 68321,669	San Giustino: 3654352,7878	Montone: 97453,629
Fratta Todina: 1405912,001	Gubbio: 2881536,3378	Scheggia e Pascelupo: 92686,581
Trevi: 2504021,9724	Bettona: 2829256,2298	Monte Santa Maria Tiberina: 52690,326
Preci: 16576,326	Paciano: 1639563,562	Pietralunga: 246165,062
		Citerna: 393100,89

Table 3. Theoretical photovoltaic energy production for municipalities of Lecce province. It was computed using data on the total photovoltaic power installed in every one of the Italian municipality; Referred data are updated to 30 June 2011. It must be said that the Atlasole database is constantly updated by the GSE.

Photovoltaic Energy (*KWh/y*) in Treviso province municipalities		
Follina: 573080,6576	Gorgo al Monticano: 544670,885	Montebelluna: 2868976,5368
Resana: 2160255,0288	Giavera del Montello: 974623,9822	Motta di Livenza: 2527787,2994
Ponte di Piave: 791220,9778	Asolo: 704458,667	Volpago del Montello: 1510711,125
Trevignano: 821378,668	Maser: 264460,1366	San Zenone degli Ezzelini: 1202145,6084
Caerano di San Marco: 1048791,304	Borso del Grappa: 378549,4482	Ormelle: 359205,2156
San Polo di Piave: 1019326,2618	Crocetta del Montello: 1330823,3092	Spresiano: 1172480,9206
Meduna di Livenza: 358277,271	Nervesa della Battaglia: 2782819,2744	Oderzo: 1912483,6346
Mareno di Piave: 1088789,6888	Paderno del Grappa: 291552,8594	Fonte: 535086,8776
Valdobbiadene: 1252951,3392	Crespano del Grappa: 241328,7492	Arcade: 399183,2284
Orsago: 439583,9602	Fontanelle: 1502586,7714	Zenson di Piave: 326247,394
Colle Umberto: 1031921,2508	Monfumo: 67916,1736	Istrana: 859223,7324
Mogliano Veneto: 1458842,9944	Cornuda: 558426,0594	Carbonera: 1725000,1186
Casale sul Sile: 1457118,5046	Castelcucco: 800506,5354	San Biagio di Callalta: 906793,371
Zero Branco: 1585091,3342	Vazzola: 971910,4318	Vedelago: 3123654,039
Preganziol: 1221363,5346	Santa Lucia di Piave: 321879,6372	Castello di Godego: 1289155,439
Roncade: 1298105,8772	Susegana: 736859,3144	Salgareda: 963963,3146
Casier: 840738,1796	Possagno: 382550,509	Villorba: 2286396,4156
Morgano: 411870,91	Pederobba: 732829,7328	Cessalto: 548989,749
Quinto di Treviso: 921693,4518	Cavaso del Tomba: 339821,2576	Ponzano Veneto: 2391523,0658
Monastier di Treviso: 481009,4036	Vidor: 875281,9614	Breda di Piave: 906385,931
Silea: 864474,6154	Moriago della Battaglia: 684566,4276	Chiarano: 548241,078
Treviso: 3320145,0348	Sernaglia della Battaglia: 817190,1848	Riese Pio X: 1867008,2376

Castelfranco Veneto: 3522677,3472	Gaiarine: 2574585,8578	Loria: 1162093,2378
Paese: 5245329,5928	Conegliano: 1720958,3138	Altivole: 2236252,7748
Revine Lago: 731583,985	San Vendemiano: 902205,5966	Maserada sul Piave: 654684,778
Fregona: 305781,6828	Pieve di Soligo: 1617355,4892	Povegliano: 599359,519
Tarzo: 494907,182	Farra di Soligo: 947745,1654	Tarzo: 494907,182
Sarmede: 482445,6296	San Pietro di Feletto: 445014,1168	Sarmede: 482445,6296
Vittorio Veneto: 4191583,8184	Segusino: 254568,512	Vittorio Veneto: 4191583,8184
Godega di Sant'Urbano: 1167439,8692	Cordignano: 1884252,117	San Fior: 712031,958
Miane: 315684,512	Cappella Maggiore: 539039,0456	Refrontolo: 373649,9822
Godega di Sant'Urbano: 1167439,8692	Cison di Valmarino: 174471,9196	

References

[1] Albért R., Barabási A. L., Statistical mechanics of complex networks. Rev. Mod. Phys. 2002;74:47-97.

[2] Caldarelli G., Scale Free Networks. Cambridge, UK: Cambridge University Press; 2007.

[3] Petrarca S., Cogliani E., Spinelli F., La radiazione globale al suolo in Italia. Roma, IT: Edizioni ENEA; 2000.

[4] Goulias K. G., Transport system planning: methods and applications. U.S.A: CRC Press; 2003.

[5] Compilation of best research solar cell efficiencies. Data compiled by Lawrence Kazmerski, National Renewable Energy Laboratory (*NREL*). – Available at:<http://upload.wikimedia.org/wikipedia/commons/7/74/PVeff%28rev100921%29.jpg>[accessed 24.1.2012]

[6] SAPEI il cavo dei record – Available at:<http://www.sapei.it/Home.aspx> [accessed 20.1.2012].

[7] GSE Atlasole – Available at:<http://atlasole.gse.it/atlasole/> [accessed 20.1.2012].

[8] TERNA Dati statistici – Available at: <http://www.terna.it/default.aspx?tabid=418>.[accessed 20.1.2012].

[9] ENEA Archivio climatico DBT – Available at: <http://clisun.casaccia.enea.it/Pagine/Radiazione.htm>.[accessed 20.1.2012].

[10] ISTAT Codici dei comuni, delle provincie e delle regioni – Available at: <http://www.istat.it/it/archivio/6789>.[accessed 20.1.2012].

[11] Comuniverso – Available at: <http://www.comuniverso.it/>.[accessed 20.1.2012].

[12] ENEA-Archivio dei comuni: – Available at: <http://clisun.casaccia.enea.it/Pagine/Comuni.htm>.[accessed 20.1.2012].

[13] GSE Statistical Office, Statistical report 2010 - Renewable energy power-installations. Rome, November 2011.

[14] International Energy Agency, Key world energy statistics 2011, Paris 2011 – Available at:<http://www.iea.org/textbase/nppdf/free/2011/key_world_energy_stats.pdf>.[accessed 27.01.2012].

[15] TERNA, Verso la rete del futuro, nuove idee per una rete elettrica intelligente e a basso impatto ambientale – Available at: <http://www.terna.it/LinkClick.aspx?fileticket=rF4Xri6AY8c%3D&tabid=3664&mid=17871>. [accessed 29.03.2012].

[16] Terna S.p.a. and Gruppo Terna, Dati Statistici Sull'Energia Elettrica in Italia, 2010 – Available at:<http://www.iea.org/textbase/nppdf/free/2011/key_world_energy_stats.pdf> [accessed 20.04.2012].

[17] Bravi M., Parisi M.L., Tiezzi E., Basosi R., Life cycle assessment of a micromorph photovoltaic system, Energy 36 (2011) 4297-4306

[18] Photovoltaic Geographical Information System, Joint Research Centre, Institute for Energy and Transport, European Commission – Available at:< http://re.jrc.ec.europa.eu/pvgis/> [accessed 20.04.2012].

Design of a multi-purpose building "to zero energy consumption" according to european directive 2010/31/ce: architectural and plant solutions

Umberto Desideri[1], Livia Arcioni[1], Daniela Leonardi[1], Luca Cesaretti [2],Perla Perugini, Elena Agabitini, Nicola Evangelisti

[1] University of Perugia, Dept. of Industrial Engineering, Perugia, Italy, arcioni@tre-eng.com
[2] Municipality of Città della Pieve,ing.lucacesaretti@trepuntozero.it

Abstract

Considering the significant impact that the residential sector has on energy consumption, it is particularly important to implement policies aimed at improving energy efficiency in buildings for saving primary energy, and also to spread the concept of sustainable development through the use of appropriate technology and proper project criteria for new constructions. For these reasons the Municipality of Città della Pieve promoted the creation of a "Renewable Energy Park" in a deprived area of its territory, so that there were the main technologies for the production of green energy. In this context, it could not be lacking an educational/demonstrative "zero energy consumption" building for multifunctional activities realized with the most innovative techniques to save energy. The building will exemplify the optimization of the benefits derived from improved energy efficiency in synergy with systems of energy production from renewable sources, such as to make possible the transition from "passive" building to get to "active" building. In this paper we describe the technical solutions adopted both in the building envelope and the system concept for the project of that "zero energy consumption" building according to Directive 2010/31/CE. In order to validate the proposed solutions, it has also been carried out a simulation of the behaviour of the building in summer and winter so that it is possible to assess the actual benefits obtained both in terms of energy and in economic terms following the adoption of the proposed solutions.

Keywords

Sustainability, building, insulation materials, energetic performances

1. Introduction and regulatory background

The precarious state of health of our planet and the awareness of the limited non-renewable energy sources, made it inevitable a reform of the human activities' process of development, directed toward a policy of energy saving and promoting the use of alternative energy sources [1]. Data from ENEA MSE show that the building sector in Italy consumed in 2008 about 45 Mtoe of energy out of a total of 192 Mtoe, showing an increase from about 42 Mtoe required in 2005. From this emerges that civilian use of energy have continued to grow up despite the economic crisis of these years that, however, have affected other fields [2].

Considering the impact of residential sector in the emissions of climate-altering gases and in the use of primary energy, it is of main importance to implement policies aimed to improve the energy efficiency of buildings, thus saving primary energy. It is also important to disseminate the concept of sustainable development through the use of appropriate technology and appropriate design criteria for new constructions and for the rehabilitation of existing ones [3].

In recent years, several agreements were signed at international level, starting with the Geneva Convention of 1979, to arrive in the 1997 to Kyoto Protocol. This document defines timing and extent of the reduction of greenhouse gases emissions by 2012, and explicitly identifies the policies and actions to undertake. In the EU context, this is a new reference frame for the development of

standards related to energy conservation, to the climate change and to the management of environmental resources and energy. In this perspective, the Energy Certification of buildings determined by the European Directive 2002/91/EC assumes particular importance [4]. The creation of an energy label associated to the buildings, allows to classify them according to their energy performance and allows to limit consumption during the construction and/or restructuring. The recently published Directive 2010/31/UE [5] integrates the 2002/91/EC and promotes the improvement of buildings' energy performance in the Union. It is also applicable to all types of business, both in the civilian and industrial sector. In the cost-benefits analysis perspective, already provided by Directive 2002/91, Directive 2010/31 defines the evaluation of energy performance level in relation to costs (Art. 4). The obligation to build near-zero energy buildings starts on December 31, 2020, for private homes, and on Dec. 31, 2018, for the local government buildings, whether occupied or not (Art. 9). The limit size of the buildings surface subject to important renovations disappears and it is established by Directive 2002/91 to 1000 m^2. Beyond this limit there is the obligation to comply with the minimum energy performance requirements set by the State (Art 7). Besides, Directive 2010/31 introduces the obligation to report, on all the advertisements of commercial media, the energy performance indicator in cases of sale and lease (Art. 12). Lastly, the Member States have the chance of reducing the frequency of heating systems inspections in the presence of an electronic system of control (art. 14).
The measures to be undertaken vary depending on the type of building. For new buildings it is necessary to submit, before work, an assessment of technical, economic and environmental feasibility for the use of alternative energy production systems. It is fundamental to take into consideration: the decentralized energy supply systems based on renewable energy sources; cogeneration; urban or collective district heating or cooling , particularly if it is based wholly or partly on renewable energy, heat pumps. The preliminary study, which must be documented and made available for inspection, can be made for individual buildings, groups of similar buildings or for common types of buildings which are in the same area. In the case of existing buildings, a renovation can be defined as important and therefore be subject to the requirements for new buildings in two cases: with regard to the building envelope or buildings' technical systems, the cost of the renovation exceeds 25% of the value of the building, excluding the value of the land upon which it is located; on the other hand, the renovation concerns more than 25% of the building envelope. With regard to the Energy Performance Certificate, it allows to evaluate and compare the energy performance of different buildings / housing units with the same method of judgment. The novelty is that, in case of sale or lease, the energy performance indicator contained in the certificate of the building or building unit, is shown in all advertisements of commercial media in Italy. The directive is in effect from 8 July 2010, but States of EU have time until July 9, 2012 to adopt it.
This article concerns the study of plant and architectural solutions aimed to the creation of a multipurpose building in a near zero consumption to be realized in a town of central Italy. This building is part of a project for the upgrading of a degraded industrial area, where will be created a renewable energy park.
The main objective of this project is to promote, on a broader scale, the use of technologies aimed at energy savings while providing the same level of service and to stimulate the energy production from renewable sources; for this purpose, several measures of energy production from renewable energy sources, such as solar and wind power plants, will be designed, constructed, managed and monitored. The Park project will also involves an educational course and a training center for young people from Città della Pieve and neighboring towns, in order to sensitize the community on these issues.

2. Case study

2.1 General framework

The project is set in the territory of Città della Pieve in Umbria on a hill at 508 m sea-level dominating the Valdichiana and Trasimeno Lake. A town with about 7,800 inhabitants and a territorial extension equal to 111 square kilometers which is situated on the border between two regions, Umbria and Tuscany, and three provinces, Perugia, Terni and Siena. The hill is like a plateau (Fig. 1), characterized by ridges alternating with deep ditches with layers of sands and conglomerates and large amounts of fossil fuels. This is the area where, several geological ages ago, there was the ancient delta of the Tiber.

Figure 1- landscape of Città della Pieve

The area identified by the city Administration for the implementation of the Technology Park for Energy and Environmental Sustainability, is located in the north of the village of Ponticelli, and covers an area of approximately 9 ha and is located in a flat depression bounded to the east by the channels Chiana and Astrone and to the west by the two railway lines Rome-Florence. To the south there is an industrial area in a strong deteriorating state with some disused craft buildings.
The whole area is particularly suited for the creation of a Technology Park for Energy and Environmental Sustainability. The park project involves the construction of an educational course and a training center for young people from Città della Pieve and surrounding municipalities. In detail, the functional program for the entire area provides the realization of:

- No.2 fixed solar fields with peak powers respectively of 900 kW and 800 kW for a total of 1700 kWp;
- No.3 “Sunflowers” made up of three sail of 12 kWp for every biaxial solar tracker, for the production of electricity in addition to the n. 2 fixed solar fields;
- No.4 micro-wind blades, two with horizontal and two with vertical axis, for a peak power of not more than 10 kWp;
- A multipurpose building designed in a single floor for education and training (about 50/60 sqm), built with green building techniques and completely sustainable. It will be a passive building designed with lightweight technologies and it will be the best expression of contemporary architecture in compliance with European Directive 2010/31/CE.

Thereafter, may be also realized an experimental section in which it will be possible to monitor some technologies, still in testing phase, to make them usable by public and private entities wishing to implement interventions in pilot scale. So it will be possible to create an attraction pole for all companies operating in the business. Companies will thus benefit from incentives and support in both financial and bureaucratic fields and in the connection with academic research and innovation.
Subject of this work is the analysis of solutions to “near-zero energy” suggested for the multipurpose building.

2.2 Architectural-Structural Analysis

The multi-purpose building at the service of the Renewable Energy Park was designed with architectural solutions that allow to take into account the context in which it is built, the energy conservation and the use of low environmental impact materials.

The building is constituted by a single floor, made in a raised position compared to the ground level through the presence of a ventilated crawl space 120 cm high. There are two spaces used for teaching purposes:

1. an interior space which consists of a multipurpose hall and an exhibition hall. The two rooms are characterized by large windows that allow an optimum observation of the external technological plants;
2. an outdoor space, located to the west, consisting of a staircase covered with photovoltaic panels made of polycrystalline silicon, for a pleasant use in summer.

Since the extent of glazing surfaces is considerable, the design includes low emissive elements to offer a comfortable shielding from solar radiation, especially during the summer. The windows' frames are made of aluminum in modules of 120 x 180 cm.

In addition, there is also a reinforced concrete septum that allows to isolate the building, visually and acoustically, from the nearby railway line. This septum is also the structural technological backbone on which are installed technical plants of the educational areas, in the south-west, and the mechanical room, containing electrical panels, on the east façade.

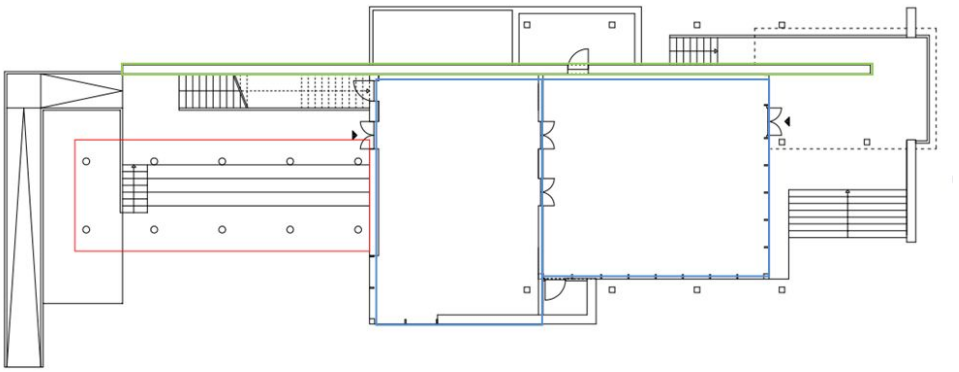

Legend:

- Green: reinforced concrete septum ;
- Blue: interior rooms;
- Red: outdoor pergola.

Figure 1 - Ground Floor: educational and external areas and reinforced concrete septum

Figure 1 shows the plan of the ground floor where is possible to identify the reinforced concrete septum, the interior rooms and the external pergola.

The building's roof is on two levels and it is made up with different construction types (Figure 2). In particular, there are:

1. an accessible green roof, to cover the exhibition hall, made with a suitable stratigraphy and placed at 4.5 m;
2. a not accessible green cover, positioned above the right entrance's porch;
3. a not accessible self-supporting cover over the multipurpose room, with an average height of 6,15 m with slope equal to 2% in the direction of the septum. On this cover there is also a solar-thermal integrated solution (Figure 3);
4. a photovoltaic roof, to cover the external pergola on the left, made of steel structural elements.

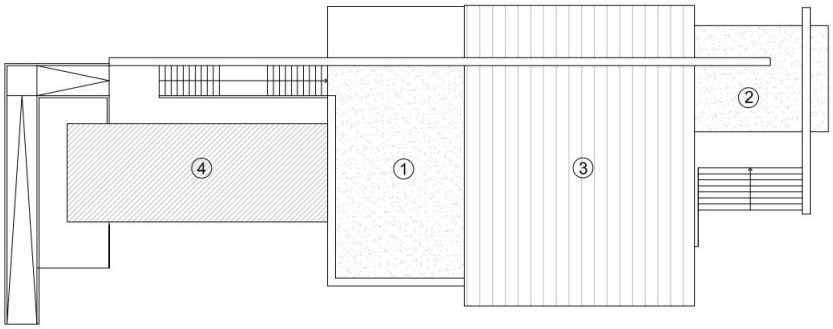

Figure 2 - Plan of the coverage

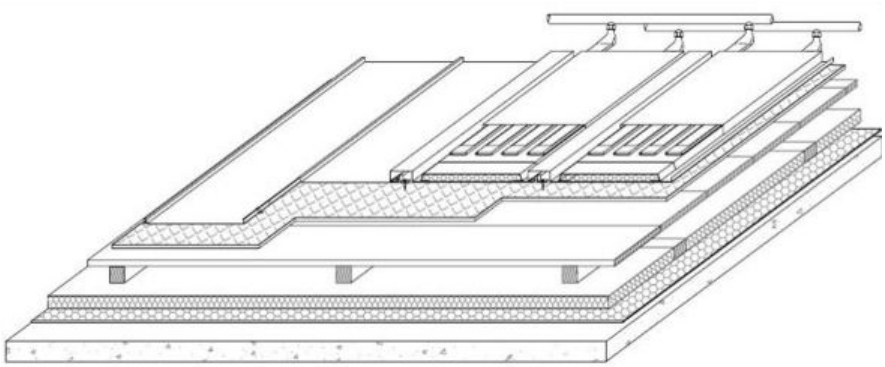

Figure 3 - Detail of the thermal solar integrated cover

From the structural point of view, the design of the complex was performed by limiting the use of hydraulic binders and traditional materials such as concrete and masonry.
The building presents a punctual structure with lamellar wood pillars of size 24 x 24 cm connected directly to the foundation platform. The point elements were also used in the definition of outer space in particular for the two porches.
In addition to the point structure, were also designed some continuous self-supporting elements (walls) that realize the internal division and define, together with windows, the perimeter of the rooms.
With the exception of the septum, the foundation (a reinforced concrete strip foundation that retrace the perimeter of the structure), the low walls (which allow to raise up the floor from ground level) and external walls of the technical services room (made of masonry), the remaining part of the structure was made using a dry technology.
The building's roof, set on two levels with different lights, was made of beams of different sizes: 60 x 24 cm first level, 90 x 24 cm second level .
The building will then be equipped with disabled access.
All the solutions, both in terms of materials and plants solution, are inspired by the principles of bio-architecture, thus creating an element of very low environmental impact and high energy self-sufficiency.

2.3 Building packages' stratigraphy

The energy analysis, performed in accordance with the DPR April 2, 2009 No. 59 came into force on June 25, 2009 [6] for the values of transmittance and according to UNI EN ISO 13788 [2] for Thermohygrometric testing, has led to the choice of particular stratigraphy for the building packages. The study was carried out through a specific software (Edilclima EC700), which allowed the determination of the thermal performance and the energy class of the building.

Below there are the details of the Construction layers of the building elements used. In particular, in Table 1, are shown the details of the walls.

Wall	Layer description	Depth (mm)	D_{TOT} (mm)	U (W/m^2K)	U_{LIMIT} (W/m^2K)	Picture
Concrete reinforced septum	Reinforced concrete	400	563	0.24	0.34	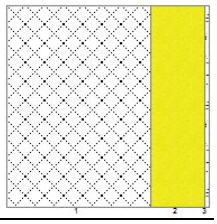
	Feldspar mineral fibers	150				
	Plasterboard	13				
Toilet facilities/technical premises' dividing wall	lime and gypsum plaster	10	331	0.219	0.8	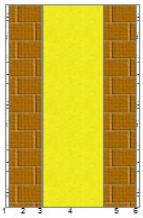
	Brickwork, internal wall	80				
	Bitumen felt/sheet vapour barrier	0.5				
	Feldspar mineral fibers	150				
	Brickwork, outer wall	80				
	lime and gypsum plaster	10				
Dry wall	Plasterboard	13	314	0.179	0.34	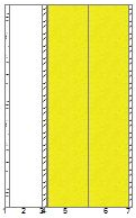
	Non-ventilated air gap	80				
	OSB panels	10				
	Bitumen felt/sheet vapour barrier	0.5				
	Feldspar mineral fibers	100				
	Feldspar mineral fibers	100				
	OSB panels	10				
Toilet facilities' outer wall	lime and gypsum plaster	15	451	0.194	0.34	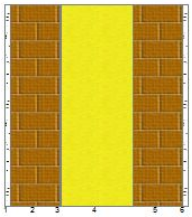
	Brickwork, internal wall	120				
	Bitumen felt/sheet vapour barrier	0.5				
	Feldspar mineral fibers	180				
	Brickwork, outer wall	120				
	lime and gypsum plaster	15				

Table 1 – Walls' stratigraphy

The calculations show that the average transmittance of the walls is equal to 0.208 W/m2K, that the verification of absence of surface condensation is satisfied and that the interstitial condensations of opaque walls are limited to the evaporable amount.
In the following part, there are the stratigraphy of the proposed solutions for the covers (Table 2). The self-supporting cover is realized with panels composed by an insert of non-combustible mineral wool covered with a vapor barrier which allows to achieve excellent thermal insulation values.
The extensive green roof is a system that combines thermal insulation, energy saving, mitigation of environmental impact and water drainage system. It is particularly suitable for all those coverings that can not be subject to frequent maintenance, because it does not require an irrigation systems.

The vegetation used, *sedum*, easily adapts to the weather conditions because it can regenerate itself quickly and it can resist to long dry periods.
The estimated cost is around 100 € / m2 for a total of 8000 €.
At the ground floor has been suggested the insertion of a conventional ventilated attic made up with cupolex and underfloor heating, as shown in Table 2.

Covers	Layer description	Depth (mm)	D_{TOT} (mm)	U (W/m^2K)	U_{LIMIT} (W/m^2K)	Picture
Self-supporting cover	Fir wood	10	221	0.179	0.3	
	Feldspar mineral fibers	200				
	Bitumen felt/sheet vapour barrier	0.5				
	Fir wood	10				
Green roof	Wet soil	70	506	0.172	0.3	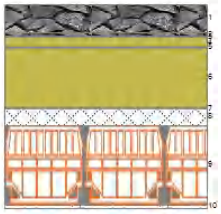
	Living loose pumice	10				
	Nonwoven fabric	1,3				
	Extruded polystyrene	24				
	Polyester fabric	0.5				
	Extruded skinless polystyrene	150				
	Bitumen felt/sheet vapour barrier	0.,5				
	Sand and gravel concrete	40				
	Brick floor	200				
	Lime and chalk plaster	10				
Airy floor	Ceramic tiles	1	362	0.194	0.33	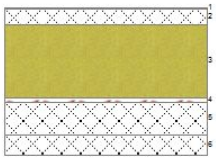
	Lean concrete	40				
	Extruded polystyrene in plates	180				
	Thermoliving 3B	11				
	Lean concrete	80				
	Screed coat	50				

Table 2 - Covers and airy floor

The calculation shows that the average transmittance of the covers is equal to 0.176 W/m^2 and that the thermohygrometric tests are met.
The glass wall is equipped with a continuous insulating glass with double function of low emissivity and solar control. This glass gives to the wall reinforced thermal insulation properties in winter and sun protection in summer. The glass is made through a process which provides the presence of an airtight space filled with insulating gas (argon 90%) between the two panes, allowing to reach a transmittance value of 1.1 W/m^2K.
In winter, the glass provides a thermal insulation three times higher than a normal double glazing allowing a reduction in heating costs. Besides, the ability to achieve greater comfort in the proximity of the glass walls, reduces the risk of condensation inside. It also protect the environment by reducing greenhouse gas emissions and allows to have large windows yet respecting the constraints of regulations existing on thermal matter [5]. In summer, the glass reduces by twice the direct transmission of solar heat allowing the maintenance of a pleasant indoor temperature, limiting

the costs for air conditioning and reducing the transmission of ultraviolet radiation. In particular, the free solar contribution both on opaque elements and glass windows elements has been calculated. This value is equal to 32371 kWh for the entire summer season (April 15 - October 15), as measured according to UNI TS11300. This thermal load is brought down, as well as the sensible load and the latent load, through the use of the air conditioning, which is able to maintain an internal temperature of at most 5° C lower than the outdoor temperature.
The aluminum frame has permeability class 4 according to UNI EN 12207 [9] and transmittance equal to 1.34 W/m^{2}K. The total transmittance takes account of the features of glass package and aluminum frame and reach the value of 1.274 W/m^{2}K (Table 3). The average transmittance of the glass walls is equal to 1.407 W/m^{2}K.

Building package	$Depth_{TOT}$ (mm)	U (W/m^{2}K)	Permeability class	U_{LIMIT} (W/m^{2}K)	$U_{GLASS\ ONLY}$ (W/m^{2}K)	$U_{LOOM\ ONLY}$ (W/m^{2}K)
Continuous insulating glass wall	28	1.274	4	2.2	1.1	1.34

Table 3 - Glass wall

2.4 Plant choices

Plant choices have been made by pursuing the theme of environmental sustainability that is improvement of building energy performance, trying to combine the aesthetic and energy options. These reasons have led to the inclusion of a photovoltaic system, that makes a sort of technological bower, and of an integrated solar cover which can be used both for the production of hot water and for the operation of underfloor heating. These systems can significantly reduce consumptions of the building.
In particular, the solar thermal cover is an innovative system made entirely of copper. The surface of the cover absorbs the heat of solar energy which is then transmitted to a system of pipes located under the roof covering. Inside the tubes flows a fluid (water + 40% ethylene glycol) at a pressure of 1 bar that transfers heat through a stainless steel coil, to the water contained in the storage tank and from there to the entire thermal system. The water is stored at a temperature of about 50° C, to be then sent to the users. This solution is ideal not only for residential building but also for sports facilities, public buildings, hotels and multi-purpose complex as in this case.
According to the size of the cover, 24 solar collectors have been provided. Their dimensions are 46,7 cm x 5 m and in each one flows, through the ovoid section, an operating flow rate of 87 l/h for a total of 2088 l/h.
This flow rate satisfies completely hot water demand and partly heating demand (3729.78 l/h).
Table 4 shows the percentages of the requirements of Domestic Hot Water and Heating met by solar thermal cover.

Domestic Hot Water	Heating

Months	Primary Energy (excluding solar energy) [kWh]	Coverage Percentage [%]	Primary Energy (excluding solar energy) [kWh]	Coverage Percentage [%]
Jan.	29	98.7	1534	6.3
Feb.	25	100.0	961	9.7
Mar.	26	98.7	207	41.6
Apr.	23	100.0	15	99.1
May	23	95.1	0	0.0
June	21	98.3	0	0.0
July	21	95.1	0	0.0
Aug.	21	95.1	0	0.0
Sept.	21	98.3	0	0.0
Oct.	23	98.7	0	0.0
Nov.	24	100.0	275	30.3
Dec.	28	98.7	1416	6.5

Table 4 – Percentages of the requirements covered by solar thermal cover

With regard to the PV system, the choice is to include 30 polycrystalline panels with peak power of 285 W for a total output of 8 kW.
They have been installed with southwest exposure following the inclination of technological bower of 15°. In Figure 4 is reported the graph of the monthly production of the plant.

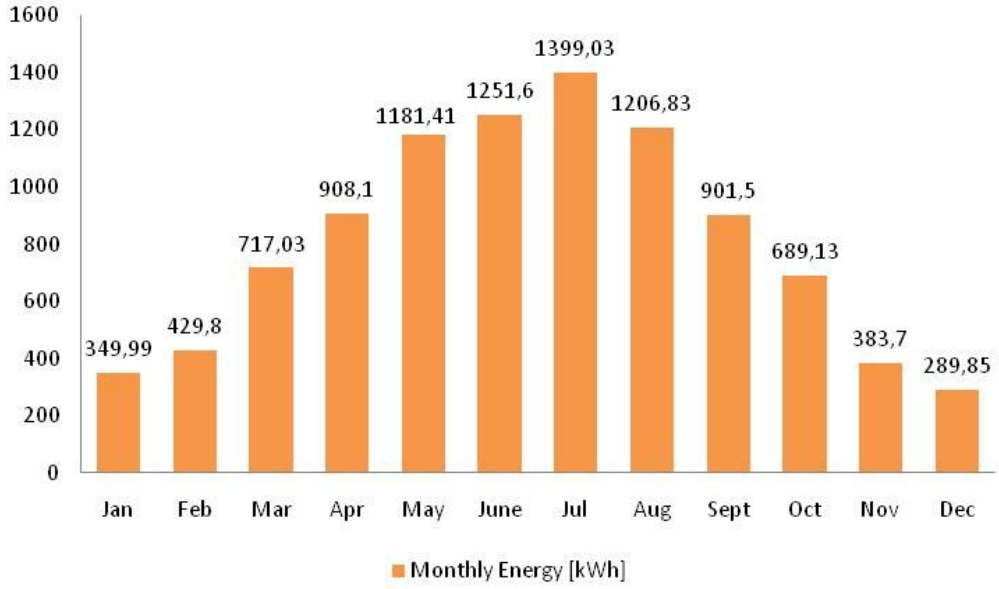

Figure 4 - Energy monthly produced by the PV plant

The cost of single panel is € 331.21 for a total of € 9936.39, that is € 1242 / kW.
The energy requirements of the heat pump is entirely covered by the energy produced by the photovoltaic system, in particular the heat pump has an absorption of 4 kW in wintertime and of 5.4 kW in summertime.
The features of the heat pump are reported below (Table 5).

Features:	Electric demand:

Nominal power (kW)	COPe	Average power of auxiliaries (W)	Electric power of circulating pumps (W)
16.30	3.94	70	250

Table 5 - Features of the heat pump.

3. Calculation results

3.1 Calculation Methodology

This study used Edilclima EC700, a software elaborated by Edilclima software house. The thermo-physical parameters refer to an internal database (coming from UNI Standards) or to manual input. The thermal-bridges are calculated by a parametric method called "Atlas of thermal-bridges" which follows UNI 14683 Standard [14].

The heating and domestic hot water plant inputs are expressed in global thermal-efficiency or for each plant subsystem and they are referred to UNI TS 11300 part 2 or producer technical database. The outputs are:

a) wintertime power, for the sizing of the heating system according to UNI EN 12831;
b) useful and primary energy winter heating, according to technical specifications UNI/TS 11300 part 1 and 2;
c) useful energy for summer cooling, under the technical specification UNI/TS 11300-1;
d) useful and primary energy for domestic hot water production, according to UNI/TS 11300-2.

Climate data considered in this study come from the Archive of Software and are based on the UNI 10349. They include: winter and summer design temperature, summer design humidity, wind speed, average monthly temperature, monthly average solar irradiance for 9 directions, the monthly average vapor pressure, altitude, latitude, longitude, climate zone, wind area, degree days.

The standard input conditions are UNI TS 11300 standard input data. The input data used are:

- Hours of heating plant operation: 24 h/day;
- Hours of cooling plant operation: 12 h/day;
- Number of days of heating plant operation: 183 day;
- Outside project temperature in winter: -2°C.
- Outside project temperature in summer: 29.5°C;
- Inside project temperature in winter:20°C.
- Inside project temperature in summer: 26°C;
- Indoor dry bulb temperature: 25° C;
- Winter indoor relative humidity: 60%;
- Summer indoor relative humidity: 50%;
- Air exchange peak: 0,5 vol/h;
- Number of persons/m^2: 0,25 persons/m^2;
- Sensible heat per person: 64W/person;
- Latent heat per person: 46W/person.

For the calculation of the energy performance, the internal space has been divided into 2 thermal zones (Figure 5):

1. air-conditioned area, which includes the exhibition room, the multipurpose room and toilet facilities (A);
2. non-heated area, represented by the equipment room (B).

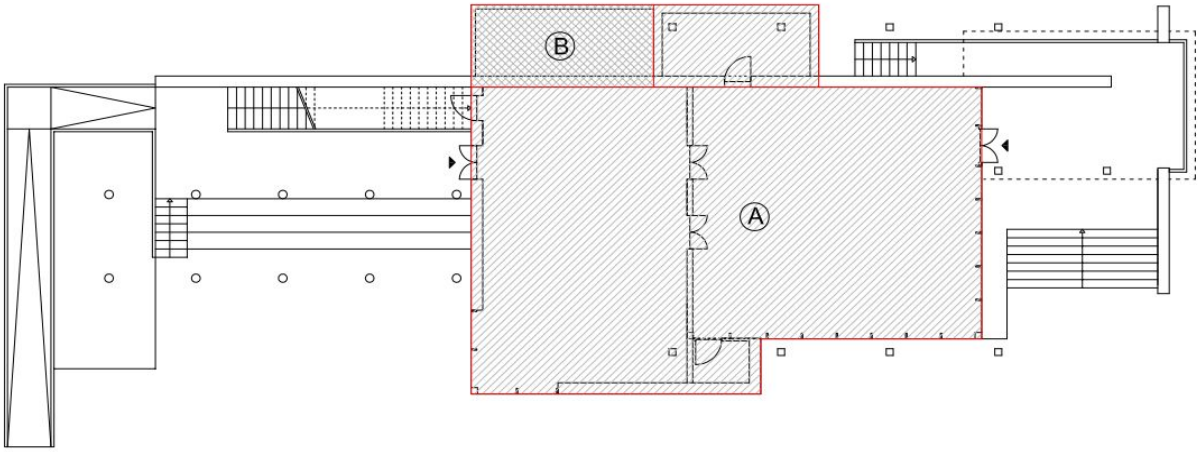

Figure 5 - Identification of the air-conditioned and non air-conditioned area

3.2 Settings

In this article the energy performance of multi-purpose building have been evaluated, using the software Edilclima EC700 and considering different settings [11, 12, 13]:

1. Setting 1: This scenario considers a building realized with Construction layers of the building elements reported in section 2 (Building on "near-zero" consumption), and the use of renewable energy sources (photovoltaic and solar thermal cover);
   - 1.a Setting 1.a: Building on "near-zero" consumption with only solar thermal cover;
   - 1.b Setting 1.b: Building on "near-zero" consumption without renewable energies.
2. Setting 2: This scenario regards a building constructed with Construction layers of the building elements with transmittance value according to law limits, and the use of renewable energy sources (solar thermal cover), in which:
   - The depth of the insulating layers and the full-length window reach the limit values of transmittance provided for the rules about vertical and horizontal opaque components and windows (DPR 59/09 [5]);
   - Absence of the photovoltaic system, due to the use of a non electrical heating system;
   - Replacement of the heat pump with a conventional Plant.
   - 2.a Setting 2.a: Building according to the limits of law without renewable energies.

Setting n. 1

The results of the evaluations are reported below (Table 6).

Heating service		
Annual primary energy demand	3942	kWh/year
Annual consumption of electricity	1813	kWh_e/year
Hot water service		
Annual primary energy demand	5	kWh/year
Annual consumption of electricity	2	kWh_e/year
Thermal solar system		
Manufacturability of the solar panels (hot water)	534	kWh/year
Percentage coverage (hot water)	98.2	%
Manufacturability of the solar panels (heating)	778	kWh/year
Percentage coverage (heating)	10.6	%

Photovoltaic system		
Electricity from photovoltaic system	9708	kWh/year
Total electrical demand	1816	kWh/year
Electricity from main	0	kWh/year
Electricity produced and not consumed	7892	kWh/year
Energy primary index (EPi)	0	kWh/m^{3}year
Energy primary index provided for the rules (D.Lgs. 192/05)	21.26	kWh/m^{3}year

Table 6 - Energetic ratings Setting 1

From the analysis of results follows that the annual consumption of electricity for heating and hot water amount respectively to about 1813 kWh/year and 2 kWh/year, for a total of 1816 kWh/year. The PV system can produce 9708 kWh/year, of which 7892 kWh/year are not consumed but put in the mains.
For this reason, the building can be considered as a zero consumption structure.

Setting n. 1.a
The results of the evaluations reported below (Table 7) are referred to the case that the photovoltaic system is removed and the consumption of the building is fully covered by the mains.

Heating service		
Annual primary energy demand	3942	kWh/year
Annual consumption of electricity	1813	kWh$_e$/year
Hot water service		
Annual primary energy demand	5	kWh/year
Annual consumption of electricity	2	kWh$_e$/year
Thermal solar system		
Manufacturability of the solar panels (hot water)	534	kWh/year
Percentage coverage (hot water)	98.2	%
Manufacturability of the solar panels (heating)	778	kWh/year
Percentage coverage (heating)	10,6	%
Energy primary index (EPi)	3.68	kWh/m^{3}year
Energy primary index provided for the rules (D.Lgs. 192/05)	21.26	kWh/m^{3}year

Table 7 - Energetic ratings Setting 1.a

Setting n. 1.b
The results of the evaluations are reported below (Table 8). In this case there is an increase of 16% of annual consumption of electricity due to the absence of the solar thermal system in addition to underfloor heating. The annual consumption of electricity increases from 1816 kWh/year to the value of 2158 kWh/year.

Heating service		
Annual primary energy demand	4408	kWh/year
Annual consumption of electricity	2027	kWh$_e$/year

Hot water service		
Annual primary energy demand	284	kWh/year
Annual consumption of electricity	131	kWh_e/year
Energy primary index (EPi)	4.11	kWh/m^3year
Energy primary index provided for the rules (D.Lgs. 192/05)	21.26	kWh/m^3year

Table 8 - Energetic ratings Setting 1.b

Setting n. 2

For the setting n. 2, the analysis has been performed considering building packages with transmittance values near to the rules limits [6]. The percentage differences in terms of depth of insulating material and in terms of thermal transmittance of the packages have been reported in Table 9.

Building package	Insulating layer	Depth (mm)	$Depth_{STANDARD}$ (mm)	Δ S %	U (W/m^2K)	$U_{STANDARD}$ (W/m^2K)	Δ U %
Reinforced concrete septum	Feldspar mineral fibers	150	100	33	0.24	0.344	30
Dividing wall facilities – technical premises	Feldspar mineral fibers	150	80	47	0.219	0.354	38
Drywall	Feldspar mineral fibers	100	40	60	0.179	0.351	49
	Feldspar mineral fibers	100	50	50			
External wall of facilities	Feldspar mineral fibers	180	90	50	0.194	0.343	43
Self-supporting cover	Feldspar mineral fibers	200	110	45	0.179	0.310	42
Green roof	Extruded skinless polystyrene	150	60	60	0.172	0.317	46
Airy floor	Extruded polystyrene in plates	180	100	44	0.194	0.316	39

Table 9 - Depth of the insulating layers and transmittances of building packages Setting n.2

The percentage differences in terms of thermal transmittance of the insulating glass wall has been reported in Table 10.

Building package	Depth (mm)	$U_{GLASS\ ONLY}$ (W/m^2K)	$U_{FRAME\ ONLY}$ (W/m^2K)	U (W/m^2K)	$U_{GLASS\ ONLY\ STANDARD}$	$U_{FRAME\ ONLY\ STANDARD}$	$U_{STANDARD}$ (W/m^2K)	Difference % U

					(W/m^{2}K)	(W/m^{2}K)		
Continuous insulating glass wall	28	1.1	1.340	1.274	1.7	4.4	2.258	44

Table 10 - Depth and transmittance of the glass wall Setting n.2

The average values of transmittance of different building packages reached in setting n.1 and in setting n.2 are reported in Table 11.

	Setting n.1	Setting n.2	
	$U_{AVERAGE}$ (W/m^{2}K)	$U_{AVERAGE}$ (W/m^{2}K)	Δ U %
Walls	0.208	0.347	67
Covers	0.176	0.314	78
Floors	0.192	0.311	62
Glass walls	1.407	2.056	46

Table 11 - Average values of transmittance

The technical features of the traditional boiler, that in Setting n. 2 replaces the heat pump, are reported in Table 12:

Features:		
Nominal power of furnace	**28.00**	kW
Efficiency at nominal power	**93.20**	%
Efficiency at intermediate power	**94.10**	%
Electric demand:		
Electric power burner	**120**	W
Electric recovery factor	**0.80**	-
Electric power of circulating pumps	**0**	W
Electric recovery factor	**0.80**	-

Table 12 - Features of the traditional boiler

The results of the simulation on Setting n. 2 are reported in Table 13:

Heating service		
Annual primary energy demand	16087	kWh/year
Annual consumption of fuel	1597	Nm³
Annual consumption of electricity	100	kWh_e/year
Hot water service		
Annual primary energy demand	11	kWh/year
Annual consumption of fuel	1.1	Nm³
Annual consumption of electricity	0	kWh_e/year
Thermal solar system		
Manufacturability of the solar panels (hot water)	534	kWh/year
Percentage coverage (hot water)	98.0	%
Manufacturability of the solar panels (heating)	961	kWh/year
Percentage coverage (heating)	6.4	%
Energy primary index (EPi)	15	kWh/m^{3}year

Energy primary index provided for the rules (D.Lgs. 192/05)	21.26	kWh/m^{3}year

Table 13 - Energetic ratings Setting 2

Compared to Setting n.1, there is an increase of annual primary energy demand equal to 12145 kWh/year for heating service and to 6 kWh/year for hot water service. This second increase is however reduced because the building is still provided with solar thermal system.

Setting n. 2.a
In this simulation, the solar thermal cover is removed. The results are reported in Table n. 14:

Heating service		
Annual primary energy demand	17192	kWh/year
Annual consumption of fuel	1707	Nm³
Annual consumption of electricity	105	kWh$_e$/year
Hot water service		
Annual primary energy demand	583	kWh/year
Annual consumption of fuel	58.2	Nm³
Annual consumption of electricity	2	kWh$_e$/year
Energy primary index (EPi)	17	kWh/m^{3}year
Energy primary index provided for the rules (D.Lgs. 192/05)	21.26	kWh/m^{3}year

Table 14 - Energetic ratings Setting 2.a

In this case, the increase of primary energy demand from 11 kWh/year in Setting n. 2 to 583 kWh/year in Setting n. 2.a, is due primarily to hot water service that, in the previous simulation, was covered for 98% by the integrated solar thermal solution.

4. Conclusions

The analysis made in this article relate to the architectural and plant solutions of a multipurpose building on "near-zero" consumption. Different plant solutions and different architectural solutions have been evaluated to compare the consumption in the various solutions suggested.
The values of global primary energy demand for winter heating in the different settings considered have been summarized in Table 15:

	EP_{gl} (kWh/m^{3}year)	$EP_{gl,average}$	Δ $EP_{gl,average}$ %
setting n.1	0		
setting n.1.a	3.68	2.7	
setting n.1.b	4.38		504
setting n.2	15.01	16.3	
setting n.2.a	17.59		

Table 15 - Percentage increase of $EP_{gl,average}$

Furthermore, the use of renewable sources, combined with the use of building packages with high performance and with high efficiency plants, allows to obtain in all settings analyzed low emissions of CO_2 (Table 16).

	$kgCO_2/m^3$year
setting n.1	0

setting n.1.a	1.6
setting n.1.b	1.9
setting n.2	3
setting n.2.a	3.51

Table 16 - Emissions of CO_2

Thanks to the combination of these elements, which allow the building to reach energy self-sufficiency, the design assumptions applied in Setting n.1. make the multipurpose building a structure on zero consumption with zero emissions of CO_2.
Moreover is very interesting to analyze the situation of the costs of a building realized with a "near-zero" consumption and a "traditional" building. The estimated costs taking in account the elements listed below:

- Construction works;
- Sanitary water systems, and sewer;
- Mechanical plants;
- Electrical plants.

The building costs for a "near zero" consumption building is around 1700.00 €/m^2 (for a total amount of 255,000.00 € VAT excluded) instead a traditional construction building that is about 1400.00€/m^2 (for a total amount of 210,000.00 € VAT excluded). Considering the current market price of thermal and electric kWh, the difference in terms of operating costs between the two solution must be estimated at about 5500.00 €/year. So is it possible to evaluate the pay-back period of the investment is 8.2 years.

Acknowledgments

We would like to thank Municipality of Città della Pieve for its contribution in the present work.

References

[1] S. Stanghellini, "Qual è il senso dell'espressione "città sostenibile?"", relazione presentata al convegno "Sviluppo sostenibile e città", Venezia, 29 ottobre 1997.

[2] Meadows, D.H., Meadows, D. L. Randers, J., & Behrens, W.W., The limits to growth, New York Universe, III 1972.

[3] Lester Brown, J. Lrsen, B. Fischlowitz-Roberts, Bilancio Terra. Gli effetti ambientali dell'economia localizzata, Ed. Ambiente, 2004

[4] Direttiva 2002/91/CE del Parlamento Europeo e del Consiglio del 16 dicembre 2002 sul rendimento energetico nell'edilizia

[5] Direttiva 2010/31/UE del Parlamento Europeo e del Consiglio del 16 dicembre 2002 sul rendimento energetico nell'edilizia

[6] DPR 59/09, Decreto del Presidente della Repubblica n. 59 del 2 Giugno 2009

[7] UNI EN ISO 13788, Prestazione igrometrica dei componenti e degli elementi per l'edilizia – Temperatura superficiale interna per evitare l'umidità superficiale critica e condensazione interstiziale – Metodo di calcolo

[8] UNI TS 11300 - 1 – 2, Prestazione energetica degli edifici - Determinazione del fabbisogno di energia primaria e dei rendimenti per la climatizzazione invernale e per la produzione di acqua calda sanitaria

[9] UNI EN 12207, Classificazione della permeabilità dell'aria

[10] DL 192/05, attuazione della direttiva 2002/91 CE relativa al rendimento energetico nell'edilizia

[11] Desideri U., Proietti S., 2002, "Analysis of energy consumption in the high schools of a province in central Italy", Energy and Building, Vol 34, pp. 1003-1016, Elsevier. DOI:10.1016/S0378-7788(02)00025-7

[12] Butala V., Novak P., 1999, "Energy consumption and potential energy savings in old school buildings", Energy and Buildings, Vol 29, pp. 241–246, Elsevier. DOI:10.1016/S0378-7788(98)00062-0

[13] Proietti S., Desideri U., 2003, "Analysis and simulation of distributed cogeneration in the school sector", Proceedings of ECOS 2002 International Conference on Efficiency, Cost, Optimization, Simulation and Environmental Impact of Energy Systems, July 2-7, 2003, Berlin, Germany.

[14] Tronchin L., Fabbri K., 2010, "A Round Robin Test for buildings energy performance in Italy", Energy and Buildings, Vol. 42, pp. 1862–1877.

Effect of Initial Systems on the Renewal Planning of Energy Supply Systems for a Hospital

Shu Yoshida[a], Koichi Ito[b], Yoshiharu Amano[b], Shintaro Ishikawa[c], Takahiro Sushi[c] and Takumi Hashizume[b]

[a] *Energy Use Research and Development Center, The Kansai Electric Power Co., Inc., Osaka, Japan, yoshida.shuu@e2.kepco.co.jp,* ***CA***
[b] *Research Institute for Science and Engineering, Waseda University, Tokyo, Japan*
[c] *Graduate School of Fundamental Science Engineering, Waseda University, Tokyo, Japan*

Abstract:

In recent years, many types of energy supply systems have come into use in various buildings for space-heating/cooling and hot water supply. Lifetimes of buildings are generally more than 60 years, but those of energy supply systems are around 15~25 years. Therefore, these systems must be renewed several times during lifetimes of buildings. In the study, this renewal planning problem is formulated mathematically as an optimization one, in which the objective function to be minimized is the average value of annual total cost during system's evaluation period. Namely, this optimization problem is formulated as a large-scale mixed-integer linear programming problem, and the programming language AMPL solver is adopted here as the solving tool to derive the numerical solution.

A numerical study is carried out for a hospital with the total floor area of 25 000m^2, where electrical (e.g., heat pump) and gas (e.g., gas engine cogeneration) systems are compared together with their hybrid system. The analysis is particularly focused on the influence of initial system's difference on the renewal planning of energy supply system.

Through this study, the following results are mainly obtained:

a) If the initial system is gas one, it is better to renew it to the electrical one as soon as possible due to relatively low energy efficiency of gas utilizing pieces of equipment, the high price of gas input energy in Japan, and so on.

b) If the initial system is electrical one, the optimal renewal year becomes relatively later year, because it is economically better to use the initially installed high efficiency system as long as possible.

c) Theoretically, the hybrid system is of course the best renewal one. However, there is no economic difference between the hybrid and the electrical systems.

Keywords:

Energy supply system, Hospital, Initial system, Optimization, Renewal planning.

1. Introduction

In recent years, various types of energy supply systems have come into use in various buildings such as electrical systems with heat pumps and gas systems with gas-engine cogeneration for space-heating/cooling and hot water supply. Lifetimes of these buildings are in general more than 60 years, and they are becoming longer and longer recently in Japan. On the other hand, lifetimes of these energy supply systems are about 15~25 years, and they must be renewed several times during lifetimes of buildings.

In the past, lots of planning problems were studied on energy supply systems installed newly into buildings by applying various types of mathematical optimization methods [1]. However, scarcely few theoretical studies have been done on the renewal planning problem of energy supply systems for buildings in spite of its engineering importance. Up to the present, the authors have investigated on some renewal planning problems of energy supply systems for building by applying the mathematical optimization method. Namely, they are a renewal problem of an energy supply system for an office building from economical viewpoint [2], a comparative study on alternative renewal plans for different types of energy supply systems [3], a multi-stage renewal planning problem [4], an impact analysis of carbon tax on the renewal planning [5], and a multi-objective renewal planning problem from economic and environmental viewpoints [6].

In the renewal planning of these systems, it becomes necessary to consider many factors such as the long term economy of the system, the deterioration of each pieces of existing equipment, candidate pieces of new equipment with upgraded efficiency reflecting the technology improvement, the system's renewal year, the structure of renewal system, etc. It is also necessary to consider the system's operational policy for hourly and seasonally changing energy demands through one year.

In addition, the structure of initially existing system (say shortly as initial system) has strong influence on the renewal planning. However, this important factor has not been studied up to present. Therefore, the purpose of this paper is mainly focused on the analysis of the influence of initial system's structure on the renewal planning problem.

In the following, this renewal planning problem is formulated mathematically as an optimization one, in which the objective function to be minimized is the average value of annual total cost during system's evaluation period. A numerical study is carried out for a hospital with the total floor area of 25 000m^2, where electrical, gas and their hybrid systems are compared as initial systems of renewal planning problems.

2. Optimal renewal planning problem

The optimal renewal planning method proposed here can help rational decision makings by determining the appropriate renewal year, the renewal system's structure, equipment capacities, and the system's operational strategy so as to minimize the mean value of annual total cost of the system during the evaluation period. Let us briefly explain here the framework and the mathematical formulation of the planning problem and its solution method.

2.1. Framework of problem

The framework of the optimal renewal planning problem is shown in Fig. 1. Here, the horizontal axis t is the year variable, and the initial system X_0 is constructed at $t = 0$ y. The present planning year is set as $t = t_p$, and the system will be evaluated economically during the period from $t = t_p$ to $t = t_p+T$. In other words, T means the total evaluation period of the system in this renewal planning problem. The initial system X_0 will be renewed to the renewal system X_1 at $t = \tau$ ($t_p \leq \tau < t_p + T$). In this renewal year, some pieces of equipment are determined to be discarded from X_0, but some others will continue in use and will form a part of the renewal system X_1 as shown in Fig. 1.

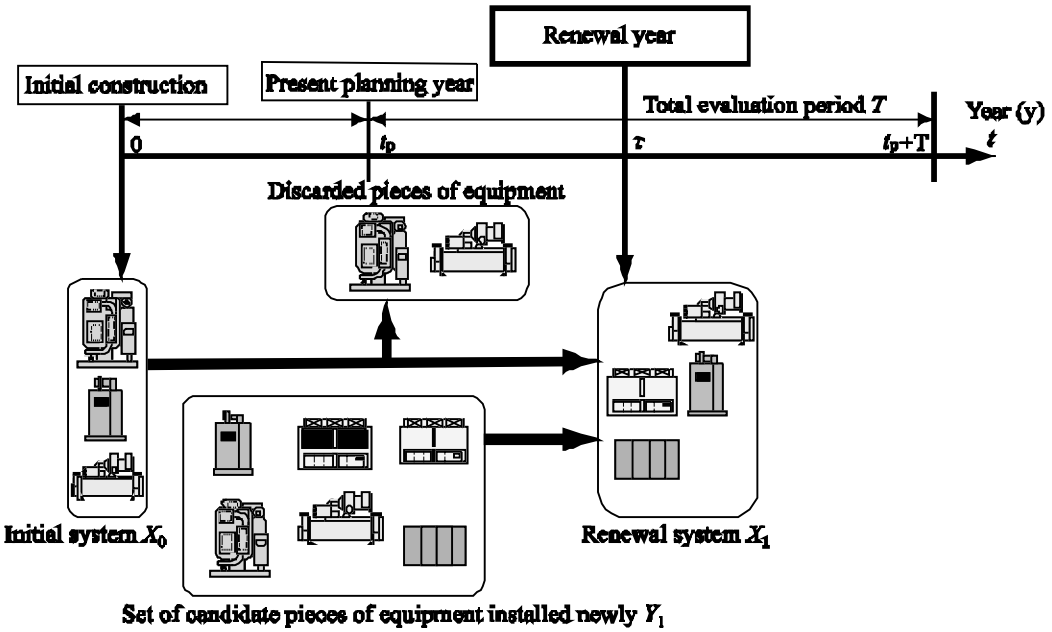

Fig. 1. Framework of the renewal planning problem

In addition, from the set of candidate pieces of equipment installed newly at the renewal year Y_1, some pieces of equipment are selected and the others are not. Thus, the renewal system X_1 is composed by combining pieces of equipment which are not discarded from X_0 and those selected from Y_1.

2.2. Mathematical formulation

2.2.1. Decision variables and constraints

Decision variables that will be determined by the optimization problem are composed of continuous and binary variables which are defined at $t = \tau$. The continuous variables contain as follows; i.e., the vector composed of capacities of each pieces of equipment $\boldsymbol{x}$, vectors composed of input and output energy flow rates of each pieces of equipment $\boldsymbol{u}$ and $\boldsymbol{v}$, respectively, and the vector composed of utility maximum contract demands $\boldsymbol{y}$. The binary variables mentioned above are expressed by the vector composed of ones related to the selection of each pieces of equipment to construct the renewal system X_1. In this study, energy demands are assumed to change hourly and monthly, but for the simplicity of the analysis, it is assumed that they don't change yearly through the system's evaluation period. However, as the system's structure changes at the renewal year $t=\tau$, and the performance characteristics of each pieces of existing equipment deteriorate year by year, the system's operational policy changes in each year. In this study, the performance improvement and the deterioration of each pieces of equipment are expressed by vectors of rates $\boldsymbol{\alpha}$ and $\boldsymbol{\beta}$ %/y, respectively, and their performance characteristic values change linearly year by year according to these rates.

Next, as constraints of this optimization problem, the first set of equations consists of performance characteristics of each pieces of equipment and their upper and lower limits of output energy flow rates formulated by the following equations; i.e.,

$$\begin{aligned} &\boldsymbol{v} = \boldsymbol{P} \cdot \boldsymbol{u}, \\ &0 \le \boldsymbol{v} \le \boldsymbol{x}, \end{aligned} \qquad (1)$$

where $\boldsymbol{P}$ is the diagonal matrix composed of performance characteristic values of each pieces of equipment.

The second set of equations consists of energy balance relationships of energy flow rates at each junction. The third one is related to those of energy supply demand relationships. The last set of equations consists of relationships among input values of utility and their maximum contract demands in addition to the selection of utility rates.

2.2.2. Objective function

The objective function to be minimized is the average annual total cost from a long-term economic viewpoint. It is evaluated as the sum of annual capital, operational, and maintenance costs based on the annualized costs method [7] as shown in Fig. 2 during the system's evaluation period formulated by the following equation:

$$J = C(\boldsymbol{\delta}, \boldsymbol{x}) + O(\boldsymbol{y}, \boldsymbol{u}, \boldsymbol{v}) + M(\boldsymbol{x}, \boldsymbol{u}, \boldsymbol{v}), \qquad (2)$$

where C expresses the annual capital cost and is a function of both vectors composed of binary variables related to the selection of each pieces of equipment $\boldsymbol{\delta}$ and their capacities $\boldsymbol{x}$, respectively. In the calculation of C, it is necessary to take into account construction and discarding costs of each pieces of equipment at τ, and they are expressed by multiplying construction and discarding cost ratios γ and μ to each equipment cost, respectively. In Eq.(2), O expresses the average value of annual operational cost (=input energy cost) and is a function of the vector composed of utility maximum contract demands $\boldsymbol{y}$, and input and output energy flow rates $\boldsymbol{u}$ and $\boldsymbol{v}$, respectively. As the annual operational cost changes year by year, this average value during the evaluation period becomes relatively complex. Moreover, M expresses the annual maintenance cost and is a function of $\boldsymbol{x}$, $\boldsymbol{u}$, and $\boldsymbol{v}$.

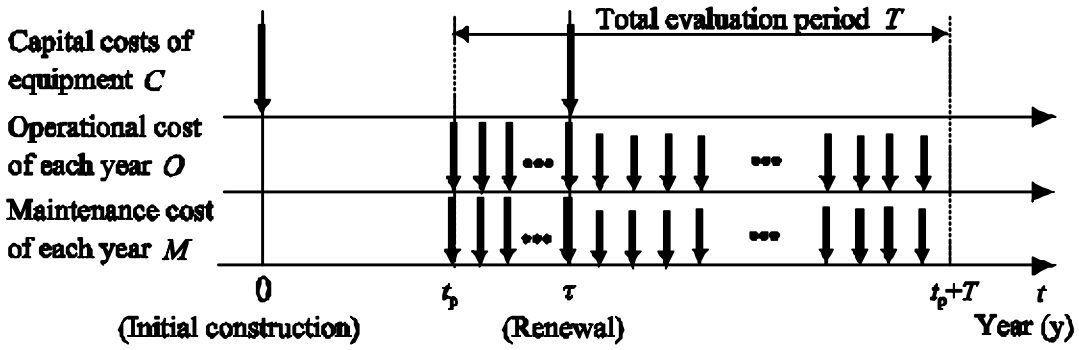

Fig. 2. Economic evaluation of the renewal system

It is of course necessary to consider interest rate i %/y, and the residual value of each piece of the equipment at the end of the total evaluation period. Concerning the latter, by denoting the statutory useful lifetime of equipment as κ, the residual cost ratio at the end of κ is set as ε, and its value is assumed simply to be equal for all pieces of equipment. In this place, it is assumed here that each pieces of equipment can be used after the end of κ though its maintenance cost arises $(1 + \theta)$ times higher stepwisely, where θ is the increasing rate of maintenance cost of equipment after the end of κ.

Lastly, in the practical renewal planning of energy supply systems, it is generally necessary to assume that the system has the surplus supplying capacity for each category of energy demands by taking the deterioration of equipment and the uncertainly of energy demands. In this paper, this necessary surplus capacity is simply reflected by the surplus rate of system's capacity λ, where this rate is simply assumed to take all equal value for all categories of energy demands.

2.2.3. Solution method

From sections 2.2.1 and 2.2.2, the renewal planning problem of the energy supply system can be formulated mathematically as a mixed-integer linear programming one [8]. This problem includes large numbers of continuous and binary unknown decision variables with many constraint equations. As the solving tool to derive the numerical optimal solution, the programming language AMPL solver [9] is adopted here, and this is developed by combining the branch and bound method with the simplex one of linear programming.

3. Numerical study for a hospital

3.1. Input data

A hospital with total floor area of 25 000m^2 is taken as the object of numerical example studied in this paper. The energy demands are estimated at each 24 hours on 15 representative days per year; that is, average demand days for each month, and peak demand days of electricity, space cooling and heating, respectively. For example, Fig. 3 shows the hourly energy demands on average demand days in February and August, respectively.

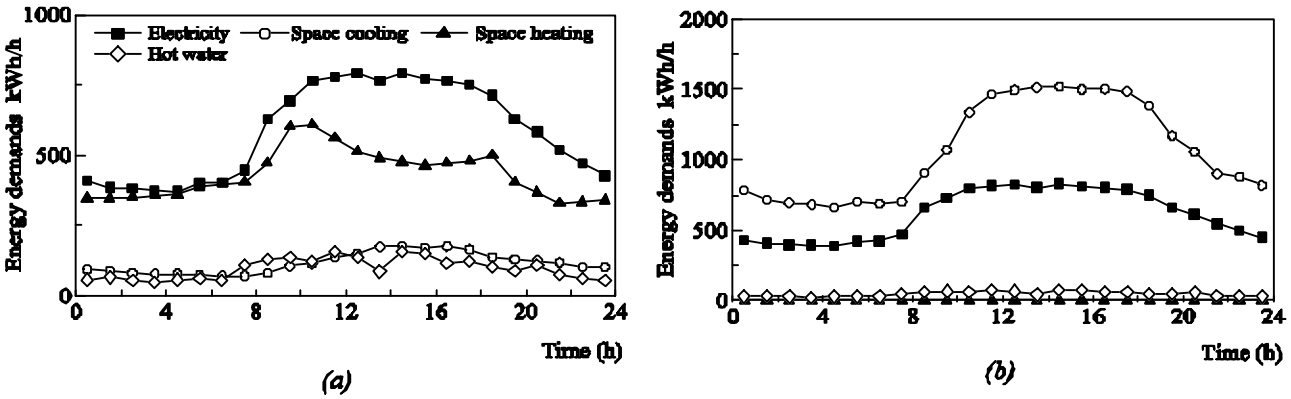

Fig. 3. Examples of hourly energy demands: a) February, b) August (Average demand days)

In this study, four initial systems are compared with one another, which are composed by combining four different types of equipment, respectively; i.e., the standard system (X_0=S_0), the gas system (G_0), the electrical system (E_0), and the hybrid system (H_0). Namely, S_0 is the system that exists really in the objective hospital and is selected as the standard for the comparison of four alternative initial systems. Explaining more in detail, S_0 is composed by a gas engine (GE), a steam absorption refrigerator (RS), a steam boiler (BS), and a hot water tank (HWT) as shown in Table 1. Next, X_0=G_0 is the system composed by GE, a gas-fired absorption refrigerator with gas engine waste heat utilization (GL), a gas-fired absorption refrigerator (RG), and HWT, X_0=E_0 is composed by an electric turbo-compression refrigerator (water cooling type) (RE), an electric heat pump using screw compressor for space heating and cooling (air cooling type) (HP), an electric heat pump using scrolling compressor for hot water supply(air cooling type) (EW), and a hot water tank for heat pump EWT, and X_0=H_0 is composed by RS, BS, a heat pump chiller using screw compressor (water cooling type) (CH), HP and HWT as shown in Table 1, respectively. The equipment capacities of these systems are also shown in Table 1, and they are determined that each initial system X_0 can supply required energy demands equivalently by applying a mathematical optimization method [1].

In the renewal planning problem, the superstructure of the renewal system is first set as shown in Fig. 4, where HB is a brine electric heat pump using screw compressor(air cooling type), and IST is an ice storage tank. The present renewal planning year is set as t_p = 7y, and each initial system X_0=S_0, G_0, E_0 or H_0 will be renewed to the respective renewal system X_1 at the renewal year $t = \tau$ as shown in Fig. 1. In this renewal year, some pieces of equipment are determined to be discarded from X_0, and some pieces are selected from the set of candidate pieces of equipment Y_1, and the renewal system X_1 will be composed by combining them. In this place, Y_1 is limited as the set of pieces of equipment indicated by the mark • for each standard(S), gas(G), electrical(E) and hybrid(H) systems as shown in Table 1, respectively. In this study, several cases of renewal plans are compared as shown in Table 2. As an example, the case G_0 - E_1 means the renewal plan where the initial system is set as X_0=G_0 shown in Table 1, and the set of candidate pieces of equipment installed newly is set as Y_1=E_1 shown in Table 1, respectively. In This place, the case S_0 - S_1 in Table 2 shows the standard case of renewal planning, where all pieces of equipment and their capacities of the renewal system X_1 are equal to those of the initial system X_0=S_0, respectively, and this renewal will be done at the year τ=15y.

In Table 3, economic values of capital and maintenance unit costs of each pieces of equipment at t=0 are shown together with their performance characteristic values, and performance improvement/deterioration rates, respectively. Rates for purchased electricity, natural gas, and water

Table 1. Alternative energy supply systems compared

	Initial system X_0				Candidate equipment Y_1			
Equipment	S_0	G_0	E_0	H_0	S_1	G_1	E_1	H_1
GE	○ 341 kW	○ 341 kW			•	•		•
RS	○ 2 780 kW			○ 1 293 kW	•	•		•
BS	○ 3 310 kW			○ 1 078 kW	•	•		•
GL		○ 783 kW				•		•
RG		○ 1 993 kW				•		•
RE			○ 1 340 kW				•	•
CH				○ 754 kW			•	•
HP			○ 1 435 kW	○ 729 kW			•	•
HB							•	•
EW			○ 302 kW				•	•
IST							•	•
EWT			○ 2 114 kWh				•	•
HWT	○ 600 kWh	○ 600 kWh		○ 600 kWh	•	•		•

○ initially existing equipment • candidate equipment installed newly

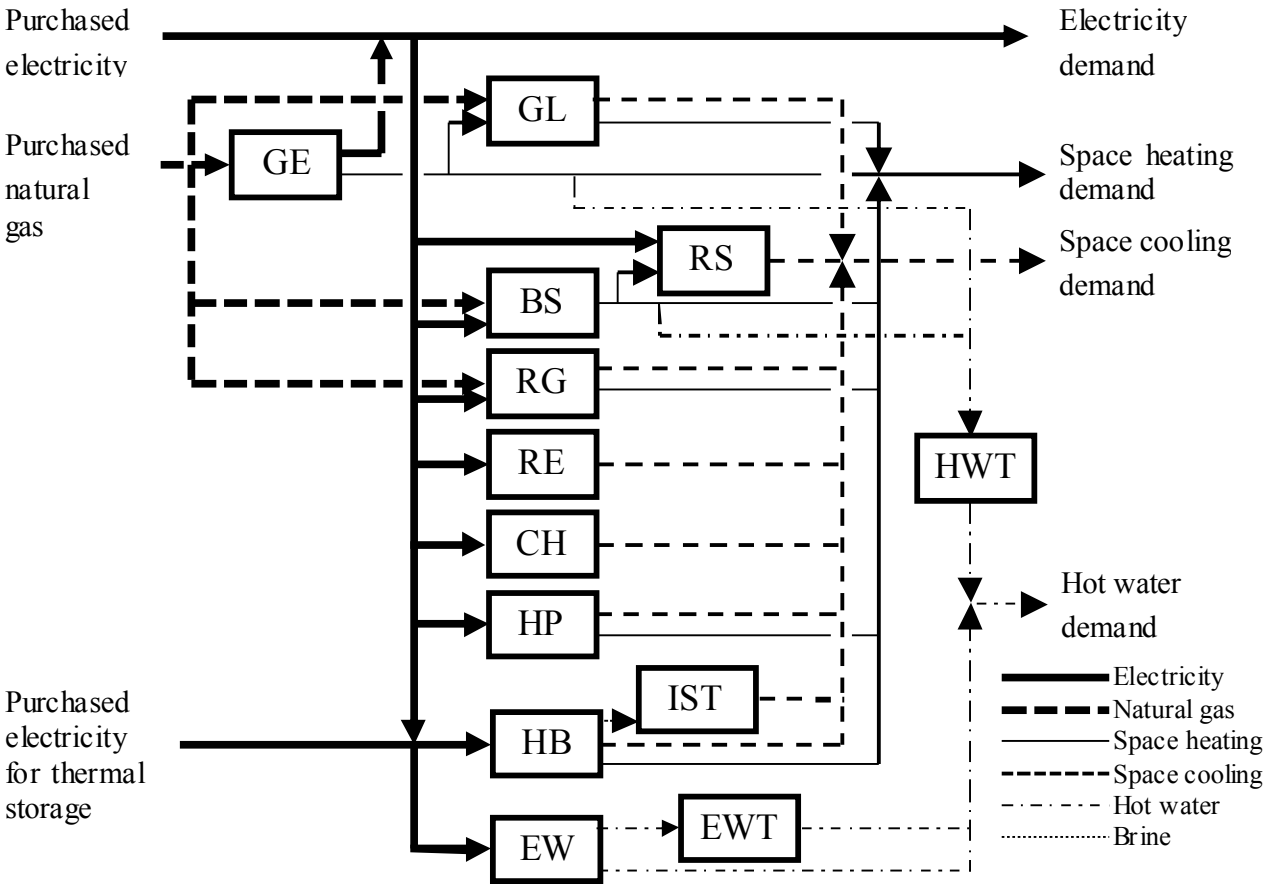

Fig. 4. Superstructure of renewal system

Table 2. Several cases of renewal plans compared

Case	Initial system X_0	Candidate equipment Y_1	Case	Initial system X_0	Candidate equipment Y_1
S_0 - S_1	Standard	Standard	E_0 - G_1	Electrical	Gas
S_0 - G_1	Standard	Gas	E_0 - E_1	Electrical	Electrical
S_0 - E_1	Standard	Electrical	E_0 - H_1	Electrical	Hybrid
S_0 - H_1	Standard	Hybrid	H_0 - G_1	Hybrid	Gas
G_0 - G_1	Gas	Gas	H_0 - E_1	Hybrid	Electrical
G_0 - E_1	Gas	Electrical	H_0 - H_1	Hybrid	Hybrid
G_0 - H_1	Gas	Hybrid			

are shown in Table 4. These data are actual rates used in the Kansai area, Japan. In evaluating the annual capital cost, it is assumed that κ=15y, and i=3%/y, respectively. The evaluation period of the system is set as T=15y, and other values of miscellaneous parameters are also shown in Table 5.

3.2. Numerical results and discussions

First of all, the optimal renewal planning problem has been solved numerically by assuming that four different types of initial system X_0= S_0, G_0, E_0 or H_0 is renewed to X_1 according to the plan shown in Table 2, respectively. Figure 5 shows the respective optimal value of annual total cost for each case of renewal system's plan mentioned above, where the annual capital cost of equipment

Table 3. Economic and performance values of each pieces of equipment (at t=0)

Equip-ment	Performance characteristic value		Performance improvement rate of equipment α %/y	Performance deterioration rate of equipment β %/y	Capital unit cost $a \times 10^3$ yen/kW $+ b \times 10^6$ yen		Maintenance unit cost yen/(kW·y)
					a	b	
GE	Power efficiency	0.31	0.0	0.50	181	0.0	3.20[#1]
	Thermal efficiency	0.45	0.0	0.0			
RS	COP	1.29	0.75	1.50	12.4	7.76	1 534
BS	Thermal efficiency	0.88	0.0	0.25	3.48	0.420	706
GL	Thermal efficiency (space cooling)	1.33	0.75	1.50	20.5	9.10	1 600
	Thermal efficiency (space cooling: Waste heat usage)	1.81	0.75	1.50			
	Thermal efficiency (space heating)	0.88	0.75	1.50			
RG	Thermal efficiency (space cooling)	1.32	0.75	1.50	19.1	7.14	1 534
	Thermal efficiency (space heating)	0.88	0.0	0.0			
RE	COP	6.12	1.00	0.50	18.4	15.8	1 230
CH	COP	5.45	1.00	0.50	23.5	1.01	1 883
HP	COP (space cooling)	4.30	1.50	0.50	39.8	0.0	1 422
	COP (space heating)	3.50	1.50	0.50			
HB	COP (brine for thermal storage)	3.35	1.50	0.50	90	1.11	2 161
	COP (space cooling)	3.97	1.50	0.50			
	COP (space heating)	3.22	1.50	0.50			
EW	COP (supplying hot water to tank)	4.10	1.50	0.50	120	0.0	1 422
	COP (supplying hot water directly)	1.86	1.50	0.50			
IST[#2]	Thermal loss (%/h)	1.0	0.0	0.0			
EWT[#2]	Thermal loss (%/h)	1.0	0.0	0.0			
HWT	Thermal loss (%/h)	1.0	0.0	0.0	5.89[#1]	0.0	0

[#1] yen/kWh
[#2] The capital initial and maintenance costs of IST and EWT are included in HB and EW, respectively.

Table 4. Rates of purchased electricity and natural gas (Kansai area, Apr. 2009)

Utility unit cost	Customer charge	Demand charge	Maximum demand charge	Energy charge
Electricity	–	1.69×10^3 yen/(kW·month)	–	(July~Sep.) 12.67 yen/kWh (Other months) 11.65 yen/kWh
Electricity for thermal storage	–	–	–	(22:00 ~ 8:00) 5.94 yen/kWh
Natural gas	25.4×10^3 yen/month	1334 yen/Nm^3·month	(7:00~10:00) 9.74 yen/Nm^3·month (10:00~7:00) 4.96 yen/Nm^3·month	79.31yen/Nm^3
Natural gas for cogeneration	8.62×10^3 yen/month	912 yen/Nm^3·month	(Dec.~Mar.) 1.33 yen/Nm^3·month	76.77yen/Nm^3
Water	–	–	–	550 yen/m^3

Table 5. Values of miscellaneous parameters

Item	Symbol	Value	Item	Symbol	Value
Present planning year	t_p	7 y	Surplus rate of system's capacity	λ	0.3
Total evaluation period of the system	T	15 y	Construction cost ratio of equipment	γ	0.4
Interest rate	i	3 %/y	Discarding cost ratio of equipment	μ	0.2
Residual cost ratio of equipment	ε	0	Increasing rate of maintenance cost after the end of statutory useful lifetime of equipment	θ	0.2
Statutory useful lifetime of equipment	κ	15 y			

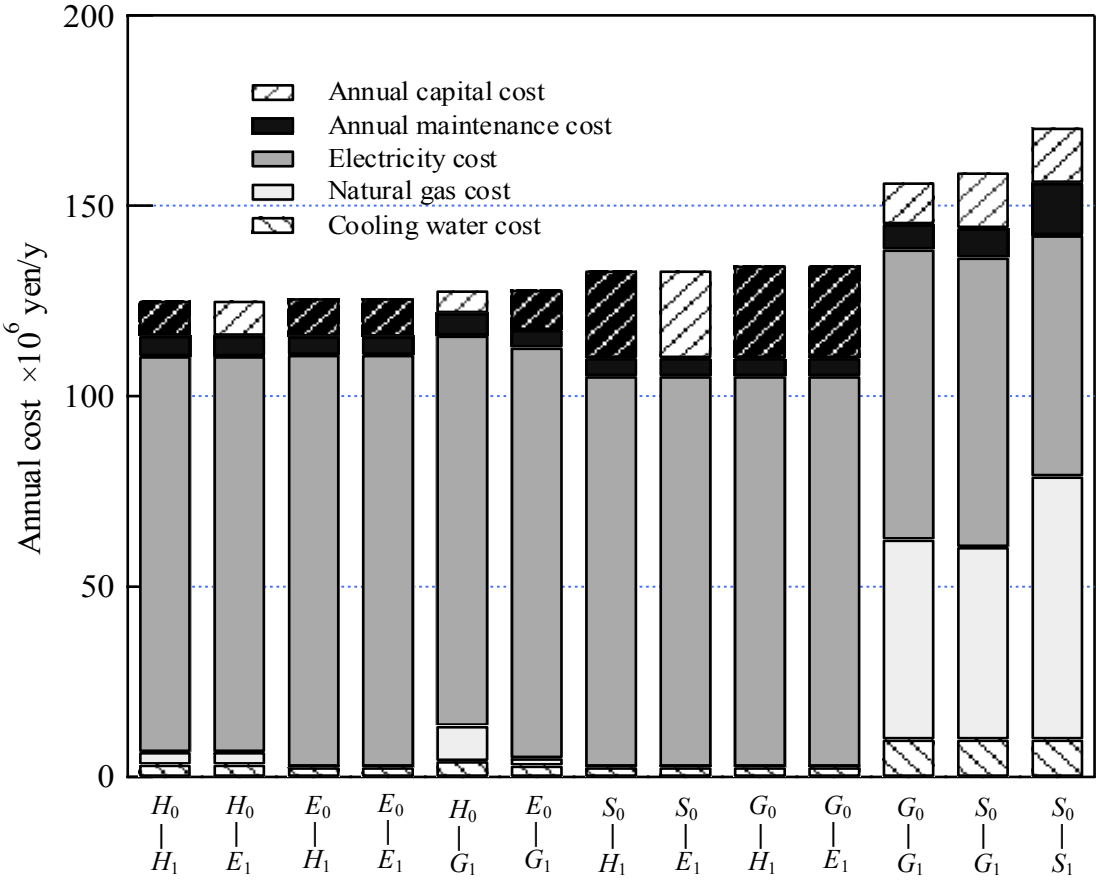

Fig. 5. Economic comparison of several renewal plans

includes the capital, construction and discarding costs. All these detailed costs are respective average values during the total evaluation period T shown in Fig. 1, which are calculated based on the annualized costs methods. In addition, the annual maintenance cost is also illustrated in this figure together with annual input energy costs of electricity and natural gas together with the cooling water cost. In Table 6, for each optimal renewal plans illustrated in Fig. 5, the optimal renewal year $\tau=\tau^*$, the annual costs, and the optimal structure of renewal system X_1 are shown, respectively.

In Table 6, for each optimal renewal plans illustrated in Fig. 5, the optimal renewal year $\tau=\tau^*$, the annual costs, and the structure of the renewal system X_1 are shown, respectively.

As shown in Fig. 5 and Table 6, the economically optimal renewal plan is H_0 - H_1 case in which it is permitted to install all candidate pieces of equipment at the renewal year $t=\tau$ as shown in Table 1. It is theoretically convinced that H system is economically superior to both E and G systems, because the candidate sets of pieces of equipment Y_1 are limited for the latter systems. However, it is very notable result that all solutions of S_0 - E_1 and S_0 - H_1, G_0 - E_1 and G_0 - H_1, E_0 - E_1 and E_0 - H_1, H_0 - E_1 and H_0 - H_1 are equal to corresponding each others, respectively. The economically worst case is S_0 - S_1, which is selected as the standard of renewal planning as explained in Section 3.1.

Next, Table 6 shows that the optimal renewal year τ^* is 7y for all cases of S_0 - E_1, S_0 - H_1, G_0 - E_1 and G_0 - H_1, respectively. All pieces of equipment of both S_0 and G_0 are composed of gas oriented ones as shown in Table 1, and this result shows that the early stage renewal is stimulated of discarding these pieces of equipment with relatively low energy efficiency, and to install pieces of electrical equipment with high energy efficiency. It is true that the electrical equipment with high performance characteristic value has high capital unit cost in general, but the ratio of the annual

Table 6. The structure of the renewal system for each optimal renewal plan (kW)

Case		S_0 - S_1	S_0 - G_1	S_0 - E_1 & S_0 - H_1	G_0 - G_1	G_0 - E_1 & G_0 - H_1	E_0 - G_1	E_0 - E_1 & E_0 - H_1	H_0 - G_1	H_0 - E_1 & H_0 - H_1
Optimal Renewal year τ^*		15	9	7	13	7	—	18	—	13
Annual total cost[#1]		170.6	158.8	133.1	156.1	134.4	125.9	125.7	126.4	125.1
Annual capital cost[#1]		14.6	14.7	23.0	11.0	24.3	9.5	10.0	5.5	9.2
Annual operational cost[#1]		142.3	136.4	105.3	138.5	105.3	111.8	110.9	115.1	110.5
Annual maintenance cost[#1]		13.7	7.7	4.8	6.6	4.8	4.6	4.8	5.8	5.4
Equipment of renewal system X_1	Initially existing equipment									
	GE	dis.[#2]	341	dis.	341	dis.	—	—	—	—
	RS	dis.	dis.	dis.	—	—	—	—	1293	dis.
	BS	dis.	dis.	dis.	—	—	—	—	1078	dis.
	GL	—	—	—	dis.	dis.	—	—	—	—
	RG	—	—	—	1993	dis.	—	—	—	—
	RE	—	—	—	—	—	1340	1340	—	—
	CH	—	—	—	—	—	—	—	754	754
	HP	—	—	—	—	—	1435	1435	729	729
	HB	—	—	—	—	—	—	—	—	—
	EW	—	—	—	—	—	302	302	—	—
	IST[#3]	—	—	—	—	—	—	—	—	—
	EWT[#3]	—	—	—	—	—	2114	2114	—	—
	HWT[#3]	600	600	600	600	600	600	600	600	600
	Equipment installed newly									
	GE	341	—	—	—	—	—	—	—	—
	RS	2780	1006	—	—	—	—	—	—	—
	BS	3310	808	—	—	—	—	—	—	—
	GL	—	—	—	—	—	—	—	—	—
	RG	—	1598	—	841	—	—	—	—	—
	RE	—	—	—	—	—	—	—	—	—
	CH	—	—	887	—	887	—	—	—	352
	HP	—	—	695	—	695	—	527	—	527
	HB	—	—	457	—	457	—	—	—	—
	EW	—	—	219	—	219	—	—	—	212
	IST[#3]	—	—	3199	—	3199	—	—	—	—
	EWT[#3]	—	—	1532	—	1532	—	—	—	1484

[#1] $\times 10^6$yen/y [#2] =discarded [#3] kWh

capital cost in the total annual cost is relatively low compared with the one of the annual operational cost (or input energy and water cost) as shown in Fig. 6. Therefore, this high capital unit cost doesn't prevent this early stage installing of new pieces of electrical equipment. However, the optimal renewal year τ^* becomes to be delayed as 9y for S_0 - G_1 and 13y for G_0 - G_1, and it is not necessary to renew these initial systems to the respective ones with gas oriented pieces of equipment very rapidly. For cases of H_0 - E_1 and H_0 - H_1, as H_0 contains both gas and electrical pieces of equipment, the optimal renewal year becomes τ^*=13y. However, for cases of E_0 - E_1 and E_0 - H_1, τ^*=18y, and it is not necessary to renew the initial system E_0 with high energy efficiency at the early year. Moreover, for cases of E_0 - G_1 and H_0 - G_1, the result in Table 6 shows that it is not necessary to renew this initial system within the system's evaluation period. In other words, it is

better economically to use the high energy efficiency system $X_0=E_0$ as long as possible, and there exists no need to renew this system to the gas one with equipment of relatively low energy efficiency.

Lastly, it is necessary to mention that from the practical engineering standpoint, the above discussed H system is rarely adopted because it arises relatively complex operational and maintenance labours and troubles in addition to the complexity of constructing this system.

4. Conclusion

In the study, the renewal planning problem of energy supply system for a hospital is formulated as a mathematical optimization one, in which the objective function to be minimized is the average value of annual total cost during the system's evaluation period. This optimization problem is a large-scale mixed-integer linear programming problem, and the programming language AMPL solver is adopted as the solving tool to derive the numerical optimal solution.

A numerical study is carried out for a hospital with the total floor area of 25 000m^2, and the analysis is particularly focused on the influence of the initial system on the renewal planning. Namely, the standard, gas electrical and hybrid systems are selected as initial systems, and 13 cases of renewal plans are compared with each others.

Through this numerical study, the following results are mainly obtained:

a) It is notable result that the structure of initial system influences strongly on the optimal renewal year $t=\tau^*$.

b) Theoretically, the hybrid system is of course the best renewal one. However, there is no economic difference between the hybrid and the electrical systems.

c) If the initial system is gas one, it is better to renew it to the electrical one as soon as possible due to relatively low energy efficiency of the gas utilizing pieces of equipment, the high price of gas input energy in Japan, and so on.

d) If the initial system is electrical one, the optimal renewal year becomes relatively later year, because it is economically better to use the initial system with high energy efficiency as long as possible.

e) It is economically better not to renew the electrical system with high energy efficiency to the gas system with low efficiency during the evaluation period of the system.

Acknowledgments

The authors would like to thank members of the Research Group for Total Energy Systems Analysis, the Society of Electric Enhancement in Buildings for their support and cooperation.

Nomenclature

i Interest rate, %/y

$\boldsymbol{P}$ Diagonal matrix composed of performance characteristic values of each pieces of equipment

t Year variable, y

t_p Present planning year, y

$\boldsymbol{u}$, $\boldsymbol{v}$ Vectors composed of input and output energy flow rates of each pieces of equipment, respectively, kWh/h

$\boldsymbol{x}$ Vector composed of the capacities of each pieces of equipment, kW

$\boldsymbol{y}$ Vector composed of utility maximum contract demands, kW, m^3/h

C Annual capital cost, yen/y

E Electrical system

G Gas system

H Hybrid system

J Average annual total cost during the system's evaluation period, yen/y

M Annual maintenance cost, yen/y

O Average value of annual operational cost, yen/y

S Standard system

T Total evaluation period of the system, y

X_0 Initial system

X_1 Renewal system

Y_1 Set of candidate pieces of equipment installed newly at the renewal year

Greek symbols

$\boldsymbol{\alpha}$ Vector composed of performance improvement rates of each pieces of equipment, %/y

$\boldsymbol{\beta}$ Vector composed of performance deterioration rates of each pieces of equipment, %/y

γ Construction cost ratio

$\boldsymbol{\delta}$ Vector composed of binary variables related to the selection of each pieces of equipment

ε Residual cost ratio at the end of the statutory useful lifetime of equipment

θ Increasing rate of maintenance cost after the end of statutory useful lifetime of equipment

κ Statutory useful lifetime, y

λ Surplus rate of system's capacity for each category of energy demands

μ Discarding cost ratio of equipment

τ Renewal year, y

Subscripts and superscripts

BS Steam boiler

CH Heat pump chiller using screw compressor(water cooling type)

EW Electric heat pump using scrolling compressor for hot water supply(air cooling type)

EWT Hot water tank for heat pump

GE Gas engine

GL Gas-fired absorption refrigerator with gas engine waste heat utilization

HB Brine electric heat pump using screw compressor(air cooling type)

HP Electric heat pump using screw compressor for space heating and cooling(air cooling type)

HWT Hot water tank

IST Ice storage tank

RE Electric turbo-compression refrigerator(water cooling type)

RG Gas-fired absorption refrigerator

RS Steam absorption refrigerator

References

[1] Yokoyama R, Hasegawa K, Ito K. A MILP decomposition approach to large scale optimization in structural design of energy supply systems. 2002; Energy Conversion and Management 43: 771-790.

[2] Yoshida S, Gamou S, Ito K, Enokido T, Yokoyama R. An optimal renewal planning of energy supply system from an economic viewpoint. In: Proceedings of International Conference on Power Engineering (ICOPE); 2005; B: 1477-1483.

[3] Yoshida S, Inoue M, Okano A, Ito K, Amano Y, Hashizume T. Comparative study on renewal planning of alternative energy supply systems for a hospital. In: Proceedings of Conference ECOS; 2011:150-157.

[4] Yoshida S, Ito K, Amano Y, Matsuo K, Hashizume T, Ueta K. A multi-stage optimal renewal planning for energy supply system from an economic viewpoint. In: Proceedings of International Conference on Power Engineering (ICOPE); 2009; 3: 173-178.

[5] Amano Y, Ito K, Yoshida S, Matsuo K, Hashizume T, Favrat D, Marechal F. Impact analysis of carbon tax on the renewal planning of energy supply system for an office building. 2010; Energy 35: 1040-1046.

[6] Yoshida S, Ito K, Amano Y, Hashizume T. Multi-objective optimal renewal planning of energy supply systems for buildings from economic and environmental viewpoints. In: Proceedings of ECOS; 2008; 1545-1552.

[7] Witte L C, Schmidt P S, Brown D R. Industrial energy management and utilization. Hemisphere Pub. Corp.; 1988: 68-69.

[8] Adjiman C S, Schweiger C A, Floudas C A. In: Du D- Z, Pardalos P M, editor. Mixed-integer nonlinear optimization in process synthesis. Handbook of combinatorial optimization; 1 Doradrecht; Kluwer Academic Pub.; 1998: 1-76.

[9] Robert F, David M G, Brain W K. AMPL-A modelling language for mathematical programming. Second ed.; Thomson brooks/Cole; 2003.

Effects of insulation and phase change materials (PCM) combinations on the energy consumption for buildings indoor thermal comfort

[a]C. Tzivanidis, [b]K.A. Antonopoulos,[c]E.D. Kravvaritis

[a]National Technical University of Athens (N.T.U.A.),
School of Mechanical Engineering, Thermal Engineering Department,
Refrigeration and Air-Conditioning Laboratory, Solar Energy Laboratory
9, Heroon Polytechniou, Zografou 157 73, Athens, Greece
ctzivan@central.ntua.gr, ***CA***
[b]N.T.U.A., kanton@central.ntua.gr
[c]N.T.U.A., lkravvaritis@gmail.com

Abstract

It is known that, under usual insulation characteristics, placing a phase change material (PCM) layer at the outdoor side of buildings exterior walls insulation offers negligible profit as the latter obstructs PCM in the exchange of heat with the indoor environment. On the contrary, considerable energy profit is obtained by placing a PCM layer at the indoor side of the exterior walls insulation, provided that there is opposite fenestration, which allows PCM loading by the incoming solar radiation. If opposite fenestration does not exist, there is no solar radiation profit, as the insulation layer obstructs heat exchange between PCM and outdoor environment. However, the above known behavior of exterior walls containing PCM and insulation layers may be different if we change insulation characteristics (i.e. layers thickness and/or specific thermal conductivity). In the present study a numerical procedure has been developed for the simulation of PCM and insulation combined effect on buildings transient thermal behavior. It was found that, under winter conditions, if PCM layer is placed at the indoor side of the insulation, a proper decrease of insulation thickness will facilitate PCM loading by the solar radiation incident on the outdoor wall surface and the gain from the loading increase will be higher than the heat loss increase provoked by the decrease of insulation effectiveness. In the opposite case, i.e. if PCM is placed at the outdoor side of the insulation, it was found that the decrease of insulation effectiveness will lead to favorable results only in extreme values combinations of the parameters involved.

Keywords

Phase change materials, PCM, insulation and PCM combination, buildings thermal behavior, buildings heating energy consumption.

Nomenclature

A	Area (m^2)
B	Initial temperature field (K or ^oC)
b	Temperature width of PCM phase change
C_p or C	Thermal capacity (J/kg K)
$C_{p,eff}$	Effective thermal capacity (J/kg K)
G_T	Incident total solar radiation (W/m2)
g	Radiation heat-transfer factor (W/m2K)
H	Phase change heat (KJ/kg)
h	Convection heat transfer coefficient (W/m^2K)
k	Thermal conductivity (W/mK)
L	Normalized Radiation Losses (K or oC)
m	Mass (kg)

Q Indoor load (W)
q Heat flow (W/m^2)
R Absorbed solar radiation by a wall (W/m^2)
S Exterior tube surface (m^2)
T Temperature (K or ^oC)
T_o Equivalent outdoor temperature (K or ^oC)
T_l , T_s Temperatures at the ends of two-phase region (K or oC)
T_m , T_r PCM and reference fluid temperatures, respectively (K or oC)
t Time (s)
U Overall heat transfer coefficient of a wall or rood (W/m^2K)
v Volume (m^3)
x Cartesian coordinate (m)

Greek symbols
α Absorption coefficient for incident solar radiation
ρ Density ($kg//m^3$)
τ Fenestration transmission coefficient for solar radiation

Subscripts
a Refers to air
amb Refers to the ambient

1. Introduction

A promising heat or cool storage technique in buildings applications is related to the use of Phase Change Materials (PCM), which may provide up to five times (in case of organic PCM) or even up to ten times (in case of inorganic PCM) higher storage capacity than the conventional construction materials [1]. Classifications of organic and inorganic PCM, advantages, disadvantages, applications and general information about them may be found, among others, in refs. [2-4]. Examples from the more recent studies concerning passive PCM applications in buildings may be found in refs. [5-8]. In these, innovative ideas on the PCM use are presented, while in refs [9-12] attention focuses on parametric studies and optimizations. Refs. [13-15] refer to investigation of PCM behavior under various boundary conditions, including weather conditions (ambient temperature and solar radiation) at specified locations and days or seasons of the year. However, the literature survey showed that little work has been done on the effects of the combinations of PCM and insulation characteristics on the energy consumption for buildings heating.

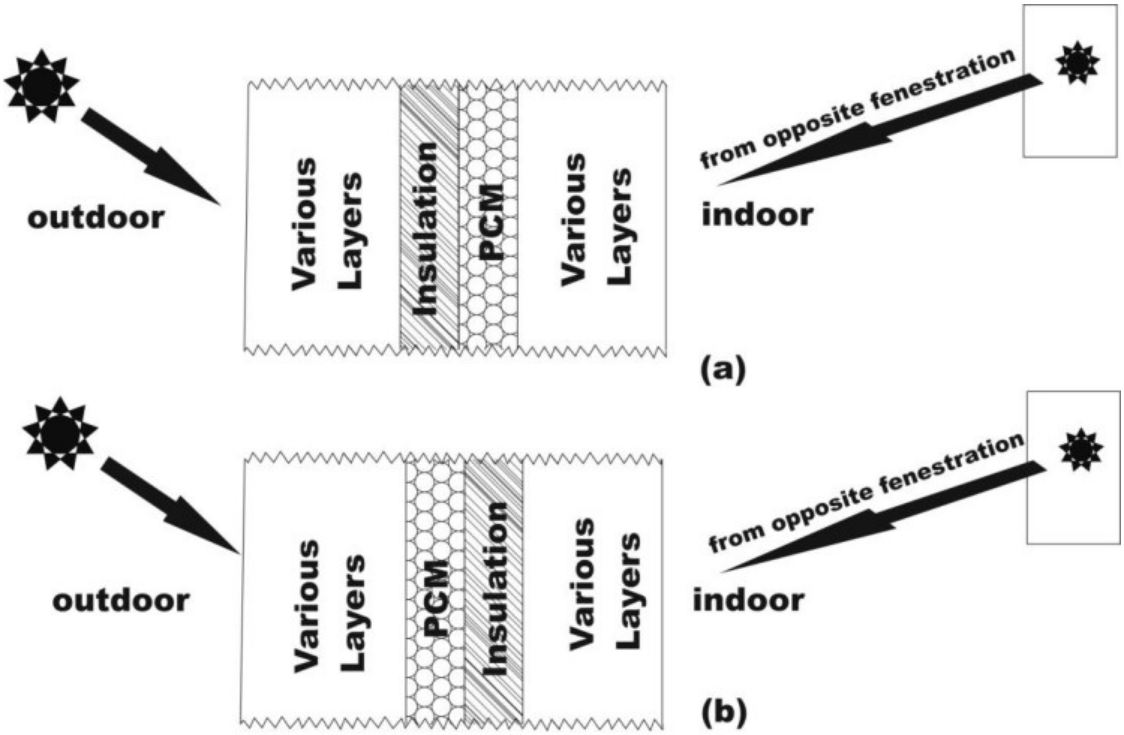

Fig. 1. Relative position of PCM – insulation layers within building's exterior walls and solar radiation incident onto the outdoor wall surface and/or the indoor wall surface through opposite fenestration. PCM layer is located at the: (a) indoor side of the insulation layer, (b) outdoor side of the insulation layer.

The objective of the present study is to contribute on the analysis of the above subject, which has received little attention thus far. In our recent publications [16,17] concerning passive PCM buildings applications, the effect of twelve parameters on heating and cooling energy consumption was investigated. One of the conclusions of the above studies was that considerable energy profit is obtained by placing a PCM layer at the indoor side of the exterior walls insulation (Fig. 1(a)), provided that there is opposite fenestration, which allows PCM loading by the incoming solar radiation. If opposite fenestration does not exist, there is no solar radiation profit, as the insulation layer obstructs PCM loading by the solar radiation incident on the outdoor surface of the exterior wall. However, the above known behavior of exterior walls containing PCM and insulation layers may be different if we change insulation characteristics (i.e. layers thickness and/or specific thermal conductivity). For example, a decrease of insulation thickness may facilitate PCM loading by the solar radiation incident on the outdoor wall surface, if PCM layer is placed at the indoor side of the insulation. In the opposite case, i.e. if PCM is placed at the outdoor side of the insulation (Fig. 1(b)), PCM loading by the incident solar radiation can easily take place but the insulation obstructs heat exchange between PCM and the indoor space. In this case a decrease of insulation thickness may facilitate heat exchange between PCM and indoor environment. The purpose of the present study is to analyze the effects of the various values combinations of insulation and PCM characteristics on buildings thermal behavior.

The above outlined transient thermal problem is analyzed by using a developed numerical procedure, which solves, by finite difference means, a set of differential equations describing buildings transient thermal behavior. The study is conducted by testing an extensive number of values combinations of PCM and insulation characteristics in a Typical Greek Reference House (TGRH) under the outdoor conditions (temperature and solar radiation) of the Athens typical winter. PCM phase change process is simulated by the Effective Thermal Capacity Model [18,19]

in conjunction with the Thermal Delay Method [20,21]. The latter has been developed by the present authors for the measurement of PCM "effective thermal capacity".

2. Simulation procedure of PCM and insulation combined effect on buildings transient thermal behavior

2.1 Transient thermal analysis of buildings

Existing codes for the transient thermal analysis of buildings, for example [22,23], required extensive modifications for the purposes of our study. Therefore, it was decided to develop a numerical procedure adjusted exactly to the present needs. The new procedure follows simulation methods developed in our previous studies, related to buildings transient thermal behavior [24-32] and tested against experimental data and other numerical predictions [17,19,28]. Only a brief description of the developed simulation procedure will be given below, containing mainly the new points introduced. It is assumed that significant temperature variations are observed only in the direction normal to buildings extended surfaces, as for example are the envelope elements (i.e. exterior walls, fenestration, roof and floor). Therefore, the instantaneous temperature $T_{ej}(t,x)$ of any layer j of envelope element e, composed of J layers (including PCM and insulation layers) at time t and depth x, measured from the outdoor surface, may be calculated from the transient one-dimensional heat conduction differential equation supplemented by the appropriate boundary conditions, i.e.

$$\rho_{ej}C_{ej}\partial T_{ej}(t,x) / \partial t = k_{ej}\partial^2 T_{ej}(t,x) / \partial x^2 \quad , \quad x_j \le x \le x_j + B_{ej} \quad , \quad j = 1, 2, \ldots, J \qquad (1)$$

$$q_{o,e}(t) = h_o[\, T_o(t) - T_{e1}(t,x)\,] \quad , \quad x = 0 \qquad (2)$$

$$q_{i,e}(t) = h_i[T_{eJ}(t,x) - T_i(t)] \; + \; \Sigma_v g_{e,v}[\, T_{eJ}(t,x) - T_v(t)] + R_e(t) \quad , \quad x = x_J + B_{eJ} \qquad (3)$$

where ρ_{ej}, c_{ej}, k_{ej} and B_{ej} denote the density, thermal capacity, thermal conductivity and thickness of each layer j of multilayer element e, respectively; and x_j, x_j+B_{ej} are the coordinates of the jth layer surfaces of element e; $T_i(t)$, $q_{i,e}(t)$ and h_i stand for the indoor air temperature, the heat flow and the convection heat-transfer coefficient at interior surface of envelope element e, respectively, while $T_o(t)$, $q_{o,e}(t)$ and h_o are the corresponding quantities for the outdoor surface. Σ_v expresses summation over indoor surfaces; $g_{e,v}$ is the radiation heat-transfer factor between indoor surface of envelope element e and any other indoor surface v of temperature $T_v(t)$. The solar radiation incident on outdoor walls or roof surface is introduced by using the sol-air temperature concept [33]. The term $R_e(t)$ expresses the part of solar radiation transmitted through any opposite fenestration, and the parts of all other radiative loads (i.e. lighting, equipment, people, etc), which are absorbed by the indoor surface of any envelope element e, apart from fenestration. For the latter, the solr-air temperature [33] $T_o(t)$ is replaced by the real outdoor temperature $T_{amb}(t)$, the term $R_e(t)$ is omitted and the parts of incident solar radiation or other radiative loads absorbed are introduced as source terms in the transient heat conduction differential equation (1). On the lower surface of floors directly in contact with the ground, or over an underground non-ventilated basement, adiabatic boundary conditions are imposed [33].

The instantaneous temperature $T_{pj}(t,x)$ of any layer j of multilayer indoor partitions (i.e. indoor walls, ceilings and floors) is calculated from the transient one-dimensional heat conduction differential equation, supplemented by the appropriate boundary conditions, i.e.

$$\rho_{pj}C_{pj}\partial T_{pj}(t,x) / \partial t = k_{pj}\partial^2 T_{pj}(t,x) / \partial x^2 \quad , \quad x_j \le x \le x_j + B_{pj} \quad , \quad j = 1, 2, \ldots, J \qquad (4)$$

$$q_{p1}(t) = h_i[T_{p1}(t,0) - T_i(t)] + \Sigma_v g_{p,v}[T_{p1}(t,0) - T_v(t)] + R_{p1}(t) \quad (5)$$
$$q_{pJ}(t) = h_i[T_{pJ}(t, x_J + B_{pJ}) - T_i(t)] + \Sigma_v g_{p,v}[T_{pJ}(t, x_J + B_{pJ}) - T_v(t)] + R_{pJ}(t) \quad (6)$$

where symbols in eq.(4) have analogous meaning as in eq.(1); $q_{p1}(t)$ and $q_{pJ}(t)$ are the heat flows at the two sides 1 and J of partition p at time t, respectively, while $T_{p1}(t,0)$ and $T_{pJ}(t, x_j+B_{pJ})$ stand for temperatures of these sides at which the convection heat-transfer coefficient is h_i ; $T_i(t)$ denotes the indoor air temperature; Σ_v expresses summation over all indoor surfaces v of temperature $T_v(t)$, and $g_{p,v}$ is the radiation heat-transfer factor between these surfaces and partitions sides. The parts of solar radiation, transmitted through opposite fenestration, and of any other radiative load (i.e. from lighting, people, equipment, etc.) which are absorbed by partition sides 1 and J are denoted by terms $R_{p1}(t)$ and $R_{pJ}(t)$, respectively.

Furniture is simulated by equivalent multilayer slabs composed of the usual furniture materials (i.e. wood, plastics, glass, textile matter, metal, etc.). The temperature distribution $T_{fj}(t,x)$ within the equivalent slabs is predicted by using the indoor partitions eqs. (4)-(6) with subscript p replaced by f.

Indoor thermal energy balance may be expressed by differential equation:

$$m_a C_a \partial T_i(t)/\partial t = Q_o(t) \quad (7)$$

where $T_i(t)$, m_a and C_a are the temperature at time t, the mass and the thermal capacity of indoor air, respectively, while $Q_o(t)$ contains the heat loads delivered to the indoor air from all sources, i.e.

$$Q_o(t) = \Sigma_e q_{i,e}(t) A_e + [q_{p1}(t) + q_{pJ}(t)]A_p + [q_{f1}(t) + q_{fJ}(t)]A_f + Q_v(t) + Q_i(t) + Q_e(t) \quad (8)$$

where the first term denotes the sum of heat flows from envelope elements e with heat transfer surfaces A_e and the second and third terms express the heat flows from indoor partitions and equivalent furniture slabs with heat-transfer surfaces A_p and A_f, respectively; $Q_v(t)$ is the ventilation and infiltration heat load; $Q_i(t)$ expresses the convective parts of loads from all indoor sources (lighting, people, equipment, etc.) as well as the parts of solar radiation and other radiative indoor loads absorbed by the indoor air. The last term $Q_e(t) \geq 0$ or $Q_e(t) < 0$ is the heat power provided by the heating or cooling equipment, respectively.

Equations (1)-(8), together with the equations for the equivalent furniture slabs, form a set of differential equations, which is solved as described very briefly below (details may be found in ref. [34]. First, initial conditions ($t=t_o=0$) are prescribed for the temperature fields $T_{ej}(t_o,x)$, $T_{pj}(t_o,x)$ and $T_{fj}(t_o,x)$ within the envelope, indoor partitions and equivalent furniture slabs, respectively, as well as for the indoor air temperature $T_i(t_o)$. Then, the temperature fields $T_{ej}(t_o+\Delta t , x)$, $T_{pj}(t_o+\Delta t , x)$ and $T_{fj}(t_o+\Delta t , x)$ at the next time level $t=t_o+\Delta t$ are calculated by employing a usual implicit finite-difference technique [35]. The indoor air temperature $T_i(t+\Delta t)$ at any time level $t+\Delta t$ is calculated from the discretized form of differential eq.(7), using the known temperature fields of the previous time level, i.e.

$$T_i(t+\Delta t) = T_i(t) + Q_o(t)\Delta t/m_a C_a \quad (9)$$

The above step is repeated until the 24-hours period is completed. Then, solution is repeated with identical outdoor conditions until convergence to the "periodic steady-state" is obtained, in which solution repeats itself every 24 hours. Convergence criterion was set to 0.01^oC. Grid dependence tests defined space grid finess $\Delta x=0.001$ m for the insulation layers and $\Delta x=0.002$ m for al other materials. Time step was $\Delta t=60$ s.

2.2 Simulation of PCM phase change process

The most widely-used models for the simulation of phase change process in numerical calculations are the Enthalpy Method [36] and the Effective Thermal Capacity Method [18,19]. The former, which is based on a numerical solution of the enthalpy transport differential equation, is suitable for predicting details related to the mechanism of phase change process. In the present study, phase change is interesting only as a macroscopic phenomenon without need of predicting further details. Therefore, the Effective Thermal Capacity Method has been selected, as it is simpler and more easily incorporated into the numerical procedure than the Enthalpy Method. The selected method considers that PCM thermal capacity during phase change is a function of temperature, usually called "the effective thermal capacity function" $C_{p,eff}(T)$. The only difficulty is that the $C_{p,eff}(T)$ function for any PCM used, should be known. Functions $C_{p,eff}(T)$ for the PCM used in the present study have been determined experimentally using the "Thermal Delay Procedure", developed by the present authors and described in ref. [20,21]. For completeness reasons, a very brief outline of the developed procedure is given below together with an example of $C_{p,eff}(T)$ function derived and used in the present analysis.

According to our "Thermal Delay Procedure", which is an improved version of the well-known T-history method [37], two glass tubes containing liquid PCM and a reference fluid, respectively, are cooled until the complete PCM solidification within a controlled environment test chamber of constant temperature T_a, lower than the PCM solidification temperature T_s. The PCM and reference fluid temperatures $T_{m,k}$ and $T_{r,k}$ respectively, are measured during the cooling process at any time t_k , with a time step $(t_{k+1} - t_k)$. The effective thermal capacity corresponding to temperature $T= (T_{m,k} + T_{m,k+1})/2$ is calculated from equation [20,21,30]:

$$C_{p,eff}(T)=M\,(T_{r,k} -T_{r,k+1})(T_{m,k}+T_{m,k+1}-2T_a) / (T_{m,k}-T_{m,k+1})(T_{r,k}+T_{r,k+1}-2T_a) - N \quad (10)$$

where,

$$M = (m_{tr}C_{ptr} + m_rC_{pr})A_{tm} / m_mA_{tr} \quad (11)$$

$$N = m_{tm}C_{ptm} / m_m \quad (12)$$

In the above equations m_m and m_r are the PCM and reference fluid mass, respectively; C_{pr} is the reference fluid heat capacity; m_{tm}, C_{ptm} and A_{tm} denote the mass, heat capacity and exterior surface of the tube containing the PCM, while m_{tr}, C_{ptr} and A_{tr} stand for the corresponding quantities for the tube containing the reference fluid.

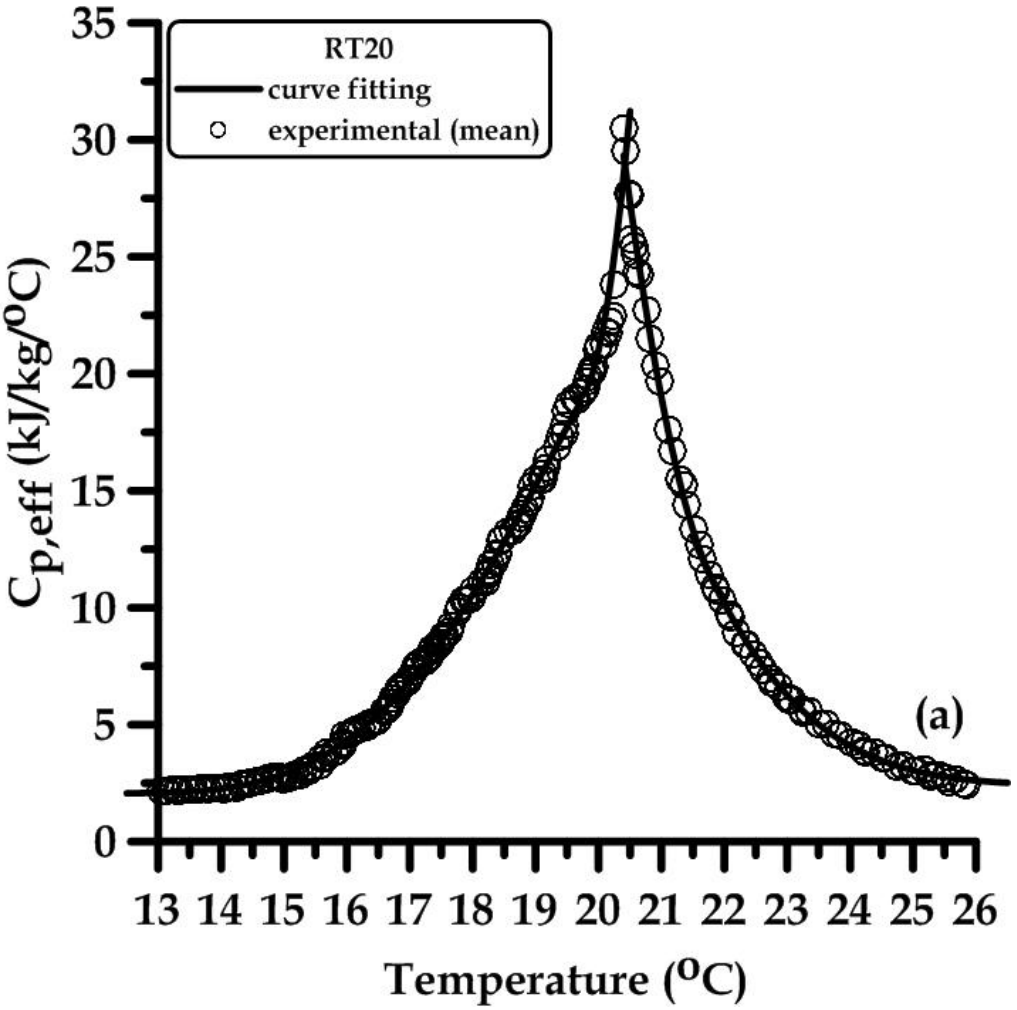

Fig. 2. Experimentally determined effective thermal capacity function $C_{p,eff}(T)$ for Rubitherm paraffin RT20 [38].

An example of experimentally determined effective thermal capacity function $C_{p,eff}(T)$, for Rubitherm Company [38] paraffin under trade name RT20 is shown in Fig. 2. The point symbols correspond to the experimentally derived values ($C_{p,eff}$, T) according to eq.(10), while the line represents an analytical approximation by curve fitting to the ($C_{p,eff}$, T) points, given below

$$C_{p,eff}(T) = 444.4711352 - 170.5210626T + 25.80658991T^2 - 1.912462169T^3 + 0.06910480624T^4 - 0.0009667426392T^5 \quad \text{for } 15^oC \leq T \leq 19.5^oC \tag{13}$$

$$C_{p,eff}(T) = 5529.086311 - 565.4394794T + 14.50378915T^2 \quad \text{for } 19.5^oC < T \leq 20.5^oC \tag{14}$$

$$C_{p,eff}(T) = 3780.001949 - 342.8478233T + 7.797040983T^2 \quad \text{for } 20.3^oC < T \leq 22^oC \tag{15}$$

$$C_{p,eff}(T) = 3735.906512 - 536.9879458T + 28.98735267T^2 - 0.6959772441T^3 + 0.006270432248T^4 \quad \text{for } 21.5^oC < T \leq 26^oC \tag{16}$$

Figure 2 also shows that the value of $C_{p,eff}(T)$ function remains constant before and after phase change region, thus providing a way to determine the temperatures T_s and T_l at the ends of the two phase region, as well as the solid and liquid PCM thermal capacities C_{ps} and C_{pl} , respectively. These values and the values of $C_{p,eff}(T)$ are used in eq.(1) for the thermal capacity C_{ej} when j denotes the PCM layer.

3. Typical Greek Reference House (TGRH)

The values combinations effects of insulation and PCM characteristics on the heating energy consumption of buildings will be examined by conducting tests on a Typical Greek Reference House (TGRH). Definition of the TGRH has been obtained by conducting a limited research on Greek Houses and "averaging" their characteristics taking also into account the related Hellenic Directive published in the Official Government Gazette Issue 407/9-4-2010, which is based on the European Union Directive 91/2000 on the energy performance of buildings. Although TGRH characteristics are similar to those used in previous studies on related subjects [16,17,39], they are repeated below very briefly for the sake of completeness: 100 m^2 detached one-storey house of square shape with roof composed of 2 cm interior finishing layer, 15 cm reinforced concrete slab, W_i = 4 cm insulation thickness with specific thermal conductivity k_i=0.038 W/mK, and 10 cm of usual exterior waterproof and concrete mixtures layers; floor constructed from 10 cm upper floor tiles with cement mixture sub-layers, 4 cm insulation layer, 10 cm reinforced concrete slab and adiabatic condition at the lower boundary [33]; exterior walls composed of 2 cm exterior finishing layer, 9 cm brickwork, insulation of the same thickness W_i and thermal conductivity k_i as in the roof, 9 cm brickwork and 2 cm interior finishing layer; indoor walls of 20 m length made of single bricks with 2 cm finishing layers on both sides; outdoor and indoor convection coefficients 16 W/m^2 ^{o}C and 8 W/m^2 ^{o}C, respectively; light-coloured exterior envelope surface with absorption coefficient for solar radiation 0.44; the four sides of the house are oriented towards the four main orientations and each one is composed of P_f=25% fenestration with overall heat transfer coefficient U_f=3.5 W/m^2 K; constant ventilation of 0.5 indoor air change per hour; 0.85 fenestration transmission coefficient for solar radiation; 5% of the transmitted solar radiation is absorbed by the indoor air, while the remaining radiation is absorbed by the wall opposite to fenestration and released later. The typical year hourly values of ambient temperature and solar radiation for the Athens area have been used, taken from refs [40-42]

4. PCM layer located at the exterior walls

The analysis made in our previous publications [16, 17], supported also by additional tests in the present study, showed that considerable energy saving is obtained by adding PCM to interior or exterior walls opposite fenestration. The attention of the present study is focused on the exterior walls and especially on the effects of the combinations of PCM and insulation characteristics as well as on the relative position of insulation and PCM layers on the energy consumption for building heating. As implied in the introduction, considerable energy profit is obtained by placing a PCM layer at the indoor side of exterior walls insulation (Fig. 1(a)), provided that there is opposite fenestration, which allows PCM loading by the incoming solar radiation. If PCM layer is placed at the outdoor side of the insulation (Fig. 1(b)), its loading by the solar radiation incident onto buildings envelope, can easily take place but the insulation obstructs heat exchange between PCM and indoor space, unless a decrease of insulation effectiveness is made. The following analysis is based on the predictions obtained by the developed simulation model and the corresponded computer code presented in Section 2. Both cases of PCM -insulation relative positions, shown in Fig. 1, are examined in the following two sections.

4.1 PCM layer located at the indoor side of exterior walls insulation

A schematic representation of the physical situation examined is shown in Fig. 1(a). Although an extended number of values combinations of the parameters involved have been tested, only the most important cases are presented for space limitation reasons. These correspond to: (i) a passive heating system (i.e. term $Q_e(t)$ in eq. (8) is set to zero); (ii) PCM properties are as follows: phase change temperature range from 9.5°C to 14.5°C, 2 cm PCM layer thickness, 1 W/mK thermal conductivity, 140 kJ/kg phase change heat; (iii) solar radiation is reduced by 50% to simulate shading from adjacent buildings or other obstacles as well as the mean cloudy Athens 21 January [41,42]; (iv) the TGRH described in Section 3 is modified so that fenestration percentages on the south, east and west sides are 10%, 5% and 5%, respectively. No fenestration exists on the north exterior wall.

The most important cases, which present theoretical and practical interest, are related to the locations of indoor walls within the TGRH, as follows:
(a) Figure 3 shows the predicted indoor air temperature as a function of the time for 1 cm and 4 cm insulation layer thicknesses, for the TGRH case illustrated within the same figure: PCM layer is located at the indoor side of exterior walls insulation (PCM IN) and only a N-S direction interior wall exists, which does not enable solar radiation, entering through the east and west direction fenestration, to be absorbed by the PCM of the west and east exterior walls, respectively. Therefore, only the north wall PCM layer is loaded by the solar radiation entering through the south fenestration. The south, east and west walls PCM layers are also loaded by the solar radiation incident on the buildings envelope but to a much lesser extent, as the insulation layers, which are located at the outdoor sides of the PCM layers, obstruct their loading. The figure shows that by decreasing insulation layers thickness from 4 cm to 1 cm, an increase of PCM loading is obtained which leads to about 0.3°C indoor temperature increase.

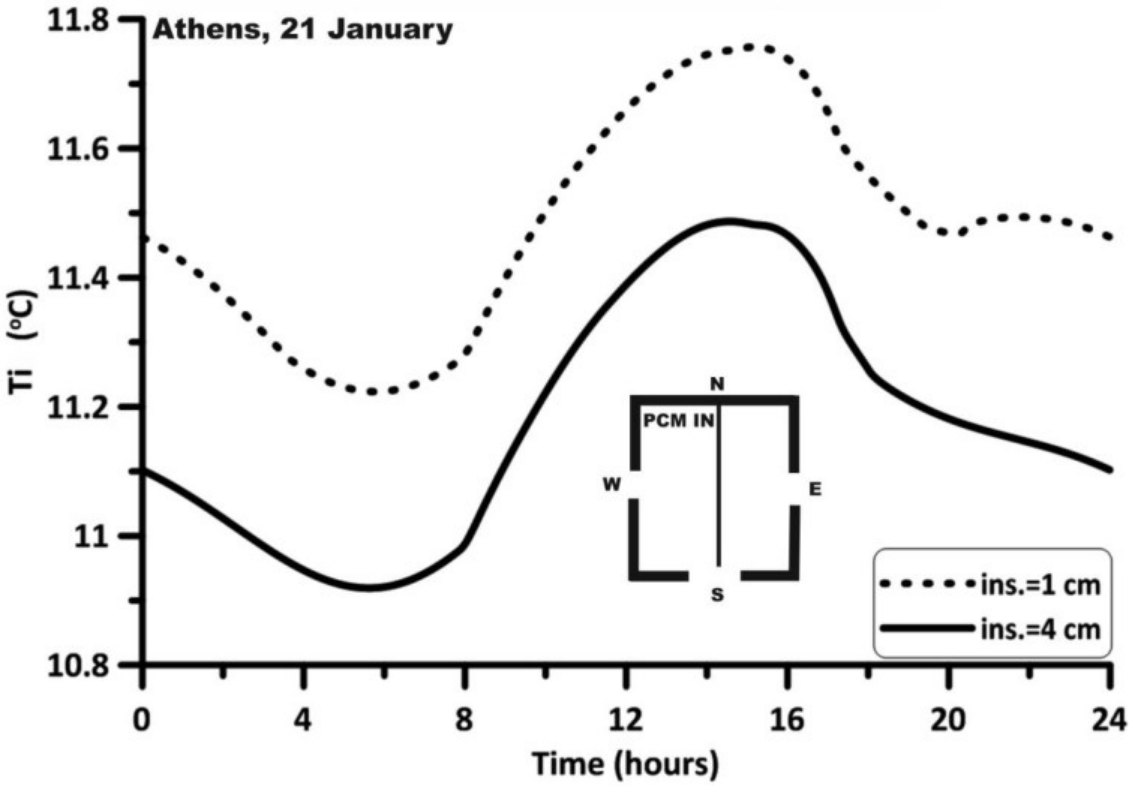

Fig. 3. Predicted indoor air temperature in terms of the time for 1 cm and 4 cm insulation layers thicknesses. PCM layers are located at the indoor sides of the insulation layers and only a N-S direction interior wall exists.

(b) Analogous results are shown in fig. 4, but here the indoor wall is located in the E-W direction. Now, the east and west walls PCM layers are loaded by the solar radiation entering through the west and east fenestration, respectively. Also, solar radiation incident onto the building envelope provides a low loading, which increases with decreasing insulation thickness, but the gain obtained is again small (≈ 0.4°C indoor temperature increase).

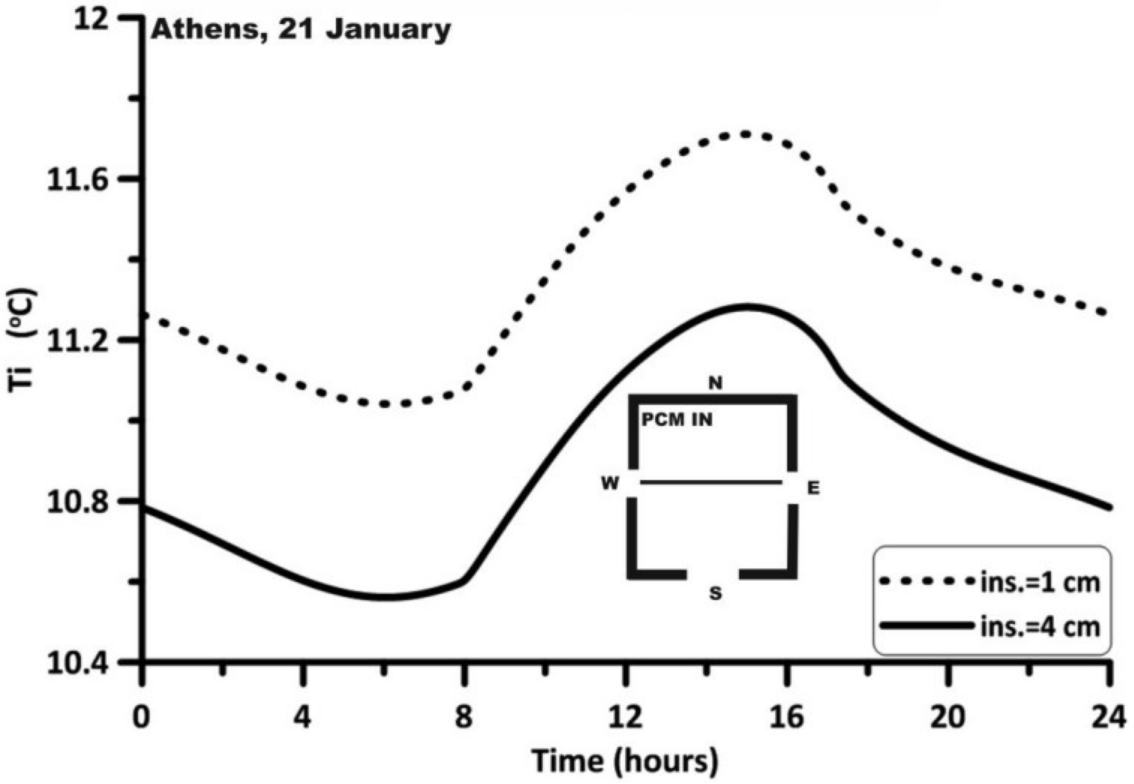

Fig. 4. As in Fig. 3, but with only an E-W direction interior wall.

(c) Indoor walls have been totally removed in Fig. 5, so that the north, east and west walls PCM layers are loaded by the solar radiation entering through south, west and east fenestration, respectively. Also, radiation incident onto the buildings envelope provides a low loading, which increases with decreasing insulation thickness. Here, the gain obtained by the decrease of the insulation thickness is lower than that of the previous cases (i.e. less than 0.2°C indoor temperature increase). This happens because, when PCM is loaded from both sides, the insulation effect decreases owing to the lower temperature differences between PCM and adjacent layers.

(d) In the case of Fig. 6, indoor walls of N-S and E-W directions have been inserted, which do not allow PCM loading by the solar radiation entering though the fenestration. Now, PCM loading is exclusively obtained by the solar radiation incident onto buildings envelope. Therefore, insulation effect is more pronounced, i.e. a decrease of insulation layer thickness from 4 cm to 1 cm provokes an indoor temperature increase of about 0.7°C.

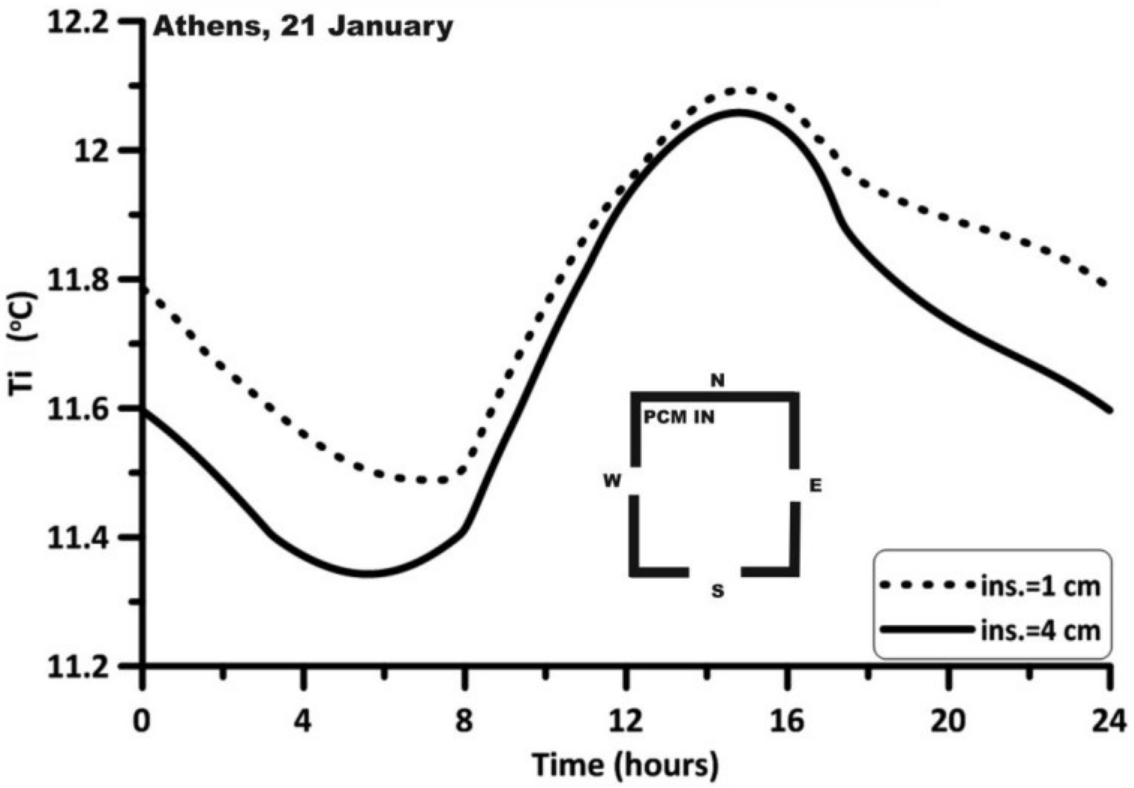

Fig. 5. As in Fig. 3, but without interior walls.

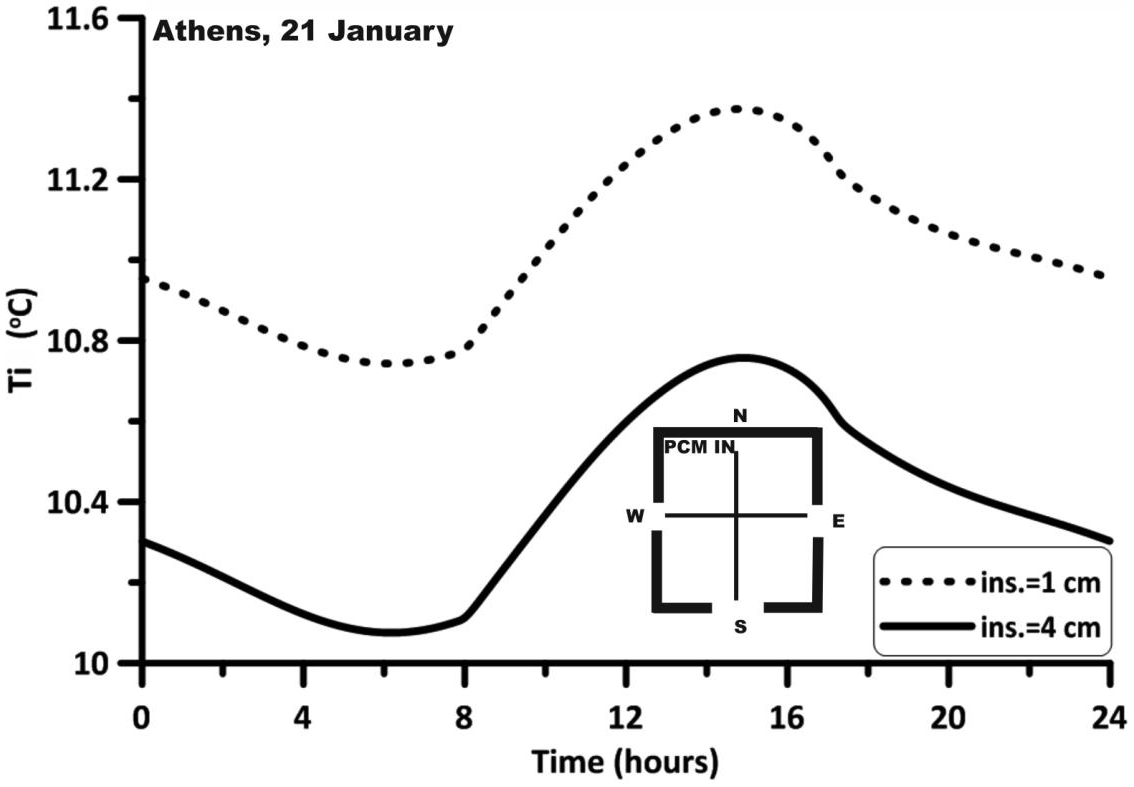

Fig. 6. As in Fig. 3, but with interior walls of N-S and E-W directions.

4.2 PCM layer located at the outdoor side of exterior walls insulation

A schematic representation of the physical situation examined is shown in Fig. 1(b). In this case, the effect of insulation layer thickness and/or specific thermal conductivity on PCM effectiveness is lower and in some cases opposite to that of the previous cases depending on the construction and operational parameters of the problem. Therefore, decreases of the insulation layer thickness provoke slightly higher or lower indoor temperature. An example is shown in fig. 7, where the TGRH appears with indoor walls of N-S and E-W directions. Therefore, PCM loading is exclusively obtained by the solar radiation incident onto buildings envelope. Here, PCM loading by the incident solar radiation can easily take place but the insulation layers, which are located at the indoor PCM sides, obstruct heat exchange between PCM and the indoor space. In the present example a decrease of the insulation layers thickness form 4 cm to 1 cm provokes an increase of the indoor temperature from 0.02°C to 0.21 °C.

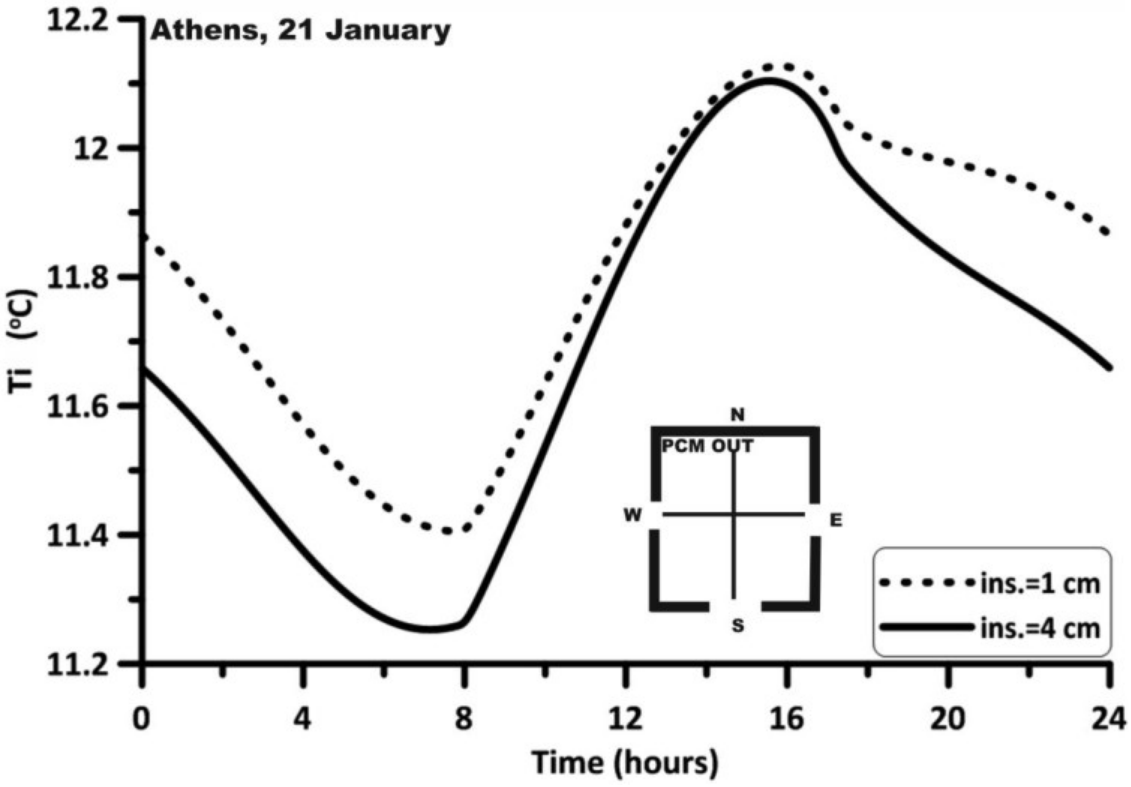

Fig. 7. As in Fig. 3, but with interior walls of N-S and E-W directions and PCM layers located at the outdoor sides of the insulation layers.

5. CONCLUSION

A numerical procedure has been developed for the simulation of PCM and insulation combined effect on buildings transient thermal behavior. The procedure is based on a finite-difference solution of a set of differential equations describing buildings transient thermal behavior. Phase change process is simulated by the "Effective Thermal Capacity Method" [18,19], in which the "effective thermal capacity function" $C_{p,eff}(T)$ of the various PCM, tested in the present study, has been determined experimentally using the "Thermal Delay Procedure", developed by the present authors [20,21].

The present analysis was made under passive heating conditions and refers to the exterior walls where insulation layers are located in all contemporary buildings. Characteristic predictions

are shown in Figs. 3-7, although a great volume of cases has been solved referring to extended ranges of the parameters involved, i.e. PCM thermophysical properties, buildings design, construction and operational parameters and weather conditions including shading and cloudiness conditions along the Athens typical winter. The results presented (Figs. 3-7) correspond, in some way, to the mean values of the parameters examined. Predictions corresponding to the extreme values of the parameters ranges examined differ up to 30% of the predictions presented.

For the heating period it was found that, if PCM layer is placed at the indoor side of the insulation (Fig. 1(a)), a proper decrease of insulation thickness will facilitate PCM loading by the solar radiation incident on the outdoor wall surface and the gain from the loading increase will be higher than the heat loss increase provoked by the decreased insulation effectiveness. For example, during the typical Athens January, a decrease of the insulation layer thickness from 4 cm to 1 cm will provide an indoor air temperature increase up to 1 ^{o}C, depending on PCM thermophysical properties, climatological conditions and operational and construction parameters, as well as the design of the buildings.

In the opposite case, i.e. if PCM is placed at the outdoor side of the insulation (Fig. 1(b)), it was found that a decrease of insulation layer thickness will facilitate heat exchange between the loaded PCM and indoor environment but the gain obtained may be lower of higher than the heat loss increase provoked by the decrease of insulation effectiveness. For example, during the typical Athens January, a decrease of insulation layer thickness from 4 cm to 1 cm will provide an indoor air temperature change ΔT in the range $-1<\Delta T<1$, depending on PCM thermophysical properties, weather conditions and operational and construction parameters as well as the design of the buildings.

It is concluded that PCM effectiveness is higher if PCM layers are located at the indoor sides of the exterior walls insulation layers than at the outdoor sides. The effect of insulation layer thickness and/or thermal conductivity on PCM effectiveness is considerable only under proper values combinations of PCM thermophysical properties, buildings design, construction and operational parameters, as well as climatological conditions. The proper parameters combinations may be found by the finite-difference simulation procedure developed in the present study. The existence of fenestration opposite exterior walls highly improves PCM effectiveness.

References

[1] Zalba B, Marín JM, Cabeza LF, Mehling H. Review on thermal energy storage with phase change: materials, heat transfer analysis and applications, Applied Thermal Engineering 2003;23:251–283.

[2] Khudhair AM, Farid MM. A review on energy conservation in building applications with thermal storage by latent heat using phase change materials, Energy Conversion and Management 45 (2004) 263–275.

[3] Abhat A. Low temperature latent heat thermal energy storage: Heat storage materials. Solar energy 1983;30:313-332.

[4] Lane GA. Solar Heat Storage: Latent Heat Materials, 1983, Vol. I, Background and Scientific Principles, CRC Press.

[5] Medina MA, King JB, Zhang M. On the heat transfer rate reduction of structural insulated panels (SIPs) outfitted with phase change materials (PCMs). Energy 2008; 33:667-678.

[6] Borreguero AM, Carmona M, Sanchez ML, Valverde JL, Rodriguez FJ. Improvement of the thermal behaviour of gypsum blocks by the incorporation of microcapsules containing PCMS obtained by suspension polymerization with an optimal core/coating mass ratio. Applied Thermal Engineering 2010; 30:1164-1169.

[7] Chen C, Guo H, Liu Y, Yue H, Wang C. A new kind of phase change material (PCM) for energy-storing wallboard. Energy and Buildings 2008; 40:882-890.

[8] Evers AC, Medina MA, Fang Y. Evaluation of the thermal performance of frame walls enhanced with paraffin and hydrated salt phase change materials using a dynamic wall simulator. Building and Environment 2010;45:1762-1768.
[9] Kuznik F, Virgone J, Noel J. Optimization of a phase change material wallboard for building use. Applied Thermal Engineering 2008;28:1291-1298.
[10] Khalifa AJN, Abbas EF. A comparative performance study of some thermal storage materials used for solar space heating. Energy and Buildings 2009;41:407-415.
[11] Potvin FM, Gosselin L. Thermal shielding of multilayer walls with phase change materials under different transient boundary conditions. Int. Journal of Thermal Sciences 2009;48:1707-1717.
[12] Liu H, Awbi HB. Performance of phase change material boards under natural convection. Building and Environment 2009;44:1788-1793.
[13] Shilei Lv, Neng Z, Guohui F. Impact of phase change wall room on indoor thermal environment in winter. Energy and Buildings 2006;38:18-24.
[14] Huang MJ, Eames PC, Hewitt NJ. The application of a validated numerical model to predict the energy conservation potential of using phase change materials in the fabric of a building. Solar Energy Materials and Solar Cells 2006;90:1951-1960.
[15] Kuznik F, Virgone J. Experimental assessment of a phase change material for wall building use. Applied Energy 2009;86:2038-2046.
[16] C. Tzivanidis, K.A. Antonopoulos, E.D. Kravvaritis, Numerical evaluation of the degree of phase change materials exploitation in building passive solar heating and cooling, 24th Int. Conf. ECOS 2011, Novi Sad, Serbia, pp. 2007-2021.
[17] E.D. Kravvaritis, K.A. Antonopoulos, C. Tzivanidis, Solar energy management using PCM passive systems in the Athens area buildings, Energy Conversion & Management, under publication 2012.
[18] Darkwa K, O'Callaghan PW. Simulation of phase change drywalls in a passive solar building, Applied Thermal Engineering 2006;26:853-858.
[19] Kuznik F, Virgone J, Roux JJ. Energetic efficiency of room wall containing PCM wallboard: A full-scale experimental investigation. Energy and Buildings 2008;40:148-156.
[20] Kravvaritis ED, Antonopoulos KA, Tzivanidis C. Improvements on the measurement of the thermal properties of phase change materials (PCM), Meas. Sci. Technol. 2010;21045103(9pp).
[21] Kravvaritis ED, Antonopoulos KA, Tzivanidis C. Experimental determination of the effective thermal capacity function and other thermal properties for various phase change materials using the thermal delay method. Applied Energy, under publication 2012.
[22] TRANSYS, A transient simulation program, Solar energy laboratory, University of Wisconsin, Madison, WI, U.S.A., 1990.
[23] EPS-r, A transient simulation program, Energy Systems Research Unit (ESRU), Strathclycle University, Glascow, 1998.
[24] K.A. Antonopoulos, C. Tzivanidis, Finite-difference prediction of transient indoor temperature and related correlation based on the building time constant, Int. Journal of Energy Research 20 (1996) 507-520.
[25] K.A. Antonopoulos, Analytical and numerical heat transfer in cooling panels, Int. J. Heat Mass Transfer 35 (1992) 2777-2782.
[26] K.A. Antonopoulos, F. Democritou, Periodic steady-state heat transfer in cooling panels, Int. J. Heat and Fluid Flow 14 (1993) 94-100.
[27] K.A. Antonopoulos, C.Tzivanidis, Numerical solution of unsteady three-dimensional heat transfer during space cooling using ceiling-embedded piping, Energy 22 (1997) 59-67.
[28] K.A. Antonopoulos, M. Vrachopoulos, C. Tzivanidis, Experimental and theoretical studies of space cooling using ceiling-embedded piping, Applied Thermal Engineering 17 (1997) 351-367.
[29] C. Tzivanidis, K.A. Antonopoulos, E.D. Kravvaritis, Parametric analysis of space cooling systems based on night ceiling cooling with PCM-embedded piping, Int. J. of Energy Research (in press), Wiley on line Library DOI:10.1002/er.1777.

[30] C. Tzivanidis, K.A. Antonopoulos, E.D. Kravvaritis, Transient three-dimensional numerical solution of night ceiling cooling using PCM-embedded piping. J. of Energy Engineering, under publication, 2012.
[31] K.A. Antonopoulos, E. Koronaki, Envelope and indoor thermal capacitance of buildings, Applied Thermal Engineering 19 (1999), 743-756.
[32] K.A. Antonopoulos, E. Koronaki, Effect of indoor mass on the time constant and thermal delay of buildings, Int. J. of Energy Research, 24 (2000) 391-402.
[33] American Society of Heating, Refrigerating and Air-Conditioning Engineers. ASHRAE Fundamentals, Atlanta, GA, 1993.
[34] C. Tzivanidis, K.A. Antonopoulos, F. Gioti, Numerical simulation of cooling energy consumption in connection with thermostat operation mode and comfort requirements for the Athens buildings, Applied Energy, under publication, 2012.
[35] S.V. Patankar, Numerical Heat Transfer and Fluid Flow, Hemisphere Publishing Corporation, McGraw-Hill Book Company, 1980.
[36] Costa M, Buddhi D, Oliva A. Numerical simulation of a latent heat thermal energy storage system with enhanced heat conduction, Energy Comers. Mgmt. 1998;39:319 – 330.
[37] Yinping Z, Yi J, Yi J: A simple method the T –history method, of determining the heat of fusion, specific heat and thermal conductivity of phase-change materials, Meas. Sci. Technol. 1999;10:201–205.
[38] www.rubitherm.com
[39] C. Tzivanidis, K.A. Antonopoulos, F. Gioti, Computational analysis of the envelope parameters effects on the transient heating energy consumption of buildings, 24th Int. Conf. ECOS 2011, Novi Sad, Serbia, pp. 1894-1908.
[40] Kouremenos DA, Antonopoulos KA, Rogdakis E. Performance of solar NH_3/H_2O absorption cycles in the Athens area. Solar Energy 1987;39:187-195.
[41] Kouremenos DA, Antonopoulos KA, Domazakis ES. Solar radiation correlations for the Athens, Greece, area. Solar Energy. 1985;35:259-269.
[42] Kouremenos DA, Antonopoulos KA, Doulgerakis S. Direct and diffuse solar radiation correlations for tilted surfaces in the Athens, Greece. Solar Energy, 1987; 38:203-217.

Energetic evaluation of a smart controlled greenhouse for tomato cultivation

N.Van den Bulck[a], M. Coomans[b], L. Wittemans[c], K. Goen[d], J. Hanssens[e], K. Steppe[f], H. Marien[g], J. Desmedt[h]

[a] Flemish Institute for Technological Research (VITO), Mol, Belgium, nickey.vandenbulck@vito.be
[b] Flemish Institute for Technological Research (VITO), Mol, Belgium, mathias.coomans@vito.be
[c] Research Station for Vegetable Production, Sint-Katelijne-Waver, Belgium, Lieve.wittemans@proefstation.be
[d] Research Center Hoogstraten, Hoogstraten, Belgium, Kris.Goen@proefcentrum.be
[e] Lab. of Plant Ecology, Dpt. of Applied Ecology and Environmental Biology, Ghent University, Ghent, Belgium, jochen.hanssens@ugent.be
[f] Lab. of Plant Ecology, Dpt. of Applied Ecology and Environmental Biology, Ghent University, Ghent, Belgium, kathy.steppe@ugent.be
[g] Katholieke Hogeschool van de Kempen, Geel, Belgium, herman.marien@khk.be
[h] Flemish Institute for Technological Research (VITO), Mol, Belgium, johan.desmedt@vito.be

Abstract:

Greenhouse plant cultivation is an energy-demanding industry, especially in colder regions like Western Europe. The increase in yield and the year-round production of greenhouse cultivation comes with high investment and operational costs in comparison to other agricultural activities. Due to the high percentage of energy costs in the total production cost, alternative energy systems are needed. An innovative ventilation system can provide optimal climatic conditions inside the greenhouse without the excessive heat loss of a traditional installation. Therefore, an innovative ventilation-concept has been implemented in the Research Station for Vegetable Production at Sint-Katelijne-Waver, Belgium, and results have been compared to a traditional operated greenhouse compartment. The pilot compartment is equipped with double thermal screens, which reduce the heat loss to the ambient environment. Furthermore, the mechanical ventilation enables the extensive use of these double screens together with a better control of the incoming air rate compared to the traditional ventilation method of opening greenhouse windows. In both the ventilated and traditional greenhouse, temperature, relative humidity, CO2 concentration, energy consumption and control strategies were registered during the first year of use in 2010. In this paper these measurements are presented to determine the potential of the concept in terms of energy savings, improved yield and investment costs.

Keywords:

Greenhouse; Ventilation; Energy management; Tomato

1. Introduction

Greenhouse farming is an energy consuming part of horticulture in Flanders, Belgium. By maintaining a stable indoor climate, it becomes possible to obtain large crop yields throughout the year [1]. However, greenhouses require high investments and are accompanied by significant energy consumptions when using additional heating. According to Ghosal et al. [2], a shift should be made to low-cost heating systems. New available technologies include phase changing materials, use of a rock bed, a ground air collector, an earth-to-air-heat exchanger system and an aquifer coupled cavity flow heat exchanger system. Several systems were surveyed and evaluated by Sethi and Sharma [1]. They concluded that the use of these heating systems involves high installation and operational costs that the user has to bear. Due to the increase and instability of energy prices and ongoing pressure from international competition, it remains of importance to search for energy efficient solutions without reducing yield or crop quality.

Most modern greenhouses are using thermal screens to reduce thermal losses. The screens decrease the convective heat transfer and, to lesser extent, the radiative losses. The resulting insulation improvements can save significant quantities of fuel, especially during night heating [3]. Applying multiple screens will result in a better insulation performance than merely improving screen radiation characteristics [1] and allows for more intensive screening due to different screen characteristics. Some disadvantages of screens include poor mechanical reliability, incomplete sealing after closure and condensation damage to curtains and plants [1]. Intensive screening may also lead to higher humidity levels as it restricts indoor air movement and diminishes dehumidification by condensation on the greenhouse surface. Excessive humidity may increase the probability of plant infection with fungal diseases e.g. Botrytis and will enhance mineral depletion [4,5]. In addition, crop growth may be affected, anatomical changes may occur and plant development can be distributed or delayed. High levels of humidity directly affect the crop yield and quality, making it an important factor in greenhouse horticulture and a restrictive factor for the use of thermal screens.

Humidity control in greenhouses is mostly achieved by natural ventilation. Moist indoor air is replaced with dry outside air by opening the greenhouse windows. This dehumidification process is ideal when excess heat is available (e.g. summer), but energy loss occurs when warm greenhouse air is replaced by colder outside air (e.g. winter), lowering indoor temperature and thus diminishing the effects of thermal screening [6]. Besides ventilation, one should also consider indoor temperature and concentration of gases such as CO_2 when striving towards optimal humidity control [5]. Greenhouses employing natural ventilation are considered to be 'open' systems. While it provides a cost effective means to maintain the indoor climate, the efficiency is dependent on several environmental parameters such as wind speed and direction, temperature distribution, window geometry, ... which makes the natural ventilation process difficult to control [5,7,8]. Greenhouse dehumidification and cooling can therefore easily exceed demand, resulting in higher energy consumptions [8]. Some studies describe open greenhouses to be less efficient when cooling is needed on sunny days without wind [9,10]. Additionally, an open window can cause a local cold downdraught, which can result in crop damage [11].

When eliminating natural ventilation by keeping the windows shut as much as possible, the greenhouse can be operated as a 'closed' system. Humidity and temperature should then be controlled by a mechanical ventilation unit. Opposed to natural ventilation, fan driven ventilation has shown no significant dependency on the external wind and the internal buoyancy forces [12]. This independency manifests itself in an increased control over ventilation rates. Carpenter and Bark [13] showed that mechanical air circulation reduces the vertical temperature gradients and eliminates the high temperature build-up in the ridge area of the greenhouse. Moreover, mechanical ventilation can reduce the inside temperature significantly during warm conditions [14].

Sealing off the greenhouse and improving thermal insulation with screens may not guarantee an overall energy reduction. A study conducted by the University of Wageningen discussed the monitoring of nine closed and semi-closed greenhouses [15]. Total heat demand of the closed system proved to be slightly higher than that of an open system. Additionally, mechanical ventilation (and dehumidification in particular) used a fair amount of electricity. The benefits of an improved insulation might therefore be outweighed, making the system economically unviable. It was recommended to add natural ventilation as an option for climate control next to the ventilation system. Raaphorst et al. [16] concluded that a realistic return on investment could be achieved with higher gas prices and / or lower electricity prices. The energy savings are primarily obtained by the application of multiple thermal screens, which is made possible by controlled dehumidification with a ventilation unit. An alternative solution is thus found in the combination of natural ventilation with a mechanical ventilation system. A so called 'semi-closed' system provides an inexpensive control of the indoor climate and can switch between natural or mechanical ventilation depending on energetic and economical considerations. The purpose of the mechanical ventilation is to postpone the need for natural ventilation, which should allow for an increase in thermal screen usage and a reduction of heat demand.

This paper reports on the results obtained in the Research Station for Vegetable Production at Sint-Katelijne-Waver, Belgium, for the growing season of 2010. It involves a semi-closed greenhouse that uses a ventilation unit in combination with two retractable thermal screens. The results are compared to a reference greenhouse that only uses natural ventilation for climate control. An overview of the technical installation is presented along with an analysis of energy use and system performance.

2. System description

2.1. Greenhouse configuration

The greenhouse at the research facility has been divided into several compartments. A 'ventilated' compartment is equipped with a 'ClimecoVent' system and is located in compartment 1, as shown in Fig.1. The installation consists of two thermal screens in combination with a mechanical ventilation unit. The ClimecoVent installation is commercially available and has been selected for its potential to reduce energy costs without strongly increasing initial expenditures or sacrificing yield and thus profitability of the greenhouse. The ventilated compartment is monitored alongside a 'reference' compartment that is also equipped with two screens, but uses natural ventilation to maintain the indoor climate. The reference case is located in compartment 6 and has the same dimensions and crop characteristics.

An important difference between the compartments is found in their location within the greenhouse. While compartment 6 is enclosed by three other heated compartments and has one side bordering the hallway, compartment 1 is adjacent to only one heated compartment, a non-heated hallway, a ventilation unit and an exterior wall. Because of this significant difference in boundary conditions, the ventilated compartment will face more heat loss through its boundary walls than the reference case. This was confirmed by measurements taken during a winter period under specific conditions (closed compartments, no screens, no crops, equal temperature). The difference in energy consumption was estimated at 20 % in favour of the reference greenhouse.

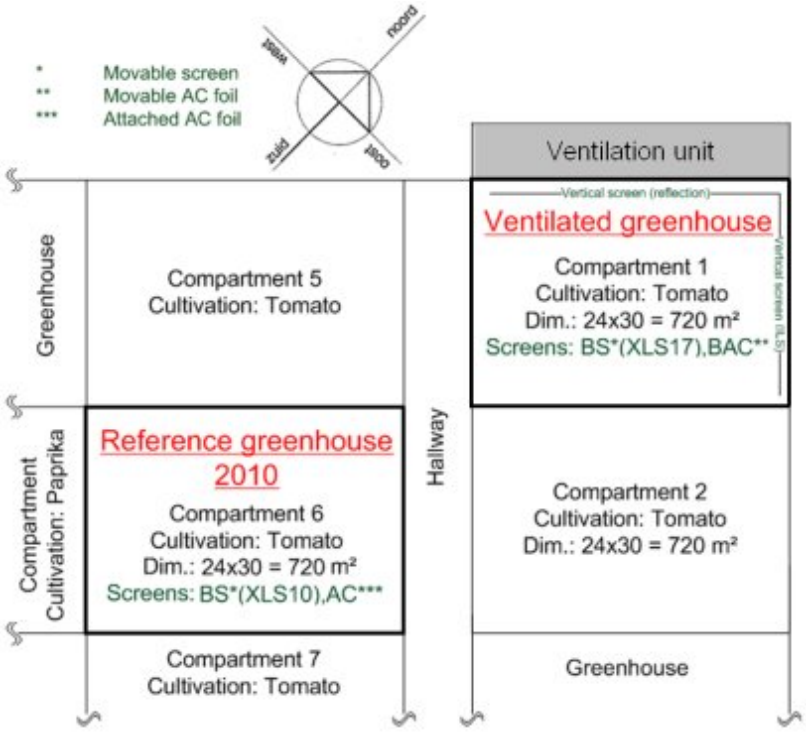

Fig.1. Sketch of the Research Station for Vegetable Production.

2.2. Experimental set-up and monitoring

2.2.1. Thermal screens

The ventilated and reference greenhouse are both equipped with two thermal screens as given in Table 1. In the ClimecoVent concept of the ventilated greenhouse, two movable screens are used. One is a 'XLS 17 firebreak' screen which has high thermal insulating qualities at the cost of optical transmission and could therefore only be closed during night-time to prevent crop damage due to light deficiencies. The second screen is an AC foil (anti-condensation foil) which has a high optical transmission, making it suitable for day and night use, but has low insulation properties.

The reference greenhouse is also equipped with an AC foil, although it cannot be moved automatically. The foil is attached to the greenhouse deck manually, and is therefore used for one consecutive period, mostly during the colder months of the growing season. The reference compartment is also equipped with a 'XLS 10 ultra revolux' screen, which has lesser insulation capabilities then the XLS 17 screen, but has an optical transmission factor close to that of the AC foil.

Table 1. Light transmittance and energy saving characteristics of used screens.

	☼	☁	≋
Compartment 1: 'ventilated' greenhouse			
XLS 17 FIREBREAK	*25%*	*24%*	*67%*
RETRACTABLE AC FOIL	*≈90%*		
Compartment 6: reference greenhouse			
XLS 10 ULTRA REVOLUX	*83%*	*75%*	*47%*
ATTACHED AC FOIL	*≈90%*		

☼ – Light transmission in sunlight
☁ – Light transmission when overcast
≋ – Energy saving

2.2.2. Ventilation

The ventilation unit (part of the ClimecoVent system) of the ventilated greenhouse is placed at the centre of the outer wall and has three intake ducts as presented in Fig.2. One is positioned at the exterior of the compartment, enabling the intake of outside air that is used for dehumidification or cooling. The other two ducts are arranged above and below the thermal screens at the inner side of the greenhouse. The ventilation unit has the ability of mixing three air streams by controlling the valves of the intake ducts. After mixing, the supply air to the greenhouse will pass along a low temperature heat exchanger, which can preheat the air before entering the indoor distribution system. A ventilator will force the conditioned air through a set of air hoses, distributed across the ventilated greenhouse. The system is designed for a maximum air rate of $10 m^3.m^{-2}.h^{-1}$. The tubes that distribute the air are located at the base of the plants below the crop gutter except for the hindmost, thus evenly dispersing the air supply over the compartment. When the ventilation unit cannot maintain a proper indoor climate, the system can switch to natural ventilation by opening the greenhouse windows.

Natural ventilation in the reference and ventilated compartments is achieved by opening small windows measuring 1.25x1.35m and larger windows measuring 2.5x1.35m, which are distributed as follows: 2 small and 2 large windows in southeast direction and 3 large windows in northwest direction.

2.2.3. Heat supply

Heat is supplied to both compartments by two tube rails and two growing tubes (Fig.2) with a length of about 27 m and a diameter of 51 mm for each growing gutter. In addition, the ventilated compartment has the ability to preheat the supply air delivered by the ventilation unit, as discussed in section 2.2.2.

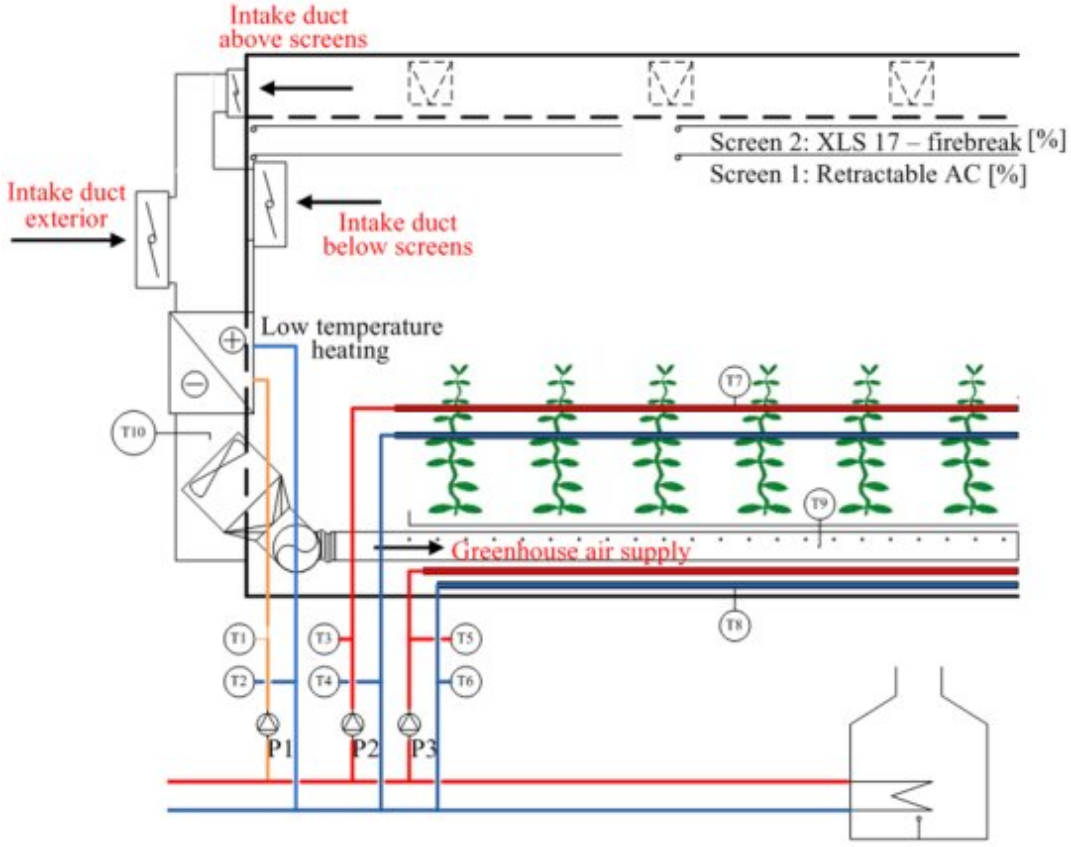

Fig.2. Overview of the experimental set-up and the monitored variables.

2.2.4. Monitoring

The compartments are controlled and monitored by a 'HortiMax' climate computer, which manages indoor climate and registers all measurements on a minute basis. Monitoring information includes weather, indoor sensors and system control variables. The weather station is located outside the research station's greenhouse and registers exterior factors such as temperature, relative humidity and solar gains. Several sensors are placed within the greenhouse to determine temperature, humidity and CO2 levels. Finally, the system control variables are based on the aforementioned measurements in combination with climate settings. They control the different technical systems such as screens or window positions and duct valve positions of the ventilation unit. From all data, a set of parameters has been selected for use during the monitoring campaign and can be found in Table A.1.

The growing season started at 6 January in both monitored compartments and ended 12 November 2010. However, irregular values for heating were registered in the pilot compartment until 12 January due to the incomplete installation of the air handling unit. As a result the monitoring campaign only considers the period from 13 January till 12 November. In order to limit the amount of data, the registered values were averaged over a five minute interval.

3. Results

3.1 Energy consumption

Total heat consumption, as shown in Fig.3, is calculated as the sum of all heating circuits: growing tubes, rail tubes and additionally the low temperature heat exchanger in the ventilated compartment. Electricity consumption of the ventilation unit and screen system has not been included in the energetic evaluation as these values are not available. Throughout the growing season of 2010, heat consumption for the ventilated greenhouse was higher as compared to the reference case, excluding months March and November. In March, problems in the reference compartment were encountered during the removal of the attached AC foil, explaining the added energy consumption. In November, growing in the ventilated compartment was ended early, resulting in lower energy consumption.

In total the ventilated greenhouse has consumed 9.6% more energy than the reference case. The higher consumption is presumably due to location differences of the compartments within the greenhouse complex. Tests taken during winter of 2009 reported up to 26.3% improved insulation properties for the reference compartment as compared to the ventilated case. When this factor is considered, the ventilated greenhouse would reduce energy consumption by 14.1%, as if it were compared to a similar located compartment. Measurements in the first half of 2011 confirmed this statement, comparing the system to a newly located reference greenhouse with similar boundary conditions. Energy savings till august 2011 were estimated at 11%.

In addition, the ventilated greenhouse uses a low temperature heat source to preheat the air supply, which stands for about 10% of its total heat consumption. At the research station, this heat is provided by the addition of an extra condensation stage to an available gas fired heating system located onsite. Heat could be generated more efficiently (e.g. geothermal heat pump), which in turn will lead to lower energy costs.

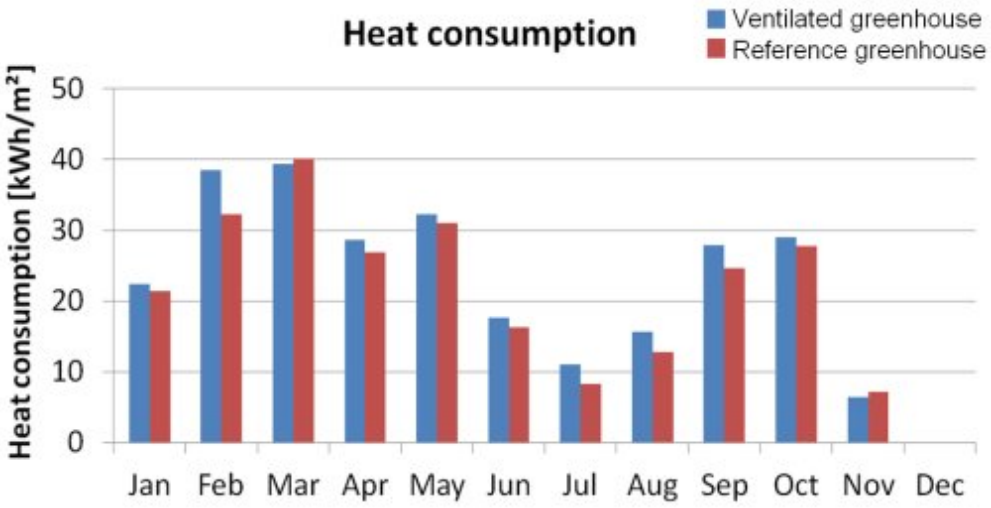

Fig.3. Total heat consumption of the monitored compartments.

3.2 System performance

3.2.1. Thermal screens

The ClimecoVent concept, used in the ventilated greenhouse, is based on energy saving through extensive thermal screen use, enabled by a heavy insulating XLS17 screen and a movable AC foil. In practice, the XLS17 screen will open at early morning, while the XLS10 screen used in the reference compartment can stay closed during daytime in certain conditions. Fig.4 shows the average daily screen positions over a 24-hour period (during a week in winter). The opening and

closing of the XLS17 screen corresponds to the time of sunrise and sunset. The average position of the XLS10 shows more variation, with increased daytime screening and slightly less use over night. Therefore, the XLS17 has a lower amount of total screening hours than the XLS10 screen, with values of respectively 934 and 1138 hours.

Nevertheless, the ventilated greenhouse can deploy its movable AC foil repeatedly during the whole of the growing season as opposed to the non-flexible attached AC foil in the reference case. This leads to a significant difference in total AC foil screening hours, with values of 2958 and 1400 hours for ventilated and reference greenhouse respectively. In Fig.4, the positional value for the attached AC foil in the reference compartment remains fixed at 100%, until its removal at the end of winter as of 12 March 2010.

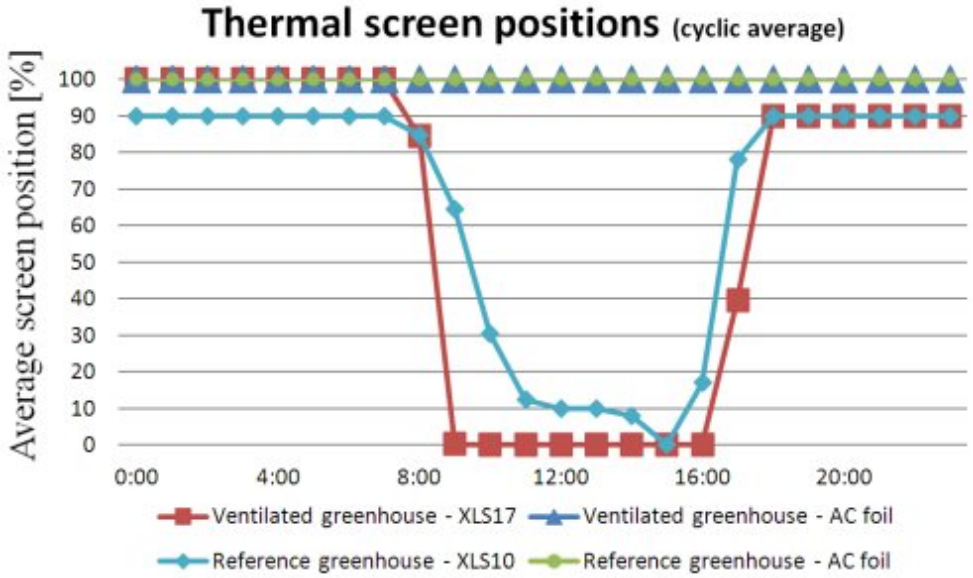

Fig.4. Cyclic averages of thermal screen positions during a winter week.

3.2.2. Natural ventilation

The amount of natural ventilation being used can be linked to the greenhouse window openings. Measured values consist of the window positions expressed as a percentage. The average leeward facing window positions in 2010 were 20 % for the ventilated compartment and 26 % for the reference case. Values for the windward facing windows were respectively 30 % and 37%. Lower values for the ventilated greenhouse indicate a reduced use of natural ventilation, in favour of mechanical ventilation usage. Detailed analyses showed a certain lag between the windows openings of the ventilated and reference compartments, indicating that mechanical ventilation is used prior to natural ventilation as it is supposed to, but seems to be insufficient to maintain the greenhouse climate.

3.2.3. Mechanical ventilation

During the introduction of the ventilated greenhouse concept at the research facility, minor start-up problems occurred. A temporary axial ventilator had to be used during the first three months of growing, delivering a small airflow and working on a fixed ventilation schedule. At night ventilation was disabled and during daytime the system was running at full capacity. This can be derived from the average ventilator revolutions shown in Fig.5. Revolutions increase from 35 to 53 % in the period of January to March, in accordance with increasing daylight time. Afterwards, when the ClimecoVent ventilation unit was installed, a new schedule was introduced imposing a minimum ventilation rate of 20 % during daytime and 0 % at night for the remainder of 2010. With the new ventilation unit, average revolutions drop to 20 % and decrease further during summer

when natural ventilation becomes a more effective solution for dehumidification and temperature control.

Intake of outside air for dehumidification occurs primarily during spring and summer, as can be seen in Fig.5. In winter, the greenhouse contains smaller crops which cause little to no evaporation. Along with low outside temperatures this results in low absolute indoor humidity. Additionally, condensation on cold greenhouse surfaces and dehumidification through air infiltration results in even lower humidity levels, reducing the need for climate control by mechanical ventilation. Measurements confirm this, since average valve positions for outdoor air intake are diminished during autumn and winter.

Fig.5 also shows a reversed use of the air valves below and above the screens. Although the valve above the screens could be used in winter periods for dehumidification through condensation on the greenhouse deck, it is mostly used in the summer. When analysing the data, a correlation can be found between opening the screens and switching from the air valve below the screens to the upper valve.

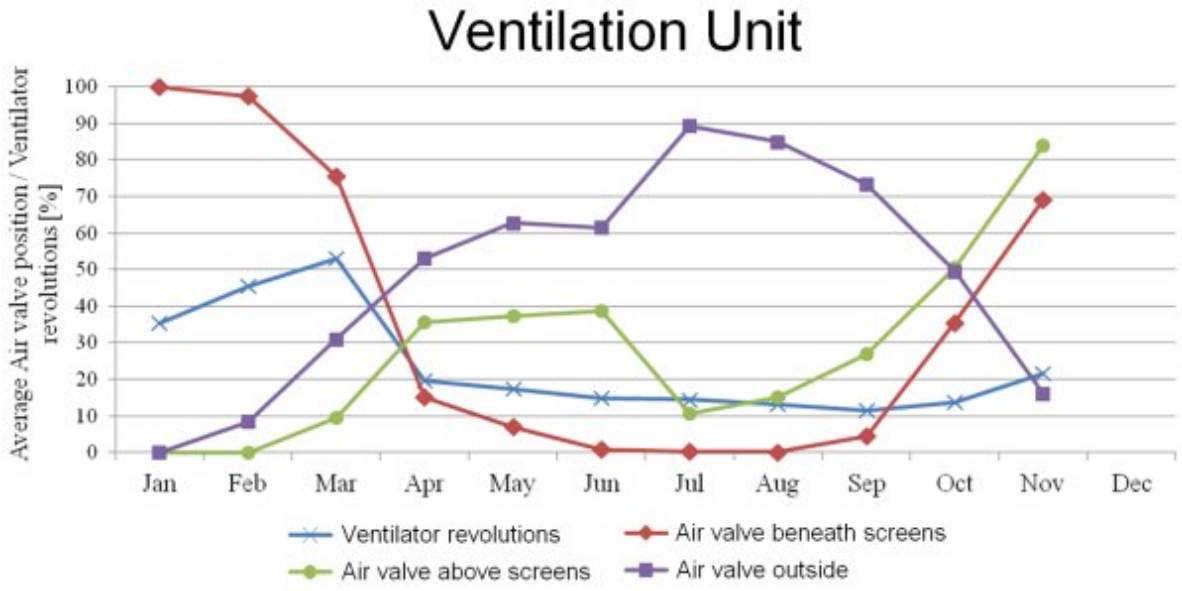

Fig.5. Average monthly valve positions and ventilator revolutions in percentage

3.3 Crop yield

The ventilated greenhouse slightly underperformed the reference case in terms of crop production during 2010. Total yield amounted to respectively 55,99 and 56,46 kg.m-². During the first weeks of growing, crop progression in the ventilated greenhouse was lagging due to excessive use of the XLS17 screen, resulting in light deficiencies at the start of growth. However, crop yield caught up and production surpassed that of the reference case until summer, as can be seen in Fig.6. The reference greenhouse equalizes total production in summer, but early crop yield is economically more interesting. During the remainder of the year, production between the two concepts proved to be almost equal, ending with a small lead in favour of the reference greenhouse. Still, the ventilated greenhouse concept has shown it can generate positive effects to the growing process, by achieving an increased production rate despite the crop damage taken at the beginning of the growing season.

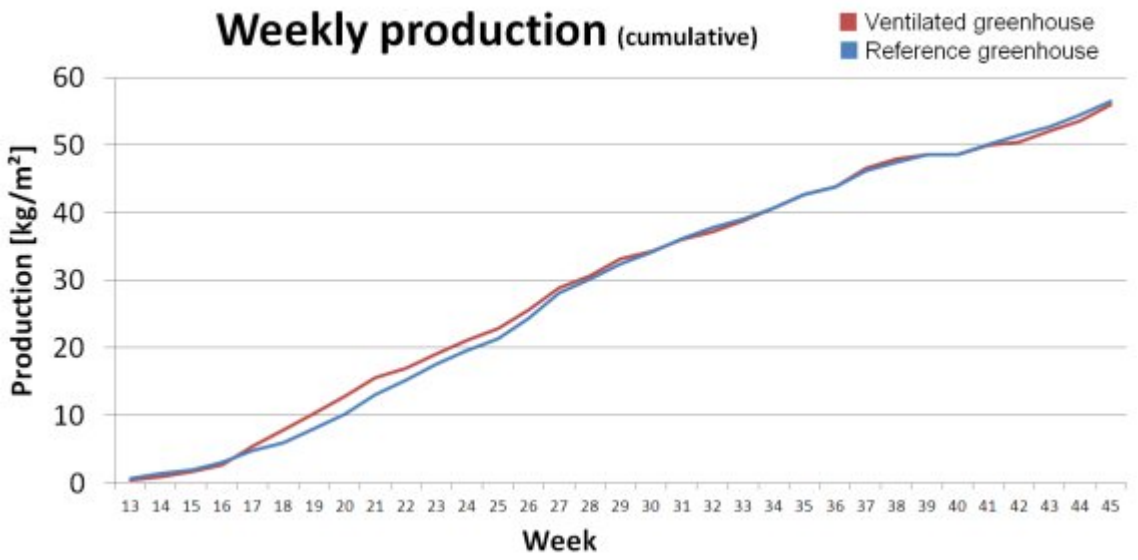

Fig.6. Weekly cumulative tomato production kg.m^{-2}

4. Discussion

It should be noted that the reference compartment used in this monitoring campaign does not represent the common greenhouses in Flanders, since it is equipped with two thermal screens while most greenhouses still lack the use of screens or use only one. Established energy savings of the ventilated greenhouse concept would therefore be more favourable when comparing them to such conventional systems. However, the investment cost of the ventilation unit needs to be justified even when comparing it to a 'best available technique' reference scenario.

The monitoring campaign of 2010 showed higher heat consumption for the mechanically ventilated compartment. Measurements confirmed that the locations of the compartments within the greenhouse complex play an important role in their insulation properties. Based on these insulation measurements, a correctional factor was deducted which indicated that energy savings would be observed when comparing the ventilated greenhouse to an identically located reference case. This was confirmed during the first half of 2011, as energy savings were reported against a similar conditioned reference compartment.

Average window positions were lower in the ventilated compartment, which indicates improved dehumidification by mechanical ventilation. Nevertheless, dehumidification capabilities of the mechanical ventilation system appear insufficient, since greenhouse windows still tend to open repeatedly, even during cold outdoor conditions.

The monitored compartments are relatively small. Humidity problems associated with thermal screening will increase with the size of the greenhouse, meaning that screening hours will reduce when dealing with a normal sized greenhouse. Therefore, the ClimecoVent concept will presumably show better use in larger greenhouses, as it enables intensive screening.

5. Conclusions

In 2010, a monitoring campaign has been conducted on two greenhouse compartments located at the Research Station for Vegetable Production at Sint-Katelijne-Waver, Belgium. One of the compartments was equipped with the commercially available ClimecoVent system, which controls indoor humidity and temperature with a mechanical ventilation unit. The other greenhouse compartment served as a reference case for comparison of the results. It was concluded that the mechanical ventilation concept delivered an equivalent crop yield, while heat consumption increased. This difference in energy use is due to differing locations of the compartments within the greenhouse complex, resulting in varied insulation properties and therefore influencing heat demand. Nevertheless, the potential of the ventilated concept has been demonstrated during the first half of the growing season of 2011, with reported energy savings in range with predictions made in 2010. The energetic performance can also be improved by implementing a more efficient low temperature heating system for preheating of the supply air. Furthermore, the ventilated compartment established a gain in crop yield during the first half of the growing season.

Appendix A

Table A.1. Monitored parameters

Measurement	Unit	Source	ClimecoVent	Reference
Outdoor temperature	°C	Weather station		
Outdoor Relative humidity	%	Weather station		
Outdoor Moisture deficit	g/m³	Weather station		
Wind speed	m/s	Weather station		
Wind direction	°	Weather station		
Standard radiation intensity	W/m²	Weather station		
Greenhouse temperature	°C	Climate box 1	x	x
Relative humidity	%	Climate box 1	x	x
Moisture deficit	g/m³	Climate box 1	x	x
CO2 concentration	ppm	Climate box 1	x	x
Window position side 1	%	System control signal	x	x
Window position side 2	%	System control signal	x	x
Window position leeward side	%	System control signal	x	x
Window position windward side	%	System control signal	x	x
Screen position XLS 17	%	System control signal	x	
Screen position AC foil	%	System control signal	x	
Screen position XLS 10	%	System control signal		x
Tube temperature lower heating circuit	°C	T9	x	x
Inlet temperature lower heating circuit	°C	T5	x	x
Outlet temperature lower heating circuit	°C	T6	x	x
Flow rate lower heating circuit	l/min	P3	x	x
Energy consumption lower heating circuit	kW	Calculated value	x	x
Tube temperature upper heating circuit	°C	T7	x	x
Inlet temperature upper heating circuit	°C	T3	x	x
Outlet temperature upper heating circuit	°C	T4	x	x
Flow rate upper heating circuit	l/min	P2	x	x
Energy consumption upper heating circuit	kW	Calculated value	x	x
Inlet temperature low temperature heating	°C	T1	x	

circuit			
Outlet temperature low temperature heating circuit	°C	T2	x
Flow rate low temperature heating circuit	l/min	P1	x
Energy consumption low temperature heating circuit	kW	Calculated value	x
Measured ventilator revolutions	%	System control signal	x
Temperature mixing room ventilation unit	°C	T10	x
Temperature supply air	°C	T9	x
Air valve below screen	%	System control signal	x
Air valve above screen	%	System control signal	x
Air valve exterior	%	System control signal	x

References

[1] V.P. Sethi, S.K. Sharma, Survey and evaluation of heating technologies for worldwide agricultural greenhouse applications, Solar Energy, Volume 82, Issue 9, September 2008, Pages 832-859, ISSN 0038-092X, 10.1016/j.solener.2008.02.010.

[2] M.K. Ghosal, G.N. Tiwari, D.K. Das, K.P. Pandey, Modeling and comparative thermal performance of ground air collector and earth air heat exchanger for heating of greenhouse, Energy and Buildings, Volume 37, Issue 6, June 2005, Pages 613-621, ISSN 0378-7788, 10.1016/j.enbuild.2004.09.004.

[3] Winspear, K.W., Bailey, B.J., 1977. Greenhouse thermal screens save fuels. Proceedings of symposium on controlled environment agriculture, Tucson, AZ, pp. 414–418.

[4] C. Kittas, T. Bartzanas, Greenhouse microclimate and dehumidification effectiveness under different ventilator configurations, Building and Environment, Volume 42, Issue 10, October 2007, Pages 3774-3784, ISSN 0360-1323, 10.1016/j.buildenv.2006.06.020.

[5] A. Mistriotis, G.P.A. Bot, P. Picuno, G. Scarascia-Mugnozza, Analysis of the efficiency of greenhouse ventilation using computational fluid dynamics, Agricultural and Forest Meteorology, Volume 85, Issues 3–4, July 1997, Pages 217-228, ISSN 0168-1923, 10.1016/S0168-1923(96)02400-8.

[6] P. Thongbai, T. Kozai, K. Ohyama, CO2 and air circulation effects on photosynthesis and transpiration of tomato seedlings, Scientia Horticulturae, Volume 126, Issue 3, 30 September 2010, Pages 338-344, ISSN 0304-4238, 10.1016/j.scienta.2010.07.018.

[7] V.P. Sethi, S.K. Sharma, Survey of cooling technologies for worldwide agricultural greenhouse applications, Solar Energy, Volume 81, Issue 12, December 2007, Pages 1447-1459, ISSN 0038-092X, 10.1016/j.solener.2007.03.004.

[8] M. Djevic, A. Dimitrijevic, Energy consumption for different greenhouse constructions, Energy, Volume 34, Issue 9, September 2009, Pages 1325-1331, ISSN 0360-5442, 10.1016/j.energy.2009.03.008.

[9] Verlodt, H., Baeten, S., El Fahem, S. and Harbaoui, Y. 1985. Influence of different static aeration systems on the diurnal climate under PE greenhouse. Acta Hort. (ISHS) 170:153-172.

[10] Silva, A.M. and Rosa, R. 1985. Means Of Cooling A Greenhouse In A Hot Climate. Acta Hort. (ISHS) 174:81-86.

[11] J. Derks, Rationeel energiegebruik door warmterecuperatie uit ventilatielucht, Innovatiesteunpunt voor land- en tuinbouw. [Dutch]

[12] M. Fuchs, E. Dayan, E. Presnov. Evaporative cooling of a ventilated greenhouse rose crop. Agriculture and Forest Meteorology, 138 (1–4) (2006), pp. 203–215.

[13] W.J. Carpenter, L.D. Bark. Temperature pattern in greenhouse heating. Florists Review (1967), pp. 17–19.

[14] Goodhind, G.W., 1965. Air movement in glass houses. Shinfield Paper No. 7, pp. 61–63.

[15] Th.H. Gieling, M.A. Bruins, J.B. Campen, H.J.J. Janssen, F.L.K. Kempkes, M.G.M. Raaphorst, A. Sapounas, Monitoring technische systemen in semi-gesloten kassen, Wageningen U.R., Rapport GTB-1008, 2010.

[16] M. Raaphorst, J. voermans, Monitoring ClimecoVent-systeem in de praktijk: Technisch, teeltkundig en economisch onderzoek naar een energiezuinige kas bij kwekerij Grenspaal B.V., Wageningen U.R., Rapport GTB-1032, 2010.

Energy Networks in Sustainable Cities: temperature and energy consumption monitoring in urban area

Luca Giaccone[a], Alessandra Guerrisi[a], Paolo Lazzeroni[a] and Michele Tartaglia[a]

[a]Politecnico di Torino – Dipartimento Energia, Torino, Italy, paolo.lazzeroni@polito.it

Abstract:

The European Commission is supporting many projects intended to improve the use of renewable energy sources and a special attention has been devoted to the case of large-scale urban areas. The Polycity project represents a significant demonstration of this energy policy, which was applied to 3 cities: Barcelona, Stuttgart and Torino. The case of Torino appears of particular relevance because it is dedicated to the improvement of energy performance of existing buildings and installations which is, in our opinion, the most frequent situation.

In particular the most qualifying characteristic of Torino project is the installation of a new combined heat and power generator (CHP), coupled with an absorption chiller, in order to supply energy more efficiently in a district which include the Housing Authority of the Province of Torino (ATC) building and 30 council buildings. The trigeneration is able to supply electricity and cooling power to the main office building and, thanks to the coupling to the existing district heating system, it provides thermal energy for space heating and hot water to the council buildings in the district.

The paper presents the analysis activities performed during Polycity project to understand the role of monitoring and control in a complex energy system with the aim of improving the efficiency and reducing the energy consumption. Further analysis in terms of economical and environmental benefits have been already described in another paper where an optimal management system was used to improve the efficiency of the plant. Here only the results analysis of the project monitoring are analysed. Particular attention has been dedicated to the analysis of temperature profiles measured in some flats of residential buildings: these data have been collected for more than one year. Possible relationships between energy consumption and temperature management have been analysed and discussed in order to improve the results.

Keywords:

Energy and temperature monitoring, Energy consumption, Social Housing, Office building.

1. Introduction

Arquata is a quarter in Torino built at the beginning of XX century which involves an area of about 87,500 m^2 dedicated to social purposes (social houses, Fig. 1).

Fig. 1. Arquata district

The building construction standards were very simple and no heating system was initially installed.

In proximity of this quarter the general office of the organization (ATC, see Fig. 2) which manages all the social houses of the Region Piedmont was built in first 70's. This building needs both heating and cooling systems and it exhibited a lot of problems of energy consumption to get satisfactory ambient conditions due to its wide glazed façades and poor insulations. The surface of this building is about 11,350 m^2.

Fig. 2. ATC office building

In recent years this set of buildings received many interventions of rehabilitation. In particular a district heating was installed: it allows to heat all the dwellings of the district and to distribute hot water in most of them; the same plant supplies heat to the ATC office building. A lot of attention was focused on the management of the overall complex energy system composed both from supply and demand side. An intelligent structure called Communal Energy Management System (CEMS) was developed in order to define the best production strategies (over a short and a long time period) in order to minimize the operation cost [1].
The Polycity project [2,3], supported by the European Commission (Sixth Framework Programme – Priority 6.1 Sustainable Energy Systems), allowed to introduce further developments by supporting the installation of a CHP which produces electric energy, released to the medium voltage grid, and heat, which enhances the thermal power produced by the existing heat plant in winter and which is used for hot water production and for supplying an absorption chiller during summer.

Reduction of primary energy consumption for space heating was one of the main goals of the project. Despite al lot of work has been carried out on the management of the supply side with reference to the actual consumption. The concept of indoor environment quality is not automatically implemented in the CEMS. For example, the thermal consumption of flats in 30 dwellings is known, but the internal temperature inside flats, which allow to understand from where this consumption value come from are not directly detected from CEMS.
In this paper the analysis of the energy behavior of inhabitants is investigated. The expected results were strictly related to many factors (insulation, intervention on frame, solar beam, external temperature, etc.), but also the inhabitant behavior can significantly influence the resulting energy demand. In fact smart and conscious users [4,5] can contribute to an effective reduction of energy consumption.
The following paper gives information on the metering system with a focus on temperature and consumption monitoring systems to investigate on the energy behavior of inhabitants of the district and of people that manage office building, in order to look for possible improvements.

2. Monitoring system

One of the main issues in the project was represented by the monitoring and analysis of heating system for the social housing and office building connected to the district heating network. Particular attention was devoted to the behavior of inhabitants of social houses and employers of office building in order to point out possible relationships between consumption for space heating and internal temperature. In this light several sensors (30) were installed in some dwellings of Arquata district for more than one year to collect the temperature profiles.

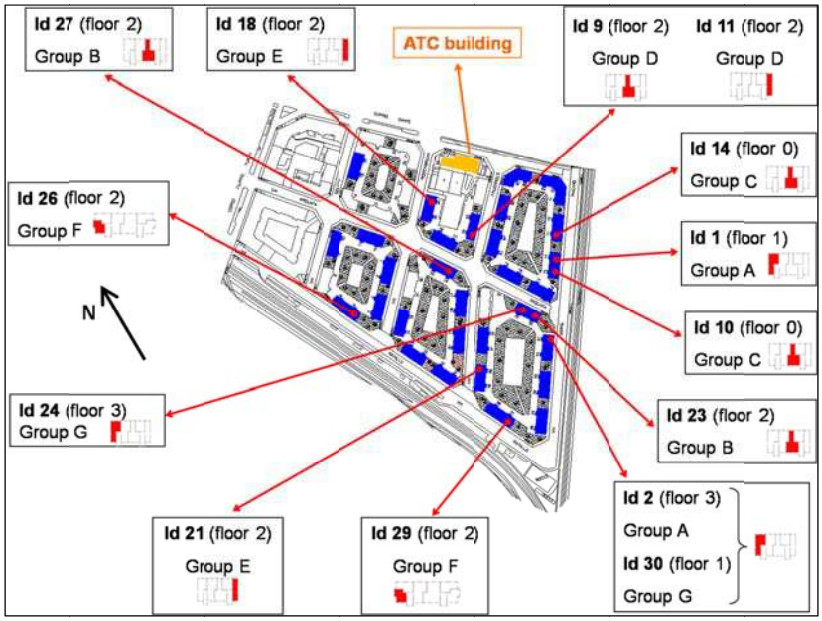

Fig. 3. Location of temperature sensors in Arquata quartier

These sensors have been located in dwellings (see Fig. 3) having different characteristics: useful floor surface, exposure with reference to the sun, number of occupants, etc. Heating systems of all the flats involved are connected to the district heating and their internal temperature is managed by inhabitants trough dedicated thermostat installed in each apartment. The thermal energy consumption of each flat has been calculated considering the measurement realized by the thermal energy metering systems installed in each end users of district heating. These measurements represent the total energy consumption of each apartment, defined as the sum of space heating and domestic hot water demand. Possible relationships between these temperature profiles and energy consumption will be investigated in the next sections.

As regards the ATC office building, only two floors (3rd and 5th) have been monitored. The thermal energy consumptions for space heating have not been considered because these data are not available. In fact only the total energy demand of the whole building is available, moreover these data take into account also the consumption of domestic hot water and space heating for some parts of the building not devoted to office use (e.g. conference hall, employers canteen, etc.). Therefore it is not possible to know the consumption of each floor of the building: extrapolation of energy consumption for space heating due only to 3rd and 5th floor can be difficult and inaccurate. Thus, only a qualitative analysis on the temperature profile has been performed for these sensors and a possible evaluation of the management of heating system can be done.
Fig. 4 shows the placement of the sensors in the ATC building.

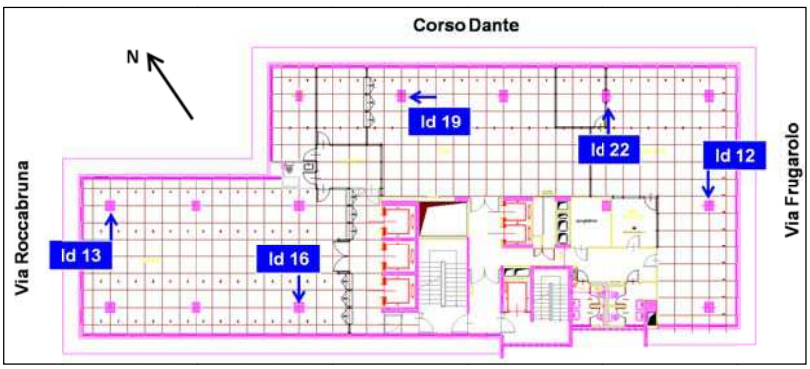

(a)

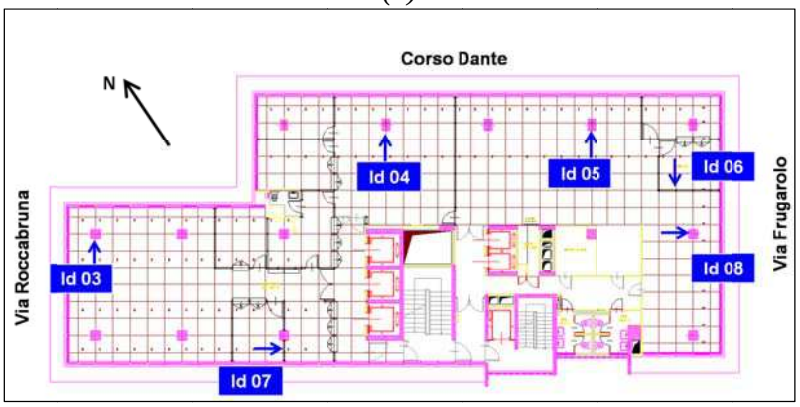

(b)

Fig. 4. Location of temperature sensors in ATC building: a) 3rd floor, b) 5th floor

2.1. Apartment energy consumption

The temperatures monitoring covers a period of one year, from July 2010 to July 2011, and the measurements of energy consumptions of end users cover a period slightly longer than one year, from June 2010 to July 2011.

Since measurements of energy consumption of the inhabitants in Arquata district take into account both the demand for space heating and domestic hot water, some corrections on the measurements have been made in order to predict energy consumption only for space heating. This means that an evaluation of domestic hot water demand has been performed considering some parameters:

- T_{WS} and T_{DHW}: average temperature (°C) of water supply and domestic hot water;
- B: average hot water consumption (liter per day per person);
- NP: number of people living in each flat.

The daily domestic hot water demand can be simply defined as follows:

(1)

where C_p is the specific heat of water. The AHSRAE Standard [6] suggests a hot water consumption of 50 l/day per person, but 30 l/day per person have been considered for people living in social housing [7]. The average temperature of water supply and hot water has been estimated as 15 °C and 50 °C respectively.

Table 1 shows the total energy consumption, for one year, of the inhabitants involved in the temperature and consumption measurements. Both energy demand for space heating and consumption for domestic hot water are supplied, in each flat, by the district heating. Thus, using (1), the estimated energy consumption for space heating has been evaluated for each living unit for the conventional heating period. For Torino the conventional heating period begins 15th October and ends 15th April (approximately 180 days) because Torino is located in zone E [8]. Specific energy consumption related to the floor space has been also considered to normalize the energy demand of each apartment.

Table 1. Energy consumption for the flats of Arquata district

N°	ID user	Number of person	Yearly energy consumption measured (kWh)	Predicted hot water energy consumption (kWh)	Predicted yearly energy consumption for space heating (kWh)	Gross heating area (m^2)	Specific energy consumption for space heating ($kWh/m^2/yr^1$)
1	ID_01	3	7135.8	659.30	6267.7	56.7	110.6
2	ID_02	3	8617.0	659.30	7748.9	58.4	132.7
3	ID_09	1	5324.0	219.77	5034.6	40.5	124.4
4	ID_10	1	12378.5	219.77	12089.1	60.7	199.2
5	ID_11	1	7342.9	219.77	7053.5	36.5	193.5
7	ID_18	2	7451.6	439.53	6872.9	36.5	188.6
8	ID_21	1	9586.4	219.77	9297.0	36.5	255.1
9	ID_23	3	3567.9	659.30	2699.8	60.7	44.5
10	ID_24	4	7686.2	879.06	6528.8	58.4	111.8
11	ID_26	2	3319.7	439.53	2741.0	38.9	70.4
12	ID_27	2	2143.6	439.53	1564.9	60.7	25.8
13	ID_29	1	6781.1	219.77	6491.7	38.9	166.7
14	ID_30	2	9120.4	439.53	8541.7	56.7	150.7

Making reference to the benchmark value of the project was equal to 90 kWh/m^2/year, the following main results are identified in the above Table 1.
Only few flats have low energy consumption (lower than the benchmark level), most of them have an energy demand between 100 and 150 kWh/m^2/year, with particular cases where consumptions reach 200-250 kWh/m^2/year. These last results suggest an inappropriate management of the flat heating system by inhabitants.

For this reason, energy consumptions and temperature measures have been analyzed in order to justify the relevant heating demand of some flats. The comparison has been focused on 7 groups of dwellings with different characteristics (flat position in building, exposure with reference to the solar beam, floor, etc.) as shown in Table 2.

Table 2. Criterion of subdivision of flats of Arquata district

Group	ID	Subdivision criteria	
A	1, 2	- similar flats - different building	- different floor (1st, 3rd) - equal exposure
B	23, 27	- similar flats - different building	- same floor (2nd) - equal exposure
C	10, 14	- similar flats - different building	- same floor (ground) - equal exposure
D	9, 11	- different flats - same building	- same floor (2nd) - equal exposure
E	18, 21	- similar flats - different building	- same floor (2nd) - equal exposure
F	26, 29	- similar flats - different building	- same floor (2nd) - equal exposure

[1] Referred to the heating period 2010 15thOctober – 2011 15thApril

G	24, 30	- similar flats - different building	- same floor (3rd) - different exposure

2.2. Temperature measurements

Fig. 5 shows the average temperature measured during the heating period for the different groups, compared to the trend of daily average external temperature [8].

The temperature profiles point out as the people living in Arquata quartier did not pay attention to the temperature control system. In fact average temperatures over 20-21 °C are shown in almost all groups and the temperature profiles are quite constant in some cases. This last trend suggests an incorrect setting of the temperature control system in the apartments by the people: day and night temperatures have been set at the same value (confirmed by inspections in each dwellings) and the setting values are too high with respect to 20 °C which is the limit value of internal temperature for residential buildings in Italy [9]. This is also due to a poor people instruction about the necessity of settings the range of internal temperature to lower values and to use different level of temperature during daytime and nighttime.

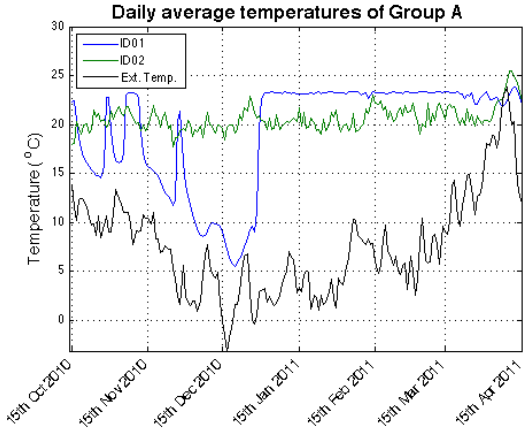

(a)

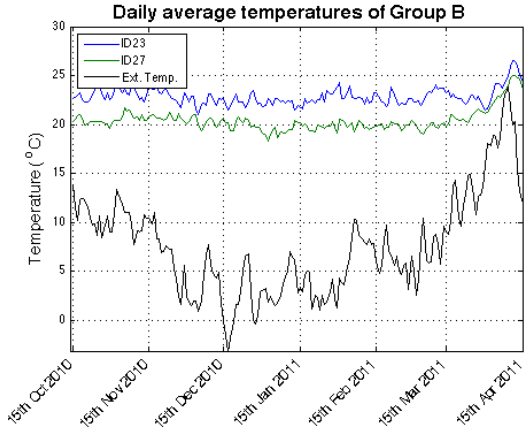

(b)

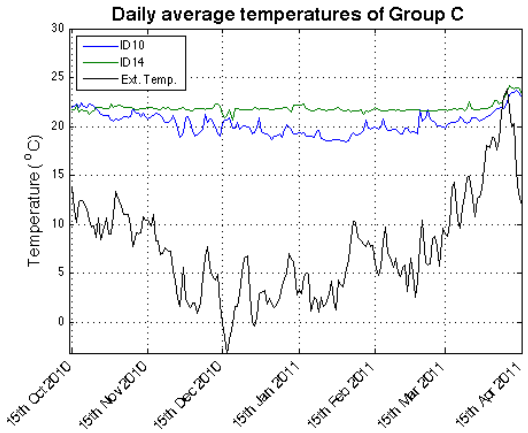

(c)

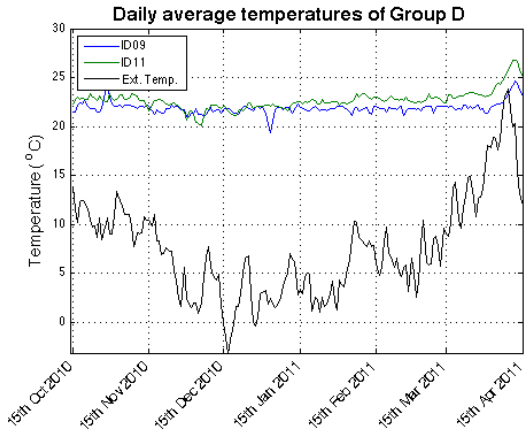

(d)

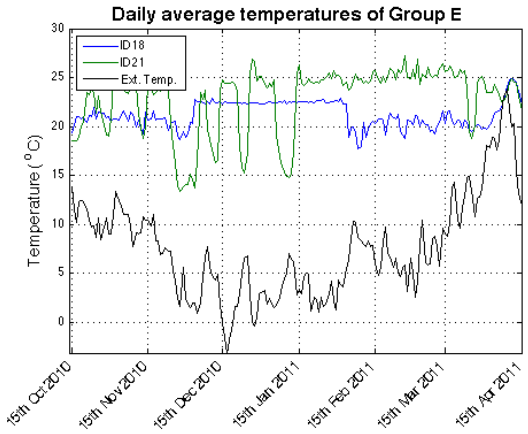

(e)

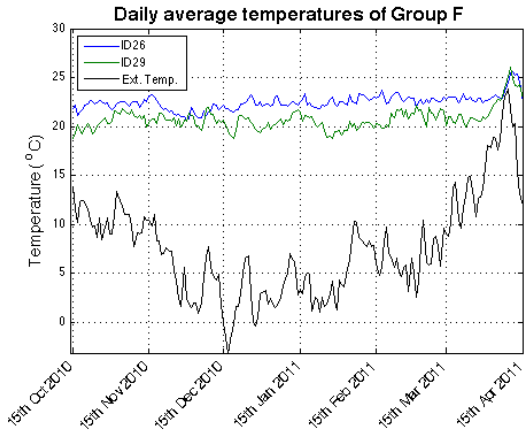

(f)

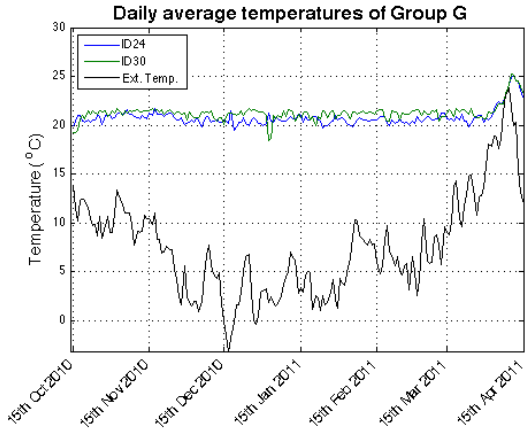

(g)

Fig. 5. Temperature profiles for different groups: a) Group A, b) Group B, c) Group C, d) Group D, e) Group E, f) Group F, g) Group G

2.3. Temperature analysis

The comparison between specific consumptions and temperature profiles allows to verify that high daily average temperatures are strictly related to high energy consumption.

Fig. 5e, for example, shows the trend for ID_21, related to the flat with the highest specific energy consumption. The average temperature in that case is more than 25 °C for almost half heating period. The same relationship can be verified for ID_10 and ID_11 (see Fig. 5c and Fig. 5d) where specific consumptions (respectively 199.2 and 193.5 kWh/m^2/year) are related to an average temperature higher than 23 °C for all the heating period. High values of average internal temperature of the flats suggest an inadequate control of temperature operated by the inhabitants, which produces wasting of energy for space heating. Fig. 6a and Fig. 6b show the trend of temperatures observed in some flats during a period of one week, from 1st to 7th January 2011 (sampling time equal to 15 minutes). The temperature profile is quite constant and over the reference value of 20 °C in almost all time steps. Thus the internal temperature was wrongly set and incorrectly managed as also confirmed by the Fig. 7 about the daily temperature profiles. In fact, Fig. 7a shows as the temperature in the flat (ID_18) is kept quite constant between 22 °C and 23 °C

(e.g. heating system is always working also during night-time), while the temperature in the second flat (Fig. 7b) shows a wrong regulation of thermostat (e.g. heating system is turned on at 9 a.m. and turned off at 2 a.m. with a setting value of internal temperature higher than 21 °C).
An accurate regulation of day and night temperature in the apartments (e.g. low set point of temperature during sleeping hour) could significantly reduce the energy consumption.
However, the measured energy consumption is low in some cases even if the temperature profiles are quite high, with evident virtuous behavior of inhabitants. Flats associated to ID_23 and ID_27 show in Table 1 relatively low energy consumptions compared to their weekly temperature profiles shown in Fig. 8. Fig. 8b and Fig. 9b show that ID_27 has an accurate setting of thermostat because the internal temperature of the flat is mainly maintained under 20 °C. Instead, Fig. 8a and Fig. 9a show a temperature profiles over 20 °C for ID_23. This situation, combined to a low energy consumption, can be due to the exposure to the south, to the central position of the flat in the building and to an appropriate thermal insulation.

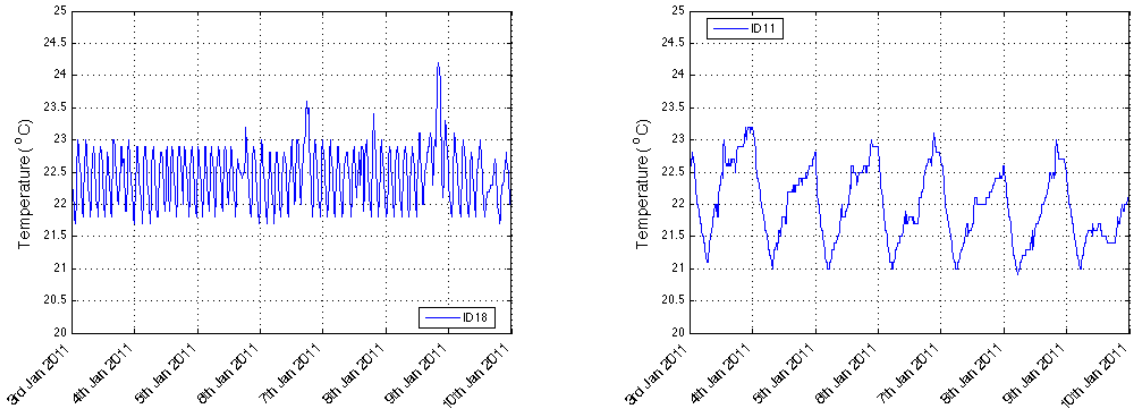

(a) *(b)*

Fig. 6. Weekly temperature profiles of two flats of Arquata district (Monday 3rd to Sunday 9th January, 2011): a) for ID_18, b) for ID_11

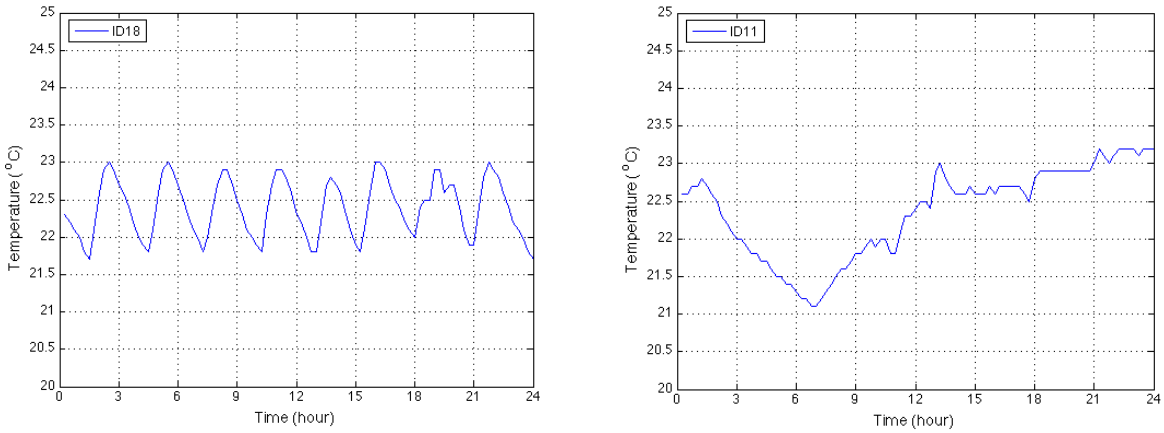

(a) *(b)*

Fig. 7. Daily temperature profiles of two flats of Arquata district (Monday 3rd January, 2011): a) for ID_18, b) for ID_11

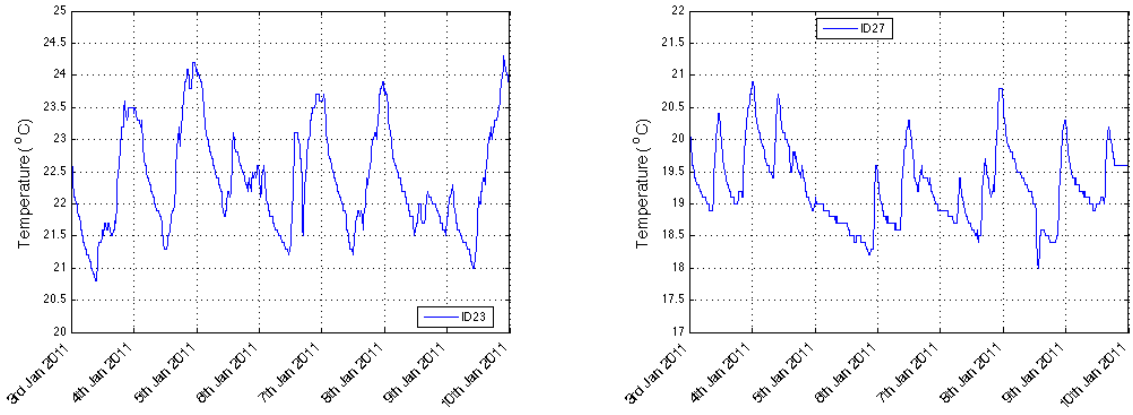

(a) *(b)*

Fig. 8. Weekly temperature profiles of two flats of Arquata district (Monday 3rd to Sunday 9th January, 2011): a) for ID_23, b) for ID_27

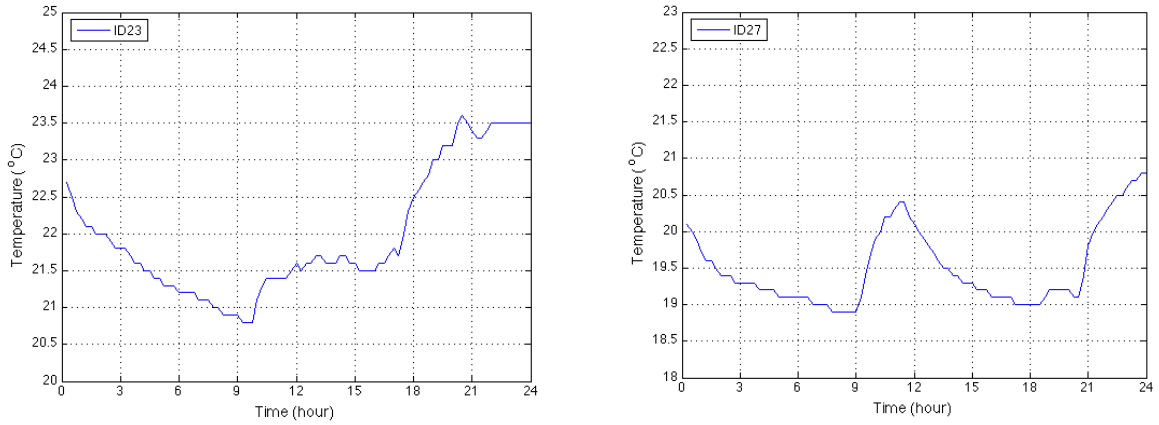

(a) *(b)*

Fig. 9. Daily temperature profiles of two flats of Arquata district (Monday 3rd January, 2011): a) for ID_23, b) for ID_27

Other analyses have been performed comparing the temperature profiles of the flats that belong to the same groups.

The flats in Group A belong to the same building and they have equal position (lateral) and exposure, but they are located at different floors.

The ID_01 is related to inhabitants out of home for a period of about half of heating season, for this reason the average temperature decrease up to 5-6 °C during that period. ID_02 shows a constant daily average temperature close to 20-21 °C. The specific consumption is almost the same for both flats, but ID_01 has a higher value due to the higher constant average temperature of about 23 °C during second half heating season.

Group B is referred to flats with lower specific energy consumption, even if the average temperatures are quite high. The flats in fact have a central position in the corresponding buildings and the contiguous apartments probably have a high setting of internal temperature, thus the heat dispersion throw the wall are very low.

The groups C and F are formed by flats with similar position, floor (ground and 2nd floor, respectively) and exposition, but are located in different buildings. The specific energy consumptions of ID_10 and ID_26 are twice than those of ID_14 and ID_29, even if the

temperature profiles are not different. This result can be probably related again to the effect of contiguous apartments, probably managed with high setting of internal temperature.
The group D is related to flats in the same building, floor and exposure, but having different position (ID_09 and ID_11 are, respectively, in central and lateral position). The temperature profiles are similar, with a daily average temperature close to 22 °C, but the specific consumption is higher for ID_11 due to the lateral position of the building.
The flats with high energy consumptions form the group E. As discussed before, the relevant level of daily average temperature significantly affects the specific consumptions. In fact the temperature profiles are relevant for ID_18 and ID_11, as shown in Fig. 6.
The flats of the last group (G), ID_24 and ID_30, have a quite constant temperature profile and significant energy consumption due to the improper regulation of the setting temperature for night and day, as mentioned before.

Similar analysis has been performed for the temperature profiles of the ATC building. However, in this case, the temperature analysis neglects the energy consumption of ATC offices and it is principally addressed to explore the trend of temperatures, because specific consumption data are not available.

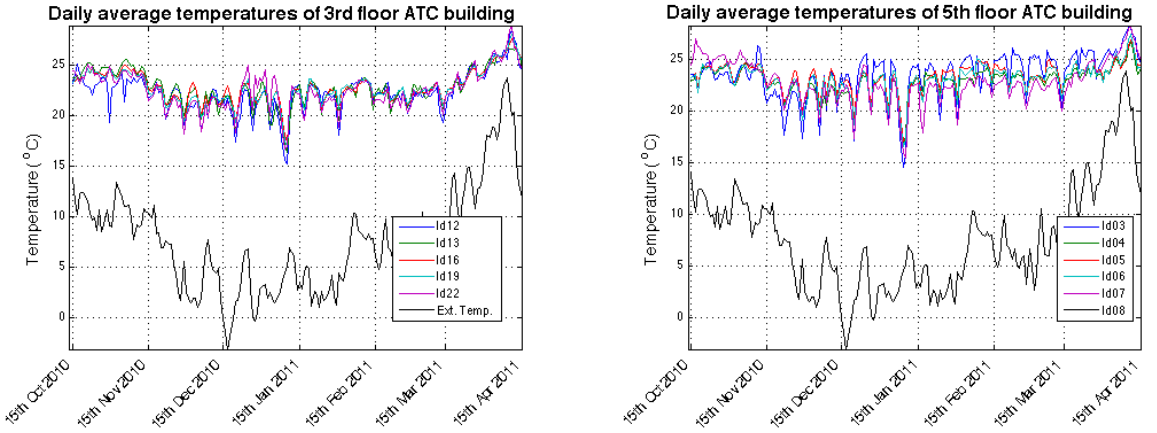

(a) *(b)*

Fig. 10. Temperature profiles for ATC office building: a) 3rd floor, b) 5th floor

Fig. 10 shows as the average temperatures in ATC offices were strongly higher than the reference internal temperature of office building (20 °C) [9] for major part of heating season. Also in this case the trends underline an incorrect management of internal temperatures, which can cause a relevant energy consumption. Fig. 11 and Fig. 12 show the trend of internal temperatures (weekly profiles from 17th to 23rdJanuary 2011 and sampling time of 15 minutes) for the sensors installed in 3rd and 5th floor of ATC building, respectively.

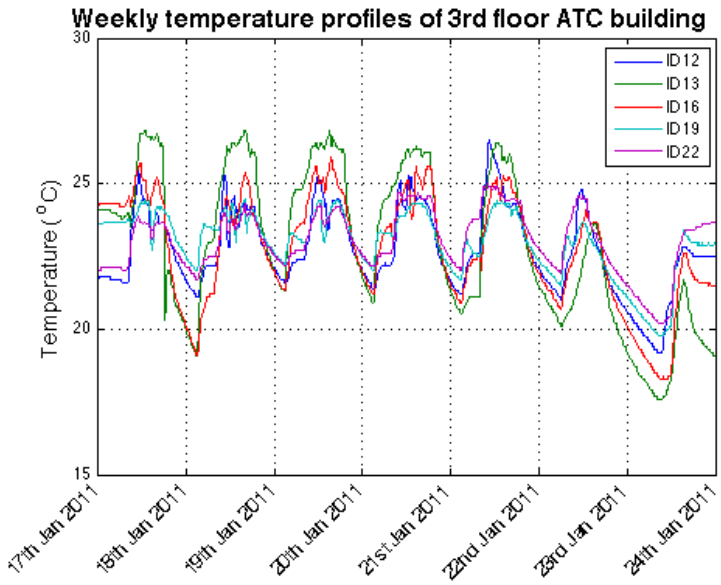

Fig. 11. Weekly temperature profiles of 3rd floor ATC building (Monday 17th to Sunday 23th January, 2011)

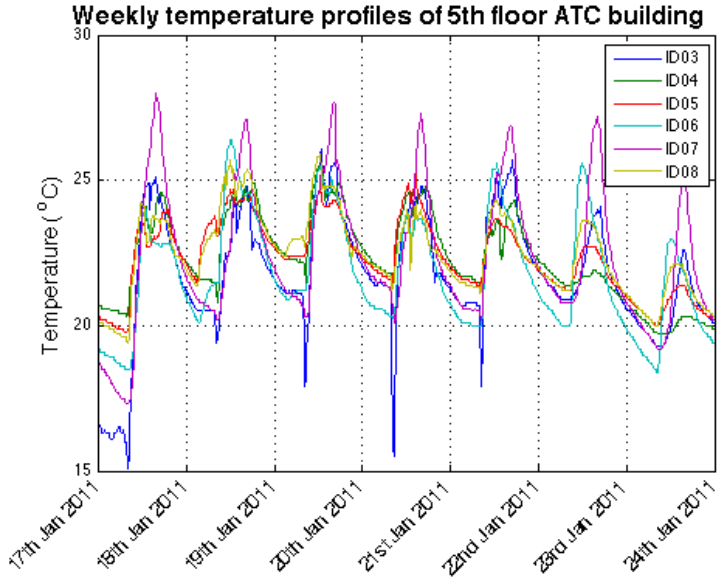

Fig. 12. Weekly temperature profiles of 5th floor ATC building (Monday 17th to Sunday 23th January, 2011)

Both in sensors of 3rd floor and in ones of 5th floor most of weekly temperatures are significantly over 20 °C during the working day. In some cases the temperature profiles is greater than 20 °C also during night-time. This management produces two different negative effects. On one hand the energy consumption becomes relevant, also during closing time when no employees are working and the offices spaces are empty. On the other hand, the high temperature in a work environment can increase the discomfort for the employees during working time.

Temperature profiles of ATC building can be also related to the operation of the heating system to identify incorrect management of the temperature control system. Fig. 13 shows when the heating system is turned on and turned off.
The 3rd floor is managed by a centralized system that controls all the fan coils. Starting and switching off time are fixed at 3 a.m. and 6 p.m. respectively (see Fig. 13a). On one hand the management could be improved retarding the switch on-timing because the building seems to have a low thermal time constant. On the other hand, the setting temperature could be reduced to a more convenient value.
The 5th floor is managed by control local systems, which act different group of fan coils. Starting and switching off time are fixed at 7 a.m. and 6 p.m. respectively (see Fig. 13b). Also in this case setting temperature could be reduced to more convenient value.

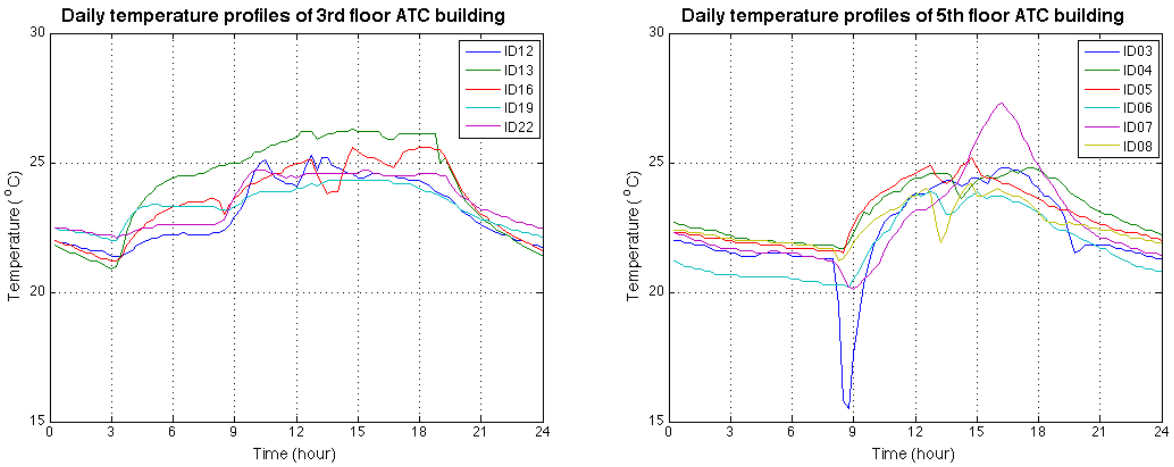

(a) *(b)*

Fig. 13. Daily temperature profiles of ATC building at Tuesday 20th January 2011: a) 3rd floor, b) 5th floor

Finally Fig. 14a shows another wrong management of space heating in 3rd floor. In fact the figure represents a Sunday temperature profile (16th January, 2011) where the switch on time was fixed at midday and energy was used to heat empty offices. A short heating time constant suggests to shift the on-timing at the beginning of the next day.
5th floor (see Fig. 14b) seems to be better managed on Sunday because the heating system was turned off during no-working day. Temperatures over 20 °C can be probably due to the solar beam effect on the temperature sensors (same effect is shown in Fig. 13b).

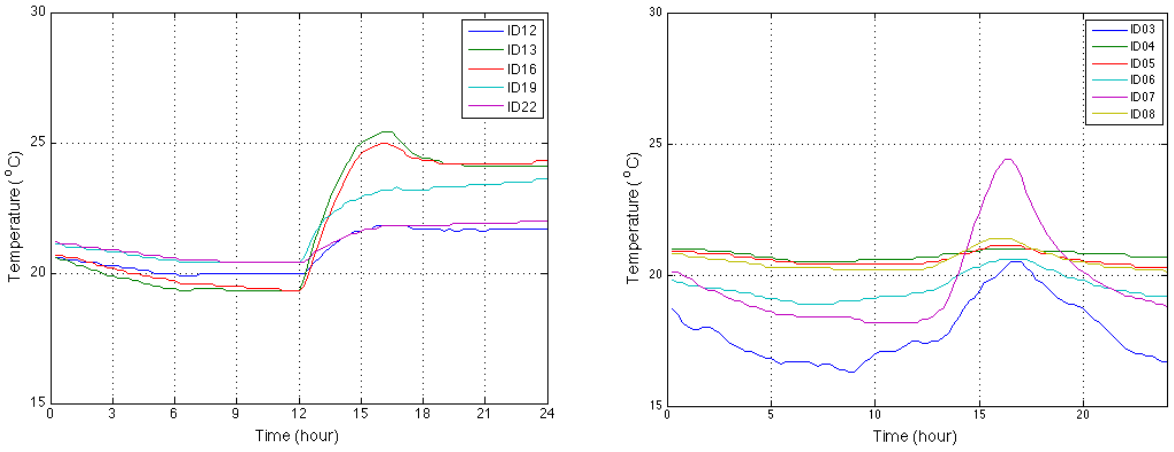

a) *b)*

Fig. 14. Daily temperature profiles of ATC building at Sunday 16th January 2011: a) 3rd floor, b) 5th floor

3. Conclusions

Temperature and consumption monitoring are good practices to investigate energy management, to reduce energy demand for space heating and to increase the comfort. In fact significant consumptions are often related to high temperature level, thus an accurate characterization of the temperature profiles allows to locate the area where improve the temperature management and reduce wasting energy for space heating.
This paper has underlined this aspects showing the links between consumptions and temperature profiles for two different type of consumers of the Polycity project: social housing and office building. For some people living in Arquata quartier, the relevant consumptions and the corresponding high temperature profiles can be related to an incorrect management of the heating systems of the flats. Particular attention has to be devoted on the education of citizens living in social housing to become smart and conscious users. This can be made by an adequate information campaign to educate the people to a right setting of the internal temperatures of the flats. For example, energetic benefits can be obtained simply reducing the internal temperature during sleep time.

Regarding ATC building the temperature profiles point out the energy waste in office building when the management system is neglected or it is wrongly used. For example, significant benefits in terms of energy consumptions for space heating could be reached by reducing the setting of internal temperature and by taking advantage of thermal inertia shifting the on-off timing of heating system. Reduction of internal temperature also allowed advantages in terms of comfort for the employees in a working place.

Refinement of energy consumption for space heating could be obtained improving information about DWH demand. Dedicated monitoring system for DHW consumption in each flat could be used to reach this goal, since detailed data on heating consumption could help to make more aware the inhabitants.

In this light, awareness is the key word to reduce the consumption. For this reason the results point out from Polycity project have led to continue the analysis of energetic behavior in social housing. The consequence of this choice is represented by the European project BECA, Balanced European Consumption Awareness [10].
Starting from the Polycity instrumentation, a more detailed monitoring system will be installed in some social houses and a web site will be developed in order to allow the knowledge of the measured profiles of the past months. In this way the inhabitants will know their own ambient conditions and consumptions and the energy managers will monitor the production of both the thermal plants and the global consumption of inhabitants. This project will involve three sites in Torino characterized by different supply and monitoring systems.

References

[1] Canova A., Cavallero C., Freschi F., Giaccone L., Repetto M., Tartaglia M., *Optimal Energy management,* IEEE Industry Application Magazine 15 (2009) 62-65.
doi:10.1109/MIAS.2009.931811
[2] Eicker U., Polycity: *Energy Networks in Sustainable C*ities, Stuttgart: Kraemer Verlag; 2011.

[3] Official website of Italian Polycity project – Available at www.Polycity-torino.info [accessed, 30th January 2012].
[4] Ueno T., Inada R., Saeki O., Tsuji K., *Effectiveness of an energy-consumption information system for residential buildings*. Applied Energy 2006; 83(8); pp. 868-883.
[5] Schweiker M., Shukuja M., *Investigation on the effectiveness of various methods of information dissemination aiming at a change of occupant behaviour related to thermal comfort and exergy consumption*. Energy Policy 2011;39(1); pp. 395-407.
[6] ASHRAE Standard (2003), *Energy-Efficient Design of Low-Rise Residential Buildings.*
[7] *Annex I – Description of work. Polycity Project.*
[8] *Meteorological database of Piedmont Region* (in Italian) – Available at www.arpa.piemonte.it/annali/meteorologici [a ccessed, 20th January 2012].
[9] D.P.R. 412/93, *Framework about design, installation, operation and maintenance of thermal plant inside buildings in order to reduce the energy consumption, in the implementation of article 4, paragraph 4, of the Law 9th January 1991, number 10* (in Italian).
[10] BECA project website – Available at www.beca-project.eu/index.php [accessed, 30th January 2012].
[11] Bellosio B., Giaccone L., Guerrisi A., Lazzeroni P., Martino M., Tartaglia M., *Energy Network in Sustainable Cities: towards a Full Integration of Renewable Systems in Urban Area*. Proc. IECON 2011, Melbourne November 2011, pp.3146-3151.

Extended Exergy Analysis of the Economy of Nova Scotia, Canada

David C. Bligh[a], V. Ismet Ugursal[b]

[a] *Dalhousie University, Halifax, Canada, DV511545@dal.ca*
[b] *Dalhousie University, Canada, Ismet.Ugursal@Dal.Ca*

Abstract:

Human societies may be modelled as very large complex systems involving multiple flows of energy and materials between different sectors. Traditional exergy analysis methods are inadequate for the analysis of such systems because they do not take non-energetic flows into account. Extended exergy analysis (EEA) allows for the inclusion of exergetic equivalents of non-energetic quantities labor, capital and the costs of environmental remediation. It is also possible within an EEA context to evaluate the efficiency of domestic household energy use with respect to the rest of the economy by considering labor as an output from all households. In this work, EEA is conducted to characterize the extraction, conversion, and end use of energy and materials in the economy of Nova Scotia, Canada, in 2006. The economy of Nova Scotia is divided into seven sectors reflecting the organization of economic data reported by Statistics Canada. The agriculture, industry, tertiary, domestic, natural resource extraction, energy conversion, and transportation sectors are each modelled according to their characteristic material and energy fluxes. A model of the structural connectivity of the economy in terms of exchanges between sectors is constructed. Equivalent values of exergy are computed for each flow of energy and material, and energy, exergy and extended exergy efficiencies are calculated for each sector of the economy of Nova Scotia and compared with those of Norway, China, Italy, Netherlands and the UK.

Keywords:

Extended exergy analysis, Exergy analysis of very large systems, Economy of Nova Scotia.

1. Introduction

1.1 – Exergy Analysis

Achieving a high level of energy efficiency is a primary objective in the design and performance evaluation of any system as the ever-increasing price of energy has shifted economic focus from the initial investment to life cycle cost.

By utilizing first and second laws of thermodynamics, the Exergy analysis provides a true measure of the efficiency of energy utilization. While the methods of exergy analysis for energy systems are well developed in the literature [1, 2], exergy analysis of economic systems are less common. Nevertheless, a number of analyses have been performed for countries like Canada [3], the United States [4], Norway [5], and others. One of the difficulties in conducting such analyses is obtaining statistical information on the national energy balance at the level of aggregation needed. The analysis of the United States for 1970 was the first of such studies, and considered the flows of energy carriers for final use in the society [4]. Wall [6, 7] devised a method of accounting for all types of material and energy flows in his analysis of Sweden, including harvested food and wood, ores and minerals, and the products of these raw materials. It is Wall's approach that is followed (though modifications are made where necessary) in the exergy analysis described in this work.

1.2 - Extended Exergy Analysis

While exergy analysis is completely satisfactory from a thermodynamic perspective, it cannot deal with non-energetic quantities labour and money, and therefore it cannot be used to analyse systems such as a national or regional economy that involves flows of non-energetic quantities. A method called Extended Exergy Analysis (EEA, also known as extended exergy accounting) was recently developed to evaluate these externalities within an exergy analysis [8]. 'Extended' refers to the inclusion of previously neglected non-energetic quantities labour, capital, and environmental remediation costs in the analysis. EEA assigns equivalent exergetic values to labour, capital, and the costs of environmental remediation of waste within a system based on the total physical exergy of materials and energy input to the system and a reference abundance of the quantity in question. In this way, a valuation in which kJ/kg is consistently equivalent to kJ/$ or kJ/hour is developed and applied to a system to quantify the externalities that are excluded from an exergy analysis.

EEA has been applied in recent years to a number of national and regional economies, including the province of Siena, Italy [9], Norway [10], the UK [11], China [12] and Netherlands [24]. In each case, the economy is divided into seven sectors: transportation, agriculture, extraction, conversion, tertiary, domestic and industry. The surrounding environment is represented as a separate sector, and other countries or regions with which the country in question might exchange mass flux, energy, capital, or labour, are represented as a sector as well.

Once all flows of material and energy, labour and capital have been identified and assigned equivalent exergetic values, the system or sector conversion effectiveness (ε_P), which is given by Sciubba [8, 13] can be computed:

$$\varepsilon_p = ee_{01} / \Sigma_j ee_{I,j} \qquad (1)$$

where ee_{O1} is the total extended exergy of the output and $ee_{I,j}$ is the sum of the equivalent exergetic inputs required to create the output. Thus, the extended exergetic cost (c_P) is simply the reciprocal of the conversion effectiveness.

Monetary flux, i.e. capital (C) is defined as [9]:

$$ee_{Cap} = \frac{e_{in,society}}{M2} \qquad (2)$$

$$C = ee_{Cap} \cdot C_{in} \qquad (3)$$

where e_{in} is the total exergy influx to the society, and M2 is the reference amount of currency available in the society, a term known to economists as "broad money", which is defined by the Bank of Canada [14] as "M2 (Gross): Currency outside banks plus bank personal deposits, bank non-personal demand and notice deposits; less interbank deposits; plus continuity adjustments.". In other words, the value of capital in terms of the exergy per monetary unit is the ratio of the total exergy consumption to the monetary circulation within that society. This flux is measured in J/$, and can be converted to a value of capital in any particular sector (C) by multiplying ee_{Cap} by the capital influx to that sector (C_{in}).

Similarly, labour flux (W) is defined as [9]:

$$W = n \cdot \frac{e_{in,society}}{n_{tot}} \quad (4)$$

where n is the flux of work-hours into a particular sector, n_{tot} is the total amount of work-hours generated in the entire system, and $e_{in,society}$ is the total exergy influx to the society. This calculation is useful when it is the exergetic value of labour in a particular sector that is under investigation. If instead the primary resource value of labour over the entire society is desired, then the total number of work hours generated in the Domestic sector ($n_{workhours,Do\ sector}$) is used:

$$ee_{lab} = \frac{e_{in,sector}}{n_{workhours,Do\ sector}} \quad (5)$$

The exergetic cost of environmental remediation is computed by the addition of a real or virtual effluent treatment process downstream of every production flux under investigation, such that the physical exergy of each effluent is reduced to zero before being returned to the environment; i.e. the reference state. Each treatment process requires material, energy, capital, and labour that must be accounted for under the principles of the EEA method [9, 13].

By its nature, EEA requires an expansion of the control volume over traditional exergy analysis. The boundaries must be sufficiently large to allow effluent from the process to exit the boundary at a state of zero physical exergy (i.e. with similar composition to the reference environment). This is accomplished by including the immediate surroundings of the process and effluent treatment in the control volume. An effluent stream can then be said to cause zero impact on the environment as it will be in thermodynamic equilibrium with the reference state before being discharged into the environment. Similarly, the control volume must include the portion of the environment from which resources and minerals are extracted. If the composition of the resource at the extraction site is known, then the chemical exergy can be computed based on the resource's chemical composition, physical state, and the Gibbs energy of formation of its constituents. If the resource is chemically indistinguishable from the reference state, then the chemical portion of exergy will be equal to zero.

Decisions on the scale of the time interval for EEA must be made on a case-by-case basis considering factors such as environmental regulations and buffering capacity of the environment. For the analysis of complex systems such as a country or region, it is convenient to use the time scale of one year, as it is done here, since most of the relevant statistics are published annually.

In an EEA, all fluxes of material and energy are assigned exergetic values according to the established literature. The sources of information and the calculation of exergetic values of all fluxes used in this work are presented in Bligh [15]. The standard reference environment (Pressure P_0 = 1.01325 bar and Temperature T_0 = 298.15 K) used by Szargut et al. [1] is used as the reference environment in this work. Gaseous components are assumed to behave as an ideal gas at standard temperature and pressure. Values of standard molar chemical exergy are given for most chemical elements and a wide selection of common chemical compounds in Szargut et al. [1]. For compounds not listed in available tables, the molar chemical exergy can be calculated from the values of chemical exergy of the constituent elements and the appropriate value of the Gibbs function of formation.

1.3 – Economic Indicators of the Economy of Nova Scotia in 2006

The latest complete set of economic and energy use and balance data for Nova Scotia is for the year 2006, therefore the EEA analysis conducted in this work is for 2006. In 2006, Nova Scotia's GDP

grew at a rate of 0.9%, similar to the growth rate in the previous four years. The distribution of the total GDP of $25.9 billion dollars amongst the sectors of the economy in 2006 was as follows: Agriculture: 3%; Extraction: 3%; Conversion: 2%; Industry: 16%; Transportation: 4%; Tertiary: 72%. The official energy balance of Nova Scotia is reported by Statistics Canada in the Report on Energy Supply and Demand [16]. The energy flows in PJ into and out of the Nova Scotian economy, as well as the energy use by each sector for 2006 are shown in Table 1.

Table 1. Energy flows of Nova Scotian economy 2006 (PJ)

SUPPLY	450.1	DEMAND	450.1
Domestic Production	214.3	Domestic Consumption	307.4
Fossil Fuels	183.3	Fossil Fuels	267.1
Coal, Coke, Coke Oven Gas	6	Coal, Coke, Coke Oven Gas	75.7
Natural Gas	141.7	Natural Gas	11.2
Crude Oil	26.7	Petroleum Products	178.2
NGLs	8.9	NGLs	2
Primary Electricity	4	Primary Electricity	3.3
Secondary Electricity	27	Secondary Electricity	37
Imported Energy	223.6	Exported Energy	142.7
Crude Oil and Refined Products	161.7	Crude Oil	10.2
Other Imports	61.9	Natural Gas	130.5
Adjustments	12.2	Other	2
		Domestic Consumption	307.4
		Industrial	23.8
		Transportation	67.5
		Domestic and Agriculture	30
		Tertiary	47.5
		Conversion	114.3
		Producer Consumption	24.3

1.4 – Scope and Objective

An exergy analysis of the economic sectors of Canada for the year 1986 was published by Rosen [3], but this analysis did not include any attempt to quantify the exergetic value of non-energetic quantities like labour and capital, and did not consider the question of waste materials deposited in the environment. Thus, for the first time an exergy and an extended exergy analysis of the Canadian economy at the provincial level was conducted by Bligh in 2011 [15] to initiate such studies and to serve as a guide for future analyses. The purpose of this analysis is to determine the efficiency with which each sector of the economy consumes natural resources, capital, labour and energy carriers, and produces products, capital, and other quantities. The year 2006 is used as the year of analysis because this is the last year for which there is a complete set of energy balance data available for Nova Scotia. The procedures used to conduct the EEA are based on the methodology developed by Sciubba [8, 9]. A brief summary of the results and a discussion are presented here. For a more detailed view, Bilgh [15] should be consulted.

2. Application of EEA to Nova Scotia

2.1. Economic Sectors of Nova Scotia

To apply EEA for a nation or other large social system, the society is broken down into seven sectors to be included in the control volume. This is a suitable disaggregation level as it includes the

five traditional economic sectors (Tertiary, Industry, Transportation, Agriculture, Domestic) as well as a sector representing the activity involved in the extraction of natural resources, and a sector representing the totality of energy conversion processes [9]. These two sectors, along with the agricultural sector, are largely responsible for societal exchanges of mass and energy with the environment. The economic activities included in each of the seven sectors of Nova Scotia are listed in Table 2. The accounting for each sector includes the import/export and transport of any raw materials or goods related to the sector activity and labour, capital and environmental remediation inputs and outputs. Major inputs to the system include commodities and energy carriers that are imported, harvested and extracted, or otherwise harnessed from the environment. Major outputs of the system are products, materials, goods, and services that are consumed or exported.

Table 2 - Activities, inputs, outputs, and main sources of data for each sector of the economy in Nova Scotia.

Sector	Major Activities	Main Inputs	Main Outputs	Data Sources
Extraction (Ex)	Oil and gas extraction (on- and off-shore), coal mining, extraction of ores and minerals	Energy carriers, primary resources	Primary resources	Report on Energy Supply and Demand in Canada
Conversion (Co)	Heat and power plants, including coal and oil/natural gas, as well as hydro, wind, solar, and geothermal, energy carrier production	Recycled waste, natural resources, energy carriers	Primary resources, secondary resources, thermal discharge	Report on Energy Supply and Demand in Canada
Industrial (In)	All industrial and manufacturing activities, excluding food processing and energy industries	Natural resources, products, resources, and energy carriers	Products, waste	Statistics Canada, Canadian International Merchandise Trade Database
Tertiary (Te)	Private and public sector services, including trade, commerce, finance, real estate, construction, schools, hospitals, hotels and tourism, entertainment, municipal engineering	Energy carriers, natural resources, and products	Labor and products	Report on Energy Supply and Demand in Canada, Provincial and Territorial Economic Accounts Review, The Input-Output Structure of the Canadian Economy
Agricultural (Ag)	Agriculture, fisheries (including fish farming), forestry, hunting, and related food processing industries. Food retail is included in Te sector	Petroleum products, electricity, and other energy carriers, natural resources	Natural resources	NS Department of Agriculture
Domestic (Do)	Households	Products, energy carriers, natural resources	Labor, waste	Provincial and Territorial Economic Accounts Review, Report on Energy Supply and Demand in Canada, CANSIM tables
Transportation (Tr)	Commercial transportation services of people and goods .	Energy carriers	Products, waste, and thermal discharge	Report on Energy Supply and Demand in Canada
Environment (E)	The natural environment (earth's crust, oceans, atmosphere)	Thermal discharge and waste	Resources	Human Activity and the Environment
Abroad (A)	The rest of Canada and Abroad	Exports to other provinces and countries	Imports from other provinces and countries	The Input-Output Structure of the Canadian Economy, Canadian International Merchandise Trade Database

The seven sectors correspond to the reporting methodologies by which Statistics Canada collects economic data, making them convenient for application to the EEA. Outside of the control volume are the environment (earth's crust, atmosphere, oceans, and the natural environment) and the Atlantic Region, the rest of Canada and other nations. Transfers of mass and energy between sectors are classified as fluxes. Fluxes between sectors (such as labour, waste, products, capital, natural

resources, heat discharges) are assigned equivalent exergetic values according to the ratio of energy to exergy as established in the literature for each type of flux.

A model of the economic activity that takes place within the Nova Scotian society is realized in this work as a series of linked data sheets [15]. Exergy balances for each sector of the society are tabulated in separate sheets and linked together to complete the picture. Each exergy flux between two sectors is represented by a flux category and a subscript listing the originating sector followed by the destination sector. For example, a flux of petroleum products from the conversion sector to the transportation sector is represented as $R_{co,tr}$, a flux of waste from the domestic sector to the tertiary sector is represented as $P_{do,te}$, and so on. Each flux is categorized according to the following:

R: resources, primary (fossil fuels, solar, wind, minerals, metals, geothermal, hydraulic) and secondary (products from petroleum refining, mineral- and metal working), and electric energy.
N: natural resources (agricultural products, wood, natural fibers, livestock, fish, game).
P: products (products and services generated by In, Tr, and Te-sectors).
T: trash fluxes (organic and inorganic waste materials) deposited in the environment.
D: discharge (combustion gases, thermal discharge including radiated heat), waste heat and mass spread in the environment at low temperature.
W: human work hours, labour
C: capital

The extended exergy of each sector is calculated after the initial exergy analysis is completed. Following the approach of Wall [6], exergy conversion efficiency is calculated by only considering output fluxes that are transferred between sectors. Thus output fluxes from conversion processes (like space heating and lighting) are not classified as outputs unless they are subsequently transferred between sectors. As such, products that are considered "final use" in a sector are accounted for in trash or discharge fluxes, with a corresponding drop in exergy content – caused by the destruction of exergy as the product is consumed.

Equivalent exergetic fluxes of the same type with the same destination and origin are summed for the analysis of each sector. For example, flows of matter from the extraction sector to the conversion sector include natural gas, coal, and crude oil, among other quantities. There may be several different types of coal or grades of oil produced by the extraction sector. At this level of disaggregation, the exergetic value of the particular flow of matter is the sum of the exergetic values of the different types of fuel that combine to make up the term reported by statistical agencies as "coal". These are tabulated on separate, linked data sheets. All flows are similarly disaggregated as is appropriate, according to the complexity of the composition of any particular flow.

2.2. Equivalent Exergy of Capital and Labor

The flux of capital from the Domestic sector to each of the other sectors is taken as the sum of the value of production [17], net subsidies [17], and depreciation (where available) [18]. The flux of capital from each sector into the Domestic sector is taken as the sum of the intermediate consumption of products and services by that sector [17], return on investment to owners or other operating surplus [17], and any capital expenditures [19]. Normally in economic analysis employees and owners are regarded as a part of the sector; in this work they are regarded to be a part of the Domestic sector, and accordingly all compensation flows from the originating sector to the Domestic sector.

The capital inflow to the Do sector should equal the outflow (as people invest in and consume the products from other sectors) minus the amount saved by households that year. As the savings rate

for 2006 in Nova Scotia was -2%, the output value from the Domestic sector was calculated to be 388.17 PJ.

The equivalent exergy (E_C) of any given capital flux (C_{in}) is calculated by multiplying by the exergy influx to the entire economy (E_{in}) divided by the reference amount of money (C_{ref}):

$$E_c = (C_{in})(E_{in}/C_{ref}) \quad (6)$$

In previous extended exergy analyses done for Norway [10], UK [11], China [12], and the province of Siena, Italy [9], the reference amount of money used was the quantity M2, or broad money, which is the amount of currency in circulation outside of banks, plus bank personal deposits and non-personal demand and notice deposits [14]. It is not possible to use a precise value of this measure for the analysis of the Nova Scotian economy as it is not calculated or published for Nova Scotia by any entity. Therefore, a value of M2 for Nova Scotia was estimated by multiplying the median of the 12 monthly values of M2 for 2006 for all of Canada [20] by the share of Nova Scotia's GDP relative to the total Canadian GDP [21]:

699,262.5 million $ x 2.2 % = 15,256.06 million $ (7)

The net exergy input to the Nova Scotian economy in 2006 is taken as the sum of all fluxes originating in either the environment or abroad (extracted, harvested, or imported) minus the total exports. This value is calculated as 316.01 PJ as shown in Table 3. These fluxes are taken directly from the exergy balance sheets presented in Bligh [15]. Thus, the exergy value of money in the Nova Scotian economy for 2006 is calculated as:

316.01 PJ ÷ 15,256.06 million $ = 20.71 MJ/$ (8)

This value is close to the value calculated by Sciubba et al. [9] for the province of Siena, Italy (18.18 MJ/USD). The capital inputs and outputs of each sector are converted to equivalent exergy using equation 6 and presented in Table 4. These fluxes are included in the extended exergy balance sheets.

Table 3 - Gross inputs and outputs to Nova Scotian economy 2006, calculated net input.

Fluxes	Energy (PJ)	Exergy (PJ)	Comments
R e,ex	0.01	0.01	Domestic coal production
R e,ex	26.75	28.89	Domestic oil production
R e,ex	140.58	146.20	Domestic NG production
R e,ex	-	0.89	Domestic minerals production
R e,co	4.31	4.31	Waterfall energy
N e,ag	38.23	41.67	Wood
N e,ag	5.62	5.62	Harvest
N e,ag	1.04	1.04	Fish
N a,ag	0.15	0.15	Food imports
N a,in	9.23	9.85	Wood
P a,in	4.27	4.41	Metals, plastic
R a,in	-	0.02	Minerals imported
R a,ex	75.75	80.30	Imported coal
R a,ex	172.85	186.67	Imported oil
R ex,a	10.18	10.99	Exported oil
R ex,a	130.50	135.72	Exported NG
R ex,a	-	0.38	Minerals exported
P in,a	46.14	46.71	Metals, minerals, etc

N ag,a	0.22	0.22	Food exports
EXTRACTED	216.54	228.63	
IMPORTED	262.25	281.41	
EXPORTED	187.03	194.02	
NET INPUT	291.76	316.01	

The equivalent exergy (E_W) of any given labour flux (W_{in}) is calculated by multiplying by the exergy influx to the entire economy (E_{in}) divided by the total number of work hours generated by the Domestic sector and input to all other sectors (W_{ref}):

$$E_w = (W_{in})(E_{in}/W_{ref}) \quad (9)$$

Labour is considered to be an output from the Domestic sector to all other sectors. Labour statistics are recorded by Statistics Canada in terms of total hours worked for all jobs [22]. The total number of hours worked for all sectors in 2006 was 777.5 million hours. Using the total exergy input to the Nova Scotian economy for 2006, the exergy value of labour for the Nova Scotian economy in 2006 is calculated as:

316.01 PJ ÷ 777,456,000 hours = 406.5 MJ/hour (10)

The labour inputs and outputs for each sector are converted to equivalent exergy using equation 9. These fluxes are included in the extended exergy balance sheets.

Table 4 - Exergetic equivalents of capital flows for each sector of the economy (PJ), Nova Scotia, 2006.

Sector	Capital Input (PJ)	Capital Output (PJ)
Extraction	36.73	51.36
Conversion	21.00	21.00
Agriculture	34.30	37.26
Industry	210.84	214.39
Transportation	67.01	76.65
Tertiary	882.24	908.00
Domestic	396.09	388.17
Total	1648.09	1696.83

2.3 Equivalent Exergy of Waste and Atmospheric Emissions

Most materials eventually end up as waste in one form or another. In Nova Scotia, approximately 40% of solid waste is diverted for recycling purposes and the rest is deposited in landfills. Since the available data is limited, in order to make a reasonable estimate of the waste generated by each sector of the Nova Scotian economy, assumptions were made about the composition and sources of waste. These assumptions are explained in detail in Bligh [15]. Thus, the resulting numbers should be used with caution. As the monitoring and auditing of waste streams improve, the information gathered will become easier to analyse.

In this analysis, the full amount of residential waste is attributed to the Domestic sector. Waste reported from industrial, commercial, and institutional sources is divided among the Agriculture, Conversion, Industry, Tertiary, and Extraction sectors according to their relative share of GDP for 2006. The Tertiary sector is additionally allocated all of the construction and demolition waste. Since there is no information on the composition of disposed waste, it is assumed that the composition of disposed waste is the same as the reported composition of diverted waste [31].

Diverted waste is accounted for under the EEA as a P-flux from the relevant sector to the Tertiary sector and is assumed that disposed waste is deposited in the environment whether in a municipal

landfill, or treated and deposited in the ocean. Disposed waste is accounted for as a T-flux from the relevant sector to the environment. Each flux relating to solid waste is included in the balance sheet of the relevant sector as either an output P-flux to the Tertiary sector or an output T-flux to the environment. The balance sheet of Tertiary sector records each solid waste P-flux as an input.

The earliest available dataset on criteria air contaminants (such as NO_x, SO_x, and CO) is from 2009, while detailed information on greenhouse gases (CO_2, CH_4, and N_2O) is available from the Environment Canada National Pollutant Release Inventory (NPRI) [23] at the provincial level for 2006. Volatile organic chemicals are recorded generally as VOC and are here assumed to be entirely composed of acetone (C_3H_6O). SO_x and NO_x are assumed to be entirely composed of SO_2 and NO_2, respectively. The largest single source of particulate matter in Nova Scotia is dust from unpaved roads, which is neglected due to a lack of information on their specific composition.

Atmospheric emissions are accounted for under the EEA as D-fluxes from the relevant sector to the environment. Each flux relating to emissions is included in the balance sheet of the generating sector as a D-flux to the environment. D-fluxes have been placed on the Input side of the generating sector's balance sheet to reflect the fact that these compounds represent a cost to that sector.

3. Results and Discussion

Energy, exergy, and extended exergy input and output fluxes for each sector of the economy were calculated and detailed results are given in Bligh [15]. Based on these results, energy, exergy and extended exergy efficiencies were determined as the ratio of output value to input value. Owing to space limitations, only the efficiency values are presented in Table 5, and extended exergy efficiencies are compared to the results from other studies in Table 6.

Table 5 - Energy, exergy, and extended exergy efficiencies of the economy of Nova Scotia, 2006.

	Energy Efficiency (%)	Exergy Efficiency (%)	Extended Exergy Efficiency (%)
Agriculture	69	69	74
Extraction	97	97	99
Conversion	62	59	61
Industry	91	88	88
Transportation	22	24	59
Tertiary	23	22	86
Domestic	5	5	126

Table 6 - Extended exergy efficiencies (%) by sector for recent analyses [9-12, 24].

	Norway (2000)	UK (2004)	Siena, Italy (2000)	China (2005)	Netherlands (2000)	Nova Scotia Canada (2006)
Extraction	94.5	91.4	33	88.3	97.1	99
Conversion	76.5	38.9	54	28.1	82.6	61
Agriculture	61.5	49.1	61	56.3	56.7	74
Industry	68.8	38.6	64	38.0	74.1	88
Transportation	62.8	31.5	26	23.9	68.6	59
Tertiary	74.6	80.0	85	54.9	61.3	86
Domestic	133.7	-	83	127.3	160.0	126

The Agriculture sector analysis results in relatively high efficiencies of approximately 70% for energy and exergy and 74% for extended exergy. The extended exergy balance sheet shows that this sector is producing large amounts of wood for transfer to the Industry sector, where it is processed into intermediate and final products for export and final consumption. A major loss of exergy in this

sector is the low conversion efficiency of animals in converting feed to protein for human consumption.

The Extraction sector efficiencies are very high mainly due to large amounts of natural gas produced and exported and large amounts of imported oil. As shown in Table 6, studies from other countries that have substantial hydrocarbon fluxes (Norway, UK and China) all found high extended exergy efficiency values for the extraction sector. The reason for such high conversion efficiencies is the fact that the extraction sector is distorted by huge values of chemical exergy corresponding to hydrocarbon production, import, and export. The 99.8% extended exergy efficiency for Nova Scotia implies that there is negligible room for improvement at only 0.2%; however this does not provide a complete and realistic picture because the scale of the hydrocarbon flux blurs the magnitude of the possible savings. If the hydrocarbon fluxes were removed from both sides of the Extraction sector balance sheet, the significance of the potential for improvement would become substantially greater.

The Conversion sector analysis results in a relatively high conversion ratio of approximately 60% for energy, exergy, and extended exergy. The balance sheet of this sector is dominated by the conversion of domestically produced and imported oil into energy carriers like fuel oils, gasoline, and diesel. Coal is the main fuel source for electricity generation in Nova Scotia, which lowers the overall efficiency relative to countries like Norway, where the main source of electricity generation is hydropower [5, 10].

The Industry sector is dominated by the wood, pulp, and paper manufacturing industries. They are the single largest users of energy carriers and are efficient at converting raw wood into intermediate and final products for domestic consumption and export. Thus Industry sector efficiencies are high due to the use of waste products for electricity and process heat generation. Also, the Industry sector is capital intensive, but generates a large output of capital in the form of wages and compensation and return on investment.

The Transportation sector energy and exergy conversion ratios are low due to the large losses involved in converting liquid energy carriers to kinetic energy for the transportation of goods and passengers. Land transportation methods, and particularly cars, have the largest effect on lowering these conversion ratios as they completely dominate the use of energy carriers in this sector. The extended exergy conversion ratio is significantly higher owing to the high rate of return on capital investment.

The Tertiary sector analysis likewise results in low energy and exergy efficiencies. There are assumed to be small losses in the transfer of products from this sector to the domestic sector, but it is the relatively inefficient end-uses of energy like space heating and cooling that result in such low energy and exergy efficiencies. The recirculation of waste materials from all other sectors to the Industry sector for reprocessing has the effect of raising these efficiencies. The extended exergy efficiency is much higher, representing the value of providing services to the Domestic sector in the form of labour and the high rate of return on capital investment.

The Domestic sector analysis results in very low energy and exergy conversion ratios of approximately 5%. Under the accounting principles followed in this work, this sector does not produce any products (besides waste) that can be quantified by their specific chemical exergy. The extended exergy conversion ratio is significantly higher, at approximately 126%, which is similar to the ratios calculated for Norway (133.7%), China (127.3%), and the Netherlands (160.0%).

The extended exergy efficiencies calculated for each sector of the Nova Scotian economy are compared with those calculated for four other extended exergy analyses conducted in recent years for three European countries and China in Table 6. This comparison indicates that there are substantial differences in the efficiencies of similar sectors throughout the world.

Discussion of Error

The production and import and export figures used in this work are taken from official Canadian statistical products generated by Statistics Canada and relevant reporting agencies. Different reports use different information gathering methods to estimate these figures, and each includes a measure of statistical error. For example, the Report on Energy Supply and Demand [16] published by Statistics Canada is the official energy balance of the country. The statistical difference between the availability and final demand of energy carriers is published as a fraction for each type of energy carrier. For Nova Scotia, this difference is zero for all energy carriers except refined petroleum carriers, where it is non-zero but suppressed due to the Privacy Act. The magnitude of production and use of refined petroleum products means that this difference would have to be substantial to have an effect on the energy or exergy conversion ratio for any sector, and so the influence of statistical errors like this can be omitted.

Material fluxes of organic matter, like wood and food, are more difficult to account exactly. The moisture content of products and resources can vary substantially during storage and transport and so assumptions have been made about the moisture and energy contents of these fluxes. Exact reporting of the production mass or volume is not always available at the provincial level. This is not due to a lack of information or lax reporting standards, but rather the restrictions placed on Statistics Canada by the Privacy Act. The exact reason why a particular figure is not publicly available is not reported for the same reason. Where possible, estimates of production are made according the relative values reported as transfers between industries in the Input-Output Structure of Canada [17].

The exergy value of capital as calculated in this work is an estimate based on an assumption about the amount of currency available in the Nova Scotia economy in 2006. The measure suggested by Sciubba et al. [9] is broad money (M2), which is not published at the provincial level for Canada. However, the calculated value is close to that calculated for the extended exergy analysis of Siena, Italy (18.18 MJ/USD) [9], another analysis at the provincial level, and that calculated for the extended exergy analysis of Norway (20.09 MJ/USD) [10].

The exergy value of labour calculated for Nova Scotia is relatively high (406.5 MJ/hour compared to those calculated for other extended exergy analyses. This value was calculated as 253.0 MJ/hour for Siena [9], 248.3 MJ/hour for the UK [11], and 71.9 MJ/hour for China [12]. Labour in Norway was calculated to have a value of 525.8 MJ/hour [10], which is close to the value calculated for Nova Scotia. This relatively high value is explained for Norway as being a result of the large role played by the energy conversion and extraction industries. This explanation is satisfactory for Nova Scotia as well.

4. Conclusion

Exergy and extended exergy analyses of the economy of Nova Scotia were conducted for 2006 considering all fluxes of materials and energy between sectors of the Nova Scotian economy. The energy, exergy and extended exergy efficiencies of each sector were calculated, discussed and compared with the results from other countries.

The results of this study show a large dissipation of high quality energy (loss of exergy) for the majority of economic activities within the province. There is room for improvement on these measures through policies directed at raising the conversion efficiency, but it is not clear that an absolute increase in exergy (or extended exergy) conversion efficiency for all sectors is beneficial for the society at large.

This is the first exergy and extended exergy analysis of the Canadian economy at the provincial level and serves as a guide for future analyses. The procedure for other provinces will be similar depending on the availability of statistical data. The procedure for the analysis of the whole of Canada may prove to be more straightforward than analysis at the provincial level owing to the abundance and fewer restrictions placed on data at the country level of aggregation.

Future studies can build on this analysis by inserting environmental remediation processes into the extended exergy analysis. In this work, only the specific chemical exergy of disposed waste and atmospheric emissions are considered as part of the extended exergy analysis. A theoretical process which brings the total exergy of each chemical compound or type of waste into equilibrium with the environment can be created, inserted where appropriate, and accounted for as an exergetic cost.

Acknowledgments

We gratefully acknowledge Professor Enrico Sciubba for useful discussions and explanations of the methods used in this work. D.C. Bligh is grateful for financial support from the Natural Sciences and Engineering Research Council of Canada through V.I. Ugursal's Discovery Grant.

References

[1] Szargut J, Morris D, Steward F. Exergy Analysis of Thermal, Chemical, and Metallurgical Processes. New York: Hemisphere Publishing Corp; 1988.

[2] Kotas TJ. The exergy method of thermal plant analysis. Essex: Anchor Brendon Ltd; 1985.

[3] Rosen MA. Evaluation of energy utilization efficiency in Canada using energy and exergy analyses. Energy 1992;17:339-50.

[4] Reistad GM. Available energy conversion and utilization in the United States. J Engineering for Power 1975;97:429-434.

[5] Ertesvåg IS, Mielnik M. Exergy analysis of the Norwegian Society. Energy 2000;25:957-973.

[6] Wall G. Exergy - a Useful Concept within Resource Accounting. Göteborg: Inst of Theoretical Physics. Rep no. 77-42;1977. Accessed Mar 9, 2011 from www.exergy.se/ftp/ex77c.pdf

[7] Wall G. Exergy—a useful concept. Göteborg, Sweden: Chalmers Univ of Tech. PhD Thesis; 1986.

[8] Sciubba E. Beyond thermoeconomics? The concept of Extended Exergy Accounting and its application to the analysis of design of thermal systems. Exergy Int J. 2001;1(2):68-84.

[9] Sciubba E, Bastianoni S, Tiezzi E. Exergy and extended exergy accounting of very large complex systems with an application to the province of Siena, Italy. J of Env Management. 2008;86:372–382.

[10] Ertesvåg IS. Energy, exergy and extended exergy analysis of the Norwegian society 2000. Energy. 2005; 30:649–75.

[11] Gasparatos, A, El-Haram, M, Horner, M. Assessing the Sustainability of the UK Society Using Thermodynamic Concepts: Part 2. Ren and Sustainable En Rev, 2009;13:956-970.

[12] Chen GQ, Chen B. Extended-exergy analysis of the Chinese society. Energy 2009; 34:1127-1144.

[13] Sciubba E. Extended-exergy accounting applied to energy recovery from waste: the concept of total recycling. Energy 2003; 28:1315–34.

[14] BoC. Backgrounders (Monetary Supply). Bank of Canada. 2011 Accessed April 11, 2011 www.bank-banque-canada.ca/en/backgrounders/bg-m2.html.

[15] Bligh DC. Extended exergy analysis of the Nova Scotian Economy 2006. Halifax, Canada: Dalhousie Univ. MASc Thesis; 2011.

[16] Statistics Canada. Table 128-0010 - Supply and demand of primary and secondary energy in natural units, annual. CANSIM (database). Accessed Jan 20, 2011 from: http://cansim2.statcan.gc.ca/cgi-win/cnsmcgi.exe?Lang=E&CNSM-Fi=CII/CII_1-eng.htm.

[17] Statistics Canada. The Input-Output Structure of the Canadian Economy 2005/2006 (Input Output). Accessed March 9, 2011 www.statcan.gc.ca/pub/15-201-x/15-201-x2009001-eng.htm.

[18] CANSIM. Statistics Canada. Table 031-0002 - Flows and stocks of fixed non-residential capital, by North American Industry Classification System (NAICS) and asset, Canada, provinces and territories, annual (dollars). CANSIM (database). Accessed April 11, 2011 www5.statcan.gc.ca/cansim/a01?lang=eng.

[19] CANSIM. Statistics Canada. Table 029-0005 - Capital and repair expenditures, by sector and province, annual (dollars). CANSIM (database). Accessed: April 11, 2011 www5.statcan.gc.ca/cansim/a01?lang=eng

[20] CANSIM. Statistics Canada. Table 176-0025: Chartered bank assets and liabilities and monetary aggregates, monthly average, seasonally adjusted; Canada; M2 (gross). CANSIM (database). Accessed April 11, 2011 www5.statcan.gc.ca/cansim/pick-choisir?lang=eng&searchTypeByValue=1&id=1760020.

[21] NS Finance. Nova Scotia Statistical Review 25th Ed, Dec. 2007. NS Dept of Finance. Accessed Aug. 5, 2011 www.gov.ns.ca/finance/publish/statsrev/2007/NSSTATS_Review_2007.pdf

[22] CANSIM. Statistics Canada. Table 383-0009 - Labour statistics consistent with the System of National Accounts, by sector, job category and North American Industry Classification System (NAICS), S-level aggregation, annual, CANSIM (database). Accessed April 11, 2011 www5.statcan.gc.ca/cansim/a01?lang=eng.

[23] Environment Canada. National Pollutant Release Inventory. Accessed March 9, 2011 www.ec.gc.ca/inrp-npri/default.asp?lang=En&n=4A577BB9-1.

[24] Ptasinski KJ, Koymans MN, Verspagen HHG. Performance of the Dutch Energy Sector based on energy, exergy and Extended Exergy Accounting. Energy 2006; 31:3135–3144

Feasibility study and design of a low-energy residential unit in Sagarmatha Park for environmental impact reduction of high altitude buildings

Umberto Desideri[a], Stefania Proietti[b], Paolo Sdringola[c] and Elisa Vuillermoz[d]

[1] Department of Industrial Engineering - Perugia University, Perugia, Italy, umberto.desideri@unipg.it
[2] Department of Industrial Engineering - Perugia University, Perugia, Italy, stefania@unipg.it
[3] Department of Industrial Engineering - Perugia University, Perugia, Italy, psdringola@mach.ing.unipg.it
[4] Ev-K2-CNR Committee, Bergamo, Italy, elisa.vuillermoz@evk2cnr.org

Abstract:

The project presented in this paper is geographically set within Sagarmatha National Park, a wide area located on the Nepalese mountainside of Everest and declared as World Heritage Site since 1979. In recent years the park was the focus of several studies and initiatives, aimed at improving the management of its many-sided ecosystem, significantly influenced by climate change and increase of human activities and tourism, which occurred from the end of the 1970s, as well as by practices that are harmful both to human health and to our environment (e.g. burn up kerosene or animal excrements in order to obtain heat).
Research work has focused on designing a residential unit that meets population needs, in terms of simplicity of realization, replicability, use of local materials, environmental compatibility and exploitation of available renewable energies. For this purpose a thorough analysis was conducted to identify the housing standard characteristic of reference context and Sherpa people, concerning indoor thermal comfort conditions, construction techniques, availability and skills of local workforce. Data necessary for the design phase were obtained through a collaboration with researchers of Ev-K2-CNR center, active at 5,050 meters a.s.l. in Nepal at the base of Mount Everest with a laboratory/observatory (known as the "Pyramid") for high-altitude meteorological studies since 1989. Climate conditions were registered by specific monitoring stations at certain times (2002-2008); during preliminary stage, these values were considered representative of the local context chosen for the project, that is Namche Bazar, a village located within the park, in a central point both from the logistic and altimetric/weather points of view.
For the residential unit under investigation, two different constructive approaches were selected and compared: earthbags and straw bales. Both techniques have several advantages, in particular availability of raw material (jute bags, soil, straw), simplicity (e.g. earthbag constructions are realized using the ancient technique of pisé, combined with flexible bags or tubes), durability, insulation performance, cost-effectiveness. Through a specific software for calculation of winter/summer thermal loads, different combinations of selections of structure and insulation were examined for both solutions, in order to achieve the optimum for the case study. Furthermore on the base of data monitored on site, a specific assessment was carried out to evaluate the potential of solar and wind resources. Aiming at entirely covering the heat and electric energy needs by exploiting renewable energy sources, various plant configurations were finally assumed.
Every single choice was made to reduce human influence on land resources, such as timber, and to improve internal and external environmental quality.

Keywords:

Energy and Environmental Sustainability, High altitude buildings, Earthbags, Straw bales, Low-energy Residential Unit.

1. Introduction

The present article describes a project started from the cooperation between the Industrial Engineering Department of the University of Perugia and the Ev-K2-CNR Committee in Bergamo.

Ev-K2-CNR is well known for the Pyramid International Laboratory-Observatory, the high altitude scientific facility located on the Nepalese side of Everest at 5050 meters a.s.l. (Fig. 1), which is one

of the world's most important centres for high-altitude meteorological studies since 1990 [1]. The project is geographically set within Sagarmatha National Park, in the region of Kumbu, a wide area located on the Nepalese mountainside of Everest and declared as World Heritage Site since 1979. In recent years the park was the focus of numerous studies and initiatives, aimed at improving the management of its many-sided ecosystem, significantly influenced by climate change and tourism increase, which occurred from the end of the 1970s, which had a considerable impact on the local economy.

The objective of this research work was to design a residential unit that meets the local people's housing needs, in terms of simplicity of realization, replicability, availability and cost-effectiveness of materials, environmental compatibility and exploitation of available renewable energies. The aforementioned goals are in line with the present management approach of the park, aimed at reducing human impact on that environment. The scarcity of energy resources in some sub-realities of the park, for example, constrains local people to burn kerosene or animals excrements in order to produce heat. This causes very important problems both for the health of inhabitants of the area and for environment, as demonstrated by results of several monitoring campaign.

Climate data were provided by the researchers of the Ev-K2-CNR centre; since the park covers a wide area, climate values were registered by specific monitoring stations during the years 2002-2008. Among different options, the choice was addressed to Namche Bazaar (Fig. 2), a village located within the park, in a central point both from a logistical and altimetric/weather point of view. During the preliminary stage, these values were considered representative of the local context chosen for the project.

Fig. 1. The Pyramid Laboratory-Observatory, Ev-K2-CNR

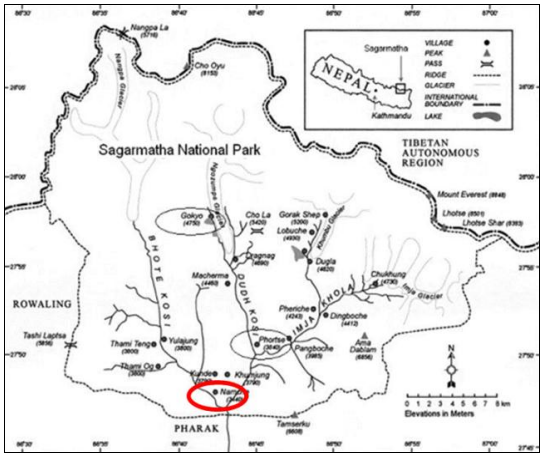

Fig. 2. Namche Bazaar, Sagarmatha National Park, Nepal

2. Site description

Sagarmatha National Park is a protected area in the Himalayas of Eastern Nepal, containing the Southern half of Everest. Sagarmatha is a Sanscrit word meaning "Mother of Universe" and it is the modern Nepali name for Mount Everest. The park lies within an area of 1148 km^2, which is located between 27° 30' 19" - 27° 06' 45" N latitude and 86° 30' 53" - 86° 99' 08" E longitude, on the border with the Tibet Autonomous Region. It ranges in elevation from 2845 m at Jorsalle to 8848 m at the summit of Mount Everest. Barren land above 5000 m is 69% of the park, while 28% is grazing land and the remaining 3% is forested; most of the park area is very rugged and steep, with its terrain cut by deep rivers and glaciers.

Unlike others, this park can be divided into different climate zones because of the rising altitude. They include a forested lower zone (alpine scrub), an intermediate one including the upper limit of vegetation growth, and the Arctic zone where no plants can grow. The indigenous Sherpa

population is about 2500 people, mainly Buddhists, whose economy is based on agriculture and trade. Their properties were legally annexed to the park [2]. Since the first time the Everest summit was reached in 1953, the inflow of tourists was continuously increasing over the years, rising from 1400 visitors in 1972 to 7492 in 1989, to over 20,000 after 2004 [3].

2.1. Conservation management

The National Park and Wildlife Conservation Act (1973), the Himalayan National Park Regulation (1979) and the Buffer Zone Organization Guidelines (1979) provide legal basis for the conservation of flora and fauna. The main objectives of the conservation management plan are to protect animals, waters and grounds, since the park has national and international importance. It is also directed to safeguard the interests of Sherpas, as well as those communities living further downstream.

As for energy consumptions within the park, some elements must be take into account in order to propose effective patterns, which could be adaptable to this territory. Due to low temperatures and atmospheric pressure, the boiling point of water decreases at higher *altitude*. Although a lower energy consumption is necessary to reach the boiling point, cooking is longer due to the lower temperature and the energy consumption is nonetheless higher. The overall energy consumption for heating and cooking is therefore higher. Moreover, there is a different availability of energy resources, such as wood (88%), kerosene (7%), LGP (2%), animal excrements (2%) and sun energy (1%). However, because of its geographic distribution, wood is more consumed by houses located at altitudes between 2500 and 3000 meters than houses at higher altitudes, where wildlife has a lower concentration and combustible materials such as kerosene, excrements and LGP are more used (Table 1). *Income* is another discriminating factor for accessing energy resources, in fact high-income families use quality resources (e.g. LGP), while low-income families are forced to use low-quality materials (e.g. animal excrements). Finally *tourism* led, on the one hand, to the introduction of renewable sources (e.g. solar thermal panels) and, on the other hand, to spread construction techniques based on cement, which are poorly effective in this case, because of too wide glass surfaces, too thin walls and lack of appropriate thermal insulation, with a consequent increase in energy demand [4].

A study concerning the distribution of consumptions among different final uses shows that 56% is associated with cooking, covered mainly by wood and electricity, followed by kerosene and LPG. Wood, animal excrements and electricity are the most used sources for space heating (34%), while LPG and solar thermal systems are more used for heating sanitary water (8%). As previously noted, the use of solar collectors is a prerogative of the hotels with economic resources necessary for their installation [4].

The use of aforementioned fuels, together with bad daily habits (e.g. rooms' inadequate ventilation, which is also favored by an architecture that prefers the use of compact rooms with few openings) and obsolete technologies (e.g. stoves are not connected to a chimneypot, so they emit pollutions directly into the room), cause high levels of indoor air pollution. This reduces the quality of life and determine a number of respiratory diseases especially in elderly people, women and children. A survey carried out by the HKKH Partnership[1] registered, for example, the highest concentration of CO (200 ppm) during cooking hours in the homes with traditional cooking stoves (Fig. 3) [5].

The increase in touristic inflow entailed a greater need for wood as both building material and fuel. Because of the lack of a regulation on the park forests conservation management, since the 1960s there was a progressive deforestation and the consequent alteration of the hydro-geological system, combined with strong impact on Sagarmatha Park's biodiversity and, therefore, on its wildlife balance [4].

Moreover, progressive worsening of water environmental conditions was registered in Kumbu in recent decades, due to uncontrolled human pressure on natural resources. The proliferation of alpine

[1] The HKKH Partnership Project aims at consolidating the institutional capacity of planning and managing the socio-ecological systems in the regions Hindu-Kush-Karakoram-Himalaya.

tourism generated accumulation of waste along the paths beaten by excursionists, which subsequently fell into torrents and rivers; in addition, organic waste is usually discarded into designated wells or trenches close to houses, and chemicals waste is generated by fertilizers used in agriculture [6].

2.2. Climate data

The data used for this project are based on values measured during CEOP Himalaya experimental project, which provides long-term monitoring of monsoons effects at higher altitudes [7]. Measurements were made every hour during the period from 01/01/2002 to 31/12/2008. Fixed on site station monitors the following parameters at different altitudes (1.5÷5 m): atmospheric pressure (P); air temperature (T); relative (U_r) and specific humidity (U_s); speed (v_V), direction, horizontal and vertical components of wind; rainwater (P_p), incident solar radiation (H_{gh}).

The data shown in table 2 are an average of the measurements made over the period between January 2004 and December 2008. Solar radiation is quite constant over the year, with a maximum value in May; there are also two peaks, which occur in June and September, respectively at the end of the pre-monsoon period and at the beginning of the post-monsoon one. The reason is that in this lapse of time, the rain and an intense cloudiness filter the sun rays , thus provoking a decrease in the measured solar radiation. Regarding the external air temperature, the annual range goes from a maximum of 23 °C to a minimum of -13 °C (punctual values). On the basis of wind speed hourly values, the related duration curve was graphed (Fig. 4); it highlights for how many hours over a year a specific speed is exceeded in the selected site.

Table 1. Daily mean per capita consumption of primary energy sources for each altitude range

Altitude, m	Wood, kg	Kerosene, kg	LGP, kg	Excrement, kg	Electricity, kWh_e
2500-3000	23.46	0.88	6.52	-	2.4
3000-3500	10.93	5.25	7.6	-	23.4
3500-4000	13.31	5.6	1.18	7.48	11.23
4000-4500	16.61	5.77	1.29	8.62	4.5
4500-5000	-	15.66	1.52	14.03	1
>5000	-	9.8	-	9.93	1

Table 2. Monthly mean values of some climatic variables

Month	P, hPa	T_e, °C	U_r, %	U_s, g/kg	v_V, m/s	P_p, mm	H_{gh}, MJ/(m^2day)
J	661.9	-1.27	66	3.24	1.46	10	13.15
F	661.2	-0.54	78	4.26	1.65	20	16.28
M	663.5	2.66	79	5.42	1.79	50	20.21
A	664.8	5.33	81	6.64	1.85	80	23.13
M	663.9	7.89	90	8.96	2.08	110	22.89
J	663.6	10.26	98	11.61	1.92	490	17.30
J	664.0	10.92	100	12.31	1.84	580	15.98
A	663.8	10.88	99	12.21	1.81	520	15.67
S	666.3	9.61	83	9.41	1.66	330	16.32
O	666.6	4.85	90	7.23	1.66	30	18.10
N	665.1	2.93	72	4.97	1.52	10	15.77
D	663.5	2.04	60	3.80	1.29	10	14.27

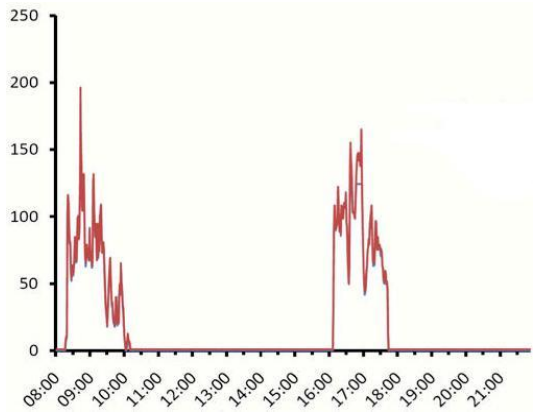

Fig. 3. Average daily trend of CO concentration (ppm)

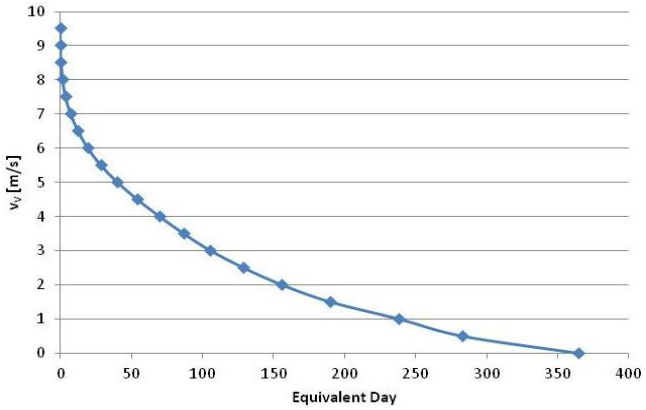

Fig. 4. Duration curve of wind

3. Construction techniques analysed for the residential unit

3.1. Architecture and local construction techniques

Part of the work involved the analysis of the construction types existing on site, in order to design a residential unit sustainable from the energy point of view (including the use of local materials) as well as integrated within the local context.

In the Himalayan region the resources used in construction are mainly wood for internal support structure, stone or soil for envelope, according to different installation techniques: compressed clay (gyang) or sun-baked mud bricks (saphang) [8]; dry masonry with different types of foundation according to the substrate type. From the architectural point of view, Sherpa villages have three distinct types of housing, one of which is the basis of the others, characterized by elongated shape, two-levels, ground floor partially adjacent to the side of the mountain. The simplest type (basic module), and consequently the most used by Sherpas, provides a single block, where ground floor is formed of store (for fodder, firewood and agricultural tools) and the stable for livestock, with a wooden staircase which leads to the upper floor, where there is a large space dedicated to domestic and social life of the family (Fig. 5). The other two housing types are obtained by adding two or more blocks to the basic module described above, thus resulting in an even more elongated or L shape house.

Therefore, in Khumbu region houses are mainly made of stone, which is abundantly present throughout the territory and derived from reclamation of agricultural soils or recovery of collapsed material or picked up along rivers, dry laid using techniques that depend on both the region and the stone typology (Fig. 6). External masonry walls are characterized by natural stone veneer facing or may be covered by a soil layer which acts as a plaster; the stone layer should be about 70-80 cm thick, however, this measure may vary within the park, given that it is a self made construction and therefore a standard process guide lacks. Wood, precious material in regions subject to excessive deforestation such as Solukhumbu, is mainly used for load-bearing structures and works of completion; concrete is used only in recent years for commercial and tourist buildings. As for floor, timber joists are disposed perpendicularly to the main girders, overlaid by floorboards; the roof is characterized by the same structural scheme, except for the specific inclination of the pitched roof. Windows have a timber frame and 3-4 mm thick single glasses; the openings are exposed to South-East in order to maximize the light in the house [9].

For the residential unit subject of study, the use of *reinforced concrete* structures was initially excluded; since it is not a technique rooted in the region, it would require the intervention of specialized technicians both in design and construction phases, option economically unattractive. About *steel*, the considerations are nearly similar, although in the design phase it was taken into

account for realizing the bearing structure, in replacement of traditional wood; the supply of certain materials in the villages immediately next to the infrastructural network could, in fact, relatively affect the final cost of the work. *Wood* could be a viable alternative, being a material which is already used in the region; however, the aforementioned considerations concerning the deforestation problems make it an unsuitable choice.

Thus, an assessment was carried out on possible sustainable construction techniques in the area described above, from an economic point of view and for the use of local material and labour.

Apart from bamboo, which is available in Nepal but not in the Khumbu region, buildings made of straw bales and earthbags were analysed. Both techniques have several advantages:

- *Material availability*. Straw for insulation is a material widely present in a region based on sheep farming such as the examined area; the same consideration applies to the jute bales, of which Nepal is a leading global manufacturer.
- *Simplicity of construction*. These types of housing may also be made by unskilled people, who do not have specific knowledge of the construction industry; they also have the advantage of being very versatile in terms of shapes, as they are not limited by the geometry of a basic element such as brick.
- *Durability*. If well protected, the filling material is generally not subject to decomposition, nest of worms or fire, therefore it is extremely durable. Some authors argue that the average life of these structures under service loads is 100 years [10].
- *Insulation performance*, through the use of materials such as straw or vermiculite.
- *Cost-effectiveness*, These building types are an inexpensive way to build, given the materials used, and therefore also represent an interesting solution in a context where the population does not have very high incomes [11].

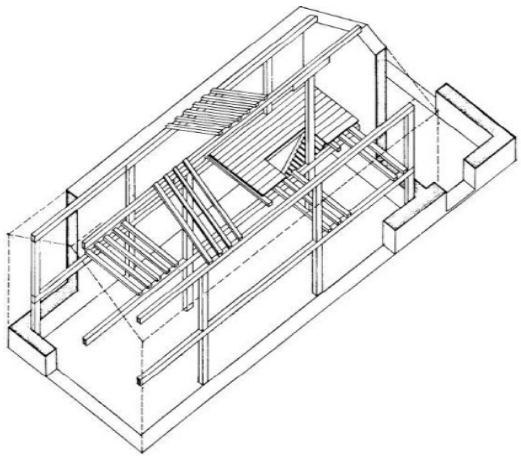

Fig. 5. Typical house perspective view

Fig. 6. Timber and stone house

3.2. Straw bale constructions

Techniques employing raw earth as building material are many and vary depending on the environmental, cultural and geographic characteristics in which they are applied, in particular: adobe, pisè, straw bales, torchis, pressed blocks, bauges [12-14].

Specifically, the straw bale technique considers the construction of a primary wall in bales of straw, supported by a timber or metal light structure, which is then covered with a layer of soil-based plaster, paying particular attention that this does not penetrate the straw; actually, the aim is to leave inside empty spaces, responsible for its insulating capacity. The technique of the soil-based plaster consists in proceeding by successive layers, with progressively finer granulometry; at the end of the process there can be a phase of smoothing and compacting of the surface. Given the predisposition

to shrinkage, an adequate presence of fibers is expected for internal plasters not subject to rain and atmospheric agents; in case of exterior plasters, it is always preferable to add a binder material such as lime and cement, which gives more stability and increases resistance to humidity and rain water [15].

3.3. Earthbag constructions

The idea of building walls with dry stacked sandbags was started about a century ago in military and civil defense; the first uses of this technique was designed to control flooding and create military trenches (temporary facilities or barriers). A leader in this field is the German architect and researcher Gernot Minke who, since 1976, began to look for solutions for using sand and gravel instead of concrete. Later, around the beginning of the 1980s, the notion of permanent houses built in bags became popular thanks to Nader Khalili, an Iranian architect, who created the technique of "Superadobe", which consists in filling the bags with a mixture of clay, sand and water that, once dry, would have constituted the bearing structure [16-17].

The bags are filled in with soil of different granulometries, which should have a 30% clay component, characterized by a low tendency to expand when subjected to humidity (i.e. kaolinite) [15]. Alternatively, in case of filling with incoherent material, this should be added with a binder, such as lime and cement. The first bags were in natural materials such as canvas or jute, while more recently polypropylene is used; they offer excellent resistance against expansion, but are subject to damage by long-term exposure to UV rays, so they must be properly protected by a plaster layer.

4. Design choices

The analysis carried out in the present study does not consider the structural aspects of the module. The possible solutions in terms of materials are represented by wood and steel; at present, it is not possible to say which is the best, since some parameters are unknown such as cost, transportability, on site workers' skills, study of loads with related impact on the structural element sizes. From an environmental point of view, due to the increasing deforestation, steel would limit the timber use in constructions.

On the basis of what is described in the previous section, it was possible to define the dimensions of an elementary residential unit (Fig. 7), for which two different design criteria were also assumed for building envelope. Given the difficulty in finding specific information about doors and windows typically used in the houses, a qualitative assessment was necessarily based on the photographic available material. The front door is supposed to be in raw fir wood (0.9 m x 2 m, 2.041 W/m^2 K), as well as windows, with double glazing 4-12-4 (no. 1, 1.5 m x 1.5 m, no. 2, 0.9 m x 1.5 m, South-facing; 2.684 W/m^2 K). Particular attention should be paid planning these elements, because it is not possible to act subsequently in a non-destructive way.

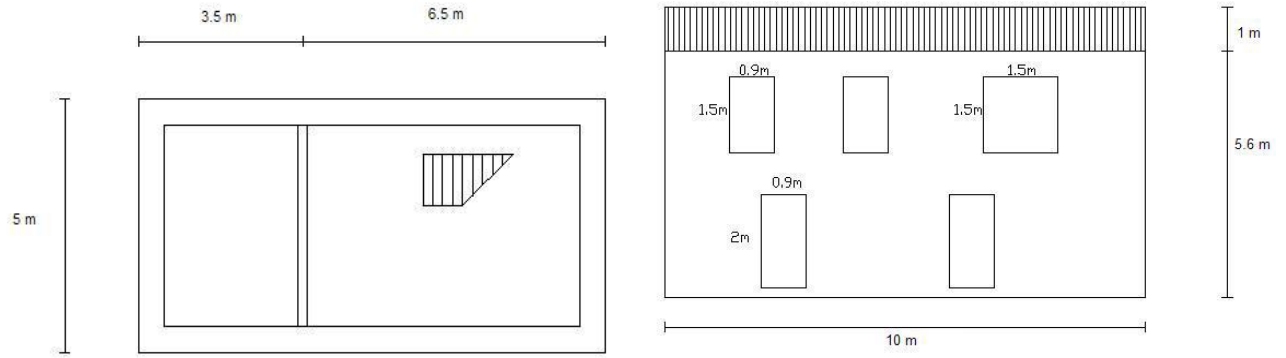

Fig. 7. Dimensions of the analysed residential unit

4.1. First design assumptions for the building envelope (S1)

The technique of straw bales requires a drying period for expelling the water contained inside. In order to evaluate the possibility to apply this technique in the Solukhumbu region, it is necessary to assess what is the most suitable period for the construction phase, depending on drying (and therefore on humidity) and on raw material workability (and thus on temperature). Based on the recorded parameters, the most binding constraint is the relative humidity, which, in the monsoon season (between June and August), reaches 100%; this forces to choose September and October as drying period, characterized by temperatures ranging between 5 °C and 12 °C and wind speed that, even if not so high, facilitates drying.

This type of external masonry veneer wall presents a good degree of insulation, according to the thickness of straw, but a reduced thermal inertia, due to the low density of straw and the thin soil layer. To solve this problem, the two properties can be separated, using the stone of the Himalayan areas in order to protect the exterior layer from atmospheric agents, thereby increasing the thermal inertia of wall assembly. The chosen solution among those analysed provides the following stratigraphy from the outside inwards: stone (30 cm), soil (2 cm), straw (45 cm), soil (2 cm), internal plaster (1 cm), for a total thickness of 80 cm and a transmittance of 0.186 W/(m^2 K). For its construction, the procedure consists in building a frame that wraps the straw bales previously stacked up. The frame, made in wood or in any material that could perform the same function, remains internal to the wall once the soil is laid mud and it is usually presented as a grid having a 50 cm pitch in both directions. A layer of soil with a high clay component is distributed on both sides, so as to close the internal straw walls; then a stone wall is built, which rests against the outer face, and finally the interior plaster is laid.

It is necessary to consider that the formation of internal condensation can cause the humidification of raw earth and for this reason vapor barriers should be used, that may inhibit the passage and avoid the wall degradation. Whereas, the exterior stagnation of rain water should be avoided by appropriate removal systems as small trenches and by raising the supporting basement. Another problem is the water rise from the foundation; in this case it may be convenient to create a draining wall plate made of sand or gravel, and create an overlying waterproof layer.

As for roofing, the chosen solution among those analysed provides the following stratigraphy from the outside inwards: board (2 cm), waterproof layer, layer of cellulose fiber such as leaves or straw (30 cm), vapor barrier, board (1 cm), for a total thickness of 33 cm and a transmittance of 0.297 W/(m^2 K).

The traditional buildings of the Khumbu region are characterized by floor made of timber joists and floorboards; the proposed solution plans of maintaining the above system, adding a lower board and filling the air gap with insulating material (e.g. 30 cm thick straw).

4.2. Second design assumption for the building envelope (S2)

The earthbag constructions have different shapes corresponding to specific needs. A dome shape gives self-bearing capacity to the structure, but it is not typical of the Solukhumbu region. Then for this case study a structure with vertical walls was considered, where the earthbags are used for the external masonry, while the roof is made of wood.

The earthbags usually provide high thermal inertia, but are characterized by a low insulating effectiveness. A possible solution is to couple them with straw layers, which determines an increased thickness of the wall structure (70-80 cm). The selected alternative, already indicated by Owen Oyger [18], consists in dividing the bag into two compartments, of which the exterior part filled in with insulation, and the interior part with soil, according to the following stratigraphy (from the outside inwards): plaster of soil and lime (1 cm), polypropylene (5 mm), soil (15 cm), polypropylene (5 mm), perlite (15 cm), polypropylene (5 mm), plaster of soil and lime (1 cm), for a total thickness of approximately 33 cm and a transmittance of 0.220 W/(m^2 K).

For this technique, specific types of foundation were tested, which could be used on site, in addition to traditional ones in lightened concrete; these are based on stabilization of the soil, already used for

filling bags, through the addition of binding materials, usually cement, asphalt emulsifiers or lime [19-20]. Even in this case it is necessary to emphasize the importance of creating something able to prevent capillary rise; this barrier can be made using commercial products or, alternatively, local materials: two alternating rows of flat stones, for example, can be laid between the foundation and the first layer of earthbags. If soil does not provide a proper drainage, a foundation trench filled with small stones, gravel or cement debris has to be created; the first row of bags is placed, paying attention that each bag is well covered by the former. Common work tools are used for tamping, which are characterized by a flat base sufficiently large to cover half bag. Generally barbed wire must be placed at every level of bags, in two rows running parallel to the direction of the wall, spaced one each other by 20 cm; this has a velcro joint effect the prevents lateral expansion due to vertical compression. In order to improve the structural solidity, the bags must be installed vertically staggered.

For the roofing, the selected solution among those analysed provides the following stratigraphy from the outside inwards: joists and roof tiles (3 cm), waterproof membrane, perlite layer (20 cm), Kraft paper, timber layer (3 cm), lime and cement plaster (2 cm), for a total thickness of 28 cm and a transmittance of 0.22 W/(m^2 K). Regarding the floor, the choice is an insulation based on the use of a perlite layer in the assembly, according to a stratigraphy similar to the one used for the roof.

5. Energy analysis

The energy assessment of the module was performed using STIMA 10 TFM software, which aims at calculating winter and summer thermal loads, on the basis of climate and geographic parameters and all technical data related to the designed structure [21]. The studied residential unit was modeled to be calculated by the software, reporting each room size, doors and windows orientation, stratigraphies of the structural elements defining the heated volume (integrating the existing library). The energy analysis was also carried out on the basis of the assumptions described in the next paragraph.

5.1. Calculations

In the Solukhumbu region, district which includes the Sagarmatha Park, for the first time an experimental campaign was recently promoted, aimed at studying thermal control methods of residents, estimating their neutral temperature and evaluating thermal comfort conditions in inner spaces. The survey campaign was conducted by giving the inhabitants a questionnaire to complete concerning comfort levels of the housing, in relation to certain internal temperatures [22]. The study brings out the following results:

- winter conditions: average recorded internal temperature 6.5 °C; comfort temperature 13.4 °C;
- summer conditions: average recorded internal temperature 17.8 °C; comfort temperature 21.1 °C.

The external design temperature was set at -13 °C, while for the ground-floor rooms (unheated) the temperature of a “cellar with doors and windows closed” (5 ° C) was assumed.

Another assumption concerns the number of people inhabiting the module upper floor, assumed equal to 6 (based on the average number of children in each Nepalese family); this figure influences the definition of the air volume exchange rate and the internal heat gains (300 MJ/month). The average daily electricity consumption was assumed about 5 kWh_e [4].

The lack of homogeneity in materials such as soil, straw, or mixture of soil and straw does not allow the definition of unique values for quantities such as thermal conductivity or density. Not knowing accurately geological features of the specific site, the authors preferred to characterize the materials with average values that can be identified in the literature (Table 3) [13, 15].

5.2. Energy balance and preliminary design

Since it is not necessary to install summer air conditioning, only the energy demand for heating in the provided configurations S1 and S2 was determined during the heating months (from October to

April) as shown in table 4. A demand of 75 MJ per day of hot sanitary water was estimated, by considering a temperature in the incoming and outgoing water respectively equal to 5 °C and 45 °C, and an average daily consumption of 37 liters per capita.

In the preliminary phase, a study was carried out about the energy generation from solar photovoltaic panels (polycrystalline silicon, 180 W_p, 1.31 m^2, 13.7% efficiency) and thermal collectors (vacuum, 12 tubes, 1.92 m^2, 63% overall efficiency), as a function of the irradiation values recorded on site. Similar considerations also involved the wind resource; the integration of the duration curve with the selected generator power curve (2 kW_e, 4 blades, 1.3 m rotor diameter, 2 m/s cut-in speed) allowed to estimate an average annual generation of 920 kWh_e.

In relation to the different design solutions to cover the maximum thermal demand (January), it is expected:

- S1: 750 liters storage of heat generated from the solar system; in particular 12 panels are installed on a total gross surface of 26.5 m^2 out of 31 available, flush mounted to the roof pitch (37°).
- S2: 800 liters storage of heat generated from the solar system; it consists of 13 panels on a total gross area of 28.7 m^2 out of 31 available, flush mounted to the roof pitch (37°).

In accordance with the issues related to indoor air quality, an electric stove is planned in place of traditional wood-burning ones, which are source of air pollution in homes. It was chosen with an electrical rating of 1.5 kW_e [23], determining an average daily total consumption of electricity equal to 8.75 kWh_e. The electricity demand is covered by a photovoltaic system composed of 8 panels (10.5 m^2 of gross surface, outside of the Southern pitch of the roof, almost completely occupied by the solar thermal plant) and by a single wind generator (8 m hub height). In any case, since the module is designed to be autonomous and not grid-connected, electrical energy storage solutions were considered (8 batteries, 12 V, 100 Ah).

Figure 8 shows the comparison between energy demand (heating and hot sanitary water) and supply via thermal solar system, both for S1 and S2 assumptions . Besides figure 9 plots electricity demand and supply via photovoltaic and wind generators, considering that the average monthly wind speed is characterized by a distribution fairly constant throughout the year.

Table 3. Materials characteristics

Material	λ, W/(m K)	μ	ρ, kg/m^3	c, kJ/(kg K)
Raw earth (Adobe)	0.635	7.5	1650	1
Raw earth (Pisè)	1.02	10.5	1950	1
Mixture of soil and straw	0.28	6	750	0.9
Straw	0.09	3	130	0.6
Fir wood	0.12	44	450	2.7
Perlite	0.04	9	150	0.84
Polypropylene	0.035	170	25	1.25
Plaster of raw earth and lime	0.8	8	1500	1.25

Table 4. Primary energy demand for heating

Month	S1, MJ	S2, MJ
O	1230	1318
N	1570	1708
D	1917	2124
J	3377	3838
F	2778	3136
M	2099	2327
A	1319	1428
Total	14,290	15,878

6. Conclusions

The work presented in this paper aimed to a preliminary study of a residential unit that allows to reduce the environmental impact of buildings at high altitude in the Nepali Sagarmatha National Park, meeting local people's needs, in terms of construction simplicity, replicability, availability and cost-effectiveness of materials, environmental compatibility and exploitation of available

renewable energies. A series of obstacles were encountered due to the complexity of gathering reliable data during the study, especially with regard to diversity of Nepali reality from a social/cultural point of view, characterized by a specific concept of housing, both in terms of construction techniques and subjective conditions of climate comfort.

Thinking of a residential unit for a different context than European one implied a thorough analysis of the existing reality, in order to design an element sustainable in terms of energy, as well as integrated within the local context. After a survey of on-site characteristics, available resources and their conservation management, straw bales and earthbag buildings were selected between the construction techniques, sustainable from an economic point of view and for the use of local material and labour.

Through the use of a specific software, several configurations for the residential unit envelope were examined; on the basis of recorded data concerning solar radiation and wind on site, a preliminary assessment was also performed to evaluate the potential generation associated with the solar and wind resources. With the purpose of achieving full coverage of heating and electricity demands by using renewable energies, different plant configurations were then assumed, which allow to reduce the use of combustibles such as wood, animal excrements and fossil fuels.

Further future developments of the project may concern an in-depth examination of structural, plant and especially economic elements of the proposed residential unit and a verification of possible solutions for partial coverage of energy demands and/or centralized management of users within the settlements, in the perspective of a dual LCA/LCC assessment.

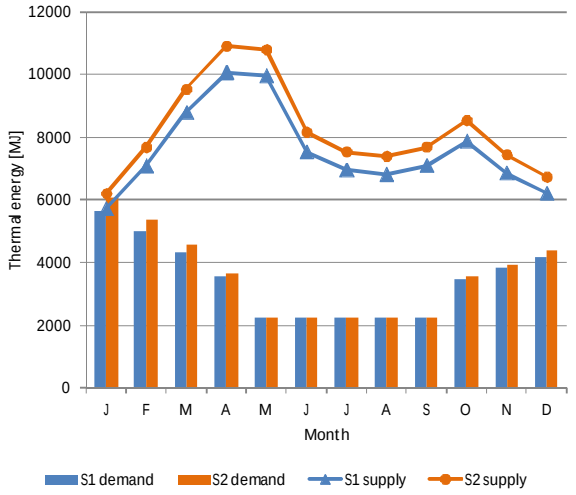

Fig. 8. Thermal energy demand vs. supply via solar system

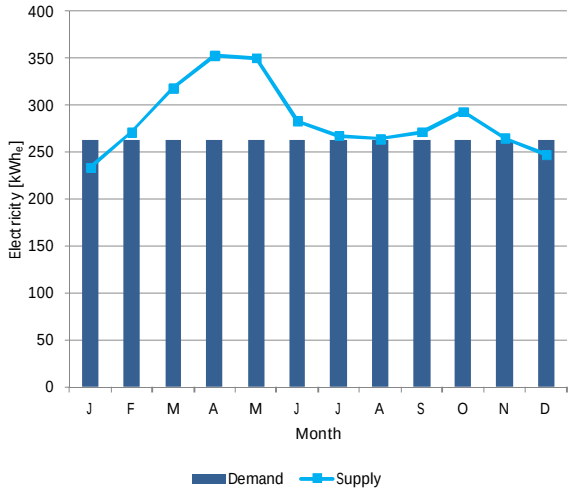

Fig. 9. Electricity demand vs. supply via photovoltaic and wind systems

Acknowledgments

Authors would like to acknowledge Simone Mariani and Stefano Paoloni for supporting the realization of this study.

Nomenclature

c	Specific heat capacity, kJ/(kg K)
H_{gh}	Incident solar radiation, MJ/(m^2 day)
LCA	Life Cycle Assessment
LCC	Life Cycle Cost
LGP	Liquefied petroleum gas

ppm Parts per million

P Atmospheric pressure, hPa

P_p Rainwater, mm

T Air temperature, °C

U_r Relative humidity, %

U_s Specific humidity, g/kg

v_V Wind speed, m/s

Greek symbols

λ Thermal conductivity, W/(m K)

ρ Density, kg/m^3

μ Resistance to steam passage

Subscripts

e Electric

p Peak

References

[1] Ev-K2-CNR Committee. Available at: <http://www.evk2cnr.org/> [accessed 10.10.2011].

[2] United Nations, Educational, Scientific and Cultural Organization, World Heritage Centre: Sagarmatha National Park. Available at: <http://whc.unesco.org/en/list/120/> [accessed 10.10.2011].

[3] Nepal S.K., Tourism in protected areas: the Nepalese Himalaya. Annals of Tourism Research 2010;27(3):661-681. doi: 10.1016/S0160-7383(99)00105-X.

[4] Salerno F., Flury B., Thakuri S., Basani M., Maskey R.K., Khanal S.N., Sapkota A., Bhuju D., Jha P.K., Bhochibhoya S., Management-Oriented Environmental Research in Sagarmatha National Park and Buffer Zone. Kathmandu, Nepal: HKKH Technical Paper, Document produced in the framework of the Project "Institutional Consolidation for the Coordinated and Integrated Monitoring of Natural Resources towards Sustainable Development and Environmental Conservation in the Hindu Kush-Karakoram-Himalaya Mountain Complex"; 2009. Available at: <http://www.hkkhpartnership.org:8080/geonetwork/srv/en/metadata.show?id=3595> [accessed 10.10.2011].

[5] Salerno F., Viviano G., Thakuri S., Flury B., Maskey R.K., Khanal S.N., Bhuju D., Carrer M., Bhochhibhoya S., Melis M.T., Giannino F., Staiano A., Carteni F., Mazzoleni S., Cogo A., Sapkota A., Shrestha S., Pandey R.K., Manfredi E.C., Energy, Forest, and Indoor Air Pollution Models for Sagarmatha National Park and Buffer Zone, Nepal – Implementation of a Participatory Modelling Framework. Mountain Research and Development 2010;30(2):113-126. doi: 10.1659/MRD-JOURNAL-D-10-00027.1.

[6] Manfredi E.C., Flury B., Viviano G., Thakuri S., Khanal S.N., Jha P.K., Maskey R.K., Kayastha R.B., Kafle K.R., Bhochhibhoya S.B., Ghimire N.P., Shrestha B.B., Gyanendra C., Giannino F., Carteni F., Mazzoleni S., Salerno F., Solid Waste and Water Quality Management Models for Sagarmatha National Park and Buffer Zone, Nepal – Implementation of a Participatory Modelling Framework. Mountain Research and Development 2010;30(2):127-142. doi: 10.1659/MRD-JOURNAL-D-10-00028.1.

[7] National Centre for Atmospheric Research Earth Observing Laboratory (NCAR/EOL). USA, EOL Data Server. Available at: <http://data.eol.ucar.edu/> [accessed 10.10.2011].

[8] Sestini V., La terra cruda, Tradizioni e tecnologie nel patrimonio architettonico himalayano (The raw earth, traditions and technologies in the Himalayan architectural heritage). Costruire in Laterizio 1998;64.

[9] Sestini V., Somigli E., Sherpa Architecture. Paris, France: UNESCO Publishing; 1978.

[10] Hart K., Geiger O., Sharing information and promoting earthbag building. Available at: <http://www.earthbagbuilding.com/> [accessed 10.10.2011].

[11] Kennedy J., Wojciechowska, P., Modular contained earth. In: Elizabeth L., Adams C., Alternative construction: contemporary natural building methods. Hoboken, NJ, USA: John Wiley & Sons; 2000.

[12] Achenza M., Sanna U., Il manuale tematico della terra cruda (Thematic handbook of raw earth). Rome, Italy: DEI; 2009.

[13] G. Bollini, Architettura in terra cruda: significato, limiti e potenzialità (Raw earth architecture: meaning, limits and potential). Proceeding of Conference "Living According to Nature: the rediscovery of straw and clay as construction materials"; 2010 Oct 9; Schio, Italy.

[14] Comandini S., Eco-architecture projects. Available at: <http://www.comandini.ch/costruzioni.html> [accessed 10.10.2011].

[15] Minke G., Building with Earth: Design and Technology of a Sustainable Architecture. Berlin, Germany: Birkhauser Basel; 2009.

[16] Wojciechowska P., Building with Earth: A Guide to Flexible-Form Earthbag Construction. White River Junction, VT, USA: Chelsea Green Publishing Company; 2001.

[17] Hunter K., Kiffmeyer, D., Earthbag Building: The Tools, Tricks and Techniques. Gabriola Island, BC, Canada: New Society Publishers; 2004.

[18] Geiger O., Insulated Earthbag Houses. Article published on 11th February 2009. Available at: <http://ezinearticles.com/?Insulated-Earthbag-Houses&id=1935442> [accessed 10.10.2011].

[19] Orazi U.S., Orazi M., Canziani A., Borghi W., Terre plastiche stabilizzate a calce: valutazione delle caratteristiche meccaniche (Plastic soils stabilised with lime: evaluation of the mechanical characteristics). Giornale di Geologia Applicata, Associazione Italiana di Geologia Applicata e Ambientale – AIGA (Italian Association of Environmental and Applied Geology) 2005;2:278-284. doi:10.1474/GGA.2005-02.0-40.0066.

[20] Manganelli G., Studio sperimentale delle terre stabilizzate con leganti idraulici; progettazione prestazionale delle miscele (Experimental study of soils stabilized with hydraulic binders: performance design of mixture) [dissertation]. Bologna, Italy: Università di Bologna; 2009.

[21] Various Authors, Stima10 User Guide; 2010.

[22] Rijal H.B., Yoshida H. , Umemiya N., Seasonal and regional differences in neutral temperatures in Nepalese traditional vernacular houses. Building and Environment 2010;45(12):2743-2753. doi: 10.1016/j.buildenv.2010.06.002.

[23] Sanchez T., Research on technology acceptance from field research in Nepal and Kenya, developed on SCORE project (Stove for Cooking, Refrigeration and Electricity supply, an affordable appliance for remote and rural communities); 2007. Available at: <http://www.score.uk.com/research/default.aspx> [accessed 10.10.2011].

Fires and Smoke Spread in Low-Income Housing in Mexico

Raul R. Flores-Rodriguez[a], Abel Hernandez-Guerrero[b], Cuauhtemoc Rubio-Arana[c] and Consuelo A. Caldera-Briseño[d]

[a] *University of Guanajuato, Salamanca, Mexico, raulfloresrdz@gmail.com*
[b] *University of Guanajuato, Salamanca, Mexico, abel@ugto.mx* ***CA***
[c] *University of Guanajuato, Salamanca, Mexico, rubioc@ugto.mx*
[d] *Autonomous University of Zacatecas, Zacatecas, Mexico, consuelo@uaz.edu.mx*

Abstract:

The spreading of fire and smoke in a 3D multi-species analysis in a typical low-income dwelling in Mexico is presented in this work. This is a highly complex phenomenon since it involves the combination of several mechanisms. The objective of this research is to provide information, through a CFD analysis, about the maximum temperatures reached inside the house, the influence of parameters on the fire control design, the pollutants generated by the fire (CO) and their scattering around the house, fire transient dynamics, etc. Time tolerance to high temperatures in a fire event is obtained. Health hazard levels, from a simple headache to increasing symptoms until death, are determined as a function of CO concentration for the different rooms in the house.

Keywords:

Fire, Smoke, Low-Income Dwellings, Pollutants Scattering, CFD Analysis.

1. Introduction

1.1. The problem of fires in homes

According to the USA National Fire Protection Association, NFPA, 93.4% of global fires occur in homes [1]; thus, new housing models seek to incorporate adequate fire protection and security systems effective in the detection, suppression or control of a fire event that could significantly increase the safety of people and the building, remembering that the main objective is to protect the lives of people.

In a typical situation in a house fire, smoke (a mixture of gases and dust created by combustion) is the cause of more than 75% of deaths [2]. The main factors that determine the damage to health and survival of the person in a fire are the high air temperatures that are reached, the combustion of certain materials containing asphyxiants and how long the victim is exposed to toxic combustion products.

1.2. Complications in the health of persons exposed in a fire: high temperature and toxic gases

Exposure to fire is an event that can produce such severe injuries in people that might even cause death, usually by the high temperatures of the surrounding air and of the combustion gases, as well as from smoke inhalation or fainting caused by poisoning and/or from severe burns in the body.

During a fire event, the environmental temperature rises above 100 °C, resulting in direct damage to the airway and respiratory system in general [3]. Most of the smoke generated in a fire is a combination of small particles in suspension and a quantity of dust floating adding to the hot gases

released by the fire, and by the complete and incomplete combustion of different materials that are in the scene. Particles facilitate the condensation of some gaseous products of combustion. Some of the suspended particles in smoke are slightly irritating, but others can be lethal to humans [4].

Carbon monoxide is a gas that is characterized by being less dense than air, colorless, odorless and tasteless, which has no irritating characteristics, since its action mechanism is asphyxiating. It originates from the incomplete combustion of carbon-containing materials in their composition. One of the main dangers of death during a fire is carbon monoxide poisoning, it is estimated that it is responsible for 80% of cases of health damage caused by smoke inhalation during a fire. In the USA it is estimated that there are about 5,600 deaths from carbon monoxide poisoning [5].

1.3. Status of housing in Mexico

The constant population growth in Mexico requires increasing attention in the development of new models of housing suitable to the current conditions of the population. The National Institute for Statistics and Geography (INEGI for its acronym in Spanish) in Mexico reported a total of 28,138,556 homes in 2010 [6]; housing with 1 and 2 bedrooms are predominant.

Table 1. Housing by number of bedrooms 2010.

Number of bedrooms	Amount
1 Bedroom	9 929 668
2 Bedrooms	11 166 348
3 Bedrooms	5 378 589
4 Bedrooms	1 211 150
5 and more bedrooms	323 620
Not specified	129 181
Total	*28 138 556*

With an average of 3.9 occupants per household, households with 1 or 2 bedrooms comprise 74.97% of all homes in Mexico. The main financial entities provided in 2011 a total of 20,400 (million US Dollars) in investments applied to housing; this shows the important development of this sector [6].

2. Computational model

2.1. Computational domain

The housing model to analyse in this study will aim to include the most typical housing standards for the average person living in low-income house in Mexico. This type of house has typically two floors, with two bedrooms, a kitchen area, living room and dining room as well as two bathrooms, with land dimensions of 6 x 9 m approximately, with a floor height of 2.6 m. The distribution of space is shown in Figure 1.

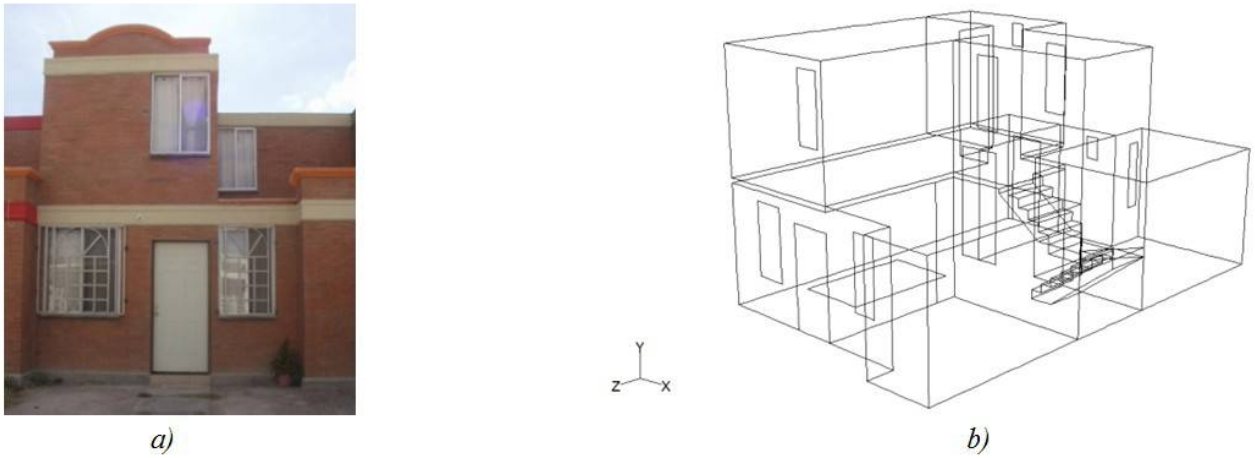

Fig. 1. Housing model analysed: a) front view and b) isometric view of the model.

2.2. Boundary conditions

The boundary conditions to comply with the most real conditions will include air vents (windows and doors), with adiabatic walls (since in Mexico the walls are made of brick). It will be assumed that the fire starts at a typical sofa in the living room.

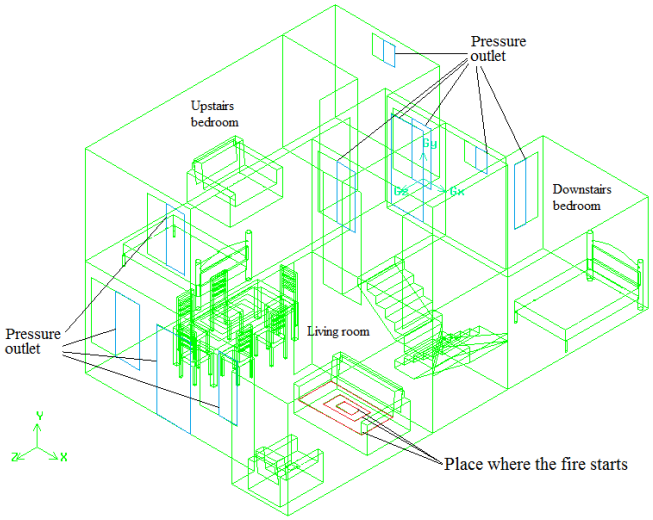

Fig. 2. Boundary conditions for the model analysed.

The most important space of analysis will be the area where the fire originates, having an area which is increased by a factor of 2, from 0.1401 m^2 for the purpose of simulating the fire, and its spreading in a couch in the living room. Air outlets are present, such as windows and doors; the pressure in these areas is considered equal to the atmospheric pressure.

2.3. Numerical procedure and considerations of the model

The presence of turbulence in the event of fire is considered in the analysis; therefore the k-epsilon model is used. In this turbulence model there are two equations, that is, there are two extra transport equations to represent the properties of fluid turbulence: kinetic energy κ and its dissipation rate ε. This allows the model to include the effects of convection and diffusion of turbulent energy. This model is popular in CFD simulation because of its robustness, computational economy and reasonable accuracy.

To perform the numerical analysis two commercial codes are used (Fluent-Gambit), in addition to the SIMPLE-C algorithm used for the discretization of the governing equations in the transient state of the fire.

Assumptions used in the modelling of the fire:

- Transient state.
- The effects of gravity are considered.
- Evolution of the power of fire.
- Fluid properties are constant.
- Heat transfer by radiation is not considered.
- Interior adiabatic walls.
- No-slip condition on the walls.

It is well understood that radiation plays an important factor in a fire, especially in a house fire; however, the analysis presented here overlooks this because the study focuses primarily on the damage caused by carbon monoxide, and the results could be considered as a first approximation. The computation model primarily sets on finding how the smoke spreads through the house.

Moreover, and seeking a practical way to model the smoke and its spreading during the fire, a ratio air/CO of 95/5 is used in the present analysis.

2.4. Source and spread of fire in the model analysed

The analysis of fire cases is a very large and extremely complicated process; many parameters are involved in the generation of a fire, however there are trends that could be used as common patterns of fire in homes; it is estimated that about 65% of fires in furniture for a home are caused by a cigarette, the rest is due to faulty electrical equipment or hot objects [7]. Thus, the procedure to simulate the fire is determined primarily by the burning of a cigarette on a sofa spreading over it. The fire area and power caused by the fire will grow to a maximum, and then stabilize to a lower value. The performance data in relation to time are taken from experimental situations performed by Babrauskas [8]; he performed testing in different materials being burnt, and for a common sofa determined the intervals shown in Table 2. His figures are used in the present study.

Table 2. Parametric data for the simulation of the fire.

Time interval [s]	Fire power [kW]	Fire area [m^2]	Smoke speed [m/s]
0-100	0.01	0.1401	0.0002
100-200	10	0.1401	0.4139
200-300	100	0.5606	1.0350
300-350	1000	0.5606	10.3500
350-400	1800	2.2425	4.5650
400-450	1000	2.2425	2.5870
450-500	600	2.2425	1.5520
500-750	200	2.2425	0.5173
750-1200	100	2.2425	0.2586
1200-1800	50	2.2425	0.1293

The previous information shows the main parameters of the source of the fire. The temperature for the mixture air/CO smoke temperature is taken as 673 K, according to the experimentally-determined temperature by Migoya [9].

It is known that there are numerous materials inside a house that are highly flammable and could be considered fire generators, especially those with which the furniture is manufactured. Since the analysis of a fire is way too wide, this work focuses attention on a particular case, with the fire starting by a lighted cigarette on the couch in the living room and then the concentration and temperature fields are tracked from place to place around the house; determining the values of the temperature field and CO concentration in the bedrooms is critical, since people could be sleeping and will inhale CO without perhaps realizing that there is a fire.

3. Analysis of results

3.1. Temperature reached in specific areas of the house

From all the parameters that define the survival, or not, of a person in a case of fire, the temperatures of the air and combustion gases are among the main ones. First, in order to know the temperature around the house, the results for the case of simulation of the typical fire conditions described above, for a time interval of 30 minutes of heat evolution, are shown in Figure 3; the figure shows the temperatures for the different rooms analysed.

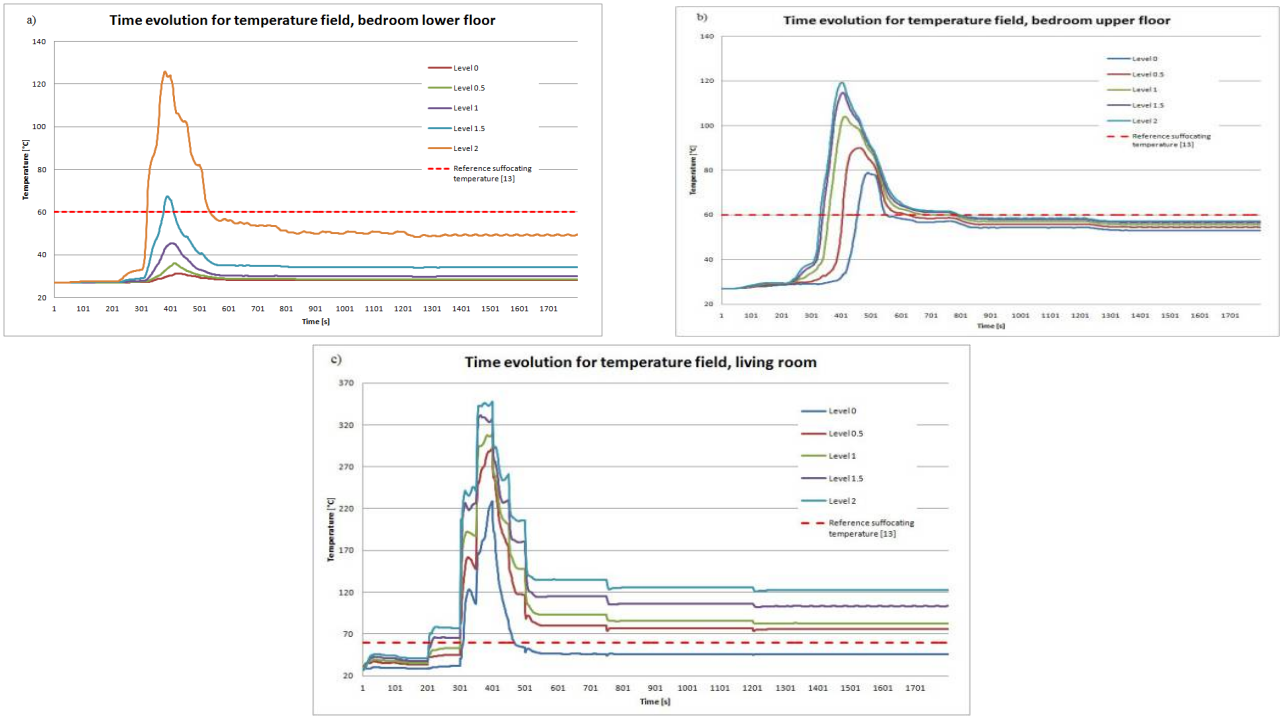

Fig. 3. Time-evolution of temperature after 30 minutes of fire spread, a) bedroom lower floor, b) bedroom upper floor, and c) living room.

Each of the graphs in Figure 3 shows the evolution of temperature during the fire for each of the places of interest at the house: the room downstairs, the bedroom in the upper floor and the living room downstairs. For each space, 5 different highs measured from the floor were chosen to obtain data: level 0 is that of the floor, level 1 corresponds to 0.5 m above the floor; level 2 corresponds to 1 m above the floor, and so on, with increments of 0.5 m, up to a height of 2 meters.

3.2. Maximum time of exposure to high temperatures

The analysis provides the average time a person can withstand at a certain temperature before the occurrence of skin damage, severe burns or hyperthermia (body temperature above 40 ° C) based on an experimental study by Purser [10]. Humidity has a significant effect on the maximum exposure time in a fire. The presence of moisture causes the effects of heat by convection to increase due to the difficulty that is added to perspiration. In wet conditions, the maximum time in minutes that a person endures can be approximated by:

$$t_{max,temp} = e^{[5.1849 - [0.0273 \cdot (T - 273)]]}, \qquad (1)$$

where the temperature is expressed in K [11]. For all the cases examined here the average temperature in each area during the fire incident is recorded, as well as the maximum time of exposition to high temperatures. These times for each room in the house are provided in Table 3.

Table 3. Average time of exposure to high air temperatures.

Room	Bedroom lower floor	Bedroom upper floor	Living room
Time [min]	68.96	40.29	13.87

It is clear that in the living room, where the fire originated, the allowable time of exposure before symptoms of fainting, breathing difficulty, dizziness, among others, caused by the hot air in the respiratory tract is less than for the other rooms.

The distribution of air temperatures 30 minutes after the fire originated is shown in Figure 4.

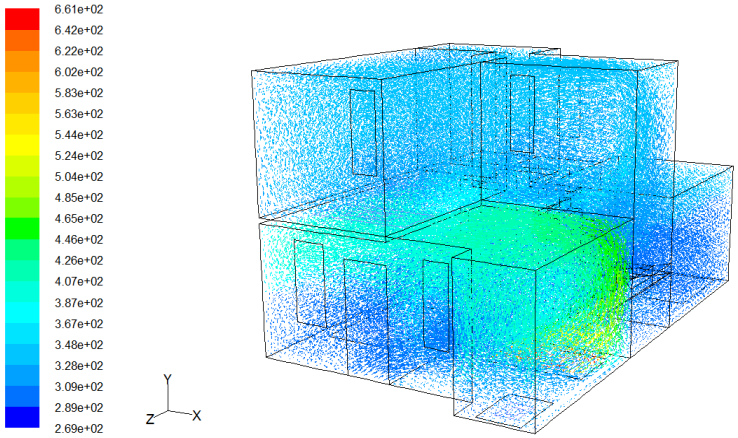

Fig. 4: Temperature distribution 30 minutes after fire started [K].

3.3. Concentration levels of CO

In fires the most common cause of death is by carbon monoxide poisoning. During a fire a large quantity of toxic substances are produced by the combustion of materials of construction, increasing the number of deaths; moreover, since oxygen is being consumed in the combustion, there will be a decrease in the amount of available air. In a fire the concentration of carbon monoxide can reach levels of about 100,000 ppm. [9]. Figure 5 shows the distribution of particles per million, ppm of CO, for a time of 1800 s (30 min) after the fire started.

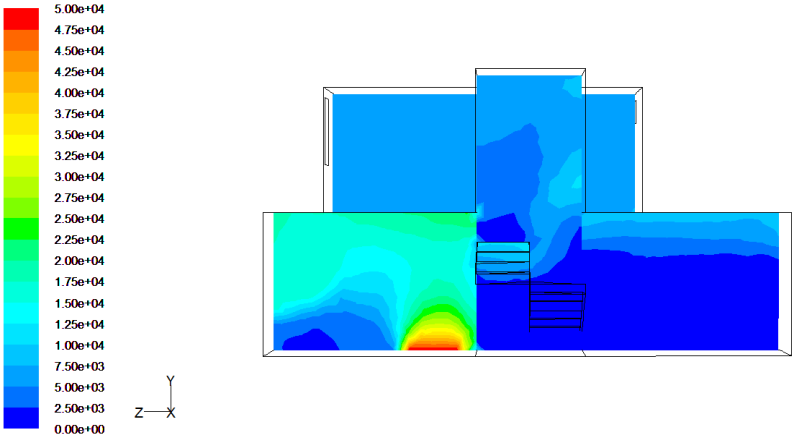

Fig. 5. CO ppm distribution 30 minutes after fire started (lateral view of the house).

It is necessary to determine the amount of particles per million of CO in each room of the house while the fire is active. This parameter is the best way to predict the time a person can withstand high concentrations of CO. The time evolution of the CO ppm concentration in each room is shown in Figure 6.

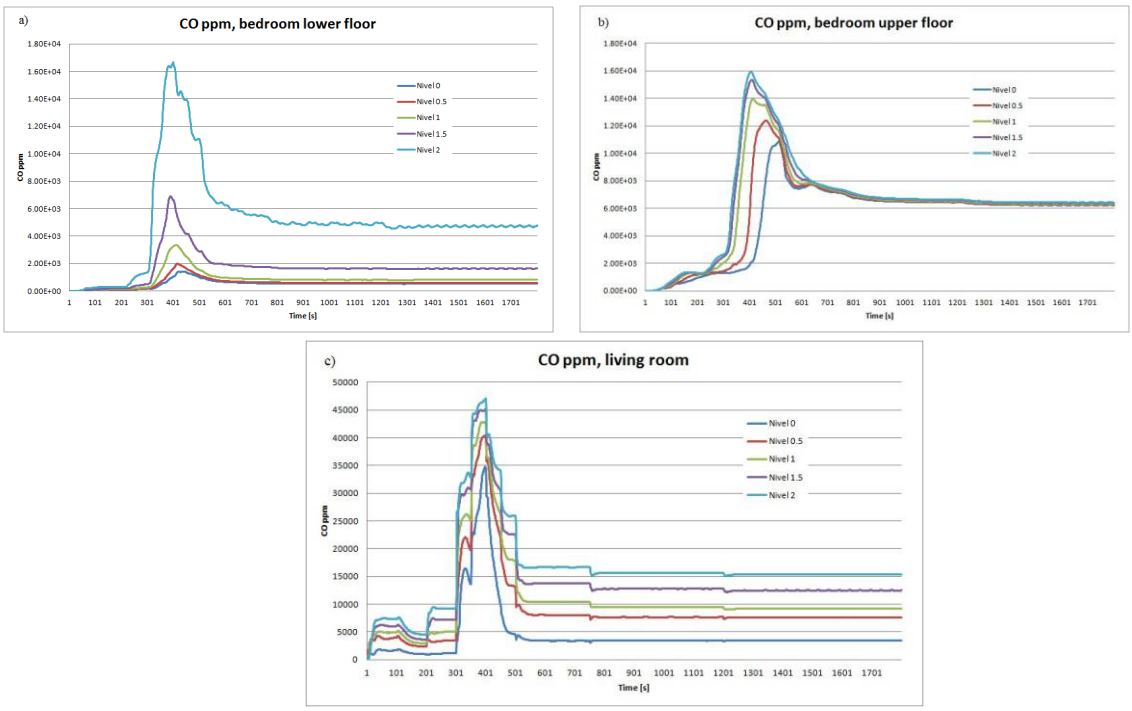

Fig. 6. Particles per million of CO as a function of time in: a) lower floor bedroom, b) upper floor bedroom, and c) living room 30 minutes after fire started.

3.4. Health hazard critical levels

High concentrations of CO in the air lead to a depletion of basic skills and finally the death of a person. An exposure to large amounts of CO beyond the normal range increases the levels of carboxyhemoglobin in the blood (COHb); the main effects of this are the reduction of the hearth and breathing rates, as well as a decrease of brain activity, leading to a certain degree of inability to react. Stewart's equation, Equation (6), predicts the concentration of COHb in the blood for small periods of time (less than an hour); this equation was derived from real human experimentation by Stewart [12]:

$$\%COHB = (3.317x10^{-5})(ppm\ CO)^{1.036}(RMV)(t). \quad (2)$$

The analysis consider that an average person (70 kg) who is sleeping will have a RMV (*Respiratory Minute Volume*) of 8.5 liters per minute; t in Equation (2) represents the estimated time of exposure to carbon monoxide. Santiago [14] reports the symptoms caused by the presence of COHb in the blood due to exposure to carbon monoxide, see Table 4, defining five levels of intensity.

Table 4. Symptoms caused by the presence of COHb in the blood [14].

COHb %	Symptoms	Level
< 10%	Asymptomatic	1
10-20%	Asymptomatic or headache	2
20-30%	Dizziness, vertigo, nausea, vomit, difficulty in breathing	3
30-40%	Visual disturbances	4
40-50%	Confusion, disorientation	5
> 50%	Coma, cardio-pulmonary dysfunction, death	6

Using Equation (2), and considering a height from the floor of 0.5 meters (position of a bed), the levels of carboxyhemoglobin in the blood reached while the fire is developing and the smog is spreading around the house, can be determined, and are shown in Figure 7.

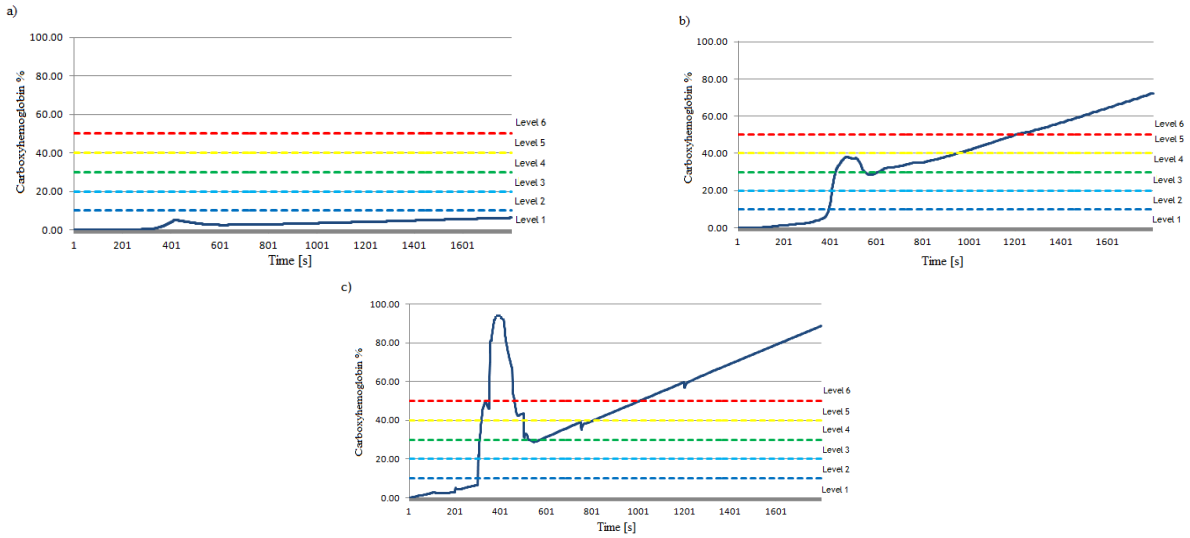

Fig. 7. Levels of carboxyhemoglobin in the blood after 30 minutes have elapsed, a) lower floor bedroom, b) upper floor bedroom, and c) living room.

It is clear that the most unfavorable place to be while the fire spreads is in the living room, since it is where the fire has originated, reaching the highest levels of carboxyhemoglobin, way above 40% to the condition where the most health hazard critical situations for people occur, and leading to their death. It is interesting to see that the upper floor bedroom is also affected greatly, due to the tendency of hot gases to rise reaching the limit of the death zone in about 1200 seconds, which is 800 seconds after the limit of death recorded in the living room; what is remarkable is that the lower floor bedroom is not affected (in terms of levels of carboxyhemoglobin) during all the fire because of its position in the house respect to the fire. Most of the smoke spreads towards the upper floor, leaving the lower floor unaffected by CO concentration.

4. Conclusions

Performing a simulation of typical fire parameters allows obtaining useful data that will allow saving lives of people who are involved in such an incident (such as the air temperature reached inside the home or building and the concentrations of carbon monoxide.) The maximum time of exposure to high temperatures that permit to withstand a fire were also calculated in this work.

Intoxication by toxic gases in a fire has a high incidence, often accompanied by a high mortality rate. Is well known that the toxic capacity of each gas is variable, with many products that can cause intoxication due to present, complete and incomplete, combustion. Thus, a large number of products could be considered and the analysis could become quite complex. In the present work the analysis focuses on the most common intoxication from a poisonous gas present in a house fire: carbon monoxide. The presence of CO in the blood of people produces carboxyhemoglobin by contact with hemoglobin in blood; high concentrations of COHb cause serious health alterations; thus, in this analysis COHb levels in the blood were obtained for the length of time of the fire.

The results indicate the places in the house where it will be dangerous to be, clearly the fumes of the fire will try to move upward towards the second floor where they concentrate and increase the CO concentrations making it a health hazard to be there, maybe even leading to death. On the contrary, being on the first floor (with the exception of the living room), will be safer since the level of CO concentrations remain low. Boundary conditions clearly change from one building (or house) to another (such as the air vents). The next aim on this study is to perform an analysis of a broad range

of conditions for air vents. Another aim will be to consider radiation in the analysis, as well as the comparison of the results with and without radiation being considered in the analysis.

The use of computational tools to analyse real problems gave a full picture of the phenomenon investigated. In this particular case, new information on the evolution of a typical fire in a low-income house representative in Mexico was obtained; thus, possible improvements to the safety features of the building can be proposed. The procedure of analysis is highly recommended because it is simple and reasonably fast, providing results such as survival time. The analysis clearly could be applied to other type of buildings, not only low-income households.

Nomenclature

T temperature, K

t time, s

RMV respiratory minute volume, lt/min

References

[1] Life Safety Code, National Fire Protection Association NFPA, 1 Batterymarch Park, PO Box 9101, Quincy, MA 02269-9101 Edition 2000.

[2] James A. Raub, Monique Mathieu-Nolf, Neil B. Hampson, Stephen R. T., Carbon monoxide poisoning: a public health perspective. National Center for Environmental Assessment, US Environmental Protection Agency, Research Triangle Park, NC 27711, USA. 1999.

[3] Asociacion Mexicana de Cirugia General (Mexican Society of General Surgery). Quemadura de vía aérea y lesión por inhalación. Avaliable at:http://www.amcg.org.mx/ [accessed 12.2.2011]

[4] Žana Ž. Stevanovića, Marija Živkovića, Nikola M., CFD modelling of fire protection system in office building. ECOS 2011 (Efficiency, Costs, Optimization, Simulation, and Environmental Impact of Energy Systems), pp. 1987-1997, Novi Sad, Serbia, July 3-7, 2011, ISBN 978-86-6055-015-8.

[5] J. Gil Cebrián, R. Díaz-Alersi Rosety, M. Jesús Coma, D. Gil Bello. Principios de urgencias, emergencias y cuidado crítico. Universidad de Burgos-FBIS, Red Universitaria de Servicios Integrados, 2005.

[6] Instituto Nacional de Estadistica y Geografia INEGI (National Institute for Statistics and Geography). Estadistica: poblacion, hogares y vivienda. Avaliable at:<http:// http://www.inegi.org.mx> [accessed 11.5.2011]

[7] Babrauskas, V., J. R. Lawson, W. D. Walton & W. H. Twilley. Upholstered furniture heat release rates measured with a furniture calorimeter. NBSIR 82-2604, USA 1992.

[8] Babrauskas, V. & Krasny, J., Fire behaviour of upholstered furniture. NBS Monograph 173. NBS, USA 1985.

[9] Migoya Valor Emilio. Modelo zonal para la simulación del movimiento de humos y gases calientes en incendios: aplicación a túneles de carretera. Tesis Doctoral. Universidad Politécnica de Madrid, Escuela Técnica Superior de Ingenieros Industriales. 2002.

[10] Purser D. A. The harmonization of toxic potency data for materials obtained from small and large fire tests and their use in calculations for the prediction of toxic hazard in fire. Proceedings of First International Fire and Materials Conference, Washington DC USA. 1992.

[11] Louise C. Speitel. Toxicity assessment of combustion gases and development of a survival model. Airport and Aircraft Safety Research and Development, Division FAA Technical Center Atlantic City International Airport. 2002.

[12] Stewart, R., Peterson, J., Baretta, E., Dodd, H., and Herrmann, A. Archives of environmental health. Volume 21, p. 154 1970.

[13] Madrzykowski Daniel, Kerber Stephen, Kumar Sunil, Panindre P. Wind, fire and high rises. Mechanical Engineering: the Magazine of ASME, Volume 132, No. 7, 2010.

[14] Blanco Marigorta E. Simulación de incendio en un túnel de carretera. Departamento de Energía, Universidad de Oviedo., Oviedo, Principado de Asturias (España), 2007.

[15] I. Santiago, "Gas poisoning". ANALES Sis San Navarra, Vol. 26, Suplemento 1. 2003.

[16] J.E. Floyd, H.R. Baum, and K.B. McGrattan, "A mixture fraction combustion model for fire simulation using CFD. Building and Fire Research Laboratory, National Institute of Standards and Technology, Gaithersburg, MD 20899, USA, 2001.

[17] Guylène Proulx, Irene M.A. Reid, Neil R. Cavan. Human behavior study: cook county administration building fire. Research Report No. 181. National Research Council Canada. October 17, 2003.

[18] Alois David, Gregory R. W. El cuerpo humano: aparato respiratorio. Enciclopedia de Salud y Seguridad en el Trabajo. 2005.

Optimal Lighting Control Strategies in Supermarkets for Energy Efficiency Applications via Digital Dimmable Technology

Salvador Acha[a], Nilay Shah[b], Jon Ashford[c] and David Penfold[d]

[a] *Imperial College London, London, UK, salvador.acha@ic.ac.uk*
[b] *Imperial College London, London, UK, n.shah@ic.ac.uk*
[c] *Sainsbury's Supermarkets Ltd, London, UK, john.ashford@sainsburys.co.uk*
[d] *Sainsbury's Supermarkets Ltd, London, UK, david.penfold@sainsburys.co.uk*

Abstract:

Electricity consumption in the UK commercial sector accounts for 19% of total annual electricity demand. This implies any step taken towards energy efficiency applications for commercial buildings can generate important reductions in both energy use and carbon emissions. Sainsbury's supermarkets, one of the UKs largest grocers, recognises the challenges climate change brings to businesses and hence is conducting efforts to reduce the operational carbon footprint of their stores. Lighting in stores is an essential service and is an important component of a stores power demand; ranging from 15 to 35% based on design features. This paper details the innovative lighting control application Sainsbury's is currently employing in its new stores with the objective to maximise the benefits digital dimmable technology possesses. Basic lighting concepts are described which explain the priorities supermarkets have when using this service, while the tradeoffs of using digital signal interface (DSI) controls are also discussed. The non-linear relationship between DSI settings, lux drawn from ballasts, and power consumed by the system are showcased as a proper understanding of this concept is paramount in achieving energy savings. In addition, using a Sainsbury's 3,300 m^2 eco-store, a thorough case study is presented in which various lighting strategy settings are applied; having very attractive results in monetary, energy, and environmental metrics without being detrimental to the shopping experience. Hence, it is proven digital dimmable technology controls can effectively provide 20 to 25% savings in lighting services if sensors and settings are established properly. Furthermore, due to the robust and fast response capability digital dimming offers, the authors argue this technology is suitable for demand side management applications that can greatly benefit the operability of the grid and as a consequence provide an additional revenue stream for businesses in a smart-grid environment.

Keywords:

Demand response, Energy efficiency, Lighting, Load control, Supermarkets, Sustainability.

1. Supermarket Challenges

Although single supermarkets do not consume large amounts of energy, when aggregated these types of businesses do become among the largest consumers of energy, particularly in developed countries such as the USA and UK. For instance, as of 1999 supermarket consumption was approximately 5% of the UK's annual energy usage and with no indication of a slowdown [1]. Therefore, within a climate change context, supermarkets today have the intriguing challenge of continuing to return value to shareholders while reducing energy consumption and carbon intensity wherever possible in their supply-chains. In the search for these savings, which will make supermarkets use energy in a 'smarter' manner, the implemented measures must be cost-effective and not impact negatively on the customer experience. Furthermore, since supermarket systems usually follow key guidelines of design and operation; the energy learning's made and successfully implemented in an individual store need to be replicable throughout their estate otherwise the aggregated benefits will be diminished.

Sainsbury's was founded in 1869 and is the third largest grocer in the UK – currently having 16% share of the food retail market [2] – its sheer size implies Sainsbury's requires substantial amounts of energy for its day to day operations. As of 2005, Sainsbury's had 505 stores throughout the UK consuming about 2 GWh of energy, emitting over 900,000 tCO_2 and paying approximately £125 million on their energy bill; Table I shows a summary of the key energy performance indicators for years 2005/2006.

Table 1. Sainsbury's supermarket energy and emissions data for 2005/2006.

Electricity Use (MWh)	Electricity CO_2 (tonnes)	Electricity Bill (£)	Natural Gas (MWh)	Natural Gas CO_2 (tonnes)	Natural Gas Bill (£)
1,554,082	840,758	118,110,260	462,132	85,032	9,242,648

As the table above suggests, Sainsbury's energy requirements are considerable; having a distribution of 77% electricity and 23% of natural gas. Recognising the energy challenges ahead, Sainsbury's has agreed to a long-term partnership with Imperial College London. The partnership aims to deliver practical solutions to reduce carbon emissions from daily operations in supermarkets. Overall, this means efforts are underway to reduce Sainsbury's impact on climate change which coincides with their 2020 sustainability targets [3]. This strategy also falls in line with ambitious UK environmental targets – 80% CO_2 reduction target by the year 2050 as established by the Department of Energy and Climate Change (DECC) [4].

1.1. The Supermarket Load Distribution

Naturally, a supermarket will consume more energy during 'trading' hours (*i.e.* opened for business) than during 'stocking' hours (*i.e.* closed for business). However it is important to clarify the intrinsic characteristics of the key loads in a store. For instance, bakery and hot foods loads are highly dependent on oven performance specifications and how staff employs them. Meanwhile, lighting load varies according to lux and ballast specification for the different store zones. Likewise, HVAC and refrigeration demands will be influenced by multiple factors such as compressor and cabinet equipment, store wall and roof specifications, external weather conditions and indoor ambient set-point temperatures just to mention a few.

Figure 1 depicts daily electricity demand of a new Sainsbury's store seen from the grids perspective. In general, the daily energy consumption does not very much from day to day since operating times do not change frequently. The power distribution has the following composition:

Refrigeration – 39%: consumes more energy during trading hours due to higher ambient temperatures from high occupancy, heating of the building, lighting heat sources, and external weather conditions

Lighting – 32%: lighting goes to trading lux levels just before store opens and then smart controls manage the sales floor lighting based on the amount of day-light coming into the store; during non-trading hours lux levels are set to a minimum to allow staff to replenish shelves

HVAC – 10%: consumes most of its energy via air handling units (AHU's) by powering fans at various speeds during trading hours; variables such as ambient and external temperatures, occupation levels, and building temperature set-points drive demand

Hot Food – 8%: activities begin in the morning by prepping fish and meat counters, high energy demand indicate oven use for meals that require it (*e.g.* chickens), work in this area winds down as store closing time approaches

Bakery – 6%: activities begin early in the morning and are usually finalised early afternoon

Others – 4%: consist of staff area energy consumption (*e.g.* manager's office, meeting rooms, etc.)

References which have also looked into load analysis in supermarkets include [5], [6], [7]; the load distribution of these publications fall in line with the one described above.

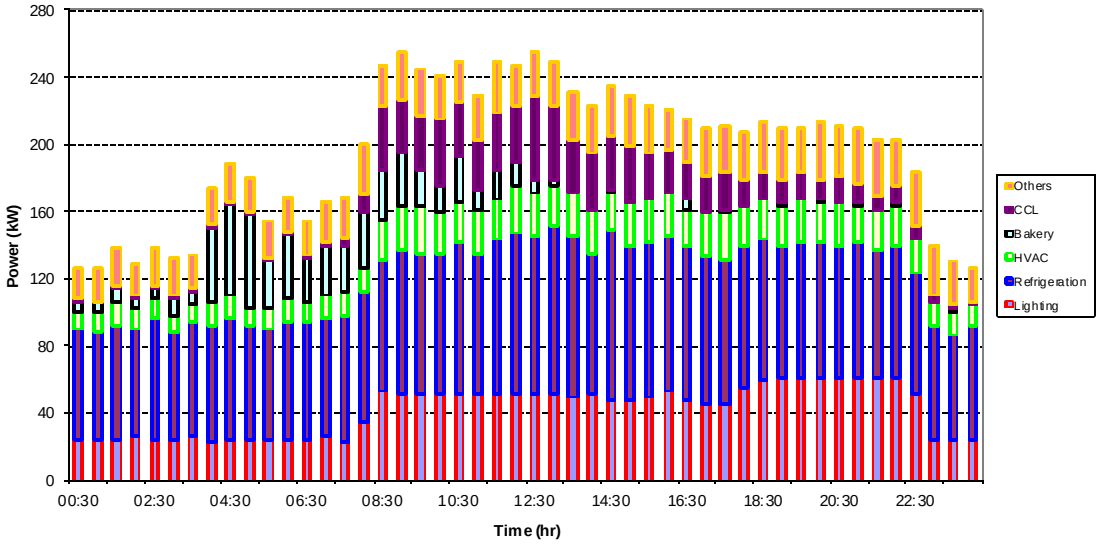

Fig. 1. Shows a typical weekday stacked chart profile of a new Sainsbury's store in March 2011.

The data for the figure shown above corresponds to a 3,300 m^2 store. For this particular day the load average is 200 kW and as it is shown the base load is stable from 11 p.m. up to 4 a.m. at about 130 kW. When bakery operations begin there is a spike in power demand which is subdued after most of the bread is made but by then the load is 160 kW. As expected, when store opens at 8 a.m. power demand rises by 50% from ramping up lights, turning on AHU's, and using hot food ovens. The trading hours from 8 a.m. till noon are the most energy intensive (peaking close to 260 kW) and then demand slowly decreases as the afternoon progresses – mainly attributed to an end of bakery and hot food activities since refrigeration and lighting demand are quite constant during trading.

1.2. Efficient Lighting Solutions in Supermarkets

Ideal lighting must provide proper levels of illumination for the desired activity to be performed inside a building with a minimum use of energy. Sainsbury's has worked on energy efficiency conservation measures regarding building design and consequently has noted that lighting load is a service where substantial energy reduction can be achieved in stores. For instance, enough sunlight falls on most buildings to provide ample illumination for the entire building hence making the most of this resource can avoid artificially lighting the store when convenient. Furthermore, the store environment can be controlled via digital dimming ballasts making it possible to ramp up or down the light intensity as desired. Thus, in recent times the lighting specification for new Sainsbury's stores has been evolving by promoting 'natural daylight' and 'digital dimmable' solutions where possible. In order to create effective daylight solutions in supermarkets two important factors must be considered [8]: *a)* meeting illumination and visual comfort requirements and *b)* properly integrating daylight features with artificial lighting.

After a couple of years of its implementation program, Sainsbury's currently has over 100 natural daylight stores promoting cost-effectiveness with the goal of obtaining economic benefits while at the same time reducing the cost and carbon content of the electricity used in supermarkets. The following formula details the philosophy applied to achieve efficient lighting:

Efficient lighting = Efficient lamps + Efficient fittings + Efficient control + Efficient light path (1)

1.3. Supermarket Lighting System Specifications

Lighting systems specifications at Sainsbury's stores are defined by the Centre of Excellence (CoE). CoE specifies natural daylight solutions for all new stores include installation of either light pipes or skylights and advanced controls; its design parameters is as follows [9]:

Natural Daylight Installation in Supermarkets

- Internal lux level at 1 metre working place: 1,200 lux
- Reflectance:
    - Ceiling: 20 to 40% dependant on ceiling cavity colour and proximity to luminaries
    - Wall/Gondola: 40%
    - Floor: 50%

All natural daylight lighting designs are issued by Sainsbury's CoE for approval before any final design is carried out. This is done with the purpose to ensure that any natural day light systems are installed to achieve maximum daylight contribution, thus benefitting the dimming system. The information required for approval by the CoE includes the following:

- Lux plot / layout for complete sales floor
- Co-ordination drawings with structural design
- Co-ordination drawings with services design
- Installation detail to roof structure
- Main structure orientation layout

It is mandatory that the light dimming system includes light lux sensors to ensure the sales floor lighting installation monitors natural daylight contribution and therefore ensures the system operates at maximum efficiency. The control logic shall be approved by Sainsbury's CoE prior to any final installation; the information required for approval will include the following aspects:

- Control schematic
- Cause and effect schedule
- Location drawing of sensors and dimming control systems
- Interface with building management system (BMS) installation

Artificial Lighting Control Requirements in Sales Floor Area

- All new lighting schemes shall be fully dimmable and will be controlled by a digital dimmable control system
- The sales floor lighting will be controlled in a single zone, unless store area is too big then CoE will define the number of zones accordingly
- The main ambient lighting level must be designed to 1000 lux and shall be dimmed to the equivalent of 900 lux for 'trading' hours
- The 'stocking' light levels shall be dimmed to the equivalent of 25% 'trading' levels
- All of the sales floor lighting is to be fed from the essential services panel with the dimming control system inhibiting the sales floor lighting to the equivalent of 25% 'trading' levels
- 15 minutes prior to store opening the sales floor area ambient lighting will go into 'trading', likewise 15 minutes after store closes the same ambient lighting will go into 'stocking'

2. Digital Dimmable Technology

2.1. Fluorescent Dimming

Currently, fluorescent lamps offer the best combination of efficiency and good lighting quality in commercial and industrial applications; although it has lately been gaining traction in residential applications as well. Fluorescent dimming has long been considered a pioneering activity that demands careful study to develop an optimal control strategy for the application at hand and thus minimises the chance of an improper installation which fails to fulfil its energy saving and adequate lighting objectives [10]. Dimming of fluorescent lighting became common practice during the 1990's and as a consequence it reduced the capital costs of equipment and incentivised major deployment across end-users.

Fluorescent dimming originally faced technical challenges of striking a proper balance of voltage and current values that guaranteed a stable operation of the lamps, making them run inefficiently and giving a wavering look, but then electronic ballasts appeared into the scene. Electronic ballasts were meaningful to fluorescent dimming applications since they can be designed to adjust voltage and current separately. For instance, the ballasts allow sending controlled pulses which regulate the amount of current feeding the lamp, while it can also establish the appropriate stating voltage applied with each lamp current cycle.

An effective dimming system will not achieve its potential energy savings and other benefits unless it is regulated to maintain lamp lux output at a minimum. Hence, state of the art dimming systems have two basic elements:

- Electronic ballasts controlling the dimming of lamps
- Light level control sensors properly allocated according to the application

Modern dimming systems can be controlled via DSI which serves to regulate lighting intensity in buildings. The dimming curve that regulates lux intensity possess a logarithmic form because it has the function to not alter the human eye perspective when lux intensity changes making it very attractive for industrial, commercial, and residential environments. However, the power variation from dimming lights does not follow a logarithmic trend and instead is a linear relationship. Both these curves can be seen in Appendix B. Combining these patterns yield the relationship between lux levels, DSI values, and electrical power demand as seen in fig 2.

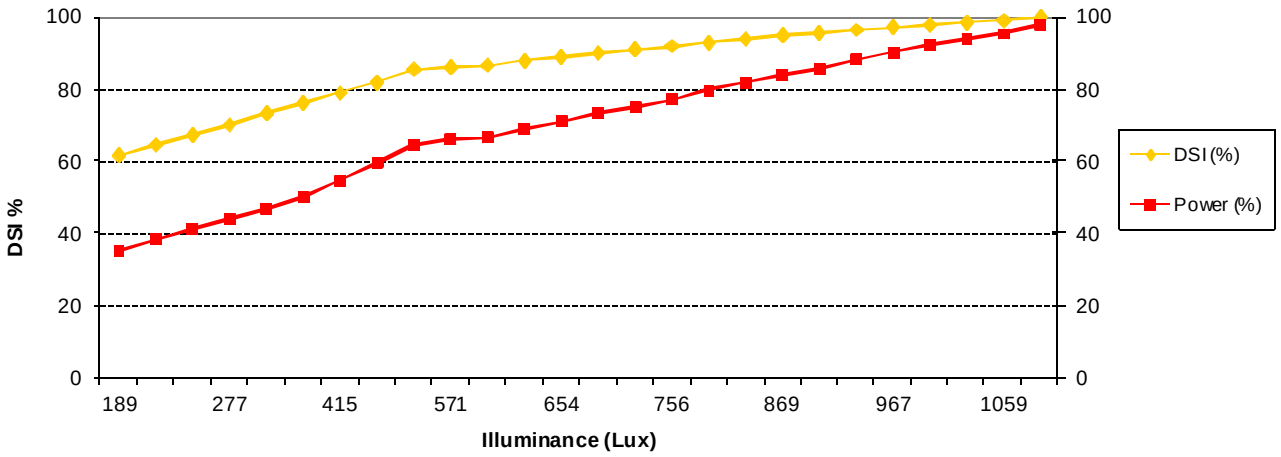

Fig. 2. Showcases interrelationships among lux intensity, DSI, and power demand percentages.

Figure 2 allows us to identify both the dimming percentages and power demand of ballasts in function of the lux it is providing. Therefore, once the lighting designer and end-user agree on a suitable range of lux levels to illuminate a specific area, it is possible to determine ideal DSI values to reach such illuminance levels and accordingly calculate the power consumption of the installed setting. The power demand formula required by ballasts can be expressed as:

$$Demand\ (kW) = [(number\ of\ lamps\ x\ lamp\ capacity\ x\ number\ of\ fittings) + (10\%\ losses)] \quad (2)$$

In order to exploit daylight features in its stores, Sainsbury's presently employs e dimming ballasts in all its new stores to regulate fluorescent lamps via the Clipsal C-bus lighting control [11].

2.2. Lighting System Controls in Supermarkets

The C-bus lighting control system is an intelligent bus wired system which uses DSI dimming protocol to control electronic ballasts. In Sainsbury's, the C-bus controllers take the sales floor dimming sensor readings, checks the code logic to make a decision, and then sends the preferred lux setting to each row of lighting on the sales floor area. Appendix A illustrates the C-bus panel schematic. In addition, auxiliary inputs are also received by the C-bus controller from the BMS (building management system) determining operating modes; these mode signals are classified as:

- *Trading*: when store is open for business, CoE trading lux levels are met
- *Stocking*: when store is closed for business, CoE stocking lux levels are met
- *Trend failed*: when Trend is at fault Clipsal defaults to 100% DSI to aware management
- *Generator*: when there is a grid failure and the stand-by generator kicks in Clipsal goes into a reduced trading lighting level (about 70% DSI)
- *Manager's route*: when no activity is to be performed during stocking in this mode lights can go to 0% DSI, hence it is employed only a couple of times throughout the year

The key variables to be used when regulating power demand in lighting systems is the dimming percentages of the different floor zones which consequently influence its corresponding lux levels; thus translating into quantifiable energy consumption. Impacts on energy savings can be estimated and modelled by knowing the rate and amount of fittings in a sales floor area and then load can be determined by employing (2). For example, taking the lighting demand from Fig 1 allows us to foresee the load profile the lighting system would have if the trading settings changed gradually from 900 to 200 lux – fig 3 depicts this data while Fig 4 shows how total store load would change.

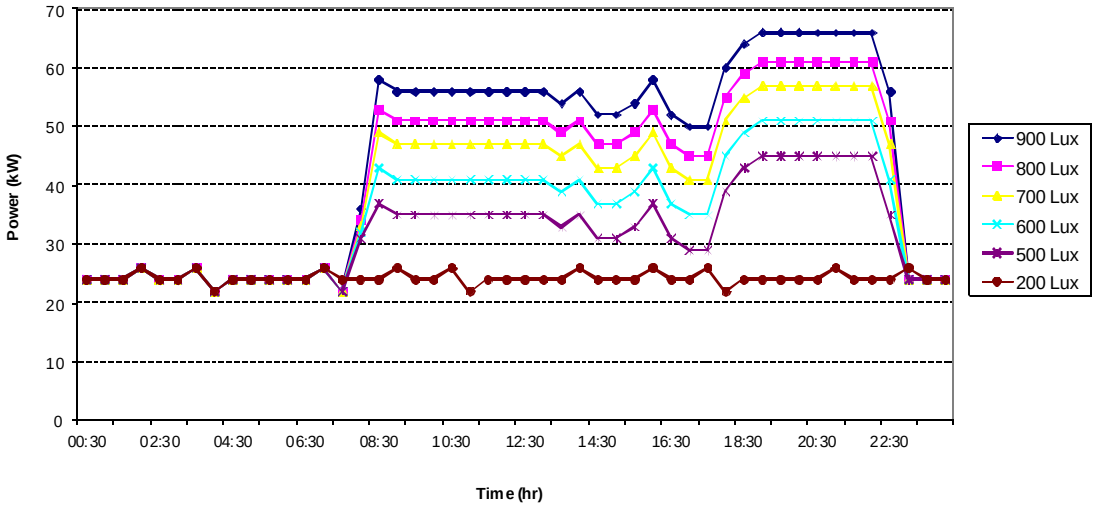

Fig. 3. Lighting load flexibility can be enhanced via digital dimmable technology.

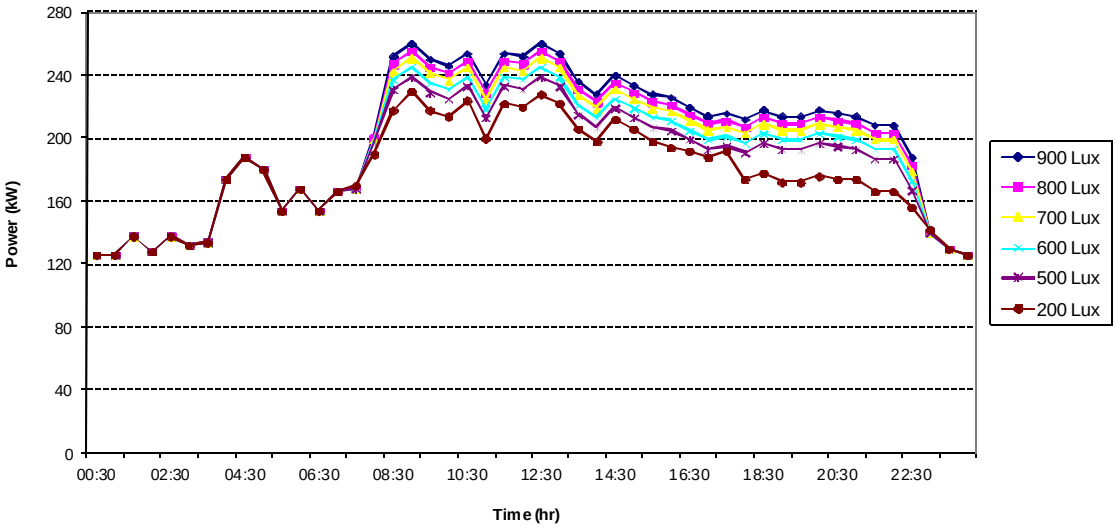

Fig. 4. Supermarkets can reduce their energy use by adopting DSI in their lighting systems.

3. Hythe: Lighting Control System Case Study

Opened in late February 2011, Hythe Sainsbury's has had the opportunity to explore and identify optimal control strategies of lighting systems by trialling different alternatives through the Clipsal C-bus system. In order to understand the impacts on store consumption from modifying lux levels a different set of operating strategies were proposed by the Imperial College team. These operation strategies have the objective of exploring the load flexibility and savings in lighting systems by learning the interrelationship between lux levels, DSI controls and energy usage.

3.1. Hythe Store Sales Floor Lighting Characteristics

Hythe has a sales floor area of 3,300 m^2 and is a carbon step change Sainsbury's store, meaning it has applied advanced building design concepts that aim at reducing its carbon footprint, such as:

- Double glazed windows in the shop front
- Reflective white ceilings and polished floor
- Circular sun pipes on the ceiling
- Extensive side windows in the general merchandise area

A review of fittings and sensor location in the sales floor area was conducted to calculate how much power sales lighting demand can draw at 100% DSI and to better understand how sensor location impacts dimming capabilities; the findings were:

- There are 722 fittings or 1444 ballasts which at 100% DSI draw a demand of 77.8 kW
    - Each fitting contains 2 x 49 W T16 lamps
- The sales floor area is divided into 8 zones which can be independently controlled by the Clipsal system – there is 1 lux sensor per zone
    - Sensors used are the C-bus 360 Degree Multi-Sensor

The eight sales floor zones described are aggregated and classified into three electrical bus bars from which energy monitoring is performed and logged via the EnergyICT database [12]. These three bus bars cover different lighting rows and are organised in the following manner:

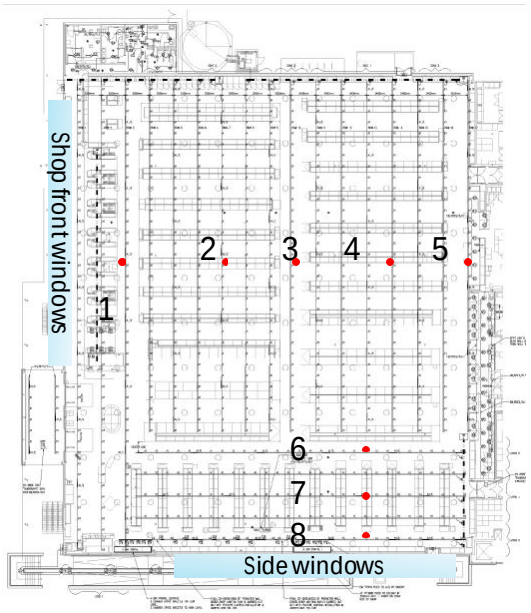

Fig. 5. Zone division and corresponding sensor location in the Hythe sales floor area.

- **BB1**: Rows 11 – 17 is the back-end of the sales floor (zones 4 and 5) with 257 fittings thus 27.70 kW is the maximum amount of power the area can draw
- **BB2**: Rows 1 – 10 is the front of the sales floor (zones 1, 2, and 3) with 320 fittings thus 34.49 kW is the maximum amount of power the area can draw
- **BB3**: Rows 18 – 22 is the right side of the sales floor (zones 6, 7, and 8) with 145 fittings thus 15.63 kW is the maximum amount of power the area can draw

Appendix C shows the power demand per bus bar the lighting system will consume according to the DSI and lux values established. These 22 rows of lighting constitute a total of 722 fittings giving a maximum demand of 77.8 kW. However, due to monitoring granularity it is possible to determine power consumption per bus bar – fig 6 illustrates the in-depth analysis detailed monitoring offers.

Fig. 6. Weekly lighting energy demand at Hythe in 30 minute intervals before installing DSI logic – non-dimmable settings fixed at 96% DSI = 900 lux.

When the Clipsal system was set up at Hythe in mid-March 2011, the following code was implemented in all zones to meet 900 lux while trading but with the possibility to dim when natural daylight was abundant:

- *if lux > 950 then 63% DSI – 120 seconds (i.e. time to implement command) – about 200 lux*
- *if lux < 850 then 96% DSI – 120 seconds (i.e. time to implement command) – about 900 lux*

3.2. Case Study Description

After studying dimming capabilities of the controls and benchmarking energy data, the Imperial College team established three trials to enhance the performance of the lighting system with the objective of reducing energy consumption, while also wondering if customers and staff would detect or complain about reducing lux levels. The trials were discussed and agreed with the Sainsbury's engineering and maintenance team, as well as its lighting contractor specialists and store management before they were carried out. The methodology undertaken consists in achieving energy savings during trading hours via two strategies. Firstly, by reducing maximum lux output and secondly by relaxing the lux bands used to dim ballasts. The following trials were conducted:

- 1st Trial – Lowering maximum lux level to 93% DSI or 790 lux (June – July 2011)
  - *if lux > 840 then 63% DSI – 120 seconds – about 200 lux*
  - *if lux < 770 then 93% DSI – 120 seconds – about 790 lux*
- 2nd Trial – Lowering maximum lux level to 90% DSI or 690 lux (August – September 2011)
  - *if lux > 770 then 63% DSI – 120 seconds – about 200 lux*
  - *if lux < 700 then 90% DSI – 120 seconds – about 690 lux*
- 3rd Trial – Lowering maximum lux level to 87% DSI or 600 lux (October – December 2011)
  - *if lux > 700 then 63% DSI – 120 seconds – about 200 lux*
  - *if lux < 630 then 87% DSI – 120 seconds – about 600 lux*

Figure 7 shows the immediate energy impacts from changing the code in the evening of the 11th of August 2011; having significant savings in peak demand and enhancing dimming capability during trading. These results demonstrate how the Clipsal system maximises the use of natural light while also reducing considerably the demand at night-time. Hence, these trials make evidently clear that even in stores that do not possess light tubes savings are possible via DSI technology.

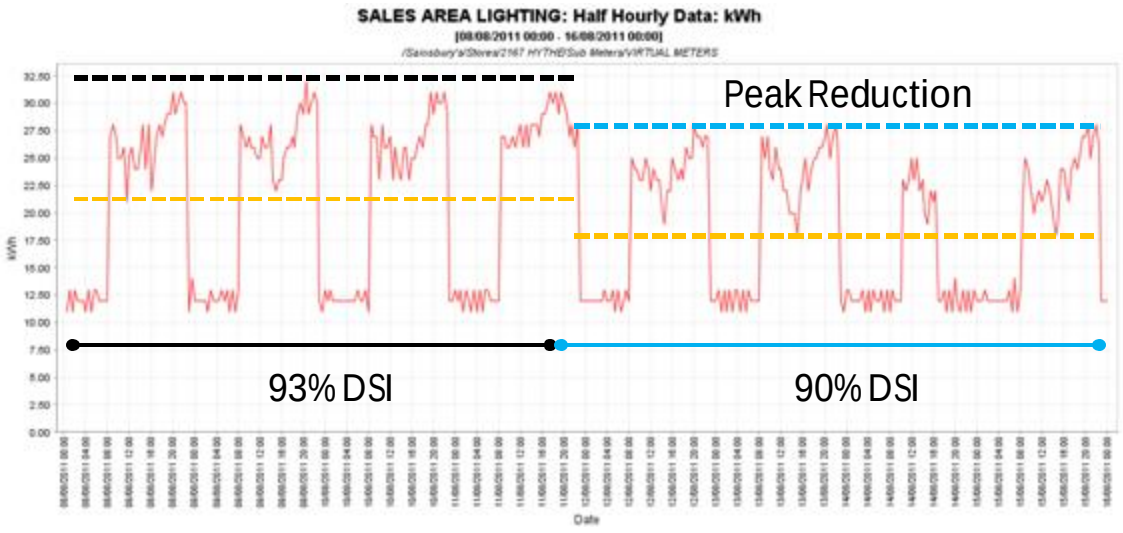

Fig. 7. By reducing maximum lux output and lowering dimming thresholds it is possible to both reduce peak lighting system demand while also enhancing its dimming capabilities.

3.3. Results Summary and Analysis

All trials were allowed to run from 4 to 6 weeks to obtain substantial results as factors such as sunshine hours per day and cloud coverage can influence the dimming capabilities of the lighting system. Likewise, it is important to factor in the moments during the year in which the trials were conducted since summer months will usually have longer days of sunshine hours and thus more dimming potential to be maximised by the controls. Figures 8 and 9 summarise these issues; Fig 8 describes a week's load profile in half-hourly intervals for each trial, while Fig 9 shows how as sunshine hours increase higher energy savings are achieved due to the effective settings applied.

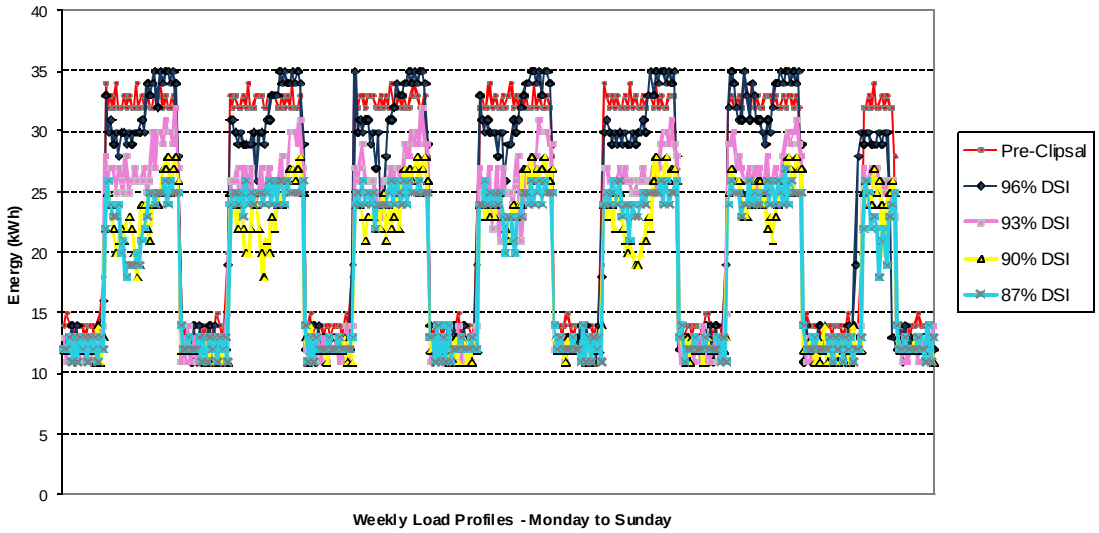

Fig. 8. Weekly results of each trial allows us to compare lighting performance under new settings.

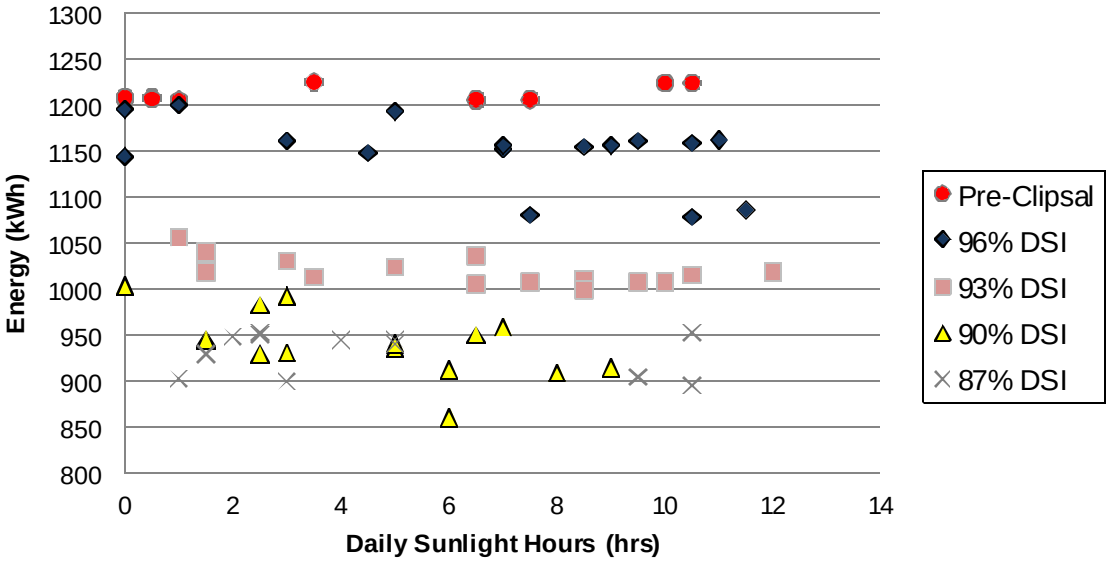

Fig. 9. Illustrates a sample of daily energy demands per trial as a function of sunshine hours.

Figures 8 and 9 demonstrate savings are quite clear once the proposed light settings have been implemented. Furthermore and equally important is the fact that no customer or staff member of the supermarket complained nor even noticed the fact that lux levels were gradually reducing as the months went by at Hythe – thus customer wellbeing and sales were not impacted negatively.

Nevertheless, an important question arose during the implementation and monitoring of the various trials: How much of the energy savings can be attributed to daylight dimming? And how much savings are due to the fact that lux levels are being reduced? In order to assess this interesting query benchmark data was taken at 96% DSI without dimming (*i.e.* flat trading profile similar to the pre-Clipsal data) and compared to profiles at 90% DSI. This comparison allowed us to separate the savings occurring during daytime and once the sun has set – the majority of the savings come from reducing maximum lux output (65%), while maximising the use of natural daylight also has a relevant contribution (35%) but just not as significant.

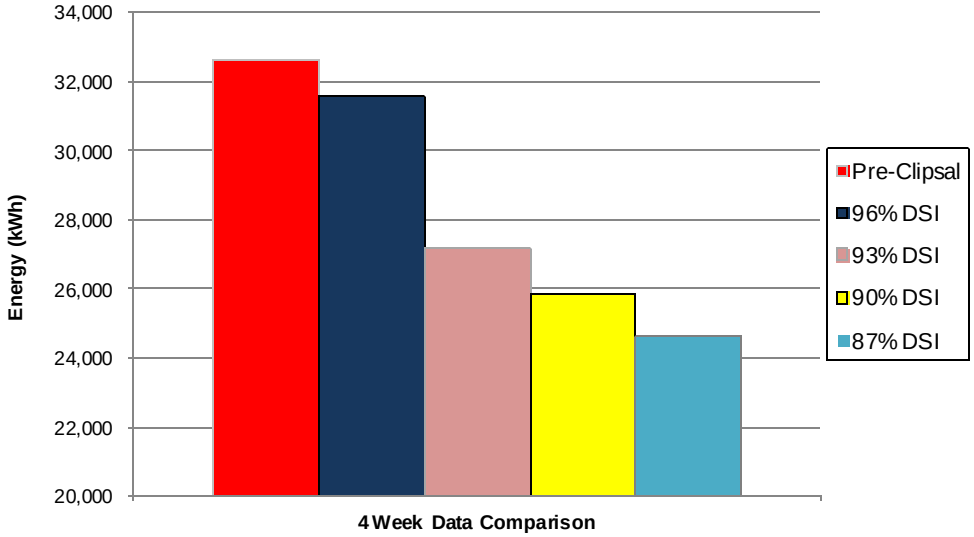

Fig. 10. Details the total energy consumed during four weeks for each light setting trialled.

Taking the four week result comparison gathered for each trial and showed in Fig. 10, it was possible to estimate annual projected performance for each light setting. Hence, Table 2 contrasts the potential benefits of the light setting strategy trialled at Hythe. The table makes special emphasis in avoided carbon emissions and its financial advantages via the Carbon Reduction Commitment (CRC) scheme implemented by DECC which plans in 2012 to begin taxing a tonne of carbon at £12 although this price could become more expensive as time progresses.

Table 2. Annual projections performance for each trial conducted at Hythe

	Pre-Clipsal	*96% DSI*	*93% DSI*	*90% DSI*	*87% DSI*
Energy Use (kWh)	424,320	410,046	353,132	335,855	320,242
Energy Bill (£)	32,715	31,615	27,226	25,894	24,691
Emissions (tCo_2)	235	228	196	186	178
CRC (£)	2,826	2,731	2,352	2,237	2,133
Total Costs (£)	**35,541**	**34,345**	**29,578**	**28,131**	**26,823**

Note: Electricity cost £0.0771 per kWh; Emissions coefficient 0.555 kg/kWh; Carbon cost £12/t [2]

The trials at Hythe are still ongoing as an astronomical clock setting is being worked upon to operate different lux level thresholds before and after the sun has set. Although important trials and associated findings are still in progress, Sainsbury's engineering and sustainability team has hailed the lighting energy trials as a success and reported results to the company's board. After assessing the retail and financial implications required for its undertaking, Sainsbury's has begun rolling-back and rolling-forward the learning's in all the stores where they have digital dimmable technology. Imperial College will continue working in conjunction with Sainsbury's to assess if Hythe's success translates effectively across the many stores where the new light settings are implemented.

4. Conclusions

Recognising the energy challenges climate change represents and being driven by its 2020 sustainability targets, Sainsbury's agreed an energy research partnership with Imperial College London to better understand how energy is used in their stores with the goal of providing insights into reducing the carbon footprint of supermarkets. After studying the principles of digital dimmable technology and the control principles applied to regulate lux levels in the sales floor area via the Clipsal C-bus system several lighting dimming trials were planned, agreed, and carried out by Imperial College at the Hythe store located in Kent, UK. The far reaching objective of the trials was to understand and identify optimal control capabilities dimming fluorescent lighting offers. Benchmark data was obtained by assessing lighting performance and controls at 900 lux (96% DSI), as a result three case studies were developed and implemented to monitor energy savings and impact on store operations by reducing lux levels during trading by going down to 790 lux (93% DSI), 690 lux (90% DSI), and 600 lux (87% DSI).

Results from the trials are very encouraging and make clear the energy efficiency capabilities of dimming technology in commercial buildings, highlighting the benefits such applications could have in industrial and residential environments. Overall, digital lighting management provides great control flexibility that allows businesses to pre-define lux level intensity and thus energy consumption according to the amount of natural day light the building can receive and the settings the user predefines.

4.1. Main Findings of the Trials

The key learning's of the lighting trials at Hythe can be summarised as follows:

- Thorough study of the system layout, communication, and logic control made it easier to develop the energy saving light settings
- Dimming capabilities depend on proper control logic and good positioning of sales floor light sensors otherwise benefits do not translate as effectively
- The lighting system at Hythe benefits greatly from light tubes on the roof, large shop front and side windows, as well as having reflective white ceiling and floor
- The Clipsal system has shown it is effective and robust in managing dimmable ballasts while also easily allowing to perform modifications to light settings
- Success of trial implementation has been due to good collaboration between partners making as a priority exploring to the fullest the dimmable technology at hand
- Substantial energy savings and lux reduction has gone unnoticed by customers and staff, hence business has not been impacted negatively
- Information gathered during the trials has fed through and enhanced the commissioning and CoE lighting requirements established by Sainsbury's
- Clipsal dial-in system is required to conduct effective remote monitoring and control
- Further energy savings are possible if BMS time settings are reduced from –/+15 minutes

4.2. Further Work on Digital Dimmable Lighting Technology

Continuation of the gathered learning's from lighting systems should not just stop at efficiency strategies that save daily energy usage. This is because if done carefully, flexible energy demand and changes to lux levels (within tolerable limits) is non-intrusive with Sainsbury's day to day business operations and therefore has big potential for further applications, such as demand side management or demand response services, given the right incentives of course. Thus, Sainsbury's with over 600 supermarkets across the UK could begin considering applying the potential it harnesses on managing its lighting load throughout its estate by aggregating flexible capacity. If made available, this load flexibility could be very valuable to power system operators who highly value security of supply such as the National Grid.

For example, if we take Hythe's lighting demand while trading (55 kW at 87% DSI) and assume remote control capability is available to trigger stocking lux levels (25 kW at 63% DSI) whenever the grid requires it then Sainsbury's has a 30 kW load flexibility to offer. If we assume the average Sainsbury's supermarket has the same load flexibility as Hythe then a total demand regulation capacity of 18,000 kW or 18 MW could be bundled altogether, most definitely a valuable resource to grid operators. This simple exercise shows the substantial amount of energy supermarkets consume and how Sainsbury's could become a relevant power broker in the UK energy market if it views its distributed store demand capacity as a single source of energy that can influence grid operations. Further work is required in this innovative field of research but it is an element worth considering and a key factor that could make commercial business enthusiastic of participating in the development of smart-grids environments as we had towards a low carbon energy future with increasing amount of intermittent renewable sources of energy in the UK fuel mix.

Acknowledgments

The authors of this paper would like to thank the sponsoring and contributing institutions of this research project without whom this valuable work had not been possible: Imperial College London, Sainsbury's, Symphony Automation, Schneider Electric, and EnergyICT.

Appendix A

Courtesy of Symphony Automation

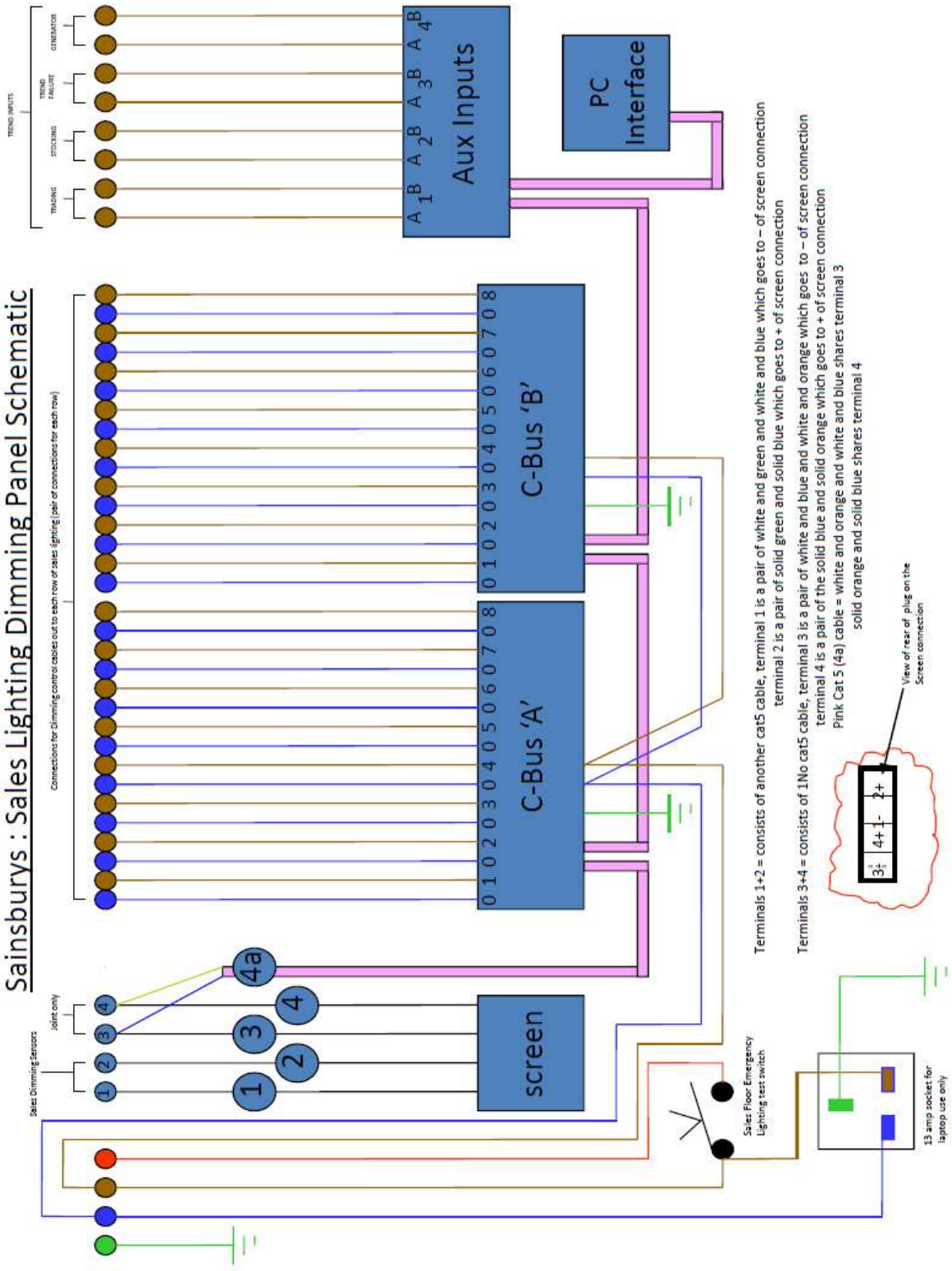

Appendix B

Courtesy of Tridonic Atco

Dimming characteristics of DSI control systems against its relative illuminance

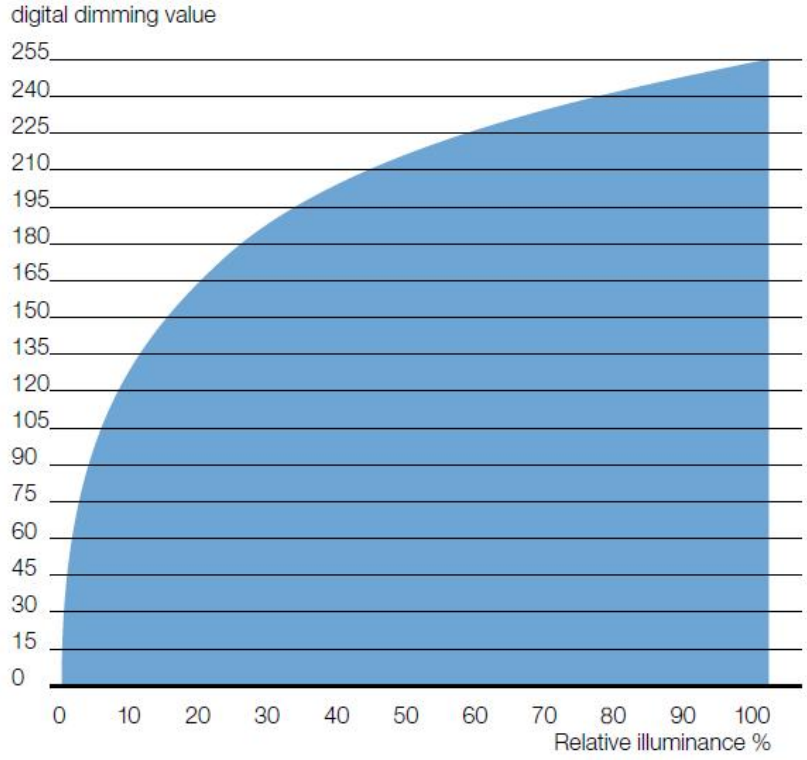

Estimated lighting energy saving as a function of DSI dimming level percentage

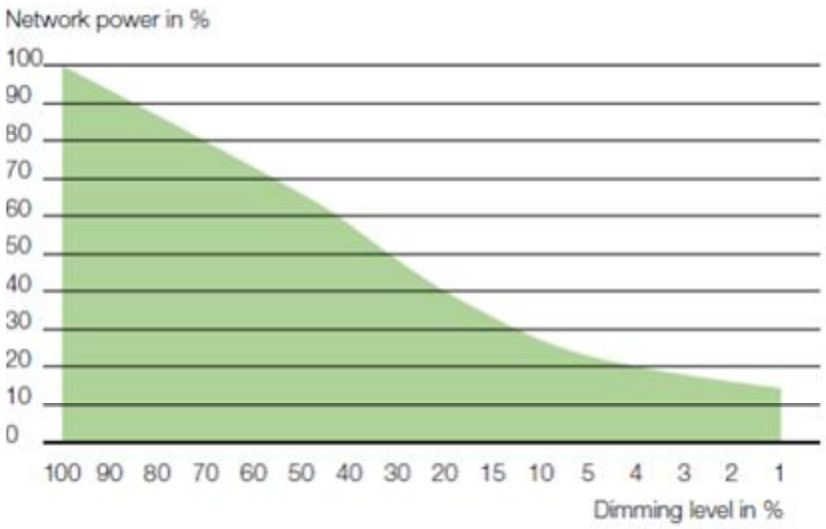

Appendix C

Lighting data relationship among key performance indicators – DSI, power, and lux values

Dimmable Technology Interrelationships		
DSI (%)	Power (%)	Lux (lx)
61.61	35.95	188.68
64.49	39.19	216.98
67.37	42.16	245.28
70.25	44.86	277.36
73.32	47.84	318.87
76.20	51.04	362.26
79.08	55.62	415.09
81.96	61.00	473.59
85.48	65.84	554.22
86.06	67.46	571.16
86.64	68.00	586.22
87.99	70.42	618.22
88.96	72.57	653.99
90.12	74.99	687.87
91.09	76.60	723.64
92.06	78.76	755.65
93.02	81.45	791.42
93.99	83.60	827.19
94.96	85.75	868.61
95.54	87.36	896.86
96.51	90.05	930.74
97.28	91.93	966.52
97.87	94.09	1000.41
98.64	95.97	1034.30
99.22	97.31	1058.78
100.00	100.00	1100.21

Hythe Lighting System Power Demand Calculation

	SF Area			SA Area		GM Area			Energy ICT Meters			
Power per Fitting (W)	Zone 1 (W)	Zone 2 (W)	Zone 3 (W)	Zone 4 (W)	Zone 5 (W)	Zone 6 (W)	Zone 7 (W)	Zone 8 (W)	BB1 (kW)	BB2 (kW)	BB3 (kW)	Total
35.23	4544.29	6763.59	1127.26	4509.06	3381.79	1056.81	3170.43	880.68	12.44	7.89	5.11	25.43
38.41	4954.30	7373.84	1228.97	4915.89	3686.92	1152.16	3456.49	960.14	13.56	8.60	5.57	27.73
41.32	5330.14	7933.23	1322.21	5288.82	3966.62	1239.57	3718.70	1032.97	14.59	9.26	5.99	29.83
43.97	5671.82	8441.77	1406.96	5627.85	4220.89	1319.03	3957.08	1099.19	15.52	9.85	6.38	31.74
46.88	6047.66	9001.17	1500.19	6000.78	4500.58	1406.43	4219.30	1172.03	16.55	10.50	6.80	33.85
50.02	6452.26	9603.37	1600.56	6402.24	4801.68	1500.53	4501.58	1250.44	17.66	11.20	7.25	36.11
54.50	7031.02	10464.77	1744.13	6976.51	5232.38	1635.12	4905.36	1362.60	19.24	12.21	7.90	39.35
59.78	7712.00	11478.33	1913.05	7652.22	5739.16	1793.49	5380.47	1494.57	21.10	13.39	8.67	43.16
64.53	8324.01	12389.23	2064.87	8259.49	6194.61	1935.82	5807.45	1613.18	22.78	14.45	9.36	46.59
66.11	8528.38	12693.41	2115.57	8462.27	6346.70	1983.34	5950.03	1652.79	23.34	14.81	9.59	47.73
66.64	8596.08	12794.17	2132.36	8529.44	6397.08	1999.09	5997.27	1665.91	23.52	14.93	9.66	48.11
69.01	8902.40	13250.09	2208.35	8833.39	6625.04	2070.33	6210.98	1725.27	24.36	15.46	10.01	49.83
71.12	9174.29	13654.76	2275.79	9103.17	6827.38	2133.56	6400.67	1777.96	25.10	15.93	10.31	51.35
73.49	9480.52	14110.55	2351.76	9407.03	7055.27	2204.77	6614.32	1837.31	25.94	16.46	10.66	53.06
75.07	9684.16	14413.64	2402.27	9609.09	7206.82	2252.13	6756.39	1876.78	26.50	16.82	10.89	54.20
77.18	9956.23	14818.58	2469.76	9879.05	7409.29	2315.40	6946.21	1929.50	27.24	17.29	11.19	55.72
79.82	10296.54	15325.08	2554.18	10216.72	7662.54	2394.54	7183.63	1995.45	28.18	17.88	11.57	57.63
81.93	10568.43	15729.75	2621.62	10486.50	7864.87	2457.77	7373.32	2048.14	28.92	18.35	11.88	59.15
84.03	10840.22	16134.28	2689.05	10756.19	8067.14	2520.98	7562.94	2100.82	29.66	18.82	12.18	60.67
85.61	11044.13	16437.78	2739.63	10958.52	8218.89	2568.40	7705.21	2140.34	30.22	19.18	12.41	61.81
88.25	11384.44	16944.29	2824.05	11296.19	8472.14	2647.54	7942.63	2206.29	31.15	19.77	12.80	63.72
90.09	11622.25	17298.23	2883.04	11532.16	8649.12	2702.85	8108.55	2252.37	31.80	20.18	13.06	65.05
92.20	11894.23	17703.04	2950.51	11802.02	8851.52	2766.10	8298.30	2305.08	32.55	20.65	13.37	66.57
94.05	12132.13	18057.12	3009.52	12038.08	9028.56	2821.42	8464.27	2351.19	33.20	21.07	13.64	67.90
95.36	12302.05	18310.03	3051.67	12206.69	9155.02	2860.94	8582.83	2384.12	33.66	21.36	13.83	68.85
98.00	12642.00	18816.00	3136.00	12544.00	9408.00	2940.00	8820.00	2450.00	34.59	21.95	14.21	70.76

References

[1] Maidment G. G., Zhao X., Riffat S. B., Prosser G., Application of combined heat-and-power and absorption cooling in a supermarket, *Applied Energy*, Volume 63, Issue 3, July 1999, Pages 169-190.

[2] J Sainsbury PLC, Annual Report and Financial Statements 2011. – Available at: <http://www.j-sainsbury.co.uk/ar11/> [accessed: 10.2.2012].

[3] J Sainsbury PLC, Sainsbury's 20 by 20 Sustainability Plan. – Available at: <http://www.j-sainsbury.co.uk/responsibility/20-by-20-commitments/> [accessed: 19.1.2012].

[4] UK HM Government, The Carbon Plan: Delivering our low carbon future. – Available at: < http://www.decc.gov.uk/en/content/cms/emissions/carbon_budgets/carbon_budgets.aspx/> [accessed: 23.1.2012].

[5] Pei Liu, Efstratios N. Pistikopoulos, Zheng Li, An energy systems engineering approach to the optimal design of energy systems in commercial buildings, Energy Policy, Volume 38, Issue 8, August 2010, Pages 4224-4231.

[6] N. Sugiartha, S.A. Tassou, I. Chaer, D. Marriott, Trigeneration in food retail: An energetic, economic and environmental evaluation for a supermarket application, Applied Thermal Engineering, Volume 29, Issue 13, September 2009, Pages 2624-2632.

[7] G.G Maidment, X Zhao, S.B Riffat, Combined cooling and heating using a gas engine in a supermarket, Applied Energy, Volume 68, Issue 4, April 2001, Pages 321-335.

[8] Wulfinghoff D., Dimming Fluorescent Lighting. Energy Efficiency Manual. New York, USA: Energy Institute Press. 1999. p. 346-378.

[9] J Sainsbury PLC, Sainsbury's Centre of Excellence: Lighting Specification Manual. 2009.

[10] Doulos L., Tsangrassoulis A., Topalis F., Quantifying energy savings in daylight responsive systems: The role of dimming electronic ballasts, *Energy and Buildings*, Volume 40, Issue 1, 2008, Pages 36-50.

[11] Schneider Electric Clipsal Integrated Systems. C-Bus Lighting Control: The new definition in lighting control. – Available at: <http://www3.clipsal.com/cis/portal/> [accessed: 30.1.2012].

[12] Energy ICT. Provider of Energy Management, Smart Grid, and Smart Metering Solutions. – Available at: < http://www.energyict.com//> [accessed: 8.2.2012].

Optimising the arrangement of finance towards large scale refurbishment of housing stock using mathematical programming and optimisation

Mark Jennings[a], Nilay Shah[b], and David Fisk[c]

[a] Department of Civil and Environmental Engineering, Imperial College London, South Kensington Campus, London SW7 2AZ, UK, m.jennings09@imperial.ac.uk CA
[b] Department of Chemical Engineering and Chemical Technology, Imperial College London, South Kensington Campus, London SW7 2AZ, UK, n.shah@imperial.ac.uk
[c] Department of Civil and Environmental Engineering, Imperial College London, South Kensington Campus, London SW7 2AZ, UK, d.fisk@imperial.ac.uk

Abstract:

The U.K. will require significant refurbishment interventions to the existing building stock if her 2050 greenhouse gas emissions targets are to be met. In parallel, the current economic recession is forcing some investors and creditors to look to new strategies of achieving healthy returns on property assets. The research presented in this paper seeks to analyse these problems using optimisation.
A mixed integer linear programming model is presented for arranging the finance for large scale refurbishment schemes. The objective function minimises the costs of arranging finance. This model feeds into a technology urban resource network model, which allows for optimised statements of the refurbishment actions to be performed, their timing, and their quantity.
An example of an urban area seeking to reduce its housing heating emissions is presented. Results suggest that division of finance, technology capacity, and organisational capacity by tenure is more appropriate than simpler representations. Overall, the optimisation models presented are thought to offer a robust method going forward for the arrangement of finance towards energy efficient refurbishment of housing stock at the large scale.

Keywords:

Optimization, MILP, Refurbishment, Buildings, Finance, Energy Efficiency.

1. Introduction

Demand side reduction is a key energy policy goal in the U.K. and reducing the heat demand of existing buildings is a policy lever to achieve this goal. There are approximately twenty-five million domestic houses in Great Britain, of which approximately 1 – 1.9% are refurbished each year [1]. Of these twenty-five million, seventeen million are privately owned, nearly four million are privately rented and four and a half million have public landlords [2]. These separate tenures offer different financial and logistical constraints to achieving energy efficient refurbishment of building stock. Refurbishment of housing stock at the large scale is argued here to be constrained in part by uninspired financial arrangements.

The line of attack taken is to optimise the major variables for separate tenures of building stock, in particular those representing activity levels of finance, financial cost, and refurbishment interventions. Whilst computer based mathematical programming has been around since just after World War 2, little work has been identified as published since then on the specific problem of arranging finance towards refurbishment interventions to existing building stock.

Gau and Kohllepp [3] use a linear programming (LP) model for use in the financial planning and management of property developments. They include a novel land-use constraint, which was

instance is particularly apt for larger scale development where land is only released after a certain number of developments have been completed. Addae-Dapaa [4] applies linear programming (LP) to the valuation of mixed used developments. However little other work has been identified using linear programming to essentially take the role of typical development appraisal software.

Mathematical programming has been employed on a more regular basis to plan refurbishment actions in housing stock (e.g. see Keirstead et al. [5] for a recent review). Initial academic studies in this area are identified from the early 1990s (e.g. [6]). Refurbishment options are typically optimised on the basis of minimisation of lifecycle cost of capital, installation, and operations. A number of previous studies conflate the process of choosing optimal refurbishment technologies with their optimal operations. For instance, Amano et al. [7] used mixed integer linear programming (MILP) to optimise the decisions of what type of equipment to choose and when to retrofit an office's energy supply but the operational policy based upon varying energy demands is also contingent upon the effect of a potential carbon tax. Conflating operational costs with capital cost risks missing the key decision maker of the models: the investor. To date, at least in the engineering literature, no studies have been identified that combine a more sophisticated finance module than a net present value or annuitisation factor with a long term refurbishment planning tool.

The models presented are a first attempt at formalizing the relationships inherent (in the U.K.) in the processes of financing and planning for refurbishment. The specific objectives of this paper are two-fold: a) to present a new optimisation framework for feedback from the international academic community, and b) to assess any limits to the use of optimisation for aiding decision making in this area. Initial results suggest that the method is robust, although there are tradeoffs between piecewise estimation accuracy and solution time of the MILP. Further results demonstrate the sensitivity of potential rates of refurbishment to both the organisational capacity (i.e. labour available and associated market), and the financing in place.

The research problem under consideration is described in greater detail, followed by a section on formulation of the models. An example is then provided and initial results are discussed. Conclusions from this use of mathematical programming to aid decision making are then offered.

2. Problem description

Each type of housing tenure has its own incentives, budgets, and organisational constraints. The financial and organisational constraints to energy efficient housing refurbishment at the large scale are of concern in this study.

Assuming that the decision to refurbish has been made, the next questions to be answered are where to get the cash, and how to plan the refurbishment interventions. The agent who initially spurs the arrangement of refurbishment finance is typically an owner occupier, public or private landlord. The agent will often seek finance from a creditor or investor. The type of creditor involved and the size of the loan available depend on a number of factors including: size of development, relationship between the agent and the creditor, agent's previous record/company guarantee, &c. See Figure 1 below. The research question of concern for this stage of the refurbishment process is what is the optimal arrangement of finance given varying financing fees?

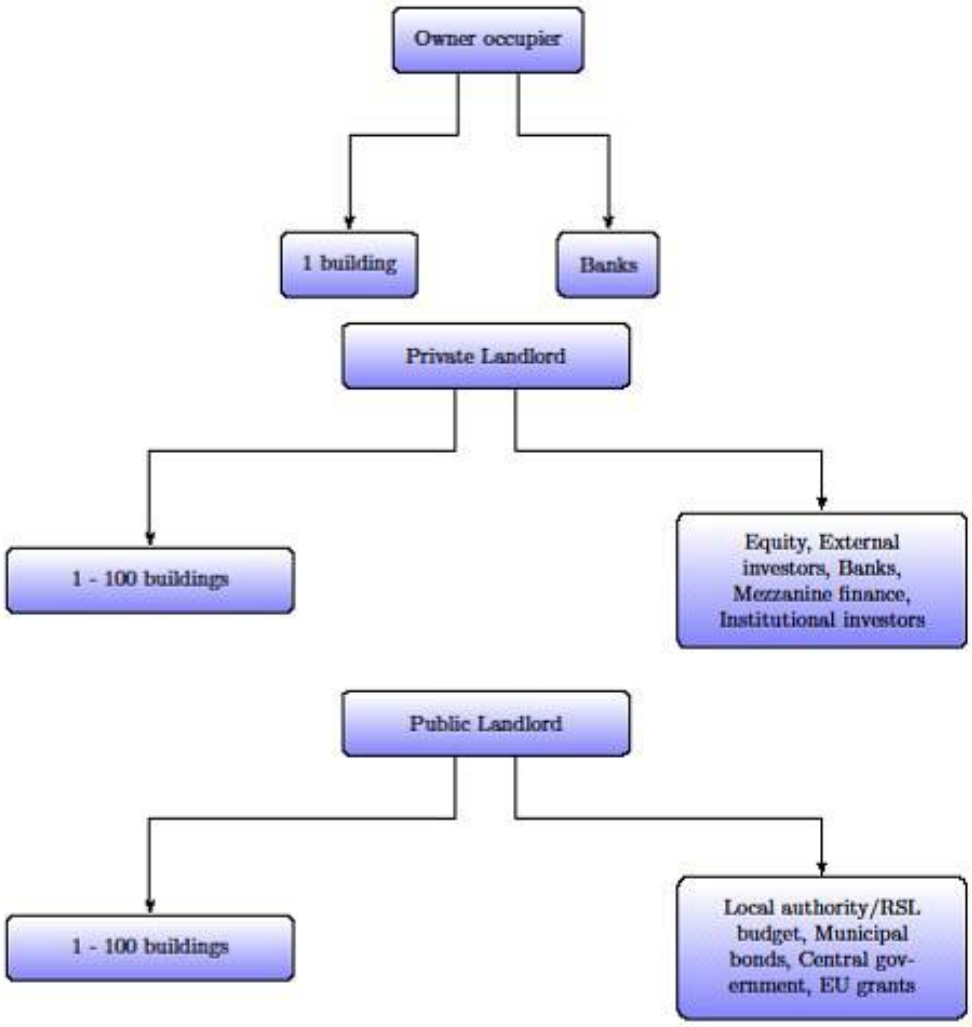

Fig. 1. A range of typical agents involved in the arrangement of finance for the refurbishment of buildings by tenure. Note: RSL denotes registered social landlord.

Once the finance is in place, the type of manager overseeing the entire refurbishment is dependent on the scale of the scheme. In typical schemes involving blocks or streets of buildings, the manager would be a property company, property developer, or house builder. For smaller schemes, a local engineering consultancy and contractor would likely suffice. The research question under study for this stage of refurbishment is what interventions should be chosen, in which order, and to what quantity? Section 3 details two mathematical programming models formulated to answer these research questions.

3. General model for financing refurbishment using mathematical programming and optimisation

The problem description led to the building of two mathematical programming models, formulated in GAMS (Version 23.3.3) and solved using the branch and bound algorithms in CPLEX (Version 12.1.0) on a cluster of LINUX central processing units. This section briefly describes the main equations and structure of both models. The financing refurbishment (FIR) model is described first followed by the description of a technology urban resource network (TURN) model. The FIR model is thought novel. The core equations of the full TURN model [8], [9] have been used here and refurbishment equations have been added to allow for changes to existing technologies and demand-side interventions [10], [11].

The FIR model seeks to optimise the financing of property refurbishment from a set of creditors over the entire span of the project. The model is temporally dynamic[1], and provides output financing costs which can feed into the TURN model. TURN is both temporally dynamic and spatially dynamic as the model allows for consideration of a set of zones, *i*. For instance, zones may have individual building heating and electricity demands, or may be aggregates of many buildings of the same tenure. The refurbishment TURN model identifies the optimal refurbishment action, when it should be performed, and in what quantity. The energy conversion technologies must meet an existing pattern of resource demands which vary in time and space [8]. These models are now described in sequence.

3.1. Financing refurbishment (FIR) model

A mixed integer linear programming (MILP) model has been built for the purposes of both codifying the primary relationships in refurbishment financing and for optimising the financing fees. An optimiser as below could be used at the development appraisal stage. There are two primary forms of development appraisal commonly used: static, and cashflow models. Static development appraisal models are often used as a first approximation of likely costs (particularly for assessing how much can be paid for the land to achieve a healthy return for the developer), before purchasing of land or hiring a professional team. A cashflow model provides a more detailed breakdown of expected costs and proceeds from the project, for a given financing stream.

The FIR model seeks to optimise the financing fees from a range of financers for refurbishment projects. The factors included in the model are based upon conversations with property developers and built asset consultancies in London. The model takes input for initial estimates of monthly costs and proceeds from a typical development appraisal (built for example in Caldes or Argus software), and selects the finance required for each month based on endogenous financing fees. Financing costs typically include but are not limited to the following costs: arrangement fees, audit fees, interest due, non-utilization fees, and exit fees.

The key decision variables in FIR are as follows (note that indices (subscripts) and parameters are outlined in the nomenclature section at the end):

- $LFac_f$ – Lending facility
- Fi_{fm} – Finance used
- TFi_{fm} – Cumulative finance used
- $IntDue_{fm}$ – Monthly interest due
- FiC_{fm} – Monthly financial cost

The objective function is that of minimising the monthly financial costs as below in (1):

$$z = \sum_f \sum_m FiC_{fm} , \tag{1}$$

If planning for the worst case, the objective function could be that of maximising the financial costs. The financial costs are calculated from the following equality constraint (2):

$$\begin{aligned} FiC_{fm} = {} & AFe_f LFac_f + AuFe_f TFi_{fm} + IntDue_{fm} + \\ & NUFe_f(LFac_f - TFi_{fm-1}) + EFe_f TFi_{fm=M} , \qquad \forall f, m \end{aligned} \tag{2}$$

The financial costs then feed into the cost balance constraint (3):

[1] The models are dynamic in that they consider discrete segments of time, repeated in order to represent a given aggregate time period (e.g. each day may be represented by six non-uniform time segments). However, these optimisation models are single-stage in nature, with decisions optimised from the point of view of the initial time period, and thus are not truly dynamic.

$$\sum_f Fi_{fm} = TC_m + \sum_f FiC_{fm}\ , \qquad \forall\, m \tag{3}$$

The total costs per month, TC_m, are a parameter estimated from a development appraisal spreadsheet, using typical inputs for a refurbishment program. An example spreadsheet is given in the Appendix. Aside from typical constraints (such as the loan facility being able to meet the monthly sum of the total costs, financing costs and a contingency) the last constraints of note estimates the interest due for each financer on a monthly basis, $IntDue_{fm}$. The monthly interest due is a product of the cumulative finance used, TFi_{fm}, and the monthly interest rate of the financer, $MInt_f$. The circumstances by which the interest rate may vary are not implicitly included in the model. The interest rate is allowed to vary on account of least cost optimization, with upper and lower bounds being provided by the modeller (5% and 8% nominal interest rates are the lower and upper bounds on the interest rate in the example given in the next section). The product of two continuous variables is a simple bilinear function, say for an arbitrary example of $x.y$ below, but its form can be changed to the following [12]:

$$u_1 = 0.5(x + y)$$
$$u_2 = 0.5(x - y) \tag{4,5,6}$$
$$u_1^{\,2} - u_2^{\,2} = x.y$$

Separable programming may be used to estimate u_1 and u_2, by q_1 and q_2. The lambda method uses the relationship between two sets of piecewise parameters, pw_p and pwe_p, to estimate the nonlinear curve, as follows for u_1 in (7 – 9):

$$u_1 = \sum_p pw_p \lambda_p \tag{7}$$

$$q_1 = \sum_p pwe_p \lambda_p \tag{8}$$

$$\sum_p \lambda_p = 1 \tag{9}$$

The lambda variables used, λ_p, are special ordered sets variables of type 2 (SOS2) meaning that only two neighbouring variables can be non-negative. This ensures the piecewise estimation is considering the correct segment of the nonlinear relationship. (7 – 9) are repeated for u_2. Finally an estimate of the product of x and y is provided, as in (10):

$$q_1 - q_2 = x.y \tag{10}$$

The process of (4 – 10) is used in FIR to provide estimates of the monthly interest due, $Intdue_{fm}$. The output of available finance from FIR now provides the maximum budget parameter for use in TURN.

3.2. Refurbishment technology urban resource network (TURN) model

The refurbishment TURN framework is formulated as a MILP to identify the optimal ordering and magnitude of integer refurbishment interventions. Integer rather than continuous variables are used to represent refurbishment interventions as it is thought more sensible to obtain discrete results for technology interventions. The TURN framework is based upon the idea of a resource-technology network whereby generic resources may be converted from one state into another by user-specified technologies [8], [9]. The model uses a hierarchical non-uniform representation of time, for example where a day could be represented by six periods of varying duration. This allows the user to model resource conversions subject to the level of detail required for the refurbishment planning. Size constraints on the problem size are dealt with in three ways. The linearization and simplification of conversion factors allow for representation of planning of technologies, without the necessary detail involved in a design optimisation. MINLP formulations are not considered in this paper. Aggregation of time periods into non-uniform periods of interest reduces the problem

size considerable, for example where 7a.m.- 9a.m. could represent the peak demand period of a weekday. Finally, aggregation of spatial configurations into zones of interest further reduces the problem size into a manageable proportion. The main equations in TURN are now provided.
The objective function for refurbishment planning is that of minimizing the gap between the actual GHG emissions produced by the building stock and an emissions reduction target, as in (11):

$$z = \sum_{m} Gap_{m} \tag{11}$$

TURN is a temporally and spatially dynamic MILP model that portrays urban energy systems (such as groups of buildings) as a system of existing resource demands and existing technologies used to convert resources from one form to another. The TURN framework describes resources, *r*, in terms of energy carriers (e.g. methane), energy demands (e.g. heat), energy by-products (e.g. GHG emissions), and so on. Technologies *j* may represent a process or operation that converts a set of input resources to a set of output resources. The resulting resource balance is described in equation (12), after Keirstead et al. [8]:

$$P_{rim} + I_{rim} = D_{rim}, \qquad \forall rim \tag{12}$$

which states that for each resource, *r*, in each zone, *i*, at each month, *m*, the net production, P_{rim}, and the amount imported from outside the city, I_{rim}, must be equal to the demand, D_{rim}. The expected impact of a technology *j* on a resource *r* is given by δ_{jr}, and the resulting demand balance is given below in (13):

$$D_{rim} = D_{rim-1} + \sum_{j} N_{jit}\delta_{jr}, \qquad \forall jrim \tag{13}$$

The current month's stock of technologies, M_{jim}, is related to the previous month's stock with changes only occurring if an intervention, N_{jim}, is chosen and if that intervention j has an effect on an existing technology j (for example a new micro-CHP would displace an existing gas condensing boiler) as shown in (14):

$$M_{jim} = M_{jim-1} + \sum_{j} N_{jit}\sigma_{jj}, \qquad \forall jim \tag{14}$$

(12 – 14) are the three major constraints of interest in this paper. Each intervention also has an associated cost, and the sum of these costs is bounded by a monthly budget. The monthly budget may be fed into TURN using output from FIR.
In general then, the systems modelled using FIR, and TURN, must satisfy certain conditions and assumptions:

- Linear programming assumptions of proportionality, non-negativity, and additivitity.
- Zones of houses are aggregated together by tenure and each zone has a minimum rate of refurbishment for each period.
- The impacts of interventions on existing resource demands are constant average values.
- Rebound effects and stochastics on demand side reductions are not included.
- The conversion factors for resources by different technologies use constant average values.

An illustrative example is now provided.

4. Example

A neighbourhood of London consists of two-hundred and five terraced houses, built by use of traditional red brick solid walls during the era of Queen Victoria (1837 – 1901). These houses have changed ownership many times since then, and as of 2012 consist of one hundred owner occupied houses, fifty-nine privately rented houses, and forty-six publically rented houses. The local council in this area of London has introduced a climate change mitigation target for 2020 with a target of a

40% reduction on 2005 levels of GHG emissions from the operation of technologies. Energy efficient refurbishment of existing housing stock is a key strategy towards meeting this target.

In this context, the local council are primarily empowered to incentivise the refurbishment of the publically owned housing stock. The owner occupiers are assumed only to refurbish their houses either when a housing technology does not work satisfactorily, or when the house is undergoing a significant renovation/extension. The average annual rate of refurbishment of both publically owned and owner occupied houses is approximately 1% (using housing renovation data as a proxy [1]).

The privately rented houses are owned by a number of private landlords, but external investors are interested in buying up this stock, refurbishing it and gaining steady returns from both the capital and rental growth. It is assumed here that institutional investors, such as insurance companies, have both the spare cash and incentive to return to the housing market in the U.K. The details and timing of the finance to be used, and its costs, are modelled using the FIR framework described in section 3.1. The timing, type, and number of refurbishment investments are then detailed using the TURN model for a given GHG emissions trajectory.

4.1. Initialisation

The proceeds and costs of the refurbishment project for the privately rented houses are pre-calculated using a bespoke spreadsheet based development appraisal. Details are provided in the Appendix. The inputs for this development appraisal come from author's estimates, interviews with U.K. stakeholders and other trade publications [13]. The refurbishment project is assumed to last twenty months, accounting for time spent arranging finance, gaining planning permission, buying the houses (assumed vacant), engineering design, the actual refurbishment construction, and finally completion/handover. The outputs of the development appraisal are the monthly costs and proceeds for input into FIR. For simplicity it is assumed that when refurbished, the fifty-nine privately rented houses will be put on the rental market for just over £300/ft^2, with a 5.8% average yield [14] when taking a 5% vacancy rate provides gross development value of £23.1 million. The total development costs (land, planning and building fees, infrastructure, construction and professional fees) less the costs of arranging finance sum up to £16.8 million. The main parameters used in FIR are given in Table 1.

Table 1. Financial parameters used in FIR

Sources: Author's estimates following interviews with U.K. stakeholders.

Note: LTGDV denotes loan to gross development value.

Financer	*Maximum LTGDV (%)*	*Minimum annual nominal interest (%)*	*Arrangement fee (% of loan)*	*Non-utilization fee (% of loan not drawn down)*	*Exit fee (% of loan)*
Property developer	20	0	0	0	0
Clearing banks	90	5.0	1.5	1.8	2.0
Institutional investors	90	5.0	1.0	1.8	1.0

The maximum monthly budgets for the privately rented refurbishments are provided by a proportion of the monthly finance available for construction costs from FIR. The maximum budgets for the owner occupiers and social landlords are assumed at £10,000/house/year and £2,500/house/year respectively.

Only the housing heating demands have been considered in this formulation of TURN. As described elsewhere [8], [10] the demands are considered for six periods per day, for three seasons per year. The project begins in winter, and continues through twenty months of varying heating

demand. Technological parameters relevant to this example are given in Table 2 below. There are no specific constraints on technology operation, such as minimum cycling periods of micro-CHP units, other than the minimum and maximum capacity factors limits related to the installed capacity of each technology. See [8], and [9] for further details. The results of the optimisation runs are presented in section 4.2. and discussed in section 5.1.

Table 2. Supply-side technological parameters used in TURN

Sources: [15–17] and author's estimates.

Technology	*Operational efficiency (min, mode, max): %*	*Installation cost (min, mode, max): k£*	*Domestic capacity (min, mode, max): kW*
Air source heat pump	1.8, 2.2, 2.6	6.0, 8.0, 10	4.0, 8.0, 16
Condensing gas boiler	0.74, 0.85, 0.90	1.0, 2.5, 4.0	10, 25, 30
Ground source heat pump	2.0, 2.5, 3.0	8.0, 15, 22	4.0, 8.0, 16
Stirling engine micro-CHP	Elec: 0.02, 0.06, 0.09 Therm: 0.60, 0.71, 0.80	4.0, 5.0, 9.0	Elec: 0.5, 1.0, 3.0 Therm: 5.0, 8.0, 15
Solar thermal		2.5, 3.5, 5.0	1.0, 2.5, 4.5

4.2. Results

Figure 2 shows two different approaches that can be taken for planning the financing of refurbishment projects, for the best case where financing costs are to be minimised and for the worst case where financing costs are to be maximised. Table 3 and Figure 2 display the main results. In the best case, the developer initially uses all the equity in month three, and the institutional investor's finance is used at a greater rate than the creditor's finance. Minimisation of financing fees allows for a saving of almost £1.0 mn, increasing the return to the property developers from 18% to 19%.

Table 3. Financial output

	Development appraisal static model:	*Optimisation model – minimising costs:*	*Optimisation model – maximising costs:*
Financing costs	£2.15 mn	£1.16 mn	£1.88 mn
Return on equity	18.0%	19.0%	15.8%

Note that most external investors/creditors will require that the developer provides equity up front, often used in the acquisition of the land/buildings before putting their own money into the scheme. It can be seen that the worst case switches the priority with the higher fees of the creditor being chosen for the majority of the financing. Still, the use of an optimised cashflow provides a lower return on equity than the static development appraisal models as the fees are calculated on a monthly basis for each cost in the cashflow version while the static model makes assumption about the appropriate compounded interest rate to apply to the aggregated costs.

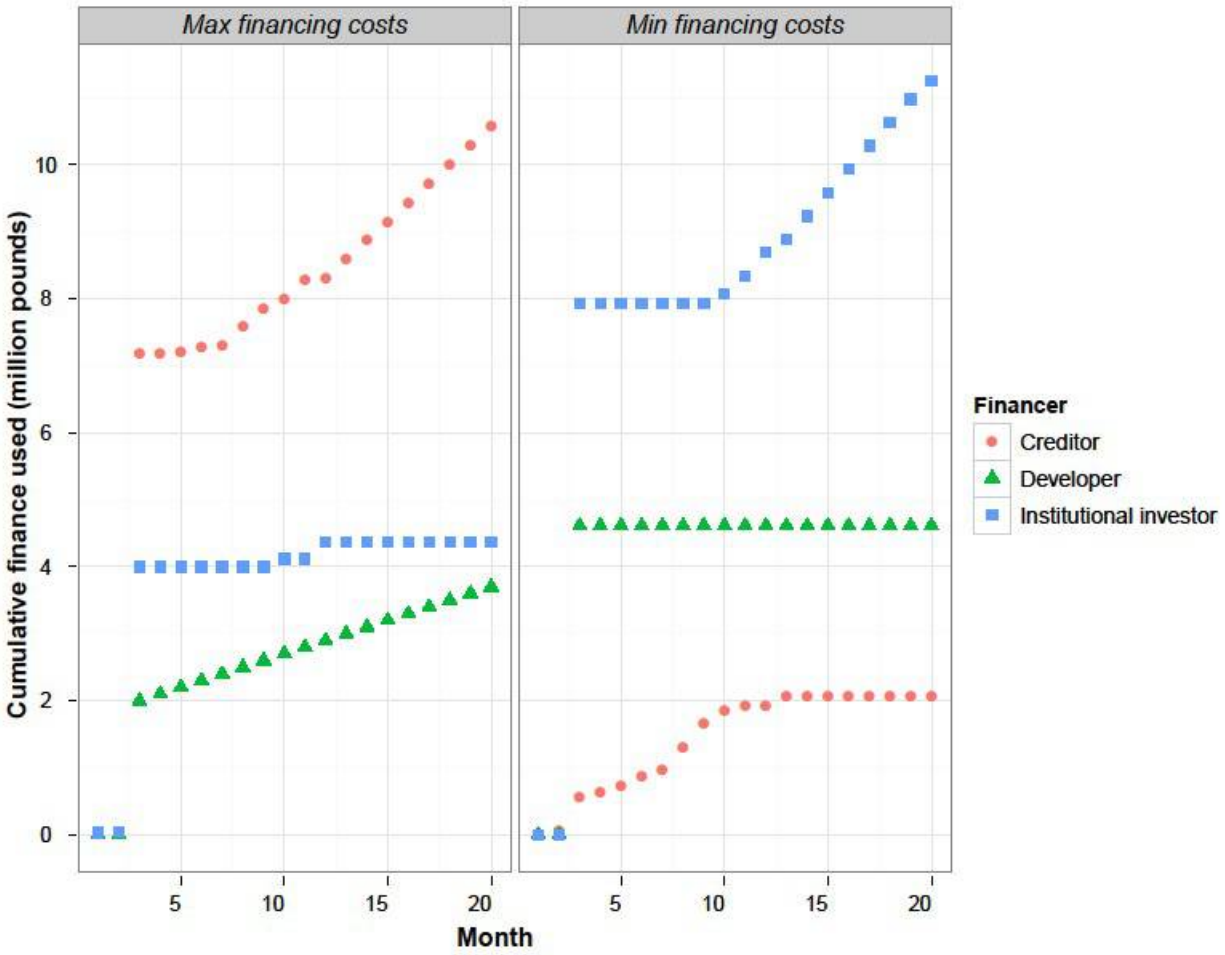

Fig. 2. Finance provided by financer, month and amount, for both objective functions.

The main inputs from the TURN model are shown in Figures 3 and 4. Figure 3 illustrates the changes in technology capacity (kW) as both a function of time (months) and tenure of buildings. The owner occupier and public landlords' building stock is refurbished at a rate that is only limited by their respective budgets. The rate of private landlord refurbishment is limited by the budget and timing of the actual construction of the refurbishment project (months seven – nineteen). It can be seen in Figure 3 that the rate at which the existing gas boilers are replaced is significantly greater than for the owner occupiers and public landlord. These results are from the minimisation of the GHG emissions gap between the targeted emissions and the actual emissions.

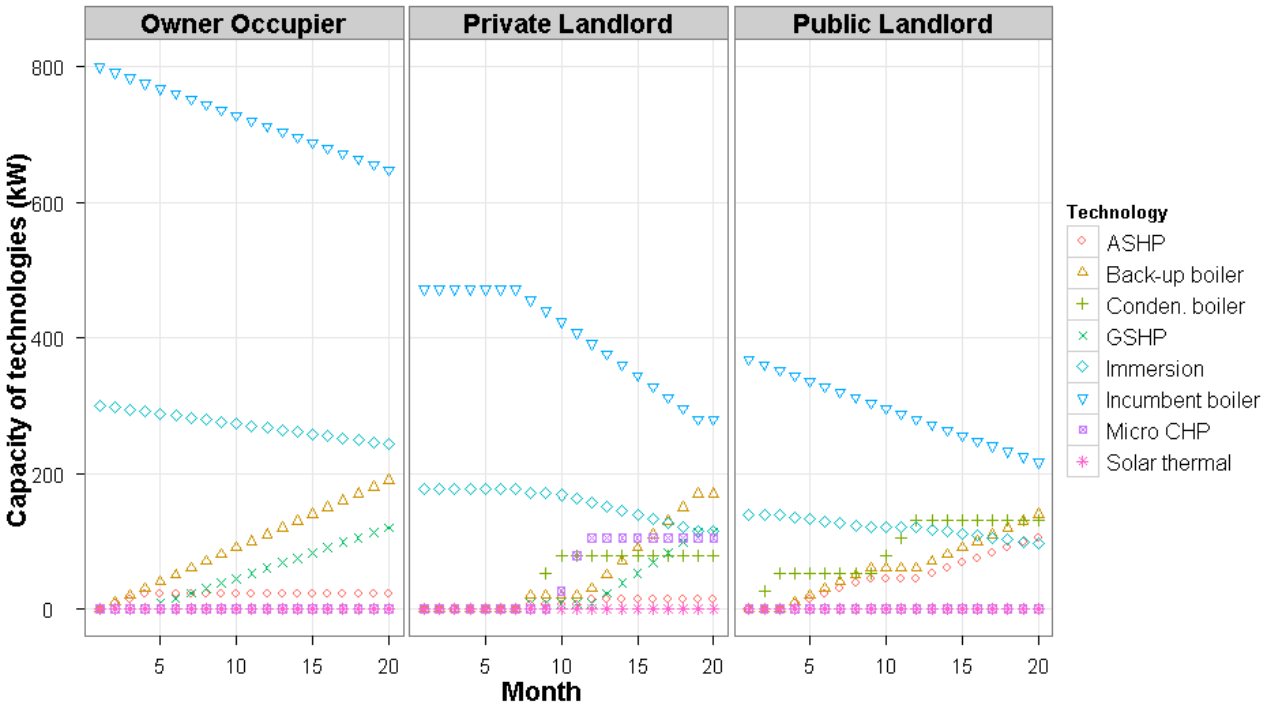

Fig. 3. Capacity changes.

Note: ASHP = air source heat pump, GSHP = ground source heat pump. Micro CHP = Micro combined heat and power unit.

Figure 4 shows the aggregated GHG emissions for the heat demand of the two hundred and five houses under the cases of minimisation and maximisation of the emissions gap. Two things are thought clear from Figure 2: a) the discretisation of time can provide robust results, as the varying emissions by season show, and b) the worst case optimisation shows significantly higher emissions than the best case optimisation. Assuming an average housing occupancy of 2.3 people [18], in the best case optimisation the emissions for a winter month are reduced from an initial 169 kg CO_2e/capita to 144 kg CO_2e/capita. These results, and others, are now discussed in the following section.

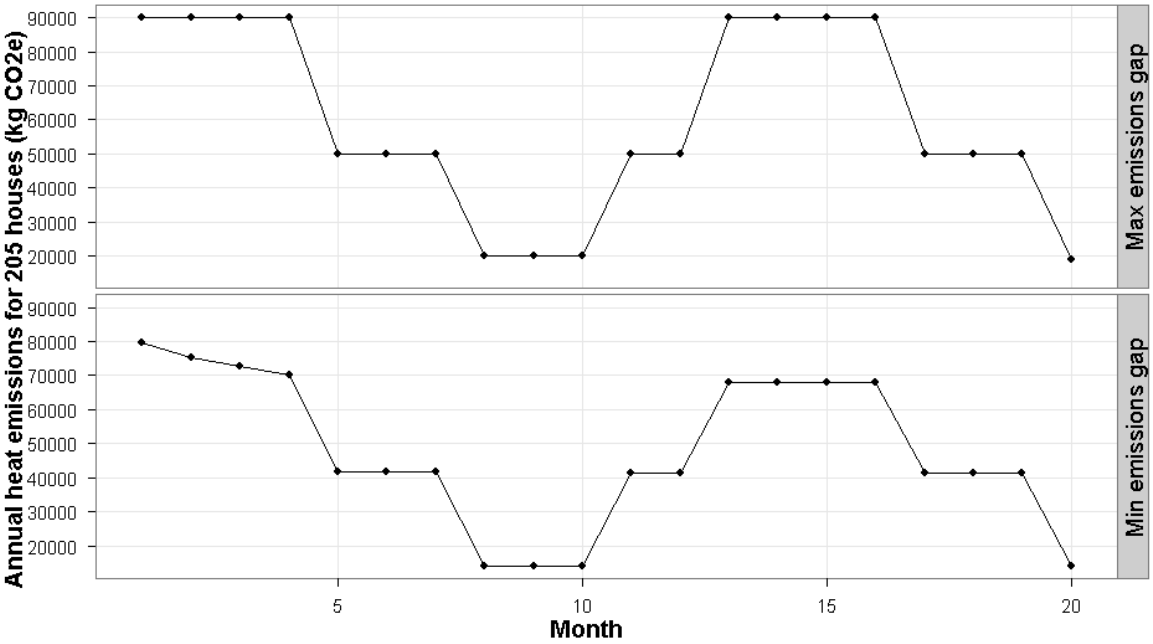

Fig. 4. Emissions reductions versus targeted emissions.

5. Discussion and conclusions

In essence, programming is a mechanical procedure by which preferred actions are chosen from a set of alternatives such that a chosen system may move from one defined state towards a pre-determined objective [19]. Programming may take place at the level of neural activity in the brain, by means of a calculator, on a spreadsheet/software program, or in the case of this study by use of mathematical programming and optimisation. The benefits of linear and integer programming over spreadsheet and mental arithmetic is both: a) the size of problem that can be modelled, and b) the efficient solution time of modern solvers and central processing units.

5.1. Example discussion

An example of a planned refurbishment scheme of two hundred and five terraced Victorian solid wall houses over a twenty month period was detailed in Section 4.1. The finance, incentives, and organisational capacity of the three tenures of house are argued here to be quite different. Finance and organisation are the foci of this study. The only formal financing being optimised in this study is that for the private landlords, who own and rent out fifty-nine of the houses. The financing of the owner occupiers and public landlords is not optimised and is assumed based on author's estimates.

Optimising the arrangement of investors, creditors, and associated interest rates is more reflective of the typical calculations used in property development. Previous optimisation models of refurbishment, where the finance module is detailed by authors, often use simple measures such as the life cycle cost or net present value with a single discount rate. The financing module here is thought a first step towards a more realistic accounting of property funding. There are a variety of investment types available given the right conditions. Modelling different mixes of investments will be useful when investors are willing to share returns and funding margins with others. Here, only institutional investors and developers were included for ease of explanation. Figure 1 shows that the size of and timing of investments can be programmed realistically, when the objective is to minimise the financing costs associated with the creditors and investors' fees.

The second model, TURN, can take the outputs of the financing optimisation, FIR, and use the output as a monthly budget for investments in refurbishment interventions, such as an Air Source Heat Pump (ASHP). The optimisation framework allows for the discrete representation of time and space, the existing housing technologies and demands, and the optimised planned order of new technologies from a set of alternatives. This powerful representation allows for a large number of scenarios to be modelled. Here, the objective function was that of minimising the gap between the actual GHG emissions (due to the heating of the 205 houses) and a targeted emissions reduction of 30%. A number of insights resulted from both: a) the process of formulating this example, and b) the results of the optimisation, shown in Figures 2 and 3.

The baseline emissions are very sensitive to the manner in which the technologies are being run. It is necessary to include appropriate capacity factors for each technology. The rate of refurbishment investments is dependent upon the finance available and the typical rate of refurbishment. The division of technology capacity by tenure is thought more appropriate for considering changes to incumbent technology capacity over time than simpler representations. In this study it was the private landlords who had the largest financial capacity and organisational capacity to change the incumbent housing stock to a more efficient standard.

5.2. Mathematical programming and optimisation discussion

Existing housing stock can be modelled as a system of resource demands, use, imports and exports, along with resource conversion technologies. Refurbishment processes may be applied to this system to improve the exergy efficiency, GHG emissions intensity, or other indicators of relative efficiency. The decisions for such a refurbishment process may be internally made, or in the case of

mathematical programming and optimisation quantitatively described and solved for a given objective.

The two models presented in this paper are both MILPs. Integer programming was used in FIR in order to estimate the nonlinear product of two continuous variables by use of the Lambda method.

The piecewise estimation of nonlinear terms can cause significant increases in solution time when using the Lambda method. This has been noted in the past [20]. There appears to be a tradeoff between accuracy and solution time, and an interesting follow-up would be a robust quantification of this tradeoff by use of additional piecewise parameters, for example where there's more curvature of the function being approximated. Furthermore the scaling of the parameters is important to retain feasible solutions. In the specific case here, the magnitude between the interest rate and the monthly finance could be up to 1e07. This led to a scaling down of the monthly finance and scaling up of the interest rate such that the relative changes in the variables could be more accurately approximated. Tightening the relaxed linear solution of the MILP by addition of extra linear constraints, as is well known [12], also allows for faster solution times.

Integers are used in TURN to provide accurate portrayal of the costs and effect of refurbishment technologies (e.g. it's difficult to buy and install half a condensing boiler!). There were no problems encountered with solution times for the given study and formulation, of which there were 456 integer variables. Further research on the extent to which both FIR and TURN are scalable will be pursued.

5.3. Conclusions

In the author's view it is clear that there is a role for mathematical programming and optimisation to robustly analyse and improve the decisions made towards financing and planning of energy efficient refurbishment of existing housing stock. The models here offer a potential stepping stone towards more robust quantification of the financing available for different tenures of housing stock.

For the given example, the type of attitude taken by the financier will determine whether a minimisation or a maximisation of creditors/investors' interest margins and fees is more appropriate for planning the arrangement of loans and cash drawdowns. Risk should be considered in the future. Nonetheless, the optimisation of which sets of finance to draw down is thought novel, and could be applied to a wide range of finance types, such as municipal bonds.

Unfortunately the example was not the result of a client's wishes, and evidence that this work is useful in real world applications is lacking. Furthermore, the extent to which both these models are scalable has not been tested, nor has the accuracy of the piecewise estimations been robustly analysed. Uncertainty analyses to stress-test these models is a further requirement. Despite these weaknesses, the models in combination are thought a strong starting point for further work in this area. A wish-list of future research items is below:

- Analysis of the limits to the method of mathematical programming and optimisation:
    - Delta method comparison to Lambda method for piecewise estimation.
    - Limits to the number of integer variables for reasonable solution times.
    - Inclusion of stochastics for key parameters.
- Improvements to the formulation of the model structure:
    - Extension of the financial module to assess fixed-income and other longer term debt products. Inclusion of rental and capital growth.
    - Inclusion of exergy coefficients in resource balance. Addition of conversion factors by mode of operation of a technology.

Acknowledgments

The financial support of BP via the Urban Energy Systems project in Imperial College is gratefully acknowledged. The comments of reviewers were particularly helpful towards the refinement of the initial draft.

Nomenclature

Indices and sets:

m	month
f	financer, i.e. investors and creditors
p	piecewise set
r	resource
i	zone, e.g. representing blocks of buildings
j	technology

User specified parameters:

AFe	arrangement fee, %
$AuFe$	audit fee, %
$NUFe$	non-utilization fee, %
EFe	exit fee, %
pw	piecewise parameter
pwe	piecewise estimation of nonlinear relationship
σ	affect of intervention on another intervention
δ	impact of a technology on a resource

Appendix A: Development Appraisal

Table A1. Static development appraisal

Sources: Author's estimates, interviews with built asset consultancies, and [13], [14], [21], [22].

Finance	*Rates/fees*		*£*
Proceeds			
Terrace refurb	Net internal area: 4,661 sq m	£304/sq m @ 5.83% yield	24,285,444
Less vacancy		5.00%	23,071,172
Gross development value (GDV)			**23,071,172**
Construction costs			
Terrace refurb	Gross internal area: 4,894 sq m	£672/sq m	3,288,682
Planning, investigation and building regulation costs			
Planning consent			295
Site investigation		1.50%	49,330
Building regulations			53,808
			103,433
Infrastructure costs			
Residential infrastructure			0
Professional fees			
Architect		5.00%	164,434
Quantity surveyor		3.00%	98,660
Structural engineer		1.00%	32,887
M&E engineer		1.00%	32,887
Geotechnical engineer		0.25%	8,222
Project manager		0.50%	16,443
Letting legal fee		1.00%	13,450
Letting agent fee		10.0%	134,505
			501,489
Return on equity		18.0%	4,152,811
Finance costs			
Debt available		60% loan to value	
Arrangement fee		1.50%	207,641
Audit/monitoring fee		0.16%	22,148
Interest		7.00%	500,345
Cost of finance			730,134
Gross development cost less land costs and interest, and equity			4,623,738
Residual land value			14,294,623
Total development cost			**18,918,361**
Land costs			
Land price	Stamp duty + legal + agent fees = 7%, compounded for 18 months		1.07*1.11 = 1.19
Land value less fees and interest			12,031,520
Cost of acquisition and interest on land			2,263,103
Net development value			23,071,172
Total development cost			18,918,361
Developer's profit			**4,152,811**

References

[1] DCLG, “Live tables on dwelling stock - Housing - Department for Communities and Local Government,” *Live tables on dwelling stock*, 2011. .

[2] DECC, “Great Britain’s housing energy fact file,” 2011.

[3] G. W. Gau and D. B. Kohlhepp, “The Financial Planning and Management of Real Estate Developments,” *Financial Management*, pp. 46–52, 1980.

[4] K. Addae-Dapaah, “Highest and best use in the valuation of mixed use development sites: a linear programming approach,” *Journal of Property Research*, vol. 22, no. 1, pp. 19-35, Jan. 2005.

[5] J. Keirstead, M. G. Jennings, and A. Sivakumar, “Review of Urban Energy System Models: Approaches, Challenges and Opportunities,” *Renewable and Sustainable Energy Reviews*, vol. 16, pp. 3847-3866, 2012.

[6] S. I. Gustafsson, B. G. Karlsson, and B. H. Sjöholm, “Differential rates for district heating and the influence on the optimal retrofit strategy for multi-family buildings,” *Heat Recovery Systems and CHP*, vol. 7, no. 4, pp. 337–341, 1987.

[7] Y. Amano et al., “Impact analysis of carbon tax on the renewal planning of energy supply system for an office building,” *Energy*, vol. 35, no. 2, pp. 1040-1046, Feb. 2010.

[8] J. Keirstead, N. Samsatli, N. Shah, and C. Weber, “The impact of CHP (combined heat and power) planning restrictions on the efficiency of urban energy systems,” *Energy*, 2011.

[9] J. Keirstead, N. Samsatli, N. Shah, and D. Fisk, “The Implications of CHP Planning Restrictions on the Efficiency of Urban Energy Systems,” in *ECOS 2010: Proceedings of the 23rd International Conference on Efficiency, Cost, Optimization, Simulation, and Environmental Impact of Energy Systems*, 2010.

[10] M. G. Jennings, D. Fisk, and N. Shah, “Optimal scheduling of low carbon investment decisions for a social housing refurbishment case study,” in *The 24th International Conference on Efficiency, Cost, Optimization, Simulation and Environmental Impact of Energy Systems*, 2011, pp. 2023-2036.

[11] M. G. Jennings, L. Munuera, D. Fisk, and N. Shah, “Optimal investment planning for low carbon domestic heating options in London: 2010 - 2050,” in *World Engineers’ Convention*.

[12] H. P. Williams, *Model Building in Mathematical Programming*, 4th ed. John Wiley & Sons, Ltd., 1999.

[13] EC Harris, *Indicative Building Costs*. 2006.

[14] Jones Lang LaSalle, “Which London postcodes offer the best returns?,” *Financial TImes*, 2012. [Online]. Available: http://www.ft.com/cms/s/2/e0a6ab7e-7d7b-11e0-b418-00144feabdc0.html#axzz1km2lmfsF. [Accessed: 12-Feb-2012].

[15] Carbon Trust, *Micro-CHP Accelerator*. 2011.

[16] SAP, “Sedbuk,” *Boiler Efficiency Database*, 2012. [Online]. Available: http://www.boilers.org.uk/. [Accessed: 17-May-2012].

[17] Energy Savings Trust, “Getting warmer: a field trial of heat pumps,” 2010.

[18] DCLG, “Housing and Planning Statistics 2010,” , Bressendan Place, London, SW1E 5DU, U.K., 2010.

[19] G. Dantzig, “Thoughts on linear programming and automation,” *Management Science*, vol. 3, no. 2, pp. 131-139, 1957.

[20] S. Messner, “Endogenized technological learning in an energy systems model,” *Journal of Evolutionary Economics*, vol. 7, no. 3, pp. 291-313, Sep. 1997.

[21] DCLG, *A Guide to the Fees for Planning Applications in England - February 2010*. 2010.

[22] DECC, “Renewable Heat Incentive: Consultation on the proposed RHI financial support scheme,” 2010.

Optimization of thermal insulation to achieve energy savings

Milorad Bojić[a], Marko Miletić[b], Vesna Marjanović[a], Danijela Nikolić[b], Jasmina Skerlić[b]

[a] *Faculty of Engineering of Kragujevac University, Kragujevac, Serbia,*
milorad.bojic@gmail.com
[b] *Faculty of Engineering of Kragujevac University, Kragujevac, Serbia,*
marko.m.miletic@hotmail.com
[b] *Faculty of Engineering of Kragujevac University, Kragujevac, Serbia,*
vmarjanovic@kg.ac.rs
[b] *Faculty of Engineering of Kragujevac University, Kragujevac, Serbia,*
danijelan@kg.ac.rs
[b] *Faculty of Engineering of Kragujevac University, Kragujevac, Serbia,*
jskerlic@gmail.com

Abstract:

Due to the current environmental situation, saving energy and reducing CO_2 emission have become the leading drive in modern research. For buildings that require heating, one of the solutions is to optimize a width of their thermal insulation layer and thus improve energy efficiency and reduce energy needs. In this paper, for a small residential house in Serbia, an optimization in the width of its thermal insulation layer is investigated by using EnergyPlus software and Hooke-Jeeves direct search method. The embodied energy of thermal insulation is taken into account. The optimization is done for the entire life cycle of the house. The results show what optimal thickness of thermal insulation yields the minimum primary energy consumption.

Keywords:

Energy efficiency, Thermal insulation, Hooke-Jeeves optimization, CO_2 emissions, EnergyPlus, life cycle

1. Introduction

Current environmental situation requires increased research in energy efficiency and energy savings in built environment due to reduced conventional fuel resources and increased CO_2 emissions, which create greenhouse effect. Therefore new projects are financed from local governments and European Union to improve energy use, increase energy production from renewable resources and decrease greenhouse gas emissions [1].

To save energy and improve energy efficiency, investigations of thermal insulation materials and their embodied energy in buildings accelerates. Monahan and Powell [2] (2011) discussed embodied energy and energy analysis during the life cycle of a house. The research included all materials that the house is built from, with part of paper that deals with thermal insulation. Yu and Kang [3], Upton [4], Thormark [5] and Gustavson [6] investigated materials, their embodied energy and greenhouse gas emission during their life cycles. Milutienė (2010) inspected embodied energy included in zero–net energy house design [7]. However, they did not optimize the thermal insulation thickness for the minimum total primary energy consumption during the life cycle of the house taking into account the embodied energy of the thermal insulation.

This paper reports a research in energy saving through an optimal use of different types of thermal insulation in a residential house. Different types of thermal insulation may be used in the house; however they have different amounts of embodied energy. The objective is to minimize the sum of the primary energy used for heating during the life cycle and the embodied energy of applied thermal insulation. The final result is the optimized thermal insulation thickness for the residential

house. EnergyPlus software is used to simulate energy flows in the house. Using GenOpt code programs the objective function. The optimization routine is an algorithm of Hooke-Jeeves optimization.

2. Scope of research

2.1. Thermal and geometrical description of the residential house

The residential house has two-storeys and four rooms. On the first storey, it has one large living room and one toilet, while on the second storey, it has two bedrooms (Figure 1).

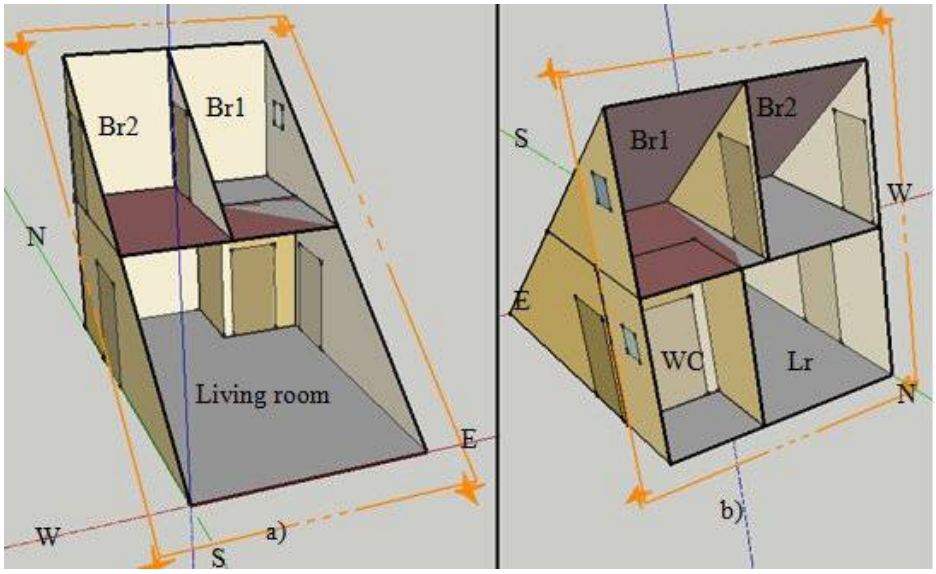

Figure 1: Geometrical definition of the residential house (Br-bedroom, Lr-Living room, WC-Bathroom) (a) South side; (b) North side.

In table 1, geometric data for area of floor by rooms are given. There is no south wall because of the sloped roof, which is under an optimal angle for a PV power generation.

Table 1. The characteristics of the used insulation material

	Floor area (m^2)	External wall area (m^2)
Living room	31.46	-
Toilet	2.95	-
Bedrooms (x2)	8.6	-
Roof	-	43.37
North wall	-	26.4
East and west wall (each)	-	23.46
Total	51.61	73.32 + 43.37

Regarding fenestration, the house has two windows, one in the bathroom and one in the bedroom 1, and it has seven doors from which three are external. The bedroom 1 is oriented toward the east, and the bedroom 2 toward the west.

2.2. Space heating of the house

According to the Serbian heating codes [8], the desired air temperatures are set in the living room and the bedrooms at 20°C, and the bathroom at 22°C, respectively. Electrical heaters with thermostatic valves heat the entire house. The heating system is designed according to the standard procedures defined in [8]. In most cases, the desired air temperatures are met in the first half of an hour of heating start. The thermostatic valves thus save energy by turning off the heaters when the air temperature is above the desired value, and then by turning on the heaters when the air temperature falls below the desired value.

3. Software used for simulation and optimization

3.1. EnergyPlus

To simulate heating, cooling, lighting, ventilation, water network and other energy flows in a built environment, EnergyPlus can be used [10]. EnergyPlus takes into account all factors that influence thermal loads in the building, such as they are electricity devices, lighting, pipes in the building, solar radiation, wind, infiltration, and shading [11]. This software is used to simulate energy behavior of the investigated house. For this house, the geometry is defined outside EnergyPlus by using Google SketchUp with an OpenStudio plug-in [12]. In the Google SketchUp environment, this geometry is shown in Figure1.

3.1.2 Mathematics

The embodied energy, in general practice, is not considered when a building is designed, specified and constructed. The embodied energy of a low-energy house is likely to contribute a greater proportion of its overall life cycle primary energy consumption during than that would be for a conventional house [2]. The embodied energy, E_{em} represents an amount of the primary energy used to create one kilogram of a material. Here, the embodied energy was calculated by using the following equation:

$$E_{emti} = A_{ti} \cdot \delta_{ti} \cdot \rho_m \cdot E_{em}\,, \qquad \text{(Eq. 1)}$$

Where A_{ti} is the area of thermal insulation (the area of the exterior walls and the roof) and in this case, it is 116.69 m^2

δ_{ti} stands for the thermal insulation thickness

ρ_m stands for the density of selected material

E_{em} stands for the embodied primary energy of selected material per kg of mass.

The annual embodied energy for the life cycle presents an embodied energy of thermal insulation divided by the number of the life cycle years, as shown in the following equation:

$$E_{aemtiy} = \frac{E_{emti}}{L_y}, \qquad \text{(Eq. 2)}$$

Where L_y stands for the number of the life cycle years.

The annual heat consumption of the house presents an annual heat consumption of the heaters in the house to sustain the desired air temperature, as shown in the following equation:

$$E_u = \sum_{d=1}^{365}\sum_{h=1}^{24} E_{uhd}\,, \qquad \text{(Eq. 3)}$$

Where E_{uhd} stands for the heat consumption in hour h on day d.

The annual primary energy consumption for heating the house presents the annual heat consumption of the house multiplied by a conversion factor from the primary energy to electricity. In Serbia, this factor is 3.04 [12]. Therefore, the primary energy consumption is calculated using the following equation:

$$E_{up} = E_u \cdot 3.04 . \quad \text{(Eq. 4)}$$

The objective function is the annual total primary energy consumption. It is the sum of the primary energy consumption for heating and the annual embodied energy, as shown in the following equation:

$$E_{sauy} = E_{up} + E_{aemtiy}, \quad \text{(Eq. 5)}$$

The total primary energy consumption is sum of the primary energy consumption and the embodied energy for the life cycle period, as shown in the following equation:

$$E_{tupy} = (E_{up} + E_{aemtiy}) \cdot L_y, \quad \text{(Eq. 6)}$$

To evaluate energy saving, the energy payback ratios are used. They present how many times the used primary energy for refurbishment is saved during the life cycle. Let us the refurbishment application to be the thermal insulation of the optimum width to the non-insulated house. The energy payback ratio X_{savedeyn} represents the amount of the saved primary energy per unit of the used embodied energy of the applied thermal insulation. The energy payback ratio is given by the following equation:

$$X_{savedeyn} = (E_{tupyn} - E_{tupyo}) / E_{emtio} . \quad \text{(Eq. 7)}$$

Where E_{tupyo} stands for the used energy when using optimized thickness of the thermal insulation layer

E_{tupyn} stands for the used energy in the house without thermal insulation

E_{emtio} stands for the embodied energy in optimal thermal insulation layer.

The energy payback ratio X_{savedeys} gives the primary energy saving per unit of the embodied energy for the second case. Then, the primary energy is saved when the customary previously thermally insulated house is additionally thermally insulated by the new thermal insulation material of the optimum width. The energy payback ratio is shown in the following equation:

$$X_{savedeys} = (E_{tupys} - E_{tupyo}) / (E_{emtio} - E_{emtis}) \quad \text{(Eq. 8)}$$

Where E_{tupys} stands for the used energy when using customary thickness of the thermal insulation layer

E_{emtis} stands for the embodied energy in the new thermal insulation layer.

3.2. GenOpt and optimization constraints

GenOpt is an optimization program used for the minimization of a function that is evaluated by an external simulation program, such as EnergyPlus, TRNSYS, SPARK, IDA-ICE or DOE-2. It has

been developed for the optimization problems where the cost function is computationally expensive and its derivatives are not available or may not even exist. GenOpt can be coupled to any simulation program that reads its input from text files and writes its output to text files. The independent variables can be continuous variables (possibly with lower and upper bounds), discrete variables, or both. Constraints on dependent variables can be implemented using penalty or barrier functions [13].

In this investigation using GenOpt, a thickness of a thermal insulation layer is optimized. A minimum thickness of the layer is taken to be 0.02m. A maximum thickness of the layer is set to 2m. The optimization method is that of Hooke-Jeeves [14]. The initial thickness for all simulations is set to 0.05m and the optimization step is 0.01. The number of step reduction is set to 4. The maximum number of iterations is set to 2000, but it is not reached (the maximum number of iterations is lower than 150 in all cases).

GenOpt reads results of simulation by EnergyPlus (the heat consumption), calculates the embodied energy, and calculates the total primary energy consumption. Then, it compares the obtained results with the results of previous calculation of the total primary energy consumption. The program checks if there is a decrease in the total primary energy consumption. After that it may automatically change the input values for the insulation thickness.

The advantage of using GenOpt instead of brute force search is in smaller time used for the optimization and in an elimination of human errors. The brute force search requires that user wait in front of computer for each simulation, compare the obtained values, and then change the value of the thickness of the insulation layer. Instead, by using GenOpt, about 50-150 simulations are automatically performed. There are 42 combinations of material type and lifecycle values. By using GenOpt, the user assistance is needed only 42 times, and in case of brute force search, the user assistance is needed about 4200 times (42 x 100) in average.

4. Thermal insulation materials

Thermal insulation materials used in the simulations represent the most common materials used in nowadays. Those materials are mineral wool, rock wool, polystyrene, polyurethane, cork, and fiberglass. Although their characteristics are discussed in literature for different regions, including New Zealand [15], the United States [16, 17], and the United Kingdom (hereafter, UK) [18, 19], the research results from Hammond and Jones [20] are taken and are representative as they are product of many years of research and the results are constantly updated and recalculated. These results are from the UK and they are taken in cooperation with their industry. Their work on the project, Inventory of Carbon & Energy (ICE) gives the embodied energy for each type of material [20]. There are no experimental and official data for embodied energy in materials in Serbia. In this study, the data from UK are taken because they can be found in the report of EU [21] from 2010. In Table 2, these values are given for each material analyzed in this investigation.

Table 2. The characteristics of the used insulation material

Material	Embodied energy, E_{em} (MJ/kg)	Density, ρ_m (kg/m^3)	Thermal conductivity,k (W/mK)	Relative/qualitative ranking ($E_{em}\rho_m k$)
Mineral wool	16.6	16	0.038	10.1
Rock wool	16.8	23	0.037	14.3
Cork	4	110	0.040	17.6
Fiberglass	28	24	0.036	24.2
Polystyrene	86.4	16	0.037	51.1
Polyurethane	101.5	24	0.028	68.2

The wall and roof types are taken from the URSA site [22]. They are given in Figure 2. In Figure 2, the wall thermal insulation layer is defined as Number 4 (left), and the roof thermal insulation layer is defined as Number 3 (right).

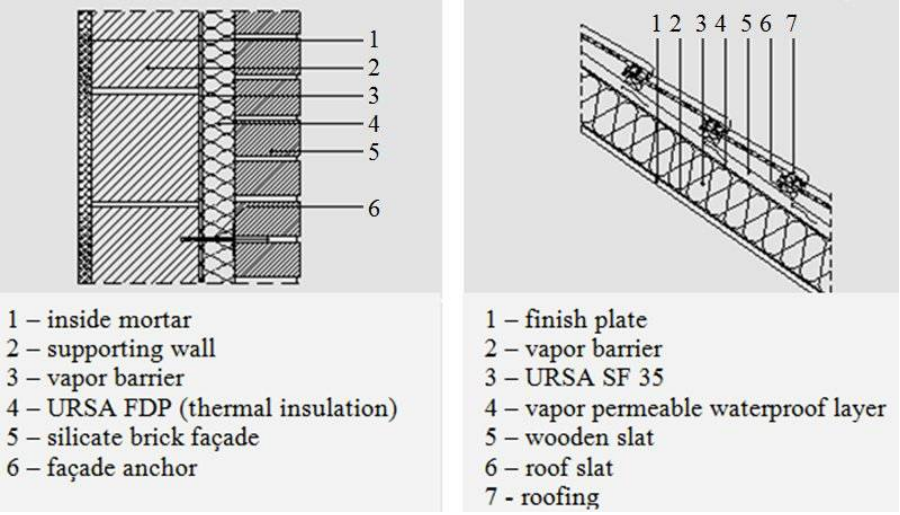

Figure 2. Wall (left) and roof (right) type by URSA

5. Results and Discussion

Figure 3 shows the optimum width of the thermal insulation layers as a function of their type and life cycle. The investigation is preformed for polyurethane, polystyrene, fibreglass, rock wool, mineral wool, and cork and the life cycles from 5 to 50 years. The optimization yields that the mineral wool layer would be the thickest and the polyurethane layer the thinnest (Figure 3). Namely, the width of the mineral wool layer is 2.5-3.5 times thicker than that of polystyrene and polyurethane.

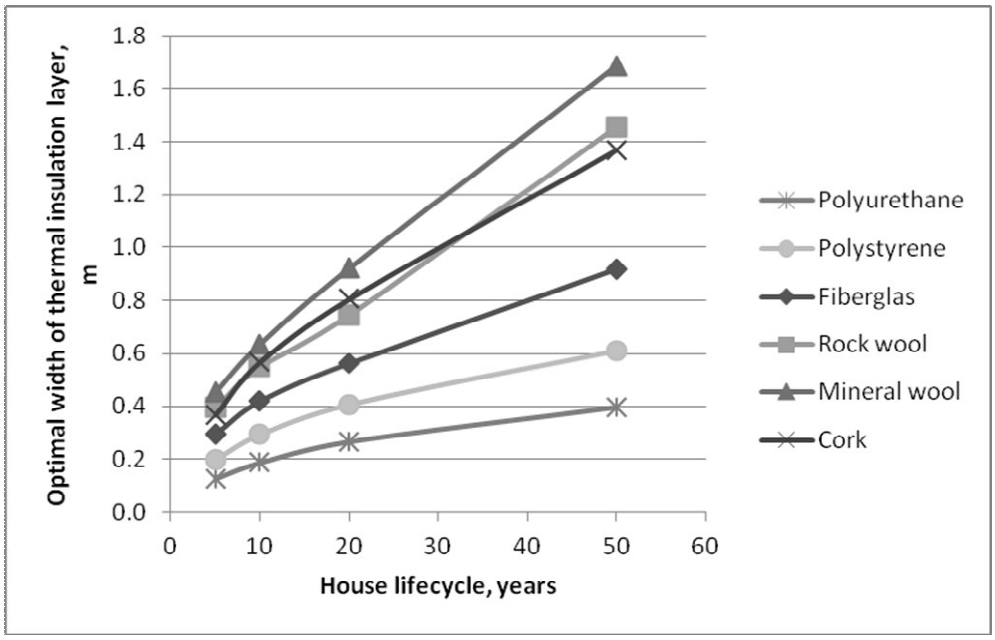

Figure 3. Optimum width of the thermal insulation layers as a function of their type and building lifecycle time

For the same thermal insulation types and life cycle range, Figure 4 shows the annual total energy consumption. It is clear that the annual total primary energy consumption is the lowest when the mineral wool is used as thermal insulation and the highest when the polyurethane is used as thermal insulation.

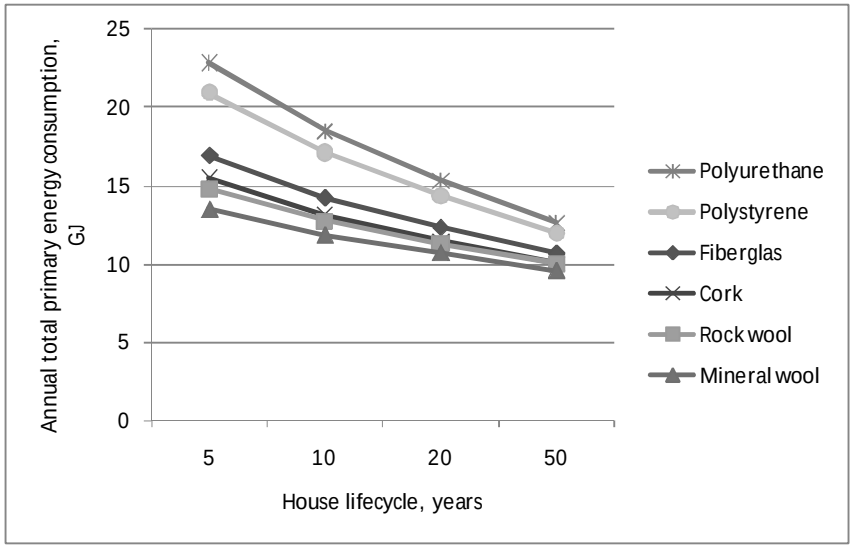

Figure 4. Annual total energy consumption vs. life cycle years and thermal insulation type

Figure 5 shows the annual total primary energy, the annual embodied energy, and the primary energy used for heating at the 50-year life cycle level for different types of thermal insulation. This figure demonstrates that the mineral wool has the smallest embodied energy and the smallest annual total primary energy used for the heating compared to that of other thermal insulation types. It is the fact that many studies have shown that building materials only contribute around 15% of the life cycle energy of a typical building. This study refers to the masonry constructions where there is the following situation. For the application of thermal insulation, the embodied energy contribution of the building materials to the total primary energy consumption will be around 27% for its lifecycle of 50 years, and around 56% for the lifecycle of 10 years. For wood constructions, it may be assumed that there is negligible amount of the used embodied energy in wood material, while the similar amount of the saved energy with thermal insulation would as that in the masonry construction. Then, the embodied energy contribution of the building materials to the total primary energy consumption would be lower and would have value of 13% for 50 years and 19% for 10 years of the life cycle. This analysis refers to the application of the optimal thickness of mineral wool for the thermal insulation.

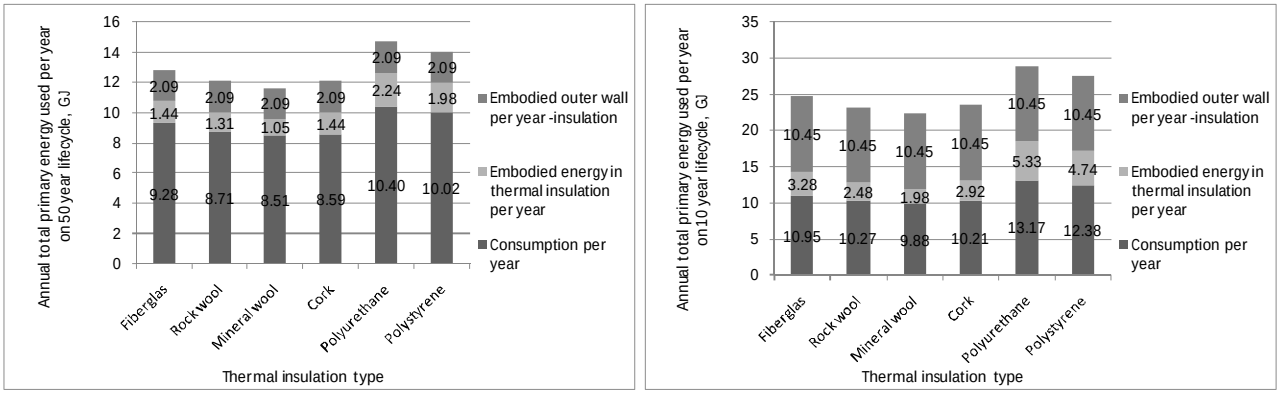

Figure 5. Annual total primary energy, annual embodied energy, and primary energy used for heating at 50-year life cycle level and at 10-year life cycle level

Figure 6 shows the total primary energy consumption for the house without, and those houses with custom and optimal thermal insulation. The thermal insulation is mineral wool. The house with the custom thermal insulation has the width for this region of 20cm of thermal insulation. All values rise in time.

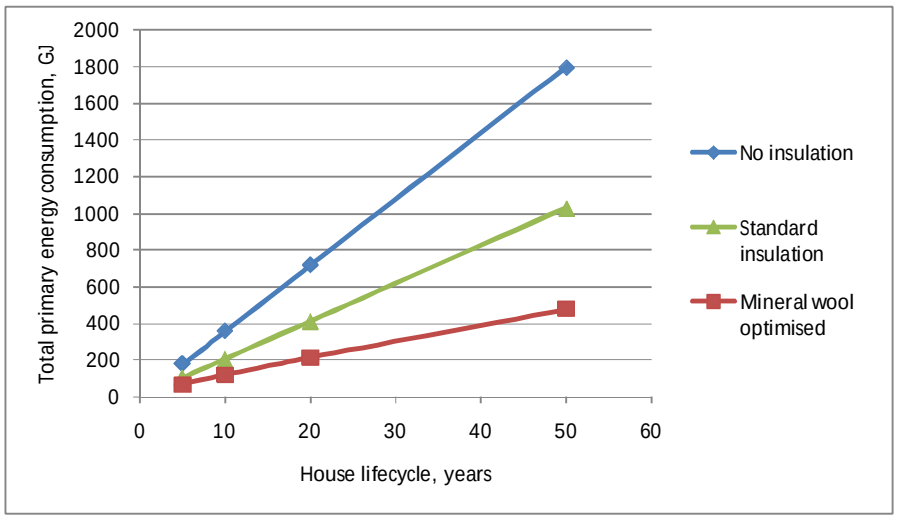

Figure 6. Total primary energy consumption for the house without, and with custom and optimal thermal insulation. The thermal insulation is mineral wool.

To evaluate energy saving on 50-year life cycle, Figure 7 shows the energy payback ratios for two refurbishment options: (1) the house with optimized thermal insulation atop the customary thermal insulation; and (2) the house with the optimized thermal insulation only. It is found that the introduction of 1 J of embodied energy to the house with the optimized thermal insulation saves 25.23 J of the primary energy ($X_{savedyn}$), whereas the introduction of 1 J of embodied energy to the house the optimized thermal insulation atop of the customary thermal insulation saves 11.96 J of the primary energy ($X_{savedys}$).

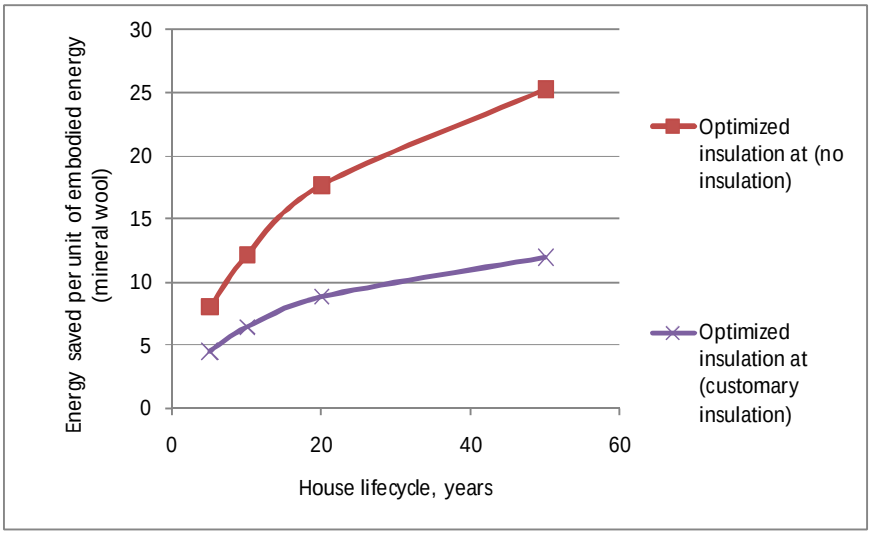

Figure 7. Energy saved per unit of the embodied energy

6. Conclusions

This paper shows that energy efficiency of the house can easily be improved by choosing proper thermal insulation width. The optimizations take into account the embodied energy in the thermal insulation. The results show that the lowest primary energy consumption is obtained by using mineral wool; however its width is the thickest when compared to all thermal insulation types. The highest primary energy consumption is obtained by using polystyrene; however its width is the thinnest. Two refurbishment options are discussed where the optimized thermal insulation of mineral wool is put to the building without any insulation and to the building with the customary width of thermal insulation, respectively. The saved energy per unit of embodied energy is as high as 10 to 25 times.

These results are obtained by using official data for embodied energy in materials in UK. However, in the future, it is important to organize research on the embodied energy in the used materials in Serbia that will take into account local conditions.

In future research, the cost and greenhouse gas emission optimization/minimization will be performed.

Acknowledgment

This paper is a result of two project investigations: (1) Project TR33015 of Technological Development of Republic of Serbia; and (2) Project III 42006 of Integral and Interdisciplinary investigations of Republic of Serbia. The first project is titled "*Investigation and development of Serbian zero-net energy house*", and the second project is titled "*Investigation and development of energy and ecological highly effective systems of poly-generation based on renewable energy sources*". We would like to thank the Ministry of Education and Science of Republic of Serbia for their financial support during these investigations.

Nomenclature

A area, m^2

C amount of carbon embodied, kg/kg

E amount of energy, J

L life cycle, years

X number of times saved

Greek symbols

δ thickness of thermal insulation, m

ρ density of material, kg/m^3

Subscripts and superscripts

a annual

d number of days

em embodied

h number of hours

m selected material

n no insulation

p primary energy

o optimized

s standard

ti thermal insulation

u used

y years

References

[1] <http://www.eib.org/about/press/2011/2011-098-european-energy-efficiency-fund-eeef-launched.htm> [accessed 15.6.2011]

[2] J. Monahan, J.C. Powell, 2011, "An embodied carbon and energy analysis of modern methods of construction in housing: A case study using a lifecycle assessment framework", Energy and Buildings 43 (2011) 179–188

[3] Chia-Jen Yu, Jian Kang, 2009, “Environmental impact of acoustic materials in residential buildings”, Building and Environment 44 (2009) 2166–2175

[4] B. Upton, R. Miner, M. Spinney, L. S. Heath, 2008, “The greenhouse gas and energy impacts of using wood instead of alternatives in residential construction in the United States”, Biomass and Bioenergy 32 (2008) 1–10

[5] Thomark, C., 2006, “The effect of material choice on the total energy need and recycling potential of a building”, Building and Environment 41 (2006) 1019–1026

[6] Gustavsson, L., Joelsson, A., 2009, “Life cycle primary energy analysis of residential buildings”, Energy and Buildings 42 (2010) 210–220

[7] Milutienė, E., 2010, “House Embodied Energy and Zero Energy Building Concept”, Environmental Research, Engineering and Management, 2010. No.4 (54), P. 62-71

[8] Todorović, B., 2005, Design of installations for central heating (in Serbian), Mašinski fakultet Beograd, Beograd

[9] Website – <http://www1.eere.energy.gov/buildings/energyplus_redirect.html>. [accessed 18.3.2009].

[10] D. Crawley, L. Lawrie, F. Winkelmann, W. Buhl, Y. Joe Huang, C. Pedersen, R. Strand, R. Liesen, D. Fisher, M. Witte, J. Glazer, EnergyPlus: creating a new-generation building energy simulation program, Energy and Buildings. 33 (2001) 319-331.

[11] <http://en.wikipedia.org/wiki/SketchUp>, [accessed 18.3.2009].

[12] Milorad Bojić, Slobodan Djordjević, Jovan Malesević, Marko Miletić, Dragan Cvetković, A simulation appraisal of a switch of district to electric heating due to increased heat efficiency in an office building, Energy and Buildings, Available online 7 April 2012, ISSN 0378-7788, 10.1016/j.enbuild.2012.04.004.

[13] <http://simulationresearch.lbl.gov/GO/>, [accessed 8.8.2011].

[14] Hooke, R.; Jeeves, T.A. (1961). "'Direct search' solution of numerical and statistical problems". Journal of the Association for Computing Machinery (ACM) 8 (2): 212–229. doi:10.1145/321062.321069.

[15] A. Alcorn, P. Wood, 1998, “New Zealand building materials embodied energy coefficients database, Volume II Coefficients”, ISBN: 1172-563X, Victoria University of New Zealand, New Zealand.

[16] <http://www.buildinggreen.com>, [accessed 10.7.2011].

[17] Sustainable Homes, 1999, “Embodied energy in residential property development”, <http://www.sustainablehomes.co.uk/upload/publication/Embodied%20Energy.pdf>, [accessed 10.7.2011].

[18] http://www.greenspec.co.uk/html/materials/insulation.html, [accessed 10.7.2011].

[19] <www.bath.ac.uk/mech-eng/sert/embodied>, [accessed 10.7.2011].

[20] Hammond, G. P. and Jones, C. I., 2008. “Embodied energy and carbon in construction materials”, Proceedings of the Institution of Civil Engineers - Energy, 161 (2), pp. 87-98, http://dx.doi.org/10.1680/ener.2008.161.2.87

[21] “Green Public Procurement - Thermal Insulation Technical Background Report”, Report for the European Commission – DG Environment by AEA, Harwell, June 2010, Owner, Editor: European Commission, DG Environment-G2, B-1049, Brussels. <http://ec.europa.eu/environment/gpp/pdf/thermal_insulation_GPP_%20background_report.pdf > [accessed 10.7.2011].

[22] <http://www.ursa.rs/>, [accessed 10.7.2011].

Residential solar-based seasonal thermal storage system in cold climate: building envelope and thermal storage

Alexandre Hugo[a] and Radu Zmeureanu[b,*]

[a]*Halsall Associates, Toronto, Ontario, Canada, ahugo@halsall.com*

[b] *Department of Building, Civil and Environmental Engineering, Faculty of Engineering and Computer Science, Concordia University, Montréal, Québec, Canada, zmeur@encs.concordia.ca* ***(CA)***

Abstract:

The reduction of electricity use for heating and domestic hot water in cold climate can be achieved by (1) reducing the heating loads through the improvement of thermal performance of house envelope, and (2) using solar energy through a residential solar-based thermal storage system. First, this paper presents the life cycle energy and cost analysis of a typical one-storey detached house, located in Montreal, Canada. Simulation of annual energy use is performed using TRNSYS 16 software. Second, several design alternatives with improved thermal resistance for walls, ceiling and windows, reduced overall air tightness, and increased window-to-wall ratio of South facing windows are evaluated with respect to the life cycle energy use, life cycle emissions and life cycle cost. The solution that minimizes the energy demand is chosen as a reference house for the study of long-term thermal storage. Third, the computer simulation of a solar heating system with solar thermal collectors and long-term thermal storage capacity is presented. Finally, the life cycle cost and life cycle energy use of the solar combisystem are estimated for flat-plate solar collectors and evacuated tube solar collectors, respectively, for the economic and climatic conditions of this study.

Keywords:

Combisystem, Heating, Solar energy, House, Envelope, Storage, Energy, Emissions, Cost, Life cycle.

1. Introduction

One of the most comprehensive studies on solar combisystems was performed within the frame of IEA-Task 26 [1] by comparing 21 different configurations. The optimization of nine combisystems under the same climatic reference conditions was performed by computer simulation using TRNSYS program. Several design strategies were recommended [2] such as: the use of low temperature heating system like a radiant floor; the increase of the insulation thickness of the storage tank to minimize the heat losses; the use of energy efficient pumps to decrease the electricity demand; and the use of stratifying devices and external heat exchangers to maintain the stratification in the storage tank. A follow up project of the IEA-Task 26 was the European project ALTENER Solar Combisystems [3]. More than 200 solar combisystems in seven European countries were installed, documented and theoretically evaluated, and 39 of them were monitored. A detailed literature review of such solar combisystems and seasonal storage approaches was presented in [4]. This paper focuses on the life cycle analysis of a solar combisystem used for seasonal thermal storage.

First, this paper presents the life cycle energy, emissions and cost analysis of a typical one-storey detached house in Montreal, Canada, where the average annual number of heating degree-days (HDD) is about 4500ºC at 18ºC outdoor temperature baseline. For comparison, the annual HDD is 2715ºC at 20ºC for Perugia, Italy. Second, several design alternatives with improved thermal resistance for walls, ceiling and windows, reduced overall air tightness, and increased window-to-wall ratio of South facing windows are evaluated with respect to the life cycle energy use, life cycle emissions and life cycle cost. The solution that minimizes the energy demand is chosen as a

reference house for the study of long-term thermal storage. Third, the performance of a solar combisystem with a long-term thermal storage capacity is investigated. The system is designed to supply hot water for the radiant floor heating system and the preparation of domestic hot water, for one year, using exclusively the solar energy. Finally, the life cycle cost, life cycle emissions and life cycle energy use of the solar combisystem is estimated for flat-plate solar collectors and evacuated tube solar collectors, respectively, for the economic and climatic conditions of this study.

2. Life cycle performance of base case house

2.1. Annual energy performance

A one-storey detached house built in the 1990's in Montreal, with the total heated floor area of 186 m^2, was used as the starting point in the development of the base case study house [4]. The house was made of wood-frame structure and brick veneer. Conventional electric baseboard heaters and an electric heater, installed in the storage tank, were used to satisfy the space heating and domestic hot water requirements.

Table 1. Thermal resistance of the exterior envelope of the base case house

Component	Thermal resistance ($m^2 \cdot C/W$)
Ceiling/roof	6.08
Above-ground walls	4.11
Foundation walls	1.09
Basement floor	0.99
Garage door (Polystyrol)	1.89
Exterior wood doors	0.47
Double glazed windows filled with argon, with aluminum frame	0.71
Overall weighted thermal resistance of all components	3.37

Four additional design alternatives of the house were developed from the initial house by incremental changes to the original house, with the goal to reduce the heating energy use, before analyzing the impact of the solar combisystem. Under those conditions, and because of limited measured data in the original house, we decided not to validate TRNSYS results with measurements. Instead, the energy use of the base case house, as estimated by TRNSYS 16 program [5], was compared with measured energy use of similar houses in the city. The simulated energy use was equal to 26,156 kWh (94,163 MJ) or 140.6 kWh/m^2 (506 MJ/m^2 of heated floor area). These values are comparable with 123.8±29.0 kWh/m^2 of normalized annual energy use monitored by Zmeureanu et al. [6] in 10 houses built in Montreal between 1986 and 1993.

2.2. Life cycle analysis of the base case house

This section presents the life cycle analysis of the base case house in terms of energy use, equivalent CO_2 emissions and cost.

2.2.1. Life cycle energy use

The life cycle energy use included the total energy input over the entire life cycle of a building and its subsystems. The life cycle in this study was 30 years as recommended by [7]. Within the scope of this study, the embodied energy due to the manufacturing of the building materials in the pre-operating phase, and the total energy use in the operating phase were evaluated. The embodied energy of plumbing, electrical, and ventilation systems was not taken into account, as those systems

were identical in the base case house and in the house with combisystem. The estimation did not consider the energy used for demolition.

The embodied primary energy that represents direct and indirect energy use to extract and transport raw materials, and fabrication of the final product was estimated using ATHENA [8]. The total embodied energy of the base case house was assessed at 566,907 MJ (Table 2), corresponding to 2,697 MJ/m^2 of total floor area, and it was equivalent to approximately five years of operating energy use. For comparison purpose, the results of other studies are cited: Haines et al. [9] estimated the embodied energy of a single-family house, complying with the Ontario Provincial Building Code, to a value of 520,000 MJ or 2,600 MJ/m^2 of floor area, while Kassab [10] found a value of 707,883 MJ or 2,286 MJ/m^2 of floor area for a duplex-apartment house built in year 2000 in Montreal. The exterior and foundation walls accounted for the highest embodied energy (1574 MJ/m^2 of wall area), followed by floors and roofs (637 MJ/m^2), foundations (355 MJ/m^2), and doors and windows (239 MJ/m^2).

The total operating primary energy use was calculated using the electricity mix of Quebec, where hydro-electricity accounted for 95.4% of the total electricity generated with the average power plant efficiency of 80%; the heavy fuel oil and nuclear accounted for 2% each with the power plant efficiency of 32.8% and 30%, respectively. Other sources such as natural gas, light fuel oil and wood had a negligible contribution, of only 0.6%, to the total power generation. The transmission and distribution losses were about 6%. The average annual efficiency of power generation plants was estimated at 73.1%, which was higher than for the conversion by using fossil fuels only. Assuming that the annual operating energy use would not change over the 30-year life span of the system, the total operating energy consumption was estimated at 3,864,000 MJ (Table 2), corresponding to 18,382 MJ/m^2 of floor area.

The life cycle energy use of the base case house, calculated as the sum of the embodied energy and the operating energy use over 30 years, was equal to 4,430,907 MJ (Table 2).

2.2.2. Life cycle emissions

The embodied emissions of the base case house were evaluated at 29.75 equivalent tons of CO_2, using the annual average values of emissions coefficients that are available with ATHENA program [8]. For detailed explanation of emissions factors, which is beyond the purpose of this paper, the reader might consult reference [8]. The exterior and foundation walls had the highest embodied energy (73 kg CO_2/m^2 of wall area), followed by doors and windows (38 kg CO_2/m^2), foundations (35 kg CO_2/m^2), and floors and roofs (32 kg CO_2/m^2).

The annual emissions due to the operating energy use were estimated at 1,875 kg of equivalent CO_2, and 56.24 tons of equivalent CO_2 over 30 years. The life cycle emissions were estimated at 85.98 tons of equivalent CO_2 emissions (Table 2).

2.2.3. Life cycle cost

The initial cost of the base house was estimated using RSMeans [11], including the total cost of building materials, labor, contractor profit and overhead cost, at $204,576 or 973 $/$m^2$ of floor area. All costs are listed in Canadian dollars. At the time of this study, the exchange rate between US and Canadian dollars was 1.01.

The operating costs included energy and maintenance costs during the life span of the building. The annual energy use was supposed to be constant during the life span of the building. The life cycle electricity cost was estimated at $46,193, calculated using the Present Worth method with the electricity rates of Hydro-Quebec [12], discount rate of 5.54%, inflation rate of 2.24% and inflation rate of electricity price of 2%. The life cycle cost of the base case house was estimated at $250,769 (Table 2).

Table 2. Life cycle profile of the base case house.

		Construction phase	Operating phase	Life cycle
Life cycle energy use	[MJ]	566,907	3,864,000	4,430,907
	[%]	13	87	100
Life cycle emissions	[Tons equiv. CO_2]	29.75	56.24	85.98
	[%]	35	65	100
Life cycle cost	[$]	204,576	46,193	250,769
	[%]	82	18	100

3. Life cycle performance of improved houses

In this section, several design alternatives are proposed in order to quantify their potential effect on a life cycle perspective. The first two design alternatives were elaborated to comply with the minimum insulation levels according to references [13,7]; they were named Quebec and MNECCH, respectively (Table 3). Since the windows of the base case house were quite small, having a window-to-wall ratio (WWR) of 0.09, a third design alternative presenting the same insulation levels and materials as the MNECCH design, but with larger windows on the South façade (WWR of 0.20), was considered. This design alternative is named MNECCH+. One last design alternative, called "best case", was proposed with higher insulation levels and "sustainable" materials.

Windows were upgraded to the best double-glazed window available in TRNSYS library, corresponding to an average U-value of 1.26 W/($m^2 \cdot ^oC$) that accounts for the centre of glass, edge-of-glass and frame. The WWR was kept at a value of 0.20 for the South façade, identical to the MNECCH+ alternative.

The air infiltration rate was reduced from 3.5 air change per hour at 50 Pa pressure difference (ach50) to 1.5 ach50. The infiltration rate of 1.5 ach50, measured by the depressurization of the house using the blower door technique, is usually given as the reference for airtight houses. The natural air infiltration rate, usually at 4 Pa pressure difference, cannot be measured, and is estimated from the value at 50 Pa pressure difference; this value is used in simulations with TRNSYS. To achieve this low infiltration rate, sprayed applied polyisocyanurate (PIR) was assumed to be used to fill the gaps around windows and doors, at the junction of the main floor framing and the foundation, and at tops of exterior and partition walls.

Using the TRNSYS and ATHENA computer programs and the RSMeans database, the life cycle energy use, life cycle emissions and life cycle cost were estimated for each design alternative of the house. Table 4 shows a summary of results and savings compared with the base case house. The "best case" design alternative was the most efficient choice, with the highest savings in terms of the life cycle energy use (33.2%), life cycle emissions (24%) and life cycle cost (2.2%).

Table 3. Summary of design alternatives of improved houses.

Building component	Design alternative				
	Base case	Quebec	MNECCH	MNECCH+	"Best case"
Air tightness [ach50]	3.5	3.5	3.5	3.5	1.5
WWR (South façade)[-]	0.09	0.09	0.09	0.20	0.20
	Thermal resistance [$m^2 \cdot °C/W$]				
Ceiling/Roof	6.08	6.08 (5.3)	7.61 (7.0)	7.61 (7.0)	7.61
Exterior walls	4.11	4.11 (3.4)	4.11 (4.1)	4.11 (4.1)	6.49
Foundation walls	1.09	2.87 (2.2)	3.56 (3.1)	3.56 (3.1)	4.74
Basement floor	0.99	1.36 (2.2)	1.36 (1.1)	1.36 (1.1)	2.82
Exterior doors	0.47	0.47	0.47	0.47	0.47
Garage door	1.89	1.89	1.89	1.89	1.89
	U-value [$W/(m^2 \cdot °C)$]				
Windows	1.40	1.40	1.40	1.40	1.26
Overall thermal resistance	3.37	3.61	4.05	4.01	5.29

Note: the number between parentheses represents the minimum thermal resistance required by the code associated with the design alternative.

4. Solar combisystem with solar thermal collectors and long-term thermal storage

The solar combisystem was installed in the "best case" design alternative (Table 4). The long term thermal storage system was designed to supply hot water for the space heating and the preparation of domestic hot water (DHW), for one year, using only the solar energy, that is, without using the auxiliary heating elements.

4.1. Description of the solar combisystem

The combisystem consisted of solar collectors (point 1 in Figure 1) of about 50 m^2 installed on the roof of the house, the heat transfer loop with antifreeze fluid and a pump (point 2), and the external heat exchanger (point 4) that transferred the heat from the primary loop into a secondary loop, which circulated the water. Hot water of the secondary loop, circulated by a pump (point 5), entered a large cylindrical storage tank (point 10) of 38,600 liters. A stratifier device improved the stratification by avoiding the mixing of water layers of different temperatures inside the tank. Hot water was supplied to radiant heating floors of the house by a variable speed pump (point 12) controlled by a thermostat installed on the first floor (point 13). An external heat exchanger (point 8) and a variable speed pump (point 7) enabled the control of domestic hot water at around 45ºC at the user-end. Detailed presentation of TRNSYS simulation was given in [14].

4.2. Energy performance of the solar combisystem

The annual house electricity use was estimated by TRNSYS at 8,300 kWh (29,880 MJ), or 45 kWh/m^2 of heated floor area (161 MJ/m^2). Compared to the annual electricity use of 18,830 kWh of the "best case" (without solar energy), this result represented a reduction of more than 50%. The ventilation had the highest contribution to the energy use as it accounted for 65.3% of the total value, followed by lighting with 14.7%, humidification with 9.2% and cooling with 8.9%. The space heating and domestic hot water production accounted for only 1.8% of the annual electricity use. The monthly electricity use of end-uses is shown in Table 5. The Heating and DHW part

represents the electricity use due to the circulating pumps for the heating and domestic hot water systems. The ventilation system had the highest contribution to the electricity use in the winter months since the outdoor air was heated up to the temperature of 20ºC. During summer, the months of July and August presented higher electricity usage by the cooling system. The energy use by electric appliances was estimated by TRNSYS by using the user-defined installed power (in kW) and the corresponding hourly schedule of usage. The radiative and convective components of heat gains from those appliances were used in the heat balance of each thermal zone of the house.

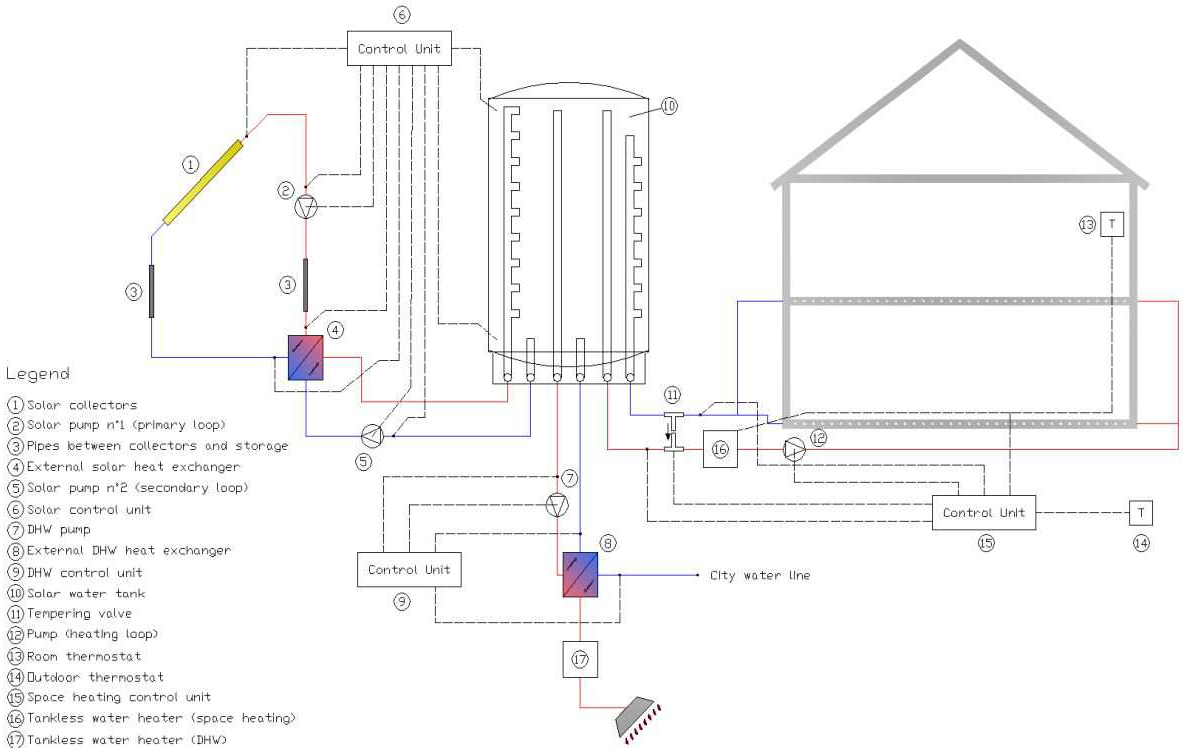

Fig. 1. Solar combisystem with long-term thermal storage.

Table 5. Monthly electricity use (kWh) in the case of solar combisystem.

End-uses	Month												
	Jan	Feb	Mar	Apr	May	Jun	Jul	Aug	Sep	Oct	Nov	Dec	Tot
Heating & DHW	24	24	29	20	4	2	1	2	1	4	18	21	150
Humidification	205	173	125	37	1	-	-	-	-	4	51	167	764
Cooling	-	-	-	-	7	146	310	231	47	-	-	-	740
Lighting	144	108	102	88	72	65	68	81	96	121	141	146	1,220
Ventilation	670	593	590	469	347	285	294	294	285	429	523	642	5,421
Total	1,035	900	846	613	432	498	673	608	429	558	732	976	8,300

4.3. Life cycle performance of solar combisystem

This section presents the life cycle cost and life cycle energy use of two solar combisystems: the design alternative no.1 with evacuated tube solar collectors, and the design alternative no.2 with

flat-plate solar collectors (Table 6). These two design alternatives had the solar fraction superior to 90%. The annual electricity use of the solar combisystem, required to provide for space heating and domestic hot water, was equal to 365 kWh (1.3 GJ) for design alternative no.1, and 567 kWh (2.0 GJ) for design alternative no.2.

Table 6. Design alternatives for solar collectors.

Design alternative	Type of solar collector	Area [m^2]	Tank volume [m^3]	$\dot{m}_{solar}$ [kg/(h·m^2)]	Tilt angle [deg]
1	Evacuated tube	47.1	34.7	25	60.0
2	Flat-plate	53.0	38.6	27	67.5

4.3.1. Life cycle cost

Since the combisystem provided for the space heating and domestic hot water, the electric baseboard heaters and the water heater were not necessary. Therefore, both design alternatives are credited with the initial costs of these systems. The cost of cross-linked polyethylene pipes (PEX) integrated in the radiant heating floor was considered. Since the flat-plate collectors were integrated to the roof, the cost of asphalt shingles was reduced.

The initial cost of the solar combisystem was estimated at $58,162 for design alternative no.1 and $39,949 for design alternative no.2 (Table 7). The main cost difference came from the collectors where the price of evacuated tubes ($35,603) represented more than twice the price of flat-plate collectors ($17,238).

The annual operating costs were estimated at $26 for design alternative no.1 (Table 8) and $40 $ for design alternative no. 2, based on the electricity use of the solar combisystem and the electricity rates of Hydro-Quebec [12].

The life cycle cost was estimated at $58,799 for design alternative no.1, and $40,939 for alternative no.2. The simple payback period of the solar combisystem was calculated as the ratio of the initial cost of the solar combisystem [$] and the annual energy savings for space and water heating [$/year], which were obtained by the use of proposed design alternative during the first year of operation. The simple payback was estimated at 79.4 years for alternative no.1 and 55.6 years for alternative no.2 (Table 8).

Compared to the simple payback period, the improved payback is a much more realistic approach as it considers the time value of money. It is defined as the period required for the cumulative savings to equal the initial cost of the system. As shown in Figure 2, the solar combisystem was not able to payback its installation costs. Yet, 50% of the installation costs were recovered after 55 years for design alternative no.1 (evacuated tube), and 34 years for design alternative no.2 (flat-plate).

If the inflation rate of electricity goes up from 2% to 4%, the curve of cumulative savings shows a different shape (Figure 3), and the payback period for design alternative no.1 is achieved after 38 years and after 26 years for design alternative no.2.

Table 7. Initial cost of the solar combisystem.

System component	Design alternative 1 [$]	Design alternative 2 [$]
Storage tank	12,031	13,023
Tank insulation	4,777	5,138
Conventional storage tank	-1,053	-1,053
Electric baseboard heaters	-3,097	-3,087
Radiant floor (PEX pipes)	2,502	2,502
Solar collectors	35,603	17,238
Shingles (credit for integrated mounting)	-	-1,201
Control unit	2,280	2,280
Pumps Stratos ECO	1,328	1,328
Pumps Stratos ECO-ST (Solar pump n^{o}1)	474	474
Tankless water heaters	1,331	1,331
Copper pipes	1,784	1,784
Piping insulation	202	202
Total	58,162	39,949

Table 8. Simple payback period of design alternatives.

Alternative	Electricity use [kWh]	Operating cost [$]	Solar savings [$]	Simple payback [years]
“Best case”	10,704	759	-	-
1	365	26	733	79.4
2	567	40	719	55.6

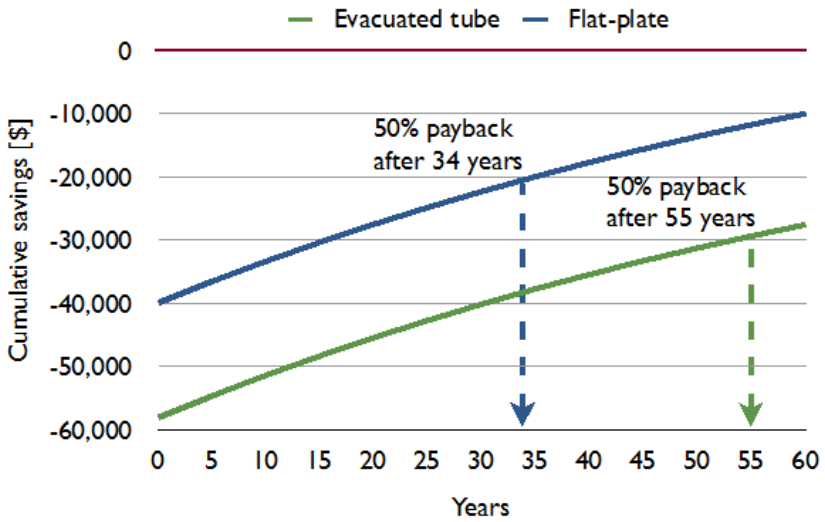

Figure 2. Cumulative savings of design alternatives and improved payback period (inflation rate of electricity of 2%).

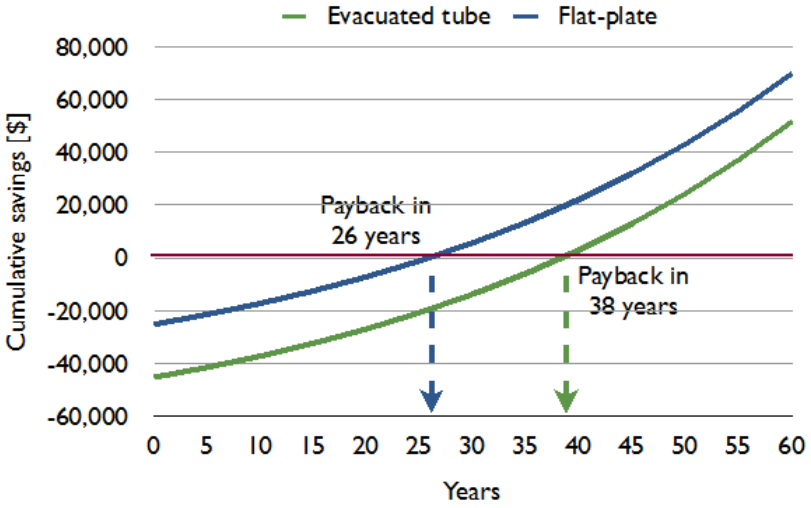

Figure 3. Cumulative savings of design alternatives and improved payback period (inflation rate of electricity of 4%).

The improved payback period of the seasonal storage system was quite long, from 55 to 38 years for design alternative no.1 (depending on the economic scenario), and from 34 to 26 years for design alternative no.2. The only way to obtain a payback period under the 30-years life span of the system is to benefit from substantial incentives. These results are seen as the direct consequence of the high initial costs of the combisystem in the context of low rates of electricity in Quebec, compared to other Canadian provinces.

4.3.2. Life cycle energy use

The embodied energy of the evacuated tube collectors was estimated at 1,521 MJ/m^2 or 71,717 MJ for the total collector area of 47.1 m^2 based on reference [15]. The average value of the embodied energy of a flat-plate collector, of 1,732 MJ/m^2, was estimated using data from several studies (Table 9). For the total collector area of 53 m^2, the embodied energy was calculated at 91,766 MJ. The storage tank was made of stainless steel (16.3 MJ/kg) and covered by 20 cm of mineral wool (15.6 MJ/kg). Copper pipes (48.7 MJ/kg) between the collectors and the storage tank had a diameter of 31.8 mm and were insulated with fiberglass (30.3 MJ/kg) over the length of 20 m. The heat exchangers were made of stainless steel (16.3 MJ/kg), and the pumps of stainless steel and grey cast iron (32.8 MJ/kg). The electric baseboard heaters previously used to heat the "best case" house were made of aluminum (58.5 MJ/kg). The embodied energy of baseboard heaters, water heaters (6,155 MJ) and roof shingles (76.6 MJ/m^2) was deducted from the total embodied energy. The embodied energy of the PEX pipes (103.0 MJ/kg), installed in the radiant floor, was considered in the analysis.
The total embodied energy of the solar combisystem was approximated at 157,870 MJ for design alternative no.1 and 134,689 MJ for design alternative no.2.

The total operating energy use over 30 years was calculated at 53.9 GJ for design alternative no. 1 and 83.8 GJ for design alternative no.2.

The life cycle energy use of the seasonal storage system, the sum of the embodied energy of the combisystem and the operating energy use over 30 years, was estimated at 188.6 GJ (design alternative no.1) and 241.6 GJ (design alternative no.2).

The energy payback time (EPT) was defined as the time (in years) in which the primary energy used to manufacture the solar combisystem was compensated by the reduction of annual electricity use [19]. With the energy payback time value of 4.9 years for design alternative no.1 and 6.0 years for design alternative no.2, the results are higher than the typical energy payback times of solar combisystems (without long-term storage capacity) ranging from 2.0 to 4.3 years [20]. Yet, such

difference is easily explained by the higher overall efficiency of power plants in Quebec (73.1%) compared to Germany (35.0%).

Table 9. Embodied energy of flat-plate solar collectors

Collector area [m^2]	Embodied energy [MJ]	[MJ/ m^2]	Country	References
2.13	3,513	1,649	Italy	[16]
1.35	2,663	1,973	Cyprus	[17]
5.00	6,408	1,282	Germany	[18]
5.00	8,633	1,727	Germany	[18]
6.15	11,450	1,862	Germany	[15]
5.76	9,790	1,700	Germany	[15]
2.00	3,604	1,802	India	[15]
	Average	1,732		

The energy yield ratio (EYR) was defined as how many times the energy invested in the manufacturing of combisystem was returned by the system in its entire life span [20]. Higher ratio values show better performance. Contrary to the energy payback time, this indicator considered the life span of the solar combisystem and hence provided more meaningful results. The EYR for design alternative no.1 was calculated at 6.1, and 5.0 for design alternative no.2. It was quite lower than the values ranging from 7.5 to 12.6 calculated for typical combisystems (without long-term storage) installed in Germany [15]. As for the EPT, this difference should be credited to the higher overall efficiency of power plants in Quebec.

4.3.3. Discussion

The life cycle cost analysis indicated that the use of proposed solar combisystem design alternatives does not result in an acceptable payback period, under the default economic conditions. However, with higher rates of inflation and with some financial incentives, the initial costs could be recovered in a shorter period of time.

The great potential of energy savings of the solar combisystem was very well demonstrated on the life cycle basis. Indeed, the energy payback time and energy yield ratio had acceptable values for such a large system. Compared to the second design alternative using flat-plate collectors, the first design alternative performed better in terms of energy payback time and energy yield ratio. Due to the higher efficiency of evacuated tube in cold climates, it required smaller solar collectors and storage tank. Therefore, less material was required for the same level of performance.

5. Conclusions

The improvement of the house envelope from the base case house to the “best case“ had as a result the reduction of the life cycle cost by $4.9/GJ of reduction of life cycle energy use. When the combisystem, design alternative no.1 was used along with the “best case” house, the life cycle cost increased by $18.7/GJ of reduction of life cycle energy use; in the case of alternative no.2, the increase was $13.3/GJ.

There are two main conclusions from this study: (1) the improvement of thermal performance of the envelope is more cost effective, and therefore should be the target before designing such complex solar combisystems; and (2) the use of a solar combisystem under the economic conditions presented in the paper is not cost effective yet. On the other hand, the energy payback shows a significant positive impact of using the solar combisystem, as the energy invested in the construction of the combisystem is recovered, through the annual operating savings, in a few years.

Acknowledgments

The authors acknowledge the financial support from Natural Sciences and Engineering Research Council of Canada and from the Faculty of Engineering and Computer Science, Concordia University.

References

[1] International Energy Agency, Solar Heating and Cooling. Available at: <http://www.iea-shc.org> [accessed March 8, 2007].

[2] Tepe, R., Bales, C., Bony, J., Pittet, T., Heimrath, R. Elements and examples of Dream Systems of solar combisystems, Technical report, International Energy Agency, Solar Heating and Cooling - Task 26, 2004.

[3] Ellehauge, K. (2003). Final report: Solar Combisystems. Technical report, Altener. Available at: http://www.elle-kilde.dk/altener-combi/[accessed October 5, 2008].

[4] Hugo, A., Computer Simulation and Life Cycle Analysis of a Seasonal Thermal Storage System in a Residential Building [Master's thesis]. Montreal, Canada: Concordia University; 2008.

[5] TRNSYS 16, 2006. A Transient Simulation Program, University of Wisconsin, Madison, Wisconsin, USA.

[6] Zmeureanu, R., Marceau, M. L., Payer, J., Derome, D., Evaluation of energy performance of nine identical row houses in Montreal. In: Proceedings of the Thermal Performance of the Exterior Envelopes of Buildings VII; 1998 December; Clearwater Beach, Florida, USA.

[7] Model National Energy Code of Canada for Houses, 1997. National Research Council of Canada. Canadian Commission on Buildings and Fire Codes. Ottawa, Canada.

[8] ATHENA, 2003. Environmental impact estimator v 3.0. Athena Sustainable Materials Institute, Ottawa, Canada.

[9] Haines, G., Org, M., Barkan, A., Pressnail, K., (2007). An economic and environmental comparison of standard versus energy efficient homes in Toronto, Canada. In: Sustainable Urban Areas; 2007; Rotterdam, Netherlands.

[10] Kassab, M., Improving the energy performance of houses in Montreal using the life-cycle analysis [Master's thesis]. Montreal, Canada: Concordia University; 2002.

[11] RSMeans, 2007. Residential Cost Data, volume 26. RSMeans Comp., Kingston, MA.

[12] Hydro-Quebec. Available at: < http://www.hydroquebec.com> [accessed 10.09.2008].

[13] Province of Quebec, 1992. Regulation respecting energy conservation in new buildings. Publications du Quebec, Quebec, Canada.

[14] Hugo, A., Zmeureanu, R., and Rivard, H., (2010) Solar Combisystem with Seasonal Thermal Storage. Journal of Building Performance Simulation 2010; 3(4):255-268.

[15] Gurzenich, D., Mathur, J., Material and energy demand for selected renewable energy technologies. Technical report, DLR - International Bureau of the BMBF; 1998.

[16] Ardente, F., Beccali, G., Cellura, M., Lo Brano, V., Life cycle assessment of a solar thermal collector. Renewable Energy 2005; 30:1031-1054.

[17] Kalogirou, S., Thermal performance, economic and environmental life cycle analysis of thermosiphon solar water heaters. Solar Energy 2008; doi:10.1016/j.solener.2008.06.005.

[18] Streicher, E., Heidemann, W., Muller-Steinhagen, H., Energy payback time – A key number for the assessment of thermal solar systems. In Proceedings of Eurosun; 2004, 20-23 June; Freiburg, Germany.

[19] Richards, B., Watt, M., Permanently dispelling a myth of photovoltaics via the adoption of a new net energy indicator. Renewable and Sustainable Energy Reviews 2007; 11:162-172.

[20] Watt, M. E., Johnson, A. J., Ellis, M., Outhred, H. R., Life-cycle air emissions from PV power systems. Progress in Photovoltaics: Research and Applications 1998; 6:127-136.

Table 4. Life cycle performance of improved houses compared with the base case house.

	Life cycle energy use [GJ]			Life cycle emissions [Tons CO_2 eq.]			Life cycle cost [$]		
Design alternative	Embodied	Operating	Life cycle	Embodied	Operating	Life cycle	Initial	Operating	Life cycle
Base case	567	129	4,431	29.75	1.87	85.98	204,576	1,878	250,769
Quebec	571	119	4,132	29.92	1.73	81.75	208,173	1,727	250,644
	+0.7%	-8.5%	-7.2%	+0.6%	-8.5%	-5.2%	+1.7%	-8.8%	+0.0%
MNECCH	558	117	4,056	29.30	1.70	80.21	209,247	1,696	250,951
	-1.6%	-10.5%	-9.2%	-1.5%	-10.5%	-7.2%	+2.2%	-10.8%	+0.1%
MNECCH+	569	115	4,033	29.92	1.68	80.35	211,001	1,677	252,239
	+0.3%	-11.5%	-9.9%	+0.6%	-11.5%	-7.0%	+3.0%	-12.0%	+0.6%
“Best case”	546	93	3,327	28.84	1.35	69.33	212,569	1,334	245,390
	-3.9%	-38.9%	-33.2%	-3.1%	-38.9%	-24.0%	+3.8%	-40.7%	-2.2%

Note: Percentages represent the increase compared with the base case house.

Simultaneous production of domestic hot water and space cooling with a heat pump in a Swedish Passive House

Johannes Persson[a], Mats Westermark[b]

[a] *Division of Energy Processes, Department of Chemical Engineering and Technology, Royal Institute of Technology, Stockholm, Sweden, tjp@kth.se*
[b] *Division of Energy Processes, Department of Chemical Engineering and Technology, Royal Institute of Technology, Stockholm, Country, mw@ket.kth.se*

Abstract:

Passive Houses have gained popularity the last ten years as a way of improving the energy efficiency in the housing stock. During the cold winter in Sweden, space heating is at times needed but a Passive House is limited to a maximum use of energy for space heating. The challenge of avoiding space heating during the cold winter climate in Sweden has pushed the design of a Passive House in a direction where problems with excessive indoor temperatures might occur summertime. This paper evaluates a comfort cooling strategy for reaching comfortable indoor climate summertime while maintaining good energy efficiency. The strategy is to use the free cooling from a heat pump while producing domestic hot water. A literature study on heat pumps for simultaneous heating and cooling (HPS) was made in order to make assumptions of the cooling and heating capacities of the HPS for the building simulations. The effect this free cooling has on the indoor climate was thereafter simulated with IDA Indoor Climate and Energy. The building model is based on an actual Passive House in the district of Lambohov in Linköping, Sweden, where continuous logging of temperatures are available. Without comfort cooling, the simulations show excessive temperatures summertime, which is consistent with field measurements from the actual house. Further, the simulation results demonstrate a substantial removal (60 – 80 %) of excessive indoor temperatures summertime with the cooling strategy implemented.

Keywords:

Passive House, Comfort cooling, Building Simulation, Heat pump.

1. Introduction

Passive Houses have gained popularity the last ten years as a way of improving the energy efficiency in the housing stock. A Passive House uses only the internal heat gains from lighting, equipment, humans and the incoming solar radiation to heat the building. This is possible through a combination of a highly insulated building envelope and a heat exchanger that heats the incoming air with the exhaust air. A Passive House has therefore no need for a traditional space heating system, but occasionally, when the temperature drops fast during a cold period, there might still be a need for additional space heating. The challenge of avoiding space heating during the cold winter climate in Sweden has therefore pushed the design of a Passive House in a direction where problems with excessive temperatures might occur summertime. The Swedish National Board of Health and Welfare recommends that the indoor temperature does not exceed 24 °C and 26 °C wintertime and summertime respectively [1]. Further, The Swedish National Board of Housing, Building and Planning recommends an indoor temperature between 23 °C and 25 °C summertime [2] and Forum for Energy Efficient Buildings recommends that the indoor temperature does not exceed 26 °C more than 10 % of the time summertime in the warmest part of the building [3].

A study by the Technical Research Institute of Sweden with temperature loggings from 20 terraced house apartments in 4 Passive Houses in Lindås, Sweden, show a mean indoor temperature of 25.2

°C summertime [4]. Some of these apartments have temperatures within good levels throughout the summer but some have periods with temperatures between 25 °C and 30 °C and there are occasions when the indoor temperature reaches above 30 °C. Dwellers in Passive Houses in the districts of Oxtorget, Glumslöv and Frillesås responded to a questionnaire study about their indoor temperature summertime. The outcome of the questionnaire gave the result that in Oxtorget 31 %, in Glumslöv 56 % and in Frillesås 11 %, respectively, claimed it was too warm during this period [5]. More reports of excessive temperatures summertime have been made from dwellers in a two-storey Passive House in Lidköping and from dwellers living on the top floor in a three-storey apartment building in Brogården, Alingsås [6]. In Lambohov, Linköping, temperature measurements from two Passive Houses also show excessive temperatures summertime. During the month of July 2010, the mean value of the exhaust air temperatures from these two apartments were 27.3 °C, Fig. 1. Further, the exhaust air temperatures from these two apartments were 26 °C or higher during 60 % of this time [7].

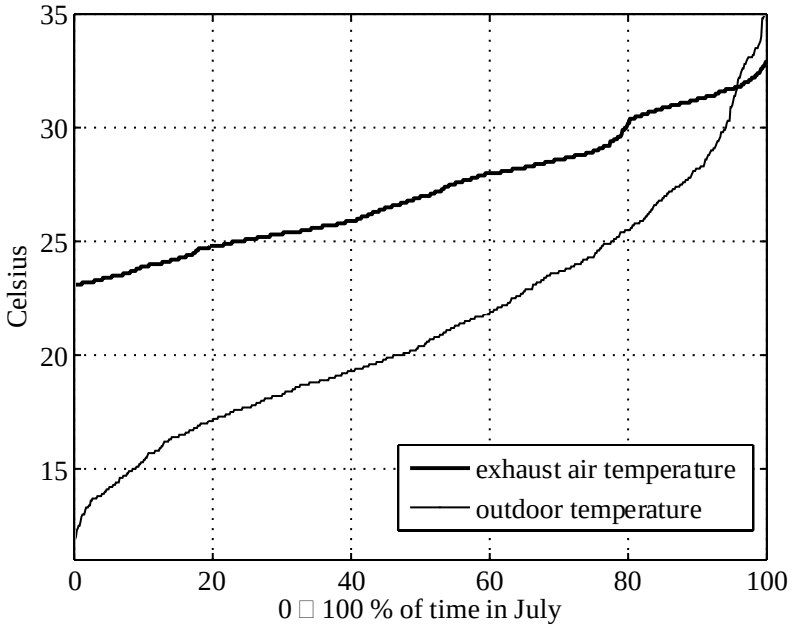

Fig. 1. Temperature logging during July from the actual Passive House in Lambohov.

In contrast to warmer countries, comfort cooling equipment is normally not installed in Swedish dwellings. However, the combination of the insulating capacity of a Passive House and the high solar gains summertime can result in excessive temperatures even in this cold climate. Methods for comfort cooling in warmer countries are normally: shading, ventilation, cooling machine, evaporative cooling, solar chimneys, earth tubes, reflectors and night time radiation cooling. This paper evaluates a comfort cooling strategy that makes use of the free cooling produced by a heat pump during its domestic hot water production. Thereafter, building simulations are carried out in order to investigate the effect this cooling has on the indoor climate in a Swedish Passive House. Especially, to what extent this space cooling can remove excessive indoor temperatures. A literature study on heat pumps for simultaneous heating and cooling (HPS) is made in order to make assumptions of the cooling and heating capacities of the HPS for the building simulations. Thereafter, a span of space cooling powers from the HPS is simulated in order to see how the indoor climate is changed with this cooling strategy implemented.

2. Methodology

In order to investigate the effect the space cooling from the heat pump has on the indoor climate in a Passive House, building simulations have been carried out using IDA Indoor Climate and Energy (ICE). The model of the Passive House in the IDA ICE-simulations is based on an actual Passive House apartment in Lambohov, Linköping, Sweden, where continuous logging of temperatures are available, see Fig. 1. Moreover, the input data in the building simulations representing the human presence and the use of electricity are based on a collection of user related data from the Swedish National Board of Housing, Building and Planning [2]. Further, a climate file from Meteonorm is used in IDA ICE to simulate the climate in Linköping.

A literature survey on heat pumps for simultaneous heating and cooling (HPS) was made in order to make assumptions of the cooling and heating capacities of the HPS for the building simulations. Thereafter, these assumption where used as input in the building simulations and the resulting effect on the indoor climate of the Passive House was simulated. When evaluating this comfort cooling strategy, the first ten days in the month of July, a period with excessive temperatures in the real Passive House was simulated as well as a longer interval of the summer months June to August. The reference case without any space cooling of the building is compared with the HPS space cooling implemented strategy after which the cooling performance is evaluated. More details are presented in Appendix.

3. Heat pumps for simultaneous production of domestic hot water and space cooling

This chapter presents theory of heat pumps for simultaneous heating and cooling along with their applications on air-conditioning and domestic hot water production. Moreover, the chapter presents information of domestic hot water use and production.

3.1. Heat pumps for simultaneous heating and cooling

A heat pump transfers heat from one medium to another in its thermodynamic cycle. It can therefore both be used for heating or cooling a medium. Heat pumps are commonly used in households for the production of space cooling, space heating and domestic hot water production. The technology has been used in households since the 1950s, however, during the 1970s oil crisis, the technology enjoyed due to its high efficiency an increased market penetration. In Sweden, the heat pump has reached a high level of market penetration for residential applications such as space heating etc. For these applications, the heat pumps most commonly use air, ground or water as heat source. Multi-functional heat pumps for various heating or cooling applications have been studied and presented in the literature, for example [8-9] present reviews of the technology. Efficiencies of more balanced thermal needs between heating and cooling is also studied in the ECBCS Annex 48 of the International Energy Agency.

This paper investigates the application of a heat pump for simultaneous production of heating and cooling (HPS), which is not possible with a standard reversible heat pump. While producing heat for domestic hot water to a household, the HPS simultaneously produces space cooling. In this combined heating and cooling process, heat is taken from the indoor air to produce domestic hot water for the household with the heat pump. While the condenser in the heat pump heats the water, the evaporator cools the indoor air. The use of heat pumps for simultaneous heating and cooling has been studied theoretically and experimentally, often with applications for various industrial, commercial and residential applications. Multi-functional heat pumps can here efficiently be used to control individual zones, providing heat to some, while cooling other zones if needed. In [10] a transcritical heat pump cycle using CO_2 as working fluid was modelled for simultaneous refrigeration and water heating for application in the food processing industry. Compared with a conventional refrigeration system and separate gas hot water boiler system, the HPS was predicted to reduce the total energy cost by 33% and the CO_2 emissions by 52%. More, efficiencies of

transcritical heat pumps with CO_2 as working fluid have further been studied for simultaneous heating and cooling of water and/or air in [11-12]. More closely related to the application in this paper, studies of HPS for the simultaneous production of space heating, space cooling and domestic hot water for residential applications have been made in [13-16]. These papers present cooling and heating capacities and comparisons of the improved system efficiencies with the HPS technology. Variable studies of supply air or water temperatures to the evaporator or the flow or refridgerants which here are CO_2, R134a or R407C are also carried out.

The indata for the simultaneous space cooling and dhw production in the simulations are in this paper similar to the properties of the HPS in [14]. This means that with an approximate evaporator inlet temperatures of the air is between 20 – 30 °C, the HPS will produce dhw water at temperatures around 55 °C while at the same time produce cooled air for space cooling of a temperature of around 12 degrees. Further, constant values of $COP_{heating}$ = 3 and $COP_{cooling}$ = 2 are used in the building simulations.

3.2. Domestic hot water production

Studies of domestic hot water use show that there are large variations among households [2]. However, there are general daily and weekly user patterns such as higher use of dhw during weekends as well as higher use on evenings and mornings. Moreover, single houses tend to use less dhw than apartment blocks [2]. The difference in the used amount of dhw origins from the number of family members in a household and their habits as well as the geographical climate, the efficiency of the dhw equipment etc. For a typical Swedish single-family house with an area of 150 m^2, the energy need to produce dhw amounts to 4500 kWh/year [17]. The Swedish National Board of Housing, Building and Planning recommend that the amount of energy needed to produce dhw does not reach over 20 [kWh/(m^2*year)]. For the 3-person household in this paper, the Swedish Passive House criteria for dhw production (18 [m^3dhw/person], 55 [kWh/m^3]) are used and results in 2970 [MWh/year] [3]. In order to avoid growth of legionella bacterias, the tank storage temperature of the dhw should reach at least 55 °C.

The simulations in this paper use a production pattern of the domestic hot water that is the same for every day of the week and constant over the 24 hours of the day. The dhw calculations are based on an household with three dwellers. Therefore, in the case with an averaged and constant dhw production, the power needed results in 2970 [kWh/year] / 8760 [h/year] = 340 W. If provided with a tank, the produced cooling could be saved for use at a later time when needed, this is however not investigated in this paper.

4. Building simulations

The building simulations in this paper have been carried out using IDA ICE. In these simulations, the input data representing the human presence, the use of electricity and domestic hot water is based on a collection of user related data from The Swedish National Board of Housing, Building and Planning [2], which applied to this household results in the internal gains of 4.6 W/m^2. The building model in the simulations is based on an actual Passive House apartment in Lambohov, Linköping, Sweden, where continuous logging of temperatures are available, see Fig. 1. It is one of two 4-room apartments in a Passive House building, both with two floors and an area of 105 m^2 with three dwellers. The ground floor has a ceiling height of 2.5 meters and the second floor has a ceiling height of 2.4 meters. The apartment has a constant air volume ventilation system that is equipped with an FTX-system that recovers the heat in the exhaust air during the heating season. Further, a climate file from Meteonorm is used in IDA ICE to simulate the climate in Linköping. In this investigation, two intervals of the summer of 2010 are simulated using two different settings of input data. The first and the longer period covers the three summer months of June to August while the second period covers the first ten days of July, a warm period with excessive temperatures in the actual Passive House. The constant production of dhw demands a constant need of 340 W, this together with the assumed values of $COP_{heating}$ = 3 and $COP_{cooling}$ = 2 gives a constant space cooling

power of 225 W. The building is simulated with two different space cooling powers, one higher than the calculated, 250 W and one lower, 150 W. This is done to capture an approximate span of varying COP values along with the varying amounts of energy that different household need for their production of dhw. In the simulations, the HPS is connected to the FTX-system and the space heating and cooling is supplied to the building via the ventilation system. The HPS is assumed to be an air to air/water system with the possibility of taking air from the outside of the building if there is a need for heating of from the inside of the building if there is a need for cooling. The HPS is also assumed to being able to heat hot water or the indoor air. The cooling system is set to control the exhaust air temperature to a maximum of 22 °C and the heating is turned off. The ventilation is set to a flow of 45 l/s demanding a power need of 60 W. More details of the input are presented in Appendix.

5. Results

Without the HPS space cooling the building simulations show excessive temperatures summertime, which is consistent with the field measurements from the actual Passive House, Fig. 1. and Fig. 2. The simulation results of the three summer months June, July and August from IDA ICE in Fig. 2 demonstrate a substantial removal of the excessive indoor temperatures when the free cooling from the evaporator in the HPS is used for space cooling. However, the excessive temperatures cannot be completely removed during the warmest summer days in these simulations. When simulating a constant space cooling power of 250 W, the amount of degree hours with excessive temperatures (>26 °C) can drastically be removed by more than 80 %. When using an assumed constant space cooling power of 150 W, the reduction of degree hours with excessive temperatures amounts to a 65 % removal. None of these simulations therefore reduce the amount of excessive temperatures to a maximum of 10 %, which is required by [3]. It is natural that the cooling results in Fig. 2, Fig. 3 and Fig. 4 show a non-linear behaviour since the counting of removed degree hours starts above 26 °C. The results from the building simulations during the warmest 10 day period of the summer show a general decrease in the exhaust air temperature of little over 1.5 °C with space cooling set on 150 W. Better results was reached with the space cooling set on 250 W where a general temperature decrease of well over 2 °C was found during the warmest 10 day period, see Fig. 4. In the same way, Fig. 2 show a decrease in the exhaust air temperature of approximately 1 to 2 °C during the long three month simulation. Both reveal that when the exhaust air temperature in the reference case without cooling exceeds 28 °C the space cooling cannot provide sufficient cooling anymore and the exhaust air temperature reaches over 26 °C.

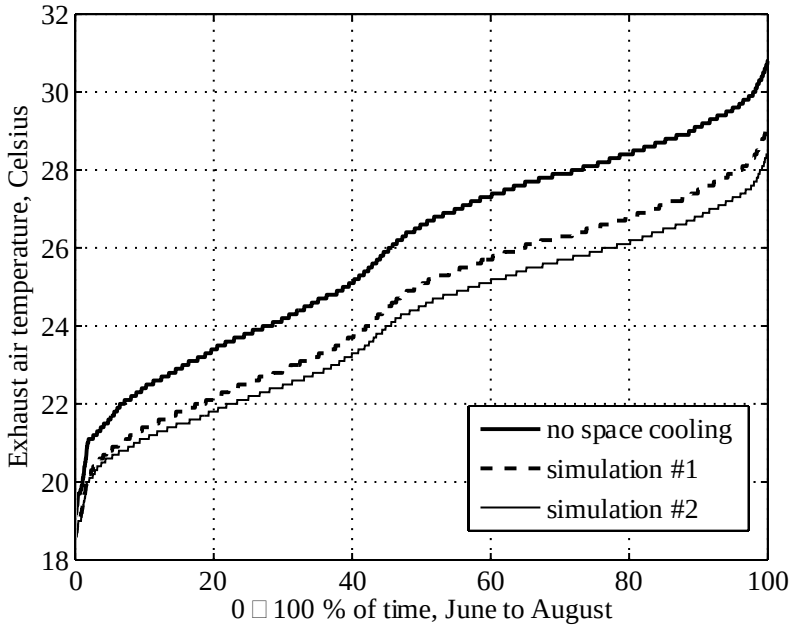

Fig. 2. The results from the building simulations with different space cooling powers. Simulation #1 provides a constant cooling of 150 W while simulation #2 provides a constant cooling of 250 W. The simulated period is June to August.

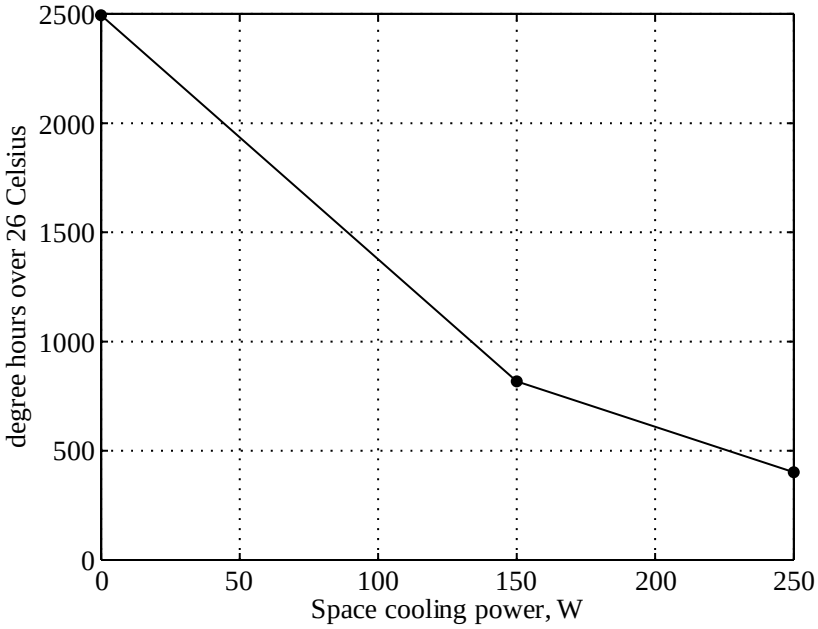

Fig. 3. The simulated reduction of degree hours as a function of the amount of space cooling, the simulated period is June to August.

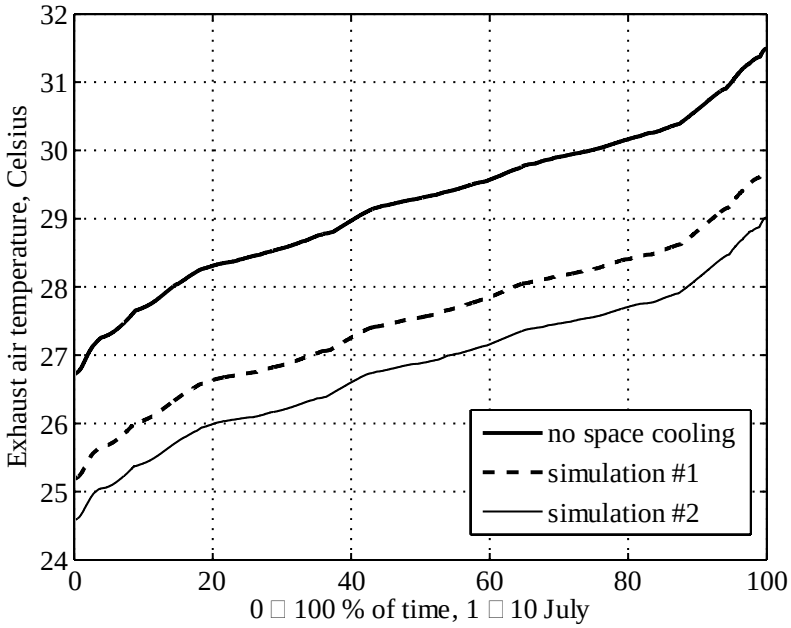

Fig. 4. The results from the building simulations with different space cooling power. Simulation #1 provides a constant cooling of 150 W and simulation #2 provides a constant cooling of 250 W. Here, the first ten days of July are simulated.

6. Conclusions

In this paper a building model based on an actual Passive House in the district of Lambohov, Linköping, Sweden was simulated with the simulation tool IDA Indoor Climate and Energy. The actual Passive House has experienced excessive temperatures during the warmer parts of the summer and would during this period have needed cooling in order to secure a comfortable and healthy indoor climate. Therefore, the alternative of providing the Passive House with cooling from a HPS while producing domestic hot water was investigated. In order to do this, a literature survey of HPS was carried out to find approximate values of the properties of the HPS.

Without the space cooling from the HPS, the simulations show excessive temperatures summertime, which is consistent with field measurements from the actual Passive House. The simulation results from the three-month period show that the HPS can remove a substantial share of the excessive indoor temperatures, Fig. 2. Further, the simulation results from the warmest 10 day period of the summer show a reduction of the indoor temperature between 1.5 to well over 2 degrees, depending on the settings of the HPS properties.

Although the building simulation with the highest power 250 W for space cooling produce results that show a drastic removal of over 80 % of the degree hours with excessive temperatures, it cannot reach an indoor climate with less than 10 % of excessive temperatures which is given as a standard by [3]. The results show that when the indoor temperature reaches above 28 °C, which it has in the actual Passive House, the HPS can not provide enough heating during the warmest part of the simulated summer without only by using the free cooling from the dhw production. The removal of excessive temperatures could however be further increased by increasing the power of the HPS even though it is not needed for the dhw production, or, by also using passive comfort cooling strategies like shading, ventilation, evaporative cooling, solar chimneys, earth tubes, reflectors and night time radiation cooling. Another strategy could be to focus the space cooling to specific rooms in the household.

Overall, the use of space cooling from the HPS improves the indoor climate summertime in the Passive House and the simulations estimate that an implementation of this storage would cut more than 60 to 80 % of the cooling need in order to remove all excessive temperatures. However, these results of the removal of excessive temperatures are sensitive to ambient climate, building properties like insulation, thermal inertia etc. and thus the cooling results will vary between buildings. Additionally, the amount of free cooling from the dhw production largely varies between households as mentioned earlier in chapter 3.2. However, if to follow the Passive House standard, there is an upper limit to the available amount of free cooling. Thus, buildings with a less amount of excessive temperatures could reach a complete removal of excessive temperatures with the HPS technology.

The heating function of the heat pump is turned off in these simulations, but the cooling system is set to control of exhaust air temperature to a maximum of 22 °C. Fig. 2 shows that the temperature sometimes drops down to nearly 18 °C. If the heating function would not have been turned off but instead controlled the exhaust air temperature not to go lower than 20 °C, it would have resulted in a smaller reduction of excessive temperatures since the house stores cooling during these hours.

Since Passive Houses effectively can contribute to increased energy efficiency in the housing stock, it is of great importance that they are well adapted to the summer climate, ensuring a comfortable living. If equipped with cooling, the Passive House could with its highly insulating capacity be able to provide an indoor climate of high quality during summertime compared with normal buildings.

References

[1] Temperaturer inomhus, The Swedish National Board of Health and Welfare, 2005.

[2] Indata för energiberäkningar i kontor och småhus en sammanställning av brukarrelaterad indata för elanvändning, personvärme och tappvarmvatten. The Swedish National Board of Housing Building and Planning, 2007.

[3] Kravspecifikation för minienergihus, Forum for Energy Efficient Buildings, 2009.

[4] Ruud, S. Lundin, L., Bostadshus utan traditionellt uppvärmningssystem – resultat från två års mätningar, Technical Research Institute of Sweden, 2004.

[5] Samuelsson, M. and Lüdeckens, T., Passivhus ur en brukares perspektiv, 2009.

[6] Janson, U., Passive houses in Sweden – From design to evaluation of four demonstration projects. Lund, Sweden, Lund University, 2010.

[7] KTC, private communications, 2010.

[8] Hepbasli, A., Kalinci, Y., A review of heat pump water heating systems, Renewable and Sustainable Energy Reviews 2009;13:1211-1229.

[9] K.J. Chua , S.K. Chou, W.M. Yang, Advances in heat pump systems: A review, Applied Energy 2010:87:3611-3624.

[10] White, S.D., Cleland, D.J., et al. A heat pump for simultaneous refridgeration and water heating, IPENZ Transactions, Vol. 24, No. 1/EMCh, 1997

[11] J. Sarkar, S. Bhattacharyya, M.R. Gopal, Performance of a transcritical CO2 heat pump for simultaneous water cooling and heating, ASHRAE Transactions, 116, 2010.

[12] J. Sarkar, Souvik Bhattacharyya, M. Ram Gopal, Simulation of a transcritical CO2 heat pump cycle for simultaneous cooling and heating applications, international journal of refrigeration 2006: 29 735-743.

[13] Elgendy, E., Schmidt, J.,Khalil, A., Fatouh, B., Performance of a gas engine heat pump (GEHP) using R410A for heating and cooling applications, Energy 2010; 35:4941-4948.

[14] Fatouh, M., Elgendy, E., Experimental investigation of a vapour compression heat pump used for cooling and heating applications, Energy 2011; 5: 2788–2795.

[15] Byrne, P., Miriel, J., Lenat, Y., Experimental study of an air-source heat pump for simultaneous heating and cooling – Part 1: Basic concepts and performance verification, Applied Energy 2011; 88: 1841-1847.

[16] Adriansyah, W., Combined air conditioning and tap water heating plant using CO2 as refrigerant, Energy and Buildings 2004; 36: 690-695.

[17] Swedish Energy Agency, Available at: <http://energimyndigheten.se/sv/hushall/Din-uppvarmning/> [accessed 2012.02.10].

Acknowledgments

This work has been carried out under the auspices of The Energy Systems Programme, which is primarily financed by the Swedish Energy Agency.

Appendix

Table A.1. *Simulation input data*

Building envelope	m^2	W/m^2K
Apartment area	105	
External wall		0.1073
Internal wall		0.6162
Internal floors		0.2259
Roof		0.08735
External floor		0.1289
Glazing		0.8800
Outer door, front		0.7500
Outer door, back		0.9000

Thermal bridges	m	W/mK
Edge beam	54	0.094
Wall corner	45	0.027

Windows & Doors	120	0.041
Wall/Joists	63	0.025

Ventilation		
Air leakage (at +/- 50 Pa)	0.24	l/s,m^2
Mechanical ventilation	45	l/s
Fan pressure	488	Pa
Fan power	60	W
Efficiency of ventilation fan	73	%
Efficiency of heat exchanger*	87	%

* During the cooling season the heat exchanger is only used if the outdoor temperature exceeds the indoor temperature

Other		
Internal gains	4.6	W/m2
Ground reflection	20	%

SOFC Micro-CHP integration in residential buildings

Umberto Desideri[a], Giovanni Cinti[b], Gabriele Discepoli[a], Elena Sisani[a] and Daniele Penchini[a]

[a] *Università degli Studi di Perugia, Perugia, Italy, fclab@unipg.itl*

Abstract:

SOFC technology has reached many of the performance goals that where indicated by scientific society and is providing several application that permits market penetration. One of the main targets is related to Micro Cogeneration Heat and Power (μ-CHP) for residential application. The integration of this system with a residential house has to be deeply investigated to individuate market targets in terms of costs and efficiency. This study evaluates the Italian market condition and analyzes the integration possibility with both thermal and electrical systems. Different solutions are investigated evaluating thermal and electrical driven logic for □-CHP SOFC based unit and the opportunity of integration with local electrical grid. Evaluation on heat and electricity storage was also considered as integration strategy. The study is based on electrical and thermal loads in typical residential users and the evaluation is based on Italian technical standards and guidelines. Several operating conditions were evaluated and compared to obtain an optimized size and integration of μCHP SOFC based solution.

Keywords:

SOFC, micro-CHP, buildings, emission, energy, sustainability.

1 Introduction

This study introduces preliminary analysis of microCHP system integration providing a feasibility study of economical and energetic operative conditions of a unit installed in a real dwelling. Integration can be realized following different strategies but the final aim is to reach economical and energetic convenience of innovative technology compared with traditional ones. The analysis focuses on an example of real apartment and evaluates the methodology to realize a study of integration between the system and the house.

Literature offers many studies on the integration between microCHP and residential dwellings. This study is important to evaluate the economical convenience in different scenarios differing in house typology, integration and tariff strategies. The results, mainly payback time prediction, individuate the target market for the producers and the economical benefits for the householders. Many of this studies are used by government to select the most effective incentive policy. While some authors focus on economical instruments for combined heat and power support [1,2], there is also a deep investigation on energetic and environmental evaluations [3–5] and many case studies, both model and experimental, that focus on the coupling of the system into the house considering real house load profiles [6–10]. The starting point of the study is the analysis of user typology. In Italy there are 11,1 million of buildings that are used for residential purpose. This buildings correspond to an average of 27 million houses, 22 million of which are regularly lived and heated. Main parts of this houses are individual, single family, while the remaining part, 900.000, is composed of multi-family residence [11]. The user is identify also by: number of inhabitants, dimension and location. The number of inhabitants has a direct influence on electrical and domestic hot water (DHW) requirements and is a parameter used to evaluate annual energy request of the building. Dwelling dimension is used to calculate annual heat demand while the geographical location gives indication on the average environmental temperatures that are usually related to heat loads. Ulterior aspects can be identified to have a more complete description of type of user: for example the type of

heating system, the insulation of the house and the typology of householder have an important impact on the utilization of the micro-CHP system. In this preliminary study this considerations are not introduced and can be added in further developments.

The integration analysis is based on information on micro-CHP working conditions and dwelling energy requirements.

2 Dwelling requirements

To produce a feasible study of the integration between building and micro-CHP, is important to correctly evaluate the trends of energy requirements of the building. Three main energy flows inlet a typical residential dwelling: electrical energy, heat for domestic hot water (DHW) and thermal energy for heating system. In addition houses usually have other energy inputs, such as natural gas for cooking purpose, but these requirements are not related with the activity of the micro-CHP but directly with the natural gas net.

The energy flow of an house is strongly dependant from both social and physical peculiarities. The habit of the people living the house can vary dramatically the load profile of all the energy flows while dimension and position of the dwelling has main impact into the heating energy requirement. Moreover the flows are also time depending due to some environmental parameters such as external temperature, season, weather condition, day/night and to some social periodic schedule: weekdays, holydays, Sundays.

The most reliable way to study the consumes of the house is the statistical study of existing data, but this information is not always available. It can be directly measured by the energy supplier or from the distributors if they install innovative instruments that measure instantaneously energy flows. This is not yet diffused in Europe and for new buildings this information cannot be provided and an estimation study has to be performed. For existing building the analysis of bills can be realized but usually there is no daily consume because suppliers calculate invoices every two months. This information can be easily obtained and in following part will be considered. Germany already developed a standard [12] that gives indications on the calculation of reference load profiles of single-family and multi-family houses for the use of CHP systems. There are additional ways to define daily load profile of an house. For example in Italy the Authority for Electric Energy and Gas provides gas standard natural gas consume profile as ratio of annual consume. This tables are divided for climate region and user typology (heating, DHW, both). This values are used by distributors to predict energy consume of standard users and to calculate relative costs but don't offer daily load profile minute by minute but permits to calculate daily requirements of heat and of DHW [13].

The annual heating requirement of an house can be predicted in many different ways. There are several commercial software available based on diffused models that calculate heat requirement depending on building insulation, structural conditions, family members and geographical location. Methods and results of this models are not investigated in this study. In addition in Italy there are several laws and standards that define how to calculate the heating requirements of an house for both heating system and domestic hot water. This standards are used to predict the yearly and monthly house requirements and are used to dimension boilers or alternative integrated system such as solar heating. Main inputs of this calculation are house location and total surface. Finally in literature [14,15] is possible to find many European data that can give an average of what are energy requirements of a standard dwelling.

In this study are considered both Italian and German standards, literature values, gas Authority profiles and some measured values. When possible a compare between different method is performed.

3 Integration study

The scheme of microCHP integration in a dwelling is simply depicted in Fig. 1.

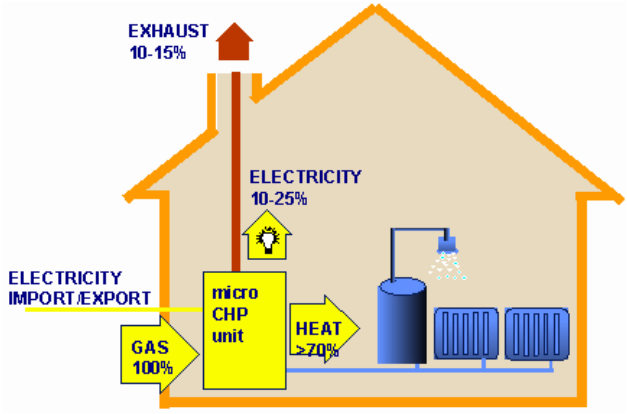

Fig. 1 Integration of micoCHP in the house

The microCHP is integrated in the house as substitution of traditional boiler and supplies energy to the heating system. A secondary boiler, integrated or external, supplies the additional heat required when the microCHP thermal power doesn't reach the building peak requirements. In general the unit supplies heat also to the DHW circuit and a thermal energy storage (TES), similar to a traditional water tank, permits to have a delay between produced heat and used hot water. If correctly dimensioned the TES allows the microCHP to operate at nominal condition most part of time.

A number of CHP operating strategies are present in the reviewed literature. They are mainly related to the tariff contract, to the size of the dwelling loads and to the opportunity of energy storage both for electrical and thermal energy. The two main dispatch strategies are heat led, where the system operates when heat load is required, and electricity led, where the unit operates when electrical load is present. Industries usually develop their products following the heat driven logic in accord also with government lows such as Energy Saving Trust [16] that present electricity as a by-product of microCHP unit heat production. In addition to these simple strategies Hawkes and Leach [17] present a "lead cost" (i.e. optimized) operation where the system is dispatched such as to minimize the cost of operation. The system can also operate so to minimize CO_2 emissions.

Following analysis is realized considering the system operation mode as heat led. The μCHP system operates only to purchase thermal energy when required. This means that there is no need of electricity profiles because all electricity is send to the grid exactly when produced. This choice is related to Italian regulations and grid development stage. The grid connection system can have priority distribution and a net metering tariff scheme. This means that there is no need to produce electricity when required because the balance is realized at the end of the year. If the system consumes all the electricity spent there is no cost for the householder, if the house consumes more electricity of the produced one differences become a cost finally if the production exceeds consumed one the difference can be paid with very small tariff or is add to next year calculation bill. There is no economical convenience in producing more electricity than the consumed one. This means that total year electrical demand is the main border condition when making economical analysis. This consideration is extremely important for selection of system electrical size and corresponding thermal one. Generally this brings to very small scale of plant (1 kWe) that permits also good thermal optimization. If we consider no modulation of the system the unit will operate always in nominal conditions and the total thermal production has to be distributed in operational hours during the all year. Note that this distribution is not required from electricity profile because of priority distribution.

Moreover considering the use of a thermal heat storage, is possible to avoid contemporarily of heat production and consume. The dimension of the storage is related to consume/production delay and total heat produced. In the study a TES able to store all the heat produced daily by the CHP was considered and calculation are realized with 24 hours total heat demand. If this value is higher of total thermal energy produced by the system the unit never stops and operates always at nominal conditions. Without storage the CHP has to go in regulation mode that can bring it to minimum working point (idle) or to shut down. As SOFCs have problems with thermal cycle and have long start-up time the study will focus on reduce on/off cycle. Finally is difficult to imagine CHP system working during summer time when only DHW is required without a storage. DHW consume usually requires high transitional slope with power demand often higher than micro-CHP one. This option is considered as less interesting for this application.

Before analyzing a specific case study some general consideration on the economics and of the integration are performed to investigate the convenience of the system compared to traditional technology. First of all following characteristic are defined:

- η_{eCHP}: microCHP electrical efficiency;
- η_{thCHP}: microCHP thermal efficiency;
- P_e: microCHP electrical power;
- P_t: microCHP thermal power;
- TER: thermal to electrical ratio. This parameter is the ratio between P_{th} and P_e but also between η_{eCHP} and η_{thCHP} as described below;
- OT: operating time. Is the ratio between the year operating microCHP hour and the total one (8760);

If we compare the microCHP with standard production of electricity and heat, we can introduce Primary Energy Save (PES), calculated as the ratio between the primary energy saved over the standard production. Considering:

- E_{CHP}: primary Energy in the CHP (Natural Gas);
- Ee: primary energy for standard electrical energy production;
- Et: primary energy for standard thermal energy production;
- ηe: standard electrical efficiency (50% for Italian standard);
- ηt. standard thermal efficiency (90% for condensing boiler);

and considering following simple equations:

$$E_{CHP} = \frac{P_e}{\eta_{eCHP}} = \frac{P_t}{\eta_{tCHP}} \;\longrightarrow\; TER = \frac{P_t}{P_e} = \frac{\eta_{tCHP}}{\eta_{eCHP}} \quad E_e = \frac{P_e}{\eta_e} \quad E_t = \frac{P_t}{\eta_t} \qquad (1)$$

PES calculation follows:

$$PES = \frac{E_e + E_t - E_{CHP}}{E_e + E_t} = 1 - \frac{\frac{P_e}{\eta_{eCHP}}}{\frac{P_e}{\eta_e} + \frac{P_t}{\eta_t}} = 1 - \frac{1}{\frac{\eta_{eCHP}}{\eta_e} + \frac{P_t}{\eta_t}\frac{\eta_{eCHP}}{P_e}} = 1 - \frac{1}{\frac{\eta_{eCHP}}{\eta_e} + \frac{\eta_{tCHP}}{\eta_t}} \qquad (2)$$

Is possible to introduce an equivalent of PES for the economical convenience. Considering:

- €e: electrical energy cost [€/kWh];
- €g: gas energy cost [€/kWh];
- R: €g/€e

Cogeneration Economical Save (CES) is defined as the ratio between the cost saved over the cost of standard solution. Note that electrical energy is valorised after transformation:

$$CES = \frac{€_e \cdot P_e + €_g \cdot E_t - €_g \cdot E_{CHP}}{€_e \cdot P_e + €_g \cdot E_t} = 1 - \frac{€_g \cdot \frac{P_e}{\eta_{eCHP}}}{€_e \cdot P_e + €_g \cdot \frac{P_t}{\eta_t}} = 1 - \frac{1}{R \cdot \eta_{eCHP} + \frac{P_t}{\eta_t}\frac{\eta_{eCHP}}{P_e}} = 1 - \frac{1}{\frac{\eta_{eCHP}}{R} + \frac{\eta_{tCHP}}{\eta_t}} \qquad (3)$$

Table 1 reports PES and CES values of the technology that are the most feasible candidates for microCHP. These are Internal combustion engine (ICE), Stirling engine, polymeric electrolyte membrane fuel cell (PEM) and SOFC based systems. An average indicative value is considered for the efficiencies while R is calculated from Italian electricity and natural gas households price as calculated in Europe Energy Portal [19]. Note that all values are positive, this means that all technologies are more convenient of standard technology both from energetic and economical point of view. Beneath all SOFC remains the most performing solution.

Table 1 PES and CES of different microCHP systems

Technology	η_e	η_{th}	**PES [%]**	**CES [%[**
ICE	0,30	0,60	21	30
Stirling	0,10	0,80	8	13
PEM	0,40	0,50	26	37
SOFC	0,50	0,40	31	42

Finally to evaluate the convenience of the solution the payback time is introduced calculated as the time required to recover with gain the initial cost of the microCHP.

Considering the definition introduced is possible to realize a preliminary sensitive analysis on some of the key parameters. Some of the value, such as initial cost and operating time, are still object of development and investigation, this section aim is only to general consideration on parameters effect. To complete the study three simple parameter referred to building specifics are introduced:

- De: is the dwelling annual electrical consumption;
- Dh: is the dwelling annual heat consumption;
- D_{TER}: is the thermal to electric ratio of the building;

Note that depending on the integration strategies the annual heat consumption can be composed of heating and/or DHW requirement.

To evaluate the optimal size of the microCHP a preliminary study of the impact of operating time was realized. The electrical microCHP size, P_e, was calculated to reach, in operating hours, an annual electrical production of the microCHP equivalent to building requirement. Results are reported in Fig. 2.

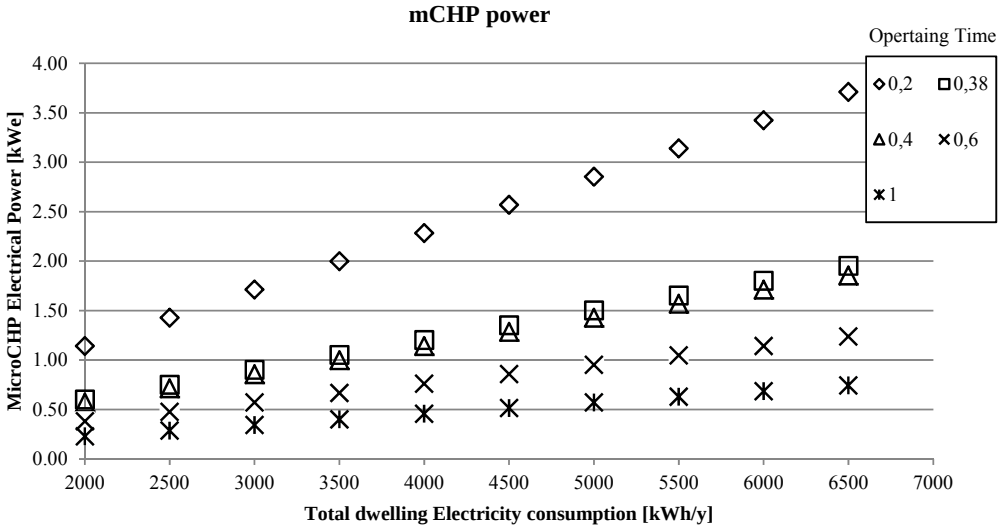

Fig. 2. Electrical power of microCHP for different dwelling consumption and operating time

Increasing operating time, the size of the system decreases due to the distribution of electrical production during the all year. Note that operating time of 0,38 is corresponding to the winter season in Italy (128 days), if the system operates 24h a day. Considering that is very unlikely to operate the system full time, OT = 1, the optimal system size is between 1 and 4 kW. If all the heat produced is used a compare between the building and the system thermal to electric ratio has to be considered. In general is better to have an heat production smaller that required one and introduce an additional boiler.

The effect of thermal building request, operating time, initial system cost and electricity cost are described in Fig. 3, Fig. 4, Fig. 5 and Fig. 6, respectively. Under each graph a table reports the values of the parameters that are kept constant. If not specified in the table P_e is calculated as previously described. In Fig. 4 two different cases are presented: in case 1 extra electricity produced is valorised with market cost while in case 2 is considered lost. Is interesting to notice how this aspect strongly effects payback time relation with operating time. If the system operates with no valorisation of current there is no reason to increase operating time that brings to the production of the only heat with η_{tCHP} that is always lower than η_t. This can justify the decision of dimensioning the system with a total electricity value smaller than De. In general the increase of the economical incoming from electricity, via increase of production, increase of electricity value or of operating time, positively changes the payback time. Note that Fig. 6 describes how electricity cost can effect payback time. Same but opposite study refers to gas cost as the ratio between this two values effect the economic analysis [20].

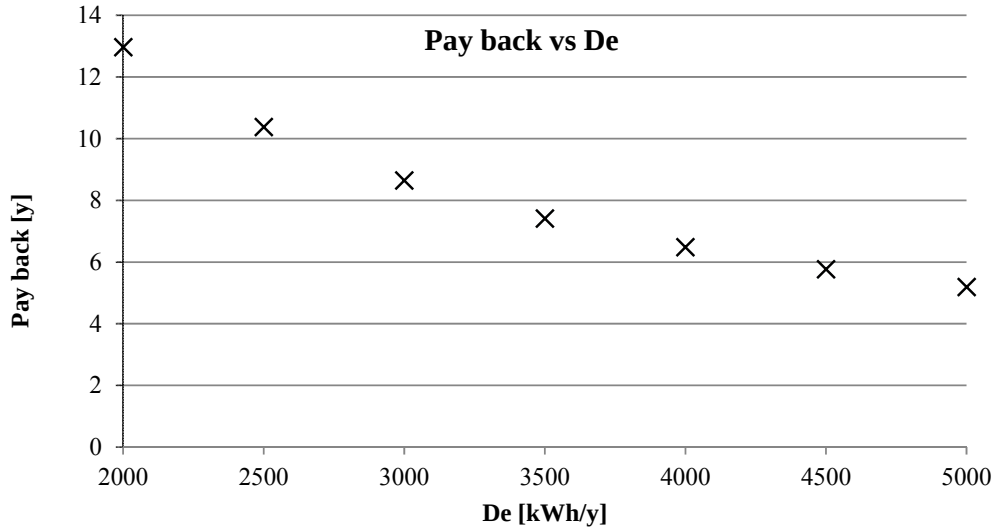

D_{TER}	Uf	TER	ηe	ηt	€e [€/kWh]	€g [€/kWh]	System cost [€]
4	0,38	0,8	0,5	0,4	0,2	0,08	3000

Fig. 3. Pay back vs. Dwelling electrical request

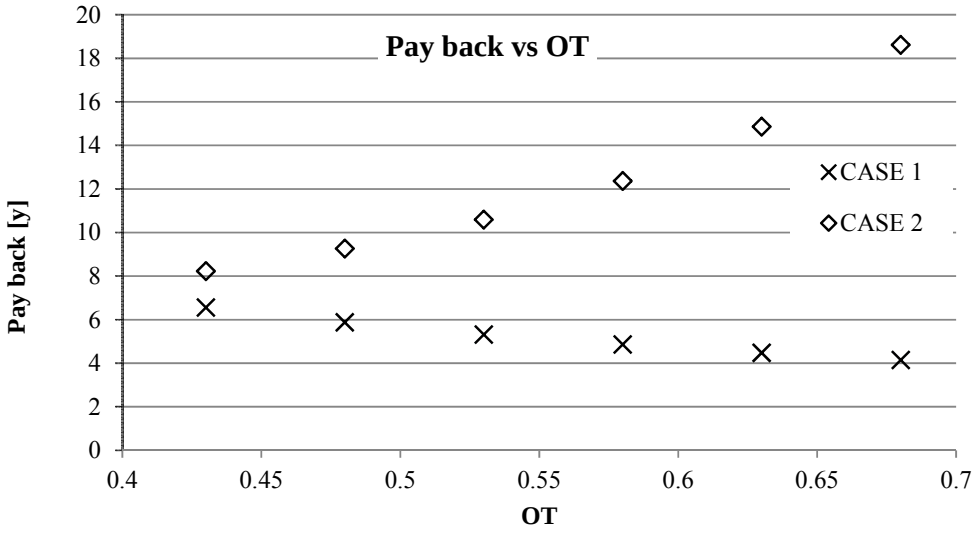

De [kWh/y]	D_{TER}	TER	ηe	ηt	€e [€/kWh]	€g [€/kWh]	System cost [€]
3500	4	0,8	0,5	0,4	0,2	0,08	3000

Fig. 4. Pay back vs. microCHP utilization factor

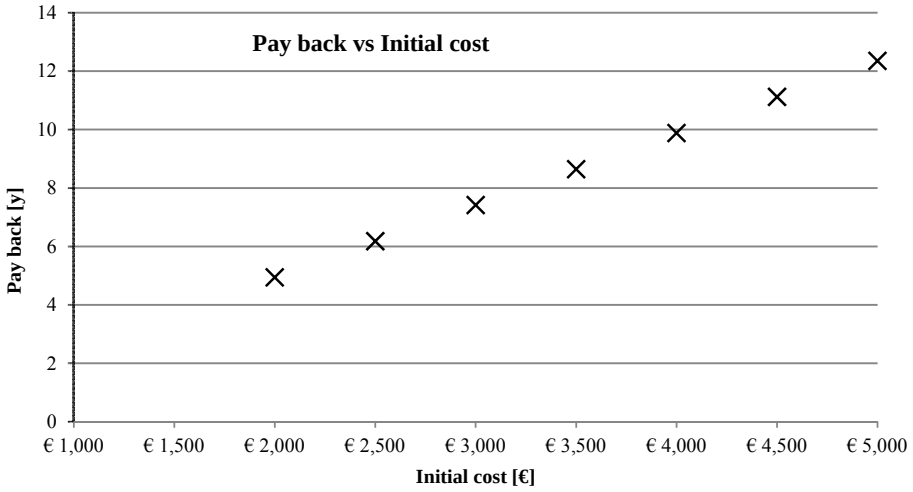

De [kWh/y]	D_{TER}	Uf	TER	ηe	ηt	€e [€/kWh]	€g [€/kWh]
3500	4	0,38	0,8	0,5	0,4	0,2	0,08

Fig. 5. Pay back vs. microCHP initial cost

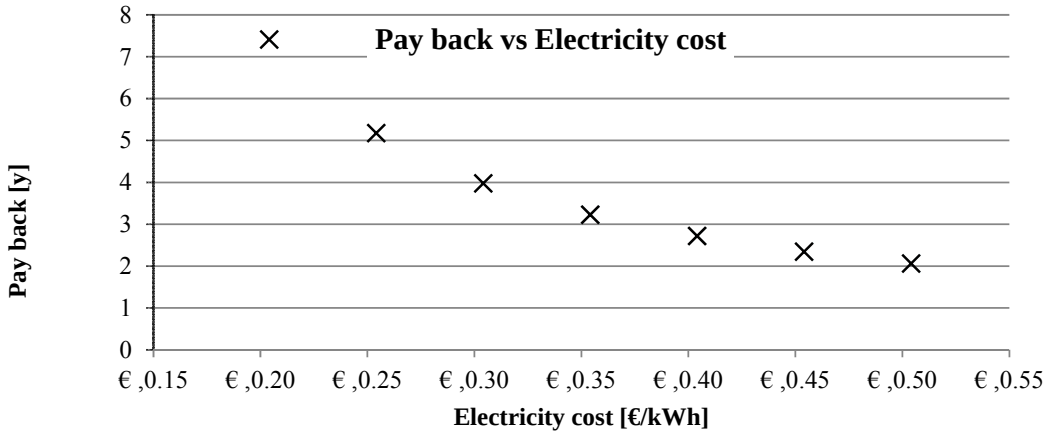

De [kWh/y]	D_{TER}	Uf	TER	ηe	ηt	€g [€/kWh]	System cost [€]
3500	4	0,38	0,8	0,5	0,4	0,08	3000

Fig. 6. Pay back vs. electricity cost

4 Case study

Let's consider a single family house, four people, of 100 m^2 located in Italy close to Perugia: climate area C. Total yearly electrical demand, calculated with VDI standard is 1750 x 4 = 7000 kWh/y. Thanks to the study of the bills of a family leaving in the house we can measure a consume of 6300 kWh/y. Both these values appear to be bigger that what is possible to find in literature [21–23]. Following indication of Annex 42 study [21] an electrical consumption of 3500 kWh can be calculated for an European standard household electricity consumption; this value is used in following calculations as the approach is more safe. Domestic Hot Water consume was calculated with several methods obtained from literature [22], VDI and Italian standard. The values are significantly different and vary from the 500 kWh per person per year up to 2000 kWh. To keep a more safe approach, less consume, we consider VDI values of 500 kWh/py with a total of 2000 kWh/y.

Space heating demand is by far the most sensitive data as it varies with the building insulation properties and family living standards. In Ref [15] a study on 193 building of five countries was performed and an average value of 175 kWh/m^2 was calculated. This value can be easily related to this typology of houses and is also consistent with Italian and German standard indications. Total heat demand is 17.500 kWh/y. Main inputs are reported in

Table .

Table 2 Example main inputs

Parameter	Value
Electricity demand [kWh/y]	3500
Domestic Hot Water [kWh/y]	2000
Annual heating energy demand [kWh/y]	17500
D_{TER}	5,6

Trends described by Italian authority was selected for defining demand profile. This data contain the daily percentage of gas average gas consumed for both heating and DHW. Values are grouped for climate area. Considering house location and typology the energy request was calculated as in Fig. 7.

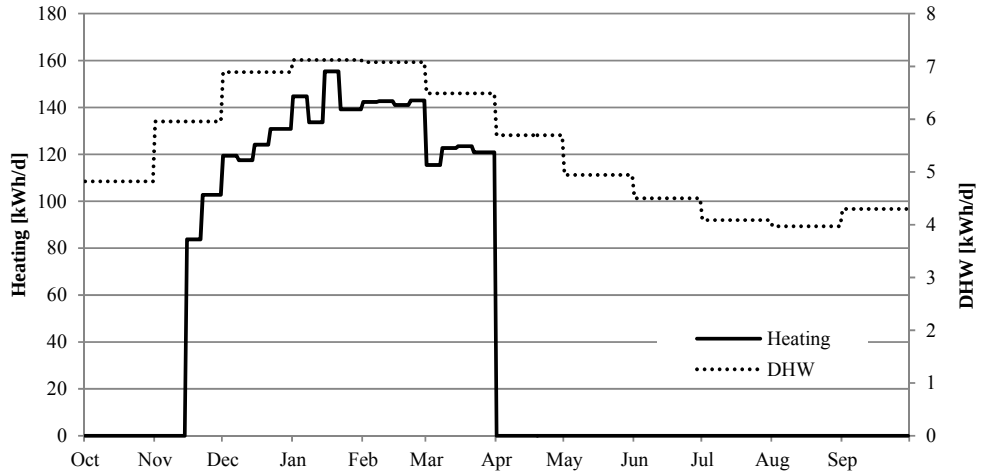

Fig. 7. Heat requirement in one year

The graph shows how the heating period is only during winter time. The exact day are usually defined by local authorities but, in general, are from October 15th to April 1st. Also domestic heat water is not constant during the year and is more concentrated on winter time. Note that in winter time there is a base request of at least 110 kWh/d corresponding to 4,5 kW. Any CHP having a thermal power lower than 4,5 kW can operate continuously during this period. Let's consider a SOFC system, with the efficiency characteristic already presented in Table 1, of 1 kWe and 0,8 kWth. If we consider this unit operating in the house we can build a curve describing operation time during the year. The heat not covered by the CHP is realized with additional boiler. Following graph, Fig 8, presents the load profiles.

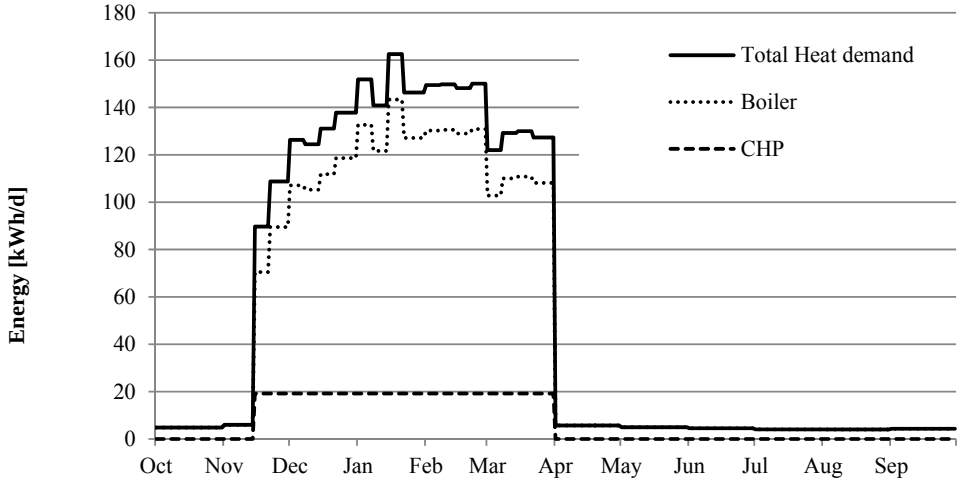

Fig. 8. Load heat profile

We can consider the system operating only during winter time or during the all year following also DHW request. In the second option in summer time the system will operate only the hours necessary to produce required heat that is stored in the water tank. We can imagine that the system operates during the night so that the hot water is ready for daily use. Total operating hours permits to calculate also produced electricity. As previously described this increase of utilization factor gives positive effect only if we give value to extra electricity produced. Table 3 compares three different solutions: only boiler, boiler plus μCHP operating only on winter, and boiler plus μCHP

operating all the time. The table introduces a new parameter: ON/OFF cycle, that is calculated as the number of shut down that have to be performed during the all year.

Table 4 Compare of system performances

Annual parameters values	Boiler + μCHP	Boiler + μCHP winter	Boiler
CHP operating hours [h/y]	4.627	3.288	-
CHP heat production [kW/h y]	3.701	2.630	-
CHP electricity production [kW/h y]	3.823	3.288	-
CHP ON/OFF cycle [/y]	229	1	-
CHP operating time	53%	38%	-
Boiler heat production [kW/h y]	15.799	16.870	19.500

This analysis shows how the utilization of winter solution permits to reduce ON/OFF cycles with a reduction of cogenerated heat and electricity. Is important also to notice how the boiler contribution to total heat remains the main one with values always higher of 85% of total energy. Total CHP electrical energy is always smaller than annual consumed.

The economical analysis can be realized considering following:

- Gas cost is evaluated as defined by Italian gas Authority with decreasing cost per unit with increasing quantity [13];
- Boiler is considered with a primary efficiency of 90% as defined for PES calculations;
- Electricity cost is evaluated as the cost of equivalent amount from regulated market as defined by electricity Italian authority [24];

Following Table presents main results. Pay back calculation was realized considering as CHP cost 3.000 € [18]. This is not the present cost of this technology but it is a feasible future market cost.

Table 4 Results of integration case study

Annual parameters values	Boiler + μCHP	Boiler + μCHP winter	Boiler
Annual electricity cost [€/y]	-299	0	1.328
Annual natural gas cost [€/y]	1.256	1.204	2.446
Total annual cost [€/y]	957	1.204	3.774
Annual saved [€/y]	729	482	-
Payback time [y]	4,12	6,62	-
Saved after 10 years [€]	4.228	1.628	-

In the payback time the cost of the additional boiler is not considered because it is a cost also in a traditional solution and is considered in both cases. As expected the best solution is the first one presented in the table but it's also the farther from the present scenario due to the number of ON/OFF cycle required to the system and the cost equivalence between used and produced electricity.

5 Conclusion

The values of this analysis are extremely interesting and offer an important starting point to perform deeper studies. The aim of this paper was to present a method for projecting the system integration in the building and to give a preliminary evaluation of system convenience. The results are positive and the concept feasibility was demonstrated. A payback time of 4 and 6 years was calculated depending on operating strategies. A deeper study can be realized improving the analysis of house

energy demand and of integration logic. Is important also to design the storage and analyze if project working conditions are confirmed. Finally it could be interesting to make a sensitive analysis on the selected value of efficiencies and power and top introduce maintenance costs that can give an additional significant contribution.

References

[1] Hawkes A. D., and Leach M. A., 2008, "On policy instruments for support of micro combined heat and power," Energy Policy, **36**(8), pp. 2973-2982.

[2] Watson J., Sauter R., Bahaj B., James P., Myers L., and Wing R., 2008, "Domestic micro-generation: Economic, regulatory and policy issues for the UK," Energy Policy, **36**(8), pp. 3095-3106.

[3] Staffell I., Ingram A., and Kendall K., 2011, "Energy and carbon payback times for solid oxide fuel cell based domestic CHP," International Journal of Hydrogen Energy, **37**(3), pp. 1-15.

[4] Peacock a, and Newborough M., 2008, "Effect of heat-saving measures on the CO2 savings attributable to micro-combined heat and power (μCHP) systems in UK dwellings," Energy, **33**(4), pp. 601-612.

[5] Cho H., Mago P. J., Luck R., and Chamra L. M., 2009, "Evaluation of CCHP systems performance based on operational cost, primary energy consumption, and carbon dioxide emission by utilizing an optimal operation scheme," Applied Energy, **86**(12), pp. 2540-2549.

[6] Magri G., Di Perna C., and Serenelli G., 2012, "Analysis of electric and thermal seasonal performances of a residential microCHP unit," Applied Thermal Engineering, **36**, pp. 193-201.

[7] Cho H., Luck R., Eksioglu S. D., and Chamra L. M., 2009, "Cost-optimized real-time operation of CHP systems," Energy and Buildings, **41**(4), pp. 445-451.

[8] Boait P., Rylatt R., and Stokes M., 2006, "Optimisation of consumer benefits from microCombined Heat and Power," Energy and Buildings, **38**(8), pp. 981-987.

[9] Dentice M., Sasso M., Sibilio S., and Vanoli L., 2003, "Micro-combined heat and power in residential and light commercial applications," Applied Thermal Engineering, **23**, pp. 1247-1259.

[10] Lee K. H., and Strand R. K., 2009, "SOFC cogeneration system for building applications, part 2: System configuration and operating condition design," Renewable Energy, **34**(12), pp. 2839-2846.

[11] Tomassetti G., Di Santo D., and Pece M., 2008, Analisi del potenziale della microcogenerazione in Italia.

[12] 4655V., "Reference load profiles of single-family and multy-family for the use of CHP systems."

[13] "http://www.autorita.energia.it/it/docs/09/139-09arg.htm." (Accessed on January 18th 2012).

[14] Beausoleil-Morrison I., 2007, Annex 42 final report an experimental and simulation-based investigation of the performance of small-scale fuel cell and combustion-based cogeneration devices serving residential buildings.

[15] Balaras C., Droutsa K., Dascalaki E., and Kontoyiannidis S., 2005, "Heating energy consumption and resulting environmental impact of European apartment buildings," Energy and Buildings, **37**(5), pp. 429-442.

[16] Harrison J., and Leach M., 2001, Domestic CHP: What are the potential benefits., London.

[17] Hawkes a, and Leach M., 2007, "Cost-effective operating strategy for residential micro-combined heat and power," Energy, **32**(5), pp. 711-723.

[18] Barbieri E. S., Spina P. R., and Venturini M., 2011, "Analysis of innovative micro-CHP systems to meet household energy demands," Applied Energy.

[19] "www.energy.eu." (Accessed on February 4th 2012).

[20] Faber A., Valente M., and Janssen P., 2010, "Exploring domestic micro-cogeneration in the Netherlands: An agent-based demand model for technology diffusion," Energy Policy, **38**(6), pp. 2763-2775.
[21] Beausoleil-Morrison I., 2010, "The empirical validation of a model for simulating the thermal and electrical performance of fuel cell micro-cogeneration devices," Journal of Power Sources, **195**(5), pp. 1416-1426.
[22] Liso V., Zhao Y., Brandon N., Nielsen M. P., and Kær S. K., 2011, "Analysis of the impact of heat-to-power ratio for a SOFC-based mCHP system for residential application under different climate regions in Europe," International Journal of Hydrogen Energy, **36**(21), pp. 13715-13726.
[23] Yao R., and Steemers K., 2005, "A method of formulating energy load profile for domestic buildings in the UK," Energy and Buildings, **37**(6), pp. 663-671.
[24] AEEG, 2011, Relazione annuale sullo stato dei servizi e sull'attività svolta.

The effect of shading of building integrated photovoltaics on roof surface temperature and heat transfer in buildings

Eftychios Vardoulakis* and *Dimitris Karamanis

University of Ioannina, Department of Environmental & Natural Resources Management, Greece,
Corresponding authors: evardoul@cc.uoi.gr, dkaraman@cc.uoi.gr

Abstract:

Urban energy use is strongly correlated with building heating, cooling and ventilation, since almost 40% of total energy use in Europe is consumed in the building sector. Almost half of total energy entering a building comes through the roof. In this study, the shading effect of building integrated photovoltaics (BIPV) on roof heat transfer was examined and quantified. The study was conducted on a university building by using a PV panel tilted on 30° angle, a set of thermocouples, hobo microdataloggers and a fully automated meteorological station. The results show that photovoltaic panels have a high impact on the roof surface temperature with a mean hourly temperature difference of 15 °C between shaded and exposed parts of the roof during the summer time. Furthermore, extensive heat transfer simulation with or without roof integrated photovoltaic shadings revealed the factors influencing the thermal and cooling loads of a building during the year. It was found that photovoltaics can reduce the daily rooftop thermal load and passively save cooling energy during the hot summer days in addition to electricity production.

Keywords:

Rooftop PV, Photovoltaics, Roof Temperature, Heat Transfer

1.Introduction

In countries with elevated temperatures during summer, like Greece, heat is the main problem of human thermal discomfort in buildings. The problem has intensively increased during the last 30 years since the lack of any urbanization plan led to uncontrollable growing with the subsequent environmental impact like the heat island effect in the major Greek cities [1-5]. The effect is lately observed regardless of the city size. Many solutions have been proposed with some of them being partially effective with specific applications today [6-9]. In the proposed solutions, the primary objective is the reduction of the buildings cooling load and the blocking of the temperature rise inside the urban spar during the summertime.

Furthermore, many projects were recently promoted by the Greek authorities with a feed in tariff system in order to increase the photovoltaic installations on building roofs (home systems of less than 10 kW) and eventually lead to their massive utilization. Rooftop building integrated photovoltaics (BIPV) have the potential to become the major alternative basic source of renewable energy in every construction and reduce the CO_2 emissions in urban environment. In this context, much research has been conducted that is mainly focused on the direct use of rooftop BIPV for energy production [10-12]. In contrast, the possible indirect benefits of rooftop PV systems such as building shading of the uncovered surface have received less attention. While a number of simulation studies have been conducted, systematic experimental measurements are limited with the exception of a recent experimental study on the roof temperature variation for a limited time period [13]. For example, it was demonstrated by heat transfer simulation into four different types of roofs, that BIPV can change the thermal resistance of a building by adding or replacing the building elements [14], [15]. For ventilated air gap BIPV, decreases of 46% and

51% occurred for the daily heat-gain and the peak-cooling load compared with the conventional roof. Simulation results also showed that building surface temperature significantly changes while urban canyon air temperature alters only marginally. Also, Yang et al. [16] developed a simulation model for the thermal performance of PV roofs and found that the cooling load component through a PV roof is about 35% of the load of a conventional roof. In the recent experimental study, air temperature sensors and a thermal infrared camera were used and interior and exterior data measurements were collected for three days [13]. Simulations showed no energy gains of the rooftop PV installation during winter (heating load) but more than 38% reduction in annual cooling load was calculated [13]. However, recent comparative simulated impact studies of roof installations [17], provided evidence that white and green roofs are more effective strategies for urban heat island mitigation than their PV covered ones.

In view of the above, the objective of the present study was to systematically investigate the temperature and heat gain variation of a rooftop PV installation on a university building during the summer and gain a better insight in the shading mechanism of roof integrated photovoltaics. PV and roof temperatures as well as meteorological parameters were recorded to estimate the differences into roof heating for shaded and non-shaded roof while the cooling and heating loads throughout the year were determined by extensive heat transfer simulation.

2. Experimental setup

Measurements were conducted in the city of Agrinio (Western Greece) during August 2011, on a building roof of the University of Ioannina. Hobo dataloggers (model: Hobo ProV2) and thermocouples (Omega TMQSS-OM075G-300) connected with a fully automated meteorological station were used to collect the temperature data.

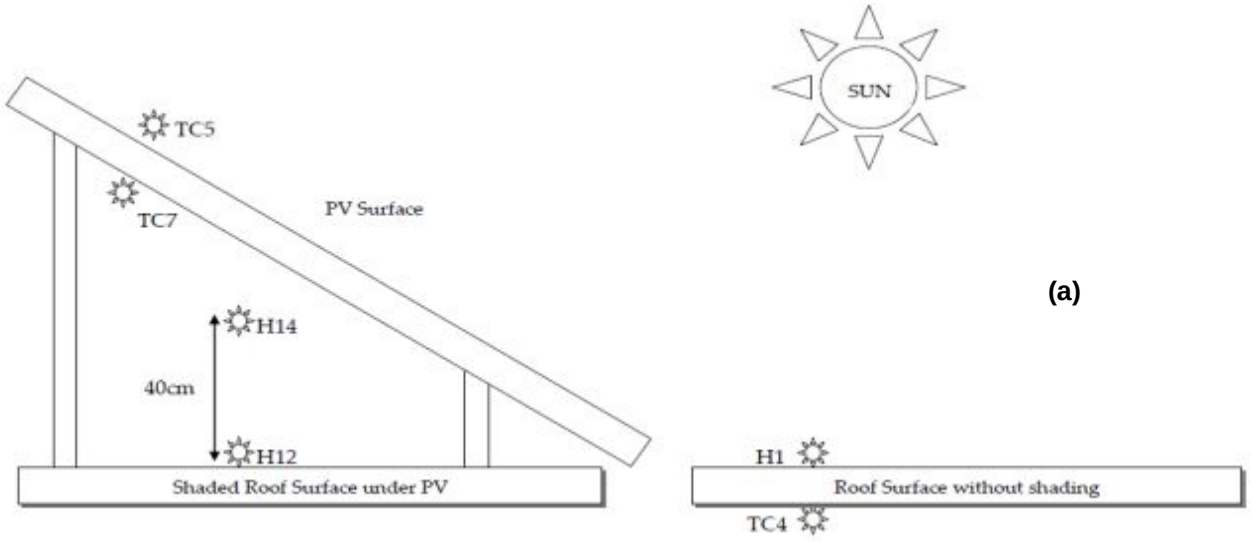

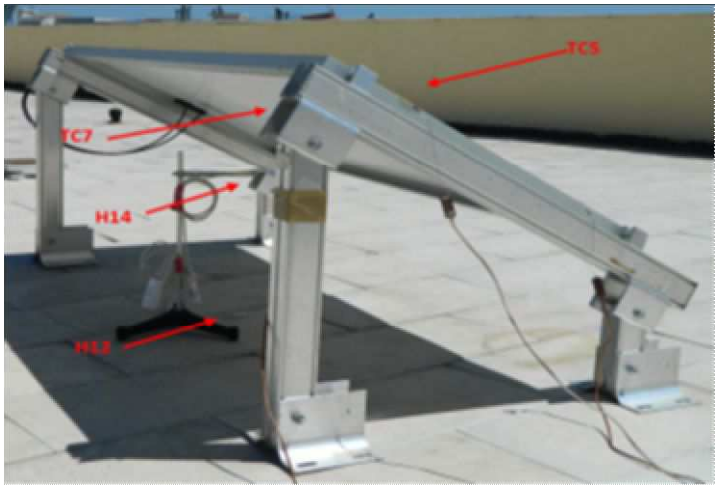

(b)

Figure 1: (a) Layout of hobo sensors and thermocouples (b) Photo from PV array

All thermocouple and meteorological signals were recorded every minute by a CR1000 datalogger (Campbell Scientific). Position and characteristics of each temperature sensor are presented in Figure 1 and Table 1.

Table 1: Position and characteristic of each sensor

Name	Accuracy (^{o}C)	Temperature Range (^{o}C)	Type	Position	Shadow
TC5	0.5	-185 to 300	Omega sensor	On PV array surface	No shading
TC7	0.5	-185 to 300	Omega sensor	Exactly behind the PV array surface	Shaded
H14	0.2	-40 to 100	Hobo Sensor	Under the PV array, 40cm over the roof surface	Shaded
H12	0.2	-40 to 100	Hobo Sensor	Under the PV module, on roof surface	Shaded
H1	0.2	-40 to 100	Hobo Sensor	On exposed roof surface	No shading
TC4	0.5	-185 to 300	Omega sensor	Exactly under the exposed roof shingle	No shading

3. Meteorological conditions

Air temperatures close to 40 ^{o}C and high solar irradiation during the summer are typical for the municipality of Agrinio, indicating the city as an ideal place to study the effects of PV shading on a roof. In the present study, data from 8 to 19 August 2011 were analyzed since it was a sunshine period (clear days without clouds) with high solar irradiation and a significant heat wave reaching air temperatures of 38 ^{o}C. Hourly mean values were exported from all the available datalogger data and were used in the following analysis.

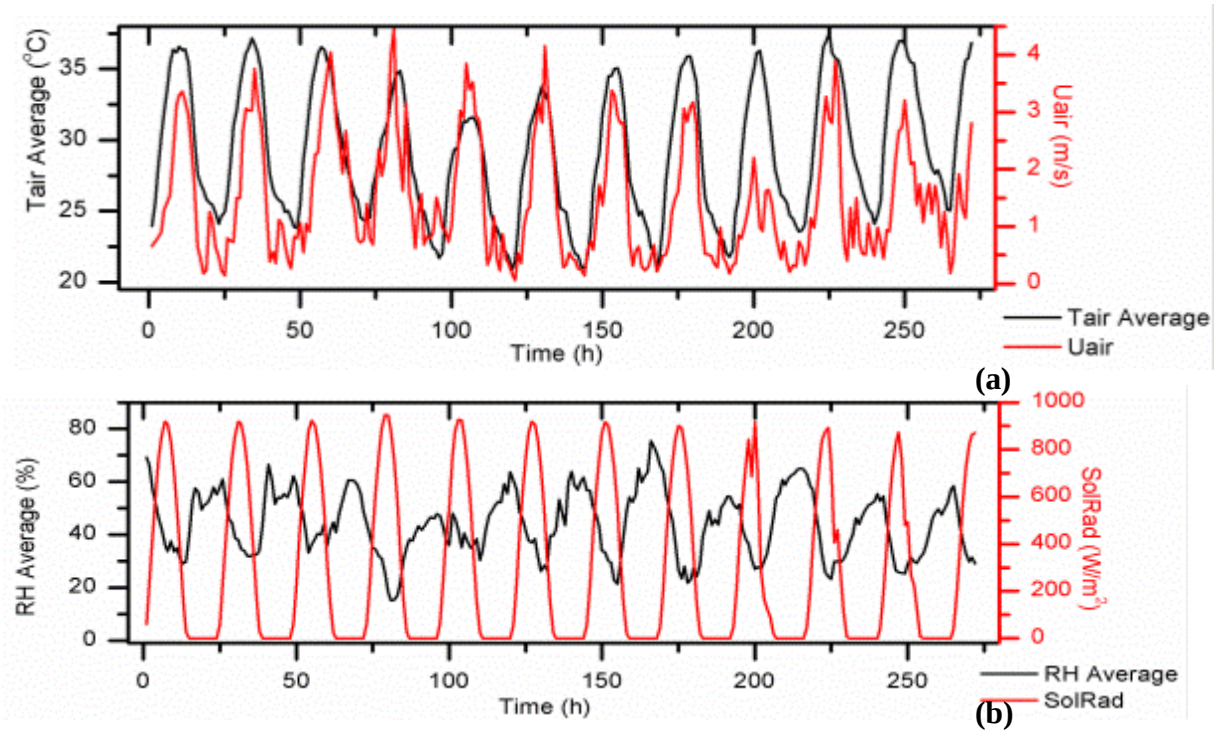

Figure 2. (a) Hourly averaged data of solar radiation and relative humidity during the experimental period. (b) Hourly averaged data of air speed and temperature from 8 to 19 August 2011

Figure 2(a) shows the solar radiation and the relative humidity (range from 30% to 70%) collected data during the testing period, while Figure 2(b) presents the air velocity and temperature data over the roof surface. It is evident from the above figures that solar radiation approached 950 W/m^2 around 1:00 pm on a daily basis while relative humidity varied from 30% to 50% during the daytime and 50% to 75% during the night of the studied period. At the beginning of the day (9:00 am), low wind dominated while wind speed increased to 3.5-4 m/s at noon (1:00 pm) and decreased to less than 1 m/s at the sunset (9:00 pm). In general, the environmental conditions of the testing period were typical for the region of Western Greece and no exceptional weather phenomena were observed.

4. PV and roof temperatures

In Figure 3a, temperature variations for roof surface with PV shading (H12) and exposed roof (H1) are presented. During the daytime, the temperature difference between shaded and exposed roof reached a maximum at 1:00 pm every day. At this time, maximum difference reached 16.2 ^{o}C on the first day of the measurements (8 August 2011) and a minimum difference of 10.7 ^{o}C on the ninth day of the measurements (16 August 2011). The opposite effect was taking place after the sunset till sunrise. Exposed roof (H1) reached lower temperature levels compared to shaded roof (H12). This difference was explained by the increased long wave radiation loss of the exposed roof surface and much more effective cooling during the night, compared to the part of the roof lying under the PV. The reason of the better and faster cooling is the increased sky view factor of the exposed roof, in addition to the shaded roof, proving that PV has also insulating properties. This result is in agreement with similar observations [13].

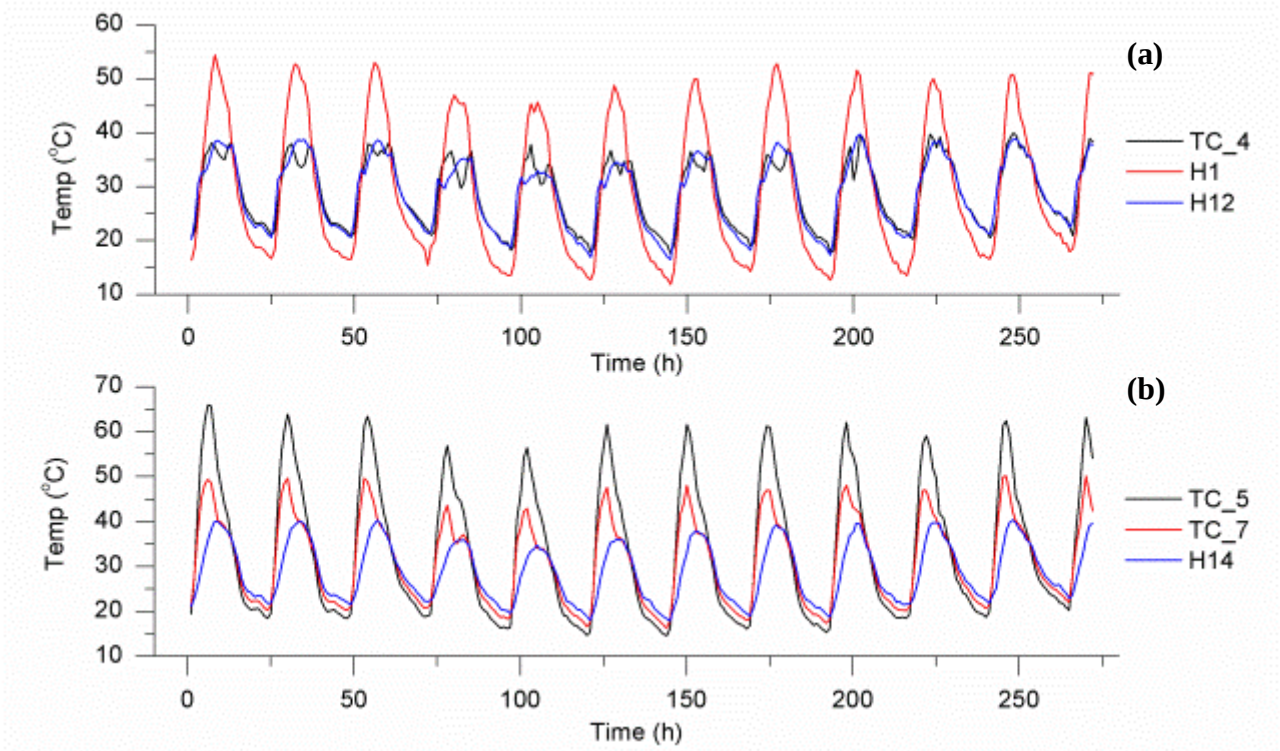

Figure 3. (a) Roof temperatures under exposed roof (TC_4), on exposed roof surface (H1) and under the PV module (H12). (b) PV temperatures over (TC_5) and under (TC_7) PV module surface. Air temperature under the PV module is also presented (H14).

The variability of the roof surface temperature was also daily monitored. On a typical summer day, exposed roof summer temperature started from the value of 16.5 ^{o}C (at 6:00 am) and reached a maximum of almost 55 ^{o}C at noon. In contrast, shaded roof temperature started to rise at 20.3 ^{o}C (at 6:00) and reached a peak at 38.6 ^{o}C (at 1:00 pm). This indicates higher rates of heat absorption from exposed roof that could potentially lead to higher degradation of the roof construction materials and buildings insulation.

Figure 3b shows the temperatures over and under the PV module surface and air temperature between the PV tilted array and the shaded roof surface. PV surface temperature (TC_5) is almost 13 ^{o}C to 15 ^{o}C hotter compared to the temperature exactly under the PV module (TC_7) at the time period of the maximum solar irradiation. This finding indicates that BIPV can act as an extra insulation over the roof during the summertime, absorbing a large amount of heat while simultaneously producing electricity.

5. Heat transfer investigation—impact of the roof integrated photovoltaics on the building's thermal behavior

Following the temperature measurements, a heat transfer simulation analysis was performed to examine the influence of BIPV in the building's cooling and heating loads during the year. The DesignBuilder [18] building energy simulation tool was used to study the shading effect of BIPV. The calculation method of the programme is based on the EnergyPlus simulation engine [19]. Due to the long time period availability and similar characteristics, Athens was selected as the simulation location and the weather data of Helenikon were used as the input meteorological parameters. A two-floor residence building of rectangular shape and 81 cm^2 flat roof was adopted for the simulation. For simulating the PV shading, six component blocks of 0.73x5.23x0.11 m^3 and high thermal and solar absorptance were installed on the flat roof at a tilt angle of 30 °. The building's energy consumption was simulated for the whole year before and after installing the PV. The set point temperature values were considered to be equal to 20 °C for the heating period

and 25 °C for the cooling period of the year. The later is higher than the value of 23.3 °C that Dominguez et al. used [13] but closer to typical values of similar studies with green roofs [20]. Double glazed windows with metal frames were considered to cover the 20% of building's surface area in each floor with typical HVAC equipment in the building. The primary outputs of the program were the cooling and heating loads of the whole building as well as the two floors separately.

Initially, the effect of the roof structural materials on the heating and cooling loads was studied. It was observed that the difference between the cooling and heating loads was maximized with the increase of the roof insulation and reflectivity. Therefore, the roof experimental conditions of 6.5 cm XPS extruded polystyrene insulation and white concrete tile covering were subsequently selected to study the monthly cooling and heating loads. Load variations as a percentage (%), because of the BIPV shading effect for the whole building and its second floor are shown in Table 2. The recorded negative values correspond to a decrease in cooling load during seven months with the BIPV installation. The cooling load reduction varied between 3.9% and 8% for the whole building while the reduction reached the value of 15.4% for the last floor. Therefore, the present study indicates that the roof BIPV leads to passive energy savings for an extended time period in addition to energy production for specific environmental conditions. Since any intervention aiming at reducing the cooling load of a building, causes an increase of its heating load, the simulation study was extended to the winter months as well. Indeed, the heating load variation after the PV installation was not negligible and reached a maximum load increase of 13.3% at March for the whole building and 21.0% for the second floor. However, it was quite small for the two main winter months of the peak heating loads, suggesting the overall beneficial shading effect of roof integrated photovoltaics. Moreover, the current simulation results agree with the results of Genchi et al. [21] but did not confirm the high percentages of cooling savings simulated by Dominguez et al. [13] or Wang et al. [14]. Therefore, loads variation is highly sensitive to the selection of the environmental parameters for the particular location, PV tilt angle installation and the building structural materials. Thus, it is proposed that a detailed simulation of the building energy loads should be performed before the BIPV installation at a particular building of a specific location in order to optimize their positive shading effects in addition to their energy production.

Table 2. The cooling and heating load variation as a percentage (%), for the whole building, as well as its second floor.

Month	**Cooling load variation (%) for the whole building**	**Cooling load variation (%) for the 2nd floor**	**Heating load variation (%) for the whole building**	**Heating load variation (%) for the 2nd floor**
January			2.9	2.7
February			13.1	16.6
March			13.3	21.0
April	-8.0	-15.4		
May	-6.0	-10.8		
June	-4.5	-7.6		
July	-3.9	-6.0		
August	-3.9	-6.2		
September	-4.2	-7.2		
October	-4.3	-8.4		
November			3.9	5.1
December			5.0	7.2

6. Conclusions

An eleven day time period of roof temperature measurements at several positions was analyzed to estimate the impact of BIPV on the roof surface temperature of a university building. The results provided direct evidence on the insulating properties of PV modules since shaded roof area achieved 16 ^{o}C lower surface temperature than the corresponding of uncovered roof under high solar irradiation. Combined with the simulation suggestions of the overall annual beneficial shading effect for the studied environmental and building conditions, the installation of PV panels on rooftops could indirectly decrease the cooling energy requirements on hot summer days in addition to the CO_2 free electricity production.

Acknowledgments

The research Project is co-funded by the European Union - European Social Fund (ESF) & National Sources, in the framework of the program "HRAKLEITOS II" of the "Operational Program Education and Life Long Learning" of the Hellenic Ministry of Education, Life Long Learning and religious affairs

NOMENCLATURE

BIPV building integrated photovoltaic

h hours

HVAC heating, ventilation and air-conditioning

PV photovoltaic

RH relative humidity (%)

SolRad solar radiation (W/m^2)

T_{air} air temperature (^{o}C)

U_{air} air speed (m/s)

XPS extrunded polysterene foam

References

[1] Santamouris, M.,Papanikolaou, N., Livada, I., Koronakis, I., Georgakis, C., Argiriou, A., Assimakopoulos, D.N., On the impact of urban climate on the energy consumption of buildings. Solar Energy 2001;70(3):201-216.

[2] Giannopoulou K., Livada I., Santamouris M., Saliari M., Assimakopoulos M., Caouris Y.G. On the characteristics of the summer urban heat island in Athens, Greece. Sustainable Cities and Society 2010;1(1):16-28.

[3] Papanastasiou D. and Kittas C., Maximum urban heat island intensity in a medium-sized coastal Mediterranean city. Theoretical and applied Climatology, accepted July 2011.

[4] Kolokotsa D., Psomas A., Karapidakis E., Urban heat island in southern Europe: The case study of Hania, Crete. Solar Energy 2009; 83 :1871-1883.

[5] Vardoulakis E., Karamanis D., Mihalakakou G., Assimakopoulos M.N., Heat island effect in Western Greece: results, statistical analysis and discussion. In: Kungolos A., Karagiannidis A., Aravossis K., Samaras P., Schramm K.W., editors. Cemepe 2011: Proceedings of the third International Conference on Environmental Management, Engineering, Planning and Economics; 2011 June 19-24; Skiathos.

[6] Vardoulakis E., Karamanis D., Assimakopoulos M.N, Mihalakakou G., Solar cooling with aluminium pillared clays. Solar Energy Materials and Solar Cells 2011; 95(8): 2363-2370.

[7] Synnefa A., Santamouris M., Livada I., A study of the thermal performance of reflective coatings for the urban environment. Solar Energy 2006; 80(8): 968-981.

[8] Meng Q., and Hu W., Roof cooling effect with humid porous medium. Energy and building 2005; 37(1): 1-9.

[9] Alvarado J.L., Terrell Jr.W., Johnson M.D., Passive cooling systems for cement-based roofs. Building and Environment 2009; 44(9): 1869-1875.

[10] Strzalka A., Alam N., Duminil E., Coors V., Eicker U., Large scale integration of photovoltaic in cities. Applied Energy 2012; Article in press.

[11] Cheng C.L., Chan C.Y. and Chen C.L., Empirical approach to BIPV evaluation of solar irradiation for building applications. Renewable Energy 2005; 30(7): 1055-1074.

[12] James P.A.B, Jentsch M.F., Bahaj A.S., Quantifying the added value of BIPV as shading solution in atria. Solar Energy 2009; 83(2): 220-231.

[13] Dominguez A., Kleissl J., Luvall J.C., Effects of solar photovoltaic panels on roof heat transfer. Solar Energy 2011; 86(9): 2244-2255

[14] Wang Y., Tian W., Ren J., Zhu L., Wang Q., Influence of a building's intergrated-photovoltaics on heating and cooling loads. Applied Energy 2006; 83: 989-1003

[15] Tian W., Wang Y., Xie Y., Wu D. Zhu L., Ren J., Effect of building integrated photovoltaics on microclimate of urban canopy layer

[16] Yang H., Zhu Z., Burnett J., Lu L., A simulation study on the energy performance of photovoltaic roof , ASHRAE Transactions 2001; 107 (2): 129-135

[17] Scherba A., Sailor D.J., Rosenstiel T.N., Wamser C.C., Modeling impacts of roof reflectivity, integrated photovoltaic panels and green roof systems on sensible heat flux into the urban environment. Building and Environment 2011; 46: 2542-2551

[18] DesignBuilder documentation, DesignBuilder user manual, version 3. UK: DesignBuilder Software Limited, 2011

[19] Crawley D.B., Lawrie L.K., Winkelmann F.C., Buhl W.F., Huang Y.J., Pedersen C.O., EnergyPlus: creating a new-generation building energy simulation program. Energy and Buildings 2001; 33 (4) : 319–331

[20] Santamouris M., Pavlou C., Doukas P., Mihalakakou G., Synnefa A., Hatzibiros A., Patargias P., Investigating and analyzing the energy and environmental performance of an experimental green roof system installed in a nursery school building in Athens, Greece. Energy 2007; 32, :1781-1788

[21] Genchi Y., Ishisaki, M., Ohashi, Y., Takahashi, H. and A. Inaba A., Impacts of Large-Scale Photovoltaic Panel Installation on the Heat Island Effect in Tokyo. 2003; Fifth Conference on the Urban Climate

The influence of glazing systems on energy performance of non-residential buildings

Cinzia Buratti[a], Elisa Moretti[b] and Elisa Belloni[c]

[a] *Department of Industrial Engineering, University of Perugia, Perugia, Italy, cburatti@unipg.it*
[b] *Department of Industrial Engineering, University of Perugia, Perugia, Italy, moretti.unipg@ciriaf.it*
[c] *Department of Industrial Engineering, University of Perugia, Perugia, Italy, belloni.unipg@ciriaf.it*

Abstract:

Glass façades have an important role in buildings both for daylighting and thermal comfort. Many studies showed that health, comfort and productivity are improved due to access to natural light. Moreover the thermal and solar transmittance, the size and the orientation of the windows are very important in the energy use in buildings. The aim of the paper is to evaluate the influence of glass components in energy saving for non-residential buildings. A multifunctional building was investigated and a dynamic thermal model was implemented by means of EnergyPlus software. The energy demand was estimated in different climatic conditions and for different building orientations both for heating and cooling. The weather data of five Italian cities (Perugia, Rome, Palermo, Milan, Bolzano) were considered. In order to evaluate the impact of windows, different kind of glazings were selected: double-glazing with low-e coating and sunlight control double glass windows. Moreover, innovative glazing systems with silica aerogel (pane and granular) in interspace were investigated as a solution for energy saving in buildings. Finally, also the effects of blind systems on the façades were evaluated.

Results showed that not only the thermal transmittance but also the solar transmittance of glazing has a large effect on thermal comfort and energy demand, depending on the chosen locality. The dynamic building models implemented in EnergyPlus software are very powerful tools and could allow to select for each scenario appropriate fenestration types, thanks to an accurate balance between energy consumption, thermal comfort and daylighting needs.

Keywords:

Building thermal performance, Energy saving, Glazing, Solar radiation, Thermal comfort

1. Introduction

Commercial and office buildings have large glass windows to provide a physical and visual connection to outside. Windows are important both for a nice view and for creating a comfortable indoor environment. Nevertheless, in the highly glazed buildings the energy demand, above all in summer, is greater than the one for buildings with conventional façades, since the glazing systems have thermal performance lower than opaque walls and are influenced by radiation [1]. Often the most effective glazing systems are characterized by low solar transmittance: they could be useful to control solar gains during summer, but in winter the reduction of solar gains can increase the heating energy demand. In this context, the unsteady state simulation programs could represent powerful tools in order to investigate the influence of different glazing solutions on thermal energy balance of the building, depending on the climate conditions [2]. The most appropriate design option could be selected considering also the shape and the exposure of the building [3].

The aim of the present paper is the energy demand analysis of a multifunctional building and the influence of different design options. The available dynamic simulation programs represent a powerful tool for evaluating the thermal and energetic performance of buildings. In the present study the building energy simulation software EnergyPlus was used.

The simulations were carried out varying the type of glazing and orientation; since the cooling demand is strongly affected by the external climate conditions, the study was performed for different climatic zones in Italy. Results were compared in terms of monthly and annual energy demand considering also the influence of different types of innovative glazing systems.

2. The case study

The case study follows a multifunctional building, built in 2005 in Perugia suburb. It consists of one basement and two floors; each floor consists of ten zones. The building has a roof garden. The total height of the building is about 10 m. The east and west façades are smaller than the others; they receive less solar radiation and at a low incident angle. A reference building was considered in the present paper, simplifying the real one and considering eight zones; the 3D model is shown in Fig.1.

A coffee bar and some shops are at the floor level, offices upstairs. Warehouses and garages are on the basement. Two room types were considered for the simulations: an office room (P1) at the first floor and a commercial one (T1) at the ground floor. Only the zones with three sides exposed to outside conditions were considered in the analysis (Fig.1). Each ground floor zone has a total area of 132 m^2; the first floor zones have a 'L' shape and a total area of about 100 m^2. The T1 zone presents a large glass wall in the south façade, for a total area of 21.5 m^2 and a door in the opposite side. Also the office zone has a large glazing in the south façade (21.5 m^2) and three windows in the opposite wall; the south façades have venetian blinds, slat-type devices with a slat-angle control mechanism. The offices have a courtyard on the back side. Outer stairs allow the access to the first floor. Windows have a sound insulating glazing system (total thickness 0.032 m). The thermal transmittance of the building opaque envelope is about 0.25 W/(m^2K). The front side walls have a copper facing; the back side walls have a black plasterwork. Moreover, 0.04 m of heat and sound insulating material are provided in perimeter walls. The first and the ground floor are clay/cement mix with insulation board. The room height is 3 m and the distance between floors is 3.5 m. The partition between zones is a gypsum plasterboard wall with a 0.2 m thickness layer of concrete block; its thermal transmittance is 0.70 W/(m^2K). The opaque envelope and glazing systems features are reported in Table 1.

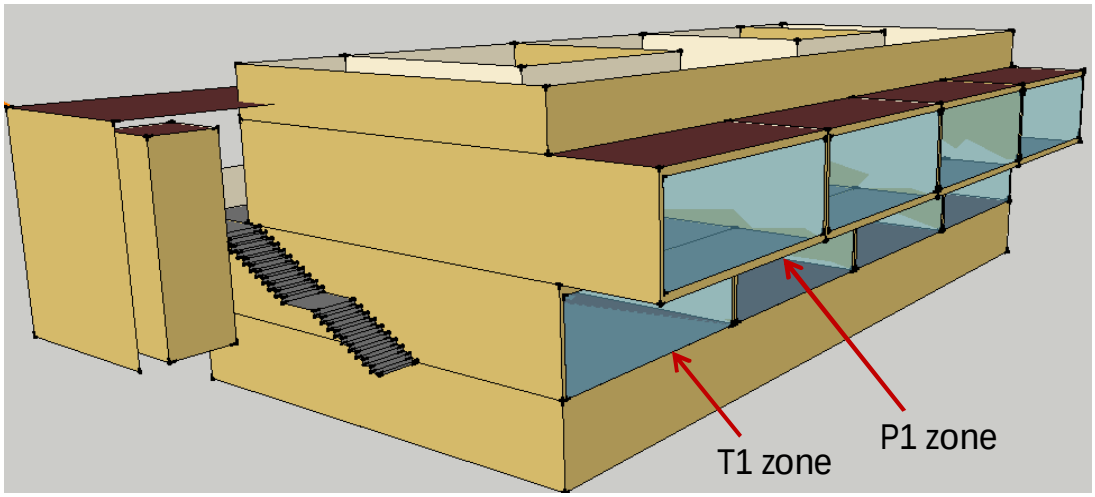

Fig. 1. 3D model implemented in EnergyPlus.

Table 1. Opaque envelope and glazing features.

Building element	*Thickness [m]*	*U – thermal transmittance [W/m^2K]*
External Wall – north façade	0.44	0.25
External Wall – south façade	0.56	0.22
Internal Wall	0.45	0.70
First floor	0.52	0.40
Roof garden	0.95	0.27
Roof	0.52	0.46
Ground floor	1.32	0.46
Glazing	0.32	2.70

3. Methodology

3.1. Building simulation model

The building performance was evaluated by means of EnergyPlus. It is a building energy simulation program; various components of building dynamics such as heating, cooling, lighting, ventilation, and energy flows can be modelled in EnergyPlus [4] and thermal loads are calculated by the heat balance method. This method takes into account all heat balances on outdoor and indoor surfaces and transient heat conduction through the building. The heat flux is evaluated by means of finite difference (FDM) and transfer function (TFM) methods. In order to predict the solar radiation on tilted surfaces, Perez model is used [5]. Several alternative methods are also proposed for defining windows and other fenestration systems in modelled buildings [6,7]. The building 3D model was implemented by means of Google SketchUp, which allows to input the geometric information.

3.2. Weather data

This building energy simulation software uses its own climate data files. The weather data are in the TMY (Typical Meteorological Year) format and they include direct normal solar radiation, global solar radiation on horizontal plane, dry bulb temperature, relative humidity, wind velocity and direction. Data are related to 1980-2005 period and they are available in the Literature. The five climatic zones investigated in this study are (see Fig.2): Perugia, Rome (middle Italy), Palermo (southern Italy), Milan, and Bolzano (northern Italy); latitude and longitude are reported in Table 2.

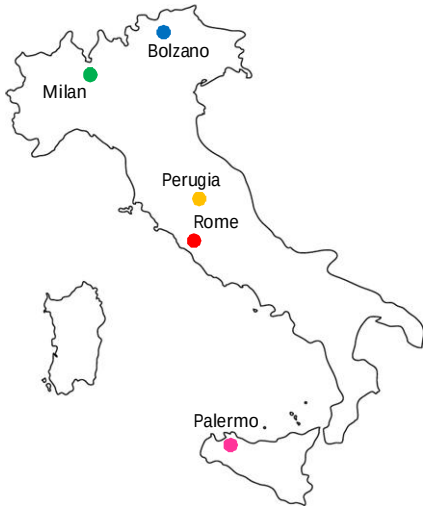

Fig. 2. The map of Italy: the geographical positions of the different examined cities.

Table 2. Monthly mean value of external air temperature and global solar radiation for five different Italian cities.

Month	***Perugia*** *43°4'N – 12°30'E*		***Rome*** *41°47'N – 12°13'E*		***Palermo*** *38°10'N – 13°6'E*		***Milan*** *45°7'N – 8°43'E*		***Bolzano*** *46°28'N – 11°19'E*	
	T [°C]	*Rad [Wh/m²]*	*T [°C]*	*Rad [Wh/m²]*	*T [°C]*	*Rad [Wh/m²]*	*T [°C]*	*Rad [Wh/m²]*	*T [°C]*	*Rad [Wh/m²]*
JAN	4.3	1152	8.3	1625	12.7	2079	0.3	1227	-1.1	943
FEB	5.4	1744	9.0	2564	11.8	3029	2.2	1870	2.0	1443
MAR	7.3	2928	10.6	3704	13.8	4164	7.5	3338	7.2	2600
APR	11.0	4272	13.3	4669	15.7	5621	10.9	3993	11.8	3631
MAY	15.4	5506	17.6	5761	19.1	6532	16.3	5607	16.2	4686
JUN	19.5	6108	21.2	6338	22.8	7268	19.7	5925	18.9	5320
JUL	22.3	6103	24.2	6805	25.5	7328	23.1	6827	21.0	5103
AUG	22.1	5125	24.4	5793	27.0	6617	22.2	5278	19.9	4282

SEP	18.5	3731	21.5	4444	24.1	4941	17.6	3783	17.2	3290
OCT	13.5	2332	17.0	2873	21.6	3662	12.5	2186	10.6	1924
NOV	9.5	1364	12.8	1908	17.2	2129	6.5	1316	4.6	974
DEC	5.3	981	9.4	1476	13.9	1811	2.2	978	-0.1	803

Table 2 shows the monthly mean values of the climatic data for the chosen cities. The maximum global solar radiation is related to Palermo (1681 kWh/m^2 per year), the minimum value (1067 kWh/m^2 per year) to Bolzano. During the summer period the external temperatures of Perugia, Milan and Bolzano are not very different; on the contrary the differences exceed more than 5°C in winter. The maximum values for external temperatures are registered for Palermo; the monthly mean external air temperature is 27° C in August.

3.3. Data and assumptions

Annual simulations were carried out for the reference building. The time step used in the simulations was 60 minutes. The convection coefficients were assumed equal to 20 W/m^{2}K for the external side and 5 W/m^{2}K for the internal one, according to UNI EN ISO 6946 [8]. Opaque building surfaces were assumed to be diffusely reflecting, whereas windows were assumed to allow specular reflection. The reflectance values for opaque surfaces were calculated from the solar and visible absorptance values of the outer material layer of the building envelope. The direct and diffuse solar radiations on the internal surfaces were distributed on the base of absorbance weighted area ratios [9].

The external wall, exposed to outside temperature conditions, was considered a heat exchanged surface (*Outdoors* is the outside boundary condition). The tested rooms represent single thermal zones; the walls between the rooms were modelled as internal surfaces and they were matched in the entire model. The floor between the basement and the low ground is an internal floor and it separates the tested rooms from a no-conditioned zone. The floor surface of the basement is exposed to the ground. A typical temperature trend was assigned to the basement, considering the external climatic conditions of the different cities.

The occupancy of five persons was assumed for the offices (P zones) and ten persons were considered for the T zones (ground floor zones) as internal loads. The presence of occupants was considered from 9.00 am to 7.30 pm for the offices and from 8.00 am to 8:00 pm for the shops every workday. The occupancy was not considered during Christmas and summer vacations. The activity level was assumed 1 met (108 W/occupant) for sitting occupants. Internal gains from lighting were taken as 3 W/m^2 for all the zones, in compliance with UNI TS 11300 standard. The schedule assumed for the use of the lights and equipment was from 8.00 to 10.00 am and from 5.00 to 7.00 pm for a typical workday. During these periods, only a 70% of the total lighting installed power was assumed, because the lights could not be turned on at the same time. During the week end no use of lights or equipment was assumed.

The considered ventilation rate was 0.68 ACH (air changes per hour) for the offices and 0.80 ACH for the ground floor zones. Moreover, in order to evaluate the annual energy demand, the ventilation rate was not considered when the HVAC system is turned on.

In the simulation, the city, the building's orientation and the façade elements (window type, shading devices, etc.) were changed, while other parameters such as building's shape, occupants' activity and schedules were the same.

For the energy demand evaluation, the cooling period was considered the same for the five cities, May 1st – September 30th. Room air set-point temperature is also based on occupancy schedules, with a daytime (7.00 am - 7.00 pm) set point of 26°C in cooling period. Different heating periods were considered for the cities. According to the Italian statutory requirements [10] in Perugia and Milan the heating period is October 15th - April 15th, in Rome it is November 1st – April 15th, in Palermo it is December 1st – March 31st, and for Bolzano it is October 1st - April 30th. The daytime set-point temperature is 20°C during the heating period. The heating and the cooling systems were switched off during the night.

4. Results and discussion

Due to the large amount of simulated building alternatives, only some representative cases related to the total energy use are presented.

In this paragraph most of the simulated alternatives are compared in order to evaluate the influence of the different parameters on the energy use [11]:

- the orientation of the building;
- the climatic zone;
- the kind of glazing.

Three different glazing surface orientations were included in this study: south, east and west. The building energy behaviour was studied in the climatic and solar radiation conditions of Perugia, Rome, Palermo, Milan, and Bolzano (different climatic zones).

Finally the energy performance of different glazing systems was investigated. The results are summarized in paragraph 4.3.

Also the shading effects of venetian blinds were accounted on the south faced transparent surfaces, only for the south façades of the offices (first floor zones).

4.1. Influence of the building orientation

The building orientation has high influence on energy use due to the large glazing façade exposure [3]. The different building orientations analysed for Perugia are the South-East 17° (the real condition), East and West orientation. For the real orientation, the monthly energy demand related to the two zones (T1 and P1) are reported in Table 3. Mainly due to the higher sunlight exposition, the first floor tends to be warmer than the ground floor. For the reference building the energy demand for heating T1 zone is about 3300 kWh, while the winter energy demand for P1 is 1768 kWh per year. The first floor is more exposed to sunlight than the ground floor, as shown in figure 1. So P1 zone has the highest summer energy demand (4716 kWh); the annual energy cooling demand is only 627 kWh for T1.

Table 3. Monthly energy demand for the reference building (kWh) – *Perugia, south-east exposure.*

Month	*T1 zone [kWh]*	*P1 zone [kWh]*
JAN	798	528
FEB	663	339
MAR	575	176
APR	129	0
MAY	0	509
JUN	54	824
JUL	306	1230
AUG	215	1208
SEP	53	945
OCT	7	0
NOV	306	115
DEC	802	609
TOTAL	**3908**	**6484**

In Fig.3 the annual energy demand for different exposures is compared for each month. The winter energy demand is similar for west and east exposures and it is higher than the one for south-east. For T1 zone the maximum summer energy need is for east exposure (1235 kWh); the minimum value is 627 kWh (south-east exposure). For the first floor (P1 zone) the maximum heating need is

for east exposure (3032 kWh); the total cooling energy demand is not very different for the several orientations (4472 - 4485 kWh), even if they have a different distribution in the summer months. In fact not only the glazing façade, but also the effects of the three windows in the opposite side are important. So the maximum monthly energy demand is for west exposure during the summer period, while the highest monthly heating demand is for east.

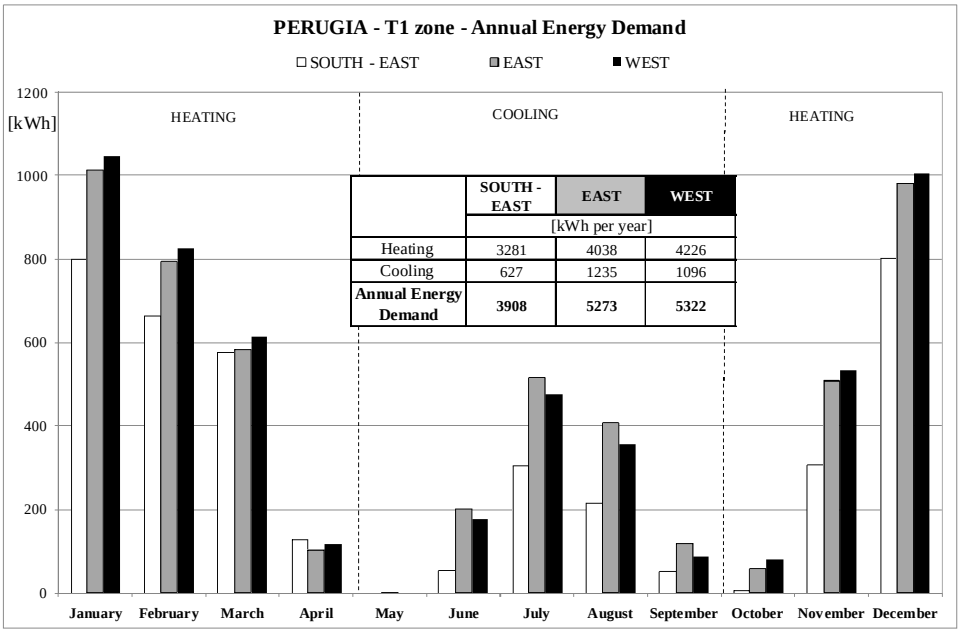

	SOUTH - EAST	EAST	WEST
	[kWh per year]		
Heating	3281	4038	4226
Cooling	627	1235	1096
Annual Energy Demand	**3908**	**5273**	**5322**

(a)

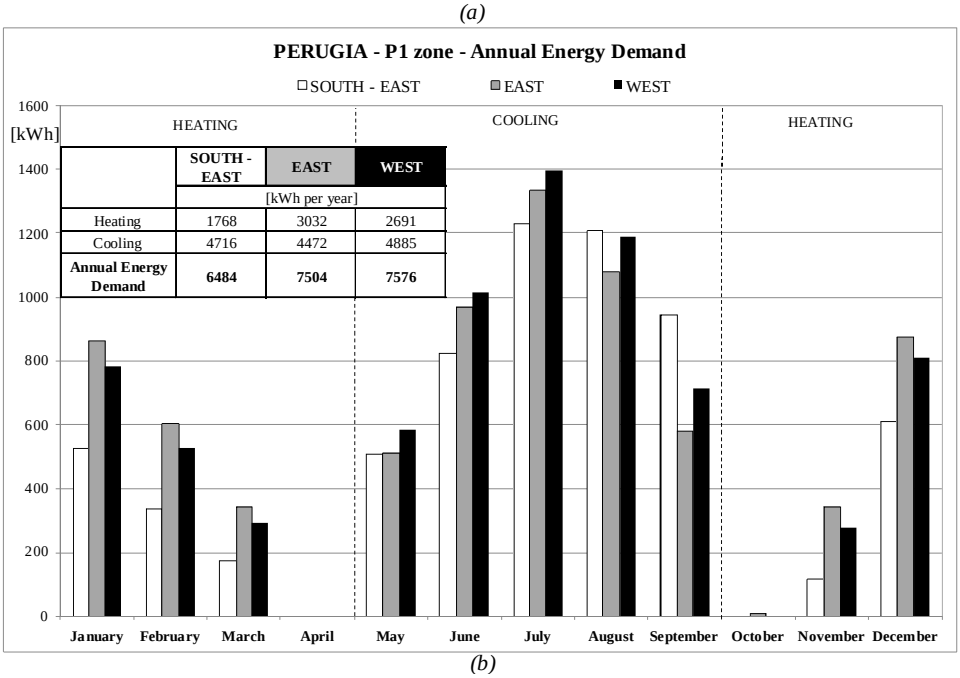

	SOUTH - EAST	EAST	WEST
	[kWh per year]		
Heating	1768	3032	2691
Cooling	4716	4472	4885
Annual Energy Demand	**6484**	**7504**	**7576**

(b)

Fig. 3. Influence of building exposures on energy monthly demand: (a) T1 zone, (b) P1 zone.

4.2. Influence of the climatic zone

The energy monthly demand, both in winter and in summer, was estimated in different climatic conditions. Only the south-east orientation of the glazing façades was considered in this analysis.

Figure 4 shows the influence of the building location on the energy annual demand.

For both the zones the cooling energy demand of Milan is higher than the one of Perugia; in fact the city of Milan has a mean global solar radiation higher than Perugia during the summer period, while the maximum temperature values are very similar.

The heating energy demand values show a very wide variation between the quite null values for Palermo and about 5000 kWh per year for Bolzano.

For T1 zone no cooling is required in May considering the exposure of the glazing which is partially screened from the first floor. During the mid-season period (April and October) the monthly heating energy demand does not exceed 180 kWh for all the cities. In P1 zone the annual energy demand values vary in the range 6146 - 7617 kWh per year. The minimum value is required for Rome, the maximum one for Bolzano because of its high heating energy demand value (3568 kWh per year). Winter energy demand peak values are obtained in January and in December for Bolzano (about 1200 kWh). Everywhere no heating is required for P1 in April. No heating is required for Palermo from October to April, because of the warm climate and the high solar radiation contribute.

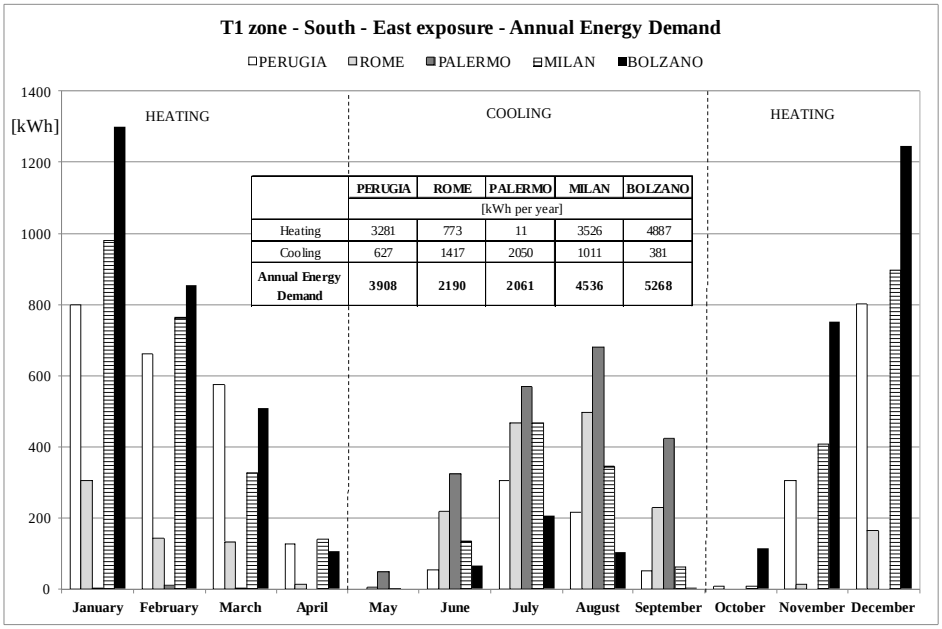

	PERUGIA	ROME	PALERMO	MILAN	BOLZANO
	[kWh per year]				
Heating	3281	773	11	3526	4887
Cooling	627	1417	2050	1011	381
Annual Energy Demand	**3908**	**2190**	**2061**	**4536**	**5268**

(a)

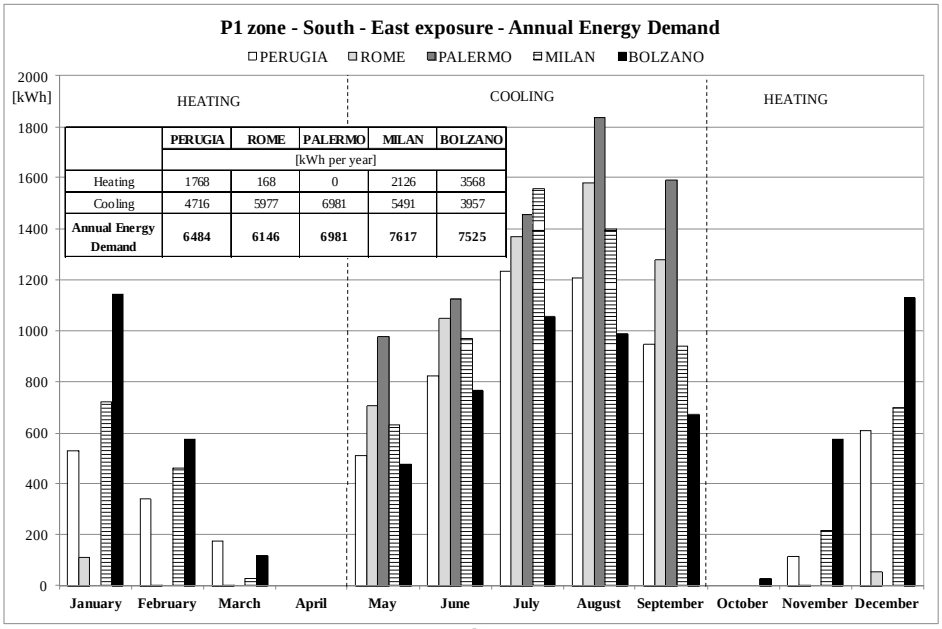

	PERUGIA	ROME	PALERMO	MILAN	BOLZANO
	[kWh per year]				
Heating	1768	168	0	2126	3568
Cooling	4716	5977	6981	5491	3957
Annual Energy Demand	**6484**	**6146**	**6981**	**7617**	**7525**

(b)

Fig. 4. Influence of building location on energy monthly demand: (a) T1 zone, (b) P1 zone.

4.3. Influence of glazing on energy saving

Finally the influence of different glazing types on annual energy demand was investigated.

In EnergyPlus the standard window modelling method includes layer-by-layer description of the optical properties of the glazing panes. Also the thermophysical properties of gas fills could be included in the model [12].

Five different types of glazing were selected; their optical and thermal properties are reported in Table 4. The first one is the standard glazing of the reference building:

- 55.1a: laminated glass with two glass panes, 5 mm thickness and PVB layer (0.38 mm);
- air space, 15 mm thickness;
- 33.1a: laminated glass with two glass panes, 3 mm thickness and PVB layer (0.38 mm).

Low-e and sunlight control glazing systems were also considered (Glazing 2 and 3); glazing 2 has a laminated glass 55.1a, 90% argon in the air space (15 mm thickness) and a low-e coated glass (6 mm). Glazing 3 has a total thickness of 32 mm (a solar control pane of 6 mm, air 15 mm, a low-e coated pane of 11 mm).

Moreover innovative glazing systems with silica aerogel in interspace were investigated (Glazing 4 and 5) (total thickness 22 cm); both kinds of aerogel were analysed: monolithic silica aerogel, thickness 14 mm, and granular aerogel, characterized by grain size in the 0.5 - 3.5 mm range [13].

Finally the effects of blind systems on the first floor façades were evaluated: external venetian blinds were defined as a series of horizontal slats. All of the slats were assumed to have the same optical properties. The overall optical properties of the blind were determined by the slat geometry (width, separation and angle) and the slat optical properties (front-side and back-side transmittance and reflectance). Slats have a cooper facing, they are perfect diffusers and the optical properties were assumed the same for the front and the back side (slat beam solar reflectance 0.7, slat diffuse solar reflectance 0.7, slat beam visible transmittance 0). It was considered a slat's width of 27 cm; the separation length between slats is 27 cm.

Blind properties for direct radiation are also sensitive to the *slat angle*. It was assumed equal to 45° in summer during the daytime (10.00 am – 8.00 pm) and horizontally oriented during the winter and in the nigh time.

Table 4. Glazing systems properties.

Glazing	*Characteristics and thickness*	*Total thickness* [m]	*τ_v – visible transmittance* [-]	*g – solar factor* [-]	*U – transmittance value* [W/m^{2}K]
1 - Standard glazing	55.1a – 15 mm air – 33.1a	0.32	0.78	0.65	2.70
2 - Low-e glazing	55.1a – 90% argon 15 mm – 6 mm low-e	0.32	0.47	0.53	1.10
3 - Solar Control	6 mm sunlight control – 15 mm air – 11 mm low-e	0.32	0.18	0.20	1.40
4 - Monolithic Aerogel	4 mm – 100% M-Aerogel 14 mm – 4 mm	0.22	0.60	0.70	0.63
5 - Granular Aerogel	4 mm – 100% G-Aerogel 14 mm– 4 mm	0.22	0.27	0.34	1.04

The effects of the different glazing systems were firstly analyzed for Perugia. The annual energy demand is showed in Fig.5 for T1 and P1 zones. The energy saved during the year by different windows, as compared to the base window (glazing 1), was calculated.

The energy saved for heating is about 60% (2000 kWh/yr) for T1 and 73% (1300 kWh/yr) for P1 considering glazing 4 (double glazing with monolithic aerogel in interspace); the heating energy saved is 40% for T1 and 50% for P1 by using the low-e glazing system. The effect of the solar

control glazing is maximum during the summer period: for T1 zone the sunlight control window saves a 40% of the cooling energy; 1525 kWh per year are saved for P1 from May to September (32%). The monolithic aerogel glazing is very effective in T1 zone. For P1 the maximum energy saving is obtained with solar control reflective window (32%). Moreover, no heating is required in October by using the low-e glazing or the glazing with silica aerogel (pane or granular).

The blind systems allow the best temperature control for the first floor during the summer period: blinds ensure the minimum value of cooling demand (1439 kWh) and the maximum energy saving value, of 69%.

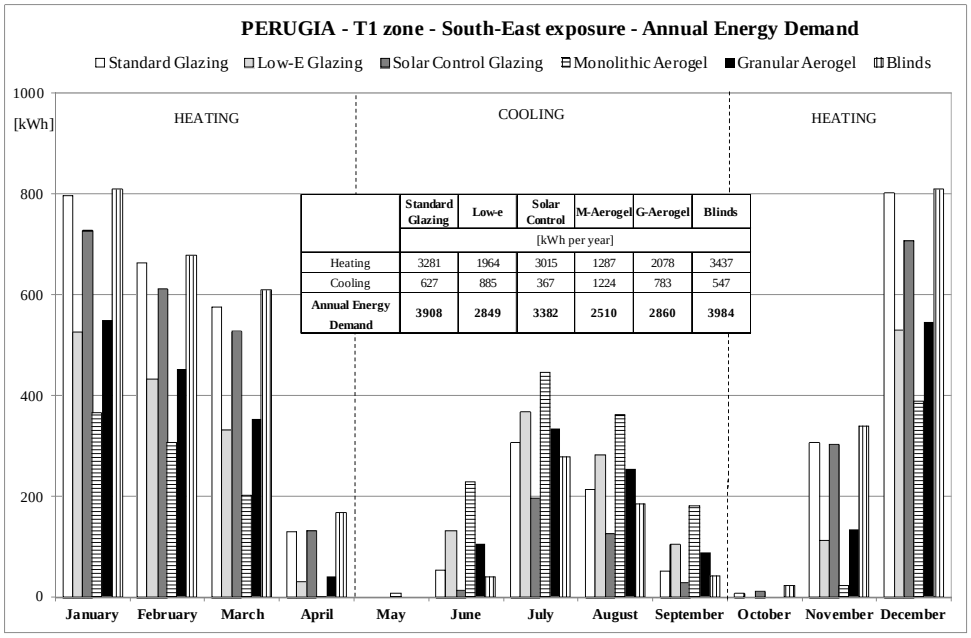

	Standard Glazing	Low-e	Solar Control	M-Aerogel	G-Aerogel	Blinds
	[kWh per year]					
Heating	3281	1964	3015	1287	2078	3437
Cooling	627	885	367	1224	783	547
Annual Energy Demand	**3908**	**2849**	**3382**	**2510**	**2860**	**3984**

(a)

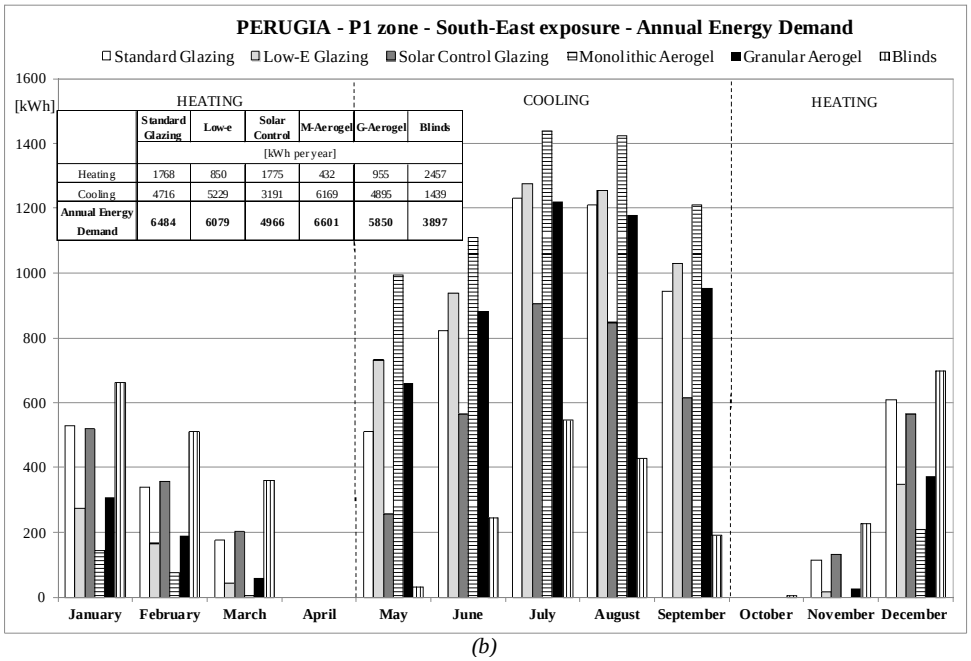

	Standard Glazing	Low-e	Solar Control	M-Aerogel	G-Aerogel	Blinds
	[kWh per year]					
Heating	1768	850	1775	432	955	2457
Cooling	4716	5229	3191	6169	4895	1439
Annual Energy Demand	**6484**	**6079**	**4966**	**6601**	**5850**	**3897**

(b)

Fig. 5. Perugia - influence of glazing systems on energy monthly demand: (a) T1 zone, (b) P1 zone.

The influence of different kinds of glazing systems was evaluated also for Palermo, as shown in Figure 6. The impact of glazing type on cooling demand is quite similar to the one of Perugia. No heating is required in P1 and the annual heating demand value for T1 is only 11 kWh, therefore only data referred to summer are reported. Also for Palermo the solar control glazing saves more energy than the other window solutions thanks to the low solar factor value: the cooling energy

saved is 32% (about 700 kWh/yr) for T1 and 27% for P1 (1900 kWh/yr). All the other glazing systems increase the annual cooling energy value for both the tested zone (cooling energy increase = 2.5 - 15%). The glazing with monolithic aerogel in interspace shows the worst behaviour in terms of cooling energy demand (8029 kWh per year for P1), due to high solar factor. Blind systems ensure the minimum value of cooling demand (3457 kWh) for the first floor.

Finally the influence of different glazing systems was evaluated for Bolzano (Fig.7).

Glazing 4 (M-aerogel in interspace) ensures the minimum value of the heating demand (2466 kWh/yr for T1 and 1684 kWh/yr for P1). Also Low-e glazing and G-aerogel glazing perform well in winter (annual heating demand of about 2300 kWh per year for P1): these types of window ensure a similar heating energy saving of 35% for P1. The annual cooling demand is not very high for the ground floor (381 kWh), but the monolithic aerogel allows an increase of 542 kWh, due to the high value of the solar factor (0.7). Finally, the shadow systems allow a cooling energy decrease of about 75% for the first floor zone and this is the best solution in terms of energy saving (annual energy demand of 5192 kWh). In fact the external mean air temperatures of Bolzano are lower than the ones of the other localities (maximum value of 21°C), but the maximum global solar radiation is high even for Bolzano (5320 Wh/m^2 in June, see Table 2). So the effect of blind systems is significant also for this city. Moreover the presence of blinds does not influence the annual energy demand of T1 zone. The sunlight control glazing requires only 5890 kWh per year for P1 (annual energy demand reduction = 22%), while the annual energy demand reduction for T1 is only 14%.

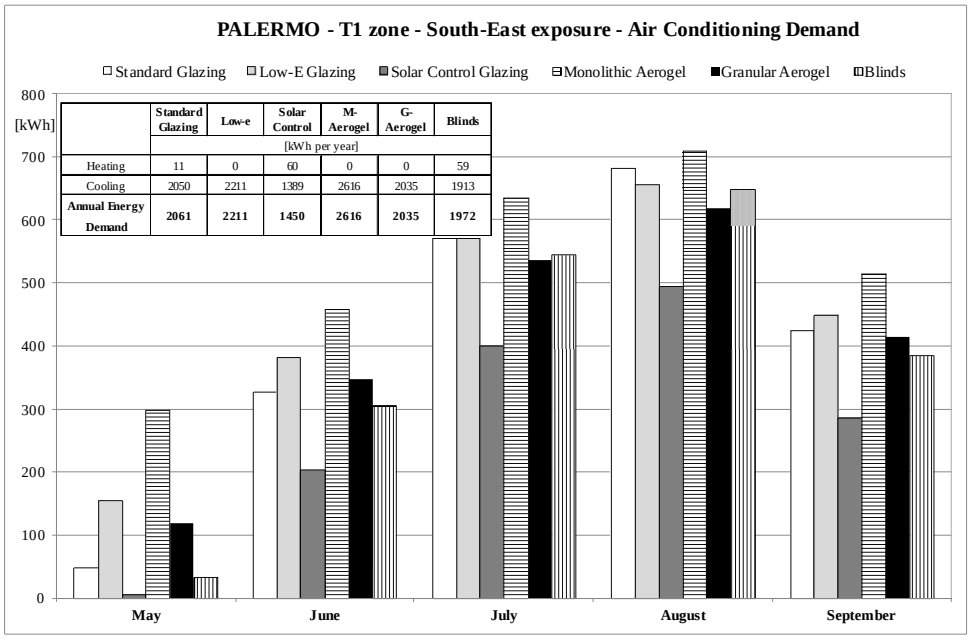

	Standard Glazing	Low-e	Solar Control	M-Aerogel	G-Aerogel	Blinds
	[kWh per year]					
Heating	11	0	60	0	0	59
Cooling	2050	2211	1389	2616	2035	1913
Annual Energy Demand	**2061**	**2211**	**1450**	**2616**	**2035**	**1972**

(a)

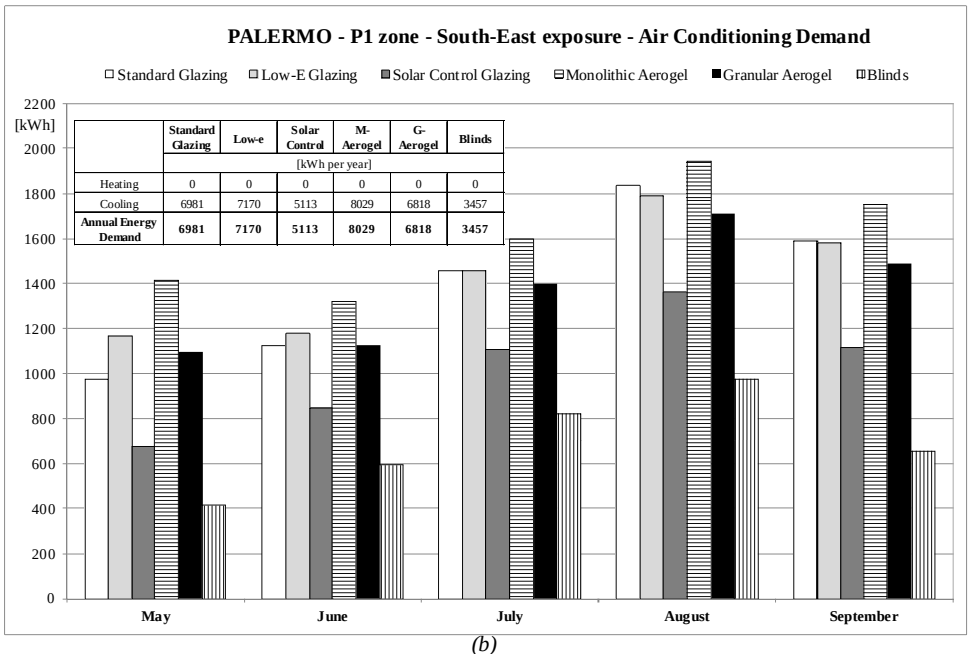

	Standard Glazing	Low-e	Solar Control	M-Aerogel	G-Aerogel	Blinds
	[kWh per year]					
Heating	0	0	0	0	0	0
Cooling	6981	7170	5113	8029	6818	3457
Annual Energy Demand	**6981**	**7170**	**5113**	**8029**	**6818**	**3457**

(b)

Fig. 6. Palermo - influence of glazing systems on cooling monthly demand: (a) T1 zone, (b) P1 zone.

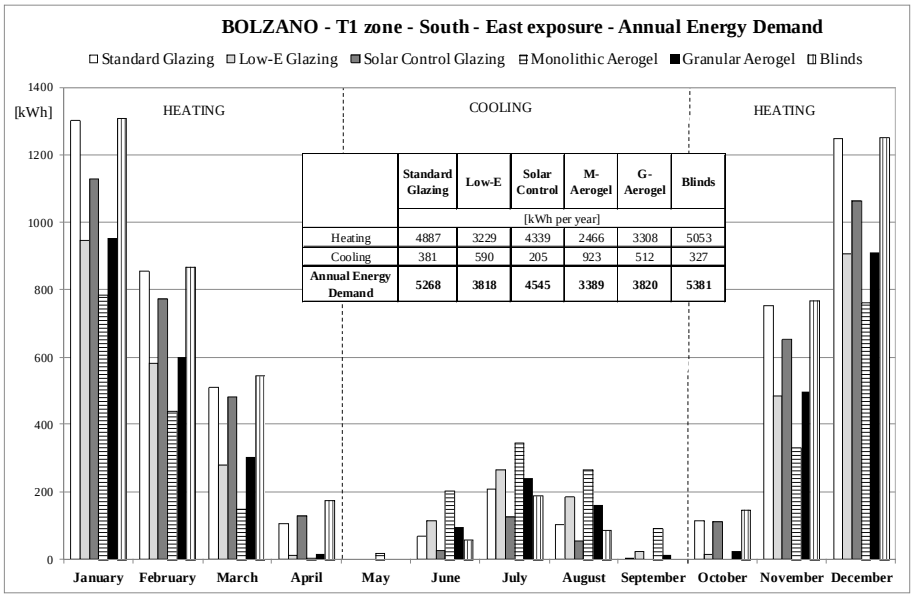

	Standard Glazing	Low-E	Solar Control	M-Aerogel	G-Aerogel	Blinds
	[kWh per year]					
Heating	4887	3229	4339	2466	3308	5053
Cooling	381	590	205	923	512	327
Annual Energy Demand	**5268**	**3818**	**4545**	**3389**	**3820**	**5381**

(a)

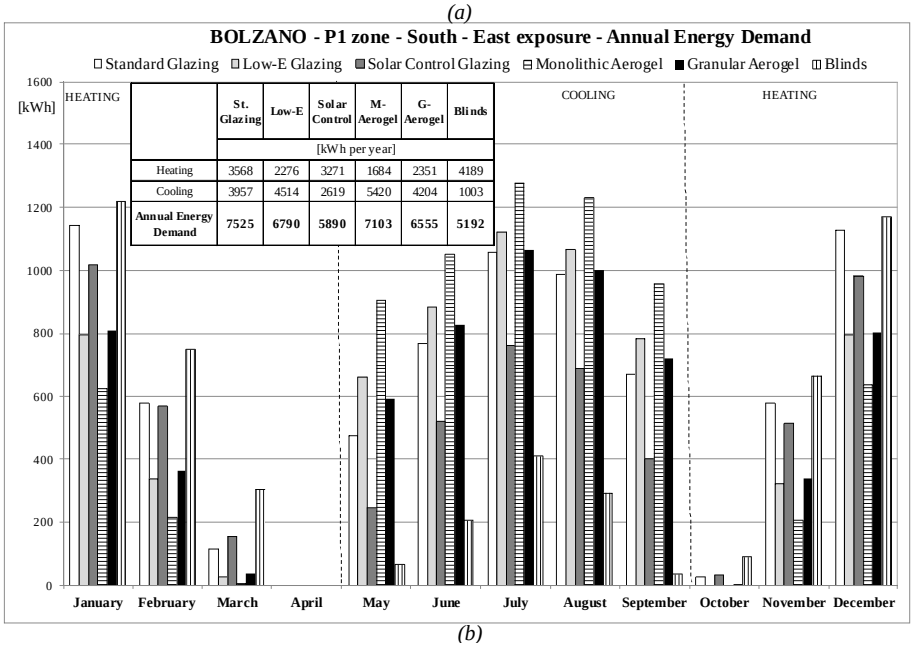

	St. Glazing	Low-E	Solar Control	M-Aerogel	G-Aerogel	Blinds
	[kWh per year]					
Heating	3568	2276	3271	1684	2351	4189
Cooling	3957	4514	2619	5420	4204	1003
Annual Energy Demand	**7525**	**6790**	**5890**	**7103**	**6555**	**5192**

(b)

Fig. 7. Bolzano - influence of glazing systems on energy monthly demand: (a) T1 zone, (b) P1 zone.

5. Conclusions

The energy efficiency of a building highly depends on the façade construction. Most of all highly glazed buildings should be studied very carefully during the design stage since different design options have a large impact on the energy efficiency. Low thermal transmittance values can be crucial to ensure acceptable heating demand and low energy use; at the same time the solar factor of windows should be thoroughly evaluated.

The aim of the present paper was to analyse the energetic performance of a multifunctional building by means of EnergyPlus simulation program. Two thermal zones were considered in the simulations: an office room (P1) at the first floor and a commercial one (T1) at the ground floor. Both the tested zones have a large glazing wall in the south façade, for a total area of 21.5 m^2. The weather data of five Italian localities (Perugia, Rome, Palermo, Milan, Bolzano) were considered in the simulations and three different exposures were evaluated for the city of Perugia. Moreover the influence of different types of glazing solutions was considered for Perugia, Palermo and Bolzano. Finally also the effects of blind systems on the façades were evaluated for the investigated building.

Results show that the heating energy demand for west and east exposures is higher than for south-east, for both the tested zones. The annual cooling demand, on the contrary, is not very different for the three exposures. The heating energy demand in the different climatic zones shows a very wide variation (quite null values for Palermo and maximum value of Bolzano), mainly due to the latitude of the city. The monthly mean values of the global solar radiation influence very much the annual cooling demand, above all for P1 zone. Energy savings with different kind of windows were also evaluated. They highly depend on the type of glass and location. Low thermal transmittance of windows is a good choice since it decreases the heating demand, while the cooling demand is not very much influenced. The annual energy saving by a particular window depends upon several factors: U-value, g-value, orientation and climatic conditions. Low g-values of windows have a great impact on the cooling demand. Externally placed blind devices are an efficient way of reducing cooling demand [3]: this is the best solution both for Perugia and Palermo, because blind systems allow an annual energy demand decrease of about 40-50%. The solar control glazing systems ensure the maximum effect in terms of energy saving for Palermo. On the contrary, the glazing with monolithic aerogel in interspace is the most efficient system for Bolzano, but only for the T1 zone. The unsteady state models implemented are very powerful tools in building design: many different solutions could be investigated and the most appropriate design option could be selected thanks to the simulation results. Thermal comfort and daylighting analysis, in addition to energy performance, will be investigated in the next phase of the study: the optimal fenestration types will be selected considering not only the energy demand but also daylighting needs and the indoor thermal comfort conditions.

References

[1] Poirazis H., Blomsterberg A., Wall M., Energy simulations for glazed office buildings in Sweden. Energy and Buildings 2008;40:1161-1170.

[2] Ebrahimpour A., Maerefat M., Application of advanced glazing and overhangs in residential buildings. Energy Conversion and Management 2011;52:212-219.

[3] Hassouneh K., Alshboul A., Al-Salaymeh A., Influence of windows on the energy balance of apartment buildings in Amman. Energy Conversion an Management 2010;51:1583-1591.

[4] Golasangimath D.V., Thermal and daylighting performance of automated split-controlled blinds. A thesis presented to the Graduate School of the University of Florida; 2009.

[5] Perez R., An Anisotropic Hourly Diffuse Radiation Model for Sloping Surfaces: Description, Performance, Validation, Site Dependency Evaluation. Solar Energy 1986, Vol. 36.

[6] Pyeongchan I., Moncef K., Henze G.P., Development of a thermal energy storage model for EenrgyPlus. Energy and Buildings 2004;36:807-814.

[7] Lyons P., Wong J., Bhandari M., A comparison of window modelling methods in EnergyPlus 4.0. Fourth International Conference of IBPSA; 2010 August 11-13; New York City.

[8] UNI EN ISO 6946. Building components and building elements - Thermal resistance and thermal transmittance - Calculation method; 2008.

[9] Gasparella A., Pernigotto G., Cappelletti F., Romagnoni P., Baggio P., Analysis and modelling of the energy performance of window and glazing systems. 65th Congresso Nazionale ATI; 2010 September 13-17; Domus de Maria – Cagliari (Italy).

[10] DPR n.412. Regolamento recante norme per la progettazione, l'installazione e la manutenzione degli impianti termici degli edifici, ai fini del contenimento dei consumi di energia, in attuazione dell'art. 4, comma 4 della legge 9 gennaio 1991, n.10; 1993 August 26.

[11] Singh M.C., Garg S.N., Energy rating of different glazings for Indian climates. Energy 2009;34:1986-1992.

[12] EnergyPlus Documentation. Version 7.0 Documentation, 2011October.

[13] Buratti C., Moretti E., Transparent insulating materials for buildings energy saving: experimental results and performance evaluation. Third International Conference on Applied Energy; 2011 May 16-18; Perugia (Italy), Press: 1421-1432.

Thermal Analysis of a Greenhouse Heated by Solar Energy and Seasonal Thermal Energy Storage in Soil

Y. Li, J. Xu, and R. Z. Wang

Institute of Refrigeration and Cryogenics, Shanghai Jiao Tong University,
800 Dong Chuan Road Shanghai, 200240, P. R. China Email : liyo@sjtu.edu.cn,

Abstract:

The use of greenhouses for crops has increased manifold over recent decades in China. To maintain a suitable environment for the production of various crops, enormous fossil fuel has been used for heating the green house in winter. A novel solar heating system with thermal energy storage in underground soil has been proposed to reduce the fossil fuel consumption. The underground soil inside the greenhouse is heated with U-bend heat exchanger by solar hot water during summer and autumn season. In winter, the greenhouse is heated by the ground and the ground tube with solar hot water from the hot water tank. A mathematical model is established to investigate the heat transfer and temperature distribution of the novel solar heated greenhouse in Shanghai winter climatic condition. The dynamic performance of greenhouse is measured in terms of the temperature histories in the greenhouse, heat loss of the greenhouse. Simulation results indicate that the heat can be effective stored in the central area of the underground soil and provide heating to the greenhouse in winter season in Shanghai weather condition.

Keywords:

Greenhouse heating, Solar energy, Seasonal thermal energy storage, Heat storage in underground soil,

1. Introduction

In China, agriculture has developed steadily with improvement of economic and living conditions. Greenhouses have been widely used to produce crops, flowers and vegetables outside the cultivation season. Massive fossil fuel has been used to maintain an appropriate temperature of the greenhouse in cold winter season [1]. Due to the rising price of fossil fuel and CO_2 emission problem, various solar heating technologies have been applied. Based on different working fluids, the heating system can be divided into water and air heating system. Based on storage technologies, water tank, underground soil, rock bed, and phase change material storage technologies have been used [2].

Therefore, in this study, an alternative composite system is proposed which can be effectively used for heating the greenhouse air in winter. The system uses the soil beneath the ground surface to store the solar thermal energy underground in the seasons that heating is not needed and to heat the greenhouse during the winter when the greenhouse temperature is lower than set temperature. The proposed heating system can make full use the solar energy available all year around.

As per the literature review, no such system is tried anywhere in the world and it is the first working system of its kind used for thermal control of an agricultural greenhouse.

Various models have been proposed to study the performance of heating in the greenhouse. Abdel-Ghany developed a simplified model which is based on a total heat balance to study three parameters used for evaluating the solar energy conversions in the greenhouse[3], they are latent heat factor, sensible heat factor and efficiency of utilization. This author also studied multiple

reflections of solar radiation between greenhouse components (i.e., the cover, humid air, plants and soil) [4]. Most researchers developed transient model to study the variation of temperature, heat transfer in the greenhouse [5-10]. Tuntiwaranuruka [5] proposed a model to soil temperature and moisture with and without rice husks in the greenhouse. Kurpaska investigated the heat losses in a substratum heating process based on a 2-D mathematical model, temperature differences in the soil space were observed, optimum values of some important design parameters have been found [6]. Pieters [7] proposed a comprehensive model named as Gembloux Dynamic Greenhouse Climate Model to study the performance of greenhouse, in his model, 1-Dimensional thermal radiation from the soil floor and the heat conduction in the soil has been considered.

The thermal energy storage in the ground using U-tubes and boreholes has been a hot topic in recent decades for central solar heating plants with seasonal heat storage [11]. Modeling of the storage subsystem and its integration with the solar heating system is essential for performance analysis and design. A comparative analysis of the heat transfer was conducted by Breger [12] from boreholes and U-tubes using analytical solutions, finite element modeling, and the available simulation model. Reuss [13] developed a computer model to simulate heat and soil moisture interactions in high temperature ground heat storages(70-90 ^{o}C). Numerical approximation by the finite-differences-method (FDM) was used to solve the differential equations. Dry-out effects in the vicinity of the heat exchangers were studied using this model.

In this paper, a model has been established to investigate the performance of the novel solar greenhouse with seasonal heat storage in the soil. The temperature profile of in the soil has been analyzed, and the influence of some important design/operational parameters on the performance of the greenhouse is reported in this study.

2. System description

Figure 1 shows the schematic diagram of solar greenhouse with seasonal heat storage in the soil considered in this study. The main focus here is to store the thermal energy obtained by the solar collector in summer and autumn seasons. The heat transfer in the underground soil has been studied. The heating system consists of the following components: (1) Evacuated tube solar collector; (2) Tank to store hot water; (3) A underground thermal energy storage system. (4) A floor heating system. Evacuated tube solar collector is chosen for its low cost and high efficiency. Also, solar energy being heat source with ground heat storage has the advantage of low maintenance as well as low the operational costs. The tank can be connected to the underground U tube and the floor heating tube. The connection and disconnection can be controlled by valve and pump.

The underground energy storage system is used for storing large quantities of solar heat collected in spring, summer and autumn to heat the greenhouse in winter. It is built just in the centre area of the underground of the green house. It is a large underground heat exchanger, which consists of an array of boreholes resembling standard drilled wells. After drilling, a plastic pipe with a “U” bend at the bottom is inserted in the borehole.

To begin with, in the seasons that greenhouse heating is not needed, solar energy gained through collector is accumulated in the hot water storage tank. When water is heated to the required temperature (for example, 333 K), the tank is connected to the underground storage system to heat the underground soil. The solar thermal energy is transferred to the underground soil. In the evening of the storage season, the higher temperature soil near the U tube releases the heat to the nearing soil. Hence, the thermal energy can be stored/accumulated into the soil steadily.

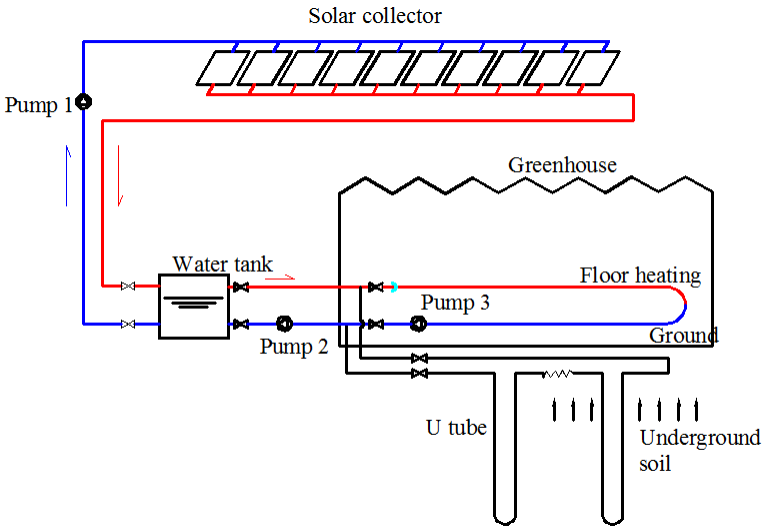

Fig. 1. Working principle of the greenhouse heating system with ground thermal energy storage

In winter, when the temperature of the greenhouse reduces to certain value, the heat in the soil releases to the ground surface and then to the green house due to the temperature difference. At the same time, the solar energy can still be collected in clear days, stored the hot water in the tank. The hot water is used to heat the greenhouse in the evening by flowing through floor heating tube. When the hot water temperature in the tank decreased to certain temperature, the underground U tube is connected to the floor heating tube to transfer the thermal energy stored in the ground to the floor heating tube and release heat to the greenhouse.

The major advantages of the proposed system over the conventional greenhouse heating system are: (i) the cost of ground storage is relative low, which significantly lowers the installation cost of the system. (ii) Greenhouse floor is also used as heat transfer area which reduce the area of floor heating tubes (iii) temperature of the soil mass is higher than air temperature, which is good for the crops growing. (iv) the storage bed is in the middle area of the green house, the heat loss to the adjacent soil is useful to maintain the greenhouse temperature.

3. Mathematical model

In order to study the evolution of heat transfer process in the underground as well as the greenhouse, a mathematical model has been developed. To simplify the model, following assumptions are made:

- Absorptivity of the enclosed air is neglected.
- The greenhouse and underground heating is assumed to be asymmetric. The heat transfer in the ground is two-dimensional. The heat transfer in the greenhouse is 1-dimensional.
- The soil and subsoil is considered to be a homogeneous while the thermal conductivity is constant.
- The physical parameters of air in the greenhouse and in the surrounding are constant during the process.
- The floor properties is the same of the soil, vegetation is not considered.

To study the performance of the greenhouse with ground heat storage, a research base case has been proposed. As shown in Fig. 2, the heat storage bed is in the central area of the greenhouse and consists 256 ducts with a length of 10 m and a space of 1.5 m. The distance from the U tube heat

exchanger to the greenhouse floor is 0.5 m to avoid overheating of soil. Other parameters used in the simulation are shown in Table 1.

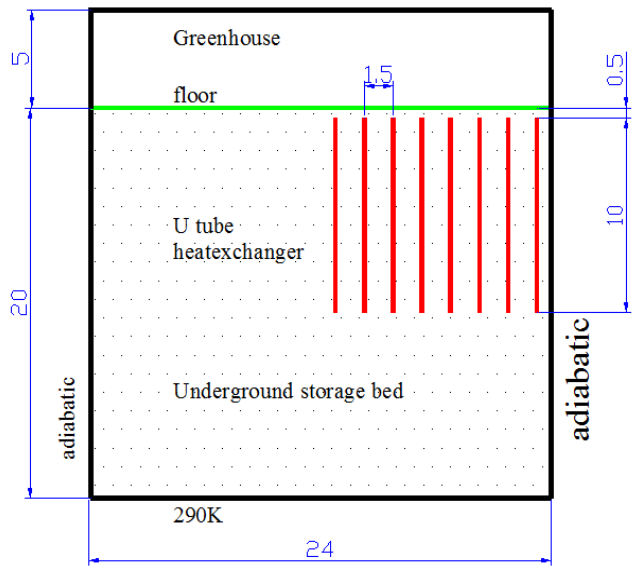

Fig. 2. Heat transfer model of the greenhouse heating system with ground thermal energy storage

The domain studied includes the greenhouse and the underground soil. The depth of underground soil domain boundary is 20 meters. The vertical plane under the wall of the greenhouse is the boundary in vertical direction. The Energy balance of the air in the greenhouse can be written as follows:

$$\rho_a V_r c_a \frac{\partial T_r}{\partial t} = h_f l_f (T_r - T_f) + h_c l_c (T_r - T_c) \tag{1}$$

Energy balance of the floor in the greenhouse can be written as follows:

$$\alpha_f \tau I_t = -k l_f \frac{\partial T_s}{\partial y} + h_f l_f (T_r - T_f) \tag{2}$$

The heat flow in the soil is given as:

$$\frac{\partial T_s}{\partial t} = k_{eff} \frac{\partial^2 T_s}{\partial x^2} + k_{eff} \frac{\partial^2 T_s}{\partial y^2} \tag{3}$$

The Typical Meteorological Year (TMY) data of Shanghai is used as input of the solar radiation and other environmental condition in the simulation. The heat collected by the solar collector for one day is calculated by:

$$Q_{c,day} = \int I_t \eta_{sc} A_{sc} dt \tag{4}$$

Heat sent to each tube:

$$Q_{t,day} = Q_{c,day} / N \tag{5}$$

Heat released to the soil for one day:

$$Q_{s,day} = \int q A_t dy dt \tag{6}$$

The time to heat the ground soil $t_{heating}$ is obtained by following condition:

$$Q_{s,day} = Q_{c,day} \tag{7}$$

The initial conditions of soil:

$$T_s(x,y,0) = T_{s0} = 290\,K \tag{8}$$

In heating phase, constant temperature is used at the heating tube is:

$$T_y(a_1,\ldots a_8) = T(x_1, y|_{-0.5}^{-10.5}, t_{heating}) = 333\,K \tag{9}$$

In non-heating period, the boundary conditions at the heating tube is:

$$q_y(a_1 \ldots a_8, y|_{-0.5}^{-10.5}, t_{non-heating}) = 0 \tag{10}$$

The boundary temperature under the heating soil is set as a constant:

$$T(x,-20) = 290\ K \tag{11}$$

The boundary conditions at the vertical planes under the wall of the green house.

$$\frac{\partial T_s}{\partial y} = 0 \qquad y = 0 \sim -20 \ \text{m} \tag{12}$$

Table 1. Values of the main greenhouse parameters used for the simulations

Parameters of the construction	
Latitude, N.	31
Length of the greenhouse, m	48
Height of the greenhouse, m	5
Parameters of the floor and the soil layer	
Heat capacity, J/kgK	1900
Density, kg/m^3	1500
Reflectance for far-infrared radiation, ρ_s	0.85
Emittance for far-infrared radiation, ε_s	0.4
Deep soil temperature, T_{ss} ^{o}C	19.75
Parameters of the inside air	
Density, kg/m^3	1.25
Heat capacity, J/kgK	1003.2
Air velocity,m/s	0.3
Parameters of ground storage bed	
The depth of U tube, m	10
U tube distance to the greenhouse floor, m	0.5
distance between the U tubes, m	1.6
Solar collector	
Area m^2	500
Thermal efficiency	0.4

4. Results and discussion

The system was simulated with a control scheme to start store heat into the soil at the beginning of June. When the water temperature in the tank is higher than 60 ^{o}C, the pump is started and hot water is circulated in the ground heating tube. During the month of June to November, all the solar energy is stored in the soil, this period is the charging period. The heating season starts in December and ends in February. The stored solar energy is drawn to the loads when the greenhouse

temperature drops below 12 °C. When the greenhouse temperature drops below 8 °C, the auxiliary heat is supplied whether heat is supplied from the tank or not.

The TMY (Typical Meteorological Year) type weather data of Shanghai is used in the simulation. Figure 3 shows the monthly average weather data for Shanghai China.

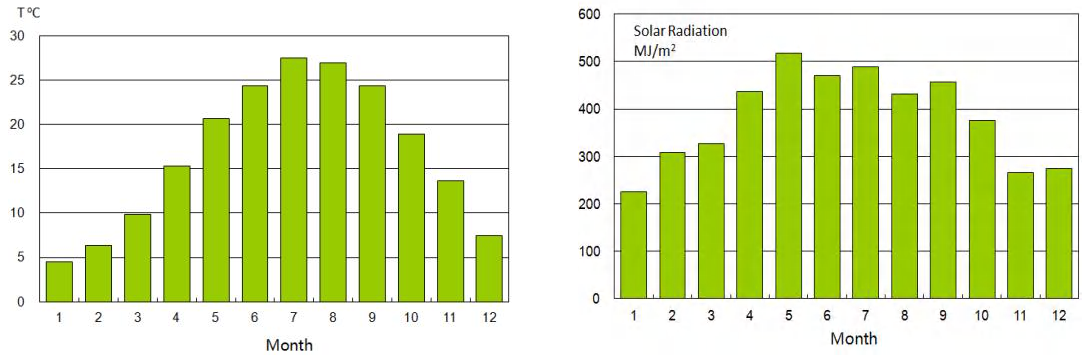

(a) (b)

Fig. 3. Month average (a) temperature (b) solar radiation of Shanghai

Figure 3 shows the temperature distribution in the ground at the end of Charging period. The highest temperature can reach 41 °C and is located in the central area, 3 meters from the floor. The heat loss is mainly in two directions top and bottom. The temperature gradation is more significant near the top side for following reason: in the top side, heat is transferred from the soil to the air by convection. While in the bottom side of the heating tube, the thermal energy is transferred by conduction of soil, which has very low thermal conductivity. In Fig. 3, it can also observed that near the vertical boundary under the wall of the greenhouse, the temperature is almost the same as the outside soil area, which means the adiabatic assumption is appropriate. Similarly, the temperature variation at the depth of 20 m is very small, meaning that the constant temperature assumption is valid.

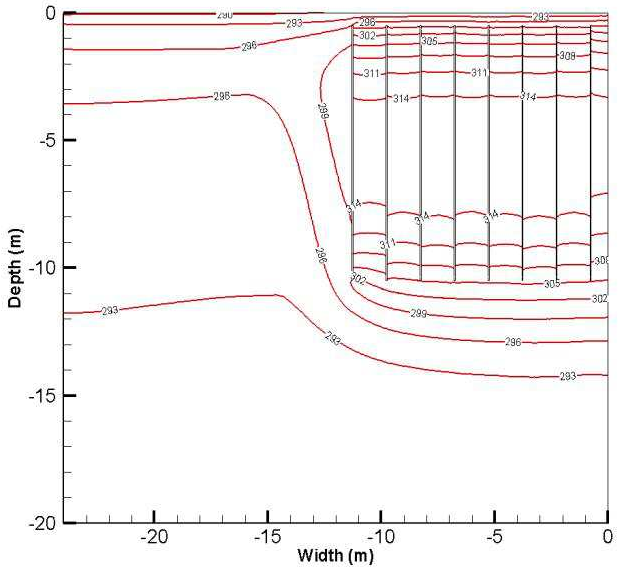

Fig. 4. Temperature distribution in the ground at the end of Charging period

Figure 5 shows the temperature history of typical point in the soil bed. In the initial period of heating, the soil temperature rise fast. With the increase of the soil temperature, the heat loss increase steadily. Hence, the rate of temperature rise reduces. This is due to two reasons: 1) the

temperature difference between the hot water and the soil adjacent to the tube reduce. 2) the heat loss increase with the increase in soil temperature and reduce in environmental temperature.

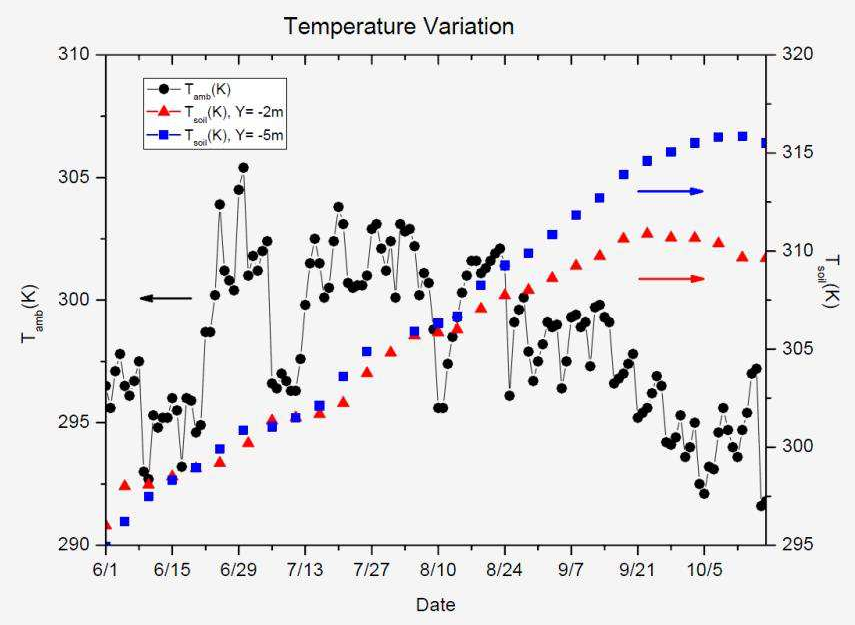

Fig. 5. Temperature history in the soil storage bed at the depth of 2m and 5m between the heating tube.

Figure 6 shows the history of the thermal energy stored in soil bed during charging period and the heat loss due to convection. It is obviously, that the heat can be accumulated in the soil steadily till the end of September. It can also be found that the heat loss due to convection can be positive in some periods in June and August, which means the heat is transferred to the soil from the air. This is mainly due to higher temperature of the greenhouse air. It can also observed in Fig. 6 that the increase of heat accumulated in the soil is almost stopped, although the solar thermal energy is still added into the soil. The reason is that, with the temperature difference between the soil and the air increase, the heat loss also increases. The heat collected by solar collector is almost equal to the heat loss. Hence, the heat stored in the soil doesn't increase.

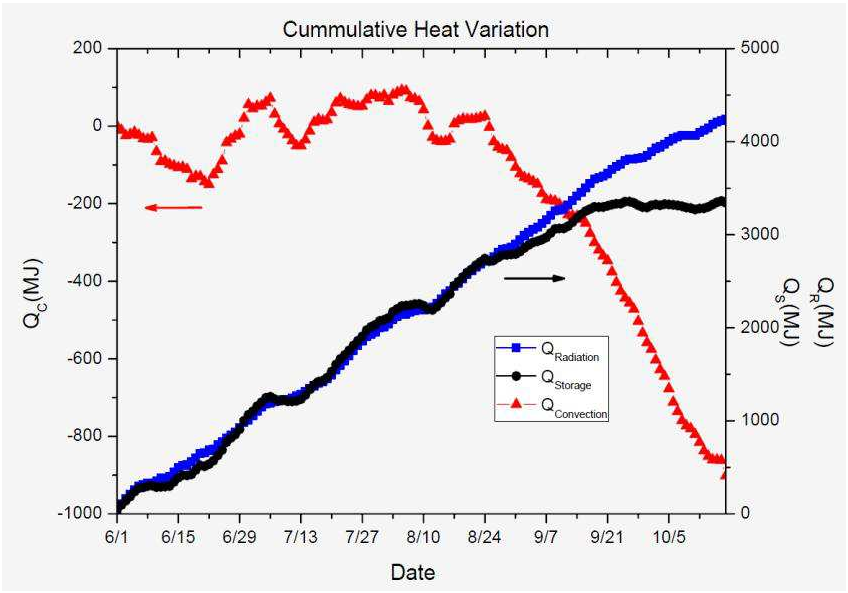

Fig. 6. Variation of heat stored in the soil storage bed and the heat loss.

5. Conclusions

A novel solar greenhouse with seasonal heat storage in the soil has been proposed in this paper. A mathematical model has been developed to investigate the performance of the system. In Shanghai Typical Meteorological Year weather condition, with heat storage starting in June 1, the simulation results indicate that the solar thermal energy can be effectively stored in the soil. The accumulation of stored heat energy doesn't increase at the end of October due to increased heat loss. The stored thermal energy can be transferred to the greenhouse floor by conduction to keep the greenhouse temperature higher than conventional greenhouse in winter.

Nomenclature

A area (m^2)

c specific heat, J/(kg K)

h heat transfer coefficient, W/(m^2 K)

h_f convective heat transfer coefficient from floor to greenhouse air (W/m^2 K) (=2.8 + 3.0v)

I_t solar radiation falling on greenhouse cover (W/m^2)

k thermal conductivity of ground (W/m K)

M_a total mass of air in greenhouse enclosure (kg)

N number of tube

Q thermal energy (J)

q heat transfer rate (W/m^2)

r reflectivity (dimensionless) (decimal)

T temperature (K)

V volume (m^3)

t time (s)

x horizontal direction

y vertical direction

Greek symbols

α absorptivity of the ground, dimensionless

τ transmissivity of the greenhouse cover, dimensionless

ρ density of air, kg/m^3

η efficiency

Subscripts and superscripts

a air

day one day

e environment

eff effective property

f floor of greenhouse

r greenhouse room

R radiative

s soil

sc solar collector

sky sky

t tube

References

[1] Critten D.L., Bailey B.J., A review of greenhouse engineering developments during the 1990s Agricultural and Forest Meteorology 2002; 112:1–22

[2] Sethi V.P., Sharma S.K., Survey and evaluation of heating technologies for worldwide agricultural greenhouse applications. Solar Energy 2008; 82(9):832-859

[3] Abdel-Ghany A. M., Solar energy conversions in the greenhouses, Sustainable Cities and Society 2011; 1:219– 226.

[4] Abdel-Ghany A.M., Al-Helal I.M., Solar energy utilization by a greenhouse: General relations. Renewable Energy 2011;36:189-196.

[5] Tuntiwaranuruka U., Thepaa S., Tiab S., Bhumiratanab S., Modeling of soil temperature and moisture with and without rice husks in an agriculture greenhouse Renewable Energy 2006;31:1934–1949.

[6] Kurpaska S., Slipek Z. Optimization of Greenhouse Substrate Heating, Journal of agriculture Engineering Research 2000;76:129-139

[7] Pieters J. G., Deltours J. M., Performances of Greenhouses with the Presence of Condensation on Cladding Materials, Journal of agriculture Engineering Research 1997;68:125-137.

[8] Sethi V.P., Sharma S.K., Thermal modeling of a greenhouse integrated to an aquifer coupled cavity flow heat exchanger system, Solar Energy 2007; 81 :723–741.

[9] Singh R.D., Tiwari G.N., Thermal heating of controlled environment greenhouse: a transient analysis Energy Conversion and Management 2000;41(5):505-522.

[10] Kurpaska S., Slipek Z ., Mathematical Model of Heat and Mass Exchange in a Garden Subsoil during Warm-air Heating, Journal of agriculture Engineering Research 1996;65:305 – 311

[11] Bauer D., Marx R., Nußbicker-Lux J., Ochs F., Heidemann W., Muller-Steinhagen H., German central solar heating plants with seasonal heat storage, Solar Energy 2010;84:612–623.

[12] Breger D. S., Hubbell J. E., Hasnaoui H. and Sunderland J. E. Thermal energy storage in the ground: comparative analysis of heat transfer modelling using U-tubes and boreholes. Solar Energy 1996; 56(6): 493-503.

[13] Reuss M., Beck M. and Mijller J. P., Design of a seasonal thermal energy storage in the ground, Solar Energy 1997;59(4-6):247-257.

Thermodynamic analysis of a combined cooling, heating and power system under part load condition

Qiang Chen[a], Jian-jiao Zheng[b], Wei Han[c], Jun Sui[d], and Hong-guang Jin[e]

[a] *Institute of Engineering Thermophysics, Beijing, P. R. China, workchenqiang@126.com*
[a] *Graduate University of Chinese Academy of Sciences, Beijing, P. R. China, workchenqiang@126.com*
[b] *Institute of Engineering Thermophysics, Beijing, P. R. China, zhengjianjiao@iet.cn*
[b] *Graduate University of Chinese Academy of Sciences, Beijing, P. R. China, zhengjianjiao@iet.cn*
[c] *Institute of Engineering Thermophysics, Beijing, P. R. China, hanwei@mail.etp.ac.cn*
[d] *I Institute of Engineering Thermophysics, Beijing, P. R. China, suijun@mail.etp.ac.cn*
[e] *Institute of Engineering Thermophysics, Beijing, P. R. China, hgjin@mail.etp.ac.cn*

Abstract:

Combined cooling, heating, and power (CCHP) system is a potential way to utilize fossil fuel more efficiently and release less green house gas. However, the thermodynamic performance of CCHP system will deteriorate dramatically under the part-load condition than that under the rated condition. The CCHP system investigated in the current study consists of a small-scale gas turbine, an exhaust-fired double-effect absorption chiller, and a heat exchanger. The gas turbine generates electrical power. The exhaust gas of the gas turbine at high temperature is introduced to the absorption refrigerator to generate the cooling energy for building air conditioning. The waste heat of the exhaust gas of the absorption chiller is recovered in the heat exchanger to generate hot water. Three indicators: fuel energy saving ratio, energy level difference, and trigeneration carbon dioxide emission ratio are employed to evaluate the performance of CCHP system with respect to the reference system using conventional technologies. In this study, the thermodynamic and energy level analyses of the CCHP system are investigated under the rated and part-load conditions. The energy level analysis is implemented on the energy conversion progresses to reveal the mechanisms of the deterioration of the CCHP performance under part-load conditions. The results showed that the combustor of the small-scale gas turbine mainly contributed to the deteriorated performance of the CCHP system. The potential to enhance the off-design performance of the CCHP system is pointed out. The results provided a new direction for improving the off-design performance of the CCHP system.

Keywords:

CCHP system, Trigeneration CO_2 emission ratio, Double-effect absorption chiller, Energy level analysis, Exergy

1. Introduction

The combined cooling, heating, and power (CCHP) systems are integrated energy systems that produce electricity, cooling, and heating simultaneously, which is also referred to as trigeneration [1, 2]. In a CCHP plant, the exhaust heat of a power generation unit was recovered for further utility, such as cooling and heating, among others, instead of ejecting to the environment as that in a conventional power plant. In China, CCHP has a great potential in issues concerning the sustainable energy system transition [3]. With the availability of gas turbine spanning an increasingly wide range of capacities, the utilization of CCHP has becoming increasingly attractive via a combination of gas turbines and absorption chillers [4-6].

J. Bassols et al. [7] have presented the application of CCHP systems driven by gas turbine in the food industry. Andreas Poullikkas [8] have given an overview of the current and future sustainable gas turbine technologies in distributed energy. R.Z. Wang et al. [9] analyzed the problem of optimal energy management in the CCHP system, and concluded that the operation of the turbine may not

be optimized when the electric-to-gas cost ratio is very low. The energy system consists of a gas turbine, an absorption chiller, and a heat recovery boiler. Abdul Khaliq [10, 11] performed a second law performance analysis on the gas turbine trigeneration system, which consists of a gas turbine, a heat recovery steam generator, and a single effect absorption chiller. The effect of the parameters, such as the pressure ratio and the process steam pressure on the thermodynamic performance of the system, were studied. The exergy destruction on each component of the system was calculated under a different pressure ratio of the gas turbine.

The integration of a micro gas turbine that is coupled directly with the double-effect water-LiBr absorption chiller is another emerging technology for the spread of distributed energy. In this type of CCHP system, fresh air or oxygen is supplied to the additional gas post combustion to drive the gas fired absorption chiller. J. Carles Brunoet al. [12] compared the different configuration, and the Coefficient of Performance (COP) of the chillers is found to be higher than that in a single effect configuration. A wider range of chilled water production is also available because of the decoupled chillers. Huicochea A. et al [13] evaluated the theoretical performance of a CCHP system consisting of a micro gas turbine and a double-effect absorption chiller. Experimental data was used from the manufacturer to determinethe performance of the micro gas turbine. Different operating conditions such as the ambient temperature, generation temperatures, and micro gas turbine fuel mass flow were taken into consideration. The default configuration has a low exhaust gas temperature from the prime mover, which is difficult to drive a double-effect absorption chiller.

In recent years, a wide consensus exists about the environment protection and the energy security. The CCHP system has benefits in terms of green house gas (GHG) emission reduction with respect to the separate production (SP) as a result of their enhanced energy performance. The potential of CCHP systems for reducing the emission of hazardous GHG have been investigated [14, 15]. Mago et al. [16, 17] analyzed the optimum operation of CCHP system from the perspective of the environmental impact, energy savings, and operation cost. PierluigiMancarella and Gianfranco Chicco [18] set up the global and local emission impact model for the distributed cogeneration system, and analyzed an application based on the emission characteristics of a real micro gas turbine.

As for the configuration of the CCHP system, an auxiliary boiler or electric compressor chiller is integrated generally to meet the heating or cooling load. In addition, the system was connected to the grid to sell the excess electricity or import electricity from the grid. A few studies exist on the off-design performance of the CCHP system. Another problem involves the frequent use of constant engine efficiencies or empirical efficiency curves of equipments in the simulations of the performance evaluation of CCHP systems, which decreases the accuracy in the operation decision.

This paper aims to discover the mechanism of the off-design performance deterioration and locate the irreversibility for the CCHP system by the exergy and energy level difference analysis. In the study, a CCHP system was simulated based on the off-design models of the small-scale gas turbine and the absorption chiller. The performance of a CCHP system was evaluated by three indicators, including fuel utility efficiency, fuel energy saving ratio (FESR), and the trigeneration CO_2 emission reduction indicator (TCO_2ER).

2. Description of system

The CCHP system invested in the present study consists of a small-scale gas turbine, a double-effect absorption water-LiBr chiller, and a heat exchanger. The exhaust gas from the small-scale gas turbine at high temperature is introduced to the generator of the absorption system. The exhaust gas from a double-effect chiller at lower temperature then passes through a heat exchanger to produce hot water. The schematic diagram of the CCHP system is shown in Fig. 1.

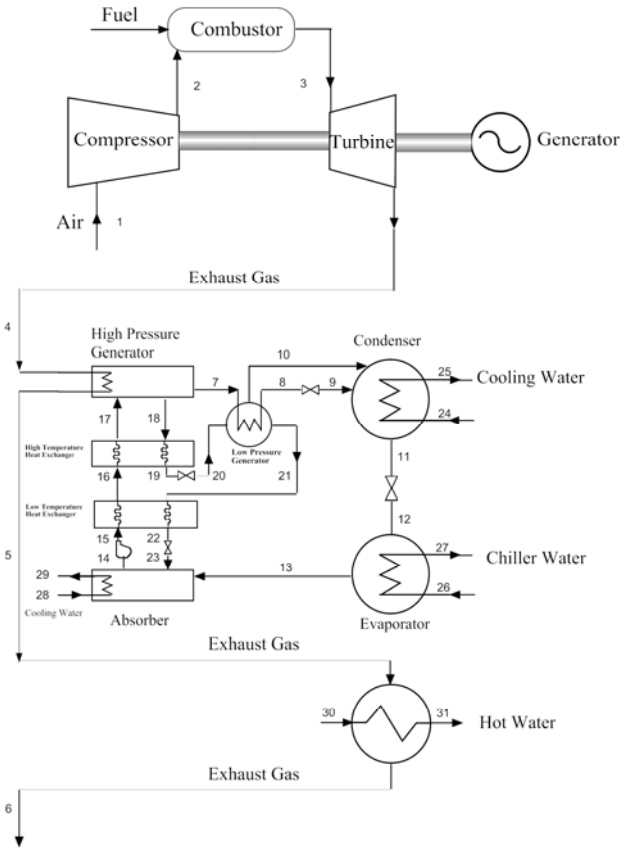

Fig. 1 Schematic diagram of the CCHP system

A small-scale gas turbine, having a centrifugal compressor and a radial inflow turbine with power output of 1747 kW, was investigated. As shown in Fig. 1, air is induced into the centrifugal compressor through an inlet duct. The compressed air then flows toward the combustion chamber with a constant combustion efficiency of 0.97. After combustion, the hot gases enter the radial inflow turbine nozzles to drive the external load and the centrifugal compressor. The stack gas with high temperature is ejected to a double-effect absorption chiller to recover waste heat.

The schematic diagram of a double-effect H_2O-LiBr absorption chiller that is activated by an exhaust gas was shown in Fig. 1. The main components of the absorption system includes a condenser (CON), an evaporator (EVA), an absorber (ABS), a solution pump, a high temperature heat exchanger (HTHE), a low temperature heat exchanger (LTHE), a high pressure generator (HPG), a low pressure generator (LPG), two solution reducing valves and two refrigerant expansion valves.

The exhaust gas at high temperature flowed into the HPG to generate the primary steam and a concentrated working solution. In the solution circulation, the weak solution (in which the absorbent concentration is low) produced in the absorber is pumped through the LTHE and HTHE to recover the surplus heat of the medium concentration solution from LPG and the strong concentration solution from HPG. The weak solution then is introduced to the HPG, where it is heated and concentrated into medium concentration solution by exhaust gas, and generates high-pressure refrigerant steam. The medium concentration solution then passes through the HTHE and enters the LPG after decreasing the pressure, where the medium concentration solution is further concentrated into a strong solution. The strong solution enters the absorber after cooled in the LTHE. In the refrigerant circulation, the refrigerant steam from the HPG condenses in the LPG and low-pressure refrigerant steam is generated. The high-pressure refrigerant water and low-pressure refrigerant steam are sent to the condenser. The refrigerant water is throttled and introduced to the

evaporator for cooling generation. Finally, the refrigerant steam is absorbed by strong solution in the absorber.Then, the exhaust gas entered into the heat exchanger for further utility.

A heat exchanger was adopted in the CCHP system to produce hot water using the low-grade waste heat. The apparatus was affected by many factors, such as the temperature of the exhaust gas, the mass flow for both cold and hot sides, and ambient temperature. The heat exchanger should meet the condition wherein the outlet temperature of the exhaust gas is 90 °C to make a simplified analysis on the CCHP system. The exhaust gas from the absorption chiller enters into the heat exchanger to produce hot water, and then ejected to the environment.

3. Mathematical model and CCHP system

3.1. Thermodynamic analysis

The general energy and exergy analysis relations for the system, equipment, and the parts of the equipment are given below. The performance of the gas turbine was simulated based on the explicit analytical solution [19, 20] and the literature [21], which was given in Appendix A. As for the double-effect absorption chiller, the performance was simulated by the specific mass and energy balance [22], of which the flow diagram was shown in Fig. 1.

The energy and exergy rate balances for any control volume at steady state can be expressed as [23]:

$$\dot{Q}-\dot{W}+\sum_{in}\dot{m}_{in}h_{in}-\sum_{out}\dot{m}_{out}h_{out}=0, \qquad (1)$$

$$\sum_{i=1}^{n}(\varepsilon_Q)_i+\sum_{in}\dot{m}_{in}\varepsilon_{in}-\sum_{out}\dot{m}_{out}\varepsilon_{out}-\dot{W}-\dot{E}x_D=0, \qquad (2)$$

where $\dot{W}$ and $\dot{Q}$ are the net rates of energy transfer by heat and work, e and ε are the specific energy and exergy, $\dot{m}_{in}$ is the mass rate, and $\dot{E}x_D$ is the destroyed exergy.

The net power output of a small-scale gas turbine is given by:

$$\dot{W}_{net}=(1+f)m_{air}(h_3-h_4)-m_{air}(h_2-h_1), \quad (3)$$

The working fluid of gas and air for the Brayton cycle was issued in detail in theliterature [24, 25].

The refrigeration cold product (Q_E) can be obtained by the following equation:

$$\dot{Q}_E=COP(1+f)m_{air}(h_4-h_5), \qquad (4)$$

The hot water produced by the heat exchanger can be written as:

$$\dot{Q}_{HW}=\sigma(1+f)m_{air}(h_5-h_6), \qquad (5)$$

where the effectiveness of the heat exchanger σ is taken to be constant at 0.9, and the enthalphy of the exhaust gas ejected to the environment was assumed to be the enthalphy of the gas at 90 °C.

3.2. Exergy destruction model

The CCHP system was assumed to be operated in a steady state, steady flow condition, and all non-reacting gases can be assigned arbitrarily as zero thermomechanicalenthalphy, entropy, and exergy at a condition of ambient temperature and pressure, regardless of their chemical composition. Transforming Eq. (2), the following expression can be achieved for the general exergy destruction:

$$\dot{E}x_D = \sum_{i=1}^{n}(\varepsilon_Q)_i + \sum_{in}\dot{m}_{in}\,\varepsilon_{in} - \sum_{out}\dot{m}_{out}\,\varepsilon_{out} - \dot{W} \quad , \qquad (6)$$

The general exergy of the working fluid in the above equations can be calculated by:

$$\varepsilon_x = (h - h_{amb}) - T_{amb}(s - s_{amb}) , \qquad (7)$$

An approximate formulation for the chemical exergy of gaseous hydrocarbon fuels as C_aH_b on a unit mass basis is given as:

$$\varepsilon_{x,fuel} = LHV_{NG}A_{NG} \approx LHV_{NG}\cdot(1.033 + 0.0169\frac{b}{a} - \frac{0.0698}{a}) , \quad (8)$$

where A denotes the fuel chemical energy level [26, 27].

Appling the general exergy destruction equation to each component of the main equipment of the CCHP system,

$$\dot{E}x_{D,cmp} = \dot{W}_{cmp} - \dot{m}_{air}\cdot\varepsilon_{x2,air} + \dot{m}_{air}\cdot\varepsilon_{x1,air} , \qquad (9)$$

where, $\dot{W}_{cmp} = \dot{m}_{air}\cdot(h_2 - h_1)$, $\varepsilon_{x1,air} = 0$, (10)

$$\dot{E}x_{D,comb} = (1+f)\cdot\dot{m}_{air}\cdot\varepsilon_{x3,gas} - \dot{m}_{air}\cdot\varepsilon_{x2,air} - f\cdot\dot{m}_{air}\cdot\varepsilon_{x2,fuel} , \quad (11)$$

$$\dot{E}x_{D,turbo} = (1+f)\cdot\dot{m}_{air}\cdot\varepsilon_{x3,gas} - \dot{W}_{turbo} - (1+f)\cdot\dot{m}_{air}\cdot\varepsilon_{x4,gas} , \qquad (12)$$

where, $\dot{W}_{turbo} = (1+f)\cdot\dot{m}_{air}\cdot(h_3 - h_4)$, (13)

$$\dot{E}x_{D,HPG} = (1+f)\cdot\dot{m}_{air}\cdot(\varepsilon_{x4,gas} - \varepsilon_{x5,gas}) + \dot{m}_{s,17}\cdot\psi_{x,17} - \dot{m}_{w,7}\cdot\psi_{x,7} - \dot{m}_{s,18}\cdot\psi_{x,18} , \quad (14)$$

$$\dot{E}x_{D,LPG} = \dot{m}_{w,7}\cdot\psi_{x,7} + \dot{m}_{w,20}\cdot\psi_{x,20} - \dot{m}_{s,8}\cdot\psi_{x,8} - \dot{m}_{w,21}\cdot\psi_{x,21} - \dot{m}_{s,10}\cdot\psi_{x,10} , \qquad (15)$$

$$\dot{E}x_{D,CON} = \dot{m}_{w,9}\cdot\psi_{x,9} + \dot{m}_{w,10}\cdot\psi_{x,10} + \dot{m}_{cow,24}\cdot\psi_{x,24} - \dot{m}_{cow,25}\cdot\psi_{x,25} , \qquad (16)$$

$$\dot{E}x_{D,EVA} = \dot{m}_{w,12}\cdot\psi_{x,12} + \dot{m}_{chw,26}\cdot\psi_{x,26} - \dot{m}_{w,13}\cdot\psi_{x,13} - \dot{m}_{chw,27}\cdot\psi_{x,27} , \qquad (17)$$

$$\dot{E}x_{D,ABS} = \dot{m}_{w,13}\cdot\psi_{x,13} + \dot{m}_{s,23}\cdot\psi_{x,23} + \dot{m}_{cow,28}\cdot\psi_{x,28} - \dot{m}_{cow,29}\cdot\psi_{x,29} - \dot{m}_{s,14}\cdot\psi_{x,14} , \quad (18)$$

$$\dot{E}x_{D,LTHE} = \dot{m}_{s,15}\cdot\psi_{x,15} + \dot{m}_{s,21}\cdot\psi_{x,21} - \dot{m}_{s,16}\cdot\psi_{x,16} - \dot{m}_{s,22}\cdot\psi_{x,22} , \quad (19)$$

$$\dot{E}x_{D,HTHE} = \dot{m}_{s,16}\cdot\psi_{x,16} + \dot{m}_{s,18}\cdot\psi_{x,18} - \dot{m}_{s,17}\cdot\psi_{x,17} - \dot{m}_{s,19}\cdot\psi_{x,19} , \quad (20)$$

$$\dot{E}x_{D,Valve} = \dot{E}x_{D,V1} + \dot{E}x_{D,V2} + \dot{E}x_{D,V3} + \dot{E}x_{D,V4} , \qquad (21)$$

where, $\dot{E}x_{D,V} = \dot{m}_{in}\cdot\psi_{in} - \dot{m}_{out}\cdot\psi_{out}$, (22)

$$(1+f)\cdot \dot{m}_{air}\cdot \varepsilon_{x5,gas} = (1+f)\cdot \dot{m}_{air}\cdot \varepsilon_{x6,gas} + \dot{m}_{hw,31}\cdot \psi_{x,31} - \dot{m}_{hw,30}\cdot \psi_{x,30} + \dot{E}x_{D,HE}, \quad (23)$$

3.3. Energy level *ΔA*

A new method has been developed based on the concept of energy level to determine the mechanism of the change in the thermodynamic performance for the CCHP system under off-design conditions. The method was proposed first by Ishida in 1982 and was applied successfully in studies on chemical and thermal systems [28, 29]. The energy level is an intensive value and represents the energy quality.

The definition of the energy level *A* is given by

$$A = \frac{\Delta E}{\Delta H} = 1 - \frac{T_0 \Delta S}{\Delta H}, \quad (24)$$

where *ΔE* and *ΔS* represent the exergy change and entropy change, respectively, and *ΔH* is the amount of transformed energy/enthalpy.

An energy donor and an energy acceptor exist for an energy-transformation system. For the system consisting of an energy donor and an energy acceptor,

$$\Delta H_{ed} + \Delta H_{ea} = 0, \Delta S_{ed} + \Delta S_{ea} \geq 0 \quad (25)$$

The relationship between the exergy change for both sides can be written as:

$$\Delta E_{ed} + \Delta E_{ea} = (\Delta H_{ed} - T_0 \Delta S_{ed}) + (\Delta H_{ea} - T_0 \Delta S_{ea}) = -T_0 (\Delta S_{ed} + \Delta S_{ea}) \leq 0, \quad (26)$$

Then, the exergy destruction can be written as:

$$\Delta E = -\Delta E_{ed} - \Delta E_{ea} = \Delta H_{ea} \left(-\frac{\Delta E_{ed}}{\Delta H_{ea}} - \frac{\Delta E_{ea}}{\Delta H_{ea}}\right) = \Delta H_{ea} \left(\frac{\Delta E_{ed}}{\Delta H_{ed}} - \frac{\Delta E_{ea}}{\Delta H_{ea}}\right), \quad (27)$$

Combining Eq. (24), Eq. (26), and Eq. (27), the equation may be rewritten as:

$$\Delta E = \Delta H_{ea} (A_{ed} - A_{ea}) = \Delta H_{ea} \Delta A \geq 0, \quad (28)$$

The exergy of the energy is concluded to decrease always, and the energy level difference *ΔA* can be treated as the driving force of the process. Applying the general energy level difference equation to each component of the main equipment of the CCHP system, the energy level difference can be achieved for the whole system.

3.4. System performance indicators

The environmental impact of the CCHP system was evaluated by the TCO_2ER indicator, which was given by the following equation:

$$TCO_2ER = \frac{(m_{co_2})_{sp} - (m_{co_2})_{cchp}}{(m_{co_2})_{sp}} = \frac{(m_{co_2})_{sp} - (m_{co_2})_{cchp}}{(m_{co_2})_{sp}^{W} + (m_{co_2})_{sp}^{C} + (m_{co_2})_{sp}^{Q}}, \quad (29)$$

The amount of CO_2 emission from the CCHP system and the conventional separation system can be determined using the emission conversion factor as follows:

$$(m_{co_2})_{cchp} = (\mu_{co_2,cchp})^{F} \cdot F, \quad (30)$$

$$(m_{co_2})_{sp}^{W} = (\mu_{co_2,sp})^{W} \cdot W, \quad (31)$$

$$(m_{co_2})_{sp}^{\ Q} = (\mu_{co_2,sp})^{Q} \cdot Q, \qquad (32)$$

$$(m_{co_2})_{sp}^{\ C} = (\mu_{co_2,sp})^{W} \cdot C = (\mu_{co_2,sp})^{W} \frac{C}{COP^{sp}}, \qquad (33)$$

where μ is the emission conversion factor, in (g/kWh).

For a thermodynamic analysis of the CCHP system, the first two important indicators are fuel utilization efficiency and the FESR. Their expressions can be written by the following equation:

$$\eta = \frac{\dot{W} + \dot{Q} + \dot{C}/COP}{f \cdot \dot{m}_{air} \cdot LHV_{NG}}, \qquad (34)$$

The FESR is defined as the ratio of the saving energy of CCHP system in comparison with the SP system to the energy consumption by the SP system, and is expressed as:

$$FESR = \frac{F^{SP} - F^{CCHP}}{F^{SP}} = 1 - \frac{F^{CCHP}}{(\dot{W}/\eta_g)^{SP} + (\dot{Q}/\eta_b)^{SP} + (\dot{C}/\eta_g COP_e)^{SP}}, \qquad (35)$$

4. Results and discussion

4.1. System Performance

The performance of a CCHP system, consisting of a small-scale gas turbine, a double-effect absorption chiller driven by gas, and a heat exchanger, was studied. The specific technical parameters for the CCHP system and the SP system were listed in Table 1.

Table 1.Specific technical parameters of the CCHP and the SP

Item	Variable	Sysmbo	Value
CCHP	Gas turbine efficiency,%	η_e	27.1
	Rated power, kW	W	1748
	Absorption chiller COP	COP_a	1.3
	Rated cooling load, kW	C	4204
	Effective of the heat exchanger		1
SP	Overall generation efficiency,%	η_g	33
	Boiler efficiency,%	η_b	80
	Electricicalchiller COP	COP_e	5
CO_2 factor	Natural gas, g/kWh	$\mu_{co2,cchp}$	220
	Electricity of the grid, g/kWh	$\mu_{co2,e}$	968

The pressure, temperature, mass flow, and composition of the main points in Fig. 2 are listed in Table 2 when the CCHP system was operated at design point. To assess the part load performance of the CCHP system, a simulation model of the small scale gas turbine was adopted to predict the part load performance, which is presented in Appendix A. As for the double effect H2O-LiBr absorption chiller, the off design performance could be caculated based on the energy and mass balance. Details regarding the equations adopted to simulate the absorption chiller are available in reference [22]. The detailed expressions of the state parameters of LiBr-H_2O can be obtained from the correlations provided by ASHRAE (1998). When the load level of small gas turbine dropped, CCHP system was operated undert part load conditions and the state of main points in Fig.2 for the load level of 76.7% was presented in Table 3.

Table 2.Key point Parameters of the CCHP system at full load

Point	Mass (kg/s)	Temp(°C)	Pressure(kPa)	LiBr (%)	CO2 (%)	H2O (%)	O2 (%)	N2 (%)
1	7.5	25.0	101.3				21.00	79.00
2	7.5	289.3	709.3				21.00	79.00
3	7.6291	980.0	695.1		3.014	6.028	14.29	76.67
4	7.6291	568.8	101.3		3.014	6.028	14.29	76.67
5	7.6291	185.5	101.3		3.014	6.028	14.29	76.67
6	7.6291	90	101.3		3.014	6.028	14.29	76.67
7	0.9927	156.9	108.6			100		
8	0.9927	101.9	108.6			100		
9	0.9927	40.19	7.455			100		
10	0.8032	92.54	7.455			100		
11	1.796	40.19	7.455			100		
12	1.796	40.19	0.8531			100		
13	1.796	4.676	0.8531			100		
14	18.22	40.16	0.8531	58.87				
15	18.22	40.16	108.6	58.87				
16	18.22	79.12	108.6	58.87				
17	18.22	142.1	108.6	58.87				
18	17.23	161.6	108.6	61.95				
19	17.23	91.49	108.6	61.95				
20	17.23	91.49	108.6	61.95				
21	16.43	96.1	7.455	64.98				
22	16.43	48.56	7.455	64.98				
23	16.43	48.56	7.455	64.98				
24	116	32				100		
25	116	36.68				100		
26	172.7	12.81				100		
27	172.7	7				100		
28	265	32				100		
29	265	36.66				100		

♣ The composition of the working fluid (1-6) was molar basis percentage, whereas others were mass basis percentage.

Table 3.Key point Parameters of the CCHP system at part load of 76.7%

Point	Mass (kg/s)	Temp(°C)	Pressure(kPa)	LiBr (%)	CO2 (%)	H2O (%)	O2 (%)	N2 (%)
1	7.8	25	101.3		1	7.8	25	101.3
2	7.8	287.7	101.3		2	7.8	287.7	101.3
3	7.9082	857.22	686.8		3	7.9082	857.22	686.8
4	7.9082	486.21	101.3		4	7.9082	486.21	101.3
5	7.9082	169.8	101.3		5	7.9082	169.8	101.3
6	7.9082	90	101.3		6	7.9082	90	101.3
7	0.8324	145.4	108.6		7	0.8324	145.4	108.6
8	0.8324	94.69	108.6		8	0.8324	94.69	108.6
9	0.8324	38.9	7.455		9	0.8324	38.9	7.455
10	0.687	86.94	7.455		10	0.687	86.94	7.455
11	1.519	38.9	7.455		11	1.519	38.9	7.455
12	1.519	38.9	0.8531		12	1.519	38.9	0.8531
13	1.519	5.028	0.8531		13	1.519	5.028	0.8531
14	18.06	38.9	0.8531	57.72	14	18.06	38.9	0.8531
15	18.06	38.9	108.6	57.72	15	18.06	38.9	108.6
16	18.06	75.49	108.6	57.72	16	18.06	75.49	108.6
17	18.06	132.7	108.6	57.72	17	18.06	132.7	108.6
18	17.23	149	108.6	60.51	18	17.23	149	108.6
19	17.23	86.53	108.6	60.51	19	17.23	86.53	108.6
20	17.23	86.53	108.6	60.51	20	17.23	86.53	108.6
21	16.54	89.76	7.455	63.03	21	16.54	89.76	7.455
22	16.54	46.53	7.455	63.03	22	16.54	46.53	7.455
23	16.54	46.53	7.455	63.03	23	16.54	46.53	7.455
24	116	32			24	116	32	
25	116	35.94			25	116	35.94	
26	172.7	11.93			26	172.7	11.93	
27	172.7	7			27	172.7	7	
28	265	32			28	265	32	
29	265	35.94			29	265	35.94	

♣ The composition of the working fluid (1-6) was molar basis percentage, whereas others were mass basis percentage.

Figure 1 shows the utility of the energy released by the combustion reaction of the chemical fuel in combustor. As seen in Fig.1, when the CCHP was operated under the design condition, the maximum energy was used to drive a double-effect absorption chiller, and then followed by power, wherein the exhaust gas was smallest. However, for the off-design condition, the electricity is decreased, and the amount of the energy ejected to the environment was considerable. The overall fuel utility efficiency of the CCHP system ranged from 80% to 90% using a heat exchanger to recover the low-grade energy. The overall fuel utility efficiency of the CCHP system is 65%-75% without a heat exchanger. Figure3 shows the exergy distribution among the main equipment of the CCHP system. The exergy of the exhaust gas from the double-effect chiller was very small compared to the other equipment.

A conventional SP is compared to the CCHP to calculate the FESR of the CCHP system, as listed in Table 3.The variation of the FESR of the CCHP system under different load levels was presented in Fig. 4. For the design point, the FESR had a value as high as 26.6%. The lower the load level was, the smaller is the FESR value. When the load level decreased to approximately 30% of the full load level, the FESR is zero, which means that the energy saving performance of the CCHP system was identical to the SP system. As for the load level of 19%, the performance of the CCHP system has deteriorated considerably with the FESR value of -7.4%.

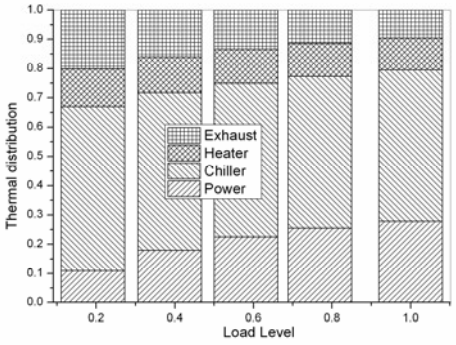

Fig. 2 The energy distribution under different load levels

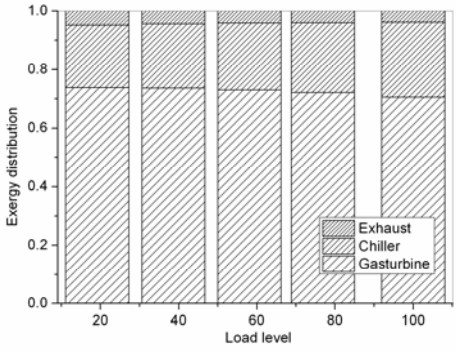

Fig. 3 The exergy distribution under different load levels

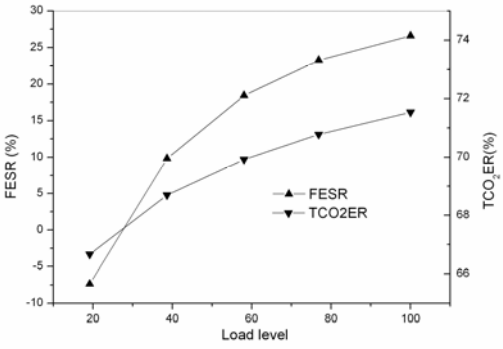

Fig.4 FESR and TCO2ER of the CCHP system

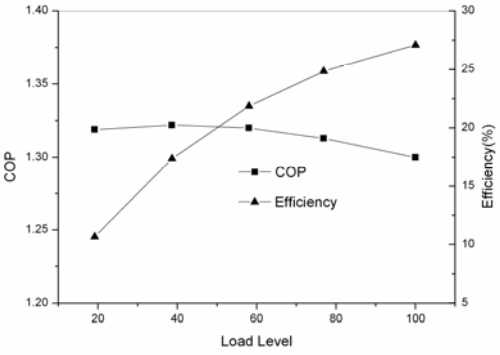

Fig. 5 Components performance under different load levels

The environmental performance of the CCHP system is shown in Fig. 4. The TCO_2ER improves the performance for all the load level ranges, even if the FESR of the CCHP is negative. For instance, the TCO2ER is 67% for the load level of 19%, whereas -7.4% for the FESR. The CO_2 emission reduction ranging from approximately 67% to 72% is concluded to be excellent for every loading level. The lower emission conversion factor of the natural gas resulted in a good enviromental performance.

The variation of the performance for the gas turbine and the double-effect absorption chiller under off-design performance was shown in Fig. 5. As can be seen, the efficiency of the small-scale gas turbine changed dramatically, wheareas the performance of the double-effect absorption chiller has changed slightly. The efficiency ranged from 27.1% at the full load to 11% at 19% of the full load. As shown in Fig.5, the COP of the absorption chiller increased slightly with the decreasing load level of the CCHP system, and then decreased slightly with the continuing decrease of the load level. Therefore, the performance deterioration in the FESR and the TCO_2ER was mainly due to the bad performance of the gas turbine under off-design condition.

4.2. Component performance and exergy destruction

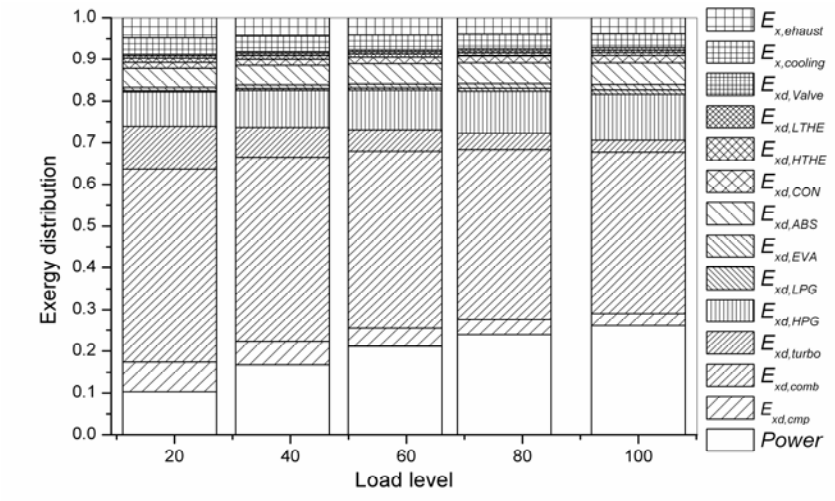

Fig. 6. Effect of the variation of load levels on the exergy distribution among different components

Figure 6 shows the exergy distribution of the exergy input by the fuel. As can be seen, power and cooling exergy ($E_{x,cooling}$) was two types of useful exergy product, exergy of the flue gas ($E_{x,exhaust}$) was exergy loss ejected to enviroment, wheareas others are exergy destruction in different components. Under the part load condition, the combustor was found to have the largest exergy destruction, followed by HPG, absorber, and compressor. When the power output of the gas turbine decreases, the fuel added to the combustor decreases as well. As the load level decreases the exergy destruction in combustion chamber increases, because the mean temperature of the working fluid decreases. For the double effect absorption chiller, the exergy destruction in HPG decreases, and the cooling exergy output increases, significantly. So, the COP of the absorption chiller remains constant under part load condition, and the chiller makes a positive contribution to the performance enhancement of the CCHP system.

Table 2 shows the exergy destruction in each component of the CCHP system with the changing load levels for the same unit electricity. It can be also found that the exergy destruction in combustor was largest and increased with the decreasing load level, which resulted in the performance deterioration of the small-scale gas turbine as illustrated in Fig.5.

Table 2.Exergy destruction per unit electricity in different components of the CCHP system

Component	Load level *(%)*				
	100	76.7	58.1	38.6	19.2
$E_{dx,cmp}$, kW/kW	0.11156	0.15175	0.20929	0.32887	0.69576
$E_{dx,comb}$, kW/kW	1.48261	1.70162	2.0119	2.63872	4.50355
$E_{dx,turbo}$, kW/kW	0.10885	0.15984	0.24177	0.42143	0.98887
$E_{dx,HPG}$, kW/kW	0.42077	0.4205	0.44755	0.5269	0.80344
$E_{dx,LPG}$, kW/kW	0.03918	0.03031	0.02629	0.02466	0.02882
$E_{dx,EVA}$, kW/kW	0.04756	0.04454	0.04503	0.0501	0.0716
$E_{dx,ABS}$, kW/kW	0.20258	0.21248	0.23378	0.28514	0.45395
$E_{dx,CON}$, kW/kW	0.06682	0.06715	0.0726	0.08773	0.13911
$E_{dx,HTHE}$, kW/kW	0.03134	0.03425	0.03991	0.05273	0.0933
$E_{dx,LTHE}$, kW/kW	0.02291	0.02359	0.02712	0.03595	0.06435
$E_{dx,Valve}$, kW/kW	0.02193	0.02079	0.02155	0.02501	0.03811
$E_{dx,EXHAUST}$, kW/kW	0.14703	0.16448	0.19416	0.25953	0.4644

4.3. Energy level analysis

Table 3 presents the energy level analysis results for different load levels for all the components of the CCHP system. When the CCHP system was operated at the design condition, the energy level difference ΔA in the combustor is the largest with a value of 0.3871, followed by the HPG with a value of 0.2274, and then the compressor of the small-scale gas turbine with a value of 0.0972. The magnitude of the energy level difference ΔA in other equipments of the CCHP system is small, and can be shown easily with an order of magnitude on the first column of Table 3. The improvement of the design performance of the CCHP system lies mainly in the combustor of the gas turbine and the HPG of the double-effect water-LiBr absorption chiller.

The energy level difference ΔA for each component under off-design condition was obtained in the analysis, and the trend of the energy level difference ΔA for different load levels could also be evaluated. The change of ΔA for all the components of the small-scale gas turbine is positive, whereas the trend for all the components of a double-effect absorption chiller is negative. This phenomenon implies that the performance of the absorption chiller tends to produce good performance under the off-design conditions, and the performance of the gas turbine tends to deteriorate under the same conditions. The analysis results can be used to explain the opposite performance characteristics of the main equipment illustrated in Fig. 6.

Table 3.Energy level difference analysis on different components of the CCHP system

	The energy level difference ΔA				
ITEM	ΔA_1	ΔA_2	ΔA_3	ΔA_4	ΔA_5
Level	*100%*	*76.87%*	*58.05%*	*38.64%*	*19.17%*
Cmp	0.0972	0.09777	0.09903	0.10092	0.10336
Comb	0.3871	0.40755	0.42434	0.44262	0.46266
Turbo	0.05048	0.06257	0.0778	0.09946	0.12904
HPG	0.2274	0.2081	0.1924	0.1755	0.1574
LPG	0.02921	0.02063	0.01556	0.01138	0.0079
EVA	0.01978	0.01679	0.01467	0.01263	0.01063
ABS	0.0685	0.06533	0.06225	0.05878	0.05503
CON	0.05146	0.0472	0.04425	0.04144	0.03874
HTHE	0.02419	0.02229	0.02098	0.01974	0.01853
LTHE	0.02862	0.02404	0.02179	0.02007	0.01862

The trend of the energy level difference ΔA for each component indicates the driving force change of the component itself. From the results listed in Table 3, the potential to enhance the off-design performance of the gas turbine lies in the combustor. As for the double-effect absorption chiller adopted in the CCHP system, the key factor for the off-design performance is the HPG.

4. Conclusions

A CCHP system for the production of electricity, cooling load, and hot water has been analyzed. The off-design performance of a small-scale gas turbine and a double-effect water-LiBr absorption chiller is simulated. A conceptual heat exchanger to produce hot water is introduced to recover the low-grade waste heat in the exhaust gas. The fuel utility efficiency and FESR were used to evaluate the thermodynamic performance of the CCHP system. The TCO_2ER indicator evaluated the environmental impact of the system. The exergy analysis and the energy level difference analysis were performed on the equipment and each components of the CCHP system. The following conclusions are drawn from the analysis results of the system.

(1) The CCHP system is not always an energy-saving system. The results showed that the FESR is approximately zero when the load level of the system has decreased to 30% of the full load. The results of the TCO_2ER indicator in the assessment of the emission impact showed that the CCHP system is always environment-friendly for all the load levels, and the TCO_2ER ranged from 66.7% to 71.5% as the load increased from 19% to full load. From thermodynamic point of view, the performance deterioration of CCHP system becomes not energy-saving, because the performance deterioration of the gas turbine under part load condition as described in this study.

(2) The exergy destruction in the combustor is the largest among all the components of the CCHP system.

(3) The heat exchanger has a direct impact on the fuel utility efficiency of the CCHP system, which was enhanced by 10% for all the load level ranges. However, the exergy destruction by the exhaust gas from the absorption chiller is considerably small.

(4) The energy level analysis was conducted on each component of the CCHP system, and the mechanism of the off-design performance deterioration for the CCHP system is determined. Under part load condition, the energy level difference ΔA in the combustor increased and resulted in the performance deterioration of the CCHP system.

Acknowledgments

The authors gratefully acknowledge the support from the National Key Fundamental Research Project (Contract No. 2010CB227306) and the National Natural Science Foundation of China (Contract No. 51176185).

Appendix A

The gas turbine engine is a complex assembly of a variety of components and the complexity of aerothermodynamic analysis makes it impossible to mathematically solve the optimization equations involved in various gas turbine cycles. In the present work, according to an explicit analytical solution [19], a simulation program written in FORTRAN code was developed for the prediction of the small scale gas turbine. The computer program basically satisfies the matching conditions analytically between the various gas turbine components to produce the equilibrium running line. A set of performance maps is used to describe the off design of the compressor, and the turbine. The maps described in reference [20], were obtained from a simplified set of analytical equations that represents a compromise between calculation costs and accuracy of the results.

1. Model description

1.1. Compressor

The temperature at the end of compression T_2 and power consumed by the compressor are calculated by the Eq. (A.1) and Eq. (A.2).

$$T_2 = T_1 \pi_{cmp}^{\frac{k-1}{\eta_{cmp} \cdot k}}, \qquad \text{(A.1)}$$

$$\dot{w}_{cmp} = \dot{m}_{cmp} \cdot c_{p,air} \cdot (T_2 - T_1), \qquad \text{(A.2)}$$

The characteristic map of the compressor was calculated by the analytical equations, which is shown in Fig. A.1.

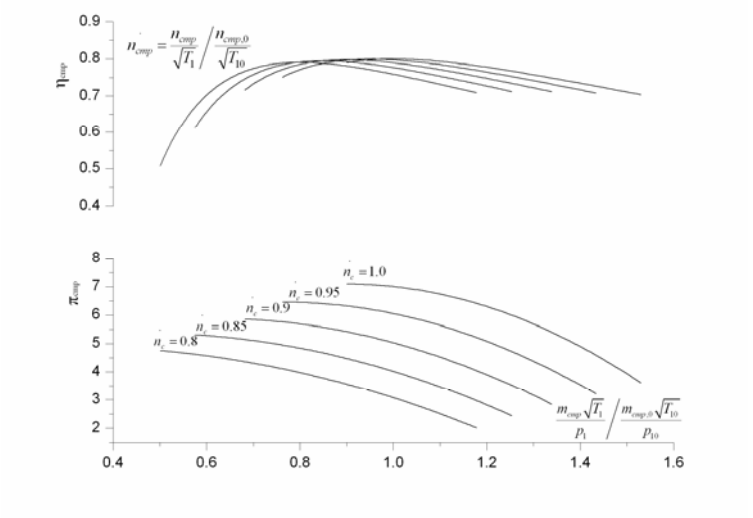

Fig. A.1 Compressor characteristic maps

1.2 Turbine

The temperature at the end of compression T_4 and power consumed by the compressor are calculated by the Eq. (A.3) and Eq. (A.4). The isentropic efficiency and the mass flow of the turbine are presented in Turbine characteristics map (Fig. A.2).

$$T_4 = \frac{T_3}{\pi_t^{\frac{k-1}{\eta_t \cdot k}}}, \qquad \text{(A.3)}$$

$$\dot{w}_{turbo} = \dot{m}_{turbo} \cdot c_{p,gas} \cdot (T_3 - T_4), \qquad \text{(A.4)}$$

A Flugel formula is used to describe the correlation between the mass flow, the pressure ratio and the rotational speed of the turbine [19]

$$\frac{\dot{m}_{turbo}}{\dot{m}_{turbo,0}} = \sqrt{1.4 - 0.4\frac{n_{turbo}}{n_{turbo,0}}} \cdot \sqrt{\frac{T_{30}}{T_3}} \cdot \sqrt{\frac{\pi_{turbo}{}^2 - 1}{\pi_{turbo,0}{}^2 - 1}}, \qquad \text{(A.5)}$$

The efficiency characteristic of the turbine is defined as [19]

$$\dot{\eta}_t = [1 - t_4(1 - \dot{n}_t)^2]\frac{\dot{n}_t}{\dot{G}_t}(2 - \frac{\dot{n}_t}{\dot{G}_t}), \qquad \text{(A.6)}$$

where

$$\dot{G}_t = \frac{\dot{m}_{turbo}\sqrt{T_3}}{p_3} \Big/ \frac{\dot{m}_{turbo,0}\sqrt{T_{30}}}{p_{30}}, \qquad \text{(A.7)}$$

$$\dot{n}_{turbo} = \frac{n_{turbo}}{\sqrt{T_3}} \Big/ \frac{n_{turbo,0}}{\sqrt{T_{30}}}, \qquad \text{(A.8)}$$

$$\dot{\eta}_{turbo} = \frac{\eta_{turbo}}{\eta_{turbo,0}} \text{ (A.7)}, \qquad \text{(A.9)}$$

T_4 is an undetermined constant, which was set to 0.3 for a small scale gas turbine.

1.3 Equilibrium conditions

Gas turbine steady running should maintain the following equilibrium conditions

$$\pi_{turbo} = \varphi \cdot \pi_{cmp}, \qquad \text{(A.10)}$$

$$G_{turbo} = G_{cmp}, \qquad \text{(A.11)}$$

$$n_{turbo} = n_{cmp}, \qquad \text{(A.12)}$$

The pressure recovery coefficient φ is usually chosen to be constants.

2. The running strategy of the small scale gas turbine

A small-scale gas turbine composed of a centrifugal compressor and a radial inflow turbine with a power output of 1.7 MW was investigated, whose techanial specifications were listed in Table 2. Since the small scale gas turbine was operated for the electricity, the compressor was run on the constant speed line of the characteristic map (Fig. A.1).

Nomenclature

A energy level

C cooling load flow, kW

c specific heat, J/(kg K)

$\dot{E}x$ Exergy destruction, kW

e total energy flow, kW/kg

f fuel to air ratio

h enthalphy, kJ/kg

$\dot{m}$ mass flow rate, kg/s

n turbine speed

$\dot{Q}$ heat flow rate, kW

$\dot{W}$ work flow rate, kW

S entropy, kJ/(kg K)

T temperature, K

Greek symbols

η efficiency

ε exergy for the gas turbine working flow

Ψ exergy for the absorption chiller working flow

μ emission conversion factor

σ the effectiveness of the heat exchanger

Subscripts and superscripts

ABS absorper

amb ambient condition

cmp compressor

comb combustor

CON condenser

des exergy destruction

ea energy acceptor

ed energy donor

EVA evaporator

fuel fuel supplied in combustor

HPG high pressure generator

HTHE high temperature heat exchanger

in input

LPG lower pressure generator

LTHE lower temperature heat exchanger

net the net work output

SP separate production

turbo turbine

out output

V valve

0 design value

1, 2 3,... state point in the Fig. 1

References

[1] Chicco G., Mancarefla P., Distributed multi-generation: A comprehensive view. Renew Sust Energ Rev 2009; 13(3):535-51.

[2] Mago PJ., Chamra LM., Hueffed A., A review on energy, economical, and environmental benefits of the use of CHP systems for small commercial buildings for the North American climate. Int J Energy Res 2009; 33(14):1252-65.

[3] Chai Q., Zhang X., Technologies and policies for the transition to a sustainable energy system in china. Energy 2010; 35(10):3995-4002.

[4] Romier A.. Small gas turbine technology. Appl Therm Eng 2004; 24(11-12):1709-23.

[5] Wu DW., Wang RZ., Combined cooling, heating and power: A review. Prog Energy Combust Sci 2006; 32(5-6):459-95.

[6] Gupta KK., Rehman A., Sarviya RM. Bio-fuels for the gas turbine: A review. Renew Sust 2010; 14(9):2946-55.

[7] Bassols J., Kuckelkorn B., Langreck J., Schneider R, Veelken H. Trigeneration in the food industry. Appl Therm Eng 2002; 22(6):595-602.

[8] Poullikkas A., An overview of current and future sustainable gas turbine technologies. Renewable & Sustainable Energy Reviews 2005; 9(5):409-43.

[9] Kong XQ., Wang RZ., Huang XH., Energy optimization model for a CCHP system with available gas turbines. Appl Therm Eng 2005; 25(2-3):377-91.

[10] Khaliq A., Kumar R., Thermodynamic performance assessment of gas turbine trigeneration system for combined heat cold and power production. Journal of Engineering for Gas Turbines and Power-Transactions of the ASME 2008; 130(2):1-4.

[11] Khaliq A., Exergy analysis of gas turbine trigeneration system for combined production of power heat and refrigeration. Int J Refrig-Rev Int Froid 2009; 32(3):534-45.

[12] Carles Bruno J., Valero A., Coronas A., Performance analysis of combined microgas turbines and gas fired water/LiBr absorption chillers with post-combustion. Appl Therm Eng 2005; 25(1):87-99.

[13] Huicochea A., Rivera W., Gutierrez-Urueta G., Bruno JC., Coronas A., Thermodynamic analysis of a trigeneration system consisting of a micro gas turbine and a double effect absorption chiller. Appl Therm Eng 2011; 31(16):3347-53.

[14] Chicco G., Mancarella P., Assessment of the greenhouse gas emissions from cogeneration and trigeneration systems. Part I: Models and indicators. Energy 2008; 33(3):410-7.

[15] Mancarella P., Chicco G., Assessment of the greenhouse gas emissions from cogeneration and trigeneration systems. Part II: Analysis techniques and application cases. Energy 2008; 33(3):418-30.

[16] Mago PJ., Chamra LM., Analysis and optimization of CCHP systems based on energy, economical, and environmental considerations. Energy and Buildings 2009; 41(10):1099-106.

[17] Mago PJ., Fumo N., Chamra LM., Performance analysis of CCHP and CHP systems operating following the thermal and electric load. Int J Energy Res 2009; 33(9):852-64.

[18] Mancarella P., Chicco G., Global and local emission impact assessment of distributed cogeneration systems with partial-load models. Appl Energy 2009; 86(10):2096-106.

[19] Zhang N., Cai RX., Analytical solutions and typical characteristics of part-load performances of single shaft gas turbine and its cogeneration. Energy Convers Manage 2002; 43(9-12):1323-37.

[20] Wang W., Cai RX., Zhang N., General characteristics of single shaft microturbine set at variable speed operation and its optimization. Appl Therm Eng 2004; 24(13):1851-63.

[21] Al-Hamdan QZ., Ebaid MSY., Modeling and simulation of a gas turbine engine for power generation. Journal of Engineering for Gas Turbines and Power-Transactions of the ASME 2006; 128(2):302-11.

[22] S.C K., A A., Energy and exergy analysis of single effect and series flow double effect water-lithium bromide absorption refrigeration systems. International Journal of Refrigeration 2009(32):2147-58.

[23] Bejan A., Fundamentals of exergy analysis, entropy generation minimization, and the generation of flow architecture. International Journal of Energy Research 2002; 26(7):545-65.

[24] Heiser WH., Huxley T., Bucey JW., The Brayton Cycle Using Real Air and Polytropic Component Efficiencies. Journal of Engineering for Gas Turbines and Power 2011; 133(11):111702.

[25] Young JB., Wilcock RC., Modeling the air-cooled gas turbine: Part 1 - General thermodynamics. Journal of Turbomachinery-Transactions of the ASME 2002; 124(2):207-13.

[26] Szargut J., Chemical exergies of the elements. Appl Energy. 1989; 32(4):269-86.

[27] Balli O., Aras H., Hepbasli A., Thermodynamic and thermoeconomic analyses of a trigeneration (TRIGEN) system with a gas-diesel engine: Part I - Methodology. Energy Conversion and Management 2010; 51(11):2252-9.

[28] Gao L., Jin HG., Liu ZL., Zheng DX., Exergy analysis of coal-based polygeneration system for power and chemical production. Energy 2004; 29(12-15):2359-71.

[29] Jin HG., Han W., Gao L., Multifunctional energy system (MES) with multifossil fuels and multiproducts. Journal of Engineering for Gas Turbines and Power-Transactions of the ASME 2007; 129(2):331-7.

Baffle as a cost-effective design improvement for volatile combustion rate increase in biomass boilers of simple construction

Borivoj Stepanov[a], Ivan Pešenjanski[b] and Biljana Miljković[c]

[a] *Faculty of technical sciences, Novi Sad, Serbia, bstep@uns.ac.rs*
[b] *Faculty of technical sciences, Novi Sad, Serbia, ivpes@uns.ac.rs*
[c] *Faculty of technical sciences, Novi Sad, Serbia, bmilj@uns.ac.rs*

Abstract:

Boilers from low-cost market segment in Serbia are having simple fire-box design, water cooled walls, are operated with high air excess values for achievement of targeted heat outputs. They are cheap, perform heating duties but at the cost of efficient fuel utilization and emission. Purpose of this research is to investigate influence of baffles, which are not present in the current design, onto one of the major parameters of combustion, gas residence time in boiler. Common fuel in Serbian northern province Vojvodina is straw, which has a high volatile content. Through increase of flue gas residence time app. 50% of energy contained in fuel that is released with volatiles could be more effectively utilized. For calculation of residence time and due to complexity of combustion phenomena, method of cold flow computational fluid dynamics simulations is applied. Results for different baffle positions, dimensions and flow rates show from up to 17% decrease to up to 13 % increase of residence time. From these two design parameters and one operating parameter, most significant changes has caused vertical position of the baffle, followed by importance with length of the baffle, and least important showed to be the mass flow, which did not change the trend of increase or decrease of residence time for varying design changes. So conclusion of this research is that baffles should be used but with its correct positioning and having under analysis also two important factors such are lining as it prevents gas mixture temperature drop under the ignition point and a pressure drop that has to be covered by additional natural or artificial draft increase.

Keywords:

Combustion improvement, Residence time, Low-cost measures, Baffle, Cold flow, CFD

1. Introduction

Small-scale boilers are much smaller in size compared to boilers powering turbines or industrial processes but the complexity of the phenomena occurring inside them is the same. Previous authors' research [1] in this field lead to the methodology for application of computational fluid dynamics for study of one important aspect of combustion, i.e. residence time. In that paper major parameter was secondary air nozzle angle and flow rate. This paper is about baffles, and seeks to answer the question why there are not in wider use in domestic low-cost boilers.

Three following quotes, first from the major furnace textbook, second from the incinerator design field and the last from the stove improvement research shed light onto the existence of the problem that is to be discussed in this paper.

"Length of the gas flow path is sometimes referred to as „residence time", but the term is often misinterpreted because the time in the furnace is not just a function of the gas flow path but also the velocity of the gases." [2]

"The value of knowing the gas residence times in large municipal incinerators and the serious error imposed by the traditional use of gas volume flow rate based average residence time with regard to these incinerators are recognized." [3]

"Effect of baffles is unpredictable."[4]

1.1 - Baffles

Baffle is a metal plate installed in combustion chamber that extends from rear or front side of the chamber. Purpose of a baffle is to force gases to take the longer path before exiting the combustion chamber. This increases the length of the flow path, but it is questionable does it leads to increase of hot gas residence time, as in the channel outlined by the baffle and the top furnace side average velocity is greater then the average velocity in unbaffled design, and this has a negative influence on the residence time.

Residence or retention time in a combustion chamber without baffles is calculated through division of chamber volume with volumetric flow rate. Baffle is a thin plate of fire resistant metal. It does not change the volume significantly, but it changes flow path, and the abovementioned formula does not apply.

Beside the influence onto flow path and residence time baffles can promote combustion also through mixing improvement as they bring the reactants closer together and as they create turbulence, or through higher temperature as they prevent cooling of the primary zone through act of barrier between it and cooled parts of furnace walls.

Usage of baffles in stoves design was introduced by Norvegian company Jotul in the ’70s in the time of oil crisis. Efficiency of this then new „Scandinavian“ baffle pass design lead to significant increase of efficiency. Producer stated the efficiency of one of its stoves Jotul 118 at 76 procent.

1.2 – Boiler efficiency current stand

According to the performed tests reported in [5, 6], straw bales boilers efficiencies are in the range from 31 to 73%, and excess air values on the other hand in the range from 1.3 to 8.8.

Biomass as a fuel, when compared to coal, has a lower energy density and it is more difficult to handle. Its chemical composition causes deposits resulting from combustion, slagging and fouling are the problems with which engineers are confronted. Important property of straw is volatiles content. For wheat straw, volatile content is 71 %, ash 8.9, fixed carbon 20%, according to [7]. Similar data can be found in [8]. So approximately we have a gaseous-like solid fuel, and this fact should be taken into account when designing a furnace, if efficient and eco-friendly boiler is to be made.

In low-cost boiler market segment boilers with box type furnace and water cooled walls are common. For this design is of interest to study the effect of baffle instalment.

1.3 – Tests on baffles

Question is how efficient baffles are. Available testing results are rare. The exception that proves the rule is the work done by Jay Shelton. He has performed great number of testings on different stoves. Results are published in [4]. Conclusions drawn from tests can be summoned in one statement: “Effect of baffles is unpredictable and that there are so many possible design configurations”. Results from tests of two Scandinavian stoves are presented, a large and small model of the same design. With and without baffle present, as also over a range of power inputs. Results show the following effects. In a larger stove baffle had little effect on any of the three energy efficiencies – combustion, heat transfer and overall. In case of the smaller stove overall energy efficiency is improved by 2 percentage points.

The next figure shows how many design variations can baffle create to a simple combustion/heating device - vertical drum stove.

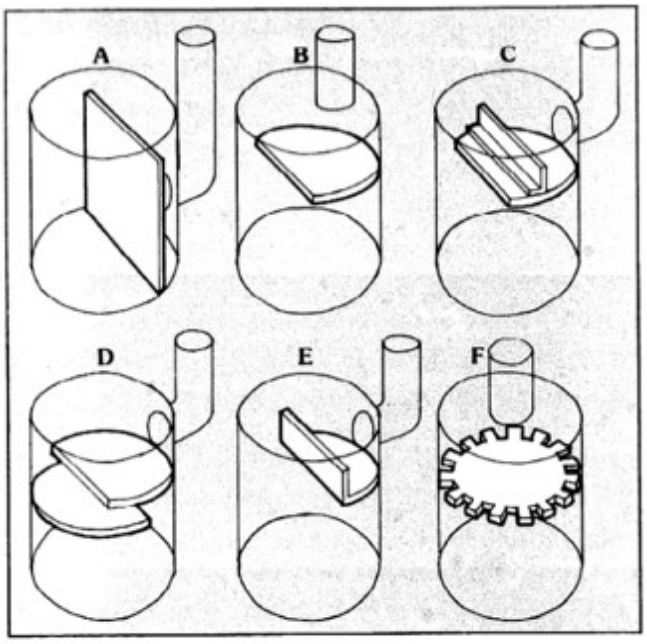

Fig. 1. Various baffle arrangements for vertical drum stoves [9]

1.4 – Baffles in use today

Baffles are present in contemporary design, what can be seen in number of studies where this design detail is presented [10, 11 and 12], as in modern biomass boilers. Papers in which their different configurations are studied are rare [13]. In studies [14, 15] problem which is at core of this paper is stated as „maximising residence time of combustion gases in the secondary chamber by improving firebox configuration and baffle locations“. In the [16] flow in stoves with baffles is known under name S-flow named. Residence time has been studied in 60 and 70-s, [17, 18] It is worth mentioning that the cold flow approach has been implemented in [17].

2. Method

2.1. CFD software

The present paper is based on the commercial STAR-CCM+ code from CD adapco Group. CFD solver used for solving problems involving flow (of fluids or solids), heat transfer and stress. It has ability to tackle problems involving multi-physics and complex geometries. Computer processor used for performing simulation runs was Intel Pentium E2140 1M Cache, 1.60 GHz, 800 MHz FSB dual core processor.

2.2. Lagrange particle tracking for residence time calculation

STAR-CCM+ uses Lagrangian/Eulerian framework [19] for describing multiphase problems. The physics continuum is a continuous phase whose governing equations are expressed in Eulerian form. Lagrangian approach is applied for modelling of arbitrary number of dispersed phases. Particle-like elements known as parcels are followed through the continuum, with the state of each parcel updated according to a selected set of models and optionally recorded as a track.

These phases can be massless. So these fluid particles, which simply move with the continuous phase, without influencing each other or the continuous phase. In this paper massless phase has been utilized. Velocity of the massless particle is equal to the one of surrounding fluid.

$$v_p = v \tag{1}$$

2.3. Cold flow approach

Cold flow is known by other names: isothermal flow, non-reacting flow, and they all refer to modelling flow without taking into account the reactions.

In order to determine the effects of design parameters on combustion researchers have frequently used cold-flow simulations. Examples are referenced in [20], and are namely works from field of waste incineration [21, 22, 23, 24 and 25]. The cold flow models are extremely useful, because they provide a reasonable amount of information while minimizing the complexities and efforts. [20]

It is obvious, however, that real incinerator performance cannot be reproduced with cold-flow models. Some of the major problems include the density variation of combustion gases (typically a function of the temperature and the combustion stoichiometry), the heat generation associated with the chemical reaction and the heat transfer between the wall, the waste bed and the combustion gases (probably with the products of incomplete combustion).[20] Independently from the above stated recommendation has been made [26] to include in the model dependence of gases density of height, but convergence difficulties have not been surpassed by the author.

It is of importance to note the example from industry, where Steinmueller, renown incinerator producer, has relied heavily on extensive cold-flow modelling and in-furnace field measurements to optimize the design and operation of their systems in order to ensure high temperatures and uniform mixing conditions.[27]

2.4. Description of geometry and physics model

Nine different geometry cases has been studied, each determined by the vertical position and the distance from the side of the baffle. In each case baffle extends from one side. Dimensions are: 1 x 1 x1 m (height x width x length). Recommended furnace heat load per volume unit is taken from [28] for the hand stoked boilers. For the given heat load according air flows are calculated for different air excess values. They are 0.16, 0.24, 0.32, 0.40 and 0.48 kg/s.

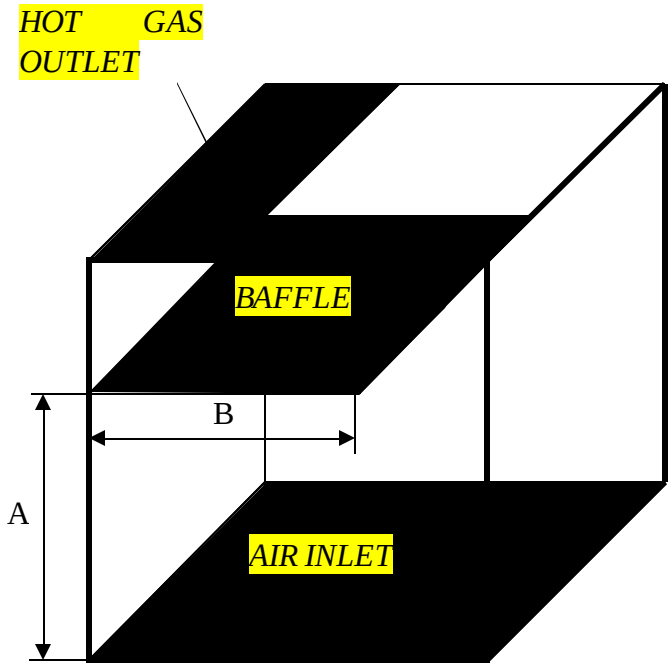

Fig. 2. Geometry of the problem

Two main parameters determine the geometry. It is A which is the height at which the baffle is positioned in the firebox, and B which is the width of the baffle. The A parameter in the simulations

takes the following values: A1: 0.7m; A2: 0.8m; A3: 0.9m, and the B parameter takes: B= B1: 0.7m; B2: 0.8m; B3: 0.9m. Combination of these values leads to the Cases:

Case 1: A1 & B1; Case 2: A1 & B2; Case 3: A1 & B3; Case 4: A2 & B1; Case 5: A2 & B2; Case 6: A2 & B3; Case 7: A3 & B1; Case 8: A3 & B2; Case 9: A3 & B3.

Base case named Case 0 is the one without baffle. Ten cases from Case 0 to Case 9 has been calculated for each selected mass flow. In total 50 simulations have been performed.

Flow turbulence is modelled using Reynolds-Averaged Navier-Stokes turbulence models. Closure is done through usage of Realizable Two-Layer K-Epsilon Model. The Coupled Flow model is applied which solves the conservation equations for mass and momentum simultaneously using a time- (or pseudo-time-) marching approach. [19]

3. Results

In the following table and accompanying graph are presented results from average residence time calculation.

Table 1. Average residence time for different geometries and mass flows

Average residence time [s] t_{CFD}		Mass flow [kg/s] 0.16	0.24	0.32	0.4	0.48
Case	0	7.62	5.08	3.81	3.05	2.55
Case	1	6.97	4.61	3.49	2.79	2.32
Case	2	6.54	4.37	3.28	2.62	2.18
Case	3	6.51	4.26	3.19	2.55	2.12
Case	4	7.35	4.88	3.67	2.95	2.45
Case	5	7.23	4.82	3.62	2.89	2.41
Case	6	7.32	4.83	3.61	2.88	2.4
Case	7	7.94	5.28	3.95	3.15	2.61
Case	8	8.14	5.29	3.91	3.14	2.61
Case	9	8.65	5.7	4.25	3.35	2.73
Air density [kg/m³]		1.18415				
$t_{calc.Case\,0}$*		7.4	4.93	3.7	2.96	2.47
$(t_{calc.Case\,0} - t_{CFD\ \ Case\,0})/t_{CFD\ \ Case\,0}$**		-0.03	-0.03	-0.029	-0.031	-0.035

* $t_{calc.Case\,0} = \frac{V}{\dot{m}/\rho_{Air}}$, where V, $\dot{m}$ and ρ_{Air} are volume of the combustion chamber, air mass flow and air density.

** differences appear as a result of influence on the average value of the tracks which end in a recirculation flows

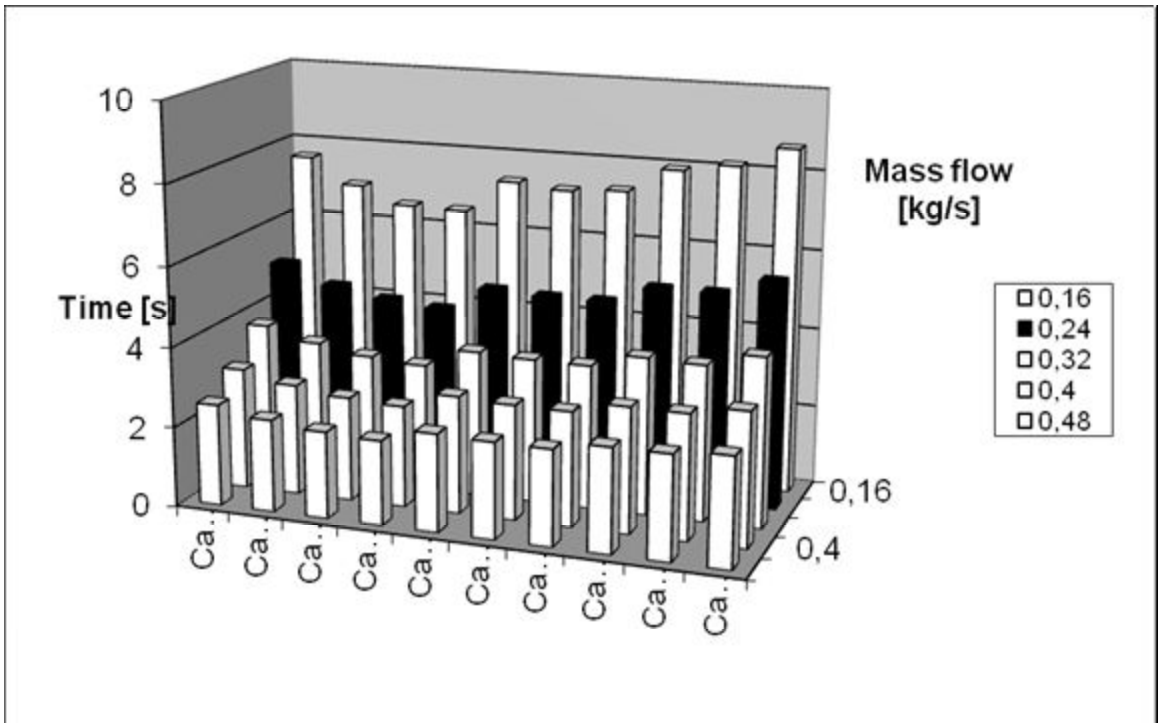

Fig. 3. Average residence time for different geometries and mass flows

The following table and accompanying graph present the same results as above, just in relative values. Base value is residence time for the Case 0.

Table 2. Average residence time for different geometries and mass flows presented in relative units (base case Case 0- baffles case)

t_{rel} *		Mass flow [kg/s]				
		0.16	0.24	0.32	0.4	0.48
Case	1	-8.5	-9.3	-8.4	-8.5	-9
Case	2	-14.2	-14	-13.9	-14.1	-14.5
Case	3	-14.6	-16.1	-16.3	-16.4	-16.9
Case	4	-3.5	-3.9	-3.7	-3.3	-3.9
Case	5	-5.1	-5.1	-5	-5.2	-5.5
Case	6	-3.9	-4.9	-5.2	-5.6	-5.9
Case	7	4.2	3.9	3.7	3.3	2.4
Case	8	6.8	4.1	2.6	3	2.4
Case	9	13.5	12.2	11.5	9.8	7.1

* Relative residence time $t_{rel} = (t_{CFD\ \ Case\,i} - t_{CFD\ \ Case\,0}) / t_{CFD\ \ Case\,0}$

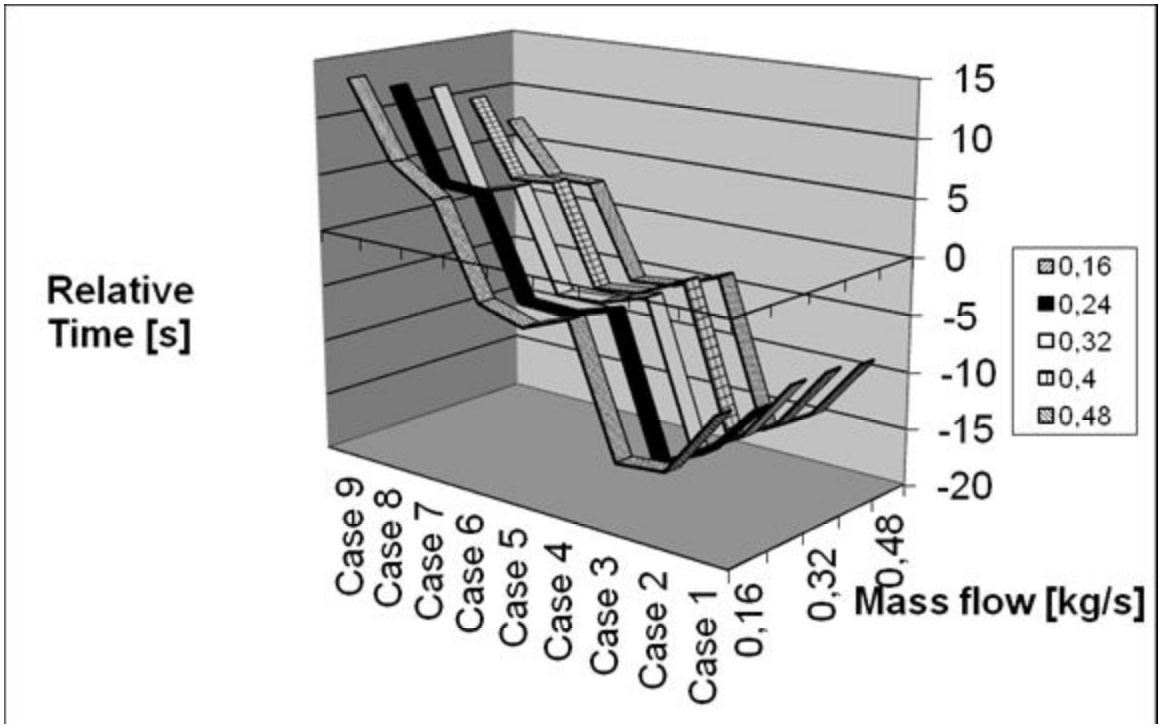

Fig. 4. Average residence time for different geometries and mass flows presented in relative units (base case Case 0- unbaffled case)

The following table shows the influence of the baffle length on residence time at different positions . For the case of baffles at lowest position present is sharp drop in residence time with increase of length, at the medium height values vary slightly, and at the highest position present is sharp rise.

*Table 3. Influence of baffle length on average residence time **

Baffle ..	Average residence time [s] = t_{CFD}		Mass flow [kg/s] 0.16	0.24	0.32	0.4	0.48
.. Position 1	Case	1	0	0	0	0	0
	Case	2	-6.2	-5.2	-6.1	-6.1	-6
	Case	3	-6.6	-7.4	-8.4	-8.6	-8.7
.. Position 2	Case	4	0	0	0	0	0
	Case	5	-1.6	-1.2	-1.5	-1.9	-1.7
	Case	6	-0.3	-1.1	-1.7	-2.2	-2.1
.. Position 3	Case	7	0	0	0	0	0
	Case	8	2.5	0.4	-1	-0.3	0
	Case	9	9	8	7.5	6.6	4.7

**base case always the first case at the given vertical position, i.e. Case 1, Case 4 and Case 7, i.e.* $((t_{calc.case} - t_{calc.base\ case})/t_{calc.base\ case})$

The following table shows the influence of the baffle position on residence time for different baffle lengths. At all lengths there is a trend of increase of residence time when the baffle is installed higher. Longer the baffle this increase is even greater.

*Table 4. Influence of baffle position on average residence time ***

Baffle ..	Average residence time [s] = t_{CFD}		Mass flow [kg/s] 0.16	0.24	0.32	0.4	0.48
.. Length 1	Case	1	0	0	0	0	0
	Case	4	5.4	6	5.3	5.7	5.5
	Case	7	13.8	14.5	13.3	12.8	12.2
.. Length 2	Case	2	0	0	0	0	0
	Case	5	10.6	10.5	10.4	10.4	10.3
	Case	8	24.5	21.3	19.4	19.8	19.3
.. Length 3	Case	3	0	0	0	0	0
	Case	6	12.4	13.2	13	13	13.1
	Case	9	32.8	33.6	33.1	31.5	28.6

base case is always the first case of the given length, i.e. Case 1, Case 2 and Case 3 (($t_{calc.case}$ - $t_{calc.base\ case}$)/ $t_{calc.base\ case}$)

4. Discussion

Results show that baffles can cause increase as also decrease of the residence time when installed. Values range from -17 percentage points to +13 for the CFD tested designs change relative to the case without baffles.

The most influential factor is the vertical position of the baffle, followed by its length. Where length can induce negative and positive changes depending on the position, higher position causes always positive changes. Mass flow does not influence significantly the trend of increase or decrease of residence time.

Practice in Serbia shows that small boiler producers prefer not to use this measure. One can assume that tests could have been done with unsatisfactory results. First reason for that is the increase in pressure drop. Baffles are in a way like a throttling device for hot gases. So in order to have the same air flow, then higher chimney has to be built or fan must be installed. Without these measures, situation deteriorates in respect of heat output. Second reason is concerning hot gas temperatures. As additional time is provided for them for flow in furnace, there is a possibility that they cool under the ignition temperature. In that case even with perfect mixing of overstoichiometric quantity of air with combustibles does not lead to combustion. And this case is more realistic, as the air excess ratio is greater, which in turn lowers the adiabatic flame temperature. And one another aspect is present, water cooled furnace walls that cool gases faster. Recommendation for this case would be to introduce lining which would act as inhibitor of cooling the gases under the ignition temperature. Lining should not cover the whole furnace.

If correctly applied this measure could lead to usage of lower air excess values, without consequence of losing on heat output.

Acknowledgments

This work has been done in the frame of the project „Development of methods, sensors and systems for monitoring of quality of water, air and land", for the Republic of Serbia Ministry of science and technology. (Project No III 43008)

References

[1] Stepanov B., Pešenjanski I., Miljković B., Gas residence time analysis for efficiency improvement of small-scale straw fired boilers. In: Bojić M., Lior N., Petrović J., Stefanović G., Stevanović V., editors. ECOS 2011: Proceedings of the 24th International Conference on Efficiency, Cost, Optimization, Simulation, and Environmental Impact of Energy Systems; 2011 July 4-7; Novi Sad, Serbia. Niš, Faculty of mechanical engineering:1300-10.

[2] W. Trinks, M. H. Mawhinney, R. A. Shannon, R. J. Reed and J. R. Garvey, Saving energy in industrial furnace systems. In: W. Trinks et al.. Industrial Furnaces, Sixth edition. Hoboken, N.J., USA: John Wiley & Sons, Inc. 2004. p. 175-242.

[3] Nasserzadeh V, Swithenbank J, Schofield G, Scott D W, Loader, A. Effects of high speed jets and internal baflees on the gas residence times in large municipal incinerators, Environmental Progress, 1994;13 (2): 124-133.

[4] Shelton J., Jay Shelton's solid fuels encyclopedia. Garden Way Publishing, Charlotte, Vt, USA; 1983.

[5] Martinov M, Tešić M, Brkić M., Efficiency and emission of crop residues combustion facilities in Serbia – Status and needed measures for improvement, Thermal Science 2006; 10, Suppl., No. 4: 189-194.

[6] Pešenjanski I, Stepanov B. Test results for a 250 KW bio-mass energy boiler and suggested technical and organizational measures to increase energy efficiency of current boiler installations, Savremena poljoprivredna tehnika 2005; 31(4): 197-203.

[7] Ebeling J, Jenkins B: Thermocemical properties of biomass fuels. Agricultural and natural resources communication services webserver - Available at:<ucce.ucdavis.edu/files/repositoryfiles/ca3905p14-62863.pdf >[accessed 15.3.2011.].

[8] Domalski E, Jobe T, Milne T. Thermodynamic data for biomass conversion and waste incineration. Boulder, US: National bureau of standards; 1986 Sept. Technical report No.: SERI/SP-271-2839

[9] Wick O., Wik M., Wood stoves : how to make and use them. Northwest Pub. Co. Anchorage, Alaska, USA; 1977.

[10] Hartmann H., Reisinger K., Thuneke K., Hoeldrich A., Rossmann P., Handbuch Bioenergie-Kleinanlagen. Fachagentur Nachwachsende Rohstoffe e.V. (FNR) – Available at:<www.tfz.bayern.de/sonstiges/17745/handbuch_komplett.pdf > [accessed 30.1.2012.].

[11] Dimaczek G., Quicker P., Mocker M., Kleinfeuerungsanlage für Getreide und Stroh abschlussbericht für Fachagentur Nachwachsende Rohstoffe e.V. Gülzow. ATZ Entwicklungszentrum- Available at:< http://www.fnr-server.de/ftp/pdf/berichte/22019303.pdf > [accessed 30.1.2012.].

[12] Eltrop L., Raab K., Schneider S., Schroeder G., Kaltschmitt M., Leitfaden Bioenergie - Planung, Betrieb und Wirtschaftlichkeit von Bioenergieanlagen. Fachagentur Nachwachsende Rohstoffe – Available at <http://fnr-server.de/cms35/fileadmin/biz/pdf/leitfaden/leitfaden_bioenergie.pdf> [accessed 30.1.2012.].

[13] Nasserzadeh V, Swithenbank, J . Design optimization of a large municipal solid waste incinerator, Waste Menagement, 1991; 11: 249-261.

[14] Scott A. J., Real-life emissions from residential wood burning appliances in New Zealand - Available at <http://ecan.govt.nz/publications/Reports/air-report-emissions-residential-wood-burning-appliances-nz-000805.pdf> [accessed 30.1.2012.].

[15] Todd J. J., Research relating to regulatory measures for improving the operation of solid fuel heaters. Eco-energy options, Prepared for the New South Wales Department of Environment and Conservation– Available at

<http://www.environment.nsw.gov.au/resources/woodsmoke/execsummary_toddreport.pdf>[accessed 30.1.2012.].

[16] Van Loo S., Koppejan J. (eds.), Handbook of biomass combustion and co-firing. Twente, the Netherlands: Twente university press; 2002.

[17] Beer J. M., Lee K. B., The Effect of the Residence Time Distribution on the Performance and Efficiency of Combustors. Symposium (International) on Combustion 1965; 10 (1): 1187-1202.

[18] Swithenbank J., Poll I., et al.,Combustion design fundamentals. Symposium (International) on Combustion 1973; 14(1): 627-638

[19] Star CCM+ manual, CD-Adapco. Melville, NY, USA.

[20] Han J-H, Jeong K, Choi J H, Choi S. A hot-flow model analysis of the msw incinerator. International journal of energy research, 1997; 21: 899-910.

[21] Fehr M, Vaclavinek, J. A cold model analysis of solid waste incineration. International journal of energy research, 1992; 16: 277-283.

[22] Choi S, Lee J S, Kim S K, Shin D H. Cold flow simulation of municipal waste incinerators. In Proceedings of 25th Int. Symp. On Combustion; 1994. The Combustion Insitute, Irvine, California, U.S.A.

[23] Ravichandran M, Gouldin F C. Numerical Simulation of Incinerator Overfire Mixing. Combustion Science & technology, 1992; 85: 165-185.

[24] Nasserzadeh V, Swithenbank, J . Design optimization of a large municipal solid waste incinerator, Waste Menagement, 1991; 11: 249-261.

[25] Nasserzadeh V, Swithenbank J, Schofield G, Scott D W, Loader, A. Effects of high speed jets and internal baflees on the gas residence times in large municipal incinerators, Environmental Progress, 1994;13 (2): 124-133.

[26] Personal communication with PhD mentor professor Pešenjanski

[27] Seeker W R, Lanier W S, Heap M P. Municipal waste combustion study: Combustion control of MSW combustors to minimize emission of trace organics. New York, US; EPA, 1987 May. Technical report: EPA/530-SW-87-021x.

[28] Brkić Lj., Živanović T., Termički proračun parnih kotlova. Beograd, Srbija. Mašinski fakultet; 1984.

Characterization of CH_4-H_2-air mixtures in the high-pressure DHARMA reactor

Vincenzo Moccia[a], Jacopo D'Alessio[b]

[a] *Istituto Motori – C.N.R., Napoli, Italy, v.moccia@im.cnr.it* ***CA***
[b] *Istituto Motori – C.N.R., Napoli, Italy, j.dalessio@im.cnr.it*

Abstract:

Experimental characterization of the burning behavior of gaseous mixtures has been carried out, analyzing spherical expanding flames. Tests were performed in the DHARMA (Device *for* Hydrogen-Air Reaction Mode Analysis) laboratory of Istituto Motori - CNR. Based on a high-pressure, constant-volume bomb, the activity is aimed at populating a systematic database on the burning properties of CH_4, H_2 and other species of interest, in conditions typical of i.c. engines and gas turbines. High-speed shadowgraph is used to record the flame growth, allowing to infer the laminar burning parameters and the flame stability properties. Mixtures of CH_4, H_2 and air have been analyzed at initial temperature 293÷305 K, initial pressure 3÷18 bar and equivalence ratio ϕ=1.0. The amount of H_2 in the mixture was 0%, 20% and 30%. The effect of the initial pressure and of the Hydrogen content on the laminar burning velocity and the Markstein length has been evaluated: the relative weight and mutual interaction has been assessed of the two controlling parameters. Analysis has been carried out of the flame instability, expressed in terms of the critical radius for the onset of cellularity, as a function of the operating conditions.

Keywords:

Combustion, Laminar burning velocity, Hydrogen, Methane, Shadowgraph.

1. Introduction

No matter the claim and the quest for new answers to the needs of an energy-thirstier society, thermal conversion systems will play a key role in the energy supply chain. This awareness, along with the urgent need of CO2 reduction (currently the main driver of technology advance), has some direct implications: introduction in the energy cycle of CO2-neutral fuels (biomass-derived) and design/development of more efficient conversion systems. The latter point can be anticipated to have a larger practical impact than the former, given the majority of energy sources will be represented by fossil fuels for many years to come.

Sometimes placed in the category of "alternative" fuels, methane (CH4) is indeed a hydrocarbon, sporting the peculiarity of the lowest C/H ratio, if compared to other fuels: by trivial reasoning, the less the carbon, the less the CO2. This feature has boosted a renewed attention to CH4, which represents the main constituent of natural gas. CH4 has been used with heat engines for a long time, even if with the status of a "niche" solution: as a fuel for i.c. engines, it offers some advantages over gasoline, having wider flammable limits and better anti-knock characteristics, at the cost of a lower flame speed. A feasible opportunity to overcome the limits of CH4 is offered by H2: adding H2 to CH4 (or natural gas) can improve the flame speed/stability and lower the lean operating limit. The overall effect is to extend the stable operation map to extreme conditions (e.g. high EGR).

Crucial for the development and design of i.c. engines and gas turbine combustors is the knowledge of laminar combustion properties: they offer the basis for modelling and simulation of flame-turbulence interaction. Data on the combustion properties of gaseous fuels are widely available in the literature [1-8], but hardly in a systematic form: filling this gap is the scope of the DHARMA (Device for Hydrogen-Air Reaction Mode Analysis) project, aiming at generating a comprehensive and coherent grid of data on the combustion properties of CH4 and H2, obtained in conditions as close as possible to those of actual engines.

The project relies on an optically accessible constant-volume bomb (static P ≤ 20 MPa), where test are carried out on spherical expanding flames; the operating conditions (P0, T0), the equivalence ratio, the relative composition of the mixture, the ignition energy can be varied in a meaningful range. A shadowgraph setup, based on a c.w. laser source and a CMOS camera, is used to follow the flame growth with high time and space resolution. A high-frequency dynamic pressure sensor allows to record the combustion pressure. Operation of the reactor and the various subsystems is fully automated, for the sake of safety and repeatability.
Experimental results are presented for the combustion in air of CH4-H2 mixtures: the H2 percentage varied from 0% to 30% (vol.); the initial pressure varied between 3 and 18 bar. The tests were performed at room temperature (293÷305 K), with stoichiometric mixtures. Data analysis yielded the (unstretched) laminar burning velocity and the Markstein length; the evaluation was carried out of the critical radius for the onset of cellularity, offering further details on flame properties.

2. Experimental setup and procedures

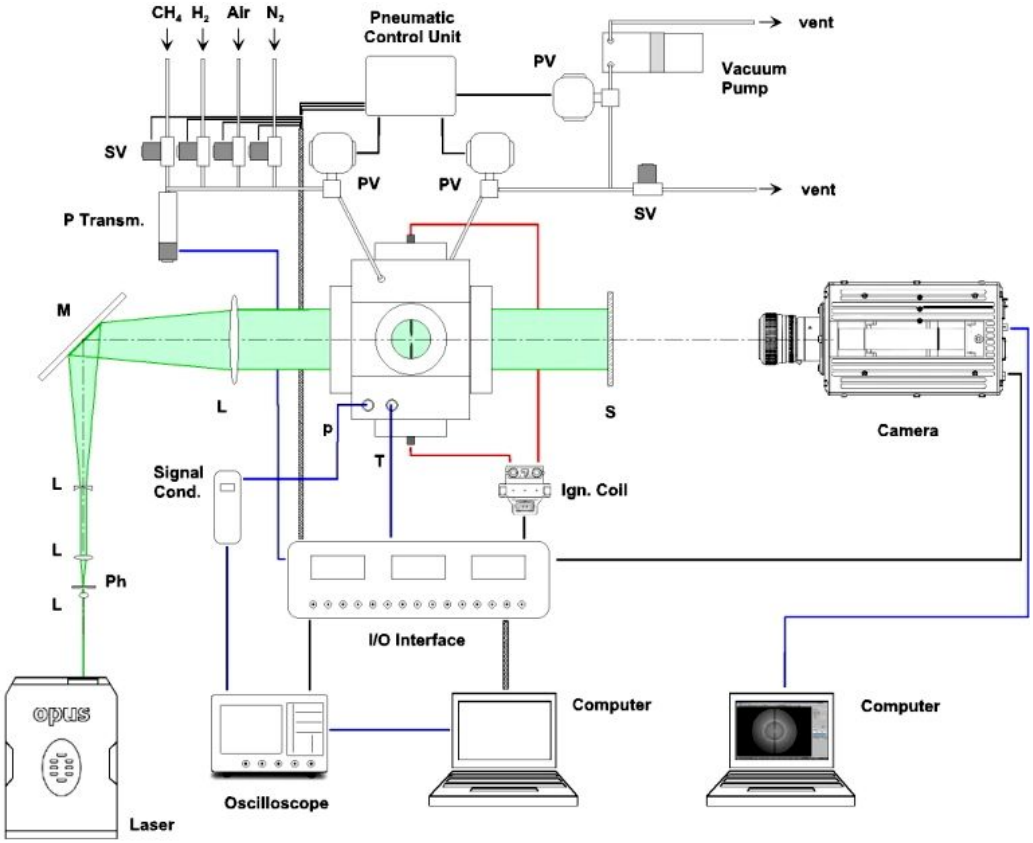

Fig. 1. Layout of the experimental apparatus.

The general arrangement of the experimental layout is shown in Fig. 1: a detailed description is given in [9]. The heart of the DHARMA laboratory is a constant-volume test reactor, made of stainless steel (AISI 316): the cylindrical chamber (i.d. = 0.070 m, h = 0.090 m) is rated for a maximum pressure of ≤ 20 MPa (static). A total of 6 optical accesses are available: the larger viewports (d = 0.065 m) are located normal to the chamber axis, providing nearly full access to chamber bore; smaller diameter ports are positioned on the chamber side, along two orthogonal axes. Hi-grade quartz windows (0.085 m diameter, 0.030 m thick) are installed in the main ports, the smaller side ports can be fitted either with quartz windows (0.049 m diameter, 0.020 m thick) or with a variety of stainless steel adapters (i.e. transducers, electrodes, sampling ports, etc.).

Four additional service ports are available, e.g. for the intake of the combusting mixture and the vent of the exhaust gases.
The mixture is ignited with an automotive inductive ignition system (energy ≤ 60 mJ): the energy of discharge can be varied adjusting the time of charge (dwell time) of the coil. The spark discharge takes place in the center of the chamber between two pointed-tip tungsten electrodes (0.001 m diameter), with a 0.001 m gap.
Pressure signal during the combustion events is detected by a high-frequency dynamic pressure transducer (resonant frequency ≥500 kHz, rise time ≤ 1 μs, sensitivity 14.5 mV/mbar). The sensor is pre-amplified and coupled to a matching signal conditioner (1MHz, 1:1 gain). Output voltage signal is acquired with a 200 MHz digital oscilloscope, interfaced to the main computer.
A metal-shielded, type K thermocouple is used to monitor the temperature of the gases, save for the combustion phase.
The gas handling system was designed to prepare combustible mixtures of variable composition with high accuracy, spanning a range of initial pressures which included values of relevance in spark-ignition engine operation.
High purity gases (CH_4: 99.9995%, H_2: 99.999%, dry air: 99.999%, N_2: 99.9995%) are used to prepare the mixtures, relying on the partial pressures method [2]: the amount of each gas is metered by a solenoid valve, controlled by a high-resolution (100 MHz) counter/timer board installed in the main computer. The pressure is monitored by a high-accuracy pressure transmitter (0-30 bar, accuracy ±0.08% FS). The gas supply system allows to prepare combustible mixtures up to 30 bar. After each test, the system is vented, N_2 purged and pumped down to 10^{-2} mbar. All the systems operate with a high degree of automation, to maximize safety and repeatability of the tests.
The entire lab conforms to current safety standards on the use of combustible gases, and is fully provided with interconnected gas leak sensors, cylinder cut-off devices and forced venting systems.
A parallel-beam direct shadowgraph layout [10] was set up for the analysis of spherical expanding flames. A Diode-Pumped Solid-State c.w. laser (2W @532nm) is used as the light source. High-resolution, time-resolved image acquisition is accomplished by means of a CMOS camera (*Photron SA-5*, 1024x1024 pixel, 1000000 fps, shutter time ≥ 368 ns), interfaced to an independent workstation.

3. Theoretical Background

The shadowgraph images of the spherical expanding flame allow to evaluate the laminar burning parameters, according to a well-known approach [2-3, 5-8, 11-13]. The time evolution of r_u (the flame radius on the *unburned* gas side) is obtained through frame-by-frame processing, assuming the luminous front in the shadowgraph corresponds to the radius on the unburned gas side [12, 13]. The *stretched* flame speed V_s can then be evaluated as

$$V_s = \frac{dr_u}{dt} \qquad (1)$$

The obtained speed includes the stretch effects associated to the propagation of a flame surface, which experiences curvature and flow dynamic strain [14-18]. The flame stretch α is defined as the relative rate of change of the flame area: for a spherically expanding laminar flame it can be expressed as:

$$\alpha = \frac{1}{A}\frac{dA}{dt} = \frac{2}{r_u}\frac{dr_u}{dt} = 2\frac{V_s}{r_u} \qquad (2)$$

As originally suggested by Markstein, the relationship between flame speed and stretch is linear; it can be expressed after Clavin [17] as:

$$V_s = V_{s0} - L_b \cdot \alpha \qquad (3)$$

where V_{s0} is the unstretched flame speed and L_b is the burned gas Markstein length, which indicates how and to what extent the flame is influenced by the stretch. Positive L_b are associated to flames with speed decreasing with stretch (which are stable), while in the case of negative L_b the flame speed tends to increase with stretch, becoming unstable; moreover, the magnitude of L_b indicates to what extent the flame propagation is influenced by the stretch. According to (3), by plotting V_s against α, the unstretched flame speed V_{s0} can be estimated as the value assumed by V_s at $\alpha = 0$, and L_b as the gradient of the best straight line fit.

The unstretched flame speed V_{s0} refers to the limiting case of a plane flame front, with infinite radius and negligible curvature: in such a case, V_{s0} can be related to the unstretched laminar burning velocity u_{l0} through the following relation:

$$u_{l0} = V_{s0} \frac{\rho_b}{\rho_u} \qquad (4)$$

where ρ_b is the density of burned gases and ρ_u the density of unburned gases. As far as the flame analysis is concerned, this relation only holds in the constant-pressure phase of flame propagation.

4. Results and discussion

In the following, results are illustrated of the combustion behaviour of CH_4 and of CH_4-H_2 mixtures, characterized by a H_2 content of 20% and 30% in volume: these are the limits currently agreed upon by the automotive industry for the potential evolution of CH_4-fueled engines, optimizing the trade-off between the extra technical complexity and the performance benefits [19, 20]. The initial temperature T_0 varied in the range 293÷305 K, while the initial pressure P_0 was set at 3, 6, 12 and 18 bar (abs.). Being targeted to the development of automotive internal combustion engines, operating with closed-loop three-way catalyst, the study was limited to stoichiometric air-fuel mixtures (equivalence ratio $\phi = 1.0$).

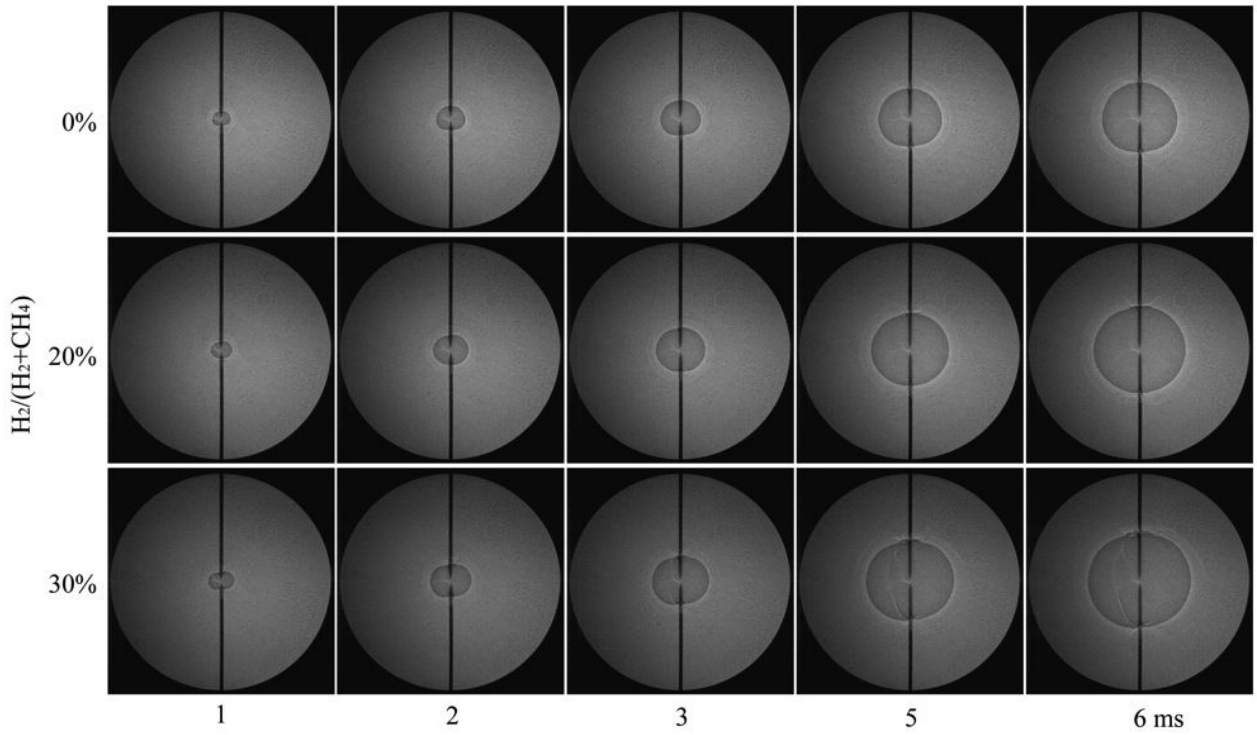

Fig. 2. Evolution of flame in the isobaric phase for stoichiometric CH_4 and H_2-enriched mixtures (20% and 30% vol.) at 3 bar and room temperature. Window dia. 65mm.

4.1. Laminar burning properties

Time-resolved shadowgraph images of spherical expanding flames were used to infer the laminar flame parameters. As stated earlier, laminar analysis can be meaningfully carried out in the constant-pressure phase only, before the chamber pressure shows a sensible increment. Moreover, as stated by Bradley et al. [4], the early stages of the flame kernel growth are affected by the spark energy release, and cannot be taken into account in the evaluation of laminar flame properties. The resulting measurement time-window starts after the ignition disturbances are over, and ends when the pressure shows an appreciable rise: the spanning of this phase depends on the experimental conditions. In the present case, spark energy was 20 mJ: being delivered by an inductive ignition coil, only a small fraction of this energy is released in the breakdown phase, which governs the early kernel growth [21, 22]: the extent of the ignition disturbances can be expected to be accordingly limited. The resulting range for data analysis was comprised between ~2.5mm and ~9.5mm (corresponding to ~27% of the chamber radius).

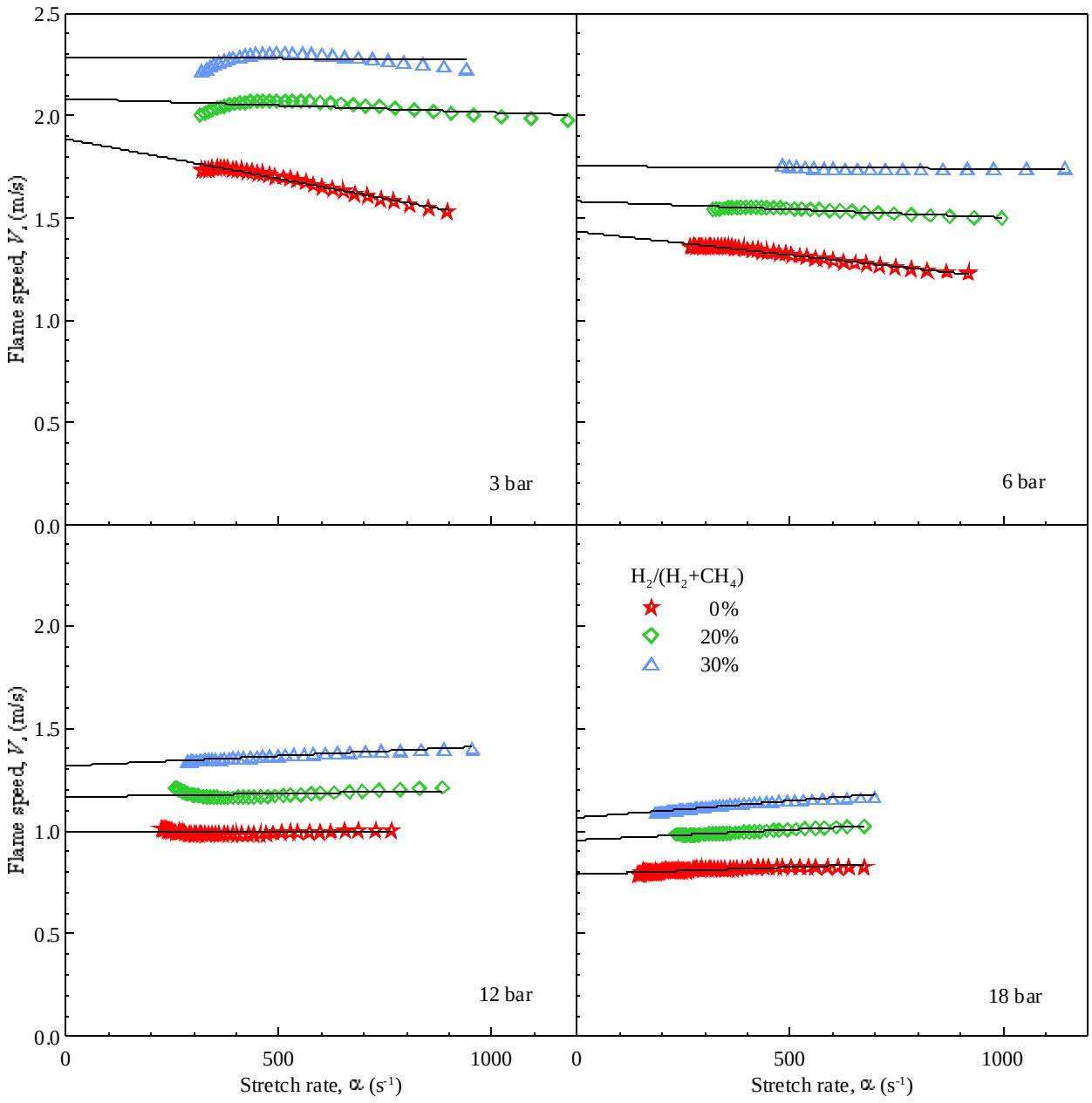

Fig. 3. Flame speed as a function of the stretch rate, obtained at different starting pressure, for stoichiometric CH_4 and H_2-enriched mixtures (20% and 30% vol.) at room temperature.

Figure 2 shows three sets of frames, describing the flame development in the laminar, isobaric phase, at P_0 = 3 bar. The combustion behaviour is compared for CH_4 and H_2-CH_4 mixtures with a H_2 content of 20% and 30% vol. Recording speed was 7000 fps (143 μs between consecutive frames) with a shutter speed of 1 μs; optical magnification ratio was 3.27:1, resulting in a spatial resolution of 15.3 pixel/mm. Flames are smooth and virtually free of wrinkles, the crack shown for the 30% mixture is the self-similar development of initial ignition disturbances. The effect of H_2 addition can be appreciated in the increased size of the flame ball at a given time.

An image processing routine has been implemented to infer the flame radius r_u from the shadowgraph data: for each frame, the flame contour is traced and the area of the projected flame ball is evaluated; the radius is estimated as that of a circle of equal area to the flame. The evolution of the flame radius r_u can then be plotted as a function of time, offering the basis for the evaluation of the stretched flame speed V_s: the latter is obtained from derivation of a polynomial fit of the above-defined data subset, following (1) [7].

Being known V_s and r_u, the stretch rate α can be evaluated after (2): the plot of the stretched flame speed against α is shown in Fig. 3 for CH_4 and CH_4-H_2, at different starting pressure: each set of data corresponds to a single, time-resolved combustion event, which has been selected as representative of the test conditions (P_0, T_0, % H_2, ϕ).

According to (3), linear-fit extrapolation of the flame speed to α = 0 gives the unstretched flame speed V_{s0}, while the slope of the fit allows to estimate the burned gas Markstein length L_b.

Figure 3 shows the distinct effect of the starting pressure and of the Hydrogen percentage on the flame characteristics: increasing the pressure has a detrimental effect on the flame speed, which, on the other hand, always benefits from the addition of H_2, even in limited amounts.

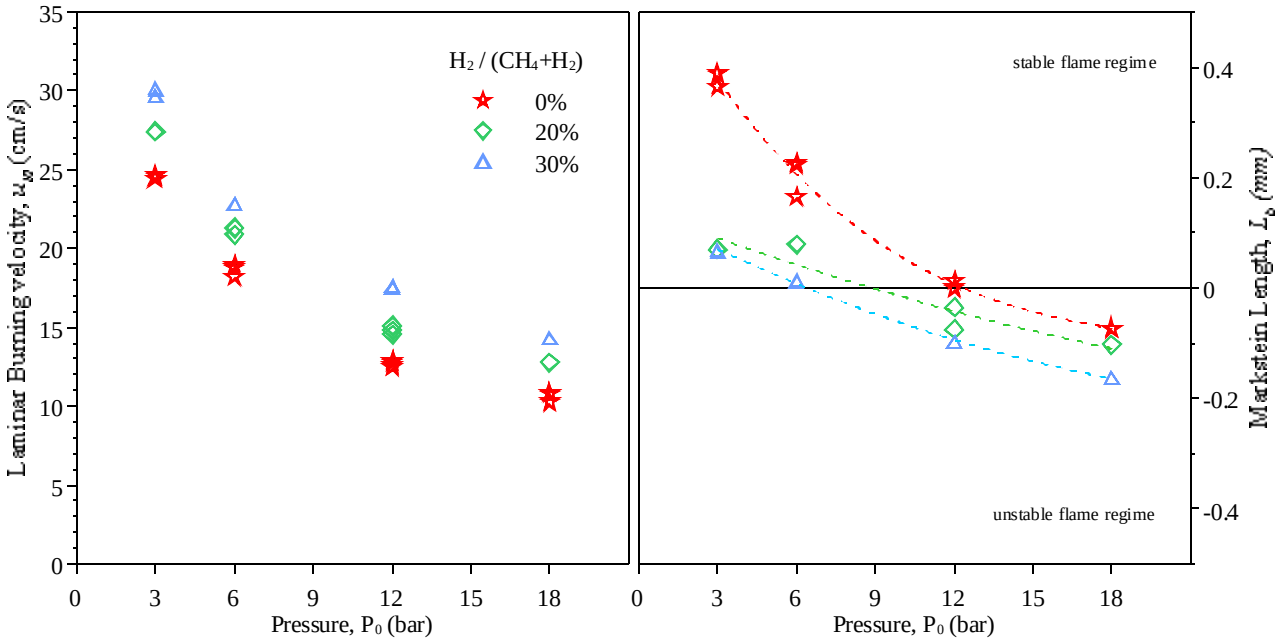

Fig. 4. Unstretched laminar burning velocity (left) and burned-gas Markstein length (right) as a function of the starting pressure, for stoichiometric CH_4 and H_2-enriched mixtures (20% and 30% vol.) at room temperature.

The corresponding values of the unstretched laminar burning velocity u_{l0} were obtained through (4), where the expansion factor ρ_u/ρ_b was evaluated from the properties of the reactant species and of equilibrated adiabatic products. The u_{l0} and L_b values are summarized in Fig. 4 as a function of initial pressure, for pure and H_2-enriched CH_4.

As the starting pressure is increased from 3 to 18 bars, a decrease of the laminar burning velocity can be observed: the value at 18 bar being about 40% of 3 bar. The addition of Hydrogen to

Methane allows a net gain of burning velocity in all the cases. This gain has the effect of shifting to higher values the curve of u_{l0} vs. P_0.
Aside from the effect on the magnitude of u_{l0}, as the starting pressure increases, the flame gets more and more unstable, as evidenced by the decreasing Markstein length: in the case of pure CH_4, L_b assumes values close to zero at 12 bar, falling in the unstable regime for larger values. Adding H_2 to CH_4 has the anticipated effect [4] of increasing flame instability: due to the combined synergy of initial pressure and Hydrogen content, high-pressure H_2-CH_4 flames fall systematically in the unstable regime.

4.2. Flame stability and cellular structures

The propensity of a flame to get unstable, as expressed by the burned-gas Markstein length L_b, can be inferred from the analysis of the expanding flame in the laminar (isobaric) regime, when, almost by definition, there is little or no sign of flame distortion (see e.g. Fig. 2). Experimental evidence of instability appears later, when the flame travelling the chamber volume may go through various stages of morphological alterations, characterized by the appearance of large cracks and, eventually, fine cellular structures [23-27].

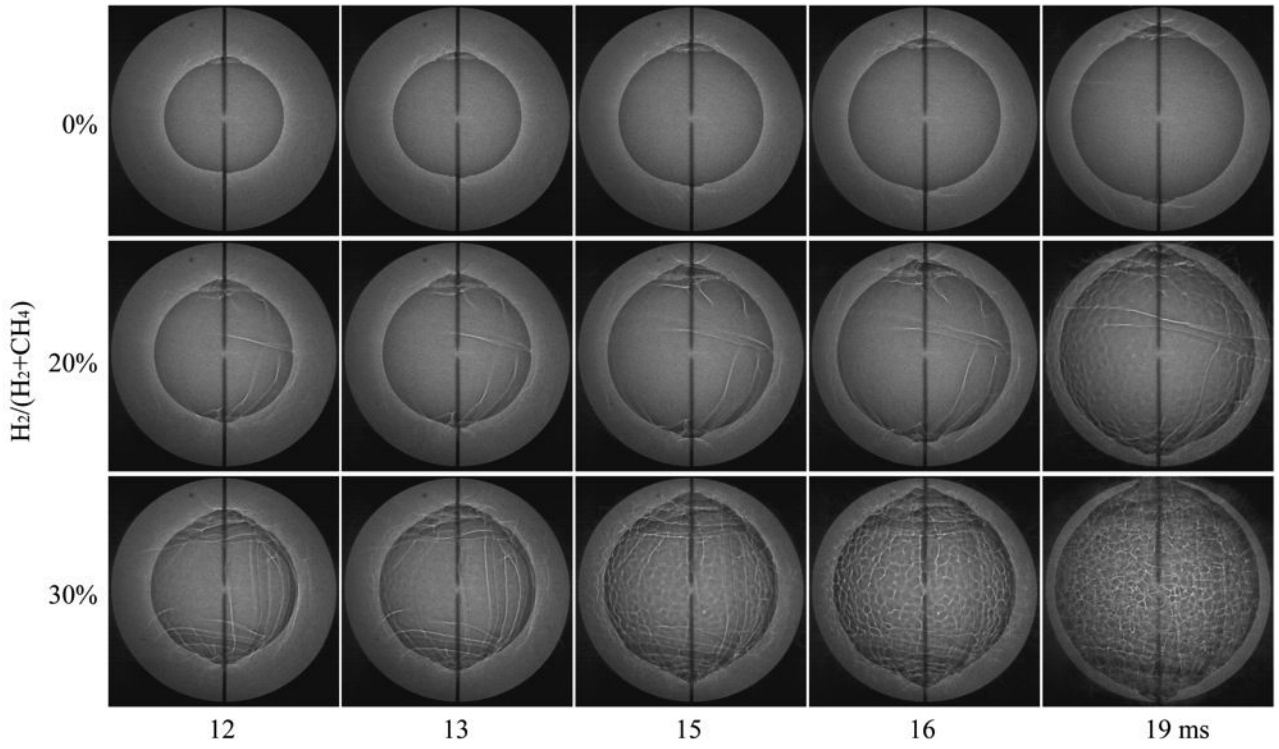

Fig. 5. Evolution of flame instability for stoichiometric CH_4 and H_2-enriched mixtures (20% and 30% vol.) at 6 bar and room temperature. Window dia. 65mm.

Figure 5 shows three sets of frames obtained in the case of pure and H_2-enriched CH_4 mixtures at 6 bar, at selected times after the spark: they were recorded at 7000 fps (143 μs between consecutive frames) and 1024x1024 pixel, with a shutter speed of 1 μs; optical magnification ratio was 3.27:1, resulting in a spatial resolution of 15.3 pixel/mm.
At moderate values of the initial pressure (P_0 = 6 bar), the CH_4 flame keeps its laminar shape until it reaches the chamber walls. The addition of H_2 to the mixture, even in limited amount (20%), is associated to the appearance of large cracks on the flame surface. The latter effect gets more striking as long as the flame travels the chamber, with the cracks being suddenly integrated by cellular structures [24, 27].
When the initial pressure gets larger, according to the findings shown in Fig. 4, the flame gets more unstable, even with pure CH4. This behaviour is shown in Fig. 6, which reports three sets of frames

obtained for the same mixtures at P_0 = 12 bar: no matter the mixture composition, in all the cases the flame exhibits deviations from the laminar morphology, which take place earlier in the process (that is at smaller radii). The typical sequence of large cracks followed by smaller, uniformly distributed "cells" is always present; the main difference is in the characteristic times, which get shorter as the amount of H_2 increases, leading to an earlier appearance of cellular structures.

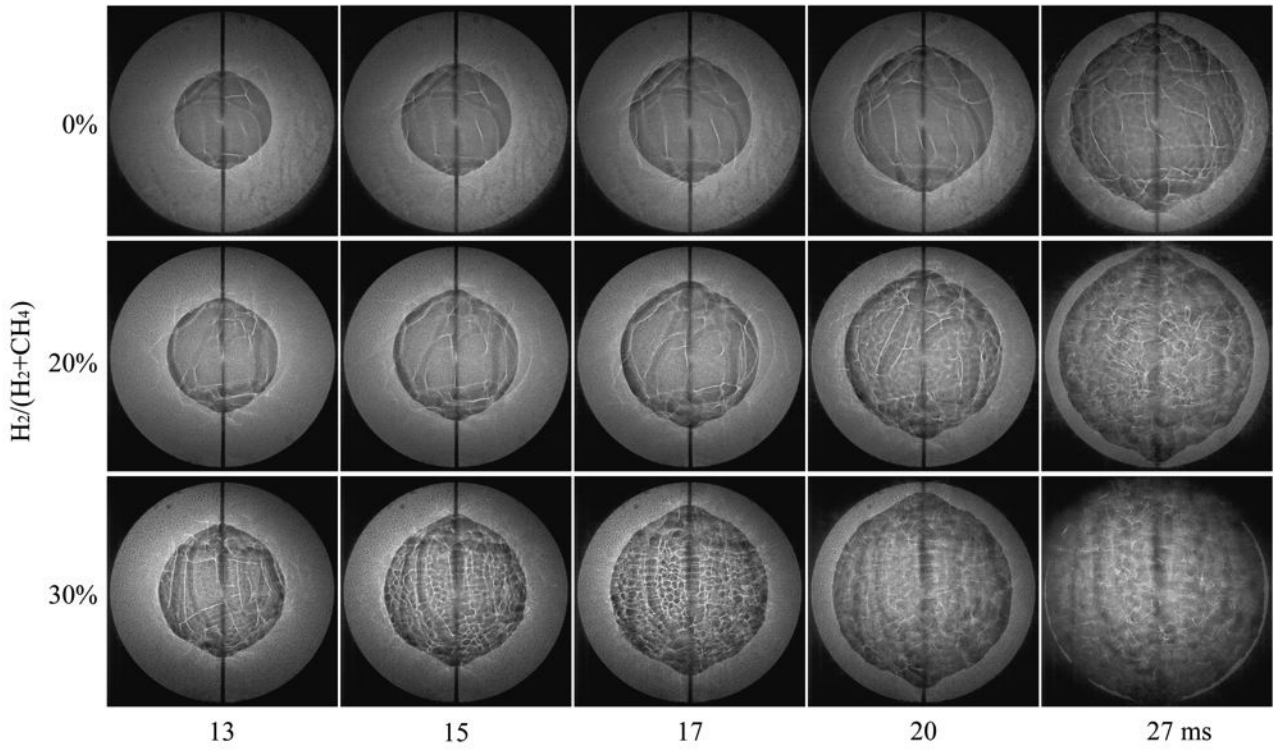

Fig. 6. Evolution of flame instability for stoichiometric CH_4 and H_2-enriched mixtures (20% and 30% vol.) at 12 bar and room temperature. Window dia. 65mm.

As suggested by Law et al.[27], two characteristic instants can be identified: the first is related to the branching of large cracks across the flame surface, the second to the sudden appearance of cells, almost uniformly over the same surface, with a characteristic size much smaller than the large cracks. Following the convention of Law et al. [27], we chose to adopt the second instant as representative of the flame loosing stability: this allows to define the critical radius r_{cr} for the onset of instability.

Figure 7 reports the values of r_{cr} evaluated in the current range of operating conditions as a function of the H_2 content, at different starting pressures. Whatever the amount of H_2 in the mixture, flames at P_0 = 3 bar always show a laminar behaviour, hence the lack of data points for this case. At P_0 = 6 bar, a cellular structure appears with pure CH_4, when the flame reaches the chamber wall: these points were omitted, since they are likely influenced by additional phenomena, like flame-wall interaction. The data confirm the trends of the Markstein length obtained by flame stretch analysis (shown in Fig. 4): they allow to assess the effect of increasing pressure on flame instability, which shows up as a progressive reduction of the critical radius: the resulting picture is of a flame which departs earlier from the laminar regime, and mostly develops under a wrinkled regime, even in quiescent atmosphere. As anticipated, adding H_2 to CH_4 further reduces r_{cr}, i.e. increases instability, even if the effect gets less marked as the pressure is increased: adding 30% of H_2 to CH_4 reduces r_{cr} by 24% at 12 bar and by 21.5% at 18 bar.

As far as the observed instabilities are concerned, it's well established that flame cellularity can be hydrodynamic and thermo-diffusive in nature (if one neglects the body-force effects). The thermo-diffusive instability originates from the diffusive disparity of heat conduction from the flame and reactant diffusion towards the flame [17]. A fitting parameter representing the effect of non-

equidiffusion is the flame Lewis number (*Le*) defined as the ratio of the heat diffusivity of the mixture to the mass diffusivity of the limiting reactant [16-18]. Values of *Le* equal or larger than a critical value *Le** (typically slightly less than unity) correspond to flames which are diffusionally stable, while for *Le* < *Le** the flames are unstable and diffusional cellularity is evidenced in the very early stages of flame development. The hydrodynamic instability is associated to the thermal expansion of the gas: it is enhanced when the thermal expansion ratio is increased and the flame thickness is decreased [26].

The current set of measurements, obtained in stoichiometric conditions (ϕ = 1.0), were characterized by *Le* always above unity (~1.25). The expansion ratio ρ_u/ρ_b was almost constant (~ 7.6). Flame thickness for CH_4 decreased by an order of magnitude, increasing the pressure from 3 to 18 bar; moreover, in all cases, the addition of 30% (vol.) of H_2 caused a reduction of ~20% of flame thickness. The experimental results show flames remaining smooth after ignition (Le > 1), and later developing cells on the surface: in the light of the above considerations, this behaviour suggests that the observed cellularity should be essentially attributed to hydrodynamic instabilities [8, 23-29].

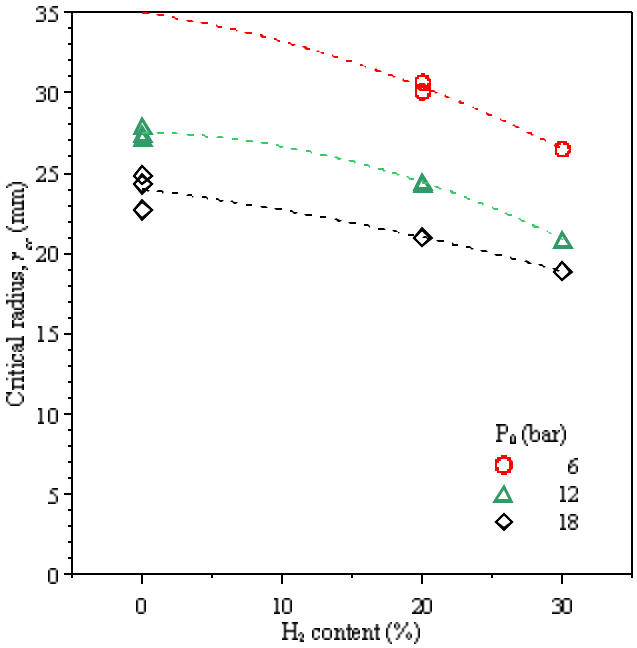

Fig. 7. Critical radius for the onset of flame instability as a function of H_2 content in CH_4-H_2 mixtures, at different starting pressure.

Summary

The effect has been analyzed of the initial pressure and H_2 content on the combustion of stoichiometric CH_4-H_2 mixtures. Laminar burning parameters (unstretched burning velocity and Markstein length) and flame instability characteristics were evaluated for mixtures with different H_2 percentage (0%, 20% and 30%), equivalence ratio ϕ = 1, initial temperature T_0 = 293÷305 K and initial pressure P_0 = 3÷18 bar. The main findings can be summarized as follows:

- Increasing the pressure, the laminar burning velocity decreases and the Markstein length becomes negative: in the case of CH_4, when P_0 is raised from 3 to 18 bar, u_{l0} is reduced of ~40%; in the same conditions L_b shifts from about 0.38 to -0.074, meaning the flame develops in the unstable regime.
- The addition of H_2 to CH_4 has a positive effect on the burning velocity: at 3 bar, u_{l0} increases by 20% if the amount of H_2 in the mixture is 30%: the effect is proportionally stronger at higher pressure (+40% at 18 bar). The Markstein length of H_2-enhanced mixtures is shifted to smaller values, if compared to pure CH_4, and gets negative at P_0 > 6 bar.

- The critical radius for the onset of cellularity was found to decrease when either the pressure or the H_2 content in the mixture were increased. No matter the amount of H_2, no sign of instability was observed at $P_0 = 3$ bar: conversely, for $P_0 > 6$ bar the flame get increasingly unstable.

Acknowledgments

The research was partially supported by the Italian Ministry of Economic Development within the framework of the Program Agreement MiSE-CNR "Ricerca di Sistema Elettrico".

Nomenclature

A flame area, mm^2

Le Lewis number

L_b burned gas Markstein length, mm

P pressure, bar

r_{cr} critical flame radius, mm

r_u cold flame front radius, mm

T temperature, K

u_{l0} unstretched laminar burning velocity, cm/s

V_s stretched flame speed, m/s

V_{s0} unstretched flame speed, m/s

Greek symbols

α flame stretch rate, 1/s

ϕ equivalence ratio

ρ gas density, kg/m^3

Subscripts and superscripts

0 initial

b burned gas

u unburned gas

References

[1] Lewis B., von Elbe G., Determination of the Speed of Flames and the Temperature Distribution in a Spherical Bomb from Time-Pressure Explosion Records. J. Chem. Phys. 1934;2(5):283-290.

[2] Milton B.E., Keck J.C., Laminar Burning Velocities in Stoichiometric Hydrogen and Hydrogen-Hydrocarbon Gas Mixtures. Combust. Flame 1984:58(1):13-22.

[3] Dowdy D.R., Smith D.B., Taylor S.C., Williams A., The use of expanding spherical flames to determine burning velocities and stretch effects in hydrogen/air mixtures. Symp. (Int.l) on Combustion 1991;23(1):325-332.

[4] Bradley D., Gaskell P.H., Gu, X.J., Burning velocities, markstein lengths, and flame quenching for spherical methane-air flames: A computational study. Combust. Flame 1996;104(1-2):176-198.

[5] Hassan M.I., Aung K.T., Faeth G.M., Measured and predicted properties of laminar premixed methane/air flames at various pressures. Combust. Flame 1998;115(4):539-550.

[6] Gu X.J., Haq M.Z., Lawes M., Woolley R., Laminar Burning Velocity and Markstein Lengths of Methane–Air Mixtures. Combust. Flame 2000;121(1-2):41-58.

[7] Halter F., Chauveau C., Djebaili-Chaumeix N., Gokalp I., Characterization of the effects of pressure and hydrogen concentration on laminar burning velocities of methane-hydrogen-air mixtures. Proceedings of the Combustion Institute 2005;30(1):201-208.

[8] Verhelst S., Woolley R., Lawes M., Sierens R., Laminar and unstable burning velocities and Markstein lengths of hydrogen-air mixtures at engine-like conditions. Proceedings of the Combustion Institute 2005;30(1):209-216.

[9] Moccia V., D'Alessio J., Evaluating the Burning Velocity of Gaseous Fuels for Engine Applications: the DHARMA Project. SAE Paper 2011-24-0056.

[10] Settles G.S., Schlieren and Shadowgraph Techniques. Berlin, DE: Springer; 2001.

[11] Huang Z., Zhang Y., Zeng K., Liu B., Wang Q., Jiang D., Measurements of laminar burning velocities for natural gas-hydrogen-air mixtures. Combust. Flame 2006;146(1-2):302-311.

[12] Parsinejad F., Keck J., Metghalchi H., On the location of flame edge in Shadowgraph pictures of spherical flames: a theoretical and experimental study. Exp. Fluids 2007;43(6):887-894.

[13] Tahtouh T., Halter F., Mounaïm-Rousselle C., Measurement of laminar burning speeds and Markstein lengths using a novel methodology. Combust. Flame 2009;156(9):1735-1743.

[14] Karlovitz B., Denniston Jr. D.W., Knapschaefer D.H., Wells F.E., Studies on Turbulent Flames : A. Flame Propagation Across Velocity Gradients, B. Turbulence Measurement in Flames. Symp. (Int.l) on Combustion 1953;4(1):613-620.

[15] Strehlow R.A., Savage L.D., The Concept of Flame Stretch. Combust. Flame 1978;31:209–211.

[16] Matalon M., On Flame Stretch, Combust. Sci. Technol. 31(3):169–181, 1983.

[17] Clavin P., Dynamic behavior of premixed flame fronts in laminar and turbulent flows. Prog. Energy Combust. Sci. 1985;11(1):1–59.

[18] Law C.K., Sung C.J., Structure, aerodynamics, and geometry of premixed flamelets. Prog. Energy Combust. Sci. 2000;26(4-6):459-505.

[19] Akansu S.O., Kahraman N., Çeper N., Experimental study on a spark ignition engine fuelled by methane-hydrogen mixtures. Int. J. Hydrogen Energy 2007;32(17):4279-4284.

[20] Kahraman N., Çeper B., Akansu S.O., Aydin K., Investigation of combustion characteristics and emissions in a spark-ignition engine fuelled with natural gas-hydrogen blends. Int. J. Hydrogen Energy 2009;34(2):1026-1034.

[21] Maly R., Vogel M., Initiation and propagation of flame fronts in lean CH4-air mixtures by the three modes of the ignition spark, Symp. (Int.l) on Combustion 1979;17(1):821-831.

[22] Borghese A., Diana M., Moccia V., Tamai R., Early Growth of Flames, Ignited by Fast Sparks. Combust. Sci. Technol. 1991;76(4-6):219-231.

[23] Groff E.G., The cellular nature of confined spherical propane-air flames. Combust. Flame 1982;48:51-62.

[24] Bradley D., Harper C.M., The development of instabilities in laminar explosion flames. Combust. Flame 1994;99(3-4):562-572.

[25] Tse S.D., Zhu D.L., Law C.K., Morphology and burning rates of expanding spherical flames in H2/O2/inert mixtures up to 60 atmospheres. Proceedings of the Combustion Institute 2000;28(2):1793-1800.

[26] Kwon O.C., Rozenchan G., Law C.K., Cellular instabilities and self-acceleration of outwardly propagating spherical flames. Proceedings of the Combustion Institute 2002;29(2):1775-1783.

[27] Law C.K., Jomaas G., Bechtold, J.K., Cellular instabilities of expanding hydrogen/propane spherical flames at elevated pressures: theory and experiment. Proceedings of the Combustion Institute 2005;30(1):159-167.

[28] Hu E.J., Huang Z.H., He J.J., Zheng J.J., Miao H.J., Measurements of laminar burning velocities and onset of cellular instabilities of methane–hydrogen–air flames at elevated pressures and temperatures. Int. J. Hydrogen Energy 2009;34(13):5574-5584.

[29] Vu T.M., Park J., Kwon O.B., Kim J.S., Effects of hydrocarbon addition on cellular instabilities in expanding syngas-air spherical premixed flames. Int. J. Hydrogen Energy 2009;34(16):6961-6969.

Development of a concept for efficiency improvement and decreased NOX production for natural gas-fired glass melting furnaces by switching to a propane exhaust gas fired process

Jörn Benthin[a], Anne Giese[a]

[a] *Gaswärme-Institut e.V, Essen, Germany, benthin@gwi-essen.de*

Abstract:

The melting of glass is a very energy-intensive process. Very high standards for the security of gas-supply and technical quality of glass melting tanks are set. Air preheating is a common method to achieve the required high melting temperatures with minimum energy consumption. Regenerative and recuperative systems can be used. Regenerative glass melting furnaces are widespread and lead to a high firing efficiency and reduced energy consumption. The resulting high local flame temperature increases NOX emissions. Conventional methods for NOx reduction in regenerative glass furnaces are pushed to their limits. On the one hand the designers, builders and operators of glass melting tank equipment like to react flexibly on the present and future situation of the gas market and ensure security of supply. On the other hand they like to improve both the efficiency of the process and the glass quality and like to reduce the pollutant emissions as well. As part of a cooperation project with its project partners IWG engineering company Wagenbauer Zwiesel, Heinz Glas GmbH Kleintettau and the Gaswärme-Institut e. V. Essen, with regard to these needs, a concept for the conversion of natural gas-fired glass melting furnaces to propane gas-fired and the associated NOX optimization was developed. The ability of the NOX reduction by exhaust gas recirculation in regeneratively fired glass furnaces has been demonstrated with great success in previous studies [1]. Within the project, several measurement campaigns were conducted at operational industrial glass melting tanks, a test tank and the experimental facilities of the GWI where temperature and species distributions were measured. The data obtained are used to validate the CFD simulation models created with the help of the gained data of propane gas-fired burners and their impact on technology, heat transfer and pollutant emissions, etc. are investigated and applied to real glass melting tanks. Initial findings have already been implemented on a small experimental tank. The design of the conversion to propane gas-firing, including the control and regulation devices represents the completion of the project.

Keywords:

Glass Melting Furnace, Energy Efficiency, Sustainability, NOX Emissions

1. Introduction

The melting of glass is a very energy-intensive process. Very high standards for the security of gas supply and technical quality of glass melting tanks are set.

With the liberalization of the European gas market and the diversification of gas supply sources, fluctuations in the gas composition in the public grids may increase in the future. The changes in combustion properties due to changes in the composition of natural gas have implications for both the process control and emissions, particularly in sensitive thermal processes such as glass production, where the flame is used as a tool and small changes in the species concentrations and temperatures can have significant influence on the process.

Another crucial problem regarding the security of gas supply was shown in recent years. A disruption of gas supply can cause serious economic damage for industrial facilities that require continuous operation. Considering the liberalization of gas market, ensuring the gas supply is of growing importance. The high value of the gas supply became clear not at least in connection with

the Russian-Ukrainian gas dispute in early 2009. In the gas sector - unlike in the electricity sector - alternative energy sources exist which can replace natural gas in its fields of application.
This is especially true in the main area of use, the heating market. However, conversion processes are costly and not always possible on short notice in most cases. In this respect, the avoidance of gaps in the gas sector has a high priority. By replacing the fuel natural gas with a defined fuel such as propane, the effect of future expected gas quality variations in gas composition due to the liberalization of gas markets and the diversification of gas supply sources should be avoided. The question of backup solutions to ensure the production operation is therefore becoming increasingly urgent. For existing facilities, particularly with regenerative U-fired furnaces and cross burner tanks which are mature in their burner combustion chamber configuration in terms of optimal heat transfer, the implementation of new burner systems may involve a high risk for operators. Since the glass melting furnaces tend to be operated at very near-stoichiometric conditions for efficiency reasons, it can at worst lead to redox reaction in the glass melt, thus endangering the entire production line.
The aim of this research project was to develop a concept and an implementation plan for the steps necessary for the conversion of conventional natural gas-fired glass melting furnaces to an alternative firing with propane gas.

2. Procedure

In early 2010 the research project began with the first basic research on the impact of fuel switching in glass tanks. Part one was the investigation of the burner systems used by the project partner Heinz glass in the experimental facilities of GWI. The aim was to investigate whether existing burner technology can be used. The necessary amounts of exhaust gas, air and generator gas respectively which has to be added to the propane were calculated in order to reach the same Wobbe index as natural gas. Comparative measurements were carried out with natural gas H and propane-nitrogen-carbon dioxide or propane-air mixtures. In addition to the analysis of the spectral radiative properties and UV flame visualization, the two-dimensional distributions of temperature and species concentrations were recorded.
The two-dimensional distributions were measured with a 2 m long water cooled measuring probe. A steady state was assumed and a two-dimensional matrix with 215 measuring points in the burner cross section was recorded. For each point in the matrix the following values were recorded the concentration of CO_2, O_2, CO, NO_x and the temperature. The program Origin was used to interpolate between the 215 points and generate a two-dimensional plot as seen in Fig. 1. The exhaust gas emissions of the various test runs are compared in Table 1.

Table 1: Experimental results at the GWI test furnace

	CO_2	O_2	CO	NO_x	T	CO	NO_x
	[Vol.-%]	[Vol.-%]	[ppm]	[ppm]	[°C]	[ppm] related to 8 % O_2	[ppm] related to 8 % O_2
Natural Gas	10,24	3,05	26,20	1563,80	1448	18,97	1132,37
Propane - Exhaust Gas	11,97	2,87	23,33	829,00	1433	16,73	594,32
Propane - Air	11,87	2,71	25,10	629,90	1411	17,84	447,64
Propane - Generator Gas	12,32	1,77	26,00	815,00	1427	17,58	550,96

These measurements were used as reference for a series of CFD simulations. Experimental and simulation results were compared with each other (Fig. 2) to validate the simulations and verify their applicability to real systems.

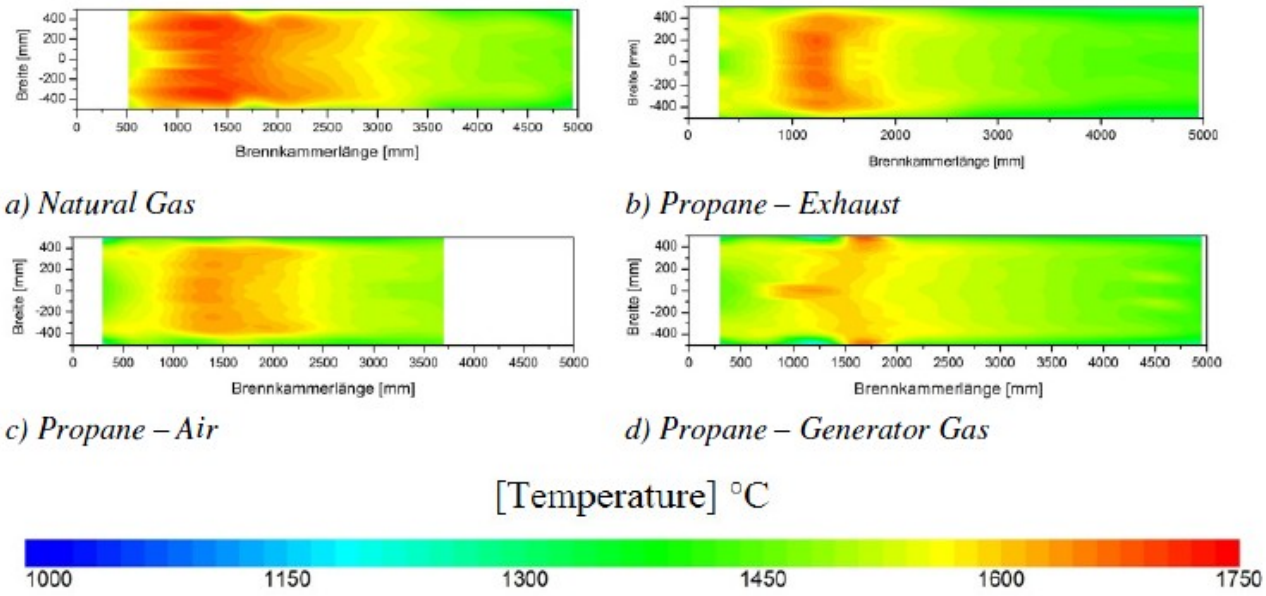

Figure 1: measured temperature distribution of different fuel mixtures

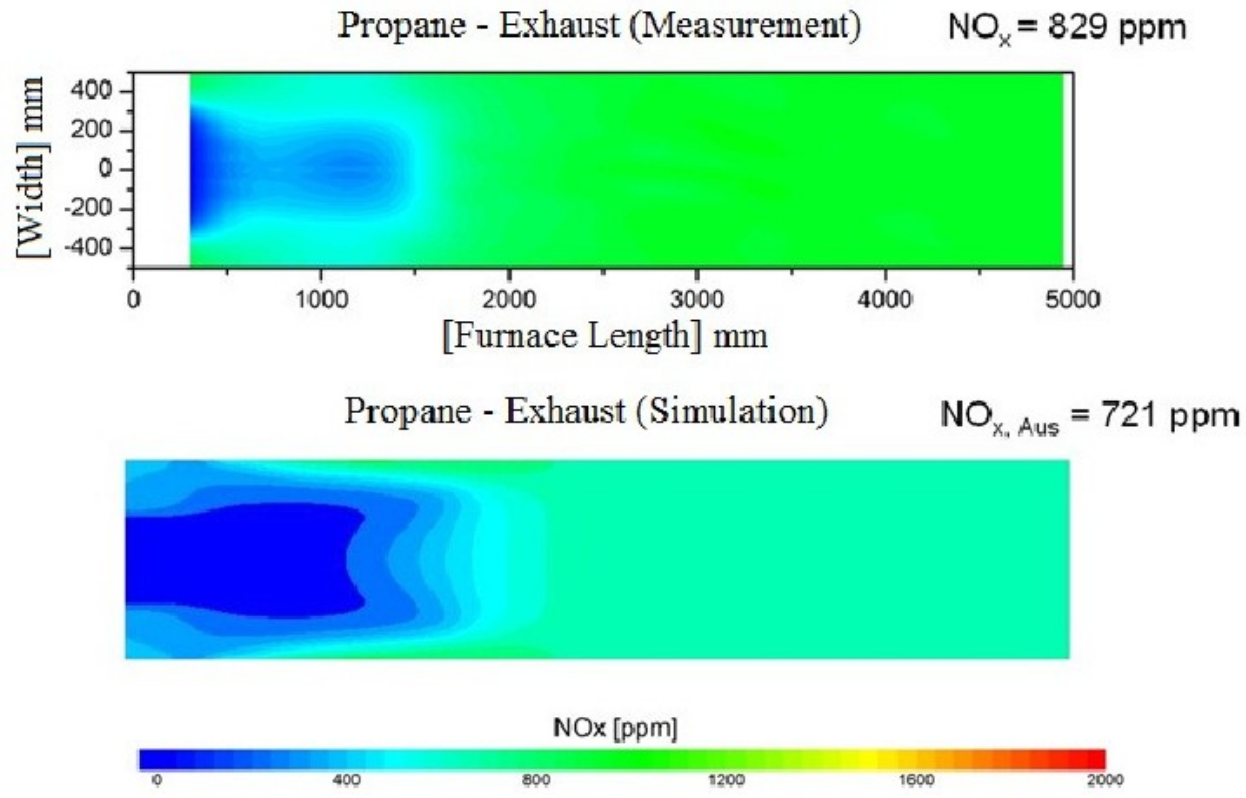

Figure 2: Comparison of NO_x emissions between measurement and calculation.

The simulations with different model combinations were compared for their applicability and quality of results. Attention was focused on the mechanisms of turbulence, reaction, radiation, and pollutant formation. Based on both the findings of experiments and the simulations at GWI the first field tests on a small experimental glass furnace were conducted. The test facility was designed and built by the project partners (Figure 3).

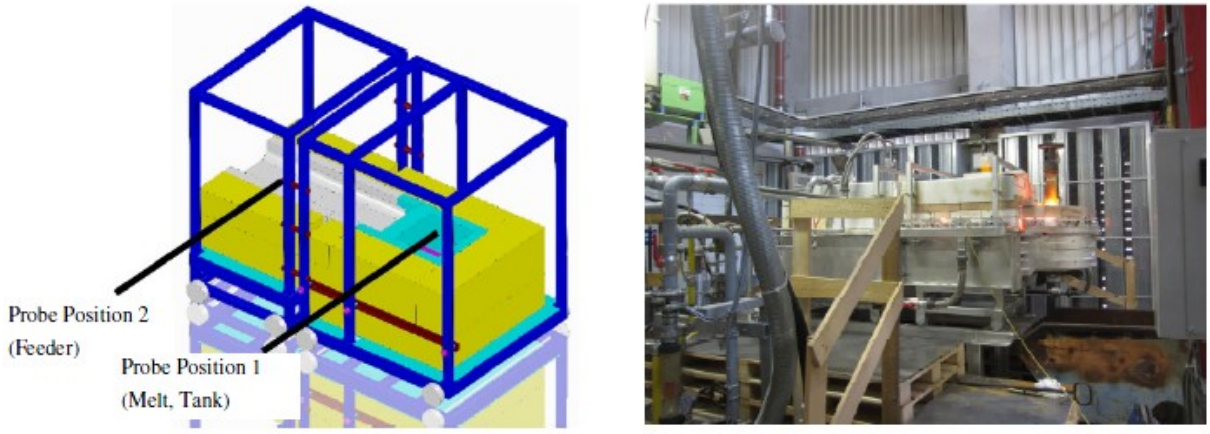

Figure 3: Experimental glass melting tank

The aim of this measurement campaign was to determine the effects of the altered firing approach on glass quality, pollutant emissions, flame parameters and ignition behaviour in a real glass melting tank. In addition, the load and switching behaviour as well as varying the composition of the fuel gas were tested.

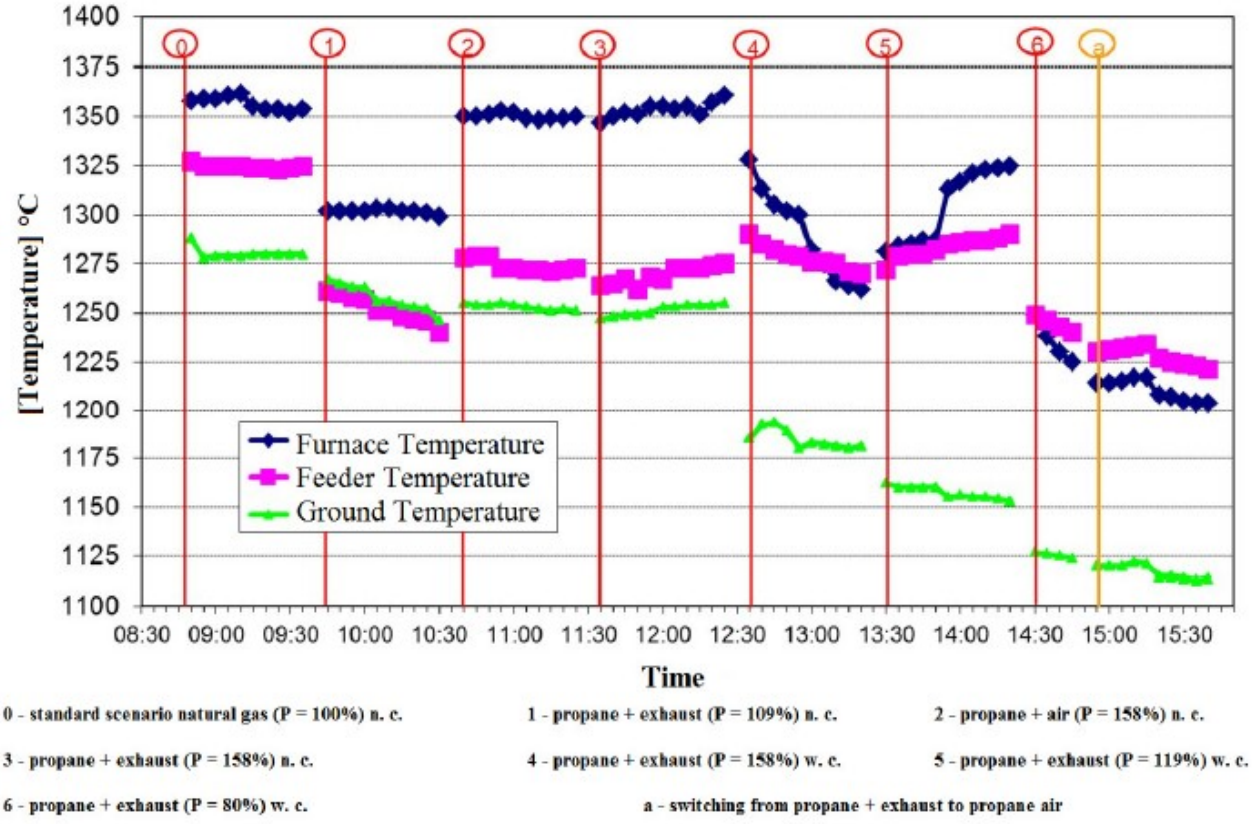

Figure 4: Time course of temperature in the experimental glass melting tank

The internal addition of exhaust turned out to be difficult during the investigations. Depending on the sampling location in the regenerator flue gas line from the tank to the chimney of the plant, the O_2 content in exhaust gas rose steadily. After cooling and filtration systems, the oxygen content went over 18 vol.%. This amount of inleaked air would not have been productive for the planned investigations. The withdrawal right behind the regenerators has led to considerable problems regarding the water content and the resulting condensation. A water separation had to be designed

and built for this extra amount of water. Another problem was the admixture of the exhaust gas to the fuel, which had a very low pressure in comparison with the fuel propane. An additional compressor was insufficient, and the admixture had to be realized through injector nozzles. After the modifications were done, the measurements could be performed.

During the readjustment of the premix burner in the feeder area to propane gas it was necessary to ensure that the default setting for the mixing ratio of air and fuel had to be changed because otherwise a considerable excess of air would have been the result.

In Figure 4 is an example of the temperature dependence of the glass melting furnace (floor, feeder and furnace element) shown for various fuels and loads while Figure 5 presents the O_2 and NO_x concentrations over the feeder. The abbreviation n. c. stands for no cullets used and w. c. for glass melting with cullets.

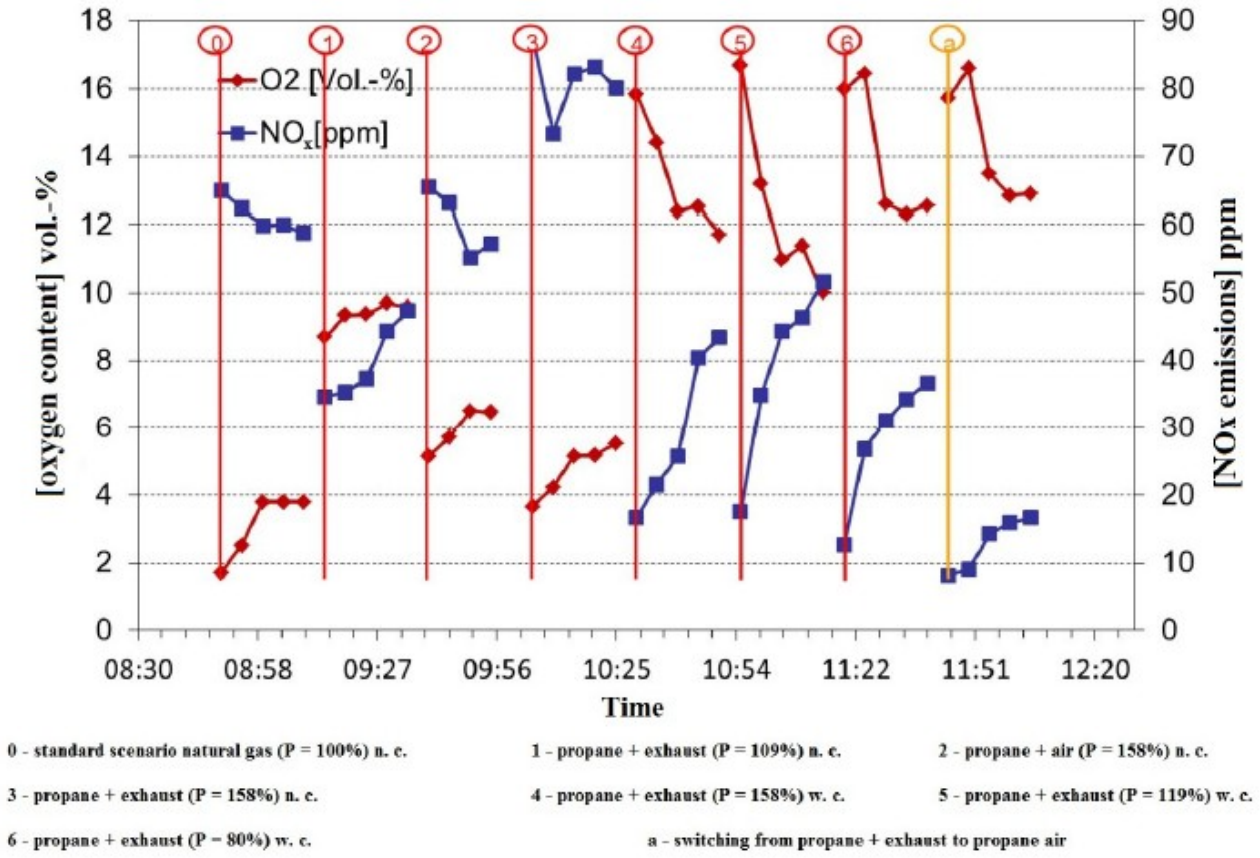

Figure 5: Time course of O_2 and NO_x in the feeder in the experimental glass melting tank

The results of the tests at the GWI test rig are confirmed by investigations at the experimental glass melting tank. The temperature in the reaction zone drops when switching from natural gas to propane if the same load of the burners is maintained. This also means a drop in temperature in the glass melt, see bottom temperature in Figure 4 A balance can be created when the power output of the propane firing is considerably increased, in the case of the experimental glass furnace to approximately 160% of gas output. It is assumed that one reasons for this drop in temperature is the different radiation characteristics of a propane flame. The higher heat capacity of CO_2 compared to nitrogen might also be a cause of this behaviour. The CO_2 content in the exhaust gas increases from about 8.6 vol.-% for natural gas to 10.8 vol.-% in the wet flue gas for the propane-gas mixture.

3. Conclusion

The national and international demand for backup systems to ensure and secure the fuel offer is constantly growing due to the politically uncertain situation in some gas supplying countries. By replacing the natural gas with a defined fuel such as propane, the effect of future expected gas quality variations in gas composition due to the liberalization of gas markets and the diversification of gas supply sources should be avoided.

Within the project the basic application of a propane-gas mixture has been shown to be capable for backup system. The used burners can be used.

Difficulties arise from the temperature drop in the reaction zone and thus in the glass melt. This must be addressed by increasing the thermal load of the burners and thus increased fuel consumption has to be taken into account.

Furthermore, the establishment of such a system has to note the following points:

1. The O_2 content of the exhaust gas which should be admixed depends on the location of removal.
2. A water trap or additional cooling must be provided to handle the increased condensation.
3. The addition of the exhaust gas to the almost non-pressurized propane needs to be carried out by means of additional measures (compressors, injector nozzles, etc.).

4. References

[1] A.Giese: Energieeinsparung und NO_x-Minderung an regenerativ befeuerten Glasschmelzwannen durch verdünnte Verbrennung - Verdünnte Verbrennung Final Report AiF-Nr.: 14755 N, 2008

[2] B. Fleischmann; A. Giese: Verbesserung des direkten Wärmeeintrages in die Glasschmelze durch Optimierung der Verbrennungsparameter bei unterschiedlichen Befeuerungsarten. Final Report AiF-Nr.: 15015 N, 2008

Experimental analysis of inhibition phenomena management for Solid Anaerobic Digestion Batch process

Francesco Di Maria[a], Giovanni Gigliotti[b], Alessio Sordi[a], Caterina Micale[a], Claudia Zadra[b], Luisa Massaccesi[b]

[a] *Dipartimento di Ingegneria Industriale, Perugia, Italy, fdm@unipg.it*
[b] *Dipartimento di Scienze Agrarie ed Ambientali, Perugia, Italy, gigliott@unipg.it*

Abstract:

Solid Batch Anaerobic Digestion (SADB) is an interesting process that can lead to the production of quite high bio-methane from several biodegradable substrates. In particular the limited production of waste liquids discharged by the reactors, along with light pre-treatment requirement, makes this process suitable for a high spreading potential in many European regions. Unfortunately, some inhibition phenomena occur when the anaerobic digestion is performed with high Total Solids concentration, as in the SADB. These phenomena can affect negatively both the stability and the viability of the process. Among the different solution exploitable for managing these phenomena, the one based on percolate recirculation seems to be very interesting. The experimental runs conducted exploiting the Organic Fraction of Municipal Solid Waste, shows that the recirculation leads to a significant reduction of the Volatile Fatty Acids concentration along with an higher biogas production rate and stability. The biogas produced in the test with percolate recirculation is double and the VFA concentration results to be significantly lower.

Keywords:

Biogas, Solid Anaerobic Digestion Batch, Volatile Fatty Acids

1. Introduction

Anaerobic digestion is one of the technologies that seem to have a very high potential for contributing to the whole renewable energy production [1], [2]. The biogas produced by the bacterial activity in absence of oxygen, under given conditions, can have a high methane content [3], [4], [5], [6] and can be exploited as fuel in ICE, leading to high energetic efficiency even thou in low size facilities. Many questions still remain open about the AD to energy plants, concerning viability, costs and process stability [5], [7], [8], [9]. The most diffused technologies for AD process are represented by the wet or dry processes [10]. Wet process usually works with TS content inside the anaerobic reactor not higher than 10-15% w/w. Semi-dry process reactors are able to work with TS% up to 20% w/w. The large fraction of the AD plants works at mesophilic conditions, with a temperature inside the reactor of about 308K, even if the number of plants working at thermophilic conditions (*i.e.* 328K) is growing [10]. High humidity levels are necessary for achieving both higher process efficiency, in terms of biomethane production per kg of VS, but also for allowing a continuos feeding of the digester. From the other hand, this advantages leads to the production of a large amount of liquids discharged by the process. The management of this huge liquid fractions, depending on the feedstock origin and on the area in which the plants operates [10], [11] (*i.e.* spreading on field), can represent a relevant problem, both from the environment and from the O&M point of view. Increasing the TS content reduces the amount of liquids from the AD process. Passing from TS of 10 to 20% w/w leads to a significant but not decisive reduction of the problem. Furthermore, when working with biomasses with high impurities and low humidity contents, very important pre-treatments are required for achieving the features require by the wet or dry reactors.

Depending on biomass quality [12], shredding, grinding, screaning, diluition and pulping can be necessary for achieving the adequate fluidity and impurities concentration reduction necessary for pumping and mixing operations. All these operations represent further increase in plant complexity, investment and management costs. A possible solution to these problems can be represented by the adoption of Solid Anaerobic Digestion Batch process. In this case the biomass need very poor pre-treatments, usually not more than mixing with shredded wood, and can be processed with TS content higher than 25% up to 50%. In this condition the digestate produced by the process, due to its low humidity, has a quite high consistency, being able to maintain its shape when arranged in open heap. Also the liquid discharged by the process [5] is narrowed, generally lower than 10%w/w. The management of the solid digestate, for several applications, is more environmentally and economically sound than the liquid one. The increase in the number of SADB reactors together with a lower automation level in biomass handling, seems to be an acceptable disadvantage for all that application that lack agricultural field or treats biodegradable substrates classified as waste. Another important aspect that has to be carefully analysed for AD working with high TS content, is represented by some biochemical inhibition phenomena that can affects both biomethane yield and process stability [13], [14]. Some solutions are possible for reducing the relevance of this phenomenon [13], [14], as increasing the amount of inoculums exploited for starting the AD process in each SADB reactor. This is a possible solution but in some cases can lead to an unacceptable increase of the reactor volume. A second possible approach can be represented by the percolation system. This paper is focused on the analysis of the inhibition phenomena comparison between a SADB process with and without percolation. Two parallel experimental tests have been started exploiting the same MSWOF mixture and I, and all the main process parameters have been controlled and measured.

2. System description and Methods

2.1. The SADB

The Solid Anaerobic Digestion Batch [5], known also as Solid State AD [14] or High Solids AD [13], is an AD process performed with biodegradable materials with a TS content higher than 25% up to 50% w/w. In this condition the material is able to maintain its shape when arranged in open heap due to its low humidity content. TS higher than 50% implies a to much low humidity content that inhibits the bacterial activity.

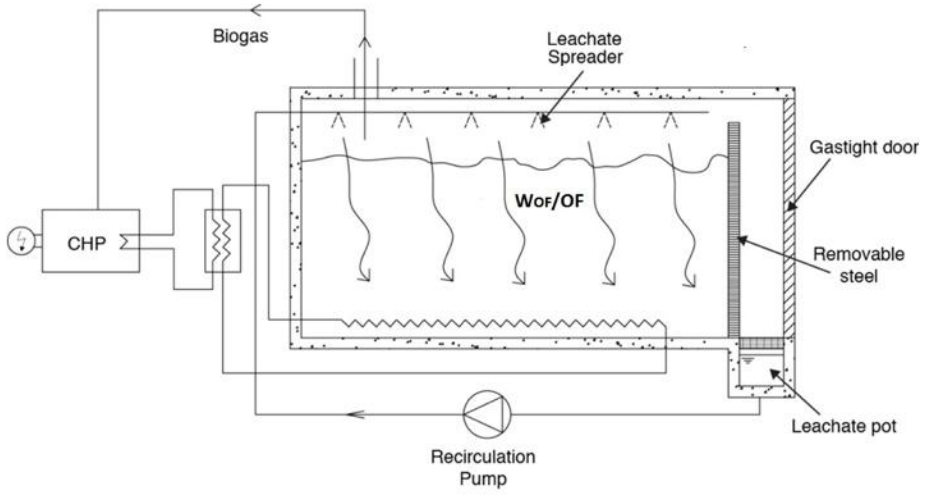

Fig. 1. SADB biocell schematic.

The most diffused reactors for SADB are represented by concrete, gastight biocells (Fig. 1), with a door through which the material can be charged and discharged.

The process is performed in static condition excepting a timed percolate spreading on the top of the material under treatment. The percolate exploited for spreading operation arises also from the one produced by previous AD processes.
Inside the biocell all the main parameters can be controlled and measured, as T, P, Humidity, CH_4, O_2, H_2S, CO_2.
Usually, the AD is performed at mesophilic conditions (308K), and the heat required by the process is recovered from the CHP fuelled by the produced biogas.
Full scale SADB have from 6 to 12 biocells with a gross volume ranging from 600 to 1200 m^3, depending on the amount of mass treated.

2.2. Biomass characterization

The biomass exploited in the runs is represented by the MSWOF arising from source segregated collection. This material has been mixed with 30% w/w of bark, for giving to the material the required level of porosity, and mixed with an equal weight of inoculums arising from previous SADB laboratory tests. The MSWOF has also been characterized by means of the main rapid biodegradable, the Fines (20mm) and inert components.

The TS have been evaluated measuring the weight loss, on wet basis, before and after heating at 378.14 K for 24 h three different samples of the mixture. VS content has been evaluated, as weight loss, by heating at 823.14 K for 24 h the TS samples obtained from the previous analysis. The mixture TOC content was determined by the Springer and Klee wet dichromate oxidation method, while Total Nitrogen (TN) was obtained by Kjeldahl method. Phosphorus assimilated was extracted with 0.5 M $NaHCO_3$ solution at pH 8.5 then was analysed with a spectrophotometer. To perform the analysis of heavy metals content, samples were digested according to the US EPA 3050B method [15]. Heavy metals concentrations were determined by flame atomic absorption spectrophotometry using a Shimadzu AA-6800 apparatus.

2.3. Experimental tests

Two parallel tests have been contemporary started, exploiting the mixture showed in Table 1. One test has been performed inside a large laboratory AD apparatus, designed for reproducing, in the most suitable way, the same SADB conditions of full scale facility (Fig. 2). This apparatus consist of a 100 litre cylindrical, gas tight AD reactor, with a removable top. The material under treatment is supported by a steel grate for separating the solid phase from the percolate that is collected and stored at the bottom of the reactor. A timed circulation pump provides to spread on the top of the material the percolate. A tap allows to samples the stored liquid. Test has been started by introducing in the reactor bottom, 10 litres of only pure demineralised water. Biogas produced is firstly piped in a moisture separator and then to a thermal gas flow meter (0.01% FS). The biogas methane content has been evaluated by an infrared sensor (±2%). Mesophilic conditions (308±2K) have been kept by the aid of a thermal band, embracing the reactor, controlled by a TDR. All data are measured and stored in a dedicate PC. Second test was started by utilizing 10 gastight bottles of 1 litres volume each one. The bottles where maintained at mesophilic condition by a thermal bath. Two bottles were also equipped by a gasometer apparatus for evaluating the biogas produced during the test.

Table 1. MSWOF and AD mixture composition

Parameter	*Value*	*Unit*
	MSWOF components	
Rapid biodegradable	93	%w/w
Inert	7	%w/w
	AD mixture	
MSWOF/I	1	kg/kg (wb)
Bark/MSWOF	30	%w/w (wb)

The main parameters evaluated during the runs are represented by the biogas production and by the evolution of the VFA concentration. At given number of days of treatment, about 500ml of percolate have been withdrawn from the experimental apparatus, and contemporary the content of a bottle was examined. The bottles with gasometer apparatus where examined last. VFA extraction of the bottle content was performed by extraction with demineralised water. Then the samples where firstly centrifuged at 5000 rpm, then filtered at 0.45 nm and finally analyzed with gaschromatograph. VFA up to 7 Carbon atoms where investigated.

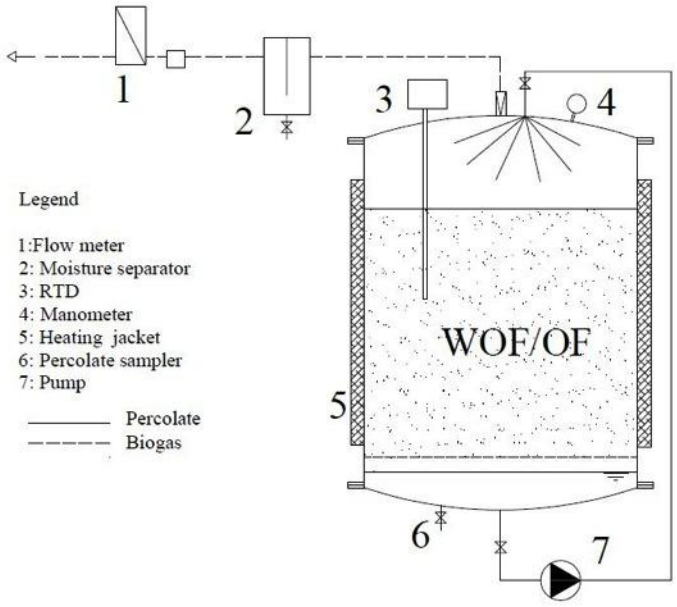

Fig. 2. SADB experimental apparatus.

3. Main results and discussion

The characterization of the I and of the MSWOF (Table 2) shows that the TS content of the I is of about 38% w/w whereas the TS content of the MSWOF is of about 27%. The ratio of the kg VS of MSWOF and I exploited in the tests is of 0.71, with mass ratio, on wet basis, of 1:1. The pH of the I is quite alkaline whereas the pH of the MSWOF results definitely acid.

Table 2. I and MSWOF characterization

Parameter	*I*	*MSWOF*	*Unit*
Humidity	62.28	72.67	% w/w
VS	95.04	93.27	% db
pH	8.90	4.97	-
N	1.03	2.67	% db
C/N	40.78	10.90	-

The BY of the SADB experimental apparatus results to be higher than the one produced by the same mixture in the bottles laboratory test (Fig. 3). During the first 7-10 days, the biogas rate per kg of VS results very similar for the two runs. After this initial period, the SADB apparatus biogas rate becomes decisively higher than the one produced by the bottles. This trend is also confirmed by the daily biogas production curves (Fig. 4). Infact, during the first 7-10 days the daily biogas rates curves overlaps with a high precision. After this period, the two curves become decisively divergent until 22nd day of the process. Infact, after 20 days, the SADB daily production curve achieve a maximum whereas the bottles one a minimum value. In the successive days the SADB curve show

a constant decrease (Fig. 4) whereas the bottles curve shows a growing trend, even if with a significant fluctuation around the mean value. Furthermore, this fluctuation seems to have a growing trend around the last days of the AD process. This behaviour is the consequence of the strong VFA concentration during the process. The TVFA concentration in the both tests is very similar, around 20,000 mg/l, until the 5th day (Fig. 5). Then, the TVFA concentration in the percolate of the SADB decrease significantly, achieving a concentration lower than 5,000 mg/l after the 25th day. The TVFA concentration in the bottles runs, without percolation, continues to rise constantly until the 30th day reaching a maximum value higher than 42,000 mg/l. After this maximum value the TVFA concentration show a decreasing trend, even if with significant oscillation. This phenomenon justifies the strong instability in the daily biogas production for the Bottles runs.

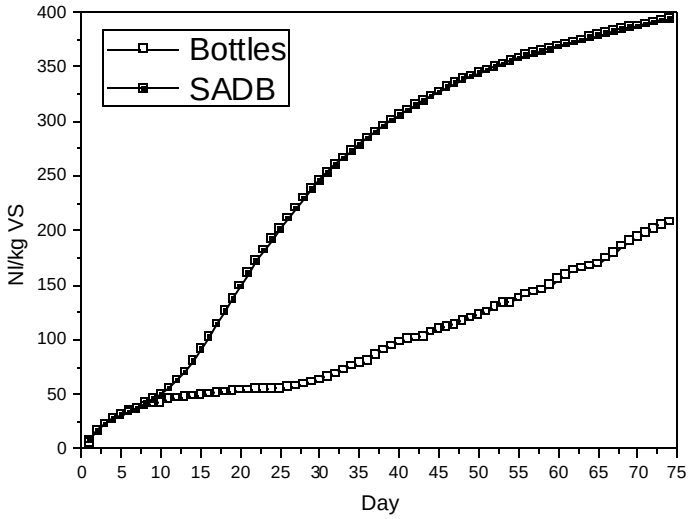

Fig. 3. BY for the SADB experimental apparatus and bottles runs.

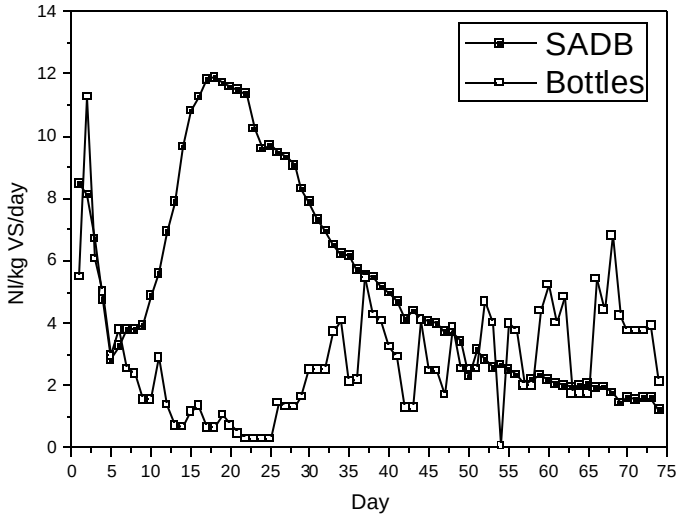

Fig. 4. Daily biogas rate for the SADB experimental apparatus and Bottles runs.

In more detail, has shown by Figure 6, the Acetic and Butyric acid concentration remains higher than 10,000 mg/l for a very long period. Also the Valeric and Propionic acid (Fig. 7) has a

significantly higher concentration during the whole bottle test compared to the one measured in the SADB apparatus. The significant variation of the different VFA, causes the strong instability of the daily biogas production instead of the one achieved in the SADB apparatus.

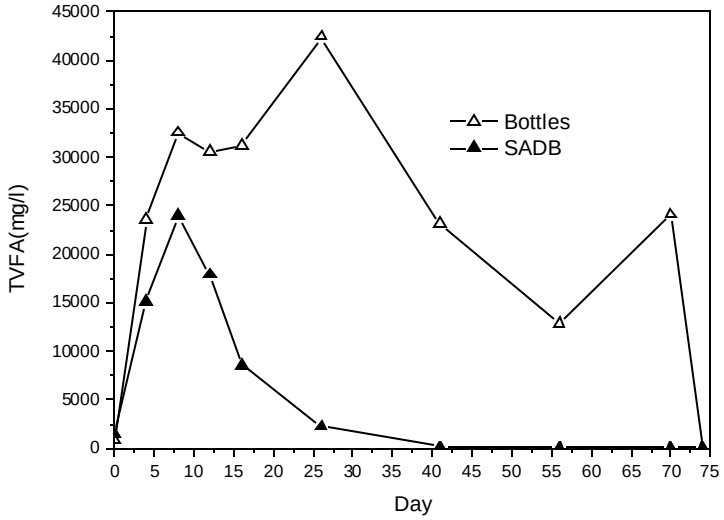

Fig. 5. TVFA evolution in the SADB experimental apparatus and Bottles runs.

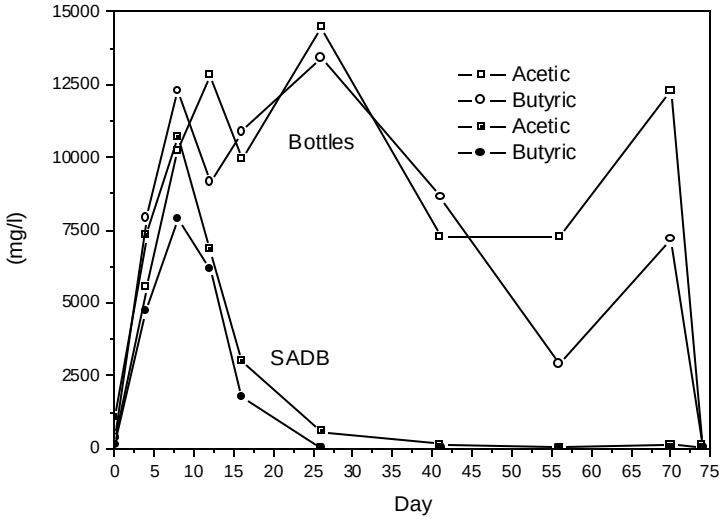

Fig. 6. Acetic and Butyric acids concentration evolution in the SADB experimental apparatus and Bottles runs.

The experimental results show the higher biogas production and process stability of the process performed in the SADB apparatus. The main difference occurring among the two tests is represented by the presence of the percolate recirculation in the SADB apparatus. Infact, a fraction of the VFA produced are solubilised in the periodically recirculated percolate, reducing its concentration and inhibition effect in the solid phase of the SADB reactor. Furthermore, in the percolate stored at the bottom of the reactor, a second wet AD process take places. The high humidity at which this second process takes places, allows a rapid metabolism of the acids leading to a higher total biogas rate. This phenomenon contributes also to the higher stability shown by the process performed in the SADB apparatus.

In the bottles runs, the AD process occurs with percolate in static conditions. This means that the solid and the liquid phase are not physically separated. During the fermentation phase, the alcohols

and VFA produced are continuosly solubilised in the liquid phase, leading to a very high concentration. This causes a process inhibition both in the liquid phase and at the solid particle surface. These preliminary results show that the percolate recirculation is able to reduces SADB inhibition phenomenon, increasing both process stability and biogas yield. This is an aspect of fundamental importance in the management of full scale SADB reactors, able to ensure a quite efficient and viable SADB process. Further positive effects of percolate recirculation can also lead to a significant reduction of I needs, with a consequent reduction in full scale investment costs.

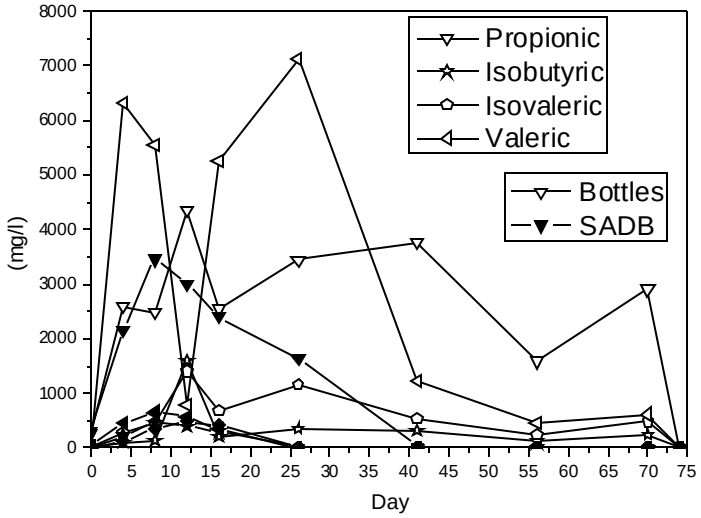

Fig. 7. Propionic, Isobutyric, Isovaleric and Valeric acids concentration evolution in the SADB experimental apparatus and in the Bottles runs.

4. CONCLUSION

The effect of percolate recirculation results to be very positive for Solid Batch Anaerobic Digestion, mainly as a consequence of a strong reduction of the inhibition phenomenon induced by high Volatile Fatty Acids Concentration. In the first days of the process, the absence of recirculation can lead to a TVFA concentration higher than 40,000 mg/l with a quite null biogas production. This strong inhibiton conditions lasts for more than 40 days. Percolate recirculation leads to a TVFA peck of about 20,000 mg/l that is then rapidly reduced till quite null concentration in about 45 days. Further biogas production achieves about 400 Nl/kgVS instead of about 150 achieved by the test without recirculation. This results shows how the percolate recirculation can represent an interesting and sustainable solution to SADB inhibition phenomena reduction, instead of other solution as the increase of the amount of inoculums exploited per each cycle.

Nomenclature

AD	Anaerobic Digestion
BY	Biogas Yield (Nl/kgVS)
CHP	Combined Heat and Power
I	Inoculum
ICE	Internal Combustion Engine
COD	Chemical Oxygen Demand (mg/l)
MSWOF	Municipal Solid Waste Organic Fraction
N	Nitrogen

O&M	Operating and Maintenance
P	Phosphorous
SADB	Solid Anaerobic Digestion Batch
TDR	Temperature Detection Resistance
T	Temperature (K)
TN	Total Nitrogen (%TS)
TOC	Total Organic Carbon (%TS)
TP	Total Phosphorous (%TS)
TS	Total Solids (%w/w)
TVFA	Total Volatile Fatty Acids (mg/l)
VFA	Volatile Fatty Acids (mg/l)
VS	Volatile Solids (%TS)

References

[1] Directive 2001/77/CE of the European Parliament and of the Council of 27 September 2001 on the promotion of the electricity produced from renewable energy sources in the internal electricity market. Official Journal of the European Communities 27.10.2001.

[2] Beurskens L.W.M., Hekkenberg M., Vethman P., ECN – Renewable Energy Projection as Published in the National Renewable Energy Action Plans of the European Members States – Available at: < http://www.ecn.nl/docs/library/report/2010/e10069.pdf>.[accessed 24.12.2011].

[3] Amon T., Amon B., Kryvoruchko V., Machmuller A., Hopfner-Sixt K., Bodiroza V., Hrbek R., Firedel J., Potsch E., Wagentristl H., Schreiner M., Zollotsch W., Methane production through anaerobic digestion of various energy crops grow in sustainable crop rotations. Bioresource Technology 2007; 98: 3204-3212.

[4] Lastella G., Testa C., Cornacchia G., Notornicola M., Voltasio F., Anaerobic digestion of semi-solid organica waste: biogas production and its purification. Energy Conversion and Management 2002; 43: 63-75.

[5] Di Maria F., Sordi A., Micale C., Energy production from mechanical biological treatment and composting plants exploiting solid anaerobic digestion batch: an Italian case study. Energy Conversion and Management 2012; 56: 112-120.

[6] Desideri U., Di Maria F., Leonardi D., Proietti S., Sanitary landfill energetci potential analysis: a real case study. Energy Conversion and Management 2003; 27 (5): 1969-1981.

[7] Walla C., Schneeberger W., The optimal size for biogas plants. Biomass and Bioenergy 2008; 32: 551-557.

[8] Vervaeren H., Hostyn K., Ghekiere G., Willems B., Biological ensilage additives as pretreatment for maize to increase the biogas production. Renewable Energy 2010; 35: 2089-2093.

[9] Gebrezgabher S.A., Meuwissen M.P.M., Prins B.A.M., Lansink A.G.J.M.O., Economic analysis of anaerobic digestion – A case of Green power biogas plant in The Netherlands. NJAS Wageningen Journal of Life Sciences 2010; 57: 109-115.

[10] De Baere L, Mattheeuws B, Anaerobic digestion in Europe: State of the art 2010. ORBIT 2010: Proceeding of the 7th International Conference on Organic Resource in the Carbon Economy; 2010 June 29 july 3; Heraklion, Crete.

[11] Di Maria F., Pavesi G., Leombruni S., Improvement of an existign anaerobic digestion plant: technical and economic analysis. ORBIT 2008: Proceeding of the 6th International Conference on Moving Organic Waste Recycling towards Resource Management and for the Bio-based Economy; 2008 October 13-15; Wageningen, The Netherlands.

[12] Vinot M, Perez CA, Turm P, Maillo A. Improvements in anaerobic digestion units and in pre-treatments performances beforehand. Venice 2010: Proceedings of the Third International Symposium on Energy From Biomass and Waste; 2010 November 8-11;Venice, Italy.

[13] Schievano A., D'Imporzato G., Malagutti L., Fragali E., Ruboni G., Adani F., Evaluating inhibition conditions in high-solids anaerobic digestion of organic fraction of municipal solid waste. Bioresource Technology 2010; 101: 5728-5732.

[14] Di Maria F., Sordi A., Micale C., Optimization of Solid State Anaerobic Digestion by Inoculum Recirculation: the Case of an Existing Mechanical Biological Treatment Plant. doi: 10.1016/j.apenergy.2011.12.093

[15] US EPA 3050 B (1996), Environmental Protection Agency.

Experimental investigations of the combustion process of n-butanol/diesel blend in an optical high swirl CI engine

S. S. Merola [a], G. Valentino [b], C. Tornatore [c], L. Marchitto [d], F. E. Corcione [e]

Istituto Motori -CNR, Napoli, Italy
[a] s.merola@im.cnr.it; [b] g.valentino@im.cnr.it; [c] c.tornatore@im.cnr.it
[d] l.marchitto@im.cnr.it; [e] f.corcione@im.cnr.it

Abstract:
In diesel engines, fuel is injected into the engine cylinder close to the end of the compression stroke. During a phase known as ignition delay, the fuel spray atomizes into small droplets, vaporizes, and mixes with air. As the piston continues moving towards TDC, the mixture temperature reaches the fuel ignition point, causing instantaneous ignition of some pre-mixed amount of fuel and air. The balance of fuel that does not burn in premixed combustion is consumed in the rate-controlled combustion phase, also known as diffusion combustion. Fuel composition, charge dilution, injection pressure as well as injection timing are the main factors that influence combustion and emission formation in the compression ignition engine.
In order to evaluate the effects of these factors on in-cylinder spray combustion and soot formation, UV-visible digital imaging and natural emission spectroscopy were applied in a single cylinder high swirl compression ignition engine. The engine was optically accessible and equipped with a common rail multi-jets injection system. Combustion tests were carried out using commercial diesel and a blend of 80% diesel with 20% n-butanol (BU20). Two injection pressures (70 and 140 MPa), two injection timings (11 CAD BTDC and 3 CAD BTDC) and a low and high EGR rate were tested.
UV-visible emission spectroscopy was used for the detection of the chemical markers of combustion process. Chemiluminescence signals, due to OH, HCO and CO2 emission bands were detected. OH emission was correlated to NO measured at the exhaust. The soot spectral feature in the visible wavelength range was correlated to soot engine out emissions.

Keywords:
Optical diagnostics; UV-visible spectroscopy; Combustion process; Common Rail CI engine; Diesel/butanol blend

1. Introduction

The use of alternative fuels (as biodiesel, ethanol, methanol) for light and heavy duty engines to approach the target of ultra low NOx and PM emissions without fuel economy penalty was widely investigated [1 - 2, 3, 4, 5]. Although a dominant role in diesel substitutes is played by biodiesel produced from animal fats, algae or non-food crop plants, alcohols have become the most popular replacement to fossil fuels due to a variety of locally available feedstock. It is recent the growing interest in the butanol as a viable alternative either single or blended with conventional based fuels to help decrease the demand for non-renewable petroleum [6]. Like ethanol, butanol can be produced both by petrochemical and fermentative processes [7]. The production of bio-butanol by fermentation offers certain advantages in comparison with bio-ethanol: higher energy content, lower water adsorption and corrosive properties, better blending abilities and the ability to be used in conventional internal combustion engines without the need for modification. Although bio-butanol could not compete on a commercial scale with butanol produced synthetically and almost all production ceased as the petrochemical industry evolved, the increasing interest in use of bio-butanol as a transport fuel has induced a number of companies to explore novel alternatives to traditional ABE fermentation, which would enable bio-butanol to be produced on an industrial

scale. Regarding the automotive use of butanol, scientific literature reports several experimental investigations to evaluate the effects of using blends of n-butanol with conventional diesel fuel on the performance, exhaust emissions, and combustion behaviour also in transient conditions [8 - 9, 10, 11, 12]. The almost totality of these studies consisted in the evaluation of performance, fuel consumption and exhaust emissions for different engine operating conditions. The aim of this paper is the better comprehension of phenomena correlated with butanol–diesel combustion in CI engine. In previous works [13, 14] cycle resolved visualization, UV-visible imaging were applied in an optically accessible high swirl multi-jets compression ignition engine fuelled with a commercial diesel and a blend of 80% diesel with 20% n-butanol (BU20). Combustion process was studied from the injection until the late combustion phase fixing the injection pressure at 70MPa and changing the injection timing and EGR rate in order to investigate low temperature combustion in partially premixed regime and in mixing controlled one. In this paper the effect of BU20 in the same c.i. engine was studied by UV-visible imaging and natural emission spectroscopy fixing two injection pressures (70 and 140 MPa) for two injection timings and high EGR rate. The spectroscopic methodology was applied to follow in the combustion chamber the formation and the evolution until the exhaust of the principal compounds and radical species to characterize the combustion process. OH and soot emission were correlated with the engine parameters and with the NOx and particulate engine out emissions, measured by conventional methods.

2. Experimental set-up

The experiments were carried out in an external high swirl optically accessed combustion bowl connected to a single cylinder 2-stroke high pressure common rail compression ignition engine. The main engine specifications are reported in Table 1. The external combustion bowl (50 mm in diameter and 30 mm in depth) is suitable to stabilize, at the end of compression stroke, swirl conditions to reproduce the fluid dynamic environment similar to a real direct injection diesel engine. The implication of “cylindrical bowl” is related to the peculiar design of the prototype engine that has a large displacement as an air compressor.

The main cylinder, connected to the external “swirled bowl” through a tangential duct, allows to supply compressed air flow to the bowl as the piston approaches TDC. The air flow, coming from the cylinder, is forced within the combustion chamber by means of the tangential duct. In this way, a counter clockwise swirl flow, with the rotation axis about coincident to the symmetry axis of the chamber, is generated. The injector was mounted within this swirled chamber with its axis coincident to the chamber axis; in this way the fuel, injected by the nozzle, is mixed up through a typical interaction with the swirling air flow. The combustion process starts and mainly proceeds in the chamber. As soon as the piston moves downward, the flow reverses its motion and the hot gases flow through the tangential duct to the cylinder and finally to the exhaust ports. The combustion chamber provides both a circular optical access (50 mm diameter), on one side of it, used to collect images and a rectangular one (size of 10 x 50 mm) at 90°, outlined on the cylindrical surface of the chamber, used for the laser illumination input. The injection equipment includes a common rail injection system with a solenoid controlled injector located on the opposite side of the circular optical access. The nozzle is a micro-sac 7 hole, 0.141 mm diameter, 148° spray angle nozzle. An external roots blower provided an intake air pressure of 0.217 MPa with a peak pressure within the combustion chamber of 4.9 MPa under motored conditions.

Table 1 - Specifications of the engine

2-stroke single cylinder ci engine	
Cylindrical Bowl (mmxmm)	50x30
Bore (mm)	150
Stroke (mm)	170
Connecting Rod (mm)	360
Compression ratio	10.1:1
Air supply	Roots blower
Abs. intake air pressure (MPa)	0.217
Bosch Injector nozzle	7/0.141/148°

In the preliminary phase of the work, combustion process visualization was obtained using an intensified CCD camera equipped with a quartz lens (UV-Nikon 78-mm), collecting the light emission that passes through the optical access of the combustion chamber. The electronically gated ICCD camera had an array size of 512 x 512 pixels with a pixel size of 19x19 μm and 16-bit dynamic range digitization at 100 kHz. The match between the ICCD and the lens allowed 185 μm spatial resolution. The camera spectral range spread from UV (180 nm) until visible (700 nm). The line-of-sight light emission measurements were performed in the whole ICCD spectral range. The ICCD is not a cycle resolved detector, hence each acquisition was carried out at a fixed crank angle for different engine cycles setting the exposure time at 5μs. The temporal difference between two images was 50μs. The intensifier gain was adjusted so that the brightest region of images was on the threshold of the detector saturation and it was the same for all the engine tests. Pictures of the experimental apparatus for the optical investigations are reported in Figure 1.

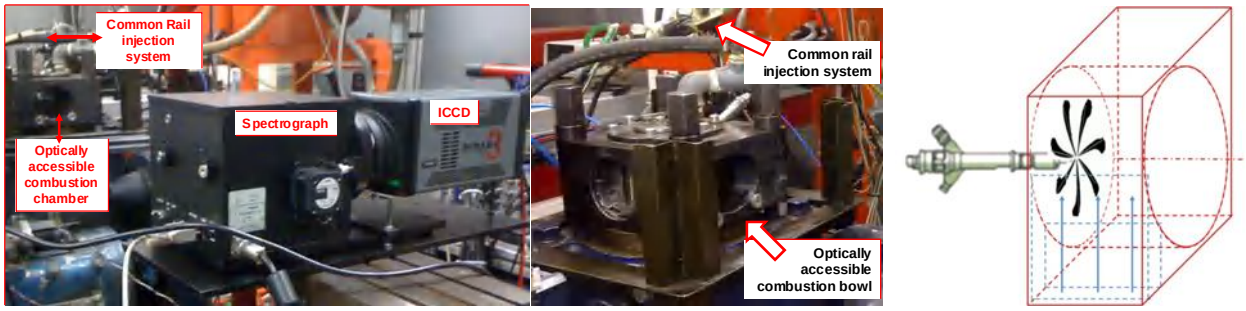

Figure 1 - Experimental apparatus for the optical investigations and drawing of injector position in the optically accessible combustion chamber.

For spectroscopic investigations, the radiative emissions from the combustion chamber were focused by a 78 mm focal length, f/3.8 UV Nikon objective onto the micrometer controlled entrance slit of a spectrometer with 150 mm focal length and 600 groove/mm grating. From the grating the radiations were detected by an intensified ICCD camera (array size of 1024 x 1024 pixels with a pixel size of 13x13 μm and 16-bit dynamic range digitization at 100 kHz). The exposure time was fixed at 41.6 μs and the dwell time between two consecutive acquisitions was set at 166 μs. The central wavelength of the grating was fixed at 300 nm and 400 nm, respectively, in order to cover the spectral range from UV to visible. Spectroscopic investigations were carried out in the central region of the combustion chamber. For a better post-detection analysis the binning of 8 spectra was performed in correspondence to 8 chamber locations. The spectra were corrected for the optical setup efficiency using a deuterium lamp with a highly uniform full spectrum. The wavelength calibration was performed using a mercury lamp. The time evolution of combustion products was evaluated from spectroscopy investigations using a post-processing procedure. For each chemical species with well-resolvable narrow emission bands, the height of the band expressed in counts was evaluated after the subtraction of emission background and other species contribution. Thus OH emission was evaluated as height of the 310 nm band system after the subtraction of the emission background, evaluated as the mean value between the emissions measured at 300 nm and 320 nm, respectively. For broadband emission the mean intensity, at specific wavelength range, was considered. Thus, soot emission was evaluated as mean intensity at 530-532 nm. A routine, developed in Labview environment, allowed to simultaneously evaluate the emissions of the selected compounds and species for each spectrum and each time. Moreover, OH and soot emissions were calculated as average on all the spectra.
A crank angle encoder signal synchronized the cameras and the engine, through a delay unit. The AVL Indimodul recorded the TTL signal from camera acquisitions together with the signal acquired by the pressure transducer. In this way, it was possible to determine the crank angles where optical

data were detected. Results of the in-cylinder pressure were computed averaging 300 consecutive engine cycles. Exhaust gaseous emissions were acquired by the AVL DiGas 4000 analyzer for NOx (1 ppm resolution), the Smoke Meter AVL 415S was used for FSN and soot concentration (0.01 mg/m³ resolution) measurements. All combustion tests were carried out running the engine at the fixed speed of 500 rpm, injecting a constant fuel amount of 30mg ±1% at the pressure of 70 MPa and 140 MPa. Tests were carried out setting the electronic start of injection (SOI) of 11 CAD BTDC and 3 CAD BTDC. EGR rate was changed from 0% to 50% corresponding to 21 and 17% of O_2 at intake, respectively. Combustion tests were carried out using two fuels. The baseline fuel was the European low sulphur (10 ppm) commercial diesel with a cetane number of 52. The blend was composed by 80% of baseline diesel and 20% of n-butanol by volume and denoted as BU20 (cetane number 44) [15].

3. Results and discussion

Diesel combustion process is very complex due to the several physical and chemical phenomena that occur [16]. The efficiency of diesel combustion and its associated pollutant emissions are mainly affected by the fuel injection process, as well as by the fuel properties. The combustion process is usually described as consisting of three distinct phases: ignition delay, premixed combustion and mixing controlled combustion. Ignition delay is the time taken after the start of injection for the pre-ignition processes to produce the ignition nuclei and detectable combustion. The duration of the ignition delay is one of the most important criteria because it has a great effect on the combustion process, mechanical stresses, engine noise and exhaust emissions. Premixed combustion refers to the combustion of a portion of the fuel injected during the ignition delay period. Mixing controlled combustion is the phase in which the fuel, that has not burnt during the premixed combustion is consumed during the concluding engine cycle. During the mixing controlled combustion phase, the fuel controls the burning rate that is influenced by the rate it mixes with air and attains the condition to burn. This phase is characterized by a lower heat release peak than that reached in the premixed phase. The rate-controlled combustion phase is often referred to as diffusion combustion. Figure 2(a-b) shows the Ignition Delay (ID) and the maximum pressure (P_{max}) measured for both fuels and for all the operating conditions.

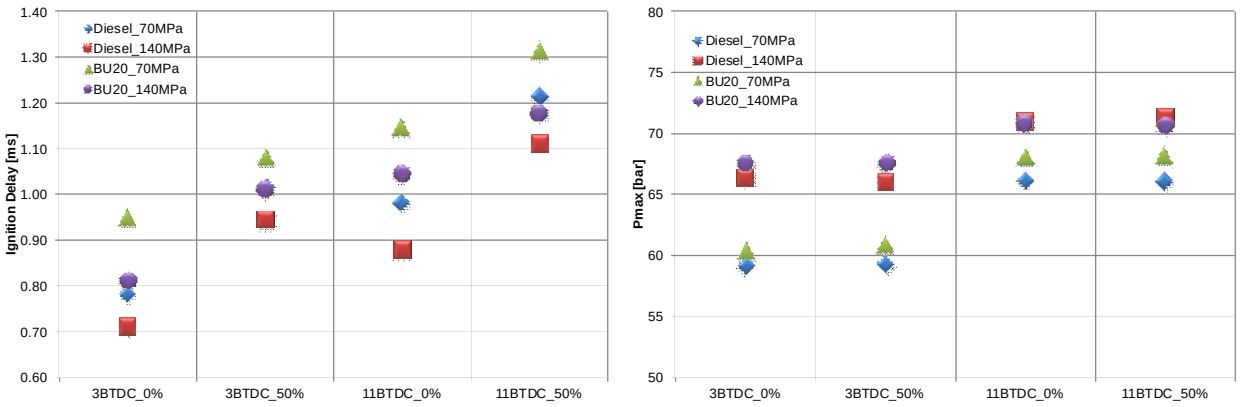

(a) (b)

Figure 2. (a) Ignition Delay (ID) and (b) pressure peak signal (P_{max}) measured for both fuels and for all the operating conditions.

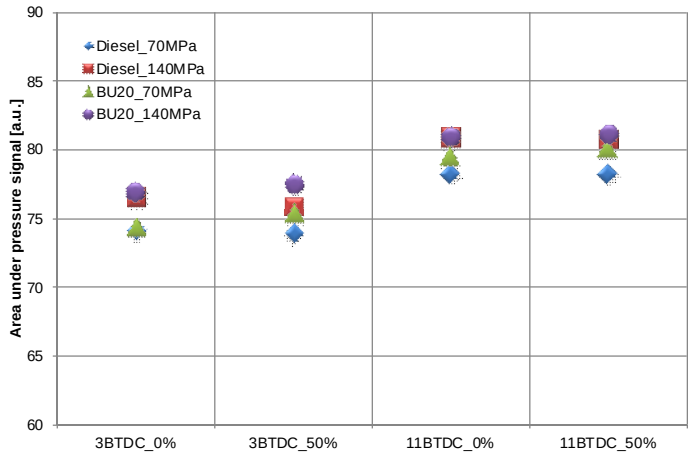

Figure 3. Pressure signal area measured for both the fuels and for all the operating conditions.

It can be observed that the combined effects of lower cetane number of BU20, which gives a longer ignition delay compared to diesel fuel, and its higher volatility contribute to increase the mixing time joined to a better mixed charge that induced a highest peak pressure. Advancing the start of injection with respect to TDC, a longer ignition delay may be observed. This trend is confirmed both at EGR=0 and 50% even if the increasing EGR rate reduced the effect of increasing injection pressure. In particular at SOI=11 CAD BTDC and Pinj=140MPa the premixed phase can be considered equivalent for both fuels and the ignition delay represents the only feature parameter.

In order to evaluate the engine efficiency of each selected operating condition, considering the used prototype engine, the areas under the combustion pressure signals were compared. The results, reported in Figure 3, were evaluated from the 300 cycles averaged pressures. As expected, at fixed SOI, the higher injection pressure induced a little increase in the engine working area. Same trend was observed advancing the start of injection at fixed injection pressure. No penalty was detected as effect of the EGR rate. For all the conditions, the engine efficiency for BU20 was higher than diesel fuel. This was due to higher BU20 volatility that improved the fuel charge mixing and reduced the amount of not completely burned fuel.

Regarding the exhaust emissions, NOx and smoke were measured for all the selected engine test conditions. The results are reported in Figures 4a and 4b for the test at 70 MPa and 140 MPa, respectively. Firstly, a strong decrease of NOx at increasing EGR rate and delayed SOI was measured for both fuels. The effect was stronger at higher injection pressure. A trade-off trend was observed for soot. The results were due to the injection of most of fuel (>50%) before the start of ignition for all the operating conditions. This produced fast burning rates once combustion started, with high rates of pressure rise and high pressure peaks. The effect was enhanced by the increase of injection pressure and by advancing of SOI that caused the NOx increase. After the premixed burning phase, part of the mixture remained rich; the higher percentage of unburned mixture induced a higher soot tendency.

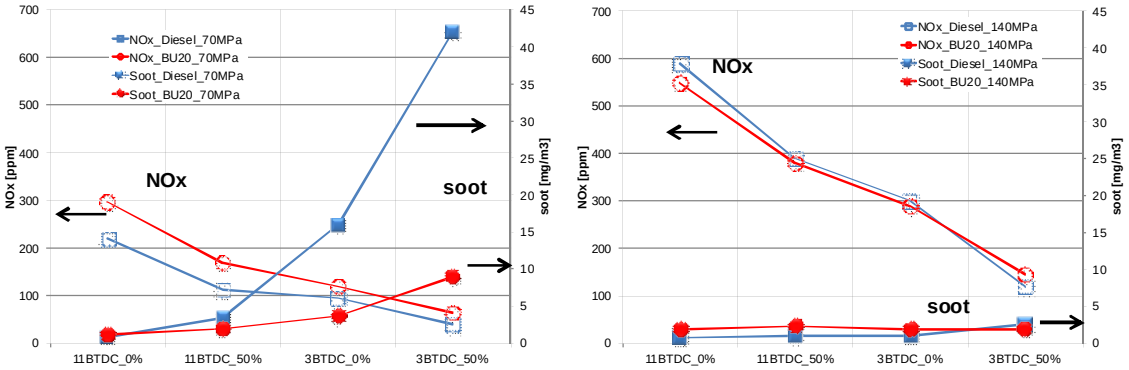

(a) (b)

Figure 4. Engine exhaust NOx and soot emission measured for both fuels and for the operating conditions with injection pressure equal to (a) 70MPa and (b) 140MPa.

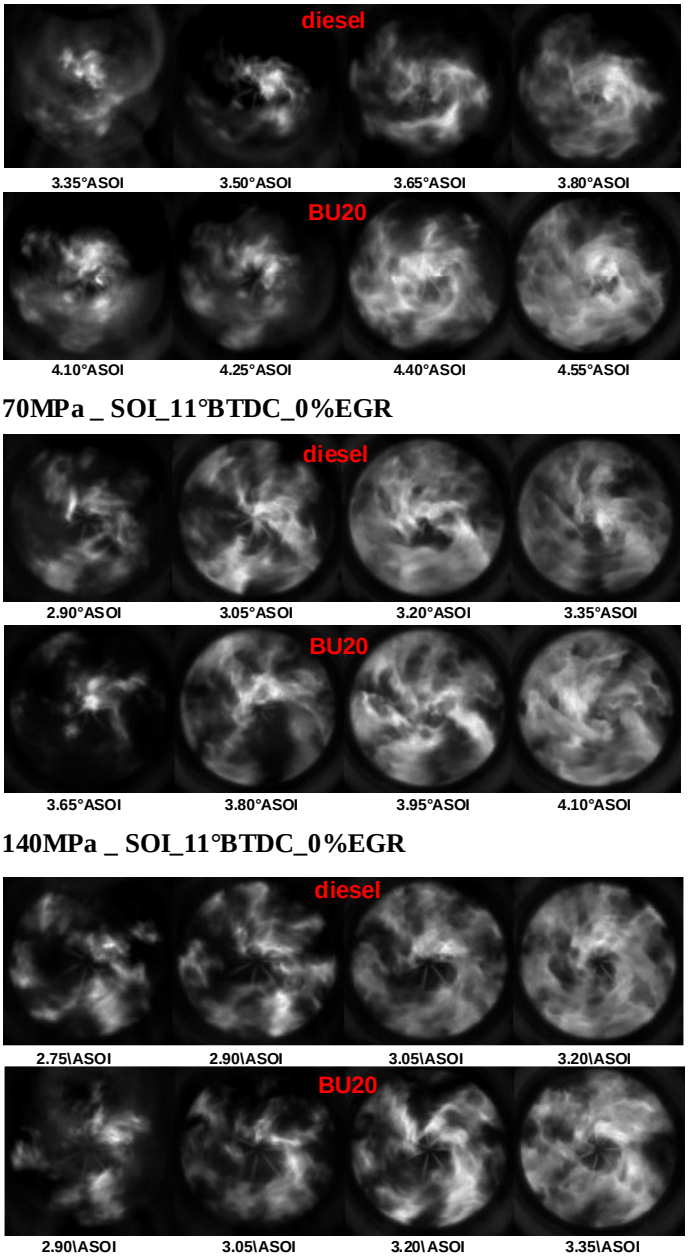

Figure 5. Selection of images detected in the first phase of ignition.

A lower carbon content fuel with a lower cetane number and higher ignition delay allowed to reduce the unburned mixture amount. Thus soot was lower for BU20 fuel than diesel for all conditions. The effect of the fuel properties on the exhaust pollutant emissions is more evident for the operating conditions with lower injection pressure and SOI=3 CAD BTDC. For both the EGR rates, the soot concentration for BU20 was about a quarter of the neat diesel. The advanced injection timing (11 CAD BTDC) allowed the ignition of a leaner mixture inducing a more complete burning. Thus, low soot concentrations were measured for both fuels without effect of injection pressure and EGR rate. On the other hand, only at the lower injection pressure the NOx emissions were acceptable. In this condition, the higher EGR rate allowed to confine the NOx emission gap between the BU20 and Diesel within 50 ppm. Thus it may be concluded that the blend BU20 with injection pressure 70MPa, injection timing of 11 CAD ATDC and at 50% of EGR allowed the best compromise between soot and NOx engine out emissions.

Figure 5 shows a selection of images detected in the first phase of ignition; UV-visible emissions were due to the first exothermic luminescence reactions. In some images, it is possible to observe fuel jets due to the self-illumination effect of the combustion process. As expected, the flame distributions in the first images demonstrated that the auto-ignition occurred near the tip of the fuel jets. Then the flame went up the direction of the spray axis, following the stoichiometric air-fuel ratio path [17]. Due to the swirl motion, the flame spreads in the combustion chamber in anticlockwise way. In agreement with the results obtained by pressure related data, the ignition delay of the BU20 was longer than the diesel fuel, at fixed operating conditions.

To better understand the outcome fuel injection mode on the combustion process, natural emission spectroscopy measurements were performed. Figure 6 shows the UV emission spectra detected at 2.90 CAD ASOI for Diesel and at 3.65 CAD ASOI for BU20 corresponding to the early stage of combustion in two locations of the combustion chamber central region. For both fuels, the injection was set at 140MPa, SOI=11 CAD BTDC with 0% EGR.

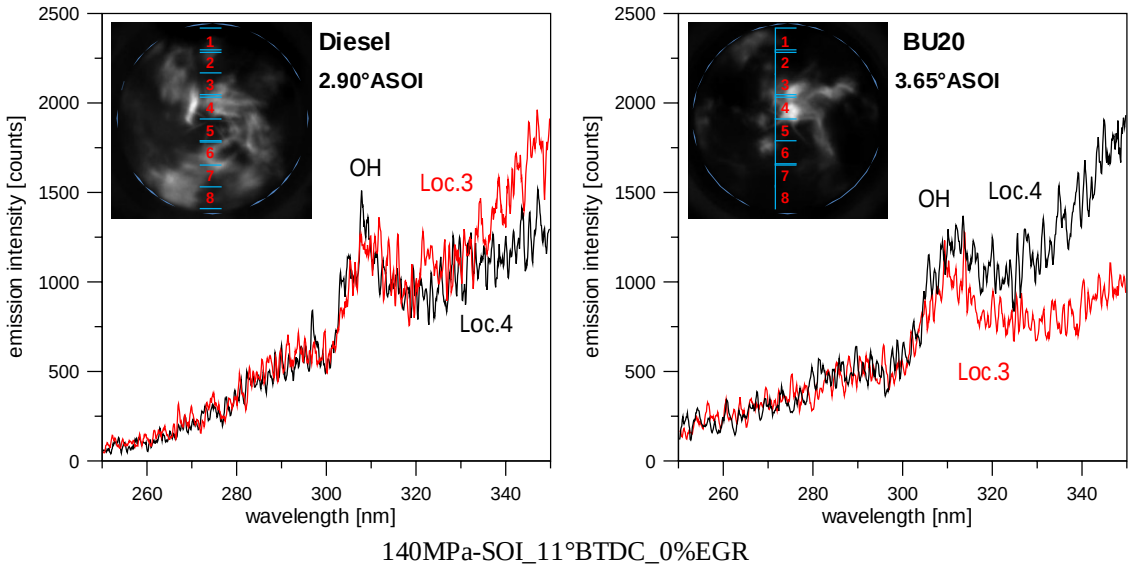

Figure 6. UV emission spectra detected in the early stage of combustion in two locations of the combustion chamber central region. For both fuels, the injection occurred at 140MPa and SOI=11 CAD BTDC with 0%EGR

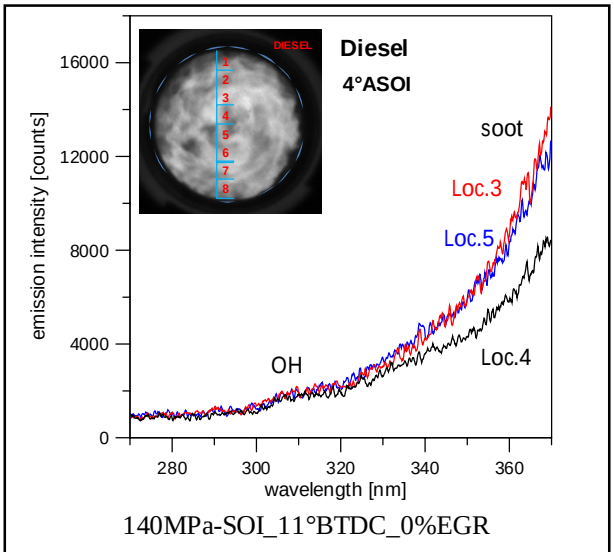

Figure 7. UV range of emission spectra detected at 4°ASOI.

For both signals, the spectral features of OH, the highest heads at 306-309 nm of OH band system (250-320 nm) were well resolved [18 - 20]. Excited OH radical was formed in the primary combustion zone by the chemiluminescent reaction: $CH + O_2 \Diamond CO + OH$.

OH was observed far from the liquid jets, in regions characterized by a large amount of fuel in the vapor phase well mixed with the air entrained in the spray, primarily around the jet. Then, it proceeded toward the injector location [17, 21, 22]. The phenomenon is fast, because the swirl moves the flame involving the whole chamber volume. It took less than 2 CAD to observe a strong soot emission in the center of the combustion chamber. Soot was characterized by a broadband feature that increased with the wavelength like a blackbody curve [23, 24]. Results reported in Figure 7 for Diesel showed the same trend of BU20 differing only in the intensity that was higher for Diesel. This confirmed the higher soot tendency of Diesel than BU20 [25]. For all the conditions the spectral behavior remained unchanged until the start of oxidation phase when the soot emission decreased and OH band system came out demonstrating OH radical as one of the principal marker of the soot oxidation [26]. As plotted in Figure 8, about 3 ms after the advanced injection timing and for the

condition at higher injection pressure, the soot was drastically reduced for BU20, while the Diesel fuel yet showed high soot emission. Similar trends were also observed for all the operating conditions.

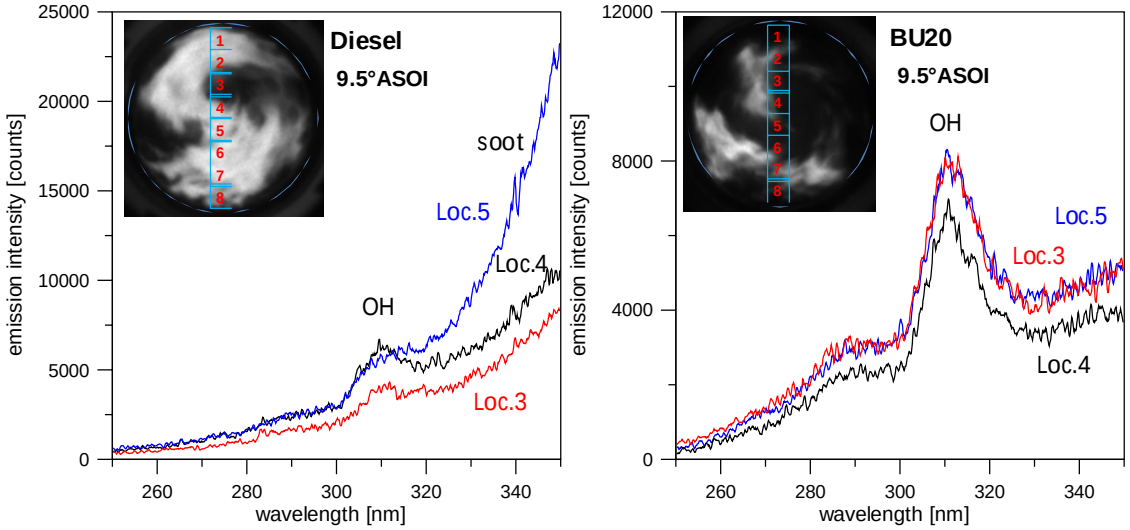

140MPa-SOI_11°BTDC_0%EGR

Figure 8. UV range of emission spectra detected at 9.5°ASOI

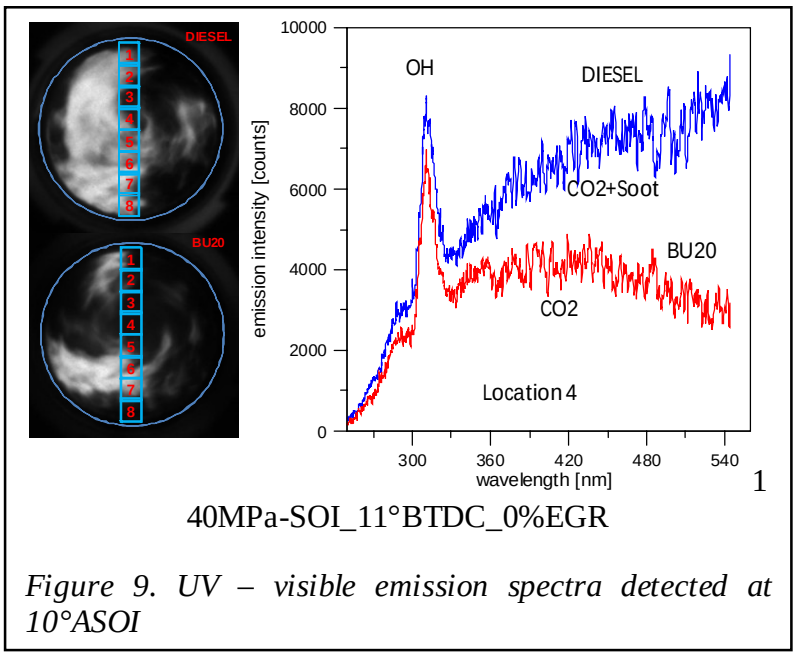

40MPa-SOI_11°BTDC_0%EGR

Figure 9. UV – visible emission spectra detected at 10°ASOI

After the soot reduction, a broadband emission form the UV to visible got highlight. The band system was related to the CO_2 chemiluminescence [27]. Even if in the flames there is not sufficient energy to excite stable atoms or molecules to high electronic states, electronic states of CO_2 can be excited during the combustion by consecutive transitions from the ground state level to intermediate vibrationally activated levels [28, 29]. The emission of CO_2* appears as a continuum, which extends from 300 nm to 600 nm with a broad maximum around 375 nm. As shown in Figure 9, at 10 CAD after the advanced injection timing the CO_2 chemiluminescence signal was well detectable together with OH emission band for BU20, while for Diesel fuel it was convoluted with soot signal. Same results were observed for the lower injection pressure and for both EGR rates. The spectroscopic data were processed, as previously described, in order to evaluate the integral evolution of OH and soot for both fuels and for all the operating conditions; the results are plotted in Figure 10-13.

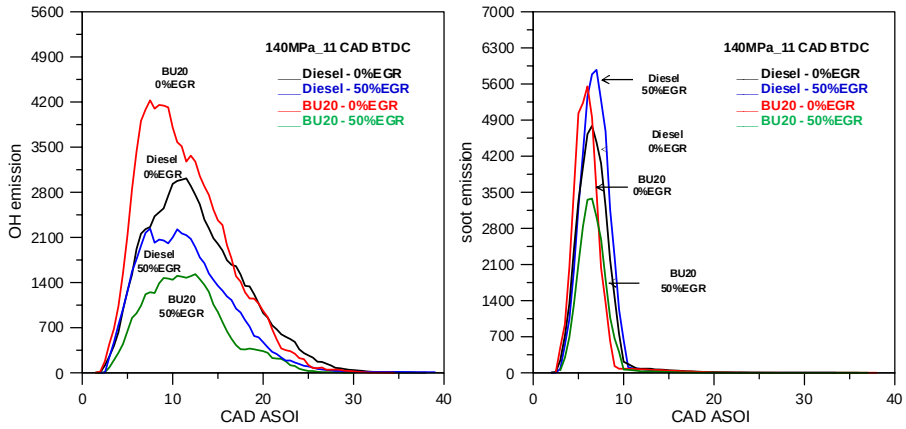

Figure 10. Integral evolution of OH and soot for both fuels at 140MPa-SOI_11°BTDC

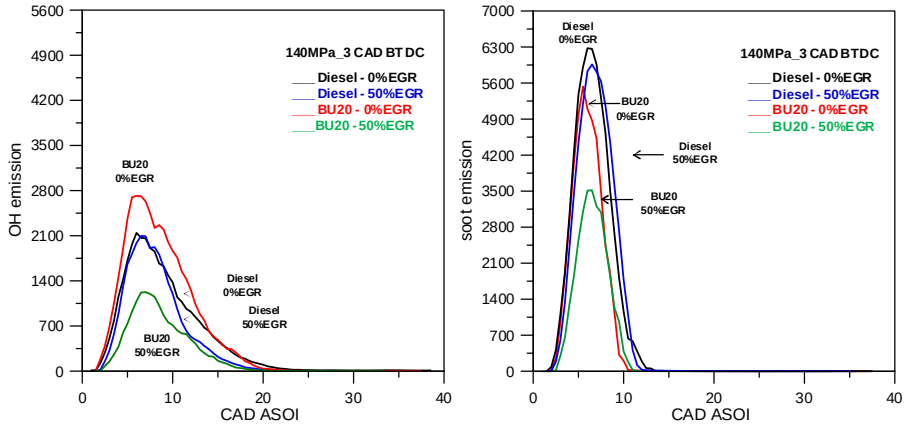

Figure 11. Integral evolution of OH and soot for both fuels at 140MPa-SOI_3°BTDC

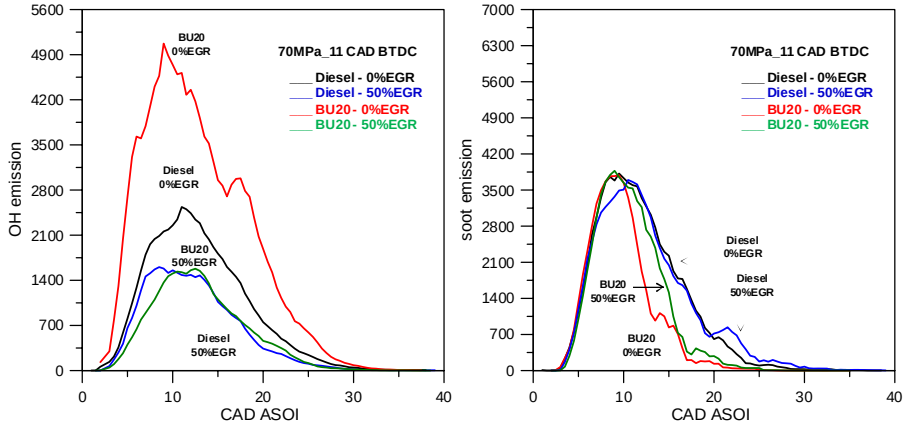

Figure 12. Integral evolution of OH and soot for both fuels at 70MPa-SOI_11°BTDC

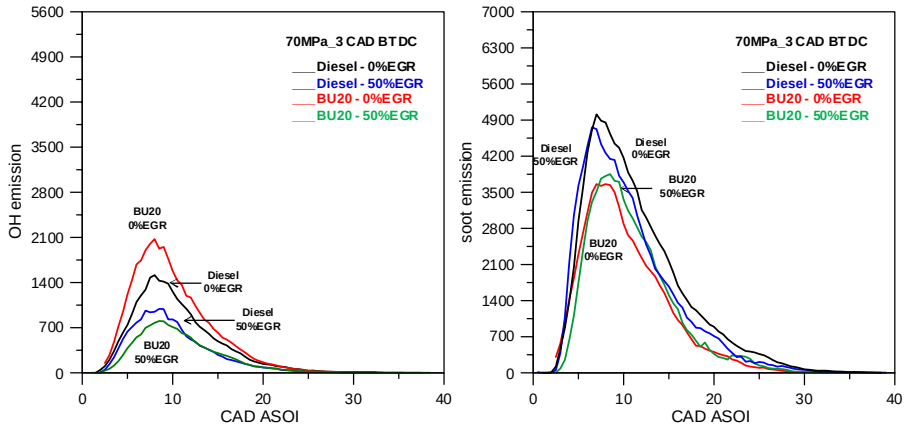

Figure 13. Integral evolution of OH and soot for both fuels at 70MPa-SOI_3°BTDC

The fuel injection timing strongly influenced OH emissions. Even if the highest OH was detected about 8 CAD after the start of injection, for all conditions, at the more advanced SOI (11 CAD BTDC) the early stages of combustion occurred during the engine compression phase. It facilitated the formation of higher OH concentration if compared to SOI=3 CAD BTDC. Regarding the injection pressure, this demonstrated a strong effect on the soot evolution. Thanks to the good fuel spray atomization and air mixture, the soot evolution was very fast for all the conditions at the injection pressure of 140MPa. Soot formation and oxidation occurred in less than 15 CAD. Due to the different carbon and oxygen contents, fuel quality and EGR rate mainly influenced the balance between the formation and the reduction of OH and soot. For all the conditions and both fuels, the optical investigations results were correlated with engine out emissions. As shown in Figure 14, the integral value of OH emission and NOx measured at the engine exhaust, presented similar trend, as expected by the extended Zeldovich mechanism [30]. Moreover, the integral value of soot, in the last combustion phase 20-30 CAD ASOI, was in agreement with exhaust soot concentration, as plotted in Figure 15.

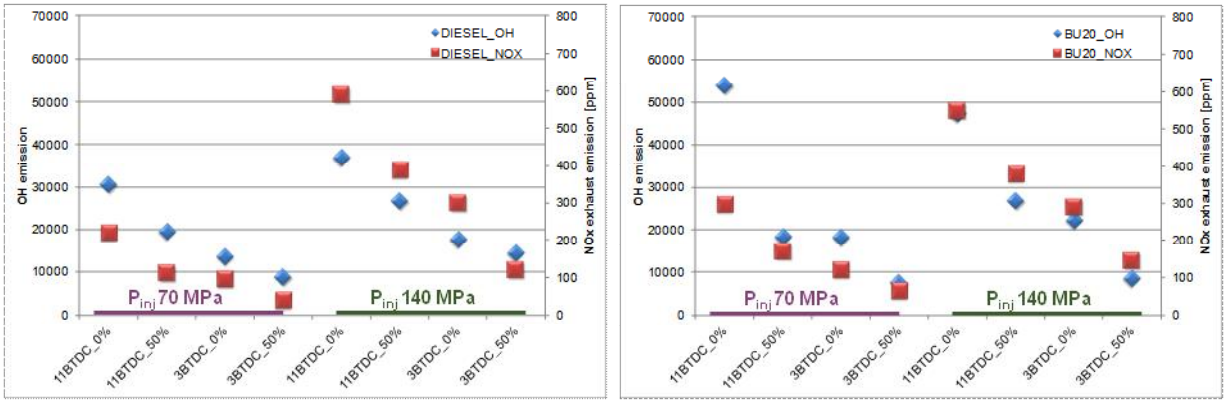

Figure 14. In cylinder OH emission and NOx exhaust emission.

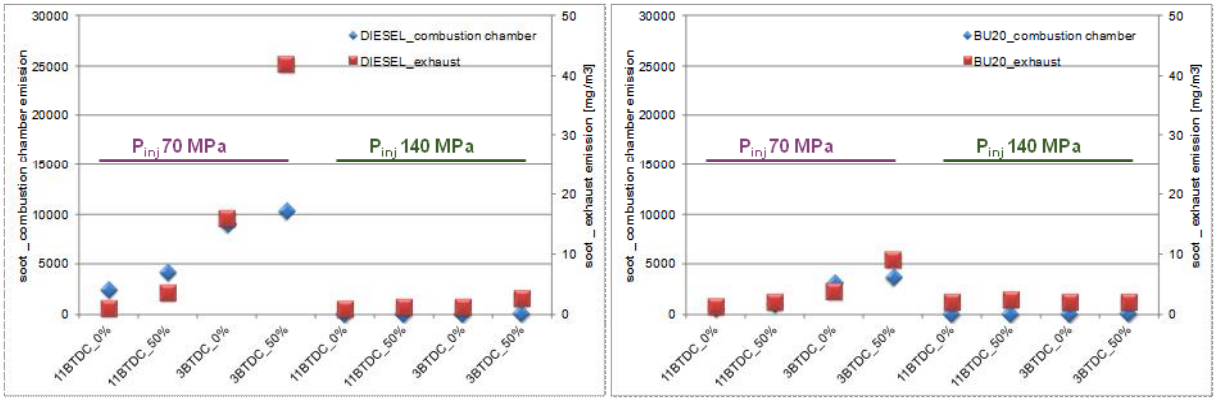

Figure 15. In cylinder soot emission and soot exhaust emission.

4. Conclusions

The combustion process of mineral diesel fuel and its blend with 20% n-butanol and their effects on diesel engine performance and emissions have been investigated.

UV-visible digital imaging and natural emission spectroscopy were applied in a single cylinder optically accessible high swirl multi-jets compression ignition engine.

Combustion tests were carried out using commercial diesel and a blend of 80% diesel with 20% n-butanol (BU20). Two injection pressures (70 and 140 MPa), two injection timings (11 CAD BTDC and 3 CAD BTDC) and a two different levels of EGR rate were tested.

UV-visible emission spectroscopy was used for the detection of the chemical markers of combustion process. Chemiluminescence signals, due to OH, HCO and CO_2 emission bands were detected. OH emission was correlated to NO measured at the exhaust. The soot spectral feature in the visible wavelength range was correlated to soot engine out emissions.

The following main conclusions can be summarized:

- For all the conditions, the engine efficiency for BU20 was higher than for diesel fuel. This was due to higher BU20 volatility that improved the fuel charge mixing and reduced the amount of not completely burned fuel.
- Soot was lower for BU20 fuel than diesel for all conditions because of a lower carbon content fuel with a lower cetane number and higher ignition delay that allows to reduce the unburned mixture amount.
- The blend BU20 with injection pressure 70MPa, injection timing of 11 CAD ATDC and at 50% of EGR allowed the best compromise between soot and NOx engine out emissions.
- UV emission spectra detected at the early stage of combustion highlight OH formation far from the liquid jets, in regions characterized by a large amount of fuel in the vapor phase well mixed with the air entrained in the spray, primarily around the jet.
- UV-visible emission spectroscopy points out the same trend of soot formation both for Diesel and BU20 differing only in the intensity that was higher for Diesel. This confirmed the higher soot tendency of Diesel than BU20.
- For all the conditions the spectral behaviour remained unchanged until the start of oxidation phase when the soot emission decreased and OH band system came out demonstrating OH radical as one of the principal marker of the soot oxidation.
- The optical investigations results were correlated with engine out emissions. The integral value of OH emission and NOx measured at the exhaust, presented similar trend, as expected by the extended Zeldovich mechanism.

– The integral value of soot, in the last combustion phase (20-30 CAD ASOI), was in agreement with exhaust soot concentration.

Acronyms

ASOI After Start of Injection
ATDC After Top Dead Centre
BTDC Before Top Dead Centre
BTDC Before Top Dead Centre
BU20 20% n-butanol and 80% gasoline blend
CAD Crank Angle Degree
CAD Crank angle degrees
CCD Charge Coupled Device
CI Compression Ignition
EGR Exhaust Gas Recirculation
ICCD Intensified Charge Coupled Device
ID Ignition Delay
SOI Start of Injection
TDC Top Dead Centre
TTL Transistor-Transistor Logic
UV Ultra Violet

Acknowledgements

The authors would like to express their sincere appreciation to Mr. A. Mazzei for the technical support in preparing the equipment and during the experiments.

References

[1] The Alternative Fuels and Advanced Vehicles Data Center (AFDC) _ <http://www.afdc.energy.gov/afdc/ > [accessed 31.01.2012].

[2] Balat M., Balat H., (2009) Recent trends in global production and utilization of bio-ethanol fuel, Applied Energy, Volume 86, Issue 11, November 2009, Pages 2273-2282

[3] Kleinová A., Vailing I., Lábaj J., Mikulec J., Cvengroš J., (2011) Vegetable oils and animal fats as alternative fuels for diesel engines with dual fuel operation, Fuel Processing Technology, Volume 92, Issue 10, October 2011, Pages 1980-1986

[4] Lapuerta M., Armas O., Rodriguez-Fernandez J. Effect of biodiesel fuels on diesel engine emissions. Progress in Energy and Combustion Science 34(2), April 2008, pp. 198-223.

[5] Pourkhesalian A.M., Shamekhi A.H., Salimi F. Alternative fuel and gasoline in an SI engine: A comparative study of performance and emissions characteristics. Fuel 9(5), May 2010, pp.1056-1063.

[6] Doğan O. The influence of n-butanol/diesel fuel blends utilization on a small diesel engine performance and emissions. Fuel 90(7), July 2011, pp. 2467-2472.

[7] Chao J., Mingfa Y., Haifeng L., Chia-fon F.L., Jing J. Progress in the production and application of n-butanol as a biofuel. Renewable and Sustainable Energy Reviews 1(8), Oct2011, pp.4080-4106

[8] Rakopoulos D.C., Rakopoulos C.D., Giakoumis E.G., Dimaratos A.M. and Kyristis D.C., 2010. Effect of butanol-diesel fuel blends on the performance and emissions of a high-speed DI diesel engine. Energy Conversion and Management 51, pp.1989–1997.

[9] Rakopoulos C.D., Dimaratos A.M., Giakoumis E.G., Rakopoulos D.C (2011) Study of turbocharged diesel engine operation, pollutant emissions and combustion noise radiation during starting with bio-diesel or n-butanol diesel fuel blends. Applied Energy, vol.88(11), November 2011, pp. 3905-3916.

[10] Rakopoulos D.C., Rakopoulos C.D., Papagiannakis R.G., Kyritsis D.C. (2011) Combustion heat release analysis of ethanol or n-butanol diesel fuel blends in heavy-duty DI diesel engine, Fuel 90, pp. 1855–1867.

[11] Rakopoulos C.D., Dimaratos A.M., Giakoumis E.G., Rakopoulos D.C. (2010) Investigating the emissions during acceleration of a turbocharged diesel engine operating with bio-diesel or n-butanol diesel fuel blends. Energy 35(12), December 2010, pp. 5173-5184.

[12] Valentino G., Corcione F.E., Iannuzzi S.E., Serra S. (2012) Experimental study on performance and emissions of a high speed diesel engine fuelled with n-butanol diesel blends under premixed low temperature combustion. Fuel 92(1), February 2012, pp.295-307.

[13] Corcione F., Valentino G., Tornatore C., Merola S. et al., "Optical Investigation of Premixed Low-Temperature Combustion of Lighter Fuel Blends in Compression Ignition Engines," SAE Technical Paper 2011-24-0045, 2011.

[14] Tornatore C., Marchitto L., Mazzei A., Valentino G., Esposito Corcione F., Merola S.S. Effect of butanol blend on in-cylinder combustion process. Part 2: compression ignition engine Journal of KONES Powertrain and Transport 2011, vol.18(3) pp. 473 – 483.

[15] Murphy M.J., Taylor J.D., McCormick R.L. (2004) Compendium of experimental cetane number data, NREL Report, NREL/SR-540-36805.

[16] Heywood J.B. Internal Combustion Engine Fundamentals, New York: McGraw-Hill, 1988.

[17] Dec J.E. and Espey C. Chemiluminescence imaging of autoignition in a DI diesel engine. SAE Paper 982685, 1998.

[18] Gaydon A.G., The Spectroscopy of Flames, Chapman and Hall ltd., 1957.

[19] Alkemade C. Th. J., Herrmann, R., Fundamentals of Analytical Flame Spectroscopy, Hilger, Bristol, UK, 1979.

[20] Dieke G.H., Crosswhite H.M. (1962). The ultraviolet bands of OH. J. Quant. Spectrosc. Radiat. Transfer, 2 pp.97-199.

[21] Dec J.E. and Coy E.B. OH radical imaging in a DI diesel engine and the sructure of the early diffusion flame. SAE Paper 960831, 1996.

[22] Singh S., Musculus M.P.B., Reitz R.D. (2009) Mixing and flame structures inferred from OH-PLIF for conventional and low-temperature diesel engine combustion, Combustion and Flame, 156(10), pp.1898-1908.

[23] Zhao H., Ladommatos N. (1998) Optical diagnostics for soot and temperature measurement in diesel engines. Progress in Energy and Combustion Science 24(3) pp.221-255.

[24] Senda J., Choi D., Iwamuro M., Fujimoto H. et al., "Experimental Analysis on Soot Formation Process In DI Diesel Combustion Chamber by Use of Optical Diagnostics," SAE Technical Paper 2002-01-0893, 2002.

[25] Pepiot-Desjardins P., Pitsch H., Malhotra R., Kirby S.R., Boehman A.L. (2008) Structural group analysis for soot reduction tendency of oxygenated fuels Original Combustion and Flame 154(1–2) pp.191-205.

[26] Nagle J., Strickland-Constable R.F. (1961). Oxidation of Carbon Between 1000°-2000°C. Proc. 5th Conf. on Carbon – Pergamon.

[27] Samaniego J.M., Egolfopoulos F.N. and Bowman C.T. (1995) CO2* Chemiluminescence in Premixed Flames. Combust. Sci. and Tech. vol. 109, pp. 183-203.

[28] Gaydon A.G. (1940) The flame spectrum of carbon monoxide. Proceedings of the Royal Society of London. Series A vol. 176 n. 967 pp. 505-521.

[29] Dixon R.N. (1963) The carbon monoxide flame bands Proceedings of the Royal Society of London. Series A vol. 275 n. 1362 pp. 431-446.

[30] Westbrook C. and Dryer F. Chemical Kinetic Modelling of Hydrocarbon Combustion. Prog. Energy Comb. Sci., page 1, 1984.

Flameless Oxidation as a Means to Reduce NO_x Emissions in Glass Melting Furnaces

Jörg Leicher[a], Anne Giese[a]

[a] Gaswärme-Institut e.V, Essen, Germany, leicher@gwi-essen.de

Abstract:

Melting glass is a very energy intensive process, with process temperatures of more than 1600°C required to melt the raw materials in the furnace. Such high temperatures are usually achieved by intensive air preheating and near stoichiometric conditions. This leads to a significant production of nitrous oxides (NOX). As the emissions of nitrous oxides are regulated be increasingly stringent environmental legislation, the glass industry is very interested in combustion techniques which reduce NOX emissions without resorting to expensive flue gas treatment while maintaining the glass quality.

In the steel industry, the so-called flameless oxidation (FLOX) combustion concept is firmly established as a state-of-the-art primary technique to reduce NOX formation in furnaces. This technology uses high momentum jets of fuel and oxidizer to generate an intense recirculation of hot, but chemically inert flue gas into the reaction zone. By mixing flue gas into the reaction zone, its shape changes from a quasi-two-dimensional flame front into a three-dimensional reaction volume. A much more homogeneous temperature distribution is obtained while the formation of hot spots can be avoided, thus significantly reducing thermal NOX emissions. The name “Flameless Oxidation” derives from the fact that no visible flame can be observed with the naked eye since the local OH concentrations are very low due to the large amounts of recirculated flue gas. Experience from the steel industry shows great promise for the introduction of this technology into other industrial sectors as a means to reduce nitrous oxide emissions.

In the course of a German research project, the Gaswärme-Institut e.V. Essen (GWI) in cooperation with several industrial partners investigated how to best introduce the flameless oxidation technique to glass melting furnaces equipped with recuperative burners, so-called unit melters. A furnace of a project partner, producing glass for compact fluorescent lamps, was chosen for conversion to FLOX burners.

Initially, there was some skepticism with regards to the applicability of a combustion process without a visible flame in a glass furnace, as normally, a slow, highly luminous flame is considered desirable in such furnaces. Also, the high gas velocities in the fuel and oxidizer jets carry the risk of blowing dust from the batch into the central recuperator. Thus, a careful design of both the new burner system as well as their positions in the furnace was necessary to avoid high gas velocities immediately above the glass bath.

In a first step, a FLOX burner system for recuperative glass melting furnaces was developed and optimized at GWI, using CFD simulations. This prototype was then tested at GWI’s semi-industrial test rig in order to verify that the new design was able to comply with the required NOX emissions limit. Compared to the burner originally mounted in the glass furnace, a reduction of almost 60 per cent was achieved.

In order to reduce the downtime of the furnace to a minimum, the exchange of the burners was planned using CFD simulations. Different configurations were simulated in order determine potential problems and an optimum burner set up was found, which was subsequently implemented on the site.

The retrofitted plant has been in operation for five years now still maintaining to produce the same glass quality as before the retrofit. The NOX emissions, on the other hand, were reduced by about 50 per cent. In addition the energy consumption of the process was reduced because an optimized burner positioning and more stable combustion allows for lower air ratios in the furnace, thus reducing fuel consumption.

Keywords:

Glass Melting Furnace, Flameless Oxidation, NO_X Emissions

1. Introduction

The melting of glass on an industrial scale is a very energy-intensive process which, depending on the glass quality being manufactured, can easily require process temperatures of more than 1600 °C. These very high temperatures are usually achieved in glass melting furnaces by means of intensive

pre-heating of the combustion air, either recuperatively (maximum air pre-heat temperatures around 800 °C) or regeneratively (maximum air pre-heat temperature 1400 °C).
These high temperatures, combined with a near-stoichiometric operation of the burners and long residence times due to the size of the furnaces and generally low flow velocities, often lead to a significant formation of nitrous oxides (NO_X). As the emission of these pollutants is strictly regulated by emission laws, the glass industry is very interested in techniques to reduce NOX emissions without resorting to costly secondary flue gas treatment. Instead, techniques are preferred which reduce NO_X formation in the furnace itself, of course without reducing the glass quality.
One such potential primary technique to reduce NO_X emissions is the so-called flameless oxidation (FLOX) technology, which is already well-established in the steel industry. Other common names for this technology are mild or colorless combustion. This technology, first developed in the 1980s [1], uses high momentum jets of fuel and air to entrain large amounts of hot, but chemically inert flue gas and mix it with fuel and combustion air. In this manner, the shape of the reaction zone is changed: instead of an almost two-dimensional reaction front, a three-dimensional reaction volume is created in which the reactants are diluted by the hot exhaust gas. The consequence of this change in the form of the reaction zone is that a much more homogeneous temperature distribution is obtained, without the temperature peaks usually found in conventional diffusion flames. As thermal NO_X formation is highly dependent on local temperature, this much more homogeneous temperature distribution drastically reduces NO_X emissions. Figure 1 shows a comparison between the standard and the FLOX modes of combustion while figure 2 shows flame images both in the visible and UV spectrum (using an OH chemoluminiscence method) of standard diffusion flames and FLOX combustion.

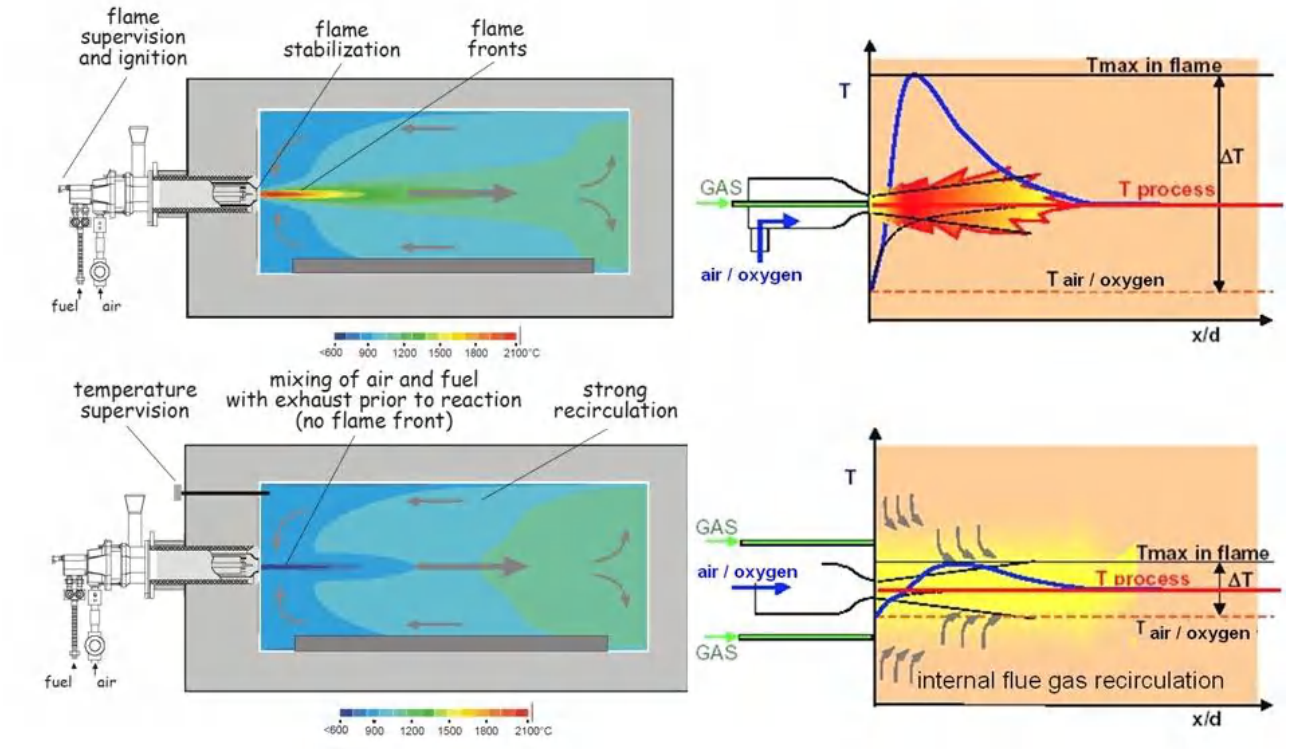

Figure 1: Principles of standard combustion (top) and flameless oxidation (bottom). On the right hand side, the temperature evolution is shown [2].

The name Flameless Oxidation derives from the fact that due to the dilution of the reaction zone, there is no visible flame while operating in FLOX mode, as can be seen on the lower left hand side of figure 2. Nevertheless, complete consumption of the fuel gas is achieved, which can be shown by

CO measurements in the exhaust gas. The different shapes of the reaction zones are visualized by the OH^* chemoluminiscence images shown on the right hand side of figure 2. While the standard combustion shows a zone of intense combustion near the burner outlet, the reaction zone in the flameless mode is lifted off the burner throat and shows a more even OH distribution.

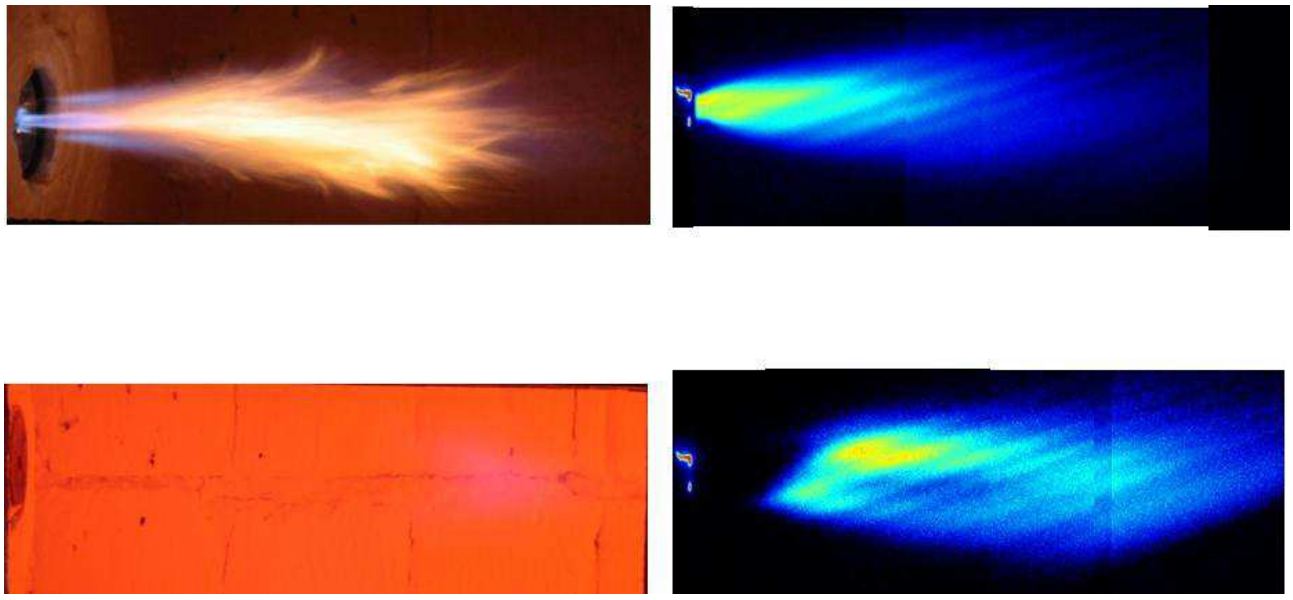

Figure 2 : Comparison of Standard (top) and FLOX (bottom) combustion modes in the visible and the UV spectrum

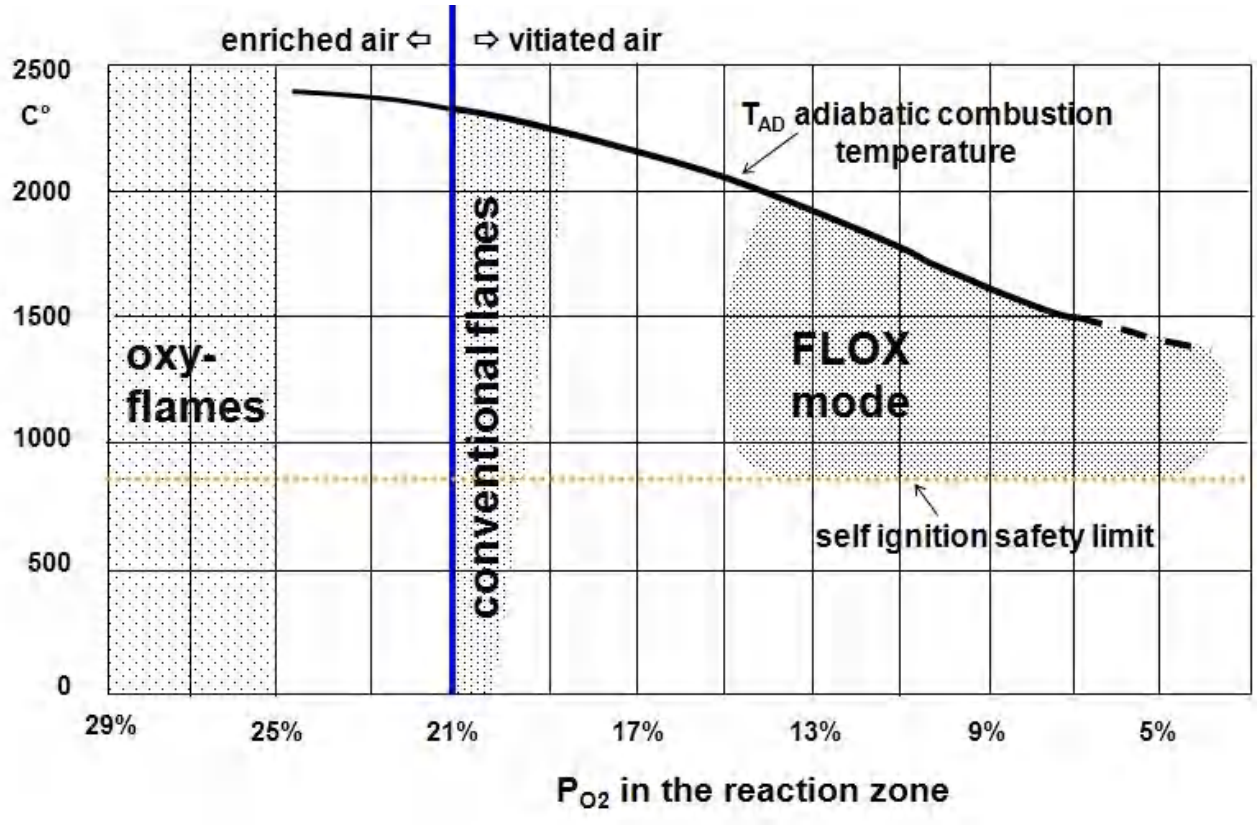

Figure 3: FLOX mode as a function of the partial pressure of O_2 [3]

As the intense mixing of the reactants with hot but chemically inert exhaust gas lifts local temperatures above the self-ignition limits, the local oxygen concentrations are reduced (cf. Fig. 3), leading to a unique form of combustion which is characterized by very homogeneous temperature and heat flux distributions, stable combustion behaviour and very low NO_X emissions. Also, noise emissions are low compared to conventional burners.
While the FLOX combustion mode has successfully established itself as a method to reduce of NO_X in many high temperature applications, the glass industry was hesitant to adopt this burner technology as flames in glass furnaces are traditionally highly luminous while the reaction zones in FLOX combustion are almost entirely invisible. However, results from a previous research project called EURONITE [4] were promising enough that a glass manufacturer (OSRAM GmbH) and a burner manufacturer (Hotwork International) could be convinced to participate in a research project called GlasFLOX which investigated the applicability of FLOX technology for glass melting furnaces.

2. The GlasFLOX Project and Test Rig Experiments

One of the defining characteristics of flameless oxidation burners is the very high momentum of the fuel jets and combustion air. It is therefore obvious that FLOX burners can only be applied to glass furnaces with recuperative air preheating because only in this configuration the required high velocities jets for the combustion air can be achieved. A schematic of such a recuperative glass melting furnace is shown in Figure 4.

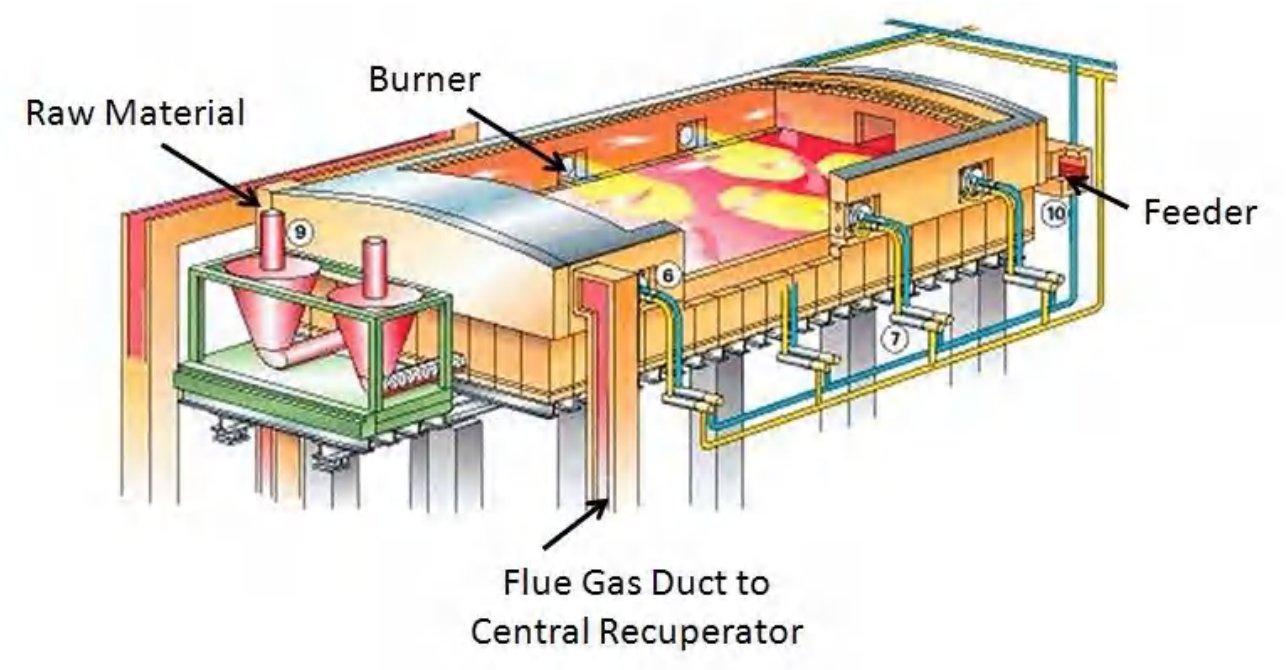

Figure 4: Schematic of a recuperative glass melting furnace

The primary objectives of the GlasFLOX project were to design a FLOX burner for operation in glass melting furnaces which would produce less than 500 mg/Nm^3 NO_X and at the same time show good behavior at partial loads. Of course, maintaining the quality of the glass was of utmost importance.

In a first step, a 500 kW FLOX burner for application in glass furnaces was designed. CFD simulations were carried out to find the optimum geometry for the burner which was then manufactured and extensively tested at one of GWI's semi-industrial test rigs in order to validate that the targeted NOX emission levels were achieved. Figure 5 shows a comparison between the

original (HWI) and the newly designed GlasFLOX burner systems. In the lower half of the figure, the CFD-calculated velocity distributions can be seen. As intended, the reduced section area leads to much higher air velocities which impart a very high momentum to the gas/air jet. The higher velocities cause higher pressure drops in the burner but these were found to be within acceptable limits.

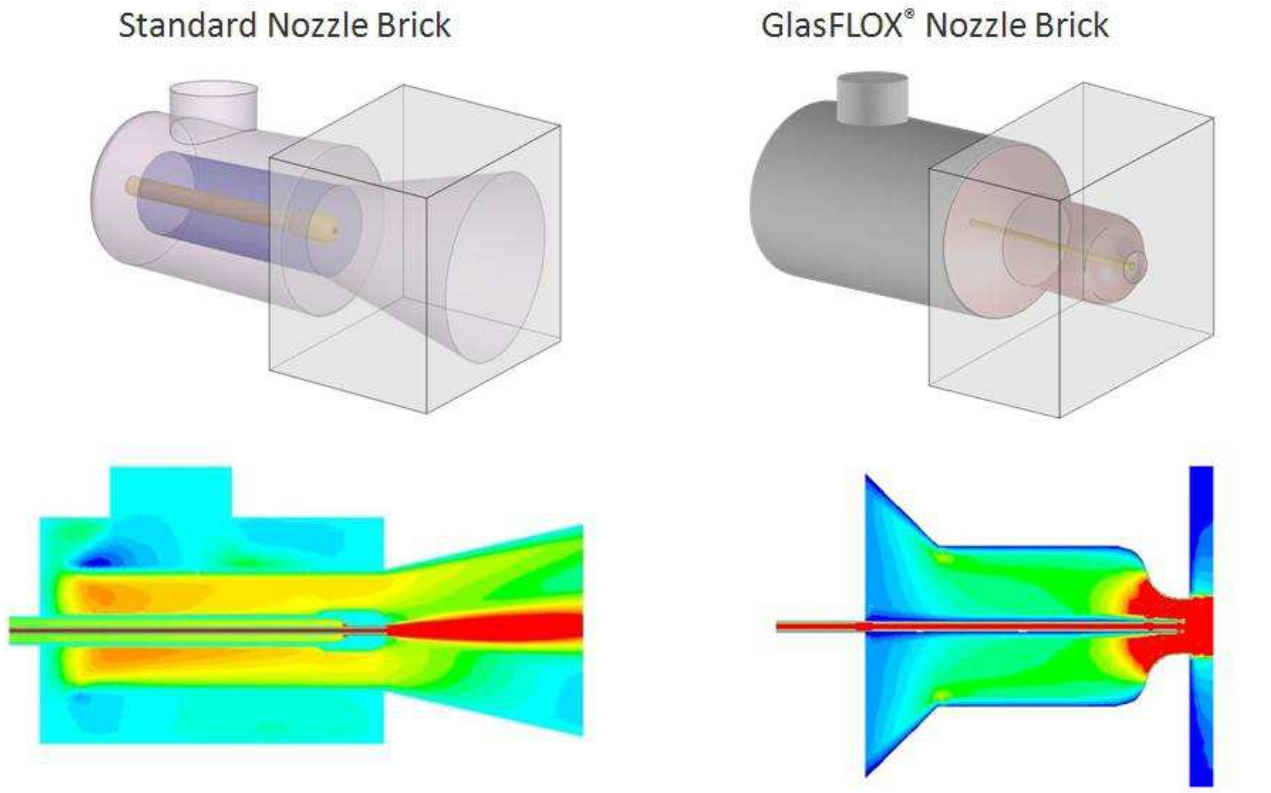

Figure 5: Comparison of the standard nozzle brick and the newly designed GlasFLOX nozzle brick with simulated velocity distributions

Numerical simulations of the original and the GlasFLOX burners showed that lower maximum temperatures were achieved in the case of the flameless oxidation burner while the temperatures of the flue gas remained almost the same. These findings were validated by measurements. The experimental investigations of both the original and new burner system in GWI's test rig prove that the GlasFLOX system was able to comply with the target emission values for NOX (cf. Figure 6), which was already significantly below the legal emission limits of 800 mg/Nm^3.

Due to these very promising results, the retrofit of an existing glass melting furnace with the new GlasFLOX burners was planned

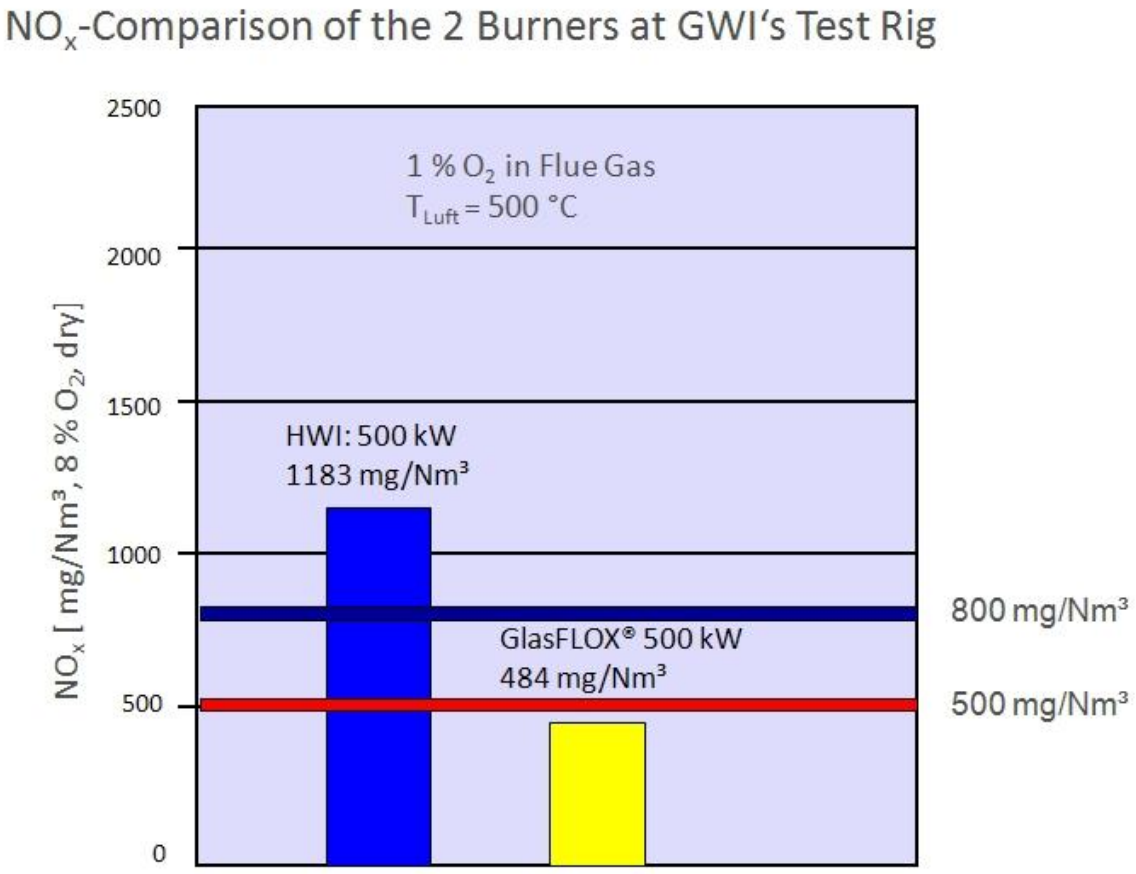

Figure 6: Measured NO_X emissions of the original (HWI) burner and the new GlasFLOX burner

3. Conversion of a Glass Melting Furnace

The glass melting furnace which was to be retrofitted with GlasFLOX burners is a side-fired furnace with ten burner positions, which are connected to a central recuperator to recover waste heat from the exhaust gas in order to preheat the combustion air. A sketch of the plant is shown in Figure7.

The process operators did not want prolonged downtimes of the plant and hence loss of production, which is why the retrofit campaign was planned in advance aided by CFD simulations of the furnace. Several configurations were simulated and evaluated.

In a first step, only four of the ten existing burners were substituted with GlasFLOX burners, those close to the batch inlet. However, simulations showed that this configuration led to increased gas velocities near the batch and the flue gas ducts. High velocities in this area are not desirable as this may lead to carry over from the dust-laden batch material into the recuperator which may cause increased wear and tear or even damage of the recuperator. Therefore, a second configuration was investigated in which all but the two burners closest to the batch inlet were swapped with GlasFLOX burners. In this way, low velocities close to batch inlet and flue gas ducts can be maintained, minimizing the risk of dust carry over into the recuperator. Figure 8 shows the various steps of the retrofit, while Figure 9 shows the calculated velocity distributions immediately above the glass melt for the various configurations [5, 6].

Also, several different alignments and configurations of the burners were simulated numerically in order to avoid collisions of the jets which might cause increased turbulence and hence disturbance of the glass bath and potential dust-ups. This was not a problem before as the burner exit velocities of the original burners were relatively low, but became important when using the flameless

oxidation burners with their much higher jet momentum. It was found that a burner alignment of 5 degrees off the burner axis was well-suited to avoid these issues.

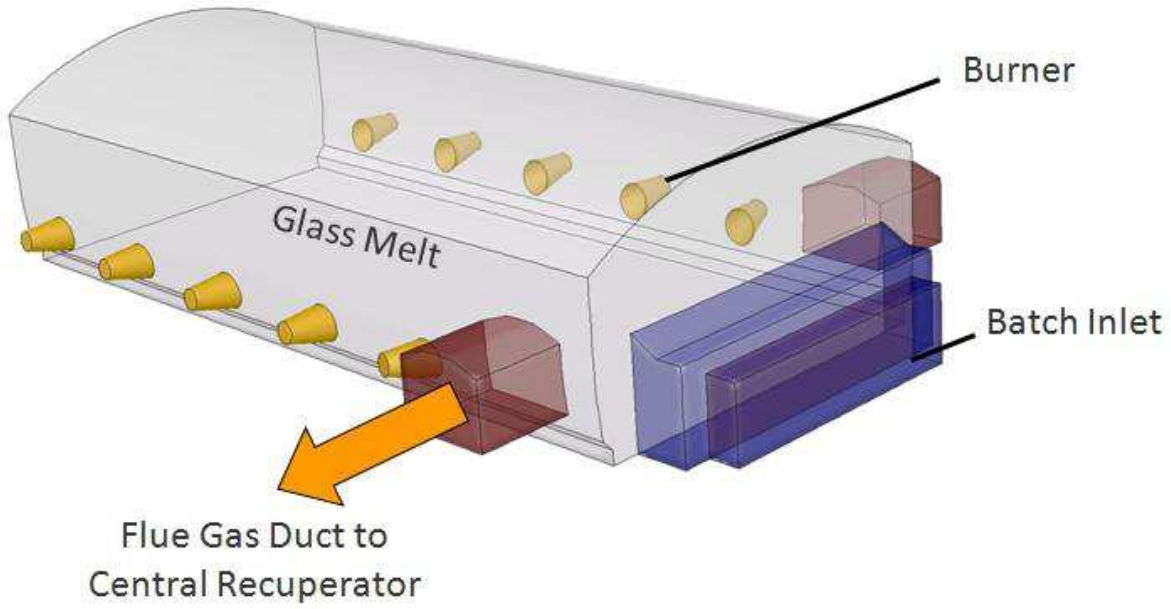

Figure 7: Schematic of a glass melting furnace

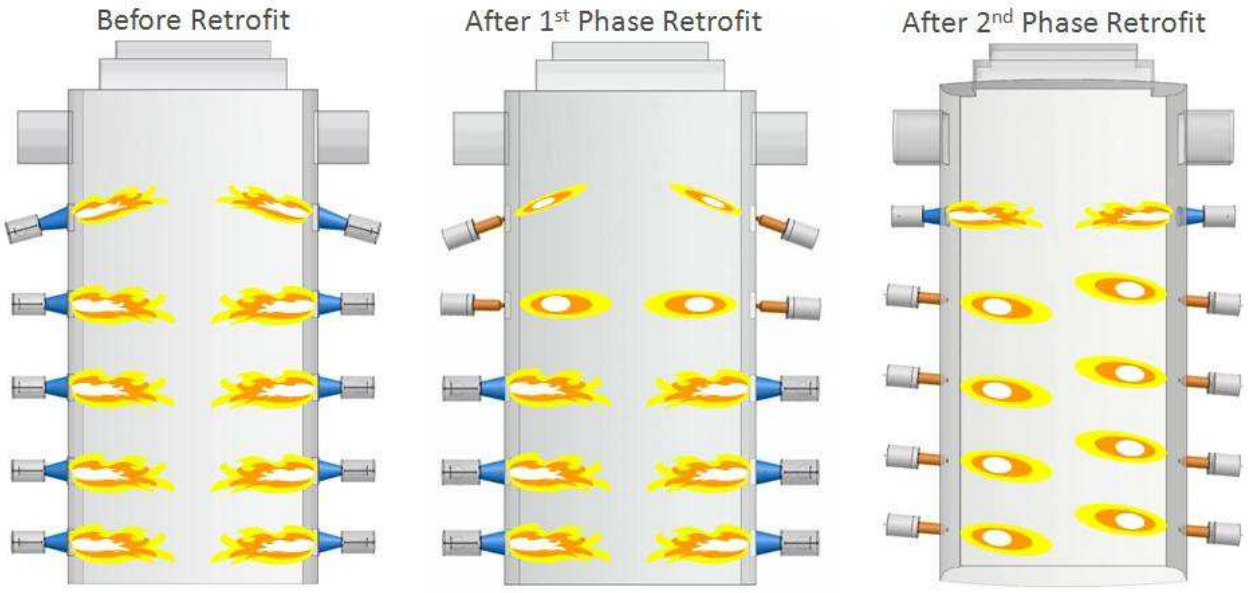

Figure 8: Burner configurations for the various retrofit phases

In the next phase, the conversion of the furnace was carried out based on the findings of the CFD simulations. Eight standard burners were replaced with GlasFLOX burners with the two burners closest to the batch inlet remaining untouched in order to maintain low gas velocities near the batch. After the retrofit, pollution emission measurements were performed in order to evaluate the impact of the new burner system on NO_X emissions. Comparisons with NO_X emission measurements taken prior the retrofit show a reduction of about 45% while maintaining constant fuel consumption and, most importantly, glass quality. Also, condensation in the flue gas ducts was found to be reduced by

about 30%. Due to the increased combustion stability inherent in the FLOX technology, it was even possible to reduce the excess air ratio.

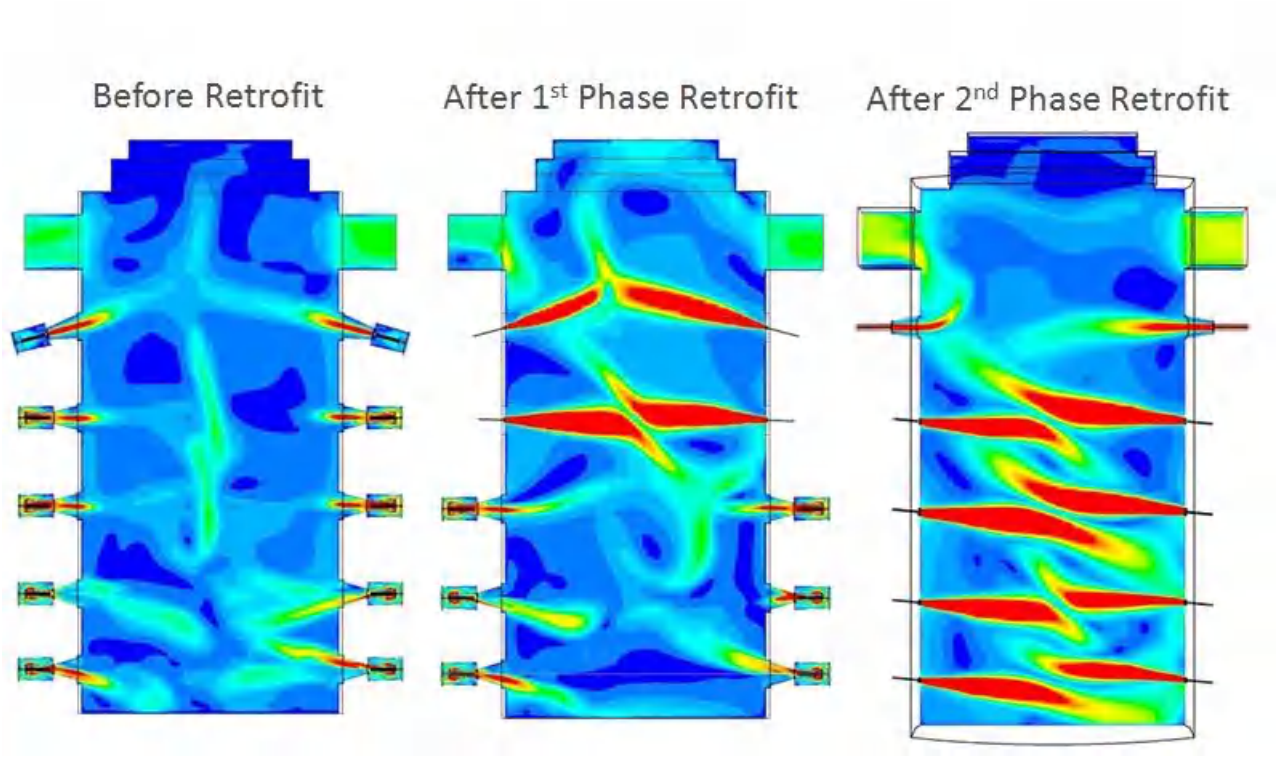

Figure 9: Simulated velocity distributions near the glass bath for the various retrofit phases

After nearly five years in operation, the plant operators are very pleased with the new burner system. NO_X emissions remain low, and there was hardly any corrosion to be found at neither the burner tips nor the nozzle bricks. The burners themselves require less maintenance than the original equipment. While there were some reservations in the beginning to the use of high momentum burners in a glass furnace due to the fear of increased dust-ups, this was found not to be the case. In fact, the amount of dust in the flue gas decreased slightly.

4. Conclusion

In the course of a research project carried out by the Gaswärme-Institut in cooperation with several industrial partners, namely OSRAM GmbH and Hotwork International AG, introduced the flameless oxidation technique into the glass industry. In the beginning, this combustion concept which has already been successfully implemented in various high temperature manufacturing processes, was regarded with some scepticism due to the lack of a visible flame and the requirement for high velocity gas flows in a glass melting furnace. However, using both experimental and numerical techniques on a lab-scale, it could be shown that this combustion concept can be successfully adapted for use in glass melting furnaces.

The subsequent conversion of the furnace to flameless oxidation operation was prepared beforehand by extensive use of CFD simulations in order to minimize the downtime of the plant. The retrofitted furnace has been operating for about five years now, with an excellent operational track record. NOX emissions are about 45% lower than before the conversion, while maintaining the same glass quality as before. While fuel consumption has not decreased, it is possible to reduce the excess air ratio in the furnace since FLOX combustion is much more stable than conventional combustion systems.

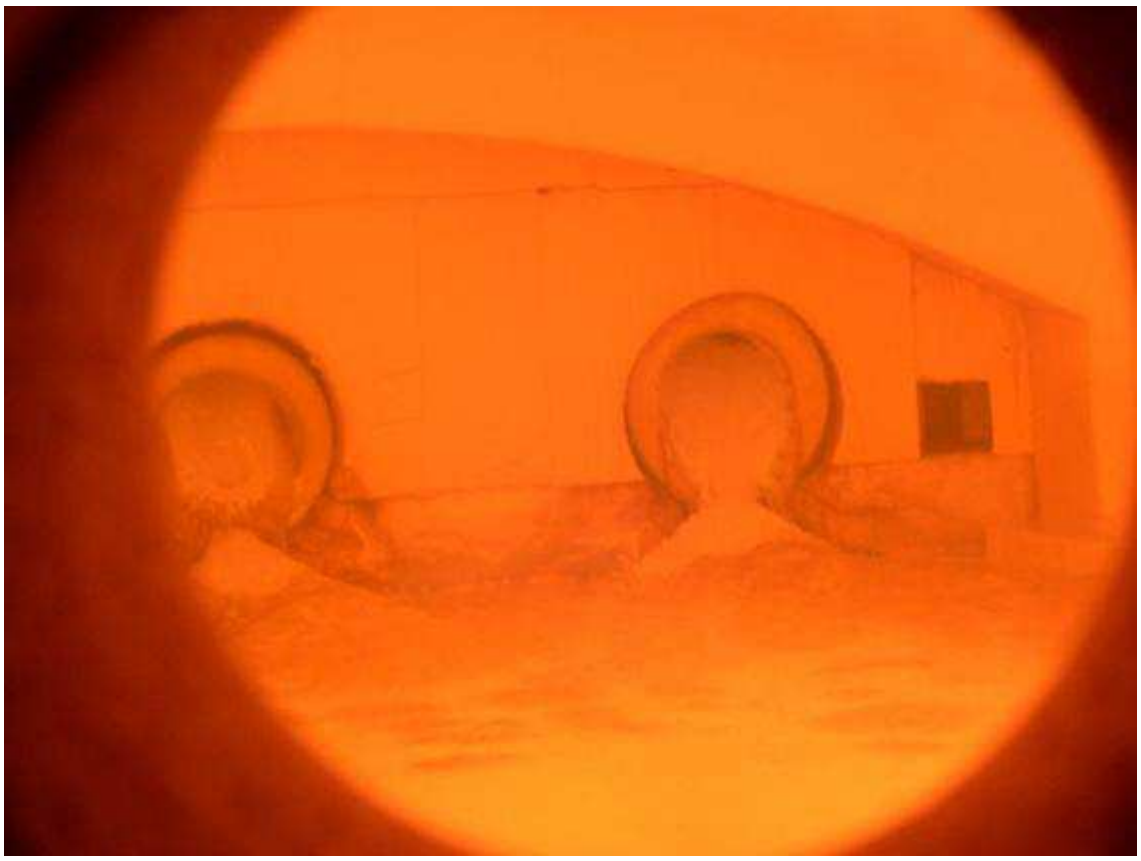

Figure 10: View into the GlasFLOX glass melting furnace

5. References

[1] Wünning, J.G.: Flammlose Oxidation von Brennstoff, PhD Thesis, RWTH Aachen, Germany, 1996

[2] Wünning, J.G: FLOX-Flameless Combustion, Thermprocess Symposium Düsseldorf, Germany, 2003

[3] Milani, A.: "Mild Combustion" techniques applied to regenerative firing in industrial furnaces, 2nd International Seminar on High Temperature Combustion, Stockholm, Sweden, 2000

[4] Flamme, M.; Kösters, M.; Scherello, A.; Kremer, H. and Boß, M.: Experimental Study of Heat Transfer Intensification in Glass Melting Furnaces. Final report of task 2.2 of the EURONITE project (JOE3CT970083). Gaswärme-Institut e.V. Essen, Germany, 2000

[5] Giese, A., Konold, U., al-Halbouni, A. Görner, K., Schwarz, G., Köster, B.; Application of Flameless Oxidation in Glass Melting Furnaces, 7th International Symposium on High Temperature Air Combustion and Gasification, Phuket, Thailand, 2008

[6] Scherello, A.; Konold, U. and Görner, K.: Anwendung der flammenlosen Oxidation für Glasschmelzwannen mit rekuperativer Luftvorwärmung – GlasFLOX®, 23. Deutscher Flammentag, 12.-13. September 2007, Berlin, VDI-Bericht 1988

Mechanism of damage by high temperature of the tubes, exposed to the atmosphere characteristic of a furnace of pyrolysis of ethane for ethylene production in the petrochemical industry

Jaqueline Saavedra [a] , Javier Trujillo Pérez francisco[b] , Lourdes Meriño Stand[c], Harbey Alexi Escobar[d], Luis Eduardo Navas [e], Juan Carlos Amézquita[f]

[a] Colombian Institute of petroleum, Ecopetrol, Santander, Colombia, Jaqueline.Saavedra@Ecopetrol.com.co
[b] Universidad Complutense of Madrid Faculty of chemical sciences, Madrid Spain, fjperez@Quim.UCM.es
[c] Department of chemical engineering, Industrial University of Santander, Bucaramanga, Colombia, loumerino2@gmail.co
[d]Management Barrancabermeja refinery, Harbey Escobar, Colombia, harbey.escobar@ecopetrol.com.co
[e] Management Barrancabermeja refinery, Colombia, Luis Eduardo Navas, Luis. Navas. Ecopetrol.com.co
[f] Department of chemical engineering, Industrial University of Santander, Bucaramanga, juancarlosamezquita@Hotmail.com .

Abstract:

In this work he took as a case study a furnace of pyrolysis of ethane for production of ethylene, which analysed different injury mechanisms, in order to determine the most critical in this process. Making a background and historical review of the process, it was determined that the carburización is the mechanism of most critical damage, which occurs primarily in the area of radiation from this type of ovens. The carburización is favoured by the undesired formation of Coke during the process. Background and historical review became an analysis of the influence of variables and factors such as temperature, time of residence, load flow, type of cargo, flow of heat and the severity of the process, the formation of Coke.

Keywords: Carburization, HP40, overheating, cooking, pyrolysis and coke.

1 Introduction

The processes of thermal pyrolysis of hydrocarbons occur at high temperatures, causing the hydrocarbons of the burden to become unstable and are decomposed into hydrogen, methane, olefins (ethylene product), aromatic and coke. The pipe from the furnace of pyrolysis of ethane to ethylene production, suffers severe corrosion at high temperature, contact gaseous vapor and hydrocarbon mixtures. The most common damage include embossing, erosion, cracking and carburización.

There are two kinds of reactions in pyrolysis process: the main reactions, which are that lead to the desired product and secondary that break down molecules of product into by-products as aromatic complex, higher olefins and Coke[1].

The environment of the process is characterized by a high activity of carbon to the inside of the pipe, where they occur reactions that involve the formation of carbon in the gas phase [2,3], which can induce the formation of layers of coke on the inner surface of the pipe, through different mechanisms [1, 2].Coke formed affects process, to generate the appearance of hotspots, increasing the pressure within the pipe drop, decreasing the efficiency and integrity of the oven, and heat

transfer, which implies increased consumption of fuel to keep constant temperature process and damage by carburización.
The carburización is one of the most critical damage mechanisms in processes of hydrocarbons at high temperature [4], which affects properties such as the coefficient of thermal expansion, magnetization, thermal conductivity, hardness and ductility, among others [5]. The carburización occurs in the tubes of the furnace of pyrolysis of ethane to produce ethylene [6], which are exposed to environments with carbon at high temperatures and where the carbon is transferred from the atmosphere of the process towards the interior of the pipe metal matrix. In the carburización mechanism, carbon atoms diffuse through the metal matrix material [7], [8]. Widespread carbon can remain without react or react with constituents of the alloy to form carbides M23C6 and M7C3 (M: METAL), intergranulares and intragranulares, mostly with chromium, affecting the structural homogeneity of the material.

2. Experimental procedure

Review of history and historical a furnace type cabin with two areas of heating, of convection and radiation, was made to analyse the different mechanisms of damage and the area in which they occur, in order to determine the most critical in the process of pyrolysis of ethane to ethylene production. They also analyze the influence of variables and factors such as temperature, residence time, load flow, type of load, heat flux and the severity of the process, the formation of Coke.

This was complemented information with thermography taken in field of pyrolysis oven, in order to define the real conditions of operation and this way, establish the diagnosis of damage.

Also made the analysis of a steel tube HP40, withdrawn from service in the furnace of pyrolysis case study, 72 000 hours of operation, which was obstructed by a thick layer of Coke, (fig. 1)

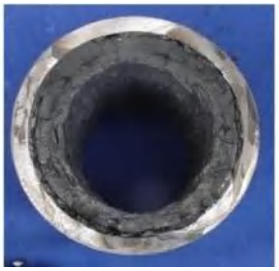

Fig 1. Length of pipe removed from service for to coking furnace pyrolysis of ethane to produce ethylene.

To assess the State of damage of steel were used techniques of non destructive analysis such as sizing, visual inspection, magnetization and destructive analysis as chemical composition and hardness.

3 Teams

The equipment used for the different analyses performed were:

- Analysis of chemical composition of the material: made by spectrometry of optical emission (EEO) technique according to standard ASTM E - 415-08 [9].
- Analysis of hardness: hardness testing were conducted in scale Brinell - HB according to standard ASTM E 10-08 [10], with an uncertainty of measurement: ± 1.31 HB, a durometer Brinell Gnehm Horgen, applying 187, 5Kgf.
- Analysis metallography: made with 6V attack 10% oxalic acid electrolyte for 10 seconds [11], according to standard ASTM E-45

- Analysis of electronic microscopy of scanning SEM: this analysis was performed with an electron microscope, Leo1450VP, equipped with system of x-ray energy dispersed OXFORD INCA [12].

4. Results and analysis of results

4.1. Analysis of history and historical

4.1.1 Mechanisms of damage

The information obtained in the revision of history and historical analyses of the process over a period of 8 years, related the frequency of failure with the affected area of the oven, as shown in the histogram of Figure 2 and it was determined that the causes for which pulled out sections of pipe from the furnace were:

- Presence of thick layers of Coke that can not be removed in the process of decoquizado with steam.
- Carburización.
- Cracking of tubes and diametrical deformation and warpage and buckling.
- Creep (creep).
- Metal dusting (accelerated Carburización).
- Excessive magnetism.

The histogram shows that had been submitted 10 failures in the pipeline in the area of radiation. Followed in frequency of failure, damage to the housing, the refractory and burners in the oven.

The analysis of the frequency of fails them, reveals that the radiation zone is indeed which presents more frequent damage. The Ues (frequency: 2) and the "Y" (frequency: 3) are part of the pipe of the coil of radiation, which has a 37.5% of failure in the radiation zone.

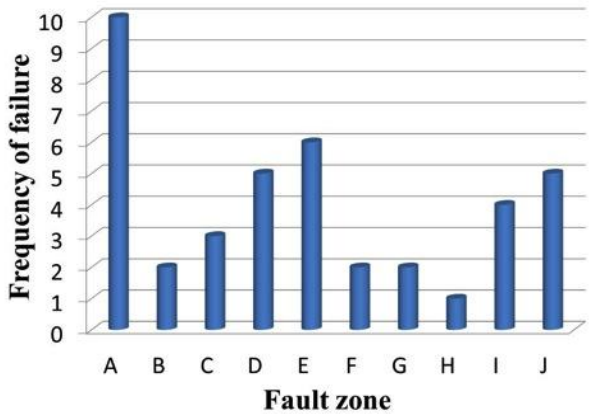

A) Pipelines - radiation zone	(F) Coil-zone convection
(B) "U" - the area of radiation	(G) Refractory-zone convection
(C) "and-radiation zone"	(H) Insulation-zone convection
(D) Refractory-zone radiation	(I) Burners
(E) Housing - re radiation area	(J) of burners Hoyas

Fig 2. Histogram of failure of the furnace case study.

4.1.2 Influence of variables of the process on formation of coke

Variables greater influence in the formation of coke in pyrolysis processes are: the severity of the process, the type of load, temperature, time of residence, heat flow, the partial pressure of hydrocarbons, whose interaction occurs on the figure 3.

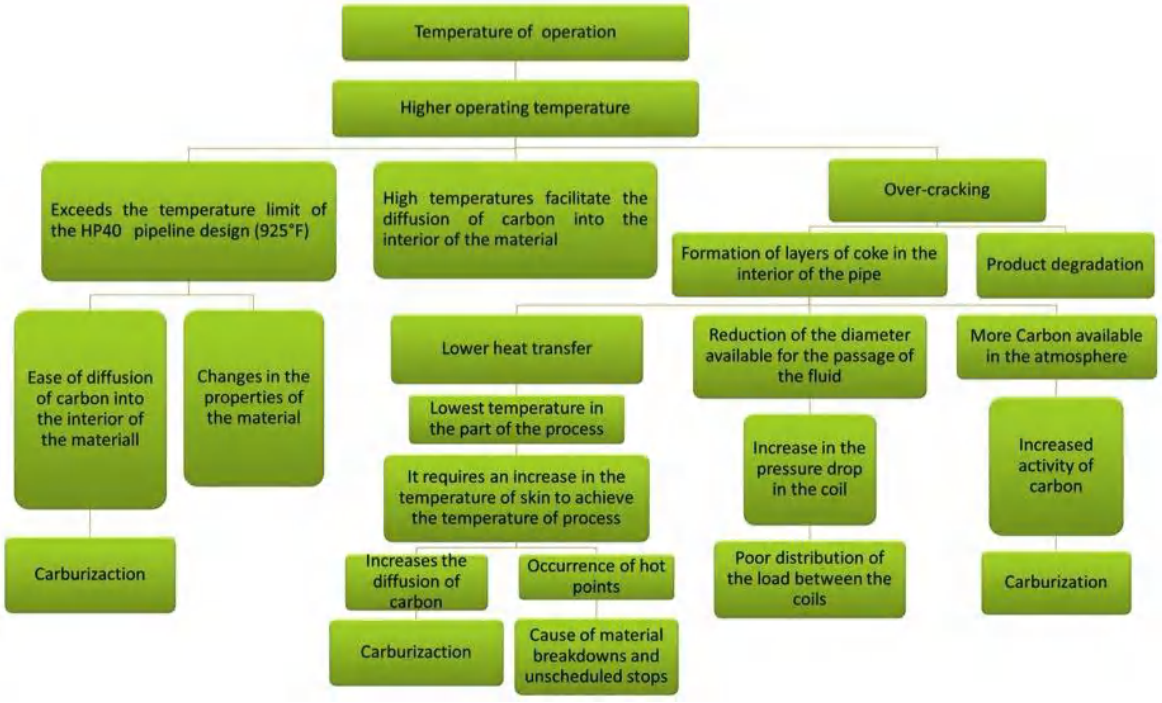

Fig 3. Operation of process variables involved in pyrolysis.

When there is this Coke, this acts as a resistance which decreases the thermal conductivity from the outside of the tube until the flow of the process (fig. 4), necessitating a greater flow of heat to maintain the required temperature of the process, which leads to sobrecalentatiento, contributing to the formation of more Coke.

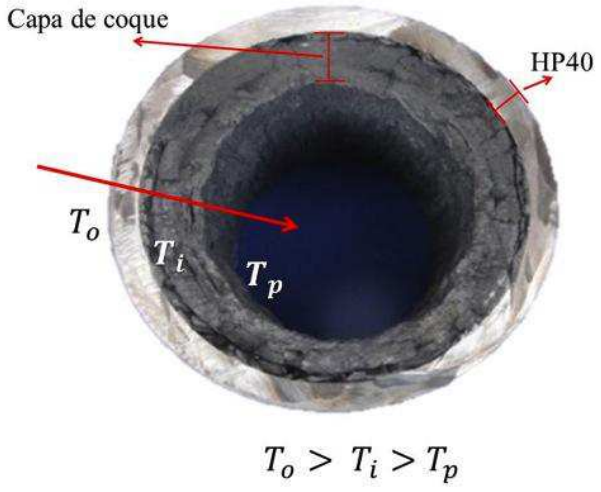

Fig. 4. Heat flow pattern through the steel HP40 and coke layer, where, To is the external temperature, Ti is the internal temperature of the tube, Tp is the temperature in the process gas.

4.2 Analysis situ of the oven

We performed a visual internal inspection into the oven, in which there were irregularities in the area of radiation as tubes: warpage and buckling in some of them. Through thermography identified the actual temperatures of operation, which notes are to reach points of up to 1057.6 ° C (1935.7 ° F), which exceed the maximum temperature design of 1010 ° C (1850 ° F according to standard API 530), Figure 5, this overheating leads to envelope pyrolysis of loading, formation of Coke, mechanisms of damage as the carburización. Coke increases the activity of carbon in the environment of the process which joined the high temperatures facilitate the diffusion of carbon into the interior of the material, cause damage by carburización.

Figure 3 shows the cyclical relationship between the high temperatures of the process and the presence of coke on the inside of the pipe, which results in effects such as: generation of an environment conducive to the emergence of damage in the alloy (such as carburización); reduction in the thermal efficiency of the oven.

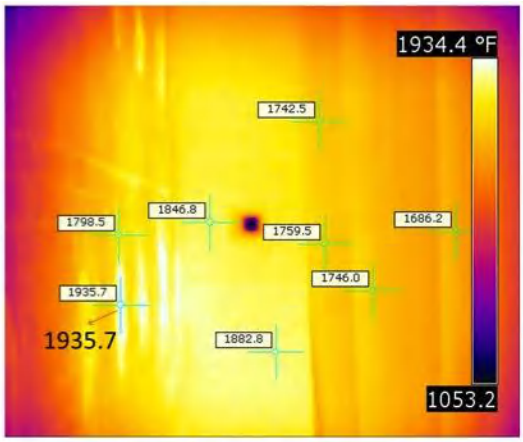

Figure 5. Thermography for the Serpentine south eastern side of the furnace of study.

4.3 Analysis of damage mechanism

High resistance materials as the HP40 tend to form a protective oxide layer which prevents the [13,14] carburización, the presence of coke in conditions of operation impaired such layer, as the elements that make up react with the carbon in the environment. In the absence of a uniform protective layer carbon diffuses towards the interior of the alloy.

The HP40 material of the pipe withdrawn from service not presented a definite profile of carburización, however there is precipitation of carbides in matrix (grain boundaries, edges of dendrites), as shown in Figure 6.

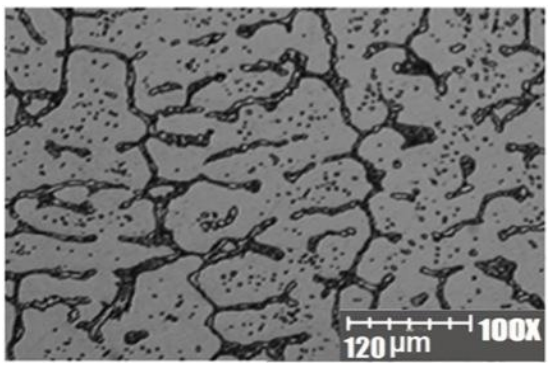

Fig 6. Metallography of the study material (steel HP40) with presence of carburization.

Carbon who has entered the matrix material, produces changes in it because it forms carbides with M23C6 and M7C3 type alloy metals (M metal), mostly with chromium [15]. These carbides introduce efforts which deform the material structure, favouring the embrittlement, magnetization, plastic deformation and change in hardness among others, eventually reducing the material life[16].

The evaluated material presented a slight magnetic response, which is higher in the inner surface which in the external, indicating a change in the microstructure of the material, the alloy has originally a ParaMagnetic behavior [17, 18], this change is due to the formation of carbides implies a redistribution of chromium [19] (mainly) in the matrix of the material.

Buckling and warpage problems found in the pipe are due to the loss of ductility of material and the elongation capacity, since carbides in matrix contribute to change the hardness of the material [20, 21]. Hardness average found for material removed from service is 188HB, while for new material is 170HB. This change in the material reduces the ability of elongation and ductility, which leads to sagging and warpage of the tubes during the thermal cycles[22].

The warpage and buckling of the pipe is also caused by the presence of Coke which hinders the heat dissipation during cooling, also acts as a thermal barrier that forces to increase the external temperature of the tubes to maintain the temperature of the process, which causes overheating, speeding up the formation of more coke and the carburización.

With background, analysis of metallic samples analysis, evidence of presence of coke and temperature exceeding those of design determined to carburización, is the mechanism of most critical damage, which occurs primarily in the area of radiation from this type of ovens.

4 Conclusions

The cooking of the pipe of pyrolysis ovens creating an environment that leads to the carburización of the pipe due to the abundant carbon available for dissemination and an increase in temperature, which must be submitted the tubes when there is a layer of Coke inside.

In the different mechanisms of failure occur in the pipe from the furnace of pyrolysis, there is one common factor involved accelerating mechanism to a greater or lesser extent, such factor is the carburización of the material. Although it does not appear as the cause of the withdrawal of the piece, it affects the deterioration of the strength of steel with mechanisms such as the creep or magnetization.

The carburización and overheating are factors contributing to damage such as plastic deformations, embrittlement, magnetization and change in hardness, the HP40 alloy tubing for the production of ethylene pyrolysis furnace.

Through the analysis of history, analysis of metallic samples, the evidence of the presence of Coke, was determined that the carburización is the mechanism of most critical damage, which occurs primarily in the area of radiation from this type of ovens.

When do not hold correct values of temperature, time of residence and severity induces a sobrepirólisis of load, speeding up the deposition of coke on the walls of the coil. Which, in turn, to reduce the transfer of heat to the process, requires to increase fuel consumption and decreases the performance of ethylene due to the fall of pressure generated by the decrease in the effective diameter of the pipe

References

[1] Albright L.F.,C. F. McConnell, k. Welther. In Thermal HydrocarbonChemistry; Eddinger, r. T. Eds.; Advances in Chemistry Series 183; American Chemical Society: Washington, D.C., 1979; pp 175-191.

[2] Albright L.F and j. C. Marekt. Mechanistic Model for Formation of Coke in Pyrolysis Units Producing Ethylene. School of Chemical Engineering, Purdue University, West Lafayette, Indiana 47907.

[3] G.C. Reyniers, G.F. Froment, F.D. Kopinke. Coke Formation in the Thermal Cracking of Hydrocarbons: Modeling of Coke Formation in Naphtha Cracking. Ind. Eng. Chem. Res. 33, 2584-2590. (1994).

[4] T. Maeda, f. X Terwijn (2005). Carburization resistance of high-CR high-Ni Weld overlayed tubes for ethylene pyrolysis furnace. In: Ethylene Producers Conference, Vol 14. 47 Session.

[5] H. M. Tawancy (2009). Degradation of mechanical strength of pyrolysis furnace tubesby high-temperature carburization in a petrochemical plant. In: Engineering Failure Analysis, Vol. 16, Issue 7 pp. 2171-2178.

[6] C. D. B. Meadowcroft and j. e. Oakey (1995). Guidelines for Plant Measurement of High Temperature Corrosion. In: European Federation of corrosion Publications, Vol. 14, pp. 1-9.

[7] Damage Mechanisms Affecting Fixed Equipment in the Refining Industry, APIRP - 571, Recommended practice 571, December 2003. In: American Petroleum Institute, First edition, pp. 3-270.

[8] ASTM G79–83 (Reapproved 1996). Standard Practice for Evaluation of Metals Exposed to Carburization Environments1

[9] ASTM E - 415-08 Standard Test Method for Atomic Emission Vacuum Spectrometric Analysis of Carbon and Low-Alloy Steel1.

[10] ASTM E 10-08 "Standard Test Method for Brinell Hardness of Metallic Materials".

[11] ASM American Society for Materials (1985). In: Metal Handbook, Properties and selection: Stainless steel. Vol 3.

[12] ECOPETROL, (2010). Colombian Institute of the oil Institute, laboratory of electron microscopy, Colombian Petroleum Institute. Report 10000048 ID0146 T67 10 103-ECP, Piedecuesta.

[13] Alvarez J. , Melo. D. Protective coatings against metal dusting. Surface & Coatings Technology, 203 (2008) 422-426.

[14] H. M. Tawancy, (2009), Degradation of mechanical strength of pyrolysis furnace tubesby high-temperature carburization in a petrochemical plant. In: Engineering Failure Analysis, vol. 16, Issue 7 pp. 2171-2178.

[15] Hall, D. et to the. Factors effecting carburization behavior of cast austenitic steels. Materials Performance, January, 1985, p. 25-26.

[16] B . Terry, j. Wright, D. Hall, (1989). A model for prediction of carburization in steels for ethylene production furnaces. Institution of corrosion science & technology, 48. Vol 29, pp. 1-18.

[17] I.C. Silva to Rebello J.M.A. BC Bruno, (b) P.J. Jacques, c B. Nystend and j. Dillee, (2008), Structural and magnetic characterization of to cast austenitic steel carburized. EM: Science Direct, Scripta Materialia, 1010-1013, pp. 1-4

[18] Saavedra J., Amezquita J.C., Díaz L.M. Evaluation of damage by carburization of a tube removed from a pyrolysis furnace. Ciencia e ingeniería Neogradadina,Vol. 20-2, pp. 19-20,Bogota, Diembre 2010.

[19] Haro SR, DL Lopez, Velasco AT RB Viramonetes.Microesturctural factors that determine the weldability of high Cr-high if HK40 alloy. Mater Chem Phys 2000; 66: 90-6

[20] Balikci Ercan, Mirschams RA. Raman a. Fracture Behavior of superalloy IN738LC with varius precipitate microstuctures. Mater Sci Eng A 1999: 265: 50 - 62

[21] Analysis of ethylene cracking tubes-Kaishu Guan failed **, Hong Xu, Zhiwen Wang-magazine Engineering Failure Analysis 12 (2005) 420-431.

Steam reforming of methane over Pt/Rh based wire mesh catalyst in single channel reformer for small scale syngas production

Haftor Orn Sigurdsson[a], Søren Knudsen Kær[b]

[a] *Aalborg University, Aalborg, Denmark, hos@et.aau.dk,* ***CA***
[b] *Aalborg University, Aalborg, Denmark, skk@et.aau.dk*

Abstract:

The purpose of this study is to investigate a small scale steam methane reformer for syngas production for a micro combined heat and power (mCPH) unit under different operational conditions. The study presents an experimental analysis of the performance of a specially built single channel of a catalytic parallel plate type heat exchanger (CPHE) reformer stack, where coated Pt/Rh based wire mesh is used as a catalyst. Heat is supplied to the endothermic reaction with infrared electric heaters. All the experiments were performed under atmospheric pressure and at stable operating conditions. The following parameters are considered in the experiment: catalyst temperature, gas hourly space velocity (GHSV) and steam to carbon ratio (S/C). The catalyst was tested at temperatures between 600 and 900°C, S/C ratios between 2 and 5 and GHSV between 319 and 2201 h-1. The experimental results are used to evaluate the effect of flow maldistribution in a CPHE reformer stack on the CH4 conversion and H2 yield.

Keywords:

Methane, steam reforming, syngas production, wire mesh catalyst, CPHE reformer.

1. Introduction

Existing production and distribution infrastructure of natural gas makes it an important potential feedstock for small scale fuel cell based combined heat and power (mCHP) applications. Several methods exist to produce hydrogen from hydrocarbons such as natural gas, including steam reforming, partial oxidation, auto thermal reforming and dry reforming. Steam reforming has high process efficiency compared to the other processes and is therefore usually the preferred option [1]. Steam reforming of methane rich natural gas is the most widely used process to produce hydrogen, amounting to about 48 % of the world hydrogen production [2].
New methods of extracting natural gas from shale have added significantly to natural gas resources, it is estimated that supply can meet rising demand at reasonable prices. In Europe natural gas accounts for 25 % of the primary energy need, natural gas could bridge the transition period required while shifting from coal and oil to renewable energy sources [3]. Methane rich biogas is regarded as an renewable and widely available alternative to fossil fuels in the future [4,5].
In a fuel cell based mCHP unit, where natural gas is used as fuel, hydrogen is produced on site in a small scale steam reformer before it is converted simultaneously into electricity and heat in the fuel cell. Catalytic parallel plate type heat exchanger (CPHE) reformer is an attractive device for small scale hydrogen production due to low production cost, low unit volume, high heat transfer capability and potential for high degree of integration with other components of the CPHE system.
Scaling of a CPHE reformer is more straightforward than in a conventional tubular reformer since the number of plates in the CPHE reformer can be increased to meet the hydrogen demand of the CPHE system. However care must be taken when increasing the amount of plates since longer manifold path can lead to flow maldistribution in the CPHE reformer. Flow maldistribution in a CPHE reformer can lead to heat maldistribution, hydrocarbon slip, increased overall pressure drop and carbon formation on the catalyst surface [6,7]. Flow maldistribution can occur in both the

reactor channels and the heating channels, flow maldistribution in the heating channels will lead to heat maldistribution in the reformer. This may lower the temperature on the catalyst in some of the catalyst channels, which will reduce the performance of the CPHE unit. The geometry of the CPHE reformer must be carefully designed to minimize flow maldistribution [8].
The CPHE reformer currently studied has 60 parallel channel with integrated coated woven wire mesh catalyst, and 61 parallel channels to provide heat to the steam reforming reactions from an external catalytic burner. Intake and exhaust manifolds are built into the CPHE reformer on the steam reforming side. The CPHE reformer has a Z-type flow arrangement, is single pass and counter current flow. An illustration of the CPHE reformer can be seen in Fig 1.

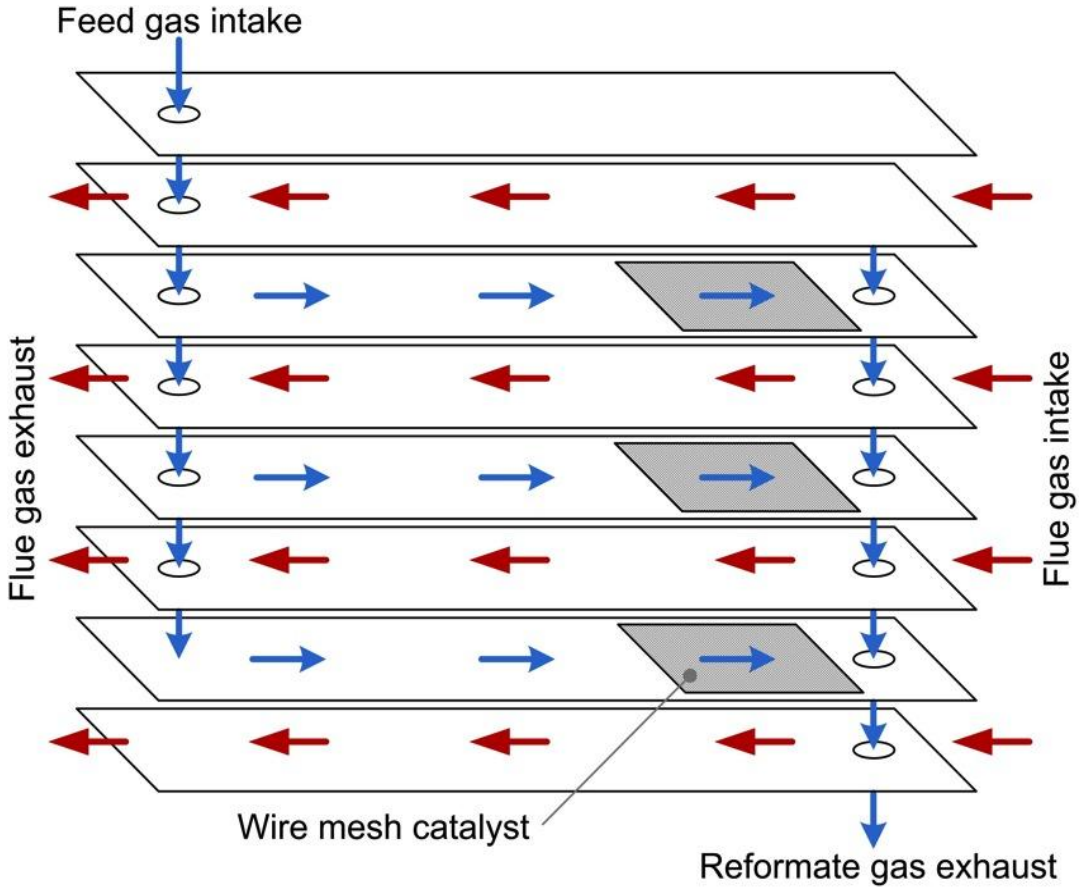

Fig 1. Layout of the CPHE reformer stack.

The present study focuses on investigating the performance of a single reactor channel at different temperatures, space velocities (SV) and steam to carbon ratios (S/C) to evaluate the effect of flow and heat maldistribution on the CPHE performance. For this purpose a specially built single channel reactor has been realized. Temperature, SV and S/C are the most important parameters in the steam reforming process. Steam reforming on a large scale is usually carried out at temperatures between 800 and 900°C and S/C between 3 and 5. In this paper we investigate the performance of the single reactor channel at temperatures between 600 and 900°C, S/C between 2 and 5 and at SV between 319 and 2201 h-1.

2. Experimental

2.1. Experimental setup and procedure

A schematic diagram of the experimental setup can be seen in Fig 2. Methane flows from the storage tank to the CH_4 mass flow controller (MFC) from where it flows to the evaporator. Demineralized H_2O is continuously pumped to the evaporator where it evaporates and mixes with

the CH_4. The evaporator is filled with 6 mm glass spheres to ensure uniform gas distribution. The feed gas is superheated to 175°C in the evaporator before it enters the reformer through the inlet tube. In the reformer the feed gas is heated up to the reactor temperature in the heat exchanger part of the reformer. The feed gas then enters the reactor part of the reformer where the reactions take place. The reactor is heated to meet the energy demand of the endothermic reactions with eight 700 W infrared heaters. The product gas from the reformer passes through a condenser before the dry gas is analyzed.

Demineralized water was supplied to the evaporator with a calibrated Grundfos dose pump. The feed flow rate of the CH_4 was controlled with Bürkert MFC with a full scale range of 0-2 nl/m. Inert nitrogen was mixed with the product gas to meet the demand of the gas analyzer, the measurements from the gas analyzer were normalized.

The evaporator is made of aluminum and is heated electrically with four 100 W tubular heaters. The reformer parts are made up of stainless steel. Temperatures of the catalyst wire mesh was measured with five N-type thermocouples. In addition three N-type thermocouples were used to measure the temperature of the feed gas in the heat exchanger. The thermocouples in the wire mesh catalyst were distributed evenly with 20 mm in between them in the centerline of the wire mesh, the first thermocouple was placed 10 mm from the catalyst opening. The tip of the thermocouples was pressed against the catalyst wire mesh to ensure good contact between the wire mesh thread and the thermocouple, and subsequently good temperature measurement. Major reactor dimensions and information can be found in Table 1.

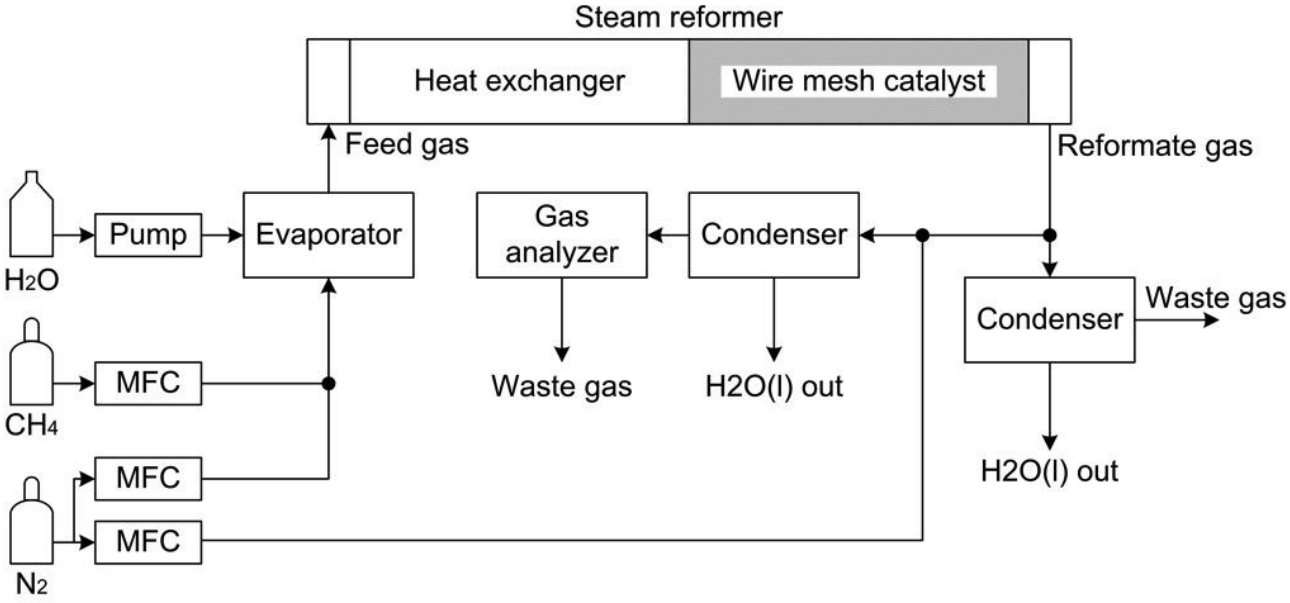

Fig 2. Schematic diagram of the experimental setup

The concentration of hydrogen in the product gas was measured using a Siemens CALOMAT 6 thermal conductivity gas analyzer, CH_4, CO and CO2 was measured using a Siemens ULTRAMAT 6 infrared analyzer. Mass flow and temperatures in the experimental reformer were controlled and recorded with LabVIEW data acquisition and control system. The product gas concentrations were continuously measured and recorded with LabVIEW, data was written to a file every two seconds.

The reformer was heated from room temperature to the working temperature at a linearly programmed rate of 4°C/min. The catalyst was purged with N_2 during heating until desired operating temperature was reached. At the desired operating temperature H_2O was fed to the nitrogen stream for approximately 5 minutes. Afterwards CH_4 was introduced gradually. Subsequently N_2 flow was reduced gradually to zero. The reformer was operated for approximately one hour at standard conditions (T = 750°C, S/C = 3.5 and GHSV = $319h^{-1}$) after startup before the experiments were performed to ensure stable operating conditions. When the reformer was stable, logging of the data was started. Every experiment lasted for approximately 10 minutes.

Table 1 Major dimensions of the experimental steam reformer

Name	Value
Reformer channel width	90 mm
Reformer channel height	1.1 mm
Reformer channel length	198 mm
Catalyst wire mesh width	88 mm
Catalyst wire mesh height	1.05 mm
Catalyst wire mesh width	88 mm
Plate thickness	0.5 mm
Catalyst wire mesh wire diameter	0.45 mm
Wire mesh void fraction	0.38
Catalyst producer	Catator
Catalyst composition	$Pt/Rh/Al_2O_3$

The steam to carbon ratio (S/C) is the total number of H_2O molecules divided by the total number of carbon atoms in the feed gas. S/C is calculated with the following equation

$$S/C = \frac{\dot{N}_{H_2O}}{\dot{N}_{CH_4}} \quad \left[\frac{\text{mol}}{\text{mol}}\right] \tag{1}$$

where $\dot{N}_{H_2O}$ and $\dot{N}_{CH_4}$ are the feed gas molar flow rates of H_2O and CH_4 respectively. To reduce coke formation on the catalyst surface the S/C ratio is normally above 3. Gas hourly space velocity (GHSV) is defined as the ratio between the void of the catalyst and the total volumetric CH_4 flow rate at the inlet. GHSV is calculated according to the following equation

$$GHSV = \frac{\dot{V}_{CH_4}}{V_{catalyst}} \quad \left[h^{-1}\right] \tag{2}$$

where $\dot{V}_{CH_4}$ is the volume flow rate of CH_4 at the inlet of the reformer and $V_{catalyst}$ is the void volume inside the catalyst. To compare the results of the experiments the conversion of CH_4 and the H_2 yield is calculated. Conversion of CH_4 is calculated as

$$X_{CH_4} = \frac{\dot{N}_{CH_4,FG} - \dot{N}_{CH_4,SG}}{\dot{N}_{CH_4,FG}} \quad [-] \tag{3}$$

where FG refers to feed gas and SG refers to synthesis gas. The H_2 yield is calculated as

$$Y_{H_2} = 0.25 \cdot \frac{\dot{N}_{H_2,SG}}{\dot{N}_{CH_4,FG}} \quad [-] \tag{4}$$

where $\dot{N}_{H_2}$ is the molar flow rate of hydrogen in the synthesis gas.

2.1. Evaluation of flow distribution in the CPHE reformer stack

Flow distribution in the CPHE reformer stack was evaluated experimentally by measuring the static pressure along the intake and exhaust manifolds with a mobile static pressure probe. Flow rates for the isothermal experiments were based on comparing Reynolds number under normal operating conditions for the CPHE reformer. The Reynolds number was based on the hydraulic diameter of the intake manifold. The dimensionless Reynolds number is defined as

$$\text{Re} = \frac{D_h \cdot V \cdot \rho}{\mu} \tag{5}$$

where D_h is the hydraulic diameter of the intake manifold, V is the velocity of the fluid entering the CPHE reformer, ρ is the density of the fluid and μ is the dynamic viscosity of the fluid. The velocity of the fluid is calculated as

$$V = \frac{\dot{m}}{\rho \cdot A_m} \tag{6}$$

where $\dot{m}$ is the mass flow rate and A_m is the cross sectional area of the intake manifold. Static pressure was measured at 20 evenly distribution positions inside the intake and exhaust manifolds. Inclined liquid nanometer filled with methanol was used to measure pressure difference between the manifolds. A Bürkert 8702 MFC supplied the reformer stack with constant flow of air. The exhaust of the reformer stack was open to the atmosphere. Fig 3 shows the static pressure probe and the CPHE reformer stack.

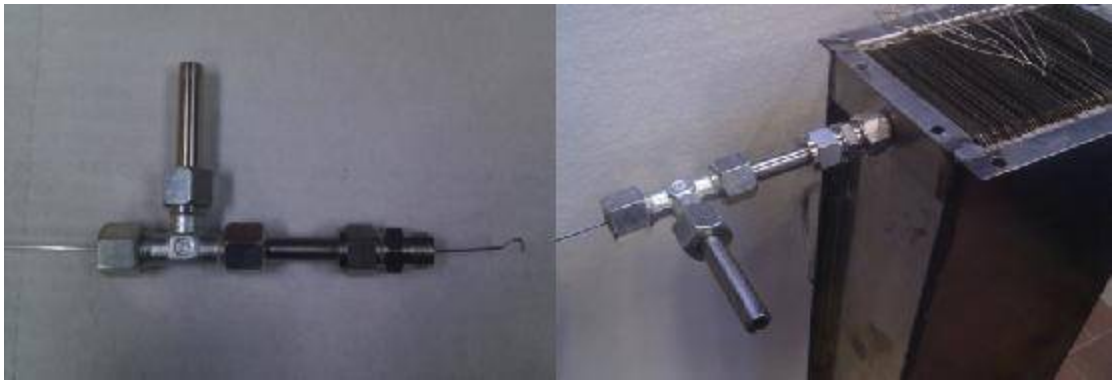

Fig 3: The static pressure probe (left) and the CPHE reformer stack (right).

Pressure drop had been measured in a single cassette at different flow rates in an earlier study [9], the results were used to evaluate the mass flow maldistribution in the reformer stack. The normalized mass flow distribution can be seen in Fig 4. Channel 1 is defined as the first channel in the flow direction in the intake manifold. It can be seen from the figure that there is a large maldistribution in the CPHE reformer. Mass flow in the last 10 channels is almost 5 times the average flow, while in the first 10 channels it is on average 0.4 times the average flow in the reverse direction. The reverse flow near the intake is caused by rapid expansion from the intake tube of the reactor to the manifold. At perfect conditions the flow in each channel would result in a GHSP of 319 h^{-1}, to evaluate the effect of flow maldistribution on the reforming process the single channel reforming experiments are performed at GHSP of up to 7 times the average channel flow rate.

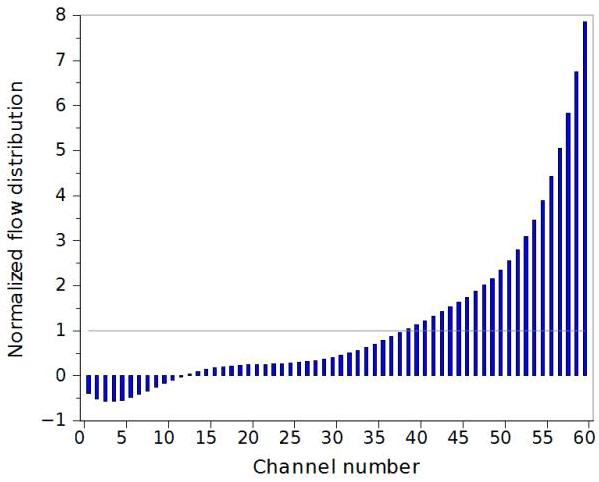

Fig 4. Flow distribution in the CPHE reformer stack under isothermal conditions.

3. Results and discussion

3.1 Catalyst stability

The performance stability of the catalyst was investigated before all other experiments were carried out. Conditions for the stability test were as follows; temperature of 750°C, steam to carbon ratio 2.0 and GHSV of 627 h^{-1}. The conditions were kept constant during the period of the experiment and the composition of the syngas was measured. It was observed that the gas composition remained steady at up to 22 h; catalyst deactivation was not observed. The results are presented in Fig 5. On dry basis the average volumetric concentration of H_2, CO, CO_2 and CH_4 in the reformate gas was 76 %, 16 %, 6.3 % and 1.4 % respectively. No significant changes could be observed in the product gas composition during the stability experiment.

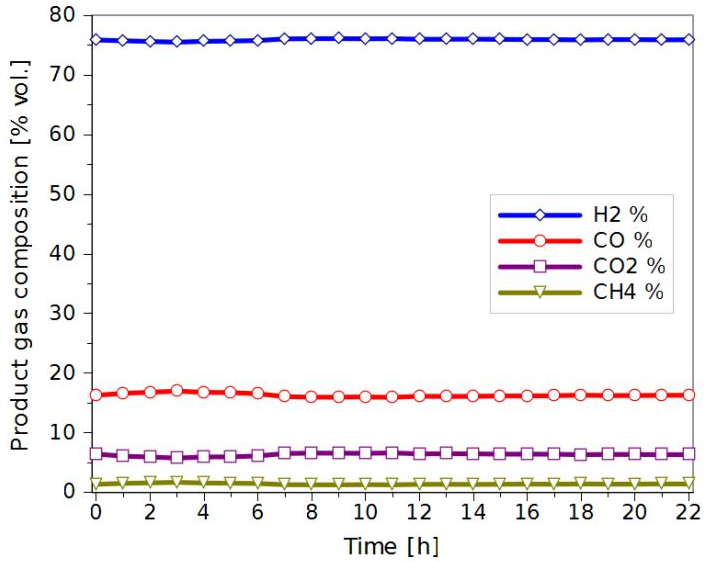

Fig 5. Composition of product gas as functions of time in hours. Conditions were as follows: catalyst average temperature 750°C, S/C ratio 3.5 and GHSV of 627 h^{-1}.

3.3. Effect of catalyst temperature

In this set of experiments the GHSV and S/C ratio is kept constant at 319 h^{-1} and 3.5 respectively while the temperature of the reformer is varied from 600 to 900°C in steps of 50°C. The syngas composition was measured with the gas analyzer and the conversion of CH_4 and H_2 yield was calculated from the results.

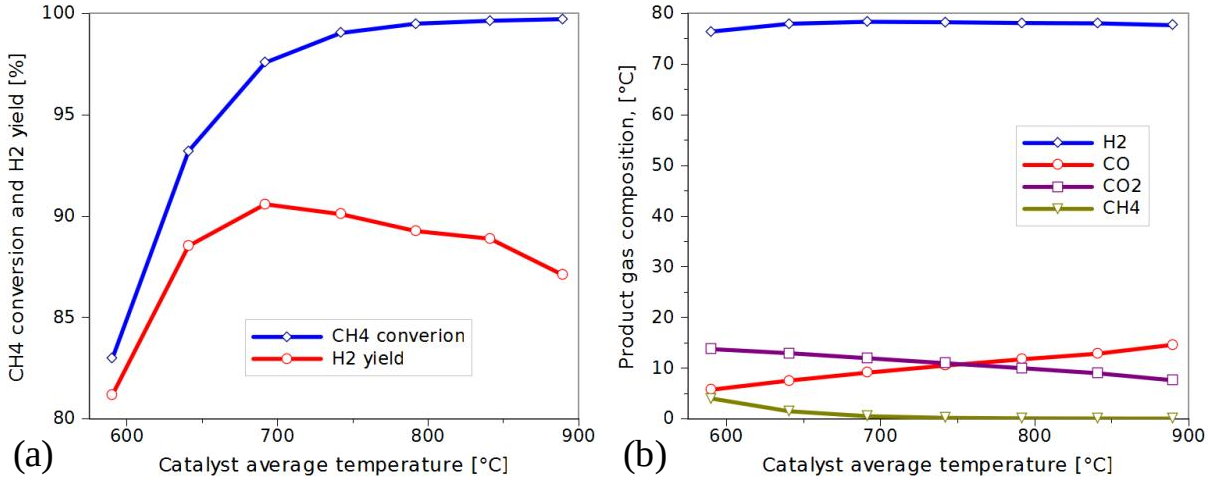

Fig 6. CH_4 conversion and H_2 yield (a) and syngas composition (b) as a function of catalyst temperature at GHSV and S/C ratio of 319 h^{-1} and 3.5 respectively.

Fig 6 (a) shows the conversion of CH_4 and H_2 yield as a function of catalyst temperature. It can be observed that as the temperature increases the conversion of CH_4 increases, until about 750°C is

reached. After that the increase in CH_4 conversion is very low. The H_2 yield has a maximum around 700°C catalyst temperature, after that it decreases. The syngas composition as a function of temperature is given in Fig 6 (b). The composition of the syngas is affected by the water gas shift (WGS) equilibrium. At lower temperatures the water gas shift (WGS) reaction occurs and the CO level in the syngas is reduced. As the temperature increases the CO conversion is lower due to equilibrium limitation. At higher temperatures the increase of H_2 production from the steam reforming reaction is lower than the decrease of H_2 production from the WGS reaction. Considering conversion of CH_4 and H_2 yield the catalyst should be kept at about 750°C, at this temperature the conversion of methane and H_2 production is high and the CO level is fairly low.

3.4. Effect of S/C ratio

In this series of experiments the S/C ratio is varied at a constant reactor temperature of 750°C and at constant space velocity of 319 h^{-1}. Conversion of CH_4 and H_2 yield can be seen in Fig 7 (a). It can be observed that the conversion of CH_4 increases slightly until S/C ratio is about 3.5, after that it stays the same until the S/C ratio reaches 5. Higher S/C ratio in the feed gas increases the selectivity toward hydrogen, the higher S/C ratio favour the production of H_2 in both the steam reforming and WGS reactions. Fig 7 (b) shows the composition of product gas as a function of S/C. The concentration of H_2 is constant at about 76 % for the different S/C ratios. On the other hand, the higher the S/C ratio is the more energy is required for the water evaporation process. The S/C ratio directly affects the efficiency of the process. Since little is gained in conversion of CH4 and H2 yield above S/C ratio of 3.5, that S/C ratio is used in the following experiments.

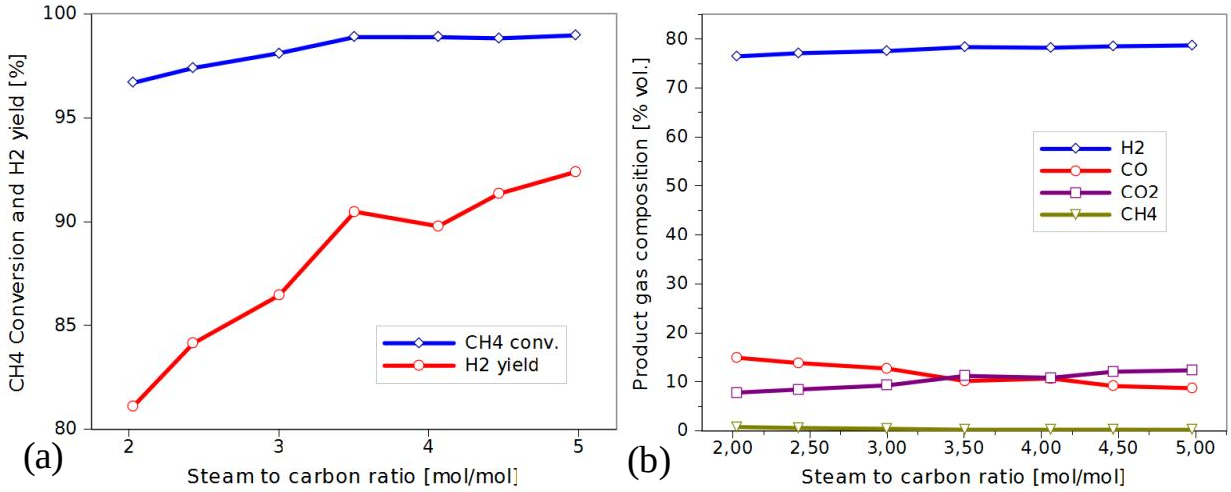

Fig 7. CH_4 conversion and H_2 yield (a) and product gas composition (b) as a function of S/C at GHSV and catalyst temperature of 319 h^{-1} and 750°C respectively.

3.5. Effect of space velocity and temperature

In this set of experiments the effect of different space velocity on the CH_4 conversion and H_2 yield and composition of the syngas at different reformate gas temperatures was studied. Experiments were performed at reformate gas temperatures of 650, 750 and 850°C and at space velocities of 319, 627, 941, 1250, 1563, 1896 and 2201 h^{-1}. The CH_4 conversion, H_2 yield and product gas composition, as a function of GHSV, can be observed in Fig 8, Fig 9 and Fig 10 for reformer temperatures of 650, 750 and 850°C respectively. It can be observed from the figures that increasing the GHSV (reducing the gas contact time with the catalyst) has a high impact on the CH_4 conversion and the H_2 yield.

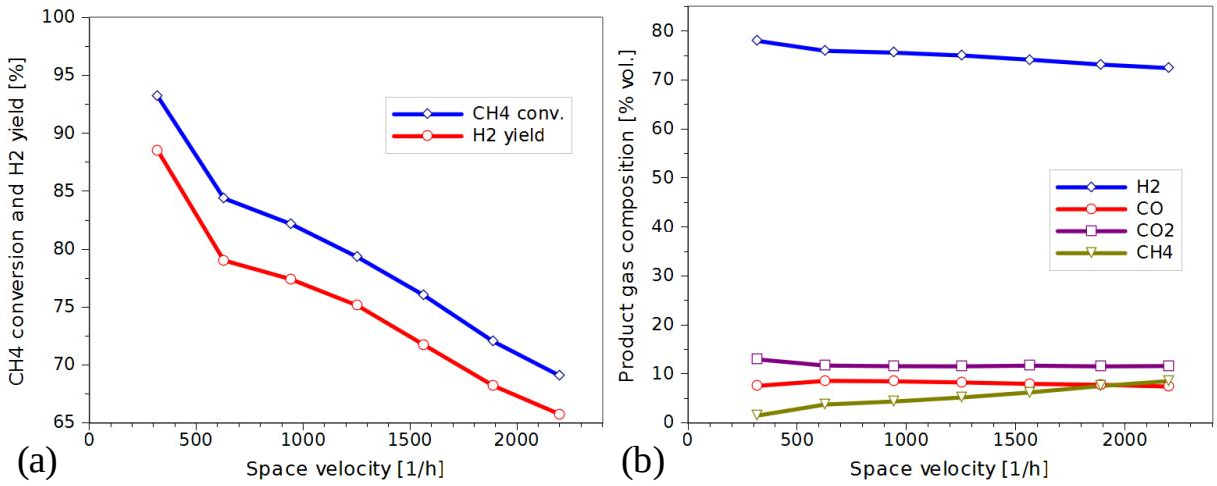

Fig 8. CH_4 conversion and H_2 yield (a) and product gas composition (b) as a function of space velocity at reformate gas temperatures of 650°C and S/C ratio of 3.5.

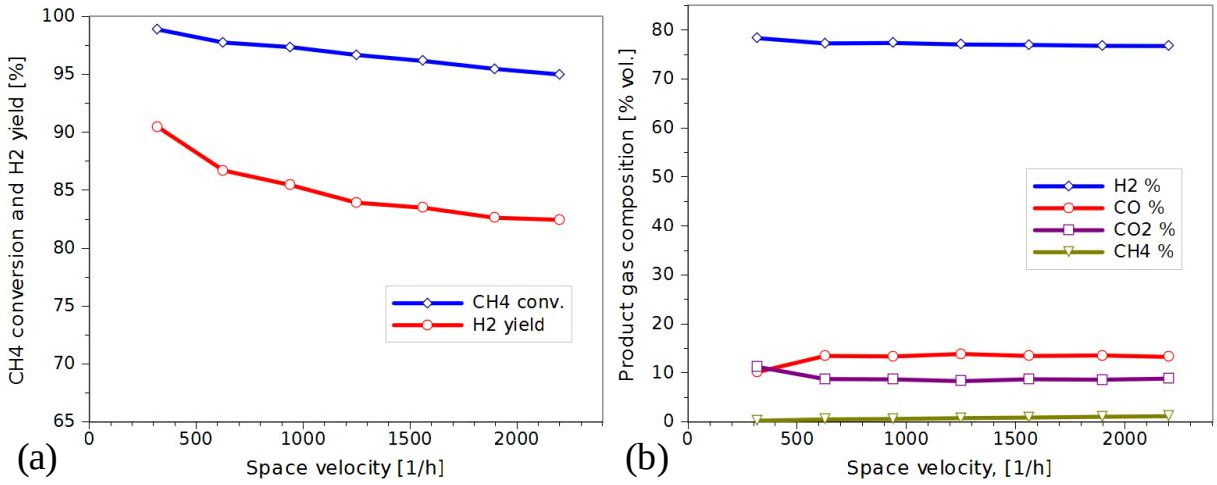

Fig 9. CH_4 conversion and H_2 yield (a) and product gas composition (b) as a function of space velocity at reformate gas temperatures of 750°C and S/C ratio of 3.5.

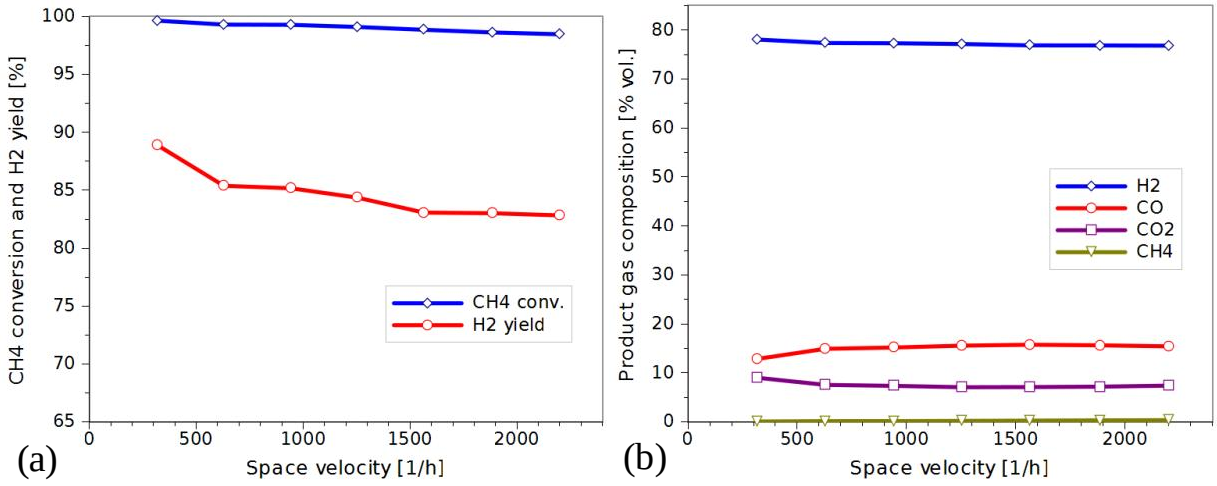

Fig 10. CH_4 conversion and H_2 yield (a) and product gas composition (b) as a function of space velocity at reformate gas temperatures of 850°C and S/C ratio of 3.5.

The impact of higher GHSV on CH_4 conversion and H_2 yield is considerable higher at lower reformate gas temperatures. The CH_4 conversion and H_2 yield drops very rapidly as the GHSV is

increased at reformate gas temperature of 650°C. However at reformate gas temperatures of 750 and 850°C the drop in CH_4 conversion and H_2 yield is not as dramatic.

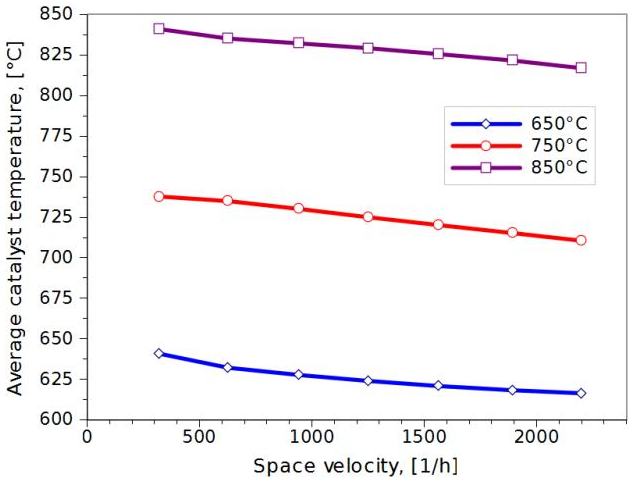

Fig 11. Average catalyst temperatures as a function of space velocity for reformate gas temperatures of 650, 750 and 850°C.

The average catalyst wire mesh temperatures as a function of GHSV are shown in Fig 11 for reformate gas temperatures of 650, 750 and 850°C. It can be observed that due to the increased catalyst load, and insufficient heat transfer from the wall to the wire-mesh, the temperature of the catalyst wire mesh drops as the GHSV is increased.

4. Conclusion

Steam reforming of methane over a Pt/Rh based wire mesh catalyst in a single channel plate reformer is investigated in the present paper, the results are summarized below.

- Experiments were performed at temperatures between 600 and 900°C, S/C ratio between 2 and 5 and at GHSP between 319 and 2201 h^{-1}.
- The catalyst temperature has a high impact on the CH_4 conversion, H_2 yield and purity of H_2. However the H_2 yield reaches a maximum between 650 and 700°C at S/C ratio of 3.5.
- CH_4 conversion and H_2 yield drops significantly at reformer temperature of 650°C when GHSV is increased above the normal operating conditions of 319 h^{-1}.
- Increasing the S/C ratio increases the CH_4 conversion and H_2 yield, however the energy demand rises rapidly since evaporating and superheating water is energy demanding.

The results show the importance of maintaining healthy flow distribution in a plate reformer since the heat input to the reforming channels would need to be increased significantly to meet the demand of the channel receiving the highest feed gas flow rates.

Catalyst deactivation was not observed in the catalyst stability test, composition of the product gas was constant throughout the experiments. It is therefore concluded that deactivation does not affect the experimental results during these experiments.

Acknowledgments

The authors would like to gratefully acknowledge the financial support from The European Regional Development Fund and the Department of Energy Technology at Aalborg University.

THE EUROPEAN UNION
The European Regional Development Fund
Investing in your future

References

[1] Gardemann U, Roes J, Heinzel A. Pollutant emissions of burners for steam reformers for residential power supply. International Journal of Hydrogen Energy 2011;36(8):5189-5199.

[2] Ewan B, Allen R. A figure of merit assessment of the routes to hydrogen. International Journal of Hydrogen Energy 2005;30(8):809-819.

[3] Weijermars R, Drijkoningen G, Heimovaara TJ, Rudolph ESJ, Weltje GJ, Wolf KH a. a. Unconventional gas research initiative for clean energy transition in europe. Journal of Natural Gas Science and Engineering 2011;3(2):402-412.

[4] Zhu B, Li X-S, Shi C, Liu J-L, Zhao T-L, Zhu A-M. Pressurization effect on dry reforming of biogas in kilohertz spark-discharge plasma. International Journal of Hydrogen Energy 2012:1-10.

[5] Rafiq MH, Hustad JE. Biosyngas production by autothermal reforming of waste cooking oil with propane using a plasma-assisted gliding arc reactor. International Journal of Hydrogen Energy 2011;36(14):8221-8233.

[6] Ahmed K, Föger K. Fuel processing for high-temperature high-efficiency fuel cells. Industrial & Engineering Chemistry Research 2010;49(16):7239-7256.

[7] Chen F, Chang M, Kuo C, Hsueh C, Yan W. Analysis of a plate-type microreformer for methanol steam reforming reaction. Energy & Fuels 2009;23(10):5092-5098.

[8] Delsman ER, Pierik A, Croon MHJM de, Kramer GJ, Schouten JC. Microchannel plate geometry optimization for even flow distribution at high flow rates. Chemical Engineering Research and Design 2004;82(2):267-273.

[9] Sigurdsson HO, Kær SK. Experimental and numerical evaluation of the by-pass flow in a catalytic plate reactor for hydrogen production. In: Proceedings of asme 2011 9th fuel cell science, engineering and technology conference. Washington: ASME, 2011.

ECOS 2012

The 25th International Conference on Efficiency, Cost, Optimization and Simulation of Energy Conversion Systems and Processes

(Perugia, June 26th-June 29th, 2012)

edited by
Umberto Desideri, Giampaolo Manfrida,
Enrico Sciubba

firenze university press
2012

ECOS 2012 : the 25th International Conference on Efficiency, Cost, Optimization and Simulation of Energy Conversion Systems and Processes (Perugia, June 26th-June 29th, 2012) / edited by Umberto Desideri, Giampaolo Manfrida, Enrico Sciubba. – Firenze : Firenze University Press, 2012.
(Proceedings e report ; 90)

http://digital.casalini.it/9788866553229

ISBN 978-88-6655-322-9 (online)

Progetto grafico di copertina Alberto Pizarro, Pagina Maestra snc
Immagine di copertina: © Kts | Dreamstime.com

Peer Review Process
All publications are submitted to an external refereeing process under the responsibility of the FUP Editorial Board and the Scientific Committees of the individual series. The works published in the FUP catalogue are evaluated and approved by the Editorial Board of the publishing house. For a more detailed description of the refereeing process we refer to the official documents published on the website and in the online catalogue of the FUP (http://www.fupress.com).

Firenze University Press Editorial Board
G. Nigro (Co-ordinator), M.T. Bartoli, M. Boddi, F. Cambi, R. Casalbuoni, C. Ciappei, R. Del Punta, A. Dolfi, V. Fargion, S. Ferrone, M. Garzaniti, P. Guarnieri, G. Mari, M. Marini, M. Verga, A. Zorzi.

© 2012 Firenze University Press
Università degli Studi di Firenze
Firenze University Press
Borgo Albizi, 28, 50122 Firenze, Italy
http://www.fupress.com/
Printed in Italy

ECOS 2012

The 25th International Conference on

Efficiency, Cost, Optimization and Simulation
of Energy Conversion Systems and Processes

Perugia, June 26th-June 29th, 2012

Book of Proceedings - Volume VIII

Edited by:
Umberto Desideri, Università degli Studi di Perugia
Giampaolo Manfrida, Università degli Studi di Firenze
Enrico Sciubba, Università degli Studi di Roma "Sapienza"

ECOS 2012 - THE 25TH INTERNATIONAL CONFERENCE ON
EFFICIENCY, COST, OPTIMIZATION, SIMULATION AND ENVIRONMENTAL IMPACT OF ENERGY SYSTEMS
JUNE 26-29, 2012, PERUGIA, ITALY
EDITED BY UMBERTO DESIDERI, GIAMPAOLO MANFRIDA, ENRICO SCIUBBA
FIRENZE UNIVERSITY PRESS, 2012, ISBN ONLINE : 978-88-6655-322-9

Advisory Committee (Track Organizers)

Building, Urban and Complex Energy Systems
V. Ismet Ugursal
Dalhousie University, Nova Scotia, Canada

Combustion, Chemical Reactors, Carbon Capture and Sequestration
Giuseppe Girardi
ENEA-Casaccia, Italy

Energy Systems: Environmental and Sustainability Issues
Christos A. Frangopoulos
National Technical University of Athens, Greece

Exergy Analysis and Second Law Analysis
Silvio de Oliveira Junior
Polytechnical University of Sao Paulo, Sao Paulo, Brazil

Fluid Dynamics and Power Plant Components
Sotirios Karellas
National Technical University of Athens, Athens, Greece

Fuel Cells
Umberto Desideri
University of Perugia, Perugia, Italy

Heat and Mass Transfer
Francesco Asdrubali, **Cinzia Buratti**
University of Perugia, Perugia, Italy

Industrial Ecology
Stefan Goessling-Reisemann
University of Bremen, Germany

Poster Session
Enrico Sciubba
University Roma 1 “Sapienza”, Italy

Process Integration and Heat Exchanger Networks
Francois Marechal
EPFL, Lausanne, *Switzerland*

Renewable Energy Conversion Systems
David Chiaramonti
University of Firenze, Firenze, Italy

Simulation of Energy Conversion Systems
Marcin Liszka
Polytechnica Slaska, Gliwice, Poland

System Operation, Control, Diagnosis and Prognosis
Vittorio Verda
Politecnico di Torino, Italy

Thermodynamics
A. Özer Arnas
United States Military Academy at West Point, U.S.A.

Thermo-Economic Analysis and Optimisation
Andrea Lazzaretto
University of Padova, Padova, Italy

Water Desalination and Use of Water Resources
Corrado Sommariva
ILF Consulting M.E., U.K

Scientific Committee

Riccardo Basosi, University of Siena, Italy
Gino Bella, University of Roma Tor Vergata, Italy
Asfaw Beyene, San Diego State University, United States
Ryszard Bialecki, Silesian Institute of Tecnology, Poland
Gianni Bidini, University of Perugia, Italy
Ana M. Blanco-Marigorta, University of Las Palmas de Gran Canaria, Spain
Olav Bolland, University of Science and Technology (NTNU), Norway
Renè Cornelissen, Cornelissen Consulting, The Netherlands
Franco Cotana, University of Perugia, Italy
Alexandru Dobrovicescu, Polytechnical University of Bucharest, Romania
Gheorghe Dumitrascu, Technical University of Iasi, Romania
Brian Elmegaard, Technical University of Denmark , Denmark
Daniel Favrat, EPFL, Switzerland
Michel Feidt, ENSEM - LEMTA University Henri Poincaré, France
Daniele Fiaschi, University of Florence, Italy
Marco Frey, Scuola Superiore S. Anna, Italy
Richard A Gaggioli, Marquette University, USA
Carlo N. Grimaldi, University of Perugia, Italy
Simon Harvey, Chalmers University of Technology, Sweden
Hasan Heperkan, Yildiz Technical University, Turkey
Abel Abel Hernandez-Guerrero, University of Guanajuato, Mexico
Jiri Jaromir Klemeš, University of Pannonia, Hungary
Zornitza V. Kirova-Yordanova, University "Prof. Assen Zlatarov", Bulgaria
Noam Lior, University of Pennsylvania, United States
Francesco Martelli, University of Florence, Italy
Aristide Massardo, University of Genova, Italy
Jim McGovern, Dublin Institute of Technology, Ireland
Alberto Mirandola, University of Padova, Italy
Michael J. Moran, The Ohio State University, United States
Tatiana Morosuk, Technical University of Berlin, Germany
Pericles Pilidis, University of Cranfield, United Kingdom
Constantine D. Rakopoulos, National Technical University of Athens, Greece
Predrag Raskovic, University of Nis, Serbia and Montenegro
Mauro Reini, University of Trieste, Italy
Gianfranco Rizzo, University of Salerno, Italy
Marc A. Rosen, University of Ontario, Canada
Luis M. Serra, University of Zaragoza, Spain
Gordana Stefanovic, University of Nis, Serbia and Montenegro
Andrea Toffolo, Luleå University of Technology, Sweden
Wojciech Stanek, Silesian University of Technology, Poland
George Tsatsaronis, Technical University Berlin, Germany
Antonio Valero, University of Zaragoza, Spain
Michael R. von Spakovsky, Virginia Tech, USA
Stefano Ubertini, Parthenope University of Naples, Italy
Sergio Ulgiati, Parthenope University of Naples, Italy
Sergio Usón, Universidad de Zaragoza, Spain
Roman Weber, Clausthal University of Technology, Germany
Ryohei Yokoyama, Osaka Prefecture University, Japan
Na Zhang, Institute of Engineering Thermophysics, Chinese Academy of Sciences, China

The 25th ECOS Conference 1987-2012: leaving a mark

The introduction to the ECOS series of Conferences states that "ECOS is a series of international conferences that focus on all aspects of Thermal Sciences, with particular emphasis on Thermodynamics and its applications in energy conversion systems and processes". Well, ECOS is much more than that, and its history proves it!

The idea of starting a series of such conferences was put forth at an informal meeting of the Advanced Energy Systems Division of the American Society of Mechanical Engineers (ASME) at the November 1985 Winter Annual Meeting (WAM), in Miami Beach, Florida, then chaired by Richard Gaggioli. The resolution was to organize an annual Symposium on the Analysis and Design of Thermal Systems at each ASME WAM, and to try to involve a larger number of scientists and engineers worldwide by organizing conferences outside of the United States. Besides Rich other participants were Ozer Arnas, Adrian Bejan, Yehia El-Sayed, Robert Evans, Francis Huang, Mike Moran, Gordon Reistad, Enrico Sciubba and George Tsatsaronis.

Ever since 1985, a Symposium of 8-16 sessions has been organized by the Systems Analysis Technical Committee every year, at the ASME Winter Annual Meeting (now ASME-IMECE). The first overseas conference took place in Rome, twenty-five years ago (in July 1987), with the support of the U.S. National Science Foundation and of the Italian National Research Council. In that occasion, Christos Frangopoulos, Yalcin Gogus, Elias Gyftopoulos, Dominick Sama, Sergio Stecco, Antonio Valero, and many others, already active at the ASME meetings, joined the core-group.

The name ECOS was used for the first time in Zaragoza, in 1992: it is an acronym for **Efficiency, Cost, Optimization and Simulation** (of energy conversion systems and processes), keywords that best describe the contents of the presentations and discussions taking place in these conferences. Some years ago, Christos Frangopoulos inserted in the official website the note that "ècos" ('οικος) means "home" in Greek and it ought to be attributed the very same meaning as the prefix "Eco-" in environmental sciences.
The last 25 years have witnessed an almost incredible growth of the ECOS community: more and more Colleagues are actively participating in our meetings, several international Journals routinely publish selected papers from our Proceedings, fruitful interdisciplinary and international cooperation projects have blossomed from our meetings. Meetings that have spanned three continents (Africa and Australia ought to be our next targets, perhaps!) and influenced in a way or another much of modern Engineering Thermodynamics.
After 25 years, if we do not want to become embalmed in our own success and lose momentum, it is mandatory to aim our efforts in two directions: first, encourage the participation of younger academicians to our meetings, and second, stimulate creative and useful discussions in our sessions. Looking at this years' registration roster (250 papers of which 50 authored or co-authored by junior Authors), the first objective seems to have been attained, and thus we have just to continue in that direction; the second one involves allowing space to "voices that sing out of the choir", fostering new methods and approaches, and establishing or reinforcing connections to other scientific communities. It is important that our technical sessions represent a place of active confrontation, rather than academic "lecturing".
In this spirit, we welcome you in Perugia, and wish you a scientifically stimulating, touristically interesting, and culinarily rewarding experience. In line with our 25 years old scientific excellency and friendship!

Umberto Desideri, Giampaolo Manfrida, Enrico Sciubba

CONTENT MANAGEMENT

The index lists all the papers contained all the eight volumes of the Proceedings of the ECOS 2012 International Conference.
Page numbers are listed only for papers within the Volume you are looking at. The ID code allows to trace back the identification number assigned to the paper within the Conference submission, review and track organization processes.

CONTENT

VOLUME VIII

VIII. 1 ENERGY SYSTEMS: ENVIRONMENTAL AND SUSTAINABILITY ISSUES

» A multi-criteria decision analysis tool to support electricity planning (ID 467) ……..... *Pag. 1*
Fernando Ribeiro, Paula Ferreira, Madalena Araújo

» Comparison of sophisticated life cycle impact assessment methods for assessing environmental impacts in a LCA study of electricity production (ID 259) ……..... *Pag. 15*
Jens Buchgeister

» Defossilisation assessment of biodiesel life cycle production using the ExROI indicator (ID 304) ……..... *Pag. 27*
Emilio Font de Mora, César Torres, Antonio Valero, David Zambrana

» Design strategy of geothermal plants for water dominant medium-low temperature reservoirs based on sustainability issues (ID 99) ……..... *Pag. 38*
Alessandro Franco, Maurizio Vaccaro

» Energetic and environmental benefits from waste management: experimental analysis of the sustainable landfill (ID 33) ……..... *Pag. 50*
Francesco Di Maria, Alessandro Canovai, Federico Valentini, Alessio Sordi, Caterina Micale

» Environmental assessment of energy recovery technologies for the treatment and disposal of municipal solid waste using life cycle assessment (LCA): a case study of Brazil (ID 512) ……..... *Pag. 62*
Marcio Montagnana Vicente Leme, Mateus Henrique Rocha, Electo Eduardo Silva Lora,Osvaldo José Venturini, Bruno Marciano Lopes, Claudio Homero Ferreira

» How will renewable power generation be affected by climate change? – The case of a metropolitan region in Northwest Germany (ID 503) ……..... *Pag. 71*
Jakob Wachsmuth, Andrew Blohm, Stefan Gößling-Reisemann, Tobias Eickemeier, Rebecca Gasper, Matthias Ruth, Sönke Stührmann

» Impact of nuclear power plant on Thailand power development plan (ID 474) ……..... *Pag. 88*
Raksanai Nidhiritdhikrai, Bundhit Eua-arporn

» Improving sustainability of maritime transport through utilization of liquefied natural gas (LNG) for propulsion (ID 496) ……..... *Pag. 102*
Fabio Burel, Rodolfo Taccani, Nicola Zuliani

» Life cycle assessment of thin film non conventional photovoltaics: the case of dye sensitized solar cells (ID 471) ……..... *Pag. 119*
Maria Laura Parisi, Adalgisa Sinicropi, Riccardo Basosi

» Low CO2 emission hybrid solar CC power system (ID 175) ……..... *Pag. 133*
Yuanyuan Li, Na Zhang, Ruixian Cai

» Low exergy solutions as a contribution to climate adapted and resilient power supply (ID 489) ……..... *Pag. 148*
Stefan Goessling-Reisemann, Thomas Bloethe

» On the use of MPT to derive optimal RES electricity generation mixes (ID 459) ……..... *Pag. 164*
Paula Ferreira, Jorge Cunha

» Stability and limit cycles in an exergy-based model of population dynamics (ID 128) ……..... *Pag. 179*
Enrico Sciubba, Federico Zullo

» The influence of primary measures for reducing NOx emissions on energy steam boiler efficiency (ID 125) ……..... *Pag. 193*
Goran Stupar, Dragan Tucaković, Titoslav Živanović, Miloš Banjac, Srđan Belošević,Vladimir Beljanski, Ivan Tomanović, Nenad Crnomarković, Miroslav Sijerčić

» The Lethe city car of the University of Roma 1: final proposed configuration (ID 45) ……..... *Pag. 206*
Roberto Capata, Enrico Sciubba

VIII. 2 POSTER SESSION

» A variational optimization of a finite-time thermal cycle with a Stefan-Boltzmann heat transfer law (ID 333) ……..... *Pag. 216*
Juan C.Chimal-Eguia, Norma Sanchez-Salas

» Modeling and simulation of a boiler unit for steam power plants (ID 545) ……..... *Pag. 217*
Luca Moliterno, Claudia Toro

» Numerical Modelling of straw combustion in a moving bed combustor (ID 412) ……..... *Pag. 218*
Biljana Miljkoviü, Ivan Pešenjanski, Borivoj Stepanov, Vladimir Milosavljeviü, Vladimir Rajs

» Physicochemical evaluation of the properties of the coke formed at radiation area of light hydrocarbons pyrolysis furnace in petrochemical industry (ID 10) ……..... *Pag. 219*
Jaqueline Saavedra Rueda , Angélica María Carreño Parra, María del Rosario Pérez Trejos, Dionisio Laverde Cataño, Diego Bonilla Duarte, Jorge Leonardo Rodríguez Jiménez, Laura María Díaz Burgos

» Rotor TG cooled (ID 121) ……..... *Pag. 220*
Chiara Durastante, Paolo Petroni, Michela Spagnoli, Vincenzo Rizzica, Jörg Helge Wirfs

» Study of the phase change in binary alloy (ID 534) ……..... *Pag. 221*
Aroussia Jaouahdou, Mohamed J. Safi, Herve Muhr

» Technip initiatives in renewable energies and sustainable technologies (ID 527) ……..... *Pag. 222*
Pierfrancesco Palazzo, Corrado Pigna

CONTENTS OF ALL THE VOLUMES

VOLUME I

I . 1 – SIMULATION OF ENERGY CONVERSION SYSTEMS

» A novel hybrid-fuel compressed air energy storage system for China's situation (ID 531)
Wenyi Liu, Yongping Yang, Weide Zhang, Gang Xu,and Ying Wu

» A review of Stirling engine technologies applied to micro-cogeneration systems (ID 338)
Ana C Ferreira, Manuel L Nunes, Luís B Martins, Senhorinha F Teixeira

» An organic Rankine cycle off-design model for the search of the optimal control strategy (ID 295)
Andrea Toffolo, Andrea Lazzaretto, Giovanni Manente, Marco Paci

» Automated superstructure generation and optimization of distributed energy supply systems (ID 518)
Philip Voll, Carsten Klaffke, Maike Hennen, André Bardow

» Characterisation and classification of solid recovered fuels (SRF) and model development of a novel thermal utilization concept through air- gasification (ID 506)
Panagiotis Vounatsos, Konstantinos Atsonios, Mihalis Agraniotis, Kyriakos D. Panopoulos, George Koufodimos,Panagiotis Grammelis, Emmanuel Kakaras

» Design and modelling of a novel compact power cycle for low temperature heat sources (ID 177)
Jorrit Wronski, Morten Juel Skovrup, Brian Elmegaard, Harald Nes Rislå, Fredrik Haglind

» Dynamic simulation of combined cycles operating in transient conditions: an innovative approach to determine the steam drums life consumption (ID 439)
Stefano Bracco

» Effect of auxiliary electrical power consumptions on organic Rankine cycle system with low-temperature waste heat source (ID 235)
Samer Maalouf, Elias Boulawz Ksayer, Denis Clodic

» Energetic and exergetic analysis of waste heat recovery systems in the cement industry (ID 228)
Sotirios Karellas, Aris Dimitrios Leontaritis, Georgios Panousis, Evangelos Bellos, Emmanuel Kakaras

» Energy and exergy analysis of repowering options for Greek lignite-fired power plants (ID 230)
Sotirios Karellas, Aggelos Doukelis, Grammatiki Zanni, Emmanuel Kakaras

» Energy saving by a simple solar collector with reflective panels and boiler (ID 366)
Anna Stoppato, Renzo Tosato

» Exergetic analysis of biomass fired double-stage Organic Rankine Cycle (ORC) (ID 37)
Markus Preißinger, Florian Heberle, Dieter Brüggemann

» Experimental tests and modelization of a domestic-scale organic Rankine cycle (ID 156)
Roberto Bracco, Stefano Clemente, Diego Micheli, Mauro Reini

» Model of a small steam engine for renewable domestic CHP system (ID 31)
Giampaolo Manfrida, Giovanni Ferrara, Alessandro Pescioni

» Model of vacuum glass heat pipe solar collectors (ID 312)
Daniele Fiaschi, Giampaolo Manfrida

» Modelling and exergy analysis of a plasma furnace for aluminum melting process (ID 254)
Luis Enrique Acevedo, Sergio Usón, Javier Uche, Patxi Rodríguez

» Modelling and experimental validation of a solar cooling installation (ID 296)
Guillaume Anies, Pascal Stouffs, Jean Castaing-Lasvignottes

» The influence of operating parameters and occupancy rate of thermoelectric modules on the electricity generation (ID 314)
Camille Favarel, Jean-Pierre Bédécarrats, Tarik Kousksou, Daniel Champier

» Thermodynamic and heat transfer analysis of rice straw co-firing in a Brazilian pulverised coal boiler (ID 236)
Raphael Miyake, Alvaro Restrepo, Fábio Kleveston Edson Bazzo, Marcelo Bzuneck

» Thermophotovoltaic generation: A state of the art review (ID 88)
Matteo Bosi, Claudio Ferrari, Francesco Melino, Michele Pinelli, Pier Ruggero Spina, Mauro Venturini

I . 2 – HEAT AND MASS TRANSFER

» A DNS method for particle motion to establish boundary conditions in coal gasifiers (ID 49)
Efstathios E Michaelides, Zhigang Feng

» Effective thermal conductivity with convection and radiation in packed bed (ID 60)
Yusuke Asakuma

» Experimental and CFD study of a single phase cone-shaped helical coiled heat exchanger: an empirical correlation (ID 375)
Daniel Flórez-Orrego, Walter Arias, Diego López, Héctor Velásquez

» Thermofluiddynamic model for control analysis of latent heat thermal storage system (ID 207)
Adriano Sciacovelli, Vittorio Verda, Flavio Gagliardi

» Towards the development of an efficient immersed particle heat exchanger: particle transfer from low to high pressure (ID 202)
Luciano A. Catalano, Riccardo Amirante, Stefano Copertino, Paolo Tamburrano, Fabio De Bellis

I . 3 – INDUSTRIAL ECOLOGY

» Anthropogenic heat and exergy balance of the atmosphere (ID 122)
Asfaw Beyene, David MacPhee, Ron Zevenhoven

» Determination of environmental remediation cost of municipal waste in terms of extended exergy (ID 63)
Candeniz Seckin, Ahmet R. Bayulken

» Development of product category rules for the application of life cycle assessment to carbon capture and storage (537)
Carlo Strazza, Adriana Del Borghi, Michela Gallo

» Electricity production from renewable and non-renewable energy sources: a comparison of environmental, economic and social sustainability indicators with exergy losses throughout the supply chain (ID 247)
Lydia Stougie, Hedzer van der Kooi, Rob Stikkelman

» Exergy analysis of the industrial symbiosis model in Kalundborg (ID 218)
Alicia Valero Delgado, Sergio Usón, Jorge Costa

» Global gold mining: is technological learning overcoming the declining in ore grades? (ID 277)
Adriana Domínguez, Alicia Valero

» **Personal transportation energy consumption (ID305)**
Matteo Muratori, Emmanuele Serra, Vincenzo Marano, Michael Moran

» **Resource use evaluation of Turkish transportation sector via the extended exergy accounting method (ID 43)**
Candeniz Seckin, Enrico Sciubba, Ahmet R. Bayulken

» **The impact of higher energy prices on socio-economic inequalities of German social groups (ID 80)**
Holger Schlör, Wolfgang Fischer, Jürgen-Friedrich Hake

VOLUME II

II . 1 – EXERGY ANALYSIS AND 2ND LAW ANALYSIS

» **A comparative analysis of cryogenic recuperative heat exchangers based on exergy destruction (ID 129)**
Adina Teodora Gheorghian, Alexandru Dobrovicescu, Lavinia Grosu, Bogdan Popescu, Claudia Ionita

» **A critical exploration of the usefulness of rational efficiency as a performance parameter for heat exchangers (ID 307)**
Jim McGovern, Georgiana Tirca-Dragomirescu, Michel Feidt, Alexandru Dobrovicescu

» **A new procedure for the design of LNG processes by combining exergy and pinch analyses (ID 238)**
Danahe Marmolejo-Correa, Truls Gundersen

» **Advances in the distribution of environmental cost of water bodies through the exergy concept in the Ebro river (ID 258)**
Javier Uche Marcuello, Amaya Martínez Gracia, Beatriz Carrasquer Álvarez, Antonio Valero Capilla

» **Application of the entropy generation minimization method to a solar heat exchanger: a pseudo-optimization design process based on the analysis of the local entropy generation maps (ID 357)**
Giorgio Giangaspero, Enrico Sciubba

» **Comparative analysis of ammonia and carbon dioxide two-stage cycles for simultaneous cooling and heating (ID 84)**
Alexandru Dobrovicescu, Ciprian Filipoiu, Emilia Cerna Mladin, Valentin Apostol, Liviu Drughean

» **Comparison between traditional methodologies and advanced exergy analyses for evaluating efficiency and externalities of energy systems (ID 515)**
Gabriele Cassetti, Emanuela Colombo

» **Comparison of entropy generation figures using entropy maps and entropy transport equation for an air cooled gas turbine blade (ID 468)**
Omer Emre Orhan, Oguz Uzol

» **Conventional and advanced exergetic evaluation of a supercritical coal-fired power plant (ID 377)**
Ligang Wang, Yongping Yang, Tatiana Morosuk, George Tsatsaronis

» **Energy and exergy analyses of the charging process in encapsulted ice thermal energy storage (ID 164)**
David MacPhee, Ibrahim Dincer, Asfaw Beyene

» **Energy integration and cogeneration in nitrogen fertilizers industry: thermodynamic estimation of the efficiency, potentials, limitations and environmental impact. Part 1: energy integration in ammonia production plants (ID 303)**
Zornitza Vassileva Kirova-Yordanova

» **Evaluation of the oil and gas processing at a real production day on a North Sea oil platform using exergy analysis (ID 260)**
Mari Voldsund, Wei He, Audun Røsjorde, Ivar Ståle Ertesvåg, Signe Kjelstrup

» Exergetic and economic analysis of Kalina cycle for low temperature geothermal sources in Brazil (ID 345)
Carlos Eymel Campos Rodriguez, José Carlos Escobar Palacios, Cesar Adolfo Rodríguez Sotomonte, Marcio Leme, Osvaldo José Venturini, Electo Eduardo Silva Lora, Vladimir Melián Cobasa, Daniel Marques dos Santos, Fábio R. Lofrano Dotto, Vernei Gialluca

» Exergy analysis and comparison of CO2 heat pumps (ID 242)
Argyro Papadaki, Athina Stegou - Sagia

» Exergy analysis of a CO2 Recovery plant for a brewery (ID 72)
Daniel Rønne Nielsen, Brian Elmegaard, C. Bang-Møller

» Exergy analysis of the silicon production process (ID 118)
Marit Takla, Leiv Kolbeinsen, Halvard Tveit, Signe Kjelstrup

» Exergy based indicators for cardiopulmonary exercise test evaluation (ID 159)
Carlos Eduardo Keutenedjian Mady, Cyro Albuquerque Neto, Tiago Lazzaretti Fernandes, Arnaldo Jose Hernandez, Paulo Hilário Nascimento Saldiva, Jurandir Itizo Yanagihara, Silvio de Oliveira Junior

» Exergy disaggregation as an alternative for system disaggregation in thermoeconomics (ID 483)
José Joaquim Conceição Soares Santos, Atilio Lourenço, Julio Mendes da Silva, João Donatelli, José Escobar Palacio

» Exergy intensity of petroleum derived fuels (ID 117)
Julio Augusto Mendes da Silva, Maurício Sugiyama, Claudio Rucker, Silvio de Oliveira Junior

» Exergy-based sustainability evaluation of a wind power generation system (ID 542)
Jin Yang, B. Chen, Enrico Sciubba

» Human body exergy metabolism (ID 160)
Carlos Eduardo Keutenedjian Mady, Silvio de Oliveira Junior

» Integrating an ORC into a natural gas expansion plant supplied with a co-generation unit (ID 273)
Sergio Usón, Wojciech Juliusz Kostowski

» One-dimensional model of an optimal ejector and parametric study of ejector efficiency (ID 323)
Ronan Killian McGovern, Kartik Bulusu, Mohammed Antar, John H. Lienhard

» Optimization and design of pin-fin heat sinks based on minimum entropy generation (ID 6)
Jose-Luis Zuniga-Cerroblanco, Abel Hernandez-Guerrero, Carlos A. Rubio-Jimenez, Cuauhtemoc Rubio-Arana, Sosimo E. Diaz-Mendez

» Performance analysis of a district heating system (ID 271)
Andrej Ljubenko, Alojz Poredoš, Tatiana Morosuk, George Tsatsaronis

» System analysis of exergy losses in an integrated oxy-fuel combustion power plant (ID 64)
Andrzej Ziębik, Paweł Gładysz

» What is the cost of losing irreversibly the mineral capital on Earth? (ID 220)
Alicia Valero Delgado, Antonio Valero

II . 2 – THERMODYNAMICS

» A new polygeneration system for methanol and power based on coke oven gas and coal gas (ID 252)
Hu Lin, Hongguang Jin, Lin Gao, Rumou Li

» Argon-Water closed gas cycle (ID 67)
Federico Fionelli, Giovanni Molinari

» Binary alkane mixtures as fluids in Rankine cycles (ID 246)
M. Aslam Siddiqi, Burak Atakan

» Excess enthalpies of second generation biofuels (ID 308)
Alejandro Moreau, José Juan Segovia, M. Carmen Martín, Miguel Ángel Villamañán, César R. Chamorro, Rosa M. Villamañán
» Local stability analysis of a Curzon-Ahlborn engine considering the Van der Waals equation state in the maximum ecological regime (ID 281)
Ricardo Richard Páez-Hernández, Pedro Portillo-Díaz, Delfino Ladino-Luna, Marco Antonio Barranco-Jiménez

» Some remarks on the Carnot's theorem (ID 325)
Julian Gonzalez Ayala, Fernando Angulo-Brown

» The Dead State (ID 340)
Richard A. Gaggioli

» The magnetocaloric energy conversion (ID 97)
Andrej Kitanovski, Jaka Tusek, Alojz Poredos

VOLUME III

THERMO-ECONOMIC ANALYSIS AND OPTIMIZATION

» A comparison of optimal operation of residential energy systems using clustered demand patterns based on Kullback-Leibler divergence (ID 142)
Akira Yoshida, Yoshiharu Amano, Noboru Murata, Koichi Ito, Takumi Hashizume

» A Model for Simulation and Optimal Design of a Solar Heating System with Seasonal Storage (ID 51)
Gianfranco Rizzo

» A thermodynamic and economic comparative analysis of combined gas-steam and gas turbine air bottoming cycle (ID 232)
Tadeusz Chmielniak, Daniel Czaja, Sebastian Lepszy

» Application of an alternative thermoeconomic approach to a two-stage vapor compression refrigeration cycle with intercooling (ID 135)
Atilio Barbosa Lourenço, José Joaquim Conceição Soares Santos, João Luiz Marcon Donatelli

» Comparative performance of advanced power cycles for low temperature heat sources (ID 109)
Guillaume Becquin, Sebastian Freund

» Comparison of nuclear steam power plant and conventional steam power plant through energy level and thermoeconomic analysis (ID 251)
S. Khamis Abadi, Mohammad Hasan Khoshgoftar Manesh, M. Baghestani, H. Ghalami, Majid Amidpour

» Economic and exergoeconomic analysis of micro GT and ORC cogeneration systems (ID 87)
Audrius Bagdanavicius, Robert Sansom, Nick Jenkins, Goran Strbac

» Exergoeconomic comparison of wet and dry cooling technologies for the Rankine cycle of a solar thermal power plant (ID 300)
Philipp Habl, Ana M. Blanco-Marigorta, Berit Erlach

» Influence of renewable generators on the thermo-economic multi-level optimization of a poly-generation smart grid (101)
Massimo Rivarolo, Andrea Greco, Francesca Travi, Aristide F. Massardo

» Local stability analysis of a thermoeconomic model of an irreversible heat engine working at different criteria of performance (ID 289)
Marco A. Barranco-Jiménez, Norma Sánchez-Salas, Israel Reyes-Ramírez, Lev Guzmán-Vargas

» Multicriteria optimization of a distributed trigeneration system in an industrial area (ID 154)
Dario Buoro, Melchiorre Casisi, Alberto de Nardi, Piero Pinamonti, Mauro Reini

» On the effect of eco-indicator selection on the conclusions obtained from an exergoenvironmental analysis (ID 275)
Tatiana Morosuk, George Tsatsaronis, Christopher Koroneos

» Optimisation of supply temperature and mass flow rate for a district heating network (ID 104)
Marouf Pirouti, Audrius Bagdanavicius, Jianzhong Wu, Janaka Ekanayake

» Optimization of energy supply systems in consideration of hierarchical relationship between design and operation (ID 389)
Ryohei Yokoyama, Shuhei Ose

» The fuel impact formula revisited (ID 279)
Cesar Torres, Antonio Valero

» The introduction of exergy analysis to the thermo-economic modelling and optimisation of a marine combined cycle system (ID 61)
George G. Dimopoulos, Chariklia A. Georgopoulou, Nikolaos M.P. Kakalis

» The relationship between costs and environmental impacts in power plants: an exergy-based study (ID 272)
Fontina Petrakopoulou, Yolanda Lara, Tatiana Morosuk, Alicia Boyano, George Tsatsaronis

» Thermo-ecological evaluation of biomass integrated gasification gas turbine based cogeneration technology (ID 441)
Wojciech Stanek, Lucyna Czarnowska, Jacek Kalina

» Thermo-ecological optimization of a heat exchanger through empirical modeling (ID 501)
Ireneusz Szczygieł, Wojciech Stanek, Lucyna Czarnowska, Marek Rojczyk

» Thermoeconomic analysis and optimization in a combined cycle power plant including a heat transformer for energy saving (ID 399)
Elizabeth Cortés Rodríguez, José Luis Castilla Carrillo, Claudia A. Ruiz Mercado, Wilfrido Rivera Gómez-Franco

» Thermoeconomic analysis and optimization of a hybrid solar-electric heating in a fluidized bed dryer (ID 400)
Elizabeth Cortés Rodríguez, Felipe de Jesús Ojeda Cámara, Isaac Pilatowsky Figueroa

» Thermoeconomic approach for the analysis of low temperature district heating systems (ID 208)
Vittorio Verda, Albana Kona

» Thermo-economic assessment of a micro CHP systems fuelled by geothermal and solar energy (ID 166)
Duccio Tempesti, Daniele Fiaschi, Filippo Gabuzzini

» Thermo-economic evaluation and optimization of the thermo-chemical conversion of biomass into methanol (ID 194)
Emanuela Peduzzi, Laurence Tock, Guillaume Boissonnet, François Marechal

» Thermoeconomic fuel impact approach for assessing resources savings in industrial symbiosis: application to Kalundborg Eco-industrial Park (ID 256)
Sergio Usón, Antonio Valero, Alicia Valero, Jorge Costa

» Thermoeconomics of a ground-based CAES plant for peak-load energy production system (ID 32)
Simon Kemble, Giampaolo Manfrida, Adriano Milazzo, Francesco Buffa

VOLUME IV

IV . 1 – FLUID DYNAMICS AND POWER PLANT COMPONENTS

» A control oriented simulation model of a multistage axial compressor (ID 444)
Lorenzo Damiani, Giampaolo Crosa, Angela Trucco

» A flexible and simple device for in-cylinder flow measurements: experimental and numerical validation (ID 181)
Andrea Dai Zotti, Massimo Masi, Marco Antonello

» CFD Simulation of Entropy Generation in Pipeline for Steam Transport in Real Industrial Plant (ID 543)
Goran Vučković, Gradimir Ilić, Mića Vukić, Milan Banić, Gordana Stefanović

» Feasibility Study of Turbo expander Installation in City Gate Station (ID 168)
Navid Zehtabiyan Rezaie, Majid Saffar-Avval

» GTL and RME combustion analysis in a transparent CI engine by means of IR digital imaging (ID 460)
Ezio Mancaruso, Luigi Sequino, Bianca Maria Vaglieco

» Some aspects concerning fluid flow and turbulence modeling in 4-valve engines (ID 116)
Zoran Stevan Jovanovic, Zoran Masonicic, Miroljub Tomic

IV . 2 – SYSTEM OPERATION CONTROL DIAGNOSIS AND PROGNOSIS

» Adapting the operation regimes of trigeneration systems to renewable energy systems integration (ID 188)
Liviu Ruieneanu, Mihai Paul Mircea

» Advanced electromagnetic sensors for sustainable monitoring of industrial processes (ID 145)
Uroš Puc, Andreja Abina, Anton Jeglič, Pavel Cevc, Aleksander Zidanšek

» Assessment of stresses and residual life of plant components in view of life-time extension of power plants (ID 453)
Anna Stoppato, Alberto Benato and Alberto Mirandola

» Control strategy for minimizing the electric power consumption of hybrid ground source heat pump system (ID 244)
Zoi Sagia, Constantinos Rakopoulos

» Exergetic evaluation of heat pump booster configurations in a low temperature district heating network (ID 148)
Torben Ommen, Brian Elmegaard

» Exergoeconomic diagnosis: a thermo-characterization method by using irreversibility analysis (ID 523)
Abraham Olivares-Arriaga, Alejandro Zaleta-Aguilar, Rangel-Hernández V. H, Juan Manuel Belman-Flores

» Optimal structural design of residential cogeneration systems considering their operational restrictions (ID 224)
Tetsuya Wakui, Ryohei Yokoyama

» Performance estimation and optimal operation of a CO2 heat pump water heating system (ID 344)
Ryohei Yokoyama, Ryosuke Kato, Tetsuya Wakui, Kazuhisa Takemura

» Performances of a common-rail Diesel engine fuelled with rapeseed and waste cooking oils (ID 213)
Alessandro Corsini, Valerio Giovannoni, Stefano Nardecchia, Franco Rispoli, Fabrizio Sciulli, Paolo Venturini

» Reduced energy cost through the furnace pressure control in power plants (ID 367)
Vojislav Filipović, Novak Nedić, Saša Prodanović

» Short-term scheduling model for a wind-hydro-thermal electricity system (ID 464)
Sérgio Pereira, Paula Ferreira, A. Ismael Freitas Vaz

VOLUME V

V . 1 – RENEWABLE ENERGY CONVERSION SYSTEMS

» A co-powered concentrated solar power Rankine cycle concept for small size combined heat and power (ID 276)
Alessandro Corsini, Domenico Borello, Franco Rispoli, Eileen Tortora

» A novel non-tracking solar collector for high temperature application (ID 466)
Wattana Ratismith, Anusorn Inthongkhum

» Absorption heat transformers (AHT) as a way to enhance low enthalpy geothermal resources (ID 311)
Daniele Fiaschi, Duccio Tempesti, Giampaolo Manfrida, Daniele Di Rosa

» Alternative feedstock for the biodiesel and energy production: the OVEST project (ID 98)
Matteo Prussi, David Chiaramonti, Lucia Recchia, Francesco Martelli, Fabio Guidotti

» Assessing repowering and update scenarios for wind energy converters (ID 158)
Till Zimmermann

» Biogas from mechanical pulping industry – potential improvement for increased biomass vehicle fuels (ID 54)
Mimmi Magnusson, Per Alvfors

» Biogas or electricity as vehicle fuels derived from food waste - the case of Stockholm (ID 27)
Martina Wikström, Per Alvfors

» Compressibility factor as evaluation parameter of expansion processes in organic Rankine cycles (ID 292)
Giovanni Manente, Andrea Lazzaretto

» Design of solar heating system for methane generation (ID 445)
Lucía Mónica Gutiérrez, P. Quinto Diez, L. R. Tovar Gálvez

» Economic feasibility of PV systems in hotels in Mexico (ID 346)
Augusto Sanchez, Sergio Quezada

» Effect of a back surface roughness on annual performance of an air-cooled PV module (ID 193)
Riccardo Secchi, Duccio Tempesti, Jacek Smolka

» Energy and exergy analysis of the first hybrid solar-gas power plant in Algeria (ID 176)
Fouad Khaldi

» Energy recovery from MSW treatment by gasification and melting technology (ID 393)
Fabrizio Strobino, Alessandro Pini Prato, Diego Ventura, Marco Damonte

» Ethanol production by enzymatic hydrolysis process from sugarcane biomass - the integration with the conventional process (ID 189)
Reynaldo Palacios-Bereche, Adriano Ensinas, Marcelo Modesto, Silvia Azucena Nebra

» Evaluation of gas in an industrial anaerobic digester by means of biochemical methane potential of organic municipal solid waste components (ID 57)
Isabella Pecorini, Tommaso Olivieri, Donata Bacchi, Alessandro Paradisi, Lidia Lombardi, Andrea Corti, Ennio Carnevale

» Exergy analysis and genetic algorithms for the optimization of flat-plate solar collectors (ID 423)
Soteris A. Kalogirou

» Experimental study of tar and particles content of the produced gas in a double stage downdraft gasifier (ID 487)
Ana Lisbeth Galindo Noguera, Sandra Yamile Giraldo, Rene Lesme-Jaén, Vladimir Melian Cobas, Rubenildo Viera Andrade, Electo Silva Lora

» Feasibility study to realize an anaerobic digester fed with vegetables matrices in central Italy (ID 425)
Umberto Desideri, Francesco Zepparelli, Livia Arcioni, Ornella Calderini, Francesco Panara, Matteo Todini

» Investigations on the use of biogas for small scale decentralized CHP applications with a focus on stability and emissions (ID 140)
Steven MacLean, Eren Tali, Anne Giese, Jörg Leicher

» Kinetic energy recovery system for sailing yachts (ID 427)
Giuseppe Leo Guizzi, Michele Manno

» Mirrors in the sky: status and some supporting materials experiments (ID 184)
Noam Lior

» Numerical parametric study for different cold storage designs and strategies of a solar driven thermoacoustic cooler system (ID 284)
Maxime Perier-Muzet, Pascal Stouffs, Jean-Pierre Bedecarrats, Jean Castaing-Lasvignottes

» Parabolic trough photovoltaic/thermal collectors. Part I: design and simulation model (ID 102)
Francesco Calise, Laura Vanoli

» Parabolic trough photovoltaic/thermal collectors. Part II: dynamic simulation of a solar trigeneration system (ID 488)
Francesco Calise, Laura Vanoli

» Performance analysis of downdraft gasifier - reciprocating engine biomass fired small-scale cogeneration system (ID 368)
Jacek Kalina

» Proposing offshore photovoltaic (PV) technology to the energy mix of the Maltese islands (ID 262)
Kim Trapani, Dean Lee Millar

» Research of integrated biomass gasification system with a piston engine (ID 414)
Janusz Kotowicz, Aleksander Sobolewski, Tomasz Iluk

» Start up of a pre-industrial scale solid state anaerobic digestion cell for the co-treatment of animal and agricultural residues (ID 34)
Francesco Di Maria, Giovanni Gigliotti, Alessio Sordi, Caterina Micale, Luisa Massaccesi

» The role of biomass in the renewable energy system (ID 390)
Ruben Laleman, Ludovico Balduccio, Johan Albrecht

» Vegetable oils of soybean, sunflower and tung as alternative fuels for compression ignition engines (ID 500)
Ricardo Morel Hartmann, Nury Nieto Garzón, Eduardo Morel Hartmann, Amir Antonio Martins Oliveira Jr, Edson Bazzo, Bruno Okuda, Joselia Piluski

» Wind energy conversion performance and atmosphere stability (ID 283)
Francesco Castellani, Emanuele Piccioni, Lorenzo Biondi, Marcello Marconi

V. 2 – FUEL CELLS

» Comparison study on different SOFC hybrid systems with zero-CO2 emission (ID 196)
Liqiang Duan, Kexin Huang, Xiaoyuan Zhang and Yongping Yang

» Exergy analysis and optimisation of a steam methane pre-reforming system (ID 62)
George G. Dimopoulos, Iason C. Stefanatos, Nikolaos M.P. Kakalis

» Modelling of a CHP SOFC power system fed with biogas from anaerobic digestion of municipal wastes integrated with a solar collector and storage units (ID 491)
Domenico Borello, Sara Evangelisti, Eileen Tortora

VOLUME VI

VI . 1 – CARBON CAPTURE AND SEQUESTRATION

» A novel coal-based polygeneration system cogenerating power, natural gas and liquid fuel with CO2 capture (ID 96)
Sheng Li, Hongguang Jin, Lin Gao

» Analysis and optimization of CO2 capture in a China's existing coal-fired power plant (ID 532)
Gang Xu, Yongping Yang, Shoucheng Li, Wenyi Liu and Ying Wu

» Analysys of four-end high temperature membrane air separator in a supercritical power plant with oxy-type pulverized fuel boiler (ID 442)
Janusz Kotowicz, Sebastian Stanisław Michalski

» Analysis of potential improvements to the lignite-fired oxy-fuel power unit (ID 413)
Marcin Liszka, Jakub Tuka, Grzegorz Nowak, Grzegorz Szapajko

» Biogas Upgrading: Global Warming Potential of Conventional and Innovative Technologies (ID 240)
Katherine Starr, Xavier Gabarrell Durany, Gara Villalba Mendez, Laura Talens Peiro, Lidia Lombardi

» Capture of carbon dioxide using gas hydrate technology (ID 103)
Beatrice Castellani, Mirko Filipponi, Sara Rinaldi, Federico Rossi

» Carbon dioxide mineralisation and integration with flue gas desulphurisation applied to a modern coal-fired power plant (ID 179)
Ron Zevenhoven, Johan Fagerlund, Thomas Björklöf, Magdalena Mäkelä, Olav Eklund

» Carbon dioxide storage by mineralisation applied to a lime kiln (ID 226)
Inês Sofia Soares Romão, Matias Eriksson, Experience Nduagu, Johan Fagerlund, Licínio Manuel Gando-Ferreira, Ron Zevenhoven

» Comparison of IGCC and CFB cogeneration plants equipped with CO2 removal (ID 380)
Marcin Liszka, Tomasz Malik, Michał Budnik, Andrzej Ziębik

» Concept of a "capture ready" combined heat and power plant (ID 231)
Piotr Henryk Lukowicz, Lukasz Bartela

» Cryogenic method for H2 and CH4 recovery from a rich CO2 stream in pre-combustion CCS schemes (ID 508)
Konstantinos Atsonios, Kyriakos D. Panopoulos, Angelos Doukelis, Antonis Koumanakos, Emmanuel Kakaras

» Design and optimization of ITM oxy-combustion power plant (ID 495)
Surekha Gunasekaran, Nicholas David Mancini, Alexander Mitsos

» Implementation of a CCS technology: the ZECOMIX experimental platform (ID 222)
Antonio Calabrò, Stefano Cassani, Leandro Pagliari, Stefano Stendardo

» Influence of regeneration condition on cyclic CO2 capture using pre-treated dispersed CaO as high temperature sorbent (ID 221)
Stefano Stendardo, Antonio Calabrò

» Investigation of an innovative process for biogas up-grading – pilot plant preliminary results (ID 56)
Lidia Lombardi, Renato Baciocchi, Ennio Antonio Carnevale, Andrea Corti, Giulia Costa, Tommaso Olivieri, Alessandro Paradisi, Daniela Zingaretti

» Method of increasing the efficiency of a supercritical lignite-fired oxy-type fluidized bed boiler and high-temperature three - end membrane for air separation (ID 438)
Janusz Kotowicz, Adrian Balicki

» Monitoring of carbon dioxide uptake in accelerated carbonation processes applied to air pollution control residues (ID 539)
Felice Alfieri, Peter J Gunning, Michela Gallo, Adriana Del Borghi, Colin D Hills

» Process efficiency and optimization of precipitated calcium carbonate (PCC) production from steel converter slag (ID 114)
Hannu-Petteri Mattila, Inga Grigaliūnaitė, Arshe Said, Sami Filppula, Carl-Johan Fogelholm, Ron Zevenhoven

» Production of Mg(OH)2 for CO2 Emissions Removal Applications: Parametric and Process Evaluation (ID 245)
Experience Ikechukwu Nduagu, Inês Romão, Ron Zevenhoven

» Thermodynamic analysis of a supercritical power plant with oxy type pulverized fuel boiler, carbon dioxide capture system (CC) and four-end high temperature membrane air seprator (ID 411)
Janusz Kotowicz, Sebastian Stanisław Michalski

VI . 2 – PROCESS INTEGRATION AND HEAT EXCHANGER NETWORKS

» A multi-objective optimization technique for co- processing in the cement production (ID 42)
Maria Luiza Grillo Renó, Rogério José da Silva, Mirian de Lourdes Noronha Motta Melo, José Joaquim Conceição Soares Santos

» Comparison of options for debottlenecking the recovery boiler at kraft pulp mills – Economic performance and CO2 emissions (ID 449)
Johanna Jönsson, Karin Pettersson, Simon Harvey, Thore Berntsson

» Demonstrating an integral approach for industrial energy saving (ID 541)
René Cornelissen, Geert van Rens, Jos Sentjens, Henk Akse, Ton Backx, Arjan van der Weiden, Jo Vandenbroucke

» Maximising the use of renewables with variable availability (ID 494)
Andreja Nemet, Jiri Jaromír Klemeš, Petar Sabev Varbanov, Zdravko Kravanja

» Methodology for the improvement of large district heating networks (ID 46)
Anna Volkova, Vladislav Mashatin, Aleksander Hlebnikov, Andres Siirde

» Optimal mine site energy supply (ID 306)
Monica Carvalho, Dean Lee Millar

» Simulation of synthesis gas production from steam oxygen gasification of Colombian bituminous coal using Aspen Plus® (ID 395)
John Jairo Ortiz, Juan Camilo González, Jorge Enrique Preciado, Rocío Sierra, Gerardo Gordillo

VOLUME VII

VII . 1 – BUILDING, URBAN AND COMPLEX ENERGY SYSTEMS

» A linear programming model for the optimal assessment of sustainable energy action plans (ID 398)
Gianfranco Rizzo, Giancarlo Savino

» A natural gas fuelled 10 kW electric power unit based on a Diesel automotive internal combustion engine and suitable for cogeneration (ID 477)
Pietro Capaldi

» Adjustment of envelopes characteristics to climatic conditions for saving heating and cooling energy in buildings (ID 430)
Christos Tzivanidis, Kimon Antonopoulos, Foteini Gioti

» An exergy based method for the optimal integration of a building and its heating plant. Part 1: comparison of domestic heating systems based on renewable sources (ID 81)
Marta Cianfrini, Enrico Sciubba, Claudia Toro

» Analysis of different typologies of natural insulation materials with economic and performances evaluation of the same buildings (ID 28)
Umberto Desideri, Daniela Leonardi, Livia Arcioni

» Complex networks approach to the Italian photovoltaic energy distribution system (ID 470)
Luca Valori, Giovanni Luca Giannuzzi, Tiziano Squartini, Diego Garlaschelli, Riccardo Basosi

» Design of a multi-purpose building "to zero energy consumption" according to European Directive 2010/31/CE: Architectural and plant solutions (ID 29)
Umberto Desideri, Livia Arcioni, Daniela Leonardi, Luca Cesaretti ,Perla Perugini, Elena Agabitini, Nicola Evangelisti

» Effect of initial systems on the renewal planning of energy supply systems for a hospital (ID 107)
Shu Yoshida, Koichi Ito, Yoshiharu Amano, Shintaro Ishikawa, Takahiro Sushi, Takumi Hashizume

» Effects of insulation and phase change materials (PCM) combinations on the energy consumption for buildings indoor thermal comfort (ID 387)
Christos Tzivanidis, Kimon Antonopoulos, Eleutherios Kravvaritis

» Energetic evaluation of a smart controlled greenhouse for tomato cultivation (ID 150)
Nickey Van den Bulck, Mathias Coomans, Lieve Wittemans, Kris Goen, Jochen Hanssens, Kathy Steppe, Herman Marien, Johan Desmedt

» Energy networks in sustainable cities: temperature and energy consumption monitoring in urban area (ID 190)
Luca Giaccone, Alessandra Guerrisi, Paolo Lazzeroni and Michele Tartaglia

» Extended exergy analysis of the economy of Nova Scotia, Canada (ID 215)
David C Bligh, V.Ismet Ugursal

» Feasibility study and design of a low-energy residential unit in Sagarmatha Park (Nepal) for envirnomental impact reduction of high altitude buildings (ID 223)
Umberto Desideri, Stefania Proietti, Paolo Sdringola, Elisa Vuillermoz

» Fire and smoke spread in low-income housing in Mexico (ID 379)
Raul R. Flores-Rodriguez, Abel Hernandez-Guerrero, Cuauhtemoc Rubio-Arana, Consuelo A. Caldera-Briseño

» Optimal lighting control strategies in supermarkets for energy efficiency applications via digital dimmable technology (ID 136)
Salvador Acha, Nilay Shah, Jon Ashford, David Penfold

» Optimising the arrangement of finance towards large scale refurbishment of housing stock using mathematical programming and optimisationg (ID 127)
Mark Gerard Jennings, Nilay Shah, David Fisk

» Optimization of thermal insulation to save energy in buildings (ID 174)
Milorad Bojić, Marko Miletić, Vesna Marjanović, Danijela Nikolić, Jasmina Skerlić

» Residential solar-based seasonal thermal storage system in cold climate: building envelope and thermal storage (ID 342)
Alexandre Hugo and Radu Zmeureanu

» Simultaneous production of domestic hot water and space cooling with a heat pump in a Swedish Passive House (ID 55)
Johannes Persson, Mats Westermark

» SOFC micro-CHP integration in residential buildings (ID 201)
Umberto Desideri, Giovanni Cinti, Gabriele Discepoli, Elena Sisani, Daniele Penchini

» The effect of shading of building integrated photovoltaics on roof surface temperature and heat transfer in buildings (ID 83)
Eftychios Vardoulakis, Dimitrios Karamanis

» The influence of glazing systems on energy performance and thermal comfort in non-residential buildings (ID 206)
Cinzia Buratti, Elisa Moretti, Elisa Belloni

» Thermal analysis of a greenhouse heated by solar energy and seasonal thermal energy storage in soil (ID 405)
Yong Li, Jin Xu, Ru-Zhu Wang

» Thermodynamic analysis of a combined cooling, heating and power system under part load condition (ID 476)
Qiang Chen, Jianjiao Zheng, Wei Han, Jun Sui, Hong-guang Jin

VII . 2 – COMBUSTION, CHEMICAL REACTORS

» Baffle as a cost-effective design improvement for volatile combustion rate increase in biomass boilers of simple construction (ID 233)
Borivoj Stepanov, Ivan Pešenjanski, Biljana Miljković

» Characterization of CH4-H2-air mixtures in the high-pressure DHARMA reactor (ID 287)
Vincenzo Moccia, Jacopo D'Alessio

» Development of a concept for efficiency improvement and decreased NOx production for natural gas-fired glass melting furnaces by switching to a propane exhaust gas fired process (ID 146)
Jörn Benthin, Anne Giese

» Experimental analysis of inhibition phenomenon management for Solid Anaerobic Digestion Batch process (ID 348)
Francesco Di Maria, Giovanni Gigliotti, Alessio Sordi, Caterina Micale, Claudia Zadra, Luisa Massaccesi

» Experimental investigations of the combustion process of n-butanol/diesel blend in an optical high swirl CI engine (ID 85)
Simona Silvia Merola, G. Valentino, C. Tornatore, L. Marchitto , F. E. Corcione

» Flameless oxidation as a means to reduce NOx emissions in glass melting furnaces (ID 141)
Jörg Leicher, Anne Giese

» Mechanism of damage by high temperature of the tubes, exposed to the atmosphere characteristic of a furnace of pyrolysis of ethane for ethylene production in the petrochemical industry (ID 65)
Jaqueline Saavedra Rueda, Francisco Javier Perez Trujillo, Lourdes Isabel Meriño Stand, Harbey Alexi Escobar, Luis Eduardo Navas, Juan Carlos Amezquita

» Steam reforming of methane over Pt/Rh based wire mesh catalyst in single channel reformer for small scale syngas production (ID 317)
Haftor Orn Sigurdsson, Søren Knudsen Kær

ECOS 2012

VOLUME VIII

A Multi-Criteria Decision Analysis Tool to Support Electricity Planning

Fernando Ribeiro [a], ***Paula Ferreira*** [b], ***Madalena Araújo*** [c]

[a] *Department of Production and Systems, University of Minho, Guimarães, Portugal, fernandor@dps.uminho.pt*
[b] *Department of Production and Systems, University of Minho, Guimarães, Portugal, paulaf@dps.uminho.pt*
[c] *Department of Production and Systems, University of Minho, Guimarães, Portugal, mmaraujo@dps.uminho.pt*

Abstract: A Multi-Criteria Decision Analysis (MCDA) tool was designed to support the evaluation of different electricity production scenarios. The MCDA tool is implemented in Excel worksheet and uses information obtained from a mixed integer optimization model. Given the input, the MCDA allowed ranking different scenarios relying on their performance on 13 criteria covering economic, job market, quality of life of local populations, technical and environmental issues. The criteria were weighted using both direct weights and trade-off analysis. In this paper, scenarios for the case of the Portuguese electricity system are presented, as well as the results of the evaluation, using the MCDA tool, relying on the input from a group of academics with background in economics, engineering and environment.

Keywords: Energy decision making, electricity generation, MCDA, Sustainable Development.

1. Introduction

Over the last two decades, international treaties, such as Kyoto Protocol, have been signed, and strategies to mitigate CO_2 emissions have arisen in all the developed world nations. At the same time, Sustainable Development is becoming part of political discourse in the European Union. According to the European Union Sustainable Development Strategy (EUSDS), Sustainable Development envisages the "continuous improvement of the quality of life of citizens through sustainable communities that manage and use resources efficiently and tap the ecological and social innovation potential of the economy, so as to ensure prosperity, environmental protection and social cohesion" [1]. As a result, the electricity production planning gets more constrained than before, resulting in a multi-objective problem [2]. What traditionally was simply a cost minimizing problem should now be evaluated also under Sustainable Development criteria.

In this paper a Multi-Criteria Decision Analysis tool, designed for the evaluation of different electricity generation scenarios, is presented. When using multi-criteria decision methodologies, one has to have in mind that best solutions for some decision makers may not be universal best solutions, as results are made upon personal judgement of different criteria. In the present work, a panel of experts on energy systems was invited to map the diversity of opinions and preferences for the future of the Portuguese electricity system. The use of the MCDA tool was demonstrated for the evaluation of possible electricity scenarios drawn for Portugal in 2020.

The criteria used cover Sustainable Development (social, cost and environmental) issues among others like visual impacts and technical issues of power systems, as addressed in section 3.2. The criteria were drawn from both interviews conducted in previous work [3] and from the literature.

Figure 1 summarizes the methodological approach to the problem. The two main blocks of the methodology are Scenario Generation and Scenario Evaluation (MCDA Tool). Sections 2 and 3

Corresponding author: Paula Ferreira, Email: paulaf@dps.uminho.pt

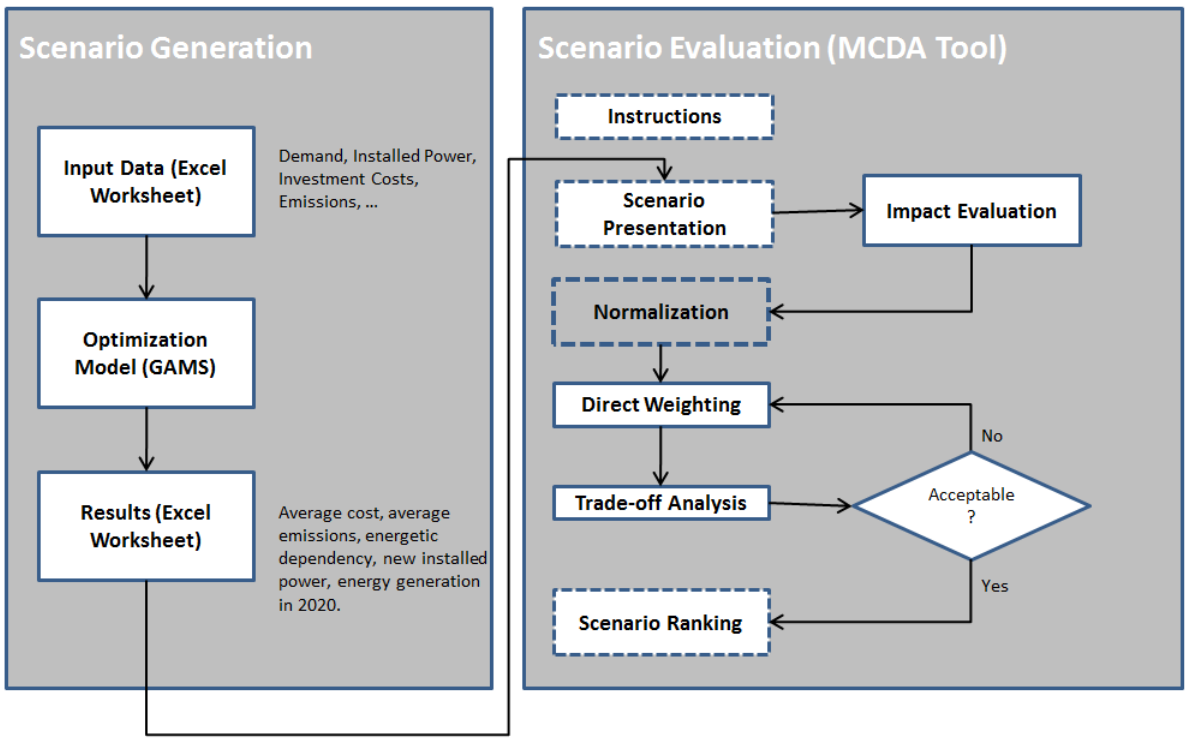

Figure 1: Evaluation of scenarios for electricity production, with MCDA evaluation

are dedicated to each one of these topics. As the Scenario Generation addesses the future of the Portuguese power generation system, the remainder of this section overviews this particular case.

1.1. Power Generation in Portugal

Electricity in Portugal is mainly generated from large hydro, thermal and wind power, as can be seen in Figure 2. Thermal power is mostly provided with coal and CCGT (combined cycle gas turbines) power plants. Special Regime Production include all the technologies benefiting from feed-in tariffs, which are in Figure 2 divided in Wind power and "Other SRP".

The Portuguese electricity system is strongly influenced by the rainfall characteristics. Although the large hydro power installed capacity remained almost unchanged between 2006 and 2010, in fact the hydro electricity production suffered strong variations.[1]

In 2007, the Portuguese state launched a new plan for installing more hydro power, known as PNBEPH (Plano Nacional de Barragens de Elevado Potencial Hidroeléctrico)[4]. It aimed to reduce the unused hydro power potential from 54% to 33% until 2020, installing new 2059 MW. This was expected to be achieved by two means: increasing installed power of already existing facilities (909 MW), and building ten new hydro power plants totaling 1150 MW of installed power. Among these projects, some include pumping capacity. The use of pumping was justified to the need to complement additional wind power to be installed: given that wind farms may produce more in off-peak hours when electricity prices are lower, this energy can be used to pump water back to dams, so that hydro power can be generated during the hours of higher consumption and higher electricity prices. In 2007 the PNBEPH forecasted that in 2010 there would be 5100 MW of installed wind power, which contrasted

[1]The yearly variation of hydro power production is reflected on the so-called "hydraulicity factor", which for an average year the equals 1.

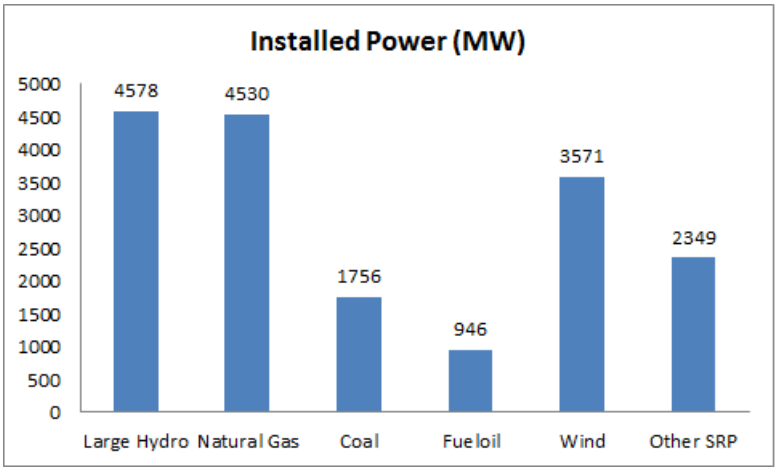

Figure 2: Installed power in Portugal, 2010. Own elaboration from www.ren.pt data. "Other SRP" include non-renewable and renewable cogeneration, biomass, small hydro, photovoltaics and wave power.

with the 3751 MW achieved in reality [5]. As a result, the completion of these plans is constrained by political and other factors (such as the fall of electricity consumption in 2010 and 2011). The future of the Portuguese power system remains uncertain, and in section 2.3 some possible scenarios for 2020 are explored.

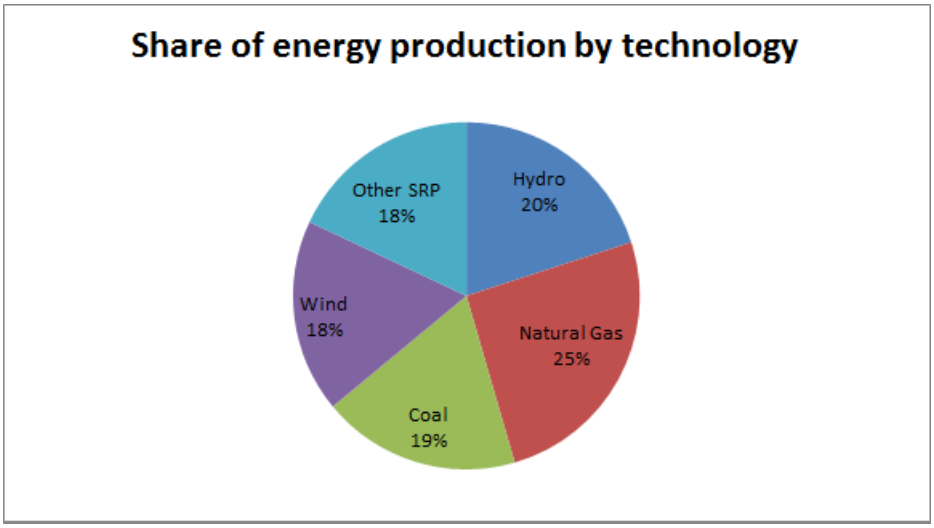

Figure 3: Electricity generation in Portugal, 2010. Own elaboration from www.ren.pt data. In order to present the numbers for a typical rainfall year, the numbers for hydro power were divided by the hidraulicity factor, which in 2010 was 1.31 [6]. The exceeding energy was assumed to be covered equally by coal and natural gas.

2. Scenario Generation

2.1. Model description

In this section the Scenario Generation phase of the methodology mentioned in Figure 1 is addressed. In short, a Mixed Integer Linear Programming (MILP) model, programmed in GAMS (General Algebraic Modeling System) was used. The input data is given in an Excel file, as well as the final results.

For the detailed description of the used model, see [7]. The source code was used to create scenarios with different characteristics, based on the cost optimization of the electricity system. These scenarios represent different possible futures for the Portuguese power generation system in a 10 year range, departing from the present characteristics of the system. A scenario is charaterized by a set of newly installed power plants of each technology, that, together with the already installed ones, will supply the electricity demand. The technologies considered as variables were hydro power, wind, natural gas and coal; on the other hand non-wind Special Regime Production was assumed to remain constant for every scenario. The remainder of this subsection contains complementary information of the given reference [7].

The demand and peak load data are presented in the Excel input file. The scenarios depend on the demand of electricity, $D_{t,m}$, which were computed according to recent forecasts, information available in the Portuguese National Renewable Energy Action Plans [8]. According to this data, demand, which was about 52 TWh in 2010, will increase 12 TWh in 10 years. The rate of the peak load growth was adjusted accordingly to the rate of consumption growth.

The present values of non-Wind Special Regime Production (SRP) installed power and generated energy, as well as expected growth are computed in the excel input worksheet, according to the information collected in the report available in the Portuguese Renewable Action Plan ([8], pages 117 and 118). Non-wind SRP includes the following technologies: non-renewable cogeneration, biomass, small hydro, photovoltaics and wave power. Therefore, a new parameter was added in the code, $srp_renewable_ratio_{t,m}$, to express the monthly percentage of renewable energy among the SRP. As addressed later in this section, this value is necessary to calculate the percentage of renewable energy generated in a given solution:

$$srp_renewable_ratio_{t,m,i} = 1 - \frac{PSRP_{t,m,i=non_renewable_cogeneration}}{PSRP_{t,m,i}} \tag{1}$$

where $PSRP_{t,m,i}$ refers to the energy generated from SRP source i, in the month m of the year t.

In order to account for the CO_2 emissions of SRP, the monthly generation of non-renewable cogeneration was multiplied by the same CO_2 emissions factor that affects CCGT groups. The value of $srp_average_emissions$ was thus calculated in order to express the emissions from the SRP in the planning period (2011 to 2020).

For calculating the SRP costs, [9] values were used (exchange ratio of 1 USD = 0.7325 EURO). From these values, the overall SRP levelized costs, $srp_levelized_cost$ were obtained, for the whole planning period:

$$srp_levelized_cost = \sum_{t,m,i} c_i \frac{P_{t,m,i}}{PSRP_{t,m,i}} \tag{2}$$

where c_i stands for the levelized cost for each SRP technology and $P_{t,m,i}$ is the monthly energy produced by SRP technology i in the month m of year t.

2.2. Scenarios

A variety of scenarios to use in the MCDA tool can be generated, and these are solutions for the model. In table 1, five possible scenarios of electricity generation in the year 2020 are presented, aiming to represent five different strategies, representative of different energy policy trends: investment in natural gas, investment in coal, investment in a mix of hydro and gas, investment in a mix of hydro and wind, and a moderated scenario following a business-as-usual approach. Obviously, none of these scenarios is likely to happen in this exact form due to the infinity of possible and distinct

combinations. However, given the present state of the Portuguese electricity system, these are five possible strategies representative of different energy policy trends. The evaluation of more scenarios demands additional input information and higher response time on the MCDA tool. In order to ensure the effective participation of experts it was decided to keep the number of scenarios low.

As the objective function of the model is the minimization of the costs, different constraints used to diversify the scenarios were created. These constraints were of two types: allowing the program to install or not power plants of a specific technology, and, on the other hand, a renewable energy quota to be met in 2020. Not using these constraints would result in the model covering the growing demand by installing only new coal power plants, the least costly solution.

Table 1: Characterization of scenarios

	Constraints		**Results**			
Scenario	**Minimum Renewable Quota**	**New installed technologies**	**New installed power**	**Cost (euro per MWh)**	**Emissions (CO2 ton per GWh)**	**External energy Dependency**
Base	45%	All technologies allowed	700MW coal, 1000MW hydro, 4400MW wind, 1180MW other SRP (all SRP excluding wind power)	25.69	262	30%
Natural Gas	Turned off	Only CCGT allowed	2350MW natural gas, 1180MW other SRP	25.24	294	53%
Coal	Turned off	Turned off	2550MW coal, 1180MW other SRP	23.75	360	55%
Hydro-Gas	45%	Only CCGT and hydro power allowed	2050MW natural gas, 2000MW hydro, 1180MW other SRP	25.96	286	45%
Maximum Renewable	70%	No coal or CCGT allowed	2000MW hydro, 4400MW wind, 1180MW other SRP	26.37	250	28%

The ”Coal” scenario is the least costly one, but also leads to the highest external energy dependency (that is, highest share of coal and natural gas) and presents the highest CO_2 emissions. The other extreme case, presenting lowest external energy dependency and less CO_2 emissions is the ”Maximum Renewable” scenario, which costs are about 11% higher than for the ”Coal” scenario.

3. Scenario Evaluation Using the Multi-Criteria Decision Analysis Tool

The MCDA tool[2] is presented on an Excel worksheet and aims to rank the suitability of electricity production scenarios according to 13 criteria. In the remainder of this section, firstly the methodology is exposed, then the MCDA tool is presented and finally applied to a case study, using the five scenarios presented in the previous section.

3.1. Methodology

A vast literature for MCDA applications to energy planning exists (see for example [10] and [11] for an overview). The proposed methodology could be summarized as direct weighting with an additive

[2]The tool is available for download in http://sepp.dps.uminho.pt/.

value function for amalgamation. As a result, it involves three phases, already mentioned in Figure 1: Impact Evaluation, Direct Weighting and Trade-off Analysis.

Impact Evaluation is the phase where a score, $score_{s,c}$ is assigned to each scenario s and criteria c. These values are then normalized, using a linear function $v_{s,c}$, so that the best values become 1 and the worst values become 0.

The user then assigns directly weights w_c to each criteria c. Finally, for every criteria c, trade-offs are presented in terms of costs, while the user is still able to change weights according to his perceptions.

The final value for the scenario s is calculated according to the Additive Value Function (AVF), as follows:

$$AVF_s = \sum w_{c_i} \times v_{s,c_i} \tag{3}$$

where the higher the value, the better the solution is.

A brief example is now presented to illustrate the calculation of a trade-off: consider, from the above scenarios, that the user is weighting only two criteria: costs and external dependency. Taking into account that "Coal" presents least cost and highest energy dependency, the opposite case of "Maximum Renewable", the normalization of these criteria would consist in $v_{coal,cost}$=1, $v_{max_renew,cost}$=0, $v_{coal,dependency}$=0, $v_{max_renew,dependency}$=1.

As can be seen in Table 2, if only two criteria are weighted and the user gives the same importance to the costs and the energy dependency, he assumes implicitly that for him it is indifferent to choose scenario "Coal" or "Maximum Renewable" scenarios. Here the notion of trade-off appears: for the user, the energy dependency of the "Maximum Renewable" scenario is worth 2,62 euro/MWh, which is the difference in cost between the scenario "Maximum Renewable" and "Coal" (26,37 minus 23,75). The calculation of the trade-off $T_{s,c}$ is performed according to the following equation:

$$T_{s,c} = \frac{w_c}{w_{cost}} \times score_{s,c} \times (26,37 - 23,75) \tag{4}$$

Since $T_{s,c}$ is already multiplied by the range of the price (the parcel on the right), its value is given in euro/MWh. The user is always given the % of the costs that this increment represents in relation of the coal solution cost: in the case of the example where costs and dependency have the same weight, T=2,62 euro/MWh and 2,62/23,75 equals 11,01%.

It is worthy observing that when the weight of the cost is equal to the weight of the external energy dependency, the scenario with best performance is the "Base", with AVF=94,79.

In case the user gives the costs a weight twice the energy dependency, he would value the energy dependency in 1,31 euro/MWh (or 5,5%) and in this case the "Coal" scenario performs better than any other.

Table 2: Calculation of additive value function (AVF) by weighting two criteria

	Scenario s				
Criteria c	**Base**	**Natural Gas**	**Coal**	**Hydro-Gas**	**Maximum Renewable**
$score_{s,cost}$	25,69	25,24	23,75	25,96	26,37
$v_{s,cost}$	0,26	0,43	1	0,15	0
$score_{s,dependency}$	30%	53%	55%	47%	28%
$v_{s,dependency}$	0,93	0,07	0	0,3	1
	w_{cost}**=**$w_{dependency}$**=80**				
AVF_s	94,79	40,47	**80**	36,09	**80**
	w_{cost}**=100,** $w_{dependency}$**=50**				
AVF_s	72,19	46,88	100	30,30	50
	w_{cost}**=40,** $w_{dependency}$**=80**				
AVF_s	84,43	23,20	40	29,90	80

3.2. The MCDA tool

The proposed MCDA tool is presented in an Excel Workbook with five Sheets, as follows:

1. General Instructions The purpose of the tool is presented, as well as a summary of each of the following pages.

2. Scenarios The scenarios are presented in the form of graphics of installed power and produced electricity. Energy dependency ratio, CO2 emissions and annualized costs are also displayed graphically.

3. Instructions Instructions for the following sheet are presented, along with an example.

4. Impact Evaluation and Weighting Here the user is presented with the 13 criteria, along with explanations of every one of them. The user then fills the required cells, according to what he percepts to be the impacts generated by each scenario. Trade-offs are presented.

5. Results Results are printed: both ranking of scenarios and contribution of each criterion is given.

In the remainder of this section the information on the sheet *Impact Evaluation and Weighting* is introduced.

The criteria, C_i, and their description, are given as follows in Table 3. Since not all the impacts can be easily agreed upon, it was decided that the user might play a role on valuing them, as detailed in Table 3, column "Scenario score $i_{s,c}$".

Information of investment, operation & maintenance of the whole group of power plants is included in a single cost criterion. Positive impacts in industry, job creation and dependency on foreign fossil fuels have been an international concern for sustainable energy decisions [11] [10] with implications at national level [8]. Diversification of the electricity mix is also seen as important for sustainability goals [12] contributing to the security of supply. Local income, visual and noise impacts, as well as land use and public health were identified as important issues for local populations' standards of living, by the authors [13]. It is sometimes argued that the intermittency of the renewables imply they are overrated in levelized costs [14]: therefore, a criteria which accounts for the dispatchable rate of power on each solution was included. According to [15], the transmission system expansion requirements may be larger when renewable energy shares are higher; as the scenarios vary respecting

to that aspect, the criteria was proposed to be evaluated. Given the importance that CO_2 emissions play in the economy nowadays, this criterion was also included.

Table 3: Description of the criteria used in the MCDA

C_i	**Name**	**Description**	**Scenario score** $i_{s,c}$
C_1	Costs	Sum of fixed and variable costs, divided by the total electricity produced during the planning period. The fixed costs are related with the investment cost applied to the new power plants and also with all fixed O&M costs. The variable costs include fuel and variable O&M costs for new and previously installed power plants.	Values in €/MWh, obtained from the MILP model. *User can not change values*.
C_2	National Industry	Impact of the scenario on the dynamics of the national industry.	Score in ordinal scale, ranging from 1 (worst) to 5 (best). *Requires user to attribute values according to own perception*.
C_3	Energy Dependency	Rate of dependency on foreign sources in year 2020, calculated as the sum of energy produced in thermal power plants (coal, natural gas and non-renewable cogeneration) divided by the total energy amount produced.	Values in %, obtained from the MILP model. *User can not change values*.
C_4	Employment	Employment created by the construction, operation and maintenance of the power plants.	Values are number of jobs. Obtained from the MILP model, based on [16]. *Although values are given, the user may attribute different values according to own perception*.
C_5	Visual Impact	Impact caused by the construction of new power plants upon the sightseeing.	Score in ordinal scale, ranging from 1 (worst) to 5 (best). *Requires user to attribute values according to own perception*.
C_6	Noise	Noise impact caused in neighbor areas by the new infra-structures.	Score in ordinal scale, ranging from 1 (worst) to 5 (best), based on [17]. *Although values are given, user may attribute values different according to own perception*.

C_7	Local Income	Rents originated by land use, for both public and private sectors.	Score in ordinal scale, ranging from 1 (worst) to 5 (best). *Requires user to attribute values according to own perception.*
C_8	Diversity of Mix	Diversity of installed power, calculated according to the Shannon-Wiener Index.	Higher values are better. Obtained from the MILP model, based on [18]. *User can not change values.*
C_9	Rate of Dispatchable Power	Ratio between the sum of installed power of coal, CCGT, dam hydro power plants, and all the installed power.	Score is given in %. Obtained from the MILP model. *User does not change values.*
C_{10}	Investment in Transmission Network	Additional investments required by the scenario. It was assumed that wind power has the worst impact, followed by hydro power, and no additional investment is required by natural gas and coal power plants.	Score in ordinal scale, ranging from 1 (worst) to 5 (best). *Although the values are given, the user may attribute different values according to own perception.*
C_{11}	CO_2 Emissions	Ratio between CO_2 emissions and the total electricity generated in the overall planning period.	Values are given in tons of CO_2 per GWh of electricity produced in the planning period. Obtained from the MILP model. *User can not change values.*
C_{12}	Land Use	Amount of land which becomes unusable by the scenario.	Values are given in 1000 km2, based on [16]. Obtained from the MILP model. *User can not change values.*
C_{13}	Public Health	Contamination of air, water, and general impact on public health.	Score is based on [17]. Obtained from the MILP model. *User can not change values.*

Figure 4 presents an example of the user's views of the MCDA tool for the C_2 criterion (National Industry). The scale for this criterion ranges from 1 (Low dynamics in industry) to 5 (Leadership of industry, resulting in capacity for exporting), and the user has assigned the following impacts for $I_{s,c}$: $I_{base,national_industry}$=4, $I_{natural_gas,national_industry}$=2, $I_{coal,national_industry}$=2, $I_{hydro-gas,national_industry}$=3, $I_{maximum_renewable,national_industry}$=5. The blue cell is the weight of the criterion, assigned as 20 in the example. The information displayed in the plot indicates that the user accepts to increase the costs in 2.20%, in order to increase the national industry dynamics from score 2 to score 5. In other words, the user wishes to increase dynamics national industry from "coal" or "national gas" levels, to the "maximum renewable" levels, and is willing to pay additional costs of 2.2% for that change. It is also implicit that the user is willing to pay more 1.47% to increase from score 2 to 4, and 0.73% to increase from 2 to 3.

Finally, the *Results* sheet contains two plots, as can be seen on Figure 5: the one on the left, showing the overall ranking for the scenarios, and the one on the right showing the contribution of each crite-

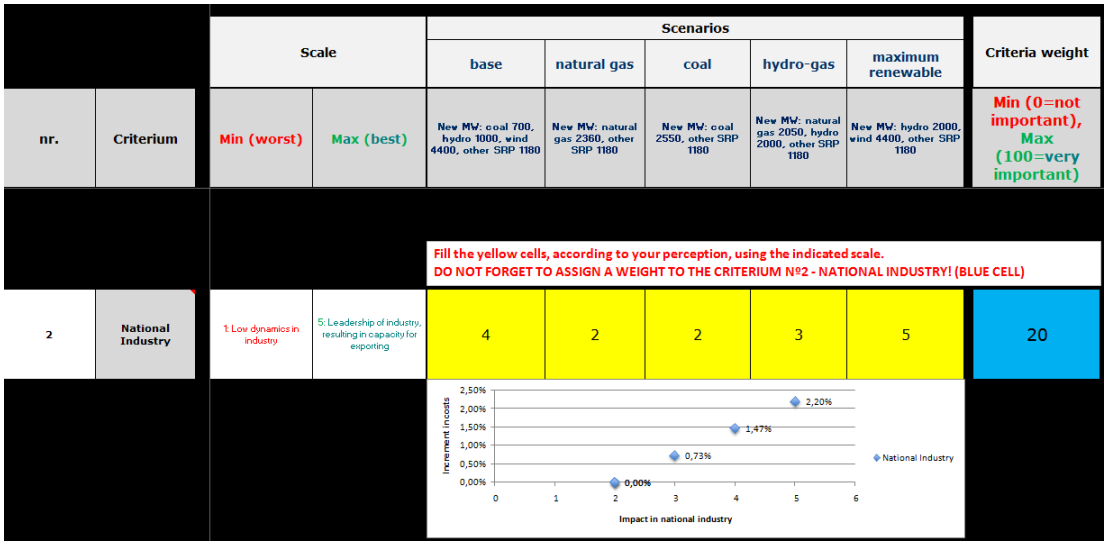

Figure 4: MCDA tool environment (Excel Sheet 4): Impacts and Criteria Weighting

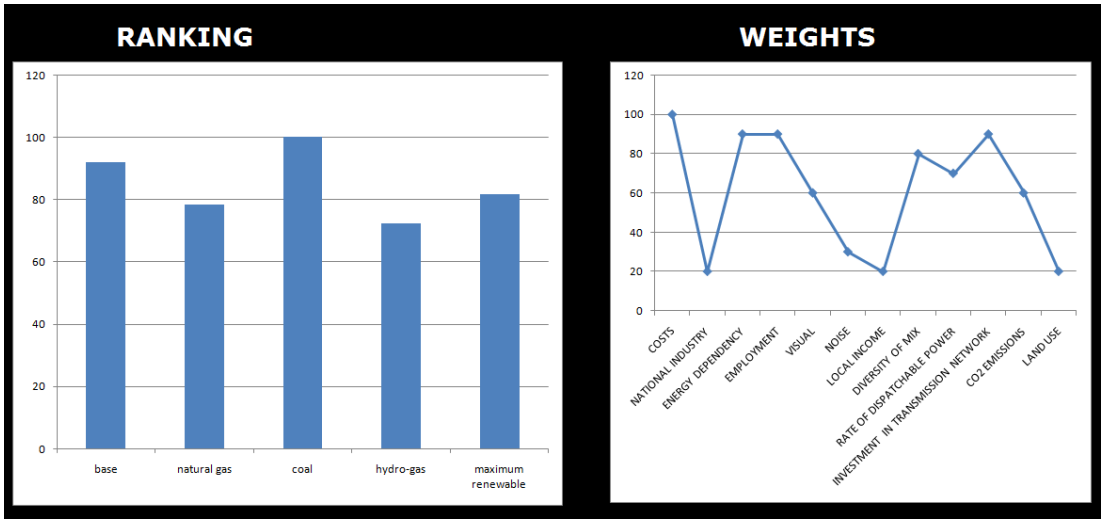

Figure 5: MCDA tool environment (Excel Sheet 5): Results. Here the user can validate his perceptions.

rion. The ranking is scaled so that the best scenario is scored by 100. On the given example, ”coal” scenario is the most rated, while the ”Cost” criterion is assigned as the most important.

4. Results

In this section the results are presented. The collaboration with academics took place in two phases. In the first place, the issues that should be included in power planning decision-making were collected with semi-structured interviews constructed over questions raised in the literature. The results of this exploratory research are described in section 2 of this report and published in [3]. In a second phase, the MCDA tool was sent by e-mail to approximately 60 academics, with background in energy, either from Economics or Engineering (Power Systems/Energy/Environment/Mechanical). The eleven experts that proceeded to the evaluation of the scenarios did it in a period of six weeks. Six of them

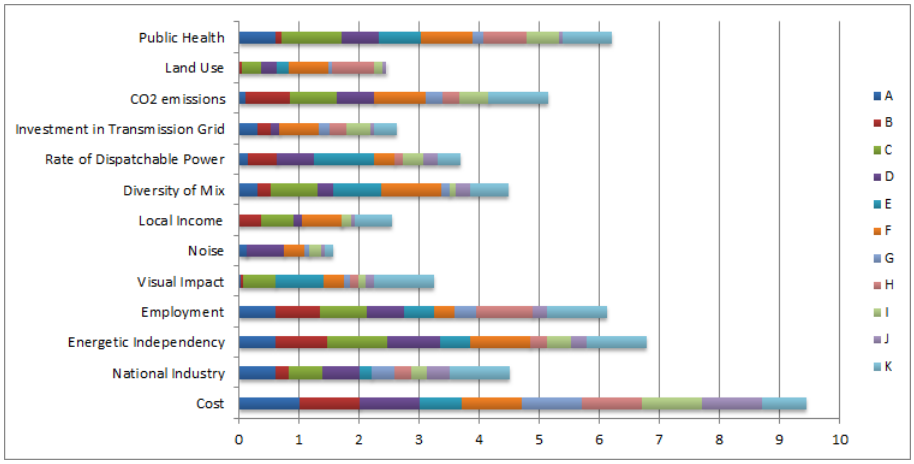

Figure 6: Aggregation of results

responded to the tool by themselves, while the other five respondents were aided in a personal interview, which they found helpful and less time-consuming. Table 4 presents the weights assigned by each respondent to each criterion.

Table 4: Criteria weights.

	Respondents										
Criterion	**A**	**B**	**C**	**D**	**E**	**F**	**G**	**H**	**I**	**J**	**K**
Costs	50	80	25	80	70	100	100	80	80	80	80
National Industry	30	20	50	50	20	25	37	30	25	30	100
Energy Independency	30	70	70	70	50	100	0	30	35	20	100
Employment	30	60	60	50	50	50	37	75	35	20	100
Visual Impact	1	5	50	0	80	50	9	20	15	10	100
Noise	6	2	25	50	0	50	9	10	20	5	30
Local income	0	30	50	10	0	75	0	10	17	5	70
Diversity of Mix	15	20	60	20	80	100	15	10	12	20	70
Rate of Dispatchable Power	7	40	25	50	100	50	30	20	30	20	50
Investment in the Transmission Grid	15	20	25	10	0	75	18	30	35	5	50
CO_2 emissions	5	60	60	50	0	90	27	30	40	0	100
Land Use	0	5	40	20	20	75	5	60	15	5	20
Public Health	30	10	70	50	70	90	18	60	45	5	85

Figure 6 aggregates the results, that were normalized for each respondent, so that the highest weight equals 1 and the lowest equals 0. Costs prevailed as the most important criterion, followed by energy dependency, followed by two social concerns: public health and employment. Least important criteria were noise, visual impact, land use and local income.

The resulting rankings are presented in Table 5. There are no dominated solutions, which means that no scenario performs always worse than any other scenario.

Even in the case that cost is regarded as the most important criterion, the best solution can either be the cheapest or the most expensive: the proof is that ”Coal” and ”Maximum Renewable”, the cheapest and the most expensive scenarios respectively, were the ones that ranked first more times (4 times each).

The only scenario that never ranked first, for any respondent, was ”Hydro-Gas”. However, it is a balanced scenario, since it only ranks in the last place twice, while ”Maximum Renewable” and ”Natural Gas” rank in the last position for three respondents’ profiles. On the other hand, ”Base” is the only scenario that never ranked last place, although only ranks first in two respondents.

Figure 7 presents the contrast between respondents favorable to ”Coal” and ”Maximum Renewable” scenarios, showing that while the former group clearly places costs high above any other criteria, the latter have five similarly valuated criteria: costs, public health, energy independency, national industry and employment.

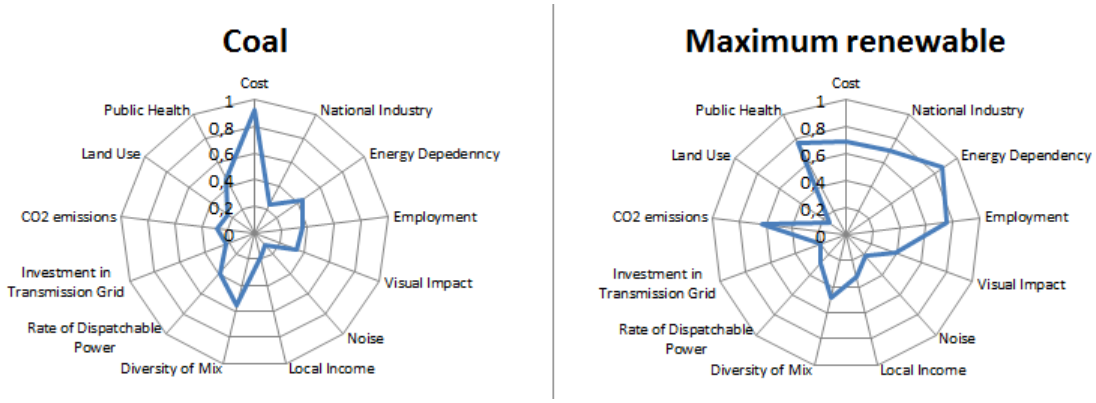

Figure 7: Average profile of respondents that chose either ”Coal” or ”Maximum Renewable” as preferred scenarios.

The obtained results confirm that costs are still the main obstacle for the incorporation of more renewable energy in electricity systems. Such as [19] case, our scenario ranking was also very sensitive to the input of costs weight.

What these results have shown is, in first place, that respondents felt it is important to trade-off costs with other criteria, hence the utility of multi-criteria methodologies. Only on rare occasions did a respondent assign zero to the weight of one criterion, but was free to do it in any criterion he wished to (if he assigned zero to all criteria besides costs, obviously the Coal scenario would be the first in the ranking, since it is the cheapest solution). Secondly, it is the magnitude of the trade-off that induces the divergence in the final rankings. For example, for the second most rated criterion, energy dependency, one respondent suggested that more information should be given when valuating this criterion (”in the worst case for fuel cost projections, how much would the price of the solution increase?”), otherwise it becomes difficult to state how much would value the criterion. However, using more information would significantly increase the response time.

5. Conclusions

In this paper, a tool to evaluate scenarios for electricity production was proposed. The tool uses multi-criteria decision analysis, and comprises a set of thirteen criteria, ranging from economic concerns,

Table 5: Scenario Ranking.

	Respondents										
Scenario	**A**	**B**	**C**	**D**	**E**	**F**	**G**	**H**	**I**	**J**	**K**
Base	2	**1**	3	2	4	2	3	**1**	4	2	2
Natural Gas	5	5	4	5	3	4	2	4	**1**	4	5
Coal	3	3	5	4	**1**	**1**	**1**	3	2	**1**	4
Hydro-Gas	4	4	2	3	2	5	4	5	3	3	3
Maximum Renewable	**1**	2	**1**	**1**	5	3	5	2	5	5	**1**

to environmental and social as well as technical issues. The methodology combines an additive value function that aggregates results from direct weighting and trade-off analysis. The proposed tool was used on the particular case of Portugal, based on a set of scenarios for the electric system in 2020. A group of experts from academia, Engineers, Economists related to the energy sector, participated in the evaluation of these scenarios. From the results obtained, most respondents would be willing to increase the costs of power generation if other issues than the economical ones were to be taken into account. This fact alone proves the utility of MCDA. The evaluated scenarios were ranked differently by respondents with different perspectives, what is not unexpected when using multi-criteria methodologies. In fact, only one of the scenarios, "Hydro-Gas", was not chosen to be the preferred by any of the eleven respondents.

Aggregating the results, cost was considered the most important criterion, even for most respondents whose preferred scenario was "Maximum Renewable". Other also important criteria were the rate of dependency on fuel sources, the employment and the public health issues. Depending on the weight assigned to these criteria, the cost loses relative importance and most expensive solutions may rank first.

Future work envisages the collection of additional information, increasing the number of experts involved. Also, being the public acceptance of different technologies a fundamental aspect to ensure the success of strategic scenarios, the work is proceeding with the evaluation of public acceptance of different electricity generation technologies.

6. Acknowledgements

This work was financed by: the QREN Operational Programme for Competitiveness Factors, the European Union - European Regional Development Fund and National Funds - Portuguese Foundation for Science and Technology, under Project FCOMP-01-0124-FEDER-011377 and Project Pest-OE/EME/UI0252/2011. Authors wish to thank all the academics that collaborated in the interviews.

References

[1] European Comission. 2011 monitoring report of the eu sustainable development strategy, 2011. European Comission.

[2] Espen and Løken. Use of multicriteria decision analysis methods for energy planning problems. *Renewable and Sustainable Energy Reviews*, 11(7):1584 – 1595, 2007.

[3] Fernando Ribeiro, Paula Ferreira, and Madalena Araújo. A methodology to address social concerns in electricity planning. In *Proceedings of the Dubrovnik Conference on Sustainable Development of Energy, Water and Environment Systems, Dubrovnik, Croatia, 25-29 September 2011.*, page 321, 2011.

[4] INAG. Plano nacional de barragens com elevado potencial hidroeléctrico. http://pnbeph.inag.pt/np4/np4/?newsId=4&fileName=pnbeph_memoria.pdf, 2007. Instituto da Água, in Portuguese.

[5] REN. A energia eólica em portugal, 2010. Redes Energéticas Nacionais, in Portuguese.

[6] REN. Informação mensal, sistema electroprodutor, 2011. Redes Energéticas Nacionais, in Portuguese.

[7] Sérgio Pereira, Paula Ferreira, and A. Ismael Vaz. Strategic electricity planning decisions. In *Proceedings of the Dubrovnik Conference on Sustainable Development of Energy, Water and Environment Systems, Dubrovnik, Croatia, 25-29 September 2011.*, page 590, 2011.

[8] República Portuguesa. Plano nacional de acÇÃo para as energias renovÁveis ao abrigo da directiva 2009/28/ce, 2009. República Portuguesa.

[9] Organization for Economic Co-operation and development/International Energy Agency, editor. *Projected Costs of Generating Energy*. Organization for Economic Co-operation and development, Paris, France, 2010.

[10] Benjamin Hobbs and Peter Meier. *Energy decisions and the environment: a guide to the use of multicriteria methods*. International series in operations research & management science. Kluwer Academic Publishers, 2000.

[11] Jiang-Jiang Wang, You-Yin Jing, Chun-Fa Zhang, and Jun-Hong Zhao. Review on multi-criteria decision analysis aid in sustainable energy decision-making. *Renewable and Sustainable Energy Reviews*, 13(9):2263 – 2278, 2009.

[12] Justin D.K. Bishop, Gehan A.J. Amaratunga, and Cuauhtemoc Rodriguez. Using strong sustainability to optimize electricity generation fuel mixes. *Energy Policy*, 36(3):971 – 980, 2008.

[13] Fernando Ribeiro, Paula Ferreira, and Madalena Araújo. The inclusion of social aspects in power planning. *Renewable and Sustainable Energy Reviews*, 15(9):4361 – 4369, 2011.

[14] Paul Joskow. Apples and oranges: Donť compare levelized cost of renewables. *The Electricity Journal*, 23(10):3 – 5, 2010.

[15] Andrew Mills, Ryan Wiser, and Kevin Porter. The cost of transmission for wind energy in the united states: A review of transmission planning studies. *Renewable and Sustainable Energy Reviews*, 16(1):1 – 19, 2012.

[16] Athanasios I. Chatzimouratidis and Petros A. Pilavachi. Multicriteria evaluation of power plants impact on the living standard using the analytic hierarchy process. *Energy Policy*, 36(3):1074 – 1089, 2008.

[17] European Commission. External costs: Research results on socio-environmental damages due to electricity and transport, 2003. European Comission.

[18] Boris Krey. Scope of electricity efficiency improvement in switzerland until 2035, 2008.

[19] G. Heinrich, L. Basson, B. Cohen, M. Howells, and J. Petrie. Ranking and selection of power expansion alternatives for multiple objectives under uncertainty. *Energy*, 32(12):2350 – 2369, 2007.

Comparison of sophisticated Life Cycle Impact Assessment Methods for Assessing Environmental Impacts in a LCA Study of Electricity Production

Jens Buchgeister

Karlsruhe Institute of Technology, Institute for Technology Assessment and Systems Analysis, Karlsruhe, Germany, Jens.Buchgeister@kit.edu

Abstract:

The methodology of life cycle assessment (LCA) has been applied widely to design for environment (DfE) of energy conversion processes. For the identification of weak points within the process in order to reduce the environmental impacts the selection of the life cycle impact assessment (LCIA) method has an influence on the LCA results.
To understand the differences between various LCIA methods a comparative analysis in general structure, extent of considered environmental aspects, and mathematical relationship for quantifying the cause-effect chain from emissions to an impact in the environment is conducted.
Furthermore the life cycle assessment is carried out in a case of electricity production by means of solid oxide fuel cell (SOFC) with integrated allothermal biomass gasification using three different LCIA methods: Eco-indicator 99, CML 2001 (baseline), and Impact 2002.
It can be presented that in this case of electricity production process the supply of biomass and the production of the SOFC have the highest environmental impacts for all applied LCIA methods.
But the divergences of the LCIA methods leads to the result that different chemical pollutants cause the highest environmental impact. For the Eco-Indicator 99 the highest contribution comes from the particles PM 2.5 whereas for CML hydrogen fluoride, for IMPACT 2002 (endpoint) dioxin (TCDD) is responsible for the highest environmental impact.
It can be shown depending on the applied LCIA method the highest contribution on the overall environmental impact can be differ. In due to the result the recommendation is made to use more than one LCIA method in order to get much more information in detail of environmental pollutants.

Keywords:

comparative analysis, electricity production, LCA, life cycle impact assessment

1. Introduction

Life cycle assessment (LCA) has been applied widely to design for environment (DfE) of energy conversion processes. For the identification of weak points within the process in order to improve the environmental performance the selection of a life cycle impact assessment (LCIA) method has an influence on the results. This knowledge is included in an ISO standard on LCA [1,2] for the part of mandatory elements in the LCIA. The current ISO standard takes into account existing uncertainties in environmental impact assessment. For this reason have been constructed a few consensus-oriented publications [3,4,5,7] over the years by working groups under the auspices of SETAC describing state of the art and best available practice on LCIA. In further consequence a number of different LCIA methods are implemented in commercial LCA software products, and are available to LCA practitioner. A general survey of LCIA methods is compiled during phase I of the international Life Cycle Initiative, a concerted project between United Nations Environment Programme (UNEP) and SETAC [8]. Furthermore has been pointed out in papers [9,10] which are carried out comparisons of a few different LCIA methods for specific case studies that main differences are existed in toxicological impacts. Therefore in a European project OMNIITOX (Operational Models aNd Information tools for Industrial applications of eco/Toxicological impact

assessments) is focused on methods for the characterisation of toxicological effects and data availability in order to improve and harmonise the practicality of toxicological impact assessment in LCA [11]. The results of the OMNIITOX project are integrated in the new designed LCIA methods Impact 2002.

The present paper reports a comparison of the three LCIA methods Eco-indicator 99 [12], CML 2001 [13], and Impact 2002 [14] based on a case of electricity production by means of SOFC with integrated allothermal biomass gasification. The goal is to reveal the causes for the differed impact results between the investigated LCIA methods.

2. Methodology

The LCA is an internationally established and standardized method for the analysis of the complete life cycle of products and services [1,2]. It analyses the consumption and emission of material flows from all process steps within the life cycle. This means the supply of the input streams, especially fuel, and the full life cycle of components. Inventories of elementary flows (i.e., consumption of natural resources and energy carriers as well as emissions) are compiled following the guidelines of international standard approaches [1,2]. The basis of the inventory result, which are calculated for the investigated life cycle processes, are the general physical laws of conservation of energy and mass. The accuracy of this procedure depends on the assumptions for each modelled process and the entire system. Based on the life cycle inventory (LCI) result the environmental impacts for various environmental impact categories are calculated by a quantitative LCIA method. An impact category describes the impact pathway between the LCI results and their environmental endpoint(s) or so-called areas of protection. It includes a cause-effect chain by using quantitative characterization indicators based on an environmental model (see figure 1). The measuring and modelling of environmental impacts are complex and it is affected by the two different main schools of approaches: endpoint and midpoint LCIA methods [6,7].

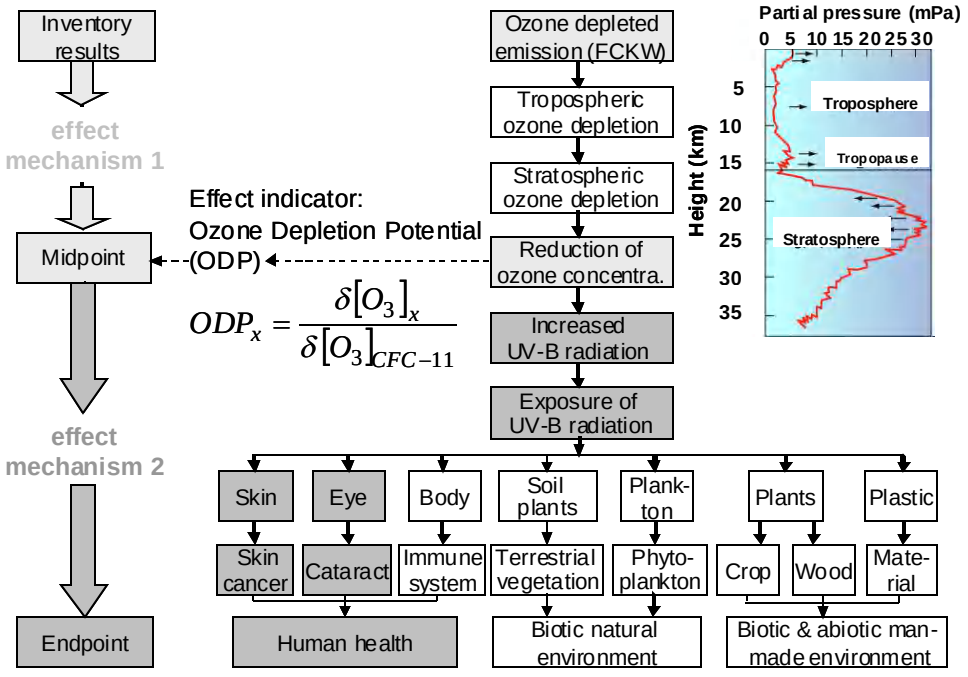

Fig. 1. Example of impact pathways of stratospheric ozone-depleting substances [adapted from 7]

The terms midpoint and endpoint mean the location of the environmental impact category indicator. In line with international standard the category indicator can be located at any point between the LCI results and the category endpoints [2]. The midpoint approach describes quantitative by the category indicator only the potential modification of the environmental state. In contrast to them the

indicator of endpoint approaches characterize based on the measurable modified environmental state to real impacts and modifications on one or more of the four defined areas of protection: human health, biotic and abiotic natural environment, biotic and abiotic natural resources, biotic and abiotic man-made environment.

To clarify the mentioned differences between midpoint and endpoint approach figure 1 presents exemplarily the complete impact pathway from the released ozone depleted substances like CFC to the area of protection for the impact category stratospheric ozone layer depletion.

The dispersion of ozone-depleting substances takes place in the troposphere. At an average of 4 years the ozone depleting emissions achieve the higher layer of more than 15 km, the stratosphere, in order to accumulate their completely [12]. During the way of ozone depleting substances from the bottom to higher air layer it comes by means of incident solar radiation to the dissociation of ozone depleting substances. Due to the dissociation chlorine and bromine atoms are generated as free radicals which reduce the ozone concentration measurable in the stratosphere. This mechanism the reduction of ozone concentration is the category indicator which is very similar for all ozone depleting substances for example CFC, HCFC or halon. For this reason the quantitative extent of reduced ozone concentration can be calculated between all these ozone depleting substances as relative reference. For the impact category stratospheric ozone layer depletion the midpoint indicator is characterized by the effect to reduce the ozone concentration (ozone depletion potential, ODP) in the stratosphere. Furthermore all released substances, which has an ODP characterized with regard to their quantitative impact in relation to the reference substance CFC-11 (trichlorfluormethane) in kg CFC-11 for stratospheric ozone depletion (on the left side of figure 1).

Due to the described effect mechanism of reduced ozone concentration in the stratosphere the solar radiation on the earth is increasing. The resulting effect is an permanent increasing of ultraviolet B (UV-B) radiation on the earth surface [20]. As rule of thumb is defined that per percent reduced ozone concentration in the stratosphere the UV-B radiation is increased nearly about 2 percent. The increasing UV-B radiation consequently leads to an increase of skin cancer for humans. The direct interrelation between UV-B radiation and different types of skin cancer is verified observed in literature [21]. In the same by health studies is known that a longer exposition of higher UV-B radiation leads for the human eye to cataract. Moreover an increasing of UV-B radiation has also an harmful impact on the plants and animals because they have also no protective mechanisms like the human. But at the moment it is not possible to quantify these impacts on plants and animals as well as for materials like plastics when it is used as building material.

That means for endpoint approaches can only quantitative operationalised the impact interrelation between human skin cancer and cataract by an continuous increasing of UV-B-radiation. For those impacts is used the concept of disability-adjusted life years (DALY) which calculate the losses of life years or an equivalent in the case of disease effects. A comprehensive description of the DALY-concept is shown in following literature [22,23].

2.1. Conclusion of comparison between midpoint and endpoint approach

In comparison between midpoint and endpoint approach to quantify the environmental impact interrelation within an impact category is pointed out that the endpoint approach needs a longer cause effect chain from the emitted emissions to the area of protections (endpoint categories) than midpoint approaches. Thereby the environmental impact is differentiated viewable on each area of protection, but currently it is not possible the specific changes within the lithosphere, hydrosphere, atmosphere and biosphere to determine in its entirety. Because there is lack of knowledge and data in order to describe the impact pathways of emission correct differentiated in space respectively the effort for data collection is too high. Furthermore leads the long cause effect chain within an endpoint approach to greater uncertainty with each additional chain link. Due to the fact that

midpoint approach currently has a lower uncertainty of mathematical function to quantify the environmental impact it have to preferable used.

As compared LCIA methods is chosen the CML 2001 method which is a classical agent of midpoint approach, the Eco-indicator 99 as agent of endpoint approach and the IMPACT 2002 method which implements both a midpoint and endpoint approach. A structural comparison of different used method is described in chapter 2.5.

2.2. Life cycle impact assessment method – CML 2001

The CML 2001 method is a classical agent of a midpoint life cycle impact assessment method. It is developed by the institute of environmental science (CML) of Leiden University. The CML has a long tradition in the methodological development of LCIA [13]. The general structure and used impact categories of the CML 2001 method (baseline) is presented in figure 2.

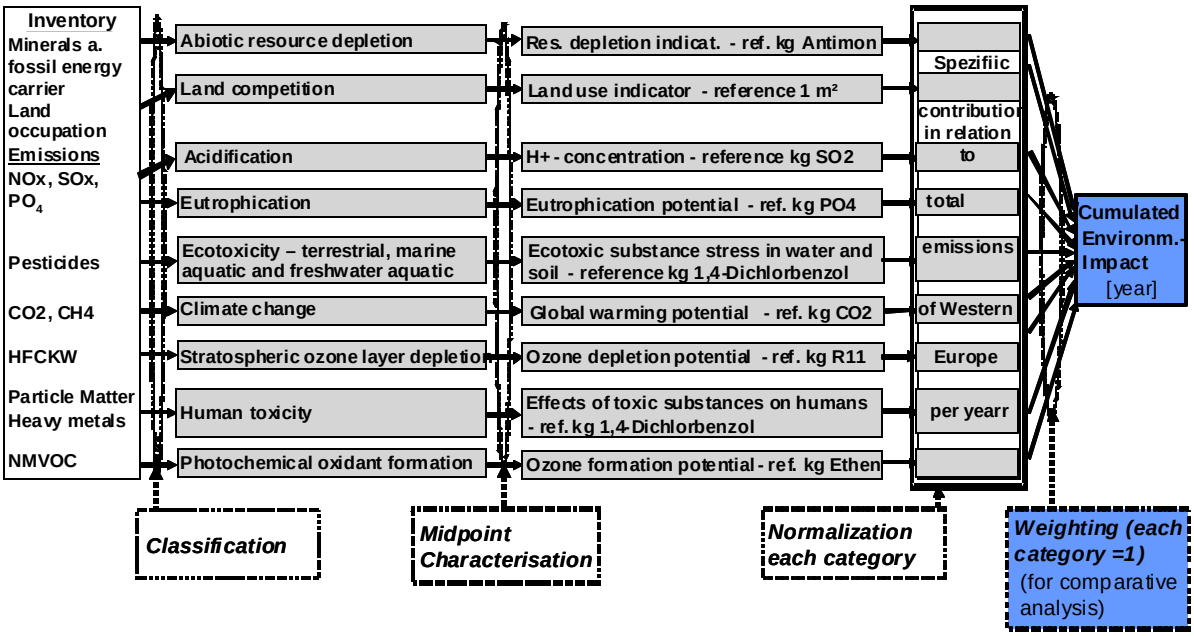

Fig. 2. General structure and used impact categories of the LCIA method CML 2001(baseline) [13]

Each impact category is characterized by an midpoint indicator which uses a defined reference substance in order to quantify the impact of a classified emission in relation to the reference substance. Usually the CML method is finished after the normalization of each impact category whereby the result shows an environmental profile of different 11 baseline impact categories (see table 1). The step of normalization calculate the specific magnitude of impact category result of the investigated system in relation to a reference information. In the case of CML 2001 method as spatial reference value the total emission of Western Europe per year is selected. Subsequently the normalized result of an impact category has the unit year.

To compare the life cycle impact assessment method CML 2001 with endpoint methods in order to quantify the environmental impact an aggregation (step of weighting) of each impact category has to integrate in the model structure. For this reason each impact category was equally weighted and can be cumulative added to the total environmental impact.

2.3 Life cycle impact assessment method – Eco-indicator 99

It is especially developed as endpoint life cycle impact assessment method to support decision-making in a design for the environment [12]. Therefore based on the three areas of protection (endpoint categories): human health, biotic and abiotic natural environment, biotic and abiotic

natural resources an aggregated value to a single score is created. The aggregation depends on a concept of different socio-culture perspectives which is developed by Hofstetter [23]. From the method developers are recommended a default weighting factor of 2/2/1 between the different endpoint categories human health, natural environment and resources [12,23]. The Eco-indicator 99 was the first developed LCIA method which calculates the environmental burden based on measurable real impacts and modifications on the three areas of protection. For this reason new concepts of environmental models like disability-adjusted life years (DALY) which calculate the losses of life years or an equivalent in the case of disease effects is applied [22,23].The structure and the considered environmental aspects are displayed in figure 3.

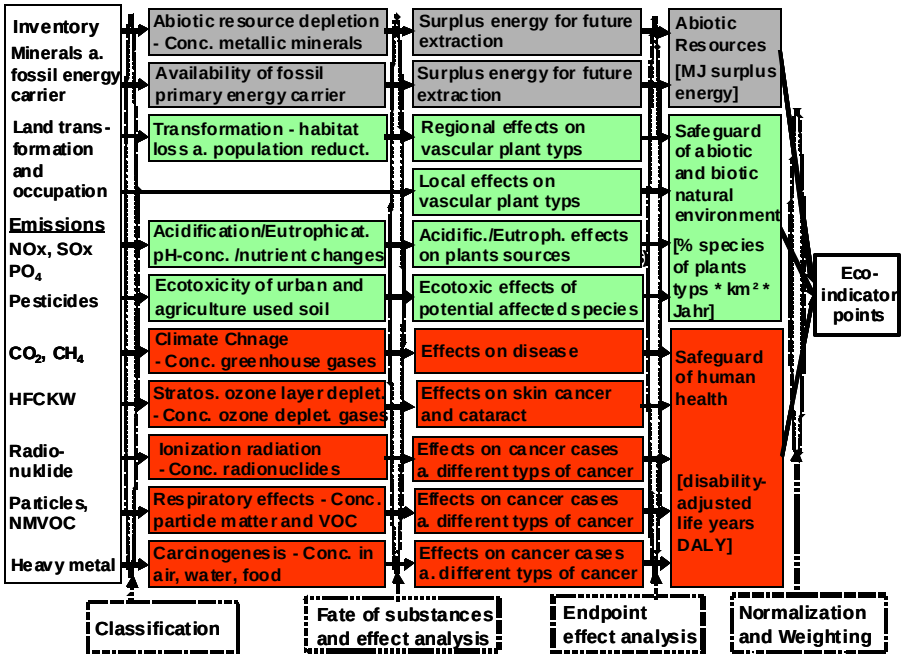

Fig. 3. General structure and used impact categories of the LCIA method Eco-indicator99 [12]

2.4 Life cycle impact assessment method – IMPACT 2002

The life cycle impact assessment method IMPACT 2002 proposes an implementation of both midpoint and endpoint approach, linking all types of inventory results via 11 midpoint categories to 4 endpoint categories: human health, abiotic and biotic natural environment, abiotic resources, and climate change [14]. The general structure and the integrated impact categories of the LCIA method IMPACT 2002 is shown in figure 4.

In difference to other endpoint LCIA methods the impact category climate change is defined as additional area of protection and therefore it is integrated as further endpoint category. The increasing relevance of the climate change is derived from the interrelation to life support functions of plants, animals, and humans. For the comparative analysis of different LCIA methods the endpoint approach of IMPACT 2002 is selected. Therefore a weighting of the four endpoint categories have to carried out which is included in the model structure of figure 4. Similar to CML 2001 each damage category was equally weighted. The result of IMPACT 2002 is expressed in points.

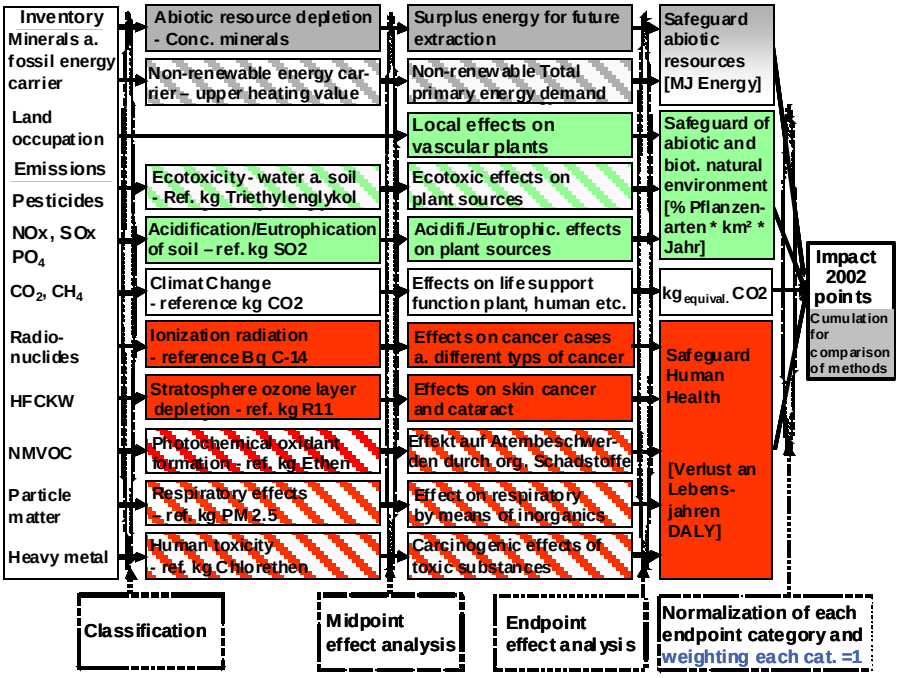

Fig. 4. General structure and used impact categories of the LCIA method IMPACT 2002 [14]

2.5 Structural comparative analysis of applied LCIA methods

In table 1 is shown a comparison of applied impact categories within the LCIA methods CML 2001 baseline, Eco-indicator 99, IMPACT 2002. The result is that the Eco-indicator 99 and IMPACT 2002 have a similar structure. In difference to the Eco-indicator 99 is the category land transformation not included as well as for the CML 2001 method.

Table 1. Comparative Analysis of applied impact categories in the LCIA methods CML 2001 baseline, Eco-indicator 99, IMPACT 2002

Impact categories	CML 2001	Eco-indicator 99	IMPACT 2002
Abiotic resources	X	X	X
Land occupation	X	X	X
Land transformation	-	X	-
Acidification and eutrophication of soil	X (two categ.)	X	X
Climate change	X	X	X
Stratospheric ozone layer depletion	X	X	X
Photochemical oxidant formation	X	X	X
Ecotoxicity in soil	X	X	X
Ecotoxicity in marine aquatic water	X	X	X
Ecotoxicity in freshwater aquatic	X	-	-
Ionization radiation	-	X	X
Human toxicity	X	X	X
Respiratory effects (by inorganic)	(human tox.)	X	X

Furthermore IMPACT 2002 has developed new environmental models for human toxicity and ecotoxicity and for non-renewable energy carriers the total primary energy content is accounted. All of these differences to the Eco-indicator 99 method are marked by hatched areas in figure 4.

The greatest structural distinctions in regard to the included environmental aspects between CML 2001 and the others methods are for the categories human toxicity and ecotoxicity. Here is the point that each method use their own environmental model to calculate the dispersion of toxic substances in the different environmental compartments [12,13,14]

3. LCA case study of electricity production

For the application of an comparative analysis of presented different LCIA methods a LCA of a thermochemical process for the conversion of biomass to electricity was carried out. The system boundary of the LCA covers all system components (see figure 5) and their respective life cycles, as well as all input streams (biomass, electricity, water) to the overall energy conversion system.

The details of the process can be found in [16]. The modelling of a similar process has been reported in [17,18]. Figure 5 shows the flowchart of the process designed for electricity generation of 1 MW alternating current. In the same figure, temperatures, pressures and mol flow rates of the material streams are presented. These values were obtained by modelling and simulation of the process described below. Biomass (wood chips) is fed to an allothermal fluidized bed gasifier (Gasifier) that is heated by an integrated burner. The flue gas of the solid oxide fuel cell (SOFC), which contains non-depleted fuel, represents the feedstock for the burner. The gasification agent is steam generated within the process. At 750°C the biomass is converted to a raw gas which mainly consists of H2, CO, CO2 and CH4. After leaving the gasifier, the raw gas enters the hot gas cleaning facility at 650°C. First it passes through a ceramic particle filter and an adsorber. Char, bed material and ash are removed in the first component, halogen and sulphur compounds are removed in the latter. Steam pulses periodically clean the particle filter. After the adsorber, steam is added to the gas in a mixer (MIX) to adjust the steam-to-gas ratio to a value of 2.5, which is necessary for tar and methane reforming and for preventing coke formation. Before the gas enters the tar reformer it has to be heated from 470 to 900°C to enable the reforming reaction to take place. This is realized in a heat exchanger (HX G4) by transferring heat from the hot anode flue gas (1000°C) from the SOFC to the tar laden gas. The tar is completely reformed to lower hydrocarbons in the catalytic tar reformer (Tar Reform.).

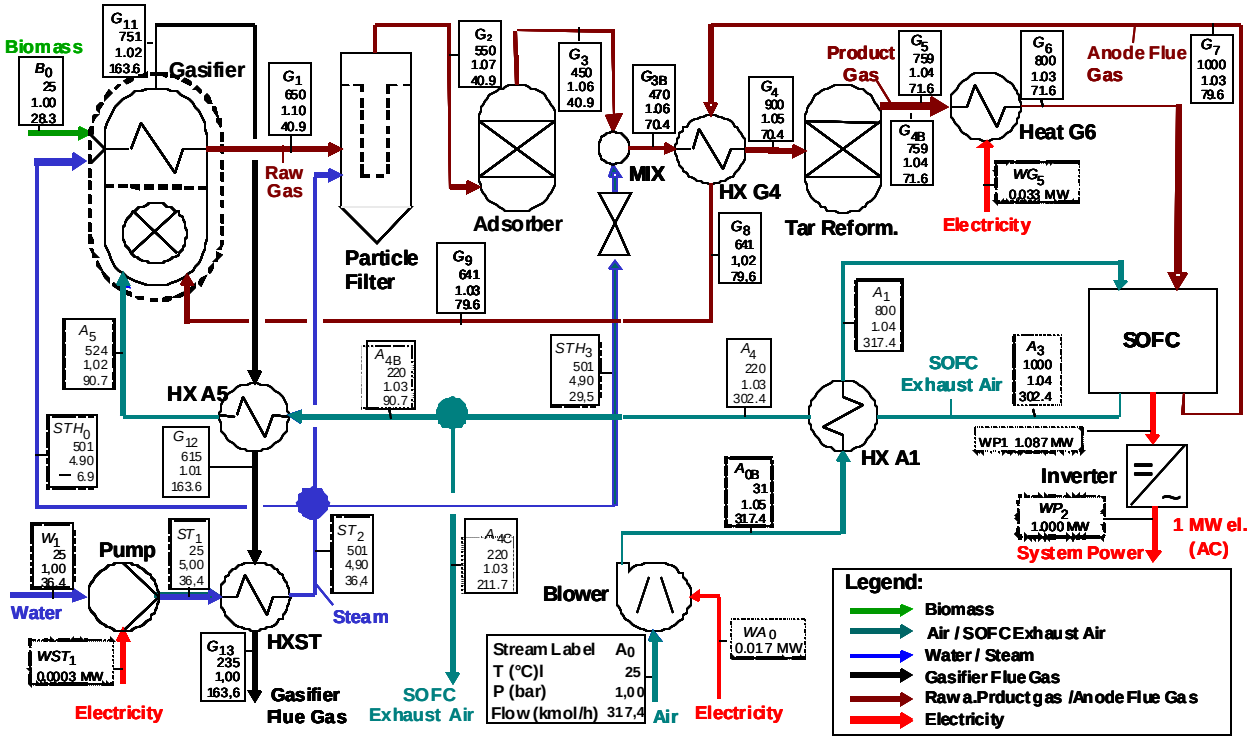

Fig. 5. Flowchart of electricity production by means of biomass conversion process

The clean gas is heated to 800°C in an electric heater (Heat G6) before entering the anode side of the SOFC. Preheated air (800°C) is supplied to the SOFC at the cathode. At an operation temperature of 1000°C the fuel cell produces direct current by oxidizing hydrogen

and carbon monoxide. Prior to that, methane was internally converted with steam to hydrogen and carbon monoxide.

The fuel utilization factor in the SOFC is 69 %. The inverter (Inverter) converts the direct current to alternating current. Ambient air is fed to the air preheater (HX A1) by an electric blower (Blower). Heat from the fuel cell exhaust air (1000°C) is transferred to the outside air. The exhaust air from the SOFC is partly released to the environment and partly preheated in another heat exchanger (HX A5) to about 520°C and fed to the burner, which is integrated into the gasifier. The hot stream in the heat exchanger is the flue gas from the burner that has previously heated the gasifier. The water supply of the system is provided by a pump (Pump) that pressurizes water to 5 bar. Following this, steam is generated from the water in a heat exchanger (HX ST) that transfers heat from the flue gas of the burner integrated into the gasifier. The gasifier model is based on a mass and energy balance and on the reforming reactions taking place in the gasifier. The fuel cell model was been adapted from a model for a tubular SOFC published in [17,18]. Depending on gas composition and operating conditions, the power output as well as the conditions and compositions of the exiting material streams of the fuel cell can be simulated.

The LCA of the system is modelled in the material flow software Umberto (version 5.5 [19]). For the case study the assumption was made that no heat demand exists outside the process in this theoretical model to simplify the calculations. Therefore, the product from the overall process is only the generated electricity. As functional unit for the LCA the production of 100 MWh of electricity has been chosen. Furthermore is assumed that the bioenergy facility investigated is situated in central Europe. All other important assumptions of parameters for the LCA are presented in table 2.

Table 2. Defined parameters and assumptions for the LCA of the case study of electricity production

Parameter	Value
Functional unit	100 MWh electricity
Lifespan of total plant	100,000 operation hours, respectively 15 years
Lifespan of solid oxide fuel cell	40.000 operation hours
heating value of biomass	19.8 MJ/kg
Density of biomass (dry)	169 kg/m³
Moisture of biomass during transport	40 %
Biomass capacity (wood chips)	500 kg/h
Transport distance of biomass	50 km

The whole LCI of the conversion process of biomass to electricity was presented in detail in [16].

3.1 Results of the compared LCIA methods

Figure 6 presents the percentage of environmental impact of all input streams and system components in relation to the total environmental impact associated with the final product for all applied LCIA methods. It shows that the supply of biomass has the highest environmental impact for all methods but the values varies from 58.7 % (Eco-indicator 99) to 45.0 % (IMPACT) and to 33.5 % (CML).

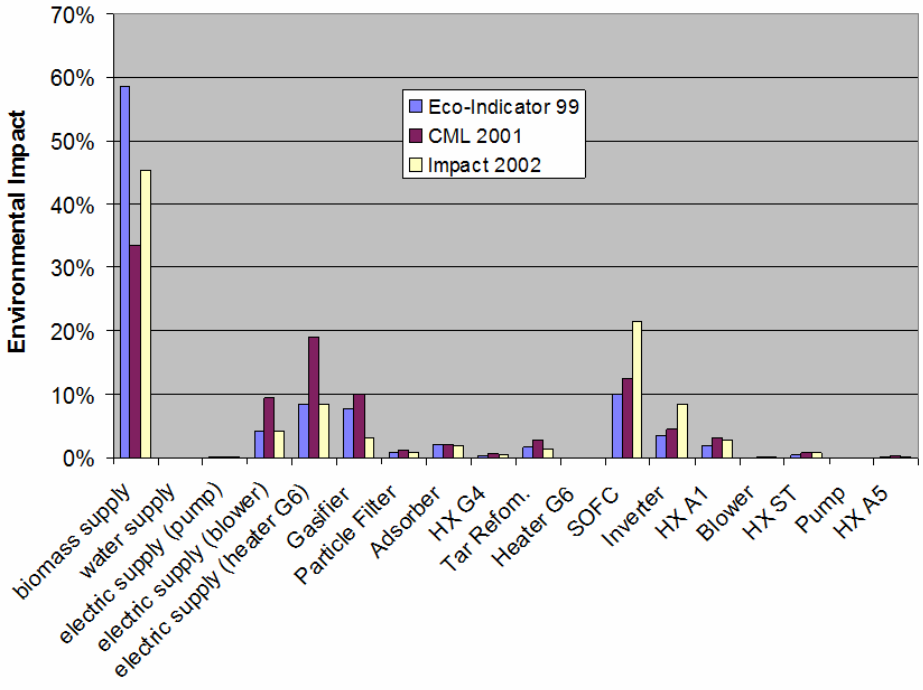

Fig. 6. Percentage of total environmental impact of input streams and system components

One reason for the highest Impact of biomass supply of all used LCIA methods can be explained by the high effort for the transport of the biomass that is transported about a distance of 50 km. Additionally the impact of land occupation especially land transformation which is only included in the Eco-indicator 99 method contributes to the highest value.

On the other hand the values for the electrical supply of the blower and heater G6 are clearly higher for the CML method during both others methods show similar values. The reason for this result is the high impact of hydrogen fluoride (HF) by the CML method. This pollutant is produced especially in fossil power plants which have the main contribution in the used EU electricity mix.

But the presented consistent results of the applied LCIA methods are not sufficient in regard to the same environmental optimization potential. For this purpose is a dominance analysis necessary in order to find out which elementary flows (emission, resource or land use) are the main contributors on the total environmental impact.

3.2 Comparative Dominance Analysis

Figure 7 presents the results of the dominance analysis for the different applied LCIA methods. For the Eco-indicator has the highest contribution the particulate matter (PM 2.5) followed by land occupation and transformation and the demand of crude oil.

During for the IMPACT method dioxin emissions (equivalent of 2,3,7,8-tetrachlorodibenzodioxin) are with over 70% responsible for the highest impact. The analysis of CML method shows that hydrogen fluoride and heavy metal emissions in water each with over 30 % exhibit the main load. The variation of main contributors in each case of applied method shows that it depend on the impact categories human toxicity and ecotoxicity which different effect models has implemented. At this crucial point recently published studies are started further development to reduce the uncertainty in these impact categories [15].

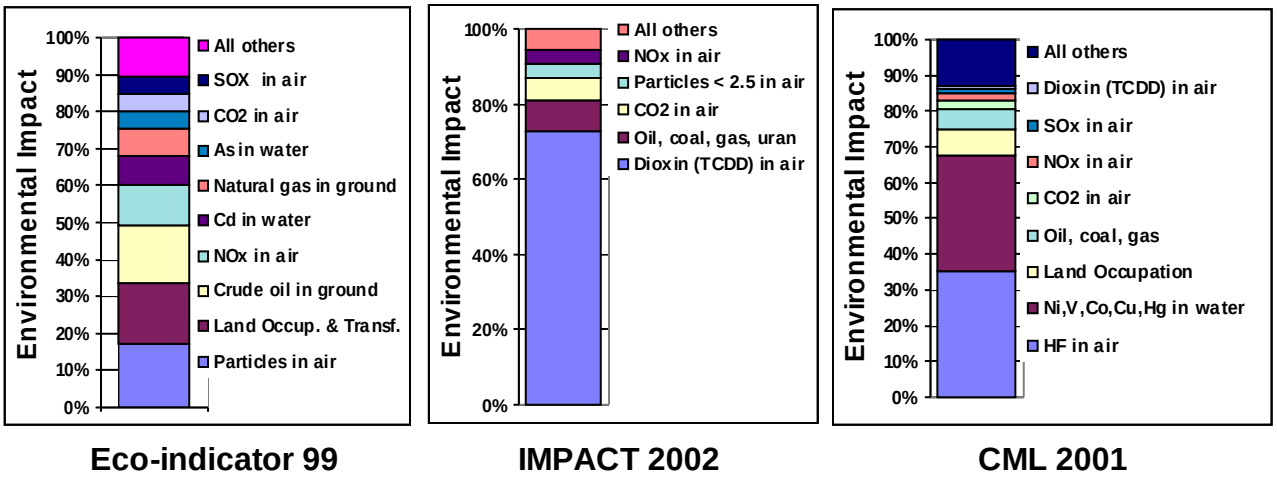

Fig. 7. Comparative dominance analysis of applied LCIA methods Eco-indicator 99, IMPACT 2002 and CML 2001

4. Conclusion

It is shown that the different life cycle impact assessment methods exhibits structural distinctions in regard to the included environmental aspects as well as for the mathematical function to quantify the environmental impact. Today neither a midpoint nor a endpoint method is available which all quantitative measurable environmental aspects could be involved. For this reason it makes sense for an analysis of environmental loads using more than one method in order to collect the environmental aspects in their broadness. Due to the fact that midpoint approach has a lower uncertainty of mathematical function to quantify the environmental impact it have to preferable used.

In the case of electricity production by means of biomass gasification with high-temperature solid oxide fuel cell is shown that all used LCIA methods provide similar results in respect of the components with the highest environmental impacts. The relevant components are the biomass supply, gasifier, SOFC, and the electricity supply of heater G6. However, the dominance analysis shows that as a function of the used LCIA method different inventory results (elementary flows) are responsible for the main contribution. All of these elementary flows are assigned to the impact categories human toxicity and ecotoxicity whose toxicity characterization models are different for each used LCIA methods. In the modelling of human toxicity and ecotoxicity have the LCA respectively LCIA method their greatest uncertainty. At this crucial point recently published studies are started further development to reduce the uncertainty in these impact categories [15].

In due to the result the recommendation is made to use more than one LCIA method in order to get much more information in detail of environmental pollutants.

References

[1] International Organization for Standardization (ISO), Environmental Management - LCA - Principles and Framework, European Standard EN ISO 14040. Geneva, Switzerland, 2006

[2] International Organization for Standardization (ISO), Environmental Management - LCA - Requirements and Guidelines, European Standard EN ISO 14044. Geneva, Switzerland, 2006

[3] Udo de Haes H.A. (ed.), Towards a methodology for Life Cycle Impact Assessment. Society of Environmental Toxicology and Chemistry (SETAC-Europe), Bruxelles, 1996

[4] Udo de Haes H.A., Jolliet O., Finnveden G., Hauschild M.Z., Krewitt W., Müller-Wenk R., Best Available Practice Regarding Impact Categories and Category Indicators in LCIA.

Background Document for the Second Working Group on LCA of SETAC-Europe (WIA-2), Part 1: Int. Journal of LCA 1999;4(2):66-74, Part 2: Int. Journal of LCA 1999;4(3):167-174

[5] Udo de Haes H.A., Jolliet O., Finnveden G., Goedkoop M., Hauschild M.Z., Hertwich E., Hofstetter P., Klöpffer W., Krewitt W., Lindeijer E., Müller-Wenk R., Olsen S., Pennington J., Steen B. (eds), Life Cycle Impact Assessment – Striving towards best practice. Society of Environmental Toxicology and Chemistry (SETAC), Pensacola, USA, 2002

[6] Bare J., Hofstetter P., Pennington D., Udo de Haes H.A., Midpoint versus Endpoint: The Sacrifices and Benefits - Life Cycle Impact Assessment Workshop Summary. Int. Journal of LCA 2000;5(6):319 - 326

[7] Jolliet O., Müller-Wenk R., Bare J., Brent A., Goedkoop M., Heijungs R., Itsubo N., Peña C., Pennington D., Potting J., The LCIA Midpoint-Damage Framework of the UNEP/SETAC Life Cycle Initiative, Int. Journal of LCA 2004;9(6):394 – 404

[8] Jolliet O., Dubreuil A., Gloria T., Hauschild M.Z., Progresses in Life Cycle Impact Assessment within the UNEP/SETAC Life Cycle Initiative. Int. Journal of LCA 2005;10(6):447-448

[9] Dreyer L.C., Niemann A.L., Hauschild M.Z., Comparison of Three Different LCIA Methods: EDIP97, CML2001 and Eco-indicator 99. Int. Journal of LCA 2003;8(4):191-200

[10] Brent A., Hietkamp S., Comparative Evaluation of Life Cycle Impact Assessment Methods with South African Case Study. Int. Journal of LCA 2003;8(1):27-38

[11] Pennington D. (ed.), OMNIITOX: Operational Models aNd Information tools for Industrial applications of eco/TOXicological impact assessment. Int. Journal of LCA 2004;9(5):281-342

[12] Goedkoop M., Spriensma R., The Eco-indicator 99: A damage oriented method for life cycle impact assessment. Methodology Report, Amersfoort, Netherlands, 2000, Available at: www.pre.nl

[13] Guinée J.B. (ed.), LCA: An Operational Guide to the ISO Standards. LCA in Perspective; Guide; Operational Annex to Guide. Centre for Environmental Science, Leiden University, Netherlands, 2001, http://www.leidenuniv.nl/interfac/cml/ssp/databases/cmlia/index.html

[14] Jolliet O., Margni M., Charles R., Humbert S., Payet J., Rebitzer G., Rosenbaum R.K., IMPACT 2002+: A New Life Cycle Impact Assessment Methodology. Int. Journal of LCA 2003;8(6):324-330

[15] Goedkoop M., Heijungs R., Huijbregts M., De Schryver A., Struijs J., van Zelm R., ReCiPe 2008 - A life cycle impact assessment method which comprises harmonised category indicators at the midpoint and the endpoint level. Report I: Characterisation, Ministry of Housing, Spatial Planning and Environment (VROM), Netherlands, 2009, Available at: www.lcia-recipe.net

[16] Meyer L., Exergiebasierte Untersuchung der Entstehung von Umweltbelastungen in Energieumwandlungsprozessen auf Komponentenebene: Exergoökologische Analyse [PhD]. Darmstadt, Germany: University of Darmstadt 2006.

[17] Panopoulos K. D. et al., High temperature solid oxide fuel cell integrated with novel allothermal biomass gasification: Part I: Modelling and feasibility study, Journal of Power Sources 2006;159(1), 570-585

[18] Panopoulos K. D. et al., High temperature solid oxide fuel cell integrated with novel allothermal biomass gasification: Part II: Exergy Analysis, Journal of Power Sources 2006;159(1), 586-594

[19] ifu Hamburg, ifeu Heidelberg, editor, Umberto –Software for Material and Energy Flow Analysis and Life Cycle Assessment. User handbook Part 1 and 2, Version 5, Hamburg, Germany, 2011 (in German)

[20] World Meteorological Organization (WMO), Scientific Assessment of Ozone Depletion: 1998. Executive summary. Global Ozone Research and Monitoring Project - Report No. 44. Geneva, Switzerland, 1999

[21] International Agency for research on cancer (IARC), Solar and Ultraviolet Radiation. Monographs on the Evaluation of carcinogenic Risks to Humans, Vol.55, Lyon, France, 1992.

[22] Murray Chr., Lopez A., The Global Burden of Disease. World Health Organisation (WHO), World Bank and Harvard School of Public Health, Boston, USA, 1996

[23] Hofstetter P., Perspectives in Life Cycle Impact Assessment. A structured Approach to Combine Models of the Technosphere, Ecosphere and Valuesphere. Kluwers Academic Publisher, Dordrecht, Netherlands, 1998

Defossilisation assessment of biodiesel life cycle production using the ExROI indicator

Emilio Font de Mora[a], César Torres[b], Antonio Valero[c] and David Zambrana[d]

*[a] Centre of Research for Energy Resources and Consumption – CIRCE, Universidad de Zaragoza, Mariano Esquillor, 15, 50018, Zaragoza (Spain), 585496@celes.unizar.es, **CA***

[b] Centre of Research for Energy Resources and Consumption – CIRCE, Universidad de Zaragoza, Mariano Esquillor, 15, 50018, Zaragoza (Spain), valero@unizar.es

[c] Centre of Research for Energy Resources and Consumption – CIRCE, Universidad de Zaragoza, Mariano Esquillor, 15, 50018, Zaragoza (Spain), ctorresc@unizar.es

[d] Centre of Research for Energy Resources and Consumption – CIRCE, Universidad de Zaragoza, Mariano Esquillor, 15, 50018, Zaragoza (Spain), zambrana@unizar.es

Abstract:

Ensuring the sustainability of biofuel´s life cycle production has become a mandatory requisite for the European Union´s Member States if they want to account the biofuels consumed in their territory for the established consumption binding 2020 targets. The EU Renewable Energy Directive puts the focus of sustainability on the reduction of greenhouse gas (GHG) emissions and the protection of high biodiversity lands and high carbon stock lands. The current legislative framework does not take into account the consumption of non-renewable resources. Starting from the paper "Assessment of biodiesel energy sustainability using the ExROI concept" published in Energy, which defined the ExROI (Exergy Return on Investment) indicator and applied it to the well-to-tank production processes of biodiesel from rapeseed, sunflower and palm oils, this paper proposes: First, extend the use of the ExROI concept, which involves exergy cost accounting, to the life cycle analysis i.e. adding the processes of the production of inputs used in the biodiesel chain; Second, extend the calculations to soybean and used cooking oil based biodiesels; Third, assessing ways to "defossilise" the production cycles to decrease their non-renewable sources consumption. This paper demonstrates that the ExROI indicator is a better indicator than the EROI (Energy Return on Investment) which only considers energy flows. Also, it shows that the life cycle production of the biodiesels considered has positive ExROI values and that the ExROI value can be improved up to 26.51 taking into account several relatively simple improvements actions. This means that for one exergy unit of non-renewable sources invested in the process more than 26 units of biodiesel can be obtained. This value evidences that biodiesel can be around five times more sustainable than fossil diesel, from the point of view of the consumption of non-renewable resources, if adequate measures are taken into account.

Keywords:

Biodiesel, FAME, Sustainability, Defossilisation, Exergy, Exergy cost, EROI, ExROI.

1. Introduction

A portfolio of alternative fuels, covering electricity, hydrogen, biofuels, methane, LPG and others, is necessary to meet the policy objectives of the European Union [1]. The National Renewable Energy Action Plans produced by the EU Member States setting the pathways to achieve the 2020 targets of the Renewable Energy Directive 2009/28/EC (RES Directive) [2], which aims at achieving a 10% use of renewable energies in transport, show that the 85% of the target for renewable energy in transport will come from first generation biofuels, i.e. conventional bioethanol and biodiesel. From these, biodiesel will play a substantial paper being 65.9% of the total target [3].

These biofuels will need to comply with the sustainability criteria set in the RES Directive which relate to the reduction of life cycle GHG emissions compared to fossil fuels, the protection of biodiversity and the exclusion of use of high carbon stock lands. Beyond these criteria, in order to ensure sustainability, it is necessary to defossilise the production life cycle as maximum, which

means substituting non-renewable fuel energy sources and derived products used in the process, by renewable energy resources and derived products.

Based on the ExROI concept, defined in a previous paper [4], this paper proposes several alternatives to defossilise the biodiesel fuel life cycle. ExROI, Exergy Return on Investment is used to calculate the ratio of non-renewable exergy consumed in the system to the exergy that the biodiesel contains. The less non-renewable exergy consumed, the higher the ExROI value will be. This definition is inversely equivalent to the non-renewable exergy cost which accounts the amount of non-renewable resources required to obtain a product.

$$ExROI = \frac{P}{C_{\mathrm{P}}^{nrs}} = \frac{1}{c_{\mathrm{P}}^{nrs}} \quad (1)$$

The ExROI concept as used in this paper conjugates two important factors, life cycle assessment and exergy cost analysis. Life cycle assessment allows taking into account all non-renewable resources required from crop cultivation to the transesterification plant (primary processes), including the production of the required inputs (secondary processes), meanwhile exergy cost analysis permits the correct cost assessment taking into account the energy quality of the production flows. Exergy allows the integration of matter and energy flows in the analysis of production systems using the same concept and units for both.

An adequate selection of the boundaries of the system is very important, as in any life cycle analysis, thus depending on the processes included in the analyses the values obtained can vary significantly. Our previous paper [4] only took into account the direct production processes, while in this paper the production processes of the inputs to the direct production stages are also taken into account; this means for example the production of fertilisers used in the cultivation of the energy crops or the production on methanol for the transesterification process. This is a more accurate way of taking into account the exergy costs, as in the previous work, the exergy costs of the inputs entering the direct production processes were assumed to be their exergy values, following the Theory of Exergy Cost [5]. By comparing the results of the previous publication with the results obtained in this one, we will be able to understand the weight that the secondary processes have in the consumption of non-renewable resources. The manufacture of machinery and equipment is not considered as this is neither considered in the sustainability criteria of the RES Directive.

This paper analyses the production life cycles of biodiesel from rapeseed, sunflower, palm, soybean and used cooking oil. Data used for carrying the calculations are mainly based on the life cycle assessment study (LCA) carried out by the JRC-EUCAR-CONCAWE consortium [6] (JEC study) which have been used by the European Commission to establish the sustainability criteria of the RES Directive and the Fuel Quality Directive (2009/30/CE) regarding the CO_2 emissions from the cultivation of the raw materials to the production of biofuel. In the cases where information was missing from the published databases, other sources of information have been used. For example, the life cycle of the used cooking oil (UCO) has been obtained from CIEMAT [7]. In the specific case of rapeseed biodiesel, a separate analysis has been produced using the SimaPro programme and EcoInvent database. This exercise will allow comparing the ExROI value obtained for one specific product using two different databases.

2. Short description of the life cycles

The biodiesel production processes vary depending on the resource. The biodiesel fuels based on energy crops, i.e. rapeseed, sunflower, palm and soybean begin by the cultivation process in order to obtain oil seeds, or fresh fruit bunches (FFB) in the case of palm plantations. In this stage,

fertilizers, pesticides and energy is consumed in different quantities for each crop. From this, each resource follows different stages that are summarised in the table 1. The processes for rapeseed, sunflower and palm oil were explained more in detail in paper [4]. The case of soybean based biodiesel is similar to the rapeseed and sunflower, but here there is no need for drying, and the transport needs increase since soybean is currently cultivated in South America and transported to Europe, where refining and transesterification take place. The extraction is done by using n-hexane for all crops except for the palm oil. In addition, in the palm oil extraction the energy is obtained by burning palm biomass residues obtaining methane and heat. In this work these flows are considered as valuable co-products.

The case of UCO is completely different. UCO is considered a residue which in case of not being used, would need to be disposed in a landfill. Given this, the previous stages before the oil becomes a residue (including the use, for example, in a frying pan) are not considered in the analysis. The life cycle starts by the collection and transport of the residue, and is followed by the recycling where the oil is filtered and decanted in order to separate solid particles and water. Once the oil is refined, it is sent to the transesterification plant.

In the transesterification process the after-treatment of biodiesel (FAME washing) and the glycerol refining are treated separately to analyse the influence of glycerol in the ExROI calculation. This is the case for all the resources except for UCO where the glycerol is not refined.

Table 1. Direct processes considered in the life cycle analysis

No. process	Rapeseed and sunflower	Palm	Soybean	UCO
1	Cultivation	Cultivation	Cultivation	Collection and transport
2	Drying	Road transport and Storage	Road and maritime Transport	Recycling
3	Transport	Extraction	Extraction	Transesterification
4	Extraction	Road transport, Depot and Maritime transport	Maritime transport	
5	Refining	Refining	Refining	
6	Pretreatment and transesterification	Pretreatment and transesterification	Pretreatment and transesterification	
7	FAME washing	FAME washing	FAME washing	
8	Glycerol refining	Glycerol refining	Glycerol refining	

3. ExROI values

The thermoeconomic model of the biodiesel production processes is represented by the productive diagrams for each of the direct processes considered in the life cycle analysis depicting the exergy flows entering and exiting each of the processes. As example, Figure 1 shows the case of rapeseed biodiesel production. Although this diagram only shows the direct processes, the exergy consumed for the production of the inputs is being accounted. From these diagrams it is possible to obtain the Fuel-Product table. Table 2 represents the Fuel-Product table for rapeseed, where F_i refers to the process *i* of the productive diagram of Fig. 1.

It is worth noticing that, as explained in [4], it has been assumed that the consumption of *replenishable* natural resources such as rain water, CO_2 and solar energy in cultivation do not add exergy to the exergy costs. By doing this, the only irreversibilities taken into account for calculating the exergy costs are the ones provided by the non-renewable materials.

From the Fuel-Product tables it is possible to obtain the production costs of each process applying the Theory of Exergy Cost [5]. Concisely, we apply its fundamentals as follows: in a specific stage of the process the exergy cost is distributed to all the products (main product and by-products) of the stage proportionally by their exergy value; there is no exergy cost allocated to the waste produced; and the exergy cost of resources entering into the system is equal to their exergy.

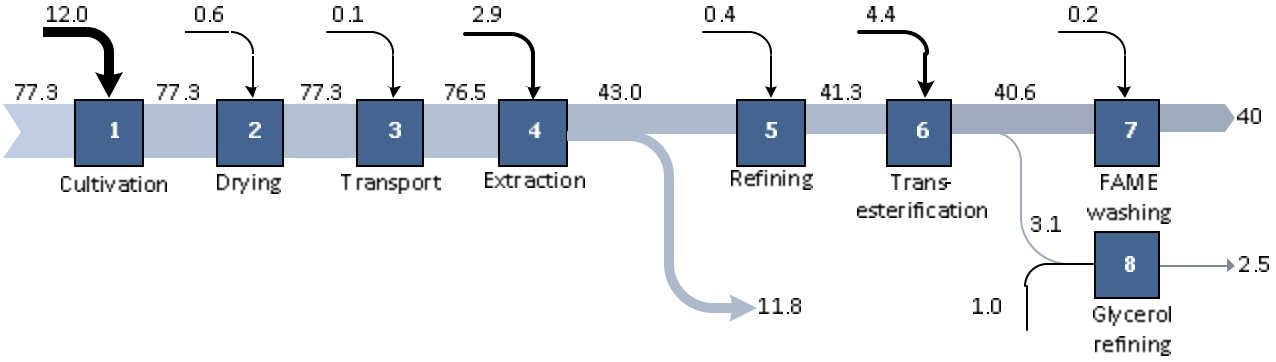

Fig. 1. Productive Diagram of rapeseed biodiesel life cycle production business as usual

Table 3 shows the production costs of each process for the rapeseed biodiesel life cycle. It is worth noticing that the non-renewable energy cost of the refined glycerol is higher than the one of the final biodiesel. This means that the ExROI of glycerol would be 1.12. The reason behind this high value is that the exergy of glycerol is low while the non-renewable exergy consumption is considerably high in the purification phase where a lot of energy is consumed in the distillation unit.

Table 2. Fuel-Product table for rapeseed biodiesel life cycle production (a) business as usual, (b) applying improvement measures (MJ/kg FAME)

(a)	F1	F2	F3	F4	F5	F6	F7	F8	F0	Total
E_0^{rs}	77.3									77.3
E_0^{nrs}	12.0	0.6	0.1	2.9	0.4	4.4	0.2	1.0		20.7
P1		77.3								77.3
P2			77.3							77.3
P3				76.5						76.5
P4					43.0				11.8	54.8
P5						41.3				41.3
P6							40.6	3.1		43.7
P7									40.0	40.0
P8									2.5	2.5
Sum	89.3	77.9	77.4	79.4	43.5	45.7	40.8	4.1	54.4	

As explained above, the inverse of the unit exergy cost of the non-renewable resources of biodiesel gives the ExROI value according to equation (1). Table 4 shows the ExROI values, unit exergy costs (c_p) and non-renewable unit exergy costs of the different biodiesel fuels (c_p^{nrs}). The non-renewable exergy cost and ExROI values are also calculated when using the exergy content of the inputs to the system instead of their exergy costs. The term "Difference" (ExROI with energy - ExROI with exergy costs) establishes the influence of the production processes of the inputs on the ExROI value. The term renewability establishes the weight of the renewable exergy costs with respect the total exergy costs.

As it can be observed in Table 4, all the biodiesel sources have ExROI values higher than one, which means that for one unit of non-renewable resources used in their production, more than one unit of biodiesel is obtained. The most sustainable one is the biodiesel produced from used cooking

oil, followed by palm, sunflower and rapeseed. The less sustainable is the soybean oil one which almost has a 1:1 relation.

Table 3. Non-renewable production costs of rapeseed based biodiesel production in the business as usual scheme and applying improvement measures (C_P in MJ/kg FAME)

		Business as usual	
Process	Product	c_P^{nrs}	C_P^{nrs}
Cultivation	Seeds	0.156	12.05
Drying	Dried seeds	0.163	12.57
Transport	Dried seeds	0.166	12.71
Extraction	Crude vegetable oil	0.282	15.49
Refining	Refined oil	0.305	12.59
Transesterification	Crude biodiesel + crude glycerol	0.387	16.93
Biodiesel drying	Final biodiesel	0.398	15.96
Gly. purification	Refined glycerol	0.890	2.22

The consideration of the production inputs (secondary processes) that enter the direct production processes plays an important role in the ExROI value as, except for the soybean oil based biodiesel, the ExROI is reduced in almost 2 units when the exergy costs, instead of the exergy values, are taken into account (see term Difference).

Table 4 also shows the EROI values of the biodiesel fuels from energy crops. As it can be observed, this indicator shows very similar values for rapeseed, sunflower and palm oil biodiesels, while these fuels have quite different ExROI values. The reason behind this is that EROI value only takes into account the consumption of energy sources while the ExROI values also considers the consumption of mass flows. The rapeseed based biodiesel consumes more mass inputs than palm and sunflower giving as a result a lower ExROI value. These results demonstrate that the ExROI concept is a better indicator of resource sustainability than the EROI concept. The value for soybean is lower and similar to the ExROI value.

The ExROI values obtained above could be considered positive news and an objective indication of which biodiesel resources should be primarily promoted. Hall et al. [8] recommend that the minimum EROI society must attain from its energy exploitation to support continued economic activity and social function is about 3:1 and therefore, biodiesel which life cycle provides an ExROI value lower than 3 should introduce measures to improve their values or be discouraged.

In addition, the ExROI values of biodiesel fuels should be compared to its direct competitor, i.e. fossil diesel fuel. According to Cleveland [9], the EROI value of gasoline (and therefore of diesel as they are products of the same process) is in the range of 6 to 10. Given this, the life cycle production processes should be defossilised in order to obtain at least the same ExROI values as fossil diesel fuel.

Table 4. EROI, ExROI and unit exergy cost (MJ/MJ) for the different types of biodiesel fuels

Source	Using Exergy Costs			Using exergy values		Difference	EROI	Renewability
	c_P	c_P^{nrs}	ExROI	c_P^{nrs}	ExROI			
Rapeseed	1.81	0.40	2.51	0.23	4.37	1.86	2.68	78
Sunflower	1.67	0.32	3.17	0.21	4.78	1.61	3.10	81

Palm	1.89	0.28	3.57	0.19	5.31	1.75	3.13	85
Soybean	1.98	0.59	1.69	0.44	2.26	0.57	1.62	70
UCO	1.42	0.22	4.54	0.16	6.44	1.91	-	84

4. Sensitivity Analysis

As it has been explained above, the results obtained are based on the consumption data of the life cycle assessments produced by the JRC, EUCAR and CONCAWE [6]. These numbers are fixed and based on specific assumptions. However, consumption in biodiesel production can vary significantly depending on many circumstances, for example, temperature and soil conditions at cultivation, carrying distance, quality of the oil at the transesterification plant, etc. This variation influences the exergy costs of the external resources entering the system and therefore the ExROI value of the product. In order to understand the effect that variations in the consumption of external resources may have in the ExROI result, a sensibility analysis is performed.

The exergy cost of the product can be calculated by the following equation:

$$\mathbf{C}_P = {}^{t}\left\langle \mathbf{P}^* \right| \mathbf{C}_e \tag{2}$$

Where P* is the product matrix and C_e is the exergy cost of the external resources entering into the system. As the external costs do not depend on the product matrix a variation in the exergy costs can be calculated by:

$$\Delta\mathbf{C}_P = {}^{t}\left\langle \mathbf{P}^* \right| \Delta\mathbf{C}_e \tag{3}$$

If π_{ij}^* is a generic element in the production matrix we obtain:

$$\Delta C_{P,i} = \pi_{ji}^* \Delta C_{e,j} \tag{4}$$

If we express equation (4) in terms of elasticity coefficient, and we only consider the non-renewable exergy costs, we obtain:

$$\frac{\%\Delta C_{P,i}^{nrs}}{\%\Delta C_{e,j}^{nrs}} = \frac{C_{e,j}^{nrs}\pi_{ji}^*}{C_{P,i}^{nrs}} \tag{5}$$

Applying this equation to rapeseed biodiesel it can be obtained that a 10% variation of the non-renewable exergy costs entering the first process (cultivation) results in a variation of 5.5% in the production costs of the biodiesel product.

On the other hand, if we calculate the impact with respect the consumption of non-renewable resources following the elasticity coefficient of eq. (6), we would obtain that an improvement on the efficiency of the system of 10% would result in an improvement of the ExROI value of 7.42%.

$$\frac{\%\Delta F_T^{nrs}}{\%\Delta k_i} = \frac{C_{F,i}^{nrs}}{F_T^{nrs}} \tag{6}$$

This value shows that in face of possible variations, errors or deviations in the introduction of non-renewable resources consumption data into the system, the exergy cost does not vary significantly and, as a result, it indicates that the ExROI value is a consistent indicator.

5. Defossilisation of rapeseed life cycle

This section analyses the impact of different actions that could be introduced in the life cycle of rapeseed based biodiesel in order to defossilise the process and obtain higher ExROI values. Given the allocation system applied as defined by the Theory of Exergy Cost, such actions should focus on reducing the consumption of non-renewable resources; decreasing the production of residues; finding a value for the residues, in order to allocate exergy costs to their flows; and reducing the amount of inputs, which reduces the exergy entering the system and therefore the exergy costs of the products. The results of the actions explained in this paragraph are gathered in table 6.

Starting from the cultivation unit, the first possible action is the use of organic fertilizers instead of inorganic fertilizers which consume high quantities of non-renewable resources. The organic fertilizer considered is compost which provides NPK, for which mass and energy consumption data have been obtained from the EcoInvent database [10]. In such a case, the ExROI value is improved (ceteris paribus) in 58%, i.e. to 3.97.

Another possibility in this stage is the selection of crop varieties with high oil contents. The JEC study considers that rape seeds have a content of oil of 0.405 kg of oil/kg of seed. If we choose a seed with an oil content of 0.445 kg of oil/kg of seed [11], which is a 9.9% higher, an ExROI of 2.56 is obtained, which is a 2% higher that the business as usual case.

Finally, if 50% of the straw produced at the site is collected and considered as a co-product of cultivation instead of a residue, the ExROI is increased up to 3.42 which is a 36% higher than the business as usual scenario. This scenario assumes that by taking half of the straw which otherwise would stay on the ground, no additional use of fertilisers to cover the potential soil quality losses are needed. This is an interesting solution to reduce the allocation of non-renewable exergy costs consumed in this stage to the main product without affecting the fertility of the soil [12].

In the oil extraction process, the most interesting action is the production of biogas from the rapeseed meal obtained. If this biogas is used in the cycle in order to reduce the use of fossil fuels the ExROI value is increased in 18%, i.e. up to 2.95.

In the transesterification unit there are many actions that can be considered. On the one hand, these relate to the substitution of fossil fuel derived methanol by other resources from renewable origin. This would be the case when methanol produced from wood or bioethanol from wheat, are used. In the first case the ExROI value would be increased by 23% (3.08) and in the second case by 14% (2.86). On the other hand, they relate to the partial reintroduction of FAME into the cycle in order to substitute the use of fossil fuels. This substitution could be direct or indirect. Direct substitution consists in the use of biodiesel instead of diesel or heavy oil in the cultivation, drying and transport processes; an indirect use consists in the use of biodiesel instead of fossil energy in the production of the inputs that enter the direct process of the biodiesel production cycle. In both cases, the ExROI is improved by 10% (2.76) and 4% (2.61), respectively, for the considered quantity of biodiesel retrofitted.

On the contrary to what could be considered, the anaerobic digestion of the glycerol of the production cycle in order to produce biogas which would be consequently used in the cycle to substitute fossil sources does not increase the ExROI value, but reduces it in -3% (2.44). This could be caused by the low biogas yield of glycerol.

If instead of producing biodiesel, we consider the refined vegetable oil as a biofuel to be used directly in adapted engines, the ExROI value of this product for which no transesterification would be needed, would be 3.28 which is a 31% higher than for biodiesel. This provides an indication of the weight that transesterification has in the biodiesel life cycle production.

All these actions applied separately do not provide an ExROI value higher than the EROI of fossil diesel fuel, according to Cleveland [9]. However, if we consider the following actions together, we can obtain an ExROI of 26.51 which is 956% higher than the reference situation and quite higher than fossil diesel fuel:

- Use of organic fertilizer instead of inorganic fertilizers;
- Conversion of rapeseed meal to biogas an use in the process;
- Use of seed varieties with high oil content;
- Use of methanol from wood in the transesterification process;
- Partial consumption of biodiesel in the cycle.

Figure 2 shows the productive diagram of this best case scenario with all the recirculations of exergy considered. Table 5 shows the non-renewable exergy costs for this scheme where the improvements have been implemented.

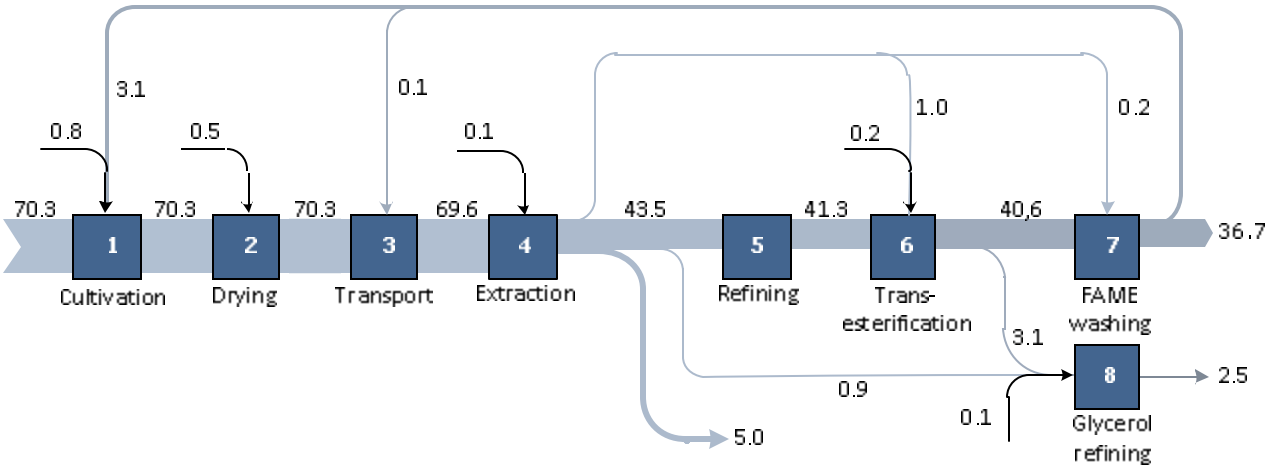

Fig.2. Productive Diagram of rapeseed biodiesel life cycle production combining several defossilisation actions

It is worth noticing that there could be situations that could worsen the ExROI of biodiesel production. For example, in the case that the glycerol produced in the transesterification process could not be sold as a product but instead treated as a residue, due to the saturation of the glycerol market. In this case, the ExROI would be reduced up to 2.33 i.e. a 7% lower than the case of glycerol being a valuable product.

To conclude the analysis, it is important to note that there are certain values and conversion factors that have not been homogenised and could vary substantially, having this variation a significant impact in the ExROI value. This could be the case for example of the exergy content of the rapeseed meal considered. In this paper, the exergy content of the meal has been considered to be 7.4 MJ/kg, which is the metabolisable energy according to [13]. This is the useful energy animals can profit of when eating the meal. If instead this value we take 21.1 MJ/kg which is the value assumed by [14] for the allocation of CO_2 emissions and energy consumption in the life cycle analysis, we obtain that for the same conditions, the ExROI value is increased in 25%, i.e. up to 3.14.

Table 5. Non-renewable production costs of rapeseed based biodiesel applying improvement measures (C_P in MJ/kg FAME)

		Improved process	
Process	Product	c_p^{nrs}	C_p^{nrs}
Cultivation	Seeds	0.013	0.92
Drying	Dried seeds	0.020	1.38
Transport	Dried seeds	0.020	1.39
Extraction	Crude vegetable oil	0.030	1.53
Refining	Refined oil	0.032	1.33
Transesterification	Crude biodiesel + crude glycerol	0.036	1.59
Biodiesel drying	Final biodiesel	0.038	1.51
Gly. purification	Refined glycerol	0.090	0.22

Finally, if EcoInvent database is used instead of the data used in the JEC study, the ExROI value obtained is equal to 2.99, which is 19% higher. EcoInvent is currently the world leading life cycle inventory data source. Taking into account this database the processes and consumption data considered in the cycle are slightly different than the ones considered in the JEC study [6]. These two last results show the need of standardise the input and conversion factors in the methodology of ExROI calculation.

Table 6. ExROI values applying improvement measures and percentage of variation compared to the business as usual scenario

Defossilisation options	ExROI	% increase
Business as usual	2.51	0
Use of organic fertilizers of biologic origin	3.97	58
Using plants with high oil content	2.56	2
Use 50% of straw as a useful co-product	3.42	36
Anaerobic digestion of meal to biogas	2.95	18
Using methanol from wood instead of fossil methanol	3.08	23
Using bioethanol from wheat instead of fossil methanol	2.86	14
Partial consumption of FAME in the cycle (direct use)	2.76	10
Partial use of FAME in the production of resources (indirect use)	2.61	4
Anaerobic digestion of glycerol to biogas	2.44	-3
PVO - Pure Vegetable oil	3.28	31
Combination of several improvement actions	26.51	956
Considering glycerol as residue	2.33	-7
Sensibility analysis: meal higher energy value. Source: I.D.A.E	3.14	25
SIMAPRO EcoInvent database	2.99	19

6. Conclusions

This paper is a continuation of paper [4] published in Energy. There the ExROI value was defined and applied to biodiesel production processes: rapeseed, sunflower and palm oil based biodiesels. Here, the number of biodiesel production processes is widened, including soybean and used cooking oil, and the boundaries of the system have been amplified to take into account not only the direct or primary processes: cultivation, transport, extraction, refining, transesterification; but also the secondary processes, i.e. the processes to produce the materials and energy used in the primary processes. With this, this paper relates the ExROI and exergy costs calculations with the life cycle analysis discipline.

The results show that biodiesel life cycles are sustainable from the point of view of the use of non-renewable resources, although improvements are necessary as the ExROI value is considered to be low in the business as usual scenario. While these values range from 1.69 for soybean biodiesel to 4.54 for biodiesel from UCO, the EROI value of diesel fossil is estimated by Cleveland to be around 6. Given this, it is considered that ExROI values higher than 6 must be achieved. This paper demonstrates that by conjugating several defossilisation improvements, which deal with the substitution of fossil materials by renewable materials, the recirculation of biodiesel and reduction of inputs, ExROI values of around 27 can be obtained, which means more than quadrupling the EROI value of fossil diesel. These measures should also be studied from an economic, social and environmental point of view in order to certify their viability. This work is currently being performed and will be shown in future publications.

Nomenclature

c unit exergy cots

C exergy cost (MJ/kg FAME)

EROI Energy return on energy investment

ExROI Exergy return on exergy investment

F Exergy of the fuel

FAME Fatty acid methyl ester (biodiesel)

FFB Fresh fruit bunches

P Exergy of the product

Subscripts and superscripts

e External resources

eq Equivalent

nrs Non renewable sources

P Product

rs Renewable sources

* Exergy cost

References

[1] CARS 21 High Level Group, Competitiveness and Sustainable Growth of the Automotive Industry in the European Union. Interim Report 2011. Brussels, 2011

[2] Beurskens L.W.M., Hekkenberg M., Vethman P., Renewable Energy Projections as Published in the National Renewable Energy Action Plans of the European Member States, Covering all 27 EU Member States with updates for 20 Member States; 2011. No ECN-E--10-069.

[3] Directive 2009/28/EC of the European Parliament and of the Council of 23 April 2009 on the promotion of the use of energy from renewable sources and amending and subsequently repealing Directives 2001/77/EC and 2003/30/EC. Official Journal of the European Union 5.6.2009.

[4] Font de Mora E., Torres C., Valero A., Assessment of Biodiesel Energy Sustainability Using the Exergy Return on Investment Concept. ECOS 2011: Proceedings of the 24th International Conference on Efficiency, Cost, Optimization, Simulation, and Environmental Impact of Energy Systems; 2011 July 4-7; Novi Sad, Serbia. Linija Projekt 481-431.

[5] Lozano, M.A., Valero, A., 1993, Theory of the exergetic cost, Energy, 18 (9), pp. 939–960.

[6] JEC - Joint Research Centre-EUCAR-CONCAWE collaboration, Well-to-Wheels Analysis of Future Automotive Fuels and Powertrains in the European Context" Version 3c, 2011. Available at : <http://iet.jrc.ec.europa.eu/about-jec/> [accessed 18.1.2012]

[7] Lechón Y., Cabal H., De la Rúa C., Lago C., Izquierdo L., Sáez R.M., Fdez. San Miguel M., Análisis de ciclo de vida de combustibles alternativos para el transporte. Fase I. Análisis de ciclo de vida comparativo del biodiesel de cereales y de la gasolina. Ministerio de Educación y Ciencia y Ministerio de Medio Ambiente, 2005.

[8] Hall C.A.S., Balogh S., Murphy D.J.R., What is the minimum EROI that a sustainable society must have? Energies 2009, 2, 25-47, doi:10.3390/en20100025.

[9] Cleveland CJ. Net energy from the extraction of oil and gas in the United States. Energy 2005;30:769-782.

[10] EcoInvent Centre, Dübendorf, Switzerland. http://www.ecoinvent.org/

[11] Life Cycle Assessment applied to first generation biofuels consumed in France. Department of Bioresources. Directorate of Renewable Energies, Energy Networks and Markets, ADEME, 2009.

[12] Christa K., Elisabeth W., Biomass report. MixBioPells project, Intelligent Energy Europe programme.

[13] Iowa Soybean Association. Comparative Composition of Various Oilseed Meals Available at: < http://www.soymeal.org/table1.htmlhttp://kinetics.nist.gov/ janaf/> [accessed 18.1.2012].

[14] Lechón Y., Herrera I., Lago C., Sánchez López J., Romero Cuadrado L., Evaluación del balance de gases de efecto invernadero en la producción de biocarburantes. Estudio Técnico PER 2011-2020; Madrid, 2011.

Design strategy of geothermal plants for water dominant medium-low temperature reservoirs based on sustainability issues

Alessandro Franco, Maurizio Vaccaro

Department of Energy and Systems Engineering
University of Pisa
Pisa, Italy
e-mail: alessandro.franco@ing.unipi.it

Abstract

A design strategy based on a multidisciplinary approach for a sustainable design of ORC power plants is proposed. The design of a geothermal plant is discussed, with reference to a case study about a geothermal area in Tuscany, in which a geothermal reservoir at 120 °C is estimated to be available at about 500 m of depth. A qualitative model of the reservoir under specific production/reinjection conditions is discussed.
Numerical simulation of geothermal reservoirs is considered an important interacting issue, also to synthesize the data and different scenarios studied. Three factors are fundamental: the maximum energy production, in the perspective of a sustainable exploitation strategy (definition of wells depth and siting, fluid rates extracted/reinjected); the chemical characterization of the fluid (to define the minimum reinjection temperature in order to prevent scaling phenomena); the definition of a reinjection strategy (flow rates, number and depths of reinjection wells and distances between them).
Key results are the temperature and pressure profiles and stored energy reduction in the reservoir during plant lifetime. A power plant output range of 250 – 500 kW is considered in order to keep the temperature decrease in the reservoir in a range of 5 - 10 °C during the expected life of the plant. The case study can be seen also as a general value example to discuss how the sustainability of the medium-low temperature geothermal resource makes the design strategy of these plants different with respect to the other renewable source based power plants.

Keywords:

Geothermal energy, Sustainability, Binary cycle power plants, Medium temperature geothermal field.

1. Introduction

The great part of geothermal resources available around the world are water dominated fields, at temperatures under 150 °C and pressures below 15 bar [1]. The total worldwide expected geothermal potential for power production has been estimated being about 200 GW, [2]. The binary cycle technology using Organic Rankine Cycle (ORC) is the most efficient solution for power production from these fields. Some manufacturers (Pratt & Whitney/UTC, Siemens) have proposed small size (0.2 MW) standard machinery and power conversion systems. This can be a key element for a large diffusion of geothermal binary cycle plants. The size and peculiarity of such plants is often different from the industrial practice of power production from renewable energy sources. Sustainability and operational parameters of the resources become fundamental issues for these utilizations, to guarantee a successful productivity of the power unit and maximize the durability.

Medium-low enthalpy geothermal resources can be available, in many areas, at relatively low depth (less than 1000 m). This circumstance allows a meaningful reduction of drilling and perforation costs on the total cost of the plant. A simulation of the geothermal reservoir and the time variations of temperature and pressure under exploitation conditions should be carried out before the design of the plant, mainly in case of ORC units utilization. This is heavily important for reservoirs at temperatures below 130 °C. Small size power plants (100 kW – 5 MW) are innovative since in traditional geothermal power industry almost only greater sizes (5-200 MW) have been used (flash systems, dry steam plants). Medium-low temperature resources, to be exploited for power purposes with ORC systems, introduce the possibility of small size units. Project sustainability, durability of

the plant and low environmental impact of this technological solution are advantageous key points, although the exploration and characterization phases will assume a huge importance. As their performances are strongly affected by changes in the external parameters (resource, environment), a reliable characterization process needs to be carried out, in order to avoid unacceptable off-design working points.

A multidisciplinary approach to geothermal projects is necessary. The interconnections between Geosciences and Energy Engineering backgrounds have been diffusely remarked, in the perspective of geothermal plants development and diffusion [3].

The main task of the geothermal utilization projects is the sustainable utilization of the reservoirs and the maximization of the durability of the resource (mainly in terms of temperature and pressure). For this reason it is very important to consider and analyze the whole *"geothermal system"* constituted by the power plant, the wells system, the geothermal reservoir and all the links between them and the environment.

The key factors governing the optimization process of the design of a plant are the definition of a sustainable mass flow rate extraction (potential assessment) and the reinjection strategy (taking into account the scaling phenomena) [4], [5]. Typical problems due to an incorrect characterization of the resource available are:

- oversizing of the plant, causing excessive extraction of fluid (the reservoir doesn't replenish the energy stored);
- unacceptable scaling phenomena (causing corrosion, productivity drop, net diameter reduction, damaging);
- excessive cooling of the reservoir or losses of fluid due to wrong reinjection strategy.

Numerical simulation of geothermal reservoirs is considered to be a very useful and strategic instrument both for two main tasks in the power production industry: the history matching of the field data (from the exploration/utilization history) and the forecast about exploitation scenarios. Its reliability depends on the accuracy of the input data (a tough problem is the definition of a reliability scale for decision making about production).

In this study the design of a geothermal plant is discussed, with reference to a case study: a geothermal area in Tuscany, in which a geothermal reservoir at about 120 °C is estimated to be available (at a depth of about 500 m). The optimal production/reinjection and global design strategy for a small size ORC based power plant is discussed.

2. Low-temperature geothermal technology and binary cycle power plants

Medium to low temperature geothermal resources are largely diffused, so that they have become very attractive for electrical power production in the last years. According to the more significant approaches in the literature, the classification of the geothermal resources depends mainly on the temperature value. In Table 1 a classification of the geothermal resources is provided. It is estimated that the major part of the geothermal energy stored worldwide is available at temperatures lower than 150 °C [1-2]. Those resource become particularly interesting when they are available at depths below 1000 m.

Table 1. Classification of the geothermal resources depending on temperature [°C]

	Muffler & Cataldi [6]	Hochstein [7]	Benderitter & Cormy [8]	Nicholson [9]	Axelsson & Gunnlaugsson [10]
Low enthalpy	< 90 °C	< 125 °C	< 100 °C	≤ 150 °C	≤ 190 °C
Medium enthalpy	90 – 150 °C	125 – 225 °C	100 – 200 °C	-	-
High enthalpy	> 150 °C	> 225 °C	> 200 °C	> 150 °C	> 190 °C

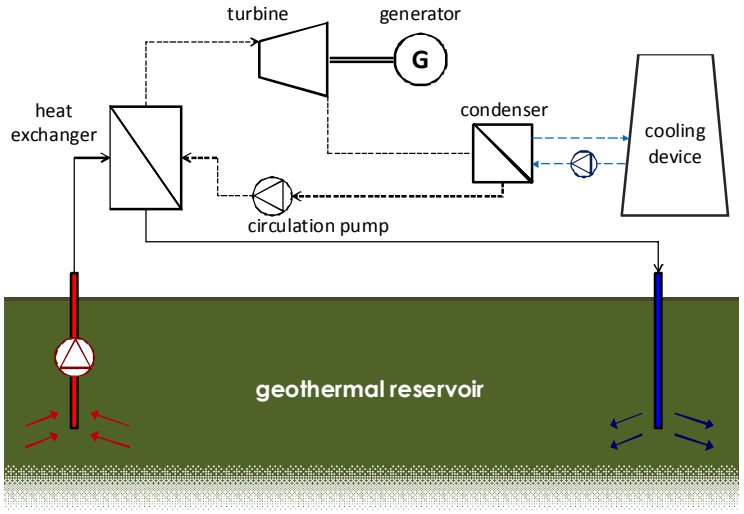

Fig. 1. Scheme of a ORC unit working on a geothermal reservoir, a doublet of withdrawal-reinjection wells is shown

Binary power plants based on Organic Rankine Cycle (ORC) are considered to be the best technology to exploit medium-low geothermal resources (mainly water dominated) at temperature below 180 °C. The operating principle of this plant is represented in the scheme of Fig. 1.
In a binary cycle power plant the heat of the geothermal fluid rate is transferred to a secondary working fluid (usually an organic fluid with a low boiling point than water at a given temperature) through an heat exchanger. The cooled geothermal fluid is then returned to the ground to recharge the reservoir, while the working fluid expands through a turbine, producing electrical power and then is condensed by exchanging heat with the environment (dry or wet cooling).

A geothermal binary power plant is characterized by high brine specific consumption β (kg of fluid extracted per unit of power produced) and low First Law efficiencies η_I (5-10%), even if Second Law efficiencies η_{II} are typically in the range 25-45%. They usually require large heat transfer surfaces both for the recovery heat exchanger and for the condensation system. The parasitic power consumption of this auxiliary system is relatively high because of the need for forced ventilation. A dry cooling system can absorb from 10-12% of gross power (under ideal conditions) to as much as 40-50% if the ambient temperature is very close to the condensation temperature. A diffused literature about this technology is available, often based on specific and local industrial application. The efficiencies of binary cycle plants are very sensible to the external thermodynamic parameters (ΔT of fluid, environmental temperature, fluid pressure, permeability changes), so the characterization of the resource available is a fundamental step.

Recently, binary power plants have been installed in Austria and Germany in applications to medium-low temperature geothermal sources (Bertani [11]). Various studies ([12-14]) demonstrates the relevance of the optimization process applied to ORC units, particularly in terms of efficiencies and fluid extraction. These plants often operate through advanced thermodynamic cycles (dual pressure level Rankine cycle or Kalina cycle) and may also use different or unconventional working fluids, such as ammonia-water mixtures (e.g. Husavik, Iceland). The characteristics of some of those plants are given in Franco [15], in which a table collecting a series of available data is present. The temperature range covered is wide (74-124 °C) so that specific brine consumption lies in the range from 44 to 200 kg/s for each MW of electricity produced.
The remarkable difference among the various plant performances can be explained in al lot of case because of the different temperature interval ($\Delta T=T_{geo}-T_{rej}$) available between the reservoir and the reinjection temperature. A scheme of temperature values of different plants is given in Fig. 2.
Till some years ago each installation was designed for specific conditions at a given location. Every system is generally tailored to specific geothermal fluid characteristics, while the medium and low temperatures applications permit to pursue the perspective of providing “standard machinery”. The possibility of “standard machinery” development is submitted to a proper characterization and

potential assessment of each local reservoir, due to the strong dependence on β, η_I and η_{II} from external parameters (environment/reservoir).

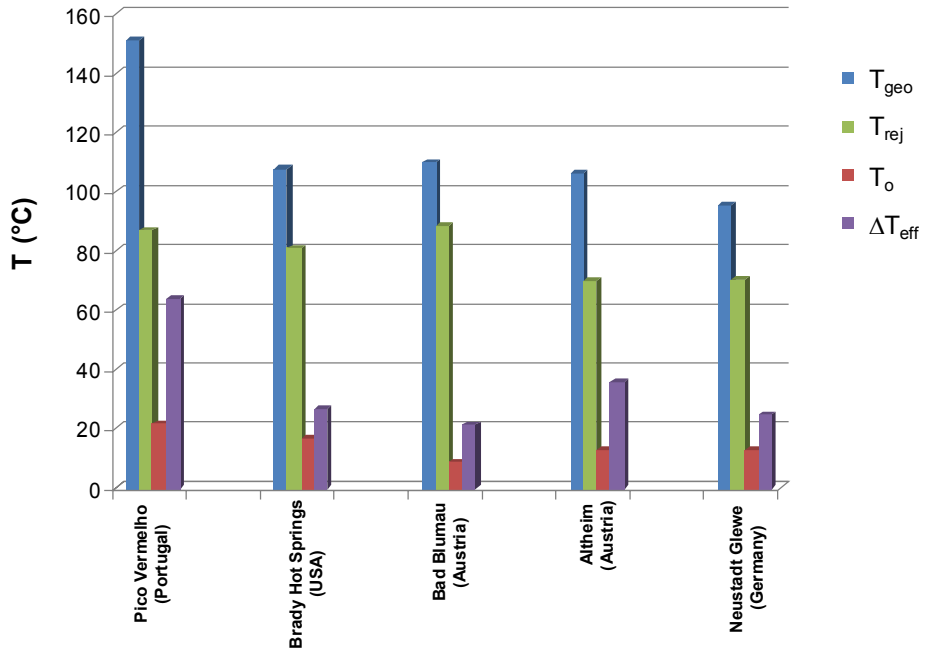

Fig. 2. Temperature values (production – reinjection – environment) in some binary plants.

2.1 Geothermal potential assessment and binary plants

A general methodology for the Geothermal Potential Assessment for every kind of geothermal field doesn't exist, although in literature a lot of different methods and reliable principles have been treated and tested, ([4], [6], [10]). Several studies are about specific geographical areas, more than general value survey and investigation techniques. A lot of instruments are available today to improve the detail of the information needed for the sustainable design of plants.

The geothermal potential of a particular area means particularly the definition of temperature (T_{geo}) and pressure (p_{geo}) of the geothermal fluid and of the maximum mass flow rate ($\dot{M}_{geo}$) that can be extracted maintaining for a long time the thermal properties of the reservoir.

A brief list of the general results that should be evaluated is here proposed: thermal energy stored (at a certain time) in the reservoir; temperature, pressure and rate of the extracted fluid; chemical composition of the fluid and saltiness (to define the reinjection temperature T_{rej}); number of wells to be drilled and mutual distances between them; time interval to have an appreciable decrease in the rate and temperature of fluid (or productivity); definition of both the "Base" resource available and of the "Effective" resource, which is useful under favourable and sustainable (economic-environmental-technological) conditions, [6]; siting of the reinjection wells (number, mutual distances and interference effects); reinjection strategy (effects of reinjection on productivity); number of wells for compensation. The total energy available is the portion extractable and favorably useful of the stored energy in the reservoir. It can be defined roughly multiplying the total energy stored for an appropriate recovery factor (R), [6]. The estimation of the recovery factor is not a trivial task, it depends from the site characterization and it can also be a result of assessment according to the individuals experience.

Let us now consider a water dominated geothermal field at moderate temperature. The energy potential of a geothermal reservoir can be first of all referred to the available temperature of the aquifer (T_{geo}). In the case of water dominated geothermal fields, the energy available can be referred to an equivalent specific thermal capacity of the reservoir (both rocks and fluid), namely $\varepsilon_{(T_{geo}-T_0)}$, which can be defined referring to the cooling down to a low temperature level, in this case the environmental temperature T_0.

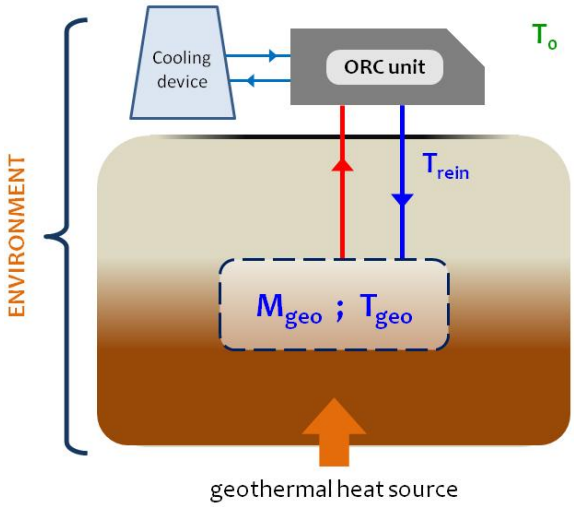

Fig. 3. Sketch of a "geothermal system" for which a geothermal potential can be defined

So if reinjection is considered, as in almost all the geothermal projects today, the useful temperature difference is $\Delta T = \left(T_{geo} - T_{rej}\right)$, being $T_{rej} < T_0$ (see Fig. 2). This means that a mass flow rate higher than $\dot{M}$ should be extracted for power production, according to the upper limit given by

$$\dot{M}^* \cdot c_p \cdot \left(T_{geo} - T_{rej}\right) \leq \dot{M} \cdot \varepsilon_{(T_{geo} - T_0)} \qquad (1)$$

It is important to understand that the upper limit for the energy potential is a function of the whole "geothermal system", as defined in the Introduction and remarked in Fig. 3

$$\Pi = f\left(geothermal\ \ system\right) \qquad (2)$$

The meaning of the last two equations is that, for a given value of maximum energy potential and for a given value of ΔT, a maximum value of mass flow rate (extracted/reinjected), M^*, can be defined. M^* clearly depends on a lot of parameters and factors (both natural and technological): permeability distribution; hydraulic linking between the production and the reinjection areas; siting of the wells; natural recharge (meteoric water) to the reservoir.
Due to the presence of this upper limit it is clear that the value of ΔT used is inversely proportional to the value of M^*. So in case of T_{rej} increasing, induced by unacceptable chemical deposition phenomena, the mass flow rate $\dot{M}$ increases, and it could reach excessive values, causing unwanted cooling down of the whole aquifer. Consequently each reservoir presents an optimal combination of mass flow rate extractable and reinjection temperature and a correct design should follow this rule.
As it can be seen, this optimization problem involves the whole "geothermal system" (plant, reservoir, environment and their mutual links), so a multidisciplinary approach become necessary.
The difference between the temperature of the reservoir (T_{geo}) and the reinjection temperature (T_{rej}), together with the geofluid availability ($\dot{M}_{geo}$ in the following, being equivalent to $\dot{M}$) and the environment reference temperature (T_0) contribute to define the exergy and energy potential of the geothermal field. The power production available from a plant can be defined according to the law

$$W_{net} = \eta_I \cdot \left[\dot{M}_{geo}(h_{geo} - h_{rej})\right] \approx \eta_I \cdot \left[\dot{M}_{geo} \cdot c_{p,geo}\left(T, p\right) \cdot (T_{geo} - T_{rej})\right] \qquad (3)$$

where η_I is the First Law Efficiency of the plant, that is a complex function of the temperature difference (T_{geo}-T_{rej}), of the condensation temperature (strongly influenced by the environmental temperature) and of the particular Organic Rankine Cycle (ORC) used in the binary plant. Considering the specific enthalpy of the geofluid η_I can be defined as follows

$$\eta_I = \frac{W_{net}}{\dot{M}_{geo}(h_{geo} - h_{rej})} \qquad (4)$$

2.2 Binary power plant design and performance parameters

An important performance parameter for the analysis of the geothermal plant is the mass flow rate to generate a fixed power output, or specific brine consumption, which is given by:

$$\beta = \frac{M_{geo}}{W_{net}} \tag{5}$$

It is inversely proportional to the First and Second Law Efficiency, which are defined as

$$\eta_I = \frac{W_{net}}{\dot{M}_{geo} \cdot \left(h_{geo} - h_{rej}\right)} \tag{6}$$

$$\eta_{II} = \frac{W_{net}}{\dot{M}_{geo} \cdot e_{geo}} = \frac{W_{net}}{\dot{M}_{geo} \cdot \left(h_{geo} - T_0 s_{geo}\right)} \tag{7}$$

Previous studies, [3-4] show that the specific brine consumption strongly depends on the difference between reservoir temperature (T_{geo}) and reinjection temperature (T_{rej}), varying from 25-40 kg/s for each MW produced in case of source temperature of 150-160 °C, up to over 100 kg/s for each MW produced in case of T_{geo} = *110 °C*. Due to the medium-low specific enthalpy entering the heat exchanger, this typical values of flow rate have to be considered in terms of design parameters and costs, particularly for small size power plants. The output power depends mainly by the thermodynamic cycle typology of the secondary fluid. Considering the schemes of Fig. 4 and 5 it is

$$W_{net} = W_{gross} - W_{pump} - W_{CS} = m_{w-fluid}\left[\Delta h_{esp} - \frac{v_{w-fluid}\left(p_{sat} - p_{cond}\right)}{\eta_{pump}}\right] - W_{CS} \tag{8}$$

$$m_{w-fluid}\left(h_3 - h_1\right) = M_{geo}\left(h_{geo} - h_{rej}\right) \tag{9}$$

A limited reduction of the temperature of the geothermal source from T_{geo} to $T^* < T_{geo}$, can be compensated by an increase of the mass flow rate extracted. This is possible if the balance

$$\dot{M}^*\left(h^* - h_{rej}\right) = \dot{M}_{geo}\left(h_{geo} - h_{rej}\right) \tag{10}$$

can be maintained even if there is a decline of temperature and pressure in the reservoir, because

$$h^* - h_{rej} \approx c \cdot \left(T^* - T_{rej}\right) \tag{11}$$

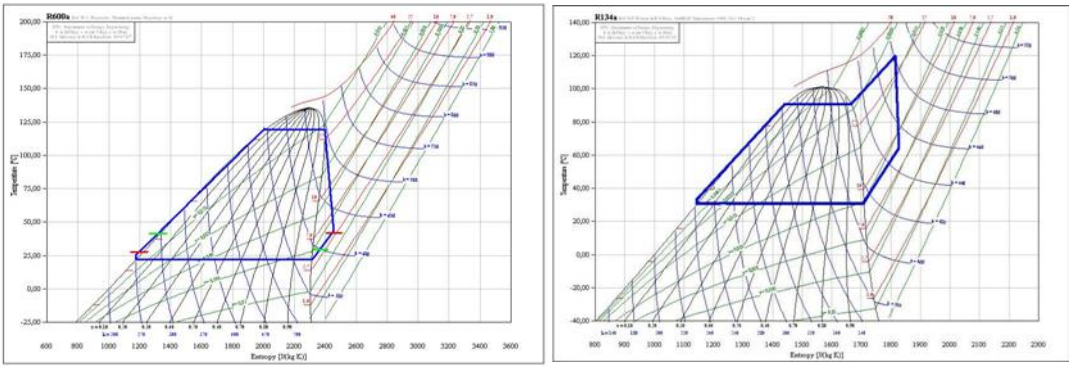

(a) (b)

Fig. 4. Thermodynamic cycles used in binary power plants (fluids R600a and R134a)

A temperature reduction of the geothermal source could cause the end of life of the plant because it could be impossible to maintain a correct pinch-point value in the heat exchanger (in Fig. 5 the decrease of the rejection temperature profile, caused by a decrease of the source temperature, cause a decrease of pinch point from the value *PP1* to the value *PP2*). This problem is important for each typology of ORC, but in particular with reference to advanced heat recovery solutions, like Rankine with superheater, Kalina and Supercritical cycles and for T_{geo} < *120-130 °C*.

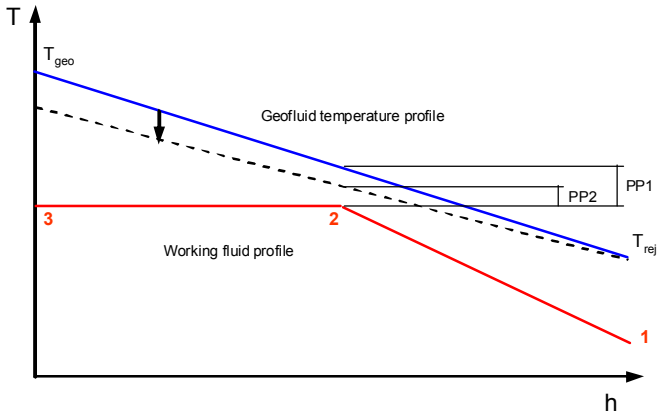

Fig. 5. Temperature profiles trend in the heat exchanger of a binary plant

3. Design strategy for binary cycle power plant

The methodology proposed has the purpose of defining peculiar targets which are characteristic of small size ORC technology. Geothermal resource is totally renewable only under particular conditions, that have to be assured by a sustainable conception of a geothermal utilization project. One of the main aspects remarked in this paper is that the evaluation of the effective sustainability and durability of a project is possible only under the appropriate values of β (considered as the main communication parameter between plant and reservoir) and of the plant size itself. This approach can be easily extended to thermal uses and medium size power plants.

As it has been previously discussed for the geothermal potential assessment, also for the reinjection strategy a general approach can't be defined for every kind of geothermal field. However general validity targets can be individuated, with the main task of maximum sustainability and useful lifetime of the plant. The mutual siting of the production and reinjection wells is often the result of a tough decision process. Numerical simulation of the reservoir circulation system is surely a useful instrument in this operation. The reinjection strategy has the role of keeping the design nominal conditions of extraction to be met for a long lifetime period. Off-design operation of such plants can be very penalizing for the efficiencies and fluid rate consumption (reservoir impoverishment).

Each coupling between a utilization plant and a particular geothermal resource would have a single optimized thermodynamic cycle and ΔT. The coupling itself is going to be considered an optimization parameter, this means that β is not given as a prescribed value. Through a numerical model, which output is the evolution and consequent response of the reservoir under a certain exploitation condition, it would be possible to globally implement this methodology. The optimization of the global "geothermal system", above described, is the synthesis of this approach. Numerical simulations can be run for forecast of future utilization or to reproduce past histories of field utilization. In forecast mode, the specific enthalpy of the geofluid extracted vs. time can be related to a model of the plant power output. Efficiency and energy production can then be estimated from this simulated parameters. A constraint to the off-design condition can be considered, for example to a minimum acceptable percentage of the nominal power output (80 % of W_{net}) to guarantee a fixed lifetime (30 years) of the plant as a possible target.

In the case of fixed design power output an increasing fluid rate should be withdrawn, if $T^* < T_{geo}$ drops, causing a decrease of the lifetime and resource durability. Connecting the numerical simulation results (temperature distribution and fluid circulation) to the plant parameters, if the working configuration is requested to be close to the nominal condition, the profiles of specific enthalpy of the geofluid extracted and power output (vs. time) should be similar.

It is evident that the elaboration of a reliable numerical model of the reservoir has a great importance for the sustainability of a geothermal project. The objective of this study is to propose a methodology for the design of a binary plant using a quite low source temperature. The methodology, of general validity, has been applied to the case of a particular area in Southern Tuscany (near Monterotondo Marittimo, Grosseto, Italy), where a geothermal resource has been

estimated to be available at 400-500 m below the ground level. The study on this field is still ongoing, by other researchers collaborating with the authors, and a detailed description will be object of a further paper. Let us define the resource by the following data (qualitatively): T_{geo} = *110 - 120 °C; p = 15 bar and* T_{rej} = *70 °C.* A condensation temperature range T_{cond} = *30 - 35 °C* is considered. The design of the plant is carried out considering the values of β used in some existing small size plants, in geothermal areas with similar resources (Table 3).

Table 3. Plants tested for adaptation at the geothermal field under analysis

	η_I %	η_{II} %	β kg/kJ	W kW	T_{sat} °C	T_{cond} °C	T_{geo} °C	T_{rej} °C
Bad Blumau (Aus)	1,89	24,57	0,1171	250	86,5	30	110	86
Wineagle (USA)	2,41	24,66	0,0899	300	66	30	110	70
Neustadt (Ger)	1,26	15,12	0,1916	230	80	30	98	78
Simbach (Ger)	0,96	15,11	0,3125	200	65,8	30	78	65

3.1. Numerical simulation of the geothermal reservoir

The models of the geothermal reservoirs are of unquestionably importance even if some limitations and criticalities are well known [3], [5] and [16]. The results reliability strongly depends from the accuracy level of the input data (thermophysical parameters, initial conditions and boundary conditions). Usually these data are known with different precision during the steps of the geothermal project, so a hard work of refinement is necessary to adapt the model to the progressive work of exploration. A schematic workflow for the realization of a numerical model is provided in Fig. 6. Calibration is an important step for the model definition. The possibility of "inverse modeling" approach is well known. It could be important to start with simple models (also lumped parameter models) to clarify the conceptual scheme and the physical consistence of the problem.

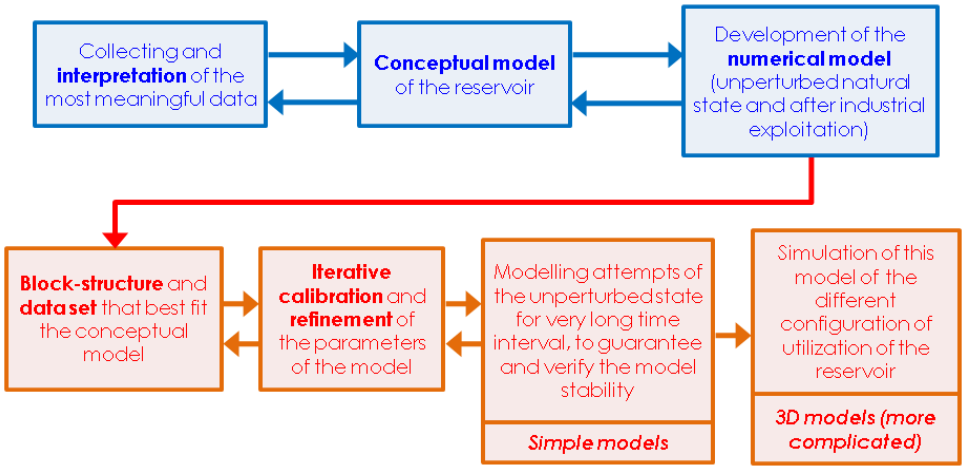

Fig. 6. Conceptual workflow for the realization of a numerical model of a geothermal reservoir

The importance of fields like the one considered is remarkable. In Italy (and generally in the proximities of the main high enthalpy fields) this kind of medium temperature reservoir are going to be exploited in the next few years by a lot of industrial subjects. A numerical model of the Monterotondo Marittimo area of Larderello field (Italy) has been realized using the commercial software Petrasim (in which is implemented the TOUGH2 simulator), [17]. The model domain extension and the various materials used are shown in Fig. 7. The conceptual model of the field is not an aim of this paper, its development is still ongoing in collaboration with other researchers. It will be covered by a further paper the authors are involved in. The model presented can be considered to be a good qualitative representation of the reservoir, and it is here used to elaborate

and underline some specific features of the sustainable design methodology of an ORC power plant. Sensitivity analysis and extension of the scale of the domain are future developments of this model.

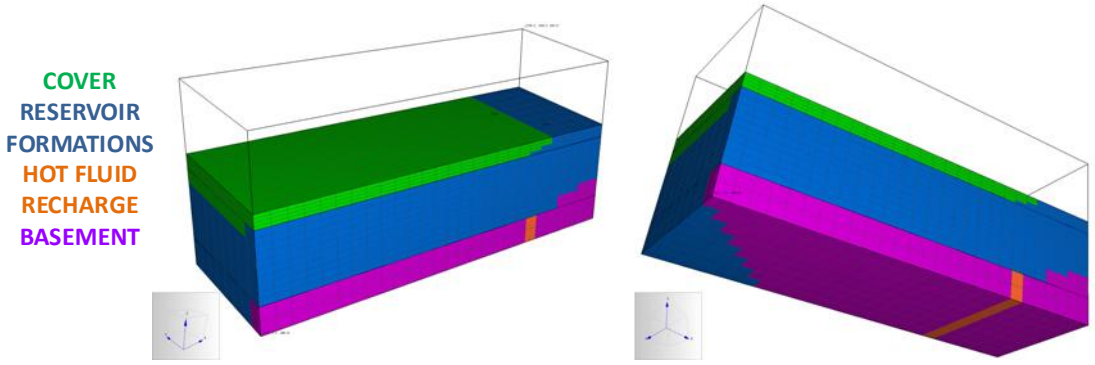

Fig. 7. Model domain and sketch of the main structural features of a numerical model grid of a geothermal reservoir

The model has been built in order to elaborate the optimal production/reinjection strategy for an ORC installation. Simulations of the natural steady-state (unperturbed) conditions of the field have been firstly run and then different exploitation scenarios have been simulated.

3.1.1. Simulation of the exploitation scenarios (ORC power plant)

The study of the particular geological structures and other exploration features will be objects of a different paper in which the authors are involved. Production scenarios have been realized to study the reservoir response to exploitation conditions and to design a possible industrial utilization of the field. The exploitation scenarios simulated are relative to production/reinjection of fluid in case of the presence of an ORC power plant with the following characteristics:

- size of the plant: 200 - 1000 kW (mass flow rate 15 - 100 kg/s)
- reinjection temperature fixed at 70 °C

Model results will be now discussed, linked to the β values and geothermal fluid mass flow rates extraction/reinjection corresponding to relative extraction temperature decrease with time and fixed power output. The value of 15 kg/s the mass flow rate is an average value for the operation of a plant like those described in Table 3, for a plant size of about 200 kW. With this low value of mass flow rate a complete sustainability of the plant is possible, because temperature reductions of 2 °C in 30 years and of about 4 °C in 50 years (Fig. 8).

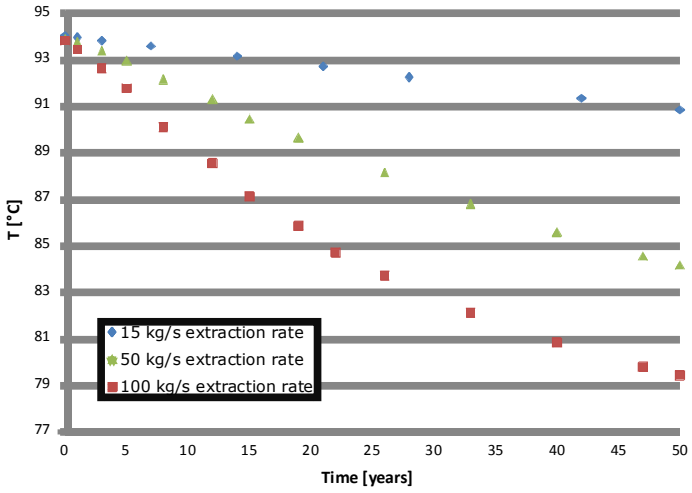

Fig. 8. Simulation of the production scenarios: temperatures at the production well (extraction/reinjection mass flow rates: 15 kg/s, 50 kg/s and 100 kg/s).

A mass flow rate extraction of 50 kg/s (for a power production of about 500 kW) determines a temperature decrease of the source of about 6 °C in 30 years and about 10 °C in 50 years, this

would be critical for the plant so a sufficient life of the plant is not assured. Besides the extraction of a mass flow rate of 100 kg/s (that would permit a power output of about 1 MW) could appear to be unsustainable for this geothermal field. The diagram of temperature reduction during the lifetime of the plant is provided in Fig. 8.

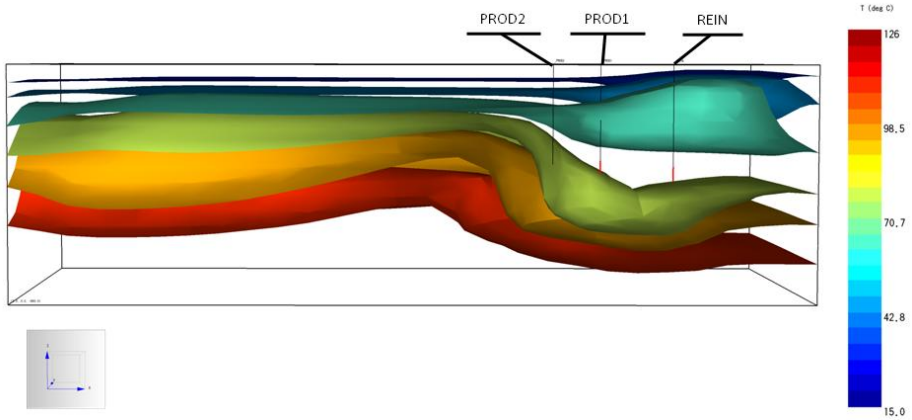

Fig. 9. Temperature iso-surfaces in the scenario with two production wells and one reinjection well.

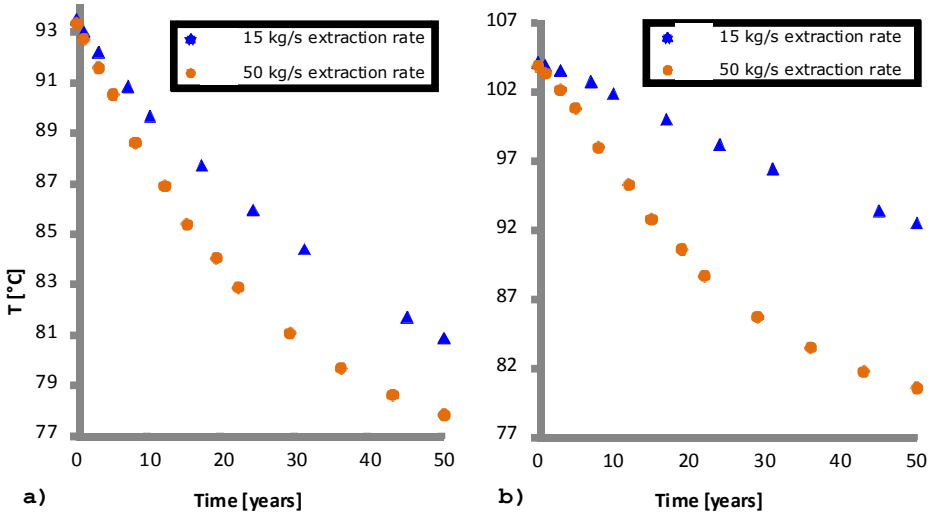

Fig. 10. Temperature evolution for the "PROD1" well (a) and for the "PROD2" well (b).

It is possible to observe temperature decreases of about 11 °C after 30 years of exploitation and 15 °C in 50 years. In both the last two cases it would be difficult to maintain a correct working of the ORC plant. A further layout scenario in which two production wells can be considered ("PROD1" and "PROD2", in Fig. 10) and one reinjection well (where the sum of the extracted flow rates is reinjected). In Figs. 9-10 the simulated extraction temperatures evolution is shown (for a period up to 50 years). For both the production wells the extraction rate of 50 kg/s is unsustainable.

4. Discussion and conclusions

The success of the application of the binary plants depends on a correct design strategy. Their efficiencies are extremely sensitive to external parameters (available ΔT of fluid, environment temperature, fluid pressure, permeability) changes. The characterization of the resource available is a fundamental initial step of each design process and it appears to be more important than the optimization of the plant itself (combination of working fluid and thermodynamic cycle).
Sustainable geothermal power production refers to the optimal extraction/reinjection fluid rate which should be maintained for a very long time, according to certain design parameters of the plant and of the wells system. This task requires an approach that join plant engineering and reservoir engineering in order to avoid overexploitation and pursuing energy-efficient utilization. Careful monitoring and exploration are essential for sustainable reservoir management. The case

study here considered has a general validity value and can be extended to more complex situations, although the model has to be considered as qualitative. Numerical simulation of geothermal reservoirs is a very useful and strategic instrument to elaborate exploitation scenarios and to define a correct reinjection strategy mainly in case of moderate temperature of the source. Its reliability strongly depends on the accuracy of the input data.

The analysis has been developed with a multidisciplinary approach to geothermal systems exploitation considering the interconnections between Geoscience and Energy Engineering, concerning in particular the geothermal energy assessment. The design of a small size geothermal plant has been carried out for the exploitation of a geothermal resource in the Larderello (Italy) geothermal area (Monterotondo Marittimo). A moderate temperature geothermal source (110-120 °C), estimated to be available at relatively low depth (400-500 m below the ground level) has been considered. The adaptability of plants size of about 200 kW or discrete multiples (up to 200 kW x 5 = 1 MW) is analyzed with the support of a numerical model of the reservoir in order to elaborate a production/reinjection strategy. According to the qualitative model elaborated, a plant size of 200 kW could be run sustainably for a period of almost 30 years; the geofluid rate is estimated to be not higher than 20 kg/s. Higher fluid rates (for example twice the previous size) would be critical for the resource durability. The extraction of a mass flow rate of 100 kg/s, that would permit a power production of the order of magnitude of 1 MW, appears to be unsustainable.

Acknowledgments

The authors want to acknowledge Vera Trinciarelli (Bachelor Degree in Energy Engineering at the University of Pisa) and Arianna Secchiari (Master Degree in Geological Sciences at the University of Pisa) among others, for their contribution in the Monterotondo numerical model.

Nomenclature

c specific heat at constant pressure, J/(kg K)

e specific exergy, J/kg

h specific enthalpy, J/kg

p pressure, bar

m mass flow rate of the working fluid, kg/s

M mass flow rate of the geothermal fluid, kg/s

Q heat flow rate, W

T temperature, °C

T_o reference temperature, K

W power. W

v specific volume, m^3/kg

Greek symbols

β specific brine consumption, kg/MJ

ε specific thermal capacity of the reservoir, kJ/kg K

ΔT temperature difference, °C

η efficiency

η_I First Law efficiency

η_{II} Second Law efficiency

Π function of the whole "geothermal system"

Subscripts and superscripts

cond at the condenser

CS of the cooling system

geo of the geothermal brine

gross gross power
liq of the saturated liquid
net net value (of the power)
pump of the pump
rej rejection
sat saturation
w-fluid of the working (organic) fluid
* value of mass flow rate, temperature and enthalpy of the reservoirs after exploitation

References

[1] Barbier E., Geothermal energy technology and current status: an overview. Renewable and Sustainable Energy Reviews 2002; 6: 3–65.

[2] Stefansson V., World Geothermal Assessment. Proceedings World Geothermal Congress 2005; 2005 Apr 24-29; Antalya, Turkey.

[3] Franco A., Vaccaro M., An integrated "Reservoir-Plant" strategy for a sustainable and efficient use of geothermal resources. Energy 2012; 37: 299-310.

[4] Axelsson G., Sustainable geothermal utilization e Case histories; definitions; research issues and modelling. Geothermics 2010; 39: 283-291.

[5] Vaccaro M., Franco A., Casarosa C., Strategies for the Sustainable Use of Geothermal Reservoirs. In: Conference Proceedings of the first Sustainable Earth Sciences Conference; 2005 Nov 8-10; Valencia, Spain.

[6] Cataldi R., Muffler P., Methods for regional assessment of geothermal resources. Geothermics 1978; 7: 53-89.

[7] Hochstein, M.P., Classification and assessment of geothermal resources. In: Dickson, M.H., Fanelli, M. editors. Small Geothermal Resources. A Guide to Development and Utilization, Rome, Italy, 1990. pp. 31–57.

[8] Benderitter Y., Cormy G. Possible approach to geothermal research and relative cost estimate. In: Dickson M.H., Fanelli M., editors. Small geothermal resources. A Guide to Development and Utilization, Rome, Italy, 1990. p. 61–71.

[9] Nicholson K., Geothermal Fluids. Springer-Verlag, New York, 1993.

[10] Axelsson G., Gunnlaugsson E. Long-term Monitoring of High- and Low-enthalpy Fields under Exploitation. World Geothermal Congress, Kyushu Japan, 2000, 226 pp.

[11] Bertani R., Geothermal power generation in the world 2005–2010 update report, Geothermics 2012, 41: 1-29.

[12] Hettiarachchi H.D.M., Golubovica M.,Woreka W.M., Yasuyuki I., Optimum design criteria for an Organic Rankine cycle using low-temperature geothermal heat sources. Energy 2007; 32: 1698–1706.

[13] Franco A., Villani M., Optimal design of binary cycle power plants for water-dominated, medium-temperature geothermal fields. Geothermics 2009; 38: 379–391.

[14] Tchanche B.F., Lambrinos Gr., Frangoudakis, A. Papadakis G., Low-grade heat conversion into power using organic Rankine cycles – A review of various applications, Renewable and Sustainable Energy Reviews 2011; 15: 3963-3979.

[15] Franco A., Power production from a moderate temperature geothermal resource with regenerative Organic Rankine Cycles. Energy for Sustainable Development 2011; 15: 411-419.

[16] O'Sullivan M.J., Pruess K., Lippman M.J., State of the art of geothermal reservoir simulation. Geothermics 2001; 30: 395-429.

[17] ThunderHead engineering. PetraSim 5 user manual. (http://www.thunderheadeng.com).

Energy and Environmental Benefits from Waste Management: Experimental Analysis of Sustainable Landfilling

Francesco Di Maria[a], Alessandro Canovai[b], Federico Valentini,[b] Alessio Sordi[a], Caterina Micale[a]

[a] *Dipartimento di Ingegneria Industriale, Perugia, Italy, fdm@unipg.it*
[b] *GESENU spa, Perugia, Italy, f.valentini@gesenu.it*

Abstract:
Sustainable landfilling is an innovative way of managing waste disposal plants, leading both to environmental and energy benefits. The rapidity of the anaerobic biodegradation process of the biodegradable fraction of urban waste can be improved by combining aerobic with anaerobic treatment. Aerobic pre-treatment of the waste, ranging from 15 to 60 days, together with leachate recirculation, can lead to the production of more than 170 Nm^3 per tonne of Volatile Solids disposed of in the landfill. The anaerobic biodegradation process can take from 3 to 14 years, depending on some differences in landfill management. Further, the total amount of renewable electrical energy able to be recovered ranges from 42 to 44 GWh, and the biomethane loss can be reduced to less than 39% of the total production.

Keywords:
Anaerobic biodegradation, Biomethane, Bioreactor, Landfill Gas, Renewable energy

1. Introduction

In the past, sanitary landfills or dumps were often the only way that Municipal Solid Waste (MSW) was managed around the world [1], [2]. As known [3], under anaerobic conditions, MSW can spontaneously generate a large amount of biological gas with a high content of methane. This phenomenon occurs when the MSW is disposed of in landfills or dumps. The management of MSW is one of the most relevant sources of anthropogenic Green House Gas (GHG) [3], from about 3 to 13% of the total amount. In the EU27 [4], the total production of MSW is about 260 Mtonnes (2008) and about 105 Mtonnes (42%) are managed directly by landfilling. Even if the amount of landfilled waste has been reduced significantly in the last years, it is, nevertheless, a current serious environmental hazard and an important source of renewable energy. The theoretical amount of Landfill Gas (LFG) able to be produced per tonne of landfilled MSW has been estimated to be about 130-160 Nm^3 [5], with a methane fraction ranging from 45 to 55 %v/v [6]. The remaining fraction is mainly carbon dioxide (from 55 to 40 %) together with other macro and micro concentration compounds [3], [6]. These values can be significantly influenced by many factors (*i.e.* waste composition, collection, pre-treatment, landfill management,…), but in any case they show the importance of the phenomenon and the need to provide suitable management to avoid risks to human health and the environment. Furthermore, the LFG is produced from the biological degradation of biodegradable waste and for this reason is considered a renewable energy source. The amount of renewable energy produced from LFG [7] in the EU25 was about 3,000 ktoe in 2010, with about 12% coming form Italy. Unfortunately, as a consequence of the most commonly used landfill management techniques, also consisting in achieving maximum separation between the

disposed waste and the external environment, a large fraction of the potential energy of LFG is missed. This is due to the loss of LFG during waste disposal activities, before and during energy recovery system implementation, and to typical inhibition phenomenon occurring once the anaerobic process starts, which can affect the methanogens phase. In fact, this last effect causes a large fraction of LFG to be produced at such a low rate for a long period of time that energy recovery is not sustainable. Furthermore, the low degradation rate of the organic material in the waste also causes a high pollutant content of the landfill leachate for a long time, making its management a serious and costly problem. All these negative aspects can be dealt with using a different management concept, based on the sustainable landfill scheme [8]. The aim of this alternative management strategy is to enhance the natural, biological process occurring in the body of the landfill in order to achieve a more rapid stabilization of the disposed waste. According to this concept, the landfill is managed as a bioreactor. This can lead to some advantages such as an increase in energy recovery from the LFG along with reduction of the time required to reach a high level of stabilization of the waste. Assuming a constant LFG potential of the waste disposed of in the landfill, theoretically a bioreactor landfill should be able to produce the same amount of gas in less time (Fig. 1). This would reduce the LFG losses, leading to further increase in recoverable energy, due to the exploitation of a larger size Internal Combustion Engine (ICE) with a greater electrical efficiency [9]. One of the methods used for enhancing biodegradation processes is recirculation of the leachate, to provide an adequate moisture content and bacterial distribution [10], [11] [12]. The enhanced bioconversion of the waste into LFG also produces an increase in the waste settlement process, leading to a further advantage, which is the increased amount of waste actually able to be disposed of in the landfill per unit of volume. Also the amount of polluting leachate can be significantly reduced. Appropriate treatment of the waste before being disposed of can improve the biological stabilization process pursued by the sustainable/bioreactor landfill management along with a reduction of LFG loss. In this study, the effect of mechanical and aerobic pre-treatment of the LFG produced from waste disposed of in a bioreactor landfill was analyzed. The study focused on the MSW collected and managed in a given Italian area, and the possible energy and environmental benefits were also been evaluated.

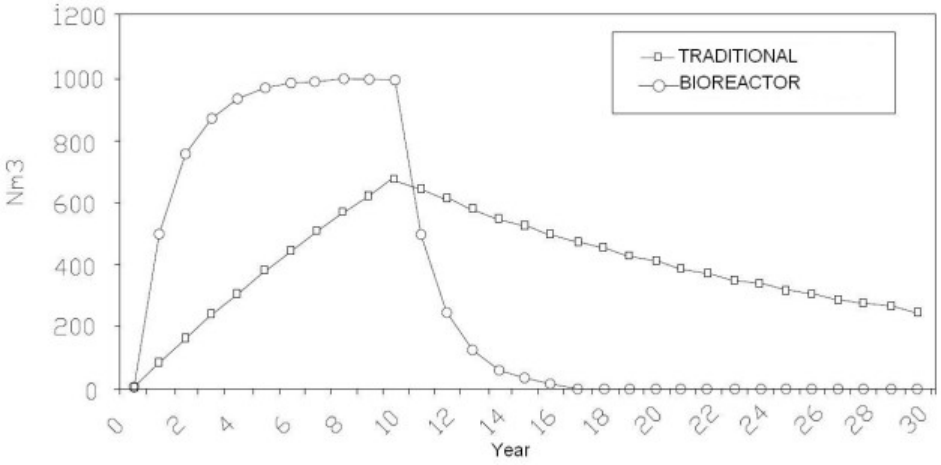

Fig. 1. Comparison of LFG production by traditional and bioreactor systems .

2. System description and Methods

2.1. The MSW management area

The MSW management system considered was Management District (MD) n°2 of the Umbria Region in central Italy (Fig. 2). The amount of waste produced in this area is about 250,000 tonnes per year and the resident population is about 350,000 inhabitants (Table 1). In MD n°2 only one Mechanical Biological Treatment (MBT) plant operates, treating the NonDifferentiated Waste (NDW) resulting after source selected collection. The aim of the MBT facility is to increase the amount of recovery of waste materials and to reduce both the mass and the reactivity of the residual waste mass before landfilling. This aim is pursued by mechanically sorting the NDW, by metal separation and size screening, followed by biological treatment. The screening is basically done using trommels with 100mm diameter holes, which produce an oversize stream of dry components (*i.e.* plastic, paper and textile), with a high Lower Heating Value (LHV) and is exploitable as fuel in co-combustion or in Waste-to-Energy (WtE) plants. The undersize stream, representing about 50% w/w of the NDW entering the plant, is rapidly biodegradable materials (*i.e.* yard trimming, household waste, kitchen residues) and is further treated in the aerobic biological section of the MBT plant. In this section aerobic biodegradation of the material stabilizes the waste along with a significant mass reduction. After this treatment the undersize material is disposed of in the existing landfill, which is close to the maximum disposal volume allowed. At the beginning of 2012, the construction of a new landfill was started, which includes leachate recirculation.

Table 1. Main features of MD n°2.

Parameter	*Value*	*Unit*
MSW (2016)	255,575	Tonnes/year
Inhabitants	349,703	-
NDW at MBT inlet	476	Tonnes/day
Undersize	50	% of NDW(1)

(1)Evaluated at trommel outlet.

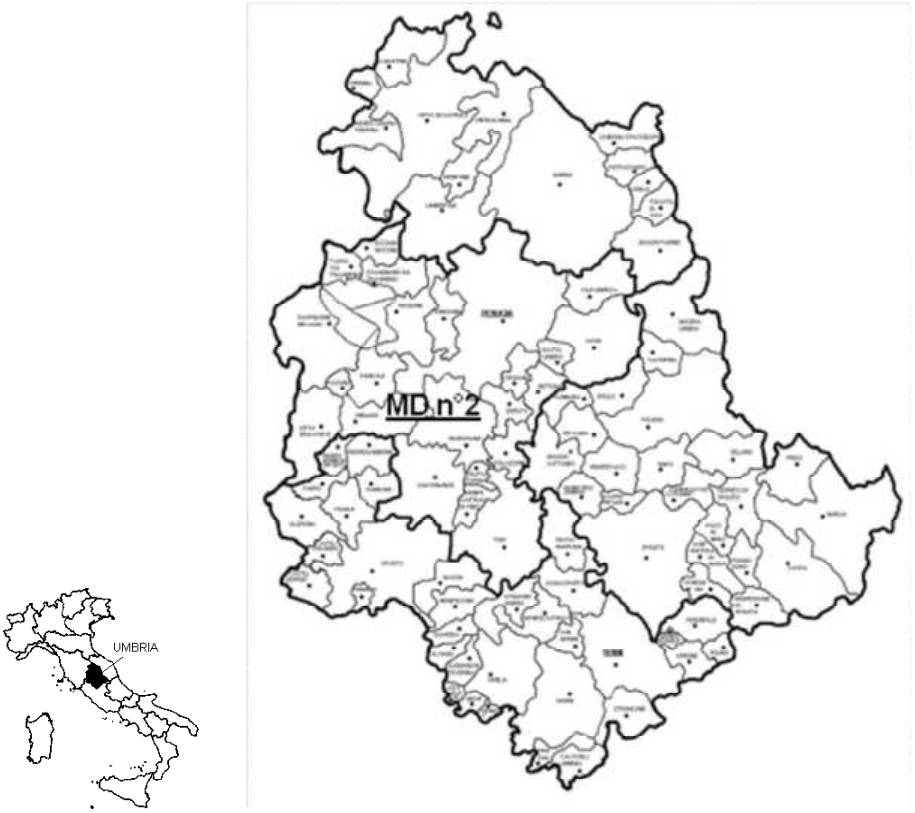

Fig. 2. Umbria region and position of Management District n° 2 (MDn°2).

Due to the large amount of the undersize and its rapid biodegradability, a large amount of LFG can be produced once it is disposed of in the bioreactor landfill. Unfortunately, due to the high Total Solids (TS) content and low pH value of the undersize, some inhibition phenomenon can occur during anaerobic degradation. To avoid or manage this, leachate recirculation and aerobic pre-treatment before disposal could be solutions. This last aspect is the focus of the present analysis.

2.2. Waste characterization

Waste samples were characterized both by make up of the components and by chemical and physical analyses. The components were analyzed manually as Non-Biodegradable (NB), Biodegradable and fines (20S) (*i.e.* particles<20mm).

The Total Solids (TS) were determined by weight loss, on wet basis, after heating the sample at 378K for 24 h. The Volatile Solids (VS) were determined by measuring the weight loss of the TS after heating at 823K for 6h [13]. All tests were done in triplicate.

2.3. Experimental tests

Three different experimental apparatus were used in the study. The first consisted in two modified bins (BIN 1, BIN 2) with a volume of 800 litres each, for simulating the aerobic pre-treatment phase. The process air was supplied through a grid at the bottom of the bin, using an electric fan to deliver 1 Nm^3/h [14]. Each bin contained about 250 kg of undersize material. The second apparatus consisted of an anaerobic vessel, working at mesophilic conditions (308K), to determine the Biogassification Potential (BP) of the undersize (Fig. 3), which is the maximum amount of biogas, in this case LFG, able to be produced by the material considered. The BP runs were started by using inoculums from previous laboratory mesophilic anaerobic digestion of cow manure. The third apparatus consisted of gastight cylindrical anaerobic reactors, with a volume of about 12 litres, and a removable top for determining the Landfill Gas Yield (LFGY) of the undersize arising from the aerobic apparatus. This is a modified incubation test as proposed by Binner and Zach [15] for determining the LFG produced by the waste considered. These anaerobic reactors process from 3 to 5 kg of undersize sample, without inoculum, and are kept at mesophilic conditions by the aid of a thermal bath. The LFGY was determined using a water displacement apparatus conceptually similar to the one shown in Figure 3 for the BP run. CH_4 and CO_2 content (%v/v) from LFGY run, were determined with infrared sensors (±1%), whereas O_2 and H_2S %v/v were determined with electrochemical cells (±2%). In this way the Bio Methane Yield (BMY) expected for the waste, once disposed of in the bioreactor landfill, was evaluated. Other LFG components were grouped in a balance term.

Table 2. Composition of the undersize.

Main Component	*Component*	*Amount (%w/w)*
NB	Plastics	3.90
	Metals	0.50
	Glass	4.30
	Others	1.10
Biodegradable	Organic & green.	29.4
	Paper & Cardboard	1.30
	Others	0.10
20S	20S	58.7

The runs consisted in evaluating the effect of 0, 15, 30, 60, 90 and 120 days of aerobic pre-treatment of samples both on the BP and on the LFGY. Also the Main Components of the undersize waste samples were determined. Simulation of the leachate recirculation process, taking place in the bioreactor landfill, was done by achieving saturated conditions. This was realized by immersing the waste in demineralised water for 24h, and then draining for 6 h before putting it in the LFGY reactor. The results obtained from the runs were also used to evaluate the energy producible from the sustainable/bioreactor landfill. The main assumptions made (Table 3) concern the fraction of LFG actually recoverable related to the total amount produced, the net electrical efficiency of the Internal Combustion Engine (ICE) and the minimum amount of the disposed waste (Min. V_{cell}) activated as bioreactor.

Table 3. Main energetic assumptions.

Parameter	*Value*	*Unit*
Fraction of LFG recoverable	0.75	Nm^3/Nm^3
ICE electrical net efficiency	35	%
Min. V_{cell}	200,000-500,00-1,000,000	m^3
Landfill Volume	1,000,000	m^3
Disposed waste density	1	tonne/ m^3
CH_4 LHV	9.58	kWh/Nm^3
Min. CH_4 rate	50,000	Nm^3/month

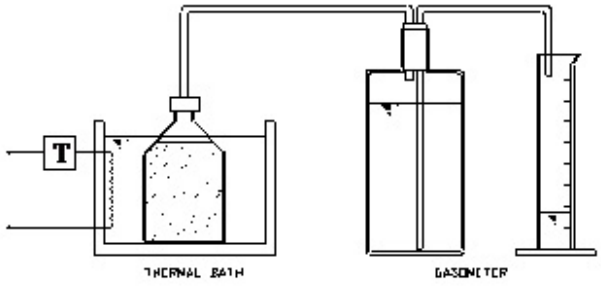

Fig. 3. Scheme of the BP experimental apparatus.

3. Main results and discussion

Table 2 reports the composition of the undersize material. All the unclassifiable fines are denoted as 20S; these include stones, metal, sand, glass, but also a large amount of biodegradable substances. For this reason, the biodegradable, together with the Organic & green Main Components represent about 90 % w/w of the entire undersize sample. Figure 4 shows the fractions %w/w of the samples withdrawn from the aerobic apparatus after different days of treatment. It can be seen that there was a constant reduction of the biodegradable fraction and a simultaneous increase of the 20S fraction. The NB fraction remained quite constant for all the samples.

During aerobic treatment the waste temperature (T) rose rapidly (Fig. 5), reaching the maximum at about 333-338 K around the 7th day. After 20 days, the temperature values dropped until reaching ambient temperature. At the same time, the moisture content of the waste decreased going from about 43% at day 0, to about 20%, at day 90. Due to the strong inhibition to the biological aerobic

process caused by the low moisture content , around day 100, about 45 litres of water were spread on the waste, causing an increase in the moisture content of the sample.
The efficiency of the methanogens activity in the LFGY run was evaluated by determining the Biogassification Efficiency (BE) expressed by eq. (1). In this way it is possible to evaluate how the aerobic pre-treatment is able to influence this important aspect of the anaerobic biological process. Figure 6 shows the BE of the samples with up to 120 days (j) of aerobic pre treatment. It was very low for the sample at day 0, and increased as the days of aerobic treatment increased.

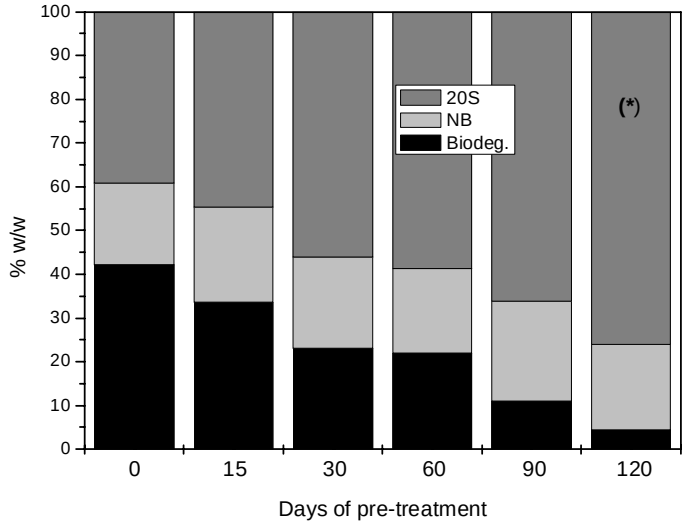

Fig. 4. Different percentages of contents of the Main Component with respect to number of days of aerobic pre-treatment.

**Addition of 18% w/w of water.*

$$BE = \frac{LFGY_j}{BP_j} \cdot 100\,(\%) \qquad (1)$$

As known, one of the main problems occurring during anaerobic biodegradation of waste disposed of in a landfill is acidification. Due to a high concentration of solids, alcoholic fermentation causes a high production of fatty acids that causes inhibition of methanogens bacterial activity along with pH reduction [16]. Aerobic treatment serves to rapidly reduce the amount of biodegradable material of the waste, reducing production of fatty acids during alcoholic fermentation and, consequently, inhibition of methanogens bacteria. This causes a reduction of the BP and an increase in the LFGY as the time of aerobic pre-treatment increases. The sample with 120 days of pre-treatment showed an opposite trend as a consequence of the addition of water process that allowed a further reduction of the amount of biodegradable substrate, during aerobic pre-treatment.
As shown in Figure 7, the longer is the aerobic pre-treatment time, greater is the amount of LFGY produced in the first days of the anaerobic process. This means that energetic exploitation of the LFG can start earlier. This advantage seems to achieve its peak for the samples with more than 90 days of treatment. Shorter times of pre-treatment led to a slower rate of LFG production in the first days of anaerobic process activation, but to a higher total LFGY. As expected, inhibition caused a very low LFGY for the day 0 samples. The amount of biomethane actually exploitable as fuel in ICE, *i.e.* with $CH_4 \geq 40\%$v/v, [16] varied significantly among the different runs, depending on the aerobic pre-treatment time (Fig. 8). The maximum biomethane yield was achieved for the runs with 15 to 30 days of aerobic pre-treatment. For longer times of aerobic treatment, the biomethane yield dropped drastically, even if the LFGY remained quite high. Furthermore, for aerobic treatment

ranging from 15 to 30 days, the biomethane production started more rapidly in comparison to the other runs.

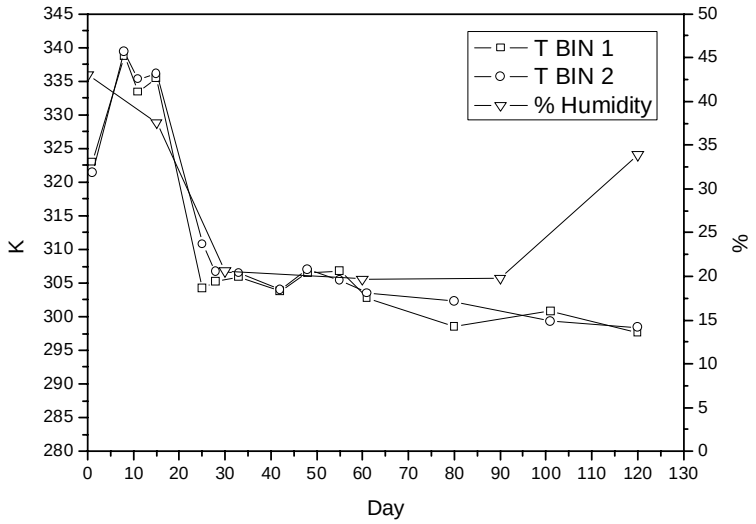

Fig. 5. Temperature (K) and moisture content (%) of the waste during aerobic pre-treatment.

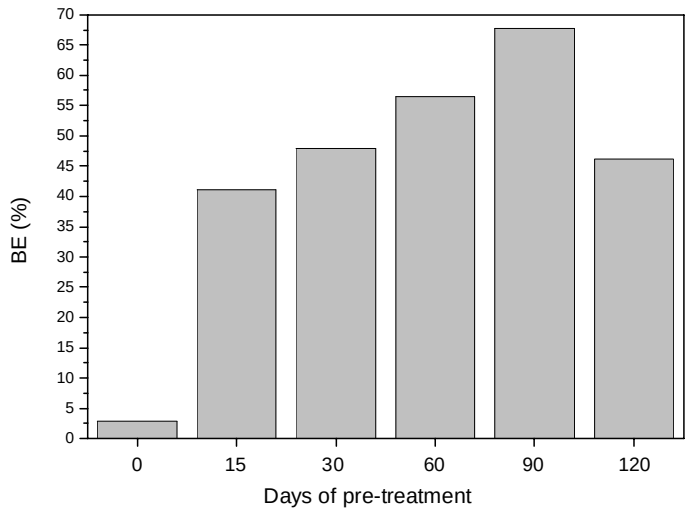

Fig. 6. BE of samples with respect to days of aerobic pre-treatment.

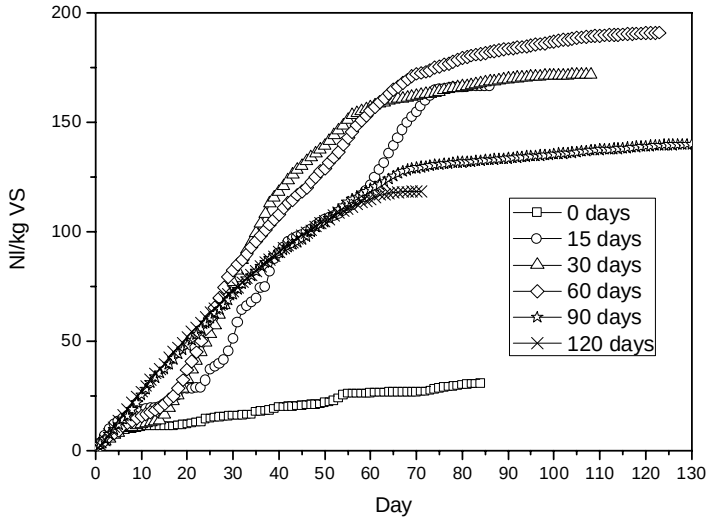

Fig. 7. LFGY with respect to days of aerobic pre-treatment.

Table 4 reports the BMY, the amount of BMY available for Energy Recovery (ERBM), eq. (2), and the amount of specific (*i.e.* per kg VS) Electrical energy ($E_{el,sp}$) recoverable (Table 3) from the bioreactor landfill with respect to the length of time of the aerobic treatment.

$$ERBM = \frac{BMY(CH_4 \geq 40\% v/v)}{BMY} \cdot 100 \quad (\%) \tag{2}$$

The best results from the energy point of view were achieved by an aerobic pre-treatment of 30 days. For this reason, evaluation of the performance of a full-scale bioreactor was based on this length of pre-treatment.

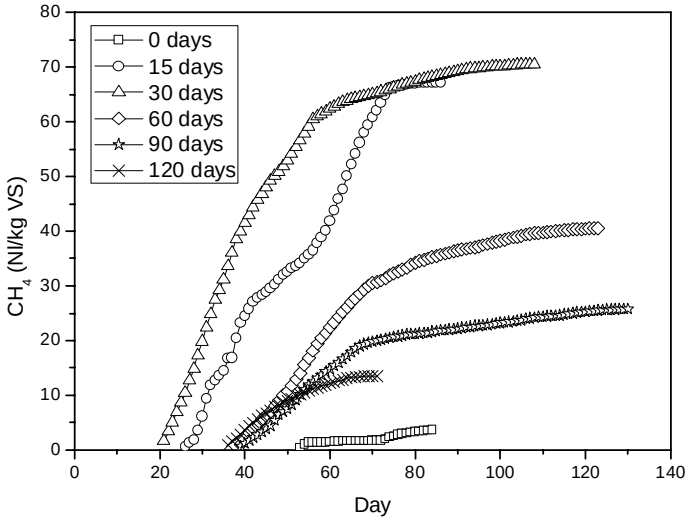

Fig. 8. Bio-Methane available for energy recovery with respect to days of aerobic pre-treatment.

Table 4. BMY, ERBM and the specific electrical energy recoverable from a bioreactor landfill with respect to length of time of aerobic pre-treatments.

Day	*BMY (Nl/kgVS)*	*ERBM (%)*	*$E_{el,\ sp}$ (Wh/kgVS)*

0	7.834	46.30	9.12
15	74.54	90.14	168.97
30	78.17	90.26	177.44
60	70.31	57.72	102.05
90	46.69	55.15	64.75
120	33.94	39.87	34.02

On the basis of the experimental daily LFG production curves and on the basis of the Landfill Gas Emission Model (LndGEM) model [18], the expected monthly bioreactor LFG production curves (Nm^3/month) were calculated. Further, considering the assumptions reported in Table 3, including the minimum monthly CH_4 rate and the amount of gas actually recoverable from the landfill, the total electrical energy production, the total amount of biomethane produced and the fraction of biomethane lost were calculated. Figure 9 shows the LFG, the total biomethane production and the monthly amount of biomethane available for energy recovery, obtained from the bioreactor landfill, assuming a Min V_{cell} of 200,000 m^3. Every 40 months leachate recirculation starts to activate the anaerobic phase. The amount of energy actually producible is about 42 GWh in about 170 months (Table 5). The biomethane produced, but not exploitable for energy recovery, is about 8,226,698 Nm^3, which is 39.55% of the total amount produced (Fig. 9). When the Min V_{cell} is 500,000 m^3 (Fig. 10), the total amount of energy recoverable is about 44 GWh (Table 5). Energy recovery is possible in two different periods of about three years each, separated by periods of about 5 years during characterized by a low LFG rate and quality (i.e. methane content). In this case the biomethane lost is 37% of the entire biomethane produced. Finally, if bioreactor is activated when the Min V_{cell} is of 1,000,000 m^3, the total amount of energy recoverable is about 45 GWh for a period of 3 years (Table 5). The biomethane lost is about 7,500,000 Nm^3, which is 36% of the total production.

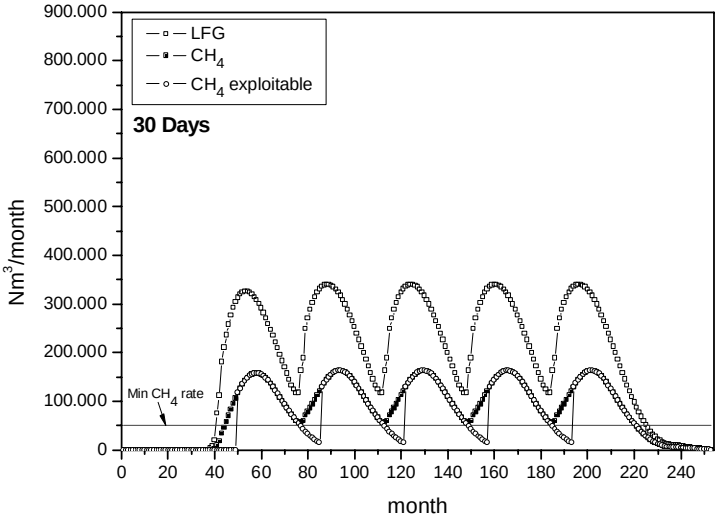

Fig. 9. Rates of LFG, biomethane and biomethane actually exploitable for a bioreactor landfill with 5 cells with a Min V_{cell} of 200,000 m^3.

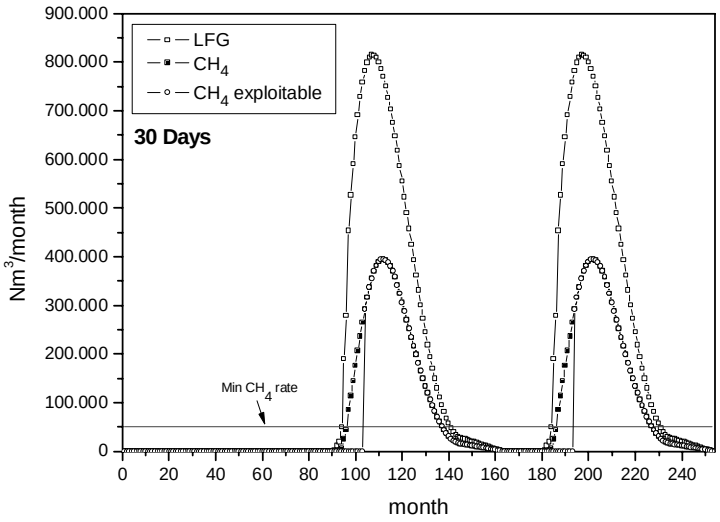

Fig. 10. Rates of LFG, biomethane and biomethane actually exploitable for a bioreactor landfill with 2 cells with a Min V_{cell} of 500,000 m^3.

3.1. Discussion

It is well known that MBT pre-treatment can produce an increase in recoverable waste material together with a reduction in the volume used for landfilling. Aerobic pre-treatment of the undersize fraction reduces the amount of the biodegradable material of the landfilled waste. This also has a positive effect on the quantity and quality of the LFG produced. Leachate recirculation creates optimal conditions for bacterial activity that can be enhanced by combining it with a suitable length of time of aerobic pre-treatment.

More efficient biological activity results in a higher LFG rate and a faster waste stabilization process. This implies both energy and environmental advantages. Waste stabilization also reduces the leachate pollutant content together with the amount of LFG loss. Furthermore, the experimental tests showed how aerobic pre-treatment can play an important role in preserving the energetic potential (*i.e.* LFGY) of landfilled waste from the time of disposal to the beginning of the energy recovery phase (*i.e.* leachate recirculation). This is another relevant aspect, which can contribute to achieving sustainable management of the landfill. In fact, during the construction phase, the amount of gaseous emissions is greatly reduced.

Another relevant question concerns the landfill management. Results show that lower is the volume of the disposed waste inside the landfill cell activated as bioreactor, lower is the amount of energy recoverable and higher is the biomethane loss. This depends on the particular effect caused both by the length of time before the methane concentration becomes ≥40%v/v and by the LFG rate suitable for energy recovery. Lower is the amount of disposed waste for the activation of a bioreactor cell, higher is the amount of biomethane lost for the aforesaid causes. Hence, theoretically, from the energy and environmental points of view, the optimal size of the minimum volume of disposed waste to be activated as bioreactor, for the landfill considered, is about 1,000,000 m^3. In practice when operating with larger volume cells, the variation in the LFG rate is very great (Figs. 10 and 11), with a very narrow maximum value. This can lead to some problems in the actual possibility of recovering the entire biogas energetic potential due to the significant variation in the size of the energy conversion system required during the energy recovery period.

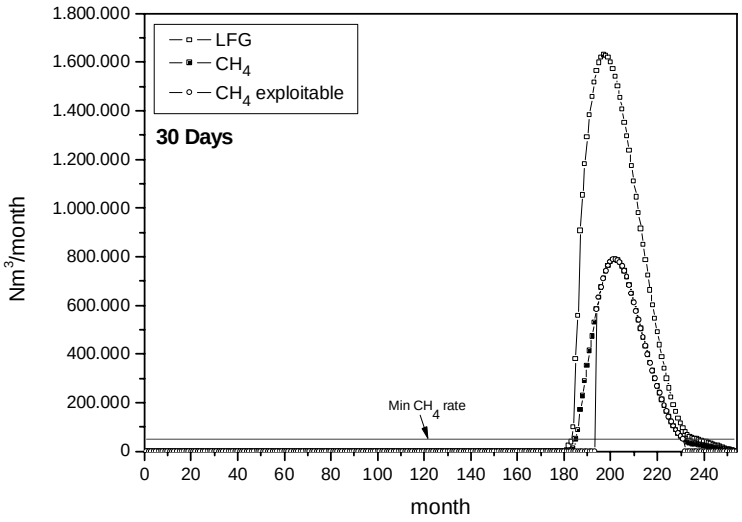

Fig. 11. Rates of LFG, biomethane and biomethane actually exploitable for a bioreactor landfill with 1 cell with a Min V_{cell} of 1,000,000 m^3.

Table 5. Total energy production, biomethane production and biomethane loss for bioreactor landfills with different Min V_{cell}

Min V_{cell}	*kWh*	*CH_4 (Nm^3)*	*% CH_4 loss*
200,000	42,162,840.28	20,800,755.21	39.55
500,000	44,044,507.48	20,800,755.21	36.85
1,000,000	44,734,951.63	20.800,755.21	35.86

4. CONCLUSION

The experimental runs showed that the aerobic pre-treatment of the MSW undersize fraction arising from mechanical sorting is an effective solution for both improving energy recovery and reducing green house gas emissions.

LFG yield ranged from 120 to 190 Nm^3 per tonne of Volatile Solids of the waste, on the average about 50 Nm^3 per tonne of disposed waste, for an aerobic pre-treatment time ranging from 15 to 120 days.

The biomethane content actually exploitable ranged from 20% to 45% of the LFG produced. The amount of LFG actually exploitable for energy purposes is also greatly influenced by the landfill managment strategy. An increase in the minimum volume of the disposed waste that is activated in a bioreactor, leads to an increase in energy recovery and a reduction in biomethane loss. The maximum energy recoverable, about 45 GWh, is achieved at a minimum volume of 1,000,000 m^3 along with a minimum biomethane loss, about 36% of the total. The anaerobic biodegradation process takes place for a period of time ranging from 3 to 14 years, depending on the different scenarios analysed, being significantly lower in comparison to the one usually achieved in traditional landfills.

Acknowledgments

The authors would like to acknowledge the SEIT for the support given for the physical and chemical analyses performed during this study.

References

[1] Themelis J.N., Ulloa P.A., Methane generation in landfills. Renewable Energy 2007; 32: 1243-1257.

[2] USEPA. (2002) EPA website. Landfill methane outreach program – Available at: <http://www.epa.gov/lmop/basic-info/index.html#a02>. [accessed 03.01.2012]

[3] Desideri U., Di Maria F., Leonardi D., Proietti S., Sanitary landfill energetic potential analysis: a real case study. Energy Conversion and Management 2003; 44 (12): 1969-1981.

[4] ISPRA, Rapporto rifiuti urbani. Edizione 2009. ISBN 978-88-448-0430-5.

[5] Di Maria F., I rifiuti e gli scarti: tecniche di gestione e di valorizzazione. Perugia, IT: Margiacchi Editore, 2011. ISBN 978-88-96663-10-3

[6] Di Maria F., Energy Recovery from Landfill Biogas: the Effect of Micro-pollutant on an Existing Plant. EWMS 2011; In proceedings of Eurasian Waste Management Symposium: 2011 November 14-16; Istanbul, Turkey.

[7] Observ'ER. The state of renewable energies in Europe. 10th EurObserv'ER Report. Paris FR; Observ'ER, 2010. ISSN 2101-9622.

[8] Cossu R., Technical evolution of landfilling. Waste Management 2010; 30: 947-948.

[9] Di Maria F., Micale C., Renewable Energy Production from Wet Landfill System as an alternative to Thermal Waste to Energy Plant: Real Case Analysis. ASME-ATI-UIT 2010; In Proceedings of the Conference on Thermal and Environmental Issue in Energy System: 2010 May 16-19; Sorrento, Italy.

[10] Benson C.H., Barlaz M.A., Lane D.T., Rawe J.M., Practice review of five bioreactors/recirculation landfills. Waste Management 2007; 27: 13-29.

[11] Hettiarachchi C.H., Meegoda J.N., Tavantzis J., Hettiaratchi P., Numerical model to predict settlement coupled with landfill gas pressure in bioreactor landfill. Journal of Hazardous Materials 2007; B139: 514-522.

[12] San I., Onay T.T., Impact of various leachate recirculation regimes on municipal solid waste degradation. Journal of Hazardous Materials 2007; B84: 259-271.

[13] Marin J, Kennedy KJ, Eskicioglu C, Effect of micowave irradiation on anaerobic degradability of model kitchen waste. Waste Management 2010; 30: 1772-1779.

[14] Di Maria F, Benavoli M, Zoppitelli M (2008) Thermodynamic analysis of the energy recovery from the aerobic bioconversion of solid urban waste organic fraction. Waste Manage; 28: 805-812.

[15] B Binner E, Zach A (1999) Biological reactivity of residual wastes and dependence on the duration of pretreatment. Waste Manage Res; 17: 543-554.

[16] Schievano A., D'Imporzato G., Malagutti L., Fragali E., Ruboni G., Adani F., Evaluating inhibition conditions in high solids anaerobic digestion of organic fraction of municipal solid waste. Bioresource Technology 2010; 101: 5728-5732.

[17] Environmental Agency, Guidance on gas treatment technologies for landfill gas engines. Environmental Agency 2010 – Available at: http://publications.environment-agency.gov.uk/PDF/GEHO0311BTON-E-E.pdf. [accessed 04.05.2012]

[18] EPA (2005) Landfill Gas Emission Model (LandGEM) version 3.02 User's Guide. EPA-600/R-05/047

Environmental assessment of energy recovery technologies for the treatment and disposal of municipal solid waste using Life Cycle Assessment (LCA): A case study of Brazil

Marcio Montagnana Vicente Leme [a], Mateus Henrique Rocha [a], Electo Eduardo Silva Lora [a], Osvaldo José Venturini [a], Bruno Marciano Lopes [b], Claudio Homero Ferreira [b].

[a] Excellence Group in Thermal Power and Distributed Generation (NEST), Federal University of Itajubá (UNIFEI), Av. BPS, 1303, Itajubá, Minas Gerais State, PO Box 50, Pinheirinho, CEP.: 37500-903.
[b] Electric Company of Minas Gerais (CEMIG), TE/AE, Av. Barbacena 1200 - 16º andar - B1 Belo Horizonte–MG CEP. 30190-131

Abstract:

The aim of this study is to compare, from an environmental point of view, different alternatives for the management of Municipal Solid Waste (MSW) generated in the town of Betim (Brazil). This 441.748 inhabitants city is located in the country South east and currently produces 200 ton of waste per day. The proposed scenarios were: landfill without biogas utilization (background scenario); landfill with biogas combustion in reciprocating engines to electricity generation; and an incineration mass burn system with energy recovery. This resulted in 3 scenarios, whose environmental behaviour was studied by applying the life cycle assessment (LCA) methodology. In accordance with the ISO 14040–14044 standards, an inventory model was developed for the main stages of the waste management life cycle. SimaPro 7.2 libraries and others were used to obtain background data for the life cycle inventory. One ton of municipal solid waste of Betim was selected as the functional unit. Environmental indicators were obtained for different impact categories (abiotic depletion, global warming, human toxicity, acidification, eutrophication and photochemical ozone depletion), which made it possible to identify the key variables in the waste management system and the scenario that offers the best environmental behaviour. Results, reliable for most of the Brazil big cities, show landfill systems as the worst waste management option and significant environmental savings at global scale are achieved from undertaking energy recovery. The best option, which presented better performance based on considered indicators, is the electricity recovery from the direct combustion of waste.

Keywords:
LCA, energy recovery, waste management, landfill biogas, waste-to-energy.

1. Introduction

The lack of a management policy of MSW in Brazil raises serious consequences from an environmental standpoint. Nowadays 60% of Brazilian cities still dump their waste in non-regulated landfills the other 40% including the biggest Brazilian cities dump their trash in regulated landfills [1]. Unregulated landfills do not have drainage systems for gas and leachate, lower sealing, and sometimes even daily soil cover. This situation brought serious environmental and social problems. In recent years, municipalities try to deploy regulated landfills in their territories, which are considered by Brazilian politics as an environmentally sound alternative.

Moreover, the European Union (EU) has, for example, introduced targets which propose to reduce the amount of landfilled biodegradable waste. The Landfill Directive [2] prevents disposal of organics to landfill by 2016. This fraction of MSW must be composted or digested [3]. Furthermore, landfilling of certain types of waste such as combustible waste or untreated organic

waste is illegal in some member states, e.g. Denmark, Sweden and Germany. Consequently, at the EU level, great efforts are made to identify alternatives to the landfilling of biodegradable waste [4].

A widespread solution for some countries is the incineration of MSW with energy recovery. This technology has undergone harsh criticism in the 80's and 90's due to high emissions of air pollutants. For this reason, strict emission limits were applied for this sector, which repressed the installation of new plants. However, the new advances in treatment technologies for air pollution control made the incineration with energy recovery attractive from an environmental standpoint and its use is being encouraged in much of the developed world. According to Psomopoulos [5] Waste-to-Energy (WTE) emissions have been reduced to a point that in 2003 the United States Environmental Protection Agency (US EPA) considered WTE a clean source of energy.

The LCA methodology was used in this work as a decision tool for treatment and disposal systems of MSW. LCA is able to provide an overview of the environmental aspects of different strategies and to compare the environmental impacts of these options. It is best known as a tool that analyzes the impacts of the life cycle of a physical product. But the approach also allows to analyze the impacts of life cycle services such as waste management. The key point in an LCA is that all products or services should have the same function, so they can be compared on the same basis [6].

This work focuses on the use of LCA for different urban solid waste management strategies with or without energy recovery that could be swiftly applied in Brazil. Unfortunately, this tool is still rarely used in the country, and studies like this, in the area of waste management, are beginning to emerge now. The paper compares waste disposal alternatives in a Life cycle perspective, considering a landfill system with subsequent use of biogas in reciprocating engines to produce electricity, and mass burn incineration system with energy recovery. In both cases no sorting phase or recycle takes place.

2. Case study

This study was performed using data from a landfill situated in Betim, a city with 441.748 thousand inhabitants located in the country's south west that produces about 52000 tons of waste annually. The landfill began operational in October 1996 and it's closing is expected to occur in 2016. The characteristics of MSW generated in the city are shown in Table 1. The production rate of biogas was determined with the methodology of IPCC [7] and the calorific value of waste from the equations found in [8] and [9]. The proportion of biogenic and fossil carbon in the MSW was estimated using information from IPCC [9]. Just like any other Brazilian city all garbage produced by the city is sent directly to landfill without any previous treatment.

Table 1. Characteristics of MSW produced in the city of Betim.

Characteristics		Components [%]	
Moisture [%]	35	Food waste	54
Volatile Solids [%]	51	Textiles	4
Ash [%]	14	Plastics	16
High heating value [kJ/kg]	14610	Rubber	1
Lower heating value [kJ/kg]	7981	Paper	10
C_{fossil} [%]	11	Cardboard	3
$C_{biogenic}$ [%]	17	Metals, glass and others	12

3. Methodology

The LCA methodology used for this work is based on the principles defined by ISO 14040 and ISO 14044 [10, 11].

3.1. Defining the purpose and scope.

The objective is to compare different alternatives for the disposal and treatment of MSW with or without energy recovery in Brazilian context. The waste entering the system has no environmental loads (collection, transportation, etc.). The functional unit of this study is 1 ton of MSW with the characteristics showed in table 1.

For scenario 1 (incineration) was considered the use of a mass burning system capable to treat 200 tons of MSW per day integrated with a boiler that generates steam for a conventional Rankine cycle that produces 400 kWh/ton of electricity per ton of waste. The waste is burned in a grate incinerator and the slag from the bottom and fly ash are sent to an inert landfill situated 54 km from the plant. The boundaries of scenario 1 are outlined in Figure 1 below. The emission control system includes a selective non-catalytic reduction fed with urea for NO_x control and dry scrubbing with lime to remove acid gases, heavy metals and dioxins, and a fabric filter to remove solid particles [12].

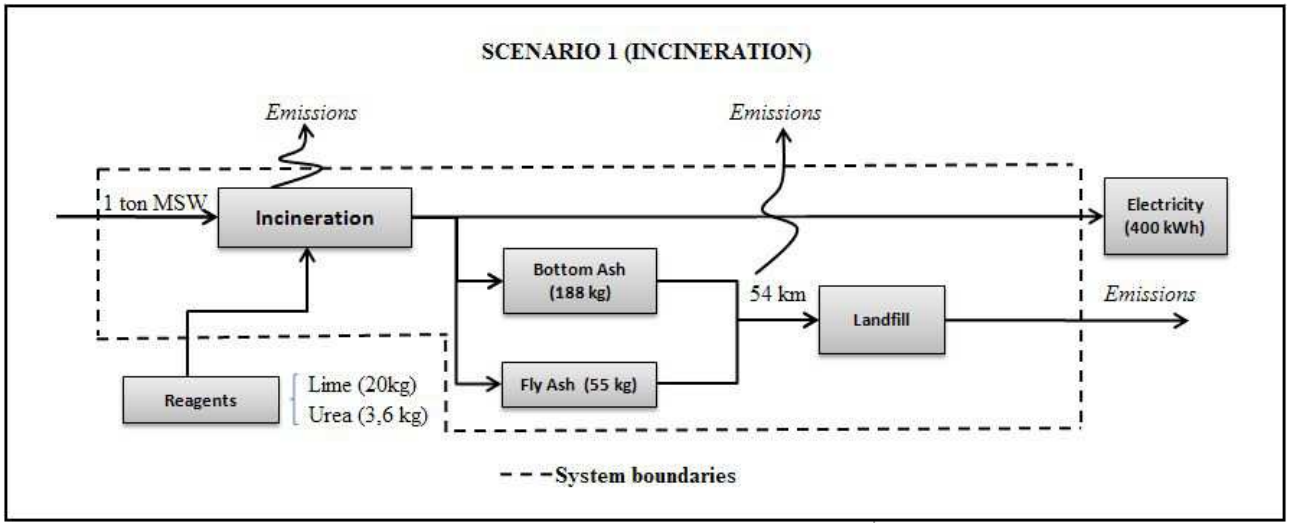

Fig. 1. Boundaries in scenario 1.

The second scenario shows the actual state of Betim landfill. The biogas generated by the site is emitted directly into the atmosphere without emissions control systems. In scenario 3 the biogas produced by the landfill is collected with 75% efficiency and sent to reciprocating engines modules and to a system of flares for backup. The boundaries of scenarios 2 and 3 are shown in Figure 2 below.

The technology considered in this study is similar to that used in landfill Betim, but in Scenarios 3 and 4, where there are power generation, information were withdrew from the bibliography of similar projects in Brazil and abroad.

In scenario 3, each generator module has 33% efficiency, produces 300 kW of electricity and has a useful life of 7 years. Over the operation life of the landfill 9 modules are installed which ensures the use of 64% of the biogas captured by the collection system, the remaining 36% are burned in the flares, the installed and available power is presented in Figure 3 and the schedule for the modules is shown in Table 2.

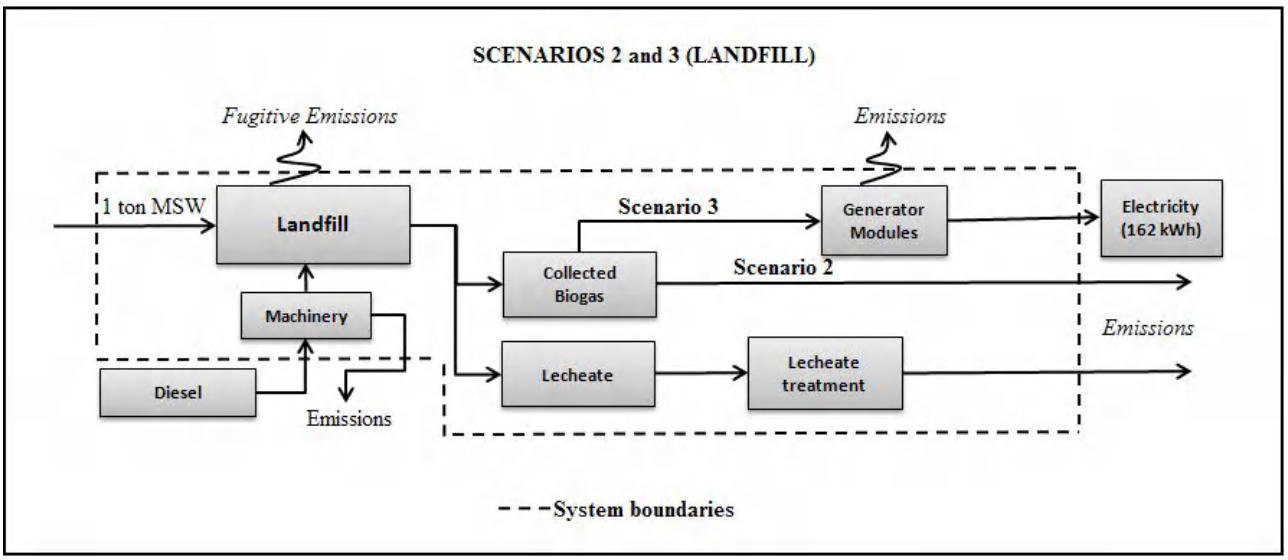

Fig. 2. Boundaries in scenarios 2 and 3.

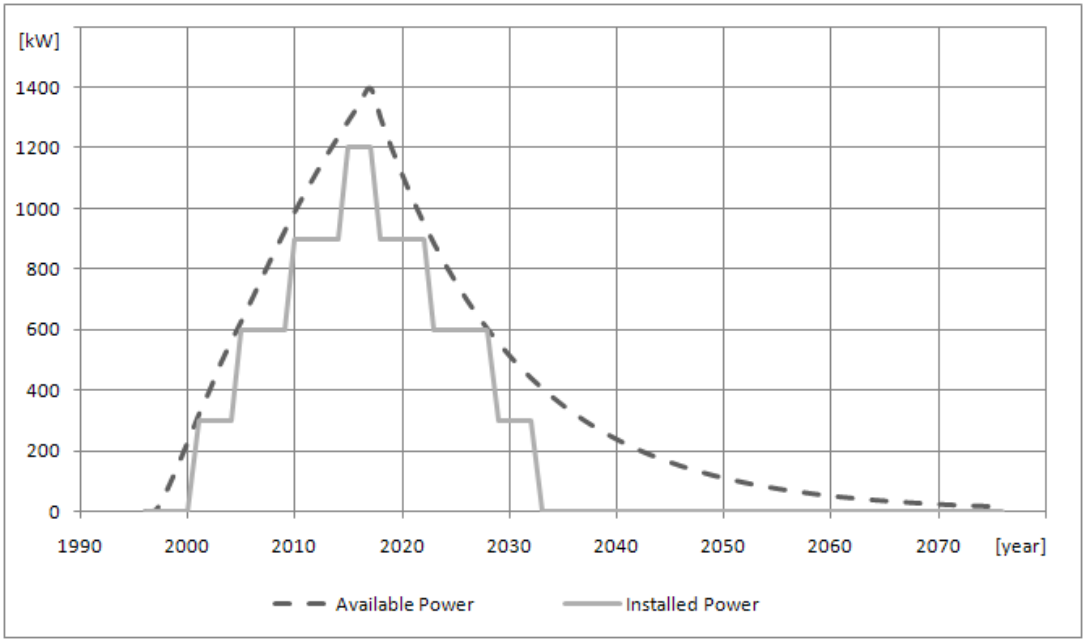

Fig. 3. Installed and available power on scenario 3.

Table 2. Schedule for the module generators in scenario 3.

	Power [kW]	Start of operation	End of operation
Module 1	300	2001	2008
Module 2	300	2005	2012
Module 3	300	2009	2016
Module 4	300	2010	2017
Module 5	300	2013	2020
Module 6	300	2015	2022
Module 7	300	2017	2024
Module 8	300	2021	2028
Module 9	300	2025	2032

In all the tree different scenarios is taken into account the emissions associated to the consumption and production of diesel, during internal movement and pressing of wastes. The environmental loads related to the production of reagents (urea and lime) are also considered.

In scenario 1, a mass burn system uses all the refuse, without prior treatment or preparation. Unlike a Refuse Derived Fuel (RDF) system that separates combustible wastes from non-combustibles such as glass and metal before burning.

3.2. Inventory Analysis

Emissions to air water and soil, consumed resources and generated energy were calculated and related to the functional unit. Emissions to water in landfills were obtained from [13] for the short period (100 years) and long period (60,000 years). The inventory of urea was taken from [14], the lime from [15] and the electricity from [16]. Emissions from the diesel used in transport and the machinery for compression and movement of MSW in landfill were obtained from [17]. Emissions to air in landfill scenarios were calculated using the equations based on the USEPA [18] report. Emissions from incineration were obtained from [19], according to the applied technology.

3.3. Impact Assessment

The evaluation was conducted until the stage of characterization. The software Simapro^{TM} 7.1.8 and the impact assessment methodology CML-2000 baseline 2000 v.2.03 (Chain Management by Life Cycle Assessment) were used for environmental impact calculation. Information about the methodology and the impact categories can be found at [20].

The chosen impact categories are present in the CMLA 2000 and are recommended for use in any LCIA. To make the study more understandable and less extensive, some categories of the CML were not considered. The evaluation method was chosen due to its easy application and understanding. Furthermore, it is a widely used and established method.

4. Results

The results of the characterization analysis per ton of MSW for each selected impact category and for each scenario are showed in Table 3 and Figure 4.

Table 3. Results of characterization in LCA.

Impact Category		Scenario 1	Scenario 2	Scenario 3
Depletion of Abiotic Resources	kg Sb eq	-0,21	0,00	-0,13
Global Warming (GWP_{100})	kg CO_2 eq	285,00	2052,00	464,00
Ozone Layer Depletion	kg CFC-11 eq	0,00	0,01	0,00
Human Toxicity	kg 1,4-DB eq	332,00	182,00	176,00
Acidification	kg SO_2 eq	0,68	0,00	11,87
Eutrophication	kg PO_4^{-3} eq	0,66	2,53	2,57

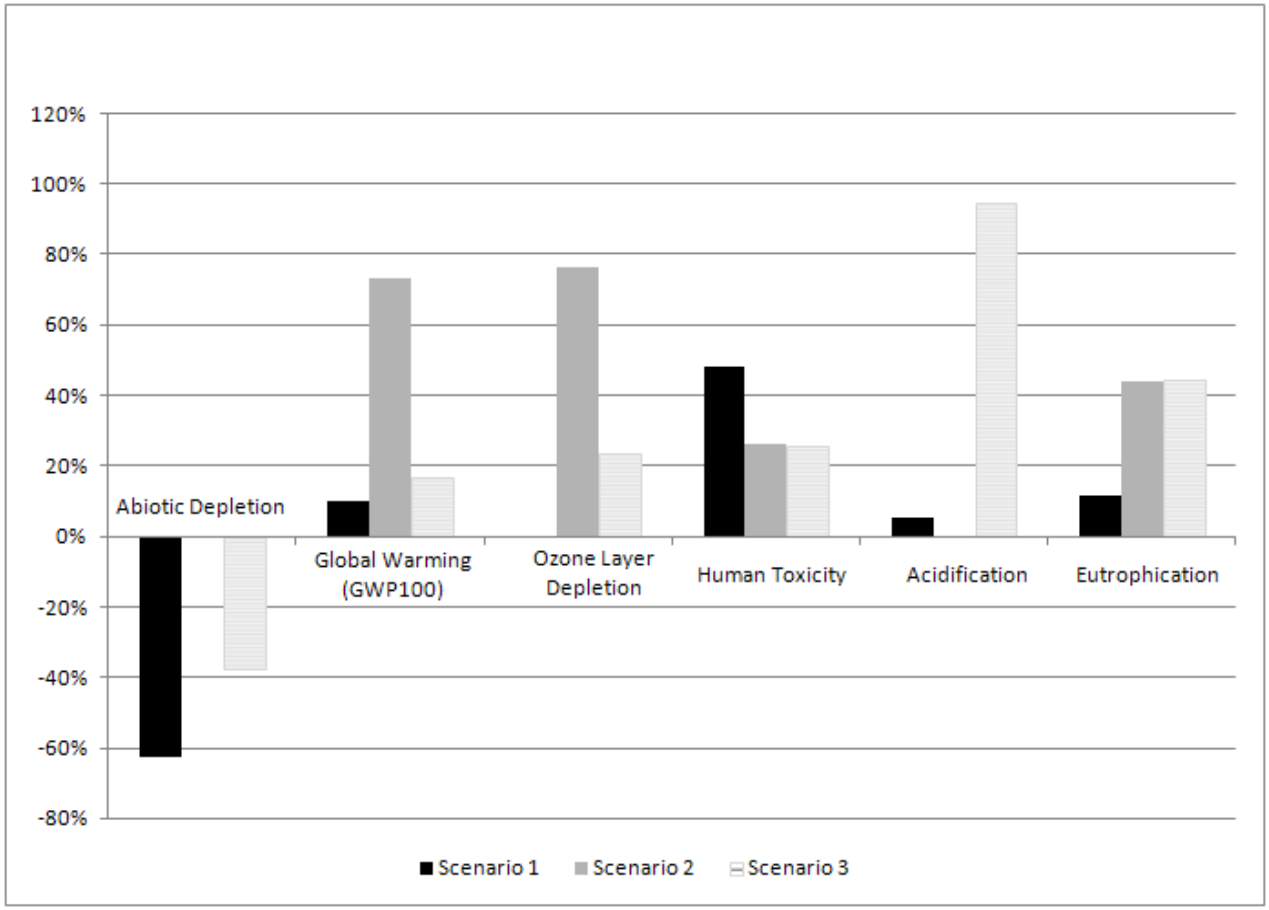

Fig. 4. Weighted results of characterization in LCA.

As reported in the table, investigated results for all impact categories are as follows:

4.1. Depletion of Abiotic Resources

In this category is considered that the energy is recovered and supplied to the Brazilian electric system what avoids the consumption of scarce natural resources to further generation of a similar amount of energy. Thus, incineration was superior to recover relatively larger amount of energy per tonne of waste compared to the landfill scenarios. Scenario 1 recovers 400 kWh per ton of MSW, scenario 3 recovers 162 kWh and in scenario 2 there is no energy recovery.

4.2. Global Warming

The lack of an emission control system for scenario 2 causes the CH_4 to be emitted directly into the atmosphere, in this scenario the methane is responsible for 92% of indicator results. In Scenario 3 the CH_4 is partially destructed but still 25% is released directly into the atmosphere as a result of fugitive emissions from the landfill. In Scenario 1 the potential impact is diminished by 86% compared to Scenario 2, the greenhouse gas emissions of this scenario are a result of the combustion of fossil carbon presented in MSW, eg. plastics and rubber.

The emissions of methane from the city landfill were calculated using the recommended methodology of UNFCCC ACM0001 – “Flaring or use of landfill gas” [22].

4.3. Ozone Layer Depletion

In Scenarios 2 and 3 the main pollutant is the CFC-12 which accounts for 93% of results for this category. These emissions are a consequence of certain products grounded as aerosol cans and polyurethane foams. In scenario 3 part of CFC-12 is destroyed in the modules and flares. In the first scenario there are no emissions of harmful compounds to the ozone layer.

4.4. Human Toxicity

The main pollutant in scenarios 2 and 3 is the emission of barium to the ground and surface water, which accounts for approximately 53% of the impact of these scenarios and 28% in scenario 1 (incineration). The difference between Scenario 1 and the other two is mainly due to the air emission of dioxins during incineration, which is 134 times greater than landfill scenarios.

4.5. Acidification

Landfill gas is rich in compounds that contain sulfur. In Scenario 3 the burning of this compound generates SO_2 emissions, gas responsible for almost the totality of the indicator results (97%). In Scenario 1, the impacts are due to the formation of SOx and NOx in the combustion of waste.

4.6. Eutrophication

For this impact category, the difference between landfill and incineration scenarios occurs due to the high organic load of water emissions from these landfills, specifically the high COD and emissions of NH_3, NO_3^- and PO_4^{-3}. The organic load of inert landfills used in scenario 1 are significantly lower compared to a common landfill.

5. Conclusion

Results show that Brazilian landfills, the solution for final MSW disposal that municipalities try to implement in their territory to get rid of non-regulated landfills, has the greatest potential to generate environmental impacts in five of the six impact categories selected in this study. Although landfills have not been compared with something revolutionary in terms of waste treatment technologies.

The energy recovery from biogas slightly diminished the environmental load of landfill, however the use of a gas cleaning phase to remove the sulfur from the gas should be recommended due to acidification problems. As 40% of Brazilian cities use landfills, we can conclude that this option is ideal for reducing the impacts of MSW in a short-term period. As Cherubini [21] results in Italy conclude, the higher the yields of energy recovered with waste disposal, the greater the environmental savings.

Some countries are establishing policies to eradicate the country's landfills and focus their efforts in implementing the "hierarchy of waste", therefore, the reduction of waste, recovery and recycling of materials and energy in it. Landfills generate an incalculable burden for future generations and should be considered as a last option for waste disposal.

The combustion of waste in Brazil is still seen as a highly polluting technology for MSW treatment, and most of the population does not approve its utilization. However, the lack of space for new landfills in metropolitan areas is causing the cities to rethink the use of WTE options. But before that, studies using a life cycle approach should be encouraged. Future works should include better waste management solutions including recycling, modern collection systems and advanced technologies for energy recovery.

Acknowledgments: This work has been funded by the Electric Company of Minas Gerais CEMIG, whose support is gratefully acknowledged. The authors would like to thank the Coordination of Improvement of Higher Education Personnel (CNPq) the National Council for Scientific and Technological Development (CAPES) and the Foundation for Research Support of Minas Gerais (FAPEMIG).

References

[1] SISTEMA NACIONAL DE INFORMAÇÕES SOBRE SANEAMENTO. Diagnóstico do manejo de resíduos sólidos urbanos – 2007. Secretaria Nacional de Informações sobre Saneamento – Brasília: MCIDADES.SNSA, SNIS, 2009.

[2] European Communities. Council directive on the landfill of waste (96/31/EEC).

[3] Murphy, J.D. and McKeoghb, E. The benefits of integrated treatment of wastes for the production of energy. Energy Volume 31, Issues 2-3, February-March 2006, Pages 294-310

[4] M. Münster, and Lunda H. Use of waste for heat, electricity and transport: Challenges when performing energy system analysis. Energy Volume 34, Issue 5, May 2009, Pages 636-644

[5] Psomopoulos C.S.; Bourka A.; Themelis N.J. Waste-to-energy: A review of the status and benefits in USA. Waste Management 29 1718–1724 (2009). See also: http://www.wte.org/userfiles/file/epaletter.pdf

[6] Finnveden G. Life Cycle Assessments of Energy from Solid Waste, APPENDIX 5. Stockholms universitet / systemekologiochfoa. September 2000.

[7] Kathiravale S., Yunus M. N. M., K. Sopian, A. H. Samsuddin and R. A. Rahman. Modeling the heating value of Municipal Solid Waste. Fuel Volume 82, Issue 9, June 2003, Pages 1119-1125

[8] Cortez L. A. B., Lora E. E. S. Gómez E. O. Biomassa para Energia. Campinas, Brazil: UNICAMP Editora da Universidade, 2008

[9] IPCC, Intergovernmental Panel on Climate Change. Guidelines for National Greenhouse Gas Inventories, Prepared by the National Greenhouse Gas Inventories Programme, Eggleston H.S., Buendia L., Miwa K., Ngara T. and Tanabe K. (eds). Published: IGES, Japan. IPCC, 2006.

[10] ISO 14040:2006 – Environmental management – Life cycle assessment – Principles and framework. 2006.

[11] ISO 14044:2006 – Environmental management – Life cycle assessment – Requirements and guidelines. 2006.

[12] Consonni S., Giugliano, M., Grosso M. Alternative strategies for energy recovery from municipal solid waste – Part A: Mass and energy balances. Waste Management 25, pg. 123–135. 2005.

[13] Doka G. Life Cycle Inventories of Waste Treatment Services. Ecoinvent report No. 13, Swiss Centre for Life Cycle Inventories, Dübendorf, December 2007.

[14] Silva, GA, Ribeiro, P.H; Kulay, L.A. Evaluation of Environmental Performance of Chemical Fertilizers in Brazil. In: XVI Brazilian Congress of Chemical Engineering, Santos. Proceedings. São Paulo, 2006. 12 p.

[15] Yokote, A.Y. Inventário do Ciclo de Vida da Distribuição de Energia Elétrica no Brasil. 2003. 369 f. Dissertação (Mestrado em Engenharia Química), Universidade de São Paulo, Escola Politécnica, São Paulo, 2003.

[16] Coltro, L.; Garcia, E. E. C.; Queiroz, G. C. Life Cycle Inventory for Electric Energy System in Brazil. International Journal of Life Cycle Assessment, v. 8, n. 5, pp. 290–296, 2003.

[17] MCT, Ministério da Ciência e Tecnologia. Emissões de gases do efeito estufa no setor energético por fontes móveis. Programa de planejamento energético da COPPE-PPE, Rio de janeiro, RJ. MCT, 2006.

[18] USEPA, United States Environmental Protection Agency. AP 42, Fifth Edition, Volume I, Chapter 2: Solid Waste Disposal, 2.4 Municipal Solid Waste Landfills, Draft Section – October, 2008.

[19] USEPA, United States Environmental Protection Agency. AP 42, Fifth Edition, Volume I, Chapter 2: Solid Waste Disposal. 2.1 Refuse Combustion, Final Section - Supplement B, October, 1996.

[20] Goedkoop, M.; Oele, M.; Schryver, A.; Vieira, M. SimaPro Database Manual Methods library. PRe´ Consultants, Netherlands, 2008.

[21] Cherubini F., Bargigli S., Ulgiati, S. Life cycle assessment (LCA) of waste management strategies: Landfilling, sorting plant and incineration. ECOS 2007. Energy. Volume 34, Issue 12, Pages 2116-2123, December 2009.

[22] UNFCCC, United Nations Framework Convention on Climate Change. Approved consolidated baseline and monitoring methodology ACM0001 “Flaring or use of landfill gas”. Avaliable on: http://cdm.unfccc.int/methodologies/DB/EYUD9R1ZAUZ2XNZXD3HQH18OK3VWIV

How will renewable power generation be affected by climate change? – The case of a metropolitan region in Northwest Germany

Jakob Wachsmuth[a], Andrew Blohm[b], Stefan Gößling-Reisemann[a], Tobias Eickemeier[a], Rebecca Gasper[b], Matthias Ruth[b], Sönke Stührmann[a]

[a] Research Center for Sustainability Studies (artec), University of Bremen, Germany, wachsmuth@uni-bremen.de
[b] Center for Integrative Research, University of Maryland, College Park, MD USA

Abstract:

Energy systems that primarily use wind and solar power production are in need of long-term storage of electricity and fully developed transmission grids. Moreover, they may be strongly affected by climate changes. We present two models that assess the impacts of climate change on solar and wind power generation and use them to evaluate climate projections based on the A1B scenario for Germany's Northwest Metropolitan Region. For these projections the seasonal profile of solar power production is not affected despite less cloud coverage during the summer, while the seasonal profile of wind power production has a more pronounced seasonal peak during the winter due to slightly increasing wind speeds. We compare the obtained seasonal profiles to different scenarios for electricity demand. For each scenario we identify the ratio of wind and solar power generation that minimizes the variance of the residual load at the monthly time scale under the premise of a full supply by wind and solar power. Our results suggest that the need for long-term storage of electricity and the need for extensions of the transmission grid will even increase because of climate change impacts in the Northwest Metropolitan Region over the next century.

Keywords:

Renewable energy sources, regional climate change, impact assessment models, seasonal load profiles.

1. Introduction

There is widespread scientific agreement that the climate will change much faster during the 21st century than in the past [1]. In order to mitigate climate change, energy systems have to be redesigned in a way that they are largely based on renewable sources. Under this premise it is very likely that wind and solar power generation will play major roles in future energy systems [2]. Both the production of wind and solar power is highly dependent on local climate conditions [3]. Thus these future energy systems may themselves be strongly affected by climate change. Moreover, climate change will probably change the seasonal profile of energy demand, in particular due to rising temperatures **Errore. L'origine riferimento non è stata trovata.**.

However, the demand change is highly dependent on the penetration of heating and cooling technologies. These penetration rates in turn do not only depend on climate alone but also on socio-economic conditions [5]. Hence, it is important to analyze the interplay of all these effects in detail. As part of the research project *"nordwest2050 - Prospects for Climate-Adapted Innovation Processes in the Metropolitan Region Bremen-Oldenburg in North Western Germany"*[1] we are

[1] nordwest2050 (<www.nordwest2050.de>) is one out of seven pilot projects on regional climate change adaptation funded by the research program "Creating Climate Change-Ready Regions" (KLIMZUG) of the German Federal Ministry of Education and Research.

building a model of the energy sector in Germany's Northwest Metropolitan Region that includes the impacts of climate change on generation and demand. The energy sector model will later be linked with similar models on agriculture and harbor and logistics. The combined model has three main purposes: (a) provision of a structured platform for data organization and dialog with stakeholders; (b) exploration of a wide range of what-if scenarios in preparation of investment and policy making; and (c) adaptive planning where the results of past actions are assessed within an ever-changing socioeconomic, technological and environmental context to guide future action **Errore. L'origine riferimento non è stata trovata.**.

The model development of the energy sector contains the building of suitable models of climate impacts on solar and wind power generation. In the context of climate change, we are particularly interested in investigating the impact on regional electricity supply systems and on times scales relevant for climate change (typically averages over 30 years). In this article we adapt existing models to this case and use them to evaluate climate projections for the Northwest Metropolitan Region.

1.1. Research on climate change impacts on the energy sector

The assessment of climate change impacts on the energy sector is a rather young topic with most research carried out in the last 20 years. In the recent review [7], Schaeffer et al. point out that while in the beginning studies focused on the impacts of climate change on energy demand, there is a rising interest in the impacts on resource endowment and electricity generation in the last years. Indeed, there are several studies on the potential impacts of of rising temperatures on electricity and heating demand (see e.g. [4]). All these studies contain implicit or explicit assumptions on expected socio-economic changes, e.g. with respect to heating, ventilating, and air conditioning equipment. Hekkenberg et al. [5] point out that this leads to an underestimation of the impacts in most of the cases as the modeling of socio-economic changes is rather intricate.

Concerning electricity generation from renewable sources, much is known about hydro and wind power, while only few studies are available on the impacts on solar power generation [7]. In a review of studies on climate impacts on wind energy, Pryor and Barthelmie [8] conclude that on the one hand, there are robust results on the impact of climate change on mean wind speeds and mean wind generation. In particular, there are studies for several different regions, with the most detailed results available for Northwestern United States [9]. On the other hand, only little research [10] has been conducted to indicate if the intra-annual and inter-annual variability of wind speeds and energy density will increase or decrease under climate change scenarios. Global trends for climate impacts on solar power generation have been analyzed by Crook et al. [11].

Due to the uncertainties about socio-economic developments the analysis of systemic aspects rather than only of certain technologies is difficult and the existing results are rather qualitative [12]. In this article we obtain first quantitative insights into climate impacts on the interplay of seasonal fluctuations in renewable electricity generation and demand by looking at the seasonal profile of the residual load. To this end, we derive a monthly profile for wind generation as in [9] and develop a similar ansatz for solar power generation. Concerning the impact of a change in demand, we restrict to a sensitivity analysis by shifting the monthly demand profile instead of tackling the deeper socio-economic modeling problems mentioned in [5].

1.2. Structure of the paper

In Section 2 we give an overview of the electricity supply and climate projections for the Northwest Metropolitan Region. To combine readability with brevity, there are no separate sections on

methodology, results and discussion. Instead, an integrated description for each of the impact assessments is given in Sections 3 to 5. In Sections 3 and 4 models for climate impacts on regional solar and wind power generation are described and the results from their application to the Northwest Metropolitan Region are presented. In Section 5 we analyze the consequences for the minimal monthly variance of the residual load in a supply scenario based on solar and wind power. In Section 6 we summarize our findings and give an outlook on future research.

2. Germany's Northwest Metropolitan Region

Germany's *Northwest Metropolitan Region* is a flat, coastal region situated between the North Sea coast and the *Wiehengebirge* mountain range. With a population of 2.7 million people and an area of about 14,000 km^2 it has strong business clusters and networks in various sectors like aeronautics, automotive, energy, food and agriculture, health, logistics and shipping, science and tourism. The region contains two urban centers with the rest of the region largely rural [12].

2.1. Electricity supply in the Northwest Metropolitan Region

In recent years electricity demand in the Northwest Metropolitan Region has averaged approximately 17,000 GWh per year (see Table 1). This estimate is based on a disaggregation of regional energy demand into the following economic sectors: industry, transport, households and other consumers (mainly the service sector) in [14]. Sufficient primary data was only available for the industrial sector. The electricity demand of the other sectors was estimated by combining available primary data on the number of different types of households for the private sector, the railway network for the transport sector, and the number of employees with average consumption rates for the service sector.

*Table 1. Final energy demand of the Northwest Metropolitan Region (own representation of [14]). *partly based on model calculations*

Final Energy Demand	**2004**	**2005**	**2006**	**2007**	**2008**	**Mean**
			GWh			
Industry	8148	7671	8088	8025	8007	7988
Transport sector*	452	477	523	525	463	488
Households*	4121	4131	4133	4132	4134	4130
Other consumers* (mainly service sector)	4565	4494	4396	4680	4665	4560
Total	**17227**	**16772**	**17140**	**17363**	**17268**	**17154**

In 2008 the net electricity generation in the Northwest Metropolitan Region totaled approximately 23,000 GWh. Much of the regional power production was from nuclear and coal fired power plants, which accounted for approximately 75.1 % of all the electricity produced in the region in 2008. Renewable technology accounted for 18.5% of all electricity produced with major contributions from wind power generation and biogas power plants [14]. In the near future a much larger proportion of the region's energy generation will come from renewable sources as a result of two factors; first, in 2011 the regions only nuclear power plant was retired, and second, each year the installed capacity of renewable energy technologies is increasing rapidly (see Fig. 1).

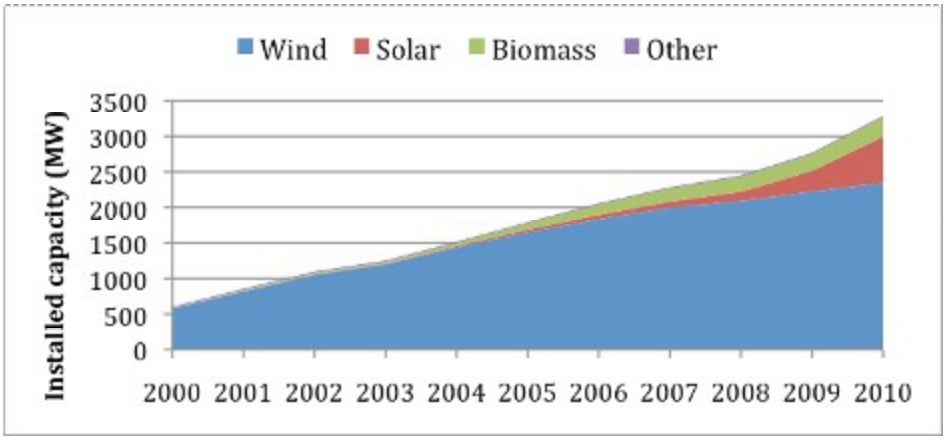

Fig. 1. Development of the installed capacity of renewables in the Northwest Metropolitan Region from 2000 to 2010 (own representation of [15]).

In 2010, renewable capacity in the region reached 3,289 MW. The dominant renewable technology in the region, as measured by proportion of total installed capacity, remains wind with more than 2,345 MW of installed capacity. However, solar capacity is on the rise with approximately 650 MW installed to date. Installed biomass capacity was surpassed by solar with approximately 273 MW of installed capacity [15].

2.2. Climate change in the Northwest Metropolitan Region

For an analysis of impacts and responses to climate change at the regional level, we draw on two regional climate models available for Germany. One of these models is REMO, developed at the Max-Planck-Institut fuer Meteorologie (MPI)[2]. The second climate model is the CLM model developed by the consortium of BTU Cottbus, Forschungszentrum GKSS, and Potsdam-Institut fuer Klimafolgenforschung Both models are operated at the MPI and capture dynamic processes in the atmosphere at several spatial scales and regional coverage [16].

Each of these climate models is run for different future scenarios of greenhouse gas concentrations derived from story lines that explain how changes in technology, demography and economic activity will unfold globally. On this basis, regional climate scenarios, which describe the evolution of the most relevant climate parameters, were developed in [17]. To incorporate uncertainties in future climate development, the regional scenarios contain mean values for one specific emission scenario (A1B, see [2]) from two different regional models, as well as the min-max range from several other models and emission scenarios. The resulting evolutions of selected climate parameters can be found in Table 2. We recall that the A1B scenario denotes one of the four illustrative emission scenarios of the IPCC. It describes a possible future development of greenhouse gas emissions consistent with an ongoing globalization, a focus on economic prosperity and a technological balance between renewable and fossil intensive energy systems.

Table 2. The evolution of the 30-year average of selected climate parameters in the climate scenarios for the Northwest Metropolitan Region ([17] and own calculations). For the time period indicated in the column header the bold numbers are the mean values of the outputs by the regional climate models CLM and REMO for the A1B scenario. The ranges of outputs for further models and emission scenarios are given in parentheses (n.e. = not evaluated).

Parameter	**2036-2065 (with respect to 1971-2000)**	**2036-2065 (absolute value)**	**2071-2100 (with respect to 1971-2000)**	**2071-2100 (absolute value)**

[2] Max-Planck-Institut fuer Meteorologie (MPI) in Hamburg, Germany (http://www.mpimet.mpg.de)

Mean temperature	**+1.5°C** (+1 to +2°C)	**10.7°C** (10.2 to 11.2°C)	**+2.8°C** (+1.9 to +4.7°C)	**12.0°C** (11.1 to 13.9°C)
Heating degree days per year[3]	**-290** (n.e.)	**3590** (n.e.)	**-491** (n.e.)	**3309** (n.e.)
Cooling degree days per year[4]	**+47** (n.e.)	**73** (n.e.)	**+97** (n.e.)	**123** (n.e.)
Heat waves per year[5]	**+0.41** (n.e.)	**0.61** (n.e.)	**+0.91** (n.e.)	**1.11** (n.e.)
Parameter	**2036-2065 (with respect to 1971-2000)**	**2036-2065 (absolute value)**	**2071-2100 (with respect to 1971-2000)**	**2071-2100 (absolute value)**
Mean wind speed (10m above ground)	**+1,8%** (0 to +2 %)	**5,8 m/s** (5,7 to 5,8 m/s)	**+2,5%** (0 to +3 %)	**5,8 m/s** (5,7 to 5,9 m/s)
Maximal wind speed (10m above ground)	**+3,8%** (n.e.)	**19,1 m/s** (n.e.)	**+11,0%** (n.e.)	**20,7 m/s** (n.e.)
Cloud coverage	**+0,1%** (-1 to +1%)	**67,6%** (66 to 68%)	**+0,7%** (-6 to +2%)	**68%** (63 to 69%)

3. Climate impacts on solar power generation

Electricity generation from a solar power plant primarily depends on three factors: (1) the amount of solar radiation received by the surface of the solar module; (2) damages to or defects of the module, and (3) the surface temperature of the module.

The amount of radiation received is directly related to the global radiation at the plant's site via the orientation and the tilt angle of the solar module [18]. Another meteorological factor in order to predict electricity generation from solar capacity is extreme weather events that may damage solar modules in a way that power generation is disrupted. Finally, high module temperatures, which are influenced by ambient air temperature, can reduce the efficiency of the module. Also, in very dry climates, excessive dust covering solar surfaces can reduce the overall efficiency [19].

3.1. A model for regional climate impacts on solar power generation

The model we present aims at capturing the major impacts of climate on the seasonal profile of solar power generation within a certain region. Therefore we do not model the technical details of electricity generation. Instead, we focus on two effects: the change in global radiation and the averaging due to the distribution of orientations and tilt angles of solar modules within a region. We recognize that we are neglecting the impacts from extreme weather events, the effect of ambient air temperature on the overall module temperature, and the effect of dust coverage. However, there is

[3] To determine the heating degree days per year take the days with a mean temperature below 15°C, subtract the mean temperature from 20°C and add up all these differences.

[4] To determine the cooling degree days per year take the days with a mean temperature above 18°C, subtract 18°C from the mean temperature and add up all these differences.

[5] Definition used here: 5 days in a row with maximal temperature above 25°C, thereof at least 3 days above 30°C.

not yet enough data available to investigate the impact of these effects. To assess these effects remains a task for future research.

In the climate projections from the regional climate model CLM, the global radiation is not explicitly given. There are several approaches to derive global radiation from total cloud coverage. We apply here the approach presented in [20], which is based on an expansion in the sine of the solar elevation angle originally carried out in [21]. For historic data on total cloud coverage and global solar radiation from the Northwest Metropolitan Region this approach led to higher correlations than the common model based on the total turbidity factor (see e.g. **Errore. L'origine riferimento non è stata trovata.**).

In order to derive the electricity generation of a particular solar module from global radiation, global radiation must be decomposed into direct and diffuse radiation. In this way the solar radiation received by the module can be calculated from its tilt angle and orientation (see e.g. **Errore. L'origine riferimento non è stata trovata.**). To investigate the solar power generation within a certain region we use regional distributions of tilt angle and orientation in order to weight the solar power generation for different orientation and tilt angle parameters.

To assess climate impacts we feed hourly data on cloud coverage into our model. The output is then aggregated to the monthly time scale and averaged over a time period relevant to climate effects, typically 30 years (see Fig. 2).

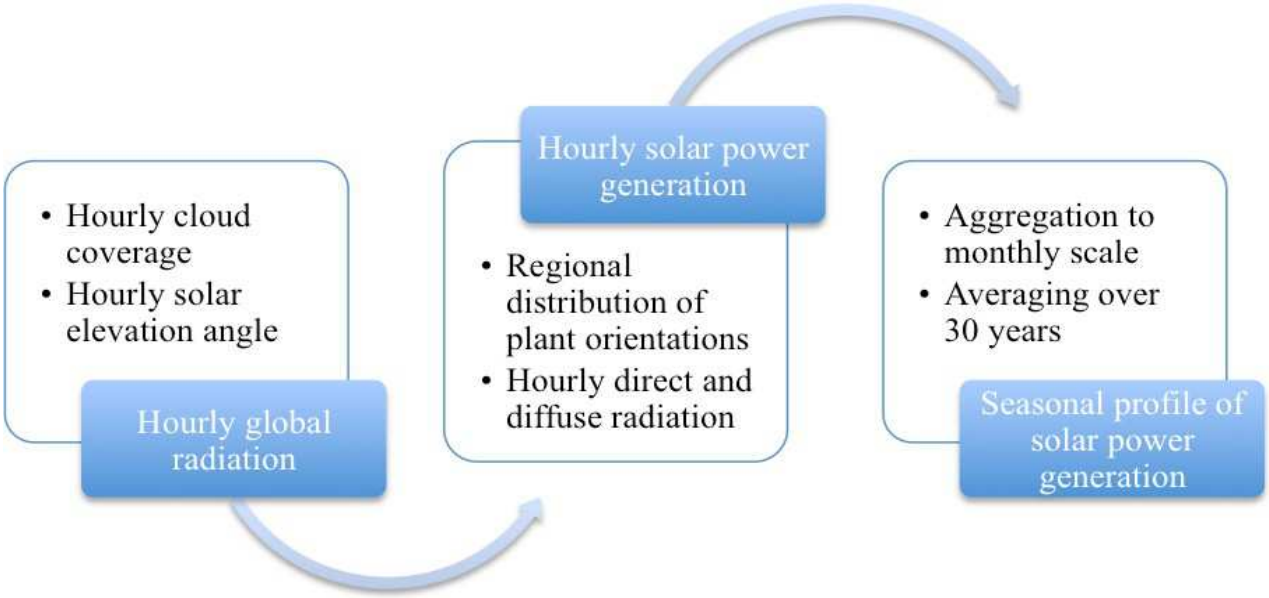

Fig. 2. Schematic representation of the climate impact model for solar power generation.

3.2. Impact on solar power plants in the Northwest Metropolitan Region

A distribution of orientations and tilt angles for the Northwest Metropolitan Region, which is needed in the model for solar power generation described above, was obtained from a German photovoltaic database [23]. For 2010, the database contains 324 solar power plants with a total installed capacity of 4,380 MW for the Northwest Metropolitan Region and neighboring counties. Plant operators provide data voluntarily, which may result in a bias towards private operators. However, they do represent the large majority of solar power plant operators in Germany [24]. We then took the current distribution as fixed for the future such that we could evaluate the relative change in generation and seasonal profile. Of course, the future distribution could differ from the status quo substantially. However, this is unlikely because modules tend to be oriented towards the south to achieve a high output, as well as to be attached to rooftops, which determines the tilt angles. Therefore the authors feel that for analyzing the relative changes the data basis is sufficient.

We then fed the historic hourly coverage data (1981-2010) for the Northwest Metropolitan Region[6] into the model. The resulting seasonal profile for solar power generation has a less pronounced peak than the one for global radiation (see Fig. 3).

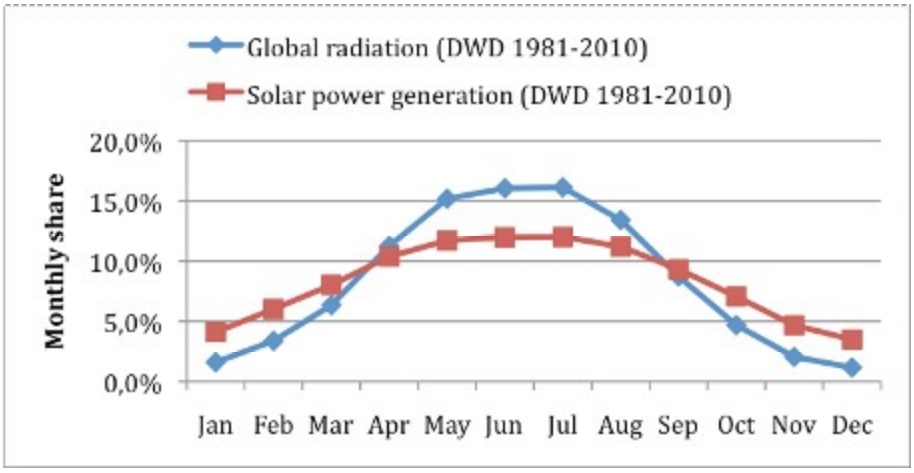

Fig. 3. The y-axis shows the monthly share of the total annual radiation and generation, respectively. The evaluation of our model with historic data shows that the monthly profile of the regional solar power generation has a less pronounced peak than the one for global radiation.

This is predominantly due to the high tilt angles of a relevant share of the modules, which makes them less efficient in summer but more efficient in winter. The distribution of orientations is less important as most modules are oriented approximately towards the south. To assess the impacts of climate change on solar power generation we use regional climate projections for the Northwest Metropolitan Region, which are based on the regional climate model CLM (cf. [16]), driven by the global emission scenario A1B (cf. [2]). In these projections, the 30-year averages of cloud coverage decrease in summer and increase in winter (see Table 3).

Table 3. Change of the seasonal cloud coverage relative to the time period 1971-2000 in the model run of CLM based on the A1B scenario.

	Climate projection	Winter (DJF)	Spring (MAM)	Summer (JJA)	Fall (SON)
Total Cloud Coverage	CLM 2036-2065	-1,1%	+2,7%	-2,6%	+0,7%
	CLM 2071-2100	+2,1%	+4,1%	-5,2%	-1,3%

Now we compare the model output for the time periods 2036-2065 and 2071-2100 to the historic data. The seasonal peak of global radiation in the summer becomes slightly more pronounced due to the decrease of cloud coverage in summer. This, however, has only a very slight effect on the solar capacity factor[7] within the region because the diverse tilt angles of solar modules within the region compensate for the shift in the profile (see Fig. 4).

[6] The historic data was provided by the German Weather Service DWD.

[7] The solar capacity factor is the ratio of the actual output of a solar power plant over a period of time and its potential output if it had operated at full nameplate capacity the entire time.

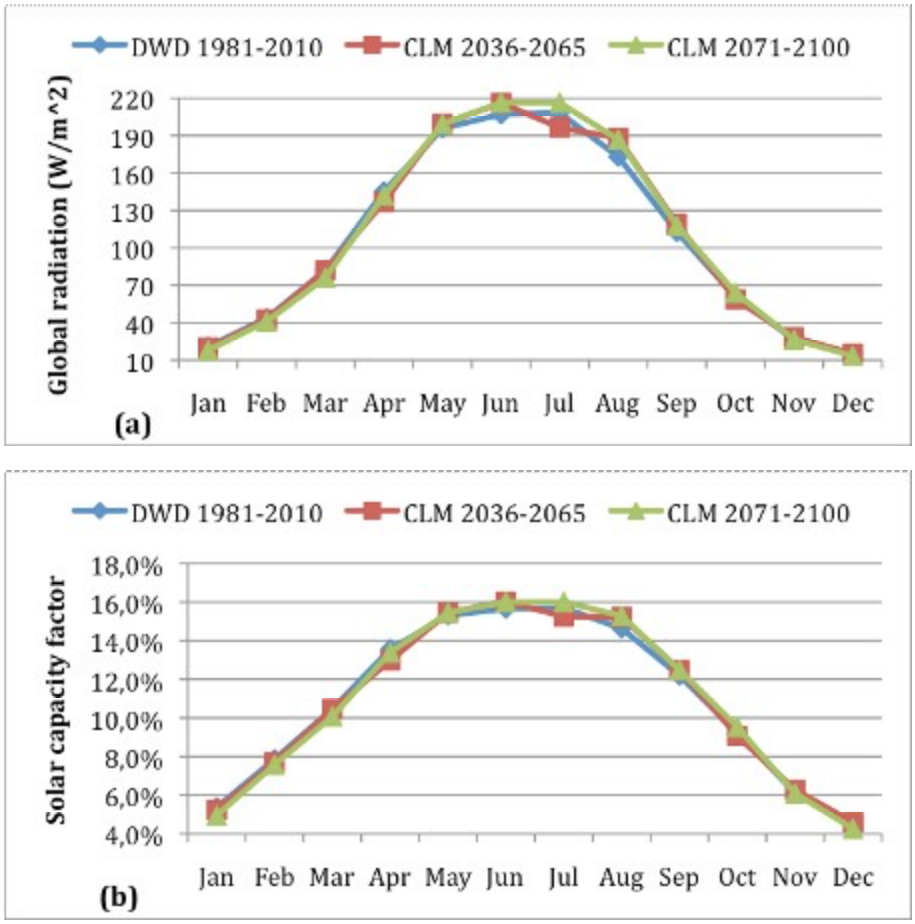

Fig. 4. The monthly profile of global radiation (a) reflect the change of seasonal cloud coverage in the regional climate projections based on the A1B scenario. This has only very little effect on the profile of the regional solar capacity factor (b) because of the diverse tilt angles of solar modules.

The decrease in cloud coverage during the summer results in an increase to annual global radiation by 0.9% through the middle of the century, which then increases to 2.0% by the end of the century. In contrast the solar capacity factor increases by only 0.4% by the end of the century (see Fig. 5). This can again be explained by the tilt of the solar modules in the region, which limit the gains.

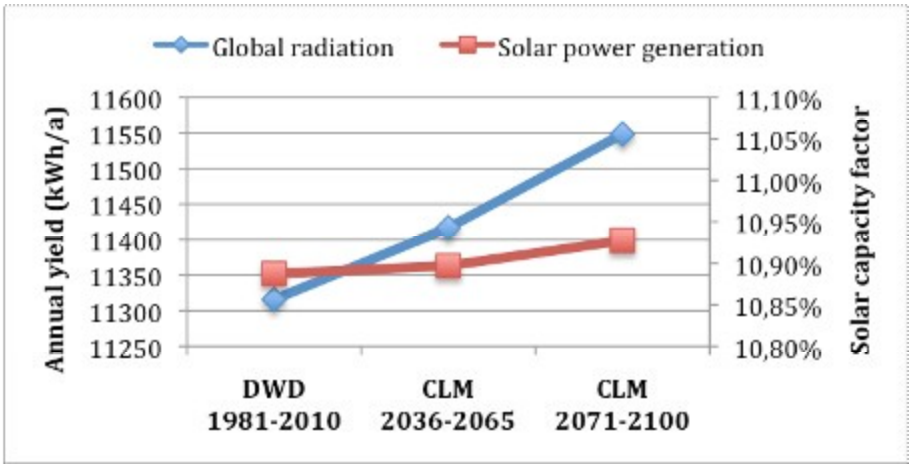

Fig. 5. The increase of global radiation in the regional climate projection based on the A1B scenario yields only a slight increase of the solar capacity factor.

4. Climate impacts on wind power generation

Wind power generation is highly dependent on climate, primarily on the mean and maximum wind speeds. Since the output of a wind power plant is proportional to the third power of the wind speed, the sensitivity with respect to changes in wind speeds is particularly high. In situations of wind speeds greater than 25-30 m/s wind power plants are usually switched off. Furthermore, frequent frost, ice and hail events can produce cracks and/or fractures in the rotor blades which can result in a decrease of power. Finally, extreme weather events (e.g. thunderstorms) may lead to a total loss of certain plants [25].

4.1. A model for regional climate impacts on wind power generation

In our model we focus on the effects of changing mean and maximum wind speeds since data on the impact of extreme weather events is limited. For an accurate assessment of the potential wind power generation at a particular site it is important to model local airflow conditions [26]. When assessing climate impacts on the wind power generation potential, this level of specificity is not achievable because of the lower spatial resolution of regional climate models. However, for a region as large as the Northwest Metropolitan Region this level of specificity is also not as useful because wind power plants may be placed at completely different sites in the future.

As in [3] we use the power curve of a standard wind turbine to map wind speeds to output power and normalize it to a capacity of 1 MW. The output of regional climate models contains hourly wind speeds at 10 m above ground. In order to apply the power curve these are rescaled to turbine height by a factor, which in addition to the turbine height, depends on the so-called surface roughness [26]. For our model we use a mean value of the rescaling factor for the addressed region. A sensitivity analysis conducted to determine the importance of the rescaling factor showed that the seasonal profile depends rather little on it[8], while obviously the annual power production strongly depends on it.

To assess climate impacts we feed hourly mean wind speeds into our model. The output is then aggregated to the monthly time scale and averaged over a time period of 30 years (see Fig. 6).

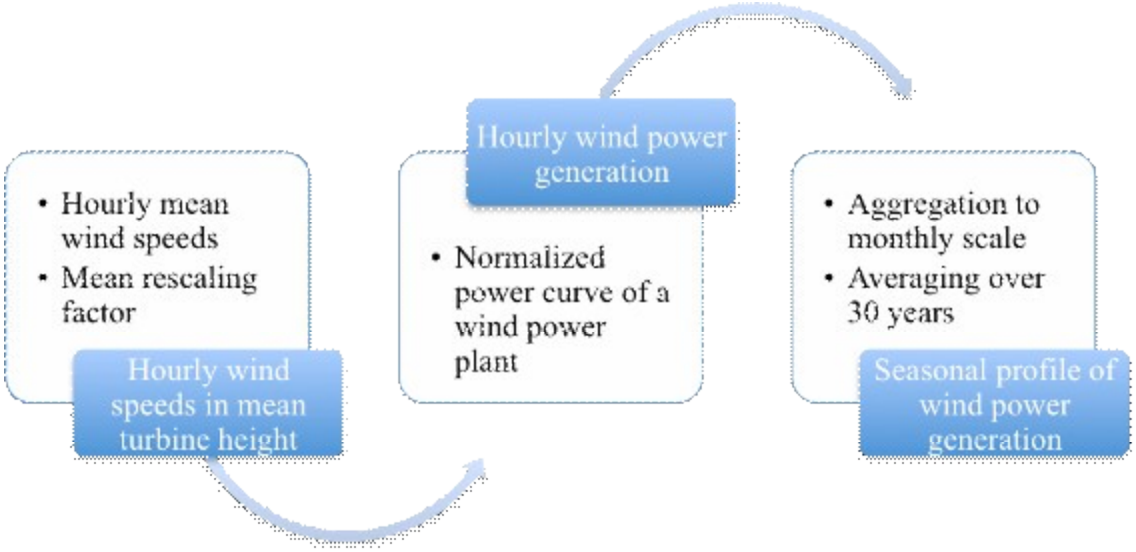

Fig. 6. Schematic representation of the climate impact model for wind power generation.

[8] Variations of the rescaling factor by 10 % led to variations of the monthly shares by less than 1.5 %.

4.2. Impact on wind power plants in the Northwest Metropolitan Region

In our assessment we distinguish inland and coastal wind sites. For both types of sites an average value for the rescaling factor has been deduced from asset master data on the wind power generation in inland and coastal parts of the Northwest Metropolitan Region [15], respectively.

We fed historic hourly wind speed data (1981-2010) for an inland site and coastal site, both within the Northwest Metropolitan Region[9], into the model for wind power generation described above. The resulting seasonal distributions are slightly different. At inland sites there is a moderate peak in February and a smaller one in October, while the pattern is reversed at coastal sites (see Fig. 7).

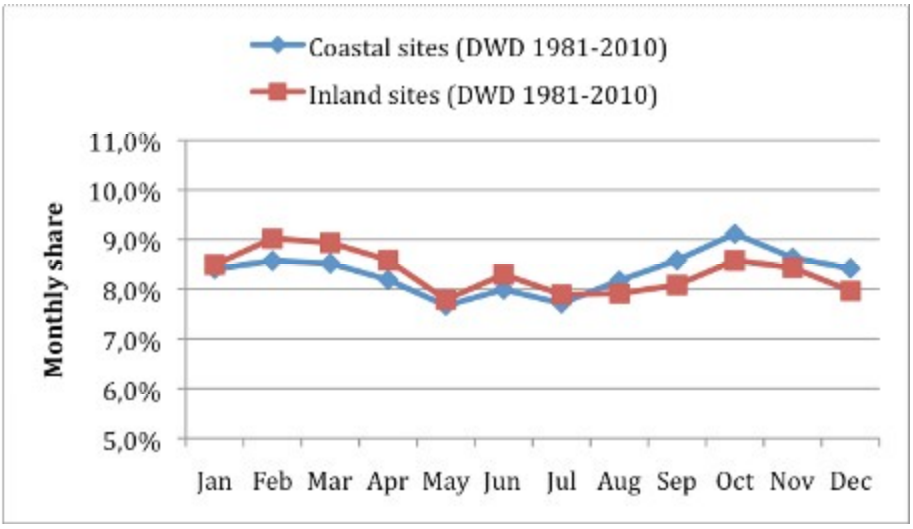

Fig. 7. The seasonal profiles of wind power generation at inland sites and coastal sites are only slightly different within the Northwest Metropolitan Region.

We next invoke the regional climate projections for the Northwest Metropolitan Region again, which are based on the regional climate model CLM (cf. [16]), driven by the global A1B emission scenario (cf. [2]). In these projections, the 30-year averages of mean wind speeds decrease in summer and an increase in the rest of the year (see ***Table 4***).

Table 4. Change of the seasonal mean wind speeds relative to the time period 1971-2000 in the model run of CLM based on the A1B scenario.

Mean Wind Speed	Climate projection	Winter (DJF)	Spring (MAM)	Summer (JJA)	Fall (SON)
Coastal sites	CLM 2036-2065	+0,9 m/s	+0,2 m/s	-0,7 m/s	+0,4 m/s
	CLM 2071-2100	+1,2 m/s	+0,1 m/s	-0,7 m/s	+0,4 m/s
Inland sites	CLM 2036-2065	+0,6 m/s	+0,2 m/s	-0,5 m/s	+0,1 m/s
	CLM 2071-2100	+0,9 m/s	+0,1 m/s	-0,5 m/s	+0,0 m/s

For both inland and coastal sites in the Northwest Metropolitan Region, the climate projections result in a pronounced peak of the capacity factor for wind power production[10] in autumn by 2050 and in an even more pronounced peak in winter by the end of the century (see Fig 8).

[9] The historic data provided by the German Weather Service DWD.

[10] The capacity factor for wind power production is the ratio of the actual output of a wind power plant over a period of time and its potential output if it had operated at full nameplate capacity the entire time.

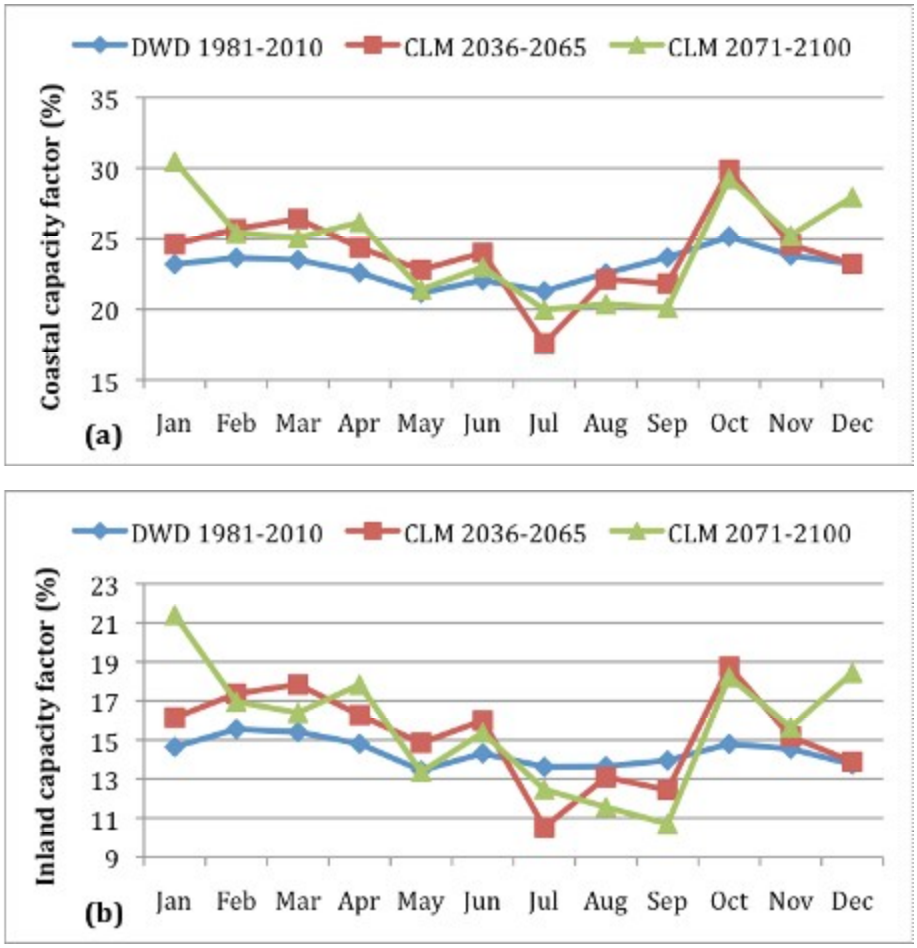

Fig 8. For both inland (a) and coastal sites (b) in the Northwest Metropolitan Region the regional climate projections based on the A1B scenario result in a pronounced peak of the capacity factor for wind power production in autumn in the mid-century and in an even more pronounced peak in winter at the end of the century.

The mean annual capacity factor for wind power generation increases in the climate scenarios. The increase at inland sites (+1.3 percentage points) and coastal sites (+1.5 p. p.) are quite similar in absolute values, but correspond to a relative increase of 9% and 6% respectively (see Fig. 9). The similar increase is probably due to the fact that the output of regional climate models has to be averaged spatially to avoid model artifacts, which smoothes the spatial variation.

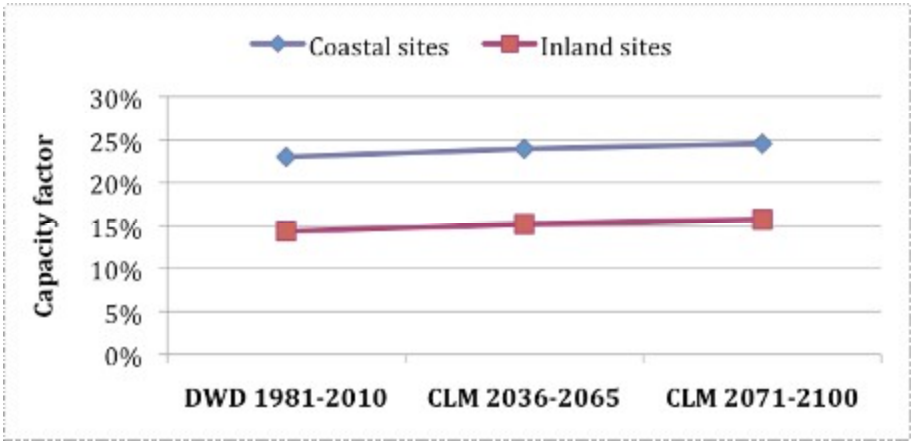

Fig. 9. The mean capacity factor in the Northwest Metropolitan Region increases both at inland sites (+1.3 perc. points) and coastal sites (+1.5 p.p.) for the projections based on the A1B scenario.

5. Climate impacts on shares of wind and solar power which minimize the variance of the residual load

In [3], shares of wind and solar power in Europe are identified that minimize the variance of the residual load on a variety of time scales (hourly, daily, weekly, monthly) under the assumption that the annual electricity demand is met by solar and wind power generation. In this section we investigate whether climate change has an effect on these "optimal shares" at the monthly and regional scale. More precisely, the goal is to assess the consequences of climate impacts on solar and wind power generation for the minimal seasonal variance of the residual load. Hence, we assume throughout this section that the average annual regional electricity demand is met by solar and wind power generation.

5.1. Minimization of the residual load's variance

The residual load in each month is defined as the difference between generation and demand. Its seasonal variance is then given by the normalized sum of the squared monthly residual loads, owing to our assumption that the mean residual load is zero. We want to minimize the seasonal variance of the residual load using seasonal profiles for solar and wind power generation. In order to calculate the monthly residual load for different shares of wind and solar power generation, we need to generate a monthly profile of the electricity demand. So let D be the annual electricity demand and D_j be the demand in the j-th month. In particular,

$$D = \sum_{j=1}^{12} D_j. \qquad (1)$$

Denoting the monthly shares of solar power generation by s_j, and those of wind power generation by w_j, we then search for S and W with

$$Var(S,W) = \tfrac{1}{12} \sum_{j=1}^{12} (s_j \cdot S + w_j \cdot W - D_j)^2 \quad \rightarrow \quad Min \qquad (2)$$

subject to the constraints

$$D = S + W, \quad S \geq 0, \quad W \geq 0. \qquad (3)$$

S and W correspond to the amounts of solar and wind power produced within a year in these equations. Since both the constraint set (3) and the variance (2) are convex, this yields a convex optimization problem. It can be solved explicitly by eliminating either S or W in (2) via (3). We note that the ratio of S and W minimizing (2) does not depend on D.

5.2. Results for optimal shares in the Northwest Metropolitan Region

We use the seasonal profile for solar power generation obtained in Section 3.2 as s_j in (2). Due to the similarity of the seasonal profiles for wind power generation at inland and coastal sites obtained in Section 4.2, an optimization between these two tends to have a minimum for either the power generated at coastal or at inland sites to be zero. However, any allowed combination of inland and coastal generation would produce more or less the same variance (2). Therefore we use only the seasonal profile for wind power generation at inland sites as w_j in (2).

To generate a monthly profile D_j of the electricity demand in the Northwest Metropolitan Region we make use of the disaggregation into the economic sectors: industry, transportation, households and other consumers (mainly the service sector) presented in Section 2.1. The profile for the industrial sector is assumed to be constant over the year because the available monthly data on

electricity consumption of the regional industry (1988-1998) has no pronounced correlations to climate parameters. The profile for the transportation sector is also assumed to be constant because regional data is available only on a yearly basis. For households and the service sector the synthetic load profiles of the BDEW for 2011[11], which are based on historical data from Germany, are aggregated to the monthly scale. The seasonal variation in the resulting load profile for the Northwest Metropolitan Region of approximately 10 % (see Fig. 10) is close to the German average, but rather weak compared to the European average of approximately 20% (see e.g. [3]).

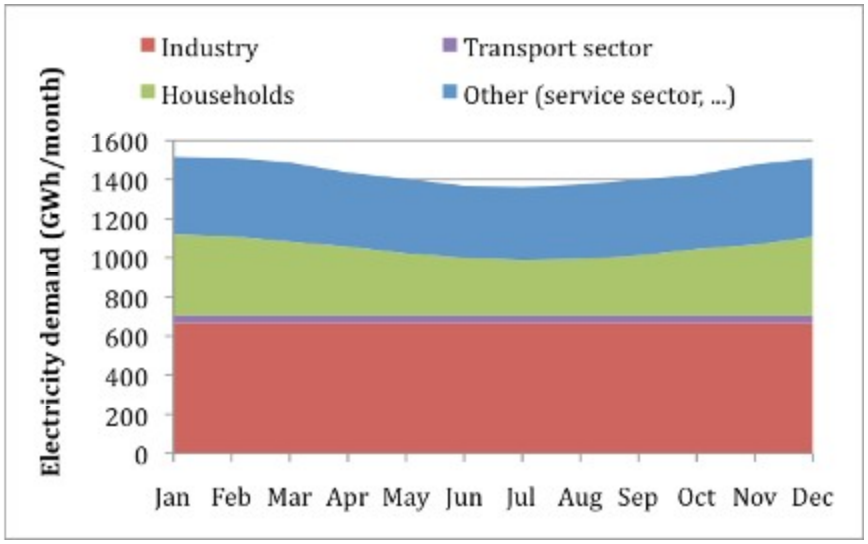

Fig. 10. The seasonal variance of the load profile in the Northwest Metropolitan Region is rather weak compared to the European average. This is mainly due to the fact that electric heating is not very common in Germany.

Concerning the assumption of an electricity supply solely based on wind and solar power we note that while the theoretical and technical potentials are sufficient within the Northwest Metropolitan Region itself [27], economic and regulatory constraints will probably prevent their exploitation. If we, however, take into account the nearby potentials for offshore wind power generation in the North Sea (with similar climate conditions), the assumption describes a relevant scenario for the mid-term future.

As a result of our calculations, in the Northwest Metropolitan Region the optimal share of solar power in a supply scenario based solely on solar and wind power would be 0 % at present. This is due to the fact that the seasonal profile of wind power generation is quite similar to that of the electricity demand. For the regional climate projections based on the A1B scenario, however, the optimal share of solar power generation increases to 13 % in the mid-century and 24 % till the end of the century because of the increasing peak of wind power generation in winter. These results should be judged carefully because other time scales will yield very different results (cf. [3]).

Moreover, the minimal standard deviation[12] of the residual load triples till the mid-century and then slightly decreases till the end of the century. This is also reflected in the yearly sum of the electricity produced in excess to the monthly demand, which is equal to the lack of electricity in the remaining months by assumption (see Table 5).

Table 5. Shares of solar and wind power generation which minimize the seasonal variance of the residual load and characteristics of the resulting residual load.

[11] The synthetic load profiles are e.g. available at < http://www.ewe-netz.de/strom/1988.php>
[12] The standard deviation is the square-root of the variance (cf. (2)).

Climate period	Share of solar power generation	Share of wind power generation	Minimal standard deviation of the residual load	Yearly sum of the power produced in excess to the monthly demand
DWD 1981-2010	0 %	100 %	59 GWh	271 GWh
CLM 2036-2065	13 %	87 %	181 GWh	921 GWh
CLM 2071-2100	24 %	76 %	154 GWh	747 GWh

5.3. The impact of a change in the seasonal demand profile

Climate impacts on electricity demand are rather intricate. At first glance the increasing cooling degree days and the decreasing heating degree days (see Section 2.2) would suggest an increasing demand for cooling in summer and a decreasing demand for heating in winter. However, the effect of the increasing amount of cooling degree days depends heavily on the penetration rate of electric air conditioning. On the one hand, this penetration rate depends on cultural habits a lot which may change due to the occurrence of extreme heat spells. On the other hand, heat-based cooling techniques like absorption refrigeration may serve to satisfy some part of the demand. Furthermore, the effect of heating degree days depends on the penetration rate of electric heating and heat pumps. Warmer winters may even entail a higher electricity demand by leading to a spread in the use of heat pumps instead of fossil-fuelled furnaces.

We plan to address the above-mentioned issues in our future research. Here we simply check the sensitivity of our results to a shift of the monthly demand profile via two scenarios: in Scenario 1 the demand in summer and in winter is balanced, in Scenario 2 the demand is highest in summer. To generate Scenario 2 the existing seasonal peak in January is shifted to July. To generate Scenario 1 we take the mean value of the present electricity demand and the demand in Scenario 2 for each month, which results in an almost constant demand profile (see Fig. 11).

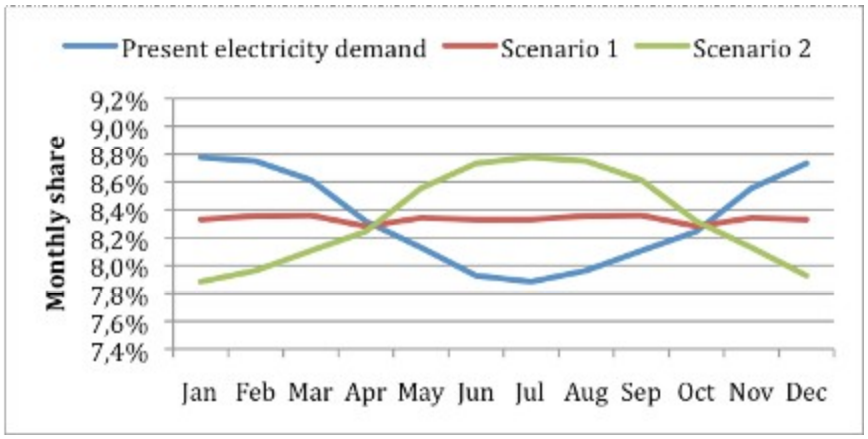

Fig. 11. Scenario 2 is generated from the present electricity demand by shifting the peak in January to July. Scenario 1 consists of the mean values of the present demand and Scenario 2.

In Scenario 1 and 2 the shares of solar power generation are significantly higher than when looking at the present profile of demand because the seasonal profile of solar generation fits better with the higher demand in summer. Nevertheless the minimal standard deviation and the yearly sum of electricity produced in excess to the monthly demand increase in a similar manner (see Table 6).

Table 6. Shares of solar and wind power generation which minimize the seasonal variance of the residual load and characteristics of the resulting residual load for two different demand scenarios.

Scenario	Climate period	Share of solar power generation	Share of wind power generation	Minimal standard deviation of the residual load	Yearly sum of the power produced in excess to the monthly demand
Scenario 1	DWD 1981-2010	6 %	94 %	61 GWh	313 GWh
	CLM 2036-2065	21 %	79 %	175 GWh	919 GWh
	CLM 2071-2100	31 %	69 %	150 GWh	700 GWh
Scenario 2	DWD 1981-2010	15%	85 %	74 GWh	354 GWh
	CLM 2036-2065	29 %	71 %	171 GWh	916 GWh
	CLM 2071-2100	38 %	62 %	148 GWh	696 GWh

6. Conclusions and Outlook

We have constructed models for solar and wind power generation which are suitable to assess the impact of climate change on the generation of renewable electricity. Using data from climate projections for the Northwest Metropolitan Region based on the A1B scenario we find that the seasonal peak of global radiation increases within the region. In contrast to that, the seasonal profile of solar power production is not significantly affected due to a wide range of the solar modules' tilt angles. The slightly higher wind speeds in the fall and winter periods strongly affect the wind power production due to its cubic dependency on wind speeds. As a consequence, the seasonal profile of wind power production forms a pronounced seasonal peak in fall till the mid of the century and an even more pronounced peak in winter till the end of the century. In future research, it would be interesting to explore these effects for other regions and climate scenarios, to which our models can be easily adapted. Furthermore, it would be valuable to collect more primary data on the correlation between solar radiation and solar modules' temperature to include the effect of a reduced efficiency for high module temperatures (cf. the introduction to Section 3).

We have compared the seasonal profiles to different scenarios for electricity demand. For each scenario we have identified the ratio of wind and solar power that minimizes the variance of the residual load at the monthly time scale. In the Northwest Metropolitan Region the optimal share of solar power in a supply scenario based solely on solar and wind power would be zero at present. With the increasing peak of wind power generation in winter, however, the optimal share of solar generation increases. This effect is even stronger in case of an increasing demand in summer. In spite of that, the minimal variance of the residual load also increases. The electricity produced in excess to the monthly demand might either be exported via the transmission grid or be stored to meet the demand in months with insufficient power generation. So our results suggest that the known need for both grid extensions and long-term electricity storage in a full supply by wind and solar power may even be increased by climate change significantly. For policy makers it is important to be aware of these potential impacts already today because of the long building times and lifetimes of large-scale infrastructure.

It is to be expected that storage of electricity on the monthly time scale will come with rather large losses. Given technology options discussed today the most likely options for electricity storage on the monthly time scale are conversion into hydrogen or methane that may be used in fuel cells or gas plants to produce electricity again, resulting in a total electric efficiency of less than 50% [28]. If large excess capacities for solar and wind power generation shall be avoided, there definitely remains a need for power plants that may be run in a flexible way. In a supply based on renewable sources biogas-fired power plants pose a valuable option because they can be run-up fast and independently of weather conditions and, hence, provide the necessary control energy.

Our results on the possible future development of solar and wind capacity factors will be fed into the Northwest Metropolitan Region model (cf. Section 1). Within this model the more intricate

issues of climate impacts on electricity demand (cf. Section 0) as well as the role of long-term storage in the regional energy system (cf. Section 5.2) may be addressed in more detail. Relevant factors have already been identified in a series of workshops with regional stakeholders. Still this will only be based on the comparison of different scenarios because of the large uncertainties about future developments that are inherent in the assessment of a socio-economic system.

The ultimate goal is to use the Northwest Metropolitan Region model to identify regional development strategies that are resilient to substantial changes of the boundary conditions, may they be related to climate change or to socio-economic developments. To this end regional stakeholders from various sectors and government officials will be asked to experiment with the parameters in the model and to reflect on their experiences. We believe that this leads to benefits for both regional stakeholders and researchers. On one hand stakeholders are able to experience possible consequences of their investment and policy decisions, while on the other hand stakeholder's expertise can be used by researchers to select the most relevant scenarios for modeling.

Acknowledgments

This paper was made possible in part through support by a grant from the German Ministry for Education and Research (Bundesministerium für Bildung und Forschung) as part of its KLIMZUG initiative. The German Weather Service (DWD) provided historic climate data. The output of the regional climate models was provided by the Climate Service Center in Hamburg. Data and model evaluations were partly carried out by our students Sven Rohrdanz and Jan-Ole Werner.

References

[1] Solomon S., Qin D., Manning M., Chen Z., Marquis M., Averyt K.B., Tignor M., Miller H.L., editors. Contribution of Working Group I to the Fourth Assessment Report of the Intergovernmental Panel on Climate Change, Cambridge, United Kingdom and New York, NY, USA: Cambridge University Press; 2007.

[2] Pachauri R.K., Reisinger A., editors. Contribution of Working Groups I, II and III to the Fourth Assessment Report of the Intergovernmental Panel on Climate Change, IPCC, Geneva, Switzerland. 2007.

[3] von Bremen L., Large-scale Variability of Weather Dependent Renewable Energy Sources. In: Troccoli A, editor. Management of Weather and Climate Risk in the Energy Industry, NATO Science Series, Springer Academic Publisher. 2010. p. 189-206.

[4] Ruth M., Lin A.C., Regional energy demand and adaptations to climate change: methodology and application to the state of Maryland, USA. Energy Policy 2006;34:2820–2833

[5] Hekkenberg M, Moll H.C., Schoot Uiterkamp A.J.M., Dynamic temperature dependence patterns in future energy demand models in the context of climate change. Energy 2009;34:1797–1806.

[6] Ruth M., Blohm A., Gasper R., Karlstetter N., Wachsmuth J., Beermann M. Eickemeier T., Gößling-Reisemann S., Akamp M., Dynamic modeling of regional climate adaptation needs and options. Annual meeting of the Western Regional Science Association. Kauai, HI. 2012.

[7] Schaeffer R., Szklo A.S., de Lucena A.F.P., Borba B.S.M.C., Nogueira L.P.P., Fleming F.P., Troccoli A., Harrison M., Boulahya M.S., Energy sector vulnerability to climate change: A review. Energy 38 (2012) 1–12.

[8] Pryor S.C., Barthelmie R.J., Climate change impacts on wind energy: a review. Renewable and Sustainable Energy Reviews 2010; 14:430–437.

[9] Sailor DJ, Smith M, Hart M. Climate change implications for wind power resources in the Northwest United States. Renewable Energy 2008;2393–406.

[10] Pryor S.C., Barthelmie R.J., Schoof J.T., Inter-annual variability of wind indices across Europe. Wind Energy 2006;9:27–38

[11] Crook J.A., Jones L.A., Forster P.M., Crook R., Climate change impacts on future photovoltaic and concentrated solar power energy output. Energy Environ. Sci., 2011;4:3101–3109.

[12] Gößling-Reisemann S., von Gleich A., Stührmann S., Wachsmuth J., Climate change and structural vulnerability of a metropolitan energy supply system – the case of Bremen-Oldenburg in Northwest Germany. Accepted for publication in J Ind Ecol.

[13] Metropolregion Bremen-Oldenburg im Nordwesten e.V., Open. Innovative. Decisive. Metropolitan Region Bremen-Oldenburg, North-West Germany – Available at:<http://www.ref60bremen.de/MPR_Broschuere_englisch.pdf> [accessed 30.01.2012].

[14] Eickemeier T., Strombilanz der Metropolregion Bremen-Oldenburg im Nordwesten [diploma thesis]. Bremen, Germany: Universität Bremen; 2012.

[15] Deutsche Gesellschaft für Sonnenenergie e.V. (DGS). Asset master data of German renewable energy facilities – Available at:<http://www.energymap.info> [accessed 30.11.2011].

[16] Schuchardt B., Wittig S., Spiekermann J., Klimaszenarien für NordWest2050. Teil 1: Grundlagen. Bremen, Germany: Bioconsult; 2010. Nordwest2050-Werkstattbericht °2.

[17] Schuchardt B., Wittig S., Spiekermann J., Klimaszenarien für NordWest2050. Teil 2: Randbedingungen und Beschreibung. Bremen, Germany: Bioconsult; 2010. Nordwest2050-Werkstattbericht °3.

[18] Klucher T.M., Evaluation of models to predict insulation on tilted surfaces. Journal of Solar Energy 1979;23(2):111-114.

[19] Zinßer B., Jahresenergieerträge unterschiedlicher Photovoltaik-Technologien bei verschiedenen klimatischen Bedingungen [dissertation]. Stuttgart, Germany: Universität Stuttgart; 2010.

[20] Ehnberg J.S.G., Bollen M.H.J., Simulation of global solar radiation based on cloud observations. Solar Energy 2005;78:157–162

[21] Nielsen L., Prahm L., Berkowicz R., Conradsen K., Net incoming radiation estimated from hourly global radiation and/or cloud observations. J. Climatol. 1981;1:255–272.

[22] Duffie J., Beckman W.A., Solar Engineering of Thermal Processes (3rd edition). Hoboken: Wiley; 2006.

[23] Solarenergie-Förderverein Deutschland e.V. Database of monthly solar power generation in Germany – Available at:<http://www.pv-ertraege.de > [accessed 30.11.2011].

[24] Klaus-Novy-Institut e.V. Marktakteure Erneuerbare – Energien - Anlagen In der Stromerzeugung – Available at:<http://www.kni.de/media/pdf/Marktakteure_Erneuerbare _Energie_Anlagen_in_der_Stromerzeugung_2011.pdf.pdf > [accessed 30.11.2011].

[25] Rothstein B., Halbig G., Weather Sensitivity of Electricity Supply and Data Services of the German Met Office. In: Troccoli A, editor. Management of Weather and Climate Risk in the Energy Industry, NATO Science Series, Springer Academic Publisher. 2010. p. 253-266.

[26] Lange M., Focken U., Physical Approach to Short-Term Wind Power Prediction, Berlin/ Heidelberg/New York: Springer. 2005.

[27] Hammerschmidt A., Osterndorf C., Wendt D., Zuch M., Potenzialanalyse für Strom und Wärme aus erneuerbaren Energien in der Metropolregion Bremen – Oldenburg im Nordwesten [seminar paper]. Bremen, Germany: Universität Bremen; 2012.

[28] Sterner M., Bioenergy and renewable power methane in integrated 100% renewable energy systems. Limiting global warming by transforming energy systems [dissertation]. Kassel, Germany: Universität Kassel; 2009.

Impact of Nuclear Power Plant on Thailand Power Development Plan

Raksanai Nidhiritdhikrai[a] and Bundhit Eua-arporn[b]

[a] Energy Research Institute, Chulalongkorn University, Bangkok, Thailand, raksanai.n@chula.ac.th
[b] Energy Research Institute, Chulalongkorn University, Bangkok, Thailand, bundhit.e@chula.ac.th

Abstract:

Negative perception on nuclear power plants has been widely acknowledged for decades. The current Thailand power development plan, in which nuclear power plant is included, is re-evaluated taking into account uncertainties on both generation and demand sides. In this paper, the impact of nuclear uncertainty is investigated from 2010 to 2030 using scenario based analysis. Energy accounting model, including methodology based on probabilistic method, is deployed to calculate system indices and handle the balance of energy. The baseline scenario, including nuclear power plants, is developed, whereas other possible scenarios, e.g., nuclear power plant postponement, nuclear power plant substitution, increase of renewable energy penetration, are simulated. Then, the impact is analyzed and compared via defined indices, e.g., reserve margin (RM), average cost, fuel diversity, and average CO_2 emission. With the obtained results, the critical system impact will be determined and used as a guideline for strategic planning and long-term preparation for Thailand power system.

Keywords:
Power Development Plan, Nuclear Power Plant, Scenario Based Analysis.

1. Introduction

An appropriate power development plan (PDP) is not only a key driving force to increase the reliability of energy supply, but also a plan to further exploit available energy potential. In Thailand, the power development plan has been implemented and periodically revised since 1982. The current PDP was revised in 2010 [1], which includes several new power plants along with 5x1,000 MW nuclear power plant [1], anticipated to be commissioned during 2020-2028 as shown in Table 1.

TABLE 1. Anticipated nuclear power plant of Thailand generation system

Plant No.	Unit size (MW)	Scheduled year	Percentage of installed capacity (%)
1	1,000	2020	2.23
2	1,000	2021	4.20
5	1,000	2024	5.71
4	1,000	2025	7.58
5	1,000	2028	8.15

However, the disaster of the nuclear power plant in Japan's Fukushima in 2011 has consequently caused Thailand to reconsider the current PDP. In this paper, the current PDP will be analysed taking into account impact of the nuclear uncertainty and options for Thailand power development based on a set of developed scenario, e.g., postponement and substitution of the nuclear power plants, increase of renewable energy. Then, the impact is comparatively analyzed through a set of predefined indices, e.g., reserve margin (RM), average cost, fuel diversity, and average CO_2 emission.

2. Scenario Definition

In this paper, scenario based method is applied to assess the impact of alternative plans on the current Thailand PDP. Details of the defined scenarios and corresponding criteria are described in Table 2, covering 9 scenarios on 3 key issues, i.e., nuclear power plant postponement, nuclear power plant substitution, and increase of renewable energy penetration.

For the renewable energy scenarios defined in Table 2, the levels of renewable energy penetration for scenarios 9 to 11 is assumed to increase linearly from 5% in 2020 to 10%, 20% and 30% respectively as shown in Fig. 1. For these scenarios, the penetration portion is maintainded 75% biomass, 15% solar, and 10% wind resources.

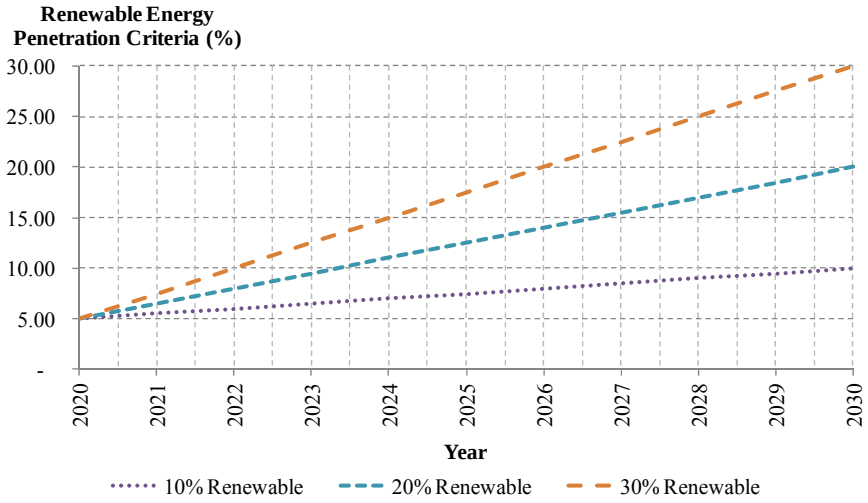

Fig. 1. Renewable energy penetration criteria

Biomass and wind generations are assumed to generate power constantly. The equivalent capacity of these generations can be illustrated by (1).

$$Equivalent\ capacity = \frac{Plant\ factor\ \times Capacity}{100} \tag{1}$$

Solar generations are assumed to generate power with constant pattern. Generation profile of solar generation is generated from solar data [2], depending on month and time of day, and used to reduce hourly load curve directly. The generation profile of 50 MW solar plant is shown for an example in Fig. 2.

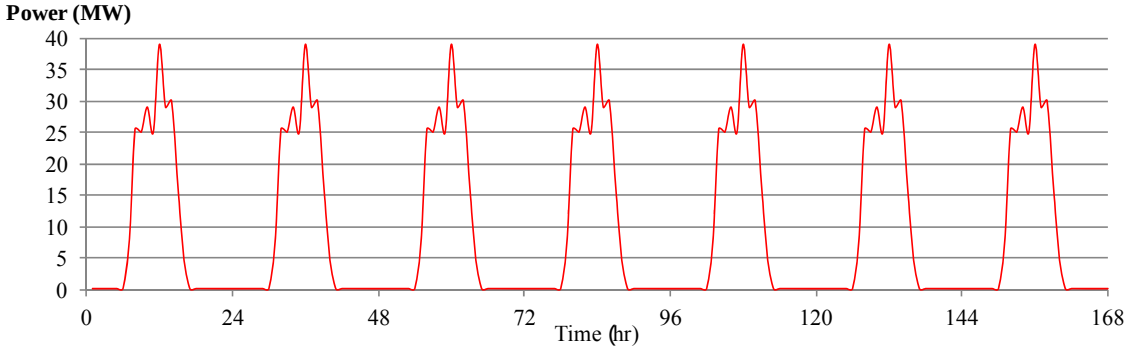

Fig. 2. Generation profile of 50 MW solar plant

TABLE 2. Developed scenarios for the current Thailand PDP

Scenario No.	Scenario name	Definition	Criteria
0	Base Case	▪ PDP2010 [1]	▪ Reserve margin is not less than 15%. ▪ Imported capacity is not more than 25%. ▪ Average CO_2 emission is not more than 0.5 $kgCO_2/kWh$
1	10% Reserve Margin	▪ Base Case + Reserve Margin ≥ 10%	▪ Same criteria as the Base Case, while reserve margin is not less than 10%, 15%, and 20% respectively. ▪ Scheduled generators are rescheduled with the same installation order as specified in Base Case scenario. ▪ Additional generators to be installed when needed.
2	15% Reserve Margin	▪ Base Case + Reserve Margin ≥ 15%	
3	20% Reserve Margin	▪ Base Case + Reserve Margin ≥ 20%	
4	Delay of Nuclear Energy	▪ Scenario 2 with 3-year delay of nuclear power plants	▪ Same criteria as the 15% Reserve Margin scenario, while nuclear power plants are delayed for 3 years.
5	No Nuclear Energy	▪ Scenario 2 with excluding of nuclear power plants	▪ Same criteria as the 15% Reserve Margin scenario, however without nuclear power plant.
6	Replacing of Nuclear Energy by Bituminous Energy	▪ Scenarios 6-8 are similar to scenario 5, with nuclear power substitution from bituminous, natural gas and imported hydro energy respectively.	▪ Same criteria as the No Nuclear Energy scenario. ▪ Optional generators powered by bituminous, natural gas, and imported hydro energy are selected when needed.
7	Replacing of Nuclear by Natural Gas Energy		
8	Replacing of Nuclear Energy by Imported Hydro Energy		
9	10% Renewable Energy	▪ Same as scenario 2 with the percentage of energy produced from all renewable resources not less than 10%, 20%, and 30% in 2030.	▪ Same criteria as the 15% Reserve Margin scenario. ▪ Levels of renewable energy penetration criteria are required to increase linearly from 5 % in 2020 to 10%, 20%, and 30% in 2030 as illustrated in Fig. 1 respectively.
10	20% Renewable Energy		
11	30% Renewable Energy		

3. Power Development Plan Analysis

In general, the PDP is analyzed to determine or reschedule future generation development to comply with the defined criteria**,** e.g., specified risk index, increase of renewable energy, demand side management. With the obtained generation development plan under the defined scenarios, expected energy production of each generator and other concerned information, e.g., reserve margin (RM), average cost, fuel diversity, and average CO_2 emission, are calculated.

The process of the PDP development, conducted on monthly based analysis, is illustrated in Fig. 3. The reliabilities criteria applied in this paper is the reserve margin defined in following section.

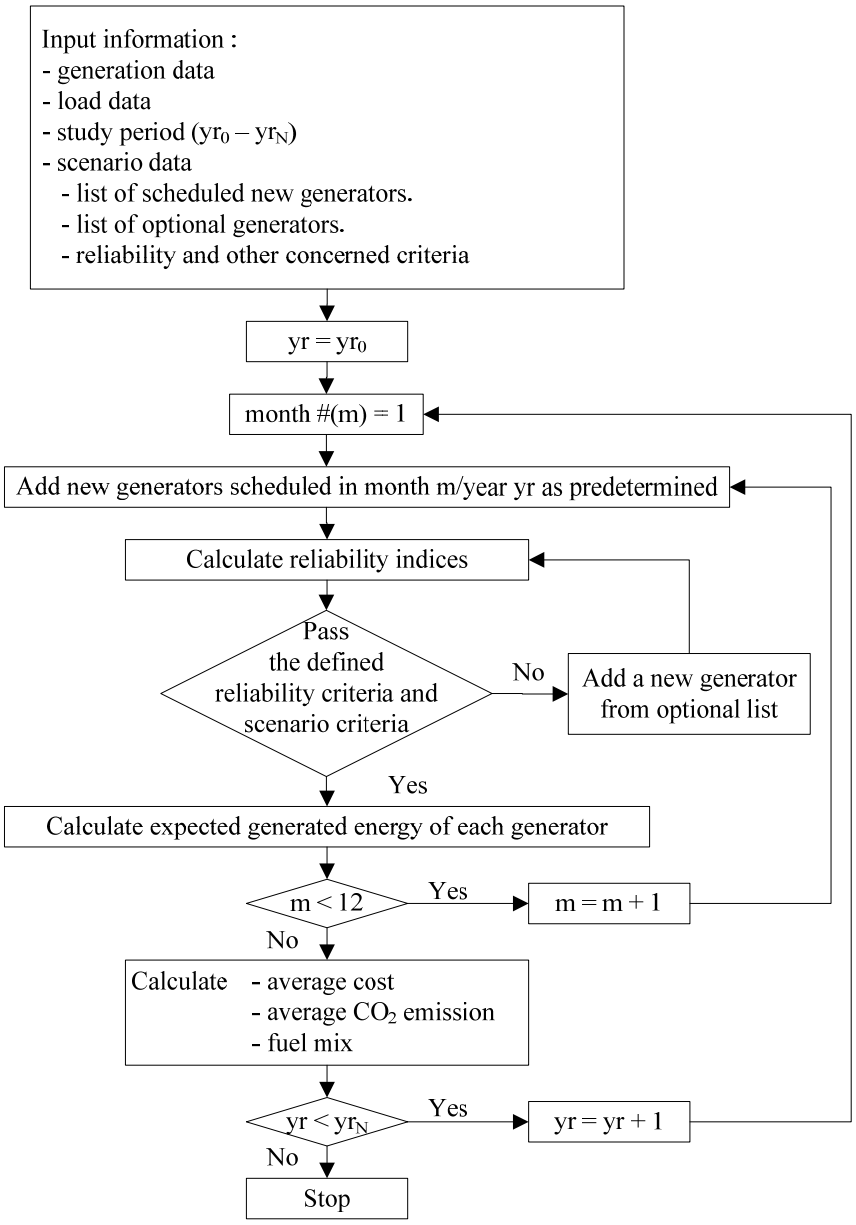

Fig. 3. Flow chart of power development plan analysis

The obtained indices under each defined scenarios, to be described in the next section, are comparatively assessed in order to determine impact of nuclear uncertainty and options for Thailand power development.

4. Concerned Indices

In this section, the considered indices, e.g., reserve margin (RM), fuel diversity, average cost, and average CO_2 emission, are summarized below.

4.1 Reserve margin

Reserve margin is the difference between dependable capacity and peak load which can be illustrated by (2).

$$RM = \frac{Dependable\ capacity - PL}{PL} \times 100 \tag{2}$$

where

RM : percentage reserve margin (%)
PL : peak load (MW).

4.2 Fuel Diversity

Fuel diversity is the standard deviation of energy percentage produced from all fuel types. This index shows the distribution of usage of fuel. A system with high fuel diversity implies unbalance fuel usage to produce most of its electricity. On the other hand, a system with low fuel diversity uses all of its fuel in same or nearby portion to produce electricity.

4.3 Economic Index

In this paper, the economic index mainly focuses on average cost, represented by (3).

$$Average\ cost = \frac{Total\ production\ cost}{Total\ generation\ energy} \tag{3}$$

4.4 Environmental Index

Environmental index proposed in this paper is focused on average CO_2 emission, which is the average amount of CO_2 emission per 1 kWh of generation. Average CO_2 emission can be obtained by (4) with the heat rate [1] and the emission factor [3] of each generator as defined in Tables 3, and 4 respectively.

$$Average\ CO_2 emission = \frac{Total\ produced\ CO_2}{Total\ generation\ energy} \left(\frac{kgCO_2}{kWh}\right) \tag{4}$$

$$Total\ \ CO_2\ production = \sum_{i=1}^{n} EPE_i \times Heat\ Rate_i \times EF_k\ \ (kgCO_2) \tag{5}$$

where

n is number of existing generators,
EPE_i is expected produced energy of generator i,
$Heat\ Rate_i$ is heat rate of generator i, and
EF_k is emission factor of fuel type k.

TABLE 3. Heat rate of generation system

Generator type No.	Generator type	Fuel Type	Heat rate	
			(kJ/kWh)	(Btu/kWh)
1	Thermal	Lignite	11,184-12,133	10,600-11,500
2	Thermal	Bituminous	9,601	9,100
3	Thermal	Natural gas	9,918-10,867	9,400-10,300
4	Thermal	Nuclear	11,606	11,000
5	Thermal	Oil	10,972	10,400
6	Gas turbine	Diesel	10,972	10,400
7	Combined cycle	Natural gas	7,174-8,220	6,800-7,800

TABLE 4. Emission factors for generation system

Fuel Type No.	Fuel Type	Emission Factor	
		($kgCO_2/kJ$)	($kgCO_2/Btu$)
1	Natural gas	0.0000543	0.0000573
2	Lignite	0.0000909	0.0000959
3	Bituminous	0.0000845	0.0000944
4	Cruel oil	0.0000755	0.0000797
5	Diesel	0.0000726	0.0000766

5. Generation System and Load Modeling

5.1 Load Model

Information of annual hourly load curve should be firstly investigated. Then the load duration curve, as shown in Fig. 4 [1], can be developed and used in conjunction with the generation system model, which will be explained in the next part, to obtain reliability indices, i.e., expected energy not supplied (EENS).

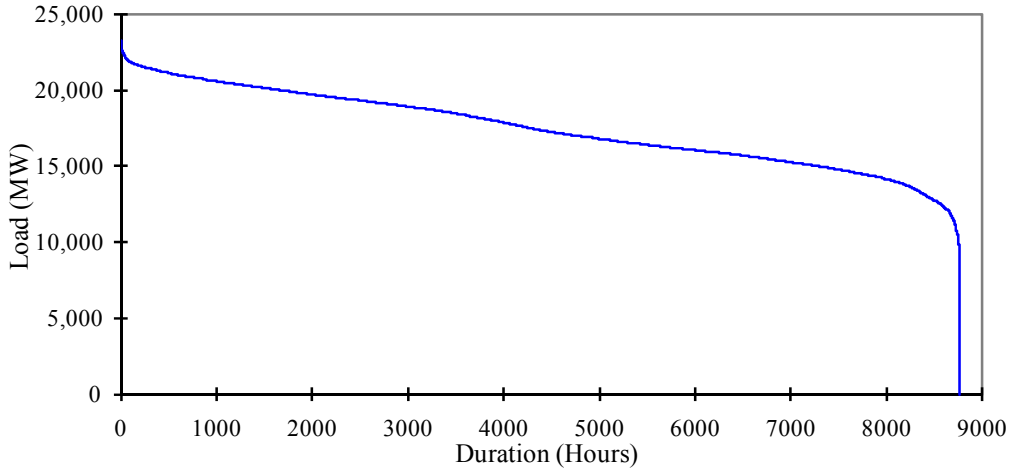

Fig. 4. Hourly load duration curve

5.2 Energy-limited Generation

In general, each generating unit is assumed to be able to generate power with sufficient fuel supply for all the considering time. However some units, e.g., hydro units, is of energy-limited type in nature since the amount of water in the reservoir, which can be discharged to generate electric energy, is varied along the considering time. Therefore these units are generally dispatched as peak-shaving units, leaving the rest of the demand to be supplied by other generating units. In this paper, the characteristic of the limited amount of energy presented as probability distribution shown in Table 5 will be considered.

TABLE 5. Energy Distribution

Plant No.	Unit size (MW)	Energy (MWh)	Cumulative probability
1	72	258,838	1.00
		448,886	0.81
		630,720	0.24
2	300	888,534	1.00
		1,348,678	0.71
		1,808,822	0.21

The peak-shaving technique [4] is firstly applied to modify the original load duration curve using a conditional probability which can be illustrated by (6).

$$D(L) = \sum_{i=1}^{N} d_i(L) \cdot P_i(C_i) \tag{6}$$

where

$D(L)$ is the duration of load L on the capacity modified curve,
$d_i(L)$ is the duration reduction of load L on the original load duration curve by MW,
C_i is output capacity of i th capacity state of the peak-shaving unit,
N is number of capacity states of peak-shaving unit, and
$P_i(C_i)$ is probability of unit's capacity of C_i.

$$D(L) = d_c(L) \cdot P\big(E(L)\big) + d_o(L) \cdot [1 - P\big(E(L)\big)] \tag{7}$$

where

$D(L)$ is the duration of the final peak-shaved curve corresponding to load of L MW,
$d_c(L)$ is the duration of capacity modified curve corresponding to load of L MW,
$d_0(L)$ is the duration on original load duration curve corresponding to load of L MW,
$E(L)$ is expected energy output of the unit, and
$P(E(L))$ is probability of energy equaling or exceeding $E(L)$.

Then energy distribution of the unit as shown in Table 5, formulated by (7) will be considered for peak load shaving. The result of the modified load duration curve can be obtained as illustrated in Fig. 5.

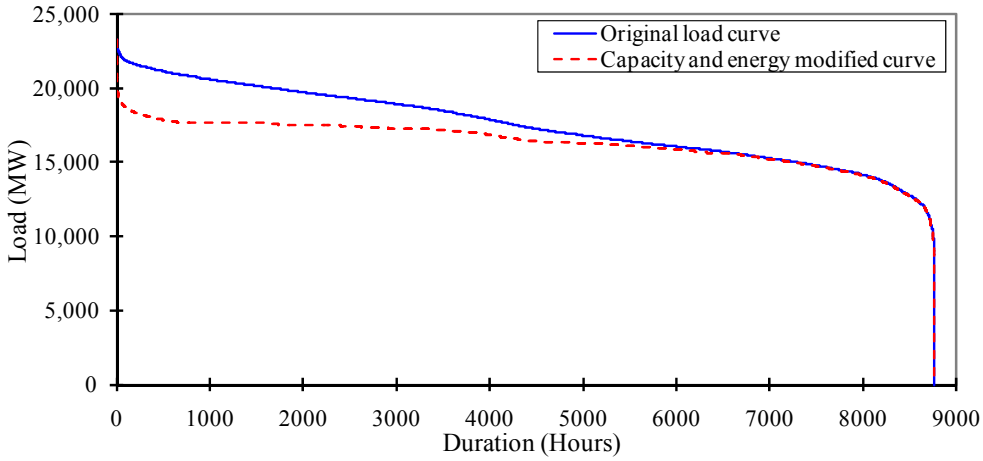

Fig. 5. Original and energy modified load duration curve

5.3 Generation System Model

The generation system model can be presented as a capacity outage probability table (COPT) [5], which is a simple array of capacity levels with their associated probabilities. The formula to obtain the cumulative probability of the X MW outage in the system can be demonstrated by (8).

$$P(X) = (1 - U) \cdot P'(X) + (U) \cdot P'(X - C) \tag{8}$$

where

$P(X)$ is cumulative probability of the capacity outage state of *X* MW after the generating unit is added,

$P'(X)$ is cumulative probability of the capacity outage state of *X* MW before the generating unit is added,

U is the unavailability of the added unit, and

C is the added unit's capacity in MW.

6. Expected Energy Production

In this paper, expected energy production from each generator is calculated for further investigation. The production is calculated using expected energy not supplied (EENS). The EENS [5] index can be obtained using the capacity outage probability table and the hourly peak load variation curve as illustrated in Fig. 6, and can be expressed mathematically by (9) and (10). The expected energy produced by each unit can be calculated by (11).

$$EENS_0 = t * \sum_{i=1}^{n} L_i \tag{9}$$

$$EENS_q = \sum_{k=1}^{N} p_k E_k \tag{10}$$

$$EEP_q = EENS_{q-1} - EENS_q \tag{11}$$

where

t is the during time period being considered,
L_i is actual load at hour i,
$EENS_0$ is the total energy demand,
$EENS_q$ is expected energy not supply of unit q,
p_k is individual probability of state k,
E_k is expected energy curtailed of state k, and
EEP_q is expected energy produced by unit q.

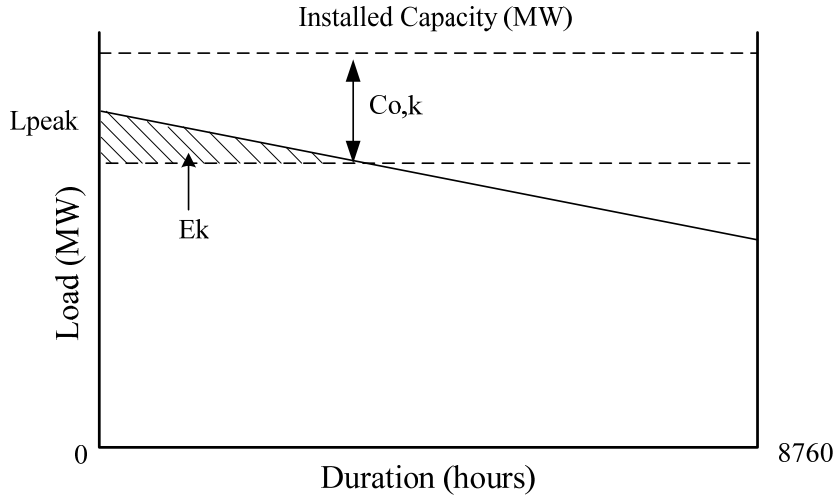

Fig. 6. EENS calculation

7. Simulation Result

The impact of nuclear power plant uncertainty during 2010 to 2030, is simulated based on the scenarios defined in Table 2, in conjunction with the power development plan (PDP2010) [1]. The system consists of 29,578.64 MW installed capacity.

In this section, the obtained results from all the scenarios defined in Table 2 are comparatively analyzed through reserve margin (RM), average cost, fuel diversity, and average CO_2 emission. The results are classified into 3 categories shown in Table 6 and illustrated in Figs 7 to15.

TABLE 6. Result categories

Category No.	Member scenario	
1	Base Case	Replacing of Nuclear Energy by Bituminous Energy
	No Nuclear Energy	Replacing of Nuclear Energy by Natural Gas Energy
	Delay of Nuclear Energy	Replacing of Nuclear Energy by Imported Hydro Energy
2	Base Case	10% Reserve Margin
	15% Reserve Margin	20% Reserve Margin
3	Base Case	10% Renewable Energy
	20% Renewable Energy	30% Renewable Energy

All the results, listed only of 2030, are summarized in Table 7, along with the corresponding indices of Base Case in 2010 and 2030.

TABLE 7. Summarized simulation results of considered scenarios in 2030

Scenario No.	Scenario name	Average cost (Baht/kWh)	Average CO_2 emission (kgCO2/kWh)	Imported energy (%)	Normalized fuel diversity
0	Base Case in 2010	2.22	0.48	4.98	2.299
0	Base Case	2.91	0.38	18.26	1.000
1	10% Reserve Margin	2.97	0.37	17.95	1.043
2	15% Reserve Margin	2.92	0.38	18.26	1.003
3	20% Reserve Margin	2.84	0.37	20.90	0.998
4	Delay of Nuclear Energy	2.93	0.38	20.03	1.034
5	No Nuclear Energy	3.00	0.44	21.72	1.227
6	Replacing of Nuclear Energy by Bituminous Energy	3.00	0.48	18.09	1.272
7	Replacing of Nuclear Energy by Natural Gas Energy	3.17	0.42	18.09	1.300
8	Replacing of Nuclear Energy by Imported Hydro Energy	2.97	0.40	23.39	1.225
9	10% Renewable Energy	3.05	0.36	13.23	0.927
10	20% Renewable Energy	3.35	0.32	14.79	0.884
11	30% Renewable Energy	3.69	0.28	12.81	1.045

If only the average cost of the substitution scenarios 6-8 is taken into account, it will be founded from Fig. 8 that the most suitable scenario is scenario 8 which provides the lowest cost.

Focusing on normalized fuel diversity, of which the fuel diversity of the considered scenario is divided by the fuel diversity of the Base Case scenario, the most suitable scenario is 20% Renewable scenario. This scenario not only increases fuel diversity, but also reduces average CO_2 emission of the system. To achieve these benefits, the average cost of electricity would be increased from 2.91 to 3.35 baht/kWh, i.e., approximately 15%.

On environmental impact or average CO_2 emission, it is found that 30% Renewable provide the most promising result, since renewable energy generated lowest CO_2 emission.

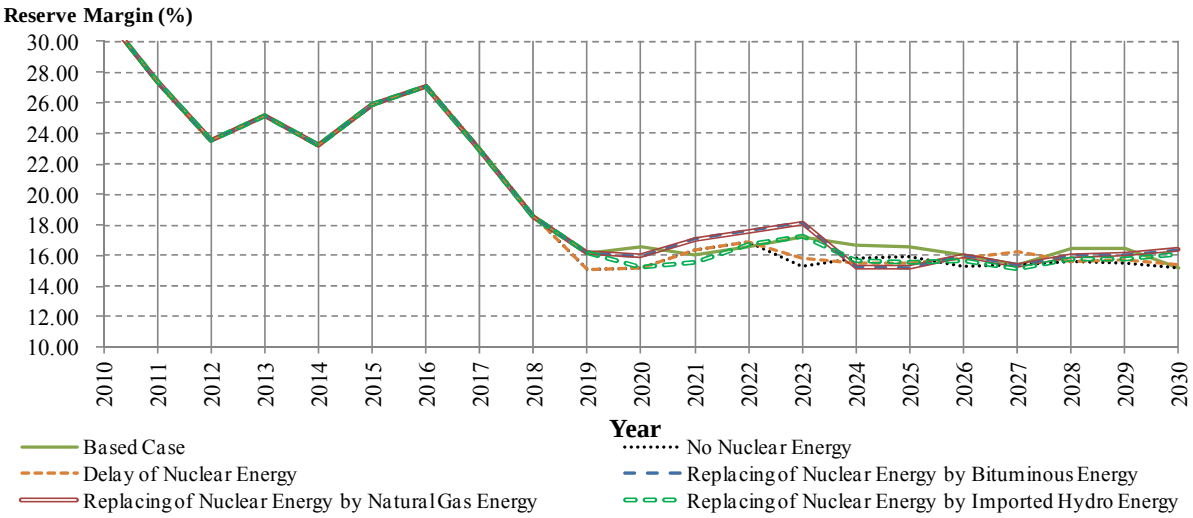

Fig. 7. Reserve margin of category 1 cases

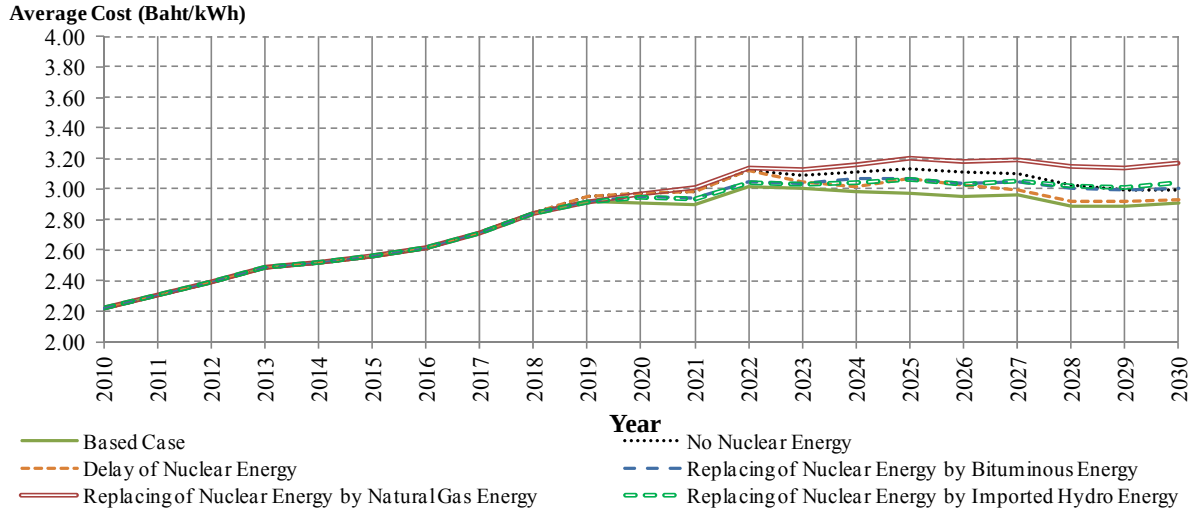

Fig. 8. Average cost of category 1 cases

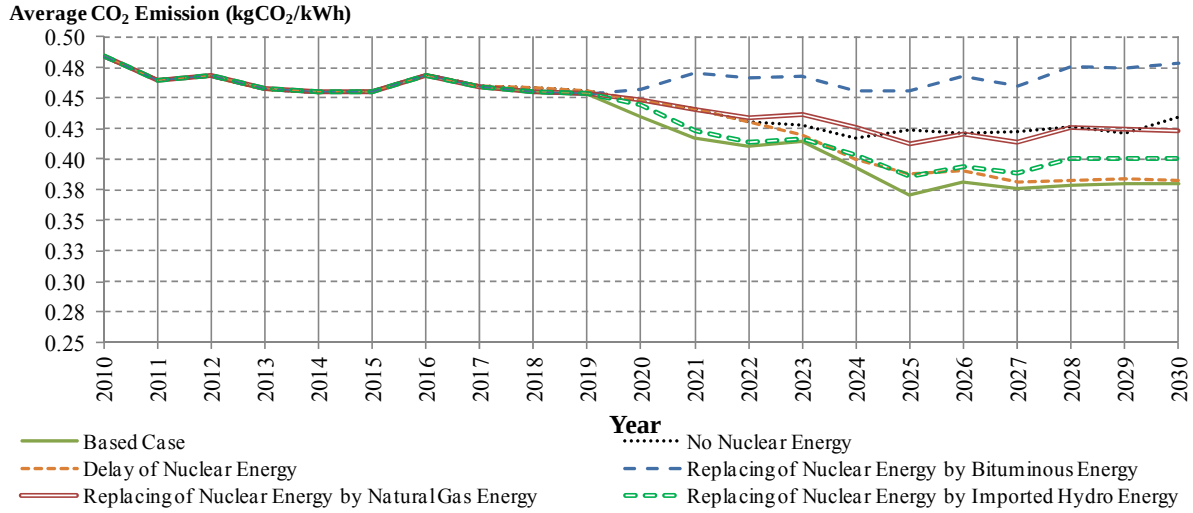

Fig. 9. Average CO_2 emission of category 1 cases

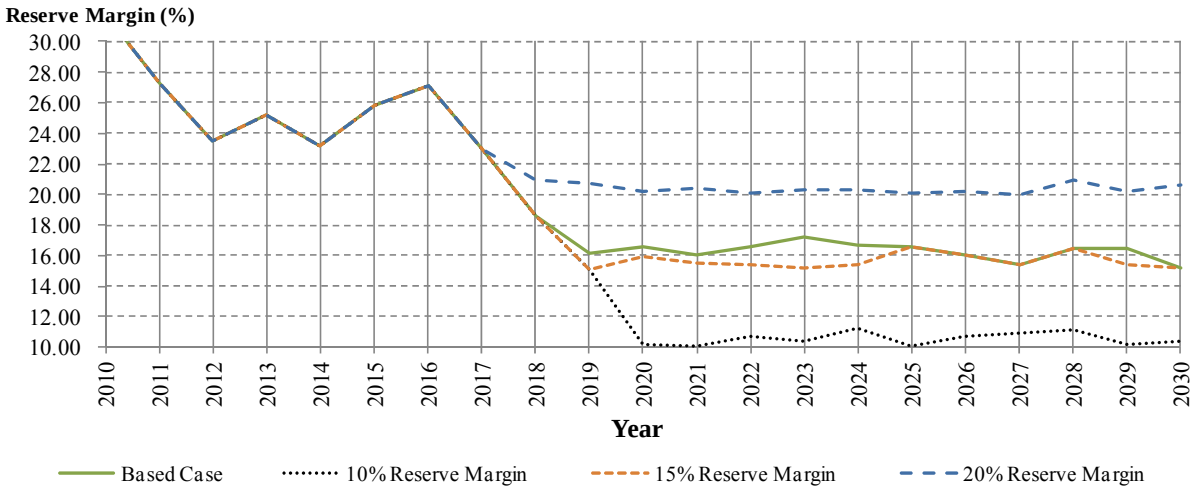

Fig. 10. Reserve margin of category 2 cases

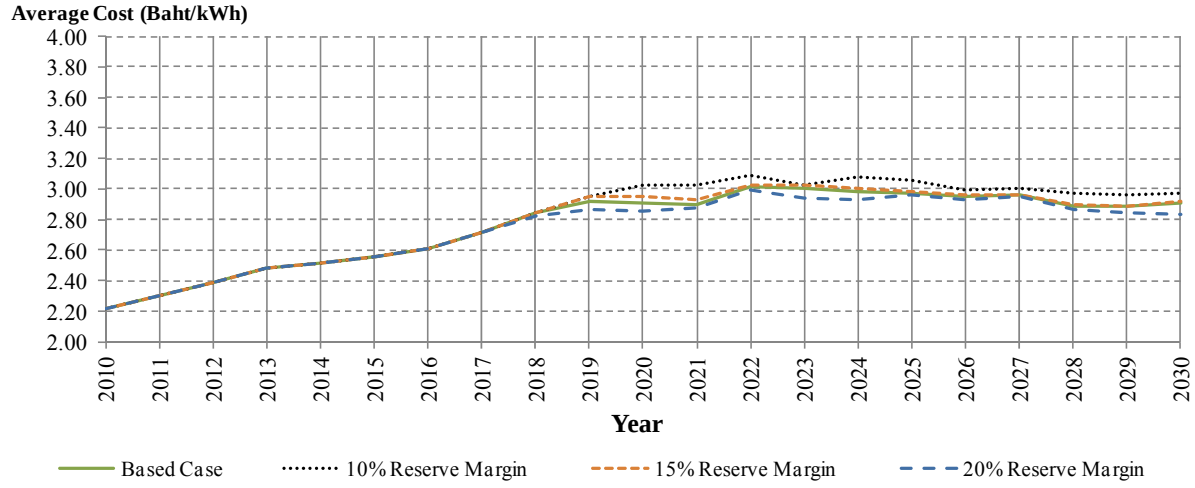

Fig. 11. Average cost of category 2 cases

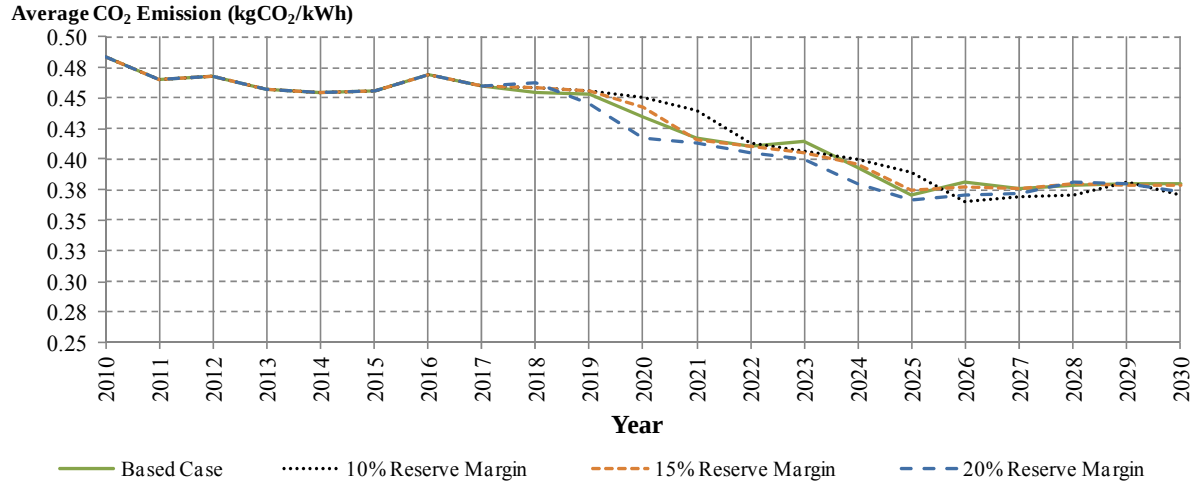

Fig. 12. Average CO_2 emission of category 2 cases

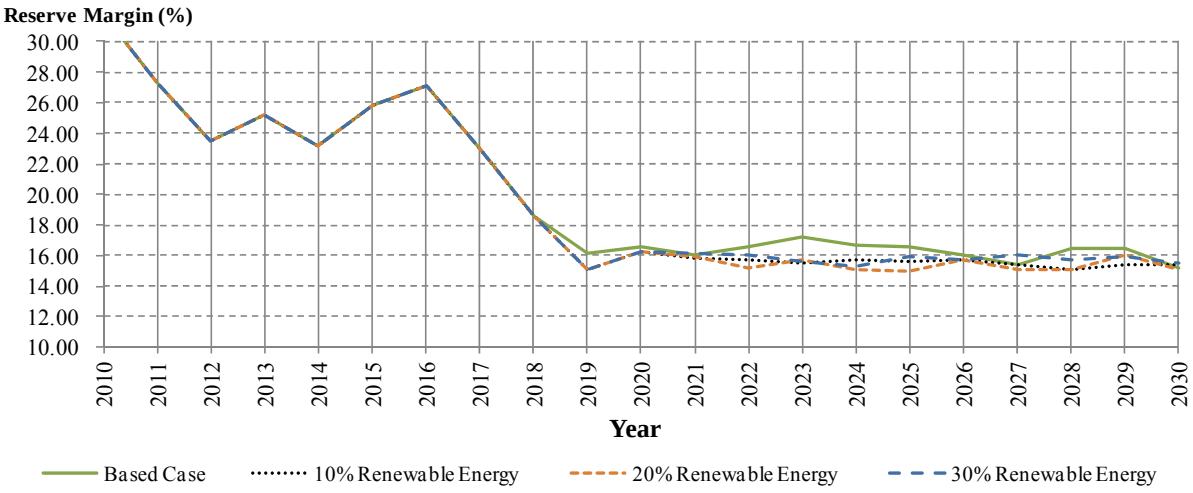

Fig. 13.Rreserve margin of category 3 cases

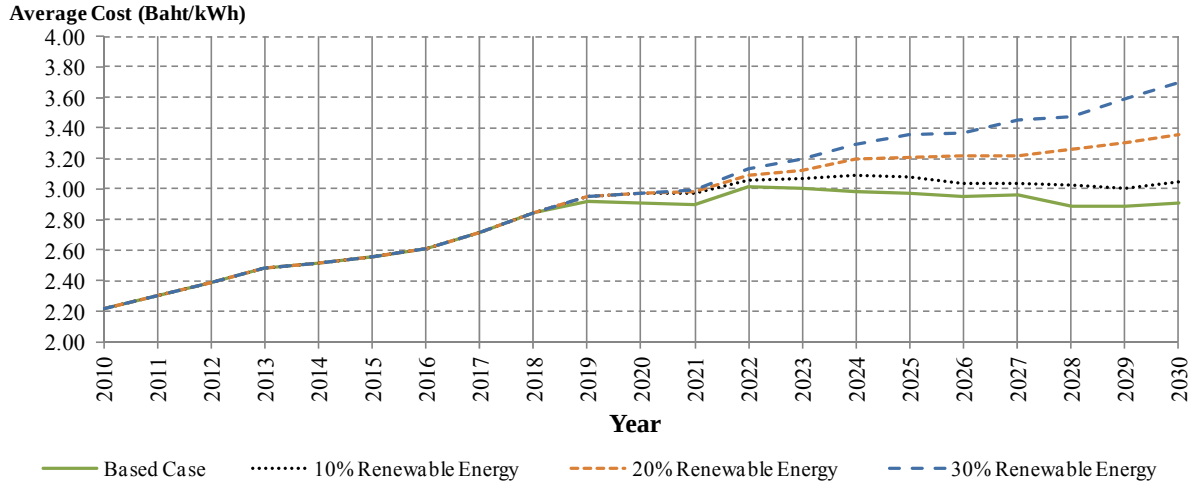

Fig. 14. Average cost of category 3 cases

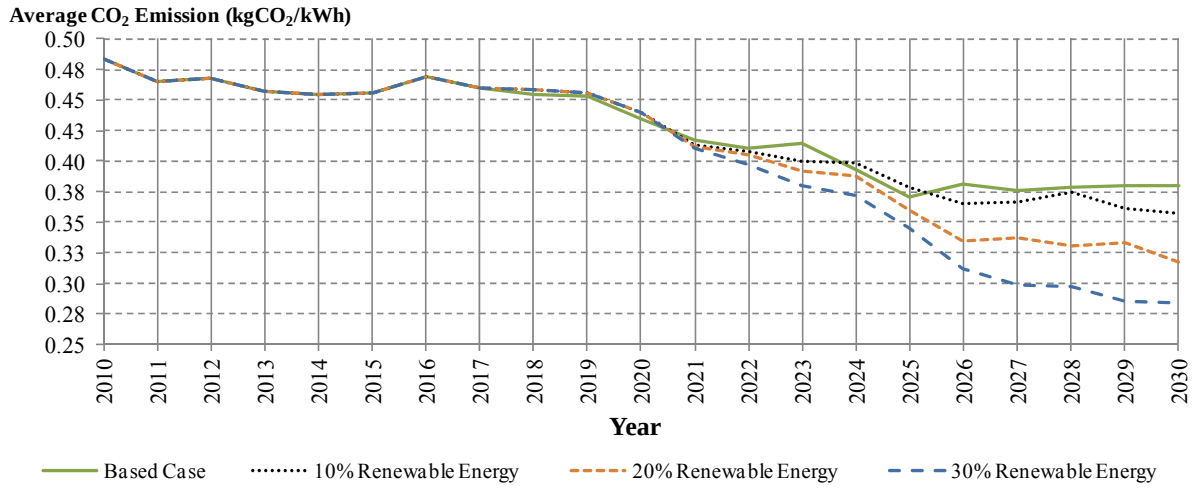

Fig. 15. Average CO_2 emission of category 3 cases

8. Conclusion

In this paper, the impacts of nuclear power plant on Thailand generation system are investigated by scenario based analysis. The obtained results show that nuclear uncertainty cannot only be relieved by importing more electricity from neighboring countries, but also maintain suitable electricity cost.

From the obtained results, the critical system impact of unclear uncertainty is determined. The results should enable the system planner to use as a guideline for strategic planning and long-term preparation for Thailand power system.

Acknowledgments

The authors would like to gratefully acknowledge the financial support from the Energy Research Institute, Chulalongkorn University, Bangkok, Thailand.

References

[1] Electricity Generating Authority of Thailand, “EGAT Power Development Plan”.

[2] R.H.B. Exell and M. Huq, “The Statistical Distribution of Hourly Solar Radiation Amounts in Thailand,” Journal of Science Society of Thailand, vol.4, no.1, pp.16-26, 1978.

[3] Intergovernmental Panel on Climate Change, “2006 IPCC Guideline for National Greenhouse Gas Inventories,” [Online], Available from: http://www.ipcc.ch.

[4] R. Billinton and P.G. Harrington, “Reliability Evaluation in Energy Limited Generating Capacity Studies,” IEEE Transactions on Power Apparatus and Systems, vol. PAS-97, no. 6, pp. 2076-2085, 1978

[5] R. Billiton and R.N. Allan, “Reliability Evaluation of Power System,” London, England: Pitman Publishing Limited, 1984.

Improving sustainability of maritime transport through utilization of Liquefied Natural Gas (LNG) for propulsion

Fabio Burel, Rodolfo Taccani, Nicola Zuliani

University of Trieste, Trieste, Italy, fburel@units.it, taccani@units.it, nzuliani@units.it

Abstract:

Today, most of the merchant vessels use Heavy Fuel Oil (HFO) for propulsion. These heavy oils are cost effective but they produce significant amounts of noxious emissions. In order to respect International Maritime Organization (IMO) rules, Liquefied Natural Gas (LNG) as fuel for ships becomes an interesting solution as it allows to reduce nitrogen and sulfur oxides emissions.
The study of the potentiality of LNG as fuel for ship propulsion is the aim of NGShiP, a research project carried out in Friuli Venezia Giulia – Italy, where the University of Trieste is a partner involved in the development of statistical model for maritime traffic data and process simulation models.
In this paper the results of the maritime traffic statistical analysis are presented. In the analysis, the world ships traffic data for the month of May of three different years (2008, 2009, 2010) have been taken into account. The study allows to identify the vessel segments and routes that can benefit most from LNG installation.
Results show that RoRo and tankers ships spend most of their sailing time in Emission Control Areas (ECA) and therefore they appear to be the best candidate for LNG installation. On this basis it has been decided to carry out an energy analysis of a tanker ship. Different energy recovery technologies have been considered and analyzed with the aim to improve ship efficiency and reduce environmental impact. Energy analysis results show that the use of LNG as fuel is interesting but important results can be obtained only if a mixture of energy saving/recovering technologies is considered. The analysis shows that an efficiency improvement as high as 15% can be achieved.

Keywords:

LNG, Ship propulsion, Maritime traffic, Liquefied Natural Gas, Energy Saving.

Introduction

Protecting the ocean environment and encouraging the development of the maritime traffic is an important challenge for the maritime industry. Currently, for economic reasons, most of the world maritime traffic consists of vessels whose engines are fed by Heavy Fuel Oil (HFO). HFOs are cost effective but contain high levels of asphalt, carbon residues, sulphur and metallic compounds, as well as having properties of high viscosity and low volatility. Due to these characteristics, during the burning process in marine diesel engines, these fuels can produce significant amounts of air pollutants such as nitrogen oxides (NO_X), sulphur oxides (SO_X), carbon monoxide (CO) and carbon dioxide (CO_2). For ships, emissions rules are imposed by the International Maritime Organization (IMO) that, through the MARPOL convention, sets limits on emissions of sulphur dioxide and nitrogen oxides both in global areas and in more restricted areas. To meet these emission requirements it is necessary to use more refined fuels or, if HFO is utilized, introduce expensive emissions reductions systems. A fuel that today is relatively cheap is Natural Gas (NG). While NG is widely used in gaseous form for industrial and domestic applications, in the maritime field the most promising solution is to use Liquified Natural Gas (LNG) [1]. In the last 40 years LNG has been used as fuel in LNG carrier [2] where the boil off gas produced inside the LNG tank is used for propulsion in traditional boiler/steam turbine system and more recently in dual fuel diesel engines. Today, attention to LNG for ships propulsion other than LNG carrier has been growing:

several studies can be found in literature and some real applications have been implemented. For example in [2] and [3], benefits and operational issues of adopting LNG as fuel for ship propulsion have been discussed. Bunkering and infrastructure related issues are presented in [4], while ship and propulsion system design are discussed in [5], [6]. These papers highlight as the use of LNG stands out from other emission reduction solutions because it appears to be the most economically advantageous. It is also interesting to observe that, if LNG is used as fuel for ships, new propulsion technologies could be considered. Among them, there has been a growing attention for marine applications of fuel cells and several demonstration studies have been carried out. At the Mechanical Engineering and Naval Architecture Department of the University of Trieste a research activity has been started recently with the aim of studying novel ship energy systems. In particular the focus is on gas fuelled systems.

Gas emissions from commercial ships

Gas emissions from commercial ships have been largely studied and results presented in different research papers such as in [7], [8], [9]. Until recently, air pollution from ships went mostly unregulated as the weight on global emission is about 3% [8]. Indeed, concern is growing as ship pollution is concentrated in relatively small areas, Baltic sea being one of the most critical [10]. In these areas diesel marine engines have come to represent an increasingly large share of air pollution. In [10] an emission forecast study, that compares the SO_2 and NO_X emissions from European Union (EU) land based systems and ships, is presented. The results are reported in Figure 1. Observing Figure 1 it is possible to conclude that, with the increasing pace of traffic, without stringent controls, shipping emissions are likely to become a large environmental problem in the coming years. Given the international nature of much of the world maritime activities, intervention to reduce sulphur and nitrogen oxides emitted by sea going vessels should be taken by the International Maritime Organization (IMO). IMO ship pollution rules are contained in the "International Convention on the Prevention of Pollution from Ships", known as MARPOL 73/78. In particular, MARPOL Annex VI sets limits on NO_X and SO_X emissions from ship exhausts, and prohibits deliberate emissions of ozone depleting substances. Both IMO and the EU recognise protected areas called Emission Control Areas (ECA) where emission limits are more stringent.

MARPOL defines limits of NO_X emission both in ECA zones and in global waters. Table 1 describe restriction on the fuel sulphur content imposed by MARPOL: sulphur content has to decrease constantly in next years. Table 2 describes restriction on the NO_X emissions which depend on the engine maximum operating speed: a three tiers reduction program has been established. Tier II is currently in effect and Tier III will come into effect in 2016, thus stepwise decreasing the allowed NO_X emission by 80% by 2016. Tier I and Tier II limits are global, while the Tier III standards apply only in ECA zones.

Table 1. Sulphur contents: global and ECA limits [11].

Date	**Global limit [% mass]**	**Date**	**ECA limit [% mass]**
Prior to 1/1/2010	4.5 %	Prior to 1/7/2010	1.5 %
After 1/1/2012	3.5 %	After 1/7/2010	1.0 %
After 1/1/ 2020	0.5 %	After 1/1/2015	0.1 %

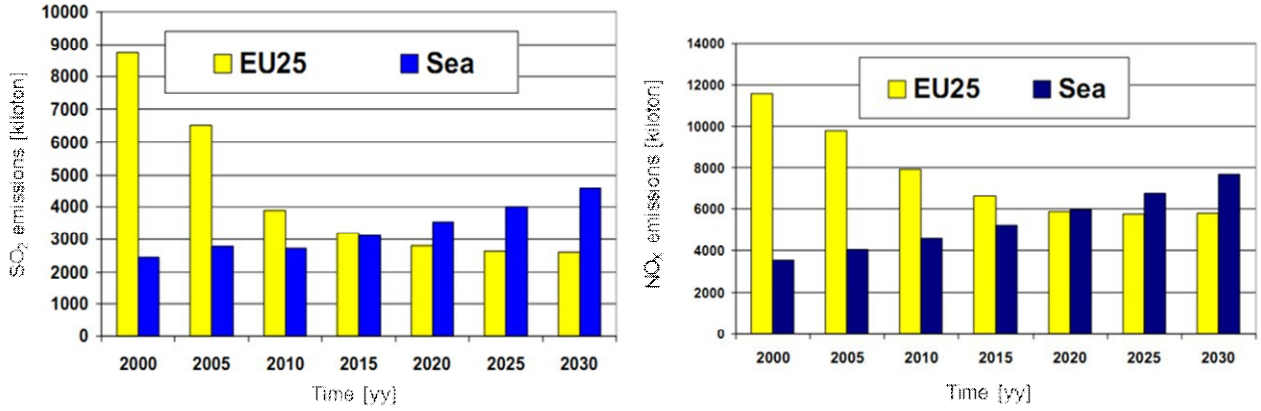

Figure 1: SO_2 emissions from European Union land based systems (EU25) compared to ships emissions (on the left) [10]; NO_X emissions from European Union land based systems (EU25) compared to ships emissions (on the right) [10].

Table 2. NO_X emissions reduction program [11].

Tier	**Date**	**NO_x limit [g/kWh]**		
		n<130	**130 ≤ n ≤2000**	**n ≥ 2000**
Tier I	2000	17.0	45 x n-0.2	9.8
Tier II	2011	14.4	44 x n-0.23	7.7
Tier III	2016*	3.4	9 x n-0.2	1.96

*Only for NO_x ECAs (TIER II apply outside of ECAs)

n = engine speed [rpm]

2.1. Approaches for reducing gas emissions from ships

In order to reduce gas emissions from existing ships, a combination of cleaner fuels, engine modifications, add-on retrofits and other measures are currently adopted. A complete review of the emission reductions options can be found in [1], [12], [13] while a summary of the emission reduction systems currently employed in ships is reported in Table 3. In particular the focus is to reduce SO_X and NO_X emissions.

Reducing SO_X emissions. Sulphur emissions are directly proportional to the sulphur content of the fuel. For this reason the first approach to reduce SO_X emission is to decrease the sulphur content in the fuel. For instance, reducing the sulphur level from 2.7% to 0.5% would reduce SO_X emissions by about 80%. Reducing the sulphur content in the fuel leads to other advantages as well: the highest portion of Particulate Matter (PM) from large marine diesels operating on HFO is from sulphate, thus sulphur fuel reduction allows reducing sulphate formation and therefore PM emissions. Furthermore, low sulphur content fuels allow utilizing more efficiently gas after-treatment measures for the reduction of NO_X. With respect with HFO, different fuels with lower sulphur content exist. In particular, Marine Diesel Oil (MDO) and Marine Gas Oil (MGO) are low sulphur content fuels. Currently, MDO is used for sailing in ECA with the current 1% sulphur limit, while in EU ports the fuel sulphur limit is 0.1% and only MGO can be used. However, the process that must be accomplished to obtain MDO/MGO is associated to higher energy requirements and then to higher costs and CO_2 emissions. For this reasons, other SO_X reduction options are used as well. Among them seawater scrubbing is a well-established control methodology that can achieve a SO_X removal level in compliance with MARPOL limits.

Reducing NO_X emissions. Different systems are available in order to reduce NO_X emissions: these systems may be classified as engine modifications, pre-engine technologies and gas after-treatment technologies. In particular, the use of Selective Catalytic Reduction (SCR), which involves

treatment of the exhaust gases with ammonia or urea in the presence of a catalyst, allows a reduction of NO_X higher than 80%.

Table 3. Gas emissions reduction obtained operating with different emission control systems and the use of LNG [10],[13].

	Emission reduction (%)			
Measure	**SO_X**	**NO_X**	**PM**	**CO_2**
Basic internal engine modifications for 2 stroke slow speed only	0	-20	0	0
Advanced internal engine modifications	0	-30	0	0
Direct water injection	0	-50	0	0
Humid air motors	0	-70	0	0
Exhaust gas recirculation + scrubbing	-93	-35	-63	0
Selective catalytic reduction (2.7% S residual oil fuel)	0	-90	0	0
Sea water scrubbing	-75	0	-25	0
Fuel switching (from 2.7% S to 1.5% S HFO)	-44	0	-18	0
Fuel switching (from 2.7% > 0.5% S HFO)	-81	0	-20	0
Low S marine diesel (from 0.5 to >0.1 % S)	-80	0	0	0
LNG	-90	-80	-100	-20

LNG for ships propulsion: benefits and technical issues

The emission reductions options above described are an effective solution for the currently operating ships, but new ships can take advantage of using a different fuel: LNG. Due to its chemical and combustion properties, the use of LNG allows a significant reduction of NO_X, SO_X, and also CO_2. In particular, compared to HFO, the use of LNG leads to the following emission advantages [3]:

- NO_X emissions are reduced by approximately 80-85%, thanks to the lean burn combustion process implemented in dual fuel internal combustion engines;
- SO_X emissions are almost completely eliminated as LNG does not contain sulphur;
- particle matter production is very low;
- CO_2 emissions are reduced by 20-30%, due to the higher hydrogen content in the molecule respect to HFO/MDO.

However, dual fuel engines can suffer from methane slip issues [14]. Methane is 21 times more powerful as a greenhouse gas than CO_2 and it partially reduces the benefits on emissions. Currently, research is focusing on reducing methane slip and an interesting study can be found in [14].

A comparison between emission reduction results obtained operating using heavy oil fuels and the use of LNG is described in [10],[13] and reported in Table 3: a switch to LNG will solve simultaneously the SO_X, NO_X and PM problems and produce an important reduction of CO_2 at the same time. This means that expensive emission reduction systems, that must be used when operating with oil fuels, can be avoided. Furthermore LNG is cheaper than oil fuels so ship operating costs are lower. This is expected to be valid in the future also, because the oil reserve that can be commercially exploited at prices the global economy has become accustomed to is limited and will soon decline [13]. Instead NG world reserves have generally witnessed a growing trend and much of the increase of reserves is attributed to new technologies that allow the extraction of stranded gas from shale fields. Current reserves are estimated to be high enough to meet worldwide demand for the next 60 years [15]. For these reasons the use of natural gas can be considered as a

way to bridge the gap between the use of current fuels and sustainable and renewable fuels. From another point of view, some technical issues when using LNG have to be taken into account. These issues are mainly consequence of LNG physical properties. LNG is mainly composed of methane thus LNG physical properties can be considered approximately equivalent to methane. A typical LNG composition is reported in Table 4 while methane physical properties are reported in Table 5. In the same table Diesel fuel is reported for comparison purpose. The most important safety issues are associated to NG storage, spillage systems and to NG flammability. NG is usually refrigerated to change its state to liquid and, during spillage, the high expansion ratio and the extreme cold temperature may cause frostbite to personnel and/or brittleness to structures. Furthermore, the wide flammability range may lead to ignition in case of gas release. However, thanks to the experience gained operating with LNG carriers, the design challenges for marine gas fuel installations have been resolved. Today, the main challenge is the broad acceptance of gas fuel as a safe means of propulsion by country and port state authorities. From this point of view, the finalization of the not yet completed International Gas Fuelled Ships code (IGF code) could lead to a wider acceptance of gas fuelled ships. A more detailed analysis on LNG safety issues can be found in [17].

Table 4. Typical LNG composition [16].

Substance	**Methane CH_4**	**Ethane C_2H_6**	**Propane C_3H_8**	**Butane C_4H_{10}**	**Nitrogen N_2**
Composition (% molar)	89.9	6.0	2.2	1.5	0.4

3.1. Keyfactors for using LNG on ships

Today, ships other than LNG carriers are using NG for propulsion. For example, in Norway, about 20 small cross fjord ferries and offshore support vessels are sailing using LNG. Among them, the "Viking Lady" is an interesting offshore vessel that uses LNG both in dual fuel engine for propulsion purposes and for feeding a fuel cell to produce electricity. Another example is the LNG powered ferry called "M/F Bergensfjord": it is a 129 meter long and 19 meter broad ship that can carry 212 cars and 587 passengers. A complete review of the LNG world fleet can be found in [18]. In principle it may be possible to design any ship to run on LNG, but today the introduction of LNG in ships depends on some key factors:

- Gas availability. Until now LNG handling is limited to gas terminals for gas carrier or to special applications. In order to introduce LNG on a large scale, a bunker infrastructure have to be built to make LNG available wherever ships operators may ask to have it. LNG bunkering installations need to be as close as possible to oil fuels bunkering: usually no "extra" stop at a refuelling station will be acceptable for any ship type. Therefore it is crucial for the introduction of LNG to have an infrastructure in place that will allow the operators to have safe, reliable and no-extra-time LNG supply in place [19].
- Ship conversion. Introduction of LNG-fuelled ships is more likely to happen by building new ships than by converting existing ships: ships usually have economic lives of 30 years or more, and it should therefore take at least 30-40 years to fully convert an established shipping segment. However a more rapid switch to cleaner technologies can be done within the ECA zones, by transfer of more polluting ships to operation in other areas.
- Emission limits (ECA zones). For economic reasons, ships which sail most of their time in ECA zones will be more economic attractive than others to introducing LNG early: future extension of emission controlled areas zones will accelerate the switch to LNG.
- The standard LNG storage tanks currently adopted occupy more space than traditional bunker tanks which also fit easily into a steel ship structure. LNG storage requires additional space since natural gas, both pressurized and liquefied, takes up roughly twice the space occupied by

diesel oil. Furthermore different safety constraints have to be fulfilled when considering an LNG plant [1].

Today, different studies aims to find which ships can most benefit from using LNG early. The ship traffic analysis and economic considerations carried out in [20],[21],[22] identifies certain ship segments:

- RoRo vessels, Product tankers and Container Vessels. The ship traffic analysis indicates that these ship segments spend most of the time sailing in ECA zones.
- Off shore support vessels. They sail most of the time in ECA zones. In particular the Norwegian government dispense offshore support vessels from paying carbon tax, if their propulsion is powered by gas.
- Cruise vessels. Although they spent most of the time not in ECA zones, having a clean image is the main incentive to use LNG.

Table 5. Methane physical properties compared to diesel fuel [3].

	Methane	**Diesel fuel**
Formula	CH_4	$_{avg.}C_{12}H_{23}$
Molecular Weight	16	200 (approx)
Composition, weight [%]		
Carbon	75	84-87
Hydrogen	25	13 -16
Density	0.717 kg/m^3 gas 415 kg/m^3 liquid	810 - 890 kg/m^3
Freezing point [°C]	-182	-40 to -1
Boiling point [°C]	-162	188 - 343
Vapour pressure at 38°C [kPa]	-	<1
Specific heat [kJ/kg K]	2.2 (300K)	1.8
Viscosity at 20°C [mPA s]	0.01	2.6 - 4.1
Lower heating value [MJ/kg]	50.0	40.8
Flash point [°C]	-188	74
Auto ignition temperature [°C]	540	316
Flammability limits, Vol. [%]		
Lower	5	1
Higher	15	6
Stoichiometric air to fuel ratio	17.2	14.7

Statistical analysis of maritime traffic

In order to find the most appropriate type of ship which can economically benefit from the installation of a LNG propulsion system, a statistical analysis of the world maritime traffic has been carried out. The aim of the statistical analysis is to find the time spent in ECA zone by each ship. Ships that spend most of their time sailing in ECA zones are more economically suitable to be fuelled with LNG. Furthermore the number of trips made by each type of ship has been considered. The analysed data cover three months of the world ship traffic of three different years: May 2008, May 2009 and May 2010. According to other studies [20] it has been decided to focus on 4 types of ships: Tanker vessels, RoRo vessels, Bulk Carrier vessels and Cruise vessels. The considered traffic

data, acquired from Lloyd's List Intelligence, made up 162,000 records and describes over 270,000 trips. A software tool has been developed in order to analyze the traffic data. The software allows to sort the data according to ship type and size, and to evaluate the time spent in ECA zones for each trip. A port to port distance matrix has been built in order to calculate each trip distance, to evaluate each ship route and in turn to calculate the time spent in ECA zone by each ship. The ports of the world, as classified by the United Nations, are more than 16,000 but in this work it has been chosen to decrease the number of considered ports to 178 "reference ports". A reference port is a port of relevant size to which other minor ports are associated. This strategy allows to reduce computational time without influencing computational accuracy. Each reference port is identified by a ECA zone code and its extension code. The software can consider both the actual ECA zones such as North Sea, Baltic Sea and North America Coasts and the ECA zone that will be established in the next future such as Mediterranean Sea, Singapore Coasts, Japan Coasts and Australia Coasts. In this work only Area 1 (North Sea, Baltic Sea) and Area 2 (North America Coasts) has been considered.

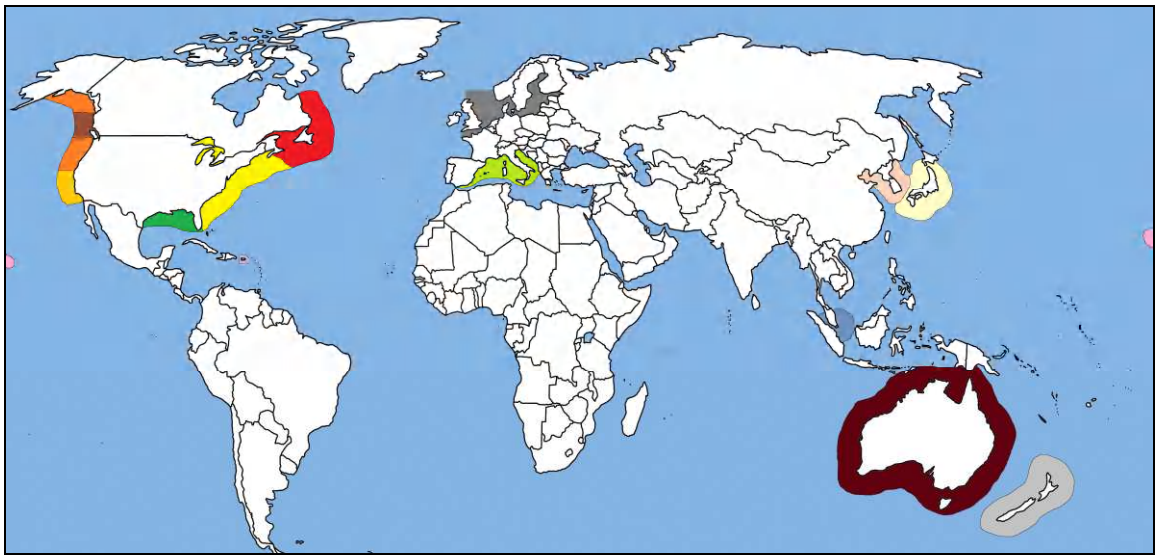

ECA Zone	ECA Area	Zone Code	Extension	ECA Zone	ECA Area	Zone Code	Extension
US East Coast / Lakes	2	1	Multiple Values	West Canada	2	9	200
US West Coast North	2	2	200	Mediterranean Sea	3	10	Multiple Values
US West Coast South	2	7	200	Singapore	4	11	200
Hawaii	2	3	200	New Zealand	5	12	200
Gulf of Mexico	2	4	200	Australia	5	13	200
Puerto Rico	2	5	200	Japan	6	14	200
North Sea / Baltic Sea	1	6	Multiple Values	Korea	7	15	200
East Canada	2	8	200				

Figure 2. Subdivision of the world in ECA areas.

4.1 Results from the statistical analysis

Figure 3 to Figure 6 show the percentage of ships that spend a specific range of time in ECA zone: Figure 3 refers to Bulk Carrier vessels, Figure 4 refers to RoRo vessels, Figure 5 refers to Tanker vessels and Figure 6 to Cruise. Ship that spend most of its time sailing in ECA zones are Very Small Bulk Carriers, Medium RoRo vessels, Very Small Tankers and Large Cruise vessels. However, it is possible to observe as a large number of ships, such as Small and Medium sizes vessels, spend more than 80% of their time in ECA zone. These results underline that a large economic market exists for LNG fuelled ships.

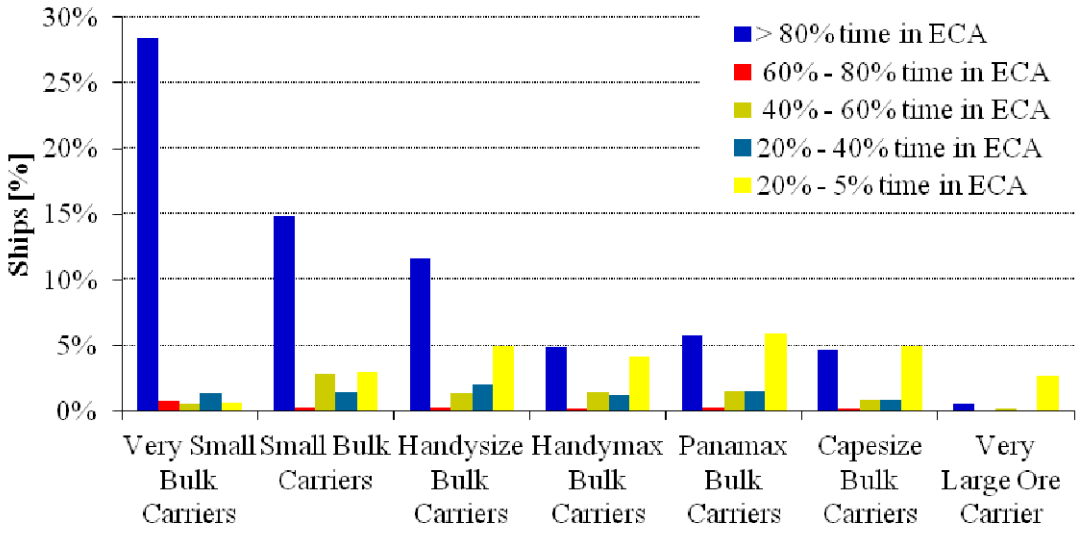

Figure 3. Time spent in ECA zones for Bulk Carriers vessels.

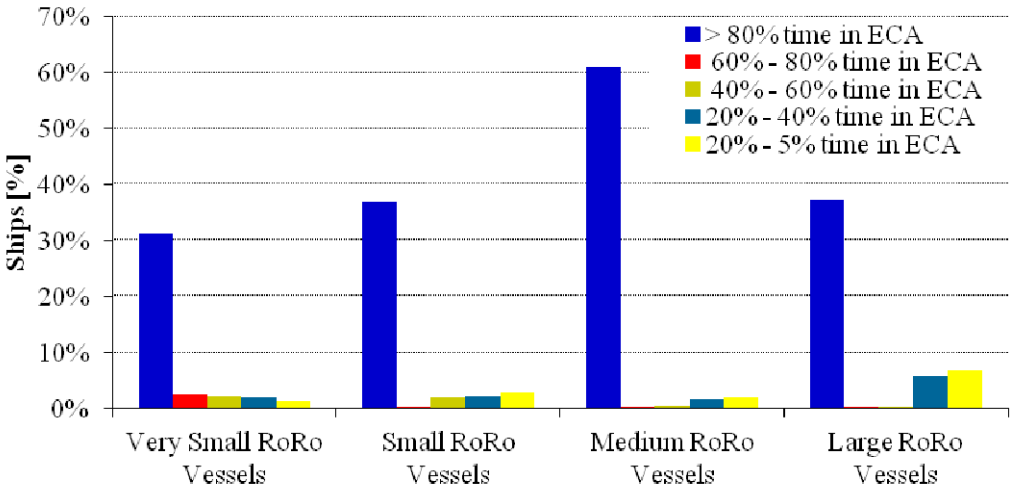

Figure 4. Time spent in ECA zones for RoRo.

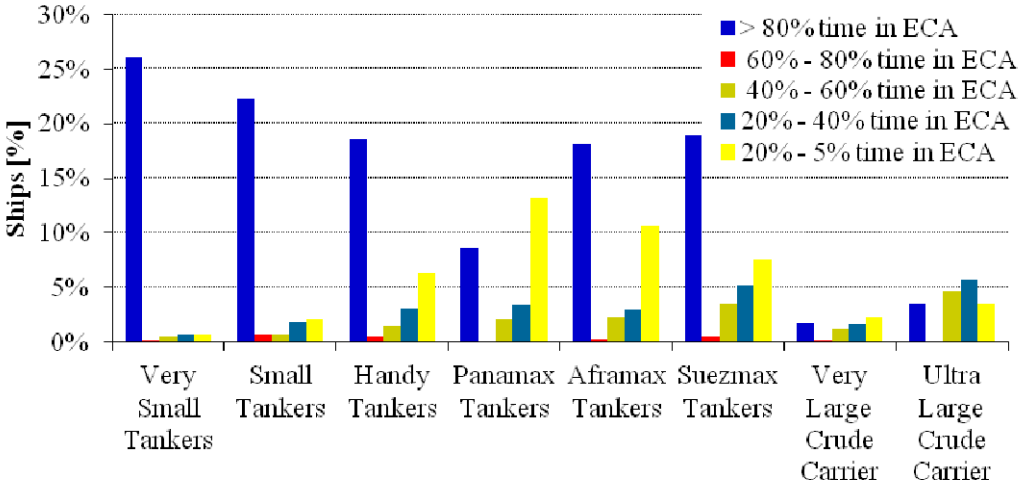

Figure 5. Time spent in ECA zones for Tanker.

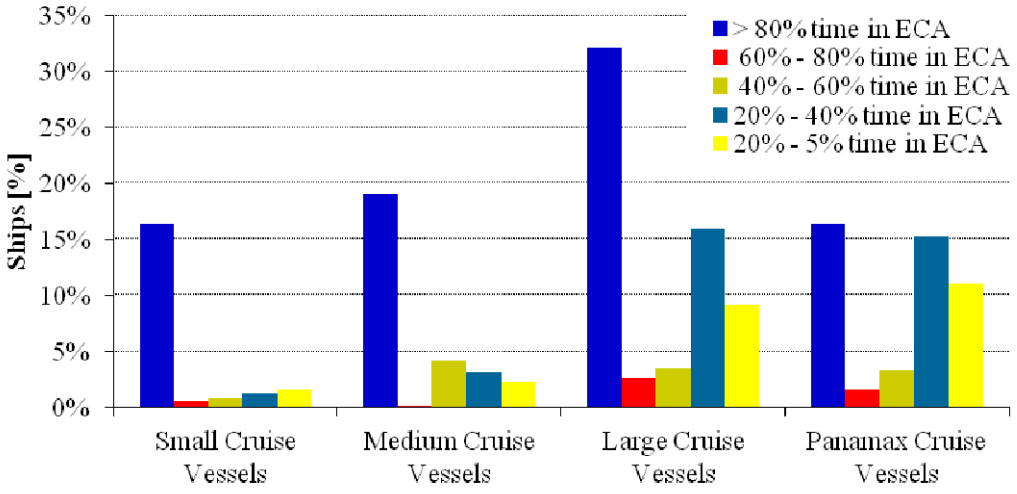

Figure 6. Time spent in ECA for Cruise vessels.

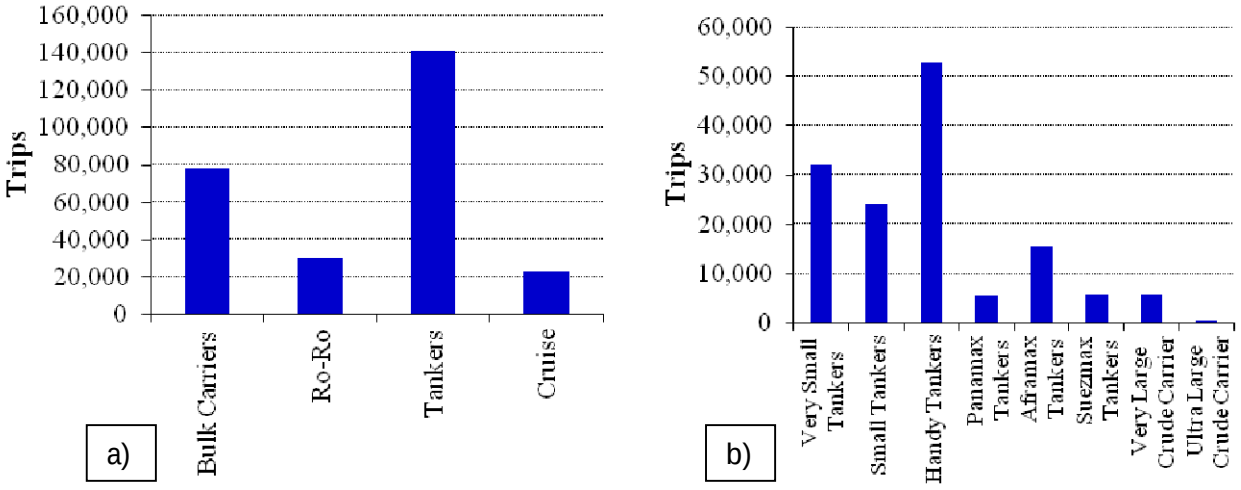

Figure 7. a) Number of trips for each vessel type; b) number of trips for each Tanker size.

Figure 7a shows the number of trips made by Bulk Carriers, Ro-Ro, Tankers and Cruise ships in the considered period: Tankers have the highest number of trips (about 140,000) followed by Bulk Carriers (79,000) and RoRo (28,000). Among the Tanker ships, the Handysize has the highest number of trips (52,000). For this reason Handy Tanker vessels have been selected as the most economically suitable ships to be fuelled with LNG.

Case study: improvements of energy efficiency on Tankers

The use of LNG instead of traditional fuels allows to reduce pollutant emissions and, at the same time, allows new energy conversion technologies to be employed on ship. Among these fuel cells are received growing attention and several demonstration studies have been carried out [22],[23]. In this paper several heat recovery technologies are considered and, the introduction of an Organic Rankine Cycle (ORC) is studied, while fuel cells will be the focus of a later work. The aim of the analysis is to evaluate the overall ship energy system efficiency, CO_2 emissions and LNG consumption. The main characteristics of the considered Tanker are described in Table 6 while the schematic layout of the energy system is shown in Figure 8: the ship is equipped with a dual fuel propulsion engine [24], two dual fuel gen-sets [24] and two gas boilers.

Table 6. Main specs of the examined tanker ship.

Dead Weight Tonnage	33,000 DWT
Length Overall	176 m
Max Breadth	31 m
Height Main Deck	17 m
Design Draft	9 m
Main Engine	Dual fuel - 8,775 kW
Gen Set	Dual fuel - 2 x 1,014 kW
Boiler 1	1,500 kW
Boiler 2	12,000 kW
Fuel	Liquefied Natural Gas

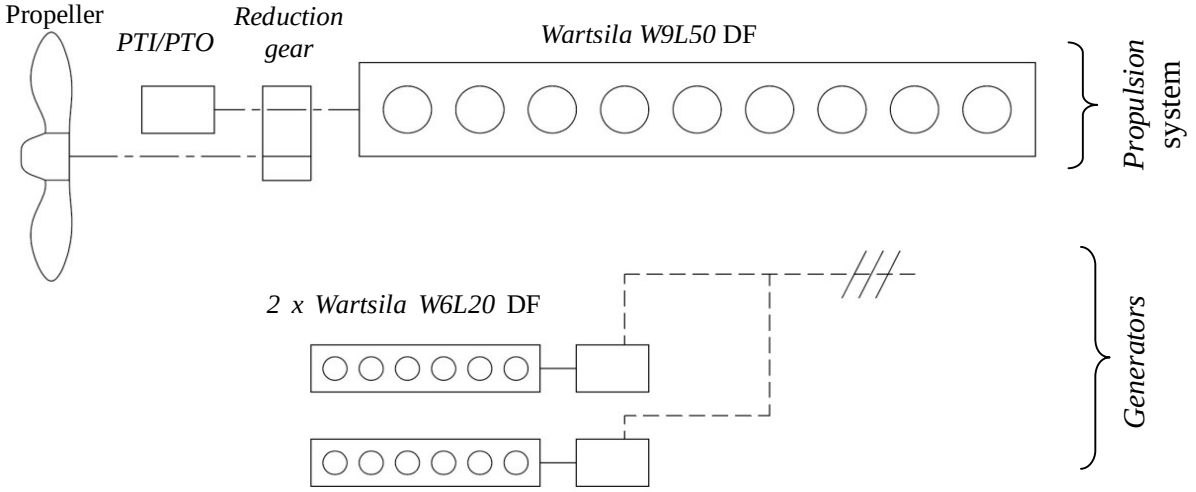

Figure 8: Layout of the energy system investigated.

Ship route considered is from Dubai (Saudi Arabia) to Hamburg (Germany) and the ship operating profile is described in Table 7. The ship is a chemical cargo carrier and cargo products have been supposed to be maintained warm at 65°C during the trip from Dubai to Hamburg, while during the ballast trip only the fuel tank (a small amount of diesel fuel that is necessary for engine pilot injection) has to be kept warm. The analysis encompasses the case in which there is no recuperative boiler. In this case the heat for cargo and fuel tank heating is provided entirely by LNG fuelled boilers which efficiency has been assumed to be 88%.

Ship propulsion power, auxiliary power and cargo heating power requirements are presented in Table 8, the pilot fuel consumption has not been taken into account in this study since it is about 1% of the LNG consumption. The thermal power required during navigation depends on speed as the amount of LNG in the evaporator is different.

Data from Table 8 have been used to calculate ship system efficiency, CO_2 emissions and LNG consumption.

Table 7. Operational profile of the considered ship.

Navigation condition	Distance covered [nm]	Time [h]	Total energy requirement [MWh]
Loading	0	24	167.1
Waiting Dubai	0	2	1.9
Maneuvering Full Load	0	1	8.4
Trip Full Load 15 kn	6,321	421	6,316.0
Trip Full Load 12 kn	346	29	344.6
Waiting Suez Full Load	0	15	107.1
Maneuvering Suez Full Load	0	2	16.9
Trip Full Load 9 kn	88	10	94.7
Unloading	0	24	167.1
Waiting Hamburg Port	0	12	9.6
Maneuvering Ballast	0	1	4.1
Trip Ballast 15 kn	6,321	421	3,122.2
Trip Ballast 12 kn	346	29	139.2
Trip Ballast 9 kn	88	10	31.3
Waiting Suez Ballast	0	15	14.0
Maneuvering Suez Ballast	0	2	4.5
Total for round trip	**13,510**	**1,018**	**10,602.7**
Yearly total (8 trips)	**108,080**	**8,144**	**84,821.2**

Table 8. Vessel power requirements during the considered navigation conditions.

Phase	Mechanical Power [kW]	Electrical Power [kW]	Thermal Power [kW]
Navigation - Full Load 15 kn	7,363	752	6,949
Navigation - Full Load 12 kn	4,400	752	6,844
Navigation - Full Load 9 kn	2,200	752	6,759
Navigation - Ballast Trip 15 kn	6,000	752	694
Navigation - Ballast Trip 12 kn	3,500	752	603
Navigation - Ballast Trip 9 kn	1,930	752	541
Maneuvering Full Load	2,018	1,782	4,645
Maneuvering Ballast	1,930	1,782	386
Waiting Full Load	0	489	6,654
Waiting Ballast	0	489	447
Harbor Cargo Handling	0	2,123	4,838
Harbor	0	470	331

System efficiency has been calculated using:

$$\eta = \frac{\sum_{i=1}^{np} P_i \cdot t_i}{FC \cdot LHV} \qquad (1)$$

Where P is the ship power requirement, t is the navigation time, FC is the fuel consumption, LHV is the lower heating value of the fuel, assumed to be 48 MJ/kg and np is the number of investigated navigation conditions which are indicated by the subscript i.

CO_2 emissions have been calculated as: $CO_2 = FC \cdot C_F$ where C_F is an *emission factor* described by the following relation: C_F = (kg CO_2) / (kg fuel). It has been assumed that C_F= 2.75 [25]. Propulsion engine, generators and boilers efficiency values have been obtained from manufacturer's data sheets [24],[26]. Main engine and gen-set specific fuel consumption at different engine loads have been taken into account (Figure 9).

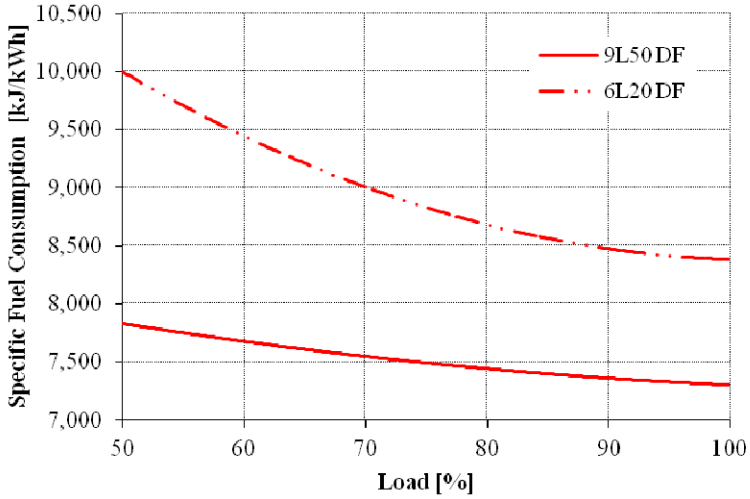

Figure 9. Main engine and gen set specific fuel consumption as function of load.

The layout of the main engine cooling circuit is shown in Figure 10: engine cooling system encompasses both a High Temperature (HT) and a Low Temperature (LT) circuit. HT cooling circuit water goes through the cylinder jackets, the cylinder heads and the first stage of the air-cooler; water in the LT circuit cools the second stage of the air-cooler and then the lubricant oil. Different heat recovering solutions have been evaluated:

- Case 1: no heat recovery;
- Case 2: heat recovery by a recovery boiler;
- Case 3: integration of an Organic Rankine Cycle;
- Case 4: integration of Organic Rankine Cycle and heat recovery from ORC condenser.

In all considered cases heat recovered from main engine LT cooling circuit is used for LNG evaporation purposes. For each case, system efficiency, CO_2 emissions and LNG consumption have been calculated and results discussed.

Case 1: no heat recovery

Only the heat recovered from the main engine LT cooling system has been taken into account. Heat recovered is used for LNG evaporation purposes. This is also the case for Tanker that does not need to heat the cargo.

Case 2: heat recovery by a recovery boiler

This solution is widely used in Tankers. In the considered case a commercial heat recovery boiler [26] has been taken into account and the exhaust gas temperature at the funnel has been assumed equal to 120°C. Furthermore, it has been assumed to recover heat from the HT main engine cooling system. Total heat recovered is used for cargo heating purposes.

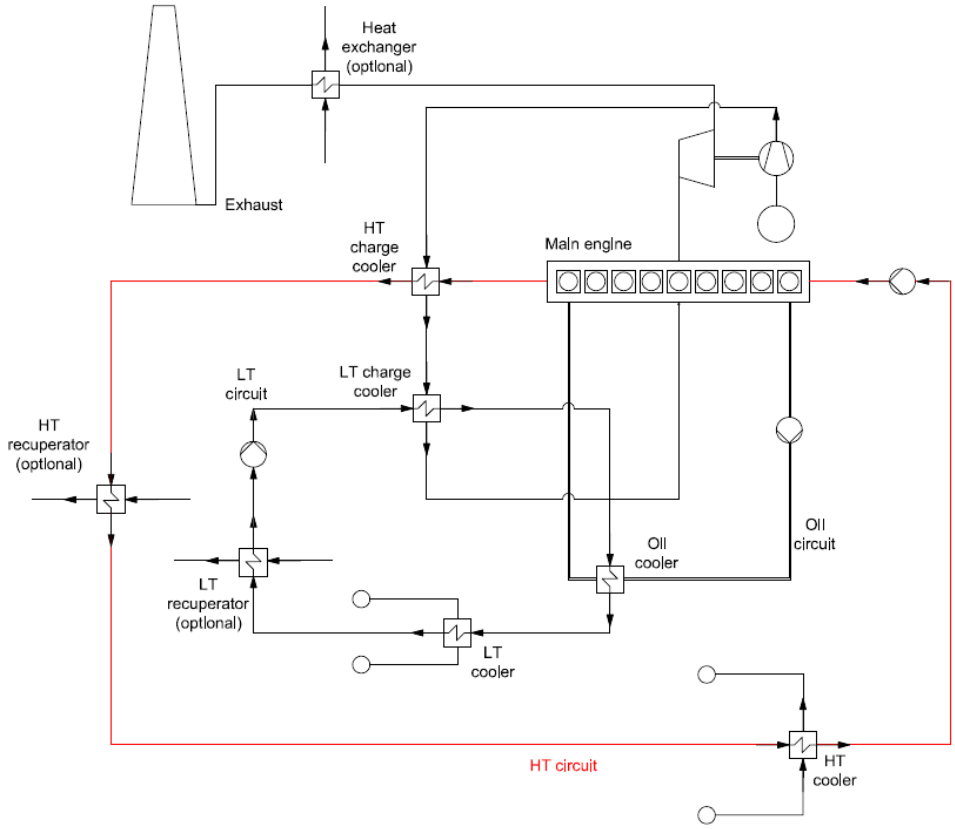

Figure 10: Simplified layout of the cooling and exhaust circuit of the propulsion engine. High Temperature (HT), Low Temperature(LT) circuits and optional exchanger for heat recovery and ORC plant.

Case 3: integration of an Organic Rankine Cycle (ORC)

An Organic Rankine Cycle is similar to a steam Rankine cycle but the working fluid is an organic mixture. A general schematic of an ORC cycle is shown in Figure 11. In comparison with water, an organic mixture fluid has some favorable characteristics such as larger molecular mass, lower critical temperature, lower critical pressure, lower condensation entropy and lower solidification temperature [27]. These characteristics allow recovering heat from low temperatures sources. The thermal power of the engine exhaust gases can be usefully utilized in an ORC system that produce electrical energy and reduce gen-sets and main engine load trough the Power Take In. In this work, it has been chosen to refer to a commercial ORC plant. Knowing the available exhaust heat power, a Turboden 7 [28] ORC plant has been selected. This ORC plant has a maximum power of 700 kWe. The exhaust gas temperature at the funnel has been assumed equal to 120°C. Furthermore, it has been assumed to recover heat from the HT main engine cooling system.

Case 4: integration of an ORC and heat recovery from ORC condenser

With respect to the previous case, heat from the ORC condenser (see Figure 11) has been also recovered. For this reason ORC condenser pressure has been assumed higher than Case 3. As a consequence, condenser temperature increases up to 100°C. This allows cargo heating by means of hot water (90°C). Nevertheless, a lower recovered electrical power has to be taken into account. Furthermore it has been assumed that, during the ballast trip, the ORC condenser pressure can be reduced in order to recover the maximum electrical energy, as there is no need for cargo heating. The minimum exhaust gas temperature at the funnel has been assumed equal to 120°C. Heat from main engine HT cooling system has been used for cargo heating.

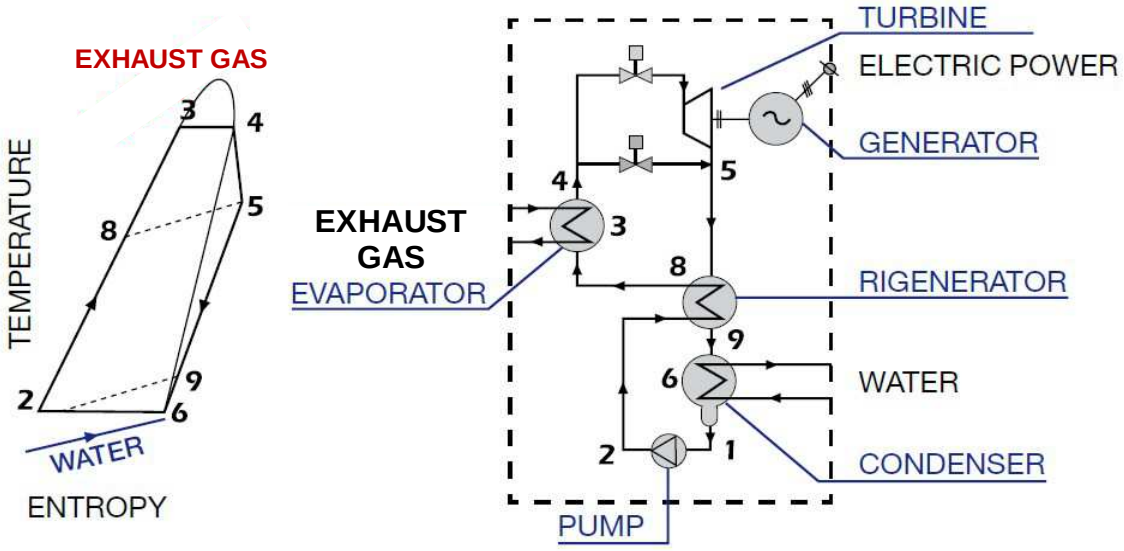

Figure 11. Temperature-entropy diagram for a generic Rankine cycle (left); ORC plant scheme (right) [28].

Results

Table 9 presents power and heat recovered as function of heat recovering solution adopted and navigation condition considered. As expected heat and electric power recovered decreases as engine load decreases. Figure 12 shows the effects of the solution adopted in terms of: a) energy efficiency, b) carbon dioxide emission and c) LNG consumption for each power plant solution examined. It should be noted that the total efficiency included both the energy for the propulsion and for the cargo heating. The mechanical efficiency has been defined as the ratio of the mechanical and electrical power over the fuel power content.

Table 9: Heat and power recovered as function of heat recovering solution adopted and navigation condition considered.

Navigation condition	Exhaust gas temp. [°C]	Exhaust gas flow [kg/s]	Boiler HR [kW]	ORC el. power [kW]	ORC+HR el. power [kW]	ORC+HR th. power [kW]	HT th. power [kW]	LT th. power [kW]
Full L. 15 kn	375	13.2	3,698	675	533	3,143	1,805	1,094
Ballast 15 kn	383	10.9	3,144	574	574	-	1,402	811
Full L. 12 kn	400	8.3	2,545	464	367	2,164	997	536
Ballast 12 kn	412	6.6	2,132	389	389	-	800	409
Full L. 9 kn	434	3.7	1,282	234	185	1,090	557	260
Ballast 9 kn	439	3.0	1,051	192	192	-	512	234

When no recovery is considered (Case 1), the efficiency of the round trip is 56.7%, the mechanical efficiency is 47%, the CO_2 emission is 30,846 ton/yy and the LNG consumption is 11,217 ton/yy. In Case 2 the mechanical efficiency is the same as Case 1, while the total efficiency increases to 68.6%. In Case 3, where the ORC is used but the heat is recovered only from the main engine, the mechanical efficiency increases, 51.4%, but the total efficiency is lower as most of the heat flows out from the ORC condenser and is not recovered for cargo heating.

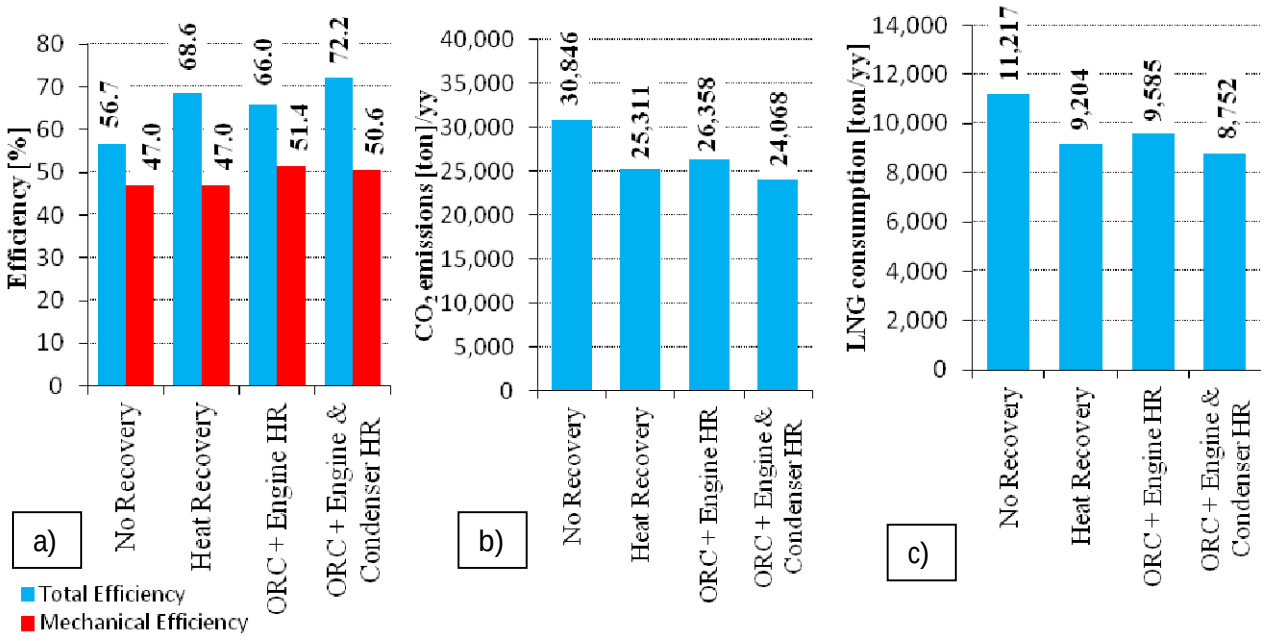

Figure 12. a)Energy efficiency, b) Carbon dioxide emission and c) LNG consumption for each power plant solution examined.

In Case 4, where the ORC is used and the condenser pressure is increased to allow a higher temperature level heat recovery that matches the cargo heating requirements, the total efficiency is the highest (72,2%) while the mechanical efficiency (50.6%) is similar to Case 3. This value correspond to an increases of about 5% respect to the typical Tanker case reproduced in Case 2. When fuel consumption is considered and assuming a fuel price of 420 €/ton [29] this means a annual saving of about 190,000 €. As above mentioned, it has been assumed that the cargo has to be maintained warm for all the sailing time. If there is not such a need fuel saving is about 9%. Obviously a complete economic analysis should be carried out to assess the return on investment considering the capital cost of the system. In particular, the LNG tank and supply system costs should be taken into account. LNG tank and supply system costs are obviously expected to be higher than conventional HFO/MDO/MGO supply systems. However, it has to be considered that expensive harmful emission reduction devices are avoided when using LNG.

Conclusions

The use of LNG for ship propulsion allows reducing NO_x, SO_x and CO_2 emissions respect to the currently adopted heavy fuel oils. In this work, the ship traffic analysis carried out highlights as a large number of ships spend more than 80% of their time in the ECA zone. In particular this is the case of Handy size Tankers and Medium size RoRo vessels that spend more than 80% of their sailing time in ECA zone. For these ships, the installation of a LNG propulsion system is an economically interesting solution in order to respect new rules on pollutant emissions scheduled for 2015-2016. The energy analysis carried out on a handy size Tanker demonstrates that several possibilities to improve ship efficiency exist. Results show that ship can reach a total efficiency of 72.2% when an ORC power plant is integrated with the propulsion system. The investigated solution allows to save about 5% in annual fuel consumption respect to the typical case of simple main engine heat recovery for cargo heating.

Nomenclature

Acronyms

ECA	Emission Controlled Area
HFO	Heavy Fuel Oils
HR	Heat Recovery
HT	High Temperature
IGF	International Gas Fuelled Ship Code
IMO	International Maritime Organization
LNG	Liquefied Natural Gas
LT	Low Temperature
MDO	Marine Diesel Oil
MGO	Marine Gas Oil
NG	Natural Gas
ORC	Organic Rankine Cycle
PM	Particulate Matter
RoRo	Roll on – Roll off
SCR	Selective Catalytic Reduction

References

[1] M.S. Eide, *"Assessment of measures to reduce future CO2 emissions from shipping"*, DNV Report, May 2010, www.dnv.com

[2] B. Curt, *"Marine Transportation of LNG"*, presentation at the Intertanko Conference March 29, 2004.

[3] A. B. Smith, *"Gas Fuelled Ships: Fundamentals, Benefits Classification & Operational Issues"*, proceedings of the first Gas Fuelled Ships Conference, Hamburg, Germany, 2010.

[4] B. Scholz, G. Würsig, *"Bunkering of LNG Fuelled Vessel Technical Challenges and Perspectives"*, proceedings of the first gas fuelled ships conference, Hamburg, Germany, 2010.

[5] I. B. Flusund, I. Hildebrand, *"Vessels Propelled by Gas Engines Driving Controllable Pitch Propellers Through Mechanical Transmission"*, proceedings of the first Gas Fuelled Ships Conference, Hamburg, Germany, 2010.

[6] O. Levander, *"Turning the Page in Ship Propulsion by Switching to LNG"*, technical presentation at the Gas as Fuel for Propulsion of Ships: Status and Perspectives Conference, March 2008, Copenhagen, Denmark.

[7] V. Eyring, J. Corbett, D. S. Lee, J. J. Winebrake, *"Brief Summary of the Impact of Ship Emissions on Atmospheric Composition, Climate, and Human Health"*, Document submitted to the Health and Environment sub-group of the International Maritime Organization, 2007..

[8] IMO, *"Study of Greenhouse Gas Emissions from Ships"*, Issue no.2 - 31, 2000.

[9] IMO,"*Second IMO GHG Study 2009*", report of the International Maritime Organization, 2009;

[10] J. Cofala, M. Amann, C. Heyes, et all. *"Analysis of Policy Measures to Reduce Ship Emissions in the Context of the Revision of the National Emissions Ceilings Directive"*, report submitted to the European Commission, DG Environment, Unit ENV/C1,2007.

[11] IMO, *"Amendments to the Annex of the Protocol of 1997 to Amend the International Convention for the Prevention of Pollution from Ships, 1973, as Modified by the Protocol of 1978 Relating thereto(Revised MARPOL Annex VI)"* , Resolution MEPC.176(58), 10 October 2008.

[12] European Federation for Transport and Environment, European Environmental Bureau, Clean Air Task Force, North Sea Foundation, *"Reducing Shipping Emissions of Air Pollution. Feasible and Cost-effective Options"*, NGO submission to the IMO's Marine Environment Protection Committee, 2005.

[13] A.H. de Ruiter, *"Sailing for Cleaner Skies. Study of LNG Fuel for Sea Vessels in Rotterdam*", master thesis in transport infrastructure and logistics, Delft University of Technology, 2008.

[14] Marintek, *"Emissions factors for CH4, NOx, particulates and black carbon for domestic shipping in Norway"*, Marintek report, November 2010.

[15] ENI, "*World Oil and Gas Review 2011"*, ENI annual report, www.eni.com.

[16] G. G. Dimopoulos, C. A. Frangopoulos "*A Dynamic Model for Liquified Natural Gas Evaporation During Marine Transportation*", International Journal of Thermodynamics, Vol. 3, pp.123-131, 2008.

[17] Y. Calogeras, *"Gaseous Fuels for Propulsion, Rules, Key Safety Considerations &Main Challenges"*, proceedings of the first Gas Fuelled Ships Conference, Hamburg, Germany, 2010.

[18] L. P. Blikom, *"A Review of The World Fleet of LNG Fuelled Ships"*, DNV web page, 2011.

[19] J. Harperscheidt, *"LNG Fuel Gas Systems for Ships other than Gas Carriers – Shipboard Systems and Infrastructure"*, proceedings of the first Gas Fuelled Ships Conference, Hamburg, Germany, 2010.

[20] Wartsila, "*In Details*", Wartsila Technical Magazine, Vol. 1, 2011, www.wartsila.com.

[21] European Maritime Safety Agency, *"The 0.1% Sulphur in Fuel Requirements from 1 January 2015 in SECAs - An Assessment of Available Impact Studies and Alternative Means of Compliance"*, Technical Report, 2010.

[22] R. Taccani, F. Burel, S. Clemente, *"LNG powered ships: energy, environmental and economic analysis"*, proceedings of the second Gas Fuelled Ships Conference, Rotterdam, The Netherlands, 2011.

[23] G. Sattler, *"Fuel Cells Going On Board"*, Journal of Power Sources, vol. 8, pag. 61-67, 2000.

[24] www.wartsila.com

[25] IMO MEPC.1/Circ.681

[26] www.aalborg-industries.com

[27] J. Bonafin, P. Pinamonti, M. Reini, P. Tremuli, *"Performance Improving of an Internal Combustion Engine for Ship Propulsion with a Bottom ORC"*, proceedings of ECOS 2010, Lausanne, Switzerland, 2010.

[28] www.turboden.com

[29] J.M. Gomes Antunes, *"Conversion of large-bore diesel engines for heavy fuel oil and natural gas dual fuel operation"*, proceedings of the second Gas Fuelled Ships Conference, Rotterdam, The Netherlands, 2011.

Life cycle assessment of thin film non conventional photovoltaics: the case of dye sensitized solar cells

Maria Laura Parisi [a], Adalgisa Sinicropi [a] and Riccardo Basosi [a,b,*]

[a] *Department of Chemistry, Università degli Studi di Siena, Siena, Italy, parisi11@unisi.it*
[b] *Center for the Study of Complex Systems (C.S.C.), Siena, Italy, riccardo.basosi@unisi.it*
** Corresponding Author*

Abstract:

Energy lies at the heart of any nation's technological, economical and social development. In recent years, energy demand has grown constantly and is bound to further increase. In this context, the interest of the scientific community is progressively moving towards renewable energy sources, with a particular focus on developing the technologies necessary for their exploitation, and towards sustainable growth. The search for alternative energy sources, able to combine efficiency, ease of use and reduced environmental impact is therefore, together with energy saving, an important challenge for our civilization. Among the various renewable energy sources available on our planet, solar energy is particularly attractive. One of the technologies available to produce electricity from solar energy is photovoltaics. With the aim of achieving a larger distribution of photovoltaics, research turned itself to the development of new technologies based on alternative materials, such as organic compounds. Some of these technologies exploit the capacity of organic dyes to liberate electrons as in natural photosynthesis. To this category belong the solar cells known as dye sensitized solar cells (DSSC), also known as Grätzel-type cells (Nature 1991). Such cells have attracted much interest, especially in the last decade, because of their potentially low cost of production. Thanks to the employment of readily available materials, produced by well-established processes, they actually present drastically lower economic and environmental costs compared with traditional silicon-based cells even though they are not efficient enough yet to be industrially competitive. An emerging challenge is to find the right set of materials to obtain DSSC of improved performances. Progress in this field requires major investments in terms of research and development aimed at the optimization of all parameters. In this study we present the preliminary results of life cycle assessment for the production of a DSSC. These results have been obtained through a multidisciplinary project for the design and synthesis of new organic sensitizers for DSSC. The life cycle assessment has been developed based on actual production data along all the project stages in order to evaluate the environmental impacts and the energy consumption associated with the production process. This analysis will be pivotal in understanding the environmental dynamics, the benefits and drawbacks associated with the production of DSSC in comparison with other photovoltaic technologies.

Keywords:
Dye sensitized solar cell, Energy, Life cycle assessment, Photovoltaic, Sustainability, Thin film.

1. Introduction

Depletion of resources and global climate change issues have led the interest of the scientific community towards clean and sustainable energy in the last decades. Among the renewable energy sources, the development of new types of solar cells for photovoltaics (PV) has been driven also by the aim of overcoming the limits of silicon shortage. One promising route for departing from the traditional solid-state cell is the dye sensitized solar cells (DSSC), assembled for the first time by the chemist Michael Grätzel in 1991 [1-4]. Such cells have attracted much academic and industrial interest, especially in the last decade, because of their potentially low cost of production. However at present, DSSC are not efficient enough to be industrially competitive. Compared with the highest efficiencies recorded for silicon-based cells, which approach 25% on a laboratory scale and 20% on a device scale, DSSC currently give efficiencies of 12% on a laboratory scale [5] and 5-6% on a larger scale [6]. Factors limiting the efficiency of the cells are mostly related to the materials

employed but also to the way in which these materials interact within the cell structure. The challenge is to find the right set of materials to obtain DSSC of improved performances. Progress in this field requires major investments in terms of research and development aimed at the optimization of all parameters. Among these, the choice of the organic sensitizer able to harvest more light by absorbing at least a part of near infrared radiation is surely one of the most critical points to face.

The development of sustainable technologies requires an overall evaluation of the product's environmental impacts and benefits. Solar cells currently on the market have undergone these environmental evaluations to be classified as sustainable sources of energy and a large number of life cycle assessment (LCA) studies on photovoltaic modules have been published in the scientific literature up to the present. Most of the previous studies were concerned with production processes and their environmental impact assessment was commonly performed from cradle to gate. From an environmental point of view, as it emerges from all LCA studies of electricity production by different energy systems, photovoltaic technologies show a clear advantage good performances with a range of 21–45 g of CO_2 equivalent emissions per kWh of produced energy for the average southern European solar irradiation [7,8]. Also a detailed comparison of energy payback times (EPBT) and emissions for different photovoltaic technologies has been carried out. In these cases the most attention has been devoted to mono-crystalline and multi-crystalline silicon modules, since they are the most often used PV technologies with a 87.4% share of the market in 2008 [8–12]. Also, inorganic thin film technologies of amorphous silicon (a-Si:H), cadmium telluride (CdTe) and copper indium diselenide (CIS) modules have been assessed [11-14]. All thin film technologies show better values of EPBT and avoided emissions, and despite their lower power conversion efficiency, their main advantage is the use of much less material in the active layer (200–300 mm for multi-Si and mono-Si, compared with approximately 10 and 1 μm for CIS and CdTe, respectively). In the near future lower material and energy consumption in the manufacturing process is likely to bring a reduction in the cost of the modules as the technology progresses through its learning curve [15,16]. The extremely high manufacturing throughput potential of hybrid and organic solar cells could have a positive impact in the markets and therefore is attracting many investors. The European Photovoltaic Technology Platform, supported by the Seventh European Framework Programme for Research and Technological Development, has included the hybrid and organic photovoltaic technologies on its roadmap. This indicates that these PV technologies are on the verge of commercialization and are already producing a rapidly developing global manufacturing base [17-18]. Though not as efficient or long-lived as solid-state PV devices, DSSC can achieve a much better performance in terms of cost per energy produced during their lifetime than any other inorganic technology.

The present paper investigates the environmental aspects of emerging DSSC PV technology under development through LCA. In addition, we report sustainability results (energy pay back time, greenhouse gas emissions and net energy ratio) published in a previous paper by the authors [19] in which we compare our case study with other thin-film and DSSC LCA studies [20-21]. The purpose of this LCA study is to identify the significant environmental aspects of the DSSC systems in particular those employing full organic sensitizers instead of metal complex dyes. The knowledge of the significant environmental aspects will be used as input in further research on the DSSC system to support the development of solar cells as a sustainable alternative for generating electric energy.

1.1 - The DSSC technology

DSSC are composed of few simple parts. First of all, there is an electrode made by a layer of nanoparticles of a semiconductor material deposited on a transparent conductive glass. Typically, nanoparticles are made of titanium dioxide, TiO_2, which is characterized by a high degree of roughness. Cells made with different materials (ZnO, CdS, CdSe only to mention a few) have also

been reported, but TiO_2 is still the most employed, since it is cheap, available on large scale and eco-compatible. TiO_2 can be found in three forms: anatase, rutile and brookite. For the use in DSSC the best one is anatase as it gives higher efficiencies. It is normally chosen because it is stable against corrosion and does not absorb light in the dye range of absorption. On the surface of the semiconductor nanoparticles are absorbed dye molecules (sensitizer) which are able to harvest light. The first DSSC described by Grätzel employed ruthenium complexes, which gave good results. However, in principle all the dyes bearing appropriate functional groups to ensure anchoring to TiO_2 and efficient electron transfer to the semiconductor can be used as sensitizers. DSSC are completed by an electrolyte solution, containing a redox couple (usually an iodide-triiodide couple I^-/I_3^-) and a counter-electrode, generally made of Pt. The sensitizer absorbs light generating an electron-hole couple which is then separated at the interface with the nanoparticle and subsequently transported to the two electrodes by the semiconductor and the electrolyte, respectively.

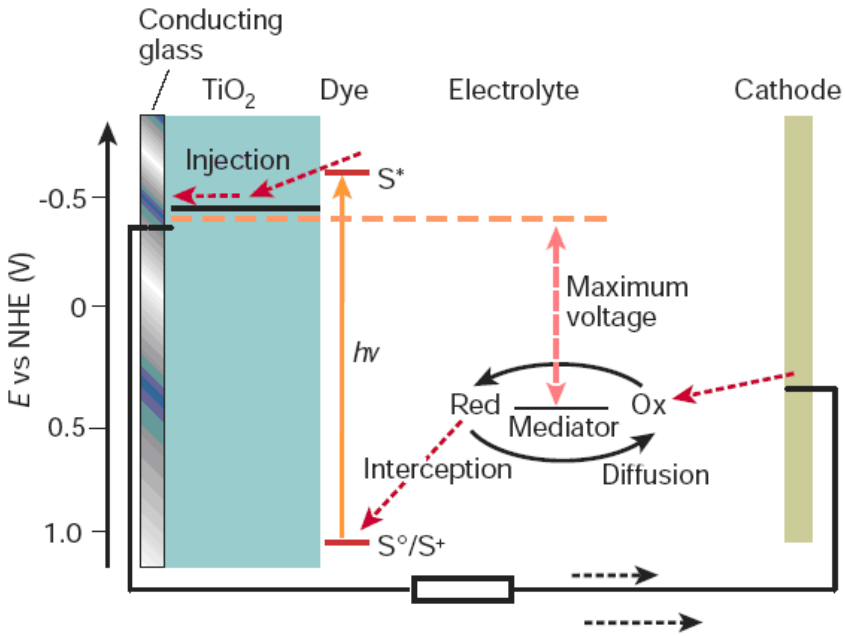

Fig. 1. DSSC functioning (source: http://www.chem.monash.edu.au/staff/bach/research.html)

From the operational point of view, conventional solar cells convert light into electricity by exploiting the photoelectric effect which takes place at the interface between the semiconductor materials. For this reason, they are strictly correlated to silicon technology (diodes, transistors, printed circuits and so on). DSSC, on the contrary, follow a different working principle, inspired by natural photosynthesis, in which light absorption and charge separation (electrons and holes) are divided (see Fig. 1): the first takes place thanks to the layer of sensitizer chemically bound to the surface of the semiconductor which, when hit by the light (as a consequence of excitation) transfers an electron to the oxide, which carries it to the glass electrode (TCO layer); at the same time, in the latter a positive charge is transferred from the dye to the redox mediator which, by oxidation, carries it to the other side of the cell onto the counter-electrode (formed by a suitable catalyst, platinum or carbon, placed on conductive glass), thereby closing the circuit and generating an electric current. From the practical point of view, the sensitized TiO_2 nanocrystals are first sintered to yield a layer, usually of about 10 µm thickness. The semiconductor layer is placed on a transparent conducting glass sheet which is crossed by the solar radiation (forward contact of the cell). On the other side of the device a second electrode (counter-electrode) is placed, and the contours of the cell are sealed, after having filled the inner space with the electrolyte solution.

1.2 – The Fotosensorg Project

The present paper investigates the environmental aspects of emerging DSSC PV technology under development through LCA. In particular it deals with results obtained in the contest of the interdisciplinary Project Fotosensorg (POR FSE 2007-2013) "Design and Synthesis of new organic sensitizers for non conventional solar cells production" developed by the Department of Chemistry at the University of Siena and the ICCOM-CNR of Firenze. The aim of the project is that of producing and characterising new molecules able to harvest a wider range light wavelenghts. In fact the opportunity to harvest more light by absorbing at least a part of infrared radiation opens up interesting perspectives toward an improvement of DSSC efficiency. The project is developed through the entire range of expertise needed to develop a project of this nature, i.e. from the synthesis of new sensitizers having innovative structural characteristics to the computational analysis of their spectroscopic and photochemical characteristics. In this context the purpose of the LCA study is to identify the significant environmental aspects of the DSSC systems in particular those employing organic sensitizers instead of metal complex dyes.

2. LCA methodology and case study

The analysis performed in this study consists of an LCA of the production phase of a photovoltaic DSSC technology panel in accordance to the relevant recommendations by the International Organization for Standardization. The LCA methodology allows one to assess the potential environmental impacts associated with a product or a service during its whole life cycle. The four phases of LCA, defined by ISO 14040 and 14044 standards [22,23], are goal and scope definition, inventory analysis, impact assessment and interpretation. The goal and scope definition defines the purpose, extent and intended audience of the study and contains a description of the system as well as geographical and time boundaries (cut-off criteria). The basis for the comparison of different systems is the functional unit of a product or service delivered. Inventory analysis consists of collection and analysis of data (such as consumed resources, electric and thermal energy use, air, water and soil emissions, by-products, etc.) associated with each process in the life cycle in order to build the life cycle inventory (LCI). When processes have more than one output, it is necessary to determine how to allocate the environmental burdens. Impact assessment evaluates the outcome of the inventory with respect to their environmental relevance. The purpose is to determine the relative importance of each of the inventory items and to aggregate them to a small set of indicators, or even to a single indicator, in order to identify the processes which contribute most to the overall impact. Two mandatory elements are considered: classification (assignment of inventory data to different impact categories) and characterization (calculation of category indicator results for each impact category using characterization factors). A series of optional elements, such as normalization and weighting may be considered in order to determine a significant final score, even if the weighting of environmental problems is difficult to estimate. Finally, an interpretation is necessary to evaluate the study for recommendations and conclusions. System boundaries for the DSSC case study are defined as in Fig. 2.

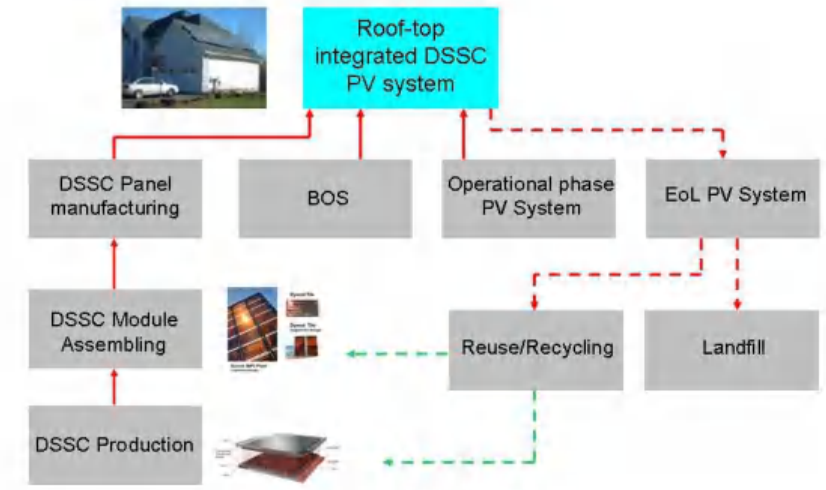

Fig. 2. System boundaries for the DSSC case study

The study carries out the analysis of the laboratory process preliminary data for the manufacturing of a DSSC and then evaluates frame and panel manufacturing process on the basis of pre-industrialisation process data extrapolated from literature and web resources. Then we assume that DSSC modules are used to deliver electricity to the grid and that the DSSC PV system is rooftop installed. Hence, emissions, material and energy usage are ascribed to the amount of kWh produced during the operational lifetime of the DSSC system. End-of-life management and recycling alternatives were not included due to lack of data for similar type of solar cell. Such investigations may assume that glass and metals are recycled allowing for reduction of mineral resources and primary energy requirements. Inorganic substances are disposed in landfills potentially offering energy recovery and the rest of polymers are incinerated.

The DSSC module manufacturing phase was analyzed by building an LCI for all the inputs (energy and material requirements) in the production process of 1 kWp of module. All calculations were performed with the SimaPro Software v 7.2 [24]. Primary data were based on preliminary and estimated production data for the cell manufacturing process developed in the project, while data for the module production process were derived from literature and web resources. Secondary data were selected from the available life cycle inventory in the Ecoinvent v 2.1 database [25, 26]. Two impact assessment methods were used to assess the potential impacts of the environmental flows collected in the inventory stage. The global warming potential (GWP_{100}) was evaluated with the Intergovernmental Panel on Climate Change (IPCC) 2007 data for a timeframe of 100 years [27], while the Cumulative Energy Demand (CED) was calculated by the method described in Ecoinvent v 2.0 by summing all fossil, nuclear, hydro and renewable energy demand into one single CED value [28]. In order to compare results from this study with those published previously in literature, the following significant indicators per unit were considered. First, the net energy ratio (NER) that is the life cycle energy output over its life cycle energy input, which stipulate the renewable energy obtained from each energy input source (most likely to be from fossil fuels). Second, the greenhouse gas (GHG) emissions, that is the calculation of the total emitted GHG during a system's life cycle divided by the total amount of electricity generated over its lifetime. Another useful parameter for comparison of renewable energy technologies is the energy pay-back time (EPBT). The EPBT value provides the number of years the energy system has to generate electricity in order to compensate for the energy used for the production of the complete system. Lastly, in order to carry out specific comparative analyses for the DSSC system, the impact method CML 2 baseline 2000 was used [29]. This method, originally developed by the Center of Environmental Science at Leiden University (Netherlands), elaborates on the problem-oriented (midpoint) approach and includes a balanced set of ten impact categories: ozone layer depletion (ODP), human toxicity, fresh water aquatic ecotoxicity, marine aquatic ecotoxicity, terrestrial ecotoxicity, photochemical oxidation, global warming (GWP_{100}), acidification, abiotic depletion and eutrophication.

3. Results and discussion

3.1. LCI analysis of production phase

3.1.1. The dye sensitized solar cell

In order to compile the LCI of the case study, all data regarding the quantities of raw material used for the DSSC manufacturing process have been collected. Our laboratory process allowed us to prepare organic solar cells of 10x5 cm. Actually there is still no massive commercial production of DSSC and thus our calculation is based on the laboratory process developed in the project and on data published by companies working on pre-industrialisation of DSSC panel and average data of similar process on industrial level [30-33]. All materials employed in the production phase are summarized in Table 1. Typically, the manufacturing steps of the cell involve low-temperature, non-vacuum processes and in particular we have considered the following process:

- Laser scribing process
- Automated hole-drilling
- Semiconductor Screen printing
- Semiconductor sintering
- Organic dye application
- Organic dye removal
- Sealant application
- Electrolyte filling
- Fill-hole sealing

Reliable life cycle inventory data for most of these processes were not available, thus the energetic input flows has been calculated according to [30-33]. For these calculations, the energy mix is taken as it is representative for the European Union for the Coordination of Transmission of Electricity (UCTE).

Table 1. Material life cycle inventory for the manufacturing of 1 m^2 of dye sensitized solar cell

Input for DSSC cell manufacturing	Quantity	Reference
Conductive solar glass	1*2 m^2	Estimation from [33] and Lab
Titanium Dioxide	29,12 g/m^2	Estimation from [33] and Lab
Platinum	0,065 g/m^2	Estimation from [33] and Lab
Iodine based electrolyte	35,1 g/m^2	Estimation from [21, 33]
Organic dye	15,959 g/m^2	Estimation from [21]
Metallization paste, silver	9,36 g/m^2	Estimation from [21] and Lab
Polyethylene (LLDPE)	32,5 g/m^2	Estimation from [21, 33]
Polyester resin	130 g/m^2	Estimation from [33] and Lab

One of the main issue regarding the LCA for the single DSSC is the contribute given by the dye and how the sensitizer has to be included in the LCI. In particular the routes for dye production are very complex and data referring to similar processes are quite a few in the available databases. In this study we consider the organic dye trimethylamine and all data regarding the industrial synthesis are derived form the Ecoinvent database. Input flows contribution to the embodied energy in MJ of equivalent primary energy for the production of DSSC are shown in Fig. 3. The largest environmental impact was found to be due to the use of primary energy for the manufacturing of

materials. As it can be seen from the diagram, the conductive solar glass production step is the most energy intensive process. The reason has to be found in the mass of glass that is necessary for the manufacturing of the cell and in the huge amount of energy required for covering glass with a conductive oxide layer (ITO). The assessment of environmental impact indicators for the DSSC production process [19], using the CML 2 baseline 2000 method, allowed us to assess that the major contributes to all impact categories is coming from the glass substrate (the production of glass consumes a lot of energy) and, to a minor extent, from the platinum counterelectrode and silver for the current-collecting grid. The impacts associated with dye, semiconductor and electrolyte are definitely really limited. Thus it is easy to understand that, working with plastic or metal substrates and different material for the counterelectrode, the overall environmental impact of DSSC manufacturing process could be further lowered.

3.1.2. Module assembling and Balance of System: toward the installation of a roof-top integrated grid-connected DSSC system

The DSSC manufacturing process is scalable using the same methods to a module composed of cells connected in series and/or parallel using additional metal contacts. Thus materials and processes employed in this production step are proportionally the same. We decided to set the dimension of the module to 80x80 cm^2 with a 70% of active area according to data published by companies working on pre-industrialisation of DSSC panel.

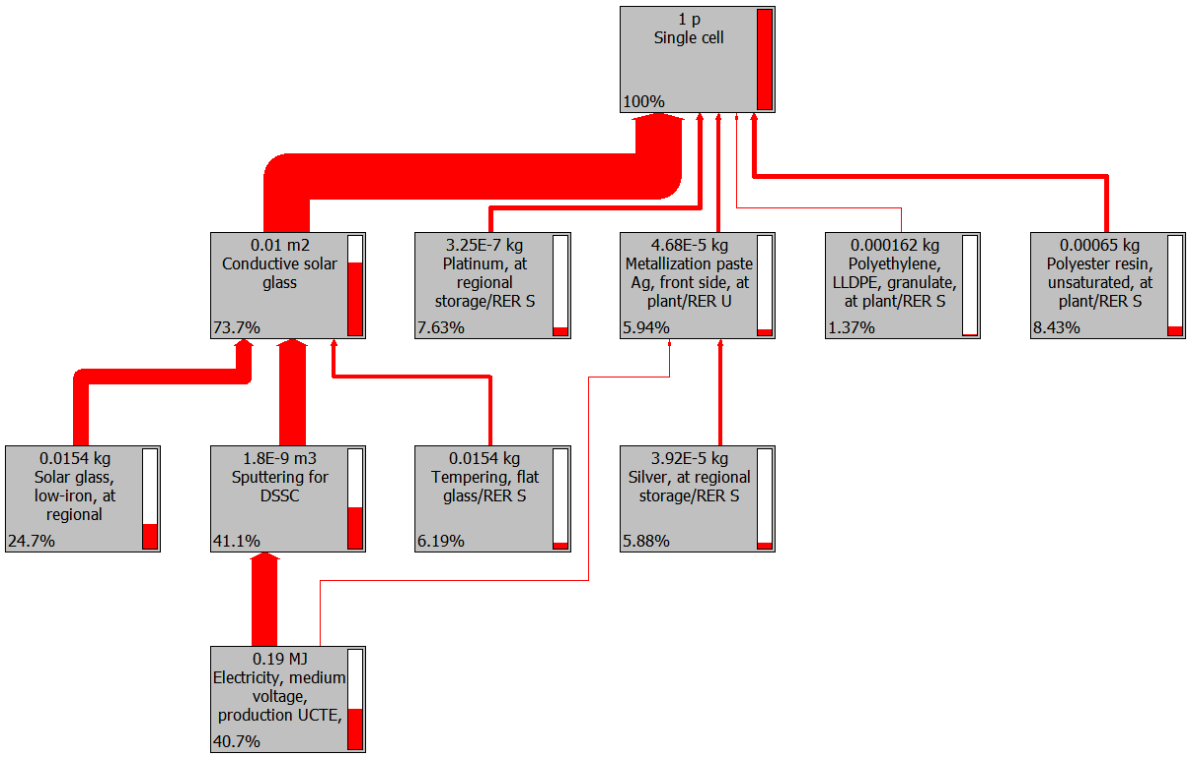

Fig. 3. Input flows contribution to the embodied energy in MJ of equivalent primary energy for the DSSC production process (cut-off 2%).

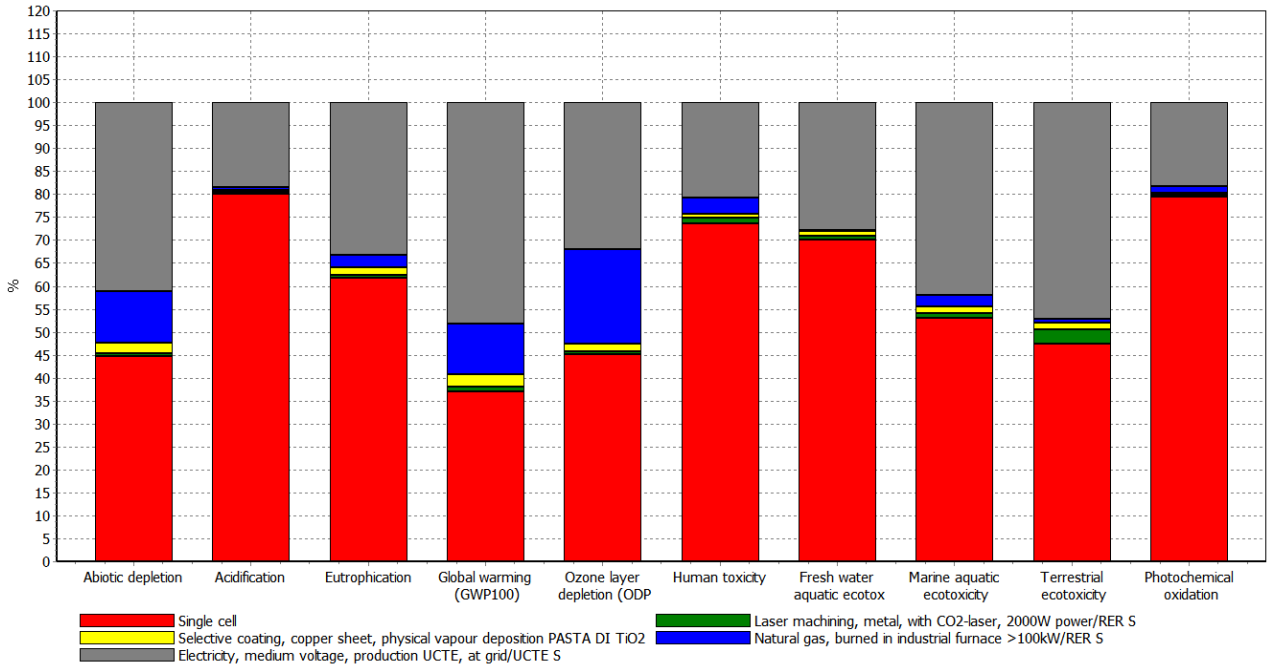

Fig. 4. Environmental impact assessment of DSSC module using the CML 2 baseline 2000 method.

Since the target of this study was to compare the environmental performance of DSSC technology with other thin film PV technologies, we considered the case study of a virtual roof-top grid-connected installation. Actually the thin film hybrid and organic solar cells inventory assumes frameless modules as DSSC are likely to be manufactured as building integrated (BIPV) products. However, for comparative purposes, aluminium frames and support steel structure (the so-called balance of system - BOS – components) have been included. The inventory of a typical BOS for a grid-connected rooftop installation was then applied to the analysis [14, 34]. In Fig. 4 we report the histogram concerning the environmental impact assessment of the DSSC module production step: also in this case the direct energy consumption in the process contributes mostly to the environmental impact. The steps that use most of the energy are the sintering of the TiO_2 layer and the glass lamination.

3.2. LCI analysis of operational phase

For the analysis of the virtual roof-top DSSC system, some assumptions have been made in order to calculate the total energy produced by the PV system during its operative lifetime. First, the efficiency of the produced DSSC PV panel is set to 8% [35] and assuming a panel area of 12,8 m^2 necessary to generate 1 kWp, the electrical energy delivered in the first year of the PV system lifetime is 1,306 kWh/year. The total amount at the end of its life cycle should be 23,774 kWh (assuming a 1% decrement per year in the conversion efficiency of DSSC module during its lifetime). Second, the irradiation level used for the calculation of the total energy produced by the PV system during its operational time is set to 1700 kWh/m^2/year. This is the typical value of European southern countries and has been chosen as a common basis for comparability with other LCA studies. Finally, we consider a 20 years lifetime for the roof-top DSSC PV system, which is comparable with other PV technologies (usually 20–30 years), supported by studies already published by companies such as Dyesol and realistic in terms of the aims for 2013 of the European Photovoltaic Technology Platform for hybrid and organic photovoltaics [17].

System losses due to the BOS and other indirect losses were assumed at 25%, that's to say the performance ratio is set equal to 0.75. Note that the actual performance ratio of DSSC systems may vary considerably with system design, shading and temperature, among other factors. The inverter

was considered to be replaced only once during the PV system lifetime.

Input flows contribution to the embodied energy in MJ of equivalent primary energy to the generated peak power in kWp are shown in Fig. 5. The network presented in this figure is the result of the analysis performed in a recent paper of the authors [19] and it's useful in this context to highlight that contributes to the final overall indicator from the panel and the BOS components are very similar. Note that in reality, framing and BOS technology are not yet well defined for large scale dye cell application, and this may be very different as compared to other photovoltaic technologies. In Table 2 we report all results obtained by the LCA analysis.

Table 2. Summary of results for DSSC system and several thin film PV technologies

	Polymer	**CdTe**	**CIS**	**MCPH**	**DSSC [21]**	**DSSC**
Irradiance (kWh/m2/year)	1700	1700	1700	1700	1700	1700
Efficiency BOS (%)	75	75	75	75	75	75
Efficiency module (%)	5	9	11	8,74	8	8
lifetime (years)	20	20	20	20	20	20
NER (E_{output}/E_{input})	15,87	13,33	7,14	24,48	23,92	12,67
EPBT (years)	1,26	1,50	2,80	0,82	0,84	1,58
GWP100 (g CO2 eq /kWh)	37,18	48,00	95,00	20,90	40,00	22,29

This data are extensively described in [19], so here we report only the most meaningful indicators for the evaluation. From the inspection of the this Table, we can see that the DSSC PV system performs similarly and sometimes even better compared to other inorganic and hybrid and organic thin film PV technologies.

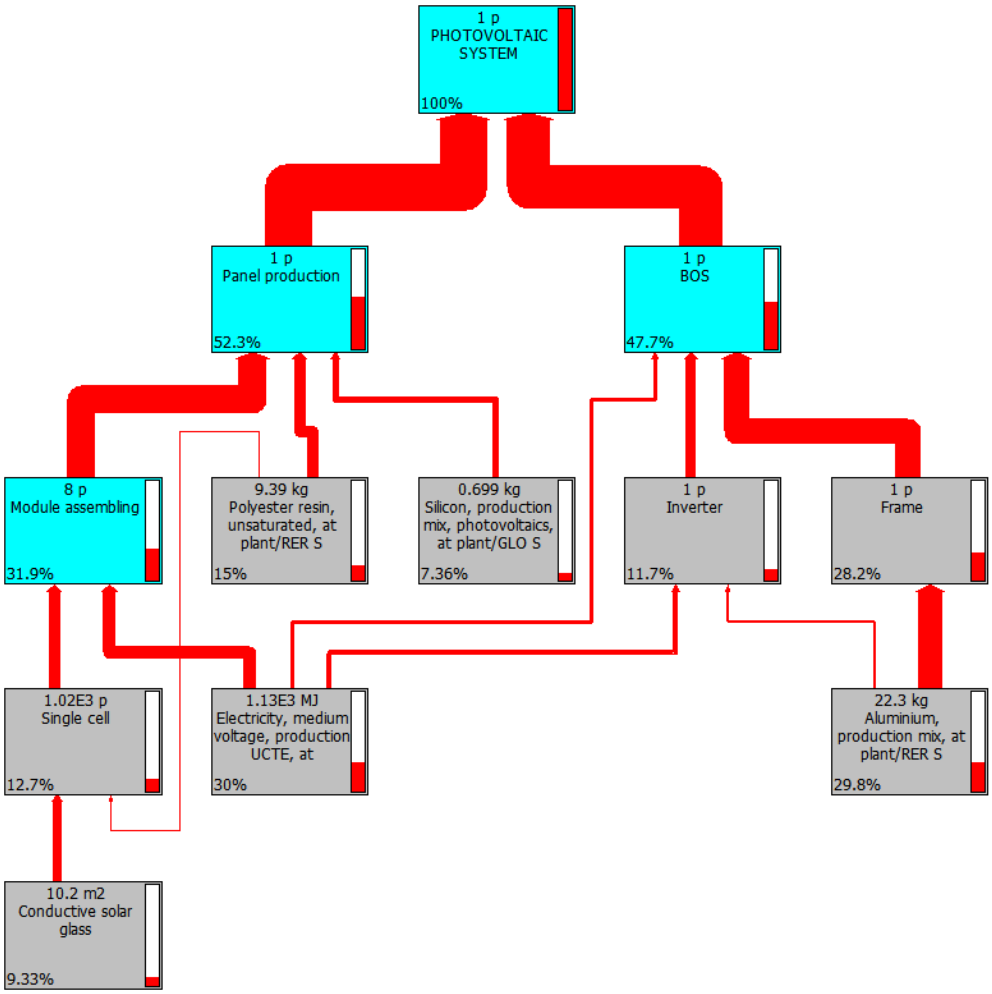

Fig. 5. Input flows contribution to the embodied energy in MJ of equivalent primary energy the generated peak power in kWp (cut-off 6%); figure from [19]

3.3. Sensitivity analysis on future DSSC efficiency and lifetime

Low cost solar cells are likely to have shorter lifetimes and lower efficiencies at the initial stage of commercialisation. A sensitivity analysis was performed to assess the impact of variations in efficiency and lifetime on the EPBT, NER and CO_2-eq/kWh results obtained from the LCA tool. Tables 3, 4 and 5 show the sensitivity analyses for the glass-glass DSSC. In each Table, values calculated for the case study are reported in bold font . The energy payback times of glass-glass DSSC devices have been calculated considering different efficiency values according to the calculations in Table 3.

Table 3. EPBT sensitivity analysis for dye sensitized solar cell.

Efficiency (%)	6	7	**8**	9	10	11	12	13
EPBT	2,11	1,81	**1,58**	1,40	1,26	1,15	1,05	0,97

With an increase of efficiency, the EPBT value becomes lower (up to 0.97) and this compares favourably with crystalline silicon which, for instance, has an EPBT of 1.5 years for PV systems with multicrystalline silicon modules installed on roofs in Southern Europe.

The results in Table 4 show that shorter lifetimes require a higher efficiency to have a high NER value. In general, if NER value is less than 1, the PV technology, which the indicator has been calculated for, is not sustainable. This is a consequence of the NER definition: the life cycle energy output over its life cycle energy input, which means that if this ratio is minor to 1, the energy produced by the PV system is less than the energy invested. Moreover, when efficiency degradation is considered, the NER values can decrease even further. The sensitivity analysis performed on our DSSC system shows sustainability is reached in every conditions with best performances in the short term for higher nominal efficiencies.

Table 4. NER sensitivity analysis for dye sensitized solar cell.

NER		Lifetime (years)															
		15	16	17	18	19	20	21	22	23	24	25	26	27	28	29	30
Efficiency (%)	**6**	7,30	7,75	8,19	8,63	9,06	9,50	9,92	10,34	10,76	11,18	11,59	11,99	12,39	12,79	13,18	13,57
	7	8,51	9,04	9,56	10,07	10,58	11,08	11,58	12,07	12,56	13,04	13,52	13,99	14,46	14,92	15,38	15,84
	8	9,73	10,33	10,92	11,51	12,09	**12,66**	13,23	13,79	14,35	14,90	15,45	15,99	16,52	17,05	17,58	18,10
	9	10,95	11,62	12,29	12,94	13,60	14,24	14,88	15,52	16,14	16,76	17,38	17,99	18,59	19,19	19,78	20,36
	10	12,16	12,91	13,65	14,38	15,11	15,83	16,54	17,24	17,94	18,63	19,31	19,99	20,66	21,32	21,97	22,62
	11	13,38	14,20	15,02	15,82	16,62	17,41	18,19	18,96	19,73	20,49	21,24	21,98	22,72	23,45	24,17	24,89
	12	14,60	15,49	16,38	17,26	18,13	18,99	19,84	20,69	21,52	22,35	23,17	23,98	24,79	25,58	26,37	27,15
	13	15,81	16,78	17,75	18,70	19,64	20,57	21,50	22,41	23,32	24,22	25,10	25,98	26,85	27,71	28,57	29,41

Similarly the thresholds for efficiency and lifetime with respect to CO_2-eq/kWh are reported in Table 5. According to [8], greenhouse emission average values for PV technologies installed in Southern Europe are comprised in the range 21 – 45 g CO_2-eq/kWh. These values could be lowered by most performing PV devices with longer lifetimes, but most of all by more efficient and environmental friendly industrial production processes [12].Values in accordance with Fthenakis et al [8] are reported in grey background in Table 5.

Table 5. g CO_2-eq/kWh sensitivity analysis for dye sensitized solar cell.

GWP_{100}		Lifetime (years)															
		15	16	17	18	19	20	21	22	23	24	25	26	27	28	29	30
Efficiency (%)	**6**	38,68	36,44	34,46	32,71	31,14	29,72	28,45	27,29	26,23	25,25	24,36	23,54	22,77	22,07	21,41	20,79
	7	33,15	31,23	29,54	28,03	26,69	25,48	24,38	23,39	22,48	21,65	20,88	20,17	19,52	18,91	18,35	17,82
	8	29,01	27,33	25,85	24,53	23,35	**22,29**	21,33	20,46	19,67	18,94	18,27	17,65	17,08	16,55	16,06	15,60
	9	25,78	24,29	22,98	21,80	20,76	19,82	18,96	18,19	17,48	16,84	16,24	15,69	15,18	14,71	14,27	13,86
	10	23,21	21,86	20,68	19,62	18,68	17,83	17,07	16,37	15,74	15,15	14,62	14,12	13,66	13,24	12,84	12,48
	11	21,10	19,88	18,80	17,84	16,98	16,21	15,52	14,88	14,30	13,78	13,29	12,84	12,42	12,04	11,68	11,34
	12	19,34	18,22	17,23	16,35	15,57	14,86	14,22	13,64	13,11	12,63	12,18	11,77	11,39	11,03	10,70	10,40
	13	17,85	16,82	15,91	15,10	14,37	13,72	13,13	12,59	12,10	11,66	11,24	10,86	10,51	10,18	9,88	9,60

4. Conclusion

In this study we performed an LCA analysis of DSSC module production by extrapolating information from the Fotosensorg Project lab processes. Our calculations allow us to assess that DSSC technology compares favourably with other PV technologies regarding the embedded energy of the PV module even for a far from optimum laboratory fabrication procedure. The main reason is

that high temperatures are not involved in the process. The embedded energy value for laboratory cell production is much less than the average value calculated for crystalline silicon technologies and it is of the same order of magnitude of thin film technologies. Thus we can expect large reductions for the DSSC technology in the large scale industrial process, giving a clear advantage to organic thin film technologies (provided that the efficiency of these industrial modules is similar to that of actual laboratory cells). In this context, much research has to be focused on alternative materials for cathodes preparation, low-temperature approaches for module manufacturing, different methods for anode deposition as well as the optimization of substrates. In additions to the advantage of process up-scaling, DSSC modules on polymer or metal substrates would probably not require an aluminium framing, thus reducing the energy requirement even further. We found also that EPBT is largely determined by the framing and BOS components and it is expected that significant differences in the EPBT will arise between grid-connected and standalone systems. Moreover recycling of glass and metals may reduce the energy requirements also drastically, but there is no practical experience yet with recycling of DSSC components.

As we showed through the sensitivity analysis, the CO_2-eq/kWh emissions are strongly correlated with the operational lifetime of DSSC modules, and values obtained for the case study are within the range of new generations PV modules.

Lastly, we point out that throughout our calculations of estimated energy output of the systems the distinction between direct and diffuse irradiation has not been taken into account here yet. When a crystalline silicon PV system is compared with hybrid and organic PV for lower levels of irradiance, a higher ratio of diffuse versus direct solar irradiance is produced and the output of the hybrid and organic PV technology will be underestimated if this issue is not taken into account. If low irradiance levels are considered, the hybrid and organic technologies are less energy-costly per installed capacity than any other PV technology even with actual laboratory processing methods and limited power conversion efficiencies.

Acknowledgments

Authors thank for financial support Project Fotosensorg (POR FSE 2007-2013) “Design and Synthesis of new organic sensitizers for non conventional solar cells production”. Useful discussions with Prof. M. Taddei (Unisi) and A. Mordini, G. Reginato and L. Zani (ICCOM-CNR) are acknowledged.

Nomenclature

BIPV	Building Integrated Photovoltaic
BOS	Balance of System
CED	Cumulative Energy Demand
DSSC	Dye Sensitized Solar cell
EPBT	Energy Pay Back Time
GHG	Green House Gas
GWP	Global Warming Potential
IPCC	Intergovernmental Panel on Climate Change
LCA	Life Cycle Assessment
LCI	Life Cycle Inventory
NER	Net Energy Ratio
PV	Photovoltaic
TCO	Transparent Conductive Oxide

References

[1] O'Regan B., Grätzel M., A Low-Cost, High Efficiency Solar Cell Based on Dye-Sensitized Colloidal TiO Films. Nature 1991;353:737-40.

[2] Grätzel M., Photoelectrochemical cells. Nature 2001;414:338–44.

[3] Bai Y., Cao Y., Zhang J., Wang M., Li R., Wang P., Nazeeruddin S. M., Grätzel M., High-performance dye-sensitized solar cells based on solvent-free electrolytes produced from eutectic melts. Nature Materials 2008;7(8):626–30.

[4] Hagfeldt A., Boschloo G., Sun L., Kloo L., Pettersson H., Dye-sensitized Solar Cell. Chemical Reviews 2010;110:6595-664.

[5] Yella A., Lee H., Tsao H., Yi C., Chandiran A., Nazzeruddin S. M., Diau E., Yeh C., Zakeeruddin S., Grätzel M., Porphyrin-sensitized solar cells with cobalt (II/III)–based redox electrolyte exceed 12 percent efficiency. Science 2011;334:629-34.

[6] National Renewable Energy Laboratory, 2008 Solar Technologies Market Report, U.S. Department of Energy, Office of Energy Efficiency and Renewable Energy; 2010 Jan.

[7] Jungbluth N., Life cycle assessment of crystalline photovoltaics in the Swiss ecoinvent database. Progress in Photovoltaics: Research and Applications 2005;13(5):429-46.

[8] Fthenakis V. M., Alsema E. A., Photovoltaics Energy Payback times, greenhouse gas emissions and external costs: 2004-early 2005 status. Progress in Photovoltaics: Research and Applications 2006;14(3):275-80.

[9] Alsema E. A., Nieuwlaar E., Energy viability of photovoltaic systems. Energy Policy 2000;28(14):999-1010.

[10] Fthenakis V. M., Kim H. C., Alsema E. A., Emissions from photovoltaic life cycles. Environmental Science & Technology 2008;42(6):2168–74.

[11] Bravi M., Parisi M. L., Tiezzi E., Basosi R., Life cycle assessment of advanced technologies for photovoltaic panels production. International Journal of Heat & Technology 2010;28(2):133-39.

[12] Bravi M., Parisi M. L., Tiezzi E., Basosi R., Life Cycle Assessment of a Micromorph Photovoltaic System, Energy 2011;36(7):4297-306.

[13] Kato K., Hibino T., Komoto K., Ihara S., Yamamoto S., Fujihara H., A life-cycle analysis on thin-film CdS/CdTe PV modules. Solar Energy Materials and Solar Cells 2001;67:279-87.

[14] Raugei M., Bargigli S., Ulgiati S., Life cycle assessment and energy pay-back time of advanced photovoltaic modules: CdTe and CIS compared to poly-Si. Energy 2007;32(8):1310-18.

[15] Dennler G., Bracec C., Socio Economics Impacts Of Low Cost PV Technologies. In Brabec C, Scherf U, Dyakonov V, editors. Organic Photovoltaics: Materials, Device Physics and Manufacturing Technologies. Germany: Wiley-VCH. 2008. pp. 531–567.

[16] Van Sark W., Alsema E. A., Junginger H. M., de Moor H. H., Schaeffer G. J., Accuracy of progress ratios determined from experience curves: the case of crystalline silicon photovoltaic module technology development. Progress in Photovoltaics: Research and Applications 2008; 16(5):441–53.

[17] Photovoltaic Technology Research Advisory Council (PV-TRAC), EU PV Technology Platform. A vision for photovoltaic technology. Brussels, Belgium: European Commission; 2005 Apr.

[18] Jäger-Waldau A., PV Status Report 2008, Research, Solar Cell Production and Market Implementation of Photovoltaics. Ispra, Italy: Institute for Energy, Renewable Energies Unit, DG Joint Research Centre; 2008 Sep. EUR - Scientific and Technical Research series - ISSN 1018-5593

[19] Parisi M. L., Sinicropi A., Basosi R., Life cycle Assessment of Grätzel-type cell production for non conventional photovoltaics from novel organic dyes. International Journal of Heat & Technology 2011;29(2):161-69.

[20] Greijer H., Karlsonb L., S. E. Lindquista, Hagfeldt A., Environmental aspects of electricity generation from a nanocrystalline dye sensitized solar cell system. Renewable Energy 2001;23(1):27-39.
[21] De Wild-Scholten M. J., Veltkamp A. C., Environmental life cycle analysis of dye sensitized solar devices; Status and Outlook. Proceedings of the 22nd European Photovoltaic Solar Energy Conference; 2007 Sept 3-7; Milan, Italy.
[22] ISO (International Organization for Standardization) 14040 standard. 'Environmental management-Life cycle assessment-Principles and framework'; 2006.
[23] ISO (International Organization for Standardization) 14044 standard. 'Environmental management-Life cycle assessment-Requirements and Guidelines'; 2006.
[24] Prè Consultants, SimaPro 7.1. Amersoort, The Netherlands, 2008 – Available at:<http://www.pre.nl>
[25] Frischknecht R., Jungbluth N., Althaus H. J., Doka G., Heck T., Hellweg S. et al., Ecoinvent v2.0: Overview and Methodology. Dübendorf, Switzerland: Swiss Centre for Life Cycle Inventories; 2007. Technical Report Ecoinvent No. 1.
[26] Jungbluth N., Dones R., Frischknecht R., Life Cycle Assessment of Photovoltaics: Update of Ecoinvent data v2.0. ESU-services Ltd., Uster, 2008.
[27] IPCC 2007 GWP 100a v 1.02, Climate Change 2007, IPCC fourth assessment report, the physical science basis.
[28] Frischknecht R., Jungbluth N., Althaus H. J., Bauer C., Doka G., Dones R., Implementation of Life Cycle Impact Assessment Methods. Dübendorf, Switzerland: Swiss Centre for Life Cycle Inventories; 2007. Technical Report Ecoinvent No. 3.
[29] Guinèe J. B., Gorrée M., Heijungs R., Huppes G., Kleijn R., De Koning A., Van Oers L., Wegener Sleeswijk A., Weidema B. P., (2001a) Life cycle assessment; An operational guide to the ISO standards; Characterisation and Normalisation Factors. Centre of Environmental Science (CML), Den Haag and Leiden, The Netherlands; 2001.
[30] Konarka Technologies Inc., USA – Available at:<http://www.konarka.com> [accessed 14.11.2011].
[31] DyeSol, Australia – Available at:< http://www.dyesol.com> [accessed 16.11.2011].
[32] Solaronix SA, Switzerland – Available at: http://www.solaronix.ch> [accessed 14.11.2011].
[33] G24 Innovations. Wales (UK) – Available at:http://www.g24i.com> [accessed 15.11.2011].
[34] Keoleian G.A., Lewis G.M., Application of life cycle energy analysis to photovoltaic module design. Progress in Photovoltaics: Research and Applications 1997;5:287-300.
[35] Pearsal N., Science, Technology and Applications Group of the EU Photovoltaic Technology Platform, A Strategic Research Agenda for Photovoltaic Solar Energy Technology, Photovoltaic Technology Platform Edition 2. Newcastle upon Tyne, UK: School of CEIS, Northumbria Photovoltaics Applications Centre. 2011 Sep. ISBN 978-92-79-20172-1.

Low CO_2 emission hybrid Solar CC power system

Yuanyuan Li [a], Na Zhang [b], Ruixian Cai [c]

[a] Institute of Engineering Thermophysics, Chinese Academy of Sciences; Graduate University of the Chinese Academy of Sciences, P.O. Box 2706, Beijing, P.R. China, marryliyuanyuan@126.com
[b] Institute of Engineering Thermophysics, CAS, P.O. Box 2706, Beijing, P.R. China, zhangna@mail.etp.ac.cn **(CA)**

[c] Institute of Engineering Thermophysics, CAS, P.O. Box 2706, Beijing, P.R. China, crx@mail.etp.ac.cn

Abstract:

Based on the principle of cascade utilization of multiple energy resources, a novel concept for gas-steam combined cycle integrated with solar thermo-chemical conversion and CO_2 capture, named low CO_2 emission hybrid Solar CC power plant (LEHSOLCC), has been proposed and analysed. The hybrid power system uses methane as its input fuel. The collected solar heat at 550°C is applied to provide heat for the endothermic methane reformation. The reforming reaction is integrated with a hydrogen separation membrane, which continuously withdraws hydrogen from the reaction zone and enables the chemical equilibrium to shift towards the product side. The pure H_2, collected in permeate side, fuel a topping Brayton cycle, and the exhaust drives a triple-pressure reheat Rankine bottoming cycle to produce additional power. The produced syngas in retentate zone is enriched with CO_2 (81.8%v) and thus can be suitable to be processed with precombustion decarbonization. In the proposed power system, the low level solar heat is first converted to syngas chemical exergy via reforming, and then released as high-temperature thermal energy in an advanced combined cycle system for power generation, thus achieving its high-efficiency heat-power conversion. To reduce the exergy destruction, special attention is paid to the thermal match of the internal heat recuperation, as well as to the thermo-chemical match between the solar heat and the reforming process.

The system is thermodynamically simulated using the ASPEN PLUS code. The results show that with 91% CO_2 captured, the specific CO_2 emission is 25 g/kWh. Exergy efficiency of 58% and thermal efficiency of 51.6% can be obtained. CO_2 capture brings about 8.4%-points thermal efficiency penalty compared with a gas-steam combined cycle system at the same technical level without CO_2 capture, but exergy efficiency remains the same level as the reference system. Fossil fuel saving ratio of 31.2% is achievable with a solar thermal share of 28.2%, and the net solar-to-electric efficiency, based on the gross solar heat incident on the collector, is about 36.4% compared with the same gas-steam combined cycle system with equivalent CO_2 removal rate by way of post-combustion decarbonization.

Keywords:

Hybrid Power System, Solar Thermal Energy, Membrane Reformer, Thermo-chemical Conversion, CO_2 capture.

1. Introduction

Solar thermal conversion is a promising technology for power generation. It is an efficient means to reduce emissions and to save fossil fuel. Generally speaking, higher working fluid temperature is preferable in power system for achieving higher heat-to-power efficiency. At low ones (~200°C or below) solar-only thermal power generation has low efficiency. For instance, the efficiency of Rankine cycle systems using organic working fluids is generally lower than 10% [1, 2]. Solar heat collected at high temperatures, however, associates with a significant increase in solar plant costs and reduced collector efficiency. In order to minish the thermo-economic gap between conventional

Corresponding author: Tel.: 86-10-82543030; fax: 86-10-82543019.
E-mail address: zhangna@mail.etp.ac.cn.

power plant technologies and solar plants, it is necessary to reduce the cost of the solar specific components and to improve the solar heat-to-electricity conversion efficiency. Solar hybrid systems, in which solar heat and fossil fuel are used in a complementary way, provide a attractive solution for achieving high efficiency converstion of solar heat.

Solar heat can be integrated into the power system either thermally or thermo-chemically. The later comprises solar upgrading of hydrocarbons by some endothermic reactions, and using the upgraded hydrogen-rich fuel to generate power in high efficiency conversion systems such as gas turbines and fuel cells. Methanol-steam reforming and methanol decomposition can achieve over 90% conversion into H_2-rich syngas at around 250℃. By taking advantage of the high conversion rates at this relatively low temperatures, Jin and co-workers proposed a combined cycle (called Solar CC) that ingeniously integrates low/mid-temperature solar thermal energy with methanol decomposition [3]. By heating the endothermic decomposition reaction, solar thermal energy is upgraded to chemical energy of the produced syngas. In a case study [3], exergy efficiency of the hybrid combined cycle system is 60.7%. The net solar-to-electricity efficiency can reach 35% with the solar thermal share of 18%, and the CO_2 emission is 310 g/kWh without regard of CO_2 capture. For natural-gas fired power plants, the methane-steam reforming generally requires above 800^{o}C with Ni-based catalyst to obtain high methane conversion. Tamme presented a high temperature (>1000^{o}C) solar hybrid system comprising solar upgrading of methane by steam reforming in solar specific receiver-reactors and utilizing the upgraded H_2-rich fuel in advanced gas-steam combined cycles [4]. In comparison to a conventional CC system, about 30% of fuel can be saved. However, due to the high temperature solar heat collection, the upgrading in energy level of solar thermal energy to syngas chemical energy is limited and the cost of the solar components is considerably high.

To avoid the high cost and low collecting efficiency caused by high temperature solar heat collection, moreover, to allow the low temperature solar heat to achieve its high-efficiency heat-power conversion, Zhang and Lior proposed a solar-assisted chemically recuperated gas turbine system (SOLRGT) with indirect solar heat upgrading [5]. Solar heat collected at ~220℃ is used to generate steam for methane reformation, thus first transformed into vapour latent heat, and then converted to the produced syngas chemical energy via the reforming reaction. The upgraded solar fuel is eventually burned in a high-efficiency power system. About 20-30% fossil fuel saving ratio can be achieved compared with a conventional chemically recuperated gas turbine system (CRGT) without solar heat contribution. However, nearly 80% of the total energy input is provided by methane, leading to 342.7g/kWh CO_2 emission.

In the SOLRGT system[5,6], the reforming section retrieves heat from the turbine exhausts at a temperature below 600^{o}C, resulting to a limited CH_4 conversion of 37.8%, far below the desired 95% conversion rate for pre-combustion decarbonization employment. Higher reforming temperature elevates methane conversion. Boosting the reaction temperature by means of supplementary firing with additional fossil fuel, however, imposes penalty on the overall system efficiency. Zhang et al proposed a zero CO_2 emission SOLRGT system [7,8] based on oxy-fuel combustion.

Besides raising reforming temperature, high CH_4 conversion can be achieved also with selective removal of reaction products, such as H_2 or CO_2. Palladium membrane, whose mechanism is based on a H_2 solution-diffusion mechanism on perm-selective film, has been applied to construct membrane reactors to shift thermodynamic equilibrium limited reactions. The investigation carried out has showed that 99% CH_4 conversion can be obtained at 550^{o}C and 3~9bar [9]. Provided that integrating the Pd membrane reactor with the SOLRGT system, the pre-combustion decarbonization may be feasible. Based on this consideration, in the present paper, we propose a low CO_2 emission hybrid Solar CC cycle (LEHSOLCC), in which solar heat collected at middle temperature (~550^{o}C) is used to heat the endothermic steam reforming of methane in a membrane reactor, achieving nearly full CH_4 conversion, realizing not only the high-efficiency cascade utilization of fuel chemical exergy and solar thermal energy, but the CO_2 capture prior to combustion with low energy

penalty. A design-point performance analysis shows that the system attains a net exergy efficiency of 58% and specific CO_2 emissions of 25 g/kWh with 91% CO_2 capture rate. Fossil fuel saving ratio of 31.2% is achievable with a solar thermal share of about 28.2%. The net solar-to-electric efficiency, based on the gross solar heat incident on the collector, is about 36.4% compared with a gas-steam combined cycle system with post-combustion decarbonization at the same fossil fuel input.

2. System configuration description

2.1. Reforming in membrane reator

Figure 1 shows the schematic diagram of methane reforming in a palladium membrane reactor. The Pd membrane is prepared via a novel electroless plating method [10]. The alumina support includes glaze and porous part to plating. One end of the support tube is sealed. The open end is applied for the introduction of a sweep gas flux and collection of permeated H_2, simultaneously.

The Pd membrane tube is located inside the center of a dense stainless steel tube reactor. An annulus chamber between the stainless steel tube and membrane tube is thus applied for reaction, which also served as the retentate side of the Pd membrane. While the inner volume of the membrane tube is the permeate zone. Diluted with silica, the catalyst is packed to construct a catalyst bed, extended over the membrane. The reactor is firstly heated to reaction temperature of 550^{o}C, after stabilizing, the mixture of methane and steam is gradually introduced to the reactor. As the reforming processes, reaction products H_2 and CO_2 in reaction zone concentrate and their pressure keep increasing. Driven by the pressure difference, H_2 moves to the permeate zone continuously, and is taken away by the sweep gas; and the impermeable CO_2 gas is collected from the bottom of the reaction zone. Note that the sweep gas flow should be countercurrent to the feed stream in order to maintain a high H_2 partial pressure drop across membrane to promote H_2 permeation.

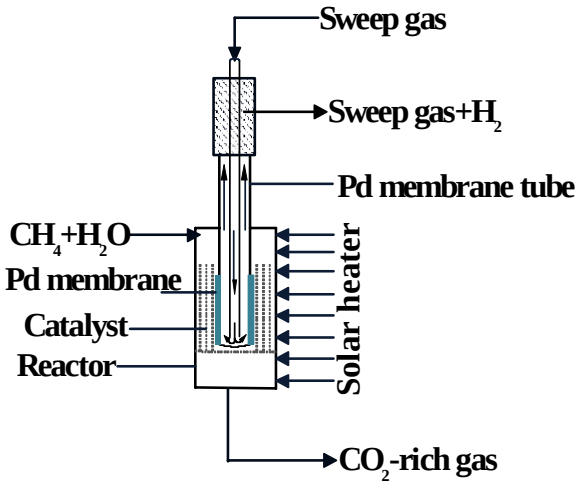

Fig. 1. Schematic diagram of membrane reformer

Figure 2 shows the principle of the membrane reformer [11]. The driving force of the membrane transport is the difference in H_2 partial pressures between the retentate and the permeate sides. The molar flow rate F of H_2 through the membrane may be described by the transport equation: $F=B \cdot A \cdot [(P_H)^n-(P_L)^n]$ [11], where B is the H_2 permeance efficiency, A is the membrane surface, and $(P_H)^n-(P_L)^n$ is the partial pressure difference across the membrane. It can be seen that separation performance of membrane depends on two factors, flux and selectivity. Flux is determined by knowing the mass of permeate collected, membrane area and the running time. H_2 selectivity represents the measure of the preferential transport of H_2. It is defined by the H_2/N_2 separation coefficient of membrane, which is determined with pure H_2 and N_2 at constant pressure drop and

temperature across the membrane. It can be found that no permeation of nitrogen across the Pd membrane is detected and an almost infinite H_2 selectivity can be obtained [9]. Moreover, the Pd membrane is experimentally characterized by gas permeation tests at different temperature and pressure using pure gases (H_2, N_2, CO, CO_2, CH_4 and H_2O). It is observed that only hydrogen permeates through the membrane [12], suggesting that Pd membrane has high H_2 permeation and separation performance. Additionally, the selectivity to a carbon product (CO or CO_2) by current reaction is defined as the ratio of molar flow rate of the selected product to the converted methane molar flow rate. To increase the CO_2 capture rate, the CO selectivity should be suppressed as far as possible.

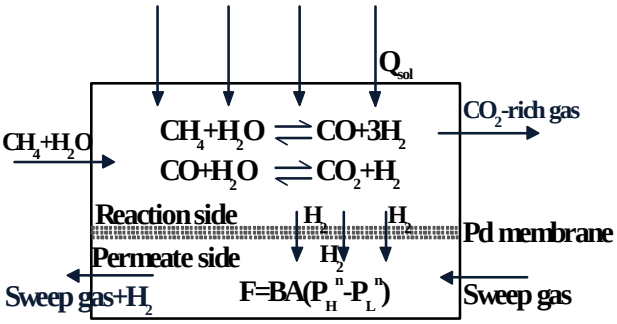

Fig. 2. Principle of the membrane reformer

2.2. Low CO_2 emission Hybrid Solar CC system

A gas-steam combined cycle integrated with solar thermo-chemical process and CO_2 capture, named LEHSOLCC (Fig. 3), has been set up to demonstrate the solar-driven-membrane reaction in power plant. A middle temperature (550^{o}C) tower-type solar collector is introduced to provide heat for the endothermic methane reforming at pressure of 9 bar and steam-to-carbon ratio of 3.5. The reformer is integrated with a hydrogen separation membrane, enabling continuously removal of hydrogen from the retentate (reaction) zone, and thus shifting the reaction to the product side. The pure H_2 (13), collected in permeate side, warms up the reforming reactants (7, 10) and fuels a topping Brayton cycle after being compressed. The CO_2-rich syngas (12) in retentate zone is first used to preheat the reforming reactants (7, 10), then cooled down to near ambient temperature and processed in a CO_2 physical absorber, where more than 90% CO_2 is removed. The remainder (22), which mainly contains 68.8%vH_2, 9%vCO, 3.8%vCH_4 and 18.4%vCO_2, is compressed, and also utilized as the fuel in the topping Brayton cycle. The gas turbine exhaust (27) eventually drives a triple-pressure reheat Rankine bottoming cycle to produce additional power. Together with the complementary make-up water (5), the condensate (18) drained from the CO_2 stream is recycled to the reformer. To reduce the exergy destruction, special attention is paid to the thermal match of the internal heat recuperation, as well as to the thermo-chemical match between the solar heat and the reforming process.

In the proposed power system, there are two stages of solar heat collection. The low level (low-temperature) solar heat (200^{o}C) evaporates the reforming water and is converted into steam latent heat, and the middle level (middle-temperature) solar heat (550^{o}C) is used to drive the endothermic reaction and transformed into syngas chemical exergy via reforming, and finally released as high-temperature thermal energy through combustion in the advanced gas-steam combined cycle system for power generation, achieving a high-efficiency heat-power conversion.

With the assistance of solar heat, the temperature match in the syngas heat recuperation process can be improved since it provides only sensible heat to the reforming reactants, leading to reduced heat transfer exergy loss. Moreover, the turbine exhaust heat is available to drive a Rankine bottoming cycle to produce additional power.

The integration of a H_2 separating membrane in the reformer achieves nearly full CH_4 conversion at middle temperature. Meanwhile, the CO_2 concentration is increased and CO_2 capture energy consumption is reduced. The system accomplishes a high-efficiency solar heat-power conversion and low-penalty pre-combustion decarbonization.

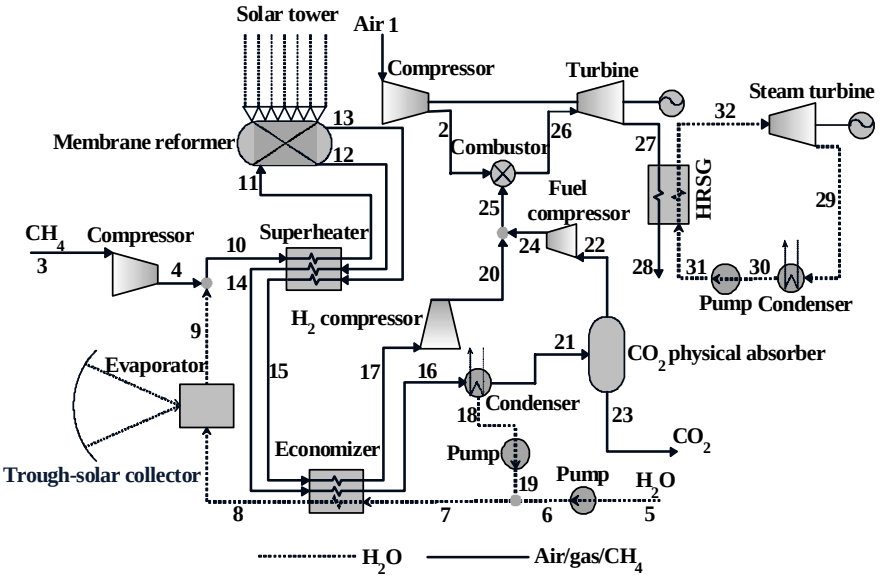

Fig. 3. Schematic diagram of LEHSOLCC system

3. Computation model and its validation

3.1. Main assumptions for the simulation

The cycles presented in the paper are modeled in ASPEN PLUS process simulation software [13]. The component models are based on the energy balance, mass balance, and species balance, with a default relative convergence error tolerance of 0.01%, which is the specified tolerance for all tear convergence variables. The RK-SOAVE and STEAM-TA thermodynamic models are selected for the thermal property calculations. The membrane reactor is modeled with a combination of Gibbs Reactor and Component Separator available in the ASPEN PLUS model library. The Gibbs Reactor determines the equilibrium conditions by minimizing Gibbs free energy, and the Separator specifies flow split fractions. The hydrogen permeation is a complex function of the partial pressure difference across the membrane and is therefore modeled with a Fortran subroutine. By assuming a certain permeability, membrane thickness and membrane area, the permeation rate can be calculated with an iterative procedure. This approach does not capture the change in flux along the length of the membrane tube, so the average flux is therefore approximated by the logarithmic mean of the flux at the inlet and outlet of the reactor [14], then it determines methane conversion and hydrogen recovery. In the solar block, the low temperature solar field is assumed to be installed with parabolic trough direct steam generation collector (DSG) [15], and the middle temperature one is with solar tower [15].

The CO_2 physical absorption in the hybrid system is based on a model developed by Lozza and Chiesa [16] using the Selexol [17] absorption medium. A conventional gas-steam combine cycle system with post-combustion decarbonization is also simulated for the purpose of performance comparison, in which CO_2 capture is accomplished using a chemical absorption process (with monoethanolamine (MEA) [18] as the absorbent). Steam is extracted from the steam turbine for the absorbent regeneration, the corresponding energy and steam demands are calculated based on the given composition of the process gas. The most relevant assumptions are summarized in Table 1.

Table 1. Main assumptions for the simulation and calculation

	Parameters	Value	Source
Gas turbine	Inlet pressure	1300°C	GT Word 2010 [20]
	Isentropic efficiency	88%	GT Word 2010 [20]
Combustor	Pressure drop (of inlet pressure)	3%	Ertesvåg et al, 2005 [21]
Heat exchanger	Minimum temperature difference	15°C	Ertesvåg et al, 2005 [21]
	Pressure loss	3%	Ertesvåg et al, 2005 [21]
Steam turbine	HP steam pressure	111bar	Ertesvåg et al, 2005 [21]
	RH/IP steam pressure	27bar	Ertesvåg et al, 2005 [21]
	LP steam pressure	4bar	Ertesvåg et al, 2005 [21]
	Condensing pressure	0.06bar	Ertesvåg et al, 2005 [21]
	HP/RH steam temperature	560°C	Ertesvåg et al, 2005 [21]
HRSG	Pinch-point temperature difference	15°C	Ertesvåg et al, 2005 [21]
	Cold side pressure drop	5%	Ertesvåg et al, 2005 [21]
	Minimum stack temperature	85°C	Ertesvåg et al, 2005 [21]
Pump	Efficiency	85%	Ertesvåg et al, 2005 [21]
Parabolic trough solar collector	Solar collector temperature	~200°C	Zhang et al, 2012 [5]
	Solar collector efficiency	62%	Zhang et al, 2012 [5]
	Minimal temperature difference	20°C	Zhang et al, 2012 [5]
Solar tower	Solar collector temperature	~550°C	Solúcar et al 2006 [16]
	Solar collector efficiency	65%	Solúcar et al 2006 [16]
	Minimal temperature difference	20°C	Solúcar et al 2006 [16]
	Direct solar radiation	940 W/m^2	Solúcar et al 2006 [16]
Membrane reformer	Reaction Pressure	9bar	Chen et al, 2008 [9]
	Pressure drop	5%	Chen et al, 2008 [9]
	Reaction temperature	550°C	Chen et al, 2008 [9]
	Steam-to-carbon ratio	3.5	Chen et al, 2008 [9]
	Membrane thickness	4μm	Chen et al, 2008 [9]
Physical absorption	CO_2-to-SELEXOL mole ratio in absorbent	0.1	Lozza et al, 2002 [17]
	Number of flash chambers	4	Lozza et al, 2002 [17]
	Last chamber pressure	to obtain 95% CO_2 removal	Lozza et al, 2002 [17]
	Number of intercoolers for CO_2 compressor	3	Lozza et al, 2002 [17]
Chemical absorption	CO_2-to-MEA mole ratio in absorbent	0.15	Lozza et al, 2002 [17]
	Minimum temperature difference at solution regenerator	10°C	Lozza et al, 2002 [17]
	Stripping pressure	1.01bar	Lozza et al, 2002 [17]
	Steam supply	3 bar	Lozza et al, 2002 [17]
	Temperature difference in reboiler	5°C	Lozza et al, 2002 [17]
	Max. gas pressure drop in absorber/stripper	4/10 kPa	Lozza et al, 2002 [17]
	Number of intercoolers for CO_2 compressor	2	Lozza et al, 2002 [17]

3.2. Validation of palladium membrane reactor

The performance of methane reforming in Pd membrane reactor mainly depends on the membrane structure and material, catalyst and working conditions (reaction temperature, reaction pressure,

steam-to-carbon molar ratio, sweep gas flux, inlet gas velocity, etc.). The Pd membrane and nickel-based catalyst are characterized by high H_2 permeance and fast kinetics, respectively. We consider in this paper only the influence of reaction conditions on the reaction performance. Figure 4 illustrates the influences of reaction temperature, pressure and steam-to-carbon ratio on methane conversion and CO selectivity at fixed gas velocity. Experimental data [9] and simulation result are plotted by dashed lines and solid lines with symbol, respectively, at the same working conditions. It can be seen that the simulation data and experiment results are in good agreement. Due to the instabilities of the experimental conditions, the experimental data of CH_4 conversion is slightly lower, and CO selectivity is higher than their corresponding simulation results, but all the relative differences are within 3%.

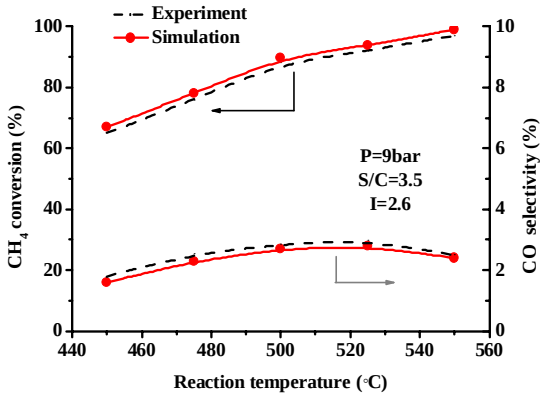

(a)

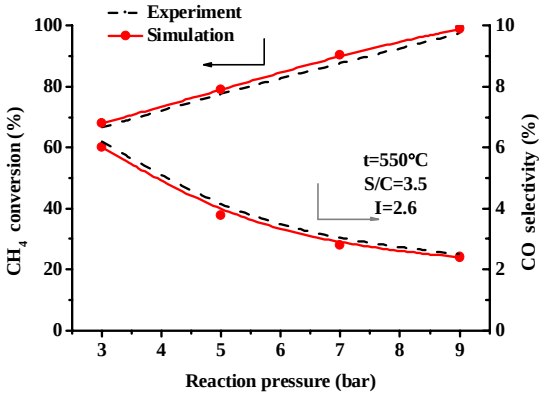

(b)

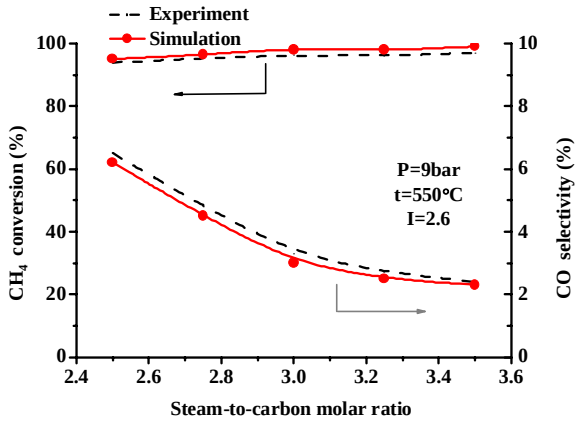

(c)

Fig. 4. Effects of working conditions on reaction performance: a) Reaction temperature, b) Reaction pressure, c) Steam-to-carbon molar ratio

Limited by both the reaction kinemics and membrane high temperature properties, membrane reaction is normally performed in the 450~600^{o}C range. As shown in Fig. 4, CH_4 conversion monotonically increases along with temperature in the calculated range. High temperature favors methane conversion and H_2 permeation, leading to high separation efficiency. Meanwhile, the behavior of H_2 permeation pulls the reaction towards the product direction, offsets the negative effect of high temperature on the shift reaction, and thus efficiently suppresses CO formation. A non-monotonic variation of CO selectivity is observed. CO selectivity first increases with reaction temperature, and then slightly decreases.

High reaction pressure is disadvantageous to CH_4 conversion in terms of thermodynamic equilibrium, but it results in a higher H_2 partial pressure in the reaction zone, and subsequently a higher driving force for H_2 permeation. Therefore, the influence of pressure is a compromise between the these two effects. It can be seen that CH_4 conversion increases and CO selectivity decreases monotonically, as the reaction pressure is varied from 3 to 9bar, indicating that the membrane permeation dominates the reaction performance.

To avoid carbon deposition, steam-to-carbon molar ratio higher than 2.5 is necessary [21], high steam addition is also favor of the methane reforming and CO shift reactions. The presence of large amount steam, however, may dilute H_2 in the reaction zone and thus hinder H_2 permeation. In the range of 2.5 to 3.5, CH_4 conversion rate grows slowly and CO formation can be suppressed efficiently, as shown in Fig. 4(c).

3.3. Gas turbine cooling model

High-temperature gas turbine performance levels are very sensitive to blade cooling requirements. In the present study, a closed-loop steam cooling (CLSC) solution is selected. The needed coolant is extracted from the high pressure steam turbine outlet, the remaining turbine exhaust steam is returned to the HRSG for reheating. After cooling the stationary and rotary hot components, the steam reaches, in practice, the reheating temperature. It is then mixed with the reheated steam from the HRSG and introduced into the intermediate pressure steam turbine section for expansion. To analyze the global performance of the cycle under investigation, a discrete (rather than differential field) model is used because of its computational convenience. The cooled turbine model with CLSC presented in previous study [22], and the refined versions of the model by Louis et al. [23] and Horlock et al. [24], is considered. It considers the turbine stage by stage, and estimates the cooling flows necessary for the stator and rotor at each stage. The stator flow is assumed to exchange heat with the main gas flow prior to flowing through the turbine, i.e., the heat exchange happens before power extraction. The rotor coolant flow cools the main stream at the rotor exit (after power extraction).

For each cooling step, the required coolant mass flow is calculated as:

$$\frac{m_c}{m_g} = 0.0156 \cdot \frac{(T_g - T_b) \cdot C_{pg}}{\varepsilon \cdot (T_b - T_c) \cdot C_{pc}}, \qquad (1)$$

where subscripts g and c refer to the main gas stream and the coolant stream, respectively. ε refers to blade cooling efficiency. For an advanced power generation gas turbine system, commonly used value for ε is 0.3. The symbol T_b refers to the turbine blade metal temperature; its value in this study is 1123K (850°C) and is kept constant in the calculation, which is validated by calibrating the model against the published performance data in [22]. The turbine in the cycle mentioned in this paper is divided into 4 stages assuming equal enthalpy drops and the first 2 stages are cooled.

4. System performance analysis and comparison

4.1. Performance criteria

The thermal efficiency of the system is defined as:

$$\eta_{th} = \frac{W_{net}}{Q_f + Q_{sol}} = \frac{W_{netl}}{m_f \cdot LHV + Q_{sol}}, \qquad (2)$$

where W_{net} is the system net power output, LHV is the fuel low heating value input, Q_{sol} is the absorbed solar heat.

Since the system input resources involve the methane chemical exergy and solar thermal energy, which is different in their energy qualities, exergy efficiency is more suitable than energy efficiency for the system performance evaluation. Assuming that methane chemical exergy is approximately equal to 1.04 times its lower heating value LHV, and the solar thermal exergy corresponds to the maximal work availability between solar collector temperature T_{sol} and ambient temperature T_0, i.e., $Q_{sol} \cdot (1\text{-}T_0/T_{sol})$. Therefore, the definition of system exergy efficiency is given as follows:

$$\eta_e = \frac{W_{net}}{E_f + Q_{sol}(1-T_0/T_{sol})} = \frac{W_{net}}{1.04 m_f \cdot LHV + Q_{sol}(1-T_0/T_{sol})}. \qquad (3)$$

The contribution of the low/mid temperature level solar heat can be measured by its share in the system total energy input:

$$X_{sol} = \frac{Q_{sol}}{Q_f + Q_{sol}} = \frac{Q_{sol}}{m_f \cdot LHV + Q_{sol}}. \qquad (4)$$

To evaluate the performance of the solar heat conversion in the proposed system, the net solar-to-electricity efficiency based on reference [3] is defined as:

$$\eta_{sol} = \frac{W_{net} - W_{ref}}{Q_{rad}} = \frac{W_{net} - Q_f \eta_{th,ref}}{Q_{rad}}, \qquad (5)$$

where $W_{ref} = Q_f \cdot \eta_{th,ref}$ is the net power output generated by a reference system with the same natural gas input. Here, a conventional natural gas fired gas-steam combined cycle power plant (CC) and a CC system with CO_2 separation from the exhaust gas (CC-Post) are chosen as reference systems.

The fossil fuel saving levels in comparison with the reference power plant, for generating the same amount of electricity, is defined as the fossil fuel saving ratio:

$$SR_f = \frac{W_{net}/\eta_{th,ref} - Q_f}{W_{net}/\eta_{th,ref}} = 1 - \frac{Q_f \cdot \eta_{th,ref}}{W_{net}}. \qquad (6)$$

4.2. System performance and discussions

4.2.1 Overall performance comparison and discussion

Using the computational assumptions and models given in section 3.1, LEHSOLCC, CC and CC-Post systems are simulated on the same basis. The main process stream data for LEHSOLCC are shown in Table 2 and the thermodynamic performance of the three systems are summarized and compared in Table 3.

It is observed that the solar heat introduced in LEHSOLCC cycle contributes 28.2% of the system total energy input, leading to a significantly increase in net power output. 31.2% and 16.4% reduction of fossil fuel input is obtained for producing the same amount of electricity in comparison with the CC-Post and CC systems, respectively. The specific CO_2 emission is 25 g/kWh, lower by

38% than that emitted by the CC-Post system at the same level of CO_2 capture rate (90%) due to the more net power output. Compared with a CC system at the same technical level and without CO_2 capture, the hybrid system has a lower thermal efficiency by 8.4%-points. The thermal efficiency penalty is due to not only power consumption for CO_2 capture and compression, but also the solar heat input, since the solar-alone system at the same collecting temperature level has a much less thermal efficiency. The second law efficiency is obviously more proper to evaluate energy system with multiple energy resources. Solar contribution at lower temperature is much lower from the view point of the second law efficiency. Evaluated by the exergy efficiency, the hybrid system is even comparable with the CC system without CO_2 capture, embodying advantages of system integration and cascade utilization of multiple energy resources.

Compared with a CC-Post system, the hybrid system exhibits better performance in terms of both thermal efficiency (by 2%-points) and exergy efficiency (by10%-points).

Table 2. Main stream states of the LEHSOLCC system (points refer to Fig.3)

point	*t* (°C)	*p* (bar)	*m* (kg/s)	Percent molar composition (%)							
				N_2	O_2	CH_4	H_2O	CO_2	CO	H_2	Ar
1	15	1	1.097	77.3	20.74		1.01	0.3			0.92
2	421.8	16.6	1.097	77.3	20.74		1.01	0.03			0.92
3	15	5	0.02			100					
4	74.2	10.06	0.02			100					
5	15	2	0.045				100				
7	15	10.59	0.08				100				
9	180.1	10.06	0.08				100				
11	530	9.76	0.1			22.2	77.8				
12	550	9.27	0.091			0.4	56.7	35.5	0.9	6.6	
13	550	4.6	0.01							100	
16	142.8	9.09	0.091			0.4	56.7	35.5	0.9	6.6	
17	142.8	4.51	0.01							100	
20	399.2	20.75	0.01							100	
21	35	9	0.055			0.8	0.1	81.8	1.9	15.3	
24	122.4	20.75	0.004			3.8	0.1	18.4	8.9	68.8	
26	1300	16.268	1.111	72.37	13.16		13.31	0.3			0.86
27	614.4	1.05	1.111	72.37	13.16		13.31	0.3			0.86
28	100.1	1.01	1.111	72.37	13.16		13.31	0.3			0.86
29	36.2	0.06	0.191				100				
32	560	111	0.191				100				

Table 3. Systems performance comparison

Items	LEHSOLCC	CC-Post	CC
Methane exergy input [kJ/mol - CH_4]	830.2	830.2	830.2
Low temperature solar heat input [kJ/mol - CH_4]	126.2	-	-
Low temperature solar exergy input [kJ/mol - CH_4]	43.4	-	-
Middle temperature solar heat input [kJ/mol - CH_4]	189.7	-	-
Middle temperature solar exergy input [kJ/mol - CH_4]	121	-	-
Steam/methane molar ratio	3.5	-	-
Solar thermal share [%]	28.2	-	-
Solar to power efficiency [%] reference to CC-Post	36.4	-	-
Solar to power efficiency [%] reference to CC	19.2	-	-
Fossil fuel saving ratio [%] reference to CC-Post	31.2	-	-
Fossil fuel saving ratio [%] reference to CC	16.4	-	-
CO_2 removal rate [%]	91	90	-
Specific CO_2 emission [g/kWh]	25	40.3	331.3

CO_2 compressor [kJ/mol-CH_4]	13.5	13	-
Net power output [kJ/mol-CH_4]	576.7	396.5	481.7
Exergy efficiency [%]	58	47.8	58
Thermal efficiency [%]	51.6	49.4	60

4.2.2 Parametric analysis

A sensitivity analysis of some key reaction parameters has been performed to quantitatively illustrate their effects on system performance. Figures 5 to 7 depict the effect of reaction temperature (Fig. 5), reaction pressure (Fig. 6) and steam-to-carbon molar ratio (Fig. 7) on solar thermal share, solar-to-electricity efficiency, fossil fuel saving ratio, system exergy efficiency and CO_2 capture rate, respectively.

As mentioned before, in the 450~550^oC temperature range, an increase in reaction temperature monotonically elevates CH_4 conversion, leading to an increasing demand of solar heat input and saving of fossil fuel. CO_2 capture rate increases as well because of higher CH_4 conversion. The energy consumption for CO_2, H_2 and syngas compression also increases. On the whole, the influence of reaction temperature on system efficiencies appears to level off.

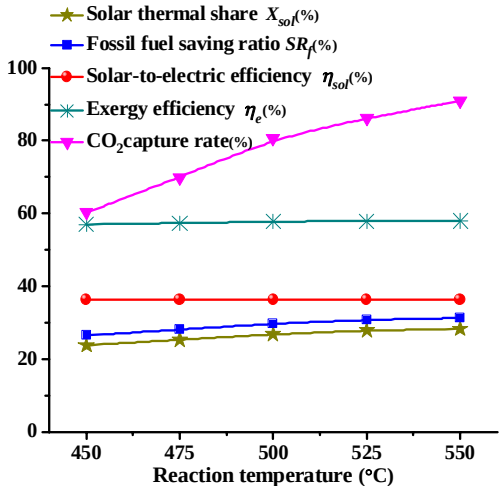

Fig. 5. Influence of reaction temperature on system performance

The effect of reaction pressure on system performance exhibits the similar trends as that of reaction temperature as shown in Fig. 6(a). As mentioned before, higher pressure on one side hinders the reforming reaction, it on the other side boosts membrane permeation, and the later dominates in the present study, an enhancement of CH_4 conversion rate is thus observed. In case of enhanced steam pressure, as shown in Fig. 6(b), the low-temperature solar heat input diminishes due to a decrease in vaporization latent heat; the middle-temperature one for the reforming reaction predominately increases, leading to the increase of overall solar input share.

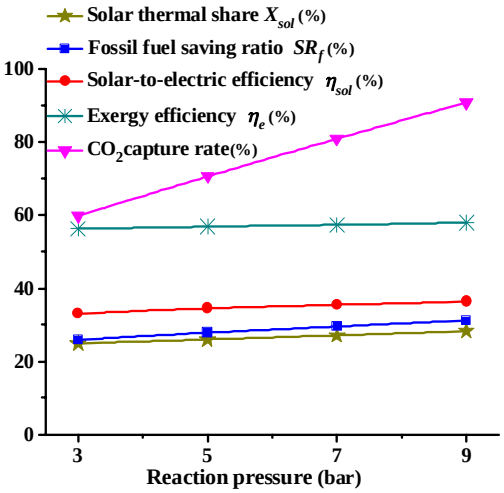

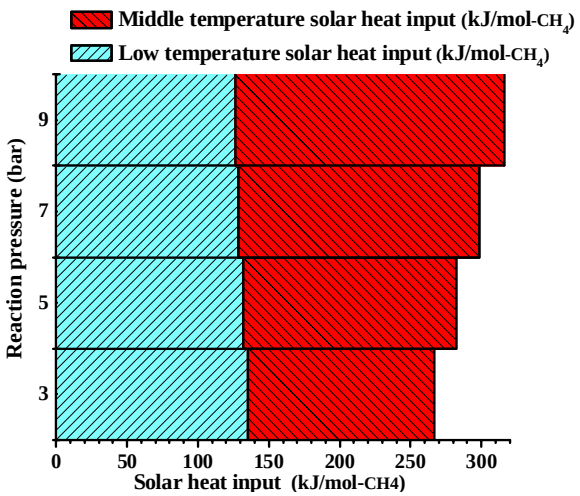

(a) *(b)*

Fig. 6. Influence of reaction pressure on system performance

At temperature of 550°C and pressure of 9bar, an enhancement in CH_4 conversion and CO_2 capture rate are observed as more reforming water is brought into the system. Solar thermal energy input increases in both water evaporation section and reforming section. Most of the imported water will be discharged in the subsequent condensation process, the working fluid mass flow rate increases slightly and yields an augment of power output. Solar-to-electricity efficiency and exergy efficiency drop slightly owning to a large solar heat input. It is noteworthy that higher steam-to-carbon ratio is not applicable, because the presence of large amount of steam causes a decline in H_2 partial pressure in the reaction zone, thus weakens reaction and system performance. However, a steam-to-carbon molar ratio more than 2 is required to avoid carbon deposition.

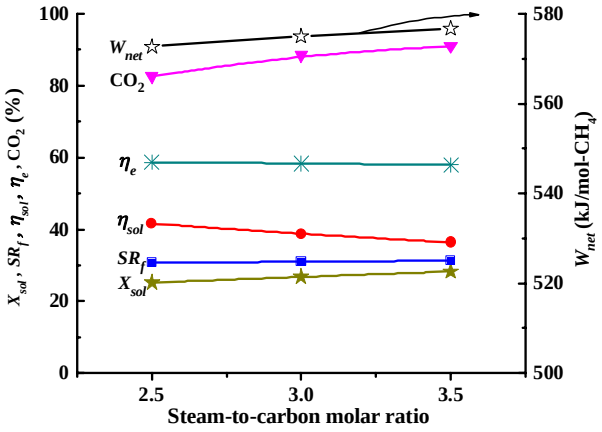

Fig. 7. Influence of steam-to-carbon molar ratio on system performance

5. Technical considerations

The hybrid power system proposed in this paper has two input resources: fossil fuel and solar heat. Solar radiation, however, is not a continuously available resource like a fossil fuel. In most of the cases, a thermal storage system or a fossil fuel backup system is needed to prolong the operation hour. In the proposed system, rather than fuelling the power block directly, the solar heat is used at low/mid temperatures to contribute to the production of syngas that can then be burned to produce heat at the high temperature for high efficiency power generation. Advantages of this concept are that it has storage capability for solar energy chemically (rather than thermally) and physical independence of the solar block to the power system, i.e., the solar assistant chemical conversion can be processed separately in the most suitable site. To ensure a stable operation, more than one solar part can be adopted to match one power block. In this case, a syngas storage subsystem is essential instead of a conventional solar heat storage system. In addition, the combined cycle can run with regular natural gas when solar heat is not available.

A parabolic trough direct steam generation collector (DSG) may be used to provide heat at ~200°C for water evaporation in order to eliminate the costly synthetic oil, intermediate heat transport piping loop and oil-to-steam heat exchanger. For middle temperature solar heat collection at 500 °C, solar tower technology is considered for the thermo-chemical solar-fuel conversion. Because of the instability and discontinuousness of solar radiation, a dynamic analysis is definitely of major importance, which evaluates performance of hybrid power plants and the compares with fossil fuelled ones from a dynamic point of view, considering the daily and seasonal variability of the

solar source and referring the results to a yearly basis. This paper focused primarily the system integration concept and the design point performance.

6. Conclusion

A novel solar-assisted hybrid system integrated with methane steam reforming and membrane separation (LEHSOLCC) has been proposed and investigated. The system mainly consists of a gas-steam combined cycle, a solar-driven membrane reformer and CO_2 absorption components. The introduction of membrane reformer breaks the limitation of temperature on reaction conversion rate and achieves a nearly full methane conversion at middle temperature. Integrated with energy conversion, CO_2 convergence and capture is accomplished with low energy penalty.

By providing heat to the endothermic methane steam reforming, solar heat collected at 550^{o}C is converted into reformed syngas chemical energy; and then released as high-temperature thermal energy in the advanced combined cycle system for power generation, thus achieving a high-efficiency heat-power conversion. The produced pure H_2, collected at the permeate side of the membrane reactor, fuels a gas/steam combined cycle. The leftover CO_2 enriched gas in the retentate zone is processed with pre-combustion decarbonization. To reduce the exergy destruction, special attention is paid to the thermal match of the internal heat recuperation, as well as to the thermo-chemical match between the solar heat and the reforming process.

The system is simulated and compared with a conventional natural-gas fired gas-steam combined cycle power plant (CC), a CC with CO_2 capture from exhaust (CC-Post). The results show that with 91% CO_2 captured, the specific CO_2 emission in the hybrid system is 25 g/kWh, lower than that in the CC-Post cycle by 36%. Exergy efficiency of 58% and thermal efficiency of 51.6% can be obtained, 10.2%- and 2.2%-points higher than the CC-Post cycle, respectively. Fossil fuel saving ratio of 31.2% is achievable with a solar thermal share of 28.2%, and the net solar-to-electricity efficiency, based on the gross solar heat incident on the collector, is about 36.4% compared with the CC-Post cycle with equivalent CO_2 removal rate. The effects of some key parameters on system performance have also been investigated.

Acknowledgments

The authors gratefully acknowledge support of the Chinese Natural Science Foundation Project (No. 51076152) and the National Key Fundamental Research Project (No. 2010CB227301).

Nomenclature

DNI direct solar radiation, W/m^2

E exergy, kW

LHV methane low heating value input, kJ/kg

m_f methane mass flow rate, kg/s

Q heat, kW

SR_f fossil fuel saving ratio

T temperature, ^{o}C

W_{net} net power output, kW

X_{sol} solar thermal share

Greek symbols

η_{col} solar collector efficiency

η_e system exergy efficiency

η_{sol} net solar-to-electricity efficiency

η_{th} system thermal efficiency

Subscripts and superscripts

a Air

f Fossil fuel

ref Reference system

rad Radiation

sol Absorbed solar heat

0 Ambient state

References

[1] Lewis NS., Toward cost-effective solar energy use. Science 2007; (315): 798-801.

[2] Jin H., Lin R., Cascade energy utilization and gas turbine integrated energy system. Beijing: Science Press; 2008.

[3] Hong H., Jin H., Ji J., Wang Z., Cai R., Solar thermal power cycle with integration of methanol decomposition and middle-temperature solar thermal energy. Solar Energy 2005; 78: 49-58.

[4] Tamme R., Buck R., Epstein M., Solar upgrading of fuels for generation of electricity. ASME Trans. Journal of Solar Energy Engineering 2001; 123: 160-3.

[5] Zhang N., Lior N., Use of low/mid-temperature solar heat for thermochemical upgrading of energy, part I: application to a novel chemically-recuperated gas-turbine power generation (SOLRGT) system. ASME J. of Engineering for Gas Turbines and Power (in press), 2012.

[6] Li Y., Zhang N., Cai R., Parametric sensitivity analysis of an SOLRGT system with the indirect upgrading of low/mid- temperature solar heat. Applied Energy (in Press), 2012.

[7] Zhang N., Lior N., Luo C., Use of low/mid-temperature solar heat for thermochemical upgrading of energy, part II: a novel zero-emissions design (ZE-SOLRGT) of the solar chemically-recuperated gas-turbine power generation system (SOLRGT) guided by its exergy analysis. ASME J. of Engineering for Gas Turbines and Power (in press), 2012.

[8] Luo C., Zhang N., Zero CO_2 Emission SOLRGT Power System. ECOS2011: Proceedings of the 24th International Conference on Efficiency, Cost, Optimization, Simulation, and Environmental Impact of Energy Systems; 2011 July 4-7; Novi Sad, Serbia. Energy (in press), 2012.

[9] Chen Y., Wang Y., Xu H., Xiong G., Efficient production of hydrogen from natural gas steam reforming in palladium membrane reactor. Applied Catalysis B: Environmental 2008; 80: 283-94.

[10] Chen Y., Wang Y., Xu H., Xiong G., Integrated one-step PEMFC-grade hydrogen production from liquid hydrocarbons using Pd membrane reactor. Ind. Eng. Chem. Res. 2007; 46(17): 5510-5.

[11] Jordal IK., Bredesen R., Kvamsdal HM., Bolland O., Integration of H_2-separating membrane technology in gas turbine processes for CO_2 capture. Energy 2004; 29: 1269-78.

[12] Iulianelli A., Manzolini G., De Falco M., Campanari S., Longo T., Liguori S., Basile A., H_2 production by low pressure methane steam reforming in a Pd-Ag membrane reactor over a Ni-based catalyst: Experimental and modeling. International Journal of Hydrogen Energy 2010; 35: 11514-24.

[13] Aspen Plus®. Aspen Technology, Inc., Version 11.1[EB/OL]-Available at:< http://www.aspentech.com/> [accessed 5.1.2009].

[14] Myers DB., Ariff GD., James BD., Lettow JS., Thomas CE., Kuhn RC,. Cost and performance comparison of stationary hydrogen fuelling appliances. Arlington, VA: National Renewable Energy Laboratory, DTI; 2002 Report No.: NREL/CP-610-32405.

[15] Zarza E., Rojas M., González L., INDITEP: The first pre-commercial DSG solar power plant. Solar Energy 2006; 80: 1270-6.

[16] Solúcar et al., 10MW solar thermal power plant for southern Spain. 2006 Nov. Technical Project No.: NNE5-1999-356.

[17] Lozza G., Chiesa P., Natural gas decarbonization to reduce CO_2 emission from combined cycles. Part 1: partial oxidation. ASME Journal of Engineering for Gas Turbines and Power 2002; 124: 82-8.

[18] Krzysztof L., Andrzej Z., Comparative analysis of energy requirements of CO_2 removal from metallurgical fuel gases. Energy 2007; 32: 521-7.

[19] Alie C., Backham L., Croiset E., et al., Simulation of CO_2 capture using MEA scrubbing: a flow-sheet decomposition method. Energy Conversion and Management 2005; 46: 475-87.

[20] Gas turbine world 2010 handbook. USA: Pequot Publishing, Inc.; 2010.

[21] Ertesvåg IS., Kvamsdal HM., Bolland O., Exergy analysis of a gas turbine combined-cycle power plant with pre-combustion CO_2 capture. Energy 2005; 30(1): 5-39.

[22] Jørgensen SL., Nielson PEH., Lehrmann P., Steam reforming of methane in a membrane reactor. Catal. Today 1995; 25:303-7.

[23] Sanjay., Singh O., Prasad BN., Influence of different means of turbine blade cooling on the thermodynamic performance of combined cycle. Applied Thermal Engineering 2008; 28: 2315-26.

[24] Louis JF., Hiraoka K., El-Masri MA., A comparative study of influence of different means of turbine cooling on gas turbine performance. GT1983: ASME international gas turbine conference; 1983 Mar 27; Phoenix, AZ, USA. ASME Paper: 83-GT-180.

[25] Horlock JH., Watson DT., Jones TV., Limitation on gas turbines performance imposed by large turbine cooling flows. ASME J. of Engineering for Gas Turbines and Power 2001; 123: 487-94.

Low Exergy Solutions as a contribution to climate adapted and resilient power supply

Stefan Gößling-Reisemann[a], Thomas Blöthe[b]

[a] *University of Bremen, Bremen, Germany, sgr@uni-bremen.de*

[b] *University of Bremen, Bremen, Germany, bloethe@uni-bremen.de*

Abstract:

The focus of our research within the climate adaptation project *nordwest2050* is on how the energy system in the metropolitan region Bremen-Oldenburg can be developed in order to maintain system services under climate change conditions and further uncertain and turbulent boundary conditions. To answer this question, we examined and evaluated currently emerging and already existing technologies. We conducted an innovation potential analysis and identified two promising innovative fields, which we call „Low Exergy Solutions", and „Resilient Energy Infrastructures". Low Exergy Solutions are characterized by the use of low exergetic ambient energy sources, or residual- and waste streams and their contribution to various energy services. Low Exergy Solutions are thus systems of matching technologies consisting of three components: an exergy source, a conversion technology and an energy service being delivered. The technologies are using waste heat and sources of material residues not currently used, thereby linking consumers and producers in regional and local networks contributing to a decentralized energy system. As a trivial example, waste heat sources with low temperature can be used for nearby space heating and other services like drying. Heat sources with higher temperatures can be used for electricity production or cooling, also across medium distances. Geothermal reservoirs can be used for local cooling and air conditioning. Results from our innovation potential analysis further show that Low Exergy Solutions contribute to climate adaptation in several ways, e.g. by decreasing the load on the electricity grid, or by providing alternatives for vulnerable energy imports. They could also make use of climate change opportunities, like increased solar heat potentials. By enlarging the diversity of the overall energy supply and by adding flexibility and redundancies, they also increase the resilience of the energy supply system.

Keywords:

Climate adaptation, Resilience, Exergy, Renewable Energy

1 Introduction

The results described here are based on work done within the climate adaptation project *nordwest2050* in the Northwest of Germany[1]. The original task was to find innovations in the energy supply system that address the climate change impacts on the system. Very soon in the process it became obvious that climate change is only one of the major uncertainties that the German energy system, and with it the Northwestern subsystem, will be experiencing in the future. The German government's decision to abandon nuclear power and its goal to have 35% of gross electricity consumption and 18% of gross energy consumption from renewable production by 2020 [1] currently alters the German energy supply system considerably. The common denominator of the coming climate change impacts and the current turbulent dynamics of the energy transition are the uncertainties surrounding them. It thus seemed wise, to not just search for innovations in the energy supply system that address climate change, but to develop design guidelines for an energy supply system that is better equipped to cope with turbulence and uncertainties. The research setup of our project was then adjusted and now incorporates

[1] See http://www.nordwest2050.de

- a two-fold **vulnerability assessment**: one with the explicit focus on climate change impacts and one with a focus on the general vulnerability of the Northwest German energy supply system
- an **innovation potential analysis** with a focus on regional innovation demands and regional potentials
- the development of **design guidelines for resilient energy systems**, i.e. systems that maintain their system services even under strong external disturbances and internal failures
- the implementation of **region specific demonstrators** to show the feasibility of short-term adaptation and resilience building
- the participatory design of a **"Roadmap of Change"** for the region, not only limited to the energy sector, but also including other sectors of the economy

The overall objective of the energy related activities in this project is to find design guidelines for the whole regional energy system. Naturally, individual analysis of technologies will have to be concise and geared towards the integration into the existing energy system and towards structural changes in the current setup. The project nordwest2050 therefore encompasses analysis and design on multiple levels of the energy system: supply chains, regional governance systems, societal needs and perceived risks, environmental impacts, conflicts with other sectors, and, of course, technologies. The results presented here should be seen in this context: as part of a larger regional transformation process which includes technological aspects as much as innovation aspects and aspects of economic feasibility and social acceptance.

In this paper, we will mainly present results from the vulnerability assessment, its consequences for the adaptation demands and innovation needs in the region, the concept of resilient energy systems and present one of the identified innovation fields for climate adaptation and resilient energy systems which we call "Low Exergy Solutions". The aim of this paper is to show how climate adaptation, building resilient energy systems and climate mitigation can simultaneously be addressed by a set of technologies chosen on the basis of scientific analysis and a guiding concept inspired by natural systems.

2 Resilient energy systems

Our understanding of a resilient energy system is based on the work by ecosystem theorists Holling, Gundersson and others [2][3][4]. There is no unique definition of resilience, so we adopted an ecosystem based definition from [5]

> Resilience „reflects the capacity (i. e. the underlying mechanisms) of [eco]systems to maintain service in the face of a fluctuating environment and human perturbation" [3][4][5]

For socio-technical systems we translated this into our definition of resilience:

> Resilience describes the ability of a system to maintain its services under stress and in a turbulent environment, i.e. even in the face of massive external perturbations and internal failures [6].

In the theoretical discussion of the resilience concept, we identified several design elements of socio-technical systems that help increase their resilience [7]:

Table 1. Design Elements for resilient socio-technical systems (abstract level)

System capabilities	System resources availability	System structure
• Adaptability • Resistance • Creativity and Design	• Energy and material • Information • Finances	• Diversity • Redundancy and modularity • Balance of positive and negative feedback mechanisms • Buffers and storage • Dampers and attenuators

These design elements can be applied to energy supply systems to direct innovations towards a more resilient design of such systems. Resilience in this sense is used as a "Leitkonzept" (guiding concept). The rather abstract design elements can further be broken down into more system specific, e.g. "Creativity and Design" translates to "Open Interfaces" in the case of resilient energy systems, meaning the ability of a resilient system to allow the integration and flexible combination of several energy carriers and infrastructure systems (gas, water, district heat, etc). The set of energy specific design elements constitutes the "Gestaltungsleitbild" (design guiding concept) of what we call *resilient energy systems*. The guiding concept should not be taken as an analytical metric. It rather points the search for innovation into a specific direction. To give an example, the diversity of an energy system is a function of the diversity of the resources it is able to use (resource diversity) as well as the diversity of the technologies comprising the system. On the resource side, a system is more resilient, the more resources it can access. Thus, innovations that enable the system to access currently unused or underutilized resources, increase the resilience of the system. The full evaluation of an innovation is however not limited to the resilience increasing effects. Other factors, like environmental risks, economic feasibility etc. have to be taken into account (see section 4). More on the use of guiding concept of resilience can be found in [7].

3 Vulnerability of the energy supply system in Germany's Northwest

In order to determine innovations enabling the adaptation of the energy supply system in Germany's Northwest to climate change, a first step was to assess the vulnerability of the system. As mentioned in the introduction, it soon became obvious that climate change is only but one of the many changes that the energy supply system is facing, all characterized by high uncertainties and possible elements of surprise. In order to analytically capture the vulnerability related to these uncertainties and surprise, we altered our vulnerability assessment by distinguishing between climate related vulnerabilities and structural vulnerabilities. Climate change vulnerabilities correspond to potential impacts from climate change, while structural vulnerabilities correspond to weak spots in the architecture of the system that make it more vulnerable to internal failures or external shocks. Without going into the details[2], a typical example for a structural vulnerability is the missing mechanism for dealing with conflicts resulting from an increasing share of renewable in the electricity sector. While e.g. the pressure on land-use in the biomass sector, the conflicts surrounding wind park sites and the issues around the intermittency related grid-stability problems are increasing, there is no consensus and no clear regulation in sight to deal with these problems. This is an architectural flaw which currently poses a threat to the stability and the future pathway of the German energy supply system in general, not just in the Northwestern parts.

[2] See [8] and [9] for a detailed discussion on the vulnerability assessment methodology.

The results of the vulnerability assessment (climate change related and structural) are summarized in Table 2. To understand the results, it is to be noted that high potential impacts and high adaptive capacity cancel each other out, while medium potential impacts can still lead to high vulnerability if adaptive capacity is low.

Table 2. Summary of results from the vulnerability assessment of the energy supply system in the Northwest of Germany. DSM = demand side management.

	Primary energy				Grid-bound energy / distribution		Demand / Applications		
	Coal	Gas	Wind	Biomass	Electric.	Gas	Heat	Cooling	DSM
Pot. impacts (climate)	Low	Low	Low	Medium	Medium	Medium	Medium	Low	Medium
pot. impacts (stuctural)	Medium	Medium	Medium	High	High	Medium	Medium	Medium	Medium
Adaptive capacity	Medium	Medium	High	Medium	Medium	Medium	Medium	Medium	High
Climate Vulnerability	Low	Low	Low	Medium	Medium	Medium	Medium	Low	Low
Structural Vulnerability	Medium	Medium	Low	High	High	Medium	Medium	Medium	Low

The structural vulnerability is generally higher than the climate change related vulnerability. One has to bear in mind though, that due to the chosen definition of structural vulnerabilities, they in some cases include vulnerabilities which result from climate change. From further analysis of the energy supply and electricity generation in the region, we deduced another structural shortcoming of the region's energy supply system: it only has a comparatively low diversity [25]. As a conclusion from this assessment, we identified several priority fields for innovation in the regional energy system:

- Reduce sensitivity, especially by providing long-term political and legal framework (biomass and electricity)
- Install conflict management tools (biomass)
- Increase resource diversity (electricity, gas, heat, cooling)
- Increase share of renewables (electricity)
- Increase storage capacity, strengthen networks and load management (electricity)
- Couple heat sources and cooling services (cooling, DSM)

These recommendations for innovation were the input for a subsequent innovation potential analysis, where regional potentials and demands where combined to derive concrete innovation candidates.

4 Innovation potential analysis

The methodology for the innovation potential analysis (IPA) has been developed within the project nordwest2050 (see [10]). It consists of four stages:

1. System definition: regional scope and cluster definition (here: the energy sector)
2. Identify innovation fields from vulnerability assessment, climate adaptation debate, innovation trends, and guiding concepts (here: resilient energy supply systems)
3. Describe the innovation system, identify and assess innovation capabilities of the regional sector
4. Identify innovation candidates and evaluate based on criteria list, choose candidates for demonstration projects

The regional scope is given by the metropolitan region Bremen-Oldenburg, a European metropolitan region consisting of counties and cities in the Northwest of Germany around the two larger cities of Bremen and Oldenburg (see www.frischkoepfe.de). Within the region, the innovation potential is mainly determined by the regional energy sector and the resources available. On the conventional side, the energy sector is characterized by two large utility companies (EWE AG and swb AG) and further utility companies operating power plants in the region. The electricity generation is currently dominated by hard coal powered conventional power plants, with wind, biomass and solar gaining quickly. The renewable generation, currently mainly wind and biomass, contributes approx. 29% to the electricity being produced in the region with 20% alone from wind and 7% from biomass (biogas plants).

4.1 Innovation needs

There are a few climate change driven innovation necessities for conventional power plants, mostly regarding cooling water availability. However, with the current regulation regime, there are hardly any new power plants being built without additional cooling towers, so that the regional cooling water availability will not pose a serious problem in the future[3]. The wind generation is hardly affected by climate change, except for the increasing likelihood of severe storms, but the climate data on this is inconclusive. The main challenges for the regional energy supply system come from structural problems, as was derived in the vulnerability assessment: especially biomass and electricity generation and distribution are affected by the uncertain regulatory and political framework and by the conflicts around the increasing renewable production and the extension of the grid.

The heat market (mainly natural gas and district heating) is affected by the decreasing number of heating degree days, which makes the extension of grids and the addition of new capacity economically less attractive. For cooling, the situation is somewhat reversed, since regional average summer temperatures are expected to rise by 1-2 degrees Celsius until 2050 and heat waves increase significantly in number, duration and temperature level [9]. With buildings becoming ever better insulated, there is a clear demand for making better use of the increasingly unused heat being generated in the regional energy system. This especially applies to the many hundred biogas plants in the region, which are almost entirely situated in rural areas with only limited connectivity to district or near-range heating networks. One long-term solution for these plants is to separate biogas generation and electricity production by either building raw gas pipelines and satellite plants or by upgrading the raw biogas to natural gas quality and feed it into the dense natural gas grid in the region. For a short term solution, it makes sense to use the heat from biogas plants for other energy services, like cooling, drying, air-conditioning, etc.

[3] This differs from other regions in Germany and Europe, see [11].

4.2 Innovation fields

With the results from the vulnerability assessment and considering the structure of the regional energy system, with its current focus on coal, wind and biomass and a rising share in renewables to come, we have derived two promising innovation fields to increase the resilience of the system:

- Low Exergy Solutions
- Resilient Energy Infrastructure

Both innovation fields address the issues raised by the vulnerability assessment, whether regarding climate change impacts or structural weaknesses and incorporate design elements from the theoretical discussion of resilient energy systems. In essence, they both should reduce the demand on the electricity network, especially in the summer time, provide a richer and more divers resource base, and provide flexibility and adaptability. While Low Exergy Solutions build on low exergetic and currently unused heat and material flows, resilient energy structures are based on interoperability of renewables with the grid, buffering and storage capacities and intelligent management of load and demand. In the following we will focus on the field of low exergy solutions only.

4.3 Low-Exergy-Solutions

The technologies for utilizing low-exergy flows are known for most applications, but they are in different stages of development. Innovation in the use of low-exergy sources is therefore needed mainly in the appropriate connection of previously unused energy sources (such as industrial waste heat, waste water heat, geothermal cooling/heating, material residues, etc.) with well-known conversion technologies (e.g. adsorption chillers, heat pumps, thermoelectric power generation, fermenters, etc.) for the provision of appropriate energy services (such as industrial cooling, air-conditioning, drying, power supply, biogas, etc.). In some cases, the conversion technologies are not yet developed or in the early phase of development, like technologies for using low exergy material flows (agricultural residues, wastes, cellulose-rich substances other than wood etc.)

We have scanned the literature on utilization technologies for low exergy flows and have identified a set of twelve technology components and six systemic combinations with promising potential for increasing the resilience of the regional energy system:

Table 3: Possible technology components and systems within the Low Exergy Solutions innovation field.

Components (sources and conversion technologies)		Systems (providing services)
Comb. heat and power	District heating grid	Biogas plant + CHP– Mobile heat
Solar thermal installations	Geothermal cooling	Biogas plant – raw gas network – satellite CHP – absorption chillers
Industrial waste heat	Long term thermal storage	Agricultural residues – biogas plant – CHP – absorption chillers
Heat pumps	Organic Rankine Cycle	Bio-energy villages (raw gas grid, CHP)
Ad-/Absorption chillers	Mobile heat storage (PCM)	Food residues – biogas plant – CHP – absorption chillers
Cellulose fermenters (RuminoTech)		RuminoTech – raw gas grid – CHP

All technologies and systemic combinations are currently assessed against a set of indicators developed in the context of the regional adaptation project. The innovation indicators include

- Status within the technology diffusion curve
- Climate mitigation potential
- Effect on vulnerability of the regional energy system
- Effect on the resilience of the regional energy system
- Plausibility of the expected effects
- Technical and economic risks
- Transferability

More indicators are currently added and final results will be published on the project website shortly (www.nordwest250.de). The pilot projects discussed below are already evaluated using the above indicators (see appendix for a graphical representation of the results).

4.3.1 Pilot projects

Basically, applications of Low-Exergy-Solutions can be established in the fields of private households, commerce and industry, and also in the public sector. We tried to derive concepts for flagship projects with broad coverage of these areas and high visibility. Since we are striving to derive options for a region wide strategy for resilient energy supply systems, it is important to engage with regional stakeholders in an early phase. The respective stakeholders then also have the best access to the regional application areas and can inform other end-users about such installations. We have started to implement three pilot projects, described below, and will continue to bring together technology developers with potential users and investors to explore the feasibility of a region wide diffusion of innovative Low Exergy Solutions. The pilot projects are accompanied by scientific analysis, e.g. measuring performance and efficiency and economic feasibility, to derive conclusions about the potential contribution of Low Exergy Solutions to a resilient regional energy supply system.

4.3.2 Pilot project 1: Cooling turkey barns and closing energy and material cycles

On an agricultural farmstead in the administrative district of Vechta, the resident farmer operates a turkey breeding facility. On this farm there are 3 turkey barns with each barn being designed for 7000 turkeys. The farmer also operates a biogas plant with a 500 kW_{el} CHP unit. The fermentation substrate of the biogas plant consists of manure from the turkeys and corn cultivated on the farm land. The biogas produced is converted into electricity by the CHP plant. The electricity is currently fed into the public grid and remunerated according to the German feed-in tariffs. The waste heat from the cogeneration units currently heats the fermentation vessel of the biogas plant, the turkey barns and the residential buildings on the farm.

4.3.2.1 Climate change considerations

In the summer, with almost no heating demand in the buildings, the heat from the cogeneration unit is currently expelled to the surroundings. On the other hand, the animals in the barn demand continuous ventilation to dissipate their accumulating body heat. With the climate change noticeably changing summer temperatures, this causes serious problems for the turkey farmer, already now. According to [12] „… a room temperature of 21 °C to 23 °C is sufficient with an

auxiliary heating system. It's also important that the animals are not to be kept warm, since too high house temperatures can speed up the heartbeat and the breathing. This is combined with a high burden on the young tissue, so that later health problems such as abdominal dropsy or bleeding can be the consequence."

In the summer, the rising ambient temperature can lead to an unacceptable increase of the temperature in the turkey barns and the animals are subject to heat stress. Even further rising temperatures can lead to the death of the turkeys, as has already happened in the recent past. With climate change it is to be expected that the mean air temperatures will continue to rise and an increase of heat waves must be expected. This has been confirmed by evaluating regional climate models [9]. A short term adaptation strategy, and implemented in this pilot project, is to air-condition the turkey barns. In the longer term, turkey breeding should be based on better suited living conditions, e.g. in less densely populated barns, to avoid the heat stress problem altogether.

4.3.2.2 Energy considerations

From an energy perspective, this pilot project seeks to demonstrate the possibility of utilizing so far unused heat sources, thereby realizing primary energy savings and closing heat and material cycles. The heat produced by the CHP drives an absorption refrigeration system for the air conditioning of the turkey barns. Approx. 400 kW thermal capacity is available for the refrigeration plant. The heat is delivered to the absorption chiller at a temperature of 95 °C (with 50 °C in the return flow). The chiller delivers cold water at a temperature of 6° C, with 12° C in the return flow. The currently planned cooling unit will use 100 kW of the thermal energy from the CHP plant to produce 70 kW of cooling energy (COP 0.7). The actual exergy efficiency can only be calculated when the plant is operational, but based on the design parameters, and the temperature levels of the heat source and the return flow of the cooling circuit, an estimate can be derived. The exergetic service of the device is the removal of 70 kW of thermal energy from the return flow at 12° C, while the exergetic input is the heat flow of 100 kW into the system at 95° plus the electrical power consumption of about 2 kW. The rational exergetic efficiency of the absorption chiller is then around 0.15. This number could be significantly improved, if the offheat from the CHP could be delivered to the absorption chiller at a higher temperature. This, however, would incur greater investments and is currently not pursued any further. Even without further improvements, the system allows using currently unused heat sources at an affordable cost.

To reduce the peak power of the absorption refrigeration system, a thermal buffer will be included. The air distribution in the stable must be carefully planned so that no "cold-" or "heat islands" be produced, which would have the risk of the animals being excessively cooled or overheated. The cooling capacity for the air conditioning system is laid out to be sufficient even till the end of the fattening period.

4.3.2.3 Regional considerations and potentials

Most absorption cooling units are currently being deployed in the North America and in Asia. However, according to [23] there is a great market potential also in Germany. The food industry in Germany alone operates around 16.500 cooling units, mainly of the compression type, from which a large portion could be substituted with absorption chillers.

With regard to the metropolitan region of Bremen-Oldenburg, there is some relevant potential for combining both of the low exergy sources in this pilot project on a larger scale: using manure for producing biogas and using offheat from the biogas CHP plants for heating and cooling. If all manure in the region was converted in conventional biogas plants, approximately 1700 GWh of electricity and 2600 GWh of thermal energy could be generated annually [26]. The absorption chiller in this example has a COP of about 0.7. So if only 25% of the potential thermal energy from manure driven biogas CHP plants could be used for cooling, using readily available absorption chillers as in this pilot project, cooling services in the order of 455 GWh could be provided. The German cooling demand is around 20,000 GWh per year [29]. Based on the number of people

living in the metropolitan region (2.7 Mio), the regional cooling demand is in the order of 660 GWh, so that approximately two thirds could be generated from this type of offheat. Compared with regular compression chillers (COP around 4), approximately 114 GWh of electrical energy could thus be substituted with offheat.

4.3.3 Pilot project 2: Geothermal cooling of a data center in Bremen

The data center operator Consultix GmbH intends to build a new data center in Bremen. The data center's waste heat must be removed from the buildings to avoid overheating of the equipment. Traditionally, this is achieved by electrically driven (compression) cooling systems. In essence, the waste heat of the servers is expelled to the ambient air by an external dry cooler. Between 50% and 150% of the electricity demand of the servers will be needed in addition in order to supply the necessary cooling [13][30]. High-quality electrical energy (100% exergy) is used to be discarded as waste heat. This is also associated with high costs, of course.

4.3.3.1 Climate change considerations

With increasing cooling needs to be expected in the future due to higher average temperatures and additional heat waves, the above mentioned problem will be aggravated. When this cooling demand is covered by compression refrigeration units, an increasing burden on the electricity grid is to be expected, adding to the already increasing burden from increasing the share of renewables in the grid. Additionally, data center operators are currently competing for the "greenest" solution. Reducing the cooling demand or meeting it in a climate friendly manner is the first and most promising objective in this context. Here, Low Exergy Solutions promise considerable potential for saving energy, reducing carbon emissions, answering the increasing cooling demand from higher temperatures and heat waves and relieving the electricity grid.

4.3.3.2 Technological solution

A natural choice for the cooling system seems to be free cooling. Here, cool air is directly used as a coolant. However, in the summer, at high ambient temperatures this technique does not suffice. An alternative could be cooling using groundwater. In this case problems arise from the aggressiveness of the groundwater and from the high iron content leading to the silting of the installation [13].

As a result, in this pilot project we propose to use geothermal probes. The geothermal probes are housed on the same site as the data center. Geothermal probes provide the possibility for cooling without the use of compression refrigeration units even in the summer. The system is ideally combined with free cooling: as long as the temperature is below 19 °C, the cooling demand is met by using ambient air. When the outside temperature rises beyond that, the waste heat is expelled using geothermal probes in the ground beneath the building. The geothermal probes will extend up to 150 m deep into the earth. In the summer period, approximately 3-4 months, when the ambient temperature is above 19 °C, the geothermal probes can also be used as a heat storage unit. In the winter months it is possible to cool down the soil with the geothermal probes again by using the stored heat for nearby residential buildings, for example. This pilot project is currently in the pre-planning phase, where geothermal surveys and test drillings are made.

4.3.3.3 Energy considerations

Since the data center is still under construction and no measurements of the cooling unit can be taken, an exergetic assessment can only be performed on design data. Towards this purpose, the air temperature in the data center is assumed to be 22° C (T_D), according to specifications regarding the optimal operation of servers. The outside temperature is assumed to be 19° C (T_0), which is the temperature where free cooling is assumed to not suffice to cool the data center. The heat removed from the data center is delivered to the ground at a temperature of 10° C (T_G). Although the ground temperature will not stay constant during the operation, for an estimate of the exergetic efficiency

the assumption should be reasonable. The actual electrical power consumption of the geothermal cooling unit is expected to be in the range from 10 to 20% of the amount of heat to be removed, i.e. the COP is around 5-10. According to the supplier of the geothermal cooling unit this is a rather conservative estimate, depending of course on ground temperature, thermal conductivity, efficiency of the pumps and other factors. With this data, the exergetic service of the unit can be derived as "heat flow Q removed at a temperature of 22° C", i.e. the exergetic service is $Q(1-T_0/T_D)$ while the exergetic input is derived from Q/COP, since only electrical energy is used. The rational exergetic efficiency then is between 0.05 and 0.09, depending on the COP. This seems rather low, but it should be compared to a compression chiller, which operates at a COP between 3 and 5, resulting in rational exergetic efficiencies between 0.03 and 0.05. One could argue, however, that the environment for this cooling unit is not really the ambient air, but the ground at 150 m depths. The reference temperature then becomes T_G and the rational efficiency improves markedly (to values between 0.17 and 0.3) due to the higher exergetic service at the same exergetic expense. If, in a second stage, the stored heat in the ground can be used to heat nearby houses or offices, the exergetic evaluation would have to include these additional services. This analysis will be done once the data center and the cooling unit is operational and measured data is available.

4.3.3.4 Regional considerations and potentials

A typical data center uses about 50% of its electricity consumption for cooling[4]. In 2008, the data centers in Germany used around 10 TWh of electricity [30], of which approximately 5 TWh are for cooling only. With the help of innovative cooling technologies, like the described geothermal cooling, the efficiency of these data centers can be improved significantly. With the above mentioned increase in the COP from 3 (on average) to between 5 and 10, the electricity consumption of data centers in Germany could be lowered by 2 to 3.5 TWh, or 20-35%, respectively. For the metropolitan region of Bremen-Oldenburg there is no data on the actual numbers of data centers available. However, based on the gross regional product compared to the German GDP, resulting in a share of 3%, the number of servers in data centers in the region should be in the order of 65000 with an electricity consumption of 300 GWh (based on data in [30]). If the above savings could be realized in all of these data centers in the region, the saved electricity would be in the order of 60 to 100 GWh. One must note, however, that geothermal cooling is not available everywhere, depending on geological conditions and space requirements for the geothermal probes. On the other hand, geothermal cooling is not limited to data centers, also hotels, offices, the food industry and other sectors are potential users. The full potential for this cooling technology in the region is currently being evaluated.

4.3.4 Pilot project 3: The use of cellulose-rich substrate in biogas plants

The third currently pursued pilot project extends the low exergy philosophy to biogenic materials: using low exergy material flows or residues to generate useful energy services. RuminoTech is an innovative biogas technology that mimicks the functions of a cow's stomach system (rumen). Different from conventional plants, based on the rear end of the biological digestive tract, the RuminoTech technology is based on the front end.

[4] http://www.google.com/about/datacenters/inside/efficiency/

4.3.4.1 Consideration of sustainability and resilience

The rumen in ruminants is one of the most efficient systems in the course of evolution for the utilization of cellulose. It uses the energy of cellulose - the main component of plant cell walls - as a motor for its metabolism. For an overview of current rumen based biogas technologies, see [15]. If humans could use cellulose more efficiently for energy and material needs, some of the many resource problems could be alleviated. Currently the technology for using rumen based biogas production is challenged by unstable biological environments, by a lack of animal mucus substitutes, and by mimicking the complex flow of fluids inside biological digestive systems [15].

The RuminoTech technology follows the principle of the rumen and is believed to have overcome the mentioned challenges. The technology has been tested on the lab-scale [16] and it is currently being scaled up to the 100 kW level. The rumen based biogas technology promises to utilize plants more effectively than classical biogas plants. The renewable raw material cellulose could thus be used for renewable energy generation without many drawbacks of conventional biomass utilization. Because the fruit of the plants is not necessary for the technology to work, the conflicts between the cultivation of food and energy crops could be avoided and one of the major controversies around sustainably using biomass would be answered. A further improvement for current biogas installations could result from feeding fermentation residues (digestates) into this technology to produce usable methane, while the nutrients would remain preserved to a large part. The inventor suggests that also straw, hay, leaves, old paper or organic residue materials can be used as a fermenting material. If realized on a larger scale, this could thus add substantially to the resource diversity of the energy system and increase its resilience. The resulting high-quality biogas can be processed with customary procedures directly to natural gas or be converted with CHP plants into electricity and heat [14]. The functioning of the technology has been demonstrated on the laboratory level and a first pilot plant is currently being developed.

In this pilot project, a demonstration plant with a capacity of 100 kW_{el} will be installed in parallel to an existing biogas plant. The available biogas plant is established in close proximity to a commercial garden centre. This opens the possibility for the RuminoTech biogas plant to be tested with different fermenting materials. The biogas produced is fed into an existing CHP plant.

4.3.4.2 Energy considerations and regional potentials

The first installation of this technology in the region will be run on digestate from a nearby conventional biogas plant. Based on first approximations, the RuminoTech technology can produce between 50 and 100 l of methane from 1 kg (dry matter) of digestate [22][5]. The conventional biogas plant (500 kW_{el}) is run on corn and produces around 2.5 t of digestate each day, enough to run the RumminoTech plant on 100% capacity. The weight of digestate is thereby reduced by approximately 50%, and the resulting residues have a very high lignin content, which can still be used energetically, e.g. as pellets in space heating systems. For the metropolitan region the potential in using digestate is significant. In the region of Bremen-Oldenburg 2.5 million tons of corn for biogas production are harvested each year, resulting in approximately 1.875 million tons of digestates with a dry matter content of 0.625 million tons. With the above mentioned 50 l methane per kg dry matter digestate, this would result in 3125 m^3 of methane which could e.g. be converted into 130 GWh of electricity, approximately 1% of the regional electricity consumption.

From a sustainability perspective, however, it is not recommendable to run the RuminoTech technology as an “afterburner” of corn based biogas plants. The RuminoTech technology offers more, especially the possibility to solve the problem between crop production for food and the production of energy. We are currently analyzing the feasibility of this concept in the regional context, determine economic and energetic efficiency, assess the flexibility of the technology and

[5] Data is scaled up from laboratory results and needs to be confirmed for the full scale unit experimentally.

explore different diffusion scenarios in the region. An estimate of the amount of straw from different grain crops is given in Table 4.

Table 4: Straw potential from different grain crops in the metropolitan region of Bremen-Oldenburg. Data based on [18]

Winter Wheat t/a	Spring wheat t/a	Winter barley t/a	Spring barley t/a	Rye t/a	Oats t/a	Triticale t/a	total amount of straw t/a
554,317	2,186	323,878	29,163	162,515	16,808	153,333	1,208,661

The RuminoTech technology is reported to produce 400 dm^3 of biogas per kg of straw [22]. This number is scaled up from laboratory experiments and has to be evaluated for the full scale unit experimentally. If the order of magnitude is correct, the straw potential in the region of Bremen-Oldenburg could be used to produce around 480 million m^3 of biogas. With an average upper heating value of 6.4 kWh/m^3 and an efficiency of 40% for the conversion to electricity, the straw produced in the region could potentially generate 1.24 TWh of electricity, or 7% of the regional consumption [27].

Other potential sources of substrate need to be evaluated in order to be able to assess the potential in applying the RuminoTech technology in the region. Based on the above given description and data, the potential is quite promising, but has to be accompanied by an integrated concept for renewable energies combining the strength of different technologies.

4.4 Conclusion and outlook

From our analysis so far we conclude that Low Exergy Solutions can play a significant role in adapting the regional energy system to climate change and to increase its resilience. The innovation potential assessment and the preliminary analysis of the above pilot projects substantiate this conclusion. Additionally, there is a relevant energy (savings) potential in the metropolitan region Bremen-Oldenburg when these technologies would be used. Nevertheless, at this stage of the project conclusions can only be preliminary and must be confirmed by analysis and evaluation of the currently installed pilot projects. Efficiencies, energy potentials and innovation criteria look promising. However, the real potential of Low Exergy Solutions for the region is depending on a large number of factors, including economic feasibility, regulation and permitting issues, social acceptance, robustness of the technologies, etc. We have to wait for the scientific evaluation of the pilot projects before we can derive robust conclusions, but there are several indications for Low Exergy Solutions being helpful in the context of climate adaptation and resilient energy systems:

- they relieve pressure on infrastructures and resources
- they diversify the energy supply
- when properly integrated, they add flexibility in delivering energy services
- they broaden the used resource base
- they increase efficiency of renewable energy conversion systems
- they consist of technologically robust components
- they save high exergetic resources (electricity/fossil fuels)
- they decrease carbon emissions

Still, there are several open questions to be answered in the pilot phase:

- do they make economic sense?
- are there ecological risks?
- can they successfully be transferred to other sites throughout the region?
- do they integrate well with existing infrastructures and technologies?

The research on Low Exergy Solutions is only one approach for increasing the regional energy system's resilience and for adapting it to climate change. In the Resilient Energy Infrastructure field for example, we also assess different storage technologies for electricity and intelligent solutions balancing demand and supply. The task of the following years will be to combine results derived from these innovations fields and organize them into a strategy for transforming the current regional energy system towards more resilience. The theoretical considerations on what constitutes a resilient system will then come back into play and have to be checked against the real-life experiences from these test cases.

4.5 References

[1] German Government, The Federal Government's energy concept of 2010 and the transformation of the energy system of 2011, Available at: <http://www.bmu.de/files/english/pdf/application/pdf/energiekonzept_bundesregierung_en.pdf > [accessed 10.02.2012].

[2] Holling, C. S., Gunderson L. H., Resilience and Adaptive Cycles. In L. H. Gunderson, C. S. Holling, Panarchy, 2002.

[3] Carpenter et al., From Metaphor to Measurement: Resilience of What to What? Ecosystems 4(8), 765–781, 2001.

[4] Folke, C. et al., Resilience and Sustainable Development: Building Adaptive Capacity in a World of Transformations. Scientific Background Paper on Resilience for the process of the World Summit on Sustainable Understanding transformations in human and natural systems. Washington: Island Press. Development on behalf of the Environmental Advisory Council to the Swedish Government, 2002.

[5] Brand, F., Ecological resilience and its relevance within a theory of sustainable development. UFZ Centre for Enviromental Research, Leipzig, 2005.

[6] Fichter, K., Gleich, A. v., Pfriem, R., Siebenhühner, B., Theoretische Grundlagen für erfolgreiche Klimaanpassungsstrategien. Nordwest2050 Berichte Heft 1. Bremen/Oldenburg: Projektkonsortium, nordwest2050, p23, 2010

[7] Stührmann S, Gleich A von, Brand U, Gößling-Reisemann S, Mit dem Leitkonzept Resilienz auf dem Weg zu resilienteren Energieinfrastrukturen. In: Decker M, Grunwald A, Knapp M, editors. Der Systemblick auf Innovation - Technikfolgenabschätzung in der Technikgestaltung. Berlin: edition sigma, 2012.

[8] Fichter, K., Gleich, A. v., Pfriem, R., Siebenhühner, B., Theoretische Grundlagen für erfolgreiche Klimaanpassungsstrategien. Nordwest2050 Berichte Heft 1. Bremen/Oldenburg: Projektkonsortium, nordwest2050, chapter 2, 2010

[9] Schuchardt, B., Wittig, S., Spiekermann, J., Klimaszenarien für ‚nordwest2050' Teil 2: Grundlagen. Nordwest2050 Werkstattbericht Nr. 3. Bremen/Oldenburg: Projektkonsortium, nordwest2050, 2010

[10] Fichter, K., Hintemann, R., Leitfaden Innovationspotenzialanalyse. Nordwest2050 Werkstattbericht Nr. 5. Bremen/Oldenburg: Projektkonsortium, nordwest2050, 2010

[11] Rothstein, B.; Parey, S.: Impacts of and adaptation to climate change in the electricity sector in Germany and France. In: Ford, J. D.; Berrang-Ford, L. (Hrsg.): Climate Change Adaptation in Developed Nations - From Theory to Practice. Heidelberg, 2011.

[12] Henk Ten Haaf, Putenmast: Produktionstechnische Tips. Dtsch. Geflügelwirtschaft und Schweineproduktion (DGS) 23, 35-37, 1992

[13] Dickehut, A., General Manager, Consultix GmbH, Informations-Technology, statement 07.02.2012

[14] Strecker, M., Rumen based process for the sustainable production of biogas. Presentation at GIDIRAT 2010, Hannover, Germany. 2010. Available at http://www.isah.uni-hannover.de/pages/aktuelles/gidirat/downloads/19_Strecker.pdf [accessed 19.05.2012]

[15] Bayané. A., Guiot, S.R., Animal digestive strategies versus anaerobic digestion bioprocesses for biogas production from lignocellulosic biomass. Reviews in Environmental Sciences and Biotechnology 10:43–62, 2011

[16] Stopp, P., Weichgrebe, D., Rosenwinkel, K.-H., Strecker, M., Breves, G., DAUMEN-Energy "Design for separation and augmented methanisation of fibres substrates – contribution to sustainable biogas production", in: Proceedings of Biogas Science 2009, Erding, Germany. Schriftenreihe der Bayerischen Landesanstalt für Landwirtschaft. 2009

[17] Gößling-Reisemann S, Gleich A von, Stührmann S, Wachsmuth J, Climate change and structural vulnerability of a metropolitan energy supply system – the case of Bremen-Oldenburg in Northwest Germany. Journal of Industrial Ecology (submitted, in review)

[18] Helmich, J., Thermo-chemische Vergasung landwirtschaftlicher Biomassen - Potenzialanalyse und Beitrag zu einer resilienten Energieversorgung in der Metropolregion Bremen-Oldenburg (Diploma thesis). Bremen, Germany: University of Bremen, 2010.

[19] Gers-Grapperhaus, C., Biogas-Aktuelle Situation in Niedersachsen. Presentation at OLEC-Meeting; 1 June 2011. Available at http://www.energiecluster.de/files/christoph_gers-grapperhaus_-_biogas_aktuelle_situation_in_niedersachsen_1.pdf [accessed 28.4.2012]

[20] Berliner Energieagentur GmbH, Machbarkeitsstudie thermische vs. konventionelle Kälteerzeugung am Bürogebäude Tiefstack der Vattenfall Europe Hamburg, Berlin, 2008.

[21] solarnext, Data leaflet „chilli Cooling Kit WFC 70", available at http://www.solarnext.eu/pdf/ger/products/111212_chillii_kit_WFC70_d.pdf [accessed 18.05.2012]

[22] Riedel, O., CEO of Victeos Group and RuminoTech GmbH: oral communication, 09.05.2012

[23] Zürich, S., Beim Kühlen bis zu 80 Prozent Primärenergie einsparen, BHKS-Almanach, 2011

[24] Landwirtschaftliches Zentrum für Rinderhaltung, Grünlandwirtschaft, Milchwirtschaft, Wild und Fischerei Baden-Württemberg (LAZBW), Einsatz von Wirtschaftsdüngern, available at http://gruenland-online.de.dedi335.your-server.de/html/duengung/wirtschaftsduenger/naehrstoffanfall/naehrstoffanfall.html [accessed 18.05.2012]

[25] Wachsmuth, J.; Gleich, A. von; Gößling-Reisemann, S.; Lutz-Kunisch, B.; Stührmann, S.: Sektorale Vulnerabilität: Energiewirtschaft. In: Schuchardt, B.; Wittig, S. (Hrsg.): Vulnerabilität der Metropolregion Bremen-Oldenburg gegenüber dem Klimawandel (Synthesebericht). nordwest2050-Berichte Heft 2, Projektkonsortium ‚nordwest2050'. S. 95-112. Bremen/Oldenburg. 2012

[26] Hammerschmidt, A. et. al., Potenzialanalyse für Strom und Wärme aus erneuerbaren Energien in der Metropolregion Bremen – Oldenburg im Nordwesten (Project report), University of Bremen, 2011

[27] Eickemeyer, T. , Strombilanz der Metropolregion Bremen-Oldenburg (Diploma thesis), Bremen, Germany: University of Bremen, 2011

[28] Deutscher kältetechnischer Verein (DKV), Final report „Energiebedarf bei der technischen Erzeugung von Kälte“. Hannover, Germany, 2002.

[29] Bettgenhäuser, K., Boermans, T., Offermann, M., Krechting, A., Becker, D., Kahles, M., Pause, F., Müller, T., Klimaschutz durch Reduzierung des Energiebedarfs für Gebäudekühlung. Umweltbundesamt Berlin, Germany. 2011.

[30] Hintemann, R.; Fichter, K.: Materialbestand der Rechenzentren in Deutschland – Eine Bestandsaufnahme zur Ermittlung von Ressourcen- und Energieeinsatz, Study for the Umweltbundesamt Berlin, 2010.

Appendix A

Evaluation of the innovation potential of selected Low Exergy Solutions

The innovation potential analysis (IPA) methodology was developed within the project nordwest2050 (see above). The evaluation phase includes an assessment based on several criteria and was performed on all technologies or combinations of technologies from section 4.3. The criteria include indicators for innovation type, climate adaptation, resilience and sustainability, feasibility, and regional transferability, Here we present the results for the above described pilot project technologies in graphical form.

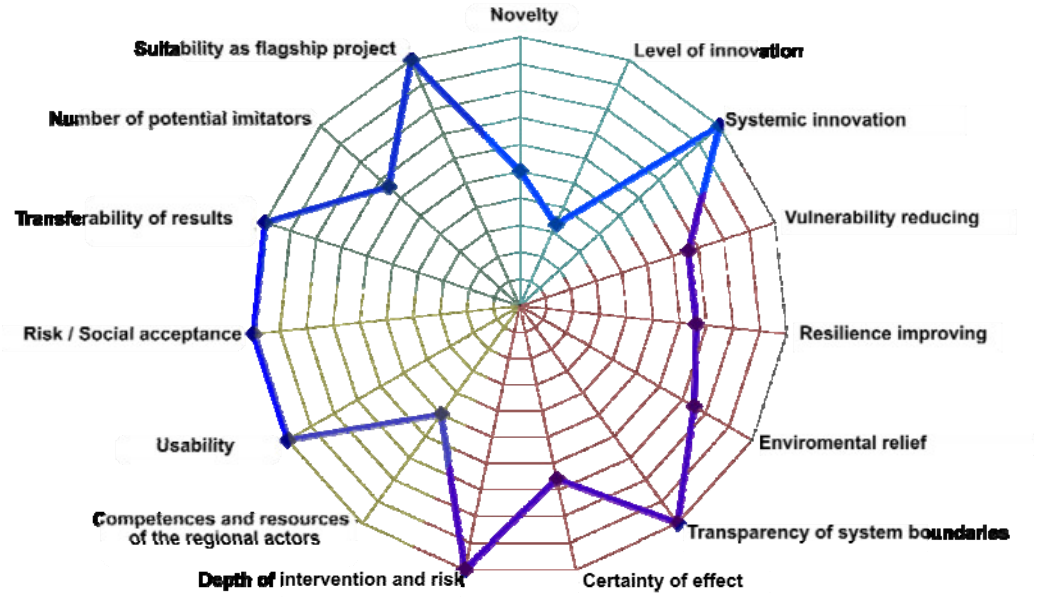

Figure 1. IPA results for Low Exergy Solution “CHP offheat from biogas plant – absorption chiller – barn cooling” (pilot project 1: “Cooling Turkey Barns”). The further outside the data point, the higher the rating in this category.

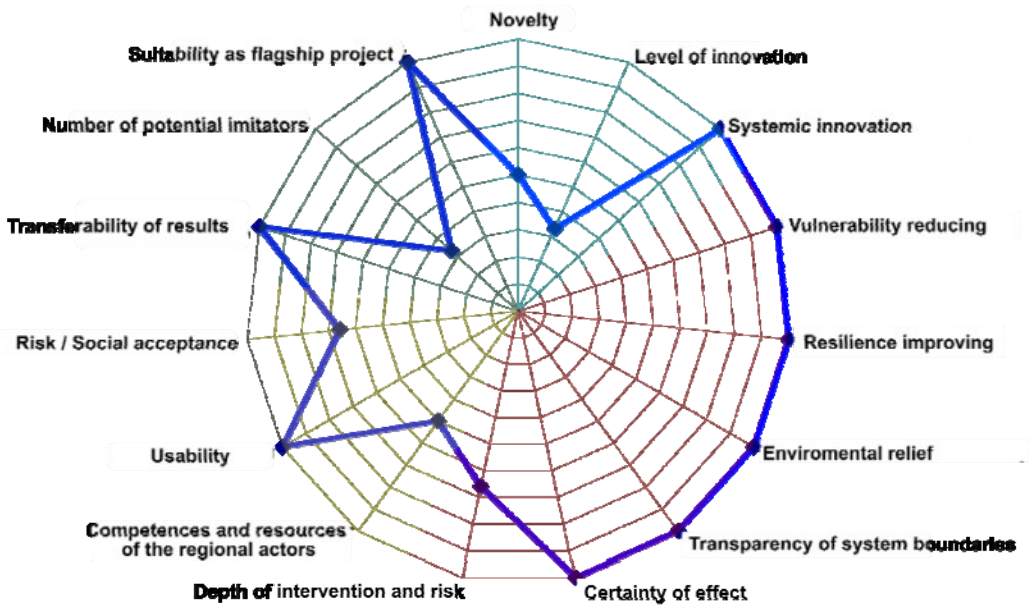

Figure 2. IPA results for Low Exergy Solution "Geothermal Cooling" (pilot project 2: "Geothermal cooling of a data center"). The further outside the data point, the higher the rating in this category.

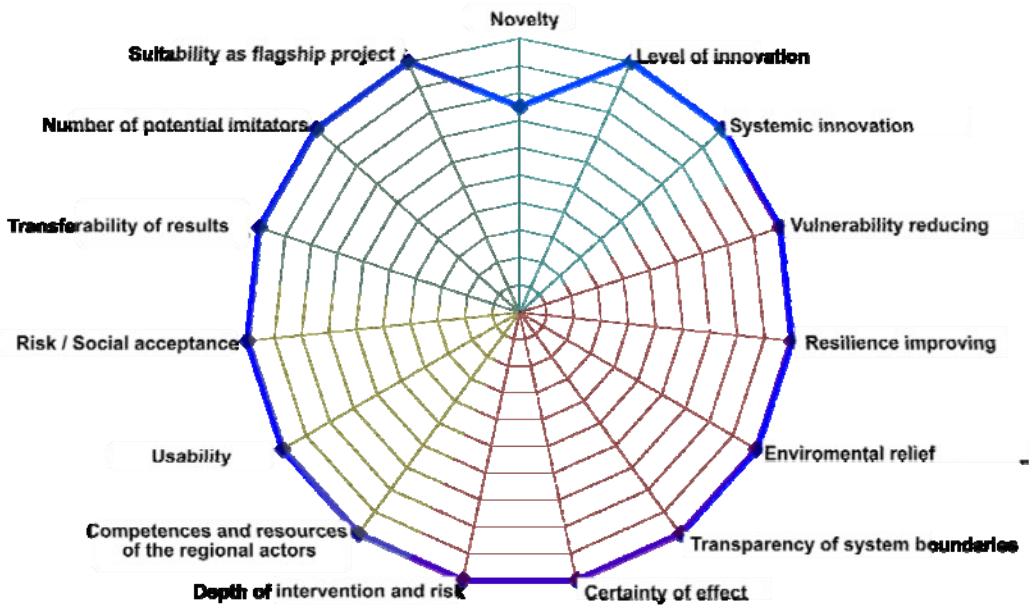

Figure 3. IPA results for Low Exergy Solution "Rumen based Biogas Plant" (pilot project 3: "Use of cellulose-rich substrate in biogas plants"). The further outside the data point, the higher the rating in this category.

On the use of MPT to derive optimal RES electricity generation mixes

Paula Ferreira[a], Jorge Cunha[b]

[a] Centre for Industrial and Technology Management, Guimarães, Portugal, paulaf@dps.uminho.pt
[b] Centre for Industrial and Technology Management, Guimarães, Portugal, jscunha@dps.uminho.pt

Abstract:

The use of modern portfolio theory (MPT) is a common practice to derive efficient frontiers and support portfolio decision making in financial markets. Although real projects present different characteristics and technical restrictions, the general objective of the decision maker is the same: to maximize the expected return minimizing the portfolio risk. Long term electricity generation decision making is characterized by high uncertainty, high impact on social welfare and a large set of diversified technologies that may be included in future scenarios. The possibility of applying MPT approach to define efficient electricity generation portfolios is explored in this paper focusing on particular in renewable energy sources (RES technologies). The use of MPT for building RES scenarios is demonstrated for the particular case of Portugal. One year hourly data concerning power output from wind, hydro and solar plants along with the power demand was collected and included in the analysis. Three different approaches were considered for designing the efficient frontiers aiming at maximizing the RES electricity generation, minimizing deviation between the demand and the RES production and minimizing the levelised cost of the RES system. The results demonstrate how this approach can be an effective tool to support decision making but put also in evidence the need to build modified MPT models in order to take into account the technical restrictions of the system.

Keywords:
Renewable electricity sources, Electricity generation, Modern portfolio theory.

1. Introduction

Electricity power planning relates to generation, transmission and distribution systems. In this paper we are focused only on the generation system.

The main goal of generation planning is to meet customers' electricity needs at least cost with an acceptable degree of safety, reliability and quality [1]. However, this is a difficult task given that generation planning deals with future decisions that have to be made in an environment of uncertainty (namely, due to electricity demand, fuel prices volatility, investment costs, regulatory framework) and such uncertainties have to be, explicitly, taken into account in electricity planning [2]. In order to achieve this goal, it is necessary to couple supply-side management programs (which involve the construction of new power plants and/or repowering of existing ones) with demand-side management programs (in order to manage the customer load demand) [3].

In short, generation planning tasks include energy and demand forecasting, supply-side management and demand-side management adjustments, analysis of alternative expansion plans, determination of the optimal strategy or portfolio strategies and the evaluation of financial implications and feasibility [1].

Traditionally, the least-cost approach has been used in generation planning. This approach is frequently based on calculating the levelised costs of electricity generation, expressed in €/MWh, for different alternative technologies (e.g. fossil fuels, nuclear, renewable) and comparing such costs in order to choose the technology with the lowest cost.

However, some criticisms to the use of this approach can be found in the literature. Firstly, the fact that electricity planning decision makers are faced both with a wider range of alternative technologies for electricity generation and different institutional framework in which they operate, coupled with a future that appears increasingly complex and uncertain [4].

Secondly, as energy markets have been liberalised, the interest in quantifying and manage market risks grew [5]. In fact, with the deregulation and liberalisation of electricity markets, with a corresponding increase in competition, electricity generation companies will no longer have a guaranteed return because the price of electricity varies depending on a number of factors. In this context, it is essential that those companies can manage electricity price risk [6].

Additionally, there is the issue of security of energy supply [7]. In fact, given the global shortage in terms of primary fuel sources, policy makers increasingly need to consider a diversification of electricity production. Simultaneously, the price volatility of fossil fuels raises the question of what are the best options in terms of energy needs of a country.

Finally, an important feature of renewable technologies is that they correspond to capital intensive investments, which translates into a relatively fixed cost structure over time, with very low (or practically zero) marginal costs, and that are uncorrelated with important risk drivers, such as fossil fuel prices [6,7].

Given these reasons, it is necessary to shift from a paradigm that seeks to evaluate different technologies for electricity production on a stand-alone basis, to one that evaluate different portfolios of technologies for electricity production [4,7]. This means abandoning the traditional least-cost approach and to adopt a new perspective of analysis based on the theory of efficient portfolios. In this context, the "mean-variance portfolio (MVP) theory is highly suited to the problem of planning and evaluating a nation’s electricity portfolio and strategies" [4]. Although, "at any given time, some alternatives in the portfolio may have higher costs while others have lower costs, yet over time, the astute combination of resources serves to minimize overall expected generating cost relative to the expected risk" [4].

In the context of electricity planning, where a combination of conventional technologies and renewable technologies is being considered, although renewables may present a higher levelised cost, it does not necessarily mean that the overall cost of the portfolio of technologies become more expensive, given the "statistical independence of renewables costs, which do not correlate (or covary) with fossil price movements" [4]. In fact, the inclusion of renewable technologies in an electricity generation portfolio is a way to reduce the cost and risk of the portfolio, although in a stand-alone basis the cost of those renewable technologies might be higher [7].

The electricity generation sector is essential for the attainment of the European renewable objectives. According to the European Union (EU) forecasts, the large hydropower will maintain its dominant position in renewable energy sources (RES) for electricity generation for the near future. However, the use of wind will continue expanding and, in 2020, the onshore and offshore wind electricity generation will overcome the hydro sector in the EU-27. Biomass/waste remains as the third RES for electricity (RES-E) technology with two digit RES share. An increase of the solar technologies is also foreseen although staying far from the wind, hydro or biomass shares [8].

The definition of optimal scenarios for RES-E to include on the grid has been frequently debated in the literature adopting multicriteria tools or electricity planning models based on cost/emissions optimization procedures. However, more recently the importance of diverse electricity technologies portfolios has been also emphasised and the use of the modern portfolio theory (MPT), previously established for the financial investment analysis, has been well applied to the electricity generation sector. This paper applies MPT as an electricity generation planning tool, in order to present optimal RES electricity generation mixes for the future, taking into account the past production pattern of each RES and optimizing the trade-off between maximizing RES output and minimizing RES variability.

The rest of the paper is organised as follows. In section 2, a brief description of the MPT reasoning and its application to electricity planning is presented. Section 3 corresponds to the empirical study undertaken, regarding the optimal RES electricity portfolios in Portugal. Finally, Section 4 draws the main conclusions of this paper and presents perspectives for future research.

2. Modern Portfolio Theory for energy decisions

2.1. Brief overview of MPT theory

Modern portfolio theory has its roots in the seminal paper by [9]. He proposed a methodology to select efficient investment portfolios based on investors' goal of maximising future expected return given a certain level of risk they were willing to take [10].

Investors in financial assets expect to earn a certain return over a given investment horizon. However, the yield actually obtained by the investor may differ from the expected return, and this represents the investment's source of risk. When deciding about his investments, the investor should consider, besides expected return, the following elements [11]: the dispersion of returns around the average return (variance), the symmetry of the distribution (skewness), and the kurtosis of the distribution. However, one of the innovations of the mean-variance model of [9], was the assumption that the distribution of returns follows a normal distribution. This has the advantage of being able to ignore those last two elements because the normal distribution is symmetric and has a kurtosis of zero. Thus, the characteristics of these investments can be measured based on only two variables: expected return and variance [11]. Therefore, assuming the assumption that investors are risk averse, having to choose between two investments with the same standard deviation but different expected returns, they always choose the one with higher expected return (and vice versa).

Thus, the mean-variance model allowed to explain the advantages that an investor has to diversify their investments among several securities (e.g. stocks or bonds). That is, instead of investing in a single asset, investing in portfolios made up of various financial assets. In fact, there are two reasons why diversification reduces the risk of investment [11]. On the one hand, as each asset included in a diversified portfolio represents a small portion of the investor's total investment, any event affecting one or a few of these assets have a more limited impact on the total value of the portfolio. On the other hand, the effect of specific events on the price of each asset included in a portfolio can be positive or negative. In large and well diversified portfolios, these effects tend to offset each other without affecting significantly the overall value of the portfolio.

One can illustrate the effects of diversification on the risk of a portfolio by examining the effect of adding more assets to the portfolio and see what happens to its variance. For example, in the case of a portfolio, P, consisting of two assets, A and B, expected return, $E(r_P)$, and variance, σ^2_P, are given by, respectively:

$$E(r_P) = \omega_A E(r_A) + \omega_B E(r_B) \quad (1)$$

and

$$\sigma^2_P = 2\omega_A{}^2\sigma^2_A + \omega_B{}^2\sigma^2_B + 2\omega_A\omega_B\rho_{AB}\sigma_A\sigma_B \quad (2)$$

where ω_A and ω_B represent the proportions invested in each asset, A and B. The last term in the expression of the variance is often written in terms of the covariance of returns between two assets: $\sigma_{AB} = \rho_{AB}\sigma_A\sigma_B$. One can see that the benefits of diversification are a function of the correlation coefficient. Thus, the lower the correlation of returns between two assets the higher the gains from diversification an investor obtain.

This reasoning can be generalised for the case of a portfolio with N assets. Thus, expected return, $E(r_P)$, and variance, σ^2_P, of the portfolio are given by:

$$E(r_P) = \sum_{i=1}^{i=N} \omega_i E(r_i)$$

(3)

and

$$\sigma_P^2 = \sum_{i=1}^{i=N} \sum_{j=1}^{j=N} \omega_i \omega_j \rho_{ij} \sigma_i \sigma_j \qquad (4)$$

We conclude, therefore, that the variance of a portfolio is partially determined by the variance of individual assets and partly by the way they move together. The latter is measured statistically by the coefficient of correlation or the covariance of the assets belonging to the portfolio. It is the term for the covariance that provides an explanation of why and in what amount diversification reduces the risk of investment. In fact, portfolios of financial assets should not be chosen only by their individual characteristics, but taking into account how the correlation between assets affects the overall risk of a portfolio [11]. Therefore, since the variances can be estimated for portfolios consisting of a large number of assets, suggests an approach to the optimal selection of portfolios in which investors make the balance between expected return and risk.

Alternative 1: If an investor can specify the maximum risk he is willing to take, the optimal portfolio is obtained maximising expected return subject to that risk level, i.e.:

$$Max \mathrm{E}(r_P) = \sum_{i=1}^{i=N} \omega_i E(r_i)$$

s.t.

$$\sigma_P^2 = \sum_{i=1}^{i=N} \sum_{j=1}^{j=N} \omega_i \omega_j \sigma_{ij} \leq \hat{\sigma}^2$$

$$\sum_{i=1}^{N} \varpi_i = 1$$

$$\varpi_i \geq 0$$

Alternative 2: If an investor specifies his desired level of expected return, the optimal portfolio is the one that minimizes the variance subject to that level of return:

$$Min \sigma_P^2 = \sum_{i=1}^{i=N} \sum_{j=1}^{j=N} \omega_i \omega_j \sigma_{ij}$$

s.a.

$$\mathrm{E}(r_P) = \sum_{i=1}^{i=N} \omega_i E(r_i) = E(\bar{r})$$

$$\sum_{i=1}^{N} \varpi_i = 1$$

$$\varpi_i \geq 0$$

The portfolios that result from this process give rise to what is called the efficient frontier, as represented in Figure 1:

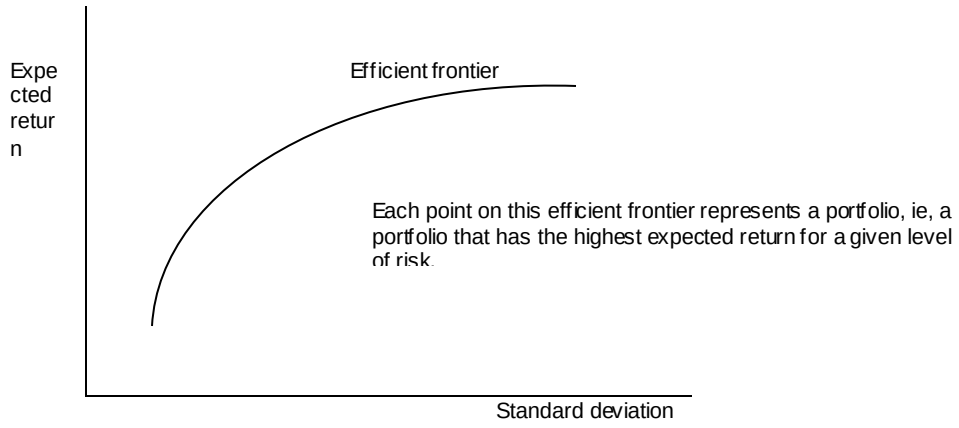

Fig. 1. – Efficient frontier

2.2. MPT applications to electricity generation

In recent years there has been a growing application of the MPT theory to electricity planning. In fact, the mean-variance model can be used to determine the optimal portfolios of electricity generation both for a company or a country. According to [5], the main idea of the MPT model is that the value of each asset can only be determined taken into account portfolios of alternative assets. Hence, energy planning should be focused more on developing efficient production portfolios and less on finding the alternative with the lowest production cost [4,7].

The MPT approach allows to analyse the impact of the inclusion of renewable technologies in the mix of generating sources of electricity. In particular, it provides a better risk assessment of alternative generation technologies, something that the traditional stand-alone least cost approach cannot do, particularly in terms of the impact of renewable energy sources in reducing the risk of the portfolio of technologies to be adopted. In fact, the MPT model allows to illustrate the trade-off between production costs and risk: the lower the cost the higher the risk, meaning that it is not possible to achieve a lower electricity production cost without assuming higher levels of risk.

It should be noted that the result of applying the mean-variance model to generation planning is not identifying a specific portfolio, but the identification of an efficient frontier where the optimal portfolios will be located. These are Pareto-optimal, that is, an increase in returns (or a decrease in costs) is only achieved by accepting an increased risk. On the other hand, an important aspect in the mean-variance model is the assumption that past events are the best guide for predicting the future. Not to say that unexpected events will not occur, but that the effect of these events is already known from past experience [7].

A study that used the MPT theory to obtain evidence about the best mix of electricity generation in Scotland was that of [12]. Based on the efficient frontier, the authors analysed the portfolios suggested in four scenarios for the electricity generation mix in 2020, seeking to clarify what role renewable technologies can play in setting up those portfolios. The main conclusions reached by those authors were that: the portfolios of electricity production corresponding to the four scenarios are not mean-variance efficient; based on MPT approach it is possible to quantify the likely scale of inefficiency; and it seems there is the opportunity to have an improvement in the generation mix in the sense of Pareto.

Another study was conducted by [13], where they tried to optimise wind power investment portfolios across countries taking into account the correlation between wind farms output located in different geographical areas. In fact, the aim is "to demonstrate the use of MVP theory as an insightful analytical approach to take into account the impact of wind output variability and correlations of wind output across different locations within a wind farm portfolio" [13]. These authors concluded that the current and projected portfolios for 2020 are far from the efficient frontier and, therefore, there is scope for wider benefits arising from greater coordination of European renewable development by providing "incentives for location of new wind farms so as to maximise the efficiency of the overall European wind portfolio".

In turn, [5] apply the MPT theory in order to optimise generation electricity portfolios but focusing their attention "on private investors' investment incentives in liberalized electricity markets, where fuel-mix diversification is a possible strategy for reducing exposure to electricity, fuel, and carbon price risks". In fact, according to these authors, the electric utilities operating in deregulated markets cannot easily pass on to the sales price changes in their production costs. Thus, utilities have to take into account the risks that may affect their profits when they have to decide about its investment projects. In this context, the risks regarding electricity, fuel and carbon prices become relevant in determining the optimal production portfolios. The results obtained by [5] demonstrated the importance of the degree of correlation between the prices of electricity, fuel and carbon in the

definition of the optimal generation mix. Hence, they concluded that "liberalized electricity markets characterized by strong correlation between electricity and gas prices […] are unlikely to reward fuel mix diversification sufficiently to make private investors' choices align with the socially optimal fuel-mix, unless investors can find counterparties with complementary risk profiles to sign long-term power purchase agreements".

Also from the perspective of a private generation company, operating in a liberalised electricity market, [6] applied the theory of efficient portfolios. In this type of markets, it is essential that utilities companies can properly manage the electricity price risk, given the strong competition among the different operators in those markets. To address this issue, [6] adopt the MPT approach in order to define the best strategy for electricity trading for a company that is considering selling in the spot market or establish bilateral contracts. The question that arises is "how to allocate energy among these potential transactions in order to maximize profits with relatively low risk" [6]. In fact, the combination of different trading strategies of electricity can be seen as constituting a portfolio which can be optimised using the MPT approach.

Finally, [4] presents a summary of the application of MPT theory in the evaluation of different electricity generation planning scenarios for the case of U.S., EU and Mexico, where was perceived that the mix of electricity generation can be improved in terms of cost and/or risk, by expanding the use of renewable technologies. The author states that "compared to existing, fossil-dominated mixes, efficient portfolios reduce generating cost while including greater renewables shares in the mix thereby enhancing energy security. Though counterintuitive, the idea that adding more costly renewables can actually reduce portfolio-generating cost is consistent with basic finance theory". It follows an important conclusion: "in dynamic and uncertain environments, the relative value of generating technologies must be determined not by evaluating alternative resources, but by evaluating alternative resource portfolios" [4].

The above mentioned papers demonstrate the possibility of adapting a financial theory on electricity planning problems. In fact, the increase of RES to electricity generation creates important challenges to grid managers due to the expected variability of the power output of most of these RES power plants. The adoption of a model based on MPT can be particularly useful for electricity systems highly RES supported, allowing to take into account both yearly seasonality and intra-daily variations of the production. This paper proposes to demonstrate the use of MPT on these systems resourcing to the particular case of the Portuguese electricity system to identify optimal RES portfolios. The aim is to optimize the trade-off between the variable production that characterize some of the RES and the return of these projects, measured according to a set of proxy variables.

3. Optimal RES electricity portfolios

The Portuguese electricity system is mainly based on a mix of thermal, hydro and wind power technologies. RES power plants represent 54% of the total installed power. The wind sector grew rapidly in the last years and an increase on the hydropower investment is also foreseen for the next years, strongly justified by the need to compensate the variable output of wind power plants. As in the EU-27, biomass represents an important RES contributor, mainly because of industrial wastes used in CHP and, in much smaller amount, by the centralized biomass power plants [14].

Some recent studies already addressed the case of electricity generation scenarios in Portugal and the use of optimization models to draw these scenarios [15,16]. However, to the authors' best knowledge no attempt has been made to use an approach close to the MPT theory to this system. In fact, most optimization models rely on the cost and/or emissions minimization of the electricity system. Functions such as the loss of load probability or the reserve margin are used to address the minimum requirements for security of supply. These functions although allowing to include the variability of RES power output do not explicitly recognize portfolio risk as a decision variable

influenced by the risk of each technology output and, most importantly, by the correlations between those risks. The general idea of this research is to present possible RES generation mixes that would ensure maximum return (or minimum cost) for each given portfolio risk level, obtaining then the efficient frontier. The use of the Portuguese case, as an electricity system strongly influenced by RES seasonality behaviour, is expected to contribute to demonstrate how MPT can provide a way to complement cost optimization models with a quantitative risk evaluation of the electricity generation portfolio.

The data used for the models was drawn from public information available on REN site (www.ren.pt), consisting of the load output of each RES power plant measured for each quarter of an hour for an one year period. For the case presented in this paper, 2010 information was considered representing 35040 measures for each technology. This allowed to capture the daily and yearly seasonality of RES technologies output and of the demand. Figures 2 to 5 show the load output of wind, small hydro, photovoltaic and small thermal power plants (including renewable and non-renewable cogeneration and biomass power plants).

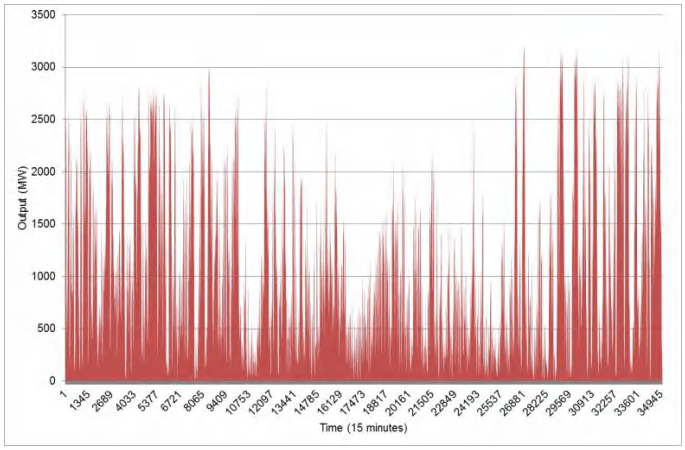

Fig. 2. Wind power load, Portugal 2010.

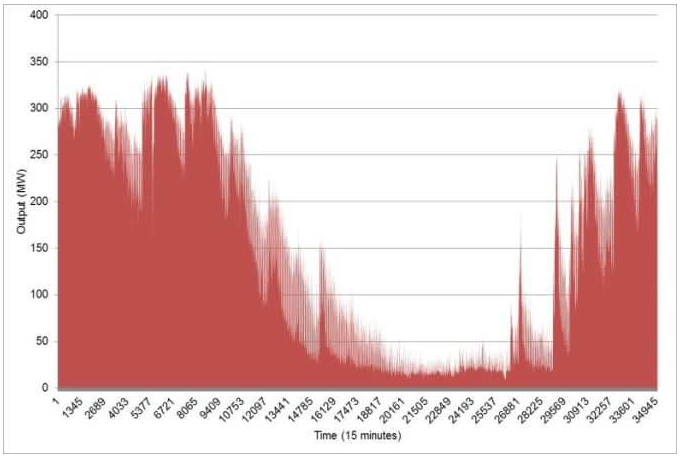

Fig. 3. Small hydro load, Portugal, 2010

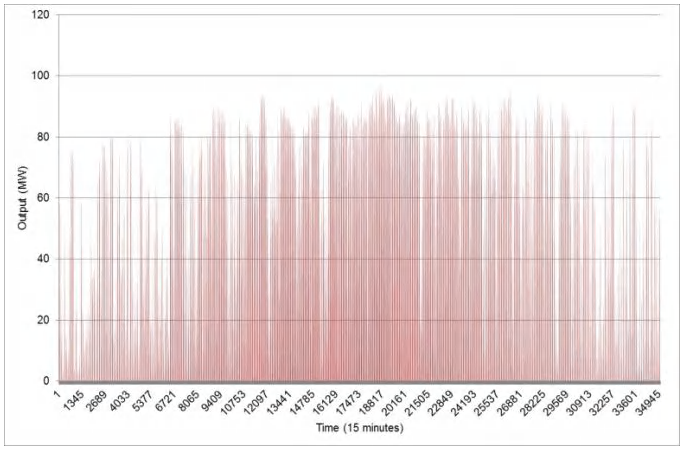

Fig. 4. Photovoltaic load, Portugal, 2010.

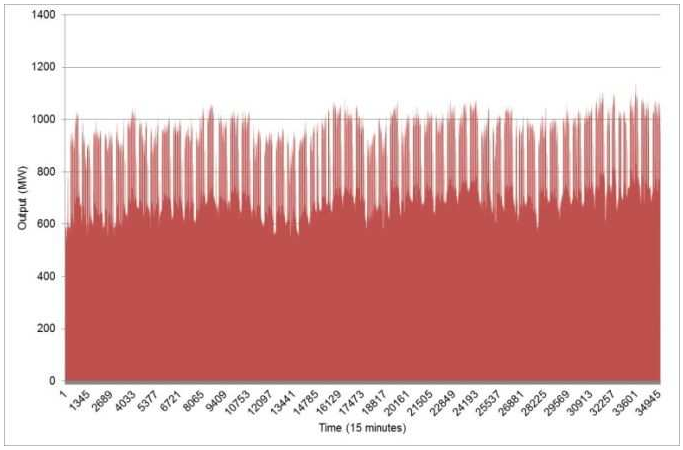

Fig. 5. Small thermal power load, Portugal, 2010

From the figures it became evident that the variability of the RES output comes mainly from the non-storage RES production, namely wind, hydro and photovoltaic power plants. The Portuguese system includes also large dams and run of river hydro plants, each one of them with some storage capacity. Although storage capacity of run of river power plants is limited, it also allows reducing the variability of the hydro power output. As for the small hydro power plants most of them do not present storage capacity and as so it was assumed that their production could represent a proxy variable for the hydro availability. Both the wind power and photovoltaic loads were assumed as proxy variables for the underlying resource availability. Being possible to storage, the variability of the biomass power output is much lower than the all the other RES and does not depend on the hourly availability of the resource. For this reason, only, wind, hydro and sun technologies are included in this analysis.

To make the variables comparable, the output of each technology was normalized by the installed power in 2010, as described in (5).

$$\mathbf{L_{i,t}} = \frac{\mathbf{Output_{i,t}}}{\mathbf{Installed\ power_i}} \quad (5)$$

Where i represents the technology (1- wind; 2- hydro; 3- photovoltaic), t represents the moment in time and $L_{i,t}$ represents the normalized variable for each technology in each quarter of an hour.

The demand was also used on the second model proposed, aiming to find the best RES solution that could meet the desired demand with the lowest deviation. For this an additional proxy variable was used to normalise the demand by the peak load, as described in (6).

$$LD_t = \frac{Demand_t}{Peak\ load} \quad (6)$$

Where $LD_{i,t}$ represents the normalized demand in each quarter of an hour.

The proxy variables included on the proposed MPT models are characterized in Table 1 and include:

- Normalized wind power output, representing the wind availability of the system.
- Normalized small hydro output, representing the hydro inflows (hydro availability) to the system.
- Normalized photovoltaic output, representing the sun availability of the system.
- Normalized demand, representing the electricity needs of the system

Table 1. Characteristics of the proxy variables for MPT model.

	Wind	Hydro	Photovoltaic	Demand
Mean (MW/Installed MW)	0,278	0,383	0,194	0,634
Standard deviation (MW/Installed MW)	0,210	0,281	0,264	0,120
Correlation coefficient				
Wind	1	0,335	-0,255	0,0019
Hydro		1	-0,152	0,0105
Photovoltaic			1	0,0080
Demand				1

In the following sections different scenarios will be presented applying models based on the MPT theory. Three different approaches were considered for designing the efficient frontiers: (1) maximizing the RES-E generation (MPT_RES); (2) minimizing the difference between demand and RES-E production (MPT_RES@Demand); (3) minimizing RES cost scenarios, according to the expected levelized cost of each technology (MPT_RES@Cost). Optimization models were built and Excel Solver was used to find optimal solutions for each problem.

3.1. MPT_RES model

For this analysis a traditional MPT model was used aiming to design the efficient frontier that can maximize the expected RES production per unit of installed capacity for each risk level. The optimisation model is described by (7) to (10).

Objective function

$$\text{Max} \quad E(L_P) = \sum_{i=1}^{3} W_i E(L_i) \quad (7)$$

Restrictions

$$\sigma(L_P) = \sqrt{\sum_{i=1}^{3} W_i^2 \sigma_i^2 + \sum_{i=1}^{3} \sum_{k=1(k\neq i)}^{3} W_i W_k \rho_{ik} \sigma_i \sigma_k} \quad (8)$$

$$\sum_{i=1}^{3} W_i = 1 \quad (9)$$

$$W_i \geq 0 \quad \forall_i \quad (10)$$

Where $E(L_p)$ represents expected return of the portfolio (RES generation per installed MW), W_i represents the share of technology i, $E(L_i)$ represents the expected i technology output (i generation per installed MW), $\sigma(L_p)$ represents the standard deviation of the portfolio, σ_i represents the standard deviation of i technology output, and ρ_{ik} represents the correlation coefficient between i and k technologies outputs.

Figure 6 and Table 2 describe the results obtained, including the efficient frontier and the characterization of a set of optimal portfolios. Figure 6 presents also the present RES (wind, hydro and photovoltaic) portfolio and the expected one in 2022, according to REN forecast [15,16].

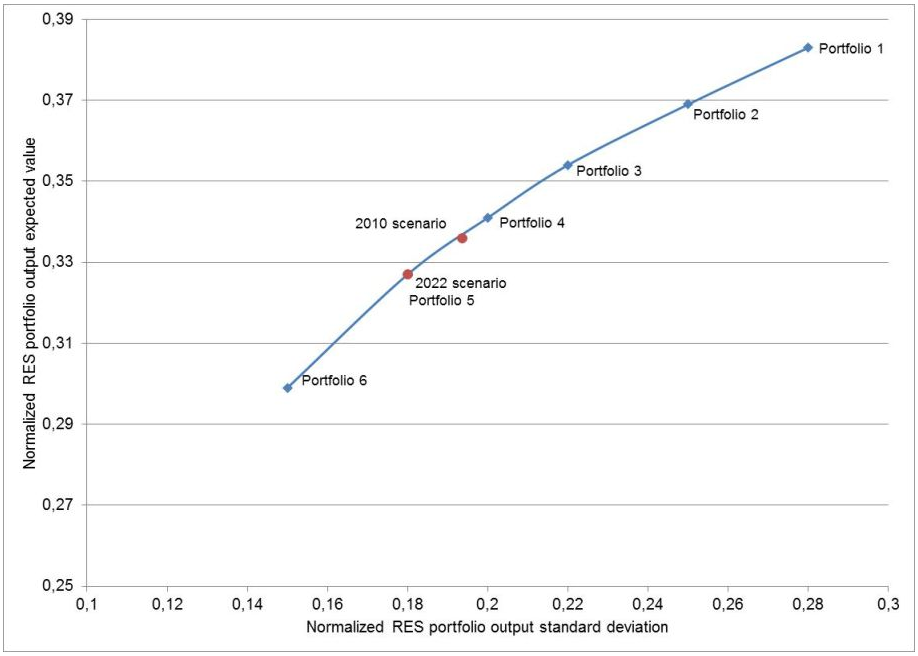

Fig. 6. Efficient frontier MPT_RES model

Table 2. Characterization of MPT_RES optimal portfolios

	$\sigma(L_p)$	$E(L_p)$	Wind	Hydro	Photovoltaic
Portfolio 1	0,28	0,383	0,30%	99,70%	0%
Portfolio 2	0,25	0,369	13,00%	87,00%	0%
Portfolio 3	0,22	0,354	27,82%	72,18%	0%
Portfolio 4	0,2	0,341	34,58%	62,50%	2,92%
Portfolio 5	0,18	0,327	36,54%	54,13%	9,33%
Portfolio 6	0,15	0,299	40,68%	37,52%	21,80%
2010 Scenario	0,194	0,336	42,03%	56,59%	1,38%
2022 Scenario	0,18	0,327	38,22%	53,46%	8,32%

3.2. MPT_RES@Demand model

For this analysis a modified MPT model was used aiming to design the efficient frontier that can minimise the deviation between the demand and the RES production in each moment. The idea is to define optimal RES portfolios that can contribute to better meet the demand in each moment, following a close load distribution pattern. The proposed optimisation model is described by (11) to (14).

Objective function

$$\text{Min } E(\text{"L"}_{\text{"P"}}) = \text{E}(\text{LD}) - \sum_{\text{"i"}=1}^{\text{"3"}} [\text{"W"}_{\text{"i"}} [\text{"E(L"}_{\text{"i"}}\text{")"}]] \quad (11)$$

Restrictions

$$\sigma(L_P)=\sqrt{\sum_{i=1}^{3} W_i^2\sigma_i^2+\sigma_d^2+\sum_{i=1}^{3}\sum_{k=1(k\neq i)}^{3} W_i W_k \rho_{ik}\sigma_i\sigma_{k-}\sum_{i=1}^{3} W_i\rho_{id}\sigma_i\sigma_d} \quad (12)$$

$$\sum_{i=1}^{3} W_i = 1 \quad (13)$$

$$W_i \geq 0 \quad \forall_i \quad (14)$$

Where, σ_d represents the standard deviation of the demand and ρ_{id} represents the correlation coefficient between i k technologies outputs and the demand.

From the reduction of risk perspective, a negative correlation between technologies is desirable to ensure their complementarity. However, but a positive correlation between RES technologies output and the demand should lead also to risk reduction under this model. The traditional standard deviation calculation was changed taking this into consideration, as may be seen in (12).

Figure 7 and Table 3 describe the results obtained, including the efficient frontier and the characterization of a set of optimal portfolios.

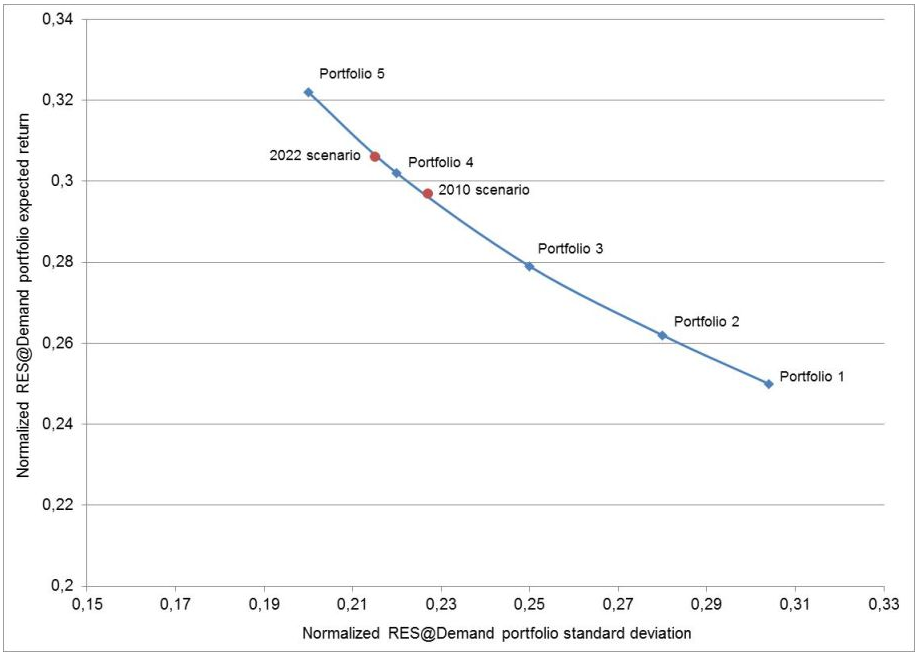

Fig. 7. Efficient frontier MPT_RES@Demand model

Table 3. Characterization of MPT_RES@Demand optimal portfolios

	$\sigma(L_p)$	$E(L_p)$	Wind	Hydro	Photovoltaic
Portfolio 1	0,304	0,25	0%	100%	0%
Portfolio 2	0,28	0,262	11,48%	88,52%	0%
Portfolio 3	0,25	0,279	27,87%	72,13%	0%
Portfolio 4	0,22	0,302	35,87%	56,40%	7,73%
Portfolio 5	0,20	0,322	38,76%	44,52%	16,72%
201 Scenario	0,227	0,297	42,03%	56,59%	1,38%
2022 Scenario	0,215	0,306	38,22%	53,46%	8,32%

3.3. MPT_RES@Cost model

This analysis is similar to the one conducted in section 3.1. However, the model is now weighted by the levelised costs of each RES technology. This way, an efficient frontier will be drawn from the optimization model with the objective goal being the minimization of the total expected cost of the RES system. The optimization model is described by (15) to (18) describe the model.

Objective function

$$\text{Min} \quad E(LC_P) = \sum_{i=1}^{3} W_i LC_i E(L_i) \tag{15}$$

Restrictions

$$\sigma(LC_P) = \sqrt{\sum_{i=1}^{3} W_i^2 LC_i^2 \sigma_i^2 + \sum_{i=1}^{3} \sum_{k=1(k\neq i)}^{3} W_i W_k \rho_{ik} \sigma_i LC_i \sigma_k LC_k} \tag{16}$$

$$\sum_{i=1}^{3} W_i = 1 \tag{17}$$

$$W_i \geq 0 \quad \forall_i \tag{18}$$

Where $E(LC_p)$ represents the expected levelised cost of the portfolio per unit of installed capacity, $\sigma(LC_p)$ represents the standard deviation of levelised cost of the portfolio and LC_i represents the levelised cost of each i technology .

Figure 8 and Table 4 describe the results obtained, including the efficient frontier and the characterization of a set of optimal portfolios.

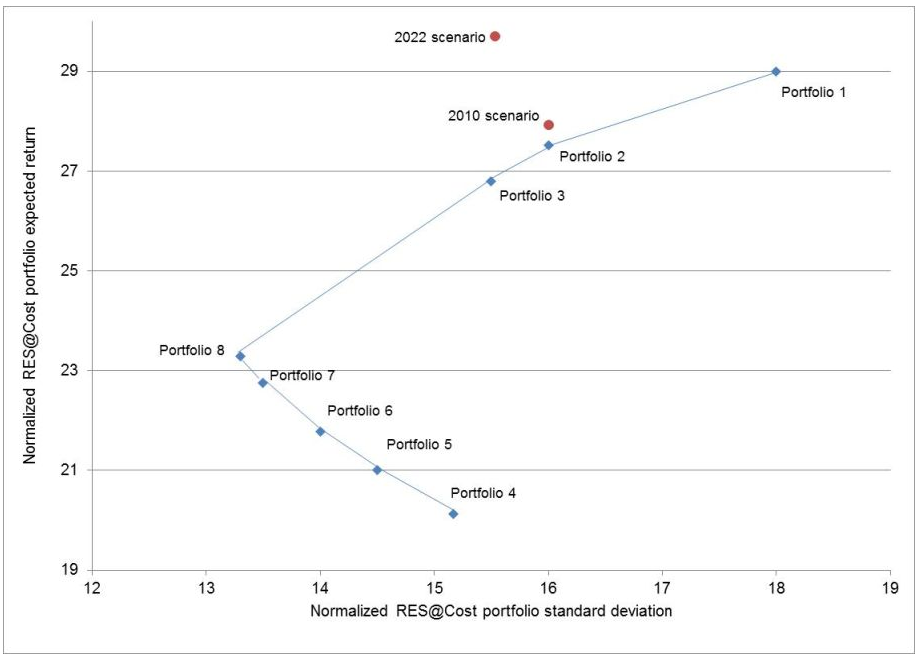

Fig. 8. Efficient frontier MPT_RES@Cost model

Table 4. Characterization of MPT_RES@Cost optimal portfolios

	$\sigma(LC_p)$	$E(LC_p)$	Wind	Hydro	Photovoltaic
Portfolio 1	18	29	31,80%	68,20%	0
Portfolio 2	16	27,51	44,84%	55,16%	0
Portfolio 3	15,5	26,8	48,80%	51,20%	0
Portfolio 4	15,17	20,13	100%	0	0
Portfolio 5	14,5	21	94,36%	5,64%	
Portfolio 6	14	21,77	89,90%	8,28%	1,82%
Portfolio 7	13,5	22,75	84,12%	12,74%	3,14%
Portfolio 8	13,3	23,29	81,03%	15,10%	3,87%
2010 Scenario	16	27,92	42,03%	56,59%	1,38%
2022 Scenario	15,53	29,71	38,22%	53,46%	8,32%

3.4. Analysis of results

The results indicate that both 2010 and 2022 scenarios [17,18] are close to the efficient frontier for MPT_RES and MPT_RES@Demand models. In fact, both these scenarios reflect the Portuguese energy policy goals of increasing RES share on the electricity system, diversifying the energy sources and promoting a strategy based on hydro reinforcement to deal with the increasing wind share. In the same way, most of the less risky scenarios described in figures 6 and 7 point to mix hydro-wind power scenarios as the more efficient ones. More risky strategies rely mainly on hydro power, the option with higher expected return but also the one with higher standard deviation. Although a positive correlation exists between wind and hydro, it does not seem to be enough to jeopardize the mix of these technologies in most of the scenarios. On the other hand, photovoltaic presents a less interesting expected value and a risk level close to the hydro one. It presents, however, the advantage of being negatively correlated to both wind and hydro. As so, less risky scenarios tend to include also this option combined with hydro and wind.

The MPT_RES@Cost present quite different results, clearly driven by the levelised cost of the technologies. A strong reliance on wind power is evident along the efficient frontier, as this is the option with less expected cost and with the lowest standard deviation when considering the levelised cost normalized by the installed power. Solutions with lower risk are characterized by a mix of wind, hydro and to a much lower extent photovoltaic technology, leading to a higher expected cost but also taking advantage of the portfolio diversification.

Particularly interesting for the MPT_RES@Cost is the comparison of portfolio 3, portfolio 4 and 2022 scenario. All of these solutions have close risk values, but very different expected levelised costs and RES structures. What seems to be the best solution (portfolio 4) is however, compromised by a 100% wind power share. From the technical point of view is a nonsense solution, due to the already existing hydro capacity and for motives of security of supply. Both portfolio 3 and 2022 scenario are much more balanced solutions, as a stronger diversity of the mix is foreseen.

The obtained results put in evidence the need to enrich the traditional MPT analysis with additional technical, legal and economic constraints when passing from financial markets to the analysis of portfolios of real projects. Traditional strategic electricity power planning cost optimization models with technical restrictions must be combined with efficient portfolio design with risk restrictions. The research project is now proceeding with this new approach into a single quantitative framework, envisaging the following elements:

- A cost objective: to minimize levelized cost of production of the electricity system as a whole.
- An environmental objective: to minimize environmental impacts, either measured by emissions or by externalities valuation.

- A risk objective: measured by the variance of the portfolio.
- A set of decision variables: share of each technology, measured by the ratio between the installed power of each technology and the total installed power of the system.
- A set of constraints: capacity limitations, legal and technical requirements and electricity demand needs.

4. Conclusion

Social welfare strongly depends on a reliable and competitive electricity system. RES technologies constitute key investments to design future scenarios or strategies for sustainable future. The raising trend of RES brings however considerable challenges to decision makers due to uncertainty of the production highly dependent on the availability of the underlying resources. This paper demonstrates the application of MPT for RES in electricity planning. This allowed to address both the expected return and the RES portfolio risk, taking into account both the standard deviation of each technology output and the correlation coefficient between technology outputs and demand needs.

The study of the Portuguese case concludes that less risky solutions are characterised by a mix of RES technologies. This mix, however, depends on the criteria used to quantify the expected return. If the maximisation of the RES contribution to the system is the goal of the planner, hydro emerges as the major contributor. On the other hand, if decisions are driven by levelised costs, hydro is penalised and wind becomes the preferable option. Photovoltaic share only becomes relevant for low risky solutions, regardless of the model used. The present Portuguese RES generation mix and the forecasted scenario for 2022 [16, 17] showed to be close to the efficient frontier for the case of MPT_RES and MPT_RES@Demand models, reflecting the diversification goal for the sector. Notwithstanding, when the levelised cost is included in the analysis, both 2010 and 2022 scenarios move away from the efficient frontier.

Although the usefulness of the MPT approach in analysing the electrical planning scenarios, has been demonstrated, it is important not to forget some limitations of this approach. For example, [12] emphasised two issues. On the one hand, the failure to consider transaction costs associated with changes in generation mix. Second, the fact that, generally, the studies carried out do not take into account the feasibility of the efficient portfolios obtained with the MPT theory in the context of existing energy infrastructure. Moreover, [7] pointed out that the characteristics of electricity generation technologies are not always comparable to the characteristics of financial assets for which the MPT theory was developed. Firstly, markets for assets (e.g. turbines, coal plants) related to electricity generation are usually imperfect in contrast with capital markets, which also make them less liquid. Secondly, financial assets are almost infinitely divisible and fungible, which does not happen with electricity generating real assets. Finally, investments in electricity production technologies tend to be lumpy, especially renewable technologies. However, [7] consider that "for large service territories or for the analysis of national generating portfolios, the lumpiness of individual capacity additions becomes relatively less significant".

Recognizing that MPT for electricity system analysis must go beyond the traditional models, future work envisages the development of a new model combining MPT with generation expansion models for electricity power planning.

Acknowledgments

This work was financed by: the QREN – Operational Programme for Competitiveness Factors, the European Union – European Regional Development Fund and National Funds-Portuguese

Foundation for Science and Technology, under Project FCOMP-01-0124-FEDER-011377 and Project Pest-OE/EME/UI0252/2011.

References

[1] Beltran H., Modern Portfolio Theory Applied to Electricity Generation Planning [Master dissertation]. Illinois, USA: University of Illinois at Urbana-Champaign; 2009.

[2] Joode J., Boots, M., Concepts of investment risks and strategies in electricity generation. Energy Research Centre of Netherlands, June 2005, ECN-061.

[3] Sedano R., Cowart, R., Power system planning and investment, New England Demand Response Initiative (NEDRI) Report, March 2003.

[4] Awerbuch A., Portfolio-Based electricity generation planning: policy implications for renewables and energy security. Mitigation and Adaptation Strategies for Global Change 2006; 11:693–710.

[5] Roques F., Newbery D., Nuttall W., Fuel mix diversification incentives in liberalized electricity markets: A Mean–Variance Portfolio theory approach. Energy Economics 2008;30:1831–1849.

[6] Liu M., Wu F., Portfolio optimization in electricity markets. Electric Power Systems Research 2007;77:1000–1009.

[7] Awerbuch S., Berger M., Applying portfolio theory to EU electricity planning and policy-making. IEA Research Paper, Paris, February 2003, Report Number EET/2003/03.

[8] European Commission, EU energy trends to 2030- Update 2009; 2010; http://ec.europa.eu/energy/index_en.htm

[9] Markowitz H., Portfolio selection. Journal of Finance 1952;7(1):77–91.

[10] Huisman R., Mahieu R., Schlichter F., Electricity portfolio management: Optimal peak/off-peak allocations. Energy Economics 2009;31:169–174.

[11] Damodaran A., Corporate finance: Theory and practice (2nd ed.). John Wiley & Son; 2001.

[12] Allan G., Eromenko I., McGregor P., Swales K., The regional electricity generation mix in Scotland: A portfolio selection approach incorporating marine technologies. Energy Policy 2011;39:6–22.

[13] Roques F.; Hiroux C., Saguan M:, Optimal wind power deployment in Europe — A portfolio approach. Energy Policy 2010;38:3245–3256.

[14] DGGE, Renováveis-Estatísticas rápidas; Janeiro 2012; www.dgge.pt (in Portuguese)

[15] Krajačić G., Neven D., Carvalho M.G., How to achieve a 100% RES electricity supply for Portugal?. Applied Energy 2011; 88(2):508-517.

[16] Pereira S., Ferreira P., Vaz A.I., Strategic Electricity Planning Decisions. Proceedings of the 6th Dubrovnik Conference on Sustainable Development of Energy, Water and Environment Systems; 2011 September 25-29; Dubrovnik, Croatia.

[17] REN, Dados Técnicos 2010; 2010; www.ren.pt (in Portuguese).

[18] REN, Plano de Desenvolvimento e Investimento da Rede de Transporte de Electricidade 2012-2017 (2022); Julho 2011; www.ren.pt (in Portuguese).

Stability and limit cycles in an exergy-based model of population dynamics

Enrico Sciubba[a], Federico Zullo[b]

[a] *Dept. of Mechanical & Aeronautical Engineering, University of Roma La Sapienza, Via Eudossiana 18, 00184 Roma, Italy. enrico.sciubba@uniroma1.it*

[b] *School of Mathematics, Statistics & Actuarial Science, University of Kent, Canterbury CT2 7NF, UK. zullo@fis.uniroma3.it*

Abstract

The long-term qualitative behaviour of most real ecological populations can be mathematically classified as either asymptotic equilibrium or limit cycling. The reasons underlying these types of behaviour have been, and are still, debated. Aim of this paper is to show that it is possible to characterize both of these behaviours through a population dynamics model, proposed and developed in previous work by the authors, in which the resource consumption is quantified solely in terms of exergy flows. A proper number of reasonable assumptions on the phenomenological characteristics of the interacting species result in different evolutionary scenarios, corresponding respectively to asymptotic stability or periodic attractors. In the case of asymptotic periodic motion the system is described by a set of non-linear, non-autonomous differential equations and an analytical investigation becomes arduous even in the simplest cases. Explicit results, both analytical and numerical, are discussed in this paper. The theoretical description is compared with the behaviour of real, well-known biological systems: the snowshoe hare-lynx predator-prey system for the periodic case and the reindeer herds of the Pribilof Islands for the case of asymptotic stability. The assumptions that must be posited to obtain a cyclic limit type behaviour in ecological populations appear to have been never recognized before and the possibility to adopt them as an universal mechanism of population cycles is discussed in the conclusions.

Keywords: sustainability, eco-systems analysis, extended exergy accounting, population dynamics, population cycles.

1 - Introduction

The concept of sustainability is inherently linked with the consideration that any analysis, be it qualitative or quantitative, of system-environment interactions unavoidably leads to the identification of a certain number of natural resources, each available in a finite amount. Since the dynamic characterization of the interplay among one or more species in a given ecological niche cannot ignore their dependence on the resources they can avail themselves of, this leads to an "intrinsic" definition of sustainability. If one adopts this point of view, there are some difficulties that preclude the construction of sufficiently detailed mathematical models that may describe, within a general framework, the outcome of the struggle for life. Indeed any model must confront itself with three well-known empirical results: i) the multiple "modes" of natural behavior detected in all existing species, that can be qualitatively categorized into interactions such as *competition*, *cooperation*, *antagonism*, *adaptation* and so on; ii) the broad variety of resources each species can

avail itself of; and iii) the natural "flexible attitude" of most species towards the *substitutability* of certain resources.

As in most modeling activities, and specifically in those attempting to treat living organisms, there exists a fundamental competition between the adoption of a completely heuristic approach, that leads to the development of several and possible unrelated *ad hoc* models, each of them focusing on the particular dynamics of a certain species, and the scientific urge for generality, that favours higher-level attempts to interpret global processes as obeying a general trend. The first approach bears the risk of describing in a sufficiently predictive way only tiny scraps of the surrounding reality, while the second, to be successful, must somehow overcome the three above stated problems. The point of view expressed in our previous papers [1-2] is that this second approach can be properly formulated by means of an exergy analysis, or, to be more precise, in terms of the concept of extended exergy (EEA, [3]), a physical quantity that allows to objectively measure and compare the different forms in which natural resources make themselves "available". Use of EEA makes it possible to use a single additive measure for the resources available to populations.

With regard to the three points raised above, it is clear that no genuinely universal approach can be mathematically formulated, because this would imply that the analyst is able to classify within general schemes even voluntary or instinctive behaviors that, especially in superior species, must be considered only in relation to a (species-specific) framework of social norms. Nevertheless, if one assumes, following Lotka [4], that consciousness is closely bound with life processes, it becomes possible to posit a somewhat general working hypothesis, formulate a proper mathematical model on its basis, and then infer from the model some global (i.e., at system level) and "local" (i.e., species-specific) consequences that must subsequently be validated by some suitable *in vivo* experiment. Such an approach has proven successful, as it was demonstrated in two previous papers [1-2], where an analysis of the sustainability concept made on the basis of a competitive model of populations dynamics was presented and discussed. The "competition" was *among* the species and *for* the available resources. The hypotheses underlying that analysis are very simple:

1) The number N of individuals in a species at a given time depends (non-linearly) on the global primary exergy resources a population can avail itself of.
2) The global primary exergy resources may be quantified by the Extended Exergy method [3].

The resulting equations, coupling the exergy rate $\dot{E}(t)$ of common resources exploited by Z populations, with their respective population sizes, read:

$$\dot{N}_i(t) = N_i(t)\left(\frac{r_i\dot{E}(t) - \mu_i\sum_{j=1}^{Z} a_{ij}N_j(t)}{\dot{E}(t) + \sum_{j=1}^{Z} a_{ij}N_j(t)}\right) \qquad 1)$$

where the dot denotes the time derivative, r_i, $i=1\ldots Z$, are the growth rates of each populations for infinitely abundant resources and μ_i's are the intrinsic mortality rate of each species when the availability of resources drops to zero. The diagonal elements a_{ii} of the system matrix can be interpreted as the specific exergy consumption rate corresponding to a "minimal survival" for the population labeled with the index "i", while the off-diagonal elements ($i\neq j$) are a measure of the strength of the competition between populations i and j ($a_{nk}=a_{kn}=0$ meaning that the two populations n and k do NOT compete). Once a well-defined scenario is provided by supplying an

independent equation for the time history of the exergy rate $\dot{E}(t)$ of the exploited resources, equations (1) determine the evolution of the Z populations. For a detailed analysis on the dynamics of competing populations governed by eqs. (1) readers are referred to [1].

In this article, on the basis of the previous assumptions, we analyze some universal behaviors in the dynamics of biological systems: the adjective "universal" implies that they are shared by a large number of case studies on the dynamics of given species populations. Indeed most of the behaviors are either limit cycles or stable equilibrium [5], [6]. As for the population cycles, many hypotheses have been developed in the last fifty years in order to clarify the physical causes underlying their dynamics. Generally speaking, three orders of difficulty are encountered: i) why does the period of the empirically observed cycles change from species to species (and, under apparently similar circumstances, even for the same species)?; ii) how can the amazing synchronic fluctuations of the numerosity of some species in a given geographical region be justified?; and iii) what is the link between a given species undergoing -or not- cycles and the state of its immediate environment?

The existing hypotheses can be classified in abiotic (weather and sunspots), biotic intrinsic (genotype or behavioral changes) and biotic extrinsic (food, parasites, predation etc.) [7-8]. Surely some of these hypotheses can explain at least partial elements of the cycles problem: for example the ten to eleven-year sunspot's cycle could explain the ten-year cycle of hares but not the four or five year cycles of voles [8]. Also, most of the proposed models do not answer all the above three questions, essentially for two reasons: first, it is very unlikely that the answer to these questions rests with one single physical explanation, and second, no model divulged to date can explain all sides of the corresponding experimental evidence.

In this paper we propose an answer to all of the three questions, obtained by positing a constructive assumption (in the sense of Popper's definition [9]): we develop and discuss a model that provides a good qualitative and an approximate quantitative description of population cycles and thus can be tested for experimental validation or falsification. To the best of our knowledge, the assumptions that constitute the scientific basis of our model have never been presented before.

As an application of our model, we present a comparison with the well-known empirical observations of the lynx-hare system [10-11].

The second issue that we consider in this paper is the asymptotic stability of the numerosity of some populations: indeed also this case is very common in both *in natura* and *in vivo* observations (see for example [6]). Our central assumption is that, since the numerosity of a population depends on the exergy resources it can avail itself of, the cause of this type of behavior must be searched in the term $\dot{E}(t)$ in eq.1. As shown in [1-2], if the evolution of this term turns out to drive the solution to an asymptotically stable point (note that this includes both scenarios with non-renewable resources and scenarios with a constant amount of renewable resources), then the populations will follow this stability and the long time picture can be either sustainable (survival of all species in certain numerical ratios) or non sustainable (there will be an extinction of some or all of the species), depending on the biotic parameters of the species. An explicit case, the reindeer herds of the Pribilof Islands [12], will be discussed in detail, both qualitatively and quantitatively. In passing, it will be shown that the proposed approach can also answer a longstanding problem about the different behaviours of two herds living in very similar niches.

2 – Limit cycles of populations as a result of differentiated exergy sources: a fundamental hypothesis.

The hare-lynx interaction is a well-known process on which an extensive body of experimental and theoretical literature exists: therefore we have chosen it as a benchmark for our model.

First of all, let us recall some well-known empirical facts, collected in a large number of publications, about population oscillations. In the case of a predator-prey system, the causes that lead to numerical fluctuations of the two species seem to be different. It is known that cycles often occur in areas of low prey diversity, where specialist predators feed primarily on a single prey species [13-15]. Indeed the diversity of mammalian prey decreases from south to north in the northern hemisphere; when there are alternative prey to hares, the lynx diet becomes differentiated. In [15] the authors take into consideration the relationship between the lynx dietary specialization and the cyclicity of their population. They come to the conclusion that an increase in specialization leads to a truly cyclic dynamics of predators, whereas when the predators can vary their diet feeding on alternative prey the dynamics is no longer cyclic. These considerations support the assumption that the lynx "track" the oscillations of the hares rather than causing them with their predatory pressure. This shifts the attention to the cause of the prey fluctuations. In [5], where about 700 time series (covering more than 25-years) of different species are analyzed, it is argued that, for mammalians, the probability to observe oscillations increases with latitude, but there are no such trends for the amplitude or the period of the oscillations. On the other hand it is also observed [16] that environments experiencing strong seasonality turn out to be more favorable to the onset of larger amplitude cycles.

Now consider the simplest case: the presence of a prey species in a given environment without predators. If our assumptions are correct and the fluctuations of the hares are not caused by the predatory pressure, it ought to be possible, depending on the type of environment (represented here by the exergy input), to observe oscillations also in this simple situation. Now let us posit that:

i) The environment *without* prey corresponds to a steady dynamic state: the exergy flow, that in presence of prey is partially exploited by the species, is, *in the absence* of this species, constant.

ii) The total exergy flow is given by the *sum* of different inputs, none of which is essential for the species survival.

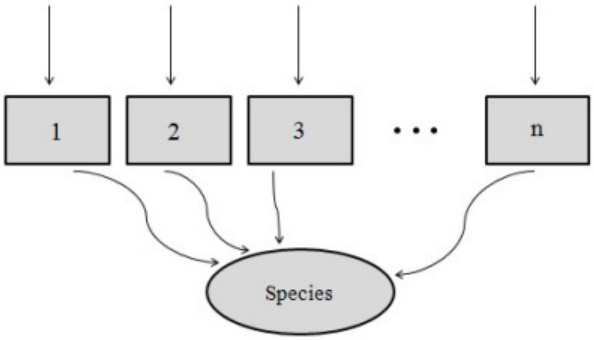

Fig. 1: The case of multiple incoming exergy sources available to a species.

In fact, the total primary exergy flow (basically, solar irradiation, water and nutrients from the soil and atmosphere/hydrosphere) will be exploited by the (biotic and abiotic) systems in that niche who will reach some steady state dynamic equilibrium (for obvious reasons, we exclude from our considerations situations in which the competition at these "elementary" scales leads to a global extinction). For assumption ii) we are thinking of an environment offering an ensemble of food sources, each of which is consumed randomly by the prey species: if the consumption of a given source is so intensive that it is completely depleted in a given time, then after this time the species will thrive on some or all of the other sources; also, if the source depleted is renewable (like the

vegetable ones), it will be in part or in total restored. As we will now show, under this assumptions the prey species will thrive on a *periodic* total exergy flow.

Thus our model assumes that when the preys are absent from their environment, the value of the "secondary" exergy flow (the one that is indeed primary for the prey species) is constant in time, say $\dot{E} = a_0 = const.$ (= assumption 1). In presence of prey $\dot{E}$ will no longer be constant, so that there is now an equation defining the variation of a around the point a_0. We need a differential equation defining the evolution in time of a. It is clear that such evolution *cannot* be determined solely by the knowledge of the initial condition $a|_{t=0}$, because one has to take into account that $a(t)$ can be a decreasing function in a neighborhood of *t=0* due to the predominance of the action of the prey with respect to the force tending to restore the resource, or can be an increasing function in the same neighborhood due to the predominance of the external input with respect to the prey consumption. This means that we need also the value of $\dot{a}|_{t=0}$, and the equation defining the evolution of $a(t)$ must be a *second order* differential equation. So we need of an equation defining $\ddot{a}$. Suppose that the prey consume their food only in an interval of time, say from t_0 to t_1; after t_1 the situation will tend to return in equilibrium as before t_0, because of the continuous primary exergy input into the system. To larger fluctuations around the point a_0 correspond larger values of the restoring force: this means that $\ddot{a}$ depends on the difference $a - a_0$, that is $\ddot{a} = F(a - a_0)$ for some function *F*. By assumption 2, we can expect that to a greater variation of a around the point a_0 there corresponds a smaller number of exergy sources. Vice versa a large number of exergy sources will correspond to smaller variations: in this case it suffices, in order to extrapolate the dynamic of the sources to expand *F* around the point a_0 and retain only the lower terms in the expansion:

$$F(a - a_0) \sim \beta - k^2(a - a_0) + \cdots. \qquad 2)$$

So that the resulting equation for a is given by:

$$\ddot{a} = -k^2(a - a_0) \qquad 3)$$

Note that the minus sign on the term k^2 is due to the "restoring" nature of the force tending to the re-establishment of the steady flow solution $\dot{E}(t) = a_0$, whereas the term β has to be zero because of the steady flow solution for $a = a_0$. The time evolution of the variable $a(t) = \dot{E}(t)$ is then given by:

$$\dot{E}(t) = a_0 + b\sin(kt + \varphi). \qquad 4)$$

According to assumption 2, the amplitude of the oscillations b must be a decreasing function of the number of food sources (Fig. 1).

Notice that the exergy flow 4) is the flow available to the prey, whether the prey represent the available exergy input for the specialist predator. If in equation 1) one substitutes *H* (= hares) for N_1, *L* (= lynxes) for N_2 and the flows for the corresponding exergy inputs, the following equations are obtained:

$$\begin{cases} \dot{H} = H\,\frac{(r_1(a_0 + b\,sin(kt)) - \mu_1 a_{11} H - \mu_1 a_{12} L)}{a_0 + b\,sin(kt) + a_{11} H + a_{12} L} \\ \dot{L} = L\,\frac{(r_2 vH - \mu_2 a_{22} L)}{vH + a_{22} L} \end{cases} \qquad 5)$$

Where, without loss of generality, we set $\varphi = 0$. The constant *v* has dimensions of J/kg and provides the conversion of the mass of the prey into exergy utilized by the predators. Obviously here $a_{21} = 0$ because the prey do not compete with the predators (hares are assumed not to feed on

each other!). The set of equations 5) is not amenable to an exact treatment: it is a system of non-linear, non-autonomous equations. So we first try an analytic approach to the simplest of the cases: the presence of prey without predators. One obtains:

$$\left\{\dot{H} = H\frac{(r_1(a_0+b\,sin(kt))-\mu_1 a_{11}H)}{a_0+b\,sin(kt)+a_{11}H}\right. \qquad 6)$$

Let us discuss some global features of this equation. Since the set $\{N_i \geq 0, i = 1..Z\}$ is an invariant submanifold for equations 1), we consider only the line $H \geq 0$. The curve $\gamma(t) = \frac{r_1(a_0+b\,sin(kt))}{\mu_1 a_{11}}$ (the grey curve in fig.2) divides the semi-plane $(H, t \geq 0)$ into two parts; in the upper one the population decreases ($\dot{H} < 0$), in the lower one the population increases ($\dot{H} > 0$): after an initial transient, the solution stabilizes and oscillates within a band width $\left(\frac{r_1(a_0-b)}{\mu_1 a_{11}}, \frac{r_1(a_0+b)}{\mu_1 a_{11}}\right)$ as in the two examples of figure 2. So, the set $\left(\frac{r_1(a_0-b)}{\mu_1 a_{11}}, \frac{r_1(a_0+b)}{\mu_1 a_{11}}\right)$ is the *attractor* of our system. Notice also in figure 2 how the solution curves decrease or increase according to their position with respect to the reference grey curve $\gamma(t) = \frac{r_1(a_0+b\,sin(kt))}{\mu_1 a_{11}}$.

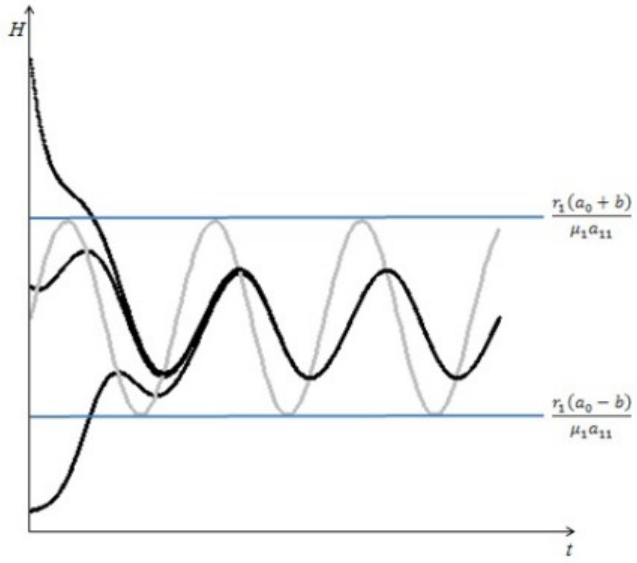

Fig.2

After an initial transient where the population presents an exponential growth or decay corresponding to an initial condition $0 < H(0) < a_0$ or $H(0) > a_0$, the population stabilizes on a given curve. As we will show this curve is indeed independent from the value of $H(0)$ in the sense that for whatever initial condition, all solutions converge on the same curve. This is clear also by inspecting fig. 2, where the evolution history of the prey population for three different initial conditions is shown.

Without loss of generality then, rather than the initial transient, we are interested in this long-term, oscillating behavior of the solution, which is independent on initial conditions. The extrapolation of this behavior can be suitably done noticing the role played by the parameter b. When $b = 0$, the set $\left(\frac{r_1(a_0-b)}{\mu_1 a_{11}}, \frac{r_1(a_0+b)}{\mu_1 a_{11}}\right)$ reduces to the point $H = H^* = \frac{r_1 a_0}{\mu_1 a_{11}}$: in this case indeed there is no oscillation in the exergy sources and the species reaches asymptotically its carrying capacity given by $H = H^*$. When b is not equal to 0, the solution oscillates within a set whose amplitude is of order b, so the oscillations will be at most of order b. This suggests to expand the dynamical variable $H(t)$ in

series of the dimensionless parameter $\frac{b}{a_0}$. After inserting the ansatz $H(t) \equiv \sum_n h_n(t) \left(\frac{b}{a_0}\right)^n$ in eq. 6) and equating the same powers of $\left(\frac{b}{a_0}\right)$, one finds that the functions $h_n(t)$ are solutions of the system:

$$\begin{cases} \dot{h}_0(a_0 + a_{11}h_0) - h_0(r_1 a_0 - \mu_1 a_{11} h_0) = 0 \\ \dot{h}_1(a_0 + a_{11}h_0) - h_1(r_1 a_0 - \mu_1 a_{11} h_0) + \dot{h}_0(a_0 \sin(kt) + a_{11}h_1) + \\ -h_0(r_1 a_0 \sin(kt) - \mu_1 a_{11} h_1) = 0 \\ \dots \\ \dots \\ a_0\left(\dot{h}_l - r_1 h_l\right) + a_0 \sin(kt)\left(\dot{h}_{l-1} - r_1 h_{l-1}\right) + a_{11} \sum_{n=0}^{l} h_{l-n}\left(\dot{h}_n + \mu_1 h_n\right) = 0 \qquad l \geq 2 \end{cases} \tag{7}$$

This system can be, in principle, solved iteratively. In fact the first equation involves only the unknown function h_0. When solved, one can insert the result into the second equation and find h_1 and iterate. Note also that only the first equation is non-linear (but indeed easily solvable), the others are linear differential equations of first order in the highest derivative, so the iteration can be carried out by using standard techniques. A further simplification in the calculations can be obtained by noticing that, if the only asymptotic solution (the oscillating one) is sought, it is possible to find the asymptotic behavior of h_{l-1} and then solve the equation for h_l. The terms containing the information about initial condition $H(0)$ will always decay exponentially in time, so in the asymptotic regime we can write:

$$\begin{cases} h_0 = \dfrac{r_1 a_0}{\mu_1 a_{11}} \\ h_1 = \dfrac{\eta}{\eta^2 + k^2}[\eta \sin(kt) - k\cos(kt)]h_0 \\ h_2 = \dfrac{\eta k^2 \left[\eta^2(5k^2 - \eta^2)\cos(2kt) + 2k\eta(k^2 - 2\eta^2)\sin(2kt) - (\eta^2 + k^2)(\eta^2 + 4k^2)\right]h_0}{2r_1(\eta^2 + 4k^2)(\eta^2 + k^2)^2} \\ \dots \\ \dots \end{cases}$$

where the convenient parameter $\eta = \frac{\mu_1 r_1}{\mu_1 + r_1}$ has been introduced. In the fig. 3 we report a plot of two numerical solutions $H(t)$ of the system 6) corresponding to two different initial conditions (grey curves), the reference curve $\gamma(t) = \frac{r_1(a_0 + b\,sin(kt))}{\mu_1 a_{11}}$ (dotted grey curve), the solution until the first order in the oscillating regime $(h_0 + \frac{b}{a_0}h_1)$ (dashed black curve) and the solution until the second order in the oscillating regime $(h_0 + \frac{b}{a_0}h_1 + \left(\frac{b}{a_0}\right)^2 h_2)$ (dotted black curve). As shown in the enlarged detail on the right, already at the second order the convergence of the series is very good, since the numerical solutions (marked in light-blue in the zoom) and the approximated one practically coincide.

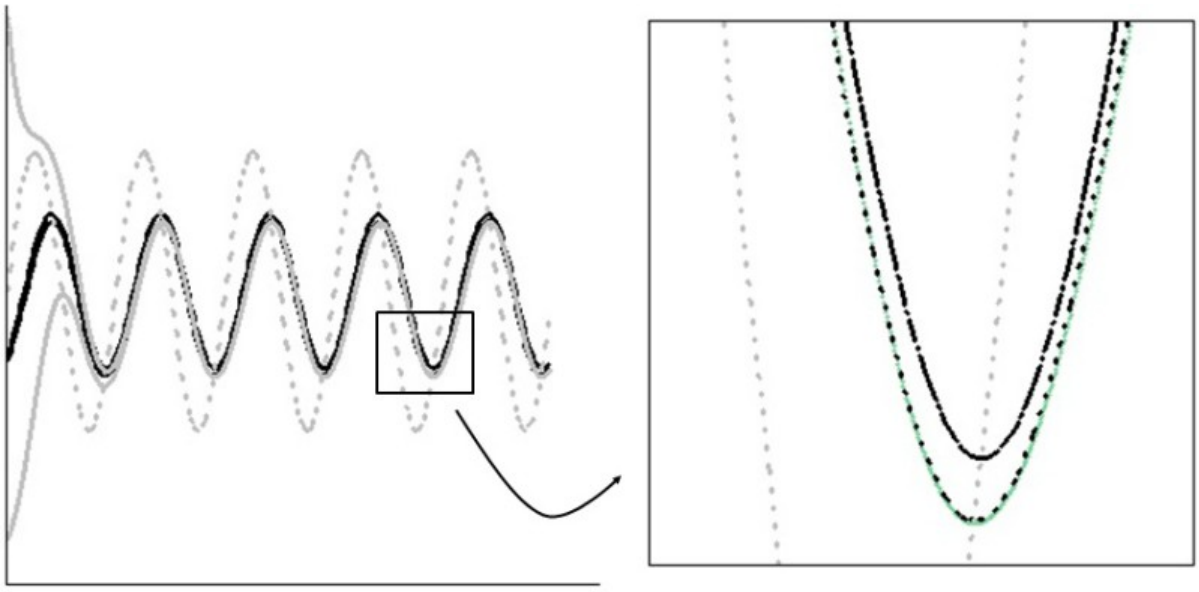

Fig. 3

We see by inspection that the mean value of $H(t)$ is affected by the oscillations only at the second order. Indeed if there are no oscillations in the exergy flow the prey would reach the carrying capacity limit given by $H^* = \frac{r_1 a_0}{\mu_1 a_{11}}$. In presence of oscillations the population is approximated by $H(t) = h_0 + \frac{b}{a_0} h_1 + \left(\frac{b}{a_0}\right)^2 h_2$ and the arithmetic mean on a period of oscillations $T = \frac{2\pi}{k}$ is given by:

$$< H >= \frac{1}{T}\int_0^T h_0 + \frac{b}{a_0} h_1 + \left(\frac{b}{a_0}\right)^2 h_2 = H^* \left(1 - \left(\frac{b}{a_0}\right)^2 \frac{\mu_1(\mu_1 + r_1)k^2}{2(\mu_1^2 r_1^2 + (\mu_1 + r_1)^2 k^2)}\right)$$

that is a bit lower than H^*. Since μ_1 and r_1 are positive, the function $\frac{\mu_1(\mu_1+r_1)k^2}{2(\mu_1^2 r_1^2+(\mu_1+r_1)^2 k^2)}$ is bounded, and more precisely:

$$0 \leq \frac{\mu_1(\mu_1 + r_1)k^2}{2(\mu_1^2 r_1^2 + (\mu_1 + r_1)^2 k^2)} \leq \frac{1}{2}$$

So that at second order, the difference between $< H >$ and H^* is at most $\frac{1}{2}\left(\frac{b}{a_0}\right)^2$. Therefore if the mean exergy flow to our population is $\dot{E} = a_0$, the mean of the numerosity of the population is not given by the value $H^* = \frac{r_1 a_0}{\mu_1 a_{11}}$ as it would be expected, but it is a bit *lower*.

Let us now introduce the predators into the picture (eq. 5)). In order to describe analytically the solution we try the approach of the series solution as before. We look at the invariant submanifold $\{H \geq 0, L \geq 0\}$. Also in this case it can be shown that the two curves $L(t)$ and $H(t)$ exponentially converge to a periodic curve with the same period of the incoming exergy and that this asymptotic behavior is again *independent* on the initial conditions, in the sense that whatever initial condition will push the solution on the same curve . For a more detailed discussion of the role played by these type of solutions in living systems we refer readers to [17] and references therein; here we wish

only to underline that, being independent from the initial condition and *globally attracting* [17], these curves and their mathematical description represent the nearest description of the notion of dynamical equilibrium developed (and observed) in ecological systems.

Inserting the series $H(t) \equiv \sum_n h_n(t)\left(\frac{b}{a_0}\right)^n$ and $L(t) \equiv \sum_n l_n(t)\left(\frac{b}{a_0}\right)^n$ into equation 5) and equating the same powers of $\left(\frac{b}{a_0}\right)$ one obtains again a linearization of the system 5), in the sense that the two terms of order 0, that is h_0 and l_0 solve a coupled non-linear system with constant coefficients, while all the pairs (h_k, l_k), $k > 0$, solve a recursive *linear* system of differential equation, depending on all the functions (h_j, l_j) , $0 \leq j < k$. Again a further simplification can be obtained by taking, in the recursive process, only the asymptotic part of each term. For the first couple of equations ($k = 0$) one obtains:

$$\begin{cases} l_0 = \frac{r_1 r_2 v a_0}{\mu_1(v r_2 a_{12} + \mu_2 a_{11} a_{22})} \\ h_0 = \frac{r_1 \mu_2 a_{22} a_0}{\mu_1(v r_2 a_{12} + \mu_2 a_{11} a_{22})} \end{cases} \qquad 8)$$

The second couple of equations, that is the equations for (h_1, l_1), shows that both h_1 and l_1 are linear combinations of $\sin(kt)$ and $\cos(kt)$, so also in this case the mean values of $L(t)$ and $N(t)$ on a period are given by $< L(t) > = l_0\left(1 + O(\frac{b}{a_0}^2)\right)$ and $< H(t) > = h_0\left(1 + O(\frac{b}{a_0}^2)\right)$, that is they differ from l_0 and h_0 only at order $(\frac{b}{a_0}^2)$. Note also that the value of l_0 is proportional to the growth rate r_2 of the predators but also to the growth rate r_1 of the prey. Vice versa the value h_0 of the prey is proportional to their growth rate r_1 and to the mortality rate μ_2 of the predators.

3-Comparisons with field data.

In this section w briefly discuss a comparison with field data. The time series for the lynx-hares is well-known (see for example [10-11]), so here we refer to this set of data, ranging from 1845 to 1935. To establish a working methodology we *assume* that the series are indeed periodic: with this assumption we mean that there exists some curve-fitting algorithm, for example the least square method, giving a set of parameters that specify which *periodic function* is the best approximation of the data.

However we can always write the periodic function as a series in sine and cosine, so we would expect, for the function $H(t)$ and $L(t)$ something like:

$$\begin{cases} H(t) = \rho_0 + \sum_{n=1}^{\infty}(\rho_n^1 \cos(nkt) + \rho_n^2 \sin(nkt)) \\ L(t) = \sigma_0 + \sum_{n=1}^{\infty}(\sigma_n^1 \cos(nkt) + \sigma_n^2 \sin(nkt)) \end{cases} \qquad 9)$$

For example at first order it can be calculated that the best least square fit for the data of the hares is given by $H(t)$= 44.81+13.96sin(0.64*t*)+24.91cos(16/25*t*), where *t* is expressed in years and *H*(*t*) is expressed in thousands.

The series 9) is the same type of the series that can be obtained, at least for reasonably low values of *n*, solving the system 5) by series expansion as explained in the previous section:

$$\begin{cases} H(t) = H_0 + \sum_{n=1}^{\infty}(H_n^1 \cos(nkt) + H_n^2 \sin(nkt)) \\ L(t) = L_0 + \sum_{n=1}^{\infty}(L_n^1 \cos(nkt) + L_n^2 \sin(nkt)) \end{cases} \qquad 10)$$

The coefficients $\left(H_n^j, L_n^j\right)$, j=1,2 and (H_0, L_0) will depend on the constants appearing in the system 5), so the matching among the coefficients of 9) and 10) will give some constraints on the constants. If one is satisfied with the first order, than there is *always* a *perfect* matching between 9) and 10) because we have an underdetermined system, that is six equations ($H_0 = \rho_0, L_0 = \sigma_{0,}\rho_n^1 = H_n^1, \rho_n^2 = H_n^2, \sigma_n^1 = L_n^1, \sigma_n^2 = L_n^2$) in ten unknowns that are the constants appearing in 5) (or, better nine unknowns because we are always free to rescale some set of constants and the system remains unchanged). The second order is more difficult to manage (and indeed we have not succeeded to represent it appropriately) because the coefficients $\left(H_2^j, L_2^j\right)$, j=1,2 depend in a very complicate manner by the constants appearing in 5) and the corresponding system of equivalence among polynomial of high order is not amenable to a close form solution even with the aid of symbolic manipulation software, This case appears though to be interesting because we have ten equations in nine unknowns.

4. Asymptotic equilibrium: the case of the reindeers of the Pribilof Islands.

The history of the reindeers herds placed by the United States on the Pribilof Islands in 1911 is well known in literature (see for example [12]). Let us recall only the essentials points of the story for what concerns our purposes. The main islands of the Pribilof group are the St. Paul island (extension about 100 km^2) and St. George Island (about 90 km^2). In 1911 25 reindeers were placed by the U.S. government on St. Paul and 15 on St. George. On the islands the reindeers did not have any predator (except for a very limited hunting by men). By the very beginning these conditions attracted the interests of ecologists because of the possibility to use the herds as a model to study the introduction of other groups on a larger scale. From this point of view the time-history of the herds can be considered as an "in natura" experiment. The lichens vegetations of the islands seems to have a large influence on the behavior of the herds. As pointed out by Palmer [18], in the winter the reindeers prefer to feed on lichens: from December to April their desirable forage consists of 75%-90% of lichens, mosses and other vegetations. Palmer concludes: "*although the lichens can not be said to be necessary for the reindeer maintenance because of their nature or nutritive qualities, yet from the standpoint of a readily accessible winter food supply they are essential*" [18]. According to this author, in an environment similar to those of the Pribilof Islands, the lichens take from 15 to 20 years to recover a grazed area; other authors (see for example Hanna [19]), based on direct inspections, lean towards much shorter period, such as 5 or 6 years. It is clear however that a continuative consumption of lichens by reindeers tends to make this resource *non-renewable*. As witnessed by Scheffer in 1951: *the food lichens are now so rare […] that diligent search is required to find representative specimens* [12]. So we can conjecture that, as concerns our model 1), we have one populations, the reindeers, thriving on non-renewable *and* renewable resources. The renewable part comes from the process of re-growing of that part of grazed food vegetables having a higher growth rate and of the lichens and mosses themselves. Indeed if the number of reindeers were not so large to consume all the food in a certain time then a carrying capacity would be reached, and in our model this carrying capacity limit is *always* associated to a renewable exergy flow exploited by the population [1-2]. Here we see also the mathematical characterization of equations 1) in the case of only one population and an exergy flow given by a mix of non-renewable and constant renewable resources. In the rest of this section we try to compare the analytical and numerical results with the time series of the reindeers herds on St. Pauls and St. George [12]. Let us report, for the sake of completeness, the equations describing the system:

$$\begin{cases} \dot{N}(t) = N(t)\left(\dfrac{r\dot{E}(t) - \mu c N(t)}{\dot{E}(t) + cN(t)}\right) \\ \dot{E}(t) = \dot{E}_{nr}(t) + \dot{E}_r = bN(t)E_{nr}(t)\left(1 - \left(\dfrac{E_{nr}(t)}{E_M}\right)\right) + \dot{E}_r \end{cases} \qquad 11)$$

We must remark that in general equation 11) are the scaled version (in time) of similar equations, where the functions N and E are premultiplied by a constant that, however, can be absorbed in the definition of time. In these formulae $N(t)$ indicates the numerosity of the population, $\dot{E}$ is the total exergy flow incoming the system, $\dot{E}_{nr}$ and $\dot{E}_r$ being respectively the non-renewable and renewable part of this exergy, E_M is the total amount of cumulative exergy available from the non-renewable resources, r is the *intrinsic* or *genetic* growth rate of the species, μ is the mortality rate for the population in the limit of vanishing resources, c is a parameter giving the specific exergy consumption rate corresponding to a "minimum survival" of the species, b is a scaling parameter indicating how fast the non-renewable part of the resources are exhausted. With *intrinsic* or *genetic* growth rate we mean that obtained as the difference between the birth rate and the mortality rate of the species when no limit is set to the availability of the resource. As a lower bound for this value we can obviously take the maximum observed growth rate for our population ($= 2.0/years$ in our case), whether as a lower bound for μ we can take the maximum of the mortality rate for our population ($\sim 0.9/years$ in our case). The true values can differ from these (they can be a little higher) since a more realistic inspection shows that the "best possible" real environment for the species is both different from the "infinite" resources scenario and the "worst" one somewhat above the "zero" resources scenario. For the value of c we have an estimate from [20] were a value of 1,735 kcal/days for non-pregnant females and 2,829 kcal/days for pregnant females is given as the mean daily energy requirement between April and May. During the winter the values can be higher, however the order of magnitude remains the same. Reported in Joule and years we have a value $c \sim 4{\cdot}10^9$ J/years. To obtain an order of magnitude for the value of E_M we can assume that the reindeers thrived only on non-renewable resources. Then the value of $c\int_{t_0}^{t_{ext}} N(\tau)d\tau$ (or the equivalent form $c\sum_i N_i$ for the discrete case), where t_{ext} is the time when the population goes extinct, gives a lower bound for E_M. For the St. Paul island we have calculated a value $E_M^{St.P} \sim 9{\cdot}10^{13}$ J, whereas for the St. George island we have a value of $E_M^{St.G} \sim 1{\cdot}10^{13}$ J. The value of b is more difficult to quantify, because it can depend, other than on the particular species under consideration, also on several environmental factors. For example a crust of ice in the winter can hinder the grazing of the reindeers. So we have carefully changed the value of this parameter to fit the experimental data. The results are shown in the following figures.

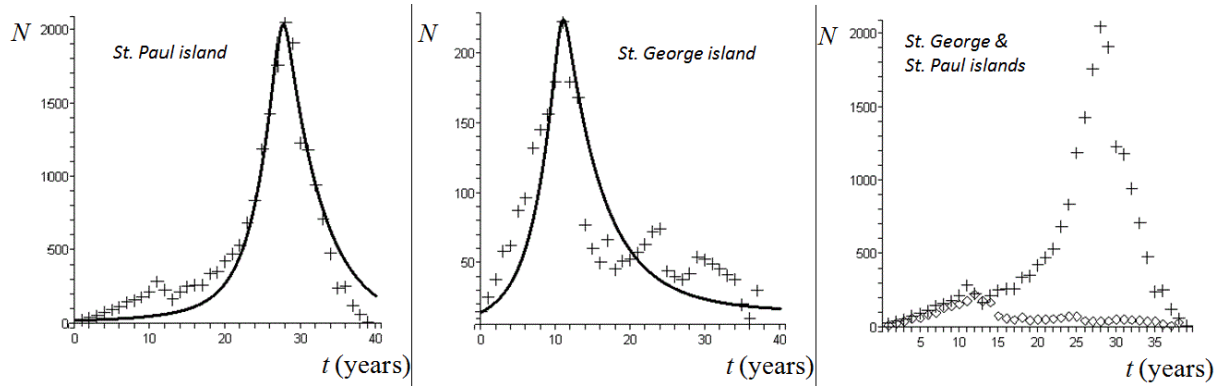

Fig.4: the time series of the reindeers herds on the Pribilof Islands.

The two plots on the left show the data on the populations from [12] (crosses) and the curve obtained by equations 11). The values of the constants are as follows: for the St. Paul island we set $r=3/years$, $\mu=2/years$, $R=4\cdot10^{9}J/years$, $c=4\cdot10^{9}J/years$, $E_M=9\cdot10^{13}J$, $b=1.35\cdot10^{-2}/years$, whereas for the St. George island we set $r=3/years$, $\mu=2/years$, $R=4\cdot10^{10}J/years$, $c=4\cdot10^{9}J/years$, $E_M=1\cdot10^{13}J$, $b=1.25\cdot10^{-1}$. In the plot on the far right we report the two populations on the same axes in order to provide a graphical representation of the very different behavior of these two herds. The initial values for $N(t)$ are given obviously by the known data ($N(0)=25$ for the St. Paul herd and $N(0)=15$ St. George herd). In order to choose a value for $E(0)$ one has to consider the role that it has on the solution of the system 11). The maximum of the functions $\dot{E}(t)$ and $N(t)$ indeed depends, both for its value and the placement, on $E(0)$. If only non-renewable resources are available, then the function $y = E_M - E(t)$ represents the value of the cumulative exergy available to the population at time t, so $y = E_M - E(0)$ is the total exergy available to the population at the initial time. A greater value of $E(0)$ corresponds to a smaller value of total exergy available, so that the maximum of $\dot{E}(t)$ will be reached sooner: an increase of $E(0)$ will displace this maximum to the left. Also, a change in the exergy available to the population will change its maximum numerosity and a larger greater value of $E(0)$ will cause a smaller value of this maximum. Summarizing we can say that greater values of $E(0)$ correspond to shifts on the left in the Cartesian plane of the maximum of $N(t)$ and $\dot{E}(t)$ and to smaller values of these maximum. These is exactly what is observed comparing the numerosities of the two herds in the right of figure 4. In our case we have taken the values $3{,}2\cdot10^{-3}E_M$ for the case of St. Paul island and $1\cdot10^{-2}E_M$ for the St. George island. There could be different physical motives for this discrepancy, but the overall effect must have been such that a portion of the food reserves was not fully accessible in the case of St. George island.

5 - Conclusions

In this paper we discuss the application of a population dynamics model previously developed in [1-2] to two different cases presenting very different behaviors in the dynamic of the populations as a response to the different type of environmental conditions in which populations live. We show that the case of a limit cycle dynamics of the population numerosity can be modeled by a time dependent external driving input to the system; the time dependence is due, in a real sense, to the action of the population on the environment. In such cases we demonstrate that the system is always attracted to the *same* curve independently from the initial conditions. This can be seen as a mathematical description of the notion of *dynamical equilibrium* developed in the realm of ecological systems (see for example [17] and references therein). Also, in section 3) we have shown that our model fits at first order in the expansion of the parameter $\left(\frac{b}{a_0}\right)$ the time series for the lynx-hares interaction [10-11], having assumed the periodicity of this series.

In the case of asymptotic stable equilibrium we have applied our model to the well documented dynamics of two reindeers populations in “closed” ecological niches. The non-trivial dependence of the population curves from the initial conditions (in particular $E(0)$), reflecting the ability of the populations to access to the food, is fully captured by the model and plays a significant role in the resulting dynamics. This is still a preliminary work needing to be refined and extended to other different species behavior, such as cooperation and parasitism, and even if the proposed model

represents only a rough description of the high complexity of ecological systems, still it shows potential to be applied to very different situations.

Acknowledgments.

One of the author (F.Z.) wish to acknowledge the financial support of the “Istituto Nazionale di Alta Matematica” (Italian National Institute for High Mathematics) as a Marie Curie scholarship holder.

References

[1] E. Sciubba, F. Zullo: Is Sustainability a Thermodynamic concept?. International Journal of Exergy 2011 - 8, No.1 pp. 68 – 85.

[2] E. Sciubba, F. Zullo: Exergy based population dynamics: a thermodynamic view of the sustainability concept. 2011. Journal of Industrial Ecology, 15, Issue 2, pp. 172–184, April 2011.

[3] E. Sciubba: ‘Beyond thermoeconomics? The concept of extended exergy accounting and its application to the analysis and design of thermal systems’, Int. J. Exergy, Vol. 1, No. 1, pp.68–84.

[4] A.J. Lotka: Elements of Physical Biology, Baltimore,Williams & Wilkins Company, 1925.

[5] B.E. Kendall, J. Prendergast, O.N. Bjørnstad: The macroecology of population dynamics: taxonomic and biogeographic patterns in population cycles; Ecology Letters, 1998, 1; pp. 160-164.

[6] M.P. Hassell, J.H. Lawton, R.M. May: Pattern of dynamical behavior in single-species populations. Journal of Animal Ecology; 1976; 45; pages 471-486.

[7] N. C. Stenseth, R. A. Ims: Population dynamics of lemmings: temporal and spatial variation: an introduction. Pages 61-96 in N. C. Stenseth and R. A. Ims, editors. The biology of lemmings. Academic Press, London, UK.

[8] E. Korpimäki, C.J. Krebs: Predation and population cycles of small mammals; Bioscience; Nov 1996; 46, 10.

[9] K.R. Popper: The Logic of Scientific Discovery, Routledge, 14th Printing, 1977. First English Ed., Hutchinson, 1959. First published as Logik Der Forschung in Vienna: Springer, 1934.

[10] C.J. Krebs, S. Boutin, R. Boonstra, A.R.E. Sinclair, J.N.M. Smith, M.R.T. Dale, K.Martin, R. Turkington: Impact of food and predation on the snowshoe hare cycle, Science. 1995; 269:1112–1115.

[11] C.S. Elton: Voles, Mice and Lemmings. Oxford, U.K.: Clarendon; 1942.

[12] V.B. Scheffer: The Rise and Fall of a Reindeer Herd, The Scientific Monthly, Vol. 73, No. 6 (Dec., 1951), pp. 356-362.

[13] L. Hansson, H. Henttonen: Rodent dynamics as community processes, Trends Ecol. Evol. 3, pp. 195-200.

[14] I. Hanski, L. Hansson, H. Henttonen: Specialist predators, generalist predators, and the microtine rodent cycle, Journal of Animal Ecology; 1991, 60, pp. 353-367.

[15] J.D. Roth, J.D. Marshall, D.L. Murray, D.M. Nickerson, T.D. Steury: Geographical gradients in diet affect population dynamics of Canada lynx, Ecology, 88(11), 2007, pp. 2736-2743.

[16] T. Klemola, M. Tanhuanpää, E. Korpimäki, K. Ruohomäki: Specialist and generalist natural enemies as an explanation for geographical gradients in population cycles of northern herbivores. Oikos 99, 2002, pages 83-94.

[17] E. Mamontov: Dynamic-equilibrium solutions of ordinary differential equations and their role in applied problems, Applied Mathematics Letters 21, 320–325.

[18] L.J. Palmer: The Alaska tundra and its use by Reindeer, U. S. Dept. of the Interior, Office of Indian Affairs, 55 pages (Mimeo).

[19] G.D. Hanna: The Reindeer Herds of the Pribilof Islands, The Sci. Monthly, 15, Issue 2, pp. 181-186.

[20] N. Tyler: Estimating the daily dry matter intake of Svalbard reindeer in late winter, Rangifer 7 (1): 29 – 32, 1987.

The Influence of Primary Measures for Reducing NO_x Emissions on Energy Steam Boiler Efficiency

Goran Stupar[a], Dragan Tucakoviæ[a], Titoslav Živanoviæ[a], Miloš Banjac[a], Srðan Beloševiæ[b], Vladimir Beljanski[b], Ivan Tomanoviæ[b], Nenad Crnomarkoviæ[b], Miroslav Sijerèiæ[b]

[a] *Faculty of Mechanical Engineering, Kraljice Marije 16, 11120 Belgrade 35, Serbia, gstupar@mas.bg.ac.rs, **CA***
[b] *Vinča Institute of Nuclear Sciences, Mike Alasa 12-14, 11001 Belgrade, Serbia*

Abstract:
Within Electric Power Utility of Serbia 1991. a thermal power plant "Kostolac B", power 2x350 MW started. Given the increased emissions of NO_x in combustion products, it is in consideration to reduce it by introducing primary measures in terms of burner reconstruction, redistribution of secondary air by furnace height and introduction of cold flue gas recirculation. Applying these measures directly affects not only the combustion process in the furnace but also the work efficiency of steam boiler. Namely, if the flue gas temperature in furnace outlet is lowered below the corresponding values, it will cause the superheater and reheater not to achieve the designed steam parameters. On the other hand, the use of cold recirculating flue gases has a beneficial effect on reducing NO_x and increases the work safety of the superheaters and reheaters, but reduces the steam boiler efficiency. In order to understand all these effects on the safety and efficiency of boiler operation, it was needed to create a software for thermal calculation of the observed steam boiler. Based on that software, this paper will display the impacts of introducing the measures for reduction of NO_x emissions on a safe and efficient operation of the steam boiler as a whole.

Keywords: steam boiler, reducing NO_x emissions, steam boiler efficiency

1. Introduction

Modern society has big energy needs. Converting energy to a form useful to people has its consequences – harmful matter created in convertion process has adverse effects to humanity and environment. One of the harmful matter groups created in conversion process is nitrogen oxide group.

Nitrogen oxides are inorganic chemical compounds where a link between nitrogen and oxygen is formed. The most frequent nitrogen oxides in the air are nitro-monoxide (NO) and nitro-dioxide (NO_2) usualy common labeled as NO_x. There are some other nitrogen oxides in the air, from which the most poluting one is nitrous-suboxide (N_2O). Others, such as N_2O_3, N_2O_4, N_2O_5, NO_3, are not contained in the air in greater quanities.

It is very important to say that most of the environmental protection regulations treat all nitrogen oxides as NO_2. Although NO_x emission level in our environment during lignite combustion is very low, but it still exceeds the European standard of 200 mg/Nm^3 [1], which will become obligatory from 2016 in Serbia.

Nitrogen oxides are very harmful compounds. Biggest source of nitrogen oxides with anthropogenic origin is fossil fuel, which is why we try hard to reduce nitrogen oxide emissions during fossil fuel combustion process. Traffic and energetics release 90% of total nitrogen oxide quantity relised by human activity. Nitrogen oxide adverse effect can be reduced easily by reducing total emission of nitrogen oxides. There are several different metods developed to reduse nitrogen oxide emission. Nitrogen oxides appear mostly through nitrogen oxidation from the air in combustion processes at high temperature ranges ("thermal NO_x") and nitrogen oxidation from the fuel ("fuel NO_x"), which appears even at lower temperature ranges. In coal steam boilers, fuel NO_x is dominant. Formation of

thermal NO_x is directly dependent to local flame temperature, while formation of fuel NO_x mostly depends on nitrogen content in fuel and reacting oxygen in the zone of particle burning.
First group of methods consists of so-called primary methods. Primary methods are based on reducing nitrogen oxide emissions before and during their formation (before and during combustion process). Primary methods are much cheaper, but less effective. Most commonly used are recirculation of combustion products, usage of low nitrogen oxide concetracion burners (Low NO_x burners), multistage combusting (OFA – Over Fire Air) or combination of those methods.
Existing NO_x reducing methods can be additionally improved and their efficiency increased by using numeric simulations. Numeric simulations compared to experimental researches are many times more cost-effective, easily doable and give satisfactory results. According to this, numeric simulations play an important role in designing new NO_x emission reduction systems that will be used on facilities in development. In this way, even in early design stages, it is possible to predict the ammount of NO_x emission, and whether the plant will satisfy the environmental regulations which are getting more and more strict.
This paper cencerns the possibility of using primary methods for NO_x reduction in outlet flue gases of energetic coal dust fired steam boilers, which refer to modification of the combusting processes in furnace of the energetic steam boilers in aspect of security and achieving work parameters of steam boiler. There was also a comparative analysis of diferent NO_x reduction methods in aspect of steam boiler efficiency. Especially for these need, a numeric modeling of combustion process was made [2,3,4], along with a termal calculation code of the steam boiler in TE "Kostolac B" [10]. The selection of tested primary methods is made in a way that, in addition to their primary task (reducing NO_x concentration in outlet gases), they do not violate the safe and efficient work of steam boiler facility.

2. Working conditions of the steam boiler

There are two exploited steam boilers in the thermal power plant "Kostolac B" that burn lignite with lower heat value of 7326,9 kJ/kg. Performances of those steam boilers are:

- Main steam mass flow rate, D=277,8 kg/s
- Main steam pressure, p_s=18,6 MPa
- Main steam temperature, t_s=540 ^oC
- Reheated steam mass flow rate, D_r=248,8 kg/s
- Reheated steam pressure, p_{rs}=4,375 MPa
- Reheated steam temperature, t_{rs}=540 ^oC
- Steam temperature at the reheated inlet, t_r=334 ^oC
- Feed water temperaure, t_{nv}=255 ^oC

Simplified steam boiler disposition is shown in Figure 1.

Flue gases made by coal combustion in furnace (1) stream over third superheater stage (3), second reheater stage (4), second superheater stage (5), first reheater stage (6) and economizer (7), and than turn into sheet duct (8), at which outlet there are two air preheaters. Flue gases are then released into the atmosphere.
Steam boilers in TE "Kostolac B" (nominal power 2x350 MW) are tower shaped with forced circulation. Furnace dimensions are 15,1 x 15,1 x 43,0 m, with solid state dross drainage and rost. Boiler is stoked with coal dust, using eight tangentially placed burners, each connected to its own fan mill (9). Burners are separated into four levels by height: lower and uper main burner (10) and two burners for coal laden vapour above (11) for burning smaller fractions of coal dust. In case of maximal permanent block power (100 % of the load) with 7 mills working, raw coal consumption is

119,13 kg/s, and hot air flow is $1050 \cdot 10^3$ Nm^3/h. Temperature of mill gases is 200 ^OC, coal dust flow per burner is 10,384 kg/s and transport fluid flow per burner is 43,726 kg/s. Hot air temperature is 288 ^OC, secondary air flow per burner is 38,2 kg/s, tercial air flow trough rost is 15,18 kg/s. Guaranteed fuel is lignite Kostolac - Drmno, technical analysis: moisture 43,93 %, mineral mater 22,25 %, volatiles 21,39 %, fixed carbon 12,43 %; elementary analysis: carbon 22,46 %, hydrogen 2,12 %, oxygen 7,7 %, nitrogen 0,9 %, burnable sulfur 0,64. Moisture content in coal dust is 8,83 %. Coal dust particles density is 1300 kg/m^3. Operational requirements data in project regime, working fuel and coal dust caracteristics are shown in [2]. Based on sifter analysis, Rozin-Ramler distribution and numerical experiments, the diameter of mono dispersal coal dust particle was taken as d_p=150 μm, for simulation purposes.

During the study, a developed model of formation and destruction of NO_x was beeing used, verified by comparison to available measurments of NO_x emission in thermo energetic facilities of TE "Kostolac B" and incorporated with earlier developed complex model of the processes in furnaces [3] of subjected blocks. For the analysis of impact the NO_x reduction measures have on the efficiency of the entire boiler plant, and the efficiency and safe work of the superheater, for achieving the designed parameters of steam, a thermal calculation code was used [10], based on Norman's method [11].

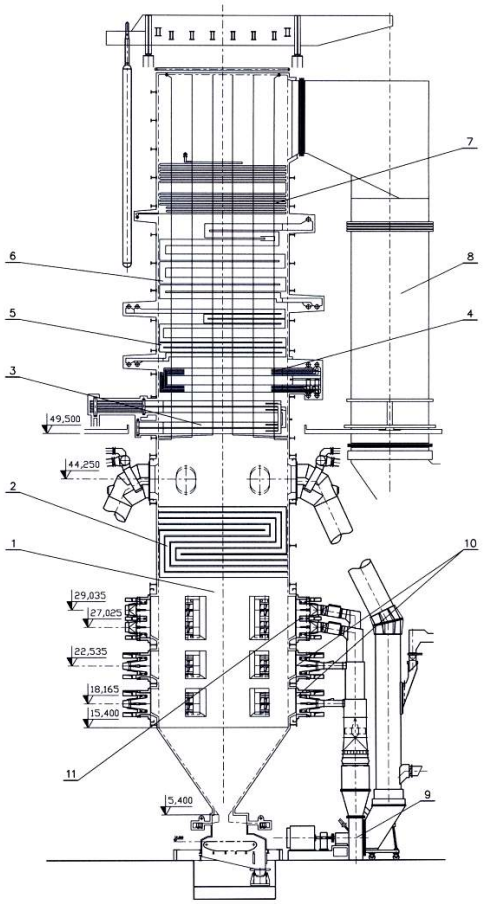

Figure 1. Disposition of the steam boiler in TP Kostolac B: 1. Furnace; 2. First superheater stage; 3. Third (output) superheater stage; 4. Second (output) reheater stage ; 5. Second superheater stage; 6. First reheater stage; 7 Economizer; 8. Sheet duct; 9. Fan mill; 10. Main burners; 11. Burner for coal laden vapour.

3. Numerical study of the possibility of NO_X reduction

Using the developed model of formation and destruction of NO_x [2,3,4], the impact of primary methods, namely, differently organized combusting processes in furnace, on reduction of NO_x emissions is numerically tested. Using a numerical simulation, the influence of different distribution of mill gases and heated air by burner levels, the impact of OFA vents and an effect of outlet gas recirculation from the steam boiler outlet on nitrogen oxide emission, was tested.

3.1. Research of the effects of diferent mill gases and air distribution to burner levels on reducing NO_X

Influence of the distribution of mill gases and air mixture on reducing the nitrogen oxide concetration was observed for three test cases (TS 1-3). In all three test cases steam boiler worked with 6 mills and designed parametars with nonworking mills on opposite walls so that the temperature field and concentration were very close to simetrical. Varied parameters are shown in Table 1.

TS-1 is a project operating mode of the boiler, therefore it is taken as reference in studying the impact of the primary methods on NO_x emission. Numerical results for gas mixtures temperature field, and O_2, HCN and NO_x concetration field in the furnace of the TE "Kostolac B" steam boiler for project conditions (TS-1) are presented in Figures 2. and 3.

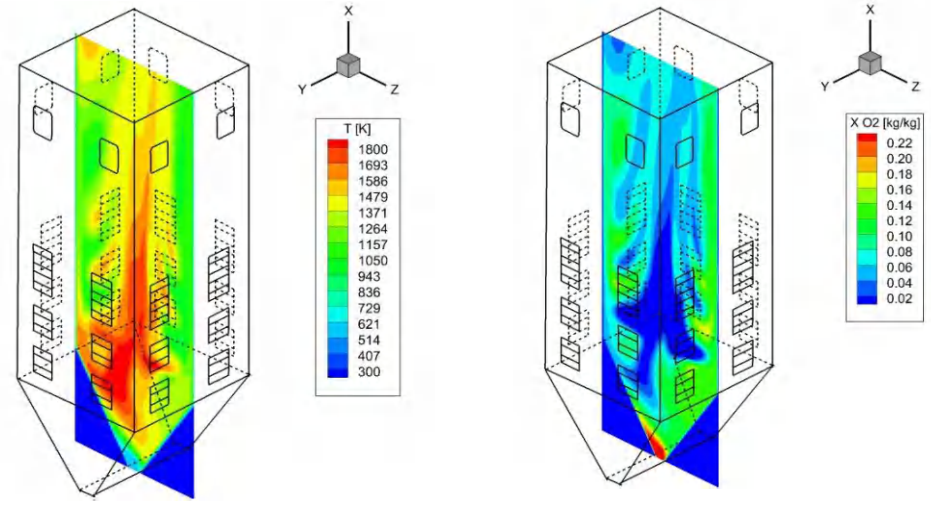

Figure 2. Gas thermal field and O_2 concetration field in furnace TEKO B for TS-1;

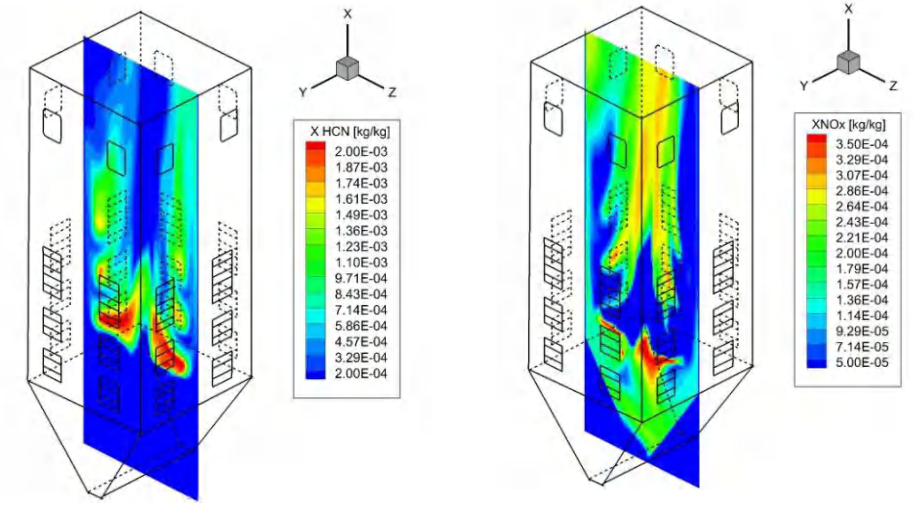

Figure 3. Concetration fields of HCN i NO_x in furnace *TEKO B for TS-1;*

Numerical results show the dependence of obtained NO_x concentration fields on gas temperatures, flame position, and field of reactants (HCN in this case) and oxygen concentration in furnance space, which, by the homogeneous reactions, produce burnable NO_x. There are also reactions of NO_x reduction with HCN. Thermal NO_x appears in a narrow area of maximum local temperatures in the furnace (T=1650K-1800K), which was expected. Thermal NO_x concetration in total NO_x emission is only a few percent. Since the fuel NO_x is much more represented then thermal NO_x (for the temperature range in the considered furnace), dependence of fuel NO_x predominantly determines the caracter of total NO_x concetration field. Figure 3 suggests a significant effect of HCN concentration (as volatiles intermediar), and therefore the nitrogen content in coal from which the HCN comes from, to NO_x content. One, narrow zone of high NO_x concentration corresponds to a maximum content of HCN is the place of introduction of most of the fuel through the lower main burners. The second, broader zone of high NO_x concentrations is noted along the flow (upwards) and corresponds to areas of intense chemical reactions of HCN consumption and forming of NO_x. In contrast to thermal NO_x the content of fuel NO_x (therefore the total NO_x) is less affected by temperature, but (besides the content of nitrogen in the fuel) it is greatly influenced by the relation of air and fuel, more precisely, the excess air (oxygen concentration field). That clearly follows from the comparison of Figure 2. with Figure 3. The NO_x concentration field does not only follow the temperature field (and HCN field) but, even more, the O_2 field. Despite the high temperatures, furnace central area does not have high concentration of NO_x because the oxygen is depleted by intensive, and relatively quick reactions of fuel combustion [5]. Numerical results for NO_x emission in the subject furnace were satisfactory matched with the results of periodic emission measurements in the TE "Kostolac B" blocks. Emission values specified by the model refer to average values at the furnace outlet, converted so they can be compared with the measurements of the steam boiler (and values defined in the standard). Numerical result of the NO_x concentration at the end of the furnace is 414.9 mg/Nm^3.

Operating mode TS-2 represents a possible case of redistribution of mill gases and combustion air, with all other input parameters unchanged, which is more preferable from the aspect of NO_x concentration. Input parameters of TS-2 mode are shown in Table 1. Figure 4. shows the appearance of gas mixture temperature field and nitrogen oxides concentration per longitudinal section of the furnace. Numerical result of the NO_x concentration at the end of the furnace is 343.6 mg/Nm^3 which is a significant improvement of the nitrogen oxides concentration in relation to the TS-1 mode.

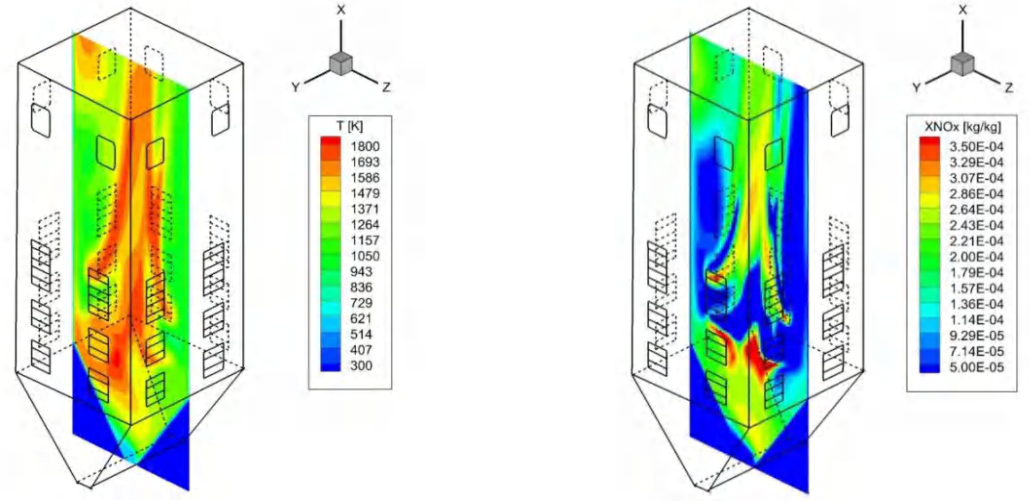

Figure 4. Gas temperature field and NO_x concentration field in furnace of TEKO B for TS-2;

Values of nitrogen oxides' concentration for three examined cases of the fuel and air distribution per burner levels are given in Table 1.

Operating mode TS-3 represents a reorganization of additional fuel intake per burner level with large amounts of fuel through the main burners. This operating mode would be more advantageous over the desired criteria to reduce the concentration of NO_x. Input parameters of TS-3 mode are shown in Table 1. Figure 5. shows the appearance of temperature field of gas mixtures and concentrations of nitrogen oxides per longitudinal section of the furnance. The numerical result for the concentration of NO_x at the end of the furnace is now further enhanced, and is 337.6 mg/Nm^3 which represents this operating mode interesting for further analysis from the viewpoint of maintaining boiler operating parameters and cost-effectiveness of this solution. In this way the numerical experiment has shown that by the favorable mill gases and distribution of combustion air can affect the reduction of nitrogen oxide concentration in the gas mixture.

Table 1. The distribution of mass fuel flow and combustion air per burner level;

Test case (TS)	Fuel distribution per burner level [%]				Transport fluid through main burners [%]	Secondary air through main burners [%]	t_{izl} [^{o}C]	NO_x Emission [mg/Nm^3]
	Main burners		Coal laden vapour burner					
	Lower	Upper	Lower	Upper				
1	45,5	24,5	19,5	10,5	57,0	67,8	1021	414,9
2	35,2	44,8	8,0	12,0	60,3	67,8	1033	343,6
3	43,2	43,2	7,9	5,7	57,4	67,8	983	337,6

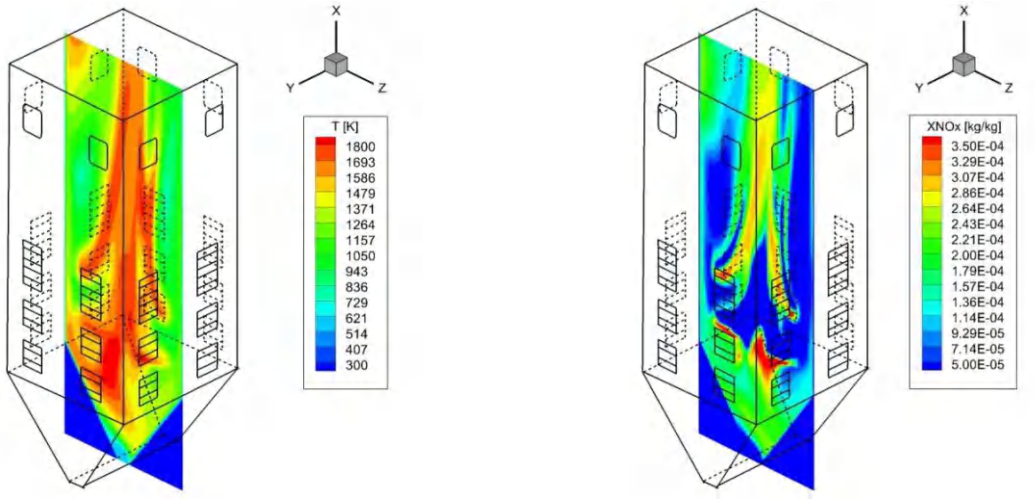

Figure 5. Gas temperature field and NO_x concentration field in furnace of TEKO B for TS-3;

3.2. Examine the influence of OFA vents on NO_X reduction

As one of the most important primary measures for reducing nitrogen oxide concentration in the mixture of gases on dust coal-fired boilers, the multilevel air intake (air stagging) is being used. This kind of measure is actually a two stage injection or two stage combustion. With this system, the total amount of the secondary combustion air is divided in two parts so that approximately 70 - 90% of air is injected through the burners and thereby the lower flame temperature and richer fuel mixtures are achieved in this zone. These two conditions allow that level of nitrogen oxides emission in burner level is less than with the classical system. The remaining 10 - 30% of the combustion air is blown in through special air vents, which are located above the burner (OFA), in

order to achieve complete combustion [8]. In this way, in the level of OFA vents, a poor mixture zone is achieved, where the emission of nitrogen oxides is less than in conventional systems. The idea is actually to delay the combustion of certan amount of fuel until the area of OFA vents where, due to the local increase of excess air, a lower temperature is achieved, which results in a lower NO_x emission [5].

This system is simulated numerically for discussed test cases. Only cases with the most optimal OFA vent parameters for the considered operating mode are shown. Figure 6. shows temperature fields of gas mixture and NO_x concentrations for TS-1 with two-stage air injection. OFA vent has the same width as the burner vent, height of 1 m, and 3 m away from the burner for coal laden vapour. The optimal flow in this case is 10% of air. In this way there was an additional reduction of nitrogen oxide emissions, to 393.8 mg/Nm^3, or 5.1% less compared to the set distribution of the working regime TS-1.

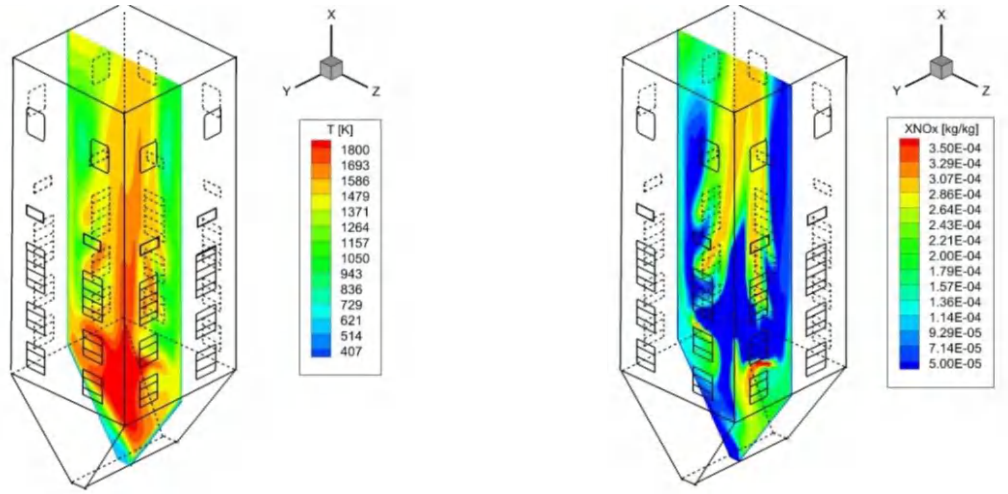

Figure 6. Gas temperature field and NO_x concetration field in furance of TEKO B for TS-1 with OFA vent;

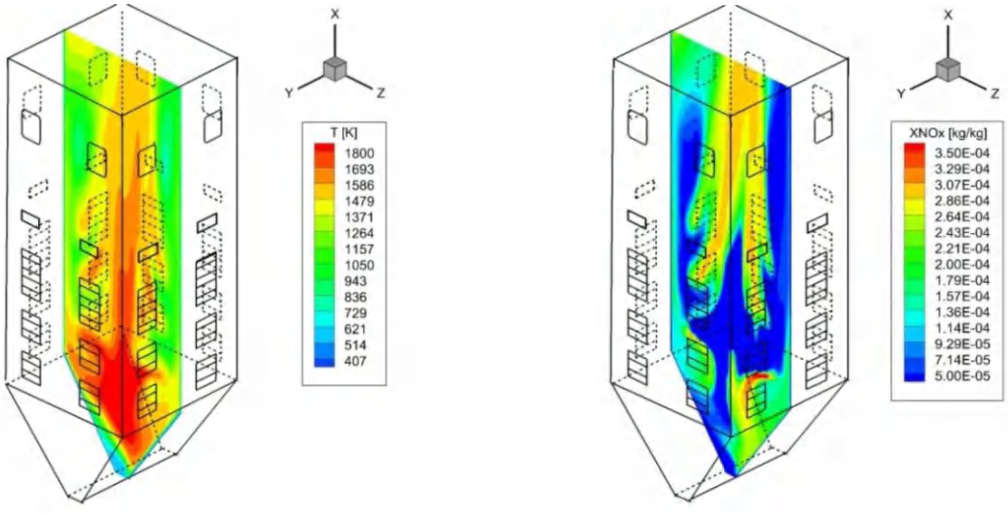

Figure 7. Gas temperature field and NO_x concetration field in furance of TEKO B for TS-2 with OFA vent;

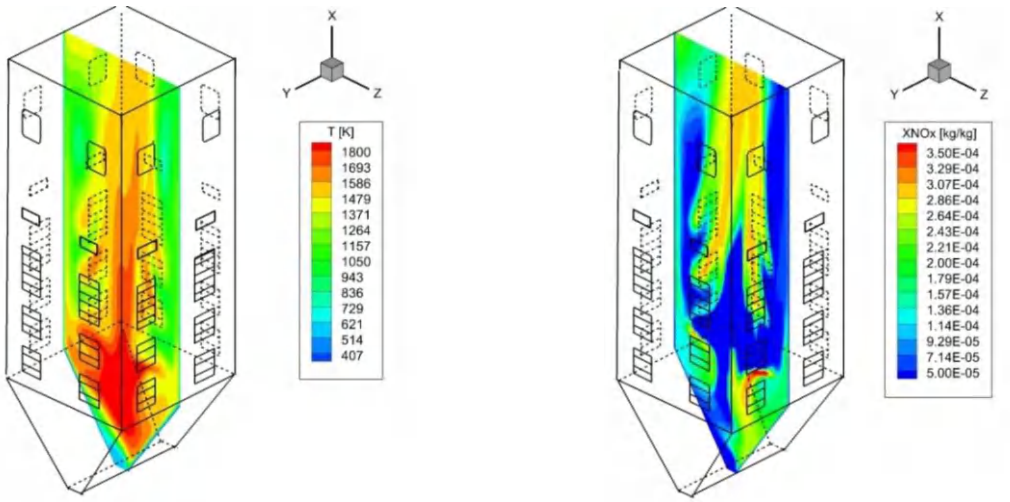

Figure 8. Gas temperature field and NO_x concetration field in furance of TEKO B for TS-3 with OFA vent;

Test case 2 is, in terms of concentration of nitrogen oxides at the furnace outlet, improved by introducing OFA vents on 6 meters from the burner for coal laden vapour. Vents are the same size as in the previous case, but the air flow through them is increased to 20%. This resulted in reduction of NO_x concentration by 11.8% from the original TS-2 and now stands at 303.2 mg/Nm^3. The temperature fields and NO_x concentration are shown in Figure 7.

In test case 3, the identical vents are installed, as with improved TS-2, but with an air flow rate of only 5%. In this case, the concentration of NO_x is reduced by 6.3% compared to the original TS-3, and is now 316.5 mg/Nm^3 in the output section of the furnace. New balance is shown in Figure 8.

3.3 Examine the influence of recirculation from the end of the boiler on reduction of NO_x

NO_x emission reduction can be achieved by recirculation of cold flue gases from boiler exits back to the combustion process. Flue gases are brought back into the primary combustion zone and in this way emission of nitrogen oxides is beeing reduced, by two mechanisms [6]:

- Flue gases acts as an inert component in the fuel-air mixture. Additional mass of cold flue gas is heated in the flame, causing a reduction of the flame temperature, while reducing the created amount of thermal nitrogen oxides,
- Introduced flue gases reduce the oxygen content in the primary combustion zone, thus reducing the created amount of nitrogen oxide.

Main disadvantage of reducing the flame temperature at flue gas recirculation is a lower overall combustion efficiency. Besides that, there is the problem of flame stability, emissions of CO and solid matter [7]. The injection of flue gas can be achieved by mixing with combustion air and fuel prior to entering the combustion zone, or may be directly introduced into the flame zone. This system enables, from technical side, an easily applicable primary measure of nitrogen oxide reduction.

Boilers of the TE "Kostolac B" operate on individual coal dust preparation system with direct blowing and drying at close process where the certan recirculation from the end of the boiler is predicted, in purpose of inertisation of mill gases and reduction of the risk of explosion [9]. This system enables, from technical side, an easily applicable primary measure of reduction of nitrogen oxides. The cold flue gases from the end of the boiler are brought into recirculation head where they mix with primary air, fuel and flue gases from the end of furnace before they are introduced into the fan mill.

The possibility of reduction of the flue gas recirculation in relation to the projected, in terms of favorable NO_x concentration, and the safe and efficient operation of the plant as a unit is considered in the test cases. This primary measure was tested by a numerical simulation with 0%, 4% and 8% of recirculated gases from the end of the boiler at on one of the working conditions measured in 2011. All prior cases were conducted with the project gas recirculation from the boiler end, which was 4.9% of the total output of flue gases (nominal load 1000 t/h).
Figure 9. shows the temperature and concentration fields of HCN, O_2 and NO_x for the three test cases of recirculation of flue gases of 0%, 4% and 8%. In the first case, when there is no recirculation, obtained content of NO_x was 748.0 mg/Nm^3, in second case, when the simulated re-circulation was 4%, it was was noted that emission was reduced by 14.1%, to 642.7 mg/Nm^3, while in the third case the recorded reduction was 23.9% compared to the reference case without circulation, and was 569.1 mg/Nm^3. In Figure 8 the effects of the characteristic mechanisms for this type of primary measures are noticeable, which are more expressed with increasing of recirculation flow.

4. The influence of the examined primary measures on operating effectiveness of the boiler

As criteria for selection of optimal primary measures (combustion modifications) to reduce NO_x emissions from the standpoint of the need for efficient operation of the complete boiler plant, as well as efficient and safe operation of super heater in terms of achieving the designed parameters of steam, we can single out the following:

- a steam boiler efficiency degree,
- an efficient and safe operation of the super heater and reheater, in terms of achieving the designed parameters of steam and
- minimum required amount of water injected into the lines of main steam and reheater steam.

In Table 2 are given the average temperatures of flue gas on the combustion chamber exit, obtained by a mathematical model for three selected test cases with low NO_x emission with and without OFA vent. Based on these temperatures, related to the nominal strain of the boiler, adjusted to the thermal calculation of the furnace in order to get identical values upon which implemented the heat boiler calculation for the projected fuel or warranted coal for the boiler.

The values that need to be analyzed according to the temperature changes of flue gases at the end of the furnace are shown in Table 2.

Table 2. Thermal calculation results according to the temperature of flue gasses on the boilers exit;

Title	Label	Unit	Test case with diferent fuel and air distribution by stages			Test case with OFA vent		
			TS-1	TS-2	TS-3	TS-1	TS-2	TS-3
Flue gass temperature in the furnance exit	$t_{l''}$	[^{o}C]	1021	1033	982	996	1000	974
Injection of the water in main steam line	D_{Hs}	[kg/s]	15,505	18,822	0	3,078	4,253	0
Main steam temperature	t_s	[^{o}C]	540	540	536	540	540	525
Injection of the water in reheated main steam line	D_{Hr}	[kg/s]	4,210	5,487	0,783	1,882	2,182	0,532

Main reheated steam temperature	t_{rs}	[°C]	540	540	540	540	540	534
Fuel consumption	B	[kg/s]	120,35	120,88	118,46	119,45	119,5	118,12
Temperature of the flue gass on boilers exit	t_{iz}	[°C]	158,9	159,3	157,7	158,2	158,4	157,1
Heat loss by the flue gass on boilers exit	q_2	[%]	11,66	11,69	11,56	11,60	11,65	11,42
Boiler efficiency	η_k	[%]	85,06	85,02	85,15	85,12	85,09	85,29

With the high temperatures of flue gases at the end of the combustion chamber, the third stage main steam superheater PP3 (Figure 1. - by the output of steam flow), receives an increased amount of heat due to the rise in the average logarithmic temperature difference of heat transmitter and receiver. In Table 2 is noted that the flue gas temperature of 1033 ℃ injecting in main steam flow line is 18.822 kg / s of water to maintain the exit temperature of main steam flow of 540 ℃. By reducing the temperature of the flue gases at the end of the combustion chamber, main steam superheater PP3 exchange a small amount of heat which leads to a reduction in the required flow of water for injecting in. The problem occurs at temperatures of flue gases at the end of the furnace below 990 ℃, since it can not achieve the design parameters of the main steam of 540 ℃, which are the primary measures applied to the TS-3, which gave good results in terms of reduced concentrations of nitrogen oxide, are disqualified as a possible solution. Above the third degree of main steam superheater, by the gas flow, the second stage of main steam reheater is set NP2 (output by the steam flow) at high temperatures of flue gases also receive an increased amount of heat. This percentage increase is slightly less than the increase that occurs in the third degree of main steam superheater. Table 2 shows that the lowering the temperature of flue gases at the end of combustion chamber, water injection in the reheated steam line are reduced, but that in all the considered cases, however, achieved subsequently superheated steam temperature at the outlet of 540 ℃. For this boiler regulation of reheated steam temperature can only be achieved by injecting water between the two levels (there is not any bifluks or trifluks). By increasing amounts of water for injecting into the reheated steam line (D_{Hr}) efficiency of the block is reduced (because the amount of injected high-pressure bypasses the turbine), but also increases fuel consumption (due to the increased amount of heat needed for local heating of injected feedwater D_{Hr}), which can be seen displayed on Table 2. In test case no. 2 there is a need for higher amount of water for injecting in into the line reheated steam, which in this case is an acceptable price for the sake of a significant reduction of NO_x emissions. By the increased heat exchange in the third stage of the steam superheater and the second stage of steam reheater at elevated temperaure of flue gases exiting the combustion chamber, flue gas temperature in front of and behind other heating surface temperatures are approaching the designed. Table 2 clearly observed that the temperature of flue gases at the end of the boiler, and therefore the boiler efficiency, slightly change the temperature of flue gases at the end of the combustion chamber, by enabling those measures applied in TS-2 are acceptable from the standpoint of efficient and safe operation of boiler the plant. This test case can be further improved by introducing OFA, so that the new reorganized combusting besides favorable concetration, further reduces the temperature of gas at the end of the combustion chamber, reduces the required amount of injection and increases efficiency. So the test case 2 with OFA vent is considered the most optimal solution. Influence of recirculation in terms of boiler plant efficiency is shown in Table 3. Giving the thermal budget for running the test cases without recirculation and with recirculation of 4% and 8%. Increasing the recirculation of flue gases from the end of the boiler and further cool the furnace and lowers the temperature of gases exiting the combustion chamber. Also, by increasing the recirculation of cold flue gas NO_x emission is reduced, however, significantly increases the temperature of flue gas exiting the boiler, leading to a reduction in boiler efficiency.

Flue gas temperature at the end of the combustion chamber is lowered, but due to the increased flue gass flow through the boiler (due to cold gas recirculation) the amount of water that is injected to regulate main and reheated steam temperature increases, which again leads to a reduction steam block efficiency and increased consumption of fuel.

Table 3. Steam boiler termal calculation results for diferent gas recirculation from at end of the boiler;

Test case	Flue gass temperature at the end of the combusting chamber, [°C]	Water injecting in the main steam line, [kg/s]	Main and reheated steam temperature, [°C]	Water injecting in the reheated steam line, [kg/s]	Fuel consumption, [kg/s]	Temperature of the gass that exits the boiler, [°C]	Output gass heat loss, [%]	Boiler efficency, [%]	NO_x emission [mg/Nm^3]	Emission reduction comparing to the case without gass recirculation (%)
0 % recirculation	1087	28,803	540	9,719	103,39	160	10,36	86,56	748,0	-
4 % recirculation	1057	24,485	540	9,109	103,71	166	10,78	86,14	642,7	14,1
8 % recirculation	1028	19,753	540	8,278	103,93	172	11,18	85,74	569,1	23,9

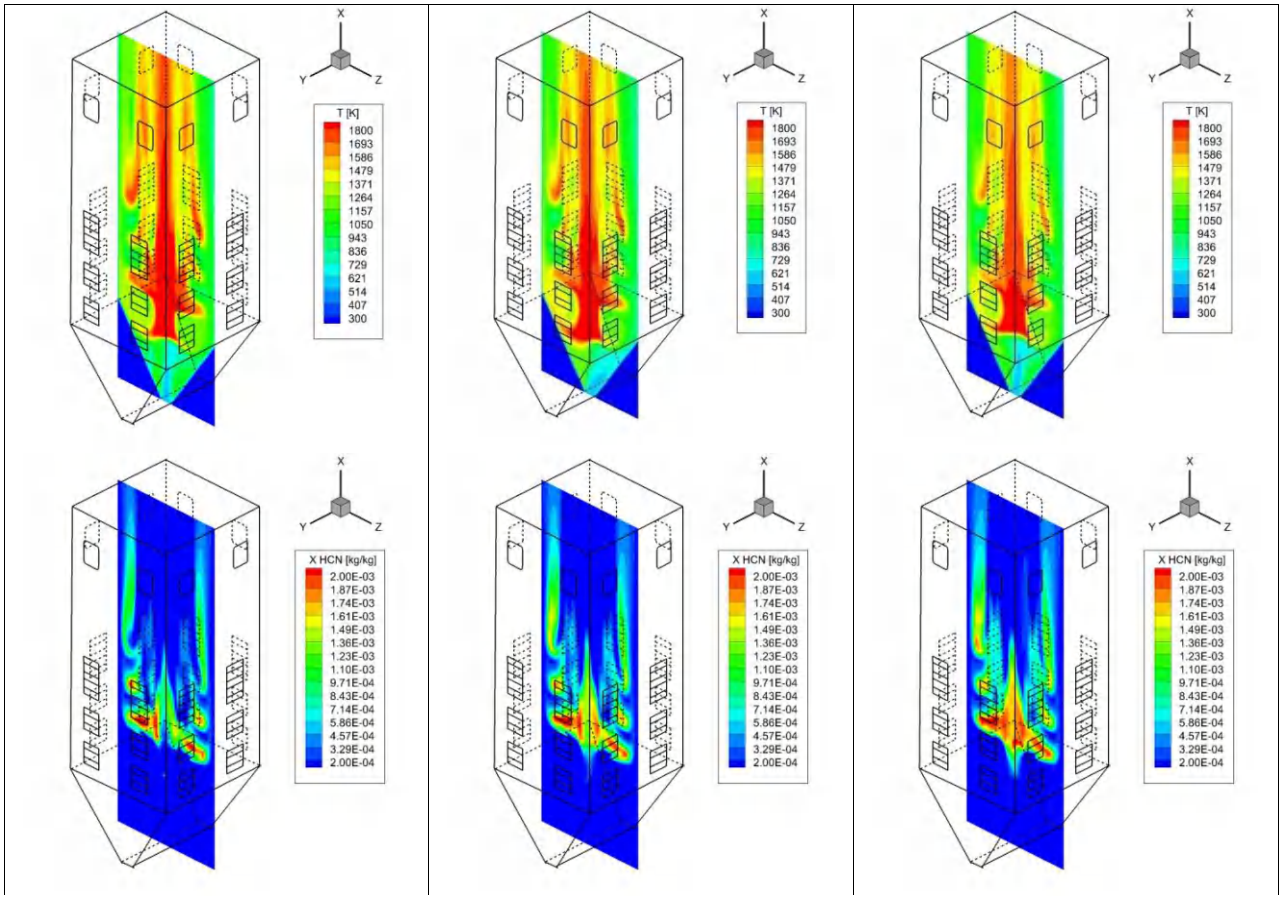

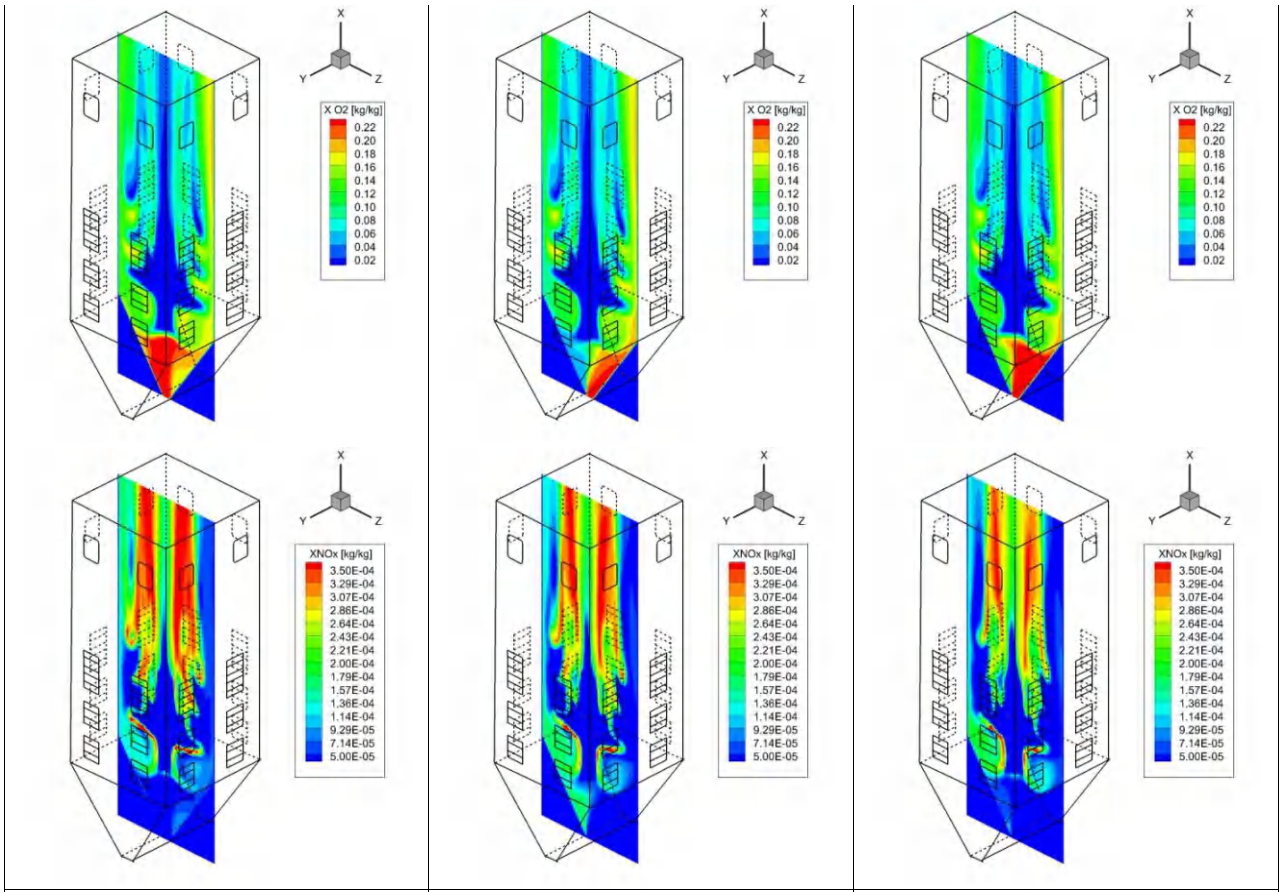

recirculation of the boiler exit flue gases: 0%	recirculation of the boiler exit flue gases: 4%	recirculation of the boiler exit flue gases: 8%

Figure 9. Temperature fields and concetration fields of HCN, O_2 i NO_x for 3 recirculation cases;

5. Conclusion

Based on the numerical simulations performed to investigate the possibility of reducing NO_x emissions, it was observed that the distribution of coal dust per burner stages and secondary air significantly affects the emission of NO_x and the exit temperature of flue gases at the end of the furnace. More coal dust passing through the main burners (85%), and control of local excess air in the burner zone, by redirecting up to 20% of heated air from the main burners to OFA vents, have a significant impact on the reduction of NO_x emissions. Cold flue gas recirculation will reduce the concentration of nitrogen oxides, but it will always result in a lower efficiency (Table 3). Numerical simulations show that optimizing the combustion process can significantly reduce NO_x emissions, and keep the temperature in furnace in the required range. In order to achieve optimum combustion process it is necessary to determine the proper distribution of coal dust and heated air to individual burners and burner stages. This can be done without large investment costs. In this way it is possible to achieve reduction of emissions by 20 - 30% without structural changes of the boiler, only by combining the tested methods of combustion process optimization.

Based on the analysis performed in the work, it can be concluded that TS-2 with OFA vents gives the best result from both considered aspects, with the possibility of increasing the recirculation from designed 4.9% to 8% which would further reduce the concentration of nitrogen oxides in flue gases at the end of combustion chamber. Based on the thermal calculation of the boiler, it can be concluded that the optimum temperature of flue gases at the end of combustion chamber should be in range of 990-1010 °C, in order to provide for safe operation of third steam superheater stage PP3,

namely to provide the necessary main steam temperature of 540 °C. At this temperature range, water injection in the reheated steam stream is minimal.
Test results show that the European standard can not be achieved using primary measures only, but with proper selection of those measures, it is possible to significally reduce the starting concentration of NO_x for use of secundary measures which require additional investment and exploitation expenses.

Acknowledgments

This work has been supported by the Republic of Serbia Ministry of Education and Science (project: “Increase in energy and ecology efficiency of processes in pulverized coal-fired furnace and optimization of utility steam boiler air preheater by using in-house developed software tools”, No. TR-33018).

References

[1] Directive 2010/75/EU European Union - limit of emissions of harmful substances into the air from large furence.

[2] Belosevic S, Sijercic M, Tucakovic D, Crnomarkovic N. A Numerical Study of a Utility Boiler Tangentially-fired Furnace under Different Operating Conditions, Fuel 87, 15-16, pp. 3331-3338.

[3] Belosevic S, Sijercic M, Oka S, Tucakovic D. Three-dimensional modelling of utility boiler pulverized coal tangentially fired furnace, INTERNATIONAL JOURNAL OF HEAT AND MASS TRANSFER 49, 19-20, p.p. 3371-3378.

[4] Belosevic S, Sijercic M, Crnomarkovic N, Tucakovic D. Numerical prediction of pulverized coal flame in utility boiler furnaces, Energy & Fuels 23, p.p. 5401-5412.

[5] Belosevic S, Sijercic M, Crnomarkovic N, Zivanovic T, Tucakovic D. Possibility of introducing the primary measures for reducing nitrogen oxide emissions from power boilers on pulverized lignite. Belgrade, Serbia: Laboratory for Thermal Engineering and Energy, Institute of Nuclear Sciences Vinca, and the Center for Thermal Engineering - Department of boilers, Faculty of Mechanical Engineering, University of Belgrade, 2011.

[6] J. Dukovic, V. Bojanic. Air pollution - a term, condition, resources, control and technological solutions. Institute for Protection and ecology - Banja Luka, Bosnia and Herzegovina, 2000.

[7] J. Baltasar, M. Carvalho, P. Coelho and M. Costa, Flue gas recirculation in a gas-fired laboratory furnace: measurements and modelling, Fuel 76, pp. 919-929

[8] Tobin, D. Moyeda, W. Zhou, R. Payne, Application of Layered Control Technologies to Significantly Reduce NOx Emissions from Coal-Fired Boilers, GE Energy, 2ndU.S.-China NOx Workshop Dalian, China, 2005.

[9] Brkic Lj, Zivanović T, Tucakovic D. Steam boilers, Faculty of Mechanical Engineering, University of Belgrade, Belgrade, Serbia 2010.

[10] Tucakovic D, Zivanovic T, Stevanovic V, Belosevic S, Galic R. A computer code for the prediction of mill gases and hot air distribution between burners sections at the utility boiler, Applied Thermal Engineering 28, 17-18, p.p. 2178-2186.

[11] Brkic Lj, Zivanovic T, Tucakovic D. Thermal calculation of steam boilers Belgrade, Serbia: Faculty of Mechanical Engineering, University of Belgrade, 2010.

The LETHE CITY CAR of the University of Roma 1: Final proposed configuration

Roberto Capata[a], Enrico Sciubba[b]

[a] *University of Roma Sapienza , Dept. of Mechanical and Aerospace Engineering, Italy, roberto.capata@uniroma1.it*

[b] *University of Roma Sapienza , Dept. of Mechanical and Aerospace Engineering, Italy, enrico.sciubba@uniroma1.it*

Abstract

A longstanding interest of the Authors' research group at UDR1 was the design, development and fielding of a road prototype of a new concept of Hybrid Series vehicle, endowed with a small Gas Turbine set as a thermal engine. This solution offers several advantages with respect to traditional internal combustion engines and even to the existing generation of Hybrid propulsive systems,: a reduced engine weight and size, lower emissions, substantially extended range, ease of maintenance, and more efficient braking energy recovery. In the LETHE (**L**ow **E**missions **T**urbo-**H**ybrid **E**ngine) the GT does not directly provide traction, but serves solely as a battery pack recharger. The vehicle is, in all respects, equivalent to a purely electric vehicle, except for the presence of an on-board recharger. Much care was placed in the design phase in the quest for an "optimal" design: first of all, an original method for identifying the most convenient degree of hybridization (ratio of the installed power of the battery pack and that of the GT) was defined and formalized, so that the resulting power balance between the two units satisfies the main design specifications, namely that of guaranteeing a practically acceptable operational life of the battery package while enabling the vehicle to complete a typical city mission (about 25-50 km) in a purely electric mode and without recharge. This paper presents a review of the previous conceptual and design results and describes in detail a possible road prototype configuration (weights, packaging of the units within the body of the vehicle, logic control unit, GT- and electric motor size and power, battery package characteristics). Some discussion is also devoted to the foreseeable impact of the deployment of a LETHE fleet on the mid-range scenario of the Italian urban transportation system.

Keywords:

Hybrid Vehicle, Ultra-Micro Gas Turbine, Vehicle emissions, CO_2 abatement, Transportation Economics

1. Introduction: a brief review of existing hybrid vehicle concepts and of current market opportunities

In the last decade, governmental incentives and the ever stricter emissions regulations have prompted some of the largest world automakers to allocate resources to the study, design, development and production of hybrid vehicles, which offer undisputed advantages in terms of emissions and fuel consumption with respect to traditional internal combustion engines. In fact, true hybrid engines are substantially smaller than conventional ICE, because they are designed to cover the vehicle's "average" power demand, which ensures proper traction for about 99% [15] of the actual driving time, and is exceeded only for prolonged mountain drives and instantaneous accelerations. When excess power is needed above this average, the hybrid vehicle relies on the energy stored in its battery pack. Hybrid cars are often equipped with braking energy recovery systems that collect the kinetic energy lost in braking, which would be dissipated into heat otherwise, and use it to recharge the battery. Smaller sizes and an (almost) constant operational curve lead to lower emissions. Moreover, a hybrid vehicle can shut down completely its gasoline engine and run off its electric motor and battery only, at least for a limited operational range: this "mixed operation" increases the net mileage and releases a substantially lower amount of pollutants over the vehicle lifetime. Due to market demand though, current commercial hybrid vehicles (HV) are mostly passenger hybrid cars equipped with a traditional ICE and an electric motor coupled in parallel. The thermal engine is normally oversized with respect to the average power, and the

surplus power needed during rapid acceleration phases is supplied by the electric motor: as a consequence, fuel savings are limited, as are global emissions, and the electric range is severely limited.

2. The LETHE@ concept

The series hybrid configuration developed by the authors' research group [2, 3], nicknamed LETHE@, is a vehicle in which two natural gas fuelled small turbogas sets are coupled to high speed electrical generators and a lead-acid battery package: the vehicle can operate in electric-only mode if requested, or in hybrid mode, where the gas turbine and the battery package operate together to satisfy the power demand [3,4]. The traction is fully electric in either operational mode. In the hybrid vehicle scheme discussed in this paper, the electronic vehicle management unit ("VMU") controls ignition and on-off switching under a Load Following logic. The VMU decides at each instant time how much of the energy produced by the GT reaches the battery package or the electric engine directly. In addition, the electric motors can also act as brakes, recovering much of the energy that is otherwise lost. In order to maximize the recovered energy and to avoid possible battery overloading, an additional dynamic storage unit has been included: a relatively small flywheel capable of storing the excess power from the regenerative braking and of releasing it at a later time according to the instantaneous power demands. The VMU performs its energy-management task on the basis of a certain number of instantaneous mission parameters: the batteries may thus provide or absorb the difference between the energy requirements of the vehicle and the GT energy production. The generator acts as a starter for the GT as well. A continuous GT control can be enforced via fuel flow control and/or employing a variable geometry GT. Since GT power modulation is affected by a substantial efficiency penalty at off-design conditions, the fuel flow control is coupled with a variable-stator turbine and the inlet guided vanes (IGV) blades for the compressor. As any other system, the GTHV has advantages and drawbacks. The following parameters ought to be considered when selecting/designing such a system:

- It is of compact size and can be comfortably mounted in the engine compartment of a sedan;
- Both the micro turbines and the electric engine have a very high power-to-weight ratio;
- The GTHV attains a very high fuel economy;
- The GTHV has a lower emission level, with effective multi-fuel capability;
- There is the possibility of improving the overall vehicle design due to weight and size savings;
- All components have a high reliability;
- The battery package has a rather low power-to-weight ratio;
- The state of charge (SOC) trend during any mission must be monitored to avoid overcharge and excessive discharge of the battery pack;
- The GT may be subjected to several ignitions during a mission, which negatively affects its mean-time-between-failure (MTBF);
- There is the necessity of monitoring and satisfying the instantaneous vehicle total power demand.

3. The degree of hybridization

The mechanical power in an series HV vehicle is typically supplied by one electric motor (EM), so that, from the traction point of view, the vehicle is in fact an electric one. The choice of the EM is a direct function of the required performance. Once the maximum required traction power is fixed, then the total power source supplied by the ICE and battery package can be calculated from the overall mission energy balance. Thus, the Hybridization Degree HD can be calculated as the ratio between the GT power and the total installed power (GT and battery package).

$$HD = P_{GT} / P_{GT+BP} \quad (1)$$

Our design target is to attain the minimum possible HD that still guarantees a good driveability under all possible conditions.

4. Simulation

Several numerical tests have been carried out to compute the vehicle performance, in two different driving missions: a combination of 10 consecutive urban cycles ECE15* and a "complex driving mission" composed of 4 consecutive extra-urban cycles EUDC* and 72 minutes of continuous highway drive at 120 km/hr. Each mission has been simulated for each of the two concept cars studied here: a "city-car" and a standard passenger sedan. The simulation computes the power balance on the basis of the imposed wheel speed and vehicle characteristics [1,2], and determines the power supplied by each system component. This process is repeated with a 1s interval, assuming that within every time interval, the power, the speed, and all other significant parameters remain constant. As mentioned above, the GT set is switched on when the SOC is lower than a set point (0.6), and switches to idling or partial load mode when the SOC reaches the maximum set point (0.8). In real operation, a manual override must also be provided, but this was not considered in the calculations. The GT load management protocol is based on the assumption that the GT sets can operate, without substantial efficiency loss, between 70% and 110% of their nominal power. Each simulation, consists of assigning first the number of modules in the battery package, then the installed power, and finally the GT power: these three values must satisfy the limitations imposed by the above- mentioned criteria of maximum power demand and maximum absorbable battery power [7]. The GTs nameplate power was iteratively adjusted until the minimal fuel consumption was obtained. This heuristic procedure was also iterated by increasing the number of battery modules, with a consequent correction of the total vehicle weight. The vehicle design specifications (Table 1) are the same as those adopted in previous papers [2,3,4]:

Table 1. GT Hybrid Vehicle (GTHV) Design Specifications

Wheel rolling radius	$R = 0.265$ m
Vehicle width	$b = 1.7$ m
Vehicle height	$H = 1.4$ m
Net front area	$S_f = 2.142$ m^2
Area ratio (S_f/S_{tot})	$\alpha = 0.9$
Aerodynamic drag coefficient	$c_x = 0.25$
Tire rolling friction coefficient	$f_r = 0.015$
Vehicle mass	$m = 1200$ kg
Equivalent mass	$m_e = 1240$ kg
Air density	$\rho = 1.18$ kg/m^3
Air intake temperature	$T = 300$ K
Minimum SOC	0.6
Maximum SOC	0.8

* EEC Directive 90/C81/01: this is a series of Regulations that prescribe both the emissions limits (adjusted every year) and the methods for testing and qualifying passenger and commercial vehicles. The test driving are in one urban cycle (European Cycle Emission) and an extra urban driving mission (Extra Urban Driving Cycle)

5. Results of the simulations

Eight different computer simulations have been performed (2 types of mission respectively simulated with 2 types of logic, and 2 types of battery recharge limit BRL).

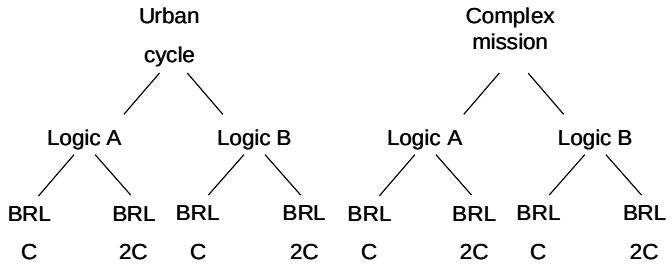

Fig.1 . Scheme of the performed simulations

The choice of the optimal configurations, within those several simulations, is a heuristic balance between the relative advantages and drawbacks of the following parameters:

- Total gross weight of the battery package;
- SOC trend during the mission;
- Number of GT ignitions during the mission;
- Instantaneous coverage of the total demand power of the vehicle;
- Size of the several devices (GT, battery package, flywheel)

6. Vehicle Hybridisation

In the vehicle hybridisation process, once the initial calculations have been completed, as indicated in previous works [1, 2], each component of the Lethe® vehicle is then individually designed. For a 30 kW electric motor, the overall dimensions of the main components are reported in table 2.

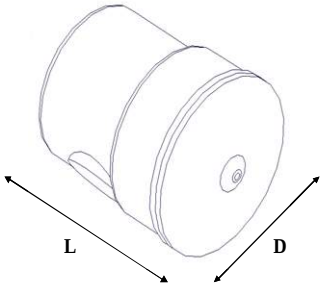

Fig. 2. Asynchronous motor da 30 kW; L = 315 mm, D = 264 mm

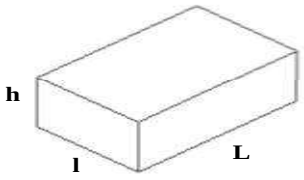

Fig. 3. Inverter; L = 410 mm, l = 340 mm, h = 138 mm

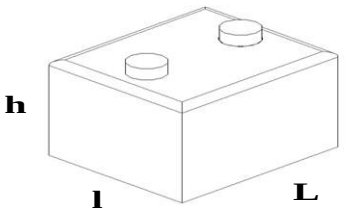

Fig. 4. GENESIS® battery module; L = 200 mm, l = 170 mm, h = 170 mm

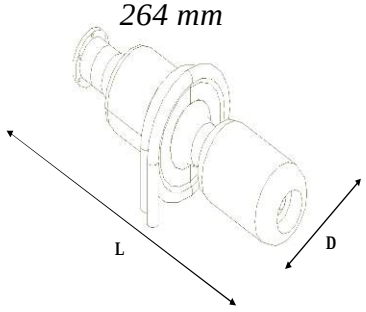

Fig. 5. Gas Turbo-generator; L = 465 mm, D = 200 mm

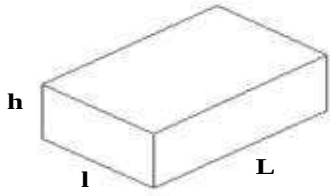

Fig. 6. Fuel tank; L = 880mm, D = 270 mm

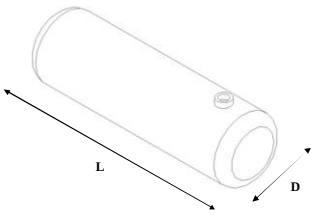

Fig. 7. Regenerator; L = 340 mm, l = 215 mm, h = 120 mm

Table 2. Components dimensions and weight

Component	Dimensions [mm]	Weight [kg]
Electric motor	Ø264 x 315	80
Inverter	410 x 340 x 138	15
Battery module	200 x 170 x 170	15
GT device	Ø200 x 465	25
Fuel tank	Ø270 x 880	37
Regenerator	340 x 215 x 120	12
(Fly wheel)[1]	Ø200 x 270	16
Total weight		200 +(16)

6.1. Note about the selection of the Gas Turbine

The design of the GT units were not a subject of this study, therefore the sizes and weights of the unit were not expressly calculated. However, in this study, is the energy balances were performed on the basis of the known characteristics of the 30 kW Capstone turbo-generator C30HEV [14], therefore the packaging reflects an excessive size, because the actual optimal degree of hybridization is about xx and would indicate the need for a xx kW turbogas set. Indeed, we assumed that the temperature (1300 K) and speed (100000 rpm) were the same as the C30HEV, therefore as an initial approximation, the sizes should be scaled respectively by a factor of 1/3. With the shape and size of the C30HEV [14] established, such an "ideal" GT group was repackaged as shown in figure 4. Its weight was also evaluated in excess, approximating it to that of a single steel cylinder (δ_{steel} = 7.87 kg/dm^3).

7. The LETHE$^{@}$ City Car

The weights and dimensions of all components are summarised in Table 3. The battery weighs 90 kg (6 modules) and is placed underneath the rear seats. The gas tank is placed in the aft section while all remaining components are housed in the front section (Figure 8). This configuration allows a weight distribution of 146 kg on the fore-axle and 127 kg on the rear axle, for a 53/47 ratio (Figure 9).

Table 3. City Car Configuration

Component	W [kg]	Dimensions [mm]
Batt. Pack (6 mod.)	90	510x400x185
E. Motor/Generator	80	Ø264x315
Inverter	15	410x340x138
GPL Fuel Tank	37	Ø270x880
Fly wheel	3	Ø200x270
Fly wheel motor	13	
GT 30 kW	23	Ø200x465
Regenerator	12	340x215x120

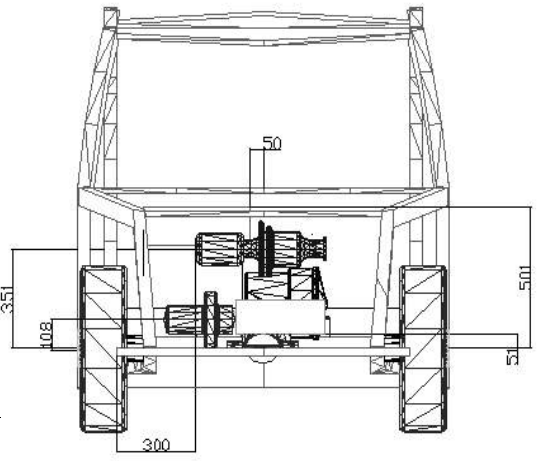

[1] The flywheel's task is that of smoothing sharp braking, downward slopes etc.. It was sized so as to obtain a compromise between storable energy and volume. Once the amount of energy that the flywheel had to absorb (20 kJ) and the maximum rotation speed (20000 rpm) were set, the weight and disk radius were computed using standard formulae [4].

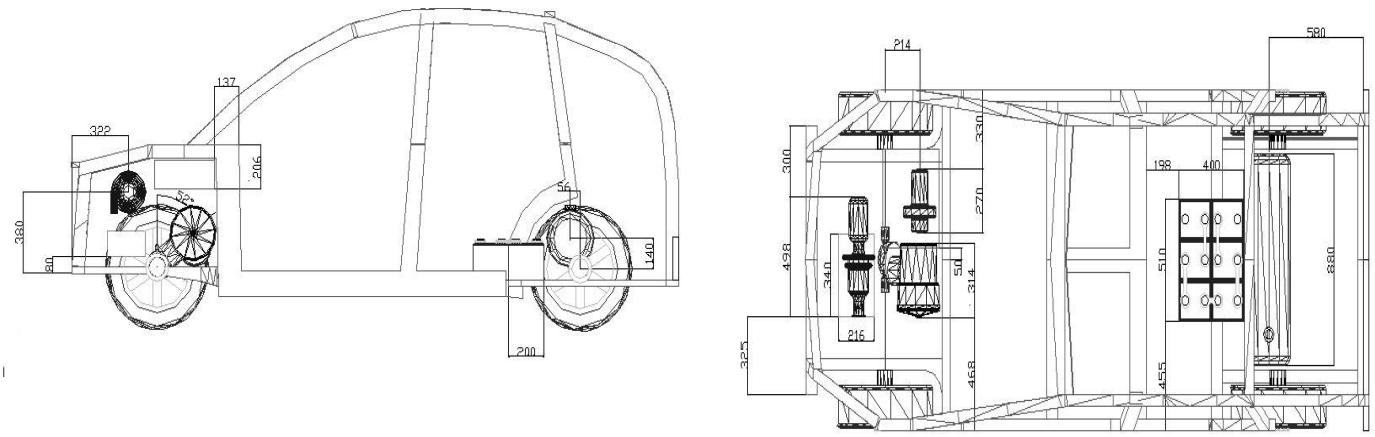

Fig. 7. Views and main dimensions (in mm) of the LETHE® City Car configuration

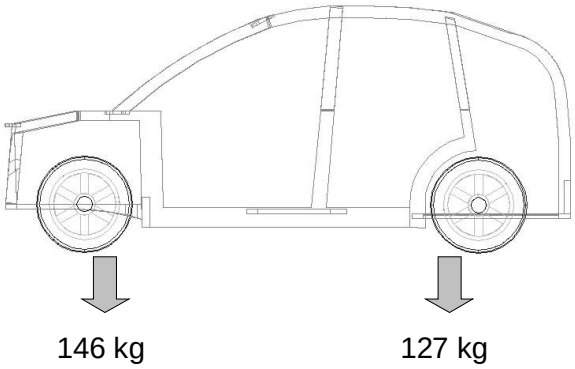

Fig. 8. Weight distribution in the LETHE® City Car configuration

8. Calculation of emissions for the LETHE@ vehicle

Pollutants emissions are linked to several factors (such as the type of fuel, the combustion temperature, the air/fuel ratio), and vary depending on operational conditions. The small amount of emissions data available on emissions at off-design conditions refer to large TG plants, where the combustion characteristics are different (pre-mixer, higher compression ratio), while the available data for small plants are only available for stationary conditions. As an initial approximation, emissions from the LETHE@ under the tested missions were estimated by comparison with emissions from the Capstone turbo-generator C30HEV [15], having presumed that our GT unit has the same inlet temperature in the turbine, same compression ratio and same speed. The Capstone data are expressed in g/kWh and refer to a fuel mass flow rate of 2.36 g/s.

Table 4. Emissions from the Capstone C30HEV unit

Emissions [g/kWh]	CNG	Propane
NOx	0,194	0,396
HC	0,313	0,313
CO	0,306	0,134
PM	0,003	0,003

It was also assumed that the GT unit is regulated by variation of the fuel capacity, maintaining the turbine inlet temperature constant. For this reason, the emissions in the Off-Design operational

mode will also be calculated using linear proportionality with emissions at the nominal point of the C30HEV, increased by a 50% safety factor .Table 5 shows the limit values for emissions set by the Directive 98/69/CE [11].

Table 5 . EURO Directives on Emissions

Normative	NO_X [g/km]	HC [g/km]	CO [g/km]	PM [g/km]
EURO 5	0,04	0,05	0,5	0,0125
EURO 4	0,08	0,1	1	0,025

Emissions for the LETHE$^{@}$ City car configuration, on urban routes, are obtained by similar calculations, and are shown in table 6.

Table 6. Emissions from the LETHE$^{@}$ City Car on urban routes

Pollutants	Emissions [g/kWh]	Emissions [g/km]
NOx	5,81E-02	6,18E-03
HC	9,39E-02	9,99E-03
CO	9,17E-02	9,75E-03
PM	9,17E-04	9,75E-05

Table 7 shows the percentage reductions of pollutant substances compared to the C30HEV and the EURO 5 Directive.

Table 7. Percentage reduction of emissions of the LETHE$^{@}$ City Car

Pollutant	C30HEV	EURO 5
NOx	-70 %	-84,5 %
HC	-70 %	-80,6 %
CO	-70 %	-98 %
PM	-70 %	-99,2 %

Such low emissions are justified by the intermittent use of the GT. On an urban mission during which 11 km are covered in 1959 seconds, the GT supplies power for only 440 seconds (including the time required to recharge the battery package at the end of the mission): therefore more than 75% of the mission is performed in electrical mode. The emissions are calculated on the entire route, considering both the electrical mode and the hybrid mode (GT switched on), and thanks to the net prevalence of electrical drive, we obtain the low emissions values displayed on Table 8.

Table 8. Lethe$^{@}$ data

Consumption			Pollutants emissions	
[km/l]	[l/100 km]	[g/kWh]	NO_x	-80%
28	3.5	171	HC	-80%
			CO	-90%
			PM	-90%

Table 9 : Capstone C30HEV (diesel fuel) emissions [15] at full load and EU limits

Emissions units	EURO 5 (2008)	EURO 6 (2013)	Capstone C30HEV
		g/kWh	
NOx	2.00	0.50	0.60
CO	1.50	1.50	1.17
PM	0.46	0.13	0.004

Table 10. LETHE® City Car emissions on urban routes and comparison to a commercial city car (SBZ srl 2011 data)

	LETHE® city car	Smart*
pollutants	Emissions [g/km]	
NOx	0.00618	0.06
HC	0.00999	n.a.
CO	0.00975	EURO V
PM	0.0000975	EURO V
CO_2	75	100

Table 11: Total emissions of a reference fleet composed by 500 gasoline vehicle, with individual annual mileage of 10000 km and comparison with a Lethe® fleet composed by 500 City cars (same mileage)

Actual commercial fleet	Total NOx emission, kg/year	total CO_2, t/year	PM10Total particulate, kg/year
Passenger sedan, gasoline	300	510	n.a.
TOTAL EMISSIONS	300	510	n.a.
LETHE® fleet	Total NOx emission, kg/year	total CO_2, t/year	PM10Total particulate, kg/year
City Car	30.9	375	450
TOTAL EMISSIONS	30.9	375	450

The analysis of table 9 indicates that the Capstone 30HEV has lower emissions in comparison with those defined by European directives (in fact, it would satisfy the EURO 6). The comparison with other current commercial vehicles (tables 10 and 11) is also positive, thanks to the peculiarity of the operational mode of the turbogas group, that is not designed to supply power to the drive train, but to recharge the battery package (range extender) or to complement the battery power during power surges.

9. Conclusions

The technical and economic feasibility of our design for a hybrid passenger sedan “LETHE” has been positively evaluated in previous papers [3,4]. The most important innovation in this project are the advantages offered by the adoption of a GT in lieu of the traditional thermal motor (ICE). This is not a complete “revolution” in the concept of cars as we know it today, but rather a simple reorganisation of the components. The energy flows management logic (VMU) for a gas-turbine-driven hybrid propulsion system has been previously described in detail [2]: it provides proper operational mode under all driving conditions. The application to possible configurations has been studied, the configurations being differentiated by the presence or absence of the dynamic storage

unit (the flywheel) and by different battery recharge modes. All simulations confirm that the LETHE vehicle is a competitive solution with respect to traditional ICE vehicles and also to other current hybrid vehicles: the calculated fuel consumptions is 29 km/l for urban cycles (compared respectively on 20 km/l for a current diesel vehicle, and 16 km/l for a gasoline sedan). All these advantages result in remarkable advantages in terms of weight, size and furthermore offer the opportunity of using a multi-fuel thermal engine (the GT) that can work with all types of liquid and gaseous fuels currently available on the market, thus reducing the economic effects of fuel price fluctuations. The analysis carried out in this article is synthetically expressed in Table 12, which shows the consumption and emissions of the LETHE hybrid according to the described procedure. This table contains data obtained by previous simulations and by the present assumptions [3, 4]: it shows a consumption reductions of about 30%, for a hybrid city car powered by methane compared to current commercial vehicles. With regard to emissions, we have highlighted the drastic reduction in all main pollutants emitted from the thermal engine compared to the values prescribed by current regulations, made possible by the optimisation of a thermal motor that operates mostly at design point. It must be underscored that it is the adoption of a Hybrid Series configuration (HS) that makes the use of GT device possible. In a global context of a simultaneous reduction of greenhouse gas emissions, of the consumption of fossil fuels, and of city pollution, it is clear that the benefits introduced by the HS vehicle would provide an immediate response to even the most stringent environmental regulations.

Nomenclature

BP Battery Package
BRC Breaking Recovery Coefficient
BRL Battery Recharge Limit
C Type of battery recharge limit
DOD Depth of Charge
EM Electric Motor
GT Gas Turbine set
GTHV Gas Turbine Hybrid Vehicle
HD Hybridization Degree
HS Hybrid Series
HV Hybrid Vehicle
ICE Internal Combustion Engine
IGV Inlet Guided Vanes
LETHE Low Emission Turbo Hybrid Electric Vehicle
MTBF Mean Time Before Failure
PM Particulate
SOC State of Charge
UDR1 University of Roma 1
VMU Vehicle Management Unit

References

[1] R. Capata et al.: *A Gas Turbine-Based Hybrid Vehicle-Part II: technological and configuration issues, JERT* , V. 125 n. 2, July 2003, 777-782

[2] R. Capata, M.Lora. *The Comparative assessment and selection of an "optimal" configuration for a Gas Turbine-Based Hybrid city car*, *JERT*.2008, vol. 129, n.2, pagg. 107-117

[3] R. Capata, A. Coccia: *Procedure for the design of a Hybrid-Series vehicle at UDR1 and the Hybridization Degree choice*. Energies 2010, vol. 3 , pagg. 450-461

[4] R. Capata, A. Coccia, M. Lora: *A proposal for the CO_2 abatement in urban areas: the UDR1–Lethe© turbo-hybrid vehicle*. Energies, Hybrid Vehicle Special Issue – Energies 2011, 4(3), 368-388; doi:10.3390/en4030368

[5] F. Ciaralli: *Evaluation and determination of efficiency index in the Combined and TurboGas Power Plant*. Master Degree Thesis (In Italian) Dept. Of Mechanical and Aerospace Engineering, University of Roma 1 "Sapienza", Rome, 2001

[6] E. Cioffarelli, E Sciubba: *A new type of gas turbine based-hybrid propulsion system-Part I: concept development, definition of mission parameters and preliminary sizing*, *Proc. AES/ASME Winter Meeting*, Orlando, FL, USA, 2000.

[7] Minotti A., E. Sciubba: *Comparison of LES calculation and experimental data for an ultra micro combustion chamber*

[8] G. Pede, ENEA (National Agency of Energy and Environment), *Personal Communication*, 2009

[9] Italian Automobile Club. Available at: <www.aci.it> [accessed 12.3.2012]

[10] Audi official web site. Available at <www.audi-club.dk> [accessed 12.12.2011]

[11] Italian gas Company web site. Available at: www.autogasitalia.it [accessed 02.02.2012]

[12] Capstone web site. Available at: www.interstatepower.us/Capstone/Document/Library/Application/Guides/480009_HEV_Application_Guide.pdf [accessed 11.11.2011]

[13] Italian Automotive Magazine web site. Available at: <www.motorbox.com/Auto/Prezzi_Nuovo> [accessed 01.12.2011]

[14] Italian Fuel Prize official website. Available at: <www.prezzibenzina.it > [accessed 01.12.2011]

[15] SBZ SrL, *Personal Communication*, 2011

[16] Ansaldo website, Products list. Available at: <www.zev.biz/azionamento_ansaldo.pdf> [accessed 14.10.2011]

[17] Burke AF: *Cycle Life Considerations for Batteries in Electric and Hybrid Vehicles***,** SAE Technical Paper Series #951951, reprinted in Electric and Hybrid Vehicles-Implementation of Technology (SP-1105); Future Transportation Technology Conference and Exposition, Costa Mesa, CA. August, 1995. Publication No. UCD-ITS-RP-95-21

A variational optimization of a finite-time thermal cycle with a Stefan-Boltzmann heat transfer law

J.C.Chimal-Eguia[a], N.Sanchez-Salas[b]
[a] Centro de Investigación en Computación del IPN, México D.F, México, jchimale@gmail.com
[b] Escuela Superior de Física y Matemáticas del IPN, México D.F., México, norma@esfm.ipn.mx,

Abstract:
In this paper we use the variational approach to study an endoreversible Curzon-Ahlborn-Novikov (CAN) heat engine under the maximum power condition. By means of this procedure we analyze the performance of a CAN heat engine with a nonlinear heat transfer law (the Stefan-Boltzmann law) to describe the heat exchanges between the working substance and its thermal reservoirs. Our results recover some previous results obtained by means of other procedures.

1. Introduction

Several authors [1-6] have pointed out that endoreversible thermal cycle models working in maximum power conditions have efficiencies which strongly depend on the heat transfer law used to describe the heat fluxes between working fluid and its surroundings. In fact, one of the most impressive results of the Curzon-Alhborn (CA) paper [7], was that the authors found very reasonable numerical results for the efficiencies of certain power plants by means of a very simple formula for the efficiency of a Carnot-like finite time heat engine in maximum power output regime. Since the CA paper, many authors have considered more realistic models to describe the heat exchanges by means of non-linear heat transfer laws [1-7]. Generally, the quantities to optimize are functional such as the work, the power and the entropy production which can be expressed as integrals over certain trajectories.
Thus, it results natural to use the variational calculus to treat optimization problems such as the ones mentioned before. By instance, in CA paper the equation which represents the efficiency of the thermal cycle was found by the maximization of the power output as a two variable function $P = P(x, y)$ with $x = T_H - T_h$ and $y = T_L - T_l$,where T_H and T_L which represents the absolute temperatures of the cold and hot reservoirs respectively (see figure 1).

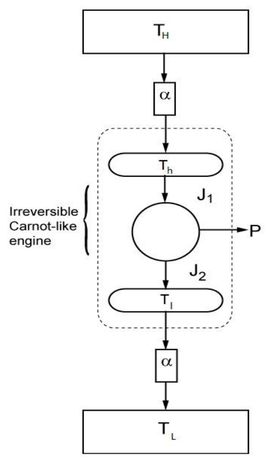

Figure 1. Diagram of the CAN endoreversible heat engine with conductances. $\alpha_1 = \alpha_2 = \alpha$

In fact, Rubin [8] could obtain the efficiency of the CA engine through the maximization of the Lagrangian with the power output as the objective function and the endoreversibility condition as the integral restriction. Later Ares de Parga et al. [9,16] use the variational approach to study a CA engine under both maximum power and maximum ecological function conditions [10]. They analyzed the performance of the CAN engine with a nonlinear heat transfer law (the Dulong and Petite law [16]), obtaining results consistent with previous obtained by means of other procedures. In this work we followed the same ideas as Ares de Parga et al., but considering a different heat transfer law, namely the Stefan-Boltzmann law, which consider only radiative effects. Using this method, we can recover all the numerical results for the Muser engine reported in Ref.[11] By means of other procedure.

2. The variational procedure

One of the most impressive results of the Curzon-Alhborn paper in 1975 [7], was that they could obtain the efficiency in the regime of maximum power output for a finite time Carnot-like thermal engine by means of a linear heat transfer. This efficiency was given by the following expression,

$$\eta_{CA} = 1 - \sqrt{\frac{T_L}{T_H}} \tag{1}$$

In 1979 Rubin [8] recovered eq. (1) by means of the application of the variational calculus to the maximization of the cycle´s power treated as the functional subject to the endoreversibility condition as restriction. In his paper, Rubin used a linear heat transfer law. Rubin´s approach consists of the maximization of a Lagrangian of the form,

$$L = W - \lambda \Delta S_W \tag{2}$$

where W is the work (power output taking the cycling period as fixed), λ is a Lagrange multiplier and is the endoreversible restriction given by,

$$\Delta S_W = \int_0^\tau \frac{\dot{q}}{T} dt = 0 \tag{3}$$

where $\dot{q}$ is a heat flux (the point means the time derivative), T is the working substance temperature and t is the time. Now assuming a Stefan-Boltzmann heat transfer law of the form,

$$q = \alpha \left(T_R^{\,n} - T^{\,n} \right) \tag{4}$$

where α is the thermal conductance and T_R is the heat reservoir temperature. Following the same procedure as Rubin, we can obtain the first variation of eq. (2), that is, $\delta L = 0$. If take into account the explicit form of equation (4) we have,

$$L = \int_0^\tau \left[\alpha (T_R^n - T^n) - \lambda \alpha \frac{(T_R^n - T^n)}{T} \right] dt \tag{5}$$

where the local equilibrium condition for the first law of thermodynamics was used. Taking the first variation of L and equalling to zero, we obtain

$$\delta L = \int_0^\tau \left[\delta T_R g(T, T_R, T_L, \lambda) - \delta T f(T, T_R, T_L, \lambda) \right] dt = 0 \tag{6}$$

which is an equation of the same form as equation (24) of Ref. [9]. Since T_R is necessarily in the interval $T_L \le T_R \le T_H$ this is a unilateral restriction [2], thus the variation of δT_R will not correspond to a physical situation and then we only consider $T_R = T_L$ or $T_R = T_H$. Therefore, in our analysis $T_R = T_H$ and T_L , which are taken as fixed and then the first term of the integrand of equation (6) vanishes- The function f in equation (6) is given by,

$$-nT^{n+1} + \lambda T^n (n-1) + \lambda T_R^n = 0 \tag{7}$$

In order to verify equation (7), we consider the special case when n=1, for this case we have,

$$T^2 - \lambda T_R = 0 \tag{8}$$

which implies that,

$$T = \pm \sqrt{\lambda T_R} \tag{9}$$

If we take $T_R = T_H$ and $T = T_h$ or ,$T = T_l$ and remembering that $\eta = 1 - \frac{T_l}{T_h}$, we obtain,

$$\eta_{CA} = 1 - \sqrt{\frac{T_L}{T_H}} \tag{10}$$

This equation is consistent with the CA case, in the limit n=1. Now, we can return to equation (7) but using now a non-linear heat transfer law, the so called Stefan-Boltzmann law (SBL), where n=4. In this case, equation 7 takes the following form,

$$4T^5 - 3\lambda T^4 - \lambda T_R^4 = 0 \tag{11}$$

As in the previous case, we can take $T_R = T_H$ and $T = T_h$ or $T = T_l$, which implies that,

$$4T_h^5 - 3\lambda T_h^4 - \lambda T_H^4 = 0 \tag{12.1}$$

and

$$4T_l^5 - 3\lambda T_l^4 + \lambda T_L^4 = 0 \tag{12.2}$$

We need to solve equations 12.1 and 12.2 for T_h or T_l respectively, and then to substitute in the endoreversible efficiency. However, equations 12.1 and 12.2 have not analytical solution, whereas the solutions of a fourth-degree equation can always be written in terms of radicals, the solutions of an arbitrary polynomial equation of degree 5 cannot, in general. Only some special classes of fifth-degree equations give rise to analytical solutions in terms if nested radicals. Therefore, in order to prove the usefulness of the variational method, we can use an approximation of the Stefan-Boltzmann engine called the Muser engine (ME) [12] introduced by Muser in 1957. This engine is a man made Stefan-Boltzmann engine in which we assume that technological skill is so good that the conversion device makes a perfect thermal contact with the second reservoir, thus, $T_l = T_L$. Taking into account this restriction, from equation 12.2 we can obtain that the Lagrange multiplier λ , that without the restriction was an additional variable, now takes the form, $\lambda = T_l$

And substituting the last equation in equation 12.1 we obtain,

$$4T_h^5 - 3T_l T_h^4 - T_l T_H^4 = 0 \tag{13}$$

This equation is the same that Muser [12] discovered in 1957, and afterwards rediscovered independently by Castañs [13] in 1976, by Jeter [14] and by De Vos and Pauwels [15] in 1981, however, we obtain it with a different method. Now if we take the endoreversible efficiency, and substitute it into equation 13 we obtain the following expression,

$$T_H^4 (1-\eta)^5 + 3T_l^4 (1-\eta) - 4T_l^4 = 0 \tag{14}$$

which is the equation 5.7 obtained by the De Vos in his famous book [11], and again as stated before, it has not analytical solution. The numerical solution of equation 15 for yields, $\eta = 0.2029$
Where, we take the same approximation as De Vos [11] for the special case of the Solar converter or Muser engine, i.e, and , the planet temperature and the effective sky temperatures respectively.

3. Concluding Remarks

In this paper we have used a simple variational procedure for obtaining the thermal efficiency of an endoreversible CAN finite time cycle in the maximum power regime. This analysis was made by means of a non linear heat transfer law (The Stefan Boltzmann law), which is consider to represent the heat exchanges between reservoirs and working substance taking into account only radiative contributions. The variational procedure allows us to obtain two algebraic equations of fifth order for the temperatures of the isothermal processes. However due to the order of the equations it is not possible to obtain analytical solutions. In order to prove our results, we take into account the Muser engine, which main characteristic is to have a perfect thermal contact with the surroundings. With the restriction mentioned before, we can reproduce the results made by other authors in particular those reported by De Vos [11] with respect to the efficiency of the engine. We believe that the variational procedure is a worthwhile method that could be used more extensively in thermodynamics particularly in finite time thermodynamics.

Acknowledgments
We would like to thanks CONACYT, EDI-IPN, and COFAA-IPN for supporting this work.

4. References

[1] Gutkowicz-Krusin D, Procaccia I and Ross J. 1978, J. Chem. Phys. 69, 2898.
[2] De Vos A. 1985, Am. J. Phys. 53 570
[3] Chen L. And Yan Z. 1989. J. Chem. Phys. 90, 3740
[4] Angulo-Brown F. and Paez-Hernandez R. 1993 J. Appl. Phys. 74 2216
[5] Arias-Hernandez L.A. and Angulo-Brown F. 1994 Rev. Mex. Fis. 40, 886.
[6] Arias-Hernandez L.A. and Angulo-Brown F. 1997 J. Appl. Phys. 81 2973
[7] Curzon F. L. and Alhborn B. 1975 Am. J. Phys. 43 22
[8] Rubin M. H. 1979 Phys. Rev. A. 19 1272
[9] Ares de Parga G. and Santillan M. 1998 Rev. Mex. Fis. 44 373
[10] Angulo-Brown F. 1991 J. Appl. Phys. 69, 7465.
[11] A. De Vos Endoreversible Therm.of Solar Energy Conversion Oxford University Press, Oxford, 1992.
[12] Muser H. 1957 Zeitschrift fur Physik 148, 380
[13] Castans M. 1976 Revista Geofisica, 35, 227-239
[14] Jeter S. 1981 Solar Energy 26, 231-236
[15] De Vos A. and Pauwels H. 1981, Applied Physics, 25, 119-125
[16] Ares De Parga G. Angulo-Brown F. Navarrete-Gonzalez T.D. 1999, Energy, 24, 2234

MODELING AND SIMULATION OF A BOILER UNIT FOR STEAM POWER PLANTS

L.Moliterno, C.Toro

University of Rome "Sapienza" , Italy

ECOS 2012

INTRODUCTION

The modeling and steady state simulation of large-size boiler units for steam power plants have been performed.
The component "boiler" has been developed and implemented into the library of a modular object-oriented process simulator, CAMEL-Pro™ to perform the simulation and the exergy analysis of the single component and of the global steam power plant. The model created is than applied to a large size steam generator for a thermal power plant of 320 MW, powered by oil and with a reheat of the steam.

MODEL

The model implemented is based on mass and energy balances and proper equations for the evaluation of the heat exchange coefficients are introduced. Energy balances are performed not only for the whole plant but also for each component in order to evaluate the distribution of the thermodynamic inefficiencies throughout the system. The equation system has been written using CAMEL-Pro™ Simulation Software which is an "Object oriented" modular code (C++) equipped with a WINDOWS-compatible and user friendly graphical user interface (C#)

Scheme of the model

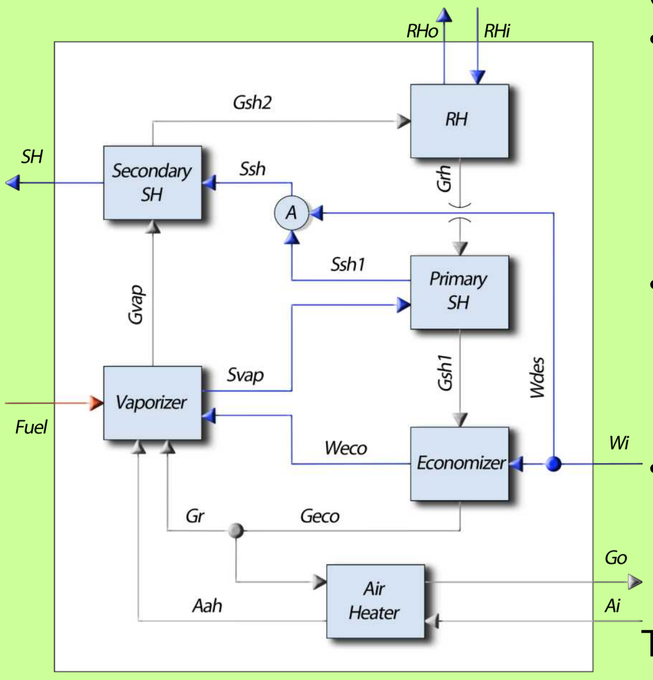

Legend :
- Air/Gas;
- Steam/Water;
- Fuel;

Unknowns

- Air/gas stream 12 unknowns (8 stream)

$$m, p, T, h, s, ex, q, (xO2), (xN2), (xCO2), (xH2O), v$$

- Steam/water stream 7 unknowns (9 stream)

$$m, p, T, h, s, ex, q$$

- Fuel 5 unknowns

$$m, LHV, (xC), (xH), \alpha$$

The problem presents 165 unknowns, 128 equation has been written, so to perform the simulation 37 boundary conditions are necessary.

Heat transfer

The heat transferred in the furnace to the vaporizer's tube banks has been calculated as a percentage of the heat introduced with fuel (Orrok's method). The emissivity of the gas necessary to calculate the radiation heat transfer has been obtained with the equation proposed from Ganapathy.

Characteristics of the generator:

320 MW nominal power;
- Oil fuel;
- Forced circulation of water;
- Pusher fan;

RESULTS

The geometric and operative data are referred to the ENEL's power plant of Sermide

Boundary condition

	Ai	SH	Wdes	Wi	RHi
m [kg/s]	?	?	5,68	278,21	231,67
p [kPa]	101,42	16654	18400	?	3498
t [K]	323,15	811,15	564,92	564,92	604,15
h [KJ/Kg]	25,54	?	1187	1187	2953
ex [KJ/Kg]	3,64	?	980	980	1719
s [KJ/Kg]	7,03	?	3,138	3,138	6,58
q [Kg/Kg]	1	?	0	0	1
v [m/s]	15	---	---	---	---
O2	0,23	---	---	---	---
N2	0,7576	---	---	---	---
H2O	0,119	---	---	---	---
CO2	0,0005	---	---	---	---

	Fuel
m [kg/s]	?
Alfa	0,0708
LHV[KJ/Kg]	40974
C	0,86
H	0,11

Destroyed Exergy (MW)

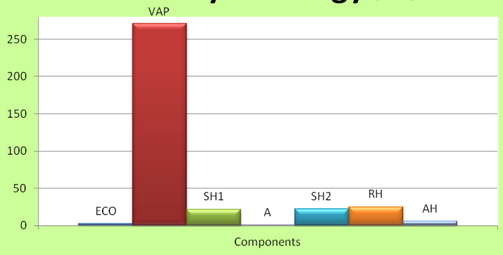

Exergetic Efficiency

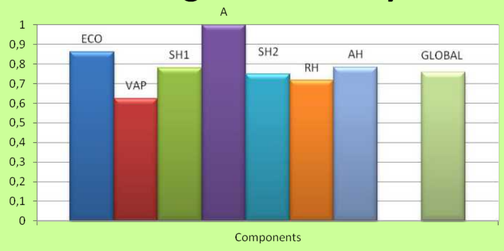

Steam

Gas

Water	Relative Error (%)
Wi	0
Weco	0,58
Svap	2,29
Ssh1	1,62
Ssh	1,85
SH	0
RHi	0
RHo	0,2

Gas	Relative Error (%)
Ai	0
Aah	3,96
Gvap	-1,23
Gsh2	0,22
Grh	-1,49
Gsh1	4,17
Geco	9,75
Go	-0,41

Comparison between simulation results and ENEL's power plant of Sermide data

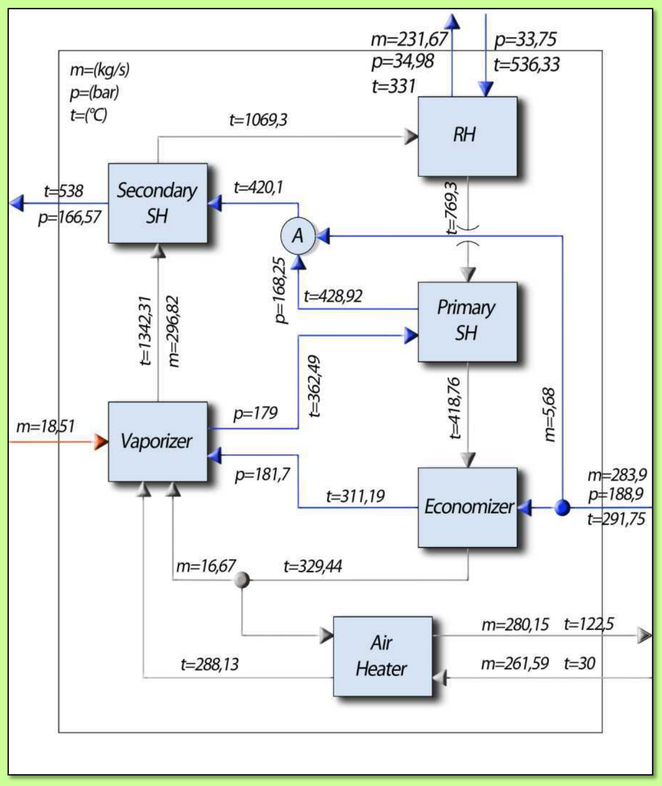

Steam Power Plant Simulation

With CAMEL-Pro™, using the component "boiler" developed, has been simulated a steam power plant high pressure side. The imagines below represent s the plant's layout in CAMEL-Pro™

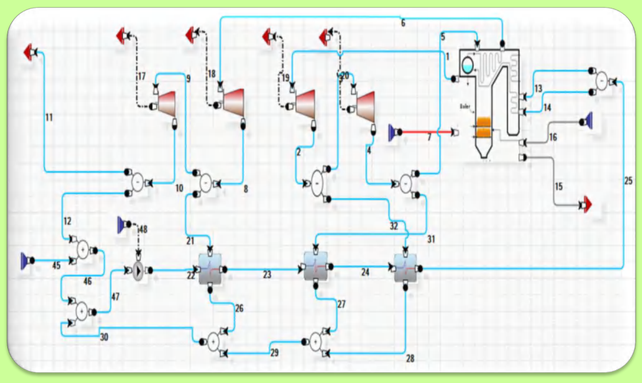

References

- *Donatello Annaratone, "Steam Generator - Description and Design" 2008 Springer-Verlag Berlin Heidelberg*
- *V.Ganapathy, "Industrial boilers and heat recovery steam generators" 2003 Marcel Dekker, Inc.*
- *http://www.turbomachinery.it, CAMEL-Pro™ Manual V.4.0*

NUMERICAL MODELLING OF STRAW COMBUSTION IN A MOVING BED COMBUSTOR

Biljana Miljković, Ivan Pešenjanski, Borivoj Stepanov, Vladimir Milosavljević, Vladimir Rajs

Faculty of Technical Sciences, Novi Sad, Serbia, bmilj@uns.ac.rs

INTRODUCTION and BECKGROUND

Combustion of wheat straw in Serbia is a perspective way of energy conversion but devices for agricultural waste combustion are still in developing phase and good enough design solution still does not exist. Since the combustion of straw for power generation is a relatively new concept, the design and operating conditions are not fully optimized. That is why grate-fired boilers burning straw are often associated with high emission levels and relatively poor fuel burnout. Mathematical modelling thereby becomes a cost-effective alternative to exhaustive testing in designing, retrofitting, analyzing and optimizing the performance of combustion systems.

A moving grate furnace is a typical way to burn solid biomass in many combustion plants and a furnace is the simplest combustion technology. Despite its apparent simplicity, direct combustion is an extremely complex process from a technological point of view.

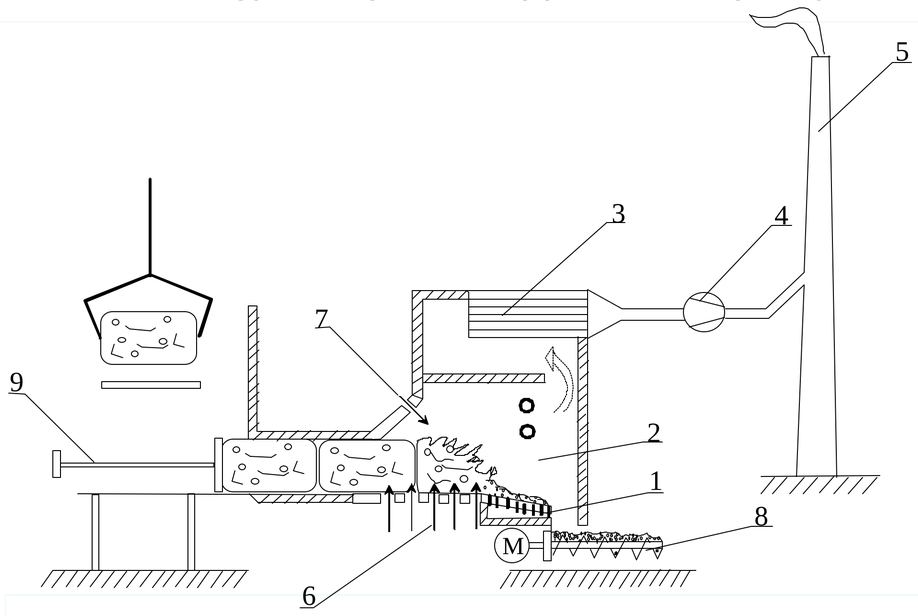

Fig 1. Real combustion equipment for bale straw

During the continual combustion process that happens in such hypothetical moving bed, moisture evaporation front, straw pyrolysis and fuel combustion front are formed, as illustrated in figure 2.

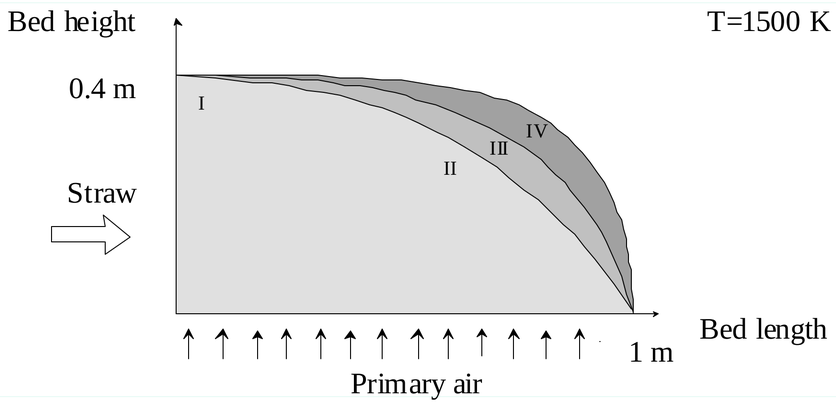

Fig 2. Contour of fuel by combustion in a horizontal bed
I-raw straw,
II-dry straw,
III-pyrolysis front,
IV-combustion front

RESULTS and DISCUSSION

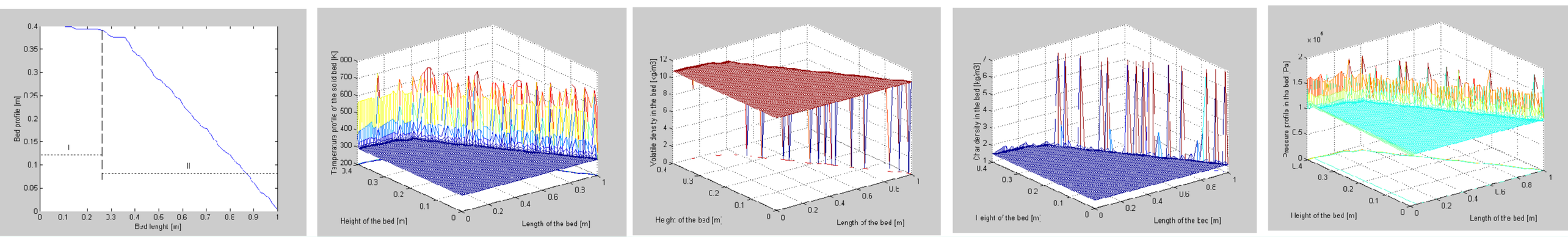

Fig 3.a) Simulated results of bed profile, b) temperature profile of solid phase, c) volatiles profile, d) char profile and e) pressure profile in the bed

1. As shown in figure 3, during combustion process in a moving bed, two stages are defined, (I) <u>the preheat stage</u> at the start of the grate, where the solid temperature of the surface layer rises sharply from room level to a peak temperature (about 550 K) and (II) <u>intense reaction stage</u> after the heating stage, where the top bed temperature starts to rise and reaches about 700 K.
2. In the preheat stage (I) drying process is finished and partially devolatilisation process, but there are no intense combustion reactions and hence no visible degradation of the bed. The heating zone in this stage stays very thin, only a few millimeters.
3. In the intense reaction stage (II), after heating, drying and devolatilisation processes, the local bed temperature rises to a peak value at which point combustion process of volatiles starts, followed by combustion of char. The heat from the char oxidation and other combustible material remains in the bed, increasing the bed temperature to a higher level than in the heating stage.

CONCLUSIONS

An original mathematical model is developed and simulations are carried out for the combustion of straw in a moving bed. Model includes: moisture evaporation, straw pyrolysis, volatiles and char combustion. The model is able to predict the influence of main processes occurring in straw bed combustion. Mathematical modelling provides detailed information on the burning processes, which is otherwise very difficult to obtain by using conventional experimental techniques.

Very important result of simulations is the time needed for complete burnout of the bed. Thus, the model can be used to perform investigations of different furnace conditions and may be used for the optimisation of existing furnaces and development of new ones.

ACKNOWLEDGMENTS

This work steams from our ongoing investigation “Development of methods, sensors and systems for monitoring of water, air and soil quality”, funded by the Serbian Ministry of Science (Project No. III 43008)

PHYSICOCHEMICAL EVALUATION OF THE PROPIERTIES OF THE COKE FORMED AT RADIATION AREA OF LIGHT HYDROCARBONS PYROLYSIS FURNACE IN PETROCHEMICAL INDUSTRY

Jaqueline Saavedra Rueda[a], Angélica María Carreño Parra[b], María del Rosario Pérez Trejos[c], Dionisio Laverde Cataño[d], Diego Bonilla Duarte[e], Jorge Leonardo Rodríguez Jiménez[f], Laura María Díaz Burgos[g]

[a]*Instituto Colombiano del petróleo, Ecopetrol, Santander, Colombia, jaqueline.saavedra@ecopetrol.com.co*
[b]*Instituto Colombiano del petróleo, Ecopetrol, Santander, Colombia, angelica.carreño@ecopetrol.com.co*
[c]*Instituto Colombiano del petróleo, Ecopetrol, Santander, Colombia, mariadelr.perez@ecopetrol.com.co*
[d]*Departamento de Ingeniería Química, Universidad Industrial de Santander, Colombia,* dionisio.laverde@correo.uis.edu.co
[e]*Departamento de Ingeniería Química, Universidad Industrial de Santander, Colombia, diegob-7@hotmail.com*
[f]*Departamento de Ingeniería Química, Universidad Industrial de Santander, Colombia, jorgerodriguez_09@hotmail.com*
[g]*UT-TIP PETROLABIN- Santander, Colombia, ladibu10@hotmail.com*

INTRODUCTION

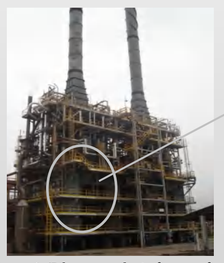

Figure 1. Ethane pyrolysis furnace for the production of ethylene.

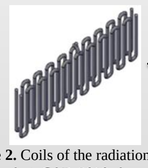

Figure 2. Coils of the radiation spot
Source: ***AutoCAD-2010. Amezquita J.C***

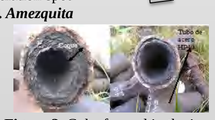

Figure 3. Coke formed in the inner walls of the tubes.

Different studies using physicochemical characterization had been focused to cokes obtained from laboratories, under controlled conditions and with magnitudes relatively small, respect to the industrial scale, what makes it more easy and predictable the analysis of heat and mass transference phenomena.

RESULTS AND DISCUSSION

Structure and infrared spectroscopy

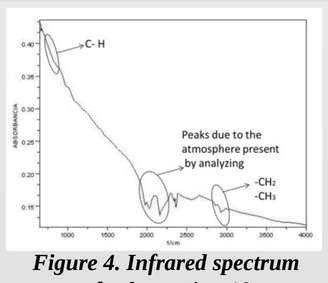

Figure 4. Infrared spectrum of coke section 10

Spectrum shows that the coke bands between 750-900 cm^{-1}, belong to typical to typical aromatic vibrations C-H bonds. Furthermore, in the region 2750-2980 cm^{-1} shows two peaks, corresponding to the vibrations of the $-CH_2$ of the $-CH_2$ and $-CH_3$ asymmetric and (alkyl) bonds, it means aliphatic chains with possible ramifications

Coke Morphology

Shows morphology a large amount of agglomerates of particles without pattern stacking, that generate spacing between the structures formed, called pores, corresponding to dark cavities present in the micrographs; these agglomerates are formed by spherical particles or globules, because the circular geometry is the more stable when condensation occurs drops of pitch.

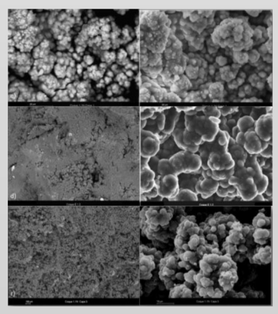

Figure 5. e) Layer 1; d) Layer 2; r) Layer 3

Layer	Average Diameter
Layer 1: Adjacent to pipe	2,2- 3,5 µm
Layer 2: Intermediate	3,5- 6,0 µm
Layer 3: Exposed to pyrolysis gas	6,0- 7,0 µm

Table 1. Average Diameter of the globules

Thermal coke stability

The reactions that take place during the heating of coke under an Inert environment, involve thermal decomposition of coke at temperatures above 600 ° C, during which the macromolecular structure is broken, generating free radicals, to form stabilized species of low molecular weight hydrocarbon.

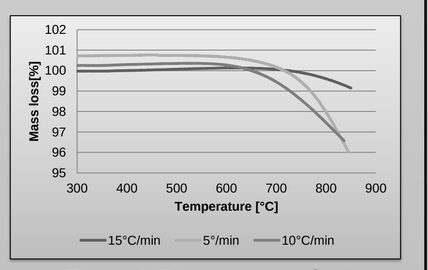

Figure 6. Thermograms of coke at different rates of heating in an inert atmosphere

Real Density and porosity of coke

Property	Valor Promedio
Real Density[g/cm3]	1,96 ± 0,01
Apparent Density [g/cm3]	1,01 ± 0,01
Pore volume [cm3/g]	0,24 ± 0,13
Porosity	31,63 ± 0,14

Table 2. Parameters calculated from the skeletal density

The porosity, influences the mechanical and physical properties of coke, because the existing pores generate spaces between its molecules. Furthermore, the porosity affeds the the kinetics of reactions, particularly in the combustion and gasification.

Coke Chemical Composition

Substance	[%w/w]
Fixed Carbon	95,68
Ash	0,37
Moisture residual	0,03
Volatile matter	3,92

Table 3. Coque proximate Analysis

Proximate Analysis

Elemental Analysis

Substance	[%p/p]
Total sulfur	<0.06
% C	97,98
% H	0,81

Table 4. Amount of sulfur, carbon e hydrogen.

Element	Layer 1	Layer 2	Layer 3
C	93.8±2,2	96,3±0,9	96,3±1,0
O	5,7±1,73	3,6±0,9	4±0,9
Fe	Tr	Tr	Tr
Al	Tr	Tr	Tr
Si	Tr	N.D	Tr
S	N.D	N.D	Tr
Ca	Tr	N.D	Tr
Cr	Tr	N.D	Tr
Ni	Tr	Tr	Tr

Table 5. Relative abundance of chemical elements Tr: Trace. N.D: not detectable

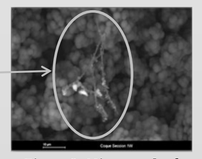

Figure 9. Micrograph of a filament present in the coke.

EDX Elemental Analysis

Combustion and calorific value of coke

$$r_c = -\frac{dC_c}{dt} = kP_{O_2}^m C_c^n \quad \Rightarrow \quad \frac{dC_c}{dt} = \frac{dC_c}{dT} * \frac{dT}{dt};\ \beta = \frac{dT}{dt}$$

k: Arrhenius kinetic rate constant

$$\ln\left[\frac{-\ln(1-\alpha)}{T^2}\right] = \ln\left[\frac{A*R}{\beta*E_a}\right] - \frac{E_a}{R}\left(\frac{1}{T}\right)$$

β [°C/min]	A [s^{-1}]	E_a [KJ/mol]	R^2
5	1,73 E+5	120,33	0,98
10	8,32 E+18	329,11	0,96
15	4,43 E+12	234,75	0,99

Table 6. Arrhenius kinetic parameters at different heating

This gives an indication of the variation of kinetics as a function of heating rate, also defined the kinetic parameters and the heating rate biggest for decoking processes.

TGA

CONCLUSIONS

- The microstructural properties, physical, chemical, morphological properties and low impurity content determined for this type of coke, infer that could be used in different kinds of industries.
- The coke formed is thermally decomposed in the pyrolysis process, ie carbon follows belonging to the matrix of coke which may cause phenomena of carburization.

REFERENCES

- ALBRIGHT, Lyle. MAREK, James. Mechanistic model for formation of coke in pyrolysis units producing ethylene. En: Ind. Eng. Chem. Res. Mayo, 1988. 27, 5, p. 755–759.
- SAAVEDRA, Jaqueline. PÉREZ, María del Rosario. CARREÑO, Angélica, DIAZ, Laura. AMÉZQUITA, Juan Carlos. LAVERDE, Dionisio. BOLÍVAR, Francisco PÉREZ, Francisco. Caracterización por técnica analítica SEM-EDX y DRX del coque producido en un horno petroquímico y análisis de su efecto sobre el mecanismo de carburización en un acero HP40. En: XII SEMINARIO LATINOAMERICANO DE ANÁLISIS POR TÉCNICAS DE RAYOS X. (15-19, Noviembre, 2010: Puebla, México).
- ALBRIGHT, Lyle. MAREK, James. Mechanistic model for formation of coke in pyrolysis units producing ethylene. En: Ind. Eng. Chem. Res. Mayo, 1988. 27, 5, p. 755–759.

Rotor TG Cooled

Chiara Durastante, Paolo Petroni, Michela Spagnoli, Vincenzo Rizzica, Jörg Helge Wirfs

Università di Roma La Sapienza, Italy

First-stage rotoric blade of an axial gas turbine

INTRODUCTION and BACKGROUND

Developing of numerical simulations whose aim is to display the velocity, pressure and temperature maps. Computation and plotting of the entropy field in the domain considered.

RESULTS

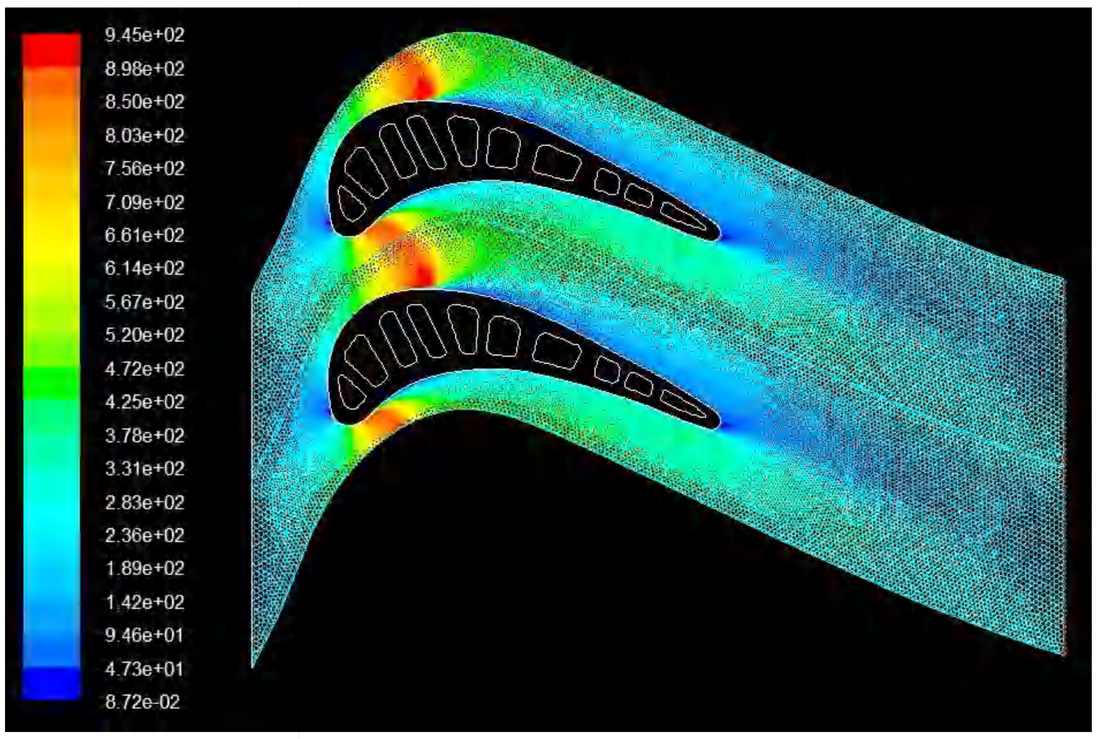

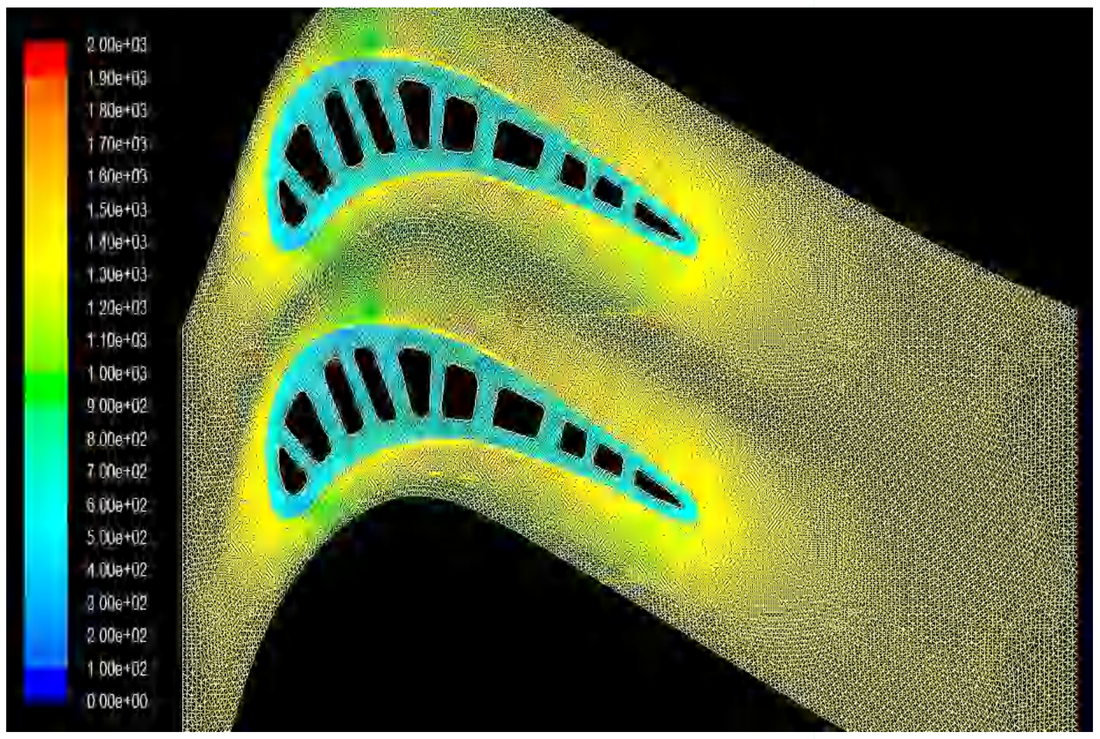

DISCUSSION

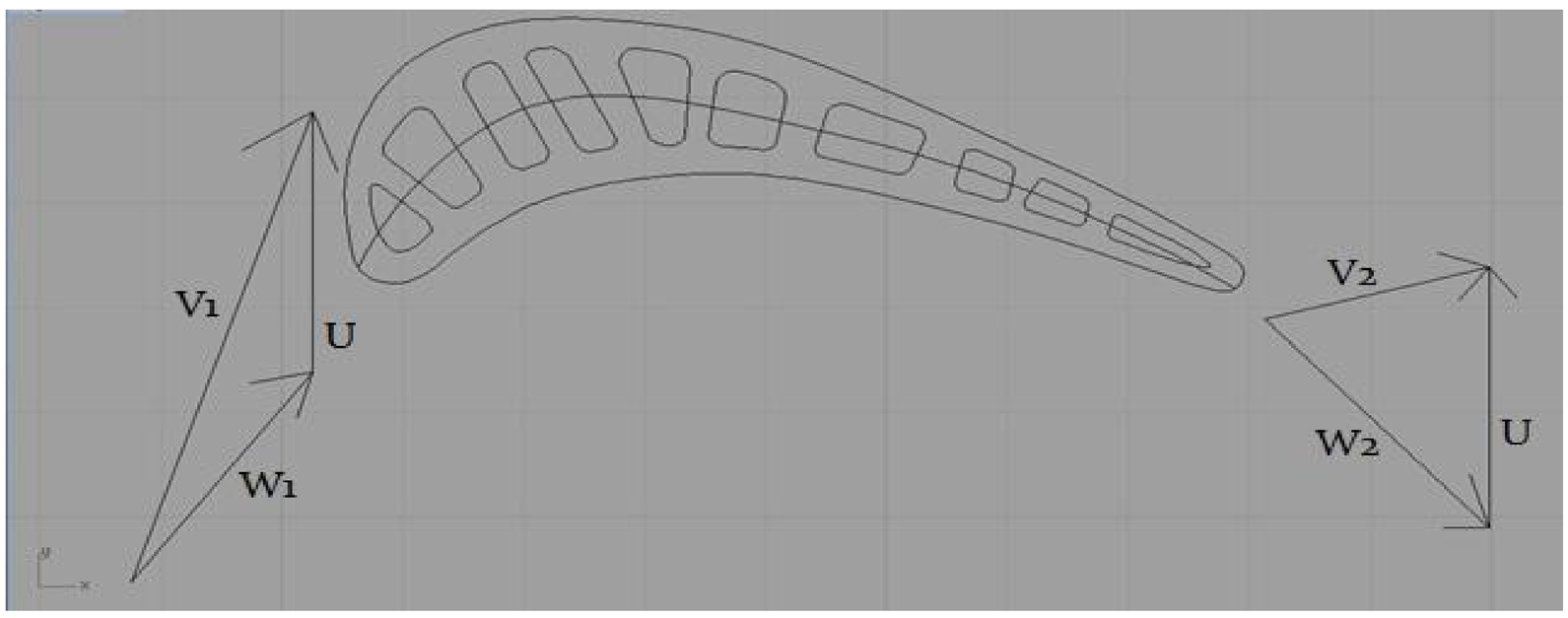

CONCLUSIONS

It's noticeable that the large thickness of the blade produces high accelerations at the entrance of the rotoric channel and determines the position of the throat section very close to the inlet section, so that the canal become soon divergent. This sets a limit to the performances but maybe there was the need of realizing the cooling passages and at the same time to assure sufficient mechanical resistance of the blade.

REFERENCES

• E. Sciubba, "*Lezioni di Turbomacchine*", Eurostampe 2001;
• R. Capata, E. Sciubba, "*Selected Design Problems in Turbomachinery*", Eurostampe 2004;
• "*Fluent 6.3 User's Guide*", Fluent Inc. 2006.

STUDY OF THE PHASE CHANGE IN BINARY ALLOY

A.Jaouahdou[a], MJ.Safi[a],H.Muhr[b]

[a] *National School of Engineering Tunisia*

[a] *LRGP-ENSIC Nancy France*

Aroussia.jaouahdou@enit.rnu.tn

Phase change in binary solution can be used as a separation process of its components (desalination or metallurgy) or to concentrate it (food concentration or pharmaceutical products). In this way, we study the effect of the initial solute concentration on the temperature, the ice growth and the concentration field in a binary solution freezing from below. Visualization of H_2O-NaCl freezing at different salt concentration and temperature field are presented.

Experimental study on a case of seawater desalination shows that we can attend 2g/l salt by improving the sweating step and adjusting some parameters. These results are used to set up a device of freezing desalination.

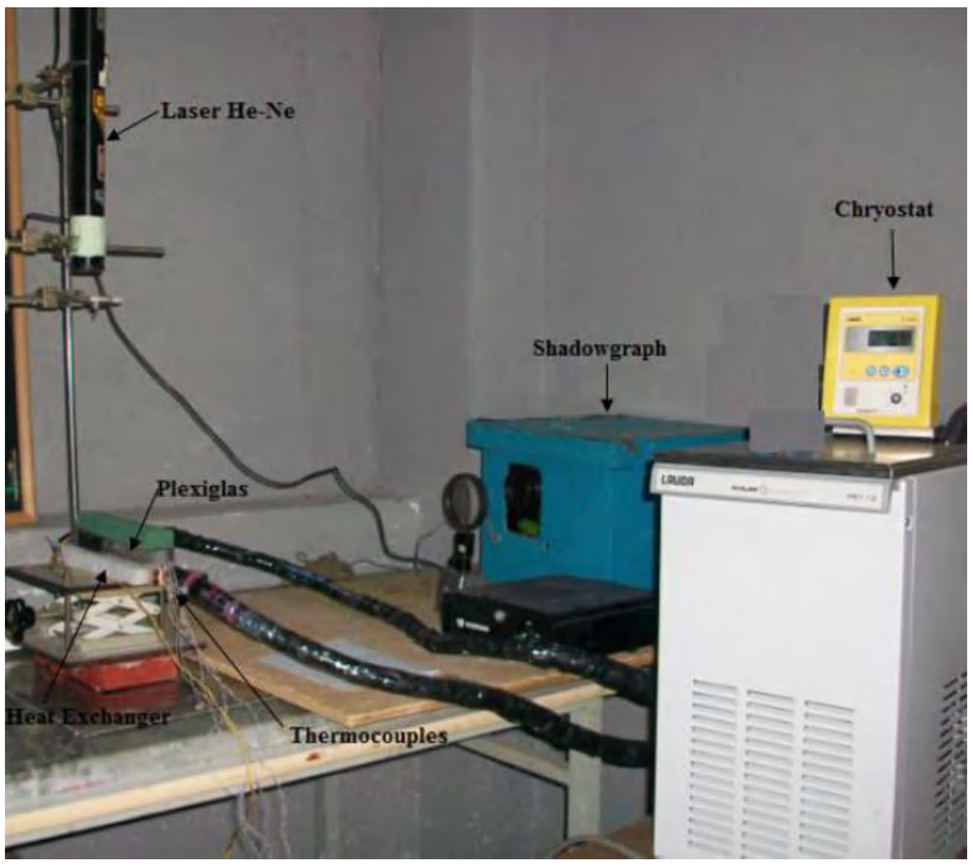

Fig.1 Experimental Setup

Experiments	C_0 (g/l)	T_∞ (°C)	T_f (°C)	Ra_{th}	Ra_{sol}
1	2	25	-6	$1.3*10^7$	$1.57*10^7$
2	10	25	-6	$6.23*10^7$	$2.16*10^7$
3	35	25	-6	$1.01*10^8$	$2.69*10^7$

Tab.1 Operating conditions

This study confirms the thermal and solutal stratification seen in freezing from below. This stratification is given by conduction thermal transfer, and can be used to perform a setup for freezing desalination.

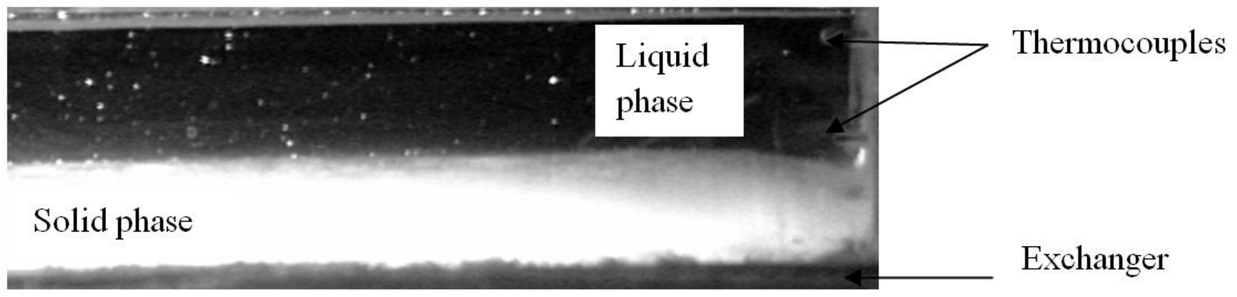

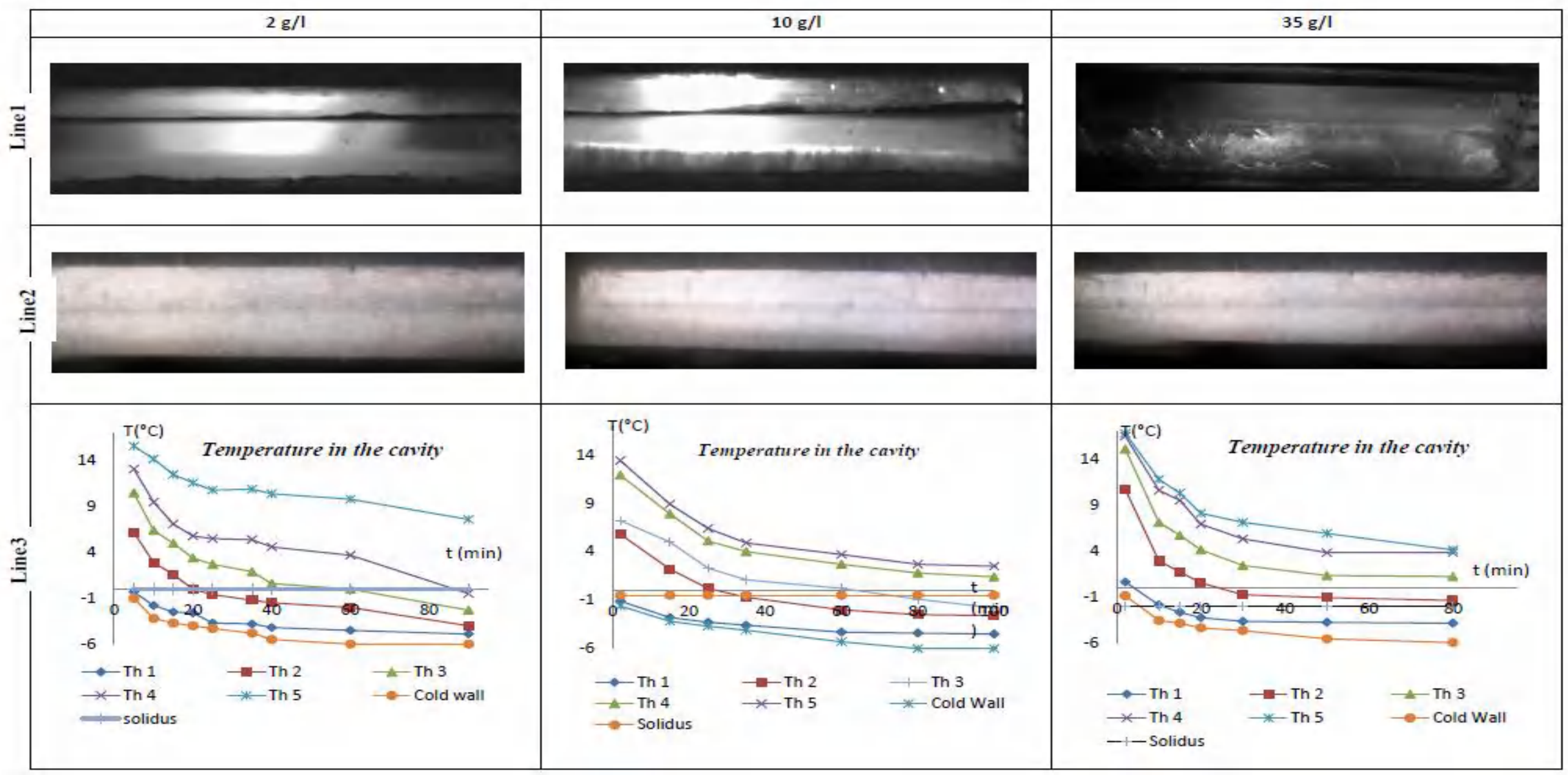

TECHNIP INITATIVES IN RENEWABLE ENERGIES AND SUSTAINABLE TECHNOLOGIES

Pierfrancesco Palazzo[a], Corrado Pigna[b]

[a] *Technip, Rome, Italy, ppalazzo@technip.com* [b] *Technip, Rome, Italy, cpigna@technip.com*

Technip, with engineering, technologies and project management, on land and at sea, safely and successfully delivers the best solutions for its clients in the energy business. Technip is present with 30,000 people in 48 countries. With a fleet of 33 vessels Technip has industrial assets on all continents. Technip 2011 revenue was € 6.8 billion

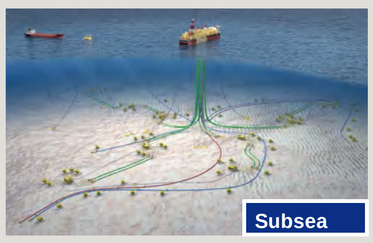

Technip stock has been reselected for the 10th consecutive year in the Dow Jones Sustainability Indexes. The Group is part of SAM's list of best performing companies in Sustainable Development and is also listed in ASPI Eurozone's Index of socially responsible groups.

MAIN MARKETS

- Biofuels (1st and 2nd generation)
- Solar power: thermal generation (concentrated solar power – CSP)
- Marine energies (offshore wind, tidal, waves)
- Carbon capture and storage
- Geothermal

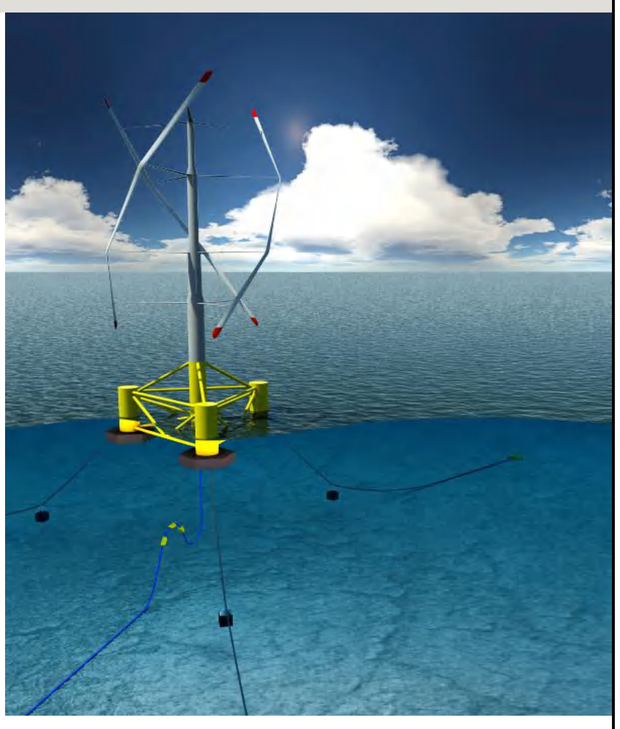

KEY REFERENCES

- Technip has recently completed on a EPCM basis, the construction of the two largest Renewable Diesel plants in the world in Singapore and Rotterdam for Neste Oil
- Technip realized on a EPCI basis the complete construction and installation of the world first floating wind turbine for Statoil

NENUPHAR's floating wind turbine: a simple and robust vertical-axis wind turbine (VAWT)

- NENUPHAR's VAWT performance comparable with conventional HAWTs
- Optimized wind turbine architecture: no yaw system , no variable pitch, no gearbox
- With a direct-drive permanent magnet generator, and a reduced number of components, NENUPHAR's VAWTs have higher availability rates than competing solutions; Failure rate is 45% lower than for conventional HAWT's
- A short and optimized floater: for a given output, the VAWT architecture allows to reduce destabilizing moments (weight and aerodynamic forces) compared to a conventional HAWT floating solution
- One standard product: sea depth > 50 m, overall height: 90 to 100 m, output: 2 to 3 MW

Technip partner of the Iberdrola – Eole-RES Consortium awarded 500 MW Saint-Brieuc Offshore Wind Project, France

Ethanol

- Hundreds of references globally
- A know-how based on the acquisition of Speichim in 2000
- Proprietary technologies

Diesel

- Close cooperation with Axens on a unique process (Esterfip-H)
- Collaboration with Neste Oil for various project using their NexBtL proprietary technology

New Generation of biofuels: Ligno-cellulosic ethanol; BtL; Others…

EUROPEAN PROJECT CACHET II LED BY BP

- 8 partners overall including Technip (leader in the design of reactor)
- Funded by EU commission under the FP7
- The project is about an Hydrogen (H2) permeable membrane reactors for pre-combustion carbon dioxide capture in both coal and gas fired power stations.
- Main benefits are :
  - Combination of efficient conversion of syngas into hydrogen fuel with capture of the remaining carbon dioxide in one reactor.
  - The carbon dioxide is produced at high pressure,reducing the compression energy for transport and storage.